# Reflections and Resolutions

**Karen Hindson**
**Editor, EurJIC**

New Year is a time for reflection on the past and resolutions for the future. This year this editorial will cover the past year but also take a look to the future.

2005 was again a good year for the *European Journal of Inorganic Chemistry*. Although the number of submissions continue to rise (ca. 7% more by September), which kept all of us in the editorial office on our toes, we concentrated this year on reducing publication times. As a start in this ongoing effort, we have reduced the time from submission to online publication by 25−30%, depending on the type of article. The Short Communications, which are defined as brief reports on topics of high significance and urgency, have benefited the most and appear online about 100 days after submission, but on average only about a month faster than the other categories. By far the most time-consuming process is the peer review and revision. In this area a balance between speed and diligence will serve our science best. More on this topic later.

The number of downloads has also steadily increased over 2005. This statistic not only reflects the attention that a particular group has attracted to its work − this attention becomes concrete later when the articles are cited in the papers of other researchers. More reliably it shows the areas which are topical at present. Chart 1a lists the five Microreviews that were downloaded most often by mid November. In addition I would like to mention two from the issues that became available late in the year and which therefore have not had the opportunity to appear in the "Top 5" stakes (Chart 1b), but within one month of publication jumped into the top 50. Chart 2a and b (see page 6) give the Short Communications and Full Papers the same honours. Thus the hot topics range from supramolecular chemistry, molecular recognition and biomimetic ligands to catalysis, nanoscience and ionic ligands. Properties useful for applications, such as magnetism, porosity, electrochemistry and luminescence feature prominently. On these topics EurJIC will also be publishing Microreviews in the near future. In this issue you can read about triazine-based ligands in supramolecular chemistry. Coming are Microreviews on host−guest and intercalation chemistry of $C_{60}$, catalysis in ionic liquids, mesoporosity and model complexes for metalloenzymes.

Two projects, started as a result of the urging of readers, have been completed in 2005. Most often I have been asked at conferences about the online accessibility of predecessor journals to EurJIC. I am therefore pleased to announce that in January all issues from the inception of *Liebigs Annalen* and *Chemische Berichte* will become available electronically as part of the Chemistry Societies Backfile Collection: 27,100 articles from *Liebigs Annalen* (from 1832 to 1997) and 57,270 articles from *Chemische Berichte* (from 1868 to 1997) will be fully searchable. In addition the reference section has been tagged so that CrossRef allows jumping to the full-text of the citation, if the publisher is a member of CrossRef and the backfile is available (to find out more about CrossRef, see www.crossref.org). The other journals

Chart 1a. Most downloaded Microreviews published in 2005 (* indicates the correspondence author).

1. Stabilization of Organometallic Species Achieved by the Use of N-Heterocyclic Carbene (NHC) Ligands; **N. M. Scott, S. P. Nolan***, *Eur. J. Inorg. Chem.* **2005**, (10), 1815−1828.
2. Ordered Meso- and Macroporous Binary and Mixed Metal Oxides; **M. A. Carreon, V. Guliants***, *Eur. J. Inorg. Chem.* **2005**, (1), 27−43.
3. Molecular Recognition: Use of Metal-Containing Molecular Clefts for Supramolecular Self-Assembly and Host-Guest Formation; **J. D. Crowley, B. Bosnich***, *Eur. J. Inorg. Chem.* **2005**, (11), 2015−2025.
4. Luminescence from Lanthanide(3+) Ions in Solution; **A. Døssing***, *Eur. J. Inorg. Chem.* **2005**, (8), 1425−1434.
5. Ionic Liquids with Fluorine-Containing Cations; **H. Xue, J. M. Shreeve***, *Eur. J. Inorg. Chem.* **2005**, (13), 2573−2580.

Chart 1b. Microreviews from later issues that attracted a high number of downloads within one month.

1. Magnetic Nanoparticle Superstructures; **M. Giersig, M. Hilgendorff**, *Eur. J. Inorg. Chem.* **2005**, (18), 3571−3583.
2. Continuous Homogeneous Catalysis; **D. Vogt** et al., *Eur. J. Inorg. Chem.* **2005**, (20), 4011−4021.

 © 2005 Wiley-VCH Verlag GmbH & Co. KGaA, Weinheim 

Chart 2a. Most downloaded Short Communications (SC) and Full Papers (FP) published in 2005.

1. SC: $Co^{II}$ Complexes of Triazine-Based Tridentate Ligands with Positive and Attractive $Co^{II/III}$ Redox Couples; **G. S. Hanan** et al., *Eur. J. Inorg. Chem.* **2005**, (7), 1223−1226.
2. FP: A New Ligand for the Formation of Triangular Building Blocks in Supramolecular Chemistry; **I. M. Müller**, **D. Möller**, *Eur. J. Inorg. Chem.* **2005**, (2), 257−263.
3. FP: Solvothermal Synthesis of NiS 3D Nanostructures; **Y Qian** et al., *Eur. J. Inorg. Chem.* **2005**, (4), 653−656.
4. FP: *N*-Ferrocenyl-Substituted Planar-Chiral N-Heterocyclic Carbenes and Their $Pd^{II}$ Complexes; **A. Togni** et al., *Eur. J. Inorg. Chem.* **2005**, (2), 347−356.
5. FP: Carbon-Rich Ruthenium Complexes Containing Bis(allenylidene) and Mixed Alkynyl-Allenylidene Bridges; **S. Rigaut, D. Touchard, P. H. Dixneuf** et al., *Eur. J. Inorg. Chem.* **2005**, (3), 447−460.
6. SC: Preparation and Characterization of $Ag@TiO_2$ Core-Shell Nanoparticles in Water-in-Oil Emulsions; **F. Liu** et al., *Eur. J. Inorg. Chem.* **2005**, (9), 1643−1648.
7. FP: Three-Dimensional Lanthanoid-Containing Coordination Frameworks: Structure, Magnetic and Fluorescent Properties; **X.-Z. You, S. Gao** et al., *Eur . J. Inorg. Chem.* **2005**, (4), 766−772.
8. FP: Synthesis, Structure, and Photophysical and Electrochemical Properties of Cyclometallated Iridium(iii) Complexes with Phenylated Bipyridine Ligands; **K. Kam-Wing Lo, V. Guerchais** et al., *Eur. J. Inorg. Chem.* **2005**, (1), 110−117.
9. FP: A Structural and Magnetic Investigation of Ferromagnetically Coupled Copper(ii) Isophthalates; **P. Cheng** et al., *Eur. J. Inorg. Chem.* **2005**, (12), 2297−2305.
10. FP: Bis(1-methylimidazol-2-yl)propionates and Bis(1-methylbenzimidazol-2-yl)-propionates: A New Family of Biomimetic N,N,O Ligands − Synthesis, Structures and $Cu^{II}$ Coordination Complexes; **R. J. M. Klein, G. van Koten** et al., *Eur. J. Inorg. Chem.* **2005**, (4), 779−787.

Chart 2b. Short Communications (SC) and Full Papers (FP) from later issues that attracted a high number of downloads within one month.

1. SC: Self-Assembly of 1-D Coordination Polymers Using Organometallic Linkers and Exhibiting Argentophilic Interactions AgI···AgI; **H. Amouri** et al., *Eur. J. Inorg. Chem.* **2005**, (19), 3808−3810.
2. FP: Structures, Photoluminescence and Theoretical Studies of Two $Zn^{II}$ Complexes with Substituted 2-(2-Hydroxyphenyl)benzimidazoles; **S.-L. Zheng, X.-M. Chen** et al., *Eur. J. Inorg. Chem.* **2005**, (18), 3734−3741.
3. FP: Multiple Regulated Assembly, Crystal Structures and Magnetic Properties of Porous Coordination Polymers with Flexible Ligands; **L. P. Jin, S. Gao et al.,** *Eur. J. Inorg. Chem.* **2005**, (20), 4150−4159.
4. FP: Self-Assembly and Characterization of Grid-Type Copper(I), Silver(I), and Zinc(II) Complexes; **V. Patroniak, J. M. Lehn** et al., *Eur. J. Inorg. Chem.* **2005**, (20), 4168−4173.

included in the Chemistry Societies Backfile Collection are *Angewandte Chemie* and the first three volumes of *Chemistry − A European Journal.* In total the Chemistry Societies Backfile Collection comprises more than 872,000 pages (see http://www3.interscience.wiley.com/cgi-bin/collectionhome/CSCOL/HOME).

Thus retrospective literature researches can be performed from the convenience of your office desk. But forward-looking searches are useful, too. Often the quickest way to become aware of new research is to check the citations to an important paper in the field. Now with "Citation Tracking" in Wiley InterScience you can do just that with ease. From the Abstract or Reference link of any article you find a new link "Citation Tracking" (see Figure 1, page 7). A click provides a list of papers that cite the article. Not only articles in Wiley InterScience are found, but also articles from all CrossRef member publishers. And the lesson to be learned from these two projects? Continue to tell us what you would like to have from our journals − we take you seriously!

An important reaction to the reflection on the past year is gratitude to our Editorial and Advisory Board members, and our peer reviewers. Their expertise and sound advice is much appreciated. To all of them, and to our readers and authors, we wish every success in your research and good ideas from reading EurJIC.

Reminiscences on the less common events uncover areas where resolutions more substantial than the usual New Year's Resolution are required. This year brought a disheartening number of cases of plagiarism. Coincidence plays a large part in its discovery before publication. Two editors select the same referee, or a referee checks a citation or looks up a reference that appears pertinent. My sincerest thanks go to those referees whose conscientious review brought unacceptable behaviour to light. Such care takes time. In the interests of all involved in chemical research, peer review must not be rushed more than expedient. On the other hand, authors have the right to know the fate of their manusacript in a timely fashion. Informing an editor if the referee report will be delayed is also an ethical tenet.

Editors, societies and publishers cooperate closely to stamp out unethical practices. All steps directed at keeping the communication of our Science fair but efficient in these times of sharp competition must be welcomed. The American Chemical Society was pioneer and their Ethical Guidelines are prominent online as a link on all their journal pages. The initiative of the many European Chemical Societies to formulate unified Guidelines including measures to be taken against offenders is praiseworthy.

On confronting the problem of plagiarism in 2005 I was reminded of an experience of mine. After my degree in Chemistry I took an elective in the Humanities with several hundred fellow students at first semester level. I was expected to cite the same reference several times in one paragraph, although to me it was obvious from the context that the text was explaining one idea. The measures taken for failure to do so could not be overlooked by any student − zero credit for the assignment. The nature of the assignments in the Humanities lends itself far more readily than in the experimental sciences to education in this aspect essential to academia. Nevertheless, the difference is striking. Nowhere in my academic career in Chemistry did I receive as clear a message in the ethics of citation and the severity

 © 2006 Wiley-VCH Verlag GmbH & Co. KGaA, Weinheim 

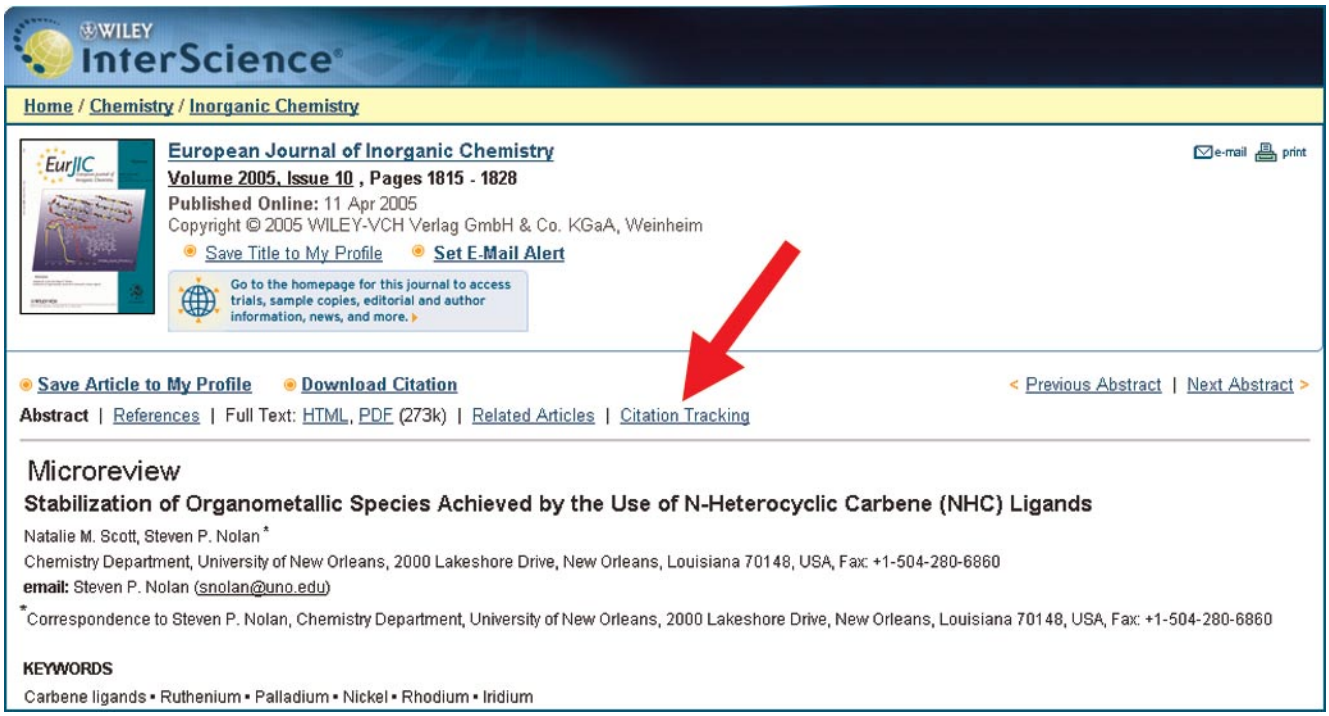


Figure 1. Abstract page of an article in Wiley InterScience showing the Citation Tracking link.

of the measures for omission. Only at a much later stage in my studies did I become conscious of the importance of references, more through my exposure to the chemical literature than through mentoring. Yet I am sure my professors are convinced that they instilled into their students the culture of citation.

At the latest when the research of a student is included in a manuscript for publication, that student must be formally educated in the ethics of publishing and the consequences of violation. All senior authors need to take this responsibility seriously, not only as an educational aim, but also as self-protection. No editor considers as excuse, or even extenuating circumstances, that the text was taken from the notes of a PhD student, although it is a fact that plagiarism has become more likely than in the days when "Copy and Paste" meant getting sticky with glue.

Changed circumstances always require an appraising reaction. This is as true in publishing as Newton's third law of motion. Let us make 2006 a turning point in awareness towards the ethics of our science.

Karen J. Hudson

 © 2005 Wiley-VCH Verlag GmbH & Co. KGaA, Weinheim 

EurJIC
European Journal of Inorganic Chemistry

Issue 1/2006

Pages 1–256

*Papers available ahead of print in Early View at www.interscience.wiley.com*

*Earliest available Table of Contents:*
*Automatically, free of charge by e-mail through*
*www.interscience.wiley.com/alerts*

## COVER PICTURE

**The cover picture shows** that addition of lanthanum(III) triflate to the red solution of a fluorescent "Nile Red" derivative results in a bathochromic shift of the intense charge-transfer band due to the formation of a chelate lanthanum(III) complex, as shown by a structure determination of crystals isolated from the resulting blue solution. details are discussed in the Short Communication by A. Døssing et al. on p. 43 ff.

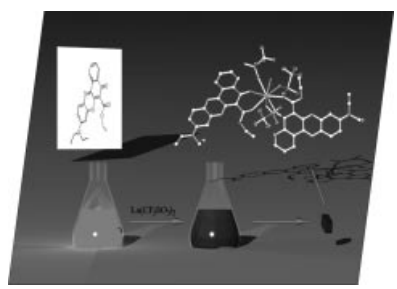

## MICROREVIEW

**Contents**

**29** **P. Gamez,* J. Reedijk***

1,3,5-Triazine-Based Synthons in Supramolecular Chemistry

**Keywords:** Supramolecular chemistry / Self-assembly / Crystal engineering / N ligands / Cyanuric chloride / 1,3,5-Triazine

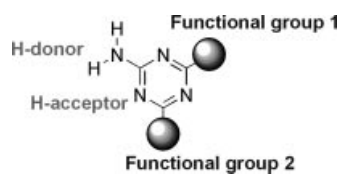


 © 2006 Wiley-VCH Verlag GmbH & Co. KGaA, Weinheim 

# SHORT COMMUNICATIONS


**43** **A. Døssing,* M. Magnussen, A. M. Frey**

Crystal Structure and Optical Properties of a Lanthanum(III) Complex of the Solvatochromic Dye "Nile Red"

**Keywords:** Lanthanum / Heterocycles / N,O ligands / Chelates


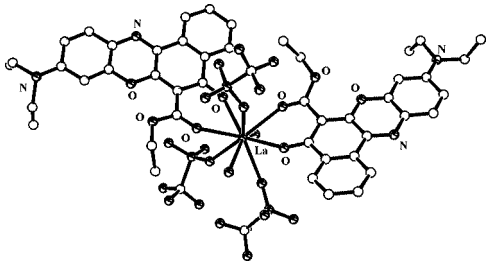


**47** **C. Ornelas, V. Vertlib, J. Rodrigues,* K. Rissanen***

Ruthenium Metallodendrimers Based on Nitrile-Functionalized Poly(alkylidene imine)s

**Keywords:** Ruthenium / Dendrimers / N ligands / Sandwich complexes


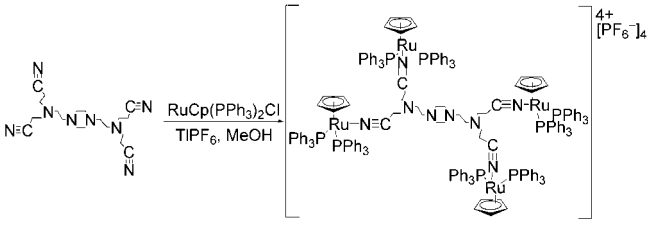


# FULL PAPERS


**51** **J. Andrieu,* J.-M. Camus, P. Richard, R. Poli, L. Gonsalvi, F. Vizza, M. Peruzzini***

Amino-phosphanes in $Rh^{I}$-Catalyzed Hydroformylation: Hemilabile Behavior of P,N Ligands under High CO Pressure and Catalytic Properties

**Keywords:** Rhodium / Amino-phosphane ligands / Hemilability / Hydroformylation catalysis


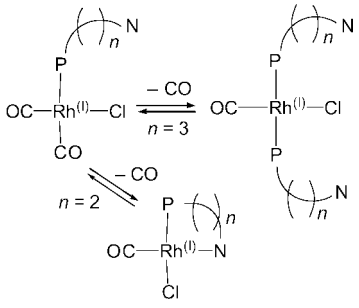



**62** **J. Andrieu,* J.-M. Camus, C. Balan, R. Poli***

Amino-phosphanes in $Rh^{I}$-Catalyzed Hydroformylation: New Mechanistic Insights Using $D_2O$ as Deuterium-Labeling Agent

**Keywords:** Rhodium / Amino-phosphane ligands / H/D isotopic exchange / Hydroformylation catalysis / Enantioselectivity


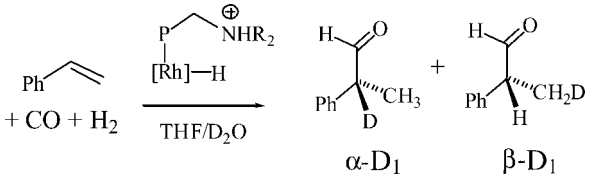



**69** **J. Oláh, F. Blockhuys, T. Veszprémi, C. Van Alsenoy***

On the Usefulness of Bond Orders and Overlap Populations to Chalcogen−Nitrogen Systems

**Keywords:** Bond order / Overlap population / Hirshfeld partitioning / Chalcogen−nitrogen systems / Bonding


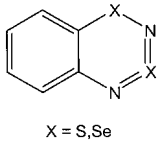

**78** **J. Díez, M. P. Gamasa,* J. Gimeno, E. Lastra,* A. Villar**

Synthesis of New Half-Sandwich Ruthenium(II) Complexes Bearing Alkenyl- and Alkynylphosphane Ligands

**Keywords:** Indenyl complexes / Phosphane ligands / Ruthenium / Sandwich complexes

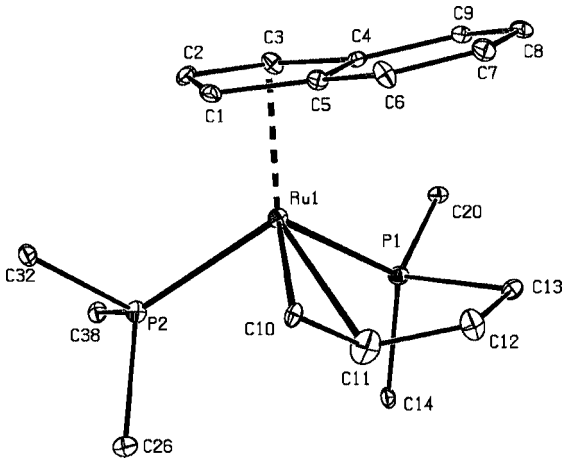


**88** **C. G. Hrib, F. Ruthe, E. Seppälä, M. Bätcher, C. Druckenbrodt, C. Wismach, P. G. Jones, W.-W. du Mont,* V. Lippolis, F. A. Devillanova, M. Bühl**

The Bromination of Bulky Trialkylphosphane Selenides $R_2R'PSe$ (R, R′ = *i*Pr and/or *t*Bu) Studied by Physical and Computational Methods

**Keywords:** Phosphane selenide dibromides / Heteronuclear NMR / Raman spectroscopy / X-ray structures / Bromine exchange / Ab initio calculations

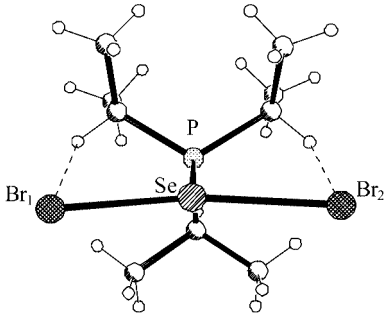


**101** **B. Wrackmeyer,* B. H. Kenner-Hofmann, W. Milius, P. Thoma, O. L. Tok, M. Herberhold***

Ferrocenylethynyltin Compounds − Characterization and Reactivity towards Triethylborane

**Keywords:** Alkynes / Boranes / Ferrocenes / NMR spectroscopy / Tin

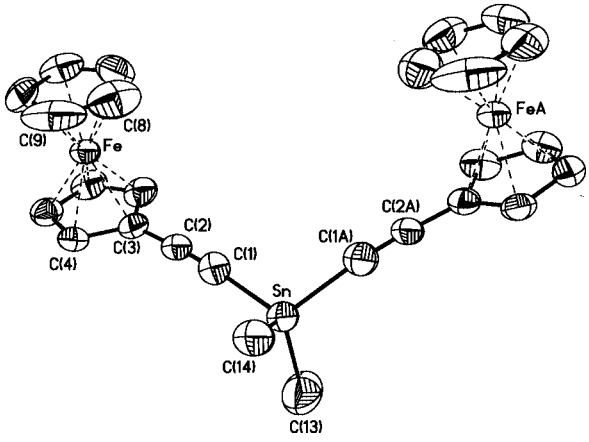


**109** **F. Wang, G. Xu,* Z. Zhang, X. Xin**

Synthesis of Monodisperse CdS Nanospheres in an Inverse Microemulsion System Formed with a Dendritic Polyether Copolymer

**Keywords:** Monodisperse nanopheres / Semiconductors / Dendrimers / X-ray diffraction / Microemulsion

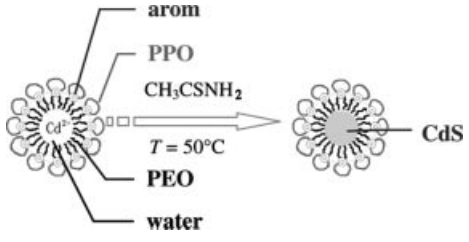


 © 2006 Wiley-VCH Verlag GmbH & Co. KGaA, Weinheim 

## 115

**J. Vicente, P. González-Herrero,***
**Y. García-Sánchez, P. G. Jones, D. Bautista**

Copper Complexes with (2,7-Di-*tert*-butylfluoren-9-ylidene)methanedithiolate: Oxidatively Promoted Dithioate Condensation

**Keywords:** Copper / Dithiolates / Phosphane ligands / S ligands

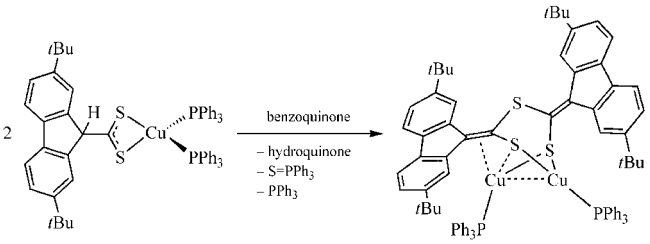


## 127

**J. Sánchez-Nieves, P. Royo,***
**M. E. G. Mosquera**

$\eta^2$-Iminoacyl and $\eta^2$-Acyl Monocyclopentadienyl Tantalum Complexes Bearing Oxo and Oxo-Borane Ligands

**Keywords:** Tantalum / Oxo ligands / Insertion reactions / Isocyanide / Carbon monoxide

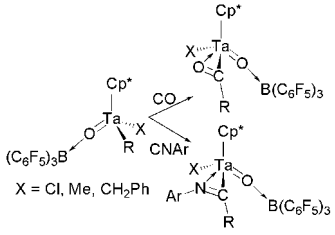


## 133

**J. Mathieu, B. Fraisse, D. Lacour,**
**N. Ghermani, F. Montaigne, A. Marsura***

An Original Supramolecular Helicate from a Bipyridine−Bipyrazine Ligand Strand and $Ni^{II}$ by Self-Assembly

**Keywords:** Magnetic properties / N ligands / Nickel / Self assembly / Supramolecular chemistry

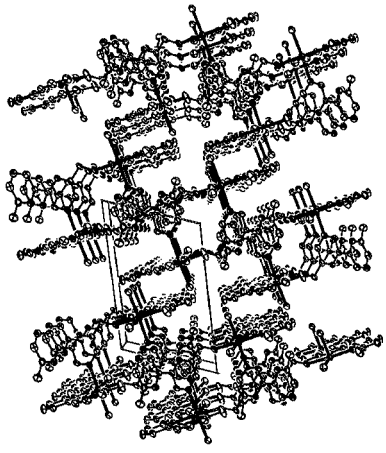

## 137

**L. Weber,* P. Bayer, S. Uthmann, T. Braun,**
**H.-G. Stammler, B. Neumann**

Reactivity of the Inversely Polarized Arsaalkenes $R-As=C(NMe_2)_2$ {R = $[(\eta^5\text{-}C_5Me_5)(CO)_2Fe]$, *t*BuC(O), 4-Et−$C_6H_4$C(O)} towards Phosphavinylidene Complexes $[\eta^5\text{-}(C_5H_5)(CO)_2M=P=C(SiMe_3)_2]$ (M = Mo, W)

**Keywords:** Arsaalkenes / Heteroallyl ligands / Molybdenum / Phosphavinylidene complexes / Tungsten

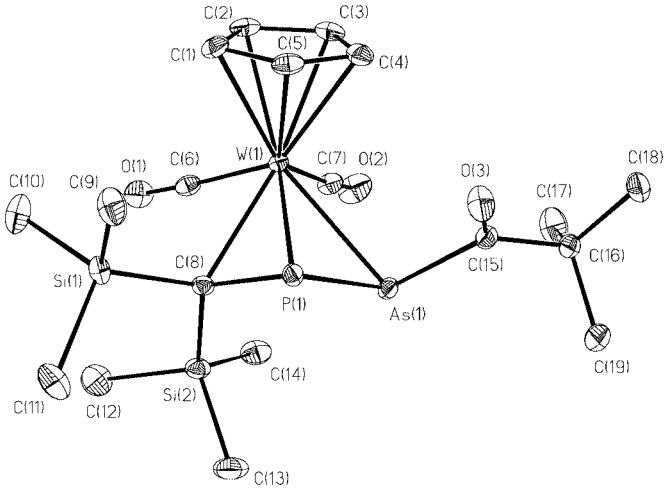


 © 2006 Wiley-VCH Verlag GmbH & Co. KGaA, Weinheim 

**144** **V. Patroniak,* A. R. Stefankiewicz, J.-M. Lehn, M. Kubicki, M. Hoffmann**

Self-Assembly and Characterization of Homo- and Heterodinuclear Complexes of Zinc(II) and Lanthanide(III) Ions with a Tridentate Schiff-Base Ligand

**Keywords:** Dinuclear complexes / Lanthanides / Tridentate Schiff-base ligand / Self-assembly / Zinc

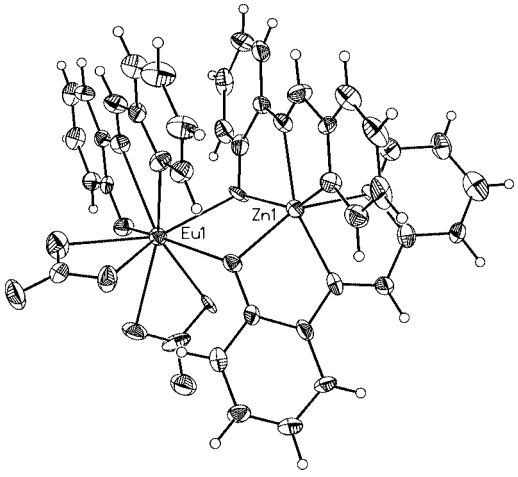


**150** **K. Binnemans,* K. Lodewyckx, T. Cardinaels, T. N. Parac-Vogt, C. Bourgogne, D. Guillon, B. Donnio***

Dinuclear Lanthanide Schiff-Base Complexes Forming a Rectangular Columnar Mesophase

**Keywords:** Columnar mesophases / Lanthanides / Liquid crystals / Metallomesogens / Rare earths

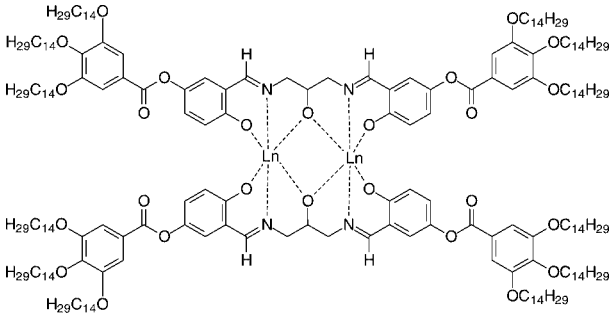


**158** **M. Paas, B. Wibbeling, R. Fröhlich, F. E. Hahn***

Silver and Rhodium Complexes of Stable, Monomeric Imidazolidin-2-ylidenes: Synthesis, Reactivity and Decomposition Pathway

**Keywords:** Carbenes / Carbene ligands / Nitrogen heterocycles / Silver / Sulfur

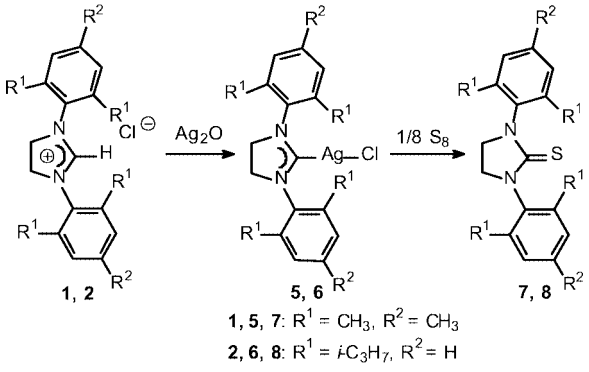


**163** **Y. Sakai, A. Shinohara, K. Hayashi, K. Nomiya***

Synthesis and Characterization of Two Novel, Mono-Lacunary Dawson Polyoxometalate-Based, Water-Soluble Organometallic Ruthenium(II) Complexes: Molecular Structure of $[\{(C_6H_6)Ru(H_2O)\}(\alpha_2\text{-}P_2W_{17}O_{61})]^{8-}$

**Keywords:** Arene ligands / Polyoxometalates / Ruthenium / X-ray diffraction

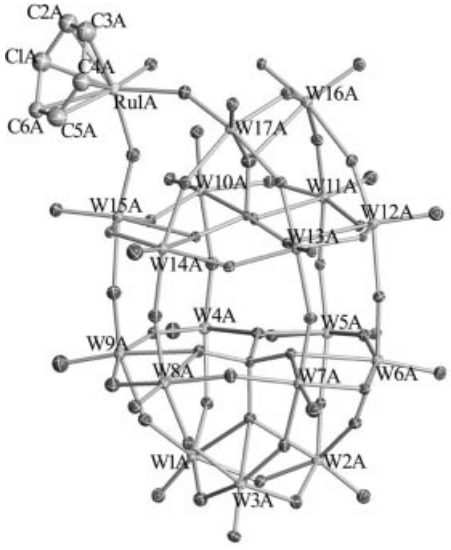


 © 2006 Wiley-VCH Verlag GmbH & Co. KGaA, Weinheim 

**172** **S. Panda, S. S. Zade, H. B. Singh,* R. J. Butcher**

The Ligation Properties of some Reduced Schiff Base Selena/Telluraaza Macrocycles: Versatile Structural Trends

**Keywords:** Chalcogenaaza macrocycles / Selenium tellurium ligands / Nickel / Palladium / Platinum

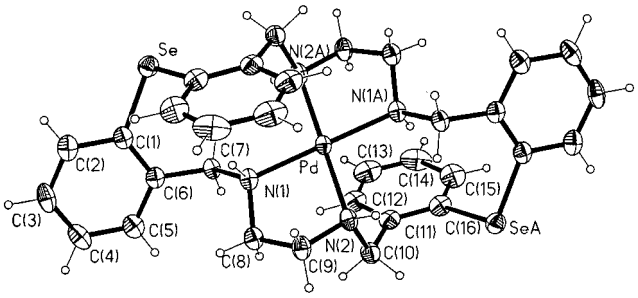


**185** **S. Triki,* J. Sala-Pala, F. Thétiot, C. J. Gómez-García, J.-C. Daran**

New, Multi-Dimensional Cu(tn)-$[M(CN)_6]^{n-}$ Cyano-Bridged, Bimetallic Coordination Materials ($M = Fe^{II}$, $Co^{III}$, $Cr^{III}$ and tn = 1,3-Diaminopropane)

**Keywords:** Bridging ligands / Cyanides / Heterometallic complexes / Magnetic properties

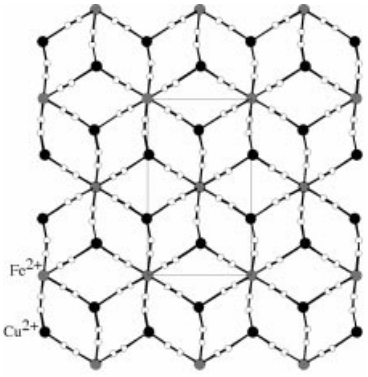


**200** **M. C. Aragoni, M. Arca, M. B. Carrea, F. Demartin, F. A. Devillanova, A. Garau, M. B. Hursthouse, S. L. Huth, F. Isaia,* V. Lippolis, H. R. Ogilvie, G. Verani**

Copper(I) Complexes with a $Cu_4S_6$- and $CuS_4$-Type Core Obtained from the Reaction of Copper(0) with $HN(SPPh_2)_2 \cdot I_2$

**Keywords:** Cluster compounds / Copper / Coordination chemistry / Phosphanes / S ligands

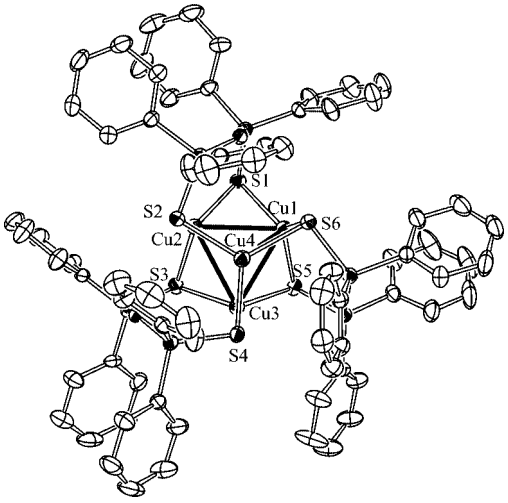


**207** **S. Xiong, L. Fei, Z. Wang, H. Y. Zhou, W. Wang, Y. Qian***

Preparation of Semiconductor/Polymer Coaxial Nanocables by a Facile Solution Process

**Keywords:** Hydrothermal synthesis / Nanostructures / Photoluminescence / Semiconductors / Tellurium

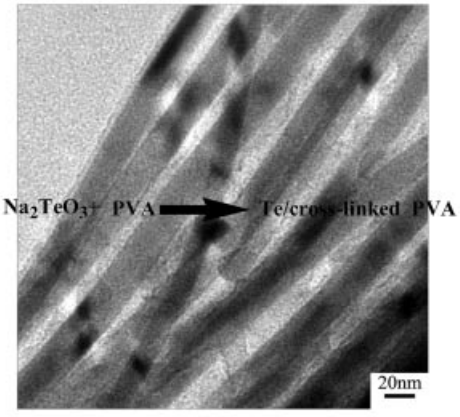


 © 2006 Wiley-VCH Verlag GmbH & Co. KGaA, Weinheim 

**213** **M. Piacenza, J. Rakow, I. Hyla-Kryspin,* S. Grimme***

Theoretical Study of the Effects of Phosphane Substituents on the Bonding Properties of Acetylene with $Ni(PR_3)_2$ (R = H, $CH_3$, F, $CF_3$, $C_6H_5$)

**Keywords:** Alkyne ligands / Density functional calculations / Nickel / Phosphane ligands

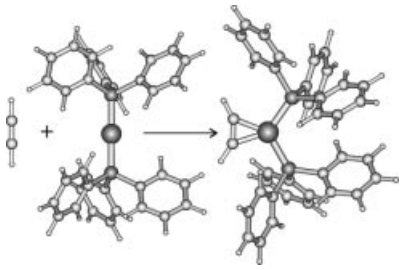

**222** **Y. Obora, Y. K. Liu, S. Kubouchi, M. Tokunaga, Y. Tsuji***

Monophosphanylcalix[6]arene Ligands: Synthesis Characterization, Complexation, and Their Use in Catalysis

**Keywords:** Calixarenes / Heterogeneous catalysis / Phosphanes / Platinum / Rhodium

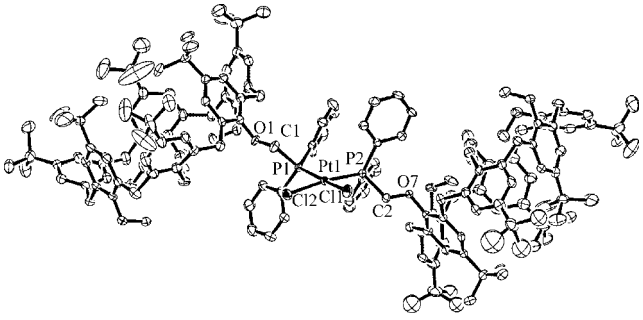


**231** **L. Quebatte, R. Scopelliti, K. Severin***

Synthesis, Structure and Reactivity of Homo- and Heterobimetallic Complexes of the General Formula $[Cp^*Ru(\mu\text{-}Cl)_3ML]$ [LM = (arene)Ru, Cp*Rh, Cp*Ir]

**Keywords:** Heterometallic complexes / Iridium / Rhodium / Ruthenium

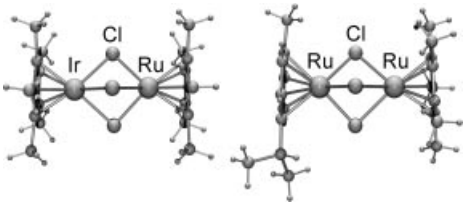


**237** **L. Lakiss, A. Simon-Masseron, F. Porcher, J. Patarin***

Mu-34: a New Porous Layered Fluorogallophosphate Material Obtained by in Situ Generation of Ethylamine

**Keywords:** Fluorogallophosphate / Ethylformamide / Solvothermal synthesis / Ethylamine / Porous layered solids / Microporous materials

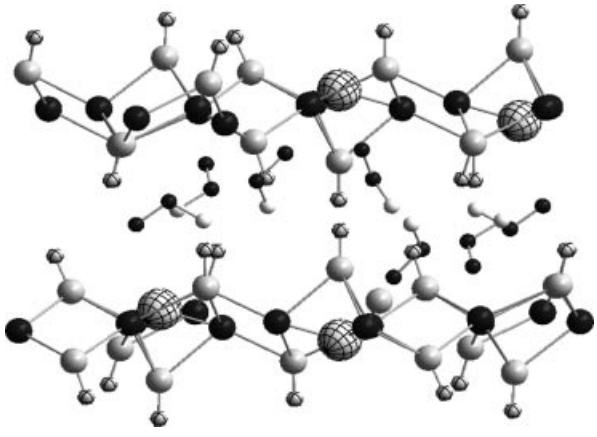

 © 2006 Wiley-VCH Verlag GmbH & Co. KGaA, Weinheim 

**244** **I. Janser, M. Albrecht,* K. Hunger, S. Burk, K. Rissanen**

Formation of Triple-Stranded Dinuclear Helicates with Dicatecholimine Ligands: The Influence of Steric Hindrance at the Spacer

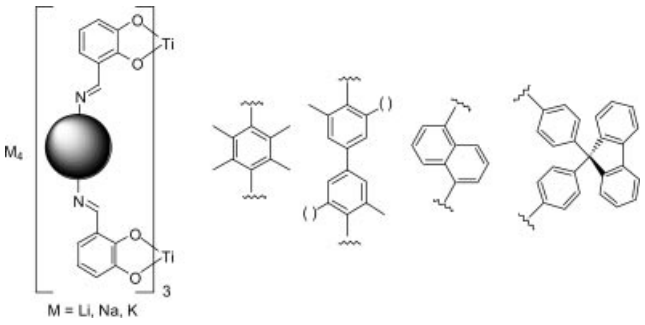


**Keywords:** Dinuclear complexes / Helicates / Mesohelicates / Self-assembly / Titanium / Bulky ligands

## 1. General Information

The *European Journal of Inorganic Chemistry (EurJIC)* is published twice monthly.

**Manuscripts should be submitted online** using our online submission service at http://www.manuscriptXpress.org. You should prepare a **single file containing all tables, graphics, supporting information (where appropriate) etc.** Acceptable file formats are **Microsoft Word, Rich Text Format, Postscript and PDF**. Avoid the use of page breaks even between the title page and the introduction. If graphics are included at the end of the manuscript, try to fit as many as possible onto a single page. The file should have margins of 2 cm and be 1.5-line spaced.

Authors can follow the progress of their manuscript on their **personal homepage**, which is created automatically upon initial registration. This homepage is the same for the family of Wiley-VCH European journals and can be used to **store the latest version of a submitted paper** and to **upload the document file after acceptance**. Your referee reports for the family of Wiley-VCH European journals are also archived here.

**No paper copies of the manuscript are required when using this system.**

- The author must inform the editor of all manuscripts submitted, soon to be submitted, or in press at other journals that have a bearing on the manuscript being submitted.
- The correspondence author of a Microreview will receive a complimentary copy of the journal along with a PDF file of his/her paper restricted to 50 printouts; the correspondence author of other articles will receive a PDF file restricted to 25 printouts. Colour figures can be reproduced. Unless the editor deems colour to be essential for the understanding of a paper, authors will be requested to make a contribution towards the costs of colour reproduction. Details will be provided after acceptance of the manuscript.
- We encourage authors to submit pictures for the cover page. A template of our cover page, **eurjiccover.pdf**, can be reached by clicking the link "For Authors" on our journal homepage (http://www.eurjic.org), to help you visualize the final effect of your design.

**IMPORTANT:** Any manuscript already available on personal/group web pages will be considered by the editors as already published and will not be accepted.

On behalf of our authors who are also US National Institutes of Health (NIH) grantees, we will deposit in PubMed Central (PMC) and make public after 12 months the peer-reviewed version of the author's manuscript. By assuming this responsibility, we will ensure that our authors are in compliance with the NIH request, and make certain that the appropriate version of the manuscript is deposited. We await the release by PMC of the protocols regarding manuscript submission. We reserve the right to change or rescind this policy.

## 2. Types of Contributions

**EurJIC publishes articles on inorganic, organometallic, bioinorganic, physical inorganic and solid-state chemistry. All contributions undergo peer review. An author may appeal against the decision on his/her manuscript, in writing. Three types of contributions are accepted for publication:**

- **Full Papers** are articles with an Experimental Section that describe a significant contribution to the development of an area of research of importance. There are no restrictions placed on the length of a Full Paper.
- **Short Communications** are brief reports on results of high significance and urgency. Generally, they are no longer than 12−16 double-spaced pages or 3−4 typeset pages. An Experimental Section (as a separate paragraph or as part of the references) is desirable; if it is not included in the paper, the experimental data should be submitted as Supporting Information for refereeing purposes, and marked as such. A justification for urgent publication should accompany submission.
- **A Microreview** introduces the reader to a particular area of an author's research through a concise overview of a selected topic. As a rule, Microreviews are written on invitation, although unsolicited articles are also welcome. It is recommended, however, to contact the editor before submitting an unsolicited Microreview. The content should balance scope with depth; it should be a focused review of 25−30 double-spaced pages or 6−8 typeset pages. Reference to important work from others that is significant to the topic should be included. Microreviews will be refereed but will have no Experimental Section.

## 3. Manuscript Preparation

### 3.1 General

The whole of the manuscript should be 1.5-line spaced and in a large script (Times New Roman, 12 pt). We recommend that you prepare your text with **Microsoft Word (PC or Macintosh versions)** (see Section 3.2). Page numbers are essential: use the automatic pagination function incorporated in your word processing software. Leave a 2-cm margin around the perimeter of each page. Consult a current issue of the journal for an overview of the format. A manuscript should comprise: ◇ Title Page ◇ Keywords ◇ Abstract ◇ Main Text including Introduction, Results and Discussion etc. ◇ Experimental Section ◇ Acknowledgments (optional) ◇ Captions ◇ Tables ◇ References ◇ Schemes and Figures ◇ Graphical Abstract ◇ For Microreviews only: Biographical sketches and a portrait-quality photograph of all authors (when several authors from one institution are involved, group photographs are preferred).

 © 2006 Wiley-VCH Verlag GmbH & Co. KGaA, Weinheim 

### 3.2 Text

The text should be typed with carriage returns (hard returns) only at the end of a paragraph, title, heading and similar features. Avoid end-of-line word divisions.

**Abbreviations and acronyms** should be used sparingly and consistently. Where they first appear in the text, the complete term — apart from the most common ones such as NMR, IR, THF, *t*Bu etc. — should also be given.

**In the Experimental Section**, quantities of reactants, solvents etc. should be included in parentheses [e.g. A solution of triphenylphosphane (500 mg, 1.91 mmol) in dichloromethane (15 mL) was added to...].

**NMR spectroscopic data** should be quoted as in the following example: $^1$H NMR (300 MHz, $C_6D_6$, 25 °C): $\delta$ = 1.3 (s, 18 H, $SiMe_3$), 0.9 (d, $^3J_{H,H}$ = 5.7 Hz, 2 H, 2-H) ppm. For each chemical shift, additional information should be given in the order: multiplicity, coupling constant, number of protons, assignment.

**The purity of all new compounds** should be verified by elemental analysis to an accuracy within ±0.4%. In special cases, for instance when the compound is unstable or not available in sufficient quantities for complete analysis, the exact relative molecular mass obtained from a high-resolution mass spectrum and a clean $^{13}$C NMR spectrum (as additional material for inspection by the referees) should be supplied.

**Symbols of physical quantities**, but not their units (e.g. *T* for temperature, *J*, $\lambda$), stereochemical information (*cis*, *trans*, *Z*, *R*), locants (*N*-methyl), symmetry and space groups ($P2_1/c$), and prefixes in formulas or compound names (*t*Bu, *tert*-butyl) **must be in italics**. Latin phrases, such as "in situ", should not.

**Stereochemical descriptors**, such as D- and L-, and molar (M) or normal (N) should be in **small capitals**. Use character formatting for italic and bold characters. Avoid any *special style sheets* to format these features. Write *capital letters* using the keyboard (shift + letter key), **not** the format "Capital letter" in Word.

**Use only characters from the Symbol and Normal Text character sets**, especially when inserting Greek letters and characters with umlauts, accents, tildes, etc.: α, ä, à, ã, Å.

There are three types of hyphens: normal dashes (-), en dashes (−), and em dashes (—). Use these as illustrated — spacing is important too — in the following examples:

| | |
|---|---|
| well-known reaction | C−H bond |
| six-membered ring | Tables 2−4 |
| 3-position of the ring | carbon−oxygen bond |
| signal-to-noise ratio | C−N stretch |
| Mo-$K_\alpha$ | Diels−Alder reaction |
| 1,2-dicyanobutane | structure−activity relationship |
| *p*-*tert*-butylphenol | 80−100 mg |
| (−)-tartaric acid | carried out at −10 °C |
| $[M^+ - CH_3]$ | $cm^{-1}$ |

Use the symbol × where appropriate, rather than the letter x:
... washed with water (2 × 150 mL) ...
Use the double quotation marks "..." rather than „...", "..." or «...».
**Graphics (including structural formulas, schemes, figures, equations and small graphical items that appear in captions) must be submitted camera-ready on separate pages after acceptance of the manuscript (see Section 3.5).**

**Lines** or **arcs**, for example to indicate ring compounds, cannot be used within the text. Another method for indicating such compounds must be devised. Please contact the Editorial Office if any help is needed.

If practical, authors should use a systematic name (IUPAC or Chemical Abstracts) for each title compound in the Experimental Section. Please try to avoid complicated, multi-line names if a simpler version (e.g. alcohol **4**, ketone **5**, compound **6**) could be used instead.

### 3.3 Tables

Use the Insert Table command from the Table menu or use the Insert Table button on the Standard toolbar for creating tables, and use tabs ONLY to move between cells.

### 3.4 References

We strongly recommend the use of the Endnotes feature of Word. If you prefer not to use this function, references should be indicated by numbers in square brackets as superscripts and, if applicable, after punctuation (example: text.[1]). Use the Format Font menu. Journal titles should be abbreviated according to the Chemical Abstracts Service Source Index (CASSI).

The Author is responsible for correct citations. The *European Journal of Inorganic Chemistry* is a member of Cross Ref. (http://www.crossref.org), a service which links reference citations to the online content that those references cite. This can only function if the citations are accurate. Please ensure that only one reference is cited under each reference number or that a composite reference is subdivided into parts a), b) etc. For example:

[1] A. Einstein, A. N. Other, *Eur. J. Inorg. Chem.* **2003**, 1−15.
[2] R. Schoenfeld, *The Chemist's English*, 3rd ed., VCH, Weinheim, **1990**, p. 111.

or

[1] a) A. Einstein, A. N. Other, *Eur. J. Inorg. Chem.* **2003**, 1−15; b) R. Schoenfeld, *The Chemist's English*, 3rd ed., VCH, Weinheim, **1990**, p. 111.

but not

[1] a) A. Einstein, A. N. Other, *Eur. J. Inorg. Chem.* **2003**, 1−15; R. Schoenfeld, *The Chemist's English*, 3rd ed., VCH, Weinheim, **1990**, p. 111.

### 3.5 Graphics

Graphics are schemes, figures, equations and small graphical items that appear in captions. Graphics differ fundamentally from the text portion of your manuscript in that they must be scanned or electronically processed. Schemes should be self-explanatory: reaction conditions should therefore be given above the arrows rather than in the caption.

In the revised version please submit **each graphic in its own file** within a graphic folder. For good reproduction, the following formats are preferred: *.cdr, *.cdx, *.tif, *.pdf, *.psd, *.ai, *.fh, *.qxd,*.pct, *.eps. The resolution should be a minimum of 300 dpi and 600 dpi for bitmap graphics.

Consult the following table for the appropriate size of lettering. Lettering smaller than 3.0 mm will reproduce poorly. Please use only one size of lettering per graphic and the same letter font for all graphics.

Table 1. Guide for preparing graphics

| Letter Size | Font | Maximum Graphic Width[a] 1-Column Format | 2-Column Format |
|---|---|---|---|
| | Times New Roman | | |
| 3.0 mm | 12 | 13 cm | 26 cm |
| **3.5 mm** | **14** | **15 cm**[b] | – |
| **4.0 mm** | **16** | **17 cm**[b] | – |
| 4.5 mm | 18 | 19 cm | – |

[a] Most graphics are in 1-column format. [b] We prefer lettering of 3.5 or 4.0 mm with maximum graphic widths of 15 or 17 cm, respectively.

 © 2006 Wiley-VCH Verlag GmbH & Co. KGaA, Weinheim 

The settings for one-column graphics constructed with Chem Draw are: Print Setup: Orientation Portrait. Caption and Label Settings: Font Times New Roman, Font Style Standard, Size 12.

**Note that the graphical abstract must be in one-column format and in black-and-white**.

These settings help ensure the correct letter-size-to-graphic-width ratio for best reproduction.
Use abbreviations such as $R^1$, $R^2$ (not $R_2$), R′, R″, Ph, Me, Et, *i*Pr, *t*Bu, Ph, Bn (benzyl), Bz (benzoyl), Hal, L, M (metal), X (heteroatom).

### 4. Crystallographic Data

Authors must deposit the data of X-ray structure analyses in a crystallographic database before submitting their manuscript, so that referees can access the information electronically. The two databases, the Cambridge Crystallographic Data Centre (CCDC) and the Fachinformationszentrum Karlsruhe (FIZ) have the same procedure for the deposition of data and both will be pleased to provide help. In general, you will receive a depository number from the database two working days after electronic deposition. Send your data to the appropriate address below and quote the standard text, including the depository number, in your manuscript.

- **For all compounds without C−H bonds:**

Fachinformationszentrum Karlsruhe (FIZ)
76344 Eggenstein-Leopoldshafen, Germany
Phone: +49-(0)7247/808-205
Fax: +49-(0)7247/808-666
E-mail: crysdata@fiz-karlsruhe.de
FTP: ftp.fiz-karlsruhe.de (under path /pub/csd)
WWW: http://www.fiz-karlsruhe.de (under "Products and Services")

Further details of the crystal-structure investigation(s) may be obtained from the Fachinformationszentrum Karlsruhe, 76344 Eggenstein-Leopoldshafen, Germany, on quoting the depository number(s) CSD-....

- **For all compounds with at least one C−H bond:**

Cambridge Crystallographic Data Centre (CCDC)
12 Union Road, Cambridge CB2 1EZ, UK
Phone: +44-(0)1223/336-408
Fax: +44-(0)1223/336-033
E-mail: deposit@ccdc.cam.ac.uk
WWW: http://www.ccdc.cam.ac.uk

CCDC-****** contains the supplementary crystallographic data for this paper. These data can be obtained free of charge from The Cambridge Crystallographic Data Centre via www.ccdc.cam.ac.uk/datarequest/cif.

**NOTE:** Please use the free online **Checkcif** service provided by the International Union of Crystallography and submit the Checkcif report along with your manuscript: http://journals.iucr.org/services/cif/checkcif.html.
Finally, before you return your revised manuscript, please update your database entry if necessary.

### 5. Electronic Supporting Information

A manuscript may include Electronic Supporting Information which will be accessible only on the WWW. Authors must keep a copy to make available to readers who do not have access to the internet. As this material [text, tables, schemes, figures **but not crystallographic (CIF) data**, which must be submitted to either the FIZ or the CCDC] undergoes the peer review process, it must be included, clearly marked as "Supporting Information to be published electronically", when the paper is submitted. The following file formats are accepted: MS Winword or ASCII (*.doc, *.txt), MS Excel (*.xls), Encapsulated Postscript (*.eps), Portable Document Format (*.pdf), graphics embedded in MS Winword; if you wish to submit other formats, please consult the Editorial Office. When preparing such material, authors should keep in mind that — once accepted — it will be made available as provided by the author and not edited. Material accepted for electronic publication will be available mostly as PDF files (Adobe Acrobat Reader required) by following the Table of Contents link of EurJIC's WWW home page. A standard text will be added on the first page of the article in the printed version:

- Supporting information for this article is available on the WWW under http://www.eurjic.org or from the author.

The supporting information file must start with the title of the paper, the authors and the CASSI abbreviation of the journal to which it was submitted (e.g. *Eur. J. Inorg. Chem.*).

### 6. Basic Keyword List

To increase the relevance of articles found by search engines of Wiley InterScience, we have compiled a keyword catalogue common to our chemistry journals that is printed here and is also available online (http://www.eurjic.org).

To assist you in finding keywords they are listed according to categories. You may choose keywords from any category. As with all such records, a few guidelines facilitate the catalogue's use, and these are briefly explained below:

1. As many as possible, but at least two, of the maximum of five keywords assigned to an article must come from this list.

2. Named reactions will be incorporated only in exceptional cases. Generally the reaction type is selected instead. For example, Diels−Alder reactions will be found under "Cycloadditions" and Claisen rearrangements under "Rearrangements".

3. Heteroanalogues of compounds are mainly classified under the C variants, for example, (hetero)cumulenes, (hetero)dienes. A few aza and phospha derivatives are exceptions.

4. Compounds with inorganic components that are central to the article are listed under the element, for instance, iron complexes under "Iron". Some group names like "Alkali metals" exist alongside the names of important members of the group like "Lithium". In such cases the group name is used for these members only when comparative studies are described. The members not appearing separately are also categorised under the group name.

5. A keyword in the form "N ligand" is only chosen if a considerable portion of the paper deals with the coordination of any ligand ligating through the atom concerned.

6. Spectroscopic methods are assigned as keywords only if the article is about the method itself, or if the spectroscopic technique has made an important contribution to the problem under investigation.

7. "Structure elucidation" is intended only if the crux of the paper is a structural elucidation or if a combination of several spectroscopic techniques were needed for conclusive solution of the structure.

8. An attempt has been made to avoid synonyms and to select more general concepts rather than specialized terms. Thus, the term "Double-decker complexes" is excluded in favour of "Sandwich complexes".

This list will be a "living" catalogue to be flexible enough to absorb the new developments in chemistry. We therefore welcome all suggestions from our authors that might improve its user-friendliness.

 © 2006 Wiley-VCH Verlag GmbH & Co. KGaA, Weinheim 

# Guidelines for Authors

### Analytical Chemistry and Spectroscopic Methods

Analytical methods
Circular dichroism
Cyclic voltammetry
Electron diffraction
Electron microscopy
Electrophoresis
ENDOR spectroscopy
EPR spectroscopy
EXAFS spectroscopy
Fluorescence spectroscopy
Gas chromatography
High-throughput screening
Ion chromatography
Ion exchange
IR spectroscopy
Isotopic labeling
Laser spectroscopy
Liquid chromatography
Luminescence
Mass spectrometry
Moessbauer spectroscopy
Neutron diffraction
NMR spectroscopy
Photoelectron spectroscopy
Plasma chemistry
Raman spectroscopy
Rotational spectroscopy
Scanning probe microscopy
Sensors
Surface analysis
Surface plasmon resonance
Trace analysis
UV/Vis spectroscopy
Vibrational spectroscopy
Water chemistry
X-ray absorption spectroscopy
X-ray diffraction
ZEKE spectroscopy

### Biological Chemistry and Chemical Biology (including Biochemistry, Bioinorganic Chemistry, Bioorganic Chemistry, Medicinal Chemistry and Molecular and Cell Biology)

Allosterism
Amino acids
Angiogenesis
Antibiotics
Antibodies
Antifungal agents
Antigens
Antisense agents
Antitumor agents
Antiviral agents
Azapeptides
Azasugars
Bioinformatics
Bioinorganic chemistry
Biological activity
Biomimetic synthesis
Bioorganic chemistry
Biophysics
Biosensors
Biosynthesis
Biotransformations
C-Glycosides
Carbohydrates
Carbon dioxide fixation
Carotenoids
Cell adhesion
Cell recognition
Cerebrosides
Chaperone proteins
Cobalamines
Cofactors
Combinatorial chemistry
Cyclitols
Cyclodextrins
Cytokines
DNA
DNA cleavage
DNA damage
DNA methylation
DNA recognition
DNA replication
DNA structures
Dopamines
Drug delivery
Drug design
Electron transport
Enzyme models
Enzymes
Fibrous proteins
Fluorescent probes
Gene expression
Gene sequencing
Gene technology
Genomics
Glycoconjugates
Glycolipids
Glycopeptides
Glycoproteins
Glycosides
Glycosylation
Growth factors
Helical structures
Heme proteins
Hormones
Hydrolases
Immobilization
Immunoassays
Immunochemistry
Immunology
Inhibitors
Ion channels
Ionophores
Isomerases
Ligases
Lipids
Lipophilicity
Lipoproteins
Liposomes
Lyases
Medicinal chemistry
Membrane proteins
Membranes
Metabolism
Metalloenzymes
Metalloproteins
Micelles
Molecular evolution
mRNA
Mutagenesis
Natural products
Neurochemistry
Neurotransmitters
Nitrogen fixation
Nitrogenases
Nucleic acids
Nucleobases
Nucleosides
Nucleotides
Oligonucleotides
Oligosaccharides
Oxidoreductases
Peptide nucleic acids
Peptides
Peptidomimetics
Pheromones
Phospholipids
Photoaffinity labeling
Photosynthesis
Phytochemistry
Polyketides
Polymerase chain reaction
Prodrugs
Prostaglandins
Protein design
Protein engineering
Protein folding
Protein models
Protein modifications
Protein structures
Proteins
Proteomics
Proton transport
Radiopharmaceuticals
Receptors
Redox chemistry
Ribonucleosides
Ribozymes
RNA
RNA recognition
RNA structures
Sensitizers
Sequence determination
Sialic acids
Siderophores
Signal transduction
Sphingolipids
Steroids
Structure−activity relationships
Terpenoids
Toxicology
Transferases
tRNA
Vesicles
Vitamins

### Catalysis

Asymmetric catalysis
Autocatalysis
Biphasic catalysis
Catalytic antibodies
Enzyme catalysis
Heterogeneous catalysis
Homogeneous catalysis
Phase-transfer catalysis
Supported catalysts

 © 2006 Wiley-VCH Verlag GmbH & Co. KGaA, Weinheim 

### Coordination Chemistry: Compound Classes

Cage compounds
Chelates
Clathrates
Cluster compounds
Cuprates
Dendrimers
Heterometallic complexes
Metallacycles
Metallocenes
Nitrogen oxides
Polyoxometalates
Sandwich complexes
Ylides

### Coordination Chemistry: Ligand Classes

Alkene ligands
Alkyne ligands
Allyl ligands
Arene ligands
As ligands
Bridging ligands
Carbene ligands
Carbonyl ligands
Carboxylate ligands
Carbyne ligands
Cyclopentadienyl ligands
Diene ligands
Dioxygen ligands
Fluorinated ligands
Hydride ligands
Isocyanide ligands
Macrocyclic ligands
N ligands
N,O ligands
N,P ligands
O ligands
Oxo ligands
Peroxo ligands
Phosphane ligands
P ligands
S ligands
Si ligands
Tridentate ligands
Tripodal ligands
Vinylidene ligands

### Coordination Chemistry: Methodology and Reactions

Carbon dioxide fixation
Chemical vapor deposition
Chiral resolution
Crystal engineering
Ligand design
Matrix isolation
Metathesis
Neighboring-group effects
Nitrogen fixation
O−O activation
Oxidation
Radical reactions
Reduction
Ring-opening polymerization
Solvent effects
Solvolysis
Substituent effects
Template synthesis

### Coordination Chemistry: Structure

Agostic interactions
Aurophilicity
Charge transfer
Cooperative effects
Coordination modes
Donor−acceptor systems
Electron-deficient compounds
Electronic structure
Electrostatic interactions
Fluxionality
Helical structures
Host−guest systems
Hydrogen bonds
Inclusion compounds
Isolobal relationship
Jahn−Teller distortion
Ligand effects
Metal−metal interactions
Multiple bonds
Noncovalent interactions
Pi interactions
Stacking interactions
Structure elucidation
Through-bond interactions
Through-space interactions

### Elements and Element Groups

Actinides
Alkali metals
Alkaline earth metals
Aluminum
Antimony
Argon
Arsenic
Barium
Beryllium
Bismuth
Boron
Bromine
Cadmium
Calcium
Carbon
Cerium
Cesium
Chalcogens
Chlorine
Chromium
Cobalt
Copper
Deuterium
Fluorine
Gallium
Germanium
Gold
Group 13 elements
Group 14 elements
Hafnium
Halogens
Helium
Hydrogen
Indium
Iodine
Iridium
Iron
Krypton
Lanthanides
Lanthanum
Lead
Lithium
Magnesium
Manganese
Mercury
Molybdenum
Neon
Nickel
Niobium
Nitrogen
Noble gases
Osmium
Oxygen
Palladium
Phosphorus
Platinum
Pnicogens
Potassium
Rare earths
Rhenium
Rhodium
Rubidium
Ruthenium
Samarium
Scandium
Selenium
Silicon
Silver
Sodium
Strontium
Sulfur
Tantalum

 © 2006 Wiley-VCH Verlag GmbH & Co. KGaA, Weinheim 

Technetium
Tellurium
Thallium
Tin
Titanium
Tungsten
Uranium
Vanadium
Xenon
Ytterbium
Yttrium
Zinc
Zirconium

### Environmental and Atmospheric Chemistry

Anions
Atmospheric chemistry
Cations
Chlorine
Computer chemistry
Crop protection agents
Cycloaddition
Denitrification
Desulfurization
Environmental chemistry
Fluorine
Gas-phase reactions
Green chemistry
Halogenation
Kinetics
Molecular dynamics
Molecular modeling
Nitrogen oxides
Oxidation
Ozone
Peroxides
Photochemistry
Photolysis
Photooxidation
Radical ions
Radical reactions
Radicals
Reaction mechanisms
Reactive intermediates
Sensors
Toxicology
Trace analysis
Waste prevention
Water chemistry

### Inorganic Chemistry

Alanes
Allotropy
Alloys
Aluminosilicates
Amalgams
Amorphous materials
Anions
Automerization
Autoxidation
Azides
Bond theory
Boranes
Borates
Carbene homologues
Carbides
Carboranes
Cations
Chain structures
Chromates
Clathrates
Cluster compounds
Cyanides
Electron-deficient compounds
Fluorides
Halides
High-pressure chemistry
Host–guest systems
Hydrates
Hydrides
Hydrothermal synthesis
Hypervalent compounds
Inclusion compounds
Intercalations
Intermetallic phases
Isoelectronic analogues
Isomers
Layered compounds
Lewis acids
Lewis bases
Main group elements
Metal–metal interactions
Mixed-valent compounds
Nitrides
Nonstoichiometric compounds
Organic–inorganic hybrid composites
Perovskite phases
Peroxides
Phosphaalkenes
Phosphaalkynes
Phosphanes
Phosphazenes
Platinates
Pnictides
Polyanions
Polycations
Polychalcogenides
Polyhalides
Polymorphism
Polyoxometalates
Radical ions
Radicals
Silanes
Silicates
Sol–gel processes
Solid-phase synthesis
Solid-state reactions
Solid-state structures
Spinel phases
Stannanes
Subvalent compounds
Synthesis design
Titanates
Topochemistry
Transition metals
Transuranium elements
Valence isomerization
Vanadates
Zeolite analogues
Zeolites
Zincates
Zintl anions
Zintl phases

### Materials Science: General

Alloys
Amorphous materials
Automerization
Block copolymers
Ceramics
Charge-carrier injection
Chemical vapor deposition
Chemical vapor transport
Clays
Cluster compounds
Colloids
Conducting materials
Copolymerization
Crystal engineering
Crystal growth
Cyclooligomerization
Cyclotrimerization
Dendrimers
Doping
Energy conversion
Fullerenes
Gels
Glasses
Holography
Imprinting
Intercalations
Interfaces
Intermetallic phases
Ladder polymers
Layered compounds
Liquid crystals
Materials science
Mechanical properties
Membranes
Mesophases
Mesoporous materials
Metal–metal interactions
Metallomesogens
Micelles
Microporous materials
Monolayers
Nanostructures
Nanotechnology
Nanotubes
Nonlinear optics
Polymerization
Polymers
Ring-opening polymerization
Scanning probe microscopy
Semiconductors
Sensitizers
Sensors
Superconductors
Surface chemistry
Thin films
Vesicles
Zeolite analogues
Zeolites

 © 2006 Wiley-VCH Verlag GmbH & Co. KGaA, Weinheim 

### Miscellaneous

History of science

### Organic Chemistry: Compound Classes

Alcohols
Aldehydes
Alkaloids
Alkanes
Alkenes
Alkynes
Allenes
Allylic compounds
Amides
Amines
Amino acids
Amino alcohols
Amino aldehydes
Amphiphiles
Anhydrides
Anions
Annulenes
Arenes
Arynes
Azides
Azo compounds
Azomethine ylides
Betaines
Biaryls
Calixarenes
Carbanions
Carbenes
Carbenoids
Carbocations
Carbocycles
Carbohydrates
Carboxylic acids
Carotenoids
Catenanes
Cations
Cavitands
Crown compounds
Cryptands
Cumulenes
Cyanides
Cyanines
Cyclodextrins
Cyclophanes
Dendrimers
Diazo compounds
Dyes/Pigments
Enols
Enones
Enynes
Fatty acids
Fragrances
Fullerenes
Fused-ring systems
Heterocycles
Hydrazones
Hydrides
Hydrocarbons
Ketones
Lactams
Lactones
Ladder polymers
Macrocycles
Mannich bases
Medium-ring compounds
Metallacycles
Natural products
Nitrogen heterocycles
Oxygen heterocycles
Peroxides
Pheromones
Phosphorus heterocycles
Phthalocyanines
Polycycles
Polymethines
Porphyrinoids
Quinodimethanes
Quinones
Radical ions
Radicals
Rotaxanes
Schiff bases
Small ring systems
Spiro compounds
Steroids
Sulfonamides
Sulfur heterocycles
Surfactants
Terpenoids
Ylides
Zwitterions

### Organic Chemistry: Methodology and Reactions

Acylation
Aldol reactions
Alkylation
Allylation
Amination
Annulation
Aromatic substitution
Aromaticity
Asymmetric amplification
Asymmetric catalysis
Asymmetric synthesis
Automerization
Autoxidation
Biomimetic synthesis
C−C activation
C−C coupling
C−H activation
C1 building blocks
Carbonylation
Carboxylation
Chiral auxiliaries
Chiral pool
Cleavage reactions
Combinatorial chemistry
Cracking
Cross-coupling
Cyclization
Cycloaddition
Cyclotrimerization
Dehydrogenation
Dihydroxylation
Dimerization
Domino reactions
Electrocyclic reactions
Electrophilic addition
Electrophilic substitution
Elimination
Ene reaction
Epoxidation
Flash pyrolysis
Glycosylation
Grignard reaction
Halogenation
Heck reaction
High-pressure chemistry
Hydroamination
Hydroboration
Hydroformylation
Hydrogen transfer
Hydrogenation
Hydrolysis
Hydrosilylation
Hydrostannation
Hydroxylation
Immobilization
Insertion
Ionic liquids
Isomerization
Lithiation
Metalation
Michael addition
Molecular diversity
Multicomponent reactions
Nucleophilic addition
Nucleophilic substitution
Olefination
Oligomerization
Oxidation
Oxygenation
Ozonolysis
Perfluorinated solvents
Pericyclic reaction
Phosphorylation
Photooxidation
Polymerization
Protecting groups
Protonation
Radical reactions
Rearrangement
Reduction
Retro reactions
Ring contraction
Ring expansion
Sigmatropic rearrangement
Solid-phase synthesis
Solvent effects
Solvolysis
Steric hindrance
Substituent effects
Synthesis design
Synthetic methods
Template synthesis
Topochemistry
Total synthesis
Transesterification
Umpolung
Wittig reactions

 © 2006 Wiley-VCH Verlag GmbH & Co. KGaA, Weinheim 

# Guidelines for Authors

### Organic Chemistry: Stereochemistry and Structures

Atropisomerism
Chemoselectivity
Chiral resolution
Chirality
Configuration determination
Conformation analysis
Conjugation
Diastereoselectivity
Enantioselectivity
Hyperconjugation
Kinetic resolution
Regioselectivity
Strained molecules
Structure elucidation
Tautomerism
Valence isomerization

### Physical Chemistry and Chemical Physics (including Electrochemistry, Kinetics, Photochemistry, Radiochemistry, Thermodynamics and Theoretical Chemistry)

Ab initio calculations
Absorption
Acidity
Adsorption
Basicity
Biophysics
Bond energy
Bond theory
Calorimetry
CARS (Coherent Anti-Stokes Raman Scattering)
Charge-carrier injection
Charge transfer
Chemisorption
Chromophores
Colloids
Computer chemistry
Conducting materials
Conical intersections
Crystal engineering
Crystal growth
Cyclic voltammetry
Density functional calculations
Donor−acceptor systems
Doping
Electrochemistry
Electron microscopy
Electron transfer
ELF (Electron Localization Function)
Energy conversion
Exchange interactions
Femtochemistry
Fluorescence
Fluorescent probes
Fractals
FRET (Fluorescence Resonance Energy Transfer)
Gas-phase reactions
Gels
Glasses
Group theory
Heats of formation
High-pressure chemistry
High-temperature chemistry
Hot-atom chemistry
Hydrophobic effect
Imaging agents
Ion pairs
Ion−molecule reactions
Ionization potentials
Isotope effects
Isotopes
Kinetics
Langmuir−Blodgett films
Laser chemistry
Lewis acids
Lewis bases
Linear free energy relationships
Liquid crystals
Liquids
Low-temperature studies
Magnetic properties
Matrix isolation
Mesophases
Metallomesogens
Metastable compounds
Microreactors
Molecular dynamics
Molecular electronics
Molecular modeling
Monolayers
Nanotechnology
Neighboring-group effects
Nonequilibrium processes
Phase diagrams
Phase transitions
Photochemistry
Photochromism
Photolysis
Physisorption
Plasma chemistry
Polarized spectroscopy
Quantum chemistry
Radiochemistry
Radiopharmaceuticals
Reaction mechanisms
Reactive intermediates
Redox chemistry
Salt effect
Semiempirical calculations
Single-molecule studies
Singlet oxygen
Sol−gel processes
Solvatochromism
Spin crossover
Statistical mechanics
Statistical thermodynamics
Structure−activity relationships
Superacidic systems
Supercritical fluids
Thermochemistry
Thermodynamics
Time-resolved spectroscopy
Transition states
Viruses
Voltammetry

### Supramolecular Chemistry

Aggregation
Host−guest systems
Molecular devices
Molecular evolution
Molecular recognition
Nanostructures
Pi interactions
Receptors
Self-assembly
Supramolecular chemistry

 © 2006 Wiley-VCH Verlag GmbH & Co. KGaA, Weinheim 

DOI: 10.1002/ejic.200500672

# 1,3,5-Triazine-Based Synthons in Supramolecular Chemistry

**Patrick Gamez*[a] and Jan Reedijk*[a]**

**Keywords:** Supramolecular chemistry / Self-assembly / Crystal engineering / N ligands / Cyanuric chloride / 1,3,5-Triazine

Interest in supramolecular chemistry has grown significantly during the past two decades. In this context, hydrogen bonding and/or coordinative interactions have been extensively used to generate self-assembled one-, two- or three-dimensional polymeric networks. Crystal structure prediction has progressed tremendously, and the challenge for the contemporary supramolecular chemist is now to produce custom-made functional (and multifunctional) materials involving intermolecular interactions. Since the early 1990s, 1,3,5-triazine derivatives have shown their potential as building blocks for the preparation of such materials. In this microreview, a selection of outstanding examples of supramolecular networks involving the 1,3,5-triazine unit are discussed, illustrating the possibility of forming remarkable architectures by means of coordination and/or hydrogen bonds and their applications in host–guest chemistry, catalysis, anion recognition, sensoring, electronics and magnetism.

(© Wiley-VCH Verlag GmbH & Co. KGaA, 69451 Weinheim, Germany, 2006)

## 1. Introduction

Supramolecular chemistry is one of the topical fields of contemporary chemistry and has first been defined in 1978 by Jean-Marie Lehn as the "chemistry of molecular assemblies and of the intermolecular bond".[1] Supramolecular chemistry is a vast interdisciplinary field of research and technology, where noncovalent bonding may be a common ground. A rapidly developing branch of supramolecular chemistry is crystal engineering, in which synthetic control is particularly required.[2,3] Nowadays, the main focus of crystal engineering is the design and synthesis of molecular building blocks whose intermolecular interactions[4] with other synthons would allow some degree of predictability regarding the form and/or function of the resulting materials.[5] For instance, the chemistry of hybrid nanostructured organic–inorganic solids involving metal–ligand coordination units is emerging as a primary research area,[6] since it offers the possibility of combining different properties at the molecular level and leading to new composite materials with unprecedented behaviour.[7,8] Furthermore, the combination of coordination chemistry with noncovalent contacts, such as hydrogen bonding[9,10] or π-interactions,[11,12] provides a powerful method for generating supramolecular networks from simple building blocks. These three types of bond are indeed important in conceiving unique frameworks, since they all involve directional interactions.[13] From the perspective of crystal engineering, the benefit of using transition-metal ions is that the shape of the coordination building unit can be controlled by choosing the coordination geometries of the metal ions properly. A more specific geometry can then be obtained by judiciously attaching suitable functional substituents to the ligands, which will act as intra- and/or intermolecular connectors. Thus inorganic–organic hybrid supramolecular assemblies with unusual network topologies should be accessible through noncovalent interactions,[14] i.e. H-bonding and π-interactions.

1,3,5-Triazine derivatives have proven their great potential in this rising area of material chemistry, both for their π-interaction abilities,[15] and for their aptitude to be involved in intricate H-bond networks.[16]

The present review deals with the background on supramolecular architectures involving the 1,3,5-triazine ring as the central building moiety. A number of triazine-containing molecules have been used in crystal engineering and have allowed outstanding new developments in the arena of tailored functional materials.[17]

[a] Leiden Institute of Chemistry, Gorlaeus Laboratories, Leiden University,
P. O. Box 9502, 2300 RA Leiden, The Netherlands
Fax: + 31-71-527-4671
E-mail: p.gamez@chem.leidenuniv.nl
reedijk@chem.leidenuniv.nl

**MICROREVIEWS:** This feature introduces the readers to the authors' research through a concise overview of the selected topic. Reference to important work from others in the field is included.

 © 2006 Wiley-VCH Verlag GmbH & Co. KgaA, Weinheim InterScience 

## 2. Preparation of 1,3,5-Triazine-Based Organic Building Blocks

1,3,5-Triazine-containing compounds have found a number of applications in medicinal chemistry,[18] herbicides,[19] catalysis[20] or polymer chemistry.[21] Sophisticated *s*-triazine derivatives can be easily prepared from the cheap, readily available cyanuric chloride, i.e. 2,4,6-trichloro-1,3,5-triazine.[22] Cyanuric chloride is definitely an excellent synthon for the straightforward preparation of highly structured multitopic molecules.[23] Indeed, each chloride atom of 2,4,6-trichloro-1,3,5-triazine can be substituted by any nucleophile (Figure 1). The first substitution is exothermic and so the reaction mixture must be cooled down to 0 °C. The second chloride substitution can be performed at room temperature. Finally, the third position is functionalized under solvent reflux.

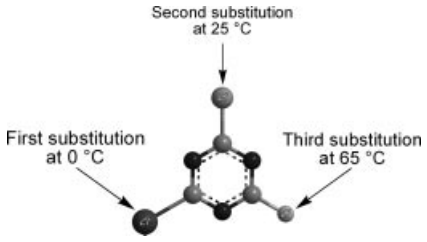


Figure 1. Differential reactivity of 2,4,6-trichloro-1,3,5-triazine.[23]

Therefore, by carefully controlling the temperature, 2,4,6-trisubstituted triazines can be synthesized by sequential, very selective addition of all kinds of nucleophiles, namely amines, alcohols, thiols or Grignard reagents (Figure 2). The yield of each substitution often exceeds 95% and the symmetric trisubstituted derivatives can even be obtained in a one pot synthesis. Various solvents can be used such as tetrahydrofuran, 1,2-dimethoxy ethane, acetonitrile, diethyl ether, and so on.

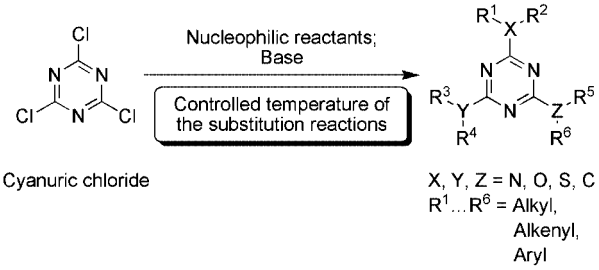


Figure 2. Preparation of polyfunctional triazine derivatives.

Numerous triazine derivatives have been prepared following this versatile synthetic pathway.[24–27]

## 3. Melamine Derivatives as Synthons for the Preparation of H-Bonded Self-Assemblies

Hydrogen bonds play a fundamental role in nature where they are particularly responsible for controlling the structure and function of many proteins, recognition of substrates by various enzymes and for the double-helix struc-

*Patrick Gamez (1967, Casablanca, Morocco) studied Chemistry at the University of Lyon in France where he obtained his first degree. In 1995, he received his D. Phil. in the field of enantioselective catalysis under the supervision of Professor M. Lemaire and was awarded the French Chemical Society Prize for his PhD research. After a period of postdoctoral research at the Max-Planck-Institut für Kohlenforschung in the group of Professor A. Fürstner and at the University of Strasbourg in the group of Dr C. Mioskowski, he joined the research group of Professor J. Reedijk. His current research interests are copper biomimetics and oxidation catalysis, and design of multidentate ligands for crystal engineering. He is (co)author of about 70 publications.*

*Jan Reedijk was born in 1943 in The Netherlands. He is currently Professor of Chemistry at the Leiden Institute of Chemistry, Leiden University, The Netherlands. After obtaining his PhD from Leiden University in 1968 (Thesis title: Methyl Cyanide as a Ligand) and a junior lectureship, he lectured in Delft University of Technology until November 1979, when he accepted his present position. During 1993 he was a visiting Professor at Cambridge University (UK), and during 2002 at the University of Louvain-la-Neuve (Belgium). His current research interests include coordination chemistry of transition-metal ions, bioinorganic chemistry (active-site structure and mechanism; models; metal–DNA interactions), applications of coordination chemistry in catalysis, medicine, ion-exchange and surface chemistry, extended (magnetic, electric) interactions in coordination compounds (dimers, clusters, chains), and molecular recognition and intermolecular interactions (catalysis, biomacromolecules). He has over 900 (co)-authored refereed research publications and patents and has supervised over 100 postdoctoral and graduate students (since 1973). Some of his major professional activities, honours and awards are: Director Leiden Institute of Chemistry (1993–2004); Member of the International Advisory Board of a number of International Conference Organisations, such as the EURASIA Conferences of Chemistry, Macromolecular Metal Complexes Conferences, EUROBIC and ICBIC. Other honours: elected as Executive Secretary of the International Coordination Chemistry Conferences (1989) and acted as President of the Royal Netherlands Chemical Society in 1990; Board member of the Chemistry Research Council (1998–2002); Elected Honorary member of the Royal Netherlands Chemical Society; Awardee of the Max Planck Research Award in Chemistry in 1992; Elected Member of the Finnish Academy of Sciences (1997); Elected Member of the Royal Netherlands Academy of Sciences (1996); Elected Member of the Academia Europaea (2004). He is and has been a member of the editorial boards of over 15 major chemistry journals, such as: Chem. Commun., Inorg. Chem., J. Chem. Soc., Dalton Trans., New J. Chem., Russian J. Coord. Chem., J. Inorg. Biochem. and the J. Biol. Inorg. Chem. He has served on several IUPAC committees on nomenclature of (bio)inorganic, biochemical, physical organic chemistry and terminology between 1978 and 1998. He is one of the founding editors of Eur. J. Inorg. Chem. (a merger from several European Chemical Society Journals).*

 © 2006 Wiley-VCH Verlag GmbH & Co. KGaA, Weinheim 

ture of DNA (Figure 3). Consequently, hydrogen bonding has become one of the most important noncovalent interactions in supramolecular chemistry.[28,29]

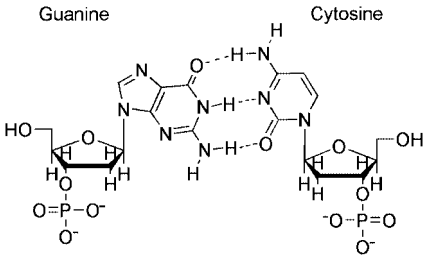


Figure 3. Watson–Crick base pairing in DNA.

Fifteen years ago, Whitesides and coworkers have shown that melamine derivatives could be used to generate outstanding aggregates.[30,31] The reaction of cyanuric acid (CA) with melamine (M) leads to the formation of an insoluble very stable (it can be heated to 450 °C without any alteration of the structure) H-bonded 2D network (Figure 4, CA·M),[30] which has been first reported in 1979 by Junichi and coworkers.[32]

In the earlier 1990s, Whitesides and coworkers have improved the preparation of this type of self-assemblies by using both substituted melamines and barbituric acids.[31] In that way, it is possible to control, by steric hindrance, the formation of the 2D frameworks. Reaction of 5,5-diethylbarbituric acid with 2-amino-4,6-(*N*-*p*-tolylamino)-1,3,5-triazine yields a linear tape (Figure 5a). If 2-amino-4,6-(*N*-*p*-methylbenzoatoamino)-1,3,5-triazine is combined with 5,5-diethylbarbituric acid, a crinkled tape is obtained (Figure 5b). Finally, with a bulkier group on the phenyl ring, i.e. *tert*-butyl, a rosette motif is achieved (Figure 5c).

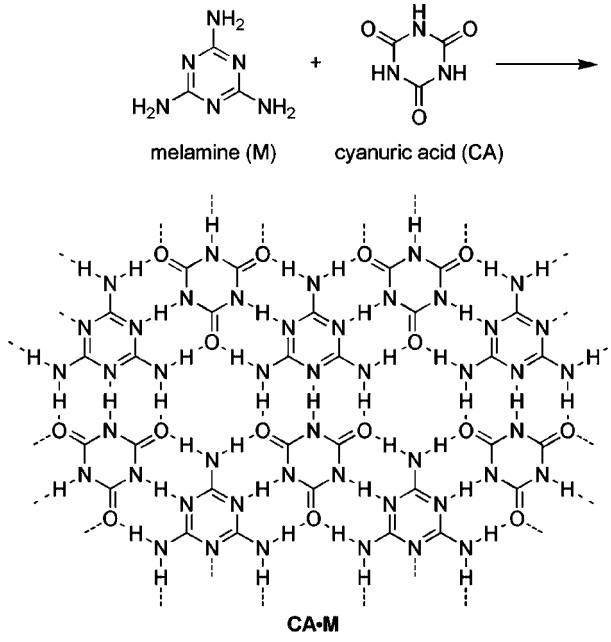


Figure 4. Self-assembly network by means of hydrogen bonds.[16,32]

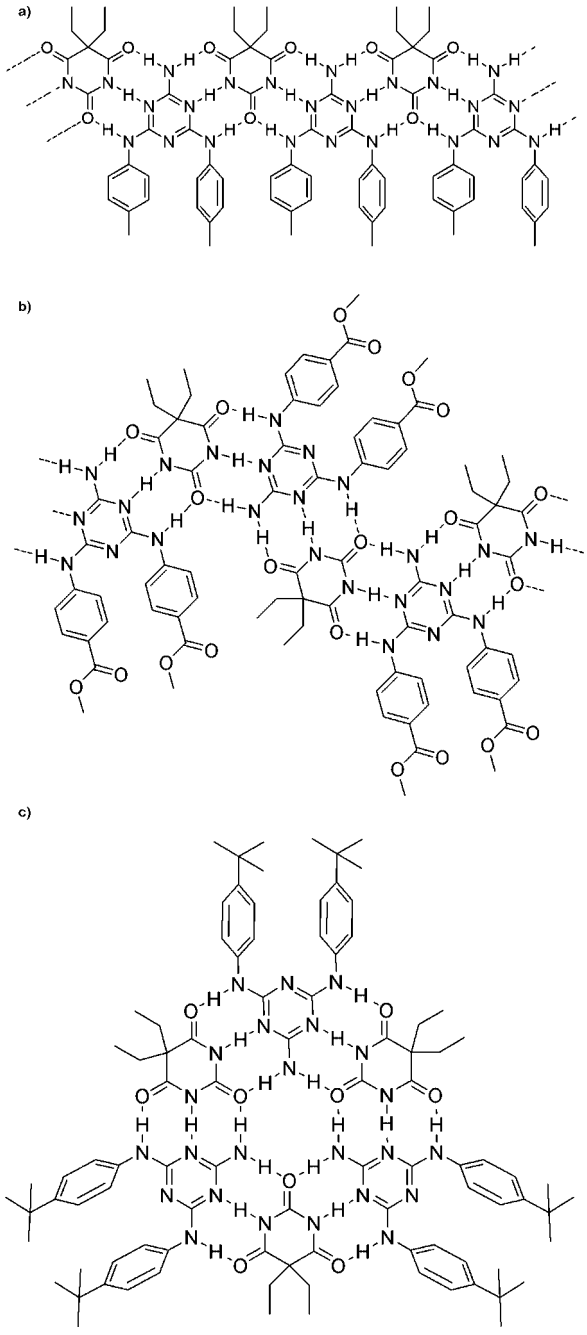


Figure 5. Structures of linear tape, crinkled tape, and rosette motifs.[16]

It has thus been evidenced that a competition takes place between nonbonded steric interactions (*para*-substituents) and a tendency for a high packing coefficient which is important in determining which type of structural motif is realized between the melamine derivative and 5,5-diethylbarbituric acid.[16] As a result, a small *para*-substituent like a methyl or a chloride group leads to a linear tape. If this substituent becomes larger than a trifluoromethyl unit, steric interactions between adjacent melamines prevent the linear structure and favour the crinkled motif where the hin

 © 2006 Wiley-VCH Verlag GmbH & Co. KGaA, Weinheim 

drance is minimized. When the size of the *para*-substituent is further increased, to a *tert*-butyl group for example, then the steric interactions are relieved in the rosette type assembly.[16]

More recently, Reinhoudt and coworkers have beautifully developed the above concept to design and prepare more intricate H-bonded networks.[33,34] Thus, molecular cage hosts can be generated by self-assembly of calixarene-based melamine derivatives and diethylbarbituric acid.[35] A non-covalent phenolic receptor has been successfully prepared by hydrogen-bonding directed association of a calixa[4]rene dimelamine compound with diethylbarbituric acid (Figure 6).[36]

For instance, the simple mixing of the building blocks **1** (1 equivalent) and DEB (2 equivalents) in an apolar solvent like chloroform or toluene produces the double rosette $\mathbf{2}_3\cdot(DEB)_6$ (Figure 7). The formation of this calixarene-bridged supramolecular structure can be followed by solution $^1H$ NMR spectroscopy.

$\mathbf{2}_3\cdot(DEB)_6$ holds six H-donor/acceptor side-arms which can act as phenol binding sites by means of H-bonds between a urea function [Figure 6, $R^1 = R^2 = CONH(CH_2)_2CH_3$] and the phenolic guest (Figure 7, G). The complexation of 4-nitrophenol by $\mathbf{2}_3\cdot(DEB)_6$ has been investigated by proton NMR spectroscopy at room temperature in $CDCl_3$. This comprehensive study clearly demonstrates that the double rosette is an *exo*-receptor able to accommodate six molecules of phenolic guest (one phenol unit per ureido group).

Last year, Meijer and coworkers reported another remarkable supramolecular rosette motif which has been evidenced by scanning tunnelling microscopy (STM).[37] For

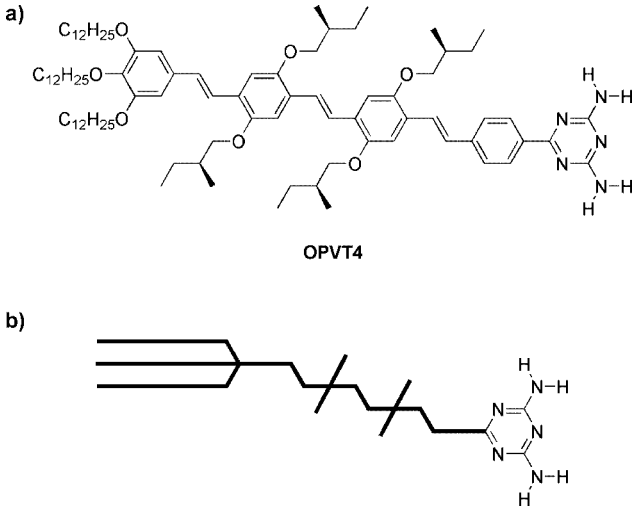


Figure 8. a) Melamine-based π-conjugated ligand OPVT4 and b) its schematic representation.[37]

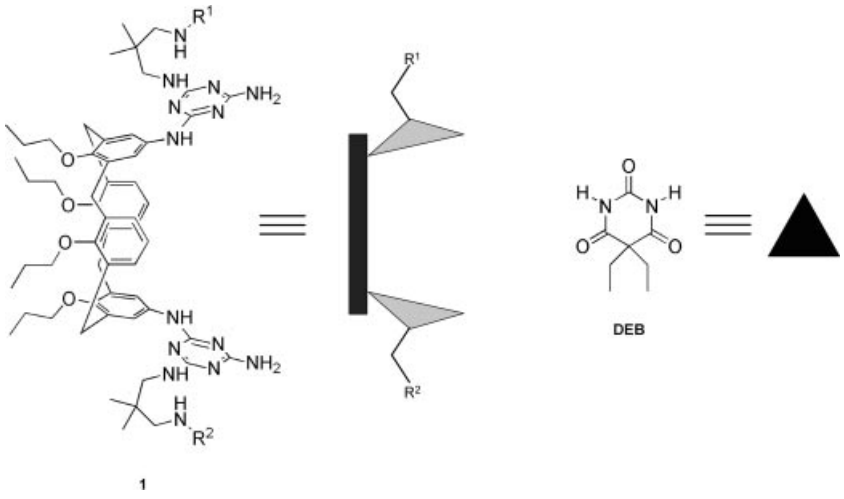


Figure 6. Building blocks for the formation of a double rosette assembly.[36]

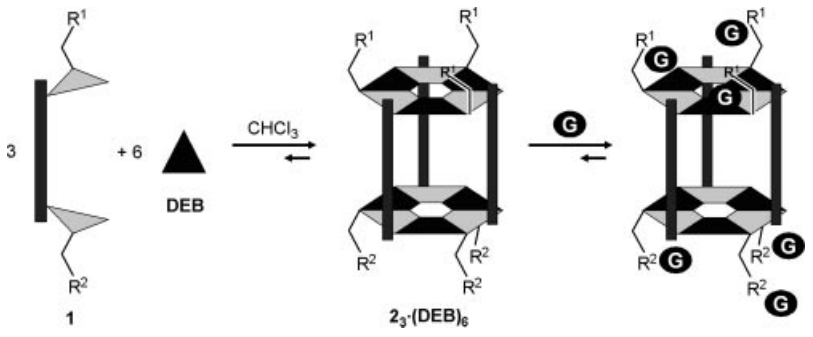


Figure 7. Schematic representation of the formation of the host–guest supramolecular double rosette system.[36]

 © 2006 Wiley-VCH Verlag GmbH & Co. KGaA, Weinheim 

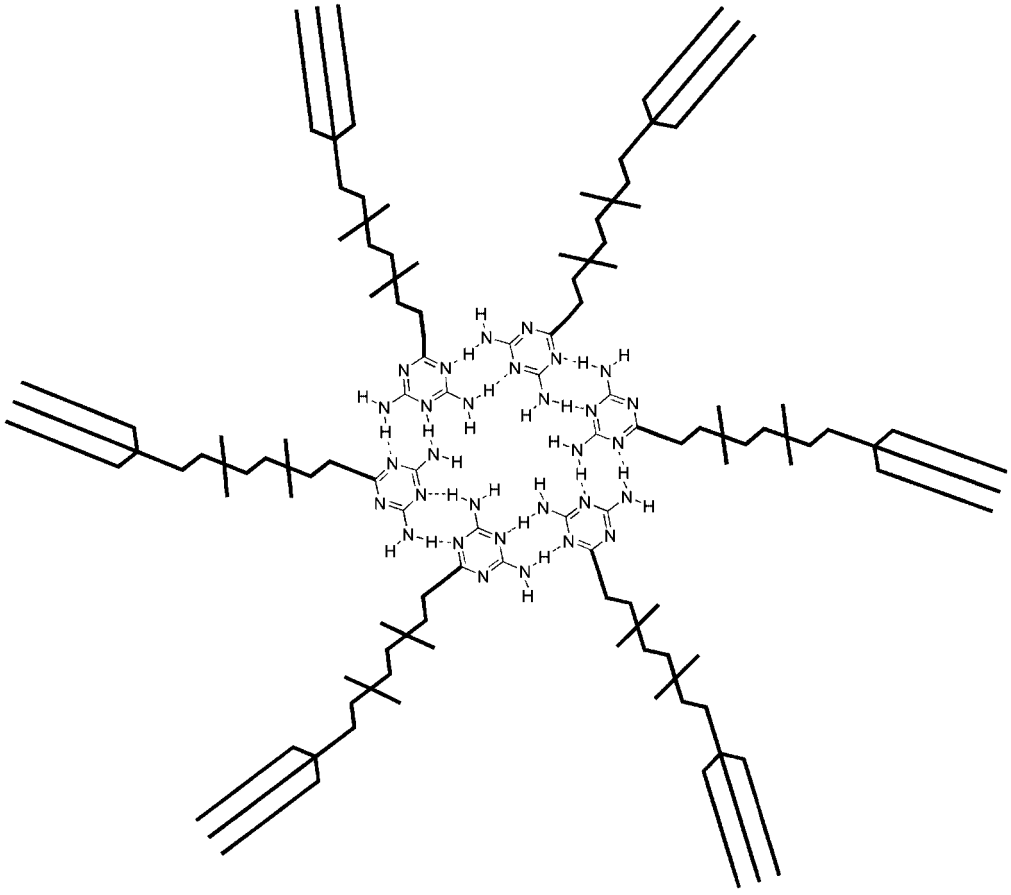

Figure 9. OPVT4 rosette.[37]

this purpose, the triazine-based ligand OPVT4 has been synthesized according to a reported procedure (Figure 8).[38] In solution in heptane, six OPVT4 molecules give a giant helical rosette with a width of about 10 nm (Figure 9).[37] This exceptional aggregation process has been followed by UV/Vis and circular dichroism (CD) in heptane and temperature-dependent measurements show that the rosette is dissociated at elevated temperature ($T$ = 305 K).

In addition, the hydrogen-bonded hexamer is chiral as proven by CD and by the counterclockwise rosette structure clearly visible in the STM images.[37] These rosettes can be stacked together to form fibres with lengths up to 10 μm as revealed by atomic force microscopy (AFM). The self-assembled tubular aggregates 6.4 nm in diameter are still soluble in heptane owing to the peripheral apolar alkyl chains (Figure 10).

The cavity generated by the formation of the hexameric rosette is about 1 nm wide and contains amine groups which would therefore find application as an ideal channel for transportation. Furthermore, the tubular stacks exhibit a well-defined and ordered π-conjugated outside shell with probable electronic properties.

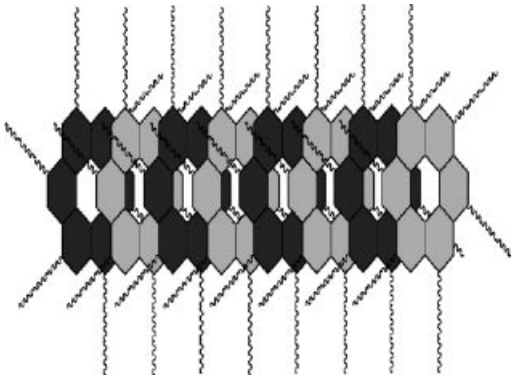

Figure 10. Rosette stacks leading to a tubular fibre.[37]

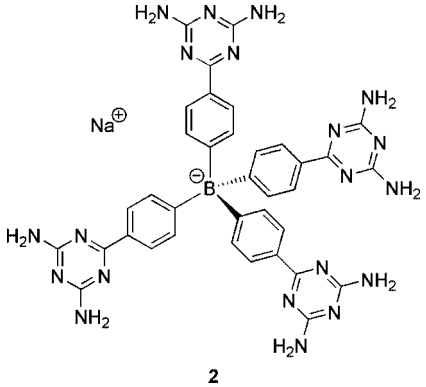

**2**

Figure 11. Sodium tetrakis[4-(2,4-diamino-[1,3,5]triazin-6-yl)-phenyl]borate (**2**·Na).[39]

 © 2006 Wiley-VCH Verlag GmbH & Co. KGaA, Weinheim 

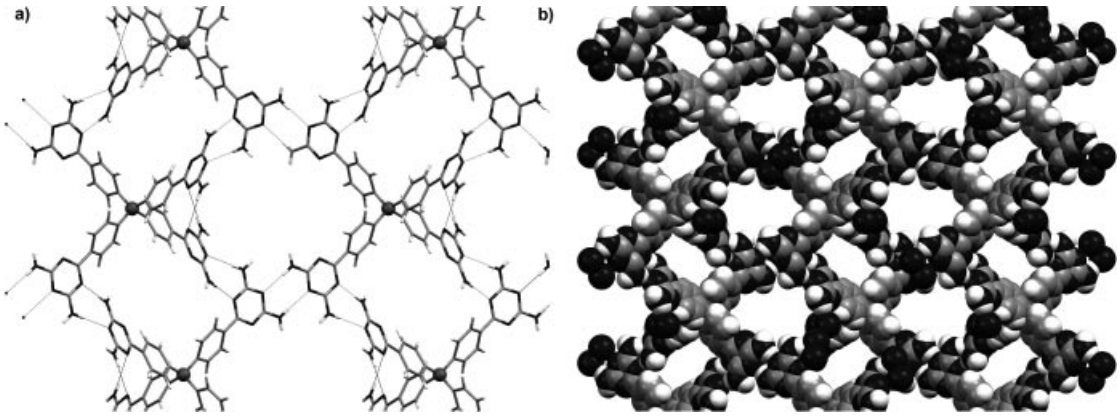


Figure 12. a) Anionic H-bonded network **2**. b) Interconnected channels.[39]

Very recently, Wuest and coworkers designed and synthesized a 3D triazine-based synthon, i.e. the tetraphenylborate Na·**2** (Figure 11).[39] The tetraphenylphosphanium salt of **2** is obtained quantitatively from the sodium salt by cation exchange. Single crystals of tecton $PPh_4$·**2** have been grown from a DMSO/toluene solution of the compound, whose solid-state structure reveals an aesthetic three-dimensional network, connected by multiple hydrogen bonds as expected (Figure 12). This anionic supramolecular architecture is extremely porous (Figure 12b), since 74% of the volume of the crystals is available for cations and guest molecules (DMSO in the present study). Materials with such great porosity are very important in the field of gas storage,[40] especially for fuel-cell applications.[41,42]

In addition, the cation can be exchanged within the crystalline solid compound. Thus, the same anionic framework is achieved when using phenazinium cation **3** (Figure 13) instead of tetraphenylphosphonium. These crystals of tecton **2** with phenazinium **3** as the counterion have been exposed to a solution of an excess of $PPh_4Br$ in DMSO for 24 h at room temperature. The resulting material remains transparent and crystalline, and diffracts with unit cell parameters analogous to those of $PPh_4$·**2**. This is an important result as a larger cation, **3**, has been replaced by a smaller one, namely tetraphenylphosphanium. Indeed, such exchange releases space within the porous material, which is available for additional neutral guest molecules. This finding gives rise to a novel approach of crystal engineering where new ionic host–guest materials can be produced by substitution of the initial cations to increase their porosity and/or physical properties without modification of their molecular arrangement.

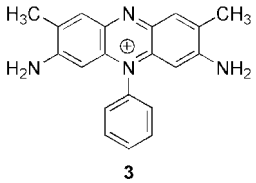


**3**

Figure 13. Phenazinium cation **3**.

## 4. 1,3,5-Triazine Derivatives as Ligands for the Preparation of Coordination Self-Assemblies

Coordination compounds from 1,3,5-triazine-based ligands are increasingly reported in the literature.[43–48] This is undoubtedly due to the ease of preparing intricate polydentate star-shaped ligands using simple and high-yielding reactions.[23] Especially one ligand, namely 2,4,6-tri(4-pyridyl)-1,3,5-triazine (Figure 14, tpt), has been extensively used in the field of crystal engineering during the past ten years.[47,49] However, novel and attractive supramolecular architectures continue to be obtained with this simple tridirectional N-donor ligand.[50] Robson's group[49] published the first crystallographically characterized coordination polymer based on tpt 24 years after it was primarily reported by Yasumoto and coworkers.[51]

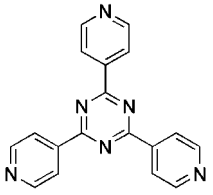


**tpt**

Figure 14. 2,4,6-tri(4-pyridyl)-1,3,5-triazine ligand (tpt).[49,51]

In 1996, Robson and coworkers described a unique system of two interpenetrating coordination networks based on tpt and copper(I) building blocks (Figure 15a).[52] The infinite (3,4)-connected network is built from repeated structural motifs with six copper centres at the corners of a regular octahedron (Figure 15b), each copper ion being shared by two adjacent motifs. This arrangement results in an infinite cubic collection of 18-Å-wide octahedral cavities filled with solvent molecules.

Almost at the same time, Fujita and coworkers reported a similar octahedral cage assembled from tpt and palladium(II) nodes.[53] The reaction of six equivalents of the $Pd^{II}$ complex **4** with four equivalents of tpt leads, in water, to the exclusive and quantitative formation of the supramolec-

 © 2006 Wiley-VCH Verlag GmbH & Co. KGaA, Weinheim 

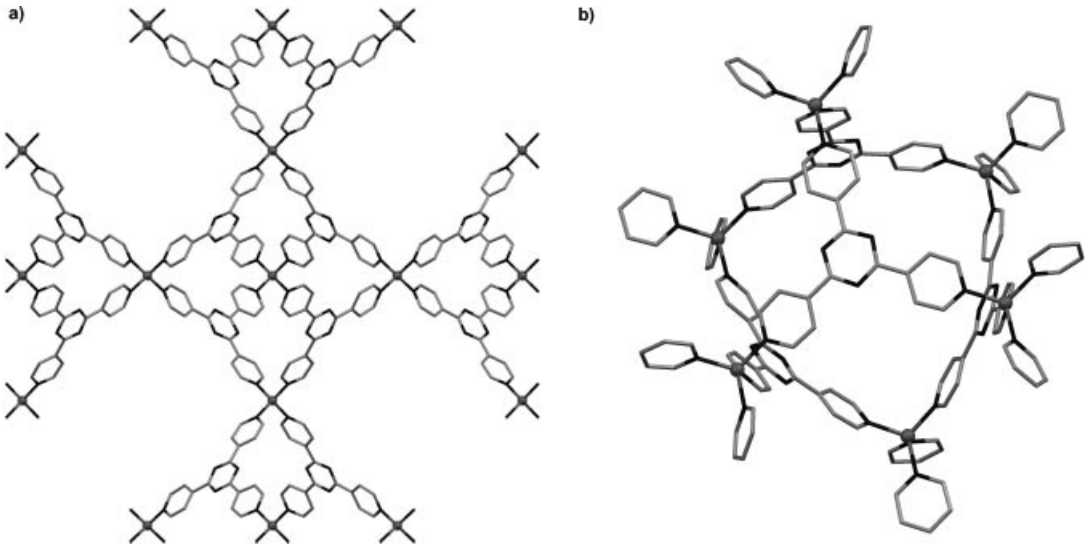


Figure 15. a) Cubic (3,4)-connected net. b) Octahedral host chamber.[52]

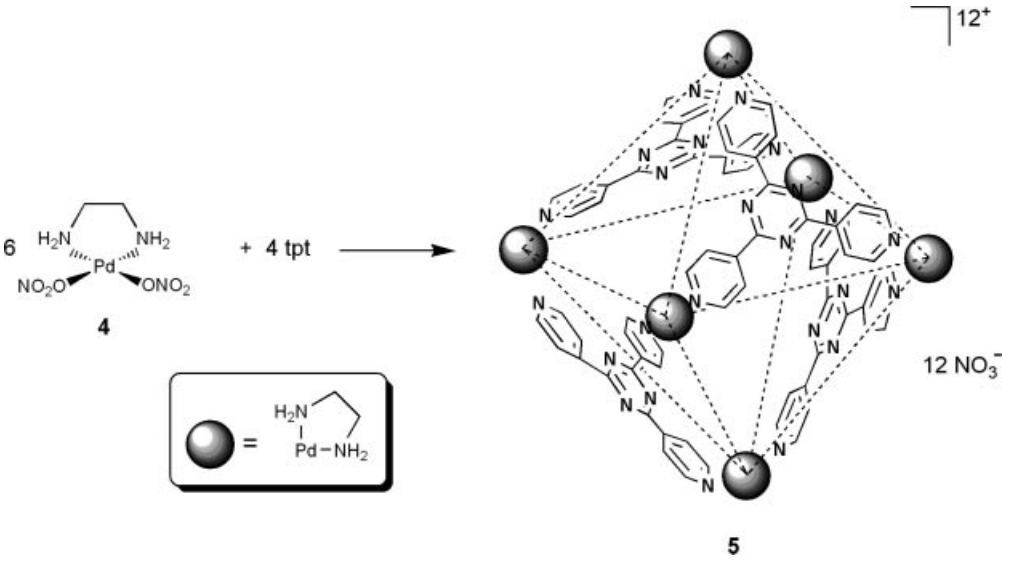


Figure 16. Self-assembly of a nanometer-scale octahedral cage.[53]

ular cage **5** (Figure 16).[53] The assembly of complex **5** has been followed by $^1$H NMR spectroscopy, which clearly demonstrated that the $M_6L_4$ compound is the thermodynamic product since its formation is not affected by the presence of an excess of **4**.

It has been shown that this coordination cage can bind efficiently various organic guest molecules[54,55] including radicals[56] as well as a water cluster[17] in its cavity. For example, *o*-carborane, an icosahedral carbon–boron cage molecule with a diameter of 8 Å, can be encapsulated in **5**.[57] This spherical, neutral molecule is apolar and insoluble in water. However, when a hexane solution of *o*-carborane is stirred with a $D_2O$ solution of **5**, four equivalents of *o*-carborane are transferred into the $D_2O$ phase to form **5**·(*o*-carborane)$_4$, as evidenced by $^1$H NMR spectroscopy. This host–guest complex has never been crystallized, but the analogous compound having 2,2′-bipyridine as *cis*-protecting ligand in place of ethylene diamine is easily crystallized in water (Figure 17).[54]

Fujita and coworkers then tried to use these cavities to perform catalytic reactions.[58] The palladium-catalyzed Wacker oxidation of styrene has been carried out in water with **5**, which can accommodate three molecules of styrene (**6**) in its cavity.[58] If the reaction is achieved at 80 °C with **4** or with **5**, only 4% of acetophenone (**7**) is detected. If the oxidation is performed in the presence of both **4** and **5**, then the yield in acetophenone is significantly increased to 86% (Figure 18a). Similarly, the ability of **5** to promote the isomerization of allylbenzene (**8**) has been examined. Once again, while the reaction does not occur in the absence of either **4** or **5**, 50% of β-methylstyrene (**9**) is obtained when a 2:1 mixture of **4** and **5** is used (Figure 18b).[59] Complex **5** acts as a phase-transfer reagent which brings the substrate, i.e. the organic molecule **6** or **8**, into the aqueous

 © 2006 Wiley-VCH Verlag GmbH & Co. KGaA, Weinheim 

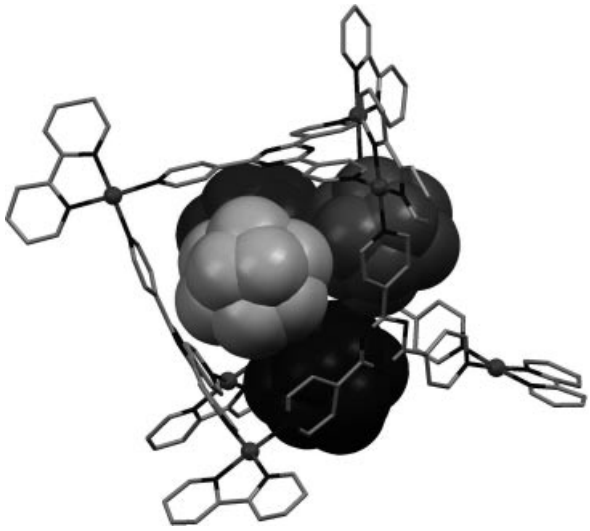

Figure 17. Encapsulation of four *o*-carborane in an $M_6L_4$ cage.[57]

phase where the palladium-mediated chemical transformation takes place. These outstanding results represent good examples of solvent-free organic reactions.

More recently, we have undertaken research investigations on coordination networks involving *s*-triazine-based N-donor ligands. For this purpose, a series of polydentate ligands have been prepared[23,60,61] according to the synthetic pathway depicted in Figure 2, and some of them are reported in Figure 19.

The simple dpyatriz ligand arises from the substitution of the three chlorides of cyanuric chloride by 2,2′-dipyridylamine and has been reported by some of us[23] and by Wang and coworkers.[62,63] Reaction of $Cu^{II}$ nitrate with dpyatriz in acetonitrile at room temperature produces a 1D ladder coordination polymer, whose crystal structure is depicted in Figure 20.[61] The polymeric compound is built up from pentanuclear copper units which are bridged by bidentate nitrate anions (Figure 20b). This uncommon molecular network[3] possesses large rectangular guest cavities with dimensions of approximately 10 × 5.5 Å, which are filled with seven acetonitrile molecules.[61] Thus, the uncoordinated solvent molecules cover 25% (652 Å$^3$) of the unit cell volume.

Thermogravimetric analysis (TGA) of the polymeric material shows 11.1% loss in weight, which exactly matches seven acetonitrile molecules. A second TGA experiment on the acetonitrile-free crystalline material left in air shows a decrease of 18.8% in weight. This decrease is attributed to the loss of water molecules rapidly taken up by the initial

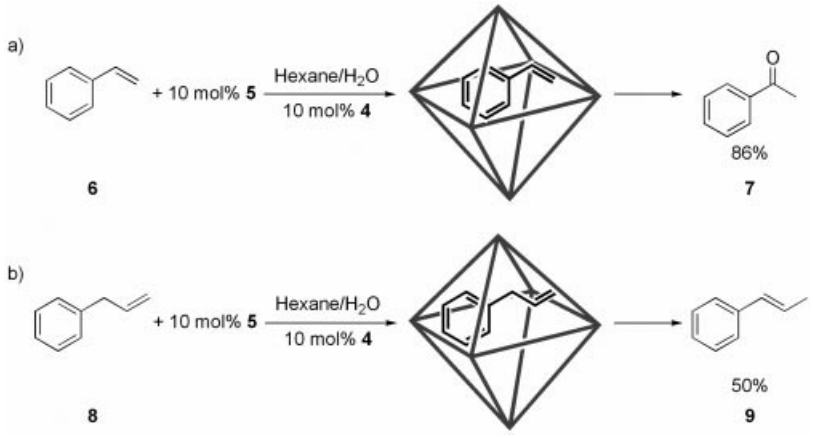


Figure 18. a) Wacker oxidation in the $M_6L_4$ cage.[59] b) isomerisation of an alkene in the $M_6L_4$ cage.[58]

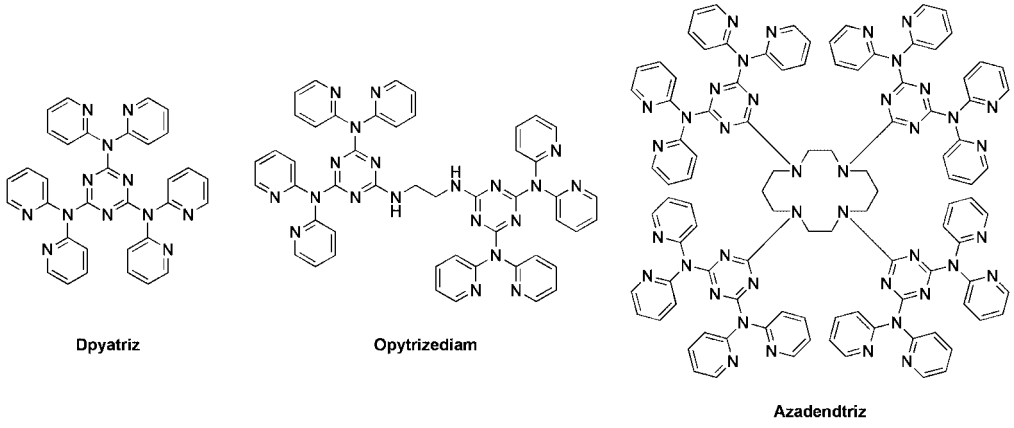


Figure 19. *s*-Triazine-based ligands used to prepare supramolecular coordination compounds.[61,64,66]

 © 2006 Wiley-VCH Verlag GmbH & Co. KGaA, Weinheim 

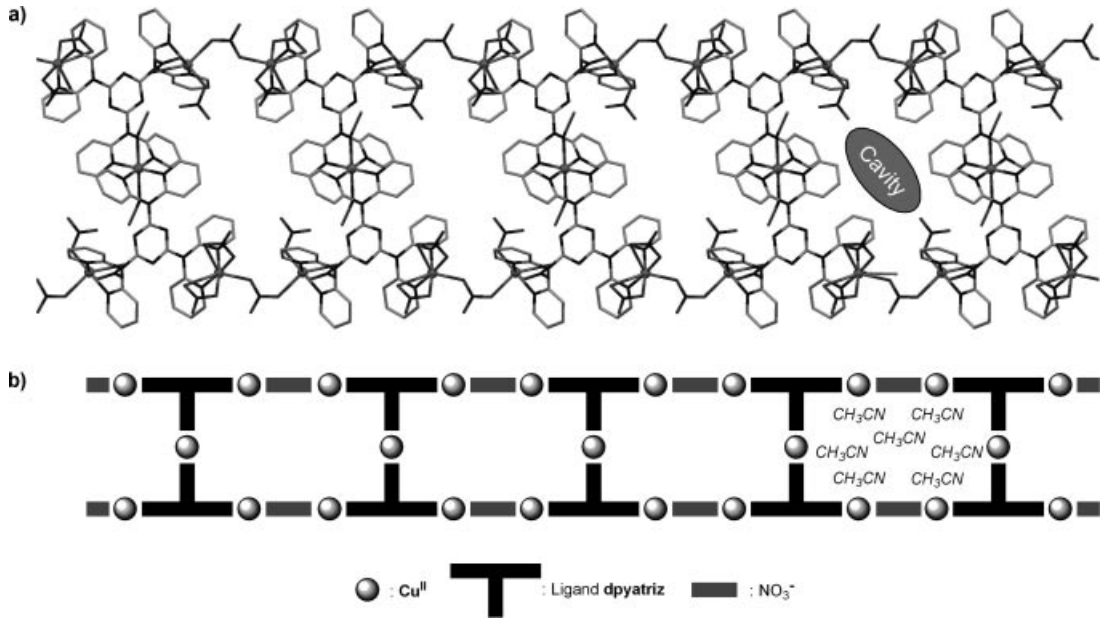


Figure 20. a) 1D ladder coordination polymer obtained from the ligand dpyatriz and $Cu(NO_3)_2$; and b) its schematic representation.[61]

material after removal of the acetonitrile molecules. This result demonstrates the possibility of using this 1D ladder coordination polymer in host–guest molecular recognition.

Another attractive coordination compound has been obtained by our group from the extended ligand opytrizediam (Figure 19). Indeed, the reaction of copper(II) chloride with this ligand in methanol leads to the formation of a 1D zigzag coordination polymer (Figure 21).[64] The polymeric compound is composed of trinuclear copper units that are connected by means of chloride bridges in a zigzag fashion, since the ligands are *up* and *down* alternated (Figure 21b). Despite its unusual arrangement,[3] this material exhibits interesting physical properties. First, a large amount of solvent molecules is present in the crystal lattice (29% of the unit cell volume, 1016 $Å^3$). The removal of these molecules may create space for the sorption of gases such as dinitrogen and dihydrogen. This is a vital feature in the field of fuel cell chemistry.[41,42,65] Second, the coordination polymer possesses ferromagnetic properties [$J$ = 6.4(1) $cm^{-1}$] inherent to the doubly chloro-bridged dicopper moieties linking the complexes to generate the infinite chain.

Recently, a very important finding in the field of anion recognition has been achieved by using the dendritic ligand azadendtriz (Figure 19).[66] Indeed, anions are ubiquitous in biochemical structures.[67,68] Contrary to that of cations, the binding of anions has received little attention. However, during the past two decades, an increasing number of anion receptors have been developed,[69,70] most likely because of their potential applications in medicine, biology, catalysis, or for the elimination of anionic polluting wastes.[71]

A number of recent publications have reported theoretical investigations on the binding of halides with the electron-deficient *s*-triazine ring.[72] All calculations clearly indicate energetically favourable noncovalent interactions between the halide and the electron-poor aromatic ring.[73,74] Consequently, *s*-triazine-based compounds are perfect candidates for the development of anion host chemistry. This

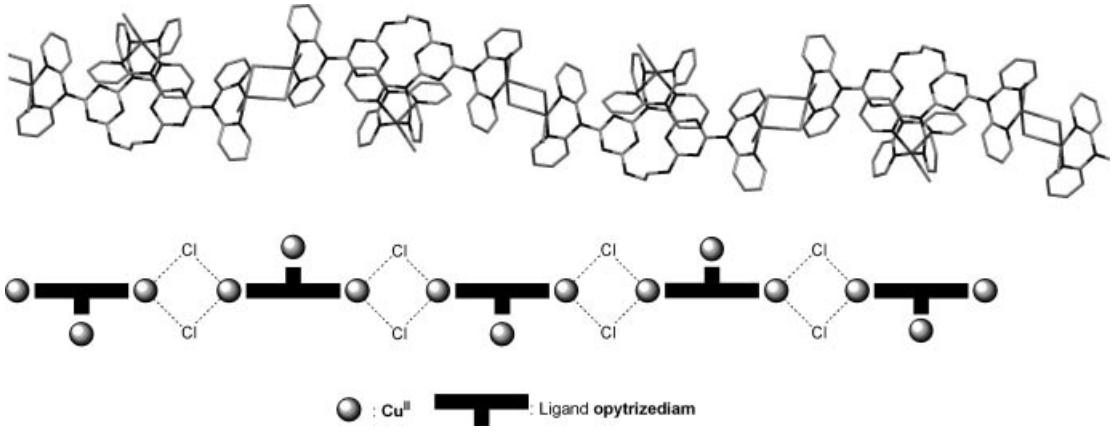


Figure 21. a) 1D zigzag coordination polymer obtained from the ligand opytrizediam and $CuCl_2$; and b) its schematic representation.[64]

 © 2006 Wiley-VCH Verlag GmbH & Co. KGaA, Weinheim 

property was recently evidenced by the first crystallographic proof of such interactions.[75]

Reaction of copper(II) chloride with the ligand azadendtriz (Figure 19) in dichloromethane/water yields the tetracopper complex depicted in Figure 22a, where the triazinyl groups are stacked two by two in a parallel mode. This is often observed in triazine rings and is known as the Piedfort effect.[76] As a result, the copper ions are coordinated by two 2,2′-dipyridylamino units from two different *s*-triazine rings, generating two aromatic baskets, each formed by four pyridines (Figure 22b). These open cavities act as anion receptors for two chlorides through anion-π interactions. In addition, the chloride ions are close to the neighbouring triazine rings (Figure 22a), suggesting electrostatic interactions between the guest and the electron-deficient triazine moieties. Thus, the combination of both electronic effects produces the first non-hydrogen-bonding artificial anionic receptor.

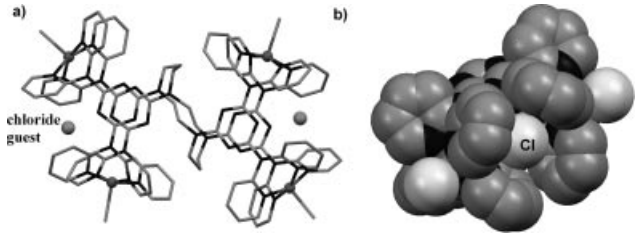


Figure 22. a) [$CuCl_2$–azadentriz] complex showing anion-binding properties; b) guest chloride anion embraced between four pyridine rings.[66]

Finally, the influence of the temperature and the pressure on the nature of the coordination framework obtained has been clearly demonstrated by using the ligand dpyatriz (Figure 19).[77] The reaction of zinc(II) nitrate with dpyatriz in acetonitrile at room temperature gives a tetranuclear zinc complex accommodating two triazine-based ligands (Figure 23).[78]

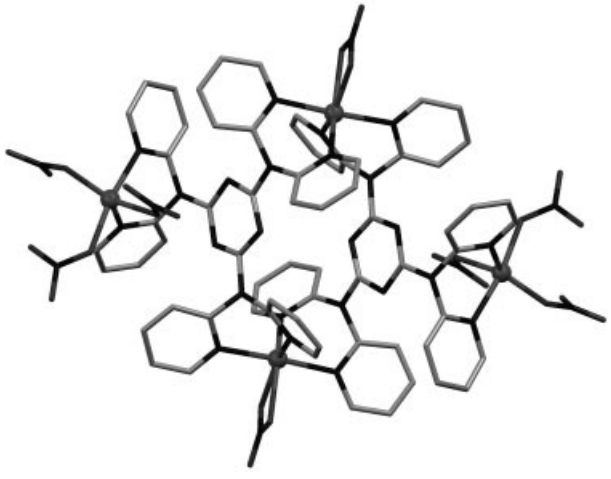

Figure 23. Tetrazinc complex obtained from the ligand dpyatriz and $Zn(^{no}3)2$ at room temperature.[78]

However, if the same reaction is performed in a sealed tube at 105 °C under autogenous pressure, a 1D polymeric chain is obtained (Figure 24).[77] The significantly different crystal packing observed at different crystallisation conditions illustrate the difficulty of anticipating a crystal structure. Crystal engineering involves various interactions between the synthons (ligand, metal ion, anion, solvent). In addition, the temperature and the pressure applied during the experiment are obviously important and hence should be considered for a better prediction of the crystal structure.

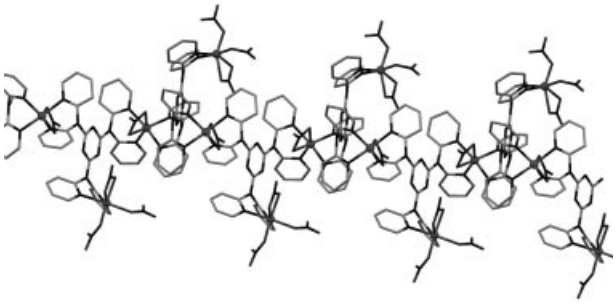

Figure 24. Coordination polymer obtained from the ligand dpyatriz and $Zn(NO_3)_2$ at 105 °C under autogenous pressure.[77]

A closely related 1D coordination polymer is achieved with copper(II) nitrate [in place of $Zn(NO_3)_2$] using the same crystallisation process, while a 1D ladder network is obtained at room temperature and normal pressure (Figure 20 and Figure 24).[61,77]

## 5. 1,3,5-Triazine Derivatives Combining Both H-Bonding and Coordination Interactions

There are only a few examples reported in the literature where the H-bonding ability of melamine derivatives has been used in combination with coordination bonds. Lehn and coworkers have described, in 1995, an ion-labelling system to detect by mass spectroscopy the formation of H-bonded networks by the binding of a metal ion, namely potassium(I).[79] The triazine **10** (Figure 25a) has been syn-

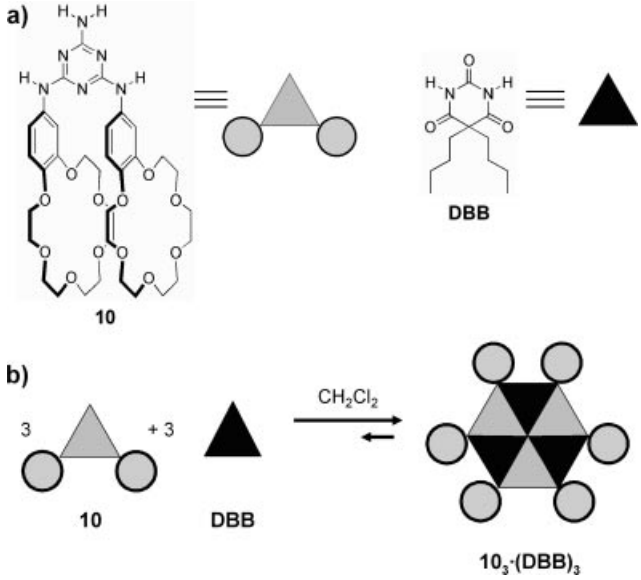


Figure 25. a) Benzocrown-containing triazine-based ligand **10**. b) Formation of the rosette assembly.[79]

 © 2006 Wiley-VCH Verlag GmbH & Co. KGaA, Weinheim 

thesized in 76% yield by reaction of two equivalents of 4′-aminobenzo[18]crown-6 with one equivalent of 6-amino-2,4-dichloro-1,3,5-triazine. The H-bonded self-assembly of **10** with 5,5-dibutylbarbituric acid (DBB) can lead to the formation of various architectures, namely linear tape, crinkled tape or rosette (Figure 5 and Figure 25b).

Equimolar $10^{-2}$ M solutions of **10** and DBB in dichloromethane are combined and treated with $KPF_6$. The resulting mixture is then analysed by electrospray mass spectrometry (ESMS), which shows ion compositions characteristic for the free ligand **10** and for the self-assemblies $\mathbf{10}_2{\cdot}(DBB)_3$, $\mathbf{10}_3{\cdot}(DBB)_2$ and $\mathbf{10}_3{\cdot}(DBB)_3$. The addition of methanol (which is known to disrupt H-networks) to this reaction mixture causes the disappearance of all peaks due to $\mathbf{10}_x{\cdot}(DBB)_y$ complexes, supporting their presence in the initial solution, since no additional assembly is observed in the gas phase (after addition of methanol). These ESMS studies clearly demonstrate the possibility of using this technique with weakly associated self-assemblies which are destroyed by protonation. The ingenious stratagem consists then of introducing a charge through cation binding to a well-designed synthon such as **10**. In that way, a component like **10** in the presence of a salt forms a neutral supramolecular coordination species that cannot be otherwise characterised by ESMS.[79]

In 1998, Reinhoudt and coworkers developed a similar labelling method for the characterisation of double rosette assemblies, comparable to $\mathbf{2}_3{\cdot}(DEB)_6$ (Figure 7), by MALDI-TOF mass spectrometry.[80] For this purpose, the ligand **11** has been prepared (Figure 26).

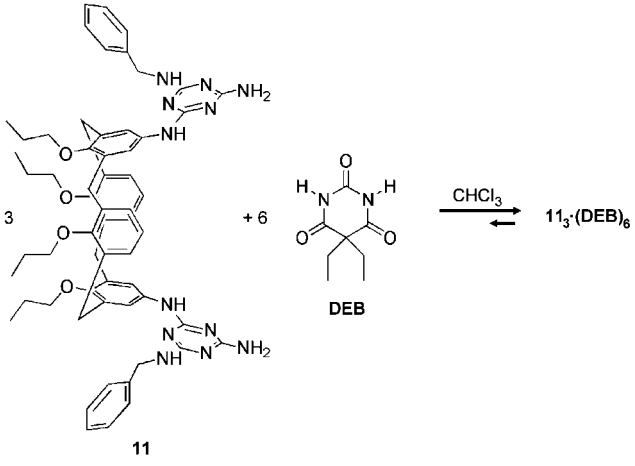


Figure 26. Components used to prepare the double rosette assembly.[80,81]

The $\mathbf{11}_3{\cdot}(DEB)_6$ adduct obtained by mixing **11** and DEB is then stirred with 1.5 equivalents of $Ag(CF_3COO)$ in chloroform for 24 h. Afterwards, the solution is analysed by MALDI-TOF mass spectrometry which shows an intense signal at $m/z$ = 4278.3 (calculated value: 4276.1), ascribed to the silver(I) complex of $\mathbf{11}_3{\cdot}(DEB)_6$ (Figure 27).[80] Moreover, these MS data are in perfect accordance with the $^1H$ NMR spectra of the hydrogen-bonded supramolecules in solution.

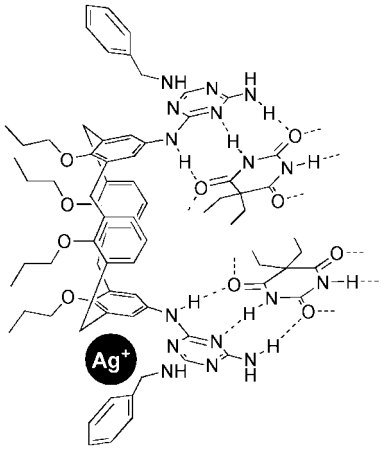


Figure 27. Proposed structure for the silver(I) complex of $\mathbf{11}_3{\cdot}(DEB)_6$. Only a small part of the double rosette is shown for clarity.[80]

This silver(I) labelling technique has been extended to a variety of hydrogen-bonded assemblies and can be considered as a powerful tool to characterise noncovalent assemblies or host–guest complexes.[81]

In 1998, Bernhardt and coworkers[82] have reported the synthesis of a remarkable ditopic triazine-based ligand, namely [6-(4′,6′-diamino-1′,3′,5′-triazinyl)-1,4,6,8,11-pentaazacyclotetradecane] (**12**, Figure 28).

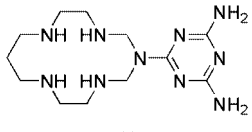

**12**

Figure 28. [6-(4′,6′-Diamino-1′,3′,5′-triazinyl)-1,4,6,8,11-pentaazacyclotetradecane] (**12**).[82,83]

As expected, this ligand can both bind a metal ion and be involved in the formation of a hydrogen network.[82,83] More recently, Bernhardt and coworkers have used this ligand to obtain a redox-active receptor for neutral guests.[84] The H-bonding abilities of the complex $[Cu(\mathbf{12})]^{2+}$ are obviously due to the presence of a melamine unit that can act as a donor–acceptor–donor entity (Figure 4). This intrinsic property has been used by Bernhardt and coworkers who have prepared a $[Cu(\mathbf{12})]^{2+}$/barbiturate adduct whose crystal structure is depicted in Figure 29.

H-bonded assemblies with barbitone and thymine (Figure 30) have also been obtained and crystallographically characterised. Solution electrochemical studies have been carried out in order to check the possibility of using $[Cu(\mathbf{12})]^{2+}$ as a redox-active receptor. The electrochemical detection is based on a shift of the redox potential of the host $[Cu(\mathbf{12})]^{2+}$ complex upon binding of the neutral guest molecule, i.e. barbitone, thymine, biuret or cytosine (Figure 30). These investigations have shown that the addition of complementary guests such as barbitone or biuret, which have an acceptor–donor–acceptor H-bonding pattern, leads to a significant shift in the $Cu^{II}/Cu^{I}$ redox potential. On the

 © 2006 Wiley-VCH Verlag GmbH & Co. KGaA, Weinheim 

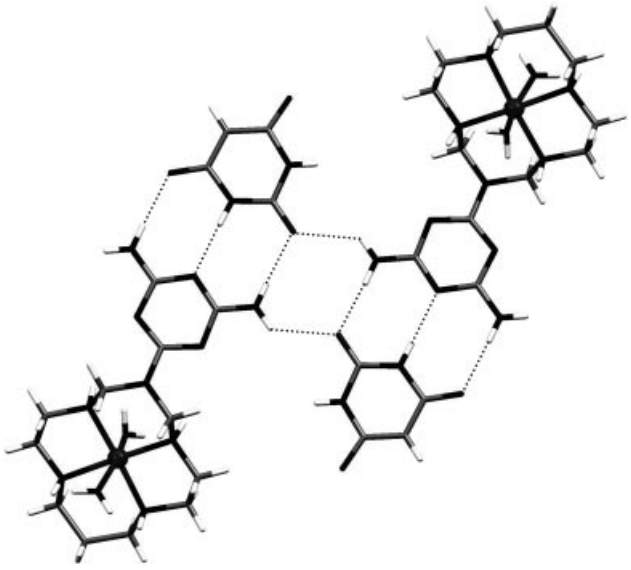

Figure 29. [Cu(**12**)]$^{+2}$/barbiturate H-bonded network.[84]

contrary, no significant shift has been observed with cytosine, which has a donor–acceptor–acceptor H-bonding pattern, mismatched with the donor–acceptor–donor pattern of [Cu(**12**)]$^{2+}$. The communication between the H-bonded element and the coordination unit of the triazine-based molecule has thus been clearly established and a host–guest selectivity has been evidenced. This type of material may be used as a sensor to detect specific polar organic compounds in solution.

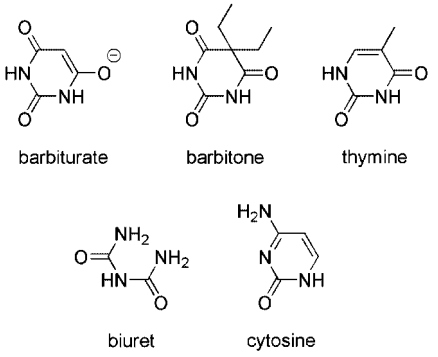


Figure 30. Guest molecules used with the complex [Cu(**12**)]$^{+2}$.[84]

## 6. Concluding Remarks

The vast development of supramolecular chemistry over the past twenty years has led to a huge diversity of chemical assemblies, obtained both by design[5] and serendipitous formation.[85] Tremendous progress has been made in the field of crystal structure prediction, using well-designed ligands and the reticular synthesis approach.[5] 1,3,5-Triazine-based synthons have proven their huge potential in this area, and the present microreview reports on some of the most remarkable examples published so far. The ability of melamine derivatives to generate H-bond networks has been elegantly applied by several research groups to produce host–guest or porous materials. The straightforward synthetic routes to generate sophisticated star-shaped polydentate N-ligands have allowed the preparation of molecular cages with applications in catalysis or separation, coordination polymers with magnetic properties or host–guest cavities, and anion hosting materials. Finally, the judicious combinations of H-bonding and coordinative interactions through the use of well-designed 1,3,5-triazine building blocks have generated functional materials with applications in mass spectrometry labelling and in sensoring. As summarized above, triazine-based supramolecules are highly promising synthons for the design and synthesis of exciting new polyfunctional compounds. The controlled preparation of hybrid inorganic–organic materials has remarkably improved since the late 1990s, and the important challenge of the contemporary supramolecular chemist is now to control the functionalization of such solids.[5] This includes the capacity to design intricate ligands which will act both as structural and functional buildings blocks to prepare custom-made materials possessing one or more specific properties, which can certainly be envisaged starting from the inexpensive, readily available 2,4,6-trichloro-1,3,5-triazine.

## Acknowledgments

Financial support from COST Action D21/003/2001 and the Dutch National Research School Combination Catalysis (HRSMC and NIOK) are thankfully acknowledged. The authors specially thank the coworkers who have been involved in the preparation and characterisation of triazine-based coordination supramolecules and whose names appear in the references list.

[1] J.-M. Lehn, *Supramolecular Chemistry: Concepts and Perspectives*, VCH, Weinheim, **1995**.
[2] A. D. Burrows, *Struct. Bonding* **2004**, *108*, 55–95.
[3] B. Moulton, M. J. Zaworotko, *Chem. Rev.* **2001**, *101*, 1629–1658.
[4] A. Gavezzotti, *Modelling Simul. Mater. Sci. Eng.* **2002**, *10*, R1–R29.
[5] O. M. Yaghi, M. O'Keeffe, N. W. Ockwig, H. K. Chae, M. Eddaoudi, J. Kim, *Nature* **2003**, *423*, 705–714.
[6] R. J. P. Corriu, *Angew. Chem. Int. Ed.* **2000**, *39*, 1376–1398.
[7] C. R. Kagan, D. B. Mitzi, C. D. Dimitrakopoulos, *Science* **1999**, *286*, 945–947.
[8] P. Gómez-Romero, C. Sánchez, *Functional Hybrid Materials*, Wiley-VCH, Weinheim, **2004**.
[9] J. D. Dunitz, A. Gavezzotti, *Angew. Chem. Int. Ed.* **2005**, *44*, 1766–1787.
[10] D. Braga, F. Grepioni, *Acc. Chem. Res.* **2000**, *33*, 601–608.
[11] P. Sozzani, S. Bracco, A. Comotti, L. Ferretti, R. Simonutti, *Angew. Chem. Int. Ed.* **2005**, *44*, 1816–1820.
[12] B. D. Wagner, G. J. McManus, B. Moulton, M. J. Zaworotko, *Chem. Commun.* **2002**, 2176–2177.
[13] P. Gamez, G. A. van Albada, I. Mutikainen, U. Turpeinen, J. Reedijk, *Inorg. Chim. Acta* **2005**, *358*, 1975–1980.
[14] S. R. Batten, R. Robson, *Angew. Chem. Int. Ed.* **1998**, *37*, 1461–1494.
[15] B. F. Abrahams, S. R. Batten, H. Hamit, B. F. Hoskins, R. Robson, *Chem. Commun.* **1996**, 1313–1314.
[16] J. A. Zerkowski, C. T. Seto, G. M. Whitesides, *J. Am. Chem. Soc.* **1992**, *114*, 5473–5475.

 © 2006 Wiley-VCH Verlag GmbH & Co. KGaA, Weinheim 

[17] M. Yoshizawa, T. Kusukawa, M. Kawano, T. Ohhara, I. Tanaka, K. Kurihara, N. Niimura, M. Fujita, *J. Am. Chem. Soc.* **2005**, *127*, 2798–2799.
[18] S. Ronchi, D. Prosperi, F. Compostella, L. Panza, *Synlett* **2004**, 1007–1010.
[19] J. M. Oliva, E. M. D. G. Azenha, H. D. Burrows, R. Coimbra, J. S. S. de Melo, M. L. Canle, M. I. Fernandez, J. A. Santaballa, L. Serrano-Andres, *ChemPhysChem* **2005**, *6*, 306–314.
[20] X. P. Hu, H. L. Chen, Z. Zheng, *Adv. Synth. Catal.* **2005**, *347*, 541–548.
[21] L. M. Pedroso, M. M. C. A. Castro, P. Simoes, A. Portugal, *Polymer* **2005**, *46*, 1766–1774.
[22] T. Carofiglio, A. Varotto, U. Tonellato, *J. Org. Chem.* **2004**, *69*, 8121–8124.
[23] P. de Hoog, P. Gamez, W. L. Driessen, J. Reedijk, *Tetrahedron Lett.* **2002**, *43*, 6783–6786.
[24] M. Arduini, M. Crego-Calama, P. Timmerman, D. N. Reinhoudt, *J. Org. Chem.* **2003**, *68*, 1097–1106.
[25] J. L. Silen, A. T. Lu, D. W. Solas, M. A. Gore, D. Maclean, N. H. Shah, J. M. Coffin, N. S. Bhinderwala, Y. W. Wang, K. T. Tsutsui, G. C. Look, D. A. Campbell, R. L. Hale, M. Navre, C. R. DeLuca-Flaherty, *Antimicrob. Agents Chemother.* **1998**, *42*, 1447–1453.
[26] T. Hayashi, A. Fujimoto, T. Kajiki, S. Kondo, Y. Yano, *Chem. Lett.* **2000**, 1018–1019.
[27] B. K. Saha, R. K. R. Jetti, S. Reddy, S. Aitipamula, A. Nangia, *Cryst. Growth Des.* **2005**, *5*, 887–899.
[28] G. A. Jeffrey, *An Introduction to Hydrogen Bonding*, Oxford University Press, Oxford, **1997**.
[29] C. R. L. P. N. Jeukens, P. Jonkheijm, F. J. P. Wijnen, J. C. Gielen, P. C. M. Christianen, A. P. H. J. Schenning, E. W. Meijer, J. C. Maan, *J. Am. Chem. Soc.* **2005**, *127*, 8280–8281.
[30] C. T. Seto, G. M. Whitesides, *J. Am. Chem. Soc.* **1990**, *112*, 6409–6411.
[31] G. M. Whitesides, J. P. Mathias, C. T. Seto, *Science* **1991**, *254*, 1312–1319.
[32] M. Kazuo, K. Hironobu, Y. Koichiso, N. Junichi, *Jpn. Kokai Tokkyo Koho* **1979**, *79*, 588.
[33] R. H. Vreekamp, J. P. M. vanDuynhoven, M. Hubert, W. Verboom, D. N. Reinhoudt, *Angew. Chem. Int. Ed. Engl.* **1996**, *35*, 1215–1218.
[34] L. J. Prins, E. E. Neuteboom, V. Paraschiv, M. Crego-Calama, P. Timmerman, D. N. Reinhoudt, *J. Org. Chem.* **2002**, *67*, 4808–4820.
[35] J. M. C. A. Kerckhoffs, F. W. R. van Leeuwen, A. L. Spek, H. Kooijman, M. Crego-Calama, D. N. Reinhoudt, *Angew. Chem. Int. Ed.* **2003**, *42*, 5717–5722.
[36] J. M. C. A. Kerckhoffs, T. Ishi-i, V. Paraschiv, P. Timmerman, M. Crego-Calama, S. Shinkai, D. N. Reinhoudt, *Org. Biomol. Chem.* **2003**, *1*, 2596–2603.
[37] P. Jonkheijm, A. Miura, M. Zdanowska, F. J. M. Hoeben, S. De Feyter, A. P. H. J. Schenning, F. C. De Schryver, E. W. Meijer, *Angew. Chem. Int. Ed.* **2004**, *43*, 74–78.
[38] P. Jonkheijm, F. J. M. Hoeben, R. Kleppinger, J. van Herrikhuyzen, A. P. H. J. Schenning, E. W. Meijer, *J. Am. Chem. Soc.* **2003**, *125*, 15941–15949.
[39] N. Malek, T. Maris, M. Simard, J. D. Wuest, *J. Am. Chem. Soc.* **2005**, *127*, 5910–5916.
[40] J. L. C. Rowsell, O. M. Yaghi, *Microporous Mesoporous Mater.* **2004**, *73*, 3–14.
[41] T. Duren, L. Sarkisov, O. M. Yaghi, R. Q. Snurr, *Langmuir* **2004**, *20*, 2683–2689.
[42] N. L. Rosi, J. Eckert, M. Eddaoudi, D. T. Vodak, J. Kim, M. O'Keeffe, O. M. Yaghi, *Science* **2003**, *300*, 1127–1129.
[43] R. Zibaseresht, R. M. Hartshorn, *Aust. J. Chem.* **2005**, *58*, 345–353.
[44] M. H. Al-Sayah, N. R. Branda, *Angew. Chem. Int. Ed.* **2000**, *39*, 945–947.
[45] M. I. J. Polson, E. A. Medlycott, G. S. Hanan, L. Mikelsons, N. L. Taylor, M. Watanabe, Y. Tanaka, F. Loiseau, R. Passalacqua, S. Campagna, *Chem. Eur. J.* **2004**, *10*, 3640–3648.
[46] Q. D. Liu, W. L. Jia, G. Wu, S. I. Wang, *Organometallics* **2003**, *22*, 3781–3791.
[47] O. Ohmori, M. Kawano, M. Fujita, *Angew. Chem. Int. Ed.* **2005**, *44*, 1962–1964.
[48] S. A. Barnett, A. J. Blake, N. R. Champness, J. E. B. Nicolson, C. Wilson, *J. Chem. Soc., Dalton Trans.* **2001**, 567–573.
[49] S. R. Batten, B. F. Hoskins, R. Robson, *Angew. Chem. Int. Ed. Engl.* **1995**, *34*, 820–822.
[50] G. J. Halder, S. M. Neville, C. J. Kepert, *CrystEngComm* **2005**, *7*, 266–268.
[51] M. Kurabaya, K. Yanagiya, M. Yasumoto, *Bull. Chem. Soc. Jpn.* **1971**, *44*, 3413–3418.
[52] B. F. Abrahams, S. R. Batten, H. Hamit, B. F. Hoskins, R. Robson, *Angew. Chem. Int. Ed. Engl.* **1996**, *35*, 1690–1692.
[53] M. Fujita, D. Oguro, M. Miyazawa, H. Oka, K. Yamaguchi, K. Ogura, *Nature* **1995**, *378*, 469–471.
[54] T. Kusukawa, M. Fujita, *J. Am. Chem. Soc.* **2002**, *124*, 13576–13582.
[55] S. Tashiro, M. Tominaga, M. Kawano, B. Therrien, T. Ozeki, M. Fujita, *J. Am. Chem. Soc.* **2005**, *127*, 4546–4547.
[56] K. Nakabayashi, M. Kawano, M. Yoshizawa, S. Ohkoshi, M. Fujita, *J. Am. Chem. Soc.* **2004**, *126*, 16694–16695.
[57] T. Kusukawa, M. Fujita, *Angew. Chem. Int. Ed.* **1998**, *37*, 3142–3144.
[58] M. Fujita, K. Umemoto, M. Yoshizawa, N. Fujita, T. Kusukawa, K. Biradha, *Chem. Commun.* **2001**, 509–518.
[59] H. Ito, T. Kusukawa, M. Fujita, *Chem. Lett.* **2000**, 598–599.
[60] P. Gamez, P. de Hoog, M. Lutz, A. L. Spek, J. Reedijk, *Inorg. Chim. Acta* **2003**, *351*, 319–325.
[61] P. Gamez, P. de Hoog, O. Roubeau, M. Lutz, W. L. Driessen, A. L. Spek, J. Reedijk, *Chem. Commun.* **2002**, 1488–1489.
[62] J. Pang, Y. Tao, S. Freiberg, X. P. Yang, M. D'Iorio, S. Wang, *J. Mater. Chem.* **2002**, *12*, 206–212.
[63] C. Seward, J. Pang, S. Wang, *Eur. J. Inorg. Chem.* **2002**, 1390–1399.
[64] P. de Hoog, P. Gamez, O. Roubeau, M. Lutz, W. L. Driessen, A. L. Spek, J. Reedijk, *New J. Chem.* **2003**, *27*, 18–21.
[65] M. Eddaoudi, H. L. Li, O. M. Yaghi, *J. Am. Chem. Soc.* **2000**, *122*, 1391–1397.
[66] P. de Hoog, P. Gamez, H. Mutikainen, U. Turpeinen, J. Reedijk, *Angew. Chem. Int. Ed.* **2004**, *43*, 5815–5817.
[67] P. D. Beer, E. J. Hayes, *Coord. Chem. Rev.* **2003**, *240*, 167–189.
[68] C. R. Bondy, P. A. Gale, S. J. Loeb, *J. Am. Chem. Soc.* **2004**, *126*, 5030–5031.
[69] K. Chellappan, N. J. Singh, I. C. Hwang, J. W. Lee, K. S. Kim, *Angew. Chem. Int. Ed.* **2005**, *44*, 2899–2903.
[70] H. Salman, Y. Abraham, S. Tal, S. Meltzman, M. Kapon, N. Tessler, S. Speiser, Y. Eichen, *Eur. J. Org. Chem.* **2005**, 2207–2212.
[71] P. D. Beer, P. A. Gale, *Angew. Chem. Int. Ed.* **2001**, *40*, 487–516.
[72] D. Quinonero, C. Garau, A. Frontera, P. Ballester, A. Costa, P. M. Deya, *J. Phys. Chem. A* **2005**, *109*, 4632–4637.
[73] M. Mascal, A. Armstrong, M. D. Bartberger, *J. Am. Chem. Soc.* **2002**, *124*, 6274–6276.
[74] D. Kim, P. Tarakeshwar, K. S. Kim, *J. Phys. Chem. A* **2004**, *108*, 1250–1258.
[75] S. Demeshko, S. Dechert, F. Meyer, *J. Am. Chem. Soc.* **2004**, *126*, 4508–4509.
[76] S. R. Batten, B. F. Hoskins, B. Moubaraki, K. S. Murray, R. Robson, *Chem. Commun.* **2000**, 1095–1096.
[77] H. Casellas, C. Massera, P. Gamez, A. M. Manotti Lanfredi, J. Reedijk, *Eur. J. Inorg. Chem* **2005**, 2902–2908.
[78] P. Gamez, P. de Hoog, M. Lutz, W. L. Driessen, A. L. Spek, J. Reedijk, *Polyhedron* **2003**, *22*, 205–210.
[79] K. C. Russell, E. Leize, A. Vandorsselaer, J. M. Lehn, *Angew. Chem. Int. Ed. Engl.* **1995**, *34*, 209–213.


 © 2006 Wiley-VCH Verlag GmbH & Co. KGaA, Weinheim 

[80] K. A. Jolliffe, M. C. Calama, R. Fokkens, N. M. M. Nibbering, P. Timmerman, D. N. Reinhoudt, *Angew. Chem. Int. Ed.* **1998**, *37*, 1247–1251.
[81] P. Timmerman, K. A. Jolliffe, M. C. Calama, J. L. Weidmann, L. J. Prins, F. Cardullo, B. H. M. Snellink-Ruel, R. H. Fokkens, N. M. M. Nibbering, S. Shinkai, D. N. Reinhoudt, *Chem. Eur. J.* **2000**, *6*, 4104–4115.
[82] P. V. Bernhardt, E. J. Hayes, *Inorg. Chem.* **1998**, *37*, 4214–4219.
[83] P. Comba, Y. D. Lampeka, A. Y. Nazarenko, A. I. Prikhod'ko, H. Pritzkow, *Eur. J. Inorg. Chem.* **2002**, 1464–1474.
[84] P. V. Bernhardt, E. J. Hayes, *Inorg. Chem.* **2003**, *42*, 1371–1377.
[85] R. E. P. Winpenny, *J. Chem. Soc., Dalton Trans.* **2002**, 1–10.
Received: July 27, 2005
Published Online: October 25, 2005

 © 2006 Wiley-VCH Verlag GmbH & Co. KGaA, Weinheim 

DOI: 10.1002/ejic.200500584

# Crystal Structure and Optical Properties of a Lanthanum(III) Complex of the Solvatochromic Dye "Nile Red"

**Anders Døssing,*[a] Magnus Magnussen,[a] and Anne Mette Frey[a]**

**Keywords:** Lanthanum / Heterocycles / N,O ligands / Chelates

A carbethoxy derivative of the push-pull chromophore benzo[*a*]phenoxazin-5-one (Nile Red) forms chelate complexes of the trivalent lanthanide ions that are stable in coordinating solvents with a bathochromic shift of the intense charge-transfer band in the Nile Red chromophore as a result. The complex formation results in quenching of the fluorescence from the free Nile Red ligand. Single crystals of a lanthanum(III) complex have been grown and the X-ray crystal structure showed that two Nile Red ligands are coordinated to the metal centre.
(© Wiley-VCH Verlag GmbH & Co. KGaA, 69451 Weinheim, Germany, 2006)

## Introduction

The benzo[*a*]phenoxazine compound Nile Red (nr) is a widely used fluorescent laser dye (Figure 1). The intense absorption band ($\varepsilon_{max} \approx 35000\ cm^{-1}\,M^{-1}$), located in the VIS range,[1] displays some charge transfer character in which electron density is moved from the diethylamino group to the carbonyl group, and nr is, accordingly, often referred to as a so-called push-pull chromophore. The positions of the absorption and emission bands are highly sensitive to the nature of the solvent (polarity and hydrogen-bond acidity), and the absorption maximum ranges from 484 nm in pentane to 629 nm in trifluoroacetic acid.[2] This solvatochromic effect has its origin in the fact that the molecule in the first excited singlet state is geometrically distorted with a significantly higher dipole moment than in the ground state. Exhibiting such twisted intramolecular charge transfer (TICT) properties nr has thus been used extensively as a polarity probe in chemical and biophysical environments.[3] Moreover, Verhoeven found recently that nr was able to sensitize a metal-centred NIR emission from the complexes [Ln(fod)$_3$(nr)] (Ln = Er or Yb, fod = 6,6,7,7,8,8,8-heptafluoro-2,2-dimethyloctane-3,5-dione) in benzene solution.[4] However, complex formation between the Lewis acids [Ln(fod)$_3$] and nr, that occurs through the carbonyl oxygen atom in nr, is weak and does not take place in more coordinating solvents such as acetonitrile (MeCN). In an attempt to overcome this obstacle we have, during our investigations in this field,[5] used a derivative of nr, namely nr-C(O)OEt shown in Figure 1. The attached carbethoxy group makes the formation of a chelate metal complex [Ln$^{III}${nr-C(O)OEt}] possible, resulting in enhanced stability of the metal complexes of nr-C(O)OEt. We present here results that show that nr-C(O)OEt forms complexes with lanthanide(III) (Ln$^{III}$) ions in coordinating solvents. Single crystals of a lanthanum(III) complex of nr-C(O)OEt have been grown, and the crystal structure of this complex has been determined. Despite the fact that nr has been widely used as a polarity probe and that the electronic structure of nr has been subject to numerous theoretical studies,[6] this contribution describes the first example of a crystal structure determination of a compound that includes an nr chromophore.

[a] Department of Chemistry, University of Copenhagen, Universitetsparken 5, 2100 Copenhagen Ø, Denmark
Fax: + 45-35320133
E-mail: dossing@kiku.dk

## Results and Discussion

The synthesis of nr-C(O)OEt has been described by Meng,[7] who prepared a whole series of nr derivatives. From an MeCN solution of nr-C(O)OEt and La(OSO$_2$CF$_3$)$_3$, single crystals of [La{nr-C(O)OEt}$_2$(OSO$_2$CF$_3$)$_3$(OH$_2$)$_2$]·H$_2$O (**1**) were grown. Figure 2 shows the molecular structure of **1**. The lanthanum(III) centre in **1** is coordinated by two molecules of nr-C(O)OEt (each bidentately coordinated as shown in Figure 1), two water molecules, and three triflate anions that are monodentately bound through the oxygen atoms. The coordination geometry is best described as tricapped trigonal prismatic. The La–O bond lengths are normal for these types of ligators. Of special note is the bonding geometry around the aliphatic, tertiary N1 and N3 atom. Firstly, the geometry is close to trigonal planar, and the C–N–C angles range from 115° to 122°, and the C–C8–N1–C and C–C31–N3–C dihedral angles range from 2° to 6° and from –170° to –178°, respectively. Secondly, the N1–C8 and N3–C31 bond lengths of 1.353(3) and 1.330(3) Å, respectively, are significantly shorter than expected for a N(sp$^3$)–C(sp$^2$) bond (1.467(2) Å in 4-aminobenzonitrile hydrochloride).[8] This can be rationalized if we take the ionic

 © 2006 Wiley-VCH Verlag GmbH & Co. KgaA, Weinheim InterScience 

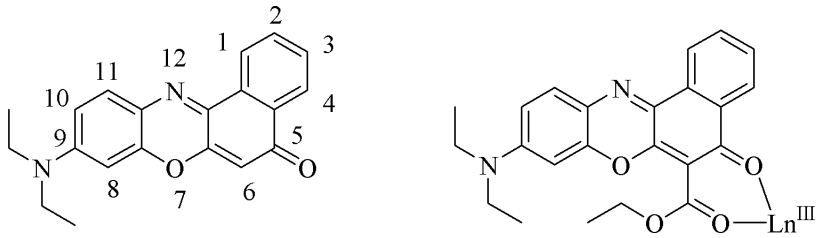


Figure 1. Structure of the ligands nr and nr-C(O)OEt; the latter ligand is chelated to a lanthanide(III) ion ($Ln^{III}$).

resonance structure shown in Figure 3 into account. Here, the lone pairs of electrons on N1 and N3 reside in a pure p orbital which is conjugated with the aromatic ring; this results in an increased order of the N1–C8 and N3–C31 bond and delocalization of a negative charge on the β-keto ester group, as shown in Figure 3. Similar behaviour was seen in other acceptor-substituted aromatic amines such as 4-(dimethylamino)benzonitrile[9] and 4-nitroso-*N*,*N*-diethylaniline[10] in which the analogous C–N bond length was 1.366(2) and 1.358(4) Å, respectively. Han et al. calculated, by density functional methods, the bond lengths of nr in the ground state and the first excited singlet state both in the gas phase and in $H_2O$ solution.[6b] It is worth noting that the bond lengths of the nr-C(O)OEt ligand in **1** agree (within 0.01 Å) with the calculated bond lengths of nr in the ground state in $H_2O$ solution. With regard to other metal complexes of nr, it should be noted in this context that Ghedini isolated the cyclometalated, square-planar complexes of the type [Pd(nr)(acac)] (acac = acetylacetonate or derivatives thereof) in which the nr ligand supposedly bidentately coordinates through the N12 and deprotonated C1 atoms (the atom numbering is taken from Figure 1).[11] No crystal structures were, however, reported.

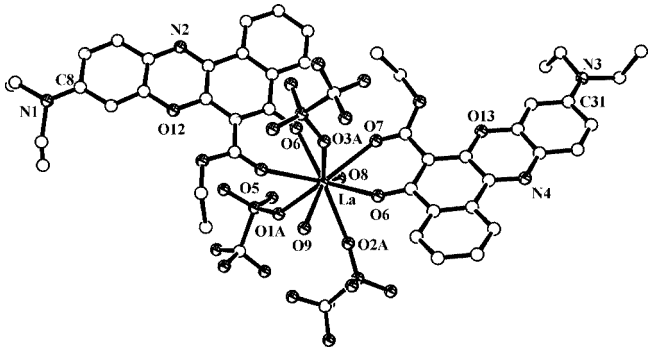


Figure 2. Molecular structure of the complex [La{nr-C(O)-OEt}$_2$($OSO_2CF_3$)$_3$($OH_2$)$_2$] with the hydrogen atoms omitted for clarity. The thermal ellipsoids are shown at the 50% probability. Ranges of bond lengths: La–O(triflate) 2.5623(16)–2.5985(16) Å, La–O(water) 2.5331(15)–2.5903(16) Å, La–O{nr-C(O)OEt} 2.4482(15)–2.5507(15) Å.

For the recording of the $^1$H NMR spectra excess $La(CF_3SO_3)_3$ was added to an acetonitrile solution of nr-C(O)OEt in order to ensure that all nr-C(O)OEt was complexed. In the $^1$H NMR spectrum of such a solution there

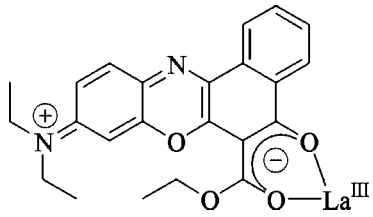

Figure 3. A resonance form of a lanthanum(III) chelate complex of nr-C(O)OEt.

are no peaks originating from free nr-C(O)OEt, and only one type of complexed nr-C(O)OEt is seen. The chemical shift values ($\delta$) for complexed and free nr-C(O)OEt are shown in Table 1. It should be noted that the chemical shifts move downfield on complexation owing to the electron-withdrawing inductive effect of the metal ion, with the exception of those for 2-H, 3-H, and 4-H. The excess $La(CF_3SO_3)_3$ in the solution favours a 1:1 stoichiometry for La/nr-C(O)OEt, but it is worth noting that the crystals that separate out from the solution after long-term storage have a stoichiometry of 1:2.

Table 1. Chemical shift ($\delta$/ppm) assignment of the $^1$H NMR spectra of nr-C(O)OEt and [$La^{III}${nr-C(O)OEt}] in $CD_3CN$ at 298 K.

| Nuclei | nr-C(O)OEt | La{nr-C(O)OEt} |
|---|---|---|
| $N(CH_2CH_3)_2$ | 1.21 | 1.40 |
| $OCH_2CH_3$ | 1.41 | 1.52 |
| $N(CH_2CH_3)_2$ | 3.48 | 3.73 |
| $OCH_2CH_3$ | 4.45 | 4.65 |
| 1-H | 8.19 | 8.38[a] |
| 2-H | 7.68 | 7.62 |
| 3-H | 7.78 | 7.62 |
| 4-H | 8.57 | 8.28[a] |
| 8-H | 6.55 | 6.59 |
| 10-H | 6.83 | 7.38 |
| 11-H | 7.61 | 7.81 |

[a] May be interchanged.

Stužka et al.[12] studied the IR spectra of various substituted benzo[*a*]phenoxazine compounds, and on the basis of that work, we assign the bands at 1640 and 1733 $cm^{-1}$ in the IR spectrum of nr-C(O)OEt as carbonyl vibrations in the keto and ester groups, respectively. An IR spectrum of a solid with the formula [La{nr-C(O)OEt}$_3$]($CF_3SO_3$)$_3$·3$H_2O$ (**2**) shows that metal complexation to the ester carbonyl oxygen atom results, in accordance with the reso-

 © 2006 Wiley-VCH Verlag GmbH & Co. KGaA, Weinheim 

nance form in Figure 3, in a significant decrease in the ester carbonyl stretching frequency; this band appears as a shoulder (at $\tilde{\nu}$ = 1694 cm$^{-1}$) on the other (keto) carbonyl vibrational band at 1658 cm$^{-1}$.

The optical spectra of nr-C(O)OEt and its lanthanum(III) complex in solution can be seen in Figure 4. The pink colour of a MeCN solution of nr-C(O)OEt ($\lambda_{abs}^{max}$ = 553 nm) changes to blue ($\lambda_{abs}^{max}$ = 622 nm) upon addition of $La(CF_3SO_3)_3$. This bathochromic shift of the charge-transfer band is a result of the interaction between the electron-rich carbonyl group and the electron-withdrawing lanthanum(III) ion that lowers the diethylamino to carbonyl oxygen charge-transfer energy. A similar behaviour with other $Ln^{III}$ ions and in other solvents is observed. With regard to the luminescence properties, solutions of nr-C(O)OEt display strong fluorescence with the emission maximum in MeCN located at $\lambda_{em}^{max}$ = 627 nm ($\lambda_{ex}^{max}$ = 553 nm). Addition of $La(CF_3SO_3)_3$ reduces the fluorescence intensity to about 10% of the original, and the emission maximum shifts to $\lambda_{em}^{max}$ = 654 nm. Earlier studies of nr[13] have shown that the fluorescence lifetime and quantum yield is reduced significantly with increasing hydrogen-bond donating power of the medium, because hydrogen bonding that involves the electrons around the carbonyl oxygen atom will promote the nonradiative deactivation pathway by vibrational excitation of the resulting O–H group. However, coordination of a lanthanum(III) ion to the carbonyl oxygen atom cannot lead to deactivation through that mechanism. Instead, intersystem crossing to a triplet state promoted by the heavy metal ion could be a possible pathway for fluorescence quenching.

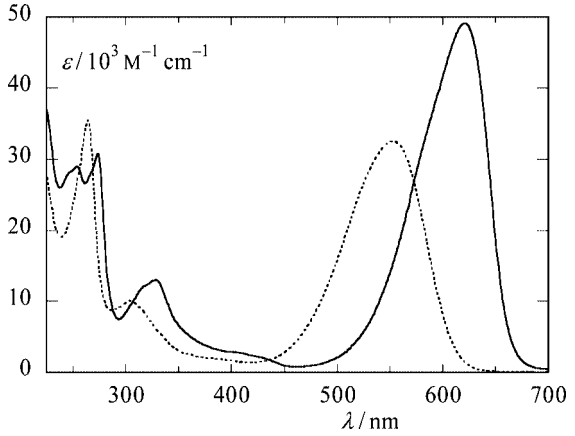


Figure 4. Optical absorption spectra of a $1.00 \times 10^{-5}$ M MeCN solution of nr-C(O)OEt before (–) and after addition of a ten-fold excess of $La(CF_3SO_3)_3$ (---).

In summary, we have shown that the present derivatisation of nr ensures that complex formation with lanthanide(III) ions *does* take place in solution. An nr chromophore might thus serve as a VIS absorbing sensitizer for the NIR emitters $Nd^{III}$, $Er^{III}$, and $Yb^{III}$. Such systems might find use as luminescent tags in biological systems and have accordingly attracted interest in recent years.[14] Our investigations in this field are ongoing, and the results will be published in due time.

## Experimental Section

**Physical Methods and Materials:** The starting material 6-carbethoxy-9-diethylamino-5*H*-benzo[*a*]phenoxazin-5-one [nr-C(O)OEt] was prepared as described in the literature.[7] Infrared spectra were obtained with a FT-IR 1760X spectrometer. $^1$H NMR studies were carried out with a Bruker 250 MHz instrument at room temperature with the $\delta$ values referenced to residual $^1$H impurities in the solvent. Optical absorption spectra were recorded with a Cary 5E UV/Vis-NIR spectrophotometer. Fluorescence spectra were recorded on a Spex Fluorolog FL3-22. Elemental analyses (C, H, N) were performed at the Department of Chemistry, University of Copenhagen.

**Single Crystals of Diaquabis(6-carbethoxy-9-diethylamino-5*H*-benzo[*a*]phenoxazin-5-one)tris(triflato-*O*)lanthanum(III) Monohydrate, [La{nr-C(O)OEt}$_2$(OSO$_2$CF$_3$)$_3$(OH$_2$)$_2$]·H$_2$O (1):** A mixture of $La(CF_3SO_3)_3$ (50 mg, 0.085 mmol), nr-C(O)OEt (10 mg, 0.026 mmol), and $CD_3CN$ (2 mL) was stirred, and undissolved $La(CF_3SO_3)_3$ was removed by centrifugation. The resulting blue solution was used for $^1$H NMR spectroscopy. After several months at 298 K, green plate crystals of **1** separated out from this solution. The crystals were isolated by decantation and dried under a flow of nitrogen.

**Tris(6-carbethoxy-9-diethylamino-5*H*-benzo[*a*]phenoxazin-5-one)lanthanum(III) Triflate Trihydrate, [La{nr-C(O)OEt}$_3$](CF$_3$SO$_3$)$_3$·3H$_2$O (2):** $La(CF_3SO_3)_3$ (200 mg, 0.34 mmol) was dissolved in dry acetonitrile (50 mL) with stirring. Then nr-C(O)OEt (50 mg, 0.13 mmol) was added, and the solution immediately turned dark blue. Slow evaporation of the solvent at room temperature over two weeks resulted in precipitation of a green microcrystalline material. The remaining mother liquor was decanted away, and the solid was washed thoroughly with water to remove excess $La(CF_3SO_3)_3$ and finally air-dried. Yield 40 mg (17%). $C_{72}H_{72}F_9LaN_6O_{24}S_3$ (1811.48): calcd. C 47.74, H 4.01, N 4.62; found C 47.81, H 3.69, N 4.63.

**X-ray Crystallography:** X-ray crystallographic study of **1**: $C_{49}H_{50}F_9LaN_4O_{20}S_3$, $M$ = 1421.02, triclinic, $P\bar{1}$, $a$ = 8.9240(9), $b$ = 13.0080(12), $c$ = 24.217(3) Å, $\alpha$ = 95.333(11), $\beta$ = 93.696(9), $\gamma$ = 90.493(9)°, $V$ = 2793.2(5) Å$^3$, $Z$ = 2, $\mu$(Mo-$K_\alpha$) = 0.987 mm$^{-1}$, 83979 reflections measured with a Nonius KappaCCD area-detector system at 122(1) K in the $\theta$ range 1.57–27.99°, 13422 unique reflections [$R$(int) = 0.0588] were used in the data analysis. The structure was solved using SHELXS-97 and refined using SHELXL-97.[15] During the refinement of **1** disorder was observed that involved one of the ethyl groups in one of the nr ligands. The disorder was resolved by refining the ethyl group in two conformations. The refinement converged at $R_1$ = 0.0293 for 12035 observed reflections with $I > 2\sigma(I)$, $wR_2$ = 0.0671 for all unique reflections, $S$ = 1.150, and an occupancy of 66% for the *cis* conformation of the disordered ethyl group. The anisotropic displacement parameters for all non-hydrogen atoms were refined. All hydrogen atoms were located in the difference Fourier map and included in the refinement riding on their parent atoms. The hydrogens on carbon were refined at idealised positions. Fourier peaks after the refinement were equal to 0.794 and –0.770 e/Å$^3$. CCDC-276918 contains the supplementary crystallographic data for this paper. These data can be obtained free of charge from The Cambridge Crystallographic Data Centre via www.ccdc.cam.ac.uk/data_request/cif.

## Acknowledgments

Mr. F. Hansen is thanked for assistance with the crystal structure determination.

 © 2006 Wiley-VCH Verlag GmbH & Co. KGaA, Weinheim 

[1] A. K. Dutta, K. Kamada, K. Ohta, *J. Photochem. Photobiol.* **1996**, *A93*, 57–64.
[2] J. F. Deye, T. A. Berger, A. G. Anderson, *Anal. Chem.* **1990**, *62*, 615–622.
[3] a) J. L. Meinershagen, T. Bein, *J. Am. Chem. Soc.* **1999**, *121*, 448–449; b) J. Hendriks, T. Gensch, L. Hviid, M. A. van der Horst, K. J. Hellingwerf, J. J. van Thor, *Biophys. J.* **2002**, *82*, 1632–1643; c) A. J. Carmichael, K. R. Seddon, *J. Phys. Org. Chem.* **2000**, *13*, 591–595; d) S. B. Ruvinov, X.-J. Yang, K. D. Parris, U. Banik, S. A. Ahmed, E. W. Miles, D. L. Sackett, *J. Biol. Chem.* **1995**, *270*, 6357–6369; e) D. L. Sackett, J. L. Knutson, J. Wolff, *J. Biol. Chem.* **1990**, *265*, 14899–14906; f) K. Goodlin, K. Johnson, L. Lefkowitz, B. W. Williams, *J. Chem. Educ.* **1994**, *71*, A8–A12.
[4] M. H. V. Werts, M. A. Duin, J. W. Hofstraat, J. W. Verhoeven, *Chem. Commun.* **1999**, 799–800.
[5] A. Døssing, *Eur. J. Inorg. Chem.* **2005**, 1425–1434 and references cited therein.
[6] a) L. C. D. Dias Jr., R. Custodio, F. B. T. Pessine, *Chem. Phys. Lett.* **1999**, *302*, 505–510; b) W.-G. Han, T. Liu, F. Himo, A. Toutchkine, D. Bashford, K. M. Hahn, L. Noodleman, *ChemPhysChem* **2003**, *4*, 1084–1094; c) C. M. Golini, B. W. Williams, J. B. Foresman, *J. Fluoresc.* **1998**, *8*, 395–404.
[7] J. Long, Y. M. Wang, T. Matsuura, J. B. Meng, *J. Heterocycl. Chem.* **1999**, *36*, 895–899.
[8] M. Colapietro, A. Domenicano, C. Marciante, G. Portaļone, *Acta Crystallogr. Sect. B* **1981**, *37*, 387–394.
[9] G. B. Jameson, B. M. Sheikh-Ali, R. G. Weiss, *Acta Crystallogr. Sect. B* **1994**, *50*, 703–707.
[10] H. J. Talberg, *Acta Chem. Scand.* **1977**, *A31*, 743–751.
[11] a) I. Aiello, M. Ghedini, M. La Deda, *J. Lumin.* **2002**, *96*, 249–259; b) M. La Deda, M. Ghedini, I. Aiello, T. Pugliese, F. Barigelletti, G. Accorsi, *J. Organomet. Chem.* **2005**, *690*, 857–861.
[12] V. Stužka, V. Šimánek, Z. Stránský, *Spectrochim. Acta A* **1967**, 2175–2183.
[13] A. Cser, K. Nagy, L. Biczók, *Chem. Phys. Lett.* **2002**, *360*, 473–478.
[14] S. Faulkner, J. L. Matthews, *Comprehensive Coordination Chemistry II* (Eds.: J. A. McCleverty, T. J. Meyer), vol. 9, Elsevier, Amsterdam, **2004**, 913–944.
[15] G. M. Sheldrick, *SHELXS-97* and *SHELXL-97*, University of Göttingen, Germany, **1997**.

Received: July 1, 2005
Published Online: September 8, 2005

 © 2006 Wiley-VCH Verlag GmbH & Co. KGaA, Weinheim 

DOI: 10.1002/ejic.200500799

# Ruthenium Metallodendrimers Based on Nitrile-Functionalized Poly(alkylidene imine)s

**Cátia Ornelas,[a] Viatcheslav Vertlib,[a] João Rodrigues,*[a] and Kari Rissanen*[b]**

**Keywords:** Ruthenium / Dendrimers / N ligands / Sandwich complexes

The preparation of the first- and second-generation of nitrile-functionalized poly(alkylidene imine) dendrimers with the organometallic ruthenium complex [Ru($\eta^5$-$C_5H_5$)($PPh_3$)$_2$Cl] peripherally attached is described. The reaction of *N*,*N*′-bis-(cyanomethyl)piperazine (**1**), *N*,*N*′-bis[*N*′′,*N*′′′-bis(cyanoethyl)aminoethyl]piperazine (**2**), or *N*,*N*,*N*′,*N*′-tetrakis(cyanoethyl)ethylenediamine (**3**) with [Ru($\eta^5$-$C_5H_5$)($PPh_3$)$_2$Cl] (**4**) in the presence of $TlPF_6$ gives the new air-stable ruthenium metallodendrimers **5**, **6**, and **7**, respectively. These stable metallodendrimers are easily prepared and represent a novel quantitative method to solidify and chromatographically purify the otherwise semi-liquid nitrile-functionalized poly(alkylidene imine) dendrimers. The compounds were fully characterized by IR and $^1$H, $^{13}$C, and $^{31}$P NMR spectroscopy, and mass spectrometry. These dendrimers represent the first example of the utilization of nitrile-functionalized poly(alkylidene imine)s as cores in the preparation of metallodendrimers.

(© Wiley-VCH Verlag GmbH & Co. KGaA, 69451 Weinheim, Germany, 2006)

## Introduction

Coordination-chemistry-based dendrimers can be easily prepared by straightforward synthetic methods by an appropriate choice of metals and ligands.[1] One of the most promising aspects of metallodendrimers[1–4] is their applicability as renewable metallodendritic catalysts,[5–7] as well as nanoscale molecular materials[8] with unusual physical or optical properties to be used as nonlinear optics (NLO) materials.[9–12]

Even though poly(propylene imine) derivatives are well known building blocks for the preparation of dendrimers,[13] the direct use of nitrile-functionalized poly(alkylidene imine) as a core for the preparation of metallodendrimers has not been reported prior to this work. In a previous work[14] we succeeded in the preparation of hexa- and nonaruthenium star-shaped complexes by using [Ru($\eta^5$-$C_5H_5$)($PPh_3$)$_2$Cl] as the organometallic ruthenium reagent. The same reasoning was followed in this work and we explored the use of nitrile-functionalized poly(alkylidene imine)s (generation 0 and 1) for the coordination to the organometallic fragment [Ru($\eta^5$-$C_5H_5$)($PPh_3$)$_2$]. The aim was the development of novel methods for the preparation of new nanoscopic molecular materials (metallodendrimer-based) with particular physical (NLO) and/or chemical properties (catalytic activity).

[a] Centro de Química da Madeira, LQCMM, Departamento de Química da Universidade da Madeira, Campus Universitário da Penteada,
9000-390 Funchal, Portugal
[b] NanoScience Center, Department of Chemistry, University of Jyväskylä,
P. O. Box 35, 40014 Jyväskylä, Finland

## Results and Discussion

The core nitrile-functionalized poly(alkylidene imine)s *N*,*N*′-bis(cyanomethyl)piperazine (**1**), *N*,*N*′-bis[*N*′′,*N*′′′-bis-(cyanoethyl)aminoethyl]piperazine (**2**), and *N*,*N*,*N*′,*N*′-tetrakis(cyanoethyl)ethylenediamine (**3**) were obtained in good yields by reaction of piperazine with chloroacetonitrile (**1**). The precursor amine for **2** was obtained by reduction of nitrile **1** with $LiAlH_4$. The piperazine and ethylenediamine were then treated with acrylonitrile under classic Michael reaction conditions.[15] The exact synthetic details of the preparation of **1**–**3** will be reported elsewhere.

These organic cores were quantitatively coordinated to the ruthenium reagent [Ru($\eta^5$-$C_5H_5$)($PPh_3$)$_2$Cl] (**4**) by substitution of chloride and coordination to the nitrile nitrogen, using a slight excess of $TlPF_6$ in methanol, resulting in the bis- and tetrakisruthenium-bonded dendrimers (Schemes 1 and 2).

These organometallic dendrimers were isolated in good yields as air-stable, yellow powders and were characterized by UV/Vis, IR, and $^1$H, $^{13}$C, and $^{31}$P NMR spectroscopy, and mass spectrometry.

The IR spectra of **5**, **6**, and **7** show, besides the characteristic band of the $PF_6^-$ counterion at 840 and 521 cm$^{-1}$, the nitrile band shifted to higher energies by 5, 14, and 21 cm$^{-1}$, respectively, when compared with the free nitrile, thus indicating similar coordination of all termini of the cores to the ruthenium fragment. These results are in accordance with the $^1$H NMR spectra, which show only one signal for C$H_2$CN shifted downfield and good relation/integrations between the protons of the ruthenium fragment and the protons of the cores. The $^{13}$C NMR spectra also show the expected signals, except for the nitrile carbon, which could

 © 2006 Wiley-VCH Verlag GmbH & Co. KgaA, Weinheim 

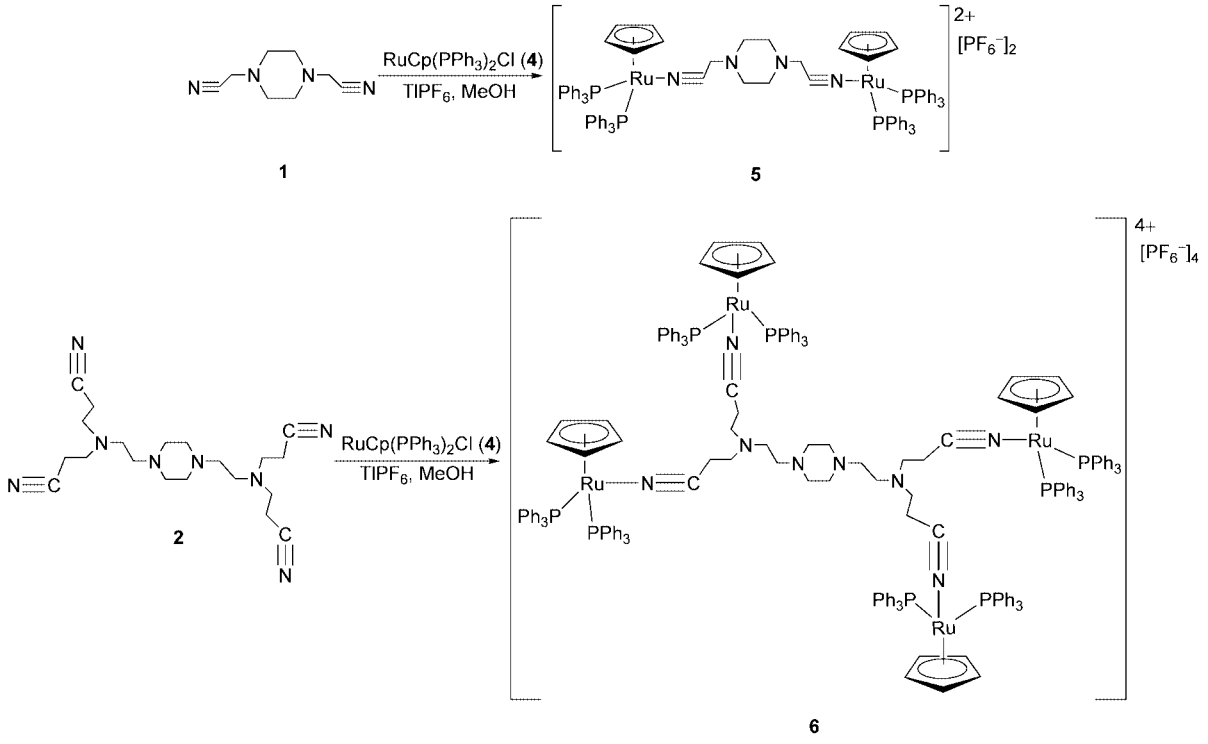


Scheme 1. First- and second-generation ruthenium metallodendrimers with piperazine cores.

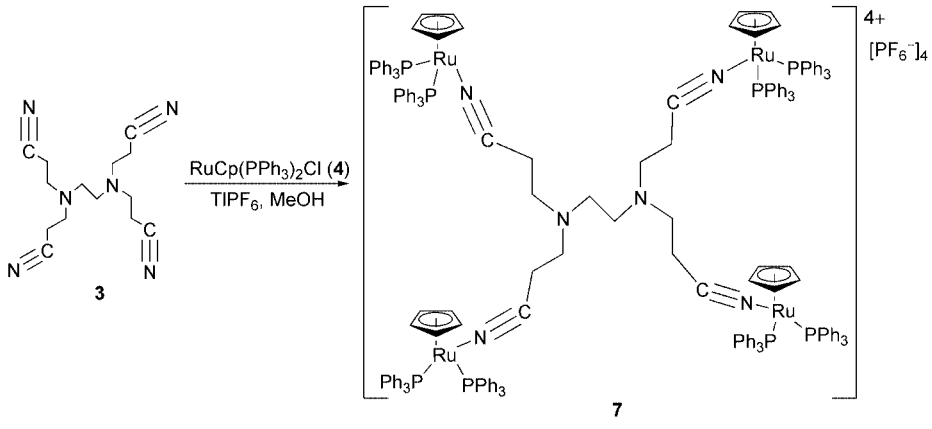


Scheme 2. A ruthenium metallodendrimer with an imine core.

not be detected due to slow relaxation. The appearance of only one Cp-ring signal at around $\delta$ = 4.5 ppm in the $^1$H NMR spectrum and only one phosphorus signal in the $^{31}$P NMR spectrum ($\delta \approx 42$ ppm) for all products is due to the equivalence of the ruthenium fragments coordinated to the cores and confirms the bis and the tetra coordination.

Clean mass spectra were obtained for all products, showing the characteristic [M$^+$] peaks at $m/z$ = 1691 (**5**), 3583 (**6**, Figure 1), and 3471 (**7**) and some peaks of typical fragmentations of the molecule in this technique (TOF-MS; see Experimental Section).

All the UV/Vis electronic spectra of the ruthenium dendrimers, recorded in ca. $10^{-5}$ M solutions of $CH_2Cl_2$, show a shoulder at around 351 nm with $\varepsilon$ values in the range 0.7–$1 \times 10^4$ M$^{-1}$ cm$^{-1}$. This behavior is probably due to a metal-to-ligand charge-transfer (MLCT) transition, since a similar transition is absent both in [Ru($\eta^5$-$C_5H_5$)($PPh_3$)$_2$Cl] and in the uncoordinated cores.

Although there is not sufficient literature data for 1:4 complex salts,[16] the conductivity measurements, together with the spectroscopic data, indicate that the assumption of 1:2 and 1:4 complex salts is correct.

 © 2006 Wiley-VCH Verlag GmbH & Co. KGaA, Weinheim 

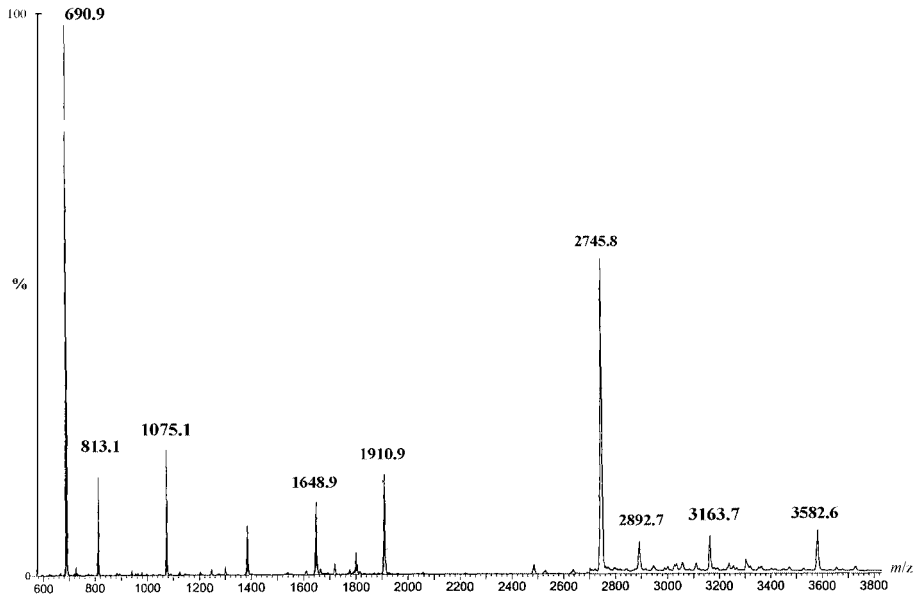


Figure 1. Mass spectrum of compound **6** showing the [$M^+$] peak at $m/z$ = 3583.

Several attempts to obtain crystals of these metallodendrimers for the elucidation of their structures in the solid state failed, producing only microcrystals unsuitable for X-ray diffraction.

## Conclusions

We have reported the preparation and characterization of the first- and second-generation poly(alkylidene imine) ruthenium dendrimers using nitrile-functionalized poly(alkylidene imine)s as cores and the organometallic fragment [Ru($\eta^5$-$C_5H_5$)($PPh_3$)$_2$] at the periphery. The easy preparation of these stable metallodendrimers represents a novel quantitative method to solidify and chromatographically purify the otherwise amorphous or semi-liquid nitrile-functionalized poly(alkylidene imine) dendrimers. The chromatographic purification of dendritic compounds is still rare and our method could be of help for purification of other dendritic nitriles. Our efforts are currently focused on the synthesis of higher generations of metallodendrimers and on the use of different metallic fragments to obtain dendrimers with different properties and applications.

## Experimental Section

**General:** All experiments were carried out under vacuum or nitrogen atmosphere by use of standard Schlenk techniques. With the exception of absolute methanol, which was used without further purification and degassed before use, all the solvents used were dried according to the usual published methods[17] and distilled prior to use. The compound [Ru($\eta^5$-$C_5H_5$)($PPh_3$)$_2$Cl] (**4**) was prepared and characterized as described in the literature.[18,19]

**Physical Measurements:** The UV/Vis spectra were recorded with a GBC-Cintra 40, UV/Vis spectrometer using 1-cm optical-path quartz cells with freshly prepared solutions of approximately $10^{-5}$ M concentration in $CH_2Cl_2$. The mass spectra (TOF-MS) were recorded on a Micromass LCT. FT-IR spectra were recorded with a Nicolet Avatar 360 FTIR spectrometer, calibrated with polystyrene, as KBr pellets; only significant bands are cited in the text. $^1$H, $^{13}$C{$^1$H}, and $^{31}$P{$^1$H} NMR spectra were recorded on a Bruker AM500 spectrometer at 500.13, 125.77, and 202.44 MHz, respectively, at 293.15 K (probe temperature). The $^1$H chemical shifts ($\delta$), reported in parts per million (ppm) downfield, are referenced to residual chloroform ($\delta$ = 7.24 ppm). The $^{13}$C{$^1$H} chemical shifts were reported in ppm relative to the carbon resonance of the deuterated NMR solvent ($CDCl_3$: $\delta$ = 77.00 ppm). The $^{31}$P{$^1$H} NMR spectra are reported in ppm downfield from external 85% $H_3PO_4$ ($\delta$ = 0.00 ppm). The elemental analysis of the complexes did not give satisfactory results after several tries and is not reported. The probable reasons for these irreproducible results are the evaporation of the possible lattice solvent molecules (MeOH, $CH_2Cl_2$, $CHCl_3$, or diethyl ether) and/or the adsorption/desorption of moisture. Conductivity measurements were made at 273.15 K on freshly made $10^{-3}$ M solutions of the complexes in nitromethane using a CRISON-microCM 2200. The cell constant was determined by measuring the resistance of an aqueous solution of KCl (0.0100 M, $\sigma$ = 0.001413 $\Omega^{-1}$ cm$^{-1}$ at 273.15 K). Molar conductivities ($\Lambda_M$) are given in units of $\Omega^{-1}$ cm$^2$ mol$^{-1}$. The accepted ranges for 1:2- and 1:4-type electrolytes under these conditions are 100–160 and 290–330 $\Omega^{-1}$ cm$^2$ mol$^{-1}$, respectively.[16]

**Synthesis of 5:** [Ru($\eta^5$-$C_5H_5$)($PPh_3$)$_2$Cl] (**4**; 0.4509 g, 0.620 mmol) and the dinitrile **1** (0.051 g, 0.310 mmol) were introduced with MeOH (30 mL), under nitrogen, into a flame-dried Schlenk flask. $TlPF_6$ (0.250 g, 0.713 mmol) was added and, after stirring the mixture for 13 h, the solvent was removed under vacuum. The product was extracted with $CH_2Cl_2$ and, after filtration, the solvent was removed under vacuum. The green product was dissolved in 10 mL

 © 2006 Wiley-VCH Verlag GmbH & Co. KGaA, Weinheim 

of $CH_2Cl_2$ and precipitated with *n*-hexane, the solution was filtered, and the yellow precipitate was washed twice with 10 mL of *n*-hexane. The yellow powder was dried under vacuum. Yield: 0.2853 g (51%). $^1$H NMR (500 MHz, $CDCl_3$): $\delta$ = 7.40–7.07 (m, $PPh_3$), 4.48 (s, 10 H, $C_5H_5$), 3.77 (s, 8 H, $CNCH_2$), 2.08 (s, 4 H, $NCH_2CH_2N$) ppm. $^{13}$C NMR (126 MHz, $CDCl_3$): $\delta$ = 135.7–133.3 ($PPh_3$), 83.8 ($C_5H_5$), 51.0 ($CNCH_2$), 48.1 ($NCH_2CH_2N$) ppm. $^{31}$P NMR (202 MHz, $CDCl_3$): $\delta$ = 42.2 (*s*, *P*$Ph_3$), –143 (m, *P*$F_6$) ppm. FT IR (KBr): $\tilde{\nu}$ = 2236 ($\nu_{CN}$), 839 and 522 $cm^{-1}$($\nu_{PF_6}$). TOF MS (ES$^+$): *m*/*z* (%) = 691 (100) [RuCp($PPh_3$)$_2$]$^+$, 855 (60) [RuCp($PPh_3$)$_2$(**1**)]$^+$, 1691 (10) **[M]$^+$**. UV/Vis ($CH_2Cl_2$): $\lambda_{max}$ [nm] ($\varepsilon$ [$M^{-1}cm^{-1}$]) = 351 ($0.8\times10^4$). $\Lambda_M$ = 157 $\Omega^{-1}cm^2mol^{-1}$.

**Synthesis of 6:** [Ru($\eta^5$-$C_5H_5$)($PPh_3$)$_2$Cl] (**4**; 0.3667 g, 0.505 mmol) and the ligand *N*,*N*′-bis[*N*′′,*N*′′′-bis(cyanoethyl)aminoethyl]piperazine (**2**; 0.047 g, 0.120 mmol) were introduced with MeOH (45 mL), under nitrogen, into a flame-dried Schlenk flask. $TlPF_6$ (0.2024 g, 0.579 mmol) was added and, after refluxing for 5 h, the mixture was stirred at room temperature for 16 h. The solvent was removed under vacuum and the product was extracted with $CH_2Cl_2$. After filtration the solvent was removed and the solid was washed twice with diethyl ether. The product was dissolved in 10 mL of $CH_2Cl_2$ and precipitated with diethyl ether. The yellow powder was dried under vacuum. Yield: 0.1933 g (45%). $^1$H NMR (500 MHz, $CDCl_3$): $\delta$ = 7.35–7.05 (m, $PPh_3$), 4.47 (s, 20 H, $C_5H_5$), 2.55 (s, 4 H, $NCH_2CH_2N$), 2.43 (s, 8 H, $NCCH_2CH_2$) 2.35 (s, 16 H, $NCH_2$) ppm. $^{13}$C NMR ($CDCl_3$, 126 MHz): $\delta$ = 135.7–127.1 ($PPh_3$), 83.5 ($C_5H_5$), 55.4 ($NCH_2CH_2N$ piperazine center), 53.1 (inner $NCH_2CH_2$), 52.3 (inner $NCH_2CH_2$), 43.5 (outer $NCH_2CH_2$), 17.9 ($CH_2CN$) ppm. $^{31}$P NMR (202 MHz, $CDCl_3$): $\delta$ = 42.4 (s, *P*$Ph_3$), –143 (m, *P*$F_6$) ppm. FT IR (KBr): $\tilde{\nu}$ = 2259 ($\nu_{CN}$), 840 and 521 $cm^{-1}$($\nu_{PF_6}$). TOF MS (ES$^+$): *m*/*z* (%) = 691 (100) [RuCp($PPh_3$)$_2$]$^+$, 813 (20) [RuCp$PPh_3$(**2**)]$^+$, 1075 (25) [RuCp($PPh_3$)$_2$(**2**)]$^+$, 1649 (15) [Cp($PPh_3$)$_2$CpRu(**2**)RuCp$PPh_3$][$PF_6$], 1911 (20) [{RuCp($PPh_3$)$_2$}$_2$(**2**)][$PF_6$], 2746 (60) [{RuCp($PPh_3$)$_2$}$_3$(**2**)][$PF_6$]$_2$, 3583 (10) [M]$^+$. UV/Vis ($CH_2Cl_2$): $\lambda_{max}$ [nm] ($\varepsilon$ [$M^{-1}cm^{-1}$]) = 350 ($1.1\times10^4$). $\Lambda_M$ = 279 $\Omega^{-1}cm^2mol^{-1}$.

**Synthesis of 7:** [Ru($\eta^5$-$C_5H_5$)($PPh_3$)$_2$Cl] (**4**; 0.2505 g, 0.345 mmol) and the ligand *N*,*N*,*N*′,*N*′-tetrakis(cyanoethyl)ethylenediamine (**3**; 0.0245 g, 0.177 mmol) were introduced with MeOH (35 mL), under nitrogen, into a flame-dried Schlenk flask. $TlPF_6$ (0.1482 g, 0.424 mmol) was added and, after refluxing for 12 h, the mixture was stirred at room temperature for 12 h. The solvent was removed under vacuum and the product was extracted with $CH_2Cl_2$. After filtration the solvent was removed and the solid was washed twice with diethyl ether. The product was dissolved in 10 mL of $CH_2Cl_2$ and precipitated with diethyl ether. The yellow powder was dried under vacuum. Yield: 0.1804 g (60%). $^1$H NMR (500 MHz, $CDCl_3$): $\delta$ = 7.31–7.06 (m, $PPh_3$), 4.47 (s, 20 H, $C_5H_5$), 2.57 (s, 8 H, $NCCH_2CH_2N$), 2.47 (s, 8 H, $NCCH_2$), 2.31 [s, 4 H, $N(CH_2)_2N$] ppm. $^{13}$C NMR (126 MHz, $CDCl_3$): $\delta$ = 136.1–128.6 ($PPh_3$), 83.8 ($C_5H_5$), 52.4 [$N(CH_2)_2N$], 49.0 ($NCH_2CH_2CN$), 18.9 ($CH_2CN$) ppm. $^{31}$P NMR(202 MHz, $CDCl_3$): $\delta$ = 42.5 (s, *P*$Ph_3$), –143 (m, *P*$F_6$) ppm. FT IR (KBr): $\tilde{\nu}$ = 2264 ($\nu_{CN}$), 840 and 521 $cm^{-1}$($\nu_{PF_6}$). TOF MS (ES$^+$): *m*/*z* = 691 (100) [RuCp($PPh_3$)$_2$]$^+$, 963 (7) [RuCp($PPh_3$)$_2$(**3**)]$^+$, 1799 (20) [{RuCp($PPh_3$)$_2$}$_2$(**3**)][$PF_6$], 2110 (18) [RuCp($PPh_3$)$_2$(**3**)(RuCp$PPh_3$)$_2$][$PF_6$]$_2$, 2372 (75) [{RuCp($PPh_3$)$_2$}$_2$-(**3**)RuCp$PPh_3$][$PF_6$]$_2$, 2634 (70) [{RuCp($PPh_3$)$_2$}$_3$(**3**)][$PF_6$]$_2$, 3471 (18) [M$^+$]. UV/Vis ($CH_2Cl_2$): $\lambda_{max}$ [nm] ($\varepsilon$ [$M^{-1}cm^{-1}$]) = 351 ($0.7\times10^4$). $\Lambda_M$ = 313 $\Omega^{-1}cm^2mol^{-1}$.

## Acknowledgments

This work was partially supported by grants from the Fundação para a Ciência e a Tecnologia (FCT) POCTI program (POCTI/QUI/41814/2001 and POCTI/CTM/41495/2001; FEDER funded). J. R. and C. O. gratefully acknowledge the Socrates/Erasmus Program for financial support. V. V. thanks FCT for giving a research assistantship grant through the POCTI/CTM/41495/2001 project. M. Sc. Anneli Roulamo is thanked for providing the nitriles, Mr. Reijo Kauppinen for the NMR, and Ms. Mirja Lahtiperä for the MS measurements.

[1] a) P. A. Chase, R. J. M. K. Gebbink, G. van Koten, *J. Organomet. Chem.* **2004**, *689*, 4016–4054; b) J. M. J. Fréchet, *Proc. Natl. Acad. Sci. USA* **2002**, *99*, 4782–4787.
[2] N. Ardoin, D. Astruc, *Bull. Soc. Chim. Fr.* **1995**, *132*, 875–909.
[3] A. W. Bosman, H. M. Janssen, E. W. Meijer, *Chem. Rev.* **1999**, *99*, 1665–1688.
[4] G. R. Newkome, E. He, C. N. Moorefield, *Chem. Rev.* **1999**, *99*, 1689–1746.
[5] D. Astruc, F. Chardac, *Chem. Rev.* **2001**, *101*, 2991–3024.
[6] G. E. Osterom, J. N. H. Reek, P. C. J. Kramer, P. W. N. M. van Leeuwen, *Angew. Chem. Int. Ed.* **2001**, *40*, 1828–1849.
[7] R. Kreiter, A. W. Kleij, R. J. M. K. Gebbink, G. van Koten, *Top. Curr. Chem.* **2001**, *217*, 163–199.
[8] V. Balzani, S. Campana, G. Denti, A. Juris, S. Serroni, M. Venturi, *Acc. Chem. Res.* **1998**, *31*, 26–34.
[9] M. G. Humphrey, C. E. Powell, M. P. Cifuentes, J. P. Morrall, M. Samoc, *Polymer Preprints* **2004**, *45*, 367–368.
[10] A. M. McDonagh, C. E. Powell, J. P. Morall, M. P. Cifuentes, M. G. Humphrey, *Organometallics* **2003**, *22*, 1402–1413.
[11] C. E. Powell, M. P. Cifuentes, J. P. Morrall, R. Stranger, M. G. Humphrey, M. Samoc, B. Luther-Davies, G. A. Heath, *J. Am. Chem. Soc.* **2003**, *125*, 602–610.
[12] H. Le Bozec, T. Le Bouder, O. Maury, I. Ledoux, J. Zyss, *J. Opt. A: Pure Appl. Opt.* **2002**, *4*, S189–S196.
[13] G. R. Newkome, C. N. Moorefield, F. Vögtle, *Dendrimers and Dendrons: Concepts, Synthesis Applications*; Wiley-VCH, Weinheim, **2001**.
[14] C. Ornelas, J. Ruiz, J. Rodrigues, D. Astruc, *Organometallics* **2004**, *23*, 4271–4276.
[15] E. Buhleier, W. Wehner, F. Vögtle, *Synthesis* **1978**, 155–158.
[16] a) J. E. Lind, J. J. Zwolenik, R. M. Fuoss, *J. Am. Chem. Soc.* **1959**, *81*, 1557–1559; b) W. J. Geary, *Coord. Chem. Rev.* **1971**, *7*, 81–122.
[17] D. D. Perrin, W. L. F. Amarego, and D. R. Perrin, *Purification of Laboratory Chemicals*, 2nd. edn., Pergamon, New York, **1980**, p. 55–59.
[18] M. I. Bruce, N. J. Windsor, *Aust. J. Chem.* **1977**, *30*, 1601–1604.
[19] C. Ornelas, C. Gandum, J. Mesquita, J. Rodrigues, M. H. Garcia, N. Lopes, M. P. Robalo, K. Nättinen, K. Rissanen, *Inorg. Chim. Acta* **2005**, *358*, 2482–2488.

Received: September 10, 2005
Published Online: November 15, 2005

 © 2006 Wiley-VCH Verlag GmbH & Co. KGaA, Weinheim 

DOI: 10.1002/ejic.200500432

# Amino-phosphanes in $Rh^{I}$-Catalyzed Hydroformylation: Hemilabile Behavior of P,N Ligands under High CO Pressure and Catalytic Properties

**Jacques Andrieu,*[a] Jean-Michel Camus,[a] Philippe Richard,[a] Rinaldo Poli,[a,b] Luca Gonsalvi,[c] Francesco Vizza,[c] and Maurizio Peruzzini*[c]**

**Keywords:** Rhodium / Amino-phosphane ligands / Hemilability / Hydroformylation catalysis

The catalytic properties of rhodium complexes containing the α-, β-, or γ-amino-phosphane ligands $Ph_2PCH_2NEt_2$ (**α-P,N-1**), $Ph_2PCH(Ar)NHPh$ [**α-P,N-2**; Ar = $\eta^6$(*o*-$C_6H_4Cl$)$Cr(CO)_3$], $Ph_2PCH_2NPh_2$ (**α-P,N-3**), $Ph_2PCH_2CH(Ph)NHPh$ (**β-P,N**), $Ph_2PCH_2$(*o*-$C_6H_4$–$NMe_2$) (**γ-P,N-1**), $Ph_2PCH$(*o*-$C_6H_4$–$CH_2NHPh$) (**γ-P,N-2**), and the α,β-diamino-phosphane ligand $Et_2NCH_2P(Ph)CH_2CH(Ph)NHPh$ (**α,β-N,P,N**), in styrene hydroformylation have been examined. The results show that the activity increases when the number of backbone carbon atoms linking P and N decreases from 3 to 1. IR and $^{31}P$ HPNMR studies in solution show that all P,N ligands adopt exclusively a $\kappa^1$-*P* coordination mode in rhodium chloride carbonyl complexes under high CO pressure. In the solid state a $\kappa^1$-*P*-α-amino-phosphane coordination has been ascertained by X-ray methods in *trans*-[RhCl(CO)(**γ-P,N-1**)$_2$]. In contrast, an equilibrium between the $\kappa^2$-*P,N* and $\kappa^1$-*P*-coordination modes has been observed as a function of the CO pressure for the complex containing the **β-P,N** ligand. The basicity of the dangling amino group also plays an important role on the catalytic activity and a mechanism involving the nitrogen function in the catalytic cycle is proposed.

(© Wiley-VCH Verlag GmbH & Co. KGaA, 69451 Weinheim, Germany, 2006)

## Introduction

Bifunctional P,N ligands are being intensively investigated because they present advantages compared to common trialkyl phosphanes in the catalytic applications of their corresponding Pd, Ni, Ru, and Ir complexes.[1–8] These ligands can be either $\kappa^1$-*P* or $\kappa^2$-*P,N* coordinated and each coordination mode can modify the catalytic properties. For example, the chelating coordination mode enhances the nucleophilic character of the metal center and subsequently promotes hydrogen oxidative addition.[7,9,10] A comparative study between α- and β-amino-phosphanes in rhodium-catalyzed hydroformylation has led to the proposal that a bidentate coordination mode accelerates aldehyde reductive elimination from $RhH_2$(acyl)(P,N).[11] The authors conclude that uncoordinated amino functions do not act as bases. In contrast, the dangling amine function in a $Pd^{II}$-coordinated $\kappa^1$-*P*-pyridinylphosphane acts as a "proton messenger" in catalytic alkyne methoxycarbonylation.[1] In another study of rhodium-catalyzed hydroformylation, it was shown that the P,N,P type, $Ph_2PCH_2N(Ar)CH_2PPh_2$, ligand is much more active than its analogous $Ph_2P(CH_2)_3$-$PPh_2$. However, a rationalization for the latter observation was not proposed.[12]

One of the key questions related to the use of bifunctional ligands, particularly those associating soft and hard donor atoms, is whether there is reversible association/dissociation of one labile function during the catalytic cycle (*hemilability* concept). In our laboratory, we have developed different pathways to chiral α- or β-P,N and mixed α,β- and β,γ-N,P,N ligands and their coordination properties have been explored in palladium(II) and rhodium(I) complexes.[13–16] Particularly, we have reported that β-P,N ligands adopt a chelating mode whereas α-P,N ligands are only P-coordinated in $Cu^{I}$ or in $Rh^{I}$ complexes.[17,18] Separate work has shown that β-P,N ligands in $Rh^{I}$ complexes can adopt a monodentate $\kappa^1$-P-[19] or a $\kappa^2$-*P,N*-coordination mode.[15,20] Nevertheless, no direct evidence for a hemilabile character has been reported so far for β-P,N ligands in $Rh^{I}$ complexes. This behavior was only suggested for a few cationic complexes of type $[Rh(COD)(\beta\text{-P,N})]^+$ in order to rationalize a rapid fluxional process.[21] Nor is it known whether the coordinated N donor in these $Rh^{I}$ complexes and in related complexes with γ-amino-phosphanes is displaced by CO under catalytic conditions. A hemilabile behavior for related chiral P,N ligands could explain the low enantioselectivities observed in asymmetric Rh-catalyzed hydroformylation.[22,23] On the other hand, an optically pure $Ru^{II}$ β-amino-phosphane complex led to higher *ee* for

[a] Laboratoire de Synthèse et Electrosynthèse Organométalliques, UMR 5188 CNRS, Université de Bourgogne, Faculté des Sciences Mirande,
9 avenue Alain Savary, 21078 Dijon, France
[b] Laboratoire de Chimie de Coordination, UPR CNRS 8241, 205 route de Narbonne, 31077 Toulouse Cedex, France
[c] ICCOM-CNR, Istituto di Chimica dei Composti Organometallici, Area di Ricerca CNR di Firenze,
10 Via Madonna del Piano, 50019 Sesto Fiorentino (Firenze), Italy
E-mail: Jacques.Andrieu@u-bourgogne.fr

 © 2006 Wiley-VCH Verlag GmbH & Co. KgaA, Weinheim 

the asymmetric reduction of ketones, whereas a related Ru-γ-amino-phosphane complex led to the same product in racemic form.[6]

We now wish to provide new information on the effect of a dangling vs. a coordinated nitrogen function of chiral P,N ligands in rhodium hydroformylation catalysis, thus helping to clarify a few previously obscure points.[11,12] Consequently, we have (i) investigated the mono- or bidentate coordination mode of P,N ligands in rhodium complexes under CO pressure by $^{31}P$ HPNMR and IR spectroscopy, (ii) examined the catalytic properties of various $Rh^{I}$–P,N complexes in styrene hydroformylation in order to establish a relation with the coordination modes, and (iii) evaluated the effect of the N basicity in P,N ligands on the formation and properties of the catalytic species.

## Results

### Coordination, IR, and $^{31}P\{^{1}H\}$ HPNMR Studies of Amino-Phosphanes in $Rh^{I}$ Complexes

We first examined whether the nitrogen donor in different P,N ligands (see Scheme 1) is coordinated under catalytic conditions. This investigation completes our recent studies on the $Rh^{I}$ coordination chemistry of P,N ligands.[15,18] Indeed, we have already reported that complex RhCl(COD)(**α-P,N-2**) (complex **1**) adopts a $\kappa^1$-*P* coordination mode both in the solid state and in solution and that an analogous monodentate coordination mode is also adopted in the dicarbonyl complex $RhCl(CO)_2$(**α-P,N-2**) (**IIα**, see Scheme 2).[18] The latter was obtained by ligand exchange from RhCl(COD)(**α-P,N-2**) (COD = 1,5-cyclooctadiene) under high CO pressure. Lowering the CO pressure did not result in the formation of a $\kappa^2$-*P,N* mononuclear product (**Iα**), but rather induces a ligand redistribution to yield $RhCl(CO)$(**α-P,N-2**)$_2$ (**IIIα**) where both α-P,N ligands are once again $\kappa^1$-*P* coordinated.

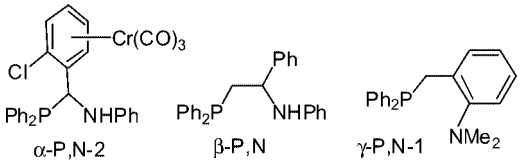


Scheme 1.

The behavior of $Rh^{I}$ complexes containing the **β-P,N** and **γ-P,N-1** ligands was first studied by IR in $CH_2Cl_2$ solution under CO (see Figure 1). Irrespective of the amino-phosphane, the IR spectrum shows two absorption bands at 2092 and at 2010 $cm^{-1}$, corresponding to the type-**II** dicarbonyl rhodium complex (named **IIγ** and **IIβ**, with the **γ-P,N-1** and **β-P,N** ligands, respectively) where the amino-phosphane is $\kappa^1$-*P* coordinated. However, the IR spectrum of **IIβ** shows an additional absorption band at 1986 $cm^{-1}$ corresponding to **Iβ**, as will be discussed in detail below.

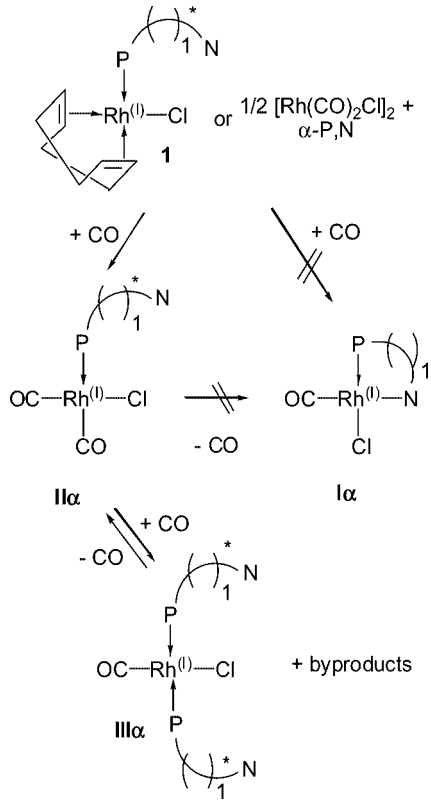


Scheme 2.

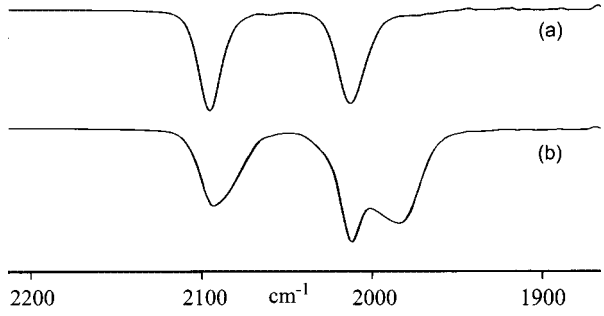


Figure 1. IR spectra of $[Rh(CO)_2Cl]_2$ + P,N ligand mixtures in 1:2 ratio prepared in $CH_2Cl_2$ under CO at room temperature, (a) with the **γ-P,N-1** ligand and (b) with the **β-P,N** ligand.

We then carried out $^{31}P\{^{1}H\}$ high pressure (HP) NMR studies for both dicarbonyl rhodium complexes **IIγ** and **IIβ** in order to confirm the IR results and to obtain additional information on their stability. When a solution of [RhCl(COD)(**γ-P,N-1**)] (complex **2**) was pressurized with CO, its doublet resonance at $\delta$ = 29.5 ppm [$^{1}J_{(Rh,P)}$ = 150 Hz] was replaced by a new one at $\delta$ = 26.9 ppm [$^{1}J_{(Rh,P)}$ = 126 Hz] (see Figure 2). The presence of a single complex is consistent with the IR data. After depressurization, complex **IIγ** evolved to complex **IIIγ**, [doublet at $\delta$ = 30.5 ppm with $^{1}J_{(Rh,P)}$ = 126 Hz] which became the only detectable product after flushing the solution for a few minutes with a dinitrogen stream (see Figure 2). The assignment of this

 © 2006 Wiley-VCH Verlag GmbH & Co. KGaA, Weinheim 

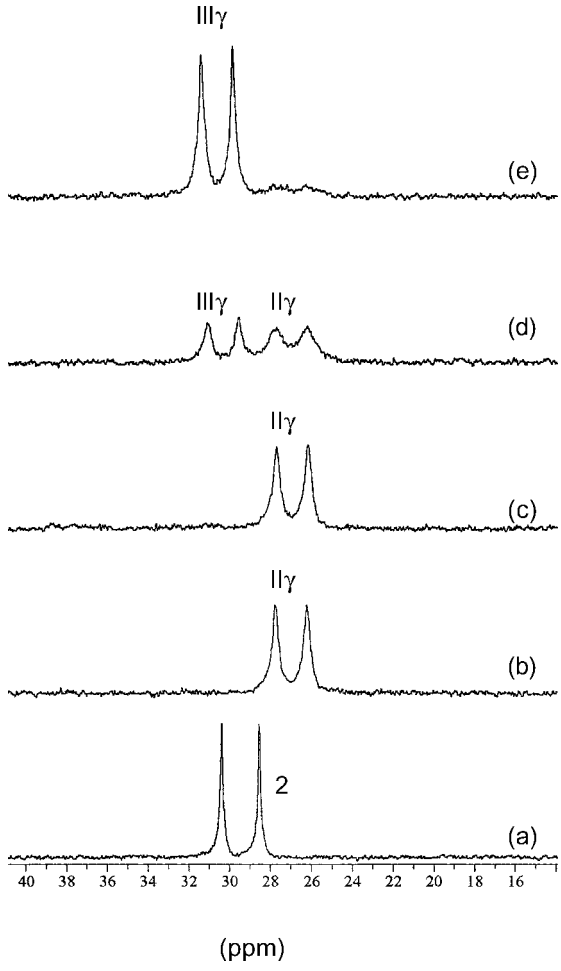


Figure 2. $^{31}P\{^{1}H\}$ HPNMR spectra under CO pressure for complex **2** in $CDCl_3$ solution. (a) Under $N_2$, (b) under CO, (c) under 20 bar of CO, (d) after depressurization, (e) solution after flushing 5 min with $N_2$.

signal to the monocarbonyl-bis-amino-phosphane rhodium complex **IIIγ** was confirmed by an X-ray structure analysis. Crystals of complex **IIIγ** (see Figure 3) were obtained upon attempting to crystallize complex **IIγ**, and their redissolution in $CDCl_3$ led to a $^{31}P$ NMR spectrum identical to spectrum (e) in Figure 2. Therefore, the final product of the NMR experiment in Figure 2 is unambiguously identified as a monocarbonyl-bis-amino-phosphane rhodium complex.

The evolution of **IIγ** to **IIIγ** must be accompanied by the formation of undefined organometallic CO-free by-products, as described previously for the analogous evolution of the **α-P,N-2** rhodium complex.[18] The $\nu_{CO}$ value at 1974 $cm^{-1}$ for **IIIγ** is close to that found for $[RhCl(CO)(PPh_3)_2]$ (1965 $cm^{-1}$),[24] thus suggesting similar electronic properties for the **γ-P,N-1** ligand and triphenylphosphane. Table 1 shows quite typical geometrical features and metric parameters for a complex of type $RhCl(CO)L_2$ (i.e.: L = trialkyl-, dialkyl-*N*-pyrrolidinyl-, or α-amino-phosphanes), namely a nearly ideal square-planar geometry around the rhodium atom with mutually *trans* phosphorus atoms.[18,24]

Table 1. Selected bond lengths [Å] and angles [deg] for **IIIγ**.

| | |
|---|---|
| Rh–P | 2.3199(7) |
| Rh–C(1) | 1.800(4) |
| Rh–Cl | 2.3681(9) |
| C(1)–O | 1.161(5) |
| | |
| P–Rh–P# | 172.83(3) |
| C(1)–Rh–P | 93.584(17) |
| C(1)–Rh–Cl | 180.0 |
| P–Rh–Cl | 86.416(17) |
| O–C(1)–Rh | 180.0 |

Symmetry transformations used to generate equivalent atoms: # $-x, y, -z + 1/2$

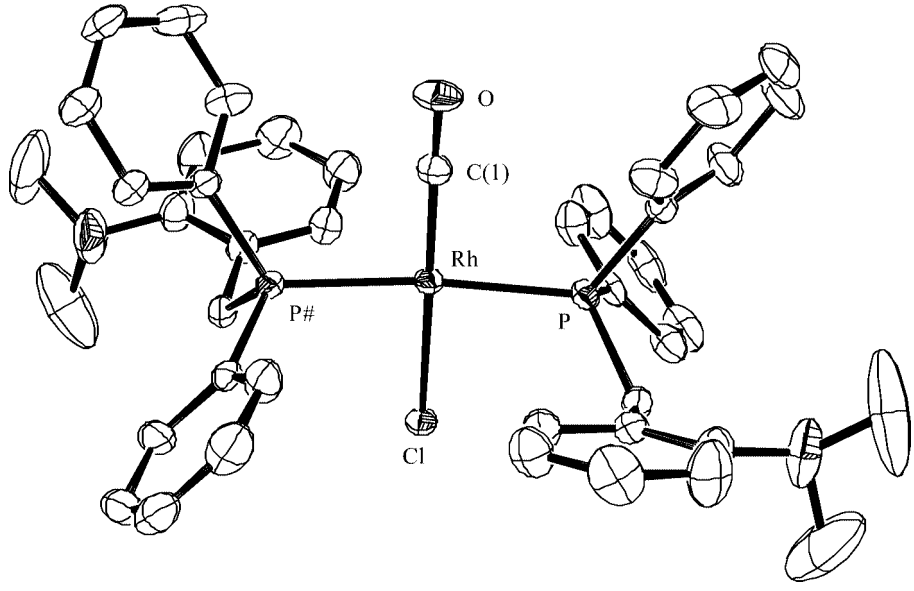


Figure 3. ORTEP view of complex **IIIγ**. Thermal ellipsoids are drawn at the 50% probability level. H atoms are omitted for clarity.

 © 2006 Wiley-VCH Verlag GmbH & Co. KGaA, Weinheim 

Worth noting in the structure is that the γ-P,N ligand does not chelate the rhodium center, contrary to what has been reported for a variety of Cu, Ru, Pd, and Rh complexes with the related ligands $Ph_2PCH_2[o\text{-}C_6H_4\text{–}N(Me)\text{-}CH_2CH_2OH]$, $Ph_2P(o\text{-}C_6H_4\text{–}CH_2NHtBu)$, $Ph_2P(o\text{-}C_6H_4\text{–}CH_2NMe_2)$, and $PhP[o\text{-}C_6H_4\text{–}CH(Me)NMe_2]_2$, respectively.[25–28] All the above results show that the α- and γ-P,N ligands adopt the same coordination mode in rhodium chloride complexes and undergo an identical ligand redistribution process (see Scheme 3).

A different situation was observed in the case of rhodium complexes containing the **β-P,N** ligand. Indeed, as mentioned above, the infrared spectrum recorded under CO shows an absorption band at 1986 $cm^{-1}$ (see Figure 1), in addition to the two carbonyl bands at 2092 and 2011 $cm^{-1}$ attributed to **IIβ**. This band corresponds to complex **Iβ**, as proven by its independent preparation and characterization (see Exp. Sect.). The simultaneous presence of **Iβ** and **IIβ** suggests the existence of an equilibrium between the two complexes under CO. This equilibrium could be followed by running two dedicated $^{31}P\{^1H\}$ NMR experiments.

The first experiment was carried out under CO on a $CDCl_3$ solution containing $[RhCl(CO)_2]_2$ and the **β-P,N** ligand. The $^{31}P\{^1H\}$ NMR spectrum showed two doublets at $\delta$ = 56 ppm [$^1J_{(Rh,P)}$ = 168 Hz] and at $\delta$ = 21 ppm [$^1J_{(Rh,P)}$ = 122 Hz] in ca. 1:2.5 ratio. The signal at $\delta$ = 56 ppm corresponds to complex **Iβ**, as verified by comparison with an authentic sample. Following the evidence provided by the IR spectrum (vide supra), the second resonance is assigned to the dicarbonyl complex **IIβ**. The second experiment was carried out under a higher CO pressure (20 bar) on a $CDCl_3$ solution containing complex [RhCl(COD)(**β-P,N**)], **3**, readily formed in situ from $[RhCl(COD)]_2$ and **β-P,N**. In this case, we observed only the doublet related to complex

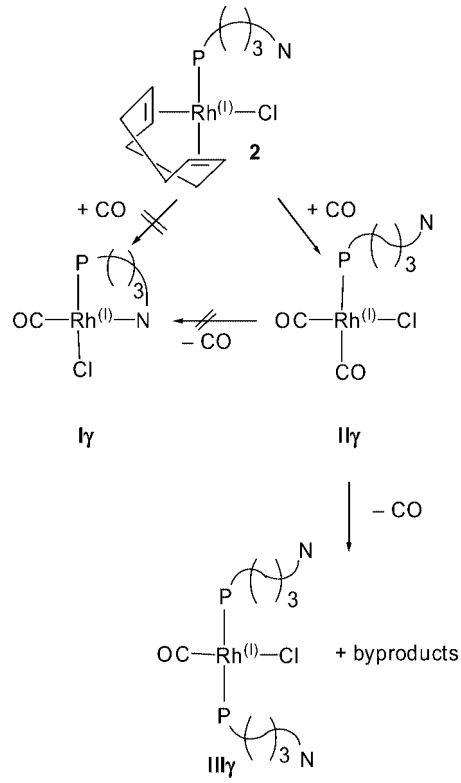


Scheme 3.

**IIβ** and no signal at $\delta$ = 56 ppm [see spectra (a) and (b), Figure 4].

After keeping the NMR solution pressurized with CO for 14 h, it was surprising to observe a new broad doublet at $\delta$ = 19 ppm [with $^1J_{(Rh,P)}$ = 168 Hz], named **II′β**, [see spectrum (c), Figure 4]. Tentatively, we attribute this broad

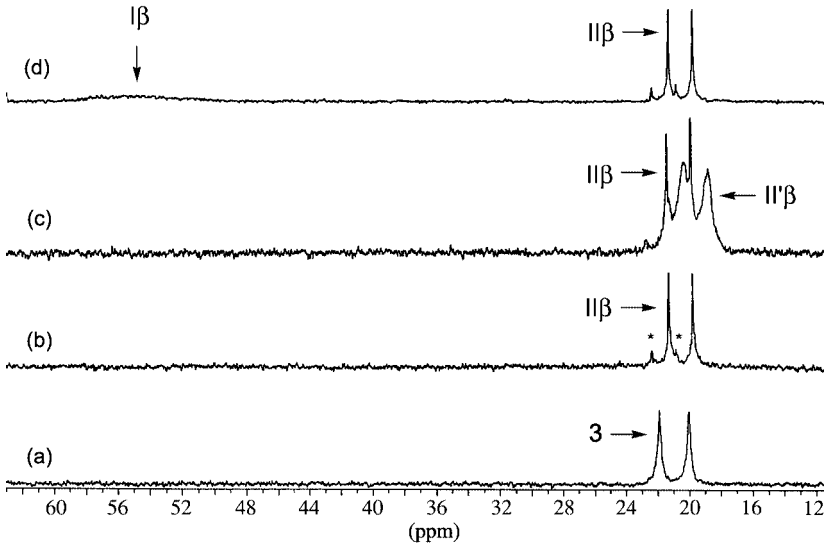


Figure 4. $^{31}P\{^1H\}$ HPNMR spectra under CO pressure of complex **3** in $CDCl_3$ solution. (a) Under $N_2$, (b) under 20 bar of CO, after 3 min, (c) under 20 bar of CO, after 14 h, (d) after depressurization. The asterisk denotes a small amount of a unidentified rhodium compound.

 © 2006 Wiley-VCH Verlag GmbH & Co. KGaA, Weinheim 

resonance to a pentacoordinate $Rh^I$ complex resulting from a further rhodium carbonylation of **IIβ** at this high CO pressure, although we have no further spectroscopic evidence to support this assignment at the moment. Depressurization of the NMR tube and purging the solution from dissolved CO with a dinitrogen stream removed the signal due to **II′β** and restored the equilibrium between complexes **Iβ** and **IIβ** [see spectrum (d), Figure 4]. The above IR and NMR observations are summarized in Scheme 4.

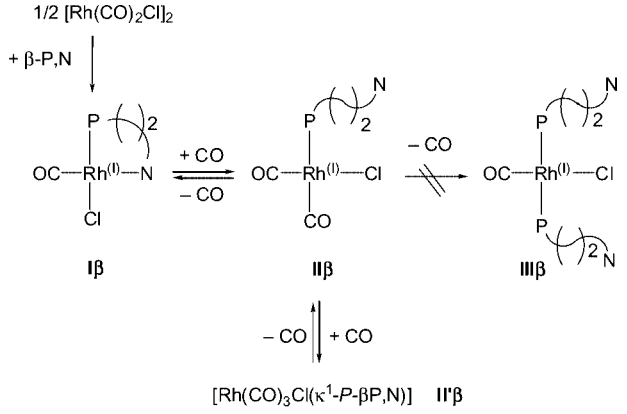


Scheme 4.

Both experiments confirm the occurrence of an equilibrium between **Iβ** and **IIβ** depending on the CO pressure as well as the hemilabile character of the **β-P,N** ligand in $Rh^I$ complexes. The combined IR and HPNMR experiments unambiguously prove the preference for keeping the amino group uncoordinated, under high CO pressure, in both β- and γ-P,N $Rh^I$ complexes, as previously shown for the related α-P,N $Rh^I$ complexes, resulting in a selective $\kappa^1$-P coordination mode. We now wish to examine the effects of the dangling amine group on the catalytic properties of the Rh-P,N hydroformylation.

## Catalytic Styrene Hydroformylation with Rh-Amino-Phosphane Complexes

The catalytic properties of different systems obtained from either $[RhCl(COD)]_2$ or $[Rh(acac)(CO)_2]$ and a variety of amino-phosphane ligands (see Scheme 5) in styrene hydroformylation tests are shown in Table 2.

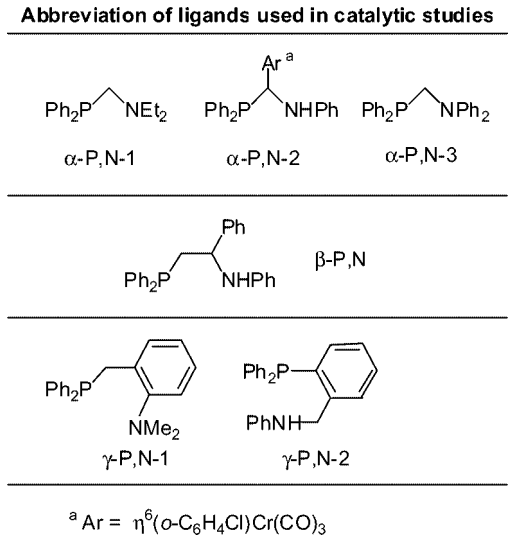


Scheme 5.

All catalytic runs were monitored by periodical withdrawal of aliquots from the autoclave. The conversion was found to be essentially linear with time, without any induction period. Thus, each reported TOF is obtained from a plot obtained by using several data points and is affected by a small error (ca. ±5%, see experimental section for details). All investigated catalysts afforded complete chemoselectivities (no product other than aldehydes are observed) and essentially the same regioselectivity, namely ca. 9:1 in favor of the branched product, which is standard for styrene hydroformylation with rhodium catalysts.[29]

A blank experiment carried out with $[RhCl(COD)]_2$ and $PPh_3$ (run 1) showed no activity whatsoever under our mild catalytic conditions. As previously reported,[30] the transformation of the chloride precursor to the catalytically active hydride complex requires an external base to trap the HCl equivalent which forms as a by-product during the initial $H_2$ activation step. The addition of one equivalent of $Ph_2NH$ or $NEt_3$ as an external base to the previous $PPh_3$-based catalyst led to a weak catalytic activity (run 2). When an amino group, on the other hand, is incorporated into the tertiary phosphane ligand (runs 3 to 7), a similar or

Table 2. Activity of $Rh^I$-P,N complexes in styrene hydroformylation catalysis.

| Run[a] | Catalytic precursor | Ligand (1 equivalent) | TOF[b] [$h^{-1}$] | b/l ratio[c] |
|---|---|---|---|---|
| 1 | $[RhCl(COD)]_2$ | $PPh_3$ | <1 | – |
| 2a | $[RhCl(COD)]_2$ | $PPh_3$ + $Ph_2NH$ | 4±0.2 | 88:12 |
| 2b | $[RhCl(COD)]_2$ | $PPh_3$ + $NEt_3$ | 10±0.5 | 87:13 |
| 3a | $[RhCl(COD)]_2$ | $Ph_2P(o\text{-}C_6H_4\text{–}CH_2NHPh)$ (**γ-P,N-2**) | 4±0.2 | 91:9 |
| 3b | $[RhCl(COD)]_2$ | $Ph_2PCH_2$ ($o\text{-}C_6H_4\text{–}NMe_2$) (**γ-P,N-1**) | 8±0.4 | 92:8 |
| 4 | $[RhCl(COD)]_2$ | $Ph_2PCH_2CH(Ph)NHPh$ (**β-P,N**) | 13±1 | 91:9 |
| 5 | $[RhCl(COD)]_2$ | $Ph_2PCH_2NPh_2$ (**α-P,N-3**) | 15±1 | 89:11 |
| 6 | $[RhCl(COD)]_2$ | $Ph_2PCH(Ar)NHPh$[d] (**α-P,N-2**) | 42±2 | 89:11 |
| 7 | $[RhCl(COD)]_2$ | $Ph_2PCH_2NEt_2$ (**α-P,N-1**) | 230±12 | 91:9 |

[a] Conditions: $[RhCl(COD)]_2$ ($2.62\times10^{-2}$ mmol) or $[Rh(acac)(CO)_2]$ ($5.23\times10^{-2}$ mmol), styrene/Rh = 1000, $CHCl_3$ (35 mL), 55 °C, *p*(syngas) = 600 psi. [b] TOF calculated from the slope of the conversions as a function of time. [c] Regioselectivity determined after complete conversion or from initial conversion rate for the faster catalytic reactions. [d] Ar = $\eta^6(o\text{-}C_6H_4Cl)Cr(CO)_3$.

 © 2006 Wiley-VCH Verlag GmbH & Co. KGaA, Weinheim 

higher (quite substantial in some cases) increase of catalytic activity resulted. Although the formation of a very active phosphane-free carbonyl species could be envisaged during the ligand scrambling process for the γ-amino-phosphane complexes **IIγ** (see Scheme 3), the lower activities observed with the complexes (runs 3a,b) indicate that either this scrambling process does not take place under the catalytic conditions (high CO pressure) or that the species formed by such a process does not possess a very high catalytic activity. The conversion rate became progressively greater as the number of carbon atoms in the ligand backbone bridging the P and N donor ends decreased from 3 to 1. A jump in activity was particularly evident on going from the γ- (3 carbon atoms) to the α-P,N ligand (1 carbon atom), with essentially identical Brønsted basicities for the dangling amino groups (runs 3a, 4, and 6). The effects of the amine basicity on the catalyst activity were then investigated.

### Nitrogen Basicity

A comparison between runs 5 and 7 shows that when the uncoordinated $NPh_2$ moiety in the α-P,N ligand is replaced by the more basic $NEt_2$ unit, the activity (TOF) increases dramatically from 15 to 230 $h^{-1}$. A similar, albeit more moderate, effect is also observed for a similar change in γ-P,N ligands in which the amino group is farther from the metallic center (see run 3a and 3b). These observations highlight the fact that the presence of an uncoordinated basic function in proximity to the metal center has a beneficial effect on the overall catalytic activity. A similar activity/basicity relationship for an uncoordinated amine function was pointed out by Reetz et al.,[12] who reported that the activity of rhodium cationic complexes in styrene or octene hydroformylation increased significantly when the dppp ligand [dppp = $Ph_2P(CH_2)_3PPh_2$] was replaced by an amino-diphosphane ligand [$Ph_2PCH_2N(Ph)CH_2PPh_2$], in which the nitrogen atom remains uncoordinated. It is to be noted that this conclusion is exactly opposite to that of Abu-Gnim and Amer, although both the ligands and conditions employed by them are apparently quite similar to ours.[11] It is possible that such a divergence comes from Amer's conclusion, which is based on the TON values. Such data are obviously less significant than the related TOF and, in addition, have been calculated from only one catalytic experiment per ligand used, with different reaction times as a function of the ligand.[11] Our straightforward interpretation of the activity results presented in Table 3 is based on the fact that all P,N ligands display an uncoordinated amine function under catalytic conditions, as demonstrated above. Additionally, the presence of the free internal base is not devoid of consequence for the catalytic efficiency because the whole system becomes more efficient as the P–N distance decreases, respectively going from γ-, β- to α-P,N ligands, and as its basicity increases.

### Rhodium Acetylacetonate Catalyst

Under the assumption that the HCl molecule originating from the chloride catalyst precursor and $H_2$ is scavenged by the dangling amine function, the latter would be converted into an ammonium function. Thus, the active catalyst would turn over in the ammonium form, rather than in the free amine form. In order to check the effect of this protonation process on the catalytic activity, experiments have also been carried out using [Rh(acac)$(CO)_2$] as the catalytic precursor. This allows the uncoordinated amine to remain in the neutral form during the catalytic cycle, since the active hydride species forms with elimination of acetylacetone rather than HCl. These experiments were only carried out with the α-P,N ligands, and the results are collected in Table 3. Generally, [Rh(acac)$(CO)_2$] is known to be a better catalytic precursor than [RhCl(COD)]$_2$ and, indeed, a comparison between runs 1 (Table 2) and 8 (Table 3) shows that this is true also in our case.

The activity in the presence of $PPh_3$ (see run 8, Table 3) remains nevertheless lower than in the presence of the α-P,N ligands (see runs 9, 10, and 11, Table 3), highlighting the beneficial effect of the free amine on the catalysis rate-determining step. We then ran an additional catalytic experiment which consisted of the addition of one equivalent of $NEt_3$ into the **α-P,N-3** rhodium chloride catalytic system. This led to better conversions (TOF = 220 $h^{-1}$, run 12) than the $NEt_3$-free system (TOF = 15 $h^{-1}$, run 5), and rather close to those obtained with the Rh-acetylacetonate catalytic precursor (TOF = 285 $h^{-1}$, run 10).

## Discussion

The new results reported in this contribution show that all P,N ligands are $\kappa^1$-P coordinated to $Rh^I$ under hydroformylation conditions, no matter the distance between the N and P atoms, and that the catalytic activity is enhanced by the proximity of the amine function and by its basicity. The role of the free amine group can be proposed at two different levels. First, we recall that no induction time is ob-

Table 3. Activity of α-P,N-based $Rh^I$ complexes in styrene hydroformylation catalysis.

| Run[a] | Catalytic precursor | Ligand (1 equivalent) | TOF[b] [$h^{-1}$] | b/l ratio |
|---|---|---|---|---|
| 8 | Rh(acac)$(CO)_2$ | $PPh_3$ | 130 ± 7 | 93:7 |
| 9 | Rh(acac)$(CO)_2$ | $Ph_2PCH(Ar)NHPh$[b] | 170 ± 9 | 88:12 |
| 10 | Rh(acac)$(CO)_2$ | $Ph_2PCH_2NPh_2$ | 285 ± 13 | 90:10 |
| 11 | Rh(acac)$(CO)_2$ | $Ph_2PCH_2NEt_2$ | 325 ± 16 | 92:8 |
| 12 | [RhCl(COD)]$_2$ | $Ph_2PCH_2NPh_2$ + $NEt_3$[c] | 220 ± 11 | 90:10 |

[a] Conditions described in Table 2. [b] Ar = $\eta^6$(*o*-$C_6H_4Cl$)$Cr(CO)_3$. [c] 1 Equivalent relative to the rhodium complex.

 © 2006 Wiley-VCH Verlag GmbH & Co. KGaA, Weinheim 

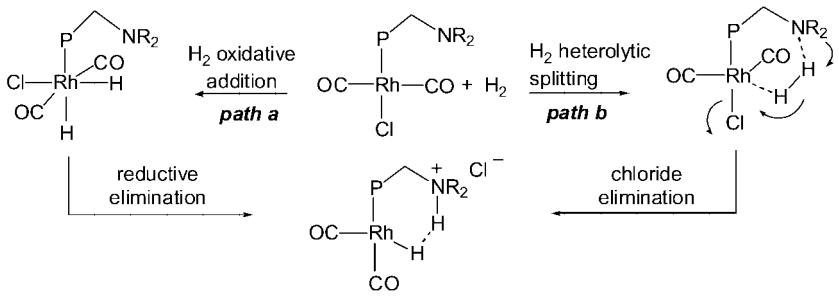


Scheme 6.

served for the generation of the catalytically active species. In order to generate the active Rh–H species, rhodium(I) chloride precursors typically show induction periods in the catalytic process because of the need to eliminate HCl after the dihydrogen oxidative addition to rhodium. The addition of an external amine favors this process and reduces or even eliminates the induction time.[30] In our own hands, $[RhCl(COD)]_2$ still affords a very active catalyst in the absence of any added phosphane ligand under the same conditions given in Table 3, but only after quite a long induction period (>3 h). It seems therefore reasonable to us that the dangling nitrogen function plays an important role in assisting the rapid formation of the Rh–H active species. We see two possible ways by which this "assistance" effect can operate. A first possibility involves, after the initial $H_2$ oxidative addition, the N-assisted promotion of HCl elimination from the intermediate $Rh^{III}$ dihydride (see Scheme 6, path a). On the other hand, an alternative mechanistic pathway could involve heterolytic cleavage of $H_2$ (see Scheme 6, path b). Indeed, many authors have proposed a base-assisted $H_2$ heterolytic splitting in relation to other catalytic processes (i.e. involving Ru,[31–34] Ir,[35] Pd,[36] and Rh[37]) over the last few years. Heterolytic splitting of $H_2$ is also shown by computational methods to be kinetically and thermodynamically more favorable than the classical dihydrogen oxidative addition for the interaction with the rhodium complex $Rh(PH_3)_2(HCO_2)$ in the presence of $NH_3$.[38] Consequently, a similar $H_2$ heterolytic activation process seems a reasonable possibility also for the rhodium hydroformylation catalytic systems here described, in particular with the basic $Ph_2PCH_2NEt_2$ ligand (see Scheme 6). In either case, the HCl produced during the activation step is likely to be trapped by the nearby amine function. However, this activation step cannot be enhancing the activity, because the chloride precursor is not the resting state of the catalytic cycle.

The second level where the external base is likely to have an effect concerns the rate-determining step of the catalytic cycle (*rds*), namely the hydrogenolysis of the rhodium acyl intermediate. Detailed kinetic and mechanistic studies carried out by van Leeuwen et al. have shown that the rate-determining step in rhodium catalyzed hydroformylation may be either the olefin insertion into the Rh–H bond or the Rh-acyl hydrogenolysis, depending on the ligand nature and on the conditions.[29,39] In the cases at hand, we have collected preliminary evidence, via H/D isotopic exchange experiments, that the hydrogenolysis is rate determining. Details of these studies are provided in a separate paper[40] In addition, no evidence for the accumulation of a hydride intermediate (as required if the olefin insertion step were rate determining) was obtained by HPNMR (vide infra).

We must now attempt to rationalize two different observations: (*i*) a proximal *free* amine function has a beneficial effect (i.e. see the experiments carried out with the acetylacetonate catalyst or with the chloride in the presence of an external base, cf. runs 12 and 2b); (*ii*) the beneficial effect is observed even when the dangling amine function is likely turned into an ammonium derivative (i.e. see all the experiments carried out with the chloride catalyst, without the use of an external base, runs 3–7).

Concerning the first point, we assume that the action of the uncoordinated amine function on the *rds* is similar to that proposed above for the activation of the chloride precursor, see Scheme 7. The greater activity could in principle be interpreted on the basis of two possible mechanistic routes. The first one (path a, Scheme 7) involves $H_2$ oxidative addition followed by aldehyde reductive elimination. On the basis of this mechanism, we would argue that the free amine ligand somehow helps either one or both of these elementary steps. However, the lack of interaction between the rhodium-acyl species and the dangling nitrogen moiety does not allow an obvious rationalization of the observed

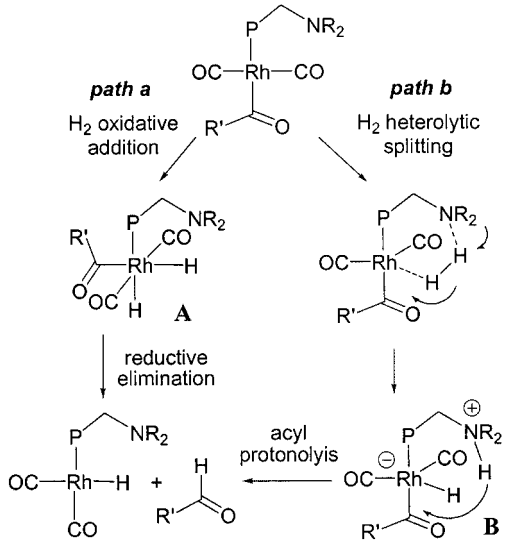


Scheme 7.

 © 2006 Wiley-VCH Verlag GmbH & Co. KGaA, Weinheim 

effect. The second pathway (path b, Scheme 7) involves a base-assisted heterolytic $H_2$ splitting, leading to a zwitterionic rhodium monohydride intermediate. The latter would be stabilized by a P,N-ligand bearing a uncoordinated ammonium end. According to this mechanism, increasing the amine basicity could lower the activation barrier leading to the zwitterionic intermediate, thereby accelerating the *rds*. The aldehyde would then be formed by protonolysis of the rhodium-acyl bond by the dangling ammonium group, rather than by a reductive elimination process.

Clearly, the accelerating effect just discussed cannot be provided when the amine function is protonated. However, it is possible to envisage a proton exchange process, whereby the ammonium hydride derivative **B** formed during the catalyst activation step may equilibrate with the amine–chloride precursor **A** to yield an inactive ammonium chloride species **D** and an active amine–hydride complex **C**, identical to that obtained from the acetylacetonate precursor (see Scheme 8). Consequently, the different accelerating effect that is observed for the chloride systems in the absence of external base (runs 3–7) may be attributed to the presence of the equilibrium species **D**, which would again operate through the same mechanism of Scheme 7, the extent of the effect being a function of the equilibrium amount of that species. Acyl complexes are known to give hydrogenolysis even without the assistance of an internal amine function. However, the presence of an internal base increases the activity of the rhodium catalyst, to a growing extent as its basicity increases (see runs 8 through 11) and could then promote the hydrogenolysis step through a mechanism encompassing the $H_2$ heterolytic splitting.

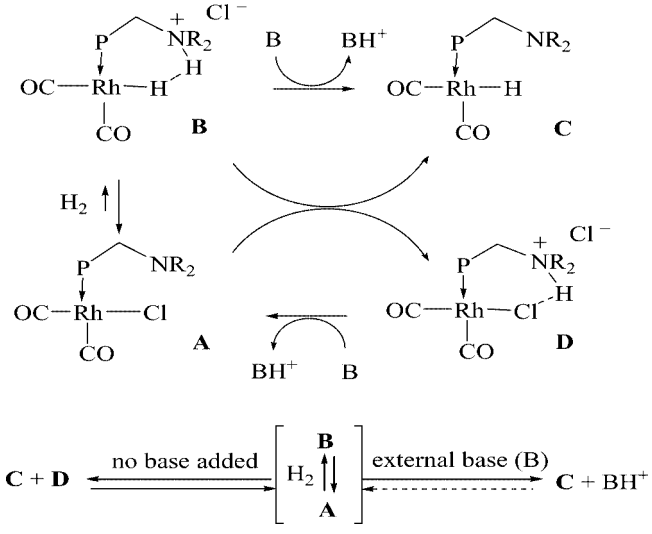


Scheme 8.

In order to obtain further mechanistic information, we have carried out a $^1H$ HPNMR study of the $[RhCl(COD)]_2$-$Ph_2PCH_2NPh_2$ mixture in $CDCl_3$ under syngas (20 atm), approaching the experimental conditions of the catalytic runs. No Rh–H species could be observed under these conditions. This observation suggests that the **A**/**B** equilibrium proposed in Scheme 8 is only weakly shifted to the Rh–H hydride species **B**. The most active species **C** would then form only in minor proportion, leading to a low catalytic activity. According to Scheme 8, the amount of **C** could be increased only upon addition of a strong external base. On the other hand, the catalytic formation of aldehyde was immediately observed after the styrene introduction into the HPNMR tube, although the hydride resonance remained undetected. The latter result is consistent with the proposition that the olefin insertion step is not the *rds* for this system.

## Conclusions

The IR and $^{31}P$ HPNMR studies reported in this contribution have shown that the coordination properties of a variety of amino-phosphane ligands in $Rh^I$ complexes depend on the length of the P,N backbone. The γ-P,N ligands behave as κ¹-*P*-α-amino-phosphanes, whereas the β-P,N amino-phosphane leads to a solution equilibrium between κ²-*P,N* and κ¹-*P*-coordination modes, depending on the CO pressure. Under hydroformylation conditions, however, all the investigated Rh-amino-phosphane precatalysts exist as monodentate $[RhCl(CO)_2(\kappa^1\text{-}P\text{-}P,N)]$ complexes with a noncoordinated nitrogen function. The reported catalytic runs demonstrate that the dangling amino group favors the formation of the Rh–H active species when using $[RhCl(COD)]_2$ as the catalytic precursor and that both the basicity of the nitrogen end and its distance from the metal center have a crucial effect on the turnover frequency. The hydride formation could occur either by $H_2$ heterolytic splitting (assisted by the nearby amino group) or by a classical oxidative addition (with the amino group assisting the subsequent HCl reductive-elimination). Theoretical calculations are currently in progress in order to elucidate the preferred mechanistic pathway. We also suggest that the dangling amino group could take an additional mechanistic function as promoter of the hydrogenolysis step through a second heterolytic $H_2$ splitting. Isotopic H/D exchange studies under catalytic conditions using chiral P,N ligands, which are reported in a separate contribution,[40] provide additional mechanistic details in hydroformylation catalysis via rhodium amino-phosphane systems.

## Experimental Section

All manipulations were carried out under purified argon using standard Schlenk techniques. All solvents were dried and deoxygenated prior to use by standard methods. Standard pressure NMR measurements [$^1H$, $^{13}C\{^1H\}$, and $^{31}P\{^1H\}$] were carried out with a Bruker DRX300 spectrometer in $CDCl_3$ at room temperature. The peak positions are reported with positive shifts in ppm downfield of TMS as calculated from the residual solvent peaks [$^1H$ and $^{13}C\{^1H\}$] or downfield of external 85% $H_3PO_4$ ($^{31}P$). The high-pressure NMR (HPNMR) spectra were recorded by using a standard 10-mm probe tuned to $^{31}P$ and $^1H$ nuclei on a BRUKER AC 200 spectrometer operating at 81 MHz. The HPNMR experiments were performed in a 10-mm sapphire tube (Saphikon Inc., NH) charged with a solution of precatalyst (10 mg of P,N ligand, plus

 © 2006 Wiley-VCH Verlag GmbH & Co. KGaA, Weinheim 

0.5 equiv. of Rh precursor) in $CDCl_3$ (2 mL) under nitrogen, after which the first spectrum (reference) was recorded at room temp. The tube was then pressurized with CO 20 atm at room temp. The variable temperature experiment was started on a Bruker AC 200 spectrometer, recording a sequence of spectra up to 80 °C. After a chosen time, the probe was cooled to room temperature and another spectrum was recorded. The last spectrum was taken after venting the tube and flushing with nitrogen. The coordinated 1,5-COD (1,5-cyclooctadiene) C and H nuclei are labeled from 1 to 8, $C^1$ and $C^2$ being *trans* to P.

**CAUTION:** *All manipulations involving high pressure are potentially hazardous. Safety precautions must be taken at all stages of NMR studies involving high pressure tubes.*

All IR spectra were recorded in $CH_2Cl_2$ solution with a Bruker IFS 66 V spectrophotometer with KBr optics and the absorption vibration bands are given in $cm^{-1}$. Elemental analyses were carried out by the analytical service of the L.S.E.O. with a Fisons Instruments EA1108 analyzer. The commercial compounds $PPh_3$, $Ph_2NH$, $[RhCl(COD)]_2$, $[Rh(acac)(CO)_2]$, and $[Rh(CO)_2Cl]_2$ were used as received. The ligands $Ph_2PCH_2NEt_2$, $Ph_2PCH_2NPh_2$, $Ph_2PCH(Ar)NHPh$ {Ar = *o*-$C_6H_4Cl$ or *o*-$C_6H_4Cl[Cr(CO)_3]$}, $Ph_2PCH_2CH(Ph)NHPh$, $Ph_2PCH_2$(*o*-$C_6H_4$–$NMe_2$) (γ-P,N-1), and $Ph_2P$(*o*-$C_6H_4$–$CH_2NHPh$) (γ-P,N-2) were prepared according to literature.[13,14,17,41–44] The synthesis of complex [RhCl(COD)(α-P,N)] **1** with α-P,N=$Ph_2PCH$(*o*-$C_6H_4Cl[Cr(CO)_3]$)NHPh has previously been described.[18]

### Synthesis of [RhCl(COD)(P,N)] Complexes

The syntheses of the [RhCl(COD)(P,N)] complexes were generally carried out as follows. A mixture of $[RhCl(COD)]_2$ and P,N ligand were dissolved in $CH_2Cl_2$ (5 mL). The yellow solution obtained was stirred for 1 h. Addition of pentane afforded yellow or orange microcrystals which were isolated and dried in vacuo.

**[RhCl(COD)(γ-P,N-1)] (2):** $[RhCl(COD)]_2$ (84.4 mg, 0.171 mmol), **γ-P,N-1** (109 mg, 0.341 mmol) gave 144 mg of **2**, yield 75%. $^1H$ NMR: $\delta$ = 8.81–7.12 (m, 14 H, arom.), 5.61 (s, 2 H, $C_8H_{12}$, olefinic protons, *trans* to P), 4.21 [d, $^2J_{(P,H)}$ = 11.6 Hz, 2 H, $PCH_2$], 2.93 (s, 2 H, $C_8H_{12}$, olefinic protons, *cis* to P), 2.48 (s, 3 H, $NCH_3$), 2.49–1.86 (m, 8 H, $C_8H_{12}$, aliph. H) ppm. $^{31}P\{^1H\}$ NMR: $\delta$ = 30.1 [d, $^1J_{(Rh,P)}$ = 150 Hz] ppm. $^{13}C\{^1H\}$ NMR: $\delta$ = 154.1–120.2 (m, 18 C, arom.), 104.3 (m, 2 C, $C^{1,2}$), 70.9 (s, 1 C, $C^5$), 70.7 (s, 1 C, $C^6$), 45.3 (s, 2 C, $NCH_3$), 33.3 (s, 2 C, $C^{3,8}$), 29.3 (s, 2 C, $C^{4,7}$), 28.5 [d, $^2J_{(P,C)}$ = 21 Hz, 1 C, $PCH_2$] ppm. $C_{29}H_{34}ClNPRh$ (565.92): calcd. C 61.55, H 6.05, N 2.48; found C 61.09, H 5.66, N 3.09.

**[RhCl(COD)(β-P,N)] (3):** $[RhCl(COD)]_2$ (85 mg, 0.172 mmol) and **β-P,N** (131 mg, 0.344 mmol) gave 152 mg of **3**, yield 80%. $^1H$ NMR: $\delta$ = 8.09–6.72 (m, 20 H, arom.), 7.02 [d, $^3J_{(P,H)}$ = 7 Hz, 1 H, NH, exchange with $D_2O$], 4.78 (m, 1 H, $NCH^c$), 3.36 [dt, $^2J_{(P,H^a)}$ = $^3J_{(H^a,H^b)}$ = 14, $^3J_{(H^a,H^c)}$ = 4 Hz, 1 H, $PCH^a$], 2.64 [t, $^2J_{(P,H^b)}$ = $^3J_{(H^b,H^a)}$ = 14 Hz, 1 H, $PCH^b$], 2.38–1.75 (m, 6 instead of 8 H, $C_8H_{12}$, aliph. H) ppm. The olefinic protons were not observed at room temp. due to an olefin rotation dynamic process. $^{31}P\{^1H\}$ NMR: $\delta$ = 21.7 [d, $^1J_{(Rh,P)}$ = 150 Hz] ppm. $^{13}C\{^1H\}$ NMR: $\delta$ = 147.1–114.9 (m, 24 C, arom.), 105.0 (s, very br., 2 C, $C^{1,2}$ of COD), 71.0 (s, very br., 2 C, $C^{5,6}$ of COD), 57.1 (s, 1 C, NCH), 37.7 [d, $J_{(P,C)}$ = 22 Hz, 1 C, PCH], 31.3 (br. s, 4 C, $C^{3,4,7,8}$ of COD) ppm. IR: $\tilde{\nu}$ = 3324 (m, $\nu_{NH}$) $cm^{-1}$. $C_{34}H_{36}ClNPRh{\cdot}0.5CH_2Cl_2$ (670.45): calcd. C 61.75, H 5.52, N 2.09; found C 62.15, H 5.77, N 2.23.

**[RhCl(CO)(β-P,N)] (Iβ):** $[RhCl(CO)_2]_2$ (36.1 mg, 0.093 mmol) and **β-P,N** (71 mg, 0.186 mmol) gave 76 mg of **Iβ**, 57% yield. $^1H$ NMR: $\delta$ = 8.22–6.83 (m, 20 H, arom.), 6.84 [d, $^3J_{(P,H)}$ = 10.8 Hz, 1 H, NH, exchange with $D_2O$], 3.91 (m, 1 H, $NCH^c$), 3.58 [dt, $^2J_{(P,H^a)}$ = $^3J_{(H^a,H^b)}$ = 14, $^3J_{(H^a,H^c)}$ = 4 Hz, 1 H, $PCH^a$], 2.86 [dt, $^2J_{(P,H^b)}$ = $^3J_{(H^b,H^a)}$ = 14, $^3J_{(H^b,H^c)}$ = 2 Hz, 1 H, $PCH^b$] ppm. $^{31}P\{^1H\}$ NMR: $\delta$ = 56.4 [d, $^1J_{(Rh,P)}$ = 168 Hz] ppm. $^{13}C\{^1H\}$ NMR: $\delta$ = 188.5 [dd, $^1J_{(Rh,C)}$ = 74, $^2J_{(P,C)}$ = 18 Hz according to CO *cis* to P,[45] 1 C, C=O], 145.7–125.5 (m, 24 C, arom.), 8.51 [d, $^2J_{(P,C)}$ = 8.6 Hz, 1 C, NCH], 38.8 [d, $J_{(P,C)}$ = 26 Hz, 1 C, PCH] ppm. IR: $\tilde{\nu}$ = 1986 $cm^{-1}$ (vs, $\nu_{CO}$) and $\nu_{NH}$ not observed. $C_{27}H_{24}ClNOPRh{\cdot}0.5CH_2Cl_2$ (590.28): calcd. C 55.90, H 4.24, N 2.37; found C 55.64, H 4.38, N 2.54.

***trans*-[RhCl(CO)(γ-P,N-1)$_2$] (IIIγ):** $[RhCl(CO)_2]_2$ (39 mg, 0.098 mmol) and **γ-P,N-1** (125 mg, 0.392 mmol) gave 113 mg of **IIIγ**, yield 71%. $^1H$ NMR: $\delta$ = 8.39–6.93 (m, 28 H, arom.), 4.40 (t not resolved, 4 H, $PCH_2$), 2.30 (s, 6 H, $NCH_3$). $^{31}P\{^1H\}$ NMR: $\delta$ = 31.20 [d, $^1J_{(Rh,P)}$ = 126 Hz] ppm. $^{13}C\{^1H\}$ NMR: $\delta$ = 188.0 [dt, $^1J_{(Rh,C)}$ = 76, $^2J_{(P,C)}$ = 14 Hz according to CO *cis* to both P,[45] 1 C, C=O], 154.2–120.1 (m, 36 C, arom.), 45.2 (s, 4 C, $NCH_3$). 26.8 [t, $J_{(P,C)}$ = 27 Hz, 2 C, $PCH_2$] ppm. IR: $\tilde{\nu}$ = 1974 (vs, $\nu_{CO}$) $cm^{-1}$. $C_{43}H_{44}ClN_2OP_2Rh$ (805.13): calcd. C 64.15, H 5.51, N 3.48; found C 64.46, H 5.55, N 3.34.

**Formation of the Unstable *cis*-[RhCl(CO)$_2$(γ-P,N-1)] (Iiγ). Method A:** A mixture of $[RhCl(CO)_2]_2$ (19.5 mg, 0.050 mmol) and **γ-P,N-1** (32 mg, 0.098 mmol) was dissolved in $CDCl_3$ (0.7 mL). After 10 min, the mixture was analyzed by $^1H$ and $^{31}P\{^1H\}$ spectroscopy showing **IIγ** as the major complex. $^1H$ NMR: $\delta$ = 7.75–7.03 (m, 14 H, arom.), 4.27 [d, $^2J_{(P,H)}$ = 12 Hz, 2 H, $PCH_2$], 2.34 (s, 6 H, $NCH_3$) ppm. $^{31}P\{^1H\}$ NMR: $\delta$ = 31.1 [14%, d, $^1J_{(Rh,P)}$ = 125 Hz] ppm for **IIIγ** and 27.4 [86%, d, $^1J_{(Rh,P)}$ = 126 Hz] ppm for **IIγ**. After ca. 0.75 h and 12 h, the $^{31}P\{^1H\}$ NMR gave 1:4.5 and 1:2 ratios respectively for the **IIIγ/IIγ** mixture complexes. The above procedure was repeated in $CH_2Cl_2$ instead of chloroform. The atmosphere was then purged with CO and monitored by infrared. After 2 min, the pure dicarbonyl was formed. No $^{13}C$ NMR spectrum was recorded due to the increase of the ratio **IIIγ/IIγ** with time. The above procedure was repeated in $CH_2Cl_2$ and a slow diffusion of pentane to the yellow solution afforded poor quality yellow crystals which were identified as the complex **IIIγ**.

**Method B:** CO was introduced into a solution of [RhCl(COD)(**γ-P,N-1**)], **1a** (35 mg, 0.061 mmol) in $CH_2Cl_2$ (4 mL). Under CO and after 2 min, the IR spectrum showed only the pure dicarbonyl complex **IIγ** at 2092 and 2010 $cm^{-1}$ (both vs, $\nu_{CO}$), and this had not changed after two days under CO.

**Formation of the Unstable *cis*-[RhCl(CO)$_2$(β-P,N)] (Iiβ). Method A:** CO was introduced into a solution of [RhCl(COD)(β-P,N)] **1b** (42 mg, 0.071 mmol) in $CH_2Cl_2$ (4 mL). An IR spectrum was recorded after 2 min and showed a mixture of monocarbonyl complex **Iβ** at 1986 $cm^{-1}$ and dicarbonyl complex [RhCl(CO)$_2$(κ-*P*-P,N)] **IIβ** at 2011 and 2092 $cm^{-1}$. The ratio between the two complexes did not change after two days under CO.

**Method B:** A mixture of $[RhCl(CO)_2]_2$ (25.6 mg, 0.066 mmol) and β-P,N (54 mg, 0.131 mmol) was dissolved in $CDCl_3$ (1 mL). After 10 min, CO was introduced into the solution and the mixture was analyzed by $^1H$ and $^{31}P\{^1H\}$ NMR spectroscopy. The NMR spectra show a mixture of **IIβ** and **Iβ** in 1:2.5 ratio. $^1H$ NMR of **IIβ**: $\delta$ = 8.12–5.63 (m, 28 H, arom.), 5.78 [d, $^3J_{(P,H)}$ = 6 Hz, 2 H, NH, exchange with $D_2O$], 4.14 (m, 2 H, NCH), 3.58 (m, 2 H, $PCH^a$), 2.45 (m, 2 H, $PCH^b$) ppm. $^{31}P\{^1H\}$ NMR of **IIβ**: $\delta$ = 21.11 [d, $^1J_{(Rh,P)}$ = 122 Hz] ppm. No $^{13}C\{^1H\}$ NMR spectrum was recorded due to the low solubility of **IIβ** in $CDCl_3$ and $(CD_3)_2CO$.

**Crystal Structure Determination of Complex IIIγ:** Intensity data were collected with a Nonius Kappa CCD at 230 K. The structure was solved by the heavy atom method and refined by full-matrix

 © 2006 Wiley-VCH Verlag GmbH & Co. KGaA, Weinheim 

least-squares methods[46] with the aid of the WINGX program.[47] Non-hydrogen atoms were anisotropically refined. Hydrogen atoms were included in calculated positions and refined with a riding model. Crystallographic data for compound **IIIγ** are reported in Table 4.

Table 4. Crystal data and structure refinement for **IIIγ**.

| Compound | **IIIγ** |
|---|---|
| Formula | $C_{43}H_{44}ClN_2OP_2Rh$ |
| $M$ | 805.1 |
| $T$ [K] | 230(2) |
| Crystal system | monoclinic |
| Space group | $C2/c$ |
| $a$ [Å] | 13.9791(4) |
| $b$ [Å] | 17.7355(8) |
| $c$ [Å] | 17.4564(8) |
| $\beta$ [°] | 110.320(2) |
| $V$ [Å$^3$] | 4058.6(3) |
| $Z$ | 4 |
| $F(000)$ | 1664 |
| $D_{calc}$ [g/cm$^3$] | 1.318 |
| Diffractometer | Enraf–Nonius KappaCCD |
| Scan type | mixture of φ rotations and $\omega$ scans |
| $\lambda$ [Å] | 0.71073 |
| $\mu$ [mm$^{-1}$] | 0.599 |
| Crystal size [mm$^3$] | 0.6×0.5×0.5 |
| $\sin(\theta)/\lambda$ max. [Å$^{-1}$] | 0.65 |
| Index ranges | $h$: –17; 18 |
| | $k$: –22; 22 |
| | $l$: –18; 22 |
| Absorption correction | SCALEPACK |
| RC = reflections collected | 11009 |
| IRC = independent RC | 4587 [$R$(int) = 0.05] |
| IRCGT = IRC and [$I > 2\sigma(I)$] | 3262 |
| Refinement method | full-matrix least squares on $F^2$ |
| Data / restraints / parameters | 4587 / 0 / 228 |
| $R$ for IRCGT | $R_1$[a] = 0.0444, $wR_2$[b] = 0.0934 |
| $R$ for IRC | $R_1$[a] = 0.0779, $wR_2$[b] = 0.1044 |
| Goodness-of-fit[c] | 1.021 |
| Largest diff. peak and hole [e·Å$^{-3}$] | 0.47 and –1.02 |

[a] $R_1 = \Sigma(||F_o| - |F_c||)/\Sigma|F_o|$. [b] $wR_2 = \{\Sigma w(F_o^2 - F_c^2)^2/\Sigma[w(F_o^2)^2]^{1/2}\}$ where $w = 1/[\sigma^2(F_o^2) + (0.053P)^2]$, $P = [\max(F_o^2,0) + 2\times F_c^2]/3$. [c] Goodness of fit = $[\Sigma w(F_o^2 - F_c^2)^2/(N_o - N_v)]^{1/2}$.

CCDC-250351 contains the supplementary crystallographic data for this paper. These data can be obtained free of charge from The Cambridge Crystallographic Data Centre via www.ccdc.cam.ac.uk/data_request/cif.

**Catalytic Runs:** The hydroformylation reactions were carried out in a 300-mL stainless-steel Parr autoclave equipped with a magnetic drive, an internal glass vessel, and an immersion tube connected to a valve for solution withdrawals under pressure. The temperature was controlled by a rigid heating mantle and a single loop cooling coil. The autoclave was purged three times under vacuum/argon before introducing the catalytic solution. The 1:1 $CO/H_2$ mixture was prepared by mixing the pure gases in a 500-mL stainless-steel cylinder before introduction into the autoclave at the desired pressure (see Table 1 and Table 2). The zero time for kinetic runs was considered as the time at which the desired pressure was reached inside the autoclave. In order to maintain temperature and pressure conditions as constant as possible during each kinetic run, only a few mL of catalytic solution mixture were carefully withdrawn each time from the autoclave. The $CHCl_3$ or THF solvent was then rotary evaporated at room temperature and the yellow-orange residue was analyzed by $^1H$ and $^{13}C\{^1H\}$ NMR spectroscopy. The experimental error on the TOF determination was carried out from the TOF values obtained from three successive runs using three times the same solution for two different catalytic systems (run, 5 and 10). The experimental error for other catalytic runs has been estimated on the basis of the determination as above.

## Acknowledgments

This work was supported by COST D29 (WG009/03) and by the EC through the contracts HPRN-CT-2002–00176 (HYDROCHEM) and MRTN-CT-2003–503864 (AQUACHEM) and the contribution is kindly acknowledged. We are also grateful to the Ministère de la Recherche, the Centre National de la Recherche Scientifique (CNRS) and the Conseil Régional de Bourgogne for support of this work. J.-M. C. thanks the Ministère de la Recherche for a Ph. D. fellowship. HPNMR measurements have been possible through the NMR service of "FIRENZE HYDROLAB": a project sponsored by a generous grant by Ente Cassa di Risparmio di Firenze.

[1] E. Drent, P. Arnoldy, P. H. M. Budzelaar, *J. Organomet. Chem.* **1993**, *455*, 247–253.
[2] K. N. Gravilov, A. I. Polosukhin, *Russ. Chem. Rev.* **2000**, *69*, 661–682.
[3] P. Denis, A. Jean, J. F. Crizy, A. Mortreux, F. Petit, *J. Am. Chem. Soc.* **1990**, *112*, 1292–1294.
[4] H. Yang, M. Alvarez, N. Lugan, R. Mathieu, *J. Chem. Soc. Chem. Commun.* **1995**, 1721–1722.
[5] J.-X. Gao, T. Ikariya, R. Noyori, *Organometallics* **1996**, *15*, 1087–1089.
[6] C. Standfest-Hauser, C. Slugovc, K. Mereiter, R. Schmid, K. Kirchner, L. Xiao, W. Weissensteiner, *J. Chem. Soc., Dalton Trans.* **2001**, 2989–2995.
[7] T. B. Rauchfuss, J. L. Clements, S. F. Agnew, D. M. Roundhill, *Inorg. Chem.* **1977**, *16*, 775–778.
[8] D. M. Roundhill, R. A. Bechtold, S. G. N. Roundhill, *Inorg. Chem.* **1980**, *19*, 284–289.
[9] J. P. Collman, *Acc. Chem. Res.* **1968**, *1*, 136–143.
[10] F. Fache, E. Schultz, M. L. Tommasino, M. Lemaire, *Chem. Rev.* **2000**, *100*, 2159–2231.
[11] C. Abu-Gnim, I. Amer, *J. Mol. Catal.* **1993**, *85*, L275–L278.
[12] M. T. Reetz, S. R. Waldvogel, R. Goddard, *Tetrahedron Lett.* **1997**, *38*, 5967–5970.
[13] J. Andrieu, C. Baldoli, S. Maiorana, R. Poli, P. Richard, *Eur. J. Org. Chem.* **1999**, 3095–3097.
[14] J. Andrieu, J.-M. Camus, J. Dietz, P. Richard, R. Poli, *Inorg. Chem.* **2001**, *40*, 1597–1605.
[15] J. Andrieu, P. Richard, J.-M. Camus, R. Poli, *Inorg. Chem.* **2002**, *41*, 3876–3885.
[16] J. M. Camus, J. Andrieu, P. Richard, R. Poli, *Eur. J. Inorg. Chem.* **2004**, 1081–1091.
[17] J. Andrieu, J. Dietz, R. Poli, P. Richard, *New J. Chem.* **1999**, *23*, 581–583.
[18] J. M. Camus, J. Andrieu, P. Richard, R. Poli, C. Baldoli, S. Maiorana, *Inorg. Chem.* **2003**, *42*, 2384–2390.
[19] X. Liu, A. H. Eisenberg, C. L. Stern, C. A. Mirkin, *Inorg. Chem.* **2001**, *40*, 2940–2941.
[20] L. Dahlenburg, R. Götz, *J. Organomet. Chem.* **2001**, *619*, 88–98.
[21] M. Valentini, K. Selvakumar, M. Wörle, P. S. Pregosin, *J. Organomet. Chem.* **1999**, *587*, 244–251.
[22] A. Aghmiz, A. M. Masdeu-Bulto, C. Claver, D. Sinou, *J. Mol. Catal. A: Chem.* **2002**, *184*, 111–119.
[23] C. Saluzzo, J. Breuzard, S. Pellet-Rostaing, M. Vallet, F. Le Guyader, M. Lemaire, *J. Organomet. Chem.* **2002**, *643*, 98–104.
[24] M. L. Clarke, G. L. Holliday, A. M. Z. Slawin, J. D. Woollins, *J. Chem. Soc., Dalton Trans.* **2002**, 1093–1103.

 © 2006 Wiley-VCH Verlag GmbH & Co. KGaA, Weinheim 

[25] J. Andrieu, B. R. Steele, C. G. Screttas, C. J. Cardin, J. Fornies, *Organometallics* **1998**, *17*, 839–845.
[26] P. Crochet, J. Gimeno, S. Garcia-Granda, J. Borge, *Organometallics* **2001**, *20*, 4369–4377.
[27] G. A. Luinstra, P. H. P. Brinkmann, *Organometallics* **1998**, *17*, 5160–5165.
[28] I. Yamada, M. Ohkouchi, M. Yamaguchi, T. Yamagishi, *J. Chem. Soc., Perkin Trans. 1* **1997**, 1869–1873.
[29] P. W. N. M. Van Leeuwen, C. Claver (Eds.), *Rhodium Catalyzed Hydroformylation*, Kluwer, Dordrecht, **2000**, vol. 22.
[30] D. Evans, J. A. Osborn, G. Wilkinson, *J. Chem. Soc. (A)* **1968**, 3133–3142.
[31] H. S. Chu, C. P. Lau, K. Y. Wong, W. T. Wong, *Organometallics* **1998**, *17*, 2768–2777.
[32] T. Ohkuma, D. Ishii, H. Takeno, R. Noyori, *J. Am. Chem. Soc.* **2000**, *122*, 6510–6511.
[33] K. Abdur-Rashid, M. Faatz, A. J. Lough, R. H. Morris, *J. Am. Chem. Soc.* **2001**, *123*, 7473–7474.
[34] L. Dahlenburg, R. Götz, *Eur. J. Inorg. Chem.* **2004**, *4*, 888–905.
[35] A. J. Lough, S. Park, R. Ramachandran, R. H. Morris, *J. Am. Chem. Soc.* **1994**, *116*, 8356–8357.
[36] P. Pelagatti, A. Bacchi, M. Carcelli, M. Costa, A. Fochi, P. Ghidini, E. Leporati, M. Masi, C. Pelizzi, G. Pelizzi, *J. Organomet. Chem.* **1999**, *583*, 94–105.
[37] D. Sellmann, G. H. Rackelmann, F. W. Heinemann, *Chem. Eur. J.* **1997**, *3*, 2071–2080.
[38] F. Hutschka, A. Dedieu, *J. Chem. Soc., Dalton Trans.* **1997**, 1899–1902.
[39] S. C. van der Slot, P. C. J. Kamer, P. van Leeuwen, J. A. Iggo, B. T. Heaton, *Organometallics* **2001**, *20*, 430–441.
[40] J. Andrieu, J. M. Camus, C. Balan, R. Poli, *Eur. J. Inorg. Chem.* **2006**, 62–68; following article.
[41] K. Isslieb, R. Kümmel, H. Oehme, I. Meisser, *Chem. Ber.* **1968**, *101*, 3612–3618.
[42] A. L. Balch, M. M. Olmstead, S. P. Rowley, *Inorg. Chim. Acta* **1990**, *168*, 255–264.
[43] T. B. Rauchfuss, F. T. Patino, D. M. Roundhill, *Inorg. Chem.* **1975**, *14*, 652–656.
[44] D. Hedden, D. M. Roundhill, *Inorg. Chem.* **1985**, *24*, 4152–4158.
[45] E. Rotondo, G. Battaglia, G. Giuseppe, C. F. Priolo, *J. Organomet. Chem.* **1993**, *450*, 245–252.
[46] G. M. Sheldrick, *SHELX97* (Includes *SHELXS97* and *SHELXL97*), Release 97–2, Programs for Crystal Structure Analysis, University of Göttingen, Göttingen, Germany, **1998**.
[47] L. J. Farrugia, *J. Appl. Crystallogr.* **1999**, *32*, 837–838.

Received: May 12, 2005
Published Online: November 22, 2005

 © 2006 Wiley-VCH Verlag GmbH & Co. KGaA, Weinheim 

DOI: 10.1002/ejic.200500448

# Amino-phosphanes in $Rh^{I}$-Catalyzed Hydroformylation: New Mechanistic Insights Using $D_2O$ as Deuterium-Labeling Agent

**Jacques Andrieu,*[a] Jean-Michel Camus,[a] Cédric Balan,[a] and Rinaldo Poli*[b]**

**Keywords:** Rhodium / Amino-phosphane ligands / H/D isotopic exchange / Hydroformylation catalysis / Enantioselectivity

In previous work, we have demonstrated that the dangling amino group in amino-phosphane ligands increases the rate of Rh-catalyzed styrene hydroformylation as a function of the amino group basicity and of the distance between the P and N functions. We now report additional stereochemical and mechanistic insights resulting from new catalytic experiments performed with Rh-α-P,N catalytic systems in the presence of $D_2O$. In addition to the expected $D_0$ product, the formation of the β-$D_1$ aldehyde, $PhCH(CH_2D)CHO$ was observed in all cases by $^1H$ and $^{13}C$ NMR spectroscopy, indicating that H/D exchange occurs for the rhodium-hydride complex. Minor amounts of a β-$D_2$ product, $PhCH(CHD_2)CHO$, were also formed under certain conditions, demonstrating the reversibility of the olefin coordination step. The composition of the aldehyde mixture is slightly affected by the nature of the catalytic precursor or the P,N ligand used. In the specific case of the α-P,N ligand [α-P,N = ($S_{Ar}$,$S_C$)-$Ph_2PCH$-{*o*-$C_6H_4Cl(Cr(CO)_3)$}NHPh], in combination with the $[RhCl(COD)]_2$ precatalyst, products $PhCD(CH_3)CHO$ (α-$D_1$) and $PhCD(CH_2D)CHO$ (α,β-$D_2$) were also produced. This result suggests a reversible deprotonation assisted by an intramolecular H-bonding interaction between the dangling ammonium function and the carbonyl moiety. This isotopic exchange process decreases the asymmetric induction from 14 to 7 % *ee* when using the enantiopure version of this ligand. Aldehydes bearing a D atom on the formyl group, e.g. $PhCH(CH_3)CDO$, were never observed. The latter observation excludes protonolysis of the rhodium-acyl intermediate as the aldehyde forming step. In addition, it also excludes a bimolecular reaction involving the rhodium-acyl and rhodium-hydride intermediates.

(© Wiley-VCH Verlag GmbH & Co. KGaA, 69451 Weinheim, Germany, 2006)

## Introduction

Metal complexes containing P,N bifunctional phosphanes have attracted considerable attention in the field of homogeneous catalysis, in particular with transition metals like Ni,[1] Pd,[2,3] Pt,[4] Ru,[5,6] Rh,[3,7] and Ir.[8–10] These ligands can be either $\kappa^1$:*P* or $\kappa^2$:*P*,*N* coordinated and each coordination mode can modify the catalytic properties. For example, when a pyridinylphosphane is only P-coordinated in a $Pd^{II}$ complex, the dangling amine function acts then as a "proton messenger" in alkyne methoxycarbonylation catalysis,[2] whereas a selective P,N chelation of a chiral phosphanediamine induces an effective chiral field in the rhodium complex leading to a higher selectivity in asymmetric hydrogenation of acrylic acid.[7]

In our laboratory, we have developed different access ways to chiral α-[11] or β-P,N[12,13] and mixed α,β- and β,γ-P,P,N[14] ligands and their coordination properties have been explored in copper(I),[15] palladium(II),[13,16] and rhodium(I) complexes[14,17,18] Recently, we have examined the coordination properties of various P,N ligands in rhodium-catalyzed hydroformylation and demonstrated the hemilabile character of β or γ-P,N ligands under CO pressure. Therefore, under these conditions, these ligands behave like their related α-P,N monophosphane ligands, for which the chelating mode is not observed under any operating conditions.[18] The presence of a dangling nitrogen group close to the rhodium metal center could promote the activation of dihydrogen by heterolytic cleavage (see Scheme 1). In this interaction, the Rh center acts as a Lewis acid, accepting $H^-$, whereas the nearby amine function acts as a Lewis base, capturing the proton.

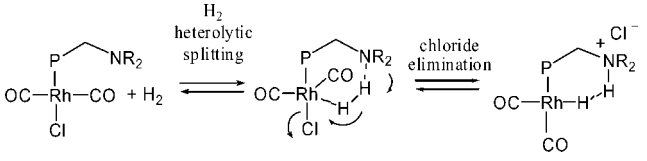


Scheme 1.

Nevertheless, even in the presence of chiral α-,[17] β-P,N[12] or other P,N ligands,[19,20] the enantioselectivity of branched aldehydes formed in styrene hydroformylation were very low (<14%). We decided to further investigate the mechanistic details of the enantioselective process by additional experiments based on H/D isotopic exchanges

[a] Laboratoire de Synthèse et Electrosynthèse Organométalliques, UMR 5188 CNRS, Université de Bourgogne, Faculté des Sciences Mirande,
9 avenue Alain Savary, 21078 Dijon, France
E-mail: Jacques.Andrieu@u-bourgogne.fr
[b] Laboratoire de Chimie de Coordination, UPR CNRS 8241, 205 route de Narbonne, 31077 Toulouse Cedex, France


© 2006 Wiley-VCH Verlag GmbH & Co. KGaA, Weinheim

using $D_2O$ as a deuterium source. Indeed, deuterioformylations performed in the presence of $D_2$ instead of $H_2$ have been most effective for elucidating mechanistic details in catalytic processes, for instance the degree of reversibility for the olefins insertion reactions into the Rh–H bond,[21–23] or the different behavior of primary, secondary, and tertiary Rh–alkyl intermediates under hydroformylation conditions.[24] In addition, the use of deuterated reagents like $D_2$, EtOD, or (*S*)-$CH_3$–CH(Ph)OD have also provided mechanistic information, respectively, in iridium-catalyzed alkane dehydrogenation,[25] in palladium-catalyzed styrene hydroalkoxycarbonylation,[26] or in metal-catalyzed hydrogen transfer from alcohols to ketones.[27] Our choice of heavy water, $D_2O$, as the source of the deuterium label was suggested by the proposed implication of ammonium functionalities, with potentially exchangeable protons, near the catalytic center, as shown in Scheme 1. Furthermore, its use would allow us not only to follow the D-incorporation into organic compounds during the catalysis, but also to obtain useful information on the stability and/or reactivity of our Rh-P,N catalysts in aqueous media.[28–30] We could then evaluate their potential for extension to biphasic conditions.[31]

## Results and Discussion

The catalytic runs were carried out using $[RhCl(COD)]_2$ or $[Rh(acac)(CO)_2]$ as precatalyst, with an equimolar amount of the α-P,N ligands $Ph_2PCH_2NR_2$ (R = Me, Ph) or $Ph_2PCH(Ar)NHPh$ [Ar = $\eta^6$(*o*-$C_6H_4Cl$)$Cr(CO)_3$], in the presence of 1000 equivalents of $D_2O$ and styrene. Control experiments were also carried out with $PPh_3$ and in the absence of phosphane ligand. In a previous contribution, we have reported the catalytic activity and linear/branched selectivity of the above systems in dry $CHCl_3$.[18] The hydroformylation experiments in the presence of $D_2O$, reported in this paper, were carried out under similar conditions with the exception of the solvent, which was changed from $CHCl_3$ to THF in order to insure homogeneous conditions in the presence of water. In Figure 1, we compare the activity of the same Rh-P,N precatalyst under the two different solvent conditions.

Neither the branched/linear regioselectivity (91/9),[18] nor the turnover frequency at the beginning of the catalytic process are affected by this solvent change. However, the catalyst starts to lose activity after ca. 5 h. Conversions of 65 and 100% were obtained respectively after one and two days, whereas a complete conversion was achieved in $CHCl_3$ after only one day (see Figure 1). Therefore, the loss of activity seems related to catalyst decay due to the presence of the large excess of water. Since a complete conversion was achieved after two days, we decided to analyze the crude aldehyde mixture by NMR spectroscopy after this period for all catalytic runs. The nature and relative proportions of the branched aldehydes are summarized in Table 1. The small relative amounts of linear aldehyde did not permit the analysis of the deuterium incorporation and these data are therefore excluded from Table 1.

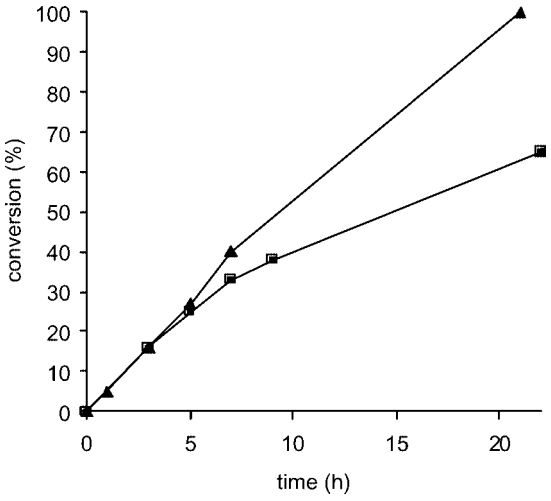


Figure 1. Conversion for the catalyzed styrene hydroformylation as a function of time: ■, in THF/$D_2O$, ▲, in $CHCl_3$. Both experiments were performed using the catalytic conditions described for run 5, Table 1.

The incorporation of the deuterium atoms either in the terminal methyl group or in the internal methyne group of the branched aldehydes was determined unambiguously by careful analysis of the primary and secondary isotope shifts and of the $J_{(CD)}$ patterns for the α- and β-C resonances in the $^{13}C\{^1H\}$ NMR spectrum (see Table 2). The relative amounts of the various products were quantified by integration of the $^{13}C\{^1H\}$ resonances affected by the secondary isotope shift, since the Overhauser effect does not depend on the substitution pattern at the adjacent C atom.[32–34] Thus, for instance, the relative proportion of compounds $PhCH(CH_3)CHO$ and $PhCH(CH_2D)CHO$ were obtained by integration of the two proton-decoupled methyne signals, whereas the relative proportions of compounds $PhCH(CH_3)CHO$ and $PhCD(CH_3)CHO$ were obtained by integration of the two proton-decoupled methyl signals.

Figure 2 shows the $^{13}C$ NMR spectra for three representative product mixtures. The mixture obtained from run 7 (Figure 2, a), as well as most other runs (see Table 1) shows only the β-$D_1$ compound in addition to the regular $D_0$ product, whereas run 5 produces a more complex mixture of deuterated aldehydes (Figure 2, c). The spectrum in Figure 2 (b) corresponds to a control mixture of $D_0$ and α-$D_1$ products, which was obtained by direct isotopic exchange between the $D_0$ aldehyde and $[PhND_3]^+[BF_4]^-$. It is to be remarked that in none of the runs was any deuterium atom found on the aldehyde function, i.e. $PhCH(CH_3)CDO$.

The ubiquitous formation of the β-$D_1$ derivative is a clear indication that $D^+$ finds its way into the hydride position during the catalytic cycle. Since the decayed catalyst (Figure 1) yields no (or a much lower amount of) new aldehyde, and since the aldehyde does not incorporate D under these conditions in the absence of the catalyst (vide infra), we can conclude that the isotopic distribution measured at the end of the experiment is not affected by the catalyst decomposition process. As this β-$D_1$ incorporation phe-

 © 2006 Wiley-VCH Verlag GmbH & Co. KGaA, Weinheim 

Table 1. Effect of the P,N ligand on the composition of deuterated aldehydes.

| Run[a] | Catalytic precursor | Ligand (1 equiv.) | 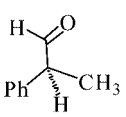 $D_0$ | 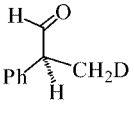 β-$D_1$ | 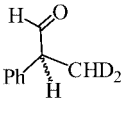 β-$D_2$ | 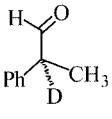 α-$D_1$ | 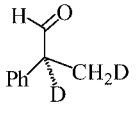 α,β-$D_2$ |
|---|---|---|---|---|---|---|---|
| 1 | $[RhCl(COD)]_2$ | no | 44% | 44% | 12% | – | – |
| 2 | $[RhCl(COD)]_2$ | $PPh_3$ | 73% | 27% | – | – | – |
| 3 | $Rh(acac)(CO)_2$ | $PPh_3$ | 87% | 13% | – | – | – |
| 4 | $[RhCl(COD)]_2$ | $Ph_2PCH_2NPh_2$ | 51% | 41% | 9% | – | – |
| 5 | $[RhCl(COD)]_2$ | $Ph_2PCH(Ar)NHPh$[b] | 60% | 20% | – | 15% | 5% |
| 6 | $[RhCl(COD)]_2$ | $Ph_2PCH(Ar)NHPh$[b] + $NEt_3$[c] | 73% | 23% | – | 4% | – |
| 7 | $Rh(acac)(CO)_2$ | $Ph_2PCH(Ar)NHPh$[b] | 75% | 25% | – | – | – |
| 8 | $[RhCl(COD)]_2$ | $Ph_2PCH_2NEt_2$ | 83% | 17% | – | – | – |
| 9 | $Rh(acac)(CO)_2$ | $Ph_2PCH_2NEt_2$ | 77% | 23% | – | – | – |

[a] Conditions: $[RhCl(COD)]_2$ ($2.62\times10^{-2}$ mmol) or $[Rh(acac)(CO)_2]$ ($5.23\times10^{-2}$ mmol), styrene/Rh and $D_2O$/Rh = 1000, plus ligand, THF (35 mL), 55 °C, *p*(syngas) = 600 psi, two days. [b] Ar = $\eta^6$(*o*-$C_6H_4Cl$)$Cr(CO)_3$. [c] P,N/$NEt_3$ ratio = 1.

Table 2. Selected $^{13}$C-NMR spectroscopic data and $J_{(CD)}$ coupling constants of deuterated compounds.

| Compounds | $C_\alpha$ δ [ppm] ($J_{(CD)}$ in Hz) | $C_\beta$ |
|---|---|---|
| $D_0$ | 51.82 | 13.43 |
| β-$D_1$ | 51.77 | 13.18 (19) |
| β-$D_2$ | 51.72 | very weak signal |
| α-$D_1$ | 51.41 (20) | 13.34 |
| α,β-$D_2$ | 51.36 (20) | 13.08 (19) |

nomenon occurs also when the phosphane ligand carries no amine function (runs 2 and 3) and even in the absence of any phosphane (run 1), a direct acid dissociation of the hydride intermediate in the protic medium or a reversible protonation to generate a dihydrogen complex or a classical dihydride intermediate (Scheme 2) appear as the most logical mechanisms for this H/D exchange.

The observation that all experiments where a phosphane ligand is present (runs 2–9) provided a greater $D_0$/β-$D_1$ ratio (≈3) than run 1 appears to be in better agreement with the hypothesis of acid dissociation. Note that the $D_0$/β-$D_1$ ratio is not greatly affected by the phosphane nature. For other processes, on the other hand, the amount of D incorporation by exchange with $D_2O$ was shown to greatly depend on the nature of the phosphane ligand and substrate.[30,35]

The formation of the β-$D_2$ product is observed only in the absence of phosphane ligand (run 1) and for run 4, using the $Ph_2PCH_2NPh_2$ ligand. The presence of this product must be the consequence of reversibility for the styrene insertion step. It is to be remarked that H elimination from the β-$D_1$-1-phenylethyl insertion product should be favored over D elimination by a kinetic isotope effect, since the C–H/D vibrational modes are stronger than those of the C···H/D and Rh···H/D interactions in the transition state.[36] The reversibility of the styrene coordination step is further confirmed by the recovery of free β-$D_1$-styrene, i.e. PhCH=CHD, when a catalytic experiment carried out under the same condition of run 1 was quenched and the organic phase analyzed after 30% conversion. The absence of α-$D_1$-styrene, i.e. $PhCD=CH_2$, indicates that the 1,2 insertion leading to the $\eta^1$-2-phenylethyl rhodium complex (precursor of the linear aldehyde) is irreversible. This is consistent with other previously reported results.[22,37,38] Reversible 2,1 styrene insertion has previously been evidenced for hydroformylation experiments carried out under $D_2$ with $Rh_4(CO)_{12}$ as the catalyst (without phosphane ligands) or with $[Rh(acac)(CO)_2]$ in the presence of the mono-, diphosphane, or (*R*,*S*)-binaphos ligand.[21,23,37,38] With the latter Rh–binaphos catalytic system, the amount of α-plus β-$D_1$-styrene was observed to increase significantly from 2 to 30% when the syngas pressure was increased from 1 to 100 atm. Our results indicate that the styrene insertion becomes less reversible in the presence of phosphane ligands, with the exception of run 4. The latter leads to quite comparable results to those of run 1 and to those of the process conducted with tetranuclear rhodium precatalysts in the absence of phosphane ligands.[38] In other previous work based on the use of mono or di-phosphane ligands, the amount of deuterium label found in styrene was reported to be very minor and to vary only slightly (from 0.1 to a few %) as a function of the phosphane nature.[21] The unusually high proportion of β-$d^2$ in run 4 could be due to a ligand dissociation, but we have no further evidence to confirm or refute this assumption at this time.

 © 2006 Wiley-VCH Verlag GmbH & Co. KGaA, Weinheim 

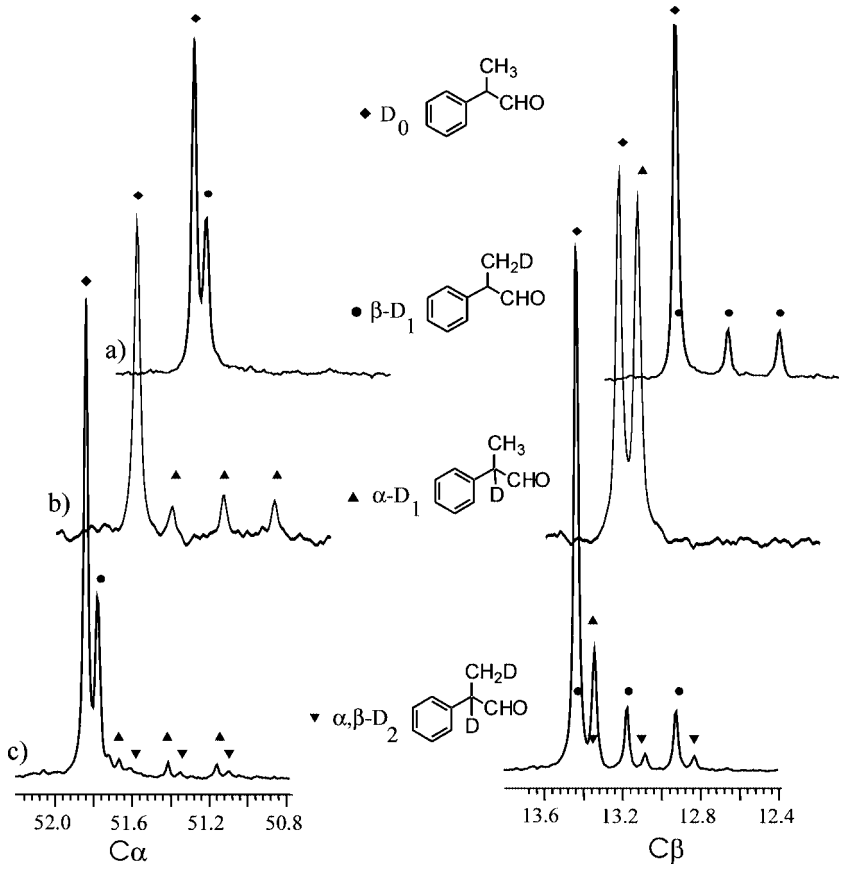


Figure 2. $^{13}C\{^1H\}$ NMR spectra of partially deuterated aldehyde mixtures. Only the peaks of the branched aldehydes are shown for clarity. $C_\alpha$ and $C_\beta$ correspond respectively to the methyne and methyl carbon atoms. (a) From run 7, after complete conversion. (b) From the reaction between $D_0$ aldehyde and 0.3 equivalent of $[PhND_3^+](BF_4^-)$, after 24 h, under catalytic conditions described in Table 1 without rhodium catalyst. (c) From run 5, after complete conversion.

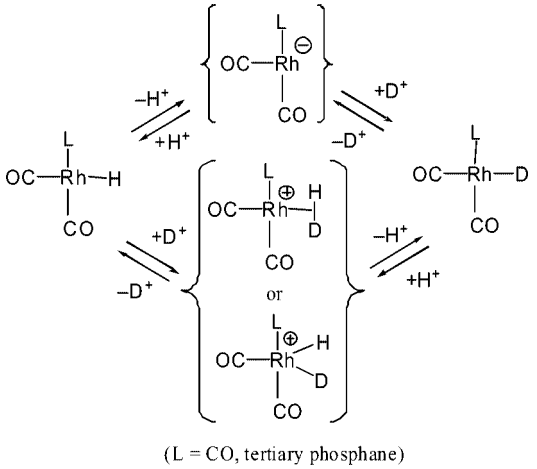


Scheme 2.

The absence of any observable deuterium incorporation into the formyl group has very important implications. As discussed above, an HCl equivalent is generated during the catalyst activation process when using the $[RhCl(COD)]_2$ precursor. This by-product will presumably be trapped by the internal amine function (see Scheme 1), since amines are more basic than water ($pK_a \approx 4.8$ for $PhNH_2Me^+$ and 10.7 for $NHEt_3^+$). The ammonium protons of the resulting Rh–ammonium species are likely to be exchanged by $D^+$ in the presence of $D_2O$, see Scheme 3.

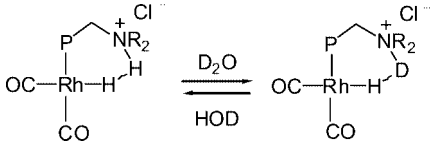


Scheme 3.

Therefore, the outcome of the catalytic runs in the presence of $D_2O$ excludes Rh–acyl protonolysis by the ammonium function as the aldehyde forming step (see Scheme 4). In other words, the amino-phosphane ligand does not act as a "proton messenger", unlike the pyridinylphosphane ligand in the palladium catalyzed alkyne methoxy-carbonylation process.[2] Furthermore, this result also excludes the possibility of a binuclear aldehyde elimination process between a rhodium acyl and a rhodium hydride species,[39,40] for this system. These observations are summarized in Scheme 4.

The hydrogen atom that becomes part of the formyl group must derive from the $H_2$ molecule involved in the hydrogenolysis step. As discussed in our recent contribution,[18] hydrogenolysis could occur either by $H_2$ oxidative addition followed by aldehyde reductive elimination

 © 2006 Wiley-VCH Verlag GmbH & Co. KGaA, Weinheim 

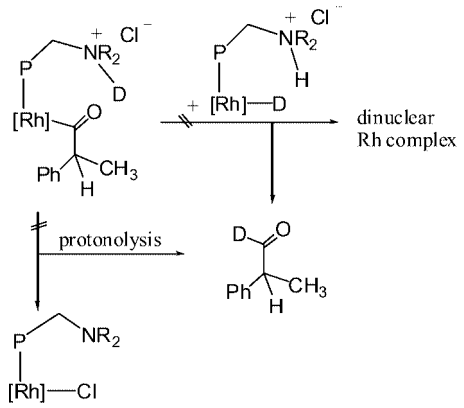


Scheme 4.

with a $Rh^{III}$ dihydride intermediate (**A**), or by $H_2$ heterolytic splitting via a zwitterionic ammonium-hydride complex (**B**), see Scheme 5. In either case, the aldehyde release from the intermediate must be faster than the H/D exchange at the site that ultimately delivers the H atom to the formyl unit.

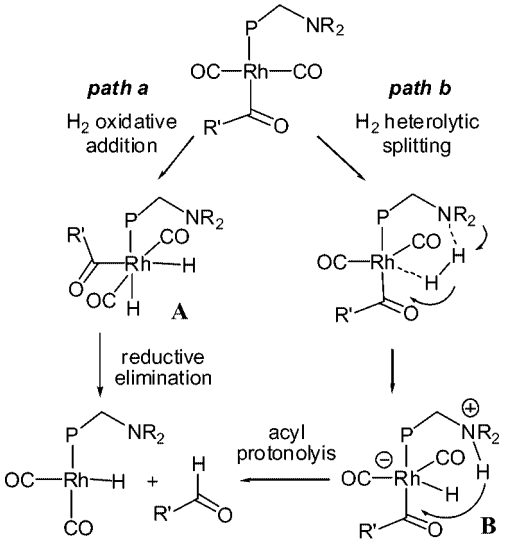


Scheme 5.

The most unexpected result of our investigation, however, is the observation of the α-$D_1$ and α,β-$D_2$ products for the [RhCl(COD)]$_2$/$Ph_2PCH(Ar)NHPh$ catalytic system (Table 1, runs 5 and 6). A possible pathway for the D incorporation from $D_2O$ at the α-position could in principle involve a β-elimination reaction from the Rh–acyl complex leading to a ketene-hydride intermediate. After Rh–H/Rh–D isotopic exchange with $D_2O$ and subsequent ketene insertion, the Rh–acyl complex with the deuterium atom at the α-position could be obtained. However, this mechanism is unlikely for three different reasons. The first one is that the high reactivity of ketene towards water[41] should lead to the related acid, which is not detected in NMR spectra. The second reason is that such a mechanism should lead to aldehydes without any *ee*.

Additional catalytic runs were performed with complexes RhCl(COD)(*S*,*S*-α-P,N) and Rh(acac)(CO)(*S*,*S* -α-P,N) prepared in situ from the chiral ligand [*S*,*S*-α-P,N = ($S_{Ar}$,$S_C$)-$Ph_2PCH\{o\text{-}C_6H_4Cl(Cr(CO)_3)\}NHPh$][17] and the rhodium precatalysts [RhCl(COD)]$_2$ and Rh(acac)$(CO)_2$, respectively. These tests, run either with RhCl(COD)(*S*,*S*-α-P,N) in $CHCl_3$ or with Rh(acac)(CO)(*S*,*S*-α-P,N) in $C_6H_6$, gave (*S*)-2-phenylpropanal with 7 and 14% *ee*, respectively. In order to verify that the low *ee* are not merely the consequence of racemization under our catalytic conditions, (*R*)-2-phenylpropanal was heated at 55 °C in $CHCl_3$ for one day. No significant change of the *ee* was observed. Thirdly, it is not possible to easily rationalize why the H/D exchange at the α position via the ketene intermediate would only be promoted by the [RhCl(COD)]$_2$/$Ph_2PCH(Ar)NHPh$ combination. Note that changing the P,N ligand to a more basic one (run 8), or changing the precursor to the acetylacetonate complex (run 7) suppresses this phenomenon.

The catalyst modifications alluded to above have an effect on the state of protonation of the dangling nitrogen atom, thus suggesting a direct role of this function in the H/D exchange at the α position. Therefore, a possible pathway for the formation of the α-$D_1$ and α,β-$D_2$ products in runs 5 and 6 could be based on the equilibrium between the Rh–acyl intermediate and its related enolate form (**A** and **B** in Scheme 6), with assistance from the ammonium function via hydrogen bonding. This assistance requires the presence of a proton-bearing ammonium functionality with sufficient acidity, thereby explaining the absence of this phenomenon when using the acetylacetonate precatalyst (the dangling amine is not protonated) or a more basic P,N ligand (insufficient acidity for the resulting ammonium function). The decreased amount of α-$D_1$ aldehyde from 15 to 4% when an addition external base is added to this catalytic system (from run 5 to run 6) is also consistent with this mechanistic proposal. A control experiment carried out under the same temperature and pressure conditions of run 5, in the presence of a catalytic amount of [$PhND_3$][$BF_4$] (0.1% vs. the aldehyde), but without the rhodium complex and the phosphane, shows no observable α-D incorporation. However, ca. 50% conversion to the α-$D_1$ aldehyde occurred when a higher amount of deuterated ammonium salt (20% vs. the aldehyde) was used under similar conditions (see Figure 2,b). Thus, H/D exchange at the α position can indeed occur in the presence of a sufficiently strong acid. Note that $PhND_3^+$ is a stronger acid than the dangling $Ph_2PCH(Ar)NPhH_2^+$ function and yet it is a less effective H/D exchange catalyst that the protonated, rhodium-coordinated amino-phosphane. This suggests cooperativity between the ammonium function and the metal center.

At this point, the enolate anion **B** can be protonated by either $H^+$ or $D^+$, originating from water or from the $-ND_2Ph^+$ fragment, leading to **A** or **C**. Further hydrogenolysis liberates the $D_0$ and α-$D_1$ aldehydes, respectively. On the basis of the basic properties of the dangling amine function, one would expect that the [RhCl(COD)]$_2$/$Ph_2PCH_2NPh_2$ (run 4) should also lead to H/D exchange

 © 2006 Wiley-VCH Verlag GmbH & Co. KGaA, Weinheim 

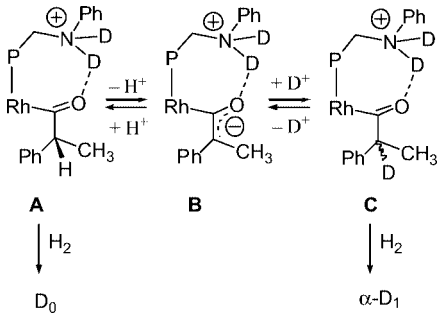


Scheme 6.

at the α position, whereas no α-$D_1$ product is observed in this case. This result is probably associated with the insufficient basicity of the N atom (e.g. the p$K_a$ of $Ph_2NH_2^+$ is 0.8 vs. 4.85 for $PhNH_2Me^+$). Thus, the liberated HCl would be trapped by the aqueous solvent in this case, rather than by the dangling amine group.

It is to be noted that Rh-enolate intermediates have also been proposed in catalytic aldolization reactions or in one-pot catalytic tandem/aldol condensation, but in both cases the enolate moiety adopts a $\eta^1$-O coordination mode rather than a $\eta^1$-C one.[42,43] The H/D exchange process on the Rh–acyl, according to the proposed Scheme 6, must necessarily be associated to an intramolecular racemization before the aldehyde liberation by hydrogenolysis. In this respect, there is a correlation between the production of α-$D_1$ aldehyde for run 5 (and its absence for run 7) in Table 1 and the reduced enantioselectivity observed with the RhCl(COD)(*S*,*S*-α-P,N) precatalyst vs. the Rh(acac)-(CO)(*S*,*S*-α-P,N) precatalyst in chloroform (discussed above).

## Conclusions

The isotopic composition of aldehyde, obtained by styrene hydroformylation using Rh-α-P,N catalytic systems in the presence of $D_2O$, allows us to obtain new stereochemical and mechanistic information for this catalytic reaction. Specifically, the absence of $PhCH(CDO)CH_3$ in all cases shows that the rhodium-acyl intermediate does not release the aldehyde product by a protonolysis process, nor by bimetallic reductive elimination. The presence of $PhCD(CHO)CH_3$ in only one catalytic experiment shows, for the first time, that a Rh–acyl racemization may be catalyzed in the presence of certain ligands. An intramolecular H-interaction between the ammonium and Rh-enolate moieties is proposed to be responsible for this process, leading to M–acyl racemization before the reductive elimination step. This is a new phenomenon to be considered for the design of new ligands for use in the efficient and highly enantioselective branched hydroformylation process. It should also be considered for the extension of existing rhodium catalyzed asymmetric hydroformylation processes to ionic liquid media such as imidazolium or ammonium salts.

## Experimental Section

**General Procedures:** All manipulations were carried out under purified argon and in the dark using standard Schlenk techniques. All solvents were dried and deoxygenated by standard methods and distilled under dinitrogen prior to use. $^1H$ and $^{13}C\{^1H\}$ NMR measurements were carried out with a Bruker AC300 spectrometer. The peak positions are reported with positive shifts in ppm downfield of TMS as calculated from the residual solvent peaks. The commercial compounds $PPh_3$, $Ph_2NH$, $[RhCl(COD)]_2$, $[Rh(acac)(CO)_2]$, and $[Rh(CO)_2Cl]_2$ were used as received without further purification. The ligands $Ph_2PCH_2NEt_2$, $Ph_2PCH_2NPh_2$, $Ph_2PCH(Ar)NHPh$ [Ar = *o*-$C_6H_4Cl\{Cr(CO)_3\}$], were prepared according to the literature.[11,15,44,45] The preparation of the optically pure version of the latter ligand, (*S*,*S*)-**1**, has been previously reported[11] The synthesis of complex [RhCl(COD)(α-P,N)] **1** with α-P,N=$Ph_2PCH$(*o*-$C_6H_4Cl[Cr(CO)_3]$)NHPh has previously been described.[17] The (*R*)-2-phenylpropanal was prepared by an oxidation reaction using the Dess–Martin reagent[46] from commercially available (*R*)-2-phenyl-1-propanol (Aldrich) according to a previously described procedure[47] (*ee* = 93% by use of the NMR chiral shift reagent $[Eu(hfc)_3]$, according to the literature[48]).

**Catalytic Runs:** The hydroformylation reactions were carried out in a 300-mL stainless-steel Parr autoclave equipped with a magnetic drive, an internal glass vessel, and an immersion tube connected to a valve for solution withdrawals under pressure. The temperature was controlled by a rigid heating mantle and a single loop cooling coil. The autoclave was purged three times under vacuum/argon before introducing the catalytic solution (see Table 1). The 1:1 CO/$H_2$ mixture was prepared by mixing the pure gases in a 500-ml stainless steel cylinder before introduction into the autoclave at the desired pressure (see Table 1). The zero time for kinetic runs was considered as the time at which the desired pressure was reached inside the autoclave. In order to maintain temperature and pressure conditions as constant as possible during each kinetic run, only a few mL of catalytic solution mixture were carefully withdrawn each time from the autoclave. The THF solvent was then rotary evaporated at room temperature and the yellow-orange residue was analyzed by proton and carbon NMR spectroscopy. For the product obtained in the presence of the optically active catalyst, the *ee* as well as the absolute configuration of the enantiomer were determined by use of the NMR chiral shift reagent $[Eu(hfc)_3]$, according to the literature.[48]

## Acknowledgments

We are grateful to the Ministère de la Recherche, to the Centre National de la Recherche Scientifique (CNRS), and to the Conseil Régional de Bourgogne for support of this work. J.-M. C. thanks the Ministère de la Recherche for a Ph. D. fellowship.

[1] P. Denis, A. Jean, J. F. Crizy, A. Mortreux, F. Petit, *J. Am. Chem. Soc.* **1990**, *112*, 1292–1294.
[2] E. Drent, P. Arnoldy, P. H. M. Budzelaar, *J. Organomet. Chem.* **1993**, *455*, 247–253.
[3] K. N. Gravilov, A. I. Polosukhin, *Russ. Chem. Rev.* **2000**, *69*, 661–682.
[4] S. M. Thompson, F. Stöhr, D. Sturmayr, G. Kickelbick, U. Schubert, *J. Organomet. Chem.* **2003**, *686*, 183–191.
[5] H. Yang, M. Alvarez, N. Lugan, R. Mathieu, *J. Chem. Soc., Chem. Commun.* **1995**, 1721–1722.
[6] J.-X. Gao, T. Ikariya, R. Noyori, *Organometallics* **1996**, *15*, 1087–1089.

 © 2006 Wiley-VCH Verlag GmbH & Co. KGaA, Weinheim 

[7] I. Yamada, M. Ohkouchi, M. Yamaguchi, T. Yamagishi, *J. Chem. Soc., Perkin Trans. 1* **1997**, 1869–1873.
[8] L. Dahlenburg, R. Götz, *Inorg. Chim. Acta* **2004**, *357*, 2875–2880.
[9] D. M. Roundhill, R. A. Bechtold, S. G. N. Roundhill, *Inorg. Chem.* **1980**, *19*, 284–289.
[10] T. B. Rauchfuss, J. L. Clements, S. F. Agnew, D. M. Roundhill, *Inorg. Chem.* **1977**, *16*, 775–778.
[11] J. Andrieu, C. Baldoli, S. Maiorana, R. Poli, P. Richard, *Eur. J. Org. Chem.* **1999**, 3095–3097.
[12] J.-M. Camus, J. Andrieu, P. Richard, R. Poli, C. Darcel, S. Jugé, *Tetrahedron: Asymmetry* **2004**, *15*, 2061–2065.
[13] J. Andrieu, J.-M. Camus, J. Dietz, P. Richard, R. Poli, *Inorg. Chem.* **2001**, *40*, 1597–1605.
[14] J. Andrieu, P. Richard, J.-M. Camus, R. Poli, *Inorg. Chem.* **2002**, *41*, 3876–3885.
[15] J. Andrieu, J. Dietz, R. Poli, P. Richard, *New J. Chem.* **1999**, *23*, 581–583.
[16] J.-M. Camus, J. Andrieu, P. Richard, R. Poli, *Eur. J. Inorg. Chem.* **2004**, 1081–1091.
[17] J.-M. Camus, J. Andrieu, P. Richard, R. Poli, C. Baldoli, S. Maiorana, *Inorg. Chem.* **2003**, *42*, 2384–2390.
[18] J. Andrieu, J.-M. Camus, P. Richard, R. Poli, L. Gonsalvi, F. Vizza, M. Peruzzini, *Eur. J. Inorg. Chem.* **2006**, 51–61; preceding article.
[19] A. Aghmiz, A. M. Masdeu-Bulto, C. Claver, D. Sinou, *J. Mol. Catal. A: Chem.* **2002**, *184*, 111–119.
[20] C. Saluzzo, J. Breuzard, S. Pellet-Rostaing, M. Vallet, F. Le Guyader, M. Lemaire, *J. Organomet. Chem.* **2002**, *643*, 98–104.
[21] T. Horiuchi, E. Shirakawa, K. Nozaki, H. Takaya, *Organometallics* **1997**, *16*, 2981–2986.
[22] K. Nozaki, T. Nanno, H. Takaya, *J. Organomet. Chem.* **1997**, *527*, 103–108.
[23] R. Lazzaroni, A. Raffaelli, R. Settambolo, S. Bertozzi, G. Vitulli, *J. Mol. Catal.* **1989**, *50*, 1–9.
[24] R. Lazzaroni, R. Settambolo, G. Uccello-Barretta, S. Scamuzzi, *J. Mol. Catal. A: Chem.* **1999**, *143*, 123–130.
[25] H. Gérard, O. Eisenstein, D. H. Lee, J. Chen, R. H. Crabtree, *New J. Chem.* **2001**, *25*, 1121–1131.
[26] C. Benedek, G. Szalontai, Á. Gömöry, S. Tõrös, B. Heil, *J. Organomet. Chem.* **1999**, *579*, 147–155.
[27] O. Pámies, J.-E. Bäckvall, *Chem. Eur. J.* **2001**, *7*, 5052–5058.
[28] S. R. Klei, J. T. Golden, T. D. Tilley, R. G. Bergman, *J. Am. Chem. Soc.* **2002**, *124*, 2092–2093.
[29] F. Joó, L. Nádasdi, A. Bényei, D. J. Darensbourg, *J. Organomet. Chem.* **1996**, *512*, 45–50.
[30] J. Bakos, R. Karaivanov, M. Laghmari, D. Sinou, *Organometallics* **1994**, *13*, 2951–2956.
[31] B. Cornils, W. A. Herrmann (Eds.), *Applied Homogeneous Catalysis with Organometallic Compounds*, VCH, Weinheim, **1996**.
[32] S. Lange, W. Leitner, *J. Chem. Soc., Dalton Trans.* **2002**, 752–758.
[33] G. C. Lloyd-Jones, *Synlett* **2001**, 161–183.
[34] W. Leitner, J. M. Brown, H. Brunner, *J. Am. Chem. Soc.* **1993**, *115*, 152–159.
[35] R. Lazzaroni, R. Settambolo, A. Caiazzo, M. A. Bennett, *Organometallics* **2002**, *21*, 2454–2459.
[36] J. Evans, J. Schwartz, P. W. Urquhart, *J. Organomet. Chem.* **1974**, *81*, C37–C39.
[37] C. P. Casey, L. M. Petrovich, *J. Am. Chem. Soc.* **1995**, *117*, 6007–6014.
[38] R. Lazzaroni, R. Settambolo, A. Raffaelli, S. Pucci, G. Vitulli, *J. Organomet. Chem.* **1988**, *339*, 357–365.
[39] M. Diéguez, C. Claver, A. M. Madseu-Bulto, A. Ruiz, P. W. N. M. Van Leeuwen, G. C. Schoemaker, *Organometallics* **1999**, *18*, 2107–2115.
[40] R. C. Matthews, D. K. Howell, W.-J. Peng, S. G. Train, W. D. Treleaven, G. G. Stanley, *Angew. Chem. Int. Ed. Engl.* **1996**, *35*, 2253–2256.
[41] M. T. Nguyen, A. F. Hegarty, *J. Am. Chem. Soc.* **1984**, *106*, 1552–1557.
[42] G. A. Slough, R. G. Bergman, C. H. Heathcock, *J. Am. Chem. Soc.* **1989**, *111*, 938–949.
[43] L. Bärfacker, D. El Tom, P. Eilbracht, *Tetrahedron Lett.* **1999**, *40*, 4031–4034.
[44] K. Isslieb, R. Kümmel, H. Oehme, I. Meisser, *Chem. Ber.* **1968**, *101*, 3612–3618.
[45] A. L. Balch, M. M. Olmstead, S. P. Rowley, *Inorg. Chim. Acta* **1990**, *168*, 255–264.
[46] R. E. Ireland, L. Liu, *J. Org. Chem.* **1993**, *58*, 2899.
[47] C. Botuha, M. Haddad, M. Larchevêque, *Tetrahedron: Asymmetry* **1998**, *9*, 1929–1931.
[48] A. M. Masdeu, A. Orejón, A. Ruiz, S. Castillón, C. Claver, *J. Mol. Catal. A: Chem.* **1994**, *94*, 149–156.

Received: May 12, 2005
Published Online: November 22, 2005

 © 2006 Wiley-VCH Verlag GmbH & Co. KGaA, Weinheim 

DOI: 10.1002/ejic.200500489

# On the Usefulness of Bond Orders and Overlap Populations to Chalcogen–Nitrogen Systems

**Julianna Oláh,[a,b] Frank Blockhuys,[a] Tamás Veszprémi,[b] and Christian Van Alsenoy*[a]**

**Keywords:** Bond order / Overlap population / Hirshfeld partitioning / Chalcogen–nitrogen systems / Bonding

Bond orders calculated using the Mayer, Wiberg or NAO methodologies are incompatible with the observed bond lengths in chalcogen–nitrogen systems. To study this discrepancy four types of bond orders and three types of (scaled) overlap populations have been used to determine the bonding in these systems. A new overlap population based on the Hirshfeld partitioning of the electron density is compared to the Mayer, Wiberg, NAO and Fuzzy bond order schemes and the Mulliken and Fuzzy overlap population schemes. The correlation between the investigated bond orders and overlap populations is excellent for common organic molecules, but the (scaled) Hirshfeld and Fuzzy overlap population schemes produce the best results for a series of chalcogen-nitrogen systems.
(© Wiley-VCH Verlag GmbH & Co. KGaA, 69451 Weinheim, Germany, 2006)

## Introduction

There has been an increasing interest in low-molecular-weight derivatives of $(SN)_x$ polymer since the latter's metallic properties[1] and low-temperature superconductivity[2] were discovered in the 1970′s. In our earlier work we have dealt with various compounds containing an $(SN)_2$ fragment such as 1,3λ⁴δ²,2,4-benzodithiadiazine (**1**),[3] its fluorinated derivatives[4] and Roesky's ketone (**4**).[5] 3λ⁴δ²,1,2,4-Benzothiaselenadiazine (**2**) and 1,3λ⁴δ²,2,4-benzodiselenadiazine (**3**), the mono- and diselena analogues of **1**, are also of considerable interest and are presently targets for synthesis.[6] Figure 1 presents structural formulas of these compounds. According to single-crystal X-ray diffraction (XRD) studies,[7] the structure of **1** is planar in the solid state, whereas both gas-phase electron diffraction (GED) and quantum chemical calculations indicate a bent structure in the gas phase.[3] Compound **1** possesses a cyclic 12π-electron system, and the deviation from the planar structure was attributed to a pseudo-Jahn–Teller distortion to minimize the antiaromaticity.[3,8] Furthermore, the energy barrier to planarity is low (1.17 kJ·mol$^{-1}$ at the HF/6-31G* level) and in the crystal phase the molecule can be flattened without great effort.

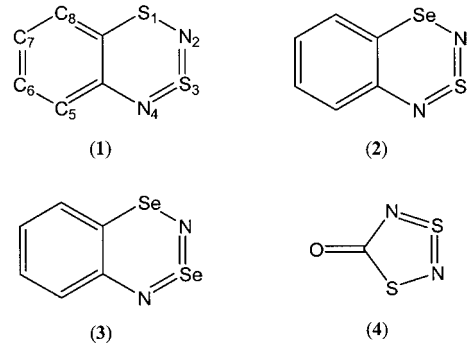


Figure 1. Structural formulas and atomic numbering of the chalcogen–nitrogen compounds under consideration. For compound **4** the formal Lewis structure is given.

Despite the different conformations in the two phases the measured (by XRD and GED) and calculated geometrical parameters of **1** reflect similar bonding. In the heteroatomic part there are two virtually equally short N=S bonds (bond length about 1.55 Å) and one longer N–S bond (bond length about 1.70 Å). On the basis of a comparison between the average bond lengths for the N=S and N–S bonds, the two short bonds could be identified as being double bonds while the longer one fell within the range for a single bond. Indeed, according to the analysis of the Cambridge Structural Database by Allen et al.,[9] an average N–S single bond lies between 1.64 and 1.70 Å, while a N=S double bond is approximately 1.54 Å long [we note that the N=S bond length is only tabulated for conjugated N=S=N systems].

In many cases, conclusions on the structures of compounds are based on bond order considerations, and therefore, it is essential to obtain reliable values for it. According to the IUPAC Compendium of Chemical Terminology, a

[a] University of Antwerp, Department of Chemistry, Universiteitsplein 1, 2610 Antwerp, Belgium
Fax: +32-3-820-23-10
E-mail: kris.vanalsenoy@ua.ac.be
[b] Budapest University of Technology and Economics, Department of Inorganic Chemistry, Gellért tér 4, 1521 Budapest, Hungary

 © 2006 Wiley-VCH Verlag GmbH & Co. KgaA, Weinheim 

bond order is a "theoretical index of the degree of bonding between two atoms relative to that of a single bond, i.e. the bond provided by one localized electron pair".[10] However, there exists no unique formula to calculate the bond order. Every bond order is partly arbitrary since it is based on a population analysis scheme which is arbitrary itself: different schemes for the partitioning of the electron density give rise to different definitions of bond orders.

Regardless of the differences between the various bond order methodologies, it is important that each one of them produces consistent results, and this is often the case for common organic molecules. This requirement is, however, not fulfilled in the case of compound **1** for which the Mayer,[11–13] Wiberg[14] and NAO (atom-atom-overlap-weighted Natural Atomic Orbital bond order)[15,16] methodologies predict a bond order value for the NS double bond which is much smaller than expected on the basis of the bond length. The same controversy is observed in the case of compounds **2**, **3** and **4**.

Since the early definition of Wiberg[14] there has been a long debate on the appropriate quantum chemical definition of bond orders (see ref.[17] and refs. 1–18 therein). Recently, Mayer and Salvador[18] have proposed bond orders based on 'fuzzy' atoms which are characterized by soft overlapping boundaries and defined using the Becke partitioning scheme. Clark and Davidson proposed a method for controlling the region of overlap between atoms and thoroughly examined the effect of the shape and sharpness of the interatomic boundaries on the obtained fuzzy atomic populations.[19] Mayer's fuzzy atom bond order, together with several other methods, was used by Clark et al.[20] in their investigation of the bonding properties of a number of actinide complexes. It was found that the fuzzy atom method[18] performed well for these compounds, even though the Natural Population Analysis (NPA) method exhibited the best performance of all the orbital-based partitioning schemes for these molecules.

Pauling was the first to suggest that bond orders can be related to bond lengths, and since then several relationships have been proposed.[21–24] These curves have found widespread applications. Among others, Lendvay[25] has reconfirmed the exponential relationship between the bond length and bond order using Equation (1),

$$n = \exp[-(r - r_0)/b] \tag{1}$$

where $n$ is the bond order, $r_0$ the equilibrium bond length of a single bond, $r$ the real bond length in the compound considered, and $b$ is a constant.

It is the purpose of this paper to address the discrepancies between observed bond lengths and the corresponding bond orders calculated using different methodologies, in particular for NS and NSe bonds in chalcogen-nitrogen compounds. For this purpose we have calculated and compared the Mulliken, Fuzzy and Hirshfeld overlap populations with the Mayer, Wiberg, NAO and Fuzzy bond orders. We have also investigated the relationship between these bond orders, overlap populations and the corresponding bond lengths. It has been known for decades that Mulliken overlap populations correlate reasonably well with Mayer bond orders,[26] even though Mayer insists that overlap populations and bond orders reflect different aspects of bonding, i.e. charge accumulation and exchange interactions, respectively. In the recent past the Hirshfeld partitioning scheme[27,28] has received considerable interest in relation to the calculation and interpretation of a variety of molecular quantities such as charges and dipoles,[28–33] enthalpies of formation,[34–36] global QMSI (quantum molecular similarity index) values[37] and Fukui functions (see ref.[38] and refs. therein).

## Theory and Computational Details

In the Hirshfeld Scheme[27,28] the number of electrons attributed to an atom A in a molecule, $N_A$, is defined as in Equation (2),

$$N_A = \int d\boldsymbol{r} \frac{\rho_A(\boldsymbol{r})}{\sum_X \rho_X(\boldsymbol{r})} \rho_M(\boldsymbol{r}) \tag{2}$$

in which $\rho_M(\boldsymbol{r})$ is the molecular density at position $\boldsymbol{r}$, $\rho_A(\boldsymbol{r})$ is the atomic density and $\sum_X \rho_X(\boldsymbol{r})$ constitutes the pro-molecular density. In a way similar to the definition of the atomic charge,[28–33] the Hirshfeld overlap population (HOP), $B_{AB}$, can be defined by Equation (3),

$$B_{AB} = \int d\boldsymbol{r} \frac{\rho_A(\boldsymbol{r})\rho_B(\boldsymbol{r})}{\left(\sum_X \rho_x(\boldsymbol{r})\right)^2} \rho_M(\boldsymbol{r}) \tag{3}$$

which is the special case of the fuzzy atom overlap population defined earlier[18] in which the weight factors have been replaced by those specified by Hirshfeld. Full geometry optimisations of the structures of all the molecules studied in this work were performed using the Gaussian 03 program package[39] applying Density Functional Theory (DFT) with the hybrid B3LYP functional[40] and the cc-pVTZ basis set; the basis set was used as it is implemented in the program. The Wiberg and NAO bond orders and the NPA charges were calculated using the NBO 3.0 program[41] as it is implemented in the Gaussian 03 program package. Mayer and Fuzzy bond orders and Mulliken and Fuzzy charges were calculated using the program Fuzzy.[42] The Hirshfeld overlap populations and stockholder charges were calculated using the BRABO program package.[43]

## Results and Discussion

### Comparison of Overlap Populations and Bond Orders for Homodiatomic and Simple Organic Molecules

In order to evaluate our new Hirshfeld overlap populations (HOP) as they are defined by Equation (3), the values

 © 2006 Wiley-VCH Verlag GmbH & Co. KGaA, Weinheim 

were compared to the corresponding Mulliken and Fuzzy overlap populations and to the Mayer, Wiberg, NAO and Fuzzy bond orders for a set of simple organic and inorganic molecules. The results have been compiled in Table 1. The values of the overlap populations are considerably smaller than those of the bond orders. In order to make comparison of the data easier, we have scaled the overlap populations in such a way that they are in line with the formal bond orders of 1, 1.5, 2, and 3 for the CC bonds in ethane, benzene, ethene, and ethyne, respectively. Therefore, these four compounds and their bond order values were used to construct a linear function between the calculated and formal bond orders and this has been presented graphically in Figure 2; the relevant data of the trendlines have been given in Table 2. Although this scaling is arbitrary it does have the advantage that it produces numbers comparable to the bond orders expected by chemical intuition. For reasons of comparison similar linear regression curves were calculated for the bond order schemes as well. Figure 2 and Table 2 indicate that the slopes of the regression lines for the Wiberg, Mayer and Fuzzy bond orders are close to 1, precluding any form of scaling. The values of the NAO bond orders and of the three overlap populations are lower in absolute value, but correlate very well linearly with the formal bond orders as can be seen from the $R^2$ values given in Table 2. On the basis of the equations of the regression lines obtained for the three overlap populations and the NAO bond orders, scaled equivalents of these were calculated, and these are also given in Table 1 as sHOP (scaled Hirshfeld overlap population), sMOP (scaled Mulliken overlap population), sFOP (scaled Fuzzy overlap population) and sNAO (scaled NAO bond order).

The bond orders and overlap populations of the different bonds in a series of substituted ethynes (RC≡CH), ethenes ($RHC=CH_2$) and ethanes ($RH_2C–CH_3$) were calculated and the changes of the bond order or overlap population as a function of the substituents (R = H, $CH_3$, F, Cl and CHO) were examined. All schemes used reflect the expected trends. For the homodiatomic molecules, basic chemical knowledge suggests that there is a single bond in $H_2$, $F_2$ and $Cl_2$, a double bond in $O_2$ and a triple bond in $N_2$; the respective bond orders are then 1, 2 and 3. The scaled Hirshfeld overlap population of 1.91 for $O_2$ is remarkable, as is the value of 1.87 obtained with the Mayer scheme; the other methods show much lower or higher values, despite the commonly accepted bond order value of 2. In contrast, the values of sHOP for both $H_2$ and $F_2$ are quite low. It is important to note that there is a significant difference between the Wiberg and Mayer bond orders on the one hand, and the Hirshfeld and Fuzzy overlap populations and the NAO bond order on the other. In each case, the Wiberg/Mayer values are very close to the formal bond order of 1 but are independent of the strength of the bond, while the Hirshfeld/NAO/Fuzzy values seem to provide additional information on the bond strength (i.e. they give larger numbers for stronger single bonds and smaller values for weaker single bonds). The Wiberg bond order of the F–F bond is 1.01 and virtually equal to that of the H–H bond, while both sNAO and sHOP suggest a weaker bond in $F_2$ which is in accordance with the small dissociation energy of the F–F bond.[44] Table 1 also contains a number of negative values which are clearly due to the scaling procedure. Even though these values have lost their quantitative meaning they are still useful on a qualitative level.

In order to compare the values of the scaled Hirshfeld overlap population with those of the other investigated quantities, the latter were plotted against the scaled Hirshfeld overlap populations in Figure 3; all carbon–carbon bonds compiled in Table 1 have been included. As can be seen from Figure 3 the Hirshfeld overlap population correlates quite well with all the other bond order and overlap population schemes except with the Mulliken overlap population. The correlation with NAO is the best.

As mentioned in the introduction, since Pauling's original suggestion several authors have confirmed the bond orders' exponential decrease with the bond length. In Figure 4 the values of the bond orders and overlap population calculated using the different methods were plotted against the

Table 1. Calculated bond lengths ($r_e$ in Å), the corresponding Hirshfeld (HOP), Fuzzy (FOP) and Mulliken (MOP) overlap populations together with their scaled equivalents (sHOP, sFOP and sMOP), and the NAO (NAO), scaled NAO (sNAO), Wiberg (WBO), Mayer (MBO) and Fuzzy (FBO) bond orders for a number of organic and diatomic compounds. See text for details. * These compounds were used for scaling.

| | | | Overlap populations | | | | | | Bond orders | | | | |
|---|---|---|---|---|---|---|---|---|---|---|---|---|---|
| | bond | $r_e$ | HOP | FOP | MOP | sHOP | sFOP | sMOP | NAO | sNAO | WBO | MBO | FBO |
| $HC\equiv CH$* | C≡C | 1.1960 | 0.82 | 0.46 | 0.83 | 3.00 | 2.96 | 2.93 | 2.00 | 3.01 | 3.00 | 2.73 | 2.85 |
| $H_2C=CH_2$* | C=C | 1.3242 | 0.59 | 0.38 | 0.62 | 1.98 | 2.11 | 2.09 | 1.43 | 1.98 | 2.05 | 1.91 | 1.97 |
| $H_3C-CH_3$* | C–C | 1.5262 | 0.37 | 0.28 | 0.33 | 0.99 | 1.09 | 0.92 | 0.90 | 1.02 | 1.05 | 0.96 | 1.14 |
| Benzene* | CC | 1.3907 | 0.49 | 0.31 | 0.49 | 1.53 | 1.33 | 1.57 | 1.16 | 1.49 | 1.44 | 1.37 | 1.37 |
| $H_3\overset{1}{C}-\overset{2}{C}\equiv\overset{3}{C}-\overset{4}{C}H_3$ | C≡C | 1.2010 | 0.80 | 0.44 | 0.52 | 2.92 | 2.76 | 1.68 | 1.94 | 2.91 | 2.78 | 2.50 | 2.64 |
| | C–C | 1.4566 | 0.44 | 0.29 | 0.52 | 1.31 | 1.19 | 1.68 | 0.97 | 1.16 | 1.09 | 1.09 | 1.20 |

 © 2006 Wiley-VCH Verlag GmbH & Co. KGaA, Weinheim 

Table 1. *(continued)*

| | | | | | | | | | | | | | |
|---|---|---|---|---|---|---|---|---|---|---|---|---|---|
| 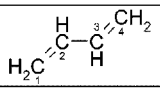 | C–C | 1.4527 | 0.44 | 0.28 | 0.42 | 1.28 | 1.10 | 1.26 | 0.96 | 1.14 | 1.13 | 1.07 | 1.19 |
| | C=C | 1.3339 | 0.57 | 0.36 | 0.60 | 1.88 | 1.87 | 2.01 | 1.37 | 1.87 | 1.89 | 1.77 | 1.82 |
| 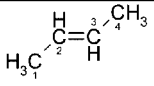 | C=C | 1.3283 | 0.57 | 0.35 | 0.65 | 1.88 | 1.82 | 2.20 | 1.38 | 1.90 | 1.92 | 1.85 | 1.83 |
| | C–C | 1.4976 | 0.40 | 0.28 | 0.36 | 1.11 | 1.06 | 1.05 | 0.89 | 1.01 | 1.06 | 0.98 | 1.14 |
| $H_3C-C\equiv C-H$ | C–C | 1.4549 | 0.44 | 0.29 | 0.39 | 1.30 | 1.19 | 1.14 | 0.98 | 1.17 | 1.10 | 1.02 | 1.20 |
| | C≡C | 1.1989 | 0.81 | 0.45 | 0.80 | 2.96 | 2.86 | 2.80 | 1.98 | 2.98 | 2.88 | 2.65 | 2.74 |
| 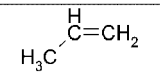 | C–C | 1.4968 | 0.40 | 0.28 | 0.36 | 1.10 | 1.06 | 1.02 | 0.90 | 1.02 | 1.06 | 0.97 | 1.14 |
| | C=C | 1.3265 | 0.58 | 0.37 | 0.64 | 1.93 | 1.97 | 2.15 | 1.41 | 1.95 | 1.98 | 1.87 | 1.90 |
| 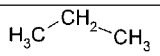 | C–C | 1.5277 | 0.36 | 0.27 | 0.34 | 0.95 | 0.94 | 0.97 | 0.85 | 0.94 | 1.04 | 0.95 | 1.11 |
| $FC\equiv CH$ | F–C | 1.2777 | 0.49 | 0.30 | 0.38 | 1.55 | 1.29 | 1.10 | 0.87 | 0.97 | 1.00 | 1.21 | 1.25 |
| | C≡C | 1.1917 | 0.82 | 0.43 | 0.64 | 3.04 | 2.67 | 2.16 | 1.95 | 2.94 | 2.84 | 2.62 | 2.64 |
| $FHC=CH_2$ | F–C | 1.3462 | 0.43 | 0.28 | 0.36 | 1.24 | 1.10 | 1.03 | 0.77 | 0.79 | 0.90 | 1.10 | 1.17 |
| | C=C | 1.3172 | 0.59 | 0.34 | 0.56 | 1.99 | 1.65 | 1.83 | 1.43 | 1.98 | 1.96 | 1.84 | 1.81 |
| $FH_2C-CH_3$ | F–C | 1.3974 | 0.38 | 0.27 | 0.33 | 1.02 | 0.91 | 0.91 | 0.62 | 0.51 | 0.85 | 1.02 | 1.11 |
| | C–C | 1.5094 | 0.38 | 0.24 | 0.33 | 1.02 | 0.68 | 0.90 | 0.90 | 1.02 | 1.04 | 0.97 | 1.05 |
| Fluorobenzene | F–C | 1.3503 | 0.42 | 0.27 | 0.39 | 1.19 | 0.95 | 1.15 | 0.76 | 0.78 | 0.89 | 1.11 | 1.11 |
| $ClC\equiv CH$ | Cl–C | 1.6424 | 0.53 | 0.34 | 0.41 | 1.72 | 1.73 | 1.24 | 0.99 | 1.19 | 1.18 | 1.29 | 1.46 |
| | C≡C | 1.1977 | 0.81 | 0.43 | 0.68 | 2.95 | 2.68 | 2.33 | 1.93 | 2.89 | 2.80 | 2.58 | 2.64 |
| $ClHC=CH_2$ | Cl–C | 1.7452 | 0.43 | 0.30 | 0.29 | 1.24 | 1.29 | 0.75 | 0.85 | 0.93 | 1.06 | 1.06 | 1.29 |
| | C=C | 1.3198 | 0.58 | 0.35 | 0.63 | 1.95 | 1.76 | 2.09 | 1.42 | 1.97 | 1.97 | 1.85 | 1.84 |
| $ClH_2C-CH_3$ | Cl–C | 1.8185 | 0.36 | 0.27 | 0.25 | 0.93 | 0.91 | 0.57 | 0.75 | 0.75 | 0.99 | 0.99 | 1.19 |
| | C–C | 1.5131 | 0.37 | 0.26 | 0.34 | 1.00 | 0.80 | 0.95 | 0.88 | 0.98 | 1.05 | 0.96 | 1.08 |
| $OHC_1-C_2\equiv C_3H$ | C–C | 1.4458 | 0.46 | 0.28 | -0.02 | 1.37 | 1.09 | -0.49 | 1.00 | 1.22 | 1.08 | 0.88 | 1.18 |
| | C≡C | 1.2012 | 0.79 | 0.44 | 0.75 | 2.90 | 2.74 | 2.60 | 1.95 | 2.92 | 2.84 | 2.63 | 2.68 |
| | C=O | 1.2066 | 0.64 | 0.40 | 0.78 | 2.19 | 2.36 | 2.71 | 1.35 | 1.83 | 1.85 | 2.18 | 2.24 |
| $OHC_1-HC_2=CH_2$ | C–C | 1.4707 | 0.42 | 0.28 | 0.16 | 1.21 | 1.01 | 0.22 | 0.95 | 1.11 | 1.07 | 0.90 | 1.14 |
| | C=O | 1.2082 | 0.64 | 0.41 | 0.00 | 2.19 | 2.39 | -0.41 | 1.34 | 1.82 | 1.83 | 2.13 | 2.23 |
| | C=C | 1.3310 | 0.57 | 0.36 | 0.00 | 1.88 | 1.86 | -0.41 | 1.37 | 1.87 | 1.91 | 1.75 | 1.83 |
| $OHC_1-H_2C_2-CH_3$ | $C_1$–$C_2$ | 1.5059 | 0.38 | 0.26 | 0.16 | 1.03 | 0.88 | 0.22 | 0.90 | 1.02 | 1.01 | 0.90 | 1.09 |
| | $C_2$–$C_3$ | 1.5223 | 0.37 | 0.27 | 0.25 | 0.97 | 0.90 | 0.61 | 0.85 | 0.93 | 1.03 | 0.95 | 1.10 |
| | C=O | 1.2040 | 0.64 | 0.41 | 0.77 | 2.19 | 2.39 | 2.66 | 1.35 | 1.85 | 1.88 | 2.20 | 2.27 |
| $CH_4$ | C–H | 1.0883 | 0.34 | 0.15 | 0.40 | 0.85 | -0.32 | 1.18 | 0.77 | 0.79 | 0.96 | 0.97 | 0.98 |
| $CH_3NH_2$ | C–N | 1.4636 | 0.39 | 0.30 | 0.34 | 1.05 | 1.25 | 0.96 | 0.83 | 0.90 | 1.03 | 0.99 | 1.27 |
| $CH_3OH$ | C–O | 1.4194 | 0.39 | 0.31 | 0.35 | 1.09 | 1.38 | 0.99 | 0.74 | 0.74 | 0.96 | 1.03 | 1.38 |
| $CH_3SH$ | C–S | 1.8304 | 0.39 | 0.29 | 0.26 | 1.06 | 1.11 | 0.64 | 0.79 | 0.83 | 1.04 | 1.01 | 1.26 |
| $CH_3SeH$ | C–Se | 1.9738 | 0.34 | 0.26 | 0.25 | 0.85 | 0.85 | 0.57 | 0.74 | 0.73 | 1.03 | 1.00 | 1.20 |
| $CH_2O$ | C=O | 1.1990 | 0.65 | 0.42 | 0.71 | 2.26 | 2.56 | 2.45 | 1.37 | 1.87 | 1.95 | 2.14 | 2.36 |
| $H_2$ | H–H | 0.7429 | 0.31 | 0.12 | 0.42 | 0.72 | -0.58 | 1.26 | 0.80 | 0.84 | 1.00 | 1.00 | 1.00 |
| $N_2$ | N≡N | 1.0914 | 0.83 | 0.47 | 0.75 | 3.07 | 3.08 | 2.60 | 1.92 | 2.88 | 3.03 | 2.93 | 3.11 |
| $O_2$ | O=O | 1.2058 | 0.57 | 0.40 | 0.16 | 1.91 | 2.29 | 0.23 | 0.94 | 1.10 | 1.52 | 1.87 | 2.49 |
| $F_2$ | F–F | 1.3976 | 0.31 | 0.29 | 0.03 | 0.69 | 1.16 | -0.28 | 0.33 | -0.01 | 1.01 | 0.96 | 1.58 |
| $Cl_2$ | Cl–Cl | 2.0231 | 0.44 | 0.39 | 0.09 | 1.29 | 2.25 | -0.04 | 0.52 | 0.33 | 1.04 | 1.07 | 1.81 |

 © 2006 Wiley-VCH Verlag GmbH & Co. KGaA, Weinheim 

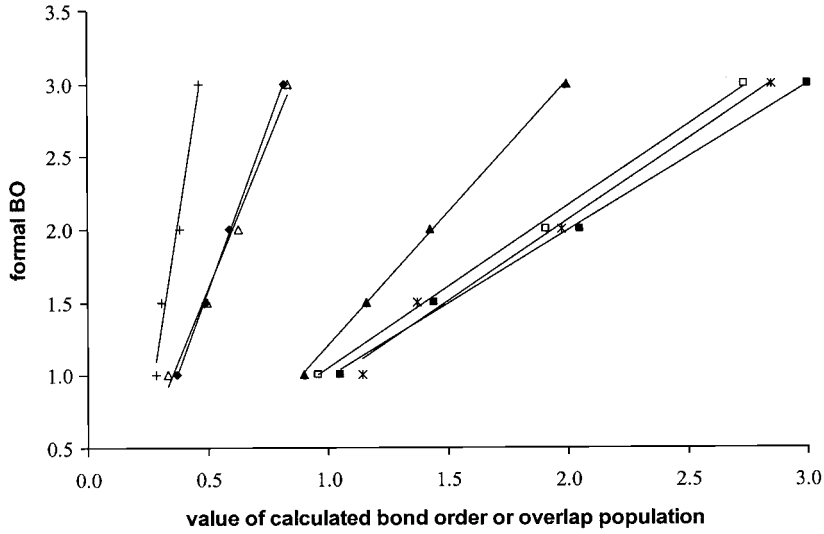


Figure 2. Calculated bond orders within the NAO (▲), Mayer (□), Fuzzy (*) and Wiberg (■) schemes and calculated overlap populations within the Hirshfeld (♦), Fuzzy (+) and Mulliken (Δ) schemes for ethane, ethene, ethyne and benzene plotted against their formal bond orders of 3, 2, 1 and 1.5. The relevant data regarding the trendlines is given in Table 2.

Table 2. Relevant data regarding the trendlines in Figure 2.

| | | Equation | $R^2$ |
|---|---|---|---|
| Bond orders | NAO (▲) | $y = 1.814\ x - 0.607$ | 1.000 |
| | Wiberg (■) | $y = 1.005\ x - 0.020$ | 0.996 |
| | Mayer (□) | $y = 1.110\ x - 0.058$ | 0.998 |
| | Fuzzy (*) | $y = 1.113\ x - 0.163$ | 0.985 |
| Overlap populations | Hirshfeld (♦) | $y = 4.518\ x - 0.686$ | 0.999 |
| | Fuzzy (+) | $y = 10.55\ x - 1.900$ | 0.977 |
| | Mulliken (Δ) | $y = 4.005\ x - 0.410$ | 0.989 |

bond length for the carbon–carbon bonds presented in Table 1. The function in Equation (4),

$$n = A \cdot \exp[-r/b] \quad (4)$$

was then fitted to the data. Compared to Equation (1) a parameter $A$ was introduced which results from two considerations. First, instead of plotting $(r - r_0)$ against $n$, only $r$ was, which resulted in a right-shift of the curve by $r_0$. This does not effect the goodness of the exponential fit, the correlation coefficients or the decay parameter $b$. Secondly, the non-scaled bond orders and overlap populations were used in these fits in order to avoid confusion because of the scaling, taking into account that the latter values are much lower than the formal bond orders, which are present in Equation (1). Table 3 contains the parameters $A$ and $b$ used in the different fits. Our results are in accordance with the earlier findings: with the exception of the Mulliken overlap population all investigated quantities decrease exponentially with the bond length, with $R^2$ values above 0.97 (except for the fuzzy overlap population). The $R^2$ values are largest for the NAO bond order and the Hirshfeld overlap population. For the Wiberg and Mayer bond orders, the

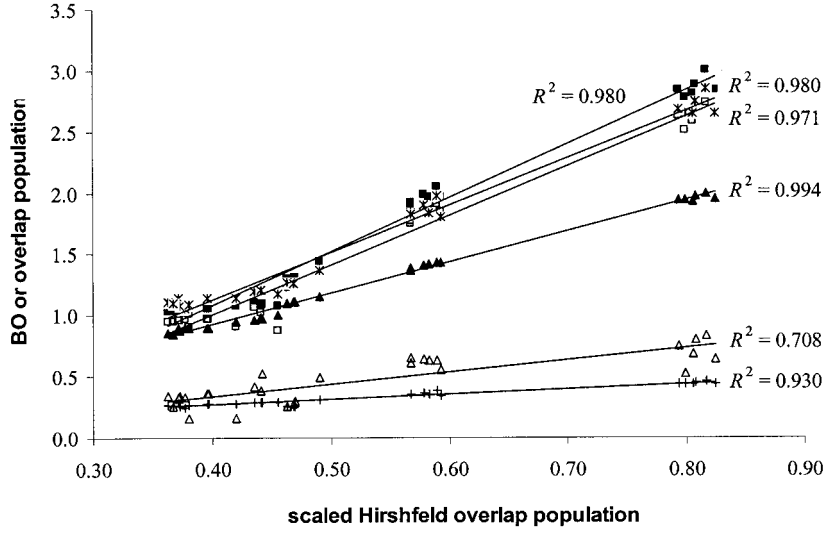


Figure 3. The scaled Hirshfeld overlap population vs. the Wiberg (■), the Fuzzy (*), the Mayer (□) and the scaled NAO (▲) bond orders and the scaled Fuzzy (+) and scaled Mulliken (Δ) overlap populations for the carbon–carbon bonds in the compounds of Table 1.

 © 2006 Wiley-VCH Verlag GmbH & Co. KGaA, Weinheim 

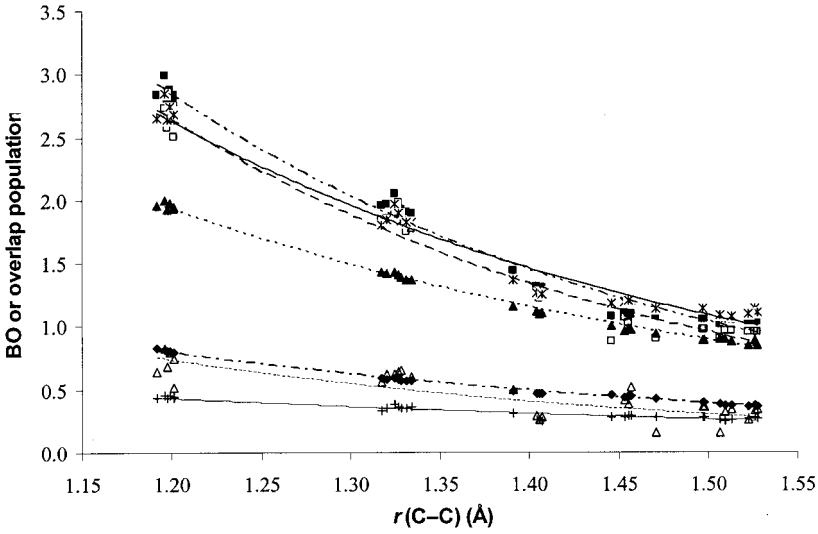


Figure 4. Exponential fit of the Wiberg (■), the Fuzzy (*), the Mayer (□) and the NAO (▲) bond orders and the unscaled Hirshfeld (♦), Fuzzy (+) and Mulliken (Δ) overlap populations vs. the *r*(C–C) of Table 1. See Table 3 for the values of the fitting parameters and the correlation coefficients.

Table 3. Parameters *A* and *b* (in Å) used in the exponential fits in the bond length vs. bond order/overlap population curves in Figure 4 and Figure 5, combined with the correlation coefficients of these fits.

| | | *r*(C–C) | | | *r*(N–S) | | |
|---|---|---|---|---|---|---|---|
| | | *A* | *b* | $R^2$ | *A* | *b* | $R^2$ |
| Bond orders | NAO (▲) | 42.11 | 0.389 | 0.994 | 112.6 | 0.337 | 0.859 |
| | Wiberg (■) | 162.10 | 0.297 | 0.973 | 3878 | 0.198 | 0.797 |
| | Mayer (□) | 157.67 | 0.293 | 0.962 | 2674 | 0.211 | 0.878 |
| | Fuzzy (*) | 88.88 | 0.341 | 0.965 | 2309 | 0.220 | 0.902 |
| Overlap populations | Hirshfeld (♦) | 13.83 | 0.419 | 0.994 | 54.32 | 0.344 | 0.989 |
| | Fuzzy (+) | 3.117 | 0.607 | 0.872 | 35.57 | 0.342 | 0.921 |
| | Mulliken (Δ) | 26.22 | 0.336 | 0.605 | 54.46 | 0.321 | 0.367 |

value of the *b* parameter is about 0.29 Å, which is close to Pauling's "universal" value of 0.26 Å.

### Chalcogen–Nitrogen Compounds

For common organic compounds, all methodologies except the Mulliken overlap population give virtually equally good results. Consequently, it is logical to investigate their performance for more exotic systems, in particular compounds **1**–**4**, which are of special interest to our research.[3–6] First, a number of simple compounds which contain formal single, double and triple NS and NSe bonds were studied. The results are given in Table 4. On the basis of these the values, the bond orders and overlap populations calculated for compounds **1**–**4** can be interpreted in the second part of this discussion.

It is important to note that while the values of the scaled Hirshfeld overlap population (sHOP) and the Wiberg and Mayer bond orders correspond to a single NX (X = O,S,Se) bond in $NH_2OH$, $NH_2SH$ and $NH_2SeH$ and a double NX bond in HN=O and HN=S, the values of the scaled NAO bond order and the Mulliken overlap population are lower, and those of both the scaled Fuzzy overlap population and the Fuzzy bond order are larger. In every case the sulfur–nitrogen bonds have a larger bond order/overlap population than the corresponding selenium–nitrogen bonds (except in the case of the scaled Mulliken overlap population) which can be explained by the fact that heavier elements do not prefer to form double or triple bonds. Furthermore, the weakening of the double bond in the N=O > N=S > N=Se series is confirmed by all except the Mayer and Mulliken schemes.

While the NS bond length is considerably shorter in HN=S=NH and HN=Se=NH than in HN=S and HN=Se, respectively (in both cases by about 0.03 Å), the Wiberg, Mayer and Fuzzy bond orders are smaller in the diimino species. The Hirshfeld and NAO methods, on the contrary, show approximately the same bond order for the di- and monoimino species. As there seems to be a contradiction between the conclusions based on bond orders and bond lengths, we calculated the ellipticity and the electron density in the bond critical points of the N=X (X = S,Se) bonds of these four molecules with the Atoms In Molecules (AIM) theory.[45,46] Table 5 collects the results. The relatively large ellipticity values for all four compounds indicates the presence of NS and NSe double bonds in the compounds, but the values obtained for HN=X=NH are particularly large. The increase of the electron density in the bond critical point upon going from the monoimino to the diimino species

 © 2006 Wiley-VCH Verlag GmbH & Co. KGaA, Weinheim 

Table 4. Calculated bond lengths ($r_e$ in Å), the corresponding Hirshfeld (HOP), Fuzzy (FOP) and Mulliken (MOP) overlap populations together with their scaled equivalents (sHOP, sFOP and sMOP) and the NAO (NAO), scaled NAO (sNAO), Wiberg (WBO), Mayer (MBO) and Fuzzy (FBO) bond orders for a number of systems containing NS and NSe bonds and compounds **1**–**4**. See text for details.

| | | | Overlap populations | | | | | | Bond orders | | | | |
|---|---|---|---|---|---|---|---|---|---|---|---|---|---|
| | bond | $r_e$ | HOP | FOP | MOP | sHOP | sFOP | sMOP | NAO | sNAO | WBO | MBO | FBO |
| $NH_2OH$ | N–O | 1.4268 | 0.34 | 0.28 | 0.17 | 0.83 | 1.06 | 0.25 | 0.61 | 0.50 | 1.00 | 0.95 | 1.38 |
| $NH_2SH$ | N–S | 1.7337 | 0.41 | 0.32 | 0.23 | 1.18 | 1.48 | 0.49 | 0.74 | 0.74 | 1.00 | 1.05 | 1.51 |
| $NH_2SeH$ | N–Se | 1.8798 | 0.36 | 0.30 | 0.24 | 0.92 | 1.25 | 0.56 | 0.68 | 0.63 | 0.97 | 1.06 | 1.47 |
| HN=O | N=O | 1.1985 | 0.61 | 0.41 | 0.34 | 2.07 | 2.37 | 0.96 | 1.18 | 1.53 | 2.02 | 1.95 | 2.40 |
| HN=S | N=S | 1.5715 | 0.59 | 0.40 | 0.36 | 1.96 | 2.31 | 1.04 | 1.12 | 1.43 | 1.97 | 1.96 | 2.37 |
| HN=Se | N=Se | 1.7210 | 0.51 | 0.37 | 0.37 | 1.61 | 1.98 | 1.09 | 1.02 | 1.24 | 1.93 | 1.97 | 2.34 |
| N≡SH | N≡S | 1.5040 | 0.69 | 0.44 | 0.56 | 2.44 | 2.77 | 1.82 | 1.37 | 1.87 | 2.13 | 2.28 | 2.61 |
| N≡SeH | N≡Se | 1.6581 | 0.60 | 0.42 | 0.54 | 2.04 | 2.51 | 1.75 | 1.22 | 1.60 | 2.07 | 2.26 | 2.58 |
| HN=S=NH | N=S | 1.5464 | 0.60 | 0.39 | 0.35 | 2.01 | 2.26 | 0.99 | 1.12 | 1.42 | 1.54 | 1.71 | 2.10 |
| | N···N | 2.5289 | 0.02 | 0.00 | -0.04 | | | | 0.00 | | 0.00 | 0.22 | 0.00 |
| HN=Se=NH | N=Se | 1.7039 | 0.51 | 0.37 | 0.39 | 1.63 | 2.01 | 1.14 | 0.99 | 1.18 | 1.50 | 1.71 | 2.07 |
| | N···N | 2.7072 | 0.01 | 0.00 | -0.03 | | | | 0.00 | | 0.00 | 0.26 | 0.00 |
| 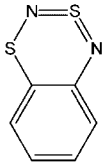 | CC | 1.4052 | 0.46 | 0.26 | 0.26 | 1.40 | 0.83 | 0.62 | 1.10 | 1.39 | 1.30 | 1.22 | 1.27 |
| | $C_{8a}$–$N_4$ | 1.4104 | 0.43 | 0.26 | 0.41 | 1.24 | 0.79 | 1.21 | 0.94 | 1.10 | 1.09 | 1.13 | 1.19 |
| | $N_4$=$S_3$ | 1.5556 | 0.59 | 0.38 | 0.46 | 1.96 | 2.13 | 1.44 | 1.09 | 1.36 | 1.39 | 1.61 | 1.91 |
| | $S_3$=$N_2$ | 1.5600 | 0.58 | 0.36 | 0.40 | 1.93 | 1.94 | 1.21 | 1.10 | 1.39 | 1.43 | 1.59 | 1.88 |
| | $N_2$–$S_1$ | 1.7032 | 0.44 | 0.30 | 0.24 | 1.32 | 1.25 | 0.53 | 0.80 | 0.85 | 0.99 | 1.05 | 1.39 |
| | $S_1$–$C_{8a}$ | 1.8098 | 0.40 | 0.26 | 0.27 | 1.11 | 0.86 | 0.67 | 0.81 | 0.86 | 0.99 | 0.98 | 1.15 |
| | $N_2$···$N_4$ | 2.6817 | 0.01 | 0.00 | -0.06 | | | | 0.00 | | 0.00 | 0.22 | 0.00 |
| 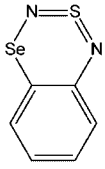 | CC | 1.4041 | 0.47 | 0.26 | 0.29 | 1.43 | 0.80 | 0.77 | 1.11 | 1.41 | 1.31 | 1.25 | 1.27 |
| | $C_{8a}$–$N_4$ | 1.4069 | 0.43 | 0.26 | 0.41 | 1.26 | 0.80 | 1.21 | 0.94 | 1.10 | 1.09 | 1.13 | 1.20 |
| | $N_4$=$S_3$ | 1.5532 | 0.59 | 0.38 | 0.46 | 1.98 | 2.13 | 1.43 | 1.09 | 1.37 | 1.41 | 1.62 | 1.92 |
| | $S_3$=$N_2$ | 1.5559 | 0.59 | 0.36 | 0.40 | 1.99 | 1.90 | 1.21 | 1.12 | 1.43 | 1.46 | 1.62 | 1.88 |
| | $N_2$–$Se_1$ | 1.8587 | 0.38 | 0.29 | 0.23 | 1.02 | 1.14 | 0.50 | 0.72 | 0.71 | 0.92 | 1.00 | 1.36 |
| | $Se_1$–$C_{8a}$ | 1.9524 | 0.35 | 0.26 | 0.26 | 0.90 | 0.80 | 0.61 | 0.79 | 0.83 | 0.97 | 0.97 | 1.12 |
| | $N_2$···$N_4$ | 2.7025 | 0.01 | 0.00 | -0.06 | | | | 0.00 | | 0.00 | 0.23 | 0.00 |
| 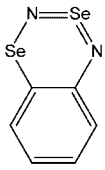 | CC | 1.4071 | 0.47 | 0.25 | 0.28 | 1.43 | 0.77 | 0.71 | 1.11 | 1.41 | 1.30 | 1.24 | 1.25 |
| | $C_{8a}$–$N_4$ | 1.3996 | 0.45 | 0.25 | 0.42 | 1.33 | 0.78 | 1.28 | 1.00 | 1.21 | 1.14 | 1.17 | 1.22 |
| | $N_4$=$Se_3$ | 1.7184 | 0.50 | 0.36 | 0.46 | 1.57 | 1.87 | 1.41 | 0.92 | 1.06 | 1.29 | 1.53 | 1.85 |
| | $Se_3$=$N_2$ | 1.7203 | 0.50 | 0.34 | 0.40 | 1.58 | 1.68 | 1.19 | 0.95 | 1.12 | 1.36 | 1.54 | 1.81 |
| | $N_2$–$Se_1$ | 1.8489 | 0.39 | 0.29 | 0.23 | 1.09 | 1.12 | 0.51 | 0.75 | 0.76 | 0.96 | 1.04 | 1.38 |
| | $Se_1$–$C_{8a}$ | 1.9557 | 0.35 | 0.25 | 0.24 | 0.89 | 0.75 | 0.57 | 0.78 | 0.81 | 0.96 | 0.95 | 1.11 |
| | $N_2$···$N_4$ | 2.9175 | 0.00 | 0.00 | -0.04 | | | | 0.00 | | 0.00 | 0.24 | 0.00 |
| 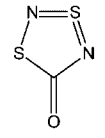 | C=O | 1.1935 | 0.66 | 0.39 | 0.78 | 2.28 | 2.22 | 2.72 | 1.39 | 1.91 | 1.74 | 2.14 | 2.15 |
| | $C_5$–$S_1$ | 1.9134 | 0.33 | 0.23 | 0.28 | 0.81 | 0.50 | 0.72 | 0.75 | 0.75 | 0.87 | 0.90 | 1.01 |
| | $S_1$–$N_2$ | 1.6397 | 0.49 | 0.32 | 0.33 | 1.52 | 1.43 | 0.92 | 0.96 | 1.14 | 1.21 | 1.28 | 1.56 |
| | $N_2$=$S_3$ | 1.5972 | 0.53 | 0.33 | 0.38 | 1.69 | 1.63 | 1.13 | 1.04 | 1.28 | 1.36 | 1.49 | 1.74 |
| | $S_3$=$N_4$ | 1.5832 | 0.54 | 0.36 | 0.43 | 1.77 | 1.87 | 1.32 | 1.03 | 1.27 | 1.28 | 1.45 | 1.74 |
| | $N_4$–$C_5$ | 1.3700 | 0.47 | 0.27 | 0.44 | 1.43 | 0.97 | 1.34 | 1.11 | 1.40 | 1.24 | 1.28 | 1.31 |
| | $N_2$···$N_4$ | 2.5642 | 0.01 | 0.00 | -0.05 | | | | 0.00 | | 0.00 | 0.18 | 0.00 |

indicates a strengthening of the N=S and N=Se bonds as well. A possible explanation for the decrease of the values of the Wiberg, Mayer and Fuzzy bond orders and the Mulliken and Fuzzy overlap populations is that these methods are much more sensitive to the valence state of the atom than the other methods; after all, HN=X contains a divalent and HN=X=NH a tetravalent chalcogen atom. As a further possibility, we checked whether there is any bonding between the two nitrogen atoms in these molecules. The Mayer bond order value of about 0.24 shows weak bonding between these atoms, but none of the other methods supports this. The overlap-population-based methodologies can not be used for non-bonded atoms as the overlap populations in theses cases are always very low if not zero.

Table 5. Ellipticity ($\varepsilon$) and electron density in the bond critical point ($\rho_{BCP}$) of the N=S and N=Se bonds in HN=S, HN=S=NH, HN=Se and HN=Se=NH.

| | $\varepsilon$ | $\rho_{BCP}$ |
|---|---|---|
| HN=S | 0.083 | 0.250 |
| HN=S=NH | 0.392 | 0.275 |
| HN=Se | 0.125 | 0.206 |
| HN=Se=NH | 0.244 | 0.220 |

 © 2006 Wiley-VCH Verlag GmbH & Co. KGaA, Weinheim 

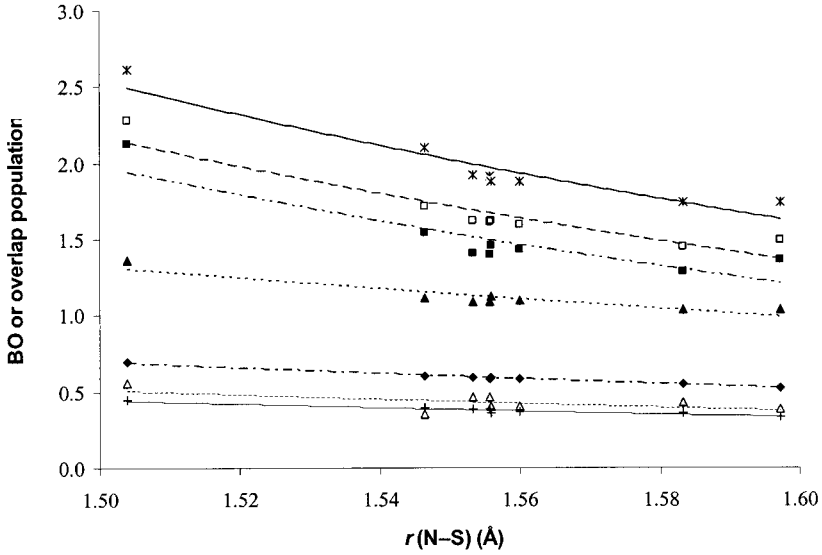


Figure 5. Exponential fit of the Wiberg (■), the Fuzzy (*), the Mayer (□) and the NAO (▲) bond orders and the unscaled Hirshfeld (♦), Fuzzy (+) and Mulliken (Δ) overlap populations vs. the *r*(N–S) of Table 4. See Table 3 for the values of the fitting parameters and the correlation coefficients.

In the second part of this discussion we will consider the bonding in compounds **1**–**4** with the above conclusion in mind. The calculated geometrical parameters and conformation of **1** are in accordance with earlier results.[3] An isolated molecule of **1** has a bent geometry and two short and one long NS bonds (see Table 4). Compounds **2** and **3** have the same conformation as **1** in the gas phase, and the bond lengths indicate similar bonding patterns in all three molecules. The scaled Hirshfeld and Fuzzy overlap populations and the Fuzzy bond orders in Table 4 are much larger than the other values for the N=S double bonds and they are in accordance with the conclusions based on the bond lengths. Only the Hirshfeld, Fuzzy bond order and NAO schemes suggest that the N=S bonds in **1** are of similar strength as those in HN=S=NH. In contrast, the Wiberg and Mayer bond orders are even smaller for the ring compounds than for HN=S=NH. As the NAO values are too small, only the scaled Hirshfeld overlap populations and Fuzzy bond orders are consistent with the conclusion based on the bond lengths. As was shown above, the AIM theory showed that for these compounds a shorter bond length indicates a stronger bond, and we can conclude that **1** contains two double and one single NS bonds. It is clear from Table 4 that the same conclusions can be drawn for compounds **2** and **3**. For the latter the bond order values have decreased in agreement with the observations made on the model compounds.

Comparison of the bond orders and bond lengths calculated for Roesky's ketone (**4**) further supports π-electron delocalisation and the aromaticity of Roesky's ketone. It was shown earlier that Roesky's ketone (**4**) is aromatic which is indicated by both the NICS value and the equalisation of the bond lengths within the ring.[5] When going from **1** to Roesky's ketone (**4**) the N=S double bond lengths increase from about 1.55 Å to about 1.58 and 1.59 Å, while the N–S single bond shortens from about 1.70 Å to about 1.64 Å. In accordance with this, the scaled Hirshfeld overlap populations of the double bonds in **4** are only 1.69 and 1.77, compared to 1.93 and 1.96 in **1**; the bond order of the single NS bond is 1.52 in **4**, while only 1.32 in **1**. The same trends can be seen in the Fuzzy, the Wiberg, the NAO and the Mayer bond orders, although the differences are far less pronounced.

Although it is known that for inorganic systems the relationship between bond order and bond length is much weaker than in organic molecules, we investigated whether Pauling's curve is applicable to our chalcogen-nitrogen systems. The calculated NS bond lengths were plotted against the values obtained from the different methodologies in Figure 5 for the tetravalent sulfur atoms; Table 3 contains the data relevant to the plots. The divalent sulfur atoms were not included in the fit, as the valence state of the atom may seriously influence this type of relationship. From Figure 5 and Table 3 it is clear that for these systems the exponential relationship between bond length and bond order/overlap population holds, but that the best correlation was found in the case of the Hirshfeld and Fuzzy overlap populations. The correlation in the case of bond orders is definitely inferior.

## Conclusions

Several types of overlap populations and bond orders were compared for a large set of common organic and diatomic molecules and applied to the description of chalcogen-nitrogen systems. It has been shown that the different overlap populations (with the exception of Mulliken) and bond orders correlate very well with bond lengths. In addition, the values obtained from the different methodologies correlate well amongst themselves. The particular use-

 © 2006 Wiley-VCH Verlag GmbH & Co. KGaA, Weinheim 

fulness of these schemes was demonstrated by examining the bonding in a set of chalcogen-nitrogen compounds which exhibit unusual bonding between heteroatoms. Only the (scaled) Hirshfeld and Fuzzy overlap population schemes produce results that are compatible with the observed bond lengths.

## Acknowledgments

This work was supported by the Flemish-Hungarian Scientific and Technological Joint Fund (TeT B-2/01, BIL 01/72 and BIL 01/17). J. O. and T. V. acknowledge financial support from OTKA Grant T048796.

[1] V. V. Walatka, M. M. Labes, J. H. Perlstei, *Phys. Rev. Lett.* **1973**, *31*, 1139–1142.
[2] R. L. Greene, G. B. Street, L. J. Suter, *Phys. Rev. Lett.* **1975**, *34*, 577–579.
[3] F. Blockhuys, S. L. Hinchley, A. Yu. Marakov, Yu. V. Gatilov, A. V. Zibarev, J. D. Woollins, D. W. H. Rankin, *Chem. Eur. J.* **2001**, *7*, 3592–3602.
[4] A. Y. Makarov, I. Y. Bagryanskaya, F. Blockhuys, C. Van Alsenoy, Y. V. Gatilov, V. V. Knyazev, A. M. Maksimov, T. V. Mikhalina, V. E. Platonov, M. M. Shakirov, A. V. Zibarev, *Eur. J. Inorg. Chem.* **2003**, 77–88.
[5] J. Van Droogenbroeck, K. Tersago, C. Van Alsenoy, S. M. Aucott, H. L. Milton, J. D. Woollins, F. Blockhuys, *Eur. J. Inorg. Chem.* **2004**, 3798–3805.
[6] A.Yu. Makarov, K. Tersago, K. Nivesanond, F. Blockhuys, C. Van Alsenoy, M. K. Kovalev, I.Yu. Bagryanskaya, Yu. V. Gatilov, M. M. Shakirov, A. V. Zibarev, *Inorg. Chem.* submitted for publication.
[7] A. W. Cordes, M. Hojo, H. Koenig, M. C. Noble, R. T. Oakley, W. T. Pennington, *Inorg. Chem.* **1986**, *25*, 1137–1145.
[8] A. Y. Makarov, I. Y. Bagryanskaya, Y. V. Gatilov, T. V. Mikhalina, M. M. Shakirov, L. N. Shchegoleva, A. Zibarev, *Heteroat. Chem.* **2001**, *12*, 563–576.
[9] F. H. Allen, O. Kennard, D. G. Watson, L. Brammer, A. G. Orpen, R. Taylor, *J. Chem. Soc., Perkin Trans. 2* **1987**, S1–S19.
[10] Compendium of Chemical Terminology, 2nd edition, **1997**.
[11] I. Mayer, *Chem. Phys. Lett.* **1983**, *97*, 270–274.
[12] I. Mayer, *Int. J. Quantum Chem.* **1986**, *29*, 73–84.
[13] I. Mayer, *Int. J. Quantum Chem.* **1986**, *29*, 477–483.
[14] K. B. Wiberg, *Tetrahedron* **1968**, *24*, 1083–1096.
[15] A. E. Reed, F. Weinhold, *J. Chem. Phys.* **1983**, *78*, 4066–4073.
[16] A. E. Reed, R. B. Weinstock, F. Weinhold, *J. Chem. Phys.* **1985**, *83*, 735–746.
[17] R. C. Bochicchio, L. Lain, A. Torre, *Chem. Phys. Lett.* **2003**, *374*, 567–571.
[18] I. Mayer, P. Salvador, *Chem. Phys. Lett.* **2004**, *383*, 368–375.
[19] A. E. Clark, E. R. Davidson, *Int. J. Quantum Chem.* **2003**, *93*, 384–394.
[20] A. E. Clark, J. L. Sonnenberg, P. J. Hay, R. L. Martin, *J. Chem. Phys.* **2004**, *121*, 2563–2570.
[21] L. Pauling, L. O. Brockway, J. Y. Beach, *J. Am. Chem. Soc.* **1935**, *57*, 2705–2709.
[22] L. Pauling, *J. Am. Chem. Soc.* **1947**, *69*, 542–553.
[23] W. Gordy, *J. Chem. Phys.* **1947**, *15*, 305–310.
[24] J. P. Paolini, *J. Comput. Chem.* **1990**, *11*, 1160–1163.
[25] G. Lendvay, *J. Mol. Struct. (THEOCHEM)* **2000**, *501–502*, 389–393.
[26] I. Mayer, *Int. J. Quantum Chem.* **1984**, *26*, 151–154.
[27] F. L. Hirshfeld, *Theor. Chim. Acta* **1977**, *44*, 129–138.
[28] B. Rousseau, A. Peeters, C. Van Alsenoy, *Chem. Phys. Lett.* **2000**, *324*, 189–194.
[29] E. N. Maslen, M. A. Spackman, *Austr. J. Phys.* **1985**, *38*, 273–287.
[30] E. R. Davidson, S. Chakravorty, *Theor. Chim. Acta* **1992**, *83*, 319–330.
[31] F. De Proft, C. Van Alsenoy, A. Peeters, W. Langenaeker, P. Geerlings, *J. Comput. Chem.* **2002**, *23*, 1198–1209.
[32] F. De Proft, R. Vivas-Reyes, A. Peeters, C. Van Alsenoy, P. Geerlings, *J. Comput. Chem.* **2003**, *24*, 463–469.
[33] M. Zwijnenburg, S. Bromley, C. Van Alsenoy, T. Maschmeyer, *J. Phys. Chem. A* **2002**, *106*, 12376–12385.
[34] A. Ruzsinszky, C. Van Alsenoy, G. I. Csonka, *J. Phys. Chem. A* **2002**, *106*, 12139–12150.
[35] G. I. Csonka, A. Ruzsinszky, J. Oláh, C. Van Alsenoy, *J. Mol. Struct. (THEOCHEM)* **2002**, *589–590*, 1–5.
[36] A. Ruzsinszky, C. Van Alsenoy, G. I. Csonka, *J. Phys. Chem. A* **2003**, *107*, 736–744.
[37] G. Boon, C. Van Alsenoy, F. De Proft, P. Bultinck, P. Geerlings, *J. Phys. Chem. A* **2003**, *107*, 11120–11127.
[38] J. Oláh, C. Van Alsenoy, A. B. Sannigrahi, *J. Phys. Chem. A* **2002**, *106*, 3885–3890.
[39] M. J. Frisch, G. W. Trucks, H. B. Schlegel, G. E. Scuseria, M. A. Robb, J. R. Cheeseman, J. A. Montgomery, Jr., T. Vreven, K. N. Kudin, J. C. Burant, J. M. Millam, S. S. Iyengar, J. Tomasi, V. Barone, B. Mennucci, M. Cossi, G. Scalmani, N. Rega, G. A. Petersson, H. Nakatsuji, M. Hada, M. Ehara, K. Toyota, R. Fukuda, J. Hasegawa, M. Ishida, T. Nakajima, Y. Honda, O. Kitao, H. Nakai, M. Klene, X. Li, J. E. Knox, H. P. Hratchian, J. B. Cross, C. Adamo, J. Jaramillo, R. Gomperts, R. E. Stratmann, O. Yazyev, A. J. Austin, R. Cammi, C. Pomelli, J. W. Ochterski, P. Y. Ayala, K. Morokuma, G. A. Voth, P. Salvador, J. J. Dannenberg, V. G. Zakrzewski, S. Dapprich, A. D. Daniels, M. C. Strain, O. Farkas, D. K. Malick, A. D. Rabuck, K. Raghavachari, J. B. Foresman, J. V. Ortiz, Q. Cui, A. G. Baboul, S. Clifford, J. Cioslowski, B. B. Stefanov, G. Liu, A. Liashenko, P. Piskorz, I. Komaromi, R. L. Martin, D. J. Fox, T. Keith, M. A. Al-Laham, C. Y. Peng, A. Nanayakkara, M. Challacombe, P. M. W. Gill, B. Johnson, W. Chen, M. W. Wong, C. Gonzalez, J. A. Pople, *Gaussian 03*, Revision B.05, Gaussian, Inc., Pittsburgh, PA, **2003**.
[40] P. J. Stephens, F. J. Devlin, C. F. Chabalowski, M. J. Frisch, *J. Phys. Chem.* **1994**, *98*, 11623–11627.
[41] E. D. Glendening, A. E. Reed, J. E. Carpenter, F. Weinhold, NBO, version 3.1.
[42] I. Mayer, P. Salvador, FUZZY, version 1.01; Girona (Italy), October **2003** and Budapest (Hungary), August **2004**.
[43] C. Van Alsenoy, A. Peeters, *J. Mol. Struct. (THEOCHEM)* **1993**, *286*, 19–34.
[44] *Handbook of Chemistry and Physics* (53rd edition), (Ed.: R. C. Weast), The Chemical Rubber Co., Cleveland, USA, **1972**–**1973**.
[45] R. F. W. Bader, *Atoms in Molecules: A quantum theory*; Oxford University Press: Oxford, **1990**.
[46] R. F. W. Bader et al., *AIMPAC: A suite of programs for the AIM theory*; McMaster University: Hamilton, Ontario, Canada, **2000**.

Received: May 31, 2005
Published Online: November 15, 2005

 © 2006 Wiley-VCH Verlag GmbH & Co. KGaA, Weinheim 

DOI: 10.1002/ejic.200500569

# Synthesis of New Half-Sandwich Ruthenium(II) Complexes Bearing Alkenyl- and Alkynylphosphane Ligands

**Josefina Díez,[a] M. Pilar Gamasa,*[a] José Gimeno,[a] Elena Lastra,*[a] and Amparo Villar[a]**

**Keywords:** Indenyl complexes / Phosphane ligands / Ruthenium / Sandwich complexes

Carbonyl substitution of the complex [RuI($\eta^5$-$C_9H_7$)$(CO)_2$] with the activated phosphanes $Ph_2PR$ (R = $CH_2CH{=}CH_2$, $CH_2CH_2CH{=}CH_2$, and C≡CPh) affords the complexes [RuI($\eta^5$-$C_9H_7$)(CO)($Ph_2PR$-κ*P*)] [R = $CH_2CH{=}CH_2$ (**1a**), $CH_2CH_2CH{=}CH_2$ (**1b**), C≡CPh (**1c**)]. The reaction of the complex [RuCl($\eta^5$-$C_9H_7$)$(PPh_3)_2$] with the corresponding phosphanes, in refluxing THF, gives the complexes [RuCl($\eta^5$-$C_9H_7$)($PPh_3$)($Ph_2PR$-κ*P*)] [R = $CH_2CH_2CH{=}CH_2$ (**2b**), C≡CPh (**2c**)] by substitution of $PPh_3$. The cationic derivatives [Ru($\eta^5$-$C_9H_7$)(L)($Ph_2PR$-κ$^3$*P,C,C*)][X] [L = CO, X = $SbF_6$, R = $CH_2CH{=}CH_2$ (**3a**), $CH_2CH_2CH{=}CH_2$ (**3b**); L = $PPh_3$, X = $PF_6$, R = $CH_2CH_2CH{=}CH_2$ (**4b**)] have been prepared by treatment of the complexes **1a**,**b** and **2b** with a halide abstractor such as $AgSbF_6$ or $NaPF_6$, respectively. Deprotonation reactions of the complexes **3b** and **4b** with cesium carbonate have been carried out, giving rise to the neutral complexes [Ru($\eta^5$-$C_9H_7$)(L)($Ph_2PCH_2CH{=}CHCH_2$-κ$^2$*P,C*)] [L = CO (**5a**), $PPh_3$ (**5b**)]. The reaction of complex **3a** with MeCN generates the complex [Ru($\eta^5$-$C_9H_7$)(MeCN)(CO)($Ph_2PCH_2CH{=}CH_2$-κ*P*)][$SbF_6$] (**6**). The vinylidene [Ru($\eta^5$-$C_9H_7$)($PPh_3$)($Ph_2PC{\equiv}CPh$-κ*P*)-{C=C(Ph)H}][$PF_6$] (**7**) and allenylidene [Ru($\eta^5$-$C_9H_7$)($PPh_3$)($Ph_2PC{\equiv}CPh$-κ*P*)(C=C=$CPh_2$)][$PF_6$] (**8**) derivatives have been synthesized by reaction of complex **2c** with phenylacetylene or 1,1-diphenylprop-2-yn-1-ol, respectively. The structures of the derivatives **1c**, **3a**, and **4b** have been determined by single-crystal X-ray diffraction analysis.
(© Wiley-VCH Verlag GmbH & Co. KGaA, 69451 Weinheim, Germany, 2006)

## Introduction

Functionalized phosphanes bearing a multiple carbon–carbon bond display a versatile behavior as ligands in coordination chemistry and have been reasonably well explored to date. Thus, alkenylphosphanes,[1] $R_2P(CH_2)_nCH{=}CH_2$ (*n* = 0–2), and alkynylphosphanes,[2] $R_2PC{\equiv}CR'$, have been used in coordination chemistry with a wide range of transition metals. Moreover, a number of ruthenium(II) complexes bearing different alkenylphosphanes, such as dicyclohexylvinylphosphane (DCVP),[3] vinyldiphenylphosphane (DPVP),[4] and allyldiphenylphosphane (ADPP)[5] have also been described and their ligand hemilabile properties have been repeatedly shown. However, the coordination properties and the hemilabile character of homoallylphosphanes have been much less exploited in the area of ruthenium chemistry. Recently, Kirchner and co-workers have studied the reactions of olefins and acetylenes with the complex [Ru($\eta^5$-$C_5H_5$)(MeCN)($Ph_2PCH_2CH_2CH{=}CH_2$-κ$^3$*P,C,C*)][$PF_6$], which give rise to interesting coupling products.[6] On the other hand, examples of complexes of ruthenium(II) with alkynylphosphanes[7] are also scarce, even though alkynylphosphanes have been extensively used in the synthesis of polynuclear complexes[2f,8] and have been reported to participate in interesting rearrangement processes, some of them involving phosphorus–carbon bond cleavage[9] or carbon–carbon bond formation.[10]

We have previously reported the synthesis and characterization of the ruthenium(II) complexes [Ru($\eta^5$-$C_9H_7$)($PPh_3$)($Ph_2PCH_2C$(R)=$CH_2$-κ$^3$*P,C,C*)][$PF_6$] (R = H, Me), which feature a κ$^3$*P,C,C* coordination mode of the allyldiphenylphosphane as well as a diastereofacial coordination of the olefin at the ruthenium center.[11] Moreover, these complexes have been demonstrated to be useful for further transformations, particularly as substrates in stereoselective nucleophilic addition[11] and intramolecular cycloaddition reactions,[12,13] which lead to interesting ruthenaphosphacyclopentane and ruthenaphosphabicycloheptene complexes, respectively. The progress of the latter reaction confirms the hemilabile character of the allyldiphenylphosphane ligand, a fact that has been corroborated by kinetic studies.[14] Continuing with these studies, we report here the synthesis of new half-sandwich indenyl complexes of ruthenium(II) containing alkenyl and alkynylphosphanes as well as some preliminary results on their reactivity.

[a] Departamento de Química Orgánica e Inorgánica, Instituto de Química Organometálica "Enrique Moles" (Unidad Asociada al C.S.I.C.), Universidad de Oviedo,
Oviedo, Spain
Fax: +34-985-103-446
E-mail: pgb@uniovi.es
elb@uniovi.es


InterScience
© 2006 Wiley-VCH Verlag GmbH & Co. KGaA, Weinheim

## Results and Discussion

### Complexes with Alkenyl and Alkynylphosphanes ($Ph_2PR$) Acting as κ*P* Monodentate Ligands

#### *Synthesis of [RuI(η⁵-C₉H₇)(CO)(Ph₂PR-κP)] [R = CH₂CH=CH₂ (1a), CH₂CH₂CH=CH₂ (1b), C≡CPh (1c)]*

The addition of the corresponding phosphane to a dichloromethane solution of the complex [RuI(η⁵-$C_9H_7$)(CO)($NMe_3$)] (prepared in situ by reaction of the complex [RuI(η⁵-$C_9H_7$)$(CO)_2$] with freshly sublimed trimethylamine oxide) generates the complexes [RuI(η⁵-$C_9H_7$)($Ph_2PR$-κ*P*)($PPh_3$)] [R = $CH_2CH=CH_2$ (**1a**), $CH_2CH_2CH=CH_2$ (**1b**), C≡CPh (**1c**)], which were isolated as air-stable red solids (78–97% yield) (Scheme 1).

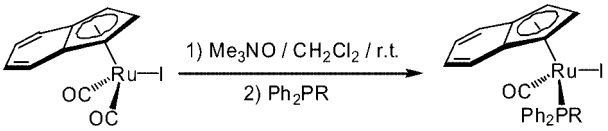


R = $CH_2CH=CH_2$ (**1a**)
$CH_2CH_2CH=CH_2$ (**1b**)
C≡CPh (**1c**)

Scheme 1.

Complexes **1a**–**c** are soluble in $CH_2Cl_2$, THF, and diethyl ether and slightly soluble in hexane. Analytical and spectroscopic data (IR and $^1H$, $^{13}C\{^1H\}$, and $^{31}P\{^1H\}$ NMR spectroscopy) support the proposed formulation (see Experimental Section for details). In particular, the IR spectra show the strong characteristic ν(CO) absorption at 1940 (**1a** and **1c**) and 1930 $cm^{-1}$ (**1b**) as well as the ν(C≡C) absorption at 2176 $cm^{-1}$ (**1c**), a singlet resonance is observed at $\delta$ = 45.0 (**1a**), 44.0 (**1b**) and 22.5 ppm (**1c**) for the phosphanes in the $^{31}P\{^1H\}$ NMR spectra, and a low-field doublet signal is observed in the $^{13}C\{^1H\}$ NMR spectra due to the carbonyl group at $\delta$ = 203.0 (**1a**), 203.5 (**1b**) and 202.4 ppm (**1c**) [$^2J_{C,P} \approx$ 20.7–21.3 Hz]. The $^{13}C\{^1H\}$ NMR spectrum of **1c** also shows two doublet signals for the alkynyl carbon nuclei at $\delta$ = 84.1 ($J_{C,P}$ = 93.6 Hz) and 108.9 ppm ($^2J_{C,P}$ = 14.4 Hz).

Slow diffusion of hexane into a solution of **1c** in diethyl ether allowed the isolation of crystals suitable for X-ray diffraction studies. An ORTEP-type representation of the molecule is shown in Figure 1. Selected bonding data are collected in the caption.

The molecule exhibits a pseudooctahedral three-legged piano-stool geometry. The η⁵-indenyl ligand displays the usual allylene coordination mode with the benzo ring oriented *trans* to the carbonyl group, as shown by the dihedral angle (1.14°) between the planes C*–C**–Ru and C*–Ru–C(10).[15]

The Ru–C(10) [1.840(4) Å] and C(10)–O(1) [1.132(5) Å] bond lengths are comparable to those found in other indenyl carbonyl ruthenium(II) complexes such as [RuI(η⁵-$C_9H_7$)(CO)($PCy_3$)] [1.817(13) and 1.142(15) Å][16] and [Ru(η⁵-1,2,3-$Me_3C_9H_4$)(CO)($PPh_3$)(C=C=$CPh_2$)][$BF_4$] [1.83(1) and 1.15(1) Å].[17]

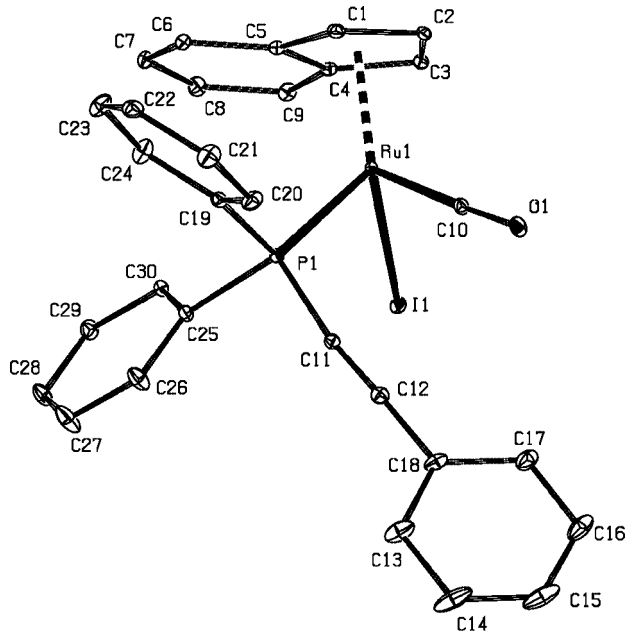


Figure 1. Molecular structure and atom-labelling scheme for complex **1c**. Non-hydrogen atoms are represented by their 10% probability ellipsoids. Hydrogen atoms and phenyl rings have been omitted for clarity. Selected bond lengths [Å]: Ru(1)–I(1) = 2.7224(4), Ru(1)–P(1) = 2.3087(9), Ru(1)–C(10) = 1.840(4), Ru(1)–C* = 1.9170, C(10)–O(1) = 1.132(5), P(1)–C(11) = 1.755(4), C(11)–C(12) = 1.210(6). Selected bond angles [°]: P(1)–Ru(1)–I(1) = 90.17(3), P(1)–Ru(1)–C(10) = 87.53(12), I(1)–Ru(1)–C(10) = 92.42(13), C*–Ru(1)–I(1) = 121.81, C*–Ru(1)–P(1) = 129.53, C*–Ru(1)–C(10) = 124.44, P(1)–C(11)–C(12) = 172.0(4), C(11)–C(12)–C(18) = 176.9(4). C* represents the centroid of atoms C(1), C(2), C(3), C(4), and C(5).

The alkynyl carbon–carbon bond length C(11)–C(12) [1.210(6) Å] is in the typical range for a carbon–carbon triple bond (1.205 Å in the free acetylene) and slightly longer than in other alkynylphosphaneruthenium complexes[7a] such as [$RuCl_2$(η⁶-*p*-cymene)($Ph_2PC\equiv CC_6H_4$-4-$CH_3$-κ*P*)] [1.198(3) Å] or [RuCl(η⁶-*p*-cymene)($Ph_2PC\equiv CtBu$-κ*P*)][OTf] [1.196(6) Å]. The alkynyl fragment of the phosphane displays a nearly linear geometry [C(11)–C(12)–C(18) = 176.9(4)°].

Both enantiomers are present in equal numbers in the crystal, as the crystal belongs to the centric space group $P\bar{1}$. The (*R*) enantiomer is shown in Figure 1.

#### *Synthesis of [RuCl(η⁵-C₉H₇)(Ph₂PR-κP)(PPh₃)] [R = CH₂CH₂CH=CH₂ (2b), C≡CPh (2c)]*

The reaction of the complex [RuCl(η⁵-$C_9H_7$)$(PPh_3)_2$] with the corresponding phosphane in refluxing THF results in the formation of the complexes [RuCl(η⁵-$C_9H_7$)($Ph_2PR$-κ*P*)($PPh_3$)] [R = $CH_2CH_2CH=CH_2$ (**2b**), C≡CPh (**2c**)], which were isolated as air-stable, red solids in 60% yield (Scheme 2). Complexes **2b**,**c** are soluble in dichloromethane and diethyl ether and insoluble in hexane, and were characterized by analytical and spectroscopic techniques (See Experimental Section for details).

 © 2006 Wiley-VCH Verlag GmbH & Co. KGaA, Weinheim 

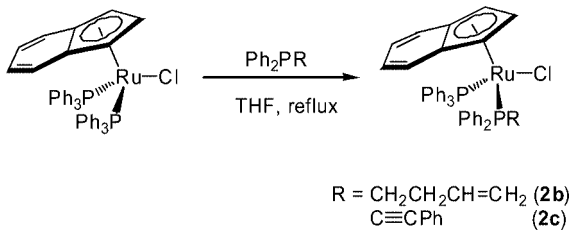


Scheme 2.

The most remarkable features of those complexes are (a) the ν(C≡C) absorption at 2168 $cm^{-1}$ in the IR spectrum for complex **2c**, (b) the expected doublets in the $^{31}P\{^1H\}$ NMR spectra at $\delta$ = 49.0 and 45.6 ppm ($^2J_{P,P}$ = 42.9 Hz) for **2b** and $\delta$ = 48.1 and 29.1 ppm ($^2J_{P,P}$ = 45.0 Hz) for **2c**, and (c) the $^{13}C\{^1H\}$NMR spectrum of **2c** shows two doublets at $\delta$ = 109.1 ($^2J_{C,P}$ = 11.5 Hz) and 87.2 ppm ($^2J_{C,P}$ = 80.7 Hz) for the acetylene carbons. One olefinic carbon appears at $\delta$ = 113.8 ppm in the $^{13}C\{^1H\}$NMR spectrum of **2b**, while the other one is overlapped by aromatic carbons.

### Complexes with Alkenylphosphanes $Ph_2P(CH_2)_nCH=CH_2$ ($n$ = 1, 2) Acting as $\kappa^3P,C,C$ Chelate Ligands: Synthesis of the Complexes $[Ru(\eta^5\text{-}C_9H_7)(L)(Ph_2PR\text{-}\kappa^3P,C,C)][X]$ [L = CO, X = $SbF_6$, R = $CH_2CH=CH_2$ (3a), $CH_2CH_2CH=CH_2$ (3b); L = $PPh_3$, X = $PF_6$, R = $CH_2CH_2CH=CH_2$ (4b)]

Due to the interest of the reactions carried out with the complex $[Ru(\eta^5\text{-}C_9H_7)(PPh_3)(Ph_2PCH_2CH=CH_2\text{-}\kappa^3P,C,C)][PF_6]$,[11–13] our interest focused on the synthesis of novel complexes with allyl- and homoallylphosphanes coordinated in a $\kappa^3P,C,C$ mode, which can be formed from complexes **1a**,**b** and **2b** by halide abstraction and subsequent olefin coordination to the metal. Thus, the treatment of complexes **1a**,**b** with $AgSbF_6$ in dichloromethane leads almost quantitatively to the complexes $[Ru(\eta^5\text{-}C_9H_7)(CO)(Ph_2PR\text{-}\kappa^3P,C,C)][SbF_6]$ [R = $CH_2CH=CH_2$ (**3a**), $CH_2CH_2CH=CH_2$ (**3b**)]. Similarly, the reaction of the complex **2b** with $NaPF_6$ in refluxing ethanol affords the complex $[Ru(\eta^5\text{-}C_9H_7)(PPh_3)(Ph_2PCH_2CH_2CH=CH_2\text{-}\kappa^3P,C,C)][PF_6]$ (**4b**) in 67% yield (Scheme 3).

Complexes **3a**,**b** and **4b** were isolated as air-stable, yellow solids that are soluble in dichloromethane and insoluble in diethyl ether and hexane. They were characterized analytically and spectroscopically (IR and $^1H$, $^{31}P\{^1H\}$, and $^{13}C\{^1H\}$ NMR spectroscopy; see Experimental Section for details).

The $^{31}P\{^1H\}$ NMR spectra show a singlet resonance for the complexes **3a** ($\delta$ = –56.4 ppm) and **3b** ($\delta$ = 74.6 ppm), while two doublet signals at $\delta$ = 69.3 [$Ph_2P(CH_2)_2CH=CH_2$] and 47.3 ppm ($PPh_3$; $^2J_{P,P}$ = 29.5 Hz) are found for complex **4b**. The phosphorus resonance of the allyldiphenylphosphane is clearly shifted upfield in the complex **3a** ($\delta$ = 74.6 ppm) in comparison with its precursor **1a** ($\delta$ = 45.0 ppm) wherein the allylphosphane acts as a monodentate ligand. However, the phosphorus resonances of the homoallyldiphenylphosphane in complexes **3b** and **4b** are shifted downfield with respect to those of the corresponding monodentate phosphanes in the complexes **1b** ($\delta$ = 44.0 ppm) and **2b** ($\delta$ = 45.6 ppm). The formation of five- (**3a**) and six-membered (**3b**, **4a**) ruthenaphosphacycles may account for the observed shift differences.[18]

Although the two olefin faces are diastereotopic when the alkenylphosphane ligands are bound in a didentate manner, the coordination to the metal is found to be completely selective, affording a sole diastereoisomer, as revealed by the analysis of the $^{31}P\{^1H\}$ NMR spectra of complexes **3a**,**b** and **4b**. Such a selectivity has also been reported previously for the complexes $[Ru(\eta^5\text{-}C_9H_7)(PPh_3)(Ph_2PCH_2CH=CH_2\text{-}\kappa^3P,C,C)][PF_6]$[11] and $[Ru(\eta^5\text{-}C_5H_5)(PPh_3)(Ph_2PCH_2CH=CH_2\text{-}\kappa^3P,C,C)][PF_6]$.[13] In addition, the $^{31}P\{^1H\}$ NMR spectra remain unchanged over a wide temperature range, thus ruling out a dynamic process between the two diastereoisomers on the NMR time scale. Contrary to these results, the analogous derivative $[Ru(\eta^5\text{-}C_5Me_5)(Ph_2PCH_2CH=CH_2\text{-}\kappa P)(Ph_2PCH_2CH=CH_2\text{-}\kappa^3P,C,C)][PF_6]$ was found to be fluxional, giving rise to a rapid equilibrium between the two diastereomeric conformations present in solution.[5c]

The relatively large difference of the $^1H$ NMR chemical shifts for the $CH_2$ geminal protons of the olefin in complexes **3a**,**b** and **4** points to a parallel orientation of the

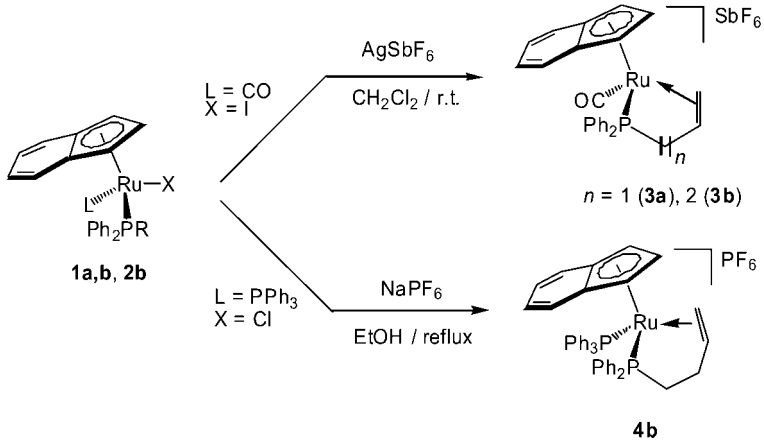


Scheme 3.

 © 2006 Wiley-VCH Verlag GmbH & Co. KGaA, Weinheim 

olefin with respect to the indenyl ring. Similar data have been reported in other cyclopentadienyl and indenyl π-olefin complexes.[19]

In order to compare the structure of the derivatives **3a** and **4b** with that of the complex $[Ru(\eta^5\text{-}C_9H_7)(PPh_3)(Ph_2PCH_2CH{=}CH_2\text{-}\kappa^3P,C,C)][PF_6]$,[11] and to find out which of the two olefin faces in the $Ph_2P(CH_2)_n\text{-}CH{=}CH_2\text{-}\kappa P$ ligand is most favored for coordination, an X-ray diffraction study was carried out. Single crystals suitable for X-ray diffraction analysis were obtained by slow diffusion of diethyl ether into a solution of complexes **3a** and **4b** in dichloromethane. The crystals belong to the centrosymmetric space groups $P\bar{1}$ (**3a**) and $P2_1/c$ (**4b**), thereby indicating the presence of a racemic mixture.

In both cases, the asymmetric unit consists of two molecules. For complex **4b**, the two molecules are conformers with identical stereochemistry, the relative configuration at the ruthenium center being $R_{Ru}$ and the olefin being coordinated through the *re* face ($R_{Ru}$*re*). However, in the case of complex **3a** the two molecules in the asymmetric unit are a pair of diastereoisomers with relative configuration ($R_{Ru}$*si*) and ($S_{Ru}$*re*) (Figure 2). For both **3a** and **4b** the more relevant structural parameters are similar in both molecules,[20] and thus only the data corresponding to one molecule will be discussed.

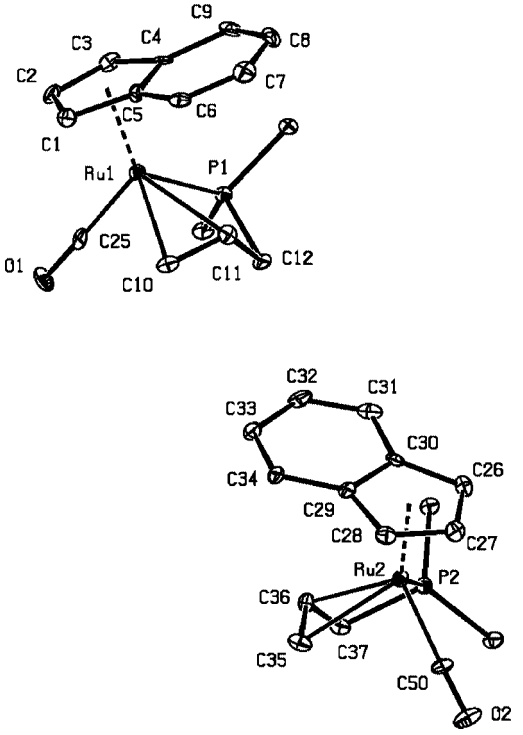


Figure 2. The two diastereoisomers found in the asymmetric unit for the cation of complex **3a** with configurations $R_{Ru}$*si* and $S_{Ru}$*re*. Non-hydrogen atoms are represented by their 20% probability ellipsoids. Hydrogen atoms and phenyl rings have been omitted for clarity.

ORTEP-type representations of the cations of one of the molecules for complexes **3a** and **4b** are shown in Figures 3 and 4, respectively. Selected bonding data are collected in Table 1.

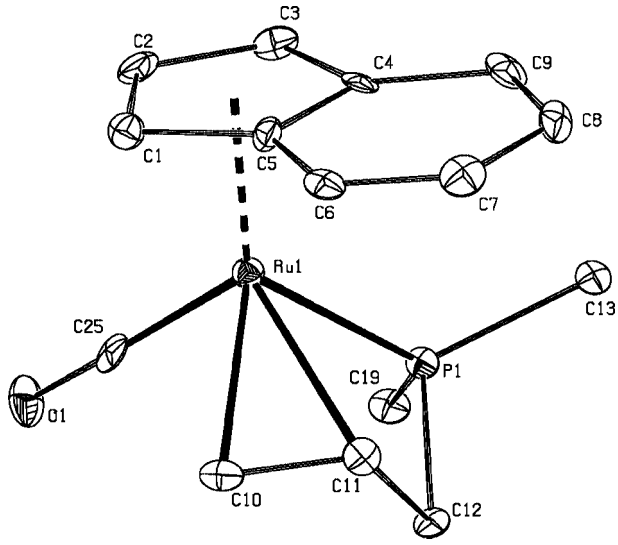


Figure 3. Molecular structure and atom-labelling scheme for the cation of complex **3a**. Non-hydrogen atoms are represented by their 10% probability ellipsoids. Hydrogen atoms and phenyl rings have been omitted for clarity.

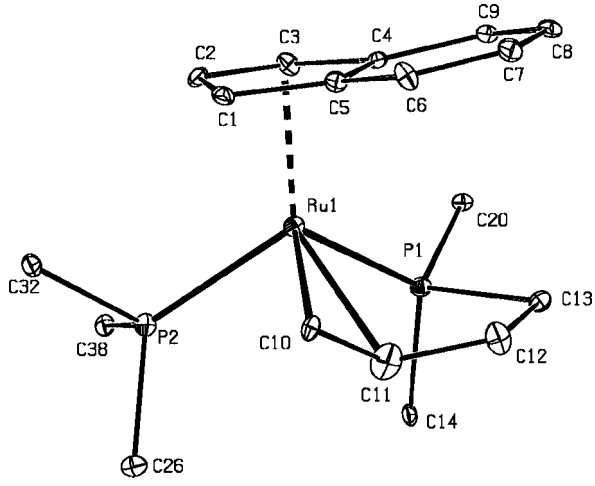


Figure 4. Molecular structure and atom-labelling scheme for the cation of complex **4b**. Non-hydrogen atoms are represented by their 10% probability ellipsoids. Hydrogen atoms and phenyl rings have been omitted for clarity.

Both structures exhibit a three-legged piano-stool geometry with the $\eta^5$-indenyl ligand displaying the usual allylene coordination mode. The Ru(1)–C(10) and Ru(1)–C(11) bond lengths reflect the coordination of the olefin to the metal center[20] [2.276(11) and 2.230(11) (**3a**) and 2.228(7) and 2.245(9) (**4b**)]. The C(10)–C(11) bond length is 1.389(17) Å in **3a** and 1.363(11) Å in **4b**, similar to that found in the complex $[Ru(\eta^5\text{-}C_9H_7)(PPh_3)(Ph_2PCH_2CH{=}CH_2\text{-}\kappa^3P,C,C)][PF_6]$.[11] It is also interesting to note that the benzo ring of the indenyl ligand is oriented almost *trans* to the CO group for complex **3a** and *trans* to the $PPh_3$ ligand for complex **4b**, as is shown by the dihedral angle between the planes C**–C*–Ru(1) and C*–Ru(1)–C(25) of 12.45° (**3a**) and C**–C*–Ru(1) and C*–Ru(1)–P(2)

 © 2006 Wiley-VCH Verlag GmbH & Co. KGaA, Weinheim 

Table 1. Selected bond lengths [Å] and bond angles [°] for **3a** and **4b**.[a]

| 3a | | 4b | |
|---|---|---|---|
| Ru(1)–C(10) | 2.276(11) | Ru(1)–C(10) | 2.228(7) |
| Ru(1)–C(11) | 2.230(11) | Ru(1)–C(11) | 2.245(9) |
| C(10)–C(11) | 1.389(17) | C(10)–C(11) | 1.363(11) |
| Ru(1)–C* | 1.9117 | Ru(1)–C* | 1.9298 |
| Ru(1)–P(1) | 2.322(3) | Ru(1)–P(1) | 2.344(2) |
| Ru(1)–C(25) | 1.860(14) | Ru(1)–P(2) | 2.301(2) |
| C(25)–O(1) | 1.148(15) | | |
| C(25)–Ru(1)–P(1) | 90.1(3) | P(1)–Ru(1)–P(2) | 102.45(8) |
| C(25)–Ru(1)–C(10) | 94.62(2) | P(2)–Ru(1)–C(10) | 88.2(2) |
| C(25)–Ru(1)–C(11) | 103.8(5) | P(2)–Ru(1)–C(11) | 96.5(3) |
| P(1)–Ru(1)–C(10) | 94.0(3) | P(1)–Ru(1)–C(10) | 107.0(2) |
| P(1)–Ru(1)–C(11) | 65.5(3) | P(1)–Ru(1)–C(11) | 71.5(3) |
| C(25)–Ru(1)–C* | 124.65 | P(2)–Ru(1)–C* | 121.41 |
| P(1)–Ru(1)–C* | 129.62 | P(1)–Ru(1)–C* | 119.18 |
| C(10)–Ru(1)–C* | 122.73 | C(10)–Ru(1)–C* | 113.8 |
| C(11)–Ru(1)–C* | 125.76 | C(11)–Ru(1)–C* | 133.40 |

[a] C* = centroid of C(1), C(2), C(3), C(4), and C(5).

11.94° (**4b**).[15] The Ru(1)–C(25) [1.860(14) Å] and C(25)–O(1) [1.148(15) Å] bond lengths for complex **3a** are similar to those found in complex **1c**.

## Reactivity of the Complexes [Ru(η$^5$-$C_9H_7$)(L)($Ph_2PR$-κ$^3$*P,C,C*)][X]

### *Deprotonation Reactions: Synthesis of [Ru(η$^5$-$C_9H_7$)(L)($Ph_2PCH_2CH$=$CHCH_2$-κ$^2$*P,C*)] [L = CO (5a), $PPh_3$ (5b)]*

The complexes [RuCl(η$^5$-$C_9H_7$)(L)($Ph_2PCH_2CH_2CH$=$CH_2$-κ$^3$*P,C,C*)][X] [X = $SbF_6$, L = CO (**3b**); X = $PF_6$, L = $PPh_3$ (**4b**)] undergo deprotonation reactions in the presence of base. Thus, the treatment of **3b** and **4b** with KO*t*Bu or $Cs_2CO_3$ in $CH_2Cl_2$ gives the neutral allylruthenium complexes [Ru(η$^5$-$C_9H_7$)(L)($Ph_2PCH_2CH$=$CHCH_2$-κ$^2$*P,C*)] [L = CO (**5a**), $PPh_3$ (**5b**)], which were isolated as yellow solids in 80–86% yield (Scheme 4).

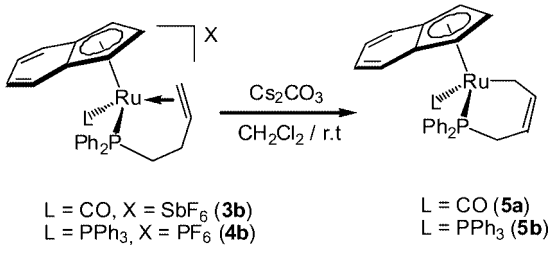


Scheme 4.

Their analytical and spectroscopic data support the proposed formulations (see Experimental Section for details).[21] The most significant spectroscopic features are (a) the IR spectrum of **5a** shows the ν(CO) absorption at 1920 cm$^{-1}$, (b) the $^{31}P\{^1H\}$ spectra of **5a** and **5b** show the resonance of the chelate-ring phosphorus atom at $\delta$ = 101.3 (singlet) and 91.8 ppm (doublet, $^2J_{P,P}$ = 33.7 Hz), respectively, and (c) the $^{13}C\{^1H\}$ NMR spectra show a high-field signal for the Ru–$CH_2$ carbon ($\delta$ = –4.1 ppm for **5a**; $\delta$ = –0.7 ppm for **5b**) and two signals for the olefinic carbons of **5a** ($\delta$ = 116.4 and 146.0 ppm; $^2J_{C,P}$ = 14.4 Hz) and **5b** ($\delta$ = 115.3 and 147.0 ppm; $^2J_{C,P}$ = 13.6 Hz). Moreover, the analogous complexes [Ru(η$^5$-$C_9H_7$)(L)($Ph_2PCH_2CH$=$CH_2$-κ$^3$*P,C,C*)][X] [L = CO, X = $SbF_6$ (**3a**); L = $PPh_3$, X = $PF_6$[11]] do not suffer deprotonation and are recovered unaltered after treatment with KO*t*Bu or $Cs_2CO_3$ under similar reaction conditions.

### *π-Olefin Exchange Reactions: Synthesis of the Complex [Ru(η$^5$-$C_9H_7$)(CO)(MeCN)($Ph_2PCH_2CH$=$CH_2$-κ*P*)]-[$SbF_6$] (6)*

The complex **3a** reacts with acetonitrile to generate the complex [Ru(η$^5$-$C_9H_7$)(CO)(MeCN)($Ph_2PCH_2CH$=$CH_2$-κ*P*)][$SbF_6$] (**6**), which was isolated as a yellow solid in 91% yield (Scheme 5).

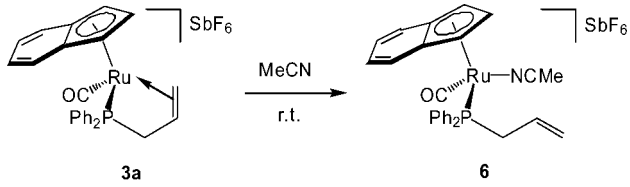


Scheme 5.

Complex **6** was characterized analytically and spectroscopically (see Experimental Section for details). In particular, its IR spectrum shows a strong ν(CO) absorption at 1977 cm$^{-1}$, a broad singlet resonance is observed at $\delta$ = 2.2 ppm for the methyl group of the acetonitrile ligand in the $^1H$ NMR spectrum, a singlet signal appears in the $^{31}P\{^1H\}$ NMR spectrum at $\delta$ = 46.9 ppm, which is in the typical range for monodentate coordination of the phosphane and in agreement with the value found for complex **1a** ($\delta$ = 45.0 ppm), and the $^{13}C\{^1H\}$ NMR spectrum shows a singlet signal at $\delta$ = 3.7 ppm for the methyl group of the acetonitrile and a low-field doublet signal at $\delta$ = 200.2 ppm ($^2J_{C,P}$ = 18.9 Hz) for the CO ligand.

This result agrees with that reported recently for the derivative [Ru(η$^5$-$C_9H_7$)($PPh_3$)($Ph_2PCH_2CH$=$CH_2$-κ$^3$*P,C,C*)]-[$PF_6$], which reacts with acetonitrile to generate a $Ph_2CH_2CH$=$CH_2$-κ*P* complex, thus emphasizing the hemilabile character of the allylphosphane.[11,14] However, all attempts to open the $Ph_2PCH_2CH_2CH$=$CH_2$-κ$^3$*P,C,C* chelate ring of derivatives **3b** and **4b** by treatment with acetonitrile were unsuccessful, probably due to the higher stability of the six-membered ring.

### *Reaction of [RuCl(η$^5$-$C_9H_7$)($PPh_3$)($Ph_2PC$≡$CPh$-κ*P*)] (2c) with Alkynes: Synthesis of Vinylidene [Ru(η$^5$-$C_9H_7$)-($PPh_3$)($Ph_2PC$≡$CPh$-κ*P*){C=C(Ph)H}][$PF_6$] (7) and Allenylidene [Ru(η$^5$-$C_9H_7$)($PPh_3$)($Ph_2PC$≡$CPh$-κ*P*)-(C=C=$CPh_2$)][$PF_6$] (8) Derivatives*

Complex **2c** reacts with terminal alkynes to give cumulenylidene complexes. Thus, the reaction of **2c** with PhC≡CH or $Ph_2C$(OH)C≡CH in the presence of $NaPF_6$ in refluxing ethanol leads to the expected vinylidene [Ru(η$^5$-

 © 2006 Wiley-VCH Verlag GmbH & Co. KGaA, Weinheim 

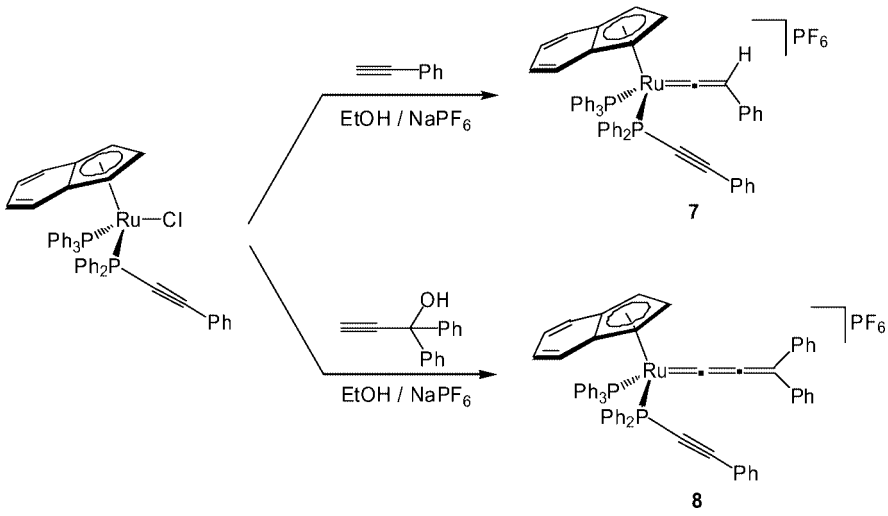


Scheme 6.

$C_9H_7$)($PPh_3$)($Ph_2PC{\equiv}CPh$-κ*P*){C=C(Ph)H}] (**7**; 82% yield) and allenylidene complexes [Ru(η$^5$-$C_9H_7$)($PPh_3$)($Ph_2P$-C≡CPh-κ*P*)(C=C=$CPh_2$)] (**8**; 76% yield) as orange and purple solids, respectively (Scheme 6).

Complexes **7** and **8** are soluble in $CH_2Cl_2$ and THF and insoluble in diethyl ether and hexane. Both complexes were characterized analytically and spectroscopically (see Experimental Section for details). In particular, some data should be noted: (a) the IR spectra show the ν(C≡C) absorption at 2171 (**7**) and 2169 cm$^{-1}$ (**8**) and the ν(C=C=C) absorption at 1931 cm$^{-1}$; (b) the $^{31}P\{^1H\}$ NMR spectra show two doublets at $\delta$ = 20.6 and 41.7 ppm ($^2J_{P,P}$ = 27.2 Hz) for complex **7** and $\delta$ = 26.0 and 48.3 ppm ($^2J_{P,P}$ = 28.7 Hz) for complex **8**; (c) the $^{13}C\{^1H\}$ NMR spectra show two signals for the alkynyl carbons at $\delta$ = 112.9 and 81.6 (**7**) and 111.3 and 81.7 ppm (**8**). A low-field pseudotriplet signal ($^2J_{C,P}$ = 18.5–16.4 Hz) is observed for the $C_\alpha$ nuclei of the cumulenic group at $\delta$ = 355.4 (**7**) and 293.2 ppm (**8**).

## Conclusions

In summary, the present work describes the synthesis of a series of chiral-at-ruthenium indenyl complexes containing alkynyl- and alkenylphosphane ligands. In the case of alkenylphosphane complexes both κ*P* and κ$^3$*P*,*C*,*C* coordination modes have been shown to occur. In complexes with κ$^3$*P*,*C*,*C*-alkenylphosphane coordination, an effective chiral recognition of a prochiral allyl group has been achieved, the olefin being coordinated to the metal in a diastereoselective way.[22]

The X-ray structure analysis of representative derivatives showing the κ$^3$*P*,*C*,*C* coordination mode has been performed and their structure compared with that of the previously described allylphosphane complexes [Ru(η$^5$-$C_9H_7$)($PPh_3$){$Ph_2PCH_2CR{=}CH_2$-κ$^3$*P*,*C*,*C*}][$PF_6$] (R = H, Me).[11] Moreover, these complexes can be used as model systems to study the diastereoselective coordination found for the alkenylphosphane ligand in $Ph_2P(CH_2)_nCH{=}CH_2$-κ$^3$*P*,*C*,*C* complexes.

The reactivity of the alkenylphosphane ligand is highly dependent on the size of the chelate ring. Thus, the complex **3a**, which contains the allylphosphane ligand $Ph_2PCH_2CHCH_2$-κ$^3$*P*,*C*,*C*, undergo ring opening upon reaction with two-electron ligands, thus emphasizing the hemilabile character of the ligand, while complexes **3b** and **4b**, with the six-membered chelate ring $Ph_2PCH_2CH_2CHCH_2$-κ$^3$*P*,*C*,*C*, undergo no transformation in acetonitrile.

The alkynylphosphane complex **1c** is able to activate terminal alkynes, leading to the formation of vinylidene [Ru(η$^5$-$C_9H_7$)($PPh_3$)($Ph_2PC{\equiv}CPh$-κ*P*){C=C(Ph)H}][$PF_6$] (**7**) and allenylidene [Ru(η$^5$-$C_9H_7$)($PPh_3$)($Ph_2PC{\equiv}CPh$-κ*P*)(C=C=$CPh_2$)][$PF_6$] (**8**) derivatives.

## Experimental Section

**General:** All manipulations were performed under an atmosphere of dry nitrogen using vacuum-line and standard Schlenk techniques. All reagents were obtained from commercial suppliers and used without further purification. Solvents were dried by standard methods and distilled under nitrogen before use. The compounds [RuCl(η$^5$-$C_9H_7$)($PPh_3$)$_2$],[23] [RuI(η$^5$-$C_9H_7$)(CO)$_2$],[24] $Ph_2PCH_2$-$CH{=}CH_2$,[25] $Ph_2PCH_2CH_2CH{=}CH_2$,[26] and $Ph_2PC{\equiv}CPh$[27] were prepared by previously reported methods. Infrared spectra were recorded with a Perkin–Elmer 1720-XFT or a Perkin–Elmer 599 IR spectrometer. The C, H, and N analyses were carried out with a Perkin–Elmer 240-B microanalyzer. NMR spectra were recorded with Bruker AC 300 and 300 DPX instruments at 300 ($^1$H), 121.5 ($^{31}$P), or 75.4 MHz ($^{13}$C) or a Bruker AC 400 instrument at 400.1 ($^1$H), 161.9 ($^{31}$P), or 100.6 MHz ($^{13}$C) with $SiMe_4$ or 85% $H_3PO_4$ as standards. DEPT experiments were carried out for all the complexes. The following atom labels have been used for the $^1$H and $^{13}C\{^1H\}$ NMR spectroscopic data.

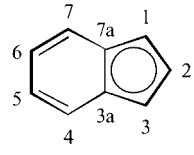


 © 2006 Wiley-VCH Verlag GmbH & Co. KGaA, Weinheim 

**Synthesis of [RuI($\eta^5$-$C_9H_7$)(CO)($Ph_2PR$-κ*P*)] [R = $CH_2CH{=}CH_2$ (1a), $CH_2CH_2CH{=}CH_2$ (1b), C≡CPh (1c)]:** Previously sublimed $Me_3NO$ (188 mg, 2.50 mmol) was added to a solution of [RuI($\eta^5$-$C_9H_7$)$(CO)_2$] (500 mg, 1.25 mmol) in $CH_2Cl_2$ (5 mL), and the mixture was stirred for 10 min at room temperature. After this time, the initial orange solution turned nearly black, and the complex [Ru($\eta^5$-$C_9H_7$)$(NMe_3)$(CO)] had formed (checked by IR spectroscopy in solution). The corresponding phosphane ligand was then added (1.5 mmol) and the reaction mixture stirred for 15–30 min. The resulting solution was evaporated to dryness and the residue extracted with toluene (2 × 20 mL) and vacuum-dried. The solid residue was then recrystallized from $CH_2Cl_2$/hexane and complexes **1a**–**c** were obtained as red solids.

**1a:** Time: 15 min. Yield: 596 mg (80%). IR (KBr): ν(CO) = 1940 $cm^{-1}$. $^1H$ NMR (300 MHz, $CDCl_3$, 18 °C): $\delta$ = 3.33 (m, 1 H, P–$CH_2$), 3.51 (m, 1 H, P–$CH_2$), 3.58 (s, 1 H, 1-H or 3-H), 4.92 (m, 2 H, =$CH_2$), 5.28 (m, 1 H, 2-H), 5.58 (m, 2 H, =CH, 1-H or 3-H), 7.29 (m, 14 H, 4,5,6,7-H, Ar) ppm. $^{13}C\{^1H\}$ NMR (75.4 MHz, $CDCl_3$, 18 °C): $\delta$ = 38.1 (d, $J_{C,P}$ = 30.3 Hz, P–$CH_2$), 70.4 (s, C-1 or C-3), 71.3 (d, $^2J_{C,P}$ = 7.1 Hz, C-1 or C-3), 89.4 (s, C-2), 110.5, 111.9 (s, C-3a, C-7a), 119.3 (d, $^2J_{C,P}$ = 11.1 Hz, =$CH_2$), 123.0–137.4 (=CH, C-4,5,6,7, Ar), 203.0 (d, $^2J_{C,P}$ = 21.2 Hz, CO) ppm. $^{31}P\{^1H\}$ NMR (121.5 MHz, $CDCl_3$, 18 °C): $\delta$ = 45.0 ppm (s). $C_{25}H_{22}IOPRu$ (597.39): calcd. C 50.26, H 3.71; found C 51.38, H 3.95.

**1b:** Time: 30 min. Yield: 596 mg (78%). IR (KBr): ν(CO) = 1930 $cm^{-1}$. $^1H$ NMR (300 MHz, $CDCl_3$, 18 °C): $\delta$ = 1.85 (m, 1 H, $CH_2$), 2.07 (m, 1 H, $CH_2$), 2.52 (m, 1 H, P–$CH_2$), 2.74 (m, 1 H, P–$CH_2$), 4.57 (s, 1 H, 1-H, 2-H or 3-H), 4.91 (m, 2 H, =$CH_2$), 5.28 (s, 1 H, 1-H, 2-H or 3-H), 5.60 (s, 1 H, 1-H, 2-H or 3-H), 5.69 (m, 1 H, =CH), 6.69 (d, $J_{H,H}$ = 8.26 Hz, 1 H, 4-H, 5-H, 6-H, or 7-H), 6.86 (t, $J_{H,H}$ = 7.4 Hz, 1 H, 4-H, 5-H, 6-H, or 7-H), 7.14–7.63 (m, 12 H, 4-H, 5-H, 6-H, or 7-H, Ar) ppm. $^{13}C\{^1H\}$ NMR (75.5 MHz, $CDCl_3$, 18 °C): $\delta$ = 28.4 (s, $CH_2$), 32.1 (d, $J_{C,P}$ = 30.5 Hz, P–$CH_2$), 70.6 (s, C-1 or C-3), 72.0 (d, $^2J_{C,P}$ = 7.4 Hz, C-1 or C-3), 89.7 (s, C-2), 111.0, 112.3 (s, C-3a, C-7a), 114.8 (s, =$CH_2$), 123.2–137.5 (=CH, C-4,5,6,7, Ar), 203.5 (d, $^2J_{C,P}$ = 21.3 Hz, CO) ppm. $^{31}P\{^1H\}$ NMR (121.5 MHz, $CDCl_3$, 18 °C): $\delta$ = 44.0 ppm (s). $C_{26}H_{24}IOPRu$ (611.42): calcd. C 51.08, H 3.96; found C 52.47, H 4.44.

**1c:** Time 30 min. Yield: 797 mg (97%). IR (KBr): ν(C≡C) = 2176, ν(CO) = 1940 $cm^{-1}$. $^1H$ NMR (300 MHz, $CDCl_3$, 18 °C): $\delta$ = 4.82 (br. s, 1 H, 1-H or 3-H), 5.57 (pseudo t, $J_{H,H}$ = 2.6 Hz, 1 H, 2-H), 5.79 (br. s, 1 H, 1-H or 3-H), 6.95–7.73 (m, 19 H, 4,5,6,7-H, Ar) ppm. $^{13}C\{^1H\}$ NMR (75.4 MHz, $CDCl_3$, 18 °C): $\delta$ = 71.0 (s, C-1 or C-3), 73.7 (d, $^2J_{C,P}$ = 9.9 Hz, C-1 or C-3), 84.1 (d, $J_{C,P}$ = 93.6 Hz, P–*C*≡C), 90.0 (s, C-2), 108.9 (d, $^2J_{C,P}$ = 14.4 Hz, P–C≡*C*), 111.0, 111.7 (s, C-3a, C-7a), 121.2–134.1 (C-4,5,6,7, Ar), 202.4 (d, $^2J_{C,P}$ = 20.7 Hz, CO) ppm. $^{31}P\{^1H\}$ NMR (121.5 MHz, $CDCl_3$, 18 °C): $\delta$ = 22.5 ppm (s). $C_{30}H_{22}IOPRu$ (657.44): calcd. C 54.81, H 3.37; found C 53.26, H 2.90.

**Synthesis of [RuCl($\eta^5$-$C_9H_7$)($PPh_3$)($Ph_2PCH_2CH_2CH{=}CH_2$-κ*P*)] (2b):** A solution of [RuCl($\eta^5$-$C_9H_7$)$(PPh_3)_2$] (500 mg, 0.64 mmol) and homoallyldiphenylphosphane (168 mg, 0.70 mmol) in THF (40 mL) was refluxed for 20 min. It was then concentrated to about 10 mL and CuI (183 mg, 0.96 mmol) was added. After 30 min at room temperature, the solution was evaporated to dryness and the residue extracted with diethyl ether (2 × 20 mL), vacuum-dried, and recrystallized from diethyl ether/hexane (1:10) to obtain complex **2b** as a red solid. Yield: 290 mg (60%). $^1H$ NMR (300 MHz, $CDCl_3$, 18 °C): $\delta$ = 0.81 (m, 1 H, $CH_2$), 0.97 (m, 1 H, $CH_2$), 1.50 (m, 1 H, $CH_2$), 2.56 (m, 1 H, $CH_2$), 4.67 (m, 4 H, 1-H, 3-H, =$CH_2$), 4.84 (t, $J_{H,H}$ = 2.0 Hz, 2-H), 5.33 (m, 1 H, =CH), 6.30 (d, $J_{H,H}$ = 8.2 Hz, 1 H, 4-H, 5-H, 6-H, or 7-H), 6.81–8.00 (m, 28 H, 4-H, 5-H, 6-H, or 7-H, Ar) ppm. $^{13}C\{^1H\}$ NMR (75.4 MHz, $CDCl_3$, 18 °C): $\delta$ = 20.3 (d, $J_{C,P}$ = 22.9 Hz, P–$CH_2$), 28.7 (d, $^2J_{C,P}$ = 8.3 Hz, $CH_2$), 61.6 (s, C-1 or C-3), 69.4 (d, $^2J_{C,P}$ = 11.4 Hz, C-1 or C-3), 90.6 (s, C-2), 109.8, 111.3 (s, C-3a, C-7a), 113.8 (s, =$CH_2$), 123.3–138.2 (=CH, C-4,5,6,7, Ar) ppm. $^{31}P\{^1H\}$ NMR (121.5 MHz, $CDCl_3$, 18 °C): $\delta$ = 45.6 (d, $^2J_{P,P}$ = 42.9 Hz), 49.0 (d, $^2J_{P,P}$ = 42.9 Hz) ppm. $C_{43}H_{39}ClP_2Ru$ (754.24): calcd. C 68.47, H 5.21; found C 67.05, H 4.30.

**Synthesis of [RuCl($\eta^5$-$C_9H_7$)($PPh_3$)($Ph_2PC{\equiv}CPh$-κ*P*)] (2c):** A solution of [RuCl($\eta^5$-$C_9H_7$)$(PPh_3)_2$] (500 mg, 0.64 mmol) and phenylalkynyldiphenylphosphane (161 mg, 0.77 mmol) in THF (55 mL) was refluxed for 10 min. The solution was then evaporated to dryness and the solid residue extracted with diethyl ether (2 × 20 mL). The solution was concentrated under vacuum and the product precipitated as a red solid upon addition of hexane; it was vacuum-dried. Yield: 307 mg (60%). IR (KBr): ν(C≡C) = 2168 $cm^{-1}$. $^1H$ NMR (300 MHz, $C_6D_6$, 18 °C): $\delta$ = 3.80, 4.29, 4.87 (s, 4 H, 1,2,3-H and 4-H, 5-H, 6-H, or 7-H), 6.84–7.87 (m, 33 H, 4-H, 5-H, 6-H, or 7-H, Ar) ppm. $^{13}C\{^1H\}$ NMR (75.4 MHz, $C_6D_6$, 18 °C): $\delta$ = 66.6 (s, C-1 or C-3), 69.5 (d, $^2J_{C,P}$ = 9.5 Hz, C-1 or C-3), 87.2 (d, $J_{P,C}$ = 80.7 Hz, P–*C*≡C), 91.8 (s, C-2), 109.1, (d, $J_{C,P}$ = 11.5 Hz, P–C≡*C*), 110.5 (s, C-3a or C-7a), 111.8 (d, $^2J_{C,P}$ = 3.8 Hz, C-3a or C-7a), 122.5–134.7 (C-4,5,6,7, Ar) ppm. $^{31}P\{^1H\}$ NMR (121.5 MHz, $C_6D_6$, 18 °C): $\delta$ = 29.1 (d, $^2J_{P,P}$ = 45.0 Hz), 48.1 (d, $^2J_{P,P}$ = 45.0 Hz) ppm. $C_{47}H_{37}ClP_2Ru{\cdot}CH_2Cl_2$ (800.27): calcd. C 65.13, H 4.44; found C 66.41, H 4.04.

**Synthesis of [Ru($\eta^5$-$C_9H_7$)(CO)($Ph_2PR$-κ$^3$*P*,*C*,*C*)][$SbF_6$] [R = $CH_2CH{=}CH_2$ (3a), $CH_2CH_2CH{=}CH_2$ (3b)]:** A solution of the complex [RuCl($\eta^5$-$C_9H_7$)($Ph_2PR$-κ$^1$*P*)(CO)] [R = $CH_2CH{=}CH_2$ (**1a**), $CH_2CH_2CH{=}CH_2$ (**1b**)] (0.82 mmol) and $AgSbF_6$ (337 mg, 0.98 mmol) in $CH_2Cl_2$ (80 mL) was stirred for 1 h at room temperature in the absence of light. A change of color from red to yellow was observed. After this time, the suspension was exposed to light for 1 h, then filtered through kieselguhr and the solvents evaporated to dryness. The solid residue was recrystallized from $CH_2Cl_2$/hexane (1:10), washed with hexane (2 × 20 mL), and vacuum-dried.

**3a:** Yield: 562 mg (97%). IR (KBr): ν(CO) = 2012, ν($SbF_6$) = 658 $cm^{-1}$. Conductivity (acetone): 123 $\Omega^{-1}cm^2mol^{-1}$. $^1H$ NMR (400.1 MHz, $CD_2Cl_2$, 18 °C): $\delta$ = 2.36 (m, 1 H, =$CH_2$), 2.82 (m, 1 H, P–$CH_2$), 3.47 (m, 1 H, =$CH_2$), 3.92 (m, 1 H, =CH), 4.43 (m, 1 H, P–$CH_2$), 5.47 (pseudo t, $J_{H,H}$ = 2.5 Hz, 1 H, 2-H), 5.85, 6.05 (s, 1 H each, 1-H, 3-H), 6.78 (d, $J_{H,H}$ = 8.6 Hz, 1 H, 4-H, 5-H, 6-H, or 7-H), 7.16–7.71 (m, 13 H, 4-H, 5-H, 6-H, or 7-H, Ar) ppm. $^{13}C\{^1H\}$ NMR (100.6 MHz, $CD_2Cl_2$, 18 °C): $\delta$ = 34.0 (d, $J_{C,P}$ = 38.2 Hz, P–$CH_2$), 55.1 (d, $J_{C,P}$ = 20.1 Hz, =CH), 57.0 (d, $J_{C,P}$ = 6.0 Hz, =$CH_2$), 73.8, 76.3 (s, C-1, C-3), 93.9 (s, C-2), 106.9, 108.9 (s, C-3a, C-7a), 122.6–134.7 (C-4,5,6,7, Ar), 202.0 (d, $^2J_{C,P}$ = 16.1 Hz, CO) ppm. $^{31}P\{^1H\}$ NMR (161.9 MHz, $CD_2Cl_2$, 18 °C): $\delta$ = –56.4 ppm (s). $C_{25}H_{22}F_6OPRuSb$ (706.24): calcd. C 42.52, H, 3.14; found C 42.12, H 3.09.

**3b:** Yield: 561 mg (95%). IR (KBr): ν(CO) = 2001, ν($SbF_6$) = 659 $cm^{-1}$. Conductivity (acetone): 144 $\Omega^{-1}cm^2mol^{-1}$. $^1H$ NMR (400.1 MHz, $CD_2Cl_2$, 18 °C): $\delta$ = 1.73 (m, 1 H, $CH_2$), 2.11 (d, $J_{H,H}$ = 8.6 Hz, 1 H, =$CH_2$), 2.66 (m, 2 H, $CH_2$ and P–$CH_2$), 3.06 (m, 1 H, P–$CH_2$), 3.13 (d, $J_{H,H}$ = 13.0 Hz, 1 H, =$CH_2$), 4.48 (m, 1 H, =CH), 5.61 (m, 1 H, 2-H), 5.87 (s, 1 H, 1-H or 3-H), 6.27 (s, 1 H, 1-H or 3-H), 6.60 (dd, $J_{H,H}$ = 8.6, $J_{H,H}$ = 1.0 Hz, 1 H, 4-H, 5-H, 6-H, or 7-H), 7.27–7.69 (m, 13 H, 4-H, 5-H, 6-H, or 7-H, Ar) ppm. $^{13}C\{^1H\}$ NMR (100.6 MHz, $CD_2Cl_2$, 18 °C): $\delta$ = 28.1 (d, $J_{C,P}$ = 6.0 Hz, $CH_2$), 38.8 (d, $J_{C,P}$ = 34.2 Hz, P–$CH_2$), 54.9 (s, =$CH_2$), 74.6, 77.8 (s, C-1, C-3), 85.2 (d, $J_{C,P}$ = 5.0 Hz, =CH), 94.7 (s, C-2), 107.5, 110.0 (s, C-3a, C-7a), 121.7–134.7 (C-4,5,6,7, Ar), 200.2 (d, $^2J_{C,P}$ = 18.1 Hz, CO) ppm. $^{31}P\{^1H\}$ NMR (162.0 MHz,

 © 2006 Wiley-VCH Verlag GmbH & Co. KGaA, Weinheim 

$CD_2Cl_2$, 18 °C): $\delta$ = 74.6 ppm (s). $C_{26}H_{24}F_6OPRuSb{\cdot}CH_2Cl_2$ (720.26): calcd. C 40.28, H 3.25; found C 40.18, H 2.78.

**Synthesis of [Ru(η⁵-C₉H₇)(PPh₃)(Ph₂PCH₂CH₂CH=CH₂-κ³*P*,*C*,*C*)][PF₆] (4b):** A solution of the complex [RuCl(η⁵-$C_9H_7$)($PPh_3$)($Ph_2PCH_2CH_2CH=CH_2$-κ*P*)] (500 mg, 0.66 mmol) and $NaPF_6$ (222 mg, 1.32 mmol) in EtOH (30 mL) was refluxed for 5 min. After this time, the solution was evaporated to dryness and the residue extracted with $CH_2Cl_2$ (2×20 mL). The solvent was then concentrated to about 2 mL and diethyl ether (20 mL) was added. The yellow solid obtained was washed with diethyl ether (2×10 mL) and vacuum-dried. Yield: 382 mg (67%). IR (KBr): ν($PF_6$) = 838 $cm^{-1}$. Conductivity (acetone): 97 $\Omega^{-1}cm^2mol^{-1}$. $^1H$ NMR (300.1 MHz, $CD_2Cl_2$, 18 °C): $\delta$ = 1.78 (d, $J_{H,H}$ = 8.8 Hz, 1 H, =$CH_2$), 2.24 (m, 2 H, $CH_2$), 2.54 (m, 2 H, $CH_2$), 3.57 (m, 1 H, =$CH_2$), 5.10 (s, 1 H, 1-H, 2-H or 3-H), 5.30 (m, 1 H, =CH), 5.37 (s, 1 H, 1-H, 2-H or 3-H), 5.51 (s, 1 H, 1-H, 2-H or 3-H), 6.79–7.69 (m, 29 H, 4,5,6,7-H, Ar) ppm. $^{13}C\{^1H\}$ NMR (75.4 MHz, $CD_2Cl_2$, 18 °C): $\delta$ = 24.4 (d, $^2J_{C,P}$ = 6.7 Hz, P–$CH_2$), 40.0 (d, $J_{C,P}$ = 33.5 Hz, $CH_2$), 79.3 (s, C-1 or C-3), 82.1 (d, $^2J_{C,P}$ = 12.0 Hz, C-1 or C-3), 87.6 (s, C-2), 97.5, 103.6 (s, C-3a, C-7a), 107.4 (d, $J_{C,P}$ = 3.4 Hz, =$CH_2$), 122.5–133.6 (=CH, C-4,5,6,7, Ar) ppm. $^{31}P\{^1H\}$ NMR (121.5 MHz, $CD_2Cl_2$, 18 °C): $\delta$ = 47.3 (d, $^2J_{P,P}$ = 29.5 Hz), 69.3 (d, $^2J_{P,P}$ = 29.5 Hz) ppm. MS (FAB+): *m*/*z* = 719 [$M^+$].

**Synthesis of [Ru(η⁵-C₉H₇)(L)(Ph₂PCH₂CH=CHCH₂-κ²*P*,*C*)] [L = CO (5a), PPh₃ (5b)]:** A solution of [Ru(η⁵-$C_9H_7$)(L)-($Ph_2PCH_2CH_2CH=CH_2$-κ³*P*,*C*,*C*)][X] [X = $SbF_6$, L = CO (**3b**); X = $PF_6$, L = $PPh_3$ (**4b**)] (0.14 mmol) and $Cs_2CO_3$ (228 mg, 0.7 mmol) in $CH_2Cl_2$ (20 mL) was stirred for 1 h at room temperature. After this time the solution was filtered through kieselguhr and the solvents evaporated to dryness. The solid residue was extracted with 20 mL of diethyl ether and precipitated with hexane. The yellow solid obtained was washed with hexane (2×10 mL) and vacuum-dried.

**5a:** Yield: 46 mg (86%). IR (KBr): ν(CO) = 1920 $cm^{-1}$. $^1H$ NMR (400.1 MHz, $C_6D_6$, 18 °C): $\delta$ = 2.19 (m, 1 H, Ru–$CH_2$) 2.35 (m, 1 H, Ru–$CH_2$), 2.69 (m, 2 H, P–$CH_2$), 4.82 (s, 1 H, 1-H or 3-H), 5.04 (s, 1 H, 2-H), 5.34 (s, 1 H, 1-H or 3-H), 5.51 (m, 1 H, =CH), 6.46 (d, $J_{H,H}$ = 8.1 Hz, 1 H, 4-H, 5-H, 6-H, or 7-H), 6.78 (m, 1 H, =CH), 6.97–7.27 (m, 13 H, 4-H, 5-H, 6-H, or 7-H, Ar) ppm. $^{13}C\{^1H\}$ NMR (100.6 MHz, $C_6D_6$, 18 °C): $\delta$ = –4.1 (d, $J_{C,P}$ = 8.8 Hz, Ru–$CH_2$), 26.8 (d, $J_{C,P}$ = 22.4 Hz, $CH_2$), 72.0 (d, $^2J_{C,P}$ = 7.2 Hz, C-1 or C-3), 74.3 (s, C-1 or C-3), 98.3 (s, C-2), 108.1 (s, C-3a, C-7a), 116.4 (s, =CH), 122.5–141.6 (C-4,5,6,7, Ar), 146.0 (d, $J_{C,P}$ = 14.4 Hz, =CH), 205.4 (d, $^2J_{C,P}$ = 16.8 Hz, CO) ppm. $^{31}P\{^1H\}$(162.0 MHz, $C_6D_6$, 18 °C): $\delta$ = 101.3 ppm (s). MS (FAB+): *m*/*z* = 485 [$M^+$ + 1].

**5b:** Yield: 80 mg (80%). $^1H$ NMR (400.1 MHz, $CD_2Cl_2$, –50 °C): $\delta$ = 0.79 (m, 1 H, Ru–$CH_2$), 1.62 (m, 1 H, P–$CH_2$), 2.43 (m, 1 H, Ru–$CH_2$), 3.30 (m, 1 H, P–$CH_2$), 3.99 (s, 1 H, 1-H or 3-H), 4.19 (s, 1 H, 1-H or 3-H), 5.15 (s, 1 H, 2-H), 5.51 (m, 1 H, =CH), 6.67 (m, 1 H, =CH), 6.92–7.66 (m, 29 H, 4,5,6,7-H, Ar) ppm. $^{13}C\{^1H\}$ NMR (100.6 MHz, $CD_2Cl_2$, –50 °C): $\delta$ = –0.7 (br. s, Ru–$CH_2$), 25.8 (d, $J_{C,P}$ = 20.4 Hz, P–$CH_2$), 71.1 (s, C-1 or C-3), 74.0 (d, $^2J_{C,P}$ = 5.4 Hz, C-1 or C-3), 93.5 (pseudo t, $^2J_{C,P}$ = 4.7 Hz, C-2), 103.8, 109.7 (s, C-3a, C-7a), 115.3 (s, =CH), 121.0–144.9 (C-4,5,6,7, Ar), 147.0 (d, $J_{C,P}$ = 13.6 Hz, =CH) ppm. $^{31}P\{^1H\}$ NMR (162.0 MHz, $CD_2Cl_2$, 18 °C): $\delta$ = 56.2 (d, $^2J_{P,P}$ = 33.7 Hz), 91.8 (d, $^2J_{P,P}$ = 33.7 Hz) ppm. MS (FAB+): *m*/*z* = 719 [$M^+$ + 1].

**Synthesis of [Ru(η⁵-C₉H₇)(MeCN)(CO)(Ph₂PCH₂CH=CH₂-κ*P*)]-[SbF₆] (6):** A solution of [Ru(η⁵-$C_9H_7$)(CO)($PPh_2CH_2CH=CH_2$-κ³*P*,*C*,*C*)][$SbF_6$] (500 mg, 0.7 mmol) in MeCN (100 mL) was stirred at room temperature for 2.5 h. The solution was then evaporated to dryness and the residue extracted with $CH_2Cl_2$ (2×20 mL). The solvent was then concentrated to about 2 mL and hexane (20 mL) was added. The yellow solid obtained was washed with hexane (2×10 mL) and vacuum-dried. Yield: 530 mg (91%). IR (KBr): ν(CO) = 1977, ν($SbF_6$) = 658 $cm^{-1}$. Conductivity (acetone): 123 $\Omega^{-1}cm^2mol^{-1}$. $^1H$ NMR (300 MHz, $CDCl_3$, 18 °C): $\delta$ = 2.23 (br. s, 3 H, $CH_3$), 3.35 (m, 2 H, P–$CH_2$), 5.15 and 5.28 (2×m, 5 H, =$CH_2$ and 1,2,3-H), 5.48 (m, 1 H, =CH), 7.22–7.68 (m, 14 H, 4,5,6,7-H, Ar) ppm. $^{13}C\{^1H\}$ NMR (75.5 MHz, $CDCl_3$, 18 °C): $\delta$ = 3.7 (s, $CH_3$), 36.6 (d, $J_{C,P}$ = 30.2 Hz, P–$CH_2$), 65.8, 67.1 (s, C-1, C-3), 93.3 (s, C-2), 109.3, 112.9 (s, C-3a, C-7a), 121.4 (d, $J_{C,P}$ = 12.1 Hz, =$CH_2$), 123.5–132.3 (C-4,5,6,7, Ar), 200.2 (d, $^2J_{C,P}$ = 18.9 Hz, CO) ppm. $^{31}P\{^1H\}$ NMR (121.5 MHz, $CDCl_3$, 18 °C): $\delta$ = 46.9 ppm (s). $C_{27}H_{25}F_6OPNRuSb$ (747.29): calcd. C 43.40, H 3.37, N 1.87; found C 42.48, H 3.67, N 1.90.

**Synthesis of [Ru(η⁵-C₉H₇)(PPh₃)(Ph₂PC≡CPh-κ*P*){=C=C(Ph)H}]-[PF₆] (7):** A solution of [RuCl(η⁵-$C_9H_7$)($PPh_3$)($Ph_2PC{\equiv}CPh$-κ*P*)] (50 mg, 0.07 mmol), $NaPF_6$ (23 mg, 0.14 mmol), and phenylacetylene (36 mg, 0.35 mmol) in EtOH (8 mL) was refluxed for 15 min. After this time the solution was evaporated to dryness and the residue was extracted with $CH_2Cl_2$ (2×10 mL). The solvent was then concentrated to about 2 mL and hexane (20 mL) was added. The orange solid obtained was washed with hexane (2×10 mL) and vacuum-dried. Yield: 58 mg (82%). IR (KBr): ν(C≡C) = 2171, ν($PF_6$) = 838 $cm^{-1}$. Conductivity (acetone): 96 $\Omega^{-1}cm^2mol^{-1}$. $^1H$ NMR (300 MHz, $CD_2Cl_2$, 18 °C): $\delta$ = 5.30, 5.54, 5.74 (s, 1 H each, 1,2,3-H), 5.94 (d, $J_{H,H}$ = 8.3 Hz, 1 H, 4-H, 5-H, 6-H, or 7-H), 6.21 (s, 1 H, =CH), 6.37 (d, $J_{H,H}$ = 8.3 Hz, 1 H, 4-H, 5-H, 6-H, or 7-H), 6.78–7.58 (m, 37 H, 4-H, 5-H, 6-H, or 7-H, Ar) ppm. $^{13}C\{^1H\}$ NMR (75.5 MHz, $(CD_3)_2CO$, 18 °C): $\delta$ = 81.6 (d, $J_{C,P}$ = 95.0 Hz, P–*C*≡C), 82.5 (s, C-1 and C-3), 100.6 (s, C-2), 112.9 (d, $^2J_{C,P}$ = 12.3 Hz, P–C≡*C*), 115.1 (s, C-3a or C-7a), 117.2 (s, $C_\beta$), 120.9 (d, $J_{C,P}$ = 2.6 Hz, C-3a or C-7a), 123.9–135.2 (Ar), 355.4 (pseudo t, $^2J_{C,P}$ = 16.4, $C_\alpha$) ppm. $^{31}P\{^1H\}$ NMR (121.5 MHz, $CD_2Cl_2$, 18 °C): $\delta$ = 20.6 (d, $^2J_{P,P}$ = 27.2 Hz), 41.7 (d, $^2J_{P,P}$ = 27.2 Hz) ppm.

**Synthesis of [Ru(η⁵-C₉H₇)(PPh₃)(Ph₂PC≡CPh-κ*P*)(=C=C=CPh₂)]-[PF₆] (8):** A solution of [RuCl(η⁵-$C_9H_7$)($PPh_3$)($Ph_2PC{\equiv}$CPh-κ*P*)] (50 mg, 0.07 mmol), $NaPF_6$ (23 mg, 0.14 mmol), and 1,1-diphenylprop-2-yn-1-ol (72 mg, 0.35 mmol) in EtOH (8 mL) was refluxed for 20 min. After this time the solution was evaporated to dryness and the residue was extracted with $CH_2Cl_2$ (2×10 mL). The solution was concentrated under vacuum and the product precipitated and washed with hexane (2×10 mL). The violet solid obtained was vacuum-dried. Yield: 59 mg (76%). IR (KBr): ν(C≡C) = 2169, ν(C=C=C) = 1931, ν($PF_6$) = 837 $cm^{-1}$. Conductivity (acetone): 133 $\Omega^{-1}cm^2mol^{-1}$. $^1H$ NMR (300 MHz, $CDCl_3$, 18 °C): $\delta$ = 5.24, 5.66, 5.72 (s, 3 H, 1,2,3-H), 6.22 (d, $J_{H,H}$ = 8.0 Hz, 1 H, 4-H, 5-H, 6-H, or 7-H), 6.88–7.84 (m, 43 H, 4-H, 5-H, 6-H, or 7-H, Ar) ppm. $^{13}C\{^1H\}$ NMR (75.5 MHz, $CD_2Cl_2$, 18 °C): $\delta$ = 80.8 (d, $J_{C,P}$ = 5.8 Hz, C-1 or C-3), 81.7 (dd, $J_{C,P}$ = 92.5, $^3J_{C,P}$ = 3.5 Hz, P–*C*≡C), 82.6 (d, $J_{C,P}$ = 7.0 Hz, C-1 or C-3), 98.4 (s, C-2), 111.3 (d, $^2J_{C,P}$ = 10.4 Hz, P–C≡*C*), 113.5 (s, C-3a or C-7a), 119.5 (d, $^2J_{C,P}$ = 2.3 Hz, C-3a or C-7a), 122.6–142.8 (Ar), 158.5 (s, $C_\gamma$), 204.9 (s, $C_\beta$), 293.2 (pseudo t, $^2J_{C,P}$ = 18.5 Hz, $C_\alpha$) ppm. $^{31}P\{^1H\}$ NMR (121.5 MHz, $CDCl_3$, 18 °C): $\delta$ = 26.0 (d, $^2J_{P,P}$ = 28.7 Hz), 48.3 (d, $^2J_{P,P}$ = 28.7 Hz) ppm.

**X-ray Crystal Structure Determination of Complexes 1c, 3a, and 4b:** Crystals suitable for X-ray diffraction analysis were obtained by slow diffusion of hexane (**1c**) or pentane (**3a** and **4b**) into a saturated solution of the complexes in dichloromethane. The most relevant crystal and refinement data are collected in Table 2. Diffraction data for **1c** were recorded with a Bruker Smart 6k CCD area-

 © 2006 Wiley-VCH Verlag GmbH & Co. KGaA, Weinheim 

Table 2. Crystal data and structure refinement for **1c**, **3a**, and **4b**.

| | **1c** | **3a** | **4b** |
|---|---|---|---|
| Chemical formula | $C_{30}H_{22}IOPRu$ | $C_{25}H_{22}F_6OPRuSb$ | $C_{43}H_{39}F_6P_3Ru$ |
| Mol. mass | 657.42 | 706.22 | 863.72 |
| $T$ [K] | 296(2) | 293(2) | 293(2) |
| Wavelength [Å] | 1.54184 | 1.54184 | 0.71073 |
| Crystal system | triclinic | triclinic | monoclinic |
| Space group | $P\bar{1}$ | $P\bar{1}$ | $P2_1/c$ |
| $a$ [Å] | 8.71010(10) | 12.1110(9) | 10.8581(13) |
| $b$ [Å] | 17.1308(3) | 13.2257(8) | 36.732(4) |
| $c$ [Å] | 17.7376(3) | 16.0508(10) | 19.627(2) |
| $\alpha$ [°] | 81.6670(10) | 80.581(4) | 90 |
| $\beta$ [°] | 77.1680(10) | 86.865(4) | 105.209(2) |
| $\gamma$ [°] | 83.3500(10) | 89.774(4) | 90 |
| $V$ [Å$^3$] | 2543.69(7) | 2532.5(3) | 7553.9(14) |
| $Z$ | 4 | 4 | 8 |
| $\rho_{calcd.}$ [g cm$^{-3}$] | 1.717 | 1.852 | 1.519 |
| $\mu$ [mm$^{-1}$] | 15.268 | 14.442 | 0.603 |
| $F$(000) | 1288 | 1376 | 3520 |
| Crystal size [mm] | 0.25 × 0.15 × 0.12 | 0.125 × 0.05 × 0.025 | 0.25 × 0.21 × 0.19 |
| $\theta$ range [°] | 2.57 to 70.62 | 2.79 to 70.06 | 1.54 to 26.12 |
| Index ranges | $-13 \le h \le 12$ | $-14 \le h \le 14$ | $-13 \le h \le 12$ |
| | $0 \le k< \le 45$ | $-15 \le k \le 16$ | $0 \le k \le 45$ |
| | $0 \le l \le 24$ | $0 \le l \le 19$ | $0 \le l \le 24$ |
| No. of reflns. collected | 16413 | 50571 | 37632 |
| No. of unique reflns. | 8462 [$R$(int) = 0.0295] | 9308 [$R$(int) = 0.066] | 14418 [$R$(int) = 0.10] |
| Completeness to $\theta_{max}$ | 86.6% | 96.7% | 95.8% |
| No. of parameters/restraints | 613/0 | 616/0 | 955/0 |
| Goodness-of-fit on $F^2$ | 0.984 | 0.959 | 0.998 |
| Weight function ($a$, $b$) | | 0.0546,13.5440 | 0.0694, 0.1691 |
| $R_1$[a] [$I > 2\rho(I)$] | 0.0312 | 0.0619 | 0.0916 |
| $wR_2$[a] [$I > 2\rho(I)$] | 0.0772 | 0.1544 | 0.1061 |
| $R_1$ (all data) | 0.0360 | 0.1074 | 0.2105 |
| $wR_2$ (all data) | 0.0800 | 0.1977 | 0.1283 |
| Largest diff peak and hole [e Å$^{-3}$] | 1.218 and-0.565 | 2.668 and –1.042 | 0.6166 and –1.115 |

[a] $R_1 = \Sigma(|F_o| - |F_c|)/\Sigma|F_o|$; $wR_2 = \{\Sigma[w(F_o^2 - F_c^2)^2]/\Sigma[w(F_o^2)^2]\}$½.

detector three-circle diffractometer (Cu-$K_\alpha$ radiation, λ = 1.5418 Å). The data were collected using 0.3°-wide $\omega$ scans with a crystal-to-detector distance of 40 mm. The diffraction frames were integrated using the SAINT package[28] and corrected for absorption with SADABS.[29] For **3a** diffraction data were recorded with a Nonius Kappa CCD single crystal diffractometer using Cu-$K_\alpha$ radiation (λ = 1.5418 Å) − the crystal-to-detector distance was fixed at 29 mm − and using the oscillation method, with 2° oscillation and 40 s exposure time per frame. The data collection strategy was calculated with the program Collect.[30] Data reduction and cell refinement were performed using the programs HKL Denzo and Scalepack[31] and absorption correction was applied by means of SORTAV.[32] Data for **4b** were collected on a Bruker Smart CCD diffractometer using graphite-monochromated Mo-$K_\alpha$ radiation (λ = 0.71073 Å). The data were collected using 0.3°-wide $\omega$ scans with a crystal-to-detector distance of 40 mm. The diffraction frames were integrated using the SAINT package[28] and corrected for absorption with SADABS.[29]

The software package WINGX was used for space group determination, structure solution, and refinement.[33] The structures were solved by Patterson interpretation and phase expansion using DIRDIF.[34] Isotropic least-squares refinement on $F^2$ using SHELXL97 was performed.[35] For all the complexes, during the final stages all non-hydrogen atoms were refined with anisotropic displacement parameters and the H atoms were geometrically located and their coordinates were refined riding on their parent atoms. The maximum residual electron density is located near to heavy atoms (Ru, I) for **1c** and near to the disordered $PF_6^-$ ions for **3a**.

The function minimized was $[\Sigma w(F_o^2 - F_c^2)/\Sigma w(F_o^2)]^{1/2}$ where $w = 1/[\sigma^2(F_o^2) + (aP)^2 + bP]$ ($a$ = 0.0512 and $b$ = 0 for **1c**, $a$ = 0.0899 and $b$ = 0 for **3a**, $a$ = 0.0228 and $b$ = 0 for **4b**) with $\sigma(F_o^2)$ from counting statistics and $P = [\mathrm{Max}(F_o^2,0) + 2F_c^2]/3$. Atomic scattering factors were taken from the International Tables for X-ray Crystallography.[36] Geometrical calculations were made with PARST.[37] The crystallographic plots were made with PLATON.[38] CCDC-276224 (**1c**), -276225 (**3a**), and -276226 (**4b**) contain the supplementary crystallographic data for this paper. These data can be obtained free of charge from The Cambridge Crystallographic Data Centre via www.ccdc.cam.ac.uk/data_request/cif.

## Acknowledgments

This work was supported by the Spanish M.C.T. (BQU2003-00255) and the Principado de Asturias (PR-01-GE-6). A. V. thanks the Spanish Ministerio de Educación, Cultura y Deporte for a scholarship.

[1] For representative examples of complexes with $R_2PCH{=}CH_2$, see the following: [M] = [Cr] and [Mo] a) P. G. Edwards, J. S. Fleming, S. S. Liyanage, S. J. Coles, M. B. Hursthouse, *J. Chem. Soc., Dalton Trans.* **1996**, 1801–1807; [Os]: b) M. Baya, M. L. Buil, M. A. Esteruelas, E. Oñate, *Organometallics* **2005**, *24*, 2030–2038; c) M. A. Esteruelas, A. I. González, A. M.

 © 2006 Wiley-VCH Verlag GmbH & Co. KGaA, Weinheim 

López, E. Oñate, *Organometallics* **2004**, *23*, 4858–4869; [Rh]: d) L. P. Barthel-Rosa, V. J. Catalano, K. Maitra, J. H. Nelson, *Organometallics* **1996**, *15*, 3924–3934. For representative examples of complexes with $R_2PCH_2CH=CH_2$, see the following: [M] = [Cr] and [Mo], see ref.[1a]; [W]: e) X. Morise, M. L. H. Green, P. C. McGowan, S. J. Simpson, *J. Chem. Soc., Dalton Trans.* **1994**, 571–578; [Pd]: f) S. J. Coles, P. Faulds, M. B. Hursthouse, D. G. Kelly, G. C. Ranger, A. J. Toner, N. M. Walker, *J. Organomet. Chem.* **1999**, *586*, 234–240. For examples of complexes with $R_2PCH_2CH_2CH=CH_2$, see the following: [M] = [Ni]: g) K. Issleib, M. Haftendorn, *Z. Anorg. Allg. Chem.* **1967**, *351*, 9–17; [Rh] and [Ir]: h) D. V. Krupenya, S. I. Selivanov, S. P. Tunik, M. Haukka, T. A. Pakkanen, *Dalton Trans.* **2004**, 2541–2549; i) P. W. Clark, G. E. Hartwell, *J. Organomet. Chem.* **1975**, *102*, 387–396.

[2] For representative examples of alkynylphosphane complexes, see the following: [M] = [Fe]: a) E. Louattani, J. Suades, A. Álvarez-Larena, J. F. Piniella, G. Germain, *J. Organomet. Chem.* **1996**, *506*, 121–127; [Mo]: b) E. Louattani, J. Suades, *J. Organomet. Chem.* **2000**, *604*, 234–240; [Rh], [Ir], and [Pt]: c) J. R. Berenguer, M. Bernechea, J. Forniés, A. García, E. Lalinde, M. T. Moreno, *Inorg. Chem.* **2004**, *43*, 8185–8198; d) J. Forniés, A. García, B. Gil, E. Lalinde, M. T. Moreno, *Dalton Trans.* **2004**, 3854–3863; e) J. Forniés, A. García, J. Gómez, E. Lalinde, M. T. Moreno, *Organometallics* **2002**, *21*, 3733–3743; [Au]: f) M. Bardaji, A. Laguna, P. G. Jones, *Organometallics* **2001**, *20*, 3906–3912.

[3] For recent examples of ruthenium complexes with DCVP see: a) D. Dorota, J. H. Nelson, *Dalton Trans.* **2005**, 92–103; b) K. Y. Ghebreyessus, J. H. Nelson, *Synth. React. Inorg. Met.-Org. Chem.* **2003**, *33*, 1329–1349.

[4] For recent examples of ruthenium complexes with DPVP see: a) D. C. Wilson, J. H. Nelson, *J. Organomet. Chem.* **2003**, *682*, 272–289; b) H. D. Hansen, J. H. Nelson, *Inorg. Chim. Acta* **2003**, *352*, 4–8; c) G. Kesete, J. H. Nelson, *Inorg. Chem. Commun.* **2003**, *6*, 1044–1047; d) D. Dorota, J. H. Nelson, *Dalton Trans.* **2003**, 449–457; e) G. Kesete, J. H. Nelson, *Organometallics* **2000**, *19*, 3387–3392; f) H. Heather, J. H. Nelson, *Organometallics* **2000**, *19*, 4740–4755.

[5] For recent examples of ruthenium complexes with ADPP see: a) D. Cuervo, M. P. Gamasa, J. Gimeno, *Chem. Eur. J.* **2004**, *10*, 425–432; b) K. D. Redwine, J. H. Nelson, *J. Organomet. Chem.* **2000**, *613*, 177–199; c) L. P. Barthel-Rosa, K. Maitra, J. Fischer, J. H. Nelson, *Inorg. Chem.* **1998**, *37*, 633–639.

[6] C. Slugovc, K. Mereiter, R. Schmid, K. Kirchner, *Organometallics* **1999**, *18*, 1011–1017.

[7] a) J. R. Berenguer, M. Bernechea, J. Forniés, A. García, E. Lalinde, *Organometallics* **2004**, *23*, 4288–4300; b) J. R. Berenguer, M. Bernechea, J. Forniés, J. Gómez, E. Lalinde, *Organometallics* **2002**, *21*, 2314–2324; c) C. J. Adams, M. I. Bruce, B. W. Skelton, A. H. White, *Inorg. Chem.* **1992**, *31*, 3336–3338; d) G. Mohamed, B. Demerseman, P. H. Dixneuf, *J. Organomet. Chem.* **1992**, *424*, 65–70.

[8] a) F. Hong, Y. Ho, Y. Chang, Y. Lai, *Tetrahedron* **2004**, *60*, 2639–2645; b) T. Baumgartner, K. Huynth, S. Schleidt, A. J. Lough, I. Manners, *Chem. Eur. J.* **2002**, *8*, 4622–4632; c) T. De Simone, R. S. Dickson, B. W. Skelton, A. W. White, *Inorg. Chim. Acta* **1995**, *240*, 323–333; d) I. Moldes, J. Ros, *Inorg. Chim. Acta* **1995**, *232*, 75–81.

[9] J. E. Davies, M. J. Mays, P. R. Raithby, K. Sarveswaran, G. A. Solan, *J. Chem. Soc., Dalton Trans.* **2001**, 1269–1277.

[10] I. Ara, J. Forniés, A. García, J. Gómez, E. Lalinde, M. T. Moreno, *Chem. Eur. J.* **2002**, *8*, 3698–3716.

[11] P. Álvarez, E. Lastra, J. Gimeno, P. Braña, J. A. Sordo, J. Gómez, L. R. Falvello, M. Bassetti, *Organometallics* **2004**, *23*, 2956–2966.

[12] P. Álvarez, E. Lastra, J. Gimeno, M. Bassetti, L. R. Falvello, *J. Am. Chem. Soc.* **2003**, *125*, 2386–2387.

[13] J. Díez, M. P. Gamasa, J. Gimeno, E. Lastra, A. Villar, *Organometallics* **2005**, *24*, 1410–1418.

[14] M. Bassetti, P. Álvarez, J. Gimeno, E. Lastra, *Organometallics* **2004**, *23*, 5127–5134.

[15] C* represents the centroid of atoms C(1), C2), C(3), C(4), and C(5); C** represents the centroid of atoms C(4), C(5), C(6), C(7), C(8), and C(9).

[16] S. García-Granda, M. Pérez-Priede, J. F. Van der Maelen, personal communication.

[17] M. P. Gamasa, J. Gimeno, C. González-Bernardo, J. Borge, S. García-Granda, *Organometallics* **1997**, *16*, 2483–2485.

[18] P. Garrou, *Chem. Rev.* **1981**, *81*, 229–266.

[19] a) J. Okuda, K. H. Zimmermann, *Chem. Ber.* **1989**, *122*, 1645–1647; b) J. W. Faller, B. V. Johnson, *J. Organomet. Chem.* **1975**, *88*, 101–113; c) J. A. Miguel-García, H. Adams, P. M. Maitlis, *J. Organomet. Chem.* **1991**, *413*, 427–444.

[20] Significant distance differences are only found in the cases of the coordination of the olefin to the ruthenium center, probably due to steric requirements. **3a**: Ru–C(10) 2.276(11) and 2.289(13); Ru–C(11) 2.230(11) and 2.263(11); C(10)–C(11) 1.389(17) and 1.395(16). **4b**: Ru–C(10) 2.228(7) and 2.253(8); Ru–C(11) 2.245(9) and 2.235(8); C(10)–C(11) 1.363(11) and 1.363(10).

[21] Complex **5b** is unstable in solution at room temperature and the NMR spectra were therefore recorded at low temperature (–50 °C).

[22] J. A. Gladysz, B. I. Boone, *Angew. Chem. Int. Ed. Engl.* **1997**, *36*, 550–583.

[23] L. A. Oro, M. A. Ciriano, M. Campo, C. Foces-Foces, F. H. Cano, *J. Organomet. Chem.* **1985**, *289*, 117–131.

[24] M. S. Loonat, L. Carlton, J. C. A. Boeyens, N. J. Coville, *J. Chem. Soc., Dalton Trans.* **1989**, 2407–2414.

[25] P. Clark, J. L. S. Curtis, P. E. Garrou, G. E. Hartwell, *Can. J. Chem.* **1974**, *52*, 1714–1720.

[26] R. S. Dickson, T. De Simona, E. M. Campi, W. R. Jackson, *Inorg. Chim. Acta* **1994**, *220*, 187–192.

[27] E. Louattani, J. Suades, R. Mathieu, *J. Organomet. Chem.* **1991**, *421*, 335–340.

[28] SAINT version 6.02 Bruker Analytical X-ray Systems, Madison, WI, **2000**.

[29] G. M. Sheldrick, *SADABS empirical absorption program*, University of Göttingen, **1996**.

[30] Collect, Nonius BV, Delft, The Netherlands, **1997**–**2000**.

[31] Z. Otwinowski, W. Minor, *Methods Enzymol.* **1997**, *276*, 307–326.

[32] R. H. Blessing, *Acta Crystallogr., Sect. A* **1995**, *51*, 33–38.

[33] L. J. Farrugia, *J. Appl. Crystallogr.* **1999**, *32*, 837.

[34] P. T. Beurskens, G. Admiraal, G. Beurskens, W. P. Bosman, S. García-Granda, R. O. Gould, J. M. M. Smits, C. Smykalla, *The DIRDIF Program System*, Technical Report of the Crystallographic Laboratory, University of Nijmegen, Nijmegen, The Netherlands, **1999**.

[35] G. M. Sheldrick, *SHELXL97: Program for the Refinement of Crystal Structures*; University of Göttingen, Göttingen, Germany, **1997**.

[36] *Tables for X-ray Crystallography*, Kynoch Press, Birminghan, U. K., **1974**, vol. IV (present distributor: Kluwer Academic Publishers, Dordrecht, The Netherlands).

[37] M. Nardelli, *Comput. Chem.* **1983**, *7*, 95–98.

[38] A. L. Spek, *PLATON: A Multipurpose Crystallographic Tool*, University of Utrecht, The Netherlands, **2005**.

Received: June 27, 2005
Published Online: November 22, 2005

 © 2006 Wiley-VCH Verlag GmbH & Co. KGaA, Weinheim 

DOI: 10.1002/ejic.200500596

# The Bromination of Bulky Trialkylphosphane Selenides $R_2R'PSe$ (R, R′ = *i*Pr or *t*Bu) Studied by Physical and Computational Methods

Cristian G. Hrib,[a] Frank Ruthe,[a] Emma Seppälä,[a] Michael Bätcher,[a] Christian Druckenbrodt,[a] Cathleen Wismach,[a] Peter G. Jones,[a] Wolf-W. du Mont,*[a] Vito Lippolis,[b] Francesco A. Devillanova,[b] and Michael Bühl[c]

**Keywords:** Phosphane selenide dibromides / Heteronuclear NMR / Raman spectroscopy / X-ray structures / Bromine exchange / Ab initio calculations

Bulky trialkylphosphane selenides *t*$Bu_3$PSe (**1a**), *i*$Pr_3$PSe (**1b**), *t*$Bu_2$(*i*Pr)PSe (**1c**) and *t*Bu(*i*$Pr)_2$PSe (**1d**) react with one equiv. of bromine providing "T-shaped" products $R_2R'P–SeBr_2$ (**2a–d**), which contain three-coordinate selenium atoms (10-Se-3). The solid compounds **2b** (bimorphic), **2c** and **2d** exhibit different extents of distortions of the $PSeBr_2$ moieties and different patterns of intermolecular soft–soft interactions. In mixtures containing **1** and **2**, exemplified by the "NMR-titration" of **1c** with molecular bromine, averaged $^{31}P$ NMR singlets and their $^{77}Se$ satellites indicate rapid intermolecular bromine exchange reactions (kinetic lability of the Se–Br bonds). Calculations modelling such bromine transfer support nucleophilic attack of $R_3PSe$ (Se → Br) on an electrophilic Br atom of $R_3PSeBr_2$. Among the phosphane selenides **1a–d**, *t*Bu(*i*$Pr)_2$PSe (**1d**) gives the largest $^{77}Se$ NMR upfield shift and *t*$Bu_2$(*i*Pr)PSe (**1c**) the lowest, that is, $^{77}Se$ NMR shifts do not correlate with increasing numbers of *tert*-butyl groups. GIAO-HF/962+(d) calculations on the $^{77}Se$ NMR shifts of compounds **1** allow correlation of surprising relative deshielding of **1c**, compared with **1b** and **1d**, with its particular population of rotamers (excluding a rotamer with *anti* arrangement of the SePCH moiety in **1c**). Bromine addition to compounds **1** leads to line broadening and extreme deshielding in the $^{77}Se$ NMR spectroscopy. Reaction of **2b** with bromine leads – inter alia – to P–Se cleavage with *P*-bromination. The structures of **1b**, **2b–d** and *t*$Bu_2$(*i*Pr)$PBr_2$ (**3c**) were determined by X-ray crystallography. In compounds **2b–d**, intramolecular C–H···Br interactions determine the conformation to a large extent.

(© Wiley-VCH Verlag GmbH & Co. KGaA, 69451 Weinheim, Germany, 2006)

## Introduction

Phosphane chalcogenides $R_2R'P=Y$ (Y = S, Se) are known to act as donors towards dihalogen molecules.[1–4] From phosphane selenides, which are stronger donors than the sulfides, a considerable number of 1:1 adducts $R_2R'PSeX_2$ have been isolated.[5–8] *Molecular* structures have recently been determined for $R_2R'PSeI_2$ (type **A**, [10-I-2], R, R′ = $C_6H_5$, $NMe_2$, $NEt_2$,[6] and R = *t*Bu, R′ = I)[7] and for $R_3PSeBr_2$ (type **B**, [10-Se-3] R, R′ = $NMe_2$, $C_6H_{11}$).[8] Ionic structures of solid 1:1 adducts of phosphane selenides with iodine involve $(R_3PSe)_2I^+$ cations with $I_3^-$ (type **C**, [10-I-2]),[5,9,10] whereas $R_3PSeI^+$ cations (type **D**) are formed as polyiodide salts (Scheme 1).[3,9,11]

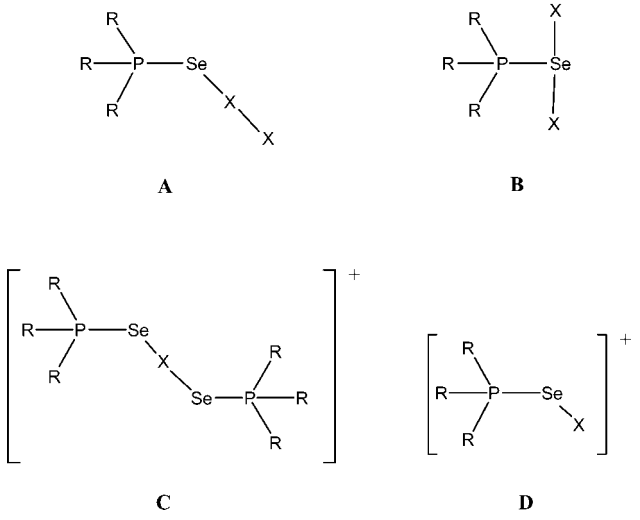


Scheme 1. Various structures of halogen adducts of phosphane selenides.

[a] Institut für Anorganische und Analytische Chemie der Technischen Universität Braunschweig,
Postfach 3329, 38023 Braunschweig, Germany
Fax: +49-531-3915387
E-mail: w.du-mont@tu-bs.de
[b] Dipartimento di Chimica Inorganica ed Analitica, Complesso Universitario di Monserrato, Università degli Studi di Cagliari, S.S. 554 Bivio per Sestu, 09042 Monserrato (CA), Italy
Fax: +39-0706754456
E-mail: devilla@unica.it
[c] Max-Planck-Institut für Kohlenforschung,
Kaiser-Wilhelm-Platz 1, 45470 Mülheim/Ruhr, Germany
Fax: +49-306-2996
E-mail: buehl@mpi-muelheim.mpg.de


© 2006 Wiley-VCH Verlag GmbH & Co. KGaA, Weinheim

Averaged $^1$H-, $^{13}$C- and $^{31}$P-solution NMR singlet signals (including their $^{77}$Se satellite doublets) and spectra, however, suggest that equilibrium mixtures of several species are present in solutions of such 1:1 adducts.[5,7,9] Until now, no reports on $^{77}$Se NMR spectra of phosphane selenide halogen adducts have appeared in the literature. It was observed that addition of a few percent of iodine to a phosphane selenide solution leads to extreme broadening of the $^{77}$Se NMR doublet signal and after further addition of iodine, the $^{77}$Se NMR signal is no longer resolvable. In the context of the present discussion on theoretical descriptions of the addition of halogens and interhalogens to P=Se or C=Se bonds, it would be desirable to study hypervalent selenium products and their dynamics in solution by $^{77}$Se NMR spectroscopy. The present study was undertaken to follow for the first time the course of stepwise bromination of three related bulky trialkylphosphane selenides in solution by $^{31}$P and $^{77}$Se NMR spectroscopy and to elucidate the role of steric effects that might determine the nature of the products. In the case of phosphane selenide–iodine reactions, slight variations of the substituents attached to phosphorus determined – in an surprising way – the nature of the 1:1 adducts (*molecular* vs. *ionic*)[5,8,9] and the particular supramolecular structures of polyiodide salts from $[R_2R'PSeI]^+$ cations.[9,11]

## Reactions

### Formation of "1:1 Adducts"

Adding $Br_2$ in titration-like fashion to solutions of phosphane selenides $R_2R'P{=}Se$ (**1a**: R, R′ = *t*Bu; **1b**: R, R′ = *i*Pr; **1c**: R = *t*Bu, R′ = *i*Pr; **1d**: R = *i*Pr, R′ = *t*Bu) in dichloromethane leads to only one averaged $^{31}$P NMR signal, with a pair of $^{77}$Se satellites, in all $^{31}$P NMR spectra of such solutions. The magnitude of $^1J(^{77}Se,^{31}P)$ decreases with increasing amounts of $Br_2$; in $CD_2Cl_2$ the magnitudes of $^1J(^{77}Se,^{31}P)$ are smaller than in comparable $C_6D_6$ solutions. $^{77}$Se NMR resonances of bromination products cannot be resolved as easily as those of the parent phosphane selenides. Adding less than 5% $Br_2$ to the solution of any of the trialkylphosphane selenides **1** leads to severe broadening of the $^{77}$Se NMR doublet signal, which is shifted slightly to a lower field compared with pure **1**. With larger amounts of $Br_2$ the $^{77}$Se NMR signal becomes too broad to be resolved. $CD_2Cl_2$ solutions of pure $iPr_3PSeBr_2$ (**2b**) and $tBu(iPr)_2PSeBr_2$ (**2d**), however, allow resolution of $^{77}$Se NMR doublet signals, and $tBu_2iPrPSeBr_2$ (**2c**) gives a single broad $^{77}$Se resonance (all about 900–1000 ppm downfield from the parent phosphane selenides) (Table 1). These observations suggest kinetic lability of $R_3PSe/Br_2$ systems, involving exchange reactions that are *fast* at the $^1$H, $^{13}$C and $^{31}$P NMR timescales (and *medium* at the $^{77}$Se NMR timescale). Crystallisation of products from **1** with $Br_2$ provides solids $R_2R'PSeBr_2$ (**2a**–**d**). In each of these compounds, bromine has been oxidatively added to selenium, which becomes "hypervalent" (structure type **B**, 10-Se-3) (vide infra).

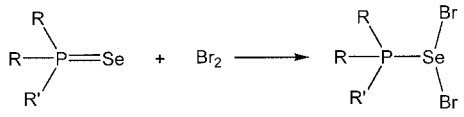


**1a**: R, R' = *t*Bu; **1b**: R, R' = *i*Pr; **1c**: R = *t*Bu, R' = *i*Pr; **1d**: R = *i*Pr, R' = *t*Bu **2a–d**

### Reactions with Excess Bromine

Addition of another equivalent of molecular bromine to the dibromides **2b** and **2c** led to their complete consumption in favour of unselective formation of new species. $^{31}$P NMR spectra of such a reaction mixture recorded immediately after addition of $Br_2$ to solutions of **2b** allowed the detection of a singlet ($\delta^{31}P$ = 72.7 ppm) with satellites exhibiting a coupling constant $^1J(^{77}Se,^{31}P)$ of ±499 Hz (5% smaller than that of **2b**). Isolating crystals from such a solution led, however, to a second polymorph of compound **2b**, and to crystals that apparently contain $iPr_3PBr^+$ cations, accompanied by severely disordered cationic P–Se species, and by bromoselenato(IV) anions ($SeBr_6^{2-}$ and $Se_2Br_9^-$). The $CH_2Cl_2$ solution from these crystals gives a $^{31}$P NMR signal ($\delta$ = 71 ppm) with $^1J(^{77}Se,^{31}P)$ = ±506 Hz, accompanied by the singlet signal of $iPr_3PBr^+$ ($\delta$ = 113.9, no $^{77}$Se satellites).[12,13] As reference compounds for the bromination products, $iPr_3PBr_2$ (**3b**)[12,13] and $tBu_2(iPr)PBr_2$ (**3c**) were prepared and characterised. Solid **3c** consists of ion pairs with weak Br···Br interactions. An attempt to generate the $iPr_3PSeBr^+$ cation from **2b** by bromide abstraction with $HgBr_2$ in $CH_2Cl_2$ solution led after two days to a mixture of products ($\delta^{31}$P 75 [very broad, $W_{1/2}$ about 85 Hz], $\delta^{31}$P = 80.0 [satellite doublet $J$ = ±430 Hz], 94.2 and 113.8). From this solution a single crystal of $[iPr_3PSe_3PiPr_3]^{2+}$ $[Hg_2Br_6]^{2-}$ (**4**) was obtained.[13b]

Table 1. Addition of bromine to **1b** and to **1c** followed by NMR (*J* values are in italics).

| Solution ($CD_2Cl_2$) | $\delta^{31}$P [ppm] $^1J(^{77}Se,^{31}P)$ [Hz] | | $\delta^{77}$Se [ppm] $^1J(^{77}Se,^{31}P)$ [Hz] | |
|---|---|---|---|---|
| $iPr_3P{=}Se$ | 70.6 | 692 | –481.5 | 690 |
| $iPr_3P{=}Se + Br_2$ | 69.8 | 521 | 409.0 | 521 |
| $iPr_3P{=}Se + 5Br_2$ | 72.7 | 499 | – | |
| $tBu_2iPrP{=}Se$ | 84.4 | 696 | –399 | 692 |
| $tBu_2iPrP{=}Se + 0.05\ Br_2$ | 83.7 | 687 | –381 | 689 |
| $tBu_2iPrP{=}Se + 0.10\ Br_2$ | 83.6 | 682 | –358, – (broad, ≈700 ± 40) | |
| $tBu_2iPrP{=}Se + Br_2$ | 82.9 | 520 | – | |

 © 2006 Wiley-VCH Verlag GmbH & Co. KGaA, Weinheim 

## $^{31}P$ and $^{77}Se$ NMR Spectra

Trialkylphosphane selenides ($R_3P$=Se) exhibit increasing $^{31}P$ downfield shifts with increasing α-branching of the alkyl groups to a lesser extent than do their parent trialkylphosphanes ($R_3P$) (Table 2).[15b] As expected, the $^{31}P$ signal of the mixed-substituted compounds $t$Bu$_2$($i$Pr)PSe (**1c**) [$\delta^{31}P$ = 79.2 and $t$Bu($i$Pr)$_2$PSe (**1d**) ($\delta$ = 85.8 ppm)] appears downfield from **1b** ($\delta$ = 72.2 ppm) but upfield from **1a** ($\delta$ = 94.7 ppm). Compared with their parent phosphanes $R_2R'P$, the $^{31}P$ resonances of phosphane selenides **1a**–**d** appear 30–50 ppm downfield, but the bromine addition products $R_2R'PSeBr_2$ (**2a**–**d**) appear slightly upfield from their respective selenides **1**. *Stepwise* addition of bromine to **1a**–**d** does not lead to new $^{31}P$ NMR signals of reaction products; the singlet signals are only shifted slightly upfield towards those of pure **2a**–**d**.

More indicative of the reaction course of phosphane selenides with electrophiles are coupling constants $^1J(^{77}Se,^{31}P)$, which are determined from satellite doublets in the $^{31}P$ NMR spectra. The magnitudes of $^{77}Se,^{31}P$ coupling constants of **1a**–**c** are comparable to those of $Me_3P$=Se or $Et_3P$=Se.[14,15b] These couplings are solvent-dependent, being about 2–3% smaller in polar solvents (e.g. acetonitrile, dichloromethane) than in benzene.[16,17]

With increasing amounts of added bromine, the $^1J$ values decrease continuously from about 700 ± 15 Hz (in the starting materials) to about 525 Hz in the 1:1 products with bromine.

In the $^{77}Se$ NMR spectra (Table 3), a straightforward correlation (like that of $\delta^{31}P$) between chemical shifts of $R_3P$=Se and increasing α-branching of the alkyl groups in **1a**–**d** does not exist. From comparison of $Me_3P$=Se ($\delta^{77}Se$ = –235[14]) via $Et_3P$=Se ($\delta^{77}Se$ = –428[15b]) to $i$Pr$_3$P=Se (**1b**, $\delta^{77}Se$ = –484[15b]), upfield shifts may be correlated with increasing α-branching. However, exchanging two $i$Pr groups of **1b** for two $t$Bu groups (in **1c**) does not lead to a further monotonic increase of $\delta^{77}Se$ (see Table 1). A comparable unexpected $^{125}Te$ NMR deshielding of $t$Bu$_3$P=Te,[15a] compared with $i$Pr$_3$P=Te, has already been recognised,[15b,16] but a conclusive explanation has not yet been given; as in the above $R_3P$=Se series, the $^{125}Te$ resonance of $t$Bu($i$Pr)$_2$P=Te appears further upfield than that of $i$Pr$_3$P=Te, whereas the $^{125}Te$ signals of the following members of the series ($t$Bu$_2$-$i$PrP=Te and $t$Bu$_3$P=Te) appear at significantly lower fields.[18]

### Calculations of $^{77}Se$ NMR Shifts

For a deeper understanding of the unexpected variation of magnitudes of $\delta^{77}Se$ and of $\delta^{125}Te$ in these sterically crowded phosphane chalcogenides, we carried out GIAO-HF/962+(d) ab initio calculations on various conformers of the known symmetric phosphane selenides **1a** and **1b** and of the new mixed-substituted compounds **1c** and **1d**.[19–22]

Qualitatively, the experimentally observed range of $^{77}Se$ NMR shieldings (**1c** < **1a** << **1b** < **1d**) reflects fairly well the calculated shift values of their energetically most favourable rotamers (**1cA** < **1a** << **1bA** < **1dA**) (Scheme 2). The range is similar (**1c**, **a** << **1b**, **d**) when the $^{77}Se$ NMR shifts are averaged according to a Boltzmann

Table 2. $^{31}P$ NMR shifts [ppm] and coupling constants $^1J$ ($^{77}Se,^{31}P$) [Hz] ($J$ values are in italics) of phosphane selenides $R_2R'PSe$ (R, R′ = $i$Pr or $t$Bu) **1a**–**d** and of phosphane selenide dibromides **2a**–**d**.

| | | $R_2R'P$ | $R_2R'PSe$ (**1**) | | $R_2R'PSeBr_2$ (**2**) | |
|---|---|---|---|---|---|---|
| | | $\delta^{31}P$ | $\delta^{31}P$ | $\lvert^1J(^{77}Se,^{31}P)\rvert$ | $\delta^{31}P$ | $\lvert^1J(^{77}Se,^{31}P)\rvert$ |
| $t$Bu$_3$P | **a** | 62.0[a] | 93.8[a]<br>93.3[b] | 709[a]<br>693[b] | 83.0[c] | 514[c] |
| $t$Bu$_2$($i$Pr)P | **c** | 46.9[a] | 84.6[a]<br>70.6[b] | 706[a]<br>692[b] | 82.9[b] | 520[b] |
| $t$Bu($i$Pr)$_2$P | **d** | 33.3[a] | 79.9[a]<br>84.4[b] | 713[a]<br>688[b] | 77.4[b] | 526[b] |
| $i$Pr$_3$P | **b** | 19.3[a] | 71.1[a]<br>79.5[b] | 709[a]<br>696[b] | 69.8[c] | 521[c] |

[a] $C_6D_6$. [b] $CD_2Cl_2$. [c] $CH_2Cl_2/C_6D_6$.

Table 3. $^{77}Se$ NMR shifts [ppm] of phosphane selenides $t$Bu$_n$($i$Pr)$_{3-n}$PSe.

| | $n$ = 3<br>$t$Bu$_3$PSe<br>**1a** | $n$ = 2<br>$t$Bu$_2$($i$Pr)PSe<br>**1c** | $n$ = 1<br>$t$Bu($i$Pr)$_2$PSe<br>**1d** | $n$ = 0<br>$i$Pr$_3$PSe<br>**1b** |
|---|---|---|---|---|
| | Experimental | | | |
| In $C_6D_6$ | –420 | –400 | –499 | –490 |
| In $CH_2Cl_2$ | –417 | –394 | –493 | –482 |
| In $CH_3CN$ | –421 | –398 | –497 | –485 |
| | Calculated (see Scheme 2) | | | |
| Most stable rotamer | –427 | –408 | –567 | –480 |
| Second most stable rotamer ($E$) | | –391 (0.5) | –492 (0.3) | –568 (0.7) |
| Boltzmann-averaged | | –403 | –500 | –519 |

 © 2006 Wiley-VCH Verlag GmbH & Co. KGaA, Weinheim 

distribution of the respective rotamers at 298 K (**1c**: –403, **1a**: –427, **1b**: –519, **1d**: –500). Compound **1c**, showing the "abnormally deshielded" $^{77}$Se signal (compared with naive expectations from linear interpolation between **1a** and **1b**) is apparently the only compound among the isopropyl derivatives in which no rotamer with *anti* arrangement of the SePCH moiety (which would be **1cC**) contributes to the rotamer-population averaged $^{77}$Se NMR shift. Our theoretically determined energies and shifts may still involve significant inaccuracies because of the approximate nature of the methods used.[21,22] Nevertheless, the good qualitative accord between the current computational and experimental results is encouraging. In addition, the MP2/962(d) relative stabilities of rotamers of **1c** correlate fairly well with those calculated previously by an empirical force field (MM2) on the parent phosphane $t$Bu$_2i$PrP.[22] It was confirmed by NMR studies on $t$Bu$_2i$PrP and its Rh$^{I}$ and Ir$^{I}$ complexes that the preferred "GA conformation" (*gauche*/*anti* $CH_3$ groups, corresponding to **1cA/1cB**)[23] of $t$Bu$_2i$PrP is essentially retained in its metal complexes.[24,25] Another interesting result from the calculated $^{77}$Se NMR shifts is the observation that the shieldings relative to **1a** increase with increasing number of *anti* hydrogen atoms (*anti* arrangement of the SePCH moieties [**1cC** < **1dB** < **1bC**]) and decrease with increasing number of *gauche* hydrogen atoms (**1cA** > **1dC** > **1bD**) in the isopropylphosphorus groups. Direct evidence on these questions can be expected from structure determinations (vide infra) combined with forthcoming solid state $^{77}$Se NMR studies.

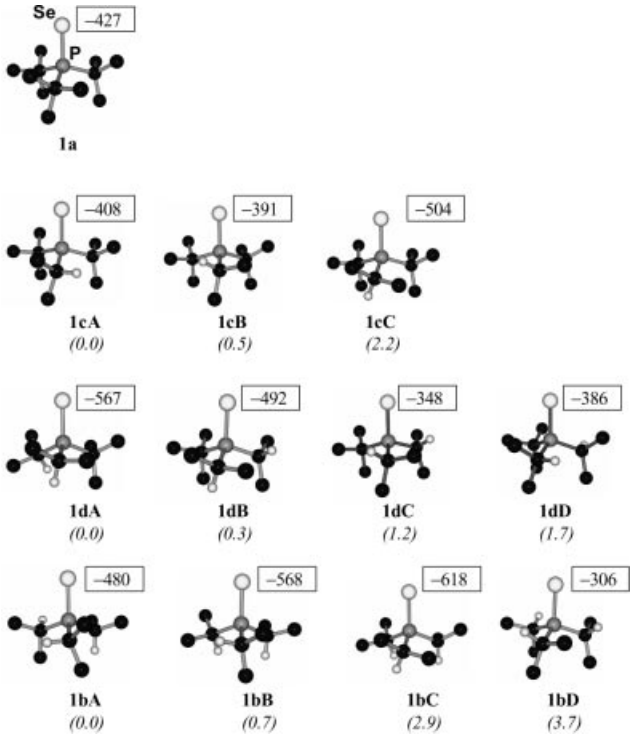


Scheme 2. Optimised rotamer structures of **1a**–**1d** (in italics: MP2-based relative energies [kcal/mol]; in boxes: GIAO-HF computed $^{77}$Se chemical shifts).

## Structure Determinations

### Phosphane Selenide Structures

The molecular structure of $t$Bu$_3$PSe (**1a**) has been determined recently,[26] but the structures of $i$Pr$_3$PSe (**1b**) and of the mixed substituted compounds **1c** and **1d** were not yet known. Differently from **1a**, which displays crystallographic $C_3$ symmetry implying twisted *tert*-butyl groups,[26] both crystallographically independent molecules of solid **1b** exhibit $C_s$ symmetry (Figure 1). Se,P and the C–H bond of one of the isopropyl groups lie within the mirror plane, and the H–C–P–Se moiety is in a *trans* arrangement. This structure is related to that of the telluride $i$Pr$_3$PTe.[15b] The fact that only one of the C–H bonds of the three isopropyl groups is in a *transoid* arrangement with respect to the PSe bond, and the two other groups display *gauche* type conformations, is in agreement with the calculated *lowest-energy* gas phase structures (**1bA** and **1bB**), but the symmetric orientation of the two twisted isopropyl groups with respect to the mirror plane is not in agreement with calculation. The increase of "1,3 dimethyl strain", also shown by the short contacts H(2A)···H(2A′) 224, H(3C)···H(3C′) 215, H(7A)···H(7A′) 220, H(8C)···H(8C′) 217 pm between the two symmetry-equivalent isopropyl groups in solid **1b**, is reflected by the expanded angle C(1)P(1)C(1′) 112° and C(6)P(1)C(6′) 113° compared with C(1)P(1)C(4) 105° and C(6)P(2)C(9) 105°. The P–C and C–C distances, however, are apparently not affected by this distortion. The related cell constants of **1b** and $i$Pr$_3$PTe (7.630, 11.856, 13.750 Å, $\beta$ = 100.29°) would suggest some similarity of packing. Figure 2 (a and b) shows the packing projected down the shortest axis in each case. Within the horizontal rows of molecules, the heights are however different; for **1b**, consecutive molecules lie at about 0, ¼, ½, ¼, 0… and for $i$Pr$_3$PTe at 0, ½, 0, ½… (in both cases for the upper row within the cell). One short methine C–H···Se interaction is observed for **1b**, namely H9···Se1 294 pm (within the asymmetric unit).

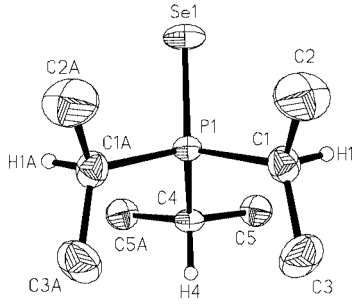


Figure 1. Structure of **1b**, molecule 1 (molecule 2 is very similar), selected bond lengths [pm] and angles [°]: P(1)–Se(1) 212.44(9), C(1)#1–P(1)–C(1) 112.20(15), C(1)#1–P(1)–C(4) 105.56(9), C(1)–P(1)–C(4) 105.56(9). Carbon atoms numbered 6–10 (see text) refer to molecule 2.

Single crystals of suitable quality for structure determinations have not yet been obtained from the mixed-substituted phosphane selenides **1c** and **1d**. A crystalline sample of $t$Bu($i$Pr)$_2$PSe (**1d**) was investigated, but poor crystal qual-

 © 2006 Wiley-VCH Verlag GmbH & Co. KGaA, Weinheim 

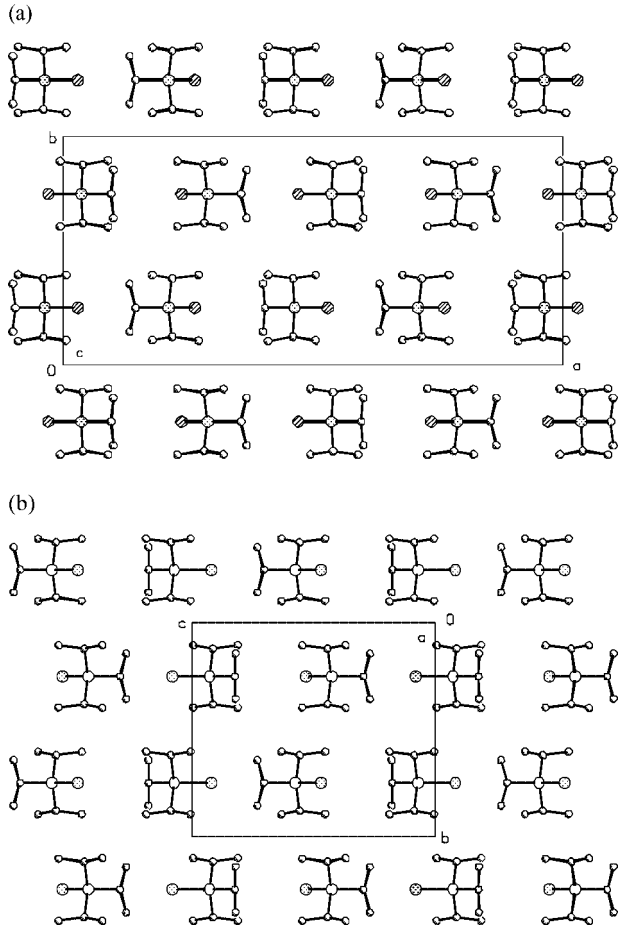


Figure 2. (a) Packing diagram in projection of $i$Pr$_3$PSe (**1b**). (b) Packing diagram in projection of $i$Pr$_3$PTe.

ity precluded a satisfactory refinement. The data indicate qualitatively that one of the isopropyl groups adopts a conformation with a *transoid* H–C–P–Se arrangement (as in calcd. structures **1dA**, **1dB**).

The crystalline bromophosphonium salt $t$Bu$_2$($i$Pr)-PBr$^+$Br$^-$ (**3c**) contains a cation that is isoelectronic with **1c**.

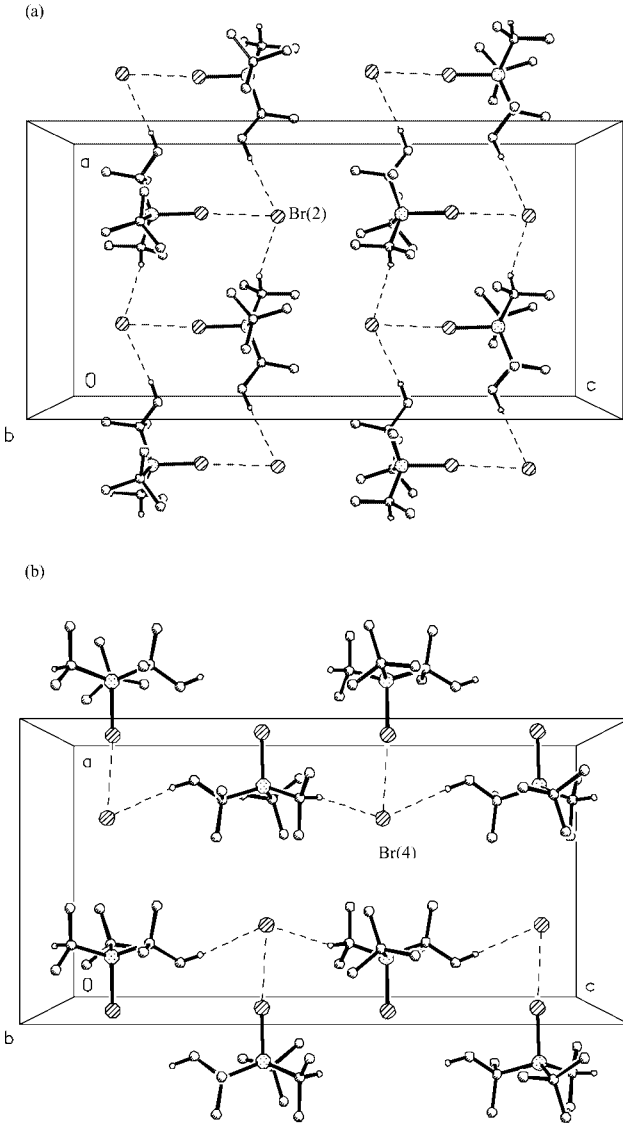


Figure 4. (a) Packing diagrams of the individual formula units of **3c** at $y \cong 0$. (b) Packing diagrams of the individual formula units of **3c** at $y \cong ½$.

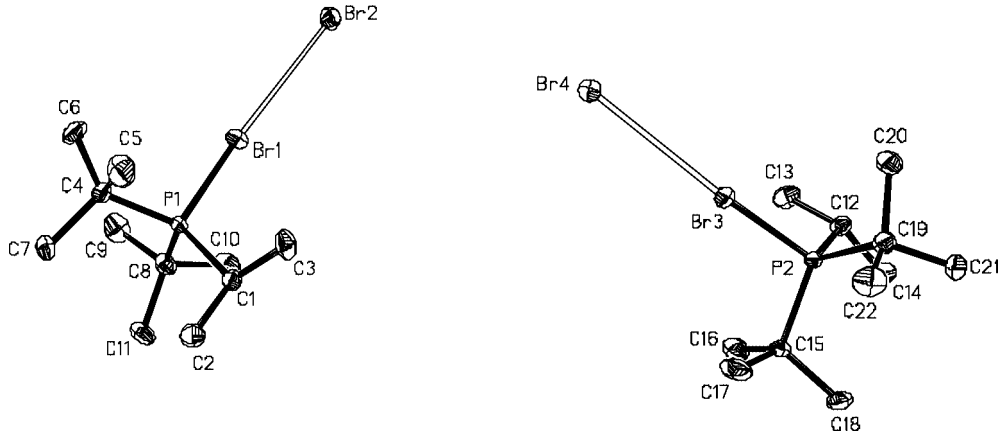


Figure 3. Structure of two ion pairs of **3c**. Selected bond lengths [pm] and angles [°]: P(1)–Br(1) 218.55(7), Br(1)–Br(2) 342.27(4), P(2)–Br(3) 218.62(6), Br(3)–Br(4) 336.79(4), P(1)–Br(1)–Br(2) 175.146(18), P(2)–Br(3)–Br(4) 174.451(18).

 © 2006 Wiley-VCH Verlag GmbH & Co. KGaA, Weinheim 

Within the asymmetric unit are two independent cation–anion pairs $t\mathrm{Bu}_2(i\mathrm{Pr})\mathrm{PBr}^+$ $\mathrm{Br}^-$ (Figure 3). Both pairs display approximately linear P–Br···Br moieties (175.5 ± 1°) with weak ($n \rightarrow \sigma^*$) Br···Br interactions (336.8 and 342.3 pm). Br(1)···Br(2) is roughly parallel to the *c* and Br(3)···Br(4) to the *a* axis. Within both $t\mathrm{Bu}_2(i\mathrm{Pr})\mathrm{PBr}^+$ cations, the H–C–P–Br moiety involving the C–H bond of the isopropyl group is in a *gauche* conformation, as predicted for selenide **1c** (calcd. structures **1cA**, **1cB**) and for the parent phosphane and its Rh and Ir complexes.[24,25] The ion pairs $t\mathrm{Bu}_2(i\mathrm{Pr})\mathrm{PBr}^+$ $\mathrm{Br}^-$ exhibit *inter*molecular C–H···Br contacts involving the bromide ions. Considering only contacts H···Br < 300 pm, Br(2) exhibits three and Br(4) four contacts, of which the shortest by far involve the methine protons [C(1)–H(1)···Br(2) 277 pm; C(12)–H(12)···Br(4) 273 pm]. Packing diagrams of the individual formula units (Figure 4, a and b) show that they occupy different regions of the cell at $y \approx 0$ and $y \approx ½$ respectively.

### Phosphane Selenide Dibromides

The discussion in the sequence **2b**, **2d**, **2c** follows the increasing steric strain with an increasing number of *tert*-butyl groups in the molecules.

From $i\mathrm{Pr}_3\mathrm{PSeBr}_2$ (**2b**), two different crystalline phases were isolated. The intended preparation of **2b** led by recrystallisation of the crude product from dichloromethane/pentane (vapour diffusion method) to monoclinic crystals ($P2_1/n$, $Z = 4$; **2b**#1). Bromination of **1b** with an excess of bromine led to a mixture of products from which two types of single crystals were collected by crystallisation from dichloromethane: about 50% of a complex material that is apparently $[(i\mathrm{Pr}_3\mathrm{PSeH}^+)_2(i\mathrm{Pr}_3\mathrm{PSeBr}^+)(\mathrm{SeBr}_6^{2-})(\mathrm{Se}_2\mathrm{Br}_9)^-]$ (partially disordered),[13b] and a few single crystals of **2b**#2 (monoclinic, $P2_1/n$, $Z = 8$).

All molecules in both phases of **2b** contain $i\mathrm{Pr}_3\mathrm{P}$ coordinated to the central selenium atoms of approximately linear BrSeBr groups ("10-Se-3" according to the J. C. Martin count).[10] The T structures around Se are distorted by unequal Se–Br bond lengths and by PSeBr angles that are larger than 90° (in the opposite sense to the distortion of the "classic" $\mathrm{ClF}_3$ structure). The latter distortion, as in previously known $\mathrm{R}_3\mathrm{PSeBr}_2$ structures, is attributed to steric repulsion between the $\mathrm{PR}_3$ substituent and the bromine atoms.

In the monomeric molecule **2b**#1 (Figure 5, a and b) the BrSeBr group differs from linearity by nearly 13° (angles PSeBr 95.5 and 96.8°) and from Se–Br equidistance by about 12 pm (252.52 and 264.35 pm). The PSe bond length is extended from 212.2 pm (**1b**) to 226.8 pm, which is very similar to that of known $\mathrm{R}_3\mathrm{PSeBr}_2$ structures.[8] The conformation of the $i\mathrm{Pr}_3\mathrm{PSe}$ group differs from that of solid *free* **1b** by lacking the formal mirror plane, but the mirror symmetry is maintained to a good approximation (r.m.s. deviation of molecular halves: 0.08 Å). One of the isopropyl groups adopts a conformation with a *transoid* H–C(1)–P–Se arrangement (as in the calculated structure **1bA**); the other two are twisted, leading to *gauche* type H–C–P–Se conformations. The orientation of the P–C(1) bond is orthogonal to the BrSeBr vector; the approximate mirror symmetry is also shown by the torsion angles [Br(1)SePC(7) –28.46(7)° and Br(2)SePC(4) 29.90(8)°]. As in solid **1b**, CPC angles involving the C atom of the *transoid* HCPSe moiety are significantly smaller (107.8, 108.7°) than that of the two other isopropyl groups [C(4)PC(7) 114.7°]. An explanation for this phenomena is the C–H···Br intramolecular interactions (see below; Figure 6, a). Three short H···Br (296–305 pm) and one short H···Se (3.02 Å) from H(1) link the molecules to form layers parallel to the *ac* plane.

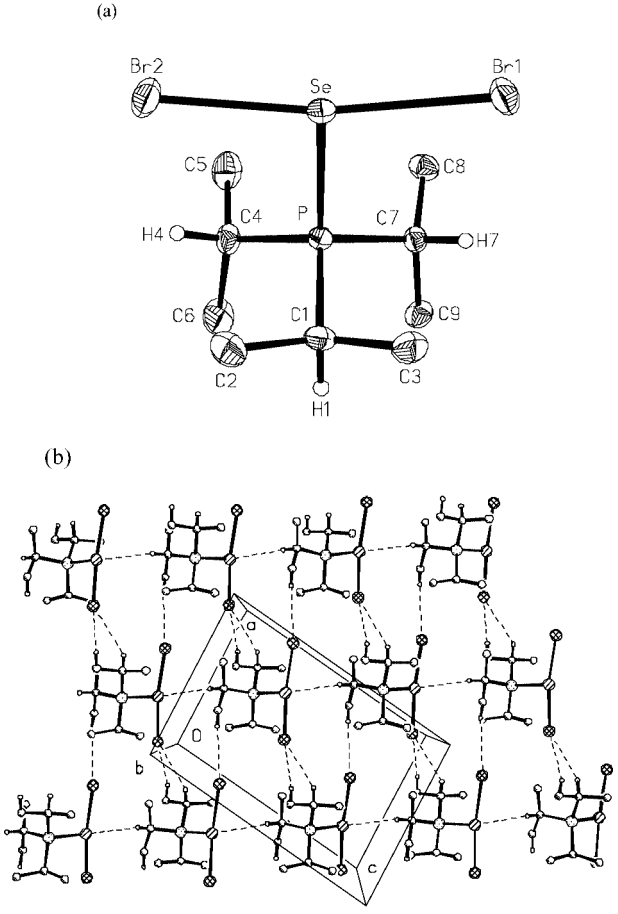


Figure 5. (a) Structure of **2b**#1, $Z = 4$, selected bond lengths [pm] and angles [°]: P–Se 226.81(5), Se–Br(1) 264.35(3), Se–Br(2) 252.52(3), P–Se–Br(1) 96.734(16), P–Se–Br(2) 95.485(16), Br(1)–Se–Br(2) 167.209(11), C(1)–P–C(7) 107.77(10), C(1)–P–C(4) 108.66(10), C(7)–P–C(4) 114.73(10). (b) Intermolecular interactions (CH···Se and CH···Br) in the packing diagram of **2b**#1.

Molecule **2b**#2 (Figure 7, a and b) involves two crystallographically independent molecules that are similar to each other (r.m.s. deviation 0.14 Å) and again display approximate mirror symmetry. The $\mathrm{SeBr}_2$ moieties are more regular than in **2b**#1, with Se···Br 257.56, 260.18 and 254.23, 260.55 pm. In contrast to **2b**#1, which has no significant short contacts of the type Se···Br and Br···Br, there are two such contacts in **2b**#2; Se(1)···Br(3) 346.23(8) within the

 © 2006 Wiley-VCH Verlag GmbH & Co. KGaA, Weinheim 

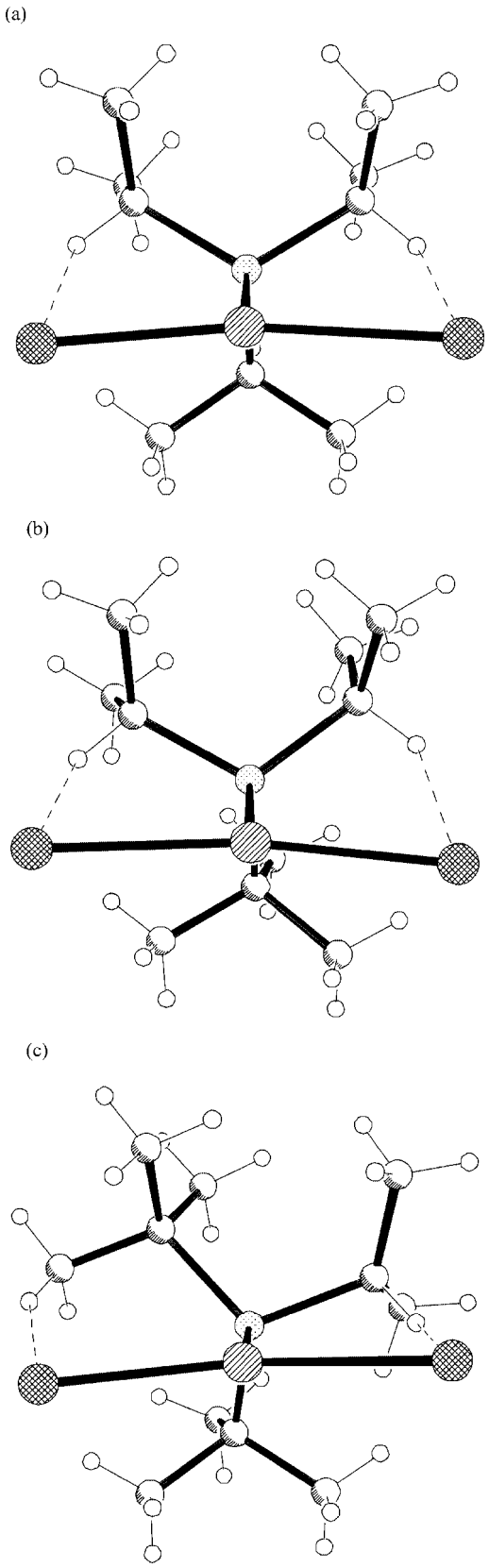


Figure 6. (a) Structure of $i$Pr$_3$PSeBr$_2$, **2b**#1, $Z$ = 4; H···Br intramolecular interactions: H(4)···Br(2) 272, H(7)···Br(1) 280 pm. (b) Structure of $t$Bu($i$Pr)$_2$PSeBr$_2$ (**2d**); H···Br intramolecular interactions: H(5)···Br(1) 299, H(8)···Br(2) 267 pm. (c) Structure of $t$Bu$_2$($i$Pr)PSeBr$_2$ (**2c**); H···Br intramolecular interactions: H(1)···Br(1) 262, H(9C)···Br(2) 271 pm.

asymmetric unit and Br(4)···Br(4′) 361.22(15) pm. The packing also involves the contact H(1)···Se(2) 303 pm and eight H···Br contacts under 315 pm. The net effect is to form layers parallel to 101.

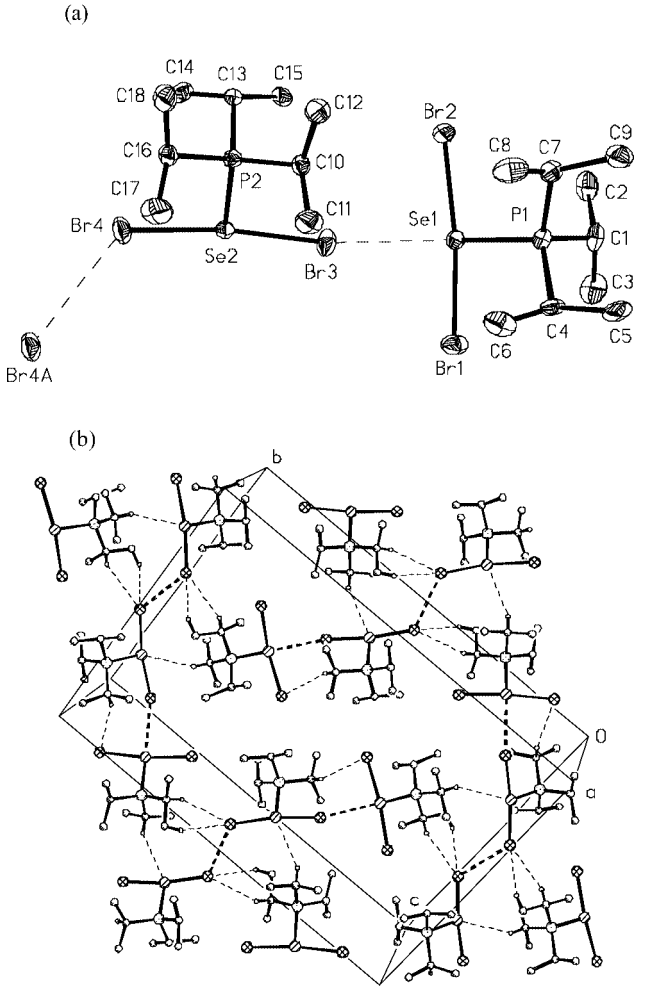


Figure 7. (a) Structure of **2b**#2, $Z$ = 8, selected bond lengths [pm] and angles [°]: P(1)–Se(1) 227.34(14), Se(1)–Br(1) 257.56(9), Se(1)–Br(2) 260.18(9), P(1)–Se(1)–Br(1) 94.36(4), P(1)–Se(1)–Br(2) 95.49(4), Br(1)–Se(1)–Br(2) 169.18(3), P(2)–Se(2) 227.15(14), Se(2)–Br(3) 260.55(9), Se(2)–Br(4) 254.23(9), P(2)–Se(2)–Br(3) 96.59(5), P(2)–Se(2)–Br(4) 95.10(5), Br(3)–Se(2)–Br(4) 168.19(3), C(4)–P(1)–C(1) 108.6(3), C(4)–P(1)–C(7) 113.2(2), C(1)–P(1)–C(7) 107.1(3), C(13)–P(2)–C(10) 109.1(3), C(13)–P(2)–C(16) 107.5(3), C(10)–P(2)–C(16) 114.8(2). (b) Intermolecular contacts involving the two types of molecules of **2b**#2.

Formal exchange of one isopropyl group by one *tert*-butyl group in **2b** affords **2d**. Compound **2d** crystallises as centrosymmetric Se–Br···Se-bridged dimers. Two T-shaped PSeBr$_2$ groups associate so that the bridging Br atom of one molecule exhibits contacts to the Se atom (382 pm) and to the bridging Br atom (388 pm) of the neighbouring molecule (Figure 8, a and b). The shorter Se–Br bond is involved in these intermolecular interactions (253.64, cf. 264.95 pm). Compound **2d** deviates significantly from mirror symmetry

 © 2006 Wiley-VCH Verlag GmbH & Co. KGaA, Weinheim 

[e.g. torsion angles C(5)–P–Se–Br(1) –36.9, C(8)–P–Se–Br(2) 24.3°]. The conformation of the $t$Bu($i$Pr)$_2$PSe group within **2d** differs from that calculated for **2d** in the gas phase. The additional methyl group in **2d** formally replaces the H atom that was part of the *trans*-H–C–P–Se moiety of **2b**; that is, both remaining isopropyl group methine protons are part of *synclinal* H–C–P–Se conformations [H(5)C(5)PSe, $\Theta$ = 73.3°; H(8)C(8)PSe, $\Theta$ = –49°] (Figure 6, b). Compared with **2b**, the additional methyl group at C(1) [*transoid* C(4)–C(1)–P–Se] enhances the 1,3-dimethyl strain towards C(6) and C(9) of the isopropyl groups leading to approximately equal CPC bond angles (110.6, 111.24, 112.9°), compared with 105/112° in **1b** and 108/115 in **2b**#1. In case of **1d**, such a conformation is expected to be about 1.2 kcal above ground state (**1dC** in Scheme 2). Compounds **2d** and **2b**#1 are not isostructural, despite the similarity of cell constants; **2d** displays four H···Br contacts <315 pm but no H···Se contacts.

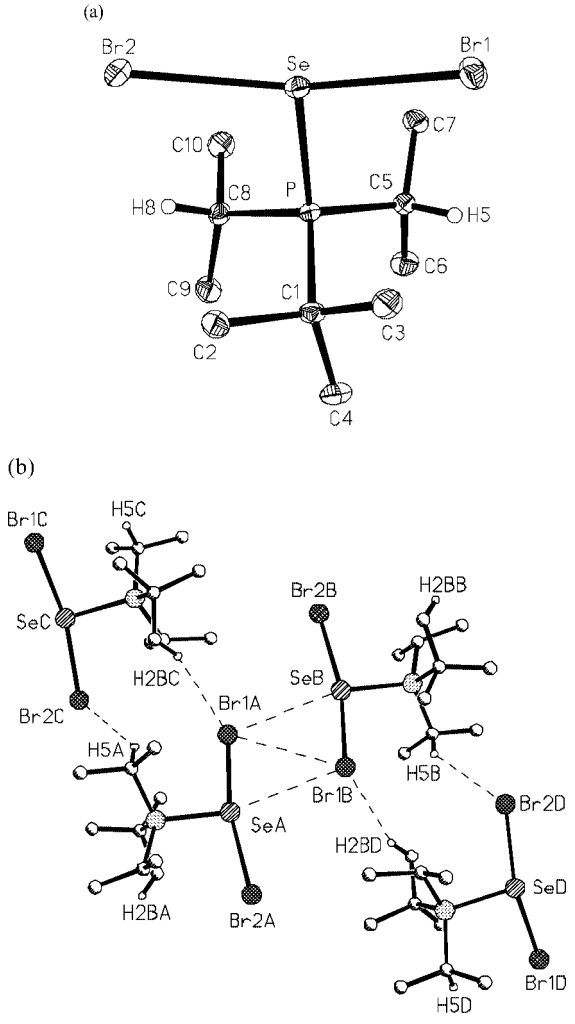


Figure 8. (a) Structure of **2d**, selected bond lengths [pm] and angles [°]: P–Se 228.67(4), Se–Br(1) 253.64(3), Se–Br(2) 264.95(3), P–Se–Br(1) 95.032(12), P–Se–Br(2) 97.462(12), Br(1)–Se–Br(2) 167.104(9), C(8)–P–C(5) 112.93(7), C(8)–P–C(1) 110.60(7), C(5)–P–C(1) 111.24(7). (b) Intermolecular interactions in the packing diagram of **2d**, selected contact distances [pm]: H(5)–Br(2) 305.3, H(2)–Br(1) 298.2, Se–Br(1) 381.68(3), Br(1)–Br(1) 388.02(4).

The structure of $t$Bu$_2$($i$Pr)PSeBr$_2$ is imprecisely determined for reasons given in the experimental section; the heavy atoms correspond closely to crystallographic mirror (pseudo)symmetry, but the light atoms do not (Figure 9, a). The reason is clearly the intramolecular hydrogen bond H(1)···Br(1) of 262 pm, cf. H(9C)···Br(2) 271 pm, from a methyl hydrogen of a butyl group (Figure 6, c). This leads to torsion angles [°] H(1)–C(1)–P–Se 42, C(1)–P–Se–Br(1) –15.8, cf. C(8)–P–Se–Br(2) 49.2; the bromine Br(1) is thus approximately synperiplanar with the isopropyl carbon C(1). The *tert*-butyl carbon C(6) is antiperiplanar to the selenium, with C(6)–C(4)–P–Se 168.2°.

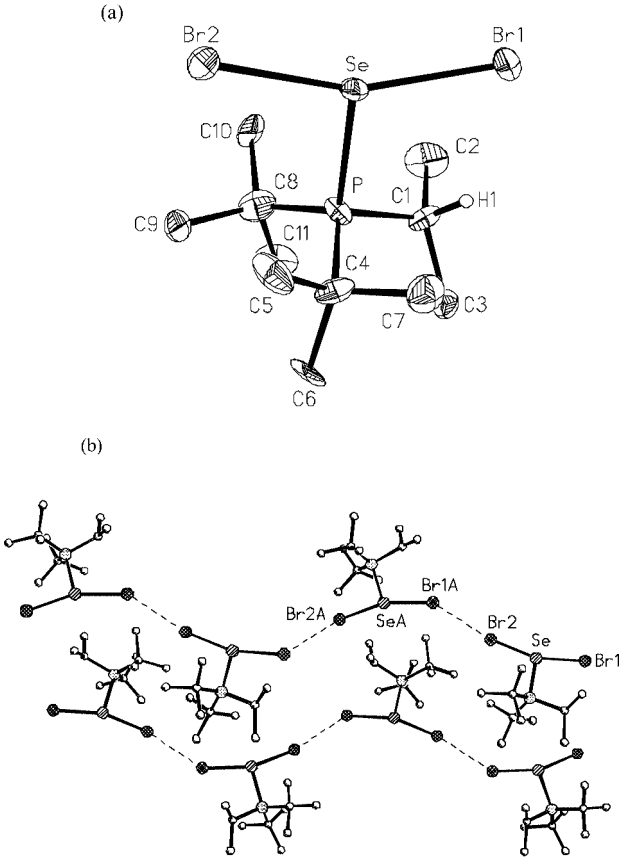


Figure 9. (a) Structure of **2c**, selected bond lengths [pm] and angles [°]: P–Se 230.39(19), Se–Br(1) 262.93(11), Se–Br(2) 255.49(11), P–Se–Br(1) 101.57(6), P–Se–Br(2) 99.22(6), Br(1)–Se–Br(2) 159.16(4), C(4)–P–C(1) 110.6(5), C(4)–P–C(8) 115.2(5), C(1)–P–C(8) 109.0(5). (b) Intermolecular interactions in the packing diagram of **2c**, array of molecules with Br···Br contacts, selected contact distances [pm]: Br(1)–Br(2) 358.90(11).

In view of inaccuracies associated with the pseudosymmetry, it would be unwise to regard light atom bond lengths and angles as reliable in detail. Among the heavy-atom dimensions, Se–Br(1) is appreciably longer than Se–Br(2) [262.93(11), 255.49(11) pm], but the angles BrSeP are almost equal [Br(2)–Se–P 99.22(6)°, Br(1)–Se–P 101.57(6)°], if rather wide.

The PSe bond is longer (230.39 pm) and the deviation of the BrSeBr group from linearity (BrSeBr 159.16°) larger

 © 2006 Wiley-VCH Verlag GmbH & Co. KGaA, Weinheim 

Table 4. Intramolecular interactions C–H···Br and important torsion angles in solid phosphane selenide dibromides [pm, °].

| | | | | |
|---|---|---|---|---|
| (**2b**#1) $i$Pr$_3$PSeBr$_2$ | H(4)···Br(2) | 272 | C(4)–P–Se–Br(2) | 29.9 |
| | H(7)···Br(1) | 280 | C(7)–P–Se–Br(1) | –28.5 |
| (**2b**#2) $i$Pr$_3$PSeBr$_2$ (mol1) | H(4)···Br(1) | 283 | C(4)–P–Se–Br(1) | –33.2 |
| | H(7)···Br(2) | 267 | C(7)–P–Se–Br(2) | 26.8 |
| (**2b**#2) $i$Pr$_3$PSeBr$_2$ (mol2) | H(10)···Br(3) | 276 | C(10)–P–Se–Br(3) | –28.6 |
| | H(16)···Br(4) | 274 | C(16)–P–Se–Br(4) | 27.4 |
| (**2c**) $t$Bu$_2i$PrPSeBr$_2$ | H(1)···Br(1) | 262 | C(1)–P–Se–Br(1) | –15.8 |
| | H(9C)···Br(2) | 271 | C(8)–P–Se–Br(2) | 49.2 |
| (**2d**) $t$Bu$i$Pr$_2$PSeBr$_2$ | H(5)···Br(1) | 299 | C(5)–P–Se–Br(1) | –36.9 |
| | H(8)···Br(2) | 267 | C(8)–P–Se–Br(2) | 24.3 |

than in any other $R_3PSeBr_2$ structure. Intermolecular Br···Br contacts (358.90 pm) between T-shaped moieties of **2c** lead, as in solid $c$-Hex$_3$PSeBr$_2$,[8] to wave-like chains (Figure 9, b) that are packed into layers in the crystal. Additionally, the contact H(7b)···Se 302 pm and four H···Br contacts <315 pm lead to a complex three-dimensional packing.

The observation of the intramolecular C–H···Br interaction in **2c** prompted us to re-assess the other structures; in most cases, the isopropyl C–H groups, the most effective donors available, form a short intramolecular contact to the bromine. Compounds with two such donors thus tend to display exact or approximate mirror symmetry (Figure 6, a and b, Table 4). Hydrogen bonds of the type C–H···halogen have previously been adduced by us as conformation-determining factors.[27]

In summary, steric strain from *tert*-butyl groups correlates with increasing deviation from linearity of the Br–Se–Br groups and with increasing P–Se distances (Table 5). We do not observe, however, a straightforward correlation of intermolecular Se···Br and Br···Br interactions, steric effects and nonequidistance of Se–Br bonds in our series of related trialkylphosphane selenide dibromides. Intramolecular hydrogen bonds of the type C–H···Br determine, to a large extent, the local molecular symmetry.

Table 5. Important bond lengths (P–Se, Se–Br) and intermolecular contacts (Br···Br, Se···Br) in solid phosphane selenide dibromides.

| | P–Se | Se–Br | Br···Br | Se···Br |
|---|---|---|---|---|
| (**1a**) $t$Bu$_3$PSe[25] | 213.3 | – | – | – |
| (**1b**) $i$Pr$_3$PSe | 212.4 | – | – | – |
| (**2b**) $i$Pr$_3$PSeBr$_2$#1 | 226.8 | 252.5, 264.4 | – | – |
| $i$Pr$_3$PSeBr$_2$#2 (mol1) | 227.3 | 257.6, 260.2 | 361.2 | 346.2 |
| $i$Pr$_3$PSeBr$_2$#2 (mol2) | 227.2 | 254.2, 260.6 | 361.2 | 346.2 |
| (**2c**) $t$Bu$_2i$PrPSeBr$_2$ | 230.4 | 255.5, 262.9 | 358.9 | – |
| (**2d**) $t$Bu$i$Pr$_2$PSeBr$_2$ | 228.7 | 253.6, 264.9 | 388.0 | 381.7 |

## Bromine Exchange Reactions

The NMR phenomena in solutions containing selenides **1** together with the dibromides **2** can be explained by bromine exchange reactions (rapid on the $^{31}$P NMR timescale, however in coalescence on the $^{77}$Se timescale) that involve Se–Br bond breaking, but do not involve P–Se bond breaking, because $^1J(^{77}Se,^{31}P)$ can be observed at all times from the $^{31}$P NMR satellites.

Bromine exchange between selenium atoms has been observed in bromine adducts of bis(arylselanyl)benzenes,[28] but the kinetic lability (bromine exchange) of phosphane chalcogenide dibromides has apparently not yet been recognised in the literature. We suppose that the mode of halogen exchange will be related to that in phosphane–dihalogen equilibrium systems ($R_3PX_2/R_3P$; X = Br, I).[29] The latter involve nucleophilic attack at halogen atoms in α position ($R_3PX^+ \leftarrow PR_3$), whereas for the phosphane selenides the same should occur in β position ($R_3PSeX^+ \leftarrow SePR_3$) from the onium centres. As shown previously, $[R_3PSeISePR_3]^+$ cations can be stable species in such equilibria.[9] Cations $[R_3PSeBrSePR_3]^+$, however, have not yet been observed as ground state species.

Support for these interpretations is provided by computations for the model compound $Me_3PSe$ and its brominated derivatives. Both types of "1:1 adducts" with $Br_2$ are minima on the potential energy surface, namely the weak donor–acceptor complex **5A** and T-shaped **5B**, the oxidative addition product (Scheme 3). The latter is computed to be more stable than the former by 13.6 kcal/mol and is characterised by a $^{77}$Se resonance ($\delta_{calc}$ = 454) downfield from that of free $Me_3PSe$. The large stabilisation of **5B** over **5A** is consistent with the exclusive occurrence of type **B** adducts with $Br_2$ (see above). Heterolytical cleavage of **5A** or **5B** into $Me_3PSeBr^+$ (**6**) and $Br^-$ is highly unfavourable in the gas phase (109.3 and 123.2 kcal/mol, respectively), but may well be facilitated by polar solvents. The halogen transfer discussed above can proceed via complex **7A**. On the HF/641(d) potential energy surface (PES), **7A**, with its asymmetrical Se–Br···Se arrangement (distances 2.37 and 3.17 Å), is a shallow minimum, about 2 kcal/mol below the $C_{2h}$ symmetric transition state **7B** with equal Se···Br distances (2.65 Å). Inclusion of electron correlation effects by the MP2 single-point energies stabilises **7B**, to 8.7 kcal/mol below the apparent minimum **7A**. It is thus very likely that the symmetrical form is the actual minimum on the true PES (a notion which is supported by an MP2/962+(d) optimisation of **7A**, which afforded symmetrical **7B**); in any event, the proposed halogen transfer reaction by the sequence **7A** ⇌ **7B** ⇌ **7A′** (Scheme 3) is indicated to be a facile process.

 © 2006 Wiley-VCH Verlag GmbH & Co. KGaA, Weinheim 

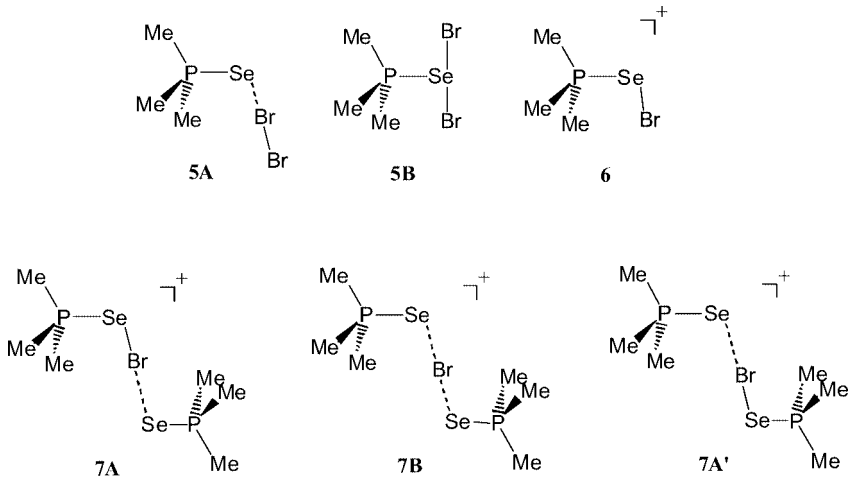


Scheme 3. Bromine transfer between $Me_3PSe$ molecules.

## Vibrational Spectra

It is well known that "T-shaped" adducts featuring a linear and symmetric Br–E–Br group (E = S, Se) show in their Raman spectra only one strong peak at around 160 $cm^{-1}$, because of the symmetric stretching vibration of the Br–E–Br system. A second lower peak at around 190 $cm^{-1}$, because of the antisymmetric vibration, appears when the Br–E–Br system is asymmetric.[30,31] This vibrational behaviour strictly resembles that observed for $[Br–X–Br]^-$ (X = I, Br) anions,[30,31] which are characterised by a very strong Raman peak at around 160 $cm^{-1}$ accompanied by a weaker one at 190 $cm^{-1}$ when these anions are slightly asymmetric. The FT-Raman spectra of **2b** and **2c** confirm the vibrational analogy between the aforementioned trihalides and the hypervalent Se adducts with $Br_2$. In fact, they are dominated by very strong peaks, at 169 and 163 $cm^{-1}$ for **2b** and **2c**, respectively, accompanied by weaker peaks at about 190 $cm^{-1}$, agreeing with the slight asymmetry of the Br–Se–Br groups observed for the two compounds by X-ray analysis. The Raman spectrum of **2d** also shows a peak at 163.9 $cm^{-1}$ accompanied by a weaker one at 190 $cm^{-1}$ with the difference that compared to **2b** and **2c** the intensity of the peak at 163.9 is much lower. In the FTIR spectra of **2b** and **2c** two broad bands at about the same frequencies of those observed in the Raman spectra are present with an increased intensity for the band because of the antisymmetric stretching of the Br–Se–Br group. For **2d**, the quality of the FTIR spectra does not provide any additional information.

The Raman spectrum of the ionic pair **3c** show a very weak peak at 180 $cm^{-1}$, which cannot be attributable to a Br–Br stretching vibration, the Br···Br distance being very long. Therefore, we think that this peak might be originated by vibration modes involving the P–Br bond and the remaining organic framework of the cation in the ionic pair.

## Discussion

GIAO-HF/962+(d) calculations on the $^{77}Se$ NMR shifts of related trialkylphosphane selenides **2a**–**d** allow an explanation of the differences between their $^{77}Se$ NMR shifts on the basis of particular conformations of their Se–P–C–H groups. The surprising $^{125}Te$ deshielding of $tBu_3PTe$ relative to $iPr_3PTe$[15] can be explained in a similar way.

All known phosphane selenide dibromides contain three-coordinate selenium in distorted T-shaped environments. Similar to related bromine adducts from precursors with C=Se bonds,[30] solid phosphane selenide dibromides tend to exhibit intermolecular Se···Br and/or Br···Br "*soft–soft interactions*". Small variations in the alkyl groups at phosphorus lead to large differences in the pattern of intermolecular contacts. In solution, phosphane selenide dibromides **2a**–**d** are kinetically labile with respect to reversible bromine transfer to their parent phosphane selenides (averaged $^1H$, $^{13}C$ and $^{31}P$ NMR signals, coalescing $^{77}Se$ signals in $R_3PSeBr_2/R_3PSe$ mixtures). Calculations show that nucleophilic attack of $R_3PSe$ at the Br atom of a $R_3PSeBr^+$ cation ($Br^+$ transfer) is a low-energy pathway for bromine exchange. $^{77}Se$ NMR signals of pure compounds $R_3PSeBr_2$ appear about 900–1000 ppm downfield from $R_3PSe$, and their $^1J(^{77}Se,^{31}P)$ coupling constants are 30% smaller than those of $R_3PSe$. Addition of electrophiles to dissolved compounds $R_3PSeBr_2$ led to a further decrease of $^1J(^{77}Se,^{31}P)$ to less than 500 Hz, but isolation of salts with $R_3PSeBr^+$ cations was not achieved.

## Experimental Section

**NMR Spectra:** NMR spectra were recorded using Bruker spectrometers AC 200, Avance 200, Avance 400 and AMX 300, with 85% $H_3PO_4$, $(CH_3)_2Se$ and $SiMe_4$ as external or internal standards. For the measurements of **1a**–**d** compounds we used 10% solution of $(CH_3)_2Se$ in $C_6D_6$ and $CD_2Cl_2$ as standards.

**FT-Raman Spectra:** FT-Raman spectra in the range 500–50 $cm^{-1}$ were recorded with a resolution of 2 $cm^{-1}$ on a Bruker RFS100 FT-Raman spectrometer, fitted with an In-Ga-As detector (room temperature) operating with a Nd-YAG laser (excitation wavelength 1064 nm; 100 mW), with a 180° scattering geometry. Infrared spectra were recorded with a Bruker IFS55 spectrometer at room temperature, purging the sample cell with a flow of dried air.

 © 2006 Wiley-VCH Verlag GmbH & Co. KGaA, Weinheim 

Polythene pellets with a mylar beam-splitter and polythene windows (500–50 $cm^{-1}$, resolution 2 $cm^{-1}$) were used.

**2a:** Bromine (330 mg, 2.1 mmol) was added slowly through a dropping funnel to a solution of $t$Bu$_3$PSe (**1b**) (590 mg, 2.1 mmol) in dichloromethane (10 mL) in a Schlenk tube. The red-orange solution was stirred for a further 2 h at room temperature, whereafter the crude product **2a** was isolated by vacuum evaporation of the solvent and purified by washing with pentane, drying by vacuum evaporation. Yield: approx. 89%; m.p. 92 °C; elemental analysis: $C_{12}H_{27}Br_2PSe$ (281.28): calcd. C 32.68, H 6.17; found C 30.62, H 5.94. MS (FAB, *o*-nitrobenzylamine matrix): *m*/*z*, pos. (%) = 57 [100, ($t$Bu)$^+$], 361 [78, ($t$Bu$_3$PSeBr)$^+$], 226 [17, ($t$Bu$_2$PSe)$^+$], 282 [33, ($t$Bu$_3$PSe)$^+$], 305 [31, ($t$Bu$_2$PSeBr)$^+$], 169 [28, ($t$BuPSe)$^+$], 89 [25, ($t$BuP)$^+$]; *m*/*z*, neg. (%) = 294 [100, {(NBA – NH$_2$) + SeBr}$^-$], 375 [85, {(NBA – NH$_2$) + SeBr$_2$}$^-$], 234 [36, (NBA + Br)$^-$], 79 [34, (Br)$^-$]; EI-MS: *m*/*z* (%) = 57 [100, ($t$Bu)$^+$], 170 [43, ($t$BuPSe)$^+$], 282 [17, ($t$Bu$_3$PSe)$^+$], 226 [17, ($t$Bu$_2$PSe)$^+$], 160 [10, (Br$_2$)$^+$], 111 [3, (PSe)$^+$]. $^{31}$P NMR (CH$_2$Cl$_2$/C$_6$D$_6$): $\delta$ = 83.0 (s, $^1J_{P,Se}$ = 514 Hz) ppm.

**2b:** Bromine (330 mg, 2.1 mmol) was added slowly through a dropping funnel to a solution of $i$Pr$_3$PSe (**1b**) (500 mg, 2.1 mmol) in dichloromethane (10 mL) in a Schlenk tube. The red-orange solution was stirred for a further 60 min at room temperature, whereafter the crude product **2b** was isolated by vacuum evaporation of the solvent and purified by washing with pentane, drying by vacuum evaporation and recrystallised by gas diffusion from dichloromethane/pentane. Yield: approx. 78%; m.p. 72 °C; elemental analysis: $C_9H_{21}Br_2PSe$ (239.20): calcd. C 27.09, H 5.30; found C 27.04, H 5.32. MS (FAB, *o*-nitrobenzylamine matrix): *m*/*z*, pos. (%) = 177 [100, ($i$Pr$_3$POH)$^+$], 319 [47, ($i$Pr$_3$PSeBr)$^+$], 353 [32, ($i$Pr$_3$PO)$_2$H$^+$], 240 [8, ($i$Pr$_3$PBr)$^+$]; *m*/*z*, neg. (%) = 232 [77, (NBA·Br)$^-$], 79 [45, (Br)$^-$]; EI-MS: *m*/*z* (%) = 160 [100, (Br$_2$)$^+$], 79 [10, (Br)$^+$], 240 [2, ($i$Pr$_3$PSe)$^+$], 43 [2, ($i$Pr)$^+$]. IR (50–500 $cm^{-1}$): 93 (s), 119 (m), 143 (s), 172 (s), 186 (s), 279 (vw), 340 (w), 417 (m), 433 (m); Raman (500–50 $cm^{-1}$): 418 (vw), 385 (vw), 270 (vw), 187 (m), 169 (vs), 145 (m), 94 (m). $^{31}$P NMR (CH$_2$Cl$_2$/C$_6$D$_6$): $\delta$ = 69.8 (s, $^1J_{P,Se}$ = 521 Hz) ppm. $^{77}$Se NMR (CH$_2$Cl$_2$/C$_6$D$_6$): $\delta$ = 409.0 (d, $^1J_{P,Se}$ = 521 Hz) ppm.

**2c:** Di-*tert*-butylisopropylphosphane selenide (0.82 g, 3.07 mmol) was dissolved in dichloromethane (40 mL) and a solution of bromine (0.50 g, 3.07 mmol) in dichloromethane (40 mL) was added. The reaction mixture was stirred at room temperature for one day. Solvent was removed in vacuo and the powdery bright orange (di-*tert*-butylisopropylphosphane selenide)–$Br_2$ complex was obtained. Yield: 1.24 g (94%); m.p. 111 °C; elemental analysis: $C_{11}H_{25}Br_2PSe$ (267.25): calcd. C 30.94, H 5.90; found: C 28.64, H 5.64. MS (FAB, *o*-nitrobenzylamine matrix): *m*/*z*, pos. (%) = 77 [100, (C$_6$H$_5$)$^+$ or (C$_3$H$_{10}$P)$^+$], 57 [88, ($t$Bu)$^+$], 136 [65, (NBA – OH)$^+$], 107 [61, (NBA – CH$_2$OH – O)$^+$], 189 [30, ($t$Bu$_2$$i$PrP + H)$^+$], 154 [28, (NBA + H)$^+$], 269 [25, ($t$Bu$_2$$i$PrPSe + H)$^+$], 212 [23, ($t$Bu$i$PrPSe + H)$^+$]; *m*/*z*, neg. (%) = 232 [100, (NBA+Br)$^-$], 153 [88, (NBA)$^-$], 81 [50, (Br)$^-$], 168 [49, (NBA + CH$_3$)$^-$], 122 [41, (NBA + H$_2$O)$^-$], 305 [35, (2NBA – H)$^-$]; EI-MS: *m*/*z* (%) = 268 [100, ($t$Bu$_2$$i$PrPSe)$^+$], 57 [95, ($t$Bu)$^+$], 156 [76, ($i$PrPSe + 2H)$^+$], 212 [40, ($t$Bu$i$PrPSe + H)$^+$], 160 [31, (Br$_2$)$^+$], 43 [10, ($i$Pr)$^+$], 81 [5, (Br)$^+$]. $^1$H NMR (CD$_2$Cl$_2$): $\delta$ = 3.97 [m, C$H$(CH$_3$)$_2$], 1.76 [d, $^3J_{H,P}$ = 16.7 Hz, C(C$H_3$)$_3$], 1.67 [dd, $^3J_{H,H}$ = 7.3, $^3J_{H,P}$ = 16.4 Hz, CH(C$H_3$)$_2$] ppm. $^{13}$C NMR (CD$_2$Cl$_2$): $\delta$ = 44.5 [d, $^1J_{C,P}$ = 13.2 Hz, $C$(CH$_3$)$_3$], 31.8 [d, $^1J_{C,P}$ = 18.5 Hz, $C$H(CH$_3$)$_2$], 30.1 [s, C($C$H$_3$)$_3$], 21.1 [d, $^2J_{C,P}$ = 3.5 Hz, CH($C$H$_3$)$_2$] ppm. $^{31}$P NMR (CD$_2$Cl$_2$): $\delta$ = 82.9 (s, $^1J_{P,Se}$ = 520.2 Hz) ppm.

**2d:** *tert*-Butyldiisopropylphosphane selenide (0.50 g, 1.97 mmol) was dissolved in dichloromethane (30 mL) and a solution of bromine (0.31 g, 1.97 mmol) in dichloromethane (30 mL) was added. The reaction mixture was stirred at room temperature for one day. The solvent was removed in vacuo and the solid orange (*tert*-butyldiisopropylphosphane selenide)–$Br_2$ complex was obtained. Yield: 0.76 g (93.39%); m.p. 74 °C; elemental analysis: $C_{10}H_{23}Br_2PSe$ (253.23): calcd. C 29.08, H 5.61; found C 29.32, H 5.66. MS (FAB, *o*-nitrobenzylamine matrix): *m*/*z*, pos. (%) = 57 [100, ($t$Bu)$^+$], 333 [90, ($t$Bu$i$Pr$_2$PSeBr)$^+$], 154 [70, (NBA + H)$^+$], 191 [65, ($t$Bu$i$Pr$_2$POH)$^+$], 136 [60, (NBA – OH)$^+$], 255 [38, ($t$Bu$i$Pr$_2$-PSe)$^+$], 307 [15, (2NBA + H)$^+$], 413 [4, ($t$Bu$i$Pr$_2$PSeBr$_2$)$^+$]; *m*/*z*, neg. (%) = 153 [100, (NBA)$^-$], 232 [95, (NBA + Br)$^-$], 306 [75, (2NBA)$^-$], 168 [42, (NBA + CH$_3$)$^-$], 122 [22, (NBA + H$_2$O)$^-$], 79 [18, (Br)$^-$], 414 [6, ($t$Bu$i$Pr$_2$PSeBr$_2$)$^-$]; EI-MS: *m*/*z* (%) = 156 [100, ($i$PrPSe + 2 H)$^+$], 57 [95, ($t$Bu)$^+$], 254 [50, ($t$Bu$i$Pr$_2$PSe)$^+$], 198 [40, ($i$Pr$_2$PSe + H)$^+$], 111 [12, (PSe)$^+$], 80 [10, (Br)$^+$]. $^1$H NMR (CD$_2$Cl$_2$): $\delta$ = 3.48 [m, C$H$(CH$_3$)$_2$], 1.55 [dd, $^3J_{H,H}$ = 6.6, $^3J_{H,P}$ = 16.9 Hz, CH(C$H_3$)$_2$], 1.52 [d, $^3J_{H,P}$ = 16.6 Hz, C(C$H_3$)$_3$] ppm. $^{13}$C NMR (CD$_2$Cl$_2$): $\delta$ = 28.6 [d, $^1J_{C,P}$ = 26.3 Hz, $C$(CH$_3$)$_3$], 25.9 [d, $^1J_{C,P}$ = 26.4 Hz, $C$H(CH$_3$)$_2$], 24.8 [s, C($C$H$_3$)$_3$], 19.8 [d, $^2J_{C,P}$ = 3.5 Hz, CH($C$H$_3$)$_2$], 17.5 [d, $^2J_{C,P}$ = 3.1 Hz, CH($C$H$_3$)$_2$] ppm. $^{31}$P NMR (CD$_2$Cl$_2$): $\delta$ = 77.4 (s, $^1J_{P,Se}$ = 526.2 Hz) ppm. $^{77}$Se NMR (CDCl$_3$): $\delta$ = 537.0 (d, $^1J_{Se,P}$ = 521.6 Hz) ppm.

**1a$^1$:** $^1$H NMR (C$_6$D$_6$): $\delta$ = 1.32 [d, $^3J_{H,P}$ = 13.9 Hz, C(C$H_3$)$_3$] ppm. $^{13}$C NMR (C$_6$D$_6$): $\delta$ = 40.9 [d, $^1J_{C,P}$ = 26.4 Hz, $C$(CH$_3$)$_3$], 30.5 [s, $C$H(CH$_3$)$_2$] ppm. $^{31}$P NMR (C$_6$D$_6$): $\delta$ = 93.8 (s, $^1J_{P,Se}$ = 708.5 Hz) ppm. $^{77}$Se NMR (C$_6$D$_6$): $\delta$ = –420.3 (d, $^1J_{Se,P}$ = 707.0 Hz) ppm.

**1a$^2$:** $^1$H NMR (CD$_2$Cl$_2$): $\delta$ = 1.41 [d, $^3J_{H,P}$ = 14.2 Hz, C(C$H_3$)$_3$] ppm. $^{13}$C NMR (CD$_2$Cl$_2$): $\delta$ = 41.0 [d, $^1J_{C,P}$ = 26.2 Hz, $C$(CH$_3$)$_3$], 30.5 [s, $C$H(CH$_3$)$_2$] ppm. $^{31}$P NMR (CD$_2$Cl$_2$): $\delta$ = 93.3 (s, $^1J_{P,Se}$ = 692.9 Hz) ppm. $^{77}$Se NMR (CD$_2$Cl$_2$): $\delta$ = –417.0 (d, $^1J_{Se,P}$ = 692.8 Hz) ppm.

**1b$^1$:** $^1$H NMR (C$_6$D$_6$): $\delta$ = 1.89 [m, $^3J_{H,H}$ = 7.0, $^2J_{H,P}$ = 10.0 Hz, C$H$(CH$_3$)$_2$], 1.03 [dd, $^3J_{H,H}$ = 7.1, $^3J_{H,P}$ = 16.0 Hz, CH(C$H_3$)$_2$] ppm. $^{13}$C NMR (C$_6$D$_6$): $\delta$ = 26.8 [d, $^1J_{C,P}$ = 38.7 Hz, $C$H(CH$_3$)$_2$], 18.2 [d, $^2J_{C,P}$ = 2.1 Hz, CH($C$H$_3$)$_2$] ppm. $^{31}$P NMR (C$_6$D$_6$): $\delta$ = 71.1 (s, $^1J_{P,Se}$ = 709.2 Hz) ppm. $^{77}$Se NMR (C$_6$D$_6$): $\delta$ = –489.9 (d, $^1J_{Se,P}$ = 707.9 Hz) ppm.

**1b$^2$:** $^1$H NMR (CD$_2$Cl$_2$): $\delta$ = 2.17 [m, $^3J_{H,H}$ = 7.1, $^2J_{H,P}$ = 10.1 Hz, C$H$(CH$_3$)$_2$], 1.16 [dd, $^3J_{H,H}$ = 7.1, $^3J_{H,P}$ = 16.2 Hz, CH(C$H_3$)$_2$] ppm. $^{13}$C NMR (CD$_2$Cl$_2$): $\delta$ = 26.8 [d, $^1J_{C,P}$ = 38.6 Hz, $C$H(CH$_3$)$_2$], 18.0 [d, $^2J_{C,P}$ = 2.2 Hz, CH($C$H$_3$)$_2$] ppm. $^{31}$P NMR (CD$_2$Cl$_2$): $\delta$ = 70.6 (s, $^1J_{P,Se}$ = 691.9 Hz) ppm. $^{77}$Se NMR (CD$_2$Cl$_2$): $\delta$ = –481.5 (d, $^1J_{Se,P}$ = 692.8 Hz) ppm.

**1c$^1$:** $^1$H NMR (C$_6$D$_6$): $\delta$ = 2.06 [m, $^3J_{H,H}$ = 7.3, $^2J_{H,P}$ = 11.9 Hz, C$H$(CH$_3$)$_2$], 1.29 [dd, $^3J_{H,H}$ = 7.3, $^3J_{H,P}$ = 14.9 Hz, CH(C$H_3$)$_2$], 1.24 [d, $^3J_{H,P}$ = 14.2 Hz, C(C$H_3$)$_3$] ppm. $^{13}$C NMR (C$_6$D$_6$): $\delta$ = 38.6 [d, $^1J_{C,P}$ = 30.1 Hz, $C$(CH$_3$)$_3$], 30.7 [d, $^1J_{C,P}$ = 31.6 Hz, $C$H(CH$_3$)$_2$], 29.2 [d, $^2J_{C,P}$ = 1.0 Hz, C($C$H$_3$)$_3$], 21.4 [d, $^2J_{C,P}$ = 2.7 Hz, CH($C$H$_3$)$_2$] ppm. $^{31}$P NMR (C$_6$D$_6$): $\delta$ = 84.6 (s, $^1J_{P,Se}$ = 706.2 Hz) ppm. $^{77}$Se NMR (C$_6$D$_6$): $\delta$ = –399.8 (d, $^1J_{Se,P}$ = 705.8 Hz) ppm.

**1c$^2$:** $^1$H NMR (CD$_2$Cl$_2$): $\delta$ = 2.26 [m, $^3J_{H,H}$ = 7.3, $^2J_{H,P}$ = 12.2 Hz, C$H$(CH$_3$)$_2$], $\delta$ = 1.45 [dd, $^3J_{H,H}$ = 7.3, $^3J_{H,P}$ = 15.6 Hz, CH(C$H_3$)$_2$], 1.34 [d, $^3J_{H,P}$ = 14.4 Hz, C(C$H_3$)$_3$] ppm. $^{13}$C NMR (CD$_2$Cl$_2$): $\delta$ = 38.8 [d, $^1J_{C,P}$ = 29.8 Hz, $C$(CH$_3$)$_3$], 31.0 [d, $^1J_{C,P}$ = 31.7 Hz, $C$H(CH$_3$)$_2$], 29.2 [d, $^2J_{C,P}$ = 0.5 Hz, C($C$H$_3$)$_3$], 21.4 [d, $^2J_{C,P}$ = 2.9 Hz, CH($C$H$_3$)$_2$] ppm. $^{31}$P NMR (CD$_2$Cl$_2$): $\delta$ = 84.4 (s, $^1J_{P,Se}$ = 687.7 Hz) ppm. $^{77}$Se NMR (CD$_2$Cl$_2$): $\delta$ = –393.8 (d, $^1J_{Se,P}$ = 688.2 Hz) ppm.

**1d$^1$:** $^1$H NMR (C$_6$D$_6$): $\delta$ = 2.0 [m, $^3J_{H,H}$ = 7.0, $^2J_{H,P}$ = 9.1 Hz, C$H$(CH$_3$)$_2$], 1.10 [d,d, $^4J_{H,H}$ = 0.2, $^3J_{H,P}$ = 14.5 Hz, C(C$H_3$)$_3$], 1.09 [dd, $^3J_{H,H}$ = 7.1, $^3J_{H,P}$ = 15.7 Hz, CH(C$H_3$)$_2$], 1.07 [dd, $^3J_{H,H}$ =

 © 2006 Wiley-VCH Verlag GmbH & Co. KGaA, Weinheim 

7.0, $^3J_{H,P}$ = 15.4 Hz, CH(C$H_3$)$_2$] ppm. $^{13}$C NMR ($C_6D_6$): $\delta$ = 35.3 [d, $^1J_{C,P}$ = 34.3 Hz, *C*(CH$_3$)$_3$], 28.2 [d, $^2J_{C,P}$ = 0.9 Hz, C(*C*H$_3$)$_3$], 26.6 [d, $^1J_{C,P}$ = 36.3 Hz, *C*H(CH$_3$)$_2$], 19.5 [d, $^2J_{C,P}$ = 1.9 Hz, CH(*C*H$_3$)$_2$], $\delta$ = 18.8 [d, $^2J_{C,P}$ = 2.1 Hz, CH(*C*H$_3$)$_2$] ppm. $^{31}$P NMR ($C_6D_6$): $\delta$ = 79.9 (s, $^1J_{P,Se}$ = 712.7 Hz) ppm. $^{77}$Se NMR ($C_6D_6$): $\delta$ = –499.2 (d, $^1J_{Se,P}$ = 711.5 Hz) ppm.

**1d²**: $^1$H NMR ($CD_2Cl_2$): $\delta$ = 2.3 [m, $^3J_{H,H}$ = 7.0, $^2J_{H,P}$ = 9.1 Hz, C*H*(CH$_3$)$_2$], 1.22 [d,d, $^4J_{H,H}$ = 0.4, $^3J_{H,P}$ = 14.6 Hz, C(C$H_3$)$_3$], 1.21 [dd, $^3J_{H,H}$ = 6.9, $^3J_{H,P}$ = 15.9 Hz, CH(C$H_3$)$_2$], 1.19 [dd, $^3J_{H,H}$ = 7.0, $^3J_{H,P}$ = 15.5 Hz, CH(C$H_3$)$_2$] ppm. $^{13}$C NMR ($CD_2Cl_2$): $\delta$ = 35.5 [d, $^1J_{C,P}$ = 34.1 Hz, *C*(CH$_3$)$_3$], 28.2 [s, C(*C*H$_3$)$_3$], 26.7 [d, $^1J_{C,P}$ = 36.3 Hz, *C*H(CH$_3$)$_2$], 19.4 [d, $^2J_{C,P}$ = 2.0 Hz, CH(*C*H$_3$)$_2$], 18.4 [d, $^2J_{C,P}$ = 2.2 Hz, CH(*C*H$_3$)$_2$] ppm. $^{31}$P NMR ($CD_2Cl_2$): $\delta$ = 79.5 (s, $^1J_{P,Se}$ = 695.8 Hz) ppm. $^{77}$Se NMR ($CD_2Cl_2$): $\delta$ = –493.2 (d, $^1J_{Se,P}$ = 694.8 Hz) ppm.

**Computational Details:** The same methods and basis sets as in two former computational studies on $^{77}$Se chemical shifts were employed.[19] Specifically, geometries were fully optimised at the restricted Hartree–Fock (HF) level employing the 641(d) basis set, that is, Binning and Curtiss' contracted [6s4p1d] basis on Se and Br,[19a] a contracted [2s] double-zeta Huzinaga basis on H (DZ),[20b] and standard 6-31G* basis on P and C.[20c,20d] All minima were characterised as such by computation of the harmonic vibrational frequencies. Single-point energy calculations for these geometries were performed at the electron-correlated second-order Møller–Plesset (MP2) level using the larger 962(d) basis, that is, a decontracted version of the 641(d) basis on Se and Br,[20a] DZ basis on H, Dunning's polarised ($\alpha_d$ = 0.75) [5s3p] basis on C,[20e] and McLean and Chandler's polarised ($\alpha_d$ = 0.465) [6s5p] basis on P.[20f] Relative energies are reported at the MP2/962(d)//HF/641(d) level (in the "level of energy evaluation // level of geometry optimisation" notation), corrected for the HF/641(d) zero-point energies (scaled by 0.9).

Magnetic shieldings were computed at the HF level with the Gauge-Including-Atomic-Orbitals (GIAO) method, as implemented[21] in the Gaussian 98 program,[22] employing the HF/641(d) geometries and 962+(d) basis, that is, the same as 962(d), but augmented with a set of diffuse s and p functions on Se ($\alpha_s$ = $\alpha_p$ = 0.022),[20a] which were shown to be beneficial in many cases.[19a] $\delta^{77}$Se chemical shifts are reported relative to $Me_2Se$, the experimental standard, for which an absolute shielding constant of 1905 ppm is obtained at the same level.

**X-ray Structure Determinations:** Numerical details are presented in Table 6. *Data collection and reduction*: Crystals were mounted in inert oil on glass fibres and transferred to the cold gas stream of the diffractometer (**1b**: Stoe STADI-4; **2b**#2, **2c**: Siemens P4; **2b**#1, **2d**, **3c**: Bruker SMART 1000 CCD). Measurements were performed with monochromated Mo-$K_\alpha$ radiation. Absorption corrections for the area detector were performed with the program SADABS, and for the serial diffractometers on the basis of $\psi$-scans. The crystal of **2c** decomposed appreciably even at low temperature and data were scaled accordingly. *Structure solution and refinement*: The structures were refined anisotropically against $F^2$ (program SHELXL-97, G.M. Sheldrick, University of Göttingen). H atoms were included with a riding model or as rigid methyl groups. *Special features of refinement*: Compound **2c** was refined as an enantiomeric twin, with Flack parameter 0.46(3); it is severely pseudosymmetric, with P, Se and Br atoms lying in a pseudomirror plane corresponding to the higher symmetry space group *Pnma*, but the alkyl groups clearly rotated out of the mirror-symmetric positions. Methyl hydrogens were placed in ideally staggered positions. Despite the use of distance restraints, the light atom bond lengths and angles were distorted and of limited reliability. CCDC-282196 (for **1b**), -282197 (for **2b**#1), -282198 (for **2b**#2), -282199 (for **2c**), -282200 (for **2d**) and -282201 (for **3c**) contain the supplementary crystallographic data for this paper. These data can

Table 6. Crystallographic data.

| | **1b** | **2b**#1 | **2b**#2 | **2c** | **2d** | **3c** |
|---|---|---|---|---|---|---|
| Formula | $C_9H_{21}PSe$ | $C_9H_{21}Br_2PSe$ | $C_9H_{21}Br_2PSe$ | $C_{11}H_{25}Br_2PSe$ | $C_{10}H_{23}Br_2PSe$ | $C_{11}H_{25}Br_2P$ |
| $M_r$ | 239.19 | 399.01 | 399.01 | 427.06 | 413.03 | 348.10 |
| Habit | colourless prism | pale orange prism | yellow tablet | red tablet | red tablet | red tablet |
| Crystal size [mm] | 0.6×0.6×0.5 | 0.27×0.2×0.13 | 0.6×0.5×0.18 | 0.4×0.3×0.2 | 0.45×0.3×0.3 | 0.3×0.2×0.1 |
| Crystal system | orthorhombic | monoclinic | monoclinic | orthorhombic | monoclinic | monoclinic |
| Space group | *Pnma* | $P2_1/n$ | $P2_1/n$ | $Pna2_1$ | $P2_1/n$ | $P2/c$ |
| $a$ [pm] | 2619.0(5) | 838.65(6) | 750.38(10) | 1586.82(15) | 755.56(6) | 1111.95(8) |
| $b$ [pm] | 1193.13(14) | 1380.23(10) | 2301.7(4) | 849.82(10) | 1412.97(12) | 1172.06(8) |
| $c$ [pm] | 744.74(15) | 1219.81(9) | 1639.7(2) | 1157.33(10) | 1351.63(10) | 2220.46(16) |
| $\beta$ [°] | 90 | 97.397(2) | 91.806(10) | 90 | 95.837(3) | 90.00(2) |
| $V$ [nm$^3$] | 2.3271 | 1.40022 | 2.8306 | 1.5607 | 1.4355 | 2.8939 |
| $Z$ | 8 | 4 | 8 | 4 | 4 | 8 |
| $D_x$ [Mg/m$^3$] | 1.365 | 1.893 | 1.873 | 1.818 | 1.911 | 1.598 |
| $\mu$ [mm$^{-1}$] | 3.3 | 8.5 | 8.4 | 7.6 | 8.3 | 5.7 |
| $F$(000) | 992 | 776 | 1552 | 840 | 808 | 1408 |
| $T$ (°C) | –100 | –130 | –100 | –100 | –140 | –130 |
| $2\theta_{max}$ | 50 | 57.1 | 50 | 50 | 61 | 60 |
| Refl. measured | 4303 | 14840 | 9982 | 2743 | 30282 | 34805 |
| Refl. indep. | 2160 | 3559 | 4974 | 2743 | 4374 | 8849 |
| Transmissions | 0.696–0.823 | 0.208–0.406 | 0.272–0.994 | 0.151–0.312 | 0.479–0.862 | 0.601–1.000 |
| $R_{int}$ | 0.043 | 0.031 | 0.069 | 0.0 | 0.032 | 0.039 |
| Parameters | 115 | 125 | 248 | 137 | 134 | 269 |
| Restraints | 0 | 45 | 90 | 161 | 0 | 0 |
| $wR$ ($F^2$, all refl.) | 0.072 | 0.048 | 0.066 | 0.089 | 0.051 | 0.075 |
| $R$ [$F$, >4$\sigma$($F$)] | 0.027 | 0.021 | 0.034 | 0.098 | 0.020 | 0.049 |
| $S$ | 1.04 | 0.97 | 0.71 | 0.855 | 1.04 | 0.99 |
| Max. $\Delta\rho$ (e/nm$^3$) | 368 | 1496 | 574 | 839 | 703 | 1649 |

 © 2006 Wiley-VCH Verlag GmbH & Co. KGaA, Weinheim 

be obtained free of charge from The Cambridge Crystallographic Data Centre via www.ccdc.cam.ac.uk/data_request/cif.

## Acknowledgments

M. B. wishes to thank Prof. W. Thiel for his continuing support and the Deutsche Forschungsgemeinschaft for a Heisenberg fellowship. Computations were performed on Compac XP1000 and ES40 workstations at the MPI Mülheim.

[1] R. A. Zingaro, E. A. Meyers, *Inorg. Chem.* **1962**, *1*, 771.
[2] D. J. Williams, K. J. Wynne, *Inorg. Chem.* **1976**, *15*, 1449.
[3] M. D. Rudd, S. V. Lindemann, S. Husebye, *Acta Chem. Scand.* **1997**, *51*, 689.
[4] M. Arca, F. A. Devillanova, A. Garau, F. Isaia, V. Lippolis, G. Verani, F. Demartin, *Z. Anorg. Allg. Chem.* **1998**, *624*, 745; W. W. Schweikert, E. A. Meyers, *J. Phys. Chem.* **1968**, *72*, 1561; D. C. Apperley, N. Bricklebank, S. L. Burns, D. E. Hibbs, *J. Chem. Soc., Dalton Trans.* **1998**, 1289.
[5] W.-W. du Mont, *Main Group Chem. News* **1994**, *2*, 18; M. Bätcher, Ph. D. thesis, University of Oldenburg, **1989**; J. Jeske, Ph. D. thesis, Techn. University of Braunschweig, **1997**.
[6] S. M. Godfrey, S. L. Jackson, C. A. McAuliffe, R. G. Pritchard, *J. Chem. Soc., Dalton Trans.* **1997**, 4499.
[7] J. Jeske, W.-W. du Mont, P. G. Jones, *Chem. Eur. J.* **1999**, *5*, 385.
[8] S. M. Godfrey, S. L. Jackson, C. A. McAuliffe, R. G. Pritchard, *J. Chem. Soc., Dalton Trans.* **1998**, 4201.
[9] E. Seppälä, F. Ruthe, W.-W. du Mont, P. G. Jones, *Chem. Commun.* **1999**, 1471.
[10] (10-Se-3) means: 10 valence electrons at the central Se atom, which has 3 substituents: C. W. Perkins, J. C. Martin, A. J. Arduengo III, W. Lau, A. Alegria, J. K. Kochi, *J. Am. Chem. Soc.* **1980**, *102*, 7753.
[11] W.-W. du Mont, A. Martens von Salzen, F. Ruthe, E. Seppälä, G. Mugesh, F. A. Devillanova, V. Lippolis, N. Kuhn, *J. Organomet. Chem.* **2001**, *623*, 14; W.-W. du Mont, A. Martens von Salzen, F. Ruthe, E. Seppälä, G. Mugesh, F. A. Devillanova, V. Lippolis, N. Kuhn, *J. Organomet. Chem.* **2001**, *628*, 280.
[12] R. Bartsch, O. Stelzer, R. Schmutzler, *Z. Naturforsch., Teil B* **1981**, *36*, 1349.
[13] a) F. Ruthe, W.-W. du Mont, P. G. Jones, *Chem. Commun.* **1997**, 1947; b) F. Ruthe, Ph. D. thesis, Techn. University of Braunschweig, **2004**.
[14] W. McFarlane, D. S. Rycroft, *J. Chem. Soc., Dalton Trans.* **1973**, 2162.
[15] a) N. Kuhn, H. Schumann, G. Wolmershäuser, *Z. Naturforsch., Teil B* **1987**, *42*, 674; b) N. Kuhn, G. Henkel, H. Schumann, R. Fröhlich, *Z. Naturforsch., Teil B* **1990**, *45*, 1010.
[16] H. Duddeck, *Prog. Nucl. Magn. Reson. Spectrosc.* **1994**, *27*, 1–323.
[17] S. W. Carr, R. Colton, *Aust. J. Chem.* **1981**, *34*, 35.
[18] C. Druckenbrodt, Ph. D. thesis, Techn. University of Braunschweig, **2000**.
[19] a) M. Bühl, W. Thiel, U. Fleischer, W. Kutzelnigg, *J. Phys. Chem.* **1995**, *99*, 4000; b) H. Fleischer, S. Glang, D. Schollmeyer, N. W. Mitzel, M. Bühl, *Dalton Trans.* **2004**, 3765.
[20] a) R. C. Binning, L. A. Curtiss, *J. Comput. Chem.* **1990**, *11*, 1206; b) S. Huzinaga, *J. Chem. Phys.* **1965**, *42*, 1293; c) W. J. Hehre, R. Ditchfield, J. A. Pople, *J. Chem. Phys.* **1972**, *56*, 2257; d) P. C. Hariharan, J. A. Pople, *Theor. Chim. Acta* **1973**, *28*, 213; e) T. H. Dunning, *J. Chem. Phys.* **1970**, *53*, 2823; f) A. D. McLean, G. S. Chandler, *J. Chem. Phys.* **1980**, *72*, 5639.
[21] J. R. Cheeseman, G. W. Trucks, T. A. Keith, M. J. Frisch, *J. Chem. Phys.* **1996**, *104*, 5497.
[22] M. J. Frisch, G. W. Trucks, H. B. Schlegel, G. E. Scuseria, M. A. Robb, J. R. Cheeseman, V. G. Zakrzewski, J. A. Montgomery, R. E. Stratman, J. C. Burant, S. Dapprich, J. M. Milliam, A. D. Daniels, K. N. Kudin, M. C. Strain, O. Farkas, J. Tomasi, V. Barone, M. Cossi, R. Cammi, B. Mennucci, C. Pomelli, C. Adamo, S. Clifford, J. Ochterski, G. A. Petersson, P. Y. Ayala, Q. Cui, K. Morokuma, D. K. Malick, A. D. Rabuck, K. Raghavachari, J. B. Foresman, J. Cioslowski, J. V. Ortiz, A. G. Baboul, B. B. Stefanov, C. Liu, A. Liashenko, P. Piskorz, I. Komaromi, R. Gomperts, R. L. Martin, D. J. Fox, T. Keith, M. A. Al-Laham, C. Y. Peng, A. Nanayakkara, C. Gonzalez, M. Challacombe, P. M. W. Gill, B. G. Johnson, W. Chen, M. W. Wong, J. L. Andres, C. Gonzales, M. Head-Gordon, E. S. Replogle, J. A. Pople, *Gaussian98*, Gaussian, Inc., Pittsburgh, PA, **1998**.
[23] **1cA** and **1cB** are very close-lying minima, and seemingly only a small rotation of the *i*Pr group is needed to convert the former into the mirror image of the latter; however, larger reorientations of the interlocking methyl groups from the *t*Bu substituents are involved in this interconversion (not visible from the plot in Scheme 2), and **1cA** and **1cB** are distinct, genuine minima (e.g. they do not collapse into the same one when tighter convergence criteria are applied in the optimisation).
[24] C. D. Rithner, C. H. Bushweller, *J. Am. Chem. Soc.* **1985**, *107*, 7823.
[25] C. D. Rithner, C. H. Bushweller, *J. Phys. Chem.* **1986**, *90*, 5023.
[26] H.-U. Steinberger, B. Ziemer, M. Meisel, *Acta Crystallogr., Sect. C* **2001**, *57*, 323.
[27] M. Freytag, P. G. Jones, *Chem. Commun.* **2000**, *4*, 277.
[28] W. Nakanishi, S. Hayashi, *J. Organomet. Chem.* **2000**, *611*, 178.
[29] W.-W. du Mont, F. Ruthe, *Coord. Chem. Rev.* **1999**, *189*, 101.
[30] M. C. Aragoni, M. Arca, F. Demartin, F. A. Devillanova, A. Garau, F. Isaia, F. Lelj, V. Lippolis, G. Verani, *Chem. Eur. J.* **2001**, *7*, 3122.
[31] F. Bigoli, A. M. Pellinghelli, P. Deplano, F. A. Devillanova, V. Lippolis, M. L. Mercuri, E. F. Trogu, *Gazz. Chim. Ital.* **1994**, *124*, 445.

Received: July 5, 2005
Published Online: November 25, 2005

 © 2006 Wiley-VCH Verlag GmbH & Co. KGaA, Weinheim 

DOI: 10.1002/ejic.200500602

# Ferrocenylethynyltin Compounds – Characterization and Reactivity towards Triethylborane

**Bernd Wrackmeyer,*[a] Barbara H. Kenner-Hofmann,[a] Wolfgang Milius,[a] Peter Thoma,[a] Oleg L. Tok,[a] and Max Herberhold*[a]**

*Dedicated to Professor Henri Brunner on the occasion of his 70th birthday*

**Keywords:** Alkynes / Boranes / Ferrocenes / NMR spectroscopy / Tin

Ferrocenylethynyl(trimethyl)tin (**1**), bis(ferrocenylethynyl)dimethyltin (**2**), tetrakis(ferrocenylethynyl)tin (**3**), and chloro(ferrocenylethynyl)dimethyltin (**4**) have been prepared and characterized in solution by $^{1}H$, $^{13}C$, and $^{119}Sn$ NMR spectroscopy. Solid-state MAS $^{13}C$ and $^{119}Sn$ NMR spectra were measured for **2** and **3**, and the molecular structure of one of the modifications of **2** was determined by X-ray analysis. The reactivity of **1**–**4** towards triethylborane has been explored. 1,1-Organoboration takes place in all cases, and the reactions are stereoselective for **1** and **4** to give the alkenes **5** and **6**, respectively, in which the stannyl and the boryl groups are in *cis*-positions at the C=C bond. In the case of **2**, the final products are the 1-stannacyclopenta-2,4-diene **7a** and the 1-stanna-4-boracyclohexa-2,5-diene **8a**, whereas the reaction of **2** with triisopropylborane leads selectively to the six-membered ring **8b**. Zwitterionic intermediates **9a**,**b**, in which the tin atom is coordinated side-on to the C≡C bond of an alkynylborate, have been detected by NMR spectroscopy. Compound **3** reacts with triethylborane to give a mixture of three spirotin compounds **10**–**12** as the final products, where the tin atom connects five- and six-membered rings.

(© Wiley-VCH Verlag GmbH & Co. KGaA, 69451 Weinheim, Germany, 2006)

## Introduction

The synthetic potential of the C≡C bond in alkynes can be further enhanced by organometallic substituents.[1] This is well known for stannyl groups,[2] and the polar Sn–C≡ bonds in alkyn-1-yltin compounds are useful for various transformations. The reactivity of such alkyn-1-yltin compounds can be modified by the nature of other substituents at the tin atom and also by the second substituent at the C≡C bond, which may be hydrogen, an alkyl or aryl group, or another organometallic substituent. In the present work, we describe the synthesis and characterization of the ferrocenylethynyltin compounds **1**–**4** (Scheme 1) and report their reactivity towards triethylborane ($BEt_3$) and, in the case of **2**, triisopropylborane ($BiPr_3$).

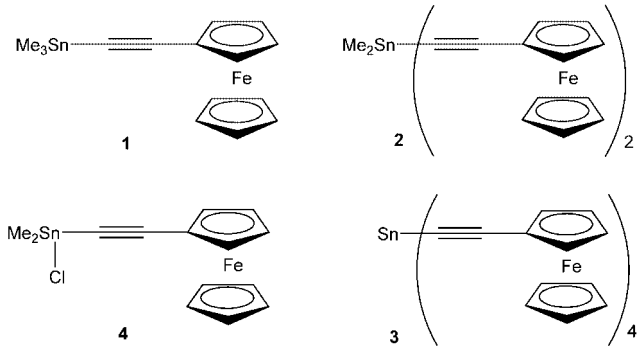


Scheme 1. The ferrocenylethynyltin compounds studied.

[a] Laboratorium für Anorganische Chemie, Universität Bayreuth, 95440 Bayreuth, Germany
Fax: +49-921-552-157
E-mail: b.wrack@uni-bayreuth.de
max.herberhold@uni-bayreuth.de

## Results and Discussion

### Synthesis and NMR Spectroscopic Characterization of the Ferrocenylethynyltin Compounds

The most convenient synthesis of **1**–**3** starts from ethynylferrocene,[3] which is first converted into the alkynyllithium reagent and then treated with tin halides. (Scheme 2). Alternatively, the reaction of ethynylferrocene with the respective tin amides[4] [e.g. $Me_3SnNEt_2$, $Me_2Sn(NEt_2)_2$ and $Sn(NEt_2)_4$] can be used to obtain **1**–**3**. The reaction of **2** with one equivalent of dimethyltin dichloride at 110 °C in the presence of a small amount of toluene leads to **4**. A slight excess (10%) of $Me_2SnCl_2$ helps to convert **2** into **4** quantitatively. Compounds **1**–**4** are orange-red solids that are well soluble (**1**, **2**, **4**) or rather insoluble (**3**) in hydrocarbons. Single crystals of complex **2** suitable for X-ray structural analysis were isolated after recrystallization from hexane. The

 © 2006 Wiley-VCH Verlag GmbH & Co. KgaA, Weinheim 

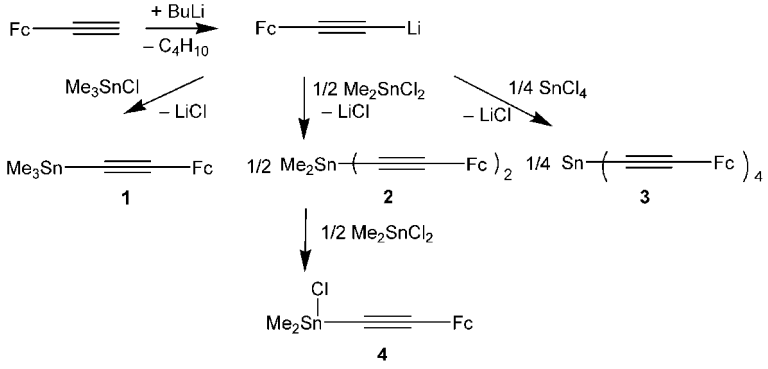


Scheme 2. Synthesis of the ferrocenylethynyltin compounds (Fc = Ferrocenyl).

Table 1. $^{13}C$ and $^{119}Sn$ NMR spectroscopic data[a] of the ferrocenylethynyltin compounds **1**–**4**.

| | $\delta^{13}C_{2,5}$ | $\delta^{13}C_{3,4}$ | $\delta^{13}C_1$ | $\delta^{13}C_{Cp}$ | $\delta^{13}C_{\equiv C-Sn}$ | $\delta^{13}C_{\equiv C-Fc}$ | $\delta^{13}C_{Me}$ | $\delta^{119}Sn$ |
|---|---|---|---|---|---|---|---|---|
| **1**[b] | 71.6 | 68.4 | 65.6 | 70.1 | 89.3 | 107.6 | –7.4 | –65.4 |
| | | | [12.8] | | [433.2] | [94.4] | [404.6] | |
| | | | | | {–58.5} | {–14.1} | {+2.7} | |
| **2** | 72.6 | 69.5 | 66.3 | 71.0 | 87.8 | 109.6 | –5.7 | –152.8[c] |
| | [5.0] | | [15.5] | | [625.9] | [134.3] | [495.1] | |
| | | | | | {–26.7} | {–2.2} | {+20.2} | |
| **3** | 72.4 | 69.7 | 63.5 | 70.7 | 82.7 | 109.8 | –- | –342.2 |
| | | | [23.4] | | [1167.3] | [241.8] | | |
| **4** | 72.8 | 69.9 | 65.0 | 71.1 | 89.7 | 111.3 | –0.1 | +21.7 |
| | [5.0] | | | | [563.6] | [133.3] | [493.4] | |

[a] In $CD_2Cl_2$ at 296 K; coupling constants $J_{^{119}Sn,^{13}C} \pm 0.5$ Hz are given in brackets; isotope-induced chemical shifts $^n\Delta^{12/13}C(^{119}Sn) \pm 0.5$ ppb in braces with a negative sign for the shift of the more heavy isotopomer to lower frequency. [b] In $CDCl_3$ at 296 K. [c] Solid-state MAS $^{119}Sn$ NMR: $\delta_{^{119}Sn}$ = –144.0 (minor) and –150.5 ppm (major).

identity of the compounds **1**–**4** in solution follows from a consistent set of NMR parameters (Table 1). Even in the case of the sparingly soluble complex **3**, the $^{13}C$ NMR spectra could be recorded for determination of the $J_{^{117/119}Sn,^{13}C}$ coupling constants (Figure 1). The large magnitude of the $^nJ_{^{119}Sn,^{13}C}$ coupling constants is typical of tetraalkyn-1-yltin derivatives.[5,6] In the cases of **1** and **2**, the $^{119}Sn$ NMR spectra were recorded in order to measure isotope-induced chemical shifts $^n\Delta^{12/13}C(^{119}Sn)$ (Figure 2). Both the $^nJ_{^{119}Sn,^{13}C}$ coupling constants and isotope-induced chemical shifts $^n\Delta^{12/13}C(^{119}Sn)$ are observed in the expected ranges of the data previously determined for other alkyn-1-yltin compounds.[5–7] This indicates that the ferrocenyl group does not exert a special influence on the bonding situation in the Sn–C≡C–Fc fragment.

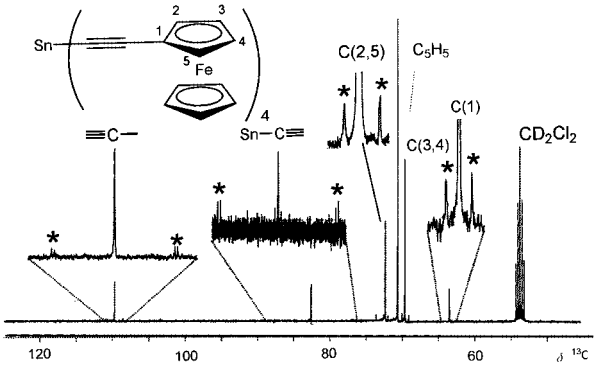


Figure 1. $^{13}C\{^1H\}$ NMR spectrum (100.5 MHz) of tetrakis(ferrocenylethynyl)tin (**3**; saturated solution in $CD_2Cl_2$) showing the $^{117/119}Sn$ satellites (marked by asterisks) for spin-spin coupling across one, two, three, and four bonds.

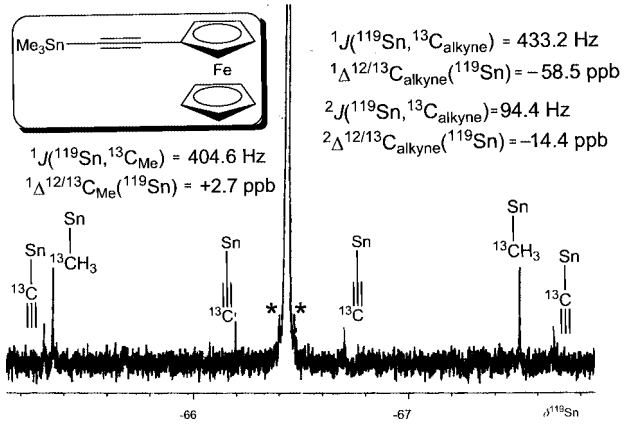


Figure 2. $^{119}Sn\{^1H\}$ NMR spectrum (refocused INEPT[25]; 186.5 MHz) of ferrocenylethynyl(trimethyl)tin (**1**; 5% in $CDCl_3$ at 296 K; acquisition time 5 s, repetition delay 2.5 s; 64 transients). The $^{13}C$ satellites are marked, and coupling constants and isotope-induced chemical shifts $\Delta^{12/13}C(^{119}Sn)$ are given. The $^{13}C$ satellites indicated by asterisks correspond to $^3J_{^{119}Sn,^{13}C_{Fc}}$ = 12.8 Hz.

### Structural Studies of Bis(Ferrocenylethynyl)Dimethyltin (2) and Tetrakis(Ferrocenylethynyl)tin (3)

The molecular structure of **2** in the solid state, determined by X-ray analysis, is shown in Figure 3. All bond

 © 2006 Wiley-VCH Verlag GmbH & Co. KGaA, Weinheim 

lengths and angles are close to the expected values, when compared with other alkynes[1a] or ferrocenyl derivatives.[8,9] The cyclopentadienyl rings are almost exactly parallel to each other, and deviate by 6.3° from the eclipsed positions. The C2–C3 bond forms an angle of 2.7° (pointing away from the iron atom) with the $C_5H_4$ plane. There are no appreciable intermolecular interactions ($d_{Fe\cdots Fe}$ = 956.6 pm). The literature does not contain structural data on comparable di(alkyn-1-yl)dimethyltin compounds.

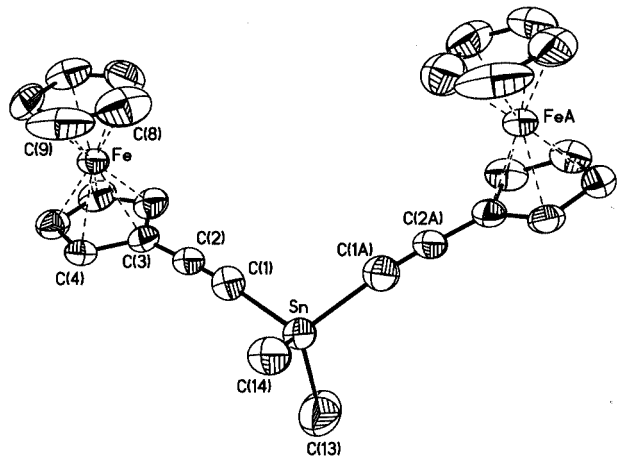


Figure 3. ORTEP representation (50% probability; hydrogen atoms have been omitted) of the molecular structure of bis(ferrocenylethynyl)dimethyltin (**2**). Selected bond lengths [pm] and angles [°]: Sn–C1 211.3(8), Sn–C13 211.3(12), Sn–C14 210.0 (12), C1–C2 119.0(9), C2–C3 141.3(9), C3–C4 143.0(8)m, C3–C7 142.2(9), C4–C5 146.1(8), C5–C6 149.2(9), Fe–centroid($C_5H_4$) 165.6, Fe–centroid($C_5H_5$) 164.4; C1–Sn–C1A 107.0(4), C1–Sn–C13 108.5(3), C1–Sn–C14 109.2(3), C13–SnC14 114.3(5), Sn–C1–C2 174.0(6), C1–C2–C3 177.1(7), centroid–Fe–centroid 178.7.

The symmetry in the solid-state structure of **2** is remarkable, and would be somewhat surprising if this structure is the sole modification of **2**. Therefore, solid-state MAS $^{13}C\{^1H\}$ and $^{119}Sn\{^1H\}$ NMR spectra were recorded (Figure 4). These measurements clearly show that the bulk material of crystalline **2** contains a second modification. There are two sites for tin with rather similar isotropic $^{119}Sn$ chemical shifts, close to the value for solutions of **2**. The solid-state MAS $^{13}C$ NMR spectrum reveals one set of alkynyl $^{13}C$ resonances, corresponding to the symmetric molecular structure found by X-ray analysis, and there are two additional sets of alkynyl $^{13}C$ resonances which can be expected for a less symmetric arrangement of the ferrocenylethynyl units in the second crystalline modification.

In the case of **3**, we have not been able to obtain single crystals so far. Only one tin site was detected in the solid-state MAS $^{119}Sn$ NMR of the microcrystalline powder of **3**, and this site shows an expectedly small chemical shift anisotropy.[10] Similarly, only one set of alkynyl $^{13}C$ resonances is observed in the solid-state MAS $^{13}C$ NMR spectrum. If there are several modifications of **3** present, it can be assumed that their structures are very similar.

## Reactivity of the Ferrocenylethynyltin Compounds Towards Triethylborane

The reactivity of Sn–C≡ bonds in alkyn-1-yltin compounds towards triorganoboranes is well documented.[11,12] The results of the reactions of **1** and **4** with triethylborane ($BEt_3$) are fully consistent with previous observations for 1,1-organoboration reactions, all of which proceed by cleavage of the Sn–C≡ bond via a borate-like zwitterionic intermediate.[12] The 1,1-ethylboration is regio- and stereospecific, and affords the alkenyltin compounds **5** and **6** in essentially quantitative yield (Scheme 3). The proposed structures follow from the NMR spectroscopic data (Table 2), and the *cis*-positions of the stannyl and boryl groups are confirmed by selective $^1H/^1H$ NOE experiments.[13]

The reaction of **2** with $BEt_3$ leads to a mixture of the stannacyclopenta-2,4-diene **7a** and the 1-stanna-4-boracyclohexa-2,5-diene **8a** in a ratio close to 1:2. This ratio was reproduced in several experiments in different solvents (toluene or $CH_2Cl_2$). The structural assignment follows conclusively from the NMR spectroscopic data (Table 3 and

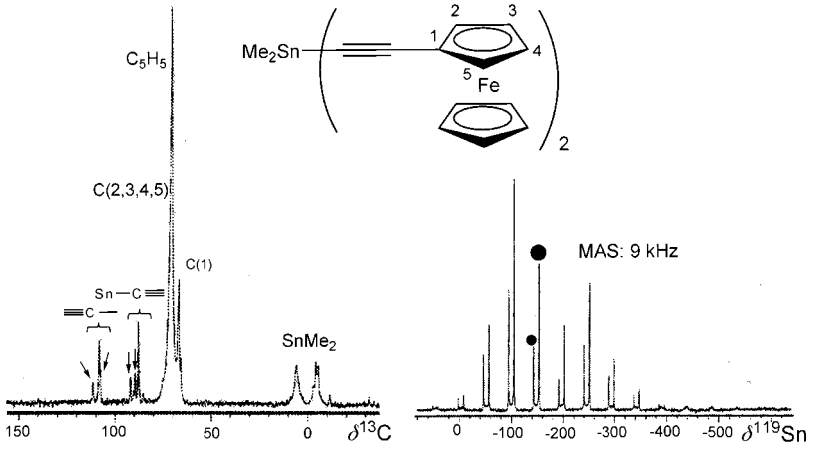


Figure 4. Solid-state VACP[27] MAS $^{13}C\{^1H\}$ (100.5 MHz) and $^{119}Sn\{^1H\}$ (149.1 MHz) NMR spectra of **2**, showing the presence of two modifications in the crystalline state. The signals for the isotropic $\delta_{^{119}Sn}$ values are marked by filled circles. The alkynyl $^{13}C$ NMR signals for the modification that is not represented by the crystal structure (Figure 3) are marked by arrows.

 © 2006 Wiley-VCH Verlag GmbH & Co. KGaA, Weinheim 

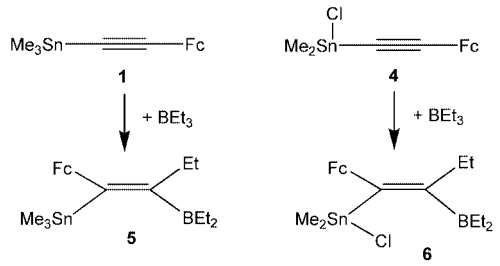


Scheme 3. 1,1-Ethylboration of the (ferrocenlyethynyl)tin compounds **1** and **4**.

Table 4), and in particular from the $^{119}$Sn and $^{13}$C NMR spectra (Figure 5).

The formation of a mixture is reminiscent of the results of the 1,1-ethylboration of bis(phenylethynyl)dimethyltin.[14] Monitoring of the reaction of **2** with $BEt_3$ by NMR spectroscopy shows that there is a fairly stable intermediate **9a** which must be regarded as the immediate precursor of the heterocycles. Zwitterionic complexes similar to **9a** have been observed before,[12] and they have been fully characterized by NMR spectroscopic data in solution,[15] in the

Table 2. $^{11}$B, $^{13}$C, and $^{119}$Sn NMR spectroscopic data[a] of the alkenyltin compounds **5** and **6**.

| | $\delta_{^{13}C}$ (Sn–C=) | $\delta_{^{13}C}$ (B–C=) | $\delta_{^{13}C}$ (Et) | $\delta_{^{13}C}$ (SnMe) | $\delta_{^{13}C}$ ($BEt_2$) | $\delta_{^{119}Sn}$ | $\delta_{^{11}B}$ |
|---|---|---|---|---|---|---|---|
| **5**[b] | 134.1<br>[543.5] | 165.3 (br) | 29,7<br>[87.3]<br>14.0<br>[10.2] | –5.7<br>[321.6] | 21.9 (br),<br>9.2 | –54.1 | 82.0 |
| **6**[c] | 136.0<br>[650.1] | 170.0 (br)<br>[65.0] | 26.4<br>[104.7]<br>14.6<br>[12.9] | 2.4<br>[348.4] | 21.8 (br)<br>10.7 | +46.4 | 76.0 |

[a] In $CD_2Cl_2$ at 296 K; coupling constants $J_{^{119}Sn,^{13}C} \pm 0.5$ Hz are given in brackets; br. denotes $^{13}$C NMR signals of carbon atoms bonded to boron. [b] Other $^{13}$C NMR spectroscopic data: $\delta$ = 90.5 [64.9] ($C_1$), 70.0 ($C_{2,5}$), 67.4 ($C_{3,4}$), 69.2 ppm ($C_5H_5$). [c] Other $^{13}$C NMR spectroscopic data: $\delta$ = 90.1 [98.3] ($C_1$), 68.9 [5.0], 70.0 ($C_5H_4$), 68.4 ppm ($C_5H_5$).

Table 3. $^{11}$B, $^{13}$C, and $^{119}$Sn NMR spectroscopic data[a] of the intermediates **9a** and **9b**.

| | $\delta_{^{13}C}$ (B–C≡) | $\delta_{^{13}C}$ (Fc-C≡) | $\delta_{^{13}C}$ (Sn–C=) | $\delta_{^{13}C}$ (B–C=) | $\delta_{^{13}C}$ (R) | $\delta_{^{13}C}$ (SnMe) | $\delta_{^{13}C}$ ($BR_2$) | $\delta_{^{11}B}$ | $\delta_{^{119}Sn}$ |
|---|---|---|---|---|---|---|---|---|---|
| **9a**[b] | 103.6<br>(br) | 128.2<br>[21.7] | 134.5<br>[679.1] | 183.9<br>(br) | 27.5<br>[137.8]<br>16.1<br>[16.1] | 1.4<br>[264.7] | 20,5<br>(br)<br>13.5 | +0.2 | 147.0 |
| **9b**[b,c] | 106.7<br>(br) | 127.4<br>[21.4] | 134.7<br>[708.5] | 192.7<br>(br) | 34.4 (CH)<br>[145.4] | 1.9<br>[272.8] | [c] | +34 | 66.0 |

[a] In $CD_2Cl_2$ at 296 K; coupling constants $J_{^{119}Sn,^{13}C} \pm 0.5$ Hz are given in brackets; br. denotes $^{13}$C NMR signals of carbon atoms bonded to boron. [b] Other $^{13}$C NMR spectroscopic data: $\delta$ = 69.0–75.0 ppm (numerous overlapping signals, not assigned, for $C_5H_5$ and $C_5H_4$). [c] Other $^{13}$C NMR signals were not assigned.

Table 4. $^{11}$B, $^{13}$C, and $^{119}$Sn NMR spectroscopic data[a] of the stannacyclopenta-3,5-diene **7a** and the 1-stanna-4-boracyclohexa-2,5-dienes **8**.

| | $\delta_{^{13}C}$ [Sn–C(2)] | $\delta_{^{13}C}$ [Sn–C(5)] | $\delta_{^{13}C}$ (B–C=) | $\delta_{^{13}C}$ (=C-Et) | $\delta_{^{13}C}$ (R) | $\delta_{^{13}C}$ (SnMe) | $\delta_{^{13}C}$ (BR) | $\delta_{^{119}Sn}$ | $\delta_{^{11}B}$ |
|---|---|---|---|---|---|---|---|---|---|
| **7a**[b] | 138.1<br>[446.0] | 136.2<br>[489.0] | 165.8<br>(br) | 152.5<br>[115.8] | 28.7<br>[55.9]<br>14.7<br>[9.5] | –5.5<br>[302.1] | 22.7 (br)<br>10.3 | +11.7 | 82.0 |
| **8a**[c] | 147.7<br>[472.0] | – | 165.7<br>(br)<br>[33.8] | – | 27.9<br>[63.5]<br>16.2<br>[9.5] | –3.9<br>[327.7] | 18.1 (br)<br>10.4 | –145.7 | 71.4 |
| **8b**[d] | 133.6<br>[452.2] | – | 174.9<br>(br) | – | 32.9<br>(CH)[d]<br>[66.1] | –3.8<br>[313.7] | [d] | –131.7 | 76.0 |

[a] In $CD_2Cl_2$ at 296 K; coupling constants $J_{^{119}Sn,^{13}C} \pm 0.5$ Hz are given in brackets; br. denotes $^{13}$C NMR signals of carbon atoms bonded to boron. [b] Other $^{13}$C NMR signals: $\delta$ = 91.1 [71.6], 88.3 [69.0] ($C_1$), 68–75 ppm (numerous overlapping signals for $C_5H_4$ und $C_5H_5$). [c] $\delta$ = 89.3 [58.9], 68–75 ppm (numerous overlapping signals for $C_5H_4$ und $C_5H_5$). [d] Other signals were not assigned owing to strong overlap.

 © 2006 Wiley-VCH Verlag GmbH & Co. KGaA, Weinheim 

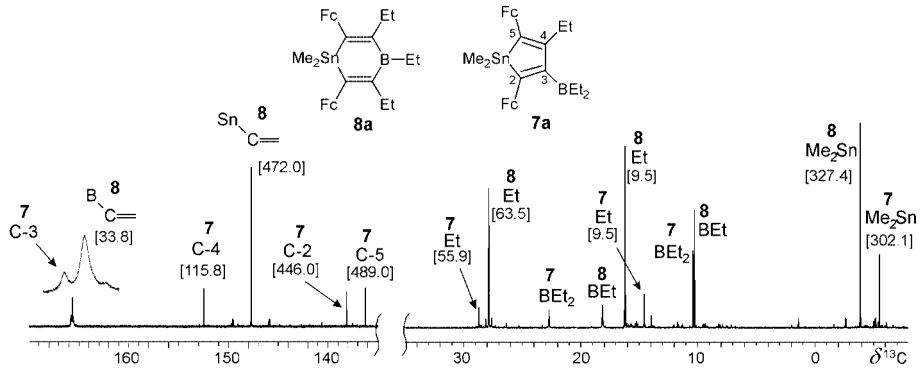


Figure 5. $^{13}C\{^1H\}$ NMR spectrum (100.5 MHz) of the mixture of products **7a** and **8a** showing the assigned $^{13}C$ NMR signals in the ranges expected for the olefinic and the aliphatic carbon atoms. $^{117/119}Sn$ satellites are indicated and $J_{^{119}Sn,^{13}C}$ coupling constants are given in brackets.

solid state,[16] and also by X-ray analysis.[15,17,18] In such related derivatives, with alkyl instead of the ferrocenyl groups, the $^{119}Sn$ resonances[15] ($\delta_{^{119}Sn}$ = +160 to +215 ppm) are found at slightly higher frequencies than for **9a** ($\delta_{^{119}Sn}$ = +147 ppm at 23 °C and +159 ppm at –20 °C). It is known, that the ferrocenyl group can stabilize a vinyl-cationic structure,[19] which may be considered for **9a** as an extreme case of unsymmetrical bridging. It should also be noted that triorganostannyl groups in the β-position to the carbocationic center exert a stabilizing effect.[20] The NMR spectroscopic evidence indicates that the ferrocenyl group stabilizes the bridged structure in **9a** much better than a phenyl group. In previous work, where the ferrocenyl was replaced with phenyl groups, the equilibrium shown for the intermediate **9a** in Scheme 4 was found, even at –10 °C, to be much more on the side of the nonbridged species[15] (cf. $\delta_{^{119}Sn}$ = +11.6 ppm and $\delta_{^{11}B}$ = +33.3 ppm at –10 °C[15] with $\delta_{^{119}Sn}$ = +147 ppm and $\delta_{^{11}B}$ = +0.2 ppm for **9a** at 23 °C).

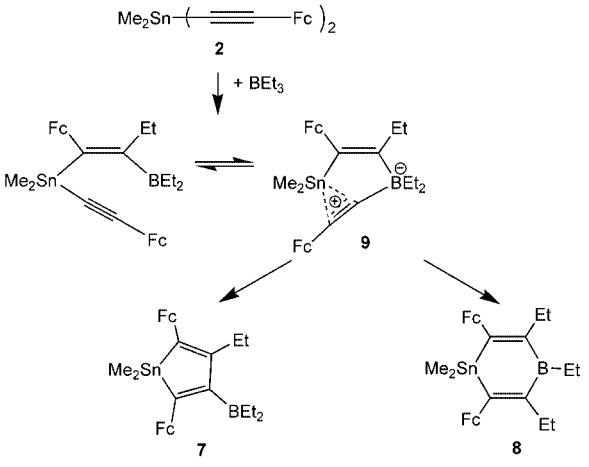


Scheme 4. 1,1-Organoboration of the bis(ferrocenylethynyl)dimethyltin (**2**).

When the reaction of **2** with triisopropylborane (B*i*Pr$_3$) was studied under similar conditions, the formation of the intermediate **9b** took place more slowly than that of **9a**. The rearrangement of **9b** was also slow (several days at room temperature); however, in contrast to the behavior of **9a**, the six-membered ring **8b** was formed selectively. The $^{119}Sn$ and $^{11}B$ NMR spectroscopic data for **9b** at room temperature ($\delta_{^{119}Sn}$ +66 ppm and $\delta_{^{11}B}$ +34 ppm) indicate that the equilibrium is shifted towards the nonbridged species.

The reaction of **3** with BEt$_3$ proceeds slowly to give a mixture of three final products, the spirotin compounds **10**–**12** (in a ratio of 45:50:5). When the progress of the reaction was monitored by $^{119}Sn$ NMR spectroscopy (see Figure 6), the $^{119}Sn$ NMR signals for various intermediates were observed. In analogy to previous work,[17,21] these were assigned to the zwitterionic intermediates **13**–**15**, which have to be considered as precursors of the final products (Scheme 5). The structural assignment of the final products is based on the $\delta_{^{119}Sn}$ values together with the observation of relevant $^{13}C$ NMR signals in the olefinic region. The latter correspond closely to those for compounds **7a** and **8a** (see Figure 5). The $^{119}Sn$ resonances differ significantly, depending on whether the tin atom is part of a five- or six-membered ring. $^{119}Sn$ nuclei as part of five-membered rings are typically deshielded.[22]

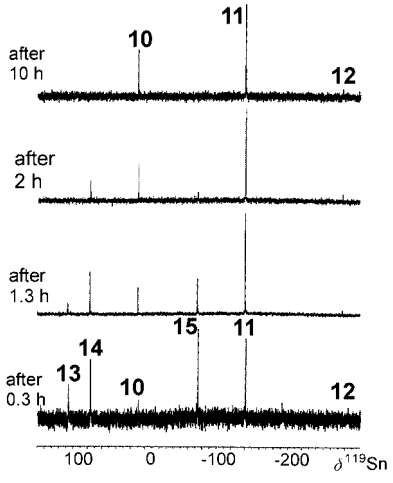


Figure 6. $^{119}Sn\{^1H$-inverse-gated$\}$ NMR spectra (149.1 MHz) of the $CD_2Cl_2$ solution from the reaction of tetrakis(ferrocenylethynyl)tin (**3**) with an excess of BEt$_3$. $^{119}Sn$ NMR signals of the zwitterionic intermediates **13**–**15** are observed in the beginning, and after 10 h at room temperature only $^{119}Sn$ NMR signals of the spirotin compounds **10**, **11** and **12** (ratio 45:50:5) are left.

 © 2006 Wiley-VCH Verlag GmbH & Co. KGaA, Weinheim 

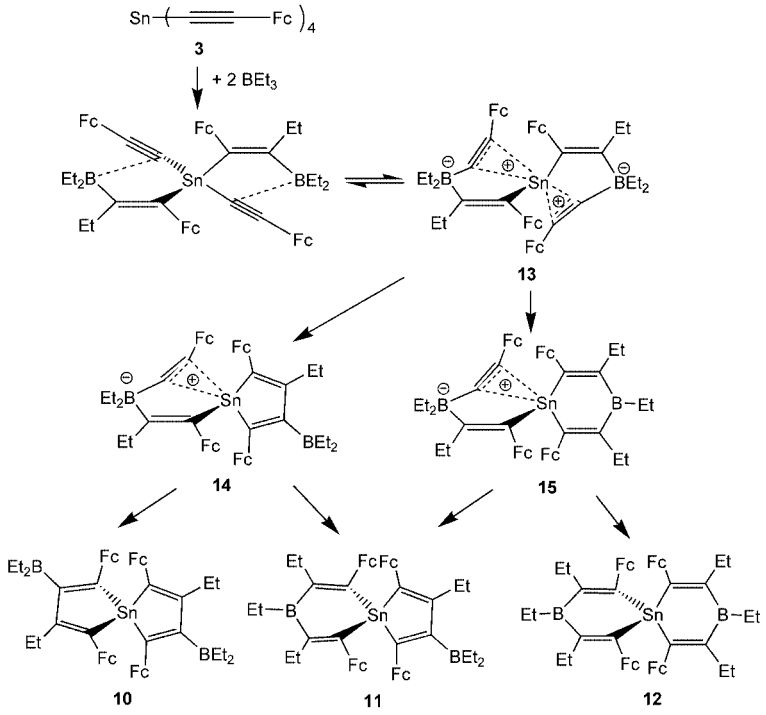


Scheme 5. 1,1-Ethylboration of tetrakis(ferrocenylethynyl)tin (**3**).

## Conclusions

All structural and spectroscopic data indicate that the ferrocenyl group does not exert any special effects on the C≡C bond in ferrocenylethynyltin compounds. This is also supported by the results of the 1,1-organoboration reactions. Novel organometallic-substituted alkenes with stannyl and boryl groups in *cis*-positions are accessible by 1,1-ethylboration of the mono(ferrocenylethynyl)tin compounds **1** and **4**. Fairly stable zwitterionic intermediates were detected in the course of 1,1-organoboration reactions of bis(ferrocenylethynyl)dimethyltin (**2**) and tetrakis(ferrocenylethylnyl)tin (**4**). These reactions give access to 1-stannacyclopenta-2,4-diene or 1-stanna-4-boracyclohexa-2,5-diene derivatives and the corresponding spirotin compounds. The product distribution is apparently dependent on the nature of the trialkylborane.

## Experimental Section

**General Procedures:** All reactions were carried out using the usual techniques to exclude oxygen and moisture. The starting materials ethynylferrocene,[3] tin amides,[23] and triisopropylborane[24] were prepared following literature procedures. BuLi, tin chlorides, and triethylborane were used as commercial products without further purification. Melting points were measured (Büchi 510 melting point apparatus) in sealed capillaries under argon and are uncorrected. Mass spectra (EI ionization, 70 eV) were obtained using a Finnigan MAT 8500 spectrometer with direct inlet. IR spectra: Perkin–Elmer, Spectrum 2000 FTIR instrument. NMR spectra: Bruker ARX 250, Bruker DRX 500 (both for $^{1}H$, $^{11}B$, $^{13}C$ and $^{119}Sn$ NMR spectra of solutions), and Varian Inova 400 (for solutions and for solid-state MAS $^{13}C$ and $^{119}Sn$ NMR spectra). $^{119}Sn$ NMR spectra of solutions were measured by using the refocused INEPT pulse sequence[25] for methyltin compounds, and by $^{1}H$ inverse-gated decoupling for all other cases. The chemical shifts are given relative to $SiMe_4$ [$\delta_{^1H}(C_6D_5H)$ = 7.15 ppm; $\delta_{^1H}(CHCl_3)$/$CDCl_3$ = 7.23 ppm; $\delta_{^1H}(CHDCl_2/CD_2Cl_2)$ = 5.33 ppm; $\delta_{^{13}C}(C_6D_6)$ = 128.0 ppm; $\delta_{^{13}C}(CDCl_3)$ = 77.0 ppm; $\delta_{^{13}C}(CD_2Cl_2)$ = 53.8 ppm], $SnMe_4$ [$\delta_{^{119}Sn}$ = 0 ppm for $\Xi(^{119}Sn)$ = 37.290665 MHz], or $BF_3{\cdot}OEt_2$ [$\delta_{^{11}B}$ = 0 ppm for $\Xi(^{11}B)$ = 32.083971 MHz]. For solid-state MAS NMR spectra, the $\delta_{^{13}C}$ and $\delta_{^{119}Sn}$ NMR spectroscopic data are given relative to external adamantane and $Sn(chex)_4$, respectively, and recalculated to the $SiMe_4$ and $SnMe_4$ scales.

**Ferrocenylethynyltrimethyltin (1):** [26] $^{1}H$ NMR (250 MHz, $CD_2Cl_2$): $\delta$ [$J_{^{119}Sn,^1H}$] = 0.31 [60.0] (s, 9 H, $SnMe_3$), 3.39, 4.13 [2m, 2×2 H, H(3,4,2,5)], 4.11 (s, 5 H, Cp) ppm. MS: *m/z* (%) = 374 (100) [$M^+$], 344 (82) [$M^+$ – 2Me], 329 (19) [$M^+$ – 3Me].

**Bis(ferrocenylethynyl)dimethyltin (2):** A THF (5 mL) solution of $Me_2SnCl_2$ (0.98 g, 4.46 mmol) was added, at 0 °C, to a solution of the Li salt of Fc-C≡C–H [prepared from 1.87 g of Fc-C≡C–H (8.92 mmol and an equimolar amount of BuLi (1.6 M in hexane)] in THF (15 mL). The mixture was kept stirring overnight, THF was removed under reduced pressure, and the residue was taken up in hexane (15 mL). After filtration, the product **2** was crystallized at –30 °C to give 1.21 g (48%) of orange crystals (m.p. 140–144 °C). $^{1}H$ NMR (400 MHz, $C_6D_6$, 296 K): $\delta$ [$J_{^{119}Sn,^1H}$] = 0.30 [68.6] (s, 6 H, $Me_2Sn$), 3.84 (m, 4 H, $C_5H_4$), 4.05 (s, 10 H, $C_5H_5$), 4.41 (m, 4 H, $C_5H_4$) ppm. IR (toluene): $\tilde{\nu}$ = 2140, 2114 $cm^{-1}$ (C≡C). MS: *m/z* (%) = 598 (80) [$M^+$], 418 (100) [$M^+$ – $SnMe_2$].

**Tetrakis(ferrocenylethynyl)tin (3):** A hexane (5 mL) solution of $SnCl_4$ (0.205 g, 1.74 mmol) was added, at 0 °C, to a solution of the Li salt of Fc-C≡C–H (prepared as above; 1.46 g, 6.94 mmol) in THF (15 mL). After stirring for 12 h at room temperature, insoluble materials were filtered off, and the solid was washed with toluene and dried to give the product **3** as an orange-yellow powder (0.877 g, 52%; m.p. 210–214 °C). $^{1}H$ NMR (400 MHz, $CD_2Cl_2$,

 © 2006 Wiley-VCH Verlag GmbH & Co. KGaA, Weinheim 

296 K): $\delta$ = 4.26 (m, 8 H, $C_5H_4$), 4.27 (s, 20 H, $C_5H_5$), 4.56 (m, 8 H, $C_5H_4$) ppm. IR (toluene): $\tilde{\nu}$ = 2147 $cm^{-1}$ (C≡C).

**Chloro(ferrocenylethynyl)dimethyltin (4):** A mixture of the stannane **2** (213 mg, 0.376 mmol) and $Me_2SnCl_2$ (90.1 mg, 0.414 mmol) in toluene (1 mL) was heated at for 1 h. After removal of the solvent and the excess of $Me_2SnCl_2$ in vacuo, the tin chloride **4** was left as a brownish-red solid that could be used without additional purification. The purity of **4** (according to NMR spectroscopic data) was ≥ 95%. $^1$H NMR (400 MHz, $C_6D_6$, 296 K): $\delta$ [$J_{^{119}Sn,^1H}$] = 0.55 [69.1] (s, 6 H, $Me_2Sn$); 4.20 (m, 2 H, $C_5H_4$); 4.22 (s, 5 H, $C_5H_5$); 4.45 (m, 2 H, $C_5H_4$) ppm.

**Organoboration the of Stannanes 1–4 with Triethylborane (General Procedure):** A twofold excess of $BEt_3$ (four equivalents were used in the case of **3**) was added, at –78 °C, to a solution of the respective alkyn-1-yltin compound **1**–**4** (0.2–0.4 mmol) in $CH_2Cl_2$ and the reactions were monitored by $^{119}$Sn NMR spectroscopy. For multinuclear NMR characterization of the zwitterionic intermediates **9a** and **9b** the same reactions were carried out with 0.1 mmol of **2** in $CD_2Cl_2$. The reaction of **2** with B*i*Pr$_3$ was also done on a small scale (0.05 mmol) in $CD_2Cl_2$ for NMR studies.

**5:** Orange-red oil. $^1$H NMR (500.1 MHz. $CDCl_3$, 296 K): $\delta$ [$J_{^{119}Sn,^1H}$] = 0.05 [53.0] (s, 9 H, $Me_3Sn$), 2.19, 0.85 (q and t, 2 H and 3 H, =C-Et), 1.30, 1.11 (m and t, 10 H, $BEt_2$), 3.85–4.00 (m, 4 H. $C_5H_4$), 3.83 (s, 5 H, $C_5H_5$) ppm.

**6:** Orange-red, waxy solid.: $^1$H NMR (400 MHz, 296 K, $CD_2Cl_2$): $\delta$ [$J_{^{119}Sn,^1H}$] = 0.59 [55.0] (s, 6 H, $Me_2Sn$); 2.21 [8.5], 0.86 (q and t, 2 H nd 3 H, =C-Et), 1.36, 1.16 (m and t, 4 H and 6 H, $BEt_2$), 3.87 (s, 5 H, $C_5H_5$), 3.9–4.0 (m, 4 H, $C_5H_4$) ppm.

**7a:** Obtained as a mixture with **8a**. $^1$H NMR (400 MHz, 296 K, $CD_2Cl_2$): $\delta$ [$J_{^{119}Sn,^1H}$] = 0.73 [52.6] (s, 6 H, $Me_2Sn$), 0.9 1.1 (m, 9 H, Et, $BEt_2$), 1.5 (q, $^3J_{^{119}Sn,^1H}$ = 7.6 Hz, 4 H, $BEt_2$), 2.2 (q, $^3J_{^{119}Sn,^1H}$ = 7.6 Hz, 2 H, Et), 4.18 (s, 10 H, $C_5H_5$), 4.1–4.3 (m, 8 H, $C_5H_4$) ppm.

**8a:** Obtained as a mixture with **7a**. $^1$H NMR ($CD_2Cl_2$, 296 K): $\delta$ [$J_{^{119}Sn,^1H}$] = 0.53 [52.6] (s, 6 H, $Me_2Sn$), 0.9–1.1 (m, 9 H, Et, BEt), 1.5 (q, 2 H, BEt), 2.2 (q, 4 H, Et), 4.18 (s, 10 H, $C_5H_5$), 4.1–4.3 (m, 8 H, $C_5H_4$) ppm.

**10:** Obtained as a mixture with **11** and **12**. $^{13}$C{$^1$H} NMR (125.8 MHz, $CD_2Cl_2$, 296 K): $\delta$ [$J_{^{119}Sn,^{13}C}$] = 22.9 (br), 9.9 ($BEt_2$). 28.3 [67.3], 16.2 [9.6] (Et), 68.9–69.9 (overlapping signals for $C_5H_4$ and $C_5H_5$), 87.6 [71.4] [$C_5H_4$-(1)], 89.9 [72.8] [$C_5H_4$-(1)], 134.2 [454.7] (C-1), 165.3 [43.6] (br) (C-2), 152.3 [117.8] (C-3), 139.0 [473.8] (C-4) ppm. $^{119}$Sn{$^1$H inverse-gated} NMR (149.1 MHz, $CD_2Cl_2$, 296 K): $\delta$ = 10.3 ppm.

**11:** Obtained as a mixture with **10** and **12**. $^{13}$C{$^1$H} NMR (125.8 MHz, $CD_2Cl_2$, 296 K): $\delta$ [$J_{^{119}Sn,^{13}C}$] = 22.3 (br), 9.9 ($BEt_2$); 18.4 (br), 8.3 (BEt); 28.5 [57.6], 13.6 [10.1] (3-Et), 28.4 [56.4], 14.4 [9.5] (7-Et), 68.9–69.9 (overlapping signals for $C_5H_4$ and $C_5H_5$), 87.5 [79.7], 88.2 [71.0] [1,4-$C_5H_4$-(1)], 89.7 [76.1] [6-$C_5H_4$-(1)], 137.1 [409.0] (C-1), 164.5 [44.4] (br) (C-2), 153.7 [117.6] (C-3), 141.1 [428.8] (C-4), 150.0 [441.5] (C-6), 167.3 [36.6] (br) (C-7) ppm. $^{119}$Sn{$^1$H inverse-gated} NMR (149.1 MHz, $CD_2Cl_2$, 296 K): $\delta$ = –139.6 ppm.

**12:** A small amount as a mixture with **10** and **11**. $^{13}$C NMR (125.8 MHz, $CD_2Cl_2$, 296 K): $\delta$ = 18.6 (br), 8.2 (BEt), 28.5, 14.3 (2-Et), 68.9–69.9 (overlapping signals for $C_5H_4$ and $C_5H_5$), 87.9 [1-$C_5H_4$-(1)], 152.4 (C-1), 166.1 (br) (C-2) ppm. $^{119}$Sn{$^1$H} NMR (149.1 MHz, $CD_2Cl_2$, 296 K): $\delta$ = –275.7 ppm.

**X-ray Crystallography:** An orange-colored crystal of compound **2** of dimensions 0.18 × 0.16 × 0.12 $mm^3$ was sealed in a glass capillary under argon and measured on a Siemens P4 four-circle diffractometer at 293(2) K with Mo-$K_\alpha$ radiation (graphite monochromator). The structure was solved by direct methods and refined by a full-matrix least-squares procedure. A numerical absorption was carried out. The positions of the hydrogen atoms were calculated and refined isotropically by applying the riding model. All non-hydrogen atoms were refined anisotropically revealing $wR^2$ = 0.124 and $R1$ = 0.056 as final $R$ values. The final difference map had no peaks of chemical significance (min./max. residual electron density –0.76/0.62 e $10^{-6}$ $pm^{-3}$).
CCDC-275737 contains the supplementary crystallographic data for this paper. These data can be obtained free of charge from The Cambridge Crystallographic Data Centre via www.ccdc.cam.ac.uk/data_request/cif.

## Acknowledgments

This work was supported by the Deutsche Forschungsgemeinschaft.

[1] a) *Modern Acetylene Chemistry* (Eds.: P. J. Stang, F. Diederich), Wiley-VCH, Weinheim, **1995**; b) L. Brandsma, *Acetylenes, Allenes and Cumulenes*, Elsevier, Amsterdam **2003**.
[2] a) A. G. Davies, *Organotin Chemistry*, 2nd Edition, Wiley-VCH, **2004**; b) M. Pereyre, J.-P. Quintard, A. Rahm, *Tin in Organic Synthesis*, Butterworth, London, **1987**.
[3] a) K. Schlögl, W. Steyrer, *Monatsh. Chem.* **1965**, *96*, 1520–1535; b) G. Doisneau, G. Balavoine, T. Fillebeen-Khan, *J. Organomet. Chem.* **1992**, *425*, 113–117.
[4] a) K. Jones, M. F. Lappert, *J. Organomet. Chem.* **1965**, *3*, 295–307; b) K. Jones, M. F. Lappert, *Proc. Chem. Soc. London* **1964**, 22–23.
[5] B. Wrackmeyer, K. Horchler, *Prog. Nucl. Magn. Reson. Spectrosc.* **1990**, *22*, 209–253.
[6] B. Wrackmeyer, *J. Magn. Reson.* **1981**, *42*, 287–297.
[7] S. Kerschl, A. Sebald, B. Wrackmeyer, *Magn. Reson. Chem.* **1985**, *23*, 514–520.
[8] M. Herberhold, in *Ferrocenes* (Eds.: A. Togni, T. Hayashi), Wiley-VCH, Weinheim, **1995**, pp. 219–278.
[9] a) K. Wurst, O. Elsner, H. Schottenberger, *Synlett* **1995**, 833–834; b) T. Steiner, M. Tamm, A. Grzegorzewski, N. Schulte, N. Veldman, A. M. M. Schreurs, J. A. Kanters, J. Kroon, J. van der Maas, B. Lutz, *J. Chem. Soc., Perkin Trans. 2* **1996**, 2441–2446.
[10] E. Klaus, A. Sebald, *Magn. Reson. Chem.* **1994**, *32*, 679–690.
[11] B. Wrackmeyer, *Rev. Silicon, Germanium, Tin Lead Compd.* **1982**, *6*, 75–148.
[12] B. Wrackmeyer, *Coord. Chem. Rev.* **1995**, *145*, 125–156.
[13] a) J. K. M. Sanders B. K. Hunter, *Modern NMR Spectroscopy*, 2nd Edition, Ch. 6, Oxford University Press, Oxford, **1993**; b) K. Stott, J. Keeler, Q. N. Van, A. J. Shaka, *J. Magn. Reson.* **1997**, *125*, 302.
[14] S. Kerschl, B. Wrackmeyer, *Z. Naturforsch., Teil B* **1984**, *39*, 1037–1041.
[15] B. Wrackmeyer, S. Kundler, R. Boese, *Chem. Ber.* **1993**, *126*, 1361–1370.
[16] B. Wrackmeyer, G. Kehr, A. Sebald, J. Kümmerlen, *Chem. Ber.* **1992**, *125*, 1597–1603.
[17] B. Wrackmeyer, S. Kundler, W. Milius, R. Boese, *Chem. Ber.* **1994**, *127*, 333–342.
[18] B. Wrackmeyer, G. Kehr, R. Boese, *Angew. Chem.* **1991**, *103*, 1374–1376; *Angew. Chem. Int. Ed. Engl.* **1991**, *30*, 1370–1372.
[19] a) H.-U. Siehl, in *Stable Carbocation Chemistry* (Eds.: G. K. S. Prakash, P. v. R. Schleyer), Wiley, New York, **1997**, pp. 165–196; b) E. W. Koch, H.-U. Siehl, M. Hanack, *Tetrahedron Lett.* **1985**, *26*, 1493–1496; c) T. S. Abram, W. E. Watts, *J. Chem. Soc., Perkin Trans. 1* **1977**, 1532–1536.
[20] Hyperconjugative stabilizing effects are well documented for silyl, germyl, and stannyl groups in β-positions. For some lead-

 © 2006 Wiley-VCH Verlag GmbH & Co. KGaA, Weinheim 

ing references, see: a) J. B. Lambert, Y. Zhao, H. Wu, *J. Org. Chem.* **1999**, *64*, 2729–2736; b) V. Gabelica, A. J. Kresge, *J. Am. Chem. Soc.* **1996**, *118*, 3838–3841; c) Y. Apeloig, R. Biton, A. Abu-Freih, *J. Am. Chem. Soc.* **1993**, *115*, 2522–2523; d) H.-U. Siehl, F. P. Kaufmann, *J. Am. Chem. Soc.* **1992**, *114*, 4937–4939; e) A. Berndt, *Angew. Chem.* **1993**, *105*, 1034–1058; *Angew. Chem. Int. Ed. Engl.* **1993**, *32*, 985–1009; f) T. Müller, R. Meyer, D. Lennartz, H.-U. Siehl, *Angew. Chem.* **2000**, *112*, 3203–3206; *Angew. Chem. Int. Ed.* **2000**, *39*, 3074–3077.

[21] R. Köster, G. Seidel, I. Klopp, C. Krüger, G. Kehr, J. Süß, B. Wrackmeyer, *Chem. Ber.* **1993**, *126*, 1385–1396.

[22] a) B. Wrackmeyer, *Annu. Rep. NMR Spectrosc.* **1985**, *16*, 73–186; b) B. Wrackmeyer, *Annu. Rep. NMR Spectrosc.* **1999**, *38*, 203–264.

[23] M. F. Lappert, A. R. Sanger, R. C. Srivastava, P. P. Power, *Metal and Metalloid Amides: Synthesis, Structure, and Physical and Chemical Properties*, Wiley, New York, **1980**.

[24] E. Krause, P. Nobbe, *Ber. Dtsch. Chem. Ges.* **1931**, *64*, 2112–2116.

[25] a) G. A. Morris, R. Freeman, *J. Am. Chem. Soc.* **1979**, *101*, 760–762; b) G. A. Morris, *J. Am. Chem. Soc.* **1980**, *102*, 428–429; c) D. P. Burum, R. R. Ernst, *J. Magn. Reson.* **1980**, *39*, 163–168.

[26] a) U. H. F. Bunz, V. Enkelmann, *Organometallics* **1994**, *13*, 3823–3833; b) P. Stepnicka, L. Trojan, J. Kubista, J. Ludvik, *J. Organomet. Chem.* **2001**, *637–639*, 291–299.

[27] a) G. Metz, X. Wu, S. O. Smith, *J. Magn. Reson., Ser. A* **1994**, *110*, 219–227; b) O. B. Peersen, X. Wu, S. O. Smith, *J. Magn. Reson., Ser. A* **1994**, *106*, 127–131.

Received: July 6, 2005
Published Online: November 11, 2005

 © 2006 Wiley-VCH Verlag GmbH & Co. KGaA, Weinheim 

DOI: 10.1002/ejic.200500603

# Synthesis of Monodisperse CdS Nanospheres in an Inverse Microemulsion System Formed with a Dendritic Polyether Copolymer

**Fang Wang,[a] Guiying Xu,*[a] Zhiqing Zhang,[a] and Xia Xin[a]**

**Keywords:** Monodisperse nanospheres / Semiconductors / Dendrimers / X-ray diffraction / Microemulsion

Nanosized CdS spheres with diameters of about 25, 40, and 50 nm have been synthesized in three inverse microemulsions formed with a dendritic amphiphilic copolymer ($H_2O$/SD31/*n*-butanol/*n*-heptane) through the reaction of cadmium chloride ($CdCl_2$) with the $S^{2-}$ ions that were slowly released from thioacetamide (TAA). X-ray powder diffraction (XRD), transmission electron microscopy (TEM), and UV/Vis absorption and photoluminescence (PL) spectroscopy were used to characterize the CdS nanospheres obtained. TEM and XRD studies showed that monodisperse CdS nanospheres with the zinc blende structure were produced, and the size of the CdS spheres increased with increasing water-core size because of the increasing [water]/[dendrimer] mass ratio ($\omega$). The blue-shift of the maxima in the UV/Vis absorption and PL spectra indicated that the CdS spheres consisted of primary CdS nanocrystals showing a quantum confinement effect. The viscosities of the three microemulsions were also determined by rheological measurements. The viscosity of the inverse microemulsion system decreased as $\omega$ increased. The water core of the inverse microemulsion provided a soft template for the precipitation of CdS spheres.

(© Wiley-VCH Verlag GmbH & Co. KGaA, 69451 Weinheim, Germany, 2006)

## Introduction

Nanocrystals have attracted broad attention from researchers in various disciplines.[1] They exhibit size-dependent characteristics and often display novel electronic, magnetic, optical, chemical, and mechanical properties that cannot be obtained in their bulk counterparts. Among the various nanocrystals, semiconductor nanocrystals, represented by Group II–IV nanocrystals with either zinc blende or wurtzite structures, have been the most studied because of their nonlinear optical and luminescence properties, quantum size effect, and other important physical and chemical features.[2,3] Altering the size of the particles changes the degree of the confinement of the electrons and affects the electronic structure of the solid, especially the bandgap edges, which can be tuned by varying the particle size. Chalcogenides such as CdS,[4–14] ZnS,[15–21] HgS,[22–24] PdS,[25–29] and MnS,[30,31] have been intensively investigated. Among these inorganic nanoparticles, CdS nanoparticles have received great attention. CdS, as an important Group II–IV semiconductor compound with a wide bandgap (energy = 2.53 eV), has attracted much research interest due to its excellent properties of luminescence and photochemistry.

To date, various methods have been developed to synthesize nanoparticles of CdS semiconductors. Recently, solvothermal or hydrothermal methods,[32] evaporation processes,[33] mesoporous silica and monoliths,[34] and sol–gel methods[35] have been utilized to prepare CdS. Other methods involve arrested precipitation from simple inorganic ions using polyphosphate and low-molecular-weight thiols as stabilizers.[36–38] Surfactants,[39] block copolymers,[40] and dendrimers[41] have also been used as specific stabilizers and soft templates for the synthesis of CdS nanoparticles in solution. However, water-in-oil microemulsions with nanometer-sized water cores are well-suited for nanoparticles. As the method that uses such microemulsions works in mild and normal environments, it is advantageous and considered to have good viability. No special conditions of pressure, irradiation, etc. are required.[42] Many kinds of CdS nanoparticles have been synthesized by this method.[43] The nanowater core acts as a nanoreactor, and the size of the prepared nanoparticles can be controlled.[44]

In previous studies, microemulsions were generally composed of low-molecular-weight surfactants. However, amphiphilic macromolecules, in particular amphiphilic dendrimers, can also be used to prepare microemulsions. Dendrimers are defined as macromolecules containing highly branched and dimensional structures with a large number of reactive terminal groups.[45] Water-soluble amphiphilic dendrimers have attracted considerable attention due to their unique properties and as new polymeric materials for applications in many areas such as the preparation of micelles, liquid crystals, microemulsions, and molecular encapsulation.[46,47] The synthesis of an amphiphilic dendritic polyether copolymer and its demulsification on crude oil were studied in our previous work.[48]

[a] Key Laboratory of Colloid and Interface Chemistry of the Ministry of Education, Shandong University,
Jinan 250100, People's Republic of China
Fax: +86-531-8564750
E-mail: xuguiying@sdu.edu.cn

 © 2006 Wiley-VCH Verlag GmbH & Co. KgaA, Weinheim 

In this article, we prepared water-in-oil microemulsions with an amphiphilic dendritic polyether copolymer SD31 as a microreactor to synthesize CdS nanoparticles and tested the feasibility of this method. As a result, nanosized monodisperse CdS spheres with diameters of 25–50 nm were obtained. The dimension of the CdS nanospheres encapsulated in microemulsion droplets could be controlled by varying the water-core size, i.e., varying the [water]/[dendrimer] mass ratio ($\omega$). The effects of the variation of $\omega$ on the synthesis were carefully examined and found to shed light on the mechanism of formation.

## Results and Discussion

Typical TEM images of CdS spheres with different sizes obtained in three different microemulsions are presented in Figure 1, which shows that the shape of all the products is spherical. However, the size is varied. The diameter of the spheres synthesized in microemulsion A is around 25 nm (Figure 1a and b), while the sphere diameters of other two samples synthesized in microemulsions B and C are about 40 and 50 nm, respectively (Figure 1c and d, e and f). It could be concluded that the size of the products increased as the [water]/[dendrimer] mass ratio ($\omega$) increased. The size of w/o microemulsion droplets is highly dependent on the concentration of each constituent in the microemulsion. However, it is recognized that the water-core size is dominantly characterized by the [water]/[surfactant] ratio, rather than the actual concentration. The radius of the water core is found to follow an approximately linear relationship with the [water]/[surfactant] ratio,[49] because the size of the water core of the microemulsion increases as $\omega$ increases. The larger water core acts as a nanoreactor that induces larger particle growth.[50] These properties and their reasons are discussed in detail below.

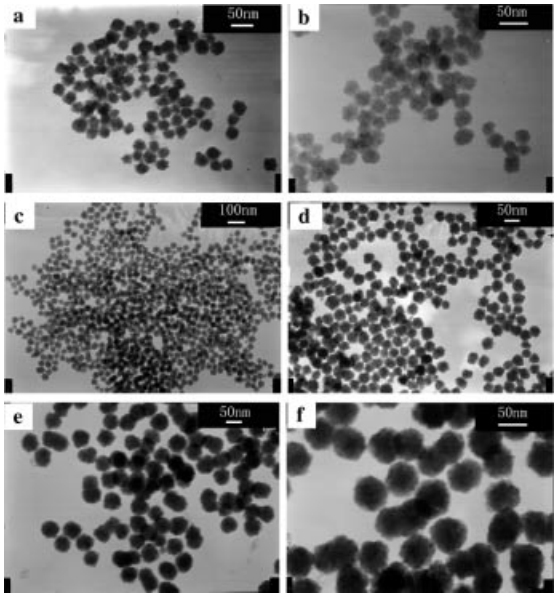


Figure 1. TEM images of CdS spheres obtained in three microemulsions with different [water]/[dendrimer] mass ratios ($\omega$): (a and b) products from microemulsion A ($\omega$ = 0.19); (c and d) products from microemulsion B ($\omega$ = 0.21); (e and f) products from microemulsion C ($\omega$ = 0.24).

The wide-angle XRD patterns for the CdS nanospheres prepared in the three microemulsions are shown in Figure 2. Diffraction peaks assigned to the (111), (200), (220), and (311) planes of bulk cubic CdS are observed for samples produced from microemulsions B and C. For the smallest sample produced from microemulsion A, the diffraction peaks are not obvious except for that of the (111) plane, which indicates incomplete crystallization of CdS and lattice defects. The diffraction peaks are fairly broad. We estimated roughly the average crystallite sizes of the primary particles by line-width analysis of the (111) diffraction peaks. Applying the Scherrer formula yielded particle sizes of 1.2, 1.6, and 2.7 nm for syntheses carried out in microemulsions A, B, and C, respectively.

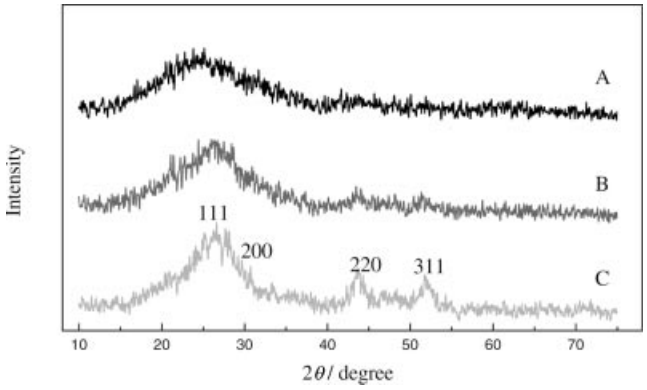


Figure 2. XRD patterns of CdS spheres obtained in the three microemulsion systems.

Figure 3 shows the intensities and wavelengths of the UV/Vis absorption peaks of the CdS spheres at various times during the process of formation. After addition of TAA, the mixture was kept at constant temperature (50 °C), and UV/Vis spectra were recorded at various time intervals. In the beginning, the solution was colorless, and there was no obvious peak in the absorption spectrum. After 30 min, the solution became slightly yellow, and an absorption peak appeared in the spectrum along with a considerable increase in absorbance. In Figure 3a, curves A′, B′, and C′ show that the absorption intensity increased with time, indicating a gradual formation of CdS particles accompanying the release of $S^{2-}$ ions from TAA. However, the position of the absorption peak was different in the three systems (Figure 3a, curves A, B, and C). The absorption peak of CdS synthesized in microemulsion A was at about 420 nm and the peak was obvious and sharp. With increasing time, the wavelength of the absorption peak remained essentially unchanged, even though the absorption intensity increased continuously, suggesting the formation of more and more CdS particles and the possible presence of large aggregates of the primary CdS particles, but the size of the primary CdS particles remained unchanged. The absorption of CdS obtained in microemulsion B displayed a shoulder peak close to 410 nm, and the absorption band of CdS obtained

 © 2006 Wiley-VCH Verlag GmbH & Co. KGaA, Weinheim 

in microemulsion C was at wavelengths no longer than about 390 nm in the beginning. Curves B and C (Figure 3a) show that the absorption peaks continuously shifted towards higher wavelengths upon further heating of the solutions. This red-shifting phenomenon indicates that the primary CdS particles grew gradually and then aggregated to form larger particles due to the quantum confinement effect. From the changes in the UV/Vis spectra of the three microemulsions, it can be deduced that the mechanism of formation of the CdS spheres was different in each system. In microemulsion A, once the CdS particles nucleated, the particles ceased growing, but more CdS particles formed or aggregated. In microemulsions B and C, although the CdS particles initially nucleated were smaller than those in microemulsion A, the primary particles grew gradually and also aggregated to form larger particles.

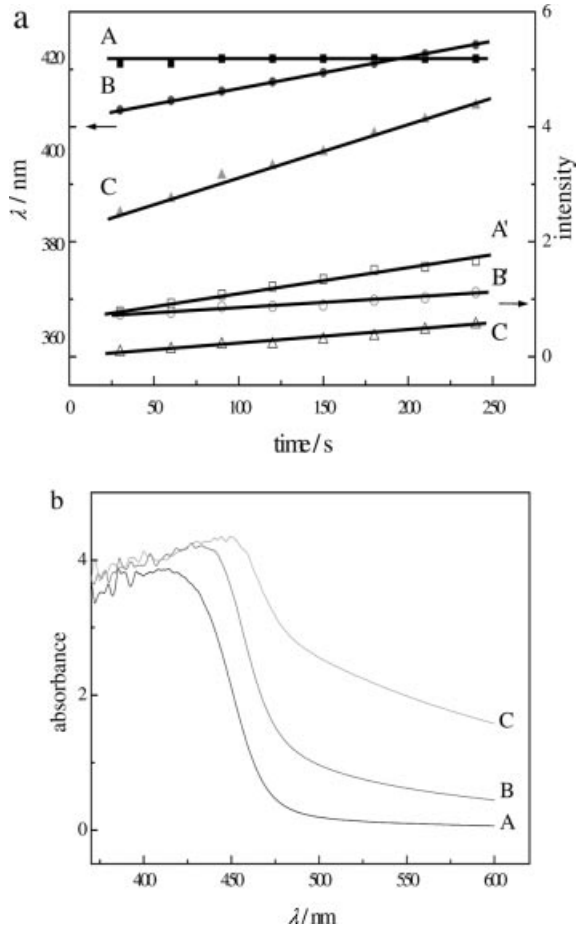


Figure 3. (a) Graphs of the wavelengths and intensities of the UV/Vis absorption peaks of the CdS products formed in the three microemulsions at earlier stages: curves A, B, and C show wavelength vs. time; curves A′, B′, and C′ show intensity vs. time. (b) UV/Vis absorption spectra of the final CdS products in the three microemulsions after eight hours. A and A′ represent microemulsion A ($\omega$ = 0.19); B and B′ represent microemulsion B ($\omega$ = 0.21); C and C′ represent microemulsion C ($\omega$ = 0.24).

Figure 3b shows the UV/Vis absorption spectra of the CdS products in the three microemulsions after eight hours. As shown in Figure 3b, the absorption spectra of the final products have peaks at 420 (microemulsion A), 440 (microemulsion B), and 450 nm (microemulsion C), which are all considerably blue-shifted relative to the absorption onset of bulk CdS (ca. 515 nm) because of the quantum confinement effect. It was interesting that CdS particles in microemulsions B and C were larger than those in microemulsion A in the end, so that the wavelength of the absorption maximum increased from A to C. The absorption peaks of B and C are obviously red-shifted relative to their initial positions, indicating the growth of the primary particles. The spectra of B and C also show a long absorption tail due to scattering by the particles in the dispersion. The absorption intensity increased with increasing particle size because of light scattering in the presence of bigger particles. From the experimental correlation between the onset of absorption and the particle diameter for CdS, the particle size of CdS nanocrystals was estimated to be about 2–3 nm and to increase from A to C.[36] These values follow the same trend as the results of XRD, which exhibit a quantum confinement effect.

The PL spectra of the CdS spheres are shown in Figure 4. The broad emission beginning around 430 nm is significantly blue-shifted from the emission of bulk CdS (ca. 520 nm). The broad PL peak observed is commonly attributed to the recombination of charged carriers trapped in the surface states and is related to the size of the CdS nanoparticles; that is, the PL bands of smaller nanoparticles appear at shorter wavelengths. Therefore, the PL emission of the CdS spheres indicates that they actually consist of primary CdS nanocrystals showing a quantum confinement effect.

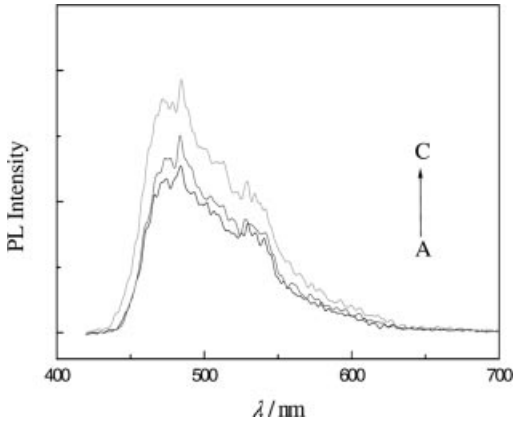


Figure 4. Photoluminescence spectra of CdS spheres obtained in three microemulsions after 8 h ($\lambda_{ex}$ = 400 nm).

Figure 5, which shows the stress at different shear rates, depicts the key results from steady-shear rheological measurements. During the experiments of shear rates, the three microemulsion systems were all Newtonian fluids. The relatively high viscosity was due to amphiphilic dendrimer content. It can be seen that shear stress increased as shear rate increased. In addition, the viscosity of the three microemulsions decreased with increased [water]/[dendrimer] mass ratio ($\omega$). This property of the microemulsion can be used to explain the different size of the products. High viscosity led to low ion flow and ion exchange, which affected the growth

 © 2006 Wiley-VCH Verlag GmbH & Co. KGaA, Weinheim 

of CdS particles in the water core and further reduced the possibility of large aggregates of the primary CdS particles. The larger particles were obtained for microemulsion C with lower viscosity. This result is consistent with the observations of the TEM images and the UV/Vis absorption spectra.

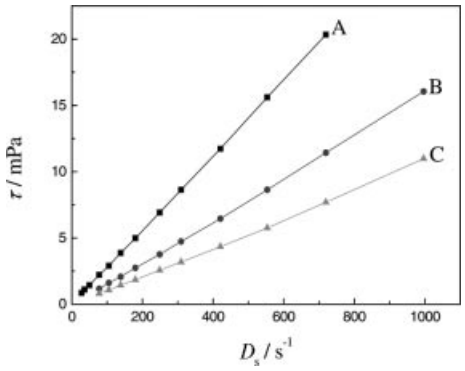


Figure 5. Shear stress vs. shear rate curves for the three microemulsion systems without CdS particles. (A) microemulsion A ($\omega$ = 0.19), (B) microemulsion B ($\omega$ = 0.21), (C) microemulsion C ($\omega$ = 0.24).

On the basis of the above observations and the monodisperse nanosphere structure we were able to propose a possible mechanism, as shown in Scheme 1. In the inverse microemulsion $H_2O$/SD31/*n*-butanol/*n*-heptane, the hydrophilic PEO of the amphiphilic dendritic polyether copolymer SD31 formed the water core, and the hydrophobic PPO and arom parts were oriented outwards. The cadmium ions that were initially dissolved in the water core reacted with the $S^{2-}$ ions that were slowly released from thioacetamide (TAA). Monodisperse CdS nanospheres were obtained because the reaction was restricted to the nanowater core.

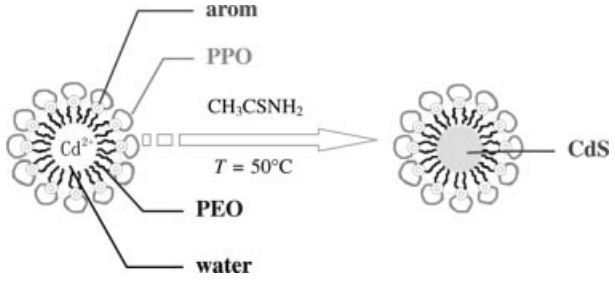


Scheme 1. Proposed mechanism for the formation of monodisperse CdS nanospheres; PEO = poly(ethylene oxide), PPO = poly(propylene oxide), arom = bisphenol A.[48]

## Conclusions

Nanosized CdS spheres were facilely synthesized in water-in-oil microemulsions prepared by amphiphilic dendrimers through the slow release of $S^{2-}$ ions from thioacetamide under heating. It was shown that the nanometer-sized water cores are well-suited for nanoparticle synthesis. Particle growth occurs within the water core of the microemulsion, and the precursors of the semiconductor particles are water-soluble. The sizes of the CdS spheres obtained in three different systems are diverse, but all spheres are composed of cubic CdS crystals of the zinc blende structure. It was revealed that the diameter of the CdS spheres increased as the [water]/[dendrimer] mass ratio ($\omega$) increased, i.e., as the water-core size increased. The viscosity of the three microemulsions decreased with increased $\omega$, which affected the flow and exchange of the ions. High viscosity led to low ion flow and induced small particles to form, preventing the particles from aggregating. It is expected that this convenient synthetic route to CdS spheres may be readily extended to the fabrication of other metal chalcogenide semiconductor nanoparticles.

## Experimental Section

**Materials:** Unless otherwise noted, all chemicals were reagent grade and were used as received without purification. Amphiphilic dendritic polyether copolymer SD31 (MW = 10600 g mol$^{-1}$) was synthesized as per ref.[48] and the molecular structure is shown schematically in Figure 6. Thrice distilled water was used in all experiments.

**Determination of the Phase Diagram:** The quasiternary phase diagram was constructed at room temperature (25 ± 1 °C). SD31 and the cosurfactant, *n*-butanol, were combined in the mass ratio1:2. Then *n*-heptane was combined with the above mixture in the mass ratios 9:1, 8:2, 7:3, 6:4, 5:5, 4:6, 3:7, 2:8, and 1:9 and shaken vigorously. Water was gradually added dropwise to the above 10 samples under shaking, and then the samples were left to settle for two days. The formation of water-in-oil microemulsions was determined through visual observation, which revealed the phase transformation or phase separation of the ternary system. The quasiternary phase diagrams of the systems are given in Figure 7.

**Synthesis of CdS Nanoparticles:** In the water-in-oil microemulsion region, three systems (see Figure 7 A, B, and C) with the same amount of water (6% wt.) but different [water]/[dendrimer] mass ratios ($\omega$) were selected as nanometer-sized reaction cores to synthesize CdS. In a typical experiment, microemulsion A, containing $CdCl_2$ solution (1.44 mL, 0.1 M), dendrimer SD31 (7.5 g), and *n*-butanol (15 g), was prepared. Thioacetamide (TAA) solution (1.44 mL, 0.1 M in ethanol) was added to microemulsion A whilst stirring until a homogeneous mixture formed. Then the final microemulsion was sealed and placed under constant temperature (50 °C) for 8 h, where the slow release of $S^{2-}$ ions from TAA led to the formation of CdS particles. The resulting solution was centrifuged at 12000 rmp, washed with ethanol under sonication, and separated by repeated centrifugation. The final product was dried to yield a powder at 50 °C. Microemulsion B was composed of $CdCl_2$ (1.60 mL, 0.1 M), dendrimer SD31 (7.5 g), *n*-butanol (15 g), and *n*-heptane (2.5 g), while microemulsion C was composed of $CdCl_2$ (1.68 mL, 0.1 M), dendrimer SD31 (7 g), *n*-butanol (14 g), and *n*-heptane (5.3 g).

**Characterization:** Transmission electron microscopy (TEM, JEM100-CXII) was used to directly observe the morphology and size of products. Powder X-ray diffraction (XRD) patterns were recorded with a Rigaku D/Max 2200-PC diffractometer with Cu-$K_\alpha$ radiation ($\lambda$ = 1.5418 Å) and a graphite monochromator at ambient temperature. UV/Vis absorption spectra were obtained with

 © 2006 Wiley-VCH Verlag GmbH & Co. KGaA, Weinheim 

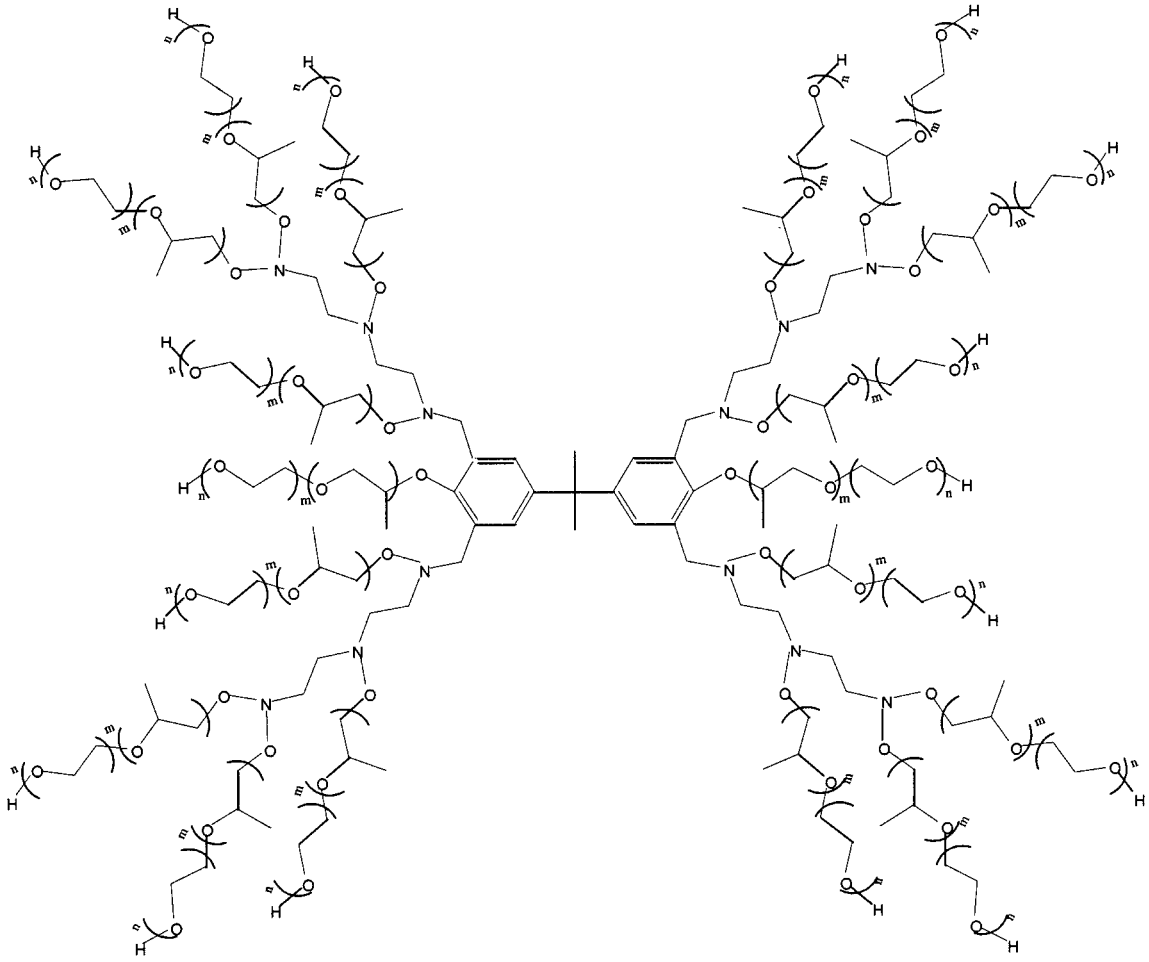

Figure 6. The molecular structure of the amphiphilic dendrimer SD31.

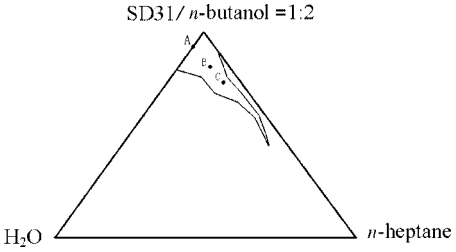


Figure 7. Ternary phase diagram of the $H_2O$/SD31/*n*-butanol/*n*-heptane system. Inset shows the water-in-oil (w/o) inverse microemulsion region. A ($\omega$ = 0.19), B ($\omega$ = 0.21), and C ($\omega$ = 0.24) were the three microemulsions used in nanoparticle synthesis.

a Hitachi U-4100 dual-beam grating spectrophotometer with a 10-mm quartz cell. PL spectra were obtained with a Perkin-Elmer LS-55 fluorescence spectrophotometer. The excitation wavelength $\lambda_{ex}$ was 400 nm, and the bandwidths of excitation and emission were both 10 nm. Fluorescence measurements were obtained on suspensions in quartz cuvettes. Shear stress versus shear rate rheological data was measured with an NXS-11A rotary viscometer.

## Acknowledgments

The authors gratefully acknowledge financial support from the National Natural Science Foundation of China (20573067).

[1] a) K. J. Klabunde, *Nanoscale Materials in Chemistry*, Wiley-Interscience, New York, **2001**; b) J. H. Fendler, *Nanoparticles and Nanostructured Films*, Wiley-VCH, Weinheim, Germany, **1998**; c) A. L. Rogach, D. V. Talapin, E. V. Shevchenko, A. Kornowski, M. Haase, H. Weller, *Adv. Funct. Mater.* **2002**, *12*, 653–664.

[2] J. Joo, H. B. Na, T. Yu, J. H. Yu, Y. W. Kim, F. Wu, J. Z. Zhang, T. Hyeon, *J. Am. Chem. Soc.* **2003**, *125*, 11100.

[3] W. Wang, I. Germanenko, M. S. El-Shall, *Chem. Mater.* **2002**, *14*, 3028–3033.

[4] T. F. Towey, A. Khan-Lodi, B. H. Robinson, *J. Chem. Soc., Faraday Trans.* **1990**, *86*, 3757–3762.

[5] a) T. Trindade, P. O'Brien, X. Zhang, *Chem. Mater.* **1997**, *9*, 523–530; b) C. S. Yang, D. D. Awschalom, G. D. Stucky, *Chem. Mater.* **2001**, *13*, 594–598; c) H. Zhao, E. P. Douglas, *Chem. Mater.* **2002**, *14*, 1418–1423.

[6] a) R. Rossetti, R. Hull, J. M. Gibson, L. E. Brus, *J. Chem. Phys.* **1985**, *82*, 552–559; b) R. Rossetti, J. L. Ellison, J. M. Gibson, L. E. Brus, *J. Chem. Phys.* **1984**, *80*, 4464–4469.

[7] M. Ohtaki, K. Oda, K. Eguchi, H. Arai, *Chem. Commun.* **1996**, 1209–1210.

[8] a) C. B. Murray, D. J. Norris, M. G. Bawendi, *J. Am. Chem. Soc.* **1993**, *115*, 8706–8715; b) C. J. Barrelet, Y. Wu, D. C. Bell, C. M. Lieber, *J. Am. Chem. Soc.* **2003**, *125*, 11498–11499; c) Y. C. Cao, J. Wang, *J. Am. Chem. Soc.* **2004**, *126*, 14336–14337.

[9] a) T. Torimoto, H. Kontani, Y. Shibutani, S. Kuwabata, T. Sakata, H. Mori, H. Yoneyama, *J. Phys. Chem. B* **2001**, *105*, 6838–6845; b) L. F. Dong, T. Gushtyuk, J. Jiao, *J. Phys. Chem. B*

 © 2006 Wiley-VCH Verlag GmbH & Co. KGaA, Weinheim 

**2004**, *108*, 1617–1620; c) T. Gao, T. H. Wang, *J. Phys. Chem. B* **2004**, *108*, 20045–20049.
[10] a) H. Y. Zhao, E. P. Douglas, B. S. Harrison, K. S. Schanze, *Langmuir* **2001**, *17*, 8428–8433; b) Y. J. Hsu, S. Y. Lu, *Langmuir* **2004**, *20*, 23–26.
[11] X. J. Zhang, Q. R. Zhao, Y. P. Tian, Y. Xie, *Cryst. Growth Des.* **2004**, *4*, 355–359.
[12] D. Dorfs, A. Eychmuller, *Nano Lett.* **2001**, *1*, 663–665.
[13] T. J. Boyle, S. D. Bunge, T. M. Alam, G. P. Holland, T. J. Headley, G. Avilucea, *Inorg. Chem.* **2005**, *44*, 1309–1318.
[14] U. S. Jeng, Y. S. Sun, H. Y. Lee, C. H. Hsu, K. S. Liang, S. W. Yeh, K. H. Wei, *Macromolecules* **2004**, *37*, 4617–4622.
[15] X. Li, J. R. Fryer, D. J. Cole-Hamilton, *J. Chem. Soc., Chem. Commun.* **1994**, 1715–1716.
[16] a) V. Sankaran, J. Yue, R. E. Cohen, R. R. Schrock, R. J. Silbey, *Chem. Mater.* **1993**, *5*, 1133–1142; b) M. R. Knecht, D. W. Wright, *Chem. Mater.* **2004**, *16*, 4890–4895.
[17] a) R. K. Rana, L. Zhang, J. C. Yu, Y. Mastai, A. Gedanken, *Langmuir* **2003**, *19*, 5904–5911; b) Y. R. Ma, L. M. Qi, J. M. Ma, H. M. Cheng, *Langmuir* **2003**, *19*, 4040–4042.
[18] L. S. Li, N. Pradhan, Y. J. Wang, X. G. Peng, *Nano Lett.* **2004**, *4*, 2261–2264.
[19] X. Chen, H. Xu, N. Xu, F. Zhao, W. Lin, G. Lin, Y. Fu, Z. Huang, H. Wang, M. Wu, *Inorg. Chem.* **2003**, *42*, 3100–3106.
[20] D. F. Moore, Y. Ding, Z. L. Wang, *J. Am. Chem. Soc.* **2004**, *126*, 14372–14373.
[21] P. Hu, Y. Liu, L. Fu, L. Cao, D. Zhu, *J. Phys. Chem. B* **2004**, *108*, 936–938.
[22] K. A. Higginson, M. Kuno, J. Bonevich, S. B. Qadri, M. Yousuf, H. Mattoussi, *J. Phys. Chem. B* **2002**, *106*, 9982–9985.
[23] B. Pal, S. Ikeda, B. Ohtani, *Inorg. Chem.* **2003**, *42*, 1518–1524.
[24] X. Chen, X. Wang, Z. Wang, X. Yang, Y. Qian, *Cryst. Growth Des.* **2005**, *5*, 347–350.
[25] Y. Wang, N. Herron, *J. Phys. Chem.* **1987**, *91*, 257–260.
[26] a) M. Moffitt, A. Eisenberg, *Chem. Mater.* **1995**, *7*, 1178–1184; b) R. Tassoni, R. R. Schrock, *Chem. Mater.* **1994**, *6*, 744–749.
[27] S. Gallardo, M. Gutierrez, A. Henglein, E. Janata, *Ber. Bunsenges. Phys. Chem.* **1989**, *93*, 1080–1090.
[28] F. Gao, Q. Lu, X. Liu, Y. Yan, D. Zhao, *Nano Lett.* **2001**, *1*, 743–748.
[29] A. Berman, N. Belman, Y. Golan, *Langmuir* **2003**, *19*, 10962–10966.
[30] J. Lu, P. F. Qi, Y. Y. Peng, Z. Y. Meng, Z. P. Yang, W. C. Yu, Y. T. Qian, *Chem. Mater.* **2001**, *13*, 2169–2172.
[31] Y. W. Jun, Y. Y. Jung, J. Cheon, *J. Am. Chem. Soc.* **2002**, *124*, 615–619.
[32] a) J. Yang, J.-H. Zeng, S.-H. Yu, L. Yang, G.-E. Zhou, Y.-T. Qian, *Chem. Mater.* **2000**, *12*, 3259–3263; b) P. Zhang, L. Gao, *Langmuir* **2003**, *19*, 208–210.
[33] a) C. Ye, G. Meng, Y. Wang, Z. Jiang, L. Zhang, *J. Phys. Chem. B.* **2002**, *106*, 10338–10341; b) G. Shen, C.-J. Lee, *Cryst. Growth Des.* **2005**, *5*, 1085–1089; c) J. Zhang, F. Jiang, L. Zhang, *J. Phys. Chem. B.* **2004**, *108*, 7002–7005.
[34] a) S. Besson, T. Gacoin, C. Ricolleau, C. Jacquiod, J.-P. Boilot, *Nano Lett.* **2002**, *2*, 409–414; b) W. Xu, Y. Liao, D. L. Akins, *J. Phys. Chem. B.* **2002**, *106*, 11127–11131; c) C. Tura, N. Coombs, O. Dag, *Chem. Mater.* **2005**, *17*, 573–579; d) Z. Zhang, S. Dai, X. Fan, D. A. Blom, S. J. Pennycook, Y. Wei, *J. Phys. Chem. B.* **2001**, *105*, 6755–6758.
[35] a) P. Xue, R. Lu, Y. Huang, M. Jin, C. Tan, C. Bao, Z. Wang, Y. Zhao, *Langmuir* **2004**, *20*, 6470–6475; b) T. Gacoin, K. Lahlil, P. Larregaray, J.-P. Boilot, *J. Phys. Chem. B.* **2001**, *105*, 10228–10235.
[36] T. Vossmeyer, L. Katsikas, M. Giersig, I. G. Popovic, K. Diesner, A. Chemseddine, A. Eychmüller, H. Weller, *J. Phys. Chem.* **1994**, *98*, 7665–7673.
[37] L. Spanhel, M. Hasse, H. Weller, A. Henglein, *J. Am. Chem. Soc.* **1987**, *109*, 5649–5655.
[38] J. Rockenberger, L. Troger, A. Kornowski, T. Vossmeyer, A. Eychmüller, J. Feldhaus, H. Weller, *J. Phys. Chem. B* **1997**, *101*, 2691–2701.
[39] a) Y.-W. Jun, S.-M. Lee, N.-J. Kang, J. Cheon, *J. Am. Chem. Soc.* **2001**, *123*, 5150–5151; b) O. Dag, S. Alayoglu, C. Tura, O. Celik, *Chem. Mater.* **2003**, *15*, 2711–2717; c) B. A. Simmons, S. Li, V. T. John, G. L. McPherson, A. Bose, W. Zhou, J. He, *Nano Lett.* **2002**, *2*, 263–268.
[40] a) H. Zhao, E. P. Douglas, B. S. Harrison, K. S. Schanze, *Langmuir* **2001**, *17*, 8428–8433; b) L. Qi, H. Colfen, M. Antonietti, *Nano Lett.* **2001**, *1*, 61–65; c) Y. Ma, L. Qi, J. Ma, H. Cheng, W. Shen, *Langmuir* **2003**, *19*, 9079–9085; d) C.-S. Yang, D. D. Awschalom, G. D. Stucky, *Chem. Mater.* **2002**, *14*, 1277–1284.
[41] a) J. Huang, K. Sooklal, C. J. Murphy, H. J. Ploehn, *Chem. Mater.* **1999**, *11*, 3595–3601; b) L. H. Hanus, K. Sooklal, C. J. Murphy, H. J. Ploehn, *Langmuir* **2000**, *16*, 2621–2626; c) B. I. Lemon, R. M. Crooks, *J. Am. Chem. Soc.* **2000**, *122*, 12886–12887.
[42] a) S. P. Moulik, G. C. De, A. K. Panda, B. B. Bhowmilk, A. R. Das, *Langmuir* **1999**, *15*, 8361–8367; b) M. P. Pileni, *J. Phys. Chem.* **1993**, *97*, 6961–6973.
[43] a) T. Hirai, M. Miyamoto, I. Komasawa, *J. Mater. Chem.* **1999**, *9*, 1217–1219; b) S. Y. Lu, M. L. Wu, H. L. Chen, *J. Appl. Phys.* **2003**, *93*, 5789–5793; c) H. Sato, Y. Tsubaki, T. Hirai, I. Komasawa, *Ind. Eng. Chem. Res.* **1997**, *36*, 92–100; d) M. Tata, S. Banerjee, V. T. John, Y. Waguespack, G. L. McPherson, *Colloids Surf., A* **1997**, *127*, 39–46.
[44] X. L. Fang, C. F. Yang, *J. Colloid Interface Sci.* **1999**, *212*, 242–251.
[45] M. Okazaki, L. Washio, Y. Shibasaki, M. Ueda, *J. Am. Chem. Soc.* **2003**, *125*, 8120–8121.
[46] Z. Bo, J. Qiu, J. Li, A. D. Schluter, *Org. Lett.* **2004**, *6*, 667–669.
[47] F. Gröhn, B. J. Bauer, E. J. Amis, *Macromolecules* **2001**, *34*, 6701–6707.
[48] Z. Q. Zhang, G. Y. Xu, F. Wang, S. L. Dong, Y. J. Chen, *J. Colloid Interface Sci.* **2005**, *282*, 1–4.
[49] B. H. Robinson, C. Toprakcioglu, J. C. Dore, P. Chieux, *J. Chem. Soc., Faraday Trans. 1* **1984**, *80*, 13–28.
[50] A. K. Panda, B. B. Bhowmik, A. R. Das, S. P. Moulok, *Langmuir* **2001**, *17*, 1811–1816.

Received: July 7, 2005
Published Online: November 11, 2005

 © 2006 Wiley-VCH Verlag GmbH & Co. KGaA, Weinheim 

DOI: 10.1002/ejic.200500613

# Copper Complexes with (2,7-Di-*tert*-butylfluoren-9-ylidene)methanedithiolate: Oxidatively Promoted Dithioate Condensation[‡]

**José Vicente,[a] Pablo González-Herrero,*[a] Yolanda García-Sánchez,[a] Peter G. Jones,[b] and Delia Bautista[c]**

**Keywords:** Copper / Dithiolates / Phosphane ligands / S ligands

The reaction of $[Cu(NCMe)_4]PF_6$ with piperidinium 2,7-di-*tert*-butyl-9*H*-fluorene-9-carbodithioate (pipH)[$S_2C$(*t*Bu-Hfy)] (**1**; *t*Bu-Hfy = 2,7-di-*tert*-butylfluoren-9-yl), affords $[Cu_n\{S_2C(t\text{Bu-Hfy})\}_n]$ (**2**), which reacts with various P ligands to give $[Cu\{S_2C(t\text{Bu-Hfy})\}L_2]$ [L = $PPh_3$ (**3a**), $PCy_3$ (**3b**), P*i*$Pr_3$ (**3d**); $L_2$ = 1,1′-bis(diphenylphosphanyl)ferrocene (dppf, **3c**), bis(diphenylphosphanyl)methane (dppm, **3e**)]. Compounds **3a**–**c** react with atmospheric oxygen and moisture in the presence of $NEt_3$ to give the dinuclear complexes $[Cu_2\{[SC=(t\text{Bu-fy})]_2S\}L_2]$ [*t*Bu-fy = 2,7-di-*tert*-butylfluoren-9-ylidene; L = $PPh_3$ (**4a**), $PCy_3$ (**4b**); $L_2$ = dppf (**4c**)], which contain a new dithiolato ligand formally resulting from the condensation of two dithioato ligands with loss of a sulfide ion and two protons. Neutral $Cu^I$ dithiolate complexes of the type $[Cu_4\{S_2C=(t\text{Bu-fy})\}_2L_4]$ [$S_2C$=(*t*Bu-fy) = [2,7-di-*tert*-butylfluoren-9-ylidene)methanedithiolate; L = $PPh_3$ (**5a**), $P(C_6H_4OMe\text{-}p)_3$ (**5b**), P*i*$Pr_3$ (**5d**) or $L_2$ = dppf (**5c**)] were obtained by treating **1** with $[Cu(NCMe)_4]PF_6$, the corresponding phosphane, and piperidine in a 1:2:2:1 molar ratio. The reaction of **1** with $Cu(ClO_4)_2{\cdot}6H_2O$ and $(Pr_4N)OH$ in a 2:1:2 molar ratio gives the $Cu^{II}$ complex $(Pr_4N)_2[Cu\{S_2C=(t\text{Bu-fy})\}_2]$ [$(Pr_4N)_2$**6**], which readily oxidizes to the $Cu^{III}$ complex $Pr_4N[Cu\{S_2C=(t\text{Bu-fy})\}_2]$ ($Pr_4N$**7**) in the presence of atmospheric oxygen and moisture. The salt PPN**7** [$PPN^+$ = $(Ph_3P)_2N^+$] was obtained from **1**, $CuCl_2{\cdot}2H_2O$, PPNCl, and piperidine in a 2:1:1:2 molar ratio under aerobic conditions. The crystal structures of **3a**, **3c**·$CH_2Cl_2$, **4a**·$4Me_2CO$, and **4c**·$CH_2Cl_2$ have been determined by X-ray diffraction studies.

(© Wiley-VCH Verlag GmbH & Co. KGaA, 69451 Weinheim, Germany, 2006)

## Introduction

The importance of copper complexes and clusters with thiolato ligands is associated with their use as models for the understanding of the structure, bonding, and function of the active sites of copper–sulfur enzymes and proteins,[1–6] which perform crucial functions such as electron-transfer and dioxygen transport to redox systems and copper transport and delivery.[7–11] Among the variety of sulfur ligands employed for the synthesis of copper complexes, 1,1-ethylenedithiolates ($XYC=CS_2^{2-}$) and related dithio ligands have received special attention because of their ability to form high-nuclearity clusters, some of which have found industrial applications as antioxidant additives for lubricant oils.[12–20] Previously described 1,1-ethylenedithiolates that have been used for the preparation of copper complexes are limited to those with X = Y = CN (*i*-mnt), $CO_2R$ [R = Me (dmd), Et (ded), *t*Bu (*t*Bu-ded)] and X = CN and Y = $P(O)(OEt)_2$ (cpdt). The anionic $Cu^I$ clusters $[Cu_8(i\text{-mnt})_6]^{4-}$,[12,13,19] $[Cu_8(ded)_6]^{4-}$,[14] and $[Cu_8(t\text{Bu-ded})_6]^{4-}$[15,16] stand out as the best-studied 1,1-ethylenedithiolato complexes of copper, and theoretical calculations have been carried out in order to understand the bonding in the $Cu_8S_{12}$ core.[21,22] The tetranuclear cluster $[Cu_4(i\text{-mnt})_4]^{4-}$ has been obtained from the reaction of the sulfur-rich dithiolato cluster $[Cu_6\{S_3C=C(CN)_2\}_6]^{6-}$ with triphenylphosphane.[19] Clusters of higher nuclearities have been obtained by protonation of $[Cu_8(ded)_6]^{4-}$ and $[Cu_8(t\text{Bu-ded})_6]^{4-}$.[15,16] A series of clusters of $Cu^I$ with the cpdt ligand and bis(diphenylphosphanyl)methane (dppm) has also been prepared from the reaction between $[Cu_2(dppm)_2(NCMe)_2](PF_6)_2$ and $K_2$cpdt.[23] The $Cu^{II}$ complexes are represented by the mononuclear species $[Cu(i\text{-mnt})_2]^{2-}$,[12,24] $[Cu(ded)_2]^{2-}$,[25,26] and [Cu(*i*-mnt)(N–N)] (N–N = 1,2-ethanediamines).[27] The $Cu^{III}$ complex $[Cu(ded)_2]^-$ has also been prepared by the oxidation of $[Cu(ded)_2]^{2-}$ with $H_2O_2$, $I_2$, or $Cu^{2+}$ ions.[25,26]

Part of our recent research in this field has been devoted to the coordination chemistry of the (fluoren-9-ylidene)me-

[‡] (Fluoren-9-ylidene)methanedithiolato Complexes, 3. Part 1: Ref.[28] Part 2: Ref.[29]

[a] Grupo de Química Organometálica, Departamento de Química Inorgánica, Facultad de Química, Universidad de Murcia, Apdo. 4021, 30071 Murcia, Spain
E-mail: jvs1@um.es; pgh@um.es
URL: http://www.um.es/gqo
[b] Institut für Anorganische und Analytische Chemie, Technische Universität Braunschweig, Postfach 3329, 38023 Braunschweig, Germany
E-mail: p.jones@tu-bs.de
[c] SACE, Universidad de Murcia, Apdo. 4021, 30071 Murcia, Spain

Supporting information for this article is available on the WWW under http://www.eurjic.org or from the author.

 © 2006 Wiley-VCH Verlag GmbH & Co. KgaA, Weinheim 

thanedithiolato ligand and its 2,7-disubstituted derivatives. These ligands have revealed remarkable differences with respect to the previously used 1,1-ethylenedithiolates; these differences are largely attributable to the absence of strongly electron-withdrawing substituents and affect the photophysical properties and redox behavior of their metal complexes.[28,29] Given the multiple coordination possibilities and stoichiometries observed for copper/dithiolate systems, we thought it of interest to carry out an initial exploration of the chemistry of copper complexes with (2,7-di-*tert*-butylfluoren-9-ylidene)methanedithiolate [(*t*Bu-fy)=$CS_2^{2-}$ (**I**) Scheme 1], and to study the effects of the strongly electron-donating character of this ligand on their structures and reactivity. In this paper, we describe the preparation of a series of $Cu^{I}$ complexes with 2,7-di-*tert*-butyl-9*H*-fluorene-9-carbodithioate [(*t*Bu-Hfy)$CS_2^-$ (**II**), the protonated precursor of **I**] obtained from the piperidinium salt (pipH)[(*t*Bu-Hfy)$CS_2$] (**1**), which, upon deprotonation in the presence of an oxidizing agent, afford dinuclear complexes with the new ligand S[(*t*Bu-fy)=$CS]_2^{2-}$ (**III**), formally resulting from the condensation of two dithiolates with loss of a sulfide ion and two protons. The direct syntheses of $Cu^{I}$, $Cu^{II}$, and $Cu^{III}$ complexes containing the (*t*Bu-fy)=$CS_2^{2-}$ ligand from **1** and suitable copper precursors are reported.

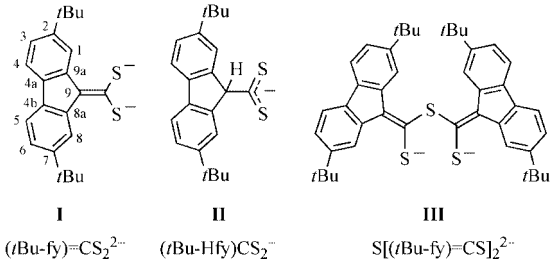


Scheme 1.

## Results and Discussion

### Copper(I) Complexes with the (*t*Bu-Hfy)$CS_2^-$ Ligand

The previously described metal complexes with the (fluoren-9-yliden)methanedithiolato ligand and its 2,7-disubstituted analogs were obtained by treating appropriate metal precursors with the corresponding piperidinium fluorene-9-carbodithioate in the presence of a base. The deprotonation of the dithiolato ligand to form the corresponding dithiolate takes place after its coordination to the metal center, which increases the acidity of the H9 atom on the fluoren-9-yl moiety. In some cases, dithioato complexes have been obtained when the reactions are carried out in the absence of a base.[28] The synthesis of $Cu^{I}$ complexes with (*t*Bu-Hfy)-$CS_2^-$ was undertaken in order to use them as precursors for the preparation of complexes with the dithiolato ligand (*t*Bu-fy)$CS_2^{2-}$.

The reaction of the piperidinium dithioate **1** with $[Cu(NCMe)_4]PF_6$ in a 1:1 molar ratio in MeCN gave the dark brown complex $[Cu_n\{S_2C(tBu\text{-}Hfy)\}_n]$ (**2**; Scheme 2), which precipitated in almost quantitative yield. Complex **2** is scarcely soluble in most organic solvents and all attempts to grow crystals suitable for X ray diffraction studies were unsuccessful. Its $^1H$ NMR spectrum displays only one set of signals for the dithioato ligand, suggesting a highly symmetrical oligomeric structure. A tetrameric structure has been found for the related copper(I) dithioate $[Cu_4(S_2CC_6H_4Me\text{-}p)_4]$[30] (Figure 1, a). Compound **2** was

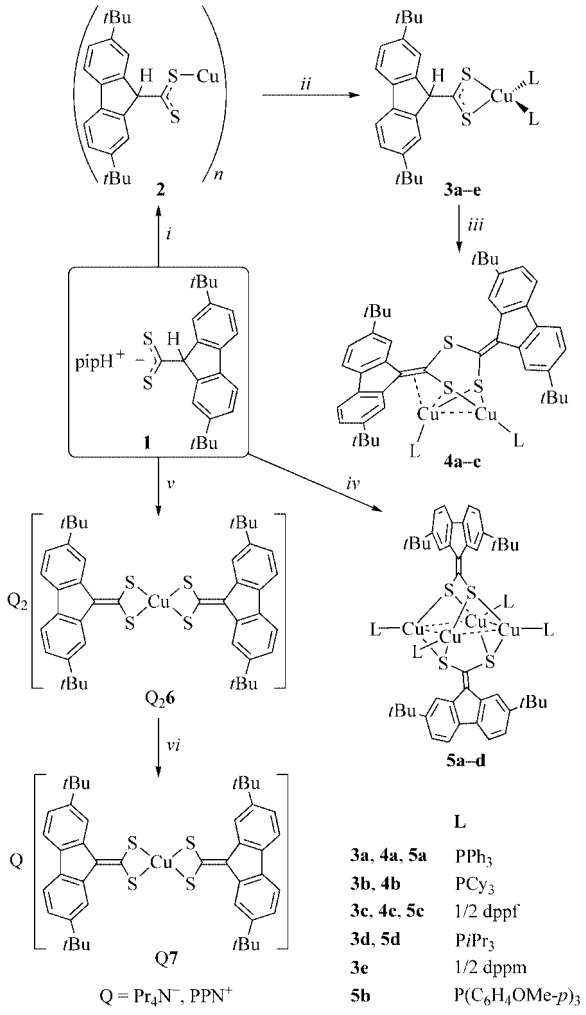


Scheme 2. (i) $[Cu(NCMe)_4]PF_6$; (ii) 2L; (iii) $NEt_3$, $O_2$ (air) or 1/2 1,4-benzoquinone; (iv) 2 $[Cu(NCMe)_4]PF_6$, 2L, pip; (v) 1/2 $Cu(ClO_4)_2{\cdot}6H_2O$, $(Pr_4N)OH$ or 1/2 $CuCl_2$, PPNCl, pip; (vi) $O_2$ (air).

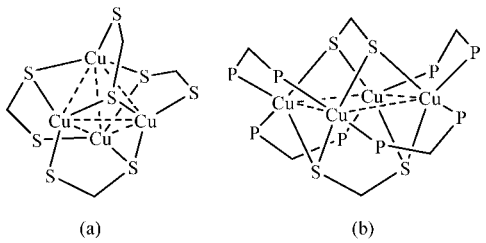


Figure 1. Structures of the $Cu_4S_8$ core in $[Cu_4(S_2CC_6H_4Me\text{-}p)_4]$ (a) and the $Cu_4S_4P_8$ core in $[Cu_4(cpdt)_2(dppm)_4]$ (b).

 © 2006 Wiley-VCH Verlag GmbH & Co. KGaA, Weinheim 

employed as starting material for the preparation of the series of complexes [Cu{$S_2C$(*t*Bu-Hfy)}$L_2$] with L = $PPh_3$ (**3a**), $PCy_3$ (**3b**), P*i*$Pr_3$ (**3d**), or $L_2$ = dppf (**3c**), dppm (**3e**). The products were obtained as salmon-pink or orange solids from the reactions of **2** with the corresponding phosphane (1:2) or diphosphane (1:1) and isolated in moderate to high yields.

### Deprotonation and Oxidation of Dithioato Complexes. Dithiolate Condensation

The deprotonation of the dithioato ligand (*t*Bu-Hfy)$CS_2^-$ in complexes **2** and **3a**–**e** was attempted by using $NEt_3$ as the base. The expected results of these reactions included the formation of anionic clusters. In the case of **3a**–**e**, anionic complexes of the type [Cu{$S_2C$=(*t*Bu-fy)}$(PR_3)_2$]$^-$ were expected as the primary products, since an analogous mononuclear complex with the *i*-mnt ligand has been described.[31] However, complexes **2** and **3a**–**e** were recovered unchanged after treatment with $NEt_3$ in MeCN or THF under an inert atmosphere. A different, unexpected result was obtained when the reactions were carried out in the presence of atmospheric oxygen and moisture. Thus, under these conditions, treatment of **3a** with $NEt_3$ in a 1:1 molar ratio in MeCN led to the gradual formation of a green solution from which a yellowish orange solid precipitated after 4 h. The X-ray structure analysis of a single crystal of this product revealed the formation of the dinuclear complex [$Cu_2${[SC=(*t*Bu-fy)]$_2$S}$(PPh_3)_2$] (**4a**), which contains only one $PPh_3$ per Cu and a new dithiolato ligand that formally results from the condensation of two (*t*Bu-Hfy)$CS_2^-$ ligands with loss of a sulfide ion and two protons (Scheme 2). The yield of **4a** was 67% after recrystallization. The oily residue obtained by evaporation of the supernatant contained $Ph_3P$=S, $Ph_3P$=O, and free $PPh_3$ as the major components, as determined by $^1$H and $^{31}$P NMR spectroscopy. Additionally, a very small amount of the dithiolato complex [$Cu_4${$S_2C$=(*t*Bu-fy)}$_2(PPh_3)_4$] (**5a**; see below) was produced. The formation of **4a** also took place when stirring **3a** in MeCN under aerobic conditions in the absence of $NEt_3$, but the reaction was much slower. It is therefore clear that an oxidant is required for this reaction to take place and that the deprotonation does not require an added base. Finally, the reaction of **3a** with the oxidant base 1,4-benzoquinone in a 2:1 molar ratio was carried out under a nitrogen atmosphere in MeCN at room temperature. Under these conditions, the gradual formation of a yellowish orange precipitate of **4a** was observed within seven hours. The product was isolated in 73% yield after recrystallization and the compounds $Ph_3P$=S, 1,4-hydroquinone, and free $PPh_3$ were identified by $^1$H and $^{31}$P NMR spectroscopy as the major components present in the supernatant.

The analogous complexes [$Cu_2${[SC=(*t*Bu-fy)]$_2$S}$L_2$] with L = $PCy_3$ (**4b**) or $L_2$ = dppf (**4c**) were similarly obtained by stirring suspensions of **3b** or **3c**, respectively, in MeCN in the presence of $NEt_3$ and atmospheric oxygen. The yield of **4b** (75%) was appreciably higher than of **4c** (51%) because of the formation of considerable amounts of the dithiolato complex [$Cu_4${$S_2C$=(*t*Bu-fy)}$_2$(dppf)$_2$] (**5c**; see below). Under the same conditions, compound **2** or the dppm derivative **3e** did not give products of definite composition, while in the case of the P*i*$Pr_3$ derivative **3d** a mixture that contained the corresponding dithiolato complex **5d** as the main component was obtained.

A possible reaction path leading to the formation of **4a**–**c** is outlined in Scheme 3. It is very likely that in the initial steps the deprotonation and oxidation of the dithioato complexes **3a**–**c** to give a $Cu^{II}$ intermediate (**A**) take place, which would account for the green color of the initial reaction mixtures. This species can be considered an oxidized analog of the reported $Cu^{I}$ complex [Cu(*i*-mnt)$(PR_3)_2$]$^-$.[31] It is well known that the combination of $Cu^{II}$ with thiolates usually results in reduction to $Cu^{I}$ and formation of disulfides.[10,32,33] Such a process would cause intermediate **A** to dimerize and form a disulfide-bridged dinuclear species such as **B**, which would subsequently undergo sulfur abstraction by one of the phosphanes to give the final monosulfide-bridged dithiolate. Tetraalkylthiuram disulfides $R_2NC(S)SSC(S)NR_2$ have been reported to undergo a similar reaction when treated with $Cu^{I}$ halides in the presence of $PPh_3$, which leads to the formation of complexes containing the corresponding monosulfide $R_2NC(S)SC(S)NR_2$.[34] The formation of the condensed ligand in **4a**–**c** is also related to the well-established reactions of organic disulfides with phosphanes, which afford thioethers and phosphane sulfide, although they usually require more vigorous reaction conditions, such as refluxing in high boiling point solvents.[35–37]

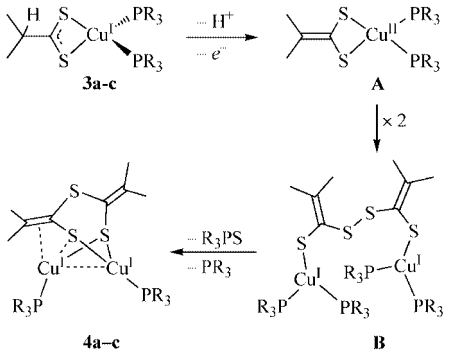


Scheme 3. Proposed reaction path for the formation of **4a**–**c** from **3a**–**c**. *t*Bu-fy groups have been omitted for clarity.

In contrast, similar sulfide-bridged dithiolato ligands have not been produced from previously described dithioato complexes of the type [Cu($S_2$CR)$(PR'_3)_2$] containing a hydrogen atom in the β position, such as those with R = Me,[38] or CH=C(OH)$C_6H_4$Me-*p*.[39] Both the presence of the relatively acidic H9 hydrogen atom in (*t*Bu-Hfy)$CS_2^-$ and the electron-donating ability of (*t*Bu-fy)=$CS_2^{2-}$ appear to be crucial for the initial deprotonation/oxidation steps leading to **4a**–**c**.

 © 2006 Wiley-VCH Verlag GmbH & Co. KGaA, Weinheim 

### Copper(I) Complexes with the (*t*Bu-fy)=$CS_2^{2-}$ Ligand and Phosphanes

The neutral $Cu^I$ complexes $[Cu_4\{S_2C=(tBu\text{-}fy)\}_2L_4]$ [L = $PPh_3$ (**5a**), $P(C_6H_4OMe\text{-}p)_3$ (**5b**) and $PiPr_3$ (**5d**) or $L_2$ = dppf (**5c**)] were obtained by treating **1** with $[Cu(NCMe)_4]PF_6$, the corresponding phosphane, and piperidine in a 1:2:2:1 molar ratio in MeCN (Scheme 2). The products precipitate in this solvent as bright yellow (**5a**,**b**,**d**) or yellowish orange (**5c**) microcrystalline solids and can be isolated in moderate to high yields. Compounds **5a**–**d** display a moderate stability in solution, which depends on the phosphane; thus, the $PiPr_3$ complex **5d** is the least stable and decomposes in $CDCl_3$ within 2 h, while the $CDCl_3$ solutions of the $P(C_6H_4OMe\text{-}p)_3$ complex **5b** are stable for more than 24 h. The preparation of analogous complexes with $PCy_3$ or dppm did not succeed under similar conditions, probably because of their lower stabilities.

The structures of **5a**–**d** could not be determined by X-ray diffraction studies because the crystals were not of sufficient quality or presented severe twinning problems. However, their composition and the copper/dithiolate/phosphane ratio were unambiguously determined by means of elemental analyses and $^1H$ NMR spectroscopy (see Experimental Section for details). The $^1H$, $^{13}C$, and $^{31}P$ NMR spectroscopic data are consistent with highly symmetrical structures containing equivalent dithiolato ligands and phosphanes. Given the preference of $Cu^I$ for a trigonal planar or tetrahedral coordination geometry and its tendency to form high nuclearity thiolato complexes with extensive cuprophilic interactions, a dinuclear formulation for **5a**–**d** is unlikely. Evidence for a tetranuclear formulation was obtained from their positive-ion FAB mass spectra. The tetranuclear $[M^+]$ ions are observed with very low relative abundances for **5b** ($m/z$ = 2368) and **5c** ($m/z$ = 2068). Heavier ions are not observed, except for the $[M + Cu]^+$ ions. All four complexes undergo very extensive fragmentations in FAB, which result in the loss of phosphane ligands and $CuL^+$ units and/or the cleavage of C–S bonds to form sulfide complexes, most of which are tetranuclear. Significantly abundant fragments that support the tetranuclear formulation are $[Cu_4\{S_2C=(tBu\text{-}fy)\}_2L_3]^+$ for **5b**, $[Cu_4S\{S_2C=(tBu\text{-}fy)\}L]^+$ and $[Cu_4S\{S_2C=(tBu\text{-}fy)\}_2L]^+$ for **5a**,**b**, $[Cu_4\{S_2C=(tBu\text{-}fy)\}_2L]^+$ and $[Cu_4\{S_2C=(tBu\text{-}fy)\}_2]^+$ for **5a**,**d**, and $[Cu_4S\{S_2C=(tBu\text{-}fy)\}(dppf)_2]^+$ for **5c** (see Supporting Information). Tetranuclear structures have been found for the related complexes $[M_4(cpdt)_2(dppm)_4]$ (M = Cu[23] and Ag[40]), $[Ag_4(i\text{-}mnt)_2(dppm)_4]$,[41] and $[Cu_4(CS_3)_2(dppm)_4]$,[42] which have their metal atoms in a nearly planar arrangement and the dithiolato ligands acting as bridging tetradentate ligands above and below the $M_4$ core (Figure 1, b). The structures of **5a**–**d** probably have similar $Cu_4S_4$ cores but with four phosphane groups instead of eight (Scheme 2), which would be consistent with their NMR spectroscopic data.

Complexes **5a**–**d** are luminescent at room temperature in the solid state and also in solution at 77 K. Their excitation and emission properties are currently under investigation and a complete study will be reported elsewhere.

### Copper(II) and Copper(III) Complexes with the (*t*Bu-fy)=$CS_2^{2-}$ Ligand

The poorly soluble $Cu^{II}$ complex $(Pr_4N)_2[Cu\{S_2C=(tBu\text{-}fy)\}_2]$ [$(Pr_4N)_2$**6**] precipitated as a brown solid upon treatment of the dithioate **1** with $Cu(ClO_4)_2{\cdot}6H_2O$ and $(Pr_4N)OH$ in a 2:1:2 molar ratio in MeCN under an inert atmosphere, (Scheme 2). Although [$(Pr_4N)_2$**6**] is air stable in the solid state, it is slowly oxidized by atmospheric oxygen to the $Cu^{III}$ complex $[Cu\{S_2C=(tBu\text{-}fy)\}_2]^-$ (**7**) when suspended in MeCN or $CH_2Cl_2$. Thus, the green salt $Pr_4N$**7** was obtained almost quantitatively by bubbling air through an MeCN suspension of $(Pr_4N)_2$**6**. Alternatively, $Pr_4N$**7** was obtained in high yield when the reaction of **1** with $Cu(ClO_4)_2{\cdot}6H_2O$ and $(Pr_4N)OH$ was carried out under atmospheric conditions. The salt PPN**7** was similarly obtained from **1**, $CuCl_2{\cdot}2H_2O$, PPNCl, and piperidine in a 2:1:1:2 molar ratio. The only previously reported $Cu^{III}$ complex with a 1,1-ethylenedithiolato ligand is $[Cu(ded)_2]^-$, which was prepared from the oxidation of $[Cu(ded)_2]^{2-}$ with $H_2O_2$, $I_2$, or $Cu^{2+}$ ions.[25,26] In comparison, the formation of the $Cu^{III}$ complex **7** takes place under milder conditions and represents an uncommon example of aerobic oxidation of a $Cu^{II}$ complex. We have previously observed that the (fluoren-9-ylidene)methanedithiolato ligand and its 2,7-disubstituted derivatives facilitate the oxidation of $Au^I$ to $Au^{III}$ [28] and $Pt^{II}$ to $Pt^{IV}$,[29] which can be attributed to their stronger electron-donating character as compared with other, more commonly studied 1,1-ethylenedithiolato ligands.

### Crystal Structures of the Complexes

The crystal structures of **3a** (Figure 2), **3c**·$CH_2Cl_2$ (Figure 3), **4a**·$4Me_2CO$ (Figure 4), and **4c**·$CH_2Cl_2$ (Figure 5) were solved by X-ray diffraction studies. Selected bond lengths and angles are listed in Tables 1, 2, and 3. The molecular structures of **3a** and **3c** show the copper atom in a distorted tetrahedral environment. The main distortion originates from the constraints imposed by the four-membered chelate ring, which lead to S–Cu–S angles of 74.48(2)° (**3a**) and 74.38(3)° (**3c**). The steric hindrance of the $PPh_3$ ligands leads to a relatively wide P(1)–Cu–P(2) angle of 129.25(3)° in **3a**. The chelating dppf ligand in **3c** adopts a staggered conformation leading to a bite angle of 112.76(4)°, which is closer to the ideal value for a tetrahedral geometry. Similar coordination environments around the Cu atom and Cu–S bond lengths have been found in the analogous dithioato complexes $[Cu(S_2CR)(PPh_3)_2]$ [R = Me,[38] Ph,[43] *p*-To,[30] $C_5Me_5$[44] $CO_2Me$[45] and $CH{=}C(OH)C_6H_4Me\text{-}p$].[39]

 © 2006 Wiley-VCH Verlag GmbH & Co. KGaA, Weinheim 

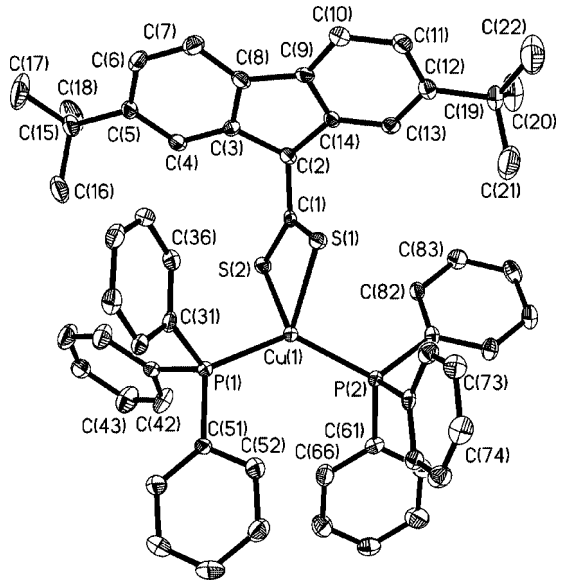


Figure 2. Thermal ellipsoid plot (50% probability) of complex **3a**. H atoms have been omitted for clarity.

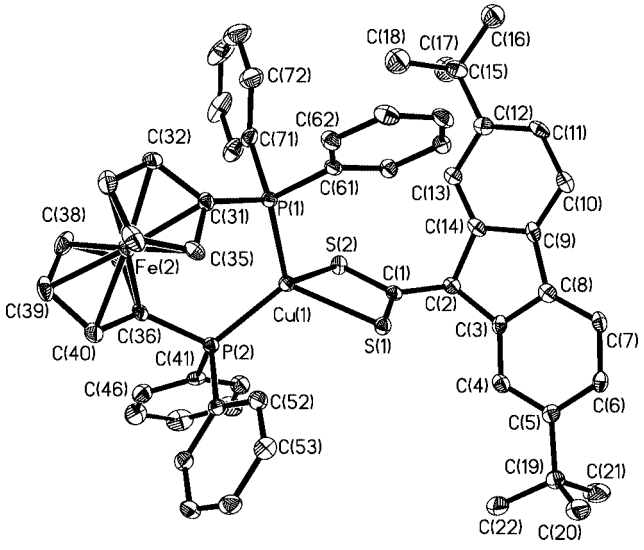


Figure 3. Thermal ellipsoid plot (50% probability) of complex **3c**. H atoms have been omitted for clarity.

Complexes **4a** and **4c** exhibit essentially the same structural arrangement for the $Cu_2\{[SC=(t\text{Bu-fy})]_2S\}$ unit as the condensed dithiolato ligand coordinates to the two copper atoms in different ways. The atom Cu(1) is bonded to the two terminal sulfur atoms S(1) and S(2) and one $PPh_3$ ligand (or one of the $PPh_2$ units of dppf), resulting in a slightly distorted trigonal planar geometry, whereas the atom Cu(2) is attached to the other $PPh_3$ ligand or the second $PPh_2$ unit, and to the dithiolato ligand through the C(29)=C(30) double bond and the terminal S(1) atom, which thus bridges the two copper atoms. The coordination around Cu(2) is also trigonal planar if we consider the atoms S(1), P(1), and the C(29)=C(30) bond centroid. The Cu(1)–S(2) and Cu(2)–S(1) bond lengths are very similar [range 2.2156(10)–2.2659(9) Å] and slightly shorter than the

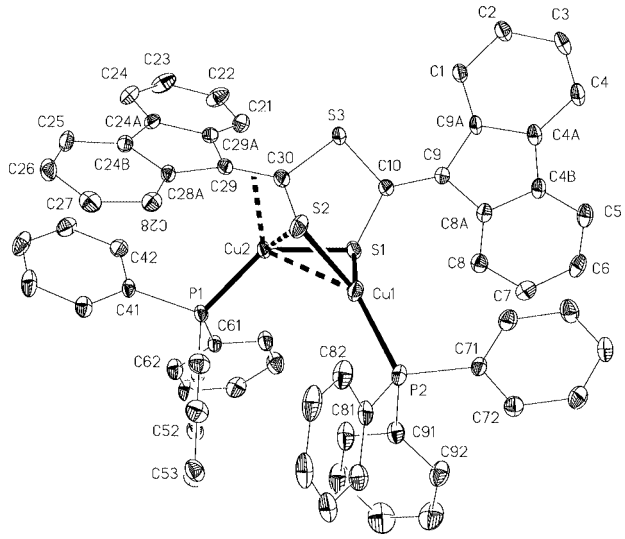


Figure 4. Thermal ellipsoid plot (30% probability) of complex **4a**. H atoms and *t*Bu groups have been omitted for clarity.

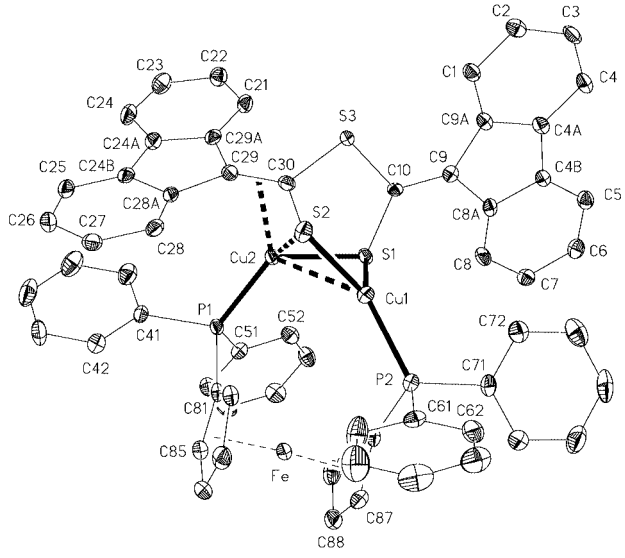


Figure 5. Thermal ellipsoid plot (50% probability) of complex **4c**. H atoms and *t*Bu groups have been omitted for clarity.

Table 1. Selected bond lengths [Å] and angles [°] for **3a** and **3c**·$CH_2Cl_2$.

| | **3a** | **3c**·$CH_2Cl_2$ |
|---|---|---|
| Cu(1)–S(1) | 2.3901(8) | 2.4196(9) |
| Cu(1)–S(2) | 2.4357(8) | 2.3806(10) |
| Cu(1)–P(1) | 2.2449(7) | 2.2433(9) |
| Cu(1)–P(2) | 2.2413(8) | 2.2325(10) |
| S(1)–C(1) | 1.674(3) | 1.680(4) |
| S(2)–C(1) | 1.693(3) | 1.694(3) |
| C(1)–C(2) | 1.520(4) | 1.520(5) |
| S(1)–Cu(1)–S(2) | 74.48(2) | 74.38(3) |
| P(1)–Cu(1)–P(2) | 129.25(3) | 112.76(4) |
| S(1)–C(1)–S(2) | 120.30(16) | 118.7(2) |

Cu(1)–S(1) distance [2.3413(10) (**4a**) or 2.3298(11) Å (**4c**)]. There is also an appreciably longer Cu(2)–S(2) distance of 2.7336(9) (**4a**) or 2.7878(11) Å (**4c**), which is indicative of a much weaker interaction. The distance of Cu(1) to the

 © 2006 Wiley-VCH Verlag GmbH & Co. KGaA, Weinheim 

Table 2. Selected bond lengths [Å] and angles [°] for **4a**·4Me$_2$CO.

| | | | |
|---|---|---|---|
| Cu(1)–P(2) | 2.2053(9) | Cu(2)–S(2) | 2.7336(9) |
| Cu(1)–S(2) | 2.2576(9) | S(1)–C(10) | 1.773(3) |
| Cu(1)–S(1) | 2.3413(10) | S(2)–C(30) | 1.763(3) |
| Cu(1)–Cu(2) | 2.6999(5) | S(3)–C(10) | 1.769(3) |
| Cu(2)–C(30) | 2.087(3) | S(3)–C(30) | 1.773(3) |
| Cu(2)–P(1) | 2.2069(8) | C(9)–C(10) | 1.360(4) |
| Cu(2)–C(29) | 2.255(3) | C(29)–C(30) | 1.401(4) |
| Cu(2)–S(1) | 2.2659(9) | | |
| P(2)–Cu(1)–S(2) | 128.30(4) | C(10)–S(1)–Cu(1) | 89.29(11) |
| P(2)–Cu(1)–S(1) | 128.92(3) | Cu(2)–S(1)–Cu(1) | 71.73(3) |
| S(2)–Cu(1)–S(1) | 102.76(3) | C(30)–S(2)–Cu(1) | 98.61(10) |
| P(1)–Cu(2)–S(1) | 124.26(3) | Cu(1)–S(2)–Cu(2) | 64.68(2) |
| P(1)–Cu(2)–S(2) | 124.23(3) | C(10)–S(3)–C(30) | 103.78(14) |
| S(1)–Cu(2)–S(2) | 91.42(3) | S(3)–C(10)–S(1) | 115.50(16) |
| C(10)–S(1)–Cu(2) | 105.47(10) | S(2)–C(30)–S(3) | 116.71(16) |

Table 3. Selected bond lengths [Å] and angles [°] for **4c**·$CH_2Cl_2$.

| | | | |
|---|---|---|---|
| Cu(1)–P(2) | 2.1821(10) | Cu(2)–S(2) | 2.7878(11) |
| Cu(1)–S(2) | 2.2156(10) | S(1)–C(10) | 1.757(3) |
| Cu(1)–S(1) | 2.3298(11) | S(2)–C(30) | 1.774(4) |
| Cu(1)–Cu(2) | 2.7568(6) | S(3)–C(10) | 1.772(3) |
| Cu(2)–C(30) | 2.114(3) | S(3)–C(30) | 1.790(3) |
| Cu(2)–P(1) | 2.2172(10) | C(9)–C(10) | 1.369(5) |
| Cu(2)–S(1) | 2.2529(9) | C(29)–C(30) | 1.396(5) |
| Cu(2)–C(29) | 2.256(3) | | |
| P(2)–Cu(1)–S(2) | 137.20(4) | C(10)–S(1)–Cu(1) | 92.13(12) |
| P(2)–Cu(1)–S(1) | 118.41(4) | Cu(2)–S(1)–Cu(1) | 73.94(3) |
| S(2)–Cu(1)–S(1) | 103.77(4) | C(30)–S(2)–Cu(1) | 98.77(11) |
| P(1)–Cu(2)–S(1) | 118.84(4) | Cu(1)–S(2)–Cu(2) | 65.71(3) |
| P(1)–Cu(2)–S(2) | 127.88(4) | C(10)–S(3)–C(30) | 104.51(15) |
| S(1)–Cu(2)–S(2) | 89.76(3) | S(1)–C(10)–S(3) | 117.10(18) |
| C(10)–S(1)–Cu(2) | 106.48(11) | S(2)–C(30)–S(3) | 115.10(19) |

C(29)=C(30) bond centroid of 2.056 (**4a**) or 2.072 Å (**4c**) is close to the upper limit of the range found for the majority of alkene complexes of copper(I) in the Cambridge Structural Database (1.840–2.110 Å).[46] The bond length of the uncoordinated C(9)=C(10) double bond [1.360(4) (**4a**) or 1.369(5) Å (**4c**)] is similar to the corresponding distances found for 1,1-ethylenedithiolato ligands,[28] which are usually close to the higher limit of the range found for C(sp$^2$)=C(sp$^2$) double bonds (1.294–1.392 Å),[47] whereas the C(29)–C(30) distance of 1.401(4) (**4a**) or 1.396(5) Å (**4c**) is slightly longer, as expected for a coordinated C=C bond. The Cu(1)–Cu(2) distance of 2.6999(5) (**4a**) or 2.7568(6) Å (**4c**) is slightly shorter than the sum of the van der Waals radii for Cu (2.80 Å[48]) and typical of the cuprophilic interactions found in numerous di- or polynuclear copper(I) complexes with bridging thiolato ligands.[49–53] The planes S(1)–C(10)–S(3) and S(3)–C(30)–S(2) form an angle of 75° (**4a**) or 77° (**4c**). The fluoren-9-ylidene fragments are nearly planar, with their respective mean planes being perpendicular to each other [89° (**4a**) or 90° (**4c**)] and slightly rotated with respect to the corresponding S–C–S planes. The dppf ligand in **4c** adopts an eclipsed conformation, with the P(1)–C(81) and P(2)–C(86) bonds rotated by 79° with respect to each other. This results in a large distance between both phosphorus atoms (5.275 Å) and allows the flexible dppf ligand to bridge the copper atoms in such a way that the $PPh_2$ groups occupy the same positions as the two independent $PPh_3$ ligands in **4a** (P···P = 5.438 Å).

## NMR Spectra

The $^1$H and $^{13}$C{$^1$H} NMR spectra of complexes **2** and **3a**–**e** show one set of signals for the protons and carbon atoms of the dithioato ligand, which are slightly modified with respect to those of the free dithioate **1**,[54] with the 9-H resonance in the range $\delta$ = 5.35–5.68 ppm and the *C*S$_2$ resonance in the range $\delta$ = 251.5–259.3 ppm. On the basis of these data, complex **2** most probably has a highly symmetrical oligomeric structure (see above).

The crystal structures of **4a** and **4c** show that the condensed ligand contains two *t*Bu-fy groups in different environments. Because the rotation around the C9=CS$_2$ double bonds is expected to be hindered at room temperature, the two halves of each of these groups are not equivalent. Therefore, if their solid-state structures were retained in solution, the $^1$H and $^{13}$C{$^1$H} NMR spectra of **4a**–**c** should display the resonances corresponding to four different *t*Bu groups, four sets of signals for the aromatic H and C atoms, and two signals for both the C9 and CS$_2$ atoms. Additionally, two different resonances should be expected in the $^{31}$P NMR spectra. However, the $^1$H, $^{13}$C{$^1$H}, and $^{31}$P{$^1$H} NMR spectra of **4a**–**c** reveal that the *t*Bu-fy groups are equivalent in solution, as are the two $PPh_3$ or $PCy_3$ ligands in **4a**,**b** or the $PPh_2$ groups of the dppf ligand in **4c**. Thus, the $^1$H NMR spectra show only two singlets for the *t*Bu groups and two sets of resonances for the aromatic protons; the two signals corresponding to the 1-H and 8-H atoms are considerably downfield-shifted, as is the case for coordinated (fluoren-9-ylidene)methanedithiolato ligands,[28] and also the most affected by the lack of symmetry of the *t*Bu-fy groups, appearing at very different chemical shifts (ranges $\delta$ = 9.61–9.71 and 8.55–8.69 ppm, respectively). The $^{13}$C{$^1$H} NMR spectra show two sets of resonances for the carbon atoms of the ligand except for the C-9 and CS$_2$ atoms, each of which gives rise to only one resonance; the CS$_2$ resonance appears as a slightly broad signal for **4a**,**b**, but in the case of **4c** resolves as a triplet because of coupling with two equivalent phosphorus atoms. The $^{31}$P NMR spectra show a relatively broad singlet. The dppf ligand in **4c** gives rise to six multiplets in the room temperature $^1$H NMR spectrum corresponding to the two inequivalent Ph rings of each $PPh_2$ group, and four broad resonances corresponding to the protons of the two equivalent Cp rings. This means that the diphosphane is essentially rigid in solution and does not undergo the fluxional process observed in **5c** (see below) and other metal complexes with bridging dppf,[55–60] which involves a conformation change leading to the equivalence of the phenyl groups and the two $H_\alpha$ and $H_\beta$ atoms of the Cp rings on the NMR timescale. The absence of any dynamic process affecting the dppf ligand was further confirmed by a variable-temperature NMR study of **4c**, which revealed no changes in the $^1$H and $^{31}$P resonances arising from this diphosphane between –65 and +50 °C in $CDCl_3$.

 © 2006 Wiley-VCH Verlag GmbH & Co. KGaA, Weinheim 

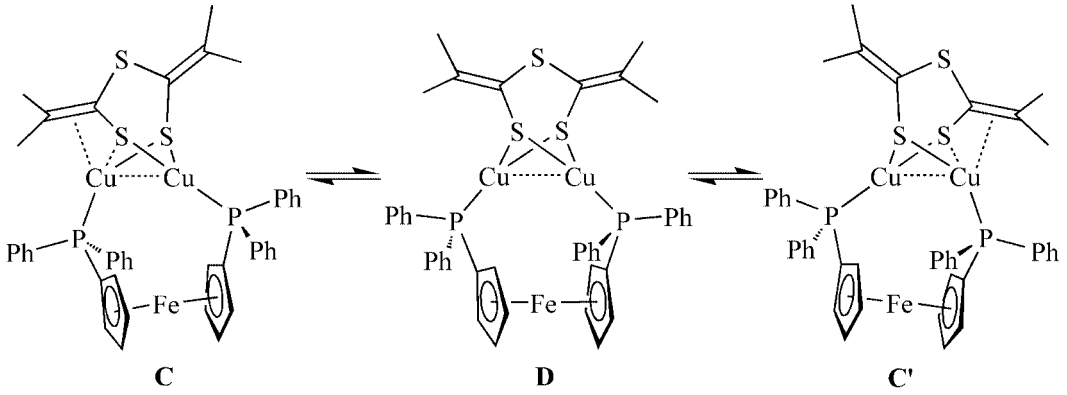


Scheme 4. *t*Bu-fy groups have been omitted for clarity.

In view of these observations, the two possible explanations for the NMR spectroscopic data of **4a**–**c** are: (*i*) the existence of a dynamic process mainly affecting the $Cu_2\{[SC=(t\text{Bu-fy})]_2S\}$ unit that causes the copper atoms to interchange their coordination environments, or (*ii*) a different, symmetrical structure of the complexes in solution. The possible dynamic process is represented in Scheme 4 for **4c**. The transition from the solid state form **C** (or its equivalent **C**′) to the intermediate, $C_2$-symmetrical form **D** requires only minor rearrangements of the molecules involving the rupture of the relatively weak coordination of C(29)=C(30) to Cu(2) and the strengthening of the Cu(2)–S(2) interaction to form a symmetrical bridge, while retaining the conformation of the dppf ligand. However, the $^1H$ and $^{31}P$ NMR spectra of **4a**–**c** show that the signals arising from the condensed ligand and the phosphorus atoms do not split, even at –90 °C in $CD_2Cl_2$, which could be due to a very low activation energy and/or to negligible differences in the chemical shifts of the H nuclei of the inequivalent *t*Bu-fy groups (or the P nuclei of the phosphanes) in form **C**. The possibility that the actual structure in solution is form **D** would also be consistent with the experimental observations; in this case, the arrangement found in the solid-state structures would most probably be a consequence of packing forces in the crystals.

The $^1H$ and $^{13}C\{^1H\}$ NMR spectra of complexes **5a**–**d** display very similar sets of resonances for the protons and carbon atoms of the $(t\text{Bu-fy})=CS_2^{2-}$ ligand, which indicate that all of them have similar structures with equivalent and symmetrical dithiolates. The resonances of the 1-H and 8-H atoms are typically downfield-shifted (range $\delta$ = 9.37–9.54 ppm). The resonances of the Ph and Cp protons of the dppf ligand in **5c** are observed as broad signals at room temperature, suggesting fluxional behavior. At –40 °C, the Cp resonances resolve into four signals, while the Ph rings give rise to five broad signals, indicating that the two Cp rings and $PPh_2$ groups of each dppf are equivalent, while the two Ph rings of each $PPh_2$ group are not. The fluxional behavior of a bridging dppf ligand has been observed previously and thoroughly described for other di- or polynuclear complexes.[55–60] The opposite twisting of the two halves of the ferrocene fragment around the Cp centroid–centroid axis, together with the concerted twist around the P–$C_{ipso(Cp)}$ and P–Cu bonds, causes the two $H_\alpha$ and $H_\beta$ atoms and the Ph rings on each $PPh_2$ group to exchange their positions. The resonances of the protons of the dithiolato ligands in **5c** remain practically unchanged between –40 and 25 °C.

The $^1H$ NMR spectrum of the $Cu^{II}$ complex $(Pr_4N)_2$**6** in $CDCl_3$ shows broad signals for the $Pr_4N^+$ cation, while the resonances corresponding to the ligand protons are not observed, which can be attributed to its paramagnetic nature. The $^1H$ and $^{13}C$ NMR spectroscopic data of the Q**7** salts (Q = $Pr_4N^+$, $PPN^+$) are fully consistent with a square-planar structure. The chemical shifts of the H and C resonances of the dithiolato ligand are very similar to those observed for the analogous $Au^{III}$ complex.[28]

## IR Spectra

The solid-state infrared spectrum of the dithioato complex **2** displays one band at 975 $cm^{-1}$ assignable to one of the two $\nu(CS_2)$ modes,[43] while for the phosphane complexes **3a**–**e** the corresponding absorption appears around 1010 $cm^{-1}$. The dinuclear complexes **4a**–**c** give rise to one band associated with the $C=CS_2$ double bonds at around 1500 $cm^{-1}$. The expected $\nu(C=CS_2)$ band[61] arising from the $(t\text{Bu-fy})=CS_2^{2-}$ ligand in complexes **5a**–**d** occurs in the range 1482–1490 $cm^{-1}$, while for the $Cu^{II}$ complex $(Pr_4N)_2$**6** it is observed at 1480 $cm^{-1}$ and for the $Cu^{III}$ salts Q**7** at 1548 ($Pr_4N^+$) or 1552 $cm^{-1}$ ($PPN^+$). We have previously shown that the variations in the energies of the $\nu(C=CS_2)$ bands can be attributed to the oxidation state of the metal center and the nature of the ligands attached to it, which affect the strength of the $\pi$ component of the $C=CS_2$ bond.[28] Usually, a higher oxidation state and/or the presence of weaker donor ligands increase the energy of the $\nu(C=CS_2)$ band, which is consistent with the high energy observed for the $Cu^{III}$ complex. The spectra of the salts Q**7** also show one intense band at 416 ($Pr_4N^+$) or 420 $cm^{-1}$ ($PPN^+$) assignable to the $\nu$(Cu–S) mode.

 © 2006 Wiley-VCH Verlag GmbH & Co. KGaA, Weinheim 

### Electronic Absorption Spectra

The UV/Visible absorption spectra of compounds **2**–**7** were measured in the range 200–700 nm in $CH_2Cl_2$ at 298 K. All of them display the bands arising from the aromatic part of the dithioato or dithiolato ligands at around 230, 260–270 and 300 nm.[28] The bands above 300 nm are listed in Table 4. The low intensity band centered at about 360 nm for dithioato complexes **3a**–**d** is probably the result of the modification of the band observed for the free dithioate **1b** at 346 nm, which arises from n–π* transitions within the $CS_2^-$ group. In the case of **3e** ($L_2$ = dppm) this band appears at 391 nm. The spectrum of compound **2** shows two very broad bands at 393 and 438 nm, which are probably also related to these transitions.

Table 4. Electronic absorption data for compounds **2**–**7** in $CH_2Cl_2$ solution (ca. $5\times10^{-5}$ M) at 298 K ($\lambda > 300$ nm).

| Compound | $\lambda$ [nm] ($\varepsilon$ [$M^{-1}cm^{-1}$]) |
|---|---|
| **2** | 393, 438[a] |
| **3a** | 353 (5200) |
| **3b** | 360 (6000) |
| **3c** | 356 (6800) |
| **3d** | 357 (6100) |
| **3e** | 391 (4100) |
| **4a** | 369 (20900), 409 (24600), 467 (sh, 9000) |
| **4b** | 372 (sh, 20700), 407 (22700), 500 (sh, 7800) |
| **4c** | 367 (19800), 403 (29100), 452 (sh, 9300) |
| **5a** | 415 (sh, 36300), 435 (42200) |
| **5b** | 418 (sh, 36900), 440 (48000) |
| **5c** | 411 (sh, 31700), 442 (37400) |
| **5d** | 423 (sh, 63800), 442 (76800) |
| $(Pr_4N)_2$**6** | 399 (36800), 430 (62500) |
| $Pr_4N$**7** | 376 (16200), 397 (43600), 451 (64100) |
| PPN**7** | 377 (29900), 397 (51300), 451 (67100) |

[a] Accurate concentration and $\varepsilon$ values could not be measured for this compound because of its very low solubility.

The absorptions of complex **4a** above 300 nm occur as broad, medium-intensity bands at 369 and 409 nm, with a shoulder at 467 nm. The analogous complexes **4b** and **4c** show a very similar pattern. The probable origins of these bands are intraligand transitions associated with the $C{=}CS_2$ units and ligand-to-metal charge-transfer transitions (LMCT), which are usually observed in this region for $Cu^I$ complexes with sulfur donor ligands.[62]

The spectra of the dithiolato complexes **5a**–**d** display a very intense absorption band at around 440 nm, with a shoulder on the higher energy slope between 411 and 420 nm. Very similar absorptions have been observed for neutral $Au^I$–phosphane complexes containing the (fluoren-9-yliden)methanedithiolato ligand or its substituted derivatives (415 nm), which are assignable to LMCT transitions.[28]

The absorption spectra of the $Cu^{III}$ salts Q**7** are almost identical and show two medium intensity bands at 377 and 397 nm and a very intense band at 450 nm. The two higher energy bands appear with very little differences from those in the spectra of other square-planar $Au^{III}$ and $Pt^{II}$ complexes containing the ($t$Bu-fy)$=CS_2^{2-}$ ligand and can be assigned to intraligand transitions associated with the $C{=}CS_2$ unit. The lowest-energy band can be assigned to a metal-to-ligand charge-transfer (MLCT) transition by analogy with other isoelectronic bis(dithiolato) complexes.[24] The $Au^{III}$ and $Pt^{II}$ complexes with the same dithiolato ligand show this band at 410[28] or 490 nm,[29] respectively. The absorption spectrum of the $Cu^{II}$ complex $(Pr_4N)_2$**6** is similar to those of the Q**7** salts, except for the lowest-energy band, which is observed at 430 nm.

## Conclusions

The series of complexes [Cu{$S_2C$($t$Bu-Hfy)}$L_2$] [L = $PPh_3$ (**3a**), $PCy_3$ (**3b**), P$i$Pr$_3$ (**3d**); $L_2$ = dppf (**3c**), dppm (**3e**)] were prepared by the reaction of the oligomeric compound [$Cu_n${$S_2C$($t$Bu-Hfy)}$_n$] (**2**) with different P ligands. Compounds **3a**–**c** react with atmospheric oxygen in the presence of $NEt_3$ to give the dinuclear complexes [$Cu_2${[SC=($t$Bu-fy)]$_2$-S}$L_2$] [L = $PPh_3$ (**4a**), $PCy_3$ (**4b**); $L_2$ = dppf (**4c**)], containing a novel, sulfide-bridged dithiolato ligand, formally resulting from the condensation of two dithioato ligands with loss of a sulfide ion and two protons. The proposed reaction path for the formation of **4a**–**c** involves the initial deprotonation and oxidation of **3a**–**c**, the formation of a disulfide-bridged dinuclear species and the subsequent sulfur abstraction by one of the phosphane ligands. The first family of Cu complexes with the (2,7-di-*tert*-butylfluoren-9-ylidene)-methanedithiolato ligand has been prepared, including a series of $Cu^I$ complexes of the type [$Cu_4${$S_2C$=($t$Bu-fy)}$_2L_4$] [L = $PPh_3$ (**5a**), P($C_6H_4$OMe-$p$)$_3$ (**5b**), P$i$Pr$_3$ (**5d**) or $L_2$ = dppf (**5c**)] and salts of the $Cu^{II}$ complex [Cu{$S_2C$=($t$Bu-fy)}$_2$]$^{2-}$ (**6**) and the $Cu^{III}$ complex [Cu{$S_2C$=($t$Bu-fy)}$_2$]$^-$ (**7**).

## Experimental Section

**General Considerations, Materials, and Instrumentation:** All reactions were carried out at room temperature under an atmosphere of nitrogen using Schlenk techniques, except in the cases indicated. Solvents were dried by standard methods and distilled under nitrogen before use. The compounds [Cu(NCMe)$_4$]$PF_6$ [63] and (pipH)[($t$Bu-Hfy)$CS_2$][54] (**1**) were prepared following published procedures. All other reagents were obtained from commercial sources and used without further purification. NMR spectra were recorded on Bruker Avance 200, 300, or 400 spectrometers at 298 K, unless otherwise indicated. Chemical shifts are referenced to internal TMS ($^1$H and $^{13}$C{H}) or external 85% $H_3PO_4$ ($^{31}$P{H}). The assignments of the $^1$H and $^{13}$C{H} NMR spectra were made with the help of HMBC and HSQC experiments. Scheme 1 shows the atom numbering of the dithiolato ligand. Melting points were determined on a Reichert apparatus and are uncorrected. Elemental analyses were carried out with a Carlo Erba 1106 microanalyzer. Infrared spectra were recorded in the range 4000–200 $cm^{-1}$ on a Perkin–Elmer 16F PC FT-IR spectrophotometer as Nujol mulls between polyethylene sheets or KBr pellets. UV/Visible absorption spectra were recorded on an Unicam UV500 spectrophotometer. FAB mass spectra were recorded on a VG Autospec 500 mass spectrometer using 3-nitrobenzyl alcohol as matrix.

**[$Cu_n${$S_2C$($t$Bu-Hfy)}$_n$] (2):** Dithioate **1** (473 mg, 0.99 mmol) was added to a solution of [Cu(NCMe)$_4$]$PF_6$ (359 mg, 0.96 mmol) in MeCN (20 mL). An immediate reaction was observed, with forma-

 © 2006 Wiley-VCH Verlag GmbH & Co. KGaA, Weinheim 

tion of a dark brown precipitate. The mixture was stirred for 30 min and the solid collected by filtration, washed with MeCN (2×2 mL), and vacuum-dried to give **2**. Yield: 389 mg (97%), m.p. 184 °C (dec.). IR (Nujol): $\tilde{\nu}$ = 975 $cm^{-1}$ ($CS_2$). $^1H$ NMR (400.9 MHz, $CDCl_3$): $\delta$ = 7.61 (d, $^3J_{H,H}$ = 8.0 Hz, 2 H, 4-H, 5-H), 7.47 (br., 2 H, 1-H, 8-H), 7.42 (dd, $^3J_{H,H}$ = 8.0, $^4J_{H,H}$ = 1.5 Hz, 2 H, 3-H, 6-H), 5.68 (s, 1 H, 9-H), 1.29 (s, 18 H, *t*Bu) ppm. $^{13}C\{^1H\}$ NMR (50.3 MHz, $CDCl_3$): $\delta$ = 259.3 ($CS_2$), 150.5 (C-2, C-7), 144.6 (C-8a, C-9a), 138.5 (C-4a, C-4b), 125.4 (C-3, C-6), 121.6 (C-1, C-8), 119.2 (C-4, C-5), 71.3 (C-9), 35.0 (*C*$Me_3$), 31.5 (C*Me*$_3$) ppm. $C_{22}H_{25}CuS_2$ (417.12): calcd. C 63.35, H 6.04, S 15.37; found C 62.95, H 6.06, S 15.21.

**[Cu{$S_2$C(*t*Bu-Hfy)}($PPh_3$)$_2$] (3a):** $PPh_3$ (90 mg, 0.34 mmol) was added to a suspension of **2** (64 mg, 0.15 mmol) in $CH_2Cl_2$ (15 mL) and the mixture was stirred for 1 h. Partial evaporation of the resulting orange solution and addition of methanol (15 mL) led to the precipitation of a pale-pink solid, which was filtered off, washed with methanol (2×2 mL), and vacuum-dried to give **3a**. Yield: 104 mg (72%), m.p. 120 °C (dec.). IR (Nujol): $\tilde{\nu}$ = 1011 $cm^{-1}$ ($CS_2$). $^1H$ NMR (400.9 MHz, $CDCl_3$): $\delta$ = 7.84 (s, 2 H, 1-H, 8-H), 7.63 (d, $^3J_{H,H}$ = 8.0 Hz, 2 H, 4-H, 5-H), 7.40 (d, $^3J_{H,H}$ = 7.8 Hz, 2 H, 3-H, 6-H), 7.28–7.22 (m, 18 H, *o*-H + *p*-H, Ph), 7.10 (m, 12 H, *m*-H, Ph), 5.38 (s, 1 H, 9-H), 1.26 (s, 18 H, *t*Bu) ppm. $^{13}C\{^1H\}$ NMR (50.3 MHz, $CDCl_3$): $\delta$ = 256.4 ($CS_2$), 149.3 (C-2, C-7), 144.7 (C-8a, C-9a), 138.5 (C-4a, C-4b), 133.6 (C-1 + C-2, C-6, Ph), 129.3 (C-4, Ph), 128.3 (C-3, C-5, Ph), 124.4 (C-3, C-6), 123.2 (C-1, C-8), 118.8 (C-4, C-5), 71.3 (C-9), 34.9 (*C*$Me_3$), 31.6 (C*Me*$_3$) ppm. $^{31}P\{^1H\}$ NMR (162.3 MHz, $CDCl_3$): $\delta$ = 0.66 ppm (br). $C_{58}H_{55}CuP_2S_2$ (941.70): calcd. C 73.98, H 5.88, S 6.81; found C 73.79, H 5.94, S 6.47.

**[Cu{$S_2$C(*t*Bu-Hfy)}($PCy_3$)$_2$] (3b):** This salmon-pink compound was prepared as described for **3a**, from **2** (198 mg, 0.47 mmol) and $PCy_3$ (270 mg, 0.96 mmol). Yield: 391 mg (84%), m.p. 120 °C (dec.). IR (Nujol): $\tilde{\nu}$ = 1014 $cm^{-1}$ ($CS_2$). $^1H$ NMR (400.9 MHz, $CDCl_3$): $\delta$ = 7.89 (br., 2 H, 1-H, 8-H), 7.57 (d, $^3J_{H,H}$ = 8.0 Hz, 2 H, 4-H, 5-H), 7.35 (d, $^3J_{H,H}$ = 8.0 Hz, 2 H, 3-H, 6-H), 5.35 (s, 1 H, 9-H), 1.87–1.55 (m, 30 H, Cy), 1.37 (br. s, 30 H, *t*Bu + Cy), 1.18 (br. s, 24 H, Cy) ppm. $^{13}C\{^1H\}$ NMR (300.1 MHz, $CDCl_3$): $\delta$ = 251.5 ($CS_2$), 148.8 (C-2, C-7), 145.2 (C-8a, C-9a), 138.5 (C-4a, C-4b), 124.1 (C-3, C-6), 123.1 (C-1, C-8), 118.5 (C-4, C-5), 71.7 (C-9), 34.9 (*C*$Me_3$), 33.5 (C-1, Cy), 31.6 (C*Me*$_3$), 30.1 (C-2, C-6, Cy), 27.8 (C-3, C-5, Cy), 26.4 (C-4, Cy) ppm. $^{31}P\{^1H\}$ NMR (162.3 MHz, $CDCl_3$): $\delta$ = 12.64 ppm. $C_{58}H_{91}CuP_2S_2$ (977.99): calcd. C 71.23, H 9.38, S 6.56; found C 71.12, H 9.20, S 6.26.

**[Cu{$S_2$C(*t*Bu-Hfy)}(dppf)] (3c):** dppf (351 mg, 0.63 mmol) was added to a suspension of **2** (262 mg, 0.63 mmol) in $CH_2Cl_2$ (15 mL) and the mixture was stirred for 1 h. Partial evaporation of the resulting orange solution (5 mL) and addition of pentane (30 mL) led to the precipitation of an orange solid, which was filtered off, washed with pentane (2×5 mL), and vacuum-dried to give **3c**. Yield: 541 mg (89%), m.p. 198 °C (dec.). IR (Nujol): $\tilde{\nu}$ = 1010 $cm^{-1}$ ($CS_2$). $^1H$ NMR (400.9 MHz, $CDCl_3$): $\delta$ = 7.87 (br. s, 2 H, 1-H, 8-H), 7.63 (d, $^3J_{H,H}$ = 8.0 Hz, 2 H, 4-H, 5-H), 7.56 (m, 8 H, *o*-H, Ph), 7.39 (dd, $^3J_{H,H}$ = 8.0, $^4J_{H,H}$ = 1.3 Hz, 2 H, 3-H, 6-H), 7.32 (m, 4 H, *p*-H, Ph), 7.23 (m, 8 H, *m*-H, Ph), 5.48 (s, 1 H, 9-H), 4.27 (br., 4 H, 3-H, 4-H, Cp), 4.14 (br., 4 H, 2-H, 5-H, Cp), 1.21 (s, 18 H, *t*Bu) ppm. $^{13}C\{^1H\}$ NMR (75.4 MHz, $CDCl_3$): $\delta$ = 256.5 ($CS_2$), 149.5 (C-2, C-7), 145.1 (C-8a, C-9a), 138.5 (C-4a, C-4b), 134.8 (vt, *N* = 31.0 Hz, C-1, Ph), 133.9 (vt, *N* = 16.8 Hz, C-2, C-6 Ph), 129.6 (C-4, Ph), 128.3 (vt, *N* = 9.6 Hz, C-3, C-5, Ph), 124.4 (C-3, C-6), 122.8 (C-1, C-8), 118.7 (C-4, C-5), 77.8 (vt, *N* = 37.7 Hz, C-1, Cp), 73.9 (vt, *N* = 10.8 Hz, C-2, C-5, Cp), 71.6 (br., C-9), 71.5 (br., C-3, C-4, Cp), 34.8 (*C*$Me_3$), 31.5 (C*Me*$_3$) ppm. $^{31}P\{^1H\}$ NMR (75.5 MHz, $CDCl_3$): $\delta$ = –13.33 ppm. $C_{56}H_{53}CuFeP_2S_2$ (971.51): calcd. C 69.23, H 5.50, S 6.60; found C 69.03, H 5.57, S 6.32.

**[Cu{$S_2$C(*t*Bu-Hfy)}(P*i*Pr$_3$)$_2$] (3d):** P*i*$Pr_3$ (167 μL, 0.88 mmol) was added to a suspension of **2** (182 mg, 0.44 mmol) in MeOH (8 mL) and the mixture was stirred for 2 h. A salmon-pink precipitate formed, which was filtered off, washed with methanol (2×2 mL), and vacuum-dried to give **3d**. Yield: 269 mg (84%), m.p. 110 °C (dec.). IR (Nujol): $\tilde{\nu}$ = 1012 $cm^{-1}$ ($CS_2$). $^1H$ NMR (400.9 MHz, $CDCl_3$): $\delta$ = 7.72 (s, 2 H, 1-H, 8-H), 7.58 (d, $^3J_{H,H}$ = 7.9 Hz, 2 H, 4-H, 5-H), 7.36 (d, $^3J_{H,H}$ = 7.9 Hz, 2 H, 3-H, 6-H), 5.46 (s, 1 H, 9-H), 2.13 (m, 6 H, C*H*$Me_2$), 1.35 (s, 18 H, *t*Bu), 1.22 (m, 36 H, CH*Me*$_2$) ppm. $^{13}C\{^1H\}$ NMR (75.5 MHz, $CDCl_3$): $\delta$ = 252.8 ($CS_2$), 149.1 (C-2, C-7), 145.9 (C-8a, C-9a), 138.4 (C-4a, C-4b), 124.4 (C-3, C-6), 122.1 (C-1, C-8), 118.7 (C-4, C-5), 72.4 (C-9), 34.9 (*C*$Me_3$), 31.6 (C*Me*$_3$), 23.6 (*C*H$Me_2$), 20.1 (CH*Me*$_2$) ppm. $^{31}P\{^1H\}$ NMR (162.3 MHz, $CDCl_3$): $\delta$ = 21.93 ppm. $C_{40}H_{67}CuP_2S_2$ (737.60): calcd. C 65.14, H 9.16, S 8.69; found: C 65.01, H 9.23, S 8.56.

**[Cu{$S_2$C(*t*Bu-Hfy)}(dppm)] (3e):** This orange compound was prepared as described for **3c**, from **2** (262 mg, 0.63 mmol) and bis(diphenylphosphanyl)methane (251 mg, 0.65 mmol). Yield: 415 mg (82%), m.p. 151 °C (dec.). IR (Nujol): $\tilde{\nu}$ = 1010 $cm^{-1}$ ($CS_2$). $^1H$ NMR (400.9 MHz, $CDCl_3$): $\delta$ = 7.70 (br., 2 H, 1-H, 8-H), 7.59 (d, $^3J_{H,H}$ = 8.0 Hz, 2 H, 4-H, 5-H), 7.35 (d, $^3J_{H,H}$ = 8.0 Hz, 2 H, 3-H, 6-H), 7.20 (br. m, 8 H, *o*-H, Ph), 7.13 (br. m, 4 H, *p*-H, Ph), 6.96 (br. m, 8 H, *m*-H, Ph), 5.61 (s, 1 H, 9-H), 3.00 (s, 2 H, $CH_2$), 1.23 (s, 18 H, *t*Bu) ppm. $^{13}C\{^1H\}$ NMR (75.5 MHz, $CDCl_3$): $\delta$ = 256.1 ($CS_2$), 149.3 (C-2, C-7), 145.8 (C-8a, C-9a), 141.8 (C-4a, C-4b), 138.4 (C-1, Ph), 135.0 (C-2, C-6 Ph), 129.1 (C-4, Ph), 128.1 (C-3, C-5, Ph), 124.2 (C-3, C-6), 122.4 (C-1, C-8), 118.7 (C-4, C-5), 71.4 (C-9), 34.8 (*C*$Me_3$), 31.6 (C*Me*$_3$) ($CH_2$ of dppm not observed) ppm. $^{31}P\{^1H\}$ NMR (162.3 MHz, $CDCl_3$): $\delta$ = –12.42 ppm. $C_{47}H_{47}CuP_2S_2$ (801.52): calcd. C 70.43, H 5.91, S 8.00; found C 70.18, H 6.21, S 7.76.

**[$Cu_2${[SC=(*t*Bu-fy)]$_2$S}($PPh_3$)$_2$] (4a). Method A:** $NEt_3$ (22 μL, 0.17 mmol) was added to a suspension of **3a** (160 mg, 0.17 mmol) in MeCN (10 mL) and the mixture was stirred under atmospheric conditions for 4 h. The poorly soluble starting material slowly reacted to give a green solution, from which a yellowish orange solid gradually precipitated. The suspension was cooled to –15 °C and the solid collected by filtration and washed with cold MeCN (3×4 mL). Recrystallization from $CH_2Cl_2$/MeCN gave orange crystals of **4a**, which turned red upon drying under vacuum. Yield: 76 mg (67%).

**Method B:** A solid mixture of **3a** (203 mg, 0.22 mmol) and 1,4-benzoquinone (12 mg, 0.11 mmol) was suspended in MeCN (10 mL) and stirred for 7 h under an atmosphere of nitrogen. The reaction took place gradually to give a yellowish orange precipitate, which was isolated and purified as described for method A to give red crystals of **4a**. Yield: 104 mg (73%), m.p. 145 °C (dec.). IR (Nujol): $\tilde{\nu}$ = 1506 $cm^{-1}$ (C=$CS_2$). $^1H$ NMR (400.9 MHz, $CDCl_3$): $\delta$ = 9.64, 8.66 (both d, $^4J_{H,H}$ = 1.4 Hz, 2 H each, 1-H, 8-H), 7.48, 7.40 (both d, $^3J_{H,H}$ = 8.0 Hz, 2 H each, 4-H, 5-H), 7.24–7.16 (m, 10 H, 3-H, 6-H + C-4, Ph), 7.06 (m, 12 H, C-2, C-6, Ph), 6.94 (m, 12 H, C-3, C-5, Ph), 1.25, 1.14 (both s, 18 H each, *t*Bu) ppm. $^{13}C\{^1H\}$ NMR (75.45 MHz, $CDCl_3$): $\delta$ = 148.9, 148.8 (C-2, C-7), 140.1, 139.1 (C-8a, C-9a), 138.8 (br., $CS_2$), 136.4, 136.2 (C-4a, C-4b), 133.5 (d, $^2J_{C,P}$ = 15.0 Hz, C-2, C-6, Ph), 132.0 (C-9), 130.9 (d, $^1J_{C,P}$ = 38.4 Hz, C-1, Ph), 129.8 (C-4, Ph), 128.4 (d, $^3J_{C,P}$ = 10.0 Hz, C-3, C-5, Ph), 123.8, 123.7, 123.0, 122.9 (C-1, C-8, C-3, C-6), 118.1, 117.9 (C-4, C-5), 34.9, 34.8 (*C*$Me_3$), 31.6, 31.4 (C*Me*$_3$) ppm.

 © 2006 Wiley-VCH Verlag GmbH & Co. KGaA, Weinheim 

$^{31}P\{^1H\}$ NMR (162.3 MHz, $CDCl_3$): $\delta$ = 7.38 ppm. $C_{80}H_{78}Cu_2P_2S_3$ (1324.7): calcd. C 72.53, H 5.94, S 7.26; found C 72.56, H 5.88, S 7.03.

**$[Cu_2\{[SC=(tBu\text{-}fy)]_2S\}(PCy_3)_2]$ (4b):** $NEt_3$ (30 μL, 0.24 mmol) was added to a suspension of **3b** (215 mg, 0.22 mmol) in MeCN (8 mL) and the mixture was stirred under atmospheric conditions for 4 h. A red precipitate gradually formed, which was filtered off and washed with MeCN (3×4 mL). The crude product was recrystallized from $CH_2Cl_2$/MeCN and vacuum-dried to give **4b** as a red microcrystalline solid. Yield: 113 mg (75%), m.p. 134 °C (dec.). IR (KBr): $\tilde{\nu}$ = 1498, 1486 $cm^{-1}$ (C=$CS_2$). $^1H$ NMR (400.9 MHz, $CDCl_3$): $\delta$ = 9.61, 8.55 (both d, $^4J_{H,H}$ = 1.5 Hz, 2 H each, 1-H, 8-H), 7.61, 7.57 (both d, $^3J_{H,H}$ = 8.0 Hz, 2 H each, 4-H, 5-H), 7.33, 7.20 (both dd, $^3J_{H,H}$ = 8.0 Hz, $^4J_{H,H}$ = 1.5 Hz, 2 H each, 3-H, 6-H), 1.67 (br. m, 6 H, CH, Cy), 1.60 (br. m, 24 H, $CH_2$, Cy), 1.42, 1.19 (both s, 18 H each, *t*Bu), 1.16–0.99 (br. m, 36 H, $CH_2$, Cy) ppm. $^{13}C\{^1H\}$ NMR (75.45 MHz, $CDCl_3$): $\delta$ = 148.9, 148.7 (C-2, C-7), 140.9 (C-8a, C-9a), 140.6 (br., $CS_2$), 139.5 (C-8a, C-9a), 136.5, 135.8 (C-4a, C-4b), 131.7 (C-9), 123.8, 123.5, 122.9, 122.5 (C-1, C-8, C-3, C-6), 117.9, 117.8 (C-4, C-5), 35.1, 34.9 (*C*$Me_3$), 32.1 (d, $^1J_{C,P}$ = 16.8 Hz, C-1, Cy), 31.8, 31.6 (C*Me*$_3$), 30.1 (vdd, *N* = 44.1 Hz, C-2, C-6, Cy), 27.4 (d, $^3J_{C,P}$ = 11.0 Hz, C-3, C-5, Cy), 25.9 (C-4, Cy) ppm. $^{31}P\{^1H\}$ NMR (162.3 MHz, $CDCl_3$): $\delta$ = 21.9 ppm. $C_{80}H_{114}Cu_2P_2S_3$ (1361.0): calcd. C 70.60, H 8.44, S 7.07; found C 70.37, H 8.63, S 7.84.

**$[Cu_2\{[SC=(tBu\text{-}fy)]_2S\}(dppf)]$ (4c):** $NEt_3$ (21 μL, 0.17 mmol) was added to a suspension of **3c** (160 mg, 0.16 mmol) in MeCN (8 mL) and the mixture was stirred for 24 h. The reaction took place gradually to give a brown suspension. The solvent was removed under vacuum and the residue was stirred in $CH_2Cl_2$ (10 mL) for 7 h. The dark-brown solution was filtered through Celite and concentrated to about 4 mL. Addition of acetone (12 mL) led to the slow precipitation of an orange solid, which was filtered off, washed with acetone (3×2 mL), and vacuum-dried to give **4c**. Yield: 57 mg (51%), m.p. 200 °C (dec.). IR (Nujol): $\tilde{\nu}$ = 1504 $cm^{-1}$ (C=$CS_2$). $^1H$ NMR (400.9 MHz, $CDCl_3$): $\delta$ = 9.71, 8.69 (both d, $^4J_{H,H}$ = 1.5 Hz, 2 H each, 1-H, 8-H), 7.77 (m, 4 H, *o*-H, Ph), 7.46–7.37 (m, 8 H, 4-H, 5-H + *m*-H, *p*-H, Ph), 7.27 (d, $^3J_{H,H}$ = 8.0 Hz, 2 H, 4-H, 5-H), 7.23 (dd, $^4J_{H,H}$ = 1.7, $^3J_{H,H}$ = 8.0 Hz, 2 H, 3-H, 6-H), 7.14–7.09 (m, 4 H, 3-H, 6-H + *p*-H, Ph), 6.83 (m, 4 H, *m*-H, Ph), 6.52 (m, 4 H, *o*-H, Ph), 5.34 (br., 2 H, Cp), 4.22 (br., 2 H, Cp), 3.94 (br., 2 H, Cp), 3.47 (br., 2 H, Cp), 1.25, 1.24 (both s, 18 H each, *t*Bu) ppm. $^{13}C\{^1H\}$ NMR (100.8 MHz, $CDCl_3$): $\delta$ = 149.0, 148.6 (C-2, C-7), 140.2 (t, $^3J_{C,P}$ = 4.1 Hz, $CS_2$), 140.0, 139.1 (C-8a, C-9a), 136.3 (C-4a, C-4b), 134.4 (d, $^2J_{C,P}$ = 15.5 Hz, C-2, C-6, Ph), 132.4 (d, $^1J_{C,P}$ = 38.5, C-1, Ph), 131.0 (d, $^2J_{C,P}$ = 14.5 Hz, C-2, Ph), 130.65 (C-4, Ph), 130.63 (C-9), 128.9 (C-4, Ph), 128.4 (d, $^3J_{C,P}$ = 10.4 Hz, C-3, C-5, Ph), 128.2 (d, $^3J_{C,P}$ = 9.7 Hz, C-3, C-5, Ph), 123.7, 123.6, 123.2, 123.0 (C-1, C-8, C-3, C-6), 118.3, 117.9 (C-4, C-5), 80.2 (br. d, $J_{C,P}$ = 27.8 Hz, CH, Cp), 72.9 (d, $J_{C,P}$ = 3.4 Hz, CH, Cp), 72.7 (d, $^1J_{C,P}$ = 44.1 Hz, C-1, Cp), 71.9 (d, $J_{C,P}$ = 9.9 Hz, CH, Cp), 71.4 (br., CH, Cp), 34.94, 34.89 (*C*$Me_3$), 31.62, 31.60 (C*Me*$_3$) ppm. $^{31}P\{^1H\}$ NMR (162.3 MHz, $CDCl_3$): $\delta$ = –1.39 ppm. $C_{78}H_{76}Cu_2FeP_2S_3$ (1354.5): calcd. C 69.16, H 5.66, S 7.10; found C 69.28, H 5.77, S 6.91.

**$[Cu_4\{S_2C=(tBu\text{-}fy)\}_2(PPh_3)_4]$ (5a):** A solid mixture of $[Cu(NCMe)_4]PF_6$ (239 mg, 0.64 mmol), $PPh_3$ (177 mg, 0.67 mmol), and **1** (163 mg, 0.34 mmol) was suspended in MeCN (15 mL) and treated with piperidine (36 μL, 0.36 mmol). The resulting orange suspension was stirred for 1 h, whereupon a yellow precipitate formed, which was filtered off, washed with MeCN (3×5 mL), and vacuum dried to give **5a** as a bright-yellow microcrystalline solid. Yield: 228 mg (71%), m.p. 123 °C (dec.). IR (KBr): $\tilde{\nu}$ = 1482 $cm^{-1}$ (C=$CS_2$). $^1H$ NMR (400.9 MHz, $CDCl_3$): $\delta$ = 9.37 (d, $^4J_{H,H}$ = 1.4 Hz, 4 H, 1-H, 8-H), 7.60 (d, $^3J_{H,H}$ = 7.9 Hz, 4 H, 4-H, 5-H), 7.25–7.18 (m, 28 H, 3-H, 6-H + *o*-H, Ph), 6.97 (t, $^3J_{H,H}$ = 7.3 Hz, 12 H, *p*-H, Ph), 6.72 (t, $^3J_{H,H}$ = 7.0 Hz, 24 H, *m*-H, Ph), 1.03 (s, 36 H, *t*Bu) ppm. $^{13}C\{^1H\}$ NMR (75.4 MHz, $CDCl_3$): $\delta$ = 157.9 (br., $CS_2$), 147.7 (C-2, C-7), 140.9 (C-8a, C-9a), 135.7 (C-4a, C-4b), 133.8 (d, $^2J_{C,P}$ = 14.6 Hz, C-2, C-6, Ph), 133.3 (C-9), 132.6 (d, $^1J_{C,P}$ = 30.7 Hz, C-1, $PPh_3$), 129.3 (C-4 $PPh_3$), 128.2 (d, $^3J_{C,P}$ = 9.1 Hz, C-3, C-5, $PPh_3$), 124.8 (C-1, C-8), 121.3 (C-3, C-6), 116.9 (C-4, C-5), 34.8 (*C*$Me_3$), 31.8 (C*Me*$_3$) ppm. $^{31}P\{^1H\}$ NMR (162.3 MHz, $CDCl_3$): $\delta$ = –4.04 ppm. $C_{116}H_{108}Cu_4P_4S_4$ (2008.5): calcd. C 69.37, H 5.42, S 6.39; found C 69.16, H 5.56, S 6.25.

**$[Cu_4\{S_2C=(tBu\text{-}fy)\}_2\{P(C_6H_4OMe\text{-}p)_3\}_4]$ (5b):** This yellow compound was obtained as described for **5a**, from $[Cu(NCMe)_4]PF_6$ (235 mg, 0.63 mmol), **1** (152 mg, 0.32 mmol), and tri-*p*-methoxyphenylphosphane (227 mg, 0.64 mmol). Yield: 331 mg (89%), m.p. 167 °C (dec.). IR (KBr): $\tilde{\nu}$ = 1498 $cm^{-1}$ (C=$CS_2$). $^1H$ NMR (400.9 MHz, $CDCl_3$): $\delta$ = 9.53 (d, $^4J_{H,H}$ = 1.4 Hz, 4 H, 1-H, 8-H), 7.63 (d, $^3J_{H,H}$ = 7.9 Hz, 4 H, 4-H, 5-H), 7.19 (m, 28 H, 3-H, 6-H + *o*-H, $C_6H_4OMe$-*p*), 6.24 (d, $^3J_{H,H}$ = 7.8 Hz, 24 H, *m*-H, $C_6H_4OMe$-*p*), 3.45 (s, 36 H, OMe), 1.02 (s, 36 H, *t*Bu) ppm. $^{13}C\{^1H\}$ NMR (100.8 MHz, $CDCl_3$): $\delta$ = 160.2 (C-4, $C_6H_4OMe$-*p*), 148.0 (C-2, C-7), 141.3 (C-8a, C-9a), 135.4 (C-4a, C-4b), 135.2 (d, $^2J_{C,P}$ = 16.2 Hz, C-2, C-6, $C_6H_4OMe$-*p*), 132.6 (C-9), 125.2 (C-1, C-8), 124.5 (d, $^1J_{C,P}$ = 35.0 Hz, C-1, $C_6H_4OMe$-*p*), 120.9 (C-3, C-6), 117.0 (C-4, C-5), 113.9 (d, $^3J_{C,P}$ = 10.2 Hz, C-3, C-5, $C_6H_4OMe$-*p*), 54.8 (OMe), 34.8 (*C*$Me_3$), 31.7 (C*Me*$_3$) ppm; *C*$S_2$ not observed. $^{31}P\{^1H\}$ NMR (162.3 MHz, $CDCl_3$): $\delta$ = –8.26 ppm. $C_{128}H_{132}Cu_4P_4S_4$ (2176.8): calcd. C 64.90, H 5.62, S 5.41; found C 64.66, H 5.68, S 5.36.

**$[Cu_4\{S_2C=(tBu\text{-}fy)\}_2(dppf)_2]$ (5c):** This yellowish orange microcrystalline compound was obtained as described for **5a**, from $[Cu(NCMe)_4]PF_6$ (234 mg, 0.63 mmol), dithioate **1** (154 mg, 0.32 mmol), and dppf (177 mg, 0.32 mmol). The product was purified by recrystallization from $CH_2Cl_2$/acetone and dried at 60 °C for 4 h. Yield: 255 mg (78%), m.p. 198 °C (dec.). IR (KBr): $\tilde{\nu}$ = 1490 $cm^{-1}$ (C=$CS_2$). $^1H$ NMR (400.9 MHz, $CDCl_3$): $\delta$ = 9.54 (d, $^4J_{H,H}$ = 1.5 Hz, 4 H, 1-H, 8-H), 7.71 (d, $^3J_{H,H}$ = 7.9 Hz, 4 H, 4-H, 5-H), 7.46 (br., 16 H, *o*-H, Ph), 7.23 (dd, $^3J_{H,H}$ = 7.9, $^4J_{H,H}$ = 1.5 Hz, 4 H, 3-H, 6-H), 7.12 (br., 8 H, *p*-H, Ph), 6.91 (br., 16 H, *m*-H, Ph), 4.80 (br., 8 H, Cp), 3.86 (br., 8 H, Cp), 1.06 (s, 36 H, *t*Bu) ppm. $^{13}C\{^1H\}$ NMR (100.8 MHz, $CDCl_3$): $\delta$ = 157.5 (app t, $^3J_{C,P}$ = 8.5 Hz, $CS_2$), 148.1 (C-2, C-7), 141.1 (C-8a, C-9a), 135.8 (C-4a, C-4b), 134.3 (br., C-1, Ph), 133.9 (C-9), 133.2 (br., C-2, C-6, Ph), 129.2 (C-4, Ph), 128.2 (d, $^3J_{C,P}$ = 9.3 Hz, C-3, C-5, Ph), 124.9 (C-1, C-8), 121.6 (C-3, C-6), 117.3 (C-4, C-5), 74.1 (d, $^2J_{C,P}$ = 36.6 Hz, C-1, Cp), 71.6 (d, $^3J_{C,P}$ = 5.2 Hz, CH, Cp), 34.9 (*C*$Me_3$), 31.9 (C*Me*$_3$) ppm. $^{31}P\{^1H\}$ NMR (162.3 MHz, $CDCl_3$): $\delta$ = –14.49 ppm. $C_{112}H_{104}Cu_4Fe_2P_4S_4$ (2068.1): calcd. C 65.05, H 5.07, S 6.20; found C 65.01, H 5.22, S 6.05.

**$[Cu_4\{S_2C=(tBu\text{-}fy)\}_2(PiPr_3)_4]$ (5d):** This bright-yellow microcrystalline compound was obtained as described for **5a**, from $[Cu(NCMe)_4]PF_6$ (335 mg, 0.90 mmol), **1** (214 mg, 0.45 mmol), and P*i*$Pr_3$ (172 μL, 0.90 mmol). Yield: 241 mg (67%), m.p. 171 °C (dec.). IR (KBr): $\tilde{\nu}$ = 1482 $cm^{-1}$ (C=$CS_2$). $^1H$ NMR (400.9 MHz, $CDCl_3$): $\delta$ = 9.61 (s, 4 H, 1-H, 8-H), 7.60 (d, $^3J_{H,H}$ = 7.8 Hz, 4 H, 4-H, 5-H), 7.18 (d, $^3J_{H,H}$ = 7.8 Hz, 4 H, 3-H, 6-H), 1.98 (m, 12 H, C*H*$Me_2$), 1.35 (s, 36 H, *t*Bu), 1.14 (m, 72 H, CH*Me*$_2$) ppm. $^{31}P\{^1H\}$ NMR (162.3 MHz, $CDCl_3$): $\delta$ = 22.85 ppm. $C_{80}H_{132}Cu_4P_4S_4$ (1600.27): calcd. C 60.04, H 8.31, S 8.01; found C 59.86, H 8.32, S 7.69.

 © 2006 Wiley-VCH Verlag GmbH & Co. KGaA, Weinheim 

Table 5. Crystallographic data for **3a**, **3c**·$CH_2Cl_2$, **4a**·4$Me_2CO$, and **4c**·$CH_2Cl_2$.

| | **3a** | **3c**·$CH_2Cl_2$ | **4a**·4$Me_2CO$ | **4c**·$CH_2Cl_2$ |
|---|---|---|---|---|
| Formula | $C_{58}H_{55}CuP_2S_2$ | $C_{57}H_{55}Cl_2CuFeP_2S_2$ | $C_{92}H_{102}Cu_2O_4P_2S_3$ | $C_{79}H_{78}Cl_2Cu_2FeP_2S_3$ |
| Mol. wt. | 941.62 | 1056.36 | 1556.94 | 1439.36 |
| $T$ [K] | 100(2) | 100(2) | 133(2) | 133(2) |
| $\lambda$ [Å] | 0.71073 | 0.71073 | 0.71073 | 0.71073 |
| Cryst syst | orthorhombic | orthorhombic | triclinic | monoclinic |
| Space group | $P2_12_12_1$ | $Pbca$ | $P\bar{1}$ | $P2_1/n$ |
| $a$ [Å] | 9.9445(5) | 15.2475(4) | 13.901(2) | 16.998(2) |
| $b$ [Å] | 19.6841(9) | 18.7570(5) | 17.245(2) | 18.785(2) |
| $c$ [Å] | 24.5657(12) | 35.9456(11) | 18.922(2) | 21.544(2) |
| $\alpha$ [°] | 90 | 90 | 103.664(5) | 90 |
| $\beta$ [°] | 90 | 90 | 96.463(5) | 96.539(4) |
| $\gamma$ [°] | 90 | 90 | 100.832(5) | 90 |
| $V$ [Å$^3$] | 4808.7(4) | 10280.3(5) | 4270.0(9) | 6834.8(13) |
| Z | 4 | 8 | 2 | 4 |
| $\rho_{calcd.}$ [Mg m$^{-3}$] | 1.301 | 1.365 | 1.211 | 1.399 |
| $\mu$ [mm$^{-1}$] | 0.646 | 0.980 | 0.657 | 1.087 |
| $R_1$[a] | 0.0414 | 0.0584 | 0.0495 | 0.0558 |
| $wR_2$[b] | 0.1046 | 0.1321 | 0.1372 | 0.1374 |

[a] $R_1 = \Sigma||F_o| - |F_c||/\Sigma|F_o|$ for reflections with $I > 2\sigma(I)$. [b] $wR_2 = \{\Sigma[w(F_o^2 - F_c^2)^2]/\Sigma[w(F_o^2)^2]\}^{0.5}$ for all reflections; $w^{-1} = \sigma^2(F_2) + (aP)^2 + bP$, where $P = (2F_c^2 + F_o^2)/3$ and $a$ and $b$ are constants set by the program.

**$(Pr_4N)_2$[Cu{$S_2C$=(*t*Bu-fy)}$_2$] [$(Pr_4N)_2$6]:** A previously degassed 1.0 M solution of ($Pr_4N$)OH in water (0.60 mL, 0.60 mmol) and a solution of $Cu(ClO_4)_2$·$6H_2O$ (85 mg, 0.23 mmol) in MeCN (5 mL) were added successively to a solution of **1** (234 mg, 0.49 mmol) in MeCN (10 mL). Reaction was observed to give a dark-brown suspension, which was stirred for 5 min. The supernatant was decanted and the precipitate was washed with MeCN (3 × 5 mL) and vacuum-dried to give $(Pr_4N)_2$**6** as a brown powder. Yield: 208 mg (79%), m.p. 237 °C (dec.). IR (KBr): $\tilde{\nu}$ = 1480 cm$^{-1}$ (C=$CS_2$). $C_{68}H_{104}CuN_2S_4$ (1141.4): calcd. C 71.56, H 9.18, N 2.45, S 11.24; found C 71.36, H 9.23, N 2.50, S 11.45.

**$Pr_4N$[Cu{$S_2C$=(*t*Bu-fy)}$_2$] ($Pr_4N$7):** A solution of **1** (607 mg, 1.27 mmol) in MeCN (15 mL) was treated successively with a 1.0 M solution of ($Pr_4N$)OH in water (1.4 mL, 1.4 mmol) and Cu($ClO_4)_2$·$6H_2O$ (228.7 mg, 0.617 mmol). The resulting brown suspension was stirred for 2.5 h under atmospheric conditions, whereupon a green precipitate formed, which was filtered off, washed with MeCN (3 × 3 mL), and vacuum-dried to give $Pr_4N$**7**. Yield: 544 mg (92%), m.p. 233 °C (dec.). IR (Nujol): $\tilde{\nu}$ = 1548 cm$^{-1}$ (C=$CS_2$), 416 (Cu–S). $^1$H NMR [400.9 MHz, $(CD_3)_2CO$]: $\delta$ = 8.46 (d, $^4J_{H,H}$ = 1.3 Hz, 4 H, 1-H, 8-H), 7.68 (d, $^3J_{H,H}$ = 8.0 Hz, 4 H, 4-H, 5-H), 7.29 (dd, $^3J_{H,H}$ = 8.0, $^4J_{H,H}$ = 1.7 Hz, 4 H, 3-H, 6-H), 3.31 (m, 8 H, $NCH_2$), 1.78 (m, 8 H, $CH_2$), 1.39 (s, 36 H, *t*Bu), 0.95 (t, $^3J_{H,H}$ = 7.2 Hz, 12 H, Me, $Pr_4N^+$) ppm. $^{13}$C{$^1$H} NMR [75.5 MHz, $(CD_3)_2CO$]: $\delta$ = 154.1 ($CS_2$), 149.6 (C-2, C-7), 140.2 (C-8a, C-9a), 135.7 (C-4a, C-4b), 128.2 (C-9), 122.8 (C-3, C-6), 120.7 (C-1, C-8), 119.2 (C-4, C-5), 35.4 ($CMe_3$), 32.1 ($CMe_3$) ppm. $C_{56}H_{76}CuNS_4$ (955.03): calcd. C 70.43, H 8.02, N 1.47, S 13.43; found C 70.66, H 8.29, N 1.50, S 13.79.

**PPN[Cu{$S_2C$=(*t*Bu-fy)}$_2$] (PPN7):** Piperidine (46 μL, 0.46 mmol) and $CuCl_2$·$2H_2O$ (34 mg, 0.20 mmol) were added successively to a solution of **1** (212 mg, 0.45 mmol) and PPNCl (130 mg, 0.23 mmol) in MeCN (15 mL). The resulting red solution was stirred for 1 h under atmospheric conditions, after which time a green solid precipitated. The product was filtered off, washed with ethanol (3 × 2 mL) and diethyl ether (2 mL), and vacuum-dried to give PPN**7**. Yield: 184 mg (63%), m.p. 238 °C (dec.). IR (Nujol): $\tilde{\nu}$ = 1552 cm$^{-1}$ (C=$CS_2$), 420 (Cu–S). $^1$H NMR [400.9 MHz, $(CD_3)_2$-CO]: $\delta$ = 8.46 (d, $^4J_{H,H}$ = 1.4 Hz, 4 H, 1-H, 8-H), 7.72–7.65 (m, 22 H, 4-H, 5-H + $PPN^+$), 7.56–7.51 (m, 12 H, $PPN^+$), 7.28 (dd, $^4J_{H,H}$ = 1.7, $^3J_{H,H}$ = 8.0 Hz, 4 H, 3-H, 6-H), 1.38 (s, 36 H, *t*Bu) ppm. $^{13}$C{$^1$H} NMR [75.5 MHz, $(CD_3)_2CO$]: $\delta$ = 154.3 ($CS_2$), 149.6 (C-2, C-7), 140.3 (C-8a, C-9a), 135.7 (C-4a, C-4b), 128.2 (C-9), 122.7 (C-3, C-6), 120.7 (C-1, C-8), 119.1 (C-4, C-5), 35.4 ($CMe_3$), 32.1 ($CMe_3$) ppm. $C_{80}H_{78}CuNS_4$ (1245.3): calcd. C 73.50, H 6.01, N 1.07, S 9.81; found: C 73.50, H 5.80, N 1.10, S 9.52.

**X-ray Structure Determinations:** Crystals of **3a**, **3c**·$CH_2Cl_2$, **4a**·4$Me_2CO$, and **4c**·$CH_2Cl_2$ suitable for X-ray diffraction studies were obtained from chloroform/pentane (**3a**), $CH_2Cl_2$/hexane (**3e**), acetone/hexane (**4a**), or $CH_2Cl_2$/pentane (**4c**). Numerical details are presented in Table 5. The structures of **3a** and **3c** were measured on a Bruker Smart APEX diffractometer, and those of **4a** and **4c** on a Bruker SMART 1000 CCD diffractometer. Data were collected using monochromated Mo-$K\alpha$ radiation in $\omega$-scan mode. The structures were solved by direct methods and refined anisotropically on $F^2$ using the program SHELXL-97 (G. M. Sheldrick, University of Göttingen, Germany). Restraints to local aromatic ring symmetry or light-atom displacement factor components were applied in some cases. The methyl groups were refined using rigid groups, and the other hydrogen atoms were refined using a riding model. *Special features of refinement*: For compound **3a**, the Flack parameter is 0.047(10). For compounds **3c**, **4a**, and **4c** the Me groups of one *t*Bu group are disordered over two positions. The solvent in the crystals of **4a** was so badly resolved that no sensible refinement model could be developed. For this reason the program SQUEEZE (A. L. Spek, University of Utrecht, Netherlands) was used to remove the effects of the solvent mathematically. The solvent content of four acetone molecules is only an approximate estimate. The dichloromethane molecule in **4c** is disordered over two positions.

CCDC-277675 (**3a**) -277674 (**3c**·$CH_2Cl_2$), -277676 (**4a**·4$Me_2CO$), and -277673 (**4c**·$CH_2Cl_2$) contain the supplementary crystallographic data for this paper. These data can be obtained free of charge from The Cambridge Crystallographic Data Centre via www.ccdc.cam.ac.uk/data_request/cif.

**Supporting Information** (see footnote on the first page of this article): Positive ion FAB mass spectra of **5a**–**d**.

 © 2006 Wiley-VCH Verlag GmbH & Co. KGaA, Weinheim 

## Acknowledgments

We thank the Ministerio de Ciencia y Tecnología (Spain) and FEDER (BQU2001-0133 and CTQ2004-05396) for financial support. P. G.-H. thanks the Ministerio de Educación y Ciencia (Spain) and the Universidad de Murcia for a contract under the Ramón y Cajal Program. Y. G.-C. thanks the Ministerio de Educación y Ciencia (Spain) for a grant.

[1] G. Henkel, B. Krebs, *Chem. Rev.* **2004**, *104*, 801–824.
[2] B. Krebs, G. Henkel, *Angew. Chem. Int. Ed. Engl.* **1991**, *30*, 769–788.
[3] K. Fujisawa, S. Imai, S. Suzuki, Y. Moro-oka, Y. Miyashita, Y. Yamada, K.-i. Okamoto, *J. Inorg. Biochem.* **2000**, *82*, 229–238.
[4] J. Hanss, H. J. Kruger, *Angew. Chem. Int. Ed. Engl.* **1996**, *35*, 2827–2830.
[5] K. Fujisawa, S. Imai, N. Kitajima, Y. Moro-oka, *Inorg. Chem.* **1998**, *37*, 168–169.
[6] A. F. Stange, A. Klein, K. W. Klinkhammer, W. Kaim, *Inorg. Chim. Acta* **2001**, *324*, 336–341.
[7] E. I. Solomon, U. M. Sundaram, T. E. Machonkin, *Chem. Rev.* **1996**, *96*, 2563–2605.
[8] R. H. Holm, P. Kennepohl, E. I. Solomon, *Chem. Rev.* **1996**, *96*, 2239–2314.
[9] E. I. Solomon, D. W. Randall, T. Glaser, *Coord. Chem. Rev.* **2000**, *200*, 595–632.
[10] W. Kaim, J. Rall, *Angew. Chem. Int. Ed. Engl.* **1996**, *35*, 43–60.
[11] D. L. Huffman, T. V. O'Halloran, *Annu. Rev. Biochem.* **2001**, *70*, 677–701.
[12] J. P. Fackler Jr., D. Coucouvanis, *J. Am. Chem. Soc.* **1966**, *88*, 3913–3920.
[13] L. E. McCandlish, E. C. Bissell, D. Coucouvanis, J. P. Fackler Jr., K. Knox, *J. Am. Chem. Soc.* **1968**, *90*, 7357–7359.
[14] F. J. Hollander, D. Coucouvanis, *J. Am. Chem. Soc.* **1977**, *99*, 6268–6280.
[15] D. Coucouvanis, D. Swenson, N. C. Baenziger, R. Pedelty, M. L. Caffery, *J. Am. Chem. Soc.* **1977**, *99*, 8097–8099.
[16] D. Coucouvanis, D. Swenson, N. C. Baenziger, R. Pedelty, M. L. Caffery, S. Kanodia, *Inorg. Chem.* **1989**, *28*, 2829–2836.
[17] C. W. Liu, T. Stubbs, R. J. Staples, J. P. Fackler Jr., *J. Am. Chem. Soc.* **1995**, *117*, 9778–9779.
[18] I. Haiduc, D. B. Sowerby, S. F. Lu, *Polyhedron* **1995**, *14*, 3389–3472.
[19] C. W. Liu, R. J. Staples, J. P. Fackler Jr., *Coord. Chem. Rev.* **1998**, *174*, 147–177.
[20] J. P. Fackler Jr., R. J. Staples, C. W. Liu, R. T. Stubbs, C. Lopez, J. T. Pitts, *Pure Appl. Chem.* **1998**, *70*, 839–844.
[21] A. Avdeef, J. P. Fackler Jr., *Inorg. Chem.* **1978**, *17*, 2182–2187.
[22] M. T. Garland, J. F. Halet, J. Y. Saillard, *Inorg. Chem.* **2001**, *40*, 3342–3350.
[23] C. W. Liu, B. J. Liaw, J. C. Wang, L. S. Liou, T. C. Keng, *J. Chem. Soc., Dalton Trans.* **2002**, 1058–1065.
[24] B. G. Werden, E. Billig, H. B. Gray, *Inorg. Chem.* **1966**, *5*, 78–81.
[25] F. J. Hollander, M. L. Caffery, D. Coucouvanis, *J. Am. Chem. Soc.* **1974**, *96*, 4682–4684.
[26] D. Coucouvanis, F. J. Hollander, M. L. Caffery, *Inorg. Chem.* **1976**, *15*, 1853–1860.
[27] H. H. Alkam, A. Hatzidimitriou, C. C. Hadjikostas, C. Tsiamis, *Inorg. Chim. Acta* **1997**, *256*, 41–50.
[28] J. Vicente, P. González-Herrero, Y. García-Sánchez, P. G. Jones, M. Bardají, *Inorg. Chem.* **2004**, *43*, 7516–7531.
[29] J. Vicente, P. González-Herrero, M. Pérez-Cadenas, P. G. Jones, D. Bautista, *Inorg. Chem.* **2005**, *44*, 7200–7213.
[30] A. Camus, N. Marsich, A. M. M. Lanfredi, F. Ugozzoli, *Inorg. Chim. Acta* **1989**, *161*, 87–96.
[31] W. P. Su, M. C. Hong, R. Cao, H. Q. Liu, *Acta Crystallogr., Sect. C.* **1998**, *54*, 337–338.
[32] M. D. Janssen, D. M. Grove, G. Van Koten, *Progr. Inorg. Chem.* **1997**, *46*, 97–149.
[33] L. M. Nguyen, M. E. Dellinger, J. T. Lee, R. A. Quinlan, A. L. Rheingold, R. D. Pike, *Inorg. Chim. Acta* **2005**, *358*, 1331–1336.
[34] L. I. Victoriano, M. T. Garland, A. Vega, C. López, *J. Chem. Soc., Dalton Trans.* **1998**, 1127–1131.
[35] F. Challenger, D. Greenwood, *J. Chem. Soc.* **1950**, 26–30.
[36] C. G. Moore, B. R. Trego, *Tetrahedron* **1962**, *18*, 205–218.
[37] A. Schönberg, M. Z. Barakat, *J. Chem. Soc.* **1949**, 892–894.
[38] T. C. Deivaraj, J. J. Vittal, *Acta Crystallogr. Sect. E* **2001**, *57*, M566–M567.
[39] I. García-Orozco, J. G. López-Cortés, M. C. Ortega-Alfaro, R. A. Toscano, G. Penieres-Carrillo, C. Álvarez-Toledano, *Inorg. Chem.* **2004**, *43*, 8572–8576.
[40] C. W. Liu, B. J. Liaw, J. C. Wang, T. C. Keng, *Inorg. Chem.* **2000**, *39*, 1329–1332.
[41] W. P. Su, M. C. Hong, R. Cao, J. T. Chen, D. X. Wu, H. Q. Liu, J. X. Lu, *Inorg. Chim. Acta* **1998**, *267*, 313–317.
[42] A. M. M. Lanfredi, A. Tiripicchio, A. Camus, N. Marsich, *J. Chem. Soc., Chem. Commun.* **1983**, 1126–1128.
[43] A. Camus, N. Marsich, G. Nardin, *J. Organomet. Chem.* **1980**, *188*, 389–399.
[44] H. Otto, H. Werner, *Chem. Ber.* **1987**, *120*, 97.
[45] P. Strauch, B. Dempe, R. Kempe, W. Dietzsch, J. Sieler, E. Hoyer, *Z. Anorg. Allg. Chem.* **1994**, *620*, 498–504.
[46] F. H. Allen, *Acta Crystallogr., Sect. B: Struct. Sci.* **2002**, *58*, 380–388.
[47] F. H. Allen, O. Kennard, D. G. Watson, L. Brammer, A. G. Orpen, R. Taylor, *J. Chem. Soc., Perkin Trans. 2* **1987**, S1.
[48] A. Bondi, *J. Phys. Chem.* **1964**, *68*, 441–451.
[49] D. M. Knotter, M. D. Janssen, D. M. Grove, W. J. J. Smeets, E. Horn, A. L. Spek, G. van Koten, *Inorg. Chem.* **1991**, *30*, 4361–4366.
[50] A. M. M. Lanfredi, A. Tiripicchio, A. Camus, N. Marsich, *J. Chem. Soc., Dalton Trans.* **1989**, 753–756.
[51] I. Schroter-Schmid, J. Strähle, *Z. Naturforsch., Teil B* **1990**, *45*, 1537–1542.
[52] M. Baumgartner, W. Bensch, P. Hug, E. Dubler, *Inorg. Chim. Acta* **1987**, *136*, 139–147.
[53] M. Baumgartner, H. Schmalle, E. Dubler, *Inorg. Chim. Acta* **1993**, *208*, 135–143.
[54] J. Vicente, P. González-Herrero, Y. García-Sánchez, M. Pérez-Cadenas, *Tetrahedron Lett.* **2004**, *45*, 8859–8861.
[55] S. L. Lam, Y. X. Cui, S. C. F. Auyeung, Y. K. Yan, T. S. A. Hor, *Inorg. Chem.* **1994**, *33*, 2407–2412.
[56] D. Cauzzi, C. Graiff, C. Massera, G. Predieri, A. Tiripicchio, D. Acquotti, *J. Chem. Soc., Dalton Trans.* **1999**, 3515–3521.
[57] S. M. Draper, C. E. Housecroft, A. L. Rheingold, *J. Organomet. Chem.* **1992**, *435*, 9–20.
[58] I. D. Salter, S. A. Williams, T. Adatia, *Polyhedron* **1995**, *14*, 2803–2817.
[59] I. D. Salter, V. Sik, S. A. Williams, T. Adatia, *J. Chem. Soc., Dalton Trans.* **1996**, 643–652.
[60] S. W. A. Fong, T. S. A. Hor, *J. Clust. Sci.* **1998**, *9*, 351–392.
[61] K. A. Jensen, L. Henriksen, *Acta Chem. Scand.* **1968**, *22*, 1107–1128.
[62] H. Xu, J. H. K. Yip, *Inorg. Chem.* **2003**, *42*, 4492–4494.
[63] G. J. Kubas, *Inorg. Synth.* **1979**, *19*, 90–92.

Received: July 11, 2005
Published Online: November 11, 2005

 © 2006 Wiley-VCH Verlag GmbH & Co. KGaA, Weinheim 

DOI: 10.1002/ejic.200500643

# $\eta^2$-Iminoacyl and $\eta^2$-Acyl Monocyclopentadienyl Tantalum Complexes Bearing Oxo and Oxo-Borane Ligands

**Javier Sánchez-Nieves,[a] Pascual Royo,*[a] and Marta E. G. Mosquera[a][‡]**

*Dedicated to J. Antonio Abad, an excellent scientist and friend*

**Keywords:** Tantalum / Oxo ligands / Insertion reactions / Isocyanide / Carbon monoxide

Alkyl-chloro ligand exchange by the reaction of [TaCp'$R_2${O·B($C_6F_5$)$_3$}] (R = $CH_2Ph$, Me) with $Ph_3CCl$ gave the monoalkyl compounds [TaCp'RCl{O·B($C_6F_5$)$_3$}] (R = $CH_2Ph$, Me). Insertion of CNAr (Ar = 2,6-$Me_2C_6H_3$) and CO into a Ta–C bond of the mono- and dialkyl complexes gave the iminoacyl compounds [TaCp'X{$\eta^2$-C(R)=NAr}{O·B($C_6F_5$)$_3$}] (X = R = $CH_2Ph$, Me; X = Cl, R = $CH_2Ph$) and the acyl compounds [TaCp'X{$\eta^2$-C(R)=O}{O·B($C_6F_5$)$_3$}] (X = R = $CH_2Ph$, Me; X = Cl, R = $CH_2Ph$), respectively. The related chloro compound [TaCp'Cl{$\eta^2$-C(Me)=NAr}{O·B($C_6F_5$)$_3$}] was isolated from the reaction of the oxo derivative [TaCp'Cl{$\eta^2$-C(Me)=NAr}(O)] with the Lewis acid B($C_6F_5$)$_3$. Addition of CNAr or pyridine to [TaCp'($CH_2Ph$){$\eta^2$-C($CH_2Ph$)=NAr}{O·B($C_6F_5$)$_3$}] afforded the borane-free complex [TaCp'($CH_2Ph$){$\eta^2$-C($CH_2Ph$)=NAr}(O)] and the acid-base adduct L·B($C_6F_5$)$_3$ (L = py, CNAr). The molecular structures of [TaCp'Cl{$\eta^2$-C(Me)=NAr}{O·B($C_6F_5$)$_3$}] and [TaCp'($CH_2Ph$){$\eta^2$-C($CH_2Ph$)=O}{O·B($C_6F_5$)$_3$}] were obtained from X-ray diffraction studies.

(© Wiley-VCH Verlag GmbH & Co. KGaA, 69451 Weinheim, Germany, 2006)

## Introduction

The formation of C–C bonds through insertion of isocyanides (CNR) and carbon monoxide (CO) into M–C bonds is well-documented, and this reaction initially affords iminoacyl and acyl complexes, respectively.[1] For a given metal atom, the stability and further evolution of these compounds are determined by the nature of the ancillary ligands. Many reaction pathways may follow to give a broad variety of products:[1] (a) migratory insertion of a second alkyl or aryl group to give $\eta^2$-imine or $\eta^2$-ketene complexes;[2–5] (b) intra- or intermolecular coupling of iminoacyl or acyl units affording diaza- or dioxobutene complexes;[6,7] (c) transfer of the NR or O moieties to the metal centre;[8–11] (d) insertion of a second CNR[12–16] or CO[17] molecule into the new M–C bond formed after the first insertion process and (e) hydrogen migration.[18,19]

We reported the results of our studies on the insertion reactions of CNR into the Ta–C(methyl) bond of monocyclopentadienyl complexes of the type [TaCp*$Cl_xMe_{4-x}$][8–10] for which processes (a) and (c) were observed. Similar reactions with imido compounds of the type [TaCp*MeX(N*t*Bu)] (X = Cl, Me, OR, NH*t*Bu) gave the imine-$\eta^2$-iminoacyl derivatives [TaCp*(N*t*Bu)X{$\eta^2$-C[C(Me)=NR]=NR}].[20] With regard to the CO insertion reactions, double migration of the alkyl group [process (a)] was observed for [TaCp*$Cl_2Me_2$],[10] whereas the coupling of the acyl groups [process (b)] occurred for [TaCp*$Me_2$(NR)] (R = 2,6-$Me_2C_6H_3$) to give the dinuclear compound [TaCp*(NR)Me]$_2${μ-$\eta^2$-OC(Me)=C(Me)O},[10] and ligand exchange [process (c)] for complexes [TaCp*ClMe(NR)] (R = 2,6-$Me_2C_6H_3$,[10] *t*Bu)[11] led to the oxo compounds [TaCp*Cl(O){$\eta^2$-C(Me)=NR}]. Furthermore, the $\eta^2$-(methyl)acyl complexes remained elusive and were only detected as intermediates by NMR spectroscopy, whereas the related $\eta^2$-iminoacyl complexes are stable.

It was observed that for monocyclopentadienyl imido tantalum derivatives addition of a second CNR molecule into the iminoacyl compounds [TaCp*(NR)X{$\eta^2$-C(Me)=NR}] (R = 2,6-$Me_2C_6H_3$, *t*Bu; X = Cl, Me) resulted in differing behaviours depending on the R group of the imido ligand. No reaction was found for R = 2,6-$Me_2C_6H_3$,[10] whereas a second insertion occurred for R = *t*Bu.[20] Conversely, the imido complexes [TaCp*MeX(NR)] (R = 2,6-$Me_2C_6H_3$, *t*Bu; X = Cl, Me) reacted with CO to give the dinuclear compound [TaCp*(NR)Me]$_2${μ-$\eta^2$-OC(Me)=C(Me)O} for X = Me[10] and one of the few mononuclear derivatives [TaCp*Cl(O){$\eta^2$-C(Me)=NR}] containing a terminal tantalum-oxo double bond for X = Cl.[10,11]

The versatility and potential applications of all these results determined by the R and X substituents of the imido

[a] Departamento de Química Inorgánica, Universidad de Alcalá, Campus Universitario,
28871 Alcalá de Henares, Madrid, Spain
Fax: +34-91-885-4683
E-mail: pascual.royo@uah.es
[‡] X-ray diffraction studies.

 © 2006 Wiley-VCH Verlag GmbH & Co. KgaA, Weinheim 

complexes [TaCp*MeX(NR)] led us to extend our studies to similar insertion reactions of CNR and CO into the Ta–alkyl bonds of the related oxo-borane compounds [TaCp*$X_2${O·B($C_6F_5$)$_3$}] that have recently been isolated.[21]

## Results and Discussion

The monoalkyl oxo-borane compounds [TaCp*RCl{O·B($C_6F_5$)$_3$}] (R = $CH_2Ph$ **1c**, Me **1d**) were synthesised by an alkyl-chloro metathesis reaction of [TaCp*$R_2${O·B($C_6F_5$)$_3$}] (R = $CH_2Ph$ **1a**, Me **1b**) with one equiv. of $Ph_3CCl$ as chlorinating agent (Scheme 1). The reaction for **1c** proceeded smoothly at room temperature to give a pale yellow solid in good yield, whereas complex **1d** could not be isolated in the solid state. The formation of **1d** was demonstrated on a small scale by $^1$H NMR spectroscopy with a $C_6D_6$ solution of **1b** that was treated with $Ph_3CCl$ and heated to 40 °C. All attempts made to obtain the monomethyl complex through alkylation of [TaCp*$Cl_2${O·B($C_6F_5$)$_3$}] and redistribution reactions between [TaCp*$Cl_2${O·B($C_6F_5$)$_3$}] and [TaCp*$Me_2${O·B($C_6F_5$)$_3$}] failed. The $^{11}$B and $^{19}$F NMR spectra of complexes **1c** and **1d** are consistent with the presence of a tetracoordinate boron atom,[21–31] and the $^1$H NMR spectra with the monosubstitution of only one of the alkyl ligands.

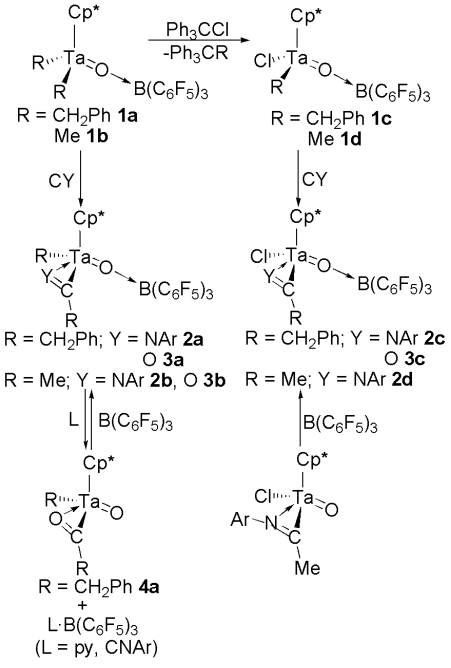


Scheme 1.

The alkyl complexes [TaCp*$R_2${O·B($C_6F_5$)$_3$}] (R = $CH_2Ph$ **1a**, Me **1b**) and [TaCp*($CH_2Ph$)Cl{O·B($C_6F_5$)$_3$}] (**1c**) immediately reacted at room temperature with one equiv. of the isocyanide CNAr (Ar = 2,6-$Me_2C_6H_3$) to give the corresponding $\eta^2$-iminoacyl compounds [TaCp*X{$\eta^2$-C(R)=NAr}{O·B($C_6F_5$)$_3$}] (X = R = $CH_2Ph$ **2a**, Me **2b**; X = Cl, R = $CH_2Ph$ **2c**) in high yields by insertion of the isocyanide ligand into a Ta–C bond (Scheme 1). These pale yellow complexes are air and thermally stable in solution. The $^{13}$C NMR resonance at ca. $\delta$ = 240 ppm is the most apparent spectroscopic feature and confirms the presence of the $\eta^2$-iminoacyl ligand in complexes **2**.

We previously reported[10] on the isolation of the related oxo complex [TaCp*Cl{$\eta^2$-C(Me)=NAr}(O)] from the reaction of the monomethyl compound [TaCp*ClMe(NAr)] with CO through a process that involved insertion of CO into the Ta–Me bond and further rearrangement of the $\eta^2$-acyl intermediate with intramolecular oxo-imido exchange. Since the starting oxo-borane chloro-methyl complex could not be isolated, thus preventing access to the oxo-borane compound [TaCp*Cl{$\eta^2$-C(Me)=NAr}{O·B($C_6F_5$)$_3$}] (**2d**) by insertion of CNAr into the Ta–C bond of the corresponding alkyl-chloro compound, we tried to obtain this compound by an alternative route. With this aim, we investigated the reaction of the oxo iminoacyl compound [TaCp*Cl{$\eta^2$-C(Me)=NAr}(O)] with B($C_6F_5$)$_3$, which afforded **2d** in high yield. The formation of **2d** was confirmed by $^{13}$C and $^{19}$F NMR spectroscopy. The $^{13}$C NMR spectrum shows the resonance corresponding to the $C_{sp^2}$ atom of the $\eta^2$-iminoacyl ligand ($\delta$ = 240.1 ppm) to be slightly low-field shifted with respect to that of the starting compound [TaCp*Cl{$\eta^2$-C(Me)=NAr}(O)] ($\delta$ = 236.8 ppm). An analogous behaviour was observed in the $^1$H NMR spectrum for the methyl-iminoacyl group, which was shifted from $\delta$ = 2.65 ppm in [TaCp*Cl{$\eta^2$-C(Me)=NAr}(O)] to $\delta$ = 2.94 ppm in **2d**.

The molecular structure of compound [TaCp*Cl{$\eta^2$-C(Me)=NAr}{O·B($C_6F_5$)$_3$}] (Ar = 2,6-$Me_2C_6H_3$) (**2d**) was obtained by X-ray diffraction studies. Figure 1 depicts an ORTEP drawing of **2d** with selected bond lengths and angles. Compound **2d** exhibits the typical geometry known for group 5 half-sandwich iminoacyl compounds with a tetrahedral coordination environment around the tantalum atom. Considering the centroid of the Cp* ring and the midpoint of the C(10)–N bond as coordination sites, the other two positions are occupied by the chloro and oxo ligands. The N atom of the $\eta^2$-iminoacyl group is located in a *trans* position with respect to the oxo ligand, as in analogous half-sandwich imido complexes and in [TaCp*Cl{$\eta^2$-C(Me)=NAr}(O)]. Furthermore, the oxygen atom is attached to the boron atom of the B($C_6F_5$)$_3$ group.

All the values of the bond lengths and angles of compound **2d** are very close to the corresponding bond lengths and angles found for the parent compound [TaCp*Cl{$\eta^2$-C(Me)=NAr}(O)][10] except for the Ta–O bond, which is longer in [TaCp*Cl{$\eta^2$-C(Me)=NAr}(O)] [1.731(7) Å] than in **2d** [1.809(5) Å] as a consequence of the coordination of the oxygen atom to the B($C_6F_5$)$_3$ ligand.[21,23–28,30,31] The linear Ta–O–B angle [174.4(6)°] and the B–O bond length [1.52(1) Å] are typical of oxo-borane compounds.[21–31] The Ta–O bond in **2d** is longer than that in the oxo-borane compound [TaCp*$Cl_2${O·B($C_6F_5$)$_3$}][21] [1.784(2) Å]. This bond length is similar to the lower end of the range of Ta–O bond lengths for compounds with Ta–O–Ta bridges (1.82–2.10 Å)[32–35] and with terminal Ta–OH bonds (1.85–1.97 Å).[36–38] However, the single bond Ta–O distances are ca. 2.18 Å,

 © 2006 Wiley-VCH Verlag GmbH & Co. KGaA, Weinheim 

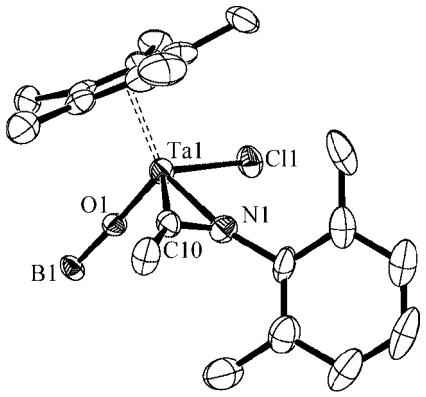


Figure 1. ORTEP diagram of the X-ray structure of compound **2d**. Thermal ellipsoids are drawn at the 50% level, and hydrogen atoms and $C_6F_5$ groups have been omitted for clarity. Selected bond lengths [Å] and angles [°]: Ta–O 1.809(5), Ta–N 2.127(7), Ta–C(10) 2.120(9), Ta–Cl 2.392(2), B–O 1.525(11), N–C(10) 1.26(1), N–Ta–C(10) 34.5(3), C(10)–N–Ta 72.4(5), N–C(10)–Ta 73.1(5), B–O–Ta 174.4(6).

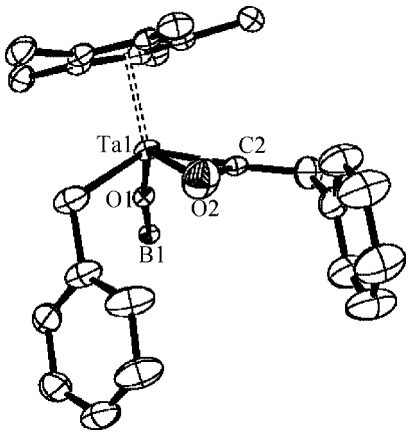


Figure 2. ORTEP diagram of the X-ray structure of compound **3a**. Thermal ellipsoids are drawn at the 50% level, and hydrogen atoms and $C_6F_5$ groups have been omitted for clarity. Selected bond lengths [Å] and angles [°]: Ta–O(1) 1.816(2), Ta–O(2) 2.110(3), Ta–C(1) 2.229(4), Ta–C(2) 2.011(3), B–O(1) 1.512(4), O(2)–C(2) 1.209(4), O(2)–Ta–C(2) 34.02(12), C(2)–O(2)–Ta 68.5(2), O(2)–C(2)–Ta 77.5(2), B–O(1)–Ta 173.02(19).

and thus a bond order of two should be considered for the Ta–O bond in **2d**.

The reaction of the dialkyl [TaCp*$R_2${O·B($C_6F_5$)$_3$}] (R = $CH_2$Ph **1a**, Me **1b**) and the monobenzyl [TaCp*($CH_2$Ph)Cl{O·B($C_6F_5$)$_3$}] (**1c**) complexes with CO in toluene gave the η²-acyl compounds [TaCp*X{η²-C(R)=O}{O·B($C_6F_5$)$_3$}] (X = R = $CH_2$Ph **3a**, Me **3b**; X = Cl, R = $CH_2$Ph **3c**) after ca. 24 h at room temperature in moderate yields (Scheme 1). These pale yellow compounds were air and thermally stable below 120 °C for several hours. The $^{13}$C NMR spectra showed a resonance at ca. $\delta$ = 305 ppm corresponding to the $C_{sp^2}$ atom of the η²-acyl fragment. The slowness of the insertion reactions of CO is in contrast with the rapid transformations observed for complexes **1** with isocyanide and the behaviour observed[10,11] for the reactions of the imido compounds [TaCp*MeX(NR)] (R = 2,6-$Me_2C_6H_3$, *t*Bu; X = Cl, Me) with CO. This difference may be attributed to the lower oxophilicity of the tantalum atom in compounds **1** that is caused by the presence of the oxo ligand.

The X-ray structure of compound **3a** is shown in Figure 2. The environment around the Ta atom is analogous to that described for compound **2d** (see above) with the oxygen atom of the acyl group located *trans* to the oxo-borane ligand, as expected. The Ta–O(1) bond length of 1.816(2) Å is similar to that observed for compound **2d**, and the O(1)–B bond length [1.512(4) Å] and Ta–O(1)–B angle [173.0(2)°] have values that are normally seen for these types of compounds.[21–31]

The whole set of angles and bond lengths of the [Ta-(η²-acyl)] group is in line with compounds of this type[1] and is similar to those found in the other two tantalum-acyl complexes for which X-ray structures are known, [TaCp*Me{η²-C($CH_2CMe_2$Ph)=O}{N(2,6-$Me_2C_6H_3$)}][39] and [TaCp*$Cl_3${η²-C($CH_2CMe_3$)=O}].[40] However, in the particular case of the isostructural imido derivative [TaCp*Me{η²-C($CH_2CMe_2$Ph)=O}{N(2,6-$Me_2C_6H_3$)}], the Ta–O bond [2.21(1) Å] is slightly longer than the corresponding bond in compound **3a** [2.110(3) Å], because of the different *trans* effect and higher donor capacity of the imido ligand.

The insertion of a second CNAr or CO molecule into these new acyl and iminoacyl oxo-borane complexes was not observed, in contrast with the behaviour observed for the analogous *tert*-butyl imido complexes.[20] Rather, all complexes **2**–**3** released the acid-base adduct L·B($C_6F_5$)$_3$ (L = py, CNAr) in the presence of donor ligands such as isocyanide or pyridine.[41] Only in the case of compound **2a** were we able to isolate the borane-free 18-electron compound [TaCp*($CH_2$Ph){η²-C($CH_2$Ph)=NAr}(O)] (**4a**), with a terminal oxo-tantalum bond. The remaining oxo-borane complexes decomposed under similar conditions. The $^{13}$C NMR spectrum of the new oxo iminoacyl compound **4a** showed the η²-iminoacyl $C_{sp^2}$ resonance at $\delta$ = 240.3 ppm. A comparison of this $^{13}$C resonance and that assigned to the $CH_2$–iminoacyl group in the $^1$H NMR spectrum with the corresponding resonances in the parent compound **2a**, showed a behaviour that is opposite to that observed for **2d** and [TaCp*Cl{η²-C(Me)=NAr}(O)].

## Conclusions

The dialkyl oxo-borane compounds [TaCp*$R_2${O·B($C_6F_5$)$_3$}] can be transformed into the monoalkyl derivatives [TaCp*RX{O·B($C_6F_5$)$_3$}] by alkyl-chloro exchange with $Ph_3CCl$. All of these complexes reacted with one molecule of isocyanide or carbon monoxide to give the η²-iminoacyl or η²-acyl compounds, respectively. No further insertion processes have been observed. This behaviour is analogous to that observed for the imido compounds [TaCp*MeX(NR)] (R = 2,6-$Me_2C_6H_3$; X = Cl, Me), although in the oxo-borane compounds the insertion of CO gave stable η²-acyl derivatives because of the presence of a Ta–O multiple bond, which prevents further rearrangement.

 © 2006 Wiley-VCH Verlag GmbH & Co. KGaA, Weinheim 

## Experimental Section

All manipulations were carried out under argon, and solvents were distilled from appropriate drying agents. NMR spectra were recorded at 300.13 ($^1$H NMR), 188.31 ($^{19}$F NMR), 75.47 ($^{13}$C NMR) and 128.38 Hz ($^{11}$B NMR) at room temperature with a Varian Unity 300 ($^1$H, $^{13}$C, $^{19}$F) or Bruker Advance 400 ($^{11}$B NMR) instrument. Chemical shifts ($\delta$, $CDCl_3$) are given in ppm, relative to internal TMS ($^1$H and $^{13}$C NMR), and external $CFCl_3$ ($^{19}$F NMR) and $BF_3{\cdot}OEt_2$ ($^{11}$B NMR). Elemental analyses were performed with a Perkin–Elmer 240C instrument. Compounds [TaCp*Me$_4$],[42] [TaCp*(CH$_2$Ph)$_2${O·B(C$_6$F$_5$)$_3$}],[21] [TaCp*Me$_2${O·B(C$_6$F$_5$)$_3$}],[21] [TaCp*Cl{$\eta^2$-C(Me)=NAr}(O)][10] and B(C$_6$F$_5$)$_3$[43] were prepared by literature methods, and H$_2$O·B(C$_6$F$_5$)$_3$[44] was prepared from H$_2$O and B(C$_6$F$_5$)$_3$ in toluene at room temperature and used in situ without further purification.

**[TaCp*Cl(CH$_2$Ph){O·B(C$_6$F$_5$)$_3$}] (1c):** A suspension of $Ph_3CCl$ (0.14 g, 0.50 mmol) and [TaCp*(CH$_2$Ph)$_2${O·B(C$_6$F$_5$)$_3$}] (**1a**) (0.50 g, 0.49 mmol) in toluene (5 mL) was stirred overnight at room temperature, with a colour change from yellow to brown. Later, all volatile components were removed under vacuum until the volume was ca. 1 mL, leaving a dark oil that was washed with hexane (2 × 10 mL) to yield **1c** as a brownish solid (0.36 g, 76%). $C_{35}H_{22}BClF_{15}OTa$ (970.75): calcd. C 43.31, H 2.28; found C 42.99, H 2.25. $^1$H NMR: $\delta$ = 2.14 (s, 15 H, C$_5$*Me*$_5$), 2.52 (d, $^2J_{H,H}$ = 14.0 Hz, 1 H, C*H*$_2$Ph), 2.80 (d, $^2J_{H,H}$ = 14.0 Hz, 1 H, C*H*$_2$Ph), 6.74 (m, 2 H, C$_6$*H*$_5$), 7.02 (m, 3 H, C$_6$*H*$_5$) ppm. $^{11}$B NMR: $\delta$ = 0.10 [O·B(C$_6$F$_5$)$_3$] ppm; $^{13}$C NMR{$^1$H}: $\delta$ = 11.5 (C$_5$*Me*$_5$), 82.3 (*C*H$_2$Ph), 125.7 (*C*$_5$Me$_5$), 127.1 (*C*$_6$H$_5$), 128.2 (*C*$_6$H$_5$),128.3 (*C*$_6$H$_5$), 131.4 (*C*$_6$H$_5$), 135.0 (*C*$_6$F$_5$), 138.3 (*C*$_6$F$_5$), 145.9 (*C*$_6$F$_5$), 149.1 (*C*$_6$F$_5$) ppm; $^{19}$F NMR: $\delta$ = –132.9 (*o*-C$_6$F$_5$), –157.7 (*p*-C$_6$F$_5$), –163.3 (*m*-C$_6$F$_5$) ppm.

**[TaCp*ClMe{O·B(C$_6$F$_5$)$_3$}] (1d):** A solution of $Ph_3CCl$ (0.080 g, 0.028 mmol) and [TaCp*Me$_2${O·B(C$_6$F$_5$)$_3$}] (**1d**) (0.025 g, 0.028 mmol) in $C_6D_6$ was heated at 45 °C for 18 h. Total transformation of **1b** to **1d** was then observed. $^1$H NMR ($C_6D_6$): $\delta$ = 1.26 (s, 3 H, Ta–*Me*), 2.13 (s, 15 H, C$_5$*Me*$_5$) ppm. $^{11}$B NMR ($C_6D_6$): $\delta$ = 0.05 [O·B(C$_6$F$_5$)$_3$] ppm. $^{19}$F NMR ($C_6D_6$): $\delta$ = –133.0 (*o*-C$_6$F$_5$), –157.2 (*p*-C$_6$F$_5$), –163.3 (*m*-C$_6$F$_5$) ppm.

**[TaCp*(CH$_2$Ph){$\eta^2$-C(CH$_2$Ph)=NAr}{O·B(C$_6$F$_5$)$_3$}] (Ar = 2,6-Me$_2$C$_6$H$_3$) (2a):** A solution of [TaCp*(CH$_2$Ph)$_2${O·B(C$_6$F$_5$)$_3$}] (**1a**) (0.50 g, 0.49 mmol) in toluene (5 mL) was treated with CNAr (0.065 g, 0.50 mmol), and the mixture was stirred for 1 h at room temperature. All volatile components were removed under vacuum, and the remaining solid was washed with hexane (2 × 10 mL) to give **2a** as a white solid (0.49 g, 87%). $C_{51}H_{38}BF_{15}NOTa$ (1157.59): calcd. C 52.91, H 3.31, N 1.21; found C 52.67, H 3.21, N 1.09. $^1$H NMR: $\delta$ = 1.34 (s, 3 H, *Me*$_2$C$_6$H$_3$), 1.41 (s, 3 H, *Me*$_2$C$_6$H$_3$), 1.93 (s, 15 H, C$_5$*Me*$_5$), 2.78 (d, $^2J_{H,H}$ = 12.5 Hz, 1 H, Ta–C*H*$_2$Ph), 2.93 (d, $^2J_{H,H}$ = 12.5 Hz, 1 H, Ta–C*H*$_2$Ph), 4.46 (d, $^2J_{H,H}$ = 17.4 Hz, 1 H, C–C*H*$_2$Ph), 4.56 (d, $^2J_{H,H}$ = 17.4 Hz, 1 H, C–C*H*$_2$Ph), 6.47–7.03 (m, 13 H, C$_6$*H*$_3$ and C$_6$*H*$_5$) ppm. $^{13}$C NMR{$^1$H}: $\delta$ = 11.1 (C$_5$*Me*$_5$), 17.6 (*Me*$_2$C$_6$H$_3$), 18.8 (*Me*$_2$C$_6$H$_3$), 42.2 (C–*C*H$_2$Ph), 54.8 (Ta–*C*H$_2$Ph), 120.1 (*C*$_5$Me$_5$), 123.5–149.2 (*C*$_6$H$_5$, Me$_2$*C*$_6$H$_3$ and *C*$_6$F$_5$), 237.7 (Ta–*C*=N) ppm. $^{19}$F NMR: $\delta$ = –130.7 (*o*-C$_6$F$_5$), –158.3 (*p*-C$_6$F$_5$), –163.8 (*m*-C$_6$F$_5$) ppm. IR (KBr): $\tilde{\nu}$ = 1601 (C=N) cm$^{-1}$.

**[TaCp*Me{$\eta^2$-C(Me)=NAr}{O·B(C$_6$F$_5$)$_3$}] (Ar = 2,6-Me$_2$C$_6$H$_3$) (2b):** The procedure used for **2a**, but starting from [TaCp*Me$_2${O·B(C$_6$F$_5$)$_3$}] (**1b**) (0.50 g, 0.57 mmol) and CNAr (0.079 g, 0.060 mmol), gave **2b** (0.52 g, 91%). $C_{39}H_{30}BF_{15}NOTa$ (1005.41): calcd. C 46.59, H 3.09, N 1.39; found C 46.40, H 3.00, N 1.28. $^1$H NMR: $\delta$ = 0.79 (s, 3 H, Ta–*Me*), 1.48 (s, 3 H, *Me*$_2$C$_6$H$_3$), 1.69 (s, 3 H, *Me*$_2$C$_6$H$_3$), 1.95 (s, 15 H, C$_5$*Me*$_5$), 2.72 (s, 3 H, C–*Me*), 7.06 (m, 2 H, Me$_2$C$_6$*H*$_3$), 7.13 (m, 1 H, Me$_2$C$_6$*H*$_3$) ppm. $^{13}$C NMR{$^1$H}: $\delta$ = 11.0 (C$_5$*Me*$_5$), 17.2 (*Me*$_2$C$_6$H$_3$), 18.6 (*Me*$_2$C$_6$H$_3$), 20.0 (Ta–*Me*), 31.6 (C–*Me*), 118.7 (*C*$_5$Me$_5$), 127.6–148.8 (Me$_2$*C*$_6$H$_3$ and *C*$_6$F$_5$), 238.3 (Ta–*C*=N) ppm. $^{19}$F NMR: $\delta$ = –131.7 (*o*-C$_6$F$_5$), –158.4 (*p*-C$_6$F$_5$), –163.8 (*m*-C$_6$F$_5$) ppm. IR (KBr): $\tilde{\nu}$ = 1629 (C=N) cm$^{-1}$.

**[TaCp*Cl{$\eta^2$-C(CH$_2$Ph)=NAr}{O·B(C$_6$F$_5$)$_3$}] (Ar = 2,6-Me$_2$C$_6$H$_3$) (2c):** The procedure used for **2a**, but starting from [TaCp*Cl(CH$_2$Ph){O·B(C$_6$F$_5$)$_3$}] (**1c**) (0.50 g, 0.52 mmol) and CNAr (0.072 g, 0.55 mmol), gave **2c** (0.51 g, 89%). $C_{44}H_{31}BClF_{15}NOTa$ (1101.91): calcd. C 47.96, H 2.84, N 1.27; found 47.00, H 2.75, N 1.24. $^1$H NMR: $\delta$ = 1.55 (s, 3 H, *Me*$_2$C$_6$H$_3$), 1.64 (s, 3 H, *Me*$_2$C$_6$H$_3$), 2.09 (s, 15 H, C$_5$*Me*$_5$), 4.59 (d, $^2J_{H,H}$ = 18.5 Hz, 1 H, C–C*H*$_2$Ph), 4.72 (d, $^2J_{H,H}$ = 18.5 Hz, 1 H, C–C*H*$_2$Ph), 6.76–7.06 (m, 8 H, C$_6$*H*$_3$ and C$_6$*H*$_5$) ppm. $^{13}$C NMR{$^1$H}: $\delta$ = 11.4 (C$_5$*Me*$_5$), 17.8 (*Me*$_2$C$_6$H$_3$), 21.4 (*Me*$_2$C$_6$H$_3$), 43.3 (C–*C*H$_2$Ph), 123.2 (*C*$_5$Me$_5$), 125.3–149.2 (*C*$_6$H$_5$, Me$_2$*C*$_6$H$_3$ and *C*$_6$F$_5$), 236.7 (Ta–*C*=N) ppm. $^{19}$F NMR: $\delta$ = –130.6 (*o*-C$_6$F$_5$), –157.9 (*p*-C$_6$F$_5$), –163.4 (*m*-C$_6$F$_5$) ppm. IR (KBr): $\tilde{\nu}$ = 1644 (C=N) cm$^{-1}$.

**[TaCp*Cl{$\eta^2$-C(Me)=NAr}{O·B(C$_6$F$_5$)$_3$}] (Ar = 2,6-Me$_2$C$_6$H$_3$) (2d):** A solution of [TaCp*Cl{$\eta^2$-C(Me)=NAr}(O)] (0.25 g, 0.49 mmol) and B(C$_6$F$_5$)$_3$ (0.28 g, 0.51 mmol) in toluene (5 mL) was stirred at room temperature for 1 h. Later, the solution was filtered, layered with hexane (5 mL) and cooled to –10 °C, obtaining **2d** as yellow crystals (0.40 g, 74%). $C_{38}H_{27}BClF_{15}NOTa{\cdot}(C_7H_8)_2$ (1210.09): calcd. C 51.61, H 3.58, N 1.16; found C 51.01, H 3.22, N 1.19. $^1$H NMR: $\delta$ = 1.62 (s, 3 H, *Me*$_2$C$_6$H$_3$), 1.91 (s, 3 H, *Me*$_2$C$_6$H$_3$), 2.18 (s, 15 H, C$_5$*Me*$_5$), 2.94 (s, 3 H, C–*Me*), 7.13 (m, 2 H, Me$_2$C$_6$*H*$_3$), 7.20 (m, 1 H, Me$_2$C$_6$*H*$_3$) ppm. $^{13}$C NMR{$^1$H}: $\delta$ = 11.5 (C$_5$*Me*$_5$), 17.6 (*Me*$_2$C$_6$H$_3$), 19.2 (C–*Me*), 21.1 (*Me*$_2$C$_6$H$_3$), 113.3 (*C*$_5$Me$_5$), 128.7–149.4 (Me$_2$*C*$_6$H$_3$ and *C*$_6$F$_5$), 240.1 (Ta–*C*=N) ppm. $^{19}$F NMR: $\delta$ = –131.5 (*o*-C$_6$F$_5$), –158.4 (*p*-C$_6$F$_5$), –164.0 (*m*-C$_6$F$_5$) ppm. IR (KBr): $\tilde{\nu}$ = 1638 (C=N) cm$^{-1}$.

**[TaCp*(CH$_2$Ph){$\eta^2$-C(CH$_2$Ph)=O}{O·B(C$_6$F$_5$)$_3$}] (3a):** A flask containing a solution of [TaCp*(CH$_2$Ph)$_2${O·B(C$_6$F$_5$)$_3$}] (**1a**) (0.50 g, 0.49 mmol) in toluene (10 mL) was charged with CO, and the mixture was stirred for 24 h at room temperature. The solution was then filtered, all volatile components were removed under vacuum to leave ca. 4 mL of solution and the solution was layered with hexane (4 mL) and cooled to –10 °C to give **3a** as yellow crystals (0.39 g, 70%). $C_{43}H_{29}BF_{15}O_2Ta{\cdot}C_7H_8$ (1146.56): calcd. C 52.38, H 3.25; found C 52.43, H 3.17. $^1$H NMR: $\delta$ = 1.88 (s, 15 H, C$_5$*Me*$_5$), 2.54 (d, $^2J_{H,H}$ = 12.1 Hz, 1 H, Ta–C*H*$_2$Ph), 2.70 (d, $^2J_{H,H}$ = 12.1 Hz, 1 H, Ta–C*H*$_2$Ph), 4.59 (d, $^2J_{H,H}$ = 19.4 Hz, 1 H, C–C*H*$_2$Ph), 4.88 (d, $^2J_{H,H}$ = 19.4 Hz, 1 H, C–C*H*$_2$Ph), 6.70–6.90 (m, 6 H, C$_6$*H*$_5$), 7.20–7.45 (m, 4 H, C$_6$*H*$_5$) ppm. $^{13}$C NMR{$^1$H}: $\delta$ = 10.8 (C$_5$*Me*$_5$), 49.2 (C–*C*H$_2$Ph), 60.0 (Ta–*C*H$_2$Ph), 120.0 (*C*$_5$Me$_5$), 123.5–148.9 (*C*$_6$H$_5$ and *C*$_6$F$_5$), 306.9 (Ta–*C*=O) ppm. $^{19}$F NMR: $\delta$ = –133.0 (*o*-C$_6$F$_5$), –157.7 (*p*-C$_6$F$_5$), –163.4 (*m*-C$_6$F$_5$) ppm. IR (KBr): $\tilde{\nu}$ = 1643 (C=O) cm$^{-1}$.

**[TaCp*Me{$\eta^2$-C(Me)=O}{O·B(C$_6$F$_5$)$_3$}] (3b):** The procedure used for **3a**, but starting from [TaCp*Me$_2${O·B(C$_6$F$_5$)$_3$}] (**1b**) (0.50 g, 0.57 mmol) and CO, gave **3b** as a white solid (0.41 g, 80%). $C_{31}H_{21}BF_{15}O_2Ta$ (902.23): calcd. C 41.27, H 2.35; found C 40.87, H 2.30. $^1$H NMR: $\delta$ = 0.81 (s, 3 H, Ta–*Me*), 1.90 (s, 15 H, C$_5$*Me*$_5$), 3.23 (s, 3 H, C–*Me*) ppm. $^{13}$C NMR{$^1$H}: $\delta$ = 10.6 (C$_5$*Me*$_5$), 28.7 (Ta–*Me*), 37.6 (C–*Me*), 119.4 (*C*$_5$Me$_5$), 134.3–149.8 (*C*$_6$F$_5$), 313.8 (Ta–*C*=O) ppm. $^{19}$F NMR: $\delta$ = –133.2 (*o*-C$_6$F$_5$), –157.7 (*p*-C$_6$F$_5$), –163.4 (*m*-C$_6$F$_5$). IR (KBr): $\tilde{\nu}$ = 1644 (C=O) cm$^{-1}$.

 © 2006 Wiley-VCH Verlag GmbH & Co. KGaA, Weinheim 

**[TaCp*Cl{η²-C(CH₂Ph)=O}{O·B(C₆F₅)₃}] (3c):** The procedure used for **3a**, but starting from [TaCp*Cl(CH₂Ph){O·B(C₆F₅)₃}] (**1c**) (0.50 g, 0.52 mmol) and CO, gave **3c** as a yellowish solid (0.40 g, 78%). $C_{36}H_{22}BClF_{15}O_2Ta$ (998.76): calcd. C 43.29, H 2.22; found C 43.17, H 2.24. $^1$H NMR: $\delta$ = 2.05 (s, 15 H, $C_5Me_5$), 4.41 (d, $^2J_{H,H}$ = 19.0 Hz, 1 H, C–C$H_2$Ph), 4.91 (d, $^2J_{H,H}$ = 19.0 Hz, 1 H, C–C$H_2$Ph), 7.05–7.40 (m, 5 H, $C_6H_5$) ppm. $^{13}$C NMR{$^1$H}: $\delta$ = 10.5 ($C_5Me_5$), 49.2 (C–$C$H$_2$Ph), 123.7 ($C_5$Me$_5$), 127.8–130.0 ($C_6$H$_5$), 135.8, 138.3, 139.2, 141.7, 146.8 and 150.1 ($C_6F_5$), 310.5 (Ta–$C$=O) ppm. $^{19}$F NMR: $\delta$ = –132.5 ($o$-$C_6F_5$), –156.9 ($p$-$C_6F_5$), –162.9 ($m$-$C_6F_5$) ppm. IR (KBr): $\tilde{\nu}$ = 1658 (C=O) cm$^{-1}$.

**[TaCp*(CH₂Ph){η²-C(CH₂Ph)=NAr}(O)] (Ar = 2,6- Me₂C₆H₃) (4a):** A solution of [TaCp*(CH$_2$Ph){η$^2$-C(CH$_2$Ph)=NAr}-{O·B(C$_6$F$_5$)$_3$}] (**2a**) (0.25 g, 0.22 mmol) in toluene (5 mL) was treated with pyridine (0.026 g, 0.33 mmol), and the mixture was stirred for 2 h at room temperature. All volatile components were removed under vacuum until ca. 1 mL remained, and hexane (10 mL) was added to precipitate a white solid that was washed with a hexane/toluene mixture (2 × 10 mL, 9:1) to give **4a** (0.10 g, 72%). $C_{33}H_{38}NOTa$ (645.62): calcd. C 61.39, H 5.93, N 2.17; found C 61.00, H 5.83, N 2.21. $^1$H NMR: $\delta$ = 1.25 (s, 3 H, $Me_2C_6H_3$), 1.72 (d, $^2J_{H,H}$ = 11.9 Hz, 1 H, Ta–C$H_2$Ph), 1.80 (s, 3 H, $Me_2C_6H_3$), 1.99 (s, 15 H, $C_5Me_5$), 2.77 (d, $^2J_{H,H}$ = 11.9 Hz, 1 H, Ta–C$H_2$Ph), 3.75 (d, $^2J_{H,H}$ = 17.6 Hz, 1 H, C–C$H_2$Ph), 4.25 (d, $^2J_{H,H}$ = 17.6 Hz, 1 H, C–C$H_2$Ph), 6.50–7.26 (m, 13 H, $C_6H_3$ and $C_6H_5$) ppm. $^{13}$C NMR{$^1$H}: $\delta$ = 10.9 ($C_5Me_5$), 17.2 ($Me_2C_6H_3$), 18.4 ($Me_2C_6H_3$), 39.3 (C–$C$H$_2$Ph), 48.8 (Ta–$C$H$_2$Ph), 121.1 ($C_5$Me$_5$), 126.1–149.8 ($C_6$H$_5$ and Me$_2C_6$H$_3$), 240.3 (Ta–$C$=N) ppm. IR (KBr): $\tilde{\nu}$ = 1631 (C=N) cm$^{-1}$.

**Crystal Structure Determination for 2d and 3a:** Selected crystals were covered with perfluoropolyether oil and mounted on a Nonius KAPPA-CCD single crystal diffractometer. The crystal structure was solved by direct methods and refined using full-matrix least-squares on $F^2$ (SHELXL-97). All non-hydrogen atoms were anisotropically refined. Hydrogen atoms were geometrically placed and left riding on their parent atoms. Two molecules of toluene crystallised with every molecule of **2d**; both solvent molecules were found in the difference Fourier map but one of them was very disordered and it was not possible to get a chemically sensible model for it, so the Squeeze procedure[45] was used to remove its contribution to the structural factors. In **3a** some restraints on the solvent molecule were applied. Crystal data for both compounds are given in Table 1. CCDC-272817 (for **2d**) and CCDC-272818 (for **3a**) contain the supplementary crystallographic data for this paper. These data can be obtained free of charge from The Cambridge Crystallographic Data Centre via www.ccdc.cam.ac.uk/data_request/cif.

Table 1. Crystallographic data for compounds **2d** and **3a**.

| Compound | **2d** | **3a** |
|---|---|---|
| Empirical formula | $C_{52}H_{43}BClF_{15}NOTa$ | $C_{50}H_{37}BF_{15}O_2Ta$ |
| Formula mass | 1210.08 | 1146.56 |
| $\lambda$ [Å] | 0.71069 | 0.71069 |
| Crystal system | triclinic | triclinic |
| Space group | $P\bar{1}$ | $P\bar{1}$ |
| $T$ [K] | 200(2) | 150(2) |
| $a$ [Å] | 9.565(1) | 12.739(2) |
| $b$ [Å] | 13.7547(3) | 13.171(2) |
| $c$ [Å] | 19.545(3) | 15.104(2) |
| $\alpha$ [°] | 77.483(7) | 88.20(1) |
| $\beta$ [°] | 79.50(1) | 82.58(2) |
| $\gamma$ [°] | 71.389(4) | 63.20(1) |
| $V$ [Å$^3$] | 2361.1(5) | 2242.1(6) |
| $Z$ | 2 | 2 |
| Calcd. density [mg m$^{-3}$] | 1.572 | 1.698 |
| Absorption coefficient [mm$^{-1}$] | 2.478 | 2.555 |
| $\theta$ range [°] | 3.52–27.50 | 3.61–27.50 |
| Reflections collected/unique reflections | 13375/8067 | 19150/10201 |
| $R$(int.) | 0.0863 | 0.0228 |
| Data/restraints/parameters | 8067/3/586 | 10201/239/622 |
| GOF | 1.101 | 1.042 |
| Final $R$ indices | $R_1$ = 0.0575 | $R_1$ = 0.0292 |
| [$I > 2\sigma(I)$] | $wR_2$ = 0.1211 | $wR_2$ = 0.0678 |
| Largest diff. peak/hole [e Å$^{-3}$] | 1.596/–1.899 | 1.303/–1.364 |

## Acknowledgments

We gratefully acknowledge the Ministerio de Educación y Ciencia (project MAT2004–02614) and DGUI-Comunidad de Madrid (project GR/MAT/0622/2004) (Spain) for financial support.

[1] L. D. Durfee, I. P. Rothwell, *Chem. Rev.* **1988**, *88*, 1059.
[2] R. Lai, S. Lebot, F. Djafri, *J. Organomet. Chem.* **1991**, *410*, 335.
[3] M. H. P. Rietveld, H. Hagen, L. van de Water, D. M. Grove, H. Kooijman, N. Veldman, A. L. Spek, G. van Koten, *Organometallics* **1997**, *16*, 168.
[4] A. Castro, M. V. Galakhov, M. Gómez, P. Gómez-Sal, A. Martín, F. Sánchez, P. Velasco, *Eur. J. Inorg. Chem.* **2000**, 2047.
[5] R. Fandos, I. López-Solera, A. Otero, A. Rodríguez, M. J. Ruiz, P. Terreros, *Organometallics* **2004**, *23*, 5030.
[6] L. Kloppenburg, J. L. Petersen, *Organometallics* **1997**, *16*, 3548.
[7] A. Sebastián, Ph. D. thesis, Alcalá University (Alcalá de Henares), **2004**.
[8] M. V. Galakhov, M. Gómez, G. Jiménez, M. A. Pellinghelli, P. Royo, A. Tiripicchio, *Organometallics* **1994**, *13*, 1564.
[9] M. V. Galakhov, M. Gómez, G. Jiménez, P. Royo, M. A. Pellinghelli, A. Tiripicchio, *Organometallics* **1995**, *14*, 2843.
[10] M. Gómez, P. Gómez-Sal, G. Jiménez, A. Martín, P. Royo, J. Sánchez-Nieves, *Organometallics* **1996**, *15*, 3579.
[11] J. Sánchez-Nieves, Ph. D. thesis, Alcalá University (Alcalá de Henares), **2000**.
[12] L. Kloppenburg, J. L. Petersen, *Polyhedron* **1995**, *14*, 69.
[13] C. Valero, M. Grehl, D. Wingbermuhle, L. Kloppenburg, D. Carpenetti, G. Erker, J. L. Petersen, *Organometallics* **1994**, *13*, 415.
[14] F. J. Berg, J. L. Petersen, *Organometallics* **1993**, *12*, 3890.
[15] F. J. Berg, J. L. Petersen, *Organometallics* **1991**, *10*, 1599.
[16] F. J. Berg, J. L. Petersen, *Organometallics* **1989**, *8*, 2461.
[17] N. S. Radu, M. P. Engeler, C. P. Gerlach, T. D. Tilley, A. L. Rheingold, *J. Am. Chem. Soc.* **1995**, *117*, 3621.
[18] S. M. Beshouri, D. E. Chebi, P. E. Fanwick, I. P. Rothwell, J. C. Huffman, *Organometallics* **1990**, *9*, 2375.
[19] M. I. Alcalde, M. P. Gómez-Sal, P. Royo, *Organometallics* **1999**, *18*, 546.
[20] J. Sánchez-Nieves, P. Royo, M. A. Pellinghelli, A. Tiripicchio, *Organometallics* **2000**, *19*, 3161.
[21] J. Sánchez-Nieves, L. M. Frutos, P. Royo, O. Castaño, E. Herdtweck, *Organometallics* **2005**, *24*, 2004.
[22] A. R. Siedle, R. A. Newmark, W. M. Lamanna, J. C. Huffman, *Organometallics* **1993**, *12*, 1491.
[23] J. R. Galsworthy, M. L. H. Green, M. Muller, K. Prout, *J. Chem. Soc., Dalton Trans.* **1997**, 1309.
[24] J. R. Galsworthy, J. C. Green, M. L. H. Green, M. Muller, *J. Chem. Soc., Dalton Trans.* **1998**, 15.
[25] L. H. Doerrer, J. R. Galsworthy, M. L. H. Green, M. A. Leech, *J. Chem. Soc., Dalton Trans.* **1998**, 2483.
[26] L. H. Doerrer, J. R. Galsworthy, M. L. H. Green, M. A. Leech, M. Muller, *J. Chem. Soc., Dalton Trans.* **1998**, 3191.
[27] G. Barrado, L. Doerrer, M. L. H. Green, M. A. Leech, *J. Chem. Soc., Dalton Trans.* **1999**, 1061.

 © 2006 Wiley-VCH Verlag GmbH & Co. KGaA, Weinheim 

[28] Y. Han, C. J. Harlan, P. Stoessel, B. J. Frost, J. R. Norton, S. Miller, B. Bridgewater, Q. Xu, *Inorg. Chem.* **2001**, *40*, 2942.
[29] D. Neculai, H. W. Roesky, A. M. Neculai, J. Magull, B. Walfort, D. Stalke, *Angew. Chem. Int. Ed.* **2002**, *41*, 4294.
[30] F. Wolff, R. Choukroun, C. Lorber, B. Donnadieu, *Eur. J. Inorg. Chem.* **2003**, 628.
[31] M. J. Sarsfield, M. Helliwell, *J. Am. Chem. Soc.* **2004**, *126*, 1036.
[32] M. H. Chisholm, J. C. Huffman, L. S. Tan, *Inorg. Chem.* **1981**, *20*, 1859.
[33] P. Jernakoff, C. D. de Bellefon, G. L. Geoffroy, A. L. Rheingold, S. J. Geib, *Organometallics* **1987**, *6*, 1362.
[34] M. Herberhold, J. Peukert, W. Milius, *J. Prakt. Chem. Chem.-Ztg.* **1999**, *341*, 797.
[35] S. W. Schweiger, D. L. Tillison, M. G. Thorn, P. E. Fanwick, I. P. Rothwell, *J. Chem. Soc., Dalton Trans.* **2001**, 2401.
[36] A. I. Gouzyr, H. Wessel, C. E. Barnes, H. W. Roesky, M. Teichert, I. Uson, *Inorg. Chem.* **1997**, *36*, 3392.
[37] R. E. Blake, D. M. Antonelli, L. M. Henling, W. P. Schaefer, K. I. Hardcastle, J. E. Bercaw, *Organometallics* **1998**, *17*, 718.
[38] R. W. Quan, J. E. Bercaw, W. P. Schaefer, *Acta Crystallogr., Sect. C: Cryst. Struct. Commun.* **1991**, *47*, 2057.
[39] A. Castro, M. V. Galakhov, M. Gómez, P. Gómez-Sal, A. Martín, F. Sánchez, *J. Organomet. Chem.* **2000**, *595*, 36.
[40] T. Y. Meyer, L. R. Garner, N. C. Baenziger, L. Messerle, *Inorg. Chem.* **1990**, *29*, 4045.
[41] W. A. Piers, *Adv. Organomet. Chem.* **2005**, *52*, 1.
[42] R. D. Sanner, S. T. Carter, W. J. Bruton, *J. Organomet. Chem.* **1982**, *240*, 157.
[43] S. Lancaster, www.syntheticpages.org, **2003**, 216.
[44] L. H. Doerrer, M. L. H. Green, *J. Chem. Soc., Dalton Trans.* **1999**, 4325.
[45] P. Vandersluis, A. L. Spek, *Acta Crystallogr. Sect. A* **1990**, *46*, 194.

Received: July 19, 2005
Published Online: November 11, 2005

 © 2006 Wiley-VCH Verlag GmbH & Co. KGaA, Weinheim 

DOI: 10.1002/ejic.200500660

# An Original Supramolecular Helicate from a Bipyridine–Bipyrazine Ligand Strand and $Ni^{II}$ by Self-Assembly

**Julien Mathieu,[a] Bernard Fraisse,[b] Daniel Lacour,[d] Noureddine Ghermani,[c] François Montaigne,[d] and Alain Marsura*[a]**

*Dedicated to the memory of Professor Claude Selve*

**Keywords:** Magnetic properties / N ligands / Nickel / Self assembly / Supramolecular chemistry

A new discrete supramolecular pseudo-helicate has been obtained from a saturated heterotopic methylbipyrazyl–methylbipyridyl ligand strand and $NiCl_2$. The X-ray structure of the dinuclear complex shows the 2-oxapropylene bridge oxygen atoms are engaged in coordination to the octahedral metal centre and a selective ligand inter-strand orientation is promoted in the complex. The crystal packing shows a perfect regular linear arrangement of the asymmetric units giving a packing of interacting molecules having well-defined rectangular and polygonal open channels. Although a paramagnetic behaviour is observed above 10 K, below this temperature a significant deviation of this behaviour suggests the presence of an $Ni^{II}$–$Ni^{II}$ magnetic coupling.

(© Wiley-VCH Verlag GmbH & Co. KGaA, 69451 Weinheim, Germany, 2006)

## Introduction

Over the last ten years of intensive research, numerous supramolecular architectures obtained by self-assembly processes have been reported in the literature, and several reviews[1–6] give an overview of these compounds and their properties. Looking at exploratory investigations, one can see that the didentate heterocyclic 2,2′-bipyridine ligand has played a central role in the spontaneous formation of the main, from simple to sophisticated, supramolecular inorganic architectures.[7,8] A variety of discrete and highly organised species have been obtained by means of ligands designed to afford a well-defined architecture of a single type with given metal ions.[7,8] Famous examples in the literature involve oligobipyridine strands, which lead to double-stranded, triple-stranded or circular helical complexes depending on the metal ion coordination geometry and the nature of the spacer between the bipyridine nuclei.[9–12] Recently, we have studied the self-assembly of sequential 2-oxapropylene-bridged bipyridine–bidiazine ligand strands with tetracoordinate metal ions into selectively oriented H-H (head-to-head) or H-T (head-to-tail) double-stranded helicates.[13,14]

## Results and Discussion

As far as we know no supramolecular inorganic architectures obtained by spontaneous self-assembly of sequential 2-oxapropylene-bridged bipyridine–bidiazine ligand strands with an $Ni^{II}$ cation have been reported in the literature. The formation of the metal complexes was monitored by UV/Vis spectrophotometric titration of a solution of the heterotopic bipyridine–bipyrazine ligand **1**[13,14] at room temp. with $NiCl_2$ (Figure 1) in dry acetonitrile.

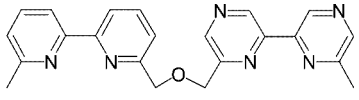

Ligand **1**

[a] GEVSM, UMR CNRS 7565; Structure et Réactivité des Systèmes Moléculaires Complexes, Université Henri Poincaré Nancy-1,
5, rue A. Lebrun, B. P. 403, 54250 Nancy Cedex, France
Fax: +33-3-8368-2345
E-mail: Alain.Marsura@pharma.uhp-nancy.fr
[b] Laboratoire SPMS UMR CNRS 8580, Ecole Centrale Paris, 1, Grande Voie des Vignes, 92295 Châtenay-Malabry, France
Fax: +33-1-4113-1437
E-mail: fraisse@spms.ecp.fr
[c] Laboratoire de Physique Pharmaceutique UMR 8612 Université Paris XI, Faculté de Pharmacie
5, Rue J. B. Clément, 92296 Châtenay-Malabry Cedex, France
Fax: +33-1-46835882
E-mail: noureddine.ghermani@cep.u-psud.fr
[d] Laboratoire de Physique des Matériaux, UMR 7556, Université Henri Poincaré Nancy-1, Faculté des Sciences,
Bd des Aiguillettes B. P. 239, 54506 Vandoeuvre-les-Nancy Cedex, France
Fax: +33-3-83684801
E-mail: montaigne@lpm.u-nancy.fr

 © 2006 Wiley-VCH Verlag GmbH & Co. KgaA, Weinheim 

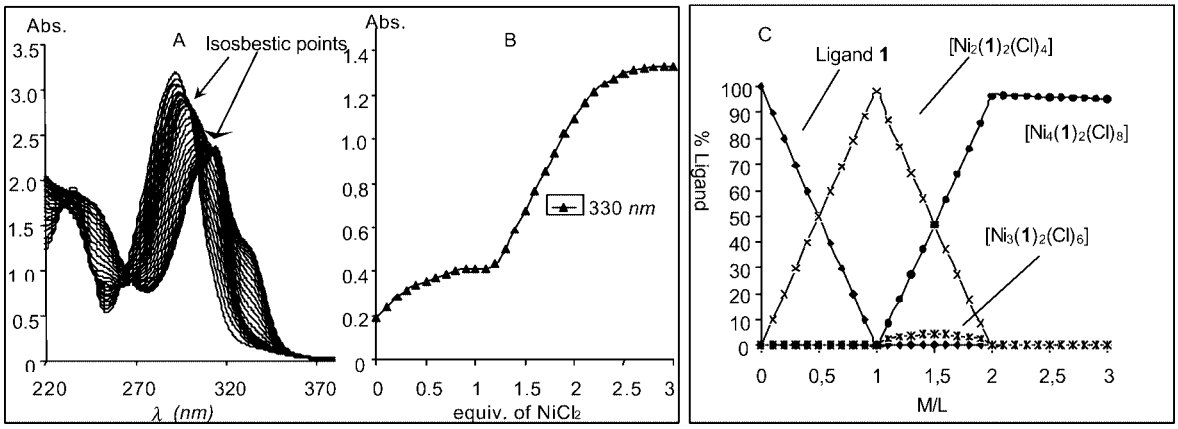


Figure 1. Spectrophotometric titration of the ligand **1** ($10^{-4}$ M) with $NiCl_2$ ($6\times10^{-3}$ M) in MeCN: (A) UV/Vis absorption spectra; (B) plot of absorbance vs. added salt at 330 nm; (C) calculated ligand speciation curves in $CH_3CN$ for ligand **1** and [$Ni^{II}$/ligand **1**] in the range 0.1–3.0.

The titration spectra of ligand **1** display two successive isosbestic points between 220 and 400 nm over the complete titration range. On the addition of $NiCl_2$, a red shift of the absorption spectrum occurs, and a strong absorption and a marked shoulder appear distinctly and successively at $\lambda_{max}$ = 315 ($\varepsilon$ = 21500) and 333 nm ($\varepsilon$ = 12600), thereby indicating the effective coordination of the $Ni^{II}$ ions. The titration plot [Figure 1(B)] shows the formation of a first species with a composition of approximately one Ni ion for 1 equiv. of **1**, in agreement with the X-ray structure of the isolated nickel complex **2**. This is followed by the appearance of a second species upon addition of a second equivalent of $Ni^{II}$ to reach a composition of about two Ni atoms for every equivalent of **1**. UV titration and analysis of the data indicate that the second species could be the complex $[Ni_4(\mathbf{1})_2Cl_8]$, which corresponds to coordination of the remaining nitrogen sites (Figure 2). The binding constants $\log(\beta_{ml})$ for the species $M_mL_l$ were calculated with the SPECFIT program:[15] $[Ni_2(\mathbf{1})_2Cl_4]$ $\log(\beta_{22}) = 34.5\pm0.5$; $[Ni_3(\mathbf{1})_2Cl_6]$ $\log(\beta_{32}) = 41.6\pm1.4$; $[Ni_4(\mathbf{1})_2Cl_8]$ $\log(\beta_{42}) = 51.0\pm2.3$. The distribution curves computed from the formation constants show that the $[Ni_2(\mathbf{1})_2Cl_4]$ and $[Ni_4(\mathbf{1})_2Cl_8]$ complexes are formed quantitatively for M/L = 1 and 2, respectively. According to the speciation [Figure 1(C)], the formation of $[Ni_3(\mathbf{1})_2Cl_6]$ can be neglected.

Figure 2. Proposed structure of the complex $[Ni_4(\mathbf{1})_2Cl_8]$.

ES-MS studies of the MeCN or $CH_2Cl_2$ solutions revealed the presence of ions that could be assigned to $[\{Ni_2(\mathbf{1})_2Cl_2\}]^{2+}$, $[\{Ni_2(\mathbf{1})_2Cl_3\}]^{+}$ and $[\{Ni_3(\mathbf{1})_2Cl_5\}]^{+}$ (all charges were confirmed by partial mass isotopomer distributions and corresponding simulated profiles). This shows unambiguously that the discrete complex **2** contains two ligands and two $Ni^{II}$ ions.

The Ni complex **2** crystallises in the centrosymmetric $P\bar{1}$ space group. The asymmetric unit contains one nickel ion, one bipyridine (bpy) and one bipyrazine (bpz) ligand. The two parts of the dinuclear Ni helicate are related by a centre of inversion, as shown in the ORTEP[16] diagram (Figure 3). In this double-stranded complex, each Ni ion is in a pseudo-octahedral coordination that involves two chlorine anions, two nitrogen atoms of the bipyridine ligand, one nitrogen atom of the bipyrazine molecule and the bridging oxygen atom, which means that the bpz N4, N5 and N6 nitrogen atoms are not connected to any metal centre. The metal–ligand bonds are Ni–N1 = 2.010(6), Ni–N2 = 2.113(5), Ni–N3 = 2.242(7), Ni–O1 = 2.290(5), Ni–Cl2 = 2.327(2) and Ni–Cl1 = 2.369(2) Å.

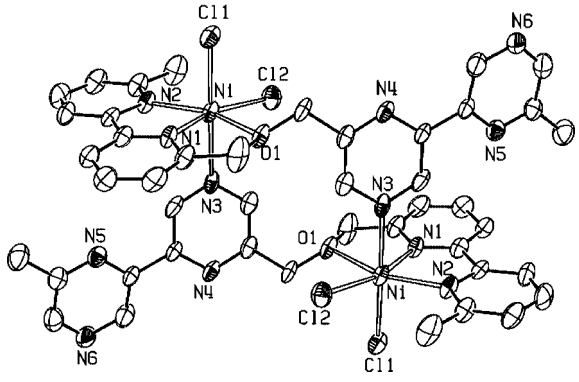


Figure 3. ORTEP drawing of the $Ni^{II}$ complex (H atoms have been omitted for clarity). Thermal ellipsoids are at the 50% probability level.

The distorted octahedra of Ni are characterised by internal angles varying from 74.9(2)° (N1–Ni–O1) to 94.7(1)° (Cl1–Ni–Cl2). In comparison, Ni–N bonds with bpy ligands are found in the range from 2.060 to 2.078 Å in the

 © 2006 Wiley-VCH Verlag GmbH & Co. KGaA, Weinheim 

bis[3,6-(dipyrid-2-ylmethyl)pyridazine]nickel dinuclear helicate,[17] where the metal ion is also octahedrally coordinated. In our Ni complex, the bpy ligand is rigorously planar whereas the bpz one has an N5–C–C–N4 torsion angle of –162.4(7)° (see Figure 3). The metal–metal distance in our Ni complex is 6.96 Å and is much longer than those found in our previous Ag and Cu helicate structures.[13,14] Figure 4 depicts the crystal packing of the (bpy–bpz)Ni complex. The regular linear arrangement of the helicates along the *b* axis gives rise to open rectangular and polygonal channels in the structure. The closest ligand distances found are between two bpy moieties (5.96 Å).

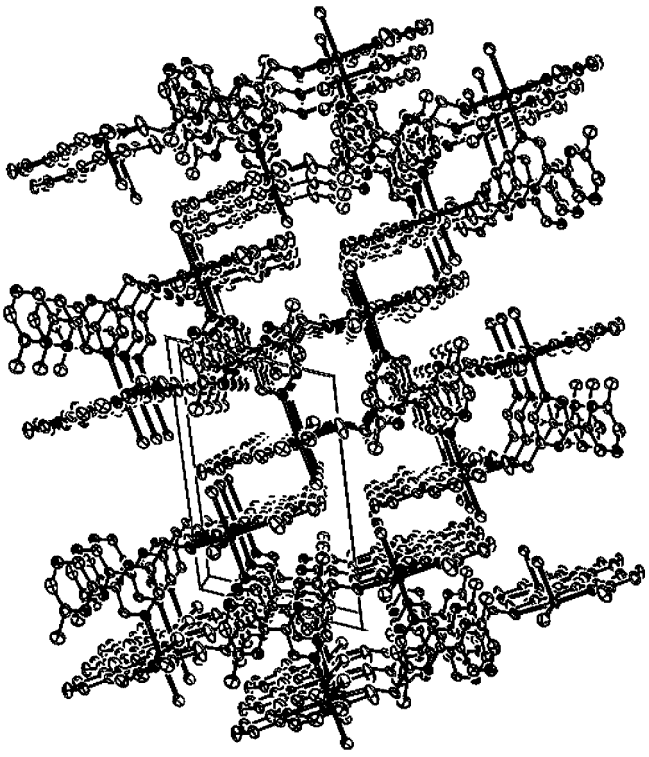

Figure 4. Crystal packing viewed along the *b* axis (Ni bonds are in bold).

### Monocrystal Magnetic Properties

Both the magnetic moment and the AC and DC magnetic susceptibility ($\chi$) of single crystals of the nickel complex **2** were investigated from 2 K to room temperature. Above 100 K the sample magnetic moment is lower than the diamagnetic signal originating from the sample holder and so is close to zero ($< 2\times10^{-7}$ A m$^2$). A plot of the $\chi T$ product vs. $T$ is shown in Figure 5(A) for temperatures between 2 K and 100 K. Figure 5(B) presents the measured magnetic moment vs. the field/temperature ratio for different applied fields and temperatures. The $\chi T$ product is constant from 100 K to about 10 K and the magnetic moment vs. the field/temperature ratio curves are superimposed. This suggests a simple paramagnetic behaviour in this temperature range. Below 10 K, $\chi T$ varies strongly with the temperature, indicating that the sample is not in a paramagnetic regime anymore. This is confirmed by the data set presented in Figure 5(B). Indeed, the magnetic moment vs. the field/temperature curves are not superimposed anymore below 10 K. The continuous line presented in Figure 5(B) is the Brillouin function calculated for two isolated $S = 1$ nuclei with a Landé factor of $g = 2.57$. Below 10 K, the measured magnetic moment is always smaller than expected, suggesting an antiferromagnetic interaction.

Recently, weak magnetic exchange between two $Ni^{II}$ metal centres operating in some diazine complexes over six bonds and over large Ni–Ni internuclear distances up to 6.6 Å has been reported.[18] It is interesting to note that such a weak coupling is maintained at higher internuclear distances in our case, with values of 6.9 Å for the intra-helicate Ni–Ni distance and up to 9.4 Å for the inter-helicate distance.

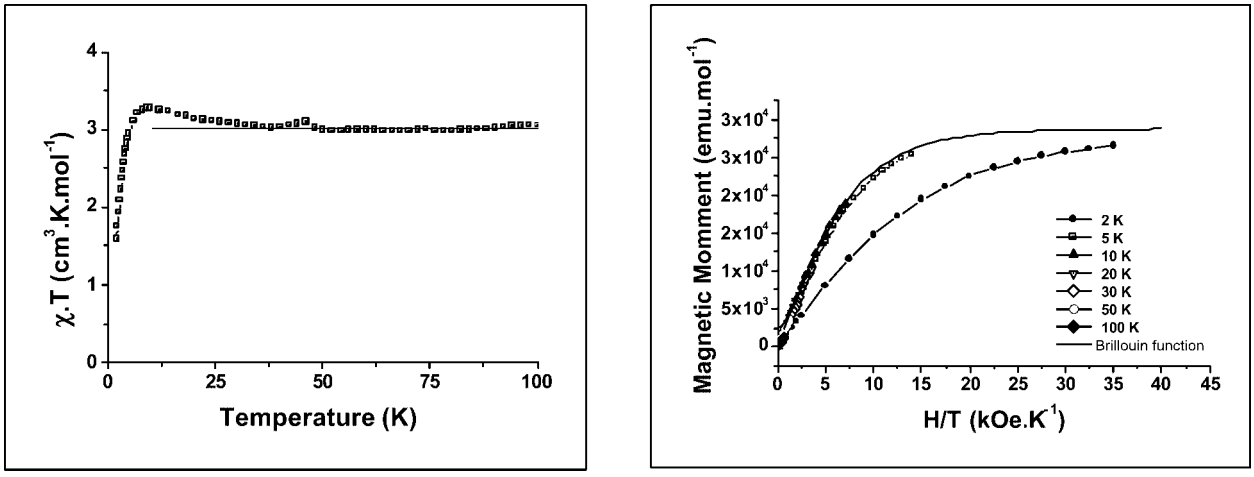


Figure 5. (A, left) DC magnetic susceptibility temperature product vs. temperature. The straight line corresponds to the behaviour expected in a paramagnetic regime. (B, right) Magnetic moment vs. applied field/temperature ratio for different temperatures. The lines between dots are guides for the eyes. The continuous line corresponds to a Brillouin function calculated for two isolated $S = 1$ nuclei (see text).

 © 2006 Wiley-VCH Verlag GmbH & Co. KGaA, Weinheim 

## Conclusions

In contrast to previously reported double-stranded helicates, afforded by the self-assembly of tetracoordinate cations and homotopic or heterotopic bis(didentate) ligands, the nickel cation gives a new discrete assembly involving oxygen atoms of the 2-oxapropylene bridges and two chlorine atoms in a hexacoordinate mode with the metal ion, and so satisfies the "maximum occupation of sites" principle. Moreover, as observed previously with the same heterotopic sequence,[13,14] one can notice a selective interstrand orientation which promotes exclusively $Ni^{II}$ coordination between a bipyrazine and a bipyridine unit in the system. From a magnetic point of view, both observation of a simple paramagnetic behaviour and the deviation from this behaviour below 10 K suggest the presence of a weak, antiferromagnetic $Ni^{II}$–$Ni^{II}$ interaction. In light of these first results, and in order to build a new library of supramolecular systems, complexation studies with other ligands and potentially hexacoordinated metal centres along with deeper investigations of their physical properties are now underway.

## Experimental Section

**General Remarks:** The synthesis of heterotopic ligand **1** has been described by us previously.[13] UV/Vis spectra were recorded with a UVmC$^2$ Safas spectrometer. Mass spectra (ES) were recorded with a Micromass Platform spectrometer. Elemental analyses were obtained with a Perkin–Elmer 240C CHN-O-S analyser.

**$[Ni_2(1)_2Cl_4]$ (2):** $NiCl_2{\cdot}6H_2O$ (31 mg, 0.13 mmol) was added to the ligand **1** (50 mg, 0.13 mmol) in anhydrous $CH_3CN$ (10 mL) under argon. The green solution was stirred at room temp. and, after evaporation of the solvent, the solid residue was crystallised by slow diffusion of diethyl ether into an acetonitrile/chloroform solution. After 2 d, suitable green crystals were obtained. UV/Vis ($CH_3CN$): $\lambda_{max}$ ($\varepsilon$) = 298 nm (28300), 315 (23500), 333 (shoulder) (12600). ESI MS: $m/z$ = 1122.2 [{$Ni_3$(**1**)$_2Cl_5$}]$^+$, 992.6 [{$Ni_2$(**1**)$_2$-$Cl_3$}]$^+$, 478.6 [{$Ni_2$(**1**)$_2Cl_2$}]$^{2+}$. $C_{44}H_{40}Cl_4N_{12}Ni_2O_2$ (1029.4): calcd. C 51.29, H 3.88, N 16.32; found C 50.85, H 3.95, N 15.97.

**Magnetic Measurements:** Both the magnetic moment and the DC magnetic susceptibility ($\chi$) of single crystals of the $Ni^{2+}$ pseudohelicate were investigated from 2 K up to room temperature. The sample mass was 2.4 mg. The magnetic moment evolution with temperature (denoted $T$ as mentioned above) was monitored by SQUID magnetometry in a magnetic field of 0.1 T. The small magnetic contribution originating from the substrate holder was subtracted from the analysed data.

**X-ray Crystallographic Study:** The crystal structure of $C_{44}H_{40}Cl_4N_{12}Ni_2O_2$ [$\rho_{calcd.}$ = 1.61 g cm$^{-3}$, $\mu$(Mo-$K_\alpha$) = 1.19 mm$^{-1}$] was determined from a single-crystal X-ray diffraction experiment performed with an Enraf–Nonius CAD-4F diffractometer (Mo-$K_\alpha$ radiation, $\lambda$ = 0.71073 Å) at room temperature. A large crystal (green, 0.60 × 0.50 × 0.30 mm) was chosen for the experiments. The compound crystallised in the triclinic space group $P\bar{1}$, $Z$ = 1. The unit-cell parameters were obtained by least-squares fit to setting angles of 25 reflections in the range $8° < 2\theta < 30°$. Cell parameters: $a$ = 8.647(2), $b$ = 10.063(8), $c$ = 13.658(4) Å, $\alpha$ = 106.78(4)°, $\beta$ = 106.76(2)°, $\gamma$ = 96.98(4)°, $V$ = 1062(1) Å$^3$. The $\omega$-$2\theta$ scan mode was used to record the diffraction intensities. Three standard reflections were monitored every 2 h in order to control the intensity decay, which did not occur significantly. 6409 reflections were collected up to $2\theta_{max}$ = 59.96°. Lorentz-polarisation corrections and data reduction were performed using the WINGX package[19] for CAD4 collected intensities. The structures were solved by direct methods using the SIR92 program[20] and refined by the full-matrix least squares based on $F^2$ using SHELX97.[21] Thermal displacements of non-hydrogen atoms were refined anisotropically. Hydrogen atoms were included at their idealised positions. During the last cycles of refinement, the best results were obtained with empirical absorption corrections using the XABS2 program in the WINGX package.[19] The final statistical factors were $R1$(all data) = 0.214, $wR2$ = 0.308 for 6166 data and 289 parameters, $R1[F^2 > 2\sigma(I)]$ = 0.0906 for 3009 data with $F^2 > 2\sigma(I)$ and the final residual densities in the unit cell were +1.47 and –1.66 e Å$^{-3}$. CCDC-234807 contains the supplementary crystallographic data for this paper. These data can be obtained free of charge from The Cambridge Crystallographic Data Centre via www.ccdc.cam.ac.uk/data_request/cif.

## Acknowledgments

We would like to thank the French MESR and the CNRS for support, J. M. Ziegler and D. Bouchu for recording the mass spectra, and Mrs. N. Marshall for correcting the manuscript.

[1] J.-M. Lehn, *Supramolecular Chemistry*, VCH, Weinheim, **1995**.
[2] A. F. Williams, *Chem. Eur. J.* **1997**, *3*, 15–25.
[3] M. Albrecht, *Chem. Rev.* **2001**, *101*, 3457–3497.
[4] M. D. Ward, *Annu. Rep. Prog. Chem. Sec. A* **2000**, *96*, 345–385.
[5] J.-M. Lehn, *Chem. Eur. J.* **2000**, *6*, 2097–2102.
[6] C. Piguet, G. Bernardinelli, G. Hopfgartner, *Chem. Rev.* **1997**, *97*, 2005–2062.
[7] C. Kaes, A. Katz, M. W. Hosseini, *Chem. Rev.* **2000**, *100*, 3553–3590 and references cited therein.
[8] D. P. Funeriu, J.-M. Lehn, K. M. Fromm, D. Fenske, *Chem. Eur. J.* **2000**, *6*, 2103–2111.
[9] R. Kramer, J.-M. Lehn, A. Marquis-Rigault, *Proc. Natl. Acad. Sci. USA* **1993**, *90*, 5394–5398.
[10] B. Hasenknopf, J.-M. Lehn, N. Boumediene, E. Leize, A. van Dorsselaer, *Angew. Chem. Int. Ed.* **1998**, *37*, 3265–3268.
[11] B. Hasenknopf, J.-M. Lehn, N. Boumediene, A. Dupont-Gervais, A. van Dorsselaer, B. Kneisel, D. Fenske, *J. Am. Chem. Soc.* **1997**, *119*, 10956–10962.
[12] B. Hasenknopf, J.-M. Lehn, B. Kneisel, G. Baum, D. Fenske, *Angew. Chem. Int. Ed. Engl.* **1996**, *35*, 1838.
[13] J. Mathieu, A. Marsura, N. Bouhmaida, N. Ghermani, *Eur. J. Inorg. Chem.* **2002**, 2433–2437.
[14] J. Mathieu, N. Ghermani, N. Bouhmaida, B. Fenet, A. Marsura, *Eur. J. Inorg. Chem.* **2004**, 5338–5346.
[15] Log $\beta$ values were calculated using the SPECFIT® program v3.0, Spectrum Software Associates, **1993**–**2001**.
[16] M. N. Burnett, C. K. Johnson, ORTEP-III report ORNL-6895, **1996**, Oak Ridge International Laboratory, Tennessee, USA.
[17] C. J. Sumby, P. J. Steel, *Inorg. Chem. Commun.* **2003**, *6*, 127–130.
[18] Z. Xu, L. K. Thompson, V. A. Milway, L. Zhao, T. Kelly, D. O. Miller, *Inorg. Chem.* **2003**, *42*, 2950–2959.
[19] L. J. Farrugia, *J. Appl. Crystallogr.* **1999**, *32*, 837–838.
[20] A. Altomare, G. Cascarano, C. Giacovazzo, A. Guagliardi, *J. Appl. Crystallogr.* **1993**, *26*, 343–350.
[21] G. M. Sheldrick, *SHELXL97* and *SHELXS97, Program for the Refinement of Crystal Structures*, University of Göttingen, Germany, **1997**.

Received: July 25, 2005
Published Online: November 22, 2005

 © 2006 Wiley-VCH Verlag GmbH & Co. KGaA, Weinheim 

DOI: 10.1002/ejic.200500674

# Reactivity of the Inversely Polarized Arsaalkenes R–As=C(NMe$_2$)$_2$ {R = [(η$^5$-C$_5$Me$_5$)(CO)$_2$Fe], *t*BuC(O), 4-Et–C$_6$H$_4$C(O)} towards Phosphavinylidene Complexes [η$^5$-(C$_5$H$_5$)(CO)$_2$M=P=C(SiMe$_3$)$_2$] (M = Mo, W)

**Lothar Weber,*[a] Philipp Bayer,[a] Stefan Uthmann,[a] Thomas Braun,[a] Hans-Georg Stammler,[a] and Beate Neumann[a]**

**Keywords:** Arsaalkenes / Heteroallyl ligands / Molybdenum / Phosphavinylidene complexes / Tungsten

The reaction of the phosphavinylidene complexes [Cp(CO)$_2$-M=P=C(SiMe$_3$)$_2$] [Cp = C$_5$H$_5$, M = Mo (**2**), W (**3**)] with the ferrioarsaalkene [Cp*(CO)$_2$Fe–As=C(NMe$_2$)$_2$] (**1a**) (Cp* = C$_5$Me$_5$) afforded the novel η$^3$-2-phospha-1-arsaallyl complexes [η$^3$-{[Fe]–As–P–C(SiMe$_3$)$_2$}M(CO)$_2$Cp] {M = Mo, [Fe] = [Cp*(CO)$_2$Fe] (**4a**);W (**5a**)}. Similarly, treatment of equimolar amounts of **3** with arsaalkene *t*Bu–C(O)–As=C(NMe$_2$)$_2$ (**1b**) gave rise to the formation of [η$^3$-{*t*BuC(O)–As–P–C(SiMe$_3$)$_2$}-W(CO)$_2$Cp] (**5b**) by an arsinidene transfer process. In contrast to this, the more reactive arsaalkene 4-Et–C$_6$H$_4$C(O)–As=C(NMe$_2$)$_2$ (**1c**) and complex **3** underwent reaction to give the cyclic phosphenium complex [Cp(CO)$_2$W=P–O–C$^a$(4-Et–C$_6$H$_4$)=As–C$^b$(SiMe$_3$)$_2$(*P*–*C$^b$*)] (**6**). The novel compounds **4a**, **5a**, **5b**, and **6** were characterized by elemental analyses and by means of spectroscopy (IR, $^1$H, $^{13}$C, $^{31}$P NMR). Moreover, the molecular structures of **4a**, **5b**, and **6** were elucidated by X-ray diffraction analyses.

(© Wiley-VCH Verlag GmbH & Co. KGaA, 69451 Weinheim, Germany, 2006)

## Introduction

The search for novel ligand systems remains an important target for both academic and industrial reasons. Prominent examples are N-heterocyclic carbenes, which, as ancillary ligands in transition-metal complexes, have significantly improved the efficiency of a number of catalyzed processes.[1] Other remarkable examples concern phosphaalkenes, phospholyl compounds, and phosphinines, which have recently emerged from the status of laboratory curiosities to become valuable ligands in complex catalysis.[2] Compared to a plethora of synthetically useful η$^3$-allyl complexes[3,4] only a few coordination compounds with η$^3$-1-phosphaallyl ligands such as **I**[5] or η$^3$-1,3-diphosphaallyl ligands such as **II**[6] and **III**[7] have been described. In the dinuclear complexes of type **IV** the 1,3-diphosphaallyl unit is incorporated in a 2,4-phospha-1-metallabutadiene ligand (Scheme 1).[8]

Complex **III** exhibits catalytic activity in ethylene polymerization.[7] Whereas 1,2-diphosphaallyllithium compounds[9] and η$^1$-complexes of the isomeric 1,2-diphosphaallyl ligand **V** have been known for some years,[10] a paper concerning η$^3$-complex **VI** was only recently published.[11]

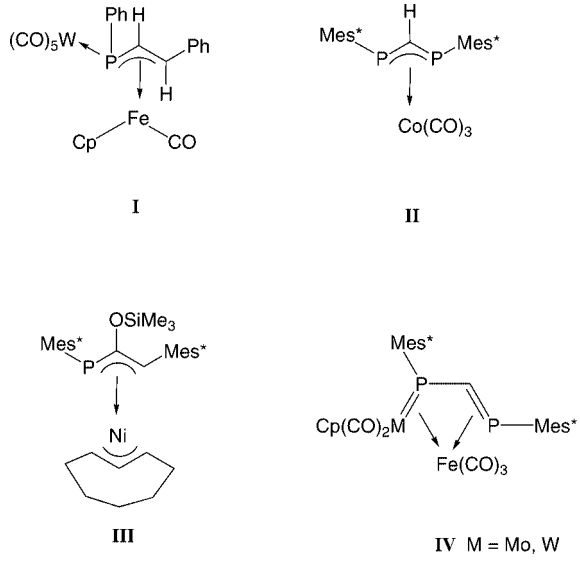


Scheme 1. (Heteroallyl)transition-metal complexes.

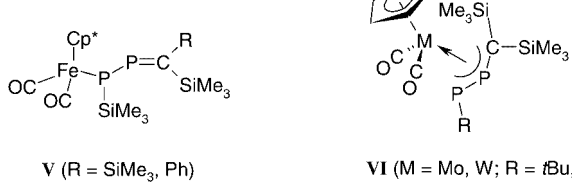


[a] Fakultät für Chemie der Universität Bielefeld, Universitätsstrasse 25, 33615 Bielefeld, Germany
Fax: +49-521-106-6146
E-mail: lothar.weber@uni-bielefeld.de

 © 2006 Wiley-VCH Verlag GmbH & Co. KgaA, Weinheim InterScience 

In this paper we report on the reactivity of inversely polarized arsaalkenes R–As=C(NMe$_2$)$_2$ [**1**: **a**: R = Cp*(CO)$_2$-Fe, **b**: *t*BuC(O), **c**: 4-Et–C$_6$H$_4$C(O)] with phosphavinylidene complexes [Cp(CO)$_2$M=P=C(SiMe$_3$)$_2$] (**2**: M = Mo; **3**: M = W),[12] whereby the first complexes with $\eta^3$-2-phospha-1-arsaallyl ligands are formed. Part of this work has previously been published in a short communication.[13]

## Results and Discussion

Treatment of complexes [Cp(CO)$_2$M=P=C(SiMe$_3$)$_2$] (**2**: M = Mo; **3**: M = W) with an equimolar amount of ferrioarsaalkene [Cp*(CO)$_2$Fe–As=C(NMe$_2$)$_2$] (**1a**)[14] in toluene solution over a temperature range of –30 °C to ambient temperature afforded the deep red crystalline $\eta^3$-2-phospha-1-arsaallyl complexes **4a** (35% yield) and **5a** (52% yield). Purification of the products was effected by column chromatography on Florisil with a mixture of hexane/diethyl ether (2:1, v/v) (**4a**) or pentane/diethyl ether (5:1, v/v) (**5a**) as eluents. The air- and moisture-sensitive complexes are well soluble in saturated hydrocarbons, ethereal and aromatic solvents. Analogously, reaction of compound **1b** with an equimolar amount of **3** gives rise to the formation of heteroallyl complex **5b** as an orange solid in 63% yield (Scheme 2). Tetrakis(dimethylamino)ethene is formed as a by-product. After removal of toluene from the reaction mixture, a few drops of the alkene were distilled off and identified by comparison of the $^1$H and $^{13}$C NMR spectra with those of an authentic sample.

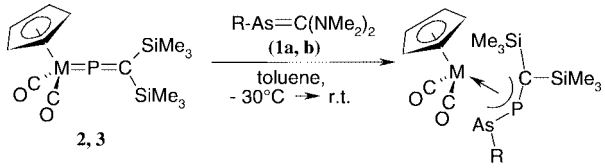


| | R | M |
|---|---|---|
| **4a** | Cp*(CO)$_2$Fe | Mo |
| **5a** | Cp*(CO)$_2$Fe | W |
| **5b** | *t*Bu-C(O) | W |

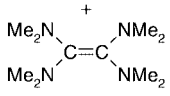


Scheme 2. Formation of the 2-phospha-1-arsaallyl complexes **4a**, **5a**, **5b**.

A singlet at $\delta$ = 4.1 ppm in the $^{31}$P{$^1$H} NMR spectrum of **4a**, a doublet in the $^{13}$C{$^1$H} NMR spectrum at $\delta$ = 49.9 ppm ($J_{P,C}$ = 105 Hz), and singlets in the $^1$H NMR spectrum for two different trimethylsilyl groups ($\delta$ = 0.26, 0.61 ppm), the pentamethylcyclopentadienyl ($\delta$ = 1.46 ppm) and the cyclopentadienyl ligands ($\delta$ = 5.10 ppm) as well as the absence of resonances due to the C(NMe$_2$)$_2$ fragment indicate the combination of the phosphavinylidene unit of **2** and the arsanediyl group of **1a** to a novel ligand system in complex **4a**. Accordingly, the tungsten analogue **5a** and the (pivaloylphosphaarsaallyl)tungsten complex **5b** display singlets at $\delta$ = –18.7 and –8.9 ppm in the $^{31}$P{$^1$H} NMR spectrum. This high-field position is typical for $^{31}$P{$^1$H} resonances of $\eta^3$-phosphaallyl complexes of tungsten as evident from [$\eta^3$-(2,4,6-*t*Bu$_3$C$_6$H$_2$PCHCH$_2$)W(CO)$_2$Cp] ($\delta$ = –48.9 and –28.0 ppm for both isomers).[15] In the $\eta^3$-1,2-diphosphaallyl complex **VI** the resonances for the central P atom were observed at $\delta$ = –6.8 ppm (M = Mo, R = *t*Bu) and $\delta$ = –61.6 ppm (M = W, R = *t*Bu).[11] In the $^{13}$C{$^1$H} NMR spectra of **4a**, **5a**, and **5b** the carbon atoms of the 2-phospha-1-arsaallyl ligands appear as doublets at $\delta$ = 49.9 ppm ($J_{P,C}$ = 105.0 Hz), 35.7 ($J_{P,C}$ = 101.2 Hz), and 31.8 ($J_{P,C}$ = 98.5 Hz) ppm. The $^{13}$C NMR resonances of the carbonyl ligands were observed at $\delta$ = 234.0 (s), 236.0 (s) (Mo–CO); 216.7 (s), 218.65 (d, $J_{P,C}$ = 11.5 Hz) (Fe–CO) for **4a**, at $\delta$ = 222.7 (s), 224.6 (s) (W–CO); 217.1 (s), 219.0 (s) (Fe–CO) for **5a**, and at $\delta$ = 222.8 (s), 223.9 (s) for **5b**. A $^{13}$C NMR doublet at δ = 233.5 ($J_{P,C}$ = 4.1 Hz) ppm in the spectrum of **5b** was attributed to the acylic carbonyl group. These resonances are shifted to a lower field relative to those of precursors **2** ($\delta$ = 230.4 ppm)[12b] and **3** ($\delta$ = 218.9 ppm)[12b] indicating the improved donor capacity of the $\eta^3$-2-phospha-1-arsaallyl ligands over the phosphavinylidene system. Similar observations were made with the $\eta^3$-1,2-diphosphaallyl complexes of type **VI** [e.g., M = Mo, R = *t*Bu; $\delta^{13}$CO = 234.3 (s), 235.5 (s) ppm]. This is also mirrored by the carbonyl stretching frequencies in the IR spectra of **4a**, **5a**, and **5b**, which are observed as intense bands at $\tilde{\nu}$= 1929, 1850 cm$^{-1}$ (**4a**), at $\tilde{\nu}$= 1923, 1843 cm$^{-1}$ (**5a**), and at $\tilde{\nu}$= 1941, 1874 cm$^{-1}$ (**5b**). The differences between the ν(CO) absorptions of **5a** and **5b** are due to the electron-donating iron substituent in **5a** and the electron-withdrawing pivaloyl group in **5b**. The corresponding bands in the precursors **2** and **3** appear at $\tilde{\nu}$= 1944, 1882 cm$^{-1}$ (KBr) and 1952, 1880 cm$^{-1}$ (*n*-hexane).[12b] In the IR spectrum of 1,2-diphosphaallyl complexes **VI** ν(CO) bands were registered at $\tilde{\nu}$= 1943, 1877 cm$^{-1}$ (M = Mo; R = *t*Bu) and at $\tilde{\nu}$= 1938, 1851 cm$^{-1}$ (M = W; R = *t*Bu).[11]

Single crystals of **4a** and **5a** suitable for an X-ray diffraction analysis were grown from a 1:9 mixture of diethyl ether/*n*-pentane at –30 °C. Compound **5a** is isostructural to **4a**, and only the latter will be discussed in detail.

The analysis (see Figure 1) displays a molecule with a distorted piano-stool geometry [As(1)–Mo(1)–C(20) = 63.87(7)°, C(20)–Mo(1)–C(21) = 80.83(11)°, C(21)–Mo(1)–C(13) = 69.07(9)°], with two nearly linear carbonyl ligands [Mo(1)–C(20)–O(3) = 170.9(2)°, Mo(1)–C(21)–O(4) = 175.7(2)°]. The most interesting part of the molecule is the unprecedented 2-phospha-1-arsaallyl ligand which is unsymmetrically linked to the metal atom in an $\eta^3$-fashion through bonds Mo(1)–As(1) [2.7644(3) Å], Mo(1)–P(1) [2.4940(6) Å], and Mo(1)–C(13) [2.420(2) Å]. The latter bond length significantly exceeds the Mo(1)–C distances of the [CpMo] part of the molecule [2.316(2)–2.371(2) Å]. In the (1,2-diphosphaallyl)molybdenum complex **VI** the corresponding Mo–C bond length was determined to be 2.437(1) Å.[11] The distances between the Mo atom and the terminal carbon atom in **4a** as well as in **VI** clearly exceed the corresponding Mo–C bond lengths in 1-phosphaallyl complex **VII** [2.357(3) Å].[5c]

 © 2006 Wiley-VCH Verlag GmbH & Co. KGaA, Weinheim 

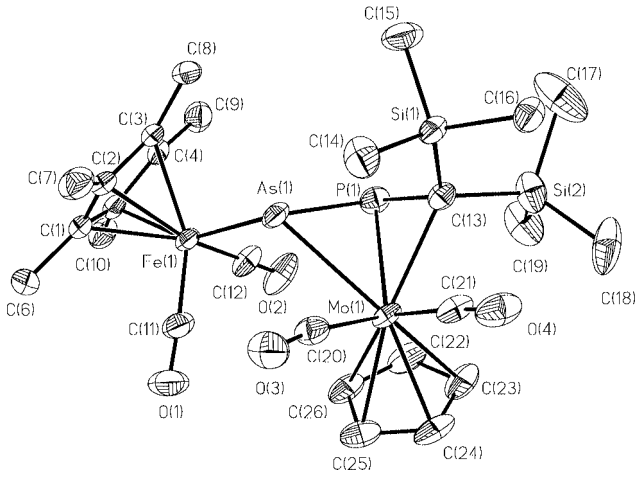


Figure 1. Molecular structure of **4a** in the crystal. Selected bond lengths [Å] and angles [°]: Mo(1)–C(20) 1.953(2), Mo(1)–C(21) 1.959(2), Mo(1)–C(13) 2.420(2), Mo(1)–P(1) 2.4940(6), Mo(1)–As(1) 2.7644(3), P(1)–As(1) 2.2507(7), P(1)–C(13) 1.791(2), As(1)–Fe(1) 2.4098(4), C(13)–Si(1) 1.898(2), C(13)–Si(2) 1.895(2), C(20)–Mo(1)–C(21) 80.83(11), C(21)–Mo(1)–C(13) 69.07(9), C(20)–Mo(1)–As(1) 63.83(7), As(1)–P(1)–C(13) 99.15(7), P(1)–As(1)–Fe(1) 106.59(2), P(1)–C(13)–Si(1) 120.88(12), P(1)–C(13)–Si(2) 108.67(11).

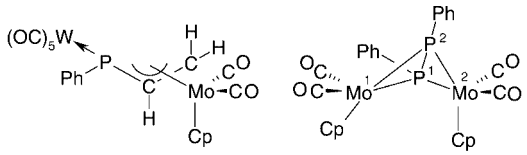


**VII** **VIII**

The metal–phosphorus distances in both complexes **4a** [2.4940(6) Å] and **VI** (M = Mo) [2.4960(3) Å] are identical, and intermediate between the Mo–P bond lengths Mo(1,2)–P(1) [2.466, 2.470 Å] and Mo(1,2)–P(2) [2.542, 2.546 Å] in **VIII**.[16] The Mo(1)–As(1) bond in **4a** is lengthened when compared with the Mo–As contacts in tetrahedrane **IX** [2.531(3), 2.645(3) Å].[17]

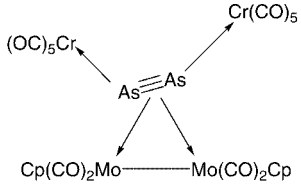


**IX**

Due to the π-interaction with a metal atom, the As–P distance within the 2-phospha-1-arsaallyl ligand in **4a** [2.2507(7) Å] is longer than the unsupported As=P double bonds in the structurally characterized compounds {$(Me_3Si)_2CH$}As=P(2,4,6-$tBu_3C_6H_2$) [2.124 Å][18] or [Cp*-$(CO)_2$FeAs{$Cr(CO)_5$}=P(2,4,6-$tBu_3C_6H_2$)] [2.155(1) Å].[19]

The bond length P(1)–C(13) in **4a** [1.791(2) Å]–as is also found in **VI** (M = Mo) [1.7875(12) Å]–is elongated with respect to a localized and unsupported P=C double bond (1.65–1.72 Å),[20] but is clearly shorter than a P–C single bond (av. 1.85 Å).[21] In **VII** the corresponding bond length was determined to be 1.755(3) Å.[5c] The atoms Fe(1) and Si(2) in **4a** are directed towards the phosphorus atom enclosing angles Fe(1)–As(1)–P(1) [106.59(2)°], As(1)–P(1)–C(13) [99.15(7)°], and P(1)–C(13)–Si(2) [108.67(11)°]. Substituent $Si(1)(CH_3)_3$ at C(13) is located above the plane defined by the atoms As(1), P(1), and C(13) with an angle P(1)–C(13)–Si(1) of 120.88(12)°.

From the view-point of the Wade–Mingos rules molecule **4a** as well as the related compounds **5a** and **5b** possess four skeleton atoms and 14 skeleton electrons and thus have to be regarded as *arachno* clusters.[22] Orange single crystals of the ($\eta^3$-2-phospha-1-arsaallyl)tungsten complex **5b** were grown from diethyl ether/*n*-pentane (1:5) at –30 °C (see Figure 2). The analysis shows a molecule, the core of which is similar to that of **4a** with the pivaloyl substituent and the group $Si(1)Me_3$ directed towards the central atom P(1) of the $\eta^3$-heteroallyl ligand. The bonds As(1)–P(1) [2.269(1) Å] and P(1)–C(8) [1.806(2) Å] within the 2-phospha-1-arsaallyl ligand of **5b** are slightly longer than in **4a**. The bond As(1)–C(15) to the carbonyl carbon atom of the pivaloyl substituent [2.063(2) Å] is markedly elongated when compared with the As–C(O) contact in the precursor arsaalkene [1.938(4) Å].[23] The sum of single bond radii of As and C is 1.98 Å.[24] The formal As=C double bond of precursor **1b** was elongated to 1.924(5) Å[23] [in Cp*$(CO)_2$Fe–As=C$(NMe_2)_2$: As–C = 1.876(8) Å].[14] The bond length C(15)–O(3) is that of a localized carbonyl group.[24] The atoms C(15) and Si(1) are located in the plane defined by the atoms C(8), P(1), and As(1). These atoms are attached to the tungsten center by bonds W(1)–As(1) [2.759(1) Å], W(1)–P(1) [2.498(1) Å], and W(1)–C(8) [2.439(2) Å]. They are all well comparable to those in **5a**: W(1)–As(1) [2.7854(2) Å], W(1)–P(1) [2.4955(5) Å], and W(1)–C(8)

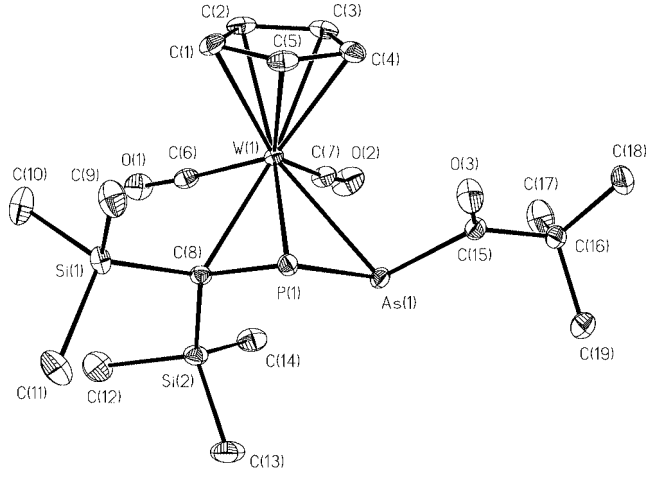


Figure 2. Molecular structure of **5b** in the crystal. Selected bond lengths [Å] and angles [°]: W(1)–C(6) 1.968(2), W(1)–C(7) 1.977(2), W(1)–C(8) 2.439(2), W(1)–P(1) 2.498(1), W(1)–As(1) 2.759(1), P(1)–C(8) 1.806(2), P(1)–As(1) 2.269(1), As(1)–C(15) 2.063(2), C(8)–Si(1) 1.912(2), C(8)–Si(2) 1.922(2), O(3)–C(15) 1.214(2), C(15)–C(16) 1.541(2), C(6)–W(1)–C(7) 80.30(8), C(6)–W(1)–C(8) 67.13(7), C(7)–W(1)–As(1) 67.62(6), C(8)–P(1)–As(1) 97.66(6), P(1)–As(1)–C(15) 93.86(5), As(1)–C(15)–O(3) 122.37(13), O(3)–C(15)–C(16) 122.47(16), As(1)–C(15)–C(16) 115.07(12), P(1)–C(8)–Si(1) 107.49(9), P(1)–C(8)–Si(2) 122.05(10), Si(1)–C(8)–Si(2) 114.60(9).

 © 2006 Wiley-VCH Verlag GmbH & Co. KGaA, Weinheim 

[2.411(2) Å]. The W–As π-bonds in [η¹:η²-PhAs=AsPhW(CO)$_5$]$_2$ [2.728(4) and 2.769(4) Å] are similar to the W–As bond length in **5b**. The W–P π-bond length in η³-{2,4,6-*t*Bu$_3$C$_6$H$_2$–P(O)CHCH$_2$}W(CO)$_2$Cp [2.488(1) Å] is also in good agreement with the respective atom distance in **5b**.[25] The W(1)–C(8) bond in **5b** [2.439(2) Å], however, is markedly lengthened in comparison to those in η³-{2,4,6-*t*Bu$_3$C$_6$H$_2$P(O)CHCH$_2$}W(CO)$_2$Cp [2.344(5), 2.335(4) Å].[25]

To the best of our knowledge compounds **4a**, **5a**, and **5b** are the first η³-2-phospha-1-arsaallyl complexes. One η¹-2-phospha-1-arsaallyl complex (η⁵-C$_5$Me$_5$)(CO)$_2$FeAs(SiMe$_3$)–P=C(SiMe$_3$)$_2$ was recently described.[26] 2-Phospha-1-arsapropenes are rare compounds. To the best of our knowledge there are two accounts in the literature of such species. Thermolabile Ph$_2$As–P=C(Ph)SiMe$_3$[27] decomposes within 1 d to Ph$_4$As$_2$ and a diphosphabicyclobutane, whereas *t*Bu$_2$As–P=C(SiMe$_3$)$_2$ is stable at ambient temperature.[28]

Reaction of phosphavinylidene complex **3** with the more reactive arsaalkene 4-Et–C$_6$H$_4$C(O)As=C(NMe$_2$)$_2$ (**1c**) in diethyl ether took a completely different course. Here the cyclic phosphenium complex **6** was isolated as red crystals in 41% yield. (Scheme 3).

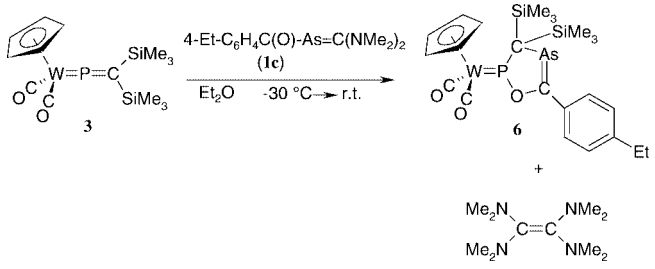


Scheme 3. Formation of the phosphenium complex **6**.

The $^{31}$P{$^{1}$H} NMR spectrum of **6** displays a singlet at $\delta$ = 313.2 ppm with $^{183}$W satellites ($J_{P,W}$ = 728 Hz), which indicates the presence of a W=P double bond. The data are comparable with the $^{31}$P NMR spectra of complexes **Xa**, **b** ($\delta$ = 306.4 ppm; 244.8 ppm, $J_{P,W}$ = 604 Hz)[29] and **IV** (M = Mo: $\delta$ = 304 ppm; M = W: $\delta$ = 246.8 ppm, $J_{P,W}$ = 638 Hz).[8]

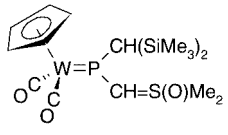


**Xa**: M = Mo
**Xb**: M = W

Both silyl groups are chemically and magnetically equivalent giving rise to a singlet at $\delta$ = 0.47 ppm in the $^{1}$H NMR spectrum and a singlet at $\delta$ = 1.9 ppm in the $^{13}$C{$^{1}$H} NMR spectrum of the compound. A doublet of low intensity at $\delta$ = 60.1 ppm ($J_{P,C}$ = 50.3 Hz) is due to a quaternary carbon atom adjacent to the P atom. The two chemically and magnetically equivalent carbonyl ligands give rise to a singlet at $\delta$ = 226.9 ppm with $^{183}$W satellites ($J_{W,C}$ = 183 Hz). A singlet at $\delta$ = 222.8 ppm is assigned to the $^{13}$C nucleus of an As=C double bond. This value falls in the range of $\delta$ = 200.6 ppm in MesAs=CHNMe$_2$ to $\delta$ = 241.5 ppm in Me$_3$Si-As=C(OSiMe$_3$)*t*Bu.[30] The IR spectrum in the region of the CO stretching modes is characterized by two intense bands at $\tilde{\nu}$ = 1938, 1859 cm$^{-1}$. No bands are found for the $\tilde{\nu}$(CO) mode of an acylarsane (e.g., $\tilde{\nu}$ = 1660 cm$^{-1}$ in **5b**). Yellow single crystals of compound **6** (Figure 3) were obtained from a diethyl ether solution at –30 °C. The analysis displays a molecule with a distorted piano-stool geometry [P(1)–W(1)–C(1) 95.1(1)°, P(1)–W(1)–C(2) 96.2(1)°, C(1)–W(1)–C(2) 84.6(1)°] with two nearly linear carbonyl ligands [W(1)–C(1)–O(1) 177.8(3)°, W(1)–C(2)–O(2) 175.1(2)°].

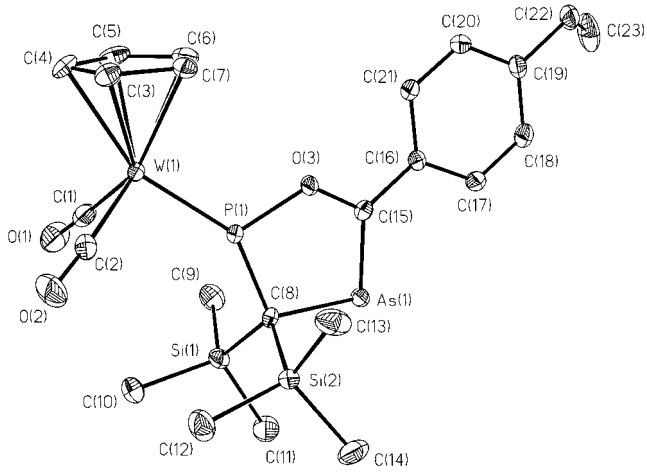


Figure 3. Molecular structure of **6** in the crystal. Selected bond lengths [Å] and angles [°]: W(1)–C(1) 1.976(3), W(1)–C(2) 1.960(3), W(1)–P(1) 2.232(1), P(1)–O(3) 1.698(2), O(1)–C(1) 1.159(3), O(2)–C(2) 1.164(3), O(3)–C(15) 1.372(3), C(15)–C(16) 1.472(3), As(1)–C(15) 1.832(2), As(1)–C(8) 2.023(2), C(8)–Si(1) 1.932(3), C(8)–Si(2) 1.941(3), C(1)–W(1)–C(2) 84.6(1), C(1)–W(1)–P(1) 95.1(1), C(2)–W(1)–P(1) 146.0(1), W(1)–P(1)–O(3) 114.2(1), W(1)–P(1)–C(8) 146.0(1), O(3)–P(1)–C(8) 99.8(1), P(1)–C(8)–As(1) 106.7(1), C(8)–As(1)–C(15) 92.1(1), As(1)–C(15)–O(3) 118.5(2), P(1)–O(3)–C(15) 118.7(1), O(3)–C(15)–C(16) 114.5(2), As(1)–C(15)–C(16) 127.0(2).

The third leg is represented by a 1,2,4-oxaphospharsolenium ligand which is linked to the metal atom through a W=P double bond of 2.232(1) Å. The bond length lies between those in [Cp(CO)$_2$W=PO$^a$–CMe$_2$–CMe$_2$–O$^b$(*P*–*O*$^b$)] [2.181 Å][31] and Cp(CO)$_2$W=P(*t*Bu)$_2$ [2.284(4) Å].[32] This ring ligand without precedent features an As–C(15) double bond of 1.832(2) Å, which is well comparable to the As–C separation in the metalloarsaalkene [Cp(CO)$_2$Fe–As=C(OSiMe$_3$)*t*Bu] [1.821(2) Å].[33] The bond length C(15)–O(3) [1.372(3) Å] is similar to the one in the metalloarsaalkene [1.356(3) Å], both being shorter with respect to an sp$^2$ C–O single bond (ca. 1.41 Å).[34] The contacts P(1)–O(3) [1.698(2) Å] and P(1)–C(8) [1.814(2) Å] are markedly shorter than the sum of the covalent radii (1.76 and 1.87 Å) but still reflect bond orders of unity. The five-membered ring is slightly puckered (sum of endocyclic angles 535°). The plane defined by the atoms P(1), O(3), and C(8) bisects the angle C(1)–W(1)–C(2), enclosing angles of 43° with vector W(1)–C(1) and 41° with vector W(1)–C(2).

 © 2006 Wiley-VCH Verlag GmbH & Co. KGaA, Weinheim 

### Mechanisms

It is conceivable that the formation of complexes **4a**, **5a**, and **5b** is initiated by the nucleophilic attack of the arsaalkene through its As atom on the phosphorus center of precursors **2** and **3** to give adduct **A**. Extrusion of $C(NMe_2)_2$ would lead to intermediate **B**. A σ/π-type rearrangement of **B** affords the final products (see Scheme 4).

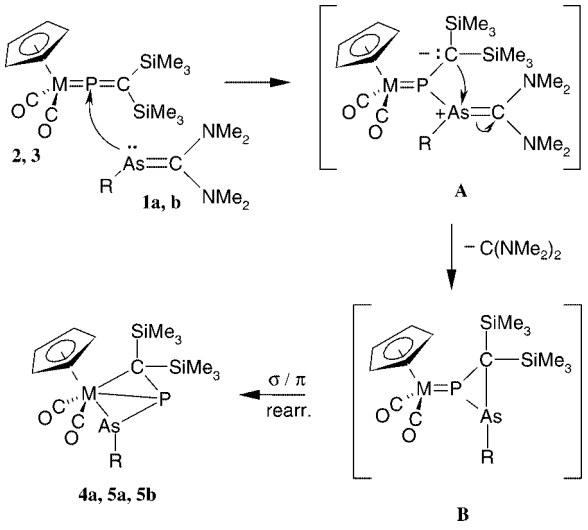


Scheme 4. Proposed mechanism for the formation of **4a**, **5a**, and **5b**.

The formation of the functionalized phosphenium complex **6** may be initiated by the nucleophilic attack of arsaalkene **1c** through its electron-abundant arsenic atom at the phosphorus center of **3** affording zwitterion **C**, which collapses to phospharsirenium complex **D**. Incorporation of the carbonyl group into the As–P bond of the strained ring leads to the observed product **6** (Scheme 5).

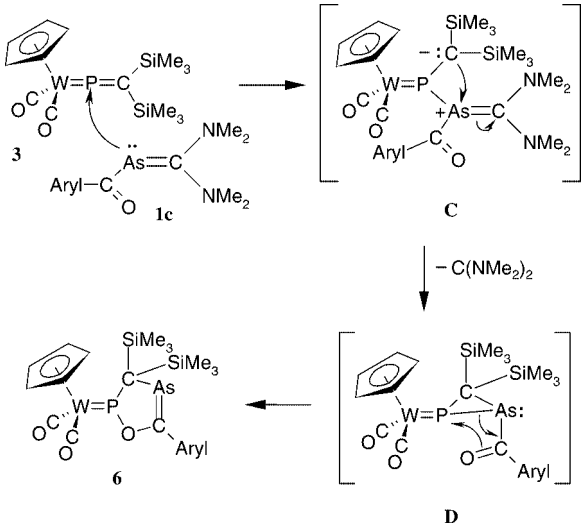


Scheme 5. Proposed mechanism for the formation of **6**.

## Conclusions

Transition-metal-induced cleavages of inversely polarized arsaalkenes to give cyclotriarsanes[35] or an $\eta^2$-diarsene complex[36] were observed. Here the smooth generation of $\eta^3$-2-phospha-1-arsaallyl complexes **4a**, **5a**, **5b**, and complex **6** featuring the 1,2,4-oxaphospharsolenium ligand underlines the ability of arsaalkenes to act as convenient sources for arsanediyl (arsinidene) units under mild conditions.

## Experimental Section

**General:** All manipulations were performed under dry, oxygen-free nitrogen using standard Schlenk techniques. Solvents were rigorously dried with an appropriate drying agent and freshly distilled under $N_2$ before use. The following compounds were prepared according to literature procedures: $[Cp(CO)_2M{=}P{=}C(SiMe_3)_2]$ [M = Mo (**2**), W (**3**)],[12] $[Cp^*(CO)_2Fe{-}As{=}C(NMe_2)_2]$ (**1a**),[14] $Me_3Si{-}As{=}C(NMe_2)_2$.[14] IR: Bruker FT-IR VECTOR 22. $^1$H-, $^{13}$C-, and $^{31}$P NMR ($C_6D_6$, room temp.): Bruker AM Avance DRX 500 ($^1$H: 500.13 Hz; $^{13}$C: 125.75 MHz; $^{31}$P: 202.46 MHz); references: $SiMe_4$ ($^1$H, $^{13}$C), 85% $H_3PO_4$ ($^{31}$P). Florisil (Merck), pivaloyl chloride, and 4-ethylbenzoyl chloride were purchased commercially.

***t*BuC(O)As=C(NMe$_2$)$_2$ (1b):** A solution of pivaloyl chloride (0.18 g, 1.50 mmol) in *n*-pentane (10 mL) was added dropwise to a chilled solution (–30 °C) of $Me_3SiAs{=}C(NMe_2)_2$ (0.37 g, 1.50 mmol) in *n*-pentane (30 mL). A yellow precipitate separated. Stirring was continued for 30 min, and the solvent was decanted. The precipitate was washed twice with cold *n*-pentane (30 mL, –30 °C) and dried in vacuo to afford 0.27 g (69%) of **1b** as a pale yellow solid. IR (Nujol): $\tilde{\nu}$= 1584, 1530 cm$^{-1}$. $^1$H NMR: $\delta$ = 1.40 (s, 9 H, *t*Bu), 2.65 (s, 12 H, $NCH_3$) ppm. $^{13}C\{^1H\}$ NMR: $\delta$ = 27.9 [s, $C(CH_3)_3$], 43.5 (s, $NCH_3$), 49.8 [s, $C(CH_3)_3$], 210.7 (s, $CN_2$), 240.1(s, CO) ppm. Because of the pronounced thermolability of the compound it was not possible to obtain reliable elemental analyses.

**[Cp(CO)$_2$Mo{η$^3$-[Cp*(CO)$_2$Fe]AsPC(SiMe$_3$)$_2$}] (4a):** A solution of **1a** (0.76 g, 1.81 mmol) in toluene (20 mL) was added dropwise to a well-stirred chilled solution (–30 °C) of **2** (0.72 g, 1.81 mmol) in toluene (25 mL). It was slowly warmed to ambient temperature and stirring was continued for 12 h. The reaction mixture was freed from solvent and volatile components. The black residue was dissolved with diethyl ether (10 mL), then Florisil was added (5 g) and the slurry was concentrated to dryness. The coated Florisil was transferred to the top of a column ($d$ = 1.5 cm, $l$ = 6 cm) charged with Florisil (20 g). A dark red zone was eluted with a 2:1 mixture of diethyl ether/*n*-pentane. Removal of solvents from the eluate afforded 0.46 g (35%) of dark red crystalline **4a**. IR (KBr): $\tilde{\nu}$= 1850, 1929, 1977 cm$^{-1}$ (C≡O). $^1$H NMR: $\delta$ = 0.26 (s, 9 H, $SiMe_3$), 0.61 (s, 9 H, $SiMe_3$), 1.46 (s, 15 H, $C_5Me_5$), 5.10 (s, 5 H, Cp) ppm. $^{13}C\{^1H\}$ NMR: $\delta$ = 4.27 (s, $SiCH_3$), 4.35 (s, $SiCH_3$), 9.4 [s, $C_5(CH_3)_5$], 49.9 (d, $J_{P,C}$ = 105 Hz, $PCSi_2$), 91.2 (s, Cp), 95.6 [s, $C_5(CH_3)_5$], 216.7 (s, FeCO), 218.65 (d, $J_{P,C}$ = 11.5 Hz, FeCO), 234.3 (s, MoCO), 236.8 (s, MoCO) ppm. $^{31}P\{^1H\}$ NMR: $\delta$ = 4.1 (s) ppm. $C_{26}H_{38}AsFeMoO_4PSi_2$ (728.44): calcd. C 42.87, H 5.26; found C 43.17, H 5.29.

**[Cp(CO)$_2$W{η$^3$-[Cp*(CO)$_2$Fe]AsPC(SiMe$_3$)$_2$}] (5a):** Analogously, the combination of **1a** (0.76 g, 1.81 mmol) in toluene (20 mL) with **3** (0.89 g, 1.81 mmol) in toluene (25 mL) at –30 °C and identical workup [Florisil, diethyl ether/*n*-pentane (5:1)] afforded 0.77 g (52%) of dark red crystalline **5a**. IR (KBr): $\tilde{\nu}$= 1843, 1923, 1975 cm$^{-1}$ (C≡O). $^1$H NMR ($C_6D_6$): $\delta$ = 0.25 (s, 9 H, $SiMe_3$), 0.66

 © 2006 Wiley-VCH Verlag GmbH & Co. KGaA, Weinheim 

Table 1. Crystal data and data collection parameters.

| Compound | **4a** | **5b** | **6** |
|---|---|---|---|
| Empirical formula | $C_{26}H_{38}AsFeMoO_4PSi_2$ | $C_{19}H_{32}AsO_3PSi_2W$ | $C_{23}H_{32}AsO_3PSi_2W$ |
| $M_r$ [g mol$^{-1}$] | 728.42 | 654.37 | 702.41 |
| Crystal dimensions [mm] | 0.25 × 0.25 × 0.24 | 0.28 × 0.22 × 0.22 | 0.38 × 0.32 × 0.20 |
| Crystal system | monoclinic | monoclinic | monoclinic |
| Space group | $P2_1/n$ | $P2_1/c$ | $C2/c$ |
| $a$ [Å] | 12.9620(1) | 12.9170(18) | 25.798(4) |
| $b$ [Å] | 18.3280(2) | 10.7550(6) | 16.597(2) |
| $c$ [Å] | 13.7430(2) | 17.904(3) | 15.674(3) |
| $\beta$ [°] | 104.2460(8) | 93.036(13) | 126.137(8) |
| $V$ [Å$^3$] | 3164.49(6) | 2483.8(6) | 5420.0(15) |
| $Z$ | 4 | 4 | 8 |
| $\rho_{calcd.}$ [g cm$^{-3}$] | 1.529 | 1.750 | 1.722 |
| $\mu$ [mm$^{-1}$] | 2.047 | 6.150 | 5.643 |
| $F(000)$ | 1480 | 1280 | 2752 |
| $\theta$ [°] | 2.95–30.00 | 3.30–30.00 | 3.02–27.50 |
| No. refl. collected | 18141 | 87578 | 81627 |
| No. refl. unique | 9224 | 7234 | 6231 |
| $R$ (int) | 0.0186 | 0.0501 | 0.0453 |
| No. refl. [$I > 2\sigma(I)$] | 7859 | 6307 | 5302 |
| Refined parameters | 336 | 253 | 287 |
| GOF | 1.035 | 1.061 | 1.141 |
| $R_F$ [$I > 2\sigma(I)$] | 0.0318 | 0.0167 | 0.0173 |
| $wR_{F2}$ [$I > 2\sigma(I)$] | 0.0757 | 0.0326 | 0.0364 |
| $\Delta\rho_{max/min}$ [e·Å$^{-3}$] | 0.970/–0.829 | 0.652/–0.573 | 0.979/–0.790 |

(s, 9 H, $SiMe_3$), 1.47 (s, 15 H, $C_5Me_5$), 5.13 (s, 5 H, Cp) ppm. $^{13}C\{^1H\}$ NMR ($C_6D_6$): $\delta$ = 4.4 (d, $J_{P,C}$ = 9.2 Hz, $SiCH_3$), 9.5 [s, $C_5(CH_3)_5$], 10.1 (s, $SiCH_3$), 35.7 (d, $J_{P,C}$ = 101.2 Hz, $PCSi_2$), 89.6 (s, Cp), 95.6 [s, $C_5(CH_3)_5$], 217.1 (s, FeCO), 219.0 (s, FeCO), 222.7 (s, WCO), 224.6 (s, WCO) ppm. $^{31}P\{^1H\}$ NMR ($C_6D_6$): $\delta$ = –18.7 (s) ppm. $C_{26}H_{38}AsFeO_4PSi_2W$ (816.35): calcd. C 38.26, H 4.49; found C 38.68, H 4.90.

**[Cp(CO)$_2$W{η$^3$-{*t*BuC(O)}AsPC(SiMe$_3$)$_2$}] (5b):** A chilled solution (–30 °C) of arsaalkene **1b** (1.81 mmol) in diethyl ether (20 mL) was added dropwise to a well-stirred cold solution (–30 °C) of complex **3** (0.89 g, 1.81 mmol) in diethyl ether (25 mL). Stirring at –30 °C was continued for 4 h before the reaction mixture was slowly warmed to room temp. After 12 h of stirring, solvent and volatile components were removed in vacuo. The black residue was dissolved in diethyl ether (10 mL). Florisil (5 g) was added and the slurry was concentrated to dryness. As described earlier, the crude material was chromatographed on a Florisil column ($d$ = 1.5 cm, $l$ = 6 cm) charged with Florisil (20 g). An orange-red zone was eluted with a diethyl ether/pentane mixture (5:1). Removal of solvents from the eluate afforded 0.75 g (63%) of orange crystalline **5b**. IR (KBr): $\tilde{\nu}$= 1941, 1874 (C≡O), 1660 (C=O) cm$^{-1}$. $^1H$ NMR: $\delta$ = 0.16 (d, $J_{P,H}$ = 1.6 Hz, 9 H, $SiMe_3$), 0.45 (s, 9 H, $SiMe_3$), 1.05 (s, 9 H, *t*Bu), 4.96 (s, 5 H, Cp) ppm. $^{13}C\{^1H\}$ NMR: $\delta$ = 4.0 (d, $J_{P,C}$ = 9.7 Hz, $SiCH_3$), 8.5 (s, $SiCH_3$), 26.2 [s, $C(CH_3)_3$], 31.8 [d, $J_{P,C}$ = 98.5 Hz, $C(SiMe_3)_2$], 50.1 [s, $C(CH_3)_3$], 90.1 (s, Cp), 222.8 (s, WCO), 223.9 (s, WCO), 233.53 (d, $J_{P,C}$ = 4.1 Hz, AsCO) ppm. $^{31}P\{^1H\}$ NMR: $\delta$ = –8.9 (s) ppm. $C_{19}H_{32}AsO_3PSi_2W$ (654.38): calcd. C 34.87, H 4.93; found C 34.82, H 4.92.

**[Cp(CO)$_2$W=POC$^a$(4-Et–C$_6$H$_4$)=AsC$^b$(SiMe$_3$)$_2$(*P*–*C*$^b$)] (6):** A solution of 4-ethylbenzoyl chloride (0.61 g, 3.62 mmol) in diethyl ether (10 mL) was added dropwise to a chilled solution (–30 °C) of $Me_3Si$-iAs=$C(NMe_2)_2$ (0.89 g, 3.62 mmol). Stirring was continued for 30 min to give **1c**. A solution of complex **3** (0.89 g, 1.81 mmol) in diethyl ether (20 mL) was slowly added with vigorous stirring. It was slowly warmed to room temp. and stirring was continued for 12 h. It was concentrated to dryness and the black residue was dissolved in diethyl ether (10 mL). Florisil (5 g) was added and the slurry was freed from solvent. The coated Florisil was transferred onto the top of a column ($d$ = 1.5 cm, $l$ = 6 cm) charged with Florisil (20 g). A red zone was eluted with pentane. Removal of solvents in vacuo afforded 0.52 g (41%) of deep red crystalline **6**. IR (KBr): $\tilde{\nu}$= 1859, 1938 (C≡O) cm$^{-1}$. $^1H$ NMR: $\delta$ = 0.47 (s, 18 H, $SiMe_3$), 1.01 (t, $J_{H,H}$ = 7.5 Hz, 3 H, $CH_3CH_2$), 2.30 (q, $J_{H,H}$ = 7.5 Hz, 2 H, $CH_3CH_2$), 5.15 (s, 5 H, Cp), 6.87 (d, $J_{H,H}$ = 8.2 Hz, 2 H, Ph), 7.77 (d, $J_{H,H}$ = 8.2 Hz, 2 H, Ph) ppm. $^{13}C\{^1H\}$ NMR: $\delta$ = 1.9 (s, $SiMe_3$), 15.4 (s, $CH_3CH_2$), 29.2 (s, $CH_3CH_2$), 60.1 [d, $J_{P,C}$ = 60.3 Hz, $C(SiMe_3)_2$], 89.6 (s, Cp), 124.4 (s, Ph), 128.3 (s, Ph), 128.7 (s, Ph), 147.4 (s, Ph), 222.8 (s, As=C), 226.9 (s, $J_{W,C}$ = 183 Hz, C≡O) ppm. $^{31}P\{^1H\}$ NMR: $\delta$ = 313.2 ($J_{P,W}$ = 728 Hz) ppm. $C_{23}H_{32}AsO_3PSi_2W$ (702.42): calcd. C 39.33, H 4.59; found C 39.47, H 4.69.

**X-ray Crystallography:** Crystallographic data were collected with a Nonius Kappa CCD diffractometer with Mo-$K_\alpha$ (graphite monochromator, $\lambda$ = 0.71073 Å) at 100 K. Crystallographic programs used for the structure solution and refinement were SHELXS-97,[37] SIR-97,[38] and SHELXL-97.[37] The structures were solved by direct methods and were refined by using full-matrix least squares on $F^2$ of all unique reflections with anisotropic thermal parameters for all non-hydrogen atoms. Hydrogen atoms were included at calculated positions with $U$(H) = 1.2 $U_{eq}$ for $CH_2$ groups, $U$(H) = 1.5 $U_{eq}$ for $CH_3$ groups. Crystal data for the compounds are listed in Table 1. CCDC-250373 (**4a**), -279437 (**5b**), and -279438 (**6**) contain the supplementary crystallographic data for this paper. These data can be obtained free of charge from The Cambridge Crystallographic Data Centre via www.ccdc.cam.ac.uk/data_request/cif.

[1] Review: W. A. Herrmann, *Angew. Chem.* **2002**, *114*, 1342–1363; *Angew. Chem. Int. Ed.* **2002**, *41*, 1290–1309.

[2] Review: L. Weber, *Angew. Chem.* **2002**, *114*, 583–592; *Angew. Chem. Int. Ed.* **2002**, *41*, 563–572.

 © 2006 Wiley-VCH Verlag GmbH & Co. KGaA, Weinheim 

[3] a) Review: G. Wilke, *Angew. Chem.* **1966**, *78*, 157–172; *Angew. Chem. Int. Ed. Engl.* **1966**, *5*, 151; b) S. G. Davies, M. L. H. Green, D. M. P. Mingos, *Tetrahedron* **1978**, *34*, 3047–3077.
[4] a) B. M. Trost, L. Weber, P. E. Strege, T. J. Fullerton, T. J. Dietsche, *J. Am. Chem. Soc.* **1978**, *100*, 3416–3425; b) B. M. Trost, L. Weber, P. E. Strege, T. J. Fullerton, T. J. Dietsche, *J. Am. Chem. Soc.* **1978**, *100*, 3426–3435.
[5] a) F. Mercier, J. Fischer, F. Mathey, *Angew. Chem.* **1986**, *98*, 347–348; *Angew. Chem. Int. Ed. Engl.* **1986**, *25*, 357–358; b) F. Mercier, C. Hugel-Le Goff, F. Mathey, *Organometallics* **1988**, *7*, 955–963; c) C. Hugel-Le Goff, F. Mercier, L. Ricard, F. Mathey, *J. Organomet. Chem.* **1989**, *363*, 325–333.
[6] R. Appel, W. Schuhn, F. Knoch, *Angew. Chem.* **1985**, *97*, 421–422; *Angew. Chem. Int. Ed. Engl.* **1985**, *24*, 420–421.
[7] W. Keim, R. Appel, S. Gruppe, F. Knoch, *Angew. Chem.* **1987**, *99*, 1042–1045; *Angew. Chem. Int. Ed. Engl.* **1987**, *26*, 1012–1015.
[8] H. H. Karsch, H.-U. Reisacher, B. Huber, G. Müller, K. Jörg, W. Malisch, *New J. Chem.* **1989**, *13*, 319–327.
[9] G. Bruder, Ph. D. Thesis, University of Bonn, **1989**, p. 42–44.
[10] a) L. Weber, R. Kirchhoff, R. Boese, H.-G. Stammler, B. Neumann, *Organometallics* **1993**, *12*, 731–737; b) L. Weber, R. Kirchhoff, R. Boese, *Chem. Ber.* **1993**, *126*, 1963–1968.
[11] L. Weber, G. Noveski, U. Lassahn, H.-G. Stammler, B. Neumann, *Eur. J. Inorg. Chem.* **2005**, 1940–1946.
[12] a) A. M. Arif, A. H. Cowley, C. M. Nunn, S. Quashie, N. C. Norman, A. G. Orpen, *Organometallics* **1989**, *8*, 1878–1884; b) E. Niecke, H.-J. Metternich, M. Nieger, D. Gudat, P. Wenderoth, W. Malisch, C. Hahner, W. Reich, *Chem. Ber.* **1993**, *126*, 1299–1309.
[13] L. Weber, P. Bayer, H.-G. Stammler, B. Neumann, *Chem. Commun.* **2005**, 1595–1597.
[14] L. Weber, O. Kaminski, H.-G. Stammler, B. Neumann, *Chem. Ber.* **1996**, *129*, 223–226.
[15] F. Mercier, F. Mathey, *Organometallics* **1990**, *9*, 863–864.
[16] D. Fenske, K. Merzweiler, *Angew. Chem.* **1986**, *98*, 357–358; *Angew. Chem. Int. Ed. Engl.* **1986**, *25*, 338–339.
[17] G. Huttner, B. Sigwarth, O. Scheidsteger, L. Zsolnai, O. Orama, *Organometallics* **1985**, *4*, 326–332.
[18] A. H. Cowley, J. G. Lasch, N. C. Norman, M. Pakulski, B. R. Whittlesey, *J. Chem. Soc., Chem. Commun.* **1983**, 881–882.
[19] L. Weber, D. Bungardt, R. Boese, *Chem. Ber.* **1988**, *121*, 1535–1539.
[20] Review: L. Weber, *Angew. Chem.* **1996**, *108*, 292–310; *Angew. Chem. Int. Ed. Engl.* **1996**, *35*, 271–288.
[21] D. D. C. Corbridge, *The Structural Chemistry of Phosphorous*, Elsevier Scient. Publ. Comp., Amsterdam, **1974**.
[22] a) K. Wade, *Adv. Inorg. Chem. Radiochem.* **1976**, *18*, 1–66; b) D. M. P. Mingos, *Acc. Chem. Res.* **1984**, *17*, 311–319.
[23] S. Uthmann, Ph. D. Thesis, University of Bielefeld, **1999**.
[24] H. F. Holleman, E. Wiberg, *Lehrbuch der Anorganischen Chemie*, 91st–100th ed., de Gruyter, Berlin, **1985**, p. 133.
[25] F. Mercier, L. Ricard, F. Mathey, *Polyhedron* **1990**, *9*, 2859–2861.
[26] L. Weber, O. Sommer, H.-G. Stammler, B. Neumann, G. Becker, H. Kraft, *Chem. Ber.* **1996**, *129*, 219–222.
[27] ref.[9], p. 31.
[28] O. I. Kolodyazhnyi, I. V. Shevchenko, V. R. Kuklar, *Zh. Obshch. Khim.* **1985**, *55*, 1862–1863.
[29] L. Weber, T. Matzke, R. Boese, *Chem. Ber.* **1990**, *123*, 739–745.
[30] Review: L. Weber, *Chem. Ber.* **1996**, *129*, 367–379.
[31] A. Meyer, E. Gross, W. Malisch, R. Boese, *Phosphorus Sulfur***1987**, *30*, 792.
[32] K. Jörg, W. Malisch, W. Reich, A. Meyer, U. Schubert, *Angew. Chem.* **1986**, *98*, 103–104; *Angew. Chem. Int. Ed. Engl.* **1986**, *25*, 92–93.
[33] L. Weber, G. Meine, R. Boese, D. Burngardt, *Z. Anorg. Allg. Chem.* **1987**, *549*, 73–86.
[34] U. Schubert, in: *Transition Metal Carbene Complexes*, Verlag Chemie, Weinheim, **1983**, p. 77.
[35] L. Weber, G. Dembeck, P. Lönnecke, H.-G. Stammler, B. Neumann, *Organometallics* **2001**, *20*, 2288–2293.
[36] L. Weber, M. H. Scheffer, H.-G. Stammler, B. Neumann, *Inorg. Chim. Acta* **1999**, *291*, 311–316.
[37] G. M. Sheldrick, *SHELX-97, Program for Crystal Structure Refinement*, University of Göttingen, **1997**.
[38] A. Altomare, M. C. Burla, M. Camalli, B. Carrozini, G. L. Cascarone, C. Giacovazzo, A. Guagliardi, A. G. G. Moliterni, G. Polidori, R. Rizzi, *J. Appl. Crystallogr.* **1999**, *32*, 115–119.

Received: July 28, 2005
Published Online: November 10, 2005

 © 2006 Wiley-VCH Verlag GmbH & Co. KGaA, Weinheim 

DOI: 10.1002/ejic.200500699

# Self-Assembly and Characterization of Homo- and Heterodinuclear Complexes of Zinc(II) and Lanthanide(III) Ions with a Tridentate Schiff-Base Ligand

**Violetta Patroniak,*[a,b] Artur R. Stefankiewicz,[a,b] Jean-Marie Lehn,[b] Maciej Kubicki,[a] and Marcin Hoffmann[a]**

**Keywords:** Dinuclear complexes / Lanthanides / Tridentate Schiff-base ligand / Self-assembly / Zinc

Tridentate Schiff-base ligand H**L** (L = $C_{12}H_9N_2O$) reacts with lanthanide(III) nitrates to give complexes of formulae $[M_2\mathbf{L}_3(NO_3)_3]$, where M = $Y^{3+}$ (**1**), $La^{3+}$ (**2**), $Nd^{3+}$ (**3**), $Sm^{3+}$ (**4**), $Eu^{3+}$ (**5**), $Gd^{3+}$ (**6**), $Tb^{3+}$ (**7**), $Dy^{3+}$ (**8**), $Ho^{3+}$ (**9**), $Lu^{3+}$ (**10**), and $[MM^1\mathbf{L}_3(NO_3)_x]$, where M = $Eu^{3+}$, and $M^1$ = $Dy^{3+}$ (**11**), $Zn^{2+}$ (**12**); x = 3 for **11** and 2 for **12**. The structures of the complexes have been assigned on the basis of the spectroscopic data (solution analysis) and microanalyses. In the case of complexes **3**, **5**, **8** and **12** the structures have been confirmed by X-ray crystallography. The structural analysis of the dinuclear complexes showed the presence of two metal atoms [M(1) and M(2)] and three ligands, **L**. Each lanthanide atom is coordinated to by 9 donor atoms with typical Ln–N and Ln–O distances. Zinc(II) is coordinated to by two oxygen atoms and four nitrogen atoms from two ligands. The metal ions are bridged by the phenoxo oxygen atoms of the ligands. We have obtained a heterodinuclear complex by a rapid one-step reaction. Quantum mechanical calculations indicated that the formation of heterodinuclear complex **12** is slightly favored energetically over the homodinuclear complex **5**.
(© Wiley-VCH Verlag GmbH & Co. KGaA, 69451 Weinheim, Germany, 2006)

## Introduction

Schiff-base ligands with N,O-donor sets may be employed in the metal ion directed assembly of coordination architectures.[1,2] These ligands are fascinating and versatile complexing agents because their metal complexes are known to serve as luminescent probes in the visible and near-IR spectral domains,[3,4] as precursors for doped materials where the metal centers must be at fixed distances from each other, as catalysts for specific DNA[5] and RNA[6] cleavage reactions, and as analytical sensors for the in vivo mapping of $Ca^{2+}$ concentration.[7,8] The complexes of paramagnetic ions have been tested as contrast enhancement agents, especially the complexes of gadolinium(III).[9–15] Dinuclear lanthanide complexes are continuing to attract considerable research interest due to their potential biological,[16–18] medical,[19] chemical and technological importance.[20] A dinuclear terbium(III) complex containing phthalocyanines is very good example of the effect of f-f interactions on dynamic magnetism.[21,22]

There is increasing interest in heterometallic 3d-4f complexes because of their magnetic[23,24] and luminescent properties.[25–29] Thermodynamic assembly processes lead to the strongly luminescent triple-helical heterodinuclear complexes of lanthanides (Ln = La to Lu) and zinc.[30,31] Dinuclear d-f complexes with Schiff-base ligands have been reported.[32–34] A novel synthetic approach for a $(3d)_2(4f)$ heterotrinuclear complex by transmetallation has been described.[35] We have obtained the heterodinuclear complex by a rapid one-pot reaction.

In view of the successful synthesis of the $Zn^{II}$, $Cd^{II}$,[36] and $Mn^{II}$ [37] complexes with H**L** (Figure 1), we attempted to prepare an analogous series of lanthanide complexes. Previously obtained complexes with zinc and cadmium had the M/L stoichiometry of 1:2. However, all of the syntheses that we attempted using lanthanides resulted in compounds with a M/L stoichiometry of 2:3 in the solid state, which was confirmed by X-ray analyses of complexes **3**, **5**, **8**, and **12**. The ESI-MS spectra of all the complexes included the $[M\mathbf{L}_2]^{n+}$ and $[\mathbf{L}]^+$ signals, which means that in solution significant dissociation of the $M_2\mathbf{L}_3$ complexes to mononulcear species and ligand molecules occurs. We also performed quantum mechanical calculations to gain an insight into the factors that affect the stability of heterodinuclear and homodinuclear complexes.

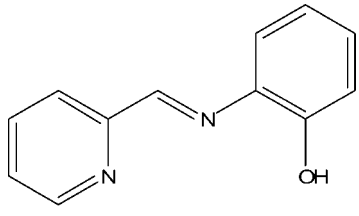


Figure 1. Structure of ligand H**L** – (*E*)-2-[(pyridin-2-yl)methyleneamino]phenol.

[a] Faculty of Chemistry, Adam Mickiewicz University, Grunwaldzka 6, 60780 Poznań, Poland
E-mail: violapat@amu.edu.pl
[b] ISIS-Université Louis Pasteur, CNRS UMR 7006, 8, Allée Gaspard Monge, B. P. 70028, 67083 Strasbourg, France

 © 2006 Wiley-VCH Verlag GmbH & Co. KGaA, Weinheim 

Herein we report that our investigations into the lanthanide coordination chemistry of the ligand **HL** have successfully demonstrated that this ligand is able to form novel dinuclear complexes. We describe and compare the structures of the complexes formed.

## Results and Discussion

### Synthesis and Characterization of the Complexes

Schiff-base ligands with N,O-donor type sets have been employed infrequently in the metal ion directed assembly of coordination architectures.[38] Ligand **HL** leads to the generation of $[M_2L_3(NO_3)_3]$, where M = $Y^{3+}$ (**1**), $La^{3+}$ (**2**), $Nd^{3+}$ (**3**), $Sm^{3+}$ (**4**), $Eu^{3+}$ (**5**), $Gd^{3+}$ (**6**), $Tb^{3+}$ (**7**), $Dy^{3+}$ (**8**), $Ho^{3+}$ (**9**), $Lu^{3+}$ (**10**), and $[MM^1L_3(NO_3)_x]$, where M = $Eu^{3+}$, $M^1$ = $Dy^{3+}$ (**11**), $Zn^{2+}$ (**12**); $x$ = 3 for **11** and 2 for **12**. The structures of the complexes have been assigned on the basis of the spectroscopic data (solution analysis), microanalyses, and in the case of complexes **3**, **5**, **8** and **12**, confirmed by X-ray crystallography.

ESI-MS is a highly sensitive and accurate analytical tool widely used for the characterization of large charged biomolecules, such as proteins and DNA. The technique has also been found to be particularly suited for the identification of large metallosupramolecular architectures present in solution, in which multiply charged ions are generated by the sequential loss of counterions resulting in characteristic isotopic patterns in the spectrum.[39] The ESI-MS investigations were performed with the complexes dissolved in acetonitrile at an approx concentration of $10^{-4}$ M. For the samarium(III) complex (**4**) the ESI mass spectrum showed a mixture of the following complexes: 1171 (5%) $[Sm_2L_3(NO_3)_3(H_2O)_5 + H]^+$, 1153 (5%) $[Sm_2L_3(NO_3)_3(H_2O)_4 + H]^+$, 546 (100%) $[SmL_2]^+$, 450 (30%) $[SmL(NO_3)(H_2O)_2]^+$, 413 (5%) $[SmL(NO_3)]^+$, 341 (5%) $[Sm_2L(NO_3)_3]^{2+}$, 253 (5%) $[Sm_2L_2(NO_3)]^{3+}$, 199 (20%) $[L]^+$. This result confirmed the previously observed behavior of lanthanide complexes in solution.[40]

### Crystallographic Characterization of Complexes 3, 5, 8, and 12

Crystals of complexes **3**, **5**, **8**, and **12** were obtained by diffusion of diethyl ether into a solution of the complex in acetonitrile. Compounds **3** (Figure 2), **5**, and **8** are isostructural. In all three complexes both lanthanide ions are nine-coordinate, albeit unsymmetrically; one of the ions is coordinated by two ligand molecules and one nitrate ion, while the other lanthanide ion binds to one ligand and two nitrate ions. The ligand molecules are tridentate, and they coordinate to the metal ions by the pyridine nitrogen atom N1, the N8 atom and by the hydroxy oxygen atom. The latter bridges the two metal ions. The bond lengths and angles are quite typical. There are also molecules of solvent (acetonitrile) in the crystal structures. In the mixed complex **12** (Figure 3), the $Eu^{III}$ ion is nine-coordinate, while the $Zn^{II}$ ion is six-coordinate and has distorted octahedral geometry.

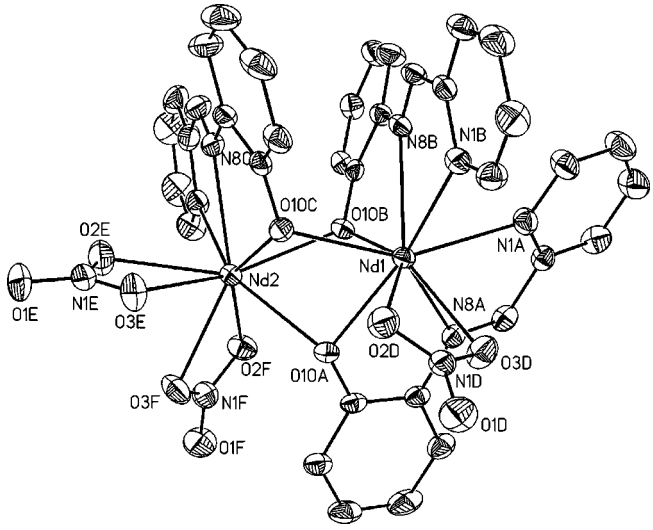


Figure 2. Anisotropic-ellipsoid representation of molecule **3** together with numbering scheme. The ellipsoids are drawn at the 50% probability level; hydrogen atoms are represented by spheres of arbitrary radii.

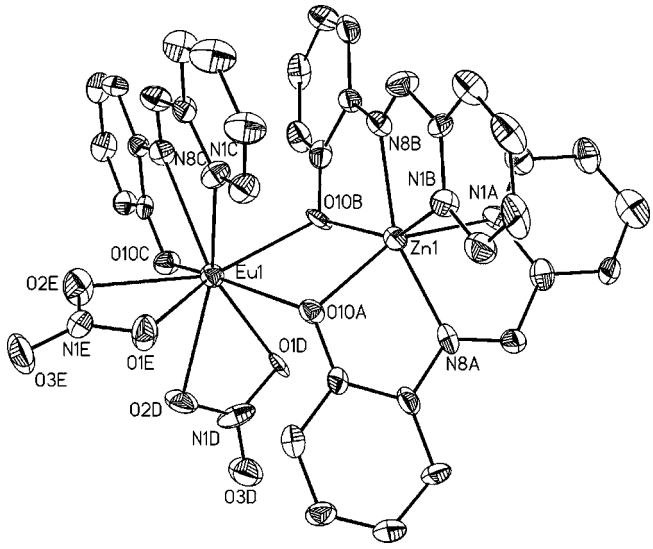


Figure 3. Anisotropic-ellipsoid representation of molecule **12** together with numbering scheme. The ellipsoids are drawn at the 50% probability level; hydrogen atoms are represented by spheres of arbitrary radii.

### Stability of Heterodinuclear and Homodinuclear Complexes

In order to assess the energy difference between heterodinuclear complex **12** and homodinuclear complex **5**, the energetics of the *fictitious* reaction of complex **12** with $Zn(NO_3)_2$, leading to the complex **5** with $Eu(NO_3)_3$, was calculated. Table 1 presents absolute energies for these species calculated with a SDD basis set. The energy difference between the species on both sides of the fictitious reaction is

 © 2006 Wiley-VCH Verlag GmbH & Co. KGaA, Weinheim 

small, about 1.8 kcal/mol, and favours the reaction leading to the heterodinuclear complex. This seems to indicate that the formation of the heterodinuclear Eu/Zn complex **12** is slightly preferred over the formation of the homodinuclear complex **5**, due to larger energy gain and thus larger thermodynamic stability of the complex **12**. This is further supported by an experimental observation − the heterodinuclear complex **12** is formed in a rapid one-step reaction.

Table 1. Absolute energies (in Hartrees) for the species involved in the fictitious reaction connecting complexes **5** and **12**.

| Molecule | Energy |
|---|---|
| $[Eu_2L_3(NO_3)_3]$ | –1779.179268 |
| $Zn(NO_3)_2$ | –342.946213 |
| $[EuZnL_3(NO_3)_2]$ | –1238.050066 |
| $Eu(NO_3)_3$ | –884.078243 |

## Conclusions

We were able to synthesize homo- and heterodinuclear zinc(II) and lanthanide(III) complexes comprising a tridentate Schiff-base ligand. The complexes were characterized in solution by ESI-MS spectroscopy. The molecular structures of complexes **3**, **5**, **8**, and **12** were investigated by X-ray crystallography, which confirmed that the coordination number is 9 for the lanthanide(III) ions, and 6 for the zinc(II) ions. Quantum mechanical calculations indicated that energetic factors slightly favour the formation of heterodinuclear as opposed to homodinuclear complexes, at least for Eu and Zn. The present results provide a facile and rapid synthetic protocol for the preparation of heterodinuclear complexes by a one-pot reaction.

In conclusion, the investigated complexes may be of use in several fields of lanthanide coordination chemistry, in nanotechnology, and as functional components of molecular electronic devices. Hydroxo-bridged Zn complexes are attractive because of their potential relevance as models for sugar-metabolizing enzymes.[41]

## Experimental Section

**General:** $CH_3CN$ was freshly distilled under argon over $CaH_2$. Ligand H**L** was prepared according to a published method.[37,42] The metal salts were used as supplied by Aldrich without further purification. Mass spectra were recorded by a Waters Micromass ZQ spectrometer in positive-ion mode. The samples were dissolved in acetonitrile ($10^{-4}$ mol dm$^{-3}$). Sample solutions were introduced into the mass spectrometer source with a syringe pump at flow rate of 40 μL min$^{-1}$ with a capillary voltage of +3 kV, and a desolvation temperature of 300 °C. The source temperature was 120 °C. The cone voltage ($V_c$) was set to 30 V to allow transmission of ions without fragmentation occuring. Scanning was performed from *m*/*z* = 200 to 1000 for 6 s, and 10 scans were summed to obtain the final spectrum. Microanalyses were obtained using a Perkin–Elmer 2400 CHN microanalyzer. IR spectra were obtained with a Perkin–Elmer 580 spectrophotometer, and are reported in cm$^{-1}$.

**Y Complex (1):** A mixture of $Y(NO_3)_3{\cdot}6H_2O$ (40 mg, 0.1 mmol) and ligand H**L** (40.0 mg, 0.2 mmol) in MeCN (15 mL) was stirred at room temperature for 24 h. The red solution was evaporated under reduced pressure to give complex **1** as an orange solid in quantitative yield. ESI-MS: *m*/*z* = 893 (5%) $[Y_2L_3(NO_3)_2]^+$, 483 (100%) $[YL_2]^+$, 366 (25%) $[YL(NO_3)(H_2O)]^+$, 348 (45%) $[YL(NO_3)]^+$, 288 (75%) $[Y_2L(NO_3)_3(H_2O)]^{2+}$, 199 (5%) $[L]^+$. IR (KBr [cm$^{-1}$]): ṽ = 3609 (OH), 3210 (OH), 3066 (CH arom), 3029 (CH imin), 1733 ($NO_3^-$), 1652 (CN), 1596 (py), 1587 (py), 1489 (py), 1470 (py), 1384 ($NO_3^-$), 1299 (py), 1272 (py), 1153 (py), 1032 (py), 870 (OH), 809 ($NO_3^-$), 750 (py), 592 (py), 536 (py). $Y_2(L)_3(NO_3)_3{\cdot}H_2O$ (973.48): calcd. C 44.25, H 3.00, N 12.95; found C 44.13, H 2.98, N 12.87.

**La Complex (2):** A mixture of $La(NO_3)_3{\cdot}6H_2O$ (44 mg, 0.1 mmol) and ligand H**L** (40.0 mg, 0.2 mmol) in MeCN (15 mL) was stirred at room temperature for 24 h. The orange solution was evaporated under reduced pressure to give complex **2** as a yellow solid in quantitative yield. ESI-MS: *m*/*z* = 533 (100%) $[LaL_2]^+$, 466 (20%) $[La_2L_3(NO_3)]^{2+}$, 398 (20%) $[LaL(NO_3)]^+$, 290 (10%) $[La_2L_3]^{3+}$, 199 (5%) $[L]^+$. IR (KBr [cm$^{-1}$]): ṽ = 3421 (OH), 3066 (CH arom), 3021 (CH imin), 1638 (CN), 1586 (py), 1567 (py), 1552 (py), 1486 (py), 1470 (py), 1451 (py), 1384 ($NO_3^-$), 1300 (py), 1265 (py), 1180 (py), 1148 (py), 868 (OH), 801 ($NO_3^-$), 748 (py), 587 (py), 526 (py). $La_2(L)_3(NO_3)_3{\cdot}H_2O$ (1073.48): calcd. C 40.28, H 2.72, N 11.74; found C 40.27, H 2.63, N 11.57.

**Nd Complex (3):** A mixture of $Nd(NO_3)_3{\cdot}6H_2O$ (45 mg, 0.1 mmol) and ligand H**L** (40.0 mg, 0.2 mmol) in MeCN (15 mL) was stirred at room temperature for 24 h. The orange solution was evaporated under reduced pressure to give complex **3** as a yellow solid in quantitative yield. ESI-MS: *m*/*z* = 1138 (5%) $[Nd_2L_3(NO_3)_3{\cdot}4H_2O]^+$, 1004 (10%) $[Nd_2L_3(NO_3)_2]^+$, 540 (50%) $[NdL_2]^+$, 471 (20%) $[Nd_2L_3(NO_3)]^{2+}$, 199 (35%) $[L]^+$, 155 (100%) $[Nd_2L(NO_3)(H_2O)]^{4+}$. IR (KBr [cm$^{-1}$]): ṽ = 3591 (OH), 3382 (OH), 3061 (CH arom), 3020 (CH imin), 1728 ($NO_3^-$), 1588 (py), 1569 (py), 1486 (py), 1465 (py), 1384 ($NO_3^-$), 1312 (py), 1182 (py), 1111 (py), 868 (OH), 803 ($NO_3^-$), 777 (py), 751 (py), 588 (py). $Nd_2(L)_3(NO_3)_3{\cdot}4H_2O$ (1138.19): calcd. C 37.99, H 3.10, N 11.08; found C 37.87, H 2.89, N 11.01.

**Sm Complex (4):** A mixture of $Sm(NO_3)_3{\cdot}6H_2O$ (45 mg, 0.1 mmol) and ligand H**L** (40.0 mg, 0.2 mmol) in MeCN (15 mL) was stirred at room temperature for 24 h. The red solution was evaporated under reduced pressure to give complex **4** as an orange solid in quantitative yield. ESI-MS: *m*/*z* = 1171 (5%) $[Sm_2L_3(NO_3)_3(H_2O)_5]$, 1153 (5%) $[Sm_2L_3(NO_3)_3(H_2O)_4]$, 557 (100%) $[SmL_2]^+$, 450 (30%) $[SmL(NO_3)(H_2O)_2]^+$, 413 (5%) $[SmL(NO_3)]^+$, 341 (5%) $[Sm_2L(NO_3)_3]^{2+}$, 253 (5%) $[Sm_2L_2(NO_3)]^{3+}$, 199 (20%) $[L]^+$. IR (KBr [cm$^{-1}$]): ṽ = 3345 (OH), 3068 (CH arom), 3021 (CH imin), 1623 (CN), 1586 (py), 1570 (py), 1559 (py), 1487 (py), 1469 (py), 1442 (py), 1384 ($NO_3^-$), 1297 (py), 1271 (py), 1185 (py), 1153 (py), 869 (OH), 808 ($NO_3^-$), 750 (py), 591 (py), 534 (py). $Sm_2(L)_3(NO_3)_3{\cdot}5H_2O$ (1168.45): calcd. C 37.01, H 3.19, N 10.79; found C 37.55, H 3.67, N 11.02.

**Eu Complex (5):** A mixture of $Eu(NO_3)_3{\cdot}5H_2O$ (43 mg, 0.1 mmol) and ligand H**L** (40.0 mg, 0.2 mmol) in MeCN (15 mL) was stirred at room temperature for 24 h. The red solution was evaporated under reduced pressure to give complex **5** as a red solid in quantitative yield. ESI-MS: *m*/*z* = 1155 (5%) $[Eu_2L_3(NO_3)_3(H_2O)_4]$, 547 (15%) $[EuL_2]^+$, 450 (100%) $[EuL(NO_3)(H_2O)_2]^+$, 253 (10%) $[Eu_2L_2(NO_3)]^{3+}$, 199 (30%) $[L]^+$. IR (KBr [cm$^{-1}$]): ṽ = 3608 (OH), 3342 (OH), 3068 (CH arom), 3025 (CH imin), 1728 ($NO_3^-$), 1596 (py), 1586 (py), 1570 (py), 1488 (py), 1467 (py), 1441 (py), 1384 ($NO_3^-$), 1297 (py), 1269 (py), 1185 (py), 1155 (py), 868 (OH), 807

 © 2006 Wiley-VCH Verlag GmbH & Co. KGaA, Weinheim 

($NO_3^-$), 778 (py), 751 (py), 590 (py). $Eu_2(\mathbf{L})_3(NO_3)_3{\cdot}4H_2O$ (1153.64): calcd. C 37.48, H 3.06, N 10.93; found C 37.43, H 2.98, N 10.87.

**Gd Complex (6):** A mixture of $Gd(NO_3)_3{\cdot}6H_2O$ (45 mg, 0.1 mmol) and ligand H**L** (40.0 mg, 0.2 mmol) in MeCN (15 mL) was stirred at room temperature for 24 h. The red solution was evaporated under reduced pressure to give complex **6** as a red solid in quantitative yield. ESI-MS: *m*/*z* = 552 (100%) $[Gd\mathbf{L}_2]^+$, 484 (30%) $[Gd_2\mathbf{L}_3(NO_3)]^{2+}$,435 (25%) $[Gd\mathbf{L}(NO_3)H_2O]^+$, 417 (80%) $[Gd\mathbf{L}(NO_3)]^+$, 199 (5%) $[\mathbf{L}]^+$. IR (KBr [$cm^{-1}$]): $\tilde{\nu}$ = 3609 (OH), 3313 (OH), 3064 (C Harom), 3025 (C Himin), 1733 ($NO_3^-$), 1595 (py), 1586 (py), 1569 (py), 1487 (py), 1468 (py), 1384 ($NO_3^-$), 1296 (py), 1270 (py), 1249 (py), 1154 (py), 868 (OH), 807 ($NO_3^-$), 778 (py), 751 (py), 590 (py). $Gd_2(\mathbf{L})_3(NO_3)_3{\cdot}H_2O$ (1110.17): calcd. C 38.95, H 2.63, N 11.36; found C 38.11, H 2.21, N 11.19.

**Tb Complex (7):** A mixture of $Tb(NO_3)_3{\cdot}6H_2O$ (45 mg, 0.1 mmol) and ligand H**L** (40.0 mg, 0.2 mmol) in MeCN (15 mL) was stirred at room temperature for 24 h. The red solution was evaporated under reduced pressure to give complex **7** as a yellow solid in quantitative yield. ESI-MS: *m*/*z* = 553 (100%) $[Tb\mathbf{L}_2]^+$, 418 (80%) $[Tb\mathbf{L}(NO_3)]^+$, 199 (20%) $[\mathbf{L}]^+$. IR (KBr [$cm^{-1}$]): $\tilde{\nu}$ = 3611(OH), 3368 (OH), 3066 (CH arom), 3026 (CH imin), 1732 ($NO_3^-$), 1594 (py), 1586 (py), 1492 (py), 1469 (py), 1384 ($NO_3^-$), 1297 (py), 1184 (py), 1108 (py), 869 (OH), 807 ($NO_3^-$), 777 (py), 750 (py), 590 (py).$Tb_2(\mathbf{L})_3(NO_3)_3{\cdot}H_2O$ (1113.52): calcd. C 38.83, H 2.63, N 11.32; found C 38.95, H 2.69, N 11.45.

**Dy Complex (8):** A mixture of $Dy(NO_3)_3{\cdot}6H_2O$ (44 mg, 0.1 mmol) and ligand H**L** (40.0 mg, 0.2 mmol) in MeCN (15 mL) was stirred at room temperature for 24 h. The orange solution was evaporated under reduced pressure to give complex **8** as an orange solid in quantitative yield. ESI-MS: *m*/*z* = 1141 (5%) $[Dy_2\mathbf{L}_3(NO_3)_2]^+$, 558 (35%) $[Dy\mathbf{L}_2]^+$, 339 (10%) $[Dy_2\mathbf{L}_3]^{3+}$, 261 (100%) $[Dy_2\mathbf{L}_2(NO_3)]^{3+}$, 199 (30%) $[\mathbf{L}]^+$, 146 $[Dy_2\mathbf{L}(NO_3)]^{4+}$. IR (KBr [$cm^{-1}$]): $\tilde{\nu}$ = 3554 (OH), 3470 (OH), 3103 (CH arom), 3027 (CH imin), 1725 ($NO_3^-$), 1555 (py), 1530 (py), 1486 (py), 1467 (py), 1384 ($NO_3^-$), 1297 (py), 1202 (py), 1106 (py), 868 (OH), 819 ($NO_3^-$), 778 (py), 751 (py), 588 (py). $Dy_2(\mathbf{L})_3(NO_3)_3{\cdot}2H_2O$ (1138.68): calcd. C 37.97, H 2.74, N 11.07; found C 37.99, H 2.78, N 11.28.

**Ho Complex (9):** A mixture of $Ho(NO_3)_3{\cdot}5H_2O$ (44 mg, 0.1 mmol) and ligand H**L** (40.0 mg, 0.2 mmol) in MeCN (15 mL) was stirred at room temperature for 24 h. The red solution was evaporated under reduced pressure to give complex **9** as a yellow solid in quantitative yield. ESI-MS: *m*/*z* = 559 (70%) $[Ho\mathbf{L}_2]^+$, 489 (5%) $[Ho_2\mathbf{L}_3(NO_3)]^{2+}$, 460 (100%) $[Ho\mathbf{L}(NO_3)(H_2O)_2]^+$, 420 (15%) $[Ho\mathbf{L}(NO_3)]^+$, 260 (40%) $[Ho_2\mathbf{L}_2(NO_3)]^{3+}$, 199 (30%) $[\mathbf{L}]^+$. IR (KBr [$cm^{-1}$]): $\tilde{\nu}$ = 3609 (OH), 3375 (OH), 3067 (CH arom), 3027 (CH imin), 1722 ($NO_3^-$), 1586 (py), 1530 (py), 1487 (py), 1469 (py), 1384 ($NO_3^-$), 1297 (py), 1185 (py), 1109 (py), 869 (OH), 808 ($NO_3^-$), 772 (py), 750 (py), 591 (py). $Ho_2(\mathbf{L})_3(NO_3)_3{\cdot}2H_2O$ (1143.54): calcd. C 37.81, H 2.73, N 11.02; found C 37.06, H 2.68, N 11.23.

**Lu Complex (10):** A mixture of $Lu(NO_3)_3{\cdot}xH_2O$ (36 mg, 0.1 mmol) and ligand H**L** (40.0 mg, 0.2 mmol) in MeCN (15 mL) was stirred at room temperature for 24 h. The red solution was evaporated under reduced pressure to give complex **10** as an orange solid in quantitative yield. ESI-MS: *m*/*z* = 569 (100%) $[Lu\mathbf{L}_2]^+$, 452 (15%) $[Lu\mathbf{L}(NO_3)(H_2O)]^+$, 434 (20%) $[Lu\mathbf{L}(NO_3)]^+$, 331 (5%) $[Lu_2\mathbf{L}_3(NO_3)]^{3+}$, 199 (5%) $[\mathbf{L}]^+$. IR (KBr, [$cm^{-1}$]): $\tilde{\nu}$ = 3611 (OH), 3335 (OH), 3055 (CH arom), 3024 (CH imin), 1732 ($NO_3^-$), 1594 (py), 1588 (py), 1570 (py), 1483 (py), 1472 (py), 1383 ($NO_3^-$), 1297 (py), 1272 (py), 1250 (py), 1154 (py), 868 (OH), 806 ($NO_3^-$), 777 (py), 752 (py), 590 (py). $Lu_2(\mathbf{L})_3(NO_3)_3{\cdot}H_2O$ (1145.60): calcd. C 37.74, H 2.55, N 11.00; found C 38.01, H 2.34, N 10.89

**Eu-Dy Complex (11):** A mixture of $Eu(NO_3)_3{\cdot}5H_2O$ (36 mg, 0.084 mmol), $Dy(NO_3)_3{\cdot}6H_2O$ (37 mg, 0.084 mmol) and ligand H**L** (50.0 mg, 0.25 mmol) in MeCN (15 mL) was stirred at room temperature for 24 h. The red solution was evaporated under reduced pressure to give complex **11** as an orange solid in quantitative yield.

Table 2. Crystal data collection and structure refinement details.

| Compound | **3** | **5** | **8** | **12** |
|---|---|---|---|---|
| Formula | $C_{36}H_{27}N_9Nd_2O_{12}{\cdot}C_2H_3N$ | $C_{36}H_{27}N_9Eu_2O_{12}{\cdot}C_2H_3N$ | $C_{36}H_{27}N_9Dy_2O_{12}{\cdot}C_2H_3N$ | $C_{36}H_{28}EuN_8O_9Zn{\cdot}2(CH_4O)$ |
| Formula weight [g mol$^{-1}$] | 1107.20 | 1122.64 | 1143.72 | 997.07 |
| Crystal system | monoclinic | monoclinic | monoclinic | monoclinic |
| Space group | $P2_1/n$ | $P2_1/n$ | $P2_1/n$ | Cc |
| *a* [Å] | 12.418(1) | 12.383(1) | 12.382(1) | 20.764(2) |
| *b* [Å] | 23.921(1) | 23.959(1) | 23.975(1) | 10.891(1) |
| *c* [Å] | 14.702(1) | 14.524(1) | 14.599(1) | 17.298(2) |
| $\beta$ [°] | 111.69(1) | 111.61(1) | 111.64(1) | 93.01(1) |
| *V* [Å$^3$] | 4058.1(8) | 4005.9(8) | 4028.5(8) | 3906.6(8) |
| *Z* | 4 | 4 | 4 | 4 |
| $D_x$ [g cm$^{-3}$] | 1.81 | 1.86 | 1.89 | 1.70 |
| μ [mm$^{-1}$] | 2.61 | 3.18 | 3.76 | 2.28 |
| Crystal size [mm] | 0.18×0.15×0.12 | 0.2×0.2×0.1 | 0.2×0.2×0.1 | 0.2×0.15×0.1 |
| $\Theta$ range [°] | 2–30 | 2–30 | 2–30 | 2–30 |
| *hkl* range | $-17 \le h \le 16$ | $-17 \le h \le 11$ | $-16 \le h \le 16$ | $-29 \le h \le 28$ |
| | $-31 \le k \le 31$ | $-32 \le k \le 32$ | $-31 \le k \le 31$ | $-14 \le k \le 7$ |
| | $-20 \le l \le 17$ | $-17 \le l \le 19$ | $-17 \le l \le 20$ | $-23 \le l \le 23$ |
| Reflections: | | | | |
| measured | 38181 | 36004 | 26034 | 18429 |
| unique ($R_{int}$) | 10602 (0.038) | 10463 (0.063) | 10144 (0.036) | 9339 (0.086) |
| with $I > 2\sigma(I)$ | 7267 | 9263 | 7160 | 4577 |
| Number of parameters | 559 | 559 | 559 | 536 |
| $R(F)$ | 0.036 | 0.063 | 0.041 | 0.060 |
| w$R(F^2)$ | 0.064 | 0.144 | 0.096 | 0.093 |
| Goodness of fit | 0.98 | 1.13 | 1.00 | 0.82 |
| max./min. Δρ [e Å$^{-3}$] | 1.67/–0.88 | 2.68/–3.50 | 1.53/–0.95 | 1.12/–0.66 |

 © 2006 Wiley-VCH Verlag GmbH & Co. KGaA, Weinheim 

ESI-MS: *m/z* = 1166 (5%) $[EuDyL_3(NO_3)]^{2+}$, 556 (100%) $[DyL_2]^+$, 547 (80%) $[EuL_2]^+$, 199 (30%) $[L]^+$. IR (KBr [$cm^{-1}$]): $\tilde{\nu}$ = 3636 (OH), 3367 (OH), 3085 (CH arom), 3025 (CH imin), 1731 ($NO_3^-$), 1564 (py), 1543 (py), 1483 (py), 1459 (py), 1384 ($NO_3^-$), 1301 (py), 1248 (py), 1102 (py), 866 (OH), 805 ($NO_3^-$), 780 (py), 751 (py), 592 (py). $EuDy(L)_3(NO_3)_3 \cdot 2H_2O$ (1128.15): calcd. C 38.33, H 2.77, N 11.17; found C 38.06, H 2.54, N 10.99.

**Eu-Zn Complex (12):** A mixture of $Eu(NO_3)_3 \cdot 5H_2O$ (36 mg, 0.084 mmol), $Zn(NO_3)_2 \cdot 6H_2O$ (16 mg, 0.084 mmol) and ligand H**L** (50.0 mg, 0.25 mmol) in MeCN (15 mL) was stirred at room temperature for 24 h. The red solution was evaporated under reduced pressure to give complex **12** as an orange solid in quantitative yield. ESI-MS: *m/z* = 1155 (5%) $[Eu_2L_3(NO_3)_3(H_2O)_4+H]^+$, 870 (5%) $[EuZnL_3(NO_3)]^+$, 545 (15%) $[EuL_2]^+$, 459 (100%) $[ZnL_2]^+$, 199 (15%) $[L]^+$. IR (KBr [$cm^{-1}$]): $\tilde{\nu}$ = 3612 (OH), 3348 (OH), 3069 (CH arom), 3027 (CH imin), 1733 ($NO_3^-$), 1569 (py), 1487 (py), 1468 (py), 1383 ($NO_3^-$), 1296 (py), 1250 (py), 1107 (py), 868 (OH), 807 ($NO_3^-$), 778 (py), 750 (py), 590 (py). $EuZn(L)_3(NO_3)_2 \cdot 4H_2O$ (1067.07): calcd. C 40.52, H 3.31, N 11.81; found C 40.21, H 3.23, N 12.02.

**Crystal Structure Determination of Complexes 3, 5, 8 and 12:** Data were collected by the ω-scan technique in the $\theta$ range of 2–30° on a KUMA KM4CCD four-circle[43] diffractometer equipped with a CCD detector, using graphite-monochromated Mo-$K_\alpha$ radiation ($\lambda$ = 0.71073 Å). Accurate cell parameters were determined by the least-squares fit of 10137 (for **3**), 13161 (for **5**), 8403 (for **8**) and 2785 (for **12**) reflections of highest intensity chosen from the complete dataset. Data were corrected for Lorentz-polarization effects[44] and for absorption.[45] The structure was solved by direct methods with SHELXS-97[46] and refined with SHELXL-97.[47] Non-hydrogen atoms were refined anisotropically. Hydrogen atoms were placed at calculated positions and refined with a 'riding model' with their isotropic thermal parameters set to 1.2 times the $U_{eq}$ of the appropriate carrier atom. Relevant crystal data and refinement details are listed in Table 2. Selected geometrical parameters for complexes **3**, **5**, **8** and **12** are listed in Table 3.

Table 3. Selected geometrical parameters.

| M | Nd (**3**) | Eu (**5**) | Dy (**8**) |
|---|---|---|---|
| M1–O10A | 2.436(2) | 2.392(4) | 2.411(3) |
| M1–O10B | 2.467(2) | 2.428(4) | 2.442(3) |
| M1–O10C | 2.408(2) | 2.363(5) | 2.367(3) |
| M1–N1A | 2.674(3) | 2.628(6) | 2.649(4) |
| M1–N1B | 2.689(3) | 2.654(6) | 2.666(4) |
| M1–N8A | 2.567(3) | 2.518(5) | 2.542(4) |
| M1–N8B | 2.581(3) | 2.534(5) | 2.547(4) |
| M1–O2D | 2.585(2) | 2.551(5) | 2.557(4) |
| M1–O3D | 2.542(3) | 2.489(5) | 2.514(4) |
| M2–O10A | 2.493(2) | 2.452(5) | 2.466(3) |
| M2–O10B | 2.461(2) | 2.399(4) | 2.414(3) |
| M2–O10C | 2.428(2) | 2.396(5) | 2.404(3) |
| M2–N1C | 2.652(3) | 2.626(6) | 2.633(4) |
| M2–N8C | 2.575(3) | 2.530(6) | 2.555(4) |
| M2–O2E | 2.560(3) | 2.524(6) | 2.537(4) |
| M2–O3E | 2.529(3) | 2.489(6) | 2.505(4) |
| M2–O2F | 2.494(2) | 2.446(5) | 2.466(3) |
| M2–O3F | 2.547(2) | 2.503(6) | 2.526(4) |
| M1–O10A–M2 | 95.49(7) | 95.0(1) | 95.0(1) |
| M1–O10B–M2 | 95.53(7) | 95.5(1) | 95.6(1) |
| M1–O10C–M2 | 97.96(8) | 97.3(2) | 97.9(1) |
| | **12** | | |
| Eu1–O10A | 2.406(7) | Zn1–O10A | 2.126(8) |
| Eu1–O10B | 2.409(6) | Zn1–O10N | 2.115(6) |
| Eu1–O10C | 2.326(6) | Zn1–N1A | 2.282(8) |
| Eu1–N1C | 2.622(9) | Zn1–N1B | 2.190(7) |
| Eu1–N8C | 2.547(7) | Zn1–N8A | 2.075(8) |
| Eu1–O1D | 2.476(6) | Zn1–N8B | 2.119(7) |
| Eu1–O2D | 2.480(7) | | |
| Eu1–O1E | 2.579(7) | | |
| Eu1–O2E | 2.510(7) | | |
| Eu1–O10A–Zn1 | 102.1(3) | | |
| Eu1–O10B–Zn1 | 102.3(2) | | |

CCDC-274721 (for **8**), -274722 (for **5**), -274723 (for **3**), and -274724 (for **12**) contain the supplementary crystallographic data for this paper. These data can be obtained free of charge from The Cambridge Crystallographic Data Centre via www.ccdc.cam.ac.uk/data_request/cif.

**Quantum Mechanical Calculations:** The set of Cartesian coordinates determined by X-ray diffraction for the atoms in complexes **5** and **12** served as a starting point for geometry optimization utilizing the density functional theory (DFT). The B3LYP method[48,49] was utilized, and a composite basis set in which Eu, and Zn were treated with a SDD basis set in which Stuttgart-Dresden pseudopotentials[50,51] substituted for the innermost electrons to account for relativistic effects was applied. Ligands atoms from the first coordination sphere were treated with a 6-31G basis set,[52] while the remaining atoms were treated with a STO-3G basis set.[53] Single point energies were calculated with a SDD basis set[50,51] for all atoms. All calculations were preformed with Gaussian 03.[54]

## Acknowledgments

This work was partially supported by grant No. 4T09A 049 24 from the Polish Ministry of Scientific Research and Information Technology.

[1] P. A. Vigato, S. Tamburini, *Coord. Chem. Rev.* **2004**, *248*, 1717–2128.
[2] W. Radecka-Paryzek, V. Patroniak, J. Lisowski, *Coord. Chem. Rev.* **2005**, *249*, 2156–2175.
[3] D. Imbert, S. Comby, A.-S. Chauvin, J.-C. Bünzli, *Chem. Commun.* **2005**, 1432–1434.
[4] V. W.-W. Yam, K. K.-W. Lo, *Coord. Chem. Rev.* **1999**, *184*, 157–240.
[5] A. Mukherjee, S. Dhar, M. Nethaji, A. R. Chakravarty, *Dalton Trans.* **2005**, 349–353.
[6] R. Häner, J. Hall, *Antisense Nucleic Acid Drug Dev.* **1997**, *7*, 423–430.
[7] W. H. Li, S. E. Fraser, T. J. Meade, *J. Am. Chem. Soc.* **1999**, *121*, 1413–1414.
[8] D. M. J. Doble, M. Melchior, B. O'Sullivan, C. Siering, J. Xu, V. C. Pierre, K. N. Raymond, *Inorg. Chem.* **2003**, *42*, 4930–4937.
[9] D. E. Reichert, J. S. Lewis, C. J. Anderson, *Coord. Chem. Rev.* **1999**, *184*, 3–66.
[10] S. Aime, L. Calabi, C. Cavallotti, E. Gianolio, G. B. Giovenzana, P. Losi, A. Maiocchi, G. Palmisano, M. Sisti, *Inorg. Chem.* **2004**, *43*, 7588–7590.
[11] J. B. Livramento, E. Tóth, A. Sour, A. Borel, A. E. Merbach, R. Ruloff, *Angew. Chem. Int. Ed.* **2005**, *44*, 1480–1484.
[12] J. Rudovský, P. Cígler, J. Kotek, P. Hermann, P. Vojtíšek, I. Lukeš, J. A. Peters, L. Vander Elst, R. N. Mueller, *Chem. Eur. J.* **2005**, *11*, 2373–2384.
[13] L. Vander Elst, I. Raynal, M. Port, P. Tisnès, R. N. Muller, *Eur. J. Inorg. Chem.* **2005**, 1142–1148.

 © 2006 Wiley-VCH Verlag GmbH & Co. KGaA, Weinheim 

[14] A. Facchetti, A. Abbotto, L. Beverina, S. Bradamante, P. Mariani, Ch. L. Stern, T. J. Marks, A. Vacca, G. A. Pagani, *Chem. Commun.* **2004**, 1770–1771.
[15] J. Xu, D. G. Churchill, M. Botta, K. N. Raymond, *Inorg. Chem.* **2004**, *43*, 5492–5494.
[16] J.-C. G. Bünzli, C. Piguet, *Chem. Rev.* **2002**, *102*, 1897–1928.
[17] C. Liu, M. Wang, T. Zhang, H. Sun, *Coord. Chem. Rev.* **2004**, *248*, 147–168.
[18] A. P. Basset, S. W. Magennis, P. B. Glover, D. J. Lewis, N. Spencer, S. Parsons, R. M. Williams, L. De Cola, Z. Pikramenou, *J. Am. Chem. Soc.* **2004**, *126*, 9413–9424.
[19] M. K. Thomson, D. M. J. Doble, L. S. Tso, S. Barra, M. Botta, S. Aime, K. N. Raymond, *Inorg. Chem.* **2004**, *43*, 8577–8586.
[20] P. M. T. Piggot, L. A. Hall, A. J. P. White, D. J. Williams, *Inorg. Chem.* **2003**, *42*, 8344–8352.
[21] R. Gheorghe, V. Kravtsov, Y. A. Simonov, J.-P. Costes, Y. Journaux, M. Andruh, *Inorg. Chim. Acta* **2004**, *357*, 1613–1618.
[22] N. Ishikawa, S. Otsuka, Y. Kaizu, *Angew. Chem. Int. Ed.* **2005**, *44*, 731–733.
[23] J.-P. Costes, F. Dahan, G. Novitchi, V. Arion, S. Shova, J. Lipkowski, *Eur. J. Inorg. Chem.* **2004**, 1530–1537.
[24] R. Koner, G.-H. Lee, Y. Wang, H.-H. Wei, S. Mohanta, *Eur. J. Inorg. Chem.* **2005**, 1500–1505.
[25] C. Piguet, G. Bernardinelli, G. Hopfgartner, *Chem. Rev.* **1997**, *97*, 2005–2062.
[26] W.-K. Lo, W.-K. Wong, J. Guo, W.-Y. Wong, K.-F. Li, K.-W. Cheah, *Inorg. Chim. Acta* **2004**, *357*, 4510–4521.
[27] M. Cantuel, G. Bernardinelli, G. Muller, J. P. Riehl, C. Piguet, *Inorg. Chem.* **2004**, *43*, 1840–1849.
[28] P. Coppo, M. Duati, V. N. Kozhevnikov, J. W. Hofstraat, L. De Cola, *Angew. Chem. Int. Ed.* **2005**, *44*, 1806–1810.
[29] X. Yang, R. A. Jones, V. Lynch, M. M. Oye, A. L. Holmes, *Dalton Trans.* **2005**, 849–851.
[30] C. Piguet, G. Bernardinelli, J.-C. Bünzli, S. Petoud, G. Hopfgartner, *J. Chem. Soc., Chem. Commun.* **1995**, 2575–2577.
[31] C. Piguet, J.-C. Bünzli, G. Bernardinelli, G. Hopfgartner, S. Petoud, O. Schaad, *J. Am. Chem. Soc.* **1996**, *118*, 6681–6697.
[32] R. E. P. Winpenny, *Chem. Soc. Rev.* **1998**, *27*, 447–452.
[33] M. Sakamoto, K. Manseki, H. Ōkawa, *Coord. Chem. Rev.* **2001**, *219–221*, 379–414.
[34] A. Golcu, M. Tumer, H. Demirelli, R. A. Wheatley, *Inorg. Chim. Acta* **2005**, *358*, 1785–1797.
[35] S. Akine, T. Taniguchi, T. Nabeshima, *Angew. Chem. Int. Ed.* **2002**, *41*, 4670–4673.
[36] D. M. Epstein, S. Choudhary, M. R. Churchill, K. M. Keil, A. V. Eliseev, J. R. Morrow, *Inorg. Chem.* **2001**, *40*, 1591–1596.
[37] N. Reddig, M. U. Triller, D. Pursche, A. Rompel, B. Krebs, *Z. Anorg. Allg. Chem.* **2002**, *628*, 2458–2462.
[38] Grid-type tetranuclear complexes have been obtained with ligands incorporating two tridentate N,O coordination subunits of type HL; see: J. Nitschke, J.-M. Lehn, *Proc. Natl. Acad. Sci. USA* **2003**, *100*, 11970–11974.
[39] I. Manet, L. Francini, S. Masiero, S. Pieraccini, G. P. Spada, G. Gottarelli, *Helv. Chim. Acta* **2001**, *84*, 2096–2107; J.-P. Costes, G. Novitchi, C. Lebrun, *J. Alloys Compd.* **2004**, *374*, 377–381.
[40] V. Patroniak, P. N. W. Baxter, J.-M. Lehn, Z. Hnatejko, M. Kubicki, *Eur. J. Inorg. Chem.* **2004**, 2379–2384.
[41] G. Parkin, *Chem. Commun.* **2000**, 1971–1985.
[42] C. G. Pitt, Y. Bao, J. Thompson, M. C. Wani, H. Rosenkrantz, J. Metterville, *J. Med. Chem.* **1986**, *29*, 1231–1237.
[43] *CrysAlisCCD*, User Guide vers. 168, Kuma Diffraction, Wrocław, Poland, **1999**.
[44] *CrysAlisRed*, Program for data reduction, Kuma CCD Diffractometer, Kuma Diffraction, Wrocław, Poland, **1999**.
[45] R. H. Blessing, *J. Appl. Crystallogr.* **1989**, *22*, 396–397.
[46] G. M. Sheldrick, *Acta Crystallogr., Sect. A* **1990**, *46*, 467–473.
[47] G. M. Sheldrick, *SHELXL-97*, Program for the refinement of crystal structures, University of Göttingen, Göttingen (Germany), **1997**.
[48] A. D. Becke, *J. Chem. Phys.* **1993**, *98*, 5648–5652.
[49] C. Lee, W. Yang, R. G. Parr, *Phys. Rev. B* **1988**, *37*, 785–789.
[50] M. Dolg, H. Stoll, H. Preuss, R. M. Pitzer, *J. Phys. Chem.* **1993**, *97*, 5852–5859.
[51] A. Bergner, M. Dolg, W. Kuechle, H. Stoll, H. Preuss, *Mol. Phys.* **1993**, *80*, 1431–1441.
[52] W. J. Hehre, R. Ditchfield, J. A. Pople, *J. Chem. Phys.* **1972**, *56*, 2257–2261.
[53] W. J. Hehre, R. F. Stewart, J. A. Pople, *J. Chem. Phys.* **1969**, *51*, 2657–2664.
[54] M. J. Frisch, G. W. Trucks, H. B. Schlegel, G. E. Scuseria, M. A. Robb, J. R. Cheeseman, J. A. Montgomery, Jr., T. Vreven, K. N. Kudin, J. C. Burant, J. M. Millam, S. S. Iyengar, J. Tomasi, V. Barone, B. Mennucci, M. Cossi, G. Scalmani, N. Rega, G. A. Petersson, H. Nakatsuji, M. Hada, M. Ehara, K. Toyota, R. Fukuda, J. Hasegawa, M. Ishida, T. Nakajima, Y. Honda, O. Kitao, H. Nakai, M. Klene, X. Li, J. E. Knox, H. P. Hratchian, J. B. Cross, V. Bakken, C. Adamo, J. Jaramillo, R. Gomperts, R. E. Stratmann, O. Yazyev, A. J. Austin, R. Cammi, C. Pomelli, J. W. Ochterski, P. Y. Ayala, K. Morokuma, G. A. Voth, P. Salvador, J. J. Dannenberg, V. G. Zakrzewski, S. Dapprich, A. D. Daniels, M. C. Strain, O. Farkas, D. K. Malick, A. D. Rabuck, K. Raghavachari, J. B. Foresman, J. V. Ortiz, Q. Cui, A. G. Baboul, S. Clifford, J. Cioslowski, B. B. Stefanov, G. Liu, A. Liashenko, P. Piskorz, I. Komaromi, R. L. Martin, D. J. Fox, T. Keith, M. A. Al-Laham, C. Y. Peng, A. Nanayakkara, M. Challacombe, P. M. W. Gill, B. Johnson, W. Chen, M. W. Wong, C. Gonzalez, J. A. Pople, *Gaussian 03, Revision C.02*, Gaussian, Inc., Wallingford, CT, **2004**.

Received: August 3, 2005
Published Online: November 28, 2005

 © 2006 Wiley-VCH Verlag GmbH & Co. KGaA, Weinheim 

DOI: 10.1002/ejic.200500702

# Dinuclear Lanthanide Schiff-Base Complexes Forming a Rectangular Columnar Mesophase

**Koen Binnemans,*[a] Katleen Lodewyckx,[a] Thomas Cardinaels,[a] Tatjana N. Parac-Vogt,[a] Cyril Bourgogne,[b] Daniel Guillon,[b] and Bertrand Donnio*[b]**

**Keywords:** Columnar mesophases / Lanthanides / Liquid crystals / Metallomesogens / Rare earths

The Schiff base $\mathbf{L}H_3$ obtained by condensation of 3-formyl-4-hydroxyphenyl-3,4,5-tris(tetradecyloxy)benzoate with 1,3-diamino-2-propanol reacts with lanthanide(III) acetate salts to form dinuclear complexes of the type $Ln_2L_2$ with the trivalent ions from the first half of the lanthanide series (Ln = Nd, Sm, Gd). These stable and neutral metallomesogens exhibit a rectangular columnar mesophase over a broad temperature range.
(© Wiley-VCH Verlag GmbH & Co. KGaA, 69451 Weinheim, Germany, 2006)

## Introduction

*N*,*N*′-Bis(salicylidene)ethylenediamine (*salen*) and similar Schiff-base ligands derived from diamines other than ethylenediamine have often been used as building blocks for metal-containing liquid crystals.[1] This work was focused mainly on copper(II), nickel(II) or oxovanadium(IV) (vanadyl) complexes that exhibit smectic mesophases,[2,3] essentially smectic A and smectic C phases, but also the more ordered smectic E phase.[2e] Similar mesomorphic properties were also observed in calamitic cobalt(II) complexes,[2g] and the enhancement of the molecular anisotropy of such $Ni^{II}$, $Cu^{II}$ and $VO^{IV}$ *salen* complexes by the use of alkylphenylazo groups results in new mesomorphic systems showing a high temperature SmC phase, and in some cases, the nematic phase.[4] Binnemans et al. reported the first mesomorphic lanthanide complexes of *salen*-type Schiff base, but owing to the elevated transition temperatures, unequivocal identification of the mesophase formed was not possible.[5] Swager and co-workers studied vanadyl complexes derived from such Schiff bases, possessing a hexacatenar structure, that exhibit a rich columnar mesomorphism,[6] whereas Binnemans et al. synthesized mixed f-d metallomesogens, derived form the related hexacatenar ligand, that contain both a transition metal ion and a lanthanide(III) ion.[7] These compounds showed a hexagonal columnar phase over a broad temperature range. Depending on the radius of the lanthanide(III) ion, either dinuclear f-d[7] or trinuclear f-d-f complexes were formed.[7,8] Note that all these complexes can be considered as adducts of a mesogenic Cu(salen) or Ni(salen) complex of a trivalent lanthanide ion. Because the Cu(salen) and Ni(salen) complexes are electrically neutral, three nitrate groups are necessary to compensate for the positive charge of the lanthanide ion in the resulting mixed f-d complexes. Additionally, if such a doubly negatively charged ligand is to be used to prepare purely lanthanide complexes, a further small inorganic anion (e.g. X = Cl, $NO_3$) has to be present to obtain electric neutrality in the corresponding LnXL complexes, otherwise neutral complexes with a different stoichiometry such as $Ln_2L_3$ type may be formed instead. By modifying the *salen*-type Schiff-base ligand, it should be possible to obtain an organic species that contains three deprotonable OH groups and which can be used as triply negatively charged anionic ligand to form neutral complexes with the trivalent lanthanide cations. Such a ligand can be obtained by condensing the aldehyde that is used to prepare the *salen*-type Schiff base, with 1,3-diamino-2-propanol instead of 1,2-diaminoethane.

In this paper, we show that the chemical modification of the *salen*-type Schiff base by using 1,3-diamino-2-propanol instead of 1,3-diaminopropane in the reaction with the appropriate 3-formyl-4-hydroxyphenyl-3,4,5-tris(tetradecyloxy)benzoate appears to be a judicious approach to prepare neutral dinuclear complexes of the type $Ln_2\mathbf{L}_2$ with trivalent lanthanide ions. Moreover, these complexes are mesomorphic and exhibit a rectangular columnar mesophase over a large temperature range, as shown by small-angle X-ray diffraction. With the help of molecular mechanics, a model for the organization of these compounds in the columns is proposed.

[a] Katholieke Universiteit Leuven, Department of Chemistry, Celestijnenlaan 200F, 3001 Leuven, Belgium
E-mail: Koen.Binnemans@chem.kuleuven.be
[b] Institut de Physique et Chimie des Matériaux de Strasbourg – Groupe Matériaux Organiques, UMR 7504 CNRS-Université Louis Pasteur,
B. P. 43, 23 rue du Loess, 67034 Strasbourg Cedex 2, France
E-mail: bdonnio@ipcms.u-strasbg.fr

 InterScience © 2006 Wiley-VCH Verlag GmbH & Co. KGaA, Weinheim 

## Results and Discussion

The Schiff-base ligand $\mathbf{L}H_3$ was obtained by condensation of the aldehyde 3-formyl-4-hydroxyphenyl-3,4,5-tris(tetradecyloxy)benzoate (1 equiv.) and 1,3-diamino-2-propanol (0.5 equiv.) in toluene, with azeotropic removal of the water. The three dinuclear lanthanide(III) complexes (Ln = Nd, Sm, Gd) were synthesized by reaction between the lanthanide acetate salt $Ln(CH_3COO)_3{\cdot}xH_2O$ (1.1 equiv.) and the Schiff base (0.5 equiv.) in chloroform at refluxing temperature. The synthesis of ligand and complexes **1**–**3** is outlined in Scheme 1.

A schematic representation of the dinuclear lanthanide(III) complexes is given in Scheme 1 (compounds **1**, **2**, **3**). Because each ligand carries a triple negative charge, the positive charge of the two trivalent lanthanide ions is counterbalanced and the dinuclear complexes are neutral; therefore no counterions are necessary. This is in contrast with

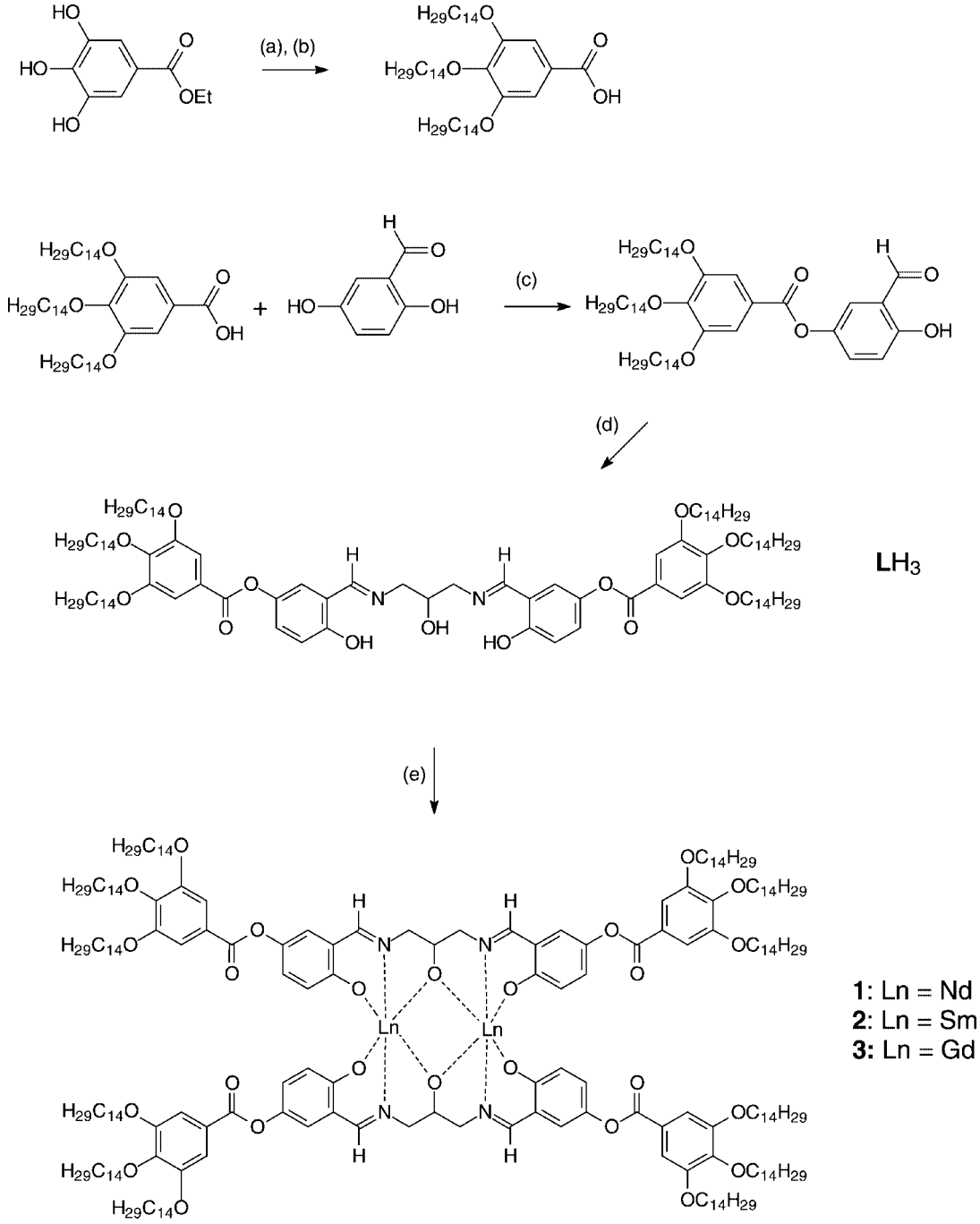


Scheme 1. Synthesis of the Schiff-base ligand and the corresponding dinuclear Ln–Ln complexes **1**–**3**. Reagents and conditions: (a) RBr (3 equiv.), $K_2CO_3$ (6 equiv.), DMF, KI (catalytic amount), reflux overnight; (b) NaOH, ethanol, reflux for 4 hours; acidification by dilute HCl solution; (c) DCC, DMAP, dichloromethane, 24 hours at room temp.; (d) 1,3-diamino-2-propanol (0.5 equiv.), glacial acetic acid (catalyst), toluene, Dean–Stark trap, 3 hours at reflux; (e) $Ln(CH_3COO)_3{\cdot}xH_2O$ (1.1 equiv.), chloroform, reflux overnight.

 © 2006 Wiley-VCH Verlag GmbH & Co. KGaA, Weinheim 

the f-d complexes with *salen*-type ligands,[7,8] the lanthanide complexes with salicylaldimine Schiff bases which have counterions such as nitrate groups.[1f,9,10] or lipophilic bis(benzimidazole)pyridine-based ligands.[11] The reasons why a dinuclear complex is formed instead of a mononuclear species are due to the tendency of the lanthanide(III) ions to achieve a high coordination number and to the nature of the ligand itself, auspicious to such a coordination mode (fused chelating parts). Typically, the coordination number of the trivalent lanthanide ions in coordination compounds is eight or nine. Also six-coordinate lanthanide(III) complexes are known, for example the tris(β-diketonato)lanthanide(III) complexes. When the ligand does not offer a sufficient number of donor atoms to the lanthanide(III) ion to achieve a high coordination number, some of the donor atoms can coordinate in a bridging mode. Alternatively, adducts can be formed with Lewis bases, such as water molecules. Unfortunately, we were unable to obtain single crystals, so that the structure of the complex is still unknown. It was also not possible to grow single crystals of similar complexes with shorter alkyl chains and due to the presence of paramagnetic ions, $^1$H NMR spectra of the complexes were not resolved. It is however unlikely to consider the structure of the dinuclear lanthanide(III) complex as totally flattened and planar (as drawn in Scheme 1) by simply considering the coordination chemistry of *d* and *f* elements and entropic phenomena. The geometric preferences of lanthanides to adopt coordination numbers higher than six support that such extended planarity is absent, and that the ligands are wrapped around the metallic centers. Thus, a more energetically favorable structure for these dinuclear species would imply the ligand to be bent or V-shaped (due to the flexible spacer), and that they are either entwined around the two metal ions as in helicates[12–14] (Figure 1a, $D_2$ symmetry) or coordinated to the two cations in such a way that a sandwich complex with a mesocate structure is formed (part b in Figure 1, $C_{2h}$ symmetry).[13] Whatever the exact structure is, it has been shown recently for some $M_2L_3$ complexes, that both species exist in equilibrium in solution, and the helicate to mesocate isomerization only requires inversion at one metal center,[15] and that this low-energy cost equilibrium may be generalized to other systems. The driving forces for the formation of helicates and/or mesocates result from the minimization of energy of the ultimate self-assembly. Such a formation depends on the metal-imposed (number and coordination geometry) and ligand-imposed constraints (type, nature of the spacer and distance between bridging units), as well as to some degree of pre-organization of the ligand. In the case of lanthanides, helicates mainly possess a three-stranded helicate $Ln_2L_3$ structure (in such case, the two lanthanide ions are wrapped by three ligands), while mesocate complexes of the type $M_2L_2$ – schematically shown in Figure 1, b – are common for both d and f elements.[13] For instance, Gelasco and Pecoraro described the crystal structure of a closely related dimeric manganese(III) complex of the Schiff base 1,3-bis(5-nitrosalicylidenimino)-2-propanol:[16] this dimeric manganese complex has a $\mu^2$-alkoxy core with a symmetric environment for the manganese(III) ions. The authors showed that the ligands adopt a hairpin conformation and that two of them wrap the two metallic ions in an antiparallel mode to form the neutral mesocate $Mn_2L_2$ complex as schematically drawn in Figure 1, b. This particular dimeric structure could be representative of the chelating mode of this type of ligand with two metallic nuclei and generalized to other dinuclear species. We have thus extrapolated this mode of chelation to the presently studied dinuclear lanthanide(III) complexes, the close proximity of the two sets of donor atoms of the bidentate bridging ligand, and the presence of the central hydroxy coordinating group slightly disfavoring the formation of the helicate structure at the expense to the mesocate one; this assumption is comforted by some molecular calculations, too (vide infra).

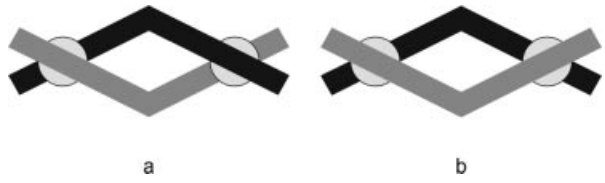


Figure 1. Schematic representation of the two possible structures given by the $Ln_2L_2$ complexes. The two bischelate bent-like ligands, may entwine the two metallic species to form a double-stranded helicate (**a**, $D_2$ symmetry) or sandwich the metal ions to form a non-helical *meso* structure or mesocate instead (**b**, $C_{2h}$ symmetry).

In this model, the two lanthanide(III) ions are in a six-coordinate environment, with the coordination polyhedron being a (distorted) octahedron. The two coordinating octahedral cages of the two lanthanide ions share a common edge, and the alkoxide group bridges the two lanthanide(III) centers (Figure 2). For a further investigation of the conformation of this dinuclear complex and to support the mesocate structure, molecular simulations were performed on both mesocate and helicate conformers (Gaussian 03, rb3lyp/3-21g**). For compatibility with the calculation bases, the lanthanide(III) cations were replaced in these models by yttrium(III), chosen because of its great proximity to the lanthanide series (located just above the lanthanum in the periodic table of elements) and for the similarity of the ionic radius between $Y^{III}$ and $Ln^{III}$. The minimization yielded two stable structures with an energetic gap of 44.9 kJ·mol$^{-1}$ in favor of the mesocate conformation. For both conformers in these theoretical structures (taken as isolated molecule in the gas phase), the angle formed by the phenyl groups of the ligands is quite wide in comparison with the manganese complex just mentioned,[16] but a search in the Cambridge Crystallographic Database shows that the very flexible *salen*-type ligand can be very distorted by packing constraints in condensed phase. It is then reasonable to propose that the present dinuclear lanthanide(III) complexes adopt preferentially a mesocate form, with the ligands in the hairpin conformation. Furthermore, with this assumption, the pinched ligand structure could be even more stabilized by intramolecular π-stacking of the benzoate rings (vide infra).

 © 2006 Wiley-VCH Verlag GmbH & Co. KGaA, Weinheim 

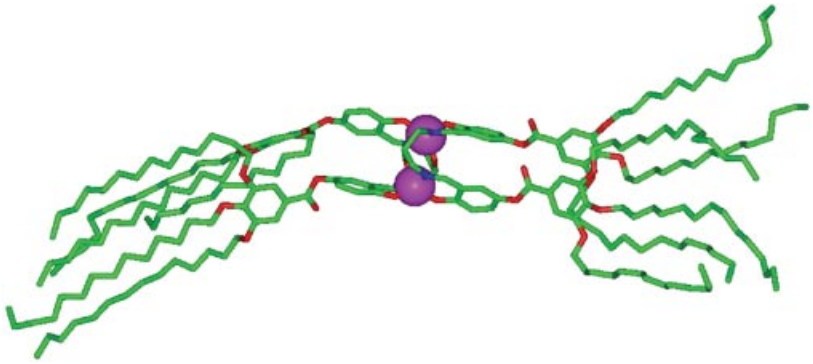

Figure 2. Minimized structure of the dinuclear diligand species (see text; purple: lanthanide cation; blue: nitrogen atom; red: oxygen atom, green: carbon atom. Hydrogen atoms have been omitted for clarity.).

The Schiff-base ligand $\mathbf{L}H_3$ is itself mesomorphic, not totally unexpected, because of its polycatenar-like molecular structure, a priori compatible with mesophase formation.[17] Observation by polarizing optical microscopy (POM) indicated a monotropic liquid-crystalline phase behavior. On heating the sample, an isotropic liquid is obtained at 82 °C, which was confirmed by an intense endothermic peak transition (82 kJ·mol$^{-1}$) in the first heating run of the DSC curve. Heating was continued above 100 °C without detecting additional thermal events, and the sample was then cooled down. At 62 °C, a phase transformation is detected by the growth of birefringent dendritic features from the isotropic liquid, remembering one of the typical texture of the hexagonal columnar phase (Figure 3). A peak of –2.50 kJ·mol$^{-1}$ in the DSC curve corresponds to this monotropic phase transition. The phase remained stable down to room temperature. On second heating, the compound cleared straight into the isotropic liquid at 62 °C, that is 20 °C lower than during the first heating. Subsequent cooling and heating repeated the behavior of the second cycle so crystallization from a solvent must result in a crystalline form that needs to rearrange on heating before it clears into the isotropic liquid. The X-ray diffractogram of the mesophase registered on cooling the sample from the isotropic liquid does not contradict the mesophase assignment made by POM, nor gives conclusive information about the mesophase symmetry, and so the mesophase remains assigned from its optical texture alone. The pattern recorded at 50 °C on cooling showed only one single, but sharp and intense small-angle diffraction peak at ca. 38 Å, which was indexed as the [10] reflection of a 2D hexagonal lattice. The liquid-like order of the aliphatic chains was confirmed by the presence of the broad scattering at ca. 4.5 Å. To conclude, the optical texture shows enough evidence that a hexagonal columnar phase was formed (Figure 3), and the thermal properties of the ligand can be summarized as follows: Cr 82 ($Col_h$ 62) I.

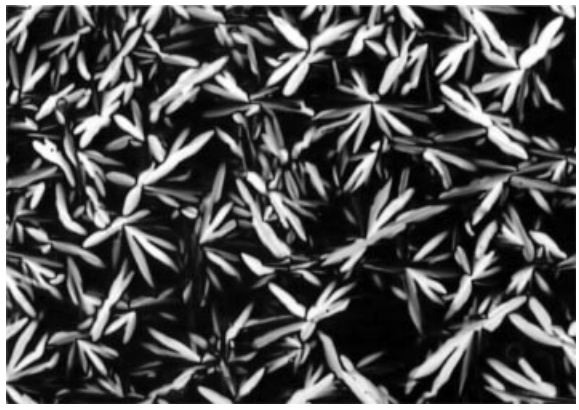

Figure 3. Optical texture of hexagonal columnar phase formed by the Schiff-base ligand $\mathbf{L}H_3$ at 58 °C.

The lanthanide(III) complexes **1**–**3** are also mesomorphic, and exhibit a mesophase over a temperature range of more than 100 °C. The clearing temperatures of the complexes could not be determined due to extensive decomposition well above 200 °C. The transition temperatures are summarized in Table 1. At room temperature, the complexes are in a semi-crystalline or *condis* (conformationally disordered) phase as revealed by XRD: only broad and diffuse scatterings were observed in the angular range of study ($0 < 2\theta < 35°$). The halo in the wide angle part at 4.5 Å corresponds to the liquid-like order of the molten chains, whereas those in the small angle part, obtained within the ratio 1:2:3 (at ca. 30.5, 15.3, and 10.2 Å) indicate some short-range layering correlations of the system. This lamellar structure is formed again on subsequent cooling/heating runs, proving the high reversibility of the phase transformation and the good thermodynamic stability of this phase. Above 100 °C, and for the three dinuclear complexes, a change in the optical texture concomitant to a phase transformation was detected. However, the optical textures observed by microscopy were not sufficiently characteristic to permit the unambiguous identification of the mesophase. With regards to the molecular structure of the complexes, which resembles to that of related dinuclear complexes constructed from hexacatenar ligands, the mesophase is likely columnar.[18] The definitive mesophase identification was achieved by temperature-dependent X-ray diffraction. The XRD pattern of the neodymium(III) complex **1** at 200 °C, chosen as representative example for the three complexes, is shown in Figure 4 and the relevant data are summarized in

 © 2006 Wiley-VCH Verlag GmbH & Co. KGaA, Weinheim 

Table 2. The X-ray pattern recorded at 200 °C was chosen instead of those recorded at lower temperatures as it provided the most suitable information. Indeed, the reflections appear to sharpen and to become more intense as the temperature was raised, a result of the temperature-induced micro-segregation. The pattern reveals two diffuse scattering halos (**5** and **6**) observed in the mid and wide-angle region. The halo at 4.5 Å (**6**), corresponds to the liquid-like order of the aliphatic chains and to the loose lateral interactions between rigid parts of the complex, whereas the other diffuse halo (**5**), corresponding to an average distance of ca 10 Å, very likely conveys to the existence of dimeric species (vide infra). In the small angle region, four large reflections were observed and indexed into a rectangular 2D lattice with the pairs of Miller's indices [*hk*] = [11], [20], [22] and [40] (Table 2). This pattern is typical for a centered rectangular lattice with a *c2mm* plane group. Since two indexations of the reflections are possible (only harmonics of the fundamental reflections were measured), we have chosen the most likely one (Table 2). The first option consists of chosing [11] = 26.0 Å and [20] = 38.25 Å, but this yields to a highly anisometric rectangular lattice, the parameters of which ($a$ = 76.5 Å and $b$ = 27.45 Å) are highly incompatible with the molecular dimensions (length, width and thickness) of the dinuclear complexes. In contrast, the other option ([11] = 38.25 Å and [20] = 26.0 Å), leads to lattice parameters that are more relevant here ($a$ = 52.0 Å and $b$ = 56.45 Å) and in agreement with the size of the complexes.

Table 1. Transition temperatures of the dinuclear lanthanide complexes.

| Compound | Ln | Transition temperatures[a] [°C] |
|---|---|---|
| **1** | Nd | X · 116 · $Col_r$-*c2mm* · 257 (dec.) |
| **2** | Sm | X · 108 · $Col_r$-*c2mm* · 227 (dec.) |
| **3** | Gd | X · 106 · $Col_r$-*c2mm* · 236 (dec.) |

[a] X: semi-crystalline lamellar solid or *condis* (conformationally disordered) phase; $Col_r$-*c2mm*: rectangular columnar phase with the centered *c2mm* symmetry; dec.: decomposition.

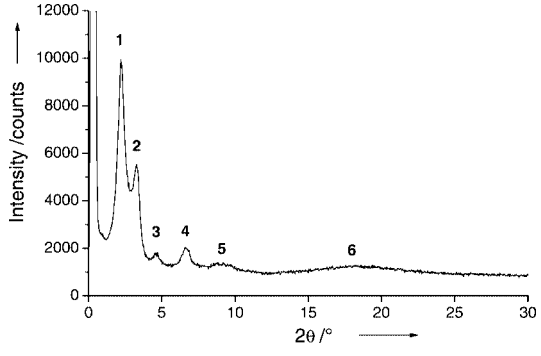


Figure 4. X-ray diffractogram of neodymium(III) complex **1** at 200 °C.

The similarity of the lattice parameters $a$ and $b$ in this case expresses that the rectangular lattice is in fact nearly square-like, that is that the cross-section of the columnar hard core (i.e. constituted of the rigid molecular parts) is not so elliptic, but rather more circular instead. In order to understand the molecular packing of the complexes in the columns and to propose a model, we first compared the molecular dimensions and volume with the columnar cross-section and rectangular cell volume of the $Col_r$ phase, and followed the methodology explained elsewhere[19] to evaluate the number of molecules per a given length of column, $h$. Of course, $h$ can be chosen arbitrarily, but in the following calculation a value of 10 Å has been assumed, corresponding to the broad signal **5** seen in the X-ray pattern (vide supra), which suggests that there is a periodicity at this distance and the breadth of the signal that there is a correlation which persists over several molecules. The minimization of the complex also showed a thickness of about 10 Å, concordant with this assumption. Thus, from the molecular volumes $V_{mol}$ of the $Ln_2L_2$ complexes (for Ln = Nd, $V_{mol}$ = 7340 Å$^3$ at 200 °C), it was found that two complexes molecular equivalents occupy the rectangular cell, 10 Å thick. Similar data were obtained for the corresponding dinuclear gadolinium and samarium complexes (see Table 2).

Table 2. XRD data of the neodymium(III) complex **1** at 200 °C.[a]

| Reflection no.[b] | $d_{exp}$[c] | [*hk*] | *I*[d] | $d_{theo}$[c] | Cell parameters[c,e] |
|---|---|---|---|---|---|
| 1 | $38.2_5$ | [11] | vs | $38.2_5$ | $Col_r$ – *c2mm* |
| 2 | 26.0 | [20] | vs | 26.0 | $a$ = 52.0 Å |
| 3 | 19.1 | [22] | m | 19.1 | $b = 56.4_5$ Å |
| 4 | $13.1_5$ | [40] | m | 13.0 | $S$ = 2.935 Å$^2$ |
| 5 | 10.0 | – | broad | – | $V_{cell}$ = 14.675 Å$^3$ |
| 6 | 4.5 | | broad | – | $N_{col}$ = 2 |

[a] For complexes **2** and **3**, similar data were obtained: Sm complex **2**: $a$ = 52.2 Å, $b$ = 56.3 Å, $V_{mol}$ = 7360 Å$^3$, $N_{col}$ = 2; Gd complex **3**: $a$ = 52.4 Å, $b$ = 56.1 Å, $V_{mol}$ = 7380 Å$^3$, $N_{col}$ = 2. [b] The numbering of X-ray reflections corresponds to the one in Figure 4. [c] $d_{exp}$ and $d_{theo}$ are the experimentally measured and theoretical diffraction spacings. Distances are given in Å. $a$, $b$ are the parameters of the $Col_r$ phase, $S$ is the lattice area and $V_{cell}$ the volume of the rectangular cellule 10 Å thick. [d] Intensity of the reflection. vs: very strong, m: medium. [e] $a$, $b$ are deduced from the measured spacings $d_{11}$ and $d_{20}$: $a = 2d_{20}$; $b = A$, with $A = \sqrt{\frac{2}{\frac{1}{d_{11}^2} + \frac{1}{d_{1\bar{1}}^2} - \frac{1}{2d_{20}^2}}}$; $d_{theor}$ is deduced from the following mathematical expression and the lattice parameters $a$ and $b$: $\frac{1}{d_{hk}} = \sqrt{\frac{h^2}{a^2} + \frac{k^2}{b^2}}$. $S = a \times b$, and $V_{cell}$ = ½×$S$×10. $N_{col}$ is the aggregation number or the number of molecular equivalents per stratum of column 10 Å thick, $N_{col} = V_{cell}/V_{mol}$.

On the basis of the molecular minimization shown above (Figure 2), it is possible to consider the formation of a dimeric species which takes an overall "bow-tie" conformation, with a thickness of approximately 10 Å, and be stabilized by lateral intermolecular interactions between the phenyl rings of the ligand strands as shown in the Figure 5. This interaction, which depends on the molecular structure, is short range and is limited in the plane to a dimeric species only because of the important number of irradiating aliphatic chains ('bow-tie'-like dimer, Figure 5), which results in the strong curvature of the hard-flexible interface and disfavors molecular associations higher than in pairs. The formation of columnar stacking is mainly driven by the

 © 2006 Wiley-VCH Verlag GmbH & Co. KGaA, Weinheim 

micro-segregation between the hard and flexible parts (Figure 6). The hard part of the dimer forms the rigid spine of the column, and the voids between these "hard" columns is filled by the homogeneous matrix of aliphatic chains. The stability of the edifice is mainly ensured by weak van der Waals interactions and by inter-dimeric interactions along the columnar axis (Figure 6). These columns then self-organize into the 2D rectangular lattice (Figure 7). A molecular dynamics model has been built from two dimers disposed respectively on the edge and at the center of a rectangular cell based on the parameters determined by XRD. Due to the incompatibility of the lanthanide ions with common forcefields used for organic compounds, and according to our previous discussion about the shape of these salen-type dimetallic complexes, the geometry of the central part of the complex was tethered to a template structure obtained from the crystallographic data of the dinuclear manganese complex mentioned above.[15] Nevertheless, each molecule was allowed to move freely from each other within the cell during the simulation. This model led to a consistent result, with a density of the packing very close to unity, similar to that of the mesophase.

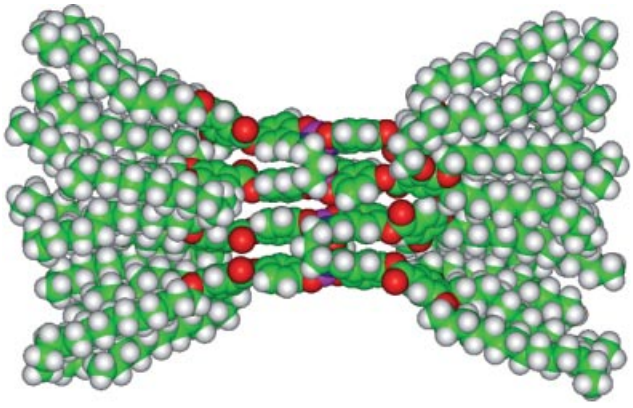

Figure 5. The 'bow-tie'-like dimeric species viewed along the columnar axis (i.e. cross-section of column).

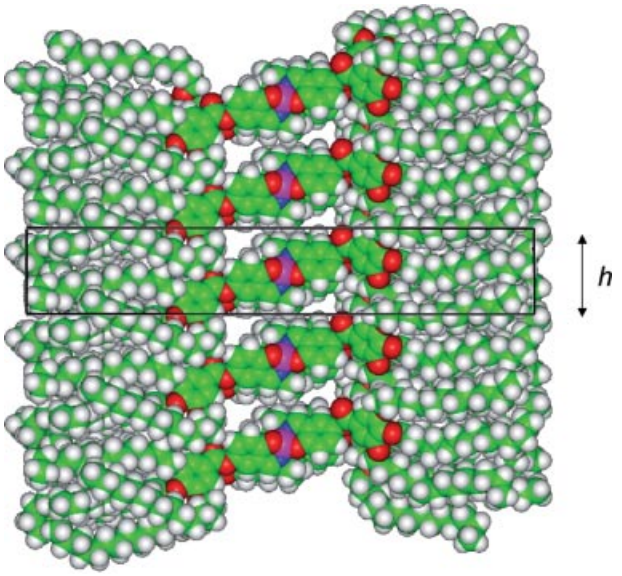


Figure 6. View of the stacking along the columnar axis, with the stacking periodicity, *h*, also representing the molecular thickness.

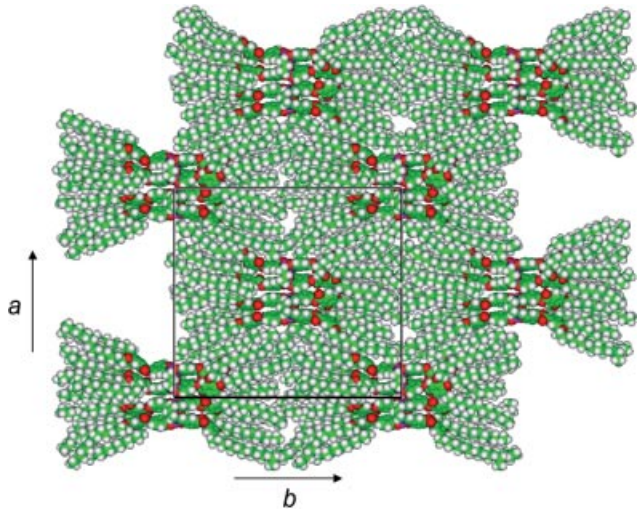


Figure 7. Arrangement of the 'bow-tie'-like dimers within the 2D rectangular lattice.

## Conclusions

In this paper, we report the first examples of neutral, liquid-crystalline dinuclear f-f complexes, i.e. complexes that contain two lanthanide ions. The ligand was designed in such a way that the resulting complexes are electrically neutral, so that no additional inorganic or organic counterions are needed to counterbalance the electric charges of the complex. Due to the synthetic methodology specifically elaborated here, only homodinuclear f-f complexes were prepared. The complexes exhibit a rectangular columnar mesophase, and a model, based on X-ray diffraction data and molecular modelling, is proposed for the molecular self-organization.

## Experimental Section

**Techniques:** The nuclear magnetic resonance (NMR) spectra were recorded on a Bruker Avance 300 spectrometer (operating at 300 MHz) and on a Bruker AMX-400 (operating at 400 MHz), using $CDCl_3$ as solvent and tetramethylsilane (TMS) as internal standard. The NMR shifts were assigned with the help of $^{13}C$ DEPT spectroscopy, two dimensional correlation spectroscopy (COSY) and proton-carbon heteronuclear multiple-quantum coherence (HMQC) spectroscopy. FTIR spectra were recorded on a Bruker IFS-66 spectrometer, using the KBr pellet method. Elemental analyses were obtained on a CE-Instrument EA-1110 elemental analyzer. MALDI-TOF mass spectra were measured on a VG Tofspec SE (Micromass, UK) equipped with a $N_2$-laser (337 nm). Optical textures of the mesophases were observed with an Olympus BX60 polarizing microscope equipped with a LINKAM THMS600 hot stage and a LINKAM TMS93 programmable temperature-controller. DSC traces were recorded with a Mettler- Toledo DSC821e module. The XRD patterns were obtained with two different exper-

 © 2006 Wiley-VCH Verlag GmbH & Co. KGaA, Weinheim 

imental set-ups, and in all cases, the powdered sample was filled in Lindemann capillaries of 1 mm diameter. A linear monochromatic Cu-$K\alpha_1$ beam ($\lambda$ = 1.5405 Å) obtained with a sealed-tube generator (900 W) and a bent quartz monochromator were used (both generator and monochromator were manufactured by Inel). One set of diffraction patterns was registered with a curved counter Inel CPS 120, for which the sample temperature is controlled within ±0.05 °C; periodicities up to 60 Å can be measured. The other set of diffraction patterns was registered on Image Plate. The cell parameters are calculated from the position of the reflections at the smallest Bragg angle, which are in all cases the most intense. Periodicities up to 90 Å can be measured, and the sample temperature is controlled within ±0.3 °C. The molecular modeling calculations were performed on a SGI Origin 2800 20 CPU computer and on an SGI Octane² calculators using Insight II and Discover 3 software from Accelrys (www.accelrys.com) with the cvff forcefield. For all models, prior to the dynamics, the systems were minimized to a gradient of 0.05 kcal mol$^{-1}$. The simulation then consisted of a 200 ps isotherm at 473 K in the NVT-PBC ensemble and with a 1 fs time step.

**Synthesis of the Schiff-Base Ligand $LH_3$:** The aldehyde 3-formyl-4-hydroxyphenyl-3,4,5-tris(tetradecyloxy)benzoate was synthesized as described elsewhere.[7] To a solution of 3-formyl-4-hydroxyphenyl-3,4,5-tris(tetradecyloxy)benzoate (1.33 g, 0.002 mol) in 200 mL of toluene was added 1,3-diamino-2-propanol (90 mg, 0.001 mol) and 5 drops of glacial acetic acid (as the catalyst). The mixture was heated for 3 hours at reflux and water formed by the reaction was removed azeotropically (Dean–Stark trap). After allowing the solution to cool down to room temperature, the solvent was removed at reduced pressure. The crude product was purified by crystallization from absolute ethanol. Yield: 80% (1.11 g). $^1$H NMR ($CDCl_3$): $\delta$ = 0.89 (m, 18 H, $CH_3$), 1.20–1.40 (m, 120 H, $CH_2$), 1.49 (m, 12 H, C*H*$_2$–$CH_2$–$CH_2$–O), 1.70–1.90 (m, 12 H, C*H*$_2$–$CH_2$–O), 3.70–3.95 (m, 4 H, N–C*H*$_2$), 4.05 (m, 12 H, $CH_2$–O), 4.30 (m, 1 H, CH), 7.01 (d, 2 H, $H_{arom}$), 7.14 (s, 2 H, $H_{arom}$), 7.16 (d, 2 H, $H_{arom}$), 7.39 (s, 4 $H_{arom}$), 8.40 (s, 2 H, C*H*=N), 13.0 (br., OH) ppm. $^{13}$C NMR ($CDCl_3$): $\delta$ = 14.1 ($CH_3$), 22.7 ($CH_2$), 26.1 ($CH_2$), 29.3–30.3 ($CH_2$), 31.9 ($CH_2$), 63.3 ($CH_2$–N), 69.3 ($CH_2$–O), 70.5 (CH), 73.6 ($CH_2$–O), 108.7 ($C_{arom}$), 117.9 ($C_{arom}$), 118.5 ($C_{arom}$), 123.7 ($C_{arom}$), 123.9 ($C_{arom}$), 126.2 ($C_{arom}$), 158.8 (C=O), 166.7 (C=N) ppm. IR (KBr): $\tilde{\nu}$ = 1641 (C=N), 1201 (C–O) cm$^{-1}$. $C_{115}H_{194}N_2O_{13}$ (1812.78): calcd. C 76.19, H 10.79, N 1.55; found C 76.18, H 10.99, N 1.42.

**Synthesis of the Lanthanide(III) Complexes:** The dinuclear lanthanide complexes (Ln = Nd, Sm, Gd) of the Schiff-base ligand **L**$H_3$ were synthesized by reaction between the lanthanide acetate salt $Ln(CH_3COO)_3{\cdot}xH_2O$ (1.1 equiv.) and the Schiff base (1 equiv.) in chloroform at refluxing temperature overnight. The acetate ions act as the base to deprotonate the ligand. The complexes were purified by crystallization from a water/ethyl acetate mixture, and were obtained in moderate yields: 74% for the Nd complex **1**, 62% for the Sm complex **2** and 49% for the Gd complex **3**. MALDI-TOF measurements show a molecular peak that corresponds to the dinuclear species with the stoichiometry [$Ln_2$**L**$_2$] for the neodymium(III) and samarium(III) complexes.

**Nd Complex 1:** $C_{230}H_{382}N_4Nd_2O_{26}$ (3907.99): calcd. C 70.69, H 9.85, N 1.43; found C 70.79, H 9.84, N 1.44. MALDI-TOF: $M_w$(isotopic) = 3907.68 *m/e*; $M_w$(found) = 3909.30 *m/e*. IR (KBr): $\tilde{\nu}$ = 1633 (C=N) cm$^{-1}$.

**Sm Complex 2:** $C_{230}H_{382}N_4O_{26}Sm_2$ (3920.23): C 70.47, H 9.82, N 1.43; found C 69.97, H 9.69, N 1.41. MALDI-TOF: $M_w$(isotopic) = 3920.71 *m/e*; $M_w$(found) = 3921.65 *m/e*. IR (KBr): $\tilde{\nu}$ = 1633 (C=N) cm$^{-1}$.

**Gd Complex 3:** $C_{230}H_{382}Gd_2N_4O_{26}$ (3934.01): C 70.22, H 9.79, N 1.42; found C 69.67, H 9.96, N 1.34. IR (KBr): $\tilde{\nu}$ = 1633 (C=N) cm$^{-1}$.

## Acknowledgments

K. B. and T. N. P.-V. thank the F.W.O.-Flanders (Belgium) for a postdoctoral fellowship. T. C. is research assistant of the F.W.O.-Flanders. Financial support by the F.W.O.-Flanders (G.0117.03) and by the K.U. Leuven (GOA, 03/03) is gratefully acknowledged. Funding for travel was obtained via a Tournesol project (Project T2004.10). C. B., D. G. and B. D. thank CNRS and ULP for support and fundings.

[1] a) *Metallomesogens, Synthesis Properties and Applications* (Ed.: J. L. Serrano), VCH, Weinheim (Germany), **1996**; b) D. W. Bruce, in: *Inorganic Materials*, 2nd ed., chapter 8, p. 429 (Eds.: D. W. Bruce, D. O'Hare), Wiley, Chichester, **1996**; c) K. Binnemans, C. Görller-Walrand, *Chem. Rev.* **2002**, *102*, 2303; d) B. Donnio, D. Guillon, R. Deschenaux, D. W. Bruce, in: *Comprehensive Coordination Chemistry II*, J. A. McCleverty, T. J. Meyer (Eds.), Elsevier, Oxford, **2003**, vol. 7 (Eds.: M. Fujita, A. Powell, C. Creutz), chapter 7.9, pp. 357–627.

[2] a) R. Paschke, H. Zaschke, A. Mädicke, J. R. Chipperfield, A. B. Blake, P. G. Nelson, G. W. Gray, *Mol. Cryst. Liq. Cryst. Lett. Sect.* **1988**, *6*, 81; b) T. D. Shaffer, K. A. Sheth, *Mol. Cryst. Liq. Cryst.* **1989**, *172*, 27; c) K. Miyamura, K. Sato, Y. Gohshi, *Bull. Chem. Soc. Jpn.* **1989**, *62*, 45; d) R. Paschke, D. Balkow, U. Baumeister, H. Hartung, J. R. Chipperfield, A. B. Blake, P. G. Nelson, G. W. Gray, *Mol. Cryst. Liq. Cryst.* **1990**, *188*, 105; e) K. Ohta, Y. Morizumi, T. Fujimoto, I. Yamamoto, K. Miyamura, Y. Gohshi, *Mol. Cryst. Liq. Cryst.* **1992**, *214*, 161; f) A. Serrette, P. J. Carroll, T. M. Swager, *J. Am. Chem. Soc.* **1992**, *114*, 1887 (Corrigendum: *J. Am. Chem. Soc.* **1993**, *115*, 11656); g) R. Paschke, S. Diele, I. Letko, A. Wiegeleben, G. Pelzl, K. Griesar, M. Athanassopoulou, W. Haase, *Liq. Cryst* **1995**, *18*, 451; h) A. B. Blake, J. R. Chipperfield, W. Hussain, R. Paschke, E. Sinn, *Inorg. Chem.* **1995**, *34*, 1125; i) R. Paschke, D. Balkow, E. Sinn, *Inorg. Chem.* **2002**, *41*, 1949; j) I. Sakata, K. Miyamura, *Chem. Commun.* **2003**, 156.

[3] N. Hoshino, *Coord. Chem. Rev.* **1998**, *174*, 77.

[4] a) I. Aiello, M. Ghedini, F. Neve, D. Pucci, *Chem. Mater.* **1997**, *9*, 2107; b) I. Aiello, M. Ghedini, M. La Deda, D. Pucci, O. Francescangeli, *Eur. J. Inorg. Chem.* **1999**, 1367.

[5] K. Binnemans, D. W. Bruce, S. R. Collinson, R. Van Deun, Yu. G. Galyametdinov, F. Martin, *Phil. Trans. Royal Soc., A* **1999**, *357*, 3063.

[6] a) A. G. Serrette, T. M. Swager, *J. Am. Chem. Soc.* **1993**, *115*, 8879; b) D. Killian, D. Knawby, M. A. Athanassopoulou, S. T. Trzaska, T. M. Swager, S. Wróbel, W. Haase, *Liq. Cryst.* **2000**, *27*, 509; c) W. Haase, D. Killian, M. A. Athanassopoulou, D. Knawby, T. M. Swager, S. Wróbel, *Liq. Cryst.* **2002**, *29*, 133.

[7] a) K. Binnemans, K. Lodewyckx, B. Donnio, D. Guillon, *Chem. Eur. J.* **2002**, *8*, 1101; b) K. Binnemans, K. Lodewyckx, *Supramol. Chem.* **2003**, *15*, 485.

[8] K. Binnemans, K. Lodewyckx, B. Donnio, D. Guillon, *Eur. J. Inorg. Chem.* **2005**, 1506.

[9] Yu. Galyametdinov, M. A. Athanassopoulou, K. Griesar, O. Kharitonova, E. A. Soto Bustamante, L. Tinchurina, I. Ovchinnikov, W. Haase, *Chem. Mater.* **1996**, *8*, 922.

[10] K. Binnemans, Yu. G. Galyametdinov, R. Van Deun, D. W. Bruce, S. R. Collinson, A. P. Polishchuk, I. Bikchantaev, W. Haase, A. V. Prosvirin, L. Tinchurina, I. Litvinov, A. Gubajdullin, A. Rakhmatullin, K. Uytterhoeven, L. Van Meervelt, *J. Am. Chem. Soc.* **2000**, *122*, 4335.

 © 2006 Wiley-VCH Verlag GmbH & Co. KGaA, Weinheim 

[11] E. Terazzi, S. Torelli, G. Bernardinelli, J.-P. Rivera, J.-M. Bénech, C. Bourgogne, B. Donnio, D. Guillon, D. Imbert, J.-C. G. Bünzli, A. Pinto, D. Jeannerat, C. Piguet, *J. Am. Chem. Soc.* **2005**, *127*, 888.
[12] a) *Supramolecular Chemistry: Concepts and Perspectives*, J.-M. Lehn, VCH, Weinheim (Germany), **1995**; b) *Supramolecular Chemistry*, J. W. Steed, J. L. Atwood, Wiley, Chichester, **2000**.
[13] a) C. Piguet, G. Bernardinelli, G. Hopfgartner, *Chem. Rev.* **1997**, *97*, 2005; b) G. F. Swiegers, T. Malefetse, *J. Chem. Rev.* **2000**, *100*, 3483; c) M. Albrecht, *Chem. Rev.* **2001**, *101*, 3457.
[14] R. Ziessel, *Coord. Chem. Rev.* **2001**, *216–217*, 195.
[15] J. Xu, T. N. Parac, K. N. Raymond, *Angew. Chem. Int. Ed.* **1999**, *38*, 2878.
[16] A. Gelasco, V. L. Pecoraro, *J. Am. Chem. Soc.* **1993**, *115*, 7928.
[17] a) J. Malthête, H.-T. Nguyen, C. Destrade, *Liq. Cryst.* **1993**, *13*, 171; b) H.-T. Nguyen, C. Destrade, J. Malthête, *Adv. Mater.* **1997**, *9*, 375.
[18] a) A. El-ghayoury, L. Douce, A. Skoulios, R. Ziessel, *Angew. Chem. Int. Ed.* **1998**, *37*, 2205; b) R. Ziessel, L. Douce, A. El-ghayoury, A. Harriman, A. Skoulios, *Angew. Chem. Int. Ed.* **2000**, *39*, 1489; c) L. Douce, R. Ziessel, *Mol. Cryst. Liq. Cryst.* **2001**, *362*, 133.
[19] a) F. Morale, R. W. Date, D. Guillon, D. W. Bruce, R. L. Finn, C. Wilson, A. J. Blake, M. Schröder, B. Donnio, *Chem. Eur. J.* **2003**, *9*, 2484; b) B. Donnio, B. Heinrich, H. Allouchi, J. Kain, S. Diele, D. Guillon, D. W. Bruce, *J. Am. Chem. Soc.* **2004**, *126*, 15258.

Received: August 4, 2005
Published Online: November 11, 2005

 © 2006 Wiley-VCH Verlag GmbH & Co. KGaA, Weinheim 

DOI: 10.1002/ejic.200500777

# Silver and Rhodium Complexes of Stable, Monomeric Imidazolidin-2-ylidenes: Synthesis, Reactivity and Decomposition Pathway

**Martin Paas,[b] Birgit Wibbeling,[c] Roland Fröhlich,[c] and F. Ekkehardt Hahn*[a]**

**Keywords:** Carbenes / Carbene ligands / Nitrogen heterocycles / Silver / Sulfur

Silver(I) complexes of the freely stable carbenes 1,3-bis(2,4,6-trimethylphenyl)imidazolidin-2-ylidene (**3**) and 1,3-bis(2,6-diisopropylphenyl)imidazolidin-2-ylidene (**4**) were prepared from the imidazolinium chlorides **1** and **2**, respectively, and silver oxide. These two air-stable and light-sensitive carbene complexes [AgCl(**3**)] (**5**) and [AgCl(**4**)] (**6**) were characterized by NMR spectroscopy, and the molecular structure of **6** was confirmed by X-ray diffraction. The imidazolidin-2-thiones **7** and **8** were obtained by reaction of the silver carbene complexes **5** and **6**, respectively, with elemental sulfur at ambient temperature. Spectroscopic evidence for the formation of the rhodium(I) complex [(cod)Rh(Cl)(**10**)] (**11**) with the sterically demanding 1,3-di-*tert*-butyl-imidazolidin-2-ylidene ligand **10** obtained in situ from 1,3-di-*tert*-butyl-imidazolinium tetrafluoroborate **9** is presented. Because of the steric demand of the carbene ligand **10**, complex **11** decomposed rapidly in solutions of chlorinated or polar solvents.

(© Wiley-VCH Verlag GmbH & Co. KGaA, 69451 Weinheim, Germany, 2006)

## Introduction

Metal complexes of N-heterocyclic carbenes have emerged as an important class of compounds with widespread applications in homogeneous catalysis.[1,2] For example, such complexes represent efficient catalysts for palladium-catalyzed carbon–carbon coupling reactions,[3,4] ruthenium-catalyzed olefin metathesis reactions,[5–7] or iridium-catalyzed transfer hydrogenation reactions.[8] In general, metal complexes of "saturated" (nonaromatic) imidazolidin-2-ylidenes[9] reveal higher catalytic activity than the analogous complexes of "unsaturated" (aromatic) imidazolin-2-ylidenes[10] or benzannulated benzimidazol-2-ylidenes.[11] This is regarded as a consequence of the stronger basicity and nucleophilicity of the nonaromatically stabilized carbene ligands. However, in contrast to unsaturated N-heterocyclic carbenes, imidazolidin-2-ylidenes can occur as carbene dimers (enetetramines) if the steric demand of their *N*-substituents is small (e.g. *N*-methyl,[12] *N*-ethyl,[12] and *N*-phenyl[13]) and the kinetic barrier for dimerization is low. Imidazolidin-2-ylidenes with bulky *N*-substituents [e.g. *N*-*tert*-butyl,[12] *N*-(2,4,6-trimethylphenyl),[14] and *N*-(2,6-diisopropylphenyl)[14]] showed no tendency to dimerize and could be isolated and characterized as monomeric compounds. Recently, a simple procedure for the formation of unsymmetrical *N*,*N*′-substituted imidazolidin-2-ylidenes was described, and it was demonstrated that only one sterically demanding *N*-substituent is sufficient to prevent the dimerization of the carbene.[15]

Initially, transition metal complexes with imidazolidin-2-ylidene ligands were synthesized by cleavage of the enetetramines under forceful conditions.[16,17] The direct formation of such carbene-metal complexes by utilization of monomeric saturated carbenes is less attractive since the free ligands are extremely sensitive towards oxygen and moisture. However, preparation of the free carbenes by in situ deprotonation of imidazolinium salts with strong bases and subsequent reaction with suitable transition-metal precursors produced an improvement. In contrast to this, transmetalation has emerged as an interesting alternative for the synthesis of numerous transition-metal carbene complexes.[18] Silver(I)-carbene complexes have turned out to be the transmetalation agent of choice and were first employed by Wang and Lin in order to prepare rhodium and palladium complexes of benzimidazol-2-ylidene ligands.[19] The analogous silver complexes of imidazolidin-2-ylidene ligands were prepared by Pytkowicz et al. from silver(I) oxide and imidazolinium salts.[20]

In this contribution we report on the preparation and characterization of silver complexes **5** and **6** (Scheme 1), along with the sterically demanding imidazolidin-2-ylidene ligands **3** and **4**. We demonstrate that complexes **5** and **6** do not react in the transmetalation reaction with $PdI_2$ and [(*p*-cymene)RuCl(μ-Cl)]$_2$, most likely because of the steric demand of the carbene ligands, which shows the limitations of the transmetalation reaction. Furthermore, the rhodium

[a] Institut für Anorganische und Analytische Chemie, Westfälische Wilhelms-Universität Münster,
Wilhelm-Klemm-Strasse 8, 48149 Münster, Germany
Fax: +49-251-8333108
E-mail: fehahn@uni–muenster.de
[b] NRW Graduate School of Chemistry,
Münster, Germany
[c] Organisch-Chemisches Institut, Westfälische Wilhelms-Universität Münster,
Corrensstraße 40, 48149 Münster, Germany

 © 2006 Wiley-VCH Verlag GmbH & Co. KGaA, Weinheim 

complex **11** with the *N*-*tert*-butyl-substituted carbene **10** is described (Scheme 3). These three complexes contain ligands that are also stable as monomeric imidazolidin-2-ylidenes when they are not coordinated to a metal center. In addition, the reaction of the complexes **5** and **6** with elemental sulfur to give imdazolidin-2-thiones is described (Scheme 2).

## Results and Discussion

The preparation of the silver complexes **5** and **6** was carried out in an analogous procedure to that described by Wang and Lin for the preparation of silver complexes with benzimidazolin-2-ylidene ligands.[19] The reaction of the imidazolinium salts **1** and **2** with 0.5 equiv. silver oxide in dichloromethane afforded the monocarbene complexes after a reaction time of 24 h (Scheme 1).

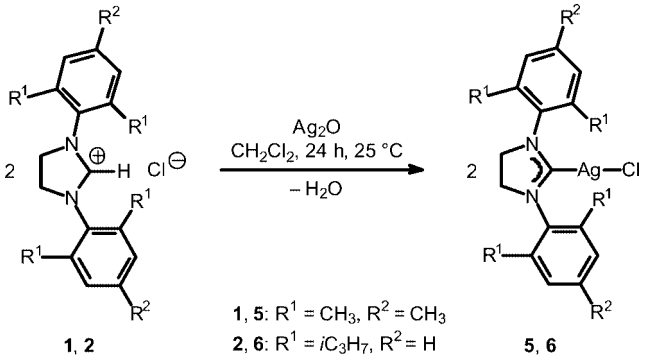


Scheme 1. Preparation of the silver carbene complexes **5** and **6**.

During the reaction, the dark suspension of silver oxide and the imidazolidinium salt became a clear and colorless solution as the silver oxide was consumed. The reaction did not require an exclusion of oxygen or moisture. This represents a substantial advantage compared with the complex synthesis using air-sensitive free carbenes and silver(I) precursors. However, complexes **5** and **6** decompose under the influence of light, as expected for silver complexes, giving the free carbenes **3** and **4** and silver chloride. Nevertheless, both novel silver carbene complexes could be fully characterized by NMR and mass spectroscopy.

Single crystals of **6**·4$CH_2Cl_2$ suitable for an X-ray diffraction analysis were obtained by layering *n*-pentane over a saturated dichloromethane solution of complex **6**. The molecular structure of the silver carbene complex **6** is depicted in Figure 1.[21] The X-ray diffraction data led, even after application of an absorption correction,[22–25] only to a poor structure model which, however, confirmed the overall composition and geometry of **6**. The quality of the X-ray data does not allow a detailed discussion of molecular parameters of **6**. Complex **6** resides on a crystallographic twofold axis that bisects the C4–C4* bond. The Ag–C2 bond in complex **6** [2.059(9) Å] is slightly shorter than the analogous bond in the silver(I) bromide complex with an *N*,*N*′-benzyl-substituted imidazolidin-2-ylidene ligand [2.09(2) Å].[20] However, the Ag–C2 bond length in **6** has a value that is similar to that found for the complex [AgCl(NHC)] (NHC = imidazolin-2-ylidene) [2.056(7) Å].[26]

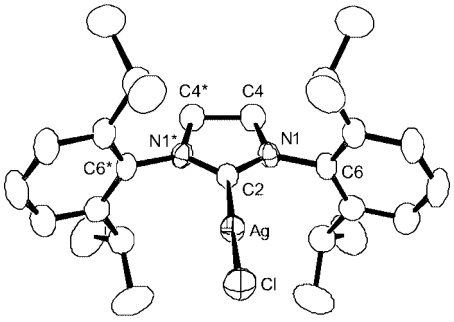


Figure 1. Molecular structure of one molecule of **6** in crystals of **6**·4$CH_2Cl_2$. Hydrogen atoms and solvent molecules have been omitted for clarity. Selected bond lengths [Å] and bond angles [°]: Ag–Cl 2.306(2), Ag–C2 2.059(9), N1–C2 1.324(7), N1–C4 1.457(8), C4–C4* 1.538(14); C2–Ag–Cl 173.5(2), C2–N1–C4 114.2(6), C2–N1–C6 123.1(5), Ag–C2–N1 125.9(4), N1–C2–N1* 107.8(8).

The transmetalation reactions with selected complexes of ruthenium and palladium {$PdI_2$, [(*p*-cymene)RuCl(μ-Cl)]$_2$} that use **5** and **6** as transmetalation agents were unsuccessful, most likely owing to the steric demand of the carbene ligands. We also studied the reactions of the complexes **5** and **6** with elemental sulfur. The imidazolidin-2-thiones **7** and **8** were obtained by simple addition of sulfur to a solution of the silver carbene complexes **5** and **6**, respectively, in dichloromethane at ambient temperature (Scheme 2).

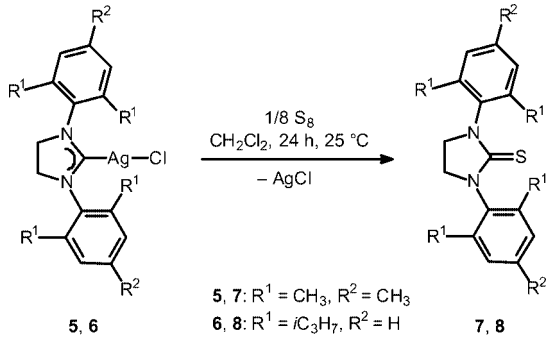


Scheme 2. Preparation of the thiones **7** and **8**.

The formation of a carbene intermediate during the reaction of complexes **5** and **6** with sulfur is very likely. This transformation represents the reverse reaction of the sequence thione reduction[27] and reaction of the free carbene with a transition metal to give transition-metal carbene complexes. The $^{13}C$ NMR spectrum of **8** reveals the characteristic resonance signal for the carbon atom of the thiocarbonyl group at $\delta$ = 184.1 ppm. Furthermore, the spectrum shows the resonance signal for the methylene carbon atom of the *N*-heterocyclic ring at $\delta$ = 50.2 ppm. The cyclic thioureas **7** and **8** were characterized by X-ray diffraction to confirm the assigned structures. Crystals of **7** and **8** were obtained by diffusion of *n*-hexane into saturated dichloromethane solutions of the thiones. Figure 2 (**7**) and Figure 3 (**8**) depict the molecular structures of the thiones.[21–25]

 © 2006 Wiley-VCH Verlag GmbH & Co. KGaA, Weinheim 

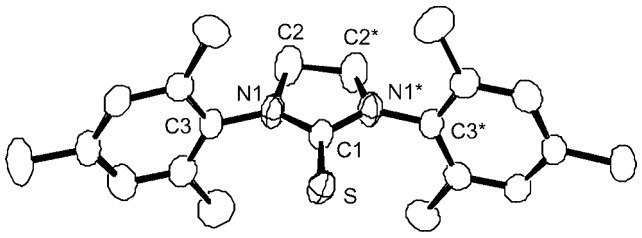


Figure 2. Molecular structure of one molecule of **7** in the crystal. Hydrogen atoms are omitted for clarity. Selected bond lengths [Å] and bond angles [°]: S–C1 1.666(2), N1–C1 1.355(2), N1–C2 1.460(2), N1–C3 1.428(2), C2–C2* 1.513(4); C1–N1–C2 112.3(1), C1–N1–C3 125.3(1), C2–N1–C3 121.96(12), S–C1–N1 126.12(9), N1–C1–N1* 107.8(2).

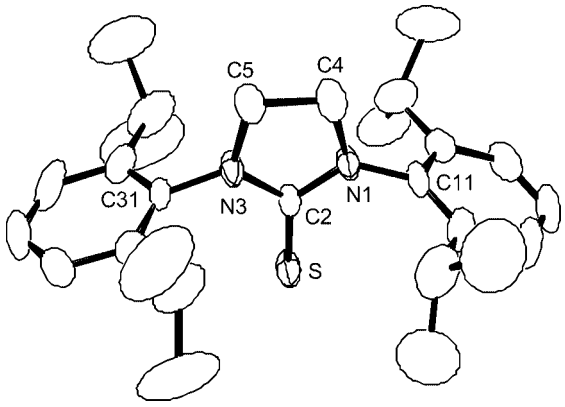


Figure 3. Molecular structure of one molecule of **8** in the crystal. Hydrogen atoms are omitted for clarity. Selected bond lengths [Å] and bond angles [°]: S–C2 1.6611(15), N1–C2 1.347(2), N1–C4 1.453(2), N1–C11 1.440(2), N3–C2 1.353(2), N3–C5 1.457(2), N3–C31 1.425(2), C4–C5 1.495(3); C2–N1–C4 112.61(13), C2–N1–C11 124.75(13), C4–N1–C11 122.63(13), C2–N3–C5 112.45(13), C2–N3–C31 126.25(13), C5–N3–C31 121.15(12), S–C2–N1 126.54(11), S–C2–N3 125.77(11), N1–C2–N3 107.69(13).

The carbon–sulfur bond lengths in both thioureas are similar to those reported for symmetrically *N*,*N*′-substituted[28] or unsymmetrically substituted spirocyclic imidazolidin-2-thiones.[15b] The N–C–N angles in thiones **7** and **8** are similar to those observed in the carbene complexes.[15]

Imidazolidin-2-thiones can act as ligands by using the sulfur atom for coordination. The molecular structure of the complex *cis*-[$PdCl_2$(**7**)$_2$] has been determined. The structure analysis reveals that coordination of the thiourea to a transition metal leaves the C–S bond length as well as the N–C–N angles of the ligand unchanged within experimental error.[29]

Complexes with *N*-*tert*-butyl-substituted imidazolidin-2-ylidenes are rare because of the steric demand of the *N*-substituents of the carbene ligand that hampers coordination and facilitates ligand dissociation from the metal center.[30] However, we found that the rhodium carbene complex **11** can be synthesized from the imidazolidinium tetrafluoroborate **9**, potassium *tert*-butoxide, and the dinuclear complex [(cod)Rh(Cl)]$_2$ by heating to reflux in THF (Scheme 3).

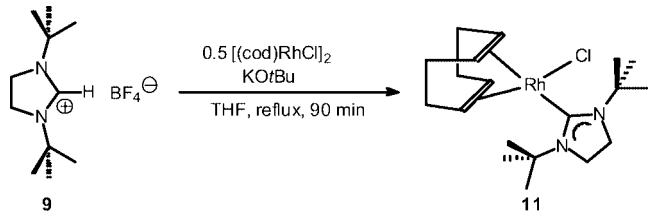


Scheme 3. Synthesis of the carbene complex **11**.

The rhodium atom in **11** is coordinated by carbene ligand **10**, which is stable in the free state and was previously isolated as such by Denk et al.[12] The *N*,*N*′-*tert*-butyl-substituted imidazolinium salt **9** is easily obtained from *N*,*N*′-di-*tert*-butylethylenediamine, triethylorthoformate, and ammonium tetrafluoroborate.[31] The $^{13}$C NMR spectrum of **11** exhibits a resonance signal for the carbene carbon atom at $\delta$ = 212.1 ppm with a $^{103}$Rh-$^{13}$C coupling constant of $^1J_{Rh,C}$ = 45 Hz. This constitutes clear evidence for complex formation. Both spectroscopic parameters are in good agreement with the analogous parameters for rhodium cod [(1*Z*,5*Z*)-1,5-cyclooctadiene] complexes with unsymmetrically *N*,*N*′-substituted carbene ligands.[15a] In comparison with rhodium complexes with benzannulated[32] and "unsaturated" (imidazolin-2-ylidene)[33] carbene ligands, the carbene carbon resonance in the $^{13}$C NMR spectrum of **11** is shifted to a lower field, whereas compared to acyclic carbene ligands,[34] a small upfield shift is observed for the carbene carbon resonance in **11**. This corroborates the expectation that the σ-donor capability of carbenes with a saturated five-membered ring is higher than that for unsaturated carbenes of the imidazolin-2-ylidene type.

Complex **11** exhibits only two resonance signals for the olefinic carbon atoms of the cod ring ($\delta$ = 68.7 ppm, $^1J_{Rh,C}$ = 15 Hz, and $\delta$ = 93.0 ppm, $^1J_{Rh,C}$ = 8 Hz). In contrast to this, the $^{13}$C NMR spectra of the rhodium complexes with unsymmetrically *N*,*N*′-substituted imidazolidin-2-ylidene ligands exhibit four signals for the olefinic carbon atoms of the cod ring, each with a $^1J$ coupling to the $^{103}$Rh nucleus.[15a] This is attributed to the loss of symmetry in the rhodium(I) complexes with unsymmetrically *N*,*N*′-substituted carbene ligands.

Rhodium complex **11** is air stable when stored as a solid, but it decomposes in solutions of dichloromethane. This lability can be rationalized by the weak bond between the rhodium atom and the carbene carbon atom, which is presumably caused by the steric demand of the *N*-*tert*-butyl substitutents of the carbene ligand. Similar observations have been made with nickel complexes of ligand **10**.[30]

## Conclusions

We have prepared the silver(I) complexes **5** and **6** along with the two monomeric imidazolidin-2-ylidenes **3** and **4**[14] starting from the imidazolinium salts **1** and **2**, respectively. The reaction of the silver complexes **5** and **6** with elemental sulfur gave the imidazolidin-2-thiones **7** and **8**, respectively. These thioureas were characterized by X-ray diffraction

 © 2006 Wiley-VCH Verlag GmbH & Co. KGaA, Weinheim 

analysis. It was shown that the rhodium(I) complex with the *N*,*N*′-*tert*-butyl-substituted imidazolidin-2-ylidene ligand **10** can be synthesized in spite of the steric bulk of this carbene ligand.

## Experimental Section

**General:** Reactions with air- and moisture-sensitive compounds or reagents were carried out in dry argon by using Schlenk and vacuum techniques. Solvents were dried by standard methods and freshly distilled prior to use. NMR spectra were recorded with a Bruker AC 200 (200 MHz) spectrometer and are reported relative to TMS as an internal standard. Mass spectra (EI) were measured with a Varian MAT 212 or a Bruker Reflex IV (MALDI) instrument. Elemental analyses (C, H, N) were obtained by using a Vario EL III elemental analyzer at the Westfälische Wilhelms-Universität Münster. The following compounds were prepared according to published procedures: 1,3-bis(2,4,6-trimethylphenyl)imidazolinium chloride (**1**),[14] 1,3-bis(2,6-diisopropylphenyl)imidazolinium chloride (**2**),[14] 1,3-di-*tert*-butyl-imidazolinium-tetrafluoroborate (**9**),[31] and {[(cod)Rh(Cl)]$_2$}.[35] All other compounds were used as purchased without further purification.

**[AgCl(3)] (5):** Silver(I) oxide (0.348 g, 1.5 mmol) was added to a solution of the imidazolinium salt **1** (1.029 g, 3.0 mmol) in dichloromethane (50 mL). The mixture was stirred at room temperature until the solid was completely consumed (24 h). The resulting solution was filtered through Celite and concentrated under vacuum. After recrystallization from dichloromethane/*n*-hexane, the silver carbene complex was obtained as a colorless solid (1.28 g, 95%). $C_{21}H_{26}N_2AgCl$ (449.8): calcd. C 56.08, H 5.83, N 6.23; found C 55.77, H 5.95, N 6.38. $^1$H NMR (200.1 MHz, $CD_3CN$): $\delta$ = 2.31 (s, 12 H, *o*-Ar–$CH_3$), 2.37 (s, 6 H, *p*-Ar–$CH_3$), 4.05 (s, 4 H, NC$H_2$C$H_2$N), 6.90, 7.08 (2×s, 4 H, Ar–H) ppm. $^{13}$C NMR (50.3 MHz, $CD_3CN$): $\delta$ = 18.1 (*o*-Ar–*C*$H_3$), 21.1 (*p*-Ar–*C*$H_3$), 51.8 ($NCH_2$), 130.1, 135.6, 137.0, 139.2 (Ar–C) ppm. The resonance for the carbene carbon atom was not observed. MS (MALDI): *m*/*z* = 719 [Ag(**3**)$_2$]$^+$.

**[AgCl(4)] (6):** Silver(I) oxide (0.348 g, 1.5 mmol) was added to a solution of **2** (1.281 g, 3.0 mmol) in dichloromethane (50 mL). The mixture was stirred at room temperature until the solid was completely consumed (24 h). It was then filtered through Celite and concentrated under vacuum. After recrystallization from dichloromethane/*n*-hexane, the silver carbene complex was obtained as a colorless solid (1.47 g, 92%). $C_{27}H_{38}N_2AgCl$ (533.9): calcd. C 60.74, H 7.17, N 5.25; found C 60.51, H 7.29, N 5.43. $^1$H NMR (200.1 MHz, $CD_3CN$): $\delta$ = 1.19, 1.27 [2×d, $^3J$(H,H) = 6.6, 7.6 Hz, 24 H, CH(C$H_3$)$_2$], 3.17 [sept, 4 H, C*H*($CH_3$)$_2$], 4.11 (s, 4 H, NC$H_2$C$H_2$N), 7.31–7.46 (m, 6 H, Ar–H) ppm. $^{13}$C NMR (50.3 MHz, $CD_3CN$): $\delta$ = 23.9, 25.5 [CH(*C*$H_3$)$_2$], 29.2 [*C*H($CH_3$)$_2$], 54.7 ($NCH_2$), 125.4, 130.7, 134.4, 148.1 (Ar–C) ppm. The resonance for the carbene carbon atom was not observed.

**1,3-Bis(2,4,6-trimethylphenyl)imidazolidin-2-thione (7):** A mixture of the silver complex **5** (0.450 g, 1 mmol) and sulfur (0.032 g, 1 mmol) was suspended in dichloromethane (50 mL) and stirred for 24 h at room temperature. After removal of silver chloride by filtration, the solvent was evaporated in vacuo. The crude product was purified chromatographically [silica gel, *n*-hexane/diethyl ether (5:1, v:v)] to give a yellow solid (0.269 g, 80%). $C_{21}H_{26}N_2S$ (338.5): calcd. C 74.51, H 7.74, N 8.28; found C 75.32, H 7.48, N 8.29. $^1$H NMR (200.1 MHz, $CDCl_3$): $\delta$ = 2.25 (s, 18 H, *p*-Ar–$CH_3$, *o*-Ar–$CH_3$), 4.00 (s, 4 H, NC$H_2$C$H_2$N), 6.99 (s, 4 H, Ar–H) ppm. $^{13}$C NMR (50.3 MHz, $CDCl_3$): $\delta$ = 17.5 (*o*-Ar–*C*$H_3$), 21.0 (*p*-Ar–*C*$H_3$), 47.5 ($NCH_2$), 129.3, 134.4, 136.3, 138.0 (Ar–C), 180.8 (C=S). MS (EI, 70 eV): *m*/*z* (%) = 338 (48) [M]$^+$.

**1,3-Bis(2,6-diisopropylphenyl)imidazolidin-2-thione (8):** A mixture of the silver complex **6** (0.534 g, 1 mmol) and sulfur (0.032 g, 1 mmol) was suspended in dichloromethane (50 mL) and stirred for 24 h at room temperature. After removal of silver chloride by filtration, the solvent was evaporated in vacuo. The crude product was purified chromatographically [silica gel, *n*-hexane/diethyl ether (5:1, v:v)] to give a yellow solid (0.262 g, 62%). $C_{27}H_{38}N_2S$ (422.7): calcd. C 76.73, H 9.06, N 6.63; found C 76.99, H 8.68, N 6.65. $^1$H NMR (200.1 MHz, $CDCl_3$): $\delta$ = 1.33, 1.37 [2×d, $^3J_{H,H}$ = 4.4, 5.2 Hz, 24 H, CH(C$H_3$)$_2$], 3.10 [sept, 4 H, C*H*($CH_3$)$_2$], 4.05 (s, 4 H, NC$H_2$C$H_2$N), 7.24–7.41 (m, 6 H, Ar–H) ppm. $^{13}$C NMR (50.3 MHz, $CDCl_3$): $\delta$ = 24.3 [CH(*C*$H_3$)$_2$], 28.9 [*C*H($CH_3$)$_2$], 50.2 ($NCH_2$), 124.2, 129.1, 134.7, 147.3 (Ar–C), 184.1 (C=S) ppm. MS (EI, 70 eV): *m*/*z* (%) = 422 (85) [M]$^+$, 407 (6) [M – $CH_3$]$^+$.

**[(cod)Rh(Cl)(10)] (11):** A solution of {[(cod)Rh(Cl)]$_2$} (0.098 g, 0.20 mmol) in THF (20 mL) was added to a suspension of the imidazolinium tetrafluoroborate **9** (0.108 g, 0.40 mmol) and potassium *tert*-butoxide (0.045 g, 0.40 mmol) in THF (20 mL). The resulting mixture was heated under reflux for 90 min. After cooling and evaporation of the solvent, the residue was suspended in toluene (10 mL) and filtered. The solvent of the filtrate was removed under vacuum, and the crude product was purified chromatographically [silica gel, hexane/ethyl acetate (5:1, v:v)] to give a yellow solid (0.067 g, 78%). $C_{19}H_{34}N_2RhCl$ (428.9): calcd. C 53.21, H 7.99, N 6.53; found C 53.56, H 7.78, N 6.59. $^1$H NMR (200.1 MHz, $CDCl_3$): $\delta$ = 1.64–1.93 [m, 8 H, cod($CH_2$)], 1.84 (s, 18 H, $CH_3$), 3.61 (s, 4 H, NC$H_2$C$H_2$N), 3.43–3.61 [m, 2 H, cod(CH)], 4.85 [m, 2 H, cod(CH)] ppm. $^{13}$C NMR (50.3 MHz, $CDCl_3$): $\delta$ = 28.2 [cod($CH_2$)], 30.8 ($CH_3$), 31.8 [cod($CH_2$)], 45.6 (N*C*$H_2$*C*$H_2$N), 57.4 [*C*($CH_3$)$_3$], 68.7 [d, $^1J_{Rh,C}$ = 15 Hz, cod(CH)], 93.0 [d, $^1J_{Rh,C}$ = 8 Hz, cod(CH)], 212.1 (d, $^1J_{Rh,C}$ = 45 Hz, NCN) ppm.

## Acknowledgments

We thank the Deutsche Forschungsgemeinschaft (IGK, 673) and the NRW Graduate School of Chemistry Münster for a predoctoral grant to M. P.

[1] B. Bourissou, O. Guerret, F. P. Gabbai, G. Bertrand, *Chem. Rev.* **2000**, *100*, 39–91.
[2] W. A. Herrmann, *Angew. Chem.* **2002**, *114*, 1342–1363; *Angew. Chem. Int. Ed.* **2002**, *41*, 1290–1309.
[3] W. A. Herrmann, M. Elison, J. Fischer, C. Köcher, G. R. J. Artus, *Angew. Chem.* **1995**, *107*, 2602–2605; *Angew. Chem. Int. Ed. Engl.* **1995**, *34*, 2371–2374.
[4] C. W. K. Gstöttmayr, V. P. W. Böhm, E. Herdtweck, M. Grosche, W. A. Herrmann, *Angew. Chem.* **2002**, *114*, 1421–1423; *Angew. Chem. Int. Ed.* **2002**, *41*, 1363–1365.
[5] M. Scholl, S. Ding, C. W. Lee, R. H. Grubbs, *Org. Lett.* **1999**, *1*, 953–956.
[6] T. M. Trnka, R. H. Grubbs, *Acc. Chem. Res.* **2001**, *34*, 18–29.
[7] A. Fürstner, *Angew. Chem.* **2000**, *112*, 3140–3172; *Angew. Chem. Int. Ed.* **2000**, *39*, 3012–3043.
[8] F. E. Hahn, C. Holtgrewe, T. Pape, M. Martin, E. Sola, L. A. Oro, *Organometallics* **2005**, *24*, 2203–2209.
[9] A. J. Arduengo III, J. R. Goerlich, W. J. Marshall, *J. Am. Chem. Soc.* **1995**, *117*, 11027–11028.
[10] A. J. Arduengo III, R. L. Harlow, M. Kline, *J. Am. Chem. Soc.* **1991**, *113*, 361–363.
[11] F. E. Hahn, L. Wittenbecher, R. Boese, D. Bläser, *Chem. Eur. J.* **1999**, *5*, 1931–1935.

 © 2006 Wiley-VCH Verlag GmbH & Co. KGaA, Weinheim 

[12] M. K. Denk, A. Thadani, K. Hatano, A. J. Lough, *Angew. Chem.* **1997**, *109*, 2719–2721; *Angew. Chem. Int. Ed. Engl.* **1997**, *36*, 2607–2609.
[13] a) H. W. Wanzlick, E. Schikora, *Chem. Ber.* **1961**, *94*, 2389–2393; b) H. W. Wanzlick, H. J. Kleiner, *Angew. Chem.* **1961**, *73*, 493.
[14] A. J. Arduengo, R. Krafczyk, R. Schmutzler, H. A. Craig, J. R. Goerlich, W. J. Marshall, M. Unverzagt, *Tetrahedron* **1999**, *55*, 14523–14534.
[15] a) F. E. Hahn, M. Paas, D. Le Van, T. Lügger, *Angew. Chem.* **2003**, *115*, 5402–5405; *Angew. Chem. Int. Ed.* **2003**, *42*, 5243–5246; b) F. E. Hahn, M. Paas, D. Le Van, R. Fröhlich, *Chem. Eur. J.* **2005**, *11*, 5080–5085.
[16] a) M. F. Lappert, *J. Organomet. Chem.* **1975**, *100*, 139–159; b) M. F. Lappert, *J. Organomet. Chem.* **1988**, *358*, 185–214.
[17] a) M. F. Lappert, P. L. Pye, G. M. McLaughlin, *J. Chem. Soc., Dalton Trans.* **1977**, 1272–1282; b) M. F. Lappert, P. L. Pye, *J. Chem. Soc., Dalton Trans.* **1977**, 1283–1291.
[18] a) S.-T. Liu, T.-Y. Hsieh, G.-H. Lee, S.-M. Peng, *Organometallics* **1998**, *17*, 993–995; b) R.-Z. Ku, J.-C. Huang, J.-Y. Cho, F.-M. Kiang, K. R. Reddy, Y.-C. Chen, K.-J. Lee, J.-H. Lee, G.-H. Lee, S.-M. Peng, S.-T. Liu, *Organometallics* **1999**, *18*, 2145–2154.
[19] H. M. J. Wang, I. J. B. Lin, *Organometallics* **1998**, *17*, 972–975.
[20] a) J. Pytkowicz, S. Roland, P. Mangeney, *J. Organomet. Chem.* **2001**, *631*, 157–163; b) J. Pytkowicz, S. Roland, P. Mangeney, G. Meyer, A. Jutand, *J. Organomet. Chem.* **2003**, *678*, 166–179.
[21] X-ray crystal structure analysis for **6**·4$CH_2Cl_2$: formula $C_{27}H_{38}N_2AgCl$·4$CH_2Cl_2$, $M$ = 873.62 g mol$^{-1}$, yellow crystal 0.20 × 0.10 × 0.05 mm, $a$ = 9.760(1), $b$ = 16.286(1), $c$ = 10.980(1) Å, $\beta$ = 103.38(1)°, $V$ = 1697.9(3) Å$^3$, $\rho_{calcd.}$ = 1.709 g cm$^{-3}$, $\mu$ = 1.329 mm$^{-1}$, $Z$ = 2, monoclinic, space group $P2_1/m$ (no. 11), Mo-$K_\alpha$ radiation, $\lambda$ = 0.71073 Å, $T$ = 198 K, 7976 reflections collected ($\pm h$, $\pm k$, $\pm l$), [(sin$\theta$)/$\lambda$] = 0.66 Å$^{-1}$, 5162 independent ($R_{int}$ = 0.044) and 3448 observed reflections [$I \geq 2\sigma(I)$], 204 refined parameters, $R$ = 0.088, $wR^2$ = 0.287, max. residual electron density 2.78 (–2.34) e Å$^{-3}$ (near disordered chlorine atoms of solvent molecules). X-ray crystal structure analysis for **7**: formula $C_{21}H_{26}N_2S$, $M$ = 338.50 g mol$^{-1}$, colorless crystal, 0.40 × 0.25 × 0.20 mm, $a$ = 16.046(1), $b$ = 7.357(1), $c$ = 16.170(1) Å, $V$ = 1908.9(3) Å$^3$, $\rho_{calcd.}$ = 1.178 g cm$^{-3}$, $\mu$ = 1.513 mm$^{-1}$, $Z$ = 4, orthorhombic, space group $Pbcn$ (no. 60), Cu-$K_\alpha$ radiation, $\lambda$ = 1.54178 Å, $T$ = 223 K, 1938 reflections collected ($-h$, $-k$, $+l$), [(sin$\theta$)/$\lambda$] = 0.62 Å$^{-1}$, 1938 independent and 1739 observed reflections [$I \geq 2\sigma(I)$], 114 refined parameters, $R$ = 0.043, $wR^2$ = 0.136, max. residual electron density 0.27 (–0.23) e Å$^{-3}$. X-ray crystal structure analysis for **8**: formula $C_{27}H_{38}N_2S$, $M$ = 422.65 g mol$^{-1}$, colorless crystal, 0.50 × 0.50 × 0.30 mm, $a$ = 19.354(1), $b$ = 6.920(1), $c$ = 20.788(1) Å, $\beta$ = 106.98(1), $V$ = 2662.8(4) Å$^3$, $\rho_{calcd.}$ = 1.054 g cm$^{-3}$, $\mu$ = 1.167 mm$^{-1}$, $Z$ = 4, monoclinic, space group $P2_1/n$ (no. 14), Cu-$K_\alpha$ radiation, $\lambda$ = 1.54178 Å, $T$ = 223 K, 15515 reflections collected ($\pm h$, $\pm k$, $\pm l$), [(sin$\theta$)/$\lambda$] = 0.59 Å$^{-1}$, 4389 independent ($R_{int}$ = 0.031) and 3874 observed reflections [$I \geq 2\sigma(I)$], 279 refined parameters, $R$ = 0.048, $wR^2$ = 0.142, max. residual electron density 0.29 (–0.23) e Å$^{-3}$. Data sets were collected with Enraf–Nonius CAD4 and Nonius KappaCCD diffractometers, the latter was equipped with a rotating anode generator. Programs used: absorption correction for CCD data, SORTAV[22] and Denzo;[23] structure solution, SHELXS-97:[24] structure refinement, SHELXL-97.[25] CCDC-282505 (**6**·4$CH_2Cl_2$), CCDC-282503 (**7**) and CCDC-282504 (**8**) contain the supplementary crystallographic data for this paper. These data can be obtained free of charge from The Cambridge Crystallographic Data Centre via www.ccdc.cam.ac.uk/data_request/cif.
[22] a) R. H. Blessing, *Acta Crystallogr. Sect. A* **1995**, *51*, 33–37; b) R. H. Blessing, *J. Appl. Cryst.* **1997**, *30*, 421–426.
[23] Z. Otwinowski, D. Borek, W. Majewski, W. Minor, *Acta Crystallogr. Sect. A* **2003**, *59*, 228–234.
[24] For SHELXS-97, see: G. M. Sheldrick, *Acta Crystallogr. Sect A* **1990**, *46*, 467–473.
[25] G. M. Sheldrick, *SHELXL-97*, Universität Göttingen (Germany), **1997**.
[26] T. Ramnial, C. D. Abernethy, M. D. Spicer, I. D. McKenzie, I. D. Gay, J. A. C. Clyburne, *Inorg. Chem.* **2003**, *42*, 1391–1393.
[27] N. Kuhn, T. Kratz, *Synthesis* **1993**, 561–562.
[28] M. K. Denk, S. Gupta, J. Brownie, S. Tajammul, A. J. Lough, *Chem. Eur. J.* **2001**, *7*, 4477–4486.
[29] D. Yang, Y.-C. Chen, N.-Y. Zhu, *Org. Lett.* **2004**, *6*, 1577–1580.
[30] R. Dorta, E. D. Stevens, N. M. Scott, C. Costabile, L. Cavallo, C. D. Hoff, S. P. Nolan, *J. Am. Chem. Soc.* **2005**, *127*, 2485–2495.
[31] S. Saba, A. M. Brescia, M. K. Kaloustian, *Tetrahedron Lett.* **1991**, *32*, 5031–5034.
[32] F. E. Hahn, T. von Fehren, L. Wittenbecher, R. Fröhlich, *Z. Naturforsch.* **2004**, *59b*, 544–546.
[33] W. A. Herrmann, C. Köcher, L. J. Gooßen, G. R. J. Artus, *Chem. Eur. J.* **1996**, *2*, 1627–1636.
[34] K. Denk, P. Sirsch, W. A. Herrmann, *J. Organomet. Chem.* **2002**, *649*, 219–224.
[35] G. Giordano, R. H. Crabtree, *Inorg. Synth.* **1980**, *28*, 88–90.

Received: September 2, 2005
Published Online: November 25, 2005

 © 2006 Wiley-VCH Verlag GmbH & Co. KGaA, Weinheim 

DOI: 10.1002/ejic.200500408

# Synthesis and Characterization of Two Novel, Mono-Lacunary Dawson Polyoxometalate-Based, Water-Soluble Organometallic Ruthenium(II) Complexes: Molecular Structure of $[\{(C_6H_6)Ru(H_2O)\}(\alpha_2\text{-}P_2W_{17}O_{61})]^{8-}$

**Yoshitaka Sakai,[a] Akira Shinohara,[a] Kunihiko Hayashi,[a] and Kenji Nomiya*[a]**

**Keywords:** Arene ligands / Polyoxometalates / Ruthenium / X-ray diffraction

The synthesis and structural characterization of a novel class of mono-lacunary Dawson polyoxometalate-(POM-)based, water-soluble organometallic complexes, which are expected to be effective homogeneous oxidation catalyst precursors in water, is described. The organometallic complexes $K_8[\{(C_6H_6)Ru(H_2O)\}(\alpha_2\text{-}P_2W_{17}O_{61})]\cdot 12H_2O$ (**1**) and $K_8[\{(p\text{-cymene})Ru(H_2O)\}(\alpha_2\text{-}P_2W_{17}O_{61})]\cdot 16H_2O$ (**2**) were successfully prepared by direct reactions of the mono-lacunary Dawson POM $K_{10}[\alpha_2\text{-}P_2W_{17}O_{61}]\cdot 19H_2O$ with the organometallic precursors $[(C_6H_6)RuCl_2]_2$ and $[(p\text{-cymene})RuCl_2]_2$, respectively, in aqueous media and characterized by complete elemental analysis, thermogravimetric and differential thermal analyses (TG/DTA), and FT-IR and solution ($^1H$, $^{13}C$, $^{31}P$, and $^{183}W$) NMR spectroscopy. The molecular structure of $[\{(C_6H_6)Ru(H_2O)\}(\alpha_2\text{-}P_2W_{17}O_{61})]^{8-}$ (**1a**), in which the binding of the cationic organometallic group $\{(C_6H_6)Ru(H_2O)\}^{2+}$ occurs through two oxygen atoms of the four available oxygen atoms in the mono-lacunary site of the POM, resulting in overall $C_1$ symmetry, was successfully determined by single-crystal X-ray analysis. Interestingly, the hydrophilicity of the organometallic precursors is greatly enhanced by binding to a mono-lacunary Dawson POM with higher hydrophilicity.
(© Wiley-VCH Verlag GmbH & Co. KGaA, 69451 Weinheim, Germany, 2006)

## Introduction

Polyoxometalates (POMs) are molecular metal oxide clusters that are of current interest as soluble metal oxides and for their application in catalysis, medicine, and materials science.[1] It has been stressed that it is important to discover more reliable and efficient procedures of synthesis before exploration of any possible new reactivity patterns.[2] The incorporation of transition metal ions into mono-lacunary Keggin and Dawson POMs has been found to give inorganic analogs of metalloporphyrin complexes[1a] and, in fact, metalloporphyrin-like catalysts that promote olefin epoxidation and aliphatic and aromatic hydroxylations have been realized.[3] The 4d or 5d transition metal ion substituted Keggin and Dawson POMs have been pointed out from the viewpoints of anticipated catalysis, in which the lacunary POM species work as π-acceptor ligands.[2]

In a separate area, water-soluble organometallic complexes that work as oxidation catalysts in water at ambient temperature are interesting from the viewpoint of green chemistry based on homogeneous catalysis by organometallic complexes.[4]

Recently, we have prepared the mono-$Ru^{III}$-substituted Dawson POM $K_7[\alpha_2\text{-}P_2W_{17}O_{61}Ru^{III}(H_2O)]\cdot 19H_2O$ as a black crystalline solid from the reaction of the mono-lacunary Dawson POM $K_{10}[\alpha_2\text{-}P_2W_{17}O_{61}]\cdot 19H_2O$ with *cis*-$[RuCl_2(DMSO)_4]$ as the ruthenium source.[5] The purity of the POM obtained here was less than 95%, which has been attributed to a serious issue involving the starting ruthenium source, i.e. some of the coordinating DMSO molecules are difficult to remove because of their strong bonding to the $Ru^{II}$ atom. Ruthenium complexes without coordinated DMSO molecules are also desirable because these DMSO molecules act as a catalyst poison during the homogeneous catalysis by the ruthenium center. POM-supported ruthenium(II) complexes such as $[Ru(DMSO)_3(H_2O)\text{-}XW_{11}O_{39}]^{6-}$ (X = Ge, Si)[6a] and $[HW_9O_{33}Ru_2(DMSO)_6]^{7-}$,[6b] prepared from *cis*-$[RuCl_2(DMSO)_4]$, have been reported and also contain some DMSO molecules coordinated to the $Ru^{II}$ atoms. For preparation of POMs that do not contain any coordinated DMSO molecules, we therefore sought other ruthenium(II) precursors without DMSO molecules, and selected the organometallic ruthenium(II) complexes $[(C_6H_6)RuCl_2]_2$ and $[(p\text{-cymene})RuCl_2]_2$.

In this work, we have obtained the novel, POM-based, diamagnetic ruthenium(II) complexes $K_8[\{(C_6H_6)Ru(H_2O)\}(\alpha_2\text{-}P_2W_{17}O_{61})]\cdot 12H_2O$ (**1**) and $K_8[\{(p\text{-cymene})Ru(H_2O)\}(\alpha_2\text{-}P_2W_{17}O_{61})]\cdot 16H_2O$ (**2**) by the direct reaction of $[\alpha_2\text{-}P_2W_{17}O_{61}]^{10-}$ with the organometallic ruthenium(II) complexes in aqueous media, and unexpectedly found that the products **1** and **2** are water-soluble. The molecular structure

[a] Department of Materials Science, Faculty of Science, Kanagawa University,
Tsuchiya 2946, Hiratsuka, Kanagawa 259-1293, Japan
Fax: +81-463-58-9684
E-mail: nomiya@chem.kanagawa-u.ac.jp
Supporting information for this article is available on the WWW under http://www.eurjic.org or from the author.

 © 2006 Wiley-VCH Verlag GmbH & Co. KgaA, Weinheim 

of the polyoxo anion $[\{(C_6H_6)Ru(H_2O)\}(\alpha_2\text{-}P_2W_{17}O_{61})]^{8-}$ (**1a**) was successfully determined by single-crystal X-ray analysis. The cationic organometallic group $\{(C_6H_6)\text{-}Ru(H_2O)\}^{2+}$ was found to be attached to two oxygen atoms of the four available oxygen atoms in the mono-lacunary site of the POM, resulting in overall $C_1$ symmetry.

Organometallic complexes supported on mono-lacunary Keggin and Dawson POMs have until now only been reported without X-ray structure analysis, such as $[(CpTi)\text{-}PW_{11}O_{39}]^{4-}$ (Cp = $C_5H_5$),[8a,8b] $[\{(C_6H_5)Sn\}PW_{11}O_{39}]^{4-}$,[8b] $[\{(RSi)_2O\}SiW_{11}O_{39}]^{4-}$ {R = $C_2H_5$, $C_6H_5$, $NC(CH_2)_3$, $C_3H_5$},[8b] $[(C_6H_5Sn)P_2W_{17}O_{61}]^{7-}$,[8b] metal–metal bonded derivatives[8c] such as $[\{CpFe(CO)_2Sn\}SiMo_{11}O_{39}]^{5-}$, $[\{[(OC)_3CoGe]_2OSiW_{11}O_{39}\}^{5-}]_n$, and $[\{(C_7H_8)_2RhSn\}\text{-}PW_{11}O_{39}]^{4-}$, and water-soluble organometallic complexes supported on tri-lacunary Keggin POM $[(CpTi)_3\text{-}XW_9O_{37}]^{7-}$ (X = Si, Ge).[8e]

As for X-ray structure analysis, POM-supported $(\eta^6\text{-arene})Ru^{2+}$ complexes have been recently reported by Proust and co-workers,[7] including $(\eta^6\text{-arene})Ru^{2+}$ complexes (arene = benzene, toluene, *p*-cymene, hexamethylbenzene) supported on mono-lacunary Keggin POMs such as $[\{[Ru(\eta^6\text{-arene})]PW_{11}O_{39}\}_2(WO_2)]^{8-}$ and $[\{Ru(\eta^6\text{-arene})(H_2O)\}\text{-}PW_{11}O_{39}]^{5-}$.[7e]

On the other hand, several saturated POMs, for example the triniobium(v)- and trivanadium(v)-substituted Keggin and Dawson POMs $[XW_9M_3O_{40}]^{n-}$ (M = Nb, V; X = Si, P) and $[P_2W_{15}M_3O_{62}]^{9-}$, have been used as molecular oxide supports for various cationic organometallic groups such as $CpTi^{3+}$, $Cp^*Rh^{2+}$, $(C_6H_6)Ru^{2+}$, $(cod)Pt^{2+}$, $(cod)Ir^+$, $(cod)\text{-}Rh^+$, $Re(CO)_3^+$, $Ir(CO)_2^+$, $Rh(CO)_2^+$, etc.[9–12] However, only a few successful X-ray structure analyses have been reported, such as $(Bu_4N)_6Na[(Cp^*Rh)(\alpha\text{-}1,2,3\text{-}P_2W_{15}Nb_3O_{62})]\cdot 10CH_3CN\cdot 10Me_2CO$[9a] and $[\{[Ag(2,2'\text{-}bpy)]_2[Ag_2(2,2'\text{-}bpy)_3]_2\}\alpha\text{-}PW_9V_3O_{40}]$.[10e]

Herein we report full details of the synthesis and unequivocal characterization of **1** and **2**, with complete elemental analysis, thermogravimetric and differential thermal analyses (TG/DTA), and FT-IR and solution ($^1H$, $^{13}C$, $^{31}P$, and $^{183}W$) NMR spectroscopy, and the molecular structure of **1a**.

## Results and Discussion

### Synthesis and Compositional Characterization

The two novel 1:1-type complexes of the cationic organometallic groups with the POM (**1** and **2**) were formed by direct reaction of the organometallic precursors $[(L)\text{-}RuCl_2]_2$ (L = $C_6H_6$, *p*-cymene) with the mono-lacunary POM $K_{10}[\alpha_2\text{-}P_2W_{17}O_{61}]$, in aqueous solution, at room temperature, under air. They were isolated as analytically pure, orange and yellow-brown powders in 24.5% (0.49 g scale) and 33.2% (0.67 g scale) yields, respectively.

The formation of **1** and **2** is represented in Equation (1).

$$1/2\ [(L)RuCl_2]_2 + K_{10}[\alpha_2\text{-}P_2W_{17}O_{61}] + H_2O \rightarrow K_8[\{(L)Ru(H_2O)\}(\alpha_2\text{-}P_2W_{17}O_{61})] + 2\ KCl \quad (1)$$

Although the organometallic precursors $[(L)RuCl_2]_2$ are insoluble in water, complexes **1** and **2** containing the organometallic fragments are water-soluble.

The molecular formulae and the 1:1-type compositions of **1** and **2** were established by complete elemental analyses (all elements, including oxygen, 100.06 and 99.7% total observed, respectively), which were carried out for the samples dried at room temperature at $10^{-3}$–$10^{-4}$ Torr overnight. The weight losses observed during drying before analysis were 3.79% for **1**, which corresponds to 10–11 adsorbed and/or hydrated water molecules, and 4.2% for **2**, which corresponds to 11–12 water molecules. In the TG/DTA measurements under atmospheric conditions, the weight loss of 3.90% observed below 124 °C in **1** corresponds to 12 water molecules and that of 6.24% observed below 189 °C in **2** corresponds to 17 water molecules, in accordance with the findings of elemental analyses plus the weight losses found before analysis (see Exp. Sect.). In these complexes, the Cl analysis (calcd. 0; found <0.1% for **1** and <0.05% for **2**) indicated no contamination by Cl atoms, thus suggesting that the reaction of Equation (1) progresses completely; complexes **1** and **2** were isolated with high purity. The diamagnetic nature of **1** and **2** was supported by solution ($^1H$, $^{13}C$, $^{31}P$, and $^{183}W$) NMR spectra; all signals were found in the region usually observed in the diamagnetic POMs.

The solid-state FT-IR measurements of $K_{10}[\alpha_2\text{-}P_2W_{17}O_{61}]$, **1**, and **2** (Figures 1a, 1b, and 1c, respectively) show the spectral patterns characteristic of the Dawson POM framework.[13] The FT-IR spectra of **1** and **2** in the polyoxometalate region are very similar to that of $K_{10}[\alpha_2\text{-}P_2W_{17}O_{61}]$, especially with regards to the multiple P–O bands (1086, 1054, and 1017 $cm^{-1}$ for **1**; 1086, 1055, and

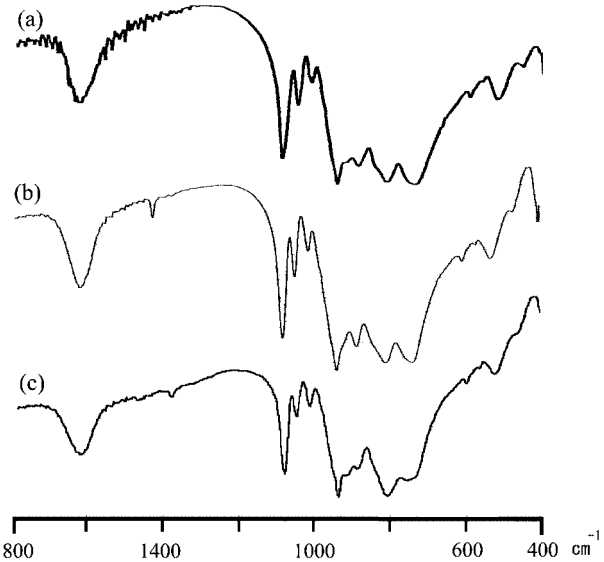


Figure 1. FT-IR spectra in the polyoxo anion regions, measured as KBr disks, of (a) $K_{10}[\alpha_2\text{-}P_2W_{17}O_{61}]\cdot 19H_2O$, (b) $K_8[\{(C_6H_6)\text{-}Ru(H_2O)\}(\alpha_2\text{-}P_2W_{17}O_{61})]\cdot 12H_2O$ (**1**), and (c) $K_8[\{(p\text{-cymene})\text{-}Ru(H_2O)\}(\alpha_2\text{-}P_2W_{17}O_{61})]\cdot 16H_2O$ (**2**).

 © 2006 Wiley-VCH Verlag GmbH & Co. KGaA, Weinheim 

1016 $cm^{-1}$ for **2**; 1085, 1052, and 1016 $cm^{-1}$ for $K_{10}[\alpha_2$-$P_2W_{17}O_{61}]$), the bands assignable to $M–O_{terminal}$ oxygen atoms (940 $cm^{-1}$ for **1**, 941 $cm^{-1}$ for **2**, and 939 $cm^{-1}$ for $K_{10}[\alpha_2$-$P_2W_{17}O_{61}]$) and in the bands assignable to edge-sharing M–O–M oxygen atoms (810 and 741 $cm^{-1}$ for **1**; 809 and 742 $cm^{-1}$ for **2**; 810 and 737 $cm^{-1}$ for $K_{10}[\alpha_2$-$P_2W_{17}O_{61}]$). No change was seen in the bands assignable to corner-sharing M–O–M oxygen atoms (885 $cm^{-1}$ for **1**, **2**, and $K_{10}[\alpha_2$-$P_2W_{17}O_{61}]$). Compared with the spectrum of $K_{10}[\alpha_2$-$P_2W_{17}O_{61}]$, the FT-IR spectra of **1** and **2** show weaker bands due to the presence of the coordinating aromatic rings at 1434 $cm^{-1}$ for **1** and 1473 and 1389 $cm^{-1}$ for **2**. The aromatic–Ru vibrational data of the precursors are observed at 1433 $cm^{-1}$ for $[(C_6H_6)RuCl_2]_2$ and at 1496, 1471, 1458, 1448, 1408, 1389, and 1362 $cm^{-1}$ for [(*p*-cymene)$RuCl_2]_2$.

### Solution NMR Spectra

The $^{31}P$ NMR spectra in $D_2O$ show clean, two-line spectra with resonances at $\delta$ = –8.36 and –14.02 ppm for **1** (Figure 2b) and at $\delta$ = –8.28 and –14.08 ppm for **2** (Figure 2c), which are different from those of $K_{10}[\alpha_2$-$P_2W_{17}O_{61}]$ at $\delta$ = –7.00 and –14.17 ppm (Figure 2a). The upfield resonance is known to be due to the phosphorus P(1) atom closer to the $W_3O_6$ cap (Figure 6b), whereas the downfield resonance is assigned to the phosphorus P(2) atom closest to the opposite site. The two-line, impressively clean $^{31}P$ NMR spectra strongly suggest the presence of a single species in solution, thereby precluding the presence of even minor, phosphorus-containing impurities in **1**, **2**, and $K_{10}[\alpha_2$-$P_2W_{17}O_{61}]$. Further, the observed $^{31}P$ chemical shifts are in the usual region for diamagnetic species of various Dawson POMs,[5,9,12b,12c] supporting the suggestion that **1** and **2** are diamagnetic $Ru^{II}$ complexes.

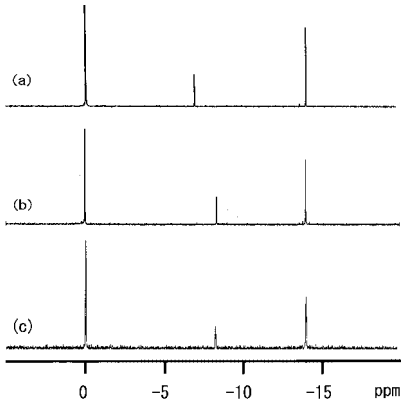


Figure 2. $^{31}P$ NMR spectra (in $D_2O$) of (a) $K_{10}[\alpha_2$-$P_2W_{17}O_{61}]$·$19H_2O$, (b) $K_8[\{(C_6H_6)Ru(H_2O)\}(\alpha_2$-$P_2W_{17}O_{61})]$·$12H_2O$ (**1**), and (c) $K_8[\{$(*p*-cymene)$Ru(H_2O)\}(\alpha_2$-$P_2W_{17}O_{61})]$·$16H_2O$ (**2**). In each case a very high level of purity is indicated (i.e., with respect to any other P-containing polyoxo anions or other materials).

The $^{183}W$ NMR spectrum of $K_{10}[\alpha_2$-$P_2W_{17}O_{61}]$ in $D_2O$ (Figure 3a) shows nine primary resonances at $\delta$ = –117.1, –140.4, –151.7, –181.0, –183.1, –218.1, –220.5, –224.0, and –242.6 with integration intensities of 2:2:2:2:1:2:2:2:2, consistent with the overall $C_s$ symmetry of the mono-lacunary Dawson structure. The $^{183}W$ NMR measurements of **1** in $D_2O$ were unsuccessful because of an insufficient concentration of the aqueous solution (see Exp. Sect.). On the other hand, the $^{183}W$ NMR spectrum of **2a**, which was derived by cation exchange of the potassium salt **2** with an excess of $NaClO_4$ (see Exp. Sect.), in $D_2O$ consists of virtually 17 lines at $\delta$ = –117.6, –125.1, –138.6, –139.0, –163.8, –177.1, –177.3, –186.5, –207.6, –217.3 (1 + 1), –218.2, –219.5, –220.6, –221.9, –239.6, and –241.6. The relative intensity of all signals, except the signals at $\delta$ = –217.3 ppm, is one (Figure 3b), thus suggesting its overall $C_1$ symmetry. These resonances are substantially different from those of $[\alpha_2$-$P_2W_{17}O_{61}]^{10–}$.

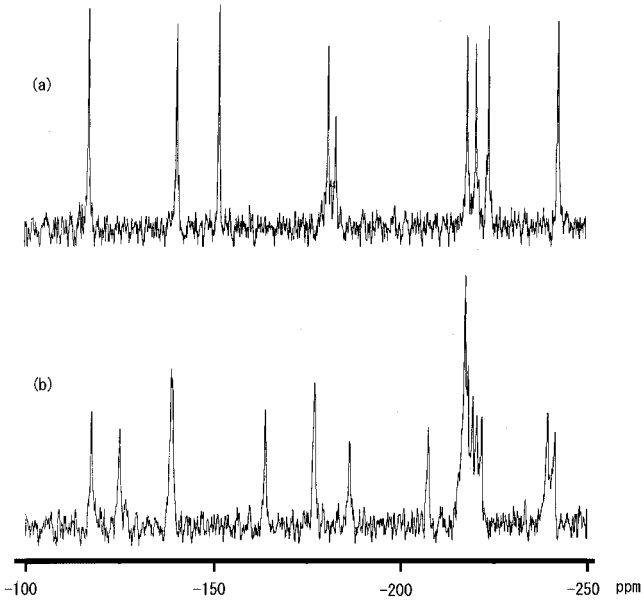


Figure 3. $^{183}W$ NMR spectra (in $D_2O$) of (a) $K_{10}[\alpha_2$-$P_2W_{17}O_{61}]$·$19H_2O$ and (b) $[\{$(*p*-cymene)$Ru(H_2O)\}(\alpha_2$-$P_2W_{17}O_{61})]^{8–}$ (**2a**), which was prepared by cation exchange of **2** using an excess amount of $NaClO_4$.

The $^1H$ (Figure 4a) and $^{13}C$ NMR (Figure 5a) spectra of **1** in $D_2O$ show single peaks at $\delta$ = 6.18 and 82.98 ppm, respectively, due to the benzene ring coordinated to the Ru atom. On the other hand, the $^{13}C$ NMR spectrum of **2** in $D_2O$ (Figure 5b) shows 10 lines due to the *p*-cymene ring coordinated to the Ru atom, thus suggesting that all carbon atoms of the coordinated *p*-cymene are inequivalent, i.e. $C_1$ symmetry. Correspondingly, the $^1H$ NMR spectrum of **2** in $D_2O$ (Figure 4b) shows that the ring protons (H2, H3, H5, H6) are inequivalent; they were actually observed as apparent three-line signals with a 1:2:1 intensity ratio. The $^1H$ and $^{13}C$ NMR spectra show the local symmetry around the coordinated benzene and the coordinated *p*-cymene, whereas the $^{31}P$ and $^{183}W$ NMR spectra show the overall symmetry of **1a** and **2a**. In the coordinated *p*-cymene ligand, all the carbon atoms are inequivalent (local symmetry

 © 2006 Wiley-VCH Verlag GmbH & Co. KGaA, Weinheim 

$C_1$) as its rotational movement is probably restricted, whereas in the coordinated benzene all the carbon atoms seem equivalent because of its free rotation on the NMR timescale. Similar observations have recently been made by the Proust group.[7e] On the other hand, the overall symmetry of **1a** is $C_1$, as revealed by single-crystal X-ray structure analysis, and that of **2a** should also be $C_1$, as suggested by the 17-line $^{183}W$ NMR spectrum.

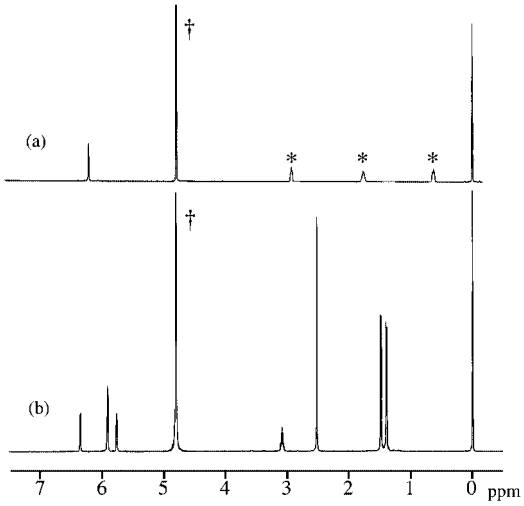


Figure 4. $^1H$ NMR spectra (in $D_2O$) of (a) $K_8[\{(C_6H_6)Ru(H_2O)\}(\alpha_2\text{-}P_2W_{17}O_{61})]\cdot 12H_2O$ (**1**), with an internal reference of DSS, and (b) $K_8[\{(p\text{-cymene})Ru(H_2O)\}(\alpha_2\text{-}P_2W_{17}O_{61})]\cdot 16H_2O$ (**2**) with an internal reference of TSP. The proton signals denoted by an asterisk in (a) are from the methylene groups of the DSS, and in both (a) and (b) the proton signals denoted by a dagger are from $H_2O$.

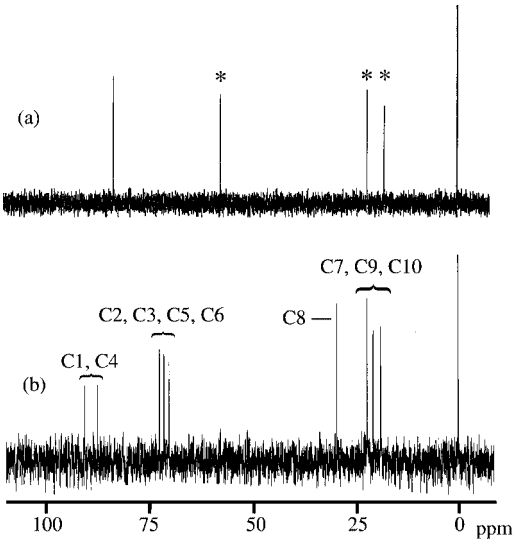


Figure 5. $^{13}C$ NMR spectra (in $D_2O$) of (a) $K_8[\{(C_6H_6)Ru(H_2O)\}(\alpha_2\text{-}P_2W_{17}O_{61})]\cdot 12H_2O$ (**1**), with an internal reference of DSS, and (b) $K_8[\{(p\text{-cymene})Ru(H_2O)\}(\alpha_2\text{-}P_2W_{17}O_{61})]\cdot 16H_2O$ (**2**), with an internal reference of TSP. The carbon signals denoted by an asterisk in (a) are from the methylene groups of the DSS.

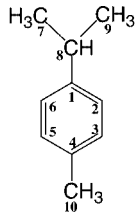


*p*-cymene ligand and its numbering

### Molecular Structure of 1a

The crystal of **1** contains discrete cluster anions, potassium cations, and lattice water molecules, all at general positions in the triclinic space group ($P\bar{1}$), except for three water oxygen atoms at special positions with a site occupancy factor fixed at 0.5. The solid-state packing of the polyoxo anion **1a** is shown in Figure 6a. The observed electron densities of the Ru and W atoms are quite different, and the data unequivocally distinguished and defined the Ru and W atoms. The 17 tungsten atoms, the one ruthenium atom, and the two P atoms were clearly identified. Thus, the main features of the molecular structure of the POM were clarified. However, the resolution obtained for the structure of the salt was limited by the poor quality of the available crystals and by the considerable disorder of the countercations and the solvent of crystallization. These features are all too common in POM crystallography.[14]

The molecular structure of **1a** is composed of the monolacunary Dawson POM unit $\alpha_2\text{-}P_2W_{17}O_{61}$ and the $\{(C_6H_6)Ru\}^{2+}$ unit, to which one oxygen atom is bonded in the form of a water molecule [Ru1A–O62A = 2.067(17) Å]. The benzene ring is disordered [C–C distances: 1.35(4)–1.47(4) Å; Ru–C distances: 2.12(3)–2.20(3) Å]. The $[(C_6H_6)Ru(H_2O)]^{2+}$ group is coordinated to only two [Ru1A–O56A (cap W) = 2.090(17) Å; Ru1A–O52A (belt W) = 2.056(18) Å] of the four available oxygen atoms (O47A, O52A, O55A, O56A) in the lacunary site of the POM support, resulting in the chiral configuration of **1a** based on $C_1$ symmetry. Thus, the polyoxo anion is found as a set of enantiomeric pairs in the unit cell (Figure 6a). As a matter of fact, there are four polyoxo anion units, denoted as units A, A′, B, and B′, in the unit cell ($Z$ = 4). The relative configurations of the benzene ring and the water molecule coordinated to the ruthenium(II) center are somewhat different between units A and B, although their polyoxo anion moieties have the same structure. Thus, the units A/A′ and B/B′ are actually the different set of enantiomeric pairs, respectively, and therefore the unit cell contains two types of the racemic mixture.

The molecular structure of unit A is depicted in Figure 6b, and that of unit B is deposited in the Supporting Information as Figure S1. Figure 6c shows a polyhedral representation of the polyoxo anion **1a**.

A few examples where only two of the four available oxygen atoms in the mono-lacunary site in the Keggin POM are utilized for coordination to the organometallic center are known. These include $[\{C_6H_5P(O)\}_2PW_{11}O_{39}]^{3-}$,[15]

 © 2006 Wiley-VCH Verlag GmbH & Co. KGaA, Weinheim 

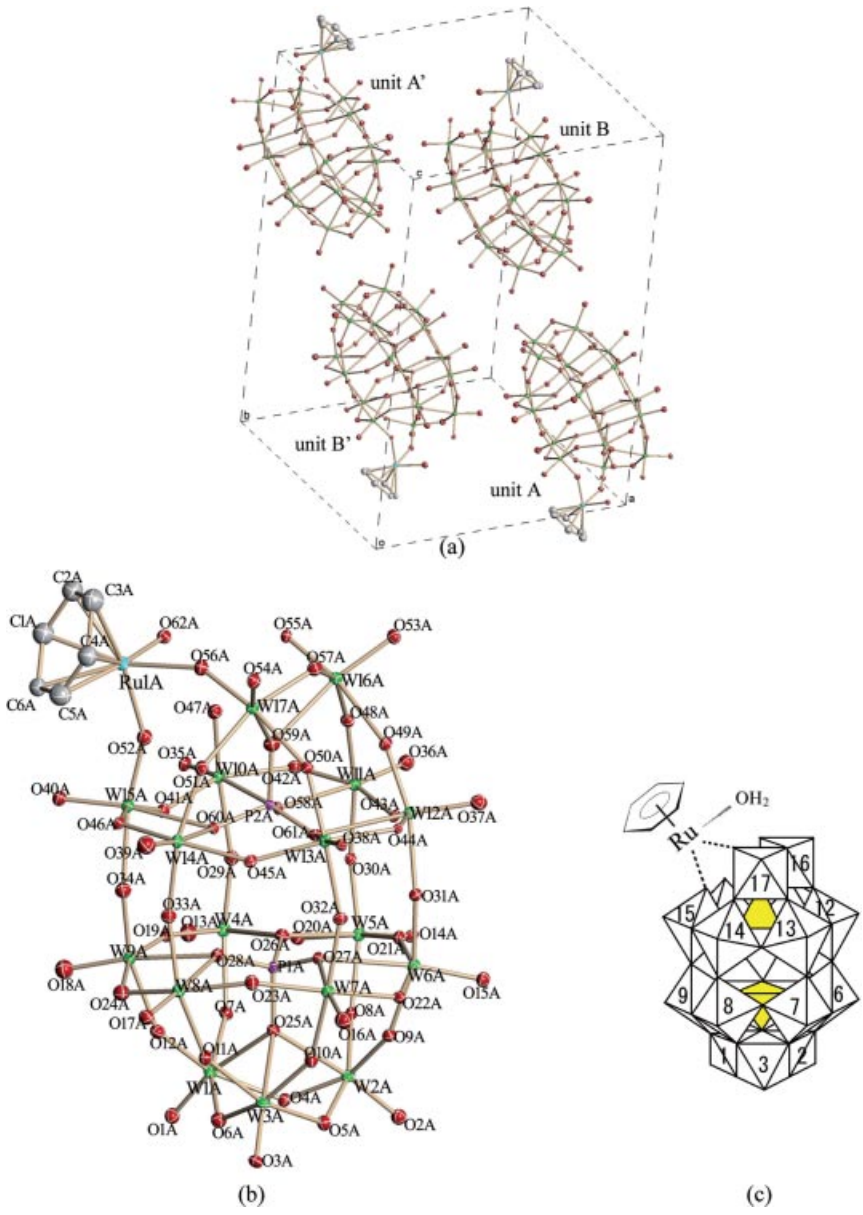


Figure 6. (a) Solid-state packing of the polyoxo anion $[\{(C_6H_6)Ru(H_2O)\}(\alpha_2\text{-}P_2W_{17}O_{61})]^{8-}$ (**1a**) (Z = 4). (b) Molecular structure of unit A in **1a** with 50% probability ellipsoids. (c) Polyhedral representation of the polyoxo anion **1a**. In (a), the units (A, A′) and (B, B′) are the different sets of enantiomeric pairs, and the relative configurations of the benzene ring and the water molecule coordinated to the ruthenium(II) center are somewhat different between the units (A and B), although their polyoxo anion moieties take the same structure. Thus, the unit cell contains two types of the racemic mixture. The molecular structure of unit A is depicted in (b); that of unit B is deposited in Supporting Information as Figure S1. In (c), the internal yellow tetrahedra represent the $PO_4^{3-}$ core, while the white octahedra represent the $WO_6$ fragment with a tungsten atom in the center of the octahedra and oxygen atoms at each corner. The cationic $[(C_6H_6)Ru(H_2O)]^{2+}$ group binds to two terminal oxygen atoms in the lacunary site. The two phosphorus atoms, P(2) and P(1), are defined as "close to Ru (north)" and "far from Ru (south)", respectively.

$[Ru(DMSO)_3(H_2O)XW_{11}O_{39}]^{6-}$ (X = Ge, Si),[6a] and $[\{Ru(\eta^6\text{-arene})(H_2O)\}PW_{11}O_{39}]^{5-}$.[7e]

Selected bond lengths and angles around the ruthenium(II) atom in **1a** are given in Table 1 and Table S1, with average bond lengths and angles for the Dawson POM unit in Table S2.

In the lacunary site, the W–O distances should be noted: W15A–O52A (bonding to Ru atom) = 1.775(18) Å; W15A–O40A (terminal) = 1.739(17) Å; W17A–O56A (bonding to Ru atom) = 1.772(17) Å; W17A–O54A (terminal) = 1.738(17) Å; W10A–O47A (terminal) = 1.767(17) Å; W10A–O35A (terminal) = 1.714(16) Å; W16A–O55A (terminal) = 1.728(16) Å; W16A–O53A (terminal) = 1.743(17) Å. These bond lengths indicate the double-bond character of the W–O (terminal) bonds. It is likely that the coordination of the Ru atom to the two oxygen atoms (O52A, O56A) in the lacunary site influences the W–O distances less than the distances W10A–O47A and W16A–O55A. On the other hand, the W–O distances in the $W_3$ cap and the two $W_6$ belts, i.e. the W–Ot (Ot: terminal oxy-

 © 2006 Wiley-VCH Verlag GmbH & Co. KGaA, Weinheim 

Table 1. Selected bond lengths [Å] and angles [°] around the ruthenium(II) atom in the unit A of **1a**.

| | | | |
|---|---|---|---|
| Ru1A–O62A ($H_2O$) | 2.067(17) | W15A–O52A (bonding Ru) | 1.775(18) |
| Ru1A–O56A (bonding cap W) | 2.090(17) | W10A–O47A (terminal) | 1.767(17) |
| Ru1A–O52A (bonding belt W) | 2.056(18) | W17A–O56A (bonding Ru) | 1.772(17) |
| | | W16A–O55A (terminal) | 1.728(16) |
| Ru1A–C1A | 2.15(3) | C1A–C2A | 1.44(4) |
| Ru1A–C2A | 2.16(3) | C2A–C3A | 1.37(4) |
| Ru1A–C3A | 2.20(3) | C3A–C4A | 1.47(4) |
| Ru1A–C4A | 2.15(3) | C4A–C5A | 1.35(4) |
| Ru1A–C5A | 2.12(3) | C5A–C6A | 1.42(4) |
| Ru1A–C6A | 2.15(3) | C6A–C1A | 1.41(4) |
| O52A–Ru1A–O56A | 83.4(7) | O47B–Ru1B–O57B | 83.6(6) |
| O62A–Ru1A–O52A | 79.7(7) | O62B–Ru1B–O47B | 85.1(7) |
| O62A–Ru1A–O56A | 84.0(7) | O62B–Ru1B–O57B | 79.5(7) |
| W15A–O52A–Ru1A | 149.7(10) | W10B–O47B–Ru1B | 145.3(9) |
| W17A–O56A–Ru1A | 148.3(10) | W16B–O57B–Ru1B | 150.6(10) |

gen atom), W–Oe (Oe: edge-sharing oxygen atom), W–Oc (W belt) (Oc: corner-sharing oxygen atom), and W–Oa (Oa: oxygen atom coordinated to P atom) distances, are in the normal range.[1b] The Dawson unit contains two central P atoms in an almost regular tetrahedral environment of $PO_4$: the $PO_4$ unit closest to the lacunary site [P–O distances: 1.534(19)–1.571(17) Å; O–P–O angles: 107.7(9)–111.3(9)°] and the $PO_4$ unit closest to the $W_3$ cap [P–O distances: 1.516(17)–1.568(17) Å; O–P–O angles: 106.3(9)–112.6(9) °].

The bond valence sums (BVS),[16] calculated using the observed bond lengths for **1a**, are in the range of 5.97–6.33 for the 17 W atoms and 4.84–5.00 for the two P atoms, which reasonably correspond to the formal valences of $W^{6+}$ and $P^{5+}$. Furthermore, the BVS values (2.17–1.50) of all oxygen atoms, except the O(62A) atom (0.45), which is bonded to the $Ru^{II}$ atom, show that they are not protonated. The BVS value of the O(62A) atom (0.45) suggests that this oxygen atom is part of a water molecule. These results are in good agreement with those of the related compounds, $[Ru(DMSO)_3(H_2O)XW_{11}O_{39}]^{6-}$ (X = Ge, Si)[6a] and $[\{Ru(p\text{-cymene})(H_2O)\}PW_{11}O_{39}]^{5-}$.[7e]

The molecular structure of **1a** is consistent with the results of the solution NMR spectra, and suggests that the solid-state structure of **1a** is maintained in aqueous solution.

### Bonding of the Organometallic Groups to the Mono-Lacunary POM

The $[\alpha_2\text{-}P_2W_{17}O_{61}]^{10-}$ POM support, the formula of which can also be rewritten as $[(PO_4^{3-})_2(W_{17}O_{53}^{4-})]$, suggests that it possesses enough basicity of the surface oxygen atoms, i.e. an extra four-minus negative charge in comparison with the saturated Dawson POM $[P_2W_{18}O_{62}]^{6-}$ $[(PO_4^{3-})_2(W_{18}O_{54}^{0})]$, and, therefore, the cationic organometallic groups can be covalently bonded to this POM. The present work shows that the higher hydrophilicity of the mono-lacunary POM is kept even after attachment of the cationic organometallic groups.

These features can be compared with the formation of the previously reported cationic organometallic complexes supported on the trivanadium(V)- and triniobium(V)-substituted Dawson POMs $[P_2W_{15}M_3O_{62}]^{9-}$ (M = $V^V$ and $Nb^V$; $[P_2W_{15}M_3O_{62}]^{9-} = [(PO_4^{3-})_2(W_{15}M_3O_{54}^{3-})]$), which have an extra three-minus negative charge in comparison with the parent POM $[P_2W_{18}O_{62}]^{6-}$.[9,10] It should be noted that the all-sodium salts of organometallic complexes supported on Dawson and Keggin POMs, namely $Na_7[(Cp^*Rh)(\alpha\text{-}1,2,3\text{-}P_2W_{15}Nb_3O_{62})]\cdot 7DMSO\cdot 5H_2O$[9c] and $Na_5[(Cp^*Rh)(\beta\text{-}1,2,3\text{-}SiW_9Nb_3O_{40})]\cdot 3DMSO\cdot 2H_2O$,[11d] have been prepared by crystallization from aqueous media. However, these compounds are relatively unstable in water.

The present complexes **1** and **2** can also be compared with our previous $[\alpha_2\text{-}P_2W_{17}O_{61}]$-based 1:2-type $Ru^{II}$ complex $K_{18}[Ru^{II}(DMSO)_2(\alpha_2\text{-}P_2W_{17}O_{61})_2]$, which was obtained from the reaction of *cis*-$[RuCl_2(DMSO)_4]$ with $K_{10}[\alpha_2\text{-}P_2W_{17}O_{61}]$ in ice-cooled, aqueous HCl solution.[5] Oxidation of the 1:2-type compound with $Br_2$ gave the 1:1-type $Ru^{III}$ compound $K_7[P_2W_{17}Ru^{III}(H_2O)O_{61}]$, without DMSO molecules. There are several factors in the formation of the 1:2- and 1:1-type complexes: (1) the ionic radius of the $Ru^{II}$ atom is much larger than that of the $Ru^{III}$ atom (0.82 Å for the six-coordinate, low-spin geometry[17]), and (2) the binding of several DMSO molecules to the $Ru^{II}$ atom is so strong that removal of all DMSO molecules is not easy.

## Conclusions

The cationic organometallic groups $\{(C_6H_6)Ru(H_2O)\}^{2+}$ and $\{(p\text{-cymene})Ru(H_2O)\}^{2+}$ have been covalently bound to the lacunary site of the mono-lacunary Dawson POM $[\alpha_2\text{-}P_2W_{17}O_{61}]^{10-}$. These complexes are water-soluble and stable in water. The molecular structure of $[\{(C_6H_6)Ru(H_2O)\}(\alpha_2\text{-}P_2W_{17}O_{61})]^{8-}$ (**1a**) was successfully determined. These POM complexes can be compared with the previously reported organometallic complexes supported on the multicenter active sites in the triniobium(V)- and trivanadium(V)-substituted Dawson POMs $[\alpha\text{-}1,2,3\text{-}P_2W_{15}M_3O_{62}]^{9-}$ (M = Nb, V).[9–12] The formation of complexes $K_8[\{(C_6H_6)Ru(H_2O)\}(\alpha_2\text{-}P_2W_{17}O_{61})]\cdot 12H_2O$ (**1**) and $K_8[\{(p\text{-cymene})Ru(H_2O)\}(\alpha_2\text{-}P_2W_{17}O_{61})]\cdot 16H_2O$ (**2**) brings up several interesting points: (1) the hydrophilicity of the organometallic precursors is greatly enhanced by binding to the mono-lacunary

 © 2006 Wiley-VCH Verlag GmbH & Co. KGaA, Weinheim 

Dawson POM with higher hydrophilicity, (2) the mono-lacunary POM has enough basicity of the surface oxygen atoms for the cationic species, suggesting the possible formation of other water-soluble organometallic complexes, (3) the mono-lacunary POM works as a bidentate O-donor ligand to the ruthenium centers, resulting in the formation of a chiral configuration (overall $C_1$ symmetry), and (4) the catalytic oxidation behaviors of the ruthenium(II) centers can be anticipated in water at ambient temperature. Thus, POMs **1** and **2** will be of interest as water-soluble, organometallic ruthenium(II) complexes, oxidation catalysis by which is anticipated in water.[3n] Studies in this direction are in progress and the data will be reported in due course.

## Experimental Section

**Materials:** The following were obtained as reagent grade and used as received: KCl, 85% aq. $H_3PO_4$, $Na_2WO_4{\cdot}2H_2O$, $KHCO_3$, $CH_3CN$, MeOH, EtOH, $Et_2O$ (all from Wako); $D_2O$ (Isotec); [(*p*-cymene)$Ru^{II}Cl_2]_2$ and $[(C_6H_6)RuCl_2]_2$ (both from Aldrich). The mono-lacunary POM $K_{10}[\alpha_2\text{-}P_2W_{17}O_{61}]{\cdot}19H_2O$ was prepared according to the literature and characterized accordingly.[3b,18]

**Instrumentation/Analytical Procedures:** Complete elemental analyses were carried out by Mikroanalytisches Labor Pascher (Remagen, Germany). The samples were dried at room temperature at $10^{-3}$–$10^{-4}$ Torr overnight before analysis. The C,H,N analyses were performed with a Perkin–Elmer PE2400 series II CHNS/O Analyzer (Kanagawa University). Infrared spectra were recorded with a Jasco 300 FT-IR spectrometer in KBr disks at room temperature. TG/DTA data were acquired with a Rigaku TG8101D and TAS 300 data-processing system. TG/DTA measurements were run under air with a temperature ramp of 4 °C/min between 30 and 500 °C. $^1H$ (399.65 MHz), $^{13}C\{^1H\}$ (100.40 MHz), and $^{31}P\{^1H\}$ (161.70 MHz) NMR spectra in solution were recorded in 5-mm outer-diameter tubes with a Jeol JNM-EX 400 FT NMR spectrometer using a Jeol EX-400 NMR spectroscopic data processing system. $^{31}P\{^1H\}$ (202.47 MHz) NMR spectra in solution were also recorded in 5-mm outer-diameter tubes with a Jeol ECP 500 FT NMR spectrometer using a Jeol ECP-500 NMR spectroscopic data processing system. $^1H$ and $^{13}C\{^1H\}$ NMR spectra of the complexes were measured in $D_2O$ solution with reference to internal DSS or TSP {sodium [2,2,3,3-$D_4$]-3-(trimethylsilyl)propionate}. Chemical shifts are reported as positive for resonances downfield of DSS or TSP ($\delta$ = 0 ppm). $^{31}P\{^1H\}$ NMR spectra were measured in $D_2O$ solution with reference to an external standard of 25% $H_3PO_4$ in $H_2O$ in a sealed capillary. Chemical shifts are reported as negative for resonances upfield of $H_3PO_4$ ($\delta$ = 0 ppm). $^{183}W$ NMR (16.50 MHz) spectra were recorded in 10-mm outer-diameter tubes with a Jeol JNM-EX 400 FT NMR spectrometer equipped with a Jeol NM-40T10L low-frequency tunable probe and a Jeol EX-400 NMR spectroscopic data-processing system. These spectra, measured in $D_2O$, were referenced to an external standard of a saturated $Na_2WO_4/D_2O$ solution. Chemical shifts are reported as negative for resonances upfield of $Na_2WO_4$ ($\delta$ = 0 ppm).

**Preparation of $K_8[\{(C_6H_6)Ru^{II}(H_2O)\}(\alpha_2\text{-}P_2W_{17}O_{61})]{\cdot}12H_2O$ (1):** $[(C_6H_6)RuCl_2]_2$ (0.10 g, 0.20 mmol) was added to a stirred solution of $K_{10}[\alpha_2\text{-}P_2W_{17}O_{61}]{\cdot}19H_2O$ (2.00 g, 0.41 mmol) in 50 mL of water. The brown suspension was stirred at room temperature for 1 h and then the brown powder was filtered off through a folded filter paper (Whatman No. 2). The clear brown filtrate was concentrated to a volume of about 15 mL in a rotary evaporator at 35 °C, and then placed in a refrigerator at 5 °C overnight. The brown powder formed was collected on a membrane filter (JG, 0.2 μm) and washed with $CH_3CN$ (2 × 5 mL) and then $Et_2O$ (3 × 50 mL). At this stage the yield was 1.0–1.5 g. All the brown powder was suspended in 15 mL of water at 60 °C. The suspension was cooled to room temperature and then placed in a refrigerator at 5 °C for 1 h. The yellow-brown powder that deposited was filtered off through a membrane filter (JG, 0.2 μm) and the clear brown filtrate was concentrated to about 7 mL in a rotary evaporator at 30 °C. After standing at room temperature for 30 min, the solution was passed through a folded filter paper (Whatman No. 2). The filtrate was slowly concentrated at room temperature in the dark. The orange plate-like crystals formed were collected on a membrane filter (JG, 0.2 μm), washed with $CH_3CN$ (2 × 5 mL) and $Et_2O$ (3 × 50 mL), and dried in vacuo for 2 h. The orange powder, obtained in 24.5% (0.49 g scale) yield, was soluble in water and DMSO, but insoluble in $CH_3CN$, MeOH, EtOH, and $Et_2O$. $K_8[\{(C_6H_6)Ru(H_2O)\}\text{-}P_2W_{17}O_{61}]{\cdot}2H_2O$ = $C_6H_{12}O_{64}K_8P_2W_{17}Ru$ (4709.4): calcd. C 1.53, H 0.26, Cl 0.00, K 6.64, O 21.74, P 1.32, Ru 2.15, W 66.37; found (repeat trials for C,H analysis) C 1.49 (1.47), H 0.33 (0.41), Cl < 0.1, K 6.26, O 22.1, P 1.25, Ru 2.23, W 66.4; total 100.06%. A weight loss of 3.79% was observed during the course of drying at room temperature at $10^{-3}$–$10^{-4}$ Torr overnight before analysis, suggesting the presence of 10–11 weakly solvated or adsorbed water molecules. TG/DTA data under atmospheric conditions: weight losses of 3.90% below 124 °C and 3.12% between 124 and 500 °C were observed with endothermic peaks at 30, 101, 147, and 185 °C and an exothermic peak at 481 °C; calcd. 3.71% for $x$ = 12 in $K_8[\{(C_6H_6)Ru(H_2O)\}P_2W_{17}O_{61}]{\cdot}xH_2O$. FT-IR (KBr disk, polyoxometalate region): $\tilde{\nu}$ = 1434 w, 1086 s, 1054 m, 1017 m, 940 vs, 885 s, 810 s, 741 s, 601 w, 528 w $cm^{-1}$. $^{31}P$ NMR ($D_2O$, 22.9 °C): $\delta$ = –8.36 (1 P), –14.02 (1 P) ppm. $^1H$ NMR ($D_2O$, 23.7 °C): $\delta$ = 6.18 (s, 6 H, $C_6H_6$) ppm. $^{13}C$ NMR ($D_2O$, 24.5 °C): $\delta$ = 82.98 ppm. Preparation of an aqueous solution of **1a** for $^{183}W$ NMR measurements was attempted by methods (1)–(3) described below, but a sufficient concentration of the pure form of **1a** was not attained. (1) A saturated $D_2O$ solution of **1** was prepared at 70 °C and the $^{183}W$ NMR spectrum was measured at this temperature over about 12 h. Clean signals of **1a** were not observed because of partial decomposition. Decomposition of **1** after 12 h at this temperature was also confirmed by a $^{31}P$ NMR measurement at room temperature. (2) The sodium salt of **1a** was generated in situ by reaction of the potassium salt of **1a** in aqueous solution with an excess amount of $NaClO_4$. After filtering the $KClO_4$ produced, the $^{31}P$ NMR spectrum of the filtrate was measured, which showed the two signals of **1a** as well as those due to the mono-lacunary POM $[P_2W_{17}O_{61}]^{10-}$. Partial dissociation of the supported organometallic group takes place during the metathesis reaction. On the other hand, complex **2a** was stable during the metathesis and a clean, two-line $^{31}P$ NMR spectrum of the in situ generated sodium salt of **2a** was observed. (3) The sodium salt of $[P_2W_{17}O_{61}]^{10-}$ was generated by a metathesis reaction of the potassium salt, $K_{10}[P_2W_{17}O_{61}]{\cdot}19H_2O$, with an excess amount of $NaClO_4$. Thus, an excess amount of $[(C_6H_6)\text{-}RuCl_2]_2$ was added to a stirred solution of the in situ generated sodium salt in water. The brown suspension was stirred at room temperature. for 1 h After filtration, the $^{31}P$ NMR spectrum of the filtrate was measured, which showed four signals due to **1a** and unreacted $[P_2W_{17}O_{61}]^{10-}$.

**Preparation of $K_8[\{(p\text{-cymene})Ru^{II}(H_2O)\}(\alpha_2\text{-}P_2W_{17}O_{61})]{\cdot}16H_2O$ (2):** [(*p*-cymene)$RuCl_2]_2$ (0.125 g, 0.20 mmol) was added to a stirred solution of $K_{10}[\alpha_2\text{-}P_2W_{17}O_{61}]{\cdot}19H_2O$ (2.00 g, 0.41 mmol) in 50 mL of water and the brown suspension was stirred at room temperature for 1 h. The greenish powder was then filtered off through a folded

 © 2006 Wiley-VCH Verlag GmbH & Co. KGaA, Weinheim 

filter paper (Whatman No. 2). The clear brown filtrate was concentrated to a volume of about 10 mL in a rotary evaporator at 30 °C and then placed in a refrigerator at 5 °C overnight. The yellow-brown powder formed was collected on a membrane filter (JG, 0.2 μm) and washed with $CH_3CN$ (3 × 30 mL) and then $Et_2O$ (3 × 50 mL). All the yellow-brown powder was suspended in 10 mL of ice-cooled water. The suspension was stirred for 30 min and then placed in a refrigerator at 5 °C for 30 min. The gray powder that deposited was filtered off through a membrane filter (JG, 0.2 μm) and the clear brown filtrate was added dropwise to 500 mL of ice-cooled MeOH. After stirring for 30 min, the yellow-brown powder was collected on a membrane filter (JG, 0.2 μm), washed with MeOH (3 × 50 mL) and then $Et_2O$ (3 × 50 mL), and dried in vacuo for 2 h. The yellow-brown powder, obtained in 32.7% (0.67 g scale) yield, was hygroscopic, soluble in water, but insoluble in MeOH, $CH_3CN$, and $Et_2O$. $K_8[\{(p\text{-cymene})Ru(H_2O)\}P_2W_{17}O_{61}]$ = $C_{10}H_{16}O_{62}K_8P_2W_{17}Ru$ (4729.5): calcd. C 2.54, H 0.34, Cl 0.00, K 6.61, O 21.0, P 1.31, Ru 2.14, W 66.1; found C 2.64, H 0.32, Cl < 0.05, K 6.49, O 20.6, P 1.29, Ru 2.07, W 66.3; total 99.7%. A weight loss of 4.2% was observed during the course of drying at room temperature at $10^{-3}$–$10^{-4}$ Torr overnight before analysis, suggesting the presence of 11–12 weakly solvated or adsorbed water molecules. TG/DTA data under atmospheric conditions: a weight loss of 6.24% below 189 °C with exothermic peaks at 206 and 265 °C; calcd. 6.11% for $x$ = 16 in $K_8[\{(p\text{-cymene})Ru(H_2O)\}P_2W_{17}O_{61}]\cdot xH_2O$. FT-IR (KBr disk, polyoxometalate region): $\tilde{\nu}$ = 1086 s, 1055 m, 1016 m, 941 vs, 885 s, 809 vs, 742 s, 670 w, 661 w, 601 w, 527 m, 420 w $cm^{-1}$. $^{31}P$ NMR ($D_2O$, 21.9 °C): $\delta$ = –8.28 (1 P), –14.08 (1 P) ppm. $^1H$ NMR ($D_2O$, 23.3 °C): $\delta$ = 1.40 (d, $J$ = 6.87 Hz, 3 H), 1.48 (d, $J$ = 6.87 Hz, 3 H) (H7 and H9), 2.51 (H10), 3.07 [m (7), $J$ = 6.87 Hz 3 H] (H8), 5.73 (d, $J$ = 5.96 Hz, 1 H), 5.88 (d, $J$ = 6.42 Hz, 2 H), 6.32 (d, $J$ = 5.96, 1 H) (relative intensity ratio 1:2:1, H2, H3, H5 and H6) ppm. $^{13}C$ NMR ($D_2O$, 25.8 °C): $\delta$ = 21.5, 23.5, 25.2 (C7, C9, C10), 33.6 (C8), 80.2, 81.5, 81.6, 82.9 (C2, C3, C5, C6), 99.9, 103.5 (C1, C4) ppm. $^{183}W$ NMR of **2a** as the sodium salt ($D_2O$, 22.6 °C): $\delta$ = –117.6, –125.1, –138.6, –139.0, –163.8, –177.1, –177.3, –186.5, –207.6, –217.3 (1 + 1), –218.2, –219.5, –220.6, –221.9, –239.6, –241.6 ppm; the relative intensity of all signals, except the signals at $\delta$ = –217.3 ppm, is one. The sodium salt of **2a** was prepared in 70.6% yield (0.56 g scale) by a cation-exchange reaction of the potassium salt **2** in aqueous solution with an excess amount of $NaClO_4$, followed by concentration of the filtrate in a rotary evaporator after filtering off the produced $KClO_4$ and then re-precipitation with ice-cooled ethanol. The characterization data of the sodium salt (IR and $^1H$ and $^{31}P$ NMR spectra) are in good agreement with those of **2**. On the other hand, for $^{183}W$ NMR measurements, a cation-exchange reaction of **2** performed using an excess amount of $LiClO_4$ was unsuccessful because of partial dissociation of the supported organometallic group.

**X-ray Crystallography of 1:** An orange plate crystal (0.18 × 0.06 × 0.02 mm) was surrounded by liquid paraffin (Paratone-N) to prevent its degradation. Data collection was performed with a Bruker SMART APEX CCD diffractometer at 90 K in the range 1.86° < 2$\theta$ < 56.42°. The intensity data were automatically corrected for Lorentz and polarization effects during integration. The structure was solved by direct methods (SHELXS-97)[19a] followed by subsequent difference Fourier calculation and refined by a full-matrix, least-squares procedure (SHELXL-97).[19b] Absorption correction was performed with SADABS (empirical absorption correction).[19c] Crystal data for $C_6H_{30}K_8O_{74}P_2RuW_{17}$: $M$ = 4887.56, triclinic, space group $P\bar{1}$, $a$ = 18.972(3), $b$ = 19.175(4), $c$ = 24.569(6) Å, $\alpha$ = 67.522(3)°, $\beta$ = 76.297(5)°, $\gamma$ = 88.825(3)°, $V$ = 7999(3) Å$^3$, $Z$ = 4, $D_c$ = 4.058 g cm$^{-3}$, $\mu$(Mo-$K_\alpha$) = 25.080 mm$^{-1}$. $R1$ = 0.1093, $wR2$ = 0.1779 (for all data). $R_{int}$ = 0.0595, $R1$ = 0.0773, $wR2$ = 0.1651, GOF = 1.160 [85964 total reflections, 39013 unique reflections where $I > 2\sigma(I)$]. The maximum and minimum residual densities (7.075 and –4.137 e Å$^{-3}$) were located at 0.61 Å from K8 and 0.61 Å from K10, respectively. Three water oxygen atoms (O1S, O2S and O3S) were in special position and their site occupancy factors were fixed at 0.5. The site occupancy factors of five water oxygen atoms (O24S, O25S, O26S, O27S, and O28S) and eight potassium atoms (K11, K12, K13, K14, K15, K16, K17, and K18) were also fixed at 0.5. CCDC-270035 contains the supplementary crystallographic data for this paper. These data can be obtained free of charge from The Cambridge Crystallographic Data Centre via www.ccdc.cam.ac.uk/data_request/cif.

**Supporting Information** (see also the footnote on the first page of this article): Molecular structure (Figure S1) of unit B of **1a** shown in Figure 6a in the text, and its bond lengths and angles around the ruthenium(II) atom (Table S1) and average bond lengths and angles for **1a** (Table S2).

## Acknowledgments

This work was supported by a Grant-in-Aid for Scientific Research and also by a High-tech Research Center Project, both from the Ministry of Education, Culture, Sports, Science, and Technology, Japan.

[1] a) M. T. Pope, A. Müller, *Angew. Chem. Int. Ed. Engl.* **1991**, *30*, 34–48; b) M. T. Pope, *Heteropoly and Isopoly Oxometalates*, Springer-Verlag, New York, **1983**; c) V. W. Day, W. G. Klemperer, *Science* **1985**, *228*, 533–541; d) C. L. Hill, *Chem. Rev.* **1998**, *98*, 1–2; e) T. Okuhara, N. Mizuno, M. Misono, *Adv. Catal.* **1996**, *41*, 113–251; f) C. L. Hill, C. M. Prosser-McCartha, *Coord. Chem. Rev.* **1995**, *143*, 407–455; g) for a series of 34 recent papers in a volume devoted to polyoxo anions in catalysis, see: C. L. Hill, *J. Mol. Catal.* **1996**, *114*, 1; h) R. Neumann, *Prog. Inorg. Chem.* **1998**, *47*, 317–370; i) *Polyoxometalate Chemistry from Topology via Self-Assembly to Applications* (Eds.: M. T. Pope, A. Müller), Kluwer Academic Publishers, The Netherlands, **2001**; j) *Polyoxometalate Chemistry for Nano-Composite Design* (Eds.: T. Yamase, M. T. Pope), Kluwer Academic Publishers, The Netherlands, **2002**; k) M. T. Pope, *Polyoxo anions: Synthesis and Structure*, in *Comprehensive Coordination Chemistry II* (Ed.: A. G. Wedd), Elsevier Science, New York, **2004**, vol. 4, pp. 635–678.

[2] a) X. Wei, R. E. Bachman, M. T. Pope, *J. Am. Chem. Soc.* **1998**, *120*, 10248–10253; b) C. Rong, M. T. Pope, *J. Am. Chem. Soc.* **1992**, *114*, 2932–2938.

[3] a) J. Bartis, Y. Kunina, M. Blumenstein, L. C. Francesconi, *Inorg. Chem.* **1996**, *35*, 1497–1501; b) D. K. Lyon, W. K. Miller, T. Novet, P. J. Domaille, E. Evitt, D. C. Jonson, R. G. Finke, *J. Am. Chem. Soc.* **1991**, *113*, 7209–7221; c) D. Mansuy, J.-F. Bartoli, P. Battioni, D. K. Lyon, R. G. Finke, *J. Am. Chem. Soc.* **1991**, *113*, 7222–7226; d) D. E. Katsoulis, M. T. Pope, *J. Chem. Soc., Dalton Trans.* **1989**, 1483–1489; e) C. L. Hill, X. Zhang, *Nature* **1995**, *373*, 324–326; f) H. T. Evans, Jr., T. J. R. Weakley, G. B. Jameson, *J. Chem. Soc., Dalton Trans.* **1996**, 2537–2540; g) C. L. Hill, R. B. Brown, Jr., *J. Am. Chem. Soc.* **1986**, *108*, 536–538; h) D. E. Katsoulis, M. T. Pope, *J. Chem. Soc., Chem. Commun.* **1986**, 1186–1188; i) A. M. Khenkin, C. L. Hill, *J. Am. Chem. Soc.* **1993**, *115*, 8178–8186; j) D. E. Katsoulis, M. T. Pope, *J. Am. Chem. Soc.* **1984**, *106*, 2737–2738; k) S. Ellis, I. V. Kozhevnikov, *J. Mol. Catal. A: Chem.* **2002**, *187*, 227–235; l) N. Mizuno, J.-S. Min, A. Taguchi, *Chem. Mater.* **2004**, *16*, 2819–2825; m) H. Yasuda, L.-N. He, T. Sakakura, C. Hu, *J. Catal.* **2005**, *233*, 119–122; n) C. N. Kato,

 © 2006 Wiley-VCH Verlag GmbH & Co. KGaA, Weinheim 

A. Shinohara, N. Moriya, K. Nomiya, manuscript under submission.

[4] a) S. Ogo, N. Makihara, Y. Watanabe, *Organometallics* **1999**, *18*, 5470–5474; b) N. Makihara, S. Ogo, Y. Watanabe, *Organometallics* **2001**, *20*, 497–500; c) J. Kovacs, T. D. Todd, J. H. Reibenspies, F. Joo, D. J. Darensbourg, *Organometallics* **2000**, *19*, 3963–3969; d) S. Wache, *J. Organomet. Chem.* **1995**, *494*, 235–240; e) D. J. Darensboug, F. Joo, M. Kannisto, A. Katho, J. H. Reibensies, D. J. Daigle, *Inorg. Chem.* **1994**, *33*, 200–208; f) M. Barton, J. D. Atwood, *J. Coord. Chem.* **1991**, *24*, 43–67; g) A. Avey, S. C. Tenhaeff, T. J. R. Weakley, D. R. Tyler, *Organometallics* **1991**, *10*, 3607–3613; h) J. P. Arhancet, M. E. Davis, J. S. Merola, B. E. Hanson, *J. Catal.* **1990**, *121*, 327–339; i) J. P. Arhancet, M. E. Davis, J. S. Merola, B. E. Hanson, *Nature* **1989**, *339*, 454–455; j) H. Hayashi, S. Ogo, S. Fukuzumi, *Chem. Commun.* **2004**, 2714–2715; k) S. Ogo, H. Hayashi, K. Uehara, S. Fukuzumi, *Appl. Organomet. Chem.* **2005**, *19*, 639–643.

[5] K. Nomiya, H. Torii, K. Nomura, Y. Sato, *J. Chem. Soc., Dalton Trans.* **2001**, 1506–1512.

[6] a) L.-H. Bi, U. Kortz, B. Keita, L. Nadjo, *Dalton Trans.* **2004**, 3184–3190; b) L. Bi, F. Hussain, U. Kortz, M. Sadakane, M. H. Dickman, *Chem. Commun.* **2004**, 1420–1421.

[7] a) V. Artero, A. Proust, P. Herson, R. Thouvenot, P. Gouzerh, *Chem. Commun.* **2000**, 883–884; b) V. Artero, A. Proust, P. Herson, P. Gouzerh, *Chem. Eur. J.* **2001**, *7*, 3901–3910; c) R. Villanneau, V. Artero, D. Laurencin, P. Herson, A. Proust, P. Gouzerh, *J. Mol. Struct.* **2003**, *656*, 67–77; d) D. Laurencin, E. G. Fidalgo, R. Villanneau, F. Villain, P. Herson, J. Pacifico, H. Stoeckli-Evans, M. Benard, M.-M. Rohmer, G. Suss-Fink, A. Proust, *Chem. Eur. J.* **2004**, *10*, 208–217; e) V. Artero, D. Laurencin, R. Villanneau, R. Thouvenot, P. Herson, P. Gouzerh, A. Proust, *Inorg. Chem.* **2005**, *44*, 2826–2835.

[8] a) R. K. C. Ho, W. G. Klemperer, *J. Am. Chem. Soc.* **1978**, *100*, 6772–6774; b) W. H. Knoth, *J. Am. Chem. Soc.* **1979**, *101*, 759–760; c) W. H. Knoth, *J. Am. Chem. Soc.* **1979**, *101*, 2211–2213; d) F. Zonnevijlle, M. T. Pope, *J. Am. Chem. Soc.* **1979**, *101*, 2731–2732; e) X.-H. Wang, J.-F. Liu, Y.-G. Chen, Q. Liu, J.-T. Liu, M. T. Pope, *J. Chem. Soc., Dalton Trans.* **2000**, 1139–1142.

[9] a) M. Pohl, Y. Lin, T. J. R. Weakley, K. Nomiya, M. Kaneko, H. Weiner, R. G. Finke, *Inorg. Chem.* **1995**, *34*, 767–777; b) D. J. Edlund, R. J. Saxton, D. K. Lyon, R. G. Finke, *Organometallics* **1988**, *7*, 1692–1704; c) K. Nomiya, C. Nozaki, M. Kaneko, R. G. Finke, M. Pohl, *J. Organomet. Chem.* **1995**, *505*, 23–28; d) M. Pohl, D. K. Lyon, N. Mizuno, K. Nomiya, R. G. Finke, *Inorg. Chem.* **1995**, *34*, 1413–1429; e) K. Nomiya, M. Pohl, N. Mizuno, D. K. Lyon, R. G. Finke, *Inorg. Synth.* **1997**, *31*, 186–201; f) M. Pohl, R. G. Finke, *Organometallics* **1993**, *12*, 1453–1457; g) H. Weiner, J. D. Aiken III, R. G. Finke, *Inorg. Chem.* **1996**, *35*, 7905–7913; h) T. Nagata, M. Pohl, H. Weiner, R. G. Finke, *Inorg. Chem.* **1997**, *36*, 1366–1377; i) B. M. Rapko, M. Pohl, R. G. Finke, *Inorg. Chem.* **1994**, *33*, 3625–3634; j) K. Nomiya, T. Hasegawa, *Chem. Lett.* **2000**, 410–411; k) K. Nomiya, H. Torii, C. N. Kato, Y. Sado, *Chem. Lett.* **2003**, *32*, 664–665; l) K. Nomiya, Y. Sakai, T. Hasegawa, *J. Chem. Soc., Dalton Trans.* **2002**, 252–258.

[10] a) R. G. Finke, B. Rapko, R. J. Saxton, P. J. Domaille, *J. Am. Chem. Soc.* **1986**, *108*, 2947–2960; b) R. G. Finke, B. Rapko, P. J. Domaille, *Organometallics* **1986**, *5*, 175–178; c) R. G. Finke, C. A. Green, B. Rapko, *Inorg. Synth.* **1990**, *27*, 128–135; d) R. G. Finke, M. W. Droege, J. C. Cook, K. S. Suslick, *J. Am. Chem. Soc.* **1984**, *106*, 5750–5751; e) G. Luan, Y. Li, S. Wang, E. Wang, Z. Han, C. Hu, H. Jia, *Dalton Trans.* **2003**, 233–235.

[11] a) R. G. Finke, M. W. Droege, *J. Am. Chem. Soc.* **1984**, *106*, 7274–7277; b) R. G. Finke, K. Nomiya, C. A. Green, M. W. Droege, *Inorg. Synth.* **1992**, *29*, 239–247; c) Y. Lin, K. Nomiya, R. G. Finke, *Inorg. Chem.* **1993**, *32*, 6040–6045; d) K. Nomiya, C. Nozaki, A. Kano, T. Taguchi, K. Ohsawa, *J. Organomet. Chem.* **1997**, *533*, 153–159; e) K. Nomiya, Y. Sakai, Y. Yamada, T. Hasegawa, *J. Chem. Soc., Dalton Trans.* **2001**, 52–56.

[12] a) R. G. Finke, D. K. Lyon, K. Nomiya, T. J. R. Weakley, *Acta Crystallogr., Sect C* **1990**, *46*, 1592–1596; b) K. Nomiya, M. Kaneko, N. C. Kasuga, R. G. Finke, M. Pohl, *Inorg. Chem.* **1994**, *33*, 1469–1472; c) K. Nomiya, C. Nozaki, K. Miyazawa, Y. Shimizu, T. Takayama, K. Nomura, *Bull. Chem. Soc. Jpn.* **1997**, *70*, 1369–1377; d) K. Nomiya, K. Ohsawa, T. Taguchi, M. Kaneko, T. Takayama, *Bull. Chem. Soc. Jpn.* **1998**, *71*, 2603–2610; e) K. Nomiya, T. Hasegawa, R. Noguchi, K. Nomura, M. Takahashi, H. Yokoyama, *Chem. Lett.* **2001**, 1278–1279.

[13] C. Rocchiccioli-Deltcheff, R. Thouvenot, *Spectrosc. Lett.* **1979**, *12*, 127–138.

[14] a) T. J. R. Weakley, R. G. Finke, *Inorg. Chem.* **1990**, *29*, 1235–1241; b) Y. Lin, T. J. R. Weakley, B. Rapko, R. G. Finke, *Inorg. Chem.* **1993**, *32*, 5095–5101; c) T. Yamase, T. Ozeki, H. Sakamoto, S. Nishiya, A. Yamamoto, *Bull. Chem. Soc. Jpn.* **1993**, *66*, 103–108; d) K. Nomiya, M. Takahashi, K. Ohsawa, J. A. Widegren, *J. Chem. Soc., Dalton Trans.* **2001**, 2872–2878; e) K. Nomiya, M. Takahashi, J. A. Widegren, T. Aizawa, Y. Sakai, N. C. Kasuga, *J. Chem. Soc., Dalton Trans.* **2002**, 3679–3685.

[15] G. S. Kim, K. S. Hagen, C. L. Hill, *Inorg. Chem.* **1992**, *31*, 5316–5324.

[16] a) I. D. Brown, D. Altermatt, *Acta Crystallogr., Sect. B* **1985**, *41*, 244–247; b) I. D. Brown, R. D. Shannon, *Acta Crystallogr., Sect. A* **1973**, *29*, 266–282; c) I. D. Brown, *Acta Crystallogr., Sect. B* **1992**, *48*, 553–572; d) I. D. Brown, *J. Appl. Crystallogr.* **1996**, *29*, 479–480.

[17] R. D. Shannon, C. T. Prewitt, *Acta Crystallogr., Sect. B* **1969**, *25*, 925–946.

[18] a) R. Contant, *Inorg. Synth.* **1990**, *27*, 104–111; b) T. L. Jorris, M. Kozik, N. Casan-Pastor, P. J. Domaille, R. G. Finke, W. K. Miller, L. C. W. Baker, *J. Am. Chem. Soc.* **1987**, *109*, 7402–7408.

[19] a) G. M. Sheldrick, *Acta Crystallogr., Sect A* **1990**, *46*, 467–473; b) G. M. Sheldrick, *SHELXL-97, Program for Crystal Structure Refinement*, University of Göttingen, Germany, **1997**; c) G. M. Sheldrick, *SADABS*, University of Göttingen, Germany, **1996**.

Received: May 6, 2005
Published Online: November 7, 2005

 © 2006 Wiley-VCH Verlag GmbH & Co. KGaA, Weinheim 

DOI: 10.1002/ejic.200500414

# The Ligation Properties of some Reduced Schiff Base Selena/Telluraaza Macrocycles: Versatile Structural Trends

**Snigdha Panda,[a] Sanjio S. Zade,[a] Harakesh B. Singh,*[a] and Ray J. Butcher[b]**

**Keywords:** Chalcogenaaza macrocycles / Selenium tellurium ligands / Nickel / Palladium / Platinum

The chalcogenaaza macrocycles **4**, **5** and **6** show versatility in ligation properties towards various transition metal ions. The structure of the reduced 22-membered selenaaza macrocycle **4** ($C_{32}H_{36}N_4Se_2$) has been determined. The $Ni^{II}$ complex **7** exhibits coordination by the N4Se2 donor sites. The $Pd^{II}$ complexes **8**, **9**, **10**, and **14** have been structurally characterized. The molecular structures of these complexes reveal interesting versatile ligating behaviors of the ligands. The Pd complexes **8**, **9**, and **14** display coordination by hard nitrogen donor atoms only, whereas the complex **10** showed coordination by N2Te2 donor centers. The $Pt^{II}$ complex **11** shows the formation of a cationic metallamacrocycle with C–Pt–Se linkage. The crystal structures suggest that the coordination of metal atoms to donors is determined by the geometrical arrangement around the metal and by the conformation of the macrocycle rather than by the HSAB (hard/soft acid/base) principle.

(© Wiley-VCH Verlag GmbH & Co. KGaA, 69451 Weinheim, Germany, 2006)

## Introduction

The mixed donor macrocycles have attracted considerable interest due to their high selective nature for complexation of ions. Amongst the chalcogenaaza macrocycles, oxaaza and thiaaza have been well studied[1] relative to their heavier counterparts. Incorporation of the larger Se and Te would lead to a change in the size of the cage cavity and hence allow for some interesting coordination behavior. There are only a few reports on homodonor selenium- and tellurium-containing macrocycles and their ligating behavior towards the metal ions.[2,3] Only recently, some mixed donor macrocycles incorporating selenium and tellurium have been reported.[4–7]

As part of our research on the design and synthesis of heavier chalcogenaaza macrocycles, we recently reported the synthesis and complexation studies of the selenaaza and telluraaza Schiff base macrocycles **1**–**3**.[5–7] However, these Schiff base macrocycles are prone to transmetallation and hydrolysis on treatment with metal salts, which leads to cleavage of the macrocycle. The selenaaza Schiff base macrocycle **1** forms the hydrolyzed product with the $Pd^{II}$ cation,[7] whereas the telluraaza Schiff base macrocycle **2** forms transmetallated products with $Pt^{II}$ and $Hg^{II}$ cations.[5] The hydrolysis of the selenaaza macrocycle **1** may be due to excessive strain on the ring, which is forced by the metal to adopt a planar geometry. The facile cleavage of the C–Te bond in **2** is due to strong N→Te intramolecular interactions, which activate the *trans* C–Te bond. This strong intramolecular interaction is mainly due to the presence of the $sp^2$ nitrogen atom. To synthesize stable complexes of chalcogenaaza macrocycles, we are now interested in the ligation behavior of the reduced forms of the Schiff base macrocycles **4**–**6**. The reduced forms of the macrocycles are more flexible. Also these macrocycles have only $sp^3$ hybridized atoms and can accommodate a larger range of shapes and sizes than the Schiff base macrocycles that have $sp^2$ hybridized donor atoms. In the reduced forms, the macrocycles have weaker E···N (E = Se, Te) interactions as evidenced from the multinuclear NMR spectra and single-crystal X-ray structures (vide infra). We reported, in a preliminary communication, the ligation properties of **4** and **5** with $Pd^{II}$ and $Pt^{II}$.[8] It was found that the macrocycle **4** forms a 23-membered metallamacrocycle on ligation with $Pt^{II}$, in which a C–Se bond is oxidatively added to the $Pt^{II}$ center to form a hexacoordinate $Pt^{IV}$ complex (**11**). Complexes **8** and **10** show contrasting ligation behavior of the macrocycles **4** and **5** with $Pd^{II}$. In **8**, the coordination sites are hard nitrogen donors only, whereas in **10** the coordination sites are occupied by N2Te2. In this paper, we now report a systematic study of the ligation properties of the reduced selena/telluraaza macrocycles with transition metal ions. The ligation properties of the reduced selenaaza macrocycle **4** with a series of transition metal cations ($Ni^{II}$, $Pd^{II}$, $Pt^{II}$ $Cu^{II}$, and $Hg^{II}$), the ligation properties of the telluraaza macrocycle **5** with $Pd^{II}$, and the ligation properties of the 28-membered selenaaza macrocycle **6** with $Pd^{II}$ have been investigated.

[a] Department of Chemistry, Indian Institute of Technology Bombay,
Powai, Mumbai, 400076, India
E-mail: chhbsia@chem.iitb.ac.in
[b] Department of Chemistry, Howard University,
Washington, D. C. 20059, USA

 © 2006 Wiley-VCH Verlag GmbH & Co. KGaA, Weinheim 

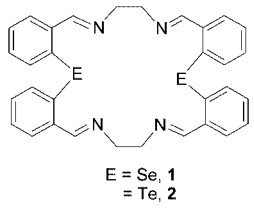


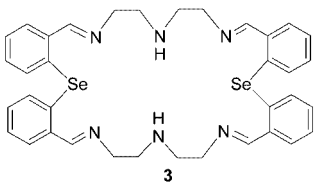


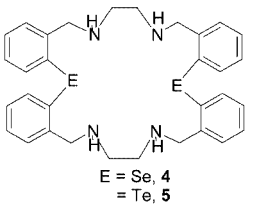


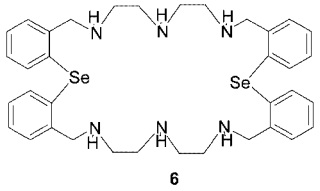


## Result and Discussion

The ligands **4**–**6** were prepared by following known procedures.[5–7] The molecular structure of the ligand **4** (Figure 1, Table 1) is centrosymmetric, and only half of the molecule represents the asymmetric unit. The structure confirms the complete reduction of the Schiff base macrocycle. Of two possible nitrogen atoms available for interaction, only one interacts weakly with the Se atom. The Se···N(1A) distance (3.01 Å) is shorter than the sum of the van der Waals radii of Se (1.99 Å) and N (1.53 Å). The transannular Se···Se distance (4.75 Å) is longer than the Se···Se distance (3.808 Å) in the parent Schiff base **1**.[7] The geometry around Se is V-shaped. The C(1B)–Se–C(1A) bond angle is 98.04°, which is smaller than that in the parent Schiff base (100.2°). The macrocycle framework is puckered so as to suit the bonding pattern of the individual atoms.

Table 1. Significant bond lengths [Å] and angles [°] for **4**.

| | | | |
|---|---|---|---|
| Se–C(1A) | 1.926(2) | Se–C(1B) | 1.938(3) |
| N(1A)–C(8A) | 1.459(3) | N(1A)–C(7A) | 1.464(3) |
| N(1B)–C(8B) | 1.460(3) | N(1B)–C(7B) | 1.475(3) |
| C(1A)–Se–C(1B) | 98.03(10) | C(8A)–N(1A)–C(7A) | 113.1(2) |
| C(8B)–N(1B)–C(7B) | 114.0(2) | C(2A)–C(1A)–Se | 120.6(2) |
| C(6A)–C(1A)–Se | 119.16(18) | N(1A)–C(7A)–C(6A) | 111.1(2) |
| C(6B)–C(1B)–Se | 120.95(19) | N(1B)–C(7B)–C(6B) | 117.1(2) |
| N(1B)–C(8B)–C(8A)# | 1110.6(2) | | |

Equimolar amounts of **4** and $Ni(OCOCH_3)_2$ in MeOH were heated to reflux for 30 min, and subsequent addition of $NH_4PF_6$ yielded a purple complex **7**, which was crystallized by slow diffusion of diethyl ether into the acetonitrile solution of the complex at room temperature (Scheme 1). The complex was soluble in MeCN, $MeNO_2$, acetone, DMSO, and DMF, and stable in air. The elemental analysis data of the complex suggest the formation of the 1:1 product. The molecular ion peak was not observed in the FAB mass spectrum of the complex, however, there are peaks centered at $m/z$ = 838 for M – $PF_6$ and at $m/z$ = 693 for M – $2PF_6$. The IR spectrum shows peaks at 840 and 557 $cm^{-1}$ corresponding to $\nu$(P–F) and $\nu$(F–P–F), respectively. The solution phase electronic spectrum (>200 nm) of the complex consists of three bands centered at 304 ($\varepsilon$ = 2400 $dm^3 mol^{-1} cm^{-1}$), 699 (15 $dm^3 mol^{-1} cm^{-1}$), and 895 nm (29 $dm^3 mol^{-1} cm^{-1}$). The solid-state absorption spectrum of the complex exhibits the same type of bands centered at 316, 564, and 894 nm. This indicates that the complex is stable in solution and in the solid state and has the same structure in both states. The $\mu_{eff}$ (B.M.) is 3.39, which is larger than the value usually observed. Larger values are

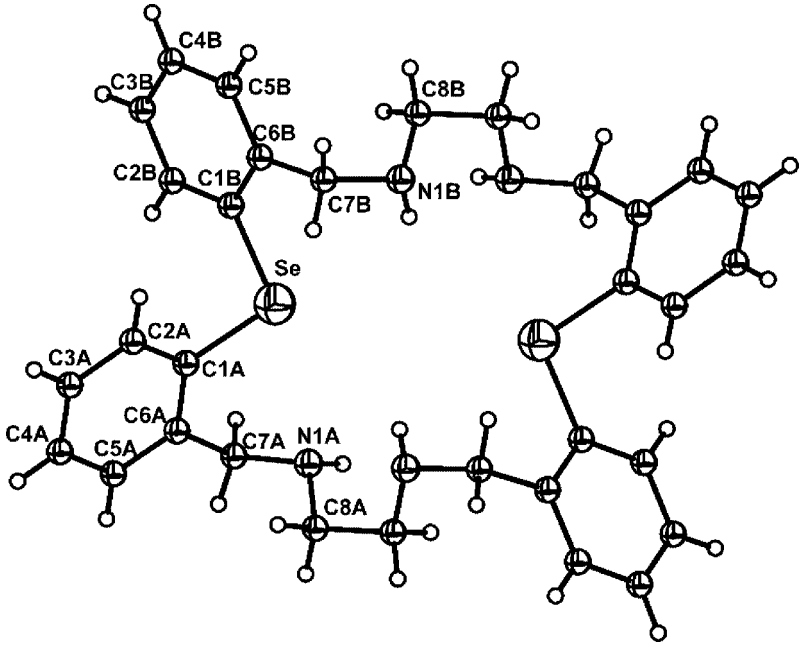


Figure 1. ORTEP diagram of the ligand **4**.

 © 2006 Wiley-VCH Verlag GmbH & Co. KGaA, Weinheim 

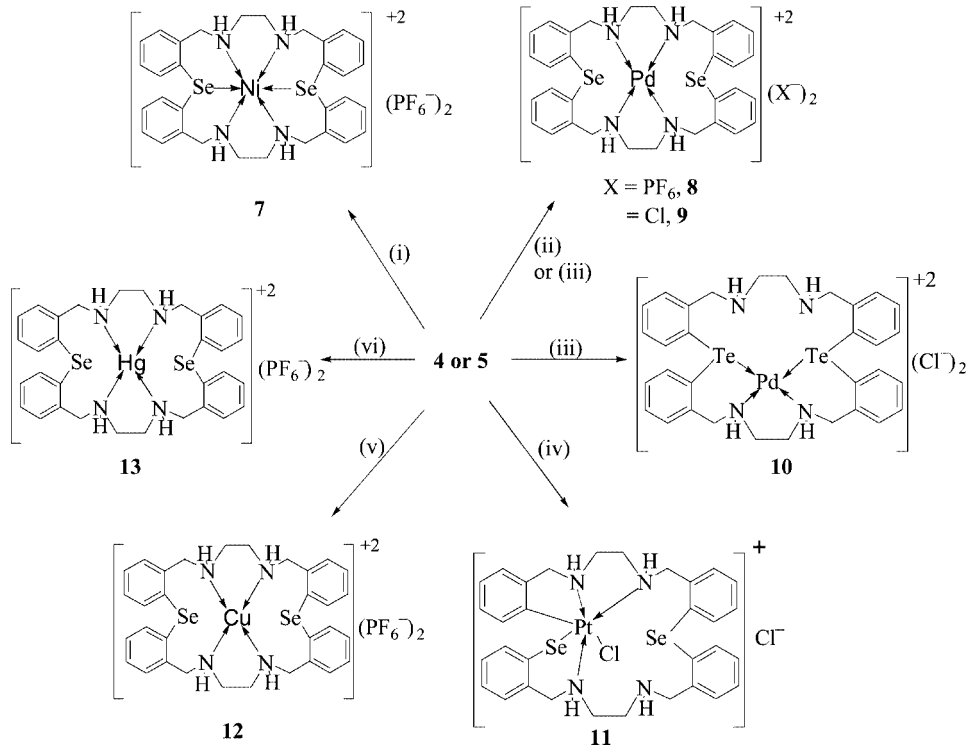


Scheme 1. Reagents: MeOH (reflux), (i) $Ni(OCOCH_3)_2$, $NH_4PF_6$; (ii) $Pd(C_6H_5CN)_2Cl_2$, $NH_4PF_6$; (iii) $PdCl_2$, (iv) $PtCl_2$; (v) $Cu(CH_3CN)_4ClO_4$, $NH_4PF_6$; (vi) $Hg(OCOCH_3)_2$, $NH_4PF_6$.

generally observed as a result of orbital contributions derived from the mixing of low-lying excited states into the ground state or because the ground state is orbitally degenerate. As expected for octahedral $Ni^{II}$ complexes, complex **7** is EPR silent.[9,10] The cyclic voltammogram of the $Ni^{II}$ complex **7** shows a quasi-reversible oxidation peak at –0.211 V and a reduction peak at –0.092 V. There is a substantial shift to a more negative potential on changing from imine to amine nitrogen donors,[7] as expected, given that this change results in a reduction of π-acceptor ability.[11]

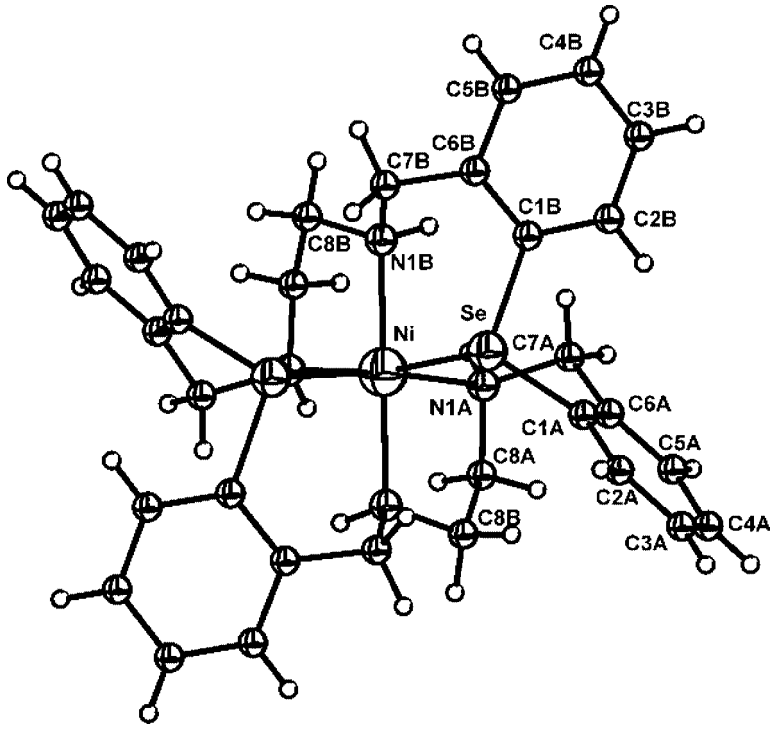


Figure 2. ORTEP diagram for **7**.

 © 2006 Wiley-VCH Verlag GmbH & Co. KGaA, Weinheim 

There are very few reports on the molecular structures of Ni complexes of selenium-containing macrocycles. This is the third example of the molecular structure of a nickel complex with a selenium-containing macrocycle.[7] The molecular structure (Figure 2, Table 2) is centrosymmetric and is similar to that of the $Ni^{II}$ complex of the parent ligand. The structure shows that the $Ni^{II}$ ion occupies the macrocyclic cavity and is bonded to all four nitrogen and two selenium donors of the macrocycle thus adopting an octahedral geometry. The bond lengths are: Ni–N(1B) 2.104(2) Å, Ni–N(2B) 2.104(2), Ni–N(1A) 2.115(2), Ni–N(2A) 2.115(2), Ni–Se 2.6189(4) Å. The Ni–Se bond length is comparable to Ni–Se distances in *trans*-[$NiCl_2$(Me-$SeCH_2CH_2SeMe_2$)][12] and is also comparable to that observed for the parent Schiff base Ni complex.[7] The C–Se–C bond angle is 101.73(10)°, which is larger than that of the parent Schiff base Ni complex [97.1(7)°]. The two Se atoms are *cis* to each other in the distorted octahedral geometry as they are in the parent Schiff base Ni complex.

Table 2. Significant bond lengths [Å] and angles [°] for **7**.

| | | | |
|---|---|---|---|
| Ni–N(1B) | 2.104(2) | Ni–N(1A) | 2.115(2) |
| Ni–Se | 2.6189(4) | | |
| N(1B)#1–Ni–N(1B) | 173.22(12) | N(1B)–Ni–N(1A)#1 | 83.53(8) |
| N(1B)–Ni–N(1A) | 91.81(8) | N(1A)#1–Ni–N(1A) | 93.54(12) |
| N(1B)#1–Ni–Se | 96.36(6) | N(1B)–Ni–Se | 88.74(5) |
| N(1A)#1–Ni–Se | 170.30(6) | N(1A)–Ni–Se | 92.56(6) |
| Se–Ni–Se#1 | 82.435(18) | | |

The corresponding palladium complexes **8** and **9** were obtained by the reaction of $Pd(C_6H_5CN)_2Cl_2$ and $PdCl_2$, respectively, with 1 mol of ligand **4** in refluxing methanol, followed by the addition of excess $NH_4PF_6$ in the case of **8** (Scheme 1). The complexes are soluble only in DMSO. The elemental analysis data suggest the formation of a 1:1 complex. The crystals were grown from DMSO/ether. The peaks at 843 and 558 $cm^{-1}$ in the IR spectrum confirms the presence of a $PF_6^-$ ion. The molecular ion peak of complex **8** is not observed in its FAB mass spectrum; peaks at *m*/*z* = 886 and 735 correspond to M – $PF_6$ and M – 2 $PF_6$, respectively. The ESI-MS spectrum of **9** exhibits a peak at *m*/*z* = 840, which corresponds to M + $2H_2O$, and a peak at *m*/*z* = 741, which corresponds to M – 2Cl. The $^1$H- and $^{13}$C NMR spectra for both **8** and **9** are too complicated for complete analysis. The $^{77}$Se NMR spectra of **8** and **9** display peaks at 869 and 787 ppm, respectively. As the $^{77}$Se NMR spectra of both complexes exhibit single signals, which were shifted downfield relative to that of the free ligand ($\delta$ = 329 ppm), it is possible that metal coordination to selenium occurs in solution. Variable-temperature $^1$H NMR spectroscopy was carried out on **8** at higher temperatures (20 °C–120 °C) in DMSO solution (Figure 3). As the temperature was increased, line broadening resulted in the coalescence of the peaks. Upon cooling to room temperature, the original spectrum was restored. The coalescence phenomena of the spectra may occur as a result of the fluxional behavior of the complex in solution. The only fluxional process that achieves this result is one in which the metal effectively hops between the six donor sites of the macrocycle, as illustrated in Scheme 2. This hopping of the $Pd^{II}$ center between the N4Se2 coordination sites is similar to that reported by McAuley et al.,[13] where, in a square-planar palladium complex, the $Pd^{II}$ center hops between any four of the six donor sites. However, an N3Se coordination is ruled out, since the $^{77}$Se NMR spectrum shows a single peak. The $^1$H NMR spectra at ambient and high temperatures do not exhibit any resonances that could be assigned to the free ligand in solution, which suggests that the interconversion does not proceed though a dissociative mechanism.

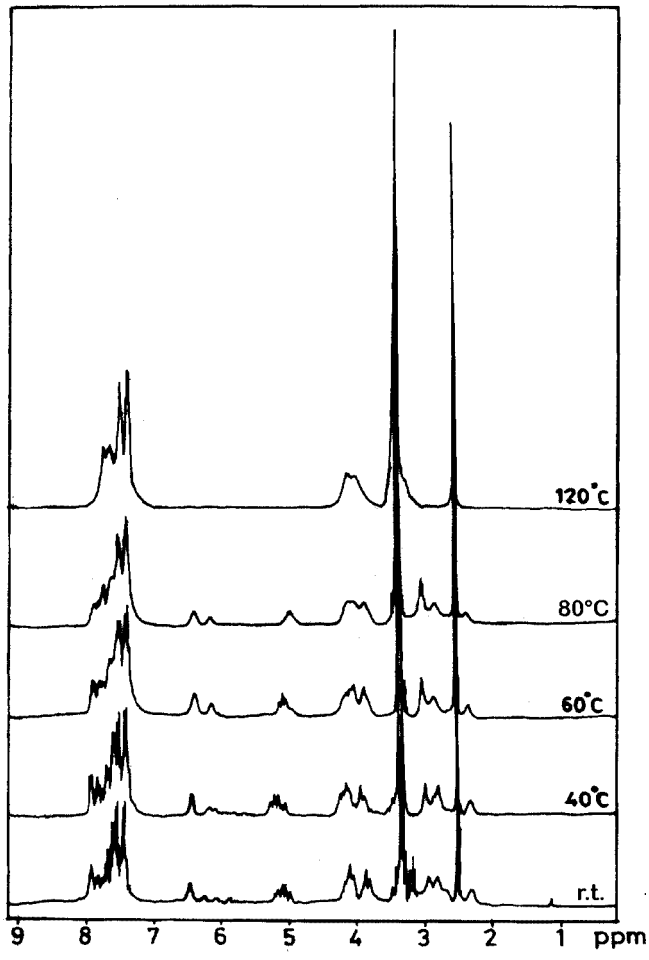


Figure 3. Variable-temperature $^1$H NMR ([$D_6$]DMSO, 300 MHz) spectra of **8**.

Since complexes **8** and **9** are isostructural (Figure 4, Figure 5, Table 3, Table 4), the crystal structure of only **8** will be discussed, and major differences between the structures will be highlighted. Both structures are centrosymmetric like the parent macrocycle **4**, and only half of the molecule represents the asymmetric unit. The cation adopts a square-planar geometry and is coordinated to the four nitrogen atoms. The N–Pd–N bond angles are ca. 180° and ca. 90°. The Pd–N bond lengths are in good agreement with the sum of the single-bond covalent radii of Pd (1.31 Å) and N (0.75 Å).[14] However, these bond lengths are slightly longer than that observed for the hydrolyzed parent Schiff base [2.019(6) Å],[7] which has $sp^2$ hybridized N donor atoms. In the solid-state molecular structures, the palladium atom

 © 2006 Wiley-VCH Verlag GmbH & Co. KGaA, Weinheim 

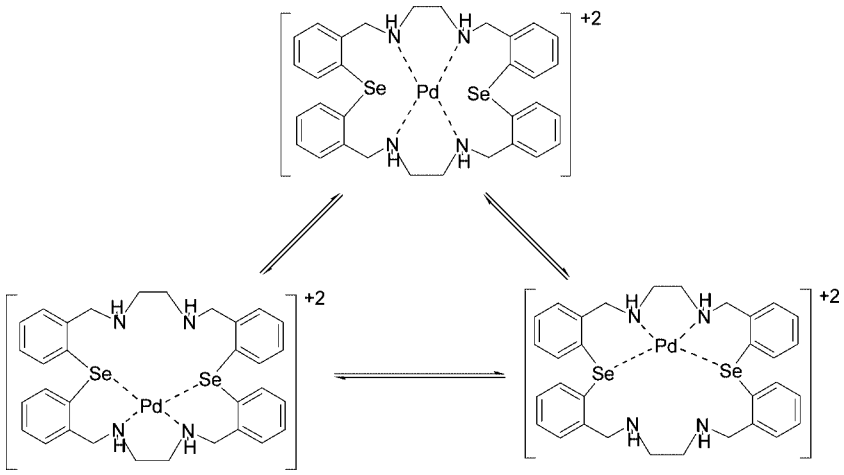

Scheme 2. Fluxional process for **8** in solution.

does not coordinate to the Se atom. This is in contrast to the solid-state structures of $Pd^{II}$ complexes of the mixed donor Se/Te macrocycles that contain O or P, in which $Pd^{II}$ coordinates to the soft Se/Te donor centers.[4] This anomalous behavior may be due to the formation of stable five-membered chelate rings rather than to the formation of six-membered chelate rings that would result in coordination to the Se donors. In this case, the absence of any interaction between the Se and $Pd^{II}$ atoms probably results from the conformational requirement of the ligand around the central $Pd^{II}$ atom for coordination with donor atoms, as well as the chelate ring effect. Complex **9** crystallizes with two waters of crystallization; however, there is no hydrogen bonding between the water molecules and the chloride counterions. The transannular Se···Se bond length of **8** is 9.310 Å and that of **9** is 9.670 Å.

Equimolar amounts of **5** and $PdCl_2$ in MeOH were heated to reflux for 15 min to yield a clear solution of the complex **10**; brown crystals were obtained by slow diffusion of diethyl ether into the reaction mixture at room temperature (Scheme 1). Complex **10** is not very soluble in $CH_3CN$ and $CH_3NO_2$ but highly soluble in DMSO. The elemental analysis data confirm the formation of a 1:1 complex. The molecular ion peak of complex **10** is not observed in its ESI

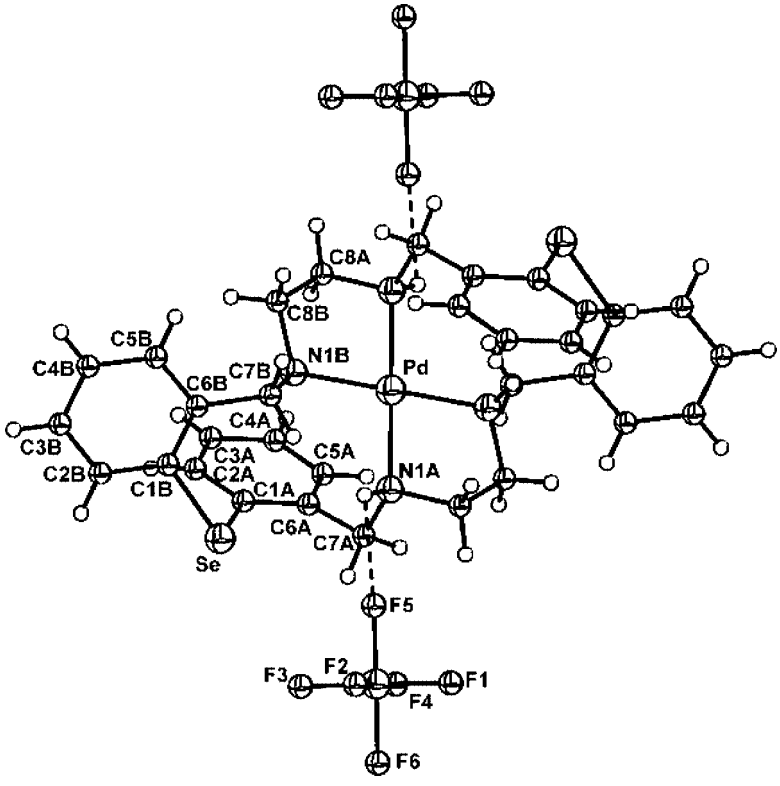


Figure 4. ORTEP diagram for **8**.

 © 2006 Wiley-VCH Verlag GmbH & Co. KGaA, Weinheim 

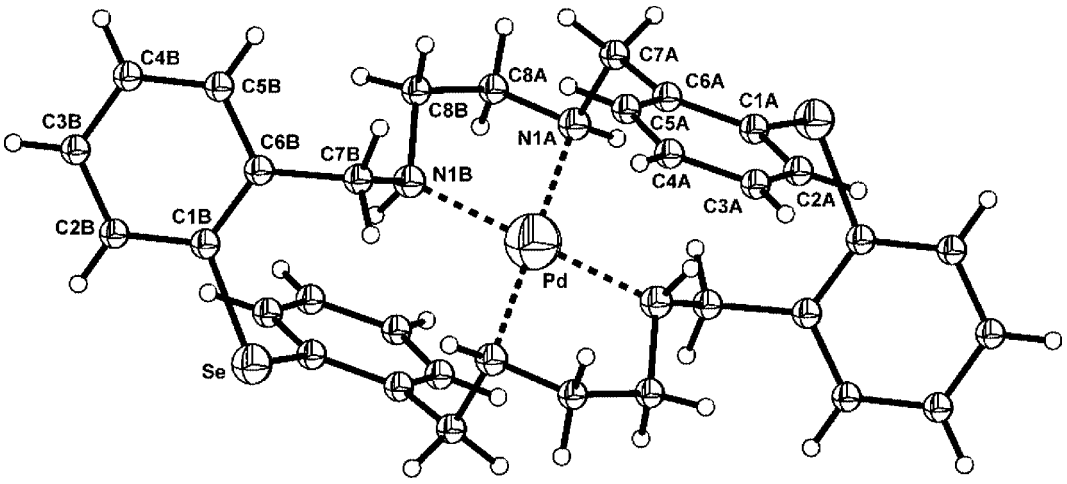


Figure 5. ORTEP diagram of **9**.

Table 3. Significant bond lengths [Å] angles [°] for **8**.

| | | | |
|---|---|---|---|
| Pd–N(1B) | 2.063(2) | Pd–N(1A) | 2.066(3) |
| N(1B)–Pd–N(1B)#1 | 180.000(1) | N(1B)–Pd–N(1A)#1 | 83.73(10) |
| N(1B)#1–Pd–N(1A)#1 | 96.27(10) | N(1B)–Pd–N(1A) | 96.27(10) |

Table 4. Significant bond lengths [Å] and angles [°] for **9**.

| | | | |
|---|---|---|---|
| Pd–N(1) | 2.072(4) | Pd–N(2) | 2.060(5) |
| N(2)#1–Pd–N(2) | 180.0(2) | N(2)#1–Pd–N(1) | 96.90(18) |
| N(2)–Pd–N(1) | 83.10(18) | | |

mass spectrum; the highest peak at $m/z$ = 838 corresponds to the M – 2Cl fragment. The $^{125}$Te NMR spectrum of complex **10** in [$D_6$]DMSO shows a peak at $\delta$ = 710 ppm, which disappeared after half an hour due to decomposition of the complex. A complex pattern of signals that were difficult to assign was observed in the $^1$H and $^{13}$C NMR spectra.

An ORTEP diagram of compound **10** is shown in Figure 6, and selected bond lengths and angles are given in Table 5. The molecule crystallizes with seven waters of crystallization. The $Pd^{II}$ cation adopts a square-planar geometry and is coordinated to the two nitrogen and two tellurium atoms. The tellurium atoms are slightly disordered. The Pd–N(1A) [2.114(6) Å] and Pd–N(2A) [2.118(8) Å] are slightly longer than the sum of the single bond covalent radii of Pd (1.31 Å) and N (0.75 Å).[14] However, these bond lengths are well within the sum of van der Waals radii. The Te–Pd bond lengths [Te(1A)–Pd 2.5770(16) Å, Te(2A)–Pd 2.5675(12) Å, Pd–Te(1B) 2.480(7) Å, and Te(2B)–Pd 2.431(4) Å] are significantly shorter than the sum of covalent radii (2.68 Å) and are comparable to those in the parent Schiff base macrocycle Pd complex.[5] The N–Pd–N, Te–Pd–Te, and N–Pd–Te bond angles are close to 90° and 180°. The coordination to Te in **10** may be due to the greater σ-donor property of the Te than Se, which leads to a stronger soft–soft interaction and stabilization of the six-membered chelate ring. The packing diagram (Figure 7) shows that the water molecules are sandwiched between the complexes and that there is extensive hydrogen bonding between the N–H hydrogen atom, chloride counterion, and the water molecules.

Equimolar amounts of **4** and $PtCl_2$ in MeOH were heated to reflux for 15 min to yield a clear solution of the complex **11**; brick-red crystals were obtained by slow diffusion of diethyl ether into the reaction mixture at room temperature (Scheme 1). The complex formed was not very soluble in most of the organic solvents and only partially soluble in MeOH. The elemental analysis data suggest the formation of a 1:1 complex. The molecular ion peak of complex **11** is absent in its ESI mass spectrum; the highest peak observed at $m/z$ = 863 corresponds to M – (Cl + 2 $H_2O$). The $^1$H and $^{13}$C NMR spectra of complex **11** are too complicated for complete analysis. As complex **11** is only partially soluble in MeOH, no satisfactory $^{77}$Se NMR spectrum could be recorded even after overnight data acquisition.

The X-ray crystal structure of **11** (Figure 8, Table 6) clearly suggests the formation of a novel 23-membered metallamacrocyclic complex. The geometry around $Pt^{IV}$ is octahedral.[8] The Pt–N bond *trans* to Pt–Se is longer (ca. 0.15 Å) than the other two Pt–N bonds because of the strong *trans* influence of –SePh.[15] The Pt–C bond length [2.010(4) Å] is shorter than those of the reported $Pt^{IV}$ selenolate compounds,[15–17] whereas the Pt–Cl bond length [2.4291(12) Å] is longer than those in related compounds.[16] This lengthening of the Pt–Cl bond and the shortening of the C–Pt bond may be ascribed to the stronger *trans* influence of phenyl ring than of Cl. The behavior of the macrocycle to form the cationic $Pt^{IV}$ complex by oxidative addition of the C–Se bond to the $Pt^{II}$ center is in contrast to those of the reported stable $Pt^{II}$ and $Pt^{IV}$ complexes with homodonor and mixed donor cyclic selenoether ligands.[4,18] The facile oxidative addition in this case may be facilitated by the more polar nature of C–Se bond that results from the N→Se intramolecular interaction present in the parent macrocycle (vide supra). Though the oxidative addition of halogens and alkyl halides to the $Pt^{II}$ center are

 © 2006 Wiley-VCH Verlag GmbH & Co. KGaA, Weinheim 

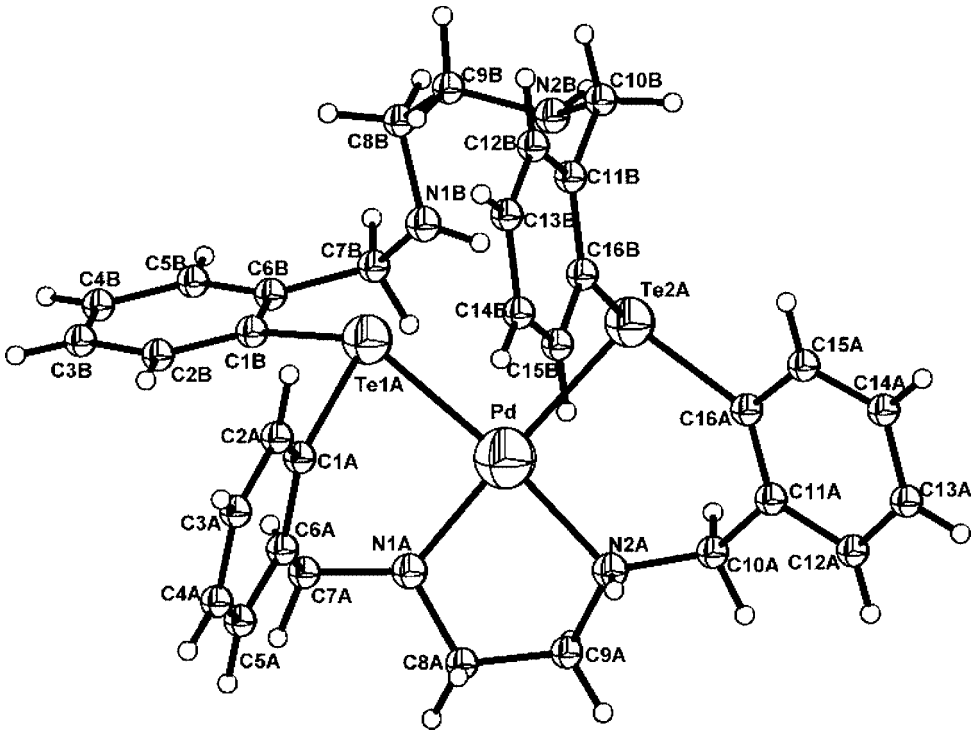


Figure 6. ORTEP diagram of **10**.

Table 5. Significant bond lengths [Å] and angles [°] for **10**.

| | | | |
|---|---|---|---|
| Te(1A)–Pd | 2.5770(16) | Te(2A)–Pd | 2.5675(12) |
| Pd–Te(1B) | 2.480(7) | Pd–Te(2B) | 2.431(4) |
| Pd–N(1A) | 2.114(6) | Pd–N(2A) | 2.118(8) |
| Te(1A)–Pd–Te(2A) | 89.67(5) | N(1A)–Pd–Te(1A) | 94.34(18) |
| N(1A)–Pd–N(2A) | 83.9(3) | N(2A)–Pd–Te(2A) | 94.0(2) |
| N(2A)–Pd–Te(1A) | 164.18(19) | N(1A)–Pd–Te(2A) | 172.18(18) |

common,[19] this is the second example of oxidative addition of C–Se bond to $Pt^{II}$.

Complex **12** was obtained by the reaction of $Cu(CH_3CN)_4ClO_4$ with 1 mol of ligand **4** in refluxing methanol, followed by the addition of excess $NH_4PF_6$. The complex is soluble in DMSO, MeCN, and $MeNO_2$. The crystals obtained from DMSO lose luster after removal of the solvent.

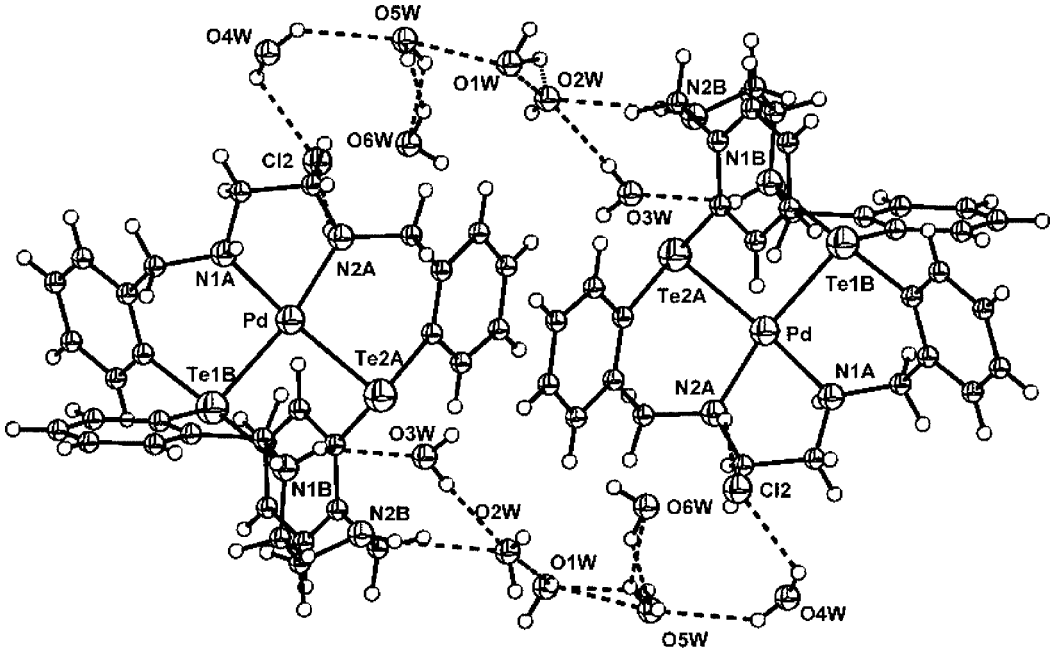


Figure 7. Packing diagram of **10**.

 © 2006 Wiley-VCH Verlag GmbH & Co. KGaA, Weinheim 

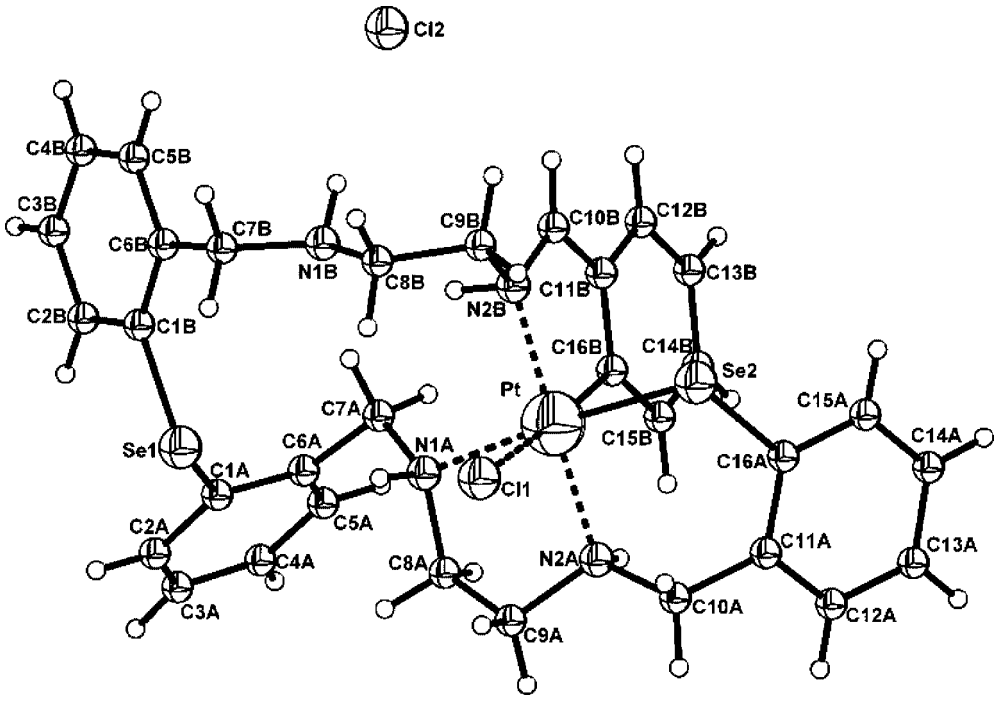


Figure 8. ORTEP diagram of **11**.

Table 6. Significant bond lengths [Å] and angles [°] for **11**.

| | | | |
|---|---|---|---|
| Pt–C(16B) | 2.010(4) | Pt–N(2B) | 2.039(4) |
| Pt–N(2A) | 2.050(4) | Pt–N(1A) | 2.180(3) |
| Pt–Se(2) | 2.4165(6) | Pt–Cl(1) | 2.4291(12) |
| Se(1)–C(1A) | 1.917(4) | Se(1)–C(1B) | 1.924(5) |
| Se(2)–C(16A) | 1.897(5) | | |
| C(16B)–Pt–Se(2) | 88.53(11) | C(16B)–Pt–N(2B) | 81.51(17) |
| N(2A)–Pt–Se(2) | 93.87(9) | N(2A)–Pt–N(1A) | 82.37(12) |
| N(2B)–Pt–N(1A) | 97.26(13) | | |

The elemental analysis data confirm the formation of a 1:1 complex. Complex **12** was found to be a 1:2 electrolyte in acetonitrile ($\Lambda_{M,}$ 393 $\Omega^{-1}\,cm^2\,mol^{-1}$). The infrared spectrum of the complex exhibits two NH stretching vibrations at 3301 and 3235 $cm^{-1}$ as sharp singlets and a bending vibration at 1629 $cm^{-1}$ as a broad singlet, while the IR spectrum of the ligand shows the stretching vibrations at 2794–3323 $cm^{-1}$ (sharp multiplets) and the bending vibration at 1687 $cm^{-1}$(sharp singlet). This implies that N–H of the ligand is involved in coordination to the metal center. The peaks at 843 and 557 $cm^{-1}$ confirm the presence of $PF_6$ in the complex. The solution-phase electronic spectrum (>200 nm) of the complex consists of two intense bands centered at 298 ($\varepsilon$ = 2485 $dm^3\,mol^{-1}\,cm^{-1}$) and 583 nm (148 $dm^3\,mol^{-1}\,cm^{-1}$), which can be assigned to the intraligand π–π* transitions. The reflectance spectrum of the solid sample exhibits the same type of bands centered at 315 and 584 nm. This indicates that the complex is stable in solution. The observed magnetic susceptibility value for the complex is 1.79 BM. This value is close to that for the square-planar copper complexes (1.84 BM).[20] The electron spin resonance spectrum further confirms the square-planar geometry of the complex. The spectrum of the powdered form is not well resolved; however, at the temperature for liquid nitrogen, an anisotropic ESR spectrum is obtained. The spectrum exhibits a line shape that is typical for a mononuclear $Cu^{II}$ complex with a $d_{x^2-y^2}$ ground state. The $g_\perp$ value for the complex is 2.052. The value for $A_\parallel$ was calculated from the difference between the peak positions i.e. 180G. The $g_z$ value is 2.24. This $g_z$ value is greater than that of $g_\perp$. The anisotropic value for $g_x$ and $g_y$ has not been resolved and no $A_\perp$ hyperfine constant was observed. The quotient $(g_z \times 10^4)/A_\parallel$ is an indication of the stereochemistry of the chelates in solution.[21] It has been suggested that this quotient may be an empirical index of tetrahedral distortion from tetragonal geometry, i.e. values that are lower than 140 are observed for square-planar structures and those that are higher than 150 for tetrahedral complexes. A value of 124 for **12** indicates a square-planar geometry. The $Cu^{II}$ complexes of tetraaza macrocyclic ligands generally exhibit irreversible redox processes. The $Cu^{II}$ complex **12** is reduced directly to $Cu^0$ by a single two-electron process at –0.524 V. Such behavior may stem from the higher flexibility of the ligand, which does not allow the $Cu^I$ complex to be kinetically stable and enables the reduction of the $Cu^{II}$ center directly to $Cu^0$.[22]

The reaction of $HgCl_2$ with ligand **4** gave an insoluble white product, which was not soluble in any of the common solvents. However, when the reaction was performed with $Hg(OCOCH_3)_2$, a white product **13** was obtained, which is soluble in MeCN and $MeNO_2$, and decomposes in DMSO. The elemental analysis data suggest the formation of a 1:1 complex. The IR spectrum shows a broad multiplet in the region of NH stretching (2911–3671 $cm^{-1}$). The peaks at 841 and 558 $cm^{-1}$ correspond to $\nu$(P–F) and $\nu$(F–P–F), respectively. The molecular ion peak of complex **13** is not

 © 2006 Wiley-VCH Verlag GmbH & Co. KGaA, Weinheim 

observed in the ESI mass spectrum, as is the case for the other complexes; the peak observed at $m/z$ = 981 is assigned to M – $PF_6$, and the peak at $m/z$ = 834 corresponds to M – 2 $PF_6$. This indicates the formation of the complex with two $PF_6$ counterions, and the peak at $m/z$ = 635 shows that the macrocycle remains intact. The broadening of the $^1$H NMR signal in the aliphatic region indicates the presence of molecular motion, which is somewhat slow on the NMR time scale. The existence of isomeric species in solution is also a possibility. The $^{13}$C NMR shows the expected number of peaks. The $^{77}$Se NMR spectrum exhibits a single signal at $\delta$ = 315 ppm, which indicates that there is no interaction between Se and $Hg^{II}$. The $Hg^{II}$ complex **13** shows two irreversible reduction peaks at 0.505 and 0.032 V, which implies the sequential reduction of $Hg^{II}$ to $Hg^{I}$ and then to $Hg^0$.

Reaction of ligand **6** with 1 and 2 equiv. Pd(COD)$Cl_2$, followed by the addition of $NH_4PF_6$ afforded the complexes **14** and **15** in a 1:1 and 1:2 (ligand/metal) ratio, respectively (Scheme 3).

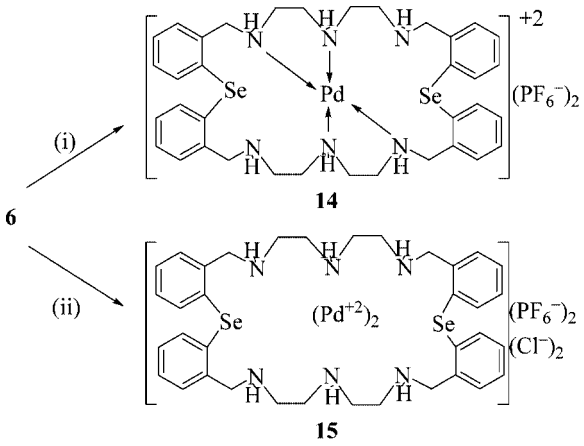


Scheme 3. Reagents: MeOH (reflux), (i) **6**:Pd(COD)$Cl_2$ (1:1), $NH_4PF_6$; (ii) **6**:Pd(COD)$Cl_2$ (1:2), $NH_4PF_6$.

Complex **14** is light yellow, whereas complex **15** is yellow. The complexes are not very soluble in all solvents even on prolonged heating. Due to the partial solubility of the complexes, complete characterization of the complexes was difficult. The elemental analysis data for **14** and **15** suggest the formation of 1:1 and 1:2 (ligand/metal) complexes respectively. The IR spectra exhibit peaks in the range 840–849 and at 556 $cm^{-1}$, which correspond to $\nu$(P–F) and $\nu$(F–P–F), respectively. In the ESI mass spectrum of complex **14**, the molecular ion peak is observed at $m/z$ = 1116.88, and the peaks for [M – $PF_6$], [M – 2 $PF_6$], and [M – (Pd + 2 $PF_6$)] are observed at $m/z$ = 971.9, 826.9, and 719, respectively. However, for complex **15**, no molecular ion peak is observed; peaks at $m/z$ = 1148.96, 1112.95, 1075.95, and 928.98 are observed for [M – $PF_6$], [M – ($PF_6$ + Cl)], [M – ($PF_6$ + 2 Cl)], and [M – 2 ($PF_6$ + Cl)]. Due to the poor solubility of complexes, it was challenging to record the $^{77}$Se NMR spectrum of the complexes. The $^{77}$Se NMR spectrum of complex **14** was recorded in 50% $CD_3CN/CD_3OD$ solution and shows one peak at $\delta$ = 303 ppm after long data accumulation. However, the $^{77}$Se NMR spectrum of compound **15** could not be recorded. The $Pd^{II}$ complexes did not show well-defined redox processes that could be interpreted.

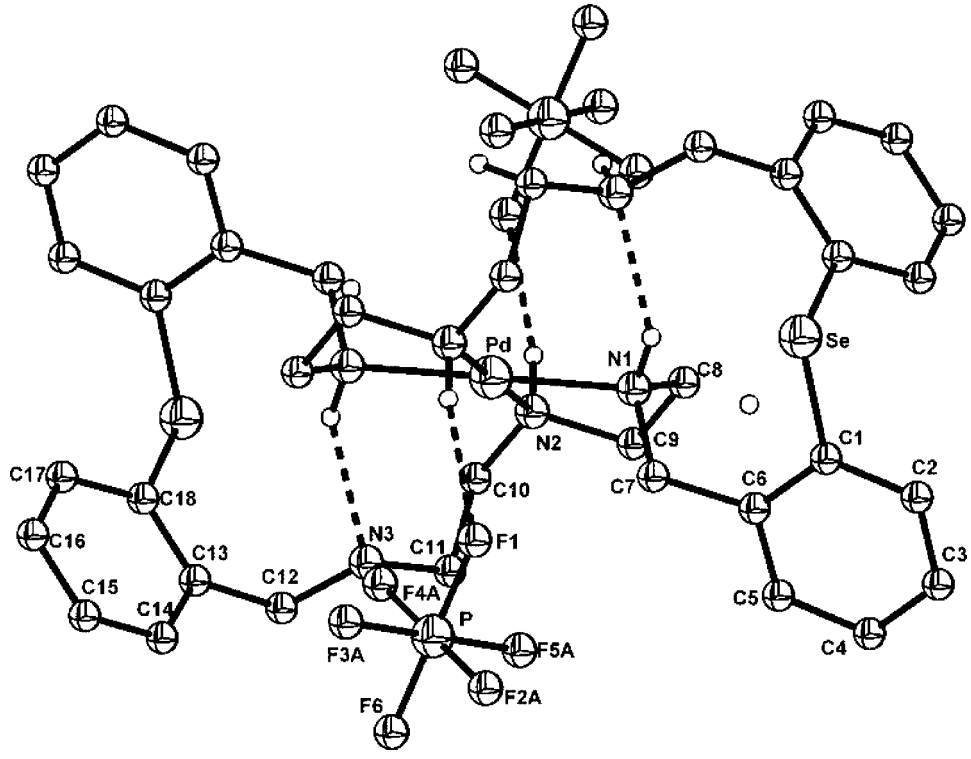


Figure 9. ORTEP diagram of **14**.

 © 2006 Wiley-VCH Verlag GmbH & Co. KGaA, Weinheim 

The ORTEP view of compound **14** is shown in the Figure 9, and selected bond lengths and angles are given in the Table 7. The molecule is centrosymmetric: only half of the molecule represents the asymmetric unit, and there is one molecule per unit cell. The cation adopts a square-planar geometry and coordinates to four nitrogen atoms out of the possible N6Se2 coordination sites. The N(1)–Pd–N(1)# and N(2)–Pd–N(2)# bond angles are 180°. The N(1)–Pd–N(2) bond angle is 84.05(13)°, and these atoms are part of a five-membered ring containing two nitrogen donor atoms. The N(1)–Pd–N(2)#1 bond angle is 95.95(13)°, and these atoms are part of a 13-membered ring containing an Se atom. The Pd–N(1) and Pd–N(2) bond lengths are 2.067(3) and 2.081(3) Å, respectively, and are marginally longer than the sum of the covalent radii of Pd (1.31 Å) and N (0.75 Å); however, they are much shorter than the sum of the van der Waals radii. The phenyl rings and the two selenium atoms bend away from the square plane that contains the Pd cation. The transannular distance between the two Se atoms is 10.422 Å.

Table 7. Significant bond lengths [Å] angles [°] for **14**.

| | | | |
|---|---|---|---|
| Pd–N(1) | 2.067(3) | Pd–N(2) | 2.081(3) |
| N(1)–Pd–N(1)#1 | 180.0 | N(1)–Pd–N(2) | 84.05(13) |
| N(1)#1–Pd–N(2) | 95.95(13) | | |

The synthesis of the $Pt^{II}$ analogues of **14** and **15** has been attempted. Though elemental analysis, and IR and ESI mass spectrometry show the formation of the desired complexes, no satisfactory NMR spectra could be obtained because of the highly insoluble nature of the complexes. Attempts to get suitable crystals were also unsuccessful.

## Conclusions

In conclusion, macrocycle **4** shows versatile coordination behavior towards the metal cations $Ni^{II}$, $Pd^{II}$, $Pt^{II}$, $Cu^{II}$, and $Hg^{II}$. In general, molecular structures of the complexes show that the coordination behavior of the metal ions towards the donors is determined by the geometrical arrangement of the ligands around the metal atom, by the stability of the chelate ring formed by metal coordination, and to a lesser extent, by the HSAB principle.

## Experimental Section

**General:** All reactions were carried out under nitrogen or argon using standard vacuum line techniques. Solvents were purified and dried by standard procedures[23] and were freshly distilled prior to use. Melting points were recorded in capillary tubes and are uncorrected. The $^1H$ (299.4), $^{13}C$ (75.42), and $^{77}Se$ (57.22) NMR spectra were recorded in [$D_6$]DMSO or $CD_3CN$ on a Varian VXR 300S spectrometer. Chemical shifts cited were referenced to TMS ($^1H$, $^{13}C$) as internal and $Me_2Se$ ($^{77}Se$) as external standards. The elemental analysis was performed on a Carlo–Erba model 1106 and Eager 300 EA1112 elemental analyzers. The IR spectra were recorded as KBr pellets with a Thermo Nicolet Avatar 320 FTIR spectrometer. The UV/Vis spectra in solution were recorded with 3-cm path length quartz cells on a UV-260 Shimadzu spectrophotometer, and reflectance spectra were recorded with a UV-160A spectrophotometer. The electronic spectra of all the complexes were recorded at room temperature in acetonitrile. The spectra were recorded in the range 200–1100 nm. The FAB mass spectra were recorded on a JEOL SX 102/DA-6000 mass spectrometer/data system using Argon/Xenon (6 KV, 10 mA) as the FAB gas. The ESI mass spectra were recorded at room temperature with a Q-Tof micro (YA-105) micromass spectrometer. The magnetic susceptibility of the complexes **7** and **12** was studied at room temperature. Complex $Hg[Co(SCN)_4]$ was used as the standard. The EPR spectra were recorded at room temperature and at the temperature for liquid nitrogen. TCNQ was taken as the standard. $Cu(CH_3CN)_4ClO_4$, $Pd(C_6H_5CN)_2Cl_2$, and $Pd(COD)Cl_2$ were prepared by literature procedures.[24] All the complexes were vacuum dried after preparation. The solution electrical conductivity was measured using a Elico CM-180 Conductivity meter with KCl solution in water as standard. Cyclic voltammetric (CV) experiments were performed on a CH instruments electrochemical analyzer with a three-electrode device. The experiments were performed with a glassy carbon working electrode, a platinum counter electrode, and a standard Ag/AgCl reference electrode. Tetrabutylammonium perchlorate (Aldrich) was used as the supporting electrolyte. All solutions were purged with nitrogen before the CV data were recorded. Measurements were recorded with 0.1 M $NBu_4ClO_4$ in acetonitrile with a sample concentration 0.05 mM. Ferrocene was taken as the standard.

**Syntheses**

Ligands **4**, **5**, and **6** were prepared following known procedures.[6,7]

**[$NiC_{32}H_{36}N_4Se_2P_2F_{12}$] (7):** $Ni(OCOCH_3)_2$ (0.026 g, 0.15 mmol) was added to ligand **4** (0.1 g, 0.15 mmol) in methanol (20 $cm^3$). The reaction mixture was then heated to reflux for 30 min. The resulting reaction mixture was filtered, and to the filtrate excess $NH_4PF_6$ was added to give the complex as a purple powder. Crystallization from an acetonitrile solution by diffusion of diethyl ether afforded purple crystals of the complex. Yield: 0.078 g, 52%. M.p. 269 °C (d.). Magnetic susceptibility: 3.39$\mu_B$. IR (KBr): $\tilde{\nu}_{max}$ = 3286 (m), 2923 (s), 1641 (b), 1461 (m), 1308 (w), 1083 (m), 951 (w), 840 (s), 760 (s), 557 (s) $cm^{-1}$. $\lambda_{max}$ (MeCN; $\varepsilon$/$dm^3 mol^{-1} cm^{-1}$): 304 (2400), 699 (15) and 895 (29) nm. FAB MS: *m*/*z* = 839 [M – $PF_6$], 693 [M – 2 $PF_6$]. $C_{32}H_{36}N_4Se_2NiP_2F_{12}$ (983.2): calcd. C 39.09, H 3.69, N 5.69; found C 38.41, H 3.60, N 7.05.

**[$PdC_{32}H_{36}N_4Se_2P_2F_{12}$] (8):**[8] Complex **8** was prepared in a manner similar to that of **7**, but with the metal precursor $Pd(C_6H_5CN)_2Cl_2$. Cream-coloured crystals were obtained from a DMSO/ether solution. Yield: 0.087 g, 56%. M.p. 247–249 °C (d.). IR (KBr): $\tilde{\nu}_{max}$ = 3426 (b), 3220 (m), 2924 (w), 1631 (w), 1449 (m), 1020 (w), 843 (s), 764 (s), 558 (s) $cm^{-1}$. $^{77}Se$ NMR ([$D_6$]DMSO): $\delta$ = 869 ppm. FAB MS: *m*/*z* = 886 [M – $PF_6$], 738 [M – 2 $PF_6$]. $C_{32}H_{36}N_4Se_2PdP_2F_{12}$: calcd. C 37.28, H 3.52, N 5.43; found C 36.88, H 3.68, N, 5.02.

**[$C_{32}H_{40}Cl_2N_4O_2PdSe_2$] (9):** $PdCl_2$ (0.027 g, 0.15 mmol) was added to **4** (0.1 g, 0.15 mmol) in MeOH (20 $cm^3$), and heated to reflux for 30 min. The reaction mixture was filtered. The solvent volume was reduced to 2 $cm^3$ in vacuo, followed by diffusion of diethyl ether to afford yellowish crystals of the complex. Yield: 0.075 g, 61%. M.p. 225 °C (d.). IR (KBr): $\tilde{\nu}_{max}$ = 3426 (s), 3226 (s), 3052 (m), 2849 (s), 1632 (s), 1464 (s), 1440 (s), 1340 (w), 1199 (w), 1025 (s), 755 (s), 633 (w), 452 (w) $cm^{-1}$. $^{77}Se$ ([$D_6$]DMSO): $\delta$ = 787 ppm. ESI-MS: *m*/*z* = 840 [M + 2 $H_2O$], 741 [M – 2 Cl]. $C_{32}H_{40}Cl_2N_4O_2PdSe_2$ (847.9): calcd. C 45.34, H 4.76, N 6.61; found C 45.58, H 5.05, N 6.27.

 © 2006 Wiley-VCH Verlag GmbH & Co. KGaA, Weinheim 

**[$PdC_{32}H_{36}N_4Te_2Cl_2$] (10):**[8] This complex was prepared in a manner similar to that described for **9** and was isolated as brownish red crystals from a methanol/ether solution. Yield: 0.2 g, 78%. M.p. 196 °C (d.). IR (KBr): $\tilde{\nu}_{max}$ = 3417 (s, br), 3320 (s), 3049 (m), 2881 (s), 2850 (s), 1621 (m), 1439 (s), 1205 (m), 1120 (m), 837 (s), 752 (s) $cm^{-1}$. ESI-MS: *m*/*z* = 838 [M – 2 Cl]. $C_{32}H_{36}N_4Te_2PdCl_2H_2O$: calcd. C 41.45, H 4.13, N 6.04; found C 40.88, H 4.22, N 5.77.

**[$PtC_{32}H_{40}N_4O_2Se_2Cl_2$] (11):**[8] This complex was prepared in a manner similar to that described for **9** and was isolated as red crystals by the slow diffusion of diethyl ether. Yield: 0.074 g, 52%. M.p. 252 °C (d.). IR (KBr) $\tilde{\nu}_{max}$ = 3429 (br), 2923 (s), 2848 (s), 1635 (s), 1439 (s), 1327 (s), 1105 (w), 1026 (s), 751 (s) $cm^{-1}$. ESI-MS: 863.2 [M – Cl], 827.21 [M – 2 Cl]. $C_{32}H_{40}N_4O_2Se_2PtCl_2$: calcd. C 41.05, H 4.30, N 5.98; found C 41.93, H 3.46, N 6.41.

**[$CuC_{32}H_{36}N_4Se_2P_2F_{12}$] (12):** This complex was prepared by following the method used for preparing complex **7** but with $Cu(CH_3CN)_4ClO_4$. Yield: 0.050 g, 33%. M.p. 212–214 °C (d.). Magnetic susceptibility: 1.79$\mu_B$. IR (KBr): $\tilde{\nu}_{max}$ = 3434 (m), 3301 (s), 2941 (w), 1629 (w), 1465 (s), 1347 (w), 1302 (w), 1199 (w), 1106 (m), 1042 (m), 927 (s), 843 (s), 622 (s), 760 (s), 577 (s) $cm^{-1}$. $\lambda_{max}$ (MeCN; $\varepsilon$/$dm^3\,mol^{-1}\,cm^{-1}$): 298 (2485), 583 (148). Molar conductivity (acetonitrile, 298 K): $\Lambda_M$ = 393 $\Omega^{-1}\,cm^2\,mol^{-1}$. FAB MS: *m*/*z* = 697 [M – 2 $PF_6$], 637 [M – (2 $PF_6$ + Cu)]. $C_{32}H_{36}N_4Se_2CuP_2F_{12}$ (988.1): calcd. C 38.90, H 3.67, N 5.67; found C 39.38, H 3.87, N 6.27.

**[$HgC_{32}H_{36}N_4Se_2P_2F_{12}$] (13):** This complex was prepared in a manner similar to that described for **7** but with the metal precursor $Hg(OCOCH_3)_2$. Yield: 0.066 g, 38%. M.p. 180 °C (d.). IR (KBr): $\tilde{\nu}_{max}$ = 3671 (w), 3271 (w), 2928 (w), 1587 (w), 1461 (s), 1439 (s), 1204 (w), 1018 (w), 841 (s), 760 (s), 558 (s) $cm^{-1}$. $^{13}C$ NMR ($CD_3CN$): $\delta$ = 47.1 ($CH_2NH$), 54.3 ($CH_2Ar$), 129.6, 131.3, 131.6, 135.2, 136.9 (Aromatic C) ppm. $^{77}Se$ NMR ($CD_3CN$): $\delta$ = 315 ppm. ESI-MS: *m*/*z* = 981 [M – $PF_6$], 835 [M – 2 $PF_6$]. $C_{32}H_{36}N_4Se_2HgP_2F_{12}$ (1125.1): calcd. C 34.16, H 3.22, N 4.98; found C 33.93, H 3.31, N 4.86.

**[$PdC_{36}H_{46}N_6Se_2P_2F_{12}$] (14):** Pd(COD)$Cl_2$ (0.057 g, 0.2 mmol) was added to **6** (0.15 g, 0.2 mmol) in MeOH (20 $cm^3$) and was heated to reflux for 30 min. The reaction mixture was filtered, and to the filtrate excess $NH_4PF_6$ was added. The solvent volume was reduced to 2 $cm^3$ in vacuo, followed diffusion of diethyl ether to afford colorless crystals. Yield: 0.15 g, 32%. M.p. 220 °C (d.). IR (KBr): $\tilde{\nu}_{max}$ = 3343 (br), 3236 (s), 2927 (br), 840 (s), 557 (s) $cm^{-1}$. $^{77}Se$ NMR

Table 8. Crystal data and structure refinement of **4**, **7**, **8**, and **9**.

| | **4** | **7** | **8** | **9** |
|---|---|---|---|---|
| Empirical formula | $C_{32}H_{36}N_4Se_2$ | $C_{32}H_{36}F_{12}N_4P_2NiSe_2$ | $C_{32}H_{46}F_{12}N_4P_2PdSe_2$ | $C_{32}H_{40}Cl_2N_4O_2Pd\ Se_2$ |
| $M_w$ | 635.7 | 983.22 | 1030.91 | 847.90 |
| Crystal system | Monoclinic | Tetragonal | Triclinic | Monoclinic |
| Space group | P2/*n* | P4(2)/*n* | $P\bar{1}$ | *P*21/*n* |
| *a* [Å] | 16.3985(14) | 15.5381(8) | 9.9501(14) | 11.4547(18) |
| *b* [Å] | 5.0714(4) | 15.5381(8) | 10.5010(15) | 11.4404(18) |
| *c* [Å] | 18.2454(15) | 15.2794(15) | 10.6403(16) | 12.864(2) |
| *α* [°] | 90 | 90 | 103.622(2) | 90 |
| *β* [°] | 104.4830(10) | 90 | 117.296(2) | 95.428(3) |
| *γ* [°] | 90 | 90 | 103.042(3) | 90 |
| *V* [Å$^3$] | 1469.1(2) | 3688.9(5) | 885.6(2) | 1678.2(5) |
| *Z* | 2 | 4 | 1 | 2 |
| Temperature [K] | 293(2) | 168(2) | 168(2) | 103(2) |
| Abs. coeff. [$mm^{-1}$] | 2.544 | 2.678 | 2.765 | 2.917 |
| Observed reflections [$I > 2\sigma$] | 3581 | 4501 | 5787 | 4083 |
| Final *R*(F) [$I > 2\sigma$][a] | 0.0416 | 0.0297 | 0.0330 | 0.0688 |
| *wR*($F_2$) indices [$I > 2\sigma$] | 0.0669 | 0.0568 | 0.0442 | 0.1462 |

[a] $R(F_o) = \Sigma||F_o| - |F_c||/\Sigma|F_o|$ and $wR(F_o^2) = [\Sigma w(F_o^2 - F_c^2)^2/\Sigma w(F_c^2)^2]^{1/2}$.

Table 9. Crystal data and structure refinement of **10**, **11**, and **14**.

| | **10** | **11** | **14** |
|---|---|---|---|
| Empirical formula | $C_{32}H_{50}Cl_2N_4O_7PdTe_2$ | $C_{32}H_{39}Cl_2N_4O_2Pt\ Se_2$ | $C_{36}H_{46}F_{12}N_6P_2PdSe_2$ |
| $M_w$ | 1035.26 | 935.58 | 1117.05 |
| Crystal system | Triclinic | Triclinic | Triclinic |
| Space group | $P\bar{1}$ | $P\bar{1}$ | $P\bar{1}$ |
| *a* [Å] | 12.072(6) | 9.9635(19) | 10.3868(1) |
| *b* [Å] | 13.264(6) | 10.210(2) | 10.4193(1) |
| *c* [Å] | 14.527(7) | 17.427(3) | 10.9246(1) |
| *α* [°] | 104.235(8) | 94.196(3) | 108.532(1) |
| *β* [°] | 107.668(9) | 105.466(3) | 95.200(1) |
| *γ* [°] | 110.244(8) | 106.808(4) | 108.573(1) |
| *V* [Å$^3$] | 1912.6(16) | 1613.7(5) | 1038.110(17) |
| *Z* | 2 | 2 | 1 |
| Temperature [K] | 293(2) | 103(2) | 294(2) |
| Abs. coeff. [$mm^{-1}$] | 2.169 | 6.806 | 7.152 |
| Observed reflections [$I > 2\sigma$] | 8797 | 7802 | 3127 |
| Final *R*(*F*) [$I > 2\sigma$][a] | 0.0771 | 0.0360 | 0.0433 |
| w*R*($F_2$) indices [I > 2σ] | 0.1788 | 0.0820 | 0.1172 |

[a] $R\ (F_o) = \Sigma||F_o| - |F_c||/\Sigma|F_o|$ and $wR(F_o^2) = [\Sigma w(F_o^2 - F_c^2)^2/\Sigma w(F_c^2)^2]^{1/2}$.

 © 2006 Wiley-VCH Verlag GmbH & Co. KGaA, Weinheim 

(300 MHz, $CD_3CN/CD_3OD$ (1:1), 25 °C): $\delta$ = 307 ppm. ESI-MS: 1117 [M], 972 [M – $PF_6$], 827 [M – 2 $PF_6$]. $C_{36}H_{46}N_6Se_2PdP_2F_{12}$ (1117.1): calcd. C 38.71, H 4.151, N 7.52; found C 38.95, H 3.81, N 6.56.

**$[Pd_2C_{36}H_{46}N_6Se_2P_2F_{12}Cl_2]$ (15):** The complex was prepared in a manner similar to that described for **14** and was separated as a yellowish white powder. Yield: 0.18 g, 34%. M.p. 230 °C (d.). IR (KBr): $\tilde{\nu}_{max}$ = 3409 (br), 3205 (w), 1625 (w), 1441 (s), 840 (s), 758 (s), 558 (s) $cm^{-1}$. ESI-MS: 1148.96 [M – $PF_6$], 1112.95 [M – ($PF_6$ + Cl)], 1075.95 [M – ($PF_6$ + 2 Cl)], 966.95, 928.98 [M – 2 ($PF_6$ + Cl)], 825.07 [M – (2 $PF_6$ + 2 Cl + Pd)]. $C_{36}H_{46}N_6Se_2Pd_2P_2F_{12}Cl_2$ (1294.4): calcd. C 33.41, H 3.58, N 6.49; found C 32.72, H 3.44, N 6.52.

**X-ray Crystallography:** The diffraction measurements for the ligand as well as for the complexes were performed at room temperature on a Bruker P4 diffractometer with graphite-monochromated Mo-$K_\alpha$ radiation ($\lambda$ = 0.71073 Å) (Table 7 and Table 8) The data were corrected for Lorentz, polarization, and absorption effects The structures were determined by routine heavy-atom with SHELXS 97[25] and Fourier methods, and were refined by full-matrix least-squares by means of the SHELEXL 97[26] program with anisotropic non-hydrogen atoms and a fixed isotropic thermal parameter of 0.07 $Å^2$ for hydrogen. The hydrogen atoms were partially located from difference electron-density maps and the rest were fixed at predetermined positions. Scattering factors were obtained from common sources.[27] Some details of the data collection and refinement are given in Table 8 and Table 9. CCDC-221526 (**11**), -221527 (**8**), -241757 (**4**), -241758 (**7**), -241759 (**9**), -241760 (**10**), and -241761 (**14**) contain the supplementary data for this paper. These data can be obtained free of charge from The Cambridge Crystallographic Data Centre via www.ccdc.cam.ac/uk/data_request/cif.

## Acknowledgments

We are grateful to the Department of Science and Technology (DST), New Delhi for funding this work. Additional help from the Regional Sophisticated Instrumentation center (RSIC), Indian Institute of Technology (IIT), Bombay, for 300 MHz NMR spectroscopy, RSIC, CDRI Lucknow, for the mass recording facility, and Tata Institute of Fundamental Research (TIFR), Bombay, for 500 MHz NMR spectroscopy is gratefully acknowledged.

[1] a) K. Gloe, H. Graubaum, M. Wust, T. Rambusch, W. Seichter, *Coord. Chem. Rev.* **2001**, *222*, 103–126; b) J. P. Danks, N. R. Champness, M. Schröder, *Coord. Chem. Rev.* **1998**, *174*, 417–468; c) A. J. Pearson, W. Xiao, *J. Org. Chem.* **2003**, *68*, 2161–2166; d) L. F. Lindoy, in *Progress in Macrocycle Chemistry* (Eds.: R. M. Izatt, J. J. Christensen), John Wiley & Sons, New York, **1987**, vol. 3, ch. 2; e) T. Tsuchiya, T. Shimizu, K. Hirabayashi, N. Kamigata, *J. Org. Chem.* **2003**, *68*, 3480–3485.

[2] a) A. J. Barton, N. J. Hill, W. Levason, G. Reid, *J. Am. Chem. Soc.* **2001**, *123*, 11801–11802; b) W. Levason, G. Reid, *J. Chem. Soc. Dalton Trans.* **2001**, 2953–2960; c) N. J. Hill, W. Levason, G. Reid, *Inorg. Chem.* **2002**, *41*, 2070–2076; d) R. Pietschnig, S. Schaefer, K. Merz, *Org. Lett.* **2003**, *5*, 1867–1869; e) N. J. Hill, W. Levason, R. Patel, G. Reid, M. Webster, *Dalton Trans.* **2004**, 980–981.

[3] a) E. G. Hope, W. Levason, *Coord. Chem. Rev.* **1993**, *122*, 109–170 and references cited therein; b) W. Levason, S. D. Orchard, G. Reid, *Coord. Chem. Rev.* **2002**, *225*, 159–199 and references cited therein; c) A. K. Singh, S. Sharma, *Coord. Chem. Rev.* **2000**, *209*, 49–98 and references cited therein; d) W. Levason, G. Reid, *Comprehensive Coordination Chemistry II* (Eds.: J. A. McCleverty, T. J. Meyer), Elsevier Science, **2004**, *1*, 399 and references cited therein.

[4] a) K. Kobayashi, H. Izawa, K. Yamaguchi, E. Horn, N. Furukawa, *Chem. Commun.* **2001**, 1428–1429; b) J. L. Li, J. B. Meng, Y. M. Wang, J. T. Wang, T. Matsuura, *J. Chem. Soc., Perkin Trans. 1* **2001**, 1140–1146; c) S. K. Tripathi, B. L. Khandelwal, S. K. Gupta, *Phosphorus Sulfur Silicon Relat. Elem.* **2002**, *177*, 2285–2293; d) X. Zeng, X. Han, L. Chen, Q. Li, F. Xu, X. He, Z. Zhang, *Tetrahedron Lett.* **2002**, *43*, 131–134; e) M. J. Hesford, W. Levason, M. L. Matthews, S. D. Orchard, G. Reid, *Dalton Trans.* **2003**, 2434–2442; f) M. J. Hesford, W. Levason, M. L. Matthews, G. Reid, *Dalton Trans.* **2003**, 2852–2858; g) C. Bornet, R. Amardeil, P. Meunier, J. C. Daran, *J. Chem. Soc., Dalton Trans.* **1999**, 1039–1040; h) W. Levason, M. Matthews, R. Patel, G. Reid, M. Webster, *New J. Chem.* **2003**, *27*, 1784–1788.

[5] a) S. C. Menon, H. B. Singh, R. P. Patel, S. K. Kulshreshtha, *J. Chem. Soc., Dalton Trans.* **1996**, 1203; b) S. C. Menon, A. Panda, H. B. Singh, R. J. Butcher, *Chem. Commun.* **2001**, 143; c) S. C. Menon, A. Panda, H. B. Singh, R. P. Patel, S. K. Kulshreshtha, W. L. Darby, R. J. Butcher, *J. Organomet. Chem.* **2004**, *689*, 1452–1463.

[6] a) A. Panda, S. C. Menon, H. B. Singh, R. J. Butcher, *J. Organomet. Chem.* **2001**, *623*, 87–94; b) S. Panda, H. B. Singh, R. J. Butcher, *Inorg. Chem.* **2004**, *43*, 8532–8537.

[7] A. Panda, S. C. Menon, H. B. Singh, C. P. Morley, R. Bachman, T. M. Cocker, R. J. Butcher, *Eur. J. Inorg. Chem.* **2005**, 1114–1126.

[8] S. Panda, H. B. Singh, R. J. Butcher, *Chem. Commun.* **2004**, 322–323.

[9] a) L. Sacconi, F. Mani, A. Benicicni, *Comprehensive Coordination Chemistry* (Eds.: G. Wilkinson, R. D. Gillard, J. A. McCleverty), Pergamon, **1987**, *5*, 55; b) M. Schröder, *Encyclopedia of Inorganic Chemistry* (Ed.: R. B. King), Wiley, New York, **1994**, *5*, 2395.

[10] P. B. Ayscough, *Electron Spin Resonance Chemistry*, Methuen and Co Ltd., **1967**.

[11] S. Brooker, P. D. Croucher, T. N. Davidson, G. S. Dunbar, A. J. McQuillan, G. B. Jameson, *Chem. Commun.* **1998**, 2131–2132.

[12] M. K. Davies, W. Levason, G. Reid, *J. Chem. Soc., Dalton Trans.* **1998**, 2185–2190.

[13] G. Hunter, A. McAuley, T. W. Whitecombe, *Inorg. Chem.* **1988**, *27*, 2634–2639.

[14] J. E. Huheey, E. A. Keiter, R. L. Keiter, in *Inorganic Chemistry: Principles of Structure and Reactivity* 4th ed., HarperCollins College Publishers, New York, **1993**.

[15] M. C. Janzen, M. C. Jennings, R. J. Puddephatt, *Can. J. Chem.* **2002**, *80*, 41–45.

[16] C. M. Bates, P. K. Khanna, C. P. Morley, M. D. Vaira, *Chem. Commun.* **1997**, 913–914.

[17] K.-T. Aye, J. J. Vittal, R. J. Puddephatt, *J. Chem. Soc., Dalton Trans.* **1993**, 1835–1840.

[18] a) W. Levason, J. J. Quirk, G. Reid, C. S. Frampton, *Inorg. Chem.* **1994**, *33*, 6120–6122; b) N. R. Champness, P. F. Kelly, W. Levason, G. Reid, A. M. Z. Slawin, D. J. Williams, *Inorg. Chem.* **1995**, *34*, 651–657; c) N. R. Champness, W. Levason, J. J. Quirk, G. Reid, *Polyhedron* **1995**, *14*, 2753–2758; d) R. J. Batchelor, F. W. B. Einstein, I. D. Gay, J. Gu, B. M. Pinto, X. Zhou, *Inorg. Chem.* **1996**, *35*, 3667–3674.

[19] G. K. Anderson, *Platinum-Carbon σ-bonded Complexes, in Comprehensive Organometallic Chemistry II*. (Eds.: E. W. Abel, F. G. A. Stone, G. Wilkinson), Pergamon, Oxford, **1995**, vol. 9.

[20] a) B. J. Hathaway, A. A. G. Tomilinson, *Coord. Chem. Rev.* **1970**, *5*, 1–43; b) B. J. Hathaway, D. E. Billing, *Coord. Chem. Rev.* **1970**, *5*, 143–207.

[21] C. Beguin, P. Chautemps, A. E. Marzouki, J. L. Pierre, S. M. Refaif, G. Serratrice, E. Saint-Aman, P. Rey, *J. Chem. Soc., Dalton Trans.* **1995**, 1939–1946.

 © 2006 Wiley-VCH Verlag GmbH & Co. KGaA, Weinheim 

[22] C. Bazicalupi, A. Benicini, S. Ciattini, C. Giorgi, A. Masotti, P. Paoletti, B. Valtoancoli, N. Navon, D. Meyerstain, *J. Chem. Soc., Dalton Trans.* **2000**, 2383–2392.
[23] W. L. F. Armarego, D. D. Perrin, in *Purification of Laboratory Chemicals*, Butterworth-Heinemann, The Bath Press, Bath, **1997**.
[24] a) G. K. Anderson, M. Lin, A. Sen, E. Gertz, *Inorg. Synth.* **1990**, *28*, 60; b) M. G. Simmons, C. L. Merril, L. J. Wilson, L. M. Bottoley, K. M. Kadish, *J. Chem. Soc., Dalton Trans.* **1980**, 1827–1837; c) D. Drew, J. R. Doyle, *Inorg. Synth.* **1972**, *13*, 47.
[25] G. M. Sheldrick, *SHELXS 97, Program for the Solution of Crystal Structures* University of Göttingen, **1990**.
[26] G. M. Sheldrick, *SHELXL 97, Program for Refining Crystal Structures* University of Göttingen, **1997**.
[27] International Tables for X-ray Crystallography, Birmingham, **1974**, 1, 99, 149.

Received: May 9, 2005
Published Online: November 15, 2005

 © 2006 Wiley-VCH Verlag GmbH & Co. KGaA, Weinheim 

DOI: 10.1002/ejic.200500626

# New, Multi-Dimensional Cu(tn)-$[M(CN)_6]^{n-}$ Cyano-Bridged, Bimetallic Coordination Materials (M = $Fe^{II}$, $Co^{III}$, $Cr^{III}$ and tn = 1,3-Diaminopropane)

**Smail Triki,*[a] Jean Sala-Pala,[a] Franck Thétiot,[a] Carlos J. Gómez-García,[b] and Jean-Claude Daran[c]**

**Keywords:** Bridging ligands / Cyanides / Heterometallic complexes / Magnetic properties

Reaction of the $[Fe^{III}(CN)_6]^{3-}$ anion with $[Cu^{II}(tn)(H_2O)_n]^{2+}$ (tn = 1,3-diaminopropane) affords the compounds $[\{Cu^{II}(tn)\}_2\{Fe^{II}(CN)_6\}]\cdot KCl\cdot 5H_2O$ (**1**), $[\{Cu^{II}(tn)\}_2\{Fe^{II}(CN)_6\}]\cdot 4H_2O$ (**2**), and $[\{Cu^{II}(tnH)_2(H_2O)_2\}\{Fe^{II}(CN)_6\}]\cdot 2H_2O$ (**3**). Each iron center in **1** and **2** is linked to six copper(II) ions by six cyanide bridges, while each copper ion is linked to three equivalent iron(II) ions. Despite these resemblances, the two compounds present large structural differences caused by two different orientations of the Cu–NC–Fe bridges: compound **1** has a 2D structure which can be described as successions of "$Cu_4Fe_3$" defective cubane units, while compound **2** displays a 3D arrangement. Compound **3**, in which only two *trans*-CN groups are bridging, displays a 1D structure. The tn ligand is chelating in **1**, as is usually observed in several parent compounds, but is unexpectedly a bridging ligand in **2** and a terminal protonated $tnH^+$ ligand in **3**. Thus, the dimension of the three compounds seems to depend on the tn coordination modes. For the three iron compounds **1**–**3**, the synthetic processes involve the spontaneous reduction of the paramagnetic $[Fe^{III}(CN)_6]^{3-}$ anion into the diamagnetic $[Fe^{II}(CN)_6]^{4-}$ anion. In order to avoid such diamagnetic building blocks, the paramagnetic $[Cr(CN)_6]^{3-}$ anion was used instead of the iron(III) analog, leading to $[\{Cu^{II}(tn)\}_3\{Cr^{III}(CN)_6\}_2]\cdot 3H_2O$ (**4**), which is the first 2D ferromagnet containing "-Cu–NC–Cr-" linkages. A similar study was performed using the diamagnetic $[Co(CN)_6]^{3-}$ anion, leading to $[\{Cu^{II}(tn)\}_3\{Co^{III}(CN)_6\}_2]\cdot 3H_2O$ (**5**), which is the Co analog of **4**. The magnetic properties of compounds **1**–**3** and **5** show the presence of isolated $Cu^{II}$ ions with weak ferromagnetic (**1**) or antiferromagnetic (**2**, **3**, and **5**) interactions. Compound **4** presents a long-range ferromagnetic ordering below $T_c$ = 9.5 K.

(© Wiley-VCH Verlag GmbH & Co. KGaA, 69451 Weinheim, Germany, 2006)

## Introduction

Bimetallic cyano-bridged assemblies based on polycyanometalates have attracted a great deal of attention because of their remarkable magnetic, photomagnetic, electric-field-induced conductance, catalytic, and porous properties.[1–6] Prussian blue analogs, derived from hexacyanometalate anions and hexa-solvated metal complexes, exhibit novel magnetic and electronic properties, and some of them present magnetic ordering at a critical temperature ($T_c$) as high as 376 K.[1] However, the difficulty of obtaining crystals suitable for X-ray structure determination precludes a thorough magneto-structural correlation of these 3D systems of high symmetry.[7] In order to tailor their dimensionality and connectivity, and to tune their properties, a different synthetic strategy involving two different families of cyano-bridged coordination assemblies was envisaged. The first family associates $[M(CN)_6]^{n-}$ building-block anions (M = divalent or trivalent first-row transition metal ion) and cationic assembling units of the general formula $[M'L_x(H_2O)_m]^{n+}$ (M′ = divalent first row transition metal ion; L = polyamine, macrocyclic ligand, Schiff base, ...) having selected free coordination sites, instead of simple hexa-solvated complexes;[8–11] the second one involves anionic complexes of general formula $[ML'(CN)_y]^{m-}$ as building blocks instead of the potentially hexadentate $[M(CN)_6]^{n-}$ anions.[12,13] In both families, a large number of such low-symmetry cyano-bridged assemblies display rich and fascinating structural architectures ranging from discrete polynuclear complexes[11,13] to extended 3D networks,[8–10,12] and in some cases exhibit interesting properties such as high $T_c$ magnets, high-spin molecules, or single-molecule magnets. For the first family built on $[M'L_x(H_2O)_m]^{2+}$ and $[M(CN)_6]^{n-}$ units, most of the materials are extended bimetallic compounds having a three- or four-coordinate $[M'L_x]^{2+}$ assembling block which constrains the number of adjacent hexacyanometalate building blocks to two and/or a limited dimensionality of two.[8–10] In contrast, examples in which the assembling block acts as a $\mu_4$-bridging "complex ligand" are very rare. In order to explore such extended bimetallic assemblies with higher connectivities and/or

[a] UMR CNRS 6521, Université de Bretagne Occidentale, B. P. 809, 29285 Brest Cedex, France
Fax: +33-298-017001
E-mail: triki@univ-brest.fr
[b] Instituto de Ciencia Molecular, Universitat de Valencia, Dr. Moliner 50, 46100 Burjasot, Spain
[c] Laboratoire de Chimie de Coordination, UPR CNRS 8241, 205 route de Narbonne, 31077 Toulouse Cedex, France

 © 2006 Wiley-VCH Verlag GmbH & Co. KgaA, Weinheim 

higher dimensionalities, we decided to focus on the use of two-coordinate assembling units containing the $Cu^{II}$ ion, whose versatility as regards to coordination number and geometry is well known. Reactions of the $[Fe^{III}(CN)_6]^{3-}$ anion with the $[Cu^{II}(tn)(H_2O)_n]^{2+}$ ion (tn = 1,3-diaminopropane) afford the compounds $[\{Cu^{II}(tn)\}_2\{Fe^{II}(CN)_6\}]\cdot KCl\cdot 5H_2O$ (**1**), $[\{Cu^{II}(tn)\}_2\{Fe^{II}(CN)_6\}]\cdot 4H_2O$ (**2**) and $[\{Cu^{II}(tnH)_2(H_2O)_2\}\{Fe^{II}(CN)_6\}]\cdot 2H_2O$ (**3**). Compounds **1**–**3** display 2D, 3D, and 1D structures, respectively, generated by Cu–NC–Fe bridges. For all three compounds the synthetic processes involve the spontaneous reductions of the paramagnetic $[Fe^{III}(CN)_6]^{3-}$ anion into the diamagnetic $[Fe^{II}(CN)_6]^{4-}$ anion, as previously observed for some parent complexes.[14] Therefore, despite the original structural features of these three compounds, their magnetic properties only show weak exchange couplings between $Cu^{II}$ ions through the diamagnetic $[Fe^{II}(CN)_6]^{4-}$ anion. In order to avoid this reduction, the paramagnetic $[Cr(CN)_6]^{3-}$ anion was used instead of the iron(III) analog, leading to the new compound $[\{Cu(tn)\}_3\{Cr(CN)_6\}_2]\cdot 3H_2O$ (**4**), which is the first 2D ferromagnet involving "-Cu–NC–Cr-" linkages. In order to compare with a diamagnetic $[M(CN)_6]^{3-}$ building block, similar attempts were made using the $[Co(CN)_6]^{3-}$ anion; this leads to **5**, the $Co^{III}$ analog of **4**. Herein we report the syntheses, a detailed structural discussion, and the magnetic properties of these five cyano-bridged bimetallic materials. Note that compounds **1** and **4** have recently been briefly communicated by us.[9c,10d]

## Results and Discussion

### Syntheses and Characterization

The reaction of $CuCl_2$ with $K_3[Fe^{III}(CN)_6]$ and KOH in aqueous solution in the presence of 1,3-diaminopropane (tn) affords $[\{Cu^{II}(tn)\}_2\{Fe^{II}(CN)_6\}]\cdot KCl\cdot 5H_2O$ (**1**) as brown crystals. A similar reaction with $(Et_4N)_3[Fe^{III}(CN)_6]$ and $Et_4NOH$ instead of $K_3[Fe^{III}(CN)_6]$ and KOH results in the formation of $[\{Cu^{II}(tn)\}_2\{Fe^{II}(CN)_6\}]\cdot 4H_2O$ (**2**) as prismatic black crystals. Further concentration of the filtrate afforded $[\{Cu^{II}(tnH)_2(H_2O)_2\}\{Fe^{II}(CN)_6\}]\cdot 2H_2O$ (**3**) as hexagonal, dark-green crystals after several weeks under aerobic conditions. It is likely that the synthetic procedure leading to the slow formation of **3** corresponds to a decrease of the pH by slow aerobic carbonation of the basic solution after several weeks; this allows formation of the $tnH^+$ unit since the $pK_a$ of the $tnH^+$/tn couple is around 10.5 (the pH of the solution is about 10.0).[15] Finally, the reaction of $CuCl_2$ and tn with $Cr^{III}$ or $Co^{III}$ hexacyanometalate anions in basic aqueous solution afforded compounds $[\{Cu^{II}(tn)\}_3\{Cr^{III}(CN)_6\}_2]\cdot 3H_2O$ (**4**) and $[\{Cu^{II}(tn)\}_3\{Co^{III}(CN)_6\}_2]\cdot 3H_2O$ (**5**). The crucial role of the base (KOH, $Et_4NOH$) in these experimental processes must be pointed out: the presence of this base curiously avoids the immediate precipitation of insoluble species and provides the stable two-coordinate aqueous $[Cu(tn)]^{2+}$ unit, which can then react with the hexacyanometalate anions. It is also worthy to note that all the above reactions with $[Fe^{III}(CN)_6]^{3-}$ involve, as shown by the crystal structures and magnetic measurements, its reduction into the diamagnetic $[Fe^{II}(CN)_6]^{4-}$ anion. The reason for this reduction is not clear for the moment. However, on the basis of our observations during this work and careful examination of the literature, we suggest a mechanism that successively involves (i) partial decomplexation of $CN^-$ ligands from the $[Fe^{III}(CN)_6]^{3-}$ complex which, although kinetically inert, is more reactive with regard to ligand substitution than its $Fe^{II}$ analog,[16] (ii) reduction of the aqueous $Cu^{II}$ moiety into the corresponding $Cu^{I}$ unit by the $CN^-$ ions with formation of cyanogen or cyanate,[17] and (iii) reduction of $[Fe^{III}(CN)_6]^{3-}$ into $[Fe^{II}(CN)_6]^{4-}$ by the $Cu^{I}$ species with formation of the $Cu^{II}$ species.[18] Such a $[Fe^{III}(CN)_6]^{3-}$ to $[Fe^{II}(CN)_6]^{4-}$ reduction has been observed previously for some parent $M^{II}$–L–$[Fe^{III}(CN)_6]^{3-}$ ($M = Cu^{II}$, $Ni^{II}$, $Mn^{II}$) systems.[14]

The infrared spectra of **1**–**5** exhibit the bands expected for compounds built from $[Cu(tn)]^{2+}$ and $[M(CN)_6]^{n-}$ units, the presence of the latter being clearly indicated by strong absorption bands assignable to $\nu_{CN}$ stretching vibrations in the 2000–2200 $cm^{-1}$ range. Previous studies have shown that the positions of these absorption bands in $[Fe(CN)_6]^{n-}$-containing derivatives can be used as a diagnostic tool for identifying the oxidation state of the metal ion and detecting the presence of cyanide bridges.[19] Terminal CN ligands are typically characterized by absorption bands at around 2120 $cm^{-1}$ when bonded to $Fe^{III}$ and around 2040 $cm^{-1}$ when bonded to $Fe^{II}$, the shift to lower wavenumbers upon reduction resulting from greater π back-bonding from the $Fe^{II}$ ion to the CN π* antibonding orbital.[20] Coordination of the CN ligand to a second metal ion through its nitrogen atom results in an increase of these values to around 2150–2180 $cm^{-1}$ for $[Fe(CN)_6]^{3-}$ and 2050–2110 $cm^{-1}$ for $[Fe(CN)_6]^{4-}$.[19–21] The $\nu_{CN}$ stretching vibrations are found at 2091 and 2079 $cm^{-1}$ for **1** and 2085 and 2056 $cm^{-1}$ for **2**; although unambiguous assignments are difficult, it is likely that these compounds are built from $[Fe^{II}(CN)_6]^{4-}$ units that have their six CN ligands acting as bridging units with Cu ions. For compound **3**, three absorption bands are found at 2095, 2060, and 2032 $cm^{-1}$; this is in good agreement with the presence of $[Fe^{II}(CN)_6]^{4-}$ units having at last one terminal CN ligand, as indicated by the lower wavenumber band. Similarly, compound **4** exhibits a strong absorption band at 2175 $cm^{-1}$ and two weaker ones at 2149 and 2128 $cm^{-1}$ for the bridging and terminal cyanide groups, respectively. For compound **5**, which contains the $[Co(CN)_6]^{3-}$ unit, the strongest $\nu_{CN}$ absorption is observed at 2175 $cm^{-1}$; the increase of this value with respect to the Fe compound is normal since the CN bond is strengthened as the Co–CN bond involves σ-donation from an antibonding orbital.[22] Finally, the 1,3-diaminopropane ligand is easily characterized by the presence in the IR spectrum of bands due to $\nu_{NH}$ stretching vibrations of the $NH_2$ groups in the 3350–3150 $cm^{-1}$ region and to $\nu_{CH}$ stretching vibrations of the $CH_2$ groups in the 2980–2800 $cm^{-1}$ region.[23a] For compound **3**, the supplementary weak bands observed in the 2700–2500 $cm^{-1}$ region could be tentatively

 © 2006 Wiley-VCH Verlag GmbH & Co. KGaA, Weinheim 

assigned to $\nu_{NH}$ stretching vibrations of the uncoordinated $NH_3^+$ group.

### Crystal Structures

Pertinent bond lengths and angles for compounds **1**–**5** are given in the tables below. Crystallographic data and structure-refinement parameters are given in the Experimental Section.

The crystal structure of compound **1** has been recently communicated;[9c] thus, we limit ourselves to discussing some structural features that are relevant for structural discussion of compound **2** since both present some interesting similarities despite their large structural differences. The asymmetric unit of **1** consists of one $[Fe^{II}(CN)_6]^{4-}$ anion, two $[Cu^{II}(tn)]^{2+}$ cations, one $K^+$, one $Cl^-$, and five $H_2O$ molecules, all in general positions. Figure 1 shows an ORTEP drawing of this asymmetric unit with the atom-labeling scheme and the metal-ion environments; pertinent bond lengths and bond angles are given in Table 1. The two nonequivalent copper(II) ions (Cu1 and Cu2) exhibit a $CuN_5$ geometry (Figure 1), which arises in both cases from two nitrogen atoms of the chelating tn ligand (N7 and N8 for Cu1 and N9 and N10 for Cu2) and from three nitrogen atoms of the cyano groups [N3, N4(f), and N5(d) for Cu1 and N1(a), N2, and N6(c) for Cu2]. The Cu2 ion is located in an approximately square-pyramidal geometry, as indicated by the low value of the trigonality index, $\tau$,[24] of 0.18 [$\tau = (\beta - \alpha)/60$, where $\alpha$ and $\beta$ are the two greatest basal plane angles ($\beta \geq \alpha$) when the polyhedron is viewed as a square pyramid; for a perfectly square-pyramidal geometry $\tau$ is equal to zero, and it becomes unity for a perfectly trigonal bipyramidal geometry. For Cu2, $\alpha$ = N6(c)–Cu2–N10 = 162.3(2)° and $\beta$ = N2–Cu2–N9 = 173.3(2)°]. This slightly distorted square-pyramidal geometry is in good agreement with the structural data, which indicate that the four equatorial bond lengths are equivalent [Cu2–N2 = 2.005(4), Cu2–N6(c) = 2.008(4), Cu2–N9 = 2.011(4), Cu2–N10 = 2.004(4) Å], while the Cu2–N1(a) apical bond length [2.230(5) Å] is significantly longer. For the Cu1 ion, the corresponding $\tau$ value of 0.55 [$\alpha$ = N4(f)–Cu1–N8 = 141.4(2)°, $\beta$ = N3–Cu1–N7 = 174.2(2)°] indicates that the coordination geometry of the Cu1 ion is intermediate between the two ideal geometries. This coordination geometry can be described as trigonal bipyramidal distorted square-based pyramidal in which one of the equatorial bond lengths is significantly longer [Cu1–N5(d) = 2.122(4) Å] than the other two [Cu–N4(f) = 2.027(6) and Cu1–N8 = 2.039(5) Å] and the apical bond lengths [Cu1–N3 = 2.002(4) and Cu–N7 = 2.009(4) Å].

Each iron ion, which has an almost regular octahedral geometry, is linked to six copper(II) ions by six cyanide bridges, while each copper ion is linked to three equivalent iron(II) ions. The Fe–C–N units are essentially linear while the C–N–Cu angles deviate significantly from linearity (see Table 1). This leads to an infinite $[\{Cu(tn)\}_2\{Fe(CN)_6\}]$ lamellar structure, which can also be described as a 2D layered structure generated by the defective cubane units

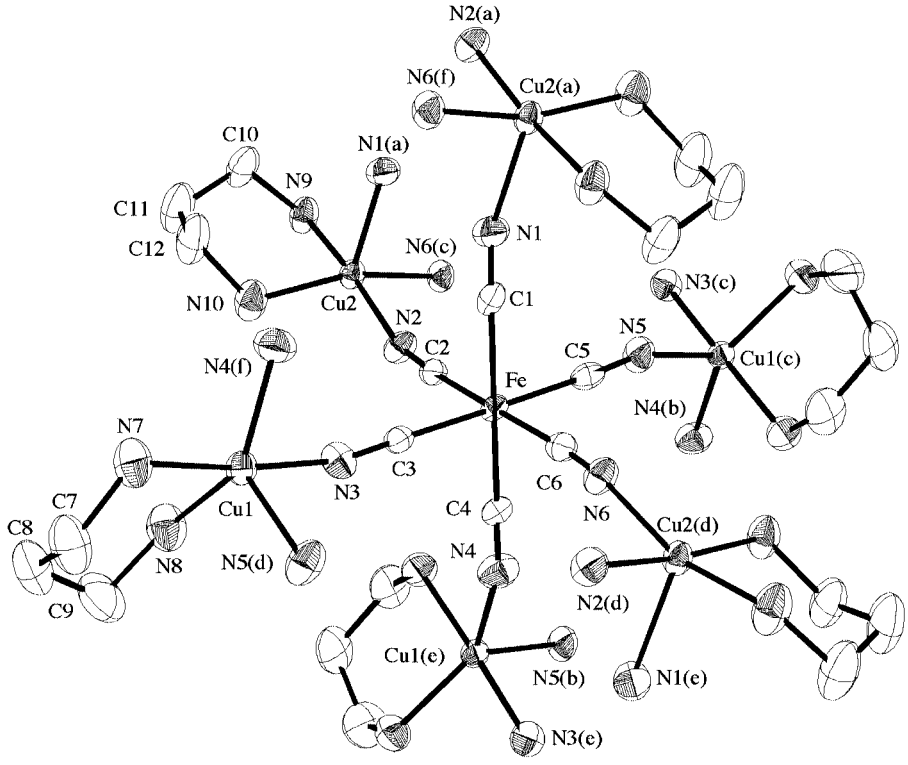


Figure 1. ORTEP view showing the atomic labeling scheme and the metal ion (M = Fe, Cu1 and Cu2) environments in compound **1** (40% probability ellipsoids). Codes of equivalent positions: (a) $-x, -y, 1 - z$; (b) $-x, -y, 2 - z$; (c) $-x, -1/2 + y, 3/2 - z$; (d) $-x, 1/2 + y, 3/2 - z$; (e) $x, 1/2 - y, 1/2 + z$; (f) $x, 1/2 - y, -1/2 + z$.

 © 2006 Wiley-VCH Verlag GmbH & Co. KGaA, Weinheim 

Table 1. Pertinent bond lengths [Å] and bond angles [°] in compound **1**.

| Fe–C–N–Cu | Fe–C | C–N | N–Cu | Fe–C–N | C–N–Cu | Fe···Cu |
|---|---|---|---|---|---|---|
| Fe–C1–N1–Cu2(a) | 1.929(6) | 1.138(8) | 2.230(5) | 175.4(4) | 156.0(4) | 5.194(1) |
| Fe–C2–N2–Cu2 | 1.918(5) | 1.145(6) | 2.005(4) | 175.3(5) | 161.2(5) | 4.980(1) |
| Fe–C3–N3–Cu1 | 1.899(4) | 1.159(6) | 2.002(4) | 178.3(4) | 162.0(5) | 4.997(1) |
| Fe–C4–N4–Cu1(e) | 1.895(6) | 1.147(8) | 2.027(6) | 178.5(4) | 160.1(4) | 4.991(1) |
| Fe–C5–N5–Cu1(c) | 1.931(4) | 1.137(6) | 2.122(4) | 176.7(5) | 159.0(5) | 5.114(1) |
| Fe–C6–N6–Cu2(d) | 1.919(5) | 1.138(6) | 2.008(4) | 175.8(5) | 163.0(5) | 4.998(1) |

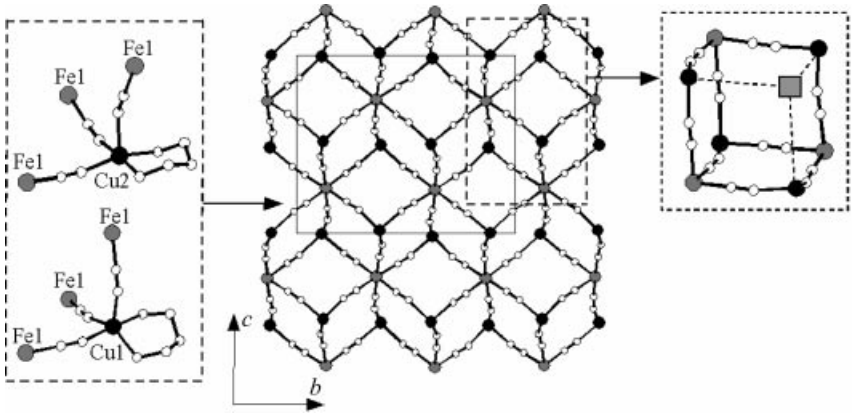


Figure 2. View of the structure of compound **1** showing the 2D arrangement generated by the square-pyramidal units of $Cu^{II}$ and a view of the "$Cu_4Fe_3$" cubane unit. The chelating tn ligands have been omitted, in the 2D arrangement, for the sake of clarity.

"$Cu_4Fe_3$", as shown in Figure 2. The distance between two neutral eclipsed parallel sheets is the *a* parameter [15.1478(3) Å], which gives rise to a large interlayer space where the chloride anions, the potassium ions, and the water molecules are accommodated. The shortest Cu···Cu distance is 6.845(1) Å.

Compound **2** crystallizes in the monoclinic system (space group $P2_1/n$); the asymmetric unit consists of one $[Fe^{II}(CN)_6]^{4-}$ anion, located at the special position (0,0,0), one $[Cu^{II}(tn)]^{2+}$ ion, and two $H_2O$ molecules, all in general positions. The copper(II) ion (Cu1) exhibits a $CuN_5$ geometry (Figure 3) arising from two nitrogen atoms of two equivalent tn ligands (N1, N5) and from three nitrogen atoms of the cyano groups (N11, N12, and N13). As for the Cu1 ion of compound **1**, the corresponding $\tau$[24] value of 0.57 [$\alpha$ = N12–Cu1–N13 = 142.9(2)°, $\beta$ = N1–Cu1–N5 = 177.0(2)°] indicates that the coordination geometry of the Cu1 ion is a trigonal bipyramidal distorted square-based pyramid with almost equivalent Cu–N bond lengths except for one of the equatorial ones [Cu–N11 = 2.228(4) Å], which is significantly longer than the other four [equatorial: Cu1–N12 = 2.001(4) and Cu1–N13 = 1.987(3) Å; apical: Cu1–N1 = 2.035(3) and Cu–N5 = 2.001(3) Å]. Examination of the N–Cu–N angles in the pseudo base plane [101.8(2), 115.3(2), 142.9(2)°] also indicates that the Cu environment deviates strongly from the ideal trigonal-bipyramidal geometry.

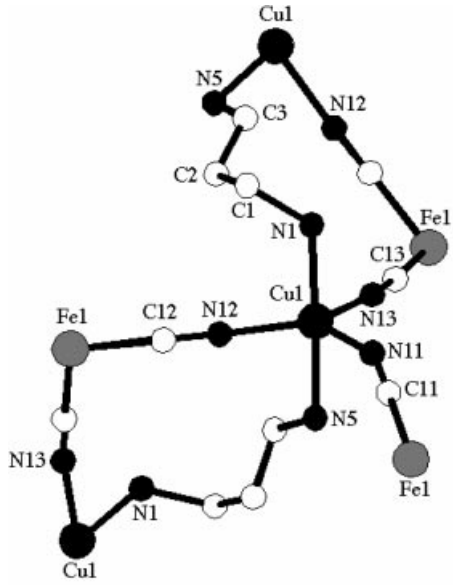


Figure 3. View of the copper ion environment in compound **2**.

As in compound **1**, the iron ion, which has an almost regular octahedral geometry, is linked to six copper(II) ions by six cyanide bridges, while the copper ion is linked to three equivalent iron(II) ions (Figure 4). This leads to a 3D

 © 2006 Wiley-VCH Verlag GmbH & Co. KGaA, Weinheim 

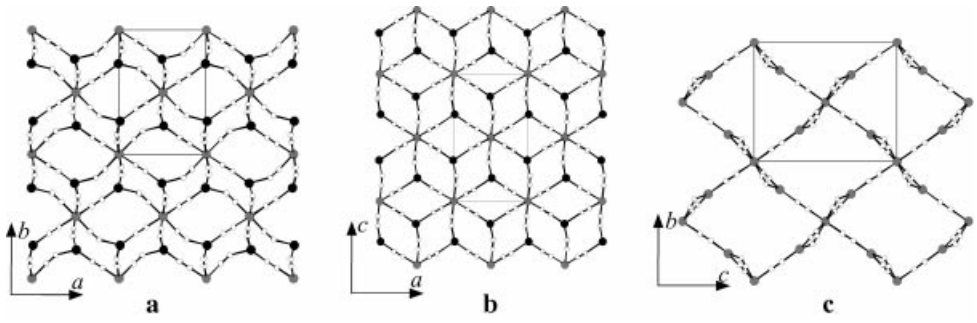


Figure 4. Projections of the structure of compound **2** in the *ab*, *ac*, and *bc* planes. In all cases, the tn ligands have been omitted for the sake of clarity.

Table 2. Pertinent bond lengths [Å] and bond angles [°] in compound **2**.

| Fe–C–N–Cu | Fe–C | C–N | N–Cu | Fe–C–N | C–N–Cu | Fe···Cu |
|---|---|---|---|---|---|---|
| Fe1–C11–N11–Cu1 | 1.930(6) | 1.157(6) | 2.228(4) | 177.5(4) | 151.8(4) | 5.149(1) |
| Fe1–C12–N12–Cu1 | 1.884(5) | 1.155(6) | 2.001(4) | 179.1(4) | 175.2(4) | 5.036(1) |
| Fe1–C13–N13–Cu1 | 1.925(4) | 1.154(4) | 1.987(3) | 177.1(5) | 168.4(5) | 5.034(1) |

arrangement in which the Fe–C–N units are essentially linear, while one of the Cu–N–C units deviates significantly from linearity (Table 2). Careful examination of this 3D arrangement shows two interesting structural features. The first one concerns the projections along the [001] and [010] directions; as shown in Figure 4, they seem to give the same lamellar structure as observed for the 2D structure of **1**. The second one concerns the unexpected coordination mode of the tn ligand; usually chelate, this unit acts in compound **2** as a bridging ligand.

To clearly describe this sophisticated structure, these two structural characteristics are detailed below. The extended structures of compounds **1** and **2** present important structural similarities: (i) they have the same chemical formula $[\{Cu^{II}(tn)\}_2\{Fe^{II}(CN)_6\}]_n$, (ii) in both structures each $Cu^{II}$ ion is linked to three $Fe^{II}$ ions while each $Fe^{II}$ ion is linked to six $Cu^{II}$ ions, and (iii) the projections of **2** along the [001] and [010] directions (parts a, b in Figure 4) seem similar to that of compound **1** along the [100] direction (Figure 2). Despite these common features, large structural differences are observed and the question now is why compound **1** displays a 2D layered structure while the structure of compound **2**, generated only by the cyanide bridges, is 3D. To clarify these differences, the best way seems to be to describe the structural arrangement of **2** on the basis of that of **1**. To simplify such complicated arrangements, the tn ligands are initially omitted. Thus, the extended arrangements of both compounds can be viewed as two different successions of the elemental units depicted in Figure 5 (trigonal pyramid for **1** and trigonal plane for **2**).

For compound **1**, the 2D structure of the "$Cu_4Fe_3$" defective cubane units depicted in Figure 2 can be easily viewed as a succession of the trigonal-pyramidal units depicted in Figure 5, while for compound **2** the trigonal planes do not allow such a structural arrangement. Thus, the projections of **2** along the [001] and the [010] directions (see a, b in Figure 4) are misleading since they are not appropriate to explain clearly the large differences between the two

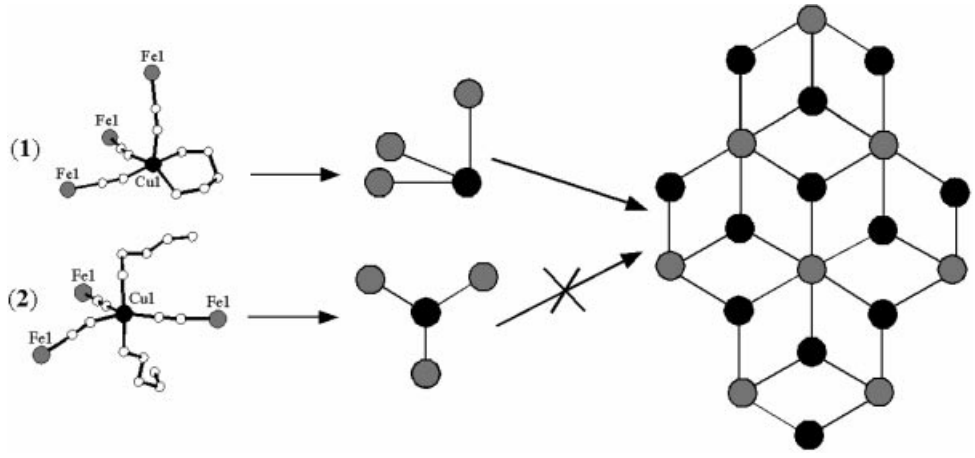


Figure 5. Schematic view showing that the 2D arrangement described as a succession of defective cubane units in compound **1** is not possible in the case of compound **2**.

 © 2006 Wiley-VCH Verlag GmbH & Co. KGaA, Weinheim 

structural arrangements. A correct description of this 3D arrangement is obtained after rotation of the unreal defective cubane unit around the *a* axis, as shown for this structure in Figure 6 (b); such a rotation shows the real geometry of this unit (Figure 6, c).

The bimetallic cyano-bridged units of **2** differ markedly from the defective cubane units observed in compound **1**, as shown by the schematic view of these units in both compounds (Figure 7).

Slight rotation around the Fe(A)–Fe(A) axis shows a nearly similar view for the structural unit and generates the 2D structure of **1**; the Cu(A) atoms are linked to the Fe(B) atoms by the CN bridges of the same unit leading, as described above, to the 2D structure parallel to the $[Cu(B)]_4$ plane. For compound **2**, a similar slight rotation around the Fe(A)–Fe(A) axis shows that the structural unit is not discrete since the Cu(A) atoms are not linked to Fe(B) atoms as observed for **1**, but linked to the Fe(A) atoms in a third direction that is orthogonal to the $[Cu(B)]_4$ plane. Finally, it is worthy to note that the unusual coordination mode of the tn ligand in compound **2** leads to a helical chain running along the [010] direction with a Cu···Cu distance of 6.719(1) Å (Figure 8). These bridges have no consequences for the structural dimension since compound **2** was described above as having a 3D structure only on the basis of the cyanide bridges.

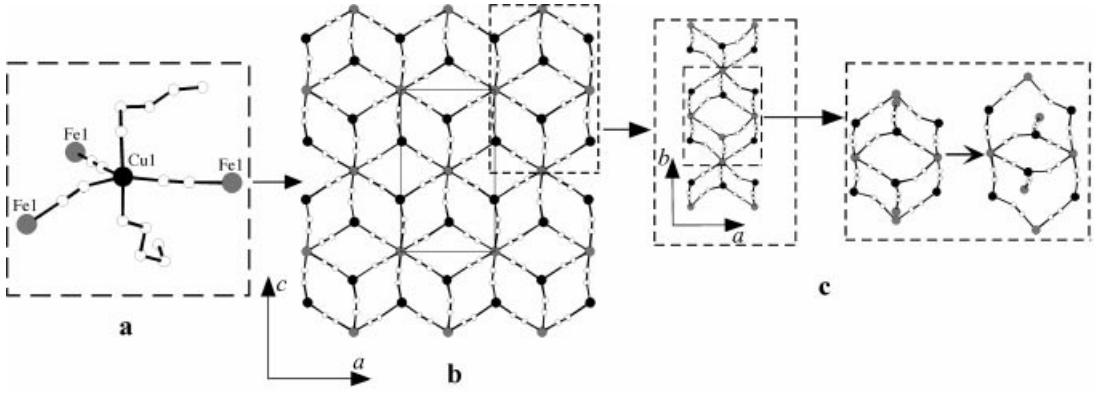


Figure 6. Careful examination of the 3D structure of compound **2**: a) scheme for the copper environment; b) projection of the structure on the *ac* plane; c) the clear structure of fragment unit after rotation around the *a* axis. In (b) and (c), the tn ligands have been omitted for the sake of clarity.

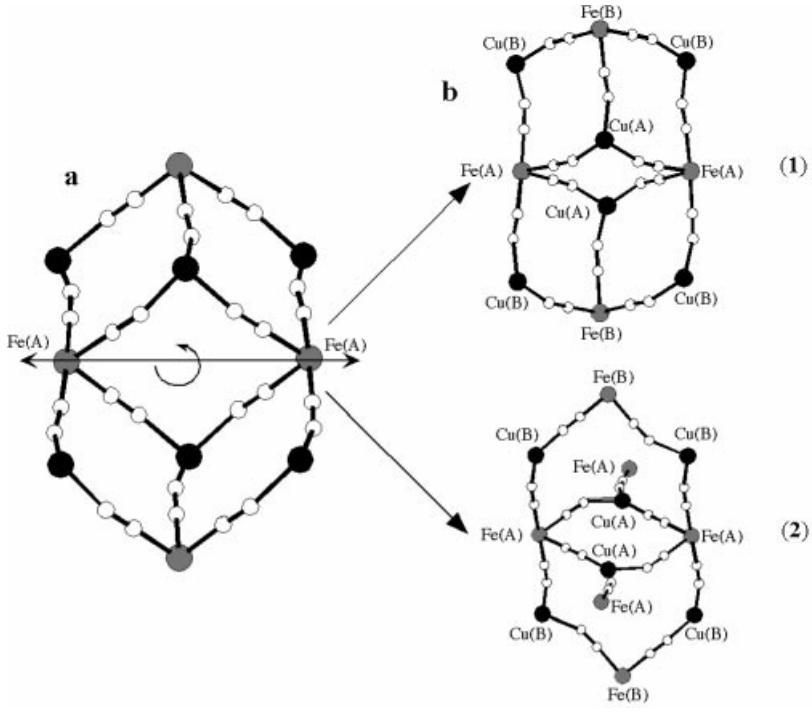


Figure 7. Fragment of the structure showing similarities and differences between compounds **1** and **2**: a) similar projections for both compounds; b) illustration of the structural differences after rotation around the Fe(A)–Fe(A) axis. The tn ligands have been omitted for the sake of clarity. A and B notations are used to indicate more clearly $[Cu(B)]_4$ and the $[Fe(A)]_4$ planes.

 © 2006 Wiley-VCH Verlag GmbH & Co. KGaA, Weinheim 

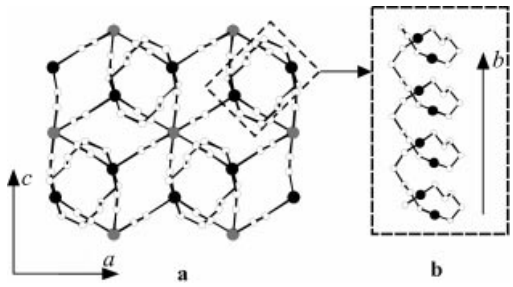


Figure 8. The bridging tn ligand in the 3D structure of compound **2**: a) projection on the *ac* plane; b) the helical chain running along the [010] direction.

Compound **3** crystallizes in the monoclinic system (space group $P2_1/n$); the asymmetric unit consists of one $[Cu(tnH)_2(H_2O)_2]^{4+}$ and one $[Fe(CN)_6]^{4-}$ unit, both localized at special positions[ (1/2,0,0) and (0,0,0) respectively], and a water molecule in a general position. Figure 9 shows this asymmetric unit with the atom labeling scheme and the coordination mode of the $[tnH]^+$ ligand. The $Cu^{II}$ ion presents a strongly elongated centrosymmetric $CuN_4O_2$ environment with four almost equivalent CuN bonds involving two N atoms of CN groups [Cu–N3 and Cu–N3$^{(b)}$: 1.961(4) Å], two N atoms of tn [Cu–N4 and Cu–N4$^{(d)}$: 2.044(4) Å], and two elongated CuO bonds [Cu–O2$^{(e)}$ and Cu–O2$^{(f)}$: 2.633(4) Å] (Figure 10). The $Fe^{II}$ ion presents an almost perfect octahedral $FeC_6$ coordination [Fe–C bond lengths from 1.914(5) to 1.921(4) Å]. The structure can be described as being formed by linear chains with alternating $[Cu(tnH)_2(H_2O)_2]^{4+}$ and $[Fe(CN)_6]^{4-}$ units linked by a CN bridge (Figure 9). Within a chain, each $[Fe(CN)_6]^{4-}$ is bonded to two Cu ions by two CN groups in a *trans* configuration while each $[Cu(tnH)_2(H_2O)_2]^{4+}$ acts as a $\mu_2$ ligand and not $\mu_3$ as described above for compounds **1**–**2**; the shortest Cu···Fe and Cu···Cu intrachain distances correspond to the *a*/2 and *a* parameter [*a* = 10.0586(4) Å], respectively. It is worthy to note that the tn unit in **3** is protonated; the $tnH^+$ ligand presents a monodentate coordination mode, with the protonated amine group being uncoordinated (Figure 9).

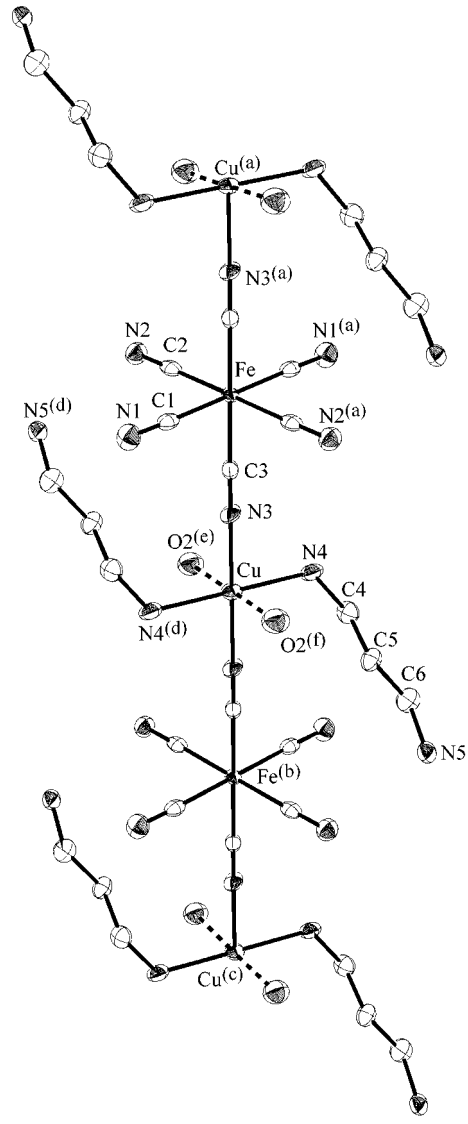


Figure 9. 1D structure of compound **3** showing the atomic labeling scheme and the terminal protonated $[tnH]^+$ ligand (30% probability ellipsoids). Codes of equivalent positions: (a) –*x*, –*y*, –*z*; (b) –1 + *x*, *y*, *z*; (c) 2 – *x*, –*y*, –*z*; (d) –1 – *x*, –*y*, –*z*; (e) –1/2 + *x*, –1/2 – *y*, –1 + *z*; (f) –1/2 – *x*, 1/2 + *y*, 1/2 – *z*.

Compounds **4** and **5** are isostructural and crystallize in the orthorhombic system (space group *Pbcn*). The asymmetric unit contains one $[M(CN)_6]^{3-}$ anion, located at a general position, and two $[Cu(tn)]^{2+}$ (Cu1 and Cu2) ions at special positions (1/2,*y*,1/4). Figure 10 shows an ORTEP drawing of this asymmetric unit with the atom-labeling scheme and the coordination polyhedra of the metal ions; pertinent bond lengths and bond angles of **4** and **5** are given in Table 3. In both structures, the Cu1 atom exhibits a distorted $CuN_5$ coordination environment (Figure 10) arising from two nitrogen atoms of a chelating tn ligand (N7, N8) and three nitrogen atoms from CN groups [N1, N2(a), and N3$^{(f)}$]. The value of the trigonality index $\tau$[24] is 0.22 for **4** [$\alpha$ = N3$^{(f)}$–Cu1–N7 = 159.2(3)°, $\beta$ = N1–Cu1–N8 = 172.4(3)°] and 0.20 for **5** [$\alpha$ = N3$^{(f)}$–Cu1–N7 = 159.1(2)°, $\beta$ = N1–Cu1–N8 = 171.0(2)°]. In agreement with these low values, the coordination geometry of the Cu1 environment can be described in both cases as distorted square-pyramidal, with an apical bond length 0.15–0.18 Å longer than the four equatorial ones. The coordination polyhedron of the Cu2 atom differs strongly from that of Cu1 and can be described as a $CuN_4N_2$ elongated octahedron generated by a $CuN_4$ equatorial plane arising from two nitrogen atoms of the chelating tn ligand [N9 and N9(a)] and two equivalent nitrogen atoms of CN groups [N4 and N4(a)], and two axial positions defined by two equivalent nitrogen atoms [N5(b) and N5(c)] of CN groups, the two axial Cu–N5 bond lengths being approximately 0.6 Å longer than the other four in both cases, as shown in Figure 10 and Table 3.

Each $M^{III}$ ion, although bound to six carbon atoms arising from one terminal and five bridging CN ligands, presents an almost regular octahedral coordination geometry, the Cr–C bond lengths being, as usually observed, 0.15–0.18 Å longer than the Co–C ones. In both cases, the ex-

 © 2006 Wiley-VCH Verlag GmbH & Co. KGaA, Weinheim 

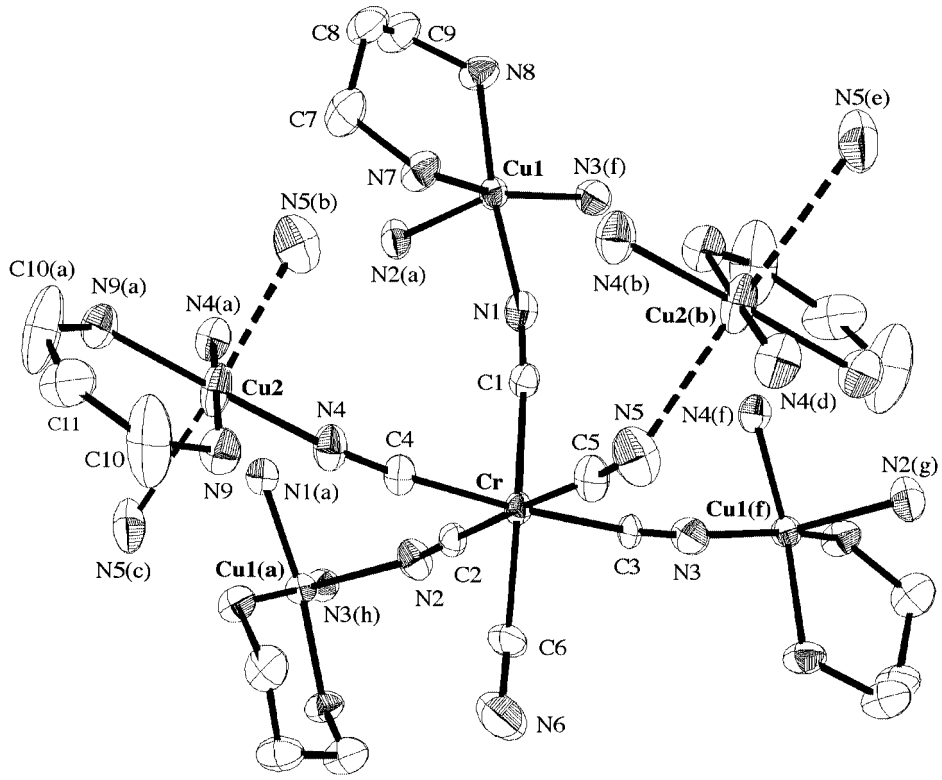


Figure 10. ORTEP view showing the atomic labeling scheme and the metal ion (Cr, Cu1, and Cu2) environments in compound **4** (40% probability ellipsoids). Codes of equivalent positions: (a) 1 – *x*, *y*, 1/2 – *z*; (b) 1 – *x*, 1 – *y*, – *z*; (c) –*x*, 1 – *y*, 1/2 + *z*; (d) *x*, 1 – *y*, –1/2 + *z*; (e) 1 – *x*, *y*, –1/2 – *z*; (f) 1 – *x*, –*y*, –*z*; (g) *x*, –*y*, –1/2 + *z*; (h) *x*, –*y*, 1/2 + *z*.

Table 3. Pertinent bond lengths [Å] and bond angles [°] in **4** and **5**.

| M–CN–Cu | M–C | C–N | M–C–N | Cu1–N | Cu2–N | Cu1–N–C | Cu2–N–C | M···Cu |
|---|---|---|---|---|---|---|---|---|
| Cr–C1–N1–Cu1 | 2.047(7) | 1.126(9) | 173.6(6) | 2.014(7) | | 171.0(6) | | 5.153(1) |
| Co–C1–N1–Cu1 | 1.885(5) | 1.141(6) | 176.5(4) | 1.977(4) | | 167.2(4) | | 4.965(1) |
| Cr–C2–N2–Cu1(a) | 2.071(7) | 1.144(9) | 174.7(6) | 2.195(7) | | 147.9(5) | | 5.164(1) |
| Co–C2–N2–Cu1(a) | 1.893(5) | 1.149(6) | 177.0(4) | 2.204(4) | | 145.1(4) | | 4.989(1) |
| Cr–C3–N3–Cu1(f) | 2.049(6) | 1.141(8) | 173.7(6) | 2.028(6) | | 172.2(6) | | 5.187(1) |
| Co–C3–N3–Cu1(f) | 1.893(5) | 1.141(6) | 175.1(4) | 2.011(4) | | 170.8(4) | | 5.015(1) |
| Cr–C4–N4–Cu2 | 2.042(7) | 1.164(8) | 173.3(6) | | 2.005(6) | | 174.7(6) | 5.190(1) |
| Co–C4–N4–Cu2 | 1.894(5) | 1.135(6) | 175.7(5) | | 2.011(4) | | 170.7(4) | 5.013(1) |
| Cr–C5–N5–Cu2(b) | 2.059(8) | 1.14(1) | 177.2(7) | | 2.569(8) | | 140.0(6) | 5.392(1) |
| Co–C5–N5–Cu2(b) | 1.884(5) | 1.152(6) | 178.5(5) | | 2.617(5) | | 140.7(4) | 5.312(1) |
| Cr–C6–N6 | 2.070(8) | 1.12(1) | 176.3(10) | | | | | |
| Co–C6–N6 | 1.888(5) | 1.153(7) | 177.1(5) | | | | | |

tended structure can be more clearly described by taking the twelve-membered tetrametallacycle M–CN–Cu–NC–M–CN–Cu–NC as the elemental unit. The molecular arrangement can be seen as a zig-zag "chain" of such "MCuMCu" cycles sharing alternatively one side (Cu1M) and one vertex (Cu1), as shown in Figure 11 (a). The adjacent "chains" are connected to each other through the CN bridges (M–C5–N5–Cu2) to lead to the neutral 2D structure depicted in part b of Figure 11.

As shown in Figure 12, the chelating tn ligands are oriented out of the plane of the bimetallic layers; this imposes a large separation between adjacent layers (adjacent layer distance: *a*/2; shortest Cu–M interlayer distance: ca. 7.0 Å), which is responsible for the presence of the nonbridging C(6)N(6) nitrile group. Careful examination of the 3D structure of $[Mn(en)]_3\{Cr(CN)_6]_2 \cdot 4H_2O$ (**6**), reported by Okawa et al.,[25] shows remarkable structural similarities with the 2D structures of **4** and **5**. Despite important differ-

 © 2006 Wiley-VCH Verlag GmbH & Co. KGaA, Weinheim 

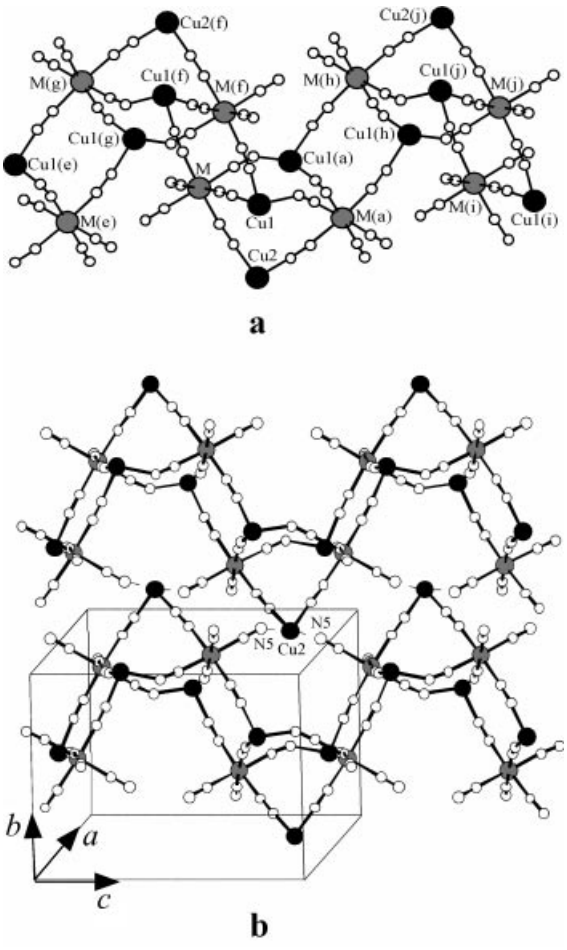


Figure 11. Structure of compounds **4** and **5**: a) schematic view of a zigzag chain unit; b) 2D arrangement. The tn chelating ligands have been omitted for clarity. Codes of equivalent positions: (a) 1 – *x*, *y*, 1/2 – *z*; (e) 1 – *x*, *y*, –1/2 – *z*; (f) 1 – *x*, –*y*, –*z*; (g) *x*, –*y*, –1/2 + *z*; (h) *x*, –*y*, 1/2 + *z*; (i) *x*, *y*, 1 + *z*; (j) 1 – *x*, –*y*, 1 – *z*.

ences related essentially to their dimensionalities, the 3D structure of **6** can be easily described from the 2D structure of **4** and **5** by taking into account that the cyano group, which is terminal in the latter [C(6)N(6)], adopts a bridging coordination mode in **6** (see Figures 10 and 12). This supplementary cyano bridge may be explained by the presence of the en ligand in **6**, which has a lower steric hindrance than the tn ligand.

### Magnetic Properties

The magnetic properties for compounds **1**–**3** and **5** are displayed in Figure 13 as the thermal variation of the $\chi_m T$ product ($\chi_m$ being the molar magnetic susceptibility per formula unit). Compounds **2**, **3**, and **5** show similar behaviors, with a constant $\chi_m T$ value from room temperature down to low temperatures (20–30 K); below this temperature, they show smooth decreases of the $\chi_m T$ product due to weak antiferromagnetic interactions between $Cu^{II}$ ions through the diamagnetic hexacyanometalate building block anions in the $d^6$ low-spin configuration {$[Fe^{II}(CN)_6]^{4-}$ for compounds **2** and **3** and $[Co^{III}(CN)_6]^{3-}$ for compound **5**}. Compound **1** displays the same behavior in the high-temperature range but shows an increase in the $\chi_m T$ value at low temperatures, which is characteristic of weak, but significant, ferromagnetic interactions between $Cu^{II}$ ions through the diamagnetic building block anion.

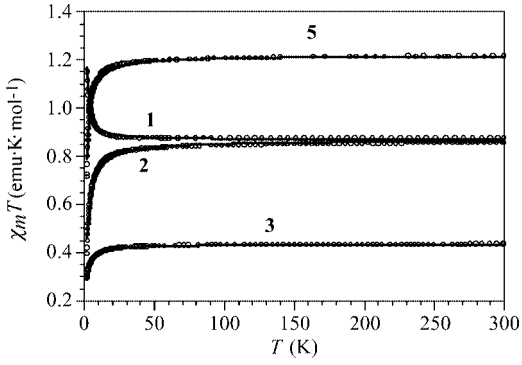


Figure 13. Thermal variation of $\chi_m T$ for compounds **1**, **2**, **3**, and **5**. Solid lines are the best fits to the Curie–Weiss law (see text).

These behaviors indicate that the four compounds behave essentially as paramagnets with weak $Cu^{II}$–$Cu^{II}$ magnetic

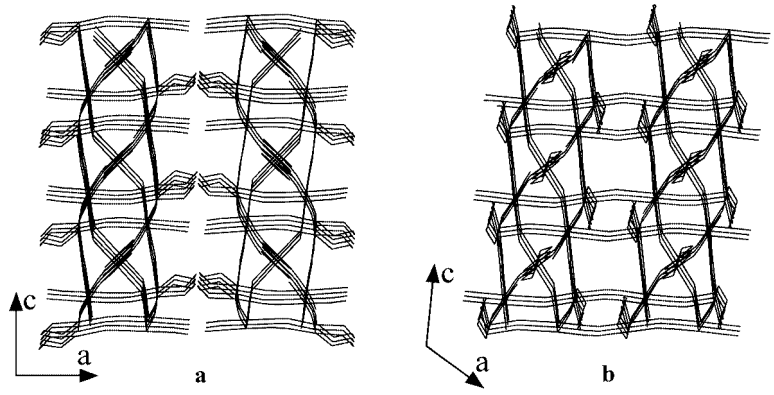


Figure 12. a) Schematic view of two adjacent layers in compounds **4** and **5** showing the nonbridging CN groups and the chelating tn ligands; b) view of the 3D arrangement of compound **6** (obtained from crystal data given in the cif file of ref.[25]); the nonbridging CN group observed in **4** and **5** is bridging here.

 © 2006 Wiley-VCH Verlag GmbH & Co. KGaA, Weinheim 

interactions, as expected from the structural data that show that the $Cu^{II}$ ions are quite well isolated due to the diamagnetic building blocks that preclude the existence of significant exchange interactions between the $Cu^{II}$ ions. Thus, for each of these four compounds, the magnetic data can be very well reproduced with a simple Curie–Weiss law: $\chi_m = C/(T - \theta)$. In all cases, this expression gives a very satisfactory agreement with the experimental data in the whole temperature range (solid lines in Figure 13) with the sets of parameters displayed in Table 4; these results corroborate the presence of weak ferromagnetic interactions in **1** and weak antiferromagnetic interactions in **2**, **3**, and **5**.

Table 4. Magnetic parameters for compounds **1**–**3** and **5**.

| | $Cu^{II}_nM$ | $C$ [emu K mol$^{-1}$] | $g$ | $\Theta$ [K] |
|---|---|---|---|---|
| **1** | $Cu^{II}_2Fe^{II}$ | 0.869(1) | 2.152 | +0.515(3) |
| **2** | $Cu^{II}_2Fe^{II}$ | 0.866(1) | 2.149 | –1.76(2) |
| **3** | $Cu^{II}Fe^{II}$ | 0.435(1) | 2.153 | –0.97(2) |
| **5** | $Cu^{II}_3Co^{III}$ | 1.218(3) | 2.081 | –0.98(2) |

A confirmation of the spin ground-state and the weak magnetic interactions in compounds **1**, **2**, **3**, and **5** comes from the isothermal magnetization of these compounds at 2 K. In all cases, the magnetization can be well reproduced with a Brillouin function for one (**3**), two (**1** and **2**), or three (**5**) independent $S = 1/2$ ions with reduced (**2**, **3**, and **5**) or increased (**1**) $g$ values accounting for the weak interactions observed at low temperatures. The magnetic behavior of **1** is similar to that observed in the previously reported compound $[Cu^{II}(en)(H_2O)\}_2\{Fe^{II}(CN)_6]\cdot 4H_2O$, which contains Cu–NC–$Fe^{II}$–CN–Cu bridges.[23b] In this compound, the nature of the ferromagnetic coupling was explained as having two possible origins: (i) intrachain interactions through the diamagnetic -NC–$Fe^{II}$–CN- bridges, or (ii) interchain interactions through double end-on cyanide bridges. As shown above, the crystal structure of **1** involves infinite 2D sheets that are eclipsed and about 15.0 Å apart. This large distance means that the adjacent sheets are well isolated and precludes consideration of any inter-sheet interaction. Thus, the weak magnetic coupling in **1** can be attributed to the interaction between $Cu^{II}$ ions through the diamagnetic -NC–$Fe^{II}$–CN- bridges. Note that such an assignment needs more experimental support but examples involving extended and discrete cyano-bridged compounds with similar diamagnetic -NC–M–CN- bridges (M = $Fe^{II}$ in $[Fe(CN)_6]^{4-}$, M = $Fe^{III}$ in $[Fe(CN)_5(NO)]^{2-}$, and M = $Co^{III}$ in $[Co(CN)_6]^{3-}$) between $Cu^{II}$ ions are very rare.[13e,23,26,27] However, such diamagnetic bridges lead to the same situation in some $Ni^{II}$–$Fe^{II}$ and $Mn^{II}$–$Fe^{II}$ bimetallic compounds;[14a,14b,26d,28] taking into consideration the electronic configuration of $Ni^{II}(t_{2g}^6e_g^2)$ or $Mn^{II}$ $(t_{2g}^3e_g^2)$ and $Fe^{II}$ $(t_{2g}^6e_g^0)$, a σ-superexchange pathway between $Ni^{II}$ (or $Mn^{II}$) ions through the empty $d_\sigma$ orbital of the $Fe^{II}$ ion was proposed to explain the ferromagnetic exchange coupling. Thus, it seems likely that a similar ferromagnetic behavior occurs in compound **1** even if the $Cu^{II}$ ion presents a nonoctahedral environment. Consequently, such ferromagnetic behavior should also occur in compounds **2** and **3** instead of the weak antiferromagnetic or the paramagnetic behavior actually observed. For compound **5**, which also involves diamagnetic bridges between $Cu^{II}$, the weak antiferromagnetic behavior observed is similar to those of a few examples recently reported.[27] Finally, on the basis of this study and on some reported examples involving diamagnetic -NC–M–CN- bridges between $Cu^{II}$ ions, we can conclude, as expected from the structural data (Cu···Cu ≥ 6.7 Å), that weak magnetic interactions occur through such diamagnetic bridges. In contrast, a clear exchange mechanism concerning the nature of the magnetic coupling needs more examples of M–$Cu^{II}$ cyano-bridged bimetallic compounds.

As expected, substitution of the diamagnetic $[Co(CN)_6]^{3-}$ anion by the paramagnetic $S = 3/2$ $[Cr(CN)_6]^{3-}$ anion results in a drastic modification of the magnetic properties, as will be shown below. The thermal variation of the molar magnetic susceptibility ($\chi_m$) of compound **4** shows an abrupt increase below about 15 K (maximum slope at about 11 K) followed by an almost saturation at low temperatures (Figure 14). This behavior suggests the presence of a long-range ordering in this compound below about 10 K. The thermal variation of the $\chi_m T$ product (per "$Cu_3Cr_2$" formula unit) shows a room-temperature value of about 5.0 emu K mol$^{-1}$, which is close to the expected value (4.875 emu K mol$^{-1}$) for three noninteracting $Cu^{II}$ ($S = 1/2$) and two $Cr^{III}$ ($S = 3/2$) ions with $g = 2$ (inset in Figure 14). On cooling the sample, the $\chi_m T$ product shows a continuous increase, which is indicative of a ferromagnetic coupling between the $Cr^{III}$ and $Cu^{II}$ ions in **4**. In fact, the magnetic susceptibility of **4** follows a Curie–Weiss law above about 100 K with $C = 4.97(1)$ emu K mol$^{-1}$ and $\theta = +46.0(2)$ K; note that the positive sign of $\theta$ confirms the presence of dominant ferromagnetic interactions between neighboring $Cr^{III}$ and $Cu^{II}$ ions. On cooling the sample further, the $\chi_m T$ product shows a maximum of about 58 emu K mol$^{-1}$ at about. 11 K; below this temperature the $\chi_m T$ product decreases sharply, due to saturation effects of the $\chi_m$ at low temperatures, to reach a value of around 15 emu K mol$^{-1}$ at 2 K (inset in Figure 14).

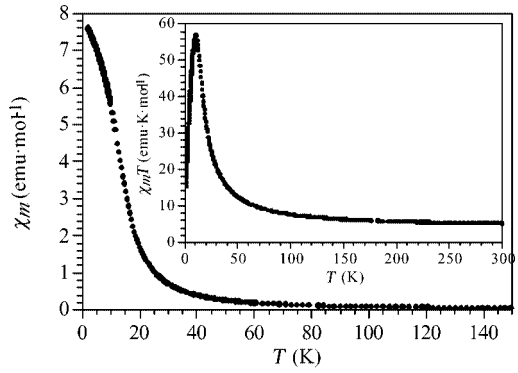


Figure 14. Thermal variations of $\chi_m$ and $\chi_m T$ (inset) for compound **4**.

To confirm the ferromagnetic nature of the long-range order transition and to determine the exact transition temperature, we performed magnetic susceptibility measure-

 © 2006 Wiley-VCH Verlag GmbH & Co. KGaA, Weinheim 

ments in an alternating field (AC susceptibility, Figure 15). These measurements show: (i) a frequency-independent peak at about 9.0 K and an additional frequency-dependent shoulder at lower temperatures in the in-phase susceptibility ($\chi'_m$) ,and (ii) a non-zero frequency-independent out-of-phase susceptibility ($\chi''_m$) below about 9.5 K that presents a frequency-dependent broad maximum at lower temperatures (3.6–4.7 K). From these data, we can conclude that compound **4** presents a ferromagnetic long-range ordering and that the ordering temperature is about 9.5 K. Furthermore, the presence of the frequency-dependent shoulders (in $\chi'_m$) and broad maxima (in $\chi''_m$) suggests that the movement of the domain walls in the ferromagnetically ordered phase is strongly hindered below about 5 K. A possible explanation is that the magnetic transition at 9.5 K corresponds to a ferromagnetic ordering within the layer (which is frequency independent, as observed in the $\chi'_m$ peak at about 9.0 K), and that at lower temperatures (below ca. 5 K) the dipolar coupling induces a 3D ferromagnetic ordering in which the domain walls are anchored.

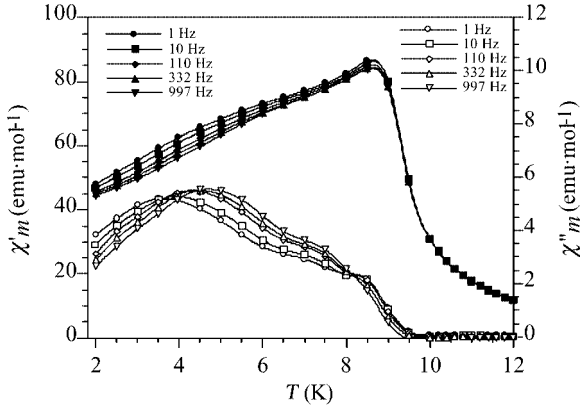


Figure 15. Thermal variation of the in-phase ($\chi'_m$, filled symbols, left scale) and out-of-phase ($\chi''_m$, empty symbols, right scale) signals of compound **4** at 1, 10, 110, 332, and 997 Hz (circles, squares, rhombs, up-triangles and down-triangles, respectively).

In this case, the frequency dependence of $\chi'_m$ can be related to the activation energy required to unlock these domain walls. This activation energy ($E_a$) can be deduced from the frequency dependence of the maximum of $\chi''_m$, which follows an Arrhenius la w, as $E_a$ = 112(2) K. An additional proof comes from the fact that the application of increasing DC fields in the AC measurements reduces the shoulder in $\chi'_m$ and the broad maximum in $\chi''_m$; both features disappear when the DC field is above about 100 mT (Figure 16). Furthermore, the temperature of these two features decreases as the DC field increases (Figure 16), indicating, as expected, that the magnetic field helps the unlocking of the domain walls. A very similar behavior has recently been observed in $[Ni(trans\text{-}C_6H_{14}N_2)_2]_3\{Fe(CN)_6]_2\cdot 2H_2O$, a similar layered cyanide-bridged bimetallic ferromagnet ($T_c$ = 14.0 K, $E_a$ = 111.6 K) with the same stoichiometric $M^{II}_3$-$M^{III}_2$ ratio[8g] and in the two pure enantiomeric derivatives of the same compound obtained with *trans*-(1*S*,2*S*)-$C_6H_{14}N_2$ and *trans*-(1*R*,2*R*)-$C_6H_{14}N_2$ ($T_c$ = 13.8 K, $E_a$ = 156 K).[8h] Note that the ordering temperature of **4** ($T_c$ = 9.5 K) is lower than that reported for the 3D compound $[Cu(EtOH)_2][Cu(en)]_2\{Cr(CN)_6]_2$ ($T_c$ = 57 K),[10e] which was previously the only known example of a cyano-bridged $Cu_3Cr_2$ ferromagnet. The difference in the ordering temperature can be related to the lower dimensionality and/or to the lower Cr–Cu exchange interactions of **4** as a result

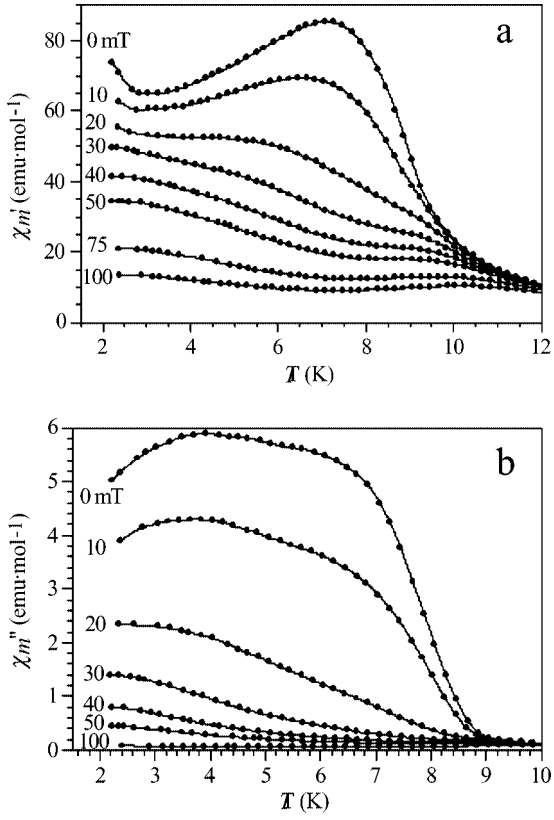


Figure 16. Thermal variation of the in-phase (a) and out-of-phase (b) signals of compound **4** at 3000 Hz with different applied DC magnetic fields.

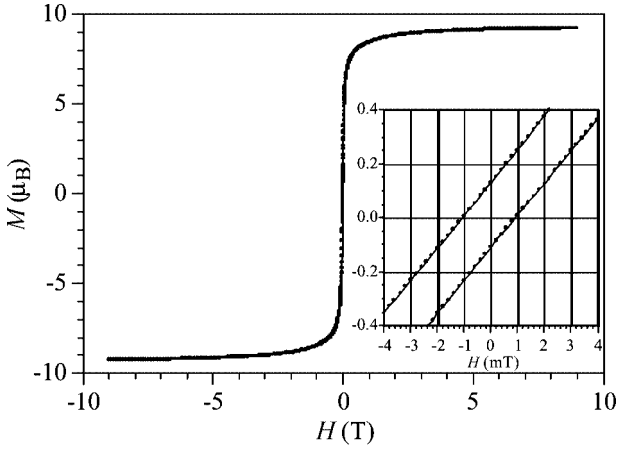


Figure 17. Hysteresis cycles at 2 K for compound **4**. The inset shows the low-field region.

 © 2006 Wiley-VCH Verlag GmbH & Co. KGaA, Weinheim 

of the different Cu–CN–Cr angles observed in both compounds.

An additional proof of the ferromagnetic nature of the long-range ordering comes from the isothermal magnetization of **4** at 2 and 5 K, which shows (i) a rapid saturation of the magnetization for magnetic fields above about 0.5 T (Figure 17), (ii) a saturation value of around 9.2 $\mu_B$, which is the expected value for the parallel alignment of three $S = 1/2$ plus two $S = 3/2$ spins with a $g$ value close to 2, and (iii) a hysteresis with small and similar coercive fields of 1.0 mT at 2 and 5 K, indicating that **4** is a soft ferromagnet.

## Conclusions

This study involves the design of some new bimetallic materials that contain a hexacyanometalate $[M(CN)_6]^{n-}$ ion and a two-coordinate $[CuL]^{2+}$ unit (L = $H_2NCH_2CH_2CH_2NH_2$). With $[Fe(CN)_6]^{3-}$, spontaneous Fe reduction was observed to afford the $[Fe(CN)_6]^{4-}$ ion. This diamagnetic building block leads to three new Cu–Fe combinations corresponding to different diamine coordination modes: chelating, bridging, and terminal, with protonation of one of the $NH_2$ groups. These three bimetallic compounds, for which magnetic properties only show weak exchange couplings between $Cu^{II}$ ions through diamagnetic hexacyanometalate bridges, have original 1D or 2D structures whose dimensionalities seems to be related to the coordination mode of the diamine unit. In order to obtain interesting magnetic behavior with paramagnetic building blocks, similar studies were performed using the $S = 3/2$ $[Cr(CN)_6]^{3-}$ building block; this leads to the first 2D ferromagnet involving Cr–CN–Cu linkages. Despite important differences related essentially to their dimensionality, this compound, $[Cu(H_2NCH_2CH_2CH_2NH_2)\}_3\{Cr(CN)_6]_2 \cdot 3H_2O$, and the recently reported $[Mn(H_2NCH_2CH_2NH_2)][Cr(CN)_6]\cdot 4H_2O$ show some remarkable structural similarities. These results, associated with some others already reported in the literature, show the ability of the $[M(CN)_6]^{n-}/[CuL]^{2+}$ system to afford a wide variety of bimetallic combinations depending not only on the nature of M and L but also on other parameters such as the pH and the nature of the counteranions. Extension of this study to other amine ligands and to other experimental conditions is in progress in order to obtain a more unified view of the structural data/magnetic behavior relationship in these bimetallic combinations.

## Experimental Section

**General:** All reagents were purchased from commercial sources and used as received. $(Et_4N)_3[Fe^{III}(CN)_6]$ and $(Et_4N)_3[Co^{III}(CN)_6]$ were prepared from the corresponding potassium hexacyanometalate in two steps via the corresponding silver salt with a procedure adapted from that reported by Le Magueres,[29] using acetonitrile as solvent instead of water. Elemental analyses were obtained from the Service Central d'Analyses (Vernaison) and Service de Micro-analyses de ICSN-CNRS (Gif-sur-Yvette). Infrared spectra were recorded in the range 4000–200 $cm^{-1}$ as KBr pellets on a FT-IR Nexus Nicolet spectrometer. Variable temperature susceptibility measurements were carried out in the temperature range 2–300 K with applied magnetic fields of 0.1 T on polycrystalline samples for all the compounds with a Quantum Design MPMS-XL-5 SQUID magnetometer. The susceptibility data were corrected for the sample holders previously measured using the same conditions and for the diamagnetic contributions of the salt, as deduced by using Pascal's constant tables. For **4**, the AC susceptibility measurements were performed in the temperature range 2–20 K with an alternating field of 0.395 mT at different frequencies in the 1–1000 Hz range with the SQUID susceptometer and with an alternating field of 1.7 mT at different frequencies in the 1–10 kHz range applying different DC magnetic fields (between 0 and 100 mT) with a Quantum Design Physical Properties Measurement System, PPMS-9.

**Synthesis of $[\{Cu^{II}(tn)\}_2\{Fe^{II}(CN)_6\}]\cdot KCl\cdot 5H_2O$ (1) (tn = 1,3-diaminopropane):** This compound was prepared as brown crystals by a procedure similar to that given below for **2**, from $K_3[Fe^{III}(CN)_6]$ (0.66 g, 2.0 mmol) and KOH (0.67 g, 12.0 mmol) instead of $(Et_4N)_3[Fe^{III}(CN)_6]$ and $Et_4NOH$. This procedure and the analytical and IR data of **1** have been previously communicated.[9c] Yield: 0.52 g (40%).

**Synthesis of $[\{Cu^{II}(tn)\}_2\{Fe^{II}(CN)_6\}]\cdot 4H_2O$ (2) and $[\{Cu^{II}(tnH)_2(H_2O)_2\}\{Fe^{II}(CN)_6\}]\cdot 2H_2O$ (3):** 1,3-Diaminopropane (1.0 mL, 12.0 mmol) was added under aerobic conditions to a concentrated aqueous solution (5 mL) of $CuCl_2\cdot 2H_2O$ (2.05 g, 12.0 mmol) with continuous stirring, leading to the immediate precipitation of a green powder. An aqueous solution of $Et_4NOH$ (0.52 g, 3.5 mmol) was then added with stirring and the resulting dark-blue solution was warmed (ca. 60 °C for about 5 min) and then filtered in order to remove the small amount of precipitate that remained. An aqueous solution (20 mL) of $(Et_4N)_3[Fe^{III}(CN)_6]$ (3.62 g, 6.0 mmol) was then added with continuous stirring. Slow concentration of the resulting solution at room temp. afforded prismatic black crystals of **2**, which were filtered and air-dried. Further evaporation afforded hexagonal dark green crystals of **3** after several weeks under aerobic conditions; these were filtered and air-dried.

**2:** Yield: 0.84 g (25%). $C_{12}H_{28}Cu_2FeN_{10}O_4$ (559.38): calcd. C 25.77, H 5.05, Cu 22.72, Fe 9.98, N 25.04; found C 25.68, H 5.02, Cu 22.61, Fe 9.85, N 25.13. IR: $\tilde{\nu}$ = 3588 m $cm^{-1}$, 3517 br, 3388 br, 3300 m, 3285 m, 3251 m, 3169 m, 2950 w, 2936 w, 2884 w, 2085 s, 2056 s, 1608 m, 1471 m, 1228 w, 1190 w, 1136 w, 1104 w, 1068 w, 1047 w, 1030 w, 667 br, 583 m, 462 br, 398 br.

**3:** Yield: 0.90 g (30%). $C_{12}H_{30}CuFeN_{10}O_4$ (497.82): calcd. C 28.95, H 6.07, Cu 12.76, Fe 11.22, N 28.14; found C 28.83, H 6.18, Cu 12.90, Fe 10.99, N 28.07. IR: $\tilde{\nu}$ = 3519 m $cm^{-1}$, 3384 br, 3277 s, 3235 s, 3166 m, 3014 br, 2979 m, 2888 m, 2819 m, 2705 w, 2613 w, 2526 w, 2492 w, 2095 s, 2060 s, 2032 s, 1685 w, 1660 w, 1618 w, 1604 m, 1497 m, 1477 w, 1411 w, 1335 w, 1242 w, 1214 m, 1144 w, 1102 w, 1062 w, 1038 w, 1004 w, 950 w, 754 m, 659 w, 584 m, 493 br, 419 w.

**Synthesis of $[\{Cu^{II}(tn)\}_3\{Cr^{III}(CN)_6\}_2]\cdot 3H_2O$ (4):** This compound was prepared as blue crystals by a procedure similar to that given below for **5**, from $(Et_4N)_3[Cr^{III}(CN)_6]$ (3.59 g, 6.0 mmol) instead of $(Et_4N)_3[Co^{III}(CN)_6]$. This procedure and analytical data have been previously communicated.[10d] Yield: 1.06 g (40%). IR: $\tilde{\nu}$ = 3627 m $cm^{-1}$, 3482 br, 3359 m, 3323 m, 3243 m, 3159 m, 2952 w, 2892 w, 2175 s, 2149 w, 2128 w, 1595 m, 1462 w, 1445 w, 1407 w, 1278 w, 1250 w, 1161 s, 1143 m, 1106 w, 1075 w, 1033 w, 1013 m, 914 m, 885 w, 677 w, 614 w, 493 s, 466 s, 378 m, 354 m.

**Synthesis of $[\{Cu^{II}(tn)\}_3\{Co^{III}(CN)_6\}_2]\cdot 3H_2O$ (5):** Under aerobic conditions, 1,3-diaminopropane (1.0 mL, 12.0 mmol) was slowly

 © 2006 Wiley-VCH Verlag GmbH & Co. KGaA, Weinheim 

Table 5. Crystallographic data and structural refinement parameters for compounds **1**–**5**.

| | **1** | **2** | **3** | **4** | **5** |
|---|---|---|---|---|---|
| Empirical formula | $C_{12}H_{30}ClCu_2FeKN_{10}O_5$ | $C_{12}H_{28}Cu_2FeN_{10}O_4$[a] | $C_{12}H_{30}FeCuN_{10}O_4$[a] | $C_{21}H_{36}Cr_2Cu_3N_{18}O_3$[a] | $C_{21}H_{36}Co_2Cu_3N_{18}O_3$[a] |
| Formula mass | 651.92 | 559.38 | 497.82 | 883.30 | 897.13 |
| Crystal system | monoclinic | monoclinic | monoclinic | orthorhombic | orthorhombic |
| Space group | $P2_1/c$ | $P2_1/n$ | $P2_1/n$ | $Pbcn$ | $Pbcn$ |
| $a$ [Å] | 15.1478(3) | 7.5721(11) | 10.0586(4) | 23.1148(4) | 22.5404(3) |
| $b$ [Å] | 14.6941(4) | 10.7215(14) | 9.0189(3) | 11.1692(6) | 10.9865(5) |
| $c$ [Å] | 12.6533(4) | 12.9266(18) | 11.9833(6) | 14.650(1) | 14.2610(8) |
| $\alpha$ [°] | 90 | 90 | 90 | 90 | 90 |
| $\beta$ [°] | 109.95(9) | 90.013(12) | 104.2(1) | 90 | 90 |
| $\gamma$ [°] | 90 | 90 | 90 | 90 | 90 |
| $V$ [Å$^3$] | 2647(1) | 1049.4(3) | 1053.8(6) | 3782.2(3) | 3531.6(4) |
| $D_c$ [g cm$^{-3}$] | 1.64 | 1.77 | 1.57 | 1.55 | 1.69 |
| $Z$ | 4 | 2 | 2 | 4 | 4 |
| $\mu$ [cm$^{-1}$] | | 27.31 | 17.38 | | 27.54 |
| Refl. measured | | 7909 | 4772 | | 17553 |
| Refl. unique/$R_{int}$ | | 2150/0.039 | 2665/0.044 | | 5888/0.063 |
| Refl. with $I > n\sigma(I)$ | | 1706 ($n$ = 2) | 1030 ($n$ = 2.5) | | 2345 ($n$ = 4) |
| $Nv$ | | 147 | 190 | | 218 |
| $R$[b] | | 0.033 | 0.036 | | 0.032 |
| $R_w$[c] | | 0.060($F_o^2$) | 0.039($F_o$) | | 0.038($F_o$) |
| GooF[d] | | 0.915 | 1.024 | | 1.122 |
| $\Delta\rho_{max}/\Delta\rho_{min}$ [e Å$^{-3}$] | | +0.779/–0.556 | +0.311/–0.536 | | +0.440/–0.747 |

[a] The asymmetric unit contains 0.5 of the chemical formula. [b] $R = \Sigma||F_o| - |F_c||/\Sigma|F_o|$. [c] $R_w(F_o) = \{\Sigma[w(F_o - F_c)^2]/\Sigma[w(F_o)^2]\}^{1/2}$, $R_w(F_o^2) = wR_2 = \{\Sigma[w(F_o^2 - F_c^2)^2]/\Sigma[w(F_o^2)^2]\}^{1/2}$. [d] GooF = $S = \{\Sigma[w(F_o^2 - F_c^2)^2]/(N_{obsd.} - N_{var})\}^{1/2}$.

added with stirring to a concentrated aqueous solution of $CuCl_2{\cdot}2H_2O$ (2.05 g, 12.0 mmol). A concentrated aqueous solution of NaOH (0.48 g, 12.0 mmol) was then added leading to a clear solution, which was boiled for five minutes and then filtered. An aqueous solution of $(Et_4N)_3[Co^{III}(CN)_6]$ (3.63 g, 6.0 mmol) was then added to the resulting blue filtrate. Slow concentration of this solution at room temp. afforded **5** as blue crystals, which were filtered and air dried. Yield: 1.48 g (55%). $C_{21}H_{36}Co_2Cu_3N_{18}O_3$ (897.13): calcd. C 28.11, H 4.04, Co 13.14, Cu 21.25, N 28.10; found C 27.98, H 4.22, Co 12.97, Cu 21.32, N 28.01. IR: $\tilde{\nu}$ = 3618 w cm$^{-1}$, 3466 br, 3366 m, 3321 m, 3232 m, 3154 m, 2953 w, 2892 w, 2175 s, 2135 m, 2125 w, 1586 m, 1458 w, 1447 w, 1407 w, 1278 w, 1259 w, 1162 s, 1143 w, 1109 w, 1077 w, 1036 w, 1013 m, 913 m, 885 w, 681 w, 668 w, 493 s, 463 s, 447 m, 433 m, 418 br.

**X-ray Crystallography:** Data for **2** were collected on an Xcalibur 1 diffractometer (Oxford Diffraction) at 180 K whereas the data for all other compounds were collected at 288 K on an Xcalibur 2 Diffractometer (Oxford Diffraction). The structures were solved by direct methods and successive Fourier difference syntheses, and were refined on $F^2$ by weighted anisotropic full-matrix least-squares methods.[30] The crystal used for compound **2** presented a pseudo-merohedral twinning with a monoclinic cell having a $\beta$ angle of nearly 90°, which emulates an orthorhombic cell with possible space group $Pmn2_1$. The structure was solved and refined using the $P2_1/n$ monoclinic space and the following twinning law: 1 0 0 0 –1 0 0 0 –1. The two components were in the ratio 0.53/0.46, which explains the pseudo-orthorhombic symmetry.

The hydrogen atoms of **1**, **2**, **4**, and **5** were calculated [$d$(C–H) = 0.95 Å], except for the hydrogen atoms of the water molecules of **1**, **4**, and **5**; the thermal parameters were taken as $U_{iso} = 1.3\,U_{equ}$(C) and therefore included as isotropic fixed contributors to $F_c$. For compound **3**, all hydrogen atoms were located in the difference Fourier map and were refined isotropically. Scattering factors and corrections for anomalous dispersion were taken from the International Tables for X-ray Crystallography.[31] The thermal ellipsoid drawings were made with the ORTEP program.[32] All calculations were performed on an Alphastation 255 4/233 computer. Pertinent crystallographic data and structural refinement parameters are listed in Table 5. CCDC-175834, -274145, -275481, -175842, and -275482 (for **1**–**5**, respectively) contain the supplementary crystallographic data for this paper. These data can be obtained free of charge from The Cambridge Crystallographic Data Centre via www.ccdc.cam.ac.uk/data_request/cif.

## Acknowledgments

The authors gratefully acknowledge the CNRS (Centre National de la Recherche Scientifique) and the framework of a French–Spanish Integrated Action (PICASSO 2004, no. 07137XK and HF2003-258) for financial support. FT thanks the Ministère de l'Education Nationale, de la Recherche et de la Technologie for a thesis grant.

[1] a) S. M. Holmes, G. S. Girolami, *J. Am. Chem. Soc.* **1999**, *121*, 5593–5594; b) O. Hatlevik, W. E. Buschmann, J. Zhang, J. L. Manson, J. S. Miller, *Adv. Mater.* **1999**, *11*, 914–918; c) E. Dujardin, S. Ferlay, X. Phan, C. Desplanches, C. Cartier dit Moulin, P. Sainctavit, F. Baudelet, F. Dartyge, P. Veillet, M. Verdaguer, *J. Am. Chem. Soc.* **1998**, *120*, 11347–11352; d) M. Vergaguer, *Science* **1996**, *272*, 698–699; e) W. R. Entley, G. S. Girolami, *Science* **1995**, *268*, 397–400; f) S. Ferlay, T. Mallah, R. Ouahes, P. Veillet, M. Verdaguer, *Nature* **1995**, *378*, 701–703.

[2] M. Pilkington, S. Decurtins, *Comprehensive Coordination Chemistry II*, vol. 7 (Eds.: J. A. McCleverty, T. J. Meyer), Pergamon Press, Oxford, **2004**, pp. 177–229.

[3] For examples of photomagnetic materials and molecular spin devices, see: a) T. Hozumi, K. Hashimoto, S.-I. Ohkoshi, *J. Am. Chem. Soc.* **2005**, *127*, 3864–3869, and references cited therein; b) A. Dei, *Angew. Chem.* **2005**, *117*, 1184–1187; *Angew. Chem. Int. Ed.* **2005**, *44*, 1160–1163; c) V. Escax, C. Cartier dit Moulin, F. Villain, G. Champion, J.-P. Itié, P. Münsch, M. Verdaguer, A. Bleuzen, *C. R. Chim.* **2003**, *6*, 1165–1173; d) O. Sato, *Acc. Chem. Res.* **2003**, *36*, 692–700; e) Y. Arimoto, S.-I. Ohkoshi, Z. J. Zhong, H. Seino, Y. Mizobe, K. Hashimoto,

 © 2006 Wiley-VCH Verlag GmbH & Co. KGaA, Weinheim 

*J. Am. Chem. Soc.* **2003**, *125*, 9240–9241; f) S. Ohkoshi, K. Hashimoto, *J. Photochem. Photobiol., C* **2001**, *2*, 71–88; g) C. Cartier dit Moulin, F. Villain, A. Bleuzen, M.-A. Arrio, P. Sainctavit, C. Lomenech, V. Escax, F. Baudelet, E. Dartyge, J.-J. Gallet, M. Verdaguer, *J. Am. Chem. Soc.* **2000**, *122*, 6653–6658; h) O. Sato, Y. Einaga, A. Fujishima, K. Hashimoto, *Inorg. Chem.* **1999**, *38*, 4405–4412; i) Z.-Z. Gu, O. Sato, T. Iyoda, K. Hashimoto, A. Fujishima, *Chem. Mater.* **1997**, *9*, 1092–1097.

[4] O. Sato, T. Kawakami, M. Kimura, S. Hishiya, S. Kubo, Y. Einaga, *J. Am. Chem. Soc.* **2004**, *126*, 13176–13177.

[5] M. J. Scott, R. H. Holm, *J. Am. Chem. Soc.* **1994**, *116*, 11357–11367.

[6] a) S. S. Kaye, J. R. Long, *J. Am. Chem. Soc.* **2005**, *127*, 6506–6507; b) L. G. Beauvais, J. R. Long, *J. Am. Chem. Soc.* **2002**, *124*, 12096–12097.

[7] W. Dong, L.-N. Zhu, H.-B. Song, D.-Z. Liao, Z.-H. Jiang, S.-P. Yan, P. Cheng, S. Gao, *Inorg. Chem.* **2004**, *43*, 2465–2467.

[8] a) M. Ohba, H. Okawa, *Coord. Chem. Rev.* **2000**, *198*, 313–328, and references cited therein; b) M. K. Saha, M. C. Morón, F. Palacio, I. Bernal, *Inorg. Chem.* **2005**, *44*, 1354–1361; c) H.-Z. Kou, B. C. Zhou, S. Gao, D.-Z. Liao, R.-J. Wang, *Inorg. Chem.* **2003**, *42*, 5604–5611; d) E. Colacio, J. M. Domínguez-Vera, F. Lloret, A. Rodríguez, H. Stoeckli-Evans, *Inorg. Chem.* **2003**, *42*, 6962–6964; e) H.-Z. Kou, B. C. Zhou, D.-Z. Liao, R.-J. Wang, Y. Li, *Inorg. Chem.* **2002**, *41*, 6887–6891; f) F. Bellouard, M. Clemente-León, E. Coronado, J. R. Galán-Mascarós, C. J. Gómez-García, F. M. Romero, K. R. Dunbar, *Eur. J. Inorg. Chem.* **2002**, 1603–1606; g) E. Coronado, C. J. Gómez-García, A. Nuez, F. M. Romero, E. Rusanov, H. Stoeckli-Evans, *Inorg. Chem.* **2002**, *41*, 4615–4617; h) K. Inoue, H. Imai, P. S. Ghalsasi, K. Kikuchi, M. Ohba, H. Okawa, J. V. Yakhmi, *Angew. Chem.* **2001**, *113*, 4372–4375; *Angew. Chem. Int. Ed.* **2001**, *40*, 4242–4245; i) J. A. Smith, J.-R. Galán-Mascarós, R. Clérac, K. R. Dunbar, *Chem. Commun.* **2000**, 1077–1078.

[9] a) E. Coronado, C. Gimenez-Saiz, A. Nuez, V. Sánchez, F. M. Romero, *Eur. J. Inorg. Chem.* **2003**, 4289–4293; b) E. Coronado, C. Giménez-Saiz, J. M. Martinez-Agudo, A. Nuez, F. M. Romero, H. Stoeckli-Evans, *Polyhedron* **2003**, *22*, 2435–2440; c) F. Thétiot, S. Triki, J. Sala-Pala, *New J. Chem.* **2002**, *26*, 196–198; d) T. Lu, H. Xiang, S. Chen, C. Su, K. Yu, Z. Mao, P. Cheng, L. Ji, *J. Inorg. Organomet. Polym.* **1999**, *9*, 165–178; e) H.-Z. Kou, D.-Z. Liao, P. Cheng, Z.-H. Jiang, S.-P. Yan, G.-L. Wang, X.-K. Yao, H.-G. Wang, *J. Chem. Soc., Dalton Trans.* **1997**, 1503–1506.

[10] a) X.-P. Shen, S. Gao, G. Yin, K.-B. Yu, Z. Xu, *New J. Chem.* **2004**, *28*, 996–999; b) H.-Z. Kou, Y.-B. Jiang, B. C. Zhou, R.-J. Wang, *Inorg. Chem.* **2004**, *43*, 3271–3276; c) M. S. El Fallah, J. Ribas, X. Solans, M. Font-Bardia, *New J. Chem.* **2003**, *27*, 895–898; d) F. Thétiot, S. Triki, J. Sala-Pala, C. J. Gómez-García, S. Golhen, *Chem. Commun.* **2002**, 1078–1079; e) H.-Z. Kou, S. Gao, J. Zhang, G.-H. Wen, G. Su, R. K. Zheng, X. X. Zhang, *J. Am. Chem. Soc.* **2001**, *123*, 11809–11810.

[11] a) C. P. Berlinguette, A. Draguescu-Andrasi, A. Sieber, H.-U. Güdel, C. Achim, K. R. Dunbar, *J. Am. Chem. Soc.* **2005**, *127*, 6766–6779; b) C. P. Berlinguette, A. Draguescu-Andrasi, A. Sieber, J. R. Galán-Mascarós, H.-U. Güdel, C. Achim, K. R. Dunbar, *J. Am. Chem. Soc.* **2004**, *126*, 6222–6223; c) H.-Z. Kou, B. C. Zhou, S.-F. Si, R.-J. Wang, *Eur. J. Inorg. Chem.* **2004**, 401–408; d) H. J. Choi, J. J. Sokol, J. R. Long, *Inorg. Chem.* **2004**, *43*, 1606–1608; e) R. Tiron, W. Wernsdorfer, F. Tuyeras, A. Scuiller, V. Marvaud, M. Verdaguer, *Polyhedron* **2003**, *22*, 2427–2433; f) V. Marvaud, C. Decroix, A. Scuiller, F. Tuyèras, C. Guyard-Duhayon, J. Vaissermann, J. Marrot, F. Gonnet, M. Verdaguer, *Chem. Eur. J.* **2003**, *9*, 1692–1705; g) R. J. Parker, K. D. Lu, S. R. Batten, B. Moubaraki, K. S. Murray, L. Spiccia, J. D. Cashion, A. D. Rae, A. C. Willis, *J. Chem. Soc., Dalton Trans.* **2002**, 3723–3730; h) K. E. Vostrikova, D. Luneau, W. Wernsdorfer, P. Ray, M. Verdaguer, *J. Am. Chem. Soc.* **2000**, *122*, 718–719; i) D. G. Fu, J. Chen, X. S. Tan, L. J. Jiang, S. W. Zhang, P. J. Zheng, W. X. Tang, *Inorg. Chem.* **1997**, *36*, 220–225.

[12] a) R. Lescouëzec, J. Vaissermann, L. M. Toma, R. Carrasco, F. Lloret, M. Julve, *Inorg. Chem.* **2004**, *43*, 2234–2236; b) L. M. Toma, F. S. Delgado, C. Ruiz-Pérez, R. Carrasco, J. Cano, F. Lloret, M. Julve, *Dalton Trans.* **2004**, *18*, 2836–2846; c) Y.-Z. Zhang, S. Gao, H.-L. Sun, G. Su, Z.-M. Wang, S. W. Zhang, *Chem. Commun.* **2004**, 1906–1907; d) R. Lescouëzec, J. Vaissermann, C. Ruiz-Pérez, F. Lloret, R. Carrasco, M. Julve, M. Verdaguer, Y. Dromzee, D. Gatteschi, W. Wernsdorfer, *Angew. Chem.* **2003**, *115*, 1521–1524; *Angew. Chem. Int. Ed.* **2003**, *42*, 1483–1486; e) L. M. Toma, R. Lescouëzec, F. Lloret, M. Julve, J. Vaissermann, M. Verdaguer, *Chem. Commun.* **2003**, 1850–1851; f) R. Lescouëzec, F. Lloret, M. Julve, J. Vaissermann, M. Verdaguer, R. Llusar, S. Uriel, *Inorg. Chem.* **2001**, *40*, 2065–2072; g) W.-F. Yeung, W.-L. Man, W.-T. Wong, T.-C. Lau, S. Gao, *Angew. Chem.* **2001**, *113*, 3121–3123; *Angew. Chem. Int. Ed.* **2001**, *40*, 3031–3033; h) N. Matsumoto, Y. Sunatsuki, H. Miyasaka, Y. Hashimoto, D. Luneau, J.-P. Tuchagues, *Angew. Chem.* **1999**, *111*, 137–139; *Angew. Chem. Int. Ed.* **1999**, *38*, 171–173.

[13] a) Z.-H. Ni, H.-Z. Kou, Y.-H. Zhao, L. Zheng, R.-J. Wang, A.-L. Cui, O. Sato, *Inorg. Chem.* **2005**, *44*, 2050–2059; b) S. Wang, J.-L. Zuo, H.-C. Zhou, Y. Song, S. Gao, X.-Z. You, *Eur. J. Inorg. Chem.* **2004**, 3681–3687; c) S. Wang, J.-L. Zuo, S. Gao, Y. Song, H.-C. Zhou, Y.-Z. Zhang, X.-Z. You, *J. Am. Chem. Soc.* **2004**, *126*, 8900–8901; d) H. Oshio, H. Onodera, T. Ito, *Chem. Eur. J.* **2003**, *9*, 3946–3950; e) J. Y. Yang, M. P. Shores, J. J. Sokol, J. R. Long, *Inorg. Chem.* **2003**, *42*, 1403–1419; f) M. P. Shores, J. J. Sokol, J. R. Long, *J. Am. Chem. Soc.* **2002**, *124*, 2279–2292; g) R. Lescouëzec, F. Lloret, M. Julve, J. Vaissermann, M. Verdaguer, *Inorg. Chem.* **2002**, *41*, 818–826; h) H. Oshio, M. Yamamoto, T. Ito, *Inorg. Chem.* **2002**, *41*, 5817–5820; i) J. J. Sokol, M. P. Shores, J. R. Long, *Angew. Chem.* **2001**, *113*, 242–245; *Angew. Chem. Int. Ed.* **2001**, *40*, 236–239.

[14] a) J.-E. Koo, D.-H. Kim, Y.-S. Kim, Y. Do, *Inorg. Chem.* **2003**, *42*, 2983–2987; b) R. J. Parker, L. Spiccia, B. Moubaraki, K. S. Murray, D. C. R. Hockless, A. D. Rae, A. C. Willis, *Inorg. Chem.* **2002**, *41*, 2489–2495; c) J. A. Smith, J. R. Galán-Mascarós, R. Clérac, J.-S. Sun, X. Ouyang, K. R. Dunbar, *Polyhedron* **2001**, *20*, 1727–1734; d) X. Sun, Z. Wang, Z. Chen, J. Bian, C. Yan, G. Xu, *Prog. Nat. Sc.* **1999**, *9*, 425–431; e) J. Zou, X. Hu, C. Duan, Z. Xu, X. You, *Transition Met. Chem. (Dordrecht, Neth.)* **1998**, *23*, 477–480; f) R. J. Parker, D. C. R. Hockless, B. Moubaraki, K. S. Murray, L. Spiccia, *Chem. Commun.* **1996**, 2789–2790.

[15] *Stability Constants of Metal-Ion Complexes. Part B: Organic ligands*, IUPAC Chemical Data Series, no. 22, Pergamon Press, Oxford, **1979**, p. 122.

[16] S. M. Nelson, *Comprehensive Coordination Chemistry*, vol. 4 (Eds.: G. Wilkinson, R. D. Gillard, J. A. McCleverty), Pergamon Press, Oxford, **1987**, pp. 217–267.

[17] A. G. Sharpe, *Comprehensive Coordination Chemistry*, vol. 2 (Eds.: G. Wilkinson, R. D. Gillard, J. A. McCleverty), Pergamon Press, Oxford, **1987**, pp. 7–14.

[18] a) I. Bertini, C. Luchinat, F. Mani, A. Scozzafava, *Inorg. Chem.* **1980**, *19*, 1333–1336; b) J. A. Fee, *Struct. Bonding (Berlin)* **1975**, *23*, 1–60; c) W. U. Malik, S. I. Ali, *Bull. Chem. Soc. Jpn.* **1961**, *34*, 1310–1313.

[19] K. Nakamoto, *Infrared and Raman Spectra of Inorganic and Coordination Compounds*, 4th ed., Wiley-Interscience, New York, **1978**.

[20] R. J. Parker, L. Spiccia, S. R. Batten, J. D. Cashion, G. D. Fallon, *Inorg. Chem.* **2001**, *40*, 4696–4704.

[21] a) M. J. Scott, S. C. Lee, R. H. Holm, *Inorg. Chem.* **1994**, *33*, 4651–4662; b) G. O. Morpurgo, V. Mosini, P. Porta, G. Dessy, V. Fares, *J. Chem. Soc., Dalton Trans.* **1981**, 111–117.

[22] P. V. Bernhardt, B. D. Macpherson, M. Martinez, *Inorg. Chem.* **2000**, *39*, 5203–5208.

 © 2006 Wiley-VCH Verlag GmbH & Co. KGaA, Weinheim 

[23] a) N. Mondal, M. K. Saha, B. Bag, S. Mitra, V. Gramlich, J. Ribas, M. S. El Fallah, *J. Chem. Soc., Dalton Trans.* **2000**, 1601–1604; b) J. Luo, M. Hong, C. Chen, M. Wu, D. Gao, *Inorg. Chim. Acta* **2002**, *328*, 185–190.
[24] a) W. Addison, T. N. Rao, J. Reedijk, J. van Rijn, G. C. Verschoor, *J. Chem. Soc., Dalton Trans.* **1984**, 1349–1356; b) M. Vaidyanathan, R. Balamurugan, U. Sivagnanam, M. Palaniandavar, *J. Chem. Soc., Dalton Trans.* **2001**, 3498–3506.
[25] M. Ohba, N. Usuki, N. Fukita, H. Okawa, *Angew. Chem.* **1999**, *111*, 1911–1914; *Angew. Chem. Int. Ed.* **1999**, *38*, 1795–1798.
[26] a) C. S. Hong, Y. S. You, *Inorg. Chim. Acta* **2004**, *357*, 3271–3278; b) N. Mondal, M. K. Saha, B. Bag, S. Mitra, G. Rosair, M. S. El Fallah, *Polyhedron* **2001**, *20*, 579–584; c) Z. Travnicek, Z. Smékal, A. Escuer, J. Marek, *New J. Chem.* **2001**, *25*, 655–658; d) F. Bellouard, M. Clemente-León, E. Coronado, J. R. Galán-Mascarós, C. Giménez-Saiz, C. J. Gómez-García, T. Woike, *Polyhedron* **2001**, *20*, 1615–1619; e) E. Colacio, J. M. Domínguez-Vera, M. Ghazi, R. Kivekäs, J. M. Moreno, A. Pajunen, *J. Chem. Soc., Dalton Trans.* **2000**, 505–509; f) H. Oshio, O. Tamada, H. Onodera, T. Ito, T. Ikoma, S. Tero-Kubota, *Inorg. Chem.* **1999**, *38*, 5686–5689; g) H.-Z. Kou, H.-M. Wang, D.-Z. Liao, P. Cheng, Z.-H. Jiang, S.-P. Yan, X.-Y. Huang, G.-L. Wang, *Aust. J. Chem.* **1998**, *51*, 661–665; h) C. Q. Liu, J. M. Shi, W. Xu, W. Xu, Y. Q. Chen, *Pol. J. Chem.* **2003**, *77*, 929–933; i) H. L. Shyu, H.-H. Wei, *J. Coord. Chem.* **1999**, *47*, 319–330; j) J. Zou, Z. Xu, X. Huang, W.-L. Zhang, X.-P. Shen, Y.-P. Yu, *J. Coord. Chem.* **1997**, *42*, 55–61.
[27] a) M. K. Saha, F. Lloret, I. Bernal, *Inorg. Chem.* **2004**, *43*, 1969–1975; b) C. R. Choudhury, S. K. Dey, S. Mitra, N. Mondal, J. Ribas, K. M. Malik, *Bull. Chem. Soc. Jpn.* **2004**, *77*, 959–964; c) V. Marvaud, C. Decroix, A. Scuiller, C. Guyard-Duhayon, J. Vaissermann, F. Gonnet, M. Verdaguer, *Chem. Eur. J.* **2003**, *9*, 1678–1691; d) B. Li, X. Shen, K. Yu, Z. Xu, *J. Coord. Chem.* **2002**, *55*, 1191–1198; e) N. Mondal, D. K. Dey, S. Mitra, V. Gramlich, *Polyhedron* **2001**, *20*, 607–613; f) M. Ferbinteanu, S. Tanase, M. Andruh, Y. Journaux, F. Cimpoesu, I. Strenger, E. Rivière, *Polyhedron* **1999**, *18*, 3019–3025.
[28] N. Fukita, M. Ohba, H. Okawa, K. Matsuda, H. Iwamura, *Inorg. Chem.* **1998**, *37*, 842–848.
[29] P. Le Magueres, PhD Thesis, **1995**, University of Rennes 1, France.
[30] a) C. K. Fair, *MolEN, An Interactive Intelligent System for Crystal Structure Analysis*, User Manual, **1985**, Enraf-Nonius, Delft, The Netherlands; b) G. M. Sheldrick, SHELX97. Programs for Crystal Structure Analysis, **1997**, University of Göttingen, Germany.
[31] *International Tables for X-ray Crystallography*, vol. 4, Kynoch Press, Birmingham, **1975**.
[32] C. K. Johnson, *ORTEP*, Rep. ONL-3794, Delft, The Netherlands, **1985**.

Received: June 24, 2005
Published Online: November 21, 2005

 © 2006 Wiley-VCH Verlag GmbH & Co. KGaA, Weinheim 

DOI: 10.1002/ejic.200500639

# Copper(I) Complexes with a $Cu_4S_6$- and $CuS_4$-Type Core Obtained from the Reaction of Copper(0) with $HN(SPPh_2)_2 \cdot I_2$

**M. Carla Aragoni,[a] Massimiliano Arca,[a] M. Bonaria Carrea,[a] Francesco Demartin,[b] Francesco A. Devillanova,[a] Alessandra Garau,[a] Michael B. Hursthouse,[c] Susanne L. Huth,[c] Francesco Isaia,*[a] Vito Lippolis,[a] Helen R. Ogilvie,[c] and Gaetano Verani[a]**

**Keywords:** Cluster compounds / Copper / Coordination chemistry / Phosphanes / S ligands

The copper(I) compounds $[Cu^I_4(L)_3]I_3$ (**1**) and $[Cu^I(HL)_2]I_3 \cdot CH_3CN$ (**2**) [HL = $HN(SPPh_2)_2$] have been obtained from the reaction of the adduct $HL \cdot I_2$ with copper(0) powder in diethyl ether solution. Compound **1** contains a tetrahedron of Cu atoms with three anionic L ligands coordinated to the coppers through the sulfur atoms to build a $Cu_4S_6$ core. The mean Cu–Cu and Cu–S bond lengths related to the $Cu_4S_6$ core in copper-loaded transcription factors CuAce1 and CuMac1, and in the model compound $[Cu_4(SPh)_6]^{2-}$, have been compared with those of the $[Cu_4(L)_3]^+$ cation, and the geometric volumes of the $Cu_4$ cores have been evaluated. The results suggest that the cation $[Cu_4(L)_3]^+$ is a possible structural model compound for the metal site in Ace1 and Mac1 transcription factors. In compound **2**, two neutral HL ligands bind a $Cu^I$ ion in an *S*,*S*′-isobidentate chelating fashion to form a slightly distorted tetrahedral $CuS_4$ core. The $^{31}P$ NMR spectroscopic data of compound **1** are consistent with the maintenance of its structure in solution. Moreover, phosphorus variable-temperature measurements indicate a change from a two-spin coupled AB system at 0 °C to an $A_2$ spin system at 40 °C. The reaction of $[Cu_4(L)_3]^+$ with HI, monitored by $^{31}P$ NMR spectroscopy, leads to the protonation of the complexed ligands at the $Cu_4$ core and formation of the cation $[Cu_4(HL)_3]^{4+}$. The protonation reaction is reversible: increasing the amount of organic base 1,8-bis(dimethylamino)naphthalene (DMAN) regenerates the starting cation $[Cu_4(L)_3]^+$.

(© Wiley-VCH Verlag GmbH & Co. KGaA, 69451 Weinheim, Germany, 2006)

## Introduction

The tetraphenyldithioimidodiphosphanic acid ligand HL, and its deprotonated derivative L, have been extensively used in coordination chemistry[1] since they feature a flexible SPNPS skeleton along with a large S···S bite that enables the formation of an unstressed six-membered, MSPNPS chelate ring with a great variety of metal ions.[1] A literature survey reveals that there have been some studies on the reaction of L with $Cu^{II}$ salts, and these have led to the synthesis of complexes $[Cu^{I,II}_3L_4]$, $[Cu^I_3L_3]$, $[Cu^I_4L_3][Cu^ICl_2] \cdot CCl_4$[2a] and, more recently, $[Cu^I_4L_3][BF_4]$.[2b] Furthermore, the ability of L to form a tetrahedral $CuS_4$ core with the $Cu^{II}$ ion has been used by Bereman et al.[3] to propose the complex $[Cu(L)_2]$ as a potential model for type-I $Cu^{II}$ sites in metalloenzymes; unfortunately, the complex was not stable for more than a few days at room temperature, either in the solid state or in solution, due to autoreduction to $Cu^I$. Recently, Woollins et al. have described three other complexes of general stoichiometry $[Cu^I_3D_3]$ (D = $[N(SPiPr_2)_2]^-$, $[N(SPiPr_2)(SPPh_2)_2]^-$ and $[N\{SP(EtO)_2\}\{SP(OPh_2)\}_2]^-$) obtained from the reaction of either $Cu^{II}$ or $Cu^I$ ions with the corresponding anionic ligand D.[4] The X-ray crystal structures of these complexes revealed that the molecules contain a six-membered $Cu^I_3S_3$ ring in their core, with each copper atom being tricoordinate in an approximately trigonal geometry resulting from the coordination of one terminal and two bridging S-donors.

The $Cu^I_xS_y$ cores[5] may be of interest as structural model compounds for the active-sites in copper(I)-containing enzymes and proteins, which are far less known or studied than the copper(II) analogues. For example, the $Cu^I_4S_6$ core is currently generating great interest since two copper-regulated transcription factors central to yeast copper homeostasis, Ace1 and Mac1, in *Saccharomyces cerevisiae*, have revealed the presence of a remarkably similar polycopper cluster in these two proteins.[6]

In this paper, we have delved into the synthesis of new copper complexes of HL and/or L using the well-tested route based on the iodine adduct of HL, $HL \cdot I_2$, as oxidising/complexing agent towards metal(0) powders. In fact,

[a] Dipartimento di Chimica Inorganica ed Analitica, Università di Cagliari,
S. S. 554 bivio per Sestu, 09042 Cagliari, Italy
[b] Dipartimento di Chimica Strutturale e Stereochimica Inorganica, Università di Milano,
via G. Venezian 21, 20133 Milano, Italy
[c] School of Chemistry, University of Southampton,
Highfield, Southampton, SO17 1BJ, UK

this kind of reaction has proved to be an interesting and promising synthetic route, as it has often led to the preparation of complexes with unusual stoichiometries and geometrical features.[7] The reaction between the $HL{\cdot}I_2$ adduct and copper(0) powder has been investigated, and the X-ray crystal structures of complexes $[Cu_4(L)_3]I_3$ (**1**) and $[Cu(HL)_2]I_3{\cdot}CH_3CN$ (**2**) are reported. The $Cu^I_4S_6$ core in complex **1** has been studied by solid-state $^{31}P$ NMR spectroscopy and solution variable-temperature NMR spectroscopy as well. The results, along with the structural data, suggest that $[Cu_4(L)_3]^+$ is a possible structural model compound for the metal site in Ace1 and Mac1 transcription factors. The reactivity of complex **1** to form the cationic complex $[Cu^I_4(HL)_3]^{4+}$ has also been evaluated as a dependence on the acid/base behaviour of the metal-complexed ligands L and HL (Scheme 1).

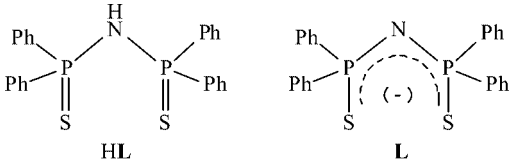


Scheme 1.

## Results and Discussion

### Syntheses and Crystal Structures of $[Cu^I_4(L)_3]I_3$ (1) and $[Cu^I(HL)_2]I_3{\cdot}MeCN$ (2)

The reaction between the adduct $HL{\cdot}I_2$ and Cu powder (1:1 molar ratio) was carried out in diethyl ether at room temperature for two days. During this time the dark-red colour of the mixture turned to pale-orange with separation of an orange powder. $^{31}P$ NMR spectroscopic analysis of the solution after two days indicated that the reaction was quantitative since no signal related to HL was detectable. The $^{31}P$ MAS NMR spectrum of the solid remaining after removal of the solvent revealed resonances at $\delta$ = 52.4, 32.9, 31.4, 30.4, 28.9 and 26.6 ppm, which are indicative of the presence of metal-complexed ligands both in their protonated, HL, and deprotonated, L, forms. Resonances in two specific ranges of the spectrum, namely $\delta$ = 60–50 and 40–20 ppm, can be considered highly diagnostic in identifying the species HL and L, respectively.[8] Treatment of the crude precipitate with $CHCl_3$ caused a partial dissolution of the solid; after slow evaporation of the solvent, orange crystals of stoichiometry $[Cu^I_4(L)_3]I_3$ (**1**) were isolated. The remaining crude precipitate was then dissolved in MeCN to produce orange crystals of $[Cu^I(HL)_2]I_3{\cdot}MeCN$ (**2**) on slow evaporation of the solvent. From the $^{31}P$ MAS NMR resonances of compounds **1** and **2** it was possible to confirm that both copper complexes are present in the orange powder separated from the ethereal reaction solution. The separation of the two complexes is, therefore, attributable to their markedly different solubility in the solvents employed. The structure of the cation of **1** has been reported before as its $CuCl_2$ and $BF_4$ salts; however, it was re-determined, and is briefly reported here, to provide a solid basis for the interpretation of the $^{31}P$ NMR measurements.

Compound **1** consists of discrete $[Cu^I_4(L)_3]^+$ cations and $I_3^-$ anions separated by normal van der Waals contacts. The molecular structure of the cation $[Cu^I_4(L)_3]^+$ is shown in Figure 1, while selected bond parameters are reported in Table 1. The cation consists of a tetrahedron of copper(I) atoms surrounded by three didentate L ligands coordinated to the copper atoms through the sulfur atoms. The arrangement of the ligands around the metal core resembles that found in $[Cu^I_4(L)_3]^+[CuCl_2]^-{\cdot}CCl_4$ (**3**),[2a] i.e. it conforms to a pseudo-trigonal idealised symmetry, with the threefold symmetry axis passing through the unique Cu(4) and the mid-point of the three remaining copper atoms (Figure 1). One sulfur atom of each ligand binds the Cu(4) atom and one of the three remaining copper atoms [Cu(1), Cu(2) and Cu(3)], while the second sulfur atom binds a couple of copper atoms of the basal plane. Thus, each copper of the basal plane is coordinated by two S atoms of the same ligand and by the sulfur atom of a different ligand. The distances of the unique Cu(4) atom to the remaining copper atoms are, on average, slightly shorter than those found between the other couples of copper atoms (2.787 vs. 2.812 Å). These values compare well with those found in the analogous complex **3** (mean values of 2.777 vs. 2.806 Å), although significant variations in the single copper–copper distances are observed in the two compounds due to local packing effects associated with different counteranions and with the presence of a solvent molecule. In **3**, the Cu–S bond lengths involving the unique Cu(4) atoms are not significantly different from each other and range from 2.257 to 2.278 Å. This range is wider in **1** (2.256–2.291 Å), with the larger Cu–S bonds being those with Cu(4). Very small changes are observed in the P–S and P–N bonds of the two compounds,

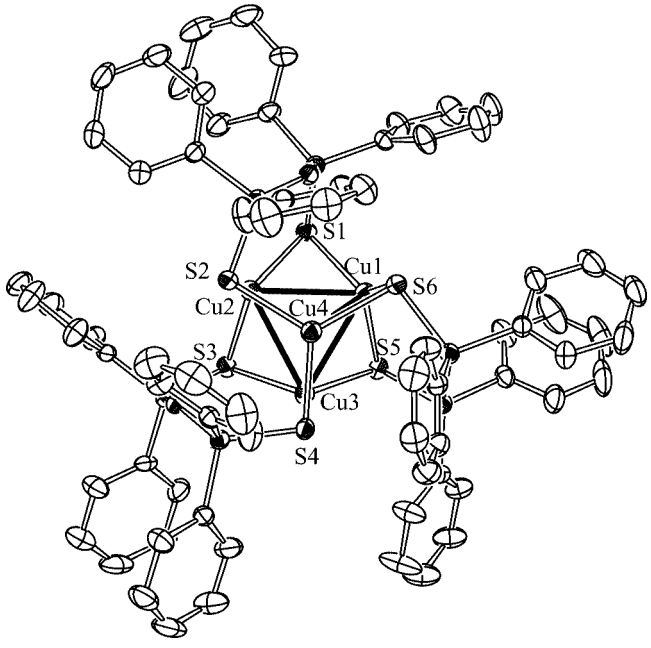


Figure 1. ORTEP drawing of the $[Cu_4(L)_3]^+$ complex cation of **1**. Thermal ellipsoids are drawn at 30% probability.

 © 2006 Wiley-VCH Verlag GmbH & Co. KGaA, Weinheim 

while a significant increase in the P–N–P angle occurs on passing from **1** to **3** (133.5° and 138.0°, respectively). The triiodide anion is slightly asymmetric and almost linear [174.60(2)°], and no I···I contacts between different anions are observed.

Table 1. Selected interatomic distances [Å] and angles [°] for compound **1**.

| | | | |
|---|---|---|---|
| Cu(1)–Cu(2) | 2.7679(8) | Cu(1)–Cu(4) | 2.8033(8) |
| Cu(1)–Cu(3) | 2.8370(9) | Cu(2)–Cu(4) | 2.7994(8) |
| Cu(2)–Cu(3) | 2.8306(8) | Cu(3)–Cu(4) | 2.7578(8) |
| S(1)–Cu(2) | 2.270(1) | S(1)–Cu(1) | 2.280(1) |
| S(2)–Cu(2) | 2.261(1) | S(2)–Cu(4) | 2.285(1) |
| S(3)–Cu(3) | 2.272(1) | S(3)–Cu(2) | 2.283(1) |
| S(4)–Cu(3) | 2.269(1) | S(4)–Cu(4) | 2.291(1) |
| S(5)–Cu(1) | 2.256(1) | S(5)–Cu(3) | 2.280(1) |
| S(6)–Cu(1) | 2.263(1) | S(6)–Cu(4) | 2.291(1) |
| P(1)–S(1) | 2.055(2) | P(2)–S(2) | 2.043(2) |
| P(3)–S(3) | 2.056(2) | P(4)–S(4) | 2.058(2) |
| P(5)–S(5) | 2.051(2) | P(6)–S(6) | 2.052(2) |
| P(1)–N(1) | 1.588(4) | P(2)–N(1) | 1.593(4) |
| P(3)–N(2) | 1.585(4) | P(4)–N(2) | 1.593(4) |
| P(5)–N(3) | 1.586(4) | P(6)–N(3) | 1.585(4) |
| I(1)–I(2) | 2.9436(9) | I(2)–I(3) | 2.8911(8) |
| Cu(2)–Cu(1)–Cu(4) | 60.32(2) | Cu(2)–Cu(1)–Cu(3) | 60.65(2) |
| Cu(4)–Cu(1)–Cu(3) | 58.54(2) | Cu(1)–Cu(2)–Cu(4) | 60.46(2) |
| Cu(1)–Cu(2)–Cu(3) | 60.88(2) | Cu(4)–Cu(2)–Cu(3) | 58.66(2) |
| Cu(4)–Cu(3)–Cu(2) | 60.11(2) | Cu(4)–Cu(3)–Cu(1) | 60.12(2) |
| Cu(2)–Cu(3)–Cu(1) | 58.47(2) | Cu(3)–Cu(4)–Cu(2) | 61.24(2) |
| Cu(3)–Cu(4)–Cu(1) | 61.34(2) | Cu(2)–Cu(4)–Cu(1) | 59.21(2) |
| Cu(2)–S(1)–Cu(1) | 74.92(4) | Cu(2)–S(2)–Cu(4) | 76.00(4) |
| Cu(3)–S(3)–Cu(2) | 76.82(4) | Cu(3)–S(4)–Cu(4) | 74.40(4) |
| Cu(1)–S(5)–Cu(3) | 77.40(4) | Cu(1)–S(6)–Cu(4) | 75.97(4) |
| P(1)–N(1)–P(2) | 133.5(2) | P(3)–N(2)–P(4) | 134.2(2) |
| P(6)–N(3)–P(5) | 132.9(2) | I(1)–I(2)–I(3) | 174.60(2) |

The molecular structure of $[Cu^{I}(HL)_2]I_3$·MeCN (**2**) is shown in Figure 2 and selected bond lengths and angles are collected in Table 2. In the complex cation $[Cu^{I}(HL)_2]^+$ the copper is coordinated by two neutral HL ligands in an *S*,*S*′-isobidentate chelating fashion, resulting in the formation of two six-membered $CuS_2P_2N$ rings; the charge is balanced by a slightly asymmetric $I_3^-$ ion. One solvent molecule (MeCN) per formula unit is also present in the structure, giving rise to weak hydrogen bonding with an imido group [N(2)–H(N2)···N(3) = 2.925 Å; N(2)–H···N(3) = 166.63°]. The $[Cu^{I}(HL)_2]^+$ cation contains a slightly distorted tetrahedral $CuS_4$ core, with S–Cu–S angles ranging from 101.10(8)° to 117.92(8)°. The four Cu–S interatomic distances are slightly different and range from 2.338(2) [Cu(1)–S(3)] to 2.376 Å [Cu(1)–S(2)]. The CuSPNPS metallacycles display a pseudo-boat conformation with a P and an S atom of the ring acting as the stern and bow of the boat,

Table 2. Selected interatomic distances [Å] and angles [°] for compound **2**.

| | | | |
|---|---|---|---|
| Cu(1)–S(1) | 2.363(2) | Cu(1)–S(2) | 2.376(2) |
| Cu(1)–S(3) | 2.338(2) | Cu(1)–S(4) | 2.352(2) |
| P(1)–S(1) | 1.962(3) | P(2)–S(2) | 1.959(3) |
| P(3)–S(3) | 1.961(3) | P(4)–S(4) | 1.963(3) |
| P(1)–N(1) | 1.666(7) | P(2)–N(1) | 1.689(6) |
| P(3)–N(2) | 1.670(7) | P(4)–N(2) | 1.675(7) |
| I(1)–I(2) | 2.9486(9) | I(2)–I(3) | 2.8786(9) |
| S(1)–Cu(1)–S(2) | 112.96(8) | S(3)–Cu(1)–S(4) | 112.62(8) |
| S(2)–Cu(1)–S(4) | 101.10(8) | S(1)–Cu(1)–S(4) | 117.92(8) |
| S(1)–Cu(1)–S(3) | 101.40(8) | S(2)–Cu(1)–S(3) | 111.22(9) |
| I(1)–I(2)–I(3) | 175.52(3) | | |
| P(1)–N(1)–P(2) | 127.4(4) | P(3)–N(2)–P(4) | 126.9(5) |
| N(1)–P(1)–C(1) | 102.7(3) | N(1)–P(1)–C(7) | 109.6(3) |
| C(1)–P(1)–C(7) | 106.5(4) | N(1)–P(1)–S(1) | 112.7(3) |
| C(1)–P(1)–S(1) | 113.6(3) | C(7)–P(1)–S(1) | 111.2(3) |
| N(1)–P(2)–S(2) | 114.6(2) | N(2)–P(3)–S(3) | 113.9(3) |
| N(2)–P(4)–S(4) | 115.0(3) | P(1)–S(1)–Cu(1) | 96.45(10) |
| P(2)–S(2)–Cu(1) | 96.60(11) | P(3)–S(3)–Cu(1) | 98.98(11) |
| P(4)–S(4)–Cu(1) | 98.01(11) | | |

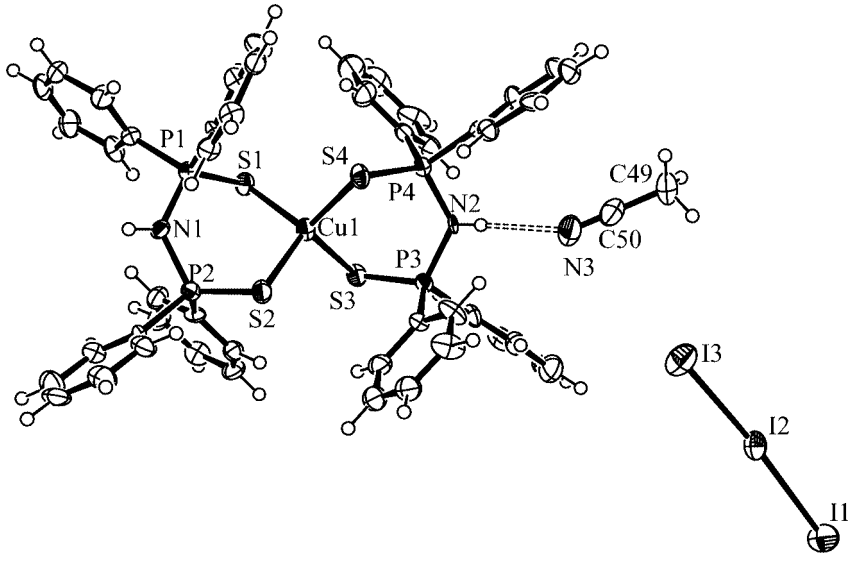


Figure 2. ORTEP plot of compound $[Cu(HL)_2]I_3$·$CH_3CN$ (**2**) showing the N(2)–H···N(3) hydrogen bond. Thermal ellipsoids are drawn at 30% probability.

 © 2006 Wiley-VCH Verlag GmbH & Co. KGaA, Weinheim 

respectively. As a result of metal complexation, some degree of π-electron delocalisation over the [Cu(SP)$_2$N] ring can be recognised from the slight increase in P–S bond lengths: from 1.937(1)–1.950(1) Å in the free ligand[9] to 1.959(3)–1.963(3) Å in **2**. Conversely, the P–N bond lengths remain substantially similar to those found in free HL [HL:[9] 1.672(2)–1.683(2) Å; **2**: 1.666(7)–1.689(6) Å].

### Solution and Solid-State $^{31}$P NMR Spectroscopy

The solid-state $^{31}$P NMR spectrum of complex **1** shows resonances at $\delta$ = 32.9 ($\Delta\nu$½ = 168 Hz), 31.4 ($\Delta\nu$½ = 134 Hz), 30.4 ($\Delta\nu$½ = 159 Hz), 28.9 ($\Delta\nu$½ = 183 Hz) and 26.6 ppm ($\Delta\nu$½ = 213 Hz), indicative of different crystallographically independent phosphorus atoms in the complex. Conversely, complex **2** shows the presence of a single resonance at $\delta$ = 52.4 ppm with a spectral line-width of 410 Hz, suggesting that the phosphorus atoms in the asymmetric unit have a closely similar environment. The variable-temperature $^{31}$P NMR spectra of **1** in $CHCl_3$ are shown in Figure 3. The spectrum recorded at 25 °C shows two distinct signals ($\delta$ = 28.5 and 28.1 ppm) with an intensity ratio of 1:1, also consistent with the maintenance of the solid structure in solution. (For $[Cu^I_4L_3][BF_4]$ in $CD_3CN$, a single broad peak at $\delta$ = 27.05 ppm has been reported, although no temperature is given).[2b] As the temperature of the solution is lowered from 25 °C to 0 °C, the $^{31}$P NMR spectra reveal two interesting spin-coupled doublets (AB system) with a $^2J_{P,P}$ coupling constant of 11.0 Hz; the spectrum at –40 °C shows that this coupling constant is temperature-invariant. The appearance of two spin-coupled doublets confirms that both phosphorus resonances are from the same complex molecule rather than from different isomers present in solution, and that the most likely explanation for this observation is the stabilisation of a conformer of the $CuS_2P_2N$ rings. As the temperature of the solution is increased to 37.5 °C, the two well-separated resonances at $\delta$ = 28.5 and 28.1 ppm coalesce ($k_{coal}$ = 126 s$^{-1}$),[10] and at 40 °C, the highest temperature reached, the phosphorus atoms become equivalent and the spectrum degenerates to an $A_2$ system. At this point, a fast exchange process on the NMR timescale makes the four copper atoms equivalent. The dynamic process that averages the phosphorus NMR resonances seems to be non-dissociative, since the reaction of **1** with HL, or with the mixed sulfur/oxygen ligand HN(SPPh$_2$)(OPPh$_2$), in the 25–40 °C ($CHCl_3$) range results in no ligand exchange. Moreover, the conductivity measured in $CHCl_3$ does not show changes in the range 25–40 °C.

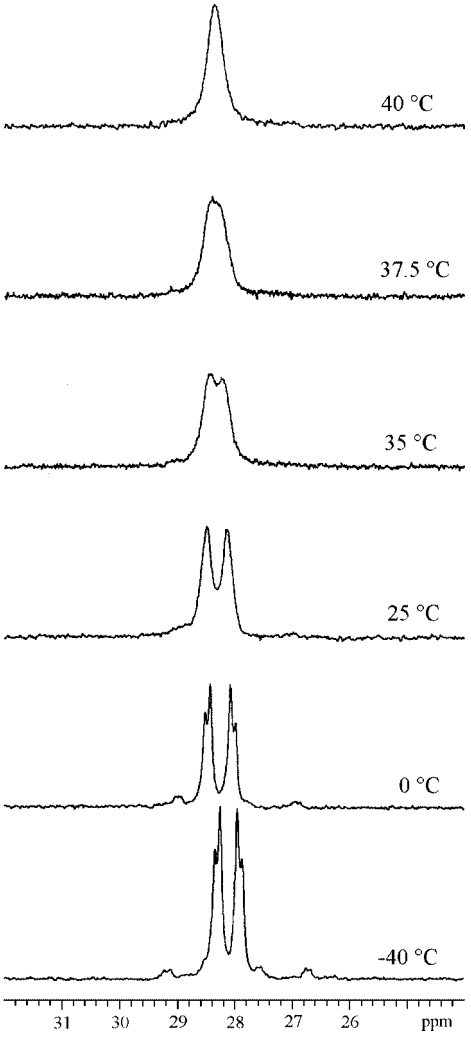


Figure 3. Variable-temperature $^{31}$P NMR spectra of complex **1** ($1.0\times10^{-2}$ M, $CDCl_3$).

### Reactivity of the $[Cu_4(L)_3]^+$ Cluster

Several studies have demonstrated that Cu activation of Ace1 and Mac1 involves formation of a tetracopper cluster within the Cu-regulatory domain. EXAFS data for CuAce1 and CuMac1[6b] suggests the presence of a distorted tetranuclear copper cluster; the $Cu^I$ ions are trigonally coordinated with Cu–S distances of about 2.25 Å and a Cu–Cu distance of 2.7 and 2.9 Å when two different Cu···Cu interactions were considered (Table 3). In this context, the $Cu_4S_6$ core in the cation $[Cu_4(L)_3]^+$ might represent a useful model compound for the metal centres in CuAce1 and CuMac1, since the mean Cu–S and Cu–Cu bond lengths (Table 3) compare well with those reported for these clusters. Moreover, unlike the copper thiolate model compound[11] $[Cu_4(SPh)_6]^{2-}$, in which the $Cu^I$ ions are chemically equivalent, the cation $[Cu_4(L)_3]^+$ contains two chemically different sets of $Cu^I$ ions [Cu(1)/Cu(2)/Cu(3) and Cu(4), respectively] that might structurally better represent the distorted tetracopper cluster within the Cu-regulatory domain. Although the two ionic complexes $[Cu_4(L)_3]^+$ and $[Cu_4(SPh)_6]^{2-}$ feature the same $Cu_4S_6$ core type, a significant difference in the "volume" of the $Cu_4$ cages is calculated from the mean Cu···Cu bond lengths (Table 3). Interestingly, the $Cu_4$ volume in the CuAce1 and CuMac1 transcriptions factors proves to be intermediate between those found in the ionic model compounds. The possibility of the $Cu_4$ cluster expanding or contracting as a result of the nature of the

 © 2006 Wiley-VCH Verlag GmbH & Co. KGaA, Weinheim 

ligands forming the $Cu_4S_6$ cores and of the charge transferred by the ligands upon it seems to be a peculiar characteristic of this species.

Table 3. Mean Cu–Cu and Cu–S bond lengths in selected copper complexes with a $Cu_4S_6$ core, and $Cu_4$ cluster volume.

| Sample | Interaction | $N$[a] | Interatomic distances [Å] | $Cu_4$ volume[b] [Å$^3$] |
|---|---|---|---|---|
| CuAce1[c] | Cu····Cu | 2 | 2.704(2) | 2.50 |
| | Cu····Cu | 1 | 2.902(6) | |
| | Cu–S | 3 | 2.251(1) | |
| CuMac1[c] | Cu····Cu | 2 | 2.705(4) | 2.50 |
| | Cu····Cu | 1 | 2.891(9) | |
| | Cu–S | 3 | 2.251(2) | |
| **1**[d] | Cu····Cu[e] | | 2.8118(8) | 2.60 |
| | Cu····Cu[f] | | 2.7868(8) | |
| | Cu–S[g] | 3 | 2.2751(1) | |
| $(Ph_4P)_2[Cu_4(SPh)_6]$[h] | Cu····Cu[i] | 3 | 2.744(4) | 2.43 |
| | Cu–S[j] | 3 | 2.261(6) | |

[a] Number of Cu–Cu and Cu–S interactions of specified distance for each copper atom. [b] Calculated as geometrical volume of the $Cu_4$ tetrahedron. [c] Interatomic distances from EXAFS data analysis, ref.[6b] [d] This work. [e] Interatomic distance calculated as the mean of the Cu(1)–Cu(2), Cu(1)–Cu(3) and Cu(2)–Cu(3) bond lengths. [f] Interatomic distance calculated as the mean of the Cu(1)–Cu(4), Cu(2)–Cu(4) and Cu(3)–Cu(4) bond lengths. [g] Value calculated as the mean of all Cu–S bond lengths. [h] Data from ref.[11] [i] Value calculated as the mean value of all Cu–Cu bond lengths. [j] Value calculated as the mean value of all Cu–S bond lengths.

Dance et al.[5,6c] have reported on the stability of $Cu^I$ tetracopper $Cu_4S_6$ clusters with small thiolate ligands and have shown that the clusters are held together by bridging thiolates and that the Cu···Cu bonding is a minor energetic factor in the stability of the clusters. In this regard, since both ligands L and HL can act as chelating agents towards a copper(I) ion, although a substantial difference in nucleophilicity is to be taken into account,[12] we thought of verifying the ability of the $Cu_4$ core to remain stable even if coordinated by a set of neutral HL ligands.

The treatment of **1** with the acid HI (55 wt.-% in water) in a mixture of MeCN and $CDCl_3$ (1:10 v:v) at 25 °C until a 1:2.8 molar ratio was reached resulted in a considerable change in the $^{31}P$ NMR spectrum of the complex (Figure 4a–d): the two distinct signals of **1** at $\delta$ = 28.5 and 28.1 ppm are lower in intensity, while a new signal at low-field ($\delta$ = 52.9 ppm) increases with the amount of HI. The latter value is strongly indicative of the formation of a new complex with all the ligands in their *N*-protonated form; interestingly, no other resonances due to copper complexes bearing L and HL ligands at the same time were detected for any molar ratio of the reagents used. Values for the $\delta$(*P*S) in the 60–50 ppm range have, in fact, been observed previously in the neutral complexes $[Pd(HL)I_2]$[13] [$\delta$(*P*S) = 56.5 ppm (MeCN/$CHCl_3$, 1:1 v:v) and $[Hg(HL)I_2]$[14] [$\delta$(*P*S) = 57.8 ppm, $CH_2Cl_2$]. To rule out that ligand protonation has caused the dismantling of the $Cu_4$ core, we also verified that the protonation reaction is reversible. The reaction of the acidic mixture with a strong base like 1,8-bis(dimethylamino)naphthalene (DMAN) causes the deprotonation of the coordinated ligands and the regeneration of the cation $[Cu_4(L)_3]^+$, as shown by the $^{31}P$ NMR peaks at $\delta$ = 28.5 and 28.1 ppm. (Figure 4, e and f). The overall reactions involving the protonation/deprotonation of the ligands in the cationic complexes $[Cu_4(L)_3]^+$ and $[Cu_4(HL)_3]^{4+}$ are summarised in Scheme 2.

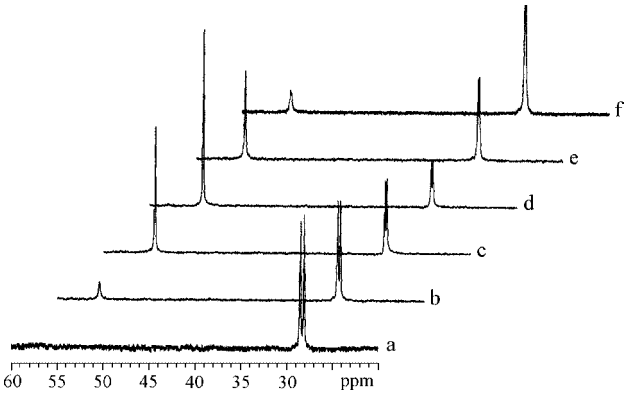


Figure 4. $^{31}P$ NMR spectra of (a) **1** ($3.4\times10^{-3}$ M); (b), (c), and (d) solution of **1** after the addition of HI to realise **1**/HI molar ratios of 1:1, 1:2 and 1:2.8, respectively; (e) the solution of (d) after addition of DMAN (**1**/HI/DMAN = 1:2.8:0.65); (f) the solution from (e) after addition of more DMAN (**1**/HI/DMAN, 1:2.8:1.3), all in MeCN/$CDCl_3$ (1:10 v:v) at 25 °C.

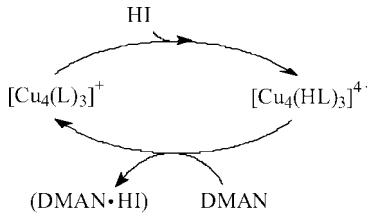


Scheme 2.

Although we were not able to isolate any solid compound from the reaction of **1** with HI, the reported results point to the ability of the $Cu_4$ cluster to be stabilised by neutral and anionic ligands.

## Conclusions

The reaction of the adduct $HL{\cdot}I_2$ with copper(0) powder under mild conditions affords complexes $[Cu^I_4(L)_3]I_3$ (**1**) and $[Cu^I(HL)_2]I_3{\cdot}CH_3CN$ (**2**). The latter compound represents a rare example of a structurally characterised complex of HL. To the best of our knowledge, only two other complexes are known in the literature, namely $[Hg(HL)I_2]$[14] and $[Ag(HL)_2BF_4]$[2b]. The copper(I) ion is coordinated by two neutral HL ligands in an *S*,*S*′-isobidentate chelating fashion to give a $CuS_4$ core. Compound **1** features a distorted tetrahedral $Cu_4$ cluster encapsulated by three bidentate anionic L ligands where only three of the four copper atoms of the $Cu_4S_6$ core are chemically equivalent. $^{31}P$ NMR variable-temperature measurements have confirmed that the solid structure is retained in solution and highlight a fast exchange process that makes all coppers equivalent ($T_{coal}$ = 37.5 °C). Interestingly, the $Cu_4S_6$ core in the cation $[Cu^I_4(L)_3]^+$ might be considered as a new structural model

 © 2006 Wiley-VCH Verlag GmbH & Co. KGaA, Weinheim 

compound for the distorted tetranuclear copper(I) cluster within the Cu-regulatory domain in proteins Ace1 and Mac1. Moreover, it constitutes a valid alternative to the higher symmetric $Cu_4S_6$ core found in the anionic copper thiolate compound $[Cu_4(SPh)_6]^{2-}$. A comparison of the "volume" of the $Cu_4$ cluster in **1** and in the anion $[Cu_4(SPh)_6]^{2-}$ reveals a significant difference that can be related to the different set and charge of the ligands complexing the $Cu_4$ unit. The stability of the $Cu_4S_6$ core in the species $[Cu_4(HL)_3]^{4+}$, obtained from the reaction of **1** with HI, was also established by $^{31}P$ NMR measurements. The expansion/contraction of the $Cu_4$ cluster may be important as regards the activation of Ace1 and Mac1 transcription factors. The electronic charge-modulation by cysteinyl residues at the metal sites in the proteins might reasonably act as a regulating device in building up, modifying or dismantling the $Cu_4$ cluster structural unit.[6b,15]

## Experimental Section

**Materials and Instrumentation:** Reagents were used as purchased from Aldrich. Diethyl ether was distilled from over $LiAlH_4$ shortly before use. Hydroiodic acid: ACS reagent, 55 wt.-% in water. $^{31}P\{^1H\}$ NMR spectra were recorded with a Varian Unity Inova 400 spectrometer operating at 161.9 MHz. The $^{31}P$ chemical shifts are referenced to an external standard of $H_3PO_4$ 85% peak ($\delta$ = 0.0 ppm). Variable-temperature $^{31}P$ NMR spectroscopic data for compound **1** were collected for a $1.0\times10^{-2}$ M solution in $CHCl_3$. $^{31}P$ MAS NMR spectra were calibrated indirectly through the $H_3PO_4$ 85% peak ($\delta$ = 0.0 ppm). IR spectra were measured as KBr (4000–400 $cm^{-1}$) or polyethylene pellets (400–50 $cm^{-1}$) on a Bruker IFS 55 FT-IR spectrometer. FT-Raman spectra were measured as solid samples on a Bruker IFS 100 spectrometer. Conductometric measurements on compound **1** ($1.0\times10^{-3}$ M in $CHCl_3$) were carried out at 20, 30 and 40 °C.

**Synthesis:** Compound HL was prepared according to ref.[16] The adduct $HL{\cdot}I_2$ was prepared in situ in freshly distilled $Et_2O$ from equimolar amounts of HL and $I_2$.

**$[Cu_4(L)_3]I_3$ (1):** A mixture of HL (0.100 g, 0.222 mmol) and $I_2$ (0.0565 g, 0.223 mmol) in $Et_2O$ (100 mL) was stirred at room temperature until complete dissolution of the reagents. Copper powder (submicron; 0.0141 g, 0.226 mmol) was then added while stirring and the mixture was allowed to react at room temperature for about 2 days. The resulting air-stable orange solid (149 mg) was isolated by suction filtration, then treated with 10 mL of $CHCl_3$ for 1 h. The mixture was filtered, and the resulting solution evaporated to dryness to give 0.100 g of **1** ($5.05\times10^{-2}$ mmol; yield 89%, based on metal). $C_{72}H_{60}Cu_4I_3N_3P_6S_6$ (1980.3): calcd. C 43.67, H 3.05, N 2.12, S 9.71; found C 44.0, H 3.1, N 2.0, S 9.6. FT-IR (KBr): $\tilde{\nu}$ = 3435 $cm^{-1}$ br. m, 3118 br. m, 3054 m, 1587 w, 1572 w, 1479 s, 1436 w, 1288 ms, 1106 vs, 1026 w, 998 w, 900 s, 788 s, 735 vs, 721 ms, 687 s, 636 m, 613 ms, 551 vs, 528 ms, 495 m, 413 w. FT-Raman (500–50 $cm^{-1}$): $\tilde{\nu}$ = 114 $cm^{-1}$. $^{31}P$ NMR ($CHCl_3$, 25 °C): $\delta$ = 28.5 and 28.1 ppm.

**$[Cu(HL)_2]I_3{\cdot}MeCN$ (2):** A mixture of HL (0.100 g, 0.222 mmol) and $I_2$ (0.0565 g, 0.223 mmol) in $Et_2O$ (100 mL) was stirred at room temperature until complete dissolution of the reagents. Copper powder (submicron; 0.0141 g, 0.226 mmol) was then added while stirring and the mixture was allowed to react at room temperature for about 2 days. The resulting air-stable orange solid was isolated by suction filtration, then treated with 10 mL of $CHCl_3$ for 1 h. The mixture was filtered, the separated solid compound washed with $CHCl_3$ and then dissolved in $CH_3CN$ (5 mL); slow evaporation of the solution afforded orange crystals of **2** (0.030 g, $2.08\times10^{-2}$ mmol; yield 10%, based on metal). $C_{50}H_{45}CuI_3N_3P_4S_4$ (1348.3): calcd. C 43.38, H 3.28, N 3.04, S 9.26; found C 43.5, H 3.2, N 3.1, S 9.0. FT-IR (KBr): $\tilde{\nu}$ = 3435 $cm^{-1}$ br. vs, 3052 w, 1477 m, 1435 vs, 1385 m, 1205 vs, 1177 s, 1106 vs, 1026 w, 998 w, 913 w, 874 w, 743 m, 721 m, 693 vs, 550 vs, 531 m, 493 m, 414 w. FT-Raman (500–50 $cm^{-1}$): $\tilde{\nu}$ = 135 $cm^{-1}$ (2.8), 112 (10), 79br (1.6) (relative intensities in parentheses, highest value: 10). $^{31}P$ NMR (MeCN): $\delta$ = 52.9 ppm.

**X-ray Crystallography:** Crystal data and details of the refinement for compounds **1** and **2** are reported in Table 4. Diffraction data were collected on a Bruker SMART CCD diffractometer at room temperature for compound **1** and at 120(2) K on a Bruker–Nonius area-detector diffractometer for compound **2**, using graphite-monochromated Mo-$K_\alpha$ radiation ($\lambda$ = 0.71073 Å). Cell parameters and orientation matrix were obtained from least-squares refinement of reflections measured in the range $2.23 < \theta < 22.41°$ for **1** and $2.91 < \theta < 27.48°$ for **2**. An absorption correction was applied using the SADABS routine[17] for **1** and the SORTAV algorithm[18] for **2**. The structures were solved by direct methods and refined on $F^2$ by using the SHELX[19] program implemented in the WinGX suite.[20] Anisotropic displacement parameters were assigned to all non-hydrogen atoms. Hydrogen atoms were included in the structure using the riding model.

Table 4. Crystal data and details of refinements for complexes **1** and **2**.

| Compound | **1** | **2** |
|---|---|---|
| Chemical formula | $C_{72}H_{60}Cu_4I_3N_3P_6S_6$ | $C_{50}H_{45}CuI_3N_3P_4S_4$ |
| Mol. wt. | 1980.27 | 1348.25 |
| Crystal system | monoclinic | monoclinic |
| Space group | $P2_1/c$ | $P2_1/c$ |
| $a$ [Å] | 14.139(1) | 16.9869(5) |
| $b$ [Å] | 16.847(1) | 17.0247(6) |
| $c$ [Å] | 32.955(2) | 20.6025(7) |
| $\beta$ [°] | 98.24(1) | 112.858(2) |
| $V$ [Å$^3$] | 7768.8(9) | 5490.3(3) |
| $Z$ | 4 | 4 |
| $\rho_{calcd}$ [Mg m$^{-3}$] | 1.693 | 1.675 |
| $\mu$(Mo-$K_\alpha$) [mm$^{-1}$] | 2.599 | 2.390 |
| Transmission factors | 0.714–1.000 | 0.9538–0.6730 |
| Collected reflections | 70186 | 65960 |
| Unique refl. with $I > 2\sigma(I)$ | 10022 | 12392 |
| Final $R$ and $wR_2$ indices | 0.0493–0.1291 | 0.0850–0.1054 |
| Max. and min. final $\Delta\rho$ | –1.244, 1.555 | –0.802, 0.723 |

CCDC-271849 (for **1**) and -271850 (for **2**) contain the supplementary crystallographic data for this paper. These data can be obtained free of charge from The Cambridge Crystallographic Data Centre via www.ccdc.cam.ac.uk/data_request/cif.

## Acknowledgments

M. B. H., S. L. H, and H. R. O. thank the UK EPSRC for support of the crystallographic study.

[1] a) I. Haiduc, *Comprehensive Coordination Chemistry II* (Ed.: A. B. P. Lever), Elsevier Pergamon, Amsterdam, Oxford, **2004**, vol. 1, p. 323–347; b) C. Silvestru, J. E. Drake, *Coord. Chem. Rev.* **2001**, *223*, 117–216, and references cited therein.

 © 2006 Wiley-VCH Verlag GmbH & Co. KGaA, Weinheim 

[2] a) C. P. Huber, M. L. Post, O. Siiman, *Acta Crystallogr., Sect. B* **1978**, *34*, 2629–2632; b) H. Liu, A. G. Bandeira, M. J. Calhorda, M. G. B. Drew, V. Felix, J. Novosad, F. Fabrizi de Biani, P. Zanello, *J. Organomet. Chem.* **2004**, *689*, 2808–2819.
[3] R. D. Bereman, F. T. Wang, J. Najdzionek, D. M. Braitsch, *J. Am. Chem. Soc.* **1976**, *98*, 7266–7268.
[4] D. J. Birdsall, A. M. Z. Slawin, J. D. Woollins, *Inorg. Chem.* **1999**, *38*, 4152–4155.
[5] In the case of thiolate ligands, the following multimetallic cuprous thiolate species have been characterised: $Cu_3S_3$, $Cu_4S_4$, $Cu_4S_6$, $Cu_5S_6$, $Cu_5S_7$, $Cu_6S_8$, $Cu_8S_8$, $Cu_8S_{12}$ and $Cu_{12}S_{12}$: I. G. Dance, *Polyhedron* **1986**, *5*, 1037–1104, and references cited therein.
[6] Both Ace1 and Mac1 bind four $Cu^{I}$ ions in their Cu-regulatory domains; at high copper concentrations, copper-loaded Ace1 binds to DNA and activates expression of copper metallothioneins that protect the cell from copper toxicity. In contrast, $Cu^{I}$ binding to Mac1 inhibits its function as a transcriptional activator. a) R. L. Lieberman, A. C. Rosenzweig, *Comprehensive Coordination Chemistry II* (Ed.: A. B. P. Lever), Elsevier Pergamon, Amsterdam, Oxford, **2004**, vol. 8, p. 195–211; b) K. R. Brown, G. L. Keller, I. J. Pickering, H. H. Harris, G. N. George, D. R. Winge, *Biochemistry* **2002**, *41*, 6469–6476; c) I. J. Pickering, G. N. George, C. T. Dameron, B. Kurz, D. R. Winge, I. G. Dance, *J. Am. Chem. Soc.* **1993**, *115*, 9498–9505.
[7] G. L. Abbati, M. C. Aragoni, M. Arca, M. B. Carrea, F. A. Devillanova, A. Garau, F. Isaia, V. Lippolis, M. Marcelli, C. Silvestru, G. Verani, *Eur. J. Inorg. Chem.* **2005**, 589–596, and references cited therein.
[8] D. Cupertino, R. Keyte, A. M. Z. Slawin, D. J. Williams, J. D. Woollins, *Inorg. Chem.* **1996**, *35*, 2695–2697.
[9] S. Husebye, K. Maartmaan-Moe, *Acta Chem. Scand. Ser. A* **1983**, *37*, 439–441.
[10] H. Günther, *NMR Spectroscopy*, John Wiley & Sons, **1995**, 2nd ed., chapter 9, p. 335–389..
[11] M. Baumgartner, W. Bensch, P. Hug, E. Dubler, *Inorg. Chim. Acta* **1987**, *126*, 139–147.
[12] The calculated NBO charges on the sulfur donor atoms of the model compounds $HN(SPH_2)_2$ and $[N(SPH_2)_2]^-$ are –0.486 and –0.707 e, respectively: G. L. Abbati, M. C. Aragoni, M. Arca, F. A. Devillanova, A. C. Fabretti, A. Garau, F. Isaia, V. Lippolis, G. Verani, *Dalton Trans.* **2003**, 1515–1519.
[13] G. L. Abbati, M. C. Aragoni, M. Arca, F. A. Devillanova, A. C. Fabretti, A. Garau, F. Isaia, V. Lippolis, G. Verani, *J. Chem. Soc., Dalton Trans.* **2001**, 1105–1110.
[14] M. C. Aragoni, M. Arca, F. Demartin, M. B. Carrea, F. A. Devillanova, A. Garau, F. Isaia, V. Lippolis, G. Verani, *Eur. J. Inorg. Chem.* **2004**, 4660–4668.
[15] M. Good, R. Hollenstein, M. Vasak, *Eur. J. Biochem.* **2001**, *197*, 655–659.
[16] A. Schmidpeter, R. H. Bohm, H. Groenger, *Angew. Chem.* **1964**, *76*, 870–871.
[17] G. M. Sheldrick, *SADABS, Area-Detector Absorption Correction Program*, Bruker AXS, Inc., Madison, WI, USA, **2000**.
[18] a) SORTAV: R. H. Blessing, *Acta Crystallogr. Sect. A* **1995**, *51*, 33–37; b) R. H. Blessing, *J. Appl. Crystallogr.* **1997**, *30*, 421–426.
[19] G. M. Sheldrick, *SHELX-97, Program for Crystal Structure Refinement*, University of Göttingen, Germany, **1997**.
[20] L. J. Farrugia, *J. Appl. Crystallogr.* **1999**, *32*, 837–838.

Received: July 19, 2005
Published Online: November 22, 2005

 © 2006 Wiley-VCH Verlag GmbH & Co. KGaA, Weinheim 

DOI: 10.1002/ejic.200500654

# Preparation of Semiconductor/Polymer Coaxial Nanocables by a Facile Solution Process

**Shenglin Xiong,[b] Linfeng Fei,[a] Zhenghua Wang,[b] Hong Yang Zhou,[b] Weizhi Wang,[b] and Yitai Qian*[a,b]**

**Keywords:** Hydrothermal synthesis / Nanostructures / Photoluminescence / Semiconductors / Tellurium

We report on the preparation of ultralong semiconductor tellurium/cross-linked PVA coaxial nanocables with a core 20–30 nm in diameter and a surrounding sheath about 5–20 nm in thickness by a simple hydrothermal process. The length of these nanocables can be up to 500–800 μm. In the present synthesis PVA was used as the reducing agent to react with $Na_2TeO_3$, and it also serves as the capping reagent and the source of the sheaths. The synergistic effects of the interaction of cross-linked PVA with the tellurium nanowires could play an important role in the formation of the morphology of the resulting products.

(© Wiley-VCH Verlag GmbH & Co. KGaA, 69451 Weinheim, Germany, 2006)

## Introduction

Nanomaterials with a core/sheath structure as another new type of one-dimensional nanostructures have, in recent years, been attracting more and more interest since these heterostructured nanostructures are constructed of cores and shells of different chemical compositions, which could further improve their functions by the preparation of the core and sheath from different materials.[1–5] In particular, coaxial nanocables with a wire/sheath structure are a kind of potentially useful 1D nanostructure. Recently, some methods have been developed to synthesize nanocables having coaxial structures. For example, $Si/SiO_2$ nanocables and three-layered nanocables consisting of silicon carbide (SiC) cores, amorphous silica intermediate layers, and sheaths of boron nitride and carbon (BNC) have been prepared by a laser ablation method,[6] and a $\beta$-$SiC/SiO_2$ nanocable has been obtained by a carbothermal reduction method.[7] In addition, several solution-based methods have also been developed to generate polymer/polymer, semiconductor/polymer, and metal/polymer nanocables at relatively low temperatures. For instance, polypyrrole/poly(methyl methacrylate) coaxial nanocables have been synthesized by sequential polymerization of monomers within the channels of mesoporous silica, followed by dissolution of the template.[8] CdSe/poly(vinyl acetate) hybrid nanocables have been obtained by growing the semiconductor nanowires inside polymer tubules.[9] Gold nanorods have recently been coated with polystyrene or silica to form cable-like structures,[10] and layer-by-layer deposition of oppositely charged species on nickel nanorods has been adopted to prepare nickel/composite nanocable structures.[11] $Ag/SiO_2$ nanocables can be formed by using a sol–gel method to coat Ag nanowires with amorphous silica,[12] and silver/carbon nanocables can be synthesized by a hydrothermal carbonization co-reduction (HCCR) technique.[13] Very recently, a one-step synthesis of silver/cross-linked PVA nanocables by in situ reduction of $Ag^+$ and $Ag^+$-catalyzed cross-linking of PVA chains under hydrothermal conditions inspired us to evaluate whether such a simple route can be applied to semiconductor/polymer nanocables.[14] Our experimental results are in good agreement with our expectations.

Based on the above idea and strategy, we successfully synthesized ultralong and uniform semiconductor tellurium/polymer nanocables with a 25–35 nm core and 30–40 nm diameter sheath and lengths of 500–800 μm by a facile hydrothermal reduction process using PVA and $Na_2TeO_3$ as starting material at relatively low temperature via a solid solution-solid transformation and the synergistic soft–hard template mechanism. Surprisingly, we found that the aspect ratio of the nanocables with semiconductor tellurium as core and polymer as shell is between 10 and 20000, which may stem mainly from their geometry-dependent properties, and may suggest their use as attractive basic building blocks that can be applied in a variety of applications.[15] In addition, an interesting feature of some nanocables is their tendency to entangle with each other to form raft-like cable bundles in a parallel fashion. The mechanism of formation of these tellurium nanostructures is discussed. To the best of our knowledge, the synthesis of flexible tellurium/poly-

[a] Hefei National Laboratory for Physical Sciences at Microscale and Department of Chemistry, University of Science and Technology of China,
Hefei, Anhui, 230026, China
Fax: +86-551-360-7402
E-mail: ytqian@ustc.edu.cn
[b] Department of Chemistry, University of Science and Technology of China,
Hefei, Anhui, 230026, China

 © 2006 Wiley-VCH Verlag GmbH & Co. KgaA, Weinheim 

mer nanocables has not yet been reported. Meanwhile, this synthetic method may be applied to the fabrication of other semiconductor/polymer nanostructures.

## Results and Discussions

The panoramic morphology of tellurium was observed by field-emission scanning electron microscopy (FESEM), in which the solid samples were mounted on a copper mesh without any dispersion treatment. Parts a and b in Figure 1 show that the final product is composed of nanowires in high yields (close to 100%), with lengths up to 500–800 μm and a uniform morphology. Higher magnification FSEM images (Figure 1, b) indicate that the average diameter of an individual nanowire is about 25–35 nm. TEM images (Figure 1, c–e) reveal that all wires are actually a composite comprised of a smooth core about 25–35 nm in diameter and a surrounding sheath about 5–10 nm in thickness, from which the contrast between surrounding polymer and inner core can be easily observed. One can see that the sheath has a relatively uniform thickness over the entire surface of each nanowire, including both ends, as shown in Figure 1 (c–e). FESEM and TEM both demonstrate that some bundles of cables are formed, and each bundle is composed of several nanocables packed in a parallel fashion (Figure 1, b–d). More-detailed TEM observations revealed that the nanocables structures have a closed end, as shown in Figure 1, e. It is clear that the uniformity in lateral dimension, the level of perfection, and the richness in quantity are obviously due to a good growth environment for the tellurium nanostructures in the current system (see part a in Figure 1).

The as-obtained samples were also examined by XRD (Figure 2). All the reflection peaks in a $2\theta$ range from 20° to 70° can be readily identified with the hexagonal phase of tellurium, with calculated lattice parameters $a$ = 4.457 and $c$ = 5.927 Å, which shows good consistency with the reported data (JCPDS 36-1452).

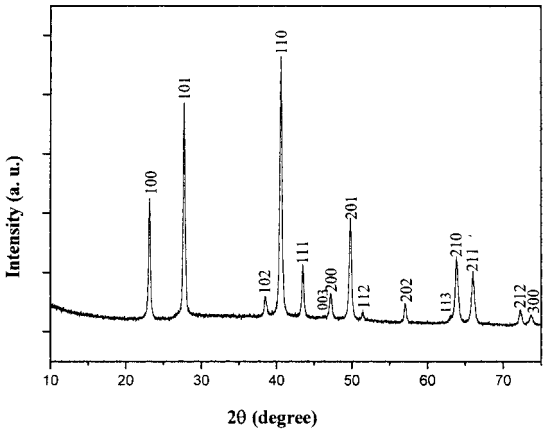


Figure 2. XRD patterns of the nanocables obtained at 180 °C for 24 h.

Further evidence for the surface composition of the samples was obtained from the X-ray photoelectron spectra of the products. The results are shown in Figure 3. The spectra of the nanocables show two strong peaks at 284.60 and 532.10 eV corresponding to the C 1s and O 1s binding energies of the obtained sample, respectively. However, the binding energy at 573.6 and 583.8 eV for $Te^0$ $3d_{5/2}$ and $3d_{3/2}$, respectively, are quite weak and almost cannot be detected. These XPS results confirm that the tellurium nanowires are confined within shells of the cross-linked PVA. The IR spectrum for the as-obtained nanocables is shown in Figure 4. Several absorption peaks located at about 3449, 2923, and 1461 $cm^{-1}$ in Figure 4 correspond to the O–H stretching vibration [ν(O–H)], the C–H stretching vibration [ν(C–H)], and the C–H bending vibration [δ(C–H)], respectively, as in the IR spectrum of pure PVA, while the wide absorption peak at about 1097 $cm^{-1}$ can be assigned to the $\nu_{as}$(C–O–

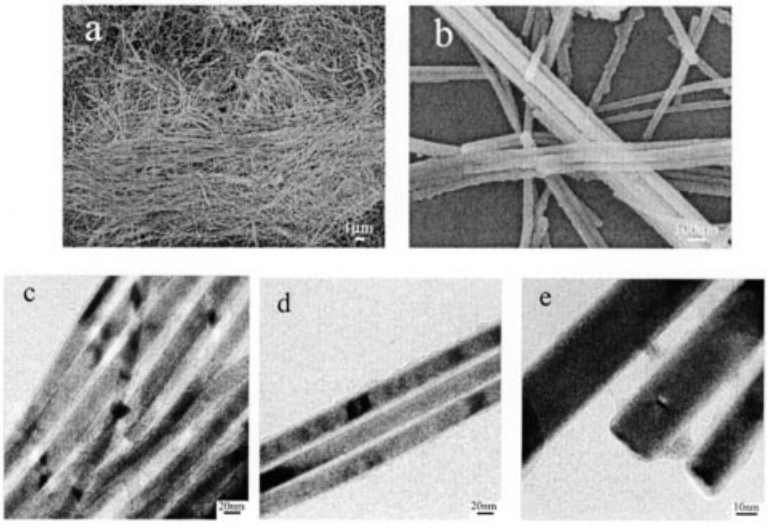


Figure 1. FESEM and TEM images of the nanocables: (a) general view of the cables; (b) magnified FESEM image of the cables; (c–e) TEM images of the cables, clearly revealing the inner core–shell structure.

 © 2006 Wiley-VCH Verlag GmbH & Co. KGaA, Weinheim 

C) absorption of cross-linked PVA. These results confirm that coating of the tellurium nanowires with cross-linked PVA has been achieved using the current hydrothermal method.

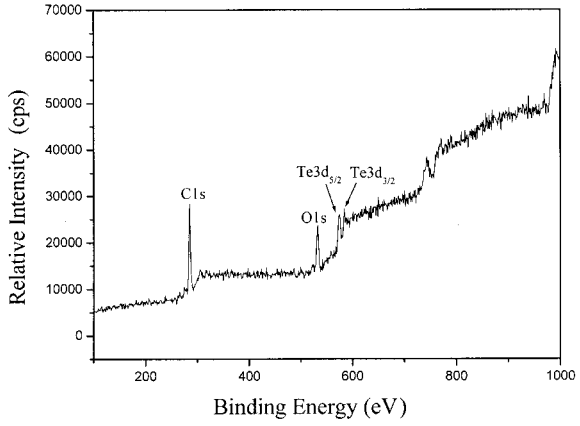


Figure 3. XPS spectrum of the nanocables obtained at 180 °C for 24 h.

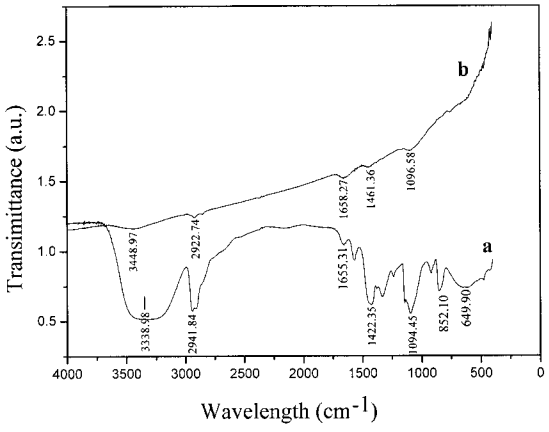


Figure 4. FTIR spectra: (a) pure PVA; (b) the nanocables obtained after reaction at 180 °C for 24 h.

The structure and morphology of the as-obtained nanocables were further observed by high-resolution TEM (HRTEM) and selected-area electron diffraction (SAED), in which the sample was treated by ultrasonic dispersion in ethanol for 15 min and then put onto a copper mesh. Figure 5 (a) shows a typical TEM image of the nanostructures, which confirms that they are composed of a very uniform diameter of the crystalline core surrounded by an amorphous coating. The average diameter of the core of this nanowire is about 25 nm, and the total diameter including the amorphous sheath is about 35 nm. The HRTEM image in Figure 5 (c) recorded from the core tellurium nanowires reveals that the core nanowire shown in the image is about 0.20 nm, which agrees with the (003) lattice planes of t-Te. Figure 5 (b) shows the corresponding ED pattern of the core tellurium nanowires, which was obtained by focusing the electron beam along the [1$\bar{1}$0] zone axis of an individual cable. Moreover, the SAED patterns taken from various regions of the core nanowire are essentially the same. The HRTEM image and ED pattern both demonstrate that the core tellurium nanowire is single-crystalline, with the growth direction along [001]. The perfect diffraction pattern and lattice fringes indicate that the core nanowire is well-crystallized.

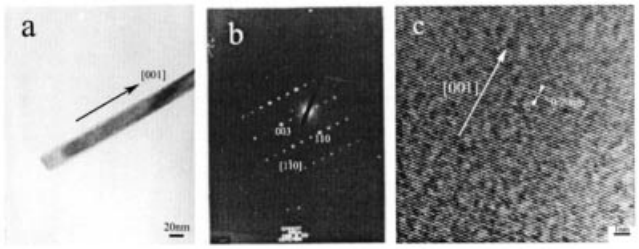


Figure 5. The electron diffraction pattern and HRTEM image of a typical nanocable. HRTEM image (c) taken from the edge of the core tellurium nanowire (a) with growth direction [001], fringe spacing d = 0.2 nm, showing that the core tellurium nanowire is structurally uniform, dislocation free, and single-crystalline. The corresponding ED pattern (b) was obtained from the same tellurium nanostructure, indicating the growth direction and the single-crystalline nature of the core tellurium nanowire.

Further advancement of this approach to nanocables' synthesis requires a clear understanding of the nucleation and growth mechanism. We therefore investigated the evolution of Te nanostructures (taken at the early stages) by TEM. Figure 6 shows the scenarios for the formation of Te nanostructures prepared by the hydrothermal treatment at different times. These images clearly show the evolution of tellurium nanostructures from nanoparticles to nanowires (cables) over time at 180 °C. After heating for 3.5 h, a gray precipitate was formed. The TEM results demonstrated that a large number of irregular nanoparticles with sizes of 10–20 nm and their larger aggregates had formed (Figure 6, a). The SAED patterns (insets of Figure 6, a) clearly reveal that the initial product of the reduction reaction was a mixture of amorphous Te (a-Te) colloids and t-Te nanocrystals. In addition, the colorless solution changed to a yellow-brown color, which implies that PVA has been oxidized by $Na_2TeO_3$ into cross-linked PVA, which is insoluble in water. After 5 h, the products were composed of a mixture of spherical nanoparticles and a small fraction of nanowires. Figure 6 (b) is a typical TEM image of the sample taken from the solution at this stage. It is clear that these nanowires have diameters of about 30 nm and lengths of several hundreds of nanometers. The ED pattern (insets of Figure 6, b) shows that these nanowires are single crystalline t-Te and that the spherical nanoparticles are composed of a mixture of a-Te and t-Te nanoparticles (marked by arrow). After heating for 8 h, nanowires with diameters of about 30 nm and lengths of up to several micrometers can be distinctly observed (Figure 6, c). In addition, at this stage the products also contain a small quantity of nanparticles (less than 10%). Further extending the heating time led to the formation of ultralong nanowires. Figure 6 (d) is a typical TEM image of a sample prepared after heating for 24 h, indicating that the obtained products are dominated by the ultralong wire-like nanostructures. These nanowires are uni-

 © 2006 Wiley-VCH Verlag GmbH & Co. KGaA, Weinheim 

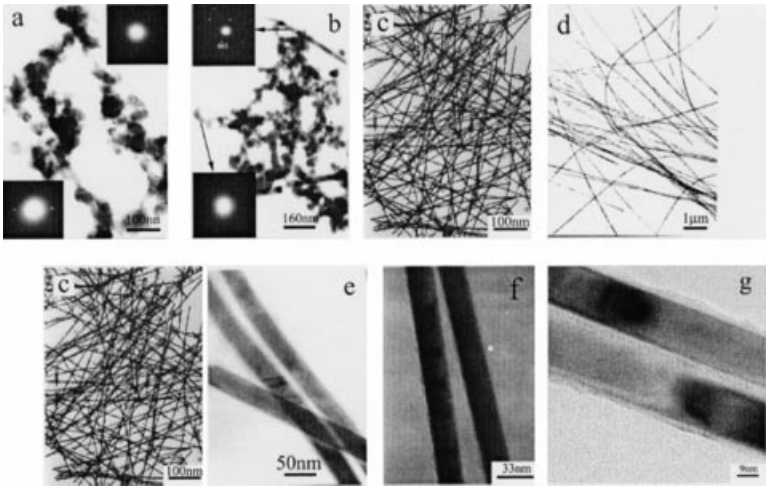


Figure 6. TEM images of Te nanostructures generated by the hydrothermal process after different times: (a) 3.5 h [the insets in Figure 6, part a, show the ED patterns, which indicate that both t-Te (bottom left) and a-Te nanoparticles (upper right) coexist in the initial products]. (b and e) 5 h, a few short nanowires can be observed. (c and f) 8 h and (d and g) 24 h. The insets in Figure 6, part b, are the ED patterns, which reveal that both t-Te nanowires/nanoparticles (upper left) and a-Te nanoparticles (bottom left) coexist in this product (as indicated by arrows).

form in diameter (25–35 nm) and their lengths extend to hundreds of micrometers. From Figure 6 (b–d) one can see that the growth of these nanowires along the longitudinal direction is quite quick, while the growth of their lateral dimensions is very slow and the diameter of nanowires almost does not change during the whole reaction. In addition, one can see that all these nanowires are actually a composite comprised of a core–sheath structure (see Figure 6, e–g), which suggests that the growth of wires and the formation of core–sheath structures occurs simultaneously. Furthermore, the lengths of these nanocables are mainly determined by the original tellurium nanowires and can be as long as several hundreds of micrometers.

As we all know, PVA chains crosslink after treatment at high temperature (250 °C); however, in the absence of $Na_2TeO_3$, we found that hydrothermal treatment of a PVA solution cannot make it cross-linked at 180 °C or even 200 °C, while the cross-linking reaction occurs at 160–180 °C in the presence of $Na_2TeO_3$. These results clearly demonstrate that the current hydrothermal process is an efficient method for promoting the cross-linking reaction. In this hydrothermal process, PVA can be oxidized by $Na_2TeO_3$ at 160–180 °C into cross-linked PVA, which is insoluble in water. As a result, the presence of $Na_2TeO_3$ is essential for the formation of cross-linked PVA and the formation of cables. In addition, when PVA was not added to the reaction system, we found that the reaction could not be initiated at all. In fact, PVA could serve as both reducing reagent and capping reagent in the present synthesis. $Na_2TeO_3$ can be reduced by PVA at 180 °C into tellurium nanoparticles and further grow into nanowires with the assistance of PVA; in turn, the tellurium nanowires serve as a hard template on which the core–sheath structures will form. It is reasonable to assume that, under the present hydrothermal conditions, the formation of the hybrid nanostructures is by synergistic growth, as both the growth of wires and the formation of core–sheath structures occur at the same time and are tightly linked to each other. The good agreement between the experimental data and our expectations suggests that it should be possible to rationally choose appropriate reaction

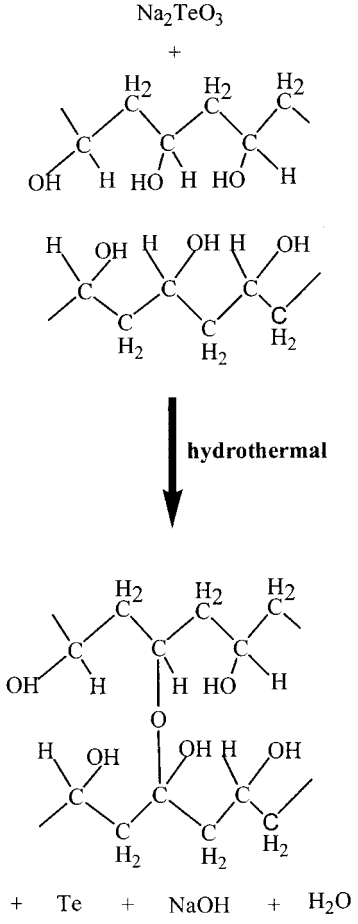


Scheme 1.

 © 2006 Wiley-VCH Verlag GmbH & Co. KGaA, Weinheim 

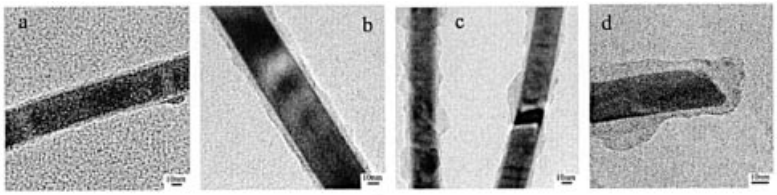


Figure 7. TEM images of tellurium/PVA coaxial nanocables obtained after the coating reaction had processed for (a) 8, (b) 24, (c) 36, and (d) 48 h, clearly showing that the thickness of the sheath increases from 2 to 10–20 nm.

systems for the synthesis of nanocables. In addition, it is worth pointing out that the pH value remains almost the same (10.40 for the starting initial solution to 9.42 for the residual solution) during reaction, thus suggesting that the solution after reaction is still more basic. According to the above results, the reaction that occurs under the current hydrothermal conditions can be formulated as shown in Scheme 1.

The final morphology of the tellurium nanostructures synthesized by the hydrothermal process is highly reliant on the amount of PVA added to the reaction solution. A number of experiments were performed with a procedure similar to that mentioned in the Experimental Section, and we found that the amount of PVA was crucial for the formation of nanocables, with the amount of PVA (5 mL) being suitable for the formation of cables. When the amount of PVA was relatively high (10 mL), no cables and only short tellurium nanorods were obtained as the final products (data not shown). The absence of nanowires (or cables) in the final product could be attributed to the high concentration of PVA, which might lead to the formation of a thick coating over the surface of the nanoparticles. Therefore, the selectivity of the interaction between PVA and various crystallographic planes is weakened, and anisotropic growth can essentially not be induced.

The thickness of the sheath can also be controlled by changing the reaction time. Figure 7 (a–d) show a set of TEM images of the cables that were obtained after different periods of time, and reveal that the thickness of the sheath can be increased by up to 10–20 nm by increasing the reaction time to 48 h. In addition, the amount of PVA and concentration of $Na_2TeO_3$ also play a key role in the formation of tellurium nanostructures. The reaction of $Na_2TeO_3$ (2 mmol) with less PVA (1 mL), with the other conditions remaining the same, gives only tellurium nanoparticles; no nanocables were observed. Moreover, if less $Na_2TeO_3$ (0.5 mmol) was used, with the other conditions remaining unchanged, no cables were obtained.

On the basis of the above results, we propose that the formation of tellurium nanocables follows the PVA-assisted solid solution-solid (SSS) transformation and the synergistic soft–hard template (SSHT) mechanism. It is clear that PVA is responsible for both the formation of tellurium nanoparticles and the subsequent oriented growth of tellurium nanowires. Firstly, the a-Te and t-Te nanoparticles a produced by the reduction of $TeO_3^{2-}$ by PVA at 180 °C. The colloids of a-Te would dissolve into the solution due to their higher free energies than those of t-Te nanocrystals. This dissolved Te (at the expense of a-Te) colloid subsequentlyforms crystalline nanowires on the seeds of t-Te due to the assistant of PVA and the anisotropic nature along the [001] direction.[16] In turn, the tellurium wires serve as a template on which cross-linked PVA forms. In addition, the newly formed cross-linked PVA will act as an effective bridge to connect nearby single cables to form raft-like cable bundles in a parallel fashion. It is worth mentioning that the growth of nanowires and the formation of core–sheath structures occur at the same time (see Figure 6, e–g).

## Conclusions

In conclusion, we have demonstrated a facile hydrothermal synthesis of ultralong nanocables with tellurium as cores and cross-linked PVA as sheaths in high yield. In the present system, the synergistic actions of both the stabilization of PVA and the binding interaction of cross-linked PVA with the tellurium nanowires could play a key role in the formation of the morphology of the resulting products. The current elegant nanocables with a high aspect ratio may have potential technological applications in nanoscience and nanotechnology. Meanwhile, we believe that the present convenient method could be extended to prepare other semiconductor/polymer or metal/polymer coaxial cables by an appropriate choice of reaction system and experimental conditions. Further work in this area is in progress.

## Experimental Section

**Synthesis:** In a typical experimental procedure, analytically pure $Na_2TeO_3$ (2 mmol) and 5 mL of PVA (5 wt.-%) solution were put into 40 mL of distilled water at room temperature to form a clear solution, which was then stirred strongly for about 0.5 h and transferred into a 50-mL Teflon-lined stainless-steel autoclave. The autoclave was sealed and maintained at 180 °C for 24 or 48 h and then air-cooled to room temperature naturally. A large quantity of black-gray, wire-like flocculent material was found floating on the top of the solution. This material was collected and washed with distilled water and anhydrous alcohol several times to remove ions and possible remnants in the final product. It was then dried in a vacuum oven at 60 °C for 4 h.

**Characterization:** The X-ray powder diffraction (XRD) analysis was performed with a Japanese Rigaku D/max-γA rotating anode X-ray diffractometer equipped with monochromatic, high-intensity Cu-$K_\alpha$ radiation ($\lambda$ = 1.54178). The X-ray photoelectron spectra (XPS) were collected on an ESCALab MKII X-ray photoelectron

 © 2006 Wiley-VCH Verlag GmbH & Co. KGaA, Weinheim 

spectrometer, using nonmonochromatized Mg-$K_\alpha$ X-rays as the excitation source. Field emission scanning electron microscope (FESEM) images were taken on a JEOL JSM-6300F SEM. Transmission electron microscopy and electron diffraction (ED) patterns were taken with a Hitachi Model H-800 instrument using an accelerating voltage of 200 kV with a tungsten filament. TEM and high-resolution TEM (HRTEM) were obtained on a JEOL-2010 transmission electron microscope at an acceleration voltage of 200 kV. Infrared (IR) analysis of the precursor was conducted on a Magna IR-750FT Spectrometer ranging from 400 to 4000 $cm^{-1}$ at room temperature with the samples mulled in KBr wafer.

## Acknowledgments

The financial support of this work by the National Natural Science Foundation of China, the 973 Project of China, and a State Key Project of fundamental research of nanomaterials and nanostructures, is gratefully acknowledged.

[1] F. Caruso, *Adv. Mater.* **2001**, *13*, 11–22.
[2] Y. Xia, B. Gates, Y. D. Yin, Y. Lu, *Adv. Mater.* **2000**, *12*, 693–713.
[3] J. J. Schneider, *Adv. Mater.* **2001**, *13*, 529–533.
[4] W. Schärtl, *Adv. Mater.* **2000**, *12*, 1899–1908.
[5] C. J. Kiely, J. Fink, J. G. Zheng, M. Brust, D. Bethell, D. J. Schiffrin, *Adv. Mater.* **2000**, *12*, 640–643.
[6] A. M. Morales, C. M. Lieber, *Science* **1998**, *279*, 208–211.
[7] a) G. W. Meng, L. D. Zhang, C. M. Mo, S. Y. Zhang, Y. Qin, S. P. Feng, H. J. Li, *J. Mater. Res.* **1998**, *13*, 2533–2538; b) L. D. Zhang, G. W. Meng, F. Phillipp, *Mater. Sci. Eng. A* **2000**, *286*, 34–38.
[8] J. Jang, B. Lim, J. Lee, T. Hycon, *Chem. Commun.* **2001**, 83–84.
[9] Y. Xie, Z. Qiao, M. Chen, X. Liu, Y. Qian, *Adv. Mater.* **1999**, *11*, 1512–1515.
[10] S. O. Obare, N. R. Jana, C. J. Murphy, *Nano Lett.* **2001**, *1*, 601–603.
[11] K. S. Mayya, D. I. Gittins, A. M. Dibaj, F. Caruso, *Nano Lett.* **2001**, *1*, 727–730.
[12] Y. Yin, Y. Lu, Y. Sun, Y. Xia, *Nano Lett.* **2002**, *2*, 427–430.
[13] S. H. Yu, X. J. Cui, L. Li, K. Li, B. Yu, M. Antonietti, H. Cölfen, *Adv. Mater.* **2004**, *16*, 1636–1640.
[14] L. B. Luo, S. H. Yu, H. S. Qian, T. Zhou, *J. Am. Chem. Soc.* **2005**, *127*, 2822–2823.
[15] a) P. M. Ajayan, *Chem. Rev.* **1999**, *99*, 1787–1800; b) S. Link, M. A. El-Sayed, *J. Phys. Chem. B* **1999**, *103*, 8410–8426; c) Y. Zhang, K. Suenaga, C. Colliex, S. Iijima, *Science* **1998**, *281*, 973–975.
[16] L. Berg, V. Haase, I. Hinz, G. Kirschstein, H. J. Richter-Ditten, J. Wagner, *Gmelin Handbook of Inorganic Chemistry* (Eds.: G. Czack, D. Koschel, H. K. Kugler), Springer-Verlag, Berlin, **1983**, vol. 8, pp. 1–223.

Received: July 23, 2005
Published Online: November 17, 2005

 © 2006 Wiley-VCH Verlag GmbH & Co. KGaA, Weinheim 

DOI: 10.1002/ejic.200500661

# Theoretical Study of the Effects of Phosphane Substituents on the Bonding Properties of Acetylene with $Ni(PR_3)_2$ (R = H, $CH_3$, F, $CF_3$, $C_6H_5$)

**Manuel Piacenza,[a] Julia Rakow,[a] Isabella Hyla-Kryspin,*[a] and Stefan Grimme*[a]**

**Keywords:** Alkyne ligands / Density functional calculations / Nickel / Phosphane ligands

The bond-formation processes between the $d^{10}$ metal fragments $Ni(PR_3)_2$ (R = H, $CH_3$, F, $CF_3$, Ph) and acetylene have been studied by density functional theory with the BP86 functional and large TZV(2df,2pd) basis sets. The Ni–acetylene bonds have been analyzed in terms of distortion and intrinsic interaction energies within the Dewar–Chatt–Duncanson model of bonding. The intrinsic interaction energies have been corrected for basis set superposition error (BSSE). Linear relationships have been found between the intrinsic interaction energies and the distances of the Ni–C and C≡C bonds as well as with the acetylene–nickel π-backbonding. No linear relationship with respect to the total interaction energies was found. Despite using large basis sets, BSSE still contaminates the interaction energies by 5–10 %. For the $PR_3$ ligands, the BSSE-corrected intrinsic interaction energies of acetylene bonding increase in the order $P(CF_3)_3 < PF_3 < PPh_3 < PH_3 < P(CH_3)_3$ from 58.9 to 77.9 kcal mol$^{-1}$, while the total interaction energies range from 32.9 to 42.4 kcal mol$^{-1}$ in the order $PPh_3 < P(CF_3)_3 < P(CH_3)_3 < PH_3 < PF_3$. These results reveal that the total influence of $PH_3$ and $PPh_3$ on the thermodynamics of the acetylene bonding is different and therefore in this sense $PH_3$ is not a good model of $PPh_3$ in theoretical calculations.

(© Wiley-VCH Verlag GmbH & Co. KGaA, 69451 Weinheim, Germany, 2006)

## Introduction

Alkynes and tertiary phosphanes coordinated to transition metals (TM) have been the subject of extensive experimental and theoretical studies.[1,2] This can be attributed to the specific reactivities of these species, which in the field of organometallic synthesis and catalysis give rise to a wide variety of products.[3,4] Because of the early work of Reppe et al.,[5] it is well known that nickel complexes promote the reactivity of the acetylene triple bond in several catalytic processes such as carbonylation, cyclooligomerization, and cooligomerization. Common to these processes is the presence of acetylene complexes with low-valent $Ni(PR_3)_2$ fragments, where R is mostly a bulky alkyl or aryl group.[3i,6]

In general, the reactivities of coordinated ligands are discussed in terms of steric and electronic effects, although the distinction between them is not always straightforward because both effects are interconnected. The steric properties of $PR_3$ ligands are usually measured by the cone angle, $\theta$, introduced by Tolman.[7] The steric effects for acetylene are less important, but in the case of alkynes with bulky substituents they may also influence the bonding.[8] The electronic effects of alkynes and phosphanes are inherently connected with the Dewar–Chatt–Duncanson (DCD) model,[9] i.e., with the ability of ligands to act as electron density donors and acceptors. Thus, the electronic contribution to a TM–P bond stems from two factors: a σ-donation from the phosphorus lone-pair orbital to empty metal orbitals, and a π-back-donation from occupied metal orbitals to the virtual σ* P–R MOs of the $PR_3$ ligands.[10] It is clear that electron-withdrawing substituents change the basicity of the $PR_3$ ligands and consequently their ability for σ-donation. The classification of donor/acceptor properties of $PR_3$ ligands has long been of interest in both experimental[7,10b,10c,11] and theoretical studies.[2f,2h,12] Due to the presence of a double π-system in alkyne ligands, two donor and two acceptor interactions are possible. As a result, alkynes exhibit a remarkable flexibility of coordination modes, and are able to act as two- or four-electron donors and to occupy up to four coordination sites.[13,14]

In the present work we are interested in the structural, electronic, and energetic properties of the bond-formation processes shown in Scheme 1.

The chosen phosphane substituents offer a broad variety of steric and electronic effects. While theoretical investigations of the effects of phosphane substituents on direct $TM–PR_3$ bonds are more common,[2f,h,12] investigations of the inductive effects on bonding of other ligands are scarce.[2l] To the best of our knowledge, a systematic study of the inductive effect of phosphane substituents on acetylene bonding in complexes **c**, including electron withdrawing and sterically demanding substituents, has not been reported so far. Furthermore, our chosen substituents should provide insight into the question of whether the $PH_3$

[a] Organisch-Chemisches Institut der Universität Münster, Corrensstr. 40, 48149 Münster, Germany
E-mail: ihk@uni-muenster.de
grimmes@uni-muenster.de

 © 2006 Wiley-VCH Verlag GmbH & Co. KgaA, Weinheim 

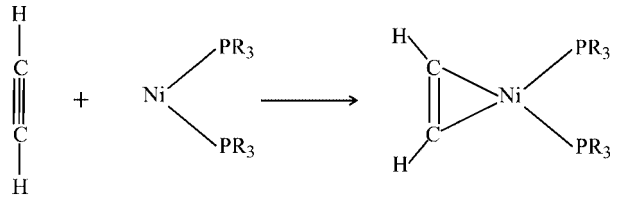

**a** **b** **c**

R = H (**1**), $CH_3$ (**2**), $CF_3$ (**4**), $C_6H_5$ (**5**)

Scheme 1.

ligand, which is frequently used in theoretical studies as a model for bulky organophosphanes,[2,4a,15] is a good substitute for the $PPh_3$ ligand, which is more common in experimental studies.

## Results and Discussion

Before we discuss our results in more detail, we present a simplified picture (Figure 1) of the well known DCD model for the donor–acceptor interactions between the valence π-MOs of acetylene (**a**) and the metal fragments $Ni(PR_3)_2$ (**b**).

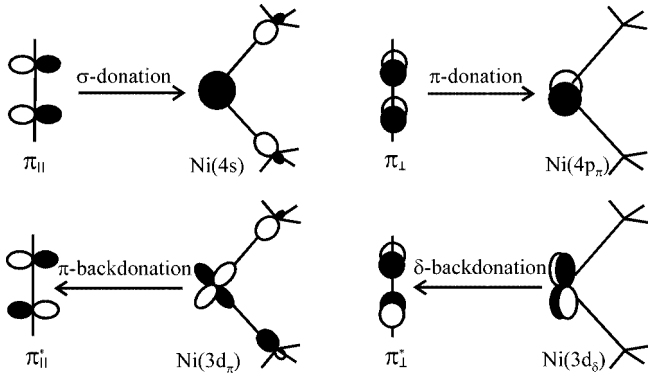


Figure 1. Simplified representation of the DCD model for synergic donor–acceptor interactions between valence MOs of acetylene and $Ni(PR_3)_2$.

Since the nickel 3d levels are fully occupied in complexes **b**, the donation of electron density from acetylene in-plane ($\pi_\parallel$) and out-of-plane ($\pi_\perp$) MOs can take place to the empty nickel levels with predominant 4s and 4p character (Figure 1 top). In these L → TM donation interactions the occupied nickel 3d levels can participate due to second-order mixing only, i.e., due to three-orbital two-electron interactions.[16] In complexes **c** two occupied Ni 3d levels may be involved in backbonding interactions with the empty $\pi_\parallel$* and $\pi_\perp$* MOs of acetylene (Figure 1 bottom). From previous investigations it is well known that the contributions from the out-of-plane L → TM π-donation and M →L δ-back-donation are by far less important than those from the in-plane σ-donation and π-back-donation interactions.[2]

Contrary to homoleptic acetylene–nickel compounds,[13d–13f] complexes **c** prefer a planar molecular structure over a twisted one (Scheme 2).[6,8] In structure **c** the acetylene, nickel, and phosphorus atoms are placed in the same plane while in the twisted structure **c′** the acetylene is rotated by 90° around the $C_2$ axis. Previous calculations on the model complex **1c** have shown that backbonding interactions from the nickel $3d_\pi$ orbital to the acetylene in-plane $\pi_\parallel$* MO account for the stability and preferred molecular geometry of this class of compounds.[2a–2e,2i,2k] In the planar geometry **c** the acetylene–nickel in-plane π-backbonding interaction is enforced by electron density donation from a phosphorus lone-pair out-of-phase combination, which in the twisted geometry **c′** is not possible (Scheme 2).

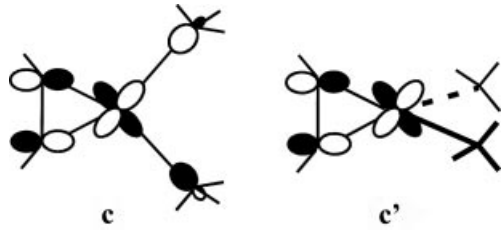

**c** **c'**

Scheme 2.

In order to find out the preferred arrangements of the phosphane ligands in the planar molecular structure of the acetylene complexes **1c**–**5c** and their molecular fragments **1b**–**5b** we first investigated the rotation of the $PR_3$ ligands around the Ni–P bond. For **1b**–**4b** and **1c**–**4c** we considered one $C_s$-symmetric and two $C_{2v}$-symmetric rotamers (Scheme 3). Complexes **5b** and **5c** were optimized in $C_s$ and $C_1$ symmetry. For the sake of clarity the lowest energy structures of **5b** and **5c** are shown in Figure 2; the relative energies of the optimized conformers are presented in Table 1 and selected optimized parameters of the lowest energy structures are collected in Table 2. The energetics for the bond formation between acetylene (**a**) and $Ni(PR_3)_2$ (**b**) are summarized in Table 3 and the results of NBO population analyses in Tables 4 and 5.

From Table 1 it is evident that the different rotamers of **1b**–**4b** and **1c**–**4c** are energetically almost equivalent and the lowest energy structures adopt $C_{2v}$ symmetry. For **1b**–**4b**, **1c**, and **3c** the energy differences are below 0.3 kcal mol$^{-1}$ and for **2c** and **4c** they are only slightly larger [0.7 kcal mol$^{-1}$ (**2c**), 0.9 kcal mol$^{-1}$ (**4c**)]. Due to the steric requirements of the $PPh_3$ ligands, **5b** and **5c** prefer nonsymmetric over $C_s$-symmetric structures, which are less stable by 9.5 and 2.2 kcal mol$^{-1}$, respectively (Table 1).

From Table 1 it is also evident that the lowest energy rotamers of the complexes **2c**–**5c** and the metal fragments **2b**–**5b** are characterized by the same conformation of the phosphane ligands. Although the preferred conformation of the phosphane ligands in the metal fragment **1b-2** differs from that in the complex **1c-1**, the energy difference between **1b-1** and **1b-2** (0.1 kcal mol$^{-1}$) is not relevant for our discussion.

The experimental molecular structures of **1c**–**4c** are not known and only that of **5c** has been determined by X-ray

 © 2006 Wiley-VCH Verlag GmbH & Co. KGaA, Weinheim 

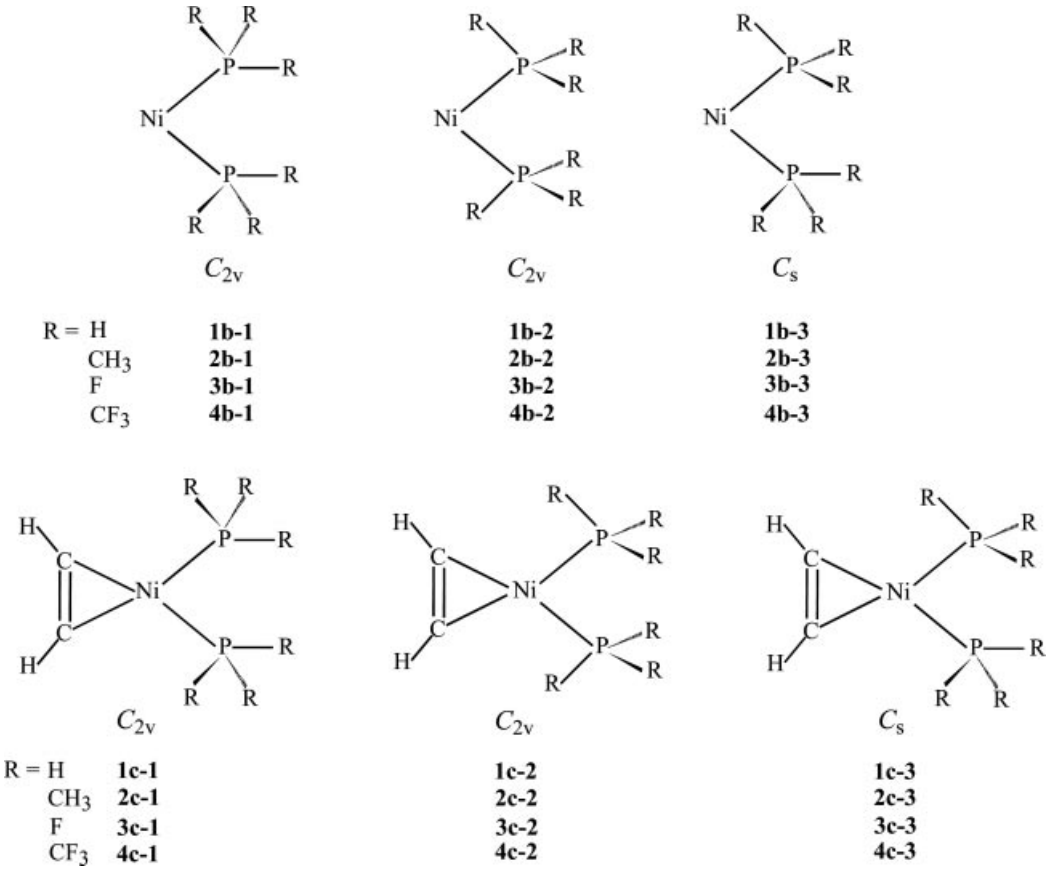


Scheme 3.

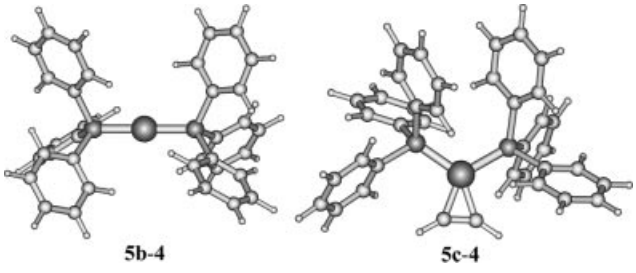


Figure 2. Optimized unsymmetrical molecular structures of **5b** and **5c**.

Table 1. Relative energies [kcal mol$^{-1}$] of the BP86/TZV(2df,2pd)-optimized rotamers of the metal fragments $Ni(PR_3)_2$ (**b**) and the acetylene complexes $C_2H_2Ni(PR_3)_2$ (**c**).

| | | R = H | | R = $CH_3$ | | R = F | | R = $CF_3$ | | R = $C_6H_5$ | |
|---|---|---|---|---|---|---|---|---|---|---|---|
| Symm. | *n* | **1b-*n*** | **1c-*n*** | **2b-*n*** | **2c-*n*** | **3b-*n*** | **3c-*n*** | **4b-*n*** | **4c-*n*** | **5b-*n*** | **5c-*n*** |
| $C_{2v}$ | 1 | 0.1 | 0.0 | 0.0 | 0.0 | 0.1 | 0.1 | 0.0 | 0.0 | | |
| $C_{2v}$ | 2 | 0.0 | 0.2 | 0.0[a] | 0.7 | 0.0 | 0.0 | 0.0[a] | 0.9 | | |
| $C_s$ | 3 | 0.3 | 0.2 | 0.3 | 0.1 | 0.1 | 0.0[a] | 0.0[a] | 0.2 | 9.5 | 2.2 |
| $C_1$ | 4 | | | | | | | | | 0.0 | 0.0 |

[a] Relative energies $\Delta E \leq 0.02$ kcal mol$^{-1}$.

Table 2. Selected optimized parameters of the most stable rotamers of the metal fragments $Ni(PR_3)_2$ (**b**), the acetylene complexes $C_2H_2Ni(PR_3)_2$ (**c**), and acetylene (**a**) in comparison with experimental data, where available.

| R | Structure | Ni–P [Å] | Ni–C [Å] | C≡C [Å] | P–Ni–P ($\beta$) [°] | H–C–C ($\alpha$) [°] |
|---|---|---|---|---|---|---|
| H | **1b-2** | 2.084 | | | 148.4 | |
| | **1c-1** | 2.145 | 1.903 | 1.278 | 107.8 | 148.4 |
| $CH_3$ | **2b-1** | 2.113 | | | 167.2 | |
| | **2c-1** | 2.161 | 1.879 | 1.286 | 114.8 | 145.2 |
| F | **3b-2** | 2.054 | | | 131.2 | |
| | **3c-2** | 2.094 | 1.914 | 1.269 | 108.1 | 152.5 |
| $CF_3$ | **4b-1** | 2.080 | | | 144.7 | |
| | **4c-1** | 2.130 | 1.931 | 1.266 | 121.1 | 152.2 |
| $C_6H_5$ | **5b-4** | 2.132 | | | 179.9 | |
| | **5c-4** | 2.185/2.189 | 1.902/1.911 | 1.279 | 115.6 | 148.5/149.2 |
| | **5c-4**(exp)[a] | 2.153/2.166 | 1.873/1.882 | 1.239 | | 148.0 |
| | $C_2H_2$ | | | 1.207 | | 180.0 |
| | $C_2H_2$(exp) | | | 1.203 | | 180.0 |

[a] X-ray data from ref.[6]

 © 2006 Wiley-VCH Verlag GmbH & Co. KGaA, Weinheim 

Table 3. Calculated energies [kcal mol$^{-1}$] for the reaction of acetylene (**a**) with $Ni(PR_3)_2$ (**b**) to give the complexes **c**, together with counterpoise corrected $\Delta E_3^{CP}$ and $\Delta E^{CP}$ values.[a]

| R | Compl. | $\Delta E_1$ | $\Delta E_2$ | $\Delta E_3$ | $\Delta E$ | $\Delta E_3^{CP}$ | $\Delta E^{CP}$ |
|---|---|---|---|---|---|---|---|
| H | **1c-1** | +18.4 | +13.1 | –78.6 | –47.1 | –71.1 | –39.6 |
| $CH_3$ | **2c-1** | +22.1 | +16.8 | –84.0 | –45.1 | –77.9 | –39.0 |
| $CH_3$[b] | **2c-1** | +22.5 | +15.7 | –126.3 | –88.1 | –108.8 | –70.6 |
| F | **3c-2** | +14.6 | +7.6 | –70.2 | –48.0 | –64.6 | –42.4 |
| $CF_3$ | **4c-1** | +14.1 | +8.3 | –62.6 | –40.2 | –58.9 | –36.5 |
| $C_6H_5$ | **5c-4** | +18.1 | +16.9 | –71.0 | –36.0 | –67.9 | –32.9 |

[a] See Experimental Section for definition of the particular energy components. [b] Results obtained with the SV(d) basis set.

Table 4. Calculated occupancies of acetylene π, phosphorus lone-pair [Lp.(P)] and σ*(P–R) NBOs in complexes **1c**–**5c**.

| | | $C_2H_2$ | | | | $PR_3$ | |
|---|---|---|---|---|---|---|---|
| R | Compl. | $\pi_\parallel$ | $\pi_\perp$ | $\pi_\parallel$* | $\pi_\perp$* | Lp.(P) | σ*(P–R) |
| H | **1c-1** | 1.838 | 1.965 | 0.509 | 0.032 | 1.694 | 0.244 |
| $CH_3$ | **2c-1** | 1.840 | 1.967 | 0.587 | 0.037 | 1.576 | 0.322 |
| F | **3c-2** | 1.836 | 1.956 | 0.456 | 0.024 | 1.505 | 0.653 |
| $CF_3$ | **4c-1** | 1.826 | 1.957 | 0.418 | 0.026 | 1.617 | 0.682 |
| $C_6H_5$ | **5c-4** | 1.842 | 1.963 | 0.520 | 0.039 | 1.581 | 0.380 |

crystallography.[6] Although the optimized bond lengths of **5c-4** are slightly longer than the experimental values (Table 2) the differences are not large (0.03–0.04 Å), and the most important geometrical features are well reproduced by the calculations. Taking into account that the theoretical data refer to the gas phase and are not subject to crystal-packing forces, such small deviations are understandable and are not considered relevant. Furthermore, it is well known that the BP86 functional usually slightly overestimates the bond lengths. The optimized bond lengths and angles of **1c-1** and **2c-1** are in good agreement with results obtained at different levels of theory in previous calculations.[2e,2i,2l]

The Ni–P bonds of **3c-2** (2.094 Å) and **4c-1** (2.130 Å) are shorter than those of **1c-1** (2.145 Å), **2c-1** (2.161 Å), and **5c-4** (2.185/2.189 Å). An opposite effect is observed for the nickel–acetylene bonds, where for complexes with electron-withdrawing substituents in the phosphane ligands the Ni–C bonds are longer [1.914 (**3c-2**) and 1.931 Å (**4c-1**)] than in the other investigated compounds (1.897–1.903 Å). The shortening of the Ni–P bonds as well as the lengthening of the Ni–C bonds of **3c-2** and **4c-1** vs. **1c-1**, **2c-1**, and **5c-4** can be well understood in the framework of the DCD model. The calculated occupancy of the σ*(P–R) NBOs of **3c-2** (0.653) and **4c-1** (0.682) is significantly higher than in the remaining compounds (0.244–0.380; Table 4). Thus, with respect to **1c-1**, **2c-1**, and **5c-4**, the Ni–σ*(P–R) back-bonding interactions of **3c-2** and **4c-1** are stronger. It is clear that an enhancement of Ni–σ*(P–R) backbonding shortens the Ni–P bonds and diminishes the competitive Ni–acetylene backbonding, which, in turn, leads to longer Ni–C bonds. Indeed, the occupancy of acetylene π* NBOs of **3c-2** and **4c-1** is significantly lower than that of **1c-1**, **2c-1**, and **5c-4** (Table 4).

Our results are consistent with the experimental observation that π-acceptor phosphanes normally exhibit shorter TM–P bonds.[17] Furthermore, Table 2 shows that substitution of $PH_3$ by $P(CH_3)_3$ and $PPh_3$ results in an elongation of the Ni–P bonds. It is interesting to note that similar properties have been observed in theoretical studies of $[Fe(CO)_4PR_3]$ compounds.[2f]

The coordination of acetylene (**a**) with $Ni(PR_3)_2$ (**b**) results in molecular deformations, which are obviously endothermic processes (Scheme 4, Table 3). Independent of the phosphane ligands, the deformation of acetylene ($\Delta E_1$) requires more energy than that of the metal fragments $Ni(PR_3)_2$ ($\Delta E_2$) (Table 3).

In complexes **c** acetylene is no longer linear and adopts a *cis* bent structure **d** with a significantly elongated C≡C bond (Table 2). The reasons for the deviation from linearity of coordinated alkynes are similar to those for the pyramidalization of complexed alkenes and have been discussed in detail in the literature.[14a,14b,18] Since, according to NBO population analyses, the electron-density distributions in acetylene with a deformed geometry **d** are the same as for the equilibrium geometry **a**, one can ask whether the deformation energy, $\Delta E_1$, as well as the geometrical changes of the HC≡C bond angle, $\Delta\alpha$, and the C≡C bond length, $\Delta R_{C\equiv C}$, are influenced by the chemical nature of the phosphane ligands. In Figure 3 we present the deformation energies, $\Delta E_1$, as a function of $\Delta\alpha$ and $\Delta R_{C\equiv C}$. From this figure it is evident that almost perfect linear correlations are found.

The $\Delta E_1$ values increase in the order: $P(CF_3)_3 \geq PF_3 >> PPh_3 \geq PH_3 >> P(CH_3)_3$. Thus, phosphanes with electron-withdrawing substituents cause the smallest deformation of the acetylene ligand. Furthermore, the above ordering of the phosphane ligands essentially agrees with the predicted decrease of π-backbonding and an increase of σ-bonding contributions to the Fe–$PR_3$ bonds.[2f] It should also be noted that the inductive effects from the $PH_3$ and $PPh_3$ ligands on acetylene deformation are very similar, as re-

Table 5. Change of NBO occupancies in **1c**–**5c** relative to those of acetylene (**d**) and the corresponding molecular fragments **1e**–**5e**.[a]

| R | Compl. | $\pi_\parallel$ | $\pi_\perp$ | $\pi_\parallel$* | $\pi_\perp$* | 3s+3d$_\sigma$[b] | 3d$_\pi$[b] | 3d$_\delta$[b] | Lp | σ*(P–R) |
|---|---|---|---|---|---|---|---|---|---|---|
| H | **1c-1** | –0.16 | –0.04 | +0.51 | +0.03 | +0.14 | –0.33 | +0.01 | –0.16 | –0.04 |
| $CH_3$ | **2c-1** | –0.16 | –0.03 | +0.58 | +0.04 | +0.09 | –0.34 | +0.01 | –0.12 | –0.04 |
| F | **3c-2** | –0.16 | –0.04 | +0.46 | +0.02 | +0.16 | –0.27 | +0.02 | –0.14 | –0.06 |
| $CF_3$ | **4c-1** | –0.17 | –0.04 | +0.42 | +0.03 | +0.12 | –0.24 | +0.02 | –0.10 | –0.02 |
| $C_6H_5$ | **5c-4** | –0.16 | –0.04 | +0.52 | +0.04 | +0.09 | –0.30 | +0.02 | –0.06 | –0.03 |

[a] Positive sign means an increase of NBO population due to complexation. [b] For the placement of the acetylene, nickel, and phosphorus atoms in the *yz*-plane, d$_\sigma$, d$_\pi$, and d$_\delta$ mean the d$_{z^2}$ d$_{yz}$, and d$_{xy}$ NBOs, respectively.

 © 2006 Wiley-VCH Verlag GmbH & Co. KGaA, Weinheim 

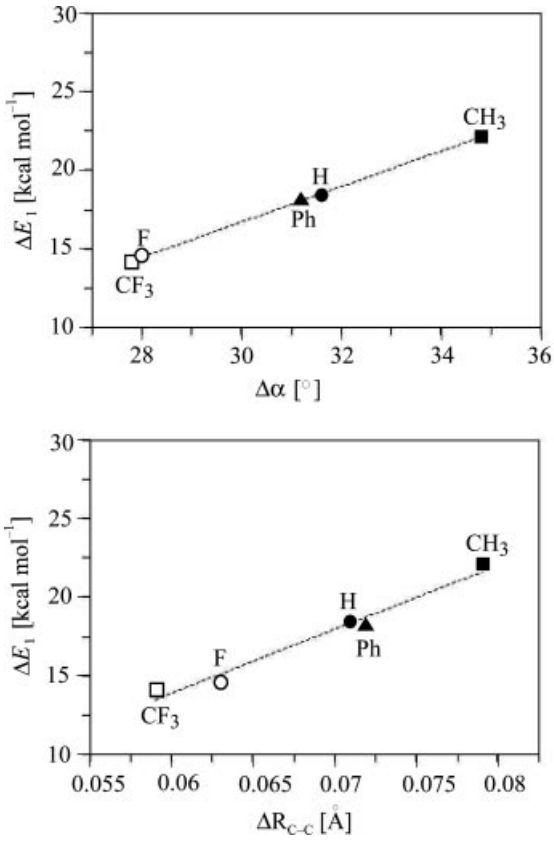


Figure 3. Deformation energy of acetylene ($\Delta E_1$) as a function of the changes in the HC≡C bond angle $\Delta\alpha$ (top) and the C≡C bond length $\Delta R_{C\equiv C}$ (bottom) for the transformation from the equilibrium geometry **a** to the geometries **d** of the $[C_2H_2Ni(PR_3)_2]$ complexes **c** (R = H, $CH_3$, F, $CF_3$, and Ph).

flected by the very close $\Delta E_1$, $\Delta\alpha$, and $\Delta R_{C\equiv C}$ values (Figure 3).

The optimized structures of the metal fragments **1b**–**4b** are bent, where the P–Ni–P bond angles, $\beta$, range from 131° to 167°, while **5b** prefers a linear arrangement of the P–Ni–P unit (Table 2, Figure 2). Our bent structures of **1b**–**4b** agree well with those obtained in an all-electron B3LYP study,[19] but are in disagreement with previous BP86/TZV and B3LYP/LANL2DZ calculations, where linear arrangements were found for the equilibrium geometries of **1b** and **2b**.[2e,2l] Nevertheless, the deformation energies, $\Delta E_2$, of **1b-2** (+13.1 kcal mol$^{-1}$) and **2b-1** (+16.8 kcal mol$^{-1}$) are very close to those reported for the linear structures (12.7 and 16.4 kcal mol$^{-1}$, respectively).[2l] This suggests that the energies of **1b-2** and **2b-1** with a linear P–Ni–P unit should be close to those of the global-minimum bent structures with $\beta$ angles of 148.4° and 167.2°, respectively (Table 2).

In Figure 4 we show the correlation between the deformation energies, $\Delta E_2$, and the $\Delta\beta$ values for the transformation of the $Ni(PR_3)_2$ equilibrium structures **b** into geometries **e**, i.e., to those that they adopt in the corresponding complexes **c** (Scheme 4). Although the $Ni(PPh_3)_2$ fragment bends more strongly upon coordination with acetylene than the $Ni[P(CH_3)_3]_2$ one, the deformation energies, $\Delta E_2$, are the same for both molecular units. This can be attributed to the fact that the distortion from the equilibrium structures **b** to geometries **e** leads not only to geometrical changes but also to different electron-density distributions. For the same reasons, no correlation was found between the $\Delta E_2$ values and the changes in the Ni–P bond lengths. Similar to the $\Delta E_1$ values of acetylene, the lowest $\Delta E_2$ values are obtained for metal fragments with electron-withdrawing substituents (F and $CF_3$).

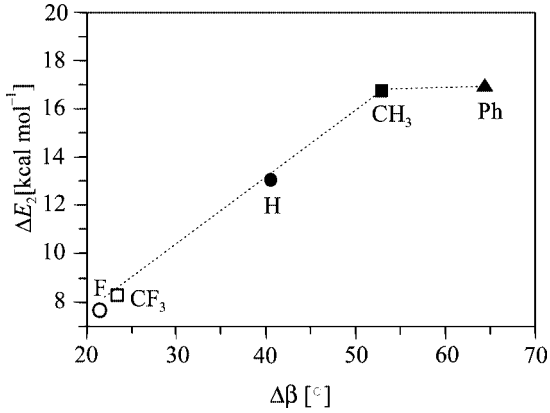


Figure 4. Deformation energy, $\Delta E_2$, as a function of the change in the P–Ni–P bond angle, $\Delta\beta$, for the transformation of the $Ni(PR_3)_2$ (R = H, $CH_3$, F, $CF_3$, Ph) metal fragments from the equilibrium geometries **b** to complex geometries **e**.

Despite using large and flexible basis sets in our studies, the intrinsic interaction energies, $\Delta E_3$, suffer from significant BSSE (Table 3). The BSSE contamination differs from one complex to the other. Thus, in the case of **3c-2** and **5c-4**, for example, the counterpoise corrections increase the difference of the bond-formation energies [$\Delta\Delta E_3 = \Delta E_3$(**3c-2**) – $\Delta E_3$(**5c-4**)] from 0.8 to 3.3 kcal mol$^{-1}$, while an opposite effect is observed for **5c-4** and **1c-1**. The $\Delta\Delta E_3$ values of **5c-4** and **1c-1** diminish from 7.6 to 3.2 kcal mol$^{-1}$ due to counterpoise corrections. Since relative energies are important for our discussion, in the following we will only consider the counterpoise corrected interaction energies. (Note that in theoretical investigations on TM compounds BSSE corrections are rather rarely taken into account, and when low-quality basis sets are used this may lead to wrong conclusions.) As an example, we recalculated the bond-formation process of **2c-1** by using the SV(d) basis set (Table 3). Although the use of the SV(d) basis set does not significantly change the distortion energies $\Delta E_1$ and $\Delta E_2$, the intrinsic interaction energy $\Delta E_3$ (–126.3 kcal mol$^{-1}$) is largely overestimated as compared with the TZV(2df,2pd) value (–84.0 kcal mol$^{-1}$) and the BSSE contamination increases from 7.2% [TZV(2df,2pd)] to 13.9% [SV(d)] (Table 3).

In accord with the DCD model from Scheme 1, the bond-formation processes between acetylene (**d**) and the metal fragments $Ni(PR_3)_2$ (**e**) are accompanied by donor–acceptor interactions between both molecular fragments (Table 5).

The data from Table 5 confirm the very weak nature of the acetylene–nickel out-of-plane π-donation and δ-back-

 © 2006 Wiley-VCH Verlag GmbH & Co. KGaA, Weinheim 

donation interactions. The change in occupancy of acetylene $\pi_\perp$ and $\pi_\perp$* NBOs is much smaller than that of the $\pi_\parallel$ and $\pi_\parallel$* NBOs. In complexes **1c**–**5c**, the decrease of the occupancy of the acetylene $\pi_\parallel$ NBO is of the same magnitude and, consequently, the acetylene–nickel σ-donation interaction cannot be responsible for the different bond strengths. However, sufficiently large differences in NBOs' occupancies are discernible for acetylene–nickel π-backbonding interactions (Table 5). The increase of the occupancy of the acetylene $\pi_\parallel$* NBO as well as the decrease of the occupancy of the relevant Ni 3d$_\pi$ level shows a linear correlation with the intrinsic interaction energies, $\Delta E_3^{CP}$ (Figure 5). It should also be noted that analogous correlations of the entire interaction energies, $\Delta E^{CP}$, are not found.

The changes of bond lengths during bond-formation or bond-breaking processes are often correlated with the bond strengths, i.e., with the corresponding $\Delta E$ or, more rigorously, $\Delta E^{CP}$ values. From the bottom of Figure 6, it is evident that such correlations do not exist either for the newly formed Ni–C bonds or for the elongation of the acetylene triple bond. However, a linear relationship is found with the intrinsic interaction energies $\Delta E_3^{CP}$ (Figure 6, top) for which the ordering of the $PR_3$ ligands [$P(CF_3)_3 < PF_3 < PPh_3 < PH_3 < P(CH_3)_3$] is the same as found for acetylene deformation energies $\Delta E_1$ (Figure 3) or acetylene–nickel in-plane π-backbonding (Figure 5).

In agreement with the opinion of other authors,[2l] these findings point to the conclusion that the intrinsic interaction energies provide a better insight into the chemical nature of the ligand–metal bonds than the usually used $\Delta E$ ($\Delta E^{CP}$) or $D_e$ values. We are aware that the DCD model represents a simplified picture of the acetylene bonding as well as that the intrinsic interaction energies may be further decomposed into contributions from Pauli repulsion and electrostatic and orbital interaction terms. Nonetheless, the correlations from Figures 5 and 6 support the DCD bonding model for the nickel compounds investigated here.

The thermodynamics of bond-formation or bond-breaking processes depend upon the total interaction energies ($\Delta E^{CP}$ or $D_e$). In the case of the $PH_3$ and $PPh_3$ ligands the $\Delta E^{CP}$ values for acetylene bonding differ by 6.7 kcal mol$^{-1}$ and therefore $PH_3$ cannot be considered as a good model for $PPh_3$. It is evident from Table 3 that this difference stems from the deformation energies, $\Delta E_2$, of the $Ni(PH_3)_2$ and $Ni(PPh_3)_2$ fragments and the corresponding intrinsic interaction energies, $\Delta E_3^{CP}$. Upon going from **5c-4** to **1c-1** the deformation energy, $\Delta E_2$, decreases by 3.8 kcal mol$^{-1}$, the intrinsic interaction energy $\Delta E_3^{CP}$ increases by 3.2 kcal mol$^{-1}$, and the deformation energy of acetylene, $\Delta E_1$, changes by only –0.3 kcal mol$^{-1}$ (Table 3). On the other hand, similar $\Delta E^{CP}$ values to those of **1c-1** and **2c-1** do not necessarily indicate a very similar chemical nature of the acetylene bonding. **1c-1** and **2c-1** have almost the same $\Delta E^{CP}$ values (–39.6 and –39.0 kcal mol$^{-1}$, respectively), but their $\Delta E_3^{CP}$ values differ by 6.8 kcal mol$^{-1}$ (Table 3). Finally, it should be noticed that the influence of phosphanes on the bonding properties of other ligands is not necessarily the same as in cases involving cleavage or formation of TM–P bonds. Thus, for example, the $\Delta E^{CP}$ values calculated for the cleavage of the Fe–$PH_3$ and Fe–$P(CH_3)_3$ bonds differ by about 10 kcal mol$^{-1}$, but with respect to $PPh_3$ the Fe–$PH_3$ bond is only 0.5 kcal mol$^{-1}$ stronger.[2f] Since the computational advantage of using H instead of Ph is clear, one can ask whether the change of the cone angle of $PH_3$ may lead to a better model for $PPh_3$. Unfortunately, such changes affect the electronic structure and all energy components. Test calculations on **1c-1** with various cone angles of the $PH_3$ ligands have shown that it is not possible to predict whether and which contributions add up or cancel out without computational knowledge about the $PPh_3$ compound. Therefore, computational model systems should rather be avoided. In our case, calculations on the $PH_3$ com-

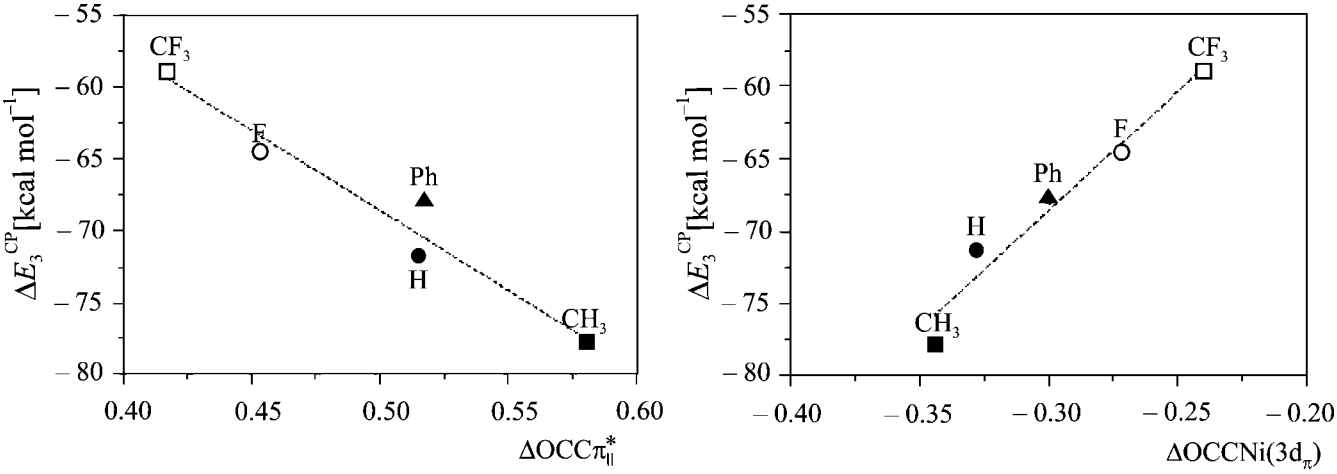


Figure 5. Correlation between intrinsic interaction energies, $\Delta E_3^{CP}$, and changes of the occupancy of acetylene $\pi_\parallel$* NBO and the Ni 3d$_\pi$ level in complexes **1c**–**5c** relative to $C_2H_2$ (**d**) and the metal fragments $Ni(PR_3)_2$ (**e**) (R = H, $CH_3$, F, $CF_3$, Ph).

 © 2006 Wiley-VCH Verlag GmbH & Co. KGaA, Weinheim 

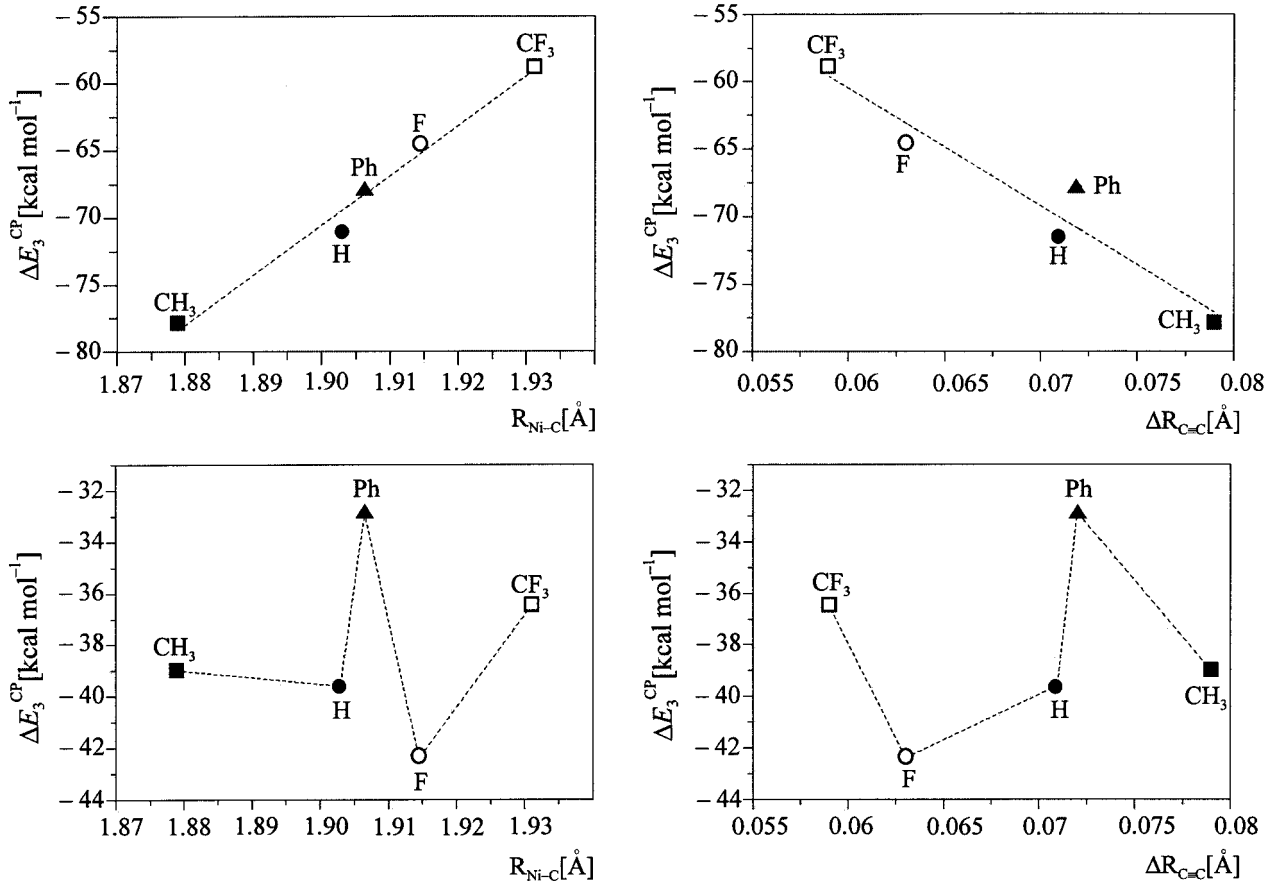


Figure 6. Correlation of the Ni–C bond lengths and the elongation of the C≡C bonds with the interaction energies $\Delta E_3^{CP}$ (top) and $\Delta E^{CP}$ (bottom) for the complexes $(C_2H_2)Ni(PR_3)_2$ (**c**) (R = H, $CH_3$, F, $CF_3$, Ph).

pound **1c-1** with the cone angles of $PPh_3$ from **5c-4** did not improve the model character of the $PH_3$ substitute.

### Concluding Remarks

In this study we have investigated the structures and energetics for the bond-formation processes between acetylene and the metal fragments $Ni(PR_3)_2$. We were interested in the question of how the substituents R (H, $CH_3$, F, $CF_3$ and Ph) in the phosphane ligands influence the nickel–acetylene bonding as well as whether the $PPh_3$ ligand may be modeled in computational studies by smaller, i.e., computationally less demanding, phosphanes. The bond-formation processes were analyzed in terms of distortion energies of acetylene ($\Delta E_1$) and $Ni(PR_3)_2$ ($\Delta E_2$), intrinsic interaction energies ($\Delta E_3$), and the DCD model. We have shown that despite using large TZV(2df,2pd) basis sets, BSSE still contaminates the $\Delta E_3$ values by 5–10% and therefore should be considered in accurate studies, especially in cases where double-ς basis sets with only a single polarization function are used. The effects of phosphane substituents on nickel–acetylene bonding cannot be correlated with total interaction energies ($\Delta E^{CP}$ or $D_e$), although linear correlations were found between the intrinsic interaction energies $\Delta E_3^{CP}$ and (i) the acetylene–nickel in-plane π-backbonding interactions, (ii) the distances of the newly formed Ni–C bonds, and (iii) the elongation of the acetylene triple bond. In these correlations the $\Delta E_3^{CP}$ values change in the order $P(CF_3)_3 < PF_3 < PPh_3 < PH_3 < P(CH_3)_3$. The total interaction energies increase in the order $PPh_3 < P(CF_3)_3 < P(CH_3)_3 < PH_3 < PF_3$. The effects of the phosphane ligands $PPh_3$ and $PH_3$ on the thermodynamics of acetylene bonding are different and therefore $PH_3$ cannot be regarded as a good substitute of $PPh_3$. The differences stem in an almost equal footing from the deformation energies of the metal fragments ($\Delta E_2$) and the intrinsic interaction energies ($\Delta E_3^{CP}$).

## Experimental Section

**Calculational Details:** The geometry optimizations of the complexes $C_2H_2Ni(PR_3)_2$ (**c**) and their molecular fragments $C_2H_2$ (**a**) and $Ni(PR_3)_2$ (**b**) were carried out with the TURBOMOLE 5.6 suite of programs.[20] As a quantum chemical method we have used density functional theory (DFT)[21] with the gradient-corrected BP86 functional[22] and the RI approximation which takes advantage of density fitting for the calculations of the Coulomb integrals.[23] All atoms were described with an all-electron valence triple-ς basis set augmented with polarization functions: (17s11p6d1f)/[6s4p3d1f] for Ni, (14s9p2d1f)/[5s5p2d1f] for P, (11s6p2df)/[5s3p2df] for C and F, and (6s2pd)/[3s2pd] for H, which we denote as TZV(2df,2pd). These basis sets, together with the corresponding auxiliary basis

 © 2006 Wiley-VCH Verlag GmbH & Co. KGaA, Weinheim 

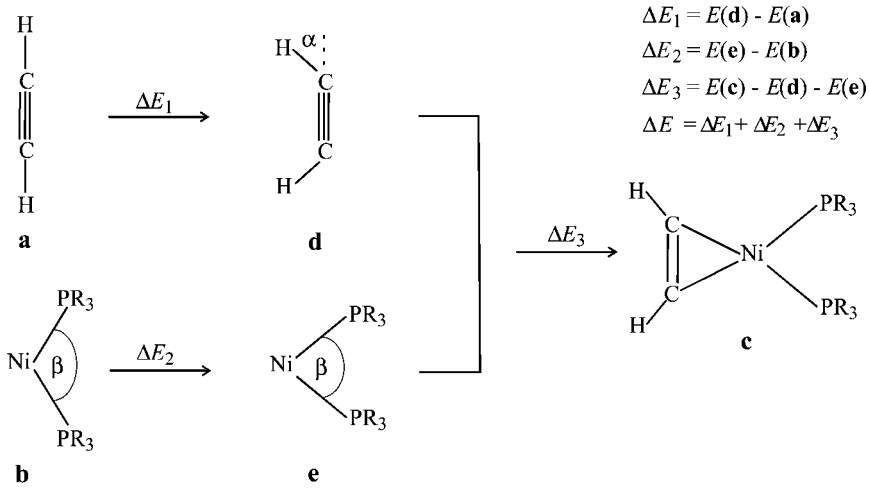


Scheme 4.

sets for the RI approximation, were taken from the TURBOMOLE basis set library.[24] Note that the TZV(2df,2pd) basis sets used here are of significantly higher quality than those employed in many previous theoretical studies on TM compounds of similar size.

The nature of ligand–metal bonds is usually discussed in terms of bond dissociation energies, $D_e$. It is obvious that the bond-formation energy of acetylene (**a**) with fragments $Ni(PR_3)_2$ (**b**) to give the complexes **c**, $\Delta E$, is equal to the negative of the dissociation energy $D_e$, see Equation (1).

$$-D_e = \Delta E = E(\mathbf{c}) - [E(\mathbf{a}) + E(\mathbf{b})] \quad (1)$$

$E(\mathbf{c})$, $E(\mathbf{a})$, and $E(\mathbf{b})$ are the total energies of the corresponding equilibrium structures. In order to obtain deeper insight into acetylene–nickel bonding, the bond-formation energy, $\Delta E$, was partitioned into deformation (also called preparation) energies ($\Delta E_1$ and $\Delta E_2$) and the intrinsic interaction energy ($\Delta E_3$), as shown in Scheme 4.

$\Delta E_1$ and $\Delta E_2$ are the energies that are necessary to transform acetylene (**a**) and $Ni(PR_3)_2$ (**b**) from their equilibrium geometries into the geometries that they adopt in the complexes **c**. $\Delta E_3$ represents the intrinsic interaction energy between the two "prepared" fragments **d** and **e** in the complex **c**. This partitioning scheme allows us to correct the intrinsic interaction energy ($\Delta E_3$) and, consequently, the bond-formation energy, $\Delta E$, for basis set superposition error (BSSE). The BSSE was calculated according to the counterpoise method[25] and the corrected energies are denoted as $\Delta E_3^{CP}$ and $\Delta E^{CP}$. The bond-formation processes were calculated for the closed-shell singlet states of the complexes **c** and their molecular fragments **a**,**d** and **b**,**e**. The electron-density distributions in complexes **c** and the molecular fragments **a**,**d** and **b**,**e** were investigated with the help of natural bond orbital (NBO) procedures.[26] Calculations of the harmonic frequencies for the equilibrium structures were carried out with the SNF program.[27]

## Acknowledgments

This work was supported by the Deutsche Forschungsgemeinschaft in the framework of the SFB 424 ("Molekulare Orientierung als Funktionskriterium in chemischen Systemen").

[1] a) F. R. Hartley, *Comprehensive Organometallic Chemistry* (Ed.: G. Wilkinson), Pergamon Press: Oxford, **1982**; b) P. W. Jolly, G. Wilke, *The Organic Chemistry of Nickel*, Academic Press, New York, **1975**; c) W. Reppe, *Neue Entwicklungen auf dem Gebiet des Acetylens und Kohlenmonooxids*, Springer-Verag, Berlin, **1979**.

[2] a) T. A. Albright, R. Hoffmann, J. C. Thibault, D. L. Thorn, *J. Am. Chem. Soc.* **1979**, *101*, 3801–3812; b) K. Kitaura, S. Sakaki, K. Morokuma, *Inorg. Chem.* **1981**, *20*, 2292–2297; c) T. Ziegler, *Inorg. Chem.* **1985**, *24*, 1547–1552; d) Z. Lin, M. B. Hall, *J. Am. Chem. Soc.* **1992**, *114*, 2928–2932; e) J. Li, G. Schreckenbach, T. Ziegler, *Inorg. Chem.* **1995**, *34*, 3245–3252; f) Ò. González-Blanco, V. Branchadell, *Organometallics* **1997**, *16*, 5556–5562; g) H. Jacobsen, H. Berke, *Chem. Eur. J.* **1997**, *3*, 881–886; h) R. Schmid, W. A. Herrmann, G. Frenking, *Organometallics* **1997**, *16*, 701–708; i) I. Hyla-Kryspin, J. Koch, R. Gleiter, T. Klettke, D. Walther, *Organometallics* **1998**, *17*, 4724–4733; j) F. Nunzi, A. Sgamellotti, N. Re, C. Floriani, *Dalton. Trans.* **1999**, 3487–3491; k) G. Frenking, N. Fröhlich, *Chem. Rev.* **2000**, *100*, 717–774; l) C. Massera, G. Frenking, *Organometallics* **2003**, *22*, 2758–2765.

[3] a) G. Wilke, *Angew. Chem.* **1957**, *69*, 397–398; b) G. Wilke, G. Herrmann, *Angew. Chem.* **1962**, *74*, 693–694; *Angew. Chem. Int. Ed. Engl.* **1962**, *1*, 549–550; c) E. J. Corey, M. F. Semmelhack, *J. Am. Chem. Soc.* **1967**, *89*, 2755–2757; d) G. Wilke, *Pure Appl. Chem.* **1968**, *17*, 179–194; e) P. W. Jolly, I. Tkatchenko, G. Wilke, *Angew. Chem.* **1971**, *83*, 328–329; *Angew. Chem. Int. Ed. Engl.* **1971**, *10*, 328–329; f) M. F. Semmelhack, P. M. Helquist, L. D. Jones, *J. Am. Chem. Soc.* **1971**, *93*, 5908–5910; g) M. F. Semmelhack, *Org. React.* **1972**, *19*, 115–198; h) M. F. Semmelhack, P. M. Helquist, J. D. Gorzynski, *J. Am. Chem. Soc.* **1972**, *94*, 9234–9236; i) G. Wilke, *Angew. Chem.* **1988**, *100*, 189–211; *Angew. Chem. Int. Ed. Engl.* **1988**, *27*, 185–207 and references cited therein.

[4] See also: a) M. Torrent, M. Solà, G. Frenking, *Chem. Rev.* **2000**, *100*, 439–493 and references cited therein; b) W. Siebert, G. Wilke, *J. Organomet. Chem.* **2002**, *641*, 1–2.

[5] a) W. Reppe, W. Sweckendiek, *Justus Liebigs Ann. Chem.* **1948**, *560*, 104–116; b) W. Reppe, O. Schlichting, H. Meister, *Justus Liebigs Ann. Chem.* **1948**, *560*, 93–104; c) W. Reppe, O. Schlichting, K. Klager, T. Toepel, *Justus Liebigs. Ann. Chem.* **1948**, *560*, 1–92.

[6] K. R. Pörschke, Y.-H. Tsay, C. Krüger, *Angew. Chem.* **1985**, *97*, 334–335; *Angew. Chem. Int. Ed. Engl.* **1985**, *24*, 323–324.

[7] C. A. Tolman, *J. Am. Chem. Soc.* **1970**, *92*, 2953–2956.

 © 2006 Wiley-VCH Verlag GmbH & Co. KGaA, Weinheim 

[8] a) K. R. Pörschke, R. Mynott, K. Angermund, C. Krüger, *Z. Naturforsch., Teil B* **1985**, *40*, 199–209; b) U. Rosenthal, G. Oehme, H. Görls, V. V. Burlakov, A. V. Polyakov, A. I. Yanovsky, Yu. T. Struchkov, *J. Organomet. Chem.* **1990**, *389*, 409–416: c) U. Rosenthal, G. Oehme, H. Görls, V. V. Burlakov, A. V. Polyakov, A. I. Yanovsky, Yu. T. Struchkov, *J. Organomet. Chem.* **1990**, *390*, 113–120; d) T. Bartic, B. Happ, M. Iglewsky, H. Bandmann, R. Boese, P. Heimbach, T. Hoffmann, E. Wenschuh, *Organometallics* **1992**, *11*, 1235–1241: e) U. Rosenthal, C. Nauck, P. Arndt, S. Pulst, W. Baumann, V. V. Burlakov, H. Görls, *J. Organomet. Chem.* **1994**, *484*, 81–87.

[9] a) M. J. S. Dewar, *Bull. Soc. Chim. Fr.* **1951**, C71–C79; b) J. Chatt, L. A. Duncanson, *J. Chem. Soc.* **1953**, 2939–2947.

[10] a) S.-X. Xiao, W. C. Trogler, D. E. Ellis, Z. Berkovitch-Yellin, *J. Am. Chem. Soc.* **1983**, *105*, 7033–7037; b) J. A. Tosell, J. H. Moore, J. C. Giordan, *Inorg. Chem.* **1985**, *24*, 1100–1103; c) B. J. Dunne, R. B. Morris, A. G. Orpen, *J. Chem. Soc. Dalton Trans.* **1991**, 653–661.

[11] a) P. B. Dias, M. E. Minas de Piedade, J. A. Martinho Simões, *Coord. Chem. Rev.* **1994**, *135/136*, 737–807: b) R. S. Drago, *Organometallics* **1995**, *14*, 3408–3417; c) S. P. Wang, M. G. Richmond, M. Schwarz, *J. Am. Chem. Soc.* **1992**, *114*, 7595–7596; d) J. Bartholomew, A. L. Fernandez, B. A. Lorsbach, M. R. Wilson, W. P. Giering, *Organometallics* **1996**, *15*, 295–301.

[12] a) D. S. Marynick, *J. Am. Chem. Soc.* **1984**, *106*, 4064–4065; b) M. R. A. Blomberg, U. B. Brandemark, P. E. M. Siegbahn, K. B. Mathisen, G. Karlström, *J. Phys. Chem.* **1985**, *89*, 2171–2180; c) T. L. Brown, *Inorg. Chem.* **1992**, *31*, 1286–1294; d) G. Pacchioni, P. S. Bagus, *Inorg. Chem.* **1992**, *31*, 4391–4398; e) M.-G. Choi, T. L. Brown, *Inorg. Chem.* **1993**, *32*, 5603–5610; f) O. D. Häberlen, N. Rösch, *J. Phys. Chem.* **1993**, *97*, 4970–4973; g) P. Fantucci, S. Polezzo, M. Sironi, A. Bencini, *J. Chem. Soc. Dalton Trans.* **1995**, 4121–4126.

[13] a) O. S. Mills, B. W. Shaw, *J. Organomet. Chem.* **1968**, *11*, 595–699; b) Y. Wang, P. Coppens, *Inorg. Chem.* **1976**, *15*, 1122–1127; c) R. J. Restiva, G. Ferguson, T. W. Ng, A. Carty, *Inorg. Chem.* **1977**, *16*, 172–176; d) D. Walther, A. Schmidt, T. Klettke, W. Imhoff, H. Görls, *Angew. Chem.* **1994**, *106*; 1421–1424; *Angew. Chem. Int. Ed. Engl.* **1994**, *33*, 1373–1376; e) D. Walther, T. Klettke, H. Görls, *Angew. Chem.* **1995**, *107*, 2022–2023; *Angew. Chem. Int. Ed. Engl.* **1995**, *34*, 1860–1861; f) D. Walther, T. Klettke, A. Schmidt, *Organometallics* **1996**, *15*, 2314–2319.

[14] a) D. M. Hoffman, R. Hoffmann, *J. Chem. Soc. Dalton Trans.* **1982**, 1471–1482; b) D. M. Hoffman, R. Hoffmann, R. Fisel, *J. Am. Chem. Soc.* **1982**, *104*, 3858–3875; c) D. J. Underwood, M. Nowak, R. Hoffmann, *J. Am. Chem. Soc.* **1984**, *106*, 2837–2847; d) J. Koch, I. Hyla-Kryspin, R. Gleiter, T. Klettke, D. Walther, *Organometallics* **1999**, *18*, 4942–4948.

[15] S.-Q. Niu, M. B. Hall, *Chem. Rev.* **2000**, *100*, 353–405 and references cited therein.

[16] T. A. Albright, J. K. Burdett, M.-H. Whangbo, *Orbital Interactions in Chemistry*, Wiley, New York, **1985**.

[17] a) H.-Y. Liu, K. Eriks, A. Prock, W. P. Giering, *Organometallics* **1990**, *9*, 1758–1766; b) K. G. Moloy, J. L. Peterson, *J. Am. Chem. Soc.* **1995**, *117*, 7696–7710.

[18] K. Morokuma, W. T. Borden, *J. Am. Chem. Soc.* **1991**, *113*, 1912–1914.

[19] J. Koch, Dissertation: Der Mechanismus der $Ni^0$-katalysierten Hydrocyanierung von Ethen und Propen, Quantenchemische Modellrechnungen, University of Heidelberg, **1997**.

[20] a) R. Ahlrichs, M. Bär, H.-P. Baron, R. Bauernschmitt, S. Böcker, M. Ehrig, K. Eichkorn, S. Elliot, F. Furche, F. Haase, M. Häser, H. Horn, C. Huber, U. Huniar, M. Kattannek, C. Kölmel, M. Kollwitz, K. May, C. Ochsenfeld, H. Öhm, A. Schäfer, U. Schneider, O. Treutler, M. von Arnim, F. Weigend, P. Weis, H. Weiss, TURBOMOLE, Ver. 5.6; University of Karlsruhe, **2003**.; b) M. von Arnim, R. Ahlrichs, *J. Comput. Chem.* **1998**, *19*, 1746–1757.

[21] R. G. Parr, W. Yang, *Density-Functional Theory of Atoms and Molecules*, Oxford University Press, Oxford, **1989**.

[22] a) A. D. Becke, *Phys. Rev. A* **1988**, *38*, 3098–3100; b) J. P. Perdew, *Phys. Rev. B* **1986**, *33*, 8822–8824.

[23] a) K. Eichkorn, O. Treutler, H. Öhm, M. Häser, R. Ahlrichs, *Chem. Phys. Lett.* **1995**, *242*, 652–660; b) O. Treutler, R. Ahlrichs, *J. Chem. Phys.* **1995**, *102*, 346–354.

[24] The basis sets are available from the TURBOMOLE homepage http://www.turbomole.com via the FTP Server Button in the subdirectories basen and jbasen (auxiliary basis set for RIDFT calculations).

[25] S. F. Boys, F. Bernardi, *Mol. Phys.* **1970**, *19*, 553–566.

[26] a) J. P. Foster, F. Weinhold, *J. Am. Chem. Soc.* **1980**, *102*, 7211–7218; b) A. E. Reed, F. Weinhold, *J. Chem. Phys.* **1983**, *78*, 4066–4073; c) A. E. Reead, R. B. Weinstock, F. Weinhold, *Chem. Rev.* **1988**, *88*, 899–926; e) J. E. Carpenter, F. Weinhold, *J. Mol. Struct. (THEOCHEM)* **1988**, *169*, 41.

[27] C. Kind, M. Reiher, J. Neugebauer, B. Hess, SNF (Vers.2.2.1), A program for numerical frequency analyses, University of Erlangen, **2002**.

Received: July 25, 2005
Published Online: November 17, 2005

 © 2006 Wiley-VCH Verlag GmbH & Co. KGaA, Weinheim 

DOI: 10.1002/ejic.200500673

# Monophosphanylcalix[6]arene Ligands: Synthesis Characterization, Complexation, and Their Use in Catalysis

Yasushi Obora,[a] Yun Kui Liu,[a] Sho Kubouchi,[a] Makoto Tokunaga,[a] and Yasushi Tsuji*[a]

**Keywords:** Calixarenes / Heterogeneous catalysis / Phosphanes / Platinum / Rhodium

Novel phosphanylcalix[6]arenes having mono-*O*-diphenylphosphanylmethyl (**3**) and mono-*O*-(4-diphenylphosphanylphenyl)methyl substituents (**5**) have been synthesized. The structures of these monophosphanylcalix[6]arenes were determined by NMR spectroscopy, mass spectrometry, and X-ray crystal structure analysis. The X-ray structure reveals that **3** adopts a flattened 1,2,3-alternate conformation in the crystalline state, while the NMR spectra show that **3** and **5** have a cone conformation in solution. Structure optimization and energy calculations for **3** and **5** at the B3LYP/LANL2DZ-CONFLEX5/MMFF94s level of theory show that the cone conformation is slightly more stable than the 1,2,3-alternate conformation by 0.36 kcal mol$^{-1}$ for **3** and 0.96 kcal mol$^{-1}$ for **5**. Complexation of **3** with $[PtCl_2(COD)]$ and $[Rh(COD)_2]BF_4$ gives *cis*-coordinated $[PtCl_2(\mathbf{3})_2]$ and $[Rh(COD)(\mathbf{3})_2]BF_4$, respectively. The X-ray analysis of $[PtCl_2(\mathbf{3})_2]$ shows that **3** adopts a cone conformation upon complexation. Combination of **3** and **5** with $[Rh(COD)_2]BF_4$ provides an active catalyst for the hydroformylation of a variety of terminal alkenes.

(© Wiley-VCH Verlag GmbH & Co. KGaA, 69451 Weinheim, Germany, 2006)

## Introduction

Calixarenes are macrocyclic compounds having well-defined cavities, and a number of synthetic procedures for their selective functionalization have been developed.[1] In particular, phosphanylcalixarenes,[2] namely phosphanes bearing calixarene moieties, have received considerable attention. Phosphane ligands in general play an important role in transition-metal-catalyzed reactions, and a wide variety of phosphanes have been prepared to realize high catalytic activity and selectivity.[3,4] The phosphanylcalixarenes are attractive ligands since they integrate the strong coordination ability of phosphanes and the unique cavity of the calixarenes to create a spatially confined environment upon complexation with transitional metals.[2]

As far as the size of the cavity is concerned, major attention has been paid to phosphanylcalix[4]arenes[5] due to their rigid conformations. As for the phosphanylcalix[4]arenes, we have reported $Pt^{II}$ and $Pd^{II}$ complexes of a bis(diphenylphosphanyl)calix[4]arene,[6a] solid-state and solution structures of a tetrakis(diphenylphosphanyl)calix[4]arene,[6b] and an $Ru^{II}$ complex of a tetrakis(diphenylphosphanylmethyl)calix[4]arene.[6c] Calix[6]arenes having larger cavities generally display more flexible and variable conformations[7] than calix[4]arenes. Therefore, the chemistry of phosphanylcalix[6]arenes[8] is essentially unexplored owing to their intricacy. We recently synthesized 1,3,5-triphosphanylcalix[6]arene, which functions as a tripodal phosphane ligand to afford novel, capsule-shaped $Ir^{I}$ and $Rh^{I}$ complexes.[9]

In the present study, we describe the synthesis and characterization of novel phosphanylcalix[6]arenes having mono-*O*-diphenylphosphanylmethyl (**3**) and mono-*O*-(4-diphenylphosphanylphenyl)methyl substituents (**5**) as the first examples of a calix[6]arene moiety bearing monodentate phosphane ligands.[10] The monodentate phosphanes are an important class of ligands in transition-metal-catalyzed reactions.[3,11] Furthermore, we have synthesized $Pt^{II}$ and $Rh^{I}$ complexes of **3**, and found that the $Rh^{I}$ complexes of **3** and **5** are active catalysts in the hydroformylation of terminal alkenes.

## Results and Discussion

The monophosphanylcalix[6]arene ligands **3** and **5** were prepared as shown in Scheme 1. According to the reported synthetic procedure for phosphanylcalix[4]arenes[5n,12] and triphosphanylcalix[6]arenes,[9] **3** was prepared as follows. Reaction of **1**[13] with $Ph_2P(O)CH_2OTs$[14] with NaH as a base, in toluene at 90 °C for 2 d, gave the phosphane oxide **2** in 95% yield. Reduction of **2** was carried out with $PhSiH_3$

[a] Catalysis Research Center and Division of Chemistry, Graduate School of Science Hokkaido University, CREST, Japan Science and Technology Agency (JST),
Sapporo 001-0021, Japan
Fax: +81-11-706-9156
E-mail: tsuji@cat.hokudai.ac.jp

Supporting information for this article is available on the WWW under http://www.eurjic.org or from the author.



© 2006 Wiley-VCH Verlag GmbH & Co. KGaA, Weinheim

in toluene under reflux to afford **3** in 90% yield. With regard to the synthesis of **5**, the corresponding phosphane oxide (**4**) was prepared from **1**, $Ph_2P(O)C_6H_4CH_2Br$,[15] and NaH in DMF at 50 °C for 20 h by modifying the reported procedure for mono-*O*-benzylation of calix[6]arenes.[16] The desired phosphane (**5**) was obtained in 82% yield after reduction of **4** with $PhSiH_3$.

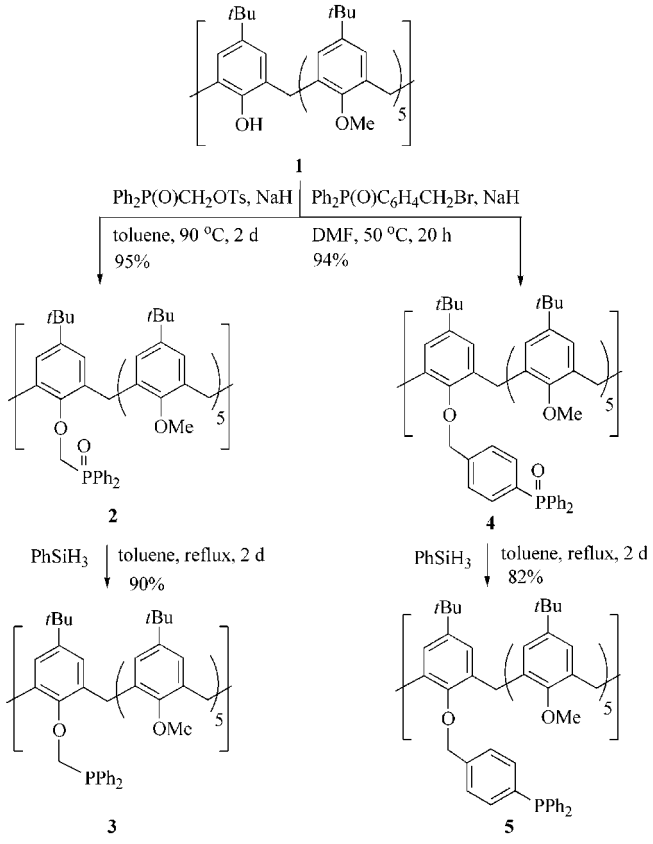


Scheme 1.

These phosphane compounds (**3** and **5**) were characterized by means of NMR spectroscopy, mass spectrometry, elemental analysis, and X-ray crystal structure analysis. The $^{31}P\{^1H\}$ NMR spectra (in $CDCl_3$) of **3** and **5** at 25 °C display single resonances at $\delta$ = –16.5 and –5.6 ppm assignable to alkyldiaryl- and triarylphosphanes, respectively. The ESI or FD mass spectra of **3** and **5** show peaks at *m*/*z* = 1264 $[M + Na]^+$ (for **3**) and 1318 $[M^+]$ (for **5**). The X-ray structure of **3** is shown in Figure 1. The crystallographic data are listed in the Experimental Section and selected atom distances and bond angles of **3** in Table 1. The X-ray structure shows that **3** adopts a 1,2,3-alternate conformation in which three pairs of diametrically opposite phenyl rings (**A** vs. **D**, **B** vs. **E**, and **C** vs. **F**) orient *anti* to each other.[17] Four of these aromatic rings (**A**, **C**, **D**, and **F**) almost stand up in pinched positions whereas the other two aromatic rings (**B** and **E**) splay outwards in flattened positions. Thus, the dihedral angles between the aromatic rings (**A**–**F**) and the calixarene reference plane (the average plane defined by the six bridging methylene carbon atoms; the maximum deviation is 0.2162 Å) are 84.3(1)°, 137.2(1)°, 66.9(1)°, 73.4(1)°, 136.2(1)°, and 68.7(1)°, respectively. This structure can also be designated as a (u,uo,u,d,do,d) conformation, as suggested by Gutsche.[18] Similar 1,2,3-alternate conformations in the crystalline state have also been reported for several hexasubstituted calix[6]arene derivatives.[19]

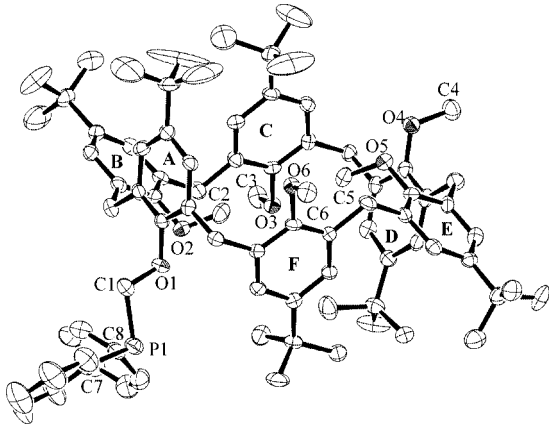


Figure 1. ORTEP drawing of the molecular structure of **3** with thermal ellipsoids at 50% probability levels. Hydrogen atoms have been omitted for clarity.

Table 1. Selected bond lengths [Å] and angles [°] for **3**.

| | | | |
|---|---|---|---|
| P(1)–C(1) | 1.863(6) | P(1)–C(7) | 1.825(6) |
| O(1)–C(1) | 1.420(6) | O(2)–C(2) | 1.431(7) |
| O(3)–C(3) | 1.436(6) | O(4)–C(4) | 1.440(6) |
| O(5)–C(5) | 1.413(7) | O(6)–C(6) | 1.433(7) |
| C(7)–P(1)–C(8) | 102.2(2) | P(1)–C(1)–O(1) | 105.8(3) |

To elucidate the structures of **3** and **5** in solution, $^1H$ and $^{13}C\{^1H\}$ NMR spectra of **3** and **5** were measured in $CDCl_3$ at 25 °C. All the $^1H$ and $^{13}C$ resonances were completely assigned by means of HMBC[20] 2D NMR spectroscopy. In solution, both compounds **3** and **5** show quite similar NMR spectra in terms of the conformation of calix[6]arene moieties. The $^1H$ NMR spectrum of **3** exhibits axial bridging methylene proton resonances as three doublets at $\delta$ = 4.03, 4.19, and 4.35 ppm in a 1:1:1 ratio, and the corresponding equatorial proton resonances as three doublets at $\delta$ = 3.85, 3.70, and 3.48 ppm in a 1:1:1 ratio, with geminal couplings ($J$ = 14–15 Hz). Similarly, the $^1H$ NMR spectrum of **5** displays signals of three axial bridging methylene protons at $\delta$ = 4.04, 4.16, and 4.43 ppm and of three equatorial protons at $\delta$ = 3.81, 3.68, and 3.51 ppm as doublets. With regard to the bridging methylene resonances in the $^1H$ NMR spectra, the difference of the chemical shift ($\Delta\delta$) between the axial and the equatorial pairs is dependent on the orientation of the two adjacent aromatic rings.[21] The $\Delta\delta$ values (0.87, 0.49, and 0.18 ppm for **3** and 0.92, 0.48, and 0.23 ppm for **5**) are quite similar to the values reported for mono-*O*-benzyl-substituted calix[6]arene (0.94, 0.50, and 0.21 ppm), which was assigned a cone conformation in solution.[22] Furthermore, the *tert*-butyl protons appear as four singlet peaks in a 1:1:2:2 ratio ($\delta$ = 0.92, 1.27, 1.06, and 1.30 ppm for **3** and $\delta$ = 0.97, 1.23, 1.02, and 1.24 ppm for **5**), and the methoxy

 © 2006 Wiley-VCH Verlag GmbH & Co. KGaA, Weinheim 

protons as three singlet peaks in a 1:2:2 ratio ($\delta$ = 2.81, 2.50, and 3.26 ppm for **3** and $\delta$ = 2.76, 2.49, and 3.22 ppm for **5**) in the $^1$H NMR spectra. It is well known that a signal arising from the bridging methylene carbon atoms (Ar-$CH_2$-Ar) appears at $\delta \approx 31$ ppm in the $^{13}C\{^1H\}$ NMR spectrum when two adjacent aryl rings are in the *syn* orientation, and close to $\delta$ = 37 ppm for the *anti* orientation.[22,23] Here, the bridging methylene carbon resonances appear at $\delta$ = 30.38, 30.48, and 30.64 ppm for **3** and $\delta$ = 30.42, 30.76, and 30.80 ppm for **5** in 1:1:1 ratios, with no methylene resonances at $\delta$ = 36–38 ppm. The ROESY spectrum of **3** at 25 °C shows that all the equatorial protons have ROE correlations with one of the aromatic protons of the calixarene moiety; no ROE correlation was observed between the axial protons and the aromatic protons (see Figure S2 in the Supporting Information). Variable-temperature $^{13}C\{^1H\}$NMR spectra of **3** in the range from –50 to 25 °C showed that the bridging methylene carbon signals ($\delta$ = 29–31 ppm) remained virtually unchanged, whereas the $^1$H NMR spectra showed that two pairs of bridging methylene doublets ($\delta$ = 4.19/3.70 and 4.03/3.85 ppm) became slightly broadened, while the remaining pair ($\delta$ = 4.35/3.48 ppm) remained as a sharp peak on lowering the temperature to –50 °C. All these NMR spectroscopic data clearly indicate that **3** and **5** adopt a cone conformation[22–24] in solution.[25]

The CPMAS solid-state $^{13}C\{^1H\}$ NMR spectra of **3** (Figure 2) and **5** (as a powder, not a single crystal) show comparable chemical shifts to the solution spectra, although the resonances in the solid state are considerably broader ($\Delta\nu_{1/2}$ = 50–180 Hz). The diagnostic bridging methylene carbon resonances appear at $\delta \approx 30.5$ ppm ($\Delta\nu_{1/2}$ = 172 Hz) for **3** and $\delta \approx 31.1$ ppm (for **5**), rather than at $\delta$ = 36–38 ppm, thus indicating that **3** and **5** have the same cone structure in the solid state as in solution.

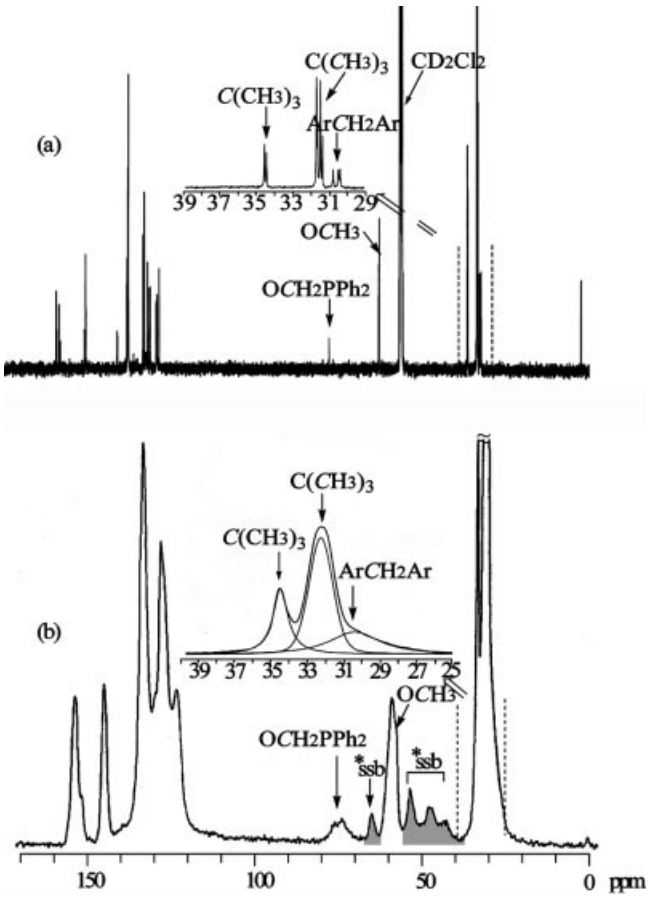


Figure 2. $^{13}C\{^1H\}$ NMR spectra of **3** at 25 °C: (a) measured in $CD_2Cl_2$; (b) measured in the solid state (CPMAS). *ssb: spinning side-band.

The structural differences between the solution (cone), powder (cone), and the single crystal (1,2,3-alternate) suggest that the energy difference between these conformations is very small. Thus, an MO calculation was carried out for the 1,2,3-alternate (Figure 3a for **3**; Figure 3d for **5**) and the cone conformations (Figure 3b for **3**; Figure 3e for **5**) as well as a common 1,3,5-alternate[18] conformation (Figure 3c for **3**; Figure 3f for **5**). In each conformation, conformational analysis of **3** and **5** was carried out by CONFLEX5[26]/MMFF94s[27] to find the lowest-energy structure. The structures were then further optimized by DFT calculations at the B3LYP[28]/LANL2DZ[29] level. The optimized structures are shown in Figure 3a–f, which reproduce the characteristic structural features: (u,uo,u,d,do,d) for the 1,2,3-alternate (Figure 3a and d), (u,u,u,u,u,u) for the cone (Figure 3b and e), and (u,di,u,d,ui,d)[18] for the 1,3,5-alternate conformation (Figure 3c and f). The energy calculations on these optimized structures at the same level (B3LYP/LANL2DZ) revealed that the energy difference between the 1,2,3-alternate and the cone conformations is very small: the latter is slightly more stable than the former but only by 0.36 (for **3**) and 0.96 kcal mol$^{-1}$ (for **5**). However, the 1,3,5-alternate conformation is considerably less stable (11.93 kcal mol$^{-1}$ for **3** and 12.67 kcal mol$^{-1}$ for **5**) than the cone conformation. This result can explain why no 1,3,5-alternate conformations were observed for **3** and **5** and that facile conformational interconversion between the 1,2,3-alternate and the cone takes place to afford the 1,2,3-alternate conformation in the crystal structure, possibly by a preferential crystallization of this conformation.[30]

The $^{13}$C NMR chemical shifts of **3** were calculated by the GIAO (Gauge-Independent Atomic Orbital)[31] method at the HF/6-31G(d) level of theory for the optimized cone (Figure 3b) and the 1,2,3-alternate (Figure 3a) structures. As shown in Table 2 and Figure 4, the calculated chemical shifts of the cone structure are in good correlation with the values observed in $CD_2Cl_2$ ($r^2$ = 0.996), thereby indicating that the calculation is reliable, although the calculated values are smaller than the observed ones by 1.5–5 ppm. It is noteworthy that among the six bridging methylene carbon atoms of the 1,2,3-altenate structure, the calculated chemical shifts of the four carbon atoms ($\delta$ = 28.04, 28.44, 28.45, and 28.46 ppm) of the *syn* orientation are definitely smaller than those of the two carbon atoms of the *anti* orientation ($\delta$ = 32.40 and 32.42 ppm). Such explicit differences would warrant the aforementioned diagnostic bridging methylene carbon resonances of the *syn* and *anti* orientations.

 © 2006 Wiley-VCH Verlag GmbH & Co. KGaA, Weinheim 

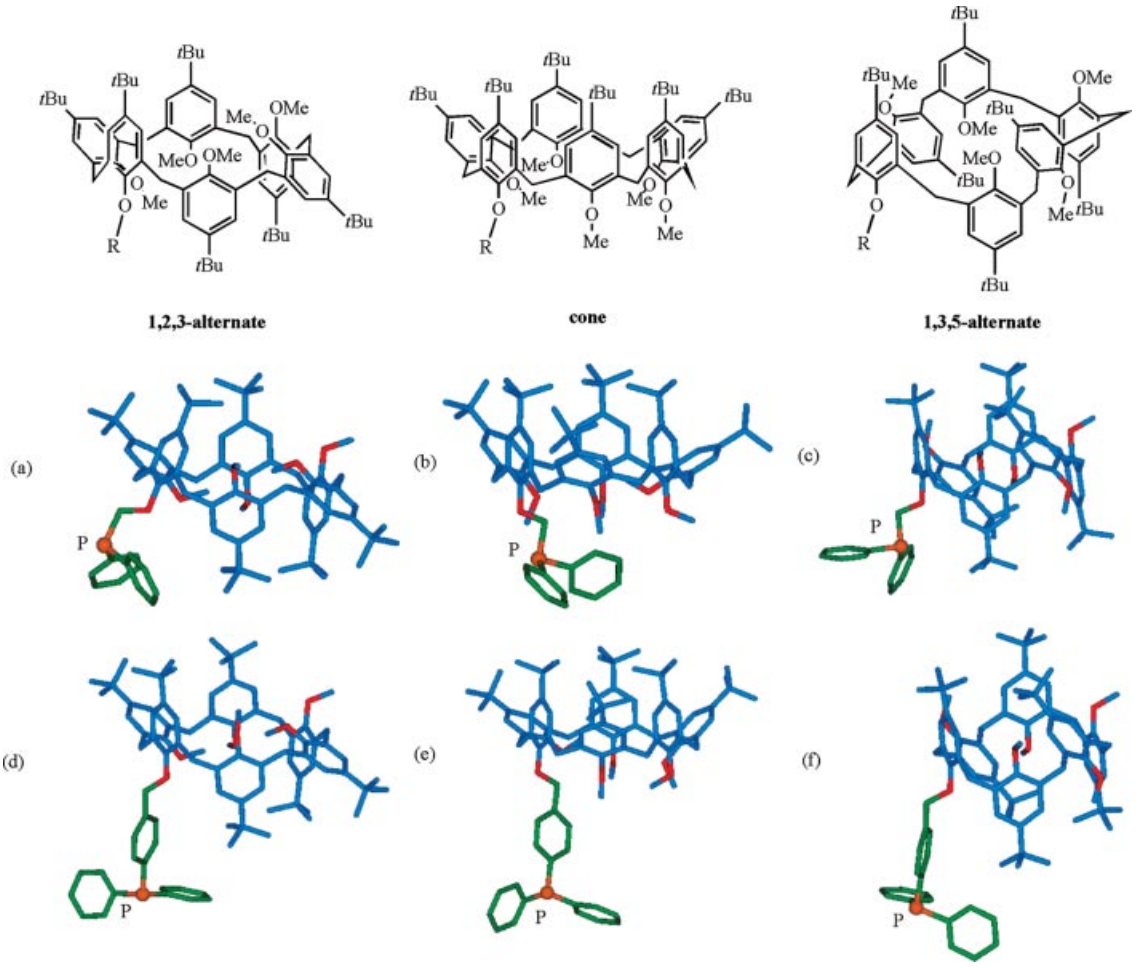


Figure 3. Conformers and optimized structures (B3LYP/LANL2DZ–CONFLEX5/MMFF94s) of **3** [(a) 1,2,3-alternate, (b) cone, (c) 1,3,5-alternate] and **5** [(d) 1,2,3-alternate, (e) cone, (f) 1,3,5-alternate].

Table 2. GIAO calculation of $^{13}C$ NMR chemical shifts [ppm] of **3** at the HF/6-31G(d) level for the cone and the 1,2,3-alternate conformers.

| | Cone | | 1,2,3-Alternate |
|---|---|---|---|
| | Calculated | Experimental[a] | Calculated |
| Ar–$CH_2$–Ar | 27.24 (*syn*) | 30.81 (–3.57) | 28.04 (*syn*), 28.44 (*syn*) |
| | 28.65 (*syn*) | 30.44 (–1.79) | 28.45 (*syn*), 28.46 (*syn*) |
| | 29.05 (*syn*) | 30.53 (–1.48) | 32.40 (*anti*), 32.42 (*anti*) |
| $(CH_3)_3C$–Ar | 28.12 | 31.48 (–3.36) | |
| | 28.23 | 31.38 (–3.15) | 28.32, 28.33, 28.36 |
| | 28.68 | 31.68 (–3.00) | 28.46, 28.68, 28.72 |
| | 28.69 | 31.63 (–2.94) | |
| $(CH_3)_3C$–Ar | 31.21 | 34.34 (–3.13) | |
| | 31.28 | 34.34 (–3.06) | 31.38, 31.40, 31.41 |
| | 31.43 | 34.43 (–3.00) | 31.43, 31.47, 31.65 |
| | 31.43 | 34.43 (–3.00) | |
| $CH_3O$–Ar | 55.18 | 60.20 (–5.02) | 54.09, 54.20 |
| | 55.76 | 60.24 (–4.48) | 55.09, 55.31 |
| | 55.86 | 60.37 (–4.51) | 55.33 |
| O–$CH_2$–$PPh_2$ | 73.18 | 75.02 (–1.84) | 70.80 |

[a] In $CD_2Cl_2$ at 25 °C (Figure 2a). The figures in parentheses show the difference between the calculated and experimental chemical shifts.

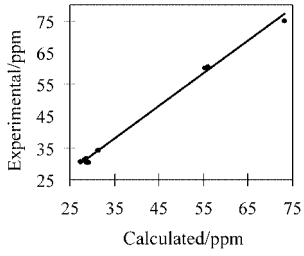


Figure 4. Correlation plots of the calculated vs. experimental $^{13}C$ NMR chemical shifts for the cone conformer.

### Preparation of Platinum(II) and Rhodium(I) Complexes of 3

$Pt^{II}$ and $Rh^{I}$ complexes of **3** were prepared. Compound **3** (2 equiv.) was treated with [$PtCl_2$(COD)] (COD = 1,5-cyclooctadiene) to afford [$PtCl_2$(**3**)$_2$] in 78% yield [Equation (1)]. Characterization of [$PtCl_2$(**3**)$_2$] was performed by NMR spectroscopy, mass spectrometry, elemental analysis, and X-ray crystal structure analysis. The ESI mass spectrum of [$PtCl_2$(**3**)$_2$] exhibits an intense signal for $[M + Na]^+$

 © 2006 Wiley-VCH Verlag GmbH & Co. KGaA, Weinheim 

($m/z$ = 2770). The structure of $[PtCl_2(\mathbf{3})_2]$ was unequivocally confirmed by X-ray diffraction. Figure 5 shows the molecular structure of $[PtCl_2(\mathbf{3})_2]$. The crystal data and selected bond lengths and angles are summarized in the Experimental Section and Table 3, respectively. In contrast to the structure of **3** (Figure 1), the two calix[6]arene moieties in $[PtCl_2(\mathbf{3})_2]$ adopt a cone conformation. The platinum atom is *cis*-coordinated by two phosphane groups and the P1–Pt–P2 bond angle is 97.6(5)°, which is comparable to the value of 98.1(3)° found in *cis*-$[PtCl_2(PMePh_2)_2]$.[32] The Cl(1)–Pt(1)–P(1) and Cl(2)–Pt(1)–P(2) angles are 170.82 (5)° and 172.15 (6)°, respectively. Thus, the geometry of the platinum center is approximately square-planar with a slightly tetrahedral distortion. The Pt–P bond lengths [2.255(1) and 2.247(2) Å] and the Pt–Cl bond lengths [2.359(2) and 2.349(1) Å] are similar to those in *cis*-$[PtCl_2(PMePh_2)_2]$[32] and other phosphanylcalixarene-based $Pt^{II}$ complexes.[33]

$$[PtCl_2(COD)] + \mathbf{3} \xrightarrow[\text{r.t., 2 h}]{CH_2Cl_2} [PtCl_2(\mathbf{3})_2] \quad (1)$$

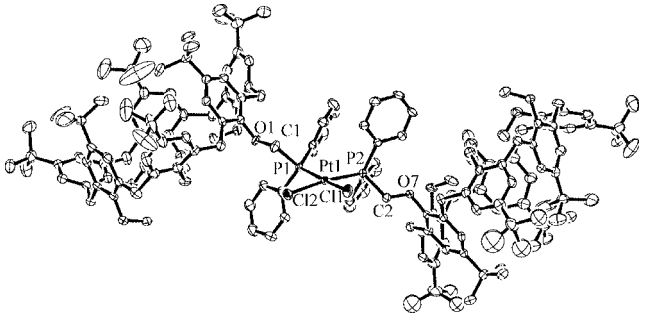


Figure 5. ORTEP drawing of $[PtCl_2(\mathbf{3})_2]$ with thermal ellipsoids at 50% probability levels. Hydrogen atoms have been omitted for clarity.

Table 3. Selected bond lengths [Å] and angles [°] for $[PtCl_2(\mathbf{3})_2]$.

| | | | |
|---|---|---|---|
| Pt(1)–P(1) | 2.255(1) | Pt(1)–P(2) | 2.247(2) |
| Pt(1)–Cl(1) | 2.350(2) | Pt(1)–Cl(2) | 2.359(2) |
| P(1)–C(1) | 1.847(7) | P(2)–C(2) | 1.857(7) |
| O(1)–C(1) | 1.430(8) | O(7)–C(2) | 1.424(7) |
| P(1)–Pt(1)–P(2) | 97.57(5) | Cl(1)–Pt(1)–Cl(2) | 87.28(6) |
| Cl(1)–Pt(1)–P(1) | 170.82(6) | Cl(2)–Pt(1)–P(2) | 172.15(6) |
| O(1)–C(1)–P(1) | 108.9(3) | O(7)–C(2)–P(2) | 109.0(4) |

In solution, the $^1H$ NMR spectrum of $[PtCl_2(\mathbf{3})_2]$ shows the bridging methylene protons as five distinct doublets with geminal couplings of 15 Hz; the other doublet is overlapped by the methoxy proton resonances. The *tert*-butyl protons appear as four singlets in a 1:1:2:2 ratio and the methoxy protons exhibit three distinct resonances with a 1:2:2 ratio. The $^{13}C$ NMR resonances of the bridging methylene carbon atoms appear at $\delta$ = 29.84, 30.33, and 30.54 ppm in a ratio of 1:1:1. All these NMR spectroscopic data indicate that the calixarene moieties of $[PtCl_2(\mathbf{3})_2]$ remain in the cone conformation in solution, as is also the case in the crystalline state (Figure 5). The $^{31}P\{^1H\}$ NMR spectrum displays a singlet peak at $\delta$ = 6.0 ppm with a $^1J_{Pt,P}$ coupling constant of 3611 Hz, which indicates the *cis* coordination of the phosphane ligand.[5a,34] When the *cis* complex was heated at 60 °C for 24 h, no *cis*/*trans* isomerization[35] was observed.

Treatment of **3** with $[Rh(COD)_2]BF_4$ in $CH_2Cl_2$ afforded $[Rh(COD)(\mathbf{3})_2]BF_4$ in 68% yield [Equation (2)]. The ESI mass spectrum of this complex shows an intense peak at $m/z$ = 2694 ($[M - BF_4^-]^+$). In the $^1H$ and $^{13}C\{^1H\}$ NMR spectra of $[Rh(COD)(\mathbf{3})_2]BF_4$ (see Experimental Section), the resonances for the bridging methylene protons and carbon atoms and the *tert*-butyl and methoxy protons indicate that the calix[6]arene moieties also maintain the cone conformation in the complex. The $^{31}P$ NMR spectrum of the complex shows a resonance at $\delta$ = 20.8 ppm ($^1J_{Rh,P}$ = 141 Hz), which is consistent with a *cis*-planar structure as was reported for $[Rh(COD)(DPPB)]BF_4$ [DPPB = 1,4-bis(diphenylphosphanyl)butane; $\delta$ =23.5 ppm ($^1J_{Rh-P}$ = 144 Hz)].[36]

$$[Rh(COD)_2]BF_4 + \mathbf{3} \xrightarrow[\text{r.t., 3 h}]{CH_2Cl_2} [Rh(COD)(\mathbf{3})_2]BF_4 \quad (2)$$

## Hydroformylation Experiments

It is known that (phosphanylcalix[4]arene)rhodium complexes have been found to be active catalysts for the hydroformylation of olefins.[5c,5g,5k,5n,5o] Phosphanylcalix[6]arenes have a larger cavity than phosphanylcalix[4]arenes; therefore, in order to examine the catalytic performance (catalytic activity and regioselectivity) of the novel monophosphanylcalix[6]arene ligands **3** and **5**, $Rh^I$-catalyzed hydroformylations of four different terminal olefins were examined [Equation (3) and Table 4]. The hydroformylation reactions were carried out with a 1:1 mixture of $CO/H_2$ (10 atm) in the presence of $[Rh(COD)_2]BF_4$ combined with **3** or **5** (olefin/Rh/P ratio = 2000:1:4) in benzene at 70 °C. When 1-hexene was employed as substrate, 1-heptanal (linear) and 2-methylhexanal (branched) were formed in 79% (with **3**) and 85% (with **5**) total yields (Entries 1 and 2). The present catalysts also show high activity in hydroformylation of styrene to afford the branched aldehyde as the major product (Entries 3 and 4). These regioselectivities (linear/branched ratios) are similar to those reported with phosphanylcalix[4]-arene ligands[5c,5g,5k,5o,5n] and conventional phosphanes.[37] In the hydroformylation of vinyl acetate and vinyl benzoate, the rhodium catalyst with **3** shows a better catalytic activity than that with **5** and affords branched aldehydes exclusively (Entries 5–8). Thus, the rhodium catalyst system combined with **3** or **5** displays a high catalytic activity for the hydroformylation of various terminal alkenes.

 © 2006 Wiley-VCH Verlag GmbH & Co. KGaA, Weinheim 

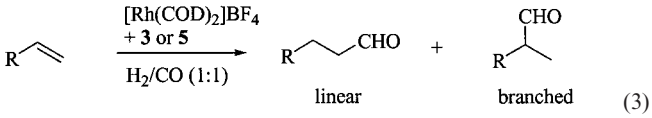


(3)

Table 4. $Rh^{I}$-catalyzed hydroformylations of terminal olefins.[a]

| Entry | Olefin | Ligand | Aldehydes [%] | Linear/branched[b] |
|---|---|---|---|---|
| 1 | 1-hexene | **3** | 79 | 66:34 |
| 2 | | **5** | 85 | 71:29 |
| 3 | styrene | **3** | 81 | 8:92 |
| 4 | | **5** | 91 | 10:90 |
| 5 | vinyl acetate | **3** | 67 | –[c] |
| 6 | | **5** | 24 | –[c] |
| 7 | vinyl benzoate | **3** | 96 | –[c] |
| 8 | | **5** | 57 | –[c] |

[a] Olefin (1.0 mmol), $[Rh(COD)_2]BF_4$ (0.005 mmol), ligand (**3** or **5**) (0.02 mmol) in benzene (2 mL) at 70 °C under 10 atm $CO/H_2$ (1:1). [b] Determined by GC. [c] No linear adduct was detected.

In conclusion, novel monophosphanylcalix[6]arene ligands having mono-*O*-diphenylphosphanylmethyl (**3**) and mono-*O*-(4-diphenylphosphanylphenyl)methyl (**5**) moieties have been prepared, and complexation of **3** with $Pt^{II}$ and $Rh^{I}$ complexes has been carried out. Conformational analysis of the ligands and complexes suggests that the cone is the most stable conformer in both solution and the solid state. However, in the crystalline state, due to a small energy difference between the cone and 1,2,3-alternate conformations, facile interconversion between these conformations takes place to afford the 1,2,3-alternate conformation by preferential crystallization of this conformer.

## Experimental Section

**General:** All reactions were performed under argon using standard Schlenk techniques. Solvents were dried and purified before use by usual methods.[38] $[Rh(COD)_2]BF_4$,[39] $[PtCl_2(COD)]$,[40] and 5,11,17,23,29,35-hexa-*tert*-butyl-38,39,40,41,42-pentamethoxycalix-[6]aren-37-ol (**1**)[15] were prepared according to literature procedures. Medium-pressure column chromatography (Yamazen YFLC-540) was performed on silica gel (Wakogel C-400HG; particle size 20–40 μm) with a UV detector (Yamazen UV-10V). Preparative-scale GPC was carried out with a Japan Analytical Industry LC-9104 instrument equipped with Jaigel-1H-40 and Jaigel-2H-40. $^1H$ (400 MHz), $^{13}C\{^1H\}$ (100 MHz), and $^{31}P\{^1H\}$ NMR (162 MHz) spectra were recorded with a Bruker ARX 400 instrument. The $^1H$ NMR spectroscopic data are referenced relative to residual protonated solvent ($\delta$ = 5.32 and 7.26 ppm in $CD_2Cl_2$ and $CDCl_3$, respectively). $^{13}C$ NMR chemical shifts are reported relative to either $CD_2Cl_2$ ($\delta$ = 53.1 ppm) or $CDCl_3$ ($\delta$ = 77.0 ppm). The $^{31}P$ NMR spectroscopic data are given relative to external 85% $H_3PO_4$. HMBC[20] 2D NMR spectra were recorded with a JEOL α-500 or a JEOL ECX-400 instrument. CPMAS solid-state $^{13}C\{^1H\}$ NMR (100 MHz) spectra were recorded with a JEOL CMXP400 or a JEOL ECX-400 instrument with magic-angle spinning at 8 kHz (for **3**) or 5 kHz (for **5**); the $^{13}C$ NMR spectroscopic data are referenced relative to hexamethylbenzene ($\delta$ = 17.4 ppm). FD and ESI mass spectra were recorded with a JEOL JMS-SX102A instrument at the GC-MS & NMR Laboratory of the Faculty of Agriculture at Hokkaido University. Elemental analysis was performed at the Center for Instrumental Analysis of Hokkaido University. Molecular-orbital calculations were performed with the Gaussian 03 program[41] on a HIT HPC-IA642/SS 1.3/3D-4G.

**5,11,17,23,29,35-Hexa-*tert*-butyl-37-(diphenylphosphanylmethoxy)-38,39,40,41,42-pentamethoxycalix[6]arene (2):** $Ph_2P(O)CH_2OTs$[14] (0.44 g, 1.1 mmol) was added to a suspension of **1**[13] (1.04 g, 1.0 mmol) and NaH (24 mg, 10 mmol) in 24 mL of toluene. The reaction mixture was heated to 90 °C and stirred at this temperature for 2 d. After cooling, the unreacted NaH was neutralized carefully by adding aq. 3% HCl. The crude product was extracted with chloroform and dried with $MgSO_4$. Analytically pure product was obtained by medium-pressure column chromatography with ethyl acetate as an eluent, followed by recrystallization from dichloromethane/ethanol (1:5). Yield: 1.20 g (95%). M.p. 172–174 °C. ESI-MS: $m/z$ = 1256 $[M]^+$. $^1H$ NMR ($CDCl_3$): $\delta$ = 0.83 (s, 9 H), 0.98 (s, 18 H), 1.26 (s, 9 H), 1.29 (s, 18 H), 2.23 (s, 6 H, OC$H_3$), 2.70 (s, 3 H, OC$H_3$), 3.32 (d, $^2J_{H,H}$ = 15 Hz, 2 H, ArC$H_2$Ar), 3.37 (s, 6 H, OC$H_3$), 3.62 (d, $^2J_{H,H}$ = 14 Hz, 2 H, ArC$H_2$Ar), 3.76 (d, $^2J_{H,H}$ = 14 Hz, 2 H, ArC$H_2$Ar), 4.12 (d, $^2J_{H,H}$ = 14 Hz, 2 H, ArC$H_2$Ar), 4.16 (d, $^2J_{H,H}$ = 15 Hz, 2 H, ArC$H_2$Ar), 4.25 (d, $^2J_{H,H}$ = 14 Hz, 2 H, ArC$H_2$Ar), 4.74 [d, $^2J_{P,H}$ = 7 Hz, 2 H, OC$H_2$P(O)$Ph_2$], 6.68 (s, 2 H), 6.77 (s, 2 H), 6.86 (s, 2 H), 7.13 (s, 2 H), 7.15 (s, 4 H), 7.45–7.58 (m, 6 H), 8.03–8.10 (m, 4 H) ppm. $^{13}C\{^1H\}$ NMR ($CDCl_3$): $\delta$ = 29.90, 30.14, 30.19, 31.05, 31.25, 31.48, 31.52, 33.97, 34.00, 34.13, 59.73, 59.86, 60.00, 71.20 [d, $^1J_{P,C}$ = 96 Hz, O*C*H$_2$P(O)$Ph_2$], 124.23, 124.47, 124.87, 126.78, 127.15, 127.43, 128.70 (d, $^2J_{P,C}$ = 11 Hz), 130.84 (d, $^1J_{P,C}$ = 110 Hz), 131.70 (d, $^2J_{P,C}$ = 9 Hz), 132.30, 132.86, 133.20, 133.24, 133.52, 133.58, 145.60, 145.64, 146.56, 151.95 (d, $^3J_{P,C}$ = 13 Hz), 153.34, 154.14, 154.32 ppm. $^{31}P\{^1H\}$ NMR ($CDCl_3$): $\delta$ = 27.9 ppm. $C_{84}H_{105}O_7P{\cdot}H_2O$ (1275.7): calcd. C 79.08, H 8.45; found C 79.44, H 8.40.

**5,11,17,23,29,35-Hexa-*tert*-butyl-37-(diphenylphosphanylmethoxy)-38,39,40,41,42-pentamethoxycalix[6]arene (3):** $PhSiH_3$ (2.78 g, 25.8 mmol) was added to a solution of **2** (1.08 g, 0.86 mmol) in 20 mL of toluene. The reaction mixture was refluxed for 2 d and then cooled down. After evaporation of the volatiles, an analytically pure product was obtained by recrystallization from dichloromethane/ethanol (1:5). Yield: 0.96 g (90%). M.p. 117–119 °C. ESI-MS: $m/z$ = 1264 $[M + Na]^+$. $^1H$ NMR ($CDCl_3$): $\delta$ = 0.92 (s, 9 H), 1.06 (s, 18 H), 1.27 (s, 9 H), 1.30 (s, 18 H), 2.50 (s, 6 H, OC$H_3$), 2.81 (s, 3 H, OC$H_3$), 3.26 (s, 6 H, OC$H_3$), 3.48 (d, $^2J_{H,H}$ = 15 Hz, 2 H, ArC$H_2$Ar), 3.70 (d, $^2J_{H,H}$ = 14 Hz, 2 H, ArC$H_2$Ar), 3.85 (d, $^2J_{H,H}$ = 15 Hz, 2 H, ArC$H_2$Ar), 4.03 (d, $^2J_{H,H}$ = 15 Hz, 2 H, ArC$H_2$Ar), 4.19 (d, $^2J_{H,H}$ = 14 Hz, 2 H, ArC$H_2$Ar), 4.35 (d, $^2J_{H,H}$ = 15 Hz, 2 H, ArC$H_2$Ar), 4.74 (d, $^2J_{P,H}$ = 4 Hz, 2 H, OC$H_2$P$Ph_2$), 6.78 (s, 2 H), 6.87 (s, 2 H), 6.93 (s, 2 H), 7.11 (s, 2 H), 7.15 (s, 2 H), 7.24 (s, 2 H), 7.34–7.38 (m, 6 H), 7.60–7.63 (m, 4 H) ppm. $^{13}C\{^1H\}$ NMR ($CDCl_3$): $\delta$ = 30.38, 30.48, 30.64, 31.15, 31.30, 31.49, 31.53, 33.99, 34.04, 34.15, 59.88, 59.92, 60.00, 74.74 (d, $^1J_{P,C}$ = 9 Hz, O*C*H$_2$P$Ph_2$), 124.20, 124.82, 125.11, 126.62, 126.78, 127.42, 128.50 (d, $^2J_{P,C}$ = 6.3 Hz), 128.83, 133.18, 133.30, 133.42, 133.45, 133.62, 136.37 (d, $^1J_{P,C}$ = 11 Hz), 145.57, 145.90, 153.25 (d, $^3J_{P,C}$ = 5 Hz), 153.56, 154.20, 154.38 ppm. $^{13}C\{^1H\}$ NMR ($CDCl_3$): $\delta$ = 30.38, 30.48, 30.64, 31.15, 31.30, 31.49, 31.53, 33.99, 34.04, 34.15, 59.88, 59.92, 60.00, 74.74 (d, $^1J_{P,C}$ = 9 Hz, O*C*H$_2$P$Ph_2$), 124.20, 124.82, 125.11, 126.62, 126.78, 127.42, 128.50 (d, $^2J_{P,C}$ = 6.3 Hz), 128.83, 133.18, 133.30, 133.42, 133.45, 133.62, 136.37 (d, $^1J_{P,C}$ = 11.4 Hz), 145.57, 145.90, 153.25 (d, $^3J_{P,C}$ = 5 Hz), 153.56, 154.20, 154.38 ppm. $^{13}C\{^1H\}$ NMR ($CD_2Cl_2$): $\delta$ = 30.44, 30.53, 30.81, 31.38, 31.48, 31.63, 31.68, 34.34, 34.43, 60.20, 60.24, 60.37, 75.02 (d, $^1J_{P,C}$ = 9 Hz, O*C*H$_2$P$Ph_2$), 124.60, 125.09, 125.41, 127.19,

 © 2006 Wiley-VCH Verlag GmbH & Co. KGaA, Weinheim 

127.40, 127.89, 128.90 (d, $^2J_{P,C}$ = 6 Hz), 129.30, 133.57, 133.69, 133.88, 133.99, 136.83 (d, $^1J_{P,C}$ = 11 Hz), 146.06, 146.37, 153.50 (d, $^3J_{P,C}$ = 5 Hz), 153.85, 154.54, 154.70 ppm. $^{31}P\{^1H\}$ NMR ($CDCl_3$): $\delta$ = –16.5 ppm. $C_{84}H_{105}O_6P{\cdot}CH_2Cl_2$ (1326.6): calcd. C 76.95, H 8.13; found C 76.91, H 8.14.

**5,11,17,23,29,35-Hexa-*tert*-butyl-37-{(4-diphenylphosphanylphenyl)-methoxy}-38,39,40,41,42-pentamethoxycalix[6]arene (4):** $Ph_2P(O)C_6H_4CH_2Br$[15] (0.782 g, 1.17 mmol) was added to a suspension of **1** (1.00 g, 0.95 mmol) and NaH (46 mg, 1.90 mmol) in DMF (25 mL). The reaction mixture was heated to 50 °C and stirred for 20 h. After cooling to room temperature, the unreacted NaH was slowly quenched with MeOH and $H_2O$. The crude product was extracted with $Et_2O$/toluene (3:1) and dried with $MgSO_4$. After filtration, the solvent was removed in vacuo and analytically pure product was obtained as a light-yellow solid by preparative GPC using chloroform as an eluent. Yield: 1.19 g (94%). FD-MS: *m*/*z* = 1334 $[M]^+$. $^1H$ NMR ($CDCl_3$): $\delta$ = 0.97 (s, 9 H), 1.01 (s, 18 H), 1.23 (s, 27 H), 2.50 (s, 6 H, $OCH_3$), 2.76 (s, 3 H, $OCH_3$), 3.21 (s, 6 H, $OCH_3$), 3.51 (d, $^2J_{H,H}$ = 15 Hz, 2 H, $ArCH_2Ar$), 3.66 (d, $^2J_{H,H}$ = 15 Hz, 2 H, $ArCH_2Ar$), 3.79 (d, $^2J_{H,H}$ = 15 Hz, 2 H, $ArCH_2Ar$), 4.05 (d, $^2J_{H,H}$ = 15 Hz, 2 H, $ArCH_2Ar$), 4.16 (d, $^2J_{H,H}$ = 15 Hz, 2 H, $ArCH_2Ar$), 4.41 (d, $^2J_{H,H}$ = 15 Hz, 2 H, $ArCH_2Ar$), 4.90 (s, 2 H), 6.82 (d, $^4J_{H,H}$ = 2 Hz, 2 H), 6.88 (s, 2 H), 6.89 (d, $^4J_{H,H}$ = 2 Hz, 2 H), 7.08 (d, $^4J_{H,H}$ = 3 Hz, 2 H), 7.11 (s, 2 H), 7.19 (d, $^4J_{H,H}$ = 3 Hz, 2 H), 7.44–7.72 (m, 14 H) ppm. $^{13}C\{^1H\}$NMR ($CDCl_3$): $\delta$ = 30.38, 30.79, 31.36, 31.43, 31.62, 31.70, 34.18, 34.22, 34.26, 59.95, 60.06, 60.11, 73.55, 124.84, 125.06, 125.31, 126.83, 127.07, 127.27, 127.37 (d, $^2J_{P,C}$ = 12 Hz), 128.63 (d, $^2J_{P,C}$ = 12 Hz), 131.27, 132.03, 132.22 (d, $^3J_{P,C}$ = 10 Hz), 132.45 (d, $^3J_{P,C}$ = 11 Hz), 133.11, 133.33, 133.52, 133.63, 133.69, 133.89, 142.17, 142.19, 145.76, 145.87, 146.34, 151.78, 153.68, 154.30, 154.38 ppm. $^{31}P\{^1H\}$NMR ($CDCl_3$): $\delta$ = 29.6 ppm. $C_{90}H_{109}O_7P{\cdot}CHCl_3$ (1453.2): calcd. C 75.21, H 7.63; found C 75.12, H 7.77.

**5,11,17,23,29,35-Hexa-*tert*-butyl-37-{(4-diphenylphosphanylphenyl)-methoxy}-38,39,40,41,42-pentamethoxycalix[6]arene (5):** A suspension of **4** (800 mg, 0.60 mmol) in toluene (12 mL) was refluxed in the presence of $PhSiH_3$ (2.2 mL, 18.0 mmol) for 2 d. The solvent was then removed under reduced pressure and the residue dissolved in $CH_2Cl_2$ (2 mL). Reprecipitation with MeOH afforded the product as a white solid. Analytically pure product was obtained by recrystallization from dichloromethane/MeOH (2:5). Yield: 646 mg (82%). FD-MS: *m*/*z* = 1318 $[M]^+$. $^1H$ NMR ($CDCl_3$): $\delta$ = 0.97 (s, 9 H), 1.02 (s, 18 H), 1.23 (s, 9 H), 1.24 (s, 18 H), 2.49 (s, 6 H, $OCH_3$), 2.76 (s, 3 H, $OCH_3$), 3.22 (s, 6 H, $OCH_3$), 3.51 (d, $^2J_{H,H}$ = 15 Hz, 2 H, $ArCH_2Ar$), 3.68 (d, $^2J_{H,H}$ = 15 Hz, 2 H, $ArCH_2Ar$), 3.81 (d, $^2J_{H,H}$ = 15 Hz, 2 H, $ArCH_2Ar$), 4.04 (d, $^2J_{H,H}$ = 15 Hz, 2 H, $ArCH_2Ar$), 4.16 (d, $^2J_{H,H}$ = 15 Hz, 2 H, $ArCH_2Ar$), 4.43 (d, $^2J_{H,H}$ = 15 Hz, 2 H, $ArCH_2Ar$), 4.86 (s, 2 H, $CH_2$), 6.82 (d, $^4J_{H,H}$ = 2 Hz, 2 H), 6.87 (s, 2 H), 6.90 (d, $^2J_{H,H}$ = 2 Hz, 2 H), 7.08 (d, $^2J_{H,H}$ = 2 Hz, 2 H), 7.11 (s, 2 H), 7.22 (d, $^2J_{H,H}$ = 2 Hz, 2 H), 7.30–7.34 (m, 12 H), 7.49–7.52 (m, 2 H) ppm. $^{13}C$ NMR ($CDCl_3$): $\delta$ = 30.42, 30.76, 30.80, 31.32, 31.39, 31.59, 34.15, 34.16, 34.24, 59.91, 60.01, 60.09, 73.94, 124.66, 125.02, 125.23, 126.86, 127.01, 127.38, 127.81 (d, $^2J_{P,C}$ = 8 Hz), 128.59 (d, $^2J_{P,C}$ = 7 Hz), 128.78, 130.19, 133.32, 133.44, 133.67, 133.72, 133.90, 133.93, 134.13, 145.71, 145.79, 146.10, 151.95, 153.64, 154.30, 154.39 ppm. $^{31}P$ NMR ($CDCl_3$): $\delta$ = –5.62 ppm. $C_{90}H_{109}O_6P{\cdot}CH_3OH$ (1349.8): calcd. C 80.97, H 8.44; found C 80.63, H 8.32.

**$[PtCl_2(3)_2]$:** A solution of ligand **3** (200 mg, 0.16 mmol) in $CH_2Cl_2$ (10 mL) was added to a solution of $[PtCl_2(COD)]$ (29.9 mg, 0.08 mmol) in 6 mL of $CH_2Cl_2$ over a period of 15 min. The solution was stirred at room temperature for 2 h. The resulting solution was then concentrated to about 0.5 mL under vacuum and the product was precipitated with ethanol (3 mL). The solid obtained was filtered and washed with ethanol to afford a pure product. Yield: 172 mg (78%). ESI-MS: *m*/*z* = 2770 $[M + Na]^+$. $^1H$ NMR ($CDCl_3$): $\delta$ = 0.76 (s, 18 H), 0.88 (s, 36 H), 1.31 (s, 18 H), 1.32 (s, 36 H), 2.03 (s, 12 H, $OCH_3$), 2.43 (s, 6 H, $OCH_3$), 3.05 (d, $^2J_{H,H}$ = 15 Hz, 4 H, $ArCH_2Ar$), 3.47–3.57 (m, 16 H, $OCH_3$ overlapped with $ArCH_2Ar$), 3.66 (d, $^2J_{H,H}$ = 15 Hz, 4 H, $ArCH_2Ar$), 3.72 (d, $^2J_{H,H}$ = 15 Hz, 4 H, $ArCH_2Ar$), 4.23 (d, $^2J_{H,H}$ = 15 Hz, 4 H, $ArCH_2Ar$), 4.30 (d, $^2J_{H,H}$ = 15 Hz, 4 H, $ArCH_2Ar$), 5.07 (br. s, 4 H, $OCH_2PPh_2$), 6.51 (br. s, 4 H), 6.69 (br. s, 4 H), 6.74 (br. s, 4 H), 7.06 (br. s, 4 H), 7.10–7.23 (m, 16 H), 7.27–7.37 (m, 4 H), 7.78–7.90 (m, 8 H) ppm. $^{13}C\{^1H\}$ NMR ($CDCl_3$): $\delta$ = 29.84, 30.33, 30.54, 31.40, 31.60, 31.98, 34.33, 34.38, 34.57, 59.82, 60.34, 77.27, 77.59, 124.24, 124.63, 125.40, 126.53, 127.49, 127.66, 128.22, 128.76, 131.90, 133.14, 133.44, 133.55, 133.93, 134.05, 135.06, 135.15, 136.37 145.87, 146.01, 146.91, 153.47, 154.70 ppm. $^{31}P\{^1H\}$ NMR ($CDCl_3$): $\delta$ = 6.0 ($^1J_{Pt,P}$ = 3611 Hz) ppm. $C_{168}H_{210}Cl_2O_{12}P_2Pt{\cdot}CH_2Cl_2$ (2834.3): calcd. C 71.62, H 7.54; found C 71.45, H 7.57.

**$[Rh(COD)(3)_2]BF_4$:** A solution of ligand **3** (100 mg, 0.08 mmol) in $CH_2Cl_2$ (12 mL) was added to a solution of $[Rh(COD)_2]BF_4$ (17.2 mg, 0.04 mmol) in 6 mL of THF over a period of 15 min. The solution was stirred at room temperature for 3 h. Removal of the solvent gave a crude product as yellow solid, which was purified by reprecipitation from $CH_2Cl_2$ solution with hexane. Yield: 72.4 mg (68%). ESI-MS: *m*/*z* = 2694 $[M - BF_4^-]^+$. $^1H$ NMR ($CDCl_3$): $\delta$ = 0.76 (s, 18 H), 0.91 (s, 36 H), 1.30 (s, 18 H), 1.34 (s, 36 H), 2.09 (s, 12 H, $OCH_3$), 2.24–2.41 (m, 8 H), 2.46 (s, 6 H, $OCH_3$), 2.58 (br., 4 H), 2.66 (d, *J* = 15 Hz, 4 H, $ArCH_2Ar$), 3.51 (s, 12 H, $OCH_3$), 3.61 (d, *J* = 14 Hz, 4 H, $ArCH_2Ar$), 3.66 (d, $^2J_{H,H}$ = 15 Hz, 4 H, $ArCH_2Ar$), 4.23 (d, $^2J_{H,H}$ = 15 Hz, 4 H, $ArCH_2Ar$), 4.30 (d, $^2J_{H,H}$ = 15 Hz, 4 H, $ArCH_2Ar$), 4.54 (br., 4 H, $OCH_2PPh_2$), 5.10 (br., 4 H), 6.46 (br., 4 H), 6.72 (br., 4 H), 6.78 (br., 4 H), 6.99 (br., 4 H), 7.16 (br., 4 H), 7.19 (br., 4 H), 7.34–7.47 (m, 12 H), 7.86–7.98 (m, 8 H) ppm. $^{13}C\{^1H\}$ NMR ($CDCl_3$): $\delta$ = 30.04, 30.27, 30.45, 31.16, 31.42, 31.62, 31.96, 32.00, 34.32, 34.40, 34.61, 60.01, 60.39, 77.62, 99.10, 124.40, 124.84, 127.60, 127.92, 128.56, 129.60, 132.02, 132.78, 132.92, 133.53, 133.88, 133.97, 134.93, 146.09, 146.78, 152.45, 153.47, 154.60 ppm. $^{31}P\{^1H\}$ NMR ($CDCl_3$): $\delta$ = 20.8 (d, $^1J_{Rh,P}$ = 141 Hz) ppm. $C_{176}H_{222}BF_4O_{12}P_2Rh{\cdot}CH_2Cl_2$ (2866.2): calcd. C 74.17, H 7.88; found C 74.27, H 7.91.

**Hydroformylation:** In a typical experiment, $[Rh(COD)_2]BF_4$ (2 mg, 0.005 mmol) and **3** (25 mg, 0.02 mmol) were introduced into a 50-mL stainless-steel autoclave (Toyo koatsu) under argon. Benzene (2 mL), decane (71 mg, 0.5 mmol, as an internal standard), and 1-hexene (84 mg, 1 mmol) were then added and the resulting solution was stirred under argon for 1 h. The autoclave was then pressurized to 10 atm with $H_2$/CO (1:1) and the reaction mixture was stirred at 70 °C for 16 h. The products were analyzed by GC and GC-MS and the structures were confirmed by spectral comparison with authentic aldehydes. The GC yields were determined by the internal standard method.

**X-ray Crystallography:** Details of the crystal data and a summary of intensity data collection parameters for **3** and $[PtCl_2(3)_2]$ are given in Table 5. Single crystals of **3** and $[PtCl_2(3)_2]$ were grown by slow diffusion of ethanol into a toluene solution of **3** and diffusion of methanol into a toluene solution of $[PtCl_2(3)_2]$. Data were collected with a Rigaku Saturn CCD diffractometer area detector with graphite-monochromated Mo-$K_\alpha$ radiation ($\lambda$ = 0.7107 Å) to a maximum $2\theta$ value of 55.0°. The structures were solved by direct methods using the program SIR2002[42] and expanded using Fou-

 © 2006 Wiley-VCH Verlag GmbH & Co. KGaA, Weinheim 

Table 5. Crystal and structure refinement data for **3** and $[PtCl_2(\mathbf{3})_2]$.

| Param | **3** | $[PtCl_2(\mathbf{3})_2]$ |
|---|---|---|
| Empirical formula | $C_{84}H_{105}O_6P{\cdot}C_7H_8{\cdot}0.5C_2H_6O$ | $C_{168}H_{210}Cl_2O_{12}P_2Pt{\cdot}4C_7H_8$ |
| Formula mass | 1356.90 | 3182.09 |
| Temperature [°C] | –160(1) | –160(1) |
| Wavelength [Å] | 0.71070 | 0.71070 |
| Crystal system | triclinic | triclinic |
| Space group | $P\bar{1}$(#2) | $P\bar{1}$(#2) |
| $a$ [Å] | 11.557(2) | 21.50(7) |
| $b$ [Å] | 12.946(6) | 24.63(10) |
| $c$ [Å] | 28.47(3) | 18.83(7) |
| $\alpha$ [°] | 81.4(1) | 100.61(8) |
| $\beta$ [°] | 79.01(12) | 106.98(5) |
| $\gamma$ [°] | 84.89(10) | 97.96(7) |
| $V$ [Å$^3$] | 4126.7(46) | 9174.8(60) |
| Z | 2 | 2 |
| $D_{calcd.}$ [g cm$^{-3}$] | 1.092 | 1.152 |
| $\mu$ [cm$^{-1}$] | 0.85 | 8.66 |
| Crystal size [mm] | 0.30 × 0.10 × 0.06 | 0.30 × 0.20 × 0.16 |
| No. of reflections measured | 33429 | 90674 |
| No. of unique reflections, $R_{int}$ | 16706, 0.045 | 90564, 0.085 |
| $R_1$[a] | 0.099[b] | 0.098[c] |
| $wR_2$ | 0.107[d] | 0.223[e] |
| GOF | 1.145 | 1.164 |

[a] $R_1 = \Sigma||F_o| - |F_c||/\Sigma|F_o|$. [b] $I > 2.3\sigma(I)$. [c] $I > 2.0\sigma(I)$. [d] $wR_2$ $[I > 2.3\sigma(I)] = [\Sigma w(|F_o| - |F_c|)^2/\Sigma wF_o^2]^{1/2}$, $w = [0.0010F_o^2 + 3.0000\sigma(F_o^2) + 0.5000]^{-1}$. [e] $wR_2$ (all data) $= [\Sigma\{w(F_o^2 - F_c^2)^2\}/\Sigma w(F_o^2)^2]^{1/2}$, $w = [\sigma^2(F_o^2) + (0.0713P)^2 + 43.3300P]^{-1}$ where $P = [\mathrm{Max}(F_o^2,0) + 2F_c^2]/3$.

rier techniques.[43] For **3**, non-hydrogen atoms except some of the solvent molecules were refined anisotropically. Hydrogen atoms were included in fixed positions. The final cycle of full-matrix least-squares refinement on $F$ was based on 8953 observed reflections [$I > 2.3\sigma(I)$] and 881 variable parameters. A Sheldrick weighting scheme was used. For $[PtCl_2(\mathbf{3})_2]$, non-hydrogen atoms except some *tert*-butyl carbon atoms and solvent molecules were refined anisotropically. Some *tert*-butyl carbon atoms were disordered over multiple positions, which were refined isotropically at fixed positions with appropriate occupation factors without hydrogen atoms. Hydrogen atoms were refined using the riding model. The final cycle of full-matrix least-squares refinement on $F^2$ was based on 41459 observed reflections (using all data) and 1785 variable parameters. Neutral-atom scattering factors were taken from Cromer and Waber.[44] Anomalous dispersion effects were included in $F_c$.[45] All calculations were performed with the CrystalStructure[46] crystallographic software package except for the refinement of $[PtCl_2(\mathbf{3})_2]$, which was performed with SHELXH-97.[47] CCDC-278415 (**3**) and -278416 $[PtCl_2(\mathbf{3})_2]$ contain the supplementary crystallographic data for this paper. These data can be obtained free of charge from The Cambridge Crystallographic Data Centre via www.ccdc.cam.ac.uk/data_request/cif.

**Supporting Information** (see footnote on the first page of this article): X-ray structure of **2** and ROESY spectrum of **3**.


[1] a) C. D. Gutsche, *Calixarenes Revisited; Monographs in Supramolecular Chemistry* (Ed.: J. F. Stoddart), Royal Society of Chemistry, Cambridge **1998**; b) V. Böhmer, *Angew. Chem. Int. Ed. Engl.* **1995**, *34*, 713; c) S. Shinkai, *Tetrahedron* **1993**, *49*, 8933; d) L. Mandolini, R. Ungaro, *Calixarenes in Action*, Imperial College Press, London, UK, **2000**.

[2] a) C. Wiser, C. B. Dielman, D. Matt, *Coord. Chem. Rev.* **1997**, *165*, 93; b) I. Neda, T. Kaukorat, R. Schmutzler, *Main Group Chem. News* **1998**, *6*, 4.

[3] a) L. Brandsma, S. F. Vasilevsky, H. D. Verkruijsse, *Applications of Transition Metals Catalysts, in Organic Synthesis*, Springer, Berlin, **1999**; b) *Homogeneous Catalysis with Metal Phosphine Complexes* (Ed.: L. H. Pignolet), Plenum, New York, **1983**.

[4] We have recently prepared a bowl-shaped phosphane and a phosphane-containing dendrimer unit, see: a) O. Niyomura, M. Tokunaga, Y. Obora, T. Iwasawa, Y. Tsuji, *Angew. Chem. Int. Ed.* **2003**, *42*, 1287; b) B. S. Balaji, Y. Obora, D. Ohara, S. Koide, Y. Tsuji, *Organometallics* **2001**, *20*, 5342.

[5] For selected recent examples of phosphanylcalix[4]arenes, see: a) S. Kim, J. S. Kim, O. J. Shon, S. S. Lee, K. M. Park, S. O. Kang, J. Ko, *Inorg. Chem.* **2004**, *43*, 2906; b) P. Kuhn, C. Jeunesse, D. Sémeril, D. Matt, P. Lutz, R. Welter, *Eur. J. Inorg. Chem.* **2004**, 4602; c) F. Plourde, K. Gilbert, J. Gagnon, P. D. Harvey, *Organometallics* **2003**, *22*, 2862; d) M. Lejeune, C. Jeunesse, D. Matt, N. Kyritsakas, R. Welter, J. P. Kintzinger, *J. Chem. Soc., Dalton Trans.* **2002**, 1642; e) C. Kunze, D. Selent, I. Neda, R. Schmutzler, A. Spannenberg, A. Börner, *Heteroatom Chem.* **2001**, *12*, 577; f) C. Dieleman, S. Steyer, C. Jeunesse, D. Matt, *J. Chem. Soc., Dalton Trans.* **2001**, 2508; g) C. Jeunesse, C. Dieleman, S. Steyer, D. Matt, *J. Chem. Soc., Dalton Trans.* **2001**, 881; h) M. Vénzina, J. Gagnon, K. Villeneuve, M. Drouin, P. D. Harvey, *Organometallics* **2001**, *20*, 273; i) M. Vénzina, J. Gagnon, K. Villeneuve, M. Drouin, P. D. Harvey, *Chem. Commun.* **2000**, 1073; j) S. Shimizu, S. Shirakawa, Y. Sasaki, C. Hirai, *Angew. Chem. Int. Ed.* **2000**, *39*, 1256; k) I. A. Bagatin, D. Matt, H. Thönnessen, P. G. Jones, *Inorg. Chem.* **1999**, *38*, 1585; l) C. B. Dieleman, C. Marsol, D. Matt, N. Kyritsakas, A. Harriman, J.-P. Kintzinger, *J. Chem. Soc., Dalton Trans.* **1999**, 4139; m) C. Wieser-Jeunesse, D. Matt, A. De Cian, *Angew. Chem. Int. Ed.* **1998**, *37*, 2861; n) C. Wieser, D. Matt, J. Fischer, A. Harriman, *J. Chem. Soc., Dalton Trans.* **1997**, 2391; o) X. Fang, B. L. Scott, J. G. Watkin, C. A. G. Carter, G. J. Kubas, *Inorg. Chim. Acta* **2001**, *317*, 276.

[6] a) K. Takenaka, Y. Obora, L. Jiang, Y. Tsuji, *Organometallics* **2002**, *21*, 1158; b) K. Takenaka, Y. Obora, L. Jiang, Y. Tsuji, *Bull. Chem. Soc. Jpn.* **2001**, *74*, 1709; c) K. Takenaka, Y. Obora, Y. Tsuji, *Inorg. Chim. Acta* **2004**, *357*, 3895.

[7] J. P. M. van Duynhoven, R. G. Janssen, W. Verboom, S. M. Franken, A. Casnati, A. Pochini, R. Ungaro, J. de Mendoza, P. M. Nieto, P. Prados, D. N. Reinhoudt, *J. Am. Chem. Soc.* **1994**, *116*, 5814, and references cited therein.


 © 2006 Wiley-VCH Verlag GmbH & Co. KGaA, Weinheim 

[8] J. F. Malone, D. J. Marrs, M. A. McLervey, P. O'Hagan, N. Thompson, A. Walker, F. Arnaud-Neu, O. Mauprivez, M.-J. Schwing-Weill, J.-F. Dozol, H. Rouquette, N. Simon, *J. Chem. Soc., Chem. Commun.* **1995**, 2151.
[9] Y. Obora, Y. Liu, L. Jiang, K. Takenaka, M. Tokunaga, Y. Tsuji, *Organometallics* **2005**, *24*, 4.
[10] For monophosphorylated ($P^V$) calix[6]arenes, see: a) R. G. Janssen, W. Verboom, S. Harkema, G. J. van Hummel, D. N. Reinhoudt, A. Pochini, R. Ungaro, P. Prodos, J. de Mendoza, *J. Chem. Soc., Chem. Commun.* **1993**, 506; b) R. G. Janssen, J. P. M. van Duynhoven, W. Verboom, G. J. van Hummel, S. Harkema, D. N. Reinhoudt, *J. Am. Chem. Soc.* **1996**, *118*, 3666.
[11] a) G. T. Grisp, *Chem. Soc. Rev.* **1998**, *27*, 427; b) T. Hayashi, *Acc. Chem. Res.* **2000**, *33*, 354.
[12] C. B. Dieleman, D. Matt, I. Neda, R. Schmutzler, A. Harriman, R. Yaftian, *Chem. Commun.* **1999**, 1911.
[13] J. de Mendoza, M. Carramolino, F. Cuevas, P. M. Nieto, P. Prados, D. N. Reinhoudt, W. Verboom, R. Ungaro, A. Casnati, *Synthesis* **1994**, 47.
[14] a) R. S. Marmor, D. Seyferth, *J. Org. Chem.* **1969**, *34*, 748; b) A. W. Spassov, Z. D. Raikov, *Z. Chem.* **1971**, *11*, 262.
[15] D. Gloyna, L. Alder, H. G. Henning, H. Koeppel, M. Siegmund, K. D. Schleinitz, *J. Prakt. Chem.* **1980**, *322*, 237.
[16] F. Pérez-Balderas, F. Santoyo-Gonzalés, *Synlett* **2001**, 1699.
[17] We also carried out an X-ray crystal structure analysis of **5**. However, partly due to crystal instability, good crystals of **5** for detailed X-ray analysis could not be obtained and the *R* value did not converge to an acceptable level. Nonetheless, a preliminary X-ray analysis showed that the structure of **5** is indeed in its 1,2,3-alternate conformation, as was observed in **3**.
[18] S. Kanamathareddy, C. D. Gutsche, *J. Am. Chem. Soc.* **1993**, *115*, 6572.
[19] a) L. N. Markovsky, V. I. Kalchenko, M. A. Vysotsky, V. V. Pirozhenko, Y. A. Simonov, A. A. Dvorkin, A. V. Iatsenko, J. Lipkowski, *Supramolecular Chem.* **1997**, *8*, 85; b) R. Ungaro, A. Pochini, G. D. Andreetti, P. Domiano, *J. Incl. Phenom.* **1983**, *1*, 135; c) F. Arnaud-Neu, E. M. Collins, M. Deasy, G. Ferguson, S. J. Harris, B. Kaitner, A. J. Lough, M. A. McKervey, E. Marques, B. L. Ruhl, M. J. Schwing-Weill, E. M. Seward, *J. Am. Chem. Soc.* **1989**, *111*, 8681.
[20] A. Bax, M. F. Summers, *J. Am. Chem. Soc.* **1986**, *108*, 2093.
[21] C. D. Gutsche, *Calixarenes; Monographs in Supramolecular Chemistry* (Ed.: J. F. Stoddart); Royal Society of Chemistry, London **1989**, pp 110–111.
[22] S. Kanamathareddy, C. D. Gutsche, *J. Org. Chem.* **1994**, *59*, 3871.
[23] C. Jaime, J. de Mendoza, P. Prados, P. M. Nieto, C. Sánchez, *J. Org. Chem.* **1991**, *56*, 3372.
[24] a) J. Magrans, A. M. Rincón, F. Cuevas, J. López-Prados, P. M. Nieto, M. Pons, P. Prados, J. de Mendoza, *J. Org. Chem.* **1998**, *63*, 1079; b) S. Kanamatharenddy, C. D. Gutsche, *J. Org. Chem.* **1992**, *57*, 3160; c) E. D. Silva, L. Memmi, A. W. Coleman, B. Rather, M. J. Zaworotko, *J. Supramol. Chem.* **2001**, *1* 135; d) E. A. Shokova, E. V. Khomich, N. N. Akhmetov, I. M. Vatsuro, Y. N. Luzikov, V. V. Kovalev, *Russ. J. Org. Chem.* **2003**, *39*, 368.
[25] A similar conformational difference between a crystalline and a solution state has also been observed for phosphane oxide analogs **2**. In the crystalline state, **2** adopts the 1,2,3-alternate structure (see Figure S1 and Table S1 in the Supporting Information), while the characteristic $^1H$ and $^{13}C\{^1H\}$ NMR resonances in $CDCl_3$ (see Exp. Sect.) show that **2** has a cone structure in the solution.
[26] a) H. Goto, E. Osawa, *J. Am. Chem. Soc.* **1989**, *111*, 8950; b) H. Goto, E. Osawa, *J. Chem. Soc., Perkin Trans. 2* **1993**, 187.
[27] a) T. A. Halgren, *J. Comput. Chem.* **1999**, *20*, 720; b) T. A. Halgren, *J. Comput. Chem.* **1996**, *17*, 490.
[28] A. D. Becke, *J. Chem. Phys.* **1993**, *98*, 5648.
[29] a) T. H. Dunning, Jr., P. J. Hay, in *Modern Theoretical Chemistry* (Ed.: H. F. Schaefer III), Plenum, New York **1976**, vol. 3, p. 1; b) P. J. Hay, W. R. Wadt, *J. Chem. Phys.* **1985**, *82*, 270; c) W. R. Wadt, P. J. Hay, *J. Chem. Phys.* **1985**, *82*, 284; d) P. J. Hay, W. R. Wadt, *J. Chem. Phys.* **1985**, *82*, 299.
[30] A. W. Kleij, B. Souto, C. J. Pastor, P. Prados, J. de Mendoza, *J. Org. Chem.* **2004**, *69*, 6394.
[31] K. Wolinski, J. F. Hinton, P. Pulay, *J. Am. Chem. Soc.* **1990**, *112*, 8251.
[32] H. Kin-Chee, G. M. McLaughlin, M. McPartlin, G. B. Bobertson, *Acta Crystallogr., Sect. B* **1982**, *38*, 421.
[33] C. Loeber, C. Wieser, D. Matt, A. De Cian, J. Fischer, L. Toupet, *Bull. Soc. Chim. Fr.* **1995**, *132*, 166.
[34] a) R. Favcz, R. Roulet, A. A. Pinkerton, D. Schwarzenbach, *Inorg. Chem.* **1980**, *19*, 1356; b) P. S. Pregosin, R. W. Kunz, *$^{31}P$ and $^{13}C$ NMR of Transition Metal Phosphine Complexes*, Springer-Verlag, Berlin, **1976**, Vol. 16.
[35] a) G. K. Anderson, R. J. Cross, *Chem. Soc. Rev.* **1980**, *9*, 185; b) P. Haake, R. M. Pfeiffer, *J. Am. Chem. Soc.* **1970**, *92*, 4996.
[36] M. P. Anderson, L. H. Pignolet, *Inorg. Chem.* **1981**, *20*, 4101.
[37] a) F. Agbossou, J.-F. Carpentier, A. Mortreux, *Chem. Rev.* **1995**, *95*, 2485; b) S. Gladiali, J. C. Bayón, C. Claver, *Tetrahedron: Asymmetry* **1995**, *6*, 1453; c) T. Bartik, H. Ding, B. Bartik, B. E. Hanson, *J. Mol. Catal.* **1995**, *98*, 117.
[38] W. L. F. Armarego, D. D. Perrin, *Purification of Laboratory Chemicals*, 4th ed., Butterworth-Heinemann, Oxford, U. K. **1997**.
[39] T. G. Shenck, J. M. Downs, C. R. C. Milne, P. B. Mackenzie, H. Boucher, J. Whealan, B. Bosnich, *Inorg. Chem.* **1985**, *24*, 2334.
[40] J. X. McDermott, J. F. White, G. M. Whitesides, *J. Am. Chem. Soc.* **1976**, *98*, 6521.
[41] M. J. Frisch, G. W. Trucks, H. B. Schlegel, G. E. Scuseria, M. A. Robb, J. R. Cheeseman, J. A. Montgomery, Jr, T. Vreven, K. N. Kudin, J. C. Burant, J. M. Millam, S. S. Iyengar, J. Tomasi, V. Barone, B. Mennucci, M. Cossi, G. Scalmani, N. Rega, G. A. Petersson, H. Nakatsuji, M. Hada, M. Ehara, K. Toyota, R. Fukuda, J. Hasegawa, M. Ishida, T. Nakajima, Y. Honda, O. Kitao, H. Nakai, M. Klene, X. Li, J. E. Knox, H. P. Hratchian, J. B. Cross, C. Adamo, J. Jaramillo, R. Gomperts, R. E. Stratmann, O. Yazyev, A. J. Austin, R. Cammi, C. Pomelli, J. W. Ochterski, P. Y. Ayala, K. Morokuma, G. A. Voth, P. Salvador, J. J. Dannenberg, V. G. Zakrzewski, S. Dapprich, A. D. Daniels, M. C. Strain, O. Farkas, D. K. Malick, A. D. Rabuck, K. Raghavachari, J. B. Foresman, J. V. Ortiz, Q. Cui, A. G. Baboul, S. Clifford, J. Cioslowski, B. B. Stefanov, G. Liu, A. Liashenko, P. Piskorz, I. Komaromi, R. L. Martin, D. J. Fox, T. Keith, M. A. Al-Laham, C. Y. Peng, A. Nanayakkara, M. Challacombe, P. M. W. Gill, B. Johnson, W. Chen, M. W. Wong, C. Gonzalez, and J. A. Pople, *Gaussian 03*, Revison A.1, Gaussian, Inc., Pittsburgh, PA, **2003**.
[42] M. C. Burla, M. Camalli, B. Carrozzini, G. L. Cascarano, C. Giacovazzo, G. Polidori, R. Spagna, *SIR2002*, **2003**.
[43] P. T. Beurskens, G. Admiraal, G. Beurskens, W. P. Bosman, R. de Gelder, R. Israel, J. M. M. Smits, *DIRDIF99, The DIRDIF-99 program system*, Technical Report of the Crystallography Laboratory, University of Nijmegen, The Netherlands, **1999**..
[44] D. T. Cromer, J. T. Waber, in *International Tables for X-ray Crystallography*, Kynoch Press, Birmingham, U. K. **1974**, vol. IV.
[45] J. A. Ibers, W. C. Hamilton, *Acta Crystallogr.* **1964**, *17*, 781.
[46] a) Crystal Structure Analysis Package, Rigaku and Rigaku/MSC, *CrystalStructure*, ver. 3.6.0., 9009 New Trails Dr., The Woodlands, TX 77381, USA, **2000**–**2004**; b) D. J. Watkin, C. K. Prout, J. R. Carruther, P. W. Betteridge, Chemical Crystallography Laboratory, Oxford, U. K., **1996**.
[47] G. M. Sheldrick, *SHELX97*, **1997**.

Received: July 28, 2005
Published Online: November 15, 2005

 © 2006 Wiley-VCH Verlag GmbH & Co. KGaA, Weinheim 

DOI: 10.1002/ejic.200500692

# Synthesis, Structure and Reactivity of Homo- and Heterobimetallic Complexes of the General Formula [Cp*Ru(μ-Cl)$_3$ML] [LM = (arene)Ru, Cp*Rh, Cp*Ir]

**Laurent Quebatte,[a] Rosario Scopelliti,[a][‡] and Kay Severin*[a]**

**Keywords:** Heterometallic complexes / Iridium / Rhodium / Ruthenium

The homo- and heterobimetallic complexes [Cp*Ru(μ-Cl)$_3$-ML] [LM = ($C_6H_6$)Ru, (cymene)Ru, (1,3,5-$C_6H_3i$Pr$_3$)Ru, Cp*Rh, Cp*Ir] were prepared by reaction of [Cp*Ru(μ-OMe)]$_2$ with $Me_3SiCl$ and subsequent addition of [LMCl$_2$]$_2$. The complexes [Cp*Ru(μ-Cl)$_3$Ru(cymene)] and [Cp*Ru(μ-Cl)$_3$-IrCp*] were characterized by single-crystal X-ray analyses. In crossover experiments with [Cp*Rh(μ-Cl)$_3$RuCl(PPh$_3$)$_2$] and [Cp*Ru(μ-Cl)$_3$Ru(1,3,5-$C_6H_3i$Pr$_3$)] in $CD_2Cl_2$, a dynamic equilibrium with the complexes [Cp*Rh(μ-Cl)$_3$RuCp*] and [(1,3,5-$C_6H_3i$Pr$_3$)Ru(μ-Cl)$_3$RuCl(PPh$_3$)$_2$] was rapidly established, demonstrating the kinetic lability of the triple chloro bridge. Upon reaction of [Cp*Rh(μ-Cl)$_3$RuCp*] with benzene, the ionic complex [Cp*Ru($C_6H_6$)][Cp*RhCl$_3$] was formed, which was characterized by X-ray crystallography.
(© Wiley-VCH Verlag GmbH & Co. KGaA, 69451 Weinheim, Germany, 2006)

## Introduction

Bimetallic complexes, in which two different metal fragments are connected by either two or three halogeno bridges, have been employed as catalyst precursors for ring-opening and ring-closing metathesis reactions,[1] for the Oppenauer-type oxidation of alcohols,[2] and for atom-transfer radical reactions.[3] The heterobimetallic Rh$^{I}$–Ru$^{II}$ complex **1**, for example, can be used as an efficient catalyst for the oxidation of secondary alcohols under mild conditions,[2a] whereas the Rh$^{III}$–Ru$^{II}$ complex **2**[3c] and the Ru$^{II}$–Ru$^{II}$ complex **3**[3a] are among the most active catalysts available for the atom-transfer radical addition of $CCl_4$ and $CHCl_3$ to olefins.

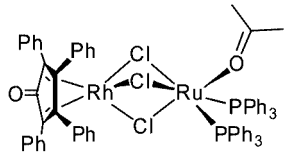


**1**

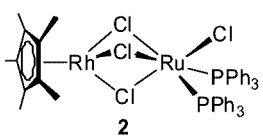


**2**

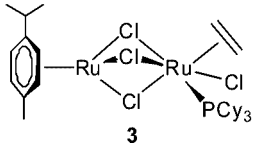


**3**

The synthesis of mixed, halogeno-bridged complexes can be accomplished by several synthetic routes.[4] Mixed complexes with two halogeno bridges are most conveniently obtained in metathesis reactions starting from the corresponding homodimeric compounds. Reactions of this kind were first described by the groups of Stone[5] and Masters[6] in the 1970s. More recent investigations have shown that this method is quite general.[7,8] Mixed complexes with three halogeno-bridges can likewise be obtained in metathesis reactions[9,10] but alternative pathways such as ligand-transfer[11] or substitution[3a,3b,12] reactions have also been explored.[4] The various methods allow the synthesis of a structurally diverse set of homo- and heterobimetallic complexes in relatively short time. This is of interest for the generation of catalyst libraries in combinatorial catalysis.[3c] In the following, we introduce a new procedure that allows the synthesis of complexes of the general formula [Cp*Ru(μ-Cl)$_3$ML] [LM = (arene)Ru, Cp*Rh, Cp*Ir] in excellent yields.

## Results and Discussion

For the synthesis of mixed complexes containing the Cp*RuCl fragment, the tetrameric complex [Cp*RuCl]$_4$ (**4**) seemed to be well suited as it is known that the chloro bridges of **4** can be easily cleaved.[13–16] The reaction of **4** with two equivalents of the dimeric half-sandwich complex [(π-ligand)MCl$_2$]$_2$ was thus expected to give the mixed complex [Cp*Ru(μ-Cl)$_3$M(π-ligand)] in an entropically favored reaction. Complex **4** can be obtained by reduction of [Cp*RuCl$_2$]$_2$ with $LiHBEt_3$[14] or with Zn.[15] Alternatively, it can be obtained by reaction of the methoxy-bridged complex [Cp*Ru(μ-OMe)]$_2$ (**5**) with $Me_3SiCl$.[16] We chose the latter method for our reactions.

For the synthesis of the homo- and heterobimetallic complexes **6**–**10**, the tetramer **4** was generated in situ by addition of $Me_3SiCl$ to complex **5** in $CH_2Cl_2$. Subsequent ad-

[a] Institut des Sciences et Ingénierie Chimiques, École Polytechnique Fédérale de Lausanne (EPFL)
1015 Lausanne, Switzerland
Fax: +41-21-693-9305
E-mail: kay.severin@epfl.ch
[‡] X-ray structural analysis.

 © 2006 Wiley-VCH Verlag GmbH & Co. KgaA, Weinheim 

dition of $[(\pi\text{-ligand})MCl_2]_2$ gave the mixed products **6**–**10** (Scheme 1). Complex **4** displays a high solubility in a variety of nonpolar organic solvents and even in hydrocarbons such as pentane. It was thus possible to use a slight excess of **5** (1.2×) with respect to the dimer $[(\pi\text{-ligand})MCl_2]_2$ because additional **4** could easily be removed by washing with pentane. The homobimetallic product **10**, on the other hand, is itself soluble in pentane. We therefore used a slight excess of $[(1,3,5\text{-}C_6H_3iPr_3)RuCl_2]_2$ (1.2×) and purified the product **10** by extraction with pentane.

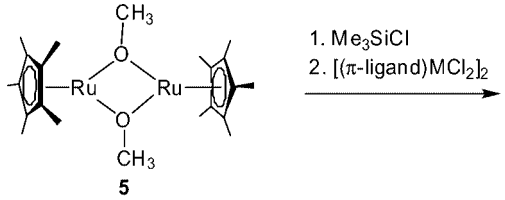


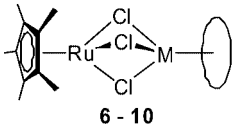


| | (π-ligand)M |
|---|---|
| **6** | $(C_6H_6)Ru$ |
| **7** | (cymene)Ru |
| **8** | Cp*Rh |
| **9** | Cp*Ir |
| **10** | $(C_6H_3iPr_3)Ru$ |

Scheme 1. Synthesis of the complexes **6**–**10**.

The new complexes **6**–**10** were characterized by $^1H$ and $^{13}C$ NMR spectroscopy and by elemental analysis. In addition, complexes **7** and **9** were analyzed by single-crystal X-ray analysis (Figures 1 and 2, respectively). The crystallographic analyses confirmed that the two metal fragments are connected by three chloro bridges. The planes defined by the π-ligands and the plane defined by the three bridging chloro ligands are nearly parallel to each other. For complex **7**, the distances of the chloro atoms to the Ru atom attached to the cymene π-ligand (Ru–Cl = 2.42–2.45 Å) are shorter than those to the Ru atom attached to the Cp* ligand (Ru–Cl = 2.50–2.56 Å). A likely explanation for this difference is the increased Lewis acidity of the (cymene)-$Ru^{2+}$ fragment compared to the $Cp^*Ru^+$ fragment. The two Ru atoms in **7** are 3.344(8) Å apart from each other. This is longer than what is found for the cationic dimer [(cymene)-$Ru(\mu\text{-}Cl)_3Ru$(cymene)]$^+$ [Ru···Ru = 3.283(3) Å].[17]

In the highly symmetrical dimer **9**, a $Cp^*Ru^+$ fragment is connected by three chloro bridges to a $Cp^*Ir^{2+}$ fragment. As was observed for **7**, the M–Cl bond lengths are shorter for the more Lewis-acidic metal fragment: the Ir–Cl distances range from 2.41 to 2.45 Å, whereas the Ru–Cl distances range from 2.50 to 2.52 Å. Complex **9** is isoelectronic with the mixed-valence $Ru^{II}$–$Ru^{III}$ complex [$Cp^*Ru(\mu\text{-}Cl)_3$-RuCp*] described by Koelle et al.,[16a,19] although due to the lack of structural data for the latter a direct comparison was not possible.

The prevalence of polynuclear ruthenium complexes with the $Ru(\mu\text{-}Cl)_3M$ structural motif suggests that the connection by three chloro bridges is thermodynamically very stable. In fact, it has been shown that some catalysts can be deactivated by the formation of face-bridged dimers.[20] In order to investigate the kinetic stability of the bimetallic complexes described above, crossover experiments were performed. Thus, a solution of complex **2** was mixed with a solution of complex **10** (both in $CD_2Cl_2$) and a $^1H$ NMR spectrum was recorded immediately after mixing. Apart from signals of the complexes **2** and **10**, the signals of two other complexes were observed (Figure 3). These were identified as the mixed complexes **8** and **11** by comparison with the $^1H$ NMR spectra of authentic samples (Scheme 2). The time-invariant integrals of the respective signals showed a nearly equimolar distribution of the four species. This suggests that a dynamic equilibrium between the four complexes is rapidly established after the mixing process.

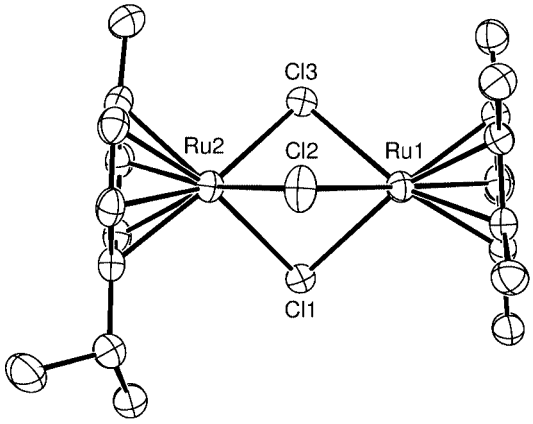


Figure 1. ORTEP[18] drawing of the molecular structure of **7** in the crystal. The hydrogen atoms have been omitted for clarity. Selected bond lengths [Å] and angles [°]: Ru1–Cl1 2.5591(13), Ru1–Cl2 2.5024(14), Ru1–Cl3 2.5075(14), Ru2–Cl1 2.4521(13), Ru2–Cl2 2.4222(13), Ru2–Cl3 2.4205(13); Ru1–Cl1–Ru2 83.70(4), Ru1–Cl2–Ru2 85.53(4), Ru1–Cl3–Ru2 85.45(4), Cl1–Ru1–Cl2 76.70(4), Cl1–Ru2–Cl2 80.23(5).

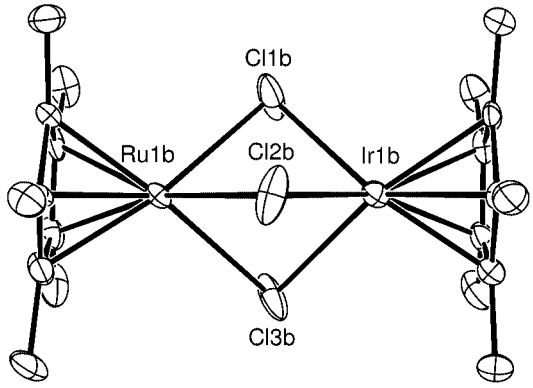


Figure 2. ORTEP[18] drawing of the molecular structure of **9** in the crystal. Only one of the two crystallographically independent molecules is shown. The hydrogen atoms have been omitted for clarity. Selected bond lengths [Å] and angles [°]: Ru1b–Cl1b 2.516(3), Ru1b–Cl2b 2.509(3), Ru1b–Cl3b 2.523(3), Ir1b–Cl1b 2.413(3), Ir1b–Cl2b 2.410(3), Ir1b–Cl3b 2.428(3); Ru1b–Cl1b–Ir1b 85.32(8), Ru1b–Cl2b–Ir1b 85.54(8), Ru1b–Cl3b–Ir1b 84.86(8), Cl1b–Ru1b–Cl2b 77.90(10), Cl1b–Ir1b–Cl2b 81.85(11).

 © 2006 Wiley-VCH Verlag GmbH & Co. KGaA, Weinheim 

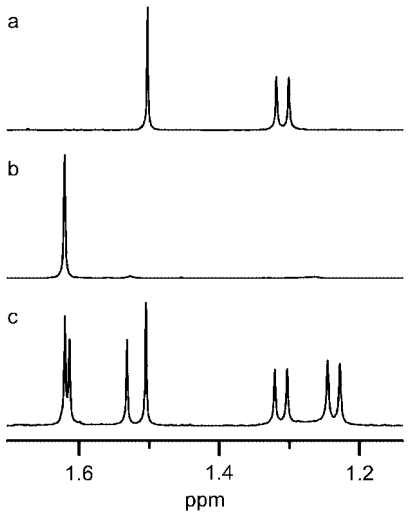


Figure 3. Part of the $^1$H NMR spectrum of a) complex **10**, b) complex **2**, and c) an equimolar mixture of complex **2** and **10**, for which the additional signals of the complexes **8** and **11** are visible.

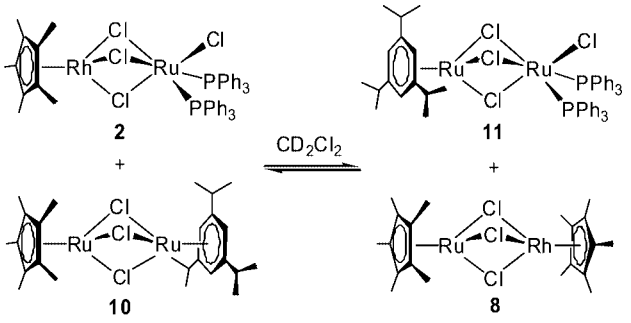


Scheme 2. In solution ($CD_2Cl_2$), complexes **2** and **10** are in a dynamic equilibrium with complexes **8** and **11**.

The results described above are in agreement with a report by Stephenson et al. in which they show that upon mixing of $[(C_6H_6)Ru(\mu\text{-}Cl)_3Ru(C_6H_6)]^+$ and $[(C_6H_6)Os(\mu\text{-}Cl)_3Os(C_6H_6)]^+$, the heterobimetallic complex $[(C_6H_6)Ru(\mu\text{-}Cl)_3Os(C_6H_6)]^+$ is obtained in equilibrium with the two homobimetallic starting materials.[21] We have previously shown that the triply bridged complex [(dcypb)$(N_2)$Ru(μ-Cl)$_3$RuCl(dcypb)] reacts rapidly with doubly bridged complexes of the general formula $[LMCl_2]_2$ [L = (cymene)Ru, Cp*Rh, Cp*Ir] to give the mixed complexes [(dcypb)ClRu(μ-Cl)$_3$ML].[9b] Taken together, these results point to the fact that $[L_nRu(\mu\text{-}Cl)_3ML'_n]$ complexes are generally very labile, despite their apparent thermodynamic stability.

Complexes **6**–**10** are soluble in a variety of organic solvents such as acetone, THF, $CH_2Cl_2$, and $Et_2O$. The very lipophilic **10** can even be dissolved in pentane. Aromatic solvents, on the other hand, are not suited because of the very high tendency of the $Cp^*Ru^+$ fragment to form sandwich complexes of the general formula [Cp*Ru(arene)]-X.[14–16,22] When complex **8** was dissolved in benzene, crystals of the ionic complex $[Cp^*Ru(C_6H_6)][Cp^*RhCl_3]$ (**12**) formed after a few hours (Scheme 3). Larger amounts of **12** could be obtained by slow diffusion of hexane into a solution of **8** in benzene.

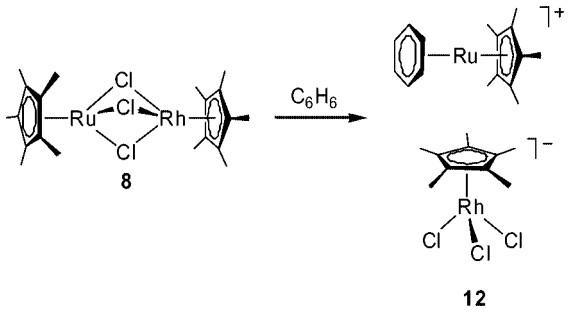


Scheme 3. The ionic complex **12** is obtained by reaction of complex **8** with benzene.

The structure of complex **12** was analyzed by single-crystal X-ray analysis (Figure 4). The bond lengths found for the cation $[Cp^*Ru(C_6H_6)]^+$ ($Ru\text{–}C_{benzene}$ = 2.21–2.22 Å; $Ru\text{–}C_{Cp^*}$ = 2.18–2.19 Å) are very similar to those reported for related $[Cp^*Ru(arene)]^+$ complexes.[22a,22d,23] The corresponding anion $[Cp^*RhCl_3]^-$ displays a typical "pianostool" geometry, with Rh–Cl bond lengths of 2.4114(14) and 2.420(2) Å, respectively. The formation of this anion is rather unusual[24] given the thermodynamic stability of the $[Cp^*Rh(\mu\text{-}Cl)_3RhCp^*]^+$ cation,[11,25] and underlines the fact that the generation of $[Cp^*Ru(C_6H_6)]^+$ is the driving force for the reaction.

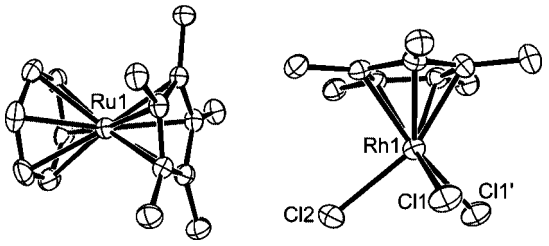


Figure 4. ORTEP[18] drawing of the molecular structure of **12** in the crystal. The hydrogen atoms have been omitted for clarity. Selected bond lengths [Å] and angles [°]: Rh1–Cl1 2.4114(14), Rh1–Cl2 2.420(2); Cl1–Rh1–Cl2 90.97(5), Cl1–Rh1–Cl1′ 91.15(7). ′: $x$, $1/2 - y$, $z$.

## Conclusions

Bimetallic complexes, in which two different metal fragments are connected by either two or three halogeno bridges, have recently emerged as a promising new class of catalysts.[1–3] New synthetic routes to generate such complexes are thus highly warranted. In this report, we have described the homo- and heterobimetallic complexes $[Cp^*Ru(\mu\text{-}Cl)_3ML]$ [LM = $(C_6H_6)$Ru, (cymene)Ru, (1,3,5-$C_6H_3iPr_3$)Ru, Cp*Rh, Cp*Ir]. They can be prepared in excellent yield by reaction of $[Cp^*Ru(\mu\text{-}OMe)]_2$ with $Me_3SiCl$ and subsequent addition of $[LMCl_2]_2$. Crossover experiments have demonstrated that these complexes undergo fast scrambling reactions with other triply bridged complexes. The dimers are thus kinetically very labile, a fact which is of importance for possible catalytic applications. In a reaction with benzene, the chloro bridge of the complex $[Cp^*Ru(\mu\text{-}Cl)_3RhCp^*]$ is cleaved in a completely asymmet-

 © 2006 Wiley-VCH Verlag GmbH & Co. KGaA, Weinheim 

ric fashion to give the cation $[Cp^*Ru(C_6H_6)]^+$ and the anion $[Cp^*RhCl_3]^-$. This type of reactivity is unusual for $[L_nRu(\mu\text{-}Cl)_3ML'_n]$ complexes but can be explained by the high intrinsic affinity of the $Cp^*Ru^+$ fragment for aromatic compounds.

## Experimental Section

**General:** All reactions were performed under an atmosphere of dry dinitrogen. The solvents and $Me_3SiCl$ were distilled from appropriate drying agents and stored under dinitrogen. The complexes $[Cp^*Ru(OMe)]_2$,[26] $[(cymene)RuCl_2]_2$,[27] $[(C_6H_6)RuCl_2]_2$,[28] $[Cp^*RhCl_2]_2$,[29] $[Cp^*IrCl_2]_2$,[29] $[(1,3,5\text{-}C_6H_3iPr_3)RuCl_2]_2$,[30] and $[Cp^*Rh(\mu\text{-}Cl)_3RuCl(PPh_3)_2]$ (**2**)[2b] were prepared according to literature procedures. An authentic sample of complex **11** was synthesized by mixing equimolar amounts of $[(PPh_3)_2ClRu(\mu\text{-}Cl)_3Ru(acetone)(PPh_3)_2]$ and $[(1,3,5\text{-}C_6H_3iPr_3)RuCl_2]_2$ in $CH_2Cl_2$.[9b] The $^1H$ and $^{13}C$ NMR spectra were recorded on a Bruker Advance DPX 400 spectrometer with the residual protonated solvent as internal standards. All spectra were recorded at room temperature.

**General Method for the Synthesis of Complexes 6–9:** $Me_3SiCl$ (71 μL, 561 μmol) was added to a solution of $[Cp^*Ru(OMe)]_2$ (100 mg, 187 μmol) in $CH_2Cl_2$ (10 mL). After addition of the respective dimer $[(\pi\text{-ligand})MCl_2]_2$ (156 μmol), the solution was stirred for 20 min. The solvent was then removed in vacuo and the resulting powder was suspended in pentane (10 mL) in order to dissolve the excess of complex $[CpRuCl]_4$. The product was isolated by filtration, washed with additional pentane (3 × 2 mL) and dried under vacuum (yield: 88–96%).

**Complex 6:** Red powder. $^1H$ NMR (400 MHz, $CD_2Cl_2$): $\delta$ = 1.50 (Cp*), 5.60 (benzene) ppm. $^{13}C$ NMR (101 MHz, $CD_2Cl_2$): $\delta$ = 10.4 ($CH_3$, Cp*), 70.9 (C, Cp*), 80.5 (benzene) ppm. $C_{16}H_{21}Cl_3Ru_2 \cdot 1/6\,C_5H_{12}$ (533.9): calcd. C 37.87, H 4.34; found C 37.96, H 4.51.

**Complex 7:** Red powder. Crystals suitable for X-ray analysis were obtained by slow diffusion of pentane into a solution of **7** in dichloromethane. $^1H$ NMR (400 MHz, $CD_2Cl_2$): $\delta$ = 1.29 [d, $^3J$ = 7.1 Hz, 6 H, $CH(CH_3)_2$], 1.51 (s, 15 H, $CH_3$, Cp*), 2.18 (s, 3 H, $CH_3$, cymene), 2.82 [sept, $^3J$ = 7.1 Hz, 1 H, $CH(CH_3)_2$], 5.21 (d, $^3J$ = 6.0 Hz, 4 H, CH), 5.43 (d, $^3J$ = 6.0 Hz, 4 H, CH) ppm. $^{13}C$ NMR (101 MHz, $CD_2Cl_2$): $\delta$ = 10.4 ($CH_3$, Cp*), 19.0, 22.4 ($CH_3$, cymene), 31.6 [$CH(CH_3)_2$], 70.6 (C, Cp*), 77.8, 78.9 (CH, cymene), 95.3, 100.3 (C, cymene) ppm. $C_{20}H_{29}Cl_3Ru_2$ (577.9): calcd. C 41.56, H 5.06; found C 41.56, H 5.23.

**Complex 8:** Red powder. $^1H$ NMR (400 MHz, $CD_2Cl_2$): $\delta$ = 1.52 (Cp*Ru), 1.61 (Cp*Rh) ppm. $^{13}C$ NMR (101 MHz, $CD_2Cl_2$): $\delta$ = 9.5, 10.5 ($CH_3$, Cp*), 70.0 (C, Cp*Ru), 93.6 (d, $^1J_{C,Rh}$ = 10.1 Hz, C, Cp*Rh) ppm. $C_{20}H_{30}Cl_3RhRu$ (580.0): calcd. C 41.36, H 5.21; found C 41.51, H 5.26.

**Complex 9:** Orange powder. Crystals suitable for X-ray analysis were obtained by slow diffusion of pentane into a solution of **9** in a mixture of dichloromethane and hexane (1:9). $^1H$ NMR (400 MHz, $CD_2Cl_2$): $\delta$ = 1.57 (Cp*), 1.58 (Cp*) ppm. $^{13}C$ NMR (101 MHz, $CD_2Cl_2$): $\delta$ = 9.5, 10.5 ($CH_3$), 70.3, 85.2 (C) ppm. $C_{20}H_{30}Cl_3IrRu$ (670.1): calcd. C 35.85, H 4.51; found C 35.99, H 4.57.

**Synthesis of Complex 10:** $Me_3SiCl$ (30 μL, 240 μmol) was added to a solution of $[Cp^*Ru(OMe)]_2$ (43 mg, 80 μmol) in $CH_2Cl_2$ (5 mL). After addition of $[(C_6H_3iPr_3)RuCl_2]_2$ (72 mg, 96 μmol), the solution was stirred for 20 min. The solvent was then removed in vacuo and the product was extracted with pentane (2 × 5 mL). The product was isolated by evaporation of the pentane and drying under vacuum. Yield: 94 mg (92%). $^1H$ MNR (400 MHz, $CD_2Cl_2$): $\delta$ = 1.31 [d, $^3J$ = 7.1 Hz, 18 H, $CH(CH_3)_2$], 1.50 (s, 15 H, $CH_3$, Cp*), 2.90 [sept, $^3J$ = 7.1 Hz, 3 H, $CH(CH_3)_2$], 5.09 (s, 3 H, CH) ppm. $^{13}C$ NMR (101 MHz, $CD_2Cl_2$): $\delta$ = 10.5 ($CH_3$, Cp*), 22.5 [$CH(CH_3)_2$],

Table 1. Crystallographic data for complexes **7**, **9**, and **12**.

| | **7** | **9** | **12** |
|---|---|---|---|
| Empirical formula | $C_{20}H_{29}Cl_3Ru_2$ | $C_{20}H_{30}Cl_3IrRu$ | $C_{26}H_{36}Cl_3RhRu$ |
| Molecular weight [g mol$^{-1}$] | 577.92 | 670.06 | 658.88 |
| Crystal size | 0.17 × 0.12 × 0.10 | 0.30 × 0.28 × 0.11 | 0.19 × 0.12 × 0.11 |
| Crystal system | monoclinic | monoclinic | orthorhombic |
| Space group | $P2_1/c$ | $I2/a$ | $Pnma$ |
| $a$ [Å] | 11.3160(6) | 27.9257(14) | 19.069(3) |
| $b$ [Å] | 17.108(3) | 10.6205(3) | 12.2265(7) |
| $c$ [Å] | 11.617(2) | 30.1330(14) | 11.346(3) |
| $\alpha$ [°] | 90 | 90 | 90 |
| $\beta$ [°] | 100.473(10) | 91.031(4) | 90 |
| $\gamma$ [°] | 90 | 90 | 90 |
| Volume [Å$^3$] | 2211.4(6) | 8935.6(7) | 2645.2(7) |
| $Z$ | 4 | 16 | 4 |
| Density [g cm$^{-3}$] | 1.736 | 1.992 | 1.654 |
| Temperature [K] | 140(2) | 140(2) | 140(2) |
| Absorption coefficient [mm$^{-1}$] | 1.730 | 6.987 | 1.510 |
| $\Theta$ range [°] | 3.00 to 25.02 | 3.19 to 25.03 | 3.25 to 25.03 |
| Index ranges | –12→ 12, –20 → 20, –13 → 13 | –33 → 33, –11 → 11, –35 → 35 | –22→ 22, –13 → 13, –13 → 13 |
| Reflections collected | 13083 | 24673 | 16451 |
| Independent reflections | 3714 ($R_{int}$ = 0.0362) | 7445 ($R_{int}$ = 0.0333) | 2352 ($R_{int}$ = 0.0444) |
| Absorption correction | semi-empirical | semi-empirical | semi-empirical |
| Max. and min. transmission | 0.8179 and 0.6935 | 0.4376 and 0.2545 | 0.8633 and 0.7484 |
| Data / restraints / parameters | 3714 / 0 / 226 | 7445 / 0 / 451 | 2352 / 0 / 152 |
| Goodness-of-fit on $F^2$ | 1.114 | 1.061 | 1.151 |
| Final $R$ indices [$I > 2\sigma(I)$] | $R_1$ = 0.0365, $wR_2$ = 0.0880 | $R_1$ = 0.0422, $wR_2$ = 0.0965 | $R_1$ = 0.0410, $wR_2$ = 0.0853 |
| $R$ indices (all data) | $R_1$ = 0.0470, $wR_2$ = 0.0955 | $R_1$ = 0.0522, $wR_2$ = 0.1001 | $R_1$ = 0.0501, $wR_2$ = 0.0896 |
| Largest diff. peak/hole [e Å$^{-3}$] | 0.739 and –0.646 | 1.778 and –1.723 | 0.941 and –0.745 |

 © 2006 Wiley-VCH Verlag GmbH & Co. KGaA, Weinheim 

32.0 [*C*H($CH_3$)$_2$], 70.3 (CH), 70.4 (C, Cp*), 106 (C, $C_6H_3iPr_3$) ppm. $C_{25}H_{39}Cl_3Ru_2$ (648.1): calcd. C 46.33, H 6.07; found C 46.30, H 6.13.

**Exchange Reactions:** Complex **10** (5.5 mg, 8.6 μmol) was dissolved in $CD_2Cl_2$ (500 μL) and a $^1$H NMR spectrum of the solution was recorded (400 MHz). A sample of complex **2** (8.7 mg, 8.6 μmol) was analyzed in the same fashion. The two solutions were subsequently mixed and immediately analyzed by $^1$H NMR spectroscopy (400 MHz).

**Synthesis of Complex 12:** Complex **8** (15.0 mg, 25.8 μmol) was dissolved in benzene (2 mL). The resulting mixture was allowed to react for 2 h, after which small crystals of complex **12** could already be observed. Slow addition of hexane (5 mL) by diffusion over 12 h resulted in the formation of crystalline **12**, which was isolated by filtration. Isolated yield: 12.5 mg (73%). The reaction was quantitative, as evidenced by $^1$H NMR analysis of the remaining solution. $^1$H NMR (400 MHz, $CD_2Cl_2$): $\delta$ = 1.57, 2.07 (Cp*), 6.05 (benzene) ppm. $^{13}$C NMR (101 MHz, $CD_2Cl_2$): $\delta$ = 9.4, 11.3 ($CH_3$, Cp*), 87.7 (benzene), 94.4 (d, $^1J_{C-Rh}$ = 14 Hz, C, Cp*Rh), 97.1 (C, Cp*Ru) ppm. $C_{26}H_{36}Cl_3RhRu$ (658.9): calcd. C 47.39, H 5.51; found C 47.55, H 5.12.

**X-ray Crystallography:** Details of the crystals and their structure refinement are listed in Table 1; relevant geometrical parameters are given in the respective figure captions. Data collection was performed at 140(2) K on a four-circle goniometer having kappa geometry and equipped with an Oxford Diffraction KM4 Sapphire CCD (**9**) or a mar345 imaging plate detector (**7** and **12**). Data reduction was carried out with CrysAlis RED, release 1.7.0.[31] An absorption correction was applied to all data sets. Structure solution and refinement were performed with the SHELXTL software package, release 5.1.[32] The structures were refined using the full-matrix least-squares on $F^2$ with all non-H atoms anisotropically defined. H atoms were placed in calculated positions using the "riding model".

CCDC-279177 to -279179 contain the supplementary crystallographic data for this paper. These data can be obtained free of charge from The Cambridge Crystallographic Data Centre via www.ccdc.cam.ac.uk/data_request/cif.

## Acknowledgments

We gratefully acknowledge support by the Swiss National Science Foundation and by the EPFL.

[1] a) B. de Clercq, F. Verpoort, *Adv. Synth. Catal.* **2002**, *344*, 639–648; b) A. Fürstner, O. Guth, A. Düffels, G. Seidel, M. Liebl, B. Gabor, R. Mynott, *Chem. Eur. J.* **2001**, *7*, 4811–4820; c) M. T. Reetz, M. H. Becker, M. Liebl, A. Fürstner, *Angew. Chem. Int. Ed.* **2000**, *39*, 1236–1239; d) J. G. Hamilton, U. Frenzel, F. J. Kohl, T. Weskamp, J. J. Rooney, W. A. Herrmann, O. Nuyken, *J. Organomet. Chem.* **2000**, *606*, 8–12; e) A. Fürstner, A. F. Hill, M. Liebl, J. D. E. T. Wilton-Ely, *Chem. Commun.* **1999**, 601–602; f) T. Weskamp, F. J. Kohl, W. Hieringer, D. Gleich, W. Herrmann, *Angew. Chem. Int. Ed.* **1999**, *38*, 2416–2419; g) E. L. Dias, R. H. Grubbs, *Organometallics* **1998**, *17*, 2758–2767.

[2] a) S. Gauthier, R. Scopelliti, K. Severin, *Organometallics* **2004**, *23*, 3769–3771; b) A. C. da Silva, H. Piotrowski, P. Mayer, K. Polborn, K. Severin, *Eur. J. Inorg. Chem.* **2001**, 685–691.

[3] a) L. Quebatte, E. Solari, R. Scopelliti, K. Severin, *Organometallics* **2005**, *24*, 1404–1406; b) L. Quebatte, M. Haas, E. Solari, R. Scopelliti, Q. T. Nguyen, K. Severin, *Angew. Chem. Int. Ed.* **2005**, *44*, 1084–1088; c) L. Quebatte, R. Scopelliti, K. Severin, *Angew. Chem. Int. Ed.* **2004**, *43*, 1520–1524; d) B. De Clerq, F. Verpoort, *Tetrahedron Lett.* **2002**, *43*, 4687–4690.

[4] For an overview see: K. Severin, *Chem. Eur. J.* **2002**, *8*, 1515–1518.

[5] M. I. Bruce, M. Z. Iqbal, F. G. A. Stone, *J. Organomet. Chem.* **1972**, *40*, 393–401.

[6] a) A. A. Kiffen, C. Masters, J. P. Visser, *J. Chem. Soc., Dalton Trans.* **1975**, 1311–1315; b) C. Masters, J. P. Visser, *J. Chem. Soc., Chem. Commun.* **1974**, 932–933.

[7] a) E. Corradi, N. Masciocchi, G. Pályi, R. Ugo, A. Vizi-Orosz, C. Zucchi, A. Sironi, *J. Chem. Soc., Dalton Trans.* **1997**, 4651–4655; b) J. D. Scott, R. J. Puddephatt, *Organometallics* **1986**, *5*, 1253–1257; c) H. C. Clark, G. Ferguson, V. K. Jain, M. Parvez, *Inorg. Chem.* **1986**, *25*, 3808–3811; d) H. C. Clark, G. Ferguson, V. K. Jain, M. Parvez, *Inorg. Chem.* **1985**, *24*, 1477–1482.

[8] a) M. Öhm, A. Schulz, K. Severin, *Eur. J. Inorg. Chem.* **2000**, 2623–2629; b) K. Polborn, K. Severin, *J. Chem. Soc., Dalton Trans.* **1999**, 759–764; c) K. Polborn, K. Severin, *Eur. J. Inorg. Chem.* **1998**, 1187–1192; d) K. Severin, K. Polborn, W. Beck, *Inorg. Chim. Acta* **1995**, *240*, 339–346.

[9] a) S. Gauthier, R. Scopelliti, K. Severin, *Helv. Chim. Acta* **2005**, *88*, 435–446; b) S. Gauthier, L. Quebatte, R. Scopelliti, K. Severin, *Chem. Eur. J.* **2004**, *10*, 2811–2821; c) A. C. da Silva, H. Piotrowski, P. Mayer, K. Polborn, K. Severin, *J. Chem. Soc., Dalton Trans.* **2000**, 2960–2963.

[10] a) T. Arthur, T. A. Stephenson, *J. Organomet. Chem.* **1981**, *208*, 369–387; b) T. Arthur, T. A. Stephenson, *J. Organomet. Chem.* **1979**, *168*, C39–C41.

[11] S. Gauthier, L. Quebatte, R. Scopelliti, K. Severin, *Inorg. Chem. Commun.* **2004**, *7*, 708–712.

[12] a) A.-R. Al-Ohaly, J. F. Nixon, *Inorg. Chim. Acta* **1985**, *103*, 83–93; b) R. A. Head, J. F. Nixon, *J. Chem. Soc., Dalton Trans.* **1978**, 909–912.

[13] a) U. Koelle, B.-S. Kang, U. Englert, *J. Organomet. Chem.* **1991**, *420*, 227–235; b) P. J. Fagan, W. S. Mahoney, J. C. Calabrese, I. D. Williams, *Organometallics* **1990**, *9*, 1843–1852; c) B. K. Campion, R. H. Heyn, T. D. Tilley, *J. Chem. Soc., Chem. Commun.* **1988**, 278–280.

[14] P. J. Fagan, M. D. Ward, J. C. Calabrese, *J. Am. Chem. Soc.* **1989**, *111*, 1698–1719.

[15] a) B. Chaudret, F. Jalón, M. Perez-Manrique, F. Lahoz, F. J. Plou, R. Sanchez-Delgado, *New J. Chem.* **1990**, *14*, 331–338; b) B. Chaudret, F. A. Jalon, *J. Chem. Soc., Chem. Commun.* **1988**, 711–713.

[16] a) U. Koelle, J. Kossakowski, *J. Organomet. Chem.* **1989**, *362*, 383–398; b) U. Koelle, J. Kossakowski, *J. Chem. Soc., Chem. Commun.* **1988**, 549–551.

[17] D. A. Tocher, M. D. Walkinshaw, *Acta Crystallogr., Sect. B* **1982**, *38*, 3083–3085.

[18] ORTEP 3 for Windows version 1.076:L. J. Farrugia, *J. Appl. Cryst.* **1997**, *30*, 565.

[19] U. Koelle, J. Kossakowski, *Inorg. Chim. Acta* **1989**, *164*, 23–32.

[20] D. Amoroso, G. P. A. Yap, D. E. Fogg, *Organometallics* **2002**, *21*, 3335–3343.

[21] T. Arthur, T. A. Stephenson, *J. Organomet. Chem.* **1981**, *208*, 369–387.

[22] a) H. Aneetha, M. Jiménez-Tenorio, M. C. Puerta, P. Valerga, V. N. Sapunov, R. Schmid, K. Kirchner, K. Mereiter, *Organometallics* **2002**, *21*, 5334–5346; b) J. W. Kriesel, S. König, M. A. Freitas, A. G. Marshall, J. A. Leary, T. D. Tilley, *J. Am. Chem. Soc.* **1998**, *120*, 12207–12215; c) A. A. Dembek, P. J. Fagan, *Organometallics* **1995**, *14*, 3741–3745; d) U. Koelle, A. Hörnig, U. Englert, *Organometallics* **1994**, *13*, 4064–4066; e) M. D. Ward, P. J. Fagan, J. C. Calabrese, D. C. Johnson, *J. Am. Chem. Soc.* **1989**, *111*, 1719–1732.

[23] A. Schmid, H. Piotrowski, T. Lindel, *Eur. J. Inorg. Chem.* **2003**, 2255–2263.

[24] In solution, the complex [(Cp*$RhCl_2$)$_2$(μ-$NH_2NMe_2$)] has been found to be in equilibrium with the ionic species [Cp*RhCl(μ-

 © 2006 Wiley-VCH Verlag GmbH & Co. KGaA, Weinheim 

$NH_2NMe_2)]^{2+}\cdot 2[Cp^*RhCl_3]^-$:W. Rigby, J. A. McCleverty, P. M. Maitlis, *J. Chem. Soc., Dalton Trans.* **1979**, 382–386.
[25] a) I. Ara, J. R. Berenguer, E. Eguizábal, J. Forniés, E. Lalinde, A. Martín, *Eur. J. Inorg. Chem.* **2001**, 1631–1640; b) K. Umakoshi, K. Murata, S. Yamashita, K. Isobe, *Inorg. Chim. Acta* **1991**, *190*, 185–191.
[26] U. Koelle, J. Kossakowski, D. Grumbine, T. D. Tilley, *Inorg. Synth.* **1992**, *29*, 225–228.
[27] M. A. Bennett, T. N. Huang, T. W. Matheson, A. K. Smith, *Inorg. Synth.* **1982**, *21*, 74–78.
[28] M. A. Bennett, A. K. Smith, *J. Chem. Soc., Dalton Trans.* **1974**, *2*, 233–241.
[29] C. White, A. Yates, P. M. Maitlis, D. M. Heinekey, *Inorg. Synth.* **1992**, *29*, 228–234.
[30] J. W. Hull, W. L. Gladfelter, *Organometallics* **1984**, *3*, 605–613.
[31] Oxford Diffraction Ltd., Abingdon, Oxfordshire, UK, **2003**.
[32] G. M. Sheldrick, University of Göttingen, Germany, **1997**; Bruker AXS, Inc., Madison, Wisconsin, 53719, USA, **1997**.

Received: August 2, 2005
Published Online: November 21, 2005

 © 2006 Wiley-VCH Verlag GmbH & Co. KGaA, Weinheim 

DOI: 10.1002/ejic.200500707

# Mu-34: a New Porous Layered Fluorogallophosphate Material Obtained by in Situ Generation of Ethylamine

**Louwanda Lakiss,[a] Angélique Simon-Masseron,[a] Florence Porcher,[b] and Joël Patarin*[a]**

**Keywords:** Fluorogallophosphate / Ethylformamide / Solvothermal synthesis / Ethylamine / Porous layered solids / Microporous materials

A new two-dimensional microporous fluorogallophosphate with porous layers, named Mu-34, has been synthesized by in situ generation of ethylamine as the structure-directing agent, the latter arising from the decomposition of ethylformamide. The fluorogallophosphate Mu-34, $Ga_6P_8O_{32}FC_{14}N_7H_{56}$ ($Z$ = 2), crystallizes in the triclinic space group $P\bar{1}$ with the following unit cell parameters: $a$ = 11.0832(6), $b$ = 11.393(6), $c$ = 21.335(1) Å, $\alpha$ = 100.62(4), $\beta$ = 99.66(5), $\gamma$ = 108.34(5)°. The structure was solved from single crystal XRD data. This new fluorogallophosphate displays porous layers with apertures delimited by 12-membered rings intercalated by protonated ethylamine molecules. Mu-34 was also characterized by powder XRD, SEM, elemental and thermal analyses, and $^{13}C$, $^{19}F$, and $^{31}P$ MAS solid state NMR spectroscopy.

(© Wiley-VCH Verlag GmbH & Co. KGaA, 69451 Weinheim, Germany, 2006)

## Introduction

Since the discovery of the microporous aluminophosphates by Wilson et al.,[1] research in the field of microporous materials has attracted considerable interest, owing to their potential uses as molecular sieves, heterogeneous catalysts, or ion exchangers.[2] The family of crystalline microporous phosphates is not limited to aluminophosphates; it also includes in particular zincophosphates and gallophosphates. These latter compounds allow a wide variety of structures to be formed, because gallium atoms can adopt 4-, 5-, and 6- coordinations. A main advance in the synthesis of these solids was achieved when fluoride anions were introduced in the starting mixture.[3] Thus, numerous fluorogallophosphates were obtained[4,5] such as cloverite, which was until now the molecular sieve with the largest 3D pore channel system.[6] In most cases $F^-$ was found to be present in the inorganic framework as terminal Ga-F groups, bridging gallium atoms or trapped into small building units such as the so-called double four rings (D4R units). In the latter case it seems that fluorine, besides its mineralizing role, plays a templating role stabilizing these units.[5–8] To date, a large number of metallophosphates with 0D, 1D, 2D, or 3D frameworks have been reported.[3–13] Some of these solids were obtained through a newly developed synthesis route that consists of the in situ formation of the structure-directing agent (SDA).[9–13] In this synthesis route, alkylformamides are introduced as the main solvents in the starting mixture and during the synthesis they partly decompose into the corresponding amine which acts as a template and is occluded in the final material. With this method, it was possible to produce the two-layered aluminophosphates, Mu-4,[9] Mu-7[10] and, more recently, the three new gallophosphates MIL30,[11] Mu-30,[12] and Ea-TREN-GaPO.[13]

In this paper, we report the synthesis, structure determination, and characterization of a new porous 2D fluorogallophosphate named Mu-34 (Mu standing for Mulhouse), which was prepared in a quasi nonaqueous medium using ethylformamide (EFD) as the main solvent. As for the other solids described above, in this case too, the in situ formation of ethylamine seems to play a key role in the formation of this solid.

## Results and Discussion

### Synthesis and Crystal Morphology

The synthesis results are summarized in Table 1. The fluorogallophosphate Mu-34 crystallizes after 4 days at 200 °C (Table 1, sample A). With a similar starting molar composition but with a longer heating period (50 days) the gallophosphate ULM-3 was obtained as a pure phase (sample B). Such a result reveals the instability of Mu-34 in this reaction medium. Under these experimental conditions, it appears that the pH has to be high enough otherwise, whatever the gallium source (GaOOH or $Ga_2O_3$), the gallophos-

[a] Laboratoire de Matériaux à Porosité Contrôlée, UMR CNRS 7016, Université de Haute Alsace,
ENSCMu, 3 rue Alfred Werner, 68093 Mulhouse Cedex, France
[b] Laboratoire de Cristallographie et Modélisation des Matériaux Minéraux et Biologiques, UMR CNRS 7036, Faculté des Sciences, Université Henri Poincaré Nancy 1,
B. P. 239, 54506 Vandoeuvre-lès-Nancy Cedex, France

Supporting information for this article is available on the WWW under http://www.eurjic.org or from the author.

 © 2006 Wiley-VCH Verlag GmbH & Co. KgaA, Weinheim 

Table 1. Syntheses performed in the system GaOOH/$H_3PO_4$/HF/ethylformamide (EFD)/Tripropylamine (TPA)/$H_2O$.[a]

| Sample (Heating time) | Molar composition of the starting mixture GaOOH | $H_3PO_4$ | HF | EFD | $H_2O$[a] | TPA | $T$ [°C] | XRD results |
|---|---|---|---|---|---|---|---|---|
| A (4 days) | 2 | 2 | 1 | 10 | 4.7 | 1 | 200 | Mu-34 |
| B (50 days) | 2 | 2 | 1 | 10 | 4.7 | 1 | 200 | ULM-3 |
| C (2 days) | 2 | 2 | 1 | 10 | 4.7 | – | 200 | Ea-TREN-GaPO + $GaPO_4$–$C_4$[b] |
| D (2 days) | 2* | 2 | 1 | 10 | 4.7 | – | 200 | Ea-TREN-GaPO + $GaPO_4$–$C_4$[b] |
| E (50 days) | 2 | 2 | 2 | 10 | 6.3 | – | 200 | ULM-4 + impurity[c] |

[a] $H_2O$ arising from the orthophosphoric acid (85% $H_3PO_4$) and hydrofluoric acid (40% HF). [b] The two phases crystallize with the same proportion. [c] Unknown phase. * The gallium source was $Ga_2O_3$.

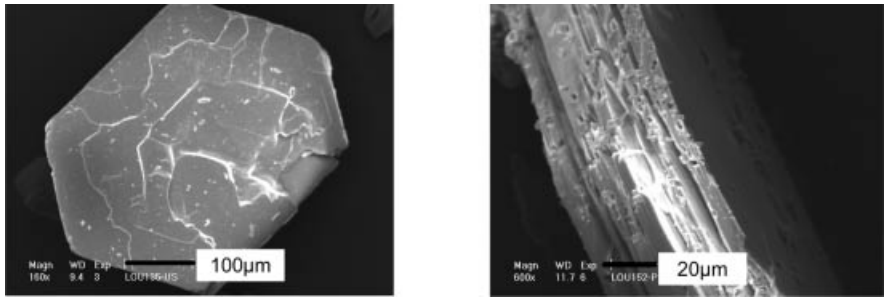


Figure 1. Scanning electron micrographs of the fluorogallophosphate Mu-34.

phates Ea-TREN-GaPO[13] and $GaPO_4$–C4[14] co-crystallize. This is clearly reflected by the experiments C and D performed in the absence of tripropylamine as a pH modifier. The presence of fluorine is also crucial. In its absence no crystalline phase is obtained. However, too large an amount leads to the formation of the gallophosphate ULM-4[15] (see sample E).

As can be seen in Figure 1, the crystals of Mu-34 display a pseudo-hexagonal shape. A close-up view shows that the crystals are in fact stacks of plate-like crystallites. This is indicative of a lamellar material.

## XRD Analysis

The experimental powder diffraction pattern of the fluorogallophosphate Mu-34 is reported in part a of Figure 2 (a). From the single crystal XRD analysis, it has been indexed in a triclinic symmetry with the following unit cell parameters: $a$ = 11.0832(6), $b$ = 11.393(6), $c$ = 21.335(1) Å, $\alpha$ = 100.62(4), $\beta$ = 99.66(5), $\gamma$ = 108.34(5)°. For comparison, the simulated XRD pattern of Mu-34 is reported in Figure 2 (b).

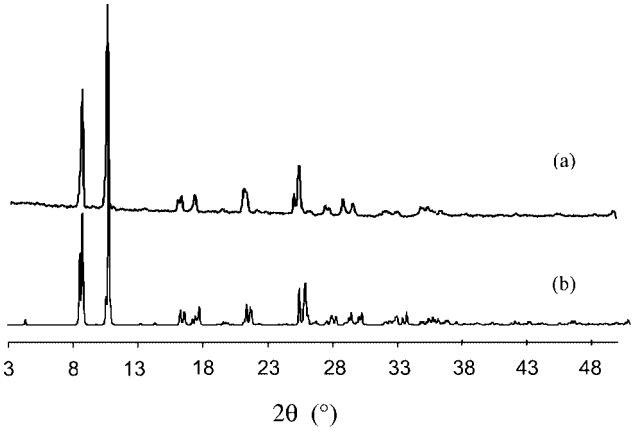


Figure 2. XRD patterns of the fluorogallophosphate Mu-34: (a) experimental pattern; (b) simulated pattern (radiation Cu-$K_\alpha$1).

## Chemical and Thermal Analyses

According to the elemental analyses, the as-synthesized Mu-34 sample has the following composition (wt.-%): Ga 27.46; P 15.56; F 1.57; N 6.19; C 10.74. Such results are in agreement with the composition obtained from the structure determination (wt.-%) Ga 27.20; P 16.11; F 1.26; N 6.37; C 10.93. The experimental C/N molar ratio equal to 2 is different from the value expected for ethylformamide (3C:1N), suggesting that the solvent partly decomposed into carbon monoxide and ethylamine (EA) during synthesis. This was later confirmed by $^{13}C$ NMR spectroscopy (see below). As previously shown for other phosphate-based materials synthesized in the presence of alkylformamide,[9–13] the in situ release of the corresponding protonated amine during the synthesis appears to be a key step in the crystallization of this lamellar gallophosphate. Indeed, experiments using ethylamine directly in the starting mixture led to the crystallization of the fluorogallophosphate ULM-3 with a nonidentified impurity.

The Ga/P molar ratio smaller than one (0.78 from chemical analyses, 0.75 from the structure determination) would indicate the presence of an interrupted framework, and more precisely the presence of terminal P=O and/or P–OH groups.

The thermal behavior of the fluorogallophosphate Mu-34 was investigated by TG/DTA thermal analyses. The TG and DTA curves of the as-synthesized fluorogallophosphate

 © 2006 Wiley-VCH Verlag GmbH & Co. KGaA, Weinheim 

Mu-34 are reported in Figure 3. The total weight loss occurs mainly in one step. However, a small weight loss close to 0.8 wt.-% appears before 200 °C. It might correspond to the loss of water molecules or fluorine (probably under the form of HF) since a weak and broad endothermic peak is observed on the DTA curve. The main weight loss (20.2 wt.-%), between 200 and 800 °C, is associated with at least three endothermic components on the DTA curve. This probably corresponds to desorption and decomposition of the organic template, to the removal of fluorine, and to the collapse of the gallophosphate framework. The exothermic signal, which is expected from the oxidation of the EA, is probably masked by the overwhelming endothermic collapse of the structure. The latter is confirmed by the XRD analysis of the residue left after heating to 800 °C, which shows that the starting material is transformed via an amorphization-recrystallization process into a cristobalite-type gallophosphate. This recrystallization might occur in two steps as reflected by the presence of two exothermic peaks on the DTA curve at 600 °C and 750 °C. Such a thermal behavior is often observed for microporous gallophosphates.[16] All of these analyses are in good agreement with the unit cell formula found by structure analysis: $[Ga_{12}(PO_4)_{16}F_2(C_2H_8N)_{14}]$.

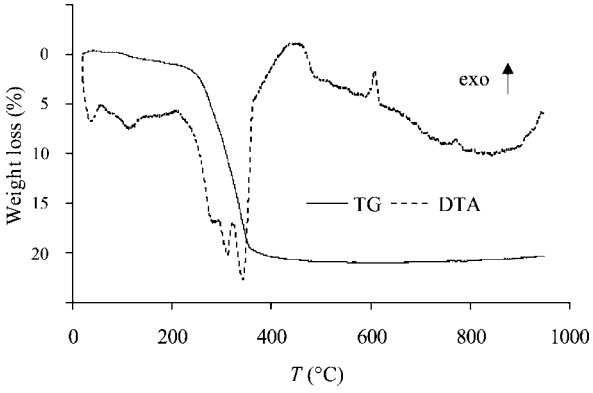


Figure 3. Thermal analysis (TG and DTA) under air of the fluorogallophosphate Mu-34.

## Structure Description

The fluorogallophosphate Mu-34 displays a 2D structure composed of porous macroanionic layers, parallel to the {–111} faces of the crystal and containing 12-membered ring apertures (12MR) arranged in a pseudo-hexagonal way (Figure 4). The asymmetric unit (not reported) contains six crystallographically distinct Ga-sites, three in fourfold coordination with oxygen atoms (Ga1, Ga5, and Ga6) and three in fivefold coordination with four oxygen atoms and one fluorine (Ga2, Ga3, and Ga4). The $GaO_4$ tetrahedra exhibit a regular geometry, with an average Ga–O bond length of 1.81(±1) Å. The $GaO_4F$ trigonal bipyramids have more disperse Ga–O bond lengths [<Ga–O> = 1.84(±3) Å] with three shorter bonds in the basal plane and a larger apical one, opposite to the Ga–F bond. Eight crystallographically distinct P-sites are also present: each phosphorus atom shares three of its oxygen atoms (labeled O1–O24) with gallium neighbors whereas the fourth oxygen atom (O25–O32) points towards the layer (Figure 5). The P–O distances involving these nonbonding oxygen atoms, 1.50(±1) Å, are typical of P=O bonds. They are significantly shorter than those involving bridging oxygen atoms [<P–O> = 1.54(±1) Å], except for O12 and O15 whose interaction with phosphorus is increased [P3–O12 = 1.503(6) Å, P4–O15 = 1.516(8) Å] as their bonding with gallium is weakened by

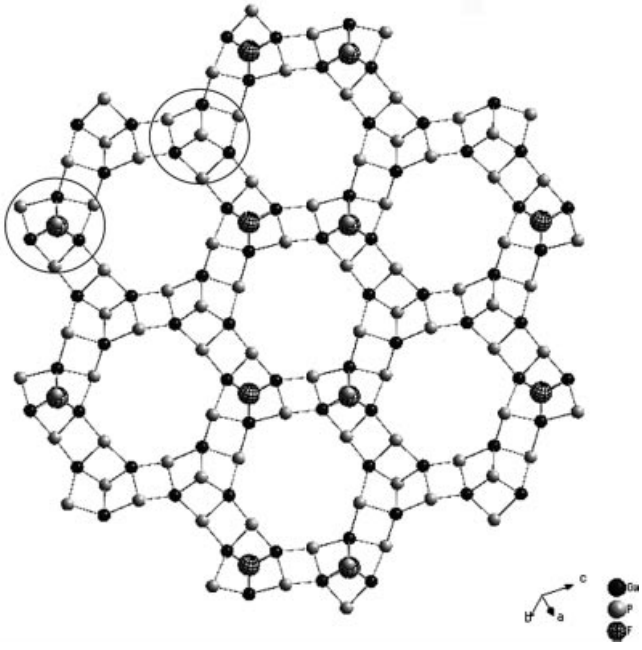

Figure 4. Projection of the structure of the fluorogallophosphate Mu-34 along the [–111] direction, showing the inorganic layers with the 12 MR openings. (For clarity, the oxygen atoms are omitted).

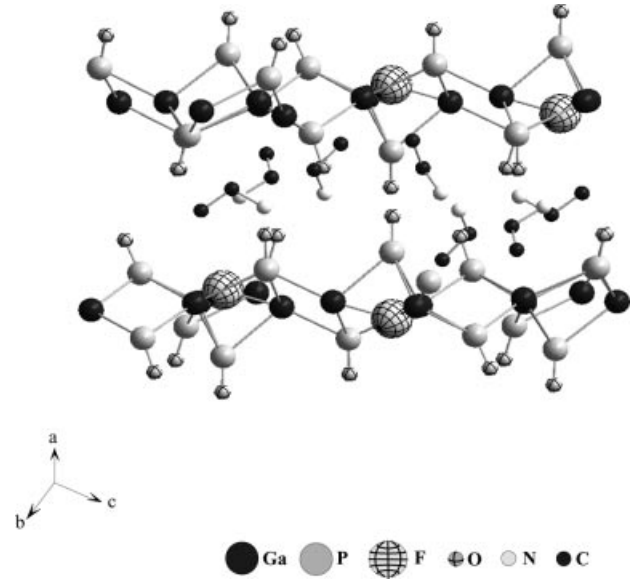


Figure 5. Projection of the structure of the fluorogallophosphate Mu-34, showing the localization of the protonated amine. (For clarity, the framework oxygen atoms are omitted except the terminal ones).

 © 2006 Wiley-VCH Verlag GmbH & Co. KGaA, Weinheim 

the presence of the supplementary fluoride ion. The crystal structure shows that all the terminal oxygen atoms act as hydrogen-bond acceptors for the seven crystallographically distinct protonated ethylamine molecules located in the interlayer space (Figure 5 and Figure 6). The positive charges of the organic molecules (see section $^{13}C$ NMR) compensate exactly the global negative charge of the layers if one considers formal $P^{+5}$, $Ga^{+3}$, $O^{2-}$, $F^{-}$ ions. As expected, in protonated ethylamine molecules, the displacement parameters are smaller for the nitrogen atoms which are precisely in interaction with O=P groups. The water molecules, which might be observed by thermal analysis, were not detected by XRD, which is not surprising considering their predictable high mobility and low site occupancy factors.

The 12-membered ring porous anionic layers can be described as resulting from the connection of two types of building units, encircled in Figure 4, via four-membered rings ($Ga_2P_2O_4$). The first type of these building units (Figure 7, left) has already been observed in other 12 MR porous layered aluminophosphates.[17–19] It is a phosphate-capped six-membered ring ($Ga_3P_3O_6$) containing three tetracoordinate gallium atoms and four tetracoordinate phosphorus ones. The second building unit is original (Figure 7, right) and consists of a phosphate and fluorine (F1) capped six-membered ring. The six-membered ring is composed of three gallium and three phosphorus atoms located on crystallographic sites Ga2, Ga3, Ga4 and P6, P7, P8, respectively. These three gallium atoms are also connected to fluorine F1 and phosphorus P1 and adopt a distorted trigonal bipyramidal geometry, the angle between apical O–Ga–F angles ranging from 177.0(3) to 178.8(3)°. Fluorine is three-coordinate to gallium atoms with one short bond [*d*(Ga3–F) = 2.080(5) Å] and two long bonds [*d*(Ga4–F) = 2.274(5) Å and *d*(Ga2–F) = 2.402(6) Å]. Such bond lengths are larger than those previously found in other fluorogallophosphates[16] [typically $1.94 < d(\text{Ga–F}) < 2.04$ Å] but the presence of the third interaction could explain the difference between these values and those reported for ideal bonds.

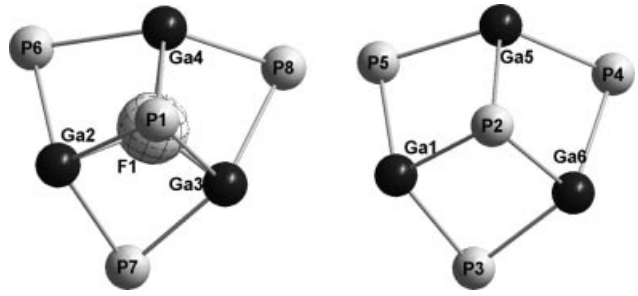


Figure 7. The two basic building units of the fluorogallophosphate Mu-34. (For clarity, the framework oxygen atoms are omitted).

### $^{13}C$ CP MAS NMR Spectroscopy

The $^{13}C$ CP MAS NMR spectrum of the fluorogallophosphate Mu-34 reported in Figure 8 shows two main

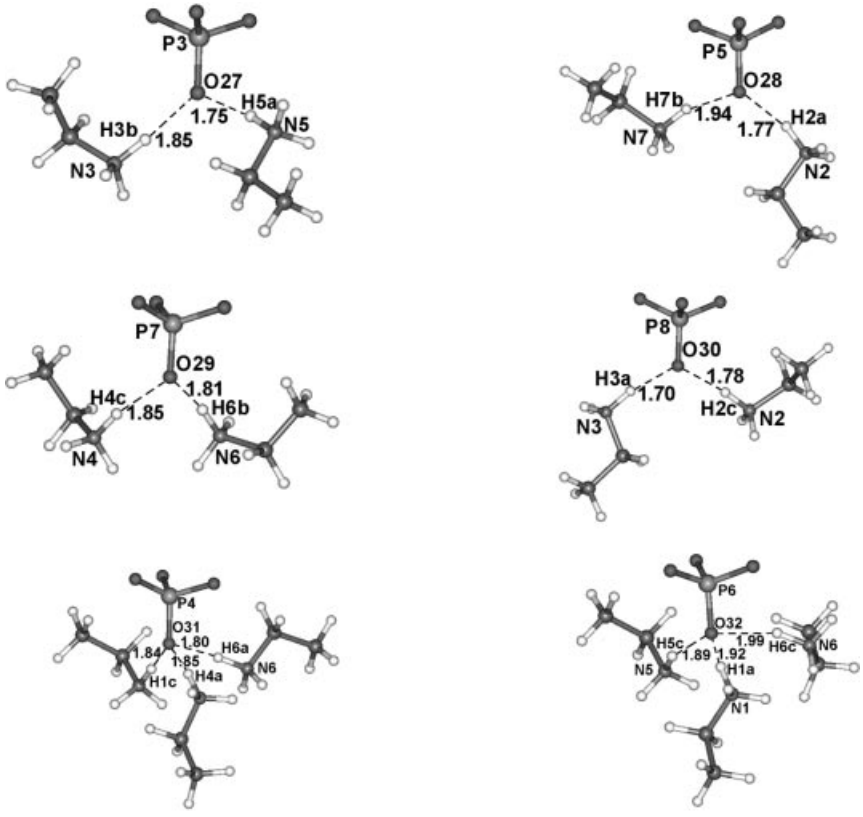


Figure 6. Hydrogen bonding scheme (dotted lines) for each phosphorus site.

 © 2006 Wiley-VCH Verlag GmbH & Co. KGaA, Weinheim 

peaks situated at $\delta$ = 15.0 and 36.4 ppm. They are assigned to the $CH_3$ and $CH_2$ groups of the ethylamine molecule, respectively.[20] No carbonyl group is observed on this spectrum (line expected at $\delta \approx 160$ ppm),[9] which means that EFD is decomposed into ethylamine (EA) and carbon monoxide under our experimental conditions. The $^{13}C$ isotropic chemical shifts for protonated and nonprotonated EA in the liquid state are at $\delta$ = 13 and 18 ppm, respectively for the methyl group, and at $\delta$ = 37 and 36 ppm, respectively for the $CH_2$ group. Thus, as suggested in the previous section, the EA occluded in Mu-34 appears to be protonated.

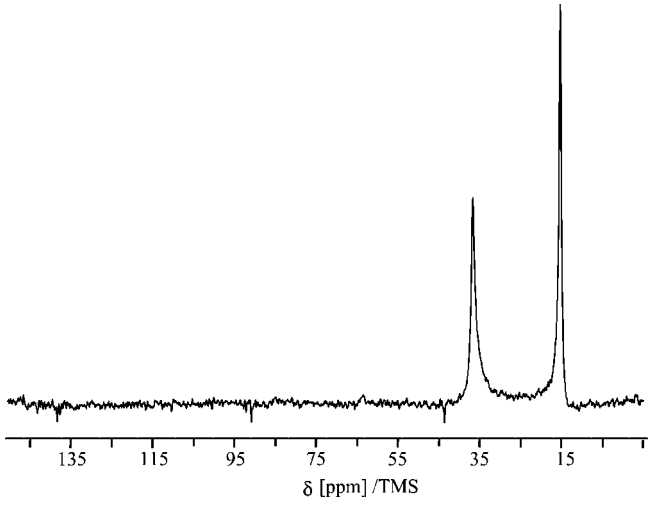


Figure 8. $^{13}C$ CP MAS NMR spectrum of the fluorogallophosphate Mu-34.

### $^{19}F$ MAS NMR Spectroscopy

The $^{19}F$ MAS NMR spectrum of the as-synthesized product, reported in Figure 9, exhibits one signal located at $\delta$ = –82 ppm. As observed for the gallophosphate Mu-28[16] and in good agreement with the crystal structure analysis, such a chemical shift value could be assigned to the three-coordinate fluorine atoms.

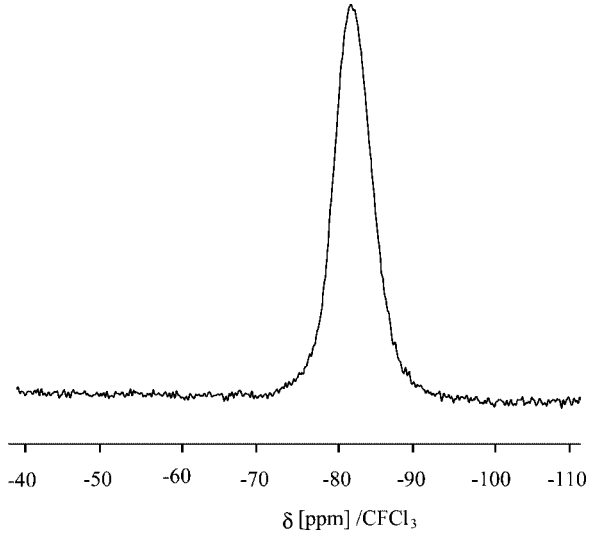


Figure 9. $^{19}F$ MAS NMR spectrum of the fluorogallophosphate Mu-34.

### $^{31}P$ MAS NMR Spectroscopy

The $^{31}P$ MAS NMR spectrum of the fluorogallophosphate Mu-34, shown in Figure 10, displays six signals at $\delta$ = 2, –2.3, –4.4, –6.6, –7.7, and –9.9 ppm. After decomposition, the relative areas are close to 1:1:1:2:1:2 respectively, indicating, in agreement with the structure determination, the existence of eight crystallographically distinct phosphorus sites. $^1H$-$^{31}P$ CP MAS NMR experiments have also been performed (spectrum not reported) and whatever the contact time (0.1, 0.05 ms) no significant difference was observed between the MAS and CP MAS spectra which means that all the atoms have the same proton environment. According to the structure and despite the low field chemical shift values observed no terminal P–OH group is present. Such a result is quite expected since all P atoms are hydrogen bonded via their P=O group (see Figure 6). A tentative assignment of the NMR peaks might be proposed on the basis of the empirical relationship between the $^{31}P$ isotropic chemical shift and the bond valence sum of the oxygen atoms connected to the phosphorus atom.[21] From the equation developed by Brown[22] and using the P–O and Ga–O bond lengths, the total oxygen bond valences [$\Sigma$s(O)] including the contribution of the hydrogen bonds[23] for the phosphorus atoms P1, P2, P3, P4, P5, P6, P7, and P8 are equal to 8.04, 8.23, 8.27, 8.48, 8.35, 8.64, 8.29, and 8.27, respectively. Consequently, the assignment of the eight NMR peaks might be made as follows. The most highfield signal is attributed to the phosphorus atom, which has the highest oxygen bond valence. Therefore, the peak at $\delta$ = –9.9 ppm, which has a relative area close to 2, could be assigned to P6 and P4 respectively [$\Sigma$s(O) = 8.48 for P4 and

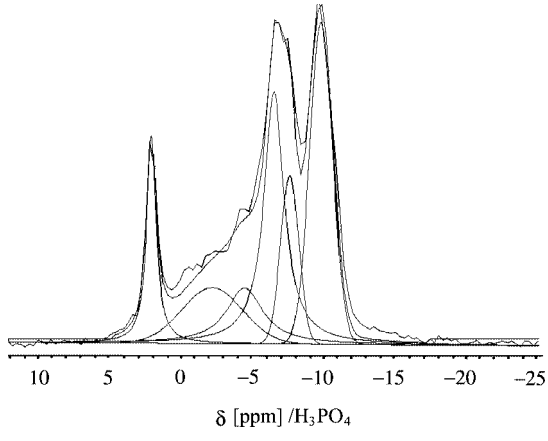


Figure 10. $^{31}P$ MAS NMR spectrum of the fluorogallophosphate Mu-34 and its decomposition.

 © 2006 Wiley-VCH Verlag GmbH & Co. KGaA, Weinheim 

8.64 for P6], the signal at $\delta$ = –7.7 ppm to P5 [Σs(O) = 8.35], and the signal at $\delta$ = 2 ppm to P1 [Σs(O) = 8.04]. Due to similar Σs(O) (8.23, 8.27, and 8.29), the other remaining signals are more difficult to assign.

## Conclusions

In this paper the synthesis and characterization of a novel fluorogallophosphate Mu-34, with a rather unusual structure, has been reported. It was prepared in a quasi nonaqueous medium using ethylformamide as the main solvent. As in several similar syntheses, the solvent decomposed during the synthesis, and the corresponding amine was found to be occluded in the final structure. The in situ release of the protonated amine during the synthesis appears to be a key step in the crystallization of this lamellar gallophosphate. Indeed, experiments using ethylamine in the starting mixture directly did not lead to the crystallization of this material.

The fluorogallophosphate Mu-34 displays porous layers built up from 4-, 6-, and 12-membered rings and resulting from the connection of two types of building units: a phosphate-capped six-membered ring and a phosphate and fluorine capped six-membered ring. It is noteworthy that in this latter unit, the fluorine atom is three-coordinate to gallium atoms. In order to compensate the negative charges of the anionic layers protonated ethylamine molecules are intercalated between. These molecules interact strongly with the inorganic layers via hydrogen bonds.

## Experimental Section

**Synthesis:** The fluorogallophosphate Mu-34 was prepared in a quasi nonaqueous fluoride medium at 200 °C from a mixture containing the ethylformamide as a precursor of the SDA (ethylamine). The molar composition of the starting mixture was 2 GaOOH : 2 $H_3PO_4$ : 1 HF : 10 ethylformamide (EFD) : 4.7$H_2O$. The amount of water arises from the phosphorus and fluoride sources. The pH value of the reaction mixture was adjusted to 4.5 with tripropylamine (TPA, Fluka 98 wt.-%), the latter presenting no structure-directing effect in the fluorine-containing gallophosphate system.[24] The amorphous gallium oxyhydroxide GaOOH was prepared by heating a gallium nitrate aqueous solution at 250 °C for 24 h. The other reactants were orthophosphoric acid (Labosi $H_3PO_4$ 85 wt.-%), hydrofluoric acid (Prolabo HF 40 wt.-%), and EFD (Fluka 99 wt.-%). The starting mixture was prepared by adding the amorphous gallium source (1.13 g) to the ethylformamide (3.65 g) under magnetic stirring. Then orthophosphoric acid (1.15 g) and hydrofluoric acid (0.25 g) were introduced. In order to increase the pH value, tripropylamine was added (0.72 g) and the mixture was stirred until it was homogeneous. Then, it was transferred to a 20 mL PTFE-lined stainless-steel autoclave and heated at 200 °C for 4 days. The product was filtered, washed with distilled water and dried at 60 °C overnight.

**Characterization:** The as-synthesized product was characterized by powder X-ray diffraction (XRD) with a STOE STADI-P diffractometer equipped with a curved germanium (111) primary monochromator and a linear position-sensitive detector using Cu-$K_\alpha$1 radiation ($\lambda$ = 1.5406 Å). The morphology and average size of the crystals were determined by scanning electron microscopy (SEM) with a Philips XL30 microscope. Elemental analyses were carried out with the Induced Coupled Plasma technique using Atomic Energy Spectroscopy (ICP AES) for Ga and P, and by coulometric and catharometric methods for C and N quantifications, respectively. Thermogravimetric (TGA) and differential thermal (DTA) analyses were performed under air with a Setaram Labsys thermoanalyser with a heating rate of 5 °C min$^{-1}$ up to 1000 °C. The $^{13}$C CP MAS NMR spectrum was recorded with a Bruker MSL 300 spectrometer and the $^{19}$F MAS, $^{31}$P MAS, and $^{31}$P CP MAS spectra with a Bruker DSX 400 spectrometer. The recording conditions are reported in Table 2. For the structure determination, a crystal plate was cut out of a larger aggregate and selected after optical examination under crossed polars. The single-crystal X-ray diffraction experiment was carried out at room temperature with an Oxford diffraction Xcalibur diffractometer equipped with a CCD detector. A full redundant Ewald sphere was collected with Mo-$K_\alpha$ radiation up to the maximum resolution $\sin\theta/\lambda_{max.}$ = 0.78 Å$^{-1}$. Bragg intensities were integrated with CrysAlis software,[25] and averaged in Laue group $P\bar{1}$ with the SORTAV program[26] after an absorption correction ($\mu$ = 3.633 mm$^{-1}$) based on the crystal shape. Data collection details are summarized in Table 3. The crystal structure was solved by direct methods using SHELXS[27] and refined with JANA2000.[28] The positions of all non-H atoms were found straightforwardly on successive Fourier maps. Hydrogen atoms were introduced in the structural model assuming ideal conformations for all protonated ethylamine molecules. Atomic displacement parameters of H atoms were restrained to 1.5 times the value of that of the heavy atom they were attached to. All bond lengths and bond angles of protonated ethylamine molecules were also restrained to the expected values observed in $CH_3$ (methyl), $CH_2$ (methylene), and $NH_3$ (amine) groups.[29] The refinement converged to $R$ = 0.0575 ($R = \Sigma||F_o| - |kF_c||/\Sigma|F_o|$) and $Rw$ = 0.0591 [$R_w = \{\Sigma w(|F_o| - |kF_c|)^2/\Sigma w(|F_o|^2)\}^{1/2}$] for 6644 reflections [$I > 3\sigma(I)$]. The supplementary crystallographic data are available online via http://www.fiz-karlsruhe.de (the reference file number is CSD-415650).

Table 2. Recording conditions of the NMR spectra.

| | $^{13}$C CP MAS | $^{31}$P MAS | $^{31}$P CP MAS | $^{19}$F MAS |
|---|---|---|---|---|
| Chemical shift reference | TMS | 85% $H_3PO_4$ | 85% $H_3PO_4$ | $CFCl_3$ |
| Frequency [MHz] | 75.47 | 161.98 | 161.98 | 376.5 |
| Pulse width [$\mu$s] | 3.7 | 3.5 | 4.5 | 2 |
| Flip angle | $\pi$ /2 | $\pi$ /2 | $\pi$ /2 | $\pi$ /2 |
| Contact time [ms] | 1 | / | 0.05–0.1 | / |
| Recycle time [s] | 8 | 30 | 10 | 20 |
| Spinning rate [Hz] | 5000 | 25000 | 25000 | 25000 |
| Number of scans | 80 | 64 | 64 | 32 |

 © 2006 Wiley-VCH Verlag GmbH & Co. KGaA, Weinheim 

Table 3. Experimental single crystal XRD data and structure analysis of the fluorogallophosphate Mu-34.

| | Mu-34 |
|---|---|
| Chemical formula (asymmetric unit) | $[Ga_6(PO_4)_8F(C_2H_8N)_7]$ |
| Cell parameters | $a$ = 11.0832(6) Å, $b$ = 11.393(6) Å, $c$ = 21.335(1) Å<br>$\alpha$ = 100.62(4)°, $\beta$ = 99.66(5)°, $\gamma$ = 108.34(5)° |
| $V$ [Å$^3$] | 2438.7(2) |
| Space group | $P\bar{1}$ |
| $Z$ | 2 |
| Crystal size [$\mu$m] | 40 × 100 × 120 |
| Diffractometer | Oxford diffraction Xcalibur 2 + Sapphire CCD |
| Radiation source, wavelength | Mo-$K_\alpha$, $\lambda$ = 0.71073 Å |
| Absorption coefficient [mm$^{-1}$] | 3.633 |
| Temperature [K] | 293 |
| Reflections measured, independent | 90333, 17034 |
| Observed reflections [$I > 3\sigma(I)$] | 6644 |
| Overall completeness ($\sin\theta/\lambda_{max.}$ = 0.78 Å$^{-1}$) | 88.7% |
| $R_{int}$ | 0.076 |
| Structure refinement [$I > 3\sigma(I)$] | $R$ = 0.0575, $Rw$ = 0.0591, goof = 2.42 |

$$R_{int} = \frac{\sum_H \sqrt{N/N-1} \sum_i^{N_{equi}} |I_i - \langle I \rangle|}{\sum_H \sum_i^{N_{equi}} |I_i|}, \quad R = \left( \sum_H^o \left| |F_{obs}| - |kF_{calc}| \right| \right) \Big/ \left( \sum_H^o |F_{obs}| \right),$$

$$Rw = \left( \left( \sum_H^o w \left( |F_{obs}| - |kF_{calc}| \right)^2 \right) \Big/ \left( \sum_H^o w |F_{obs}|^2 \right) \right)^{1/2}, \quad Gof = \left( \left( \sum_H^o w \left( |F_{obs}| - |kF_{calc}| \right)^2 \right) \Big/ (m-n) \right)^{1/2},$$

$w = 1/\sigma^2(F_{obsd.})$, $m$ is the number of reflections used, $n$ the number of parameters

**Supporting Information** (see footnote on the first page of this article): Tables S1–S3 of atomic coordinates, displacement parameters, selected bond lengths and angles.


[1] S. T. Wilson, B. M. Lok, C. A. Messina, T. R. Cannan, E. M. Flanigen, *J. Am. Chem. Soc.* **1982**, *104*, 1146.
[2] M. E. Davis, *Nature* **2002**, *417*, 813.
[3] H. Kessler, J. Patarin, C. Schott-Darie, in *Advanced Zeolite Science and Applications, Studies in Surface Science and Catalysis* (Eds.: J. C. Jansen, M. Stöcker, H. G. Karge, J. Weitkamp), Elsevier, Amsterdam, **1994**, vol. 85, p.75.
[4] G. Férey, *J. Fluorine Chem.* **1995**, *72*, 187.
[5] J. Patarin, J. L. Paillaud, H. Kessler, in *Synthesis of AlPO$_4$s and other crystalline materials, Handbook of Porous Solids* (Eds.: F. Schüth, K. S. W. Sing, J. Weitkamp), Wiley-VCH, Germany, **2002**, ch. 4.2.3, vol. 2, p. 815.
[6] M. Estermann, L. B. McCusker, Ch. Baerlocher, A. Merrouche, H. Kessler, *Nature* **1991**, *352*, 320.
[7] A. Matijasic, P. Reinert, L. Josien, A. Simon, J. Patarin, in *Zeolites and Mesoporous Materials at the Dawn of the 21st Century, Studies in Surface Science and Catalysis* (Eds.: A. Galarneau, F. Direnzo, F. Fajula, J. Vedrine), Elsevier, Amsterdam, **2001**, vol. 135, p. 142.
[8] P. Caullet, J. L. Paillaud, A. Simon-Masseron, M. Soulard, J. Patarin, *C. R. Chimie* **2005**, *8*, 245.
[9] L. Vidal, V. Gramlich, J. Patarin, Z. Gabelica, *Eur. J. Solid State Inorg. Chem.* **1998**, *35*, 545.
[10] L. Vidal, V. Gramlich, J. Patarin, Z. Gabelica, *Chem. Lett.* **1999**, 201.
[11] C. Paulet, T. Loiseau, G. Férey, *J. Mat. Chem.* **2000**, *10*, 1225.
[12] L. Lakiss, A. Simon-Masseron, V. Gramlich, J. Patarin, *Solid State Sci.* **2005**, *7*, 141.
[13] L. Lakiss, A. Simon-Masseron, J. Patarin, *Micro. Meso. Mater.* **2005**, *84*, 50.
[14] S. Feng, R. Xu, *Chem. J. Chinese Univ.* **1988**, *4*, 1.
[15] T. Loiseau, F. Taulelle, G. Férey, *Micro. Mater.* **1997**, *9*, 83.
[16] L. Josien, A. Simon-Masseron, V. Gramlich, F. Porcher, J. Patarin, *J. Solid State Chem.* **2004**, *177*, 3721.
[17] J. M. Thomas, R. H. Jones, R. Xu, J. Chen, A. M. Chippindale, S. Natarajan, A. K. Cheetham, *J. Chem. Commun.* **1992**, 929.
[18] A. M. Chippindale, A. R. Cowley, Q. Huo, R. H. Jones, A. D. Law, J. M. Thomas, R. Xu, *J. Chem. Soc. Dalton Trans.* **1997**, 2639.
[19] P. A. Barrett, R. H. Jones, *J. Chem. Commun.* **1995**, 1979.
[20] H. O. Kalinowski, S. Berger, S. Braun, *$^{13}$C NMR Spektroskopie*, Thieme, Stuttgart, **1984**, 189.
[21] A. K. Cheetham, N. J. Clayden, C. M. Dobson, J. B. Jakeman, *J. Chem. Soc. Chem. Commun.* **1986**, 195.
[22] I. D. Brown, *Structure and Bonding in Crystals*, Academic Press, New York, **1981**, ch. 14, vol. 2, p. 1.
[23] I. D. Brown, D. Altermatt, *Acta Crystallogr. Sect. B* **1985**, *41*, 244.
[24] C. Schott-Darie, Ph. D. Thesis, University of Haute Alsace, Mulhouse, **1994**.
[25] *CrysAlis* Software System, Version 1.170, Oxford Diffraction Ltd, **2003**.
[26] R. H. Blessing, *J. Appl. Cryst.* **1997**, *30*, 421.
[27] G. M. Sheldrick, *SHELXS86*, Program for the Solution of Crystal Structures, University of Göttingen, Germany, **1986**.
[28] V. Petříček, M. Dušek, *The Crystallographic Computing System JANA2000*, Institute of Physics, Praha, Czech Republic, **2000**.
[29] *International Tables for X-ray Crystallography*, Kluwer Academic Publishers, Dordrecht, vol. C, **1992**.


Received: August 5, 2005
Published Online: November 17, 2005

 © 2006 Wiley-VCH Verlag GmbH & Co. KGaA, Weinheim 

DOI: 10.1002/ejic.200500711

# Formation of Triple-Stranded Dinuclear Helicates with Dicatecholimine Ligands: The Influence of Steric Hindrance at the Spacer

**Ingo Janser,[a] Markus Albrecht,*[a] Katharina Hunger,[a,b] Simon Burk,[a] and Kari Rissanen[b]**

**Keywords:** Dinuclear complexes / Helicates / Meso-helicates / Self-assembly / Titanium / Bulky ligands

A series of new imine-bridged dicatechol ligands **3a**–**f**-$H_4$ with sterically demanding groups at the spacers are used for the formation of titanium(IV) complexes $M_4[(\mathbf{3})_3Ti_2]$. All three ligands **3a**–**c**-$H_4$ form triple-stranded dinuclear helicates. When the bulky ligands **3a**-$H_4$ or **3c**-$H_4$ are used with potassium as the countercation, oligomeric or polymeric side products are also observed. The imine-bridged ligand **3e**-$H_4$ quantitatively forms helicates $M_4[(\mathbf{3e})_3Ti_2]$ and not a $M_4L_6$ tetrahedron as observed with Raymond's analogous amide-bridged dicatechol ligand **3i**-$H_4$. NMR spectroscopic investigations at variable temperature show that ligand **3f**-$H_4$, which possesses a spiro fluorenyl group at the central unit of the spacer, forms the *meso*-helicate $M_4[(\mathbf{3f})_3Ti_2]$.

(© Wiley-VCH Verlag GmbH & Co. KGaA, 69451 Weinheim, Germany, 2006)

## Introduction

In the last two decades double- and triple-stranded helicates have been investigated very intensely as model compounds in metallosupramolecular chemistry.[1] In order to perform a systematic study on the influences of different geometric factors on the helicate formation we needed an easy way of preparing a variety of different ligands with different geometric constraints and demands. Several groups[2,3] have shown that bis(iminopyridine) ligands can be obtained by simple imine condensation from readily available starting materials. These ligands form double- or triple-stranded helicates with a series of different metal ions. Recently, we[4,5] and others[6] introduced imine condensation to obtain dicatechol ligands for the formation of helicates.[7–11]

Herein we use this concept to obtain several new ligands with different steric demands at the spacer, which can then be used for the self-assembly of triple-stranded dinuclear helicates and *meso*-helicates.

## Results and Discussion

### Synthesis and Characterisation of the Dicatechol Ligands 3a–f-$H_4$

The dicatechol ligands **3a**–**f**-$H_4$ were prepared in two different ways (Scheme 1): (i) The diamines **1a**–**1d** and 2 equiv. 2,3-dihydroxybenzaldehyde (**2**) were dissolved in toluene and heated to reflux in a Dean–Stark apparatus overnight in the presence of catalytic amounts of *p*-TosOH. Water was removed by continuous distillation of the water/toluene azeotrope. After cooling to room temperature, the precipitated product was isolated by filtration, washed with toluene, and the derivatives were obtained in 86% (**3a**-$H_4$, yellow solid), 81% (**3b**-$H_4$, red solid), 91% (**3c**-$H_4$, red solid) and 72% (**3d**-$H_4$, orange solid) yield. (ii) The diamines **1e** and **1f** and 2 equiv. 2,3-dihydroxybenzaldehyde (**2**) were dissolved in methanol. After 12 h at room temperature, the precipitated diimines were isolated by filtration in 99% (**3e**-$H_4$, red solid) or 93% (**3f**-$H_4$, red solid) yield, respectively.

The compounds were characterised by MS, elemental analysis and $^1$H NMR spectroscopy, and selected examples were also characterised by $^{13}$C NMR spectroscopy. The resonance of the imine proton is a characteristic signal in the $^1$H NMR spectra ([$D_6$]DMSO), which appears for the ligands **3a**–**f**-$H_4$ in the region of $\delta$ = 8.45–9.03 ppm. In two of the cases we were able to observe the signals for the two OH protons of the catechol moieties. For **3e**, two signals at $\delta$ = 13.17 and 9.37 ppm are detected. For **3f**, the two resonances of the OH protons can be found at $\delta$ = 13.21 and 9.23 ppm. The signal that appears downfield is assigned to the 2-hydroxy group, which forms an unsymmetric intramolecular hydrogen bond to the imine with a transfer of a proton to the nitrogen atom. At low temperatures form **A** is favoured, while form **B** is observed at higher temperatures (Scheme 2). The resonance of the 2-hydroxy group appears downfield because of shielding.[5]

[a] Institut für Organische Chemie der RWTH-Aachen,
Landoltweg 1, 52074 Aachen, Germany
Fax: +49-241-80-92385
E-mail: markus.albrecht@oc.rwth-aachen.de
[b] Nanoscience Center, Department of Chemistry, University of Jyväskylä,
Survontie 9, 40014 Jyväskylä, Finland

 © 2006 Wiley-VCH Verlag GmbH & Co. KGaA, Weinheim 

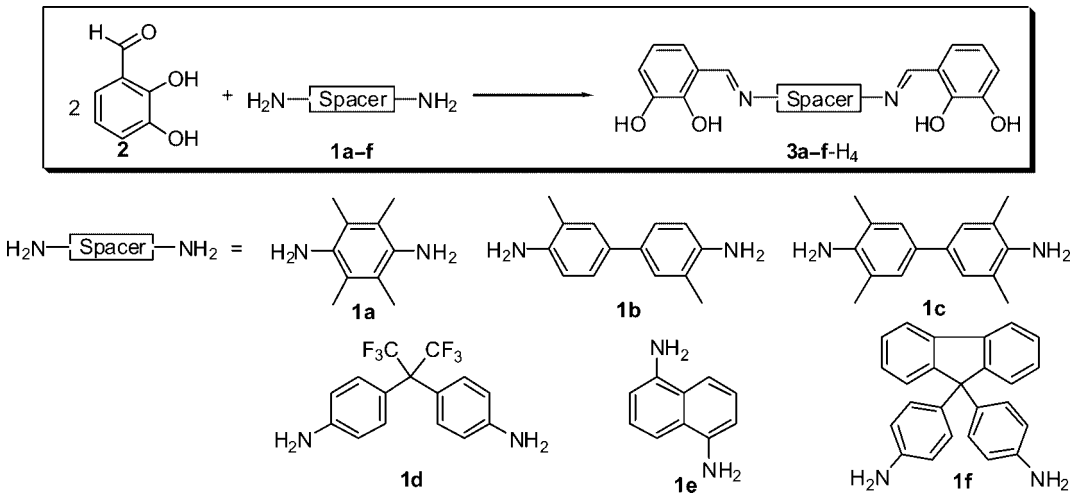


Scheme 1. Preparation of the dicatechol ligands **3a**–**f**-$H_4$ by imine condensation.

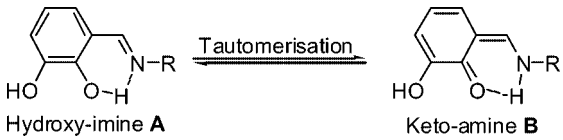


Scheme 2. Hydroxy-imine (**A**)/keto-amine (**B**) tautomerisation in Schiff base.

### Formation of Dinuclear Triple-Stranded Helicates $M_4[(3a–f)_3Ti_2]$ (M = Li, Na, K)

For the preparation of the titanium(IV) complexes $M_4[(3a–f)_3Ti_2]$, the ligands **3a**–**f**-$H_4$ (3 equiv.), $[TiO(acac)_2]$ (2 equiv.) and the corresponding alkali metal carbonate $M_2CO_3$ (2 equiv., M = Li, Na, K) were mixed in DMF (Scheme 3). Within a few minutes the solution turned orange-red and was stirred overnight at room temperature. Volatile components were removed in vacuo to obtain the complex salts $M_4[(3a–f)_3Ti_2]$ as red solids.

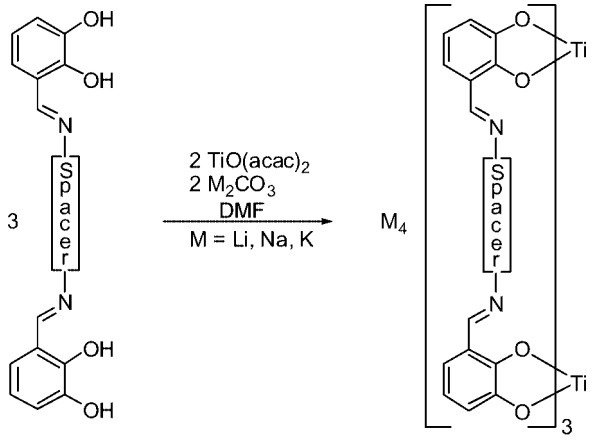


Scheme 3. Synthesis of the triple-stranded dinuclear helicates $M_4[(3a–f)_3Ti_2]$.

### *Formation and Characterisation of $M_4[(3a)_3Ti_2]$ (M = Li, Na, K)*

Ligands **3a**–**c** were introduced to study the influence of sterically demanding ligands on the self-assembly of helicates. The dinuclear complex salts $M_4[(3a)_3Ti_2]$ (M = Li, Na, K) of the phenyl-type ligand **3a** were characterised by elemental analysis, FAB MS and $^1H$ NMR spectroscopy. Positive FAB MS (3-NBA) reveals characteristic peaks at $m/z$ = 1305 $\{H_2Li[(3a)_3Ti_2]^+\}$, 1343 $\{HNa_2[(3a)_3Ti_2]^+\}$, or 1337 $\{H_2K[(3a)_3Ti_2]^+\}$. Upon complex formation, the imine proton, which appears in the $^1H$ NMR spectrum of **3a**-$H_4$ in $[D_6]$DMSO at $\delta$ = 8.45 ppm, is shifted upfield to $\delta$ = 8.10–8.16 ppm. The signals of the methyl groups of the spacer appear as a singlet at $\delta$ = 1.91 (Li), 1.91 (Na), and 1.89 ppm (K), and the catechol resonances [detected at $\delta$ = 7.03, 6.36 and 6.17 ppm (M = Li); 7.03, 6.37 and 6.19 ppm (M = Na); 6.93, 6.37 and 6.19 ppm (M =K)] appear as a doublet, triplet and doublet, respectively. No significant differences are observed for the NMR shifts of different salts of $[(3a)_3Ti_2]^{4-}$.

In earlier studies we investigated the complexation of ligand **3g**-$H_4$ with titanium(IV) ions (Figure 1). Ligand **3g**-$H_4$ possesses a phenyl spacer that is similar to that of ligand **3a**-$H_4$ but with protons instead of the four methyl groups. It could be shown that this ligand leads in a quantitative self-assembly process to the triple-stranded dinuclear helicate $M_4[(3g)_3Ti_2]$.[5]

Ligand **3a**-$H_4$ with four methyl groups at the phenyl spacer also leads to the triple-stranded dinuclear helicates $M_4[(3a)_3Ti_2]$ (M = Li, Na, K). However, in the case of the potassium salt $K_4[(3a)_3Ti_2]$, additional broad signals appear in the $^1H$ NMR sprectra ($[D_6]$DMSO) at $\delta$ = 8.28, 8.18, 7.20, 7.08, 6.17 ppm, which indicate the presence of polymeric or oligomeric species besides the triple-stranded dinuclear helicate as the main product. As can be seen from the X-ray analysis of $K_4[(3g)_3Ti_2]$ (Figure 1),[5] the complex possesses the structure of a triple-stranded dinuclear helicate. The long imine–aryl–imine spacers lead to a large sepa-

 © 2006 Wiley-VCH Verlag GmbH & Co. KGaA, Weinheim 

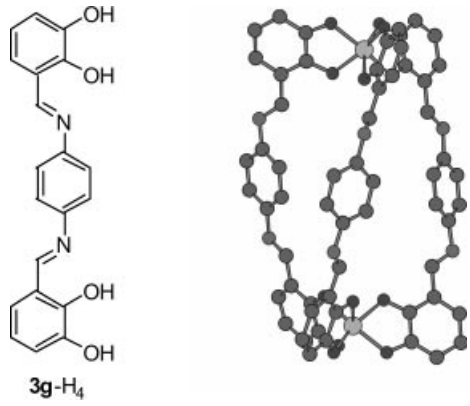


Figure 1. Ligand **3g**-$H_4$ and part of the X-ray structure of $K_4[(\mathbf{3g})_3Ti_2]$.[5]

ration of the titanium centres, and a big internal cavity is formed. As we know from other catechol-derived helicates, alkaline metal countercations are encapsulated in the interior and bind to the internal oxygen atoms of the catecholate ligands.[12,13] The coordination sphere at the cations is saturated by binding solvent molecules. It seems that the alkali cations act as a template in stabilising the formation of a triple-stranded dinuclear helicate. In the case of ligand **3a**-$H_4$, the potassium cation is not able to stabilise this formation quantitatively. The reason for this is the steric influence of the methyl groups that are probably directed into the interior of the complex, and this influence therefore suppresses the binding of big potassium cations. The lithium or sodium cations are smaller and because of this they fit into the cavity and stabilise the triple-stranded dinuclear complex more effectively.

### *Formation and Characterisation of $M_4[(3b–c)_3Ti_2]$ (M = Li, Na, K)*

In ligands **3b** and **3c** with elongated aromatic spacers, methyl groups are introduced at the *ortho* position of the imine spacers. In the presence of lithium, sodium or potassium cations, the two ligands **3b**-$H_4$ and **3c**-$H_4$ form triple-stranded helicates $M_4[(\mathbf{3b/c})_3Ti_2]$. The dinuclear complexes were characterised by elemental analysis, FAB MS and $^1H$ NMR spectroscopy. In the $^1H$ NMR spectrum of **3b**-$H_4$, the resonance for the imine proton appears at $\delta$ = 8.95 ppm and in the complexes at $\delta$ = 8.61 (Li), 8.65 (Na), and 8.60 ppm (K). The upfield shift of the resonance indicates that the conformation at the imine unit changes upon metal complexation (vide supra). The signals of the spacer can be detected for $Li_4[(\mathbf{3b})_3Ti_2]$ at $\delta$ = 7.43 (s, 6 H), 7.34 (d, $J$ = 7.5 Hz, 6 H), 7.00 (d, $J$ = 7.5 Hz, 6 H) and 2.30 ppm (s, 18 H) , for $Na_4[(\mathbf{3b})_3Ti_2]$ at $\delta$ = 7.44 (s, 6 H), 7.32 (d, $J$ = 8.0 Hz, 6 H), 7.05 (d, $J$ = 8.0 Hz, 6 H) and 2.30 ppm (s, 18 H) and for $K_4[(\mathbf{3b})_3Ti_2]$ at $\delta$ = 7.43 (s, 6 H), 7.33 (d, $J$ = 8.0 Hz, 6 H), 7.03 (d, $J$ = 8.0 Hz, 6 H) and 2.30 ppm (s, 18 H).

For the $Ti^{IV}$ complexes of ligand **3c**-$H_4$, similar MS and NMR spectroscopic results can be obtained (see Experimental Section). However, in the case of the potassium salt $K_4[(\mathbf{3c})_3Ti_2]$, additional signals appear in the $^1H$ NMR spectra ([$D_6$]DMSO) at $\delta$ = 8.57, 7.26 (br), 7.10 (br), 6.45 (br), 6.15 ppm (br), which indicate that some polymeric or oligomeric species are formed besides the triple-stranded dinuclear helicate as the main product.

In earlier studies we already investigated the coordination chemistry of the sterically less demanding ligand **3h**-$H_4$ (Figure 2) with titanium(IV) ions. Ligand **3h**-$H_4$ possesses a biphenyl spacer that is similar to ligand **3c**-$H_4$ but without the methyl substituents.[14] As we have shown, ligand **3h**-$H_4$ leads quantitatively to the formation of a triple-stranded dinuclear helicate $M_4[(\mathbf{3h})_3Ti_2]$. The X-ray structure of the complex $Na_4[(\mathbf{3h})_3Ti_2]$ shows (Figure 2) that the linear rigid ligands form a triple-stranded helicate with two similar-configured titanium(IV) complex units. Three ligands **3h**-$H_4$ wrap around the metals and adopt a conformation with the imine hydrogen atoms that point into the interior, directed towards the catecholate oxygen atoms, and therefore form a big cavity. In the solid state, two sodium cations are bound in the interior of the helicate, each binding to the internal catecholate oxygen atoms and to three DMF molecules.[14] Following this, it is reasonable to suggest that ligand **3b**-$H_4$ with its two additional methyl groups is able to form triple-stranded dinuclear complexes with lithium, sodium or potassium cations. The situation changes somewhat by using ligand **3c**-$H_4$. In the case of potassium as the countercation, the four additional methyl groups of the spacer are too big to fit into the cavity. In this case, potassium is not able to form the triple-stranded dinuclear helicate quantitatively, and therefore some oligomers and polymers are formed as side products, as is the case with ligand **3a**-$H_4$.

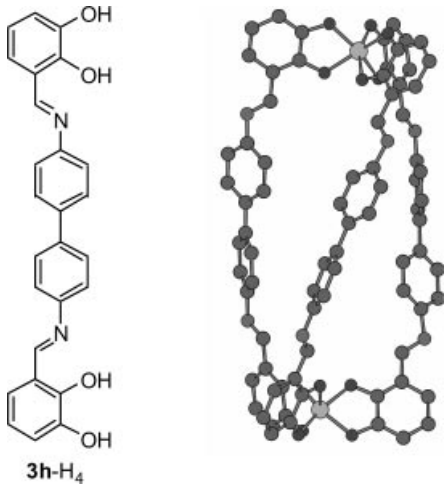


Figure 2. Ligand **3h**-$H_4$ and part of the X-ray structure $Na_4[(\mathbf{3h})_3Ti_2]$.[14]

These three examples demonstrate the influence of the spacer on the formation of the complexes. Ligand **3a**-$H_4$, with four methyl groups at the phenyl spacer, exclusively forms triple-stranded dinuclear helicates with lithium and sodium only. When potassium is the countercation both oligomeric and polymeric species can be observed. The size dependence is also observed in the yields of the three complexes $M_4[(\mathbf{3a})_3Ti_2]$. Upon coordination, the oligomeric or

 © 2006 Wiley-VCH Verlag GmbH & Co. KGaA, Weinheim 

polymeric species precipitate and the triple-stranded dinuclear helicates can be isolated by filtration in 66% (M = Li), 60% (M = Na), 37% (M =K) yield. Ligand **3b**-$H_4$, with an elongated spacer and two methyl groups in the *ortho* position of the imine spacers, forms a triple-stranded helicate in good yields (≥75%) with all three countercations. Ligand **3c**-$H_4$, with four methyl groups in the *ortho* position of the imine-spacers, leads to the formation of side products upon complexation with titanium(IV)ions and potassium as the countercations, which indicates that the cavity is too small for the four methyl groups and the big potassium cations.

### *Coordination Studies with Ligand 3d-$H_4$*

Ligand **3d** possesses two $CF_3$ groups that can act as a stereochemical probe for $^{19}F$ NMR spectroscopy. Unfortunately, we were not able to obtain triple-stranded dinuclear helicate-type compounds with ligand **3d**-$H_4$. Upon complex formation, residual water in the solvent hydrolyses the imine bond. $^1H$ NMR spectra in [$D_6$]DMSO show only resonances of the products from the cleavage reaction.

### *Formation of $M_4[(3e)_3Ti_2]$ (M = Li, Na)*

The imine-bridged dicatechol ligand **3e**-$H_4$ with a sterically demanding naphthyl spacer was introduced to study the differences from the amide-bridged dicatechol ligand **3i**-$H_4$ (Figure 3). With ligand **3i**-$H_4$, Raymond and coworkers obtained a molecular $M_4L_6$ tetrahedron, $[Ga_4\mathbf{3i}_6]^{12-}$, and no helicate was observed.[15]

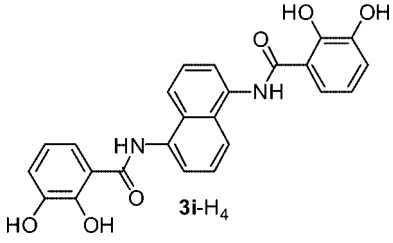


Figure 3. Ligand **3i**-$H_4$.[15]

In contrast, we obtained the triple-stranded dinuclear complexes $M_4[(\mathbf{3e})_3Ti_2]$ (M = Li, Na) in quantitative yield. Elemental analyses show the correct composition for the compounds, and characteristic peaks are observed in the positive FAB mass spectra for the dinuclear triple-stranded helicate. $^1H$ NMR spectroscopy in [$D_6$]DMSO reveals the resonances for the imine proton at $\delta$ = 8.26 (M = Li) and 8.34 ppm (M = Na), for the spacer at $\delta$ = 7.60, 7.18, and 7.02 (M = Li) and 7.65, 7.25, and 7.11 ppm (M = Na), and for the catecholate units at $\delta$ = 6.68, 6.36, and 6.12 (M = Li) and 6.78, 6.44, and 6.21 ppm (M = Na). No significant differences are observed when comparing the spectra of the complex salts $M_4[(\mathbf{3e})_3Ti_2]$ with those of different cations $M^+$. This shows that the formation of Raymond's tetrahedron in comparison to our helicate depends on the orientation of the amide versus the imine C–N group. In the case of the amide ligand **3i**, overcrowding of the spacers prevents the formation of the helicate. To explain this, we have to consider the different orientations of the imine- or amide-bridged dicatechol ligands **3e**-$H_4$ and **3i**-$H_4$ (Figure 4). We have reported earlier that the imine moiety possesses a preferred conformation **B**. In this conformation the C=N double bond is directed towards the outside of the cavity of the complex.[14] This conformation is preferred because there are electrostatic attractions between the internal catecholate oxygen atoms and the imine proton. Additional repulsion takes place between the oxygen and the imine-nitrogen lone pairs. The situation in Raymond's amide-bridged dicatechol ligand **3i**-$H_4$ is "reversed". Here an inward orientation of the amide nitrogen atom occurs (**D**), which forms an intramolecular hydrogen bond. Therefore, upon complexation of ligand **3e** with titanium(IV), a much bigger cavity is formed. In the case of the ligand **3i**-$H_4$, hydrogen bonding forces the sterically demanding naphthyl spacers into an orientation facing towards the interior of the complex. This prevents the formation of the helicate because the spacers would be forced "into each other". To prevent this, a molecular $M_4L_6$ tetrahedron is formed.[16]

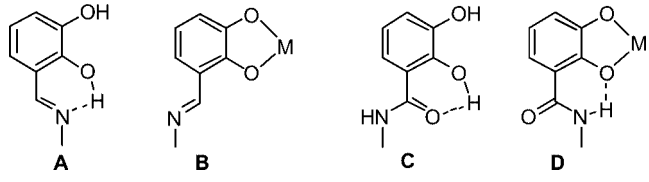


Figure 4. Possible orientations of the imine moiety in the free ligand (**A**) or in the catecholato metal complex (**B**) and of the amino moiety in the free ligand (**C**) or in the catecholato metal complex (**D**).

### *Formation of $M_4[(3f)_3Ti_2]$ (M = Li, Na, K)*

Ligand **3f**-$H_4$ possesses a big group at the central unit of the spacer and is therefore not as flexible as the related compound **3j**-$H_4$ (Figure 5). We investigated this ligand **3f**-$H_4$ in order to determine whether it is able to form *meso*-helicates with titanium(IV) and the corresponding alkali metal counterions as ligand **3j**-$H_4$ does.[14] Reaction of titanium(IV) ions with ligand **3f**-$H_4$ in the presence of an alkali metal carbonate in DMF leads to the assembly of dinuclear complex salts $M_4[(\mathbf{3f})_3Ti_2]$ in quantitative yield. The complexes $M_4[(\mathbf{3f})_3Ti_2]$ (M = Li, Na, K) were characterised by elemental analysis, ESI-MS, IR and NMR spectroscopy. In the ESI mass spectra, characteristic peaks can be detected at *m/z* = 1869 $\{Li_3[(\mathbf{3f})_3Ti_2]^-\}$, 1918 $\{Na_3[(\mathbf{3f})_3Ti_2]^-\}$, 1928 $\{HK_2[(\mathbf{3f})_3Ti_2]^-\}$. The lithium salt $Li_4[(\mathbf{3f})_3Ti_2]$ in [$D_6$]DMSO shows peaks in the $^1H$ NMR spectrum at $\delta$ = 8.53 (s, 6 H, imine), 7.89 (br., 6 H, spacer-fluorenyl), 7.48 (d, *J* = 7.3 Hz, 6 H, spacer-fluorenyl), 7.42–7.32 (m, 12 H, spacer-fluorenyl), 7.14 (d, *J* = 8.0 Hz, 12 H, spacer-phenyl), 7.04 (d, *J* = 8.0 Hz, 12 H, spacer-phenyl), 6.93 (d, *J* = 7.7 Hz, 6 H, cat), 6.30 (t, *J* = 7.7 Hz, 6 H, cat), 6.06 ppm (d, *J* = 7.7 Hz, 6 H, cat). Complex $Na_4[(\mathbf{3f})_3Ti_2]$ as well as $K_4[(\mathbf{3f})_3Ti_2]$ show similar spectra. For all three complexes, the signals for the spacer appear at room temperature as half a set of signals.

Recently, we described the formation of a triple-stranded dinuclear *meso*-helicate $M_4[(\mathbf{3j})_3Ti_2]$ with ligand **3j**-$H_4$, tita-

 © 2006 Wiley-VCH Verlag GmbH & Co. KGaA, Weinheim 

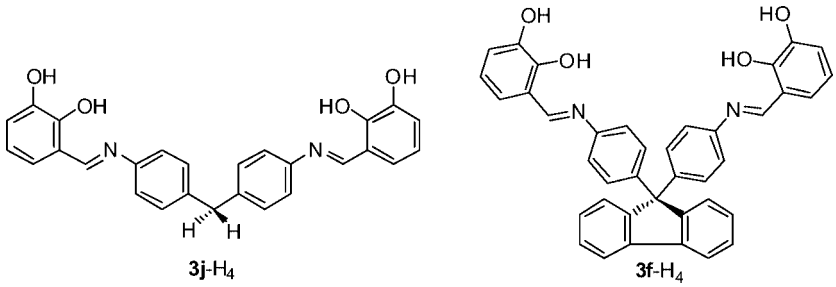


Figure 5. Ligands **3j**-$H_4$ and **3f**-$H_4$.

nium(IV) ions and the corresponding countercations ($Li^+$, $Na^+$, $K^+$).[14] The relative stereochemistry of the complex units of $M_4[(\mathbf{3j})_3Ti_2]$ was shown by X-ray diffraction as well as by NMR spectroscopy at variable temperature.

### *Temperature-Dependent NMR Spectroscopic Investigations of $Na_4[(3f)_3Ti_2]$*

For dinuclear helicate-type complexes with an odd number of $CH_2$ units in the spacer, NMR spectroscopy is a powerful tool for distinguishing between the helicate and the *meso*-helicate form.[17–22]

Figure 6 shows schematic representations of the situation that is found for dinuclear complexes with a $C_1$ unit incorporated into the spacer of either a helicate or a *meso*-helicate. In the case of the helicate, one set of signals is expected, whereas two diastereotopic groups are present in the *meso*-helicate. Therefore, we can expect two sets of signals for the substituents at the $C_1$ unit of the *meso*-helicate $[(\mathbf{3f})_3Ti_2]^{4-}$.[17–19,22]

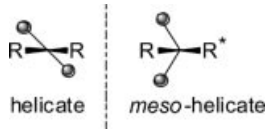


Figure 6. Schematic representation of the orientation of ligands with a $C_1$ spacer in the helicate and *meso*-helicate. Diasterotopic substituents are indicated.

As shown in Figure 5, spiro compound **3f**-$H_4$ (like **3j**-$H_4$) possesses a "C"-shaped conformation, and the *meso*-helicate should therefore be formed upon complexation with titanium(IV) ions. Thus, a full set of signals is expected for the protons of the fluorenyl group. The $^1H$ NMR spectrum of $Na_4[(\mathbf{3f})_3Ti_2]$ in [$D_4$]methanol at room temperature shows only half a set of signals (two doublets and two triplets) for the protons of the diastereotopic fluorenyl phenyl rings. Upon cooling of the NMR sample, the signals broaden and start to split. At 273 K, a full set of signals is observed, which reveals that the *meso*-helicate $Na_4[(\mathbf{3f})_3Ti_2]$ is present in solution (Figure 7).

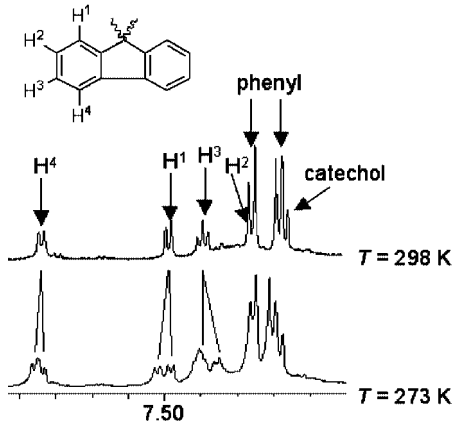


Figure 7. Temperature-dependent NMR spectrum of $Na_4[(\mathbf{3f})_3Ti_2]$ in [$D_4$]methanol at room temperature (298 K) and at 273 K. The signal of the $H^2$ proton is covered by a signal of the phenyl ring. (Two additional catechol protons are observed at $\delta$ = 6.44 and 6.51 ppm.)

## Conclusions

In this paper we demonstrated the influence of steric hindrance at the spacer of triple-stranded helicates for the self-assembly process. Therefore, a series of imine-bridged dicatechol ligands **3a**–**f**-$H_4$ with sterically demanding groups at the spacer were synthesised. The complexation of the ligands with titanium(IV)ions and the corresponding alkaline metal carbonate $M_2CO_3$ (M = Li, Na, K) has shown that the groups influence the formation of the complexes. In general, triple-stranded dinuclear complexes were formed. However, in some cases oligomeric and polymeric species could be observed as side products. In the case of a ligand with a high steric demand, it is possible that the groups of the spacer do not fit into the cavity and suppress the binding of the countercation. In this case, the cation cannot act as a template to stabilise the formation of a triple-stranded complex, and therefore oligomers or polymers are formed. The ligands **3a**-$H_4$ and **3c**-$H_4$ are bulky, and triple-stranded dinuclear helicates $K_4[(\mathbf{3a})_3Ti_2]$ or $K_4[(\mathbf{3c})_3Ti_2]$ are not obtained in quantitative yields.

Ligand **3e**-$H_4$ quantitatively formed a triple-stranded dinuclear helicate $[(\mathbf{3e})_3Ti_2]^{4-}$. The corresponding amide-bridged dicatechol ligand **3i**-$H_4$ leads to a molecular $M_4L_6$

 © 2006 Wiley-VCH Verlag GmbH & Co. KGaA, Weinheim 

tetrahedron, $K_5[Et_4N]_7[Ga_4\mathbf{3i}_6]\cdot 8H_2O$, and no helicate is observed. Here, hydrogen bonding of the amide group forces the sterically demanding naphthyl spacers to be oriented towards the interior of the complex. This prevents the formation of the helicate because the spacers would be forced "into each other". With ligand **3e**, the spacers are oriented "outwards", and the dinuclear complex can be formed.

Ligand **3f**-$H_4$ with a sterically demanding group at the central unit of the spacer quantitatively formed a *meso*-helicate. To prove this result, we used temperature-dependent NMR spectroscopy as a tool for distinguishing between the helicate and the *meso*-helicate form. This shows that the big fluorenyl group does not influence the formation of the complexes because the group is not directed into the cavity of the complex but is rather oriented outwards.

## Experimental Section

**General Remarks:** NMR spectra were recorded with a Bruker DRX 500, WM 400 or a Varian Inova 400 spectrometer. FT-IR spectra were recorded by diffuse reflection (KBr) with a Bruker IFS spectrometer. Mass spectra (EI 70 eV, FAB with 3-NBA as matrix) were recorded with a Finnigan MAT 90, 95 or 212 mass spectrometer. Elemental analyses were obtained with a Heraeus CHN-O-Rapid analyser.

**General Procedure for the Preparation of the Ligands 3a–f-$H_4$**

**Method A:** The corresponding diamine **1a**–**d** (1 mmol, 1 equiv.) and 2,3-dihydroxybenzaldehyde (**2**, 2 mmol, 2 equiv.) were heated in toluene in the presence of catalytic amounts of *p*-TosOH. Water was removed by azeotropic distillation. After cooling to room temperature, the precipitated product was isolated by filtration, washed with toluene and dried in vacuo.

**Method B:** The corresponding diamine **1e**–**f** (1 mmol, 1 equiv.) and 2,3-dihydroxybenzaldehyde (**2**, 2 mmol, 2 equiv.) were dissolved in methanol. After a few minutes, the product started to precipitate, and was then isolated by filtration after standing overnight, washed with ice-cold methanol and dried in vacuo.

**Ligand 3a-$H_4$ (Method A):** Yield: 86% of a yellow solid. $^1$H NMR ([D$_6$]DMSO): $\delta$ = 8.45 (s, 2 H), 7.07 (d, $J$ = 8.0 Hz, 2 H), 6.97 (d, $J$ = 8.0 Hz, 2 H), 6.79 (t, $J$ = 8.0 Hz, 2 H), 2.09 (s, 12 H) ppm. MS (EI, 70 eV): $m/z$ = 404 (100) $[M]^+$. $C_{24}H_{24}N_2O_4\cdot 1/2H_2O$ (413.47): calcd. C 69.72, H 6.09, N 6.78; found C 69.92, H 5.74, N 6.87.

**Ligand 3b-$H_4$ (Method A):** Yield: 91% of a red solid. $^1$H NMR ([D$_6$]DMSO): $\delta$ = 8.95 (s, 2 H), 7.70 (s, 2 H), 7.60 (d, $J$ = 8.5 Hz, 2 H), 7.48 (d, $J$ = 8.5 Hz, 2 H), 7.13 (d, $J$ = 7.5 Hz, 2 H), 6.94 (d, $J$ = 7.5 Hz, 2 H), 6.77 (t, $J$ = 7.5 Hz, 2 H), 2.44 (s, 6 H) ppm. MS (EI, 70 eV): $m/z$ = 452 (100) $[M]^+$. $C_{28}H_{24}N_2O_4\cdot 1/3H_2O$ (458.52): calcd. C 73.35, H 5.42, N 6.11; found C 73.31, H 5.17, N 6.11.

**Ligand 3c-$H_4$ (Method A):** Yield: 72% of an orange solid. $^1$H NMR ([D$_6$]DMSO): $\delta$ = 8.62 (s, 2 H), 7.48 (s, 4 H), 7.09 (d, $J$ = 8.0 Hz, 2 H), 6.97 (d, $J$ = 8.0 Hz, 2 H), 6.80 (t, $J$ = 8.0 Hz, 2 H), 2.24 (s, 12 H) ppm. MS (EI, 70 eV): $m/z$ = 480 (100) $[M]^+$. $C_{30}H_{28}N_2O_4\cdot$ 1/4toluene (503.60): calcd. C 75.72, H 6.00, N 5.56; found C 75.68, H 5.99, N 5.15.

**Ligand 3d-$H_4$ (Method A):** Yield: 81% of a red solid. $^1$H NMR ([D$_6$]DMSO): $\delta$ = 8.95 (s, 2 H), 7.53–7.44 (m, 8 H), 7.12 (d, $J$ = 8.0 Hz, 2 H), 6.96 (d, $J$ = 8.0 Hz, 2 H), 6.80 (t, $J$ = 8.0 Hz, 2 H) ppm. MS (EI, 70 eV): $m/z$ = 574 (100) $[M]^+$. $C_{29}H_{20}F_6N_2O_4\cdot$ 1/4$H_2O$ (578.98): calcd. C 60.16, H 3.57, N 4.84; found C 60.19, H 3.63, N 4.54.

**Ligand 3e-$H_4$ (Method B):** Yield: quantitative of a red solid. $^1$H NMR ([D$_6$]DMSO): $\delta$ = 13.17 (s, 2 H), 9.37 (s, 2 H), 9.03 (s, 2 H), 8.15 (d, $J$ = 7.9 Hz, 2 H), 7.71 (t, $J$ = 7.9 Hz, 2 H), 7.55 (d, $J$ = 7.9 Hz, 2 H), 7.23 (dd, $J$ = 7.4, 1.4 Hz, 2 H), 7.03 (dd, $J$ = 7.4, 1.4 Hz, 2 H), 6.86 (t, $J$ = 7.4 Hz, 2 H) ppm. MS (EI, 70 eV): $m/z$ = 398 (100) $[M]^+$. IR (KBr): $\tilde{\nu}$ = 1616, 1460, 1407, 1360, 1273, 1209, 1071, 1026, 981, 928, 781, 734, 522 cm$^{-1}$. $C_{24}H_{18}N_2O_4$ (398.42): calcd. C 72.35, H 4.55, N 7.03; found C 71.65, H 4.46, N 6.73.

**Ligand 3f-$H_4$ (Method B):** Yield: 93% of a red solid. $^1$H NMR ([D$_6$]-DMSO): $\delta$ = 13.21 (br., 2 H), 9.23 (br., 2 H), 8.88 (s, 2 H), 7.98 (d, $J$ = 7.2 Hz, 2 H), 7.52 (d, $J$ = 7.4 Hz, 2 H), 7.47–7.39 (m, 4 H), 7.34 (d, $J$ = 8.7 Hz, 4 H), 7.24 (d, $J$ = 8.7 Hz, 4 H), 7.08 (dd, $J$ = 7.8, 1.4 Hz, 2 H), 6.97 (dd, $J$ = 7.8, 1.4 Hz, 2 H), 6.79 (t, $J$ = 7.8 Hz, 2 H) ppm. $^{13}$C NMR ([D$_6$]DMSO): $\delta$ = 164.3 (CH), 150.8 (C), 149.8 (C), 147.0 (C), 146.1 (C), 144.6 (C), 140.0 (C), 129.2 (CH), 128.5 (CH), 128.4 (CH), 126.5 (CH), 123.3 (CH), 121.9 (CH), 121.2 (CH), 119.8 (C), 119.5 (CH), 119.3 (CH), 64.9 (C) ppm. MS (EI, 70 eV): $m/z$ = 588 (100) $[M]^+$. IR (KBr): $\tilde{\nu}$ = 3410, 1621, 1583, 1501, 1464, 1366, 1271, 1211, 1016, 873, 827, 735 cm$^{-1}$. $C_{39}H_{28}N_2O_4$ (588.66): calcd. C 79.57, H 4.79, N 4.76; found C 79.14, H 4.80, N 4.42.

**General Procedure for the Preparation of the Complexes $M_4[(\mathbf{3a}–\mathbf{f})_3Ti_2]$**

Ligand **3a**–**f**-$H_4$ (3 equiv.), $TiO(acac)_2$ (2 equiv.) and $M_2CO_3$ (2 equiv., M = Li, Na, K) were dissolved in DMF, and the orange mixture was stirred overnight. Volatiles were removed in vacuo to obtain the dinuclear complexes $M_4[(\mathbf{3a}–\mathbf{f})_3Ti_2]$ as red solids.

**Complex $Li_4[(\mathbf{3a})_3Ti_2]$:** Yield: 66% of a red solid. $^1$H NMR ([D$_6$]-DMSO): $\delta$ = 8.16 (s, 6 H), 7.03 (d, $J$ = 7.0 Hz, 6 H), 6.36 (t, $J$ = 7.0 Hz, 6 H), 6.17 (d, $J$ = 7.0 Hz, 6 H), 1.91 (s, 36 H) ppm. MS (pos. FAB, 3-NBA): $m/z$ = 1305 $\{H_2Li[(\mathbf{3a})_3Ti_2]^+\}$, 1299 $\{H_3[(\mathbf{3a})_3Ti_2]^+\}$, 649 $\{H_2[(\mathbf{3a})_3Ti_2]^{2+}\}$. $C_{72}H_{60}Li_4N_6O_{12}Ti_2\cdot$ 6($C_3H_7NO$)·10$H_2O$ (1943.59): calcd. C 55.62, H 6.33, N 8.65; found C 55.64, H 5.63, N 8.86.

**Complex $Na_4[(\mathbf{3a})_3Ti_2]$:** Yield: 60% of a red solid. $^1$H NMR ([D$_6$]-DMSO): $\delta$ = 8.16 (s, 6 H), 7.03 (d, $J$ = 7.0 Hz, 6 H), 6.37 (t, $J$ = 7.0 Hz, 6 H), 6.19 (d, $J$ = 7.0 Hz, 6 H), 1.91 (s, 36 H) ppm. MS (pos. FAB, 3-NBA): $m/z$ = 1343 $\{HNa_2[(\mathbf{3a})_3Ti_2]^+\}$, 1299 $\{H_3[(\mathbf{3a})_3Ti_2]^+\}$, 649 $\{H_2[(\mathbf{3a})_3Ti_2]^{2+}\}$. $C_{72}H_{60}Na_4N_6O_{12}Ti_2\cdot$ 6($C_3H_7NO$)·7$H_2O$ (1953.74): calcd. C 55.33, H 5.98, N 8.60; found C 55.15, H 5.38, N 8.86.

**Complex $K_4[(\mathbf{3a})_3Ti_2]$:** Yield: 37% of a red solid. $^1$H NMR ([D$_6$]-DMSO): $\delta$ = 8.10 (s, 6 H), 6.93 (d, $J$ = 7.0 Hz, 6 H), 6.37 (t, $J$ = 7.0 Hz, 6 H), 6.19 (d, $J$ = 7.0 Hz, 6 H), 1.89 (s, 36 H) ppm. MS (pos. FAB, 3-NBA): $m/z$ = 1337 $\{H_2K[(\mathbf{3a})_3Ti_2]^+\}$, 1299 $\{H_3[(\mathbf{3a})_3Ti_2]^+\}$, 649 $\{H_2[(\mathbf{3a})_3Ti_2]^{2+}\}$. $C_{72}H_{60}K_4N_6O_{12}Ti_2\cdot$ 6($C_3H_7NO$)·7$H_2O$ (2018.17): C 53.56, H 5.79, N 8.33; found C 53.61, H 5.30, N 8.69.

**Complex $Li_4[(\mathbf{3b})_3Ti_2]$:** Yield: quantitative of a red solid. $^1$H NMR ([D$_6$]DMSO): $\delta$ = 8.61 (s, 6 H), 7.43 (s, 6 H), 7.34 (d, $J$ = 7.5 Hz, 6 H), 7.08 (d, $J$ = 7.0 Hz, 6 H), 7.00 (d, $J$ = 7.5 Hz, 6 H), 6.38 (t, $J$ = 7.0 Hz, 6 H), 6.16 (d, $J$ = 7.0 Hz, 6 H), 2.30 (s, 18 H) ppm. MS (pos. FAB, 3-NBA): $m/z$ = 1443 $\{H_3[(\mathbf{3b})_3Ti_2]^+\}$, 721 $\{H_2[(\mathbf{3b})_3Ti_2]^{2+}\}$. $C_{84}H_{60}Li_4N_6O_{12}Ti_2\cdot 4(C_3H_7NO)\cdot 10H_2O$ (1941.53): calcd. C 59.39, H 5.61, N 7.21; found C 59.09, H 4.90, N 7.32.

**Complex $Na_4[(\mathbf{3b})_3Ti_2]$:** Yield: 75% of a red solid. $^1$H NMR ([D$_6$]-DMSO): $\delta$ = 8.65 (s, 6 H), 7.44 (s, 6 H), 7.32 (d, $J$ = 8.0 Hz, 6 H),

 © 2006 Wiley-VCH Verlag GmbH & Co. KGaA, Weinheim 

7.12 (d, $J$ = 7.5 Hz, 6 H), 7.05 (d, $J$ = 8.0 Hz, 6 H), 6.39 (t, $J$ = 7.5 Hz, 6 H), 6.18 (d, $J$ = 7.5 Hz, 6 H), 2.30 (s, 18 H) ppm. MS (pos. FAB, 3-NBA): $m/z$ = 1443 $\{H_3[(\mathbf{3b})_3Ti_2]^+\}$, 721 $\{H_2[(\mathbf{3b})_3Ti_2]^{2+}\}$. $C_{84}H_{60}Na_4N_6O_{12}Ti_2{\cdot}5(C_3H_7NO){\cdot}8H_2O$ (2042.79): calcd. C 58.21, H 5.48, N 7.54; found C 58.15, H 4.94, N 7.78.

**Complex $K_4[(3b)_3Ti_2]$:** Yield: 84% of a red solid. $^1$H NMR ([D$_6$]-DMSO): $\delta$ = 8.60 (s, 6 H), 7.43 (s, 6 H), 7.33 (d, $J$ = 8.0 Hz, 6 H), 7.10 (d, $J$ = 7.5 Hz, 6 H), 7.03 (d, $J$ = 8.0 Hz, 6 H), 6.38 (t, $J$ = 7.5 Hz, 6 H), 6.17 (d, $J$ = 7.5 Hz, 6 H), 2.30 (s, 18 H) ppm. MS (pos. FAB, 3-NBA): $m/z$ = 1443 $\{H_3[(\mathbf{3b})_3Ti_2]^+\}$, 721 $\{H_2[(\mathbf{3b})_3Ti_2]^{2+}\}$. $C_{84}H_{60}K_4N_6O_{12}Ti_2{\cdot}4(C_3H_7NO){\cdot}6H_2O$ (1998.10): calcd. C 57.71, H 5.04, N 7.01; found C 57.64, H 4.86, N 6.94.

**Complex $Li_4[(3c)_3Ti_2]$:** Yield: 75% of a red solid. $^1$H NMR ([D$_6$]-DMSO): $\delta$ = 8.30 (s, 6 H), 7.29 (s, 12 H), 7.06 (d, $J$ = 8.0 Hz, 6 H), 6.37 (t, $J$ = 8.0 Hz, 6 H), 6.17 (d, $J$ = 8.0 Hz, 6 H), 2.06 (s, 36 H) ppm. MS (pos. FAB, 3-NBA): $m/z$ = 1533 $\{H_2Li[(\mathbf{3c})_3Ti_2]^+\}$, 1527 $\{H_3[(\mathbf{3c})_3Ti_2]^+\}$, 763 $\{H_2[(\mathbf{3c})_3Ti_2]^{2+}\}$. $C_{90}H_{72}Li_4N_6O_{12}Ti_2{\cdot}5(C_3H_7NO){\cdot}16H_2O$ (2206.88): calcd. C 57.15, H 6.35, N 6.98; found C 57.25, H 5.52, N 7.27.

**Complex $Na_4[(3c)_3Ti_2]$:** Yield: 65% of a red solid. $^1$H NMR ([D$_6$]-DMSO): $\delta$ = 8.30 (s, 6 H), 7.20 (s, 12 H), 7.06 (d, $J$ = 7.5 Hz, 6 H), 6.38 (t, $J$ = 7.5 Hz, 6 H), 6.20 (d, $J$ = 7.5 Hz, 6 H), 2.06 (s, 36 H) ppm. MS (pos. FAB, 3-NBA): $m/z$ = 1549 $\{H_2Na[(\mathbf{3c})_3Ti_2]^+\}$, 1527 $\{H_3[(\mathbf{3c})_3Ti_2]^+\}$, 763 $\{H_2[(\mathbf{3c})_3Ti_2]^{2+}\}$. $C_{90}H_{72}Na_4N_6O_{12}Ti_2{\cdot}5(C_3H_7NO){\cdot}17H_2O$ (2289.09): calcd. C 55.09, H 6.21, N 6.73; found C 54.97, H 5.27, N 7.00.

**Complex $K_4[(3c)_3Ti_2]$:** Yield: 56% of a red solid. $^1$H NMR ([D$_6$]-DMSO): $\delta$ = 8.29 (s, 6 H), 7.20 (s, 12 H), 7.05 (d, $J$ = 7.5 Hz, 6 H), 6.36 (t, $J$ = 7.5 Hz, 6 H), 6.18 (d, $J$ = 7.5 Hz, 6 H), 2.06 (s, 36 H) ppm. MS (pos. FAB, 3-NBA): $m/z$ = 1566 $\{H_2K[(\mathbf{3c})_3Ti_2]^+\}$, 1527 $\{H_3[(\mathbf{3c})_3Ti_2]^+\}$, 763 $\{H_2[(\mathbf{3c})_3Ti_2]^{2+}\}$. $C_{90}H_{72}K_4N_6O_{12}Ti_2{\cdot}4(C_3H_7NO){\cdot}18H_2O$ (2298.45): calcd. C 53.30, H 5.96, N 6.09; found C 53.29, H 5.12, N 6.37.

**Complex $Li_4[(3e)_3Ti_2]$:** Yield: quantitative of a red solid. $^1$H NMR ([D$_6$]DMSO): $\delta$ = 8.26 (s, 6 H), 7.60 (d, $J$ = 8.0 Hz, 6 H), 7.18 (t, $J$ = 8.0 Hz, 6 H), 7.02 (d, $J$ = 8.0 Hz, 6 H), 6.68 (d, $J$ = 7.4 Hz, 6 H), 6.36 (t, $J$ = 7.4 Hz, 6 H), 6.12 (d, $J$ = 7.4 Hz, 6 H) ppm. MS (pos. ESI-MS, methanol): $m/z$ = 1299 $\{Li_3[(\mathbf{3e})_3Ti_2]^+\}$, 646 $\{Li_2[(\mathbf{3e})_3Ti_2]^{2+}\}$, 643 $\{HLi[(\mathbf{3e})_3Ti_2]^{2+}\}$. IR (KBr): $\tilde{\nu}$ = 3412, 1664, 1608, 1551, 1501, 1445, 1286, 1250, 1099, 1053, 924, 855, 789, 742, 712, 671, 617, 519 cm$^{-1}$. $C_{72}H_{42}Li_4N_6O_{12}Ti_2{\cdot}7(C_3H_7NO){\cdot}7H_2O$ (1944.50): calcd. C 57.45, H 5.44, N 9.36; found C 57.71, H 5.11, N 9.27.

**Complex $Na_4[(3e)_3Ti_2]$:** Yield: quantitative of a red solid. $^1$H NMR ([D$_6$]DMSO): $\delta$ = 8.34 (s, 6 H), 7.65 (d, $J$ = 7.8 Hz, 6 H), 7.25 (t, $J$ = 7.8 Hz, 6 H), 7.11 (d, $J$ = 7.8 Hz, 6 H), 6.78 (d, $J$ = 7.4 Hz, 6 H), 6.44 (t, $J$ = 7.4 Hz, 6 H), 6.21 (d, $J$ = 7.4 Hz, 6 H) ppm. MS (pos. ESI-MS, methanol): $m/z$ = 1347 $\{Na_3[(\mathbf{3e})_3Ti_2]^+\}$, 686 $\{H_2Na_4[(\mathbf{3e})_3Ti_2]^{2+}\}$, 662 $\{Na_2[(\mathbf{3e})_3Ti_2]^{2+}\}$, 640 $\{H_2[(\mathbf{3e})_3Ti_2]^{2+}\}$. IR (KBr): $\tilde{\nu}$ = 2927, 1665, 1610, 1551, 1501, 1446, 1388, 1250, 1213, 1095, 1053, 1006, 923, 854, 789, 741, 711, 666, 617, 519 cm$^{-1}$. $C_{72}H_{42}Na_4N_6O_{12}Ti_2{\cdot}7(C_3H_7NO){\cdot}5H_2O$ (1972.66): calcd. C 56.63, H 5.16, N 9.23; found C 56.99, H 4.55, N 9.14.

**Complex $Li_4[(3f)_3Ti_2]$:** Yield: quantitative of a red solid. $^1$H NMR ([D$_6$]DMSO): $\delta$ = 8.53 (s, 6 H), 7.89 (br., 6 H), 7.48 (d, $J$ = 7.3 Hz, 6 H), 7.42–7.32 (m, 12 H), 7.14 (d, $J$ = 8.0 Hz, 12 H), 7.04 (d, $J$ = 8.0 Hz, 12 H), 6.93 (d, $J$ = 7.7 Hz, 6 H), 6.30 (t, $J$ = 7.7 Hz, 6 H), 6.06 (d, $J$ = 7.7 Hz, 6 H) ppm. MS (neg. ESI-MS, methanol): $m/z$ = 1869 $\{Li_3[(\mathbf{3f})_3Ti_2]^-\}$, 1864 $\{HLi_2[(\mathbf{3f})_3Ti_2]^-\}$, 1852 $\{H_3[(\mathbf{3f})_3Ti_2]^-\}$, 932 $\{Li_2[(\mathbf{3f})_3Ti_2]^{2-}\}$. IR (KBr): $\tilde{\nu}$ = 3444, 1666, 1618, 1590, 1501, 1446, 1386, 1252, 1209, 744, 666, 599, 514 cm$^{-1}$. $C_{117}H_{72}Li_4N_6O_{12}Ti_2{\cdot}6(C_3H_7NO){\cdot}9H_2O$ (2478.17): calcd. C 65.43, H 5.37, N 6.78; found C 65.38, H 5.31, N 7.36.

**Complex $Na_4[(3f)_3Ti_2]$:** Yield: quantitative of a red solid. $^1$H NMR ([D$_6$]DMSO): $\delta$ = 8.57 (s, 6 H), 7.91 (br., 6 H), 7.44–7.31 (m, 18 H), 7.17 (d, $J$ = 8.7 Hz, 12 H), 7.06 (d, $J$ = 8.7 Hz, 12 H), 6.99 (dd, $J$ = 7.9, 1.5 Hz, 6 H), 6.34 (t, $J$ = 7.9 Hz, 6 H), 6.12 (dd, $J$ = 7.9, 1.5 Hz, 6 H) ppm. MS (neg. ESI-MS, methanol): $m/z$ = 1918 $\{Na_3[(\mathbf{3f})_3Ti_2]^-\}$, 1896 $\{HNa_2[(\mathbf{3f})_3Ti_2]^-\}$, 1874 $\{H_2Na[(\mathbf{3f})_3Ti_2]^-\}$, 1852 $\{H_3[(\mathbf{3f})_3Ti_2]^-\}$. IR (KBr): $\tilde{\nu}$ = 3442, 1666, 1615, 1588, 1499, 1445, 1386, 1252, 1211, 1093, 743, 664, 595, 513 cm$^{-1}$. $C_{117}H_{72}Na_4N_6O_{12}Ti_2{\cdot}7(C_3H_7NO){\cdot}8H_2O$ (2597.44): calcd. C 63.81, H 5.32, N 7.01; found C 63.60, H 5.35, N 7.10.

**Complex $K_4[(3f)_3Ti_2]$:** Yield: quantitative of a red solid. $^1$H NMR ([D$_6$]DMSO): $\delta$ = 8.59 (s, 6 H), 7.92 (d, $J$ = 6.9 Hz, 6 H), 7.46–7.30 (m, 18 H), 7.16 (d, $J$ = 8.7 Hz, 12 H), 7.10 (d, $J$ = 8.7 Hz, 12 H), 7.04 (d, $J$ = 7.7 Hz, 6 H), 6.34 (t, $J$ = 7.7 Hz, 6 H), 6.12 (d, $J$ = 7.7 Hz, 6 H) ppm. MS (neg. ESI-MS, methanol): $m/z$ = 1928 $\{HK_2[(\mathbf{3f})_3Ti_2]^-\}$, 923 $\{H_2[(\mathbf{3f})_3Ti_2]^{2-}\}$, 617 $\{H[(\mathbf{3f})_3Ti_2]^{3-}\}$. IR (KBr): $\tilde{\nu}$ = 3430, 1666, 1616, 1587, 1499, 1444, 1386, 1252, 1212, 1094, 781, 742, 663, 511 cm$^{-1}$. $C_{117}H_{72}K_4N_6O_{12}Ti_2{\cdot}6(C_3H_7NO){\cdot}6H_2O$ (2552.75): calcd. C 63.52, H 4.98, N 6.58; found C 63.50, H 5.04, N 6.62.

## Acknowledgments

This work was supported by the Deutsche Forschungsgemeinschaft (SPP1118). We thank C. A. Schalley (University of Bonn) for the ESI FT-ICR measurements.

[1] Reviews on helicates: a) J.-M. Lehn, A. Rigault, J. Siegel, J. Harrowfield, B. Chevrier, D. Moras, *Proc. Natl. Acad. Sci. USA* **1987**, *84*, 2565; b) J.-M. Lehn, A. Rigault, *Angew. Chem.* **1988**, *100*, 1121; *Angew. Chem. Int. Ed. Engl.* **1988**, *27*, 1095; c) C. Piguet, G. Bernardinelli, G. Hopfgartner, *Chem. Rev.* **1997**, *97*, 2005; d) M. Albrecht, *Chem. Rev.* **2001**, *101*, 3457; e) L. J. Childs, M. J. Hannon, *Supramol. Chem.* **2004**, *16*, 7; f) C. Piguet, M. Borkovec, J. Hamacek, K. Zeckert, *Coord. Chem. Rev.* **2005**, *249*, 705.

[2] a) M. J. Hannon, C. L. Painting, A. Jackson, J. Hamblin, W. Errington, *Chem. Commun.* **1997**, 1807; b) M. J. Hannon, C. L. Painting, W. Errington, *Chem. Commun.* **1997**, 307; c) M. J. Hannon, C. L. Painting, N. W. Alcock, *Chem. Commun.* **1999**, 2023; d) J. Hamblin, L. J. Childs, N. W. Alcock, M. J. Hannon, *J. Chem. Soc., Dalton Trans.* **2002**, 164; e) F. Tuna, J. Hamblin, A. Jackson, G. Clarkson, N. W. Alcock, M. J. Hannon, *Dalton Trans.* **2003**, 2141; f) N. Yoshida, H. Oshio, T. Ito, *Chem. Commun.* **1998**, 63; g) N. Yoshida, K. Ichikawa, *Chem. Commun.* **1997**, 1091.

[3] a) R. Ziessel, A. Harriman, J. Suffert, M. T. Youinou, A. De Cian, J. Fischer, *Angew. Chem.* **1997**, *109*, 2612; *Angew. Chem. Int. Ed. Engl.* **1997**, *36*, 2509; b) A. El-ghayouy, L. Douce, A. Skoulios, R. Ziessel, *Angew. Chem.* **1998**, *110*, 2327; *Angew. Chem. Int. Ed.* **1998**, *37*, 2205; c) R. Ziessel, A. Harriman, A. El-ghayouy, L. Douce, E. Leize, H. Nierengarten, A. Van Dorsselaer, *New J. Chem.* **2000**, *24*, 729.

[4] M. Albrecht, S. Kamptmann, R. Fröhlich, *Polyhedron* **2003**, *22*, 643.

[5] M. Albrecht, I. Janser, S. Kamptmann, P. Weis, B. Wibbeling, R. Fröhlich, *Dalton Trans.* **2004**, 37.

[6] J. Sanmartin, M. R. Bermejo, A. M. Garcia-Deibe, O. Piro, E. E. Castellano, *Chem. Commun.* **1999**, 1953.

[7] M. Meyer, B. Kersting, R. E. Powers, K. N. Raymond, *Inorg. Chem.* **1997**, *36*, 5179.

[8] E. J. Enemark, T. D. P. Stack, *Angew. Chem.* **1995**, *107*, 1082; *Angew. Chem. Int. Ed. Engl.* **1995**, *34*, 996.

 © 2006 Wiley-VCH Verlag GmbH & Co. KGaA, Weinheim 

[9] E. J. Enemark, T. D. P. Stack, *Angew. Chem.* **1998**, *110*, 977; *Angew. Chem. Int. Ed.* **1998**, *37*, 932.
[10] a) E. J. Enemark, T. D. P. Stack, *Inorg. Chem.* **1996**, *35*, 2719; b) M. Albrecht, *Chem. Soc. Rev.* **1998**, *27*, 281.
[11] B. Kersting, M. Meyer, R. E. Powers, K. N. Raymond, *J. Am. Chem. Soc.* **1996**, *118*, 7221.
[12] M. Albrecht, H. Röttele, P. Burger, *Chem. Eur. J.* **1996**, *2*, 1264.
[13] M. Albrecht, M. Schneider, R. Fröhlich, *New J. Chem.* **1998**, *22*, 753.
[14] M. Albrecht, I. Janser, H. Houjou, R. Fröhlich, *Chem. Eur. J.* **2004**, *10*, 2839.
[15] a) D. L. Caulder, R. E. Powers, T. N. Parac, K. Raymond, *Angew. Chem.* **1998**, *110*, 1940; *Angew. Chem. Int. Ed.* **1998**, *37*, 1840; b) D. L. Caulder, C. Brückner, R. E. Powers, S. König, T. N. Parac, J. A. Leary, K. N. Raymond, *J. Am. Chem. Soc.* **2001**, *123*, 8923.
[16] D. L. Caulder, K. N. Raymond, *Angew. Chem.* **1997**, *109*, 1508; *Angew. Chem. Int. Ed. Engl.* **1997**, *36*, 1439.
[17] M. Albrecht, S. Kotila, *Angew. Chem.* **1995**, *107*, 2285; *Angew. Chem. Int. Ed. Engl.* **1995**, *34*, 2134.
[18] M. Albrecht, M. Schneider, H. Röttele, *Chem. Ber./Recueil* **1997**, *130*, 615.
[19] M. Albrecht, *Chem. Eur. J.* **2000**, *6*, 3485.
[20] A. F. Williams, R. F. Carina, L. J. Charbonniere, P. G. Desmartin, C. Piguet, in *Physical Supramolecular Chemistry* (Eds.: L. Echegoyen, A. E. Kaifer), Kluwer, Doordrecht, **1996**.
[21] C. Provent, E. Rivara-Minten, S. Hewage, G. Brunner, A. F. Williams, *Chem. Eur. J.* **1999**, *5*, 3487.
[22] M. Albrecht, M. Schneider, *Chem. Commun.* **1998**, 137.

Received: August 9, 2005
Published Online: November 25, 2005

 © 2006 Wiley-VCH Verlag GmbH & Co. KGaA, Weinheim 

EurJIC
European Journal of Inorganic Chemistry

Issue 2/2006

Pages 257–492

*Papers available ahead of print in Early View at www.interscience.wiley.com*

*Earliest available Table of Contents: Automatically, free of charge by e-mail through www.interscience.wiley.com/alerts*

## COVER PICTURE

**The cover picture shows** that Raman spectroscopy can reveal drastically different N–N stretching frequencies in dinuclear, dinitrogen-bridged titanium complexes. In the article by F. Tuczek et al. on p. 291 ff., the recently synthesized complex [{($\eta^5$-$C_5Me_5$)Ti[$\eta^6$-$C_5H_4C$(*p*-tolyl)$_2$]}$_2$($\mu$-$\eta^1$:$\eta^1$-$N_2$)] (**1**; R. Beckhaus et al., *Eur. J. Inorg. Chem.* **2005**, 1003) is compared to the dinuclear (dinitrogen)titanium complex [{$(Me_3Si)_2$NTiCl(TMEDA)}$_2$($\mu$-$\eta^1$:$\eta^1$-$N_2$) (**3**; R. Duchateau et al., *J. Am. Chem. Soc.* **1991**, *113*, 8986). With respect to **3** [$\nu$(NN) = 1284 cm$^{-1}$], **1** exhibits an unusually high N–N stretching frequency [$\nu$(NN) = 1749 cm$^{-1}$]. These spectroscopic differences reflect different degrees of dinitrogen activation, which are explained by the fact that only one of the $N_2$ $\pi$*-orbitals is occupied in **1**, whereas both $\pi$*-orbitals are occupied in **3**.

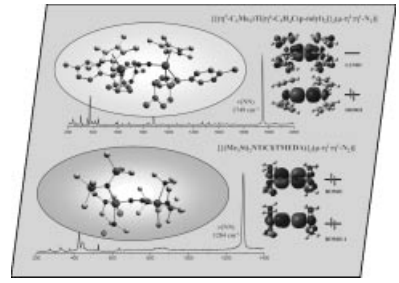

## MICROREVIEW

**Contents**

**273** **L. M. Berreau***

Bioinorganic Chemistry of Group 12 Complexes Supported by Tetradentate Tripodal Ligands Having Internal Hydrogen-Bond Donors

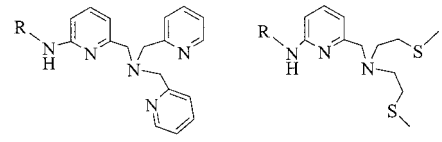

**Keywords:** Zinc / Hydrogen bonding / Hydrolysis / Cadmium / Group 12

 © 2006 Wiley-VCH Verlag GmbH & Co. KGaA, Weinheim 

# SHORT COMMUNICATION


**285** **L. Busetto, F. Marchetti, S. Zacchini, V. Zanotti***

CO Cleavage Promoted by Acetylide Addition to Vinyliminium Diiron Complexes

**Keywords:** CO cleavage / Bridging ligands / Vinyliminium / Diiron complexes


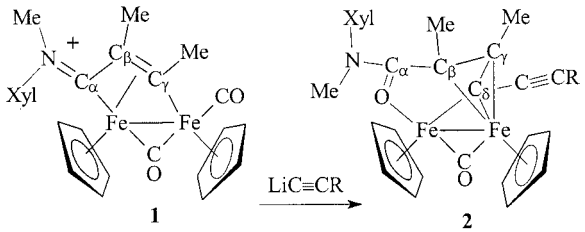


# FULL PAPERS


**291** **F. Studt, N. Lehnert, B. E. Wiesler, A. Scherer, R. Beckhaus, F. Tuczek***

Spectroscopic Comparison of Dinuclear $Ti^{+}$ and $Ti^{2+}$ μ-$\eta^1$:$\eta^1$ Dinitrogen Complexes with Cp*/Pentafulvene and Amine/Amide Ligation: Moderate versus Strong Activation of $N_2$

**Keywords:** Metallocenes / Nitrogen fixation / Titanium / Raman spectroscopy / Density functional calculations


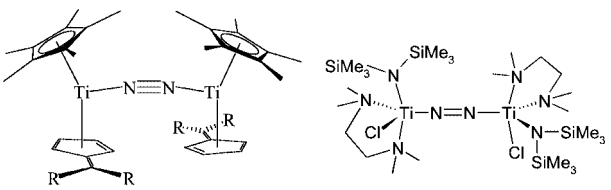


R = *p*-Tol
$>CR_2$ = adamantylidene


**298** **N. G. Naumov,* M. S. Tarasenko, A. V. Virovets, Y. Kim, S.-J. Kim,* V. E. Fedorov**

Glycerol as Ligand: The Synthesis, Crystal Structure, and Properties of Compounds $[Ln_2(H_2L)_2(H_3L)_4][Re_6Q_8(CN)_6]$, Ln = La, Nd, Gd, Q = S, Se

**Keywords:** Lanthanide(III) complexes / Glycerol / Rhenium(III) octahedral cluster / Cyanide complexes / Crystal structure


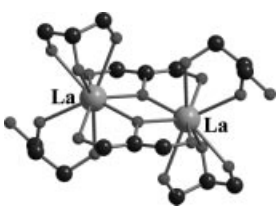



**304** **S. Del Piero, A. Melchior,* P. Polese, R. Portanova, M. Tolazzi***

*N*-Methylation Effects on the Coordination Chemistry of Cyclic Triamines with Divalent Transition Metals and Their $Co^{II}$ Dioxygen Carriers

**Keywords:** Cadmium / Cobalt / Density functional calculations / N ligands / Thermodynamics


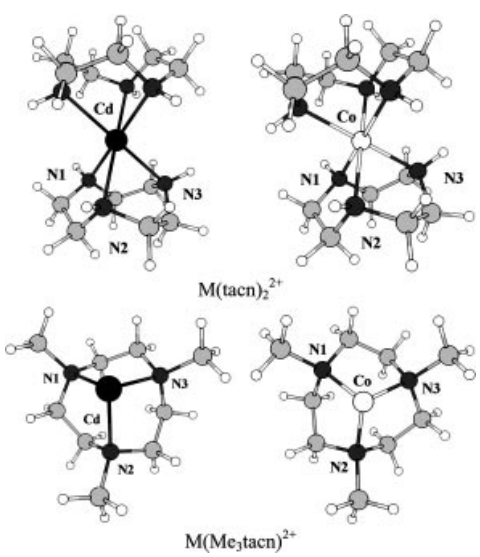

**314** **J. Romba, D. Kuppert, B. Morgenstern, C. Neis, S. Steinhauser, T. Weyhermüller, K. Hegetschweiler***

The Coordination Chemistry of 1,4-Diazepan-6-amine

**Keywords:** Chelates / Cobalt / Ligand design / N ligands / Stability constants

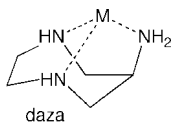


**329** **P. Talukder, S. Sen, S. Mitra,* L. Dahlenberg, C. Desplanches, J.-P. Sutter***

Evidence for Hydrogen-Bond-Mediated Exchange Coupling in an Aqua-Bridged $Cu^{II}$ Dimer: Synthesis, Magnetic Study and Correlation with Density Functional Calculations

**Keywords:** Bridging ligands / Copper / Density functional calculations / Exchange interactions / Hydrogen bonds

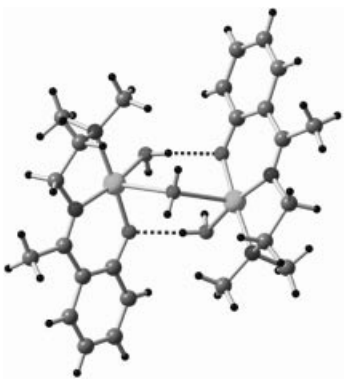

**334** **P. Aslanidis,* P. J. Cox, A. Kaltzoglou, A. C. Tsipis***

An Experimental and Theoretical (DFT) Investigation of the Coordination Mode of 2,4-Dithiouracil (2,4-dtucH$_2$) in Copper(I) Complexes with 1,2-Bis(diphenylphosphanyl)benzene (dppbz): The Crystal Structures of [Cu(μ-Br)(dppbz)]$_2$ and [CuBr(dppbz)(2,4-dtucH$_2$)]

**Keywords:** Copper / Density functional calculations / Phosphane ligands / S ligands

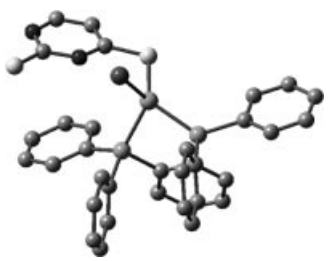

**345** **R. Ahlrichs, N. R. M. Crawford, A. Eichhöfer,* D. Fenske, O. Hampe, M. M. Kappes, J. Olkowska-Oetzel**

Synthesis and Structure of Two Ionic Copper Indium Selenolate Cluster Complexes [As(C$_6$H$_5$)$_4$]$_2$[Cu$_6$In$_4$(SeC$_6$H$_5$)$_{16}$Cl$_4$] and [As(C$_6$H$_5$)$_4$][Cu$_7$In$_4$(SeC$_6$H$_5$)$_{20}$]

**Keywords:** Cluster compounds / Density functional calculations / Mass spectrometry / X-ray diffraction

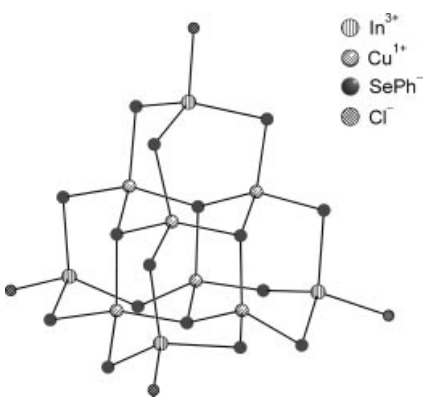


 © 2006 Wiley-VCH Verlag GmbH & Co. KGaA, Weinheim 

**351** **M. E. Burin, M. V. Smirnova, G. K. Fukin, E. V. Baranov, M. N. Bochkarev***

Neodymium(II) and Dysprosium(II) Iodides in the Reactions with Metallocenes of d-Transition Metals

**Keywords:** Dysprosium / Neodymium diiodide / Metallocenes / Reduction

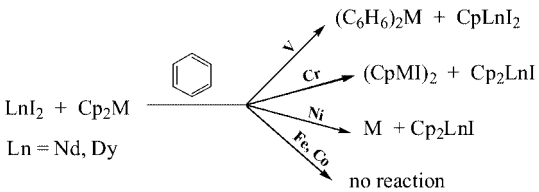


**357** **C. Desroches, G. Pilet, P. Szilágyi, G. Molnár, S. A. Borshch, A. Bousseksou, S. Parola, D. Luneau***

Tetra- and Decanuclear Iron(II) Complexes of Thiacalixarene Macrocycles: Synthesis, Structure, Mössbauer Spectroscopy and Magnetic Properties

**Keywords:** Calixarenes / Hydrothermal synthesis / Iron / Magnetic properties / Mössbauer spectroscopy

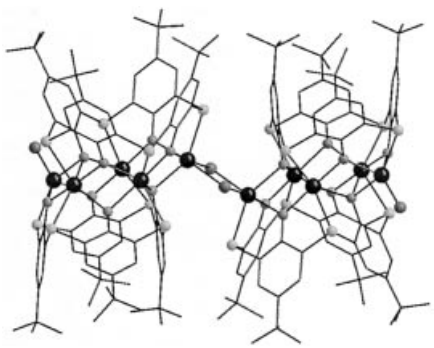

**366** **K. Nienkemper, V. V. Kotov, G. Kehr, G. Erker,* R. Fröhlich**

Chelate [2-(Iminoethyl)pyridine *N*-oxide]metal Complexes − Synthesis and Structural Comparison with Their Chemically Related 2-(Iminoethyl)pyridine-Derived Systems

**Keywords:** Chelates / Coordination chemistry / N,O ligands / Transition metals

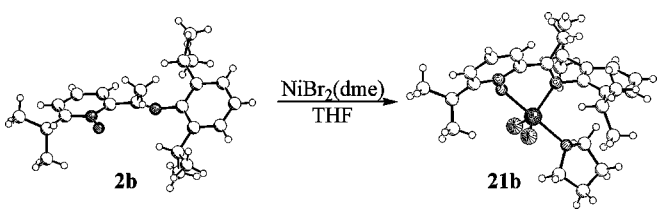


**380** **M. Bender, E. Niecke,* M. Nieger, R. Pietschnig***

Bis(stannyl)phosphanyl-Substituted Dichlorosilanes/Germanes − Potential Precursors for a Novel Strategy Toward P−Si/Ge Multiple Bonds?

**Keywords:** Silicon / Tin / Phosphorus / Hyperconjugation

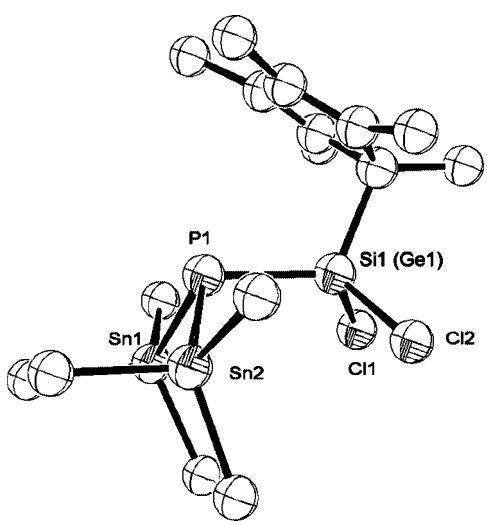


 © 2006 Wiley-VCH Verlag GmbH & Co. KGaA, Weinheim 

**385** **Z. Shi, X. Gu, J. Peng,* X. Yu, E. Wang**

From Molecular Double-Ladders to an Unprecedented Polycatenation: A Parallel Catenated 3D Network Containing Bicapped Keggin Polyoxometalate Clusters

**Keywords:** Coordination polymers / Parallel catenation / Double ladders / Hydrothermal synthesis

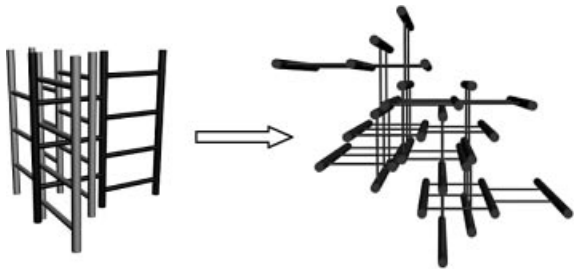

**389** **J. M. Harrowfield,* N. Lugan, G. H. Shahverdizadeh, A. A. Soudi, P. Thuéry**

Solid-State Luminescence and π-Stacking in Crystalline Uranyl Dipicolinates

**Keywords:** Uranyl luminescence / Crystal structures / π-Stacking / Dipicolinates

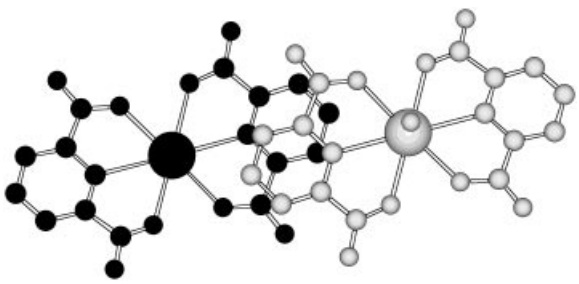

**397** **S.-T. Zheng, Y.-M. Chen, J. Zhang, J.-Q. Xu, G.-Y. Yang***

Hybrid Inorganic−Organic 1D and 2D Frameworks with $[As_6V_{15}O_{42}]^{6-}$ Polyoxoanions as Building Blocks

**Keywords:** Polyoxometalate / Vanadium / Arsenic

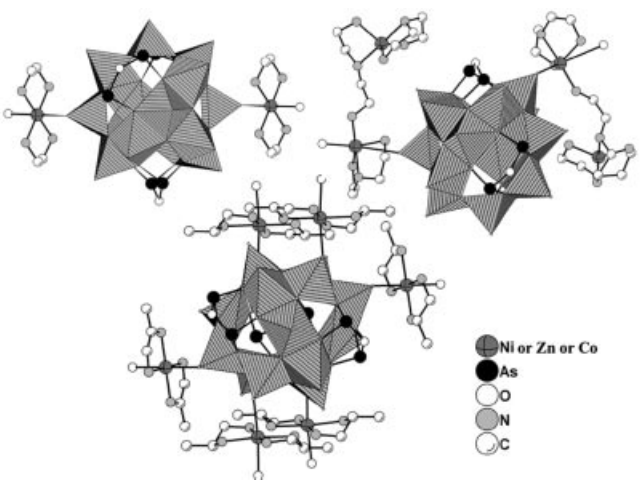


**407** **S.-Q. Bai, E.-Q. Gao, Z. He, C.-J. Fang, Y.-F. Yue, C.-H. Yan***

Manganese Azides Based on Co-Ligands with a Flexible Tail: Diverse Structural and Magnetic Properties

**Keywords:** Azides / Coordination polymers / Ligand design / Magnetic properties / Manganese

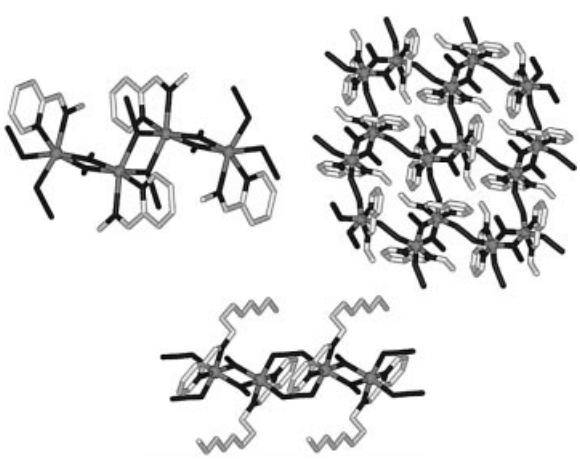

 © 2006 Wiley-VCH Verlag GmbH & Co. KGaA, Weinheim 

**416** **Z. Xiaoqing, W. Weigang, L. Fengyi, G. Maofa,* S. Zheng, W. Dianxun***

Electronic Structure of Binary Phosphoric and Arsenic Triazides

**Keywords:** Phosphorus / Arsenic / Triazides / Photoelectron spectroscopy / Ionization potentials

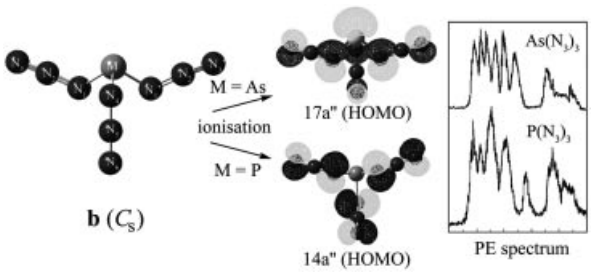


**422** **L.-C. Song,* F.-H. Su, Q.-M. Hu, E. Grigiotti, P. Zanello**

Synthesis, Characterization, and Electrochemical Properties of Novel Transition Metal–Fullerene Complexes Containing Di- and Tetraphosphane Ligands

**Keywords:** Electrochemistry / Fullerenes / Palladium / Phosphane ligands / Platinum

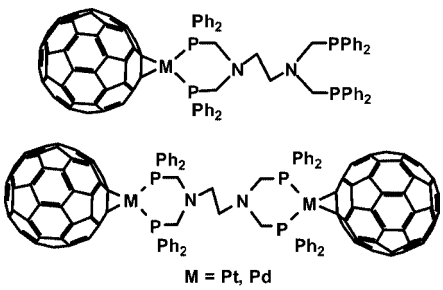


**430** **Y.-Y. Lü, L.-H. Gao, M.-J. Han, K.-Z. Wang***

Synthesis and the Effect of a Peripheral *N*-Arylcarbazole Moiety on the Acid-Base and DNA Binding Properties of a Novel Ru$^{II}$ Complex

**Keywords:** Ruthenium / N ligands / DNA / Sensors / Luminescence / UV/Vis spectroscopy

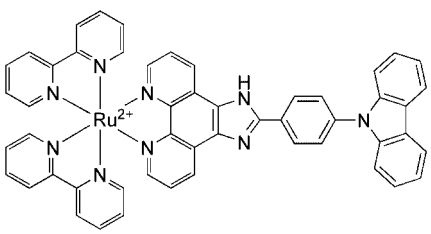

**437** **L. G. Bonnet, B. M. Kariuki***

Ionic Liquids: Synthesis and Characterisation of Triphenylphosphonium Tosylates

**Keywords:** Structure elucidation / Ionic liquids / Solid-state structures / Melting points

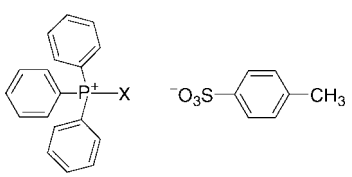

**447** **A. Rimola, M. Sodupe, J. Ros, J. Pons***

A Theoretical Study on Pd$^{II}$ Complexes Containing Hemilabile Pyrazole-Derived Ligands

**Keywords:** Pd$^{II}$ complexes / Pyrazole / Hemilabile ligands / Density functional theory

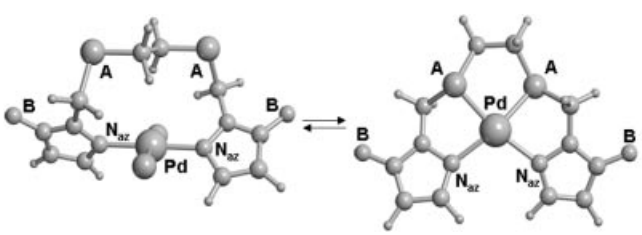


 © 2006 Wiley-VCH Verlag GmbH & Co. KGaA, Weinheim 

**455** **M. Gonschorowsky, K. Merz, M. Driess***

Cyclohexylbis(hydroxymethyl)phosphane: A Hydrophilic Phosphane Capable of Forming Novel Hydrogen-Bonding Networks

**Keywords:** (Hydroxymethyl)phosphanes / Phosphane conjugates / Phosphane sulfides / Hydrogen bonds

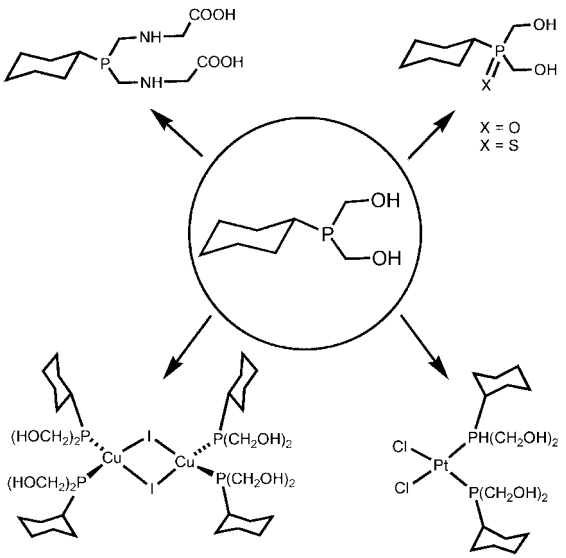


**464** **P. Srinivasan, W. K. Leong***

Reaction of the Heteronuclear Cluster $[Cp^*IrRu_3(\mu\text{-}H)_2(CO)_{10}]$ with Alkynes: Stereoselective Binding

**Keywords:** Heterometallic complexes / Ruthenium / Iridium / Alkynes / Stereoselectivity

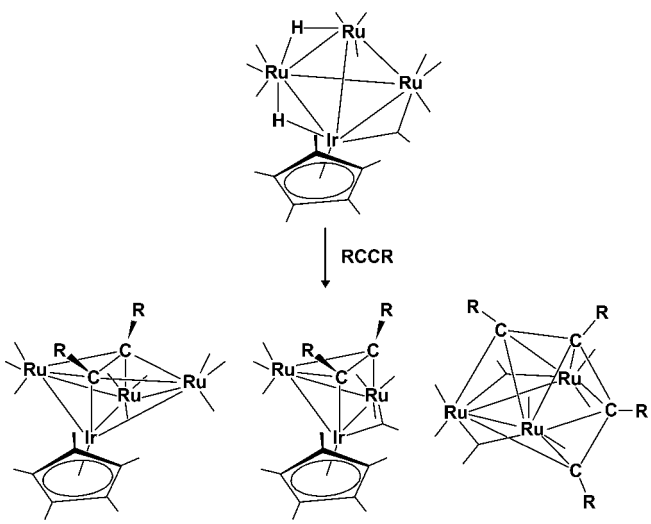


**473** **A.-S. Chauvin, F. Gumy, I. Matsubayashi, Y. Hasegawa,* J.-C. G. Bünzli***

Fluorinated β-Diketones for the Extraction of Lanthanide Ions: Photophysical Properties and Hydration Numbers of Their $Eu^{III}$ Complexes

**Keywords:** Lanthanide / Luminescence / β-diketonate / Hydration number / Extraction

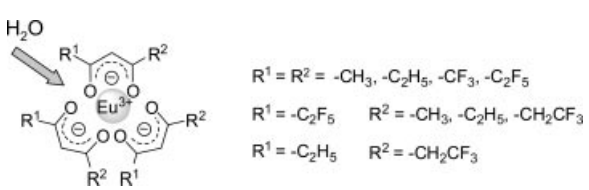


 © 2006 Wiley-VCH Verlag GmbH & Co. KGaA, Weinheim 

**481** **S. C. Manna, E. Zangrando, M. G. B. Drew, J. Ribas,* N. Ray Chaudhuri***

Syntheses, Crystal Structures and Magnetic Properties of Carboxylato-Bridged Polymeric Networks of $Mn^{II}$

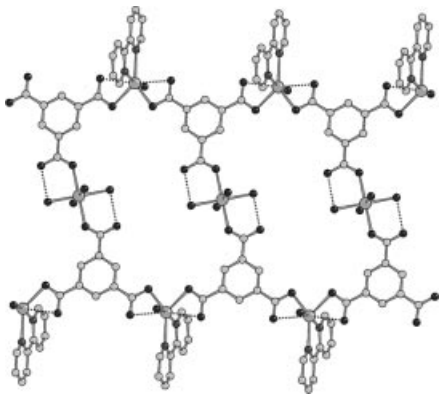

**Keywords:** Manganese(II) / Carboxylate / Crystal structure / Magnetic behavior

 © 2006 Wiley-VCH Verlag GmbH & Co. KGaA, Weinheim 

DOI: 10.1002/ejic.200500886

# Bioinorganic Chemistry of Group 12 Complexes Supported by Tetradentate Tripodal Ligands Having Internal Hydrogen-Bond Donors

**Lisa M. Berreau*[a]**

**Keywords:** Zinc / Hydrogen bonding / Hydrolysis / Cadmium / Group 12

Inspired by the proposed role of secondary hydrogen-bonding interactions in modulating the chemistry of mononuclear zinc centers in metalloenzymes, zinc complexes supported by tetradentate tripodal ligands having one or more internal hydrogen-bond donors have been prepared, characterized, and investigated for biologically relevant reactivity. Complexes of this class have been examined in terms of water activation and $CO_2$ reactivity, alcohol/alkoxide coordination, and amide methanolysis and phosphate ester hydrolysis reactivity. The results of these studies indicate that the presence of internal hydrogen-bond donors will lower the p$K_a$ of a zinc-bound water molecule, stabilize zinc alkoxide species with respect to hydrolysis, and enhance the phosphate ester cleavage reactivity of mononuclear zinc complexes. In addition, use of tripodal ligands having a single internal hydrogen-bond donor has enabled the isolation of a novel cadmium hydroxide complex and examination of its $CO_2$ chemistry, as well as the identification of a novel amide cleavage reaction which proceeds by initial formation of a deprotonated amide intermediate.
(© Wiley-VCH Verlag GmbH & Co. KGaA, 69451 Weinheim, Germany, 2006)

## Introduction

Secondary hydrogen-bonding interactions are suggested to play important roles in modulating the chemistry of mononuclear zinc centers in metalloenzymes.[1,2] For example, as outlined below for specific enzymes, these interactions have been proposed to: (1) influence the p$K_a$ of a zinc-bound water molecule, (2) orient a substrate or nucleophile for catalysis, (3) stabilize a transition state or reactive species, or (4) activate a substrate for a reaction (e.g. hydrolysis). Over the past few years, several laboratories have worked toward understanding the influence of hydrogen bonding on the chemistry of zinc centers by examining the chemistry of synthetic zinc complexes supported by novel tripodal tetradentate chelate ligands containing internal hydrogen-bond donors. In an approach akin to metal ion substitution studies of zinc enzymes, in some cases analog complexes of the heavier group 12 metals have also been prepared, characterized, and examined for biologically relevant reactivity. Overall, these studies have provided important new fundamental chemical insight with which to evaluate the proposed role of secondary hydrogen bonding in the catalytic cycles of zinc enzymes.

Carbonic anhydrases (CAs) catalyze the reversible hydration of carbon dioxide to form hydrogen carbonate. These enzymes are classified in four distinct classes, designated α-, β-, γ- and δ-CAs.[3] In the first three classes, a mononuclear zinc center mediates the hydrolysis of $CO_2$ by a two-step mechanism.[4] In the first step, a zinc-bound hy-

[a] Department of Chemistry and Biochemistry, Utah State University,
0300 Old Main Hill, Logan, UT, 84322-0300, USA
Fax: + 1-435-797-3390
E-mail: berreau@cc.usu.edu

*Lisa M. Berreau was born in Worthington, Minnesota, USA. She received her B.S. degree in chemistry from Minnesota State University, Mankato in 1990 and her Ph.D. in inorganic chemistry from Iowa State University in 1994. She was a National Institutes of Health postdoctoral fellow at the University of Minnesota for 1995–1998. She is currently an associate professor of chemistry at Utah State University, which she joined in 1998. Her laboratory uses novel ligand systems incorporating hydrogen-bond donors and/or hydrophobic substituents to investigate chemical reactions of relevance to metalloenzymes.*

**MICROREVIEWS:** This feature introduces the readers to the authors' research through a concise overview of the selected topic. Reference to important work from others in the field is included.

 © 2006 Wiley-VCH Verlag GmbH & Co. KgaA, Weinheim 

droxide serves as a nucleophile for attack on $CO_2$. The second step involves regeneration of the active site Zn–OH moiety through water activation. In the active site of a typical mammalian α-type carbonic anhydrase (e.g. carbonic anhydrase II), the resting state tetrahedral zinc center, ligated by three histidine ligands and one hydroxide/water ligand [$(N_{His})_3Zn–OH$], acts as a hydrogen-bond donor to an active-site threonine residue (Thr-199, Figure 1). This interaction is suggested to be important toward determining the p$K_a$ of the $Zn–OH_2$ moiety and orienting the hydroxide lone pair for attack on $CO_2$.[5,6] Hydrogen bonding involving Thr-199 is also suggested to be important for stabilization of the transition state and product-bound forms of the enzyme. Notably, an X-ray structure of carbonic anhydrase II shows that the zinc-bound hydroxide oxygen atom also accepts hydrogen bonds from the surrounding water molecules (Figure 1).[7]

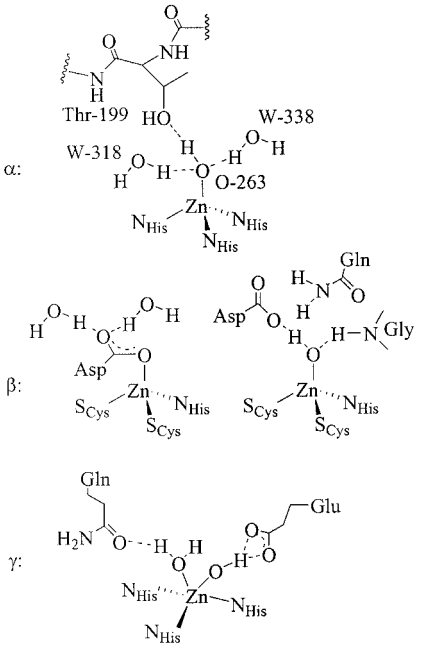


Figure 1. Active-site primary and secondary coordination environments of α-, β-, and γ-type carbonic anhydrases.

The β-type CAs contain a mononuclear zinc center ligated by two conserved cysteine residues, one conserved histidine residue, and an aspartate or water ligand (Figure 1).[8–12] On the basis of the X-ray structure of the *P. sativum* β-CA, secondary hydrogen-bonding interactions involving active site aspartate, glutamine, and glycine residues are suggested to be involved in catalysis.[9] In the γ-CA "Cam" from the archaeon *Methanosarcina thermophila*, a trigonal-bipyramidal zinc center is ligated by three histidine residues and two water/hydroxo ligands (Figure 1).[13,14] Hydrogen-bonding interactions are present between the water/hydroxo ligands and two active-site residues (Gln-75 and Glu-62). The glutamate residue has also been implicated in proton transfer and in stabilization of a hydrogen carbonate bound form of the enzyme. Finally, a δ-type carbonic anhydrase, TWCA1, from the marine diatom *Thalassiosira weissflogii*, has been identified as having an $(N_{His})_3Zn–OH_2/OH$ motif akin to α-type CAs.[15] Notably, under conditions wherein the level of TWCA1 is low in *T. weissflogii*, a putative naturally occurring, cadmium-containing carbonic anhydrase (CDCA1) has been identified.[16] The sequence of CDCA1 is significantly different from those of all other classes of CAs.[17] X-ray absorption spectroscopic studies suggest that the cadmium center in CDCA1 is tetrahedral and is ligated by two or more cysteine thiolates and a water molecule.[17]

Liver alcohol dehydrogenase (LADH) catalyzes the oxidation of alcohols to aldehydes and ketones using $NAD^+$ as a cofactor.[18] The resting state form of the enzyme contains a tetrahedral $(N_{His})(S_{Cys})_2Zn–OH_2$ center, with a nearby serine residue (Ser-48) positioned to form a hydrogen-bonding interaction with the zinc-bound water molecule (Figure 2).[18] In a proposed catalytic cycle for LADH, the active-site water molecule is replaced by the alcohol substrate.[19] An X-ray crystallographic study of $C_6F_5CH_2OH$ bound to the active-site zinc center of LADH suggests the presence of a hydrogen-bonding interaction between the hydroxy proton of the zinc-bound alcohol and the oxygen atom of Ser-48.[20] Following deprotonation of the zinc-bound alcohol, Ser-48 is proposed to form a strong hydrogen-bonding interaction with the alkoxide oxygen atom.[21,22] This interaction is then proposed to weaken upon hydride transfer and formation of a zinc-bound aldehyde or ketone product.[22] Notably, X-ray crystallographic studies of formamide-[23–25] and sulfoxide-inhibited[26,27] forms of LADH also indicate the presence of hydrogen bonding between the zinc-bound oxygen atom of the inhibitor and Ser-48.

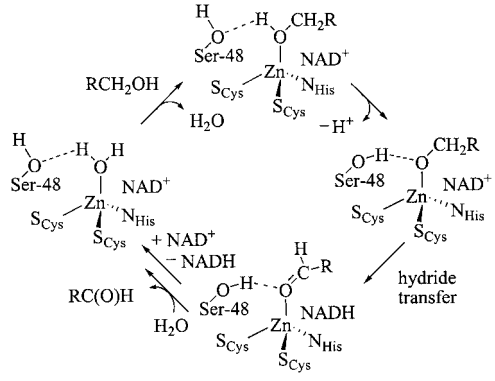


Figure 2. Hydrogen-bonding interactions proposed in the catalytic cycle of liver alcohol dehydrogenase.

Zinc enzymes that catalyze the hydrolysis of amide bonds in many cases have active-site residues within hydrogen-bonding distance of the metal-bound water and/or the substrate carbonyl group.[28,29] For example, in the active site of carboxypeptidase A, hydrogen-bonding interactions involving several residues (Glu-270, Arg-71, Arg-127, Asn-144, Arg-145, and Tyr-248) have been identified (Figure 3).[30,31]

 © 2006 Wiley-VCH Verlag GmbH & Co. KGaA, Weinheim 

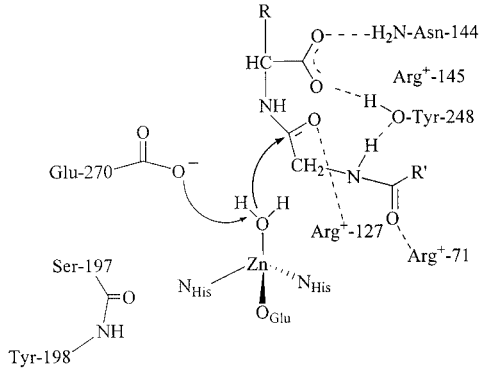


Figure 3. Proposed secondary interactions in the active site of carboxypeptidase A in the presence of substrate.

Similary, within the active site of several metalloenzymes that catalyze the hydrolysis of phosphate ester linkages, are positively charged amino acid side chains that are proposed to stabilize the transition state by hydrogen bonding and/or provide a proton for the leaving group. For example, in the catalytic cycle of alkaline phosphatase, phosphate monoester hydrolysis involves substrate interactions with arginine guanidinium and histidine imidazolium groups.[32]

In this Microreview, I summarize recent advances in the use of tripodal tetradentate ligand systems having internal hydrogen-bond donors in studies directed at evaluating the influence of secondary interactions on chemical reactions of relevance to carbonic anhydrase, liver alcohol dehydrogenase, and amide and phosphate ester hydrolyzing enzymes. In an ideal scenario, such studies would be performed using a tetrahedral enforcing ligand having internal hydrogen-bond donors, as this type of ligand would provide the most accurate mimic of both the primary and secondary coordination environment of the biological metal centers described above. However, despite recent attempts to incorporate secondary hydrogen-bond donors into tetrahedral enforcing ligands,[33] little coordination chemistry of such systems has been reported.

## Water Activation: (Aqua)- and (Hydroxo)zinc Complexes

A key step in the catalytic cycle of several zinc enzymes, including carbonic anhydrases, is the activation of a water molecule to produce a reactive Zn–OH moiety. To gauge the influence of secondary hydrogen bonding on the acidity of a metal-bound water molecule, Mareque-Rivas and co-workers have examined the acidity of a $Zn–OH_2$ moiety supported by a variety of tripodal $N_4$-donor ligands having internal hydrogen-bond donors.[34,35] For ligands having a primary amine hydrogen-bond donor [bpapa, bapapa, tapa; Figure 4 (left)], the acidity of the $Zn–OH_2$ moiety increases by ca. 0.7–0.9 $pK_a$ units per hydrogen-bond donor present in the chelate ligand. This can be rationalized by the fact that the formation of hydrogen-bonding interactions with the zinc-bound water molecule withdraws electron density from the water molecule, thus lowering the $pK_a$ value. Notably, a parallel study involving neopentylamine-appended ligands [bpnpa, bnpapa, tnpa; Figure 4 (right)] yielded a different result. Specifically, the ligand system having the largest number of internal hydrogen-bond donors (tnpa) was found to produce an (aqua)zinc complex that was intermediate in acidity between complexes supported by ligands having one (bpnpa) or two (bnpapa) internal hydrogen-bond donors. This difference may be due to steric effects involving the bulkier neopentylamine hydrogen-bond donors. In this regard, X-ray structures of zinc hydroxide complexes of both the bnpapa and tnpa ligands have been reported (Figure 5).[35,36] In $[(bnpapa)Zn–OH]ClO_4$, the zinc-bound hydroxide oxygen atom accepts two hydrogen bonds from the neopentylamine donors. These secondary interactions are characterized by a heteroatom N···O distance of ca. 2.73 Å. In $[(tnpa)Zn–OH]ClO_4$, the hydroxide oxygen atom also accepts two hydrogen bonds from the supporting chelate ligand. However, in this complex the average heteroatom distance is longer [$N···O_{avg}$ 2.82 Å; $N···O_{avg}$ 2.88 Å (two independent X-ray structures reported)].[35,36] Notably, this change in the secondary hydrogen-bonding interactions does not produce a significant difference in the Zn–O(H) bond length {$[(bnpapa)Zn–OH]ClO_4$, 1.941(3) Å; $[(tpna)Zn–OH]ClO_4$ [1.9315(8) Å, 1.957(2) Å]}.

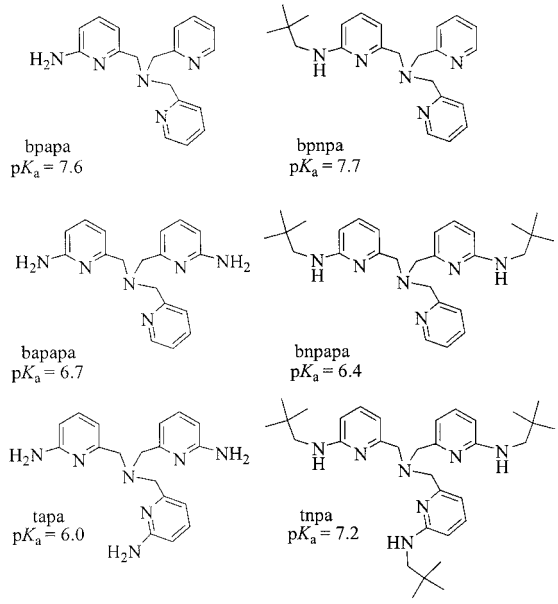


Figure 4. Tetradentate, tripodal chelate ligands having internal hydrogen-bond donors. The $pK_a$ values for the $[(ligand)Zn–OH_2]^{2+}$ complexes are given.

Chin and co-workers have determined the acidity of a zinc-bound water molecule in complexes supported by tetradentate tripodal $N_3O$-type ligands having internal hydrogen-bond donors.[37] A $Zn^{II}$ complex of the L2 ligand (Figure 6), which has two internal primary amine hydrogen-bond donors, has more acidic $pK_a$ values than a $Zn^{II}$ complex of the L1 ligand. These values, determined by potentiometric titration, are for ionization of the pendant alcohol of the chelate ligand and a zinc-bound water molecule, albeit the individual values have not been definitively as-

 © 2006 Wiley-VCH Verlag GmbH & Co. KGaA, Weinheim 

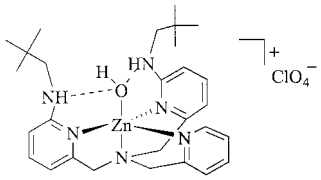


[(bnpapa)Zn-OH]$ClO_4$

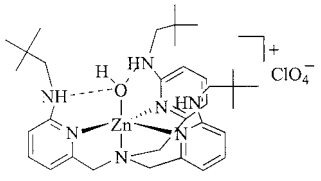


[(tnpa)Zn-OH]$ClO_4$

Figure 5. Mononuclear zinc hydroxide complexes of tripodal ligands having internal hydrogen-bond donors.

signed. As with the ligand systems described above, the enhanced acidity for the zinc-bound water molecule is attributed to secondary hydrogen-bonding interactions involving the ligand amine groups. To date, no X-ray structural characterization data has been reported for (aqua)- or (hydroxo)-zinc derivatives of the L1 or L2 ligands.

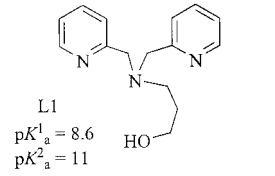


L1
$pK^1_a = 8.6$
$pK^2_a = 11$

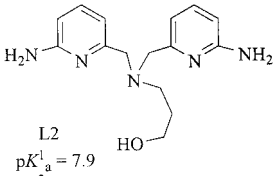


L2
$pK^1_a = 7.9$
$pK^2_a = 10$

Figure 6. $N_3O$-donor ligands. $pK_a$ values are given for the [(ligand)-Zn–$OH_2$]$^{2+}$ complexes.

## Metal Hydroxide/$CO_2$ Chemistry

As noted above, studies of both α- and γ-carbonic anhydrases suggest that $HCO_3^-$ binding to the zinc ion is stabilized by hydrogen-bonding interactions.[14,38] Interestingly, several isolated mononuclear metal hydrogen carbonate complexes also demonstrate both hydrogen-bond-donor and -acceptor interactions involving the metal-bound hydrogen carbonate ligand.[39–43] To date, a mononuclear zinc hydrogen carbonate complex of relevance to carbonic anhydrase has not been structurally characterized. However, Masuda and co-workers recently reported that a zinc hydroxide complex of the tnpa chelate ligand {[(tnpa)Zn–OH]$ClO_4$, Figure 5} undergoes reaction in the presence of $CO_2$ to produce a putative zinc hydrogen carbonate complex, which has been characterized by $^1$H and $^{13}$C NMR and electrospray mass spectrometry.[36] In the proton NMR spectrum in [$D_6$]DMSO, evidence for the formation of the hydrogen carbonate complex is derived from a shift of the neopentylamine proton resonance from δ = 9.21 ppm in the hydroxide complex to δ = 7.71 ppm in the hydrogen carbonate complex. In the $^{13}$C NMR spectrum in $CD_3OD$, a new resonance at $\delta$ = 160.8 ppm has been assigned as the sp$^2$ carbon atom of the coordinated hydrogen carbonate ligand. The strongest evidence for the formation of [(tnpa)-Zn($HCO_3$)]$ClO_4$ comes from electrospray mass spectrometry where a new isotope cluster is found at $m/z$ = 670.3. This value corresponds to the cationic formula [(tnpa)-Zn($HCO_3$)]$^+$. The reaction to produce [(tnpa)Zn($HCO_3$)]-$ClO_4$ is reversible, as purging with argon results in the regeneration of the spectroscopic signals associated with [(tnpa)Zn–OH]$ClO_4$. Recently, the same laboratory reported that [(bnpapa)Zn–OH]$ClO_4$[35,44] (Figure 5) undergoes reaction with $CO_2$ to produce a zinc hydrogen carbonate species, [(bnpapa)Zn($HCO_3$)]$ClO_4$.[45] Though not relevant to carbonic anhydrases, we note that in the presence of $H_2O_2$, this hydrogen carbonate complex undergoes further reaction with a zinc hydroperoxide intermediate, [(bnpapa)Zn–OOH]$ClO_4$, to produce a novel dinuclear zinc peroxocarbonate complex, [(bnpapaZn)$_2$($O_3$CO)]($ClO_4$)$_2$.[45] X-ray crystallographic studies of this peroxocarbonate complex indicate stabilization of peroxocarbonate dianion coordination by hydrogen-bonding interactions involving the bnpapa supporting chelate ligand.

In reactions with relevance to β-type CAs and the novel cadium-containing carbonic anhydrase that was recently reported,[16,17] we have examined the $CO_2$ reactivity of dinuclear zinc and cadmium hydroxide complexes, [(benpaZn)$_2$-(μ-OH)$_2$]($ClO_4$)$_2$[46] and [(bmnpaCd)$_2$(μ-OH)$_2$]($ClO_4$)$_2$, supported by tripodal $N_2S_2$ chelate ligands containing a single internal hydrogen-bond donor (Scheme 1).[47,48] For the zinc complex, the reaction with $CO_2$ leads to the formation of a bridging carbonate complex, [(benpaZn)$_2$(μ-$CO_3$)]-($ClO_4$)$_2$, having bidentate carbonate coordination to both zinc centers. The reaction of [(bmnpaCd)$_2$(μ-OH)$_2$]($ClO_4$)$_2$ with $CO_2$ leads to the formation of [(bmnpaCd)$_2$(μ-$CO_3$)]-($ClO_4$)$_2$, a dinuclear complex wherein the carbonate ligand is coordinated in a bidentate fashion to one Cd$^{II}$ center and in an anisobidentate mode to the other Cd$^{II}$ ion. Notably, while addition of water to the zinc carbonate complex results in the release of $CO_2$ and the regeneration of [(benpaZn)$_2$(μ-OH)$_2$]($ClO_4$)$_2$, the cadmium carbonate complex exhibits no reaction in the presence of water. This difference in reactivity may be due to several factors, including the weak nature of thioether ligation to Zn$^{II}$.[49,50] In [(benpaZn)$_2$(μ-$CO_3$)]($ClO_4$)$_2$, long Zn–S interactions [2.561(1) Å and 2.594(1) Å] suggest the possibility that a coordinated thioether may dissociate or could possibly be displaced in favor of a water ligand. Water coordination could facilitate the hydrolysis of the bridging carbonate moiety and the release of $CO_2$. Subtle differences in hydrogen-bonding interactions involving the bridging carbonate ligands in [(benpaZn)$_2$(μ-$CO_3$)]($ClO_4$)$_2$ and [(bmnpaCd)$_2$(μ-$CO_3$)]($ClO_4$)$_2$ may also contribute to the observed differences in $CO_2$ release reactivity.

 © 2006 Wiley-VCH Verlag GmbH & Co. KGaA, Weinheim 

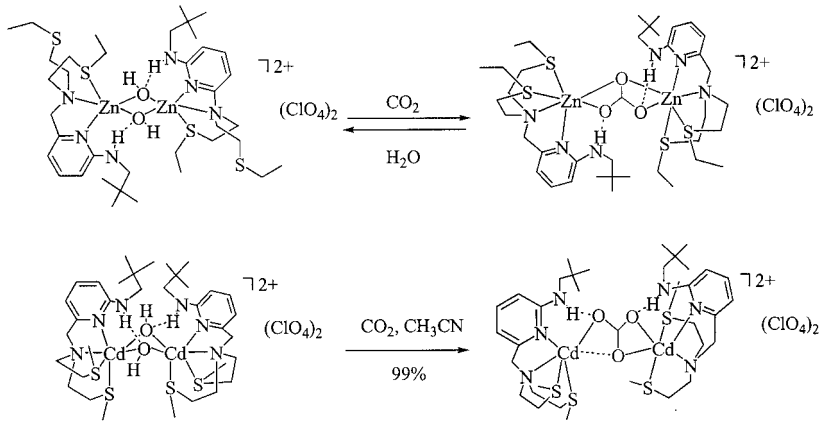


Scheme 1. $CO_2$ reactivity of $N_2S_2$-ligated zinc and cadmium hydroxide complexes.

## Nitrogen/Sulfur-Ligated Zinc–Alcohol, –Aryloxide, and –Alkoxide Complexes

Comparative structural studies of mononuclear zinc–alcohol, –formamide, and –sulfoxide complexes, supported by the $N_2S_2$-donor chelate ligands bmapa {[(6-amino-2-pyridyl)methyl]bis[2-(methylthio)ethyl]amine} and bmpa {bis-[2-(methylthio)ethyl][(2-pyridyl)methyl]amine} (Figure 7), revealed, in some cases, differences as a consequence of the presence of a hydrogen-bond-donor amine group in the former ligand.[51,52] For example, while mononuclear bmapa- and bmpa-ligated zinc–methanol complexes showed no difference in the Zn–O(alcohol) distance, a subtle elongation (ca. 0.025 Å) was identified for the Zn–O(formamide) distances in [(bmapa)Zn(DMF)]$(ClO_4)_2$ and [(bmapa)-Zn(NMF)]$(ClO_4)_2$ relative to their bmpa-ligated analogs. This bond lengthening may be due to the removal of electron density from the formamide carbonyl unit through the intramolecular hydrogen-bonding interaction, which would make the formamide a weaker donor to the cationic zinc center. However, alternative rationales for the Zn–O bond elongation in the bmapa-ligated zinc–formamide derivatives must also be considered. For example, the presence of the secondary amine group may impart additional steric hindrance that is responsible for the slight Zn–O(formamide) bond elongation. In addition, the amine substituent on the pyridyl ring of the bmapa ligand makes this heterocycle a slightly better base (pyridine: $pK_a$ = 5.14; 2-aminopyridine: $pK_a$ = 6.71) and thus a better donor to the zinc center.[53,54] This could result in a slightly decreased Lewis acidity for the zinc center in the bmapa-ligated derivatives. Overall, the degree to which each of these factors influences the neutral oxygen-donor binding properties of the $N_2S_2$-ligated zinc center remains to be fully elucidated.

As noted above, a mononuclear nitrogen/sulfur-ligated zinc–alkoxide derivative is proposed as the active species for hydride transfer in the catalytic cycle of liver alcohol dehydrogenase.[19] To examine the influence of hydrogen bonding on the formation and reactivity of nitrogen/sulfur-ligated zinc–aryloxide and –alkoxide complexes, two new tetradentate tripodal ligand systems containing one or more internal hydrogen-bond donors were employed

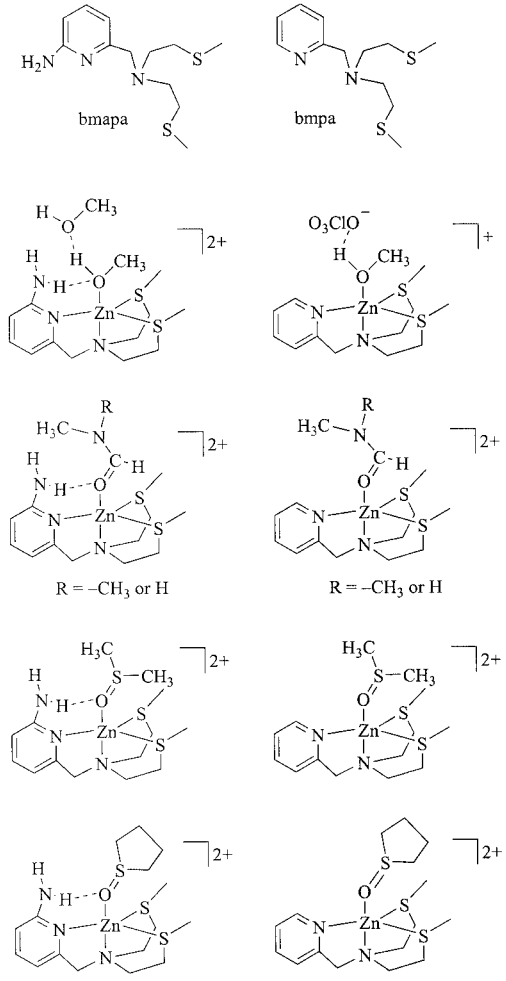


Figure 7. Zinc–alcohol, –formamide, and –sulfoxide complexes of the bmapa and bmpa ligands. All complexes have perchlorate counteranions.

(Figure 8).[46,55] Using the bmnpa and benpa ligands, a series of mononuclear $N_2S_2$-ligated zinc–aryloxide complexes were prepared and characterized.[46] In each complex, a hydrogen-bonding interaction is present between the zinc-bound aryloxide oxygen atom and the secondary amine moiety of the supporting chelate ligand. $^1$H NMR

 © 2006 Wiley-VCH Verlag GmbH & Co. KGaA, Weinheim 

studies of this family of complexes indicated that this hydrogen-bonding interaction is perturbed upon change in the basicity of the aryloxide ligand. Specifically, whereas in the *p*-methoxyphenolate complex [(benpa)Zn(*p*-$OC_6H_4OCH_3$)]$ClO_4$ the secondary amine N–H resonance is found at $\delta$ = 9.97 ppm ($CD_3CN$, ambient temperature), in the *p*-nitrophenolate complex [(benpa)Zn(*p*-$OC_6H_5NO_2$)]$ClO_4$ the same resonance is found at $\delta$ = 8.93 ppm. The downfield position of the N–H resonance in the *p*-methoxyphenolate derivative relative to the *p*-nitrophenolate analog indicates that a stronger hydrogen-bonding interaction is present in [(benpa)Zn(*p*-$OC_6H_4OCH_3$)]$ClO_4$. This is consistent with the relative basicity of the two anions (*p*-methoxyphenol: p$K_a$ = 10.2; *p*-nitrophenol: p$K_a$ = 7.14).

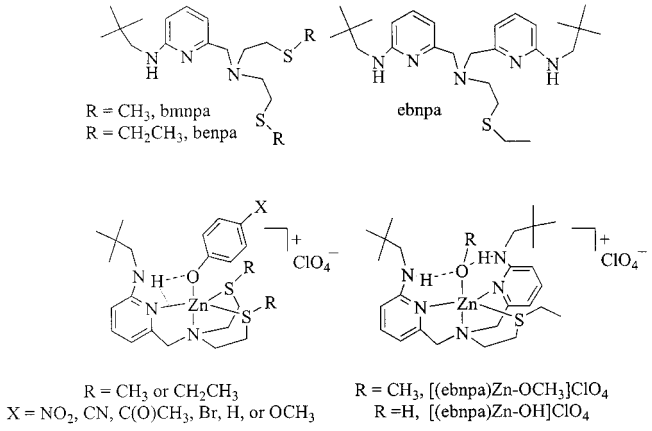


Figure 8. Top: Tripodal tetradentate nitrogen/sulfur ligands containing internal hydrogen-bond donors. Bottom: Mononuclear zinc–aryloxide and –methoxide/hydroxide complexes.

Particularly interesting results were obtained using the tripodal $N_3S$-donor ebnpa {[2-(ethylthio)ethyl]bis[(6-neopentylamino-2-pyridyl)methyl]amine} ligand (Figure 8).[55] The mononuclear zinc–methoxide and –hydroxide complexes, [(ebnpa)Zn–$OCH_3$]$ClO_4$ and [(ebnpa)Zn–OH]$ClO_4$, were isolated and characterized. Notably, determination of the equilibrium constant for the methanolysis of the hydroxide derivative revealed a value [$K_{Me}$ (304 K) = 0.30(8)] that is orders of magnitude greater than that of an equilibrium involving Zn–OH and Zn–$OCH_3$ derivatives of the hydrophobic $Tp^{tBu,Me}$ ligand [$Tp^{tBu,Me}$ = tris(3-*t*Bu-5-Me-pyrazolyl)hydroborate, Scheme 2] [$K_{Me}$ (300 K) = $1.4(2)\cdot10^{-3}$].[56,57] Examination of the temperature dependence of the equilibrium constants for the ebnpa- and $Tp^{tBu,Me}$-ligated systems yielded $\Delta H_{Me}$ = –0.9 kcal/mol and 1.2(1) kcal/mol, respectively. The negative $\Delta H_{Me}$ value for the ebnpa-ligated system indicates that spontaneous alkoxide formation will occur from a zinc hydroxide precursor at low temperature. In contrast, the positive $\Delta H_{Me}$ value for the $Tp^{tBu,Me}$-ligated system indicates that alkoxide formation from a zinc hydroxide species is thermodynamically unfavorable at all temperatures. Overall, this work has implications for the catalytic cycle of LADH as it suggests that active-site ligand effects, including hydrogen-bonding interactions involving Ser-48, likely influence the hydrolytic stability of the proposed zinc–alkoxide moiety in the catalytic cycle.

## Amide Cleavage

Secondary hydrogen-bonding interactions are proposed to play important roles in the amide hydrolysis reactions mediated by carboxypeptidase A and other metalloamidases. For example, hydrogen bonding may be involved in the activation of the amide carbonyl moiety, and/or in transition-state stabilization. To probe the influence of hydrogen bonding on amide cleavage reactivity, Mareque-Rivas and co-workers have examined the amide cleavage properties of tripodal $N_4$-ligated systems having one internal amide substrate and from zero to two internal hydrogen-bonding interactions involving the zinc-bound amide carbonyl oxygen atom (Figure 9).[58–60] X-ray crystallographic studies of [(ppbpa)Zn]$(ClO_4)_2$, [(amppa)Zn]$(ClO_4)_2$ (amppa = [(6-amino-2-pyridyl)methyl]{[6-(pivaloylamido)-2-pyridyl]-methyl}[(2-pyridyl)methyl]amine) and [(bampa)Zn]$(ClO_4)_2$ (bampa = bis[(6-amino-2-pyridyl)methyl]{[6-(pivaloylamido)-2-pyridyl]methyl}amine) revealed that each complex contains a distorted trigonal-bipyramidal zinc center with the tertiary amine and the amide oxygen donors of the chelate ligand in the axial positions.[59,61] Comparison of the zinc–ligand distances in this series of complexes indicated that as the number of internal hydrogen-bonding interactions involving the coordinated amide oxygen atom increased, the Zn–O(amide) bond elongated by ca. 0.02 Å and the Zn–N(*tert*-amine) shortened by ca. 0.02–0.03 Å

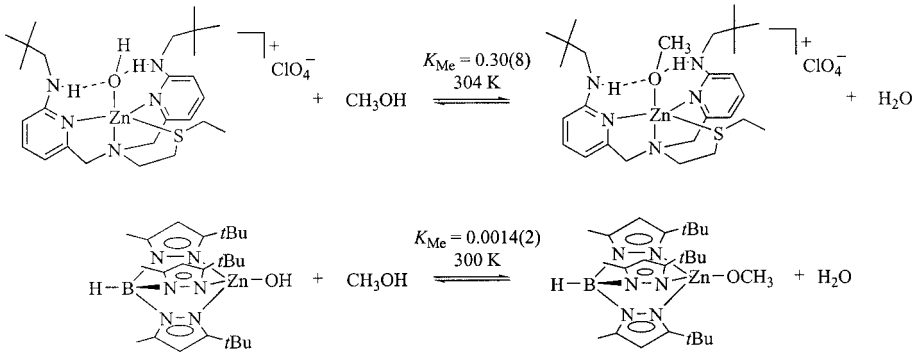


Scheme 2. Zinc–hydroxide/methoxide equilibria.

 © 2006 Wiley-VCH Verlag GmbH & Co. KGaA, Weinheim 

(Figure 9). Notably, the magnitude of this elongation of the Zn–O bond in this series of complexes per hydrogen-bond donor is identical to that found upon comparison of the Zn–O bond lengths in the $N_2S_2$-ligated zinc–formamide complexes {[(bmapa)Zn(DMF)]$(ClO_4)_2$, [(bmapa)Zn(NMF)]-$(ClO_4)_2$, Figure 7} vs. structurally similar compounds lacking the internal hydrogen-bond donor {[(bmpa)Zn(DMF)]-$(ClO_4)_2$, [(bmpa)Zn(NMF)]$(ClO_4)_2$, Figure 7}.[52] The hydrogen-bonding interactions for the complexes shown in Figure 7 and Figure 9 may all be classified as moderate hydrogen bonds.[62]

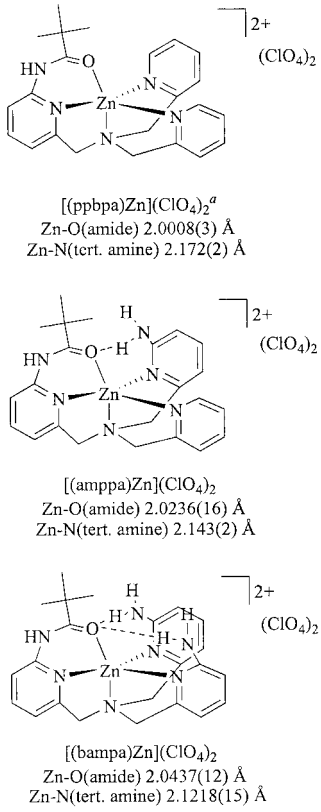


Figure 9. Amide-appended complexes containing zero to two internal hydrogen-bond donors.[63]

Treatment of the amide-appended zinc complexes shown in Figure 9 with 1 equiv. of $Me_4NOH{\cdot}5H_2O$ in methanol at 50(1) °C results in amide alcoholysis to produce 1 equiv. each of methyl trimethylacetate and $Me_4NClO_4$, and one or more zinc complexes of a modified chelate ligand having a new primary amine appendage derived from the cleavage of the amide moiety. For example, the reaction of [(ppbpa)-Zn]$(ClO_4)_2$ under the conditions cited above produces a mixture of zinc–hydroxide and –methoxide complexes of the ambpa {[(6-amino-2-pyridyl)methyl]bis[(2-pyridyl)-methyl]amine}. Mareque-Rivas and co-workers have shown that the half-life for the amide methanolysis reaction in the series of complexes shown in Figure 9 increases dramatically with the addition of each internal hydrogen-bond donor. Specifically, the half-life for the amide bond in [(ppbpa)Zn]$(ClO_4)_2$ is ca. 0.4 h, whereas for [(amppa)-Zn]$(ClO_4)_2$ and [(bampa)Zn]$(ClO_4)_2$, the half-life is ca. 9 h and ca. 320 h, respectively.[59] To interpret these results, as well as other amide cleavage studies involving similar complexes reported in the literature, we thought it essential to further investigate the reaction mechanism of amide cleavage operative in these systems. In this regard, we recently completed kinetic and mechanistic studies of the amide methanolysis reaction of [(ppbpa)Zn]$(ClO_4)_2$.[61] As depicted in Scheme 3, these studies revealed that the treatment of [(ppbpa)Zn]$(ClO_4)_2$ with 1 equiv. of $Me_4NOH{\cdot}5H_2O$ in methanol/acetonitrile solution at ambient temperature results in the stoichiometric formation of a deprotonated amide intermediate complex, [(ppbpa$^-$)Zn]$ClO_4$, which was isolated and characterized ($^1$H and $^{13}$C NMR, FTIR, and elemental analysis). Heating of analytically pure [(ppbpa$^-$)-Zn]$ClO_4$ in methanol/acetonitrile solution at 65(1) °C results in amide methanolysis. Kinetic studies of this reaction revealed a first-order dependence on both [(ppbpa$^-$)Zn]-$ClO_4$ and methanol in the rate-determining step. Analysis of the rate of decay of a $^1$H NMR signal of [(ppbpa$^-$)Zn]-$ClO_4$ as a function of time yielded activation parameters that are consistent with an intramolecular amide-cleavage process [$\Delta H^{\ddagger}$ = 15.0(3) kcal/mol, $\Delta S^{\ddagger}$ = –33(1) eu].[63] On the basis of this data and other experiments, a reaction mechanism was proposed in which the deprotonated amide species [(ppbpa$^-$)Zn]$ClO_4$ is an intermediate produced prior to the rate-limiting step.[61] The reaction of this intermediate with methanol is proposed to produce a Lewis activated type structure from which amide cleavage is initiated. The rate-determining step in this reaction pathway should be either the attack of the zinc-bound alkoxide nucleophile at the amide carbonyl carbon atom or the breakdown of the resulting tetrahedral intermediate. On the basis of these kinetic and mechanistic studies, we suggest that the slowing of the rate of amide methanolysis for the series of complexes shown in Figure 9 results from steric hindrance imparted by the hydrogen-bond donor amine groups, which limits the approach of the nucleophile to the amide carbonyl carbon atom, or from stabilization of the tetrahedral intermediate by hydrogen-bonding interactions. Further experiments directed at differentiating between these possibilities are underway.

Notably, a $Zn^{II}$ complex of the $N_2S_2$ donor ligand bmppa (Scheme 4) also undergoes amide methanolysis in the presence of $Me_4NOH{\cdot}5H_2O$ in methanol-containing solutions.[64] In addition, we have discovered that $Cd^{II}$ and $Hg^{II}$ analogs, [(bmppa)Cd$(ClO_4)$]$ClO_4$ and [(beppa)-Hg$(ClO_4)$]$ClO_4$, also undergo amide methanolysis under similar conditions.[64,65] The X-ray structures of these heavier group 12 analogs provide evidence that simultaneous amide oxygen and anion coordination can occur. Specifically, in the solid-state structures of [(bmppa)Cd$(ClO_4)$]-$ClO_4$ and [(beppa)Hg$(ClO_4)$]$ClO_4$ (Figure 10) a weak perchlorate interaction yields a six-coordinate cation having a distorted trigonal-prismatic geometry. Interestingly, the metal-bound oxygen atom of the coordinated perchlorate anion is positioned adjacent to the amide carbonyl oxygen atom in an arrangement that may be relevant to the proposed active form of the metal complexes for amide meth-

 © 2006 Wiley-VCH Verlag GmbH & Co. KGaA, Weinheim 

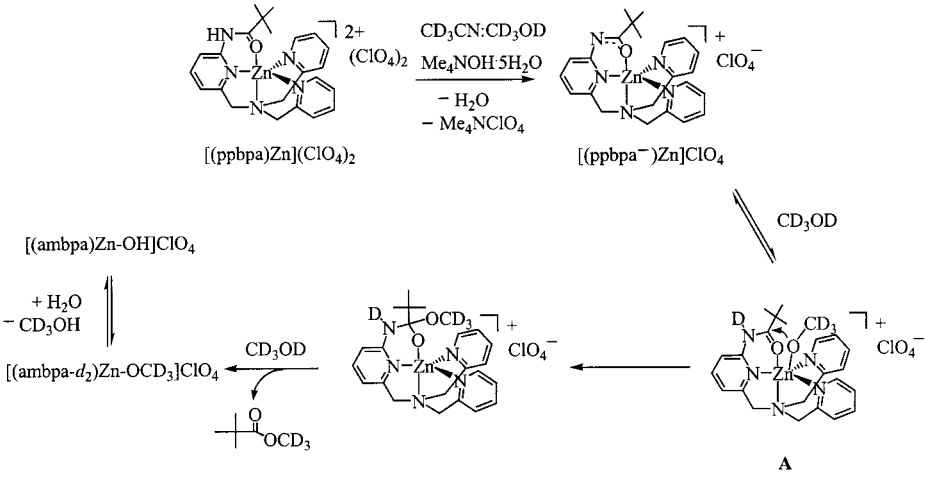


Scheme 3. Proposed mechanistic pathway of the amide methanolysis for $[(ppbpa)Zn](ClO_4)_2$.

anolysis (Scheme 3, "A"). Preliminary mechanistic studies indicate that the amide-cleavage reactions of $[(bmppa)Cd(ClO_4)]ClO_4$ and $[(beppa)Hg(ClO_4)]ClO_4$ also proceed by the formation of an intermediate deprotonated amide complex.

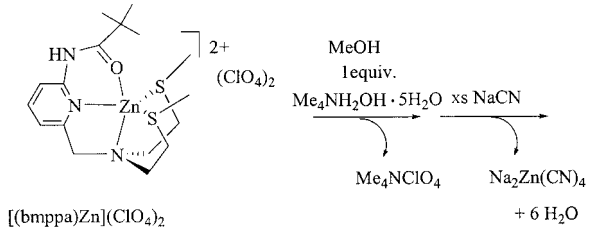


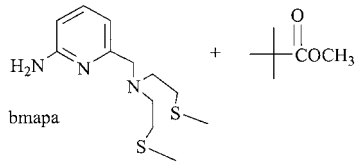


Scheme 4. Amide methanolysis reaction of $[(bmppa)Zn](ClO_4)_2$.

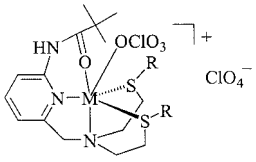


Figure 10. Drawing of the cationic portions of $[(bmppa)M(ClO_4)]ClO_4$ ($M = Cd^{II}$ or $Hg^{II}$).

The studies outlined above indicate that group 12 complexes supported by tripodal ligands having a single internal amide appendage exhibit novel amide-cleavage reactivity in basic methanol solution. This is interesting in that amide-appended tetradentate tripodal ligands have been used to stabilize a variety of 3d-metal complexes of relevance to biological systems, including metal hydroxide complexes, without any reported amide-cleavage side reactions. For example, Borovik has used amide-appended tripodal, trianionic ligands to stabilize a variety of terminal M–X (M = Fe, Mn; X = O, OH, S, Se, NHR, NR) complexes.[66,67] Masuda has also demonstrated that amide-appended tetradentate tripodal $N_4$-donor ligands can be used to stabilize a variety of novel copper– and/or iron–hydroxo, –hydroperoxo, and –alkylperoxo species.[68–73] These latter complexes are particularly interesting in that each contains the {[6-(pivaloylamido)-2-pyridyl]methyl}amine structural component within the supporting chelate ligand. Further studies are clearly needed to determine how changes in the nature of the metal ion influence the amide-cleavage reactivity.

## Phosphate Ester Coordination and Hydrolysis

There is considerable current interest in the development of synthetic compounds that catalyze the selective and/or catalytic hydrolysis of phosphate esters.[74–90] In this contribution, discussion in this area is limited to recent studies of phosphate ester coordination and hydrolysis mediated by zinc complexes of tetradentate tripodal ligands having internal hydrogen-bond donors.

Mareque-Rivas and co-workers recently compared the phosphate monoester binding properties of $[(bapapa)Zn(OH_n)]^{2+}$ ($n$ = 1 or 2; $pK_a$ = 6.7) and $[(tpa)Zn(OH_2)]^{2+}$ (Figure 11).[91] In aqueous solution at pH = 7, the former compound exhibits a higher affinity for $PhOPO_3^{2-}$ coordination ($\log K = 3.6 \pm 0.1$) than the tpa-ligated analog complex ($\log K = 4.4 \pm 0.1$). Although an X-ray structure of a phosphate monoester adduct was not reported for either system, X-ray crystallographic characterization of a zinc nitrate complex of the bapapa ligand, $[(bapapa)Zn(NO_3)]NO_3$, showed that the zinc-bound oxygen atom of the anion can participate in two moderate hydrogen-bonding interactions [O(1)···$N(amine)_{avg}$ 2.93 Å] with the supporting chelate ligand. Presumably, the bound phosphate ester monoanion can coordinate in a similar fashion.

 © 2006 Wiley-VCH Verlag GmbH & Co. KGaA, Weinheim 

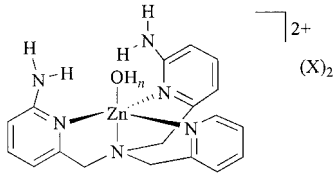

[(bapapa)Zn(H$_2$O)](X)$_2$
$n$ = 1 or 2 at pH = 7; p$K_a$ = 6.7

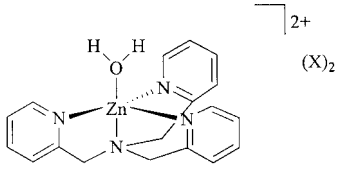

[(tpa)Zn(H$_2$O)](X)$_2$
p$K_a$ = 8.1

Figure 11. Mononuclear zinc complexes used to evaluate the influence of hydrogen bonding on the phosphate ester coordination.

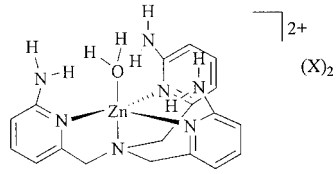

[(tapa)Zn(H$_2$O)](X)$_2$

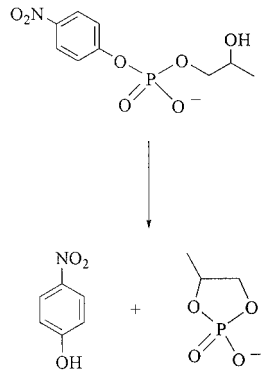

Figure 12. Top: Drawing of [(tapa)Zn(H$_2$O)](X)$_2$. Bottom: Intramolecular transesterification reaction of 2-hydroxypropyl 4-nitrophenyl phosphate.

A dinuclear zinc–phosphate diester complex, [{(bpapa)Zn}$_2$(μ-DMP)$_2$](PF$_6$)$_2$ (DBP = dibenzyl phosphate) having one internal hydrogen-bond donor per chelate ligand has been characterized by X-ray crystallography.[92] At each zinc center in [{(bpapa)Zn}$_2$(μ-DMP)$_2$](PF$_6$)$_2$, a bound phosphate diester oxygen atom accepts one hydrogen-bonding interaction from the amine group of the supporting chelate ligand. In solution [CD$_3$CN/D$_2$O (pD = 7.4)], using $^{31}$P NMR spectroscopy as a detection method, it was found that the affinity of the [(bpapa)Zn(OH/H$_2$O)]$^{2+}$ cation for DBP$^-$ was higher than that of [(tpa)Zn(H$_2$O)]$^{2+}$, which is similar to the reactivity found for the phosphate monoester binding studies described above.

In further investigations of the impact of secondary hydrogen-bonding interactions on the phosphate ester reactivity of zinc complexes, Mareque-Rivas and Williams recently reported a comparative study of the transesterification of 2-hydroxypropyl 4-nitrophenyl phosphate catalyzed by [(tapa)Zn(H$_2$O)]$^{2+}$ (Figure 12) and [(tpa)Zn(H$_2$O)]$^{2+}$ (Figure 11).[93] Notably, the rate of cyclization of the substrate is accelerated 3·10$^6$-fold by [(tapa)Zn(H$_2$O)]$^{2+}$ and 4·10$^3$-fold by [(tpa)Zn(H$_2$O)]$^{2+}$. The significant rate enhancement found for [(tapa)Zn(H$_2$O)]$^{2+}$ was attributed to enhanced stabilization of the dianionic intermediate that is formed in the rate-limiting step of the transesterification reaction, presumably by hydrogen-bonding interactions.

Studies of phosphate ester transesterification and hydrolysis have also been reported using tripodal N$_3$O-donor ligands having a variable number of internal hydrogen-bond donors.[37] Treatment of Zn$^{II}$ complexes of the L1–L3 ligands (Figure 6 and Figure 13) with bis(*p*-nitrophenyl) phosphate (BNP) results in the production of either phosphate ester transesterification or hydrolysis products, depending on the identity of the supporting chelate ligand. For L1 and L2 (Figure 6), *p*-nitrophenol and the *O*-phosphorylated chelate ligand are generated, indicating a transesterification reaction pathway involving the alkoxide moiety of the chelate ligand. For L3 (Figure 13), only phosphate ester hydrolysis products are produced.

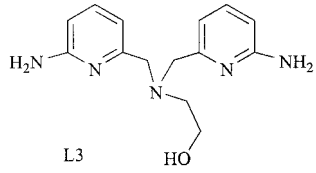

L3

Figure 13. L3 ligand.

Comparison of the reactivity of the zinc complex of L2 (second-order rate constant: 9.7·10$^{-2}$ M$^{-1}$ s$^{-1}$) vs. the spontaneous hydrolysis of BNP at pH = 7.0 and 25 °C reveals an acceleration of approximately six orders of magnitude. This rate acceleration was attributed to the involvement of an alkoxide (vs. hydroxide) nucleophile and the presence of secondary hydrogen-bonding interactions. The presence of the hydrogen-bond donors may provide additional Lewis acid activation for the zinc-bound substrate, or as suggested above, may stabilize a dianionic intermediate in the transesterification reaction. Further evidence for the impact of secondary hydrogen bonding is derived from the comparison of the second-order rate constants for BNP transesterification mediated by the zinc complex of L1 (4.2·10$^{-4}$ M$^{-1}$s$^{-1}$) vs. that of L2, which reveals a 230-fold reactivity increase. For the phosphate ester hydrolysis reaction catalyzed by the zinc complex of L3, which includes two internal hydrogen-bond donor groups, the rate acceleration is ca. 10$^5$ over that of the uncatalyzed reaction.

 © 2006 Wiley-VCH Verlag GmbH & Co. KGaA, Weinheim 

## Conclusions

Through studies of synthetic zinc complexes supported by tetradentate tripodal ligands containing one or more internal hydrogen-bond donors, chemical precedent has been elucidated which can be used to interpret the proposed roles for secondary hydrogen bonding in modulating the chemistry of mononuclear zinc centers in biological systems. For example, by using synthetic complexes, it has been determined that the presence of hydrogen-bond donors to a zinc-bound water molecule reduces the p$K_a$ of the bound water by 0.7–0.9 p$K_a$ units per secondary interaction. This result has relevance to carbonic anhydrases (CAs), where the formation of a zinc hydroxide moiety is required for $CO_2$-hydration reactivity. Hydrogen-bonding interactions are also likely important toward influencing the hydroxide and hydrogen carbonate anion coordination within the active site of CAs. In regard to the latter, spectroscopic evidence has been recently reported for the formation of a novel mononuclear zinc hydrogen carbonate complex supported by a tripodal ligand having three internal hydrogen-bond donors. Use of an $N_2S_2$-donor chelate ligand having one internal hydrogen-bond donor has enabled the isolation of a novel Cd–OH complex. This complex is reactive toward $CO_2$, thus providing the first chemical precedent relevant to the reactivity of a recently reported naturally occurring cadmium-containing carbonic anhydrase. The catalytic cycle of liver alcohol dehydrogenase is proposed to involve hydrogen-bonding interactions between a zinc-coordinated neutral oxygen donor or an alkoxide ligand and a nearby serine residue. Comparative structural studies of tripodal $N_2S_2$-ligated zinc–alcohol, –formamide, and –sulfoxide complexes revealed only minor perturbations in Zn–O bonding as a consequence of the presence of an internal hydrogen-bond donor. However, studies of the methanolysis reactivity of an $N_3S$-ligated zinc–hydroxide complex revealed that the presence of internal hydrogen-bond donors enhances the stability of a zinc–methoxide species with respect to hydrolysis. This result indicates that hydrogen bonding involving Ser-48 in LADH may play an important role in stabilizing the proposed zinc–alkoxide species.

Amide methanolysis reactivity has been identified for group 12 complexes of tetradentate tripodal $N_4$- and $N_2S_2$-donor ligands having one internal amide appendage. Kinetic and mechanistic studies of the amide methanolysis reaction of one $N_4$-ligated system indicate a novel reaction pathway involving initial formation of a deprotonated amide intermediate. Incorporation of hydrogen-bond donors into this $N_4$-donor ligand, such that they interact with the zinc-bound amide oxygen atom, significantly slows the rate of amide methanolysis. This may be the result of steric hindrance and/or hydrogen-bond stabilization of a tetrahedral intermediate. Importantly, these systems now provide a unique opportunity to systematically examine an amide-cleavage process as a function of both supporting ligand and metal ion present in the complex. Such studies are expected to provide additional insight into how secondary interactions, including hydrogen bonding, influence amide-cleavage reactions.

The presence of hydrogen-bond donors in a tetradentate tripodal $N_4$-ligated zinc complex enhances the affinity of the zinc center for coordination of a phosphate ester monoanion. In terms of phosphate ester hydrolysis reactivity, zinc complexes having internal hydrogen-bond donors have been found to exhibit significant rate enhancement over analogs lacking such secondary interactions. These combined results provide chemical precedent to support the notion that hydrogen bonding interactions play an important role in modulating biological phosphate ester cleavage reactions.

## Acknowledgments

The work in the Berreau laboratory was supported from grants from the National Science Foundation (CAREER Award CHE-0094066) and the donors of the Petroleum Research Fund (ACS-PRF 36394-G3).

[1] I. Bertini, C. Luchinat, S. Mangani, R. Pierattelli, *Comments Inorg. Chem.* **1995**, *17*, 1–15.
[2] S. Karlin, Z.-Y. Zhu, *Proc. Natl. Acad. Sci. U.S.A.* **1997**, *94*, 14231–14236.
[3] B. C. Tripp, K. Smith, J. G. Ferry, *J. Biol. Chem.* **2001**, *276*, 48615–48618.
[4] D. B. Northrop, F. B. Simpson, *Arch. Biochem. Biophys.* **1998**, *352*, 288–292.
[5] J. F. Krebs, J. A. Ippolito, D. W. Christianson, C. A. Fierke, *J. Biol. Chem.* **1993**, *268*, 27458–27466.
[6] D. W. Christianson, J. D. Cox, *Annu. Rev. Biochem.* **1999**, *68*, 33–57.
[7] K. Hakansson, M. Carlsson, L. A. Svensson, A. Liljas, *J. Mol. Biol.* **1992**, *227*, 1192–1204.
[8] S. Mitsuhashi, T. Mizushima, E. Yamashita, M. Yamamoto, T. Kumasaka, H. Moriyama, T. Ueki, S. Miyachi, T. Tsukihara, *J. Biol. Chem.* **2000**, *275*, 5521–5526.
[9] M. S. Kimber, E. F. Pai, *EMBO J.* **2000**, *19*, 1407–1418.
[10] P. Strop, K. S. Smith, T. M. Iverson, J. G. Ferry, D. C. Rees, *J. Biol. Chem.* **2001**, *276*, 10299–10305.
[11] J. D. Cronk, J. A. Endrizzi, M. R. Cronk, J. W. O'Neill, K. Y. J. Zhang, *Protein Sci.* **2001**, *10*, 911–922.
[12] A. S. Covarrubias, A. M. Larsson, M. Hogbom, J. Lindberg, T. Bergfors, C. Bjorkelid, S. L. Mowbray, T. Unge, T. A. Jones, *J. Biol. Chem.* **2005**, *280*, 18782–18789.
[13] B. E. Alber, J. G. Ferry, *Proc. Natl. Acad. Sci. U.S.A.* **1994**, *91*, 6909–6913.
[14] T. M. Iverson, B. E. Alber, C. Kisker, J. G. Ferry, D. C. Rees, *Biochemistry* **2000**, *39*, 9222–9231.
[15] E. H. Cox, G. L. McLendon, F. M. M. Morel, T. W. Lane, R. C. Prince, I. J. Pickering, G. N. George, *Biochemistry* **2000**, *39*, 12128–12130.
[16] T. W. Lane, F. M. M. Morel, *Proc. Natl. Acad. Sci. U.S.A.* **2000**, *97*, 4627–4631.
[17] T. W. Lane, M. A. Saito, G. N. George, I. J. Pickering, R. C. Prince, F. M. M. Morel, *Nature* **2005**, *435*, 42.
[18] H. Eklund, C.-I. Branden, "The Role of Zinc in Alcohol Dehydrogenase", in *Zinc Enzymes* (Ed.: T. G. Spiro), John Wiley & Sons, New York, **1983**, p. 125–152.
[19] J. P. Klinman, *Crit. Rev. Biochem.* **1981**, *10*, 39–78.
[20] S. Ramaswamy, H. Eklund, B. V. Plapp, *Biochemistry* **1994**, *33*, 5230–5237.
[21] S. Ramaswamy, D.-H. Park, B. V. Plapp, *Biochemistry* **1999**, *38*, 13951–13959.

 © 2006 Wiley-VCH Verlag GmbH & Co. KGaA, Weinheim 

[22] P. K. Agarwal, S. P. Webb, S. Hammes-Schiffer, *J. Am. Chem. Soc.* **2000**, *122*, 4803–4812.
[23] S. Ramaswamy, M. Scholze, B. V. Plapp, *Biochemistry* **1997**, *36*, 3522–3527.
[24] J. F. Schindler, K. B. Berst, B. V. Plapp, *J. Med. Chem.* **1998**, *41*, 1696–1701.
[25] H. Deng, J. F. Schindler, K. B. Berst, B. V. Plapp, R. Callender, *Biochemistry* **1998**, *37*, 14267–14278.
[26] H. Cho, S. Ramaswamy, B. V. Plapp, *Biochemistry* **1997**, *36*, 382–389.
[27] S. Al-Karadaghi, E. S. Cedergren-Zeppezauer, S. Hovmöller, K. Petratos, H. Terry, K. S. Wilson, *Acta Crystallogr., Sect. D* **1994**, *D50*, 793–807.
[28] W. N. Lipscomb, N. Sträter, *Chem. Rev.* **1996**, *96*, 2375–2434.
[29] J. E. Coleman, *Curr. Opin. Chem. Biol.* **1998**, *2*, 222–234.
[30] D. W. Christianson, W. N. Lipscomb, *Acc. Chem. Res.* **1989**, *22*, 62–69.
[31] H. Kim, W. N. Lipscomb, *Biochemistry* **1991**, *30*, 8171–8180.
[32] E. E. Kim, H. W. Wyckoff, *J. Mol. Biol.* **1991**, *218*, 449–464.
[33] Z. Shirin, C. J. Carrano, *Polyhedron* **2004**, *23*, 239–244.
[34] J. C. Mareque-Rivas, R. Prabaharan, R. T. M. de Rosales, *Chem. Commun.* **2004**, 76–77.
[35] J. C. Mareque-Rivas, R. Prabaharan, S. Parsons, *Dalton Trans.* **2004**, 1648–1655.
[36] S. Yamaguchi, I. Tokairin, Y. Wakita, Y. Funahashi, K. Jitsukawa, H. Masuda, *Chem. Lett.* **2003**, *32*, 406–407.
[37] M. Livieri, F. Mancin, U. Tonellato, J. Chin, *Chem. Commun.* **2004**, 2862–2863.
[38] A. Liljas, K. Hakansson, B. H. Jonsson, Y. Xue, *Eur. J. Biochem.* **1994**, *219*, 1–10.
[39] S. F. Hossain, K. M. Nicholas, C. L. Teas, R. E. Davis, *J. Chem. Soc., Chem. Commun.* **1981**, 268–269.
[40] H. Ito, T. Ito, *Acta Crystallogr., Sect. C* **1985**, *C41*, 1598–1602.
[41] D. J. Darensbourg, M. L. M. Jones, J. H. Reibenspies, *Inorg. Chem.* **1996**, *35*, 4406–4413.
[42] T. Yoshida, D. L. Thorn, T. Okano, J. A. Ibers, S. Otsuka, *J. Am. Chem. Soc.* **1979**, *101*, 4212–4221.
[43] R. J. Crutchley, J. Powell, R. Faggiani, C. J. L. Lock, *Inorg. Chim. Acta* **1977**, *24*, L15–L16.
[44] H. Masuda, I. Tokairin, K. Jitsukawa, H. Einaga, *J. Inorg. Biochem.* **1999**, *74*, 225.
[45] A. Wada, S. Yamaguchi, K. Jitsukawa, H. Masuda, *Angew. Chem. Int. Ed.* **2005**, *44*, 5698–5701.
[46] D. K. Garner, R. A. Allred, K. J. Tubbs, A. M. Arif, L. M. Berreau, *Inorg. Chem.* **2002**, *41*, 3533–3541.
[47] R. A. Allred, L. H. McAlexander, A. M. Arif, L. M. Berreau, *Inorg. Chem.* **2002**, *41*, 6790–6801.
[48] R. A. Allred, A. M. Arif, L. M. Berreau, *Dalton Trans.* **2002**, 300–301.
[49] C. A. Grapperhaus, T. Tuntulani, J. H. Reibenspies, M. Y. Darensbourg, *Inorg. Chem.* **1998**, *37*, 4052–4058.
[50] U. Brand, M. Rombach, H. Vahrenkamp, *Chem. Commun.* **1998**, 2717–2718.
[51] L. M. Berreau, M. M. Makowska-Grzyska, A. M. Arif, *Inorg. Chem.* **2001**, *40*, 2212–2213.
[52] M. M. Makowska-Grzyska, P. C. Jeppson, R. A. Allred, A. M. Arif, L. M. Berreau, *Inorg. Chem.* **2002**, *41*, 4872–4887.
[53] D. D. Perrin, *Dissociation Constants of Organic Bases in Aqueous Solution*, Butterworth, London, **1965**.
[54] E. A. Braude, F. C. Nachod, *Determination of Organic Structures by Physical Methods*, Academic Press, New York, **1955**.
[55] D. K. Garner, S. B. Fitch, L. H. McAlexander, L. M. Bezold, A. M. Arif, L. M. Berreau, *J. Am. Chem. Soc.* **2002**, *124*, 9970–9971.
[56] C. Bergquist, G. Parkin, *Inorg. Chem.* **1999**, *38*, 422–423.
[57] C. Bergquist, H. Storrie, L. Koutcher, B. M. Bridgewater, R. A. Friesner, G. Parkin, *J. Am. Chem. Soc.* **2000**, *122*, 12651–12658.
[58] J. C. Mareque-Rivas, R. T. M. de Rosales, S. Parsons, *Dalton Trans.* **2003**, 2156–2163.
[59] J. C. Mareque-Rivas, E. Salvagni, S. Parsons, *Dalton Trans.* **2004**, 4185–4192.
[60] J. C. Mareque-Rivas, E. Salvagni, R. Prabaharan, R. T. M. de Rosales, S. Parsons, *Dalton Trans.* **2004**, 172–177.
[61] E. Szajna, M. M. Makowska-Grzyska, C. C. Wasden, A. M. Arif, L. M. Berreau, *Inorg. Chem.* **2005**, *44*, 7595–7605.
[62] G. A. Jeffrey, *An Introduction to Hydrogen Bonding*, Oxford University Press, New York, **1997**.
[63] J. T. Groves, R. R. Chambers, Jr., *J. Am. Chem. Soc.* **1984**, *106*, 630–638.
[64] L. M. Berreau, M. M. Makowska-Grzyska, A. M. Arif, *Inorg. Chem.* **2000**, *39*, 4390–4391.
[65] M. M. Makowska-Grzyska, K. Doyle, R. A. Allred, A. M. Arif, D. C. Bebout, L. M. Berreau, *Eur. J. Inorg. Chem.* **2005**, 822–827.
[66] A. S. Borovik, *Acc. Chem. Res.* **2005**, *38*, 54–61.
[67] R. L. Lucas, D. R. Powell, A. S. Borovik, *J. Am. Chem. Soc.* **2005**, *127*, 11596–11597.
[68] L. M. Berreau, S. Mahapatra, J. A. Halfen, V. G. Young, Jr., W. B. Tolman, *Inorg. Chem.* **1996**, *35*, 6339–6342.
[69] C. E. MacBeth, B. S. Hammes, V. G. Young, Jr., A. S. Borovik, *Inorg. Chem.* **2001**, *40*, 4733–4741.
[70] A. Wada, M. Harata, K. Hasegawa, K. Jitsukawa, H. Masuda, M. Mukai, T. Kitagawa, H. Einaga, *Angew. Chem. Int. Ed. Engl.* **1998**, *37*, 798–799.
[71] S. Yamaguchi, S. Nagatomo, T. Kitagawa, Y. Funahashi, T. Ozawa, K. Jitsukawa, H. Masuda, *Inorg. Chem.* **2003**, *42*, 6968–6970.
[72] A. Wada, S. Ogo, Y. Watanabe, M. Mukai, T. Kitagawa, K. Jitsukawa, H. Masuda, H. Einaga, *Inorg. Chem.* **1999**, *38*, 3592–3593.
[73] A. Wada, S. Ogo, S. Nagatomo, T. Kitagawa, Y. Watanabe, K. Jitsukawa, H. Masuda, *Inorg. Chem.* **2002**, *41*, 616–618.
[74] J. Weston, *Chem. Rev.* **2005**, *105*, 2151–2174.
[75] J. A. Cowan, *Curr. Opin. Chem. Biol.* **2001**, *5*, 634–642.
[76] A. Sreedhara, J. A. Cowan, *J. Biol. Inorg. Chem.* **2001**, *6*, 337–347.
[77] J. R. Morrow, *Met. Ions Biol. Syst.* **1996**, *33*, 561–592.
[78] E. L. Hegg, J. N. Burstyn, *Coord. Chem. Rev.* **1998**, *173*, 133–165.
[79] G. Parkin, *Chem. Rev.* **2004**, *104*, 699–768.
[80] H. Vahrenkamp, *Acc. Chem. Res.* **1999**, *32*, 589–596.
[81] R. Krämer, *Coord. Chem. Rev.* **1999**, *182*, 243–261.
[82] J. K. Bashkin, *Curr. Opin. Chem. Biol.* **1999**, *3*, 752–758.
[83] P. Molenveld, J. F. J. Engbersen, D. N. Reinhoudt, *Chem. Soc. Rev.* **2000**, *29*, 75–86.
[84] N. Sträter, W. N. Lipscomb, T. Klabunde, B. Krebs, *Angew. Chem. Int. Ed. Engl.* **1996**, *35*, 2024–2055.
[85] N. H. Williams, B. Takasaki, M. Wall, J. Chin, *Acc. Chem. Res.* **1999**, *32*, 485–493.
[86] N. H. Williams, *Biochem. Biophys. Acta* **2004**, *1697*, 279–287.
[87] J. Suh, *Acc. Chem. Res.* **2003**, *36*, 562–570.
[88] E. Kimura, *Curr. Opin. Chem. Biol.* **2000**, *4*, 207–213.
[89] J. Chin, *Curr. Opin. Chem. Biol.* **1997**, *1*, 514–521.
[90] J. R. Morrow, O. Iranzo, *Curr. Opin. Chem. Biol.* **2004**, *8*, 192–200.
[91] J. C. Mareque-Rivas, R. T. M. de Rosales, S. Parsons, *Chem. Commun.* **2004**, 610–611.
[92] J. C. Mareque-Rivas, R. T. M. de Rosales, S. Parsons, *Dalton Trans.* **2003**, 4385–4386.
[93] G. Feng, J. C. Mareque-Rivas, R. T. M. de Rosales, N. H. Williams, *J. Am. Chem. Soc.* **2005**, *127*, 13470–13471.

Received: October 4, 2005
Published Online: December 21, 2005

 © 2006 Wiley-VCH Verlag GmbH & Co. KGaA, Weinheim 

DOI: 10.1002/ejic.200500927

# CO Cleavage Promoted by Acetylide Addition to Vinyliminium Diiron Complexes

**Luigi Busetto,[a] Fabio Marchetti,[a] Stefano Zacchini,[a] and Valerio Zanotti*[a]**

**Keywords:** CO cleavage / Bridging ligands / Vinyliminium / Diiron complexes

The vinyliminium complex [$Fe_2$\{μ-$\eta^1$:$\eta^3$-C(Me)=C(Me)-C=N(Me)(Xyl)\}(μ-CO)(CO)$(Cp)_2$][$SO_3CF_3$] (**1**; Xyl = 2,6-$Me_2C_6H_3$) reacts with LiC≡CR [R = $C_6H_4$Me = Tol, Ph, H, *n*Bu, $SiMe_3$, C(Me)=$CH_2$] affording the amido-functionalized allylidene complexes [$Fe_2$\{μ-$\kappa^1$(O):$\eta^1$(C):$\eta^3$(C)-C(C≡CR)-C(Me)C(Me)C(O)N(Me)(Xyl)\}(μ-CO)$(Cp)_2$] [R = $C_6H_4$Me = Tol, **2**; R = Ph, **3**; R = H, **4**; R = *n*Bu, **5**; R = $SiMe_3$, **6**; R = C(Me)=$CH_2$, **7**] in good yields. Labelling experiments with $^{13}$CO-enriched **1** indicate that formation of **2**–**7** occurs through cleavage of the carbon–oxygen bond of a coordinated CO ligand. The molecular structure of **2** has been determined by an X-ray diffraction study.
(© Wiley-VCH Verlag GmbH & Co. KGaA, 69451 Weinheim, Germany, 2006)

## Introduction

Recently, we described the successful preparation of bridging vinyliminium diiron complexes[1] and demonstrated the electrophilic character of the bridging ligand. Regio- and stereoselective additions of hydride ($NaBH_4$) to the μ-vinyliminium have been described in detail.[2] With the aim of extending our investigations to the addition of carbon nucleophiles, we have examined the reaction with lithium acetylides. Here, we report on the rearrangement occurring at the bridging ligand as a consequence of acetylide attack. This involves a terminally coordinated carbonyl, which undergoes CO cleavage and incorporation in the bridging ligand.

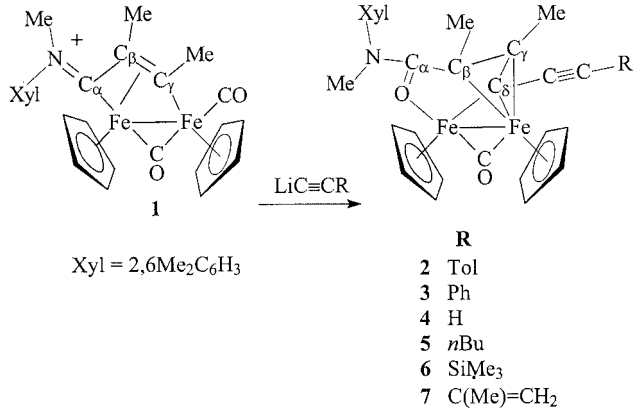


Xyl = 2,6-$Me_2C_6H_3$

**R**
**2** Tol
**3** Ph
**4** H
**5** *n*Bu
**6** $SiMe_3$
**7** C(Me)=$CH_2$

Scheme 1.

## Result and Discussion

Complex *cis*-[$Fe_2$\{μ-$\eta^1$:$\eta^3$-C(Me)=C(Me)C=N(Me)(Xyl)\}-(μ-CO)(CO)$(Cp)_2$][$SO_3CF_3$] (**1**) rapidly reacts with an excess of lithium acetylide (LiC≡CR), affording the air-stable compounds *cis*-[$Fe_2$\{μ-$\kappa^1$(O):$\eta^1$(C):$\eta^3$(C)-C(C≡CR)C(Me)-C(Me)C(O)N(Me)(Xyl)\}(μ-CO)$(Cp)_2$] (**2**–**7**), in about 60–70% yield (Scheme 1).

The molecular structure of **2** has been determined by X-ray diffraction: two different views of the molecule are shown in Figure 1, whereas relevant bond lengths and bond angles are reported in Table 1; the structure of the bridging ligand is also shown in Scheme 2.

The molecule is composed by a $Fe_2$(μ-CO)$(Cp)_2$ core with a bridging amido-functionalized allylidene μ-$\kappa^1$-(O):$\eta^1$(C):$\eta^3$(C)-{C(C≡CR)C(Me)C(Me)C(O)N(Me)(Xyl)} ligand, which is σ-coordinated to Fe(1) [Fe(1)–C(12) 1.923(4) Å] and $\eta^3$-coordinated to Fe(2) [Fe(2)–C(12) 2.004(4) Å; Fe(2)–C(21) 2.030(4) Å; Fe(2)–C(23)–2.157(4) Å], in an allyl-like fashion (see structure **A** in Scheme 2). The Fe(2)–C(23) interaction is significantly longer than that of Fe(2)–C(12) and Fe(2)–C(21), suggesting that an alternative description of the bridging ligand is possible (Scheme 2, **B**). The $C_\beta$–$C_\gamma$–$C_\delta$ sequence [C(23)–C(21)–C(12)] can be considered as a vinyl-substituted μ-alkylidene, which corresponds to a coordination mode commonly found in diiron[2] and diruthenium[3] complexes. However, because the C(12)–C(21) interaction [1.417(5) Å] is shorter than in C(21)–C(23) [1.455(6) Å] a description of the ligand as $\eta^1$:$\eta^2$-vinyl connected to an alkynyl and an amido-functionality also appears possible (structure **C**). The coordination of the amido group to Fe(1) is presumably crucial in determining the observed geometry of the bridging ligand. The oxygen atom O(2) coordinates to Fe(1) forming a five-membered oxadimetallacycle with a Fe–O

[a] Dipartimento di Chimica Fisica e Inorganica, Università di Bologna,
Viale Risorgimento 4, 40136 Bologna, Italy
E-mail: valerio.zanotti@unibo.it

 © 2006 Wiley-VCH Verlag GmbH & Co. KgaA, Weinheim 

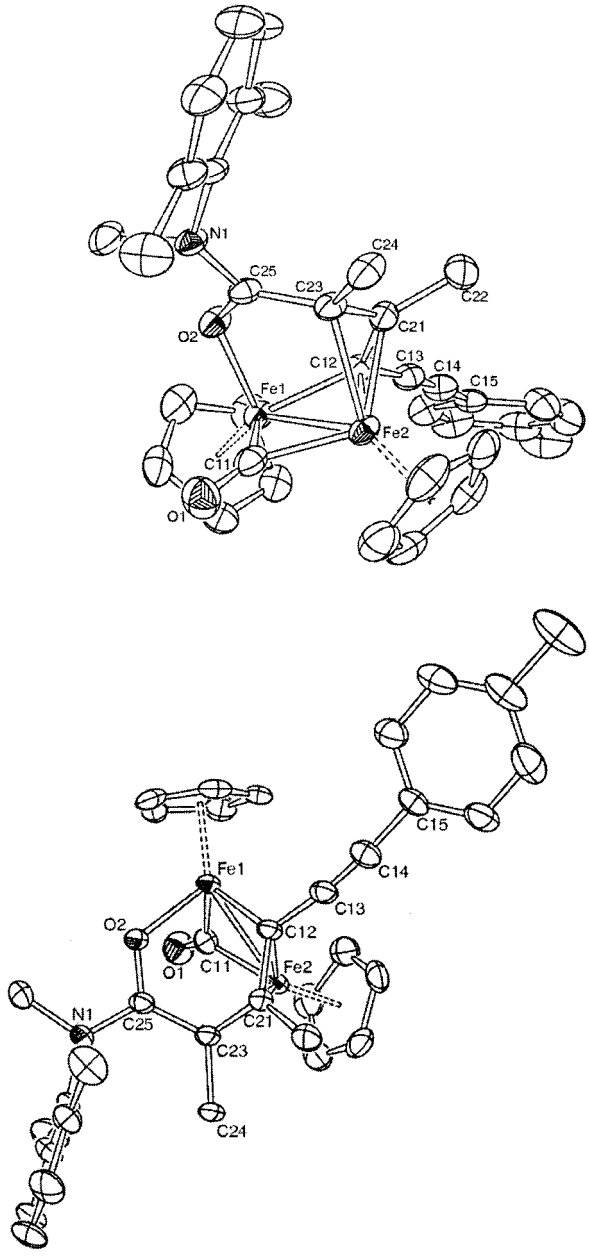


Figure 1. Different views of the molecular structure of **2** (hydrogen atoms are omitted for clarity). Displacement ellipsoids are at the 30% probability level.

Table 1. Selected bond lengths [Å] and angles [°] for complex **2**.

| | | | |
|---|---|---|---|
| Fe(1)–Fe(2) | 2.5131(8) | C(13)–C(14) | 1.191(6) |
| Fe(1)–C(11) | 1.858(5) | C(14)–C(15) | 1.443(6) |
| Fe(2)–C(11) | 1.938(5) | C(12)–C(21) | 1.417(5) |
| Fe(1)–C(12) | 1.923(4) | C(21)–C(22) | 1.506(6) |
| Fe(2)–C(12) | 2.004(4) | C(21)–C(23) | 1.455(6) |
| Fe(2)–C(21) | 2.030(4) | C(23)–C(24) | 1.529(5) |
| Fe(2)–C(23) | 2.157(4) | C(23)–C(25) | 1.464(6) |
| Fe(1)–O(2) | 1.941(3) | C(25)–O(2) | 1.267(4) |
| C(11)–O(1) | 1.205(5) | C(25)–N(1) | 1.363(5) |
| C(12)–C(13) | 1.440(6) | C(26)–N(1) | 1.477(5) |
| Fe(1)–C(11)–Fe(2) | 82.9(2) | C(22)–C(21)–C(23) | 120.7(4) |
| Fe(1)–C(12)–Fe(2) | 79.56(16) | C(21)–C(23)–C(24) | 118.8(4) |
| Fe(1)–C(12)–C(21) | 121.1(3) | C(21)–C(23)–C(25) | 115.7(4) |
| C(13)–C(12)–C(21) | 119.0(4) | C(24)–C(23)–C(25) | 119.1(4) |
| C(12)–C(13)–C(14) | 172.9(5) | C(23)–C(25)–O(2) | 121.6(4) |
| C(13)–C(14)–C(15) | 174.9(5) | C(23)–C(25)–N(1) | 124.4(4) |
| C(12)–C(21)–C(23) | 118.1(4) | O(2)–C(25)–N(1) | 114.0(4) |
| C(12)–C(21)–C(22) | 121.1(4) | C(25)–O(2)–Fe(1) | 121.1(3) |

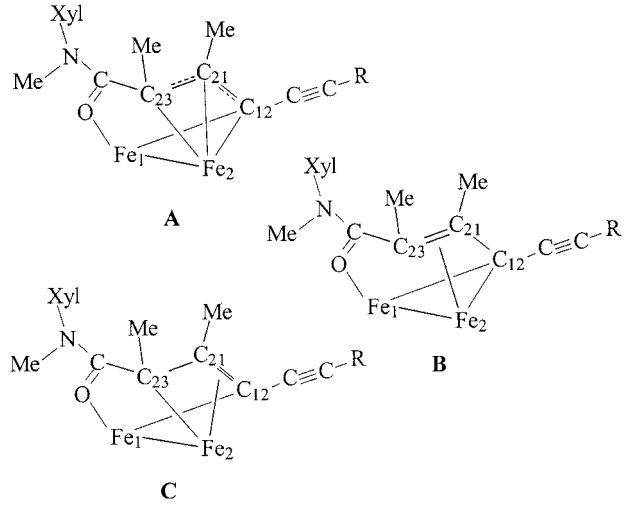


Scheme 2.

bond length [Fe(1)–O(2) 1.941(3) Å] slightly shorter than in $[Fe_2(CO)_5(\mu\text{-}PPh_2)(\mu\text{-}\eta^1(O):\eta^1(C):\eta^2(C)\text{-}\{O{=}C(N\textit{t}BuH)\text{-}CH_2\}C{=}CH_2)]$ [2.017(5) Å][4] and $[Fe_2(CO)_4(\mu\text{-}PPh_2)(\mu\text{-}dppm)\{C(CO_2\text{–}Me){=}CHC(OMe){=}O\}]$ [2.024(3) Å],[5] which contain a diiron five-membered oxametallacycle.

The spectroscopic data of **2** are in agreement with its structure: the IR spectrum (in $CH_2Cl_2$ solution) exhibits one band for the bridging carbonyl group, at 1753 $cm^{-1}$, whereas weaker absorptions at 2169 $cm^{-1}$ and 1511 $cm^{-1}$ are attributable to the C≡C and to the amide C–O interactions, respectively. NMR assignments, based on gs-HSQC, gs-HMBC and NOE experiments evidence a single $^1H$ NMR resonance for each of the six different Me groups present in **2** (at $\delta$ = 2.75, 2.42, 2.40, 2.30, 1.55 and 0.47 ppm, assigned to $C_\gamma\textit{Me}$, N*Me*, $C_6H_4\textit{Me}$, $\textit{Me}_2C_6H_3$, $C_\beta\textit{Me}$, respectively). In particular, assignments of the $C_\gamma\textit{Me}$ and $C_\beta\textit{Me}$ resonances are based on observed NOE effects between $C_6H_3\textit{Me}_2$ (Xyl) and $C_\beta\textit{Me}$. $^{13}C$ NMR resonances at $\delta$ = 179.7 and 155.5 ppm, are assigned to $C_\alpha$ and $C_\delta$, respectively. The attribution of these two signals is crucial in the later described experiment and deserves some comments: the gs-HMBC spectrum evidences correlation between the $^1H$ NMR resonance at $\delta$ = 2.42 ppm (N*Me*) and the $^{13}C$ resonance at $\delta$ = 179.7 ppm, while the $^{13}C$ NMR signal falling at $\delta$ = 155.5 ppm presents only one correlation, i.e. with the $^1H$ NMR resonance at $\delta$ = 2.75 ppm ($C_\gamma\textit{Me}$). It is worth noting that the *C*O resonance, in other analogous iron-coordinated amido functionalities, is reported at ca. 182 ppm.[4] Moreover, the $C_\gamma$ and $C_\beta$ carbon atoms give raise to signals at $\delta$ = 96.6 and 52.3 ppm, whereas the *sp* carbon atoms of the acetylenic group typically fall at $\delta$ = 104.5 and 101.6 ppm.

The reaction sequence leading to **2**–**7** is far from being obvious. One possibility is that the reaction proceeds

 © 2006 Wiley-VCH Verlag GmbH & Co. KGaA, Weinheim 

through initial attack of the acetylide to the terminal carbonyl group of **1**, originating an acyl intermediate, which further rearrange involving the μ-vinyliminium ligand. Support for this hypothesis comes from the observation that acetylides selectively attack the terminal CO in the related complexes $[Fe_2(\mu\text{-}CNMe_2)(\mu\text{-}CO)(CO)_2(Cp)_2][SO_3CF_3]$.[6] Moreover, nucleophilic attack to CO is often followed by coupling with the bridging ligands. For instance, LiC≡CPh addition to the CO in the thiocarbyne complex $[Fe_2(\mu\text{-}CSMe)(\mu\text{-}CO)(CO)_2(Cp)_2][SO_3CF_3]$ is followed by the migration of the acyl ligand, leading to the formation of the μ-carbene complexes $[Fe_2\{\mu\text{-}C(SMe)C(O)CCPh\}(\mu\text{-}CO)(CO)(Cp)_2]$.[7] Similarly, the allenyl $[Fe_2\{\mu\text{-}PPh_2\}(\mu\text{-}\eta^1{:}\eta^2\text{-}(H)C{=}C{=}CH_2)(CO)_6]$ undergoes amine addition to the terminal CO, with consequent migration of the resulting amide to the allenyl moiety.[4] The unexpected formation of **2**–**7** does not simply concern the coupling between acyl- and vinyliminium ligands: if we assume that the $C_\delta$–C≡C–R moiety in the bridging ligand of **2**–**7** originates from an acyl intermediate [C(O)C≡C–R], this implies the cleavage of the C=O.

Alternatively, the $C_\alpha$=O moiety in the bridging ligand of **2**–**7** could be originated from a migration of the terminal CO group, and acetylide addition at the $C_\alpha$ of the vinyliminium ligand. This, in turn, would require a considerable rearrangement of the iminium moiety, with 1,2 shifts of the Me and $NR_2$ groups, in order to explain the formation of **2**–**7**.

With the aim of obtaining more evidence for the reaction mechanism, we have prepared a $^{13}CO$-enriched sample of **1**, which has been reacted with Li–C≡C–Tol (see Exp. Section). The reaction yielded compound **2**, as expected, and the corresponding $^{13}C$ NMR spectrum exhibited two clearly enhanced signals at $\delta$ = 291.6 (μ-CO) and 155.8 ppm ($C_\delta$), and doublets at $\delta$ = 96.1 ($^1J_{CC}$, 50.7 Hz, $C_\gamma$), 52.4 ($^2J_{CC}$, 11.9 Hz, $C_\beta$), and 20.9 ppm ($^2J_{CC}$, 4.5 Hz, $C_\gamma Me$). Moreover, the IR spectra showed an isotopic effect for the bridging CO group and not for the $C_\alpha$=O of the bridging ligand. The above mentioned experiment indicates that the $C_\delta$ in **2** is originated from a carbonyl ligand, and implies that CO cleavage must occur at some stage of the reaction, as suggested in the former hypothesis. Interestingly, in the conversion of **1** to **2**, the three-carbon-atom chain of the bridging ligand grows by several units as a consequence of the inclusion of both the alkynyl (C≡C–Tol) group and the $C_\delta$ carbon atom, the latter originating from a CO.

Finally, it is to be remarked that reactions of organometallic complexes involving CO cleavage are of great interest, because this is considered an early and fundamental step in the heterogeneous conversion of carbon monoxide to hydrocarbons (Fischer–Tropsch process).[8] Examples, so far reported, mainly concerns: carbonyl clusters, which generally provide metal carbides,[9] polynuclear early transition-metal complexes, that take advantage of the oxophilic character of these metals for promoting CO dissociation,[10] and dinuclear tungsten complexes, with multiple metal–metal bonds.[11] Our results further support the conviction[8b] that dinuclear complexes are effective organometallic models for studying CO cleavage and C–C bond formation.

## Experimental Section

**General Remarks:** All reactions were routinely carried out under nitrogen, using standard Schlenk techniques. Solvents were distilled immediately before use under nitrogen from appropriate drying agents. Infrared spectra were recorded at 298 K with a Perkin–Elmer Spectrum 2000 FT-IR spectrophotometer and elemental analyses were performed with a ThermoQuest Flash 1112 Series EA Instrument. All NMR measurements were performed at 298 K with a Mercury Plus 400 instrument. The chemical shifts for $^1H$ and $^{13}C$ were referenced to internal TMS. The spectra were fully assigned by $^1H$,$^{13}C$ correlation measured by means of gs-HSQC and gs-HMBC experiments.[12] NOE measurements were recorded using the DPFGSE-NOE sequence.[13] All the reagents, included $^{13}CO$, were commercial products (Aldrich) of the highest purity available and used as received. Compound **1** was prepared by published methods.[1a]

**Synthesis of $[Fe_2\{\mu\text{-}\kappa^1(O){:}\eta^1(C){:}\eta^3(C)\text{-}C(C{\equiv}CR)C(Me)C(Me)C(O)N(Me)(Xyl)\}(\mu\text{-}CO)(Cp)_2]$ [R = $C_6H_4Me$ = Tol, 2; R = Ph, 3; R = H, 4; R = *n*Bu, 5; R = $SiMe_3$, 6; R = $C(Me){=}CH_2$, 7]. General Procedure:** A solution of *cis*-$[Fe_2\{\mu\text{-}\eta^1{:}\eta^3\text{-}C(Me){=}C(Me)\text{-}C{=}N(Me)(Xyl)\}(\mu\text{-}CO)(CO)(Cp)_2][SO_3CF_3]$ (**1**) (0.150 mmol), in THF (10 mL) was treated with LiC≡CR (0.350 mmol), freshly prepared from *n*BuLi and HC≡CR. The mixture was stirred for 30 min, and then it was filtered through a Celite pad. The solvent was removed under reduced pressure; hence the residue was dissolved in diethyl ether and filtered through alumina. The final product was obtained as a red powder upon removal of the solvent. Crystals of **2** suitable for X ray analysis were obtained from a hexane solution at –20 °C.

**2:** $C_{35}H_{35}Fe_2NO_2$ (613.35): calcd. C 68.54, H 5.75, N 2.28; found: C 68.46, H 5.64, N 2.33. Yield: 57 mg, 62%. $^1H$ NMR ($CDCl_3$): $\delta$ = 7.61–6.81 (m, 7 H, $Me_2C_6H_3$ and $C_6H_4Me$), 4.55, 4.08 (s, 10 H, Cp), 2.75 (s, 3 H, $C_\gamma Me$), 2.42 (s, 3 H, NMe), 2.40 (s, 3 H, $C_6H_4Me$), 2.30, 1.55 (s, 6 H, $Me_2C_6H_3$), 0.47 (s, 3 H, $C_\beta Me$) ppm. $^{13}C$ NMR{$^1H$} ($CDCl_3$): $\delta$ = 291.3 (μ-CO), 179.7 ($C_\alpha$), 155.5 ($C_\delta$), 143.1 (*ipso*-$Me_2C_6H_3$), 136.8–123.5 ($Me_2C_6H_3$ and $C_6H_4Me$), 104.5, 101.6 (C≡C), 96.6 ($C_\gamma$), 85.1, 83.5 (Cp), 52.3 ($C_\beta$), 39.5 (NMe), 22.2 ($C_\beta Me$), 21.5 ($C_6H_4Me$), 20.9 ($C_\gamma Me$), 18.2, 17.3 ($Me_2C_6H_3$) ppm. IR ($CH_2Cl_2$): $\tilde{\nu}$ = 2169 w (C≡C), 1753 vs. (μ-CO), 1511 w ($C_\alpha$O) $cm^{-1}$.

**3:** $C_{34}H_{33}Fe_2NO_2$ (599.32): calcd. C 68.14, H 5.55, N 2.34; found C 68.19, H 5.57, N 2.39. Yield: 68 mg, 76%. $^1H$ NMR ($CDCl_3$): $\delta$ = 7.71–6.82 (m, 8 H, $Me_2C_6H_3$ and $C_6H_5$), 4.56, 4.09 (s, 10 H, Cp), 2.76 (s, 3 H, $C_\gamma Me$), 2.43 (s, 3 H, NMe), 2.30, 1.56 (s, 6 H, $Me_2C_6H_3$), 0.48 (s, 3 H, $C_\beta Me$) ppm. $^{13}C$ NMR{$^1H$} ($CDCl_3$): $\delta$ = 291.0 (μ-CO), 179.7 ($C_\alpha$), 154.9 ($C_\delta$), 143.1 (*ipso*-$Me_2C_6H_3$), 135.4–126.6 ($Me_2C_6H_3$ and $C_6H_5$), 105.2, 101.4 (C≡C), 96.8 ($C_\gamma$), 85.1, 83.5 (Cp), 52.4 ($C_\beta$), 39.5 (NMe), 22.2 ($C_\beta Me$), 20.9 ($C_\gamma Me$), 18.2, 17.3 ($Me_2C_6H_3$) ppm. IR ($CH_2Cl_2$): $\tilde{\nu}$ = 2170 w (C≡C), 1751 vs. (μ-CO), 1511 w ($C_\alpha$O) $cm^{-1}$.

**4:** $C_{28}H_{29}Fe_2NO_2$ (523.23): calcd. C 64.27, H 5.59, N 2.68; found C 64.19, H 5.57, N 2.62. Yield: 56 mg, 71%. $^1H$ NMR ($CDCl_3$): $\delta$ = 7.55–6.77 (m, 3 H, $Me_2C_6H_3$), 4.48, 4.05 (s, 10 H, Cp), 3.15 (s, 1 H, C≡CH), 2.70 (s, 3 H, $C_\gamma Me$), 2.41 (s, 3 H, NMe), 2.28, 1.53 (s, 6 H, $Me_2C_6H_3$), 0.46 (s, 3 H, $C_\beta Me$) ppm. IR ($CH_2Cl_2$): $\tilde{\nu}$ = 1762 vs. (μ-CO) $cm^{-1}$.

**5:** $C_{32}H_{37}Fe_2NO_2$ (579.33): calcd. C 66.34, H 6.44, N 2.42; found C 66.30, H 6.52, N 2.36. Yield: 49 mg, 56%. $^1H$ NMR ($CDCl_3$): $\delta$ = 7.20–6.82 (m, 3 H, $Me_2C_6H_3$), 4.47, 4.02 (s, 10 H, Cp), 2.65 (s, 3 H, $C_\gamma Me$), 2.41 (s, 3 H, NMe), 2.33 (m, 2 H, C≡C$CH_2$), 2.29, 1.53 (s, 6 H, $Me_2C_6H_3$), 1.68 (m, 2 H, C≡C$CH_2CH_2$), 1.51–1.35

 © 2006 Wiley-VCH Verlag GmbH & Co. KGaA, Weinheim 

(m, 2 H, C≡CCH$_2$CH$_2$C*H*$_2$), 1.03 (t, 3 H, $^3J_{HH}$ = 7 Hz, C≡CCH$_2$CH$_2$CH$_2$C*H*$_3$), 0.44 (s, 3 H, C$_\beta$Me) ppm. $^{13}$C NMR{$^1$H} ($CDCl_3$): $\delta$ = 291.5 (μ-CO), 179.2 (C$_\alpha$), 155.8 (C$_\delta$), 143.1 (*ipso*-Me$_2$*C*$_6$H$_3$), 136.8–124.3 (Me$_2$*C*$_6$H$_3$ and *C*$_6$H$_4$Me), 110.5, 105.7 (C≡C), 96.5 (C$_\gamma$), 85.2, 83.5 (Cp), 52.4 (C$_\beta$), 39.5 (NMe), 32.5 (C≡C*C*H$_2$), 23.0 (C≡CCH$_2$*C*H$_2$), 22.2 (C$_\beta$*Me*), 20.8 (C$_\gamma$*Me*), 19.2 (C≡CCH$_2$CH$_2$*C*H$_2$), 18.3, 17.4 (*Me*$_2$C$_6$H$_3$), 14.2 (C≡CCH$_2$-CH$_2$CH$_2$*C*H$_3$) ppm. IR ($CH_2Cl_2$): $\tilde{\nu}$ = 2206 w (C≡C), 1754 vs. (μ-CO) cm$^{-1}$.

**6:** $C_{31}H_{37}Fe_2NO_2Si$ (595.41): calcd. C 62.53, H 6.26, N 2.35; found C 62.48, H 6.39, N 2.44. Yield: 63 mg, 71%. $^1$H NMR ($CDCl_3$): $\delta$ = 7.24–6.80 (m, 3 H, Me$_2$C$_6$*H*$_3$), 4.45, 4.02 (s, 10 H, Cp), 2.68 (s, 3 H, C$_\gamma$Me), 2.40 (s, 3 H, NMe), 2.28, 1.52 (s, 6 H, *Me*$_2$C$_6$H$_3$), 0.45 (s, 3 H, C$_\beta$Me), 0.39 (s, 9 H, SiMe$_3$) ppm. $^{13}$C NMR{$^1$H} ($CDCl_3$): $\delta$ = 291.0 (μ-CO), 179.5 (C$_\alpha$), 155.1 (C$_\delta$), 143.0 (*ipso*-Me$_2$*C*$_6$H$_3$), 135.4, 134.8, 128.5, 127.8, 127.3 (Me$_2$*C*$_6$H$_3$), 120.2, 104.3 (C≡C), 97.3 (C$_\gamma$), 85.4, 83.7 (Cp), 52.3 (C$_\beta$), 39.4 (NMe), 22.1 (C$_\beta$*Me*), 20.7 (C$_\gamma$*Me*), 18.2, 17.3 (*Me*$_2$C$_6$H$_3$), 1.21 (SiMe$_3$) ppm. IR ($CH_2Cl_2$): $\tilde{\nu}$ = 2101 w (C≡C), 1758 vs. (μ-CO), 1515 w (C$_\alpha$O) cm$^{-1}$.

**7:** $C_{31}H_{33}Fe_2NO_2$ (563.29): calcd. C 66.10, H 5.91, N 2.49; found C 65.99, H 5.94, N 2.50. Yield: 55 mg, 65%. $^1$H NMR ($CDCl_3$): $\delta$ = 7.23–6.80 (m, 3 H, Me$_2$C$_6$*H*$_3$), 5.47, 5.31 (m, 2 H, CH$_2$), 4.50, 4.05 (s, 10 H, Cp), 2.68 (s, 3 H, C$_\gamma$Me), 2.41 (s, 3 H, NMe), 2.28, 1.53 (s, 6 H, *Me*$_2$C$_6$H$_3$), 2.23 (s, 3 H, C≡CC*Me*), 0.45 (s, 3 H, C$_\beta$Me) ppm. $^{13}$C{$^1$H} NMR ($CDCl_3$): $\delta$ = 327.8 (μ-C), 253.9 (μ-CO), 208.1 (t-CO), 133.5–129.5 (Me$_2$*C*$_6$H$_3$), 91.4, 89.9 (Cp), 56.3 (NMe), 19.3, 18.2 (*Me*$_2$C$_6$H$_3$) ppm. IR ($CH_2Cl_2$): $\tilde{\nu}$ = 2160 w (C≡C), 1757 vs. (μ-CO), 1514 w (C$_\alpha$O) cm$^{-1}$.

**Synthesis of $^{13}$CO-Labelled 2:** The aminocarbyne complex [Fe$_2${μ-CN(Me)(Xyl)}(μ-CO)(CO)(Cl)(Cp)$_2$] (450 mg, 0.938 mmol), prepared by published method,[14] was dissolved in $CH_2Cl_2$ (10 mL). $^{13}$CO was bubbled through the solution, then $AgSO_3CF_3$ (289 mg, 1.12 mmol) was added. The mixture was stirred for 20 minutes, then it was filtered through an alumina column. Elution with methanol gave [Fe$_2${μ-CN(Me)(Xyl)}(μ-CO)($^{13}$CO)$_2$(Cp)$_2$][$SO_3CF_3$]. $^{13}$CO enrichment occurred exclusively at the terminally coordinated CO.

Conversion of $^{13}$CO labelled [Fe$_2${μ-CN(Me)(Xyl)}(μ-CO)($^{13}$CO)$_2$-(Cp)$_2$][$SO_3CF_3$] into $^{13}$C-labelled **2** was performed in further five steps, according to known procedures,[1,14] including the reaction described in this paper. The sequence included: [Fe$_2${μ-CN(Me)(Xyl)}(μ-$^{13}$CO)($^{13}$CO)(NCMe)(Cp)$_2$][$SO_3CF_3$], [Fe$_2${μ-CN(Me)(Xyl)}(μ-$^{13}$CO)($^{13}$CO)(Cl)(Cp)$_2$], $^{13}$CO-enriched **1** and $^{13}$C-labelled **2**. At each step the products were isolated and characterized to reveal the enhanced signals.

**$^{13}$C-Labelled 2:** $^1$H NMR ($CDCl_3$): $\delta$ = 7.61–6.81 (m, 7 H, Me$_2$C$_6$*H*$_3$ and C$_6$*H*$_4$Me), 4.56, 4.08 (s, 10 H, Cp), 2.76 (d, $^3J_{CH}$ = 3.66 Hz, 3 H, C$_\gamma$Me), 2.42 (s, 3 H, NMe), 2.40 (s, 3 H, C$_6$H$_4$*Me*), 2.30, 1.56 (s, 6 H, *Me*$_2$C$_6$H$_3$), 0.48 (s, 3 H, C$_\beta$Me) ppm. $^{13}$C{$^1$H} NMR ($CDCl_3$): $\delta$ = 291.6 (μ-CO), 179.7 (C$_\alpha$), 155.8 (C$_\delta$), 143.1 (*ipso*-Me$_2$*C*$_6$H$_3$), 136.8–123.5 (Me$_2$*C*$_6$H$_3$ and *C*$_6$H$_4$Me), 104.5, 101.6 (C≡C), 96.1 (d, $^1J_{CC}$ = 50.7 Hz, C$_\gamma$), 85.4, 82.9 (Cp), 52.4 (d, $^2J_{CC}$ = 11.9 Hz, C$_\beta$), 39.7 (NMe), 22.2 (C$_\beta$*Me*), 21.4 (C$_6$H$_4$*Me*), 20.9 (d, $^2J_{CC}$ = 4.5 Hz, C$_\gamma$*Me*), 18.5, 17.3 (*Me*$_2$C$_6$H$_3$) ppm. IR ($CH_2Cl_2$): $\tilde{\nu}$ = 2169 w (C≡C), 1750 vs. (μ-CO), 1717 s (μ-$^{13}$CO), 1511 w (C$_\alpha$O) cm$^{-1}$.

**X-ray Crystallographic Study:** Crystal data and collection details for **2** are reported in Table 2. The diffraction experiments were carried out with a Bruker SMART 2000 diffractometer equipped with a CCD detector using Mo-$K_\alpha$ radiation. Data were corrected for Lorentz polarization and absorption effects (empirical absorption correction SADABS).[15] Structures were solved by direct methods and refined by full-matrix least-squares based on all data using $F^2$.[16] Hydrogen atoms were fixed at calculated positions and refined by a riding model. All non-hydrogen atoms were refined with anisotropic displacement parameters.

Table 2. Crystal data and experimental details for **2**.

| Complex | **2** |
|---|---|
| Formula | $C_{35}H_{35}Fe_2NO_2$ |
| Mol. mass | 613.34 |
| $T$ [K] | 293(2) |
| $\lambda$ [Å] | 0.71073 |
| Crystal system | triclinic |
| Space group | $P\bar{1}$ |
| $a$ [Å] | 9.5614(6) |
| $b$ [Å] | 10.2070(6) |
| $c$ [Å] | 16.7137(11) |
| $\alpha$ [°] | 104.786(2) |
| $\beta$ [°] | 98.907(2) |
| $\gamma$ [°] | 101.339(2) |
| Cell volume [Å]$^3$ | 1509.76(16) |
| $Z$ | 2 |
| $D_c$ [g·cm$^{-3}$] | 1.349 |
| $\mu$ [mm$^{-1}$] | 0.992 |
| $F$(000) | 640 |
| Crystal size, mm | 0.26 × 0.23 × 0.13 |
| $\theta$ limits [°] | 1.29–26.37 |
| Reflections collected | 15228 |
| Independent reflections | 6171 ($R_{int}$ = 0.0665) |
| Data / restraints / parameters | 6171 / 0 / 367 |
| Goodness on fit on $F^2$ | 0.900 |
| $R_1$ [$I > 2\sigma(I)$] | 0.0578 |
| $wR_2$ (all data) | 0.1531 |
| Largest diff. peak and hole, e·Å$^{-3}$ | 0.733 / –0.618 |

CCDC-276446 contains the supplementary crystallographic data for this paper. These data can be obtained free of charge from The Cambridge Crystallographic Data Centre via www.ccdc.cam.ac.uk/data_request/cif.

## Acknowledgments

We thank the Ministero dell'Università e della Ricerca Scientifica e Tecnologica (M.I.U.R.) (project: "New strategies for the control of reactions: interactions of molecular fragments with metallic sites in unconventional species") and the University of Bologna for financial support.

[1] a) V. G. Albano, L. Busetto, F. Marchetti, M. Monari, S. Zacchini, V. Zanotti, *Organometallics* **2003**, *22*, 1326–1331; b) V. G. Albano, L. Busetto, F. Marchetti, M. Monari, S. Zacchini, V. Zanotti, *J. Organomet. Chem.* **2004**, *689*, 528–538.
[2] a) V. G. Albano, L. Busetto, F. Marchetti, M. Monari, S. Zacchini, V. Zanotti, *Organometallics* **2004**, *23*, 3348–3353; b) V. G. Albano, L. Busetto, F. Marchetti, M. Monari, S. Zacchini, V. Zanotti, *J. Organomet. Chem.* **2005**, *690*, 837–846.
[3] R. E. Colborn, A. F. Dyke, B. P. Gracey, S. A. R. Knox, K. A. Macpherson, K. A. Mead, A. G. Orpen, *J. Chem. Soc., Dalton Trans.* **1990**, 761–771.
[4] S. Doherty, M. R. J. Elsegood, W. Clegg, M. Waugh, *Organometallics* **1996**, *15*, 2688–2691.
[5] G. Hogarth, M. H. Lavender, *J. Chem. Soc., Dalton Trans.* **1994**, 3389–3396.
[6] V. G. Albano, L. Busetto, C. Camiletti, C. Castellari, M. Monari, V. Zanotti, *J. Chem. Soc., Dalton Trans.* **1997**, 4671–4676.

 © 2006 Wiley-VCH Verlag GmbH & Co. KGaA, Weinheim 

[7] S. Bordoni, L. Busetto, C. Camiletti, V. Zanotti, V. G. Albano, M. Monari, F. Prestopino, *Organometallics* **1997**, *16*, 1224–1232.
[8] a) P. M. Maitlis, *J. Organomet. Chem.* **2004**, *689*, 4366–4374; b) M. L. Turner, N. Marsih, B. E. Mann, R. Quyoum, H. C. Long, P. M. Maitlis, *J. Am. Chem. Soc.* **2002**, *124*, 10456–10472; c) M. J. Overett, R. O. Hill, J. R. Moss, *Coord. Chem. Rev.* **2000**, *206–207*, 581–605; d) M. W. Roberts, *Chem. Soc. Rev.* **1977**, *6*, 373–391.
[9] a) D. F. Shriver, M. J. Sailor, *Acc. Chem. Res.* **1988**, *21*, 374–379; b) C. P. Horwitz, D. F. Shriver, *J. Am. Chem. Soc.* **1985**, *107*, 8147–8153; c) C. P. Horwitz, D. F. Shriver, *Adv. Organomet. Chem.* **1984**, *23*, 219–305; d) E. L. Muetterties, J. Stein, *Chem. Rev.* **1979**, *79*, 479–490; e) B. E. Kahn, R. D. Rieke, *Chem. Rev.* **1988**, *88*, 733–745.
[10] a) D. R. Neithamer, R. E. LaPointe, T. A. Wheeler, D. S. Richeson, G. D. Van Duyne, P. T. Wolczanski, *J. Am. Chem. Soc.* **1989**, *111*, 9056–9072; b) F. Calderazzo, U. Englert, A. Guarini, F. Marchetti, G. Pampaloni, A. Segre, *Angew. Chem. Int. Ed. Engl.* **1994**, *33*, 1188–1189; c) R. L. Miller, R. Toreki, R. E. LaPointe, P. T. Wolczanski, G. D. Van Duyne, C. Roe, *J. Am. Chem. Soc.* **1993**, *115*, 5570–5588.
[11] a) R. L. Miller, P. T. Wolczanski, *J. Am. Chem. Soc.* **1993**, *115*, 10422–10423; b) M. H. Chisholm, C. E. Hammond, V. J. Johnston, W. E. Streib, J. C. Huffman, *J. Am. Chem. Soc.* **1992**, *114*, 7056–7065.
[12] W. Wilker, D. Leibfritz, R. Kerssebaum, W. Beimel, *Magn. Reson. Chem.* **1993**, *31*, 287–292.
[13] K. Stott, J. Stonehouse, J. Keeler, T. L. Hwang, A. J. Shaka, *J. Am. Chem. Soc.* **1995**, *117*, 4199–4200.
[14] V. G. Albano, L. Busetto, M. Monari, V. Zanotti, *J. Organomet. Chem.* **2000**, *606*, 163.
[15] G. M. Sheldrick, *SADABS*, Program for empirical absorption correction, University of Göttingen, Germany, **1996**.
[16] G. M. Sheldrick, *SHELX97*, Program for crystal structure determination, University of Göttingen, Germany, **1997**.

Received: October 19, 2005
Published Online: December 1, 2005

 © 2006 Wiley-VCH Verlag GmbH & Co. KGaA, Weinheim 

DOI: 10.1002/ejic.200500693

# Spectroscopic Comparison of Dinuclear $Ti^{+}$ and $Ti^{2+}$ μ-η¹:η¹ Dinitrogen Complexes with Cp*/Pentafulvene and Amine/Amide Ligation: Moderate versus Strong Activation of $N_2$

**Felix Studt,[a] Nicolai Lehnert,[a] Beatrix E. Wiesler,[a][‡] Axel Scherer,[b] Rüdiger Beckhaus,*[b] and Felix Tuczek*[a]**

**Keywords:** Metallocenes / Nitrogen fixation / Titanium / Raman spectroscopy / Density functional calculations

The two dinuclear, end-on dinitrogen-bridged titanium complexes with cp*/pentafulvene ligation, [{($\eta^5$-$C_5Me_5$)Ti($\eta^6$-$C_5H_4CR_2$)}$_2$(μ-$\eta^1$:$\eta^1$-$N_2$)], R = *p*-tolyl (**1**) and >$CR_2$ = adamantylidene (**2**), are compared to an analogous titanium dinitrogen complex with a mixed amine/amide/chloride ligand set, [{($Me_3Si)_2$NTiCl(TMEDA)}$_2$(μ-$\eta^1$:$\eta^1$-$N_2$)] (**3**; TMEDA = tetramethylethylenediamine). The N–N stretching vibrations of complexes **1** and **2** are observed at 1749 and 1755 $cm^{-1}$, respectively, indicative of a moderate activation of the dinitrogen ligand. In contrast, the N–N stretch of **3** is located at 1284 $cm^{-1}$, reflecting a much more highly activated $N_2$ ligand. These findings are in qualitative agreement with N–N bond lengths that have been observed experimentally. DFT calculations reveal that the major difference in the electronic structures of **1**, **2**, and **3** is the fact that only one of the $N_2$ π* orbitals is (doubly) occupied in the case of **1** and **2**, whereas both π* orbitals are (doubly) occupied in the case of **3**. The reason for this finding is that in **1** and **2** two of the three electrons of each $Ti^{+}$ are involved in back-bonding interactions with the terminal fulvene ligands, whereas no such interactions exist between the $Ti^{2+}$ centers of **3** and its terminal set of donor ligands.
(© Wiley-VCH Verlag GmbH & Co. KGaA, 69451 Weinheim, Germany, 2006)

## Introduction

The bonding and activation of $N_2$ by early transition-metal complexes is of continued interest.[1–4] In titanium systems dinitrogen is usually coordinated in an end-on bridging geometry.[5] The activation of the $N_2$ ligand can generally be determined by considering N–N bond lengths obtained from X-ray diffraction data and N–N stretching frequencies obtained from vibrational spectroscopy. These data allow titanium dinitrogen compounds to be divided into moderately and strongly activated species.[6] Moderately activated dinitrogen complexes are generally found for titanocene-based systems with N–N bond lengths in the range of 1.15–1.20 Å.[7–12] Strong activation, on the other hand, is observed for titanium complexes with ligand sets that are different from cyclopentadienyl, exhibiting N–N bond lengths of 1.25–1.30 Å.[13–15] A collection of N–N bond lengths of different dinitrogen complexes is given in Table 1. The two complexes with cp*/pentafulvene ligation, [{($\eta^5$-$C_5Me_5$)Ti($\eta^6$-$C_5H_4CR_2$)}$_2$(μ-$\eta^1$:$\eta^1$-$N_2$)], R = *p*-tolyl (**1**) and >$CR_2$ = adamantylidene (**2**), both have N–N bond lengths of 1.160 Å and thus can be considered to be moderately activated.[7] On the other hand, the complex [{($Me_3Si)_2$-NTiCl(TMEDA)}$_2$(μ-$\eta^1$:$\eta^1$-$N_2$)] (**3**; TMEDA = tetramethylethylenediamine) that exhibits a mixed amine/amide/chloride set of coligands has an N–N bond length of 1.29 Å and therefore activates $N_2$ to a higher degree (cf. Scheme 1).[13] This would indicate that the activation of $N_2$ is higher in compound **3**, formally a $Ti^{2+}$–$Ti^{2+}$ species, than in compounds **1** and **2**, formally $Ti^{+}$–$Ti^{+}$ complexes. At first sight this observation appears to be contradictory.

Table 1. Comparison of N–N bond lengths of different dinitrogen complexes.

| Compound | N–N bond lengths [Å] | Ref. |
|---|---|---|
| **1** | 1.160(3) | [7] |
| **2** | 1.160(5) | [7] |
| [{($\eta^5$-$C_5Me_5)_2$Ti}$_2$(μ-$\eta^1$:$\eta^1$-$N_2$)] | 1.165(14) | [8] |
| [{($\eta^5$-$C_5Me_4H)_2$Ti}$_2$(μ-$\eta^1$:$\eta^1$-$N_2$)] | 1.170(4) | [9] |
| [{($\eta^5$-$C_5H_5)_2$Ti($PMe_3$)}$_2$(μ-$\eta^1$:$\eta^1$-$N_2$)] | 1.191(8) | [10] |
| [{($\eta^5$-$C_5H_5)_2$Ti(*p*-tolyl)}$_2$(μ-$\eta^1$:$\eta^1$-$N_2$)] | 1.162(12) | [11] |
| [{[$\eta^5$-$C_5H_3(SiMe_3)_2]_2$Ti}$_2$(μ-$\eta^1$:$\eta^1$-$N_2$)] | 1.164(5) | [12] |
| **3** | 1.289(9) | [13] |
| [{($Me_3Si)_2$NTiCl($py)_2$}$_2$(μ-$\eta^1$:$\eta^1$-$N_2$)] | 1.263(7) | [14] |
| [{[$(Me_2N)$C(N*i*Pr)$_2]_2$Ti}$_2$(μ-$\eta^1$:$\eta^1$-$N_2$)] | 1.280(8) | [15] |

In order to address the above statement we investigated compounds **1**, **2**, and **3** with resonance Raman spec-

[a] Institut für Anorganische Chemie, Christian-Albrechts-Universität Kiel,
24098 Kiel, Germany
E-mail: ftuczek@ac.uni-kiel.de
[b] Institut für Reine und Angewandte Chemie, Fakultät für Mathematik und Naturwissenschaften, Carl von Ossietzky Universität Oldenburg,
Postfach 2503, 26111 Oldenburg, Germany
E-mail: ruediger.beckhaus@uni-oldenburg.de
[‡] Present address: Merck KGaA, Darmstadt

 © 2006 Wiley-VCH Verlag GmbH & Co. KgaA, Weinheim 

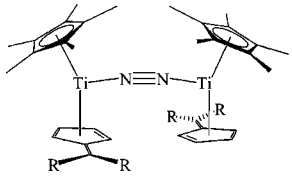

R = *p*-Tol (1)

>$CR_2$ = adamantylidene (2)

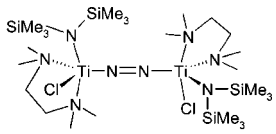

(3)

Scheme 1.

troscopy. The vibrational analysis was assisted by DFT calculations performed on structures **I** and **III**, which are models of complexes **1/2** and **3**, respectively. The UV/Vis spectra of **1/2** and **3** were interpreted on the basis of MO schemes of models **I** and **III**. The electronic-structural features leading to the observed differences in $N_2$ activation were identified through this combined spectroscopic-theoretical approach. The general implications of this result are discussed below.

## Results and Analysis

### Vibrational Spectra and Analysis

Solid-state resonance Raman spectra of complexes **1**–**3**, recorded with an excitation wavelength of 514.5 nm, are shown in Figure 1. The most intense peak in the Raman spectrum of **1** is located at 1749 $cm^{-1}$. This feature is assigned to the N–N stretching mode of the Ti–$N_2$–Ti unit on the basis of its high intensity and energetic position. The first and second overtones of this mode are found at 3475 and 5173 $cm^{-1}$, respectively. In the Raman spectrum of **2** the N–N stretching mode is identified at 1755 $cm^{-1}$ by the same arguments. The overtones are located at 3490 and 5185 $cm^{-1}$. The most prominent feature in the Raman spectrum of **3** is observed at 1284 $cm^{-1}$. Again, this peak is assigned to the N–N stretching frequency of the Ti–$N_2$–Ti unit because of its high intensity and energetic position.

DFT calculations were performed for structures **I** and **III**. In structure **I** the ligands of **1** and **2** are replaced by

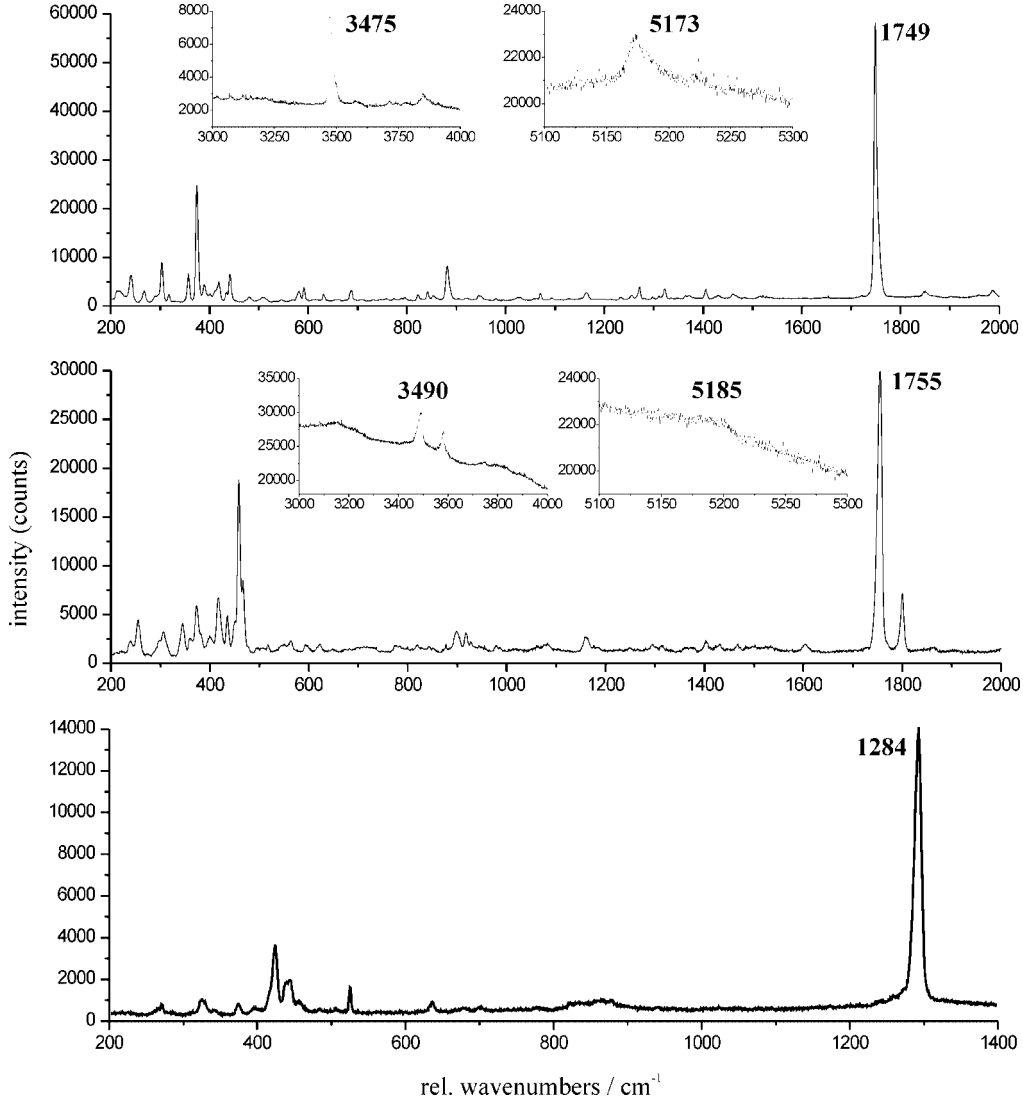


Figure 1. Top: Raman spectrum of **1**. Middle: Raman spectrum of **2**. Bottom: Raman spectrum of **3**. All Raman spectra were recorded with an excitation wavelength of 514.5 nm.

 © 2006 Wiley-VCH Verlag GmbH & Co. KGaA, Weinheim 

unsubstituted cyclopentadienyl and fulvene groups, thus providing a model system for both complexes **1** and **2**. Note, however, that in model **I** the dihedral angle between the Ct*–Ti vectors of the two halves of the dimers is approximately zero (Ct* is the center of the cp* ligand). This reproduces the structure of complex **1** but not that of complex **2**, which exhibits a twisted configuration (dihedral angles between the Ct*–Ti vectors are 19.1° and 20.0°, respectively, for the two independent molecules in the asymmetric unit). Model **III** has been simplified with respect to complex **3** by approximating the TMEDA and $(Me_3Si)_2N$ ligands through coordinated $NH_3$ and $NH_2$ groups, respectively. Structural parameters resulting from the DFT geometry optimizations are compared with the experimental values in Table 2; a comparison between the experimentally determined frequencies (see above) and the values derived from DFT (B3LYP) is given in Table 3. The calculated frequencies qualitatively reproduce the experimentally observed trend. The N–N stretching frequency of **I** is calculated at 1806 $cm^{-1}$, in good agreement with the experimentally determined value of 1749 $cm^{-1}$. The N–N stretching mode of the model complex **III** is theoretically predicted to be at a much lower energy (1371 $cm^{-1}$), in fair agreement with the corresponding peak in the Raman spectrum of **3** (1284 $cm^{-1}$). In this case the larger deviation from the experimental data probably results from the greater simplification of the terminal ligands employed in the calculation.

Table 2. Comparison of structural parameters of **1**, **2**, and **I**.

| Complex | N–N | Ti–N | Ti–Ct* | Ti–$Ct^{Fv}$ | Ti–N–N | $\theta$ |
|---|---|---|---|---|---|---|
| **1** | 1.160 | 1.999 | 2.056 | 1.965 | 170.0 | 28.3 |
| **2** | 1.160 | 2.008 | 2.064 | 1.986 | 169.8 | 31.6 |
| **I** | 1.204 | 1.916 | 2.087 | 2.043 | 176.9 | 35.7 |

Table 3. Comparison of the observed and calculated frequencies of complexes **1**–**3** with model systems **I** and **III**.

| Mode | Experimental | | | B3LYP | |
|---|---|---|---|---|---|
| | **1** | **2** | **3** | **I** | **III** |
| $\nu_{NN}$ | 1749 | 1755 | 1284 | 1806 | 1371 |
| 2 $\nu_{NN}$ | 3475 | 3490 | – | – | – |
| 3 $\nu_{NN}$ | 5173 | 5185 | – | – | – |

### Electronic Structure

An understanding of the electronic structure of complexes **1/2** and complex **3** is achieved on the basis of the MO schemes of the corresponding models **I** and **III**, respectively (Figure 2). Model **I** is oriented such that the *x* axis is directed along the N–N vector and the *y* axis along the fulvene/cyclopentadienyl ligands. Figure 2 (left) shows contour plots of important molecular orbitals of **I**. The HOMO of **I** represents a bonding combination between the $\pi_z$* orbital of dinitrogen and the metal $d_{xz}$ orbitals, forming a metal–dinitrogen π bond; this orbital has nearly equal contributions from the nitrogen p orbitals and the d functions of titanium. The LUMO of **I** is the bonding combination of the $N_2$ $\pi_y$* orbital and the metal $d_{xy}$ functions. The corresponding orbital has 19% metal and 40% nitrogen character. The LUMO+1 of **I** is an antibonding combination of the metal $d_{xz}$ orbitals with the dinitrogen $\pi_z$ orbital having 6% nitrogen character. As only one π* orbital of the dinitrogen ligand is occupied, the $N_2$ ligand has been formally reduced by the $Ti^{+}$ centers of **I** to an $N_2^{2-}$ oxidation state. The remaining electrons of the two titanium atoms are located in the two sets of $d_{z^2}$ orbitals (in-phase and out-of-phase combinations) both of which interact in a bonding fashion with fulvene π* orbitals to form two $d_{z^2}$_Fv orbitals. Both MOs have 61% fulvene character, indicative of a significant back-bonding from the metals to the fulvene ligands.

Model **III** is also oriented such that the *x* axis is along the N–N vector; the *y* axis lies in the plane of the paper, between the amino and amido ligands on the one side and the amido and chloro ligands on the other side of the dinuclear complex. The π* orbitals of the dinitrogen ligand ($\pi^*_z$ and $\pi^*_y$) form the two dinitrogen–metal π bonding combinations $\pi^*_z$_$d_{xz}$ and $\pi^*_y$_$d_{xy}$, respectively, which have nearly equal charge contributions from dinitrogen and metal d functions (Figure 2, right). Both of these orbitals are now occupied, corresponding to the HOMO–1 and the HOMO of **III**, respectively. Model **III** therefore has two metal–dinitrogen π bonds, and the dinitrogen ligand of **3** is formally reduced by its two $Ti^{2+}$ centers to a (–4) charge state. In Figure 2 the orbitals of **I** and **III** are arranged in a way that clarifies the relationship between the electronic structures of **1/2** and **3**. Evidently, the dinitrogen parts of the frontier orbitals are very similar; the major difference between the two systems lies in the fact that both π* orbitals of dinitrogen are occupied for **3**, whereas for **1** and **2** one dinitrogen π* orbital (the HOMO) is occupied and the other (the LUMO) is empty.

Table 4 summarizes the atomic charges obtained for models **I** and **III** by natural population analysis (NPA). As already inferred from the preceding orbital analysis, a significant amount of electronic charge is transferred from the titanium centers of both **I** and **III** to the bridging dinitrogen ligand. However, the negative charge on this ligand is much larger for **III** (–0.80) than for **I** (–0.24), in qualitative agreement with the fact that both π* orbitals of $N_2$ are occupied in **III** whereas only one π* orbital is occupied in **I**. As the $\pi^*$_$d_\pi$ orbitals of **I** and **III** have roughly equal contributions from the metal d orbitals and the dinitrogen π* functions, the formal charges of –2 and –4 are approximately halved, leading to approximate descriptions of the $N_2$ ligand as $N_2^{1-}$ in **1/2** and $N_2^{2-}$ in **3**. The actual charges determined by NPA (–0.24 for **I** and –0.80 for **III**; vide supra) reflect a further charge donation from lower-energy π and σ bonding orbitals of $N_2$ back into the unoccupied metal d orbitals. The titanium atoms, in turn, are calculated to have charges of +0.34 for model **I** and +1.00 for model **III**, in qualitative agreement with the different formal oxidation states obtained after interaction with $N_2$ ($Ti^{2+}$ for **I** and

 © 2006 Wiley-VCH Verlag GmbH & Co. KGaA, Weinheim 

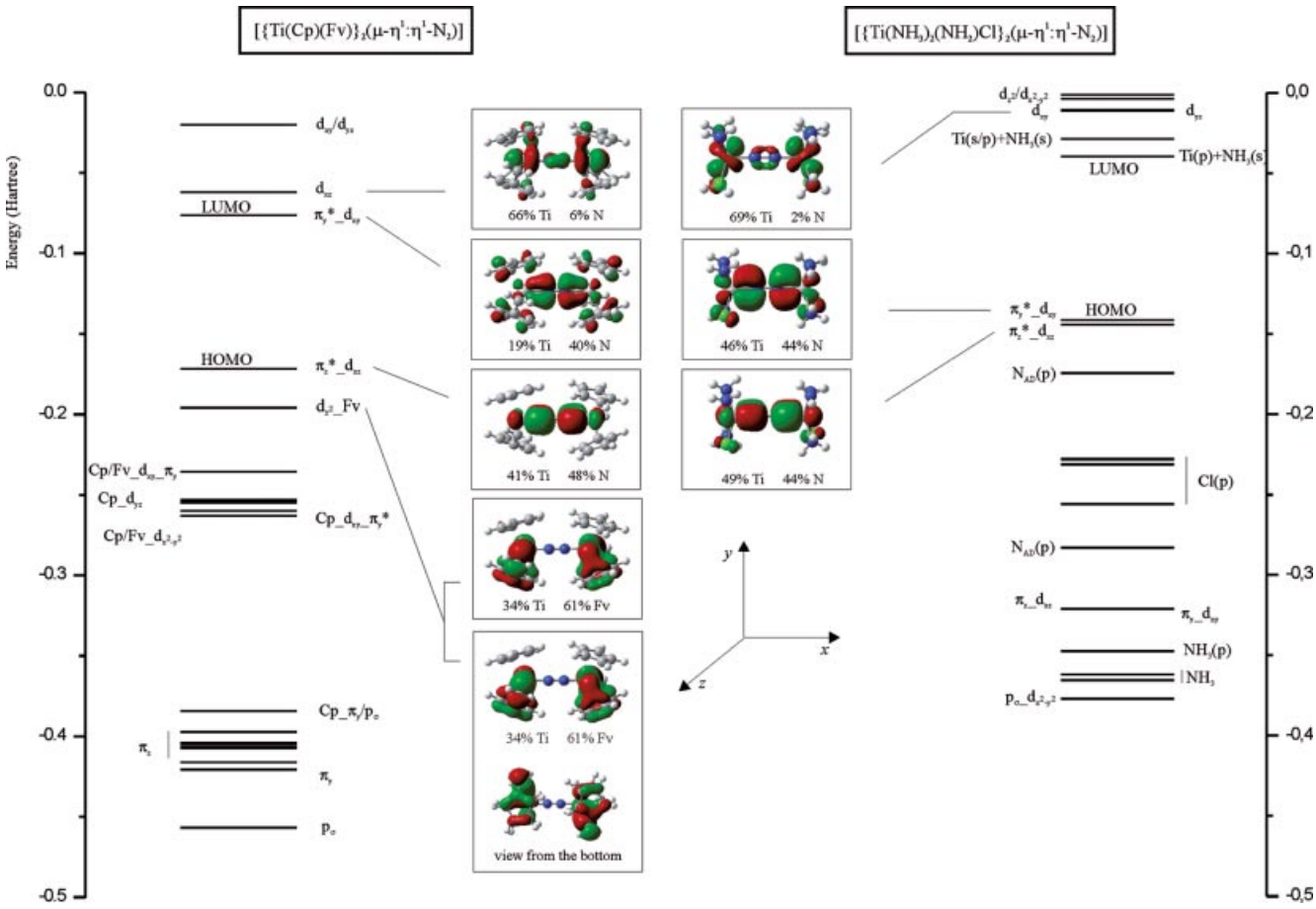


Figure 2. MO diagram of models **I** and **III** together with contour plots of important molecular orbitals of **I** and **III**.

$Ti^{4+}$ for **III**). The actual charges on the metal atoms are further influenced by donor/acceptor interactions with the terminal ligands. It can be inferred from Table 4 that the cp* ligands of **I** donate 0.93 charge units to the metal centers (resulting charge –0.07), whereas the (formally neutral) fulvene ligands act as charge acceptors (resulting charge –0.16).

Table 4. NPA charges of model systems **I** and **III**.

| Complex | Atom | | | | | | |
|---|---|---|---|---|---|---|---|
| | Ti[a] | N[a] | Cp[b] | Fu[b] | $NH_3$[b] | $NH_2$[b] | Cl[a] |
| **I** | 0.34 | –0.12 | –0.07 | –0.16 | – | – | – |
| **III** | 1.00 | –0.40 | – | – | 0.15 | –0.39 | –0.51 |

[a] Charge for each atom. [b] Charge for the corresponding ligand.

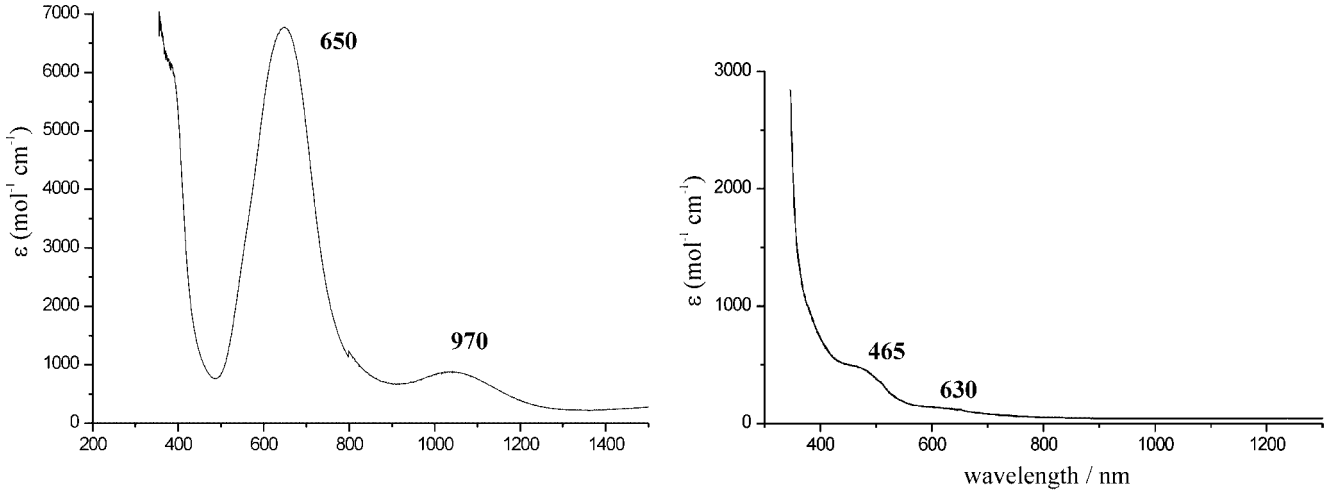


Figure 3. UV/Vis spectrum of **2** (left) and **3** (right).

 © 2006 Wiley-VCH Verlag GmbH & Co. KGaA, Weinheim 

### UV/Vis Spectroscopy

The UV/Vis spectra of **1** and **2** are very similar. The absorption spectrum of **2** (Figure 3, left) exhibits two bands at 970 ($\varepsilon$ = 900 $M^{-1}cm^{-1}$) and 650 nm ($\varepsilon$ = 6700 $M^{-1}cm^{-1}$). As there is no band at lower energies, the 970-nm band is assigned to the lowest energy transition of **2**, which corresponds to the HOMO–LUMO transition of model **I**. This transition is intrinsically of low intensity, as it involves two $\pi^*_d_\pi$ orbitals that are perpendicular to each other. The intense band at 650 nm in the UV/Vis spectrum of **2** is assigned to the symmetry- and orbital-allowed $\pi\rightarrow\pi^*$ transition from the $\pi_z^*_d_{xz}$ orbital (HOMO) to the $d_{xz}_\pi_z$ orbital (LUMO+1) of **I**. The UV/Vis spectrum of complex **3** exhibits two weak absorptions at 465 ($\varepsilon$ = 500 $M^{-1}cm^{-1}$) and 630 nm ($\varepsilon$ = 100 $M^{-1}cm^{-1}$), which are assigned to orbital-forbidden ($\pi\rightarrow\sigma$) transitions from the $\pi_y^*_d_{xy}$ and $\pi_z^*_d_{xz}$ orbitals (HOMO and HOMO–1) to unoccupied orbitals at the Ti centers. The absorption edge at 380 nm probably results from symmetry- and orbital-allowed $\pi\rightarrow\pi^*$ transitions from the central dinitrogen ligand to the Ti d functions which are therefore at a higher energy than the $\pi\rightarrow\pi^*$ transitions of **1** and **2**.

## Discussion

In the preceding section resonance Raman spectra of the moderately activated dinitrogen complexes **1** and **2** were measured and compared with the Raman spectrum of the strongly activated complex **3**. In order to theoretically determine N–N stretching frequencies and evaluate the electronic structure, DFT calculations were performed on structurally simplified models. The UV/Vis spectra of **1/2** and **3** have been interpreted on the basis of the corresponding MO schemes. The N–N stretching frequencies of complexes **1** and **2** were assigned to peaks at 1749 and 1755 $cm^{-1}$, respectively, which is supported by a DFT frequency calculation predicting the position of this mode at 1806 $cm^{-1}$. The N–N stretching mode of the strongly activated dinitrogen complex **3**, on the other hand, was identified with a peak at 1284 $cm^{-1}$ in the Raman spectrum, which is supported by a DFT prediction of 1371 $cm^{-1}$ for this mode. The difference in N–N stretching frequency between complexes **1/2** and **3** is thus large (ca. 500 $cm^{-1}$), which is in agreement with the markedly different N–N bond lengths of these compounds (1.16 Å for **1/2** and 1.29 Å for **3**). The reduction of the N–N stretching frequency of free $N_2$ at 2231 $cm^{-1}$[16] to the value observed for complexes **1** and **2** (ca. 1750 $cm^{-1}$) implies a slight elongation of the N–N bond in these compounds. The N–N stretching frequency of 1284 $cm^{-1}$ found for **3**, on the other hand, corresponds to a significant decrease of the N–N bond order which is comparable to that of a related end-on dinitrogen-bridged zirconium complex for which an N–N stretching frequency of 1211 $cm^{-1}$ and an N–N bond length of 1.30 Å have been determined.[17]

The electronic structure of strongly activated end-on $N_2$ bridged complexes was described earlier in terms of interactions of dinitrogen π and π* orbitals with metal $d_\pi$ functions. It was shown that the metal centers primarily interact with the empty π* orbitals of the $N_2$ to form two metal–dinitrogen π bonding MOs, leading to a significant charge transfer from the metals to this ligand.[18–20] This would agree with the electronic structure of **3** where both π* orbitals of the dinitrogen ligand are occupied (HOMO and HOMO–1), explaining the high degree of activation found for this complex. The electronic structures of the moderately activated complexes **1** and **2** differ from this scheme since only one π* orbital of the dinitrogen ligand is doubly occupied. The two remaining electrons of each titanium center are involved in strong back-bonding interactions with the fulvene ligands and are nonbonding with respect to the bridging dinitrogen ligand. The second π* orbital of the dinitrogen ligand thus remains unoccupied, forming the LUMO of complexes **1** and **2**.

Further information on the electronic structures of **1**–**3** can be inferred from electronic absorption spectroscopy. Inspection of the UV/Vis spectra of **2** leads to the assignment of the 970-nm band to the lowest energy transition of **I**, the HOMO–LUMO transition. On the basis of overlap considerations the intensity of this absorption band should be weak, which is in agreement with the experimental data. The 650-nm transition, on the other hand, is assigned to an electric-dipole-allowed transition from the HOMO to the LUMO+1. In complex **3** the electric-dipole-allowed transitions involving the dinitrogen ligand are located at higher energies. The MO schemes of **I** and **III** further explain the experimental findings that **1**, **2** and **3** are diamagnetic. In model **I**, which exhibits a dihedral angle of about 0° between the Ct*–Ti vectors, the two electrons in the Ti $d_{xz}$ orbitals are strongly coupled via the dinitrogen $\pi^*_z$ orbital. This is an accurate picture for complex **1** but has to be slightly modified for complex **2**, which exhibits a twisted configuration (dihedral angle between the neighboring Ct*–Ti bonds = 19.1° and 20.0° for the two independent molecules in the asymmetric unit). This reduces the interaction between the two unpaired electrons in the $d_{xz}$ orbitals via the dinitrogen $\pi^*_z$ orbital, leading in the extreme case, i.e. for a dihedral angle of 90°, to a ferromagnetic coupling ($S$ = 1 ground state).[21] Nevertheless, compound **2** is found to be diamagnetic, i.e. the same as compound **1**, demonstrating that the coupling is predominantly antiferromagnetic (ground state $S$ = 0).

To conclude, the activation of the dinitrogen ligand in **3** is found to be much larger than in **1** and **2**, in contrast to what is expected on the basis of formal oxidation states ($Ti^{+}$–$Ti^{+}$ for **1** and **2** vs. $Ti^{2+}$–$Ti^{2+}$ for **3**). It is shown in this paper that this discrepancy can be attributed to the donor/acceptor properties of the set of coligands: whereas **3** has a set of purely electron-donating ligands, strong back-bonding interactions exist between the titanium d orbitals and the fulvene π* orbitals in **1** and **2** which take up four metal d-electrons, preventing them from interacting with the bridging $N_2$ ligand. This exemplifies once again that the

 © 2006 Wiley-VCH Verlag GmbH & Co. KGaA, Weinheim 

actual degree of dinitrogen activation in transition-metal complexes depends equally on the set of ancillary ligands and the nature and oxidation state of the metal centers.[22]

## Experimental Section

**Synthesis of 1, 2, and 3:** Compounds **1**,[7] **2**,[7] and **3**[13] were synthesized by literature methods.

**Resonance Raman Spectroscopy:** Resonance Raman spectra of **1** and **2** were measured with a Dilor XY Raman spectrograph with triple monochromator and CCD detector. An Ar/Kr mixed-gas laser with a maximum power of 5 W was used for excitation. The spectra were recorded with an excitation wavelength of 514.5 nm. The spectra were measured on KBr pellets cooled to 10 K with a helium cryostat. The spectral bandpass was set to 2 $cm^{-1}$.

Resonance Raman spectra of **3** were measured on a setup involving the following components: Spectra Physics 2020 5 W $Ar^+$-laser; SPEX 1404 0.85 double monochromator equipped with a CCD camera (PI Instruments, 1024 × 256 pixels EEV chip) and a Peltier cooled RCA 31034 detector connected to a Stanford Research SR 400 photon counter allowing spectra to be recorded in spectrograph or scanning modes; liquid helium cryostat (Cryovac) for measurements from 4.2 to 300 K. The spectra were recorded at 20 K with an excitation wavelength of 514.5 nm and with the spectral bandpass set to 4.5 $cm^{-1}$.

**UV/Vis Spectroscopy:** Optical absorption spectra of **2** were obtained from the neat compound pressed between two sapphire plates. The spectra were recorded at 10 K on a Varian Cary 5 UV/Vis/NIR spectrometer. Extinction coefficients were determined by comparison with UV/Vis spectra of **2** in solution. Optical absorption spectra of **3** were obtained from a toluene solution of **3** in an ESR tube. The spectra were recorded with a Bruins Omega10 Spectrophotometer.

**Density Functional Theory Calculations:** Spin-restricted DFT calculations using Becke′s three-parameter hybrid functional with the correlation functional of Lee, Yang, and Parr (B3LYP)[23–25] were performed for the singlet ground state of model complexes **I** and **III**. Model **I** was optimized in $C_1$ symmetry. For DFT frequency calculations, model **III** was also optimized in $C_1$ symmetry, whereas the structure of model **III** used for the single point calculation was derived from the X-ray structure. The LanL2DZ basis set, which applies Dunning/Huzinaga full double-zeta (D95) basis functions[26] on first-row atoms and Los Alamos effective core potentials plus DZ functions on all other atoms, [27,28] was used for the calculations. Convergence was reached when the relative change in the density matrix between subsequent iterations was less than $1 \times 10^{-5}$ for single points and $1 \times 10^{-8}$ for optimizations. Charges were analyzed by using the natural bond orbital (NBO) formalism.[29–32] All of the computational procedures were used as implemented in the G98 package.[33] Wave functions were plotted with the visualization program Gaussview 2.1.

## Acknowledgments

F. T. thanks DFG Tu58/12-1 and Fonds der Chemischen Industrie for funding this research; R. B. thanks the Fonds der Chemischen Industrie for a scholarship kindly granted to A. S.

[1] M. D. Fryzuk, S. A. Johnson, *Coord. Chem. Rev.* **2000**, *200*, 379.
[2] B. A. MacKay, M. D. Fryzuk, *Chem. Rev.* **2004**, *104*, 385.
[3] S. Gambarotta, J. Scott, *Angew. Chem.* **2004**, *116*, 5412; *Angew. Chem. Int. Ed.* **2004**, *43*, 5293.
[4] C. M. Kozak, P. Mountford, *Angew. Chem.* **2004**, *116*, 1206; *Angew. Chem. Int. Ed.* **2004**, *43*, 1186.
[5] J. Chatt, J. R. Dilworth, R. L. Richards, *Chem. Rev.* **1978**, *78*, 589.
[6] F. Tuczek, N. Lehnert, *Angew. Chem.* **1998**, *110*, 2780; *Angew. Chem. Int. Ed.* **1998**, *37*, 2636.
[7] A. Scherer, K. Kollak, A. Lützen, M. Friedemann, D. Haase, W. Saak, R. Beckhaus, *Eur. J. Inorg. Chem.* **2005**, 1003.
[8] R. D. Sanner, D. M. Duggan, T. C. McKenzie, R. F. Marsh, J. E. Bercaw, *J. Am. Chem. Soc.* **1976**, *98*, 8358.
[9] J. M. deWolf, R. Blaauw, A. Meetsma, J. H. Teuben, R. Gyepes, V. Varga, K. Mach, N. Veldman, A. L. Spek, *Organometallics* **1996**, *15*, 4977.
[10] D. H. Berry, L. J. Procopio, P. J. Carroll, *Organometallics* **1988**, *7*, 570.
[11] J. D. Zeinstra, J. H. Teuben, F. Jellinek, *J. Organomet. Chem.* **1979**, *170*, 39.
[12] T. E. Hanna, E. Lobkovsky, W. H. Bernskoetter, P. J. Chirik, *Organometallics* **2004**, *23*, 3448.
[13] R. Duchateau, S. Gambarotta, N. Beydoun, C. Bensimon, *J. Am. Chem. Soc.* **1991**, *113*, 8986.
[14] N. Beydoun, R. Duchateau, S. Gambarotta, *J. Chem. Soc., Chem. Commun.* **1992**, 244.
[15] S. M. Mullins, A. P. Duncan, R. G. Bergman, J. Arnold, *Inorg. Chem.* **2001**, *40*, 6952.
[16] F. Rasetti, *Proc. Natl. Acad. Sci. USA* **1929**, *15*, 234.
[17] J. D. Cohen, M. Mylvaganam, M. D. Fryzuk, T. M. Loehr, *J. Am. Chem. Soc.* **1994**, *116*, 9529.
[18] C. B. Powell, M. B. Hall, *Inorg. Chem.* **1984**, *23*, 4619.
[19] M. D. Fryzuk, T. S. Haddad, M. Mylvaganam, D. H. McConville, S. J. Rettig, *J. Am. Chem. Soc.* **1993**, *115*, 2782.
[20] R. Ferguson, E. Solari, C. Floriani, D. Osella, M. Ravera, N. Re, A. Chiesa-Villa, C. Rizzoli, *J. Am. Chem. Soc.* **1997**, *119*, 10104.
[21] For some titanium dinitrogen complexes paramagnetic behavior is indeed found: $[(Cp_2Ti)_2\mu\text{-}\eta^1\text{:}\eta^1N_2]$ 1.45 $\mu_B$ (300 K); Y. G. Borodko, I. N. Ivleva, L. M. Kachapina, S. I. Salienko, A. K. Shilova, A. E. Shilov, *J. Chem. Soc., Chem. Commun.* **1972**, 1178; $[(Cp^*_2Ti)_2\mu\text{-}\eta^1\text{:}\eta^1N_2]$ 2.18 $\mu_B$ (107–298 K); J. E. Bercaw, *J. Am. Chem. Soc.* **1974**, *96*, 5087.
[22] On the basis of the strong back-bonding interaction of the fulvene ligands, it would appear justified to assign a 2– charge to the fulvene ligands. In that case the titanium centers would have a 3+ charge and be able to transfer one electron each to the dinitrogen ligand, making it an $N_2^{2-}$ unit. However, it is customary to treat the fulvene ligands as neutral.
[23] A. D. Becke, *Phys. Rev. A* **1988**, *38*, 3098.
[24] A. D. Becke, *J. Chem. Phys.* **1993**, *98*, 1372.
[25] A. D. Becke, *J. Chem. Phys.* **1993**, *98*, 5648.
[26] T. H. Dunning, Jr., P. J. Hay, in: *Modern Theoretical Chemistry* (Ed.: H. F. Schaefer III), Plenum, New York, **1976**.
[27] P. J. Hay, W. R. Wadt, *J. Chem. Phys.* **1985**, *82*, 270 and 299.
[28] W. R. Wadt, P. J. Hay, *J. Chem. Phys.* **1985**, *82*, 284.
[29] J. P. Foster, F. Weinhold, *J. Am. Chem. Soc.* **1980**, *102*, 7211.
[30] A. B. Rives, F. Weinhold, *Int. J. Quantum Chem. Symp.* **1980**, *14*, 201.
[31] A. E. Reed, R. B. Weinstock, F. Weinhold, *J. Chem. Phys.* **1985**, *83*, 735.
[32] A. E. Reed, L. A. Curtiss, F. Weinhold, *Chem. Rev.* **1988**, *88*, 899.
[33] M. J. Frisch, G. W. Trucks, H. B. Schlegel, G. E. Scuseria, M. A. Robb, J. R. Cheeseman, V. G. Zakrzewski, J. A. Montgomery, Jr., R. E. Stratmann, J. C. Burant, S. Dapprich, J. M. Millam, A. D. Daniels, K. N. Kudin, M. C. Strain, O. Farkas, J. Tomasi, V. Barone, M. Cossi, R. Cammi, B. Mennucci, C. Pomelli, C. Adamo, S. Clifford, J. Ochterski, G. A. Petersson, P. Y. Ayala, Q. Cui, K. Morokuma, P. Salvador, J. J. Dannen-

 © 2006 Wiley-VCH Verlag GmbH & Co. KGaA, Weinheim 

berg, D. K. Malick, A. D. Rabuck, K. Raghavachari, J. B. Foresman, J. Cioslowski, J. V. Ortiz, A. G. Baboul, B. B. Stefanov, G. Liu, A. Liashenko, P. Piskorz, I. Komaromi, R. Gomperts, R. L. Martin, D. J. Fox, T. Keith, M. A. Al-Laham, C. Y. Peng, A. Nanayakkara, M. Challacombe, P. M. W. Gill, B. Johnson, W. Chen, M. W. Wong, J. L. Andres, C. Gonzalez, M. Head-Gordon, E. S. Replogle, J. A. Pople, *Gaussian 98 Rev. A.11*, Gaussian, Inc., Pittsburgh, **2001**.

Received: August 2, 2005
Published Online: November 15, 2005

 © 2006 Wiley-VCH Verlag GmbH & Co. KGaA, Weinheim 

DOI: 10.1002/ejic.200500542

# Glycerol as Ligand: The Synthesis, Crystal Structure, and Properties of Compounds $[Ln_2(H_2L)_2(H_3L)_4][Re_6Q_8(CN)_6]$, Ln = La, Nd, Gd, Q = S, Se

**Nikolai G. Naumov,*[a] Maria S. Tarasenko,[a] Alexander V. Virovets,[a] Youngmee Kim,[b] Sung-Jin Kim,*[b] and Vladimir E. Fedorov[a]**

**Keywords:** Lanthanide(III) complexes / Glycerol / Rhenium(III) octahedral cluster / Cyanide complexes / Crystal structure

The interaction of aqueous solutions of octahedral cluster anions $[Re_6Q_8(CN)_6]^{4-}$ with rare earth cations in the presence of glycerol resulted in the formation of a new family of compounds $[Ln_2(H_2L)_2(H_3L)_4][Re_6Q_8(CN)_6]$ (where Ln = La, Nd, and Gd; Q = S, Se; $H_3L$ = glycerol; $H_2L^-$ = glycerolate anion). All compounds are isostructural and crystallize in the $P\bar{1}$ space group. Crystal structures are built from octahedral cluster anions $[Re_6Q_8(CN)_6]^{4-}$ and centrosymmetrical dimers $[Ln_2(H_2L)_2(H_3L)_4]^{4+}$ that have three different binding modes of glycerol.
(© Wiley-VCH Verlag GmbH & Co. KGaA, 69451 Weinheim, Germany, 2006)

## Introduction

The chemistry of octahedral cyanocluster complexes of the type $[Re_6Q_8(CN)_6]^{4-}$ (where Q = S, Se, Te) has been extensively studied over the past decade. The reactions of these anions with transition metal cations lead to the formation of cluster polymers that have Re–CN–M bridges.[1–5] The use of 3d metal complexes with chelating N-donor ligands resulted in formation of low dimensional structures [en,[6,7] trien,[8] 1,2*S*,3*S*,4-butanetetramine (threotab),[9] *N*,*N*′-bis(salicylidene)ethylenediamine (salen)[2]]. Up to now, all the compounds formed by $[Re_6Q_8(CN)_6]^{4-}$ anions and rare earth cations have 3D polymeric structures.[10–12] Attempts to use N-donor ligands were unsuccessful because of their basicity in aqueous solutions and precipitation of rare earth hydroxides.

In search of appropriate chelating ligands that are able to bind the rare earth cations, we have examined polyatomic alcohols. They are good candidates for such complexation because of their high affinity to coordinate rare earth cations, their variable steric requirements and their ability to bridge more then one metal center. The possibility of partial or full deprotonation allows the adjustment of the charge balance of the complexes. In the present work we examined glycerol, a simple, potentially tridentate ligand that may demonstrate variable chelating/bridging modes.

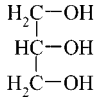

Here we report the synthesis, crystal structure and properties of a series of new compounds of composition $[Ln_2(H_2L)_2(H_3L)_4][Re_6Q_8(CN)_6]$ (Ln = La, Nd, Gd; Q = S, Se; $H_3L$ = glycerol; $H_2L^-$ = glycerolate anion), which contain $[Ln_2(H_2L)_2(H_3L)_4]^{4+}$ dimers. These dimeric structures contain three different modes of chelating glycerol molecules: bidentate, tridentate, and bridging/chelating.

## Results and Discussion

X-ray single crystal analysis shows that compounds **1**–**6** are isostructural. Their structures contain $[Re_6Q_8(CN)_6]^{4-}$ (Q = S, Se) anions and binuclear $[Ln_2(\mu\text{-}H_2L)_2(H_3L)_4]^{4+}$ cations. Both anion and cation lie in the centers of symmetry of the unit cell with the space group $P\bar{1}$.

The $[Re_6Q_8(CN)_6]^{4-}$ (Q = S, Se) anions have the typical $M_6Q_8L_6$ structure (Figure 1). The rhenium octahedron is surrounded by eight chalcogen atoms to form the cube $Q_8$. Additionally, each rhenium atom is coordinated by a terminal CN group. Bond lengths and angles are given in Table 1.

The new centrosymmetric binuclear cation $[Ln_2(H_2L)_2(H_3L)_4]^{4+}$ is shown in Figure 2, Figure 3 and Figure 4. Binding modes of $H_2L^-$ and $H_3L$ are schematically presented in Scheme 1. Two lanthanide atoms are connected by two deprotonated glycerol molecules (C9, C10, C12, O7, O8, O9) (Scheme 1a).

In structures **1**, **3**, **4**, and **6**, all ligands are ordered, while in **2** and **5** one of the carbon atoms of a bridging glycerolate ligand is disordered over two positions with equal weights. Each of the Ln atoms are additionally coordinated by two glycerol molecules as tridentate (C1, C2, C3, O1, O2, O3) and bidentate (C4, C5, C6, O4, O5, O6) ligands (Scheme 1b and c). The Ln–O bond lengths (for OH groups) lie within

[a] Nikolaev Institute of Inorganic Chemistry,
3, Lavrentieva ave., Novosibirsk 630090, Russia
Fax: +7-3832-309489
E-mail: naumov@che.nsk.su
[b] Department of Chemistry, Ewha Womans University,
Seoul 120-750, Korea
E-mail: sjkim@ewha.ac.kr

 © 2006 Wiley-VCH Verlag GmbH & Co. KGaA, Weinheim 

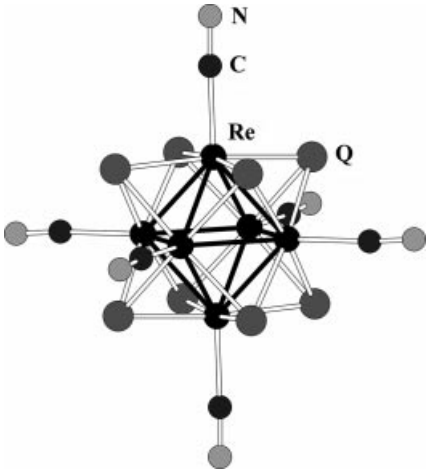


Figure 1. Structure of $[Re_6Q_8(CN)_6]^{4-}$ anions.

Figure 2. Structure of $[La_2(\mu\text{-}H_2L)_2(H_3L)_4]^{4+}$ cation. Hydrogen atoms are omitted for clarity.

2.540–2.706, 2.485–2.664, and 2.440–2.631 Å for Ln = La, Nd, and Gd, respectively. The Ln–(μ-O) bonds are distinctly shorter. The mean distances are equal to 2.397, 2.346, and 2.312 Å for Ln = La, Nd, and Gd, respectively (see Table 2). The coordination number of the $Ln^{III}$ ion in the complexes is nine, and the coordination polyhedron of lanthanide(III) may be described as a distorted tricapped trigonal prism.

In the crystal packing, there is an extensive system of hydrogen bonds between the nitrogen atoms of the CN groups and the OH groups of glycerol and glycerolate ligands (Figure 5). The shortest contacts lie within the range 2.70–3.00 Å.

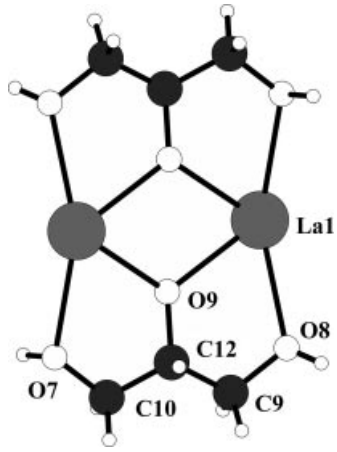


Figure 3. Centrosymmetric $[La_2(\mu\text{-}H_2L)_2]^{4+}$ fragment.

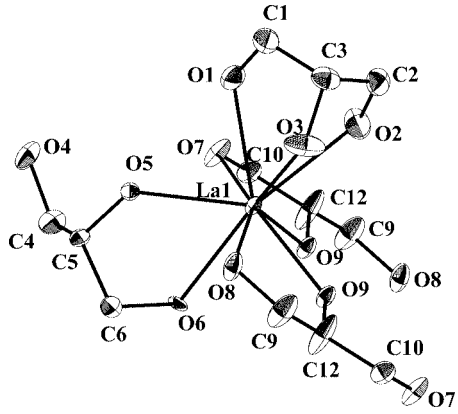


Figure 4. Environment of La in the structure of **1**. Hydrogen atoms are omitted for clarity.

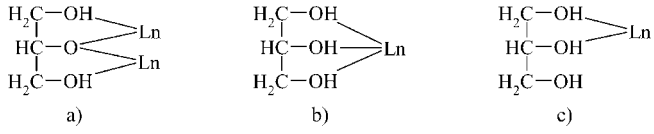


Scheme 1. Coordination modes of the glycerol molecule to lanthanide(III) cations in compounds **1**–**6**.

According to the Cambridge Structural Database (CSD V.5.25), there are no known examples of lanthanide(III) complexes bearing glycerol or glycerolate anions. Scheme 2 presents the coordination modes of glycerol and glycerolate anions ($H_2L^-$, $HL^{2-}$, and $L^{3-}$) in structurally characterized complexes of transition metals.

Table 1. Selected bond lengths [Å] in $[Re_6Q_8(CN)_6]^{4-}$ cluster anions in **1**–**6**.

| | **1** | **2** | **3** | **4** | **5** | **6** |
|---|---|---|---|---|---|---|
| Re–Re | 2.5988(5)–2.6055(5) mean 2.602(3) | 2.5971(5)–2.6055(5) mean 2.601(4) | 2.6012(4)–2.6089(4) mean 2.606(3) | 2.6319(7)–2.6368(6) mean 2.634(2) | 2.6310(4)–2.6364(4) mean 2.635(2) | 2.6312(6)–2.6356(6) mean 2.634(2) |
| Re-Q | 2.404(2)–2.414(2) mean 2.407(3) | 2.408(2)–2.4166(19) mean 2.414(5) | 2.4095(15)–2.4217(14) mean 2.415(4) | 2.5184(12)–2.5372(11) mean 2.525(6) | 2.5174(8)–2.5319(8) mean 2.523(5) | 2.5169(13)–2.5292(13) mean 2.523(4) |
| Re–C | 2.113(9)–2.126(9) mean 2.118(7) | 2.108(8)–2.132(8) mean 2.116(14) | 2.114(7)–2.118(6) mean 2.115(2) | 2.099(12)–2.119(13) mean 2.108(10) | 2.105(8)–2.127(9) mean 2.112(13) | 2.114(15)–2.128(15) mean 2.120(7) |
| C–N | 1.132(12)–1.149(12) mean 1.143(9) | 1.113(11)–1.136(10) mean 1.123(12) | 1.122(9)–1.139(8) mean 1.133(10) | 1.110(16)–1.143(15) mean 1.129(17) | 1.122(10)–1.153(10) mean 1.136(16) | 1.104(17)–1.125(17) mean 1.114(11) |

 © 2006 Wiley-VCH Verlag GmbH & Co. KGaA, Weinheim 

Table 2. Ligand environment of Ln atoms for **1**–**6**.

| | 1 | 2 | 3 | 4 | 5 | 6 |
|---|---|---|---|---|---|---|
| Ln–O(OH) [Å] | 2.540(6)–2.690(8) mean 2.595(49) | 2.485(5)–2.637(6) mean 2.540(51) | 2.440(4)–2.602(5) mean 2.509(58) | 2.546(8)–2.706(10) mean 2.605(52) | 2.474(5)–2.664(7) mean 2.558(67) | 2.425(8)–2.6310(7) mean 2.510(79) |
| Ln–($\mu_2$-O) [Å] | 2.383(6), 2.405(6) mean 2.394 | 2.330(5), 2.349(5) mean 2.340 | 2.300(4), 2.315(4) mean 2.308 | 2.388(7), 2.410(8) mean 2.349 | 2.342(5), 2.362(5) mean 2.352 | 2.301(8), 2.333(8) mean 2.317 |
| Ln–($\mu_2$-O)–Ln [°] | 111.8(2) | 112.2(2) | 112.2(2) | 111.8(3) | 112.2(2) | 112.5(3) |

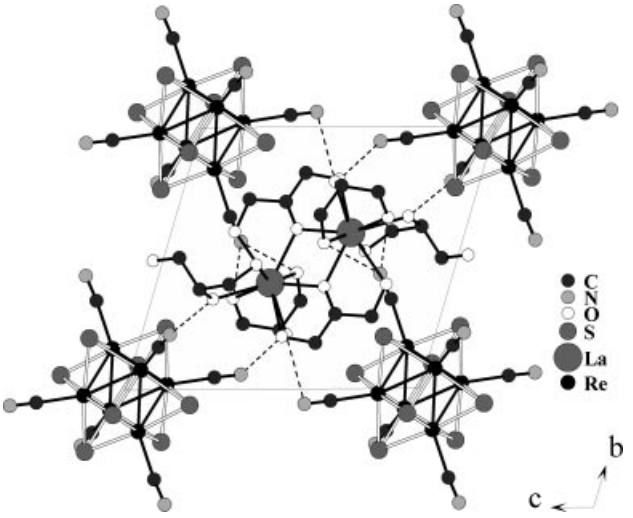


Figure 5. Crystal packing in the structure of **1**. Hydrogen atoms are omitted for clarity. Shortest N···O(OH) contacts are shown.

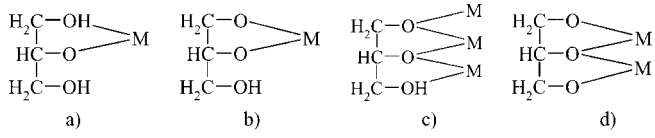


Scheme 2. Coordination modes of the glycerolate anions ($H_2L^-$, $HL^{2-}$, and $L^{3-}$) to transition metals in structurally characterized complexes; a) chelating coordination of $H_2L^-$;[13] b) chelating coordination of $HL^{2-}$;[14–17] c) chelating/bridging coordination of $HL^{2-}$;[18,19] d) chelating/bridging coordination of $L^{3-}$.[17,20]

There is only one crystal structure in which glycerol exists in the form of $[H_2L]^-$. Coordination of this ligand to a vanadium atom by one oxo- and one hydroxo group was found in oxo(propane-1,3-diol-2-olato)(salicylaldehyde hydroxyphenylmethylenehydrazonato-*N*,O,O′)vanadium(v)[13] (Scheme 2a). As in the cases of **1**–**6**, deprotonation of glycerol also occurred during crystallization in the presence of excess glycerol. The chelating coordination of $HL^{2-}$ (Scheme 2b) has been reported for several molecular complexes of platinum,[14,15] vanadium,[16] and copper.[17] The glycerolate anions $HL^{2-}$ and $L^{3-}$ often served as both chelating and bridging ligands (Scheme 2c and d). These coordination modes were encountered in numerous complexes of transition metals, e.g. Co*H*L,[18] Zn*H*L,[19] $Li_3[Cu_3L_3]\cdot 19H_2O$,[20] $Na_3[Cu_3L_3]\cdot 7H_2O$, and $Na_{10}[Cu_3L_3]_3(NO_3)\cdot 30H_2O$.[17]

## Mass Spectra

In the ESI (positive mode) mass spectra of complex **1** in glycerol/water solution several peaks appear that clearly support the proposed structure. Specifically, an intense signal at $m/z$ = 207.2 (75%) is assigned to $[La_2(\mu\text{-}H_2L)_2(H_3L)_4]^{4+}$. In addition, several mass peaks consistent with the association of this cation with glycerol molecules $\{[La_2(\mu\text{-}H_2L)_2(H_3L)_4]^{4+}\cdot(H_3L)_n\}$, $n$ = 2, 4, 6, 8 [$m/z$ = 253.3 (96%), 299.1 (100%), 345.1 (47%), 391.3 (10%)] are observed. The spectrum also contains minor peaks belonging to unidentified species. These data unequivocally confirm the presence of the $[La_2(\mu\text{-}H_2L)_2(H_3L)_4]^{4+}$ cations in solution that were observed in the solid state.

## IR Spectra

The different coordination modes of glycerol molecules and the presence of the deprotonated $H_2L^-$ species lead to changes in the vibrational frequencies of the ligand in complexes **1**-**6** relative to those of pure glycerol. In complexes **1**–**6** $\nu_{CO}$ vibrations are shifted to lower frequencies relative to those of the free ligand. For example, in complex **1** the $\nu_{CO}$ vibrations are shifted to 1095 and 1029 $cm^{-1}$, while in pure glycerol these vibrations are located at 1109 and 1034 $cm^{-1}$. The $\delta_{COH}$ vibrations centered at 1331 $cm^{-1}$ in glycerol are shifted to higher frequencies and are split into several well-defined peaks. Although the vibrational frequencies of the glycerol ligand change upon coordination in compounds **1**–**6**, these frequencies are almost insensitive to nature of lanthanide(III) ions.

The $\nu_{CN}$ vibrations of $[Re_6Q_8(CN)_6]^{4-}$ are split into three peaks and are shifted to higher frequencies relative to those of $K_4[Re_6S_8(CN)_6]$ (2117 $cm^{-1}$)[21] and $K_4[Re_6Se_8(CN)_6]\cdot 3.5H_2O$ (2107 $cm^{-1}$).[22] The $\nu_{OH}$ vibrations in **1**–**6** gave broad bands in the range 3500–3250 $cm^{-1}$ with no resolved lines in the spectra.

## Magnetic Data

Magnetic measurements carried out in the range 5–300 K show that La compounds **1** and **4** are diamagnetic, while Nd and Gd compounds **2**, **3**, **5**, and **6** are paramagnetic.

Neodymium-containing compounds **2** and **5** demonstrate complex temperature dependence of the magnetic susceptibility and effective magnetic moments. The effective magnetic moments for these complexes at 300 K are 4.61 and

 © 2006 Wiley-VCH Verlag GmbH & Co. KGaA, Weinheim 

3.91 B.M. per $Nd^{3+}$ cation (6.53 and 5.61 B.M. per $[Nd_2(H_2L)_2(H_3L)_4]^{4+}$ dimer), and 4.40 and 3.48 at 5 K – the moments gradually increase with an increase in temperature. The room-temperature values per ion appreciably exceed the usual value of 3.62 B.M. known for $Nd^{III}$.[23] Moreover, as illustrated in Figure 6a, even at 300 K the magnetic moment does not reach a plateau but continues to grow. Further studies are needed to interpret this behavior.

The effective magnetic moments for **3** and **6** at 300 K are 8.05 and 7.71 B.M. per $Gd^{III}$ cation (11.38 and 10.9 B.M. per $[Gd_2(H_2L)_2(H_3L)_4]^{4+}$ dimer), which are close to the usual value of 7.9 B.M. for isolated $Gd^{III}$ ions.[23] The behavior of the susceptibility upon a decrease in temperature of these complexes for gadolinium-containing compounds **3** and **6** is very similar. Magnetic susceptibility for these complexes can be satisfactorily described with Curie–Weiss law $\chi_M = C/(T - \theta)$. Fitting of the experimental data gave equations $\chi_M = 18.0/(T + 1.20)$ and $\chi_M = 14.83/(T + 1.10)$ for **3** and **6**, respectively. Such dependence is typical for $Gd^{III}$ ions having a half-filled shell, $4f^7$. The values of $\theta$ are comparable to those found in other O-bridged $Gd^{III}$ dimers.[24,25] The temperature-dependent magnetic data for **6** are shown in Figure 6b.

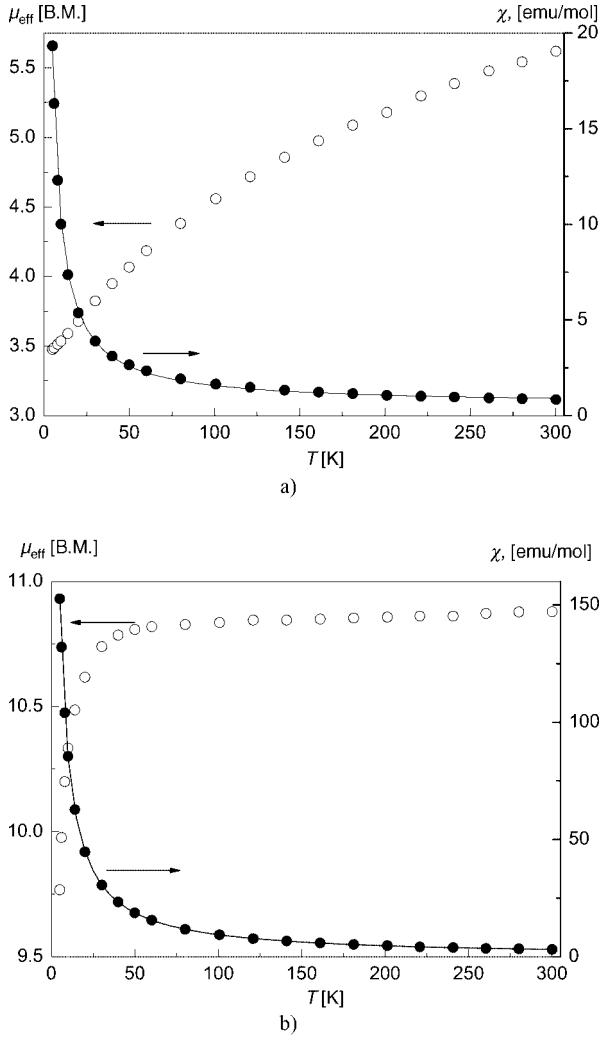


Figure 6. Magnetic susceptibility (solid circles) and effective magnetic moments (open circles) for **5** (a) and **6** (b).

Using equation

$$\theta = \frac{2S(S+1)}{3k_B}\sum_i^n z_i J_{ex,i}$$

for the case of two magnetic centers, we may estimate the exchange interactions in these dimers.[26] The values of $J$ are –0.079 and –0.073 $cm^{-1}$ for **3** and **6**, respectively, which correspond to very weak antiferromagnetic interactions between the two gadolinium cations in the $[Gd_2(H_2L)_2(H_3L)_4]^{4+}$ dimers.

## Conclusions

Glycerol molecules effectively coordinate with rare earth cations resulting in the formation of a new dimeric moiety $[Ln_2(\mu\text{-}H_2L)_2(H_3L)_4]^{4+}$. The observation of three different binding modes of glycerol in these structures demonstrates that this ligand is very attractive and potentially may form numerous complexes with rare earth cations.

## Experimental Section

### The Materials and Methods

**General:** Elemental analyses for C, H, N, and S (Carlo Erba 1106) were performed in the Laboratory of Microanalysis of the Institute of Organic Chemistry, Novosibirsk. IR spectra were recorded on KBr disks with a Scimitar FTS 2000c spectrometer in the range 4000–375 $cm^{-1}$. Magnetic susceptibility measurements for powder samples were carried out in the temperature range from 5 to 300 K in an applied magnetic field of 100 G using a Quantum Design MPMS-5 SQUID magnetometer. The starting cluster compounds $K_4[Re_6S_8(CN)_6]$[21] and $K_4[Re_6Se_8(CN)_6]\cdot 3.5H_2O$[22] were synthesized as described previously. Other reagents were used as purchased.

**Synthesis of $[La_2(H_2L)_2(H_3L)_4][Re_6S_8(CN)_6]$ (1):** To a solution of $LaCl_3\cdot 7H_2O$ (150 mg, 0.404 mmol) in $H_2O$ (20 mL) were added KOH (0.3 mL of a 0.1 M solution) and glycerol (3 mL), and the mixture was boiled for 15 min. The obtained clear solution was mixed with a solution of $K_4[Re_6S_8(CN)_6]$ (80 mg, 0.0474 mmol) in $H_2O$ (10 mL) and boiled (evaporated under heating) until the precipitation of yellow-orange compound **1**. The crystals were filtered, washed with ethanol (4 × 10 mL), and dried in air. Yield: 75.5 mg (67.5%). $C_{24}H_{46}La_2N_6O_{18}Re_6S_8$: calcd. C 12.22, H 1.97, N 3.56; found C 12.42, H 2.00, N 3.66%. IR: $\nu_{CN}$ = 2118, 2129, 2141 $cm^{-1}$; $\nu_{CO}$ = 1095, 1029 $cm^{-1}$; $\delta_{COH}$ = 1361, 1348, 1334 $cm^{-1}$.

**Synthesis of $[Nd_2(H_2L)_2(H_3L)_4][Re_6S_8(CN)_6]$ (2):** Compound **2** was prepared using the same procedure, though $NdCl_3\cdot 6H_2O$ (150 mg, 0.418 mmol) was used instead of $LaCl_3\cdot 7H_2O$. Yield: 63.0 mg (56.1%). $C_{24}H_{46}Nd_2N_6O_{18}Re_6S_8$: calcd. C 12.17, H 1.96, N 3.55; found C 12.22, H 2.06, N 3.45%. IR: $\nu_{CN}$ = 2118, 2129, 2141 $cm^{-1}$; $\nu_{CO}$ = 1095, 1028 $cm^{-1}$; $\delta_{COH}$ = 1359, 1346, 1332 $cm^{-1}$.

**Synthesis of $[Gd_2(H_2L)_2(H_3L)_4][Re_6S_8(CN)_6]$ (3):** Compound **3** was prepared using the same procedure as for **1**, though $GdCl_3\cdot 6H_2O$ (150 mg, 0.404 mmol) was used instead of $LaCl_3\cdot 7H_2O$. Yield: 66.1 mg (58.2%). $C_{24}H_{46}Gd_2N_6O_{18}Re_6S_8$: calcd. C 12.04, H 1.94,

 © 2006 Wiley-VCH Verlag GmbH & Co. KGaA, Weinheim 

Table 3. Crystal data and structure refinement for **1**–**6**.

| | **1** | **2** | **3** | **4** | **5** | **6** |
|---|---|---|---|---|---|---|
| Empirical formula | $C_{24}H_{46}La_2N_6O_{18}Re_6S_8$ | $C_{24}H_{46}N_6Nd_2O_{18}Re_6S_8$ | $C_{24}H_{46}Gd_2N_6O_{18}Re_6S_8$ | $C_{24}H_{46}La_2N_6O_{18}Re_6Se_8$ | $C_{24}H_{46}N_6Nd_2O_{18}Re_6Se_8$ | $C_{24}H_{46}Gd_2N_6O_{18}Re_6Se_8$ |
| Formula mass | 2358.17 | 2368.83 | 2394.85 | 2733.37 | 2744.03 | 2770.05 |
| Crystal system | triclinic | triclinic | triclinic | triclinic | triclinic | triclinic |
| Space group, $Z$ | $P\bar{1}$, 1 | $P\bar{1}$, 1 | $P\bar{1}$, 1 | $P\bar{1}$, 1 | $P\bar{1}$, 1 | $P\bar{1}$, 1 |
| $a$ [Å] | 10.0978(9) | 10.0906(14) | 10.1319(10) | 10.2163(10) | 10.2295(6) | 10.2521(4) |
| $b$ [Å] | 10.8864(10) | 10.8001(15) | 10.7506(12) | 10.9502(11) | 10.8649(6) | 10.7892(4) |
| $c$ [Å] | 11.8475(11) | 11.6978(16) | 11.7590(14) | 11.8852(12) | 11.8240(6) | 11.8388(5) |
| $\alpha$ [°] | 105.868(2) | 105.917(5) | 105.889(4) | 105.343(5) | 105.234(2) | 104.975(1) |
| $\beta$ [°] | 97.791(1) | 97.405(4) | 97.354(4) | 97.756(5) | 97.445(2) | 97.315(2) |
| $\gamma$ [°] | 94.010(1) | 93.980(4) | 93.793(4) | 93.614(5) | 93.566(2) | 93.411(1) |
| $V$ [Å$^3$] | 1233.3(2) | 1208.4(3) | 1214.9(2) | 1263.7(2) | 1250.9(1) | 1248.90(9) |
| $D_x$ [g/cm$^3$] | 3.175 | 3.255 | 3.273 | 3.592 | 3.643 | 3.683 |
| $\mu$ [mm$^{-1}$] | 16.756 | 17.483 | 17.982 | 21.785 | 22.375 | 22.987 |
| Crystal size [mm] | 0.15×0.10×0.10 | 0.20×0.15×0.14 | 0.33×0.20×0.15 | 0.28×0.16×0.15 | 0.05×0.06×0.10 | 0.10×0.10×0.15 |
| $2\theta$ range [°] | 1.81–25.00 | 3.39–25.00 | 1.82–25.00 | 2.91–25.00 | 1.81–25.00 | 1.80 to 25.00 |
| Reflections collected/ unique | 6373/4254 | 10141/4154 | 16883/4217 | 19948/4229 | 21168/4317 | 10800/4257 |
| $R_{int}$ | 0.0178 | 0.0296 | 0.0228 | 0.0408 | 0.0265 | 0.0334 |
| Refined parameters | 280 | 298 | 281 | 280 | 290 | 281 |
| $T_{min}/T_{max.}$ | 0.345 | 0.349 | 0.500 | 0.455 | 0.536 | 0.470 |
| $R_1/wR_2$ [$I > 2\sigma(I)$] | 0.0321/0.0761 | 0.0333/0.0854 | 0.0211/0.0532 | 0.0353/0.0834 | 0.0294/0.0793 | 0.0407/0.1058 |
| $R_1/wR_2$ (all data) | 0.0372/0.0793 | 0.0370/0.0873 | 0.0233/0.0539 | 0.0529/0.0925 | 0.0364/0.0894 | 0.0533/0.1137 |
| GoF | 1.030 | 1.037 | 1.074 | 1.015 | 1.117 | 1.057 |

N 3.51; found C 12.00, H 1.90, N 3.43%. IR: $\nu_{CN}$ = 2118, 2131, 2143 cm$^{-1}$; $\nu_{CO}$ = 1093, 1022 cm$^{-1}$; $\delta_{COH}$ = 1359, 1344 cm$^{-1}$.

**Synthesis of $[La_2(H_2L)_2(H_3L)_4][Re_6Se_8(CN)_6]$ (4):** Compound **4** was prepared using the same procedure as for **1**, though $K_4[Re_6Se_8(CN)_6]\cdot 3.5H_2O$ (100 mg, 0.0471 mmol) instead of $K_4[Re_6S_8(CN)_6]$ was used. Yield: 78.8 mg (61.2%). $C_{24}H_{46}La_2N_6O_{18}Re_6Se_8$: calcd. C 10.55, H 1.70, N 3.07; found C 10.70, H 1.90, N 3.00%. IR: $\nu_{CN}$ = 2102, 2118, 2127 cm$^{-1}$; $\nu_{CO}$ = 1095, 1031 cm$^{-1}$; $\delta_{COH}$ = 1359, 1346, 1332 cm$^{-1}$.

**Synthesis of $[Nd_2(H_2L)_2(H_3L)_4][Re_6Se_8(CN)_6]$ (5):** Compound **5** was prepared using the same procedure as for **2**, though $K_4[Re_6Se_8(CN)_6]\cdot 3.5H_2O$ (100 mg, 0.0471 mmol) instead of $K_4[Re_6S_8(CN)_6]$ was used. Yield: 89.4 mg (69.2%). $C_{24}H_{46}Nd_2N_6O_{18}Re_6Se_8$: calcd. C 12.17, H 1.96, N 3.55; found C 10.50, H 1.69, N 3.06%. IR: $\nu_{CN}$ = 2102, 2118, 2127 cm$^{-1}$; $\nu_{CO}$ = 1095, 1029 cm$^{-1}$; $\delta_{COH}$ = 1359, 1346, 1332 cm$^{-1}$.

**Synthesis of $[Gd_2(H_2L)_2(H_3L)_4][Re_6Se_8(CN)_6]$ (6):** Compound **6** was prepared using the same procedure as for **3**, though $K_4[Re_6Se_8(CN)_6]\cdot 3.5H_2O$ (100 mg, 0.0471 mmol) instead of $K_4[Re_6S_8(CN)_6]$ was used. Yield: 92.0 mg (70.5%). For $C_{24}H_{46}Gd_2N_6O_{18}Re_6Se_8$: calcd. C 10.41, H 1.67, N 3.03; found C 10.10, H 1.80, N 2.90%. IR: $\nu_{CN}$ = 2104, 2120, 2129 cm$^{-1}$; $\nu_{CO}$ = 1095, 1028 cm$^{-1}$; $\delta_{COH}$ = 1357 cm$^{-1}$.

**X-ray Structural Studies:** Diffraction measurements were carried out by standard technique on a Bruker SMART AXS diffractometer equipped with a CCD area detector (**1**) and a Buker-Nonius X8Apex CCD (**2**–**6**) using graphite-monochromated Mo-$K_\alpha$ radiation. Details of diffraction experiments, structure solution and refinement parameters are given in Table 3. Absorption corrections were applied using the SADABS program.[27,28] The crystal structures were solved independently by direct methods and then refined using the SHELX package.[29] Hydrogen atoms of CH and $CH_2$ groups were refined geometrically. Hydrogen atoms of OH groups were located from last different electron density maps and fixed. Our attempts to refine them were unsuccessful. Final refinement was done by full-matrix least-squares method. All non-hydrogen atoms were refined anisotropically. CCDC-269462 to -269467 contain the supplementary crystallographic data for this paper. These data can be obtained free of charge from The Cambridge Crystallographic Data Centre via www.ccdc.cam.ac.uk/data_request/cif.

## Acknowledgments

This work was supported by the SRC program of the Korea Science and Engineering Foundation (KOSEF) through the Center for Intelligent Nano-Bio Materials at Ewha Womans University (grant: R11-2005-008-00000-0).

[1] N. G. Naumov, A. V. Virovets, M. N. Sokolov, S. B. Artemkina, V. E. Fedorov, *Angew. Chem. Int. Ed. Engl.* **1998**, *37*, 1943–1945.
[2] Y. Kim, S. M. Park, W. Nam, S. J. Kim, *Chem. Commun.* **2001**, 1470–1471.
[3] Y. Kim, S. Kim, S. J. Kim, M. K. Lee, M. Kim, H. Lee, C. S. Chin, *Chem. Commun.* **2004**, 1692–1693.
[4] N. G. Naumov, A. V. Virovets, V. E. Fedorov, *J. Struct. Chem.* **2000**, *41*, 499–520.
[5] N. G. Naumov, D. V. Soldatov, J. A. Ripmeester, S. B. Artemkina, V. E. Fedorov, *Chem. Commun.* **2001**, 571–572.
[6] K. A. Brylev, Y. V. Mironov, N. G. Naumov, V. E. Fedorov, J. A. Ibers, *Inorg. Chem.* **2004**, *43*, 4833–4838.
[7] K. A. Brylev, G. Pilet, N. G. Naumov, A. Perrin, V. E. Fedorov, *Eur. J. Inorg. Chem.* **2005**, 461–466.
[8] K. A. Brylev, N. G. Naumov, G. Peris, R. Llusar, V. E. Fedorov, *Polyhedron* **2003**, *22*, 3383–3387.
[9] Y. V. Mironov, N. G. Naumov, K. A. Brylev, O. A. Efremova, V. E. Fedorov, K. Hegetschweiler, *Angew. Chem. Int. Ed.* **2004**, *43*, 1297–1300.
[10] M. S. Tarasenko, N. G. Naumov, A. V. Virovets, D. Y. Naumov, N. V. Kurat'eva, Y. V. Mironov, V. N. Ikorskii, V. E. Fedorov, *J. Struct. Chem. Engl.* **2005**, *46*, S134–S141.
[11] S. B. Artemkina, N. G. Naumov, A. V. Virovets, S. A. Gromilov, D. Fenske, V. E. Fedorov, *Inorg. Chem. Commun.* **2001**, *4*, 423–426.

 © 2006 Wiley-VCH Verlag GmbH & Co. KGaA, Weinheim 

[12] S. B. Artemkina, N. G. Naumov, A. V. Virovets, V. E. Fedorov, *Eur. J. Inorg. Chem.* **2005**, 142–146.
[13] S. P. Rath, K. K. Rajak, S. Mondal, A. Chakravorty, *J. Chem. Soc., Dalton Trans.* **1998**, 2097–2102.
[14] A. Appelt, A. C. Willis, S. B. Wild, *J. Chem. Soc., Chem. Commun.* **1988**, 938–939.
[15] W. T. Klooster, E. J. Voss, *Inorg. Chim. Acta* **1999**, *285*, 10–17.
[16] S. Mondal, S. P. Rath, K. K. Rajak, A. Chakravorty, *Inorg. Chem.* **1998**, *37*, 1713–1719.
[17] P. Klufers, H. Piotrowski, J. Schumacher, *Z. Anorg. Allg. Chem.* **1997**, *623*, 191.
[18] P. G. Slade, E. W. Radoslovich, M. Raupach, *Acta Crystallogr., Sect. B* **1971**, *27*, 2432–2436.
[19] T. W. Hambley, M. R. Snow, *Aust. J. Chem.* **1983**, *36*, 1249–1253.
[20] M. Klaassen, P. Klufers, *Z. Anorg. Allg. Chem.* **1993**, *619*, 661–668.
[21] N. G. Naumov, A. V. Virovets, Y. I. Mironov, S. B. Artemkina, V. E. Fedorov, *Ukr. Khim. Zh. (Russ. Ed.)* **1999**, *65*, 21–27.
[22] N. G. Naumov, A. V. Virovets, N. V. Podberezskaya, V. E. Fedorov, *J. Struct. Chem.* **1997**, *38*, 857–862.
[23] O. Kahn, *Molecular Magnetism*, VCH, New York, NY, **1993**.
[24] A. Rizzi, R. Baggio, M. T. Garland, O. Pena, M. Perec, *Inorg. Chim. Acta* **2003**, *353*, 315–319.
[25] A. Panagiotopoulos, T. F. Zafiropoulos, S. P. Perlepes, E. Bakalbassis, I. Massonramade, O. Kahn, A. Terzis, C. P. Raptopoulou, *Inorg. Chem.* **1995**, *34*, 4918–4920.
[26] S. Hatscher, H. Schilder, H. Lueken, W. Urland, *Pure Appl. Chem.* **2005**, *77*, 497–511.
[27] *APEX2* (Version 1.08), *SAINT* (Version 7.03), Bruker Advanced X-ray Solutions, Bruker AXS Inc., Madison, Wisconsin, USA, **2004**.
[28] *SADABS* (Version 2.11), Bruker Advanced X-ray Solutions, Bruker AXS Inc., Madison, Wisconsin, USA, **2004**.
[29] *SHELXTL* (Version 6.12), Bruker Advanced X-ray Solutions, Bruker AXS Inc., Madison, Wisconsin, USA, **2004**.

Received: June 22, 2005
Published Online: December 5, 2005

 © 2006 Wiley-VCH Verlag GmbH & Co. KGaA, Weinheim 

DOI: 10.1002/ejic.200500675

# *N*-Methylation Effects on the Coordination Chemistry of Cyclic Triamines with Divalent Transition Metals and Their $Co^{II}$ Dioxygen Carriers

**Silvia Del Piero,[a] Andrea Melchior,*[a] Pierluigi Polese,[a] Roberto Portanova,[a] and Marilena Tolazzi*[a]**

**Keywords:** Cadmium / Cobalt / Density functional calculations / N ligands / Thermodynamics

The thermodynamics of complex formation of $Co^{II}$ and $Cd^{II}$ ions with the triaza macrocyclic ligand 1,4,7-triazacyclononane (tacn) and its *N*-methylated derivative 1,4,7-trimethyl-1,4,7-triazacyclononane ($Me_3$tacn) has been studied in dimethyl sulfoxide (DMSO) at 298.1 K and in an ionic medium (0.1 M $Et_4NClO_4$) by means of potentiometric, UV/Vis, calorimetric and FT-IR techniques. The results are discussed by taking into account electronic and steric effects as well as solvation of the species concerned. Computational methods based on density functional theory (DFT) have been used to obtain structural information about the ligands and their complexes in order to provide further, independent insights into the effect of *N*-methylation on the coordination affinity of the ligands towards the metal ions. The computational suggestions are of great help to correlate steric effects and thermodynamic results. The kinetics of dioxygen uptake for the formation of the $Co(tacn)_2O_2$ superoxo adduct has also been studied by means of UV/Vis measurements.
(© Wiley-VCH Verlag GmbH & Co. KGaA, 69451 Weinheim, Germany, 2006)

## Introduction

In the last few years a wide variety of polyamines have been investigated in water[1–11] and in non-aqueous solvents[12–16] with the aim of studying how basicities and steric effects affect the selectivity pattern in metal coordination and for making direct comparison with the corresponding macrocyclic ligands.

As examples of these ligands' great interest and application, their potential use as sequestering agents for metals of environmental importance,[10] both toxic and essentials, and their employment as models for small molecules carriers,[16–21] such as in $Cu^{I}$ or $Co^{II}$ complexes, should be remembered.

In this context, previous studies of our group[16] on the complexation of divalent transition metal ions such as $Cd^{II}$ and $Co^{II}$ with differently *N*-alkylated linear di-, tri- and tetraamines in aprotic media have shown that: (i) the stabilities of the species formed decrease strongly with the increase of *N*-alkylation, with the enthalpy term being more responsible for that;[16a,16c] (ii) nitrogen functionalisation also strongly influences the stoichiometry and the nature of the metal complexes formed and, very interestingly, also the selectivity of these ligands (a higher affinity for $Co^{II}$ than for $Cd^{II}$ is displayed by primary and secondary polyamines, whereas the opposite is true when tertiary ones are involved);[16d] (iii) as far as cobalt(II) complexes are concerned, different *N*-alkylation of polyamines also has important effects on the behaviour of these complexes as better or worse dioxygen carriers:[16c,16e] in fact, electron transfer between the metal centre and the dioxygen depends on the electron density available at the central metal ion which, in turn, is greatly affected by the ligands;[17,20,21] (iv) steric effects due to *N*-alkylation inhibit the solvent exchange when dioxygen binding is considered, thus slowing down the oxygenation rate in the formation of the final adducts.

As an extension of this work we present here a study in the aprotic solvent dimethyl sulfoxide (DMSO) on the complex formation of $Co^{II}$ and $Cd^{II}$ ions with the simplest polyaza macrocyclic ligand 1,4,7-triazacyclononane (tacn) and its *N*-methylated derivative 1,4,7-trimethyl-1,4,7-triazacyclononane ($Me_3$tacn), whose bulky methyls cause the ligand to change both its electronic and steric properties.

Despite its small cavity size, tacn is known to show an effective, strong macrocyclic effect which is manifested in its increased thermodynamic stability with respect to chelated acyclic triamines, for example in water. In addition, a

[a] Dipartimento di Scienze e Tecnologie Chimiche, Università di Udine,
Via Cotonificio 108, 33100 Udine, Italy
Fax: +39-0432-558-803
E-mail: tolazzi@uniud.it
andrea.melchior@uniud.it

Supporting information for this article is available on the WWW under http://www.eurjic.org or from the author.

 © 2006 Wiley-VCH Verlag GmbH & Co. KGaA, Weinheim 

stronger ligand field has been observed with respect to linear analogous.[22,23] These cyclic ligands also show interesting properties as potential oxidation catalysts[24,25] due to their ability in stabilizing reaction intermediates,[24] and they influence the electron-transfer rates, which are accompanied by a change in spin-state, such as in the $Co^{II}$/$Co^{III}$ couple.[26]

Finally, tacn is ideally suited to coordinate[22,23,27] the metal-ion coordination sphere facially, thus functioning as a blocking group for three coordination sites.[22,28] Moreover, in the presence of suitable pendant arms the derivatised ligands are also very interesting as they can open-up a variety of fields of investigation, such as those of inorganic crystal engineering,[29] biological tracers,[30] MRI contrast agents[31] and the selective extraction and sequestering of metal ions.[1,23,32–34]

The aim of this work is mainly related to gaining information on the behaviour of simple triaza macrocycles that do not yet bear pendant arms and, in particular, on: (i) the macrocyclic effect in complex formation in solvating media other than water; (ii) the influence of *N*-methylation; (iii) the specific match of metal-ion size and the coordination requirements of the cyclic ligands; (iv) the effects of these preorganised ligands and of their *N*-methylation on the dioxygen affinity of their $Co^{II}$ complexes.

The effect of *N*-methylation on the coordination affinity of the ligands towards $Co^{II}$ and $Cd^{II}$, characterised by different types of electron configuration ($d^7$ and $d^{10}$), is also investigated here by computational methods using density functional theory (DFT). DFT provides an excellent framework to obtain structural information and a number of chemical reactivity indices about ligands and their complexes and is able to give results of quality comparable to those obtainable by correlated ab initio calculations. DFT has previously been used to study the influence of *N*-methylation on the structural[35] and electrochemical properties of transition-metal complexes with cyclic polyaza ligands[8] and to describe the properties of polyamines, such as their basicity, both in the gas phase[36] and in solvent models.[37] The kinetics of dioxygen uptake is also studied by means of UV/Vis measurements as far as the $Co(tacn)_2$ species is concerned as this is the only complex capable of binding $O_2$.

## Results

The structures of the ligands were optimised by DFT calculations (see Supporting Information) and were compared with X-ray data available in the literature only for $Me_3$tacn (although in its protonated forms).[38] Some of the calculated and experimental parameters of this ligand are summarised in Table 1, and show that a good match exists between optimised and available X-ray data for $Me_3$tacn. This correlation is of interest as it can be taken as a proof of the reliability of these computational results and thus gives confidence in the initial calculated structure of tacn.

Table 1. Experimental[38] and calculated values for selected structural parameters of the ligand $Me_3$tacn.

| | Distances [Å] | | | Angles [°] | |
|---|---|---|---|---|---|
| | Exp. | Calcd. | | Exp. | Calcd. |
| N–C | 1.356–1.458 | 1.457 | C–N–C | 112.4–115.1 | 113.4 |
| $N–C_{(methyl)}$ | 1.450 | 1.451 | $C–N–C_{(methyl)}$ | 110.5–115.2 | 116.4 |
| C–C | 1.403–1.488 | 1.542 | | | |

The optimised structures of the $ML^{2+}$ complexes in the gas phase, together with calculated M–N distances, are reported in Figure 1: as far as the $M(tacn)^{2+}$ structures are concerned (Figure 1a and b), the M–N distances are shorter than the X-ray ones (Cd–N = 2.351–2.382 Å;[39] Co–N = 2.127–2.157 Å[40]), and this is true especially in the case of the $Co^{II}$ complexes. This may be due to the simplified models chosen, to the limited basis sets and also because repulsive interactions present in the experimental structures are absent in the model complexes. As a matter of fact, when optimised structures of $M(tacn)_2^{2+}$ are considered (Figure 1c and d) the M–N distances are longer and very close to the experimental data.

The calculated binding energies ($E_{bind} = E_{ML^{2+}} - E_{M^{2+}} - E_L$) for the complex formation in vacuo are reported in Table 2, and the energies of the ligands in their "free" form and at the coordinates in the optimised complexes are given in Table 3.

The overall stability constants obtained after the analysis of the potentiometric (for $Cd^{2+}$) and UV/Vis data (for $Co^{2+}$) are listed in Table 4 for metal(II)–tacn and –$Me_3$tacn systems. In the same table the whole of the thermodynamic functions, with the corresponding error limits, are also reported together with the available data in water.[41] Previously published data[16a,16b] hare given for the same metal(II)–*N*,*N*′′-dimethyldiethylenetriamine (dmdien) and –*N*,*N*,*N*′,*N*′′,*N*′′-pentamethyldiethylenetriamine (pmdien) systems, which were chosen as examples of comparable secondary and tertiary linear triamines.

The spectral changes observed during reactions between $Co^{II}$ and the ligands in the presence of $Cd^{II}$ as a competitive ion,[42] under anaerobic conditions, in terms of molar absorptions of the *j* species vs. wavelengths, are similar to the previous ones[16a] and are therefore not reported. The absorption maximum for $Co(ClO_4)_2$ in DMSO occurs at 535 nm ($\varepsilon$ = 11.9 $M^{-1}cm^{-1}$) and is shifted to lower wavelengths after ligand addition, in line with an increase in the ligand field strength when $CoL_j$ species are formed.

$\Delta h_v$, the total molar enthalpy change, is plotted as a function of $R_c$ (= $C_L/C_M$, total ligand/total metal concentration) for the $Cd^{II}$– and $Co^{II}$–ligand systems in Figure 2.

The shape of the curves confirms the formation of consecutive, stable $ML_j$ complexes when L = tacn (*j* = 1,2), whereas the absence of heat evolved after $R_c$ = 1 clearly indicates that no other species are formed beyond ML when L = $Me_3$tacn. The fit between experimental and calculated (full lines) data is good.

 © 2006 Wiley-VCH Verlag GmbH & Co. KGaA, Weinheim 

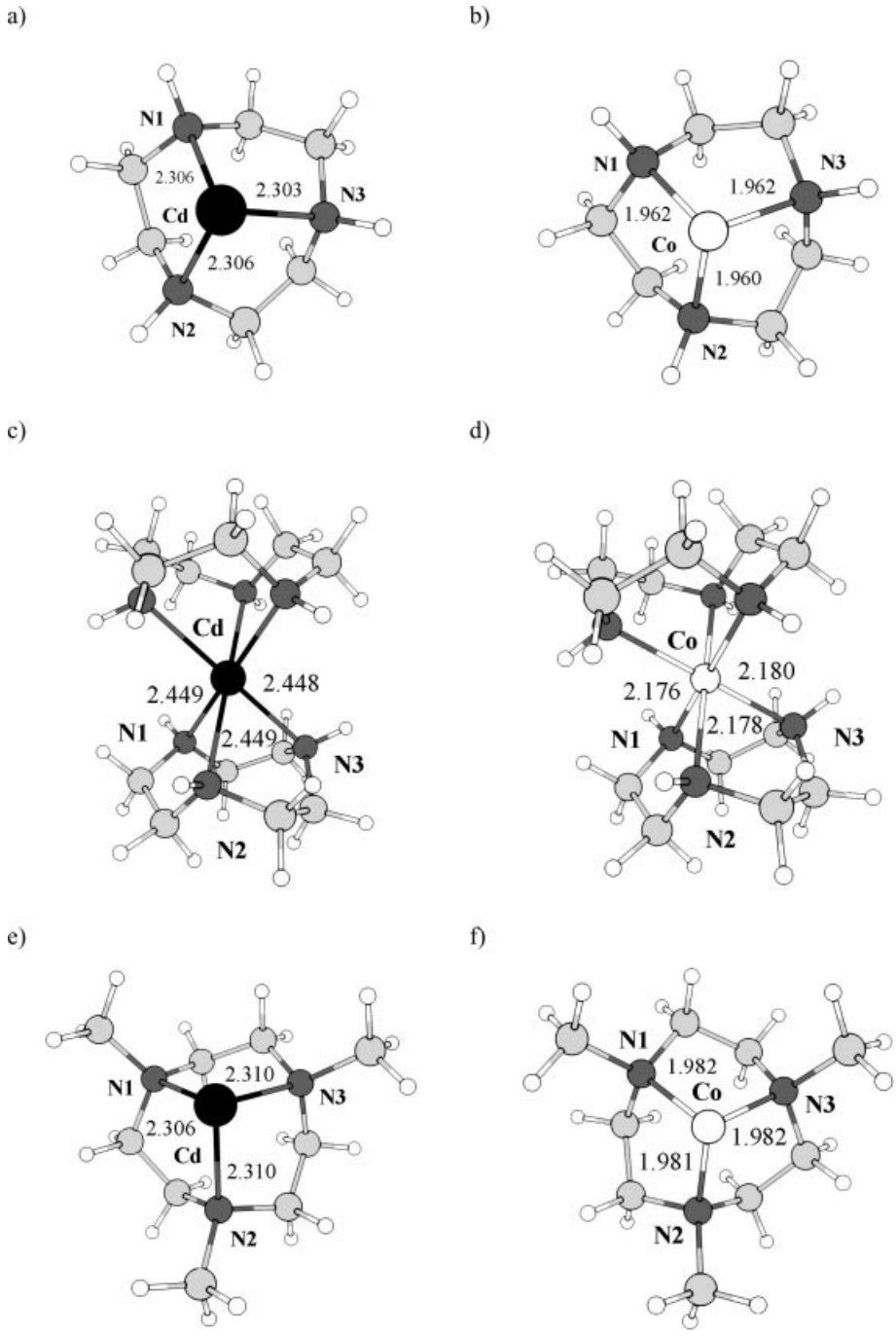


Figure 1. Optimised structures of a) $Cd(tacn)^{2+}$, b) $Co(tacn)^{2+}$, c) $Cd(tacn)_2^{2+}$, d) $Co(tacn)_2^{2+}$, e) $Cd(Me_3tacn)^{2+}$ and f) $Co(Me_3tacn)^{2+}$. Selected bond lengths are given in angstroms.

Table 2. Calculated binding energies ($E_{bind} = E_{ML^{2+}} - E_{M^{2+}} - E_L$) for $ML^{2+}$ (M = $Cd^{2+}$, $Co^{2+}$) complex formation in vacuo.

| | Binding energy [kJ mol$^{-1}$] |
|---|---|
| $Cd(tacn)^{2+}$ | –973.2 |
| $Cd(Me_3tacn)^{2+}$ | –989.7 |
| $Co(tacn)^{2+}$ | –1145.2 |
| $Co(Me_3tacn)^{2+}$ | –1196.5 |

The oxygenated spectra of a $Co(tacn)_2$ solution at different times are displayed in part a of Figure 3, while part b shows the experimental data and fitting curves for the oxygenation of $Co(tacn)_2^{2+}$ as a plot of absorbance at 336 nm vs. time. In particular, maxima at 528, 400 and 336 nm appear initially due to the fast formation of an oxygenated species and grow in intensity until about 20 min.

 © 2006 Wiley-VCH Verlag GmbH & Co. KGaA, Weinheim 

Table 3. Calculated energies [Hartree] of the optimised ML structures, free ($E_{free}$) and frozen ($E_{bound}$) at the coordinates found in the Cd and Co complexes, and strain energies $\Delta E_{strain}$ [kJ mol$^{-1}$].

| | | | | | |
|---|---|---|---|---|---|
| $Cd(Me_3tacn)^{2+}$ | $E_{bound}$ | –519.801513 | $Co(Me_3tacn)^{2+}$ | $E_{bound}$ | –519.797987 |
| | $E_{free}$ | –519.814060 | | $E_{free}$ | –519.814066 |
| | $\Delta E_{strain}$ | –32.9 | | $\Delta E_{strain}$ | –42.2 |
| $Cd(tacn)^{2+}$ | $E_{bound}$ | –401.8754428 | $Co(tacn)^{2+}$ | $E_{bound}$ | –401.8718334 |
| | $E_{free}$ | –401.8839462 | | $E_{free}$ | –401.8839619 |
| | $\Delta E_{strain}$ | –22.3 | | $\Delta E_{strain}$ | –31.8 |

Table 4. Overall stability constants and thermodynamic functions for the reactions $M^{n+} + jL \rightleftharpoons ML_j^{n+}$ ($M = Cd^{2+}$, $Co^{2+}$) in DMSO (0.1 M $NEt_4ClO_4$, 298.15 K) and in water; the errors quoted correspond to three standard deviations.

| | Complex | Log$\beta_j$ | $-\Delta G°_{\beta j}$/kJmol$^{-1}$ | $-\Delta H°_{\beta j}$/kJmol$^{-1}$ | $-T\Delta S°_{\beta j}$/kJmol$^{-1}$ |
|---|---|---|---|---|---|
| DMSO | | | | | |
| 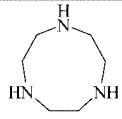 tacn | CdL | 9.56(0.02) | 54.6(0.1) | 60.6(3) | 6.0 |
| | $CdL_2$ | 18.59(0.03) | 106.1(0.2) | 130.4(3) | 24.3 |
| | CoL | 10.5(0.3) | 60(2) | 87(3) | 27 |
| | $CoL_2$ | 19.7(0.3) | 112(2) | 171(3) | 59 |
| 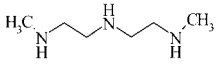 Dmdien | CdL[a] | 7.51 | 42.8 | 60.2 | 17.4 |
| | $CdL_2$[a] | 13.42 | 76.6 | 109.7 | 33.1 |
| | CoL[b] | 8.3 | 47.4 | 66.0 | 18.6 |
| | $CoL_2$[b] | 14.15 | 80.8 | 127 | 46.2 |
| 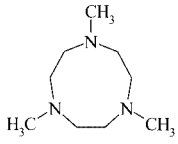 $Me_3tacn$ | CdL | 7.51(0.01) | 42.86(0.05) | 54.8(0.6) | 11.9 |
| | CoL | 7.7(0.1) | 43.9(0.6) | 74.6(1.6) | 30.7 |
| 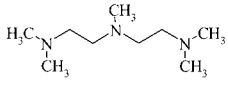 Pmdien | CdL[a] | 3.8 | 21.7 | 43.5 | 21.8 |
| | CoL[b] | 4.19 | 23.9 | 29.8 | 5.9 |
| Water | | | | | |
| 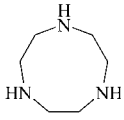 tacn | CdL[c] | 9.5 | 54.2 | 31.8[b] | –22.4 |
| | $CdL_2$[c] | 17.9 | 102.1 | | |
| | CoL[d] | 11.2 | 63.9 | | |
| | $CoL_2$[d] | 19.0 | 108.4 | | |

[a] Ref.[16b] [b] Ref.[16a] [c] Ref.[41a] [d] Ref.[41b]

This species then evolves and decreases in concentration very slowly, as can be seen from curve 3 in Figure 3a.

The best fit of the analysed experimental data reported in Figure 3b is consistent with the reaction mechanism (charges omitted) proposed in Equation (1).

Degradation reactions appear to be negligible in the time range investigated, as can also be seen from the above-described analysis of the curves (Figure 3a).

The kinetics of the process obey a second-order rate law and the values of the obtained kinetic constants, calculated by the computer treatment of the absorbance values at 336 nm, are given in Table 5 together with the equilibrium constant for the overall reaction relative to the formation of species A. This is calculated by combining the rate constants of the direct and reverse reactions at 298.1 K, which is the standard state for $O_2$ in 1 M solution.

 © 2006 Wiley-VCH Verlag GmbH & Co. KGaA, Weinheim 

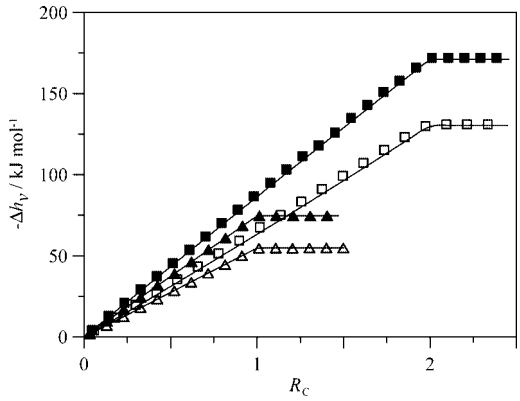


Figure 2. The total molar enthalpy changes, $\Delta h_v$, as a function of $R_c$ (= $C_L/C_M$) for $Cd^{II}$/L (open symbols) and $Co^{II}$/L (filled symbols) systems in DMSO: (□,■) L = tacn; (Δ,▲) L = $Me_3$tacn. The solid lines were calculated from the log $\beta_j$ and $\Delta H_{\beta j}°$ values in Table 1.

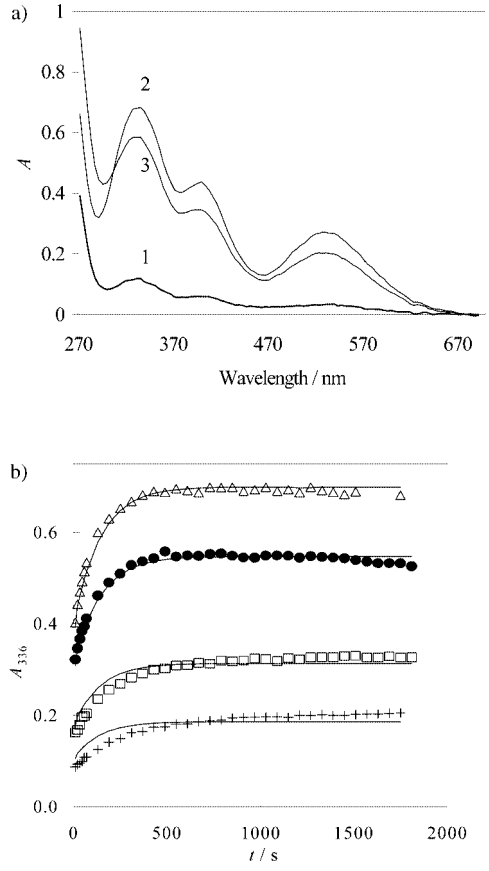


Figure 3. a) Electronic spectra of $[Co(tacn)_2{}^{2+}]$ (0.5 mM) in the presence of $P_{O_2}$ = 38 Torr after 1) 10 s, 2) 15 min, 3) 4 h; b) experimental data and fitting curves for the oxygenation of $Co(tacn)_2{}^{2+}$ in the presence of $P_{O_2}$ = 760 Torr: (+) $[Co^{2+}]$ = 0.21, [tacn] = 0.46 mM; (□) $[Co^{2+}]$ = 0.34, [tacn] = 0.72 mM; (●) $[Co^{2+}]$ = 0.58, [tacn] = 1.2 mM; (Δ) $[Co^{2+}]$ = 0.68, [tacn] = 1.4 mM. Calculated molar absorbance at 336 nm: $\varepsilon_{ML_2O_2}$ = 2.5(3)×10$^3$ M$^{-1}$ cm$^{-1}$.

$$Co(tacn)_{2(solv)} + O_{2(solv)} \underset{k_{-1}}{\overset{k_1}{\rightleftharpoons}} [Co(tacn)_2O_2]_{(solv)} \quad (1)$$
A

Table 5. Kinetic parameters for the oxygenation reactions reported in Equation (1) and thermodynamic stability constants for the reaction: $CoL_{2(solv)} + O_{2(solv)} \rightleftharpoons (CoL_2)O_{2(solv)}$ (L = tacn) in DMSO at 298.1 K and $I$ = 0.1 M. The errors in parentheses are one standard deviation.

| Complex | $k_1$ [M$^{-1}$ s$^{-1}$] | $k_{-1}$ [s$^{-1}$] | log $K_{O_2}$ |
|---|---|---|---|
| $[Co(tacn)_2O_2]^{2+}$ | 32(5) | 0.22(3) | 2.15 |

## Discussion

### DFT Calculations

The distances reported in Figure 1 show that the introduction of a methyl group on the tacn secondary nitrogens results in an elongation of the calculated M–N bond lengths (Figure 1e and f), which is more evident in the $Co^{II}$–L complexes (approx. 0.02 Å) than in the $Cd^{II}$–L complexes (approx. 0.005 Å). A similar elongation has been observed in the solid state for dinuclear $Co^{II}$ complexes of formula $[Co_2(Me_3tacn)_2X_3]$[43] for which X-ray data are available. This finding is in agreement with previous observations which show that the metal–N bond lengths increase with *N*-methylation as a consequence of steric effects in the gas phase,[44] and also of solvation effects in solution, thus leading to a stabilisation of the lower oxidation state in the $ML_j^{n+1}/ML_j^n$ redox couples.[10]

As far as the binding energies in Table 2 are concerned, it should be underlined that they are important only as far as their relative trends are conscerned: the high values found ($E_{bind}$ ≈ –970 to –1200 kJ mol$^{-1}$) cannot be compared to experimental values as environmental effects are not taken into account in the calculations, which means that additional energy terms, such as breaking of M–dmso bonds, are not considered.

Some interesting points can be outlined: i) $Co^{2+}$ binds much more strongly than $Cd^{2+}$ to the two polyamines, ii) the binding energies are higher for $Me_3$tacn than tacn for both metal ions, and iii) the difference between $Me_3$tacn and tacn is much higher when $Co^{II}$ is concerned [$\Delta E_{bindCo^{II}}$ = $E_{bind(Co–Me_3tacn)}$ – $E_{bind(Co–tacn)}$ = –51.3 kJ mol$^{-1}$; $\Delta E_{bindCd^{II}}$ = –16.5 kJ mol$^{-1}$].

Point i) may be reasonably explained by taking into account that $Co^{II}$, given its higher charge density, is a stronger Brønsted acid than $Cd^{II}$.

The higher affinity of the methylated amine for the two ions [point ii)] reflects the gas-phase basicity order of amines, which has been shown to be higher for tertiary amino groups than for secondary ones both experimentally[45] and theoretically.[35,36a,37] The effect of methyl groups on gas-phase basicity has been explained not only by the inductive effect of the $CH_3$ groups but also considering that, in the interaction of the amines with the $H^+$ ion, methyl groups are responsible for a better redistribution of the positive charge,[46] thus stabilizing the resulting cation. Even though in this case dipositive metal ions and not protons are involved, the same factors should be considered to be governing the energy trends found here.

 © 2006 Wiley-VCH Verlag GmbH & Co. KGaA, Weinheim 

As far as point iii) is concerned, the enhancement of stabilisation is probably due to a synergistic action that is effective when the stronger Brønsted acid $Co^{II}$ reacts with the stronger base $Me_3$tacn.

Steric effects due to *N*-methylation are investigated here with a particular attention to the fact that they are also reflected in the reorganisation of the ligands when they bind the metal ion, which influences their stability. Therefore, the energies of the ligands have been calculated in their "free" form and at the coordinates in the optimised complexes (Table 3): their difference $\Delta E_{strain} = E_{free} - E_{bound}$ can be considered a measure of this reorganisation. Although these differences are relatively low ($\Delta E_{strain} \approx 20$–$40\ kJ\,mol^{-1}$), they are nevertheless very important as these values are intrinsic in the ligands and therefore act in the gas phase as well as in solution.

The data for ML complexes in Table 3 mean that both ligands have to spend more energy to reorganize around $Co^{II}$ than $Cd^{II}$ ($\Delta\Delta E_{strain(L)} = \Delta E_{strain(Cd-L)} - \Delta E_{strain(Co-L)} = 9.3$ and $9.5\ kJ\,mol^{-1}$ for L = $Me_3$tacn and tacn, respectively); this is reasonable due to the larger ionic radius of $Cd^{II}$, which allows longer bond lengths and therefore lower strain, both of which imply lower steric repulsions and minor energy costs for the reorientation of the dipoles represented by N–H/$CH_3$ bonds.

To sum up, the DFT results for the gas phase forecast a higher affinity of both polyamines for $Co^{II}$ than for $Cd^{II}$, the higher difference found for $Me_3$tacn than for tacn being rationalised in terms of their gas-phase basicities. In addition, the importance of steric strain in the reorganisation of the ligands around the metals is pointed out.

## Thermodynamics

### *General Remarks*

The complex formation is accompanied by negative enthalpy values, typical of reactions between metal ions and neutral ligands in aprotic solvents.[12] The negative entropy terms found here are in line with the fact that the release of solvent molecules from the coordination sphere of the metal ions does not compensate the decrease in internal entropy of the ligand and the loss of translational entropy by the reagents upon complexation.

Thermodynamic data are available in water[41] for tacn systems, and these are also reported in Table 1. Although the enthalpy data are referred to a slightly different experimental ionic medium (0.2 M), this value nevertheless reflects different, significant effects of the two solvent media on complex formation: in water the stability with tacn is mainly due to a less favourable enthalpy term ($\Delta H°_1 = -31.8\ kJ\,mol^{-1}$), whereas the entropy term is positive. This trend has already been observed for other primary and secondary polyamines and generally results in a lower complex stabilisation in water than in DMSO.[16]

In polar solvents, where ion-pairing of counterions with metal cations and their complexes is negligible, the equilibrium constant for the complexation reaction varies with the solvation energies of the reactants (cations and ligands) and products (complexes). In many cases, the free-energy changes for ligand and complex solvation cancel each other out and the free-energy term for cation solvation is largely dominant.[12] The free-energy changes for metal-ion transfer from water to DMSO available for $Cd^{II}$ ($\Delta G°_{tr(water\rightarrow dmso)} = -60.4\ kJ\,mol^{-1}$),[47] and reasonably hypothesized to be negative for $Co^{II}$,[16a] show that these metal ions are more strongly solvated in DMSO than in water. This is in agreement with the different electron-donating abilities of the two solvent molecules, as measured by the empirical Gutmann's donor number (DN = 29.8 for DMSO and 18 for $H_2O$).[48]

In the hypothesis that the solvation energies of $Cd^{II}$ and $Co^{II}$ are the dominating solvation terms in our complexation reactions, we should expect a greater complex stability in water than in DMSO. As this does not occur, this suggests that amine solvation, rather than metal-ion solvation, plays a major role in determining the stability of tacn complexes in the two solvents. Indeed, it is known that primary and secondary amines are more solvated in water than in DMSO[15,49] and, consequently, are stronger bases in DMSO than in water. Tacn is more solvated in water, therefore complexation is a more expensive desolvation process, in terms of enthalpic contribution, but produces a greater gain in translational entropy. Accordingly, the enthalpic contribution available for the $Cd^{II}$–tacn system in water is largely less favourable than in DMSO, while the entropic one shows an opposite trend.

### *Complex Formation with Cyclic Triamines in DMSO*

Cyclisation of linear polyamines affects the stabilities and selectivities of their metal complexes: in particular, an extra stability is observed when complex formation with cyclic rather than linear polyamines is concerned. Although enthalpic and entropic arguments have been presented to account for this effect, it does not appear that one factor is unequivocally more important than the other.[3]

The results reported here show that an increase of the complex stability with both $Cd^{II}$ and $Co^{II}$ ions is effective when tacn (but also its methylated analogues) is considered with respect to the linear dmdien. This is true even if the comparison is extended to the more σ-donating primary linear triamine diethylenetriamine (dien).[16a]

This effect can be better understood by a separate analysis of the $\Delta H°$ and $\Delta S°$ contributions, which, in turn, are associated with metal, ligand and/or complex structural features.

It should be remembered that when macrocyclic rings such as 9-ane$X_3$ (X = N,O,S) are concerned, the metal ions do not enter the cavity of these small macrocycles, so that these do not represent examples of classical size-match selectivity. Rather, the metal ions are responding to the geometrical requirements for coordination out of the plane of the three donor atoms,[50] that is, the mode of coordination imposed by these ligands is stereorestrictive as they sterically constrained to facial coordination, whereas linear triamines may coordinate either facially or meridionally.

 © 2006 Wiley-VCH Verlag GmbH & Co. KGaA, Weinheim 

*1:1 Complexes*

Some important considerations can be made: (i) for the $Cd^{II}$ system with tacn, especially in the first complexation step, the extra stability with respect to the linear dmdien arises mainly from the entropy term as $\Delta H°_{\beta 1}$ is almost the same [the entropy term is far less unfavourable also when $Cd(Me_3tacn)^{2+}$ formation is considered vs. $Cd(pmdien)^{2+}$]; (ii) the opposite occurs when $Co^{II}$ complexation by the cyclic vs. the linear triamines is analysed. It must be underlined that both $Cd^{II}$ and $Co^{II}$ are octahedrally coordinated by six DMSO molecules in solution and that this coordination mode is retained in their 1:1 complexes, as indicated by UV/Vis measurements. In addition, from FT-IR spectra recorded for solutions where $R_c$ − the tacn-to-metal ratio − is varied up to 2, it can be seen that only the bands due to the bonded amine (at 3233 $cm^{-1}$) are present and no bands for free secondary (at 3345 $cm^{-1}$) amino groups could be detected, thus showing that the *N*-donor groups are all bonded to the central metal ion both in ML and $ML_2$ species.

The restricted conformational freedom of the cyclic tacn (but also $Me_3tacn$) before coordination, and hence the lower entropy loss on coordination, with respect to the linear one is one of the factors affecting this trend but certainly not the only one, as this should also influence the $Co^{II}$ system. The constraining nature of the rigid ligand, which forces a distorted octahedral structure in its facial coordination, is probably also responsible for this behaviour: in fact, with the larger $Cd^{II}$ ion (octahedral Shannon radius = 0.95 Å)[51] the steric strains of the three coordinated nitrogen atoms should be better minimised with respect to the small $Co^{II}$ ion (octahedral Shannon radius, high spin = 0.74 Å) and this may explain the great difference in entropy terms. These conclusions are also supported by the computational results in the gas phase, which show lower $\Delta\Delta E_{strain}$ values for Cd complexes than Co ones (Table 3). As a matter of fact, a special disorder has also been shown to be present in a $Cd(tacn)_2^{2+}$ solid structure,[39] and has been explained by observing that the ligands have two alternative positions which are twisted by about 56° with respect to each other.

The enthalpy values are, on the contrary, much more favourable when the $Co^{II}$–tacn system is considered with respect to $Cd^{II}$ and this should reflect stronger coordination bonds when the more (Brønsted) acidic $Co^{II}$ centre interacts with the ligands. This agrees with observed data which propose that, for metal ions which have considerable tendency for covalent bond formation, the enthalpic contribution to chelate formation can be important if their electronegativities are appreciable.[3]

Some additional points are outlined when the metal(II)–$Me_3tacn$ systems are considered: (i) a huge drop occurs in the complex stability with respect to the tacn system, and (ii) a huge gain in stability is observed as far as the complexation of the same ions with the tertiary, linear pmdien ligand are considered.

Point (i) may be explained as being due to several main reasons, especially: the different basicity of the amino group, which decreases in the order $NH_2 > NHR > NR_2$, in DMSO,[52] opposite from what occurs in gas phase; the elongation of the M–N bonds, due to the steric hindrance of the ligands[10] and the decreased solvation of the complexes as a consequence both of their increased radii and of the minor extent of hydrogen bonding brought about by the *N*-alkylated amines.[10]

The great importance of steric effects in the stability of the metal complexes formed is again clearly evident from the computational results in Table 3: the relative strain energies, in other words the repulsive forces in the $M^{II}$ complexes, are higher for $Me_3tacn$ complexes than for tacn itself ($\Delta\Delta E_{strain(tacn\rightarrow Me3tacn)}$ = 10.6 and 10.4 kJ $mol^{-1}$ for Cd and Co respectively). This destabilisation must be overcome in complex formation and thus is one of the causes of the decrease in complex stability.

As far as point (ii) is concerned, it should be remembered that data relative to pmdien agree with a bidentate behaviour of the ligand due to steric repulsions between the methyl groups.[16a,16b] In the case of $Me_3tacn$, the thermodynamic data suggest that the three nitrogens are all involved in coordination: the preorganisation of the cyclic ligand "drives" the N atoms towards the metal centre and evidently prevails over the steric repulsions between the methyl groups.

It is interesting to note that in the formation of the 1:1 complexes, $\Delta\Delta H°_1$, which is the difference between $\Delta H°_{\beta 1}{}^{Cd^{II}}$ and $\Delta H°_1{}^{Co^{II}}$ is less markedly positive for $Cd^{II}$ in the case of $Me_3tacn$ (Table 4, $\Delta\Delta H°_1$ = 19.8 kJ $mol^{-1}$) than in the case of tacn ($\Delta\Delta H°_{\beta 1}$ = 26.4 kJ $mol^{-1}$). This should once more be due to the better ability of the large $Cd^{II}$ to minimise steric hindrances. In addition, the increasingly soft nature of the tertiary amino groups should cause a less marked preference for $Co^{II}$ than for $Cd^{II}$ with respect to the secondary ones.

*1:2 Complexes*

*N*-Methylation is also responsible for the inability of $Me_3tacn$ to form an $M(Me_3tacn)_2^{2+}$ species: in fact, strong intramolecular repulsive forces would be exerted by the two rings due to non-bonding Me–Me interactions. Only one example of an $ML_2$ structure exists in the literature for this methylated ligand, namely the $Ag(Me_3tacn)_2^{+}$ complex.[53] In this case the Ag–N bond lengths are much greater (approx. 2.6 Å) and therefore the methyl groups are distant enough to allow a stabilisation of the $ML_2$ compound.

The thermodynamic data for $M(tacn)_2^{2+}$ systems show that the formation of the second complex is accompanied by a great stability (log $K_2$ = 9.03 and 9.2 for Cd and Co, respectively), which once more overcomes that relative to $M(dmdien)_2^{2+}$ complex formation. The presence of a stronger ligand-field for cyclic vs. linear triamines is evident from a comparison between the experimental UV/Vis spectra for the $Co(dmdien)_2$ and $Co(tacn)_2$ complexes: the value of $\lambda_{max}$ in the former is shifted from 535 [$\lambda_{max}$ for $Co(ClO_4)_2$ in DMSO solution] to 490 nm, whereas in the latter it is centred at 471 nm.

 © 2006 Wiley-VCH Verlag GmbH & Co. KGaA, Weinheim 

If we examine the values of the stepwise enthalpy and entropy data for M–tacn systems more deeply we can observe that the trend with both metals is in agreement with desolvation effects being more extensive in the first complexation step, and more markedly for $Cd^{II}$ than for $Co^{II}$. This desolvation effect should also play a role in explaining the low unfavourable entropy value found in the first step for Cd.

### Kinetics in Aerobic Conditions

The $k_1$ value found here for reaction (1) is slightly lower, although of the same order of magnitude, as that found for the formation of the saturated superoxo species $[Co(dien)_2O_2]^{2+}$ ($k_1$ = 69 $M^{-1}s^{-1}$), higher than that found for the formation of $[Co(dmdien)_2O_2]^{2+}$ ($k_1$ = 0.035 $M^{-1}s^{-1}$)[16h] and much lower than those found for $[CoL_2O_2]^{2+}$ [L = ethylenediamine (en), *N*,*N*′-dimethylethylenediamine (dmen)].[16e] The trend in $k_1$ values is therefore in agreement with a dissociative mechanism,[54] where a higher activation energy is required for the Co–N bond cleavage due to $O_2$ coordination in $Co(tacn)_2^{2+}$ than for the Co–$O_{(dmso)}$ bond cleavage in unsaturated $CoL_2$ complexes, the Co–N interaction being stronger than the Co–$O_{(dmso)}$ one.

The presence of steric interactions due to the methyl groups in dmdien makes the $O_2$ coordination slower[55] and this is in agreement with the $k_1$ value found for the $Co(dmdien)_2$ system with respect to $Co(tacn)_2$.

The stability constant for $O_2$ uptake is similar to that found when the secondary dmdien ligand is used [$\log K_{O_2}^{Co(dmdien)_2}$ = 2.8] and lower than that found for dien [$\log K_{O_2}^{Co(dien)_2}$ = 4.6]. The value of $\log K_{O_2}$ has been related[17] to the sum of $\log K_a$ of the ligands in water, which is a measure of the simple σ-donor ability of a ligand and therefore of the consequent electron density on the metal centre. When tacn is considered, a strongly acidic behaviour is observed for the first dissociation step due to the close proximity of the $NH_2^+$ groups, which results from the cyclic nature of the amine. Therefore, $\Sigma\log K_a$ of tacn is not available for a direct comparison with dmdien ($\Sigma\log K_a$ = 22.59) or with dien ($\Sigma\log K_a$ = 23.22). In a previous work the huge difference in stability of the dioxygen complexes of dmdien and dien systems was explained mainly by taking into account the statistical presence of a primary amino group (in dien) *trans* to the coordinated $O_2$,[16h] and this argument can also be used to explain the lower $\log K_{O_2}$ value found for the $[Co(tacn)_2O_2]^{2+}$ system with respect to $[Co(dien)_2O_2]^{2+}$. As far as the tacn and dmdien systems are compared, both possess only secondary amino groups, thus similar $\log K_{O_2}$ values are expected, as is the case. In light of the fact that the repulsion between the methyl groups in the dmdien system should lower the thermodynamic stability of the $O_2$ adduct with respect to tacn, the opposite result found here can be explained by supposing that the opening of a Co–N bond in $[Co(tacn)_2O_2]^{2+}$ causes the over-stability gained thanks to effects of "preorganisation" to partially drop.

## Conclusions

Some interesting features emerge from the combination of thermodynamic and DFT investigations. The extra stability of tacn complexes with respect to tridentate dmdien is mainly due to entropic effects for Cd, whereas the enthalpy term plays a fundamental role when Co is concerned.

This is an example of the great influence of the metal's ionic radius in satisfying the out-of-plane, facial coordination requirements of the cyclic triamine: in fact, the larger $Cd^{II}$ can better minimize steric strain, as clearly emerges from the values of the calculated strain energies in the gas phase for the same systems. On the other hand, the smaller $Co^{II}$ is more acid and achieves stronger coordination bonds than $Cd^{II}$, as confirmed by calculated binding energies of their complexes and by quite lower metal–N bond lengths in the Co–ligand systems. The enthalpy and entropy terms are therefore the result of a subtle interplay of steric and electronic effects. The *N*-methylation of tacn does not prevent $Me_3$tacn from behaving as a terdentate ligand, as occurs when linear pmdien is considered, due to a "preorganisation" of the ligand, which prevails over Me–Me steric repulsions. On the other hand, *N*-methylation, which is responsible for a less basic character of $Me_3$tacn than tacn in DMSO, causes a less marked preference for $Co^{II}$ than for the softer, larger $Cd^{II}$ with respect to tacn.

Finally, *N*-methylation strongly influences the stoichiometry of the species formed, as the $M(Me_3tacn)_2^{2+}$ (M = Co, Cd) species do not exist. As a consequence, only in the $Co(tacn)_2^{2+\cdot}$ complex does the central metal ion achieve sufficient electron density to be able to take up dioxygen.

## Experimental Section

**Materials:** $[Co(DMSO)_6(ClO_4)_2]$ and $[Cd(DMSO)_6(ClO_4)_2]$ were prepared as described previously.[16a] Tetraethylammonium perchlorate (TEAP; >97%, Aldrich ) was recrystallised from methanol and then dried under vacuum at 110 °C. The ligands tacn and $Me_3$tacn (Aldrich) were used without further purification. Dimethyl sulfoxide (99%, Aldrich) was purified by distillation according to the described procedures[16a] and stored under nitrogen over 4-Å molecular sieves. Perchlorate stock solutions of $Cd^{II}$ and $Co^{II}$ ions were prepared by dissolving weighed amounts of the adducts in anhydrous degassed DMSO; their concentrations were checked by titration against EDTA.[56]

Solutions of the ligands were prepared by dissolving weighed amounts in DMSO and standardised by thermometric titration with standard $HClO_4$ solutions. All standard solutions were prepared and stored in an MB Braun 150 glovebox under a controlled atmosphere containing less than 1 ppm of water and less than 1 ppm of oxygen. The water content in the solutions, typically 10–20 ppm, was determined with a Metrohm 684 KF Coulometer.

**Potentiometric Measurements:** All measurements employed for the determination of the stability constants of the $Cd^{II}$ complexes with tacn and $Me_3$tacn were carried out in 0.1 M $NEt_4ClO_4$ by using a thermostatted cell maintained at 298.1 ± 0.1 K, and kept under inert atmosphere in an MB Braun 150 glovebox. The concentrations of $Cd^{II}$ were obtained from the emf data of a galvanic cell measured

 © 2006 Wiley-VCH Verlag GmbH & Co. KGaA, Weinheim 

with an Amel 338 pHmeter equipped with a Weiss WCD1001 Cd ion selective electrode as working electrode and a Metrohm 6.0718.000 silver electrode as reference electrode. Aliquots of ligand solutions of known concentrations were added to solutions of cadmium(II) perchlorate only ($[Cd^{2+}]$ = 2.00–10.00 mM) of known concentration and the free-metal concentration was measured. Equilibrium was reached typically in 2–5 min. The Nernstian response of the Cd electrode was obtained in the range $10^{-7}$–$10^{-2}$ M.

The computer program Hyperquad[57] was used for the calculation of the stability constants.

**Calorimetric Measurements:** A Tronac model 87–558 precision calorimeter was checked by titration of tris(hydroxymethyl)aminomethane (tham) with a standard solution of HCl in water and used to measure the reaction heats. The experimental value of the heat of neutralisation of tham was found to be $\Delta H° = -47.58$ kJ mol$^{-1}$, in good agreement with the accepted value of $-47.53 \pm 0.13$ kJ mol$^{-1}$.[1b]

The calorimetric titrations were performed at $298.15 \pm 0.02$ K by adding known volumes of ligand solutions ([L] = 20–50 mM) to 20 mL of metal ($Cd^{II}$, $Co^{II}$) solutions ([M] = 2.00–5.00 mM). The measured heats were corrected for the dilution heat of the ligands.

The least-squares computer program Letagrop Kalle[58] was used for the calculation of the enthalpy changes.

**FT-IR Spectroscopy:** The FT-IR spectra were obtained using a Bio-Rad FTS 40 spectrometer (maximum resolution 4 cm$^{-1}$; 16 scans). Cells with barium fluoride windows (thickness of 25 μm) were used. The cells were filled and closed in a glovebox and quickly transferred to the spectrometer. Spectra were also collected for solutions containing the ligand alone.

**UV/Vis Spectrophotometric Measurements:** UV/Vis spectra were recorded with a Varian Cary 50 Spectrophotometer directly inside the glovebox when the anaerobic $CoL_j$ ($j$ = 1, 2, L = tacn; $j$ = 1, L = $Me_3$tacn) complex formation was studied. Optic fibre probes and a quartz cuvette with a path length of 1 cm (117.100 Bracco cell) were used. The data were recorded over the wavelength range 300–650 nm.

The formation constants of the $CoL_j$ complexes were obtained by performing different titrations with varying $Co^{II}$ and $Cd^{II}$ concentrations in order to obtain the best competition between the two metal ions for the same ligand and/or provide evidence of possible formation of mixed or polynuclear species, and treating the data with the Hyperquad program.[57]

The kinetics of oxygenation reactions of $Co(tacn)_2$ species were studied using an analogous apparatus by means of optic fibre probes (Hellma) of 1 cm length dipped directly into the reaction vessel. The appearance of the MLCT band(s) associated with the formation of the dioxygen adduct/s[16,17a,20,21] was followed.

The whole of the apparatus and the automatic procedure used to collect the kinetic runs, in the range 270–670 nm, were as described previously.[16e] The concentration of dissolved $O_2$ in solution was calculated assuming the validity of Henry's law[59] and a value of $2.1 \times 10^{-3}$ M for the equilibrium concentration of $O_2$ in DMSO + TEAP solution at 298 K with a partial pressure of 760 Torr of $O_2$ in the gas phase.[60] The data were analysed with the DYNAFIT program.[61]

**Computational Details:** The acyclic systems were not considered for calculations as they are flexible and give many possible coordination isomers, especially as far as the dmdien ligand is concerned. On the other hand, DFT calculations were performed on the cyclic triamines, which are more suitable to gain information about *N*-methylation effects, and on their $ML_j^{2+}$ complexes (M = Co, Cd). For this purpose, the program PC GAMESS version 6.5[62] was used with the B3LYP three-parameter hybrid density functional,[63] which has been shown to be reliable for the description of metal complexes. The split-valence basis set 6-31G+(d) was employed for the atoms of the ligands, while a 3-21G basis set was employed for the metal ions. For the $Co^{2+}$ complexes the unrestricted formalism was employed with three unpaired electrons ($S$ = 4).

All the geometries were optimised without symmetry constraints, except the $M(tacn)_2^{2+}$ complexes, which were optimised within the $C_i$ point group, until the maximum component of the gradient of the energy was below 0.0001 Hartree/Bohr and the rms gradient below 1/3 of the latter. After the optimisations, stationary points were characterised by the calculation of the vibrational frequencies in order to confirm they were local minima.

The binding energies ($E = E_{ML^{2+}} - E_{M^{2+}} - E_L$) were corrected for the basis set superposition error (BSSE) by the counterpoise correction.[64]

**Supporting Information** (see footnote on the first page of this article): Figure S1 shows the DFT-optimised structures of tacn and $Me_3$tacn with the numbering scheme and Table S1 contains the distances between all the ligands' numbered atoms.

## Acknowledgments

This work was supported by the Ministero dell'Istruzione, dell'Università e della Ricerca (MIUR, Rome) within the program COFIN 2002.

[1] a) R. M. Smith, A. E. Martell, *Critical Stability Constants*, 2nd Supplement, Plenum Press, New York, **1989**, vol. 6; b) A. E. Martell, R. M. Smith, R. J. Motekaitis, *Critically Selected Stability Constants of Metal Complexes Database*, version 5.0, **1998**.
[2] R. M. Clay, S. Corr, M. Micheloni, P. Paoletti, *Inorg. Chem.* **1985**, *24*, 3330–3336.
[3] R. Hancock, A. E. Martell, *Chem. Rev.* **1989**, *89*, 1875–1914; A. E. Martell, R. D. Hancock, R. J. Motekaitis, *Coord. Chem. Rev.* **1994**, *133*, 39–65.
[4] A. Bencini, A. Bianchi, P. Paoletti, *Coord. Chem. Rev.* **1992**, *120*, 51–85.
[5] F. C. J. M. van Veggel, W. Verboom, D. N. Reinboudt, *Chem. Rev.* **1994**, *94*, 279–299.
[6] C. Bazzicalupi, A. Bencini, A. Bianchi, V. Fusi, E. García-España, P. Paoletti, P. Paoli, B. Valtancoli, *Inorg. Chem.* **1993**, *32*, 4900–4908.
[7] G. Golub, H. Cohen, P. Paoletti, A. Bencini, D. Meyerstein, *J. Chem. Soc., Dalton Trans.* **1996**, 2055–2060.
[8] a) T. Clark, M. Hennemann, R. van Eldik, D. Meyerstein, *Inorg. Chem.* **2002**, *41*, 2927–2935; b) D. Meyerstein, *Coord. Chem. Rev.* **1999**, *185–186*, 141–147.
[9] N. Navon, A. Burg, H. Cohen, R. van Eldik, D. Meyerstein, *Eur. J. Inorg. Chem.* **2002**, 423–429.
[10] A. Bencini, A. Bianchi, P. Fornasari, C. Giorgi, P. Paoletti, B. Valtancoli, *Polyhedron* **2002**, *21*, 1329–1335.
[11] D. Dussalt, S. Friedle, L. J. Zompa, *Inorg. Chim. Acta* **2004**, *357*, 1478–1486.
[12] S. Ahrland, *The Chemistry of Non-aqueous Solvents* (Ed.: J. J. Lagowsky), Academic Press, New York, **1978**, vol. 5a.
[13] F. Arnaud-Neu, *Chem. Soc. Rev.* **1994**, *23*, 235–241.
[14] N. Heidari, A. Thaler, H. Schneider, B. G. Cox, *Inorg. Chim. Acta* **1998**, *279*, 186–191.
[15] A. Thaler, N. Heidari, B. G. Cox, H. Schneider, *Inorg. Chim. Acta* **1999**, *286*, 160–168.

 © 2006 Wiley-VCH Verlag GmbH & Co. KGaA, Weinheim 

[16] a) C. Comuzzi, M. Grespan, P. Polese, R. Portanova, M. Tolazzi, *Inorg. Chim. Acta* **2001**, *321*, 49–55; b) C. Comuzzi, M. Grespan, A. Melchior, R. Portanova, M. Tolazzi, *Eur. J. Inorg. Chem.* **2001**, 3087–3094; c) C. Comuzzi, A. Melchior, P. Polese, R. Portanova, M. Tolazzi, *Eur. J. Inorg. Chem.* **2002**, 2194–2201; d) C. Comuzzi, A. Melchior, P. Polese, R. Portanova, M. Tolazzi, *Eur. J. Inorg. Chem.* **2003**, 1948–1955; e) C. Comuzzi, A. Melchior, P. Polese, R. Portanova, M. Tolazzi, *Inorg. Chem.* **2003**, *42*, 8214–8222; f) S. Del Piero, A. Melchior, R. Portanova, P. Polese, R. Portanova, M. Tolazzi, *Dalton Trans.* **2004**, 1358–1365; g) A. Melchior, S. Peressini, R. Portanova, C. Sangregorio, C. Tavagnacco, M. Tolazzi, *Inorg. Chim. Acta* **2004**, *357*, 3473–3482; h) S. Del Piero, L. Ghezzi, A. Melchior, M. R. Tiné, M. Tolazzi, *Helv. Chim. Acta* **2005**, *88*, 839–853.
[17] a) A. F. Martell, D. T. Sawyer, *Oxygen Complexes and Oxygen Activation by Transition Metals*, Plenum, New York, **1988**; b) G. McLendon, A. E. Martell, *J. Chem. Soc., Chem. Commun.* **1975**, 223–225.
[18] H. Sugimoto, T. Nagayama, S. Maruyama, S. Fujinami, Y. Yasuda, M. Suzuki, A. Uehara, *Bull. Chem. Soc. Jpn.* **1998**, *71*, 2267–2279.
[19] R. D. Jones, D. A. Summerville, F. Basolo, *Chem. Rev.* **1979**, *79*, 139–179.
[20] E. C. Niederhoffer, J. H. Timmons, A. Martell, *Chem. Rev.* **1984**, *84*, 137–203.
[21] a) L. I. Simandi, *Dioxygen Activation and Homogeneous Catalytic Oxidation*, Elsevier, Amsterdam, **1991**; b) M. Costas, M. P. Mehn, M. P. Jensen, L. Que Jr, *Chem. Rev.* **2004**, *104*, 939–986.
[22] R. Yang, L. J. Zompa, *Inorg. Chem.* **1976**, *15*, 1499–1502.
[23] P. Chaudari, K. Wieghardt, *Prog. Inorg. Chem.* **1987**, *35*, 329–436.
[24] B. C. Gilbert, J. R. Lindsay Smith, M. S. Newton, J. Oakes, R. Pons, I. Prats, *Org. Biomol. Chem.* **2003**, *1*, 1568–1577.
[25] T. H. Bennur, D. Srinivas, S. Sivasanker, V. G. Puranik, *J. Mol. Catal. A: Chem.* **2004**, *219*, 209–216.
[26] J. W. Turner, F. A. Schultz, *J. Phys. Chem. B* **2002**, *106*, 2009–2017.
[27] P. Comba, G. N. DeIuliis, G. A. Lawrence, S. M. Luther, M. Maeder, A. L. Nolan, M. J. Robertson, P. Turner, *Dalton Trans.* **2003**, 2188–2193.
[28] a) K. P. Wainwright, *Coord. Chem. Rev.* **1997**, *166*, 35–90; b) S. F. Lincoln, *Coord. Chem. Rev.* **1997**, *166*, 255–289; c) J. M. Weeks, M. A. Buntine, S. F. Lincoln, E. R. T. Tickink, K. P. Wainwright, *J. Chem. Soc., Dalton Trans.* **2001**, 2157–2163.
[29] P. C. McGowan, T. J. Podesta, M. Thornton-Pett, *Inorg. Chem.* **2001**, *40*, 1445–1453.
[30] A. Mondal, E. L. Klein, M. A. Khan, R. P. Hauser, *Inorg. Chem.* **2003**, *42*, 5462–5464.
[31] G. Gonzales, D. H. Powell, V. Tissières, A. E. Merbach, *J. Phys. Chem.* **1994**, *98*, 53–59.
[32] R. H. Hancock, S. M. Dobson, J. C. A. Boeyens, *Inorg. Chim. Acta* **1987**, *133*, 221–231.
[33] I. V. Pletnev, *Can. J. Chem.* **1994**, *72*, 1404–1411.
[34] P. D. Beer, P. K. Hopkins, J. D. McKinney, *Chem. Commun.* **1999**, 1253–1254.
[35] L. F. Lindoy, T. Rambush, B. W. Skelton, A. H. White, *J. Chem. Soc., Dalton Trans.* **2001**, 1857–1862.
[36] a) B. Lakard, G. Herlem, B. Fahys, *J. Mol. Struct. (THEOCHEM)* **2002**, *584*, 15–36; b) A. Baeten, F. De Proft, W. Langenaeker, P. Geerlings, *J. Mol. Struct. (THEOCHEM)* **1994**, *306*, 203–221.
[37] B. Safi, K. Choho, F. De Proft, P. Geerlings, *Chem. Phys. Lett.* **1999**, *300*, 85–92.
[38] R. Willey, L. T. Daly, P. R. Meehan, M. G. B. Drew, *J. Chem. Soc., Dalton Trans.* **1996**, 4045–4053.
[39] H. Strasdeit, A.-K. Duhme, M. Weber, S. Pohl, *Acta Crystallogr., Sect. C* **1992**, *48*, 437–440.
[40] H. J. Kuppers, A. Neves, C. Pomp, D. Ventur, K. Wieghardt, B. Nuber, J. Weiss, *Inorg. Chem.* **1986**, *25*, 2400–2408.
[41] a) T. Arishima, K. Hamada, S. Takamoto, *Nippon Kagaku Kaishi* **1973**, 1119; b) M. Kodama, E. Kimura, *J. Chem. Soc., Dalton Trans.* **1978**, 1081–1085.
[42] J. C. Rossotti, H. Rossotti, *The Determination of Stability Constants*, McGraw-Hill, New York, **1961**.
[43] U. Bossek, D. Nühlen, E. Bill, T. Glaser, C. Krebs, T. Weyhermüller, K. Wieghardt, M. Lengen, A. X. Trautwein, *Inorg. Chem.* **1997**, *36*, 2834–2843.
[44] P. Comba, *Coord. Chem. Rev.* **1999**, *182*, 363–371.
[45] S. G. Lias, J. F. Liebman, R. D. Levin, *J. Phys. Chem. Ref. Data* **1984**, *13*, 695.
[46] H. Umeyama, K. Morokuma, *J. Am. Chem. Soc.* **1976**, *98*, 4400–4404.
[47] C. Kalidas, G. Hefter, Y. Marcus, *Chem. Rev.* **2000**, *100*, 819–852.
[48] V. Guttmann, *The Donor acceptor Approach to Molecular Interactions*, Plenum Press, New York, **1978**.
[49] M. R. Crampton, I. A. Robotham, *J. Chem. Res. (S)* **1997**, 22–23.
[50] R. D. Hancock, P. W. Wade, M. P. Ngwenya, A. S. de Sousa, K. V. Damu, *Inorg. Chem.* **1990**, *29*, 1968–1974.
[51] R. D. Shannon, *Acta Crystallogr., Sect. A* **1976**, *32*, 751–767.
[52] a) A. Mucci, R. Domain, R. L. Benoit, *Can. J. Chem.* **1980**, *58*, 953–958; b) R. L. Benoit, M. J. Mackinnon, L. Bergeron, *Can. J. Chem.* **1981**, *59*, 1501–1504.
[53] C. Stockheim, K. Wieghardt, B. Nuber, J. Weiss, U. Flörke, H.-J. Haupt, *J. Chem. Soc., Dalton Trans.* **1991**, 1487–1490.
[54] R. van Eldik, *Coord. Chem. Rev.* **1999**, *182*, 373–410.
[55] F. Miller, J. Simplicio, R. G. Wilkins, *J. Am. Chem. Soc.* **1969**, *91*, 1962–1967.
[56] A. I. Vogel, *Textbook of Quantitative Chemical Analysis*, 5th ed., Longman Group, London, **1989**.
[57] P. Gans, A. Sabatini, A. Vacca, *Talanta* **1996**, *43*, 1739–1753.
[58] R. Arnek, *Ark. Kemi* **1970**, *32*, 81–88.
[59] H. J. James, R. F. Broman, *Anal. Chim. Acta* **1969**, *48*, 411–417.
[60] D. T. Sawyer, G. Chiericato, C. T. Angelis, E. J. Nanni, T. Tsuchiya, *Anal. Chem.* **1982**, *54*, 1720–1724.
[61] P. Kuzmic, *Anal. Biochem.* **1996**, *237*, 260–273.
[62] a) M. W. Schmidt, K. K. Baldrige, J. A. Boatz, S. T. Elbert, M. S. Gordon, J. J. Jensen, S. Koseki, N. Matsunaga, K. A. Nguyen, S. Su, T. L. Windus, M. Dupuis, J. A. Montgomery, *J. Comput. Chem.* **1993**, *14*, 1347–1363; b) A. A. Granovsky, http://www.classic.chem.msu.su/gran/gamess/index.html.
[63] a) A. D. Becke, *J. Chem. Phys.* **1993**, *98*, 1372–1377; b) C. Lee, W. Yang, R. G. Parr, *Phys. Rev. B* **1988**, *37*, 785–789.
[64] F. F. Boys, F. Bernardi, *Mol. Phys.* **1970**, *19*, 533–566.

Received: July 28, 2005
Published Online: December 5, 2005

 © 2006 Wiley-VCH Verlag GmbH & Co. KGaA, Weinheim 

DOI: 10.1002/ejic.200500690

# The Coordination Chemistry of 1,4-Diazepan-6-amine[‡]

Jens Romba,[a] Dirk Kuppert,[a] Bernd Morgenstern,[a] Christian Neis,[a] Stefan Steinhauser,[a] Thomas Weyhermüller,[b] and Kaspar Hegetschweiler*[a]

**Keywords:** Chelates / Cobalt / Ligand design / N ligands / Stability constants

The new, tridentate, facially coordinating ligand 1,4-diazepan-6-amine (daza) has been prepared from ethane-1,2-diamine and 2,3-dibromo-1-propanol in a seven-step procedure with an overall yield of 22 %. The conformation of the free ligand has been elucidated by pH- and temperature-dependent $^1$H NMR spectroscopy and by a single-crystal X-ray structure analysis of $H_3dazaCl_3{\cdot}H_2O$. A twisted chair with a predominantly equatorial orientation of the primary amino group has been established for daza and its protonation products $H_xdaza^{x+}$ ($1 \leq x \leq 3$). The formation constants of $[M(daza)]^{2+}$ and $[M(daza)_2]^{2+}$ have been determined in aqueous solutions for M = $Ni^{II}$, $Cu^{II}$, $Zn^{II}$, $Cd^{II}$, and $Co^{II}$ by potentiometric and spectrophotometric measurements, and a remarkably high stability has been found for the bis complexes $ML_2$ in comparison to the mono complexes ML. This effect is discussed in terms of the particular steric requirements of the daza ligand. $[Cu(daza)Cl_2]$, $[Ni(daza)_2]Cl_2{\cdot}3.2H_2O$ and $[Zn(daza)_2]SO_4{\cdot}5H_2O$ have been characterized by single-crystal X-ray analyses. Aerial oxidation of $Co^{2+}$ in the presence of daza results in the formation of the inert $[Co(daza)_2]^{3+}$, which was isolated as a mixture of the *cis* and *trans* isomers. These two isomers were separated by chromatographic methods and identified by NMR spectroscopy and single-crystal X-ray structure analysis of *cis*-$[Co(daza)_2][ZnBr_4]Br{\cdot}H_2O$ and *trans*-$[Co(daza)_2]_3[ZnBr_4]_2Br_5{\cdot}4H_2O$. The redox potentials of $[Ni(daza)_2]^{3+/2+}$ (1.04 V vs. NHE) and $[Co(daza)_2]^{3+/2+}$ (–0.21 V vs. NHE) were determined by cyclic voltammetry. The values are slightly more positive than for corresponding complexes with related cyclic triamines. This effect is again discussed in terms of the particular steric requirements of these ligands.

(© Wiley-VCH Verlag GmbH & Co. KGaA, 69451 Weinheim, Germany, 2006)

## 1. Introduction

Triamines with a cyclic backbone and a restriction to facial coordination such as all-*cis*-1,3,5-cyclohexanetriamine (*cis*-tach),[1] 1,3,5-triamino-1,3,5-trideoxy-*cis*-inositol (taci),[2–4] or 1,4,7-triazacyclononane (tacn)[5,6] have received considerable attention in coordination chemistry. In particular, these ligands have been used to model the active site of metalloenzymes and to stabilize catalytically active metal centers.[7,8] In contrast to their open-chain aliphatic analogs, the restricted and well-defined coordination modes of the cyclic representatives allow a straightforward design of a specific coordination sphere, and the amino groups can readily be substituted with moieties carrying additional donor groups to give tetra-, penta-, or hexadentate chelators.[9–11]

The two triamines *cis*-tach and tacn may be regarded as the corner points of an entire series of triamine ligands containing a specific number of endocyclic (secondary) and exocyclic (primary) amino groups (Scheme 1). In view of the rich and interesting coordination chemistry opened up by *cis*-tach and tacn, it is rather remarkable that the intermediate members of this series have not received more attention as metal binding agents in coordination chemistry.[12–16] This is particularly surprising because asymmetric substitution of such species would easily open-up convenient routes to chiral derivatives and consequently to promising building blocks for new, enantioselective catalysts.

In two previous contributions,[14,15] we described the coordination chemistry of the two triamines *cis*-3,4-diaminopyrrolidine (*cis*-dap) and *cis*-3,5-diaminopiperidine (*cis*-dapi) and suggested that the seven-membered ring derivative 1,4-diazepan-6-amine (daza) would be a further, interesting member of this series. The use of *cis*-dapi as a building block for the construction of coordination polymers has meanwhile been described.[13] Substituted derivatives of 1,4-diazepan-6-amine are known as serotonine and dopamine receptor antagonists.[17] Moreover, a preliminary communication, proposing a 6-methyl-*N*,*N*′,*N*″,*N*‴-tetraacetic acid derivative of this compound as a potential Gd chelator for MRI applications, appeared very recently.[16] However, the unsubstituted 1,4-diazepan-6-amine ligand appears to be unknown, and to the best of our knowledge its coordination chemistry has hitherto not been investigated. We report here an efficient synthetic pathway for this interesting triamine and discuss its coordination properties with a range

[‡] Facially Coordinating Cyclic Triamines, 3. Part 2: Ref.[15]

[a] Anorganische Chemie, Universität des Saarlandes, Postfach 151150, 66041 Saarbrücken, Germany, Fax: +49-681-302-2663
E-mail: hegetschweiler@mx.uni-saarland.de
[b] Max-Planck-Institut für Bioanorganische Chemie, Postfach 101365, 45413 Mühlheim an der Ruhr, Germany

 © 2006 Wiley-VCH Verlag GmbH & Co. KGaA, Weinheim 

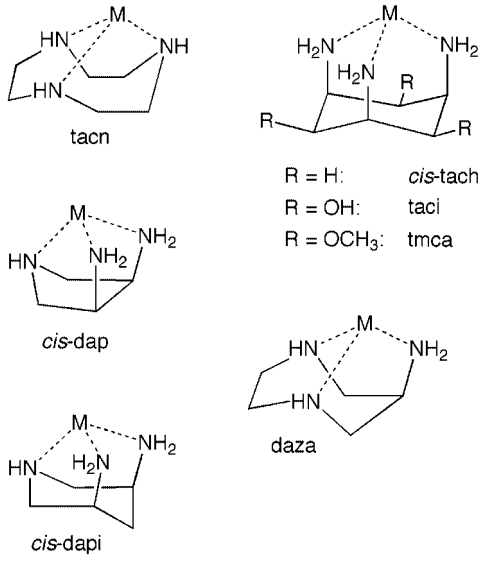


Scheme 1. Triamine ligands with a cyclic backbone.

of divalent and trivalent metal cations. The coordinating properties of the new ligand will be compared with the other cyclic triamines shown in Scheme 1, and characteristic differences will be analyzed in terms of the specific steric requirements of these compounds.

## 2. Results and Discussion

### 2.1. Preparation and Characterization of the Ligand

In previous protocols, construction of the 1,4-diazepane ring was achieved by a nitro-Mannich-type reaction.[16] We used a different approach (Scheme 2), however, and obtained the seven-membered ring by the reaction of an activated diaminoethane derivative with 2,3-dibromo-1-propanol.[18] The resulting 1,4-ditosyl-1,4-diazepan-6-ol was then transformed into the corresponding azide by converting the alcoholic OH group into a suitable leaving group followed by substitution with $N_3^-$.[19] Solutions of the azide were directly transferred into an autoclave and were hydrogenated to give the amine. Due to its potentially explosive nature, the isolation of the pure azide was usually avoided and only a small quantity of this compound was separated for characterization. The two remaining tosyl groups were finally removed in concd. aqueous hydrobromic acid, and the pure triamine was obtained as the trihydrochloride from a cation-exchange resin.

As expected, $H_3daza^{3+}$ reacts as a triprotic acid. The corresponding p$K_a$ values were determined at 25 °C by pH-metric titrations in aqueous solution for an ionic strength of 0.1 and 1 M (Table 1). The values for 0.1 M KCl and 0.1 M $KNO_3$ are closely related and an individual, direct interaction between the polyammonium cation and $Cl^-$ or $NO_3^-$ appears therefore not to be significant. The cyclic $H_3daza^{3+}$ is more acidic than the triply protonated, open-chain 3-azapentane-1,5-diamine ($H_3den^{3+}$), as shown in Table 2.[20] In particular, the second p$K_a$ value of the cyclic triamine is

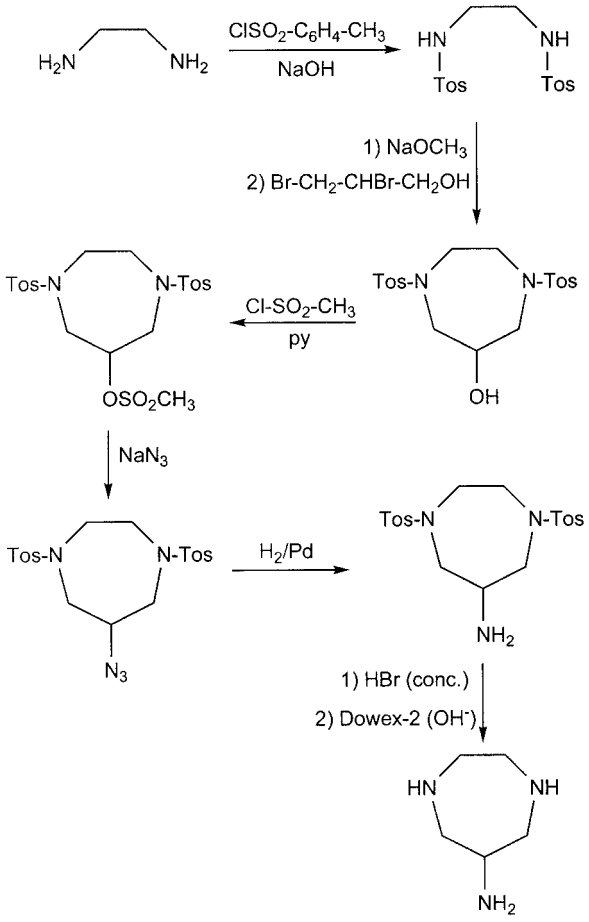


Scheme 2. Synthetic pathway for 1,4-diazepan-6-amine (daza).

considerably lower than that of the aliphatic triamine. This result is clearly a consequence of the steric constraints within the cyclic structure and can be understood in terms of simple electrostatic interactions between the positive charges located at the protonated amino groups.[15] It is also noteworthy that $H_3daza^{3+}$ is a stronger acid than $H_3(cis\text{-}dapi)^{3+}$ (Scheme 1), with a particularly pronounced effect for the first and the second deprotonation steps. The exocyclic amino groups of such ring systems preferentially adopt an equatorial orientation,[14,21] and in terms of electrostatic repulsion, it is therefore more difficult to protonate the endocyclic amino groups. These considerations are consistent with the observation that the triply protonated 1,4,7-triazacyclononane ($H_3tacn^{3+}$), where exocyclic amino groups are not present, is a strong acid that is not stable in $H_2O$.[22]

Table 1. p$K_a$ (= –log $K_a$)[a] values of $H_3daza^{3+}$ at 25 °C.

| | 0.1 M KCl | 0.1 M $KNO_3$ | 1.0 M $KNO_3$ |
|---|---|---|---|
| p$K_{a,1}$ | 3.20 | 3.18 | 3.73 |
| p$K_{a,2}$ | 6.47 | 6.44 | 6.78 |
| p$K_{a,3}$ | 9.24 | 9.24 | 9.42 |

[a] $K_{a,i} = [LH_{3-i}] \times [H] \times [LH_{4-i}]^{-1}$. The estimated standard deviations are less than 0.01.

Structural changes of polyamines in the course of protonation can be conveniently followed by $^1H$ NMR spec-

 © 2006 Wiley-VCH Verlag GmbH & Co. KGaA, Weinheim 

Table 2. Comparison of p$K_a$ values (25 °C, $\mu$ = 0.1 M) of representative triamines.

| | $H_3den^{3+}$ [a] | $H_3tacn^{3+}$ [a] | $H_3$(*cis*-dapi)$^{3+}$ [b] | $H_3$(*cis*-dap)$^{3+}$ [c] | $H_3daza^{3+}$ [d] |
|---|---|---|---|---|---|
| p$K_{a,1}$ | 4.3 | < 2 | 4.2 | 2.4 | 3.2 |
| p$K_{a,2}$ | 9.0 | 6.8 | 7.6 | 6.3 | 6.5 |
| p$K_{a,3}$ | 9.9 | 10.4 | 9.5 | 9.7 | 9.2 |

[a] From ref.[20] [b] From ref.[14] [c] From ref.[15] [d] This work, Table 1.

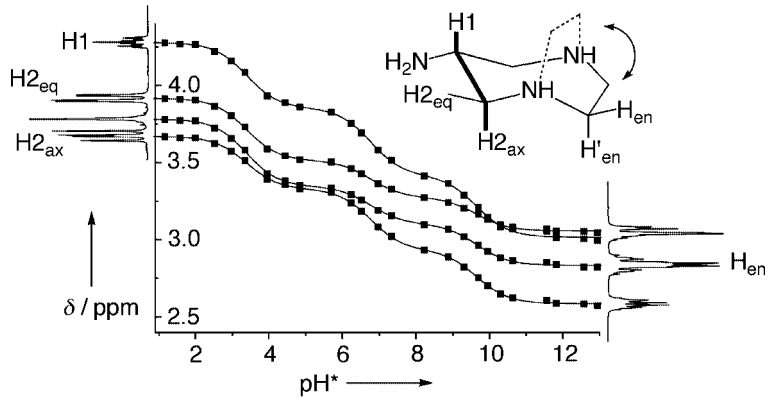


Figure 1. pH*-dependence[24] of the $^1$H NMR resonances of $H_xdaza^{x+}$ ($0 \le x \le 3$); squares correspond to experimental values; the lines were calculated (minimization of $[\delta_{obsd.} - \delta_{calcd.}]^2$). Inset: boat and chair conformations with averaged $C_s$ symmetry of $H_xdaza^{x+}$, compatible with the NMR spectroscopic data (see text); the H1–C–C–$H2_{ax}$ fragment responsible for the large vicinal coupling constant is highlighted in bold.

troscopy.[23] A series of spectra of daza as a function of pH* was recorded at 28 °C (Figure 1).[24] Assignments were established by $^1$H-$^1$H and $^1$H-$^{13}$C 2D correlation experiments, and the $\delta$ vs. pH* curves were evaluated using a least-squares procedure. The resulting apparent p$K_a$ values are 3.4, 6.8, and 9.7. Considering the different media ($D_2O$, no inert electrolyte vs. $H_2O$, 0.1 or 1 M KCl) these values agree well with the p$K_a$'s obtained from the potentiometric measurements (Table 1). It is well known that C–H protons near a basic site are deshielded in the course of protonation and this effect increases with a decreasing number of bonds between the basic site and the hydrogen atom under consideration.[25] It is possible to model this effect with a suitable set of deshielding constants and this information can then be used to identify the different tautomeric forms that are possible for the partially protonated species.[14,15] Based on such considerations, we showed that the first protonation step of daza is rather unspecific, with the proton of $Hdaza^+$ almost equally distributed over the three amino groups. For $H_2daza^{2+}$, however, the tautomer with a protonated primary amino group is strongly predominant ($\ge$ 90%).

The determination of coupling constants as a function of pH* proved helpful to follow conformational changes in the course of deprotonation.[26] At pH* < 3, H1 appears as a well-resolved, sharp triplet of triplets with two vicinal coupling constants ($J_a$ = 10.5 and $J_b$ = 3.1 Hz), indicative of an axial orientation of the hydrogen atom and thus an equatorial orientation of the primary amino group. Such a conformation of $H_3daza^{3+}$ was also observed in the crystal structure of daza·3HCl·$H_2O$ (Figure 2), where the diazepane ring adopts a twisted chair conformation (puckering parameters: $q_2$ = 0.522 Å, $q_3$ = 0.670 Å, $\theta_2$ = 41.4°, and $\theta_3$ = 193.5°).[27] The coupling constants also allowed an unambiguous identification of $H2_{eq}$ and $H2_{ax}$. As expected, the hydrogen atom with an equatorial orientation appears at higher frequency. The coupling constants change slightly with increasing pH* (pH* 4: $J_a$ = 8.4, $J_b$ = 3.7 Hz; pH* 6: $J_a$ = 7.4, $J_b$ = 4.1 Hz). As is well known, the cycloheptane ring is flexible and a variety of twisted chair and twisted boat conformations of similar energy could account for the solution structure. However, the coupling constants clearly indicate that the equatorial orientation of the primary amino group is maintained in the course of deprotonation. This assumption is also supported by the observation that an intercrossing of $H2_{eq}$ and $H2_{ax}$ in the pH* range investigated has not been noted.[14,21] Moreover, recording the spectra in MeOH/$H_2O$ (5:1) at low temperature showed only slight line broadening at 243 K, and individual signals for different conformers could not be observed.

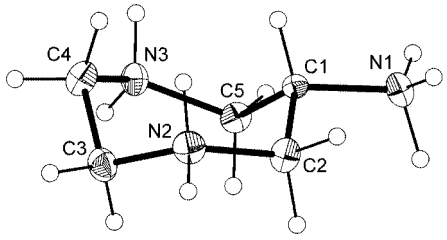


Figure 2. Molecular structure of $H_3daza^{3+}$ showing the twisted chair conformation of the seven-membered diazepane ring. The thermal ellipsoids are drawn at the 50% probability level; hydrogen atoms are shown as spheres of arbitrary size. All bond angles and bond lengths fall in the expected ranges.

 © 2006 Wiley-VCH Verlag GmbH & Co. KGaA, Weinheim 

### 2.2. Preparation and Structural Characterization of Metal Complexes

Bis complexes of $Co^{III}$ were prepared conventionally by aerial oxidation of the $Co^{II}$ precursors in aqueous solution. As is well established for $Co^{III}$–hexaamine complexes, the resulting species proved highly inert towards ligand substitution, and they could thus be used as illustrative models for studying the properties of individual isomers. Separation of different components of the reaction mixture by means of chromatographic methods yielded two major orange products, an achiral, $C_{2h}$-symmetric *trans*-$[Co(daza)_2]^{3+}$ ($\mathbf{1}^{3+}$, 25%) and a chiral, $C_2$-symmetric *cis*-$[Co(daza)_2]^{3+}$ ($\mathbf{2}^{3+}$, 20%). The two isomers could unambiguously be identified by their NMR spectra, and this assignment was further confirmed by single-crystal X-ray structure analysis (Figure 3). The crystal structures of both complexes suffered from some disorder. In the structure of the *trans* isomer, three crystallographically independent complex molecules ($\mathbf{1a}^{3+}$, $\mathbf{1b}^{3+}$, $\mathbf{1c}^{3+}$) were located, with their metal centers Co1, Co2, and Co3 all placed on twofold rotational axes. As mentioned above, the complex cation itself is centrosymmetric. It is thus noteworthy that the three complex cations are *not* placed on a crystallographic center of inversion, even though the compound crystallizes in a centrosymmetric space group. In the complex of Co1, the ligand adopts a major and a minor orientation having occupancies of 80% and 20%, respectively. In the structure of the *cis* complex $\mathbf{2}^{3+}$, the three atoms N17, C2, and C13 are placed on a crystallographic mirror plane. All other atoms are doubled, and the entire molecule was thus found to be distributed equally over two symmetry-related positions with the above-mentioned three atoms in common.

$[Ni(daza)_2]^{2+}$ ($\mathbf{3}^{2+}$) and $[Zn(daza)_2]^{2+}$ ($\mathbf{4}^{2+}$) form immediately by the simple combination of aqueous solutions of the ligand and the hydrated metal salt. Both complexes are labile. The equilibrium between individual isomers is thus rapid and it was not possible to isolate the different isomeric species in the form of solid compounds. The two complexes $\mathbf{3}^{2+}$ and $\mathbf{4}^{2+}$ were crystallized as their chloride and sulfate salts, respectively. A single crystal structure analysis showed the *trans* form for both complexes, and two crystallographically independent complex cations ($\mathbf{4a}^{2+}$ and $\mathbf{4b}^{2+}$) were located in the structure of the Zn complex. All three complex cations $\mathbf{3}^{2+}$, $\mathbf{4a}^{2+}$, and $\mathbf{4b}^{2+}$ lie on crystallographic centers of inversion, and we attribute the exclusive observation of the *trans* form to better packing of the centrosymmetric isomer.

A comparison of bond lengths and bond angles within the coordination spheres of the bis complexes $\mathbf{1a}^{3+}$–$\mathbf{1c}^{3+}$, $\mathbf{2}^{3+}$, $\mathbf{3}^{2+}$, $\mathbf{4a}^{2+}$, and $\mathbf{4b}^{2+}$ indicates some characteristic deviation from an ideal octahedral geometry. Intraligand N–M–N angles are generally smaller than 90° and interligand N–M–N angles are larger than 90°. This effect increases with the increasing ionic radius of the metal center. Moreover, the M–N bonds of the primary (exocyclic) amino groups are somewhat shorter than the M–N bonds of the secondary (endocyclic) amino groups (Table 3). We regard this effect as a consequence of the steric constraints of the ligand framework rather than a result of the different donor capacity of the two types of nitrogen donors (the secondary nitrogen donor is usually considered to be a stronger nucleophile).

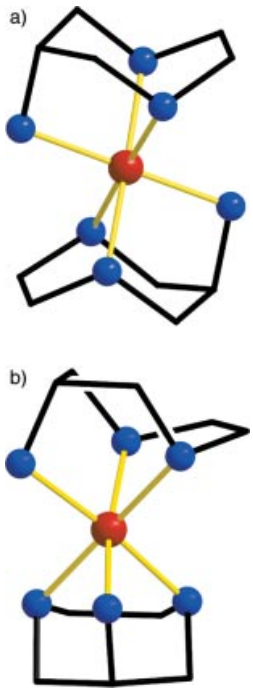


Figure 3. Molecular structure of a) the *trans*- and b) the *cis*-isomer of $[Co(daza)_2]^{3+}$ ($\mathbf{1}^{3+}$ and $\mathbf{2}^{3+}$). Color code: Co brown, N blue; the carbon skeleton is shown as a stick model (black); hydrogen atoms have been omitted for clarity. $[Ni(daza)_2]^{2+}$ ($\mathbf{3}^{2+}$) and $[Zn(daza)_2]^{2+}$ ($\mathbf{4}^{2+}$) adopt virtually the same *trans* structure as shown for the $Co^{III}$ complex $\mathbf{1}^{3+}$ (a).

The reaction of hydrated $CuCl_2$ with an excess of daza in aqueous solution resulted in the formation of a mononuclear, neutral 1:1 complex $[Cu(daza)Cl_2]$ (**5**). A crystal-structure analysis of this compound revealed a coordination number of five with a distorted square-pyramidal geometry ($\tau$ = 0.04).[28] Again, the intraligand N–Cu–N angles are significantly smaller than 90° and this effect mainly contributes to the deviation of the complex geometry from an ideal square pyramid. Complex **5** and the previously reported $[Cu(cis\text{-dapi})Cl_2]$ have closely related structures. In both complexes, the two chloro ligands and two of the nitrogen donors form the basal plane of the square pyramid. The third nitrogen donor is placed at the apex and has a considerably longer Cu–N bond (Table 3). In both structures, it is the endocyclic (secondary) nitrogen donor which forms this long bond to the apical position (Figure 4). With regard to the number of endocyclic and exocyclic nitrogen donors, the two triamine ligands *cis*-dapi (two exocyclic one endocyclic nitrogen atoms) and daza (one exocyclic, two endocyclic nitrogen atoms) are complements, and this is clearly reflected in the molecular structures of $[Cu(daza)Cl_2]$ and $[Cu(cis\text{-dapi})Cl_2]$. The free ligands *cis*-dapi and daza are both bisected by a mirror plane ($C_s$ symmetry);

 © 2006 Wiley-VCH Verlag GmbH & Co. KGaA, Weinheim 

Table 3. Synopsis of structural parameters of $H_3daza^{3+}$, *cis*-$[Co(daza)_2]^{3+}$, *trans*-$[Co(daza)_2]^{3+}$, $[Ni(daza)_2]^{2+}$, $[Cu(daza)Cl_2]$, and $[Zn(daza)_2]^{2+}$.

| | $M–N_{exo}$ (min., max., mean) [Å] | $M–N_{endo}$ (min., max., mean) [Å] | $N_{endo}–C–C–N_{endo}$ torsional angles [°] | Puckering parameters[27] $q_2$ [Å] | $q_3$ [Å] | $\theta_2$ [°] | $\theta_3$ [°] | $Q$ [Å] |
|---|---|---|---|---|---|---|---|---|
| $H_3daza^{3+}$ | | | 88.4 | 0.52 | 0.67 | 41 | 194 | 0.85 |
| *cis*-Co-daza | 1.946(8) | 1.977(8) | 0.5 | 0.59 | 0.72 | 337 | 50 | 0.93 |
| | 1.971(7) | 2.002(6) | 4.9 | 0.60 | 0.71 | 341 | 52 | 0.93 |
| | 1.959 | 1.985 | | | | | | |
| *trans*-Co-daza[a] | 1.947(3) | 1.956(3) | 6.3 (Co2) | 0.61 | 0.70 | 341 | 53 | 0.93 |
| | 1.952(3) | 2.004(3) | 0.3 (Co3) | 0.60 | 0.70 | 336 | 51 | 0.92 |
| | 1.950 | 1.980 | | | | | | |
| Ni-daza | | 2.136(3) | 0.1 | 0.57 | 0.68 | 334 | 52 | 0.88 |
| | | 2.137(2) | | | | | | |
| | 2.108(3) | 2.137 | | | | | | |
| Cu-daza | | 2.117(9) | 9.8 | 0.56 | 0.69 | 345 | 54 | 0.89 |
| | | 2.376(9) | | | | | | |
| | 1.970(11) | 2.247 | | | | | | |
| Zn-daza | 2.147(3) | 2.194(2) | 2.2 (Zn1) | 0.56 | 0.67 | 332 | 51 | 0.87 |
| | 2.148(3) | 2.234(2) | 1.4 (Zn2) | 0.55 | 0.66 | 336 | 52 | 0.86 |
| | 2.148 | 2.215 | | | | | | |

[a] Only the nondisordered ligands are considered.

however, this mirror plane is only retained in the *cis*-dapi complex, while the daza complex is devoid of any symmetry ($C_1$).

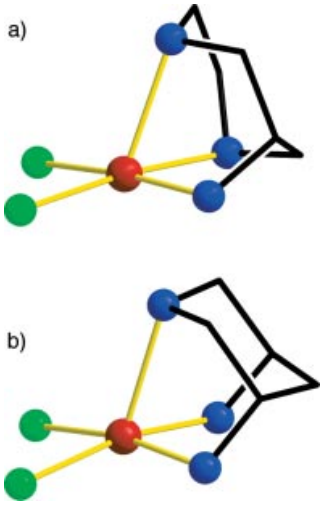


Figure 4. Molecular structure of a) $[Cu^{II}(daza)Cl_2]$ (**5**) and b) $[Cu^{II}(cis\text{-dapi})Cl_2]$ (from ref.[14]). Color code: Cu brown, N blue, Cl green; the carbon skeleton is shown by a stick model (black); hydrogen atoms have been omitted for clarity.

In all the complexes reported here the seven-membered diazepane ring adopts a regular chair conformation as indicated by the four puckering parameters $q_2$, $q_3$, $\theta_2$, and $\theta_3$ (Table 3).[27] This structural type is imposed by the tridentate coordination mode and implies an almost eclipsed orientation of the $N–CH_2–CH_2–N$ fragment (Table 3). It is noteworthy that the conformation of the corresponding five-membered chelate rings differs markedly from the well known λ/δ conformation observed in complexes with the open-chained ethane-1,2-diamine (Scheme 3), and also from the conformation that has been found for the noncoordinated ligand (Figure 2). It is thus obvious that a tridentate coordination mode of daza enforces some torsional strain within the metal complex.

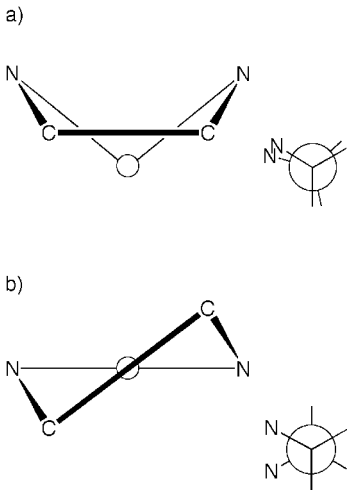


Scheme 3. Conformation of five-membered chelate rings in a metal complex with daza (a) and the open-chained ethane-1,2-diamine (b).

### 2.3. Stability of the Metal Complexes

The formation constants of daza complexes with $Co^{II}$, $Ni^{II}$, $Cu^{II}$, $Zn^{II}$, and $Cd^{II}$ were measured in aqueous media by potentiometric methods (Figure 5). A summary of these results is presented in Table 4. The main species formed in solution are $[M(daza)]^{2+}$ and $[M(daza)_2]^{2+}$. For $Cu^{II}$, however, formation of the protonated $[Cu(Hdaza)]^{3+}$ and $[Cu(daza)(Hdaza)]^{3+}$ was also verified unambiguously. As shown by their $pK_a$ values of 3.82 and 4.67, the two protonated complexes behave as acids of moderate strength.

 © 2006 Wiley-VCH Verlag GmbH & Co. KGaA, Weinheim 

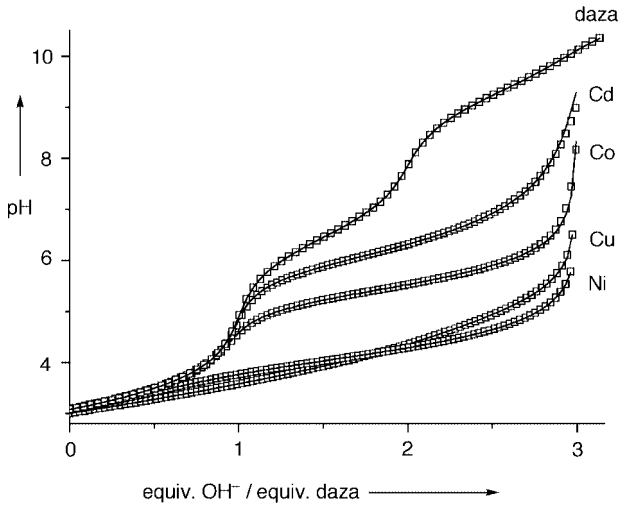


Figure 5. Titration curves (25 °C, 0.1 M KCl) of daza in the presence and absence of divalent metal cations as indicated. The total daza concentration is $2 \times 10^{-3}$ M, and (if present) the total metal concentration is $10^{-3}$ M. Squares refer to experimental values, the lines were calculated using the formation constants listed in Tables 1 and 4. The curve of the Zn complex is similar to the Co complex and has been omitted for clarity.

Table 4. Formation constants ($\log \beta_{xyz}$)[a] of daza (= L) complexes (25 °C, $\mu$ = 0.1 M).

| | $M(L)^{2+}$ $\log \beta_{110}$ | $M(HL)^{3+}$ $\log \beta_{111}$ | $M(L)_2^{2+}$ $\log \beta_{120}$ | $M(L)(HL)^{3+}$ $\log \beta_{121}$ |
|---|---|---|---|---|
| Co | 7.85(1) | – | 15.29(1) | – |
| Zn | 7.44(1) | – | 14.21(1) | – |
| Cu | 11.07(2) | 14.89(2) | 20.45(1) | 25.12(4) |
| Ni | 10.53(1) | – | 20.53(1) | – |
| Cd[b] | 6.49(2) | – | 11.65(2) | – |
| Cd[c] | 6.47(2) | – | 12.22(2) | – |

[a] $\beta_{xyz} = [M_xL_yH_z] \times [M]^{-x} \times [L]^{-y} \times [H]^{-z}$. The uncertainties given in parentheses correspond to 3σ. [b] 0.1 M KCl; the expression [M] and [ML] in the previous footnote should be interpreted as $\Sigma[MCl_i]$ and $\Sigma[MLCl_i]$, $i$ = 0, 1, respectively, see Section 2.3. [c] 0.1 M $KNO_3$.

It is well known that complexes with rigid ligands, having a cyclic backbone, often undergo ligand-exchange reactions that are slow relative to related ligands that do not have the same steric constraints. Moreover, comparatively slow substitution characteristics are well established for the $Ni^{II}$ center. Consequently, $Ni^{II}$–amine complexes such as $[Ni(cis\text{-tach})]^{2+}$ are inert,[29] and equilibration during a titration experiment is slow. In our previous investigations, a series of batch titrations were performed to investigate the $Ni^{II}$-*cis*-dapi, $Ni^{II}$-tmca, and $Ni^{II}$-taci system in aqueous solution.[14,21,30] In the $Ni^{II}$-daza system reported here, we therefore checked for complete equilibration by performing back titrations. To our surprise, the $Ni^{II}$-daza complexes proved to be labile, and an equilibration time of a few minutes after addition of an increment of titrant was sufficient even in the acidic range of the titration curve! It is well known that seven-membered rings readily undergo conformational changes, whereas six-membered chair structures, such as those observed in *cis*-dapi or taci, are rigid. The different flexibility of these ligand backbones obviously accounts for the variable lability of these tridentate systems.

In some of the titration experiments of the $Ni^{II}$ and $Cu^{II}$ complexes, the titration cell was equipped with an immersion probe, which was connected to a spectrophotometer with a diode array detector. This allowed the acquisition of additional spectrophotometric data, which were used to confirm the applied model and to evaluate the formation constants by an independent method (Figure 6). Moreover, the spectra of the individual species, which were calculated from the data, provided valuable information about the nature of the coordinated donor set. Due to the low intensity of the observed d–d transitions, the total metal concentration was increased to 10 mM and the inert electrolyte concentration was set at 1.0 M.

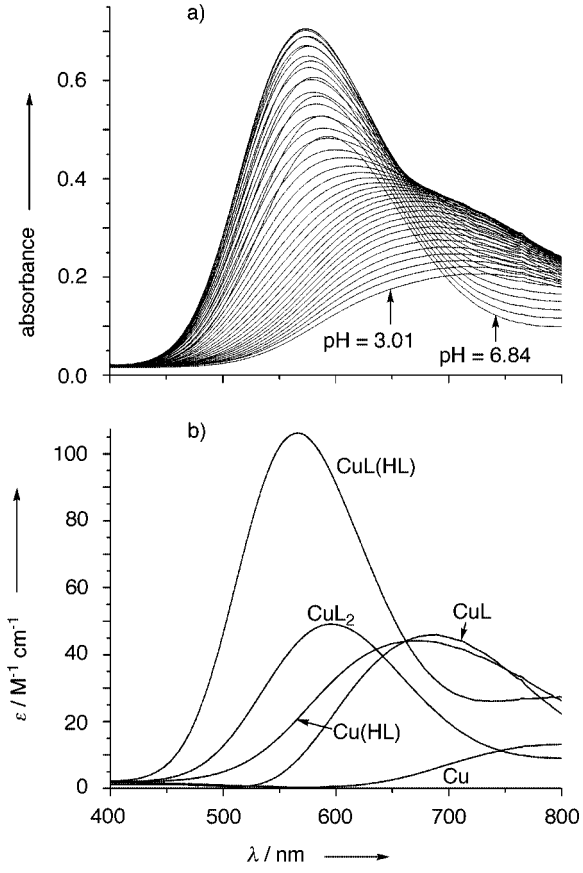


Figure 6. Determination of the formation constant $\log \beta_{xyz}$ of $[Cu_x(daza)_yH_z]^{2x+z}$ by spectrophotometric methods: a) the sample spectra of the spectrophotometric titration with total Cu/total daza = 1:2 in the range $3.0 < pH < 6.8$; b) calculated spectra of the individual $[Cu_x(L)_yH_z]^{2x+z}$ species (L = daza). The spectra of $Cu^{2+}$ was measured separately and was imported without refinement. The free ligand and its protonation products were considered as colorless.

As shown in Table 5, the agreement between the potentiometric and spectrophotometric measurements is generally good. $[Ni(daza)]^{2+}$ and $[Ni(daza)_2]^{2+}$ both exhibit the well-known three bands of a $d^8$ electron configuration, with maxima of the middle band [$^3A_{2g} \rightarrow {}^3T_{1g}(F)$ transition] at 590 and 513 nm, respectively. These values strongly sup-

 © 2006 Wiley-VCH Verlag GmbH & Co. KGaA, Weinheim 

port an octahedral triamine-triaqua-$Ni^{II}$ and hexaamine-$Ni^{II}$ chromophore, respectively (Figure 7),[31] and confirm that the tridentate coordination mode of daza observed in the crystal structure of $[Ni(daza)_2]Cl_2 \cdot 3.2H_2O$ is retained in solution. The $Cu^{II}$ complexes all show a single, broad, unresolved band. For $[Cu(daza)(Hdaza)]^{3+}$, the maximum of this band is found at 566 nm. Such a value is characteristic of a $CuN_4$ chromophore with all four nitrogen donors occupying equatorial positions, and one or two additional, weakly bonded $H_2O$ molecules in apical positions.[32] $[Cu(daza)_2]^{2+}$ exhibits a maximum at 596 nm. The corresponding red shift of about 30 nm, which follows from deprotonation of $[Cu(daza)(Hdaza)]^{3+}$, is very characteristic of the coordination of one additional nitrogen donor in one of the apical positions ("pentaamine effect").[23,33] Coordination of a sixth nitrogen donor obviously does not take place, because the maximal absorption for a tetragonally elongated $CuN_6$ chromophore would appear at even higher wavelength (around 620–640 nm).[31] As a result, we have assigned a bis-didentate coordination mode to the protonated $[Cu(daza)(Hdaza)]^{3+}$ and a combination of a didentate and tridentate coordination mode to $[Cu(daza)_2]^{2+}$. The protonated mono complex $[Cu(Hdaza)]^{3+}$ also absorbs at somewhat shorter wavelength than the nonprotonated $[Cu(daza)]^{2+}$. For these two species, the difference in wavelength is, however, relatively minor. For $Hdaza^+$, only didentate coordination is reasonable, and the red shift observed upon deprotonation is again indicative of a tridentate coordination mode for daza. Such a coordination mode is the same as that which has been observed in the solid-state structure of $[Cu(daza)Cl_2]$ (Figure 4). However, a comparison of the stability constants of $[Cu(en)]^{2+}$ ($\log \beta = 10.5$) and $[Cu(daza)]^{2+}$ ($\log \beta = 11.1$) reveals only a minor increase in stability upon going from the didentate to the tridentate ligand systems ($\Delta \log \beta = 0.6$). Obviously, the third nitrogen donor of daza undergoes only weak binding to the $Cu^{II}$ center. This is in marked contrast to the $Ni^{II}$ system, where $[Ni(daza)]^{2+}$ is considerably more stable than $[Ni(en)]^{2+}$ ($\Delta \log \beta = 3.2$).[15]

Table 5. Comparison of formation constants[a] of $Ni^{II}$– and $Cu^{II}$–daza complexes derived either from potentiometric (pot) or spectrophotometric (spec) titrations (25 °C, 1 M $KNO_3$) together with spectrophotometric data. Estimated standard deviations (3σ) are given in parentheses.

| | $x,y,z$ | $\log \beta_{xyz}$ (pot/spec) | $\lambda_{max}$ [nm]/ε [$M^{-1}cm^{-1}$] |
|---|---|---|---|
| $[Cu(daza)]^{2+}$ | 1,1,0 | 11.19(3)/11.33(9) | 682/45 |
| $[Cu(Hdaza)]^{3+}$ | 1,1,1 | 15.43(1)/15.52(6) | 674/44 |
| $[Cu(daza)_2]^{2+}$ | 1,2,0 | 20.76(1)/20.91(6) | 596/49 |
| $[Cu(Hdaza)(daza)]^{3+}$ | 1,2,1 | 25.95(2)/26.06(6) | 566/108 |
| $[Ni(daza)]^{2+}$ | 1,1,0 | 10.72(1)/10.7(1) | 590/8 |
| $[Ni(daza)_2]^{2+}$ | 1,2,0 | 20.85(1)/20.9(1) | 513/11 |

[a] $\beta_{xyz} = [M_xL_yH_z] \times [M]^{-x} \times [L]^{-y} \times [H]^{-z}$.

As noted previously for *cis*-dapi,[14] the formation constants measured for the bis complex $[Cd(daza)_2]^{2+}$ are significantly different in 0.1 M KCl or 0.1 M $KNO_3$, whereas the formation constants of the mono complex are virtually the same in the two media. This result can be explained in terms of the formation of the chloro complexes $[CdCl]^+$ and $[Cd(daza)Cl]^+$. The formation constant of $[CdCl]^+$ is known to be $K^{Cl} = [CdCl^+] \times [Cd^{2+}]^{-1} \times [Cl^-]^{-1} = 33\ M^{-1}$.[20] Conditional constants of the type $\beta_i^{cond} = \{[CdL_i] + [CdL_iCl]\} \times \{[Cd]+[CdCl]\}^{-1} \times [L]^{-i}$ may be used to describe the equilibria in the chloride medium, and $\beta_1^{cond} = \beta_1$ is thus indicative of approximately the same affinity of $Cd^{2+}$ and $CdCl^+$ for the binding of one daza ligand. The difference between $\beta_2$ and $\beta_2^{cond}$ corresponds to the value of $K^{Cl} \times [Cl^-]$ within experimental error, and this result demonstrates that $[Cd(daza)_2]^{2+}$ does not interact directly with $Cl^-$ to a significant extent, which lends strong support for a coordination number of six within the hexaamine complex.

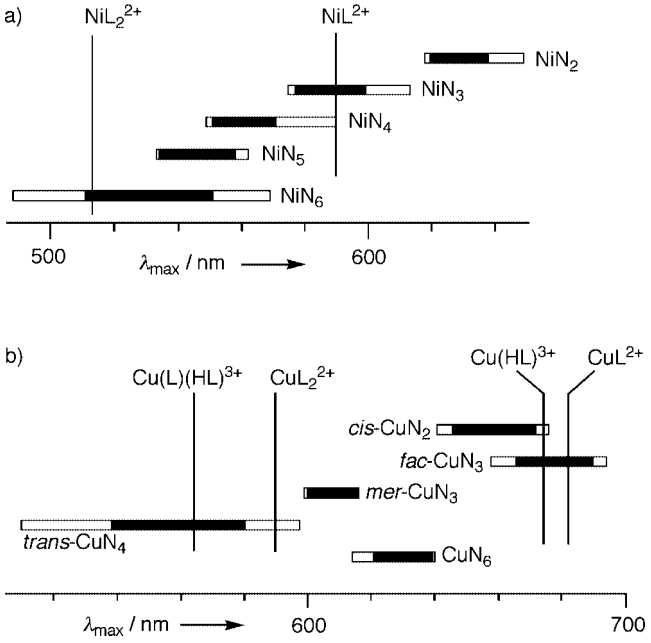


Figure 7. Correlation of the observed $\lambda_{max}$ values of the individual a) $Ni^{II}$– and b) $Cu^{II}$–daza complexes formed in aqueous solution with the $\lambda_{max}$ values of some chromophores reported in the literature.[31] Only complexes with a defined coordination environment containing a set of $sp^3$-nitrogen donors as indicated and $H_2O$ as additional ligands were considered. The data of the $Ni^{II}$ complexes refer to the $^3A_{2g}$–$^3T_{1g}(F)$ transition. Open boxes refer to the entire range reported, black boxes represent the averages ± one standard deviation.

A synopsis of the formation constants for some representative cyclic triamine ligands is given in Figure 8. The following general trends are noteworthy:

(i) With the exception of tacn, all the ligands shown have a remarkably low affinity for $Cu^{II}$ in comparison to $Ni^{II}$. For *cis*-tach, daza, and *cis*-dapi, $[Cu^{II}L]^{2+}$ is only of slightly higher stability than $[Ni^{II}L]^{2+}$ (Figure 8a). For 1,3,5-triamino-1,3,5-trideoxy-*cis*-inositol (taci), and its *O*-methylated derivative *all-cis*-2,4,6-trimethoxycyclohexane-1,3,5-triamine (tmca), the Irving–Williams order is even inverted, and the Ni complex is more stable. This effect is markedly

 © 2006 Wiley-VCH Verlag GmbH & Co. KGaA, Weinheim 

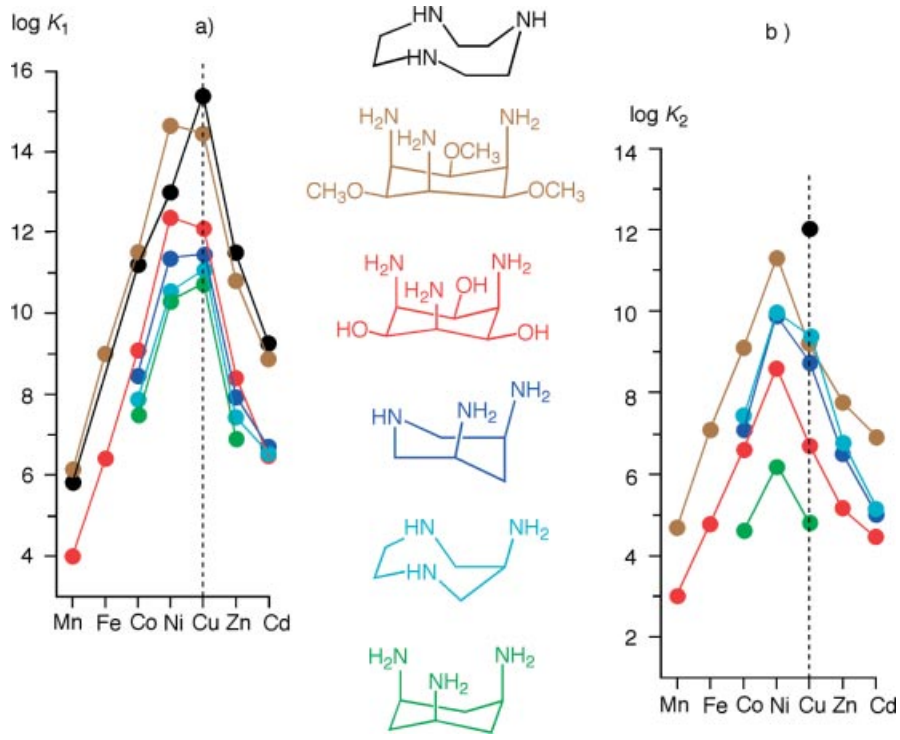


Figure 8. Survey of formation constants for complexes with divalent cations and various cyclic triamine ligands as indicated. Note that the values of the individual formation constants ($K_1 = [ML] \times [M]^{-1} \times [L]^{-1}$ and $K_2 = [ML_2] \times [ML]^{-1} \times [L]^{-1}$) rather than overall constants ($\beta_1$ and $\beta_2$) are shown. The constants of the daza complexes are from this work (Table 4), the formation constants of the other ligands are from refs.[3,14,20,21,36]

more pronounced for the addition of a second ligand moiety (Figure 8b), where a distinct maximum is now observed at $Ni^{II}$ for all the ligands. The preferred binding of $Ni^{II}$ is obviously due to the exclusive facial coordination mode of these ligands, which results in the above-mentioned weak binding of the third amine donor to the $Cu^{II}$ center.

(ii) In comparison to the other cyclic triamine ligands, the stability of the $[M(daza)]^{2+}$ species is generally low. As a matter of fact, only *cis*-tach forms 1:1 complexes of slightly lower stability. The relatively poor stability of the *cis*-tach complexes, and to a lesser extent of the *cis*-dapi complexes, is readily understood in terms of the high-energy conformation (primary amino groups all in axial positions), which is required for complex formation.[34] For taci and tmca, both chair conformations are destabilized by 1,3-diaxial repulsive interactions and metal binding does thus not require such an additional amount of energy. For daza, the primary amino group in the free ligand also has a preferred equatorial orientation (see Section 2.1), however, compared to *cis*-tach and *cis*-dapi, one would expect that much less energy is needed to bring it into an axial position. As already outlined in Section 2.2, it is the enforcement of the unfavorable chair conformation of the diazepane ring (local $C_s$ symmetry) with the eclipsed arrangement of the $N_{endo}$–$CH_2$–$CH_2$–$N_{endo}$ fragment that accounts for the low stability.

(iii) In contrast to the relatively low stability of the $[M(daza)]^{2+}$ complexes, the binding of a second ligand moiety (formation of $[ML_2]^{2+}$) is a highly favored process (Figure 8b). The ratio $\log K_1/K_2$ for the cyclohexane-based ligands *cis*-tach, taci, and tmca (excluding $Cu^{II}$) lies in the range of 2.0–4.1, whereas for daza it is 0.4–0.7. A similar behavior has previously been reported for *cis*-dapi ($\log K_1/K_2 \approx 1.4$),[14] although the ratio observed for daza is even smaller. A purely statistical approach would require that $K_1/K_2 = 16$ ($\log K_1/K_2 = 1.2$),[35] and thus it is evident that the two ligands in the $[M(daza)_2]^{2+}$ complexes show some cooperativity. As discussed previously,[14,36] the different behavior of the ligands with three exocyclic amino groups on the one hand and of *cis*-dapi and daza on the other can be explained by means of steric requirements, which result in different interligand interactions (Scheme 4). Moreover, some symbiotic behavior appears to further enlarge the binding of the second ligand.[37] The high cooperativity between the two ligand moieties in the $[M(daza)_2]^{2+}$ complexes results in some effects that are rather unusual in solution chemistry (Figure 9). For example, for ligands such as tmca, with "normal" behavior, $[ML]^{2+}$ is usually the only species that is present to a significant extent in solutions with equal concentrations of total ligand and total metal, and formation of $[ML_2]^{2+}$ is generally negligible. Furthermore, in solutions with a total metal/total ligand concentration of 1:2, the mono complex appears as the dominant species in the acidic range. In contrast, for daza, significant amounts of $[ML_2]^{2+}$ already form up to 30% in solutions with equal concentrations of total M and total L according to $2ML \rightarrow M + ML_2$, and in solutions with excess ligand $[ML]^{2+}$ appears only as a minor species within a narrow pH range.

 © 2006 Wiley-VCH Verlag GmbH & Co. KGaA, Weinheim 

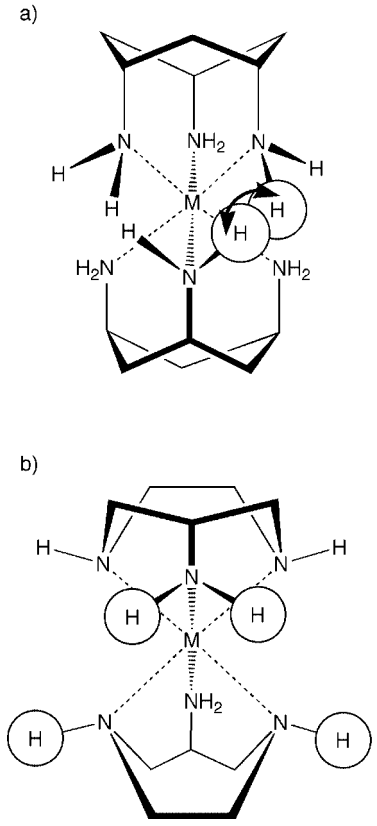


Scheme 4. Interligand repulsion in bis complexes $ML_2$ [L = *cis*-tach (a) and daza (b)].

## 2.4. Redox Properties

The redox properties of $[Co(daza)_2]^{3+/2+}$ and $[Ni(daza)_2]^{3+/2+}$ were investigated by means of cyclic voltammetry. For comparison, corresponding complexes with *cis*-dapi and taci were also studied. All the complexes investigated revealed quasi-reversible redox behavior (Figure 10), and the peak current was found to be linearly dependent on the square root of the scan rate, as expected for a diffusion-controlled process (Table 6). For the investigation of the $[Co(daza)_2]^{3+/2+}$ couple, crystalline samples of the distinct $Co^{III}$ complexes were used for the preparation of the test solutions. The *cis*- and the *trans*-isomers were investigated

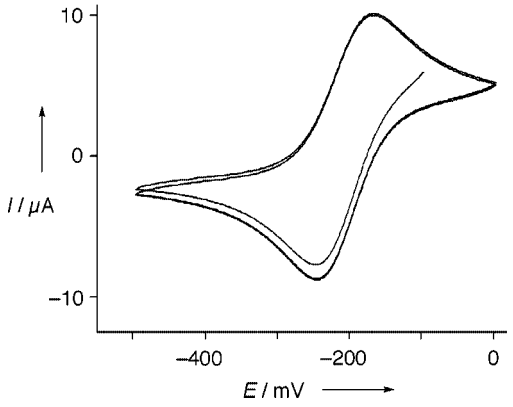


Figure 10. Cyclic voltammogram of $[Co(daza)_2]^{3+/2+}$ in aqueous solution (referenced against NHE, pH 10, 25 °C, $v$ = 50 mV s$^{-1}$).

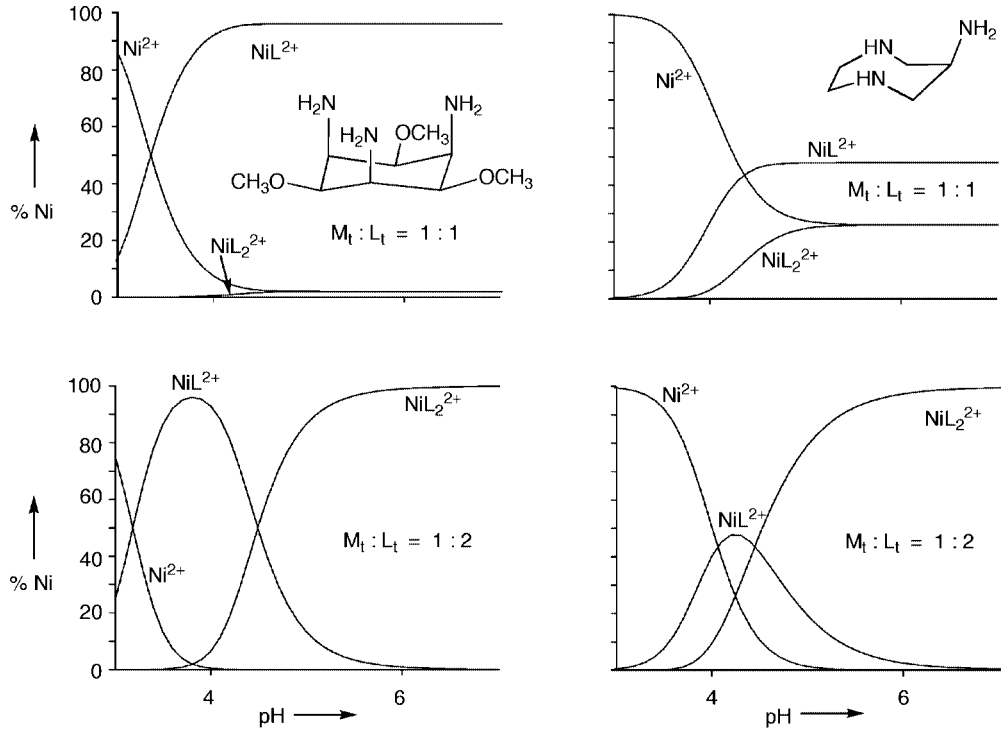


Figure 9. Illustration of the different solution properties for triamine complexes with a low (left side) and a high (right side) cooperativity between the two ligand moieties in a 1:2 complex. The species distribution was calculated for a total metal concentration of $10^{-3}$ M and a total ligand concentration of $10^{-3}$ M (top) and $2\times10^{-3}$ M (bottom). The formation constants used for the $Ni^{II}$–daza system are from this work (Table 4), the formation constants of 2,4,6-trimethoxy-1,3,5-cyclohexanetriamine are from ref.[21]

 © 2006 Wiley-VCH Verlag GmbH & Co. KGaA, Weinheim 

separately; however, the cyclic voltammograms of the two isomers did not differ to a significant extent. A similar observation has previously been reported for the $[Co(cis\text{-dapi})_2]^{3+/2+}$ system.[14]

Table 6. Electrochemical data from cyclic voltammetry for the $[CoL_2]^{3+/2+}$ and $[NiL_2]^{3+/2+}$ couples in aqueous solution.

| $[ML_2]^{3+/2+}$ | $E_{1/2}$ [V][a] | $\Delta E_p$ [mV][b] | $R$[c] |
|---|---|---|---|
| $[Co(daza)_2]^{3+/2+}$ | –0.21 | 74, 95 | 0.9998 |
| $[Co(taci)_2]^{3+/2+}$ | –0.35 | 75, 114 | 0.9995 |
| $[Co(cis\text{-dapi})_2]^{3+/2+}$ | –0.38 | 69, 91 | 0.9999 |
| $[Ni(daza)_2]^{3+/2+}$ | 1.04 | 86, 132 | 0.9978 |
| $[Ni(taci)_2]^{3+/2+}$ | 0.95 | 76, 98 | 0.9999 |
| $[Ni(cis\text{-dapi})_2]^{3+/2+}$ | 0.92 | 72, 94 | 0.9999 |

[a] Reduction potentials relative to NHE. [b] Peak separation for a scan rate of 20 mV s$^{-1}$ and 1000 mV s$^{-1}$, respectively. [c] Correlation coefficients for the linearity of $I$ vs. $\sqrt{(v)}$ in the range 20 mV s$^{-1}$ $\leq$ $v$ $\leq$ 1000 mV s$^{-1}$ with a total of eight data points for each couple.

In general, the reduction potentials of corresponding *cis*-dapi and taci complexes are in close agreement, whereas the redox potentials of the daza complexes are all somewhat more positive (Table 6). Obviously, the taci- and *cis*-dapi- (= $L^a$) complexes with divalent cations are stronger reducing agents than corresponding daza (= $L^b$) complexes, and this means that in a taci- or *cis*-dapi complex the trivalent cation is stabilized according to

$$\Delta E_{1/2} = E_{1/2}(L^a) - E_{1/2}(L^b) = -RT/F \times \{\ln[\beta_2^{III}(L^a)/\beta_2^{II}(L^a)] - \ln[\beta_2^{III}(L^b)/\beta_2^{II}(L^b)]\} = -RT/F \times \Delta\ln(\beta_2^{III}/\beta_2^{II})$$

where $\beta_2^{III}$ and $\beta_2^{II}$ stand for the formation constants of the bis complexes with the trivalent and divalent cations, respectively. For *cis*-dapi and daza, one obtains $\Delta\log(\beta_2^{III}/\beta_2^{II}) = 2.9$ for $Co^{III/II}$ and 2.0 for $Ni^{III/II}$. It is interesting to note that Hancock has proposed some characteristic size selectivity for five- and six-membered chelate rings. The steric constraints of five-membered chelate rings are more suited for the binding of a large metal cation, whereas formation of six-membered chelate rings is more favorable for small cations.[38] Since the higher oxidation state generally implies a smaller ionic size, one would thus expect a less-negative redox potential for a ligand forming exclusively five-membered chelate rings, and that is indeed what we observe. The somewhat smaller $\Delta\log(\beta_2^{III}/\beta_2^{II})$ value of Ni (in comparison to Co) can be attributed to the well-known Jahn–Teller distortion caused by the low-spin $d^7$ electron configuration. This type of distortion would destabilize the $Ni^{III}$ complex with a cyclic triamine ligand in a similar way as described for $Cu^{II}$ (see Section 2.3),[23] and this effect is obviously more pronounced for the rigid taci or dapi than for daza.

## 3. Conclusions

In this paper, we have shown that 1,4-diazepan-6-amine (daza) readily forms 1:1 and 1:2 complexes with divalent transition metal cations in aqueous solution and exhibits mainly a tridentate facial coordination mode. The specific coordinating properties of daza are as follows:

a) In contrast to the $C_{3v}$-symmetric representatives such as tacn or *cis*-tach (Scheme 1), the $C_s$-symmetric ligand daza (similar to *cis*-dapi) is of lower symmetry and thus gives rise to a more complex stereochemistry. In particular, bis complexes exist in the form of *cis*- and *trans*-isomers. Due to the labile nature of most of the metal centers used, the different forms equilibrate rapidly and cannot be isolated. For the inert $Co^{III}$, we obtained approximately equal amounts of *cis*-$[Co(daza)_2]^{3+}$ and *trans*-$[Co(daza)_2]^{3+}$ which indicates that the energy of the two isomers does not differ significantly.

b) In comparison with other triamine ligands, the stability of the complexes is not exceptionally high. As an example, the open-chained 3-azapentane-1,5-diamine (den) forms a $NiL^{2+}$ complex with a formation constant, $\log \beta_1$, of 10.55,[20] which corresponds closely to the value (10.53) found for daza (Table 4). This result was somewhat unexpected because the donor set of the daza ligand has a much higher degree of pre-orientation. In comparison to other cyclic ligands (Scheme 1), the stability of daza complexes is relatively poor. We attribute the lower stability to the unfavorable, eclipsed conformation of the $N_{endo}$–$CH_2$–$CH_2$–$N_{endo}$ moiety, which is enforced in the course of coordination. In making comments about apparent stability, however, one should note that daza is a much weaker base than, for instance, the open-chained den, and although the formation constants of the two triamines are similar, daza is a much more effective chelator in neutral or slightly acidic media.[15]

c) The cooperativity between two daza moieties of a bis complex is even higher than for *cis*-dapi, and, as a consequence, a significant amount of the bis complex is formed already if the ligand and the metal are added in a 1:1 ratio. With regard to possible applications (catalysis, modeling of the active site of a metalloenzyme), as outlined in the introduction, this high cooperativity is disadvantageous − binding of a substrate requires at least one free coordination site and the formation of the bis complexes should thus be avoided.[39] This problem can, however, be solved by adding additional substituents to some of the nitrogen donors in such a way that the steric demands, and thus interligand repulsion, disfavor the binding of a second ligand entity. This topic will be the issue of a subsequent paper.[40]

d) Compared to the *cis*-tach and *cis*-dapi backbone, the daza backbone appears to be rather flexible and this results in fast ligand-substitution behavior. The kinetics of ligand formation, although not yet studied in detail, resemble that of an open-chained ligand system.

e) The daza ligand exclusively forms five-membered chelate rings and this favors complex formation with relatively large cations. As a consequence, the redox potential of $M^{III}(daza)_x/M^{II}(daza)_x$ couples is somewhat more positive (less negative) than corresponding couples with *cis*-dapi or taci complexes.

 © 2006 Wiley-VCH Verlag GmbH & Co. KGaA, Weinheim 

## Experimental Section

**General:** The commercially available chemicals used for the synthetic work were of reagent grade quality and were used as obtained. DMSO was from Fluka (puriss., p. a.). MeOH and EtOH were purified by distillation prior to use. Dowex 50 W-X2 (100–200 mesh, $H^+$ form) and Dowex 2-X8 (50–100 mesh, $Cl^-$ form) were from Fluka. The anion resin was converted into the $OH^-$ form by treatment with 0.3 M aqueous NaOH. For the potentiometric and spectrophotometric titrations, metal salts of highest available quality (>99.95%) were used. $H_2O$ was distilled twice (quartz apparatus). UV/Vis spectra of the $Co^{III}$ complexes were measured with an Uvikon 941 spectrophotometer ($H_2O$, 25 ± 3 °C). IR spectra were recorded with a Bruker Vector 22 FT IR spectrometer equipped with a Golden Gate ATR unit. Semi-quantitative determinations of $Co^{II}$ in solution were performed with Merckoquant 10002 test strips (Merck). C,H,N analyses were performed by H. Feuerhake (Universität des Saarlandes).

**NMR:** $^1H$ and $^{13}C\{^1H\}$ NMR spectra were measured in [$D_6$]-DMSO, $CD_3OD$, or $D_2O$ at 28 °C using a Bruker DRX Avance 400 MHz NMR spectrometer (resonance frequencies: 400.13 MHz for $^1H$ and 100.6 MHz for $^{13}C\{^1H\}$). Chemical shifts are given in ppm relative to [$D_4$]sodium (trimethylsilyl)propionate ($D_2O$) or tetramethylsilane ([$D_6$]DMSO and $CD_3OD$) as internal standards ($\delta$ = 0 ppm). A Hamilton SPINTRODE glass electrode, which was calibrated with aqueous ($H_2O$) buffer solutions, was used to measure pH* directly in the NMR tube.[24] The pH* of each sample was adjusted with appropriate solutions of DCl and NaOD in $D_2O$.

**Cyclic Voltammetry:** Cyclic voltammograms were recorded at ambient temperature (25 ± 2 °C) in a BAS C2 cell (0.5 M KCl), using a BAS 100B/W2 potentiostat, a gold (for the Co complexes) or glassy carbon (for the Ni complex) working electrode, a platinum counter electrode, and an Ag/AgCl reference electrode. Sample solutions of the Co complexes were made up using solid $[CoL_2]^{3+}$ salts. The total Co concentration was 0.004 M and the pH was adjusted to 10 (KOH). Ni samples were prepared in situ using a $Ni^{II}$ salt and the trihydrochloride of the ligands (total $Ni^{II}$ = 0.012 M, total L = 0.03 M, L = daza, taci, *cis*-dapi). 0.5 M KOH was then added to bring the pH to a value of 7.

**Potentiometric and Spectrophotometric Measurements:** The titration experiments were performed at 25.0 °C under $N_2$ or Ar (for the Co complexes) as described previously.[41] Simple potentiometric titrations were carried out with total M/total daza ratios of 1:1 and 1:2 in 0.1 M KCl or 0.1 M $KNO_3$ (Figure 5). Titration experiments, which were followed by potentiometric and spectrophotometric methods, were performed in 1 M KCl. A Metrohm 665 piston burette was used for addition of the titrant (KOH, HCl or $HNO_3$), and the pH was recorded using a Metrohm glass electrode with an incorporated Ag/AgCl reference, connected to a Metrohm 713 pH/mV meter. For spectrophotometric measurements, the titration cell was equipped with an immersion probe (HELLMA), which was connected to a spectrophotometer equipped with a diode array detector (J&M, TIDAS-UV/NIR/100-1). The titrations were performed with a total metal concentration of 0.01 M and a total daza concentration of 0.02 M. A PC was used to trigger recording of a spectrum just prior to the addition of each new aliquot of base.[41]

**Calculations of Equilibrium Constants:** Equilibrium constants were generally calculated as concentration quotients (pH = –log[$H^+$]) using the computer programs HYPERQUAD and SPECFIT.[42,43] The total concentrations of the reactants and the p$K_w$ (13.78 for $\mu$ = 0.1 M, 13.77 for $\mu$ = 1.0 M)[20] were not refined. The protonation constants of the diazepane ligand were evaluated separately and were kept fixed when refining formation constants of the metal-containing species. The UV/Vis spectra of the free $Ni^{2+}$ and $Cu^{2+}$ were recorded separately and were imported as fixed data sets for the evaluation of the formation constants of the metal complexes. The free ligand and its protonation products were treated as nonabsorbing species.

***N*$^1$,*N*$^2$-Ditosyl-1,2-ethanediamine:**[44] Toluene-4-sulfonyl chloride (95 g, 0.5 mol) was suspended in diethyl ether (200 mL). The suspension was cooled with an ice bath, and a mixture of NaOH (20 g, 0.5 mol) and ethane-1,2-diamine (15 g, 0.25 mol, dissolved in 200 mL of $H_2O$) was added dropwise. The resulting white suspension was stirred overnight at room temperature. The residue was filtered off and recrystallized from MeOH (white crystals, 86.2 g, 94%). $C_{16}H_{20}N_2O_4S_2$ (368.5): calcd. C 52.15, H 5.47, N 7.60; found C 52.66, H 5.41, N 7.46. $^1H$ NMR (DMSO): $\delta$ = 2.39 (s, 6 H), 2.72 (s, 4 H), 7.38 (d, *J* = 8.2 Hz, 4 H), 7.61 (d, *J* = 8.2 Hz, 4 H) ppm. $^{13}C$ NMR (DMSO): $\delta$ = 21.0, 42.2, 126.5, 129.7, 137.4, 142.8 ppm. IR: $\tilde{\nu}$ = 664, 709, 748, 818, 875, 1020, 1058, 1092, 1153, 1188, 1240, 1292, 1307, 1330, 1404, 1452, 1496, 1598, 3282 $cm^{-1}$.

**Disodium *N*$^1$,*N*$^2$-Ditosyl-1,2-ethanediamide:** Sodium metal (4.6 g, 0.2 mol) was allowed to react with water-free MeOH (150 mL), then *N*$^1$,*N*$^2$-ditosyl-1,2-ethanediamine (36.8 g, 0.1 mol) was added. The white suspension was refluxed for half an hour, the solvent evaporated completely and the remaining white residue dried in vacuo (40.0 g, 97%). $C_{16}H_{18}N_2Na_2O_4S_2$ (412.4): calcd. C 46.60, H 4.40, N 6.79; found C 46.76, H 4.77, N 6.70. $^1H$ NMR (DMSO): $\delta$ = 2.32 (s, 6 H), 2.58 (s, 4 H), 7.18 (d, *J* = 8.0 Hz, 4 H), 7.50 (d, *J* = 8.0 Hz, 4 H) ppm. $^{13}C$ NMR (DMSO): $\delta$ = 20.9, 46.3, 126.4, 128.6, 139.2, 142.6 ppm. IR: $\tilde{\nu}$ = 658, 708, 811, 844, 884, 982, 1072, 1117, 1153 $cm^{-1}$.

**1,4-Ditosyl-1,4-diazepan-6-ol:**[18] Powdered KOH (1.9 g, 0.034 mol) was dissolved in absolute EtOH (250 mL) and 2,3-dibromo-1-propanol (3.5 mL, 0.034 mol) was added dropwise to this solution. The resulting white suspension was refluxed and disodium *N*$^1$,*N*$^2$-ditosyl-1,2-ethanediamide (14 g, 0.034 mol) was added. The mixture was refluxed for an additional six hours and the remaining solid was removed from the boiling solution by filtration. The clear solution was then cooled to 4 °C, yielding 10.1 g (70%) of colorless crystals, which were filtered off and dried in vacuo. $C_{19}H_{24}N_2O_5S_2$ (424.5): calcd. C 53.75, H 5.70, N 6.60; found C 53.38, H 5.52, N 6.31. $^1H$ NMR (DMSO): $\delta$ = 2.39 (s, 6 H), 2.85 (dd, *J* = 13.9, 8.1 Hz, 2 H), 3.11 (m, 2 H), 3.48 (m, 4 H), 3.75 (sept, *J* = 4.2 Hz, 1 H), 5.28 (br., 1 H), 7.42 (d, *J* = 8.2 Hz, 4 H), 7.67 (d, *J* = 8.1 Hz, 4 H) ppm. $^{13}C$ NMR (DMSO): $\delta$ = 20.9, 49.0, 53.0, 68.4, 126.6, 129.8, 135.5, 143.3 ppm. IR: $\tilde{\nu}$ = 610, 653, 722, 805, 911, 972, 1036, 1086, 1151, 1266, 1330, 1400, 1442, 1493, 1598, 2922, 3502 $cm^{-1}$.

**1,4-Ditosyl-1,4-diazepan-6-mesylate:** 1,4-Ditosyl-1,4-diazepan-6-ol (10 g, 0.024 mol) was dissolved in anhydrous pyridine (50 mL) and cooled to 0 °C with an ice bath. Methanesulfonyl chloride (1.87 mL, 0.024 mol) was then added dropwise to this solution. A yellow solid precipitated, and the suspension was stirred for an additional 2 h at 0 °C. 3 M HCl (200 mL) was then added and the solid turned white. Stirring was continued for a further 2 h at 0 °C. The residue was then filtered off and washed with $H_2O$. The solid was extracted with boiling EtOH and dried in vacuo. Yield: 10.6 g (88%). $C_{20}H_{26}N_2O_7S_3$ (502.6): calcd. C 47.79, H 5.21, N 5.57; found C 47.77, H 5.19, N 5.63. $^1H$ NMR (DMSO): $\delta$ = 2.39 (s, 6 H), 3.23 (m, 2 H), 3.27 (s, 3 H), 3.37 (m, 2 H), 3.53 (d, *J* = 5.1 Hz, 4 H), 4.87 (quint, *J* = 5.1 Hz, 1 H), 7.42 (d, *J* = 8.2 Hz, 4 H), 7.69 (d, *J* = 8.2 Hz, 4 H) ppm. $^{13}C$ NMR: $\delta$ = 20.9, 37.8, 50.4, 51.2, 76.7, 126.7, 129.9, 135.3, 143.6 ppm. IR: $\tilde{\nu}$ = 570, 619, 652, 702,

 © 2006 Wiley-VCH Verlag GmbH & Co. KGaA, Weinheim 

715, 743, 807, 904, 916, 949, 974, 1001, 1074, 1090, 1148, 1161, 1282, 1310, 1331, 1347, 1442, 1496, 1598 $cm^{-1}$.

**6-Azido-1,4-ditosyl-1,4-diazepane:** *Caution: Organic azides are potentially explosive. These must be handled with care and should not be isolated in large amounts*![19] Solid 1,4-ditosyl-1,4-diazepan-6-mesylate (5 g, 0.01 mol) was added to a solution of $NaN_3$ (1.95 g, 0.03 mol) in absolute DMF (100 mL). The resulting white suspension was heated to 100–110 °C for 48 h. A white solid was removed by filtration, yielding a clear, yellow solution of the desired product. A small sample to be used for IR and NMR characterization was precipitated by the addition of $H_2O$ to a few milliliters of the DMF solution. The resulting white solid was separated by filtration and air-dried. $^1H$ NMR (DMSO): $\delta$ = 2.40 (s, 6 H), 3.19 (m, 2 H), 3.39 (m, 6 H), 3.89 (m, 1 H), 7.43 (d, $J$ = 8.3 Hz, 4 H), 7.69 (d, $J$ = 8.3 Hz, 4 H) ppm. $^{13}C$ NMR (DMSO): $\delta$ = 20.9, 50.1, 50.9, 58.6, 127.0, 130.1, 135.5, 143.7 ppm. IR: $\tilde{\nu}$ = 656, 696, 720, 813, 860, 909, 958, 1036, 1090, 1158, 1245, 1306, 1332, 1381, 1455, 1494, 1599, 2110 $cm^{-1}$. The crystal structure has been published in a previous communication.[45]

**1,4-Ditosyl-1,4-diazepan-6-amine:** The experiment reported in the previous section was repeated one more time and the resulting DMF solutions of the azide were combined to one single solution. This solution was then transferred into an autoclave and hydrogenated (5 atm $H_2$) using 10% Pd/C (500 mg) as catalyst. After 48 h the catalyst was removed by filtration and the resulting solution (300 mL) was diluted with 1 L of $H_2O$. The white solid that precipitated was filtered off and dried in vacuo. This product proved to be of sufficient purity to be used for the next step, however the elemental analysis was not satisfactory. The product could be isolated as analytically pure hydrobromide by dissolving the amine in EtOH (100 mL) and adding aqueous concd. HBr (10 mL). The resulting yellow solution was filtered through Celite and the solvents evaporated to dryness. A colorless solid was obtained which was dried in vacuo (7.1 g, 70%). $C_{19}H_{25}N_3S_2O_4{\cdot}HBr$ (504.5): calcd. C 45.24, H 5.19, N 8.33; found C 45.34, H 5.38, N 8.06. $^1H$ NMR (DMSO): $\delta$ = 3.40 (m, 3 H), 3.45 (m, 4 H), 3.63 (dd, $J$ = 14.4, $J$ = 4.1 Hz, 2 H), 7.47 (d, $J$ = 8.2 Hz, 4 H), 7.72 (d, $J$ = 8.2 Hz, 4 H) ppm. $^{13}C$ NMR (DMSO): $\delta$ = 20.9, 48.9, 49.4, 50.0, 126.6, 130.1, 134.9, 143.8 ppm. IR: $\tilde{\nu}$ = 571, 653, 721, 813, 905, 967, 1030, 1089, 1152, 1330, 1449, 1494, 1597 $cm^{-1}$. The crystal structure of the free amine has been published in a previous communication.[46]

**1,4-Diazepan-6-amine·3HBr:** 1,4-Ditosyl-1,4-diazepan-6-amine (5 g, 0.012 mol) was refluxed in concd. aqueous HBr (150 mL) for 3 h. The solution was cooled to room temperature and was then concentrated to a volume of 50 mL on a rotary evaporator. A white solid crystallized which was filtered off and washed with cold EtOH. Drying in vacuo yielded 3.2 g of the trihydrobromide salt (75%). $C_5H_{16}Br_3N_3$ (357.9): calcd. C 16.78, H 4.51, N 11.74; found C 16.87, H 4.58 N 11.74. $^1H$ NMR ($D_2O$, pH < 3): $\delta$ = 3.67 (dd, $J$ = 14.1, $J$ = 10.5 Hz, 2 H), 3.77 (m, 4 H), 3.89 (dd, $J$ = 14.1, $J$ = 3.1 Hz, 2 H), 4.26 (tt, $J$ = 10.5, $J$ = 3.1 Hz, 1 H) ppm. $^{13}C$ NMR ($D_2O$, pH < 3): $\delta$ = 45.9, 47.1, 49.3 ppm. IR: $\tilde{\nu}$ = 767, 844, 864, 882, 910, 991, 1020, 1050, 1127, 1180, 1265, 1298, 1326, 1392, 1429, 1447, 1465, 1524, 1548, 2781 $cm^{-1}$.

**1,4-Diazepan-6-amine·3HCl·1.5H$_2$O:** This compound was obtained from the trihydrobromide by ion-exchange chromatography on Dowex 50. $C_5H_{16}N_3Cl_3{\cdot}1.5H_2O$ (251.6): calcd. C 23.87, H 7.61, N 16.70; found C 23.45, H 7,88, N 17.09. The $^1H$ and $^{13}C$ NMR spectra were identical with those of the trihydrobromide. IR: $\tilde{\nu}$ = 773, 852, 868, 890, 1000, 1055, 1092, 1135, 1199, 1234, 1271, 1396, 1435, 1539, 2718 $cm^{-1}$. Single crystals of composition $H_3dazaCl_3{\cdot}H_2O$, suitable for X-ray analysis were grown by slow evaporation of an aqueous solution.

**[Co(daza)$_2$]Cl$_3$:** 1,4-Diazepan-6-amine·3HBr (2.5 g, 7.0 mmol) was dissolved in $H_2O$ (50 mL), and the pH of the solution was adjusted to 8.5 by adding NaOH (1 M). Solid $CoCl_2{\cdot}6H_2O$ (0.83 g, 3.5 mmol) was then added, resulting in a red-orange solution, which was stirred in an open beaker for 3 d. The solution was tested for $Co^{2+}$ (negative), and sorbed onto Dowex 50. The column was washed successively with $H_2O$ (500 mL), aqueous 0.5 M HCl (500 mL), and aqueous 1 M HCl (500 mL). The product was then eluted from the column with aqueous 3 M HCl (500 mL). The last fraction was evaporated to dryness, and the resulting orange solid was dissolved in a small amount of $H_2O$ and sorbed onto a column of SP-Sephadex C-25 (column length: 2 m). The column was eluted with trisodium citrate (0.2 M). Beside several minor bands, two major orange bands ($\mathbf{1}^{3+}$, $\mathbf{2}^{3+}$) were observed. The two major bands were collected separately, desalted on Dowex 50 (3 M HCl), and the solvents evaporated to dryness.

***trans*-[Co(daza)$_2$]Cl$_3$·4H$_2$O (1Cl$_3$·4H$_2$O):** Yield: 25%. $C_{10}H_{26}CoCl_3N_6{\cdot}4H_2O$ (467.7): calcd. C 25.68, H 7.33, N 17.97; found C 25.75, H 7.11, N 18.52. $^1H$ NMR ($D_2O$): $\delta$ = 2.69 (d, $J$ = 13.4 Hz, 4 H), 2.88 (d, $J$ = 8.3 Hz, 4 H), 3.42 (br. s, 2 H), 3.43 (m, 4 H), 3.62 (d, $J$ = 13.4 Hz, 4 H) ppm. $^{13}C$ NMR ($D_2O$): $\delta$ = 55.7, 56.9, 62.3 ppm. IR: $\tilde{\nu}$ = 626, 780, 884, 981, 1044, 1092, 1128, 1183, 1231, 1314, 1379, 1417, 1614, 2114, 3032 $cm^{-1}$. UV/Vis: $\lambda_{max}$ ($\varepsilon$) = 335 nm (75), 470 (79).

***cis*-[Co(daza)$_2$]Cl$_3$·1.5H$_2$O (2Cl$_3$·1.5H$_2$O):** Yield: 20%. $C_{10}H_{26}Cl_3CoN_6{\cdot}1.5H_2O$ (422.7): calcd. C 28.42, H 6.92, N 19.88; found C 28.21, H 6.85, N 19.91. $^1H$ NMR ($D_2O$): $\delta$ = 2.71 (d, $J$ = 13.5 Hz, 4 H), 3.04 (m, 4 H), 3.44 (m, 4 H), 3.49 (br. s, 2 H), 3.56 (d, $J$ = 13.5 Hz, 2 H), 3.78 (m, 2 H) ppm. $^{13}C$ NMR ($D_2O$): $\delta$ = 55.6, 56.3, 57.4, 61.9 (two C atoms) ppm. IR: $\tilde{\nu}$ = 886, 988, 1048, 1092, 1151, 1230, 1285, 1316, 1356, 1444, 1496, 1590, 1981, 2051, 2165, 2323, 2430, 2754, 2875, 3030 $cm^{-1}$. UV/Vis: $\lambda_{max}$ ($\varepsilon$) = 345 nm (140), 470 (157).

Single crystals: $\mathbf{1}Cl_3{\cdot}4H_2O$ (24 mg) and $\mathbf{2}Cl_3{\cdot}1.5H_2O$ (24 mg) were separately dissolved in $H_2O$. $ZnBr_2$ (59 mg, 0.26 mmol) was added to each of the solutions. The solutions were acidified with 3 M aqueous HBr to pH < 1. Slow evaporation yielded orange crystals of composition $[\mathbf{1}]_3(ZnBr_4)_2Br_5{\cdot}4\,H_2O$ and $[\mathbf{2}](ZnBr_4)Br{\cdot}H_2O$, suitable for X-ray analysis.

**[Cu(daza)Cl$_2$]:** 1,4-Diazepan-6-amine·3HCl·H$_2$O (100 mg, 0.41 mmol) was dissolved in 1 mL of $H_2O$. $CuCl_2{\cdot}2H_2O$ (35 mg, 0.21 mmol) was added to this solution, and the pH was adjusted to 7 with 0.5 M NaOH (2 mL). The solution was then diluted with EtOH and was allowed to stand at 4 °C for a few days, yielding a small number of blue crystals which were suitable for the single crystal analysis. IR: $\tilde{\nu}$ = 666, 768, 853, 872, 966, 1041, 1098, 1149, 1319, 1444, 1605, 2848, 2871, 3167, 3242, 3300, 3322 $cm^{-1}$.

**[Ni(daza)$_2$]Cl$_2$·3.2H$_2$O:** 1,4-Diazepan-6-amine·3HCl·H$_2$O (100 mg, 0.41 mmol) was dissolved in 1 mL of $H_2O$. Solid $NiCl_2{\cdot}6H_2O$ (50 mg, 0.21 mmol) was then added and the pH was adjusted to 8 with 0.1 M KOH (12 mL). The resulting purple solution was allowed to evaporate slowly over a period of several days at room temperature, yielding a small number of purple crystals suitable for the X-ray analysis. IR: $\tilde{\nu}$ = 628, 914, 965, 1043, 1064, 1099, 1143, 1614 br, 2875, 3166, 3227, 3313 $cm^{-1}$.

**[Zn(daza)$_2$]SO$_4$·5H$_2$O:** 1,4-Diazepan-6-amine·3HBr (200 mg, 0.56 mmol) was deprotonated on Dowex 2 ($OH^-$ form). The volume of the resulting solution was reduced to 10 mL. Solid $ZnSO_4{\cdot}7H_2O$ (81 mg, 0.28 mmol) was added, and the solution was

 © 2006 Wiley-VCH Verlag GmbH & Co. KGaA, Weinheim 

Table 7. Crystallographic data for daza·3HCl·$H_2O$, [$CuLCl_2$], [$Ni(L)_2$]$Cl_2$·3.2$H_2O$, [$Zn(L)_2$]$SO_4$·5$H_2O$, *trans*-[$Co(L)_2$]$_3$($ZnBr_4$)$_2Br_5$·4$H_2O$, and *cis*-[$Co(L)_2$]($ZnBr_4$)Br·$H_2O$.

| | daza·3HCl·$H_2O$ | [$Ni(L)_2$]$Cl_2$·3.2$H_2O$ | [$CuLCl_2$] | [$Zn(L)_2$]$SO_4$·5$H_2O$ | **1**$_3$($ZnBr_4$)$_2Br_5$·4$H_2O$ | **2**($ZnBr_4$)Br·$H_2O$ |
|---|---|---|---|---|---|---|
| Formula | $C_5H_{18}Cl_3N_3O$ | $C_{10}H_{32.4}Cl_2N_6NiO_{3.2}$ | $C_5H_{13}Cl_2N_3Cu$ | $C_{10}H_{36}N_6O_9SZn$ | $C_{30}H_{86}Br_{13}Co_3N_{18}O_4Zn_2$ | $C_{10}H_{28}Br_5CoN_6OZn$ |
| $M_w$ | 242.57 | 417.63 | 249.62 | 481.88 | 2109.54 | 772.23 |
| $T$ [K] | 200(2) | 293(2) | 200(2) | 293(2) | 100(2) | 100(2) |
| Crystal system | monoclinic | monoclinic | orthorhombic | triclinic | orthorhombic | orthorhombic |
| Space group | $P2_1/n$ | $P2_1/n$ | $Pna2_1$ | $P\bar{1}$ | $Pbcn$ | $Pnma$ |
| $a$ [Å] | 12.500(2) | 8.708(2) | 16.715(3) | 8.366(2) | 15.8270(4) | 26.8941(12) |
| $b$ [Å] | 6.8580(10) | 8.826(2) | 6.9430(10) | 9.065(2) | 23.5711(6) | 8.4372(4) |
| $c$ [Å] | 14.061(3) | 12.480(2) | 7.918(2) | 15.450(3) | 16.0633(5) | 9.5817(4) |
| $\alpha$ [°] | 90.00 | 90.00 | 90.00 | 91.09(3) | 90.00 | 90.00 |
| $\beta$ [°] | 112.56(3) | 97.59(3) | 90.00 | 101.97(3) | 90.00 | 90.00 |
| $\gamma$ [°] | 90.00 | 90.00 | 90.00 | 115.54(3) | 90.00 | 90.00 |
| $V$ [Å$^3$] | 1113.1(3) | 950.8(3) | 918.9(3) | 1026.4(4) | 5992.6(3) | 2174.19(17) |
| $Z$ | 4 | 2 | 4 | 2 | 4 | 4 |
| $\rho_{calcd.}$ [g cm$^{-3}$] | 1.447 | 1.459 | 1.804 | 1.559 | 2.338 | 2.359 |
| $\mu$ [mm$^{-1}$] | 0.788 | 1.322 | 2.899 | 1.352 | 10.322 | 11.067 |
| min./max. transm. | – | – | – | 0.5931/0.9977 | 0.0769/0.4783 | 0.2882/0.5960 |
| Crystal size [mm] | 0.3×0.3×0.2 | 0.4×0.3×0.2 | 0.20×0.15×0.15 | 0.30×0.25×0.15 | 0.34×0.26×0.07 | 0.16×0.10×0.05 |
| $\theta$ range [°] | 1.86–24.06 | 2.69–25.00 | 2.44–24.06 | 2.51–25.00 | 3.68–29.00 | 2.61–28.04 |
| *hkl* ranges | –14/13 | –10/10 | –18/18 | –9/9 | –21/21 | –35/35 |
| | –7/7 | 0/10 | –7/7 | –10/10 | –32/32 | –11/11 |
| | –15/15 | 0/14 | –9/9 | 0/18 | –20/14 | –12/12 |
| Measured refl. | 6690 | 1674 | 5321 | 3603 | 30240 | 21318 |
| Unique refl. | 1682 | 1674 | 1385 | 3603 | 7545 | 2796 |
| Obsd. refl.[a] | 1177 | 1533 | 879 | 3381 | 6405 | 2550 |
| Parameters | 181 | 162 | 100 | 383 | 343 | 188 |
| $R_1$,$wR_2$ [$I > 2\sigma(I)$] | 0.0295, 0.0575 | 0.0550, 0.1277 | 0.0539, 0.1166 | 0.0402, 0.1031 | 0.0364, 0.0799 | 0.0491, 0.0946 |
| $R_1$,$wR_2$ (all data) | 0.0535, 0.0629 | 0.0579, 0.1334 | 0.0904, 0.1265 | 0.0427, 0.1062 | 0.0467, 0.0850 | 0.0556, 0.0967 |

[a] For $I > 2\sigma(I)$.

layered with acetone, yielding single crystals suitable for X-ray analysis.

**Single Crystal X-ray Diffraction Studies:**[47] Data sets were collected on the following diffractometers: STOE IPDS (daza·3HCl·$H_2O$ and [$Cu(daza)Cl_2$]), STOE STADI-4 ([$Ni(daza)_2$]$Cl_2$·3.2$H_2O$ and [$Zn(daza)_2$]$SO_4$·5$H_2O$), Nonius Kappa-CCD (*trans*-[$Co(daza)_2$]$_3$-($ZnBr_4$)$_2Br_5$·4$H_2O$, and *cis*-[$Co(daza)_2$]($ZnBr_4$)Br·$H_2O$). Graphite-monochromated Mo-$K_\alpha$ radiation ($\lambda$ = 0.71073 Å) was used throughout. The data for the two Co complexes were collected at 100(2) K, daza·3HCl·$H_2O$ and [$Cu(daza)Cl_2$] were measured at 200(2) K, and the other data sets were collected at ambient temperature. An absorption correction was performed for *cis*-[Co-($daza)_2$]($ZnBr_4$)Br·$H_2O$ (face-indexed numerical), *trans*-[Co-($daza)_2$]$_3$($ZnBr_4$)$_2Br_5$·4$H_2O$ (faced-indexed numerical), and [$Zn(daza)_2$]$SO_4$·5$H_2O$ (empirical). Further details of data collection and structure solution are summarized in Table 7. The structures were solved by direct methods (SHELXS-97) and refined by full-matrix, least-squares calculations on $F^2$ using SHELXL-97.[48] Anisotropic displacement parameters were refined for all non-hydrogen atoms. The hydrogen atoms of daza·3HCl·$H_2O$, [$Zn(daza)_2$]-$SO_4$·5$H_2O$, and [$Ni(daza)_2$]$Cl_2$·3.2$H_2O$ were located and refined isotropically. The H-atom positions of the other complexes were calculated (riding model). The disorder problems of the Co complexes **1**a$^{3+}$ and **2**$^{3+}$ are described in detail in Section 2.2. In the structure of **2**$^{3+}$, a total of 21 restraints was used to adjust corresponding bond lengths and angles of the two ligands to the same value within suitable limits (SAME instruction of SHELXL-97). Puckering parameters were calculated using the computer program PLATON.[49]

## Acknowledgments

X-ray diffraction data of $H_3dazaCl_3$·$H_2O$ and of the Ni, Cu, and Zn complexes were recorded by Dr. Volker Huch (Saarbrücken). We thank Dr. Peter Osvath (Melbourne) for valuable advice. Financial support by the Deutsche Forschungsgemeinschaft is gratefully acknowledged.

[1] a) R. F. Childers, R. A. D. Wentworth, L. J. Zompa, *Inorg. Chem.* **1971**, *10*, 302, and references cited therein; b) W. A. Freeman, C. F. Liu, *Inorg. Chem.* **1975**, *14*, 2120; c) D. Parker, K. Senanayake, J. Vepsailainen, S. Williams, A. S. Batsanov, J. A. K. Howard, *J. Chem. Soc., Perkin Trans. 2* **1997**, 1445; d) F. M. Menger, J. Bian, V. A. Azov, *Angew. Chem. Int. Ed.* **2002**, *41*, 2581; e) L. Turculet, T. D. Tilley, *Organometallics* **2004**, *23*, 1542.

[2] K. Hegetschweiler, *Chem. Soc. Rev.* **1999**, *28*, 239.

[3] M. Ghisletta, L. Hausherr-Primo, K. Gajda-Schrantz, G. Machula, L. Nagy, H. W. Schmalle, G. Rihs, F. Endres, K. Hegetschweiler, *Inorg. Chem.* **1998**, *37*, 997.

[4] a) J. Sander, K. Hegetschweiler, B. Morgenstern, A. Keller, W. Amrein, T. Weyhermüller, I. Müller, *Angew. Chem. Int. Ed.* **2001**, *40*, 4180; b) K. Hegetschweiler, R. C. Finn, R. S. Rarig Jr., J. Sander, S. Steinhauser, M. Wörle, J. Zubieta, *Inorg. Chim. Acta* **2002**, *337*, 39; c) D. Chapon, J.-P. Morel, P. Delangle, C. Gateau, J. Pécaut, *Dalton Trans.* **2003**, 2745; d) B. Morgenstern, S. Steinhauser, K. Hegetschweiler, E. Garribba, G. Micera, D. Sanna, L. Nagy, *Inorg. Chem.* **2004**, *43*, 3116; e) K. Hegetschweiler, B. Morgenstern, J. Zubieta, P. J. Hagrman, N. Lima, R. Sessoli, F. Totti, *Angew. Chem. Int. Ed.* **2004**, *43*, 3436; f) K. Hegetschweiler, A. Egli, E. Herdtweck, W. A.

 © 2006 Wiley-VCH Verlag GmbH & Co. KGaA, Weinheim 

Herrmann, R. Alberto, V. Gramlich, *Helv. Chim. Acta* **2005**, *88*, 426.
[5] P. Chaudhuri, K. Wieghardt, *Prog. Inorg. Chem.* **1987**, *35*, 329.
[6] a) J. H. Koek, S. W. Russell, L. van der Wolf, R. Hage, J. B. Warnaar, A. L. Spek, J. Kerschner, L. Del Pizzo, *J. Chem. Soc., Dalton Trans.* **1996**, 353; b) A. C. Moreland, T. B. Rauchfuss, *J. Am. Chem. Soc.* **1998**, *120*, 9376; c) C. Bolm, N. Meyer, G. Raabe, T. Weyhermüller, E. Bothe, *Chem. Commun.* **2000**, 2435; d) L. D. Slep, A. Mijovilovich, W. Meyer-Klaucke, T. Weyhermüller, E. Bill, E. Bothe, F. Neese, K. Wieghardt, *J. Am. Chem. Soc.* **2003**, *125*, 15554.
[7] a) G. Park, J. Shao, F. H. Lu, R. D. Rogers, N. D. Chasteen, M. W. Brechbiel, R. P. Planalp, *Inorg. Chem.* **2001**, *40*, 4167; b) E. A. Lewis, H. H. Khodr, R. C. Hider, J. R. Lindsay Smith, P. H. Walton, *Dalton Trans.* **2004**, 187; c) E. Boseggia, M. Gatos, L. Lucatello, F. Mancin, S. Moro, M. Palumbo, C. Sissi, P. Tecilla, U. Tonellato, G. Zagotto, *J. Am. Chem. Soc.* **2004**, *126*, 4543; d) C. Sissi, F. Mancin, M. Gatos, M. Palumbo, P. Tecilla, U. Tonellato, *Inorg. Chem.* **2005**, *44*, 2310.
[8] a) U. Bossek, T. Weyhermüller, K. Wieghardt, B. Nuber, J. Weiss, *J. Am. Chem. Soc.* **1990**, *112*, 6387; b) U. Bossek, M. Saher, T. Weyhermüller, K. Wieghardt, *J. Chem. Soc., Chem. Commun.* **1992**, 1780; c) U. Bossek, H. Hummel, T. Weyhermüller, E. Bill, K. Wieghardt, *Angew. Chem. Int. Ed. Engl.* **1995**, *34*, 2642.
[9] a) R. A. D. Wentworth, P. S. Dahl, C. J. Huffman, W. O. Gillum, W. E. Streib, J. C. Huffman, *Inorg. Chem.* **1982**, *21*, 3060; b) J. E. Bollinger, J. T. Mague, W. A. Banks, A. J. Kastin, D. M. Roundhill, *Inorg. Chem.* **1995**, *34*, 2143; c) P. Caravan, C. Orvig, *Inorg. Chem.* **1997**, *36*, 236; d) H. Luo, N. Eberly, R. D. Rogers, M. W. Brechbiel, *Inorg. Chem.* **2001**, *40*, 493; e) A. K. Nairn, R. Bhalla, S. P. Foxon, X. Liu, L. J. Yellowlees, B. C. Gilbert, P. H. Walton, *J. Chem. Soc., Dalton Trans.* **2002**, 1253; f) N. Ye, G. Park, A. M. Przyborowska, P. E. Sloan, T. Clifford, C. B. Bauer, G. A. Broker, R. D. Rogers, R. Ma, S. V. Torti, M. W. Brechbiel, R. P. Planalp, *Dalton Trans.* **2004**, 1304.
[10] a) K. Hegetschweiler, A. Egli, R. Alberto, H. W. Schmalle, *Inorg. Chem.* **1992**, *31*, 4027; b) A. Kramer, R. Alberto, A. Egli, I. Novak-Hofer, K. Hegetschweiler, U. Abram, P. V. Bernhardt, P. A. Schubiger, *Bioconjugate Chem.* **1998**, *9*, 691.
[11] a) A. E. Martell, R. J. Motekaitis, M. J. Welch, *J. Chem. Soc., Chem. Commun.* **1990**, 1748; b) C. Stockheim, L. Hoster, T. Weyhermüller, K. Wieghardt, B. Nuber, *J. Chem. Soc., Dalton Trans.* **1996**, 4409; c) R. Schnepf, A. Sokolowski, J. Müller, V. Bachler, K. Wieghardt, P. Hildebrandt, *J. Am. Chem. Soc.* **1998**, *120*, 2352; d) S. J. Brudenell, L. Spiccia, A. M. Bond, G. D. Fallon, D. C. R. Hockless, G. Lazarev, P. J. Mahon, E. R. T. Tiekink, *Inorg. Chem.* **2000**, *39*, 881; e) P. C. McGowan, T. J. Podesta, M. Thornton-Pett, *Inorg. Chem.* **2001**, *40*, 1445; f) V. Pavlishchuk, F. Birkelbach, T. Weyhermüller, K. Wieghardt, P. Chaudhuri, *Inorg. Chem.* **2002**, *41*, 4405; g) M. Li, D. Bonnet, E. Bill, F. Neese, T. Weyhermüller, N. Blum, D. Sellmann, K. Wieghardt, *Inorg. Chem.* **2002**, *41*, 3444; h) A. L. Gott, P. C. McGowan, T. J. Podesta, C. W. Tate, *Inorg. Chim. Acta* **2004**, *357*, 689.
[12] a) H. Manohar, D. Schwarzenbach, *Helv. Chim. Acta* **1974**, *57*, 519; b) H. Manohar, D. Schwarzenbach, W. Iff, G. Schwarzenbach, *J. Coord. Chem.* **1979**, *8*, 213.
[13] a) G. Seeber, A. L. Pickering, D.-L. Long, L. Cronin, *Chem. Commun.* **2003**, 2002; b) A. L. Pickering, D.-L. Long, L. Cronin, *Inorg. Chem.* **2004**, *43*, 4953.
[14] J. W. Pauly, J. Sander, D. Kuppert, M. Winter, G. J. Reiss, F. Zürcher, R. Hoffmann, T. F. Fässler, K. Hegetschweiler, *Chem. Eur. J.* **2000**, *6*, 2830.
[15] D. Kuppert, J. Sander, C. Roth, M. Wörle, T. Weyhermüller, G. J. Reiss, U. Schilde, I. Müller, K. Hegetschweiler, *Eur. J. Inorg. Chem.* **2001**, 2525.
[16] S. Aime, L. Calabi, C. Cavallotti, E. Gianolio, G. B. Giovenzana, P. Losi, A. Maiocchi, G. Palmisano, M. Sisti, *Inorg. Chem.* **2004**, *43*, 7588.
[17] a) S. Kato, H. Harada, T. Morie, *J. Chem. Soc., Perkin Trans. 1* **1997**, 3219; b) Y. Hirokawa, I. Fujiwara, K. Suzuki, H. Harada, T. Yoshikawa, N. Yoshida, S. Kato, *J. Med. Chem.* **2003**, *46*, 702.
[18] W. S. Saari, A. W. Raab, S. W. King, *J. Org. Chem.* **1971**, *36*, 1711.
[19] E. B. Fleischer, A. E. Gebala, A. Levey, P. A. Tasker, *J. Org. Chem.* **1971**, *36*, 3042.
[20] R. M. Smith, A. E. Martell, R. J. Motekaitis, *Critically Selected Stability Constants of Metal Complexes*, NIST Standard Reference Database 46; Version 8.0; Gaithersburg, MD, USA **2004**.
[21] M. Weber, D. Kuppert, K. Hegetschweiler, V. Gramlich, *Inorg. Chem.* **1999**, *38*, 859.
[22] R. Yang, L. J. Zompa, *Inorg. Chem.* **1976**, *15*, 1499.
[23] K. Hegetschweiler, O. Maas, A. Zimmer, R. J. Geue, A. M. Sargeson, J. Harmer, A. Schweiger, I. Buder, G. Schwitzgebel, V. Reiland, W. Frank, *Eur. J. Inorg. Chem.* **2003**, 1340.
[24] In this paper, the term pH* refers to the direct pH Meter reading for $D_2O$ samples (no inert electrolyte) using a pH electrode with an aqueous ($H_2O$) reference which was calibrated with aqueous ($H_2O$) buffer solutions. For the interconversion of pH* and pD see: a) R. Delgado, J. J. R. Frausto Da Silva, M. T. S. Amorim, M. F. Cabral, S. Chaves, J. Costa, *Anal. Chim. Acta* **1991**, *245*, 271; b) Z. Szakacs, G. Hägele, R. Tyka, *Anal. Chim. Acta* **2004**, *522*, 247.
[25] J. L. Sudmeier, C. N. Reilley, *Anal. Chem.* **1964**, *36*, 1698.
[26] M. Karplus, *J. Am. Chem. Soc.* **1963**, *85*, 2870.
[27] I. K. Boessenkool, J. C. A. Boeyens, *J. Cryst. Mol. Struct.* **1980**, *10*, 11.
[28] $\tau = (\alpha - \beta)/60$, where $\alpha$ is the largest and $\beta$ is the second largest bond angle within the coordination sphere. $\tau = 1$ corresponds to trigonal bipyramidal and $\tau = 0$ to a square-pyramidal coordination, see: A. W. Addison, T. N. Rao, J. Reedijk, J. van Rijn, G. C. Verschoor, *J. Chem. Soc., Dalton Trans.* **1984**, 1349.
[29] a) R. F. Childers, R. A. D. Wentworth, *Inorg. Chem.* **1969**, *8*, 2218; b) G. Schwarzenbach, H.-B. Bürgi, W. P. Jensen, G. A. Lawrance, L. Mønsted, A. M. Sargeson, *Inorg. Chem.* **1983**, *22*, 4029.
[30] K. Hegetschweiler, V. Gramlich, M. Ghisletta, H. Samaras, *Inorg. Chem.* **1992**, *31*, 2341.
[31] A. Zimmer, D. Kuppert, T. Weyhermüller, I. Müller, K. Hegetschweiler, *Chem. Eur. J.* **2001**, *7*, 917.
[32] E. Prenesti, P. G. Daniele, M. Prencipe, G. Ostacoli, *Polyhedron* **1999**, *18*, 3233.
[33] J. Bjerrum, B. V. Agarwala, *Acta Chem. Scand.* **1980**, *A34*, 475.
[34] L. Fabbrizzi, M. Micheloni, P. Paoletti, *J. Chem. Soc., Dalton Trans.* **1980**, 1055.
[35] R. Pizer, *Inorg. Chem.* **1984**, *23*, 3027.
[36] K. Hegetschweiler, R. D. Hancock, M. Ghisletta, T. Kradolfer, V. Gramlich, H. W. Schmalle, *Inorg. Chem.* **1993**, *32*, 5273.
[37] a) C. K. Jørgensen, *Inorg. Chem.* **1964**, *3*, 1201; b) R. G. Pearson, *Inorg. Chem.* **1973**, *12*, 712.
[38] R. D. Hancock, *Acc. Chem. Res.* **1990**, *23*, 253.
[39] U. Brand, H. Vahrenkamp, *Inorg. Chim. Acta* **1992**, *198–200*, 663.
[40] C. Neis, Diploma Thesis, Saarbrücken, **2005**.
[41] S. Steinhauser, U. Heinz, M. Bartholomä, T. Weyhermüller, H. Nick, K. Hegetschweiler, *Eur. J. Inorg. Chem.* **2004**, 4177.
[42] P. Gans, A. Sabatini, A. Vacca, *Talanta* **1996**, *43*, 1739.
[43] a) R. A. Binstead, B. Jung, A. D. Zuberbühler, SPECFIT/32 Version 3.0, Spectrum Software Associates, Marlborough, MA **01752**, USA, **2000**; b) H. Gampp, M. Maeder, C. J. Meyer, A. D. Zuberbühler, *Talanta* **1985**, *32*, 95.
[44] H. Stetter, E.-E. Roos, *Chem. Ber.* **1954**, *87*, 566.
[45] J. Romba, S. Steinhauser, K. Hegetschweiler, *Z. Kristallogr. - New Cryst. Struct.* **2002**, *217*, 135.
[46] J. Romba, S. Steinhauser, K. Hegetschweiler, *Z. Kristallogr. - New Cryst. Struct.* **2002**, *217*, 133.

 © 2006 Wiley-VCH Verlag GmbH & Co. KGaA, Weinheim 

[47] CCDC-279823 to -279828 (for *cis*-[Co(daza)$_2$](ZnBr$_4$)Br·H$_2$O, *trans*-[Co(daza)$_2$]$_3$(ZnBr$_4$)$_2$Br$_5$·4H$_2$O, [Cu(daza)Cl$_2$], daza·3HCl·H$_2$O, [Zn(daza)$_2$]SO$_4$·5H$_2$O, and [Ni(daza)$_2$]Cl$_2$·3.2H$_2$O, respectively) contain the supplementary crystallographic data for this paper. These data can be obtained free of charge from The Cambridge Crystallographic Data Centre via www.ccdc.cam.ac.uk/data_request/cif.
[48] a) G. M. Sheldrick, SHELXS-97, *Program for Crystal Structure Solution*, Göttingen, **1990**; b) G. M. Sheldrick, SHELXL-97, *Program for Crystal Structure Refinement*, Göttingen, **1997**.
[49] A. L. Spek, PLATON, A Multipurpose Crystallographic Tool, Utrecht University, Utrecht, The Netherlands, **2005**; see also: A. L. Spek, *J. Appl. Cryst.* **2003**, *36*, 7.

Received: August 1, 2005
Published Online: December 1, 2005

 © 2006 Wiley-VCH Verlag GmbH & Co. KGaA, Weinheim 

DOI: 10.1002/ejic.200500700

# Evidence for Hydrogen-Bond-Mediated Exchange Coupling in an Aqua-Bridged $Cu^{II}$ Dimer: Synthesis, Magnetic Study and Correlation with Density Functional Calculations

**Pritha Talukder,[a] Soma Sen,[a] Samiran Mitra,*[a] Lutz Dahlenberg,[b] Cédric Desplanches,[c] and Jean-Pascal Sutter*[c,d]**

**Keywords:** Bridging ligands / Copper / Density functional calculations / Exchange interactions / Hydrogen bonds

A rare example of a mono-aqua-bridged copper(II) dimer, namely $[Cu_2(\mu_2\text{-}H_2O)L_2(H_2O)_2](ClO_4)_2{\cdot}2H_2O$ (**1**), has been synthesised and its structure determined by single-crystal X-ray diffraction. Each $Cu^{II}$ centre is in a square-pyramidal surrounding formed by a Schiff base and a terminal $H_2O$ ligand; a second $H_2O$ ligand, which acts as a bridge, is common to two metal ions. Hydrogen bonds between the $H_2O$ ligand and the Schiff base of the adjacent centre complete the intra-dimer linkages. This compound exhibits an antiferromagnetic behaviour ($J = -13.2\ cm^{-1}$, $H = -J\boldsymbol{S}_1{\cdot}\boldsymbol{S}_2$), and density functional calculations clearly establish that the main exchange does not proceed through the bridging $H_2O$ but is mediated by the intra-dimer H-bonds.

(© Wiley-VCH Verlag GmbH & Co. KGaA, 69451 Weinheim, Germany, 2006)

## Introduction

$Cu^{II}$ centres coordinated by an O,N,N-tridentate Schiff base derived from 2-hydroxyacetophenone and 2-(dimethylamino)ethylamine can form a variety of chelates by filling out the coordination environment, resulting in a square-planar, square-pyramidal or distorted square-bipyramidal polyhedron. Depending on the proportions and physicochemical properties of the co-ligands, monomeric, dimeric, oligomeric or polymeric crystal structures are formed. Several copper(II) dimeric complexes containing a singly hydroxo-bridged system[1,2] reveal that the hydroxo group acts commonly in the $\mu_2$-O or $\mu_3$-O bridging modes. The aqua ligand almost invariably exhibits the terminal mode in copper(II) complexes, although complexes for which $H_2O$ acts as a bridge have been reported.[3–6]

There are only two $Cu^{II}$ complexes having a single aqua bridge in the CSD (July 2004). Interestingly, it has been shown that such a bridge can induce spin-exchange interactions between the linked $Cu^{II}$ centres.[3]

In our earlier articles, we have reported a mononuclear $Cu^{II}$ complex, its ferrocyanide-bridged pentanuclear complex[7] and a mononuclear $Co^{II}$ complex,[8] all containing the same Schiff base (LH), where the Schiff base acts as a tridentate chelating ligand. Here, the synthesis, structure, spectral properties and the magneto-structural correlation studies of the complex $[Cu_2(\mu_2\text{-}H_2O)L_2(H_2O)_2](ClO_4)_2{\cdot}2H_2O$ (**1**) are reported. An exchange interaction between the $Cu^{II}$ ions was found, and density functional calculations clearly establish that the main exchange does not proceed through the bridging $H_2O$ but is mediated by the intra-dimer H-bonds.

## Results and Discussion

The complex $[Cu_2(\mu_2\text{-}H_2O)L_2(H_2O)_2](ClO_4)_2{\cdot}2H_2O$ (**1**) was synthesised by mixing an aqueous solution of copper(II) perchlorate with a methanolic solution of the Schiff-base ligand LH, which was obtained by the condensation of 2-hydroxyacetophenone and 2-(dimethylamino)ethylamine.

### Crystal Structure of Complex 1

Complex **1** contains a cationic dimeric unit consisting of two $\{Cu(L)(H_2O)\}^+$ moieties bridged by one water molecule. The dinuclear cation is positioned on the twofold rotation axis of the unit cell (orthorhombic, *Fdd*2), which is shown in Figure 1. The two perchlorate counterions present in the lattice show threefold disorder. The unique $Cu^{II}$ atom adopts a (4+1) square-pyramidal geometry, formed by an O,N,N-tridentate Schiff base and an O atom of a water

[a] Department of Chemistry, Jadavpur University,
Kolkata 700032, India
Fax: +91-33-2414-6266
E-mail: smitra_2002@yahoo.com
[b] Institut für Anorganische Chemie derFriedrich-Alexander-Universität Erlangen-Nürnberg,
Egerlandstrasse 1, 91058 Erlangen, Germany
[c] Institut de Chimie de la Matière Condensée de Bordeaux – CNRS, Université Bordeaux 1,
87 Avenue du Dr. Schweitzer, 33608 Pessac, France
[d] Laboratoire de Chimie de Coordination du CNRS, Université Paul Sabatier,
205, route de Narbonne, 31077 Toulouse, France
E-mail: sutter@lcc-toulouse.fr

 © 2006 Wiley-VCH Verlag GmbH & Co. KgaA, Weinheim 

molecule in the basal plane. The apical position is occupied by the oxygen atom (O3) of the bridging water molecule. The resulting dimer, which contains one bridging water molecule, is reinforced by intra-dimer H-bonds between the $H_2O$ ligand (O2) in an equatorial position and the phenolate O atom (O1) of the adjacent $Cu^{II}$ unit [O1···O2 = 2.627(9) Å; Figure 2 and Table 1]. A number of intermolecular hydrogen bonds are also formed between the dimeric cations, the solvate $H_2O$ molecules and the $ClO_4^-$ ions. The coordination polyhedra of the two central $Cu^{II}$ atoms in **1** are uniformly square-pyramidal. The equatorial Cu1–O2(water) bond length in the basal plane of the pyramid is decreased to 1.980(8) Å (see Table 2) and the apical Cu1–O3 bond length is increased to 2.496(7) Å, resembling a Jahn–Teller effect. The Cu–O(water) lengths are comparable to the average lengths (1.95 and 2.43 Å) of these bonds in related Cu complexes reported in the Cambridge Structural Database (version 5.25.3). The Cu1–N2(imine) bond is shorter [1.959(8) Å] than the Cu1–N1(amine) bond [2.018(9) Å].

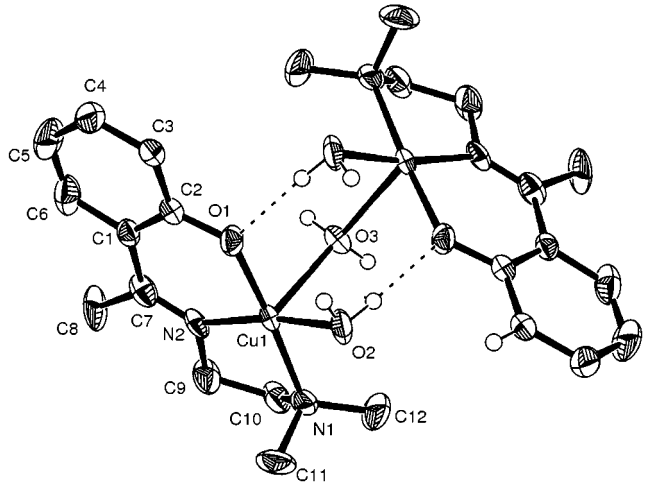


Figure 1. ORTEP view of the dinuclear cation of **1** positioned on the twofold axis of the unit cell.

The phenoxo oxygen atom (O1) is deprotonated, producing a negative charge on the Schiff-base moiety. The square base of each polyhedron is nearly planar, with the Cu atoms being shifted by 0.1171 Å from the mean plane containing the four basal atoms in the direction of the oxygen atom (O3) of the bridging water molecule. The least-squares deviations of the basal atoms from their mean plane are –0.0414, 0.0421, –0.0420 and 0.0414 Å for N1, N2, O1 and O2, respectively. The benzene ring and the six-membered metallochelate ring are puckered. The dihedral angle between the planes of the six-membered and five-membered metallochelate rings is 6.32°. The Cu–Cu distance in the dimer is 4.079 Å.

The perchlorate counterion shows threefold disorder. The disordered perchlorate counterion, the two lattice waters as well as the coordinated terminal and bridging water molecules are extensively hydrogen-bonded. The multiple hydrogen bonds are shown in Figure 2 and the interactions are listed in Table 1.

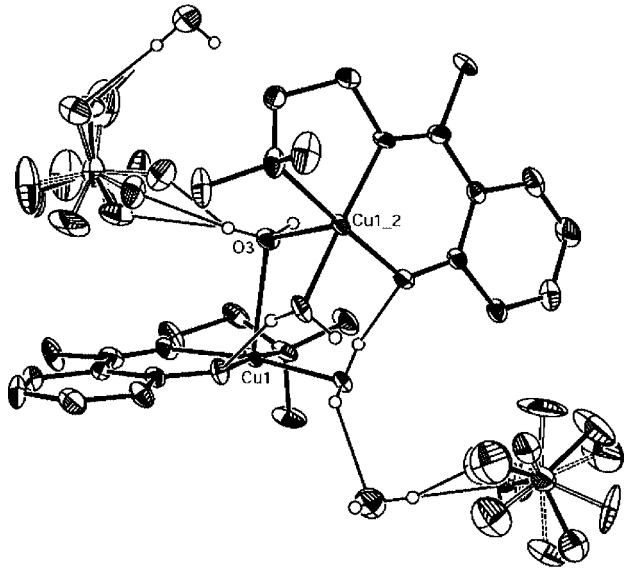


Figure 2. View of the hydrogen bonding (thin lines) in compound **1** ($ClO_4^-$ is threefold disordered).

Table 1. Hydrogen bonds for complex **1**.

| D–H···A[a] | *d*(D–H) [Å] | *d*(H···A) [Å] | *d*(D···A) [Å] | <(DHA) [°] |
|---|---|---|---|---|
| O(2)–H(2A)···O(8) | 0.85 | 2.13 | 2.644(14) | 118.9 |
| O(2)–H(2B)···O(1)#1 | 0.85 | 1.81 | 2.627(9) | 161.1 |
| O(3)–H(3)···O(4A)#1 | 0.85 | 2.27 | 3.101(18) | 165.9 |
| O(3)–H(3)···O(4B)#1 | 0.85 | 2.09 | 2.72(5) | 129.7 |
| O(3)–H(3)···O(4C)#1 | 0.85 | 2.04 | 2.88(2) | 168.0 |
| O(8)–H(8D)···O(4B)#2 | 0.85 | 2.66 | 3.24(12) | 127.2 |
| O(8)–H(8D)···O(6A)#2 | 0.85 | 1.91 | 2.76(14) | 178.8 |
| O(8)–H(8D)···O(6B)#2 | 0.85 | 2.19 | 3.04(14) | 177.3 |
| O(8)–H(8D)···O(6C)#2 | 0.85 | 1.66 | 2.46(13) | 156.2 |
| O(8)–H(8E)···O(4B)#3 | 0.85 | 2.48 | 3.25(9) | 152.3 |
| O(8)–H(8E)···O(7A)#3 | 0.85 | 1.75 | 2.54(10) | 152.5 |
| O(8)–H(8E)···O(7C)#3 | 0.85 | 2.21 | 2.90(11) | 137.5 |
| O(8)–H(8E)···O(5B)#3 | 0.85 | 2.65 | 3.34(11) | 140.0 |

[a] Symmetry transformations used to generate equivalent atoms: #1: $-x+2, -y, z$; #2: $-x+2, -y, z-1$; #3: $x, y, z-1$. The O atoms belonging to $ClO_4^-$ are O(4), O(5), O(6) and O(7).

Table 2. Selected bond lengths [Å] and angles [°] for complex **1**.

| | | | |
|---|---|---|---|
| Cu(1)–O(1) | 1.870(7) | O(1)–C(2) | 1.322(11) |
| Cu(1)–N(2) | 1.959(8) | O(2)–H(2A) | 0.850 |
| Cu(1)–O(2) | 1.980(8) | Cl(1)–O(5C) | 1.383 |
| Cu(1)–N(1) | 2.018(9) | Cl(1)–O(4B) | 1.394 |
| Cu(1)–O(3) | 2.496(7) | Cl(1)–O(5A) | 1.396 |
| | | Cl(1)–O(7A) | 1.400 |
| O(1)–Cu(1)–N(2) | 92.9(3) | O(2)–Cu(1)–N(1) | 89.7(4) |
| O(1)–Cu(1)–O(2) | 90.2(3) | O(1)–Cu(1)–O(3) | 87.4(3) |
| N(2)–Cu(1)–O(2) | 170.2(3) | N(2)–Cu(1)–O(3) | 96.5(3) |
| O(1)–Cu(1)–N(1) | 175.6(4) | O(2)–Cu(1)–O(3) | 93.0(3) |
| N(2)–Cu(1)–N(1) | 86.5(4) | N(1)–Cu(1)–O(3) | 97.1(3) |
| Cu(1)–O(3)–H(3) | 108.0 | Cu(1)–O(3)–Cu(1)#1 | 109.6(4) |

 © 2006 Wiley-VCH Verlag GmbH & Co. KGaA, Weinheim 

### Spectroscopic Properties

The IR spectrum of complex **1** shows a sharp band at 1600 $cm^{-1}$ assigned to the δ(H–OH) mode. Again, a band at 410 $cm^{-1}$ may be assigned to the $\rho_W(H_2O)$ mode and the bands at 846 and 857 $cm^{-1}$ to the $\rho_r(H_2O)$ vibrations, thereby showing presence of both coordinated and uncoordinated lattice water in the complex.[9] This also confirms the presence of hydrogen bonding in the complex.[10] The strong $\nu_{C=N}$ band occurring at 1635 $cm^{-1}$, which is shifted considerably towards lower frequencies compared to that of the free Schiff base (1650 $cm^{-1}$), suggests coordination of the imino nitrogen atom. The phenolic stretching band is found at 1258 $cm^{-1}$. The band at 1160 $cm^{-1}$ for the $\nu_3(F_2)$ $ClO_4^-$ mode is broadened and split, thus indicating the involvement of this anion in hydrogen bonding, as established from the X-ray analysis.[11] Ligand coordination to the metal centre is substantiated by two bands appearing at 405 and 332 $cm^{-1}$ for $\nu_{M-N}$ and $\nu_{M-O}$, respectively.

The electronic spectroscopic data for **1** in acetonitrile solvent are in good agreement with its geometry. A charge-transfer transition (CT) in the range 400–360 nm may be assigned to a ligand-to-metal charge-transfer transition. Much weaker, less well-defined shoulders are found in the lower energy region and are associated with d–d transitions. The d–d bands generally fall below 700 nm and are more consistent with a square-pyramidal geometry for **1**, as in certain related $Cu^{II}$ complexes.[12]

### Magnetic Properties

The temperature dependence of the molar magnetic susceptibility, $\chi_M$, for compound **1** was measured on a polycrystalline sample in the temperature range 2–300 K. The plot of $\chi_M T$ vs. $T$ for the dinuclear $Cu^{II}$ compound is shown in Figure 3. At 300 K the value of $\chi_M T$ is 0.76 $cm^3 K mol^{-1}$, in good agreement with the value expected for two non-interacting $Cu^{II}$ ions. This value decreases very slightly as the temperature is lowered to 100 K, and below this temperature it decreases rapidly to reach 0.03 $cm^3 K mol^{-1}$ at 2 K, thereby revealing the occurrence of antiferromagnetic interactions between the $Cu^{II}$ centres. A classical Bleaney–Bowers law, using the phenomenological Hamiltonian $H = -J\boldsymbol{S}_1 \cdot \boldsymbol{S}_2$, is suitable to simulate the magnetic behaviour for compound **1**, the resulting expression for $\chi_M T$ is given below. The best fit of this expression to the experimental data yields the exchange parameter $J = -13.23 \pm 0.01$ $cm^{-1}$ with $g = 2.03$.

$$\chi_M T = \frac{2Ng^2\beta^2}{k[3 + \exp(-J/kT)]}$$

The structural data for compound **1** indicate that the bridging $H_2O$ ligand is connected in an apical position to both the linked Cu ions. As a consequence, there is no overlap with the magnetic orbitals of the metal centres and the exchange interaction through this bridging ligand is expected to be very weak.[13] The magnitude found for $J$ is thus surprisingly high and suggests the occurrence of alternative exchange pathways. In order to clarify the origin of this magnetic coupling, density functional calculations were carried out.

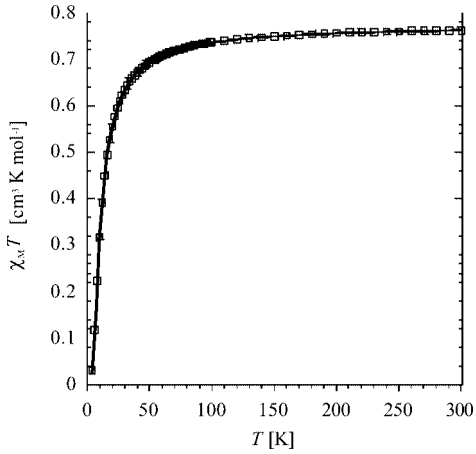


Figure 3. Experimental (□) and calculated (−) temperature dependence of $\chi_M T$ for compound **1**.

### Computational Methodology for the Density Functional Calculations

The calculated coupling constant, $J$, was deduced from two separate density functional computations carried out for the highest-spin state (triplet state for compound **1**) and for the broken-symmetry state. The hybrid B3LYP[14] functional was used, as implemented in Gaussian98.[15] The basis set used in all calculations was the triple-ζ basis-set proposed by Ahlrichs et al.[16] for transition metals and the double-ζ basis set proposed by the same authors for the other atoms.[17] The obtained $J$ values were deduced from the energy difference $E_{HS} - E_{BS} = -J$, where $E_{HS}$ and $E_{BS}$ are the energies of the high-spin and broken-symmetry states, respectively. We consider that the energy of the broken-symmetry state is a good approximation of the low-spin state energy, according to Ruiz et al.[18] The spin densities on the atoms were calculated according to the NBO method.[19]

#### *DFT Calculations for Compound 1*

Sets of calculations were carried out for the whole Cu dimer of compound **1** and for the same dimer but without the bridging $H_2O$ molecule. The isotropic interaction parameters that were obtained in both cases were very similar ($J = -8.1$ and $-7.9$ $cm^{-1}$, respectively), in rather good agreement with the experimental exchange parameter. The spin

 © 2006 Wiley-VCH Verlag GmbH & Co. KGaA, Weinheim 

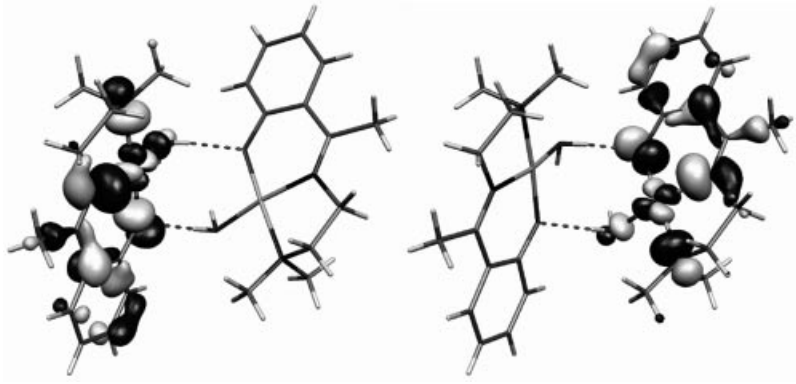

Figure 4. Localised magnetic orbitals issuing from the broken symmetry of the dehydrated compound.

density found on the two equivalent copper atoms is +0.577, whereas that located on the oxygen atoms is +0.116 for O1, +0.051 for O2 and –0.0007 for O3.

The negligible spin density on the bridging oxygen atom is in line with the very small difference in the calculated $J$ values for a dimer with and without a bridging $H_2O$ ligand. This result clearly confirms that the bridging water molecule is in no way responsible for the magnetic behaviour exhibited by the complex. In order to rationalise this behaviour, the localised magnetic orbitals issuing from the broken-symmetry state were scrutinised. These orbitals are represented in Figure 4 for the complex without the bridging $H_2O$ ligand (those of the $H_2O$-bridged system have exactly the same shapes). As expected from simple ligand-field models, the magnetic orbitals are directed towards the four short Cu–N/O distances. Indeed, in a square-pyramidal environment ($C_{4v}$ point group), the five d orbitals split into four sets: $d_{xz}$ and $d_{yz}$ (e); $d_{yx}$ ($b_2$); $d_{z^2}$ ($a_1$); and $d_{x^2-y^2}$ ($b_1$). As it is the only orbital involved in four bonds, the $d_{x^2-y^2}$ orbital has the highest energy and is singly occupied in a $d^9$ configuration. This explains the negligible influence of the bridging water molecule, which is in an apical position and therefore has no overlap with the magnetically active orbitals of the $Cu^{II}$ ions. Conversely, a significant amount of spin density is found on the oxygen atoms located in the equatorial positions (O1 and O2). The hydrogen bonds linking these atoms within a dimer (dashed lines in Figure 4) may thus provide an alternative pathway for the magnetic interaction between the two $Cu^{II}$ centres.[20] As a matter of fact, doubly H-bridged copper dimers can exhibit experimental coupling constants between limiting values of –4[21] and –94 $cm^{-1}$.[22] Different intermediate values have also been reported,[23] as well as density functional calculations on these dimers.[24] For compound **1**, the relatively weak exchange interaction is essentially due to the fact that the two basal planes of the copper geometry are not coplanar. This reduces the overlap of the magnetic orbitals, which causes decreased interactions between the two coppers centres.

This study clearly establishes that the main exchange interaction for compound **1** proceeds through the hydrogen bonds existing within the dimer, whereas the $H_2O$ ligand bridging the two Cu ions has a poor contribution.

## Conclusions

A rare example of a [(Schiff-base)$Cu^{II}$] dimer with a single $H_2O$ ligand bridging the two metal ions has been characterised. A striking feature of this compound is the absence of the $\mu_2$-coordination of the phenolato oxygen atoms often observed for such compounds. Instead, these atoms are involved in hydrogen bonds with the adjacent Cu unit, which reinforce the cohesion of the dimer. These hydrogen bonds are also the pathway for the antiferromagnetic interaction ($J$ = –13.2 $cm^{-1}$) between the Cu centres of the dimer. This is strongly supported by density functional calculations, which show that the contribution of the $H_2O$ bridge is negligible.

## Experimental Section

**Materials:** 2-Hydroxyacetophenone, 2-(dimethylamino)ethylamine and copper perchlorate were used as supplied by Aldrich. All other chemicals or solvents used were of reagent or analytical grade and used without further purification.

**Synthesis of the Ligand and Complex:** ***Caution!*** *Perchlorate salts of metal complexes with organic ligands are potentially explosive. Only a small amount of the material should be prepared and should be handled with caution*. The ligand LH was prepared by refluxing 2-hydroxyacetophenone (0.60 mL, 5 mmol) and 2-(dimethylamino)-ethylamine (0.545 ml, 5 mmol) in methanol (30 mL) for 0.5 h. The resulting mixture gave a yellow solution containing the tridentate ligand (LH). The ligand was used without further purification. The complex $[Cu_2(\mu_2\text{-}H_2O)L_2(H_2O)_2](ClO_4)_2{\cdot}2H_2O$ (**1**) was prepared by slowly adding 10 mL of a methanolic solution of LH (2 mmol) to 20 mL of an aqueous solution of copper(II) perchlorate (0.740 g, 2 mmol). The mixture was kept at room temperature. After a few days, green crystals of **1** had formed on slow evaporation of the solvent. Crystals suitable for X-ray diffraction were collected. Yield: 0.541 g (65%). $C_{24}H_{44}Cl_2Cu_2N_4O_{15}$ (826.61): calcd. C 34.9, H 5.4, N 6.8; found C 34.2, H 5.3, N 6.1.

**Physical Measurements:** Elemental analyses were carried out using a Perkin–Elmer 2400 II elemental analyser. The IR spectrum was recorded with a Perkin–Elmer Spectrum RX FTIR instrument in the range of 4000–350 $cm^{-1}$ as KBr pellets. The electronic spectrum was measured with a Perkin–Elmer Lambda-40 (UV/Vis) spectrophotometer in dichloromethane. Magnetic susceptibility measurements were carried out with a Quantum Design MPMS-5S SQUID

 © 2006 Wiley-VCH Verlag GmbH & Co. KGaA, Weinheim 

magnetometer under an applied magnetic field of 5000 Oe. Magnetic data were corrected for diamagnetic contributions estimated from Pascal tables and for the sample holder contribution.

**X-ray Data Collection and Structure Refinement:** Single crystals of the copper complex ($0.29 \times 0.22 \times 0.04$ mm) were grown from a methanol/water medium. Diffraction measurements were carried out at 153(2) K with an Enraf–Nonius CAD-4 MACH 3 diffractometer using graphite-monochromated Mo-$K_\alpha$ radiation ($\lambda$ = 0.71073 Å): orientation matrices and unit-cell parameters from the setting angles of 25 centred medium-angle reflections; collection of the diffraction intensities by ω scans. The structure was solved by direct methods and subsequently refined by full-matrix least-squares procedures on $F^2$ with allowance for anisotropic thermal motion of all non-hydrogen atoms by employing the WinGX package[25] and the relevant programs (SIR-97,[26] SHELXL-97,[27] ORTEP-3[28]) implemented therein. All hydrogen atoms were positioned geometrically and allowed to ride on their parent atoms with isotropic displacement parameters fixed at 1.2-times $U_{eq}$ of their parent atoms. $C_{24}H_{44}Cl_2Cu_2N_4O_{15}$ (826.61); orthorhombic, *Fdd*2, $a$ = 18.853(4), $b$ = 36.452(8), $c$ = 9.816(2) Å, $V$ = 6746(2) Å$^3$, $Z$ = 8, $d_{calcd.}$ = 1.628 Mg m$^{-3}$, $\mu$(Mo-$K_\alpha$) = 1.493 mm$^{-1}$; $F$(000) = 3424; $2.23° \leq \Theta \leq 25.56°$, 2482 reflections collected ($-2 \leq h \leq 22$, $-2 \leq k \leq 44$, $-2 \leq l \leq 11$; including Friedel pairs), 2075 independent reflections ($R_{int}$ = 0.0988); Completeness to $\theta$ = 25.56°: 100.0%; absorption correction: none; 267 parameters and 121 restraints ($ClO_4^-$ anion as geometrically idealised tetrahedron); final $R$ indices [$I > 2\sigma(I)$]: $R_1$ = 0.0629, $wR_2$ = 0.1738; $R$ indices (all data): $R_1$ = 0.0825, $wR_2$ = 0.1853; absolute structure parameter $x$ = –0.01(4);[29] largest difference peak/hole: 0.844/–1.478 e Å$^{-3}$. CCDC-279057 (**1**) contains the supplementary crystallographic data for this paper. These data can be obtained free of charge from The Cambridge Crystallographic Data Centre via www.ccdc.cam.ac.uk/data_request/cif.

## Acknowledgments

We gratefully acknowledge the financial assistance to P. T. and S. S. from the CSIR (New Delhi, India). The magnetic measurements and density functional computations were supported by the Centre Franco-Indien pour la promotion de la Recherche Avancée/Indo-French Centre for the Promotion of Advanced research (Project 3108-3).

[1] M. S. Haddad, S. R. Wilson, D. J. Hodgson, D. N. Hendrickson, *J. Am. Chem. Soc.* **1981**, *103*, 384–391.
[2] A. K. Patra, M. Ray, R. Mukherjee, *Polyhedron* **2000**, *19*, 1423–1428.
[3] H. Uekusa, S. Ohba, T. Tokii, *Acta Crystallogr., Sect. C* **1995**, *51*, 625–627.
[4] G. Christou, S. P. Perlepes, E. Libby, K. Folting, J. C. Huffman, R. J. Webb, D. N. Hendrickson, *Inorg. Chem.* **1990**, *29*, 3657–3666.
[5] X.-M. Chen, X.-L. Feng, X.-L. Yu, T. C. W. Mak, *Inorg. Chim. Acta* **1997**, *266*, 121–124.
[6] O. Švajlenová, J. Vančo, J. Marek, *Acta Crystallogr., Sect. C***2004**, *60*, m275–m277.
[7] N. Mondal, M. K. Saha, B. Bag, S. Mitra, G. Rosair, M. S. El Fallah, *Polyhedron* **2001**, *20*, 579–584.
[8] N. Mondal, D. K. Dey, S. Mitra, K. M. A. Malik, *Polyhedron* **2000**, *19*, 2707–2711.
[9] N. K. Karan, S. Mitra, G. Rosair, D. J. Jenkins, K. M. A. Malik, *Inorg. Chem. Commun.* **2001**, *4*, 712–715 and references cited therein.
[10] C. T. Yang, B. Moubaraki, K. S. Murray, J. D. Ranford, J. J. Vittal, *Inorg. Chem.* **2001**, *40*, 5934–5941.
[11] a) I. Chadjistamatis, A. Terzis, C. P. Raptopoulou, S. P. Perlepes, *Inorg. Chem. Commun.* **2003**, *6*, 1365–1371; b) K. Nakamoto, *Infrared and Raman Spectra of Inorganic and Coordination Compounds*, 3rd ed., John Wiley & Sons, New York, **1978**.
[12] A. B. P. Lever, *Inorganic Electronic Spectroscopy*, Elsevier, Amsterdam, **1984**, p. 553.
[13] O. Kahn, *Molecular Magnetism*, VCH Publishers, New York, **1993**, chapter 8.6.
[14] A. D. J. Becke, *J. Chem. Phys.* **1993**, *98*, 5648–5652.
[15] M. J. Frisch, G. W. Trucks, H. B. Schlegel, G. E. Scuseria, M. A. Robb, J. R. Cheeseman, V. G. Zakrzewski, J. A. Montgomery, R. E. Stratmann, J. C. Burant, S. Dapprich, J. M. Millam, A. D. Daniels, K. N. Kudin, M. C. Strain, O. Farkas, J. Tomasi, V. Barone, M. Cossi, R. Cammi, B. Mennucci, C. Pomelli, C. Adamo, S. Clifford, J. Ochterski, G. A. Petersson, P. Y. Ayala, Q. Cui, K. Morokuma, D. K. Malick, A. D. Rabuck, K. Raghavachari, J. B. Foresman, J. Cioslowski, J. V. Ortiz, B. B. Stefanov, G. Liu, A. Liashenko, P. Piskorz, I. Komaromi, R. Gomperts, R. L. Martin, D. J. Fox, T. Keith, M. A. Al-Laham, C. Y. Peng, A. Nanayakkara, C. Gonzalez, M. Challacombe, P. M. W. Gill, B. G. Johnson, W. Chen, M. W. Wong, J. L. Andres, M. Head-Gordon, E. S. Replogle, J. A. Pople, *Gaussian 98* (Revision A.11), Gaussian, Inc., Pittsburgh, PA, **1998**.
[16] A. Schaefer, C. Huber, R. Ahlrichs, *J. Chem. Phys.* **1994**, *100*, 5829–5835.
[17] A. Schaefer, H. Horn, R. Ahlrichs, *J. Chem. Phys.* **1992**, *97*, 2571–2577.
[18] E. Ruiz, J. Cano, S. Alvarez, P. Alemany, *J. Comput. Chem.* **1999**, *20*, 1391–1400.
[19] E. D. Glendening, A. E. Reed, J. E. Carpenter, F. Weinhold, *NBO*, Version 3.1.
[20] C. Rancurel, N. Daro, O. Benedi Borobia, E. Hertweck, J.-P. Sutter, *Eur. J. Org. Chem.* **2003**, 167–171.
[21] W. E. Estes, W. E. Hatfield, *Inorg. Chem.* **1978**, *17*, 3226–3231.
[22] J. A. Bertrand, T. D. Black, P. G. Eller, F. T. Helm, R. Mahmood, *Inorg. Chem.* **1976**, *15*, 2965–2970.
[23] a) J. A. Bertrand, E. Fujita, D. G. Vanderveer, *Inorg. Chem.* **1980**, *19*, 2022–2028; b) H. Muhonen, *Inorg. Chem.* **1986**, *25*, 4692–4698.
[24] C. Desplanches, E. Ruiz, A. Rodriguez-Fortea, S. Alvarez, *J. Am. Chem. Soc.* **2002**, *124*, 5197–5205.
[25] L. J. Farrugia, *J. Appl. Crystallogr.* **1999**, *32*, 837–838.
[26] A. Altomare, M. C. Burla, M. Camalli, G. L. Cascarano, C. Giacovazzo, A. Guagliardi, A. G. G. Moliterni, G. Polidori, R. Spagna, *J. Appl. Crystallogr.* **1999**, *32*, 115–119.
[27] G. M. Sheldrick, *SHELXL-97* (Release 97-2), University of Göttingen, Germany, **1998**.
[28] L. J. Farrugia, *J. Appl. Crystallogr.* **1997**, *30*, 565–566.
[29] H. D. Flack, *Acta Crystallogr., Sect. A* **1983**, *39*, 876–881.

Received: August 3, 2005
Published Online: December 1, 2005

 © 2006 Wiley-VCH Verlag GmbH & Co. KGaA, Weinheim 

DOI: 10.1002/ejic.200500726

# An Experimental and Theoretical (DFT) Investigation of the Coordination Mode of 2,4-Dithiouracil (2,4-dtucH$_2$) in Copper(I) Complexes with 1,2-Bis(diphenylphosphanyl)benzene (dppbz): The Crystal Structures of [Cu(μ-Br)(dppbz)]$_2$ and [CuBr(dppbz)(2,4-dtucH$_2$)]

**Paraskevas Aslanidis,*[a] Philip J. Cox,[b] Andreas Kaltzoglou,[a] and Athanasios C. Tsipis*[c]**

**Keywords:** Copper / Density functional calculations / Phosphane ligands / S ligands

Novel copper(I) mixed-ligand complexes containing 1,2-bis(diphenylphosphanyl)benzene (dppbz) and 2,4-dithiouracil (2,4-dtucH$_2$) ligands have been synthesised by addition of the thione ligand to the dinuclear [Cu(μ-X)(dppbz)]$_2$ intermediate in acetonitrile/methanol or acetone solution. The molecular structures of both the precursor [Cu(μ-Br)(dppbz)]$_2$ and the [CuBr(dppbz)(2,4-dtucH$_2$)] complexes were established by single-crystal X-ray diffraction. Interestingly, the structure of the thione-free dimer involves two diphosphane-chelated Cu$^I$ centres bridged by two bromide ligands, thus forming a non-planar Cu$_2$Br$_2$ core. The structure of [CuBr(dppbz)(2,4-dtucH$_2$)] corresponds to a four-coordinate Cu$^I$ centre in a tetrahedral coordination environment with the heterocyclic dithione ligand being coordinated to the metal centre in a unidentate fashion through its exocyclic sulfur donor atom. The structural, bonding and electronic properties of the model complexes [Cu(μ-X)(dppbz)]$_2$ and [CuX(dppbz)(2,4-dtucH$_2$)] (X = Cl, Br, or I) are adequately described by DFT/B3LYP computational techniques. All model dinuclear [Cu(μ-X)(dppbz)]$_2$ complexes exhibit π-type MOs delocalised over the entire four-membered Cu(μ-X)$_2$Cu ring, thereby accounting for the near equivalency of the Cu–X bonds. Moreover, the [Cu(μ-X)(dppbz)]$_2$ dimers possess a σ-type MO corresponding to weak Cu···Cu bonding interactions, which further stabilize the Cu(μ-X)$_2$Cu ring. According to our calculations, the interaction energies of the 2,4-dtucH$_2$ ligand with the Cu$^I$ centre are predicted to be about 13–16 kcal mol$^{-1}$. The coordination of the 2,4-dtucH$_2$ ligand is further stabilized by an X···H–N hydrogen bond that is perpendicular to the plane of the dppbz ligand.
(© Wiley-VCH Verlag GmbH & Co. KGaA, 69451 Weinheim, Germany, 2006)

## Introduction

The coordination chemistry of heterocyclic thiones has grown enormously in the recent past, mainly because of their relevance to biological systems.[1,2] The salient feature of these heterocyclic thioamides is their ability to bind to a metal centre in a variety of coordination modes. Along these lines a wealth of complexes exhibiting variable nuclearities and often unusual geometries have been synthesised and studied so far.[1–7] A large number of mixed-ligand complexes of the univalent coinage metals, particularly those of Cu$^I$, incorporating tertiary arylphosphanes as a second, bulky soft donor ligand have been thoroughly investigated in an attempt to understand the factors that may affect the stoichiometric and geometrical preferences of these compounds.[3] In this context, some examples of three-coordinate Cu$^I$ complexes, where the steric requirements of the phosphane ligands exert an influence on the coordination number, have also been reported.[4] Moreover, a number of halo- or thione-S-bridged dinuclear mixed-ligand complexes have been synthesised and structurally well characterised.[3,5] In contrast to the monodentate triarylphosphanes, didentate P-donor ligands, especially the oligomethylene-backboned symmetric diphosphanes formulated as Ph$_2$P(CH$_2$)$_n$PPh$_2$ ($n$ = 1, 2 or 4), favour the formation of dinuclear complexes.[6] On the other hand, the rigid *cis*-1,2-bis(diphenylphosphanyl)ethane (*cis*-dppen) and 1,3-bis(diphenylphosphanyl)propane (dppp) have been found to chelate at a single metal centre, yielding mononuclear pseudo-tetrahedral Cu$^I$ species.[7] Another didentate P-donor ligand capable of forming chelate five-membered symmetric rings is the sterically demanding 1,2-bis(diphenylphosphanyl)-benzene, hereafter abbreviated as dppbz. Although dppbz has already been used extensively as a chelating ligand for many metal centres,[8] no structurally characterised Cu$^I$ or Ag$^I$ derivatives of this rigid diphosphane, as far as we know, are currently known.

Among the heterocyclic thiones, the coordination properties of the thio derivatives of uracil, such as 2-thiouracil

[a] Aristotle University of Thessaloniki, Faculty of Chemistry, Inorganic Chemistry Laboratory,
P. O. Box 135, 54124, Thessaloniki, Greece
E-mail: aslanidi@chem.auth.gr
[b] School of Pharmacy, The Robert Gordon University,
Schoolhill, Aberdeen AB10 1FR, Scotland
E-mail: p.j.cox@rgu.ac.uk
[c] Section of Inorganic and Analytical Chemistry, Department of Chemistry, University of Ioannina,
45110 Ioannina, Greece
E-mail: attsipis@cc.uoi.gr

 © 2006 Wiley-VCH Verlag GmbH & Co. KGaA, Weinheim 

(2-tucH$_2$), 4-thiouracil (4-tucH$_2$) and 2,4-dithiouracil (2,4-dtucH$_2$) are of particular interest as these ligands have significant biological interest.[9] Very recently, the gas-phase reactivity of uracil, 2-tucH$_2$, 4-tucH$_2$, and 2,4-dtucH$_2$ towards $Cu^+$ and $Cu^{2+}$ cations has been thoroughly investigated using electronic structure calculation methods.[10] In this work we report on the synthesis, characterisation and electronic structure calculations of new copper(I) coordination compounds bearing dppbz and/or 2,4-dtucH$_2$ as ligands. In effect, what we want to address here is the coordination bonding mode of the versatile 2,4-dtucH$_2$ ligand (Scheme 1), which has two exocyclic sulfur donor atoms of different basicity that are capable of coordinating to $Cu^I$ metal centres.

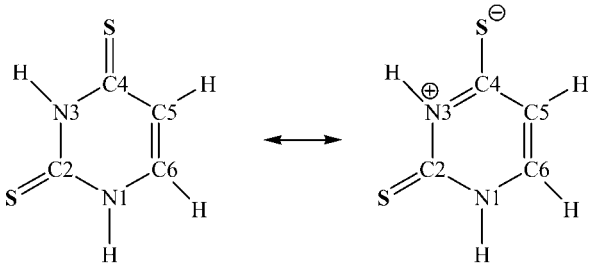


Scheme 1. Resonance structures of 2,4-dtucH$_2$.

## Results and Discussion

### Synthesis

The new compounds were prepared following a synthetic pathway that has already produced a number of mixed-ligand copper(I) halide complexes. Thus, 1 mmol of CuCl or CuBr was first treated with an equimolar quantity of dppbz to yield an intermediate adduct formulated as [CuX(dppbz)] (X = Cl, Br). This intermediate was then allowed to react with one equivalent of 2,4-dtucH$_2$ in refluxing dry acetonitrile for 2 h to afford the corresponding pure mixed-ligand complexes [CuX(dppbz)(2,4-dtucH$_2$)] (X = Cl: **1**; Br: **2**) in good yields. During the reaction of 2,4-dtucH$_2$ with CuBr, a small quantity of greenish yellow crystals was separated at the initial stages of the evaporation of the diluted acetonitrile mother liquid; their analytical and spectroscopic data were identical to those of the [CuBr(dppbz)] intermediate. In this way we were able to characterise the intermediate by X-ray crystallography as the thione-free dimer [CuBr(dppbz)]$_2$ (**3**). It should be noted that **3** is inert in the reactions with a number of heterocyclic thiones [e.g. 5-methyl-1,3,4-thiadiazole-2-thione (mtdztH) or 4-methyl-5-trifluoromethyl-4*H*-1,2,4-triazoline-3(2*H*)-thione (mftztH)]. Treatment of CuI with equimolar quantities of dppbz readily yielded the intermediate 1:1 adduct [CuI(dppbz)]$_x$ (**4**) as a white microcrystalline solid, which, however could not be converted into the corresponding [CuI(dppbz)(2,4-dtucH$_2$)] (**5**). Compound **5** was obtained following a reverse synthetic procedure, i.e., by adding a twofold excess of the 2,4-dtucH$_2$ ligand to a $Cu^I$ solution, followed by addition of dppbz. The orange-red precipitate formed before adding dppbz probably corresponds to the polymeric species [CuI(2,4-dtucH$_2$)]$_x$ (**6**), which depolymerises upon addition of dppbz to give **5** as an orange solid. The analogous polymeric species [CuBr(2,4-dtucH$_2$)]$_x$ (**7**) was also isolated as an orange-red powder following the same synthetic procedure. To investigate the ability of 2,4-dtucH$_2$ for further coordination to CuX through both exocyclic thione-S donor atoms, a series of reactions using variable stoichiometries and reaction conditions were carried out, but in all cases $Cu^I$ complexes involving 2,4-dtucH$_2$ coordination in the mono-hapto or $\mu_2$-coordination mode via the S donor atom at the 4-position were isolated.

All new complexes are diamagnetic, air-stable, microcrystalline solids that are moderately soluble in acetonitrile and only marginally soluble in chloroform and acetone. Their solutions in acetone and chloroform are non-conducting. The stoichiometry and structure of the complexes were confirmed by elemental analysis and spectroscopic measurements. Moreover, the molecular structures of [CuBr(dppbz)(dtucH$_2$)] (**2**) and [CuBr(dppbz)]$_2$ (**3**) were determined by X-ray crystallographic analyses.

### Spectroscopy

The electronic absorption spectra of the new compounds in chloroform solution at room temperature show an intense, broad band with maxima in the region of 243–255 nm, which can be attributed, with reference to the absorption bands of the uncoordinated dppbz, to intraligand $\pi^*\leftarrow\pi$ transitions on the phenyl groups of the phosphane ligand. Moreover, the spectra of compounds **1**, **2** and **5**–**7** display an additional broad band in the region of 285–310 nm, where the free thiones normally absorb. This band experiences a small red-shift as a consequence of the coordination to $Cu^I$ and may be ascribed to a thione-originating intraligand transition. The IR spectra of compounds **1**–**3**, **6** and **7**, recorded in the range 4000–250 cm$^{-1}$, all show the expected strong phosphane bands, which remain practically unshifted upon coordination. Moreover, the spectra of compounds **1**, **2** and **4**–**7** contain all of the bands required by the presence of the heterocyclic thione ligand, with shifts due to coordination indicative of an exclusive S-coordination mode.

### X-ray Structural Investigations

The X-ray crystal structures of [CuBr(dppbz)(dtucH$_2$)] (**2**) and [Cu(μ-Br)(dppbz)]$_2$ (**3**) corroborate the spectroscopic results discussed above. Selected bond distances and angles of complexes **2** and **3** are listed in Tables 1 and 2, respectively.

 © 2006 Wiley-VCH Verlag GmbH & Co. KGaA, Weinheim 

Table 1. Selected bond lengths [Å] and angles [°] for **2**.

| | | | |
|---|---|---|---|
| Cu(1)–Br(1) | 2.4366(3) | S(2)–C(2) | 1.650(2) |
| Cu(1)–P(1) | 2.2953(6) | P(1)–C(5) | 1.838(2) |
| Cu(1)–P(2) | 2.2393(6) | P(2)–C(6) | 1.833(2) |
| Cu(1)–S(1) | 2.2921(6) | C(5)–C(6) | 1.408(3) |
| S(1)–C(1) | 1.679(2) | | |
| P(1)–Cu(1)–P(2) | 86.73(2) | C(1)–S(1)–Cu(1) | 105.24(7) |
| P(1)–Cu(1)–S(1) | 108.37(2) | C(5)–P(1)–Cu(1) | 99.68(7) |
| P(2)–Cu(1)–S(1) | 120.10(2) | C(6)–P(2)–Cu(1) | 101.34(7) |
| P(1)–Cu(1)–Br(1) | 115.586(18) | P(1)–C(5)–C(6) | 117.21(16) |
| P(2)–Cu(1)–Br(1) | 118.836(18) | P(2)–C(6)–C(5) | 118.10(16) |
| S(1)–Cu(1)–Br(1) | 106.015(18) | | |
| Hydrogen bonds | | | |
| N(1)–H(1) | 0.8800 | Br(1)···N(1) | 3.3175(16) |
| NH(1)···Br(1) | 2.5100 | Br(1)···H(1)–N(1) | 152° |
| N(2)–H(2) | 0.8800 | Br(1)···N(2) | 3.1994(19) |
| NH(2)···Br(1) | 2.4300 | Br(1)···H(2)–N(2) | 146° |

Table 2. Selected bond lengths [Å] and angles [°] for **3**.

| | | | |
|---|---|---|---|
| Cu(1)–Br(1) | 2.4556(6) | Cu(1)–P(1) | 2.2586(10) |
| Cu(2)–Br(1) | 2.4958(6) | Cu(1)–P(2) | 2.2549(11) |
| Cu(2)–Br(2) | 2.4279(6) | Cu(2)–P(3) | 2.2600(11) |
| Cu(1)–Br(2) | 2.5317(6) | Cu(2)–P(4) | 2.2546(11) |
| Cu(1)–Cu(2) | 2.8410(6) | | |
| Cu(1)–Br(1)–Cu(2) | 70.022(17) | P(4)–Cu(2)–Br(2) | 118.14(3) |
| Cu(2)–Br(2)–Cu(1) | 69.859(17) | P(3)–Cu(2)–Br(1) | 108.96(3) |
| P(1)–Cu(1)–P(2) | 90.50(4) | P(3)–Cu(2)–Br(2) | 121.41 (4) |
| P(2)–Cu(1)–Br(1) | 120.66(3) | P(4)–Cu(2)–Br(1) | 110.55(3) |
| P(1)–Cu(1)–Br(1) | 121.08(3) | Br(2)–Cu(2)–Br(1) | 108.425(19) |
| P(2)–Cu(1)–Br(2) | 107.09(3) | C(13)–P(1)–Cu(1) | 102.10(12) |
| P(1)–Cu(1)–Br(2) | 109.88(3) | C(14)–P(2)–Cu (1) | 102.04(12) |
| Br(1)–Cu(1)–Br(2) | 106.417(19) | C(43)–P(3)–Cu(2) | 100.75(13) |
| P(4)–Cu(2)–P(3) | 87.86(4) | C(44)–P(4)–Cu(2) | 101.48(13) |

Compound **2** crystallises in the monoclinic space group $P2_1/c$ with four formula units in the unit cell. Figure 1 depicts a perspective of the molecule showing the atom-labelling scheme.

The tetrahedral environment of the copper atom formed by the two P atoms of the chelating dppbz unit, one Br and one of the two exocyclic S donor atoms of the dithione ligand is considerably distorted, with the largest deviation from the ideal geometry being reflected by the P(1)–Cu(1)–P(2) and P(1)–Cu(1)–Br(1) angles of 86.61(2)° and 122.05(19)°, respectively, which are markedly different from the ideal tetrahedral value of 109.4°.

As expected, the carbon atoms of the phenylene backbone and the two adjacent phosphorus atoms are coplanar and the CuPCCP five-membered ring adopts an envelope conformation with the metal atom out of the plane containing the four diphos ligand donor atoms by 1.034(1) Å. The two phenyl rings on each phosphorus atom are nearly perpendicular to each other. However, the C(17)–C(22) and C(29)–C(34) phenyl rings have their planes in an almost parallel arrangement, with a π-stacking interaction of 3.827(1) Å between them. Likewise, the inclination of the pyrimidine ring to the C(11)–C(16) phenyl ring results in a π-stacking interaction of 4.116(1) Å. The two Cu–P distances [2.2393(6) and 2.2953(6) Å] are significantly different, but are within the limits of the range expected for tetrahedrally coordinated $Cu^I$.

The coordinated 2,4-dithiouracil ligand, which adopts its most stable dithione tautomeric form (**a**, Scheme 1) is coordinated to the $Cu^I$ metal centre in a monodentate coordination mode through the S atom in the 4-position. Considering that the corresponding carbon–sulfur bond of the uncoordinated 2,4-dtuc$H_2$ has been found to be significantly longer than that in the 2-position [1.684(6) vs. 1.645(6) Å],[11] the favourable coordination of that specific sulfur atom can be interpreted as the inevitable consequence of its strong polarisation towards the amidic [–$HN^+$=C($S^-$)–] configuration (**b**). However, coordination to $Cu^I$ does not affect these two bond lengths significantly.

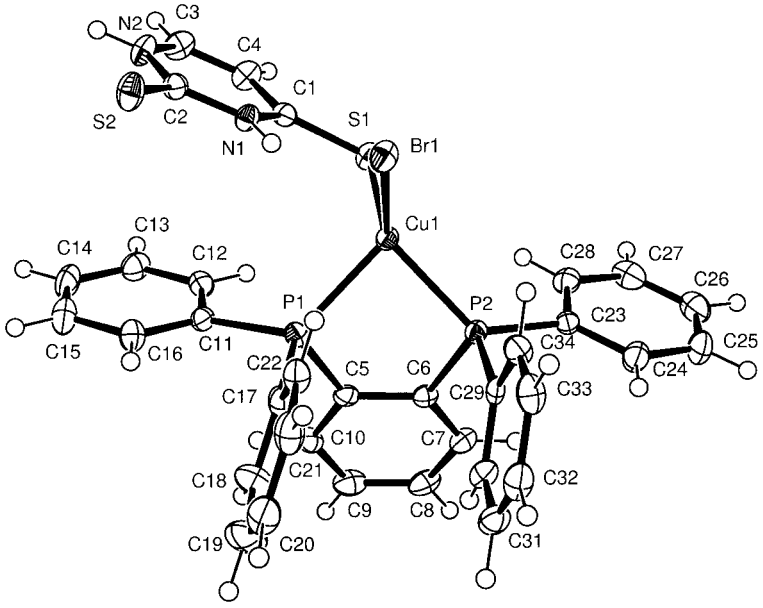


Figure 1. Structure of complex **2** together with the atom-labelling scheme (50% probability ellipsoids with hydrogen atoms omitted for clarity).

 © 2006 Wiley-VCH Verlag GmbH & Co. KGaA, Weinheim 

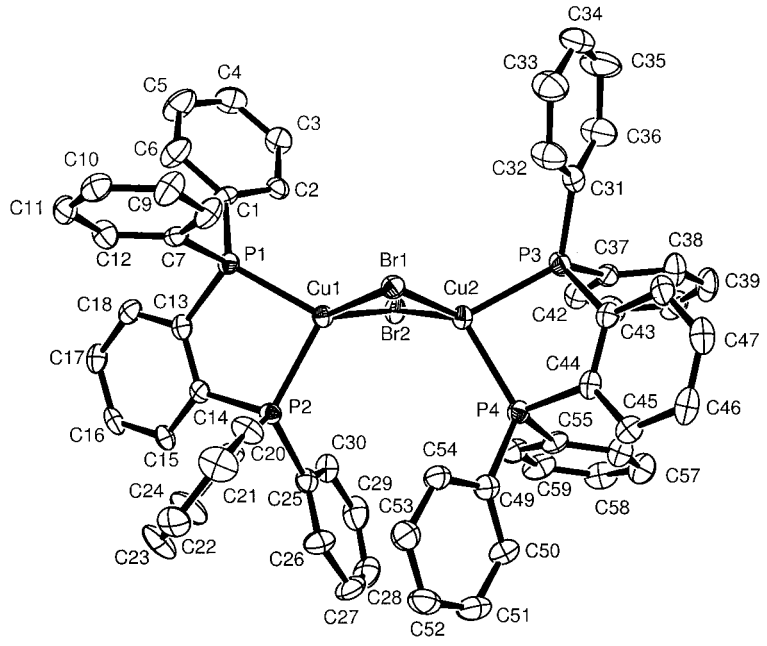


Figure 2. Structure of complex **3** together with the atom-labelling scheme (50% probability ellipsoids with hydrogen atoms omitted for clarity).

Likewise, the structural parameters within the heterocyclic backbone remain practically unaffected upon coordination.

Light-green single crystals of **3** were grown from the acetonitrile/methanol mother liquid of **2** during the earlier stages of the slow evaporation. Complex **3** crystallises in the monoclinic space group $P2_1$ with two formula units in the unit cell. The structure of **3**, together with the atom-labelling scheme, is shown in Figure 2.

The crystal structure features a dinuclear unit in which the two copper(I) centres are joined by two bromine bridges to form a four-membered $Cu_2Br_2$ core with a Cu···Cu separation distance of 2.8410(6) Å, which is suggestive of a weak metal–metal interaction, as further substantiated by the electronic structure calculations (vide infra). The strongly distorted tetrahedral coordination around each copper(I) central atom is completed by the two P donor atoms of the chelating dppbz unit.

The most salient, and quite unexpected, feature of the structure is the remarkable non-planarity within the $Cu_2Br_2$ central core. Unlike in other bromide-bridged dinuclear complexes that exhibit a strictly planar $Cu_2Br_2$ core, such as $[Cu(\mu_2\text{-Br})(tmtp)(tzdtH)]_2$ (tmtp = tri-*m*-tolylphosphane),[5] the two main planes in **3** through Br(1), Cu(1), Br(2) and Br(1), Cu(2), Br(2) form a dihedral angle of 150.10(2)°, with Br(2) being displaced from the mean plane defined by Cu(1), Br(1) and Cu(2) by 0.7201(8) Å. The same uncommon non-planarity adopted by the $Cu_2I_2$ moiety previously observed in $[Cu(\mu_2\text{-I})(dppet)]_2$ [dppet = *cis*-1,2-bis(diphenylphosphanyl)ethane] is noteworthy.[7b]

Each of the two CuPCCP five-membered chelate rings adopts the envelope conformation with the metal atoms out of the plane containing the four diphos ligand donor atoms by 0.665(3) and –0.951(2) Å for Cu(1) and Cu(2), respectively. Consequently, the bite angles of the two diphosphane units (Table 2) are clearly different, with the larger intraligand P–Cu–P angle belonging to the more distorted $C_2P_2Cu$ ring. The four individual Cu–P bonds lie in the narrow range of 2.2546(11)–2.2600(11) Å and match those observed in $[Cu(dppet)_2]PF_6$,[12] as well as in other copper(I)–diphosphane complexes having a tetrahedral coordination environment.[6,7] Moreover, there are four clearly different Cu–Br bond lengths within the $Cu_2Br_2$ backbone, lying in the range 2.4279(6)–2.5316(6) Å.

## Computational Studies Using DFT

In an attempt to understand some marked structural features of the complexes under investigation, we performed electronic structure calculations based on density functional theory for compounds **2** and **3**, as well as for some related model species. To obtain a computationally convenient size for the compounds, we used models resulting from substitution of the phenyl groups of the diphosphane ligands by H atoms. The use of such models does not alter the description of the "core" region of the compounds and is ultimately the most efficient and productive route to modelling the electronic structure and related properties of relatively big-sized copper(I) complexes. In particular, we sought an explanation for the exclusive coordination of 2,4-dithiouracil through the thione-S atom at C(4) and explored the origin of the unexpected bend of the $Cu_2Br_2$ central core in compound **3**.

### *Equilibrium Geometries, Electronic Structure and Bonding Mechanism in the Series of Model Mononuclear Complexes [CuX(dpbz)] [X = Cl, Br, or I; dpbz = 1,2-bis(diphosphanyl)benzene]*

Selected structural and electronic properties of the mononuclear complexes [CuX(dpbz)] (X = Cl, **M1**; Br, **M2**; I,

 © 2006 Wiley-VCH Verlag GmbH & Co. KGaA, Weinheim 

**M3**) computed at the B3LYP/DGDZVP level of theory are given in Table 3.

All [CuX(dpbz)] species are three-coordinate $Cu^{I}$ complexes that adopt a trigonal planar structure with the central copper(I) atom and the three donor atoms lying in a plane. As is to be expected, the Cu–X bond lengths increase upon going from the chloro to bromo to iodo derivative, which is compatible with the computed $\nu$(Cu–X) stretching vibrational frequencies at 354, 260 and 235 $cm^{-1}$, respectively. However, no other significant structural differences could be observed for the [CuX(dpbz)] (X = Cl, Br or I) complexes. Based on the HOMO–LUMO energy gap − the hardness values ($\eta$) are shown in Table 3 − one would expect the tendency for dimerisation to follow the order **M3** > **M2** > **M1**.

The most relevant molecular orbitals of the mononuclear complexes [CuX(dpbz)] related to the bonding mechanism are depicted schematically in Scheme 2. According to the natural bond orbital (NBO) population analysis, the $Cu^{I}$ centre acquires a positive natural atomic charge of about 0.61–0.7 |e|. Moreover, the natural electron configuration (*nec*) indicates that the electron density is mainly transferred to the 4s orbital of the copper(I) atom. The nature of the halide ligand does not affect the natural electron configuration of the central $Cu^{I}$ atom significantly. Interestingly, the computed bond overlap populations (*bop*) of the Cu–Br, Cu–Cl and Cu–I bonds are of almost equal size.

It can be seen that the Cu–X bond is a composite bond that acquires a partial double-bond character involving both σ and π components. The HOMO corresponds to a π*-antibonding Cu–X interaction that is strongly polarized towards the halide ligand X. Below the HOMO there is a set of σ- (HOMO–2) and π-bonding MOs (HOMO–3 and HOMO–6) that correspond to Cu–X interactions as well as describing the σ and π dative bonding of the halide ligands. Finally, the LUMO is delocalised over the benzene ring of the diphosphane ligand.

### *Equilibrium Geometries, Electronic Structure and Bonding Mechanism of the Dinuclear Compounds [Cu(μ-X)-(dpbz)]$_2$ (X = Cl, Br or I)*

Selected structural parameters and electronic properties of the dinuclear compounds [Cu(μ-Cl)(dpbz)]$_2$ (**M4**), [Cu(μ-Br)(dpbz)]$_2$ (**M5**) and [Cu(μ-I)(dpbz)]$_2$ (**M6**) computed at the B3LYP/DGDZVP level of theory are compiled in Table 4.

Table 3. Selected structural parameters and electronic properties of the mononuclear complexes [CuX(dpbz)] (X = Br or Cl) computed at the B3LYP/DGDZVP level.

| Property | [CuCl(dpbz)] (**M1**) | [CuBr(dpbz)] (**M2**) | [CuI(dpbz)] (**M3**) |
|---|---|---|---|
| $R_e$(Cu–X) [Å] | 2.175 | 2.307 | 2.500 |
| $R_e$(Cu–$P_1$) [Å] | 2.314 | 2.316 | 2.317 |
| $\theta_e$(P–Cu–X) [°] | 135.9 | 135.8 | 135.8 |
| $\theta_e$(P–Cu–P) [°] | 88.6 | 88.6 | 88.6 |
| $\mu_e$ [D] | 11.09 | 11.34 | 11.75 |
| $\eta$ [eV][a] | 1.78 | 1.70 | 1.59 |
| $q_{Cu}$[b] | 0.70 | 0.67 | 0.61 |
| $q_X$ | –0.78 | –0.75 | –0.70 |
| $q_P$ | 0.23 | 0.23 | 0.23 |
| *bop*(Cu–X)[c] | 0.25 | 0.26 | 0.28 |
| *bop*(Cu–P) | 0.21 | 0.21 | 0.21 |
| *nec*(Cu)[d] | $4s^{0.41}3d^{9.84}$ | $4s^{0.43}3d^{9.86}$ | $4s^{0.46}3d^{9.87}$ |
| *nec*(X) | $3s^{1.96}3p^{5.80}$ | $4s^{1.96}4p^{5.78}$ | $5s^{1.95}5p^{5.74}$ |
| *nec*(P) | $3s^{1.45}3p^{3.24}$ | $3s^{1.45}3p^{3.24}$ | $3s^{1.45}3p^{3.24}$ |

[a] Hardness $\eta = (\varepsilon_{LUMO} - \varepsilon_{HOMO})/2$. [b] Natural charges. [c] Mulliken bond-overlap population. [d] Natural electron configuration.

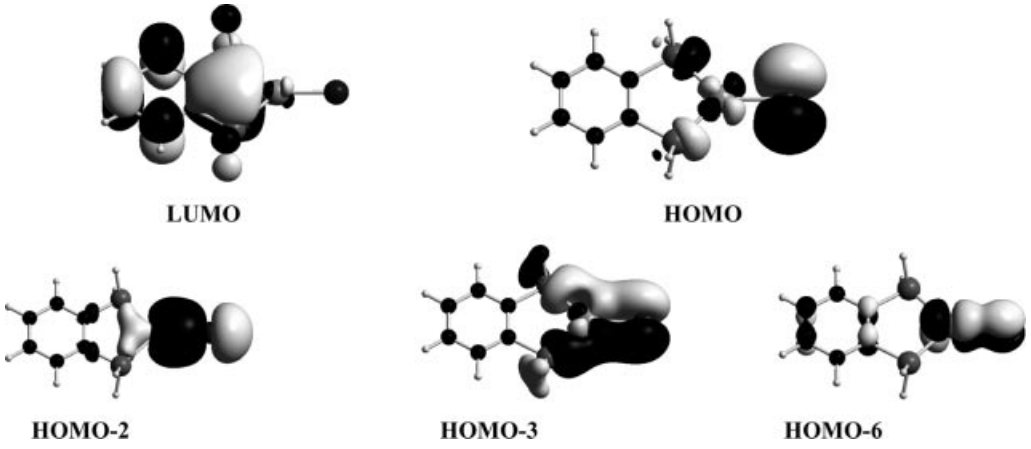


Scheme 2. The most relevant molecular orbitals of the mononuclear complex [CuBr(dpbz)] (isodensity contours of 0.03 a.u.). The relevant MOs for [CuCl(dpbz)] and [CuI(dpbz)] are analogous.

 © 2006 Wiley-VCH Verlag GmbH & Co. KGaA, Weinheim 

Table 4. Selected structural parameters and electronic properties of the dinuclear model compounds [Cu(μ-X)(dpbz)]$_2$ (X = Cl, Br or I) computed at the B3LYP/DGDZVP level.

| Property | [Cu(μ-Cl)(dpbz)]$_2$ (**M4**) | [Cu(μ-Br)(dpbz)]$_2$ (**M5**) | [Cu(μ-I)(dpbz)]$_2$ (**M6**) |
|---|---|---|---|
| $R_e$(Cu–X) [Å] | 2.402 | 2.525 | 2.720 |
| $R_e$(Cu–P$_1$) [Å] | 2.316 | 2.327 | 2.335 |
| $R_e$(Cu···Cu) [Å] | 2.972 | 2.948 | 2.887 |
| $\theta_e$(P–Cu–X) [°] | 116.2 | 114.7 | 112.4 |
| $\theta_e$(P–Cu–P) [°] | 89.1 | 88.8 | 88.5 |
| $\theta_e$(Cu–X–Cu) [°] | 76.4 | 71.5 | 64.1 |
| $\theta_e$(X–Cu–X) [°] | 103.6 | 108.5 | 115.9 |
| $\mu_e$ [D] | 0.00 | 0.00 | 0.00 |
| $\eta$ [eV][a] | 2.02 | 2.00 | 2.40 |
| $q_{Cu}$[b] | 0.75 | 0.70 | 0.62 |
| $q_X$ | –0.78 | –0.75 | –0.67 |
| $q_P$ | 0.24 | 0.24 | 0.24 |
| *bop*(Cu–X)[c] | 0.13 | 0.15 | 0.16 |
| *bop*(Cu–P) | 0.12 | 0.13 | 0.12 |
| *nec*(Cu)[d] | $4s^{0.34}3d^{9.86}$ | $4s^{0.39}3d^{9.87}$ | $4s^{0.42}3d^{9.90}$ |
| *nec*(X) | $3s^{1.95}3p^{5.82}$ | $4s^{1.95}4p^{5.78}$ | $5s^{1.94}5p^{5.72}$ |
| *nec*(P) | $3s^{1.46}3p^{3.22}$ | $3s^{1.46}3p^{3.22}$ | $3s^{1.46}3p^{3.22}$ |

[a] Hardness $\eta = (\varepsilon_{LUMO} - \varepsilon_{HOMO})/2$. [b] Natural charges. [c] Mulliken bond-overlap population. [d] Natural electron configuration.

As is to be expected, the dicopper(I) compounds adopt a "diamond like" structure of $C_{2h}$ symmetry with the plane of the Cu(μ-X)$_2$Cu "rhombus" bisecting the P–Cu–P bond angles and being perpendicular to the plane of the diphosphane ligands. The four equivalent Cu–X bonds defining the Cu(μ-X)$_2$Cu "rhombus" are elongated by about 0.2 Å compared to the corresponding Cu–X bonds of the monomers. The calculated structural parameters are in line with those of the "real" complex **3** derived from the X-ray structural analysis. However, the non-planarity of the $Cu_2Br_2$ central core of complex **3** is not observed for the $Cu_2X_2$ core in the optimised structures of the model compounds **M4**, **M5**, and **M6**, thus indicating that steric and/or crystal-packing effects in the solid state should be responsible for the $Cu_2Br_2$ folding across the Br···Br line and the non-equivalent coordination spheres around the two Cu$^I$ metal centres.

To verify this hypothesis, the rigid and relaxed PES of the "real" complex **3** and the model compound **M5** were calculated at the B3LYP/DGDZVP level of theory. It was found that the bending of the $Cu_2Br_2$ core in the "real" complex **3** and the model compound **M5** demands only 0.6 and 0.4 kcal mol$^{-1}$, respectively, thus indicating a very flat potential energy surface for both complexes. Therefore, factors such as the 4.298-Å π-stacking interaction between two almost parallel phenyl groups of the dppbz ligand could enforce the bending of the $Cu_2Br_2$ core in the real complex **3**. It should be noted that in an analogous dinuclear Ag$^I$ complex containing bulky diphosphane or diarsane ligands the folding of the Ag(μ-Br)$_2$Ag core has been attributed to steric strain in the crystal.[13] The intermetallic Cu···Cu distance follows the order **M4** > **M5** > **M6**, in line with our previous results[7a] on analogous systems with general formula [Cu(μ-X)(PH$_3$)$_2$]$_2$ (X = Cl, Br or I), as well to the observations made by Soloveichic et al.[14] in the framework of EHMO theory for the complexes [L$_n$Cu(μ-X)CuL$_n$] ($n$ = 1 or 2, L = PR$_3$). Alvarez et al.[15] have also found from MP2 and B3LYP calculations that the Cu···Cu distance in a series of [CuXL]$_2$ (X = Cl, Br or I) complexes decreases upon increasing the size of the bridging halide ligand. The X–Cu–X bond angle in **M6** was found to be more obtuse relative to that found for **M5** or **M4**, while the opposite holds true for the Cu–X–Cu bond angle (Table 4).

The computed $\nu_{sym}$(X–Cu–X) stretching vibrational frequencies at 140, 110 and 87 cm$^{-1}$ for the chloro, bromo and iodo derivatives, respectively, are compatible with the elongated Cu–X bonds in the dimers. The same also holds true for the computed $\nu_{sym}$(Cu–X–Cu) stretching vibrational frequencies at 202, 172 and 160 cm$^{-1}$ for **M4**, **M5** and **M6**, respectively.

All [Cu(μ-X)(dpbz)]$_2$ (X = Cl, Br, or I) molecules are predicted to be thermodynamically more stable than the corresponding monomers; the calculated heat of reaction $\Delta_R H$ for the dimerisation process was found to be 25–26 kcal mol$^{-1}$ at the B3LYP/DGDZVP level of theory. In addition, both **M4** and **M5** exhibit almost equal HOMO–LUMO energy gaps as well as hardness values, indicating comparable stability. On the other hand, **M6** exhibits the highest HOMO–LUMO energy gap and hardness value, and is expected to be the most stable amongst the [Cu(μ-X)(dpbz)]$_2$ (X = Cl, Br, or I) complexes.

No significant differences could be observed between the natural and net atomic charges on the Cu$^I$ bridging halide and phosphorus donor atoms of **M4**, **M5** and **M6** (Table 4). The Cu$^I$ metal centres acquire positive natural charges of about 0.6–0.8 |e|, while the halide bridging ligands acquire negative natural charges of around –0.7 |e|. According to the natural electron configurations, the electron density is mainly transferred from the valence p atomic orbitals of the bridging halide ligands to the 4s orbitals of the Cu$^I$ metal centres.

The most important MOs of the [Cu(μ-X)(dpbz)]$_2$ dimers are depicted in Scheme 3. The HOMO corresponding to π* antibonding Cu–X interactions is polarized towards the bridging halide ligands, while the LUMO is delocalised over the benzene rings of the diphosphane ligands. There

 © 2006 Wiley-VCH Verlag GmbH & Co. KGaA, Weinheim 

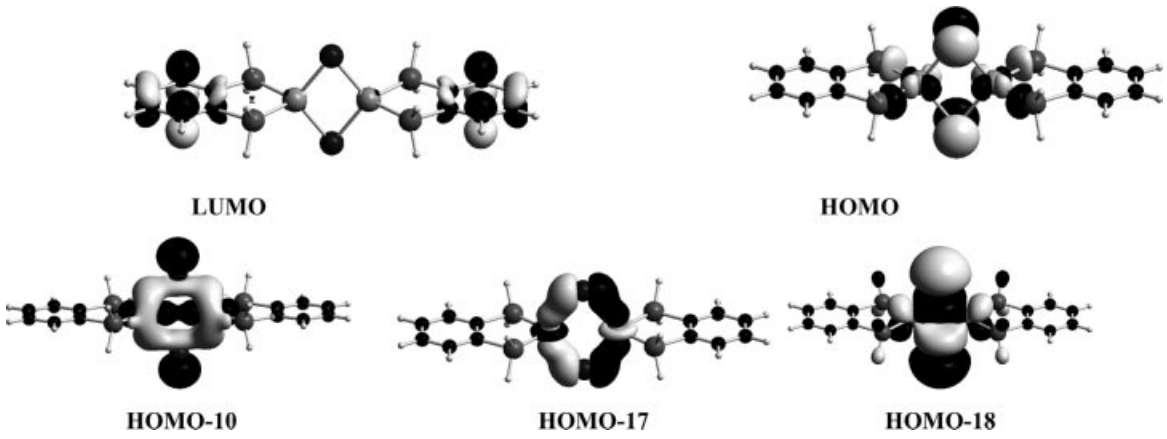


Scheme 3. The most important molecular orbitals of the dinuclear complex $[Cu(\mu\text{-}Br)(dppbz)]_2$ (isodensity contours of 0.03 a.u.). The relevant MOs for $[Cu(\mu\text{-}Cl)(dppbz)]_2$ and $[Cu(\mu\text{-}I)(dppbz)]_2$ are analogous.

are σ-type MOs (HOMO–17 and HOMO–18) delocalised over the entire four-membered $Cu(\mu\text{-}X)_2Cu$ ring. The delocalisation of the σ-electron density over the $Cu(\mu\text{-}X)_2Cu$ rhombus having eight framework electrons[16] could probably account for the almost equivalent Cu–X bonds. Interestingly, all $[Cu(\mu\text{-}X)(dpbz)]_2$ dimers exhibit a σ-type MO (HOMO–10), which suggests the existence of weak intermetallic Cu···Cu interactions.

### *Equilibrium Geometries, Electronic Structure and Bonding Mechanism of Mononuclear [CuX(dpbz)(2,4-dtucH$_2$)] (X = Cl, Br or I) Complexes*

Selected structural parameters and electronic properties of the model compounds mononuclear [CuCl(dpbz)(2,4-dtucH$_2$)] (**M7**), [CuBr(dpbz)(2,4-dtucH$_2$)] (**M8**) and [CuI(dpbz)(2,4-dtucH$_2$)] (**M9**) computed at the B3LYP/DGDZVP level of theory are summarised in Table 5.

The complexes are four-coordinate with a tetrahedral coordination environment. The calculated structural parameters of **M8** are in excellent agreement with those obtained from the X-ray structural analysis of the "real" complex **2**. The most remarkable structural difference between **M8** and **2** is the orientation of the 2,4-dithiouracil ring − in **M7**, **M8** and **M9** the plane of the 2,4-dithiouracil ring is perpendicular to the plane of the diphosphane ligand and bisects the P–Cu–P bond angle. The 2,4-dithiouracil ligand in **M7**, **M8** and **M9** is further stabilized by a hydrogen bond between the halide ligand and an H atom of the 2,4-dithiouracil. The calculated X···H distances are predicted to be 2.113, 2.302 and 2.597 Å for **M7**, **M8** and **M9**, respectively. The H-bond formation is reflected in the computed X···H *bop* values, which were found to be 0.16, 0.14 and 0.12 for **M7**, **M8** and **M9**, respectively, as well as in the existence of a MO, with a σ component (Scheme 4, **b**), describing the

Table 5. Selected structural parameters and electronic properties of the mononuclear model compounds [CuX(dpbz)(2,4-dtucH$_2$)] (X = Cl, Br or I) computed at the B3LYP/DGDZVP level.

| Property | [CuCl(dpbz)(2,4-dtucH$_2$)] (**M7**) | [CuBr(dpbz)(2,4-dtucH$_2$)] (**M8**) | [CuI(dpbz)(2,4-dtucH$_2$)] (**M9**) |
|---|---|---|---|
| $R_e$(Cu–X) [Å] | 2.324 | 2.451 | 2.647 |
| $R_e$(Cu–P$_1$) [Å] | 2.341 | 2.348 | 2.356 |
| $R_e$(Cu–S) [Å] | 2.336 | 2.346 | 2.349 |
| $\theta_e$(P–Cu–X) [°] | 105.2 | 105.4 | 105.7 |
| $\theta_e$(P–Cu–P) [°] | 88.0 | 87.8 | 87.4 |
| $\theta_e$(P–Cu–S) [°] | 120.0 | 118.8 | 116.3 |
| $\theta_e$(S–Cu–X) [°] | 114.6 | 116.7 | 120.3 |
| $\mu_e$ [D] | 6.62 | 7.14 | 8.11 |
| $\eta$ [eV][a] | 3.31 | 3.12 | 2.77 |
| $q_{Cu}$[b] | 0.71 | 0.69 | 0.65 |
| $q_X$ | –0.77 | –0.75 | –0.71 |
| $q_P$ | 0.23 | 0.24 | 0.23 |
| $q_S$ | –0.21 | –0.20 | –0.20 |
| *bop*(Cu–X)[c] | 0.17 | 0.19 | 0.21 |
| *bop*(Cu–P) | 0.15 | 0.15 | 0.15 |
| *bop*(Cu–S) | 0.20 | 0.21 | 0.20 |
| *nec*(Cu)[d] | $4s^{0.37}3d^{9.86}$ | $4s^{0.39}3d^{9.87}$ | $4s^{0.41}3d^{9.88}$ |
| *nec*(X) | $3s^{1.96}3p^{5.80}$ | $4s^{1.96}4p^{5.78}$ | $5s^{1.96}5p^{5.75}$ |
| *nec*(P) | $3s^{1.46}3p^{3.23}$ | $3s^{1.46}3p^{3.22}$ | $3s^{1.46}3p^{3.23}$ |
| *nec*(S) | $3s^{1.73}3p^{4.44}$ | $3s^{1.73}3p^{4.44}$ | $3s^{1.73}3p^{4.43}$ |

[a] Hardness $\eta = (\varepsilon_{LUMO} - \varepsilon_{HOMO})/2$. [b] Natural charges. [c] Mulliken bond-overlap population. [d] Natural electron configuration.

 © 2006 Wiley-VCH Verlag GmbH & Co. KGaA, Weinheim 

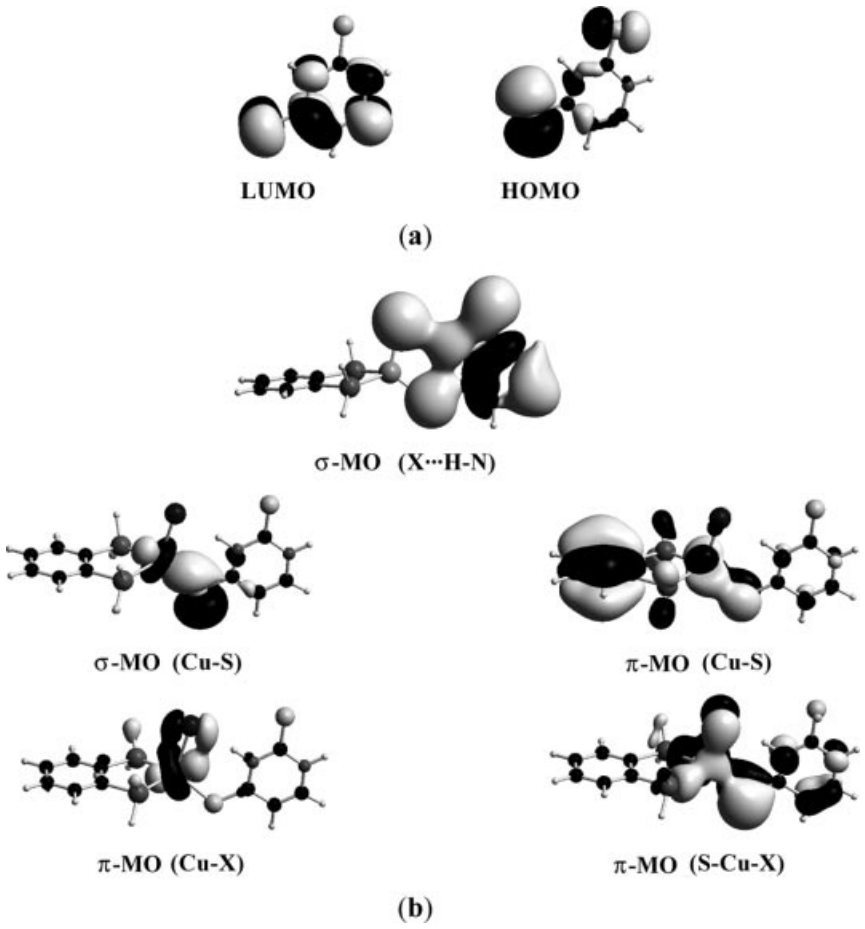


Scheme 4. The most important molecular orbitals of 2,4-dithiouracil (a) and the mononuclear compound [CuBr(dpbz)(2,4-dtucH$_2$)] (b) (isodensity contours of 0.03 a.u.). the relevant MOs for [CuCl(dpbz)(2,4-dtucH$_2$)] and [CuI(dpbz)(2,4-dtucH$_2$)] are analogous.

X···H interaction. The latter introduces an elongation to the N–H bond only about 0.03–0.02 Å in the 2,4-dithiouracil ligand with respect to that of the "free" ligand.

The computed unscaled *ν*(N–H) stretching vibrational frequencies appear at 3002, 3068 and 3160 cm$^{-1}$ for **M7**, **M8** and **M9**, respectively, while in the "free" 2,4-dithiouracil ligand it appears at 3564 cm$^{-1}$. The strong shift of the *ν*(N–H) stretching vibrational band towards lower frequencies upon coordination of the 2,4-dithiouracil ligand to the Cu$^{I}$ centre is indicative of the involvement of the H atom in H-bond formation with the halide ligand. In all [CuX(dpbz)(2,4-dtucH$_2$)] (X = Cl, Br, or I) complexes the X···H–N moiety is almost linear, the calculated X···H–N bond angle being equal to 175–177°. On the other hand, the S–Cu–X and Cu–S–C bond angles were found to be smaller, ranging from 114–120° and 110–114°, respectively. Coordination of 2,4-dithiouracil to the Cu$^{I}$ centre does not alter its structure significantly. However, in the [CuX(dpbz)(2,4-dtucH$_2$)] (X = Cl, Br, or I) complexes the coordination of the 2,4-dithiouracil through the S donor atom in the 4-position lengthens the C=S bond by about 0.03 Å. This could be attributed to electron-density transfer from the C=S group of the 2,4-dithiouracil ligand to the Cu$^{I}$ centre, leading to formation of the Cu–S coordination bond. The latter has a composite nature and exhibits both σ and π components, as can be seen from the corresponding MOs shown in Scheme 4b. The electron density is transferred from the HOMO of the 2,4-dithiouracil ligand, which is a non-bonding (lone pair) p-type MO localised mainly on the S donor atom at the 4-position and to a lesser extent on the S atom at the 2-position (Scheme 4a), to a vacant orbital of the Cu$^{I}$ metal centre, thus forming the σ(Cu←S) dative coordination bond. Obviously, the nature of the HOMO accounts well for the inability of the S atom at the 2-position to act as a second donor atom coordinated to another Cu$^{I}$ metal centre. In addition, there is π back-bonding through the interaction of an occupied orbital of the Cu$^{I}$ centre with the LUMO of the 2,4-dithiouracil ligand, which is a delocalised π*-type MO having a high contribution from the 3p orbitals of the S(4) acceptor atom (Scheme 4a). The Cu–S coordination bond is relatively weak, with a predicted bond-dissociation energy (BDE) of 16.2, 14.8 and 13.2 kcal mol$^{-1}$ for **M7**, **M8** and **M9**, respectively, at the B3LYP/DGDZVP level.

Upon coordination of the 2,4-dithiouracil ligand to the [CuX(dpbz)] (X = Cl, Br, or I) fragment the Cu–X bond is elongated by about 0.14–0.15 Å. This elongation is accompanied by a decrease of the *bop* values compared to those found for the [CuX(dpbz)] fragments. The coordination of the 2,4-dithiouracil to the Cu$^{I}$ centre of the

 © 2006 Wiley-VCH Verlag GmbH & Co. KGaA, Weinheim 

[CuX(dpbz)] fragments does not affect the natural atomic charges significantly, while the same holds true for the natural electron configurations of the respective atoms.

## Conclusions

We have described the synthesis and structural characterisation of copper(I) coordination compounds bearing 1,2-bis(diphenylphosphanyl)benzene (dppbz) and/or 2,4-dithiouracil (2,4-dtucH$_2$) as ligands. The reaction of 1,2-bis(diphenylphosphanyl)benzene (dppbz) with copper(I) halides yields [CuX(dppbz)] adducts, which for X = Br corresponds to a dimer of the formula [Cu(μ-Br)(dppbz)]$_2$ containing a non-symmetrical, bent Cu$_2$Br$_2$ core structure. The Cu···Cu separation distance of 2.8410(6) Å is indicative of weak intermetallic interactions. The latter is further corroborated by DFT calculations on the model dinuclear compound [Cu(μ-Br)(dpbz)]$_2$, which exhibits a characteristic σ-type MO (HOMO-10) describing these weak intermetallic Cu···Cu interactions. However, the non-planarity of the central Cu$_2$Br$_2$ core is not observed for the Cu$_2$X$_2$ core in the optimised model structures, thus indicating that π-stacking interactions between the two almost parallel phenyl groups of the diphosphane ligand are probably responsible for the Cu$_2$Br$_2$ folding across the Br···Br axis. The presence of σ-type MOs delocalised over the entire four-membered Cu(μ-X)$_2$Cu ring containing eight framework electrons accounts for the equivalent Cu–X bonds of the rhombus. The dimerisation energy of the [Cu(μ-X)(dpbz)]$_2$ (X = Cl, Br, or I) dimers is predicted to be 25–26 kcal mol$^{-1}$ at the B3LYP/DGDZVP level. The [CuBr(dppbz)]$_2$ dimer and its chloride and iodide analogues prove to be good precursors for the preparation of other derivatives and are used, in the course of the present study, for the synthesis of heteroleptic complexes which contain, besides the chelating dppbz, a 2,4-dithiouracil ligand. In line with theoretical predictions, the 2,4-dithiouracil ligand, which adopts the dithione form as its stable conformation, acts as a monodentate ligand that is coordinated to the metal ion exclusively through its thione-S atom at the 4-position. The nature of the HOMO − a non-bonding, lone-pair, π-type MO localised mainly on the S donor atom at the 4-position − accounts well for the inability of the S atom at the 2-position to act as a second donor to another Cu$^{I}$ centre. Moreover, the 2,4-dithiouracil ligand in the [CuX(dpbz)(dtucH$_2$)] complexes is predicted to be loosely associated with the Cu$^{I}$ centre, the interaction energies being 13–16 kcal mol$^{-1}$ at the B3LYP/DGDZVP level.

## Experimental Section

**Materials and Instrumentation:** Commercially available copper(I) chloride, bromide and iodide, and 1,2-bis(diphenylphosphanyl)benzene were used as received, while pyrimidine-2,4-dithione (Aldrich) was recrystallised from hot ethanol prior to use. All the solvents were purified by standard methods and stored over molecular sieves. IR spectra in the region of 4000–200 cm$^{-1}$ were obtained in KBr discs with a Perkin–Elmer 1430 spectrophotometer, while a Perkin–Elmer–Hitachi 200 spectrophotometer was used to obtain the electronic absorption spectra. Melting points were measured in open tubes with a STUART scientific instrument and are uncorrected. Molar conductivities, magnetic susceptibility measurements and elemental analyses for carbon, nitrogen and hydrogen were performed as described elsewhere.[17]

**Computational Details:** The structural, electronic and energetic properties of all compounds were computed with Becke's three-parameter hybrid functional[18] combined with the Lee–Yang–Parr correlation functional,[19] abbreviated as B3LYP, using the DGDZVP basis set.[20] We used the all-electron, double-zeta valence DGDZVP basis set, which is comparable with the 6-31G(d) level,[21] because it has been found previously[22] that it provides a satisfactory description of the structural and energetic properties of analogous Cu$^{I}$ complexes (overall closer to the experiment) but it is less time consuming for computations with such big-sized transition metal complexes than the larger 6-31G(d,p) basis set. No constraints were imposed on the geometry in any of the calcualtions. Full geometry optimisation was performed for each structure using Schlegel's analytical gradient method[23] and the attainment of the energy minimum was verified by calculating the vibrational frequencies that result in an absence of imaginary eigenvalues. All calculations were performed using the Gaussian 03 suite of programs.[24]

**Crystal Structure Determination:** Single crystals suitable for crystal-structure analysis were obtained by slow evaporation of acetonitrile/methanol solutions of the complexes at room temperature. X-ray diffraction data were collected on an Enraf–Nonius Kappa CCD area-detector diffractometer. The programs DENZO[25] and COLLECT[26] were used for data collection and cell refinement, respectively. Details of crystal and structure refinement are shown in Table 6. The structures were solved using the program SIR97[27] and refined with SHELX-97.[28] Molecular plots were obtained with the program ORTEP-3.[29]
CCDC-243707 (for **2**) and -269670 (for **3**) contain the supplementary crystallographic data for this paper. These data can be obtained free of charge from The Cambridge Crystallographic Data Centre via www.ccdc.cam.ac.uk/data_request/cif.

**Synthesis of Complexes 1 and 2:** 1,2-Bis(diphenylphosphanyl)benzene (223.2 mg, 0.1 mmol) was added to a suspension of CuCl or CuBr (0.5 mmol) in 30 mL of dry acetonitrile and the mixture was stirred for 2 h at 50 °C, during which time a greenish precipitate was formed. A solution of pyrimidine-2,4-dithione (0.5 mmol) in a small amount (≈20 mL) of methanol was then added and the reaction mixture was stirred under reflux for two hours, whereupon the precipitate gradually disappeared. The resulting clear solution was filtered off and left to evaporate at ambient temperature. The microcrystalline solid, which was deposited upon standing for several days, was filtered off and dried in vacuo.

**[CuCl(dppbz)(2,4-dtucH$_2$)] (1):** Orange-red solid (125 mg, 70%), m.p. 261 °C. $C_{34}H_{28}ClCuN_2P_2S_2$ (689.70): calcd. C 59.21, H 4.09, N 4.06; found C 59.75, H 4.05, N 3.93. IR: $\tilde{\nu}$ = 3446 m, 3050 m, 1599 s, 1570 vs, 1532 vs, 1480 m, 1435 m, 1342 s, 1215 s, 1198 s, 1100 s, 859 m, 741 s, 692 s, 520 s, 493 s, 467 m cm$^{-1}$. UV/Vis ($CHCl_3$): $\lambda_{max}$ (log $\varepsilon$) = 262 nm (3.68), 298 (3.69), 392 (3.31).

**[CuBr(dppbz)(2,4-dtucH$_2$)] (2):** Orange-red crystals (130 mg, 70%), m.p. 265 °C. $C_{34}H_{28}BrCuN_2P_2S_2$ (734.15): calcd. C 55.63, H 3.84, N 3.82; found C 55.91, H 3.88, N 3.79. IR: $\tilde{\nu}$ = 3457 m, 3147 w, 3070 m, 1618 m, 1599 vs, 1531 vs, 1479 s, 1435 s, 1341 m, 1215 s, 1196 vs, 1099 vs, 1068 m, 768 s, 740 s, 692 vs, 519 vs, 492 s, 441 s cm$^{-1}$.

 © 2006 Wiley-VCH Verlag GmbH & Co. KGaA, Weinheim 

Table 6. Crystal data and structure refinements for **2** and **3**.

| | **2** | **3** |
|---|---|---|
| Molecular formula | $C_{34}H_{28}BrCuN_2P_2S_2$ | $C_{60}H_{48}Br_2Cu_2P_4$ |
| Formula weight | 734.09 | 1179.76 |
| Temperature [K] | 120(2) | 120(2) |
| Wavelength [Å] | 0.71073 | 0.71073 |
| Crystal system | monoclinic | monoclinic |
| Space group | $P2_1/c$ | $P2_1$ |
| Unit cell dimensions | $a$ = 13.5328(4) Å, $\alpha$ = 90° | $a$ = 11.2105(3) Å, $\alpha$ = 90° |
| | $b$ = 14.4864(5) Å, $\beta$ = 92.407(2)° | $b$ = 18.7290(6) Å, $\beta$ = 97.6364(17)° |
| | $c$ = 16.3381(4) Å, $\gamma$ = 90° | $c$ = 12.1317(2) Å, $\gamma$ = 90° |
| Volume [Å$^3$] | 3200.12(17) | 2524.60 (11) |
| $Z$ | 4 | 2 |
| Density (calculated) [Mg m$^{-3}$] | 1.524 | 1.552 |
| Absorpt. coefficient [mm$^{-1}$] | 2.189 | 2.592 |
| $F$(000) | 1488 | 1192 |
| Crystal size [mm] | 0.52 × 0.45 × 0.10 | 0.10 × 0.10 × 0.08 |
| $\theta$ range for data collection [°] | 2.97 to 27.47° | 3.39 to 27.48 |
| Index ranges | $-17 \le h \le 17$ | $-14 \le h \le 14$ |
| | $-18 \le k \le 18$ | $-22 \le k \le 24$ |
| | $-21 \le l \le 19$ | $-15 \le l \le 15$ |
| Reflections collected | 46486 | 30939 |
| Independent reflections | 7284 [$R$(int) = 0.0538] | 10626 [$R$(int) = 0.0571] |
| Completeness to $\theta$ | 99.4% ($\theta$ = 27.47°) | 99.7% ($\theta$ = 27.48°) |
| Data / restraints / parameters | 7284 / 0 / 380 | 10626 / 1 / 613 |
| Max. and min. transmission | 0.8108 and 0.3957 | 0.8195 and 0.7816 |
| Refinement method | Full-matrix least-squares on $F^2$ | Full-matrix least-squares on $F^2$ |
| Goodness-of-fit on $F^2$ | 1.025 | 0.973 |
| Final $R$ indices [$I > 2\sigma(I)$] | $R1$ = 0.0313, $wR2$ = 0.0680 | $R1$ = 0.0374, $wR2$ = 0.0613 |
| $R$ indices (all data) | $R1$ = 0.0530, $wR2$ = 0.0739[a] | $R1$ = 0.0569, $wR2$ = 0.0666[b] |
| Largest diff peak and hole [e Å$^3$] | 0.355 and –0.415 | 0.428 and –0.610 |

[a] $w = 1/[\sigma^2(F_o^2) + (0.0379P)^2 + 0.3987P]$, where $P = (F_o^2 + 2F_c^2)/3$. [b] $w = 1/[\sigma^2(F_o^2) + (0.0184P)^2]$, where $P = (F_o^2 + 2F_c^2)/3$.

UV/Vis ($CHCl_3$): $\lambda_{max}$ (log $\varepsilon$) = 248 nm (4.09), 284 (4.31), 358 (3.94).

**Synthesis of Complexes 3 and 4:** 1,2-Bis(diphenylphosphanyl)benzene (446.5 mg, 1 mmol) was added to a suspension of copper(I) bromide or iodide (1 mmol) in 50 mL of dry acetonitrile, and the mixture was heated under reflux for 4 h. Slow evaporation of the resulting light-green solution at room temperature gave a crystalline solid, which was filtered off and dried in vacuo.

**[Cu(μ$_2$-Br)(dppbz)]$_2$ (3):** Light-green powder (550 mg, 93%), m.p. 295 °C. $C_{30}H_{24}BrCuP_2$ (589.93): calcd. C 61.08, H 4.10; found C 60.86, H 3.97. IR: $\tilde{\nu}$ = 3415 m, 3049 w, 1637 w, 1585 m, 1480 m, 1435 s, 1184 m, 1096 m, 1027 m, 750 m, 744 s, 695 s, 518 s, 497 m, 482 m cm$^{-1}$. UV/Vis ($CHCl_3$): $\lambda_{max}$ (log $\varepsilon$) = 258 nm (3.71), 293 (3.68), 351 (3.63).

**[CuI(dppbz)]$_x$ (4):** Light-green powder (541 mg, 85%), m.p. 298 °C. $C_{30}H_{24}CuIP_2$ (636.94): calcd. C 61.08, H 4.10; found C 56.15, H 3.89. IR: $\tilde{\nu}$ = 3437 m, 3048 w, 1637 m, 1585 w, 1480 m, 1434 s, 1184 w, 1156 w, 1094 m, 1027 w, 759 m, 741 s, 691 vs, 518 vs, 496 m, 480 m cm$^{-1}$ UV/Vis ($CHCl_3$): $\lambda_{max}$ (log $\varepsilon$) = 248 nm (4.35), 293 (4.16), 328 (4.07).

**Synthesis of [CuI(dppbz)(2,4-dtucH$_2$)] (5):** 1,2-Bis(diphenylphosphanyl)benzene (112 mg, 0.25 mmol) was added in small portions to a suspension of **4** (83 mg, 0.25 mmol) in 60 mL of dry acetone and the mixture was stirred for 1 h at 50 °C. The resulting clear solution was filtered and left to evaporate at ambient. The microcrystalline solid that was deposited upon standing for several days was filtered off and dried in vacuo. Orange powder (105 mg, 53%), m.p. 305 °C. $C_{34}H_{28}CuIN_2P_2S_2$ (781.16): calcd. C 52.28, H 3.61, N 3.59; found C 52.47, H 3.59, N 3.46. IR: $\tilde{\nu}$ = 3216 w, 3048 m, 1610 m, 1531 s, 1480 s, 1435 s, 1185 m, 1112 m, 1095 vs, 759 m, 742 vs, 692 vs, 518 vs, 496 s, 480 m cm$^{-1}$. UV/Vis ($CHCl_3$): $\lambda_{max}$ (log $\varepsilon$) = 248 (4.36), 330 (4.04).

**Synthesis of Complexes 6 and 7:** A solution of 2,4-dithiouracil (144 mg, 1 mmol) in a small amount (≈20 mL) of methanol was added to a suspension of CuI or CuBr (0.5 mmol) in 30 mL of dry acetonitrile and the mixture was stirred for 2 h. The orange-yellow precipitate that deposited upon cooling was filtered off, washed with small amounts of THF and dried in vacuo.

**[CuI(2,4-dtucH$_2$)]$_x$ (6):** Orange-red powder (155 mg, 93%), m.p. 295 °C. $C_4H_4CuIN_2S_2$ (334.68): calcd. C 14.36, H 1.20, N 8.37; found C 14.23, H 1.12, N 7.85. IR: $\tilde{\nu}$ = 3212 m, 3096 w, 2975 w, 1609 vs, 1528 vs, 1466 m, 1260 s, 1220 s, 1195 s, 1110 vs, 983 m, 856 m, 789 m, 692 m, 671 m, 462 m, 395 w cm$^{-1}$ UV/Vis (DMF): $\lambda_{max}$ (log $\varepsilon$) = 284 (4.07), 352 (3.75), 397 (3.04).

**[CuBr(2,4-dtucH$_2$)]$_x$ (7):** Orange-red powder (120 mg, 84%), m.p. 280 °C. $C_4H_4BrCuN_2S_2$ (287.67): calcd. C 16.70, H 1.40, N 9.74; found C 17.62, H 1.49, N 9.50. IR: $\tilde{\nu}$ = 3198 w, 3070 m, 2985 m, 2883 m, 1616 s, 1575 s, 1551 vs, 1481 m, 1220 m, 1125 s, 744 w, 693 m, 518 w cm$^{-1}$ UV/Vis (DMF): $\lambda_{max}$ (log $\varepsilon$) = 284 (4.18), 354 (3.88), 403 (3.45).

## Acknowledgments

We thank the EPSRC X-ray crystallography service at the University of Southampton for collecting the X-ray data.

[1] K. D. Karlin, J. Zubieta, *Copper Coordination Chemistry: Biochemical and Inorganic Perspectives*, Adenine Press, New York, **1983**, and references cited therein.

 © 2006 Wiley-VCH Verlag GmbH & Co. KGaA, Weinheim 

[2] B. Krebs, G. Henkel, *Angew. Chem. Int. Ed. Engl.* **1991**, *30*, 769–788.
[3] P. Karagiannidis, P. Aslanidis, D. P. Kessissoglou, B. Krebs, M. Dartmann, *Inorg. Chim. Acta* **1989**, *156*, 47–56.
[4] a) S. K. Hadjikakou, P. Aslanidis, P. Karagiannidis, A. Aubry, S. Skoulika, *Inorg. Chim. Acta* **1992**, *193*, 129–135; b) S. K. Hadjikakou, P. Aslanidis, P. Karagiannidis, D. Mentzafos, A. Terzis, *Inorg. Chim. Acta* **1991**, *186*, 199–204.
[5] a) S. K. Hadjikakou, P. Aslanidis, P. Karagiannidis, D. Mentzafos, A. Terzis, *Polyhedron* **1991**, *10*, 935–940; b) S. K. Hadjikakou, P. Aslanidis, P. Karagiannidis, A. Hountas, A. Terzis, *Inorg. Chim. Acta* **1991**, *184*, 161–166.
[6] P. J. Cox, P. Aslanidis, P. Karagiannidis, *Polyhedron* **2000**, *19*, 1615–1620.
[7] a) P. Aslanidis, P. J. Cox, S. Divanidis, A. C. Tsipis, *Inorg. Chem.* **2002**, *41*, 6875–6886; b) P. Aslanidis, P. J. Cox, S. Divanidis, P. Karagiannidis, *Inorg. Chim. Acta* **2004**, *357*, 1063–1076.
[8] a) M. Sigl, A. Schier, H. Schmidbaur, *Eur. J. Inorg. Chem.* **1998**, 203–210; b) L.-C. Song, J.-T. Liu, Q.-M. Hu, L.-H. Wenig, *Organometallics* **2000**, *19*, 1643–1647; c) W.-M. Xue, M. C.-W. Chan, Z.-M. Su, K.-K. Cheung, S.-T. Liu, C.-M. Che, *Organometallics* **1998**, *17*, 1622–1624; d) W.-M. Xue, Y. Wang, T. C. W. Mak, C.-M. Che, *J. Chem. Soc., Dalton Trans.* **1996**, 2827–2834; e) J. E. Barclay, A. Hills, T. C. W. Mak, D. L. Hughes, G. J. Leigh, *J. Chem. Soc., Dalton Trans.* **1988**, 2871–2877; f) D. Esjornson, M. Bakir, P. E. Fanwick, K. S. Jones, R. A. Walton, *Inorg. Chem.* **1990**, *29*, 2055–2061; g) J. M. Bevilacqua, J. A. Zuleta, R. Eisenberg, *Inorg. Chem.* **1994**, *33*, 258–266; h) K. D. John, K. V. Salazar, B. L. Scott, R. T. Baker, A. P. Sattelberger, *Organometallics* **2001**, *20*, 296–304; i) A. J. Paviglianiti, D. J. Min, W. C. Fultz, J. L. Burmeister, *Inorg. Chim. Acta* **1989**, *159*, 65–82; j) K. D. John, K. V. Salazar, B. L. Scott, R. T. Baker, A. P. Sattelberger, *J. Chem. Soc., Chem. Commun.* **2000**, 581–582.
[9] W. Saenger, *Principles of Nucleic Acid Structures*, Springer, New York, Berlin, Heidelberg, Tokyo, **1984**, chapter 7.
[10] a) Al M. Lamsabhi, M. Alcamí, O. Mó, M. Yáñez, *ChemPhysChem.* **2003**, *4*, 1011–1016; b) Al M. Lamsabhi, M. Alcamí, O. Mó, M. Yáñez, *ChemPhysChem.* **2004**, *5*, 1871–1878.
[11] E. Shefter, H. G. Mautner, *J. Am. Chem. Soc.* **1967**, *89*, 1249–1253.
[12] S. J. Bernes-Price, L. A. Colquhoun, P. C. Healy, K. A. Byriel, J. V. Hanna, *J. Chem. Soc., Dalton Trans.* **1992**, 3357–3363.
[13] A. Cingolani, C. Di Nicola, Effendy, C. Pettinari, B. W. Skelton, N. Somers, A. H. White, *Inorg. Chim. Acta* **2005**, *358*, 748–762.
[14] G. L. Soloveichik, O. Eisenstein, J. T. Poulton, W. E. Streib, J. C. Huffman, K. G. Caulton, *Inorg. Chem.* **1992**, *31*, 3306–3312.
[15] A. Carvajal, X.-Y. Liu, P. Alemany, J. J. Novoa, S. Alvarez, *Int. J. Quantum Chem.* **2002**, *86*, 100–105.
[16] P. Alemany, S. Alvarez, *Inorg. Chem.* **1992**, *31*, 4266–4275.
[17] P. Karagiannidis, P. Aslanidis, S. Papastefanou, D. Mentzafos, A. Hountas, A. Terzis, *Polyhedron* **1990**, *9*, 981–986.
[18] a) A. D. Becke, *J. Chem. Phys.* **1992**, *96*, 2155–2160; b) A. D. Becke, *J. Chem. Phys.* **1993**, *98*, 5648–5652.
[19] C. Lee, W. Yang, R. G. Parr, *Phys. Rev. B* **1988**, *37*, 785–789.
[20] a) N. Godbout, D. R. Salahub, J. Andzelm, E. Wimmer, *Can. J. Chem.* **1992**, *70*, 560–571; b) C. Sosa, J. Andzelm, B. C. Elkin, E. Wimmer, K. D. Dobbs, D. A. Dixon, *J. Phys. Chem.* **1992**, *96*, 6630–6636.
[21] J. Andzelm, E. Wimmer, *J. Chem. Phys.* **1992**, *96*, 1280–1303.
[22] S. K. Hadjikakou, C. D. Antoniadis, P. Aslanidis, P. J. Cox, A. C. Tsipis, *Eur. J. Inorg. Chem.* **2005**, 1442–1452.
[23] H. B. Schlegel, *J. Comput. Chem.* **1982**, *3*, 214–218.
[24] M. J. Frisch, G. W. Trucks, H. B. Schlegel, G. E. Scusseria, M. A. Robb, J. R. Cheeseman, V. G. Zakrzewski, J. A. Montgomery, T. Vreven, K. N. Kudin, J. C. Burant, J. M. Millan, S. S. Iyengar, J. Tomasi, V. Barone, B. Mennucci, M. Cossi, G. Scalmani, N. Rega, G. A. Petersson, H. Nakatsuji, M. Hada, M. Ehara, K. Toyota, F. R. J. Hasegawa, M. Ishida, T. Nakajima, Y. Honda, O. Kitao, H. Nakai, M. Klene, X. Li, J. E. Knox, H. P. Hratchian, J. B. Cross, C. Adamo, J. Jaramillo, R.Gomperts, R. E. Stratmann, O. Yazyev, A. J. Austin, R. Cammi, C. Pomelli, J. W. Ochterski, P. Y. Ayala, K. Morokuma, G. A. Voth, P. Salvador, J. J. Dannenberg, V. G. Zakrzewski, S. Dapprich, A. D. Daniels, M. C. Strain, O. Farkas, D. K. Malick, A. D. Rabuck, K. Raghavachari, J. B. Foresman, J. V. Ortiz, Q. Cui, A. G. Baboul, S. Clifford, J. Cioslowski, B. B. Stefanov, G. Liu, A. Liashenko, P. Piskorz, I. Komaromi, R. L. Martin, D. J. Fox, T. Keith, M. A. Al-Laham, C. Y. Peng, A. Nanayakkara, M. Challacombe, P. M. W. Gill, B. Johnson, W. Chen, M. W. Wong, C. Gonzalez, J. A. Pople, *Gaussian 03, Revision B.02*, Gaussian, Inc., Pittsburgh, PA, **2003**.
[25] Z. Otwinowski, W. Minor, *Methods in Enzymology*, **1997**, volume 276: *Macromolecular Crystallography, Part A* (Eds.: C. W. Carter, Jr., R. M. Sweet), Academic Press, pp. 307–326.
[26] R. Hooft, *COLLECT − Data collection software*, **1998**, Nonius B.V.
[27] A. Altomare, M. C. Burla, M. Camalli, G. L. Cascarano, C. Giacovazzo, A. Guagliardi, A. G. G. Moliterni, G. Polidori, R. Spagna, *J. Appl. Crystallogr.* **1999**, *32*, 115–119.
[28] G. M. Sheldrick, *SHELXL-97, A Program for crystal structure analysis (Release 97-2)*, University of Göttingen, Germany, **1997**.
[29] L. J. Farrugia, *J. Appl. Crystallogr.* **1997**, *30*, 565.

Received: August 15, 2005
Published Online: December 5, 2005

 © 2006 Wiley-VCH Verlag GmbH & Co. KGaA, Weinheim 

DOI: 10.1002/ejic.200500814

# Synthesis and Structure of Two Ionic Copper Indium Selenolate Cluster Complexes $[As(C_6H_5)_4]_2[Cu_6In_4(SeC_6H_5)_{16}Cl_4]$ and $[As(C_6H_5)_4][Cu_7In_4(SeC_6H_5)_{20}]$

**Reinhart Ahlrichs,[a] Nathan R. M. Crawford,[a] Andreas Eichhöfer,*[b] Dieter Fenske,[c] Oliver Hampe,[b] Manfred M. Kappes,[d] and Jolanta Olkowska-Oetzel[c]**

**Keywords:** Cluster compounds / Density functional calculations / Mass spectrometry / X-ray diffraction

The reaction of $PhSeSiMe_3$, CuCl, $InCl_3$, and $Ph_4AsCl$ in $CH_2Cl_2$ results in crystals of the structurally closely related, ionic clusters $(AsPh_4)_2[Cu_6In_4Cl_4(SePh)_{16}]$ and $(AsPh_4)[Cu_7In_4(SePh)_{20}]$, with product ratios dependent on the initial $PhSeSiMe_3$ concentration. Both molecules display a fused four-adamantoid structure related to the solid-state structure of $CuInSe_2$. Since the crystallographic analysis for $[Cu_7In_4(SePh)_{20}]^-$ remained ambiguous with respect to the assignment of one of the copper atoms, we performed a high-resolution mass spectrometric analysis as well as DFT computations to address this problem.

(© Wiley-VCH Verlag GmbH & Co. KGaA, 69451 Weinheim, Germany, 2006)

## Introduction

There has been considerable interest in the synthesis and properties of ternary transition metal chalcogenide and chalcogenolate cluster molecules. Examples for different classes of compounds include $[Cu_6In_3(SEt)_{16}](PPh_4)$,[1] $[M^I_6M^{III}_8Cl_4E_{13}(PPh_3)_6]$ ($M^I$ = Cu, Ag; $M^{III}$ = Ga, In; E = S, Se),[2] $[Cu_{11}In_{15}Se_{16}(SePh)_{24}(PPh_3)_4]$,[3] $[Ag_{26}In_{18}S_{36}Cl_6(dppm)_{10}(THF)_4][InCl_4(THF)]_2$,[4] $[Hg_{15}Cu_{20}S_{25}(P\text{-}nPr_3)_{18}]$,[5,6] $[Cu_4Nb_2Se_6(PMe_3)_8]$,[7] $[Ta_4Cu_{12}Cl_8S_{12}(PMe_3)_{12}]$[8] and $[(N,N,N',N'\text{-tmeda})_5Zn_5Cd_{11}Se_{13}(SePh)_6(THF)_2]$.[9] Interest in these compounds arises for several reasons: (a) investigation of the structural build-up of a certain composition of elements with respect to existing and nonexisting bulk phases, (b) development of precursor compounds for the production of thin films of ternary materials and (c) investigation of the properties of nano-sized species. With respect to (a), it was found that most of the cluster structures formed by elements of group 11–13–16 have, at this stage of growth, no resemblance to the bulk chalcopyrite structure of these materials. On the other hand, stable compounds such as $[Hg_{15}Cu_{20}S_{25}(PnPr_3)_{18}]$ could be formed for compositions of elements that have no stable counterpart in the bulk phase. Kanatzidis et al. studied the suitability of mixed copper indium chalcogenolates as precursor materials for the photovoltaic materials $CuInE_2$ (E = S, Se).[1,10] Corrigan et al. observed room-temperature fluorescence for the ternary 12–12′–16 cluster (12 = Zn; 12′ = Cd; 16 = Se), $[(N,N,N',N'\text{-tmeda})_5Zn_5Cd_{11}Se_{13}(SePh)_6(THF)_2]$,[9] while binary cadmium or zinc selenide clusters showed weak luminescence only at temperatures below 50 K. During recent studies, it was found that the investigation of these compounds containing complex mixtures of elements needs a combination of various investigative approaches to reach conclusions with confidence.[4]

We report herein the synthesis, structural characterization, and theoretical investigation of $[As(C_6H_5)_4]_2[Cu_6In_4(SeC_6H_5)_{16}Cl_4]$ and $[As(C_6H_5)_4][Cu_7In_4(SeC_6H_5)_{20}]$.

## Results and Discussion

### Synthesis and Structure Determination by X-ray Crystallography

Depending on the amount of $PhSeSiMe_3$ used, the reaction of CuCl, $InCl_3$ and $Ph_4AsCl$ in $CH_2Cl_2$ results in the formation of crystals of either $(AsPh_4)_2[Cu_6In_4Cl_4(SePh)_{16}]$ (**1**) or $(AsPh_4)[Cu_7In_4(SePh)_{20}]$ (**2**), as outlined in Scheme 1.

$$3\,CuCl + 2\,InCl_3 + Ph_4AsCl \xrightarrow[CH_2Cl_2]{+\,10\,PhSeSiMe_3} (AsPh_4)_2[Cu_6In_4Cl_4(SePh)_{16}]\ (\mathbf{1})$$

$$3\,CuCl + 2\,InCl_3 + Ph_4AsCl \xrightarrow[CH_2Cl_2]{+\,15\,PhSeSiMe_3} (AsPh_4)[Cu_7In_4(SePh)_{20}]\ (\mathbf{2})$$

Scheme 1.

[a] Institut für Physikalische Chemie, Lehrstuhl für Theoretische Chemie, University of Karlsruhe,
Kaiserstr. 12, 76128 Karlsruhe, Germany
[b] Institut für Nanotechnologie, Forschungszentrum Karlsruhe, Germany
Postfach 3640, 76021 Karlsruhe
Fax: +49-7247-82-6368
E-mail: andreas.eichhoefer@int.fzk.de
[c] Institut für Anorganische Chemie, University of Karlsruhe
Engesserstraße, Geb. 30.45, 76128 Karlsruhe, Germany
[d] Institut für Physikalische Chemie, University of Karlsruhe,
Kaiserstr. 12, 76128 Karlsruhe, Germany

 © 2006 Wiley-VCH Verlag GmbH & Co. KgaA, Weinheim 

Compound **1** crystallizes in the triclinic space group $P\bar{1}$ (Table 1). The tetrahedrally shaped core of the cluster anion in **1** (Figure 1) is composed of four fused distorted $\{InCu_3Se_6\}$ adamantoid cages. In this way, all six copper atoms (Cu1–Cu6) and four $\mu_3$-$SePh^-$ ligands (Se1–Se4) build a central adamantoid cage $[Cu_6(SePh)_4]^{2+}$, which is face-capped by four $[(\mu_2\text{-}SePh)_3InCl]^-$ (In1–In4, Cl1–Cl4) units through $\mu_2$-SePh ligands (Se5–Se16). All copper and indium atoms display a distorted tetrahedral coordination environment [bond angles: Se–Cu–Se 95.88(6)–124.33(7)°; Se–In–Se 100.35(4)–122.44(4)°; Cl–In–Se 102.44(8)–110.71(8)°]. The Cu-$\mu_2$-Se bonds {246.16(18) [Cu(2)–Se(6)] to 252.0(2) pm [Cu(1)–Se(8)]} are found to be slightly longer than the corresponding Cu-$\mu_3$-Se bonds ranging from 239.42(12) (Cu6–Se4) to 245.13(19) pm (Cu3–Se2). The In-$\mu_2$-SePh bond lengths range from 256.07 (In2–Se14) to 258.30(14) pm (In4–Se9), and the In–Cl bond lengths from 240.5 to 242.8 pm. The so-formed tetrahedral cluster cage is isostructural to known binary and ternary cluster molecules like $[Cd_{10}(SCH_2CH_2OH)_{16}]^{4+}$,[11] $[M_{10}E_4(SPh)_{16}]^{4-}$ (M = Zn, Cd; E = S, Se)[12,13] $[M_{10}E_4(E'Ph)_{12}(PR_3)_4]$ (M = Zn, Cd, Hg; E, E′ = S, Se, Te; R = organic group)[14–19] and $[In_{10}Se_{16}]^{6-}$.[20]

Table 1. Crystallographic data for $[As(C_6H_5)_4]_2[Cu_6In_4(SeC_6H_5)_{16}Cl_4]$ (**1**) and $[As(C_6H_5)_4][Cu_7In_4(SeC_6H_5)_{20}]$ (**2**).

| | **1**·3.5$CH_2Cl_2$ | **2**·4$CH_2Cl_2$ |
|---|---|---|
| Molecular mass [g/mol] | 4712 | 4780.3 |
| Crystal system | triclinic | tetragonal |
| Space group | $P\bar{1}$ | $I\bar{4}$ |
| $a$ [Å] | 17.660(4) | 19.428(3) |
| $b$ [Å] | 18.290(4) | |
| $c$ [Å] | 28.029(6) | 21.037(4) |
| α [°] | 88.16(3) | |
| $\beta$ [°] | 79.96(3) | |
| $\gamma$ [°] | 82.72(3) | |
| $V$ [Å$^3$] | 8842(3)) | 7940(2) |
| $Z$ | 2 | 2 |
| $T$ [K] | 190 | 190 |
| $d_{calcd.}$ [g cm$^{-3}$] | 1.770 | 2.097 |
| $\mu$(Mo-$K_\alpha$) [mm$^{-1}$] | 5.152 | 6.460 |
| $F$[000] | 4524 | 4560 |
| $2\theta_{max}$ [°] | 50 | 50 |
| Measured reflexions | 54957 | 20827 |
| Unique reflexions | 27884 | 6891 |
| $R_{int}$ | 0.0822 | 0.0762 |
| Reflexions with $I > 2\sigma(I)$ | 21130 | 6136 |
| Refined parameters | 1661 | 406 |
| $R_1[I > 2\sigma(I)]$[a] | 0.0655 | 0.0394 |
| $wR_2$(all data)[b] | 0.2299 | 0.1109 |
| Absolute structure parameter | | 0.012 |

[a] $R_1 = \Sigma||F_o| - |F_c||/\Sigma|F_o|$. [b] $wR_2 = \{\Sigma[w(F_o^2 - F_c^2)^2]/\Sigma[w(F_o^2)^2]\}^{1/2}$.

Compound **2** crystallizes in the tetragonal space group $I\bar{4}$ with a crystallographic $\bar{4}$ axis running through As(1) of the $Ph_4As^+$ cation and Cu(2)/Cu(2′) of the cluster anion. The molecular structure of the anion core, $[Cu_7In_4(SePh)_{20}]^-$, is, with the exception of two differences, very similar to the structure of **1** (Figure 2). First, the use of an excess of $PhSeSiMe_3$ leads to an exchange of the terminal chloro ligands with $SePh^-$ groups. The second, and more remarkable, difference concerns the stoichiometry and

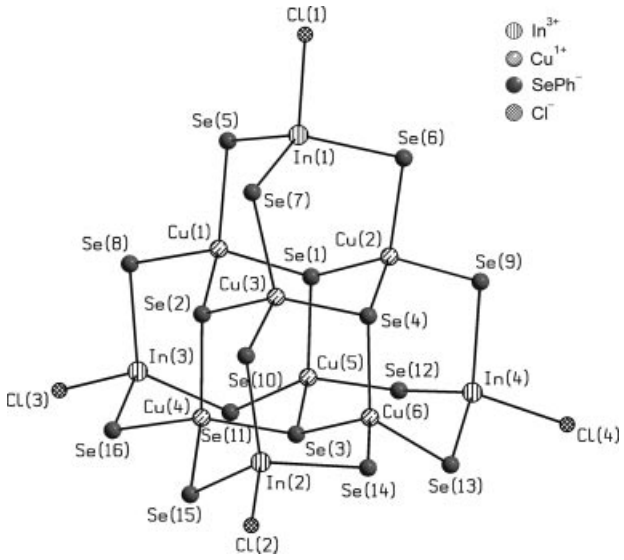


Figure 1. Molecular structure of the cluster anion $[Cu_6In_4Cl_4(SePh)_{16}]^{2-}$ in $(AsPh_4)_2[Cu_6In_4Cl_4(SePh)_{16}]$ (**1**). C and H atoms are omitted for clarity. Selected bond lengths [pm]: Cu(1)–Se(1) 243.81(17), Cu(1)–Se(2) 244.02(17), Cu(1)–Se(5) 248.25(18), Cu(1)–Se(8) 252.0(2), Cu(2)–Se(1) 242.26(18), Cu(2)–Se(4) 244.24(17), Cu(2)–Se(6) 246.16(18), Cu(2)–Se(9) 249.52(17), Cu(3)–Se(4) 2.4274(17), Cu(3)–Se(2) 245.13(19), Cu(3)–Se(10) 248.88(18), Cu(3)–Se(7) 251.0(2), Cu(4)–Se(3) 242.96(17), Cu(4)–Se(2) 244.83(18), Cu(4)–Se(16) 247.3(2), Cu(4)–Se(15) 247.86(18), Cu(5)–Se(1) 242.72(17), Cu(5)–Se(3) 243.48(17), Cu(5)–Se(11) 246.69(19), Cu(5)–Se(12) 249.57(18), Cu(6)–Se(4) 239.42(18), Cu(6)–Se(3) 241.50(19), Cu(6)–Se(13) 246.40(19), Cu(6)–Se(14) 247.37(19), In(1)–Cl(1) 240.5(3), In(1)–Se(7) 256.57(15), In(1)–Se(5) 257.27(16), In(1)–Se(6) 257.90(14), In(2)–Cl(2) 242.6(3), In(2)–Se(14) 256.07(15), In(2)–Se(15) 256.07(16), In(2)–Se(10) 257.02(16), In(3)–Cl(3) 242.8(3), In(3)–Se(16) 256.14(15), In(3)–Se(11) 256.33(14), In(3)–Se(8) 257.91(15), In(4)–Cl(4) 241.3(3), In(4)–Se(13) 256.16(15), In(4)–Se(12) 257.20(16), In(4)–Se(9) 258.30(14).

charge of the cluster anion. In the difference Fourier map, we found additional electron density on four symmetry-equivalent sites of the cluster, which were initially refined as one fourfold degenerated copper atom Cu(3). Compared to the cluster anion of **1**, this results in a reduction of the overall charge of the cluster anion from –2 to –1 if we assign the metal atoms as $In^{3+}$ and $Cu^+$. In agreement with this, we found only one tetraphenylarsonium countercation in the crystal structure. However, the observed density could also be the result of four real atoms of roughly a quarter of the atomic number and weight (e.g. oxygen). In order to maintain the overall charge of the cluster at –1, the electronic structure of the cluster must be significantly altered. Mass spectrometry and DFT computations were performed to address this problem (see further below). The additional copper atom [Cu(3)] is located in the middle of a six-membered ring [Se(4), In(1), Se(2), Cu(1′), Se(5′′) and Cu(1′′)] and has a nearly trigonal-planar coordination environment [Se–Cu–Se: 118.62(18) to 120.8(2)°]. The other copper atoms [Cu(1), Cu(2) and symmetry-equivalent positions] and indium atoms [In(1) and symmetry-equivalent positions] are all coordinated in distorted tetrahedral form by the selenium atoms of the SePh ligand [bond angles: Se–

 © 2006 Wiley-VCH Verlag GmbH & Co. KGaA, Weinheim 

Cu–Se 98.92(6)–123.55(5)°; Se–In–Se 103.23(3)–110.72(3)°]. As a consequence of the incorporation of an additional copper atom, the selenium atoms of the SePh ligands display a different set of bridging modes in **2** compared to those in **1**. Se(1), Se(1′), Se(1′′) and Se(1′′′) are terminally bonded to In(1) and its symmetry-equivalent positions. Eight SePh ligands [Se(2), Se(2′), Se(2′′), Se(2′′′), Se(4), Se(4′), Se(4′′) and Se(4′′′)] are $\mu_3$-bridging between two copper and one indium atom, whereas Se(3), Se(3′), Se(3′′) and Se(3′′′) act as $\mu_2$ bridges between two copper atoms. Se(5), Se(5′), Se(5′′) and Se(5′′′) function as $\mu_4$ bridges between four copper atoms. The Cu–SePh bond lengths range from 241.99(12) (Cu1–Se5) to 263.8(5) pm (Cu3–Se2) and the In–SePh bond lengths vary from 253.46(10) (In1–Se1) to 260.32(10) pm (In1–Se2).

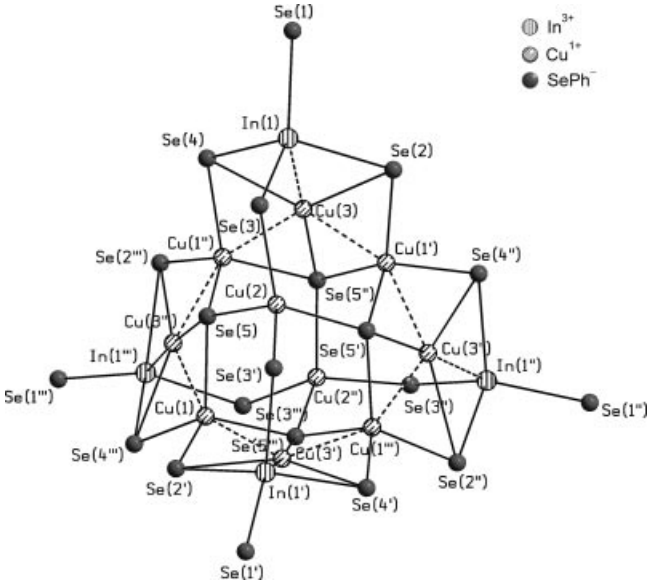


Figure 2. Molecular structure of the cluster anion $[Cu_7In_4(SePh)_{20}]^-$ in $(AsPh_4)[Cu_7In_4(SePh)_{20}]$ (**2**). C and H atoms are omitted for clarity. Selected bond length [pm] (solid lines): In(1)–Se(1) 253.46(10), In(1)–Se(3) 259.29(10), In(1)–Se(4) 260.25(9), In(1)–Se(2) 260.32(10), Cu(1)–Se(5) 241.99(12), Cu(1)–Se(5′′′) 243.92(12), Cu(1)–Se(2′) 246.77(14), Cu(1)–Se(4′′′) 250.26(14), Cu(2)–Se(5) 245.96(12), Cu(2)–Se(5′) 245.96(12), Cu(2)–Se(3′) 247.40(12), Cu(2)–Se(3) 247.40(12), Cu(3)–Se(5′′) 235.3(5), Cu(3)–Se(4) 251.5(5), Cu(3)–Se(2) 263.8(5), Se(2)–Cu(1′) 246.77(14), Se(4)–Cu(1′′) 250.26(14), Se(5)–Cu(3′′′) 235.3(5), Se(5)–Cu(1′′) 243.92(12). Weak contacts [pm] (dashed lines): Cu(1)–Cu(3′) 227.4(6), Cu(1)–Cu(3′′′) 228.4(5), In(1)–Cu(3) 261.0(5). Symmetry transformations for the generation of equivalent atoms: ′: $-x, -y-1, z$; ′′: $-y-0.5, x-0.5, -z+0.5$; ′′′: $y+0.5, -x-0.5, -z+0.5$.

Kanatzidis et al. reported the structure of a closely related singly charged cluster anion, $[Cu_6In_3(SEt)_{16}]^-$, in which one $[(\mu_2\text{-}SEt)_3InSEt]^-$ cap, which is needed to form the ideal four-fused adamantoid structure of $[Cu_6In_4(SEt)_{20}]^{2-}$, is missing.[1] Apparently, the hypothetical species of $[Cu_6In_4(ER)_{20}]^{2-}$ (E = S, Se) is unstable as the dianion.

The solid-state UV/Vis spectra of **1** and **2** (Figure 3, bottom part) are quite similar, with a first shoulder at 400 nm (3.1 eV) and a broad maximum at 310 nm (4.0 eV). In solution, one observes similar absorption features with the bands shifted to 370 nm (3.4 eV) and 265 nm (4.7 eV), respectively. As mass spectrometry indicates the existence of the intact cluster anions in solution, the shift between solid-state and solution spectra likely arises from inhomogeneities of the crystal-oil mull between the quartz plates, which has been observed for other samples.[21]

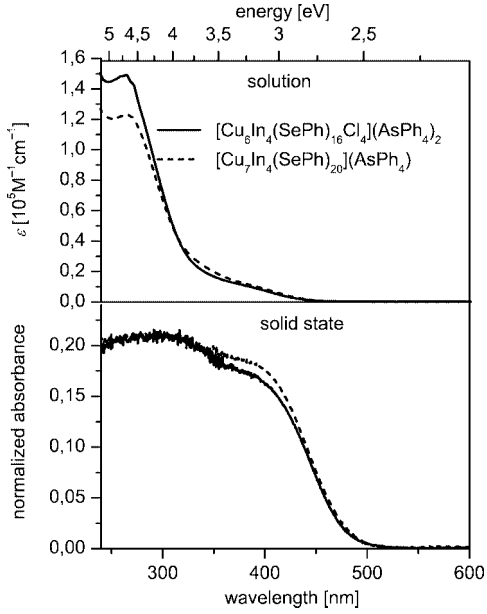


Figure 3. UV/Vis spectra of $(AsPh_4)_2[Cu_6In_4Cl_4(SePh)_{16}]$ (**1**) and $(AsPh_4)[Cu_7In_4(SePh)_{20}]$ (**2**) in solution ($CH_2Cl_2$) and in the solid state (mull in nujol between two quartz plates).

## Mass Spectrometry

The additional charge density found in the X-ray diffraction analysis of compound **2**, leading to the proposed seventh (and fourfold degenerate) copper atom Cu(3), rendered another experimental technique desirable which might give further proof of the stoichiometry and charge state. Electrospray mass spectrometry, which has been proven very powerful for this class of compounds,[22,23] was employed here in conjunction with collision-induced dissociation. The negative-ion mass spectrum of **2** (Figure 4) is governed by several strong ion signals which are all singly charged and can be clearly assigned as indicated in the graphic. The highest mass peak observed ($m/z \approx 4025$) is in complete agreement with the expected isotopomer distribution of the singly charged cluster anion $[Cu_7In_4(SePh)_{20}]^-$, as can be seen from the inset in Figure 4. We note in passing that the two small peaks marked with an asterisk and shifted by 120 amu to lower mass are due to known ligand-exchange reactions of an $SePh^-$ group with a $Cl^-$ ion in solution, as has been observed previously.[24,25] In order to answer the question whether the other strong ion signals next to the parent ion $[Cu_7In_4(SePh)_{20}]^-$ could be explained as fragments of the gas-phase ion $[Cu_7In_4$-

 © 2006 Wiley-VCH Verlag GmbH & Co. KGaA, Weinheim 

$(SePh)_{20}]^-$, we performed a collision-induced dissociation study on the $[Cu_7In_4(SePh)_{20}]^-$ cluster anion (Figure 5). Interestingly, the observed fragment ions differ significantly from the ion signals obtained by direct spraying of **2**. The fragmentation pattern indicates that the parent ion $[Cu_7In_4(SePh)_{20}]^-$ first looses sequentially two $In(SePh)_3$ units from the corner sites of the tetrahedral cluster cage (see Figure 2) with further dissociation of Cu(SePh) units. On the other hand, the four major ion peaks of Figure 4 can be formally added up pairwise {namely $[Cu_6In_3(SePh)_{19}]^-/[In(SePh)_4]^-$ and $[Cu_3In_3(SePh)_{13}]^-/[Cu_3In(SePh)_7]^-$} to give a $[Cu_6In_4$-

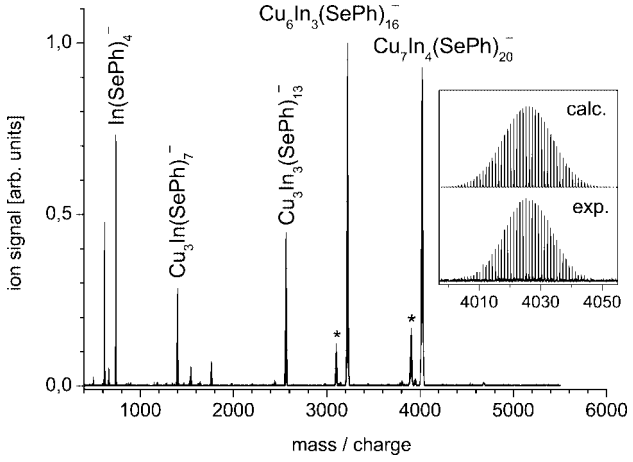


Figure 4. Negative-ion electrospray mass spectrum of **2**. The inset shows a high-resolution mass spectrum of the ion peak at $m/z \approx 4025$ displaying the isotopomer splitting in comparison to the calculated distribution expected for $[Cu_7In_4(SePh)_{20}]^-$.

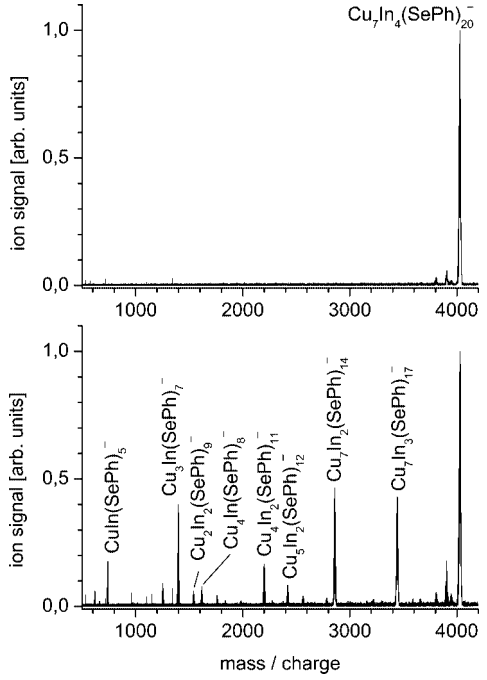


Figure 5. Mass spectrum of $[Cu_7In_4(SePh)_{20}]^-$ isolated in the ICR cell (top panel) and after collision-induced dissociation with argon (bottom panel). The fragmentation pattern can be fully described by sequential loss of $In(SePh)_3$ and Cu(SePh) units consistent with the structure shown in Figure 2.

$(SePh)_{20}]^{2-}$ entity which would rather point towards a solution-phase dissociation of **2**, i.e., loss of $Cu^+$.

However, the fragmentation pattern of **2** strongly supports the identity of the parent ion as $[Cu_7In_4(SePh)_{20}]^-$ ruling out other possibilities like the incorporation of oxygen.

## DFT Calculations

For the $Cu_7$ compound, the X-ray structure has some ambiguities in assignment. The crystallographically imposed $\bar{4}$ symmetry distributes the effective electron density of the seventh copper atom over four identical sites, but the observed density could conceivably be due to four full-occupancy oxygen atoms. There should be, however, significant structural differences between the postulated $Cu_7$ and $Cu_6O_4$ cluster cores due to the vastly different electronic structure needed to maintain the –1 overall cluster charge.

Density functional theory has been successfully applied to similar cluster compounds,[26] and should allow us to differentiate between these two putative assignments, as well as confirming that either are physically reasonable. The $Cu_6O_4$ case was quickly eliminated as it was highly unstable to geometry optimization and the electronic structure indicated a highly paramagnetic system, with essentially no HOMO–LUMO gap, contradicting the observed pale yellow color of the compound. The $Cu_7$ system was not, however, obviously the correct assignment. If addition of the seventh copper atom altered the rest of the cluster significantly from $S_4$ symmetry, the compound would be strongly disfavored from crystallizing in the observed space group.

Initial geometry optimization of the $[Cu_7In_4(SeR)_{20}]^-$ anion was simplified by replacing the phenyl rings of the selenium ligands with methyl groups.[27] Addition of a $Cu^+$ ion to one of the adamantoid faces caused strong deviations in the geometry, the seventh copper atom having burrowed into the cluster, resulting in a related structure with $C_2$ symmetry. Geometry optimization of the fully phenylselenolate-ligated cluster proceeded successfully, with the extra copper atom remaining in the center of an external adamantoid face, and no major (e.g. bond-breaking) changes when compared to the crystal structure.

To test the assumption that the observed crystal structure is indeed the superposition of four orientations of $[Cu_7In_4(SePh)_{20}]^-$, the DFT structure must be symmetrized under $S_4$ before comparison to experiment. The symmetrization procedure produced an averaged structure almost identical to that from the crystal, with an RMS distance of 13.7 pm between corresponding atoms in the superimposed structures, and well within the expected thermal motion. Calculated bonds in the cluster core tend to be consistently slightly longer than their respective distances in the crystal {calc – obs [pm]: In–Se: $4.30 \pm 1.59$; Cu–Se: $4.93 \pm 2.01$; Cu"7"–(Cu,Se): $5.15 \pm 4.35$}, as is expected when comparing gas-phase to solid-state structures. The final electronic structure (diamagnetic, HOMO–LUMO gap = 1.7 eV) is also in agreement with observations.

 © 2006 Wiley-VCH Verlag GmbH & Co. KGaA, Weinheim 

## Experimental Section

**General:** All experiments were carried out under dry nitrogen. $CH_2Cl_2$ and $CH_3CN$ were dried with $CaH_2$, followed by distillation under nitrogen. Anhydrous $InCl_3$ and $Ph_4AsCl$ hydrate were obtained from Aldrich. $Se(SiMe_3)_2$ was prepared as reported in the literature.[28] CuCl was subsequently washed with HCl, $CH_3OH$, and diethyl ether to remove traces of $CuCl_2$, and dried under vacuum. $Ph_4AsCl{\cdot}xH_2O$ was dissolved in $CH_3CN$, dried with molecular sieves, and obtained as a white solid after filtration and removal of the solvent.

**$(AsPh_4)_2[Cu_6In_4Cl_4(SePh)_{16}]$ (1):** CuCl (55 mg, 0.56 mmol), $InCl_3$ (82 mg, 0.37 mmol), and $Ph_4AsCl$ (78 mg, 0.19 mmol) were dissolved in $CH_2Cl_2$ (50 mL). After the solution was cooled to –20 °C, $PhSeSiMe_3$ (0.47 mL, 1.9 mmol) was added. The final mixture was warmed to room temperature whilst stirring to give a yellow solution. Careful evaporation of the solvent yielded **1** as yellow crystalline needles. Yield: 263 mg; 67%. $C_{144}H_{120}Cl_4Cu_6In_4Se_{16}As_2$ (4246.1): calcd. C 40.73, H 2.85; found C 40.93, H 2.92.

**$(AsPh_4)[Cu_7In_4(SePh)_{20}]$ (2):** CuCl (43 mg, 0.43 mmol), $InCl_3$ (63 mg, 0.29 mmol), and $Ph_4AsCl$ (60 mg, 0.14 mmol) were dissolved in $CH_2Cl_2$ (75 mL) and cooled to –20 °C. $PhSeSiMe_3$ (0.52 mL, 2.15 mmol) was added to give a clear, orange solution. After stirring at room temperature for 24 h, the volume was reduced to 15 mL and left to stand. A few days later, orange blocks of **2** started to crystallize. Yield: 117 mg; 43%. $C_{144}H_{120}Cu_7In_4Se_{20}As$ (4408.8): calcd. C 39.23, H 2.74; found C 38.23, H 2.73.

**Crystallography:** Crystals suitable for single-crystal X-ray diffraction were taken directly from the reaction solution of the compound and then selected in perfluoroalkylether oil. Single-crystal X-ray diffraction data of **1** and **2** were collected using graphite-monochromatized Mo-$K_\alpha$ radiation ($\lambda$ = 0.71073 Å) with a STOE IPDS II (Imaging Plate Diffraction System) equipped with a Schneider rotating anode. The structures were solved with the direct-methods program SHELXS[29] of the SHELXTL PC suite of programs, and were refined with the use of the full-matrix least-squares program SHELXL.[29] Molecular diagrams were prepared using SCHAKAL 97.[30] All Cu, In, Se, As, Cl, and C atoms of the cluster molecules were refined with anisotropic displacement parameters, while Cl and C atoms of the solvent molecules were refined isotropically. CCDC-281603 (**1**) and -281604 (**2**) contain the supplementary crystallographic data for this paper. These data can be obtained free of charge from The Cambridge Crystallographic Data Centre via www.ccdc.cam.ac.uk/data_request/cif. X-ray powder diffraction patterns (XRD) were measured with a STOE STADI P diffractometer (Cu-$K_{\alpha1}$ radiation, germanium monochromator, Debye–Scherrer geometry) in sealed glass capillaries. Simulated powder diffraction patterns for **1** and **2** were calculated on the basis of the atom coordinates obtained from single-crystal X-ray analysis by using the program package STOE WinXPOW.[31]

**Mass Spectrometry:** Mass spectrometry was performed with a 7T-Fourier transform ion cyclotron resonance (FT-ICR) mass spectrometer (Bruker Daltonics, Billerica, MA, USA), equipped with an electrospray ionization source (Analytica of Branford, Branford, CT, USA) which has been modified by us for improved ion sensitivity by means of home-built ion optics. Solutions of **1** and **2** in $CH_2Cl_2$ were prepared at a concentration of ca. 0.1 mmol/ L under nitrogen and sprayed at typical flow rates of 300µL/h. Collision-induced dissociation experiments were taken in an MS/MS mode, i.e., the parent ion of interest was first mass-selected in the ICR cell by standard ICR techniques (resonant ejection sweeps) and subjected to collisions with argon ($p = 5{\cdot}10^{-8}$ mbar) at elevated kinetic energies to induce fragmentation.

**Physical Measurements:** UV/Vis absorption spectra of cluster molecules in solution were measured with a Varian Cary 500 spectrophotometer in quartz cuvettes. Solid-state reflection spectra were measured as micron-sized crystalline powders between quartz plates with a Labsphere integrating sphere.

**Calculation Technical Details:** Density functional theory calculations were performed with the TURBOMOLE program package[32] employing the BP86 functional with the very efficient MARI-J approximation,[33] and TZVP basis set.[34] Starting geometries were adapted from the crystal structure, and then optimized with default convergence criteria. Due to electronic convergence problems, the $[Cu_6O_4In_4(SePh)_{20}]^-$ cluster was calculated spin-unrestricted with Fermi electronic occupation smearing. The metal–chalcogen core of the seven-copper cluster was symmetrized while ignoring the seventh copper atom. The pseudo-$S_4$ axis was determined by a simple linear combination of symmetry-related (in the ideal case) atom position vectors, and was then re-oriented to bring the axis in line with +$z$. The symmetry-equivalent coordinates were averaged, and the cluster was rotated about the $z$ axis to minimize differences with the X-ray data.

## Acknowledgments

This work was supported by the Deutsche Forschungsgemeinschaft (Center for Functional Nanostructures CFN).

[1] W. Hirpo, S. Dhingra, M. Kanatzidis, *Chem. Commun.* **1992**, 557–559.
[2] J. Olkowska-Oetzel, D. Fenske, P. Scheer, A. Eichhöfer, *Z. Anorg. Allg. Chem.* **2003**, *629*, 415–420.
[3] A. Eichhöfer, D. Fenske, *J. Chem. Soc., Dalton Trans.* **2000**, 941–944.
[4] R. Ahlrichs, A. Eichhöfer, D. Fenske, O. Hampe, M. M. Kappes, P. Nava, J. Olkowska-Oetzel, *Angew. Chem* **2004**, *116*, 3911–3915; *Angew. Chem. Int. Ed.* **2004**, *43*, 3823–3827.
[5] D. T. T. Tran, L. M. C. Beltran, C. M. Kowalchuk, N. R. Trefiak, N. J. Taylor, J. F. Corrigan, *Inorg. Chem.* **2002**, *41*, 5693–5698.
[6] D. T. T. Tran, N. J. Taylor, J. F. Corrigan, *Angew. Chem.* **2000**, *112*, 965–967; *Angew. Chem. Int. Ed.* **2000**, *39*, 935–937.
[7] A. Lorenz, D. Fenske, *Angew. Chem.* **2001**, *113*, 4537–4541; *Angew. Chem. Int. Ed.* **2001**, *40*, 4402; A. Lorenz, D. Fenske, *Z. Anorg. Allg. Chem.* **2001**, *627*, 2232–2248.
[8] R. Pätow, D. Fenske, *Z. Anorg. Allg. Chem.* **2002**, *628*, 1279–1288.
[9] M. W. DeGroot, N. J. Taylor, J. F. Corrigan, *J. Am. Chem. Soc.* **2003**, *125*, 864–865.
[10] W. Hirpo, S. Dhingra, A. C. Sutorik, M. Kanatzidis, *J. Am. Chem. Soc.* **1993**, *115*, 1597–1599.
[11] P. Strickler, *J. Chem. Soc. D* **1969**, 655b–656.
[12] A. Choy, D. Craig, I. G. Dance, M. L. Scudder, *J. Chem. Soc., Chem. Commun.* **1982**, 1246–1247.
[13] I. G. Dance, A. Choy, M. L. Scudder, *J. Am. Chem. Soc.* **1984**, *106*, 6285–6295.
[14] S. Behrens, M. Bettenhausen, A. Eichhöfer, D. Fenske, *Angew. Chem.* **1997**, *109*, 2874–2876; S. Behrens, M. Bettenhausen, A. Eichhöfer, D. Fenske, *Angew. Chem. Int. Ed. Engl.* **1997**, *24*, 2797.
[15] A. Eichhöfer, D. Fenske, H. Pfistner, M. Wunder, *Z. Anorg. Allg. Chem.* **1998**, *624*, 1909–1914.
[16] A. Eichhöfer, A. Aharoni, U. Banin, *Z. Anorg. Allg. Chem.* **2002**, *628*, 2415–2421.
[17] A. Eichhöfer, E. Tröster, *Eur. J. Inorg. Chem.* **2002**, 2253–2256.
[18] A. Eichhöfer, P. Deglmann, *Eur. J. Inorg. Chem.* **2004**, 349–355.
[19] M. W. De Groot, J. F. Corrigan, *Angew. Chem.* **2004**, *116*, 5469–5471; *Angew. Chem. Int. Ed.* **2004**, *43*, 5355–5357.

 © 2006 Wiley-VCH Verlag GmbH & Co. KGaA, Weinheim 

[20] Ch. Wang, X. Bu, N. Zheng, P. Feng, *Chem. Commun.* **2002**, 1344–1345.
[21] A. Eichhöfer, O. Hampe, M. Blom, *Eur. J. Inorg. Chem.* **2003**, 1307–1314.
[22] A. Eichhöfer, O. Hampe, *Chem. Phys. Lett.* **2005**, *407*, 186–191.
[23] D. Fenske, T. Langetepe, M. Kappes, O. Hampe, P. Weis, *Angew. Chem.* **2000**, *112*, 1925–1928; *Angew. Chem. Int. Ed.* **2000**, *39*, 1857–1860.
[24] T. Løver, W. Henderson, G. A. Bowmaker, J. M. Seakins, R. P. Cooney, *Inorg. Chem.* **1997**, *36*, 3711–3723.
[25] J.-J. Gaumet, G. F. Strouse, *J. Am. Soc. Mass Spectrom.* **2000**, *11*, 338–344.
[26] R. Ahlrichs, D. Fenske, M. McPartlin, A. Rothenberger, C. Schroth, S. Wieber, *Angew. Chem.* **2005**, *117*, 4002–4005; *Angew. Chem. Int. Ed.* **2005**, *44*, 3932–3936.
[27] A test optimization of the related $[Cu_6]^{2-}$ cluster converged to a geometry very close to that of the anion in the crystal structure of $Cu_7$.
[28] G. Brauer (Ed.), *Handbuch der Präparativen Anorganischen Chemie*, 3rd ed., Enke-Verlag, Stuttgart, **1975**, vol. 1, p. 372.
[29] G. M. Sheldrick, *SHELXTL PC version 5.1, An Integrated System for Solving, Refining, and Displaying Crystal Structures from Diffraction Data*, Bruker Analytical X-ray Systems, Karlsruhe, **2000**.
[30] E. Keller, *SCHAKAL 97, A Computer Program for the Graphic Representation of Molecular and Crystallographic Models*, University of Freiburg, **1997**.
[31] STOE, *WinXPOW*, STOE & Cie GmbH, Darmstadt, **2000**.
[32] R. Ahlrichs, M. Bär, M. Häser, H. Horn, C. Kölmel, *Chem. Phys. Lett.* **1989**, *162*, 165–169; O. Treutler, R. Ahlrichs, *J. Chem. Phys.* **1995**, *102*, 346–354.
[33] A. D. Becke, *Phys. Rev. A* **1988**, *38*, 3098–3100; S. J. Vosko, L. Wilk, M. Nusair, *Can. J. Phys.* **1980**, *58*, 1200–1211; J. P. Perdew, *Phys. Rev. B* **1986**, *33*, 8822–8824; erratum; J. P. Perdew, *Phys. Rev. B* **1986**, *34*, 7406; K. Eichkorn, O. Treutler, H. Öhm, M. Häser, R. Ahlrichs, *Chem. Phys. Lett.* **1995**, *242*, 652–660; M. Sierka, A. Hogekamp, R. Ahlrichs, *J. Chem. Phys.* **2003**, *118*, 9136–9148.
[34] Available at ftp://ftp.chemie.uni-karlsruhe.de/pub/.

Received: September 14, 2005
Published Online: December 1, 2005

 © 2006 Wiley-VCH Verlag GmbH & Co. KGaA, Weinheim 

DOI: 10.1002/ejic.200500543

# Neodymium(II) and Dysprosium(II) Iodides in the Reactions with Metallocenes of d-Transition Metals

**Mikhail E. Burin,[a] Marina V. Smirnova,[a] Georgy K. Fukin,[a] Eugeny V. Baranov,[a] and Mikhail N. Bochkarev*[a]**

**Keywords:** Dysprosium / Neodymium diiodide / Metallocenes / Reduction

Heating $NdI_2$ (**1**) or $DyI_2$ (**2**) with vanadocene (**3**) in benzene at 85 °C led to the formation of bis(benzene)vanadium in 10 and 24 % yields, respectively. The lanthanide products were isolated in the form of $CpLnI_2(THF)_3$ after crystallization from THF. The interaction of **2** with **3** in isopropylbenzene at 90 °C yielded a mixture of $(arene)_2V$ complexes from which a small amount of bis(isopropylbenzene)vanadium was isolated. The same reaction did not occur in mesitylene. From the reaction of **2** with **3** in molten naphthalene at 100 °C, the heterobimetallic cluster $\{[CpDy(\mu\text{-}I)_2]_7Cp_2V(\mu\text{-}I)\}$(**4**) was isolated in low yield. The reaction of $Cp_2Cr$ with **1** or **2** in benzene at ambient temperature afforded the dimer $[CpCr(\mu\text{-}I)]_2$ (**5**) and a dysprosium complex, $Cp_2DyI$ (**6**) (in the reaction with **2**). When the reaction with **2** was carried out at 80 °C, along with compound **6**, the -ate complex $\{[Cp_2DyI_2]^-[Cp_2Cr]^+\}$(**7**) was crystallized from the reaction solution. Nickelocene was reduced by **2** in benzene at 80 °C to nickel metal. The dysprosium product was isolated as solvent-free complex **6**. Ferrocene and cobaltocene did not react with **1** and **2** in benzene. The molecular structures of compounds **4**, **5**, and **7** were characterized by X-ray diffraction analysis.

(© Wiley-VCH Verlag GmbH & Co. KGaA, 69451 Weinheim, Germany, 2006)

## Introduction

The diiodides $NdI_2$ (**1**), $DyI_2$ (**2**), and $TmI_2$, which recently became available for broad chemical investigations, have proven themselves as powerful reducing reagents in reactions with various organic substrates.[1] The reactivity of these salts towards organometallic compounds has been studied. Most of the examples are metathesis reactions of $TmI_2$ with alkali-metal derivatives to give the corresponding divalent thulium complexes, $R_2Tm(solv.)_n$, or the products of their oxidation by the solvent and disproportionation.[2] The reactions of $LnI_2$ with RM {R = 2,6-*t*$Bu_2C_6H_3O$,[3] $[(Me_3Si)_2]_2N$,[3] $C_5Me_5$,[2b] $(Me_3Si)C_5H_4$,[2b] $(Me_3Si)_2C_5H_3$;[2a,2b] M = Na, K} in THF or ether, conducted in nitrogen, yielded the corresponding nitrogen-containing complexes of the type $[(R_2Ln)_2(\mu_2\text{-}N_2)]$. The addition of $Ph_2Hg$, $Ph_3GeH$, $Ph_3GeGePh_3$, or $Ph_4Sn$ to a solution of **1** or **2** in THF caused the formation of the triiodide $LnI_3(THF)_3$ and a mixture of monoiodide complexes of the type LnIRR′ containing fragments of split solvent.[4,5] Reaction of **1** with $Me_3SiCl$ in THF proceeds vigorously to give $Me_3SiH$, $Me_3SiSiMe_3$, and $Me_3SiOBu$.[6] Pentafluorophenyl germanes $(C_6F_5)_3GeH$ and $(C_6F_5)_3GeBr$ react with **1** in THF to produce a hyperbranched polymer $[(C_6F_5)_2Ge(C_6F_4)]_n$.[5] The reactivity of **1** and **2** (as well as all other $LnI_2$) towards organometallic compounds of d-transition metals has never been studied. In an effort to fill this gap, we have investigated the reactions of **1** and **2** with metallocenes of vanadium, chromium, iron, cobalt, and nickel. The second aim of this work was to develop a new way to arene complexes of these metals; therefore, the reactions were carried out in aromatic solvents. Neodymium and dysprosium diiodides were selected because they are the most active reductants among all the $LnI_2$.

[a] Razuvaev Institute of Organometallic Chemistry, Russian Academy of Sciences,
Tropinina 49, Nizhny Novgorod, 603950, Russia
Fax: +7-8312-127795
E-mail: mboch@iomc.ras.ru

## Results and Discussion

The main preparative route to bis(arene) complexes of d-transition metals is still Fischer's method – the reflux of a mixture of the metal halide, $AlCl_3$, and aluminum powder in the appropriate aromatic solvent and subsequent hydrolysis of the formed intermediates.[7] We have found that bis(benzene)vanadium can be obtained by the reaction of **1** or **2** with vanadocene (**3**) in benzene at 80 °C.[8] When the mixture was heated for 10 h, the yield of $(C_6H_6)_2V$ was 10% for **1** and 24% for **2**. An increase in reaction time did not lead to greater yields of bis(benzene)vanadium. Changing the molar ratio **2**/**3** from 2 to 4 increased the yield of $(C_6H_6)_2V$ from 15% to 24%. Despite a great excess of $LnI_2$ most of the vanadocene could be isolated from the reaction mixture. This can be explained by the heterogeneous nature of the processes: the formed lanthanide product $CpLnI_2$, sparingly soluble in benzene, covers the surface of iodide **2** and prevents it from reacting further with **3**. The neodym-

 © 2006 Wiley-VCH Verlag GmbH & Co. KgaA, Weinheim InterScience 

ium derivative has especially low solubility; therefore, only a few crystals of it were isolated as the solvated $CpNdI_2(THF)_3$ after crystallization from THF.

$$2\,LnI_2 + Cp_2V \xrightarrow{\text{benzene}} (C_6H_6)_2V + 2\,CpLnI_2$$

Ln = Nd, Dy

An attempt to use $VCl_4$ instead of **3** in this synthesis failed: the reduction of vanadium with **2** proceeds rapidly but stops at the formation of the benzene-insoluble $VCl_3$.

The mechanism of $(C_6H_6)_2V$ formation from **3** and $LnI_2$ remains unclear, but taking into account the generation of lanthanide–naphthalene–vanadium(0) complexes $[CpLn(THF)(\mu\text{-}C_{10}H_8)VCp]_n$ (Ln = Sm, Eu, Yb)[9] or the triple-decker vanadium compound $CpV(\mu\text{-}C_{10}H_8)VCp$[9a] in the reactions of **3** with other strong reductants such as lanthanide(II) naphthalenides $(C_{10}H_8)Ln(THF)_x$ suggests that reduction of **3** by **1** and **2** also proceeds via intermediates of the type $CpV(\mu\text{-}C_6H_6)LnI_2$, probably generated on a surface of $LnI_2$. However, in the reaction of **2** with **3** in molten naphthalene, where the formation of naphthalene–vanadium derivatives seemed very plausible, we were unable to isolate any arene–vanadium product although almost all of the vanadocene was consumed. The reaction readily proceeds at 100 °C to give a black solution from which only heterobimetallic cluster **4** has been isolated by crystallization from benzene. The black insoluble pyrophoric precipitate, remaining after the removal of the reaction solution, contained (according to elemental analysis and IR spectroscopy) dysprosium, vanadium, cyclopentadienyl, and arene groups. This is consistent with above supposition. Note that naphthalene–ytterbium, –samarium, and –europium are also pyrophoric.

The molecule **4** (Figure 1) is a bimetallic polynuclear complex. The metal atoms [Dy(1–3), V(1) and Dy(4–7)] are positioned at the apexes of distorted tetrahedrons and are bonded to each other by the bridging iodine atoms that form a distorted octahedron around each dysprosium atom. The iodine atoms occupy equatorial positions and the one apical position inside the cluster. The apical positions outside of the cluster are occupied by Cp ligands. The Dy(1–3) atoms, $\mu_2$-I [I(12), I(13), and I(23)] atoms, and the $\mu_3$-I(123), and $\mu_3$-I(321) atoms are located at the apexes of a distorted hexagonal bipyramid. The deviation of the Dy(1–3) and I (12, 13, and 23) atoms from the plane are 0.079 Å. The Dy(1–3)–$\mu_2$-I distances in the Dy(1–3),V(1) metallofragment vary in the range 3.0568(4)–3.1269(4) Å and are shorter than the Dy(1–3)–$\mu_3$-I distances [3.1544(4)–3.2248(4) Å]. The Dy(4, 6, 7), I(47, 67, 456) (planar location) and I(467, 654) (apical location relative to the plane) atoms in the Dy(4–7) metallofragment are also located at the apexes of a distorted hexagonal bipyramid. However there is a significant difference between the Dy(4, 6, 7)–I(47, 67, 456,467, 654) and Dy(1–3)–I (12, 13, 23, 123, 321) fragments of the cluster. The Dy(5) atom in the Dy(4, 5, 6, 7) fragment is positioned under the I(456)···I(654) edge and it interacts with these iodine atoms, whereas the vanadium atom has no additional V–I interactions. As a result, the I(654) atom is a bridging four-coordinate atom. The Dy(5, 7)–$\mu_4$-I(654) distances [3.3609(4), 3.3381(4) Å] are significantly longer than the Dy(4–7)–$\mu_2$-I [3.0407(4)–3.1261(5) Å] and Dy(4–7)–$\mu_3$-I [3.1420(4)–3.1816(5) Å] distances. It should be noted that the Dy(4, 6)–$\mu_4$-I(654) bonds [3.2191(4) and 3.2406(4), respectively] are shorter than the Dy(5, 7)–$\mu_4$-I(654) bonds. The Dy–$Cp_{center}$ and V–$Cp_{center}$ distances vary in the range 2.309(6)–2.331(6) Å and 1.934(6)–1.939(6) Å, respectively, and are typical for similar fragments ($[Cp_2DyBr]_2$, 2.327–2.360 Å;[10] $Cp_2V$, 1.918 Å;[11] $Cp_2VCl$, 1.944, 1.946 Å[12]).

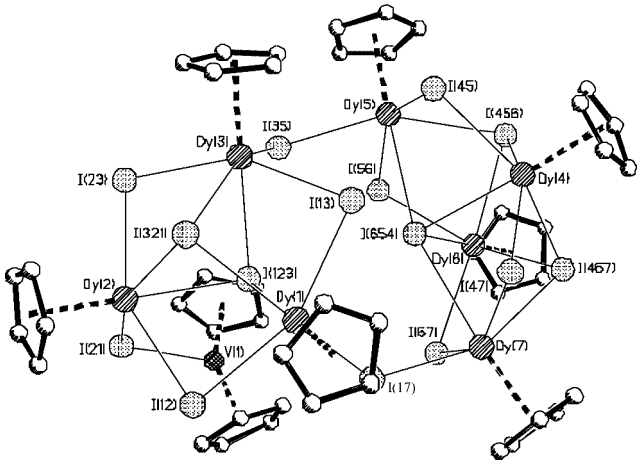


Figure 1. Molecular structure of $\{[CpDy(\mu\text{-}I)_2]_7Cp_2V(\mu\text{-}I)\}$ (**4**). Hydrogen atoms have been omitted for clarity. Relevant bond lengths [Å] and angles [°]: Dy(1)–I(12) 3.1077(4), Dy(1)–I(13) 3.0568(4), Dy(1)–I(17) 3.1451(4), Dy(1)–I(123) 3.1544(4), Dy(1)–I(321) 3.2248(4), Dy(1)–C(11–15) 2.592(5)–2.609(5), Dy(7)–I(17) 3.0583(4), V(1)–I(21) 2.8203(10), V(1)–I(1–10) 2.259(6)–2.297(6); I(13)–Dy(1)–I(12) 149.595(12), I(13)–Dy(1)–I(17) 95.692(12), I(12)–Dy(1)–I(17) 92.424(12), I(12)–Dy(1)–$Cp_{center}$ 103.5, $Cp_{center}$–V(1)–$Cp_{center}$ 142.3, I(21)–V–$Cp_{center}$ 108.6 (109.0).

No changes were observed when a mixture of **2** and **3** was heated in mesitylene at 90 °C. The same reaction in isopropylbenzene afforded a mixture of bis(arene)vanadium complexes [arene = $C_6H_6$, $C_6H_5C_3H_7$, $C_6H_4(C_3H_7)_2$] isolated as a dark brown oily liquid. A similar mixture of arene–vanadium products is formed in the reaction of $VCl_3$ with $AlCl_3$ and Al in $i\text{-}C_3H_7C_6H_5$.[13] From the reaction mixture, we were able to isolate a small amount of bis(isopropylbenzene)vanadium as yellow crystals.

Chromocene reacted with **1** in benzene at ambient temperature but did not give the expected bis(benzene)chromium. Instead, from the cherry solution, the dimer **5** was isolated as an air-sensitive, dark cherry-red crystalline solid soluble in benzene and hexane. Single crystals of **5** suitable for X-ray analysis were obtained by crystallization from hexane.

The centrosymmetric molecule **5** (Figure 2) consists of two CpCrI fragments bonded by iodine bridges. The four-membered Cr(1)I(1)Cr(1A)I(1A) cycle has a butterfly shape characteristic of similar fragments.[14] The dihedral angles between the Cr(1)I(1)I(1A) and Cr(1A)I(1)I(1A) fragments is 87.6°. The Cr(1)–I and Cr(1)–C(Cp) distances are 2.6678(5)–2.6592(5) Å and 2.242(2)–2.295(2) Å, respectively,

 © 2006 Wiley-VCH Verlag GmbH & Co. KGaA, Weinheim 

and are typical for the same type of complexes [2.671–2.707 Å for Cr–μ-I and 2.192–2.241 Å[15] for Cr–C(Cp)]. A short Cr···Cr contact [2.4921(7) Å] in the molecule indicates the existence of bonding between the two metal atoms. Similar Cr–Cr bonding has been found before in the complexes $[Cp^*Cr(\mu\text{-}Cl)]_2$ [2.642(2) Å], $[Cp^*Cr(\mu\text{-}Me)]_2$ [2.263(3) Å], and $[(Cp^*Cr)_2(\mu\text{-}Me)(\mu\text{-}Ph)]$ [2.289(4) Å].[14]

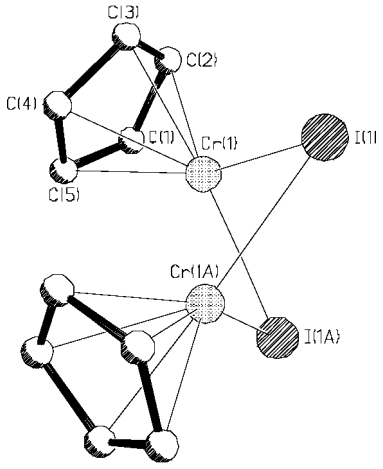


Figure 2. Molecular structure of $[CpCr(\mu\text{-}I)]_2$ (**5**). Hydrogen atoms have been omitted for clarity. Relevant bond lengths [Å] and angles [°]: Cr(1)–Cr(1A) 2.4921(7), Cr(1)–I(1) 2.6678(5), Cr(1A)–I(1) 2.6592(5), Cr(1)–C(Cp) 2.242(2)–2.295(2); Cr(1A)I(1)Cr(1) 55.787(2), I(1A)Cr(1)I(1) 94.905(2).

Increasing the reaction temperature to 80 °C did not lead to the formation of $(C_6H_6)_2Cr$. In this case, extensive transformations resulted in the formation of a green intractable mixture from which no definite products were isolated.

Similar to the neodymium salt, dysprosium iodide (**2**) reacted with $Cp_2Cr$ in benzene at room temperature to give dimer **5** and dysprosium(III) complex **6**. When the reaction was carried out at 80 °C the dimer **5** was not found in the mixture but product **6** was isolated in 34% yield. Its formation was confirmed by elemental analysis and IR spectroscopic data; however, the single crystal selected for X-ray diffraction analysis quite unexpectedly turned out to be the -ate complex $\{[Cp_2DyI_2]^-[Cp_2Cr]^+\}$(**7**), which can be considered as a combined product of $Cp_2DyI$ and $Cp_2CrI$.

According to X-ray data, molecule **7** contains the counterions $[Cp_2DyI_2]^-$ and $[Cp_2Cr]^+$ (Figure 3). The dysprosium and chromium atoms are located on the $C_2$ axis and the mirror plane, respectively. The bond angles $Cp_{cent}$–Dy(1)–$Cp_{cent}$ and I(1)–Dy(1)–I(1A) are 128.3 and 95.4°, respectively, and the distances Dy(1)–C(Cp) and Dy(1)–I vary in the ranges 2.615(4)–2.648(4) Å and 2.9818(5)–2.9926(5) Å, respectively. The Dy(1)–C(Cp) bond length in **7** is similar to the bond lengths in **4** [2.566(6)–2.637(6) Å] but the Dy–I bonds in **7** are somewhat shorter than the analogous bonds in **4**. The shortening of the Dy–I bonds in **7** probably reflects a different type of coordination of the iodine atoms in these two compounds. The iodine atoms in **7** are terminal, whereas all I atoms in **4** are bridging. The $[Cp_2Cr]^+$ cation has an ordinary geometry. To the best of our knowledge, the structure of only one complex containing the $[(Me_5C_5)_2LnI_2]^-$ anion (Ln = Yb) has been published previously.[16]

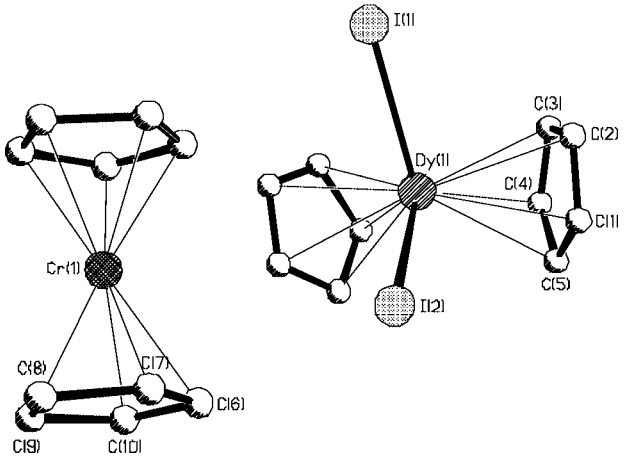


Figure 3. Molecular structure of $[Cp_2DyI_2]^-[Cp_2Cr]^+$ (**7**). Hydrogen atoms have been omitted for clarity. Relevant bond lengths [Å] and angles [°]: Dy(1)–I(1) 2.9926(5), Dy(1)–I(2) 2.9818(5), Dy(1)–C(Cp) 2.615(4)–2.648(4), Cr(1)–C(Cp) 2.188(4)–2.201(4); I(1)–Dy(1)–I(2) 95.41(1), $Cp_{center}$–Dy–$Cp_{center}$ 128.3, $Cp_{center}$–Cr–$Cp_{center}$ 179.0.

The only definite product isolated from the reaction of **2** with nickelocene in benzene at 80 °C was the dysprosium(III) complex **6**. Reduced nickel was deposited as a mirror on the walls of the reaction flask.

No transformations were observed when $Cp_2Fe$ and $Cp_2Co$ were heated with **1** or **2** in benzene at 80 °C for 10 h. Interestingly, addition of $Cp_2Fe$ to a THF solution of **2** caused immediate formation of $DyI_3$ and DyIRR' (R,R′ = fragments of THF). Ferrocene was isolated unchanged from the reaction mixture. As it was mentioned above, similar transformations have been observed before in the reactions of **1** and **2** with aromatic compounds or phenyl derivatives of mercury, germanium and tin in THF or DME.[4]

## Conclusions

The study revealed that the iodides **1** and **2** could react with metallocenes of vanadium, chromium, and nickel in nonsolvating aromatic solvents, but only in the reactions with vanadocene in benzene was the expected bis(arene) complex obtained in noticeable amounts indicative of the redox character of the transformations. In all other cases, the isolated products $CpLnI_2$, **4**, **5**, and **7** were arene-free. Formation of dimer **5** and cluster **4** reveals that most of these reactions are accompanied by Cp/I exchange. Ferrocene and cobaltocene turned out to be inert toward iodides **1** and **2** in benzene.

## Experimental Section

**General Remarks:** All procedures were performed under vacuum using standard Schlenk-tube techniques. Benzene, cumene, and mesitylene were dried by refluxing over sodium and treated with **1** for 30 min before use. Diiodides **1** and **2** were purchased from Synor

 © 2006 Wiley-VCH Verlag GmbH & Co. KGaA, Weinheim 

(Nizhny Novgorod) and used without additional purification. Vanadocene and cobaltocene were prepared according to published procedures.[17,18] Ferrocene, nickelocene, and chromocene were purchased from Aldrich. The ESR spectra were recorded with a Bruker 200D-SRC instrument. The IR spectra of the samples, prepared as Nujol mulls, were recorded with a Specord M-75 spectrometer. Melting points were determined in sealed capillaries.

**Reaction of $DyI_2$ (2) with $Cp_2V$ (3) in Benzene:** A solution of **3** (0.2 g, 1.10 mmol) in benzene (10 mL) was added to a powder of **2** (1.89 g, 4.54 mmol), and the mixture was stirred at 80 °C for 10 h. The resultant dark brown solution was separated from the precipitate by decantation, the solvent was removed by evaporation in vacuo, and the residue was extracted with hexane (2×10 mL). The extract was placed into an apparatus for sublimation, hexane was evaporated in vacuo, and the solid residue was heated gradually up to 110 °C. The sublimed mixture of violet and dark brown crystals was sublimed again. At 50–60 °C (0.1 Torr) violet crystals of **3** (0.11 g, 54%) were collected and separated [ESR (77 K): $g_\perp$ = 4.0, $A_\perp$ ($^{51}$V) = 2.8 mTs, $g$ = 2.0]. Sublimation of the remaining substance at 100–110 °C (0.1 Torr) gave dark brown crystals of $(C_6H_6)_2V$. Yield 55 mg (24%); m.p. 275–277 °C; ESR (293 K): $A_i(^{51}V)$ = 6.35 mT, $g_i$ = 1.986. The solid residue after extraction with hexane was recrystallized from THF to give $CpDyI_2(THF)_3$ (75 mg, 5%). Decomposition temperature, IR spectrum and results of elemental analysis of the product were identical to those of the previously synthesized compound.[19]

**Reaction of $NdI_2$ (1) with $Cp_2V$ (3) in Benzene:** Compound **1** (3.46 g, 8.69 mmol) reacted with compound **3** (0.35 g, 1.93 mmol), under the conditions of the previous experiment, to give $(C_6H_6)_2V$ (42 mg, 10%). The sublimation of the solid products gave unreacted **3** (0.24 g, 69%). From the solid residue after hexane extraction, a few crystals of $CpNdI_2(THF)_3$ were isolated by recrystallization from THF. Characteristics of the product were identical to those of the complex obtained in the reaction of **1** with cyclopentadiene.[19]

**Reaction of $DyI_2$ (2) with $Cp_2V$ (3) in Isopropylbenzene:** A mixture of **2** (1.01 g, 2.43 mmol), **3** (0.2 g, 1.11 mmol), and isopropylbenzene (7 mL) was stirred at 90 °C for 20 h. The resultant red-brown solution was separated from the precipitate by decantation, and cumene was removed in vacuo. A waxy residue was extracted with hexane (10 mL), and the extract was transferred into a sublimation apparatus. After evaporation of hexane, the solid products were sublimed in vacuo by gradually increasing the temperature from 20 °C to 150 °C. Unreacted **3** (57 mg, 29%), which sublimed at 50–60 °C, was collected in the top part of the apparatus. At 100–120 °C, yellow needle crystals of $(i\mathrm{PrC_6H_5})_2V$ (4 mg, 1%) sublimed; ESR (300 K): $a_i(^{51}V)$ = 6.29 mT, $g_i$ = 1.988, $A_i$(H) = 5 G.

**Reaction of $DyI_2$ (2) with $Cp_2V$ (3) in Naphthalene:** A mixture of **2** (1.6 g, 3.84 mmol), **3** (0.26 g, 1.44 mmol), and naphthalene (2.5 g) was stirred at 110–120 °C in a sealed ampoule. After 20 h, the resultant black mixture was cooled to room temperature to give a black solid from which a mixture of naphthalene and unreacted **3** was separated by sublimation in vacuo at 50–60 °C. The black residue was extracted with benzene (3×30 mL), the greenish solution obtained was concentrated to 8 mL and cooled to 8–10 °C to give violet crystals of **4**. The product was separated by decantation and dried in vacuo at room temperature. A sample of **4** isolated under these conditions contained three molecules of benzene. Yield 0.28 g (5%); m.p. >240 °C (dec.). $C_{63}H_{63}Dy_7I_{15}V$ (3910.94): calcd. C 19.20, H 1.81; found C 19.33, H 1.61. IR (nujol, KBr): $\tilde{\nu}$ = 1010 (s), 796 (s), 673 (m) cm$^{-1}$. The black residue after separation of the benzene extract was dried in vacuo at room temperature to give a black pyrophoric powder (1.35 g). IR (nujol, KBr): $\tilde{\nu}$ = 1600 (w), 1011 (m), 842 (sh), 800 (s), 677 (w), 619 (w) cm$^{-1}$.

**Reaction of $NdI_2$ (1) with $Cp_2Cr$ in Benzene (at 20 °C):** A solution of $Cp_2Cr$ (0.34 g, 0.19 mmol) in benzene (10 mL) was added to a powder of **1** (1.53 g, 0.38 mmol), and the mixture was stirred for 10 h at ambient temperature. The resultant dark-cherry solution was separated from the precipitate, and the solvent was removed in vacuo. The waxy residue was extracted with hexane (2×10 mL). Slow evaporation of hexane from the extract afforded **5** (0.18 g, 39%) as dark cherry-red crystals with m.p. 84–87 °C (dec.). $C_{10}H_{10}Cr_2I_2$ (487.90): calcd. C 24.60, H 2.05, Cr 21.32; found C 25.01, H 2.50, Cr 21.05. IR (nujol, KBr): $\tilde{\nu}$ = 3088 (w), 1011 (s), 815 (s), 784 (s), 720 (m), 665 (m), 561 (m) cm$^{-1}$.

**Reaction of $DyI_2$ (2) with $Cp_2Cr$ in Benzene (at 20 °C):** Under the conditions of the previous experiment, compound **2** (1.12 g, 2.69 mmol) was treated with $Cp_2Cr$ (0.24 g, 1.32 mmol) in benzene (8 mL). The resultant dark-cherry solution was separated from the precipitate, the solvent was removed in vacuo, and the residue was extracted with pentane. Cooling the extract to 0 °C gave **5** (0.142 g, 44%). The residue after pentane extraction was recrystallized from toluene to give **6** (0.146 g, 26%) as light yellow crystals. $C_{10}H_{10}DyI$ (739.02): calcd. Dy 38.74; found Dy 38.72. IR (nujol, KBr): $\tilde{\nu}$ = 1008 (s), 890 (w), 781 (s), 727 (m), 661 (m) cm$^{-1}$.

**Reaction of $DyI_2$ (2) with $Cp_2Cr$ in Benzene (at 80 °C):** A mixture of **2** (0.537 g, 1.29 mmol) and $Cp_2Cr$ (0.14 g, 0.77 mmol) in benzene (8 mL) was stirred at 80 °C for 12 h. The initial orange-red color of the solution gradually turned pale green. The solution was decanted from the black precipitate, and the solvent was evaporated in vacuo to leave behind a greenish powder, which was extracted with toluene. Cooling of the toluene extract in a refrigerator yielded yellow crystals of **6** (92 mg, 34%). $C_{10}H_{10}DyI$ (739.02): calcd. C 26.61, H 2.38, Dy 38.74; found C26.35, H 2.56, Dy 38.56. The IR spectrum was identical to that of the compound from the previous experiment. Among the isolated yellow crystals of **6**, a few greenish-yellow crystals were found. X-ray diffraction investigation of one of them revealed the compound to be -ate complex **7**. The amount of isolated **7** was not enough for elemental and spectroscopic analyses.

**Reaction of $DyI_2$ (2) with $Cp_2Ni$ in Benzene:** A solution of $Cp_2Ni$ (0.12 g, 0.64 mmol) in benzene (15 mL) was added to a powder of **2** (0.56 g, 1.34 mmol), and the mixture was stirred at 70 °C for 12 h. Formation of a nickel mirror on the walls of the reactor was observed. The resultant wine-colored solution was separated from the precipitate, and the latter was washed with benzene (15 mL). The reaction solution and benzene wash were combined, and the solvent was evaporated in vacuo. The solid residue was recrystallized from benzene to give **6** (0.11 g, 42%).

**X-ray Diffraction Study:** The X-ray diffraction data were collected with a SMART APEX diffractometer (graphite-monochromated, Mo-$K_\alpha$-radiation, φ-ω-scan technique, $\lambda$ = 0.71073 Å). The intensity data were integrated by the SAINT program.[20] SADABS[21] was used to perform area-detector scaling and absorption corrections. The structures were solved by direct methods and refined on $F_2$ using all reflections with the SHELXTL package.[22] All non-hydrogen atoms were refined anisotropically. The H atoms in **5** and **7** [except H(2)] were found from Fourier synthesis and refined isotropically. The H atoms in **4** and the H(2) atom in **5** were placed in calculated positions and refined in the "riding-model". In the unit cell of **4** were found the solvated molecules of benzene. The details of crystallographic, collection, and refinement data for **4**, **5**, and **7** are shown in the Table 1. The selected geometric characteristics for **4**, **5**, and **7** are given in the captions to Figure 1, Figure 2,

 © 2006 Wiley-VCH Verlag GmbH & Co. KGaA, Weinheim 

Table 1. The details of crystallographic, collection, and refinement data for **4**, **5**, and **7**.

| | **4** | **5** | **7** |
|---|---|---|---|
| Empirical formula | $C_{69}H_{69}Dy_7I_{15}V$ | $C_{10}H_{10}Cr_2I_2$ | $C_{20}H_{20}CrDyI_2$ |
| Formula mass | 3990.18 | 487.98 | 728.66 |
| Temperature [K] | 100 | 100 | 100 |
| Crystal system | monoclinic | monoclinic | monoclinic |
| Space group | *P*21/*n* | *C*2/*c* | C2/*m* |
| *a* [Å] | 17.9963(9) | 15.562(2) | 15.632(1) |
| *b* [Å] | 25.845(1) | 6.9458(11) | 16.618(1) |
| *c* [Å] | 19.965(1) | 12.763(2) | 8.2121(5) |
| *β* [°] | 105.674(1) | 111.680(3) | 102.599(1) |
| Volume [Å$^3$] | 8940.5(8) | 1282.0(3) | 2081.8(2) |
| *Z* | 4 | 4 | 4 |
| Density (calculated) [g cm$^{-3}$] | 2.964 | 2.528 | 2.325 |
| Absorption coefficient [mm$^{-1}$] | 11.086 | 6.472 | 7.048 |
| *F*(000) | 7052 | 896 | 1344 |
| Crystal size [mm] | 0.15×0.12×0.10 | 0.16×0.12×0.08 | 0.07×0.07×0.03 |
| $\theta_{max}$ range for data collection [°] | 25.00 | 29.00 | 25.00 |
| | $-21 \le h \le 21$ | $-21 \le h \le 15$ | $-18 \le h \le 18$ |
| Index ranges | $-30 \le k \le 30$ | $-9 \le k \le 7$ | $-19 \le k \le 19$ |
| | $-23 \le l \le 23$ | $-16 \le l \le 17$ | $-9 \le l \le 9$ |
| Reflections collected | 70375 | 4506 | 8265 |
| Independent reflections | 15743 ($R_{int}$ = 0.0400) | 1696 ($R_{int}$ = 0.0158) | 1910 ($R_{int}$ = 0.0295) |
| Absorption correction | SADABS | | |
| Max/min transmission | 0.4036/0.2871 | 0.6255/0.4241 | 0.8164/0.6382 |
| Refinement method | full-matrix least squares on $F^2$ | | |
| Data/restraints/parameters | 15743/31/829 | 1696/0/84 | 1910/2/150 |
| Goodness-of-fit on $F^2$ | 1.118 | 1.099 | 1.085 |
| Final *R* indices | $R_1$ = 0.0261 | $R_1$ = 0.0209 | $R_1$ = 0.0287 |
| [$I > 2\sigma(I)$] | $wR_2$ = 0.0609 | $wR_2$ = 0.0461 | $wR_2$ = 0.0673 |
| *R* indices (all data) | $R_1$ = 0.0297 | $R_1$ = 0.0245 | $R_1$ = 0.0342 |
| | $wR_2$ = 0.0622 | $wR_2$ = 0.0473 | $wR_2$ = 0.0690 |
| Largest difference peak/hole [e·Å$^{-3}$] | 1.835/–1.124 | 0.999/–0.405 | 1.388/–0.621 |

and Figure 3. CCDC-275720 (**4**), 275721 (**5**), and 275722 (**7**) contain the supplementary crystallographic data for this paper. These data can be obtained free of charge from The Cambridge Crystallographic Data Centre via www.ccdc.cam.ac.uk/data_request/cif.

## Acknowledgments

This work was supported by the Grant from the President of the Russian Federation (Program "Leading Scientific Schools", Projects No. NSh-58.2003.3, 1652.2003.3) and the Russian Fundation of Basic Research (Grant No. 04–03–32093). We gratefully acknowledge Dr. V. K. Cherkasov for recording and interpreting the ESR spectra.

[1] M. N. Bochkarev, *Coord. Chem. Rev.* **2004**, *248*, 835–851 and references cited therein.
[2] a) W. J. Evans, N. T. Allen, J. W. Ziller, *Angew. Chem. Int. Ed.* **2002**, *41*, 359–361; b) W. J. Evans, N. T. Allen, J. W. Ziller, *J. Am. Chem. Soc.* **2001**, *123*, 7927–7928; c) H. Schumann, F. Erbstein, D. F. Karasiak, I. L. Fedushkin, J. Demtschuk, F. Girgsdies, *Z. Anorg. Allg. Chem.* **1999**, *625*, 781–788; d) F. Nief, D. Turcitu, L. Ricard, *Chem. Commun.* **2002**, 1646–1647; e) F. Nief, B. T. de Borms, L. Ricard, D. Carmichael, *Eur. J. Inorg. Chem.* **2005**, 637–643; f) M. N. Bochkarev, I. L. Fedushkin, A. A. Fagin, H. Schumann, J. Demtschuk, *Chem. Commun.* **1997**, 1783–1784.
[3] a) W. J. Evans, G. Zucchi, J. W. Ziller, *J. Am. Chem. Soc.* **2003**, *125*, 10–11.
[4] M. N. Bochkarev, A. A. Fagin, G. V. Khoroshenkov, *Russ. Chem. Bull. (Engl. Transl.)* **2002**, *51*, 1909–1914.
[5] T. V. Balashova, D. M. Kusyaev, Yu. D. Semchikov, M. N. Bochkarev, *Russ. Chem. Bull. (Engl. Transl.)*, in press.
[6] A. A. Fagin, T. V. Balashova, D. M. Kusyaev, T. I. Kulikova, T. A. Glukhova, N. P. Makarenko, Y. A. Kurskii, W. J. Evans, M. N. Bochkarev, *Polyhedron*, in press.
[7] G. N. Connely, in *Comprehensive Organometallic Chemistry. Vanadium*, (Eds.: E. F. Abel, F. G. A. Stone, G. Wilkinson), Pergamon, Oxford, New York, **1982**, vol. 3, p. 783.
[8] Preliminary communication: M. N. Bochkarev, M. E. Burin, V. K. Cherkasov, *Russ. Chem. Bull. (Engl. Trans.)* **2004**, *53*, 481–482.
[9] a) M. N. Bochkarev, I. L. Fedushkin, H. Schumann, J. Loebel, *J. Organomet. Chem.* **1991**, *410*, 321–326; b) M. N. Bochkarev, I. L. Fedushkin, V. K. Cherkasov, V. I. Nevodchikov, H. Schumann, F. H. Görlitz, *Inorg. Chim. Acta* **1992**, *201*, 69–74.
[10] H. Lueken, W. Lamberts, P. Hannibal, *Inorg. Chim. Acta* **1987**, *132*, 111.
[11] M. Yu. Antipin, K. A. Lyssenko, R. Boese, *J. Organomet. Chem.* **1996**, *508*, 259.
[12] B. F. Fieselmann, G. D. Stucky, *J. Organomet. Chem.* **1977**, *137*, 43.
[13] V. A. Umilin, Yu. B. Zverev, I. I. Ermolaev, *Izv. Akad. Nauk SSSR, Ser. Khim.* **1971**, 2726.
[14] R. A. Heintz, R. L. Ostrander, A. L. Rheingold, K. H. Theopold, *J. Am. Chem. Soc.* **1994**, *116*, 11387.
[15] D. B. Morse, T. B. Rauchfuss, S. R. Wilson, *J. Am. Chem. Soc.* **1990**, *112*, 1860.
[16] P. L. Watson, J. F. Whitney, R. L. Harlow, *Inorg. Chem.* **1981**, *20*, 3271.
[17] R. B. King, *Organometallic Synthesis*, Academic Press, New York, **1965**, vol. 1.
[18] E. O. Fisher, R. Jira, *Z. Naturforsch. B* **1953**, *8*, 327.
[19] G. V. Khoroshenkov, A. A. Fagin, M. N. Bochkarev, S. Dechert, H. Schumann, *Russ. Chem. Bull. (Engl. Transl.)* **2003**, *52*, 1715–1719.

 © 2006 Wiley-VCH Verlag GmbH & Co. KGaA, Weinheim 

[20] *SAINTPlus Data Reduction and Correction Program v. 6.01*, BrukerAXS, Madison, Wisconsin, USA, **1998**a.
[21] G. M. Sheldrick, *SADABS v.2.01, Bruker/Siemens Area Detector Absorption Correction Program*, Bruker AXS, Madison, Wisconsin, USA, **1998**a.
[22] G. M. Sheldrick, *SHELXTL v. 5.10, Structure Determination SoftwareSuite*, Bruker AXS, Madison, Wisconsin, USA, **1998**.
Received: June 22, 2005
Published Online: December 1, 2005

 © 2006 Wiley-VCH Verlag GmbH & Co. KGaA, Weinheim 

DOI: 10.1002/ejic.200500640

# Tetra- and Decanuclear Iron(II) Complexes of Thiacalixarene Macrocycles: Synthesis, Structure, Mössbauer Spectroscopy and Magnetic Properties

Cédric Desroches,[a] Guillaume Pilet,[a] Petra Á. Szilágyi,[b] G. Molnár,[b] Serguei A. Borshch,[c] Azzedine Bousseksou,[b] Stéphane Parola,[a] and Dominique Luneau*[a,d]

**Keywords:** Calixarenes / Hydrothermal synthesis / Iron / Magnetic properties / Mössbauer spectroscopy

Two iron(II) complexes, namely $[Fe_4(L)_2]\cdot H_2O$ (**1**) and $[Fe_{10}(L)_4Cl_4]\cdot 2H_2O$ (**2**), have been synthesised under solvothermal conditions by treating *p-tert*-butylthiacalix[4]arene ($LH_4$) with $FeCl_2$ in methanol. Compound **1** crystallises in the orthorhombic system (space group *Immm*) with the unit-cell parameters $a$ = 17.8308(4), $b$ = 19.1372(3), $c$ = 28.8391(6) Å and $V$ = 9840.8(3) Å$^3$ ($Z$ = 2). Compound **2** crystallises in the triclinic system (space group $P\bar{1}$) with the unit-cell parameters $a$ = 13.8036(4), $b$ = 18.8373(4), $c$ = 20.1978(6) Å, $\alpha$ = 65.772(2)°, $\beta$ = 74.120(1)°, $\gamma$ = 71.922(1)° and $V$ = 4487.6(2) Å$^3$ (Z = 1). Compound **1** is a neutral tetranuclear complex and is best described as an iron(II) square sandwiched between two thiacalixarene macrocycles. Each iron centre is six-coordinate in a trigonal-prismatic geometry made up of four phenoxy oxygen atoms plus two sulfur atoms. Compound **2** is a neutral centrosymmetric decanuclear complex and may be viewed as a dimer of double chloro-bridged pentanuclear complexes. Mössbauer spectra of compounds **1** and **2** have been recorded at different temperatures between 80 and 298 K. Each sub-spectrum can be characterised by a quadrupolar doublet corresponding to different iron environments where all iron ions are in high-spin state ($S$ = 2). The hyperfine parameters (quadrupole splitting, isomer shift and line width) as well as the Mössbauer spectra area-ratios are in good agreement with the crystallographic data. The two compounds exhibit magnetic behaviours indicating that antiferromagnetic interactions occur between the iron(II) centres. The simulation of the magnetic susceptibility was done in the case of compound **1** with a single exchange coupling constant ($J$ = –4 cm$^{-1}$ and $g$ = 2.02) between the iron(II) ions [$H = -J(S_1S_2 + S_2S_3 + S_3S_4 + S_1S_4)$].

(© Wiley-VCH Verlag GmbH & Co. KGaA, 69451 Weinheim, Germany, 2006)

## Introduction

As part of our involvement in molecular magnetism[1,2] we are interested in molecular polymetallic species. One of our motivations lies in the so-called single-molecule magnets (SMMs),[3,4] which behave as single-domain magnetic particles. Their relevance as potential components of quantum computing[5] has triggered much of the recent progress in the field of molecular magnetism, as well as in those of the polynuclear complexes.[6] Many polynuclear complexes have been isolated but few exhibit SMM properties, or at temperatures that are too low for applications. Therefore, there is a real need for discovering new systems. Another motivation lies simply in the chemical point of view, where there is a general interest in finding rational routes for synthesising molecular polymetallic species in the frame of the emerging nanosciences. Up to now many clusters have been obtained serendipitously, but as more examples become available we may be expected to find some rules for predetermination.[7] The main difficulty in the formation of molecular polymetallic aggregates is to avoid the polycondensation of the metal ions, which is generally afforded by using multidentate and bulky organic capping ligands.[8]

With this in mind, we have investigated the coordination chemistry of thiacalixarene macrocycles, whose chemistry is well known by some of us.[9–12] Compared to the related calixarenes, the chemistry of thiacalixarenes is recent as the synthesis of thiacalixarenes and their sulfinyl and sulfonyl derivatives has been known only since the late 90's.[13–20] These early reports pointed out the high complexation ability of thiacalixarene macrocycles.[16,17,21,22] This was then proved by the isolation and structural characterisation of complexes of *p-tert*-butylthiacalix[4]arene with $Co^{II}$,[23,24] $Ni^{II}$,[23] $Cu^{II}$,[25] $Zn^{II}$,[24,26] $UO_2$,[27] $Nd^{III}$,[28] and also with the alkali metals.[29] These complexes are either mononu-

[a] Université Claude Bernard Lyon-1, Laboratoire des Multimatériaux et Interfaces (UMR, 5615),
Campus de La Doua, 69622 Villeurbanne Cedex, France
[b] Laboratoire de Chimie de Coordination (UPR CNRS no. 8241),
205, route de Narbonne, 31077 Toulouse Cedex, France
[c] Ecole Normale Supérieure de Lyon, Laboratoire de Chimie (UMR, 5182),
46, allée d'Italie, 69364 Lyon Cedex 07, France
[d] CEA-Grenoble, DRFMC, Service de Chimie Inorganique et Biologique,
17 rue des Martyrs 38054, Grenoble Cedex 09, France
Supporting information for this article is available on the WWW under http://www.eurjic.org or from the author.

 © 2006 Wiley-VCH Verlag GmbH & Co. KgaA, Weinheim 

clear ($UO_2$ and $Zn^{II}$),[26,27] dinuclear ($Co^{II}$ and $Ni^{II}$),[23] trinuclear ($Co^{II}$ and $Zn^{II}$)[24] or tetranuclear ($Cu^{II}$ and $Nd^{III}$).[25,28] Higher nuclearities have even been found for complexes of *p-tert*-butylthiacalix[6]arene,[30,31] with examples of tetranuclear $Ni^{II}$,[30] pentanuclear $Co^{II}$,[30] decanuclear $Cu^{II}$[31] and also some pentanuclear heterometallic[30] $Ni^{II}_4M^{II}$ (M = Mn, Co, Cu) complexes. In a few cases the magnetic properties of these complexes were also reported.[24–26,31] Despite these attractive results, thiacalixarene complexes are still somewhat scarce, which may be attributed to complications when crystallising them following conventional methods.[24] In contrast, we found that, under solvothermal conditions, *p-tert*-butylthiacalix[4]arene and its sulfonyl and sulfinyl derivatives give polynuclear complexes with most d- and f-block transition-metal ions. We recently reported the synthesis, crystal structures and magnetic properties of two tetranuclear manganese(II) complexes that we synthesised under solvothermal conditions in methanol with *p-tert*-butylthiacalix[4]arene and *p-tert*-butylsulfinylthiacalix[4]arene.[32]

In this paper we describe the syntheses, crystal structures and Mössbauer and magnetic properties of a tetranuclear complex $[Fe^{II}_4(L)_2]$ (**1**) and a decanuclear complex $[Fe^{II}_{10}(L)_4Cl_4]$ (**2**), both of which were obtained with *p-tert*-butylthiacalix[4]arene (L).

## Results and Discussion

### Synthesis

Most previously reported thiacalixarene complexes were synthesised and crystallised under conventional conditions, that is in an open vessel and below the boiling point of the solvent.[24–31] Typical solvents are $CHCl_3$ or $CH_2Cl_2$, in which the thiacalixarenes are very soluble,[15] or DMF or DMSO, where they dissolve quickly upon adding a base such as triethylamine. The down side is that the resulting complexes are also generally very soluble in those solvents, which complicates the growth of single crystals. This is generally achieved with help of a second solvent in which the thiacalixarene complexes are not or sparingly soluble, such as $CH_3CN$, EtOH or MeOH. After trials we found that these conditions and solvents did not afford a strong control of the formation of the clusters and their crystallisation. Water or alcohol are generally better solvents as regards the solubility of the metal salts. Unfortunately, under normal conditions the thiacalixarene macrocycles are sparingly soluble in these solvents This caused us to try the solvothermal synthesis method, which is known to be particularly suited for the reaction and crystallisation of materials with poor solubility as it allows high temperatures with a large panel of solvents in a way that generally favour solubilisation.[33,34] The advantage of this method is that not only is it a way to synthesise new compounds but it is also a way to get them in a crystalline form, which is generally not an easy task under normal conditions. During the last decade this method, which has long been restricted to water (hydrothermal), has undergone a real renaissance with the increasing use of non-aqueous solvents and has also proved to be particularly efficient in coordination chemistry for the synthesis of polyoxometallates,[35,36] metal clusters[37–42] or extended compounds.[43–46]

Under standard conditions we were unable to isolate any iron(II) complexes of the thiacalixarene. In contrast, under solvothermal conditions in methanol, as described in the Experimental Section, we were able to synthesise the two iron(II) compounds (**1** and **2**) reported in this paper reproducibly, in good yields and in the form of single crystals. No base was required for the deprotonation of the phenol groups for either complex. In both cases the compounds were obtained by treating $FeCl_2$ with *p-tert*-butylthiacalix[4]arene ($LH_4$). The difference in the synthesis of compounds **1** and **2** lies in the use of a different thiacalixarene/Fe ratio: for ratios from 1:2 up to 1:3 only the tetranuclear complex **1** is obtained, while compound **2** is obtained only when the thiacalixarene/Fe ratio becomes greater than 1:4. Ascorbic acid was used to avoid possible oxidation of the iron(II) ions. This was particularly required for compound **2**, which is better kept under argon. Indeed, when the reaction is carried without ascorbic acid then the isolated crystals always show some dark zones due to some oxidation of the iron(II) ions. When ascorbic acid is used no oxidation occurs, as demonstrated by the Mössbauer spectra. In contrast, compound **1** is insensitive to oxygen and can be handled without any particular care.

### Description of the Crystal Structures

#### *$[Fe^{II}_4(L)_2]\cdot H_2O$ (1)*

The crystal structure of compound **1** comprises two crystallographically independent entities called hereafter M1 and M2 and exemplified for M1 in Figure 1. One water molecule crystallises per $[Fe_4(L)_2]$ entity. A selection of interatomic distances and angles is given in Table 1.

The asymmetric unit of the M1 entity is built from two independent iron(II) ions (Fe1 and Fe2), two *tert*-butylphenoxy groups and two sulfur atoms (S1 and S2). These latter play the role of linker between the *p-tert*-butylphenoxy groups (four in total) to form the thiacalixarene macrocycle. The asymmetric unit of the M2 entity is built from only one crystallographically independent iron(II) ion (Fe3), two independent *p-tert*-butylphenoxy groups and one sulfur atom (S3). As above, these sulfur atoms link the phenoxy groups to form the thiacalix[4]arene macrocycle. Thus, each of the M1 and M2 entities is built from an iron square sandwiched between two *p-tert*-butylthiacalix[4]arene macrocycles. All phenoxy oxygen atoms are doubly bridging. The complex molecules are neutral. A similar molecular structure $[M^{II}_4(L)_2]$ has been reported previously for a tetranuclear copper(II) complex[24] and by us with manganese(II).[32]

In both entities (M1 and M2) the eight phenoxy oxygen atoms lie at the corner of a compressed square-based parallelepiped. The edges of the parallelepiped are nearly orthogonal [89.5(1)° and 90.0° for M1 and M2, respectively]. The

 © 2006 Wiley-VCH Verlag GmbH & Co. KGaA, Weinheim 

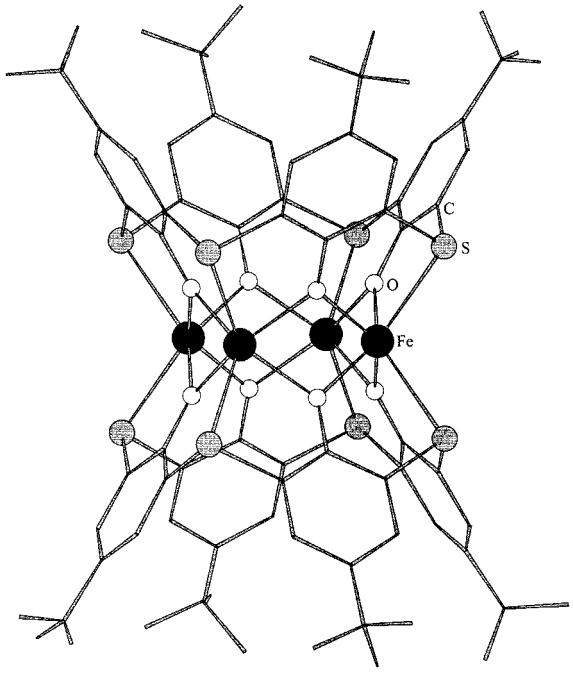


Figure 1. Molecular structure of one $[Fe_4(L)_2]$ tetranuclear iron(II) entity (M1) for compound **1**; Fe: black; S: grey; O: white.

Table 1. Selected interatomic distances [Å] and angles [°] for **1**.[a]

| | | | |
|---|---|---|---|
| Fe1···Fe2 | 3.187(3) | Fe3···Fe3 | 3.192(4) |
| Fe1–O1 | 2.04(1) [×4] | Fe2–O1 | 2.04(1) [×4] |
| Fe3–O2 | 2.03(1) [×2] | Fe3–O3 | 2.04(1) [×2] |
| Fe1–S1 | 2.639(4) [×2] | Fe2–S2 | 2.623(4) [×2] |
| Fe3–S3 | 2.621(3) [×2] | | |
| Fe1–O1–Fe2 | 102.5(6) | Fe3–O2–Fe3 | 103.36(6) |
| Fe3–O3–Fe3 | 103.6(8) | | |

[a] Numbers in square brackets indicate the number of identical bonds due to symmetry.

parallelepiped is capped above and below by the two thiacalixarene macrocycles on the square bases (Figure 1). The iron(II) ions are located in the middle and above each of the four lateral faces of the parallelepiped (Figure 1). The deviations of the iron(II) ions from the $[O_4]$ mean plane made by the four phenoxy oxygen atoms are 0.7511 (Fe1), 0.7617 (Fe2) and 0.8032 Å (Fe3).

Each iron(II) ion exhibits the same six-coordinate $[O_4S_2]$ environment (Figure 2) made by four phenoxy oxygen atoms [Fe1–O1 = 2.04(1), Fe2–O1 = 2.04(1), Fe3–O2 = 2.03(1) and Fe3–O3 = 2.04(1) Å] and two sulfur atoms [Fe1–S1 = 2.639(4), Fe2–S2 = 2.623(4) and Fe3–S3 = 2.621(3) Å]. The Fe–O bond lengths are in agreement with previously reported $Fe^{II}$–O(phenoxy) distances.[47–54] The $Fe^{II}$–S bond lengths are longer than the few previously reported for thioether complexes of high-spin iron(II) (2.20–2.29 Å).[55] This should be due to the rigidity of the macrocycle, which does not allow the sulfur atoms to come closer to the iron(II) ions. Careful analysis of the interatomic distances and angles around the iron(II) ions reveals that the coordination polyhedrons are distorted trigonal-prismatic, as shown in Figure 2. The triangular faces of the trigonal prism are defined by two phenoxy oxygen atoms and one sulfur atom belonging to the same thiacalixarene macrocycle and are equilateral. The trigonal twist angles[56] are zero but the triangular faces are not parallel and make angles of 42.16°(Fe1), 42.35°(Fe2) and 41.44°(Fe3). The four coordination polyhedra are orthogonal to each other (Figure 2). The Fe–O–Fe angles are in the range 102.5(6)–103.6(8)° (Table 1).

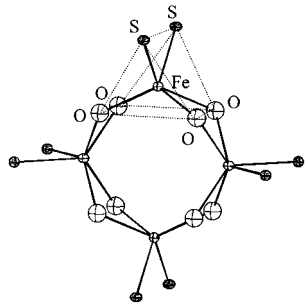


Figure 2. Representation of the iron(II) coordination polyhedra in $[Fe_4(L)_2]$ (**1**); dotted lines indicate the trigonal prism.

In the crystal the $[Fe_4(L)_2]$ entities are packed in infinite molecular chains running parallel to the *b* axis of the unit-cell in such a way that two successive molecules are rotated by 90° with respect to each.

### *$[Fe_{10}(L)_4Cl_4]\cdot 2H_2O$ (2)*

The crystal structure of compound **2** is made up of neutral, centrosymmetrical decanuclear iron(II) moieties which are dimers of two pentanuclear $[Fe^{II}_5\ (L)_2Cl_2]$ units linked by a bis-chloro bridge, as shown in Figure 3. A selection of interatomic distances and angles is given in Table 2.

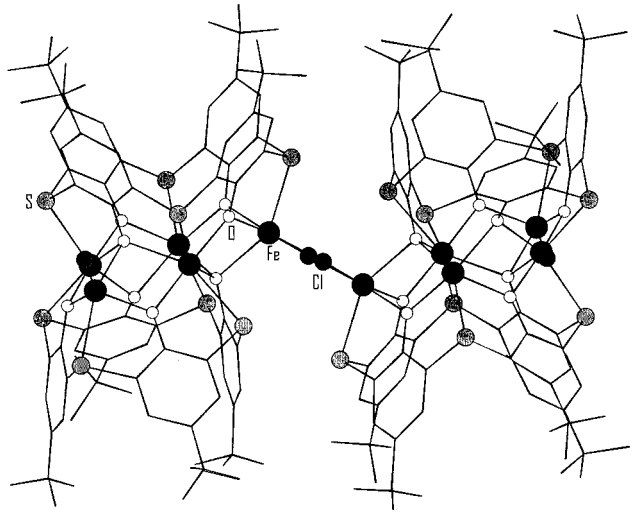


Figure 3. Molecular structure of the $[Fe_{10}(L)_4Cl_4]$ decanuclear iron(II) entities in compound **2**; Fe: black; Cl: dark grey; S: grey; O: white.

Each asymmetric $[Fe^{II}_5\ (L)_2Cl_2]$ unit comprises five iron(II) ions sandwiched between two thiacalixarene macrocycles. The coordination scheme is drastically different from that found for compound **1**, where the two thiacalixarene

 © 2006 Wiley-VCH Verlag GmbH & Co. KGaA, Weinheim 

Table 2. Selected interatomic distances [Å] and angles [°] for **2**.[a]

| | | | |
|---|---|---|---|
| Fe1–O7 | 2.079(7) | Fe1–O8 | 2.087(7) |
| Fe1–O1 | 2.231(6) | Fe2–O4 | 2.005(7) |
| Fe2–O3 | 2.034(7) | Fe2–O5 | 2.287(7) |
| Fe3–O8 | 2.012(7) | Fe3–O4 | 2.045(6) |
| Fe3–O1 | 2.218(7) | Fe3–O5 | 2.230(7) |
| Fe4–O3 | 2.032(6) | Fe4–O6 | 2.058(7) |
| Fe4–O2 | 2.064(7) | Fe4–O5 | 2.202(7) |
| Fe5–O7 | 1.996(7) | Fe5–O6 | 2.009(7) |
| Fe5–O2 | 2.213(7) | Fe5–O1 | 2.223(7) |
| Fe1–S7 | 2.520(3) | Fe2–S4 | 2.492(3) |
| Fe3–S6 | 2.633(3) | Fe3–S3 | 2.648(3) |
| Fe4–S5 | 2.532(3) | Fe4–S1 | 2.688(3) |
| Fe5–S2 | 2.502(3) | Fe5–S8 | 2.782(3) |
| Fe1–Cl2 | 2.409(3) | Fe1–Cl2#1 | 2.442(3) |
| Fe2–Cl1 | 2.225(4) | | |
| Fe1···Fe5 | 3.310(2) | Fe1···Fe3 | 3.353(2) |
| Fe1···Fe1 | 3.488(3) | Fe2···Fe4 | 3.254(2) |
| Fe2···Fe3 | 3.308(2) | Fe3···Fe5 | 3.608(2) |
| Fe3···Fe4 | 3.752(2) | Fe4···Fe5 | 3.258(2) |
| Cl2–Fe1–Cl2#1 | 88.10(1) | Fe1–Cl2–Fe1#1 | 91.9(1) |
| Fe3–O1–Fe5 | 108.7(3) | Fe4–O5–Fe3 | 115.7(3) |
| Fe3–O1–Fe1 | 97.8(3) | Fe4–O5–Fe2 | 92.9(3) |
| Fe5–O1–Fe1 | 96.0(2) | Fe3–O5–Fe2 | 94.2(3) |
| Fe5–O2–Fe4 | 99.2(3) | Fe4–O6–Fe5 | 106.5(3) |
| Fe2–O3–Fe4 | 106.3(3) | Fe1–O7–Fe5 | 108.6(3) |
| Fe3–O4–Fe2 | 109.5(3) | Fe1–O8–Fe3 | 109.8(3) |

[a] Symmetry transformations used to generate equivalent atoms: #1 $-x, -y, -z$.

macrocycles bring eight $\mu_2$-oxygen phenoxy atoms and eight sulfur atoms equally shared between the four iron(II) ions. This is sufficient to provide the charge and coordination number required by the four iron(II) centres with an identical environment. The situation is completely different for compound **2**. As in **1** there are two thiacalixarenes but they have to accommodate five iron(II) ions. The eight sulfur atoms and the eight phenoxy oxygens are not sufficient to fulfil both electro-neutrality and the iron(II) coordination. So in this case this is assumed by two extra chloride ions (Cl1 and Cl2) coordinated to Fe2 and Fe1, respectively, and by $\mu_3$-phenoxy oxygen atoms. What may seem messy at first glance, however, does show some symmetry (Figure 4). Let us consider only the asymmetric $[Fe^{II}_5(L)_2Cl_2]$ unit (Figure 4). Fe1 and Fe2 have practically the same environment of three phenoxy oxygen atoms, one sulfur atom and one chloro ligand. The difference between the two is that in the case of Fe1 the chloride ion is bridging a symmetric Fe1 ion such that Fe1 is six-coordinate with a distorted octahedral polyhedron. In the case of the Fe2 ion, however, the chloro ligand is not bridging and the Fe2 ion is only five-coordinate. It may seem surprising that Cl1 is bridging but Cl2 is not, therefore the structure was checked for possible links to neighbouring iron(II) centres; none was found. The five-coordinate geometry of Fe2 was determined by means of the geometric parameter $\tau = (\beta - \alpha)/60$, where $\beta$ and $\alpha$ are the two largest ligand–metal–ligand bond angles and $\beta > \alpha$.[57] In the case of Fe2 $\beta$ is 149.3(2)° (O5–Fe2–S4 angle) and $\alpha$ is 144.1(2)° (O3–Fe2–Cl1), which gives a $\tau$ parameter of 0.09, in agreement with a square-pyramidal geometry. The Fe4 and Fe5 ions are both six-coordinate to two sulfur atoms, three phenoxy $\mu_2$-oxygen atoms and one phenoxy $\mu_3$-oxygen atom. The Fe3 ion is also six-coordinate but is bound to two sulfur atoms, two $\mu_2$-oxo phenoxy atoms and two $\mu_3$-oxo phenoxy atoms (Figure 4). The six-coordinate geometry around Fe5 and Fe4 is a distorted octahedron. Fe3 is connected through the phenoxy oxygen atoms to the four other iron(II) ions (Fe1, Fe2, Fe4, Fe5). Fe3 and Fe1 and Fe3 and Fe2 are $\mu_2$-O and $\mu_3$-O bridged, respectively, while Fe3 and Fe4 and Fe3 and Fe5 are $\mu_3$-O bridged. Fe1 and Fe5 and Fe2 and Fe4 are $\mu_2$-O and $\mu_3$-O bridged, respectively, while Fe4 and Fe5 are doubly $\mu_2$-O bridged. Fe1 and Fe1# are doubly $\mu_2$-Cl bridged.

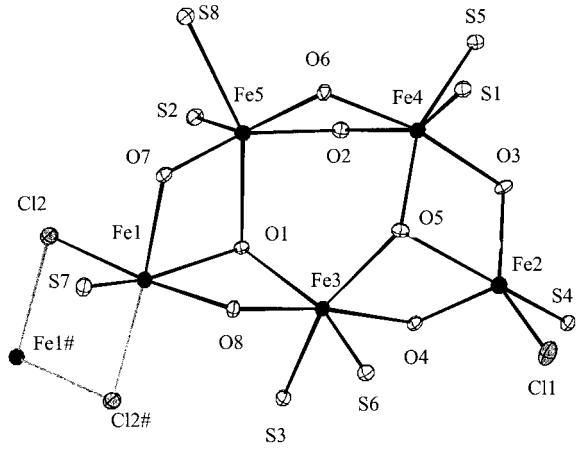


Figure 4. Representation of the coordination environment in compound **2**.

The mean value for the Fe–O($\mu_2$) bond length [2.11(10) Å] in **2** is slightly longer than that for **1** [2.04(1) Å] (Tables 1 and 2). The Fe–O($\mu_3$) bond length [2.202(7)–2.287(7) Å] and Fe–O–Fe bond angles [92.9(3)–115.7(3)°] are in the range of those previously reported.[51]

## Mössbauer Spectroscopy

### *$[Fe^{II}_4(L)_2]\cdot H_2O$ (1)*

Mössbauer spectra of compound **1** recorded at 80 and 293 K are shown in Figure 5. The Mössbauer parameters are given in Table 3. The spectra exhibit one quadrupolar doublet with characteristics of an iron(II) species in a high-spin state ($S = 2$). The four crystallographically slightly different iron centres (identical microenvironments: four oxygen and two sulfur donor atoms) are not distinguishable. The high value of the quadrupole splitting corresponding to a singlet orbital level (2.83 mm s$^{-1}$ at 80 K) can be well explained by the trigonal-prismatic geometry of these sites, which represents a very low symmetry compared to the highest, octahedral one. In addition, the relative independence of the quadrupole splitting with the temperature suggests that the ground state is well isolated.

 © 2006 Wiley-VCH Verlag GmbH & Co. KGaA, Weinheim 

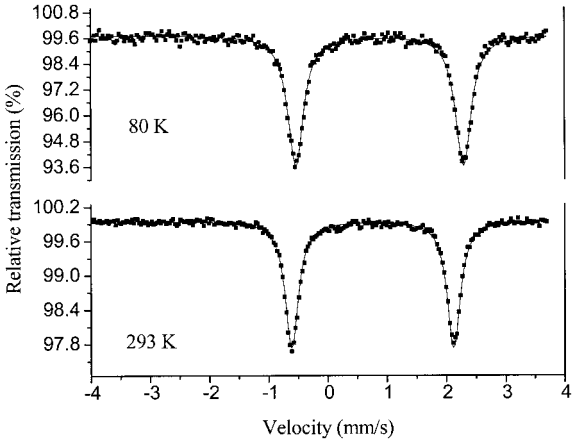


Figure 5. Mössbauer spectra of compound **1** at 80 and 293 K.

Table 3. Mössbauer parameters for compound **1**.

| $T$ [K] | $\delta$[a] [mm s$^{-1}$] | $\Delta$[b] [mm s$^{-1}$] | $\Gamma$[c] [mm s$^{-1}$] |
|---|---|---|---|
| 80 | 0.877(1) | 2.829(3) | 0.321(4) |
| 293 | 0.7568(7) | 2.733(2) | 0.271(2) |

[a] Isomer shift relative to natural iron at room temperature. [b] Quadrupole splitting. [c] Full line width at half maximum.

### *[Fe$_{10}$(L)$_4$Cl$_4$]·2H$_2$O (2)*

Mössbauer spectra of compound **2**, shown in Figure 6, were recorded at 80, 150 and 298 K. The Mössbauer parameters are given in Table 4. The shape of these spectra could indicate some texture effect (asymmetrical spectra). In order to clarify this point, another measurement was carried out at 80 K after thoroughly grinding the sample. The resulting spectrum (not shown) revealed no difference compared to the previous one. The most evident fit of these spectra would be two doublets referring to the sites with five- and sixfold coordination. Possible reasons for this behaviour are as follows: 1) a large difference in their isomer shift, 2) a large difference in their quadrupole splitting, and 3) a quadrupole splitting distribution (if the isomer shifts are the same). However, none of these hypotheses describes the global spectra properly, therefore either the molar ratio of the different sites is not in good agreement with the crystallographic data or the hyperfine parameters cannot be correlated with the X-ray structure. Fitting by three Lorentzian functions was found to describe the spectra reasonably well. The preliminary assumptions for finding the best fits were the following:

the sub-spectrum corresponding to the iron centre with fivefold coordination shows the largest quadrupole splitting;[58]

the molar ratios of the different iron microenvironments Fe1, Fe2 and (Fe3, Fe4, Fe5), as given from the X-ray structure (Figure 4), are 20, 20 and 60%;

the sub-spectrum representing three different iron centres at the same time (Fe3, Fe4 and Fe5; Figure 4) has the largest line-width because of the slight differences between these sites.

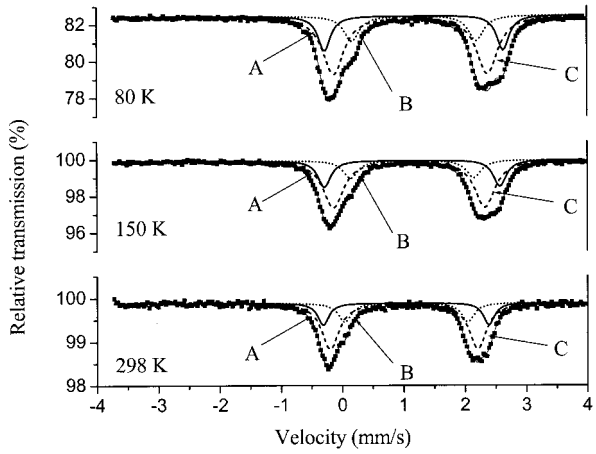


Figure 6. Mössbauer spectra of compound **2** at 80, 150 and 298 K. The sub-spectra A (solid lines), sub-spectra B (dotted lines) and sub-spectra C (dashed lines) hold for the fit of the data as explained in the text.

Table 4. Mössbauer parameters for compound **2** (fixed parameters for the fit are shown in italics).

| $T$ [K] | Fe[a] | $A/A_{tot}$[b] [%] | $\delta$[c] [mm s$^{-1}$] | $\Delta$[d] [mm s$^{-1}$] | $\Gamma$[e] [mm s$^{-1}$] |
|---|---|---|---|---|---|
| | 1 | 18.74(4) | 1.180(2) | 2.02(7) | 0.30(1) |
| 80 | 2 | 21.21 | 1.177(2) | 2.909(4) | 0.247(3) |
| | 3, 4, 5 | 60.05(5) | 1.121(1) | 2.503(5) | 0.419(6) |
| | 1 | 16.69(2) | 1.145(3) | 2.004(8) | 0.29 |
| 150 | 2 | 21.95 | 1.142(2) | 2.856(5) | 0.258(5) |
| | 3, 4, 5 | 61.36(3) | 1.093(1) | 2.466(6) | 0.405(7) |
| | 1 | 19.13 | 1.042(5) | 2.00(1) | 0.26(1) |
| 298 | 2 | 19.13 | 1.038(4) | 2.70(1) | 0.22(1) |
| | 3, 4, 5 | 61.73(1) | 1.004(2) | 2.401(7) | 0.34(1) |

[a] Iron site(s) in compound **2** (see Figure 4). [b] $A/A_{tot}$: Mössbauer spectrum area ratio. [c] Isomer shift relative to natural iron at room temperature. [d] Quadrupole splitting. [e] Full line width at half maximum.

The temperature dependence of the isomer shift of every sub-spectrum representing different iron microenvironments must be linear, following the second-order Doppler shift.[59]

The best fit is displayed in Figure 6. Each doublet represents iron(II) species in a high-spin state ($S$ = 2). Sub-spectra A represent the Fe2 iron centre within a fivefold coordination (Figure 4) because it displays the largest quadrupole splitting, sub-spectra B represent the Fe1 iron centre (Figure 4) with the apparently low molar ratio (Table 4) and sub-spectra C represent the Fe3, Fe4 and Fe5 (Figure 4) iron centres, which have the same neighbouring atoms in the ligand sphere (four oxygen and two sulfur atoms). The Mössbauer parameters of these sub-spectra should be different because of the slight differences in the crystallographic environments, although these are not resolved in the spectra. However, this doublet has a higher line-width than the other doublets (see Table 4). The isomer shift of each doublet is relatively low despite the high electronegativity of the coordinating atoms. This is due to the bridging oxygen atoms, which are coordinated to three (O1, O5) or to two (O2, O3, O4, O6, O7 and O8) different iron centres

 © 2006 Wiley-VCH Verlag GmbH & Co. KGaA, Weinheim 

at the same time, and therefore the donated electron density decreases. The relative independence of the quadrupole splitting with the temperature suggests that the electronic excited states are not populated at 298 K.

### Magnetic Properties

The results are displayed in the form of the product of the magnetic susceptibility and the temperature ($\chi T$) in Figures 7 and 8. For both compounds, all features of the curves were reproducible with different samples and no loss of water occurred during the measurements (see Experimental Section).

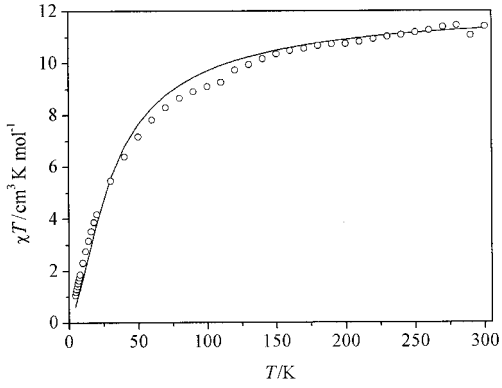


Figure 7. Temperature dependence of the product of the molar magnetic susceptibility ($\chi$) with temperature ($\chi T$) for compound **1** (circles). The solid line shows the best fit of the data.

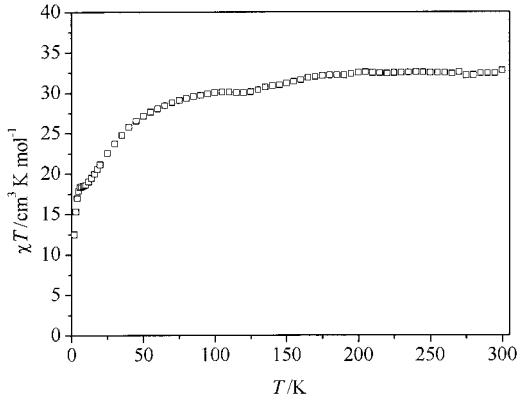


Figure 8. Temperature dependence of the product of the molar magnetic susceptibility ($\chi$) with temperature ($\chi T$) for compound **2** (squares).

### *[$Fe^{II}_4(L)_2$]·$H_2O$ (1)*

At 300 K the $\chi T$ product is 11.4 $cm^3 K mol^{-1}$ for **1** (Figure 7). This value is close to that expected for four uncoupled iron(II) ions (12.0 $cm^3 K mol^{-1}$). Upon cooling the $\chi T$ product decreases continuously down to zero while the magnetic susceptibility ($\chi$) shows a maximum at 5 K. Linearisation of the $1/\chi$ vs. $T$ curve in the range 100–300 K shows Curie–Weiss regimes with a Curie constant, $C$, of 12.9 $cm^3 mol^{-1}$, which is also close to the value expected for four uncoupled iron(II) ions (12.0 $cm^3 K mol^{-1}$). This behaviour indicates that antiferromagnetic interactions occur between the iron(II) ions. Intermolecular interactions can be ruled out because the tetranuclear cores are well separated from each other due to screening by the bulky thiacalixarene ligands. The shortest intermolecular Fe–Fe distances are longer than 16.95(3) Å.

As shown in the structural section, the four iron centres, independently of the entities M1 and M2, have identical environments, which is also in agreement with the Mössbauer study. Moreover, the Fe–O(phenoxy) bond length and the Fe–O–Fe bond angles, which are relevant to magnetic exchange couplings, do not show any striking differences. Accordingly, the magnetic data of compound **1** were analysed by considering one iron(II) square with the four exchange couplings on the edges as equal (i.e. $J = J_{12} = J_{13} = J_{34} = J_{14}$) and no diagonal interactions ($J_{13} = J_{24} = 0$), based on the Heisenberg Hamiltonian $H = -J(S_1S_2 + S_2S_3 + S_3S_4 + S_1S_4)$.

The energy levels of this Hamiltonian can be expressed as $E = -J[S(S + 1) - S_{13}(S_{13} + 1) - S_{24}(S_{24} + 1)]$, where $S$ is the total spin and $S_{13}$ and $S_{24}$ are the intermediate spins. The $S_{13}$ and $S_{24}$ values vary from 0 to 4, and for each pair of intermediate spins the total spin takes values from $|S_{13} - S_{24}|$ to $S_{13} + S_{24}$.

The best least-square fitting of the $\chi T$ vs. $T$ data with the van Vleck equation based on the above energy levels gives a poor fit, with $J = -4\ cm^{-1}$ and $g = 2.02$. However, the value of the exchange coupling is in the range of those previously reported for other $Fe^{II}$–O–$Fe^{II}$ systems.[47,48,60–62] The discrepancy between the fit with the experimental data at low temperatures is due to the fact that no zero-field splitting terms were taken into account. The apparent plateau between 100 and 120 K, which is not accounted for by the calculated curve, cannot yet be explained.

### *[$Fe_{10}(L)_4Cl_4$]·$2H_2O$ (2)*

The $\chi T$ product for this complex is 32.8 $cm^3 K mol^{-1}$. This value is slightly larger than that expected for ten uncoupled iron(II) ions (spin only 30.0 $cm^3 K mol^{-1}$) as is normally observed for high-spin iron(II) complexes. Upon cooling, $\chi T$ decreases slowly while the magnetic susceptibility ($\chi$) increases continuously without any maximum in the temperature range 300–2 K. At 9 K there is a small shoulder on the $\chi T$ curve (with a value of 18.4 $cm^3 K mol^{-1}$), then $\chi T$ decreases rapidly. Linearisation of the $1/\chi$ vs. $T$ curve in the range 100–300 K shows Curie–Weiss regimes with a Curie constant of 34 $cm^3 mol^{-1}$. This behaviour indicates that antiferromagnetic interactions also occur between the iron(II) ions in **2** that are weaker than in compound **1**. One explanation for the shoulder at 9 K is that the magnetic interaction (Fe1···Fe1#) through the bis-chloro bridge is weaker than those within the pentanuclear moieties through the phenoxy and oxo bridges. Therefore, the antiferromagnetic coupling of the $Fe^{II}$ ions within each pentanuclear moiety leads to a non-zero resultant spin, which explains the shoulder; the decrease at lower temperatures is due to the coupling through the bis-chloro bridge. We did not try to fit the magnetic data owing to the large number of mag-

 © 2006 Wiley-VCH Verlag GmbH & Co. KGaA, Weinheim 

netic interactions between the iron(II) centres in **2**. Indeed, the fitting of such a system by matrix-diagonalizing techniques is very complicated due to the high nuclearity of the cluster and its low symmetry. The Monte Carlo technique has previously been used for the magnetic data analysis of a decanuclear iron(III) cluster,[63] but the corresponding Heisenberg Hamiltonian contained only three parameters. In our case we have at least five exchange parameters to take into account and a zero-field splitting parameter must probably also be added.

## Concluding Remarks

The two iron(II) complexes reported here, which were obtained by a solvothermal route, confirm the high coordination ability of the thiacalixarene macrocycles. They are among the very few iron(II) polynuclear complexes of high nuclearities. Indeed, there are less than ten $Fe^{II}_4$ clusters[51,64–68] and, to the best of our knowledge, compound **2** is the first iron(II) decanuclear complex. It should be noted that compound **1** is particularly stable as it appears to be insensitive to oxidation by air. Both compounds exhibit weak Fe···Fe intramolecular antiferromagnetic exchange couplings. We are now engaged in a program to synthesise clusters of higher nuclearities with mixed-valence or different metals.

## Experimental Section

All chemicals and solvents were used as received; all preparations and manipulations were performed under aerobic conditions. The *p-tert*-butylthiacalix[4]arene ligand was synthesised by the published procedures.[13,14]

**Synthesis of $[Fe^{II}_4(L)_2]\cdot H_2O$ (1):** Compound **1** was isolated in the form of pale-yellow, needle-shaped crystals from the reaction of *p-tert*-butylthiacalix[4]arene ($LH_4$; 0.15 g, 0.2 mmol) with $FeCl_2$ (0.050 g, 0.4 mmol), ascorbic acid (0.07 g, 0.4 mmol) and methanol (23 mL) in a 43-mL, Teflon-lined autoclave under autogenous pressure at 170 °C for 3 d. The crystals were isolated by filtration then washed with methanol and dried in vacuo. Compound **1** is stable in air and is insoluble in common organic solvents. Yield: 66%. $C_{80}H_{90}Fe_4O_9S_8$ (1675.5): calcd. C 57.34, H 5.41, Fe 13.33, S 15.32; found C 57.77, H 5.4, Fe 13.05, S 15.6.

**Synthesis of $[Fe_{10}(L)_4Cl_4]\cdot 2H_2O$ (2):** Compound **2** was obtained in the form of pale-yellow, irregular, parallelepiped-shaped crystals from the reaction of *p-tert*-butylthiacalix[4]arene ($LH_4$; 0.15 g, 0.2 mmol) with $FeCl_2$ (0.10 g, 0.8 mmol), ascorbic acid (0.07 g, 0.4 mmol) and methanol (23 mL) in a 43-mL, Teflon-lined autoclave under autogenous pressure at 170 °C for 3 d. The crystals were isolated by filtration then washed with methanol and dried in vacuo. Compound **2** is best kept under argon and was found to be soluble in most common organic solvents ($CHCl_3$, $CH_2Cl_2$, etc.). Yield: 52%. $C_{160}H_{180}Cl_4Fe_{10}O_{18}S_{16}$ (3604.4): C 53.31, H 5.03, Cl 3.93, Fe 15.50, S 14.23; found C 53.03, H 4.87, Cl 4.05, Fe 16.05, S 14.57.

### X-ray Crystallography

**Data Collection:** Experimental details for $[Fe_4(L)_2]\cdot H_2O$ (**1**) and $[Fe_{10}(L)_4Cl_4]\cdot 2H_2O$ (**2**) are given in Table 5. Data processing was performed with the KappaCCD analysis software[69] and the lattice constants were refined by a least-squares refinement using 6303 reflections ($1.0° < \theta < 27.9°$) and 12035 reflections ($1.0° < \theta < 27.5°$) for **1** and **2**, respectively.

**Structure Solution and Refinement:** $[Fe^{II}_4(L)_2]\cdot H_2O$ (**1**) crystallises in the orthorhombic system. According to the observed systematic extinctions, the structure was solved in the *Immm* space group (no. 71). $[Fe^{II}_{10}(L)_4Cl_4]\cdot 2H_2O$ (**2**) crystallises in the triclinic system and the structure was solved in the $P\bar{1}$ space group (no. 2). The unit-cell parameters, crystal system, space group and refinement details for both of them are summarised in Table 5. Both structures were

Table 5. Crystal data and structure-refinement parameters for compounds **1** and **2**.

| | $[Fe^{II}_4(L)_2]\cdot H_2O$ (**1**) | $[Fe_{10}(L)_4Cl_4]\cdot 2H_2O$ (**2**) |
|---|---|---|
| Formula | $C_{80}H_{90}Fe_4O_9S_8$ | $Fe_{10}C_{160}H_{180}Cl_4S_{16}O_{18}$ |
| Fw ($g\,mol^{-1}$) | 1675.5 | 3604.4 |
| $T$ [K] | 293 | 293 |
| $\lambda$(Mo-$K\alpha$) [Å] | 0.71069 | 0.71069 |
| Crystal system | orthorhombic | triclinic |
| Space group | *Immm* (no. 71) | $P\bar{1}$ (no. 2) |
| $a$ [Å] | 17.8308(4) | 13.8036(4) |
| $b$ [Å] | 19.1372(3) | 18.8373(4) |
| $c$ [Å] | 28.8391(6) | 20.1978(6) |
| $\alpha$ [°] | 90 | 65.772(2) |
| $\beta$ [°] | 90 | 74.120(1) |
| $\gamma$ [°] | 90 | 71.922(1) |
| $V$ [Å$^3$] | 9840.8(3) | 4487.6(2) |
| $Z$ | 2 | 1 |
| $D$ [$g\,cm^{-3}$] | 1.130 | 1.320 |
| $\mu$ [$mm^{-1}$] | 0.680 | 1.083 |
| Crystal size [mm] | 0.015×0.015×0.025 | 0.015×0.020×0.060 |
| Reflections collected | 11680 | 26194 |
| Independent reflections | 6353 | 15841 |
| Goodness of fit on F | 1.06 | 1.20 |
| $R$[a] [$I > 3\sigma(I_o)$] | 0.1114 | 0.0578 |
| $R_w$[b] | 0.1206 | 0.0665 |
| Res. electron density [e Å$^{-3}$] | –0.98, 2.24 | –0.66, 1.09 |

[a] $R = \Sigma(|F_o| - |F_c|)/\Sigma|F_o|$. [b] $R_w = \{\Sigma[w(|F_o| - |F_c|)^2]/\Sigma[w|F_o|^2]\}^{1/2}$.

 © 2006 Wiley-VCH Verlag GmbH & Co. KGaA, Weinheim 

solved by direct methods using SIR97[70] in combination with Fourier difference syntheses and then refined against $F$ using reflections with [$I > 3\sigma(I)$] with the CRYSTALS program.[71] Hydrogen atoms were not refined and were placed either theoretically or found in the Fourier difference maps. All the thermal atomic displacements for non-hydrogen atoms and non-oxygen atoms from water molecules were successfully refined anisotropically.
CCDC-278036 (for **1**) and -278037 (for **2**) contain the supplementary crystallographic data for this paper. These data can be obtained free of charge from The Cambridge Crystallographic Data Centre via www.ccdc.cam.ac.uk/data_request/cif.

**Magnetic Measurements:** The magnetic susceptibilities were measured on bulk polycrystalline samples placed in a Teflon-capped basket, in the range 2–300 K, with a Quantum Design MPMS SQUID magnetometer operating at a field strength of 0.5 T. The data were corrected for the sample holder, the diamagnetism of the previously measured thiacalixarene macrocycle and the diamagnetism of other constituent atoms using Pascal's constants. As the compounds described in the paper contain water of crystallisation, which may be lost during the measurements, every sample was weighed before and after measurement and did not show any lost of weight. For both compounds, the magnetic measurements were also performed on several samples from different preparations.

**Mössbauer Spectroscopy:** Mössbauer spectra were recorded using a constant acceleration type spectrometer equipped with a $^{57}$Co source (15 mCi). The spectra of compounds **1** and **2** were recorded at 80 and 293 K and at 80, 150 and 298 K, respectively. Mössbauer isomer shifts are given relative to natural iron at room temperature. Least-squares fitting of the Mössbauer spectra was carried out with the assumption of a Lorentzian line-shape using MossWinn 3.0.[72]

**Supporting Information** (see footnote on the first page of this article): Figure S1. Representation of the two asymmetric moieties (M1 and M2) in compound **1**.

## Acknowledgments

The "Région Rhône-Alpes" is gratefully acknowledged for financial support and a postdoctoral fellowship to C.D. Support for magnetic measurements was provided by the "Commissariat à l'Energie Atomique" (CEA) through a "Laboratoire de Recherche Conventioné" (LRC no. DSM-03-31).

[1] P. Rey, D. Luneau, *NATO ASI Ser., Ser. C* **1999**, *518*, 145–174.
[2] D. Luneau, *Curr. Opin. Solid State Mater. Sci.* **2001**, *5*, 123–129.
[3] G. Christou, D. Gatteschi, D. N. Hendrickson, R. Sessoli, *MRS Bull.* **2000**, *25*, 66.
[4] D. Gatteschi, R. Sessoli, *Angew. Chem. Int. Ed.* **2003**, *42*, 268–297.
[5] M. N. Leuenberger, D. Loss, *Nature* **2001**, *410*, 789–793.
[6] S. K. Ritter, C. E. Washington, *Chem. Eng. News* **2004**, *82*, 29–32.
[7] R. E. P. Winpenny, *J. Chem. Soc., Dalton Trans.* **2002**, 1–10.
[8] K. S. Hagen, *Angew. Chem. Int. Ed. Engl.* **1992**, *31*, 1010–1012.
[9] C. Desroches, V. Kessler, S. Parola, *Tetrahedron Lett.* **2004**, *45*, 6329–6331.
[10] C. Desroches, C. Lopes, V. Kessler, S. Parola, *Dalton Trans.* **2003**, 2085–2092.
[11] C. Desroches, S. Parola, F. Vocanson, M. Perrin, R. Lamartine, J.-M. Letoffe, J. Bouix, *New J. Chem.* **2002**, *26*, 651–655.
[12] S. Parola, C. Desroches, *Collect. Czech. Chem. Commun.* **2004**, *69*, 966–983.
[13] H. Kumagai, M. Hasegawa, S. Miyanari, Y. Sugawa, Y. Sato, T. Hori, S. Ueda, H. Kamiyama, S. Miyano, *Tetrahedron Lett.* **1997**, *38*, 3971–3972.
[14] T. Sone, Y. Ohba, K. Moriya, H. Kumada, K. Ito, *Tetrahedron* **1997**, *53*, 10689–10698.
[15] N. Iki, C. Kabuto, T. Fukushima, H. Kumagai, H. Takeya, S. Miyanari, T. Miyashi, S. Miyano, *Tetrahedron* **2000**, *56*, 1437–1443.
[16] N. Iki, N. Morohashi, T. Suzuki, S. Ogawa, M. Aono, C. Kabuto, H. Kumagai, H. Takeya, S. Miyanari, S. Miyano, *Tetrahedron Lett.* **2000**, *41*, 2587–2590.
[17] N. Morohashi, N. Iki, A. Sugawara, S. Miyano, *Tetrahedron* **2001**, *57*, 5557–5563.
[18] N. Kon, N. Iki, S. Miyano, *Tetrahedron Lett.* **2002**, *43*, 2231–2234.
[19] N. Kon, N. Iki, Y. Yamane, S. Shirasaki, S. Miyano, *Tetrahedron Lett.* **2004**, *45*, 207–211.
[20] M. W. Hosseini, in *Calixarenes* (Eds.: M. Asfari, V. Böhmer, J. Harrowfield, J. Vicens), Kluwer Academic Publishers, Dordrecht, **2001**.
[21] N. Iki, S. Miyano, *J. Inclusion Phenom. Macrocyclic Chem.* **2001**, *41*, 99–105.
[22] N. Iki, N. Morohashi, F. Narumi, S. Miyano, *Bull. Chem. Soc. Jpn.* **1998**, *71*, 1597–1603.
[23] T. Kajiwara, S. Yokozawa, K. Ito, N. Iki, N. Morohashi, S. Miyano, *Chem. Lett.* **2001**, 6.
[24] A. Bilyk, A. K. Hall, J. M. Harrowfield, M. W. Hosseini, G. Mislin, B. W. Skelton, C. Taylor, A. H. White, *Eur. J. Inorg. Chem.* **2000**, 823–826.
[25] G. Mislin, E. Graf, M. W. Hosseini, A. Bilyk, A. K. Hall, J. M. Harrowfield, B. W. Skelton, A. H. White, *Chem. Commun* **1999**, 373–374.
[26] T. Kajiwara, S. Yokozawa, K. Ito, N. Iki, N. Morohashi, S. Miyano, *Angew. Chem. Int. Ed.* **2002**, *41*, 2076–2078.
[27] Z. Asfari, A. Bilyk, J. W. C. Dunlop, A. K. Hall, J. M. Harrowfield, M. W. Hosseini, B. W. Skelton, A. H. White, *Angew. Chem. Int. Ed.* **2001**, *40*, 721–723.
[28] A. Bilyk, A. K. Hall, J. M. Harrowfield, M. W. Hosseini, B. W. Skelton, A. H. White, *Aust. J. Chem.* **2000**, *53*, 895–898.
[29] A. Bilyk, A. K. Hall, J. M. Harrowfield, M. W. Hosseini, B. W. Skelton, A. H. White, *Inorg. Chem.* **2001**, *40*, 672–686.
[30] T. Kajiwara, R. Shinagawa, K. Ito, N. Kon, N. Iki, S. Miyano, *Bull. Chem. Soc. Jpn.* **2003**, *76*, 2267–2275.
[31] T. Kajiwara, N. Kon, S. Yokozawa, T. Ito, N. Iki, S. Miyano, *J. Am. Chem. Soc.* **2002**, *124*, 11274–11275.
[32] C. Desroches, G. Pilet, S. A. Borshch, S. Parola, D. Luneau, *Inorg. Chem.* **2005**, *44*, 9112–9120.
[33] G. Demazeau, *J. Mater. Chem.* **1999**, *9*, 15–18.
[34] A. Rabenau, *Angew. Chem. Int. Ed. Engl.* **1985**, *24*, 1026–1040.
[35] M. I. Khan, Q. Chen, H. Höpe, S. Parkin, C. J. O'Connor, J. Zubieta, *Inorg. Chem.* **1993**, *32*, 2929–2937.
[36] M. I. Khan, Q. Chen, J. Zubieta, *Inorg. Chem.* **1992**, *31*, 1556–1558.
[37] M. Molinier, D. J. Price, P. T. Wood, A. K. Powell, *J. Chem. Soc., Dalton Trans.* **1997**, 4061–4068.
[38] S. O. H. Gutschke, D. J. Price, A. K. Powell, P. T. Wood, *Angew. Chem. Int. Ed.* **1999**, *38*, 1088–1090.
[39] S. O. H. Gutschke, D. J. Price, A. K. Powell, P. T. Wood, *Inorg. Chem.* **2000**, *39*, 3705–3707.
[40] D. J. Price, A. K. Powell, P. T. Wood, *J. Chem. Soc., Dalton Trans.* **2000**, 3566–3569.
[41] E. J. L. McInnes, C. Anson, A. K. Powell, A. J. Thomson, S. Poussereau, R. Sessoli, *Chem. Commun.* **2001**, 89–90.
[42] D. J. Price, S. Tripp, A. K. Powell, P. T. Wood, *Chem. Eur. J.* **2001**, *7*, 200–208.
[43] D. Hagrman, C. Sangregorio, C. J. O'Connor, *J. Chem. Soc., Dalton Trans.* **1998**, 3707–3709.
[44] L. Pan, S. Kelly, X. Huang, J. Li, *Chem. Commun* **2002**, 2334–2335.

 © 2006 Wiley-VCH Verlag GmbH & Co. KGaA, Weinheim 

[45] R. Stähler, B.-D. Mosel, H. Eckert, W. Bensch, *Angew. Chem. Int. Ed.* **2002**, *41*, 4487–4489.
[46] R.-G. Xiong, S. R. Wilson, *J. Chem. Soc., Dalton Trans.* **1998**, 4089–4090.
[47] C. L. Spiro, S. L. Lambert, T. J. Smith, E. N. Duesler, R. R. Gagné, D. N. Hendrickson, *Inorg. Chem.* **1981**, *20*, 1229–1237.
[48] A. S. Borovik, L. Que, *J. Am. Chem. Soc.* **1988**, *110*, 2345–2347.
[49] A. S. Borovik, M. P. Hendrich, T. R. Holman, E. Münck, V. Papaefthymiou, L. Que, *J. Am. Chem. Soc.* **1990**, *112*, 6031–6038.
[50] R. A. Bartlett, J. J. Ellison, P. P. Power, S. C. Shoner, *Inorg. Chem.* **1991**, *30*, 2888–2894.
[51] S. C. Shoner, P. P. Power, *Inorg. Chem.* **1992**, *31*, 1001–1010.
[52] T. Ogihara, S. Hikichi, M. Akita, Y. Moro-oka, *Inorg. Chem.* **1998**, *37*, 2614–2615.
[53] J.-P. Costes, J. M. Clemente-Juan, F. Dahan, F. Dumestre, J.-P. Tuchagues, *Inorg. Chem.* **2002**, *41*, 2886–2891.
[54] A. K. Boudalis, J. M. Clemente-Juan, F. Dahan, J.-P. Tuchagues, *Inorg. Chem.* **2004**, *42*, 1574–1586.
[55] D. Sellmann, K. P. Peters, F. W. Heinemann, *Eur. J. Inorg. Chem.* **2004**, 581–590.
[56] E. I. Stiefel, G. F. Brown, *Inorg. Chem.* **1972**, *11*, 434–436.
[57] A. W. Addison, T. N. Rao, J. Reedijk, G. C. Verschoor, *J. Chem. Soc., Dalton Trans.* **1984**, 1349–1356.
[58] *Mössbauer Spectroscopy*, McGraw, London, **1973**.
[59] B. D. Josephson, *Phys. Rev. Lett.* **1960**, *4*, 341.
[60] J.-A. R. Hartman, R. L. Rardin, P. Chaudhuri, K. Pohl, K. Wieghart, B. Nuber, J. Weiss, V. Papaefthymiou, R. B. Frankel, S. J. Lippard, *J. Am. Chem. Soc.* **1997**, *109*, 7387–7396.
[61] P. Lainé, A. Gourdon, J.-P. Launay, J.-P. Tuchagues, *Inorg. Chem.* **1995**, *34*, 5150–5155.
[62] L. Tommasi, L. Shechter-Barloy, D. Varech, J.-P. Battioni, B. Donnadieu, M. Verelst, A. Bousseksou, D. Mansuy, J.-P. Tuchagues, *Inorg. Chem.* **1995**, *34*, 1514–1523.
[63] C. Benelli, J. Cano, Y. Journaux, R. Sessoli, G. A. Solan, R. E. P. Winpenny, *Inorg. Chem.* **2001**, *40*, 188–189.
[64] J. M. Clemente-Juan, C. Mackiewicz, M. Verelst, F. Dahan, A. Bousseksou, Y. Sanakis, J.-P. Tuchagues, *Inorg. Chem.* **2002**, *41*, 1478–1491.
[65] F. A. Cotton, L. M. Daniels, L. R. Falvello, J. H. Matonic, C. A. Murillo, X. Wang, H. Zhou, *Inorg. Chim. Acta* **1997**, *266*, 91–102.
[66] F. A. Cotton, L. M. Daniels, G. T. Jordan IV, C. A. Murillo, I. Pascual, *Inorg. Chim. Acta* **2000**, *297*, 6–10.
[67] R. A. Reynolds III, D. Coucouvanis, *Inorg. Chem.* **1998**, *37*, 170–171.
[68] K. L. Taft, A. Caneschi, L. E. Pence, C. D. Delfs, V. Papaefthymiou, S. J. Lippard, *J. Am. Chem. Soc.* **1993**, *115*, 11753–11766.
[69] Nonius, Kappa CCD Program Package: COLLECT, DENZO, SCALEPACK, SORTAV, Nonius B. V., Delft, The Netherlands, **1999**.
[70] G. Cascarano, A. Altomare, C. Giacovazzo, A. Guagliardi, A. G. G. Moliterni, D. Siliqi, M. C. Burla, G. Polidori, M. Camalli, *Acta Crystallogr., Sect. A* **1996**, *52*, C79.
[71] D. J. Watkin, C. K. Prout, J. R. Carruthers, P. W. Betteridge, *CRISTAL Issue 11*, CRISTAL Issue 11, Chemical Crystallography Laboratory, Oxford, UK, **1999**.
[72] Z. Klencsár, E. Kuzmann, A. Vértes, *J. Radioanal. Nucl. Chem.* **1996**, *210*, 105.

Received: July 19, 2005
Published Online: December 9, 2005

 © 2006 Wiley-VCH Verlag GmbH & Co. KGaA, Weinheim 

DOI: 10.1002/ejic.200500645

# Chelate [2-(Iminoethyl)pyridine *N*-oxide]metal Complexes – Synthesis and Structural Comparison with Their Chemically Related 2-(Iminoethyl)pyridine-Derived Systems

**Katrin Nienkemper,[a] Vasily V. Kotov,[a] Gerald Kehr,[a] Gerhard Erker,*[a] and Roland Fröhlich[a]**

**Keywords:** Chelates / Coordination chemistry / N,O ligands / Transition metals

The N,O-chelate ligands 2-(iminoethyl)pyridine *N*-oxide (**2a**) and 2-(iminoethyl)-6-isopropylpyridine *N*-oxide (**2b**) were prepared by conventional synthetic routes, the latter involving a variant of the Reissert–Henze reaction. Treatment of **2a** with $FeCl_2$ resulted in a deoxygenation reaction of the ligand and formation of the salt [bis{2-(iminoethyl)-pyridine}FeCl]$^+$[$FeCl_4$]$^-$ (**18a**). In contrast, the reaction of **2a** with $PdCl_2$ or $CoCl_2$ cleanly furnished the six-membered chelate [κ*N*,*O*-2(iminoethyl)pyridine *N*-oxide]$MCl_2$ complexes (**19a**, M = Pd) or (**20a**, M = Co), respectively, which were both characterised by X-ray diffraction. Treatment of **2b** with [$NiBr_2$(dme)], followed by crystallisation from THF, gave the complex [(κ*N*,*O*-**2b**)$NiBr_2$(THF)] (**21b**), which features a distorted trigonal-bipyramidal coordination geometry of the central metal atom. The reaction of **2a** with [$NiBr_2$(dme)] gave the structurally related complex [(κ*N*,*O*-**2a**)$NiBr_2$(κ*O*-**2a**)] (**21a**). The N,O-chelate Pd complex **19a** was shown to be an active catalyst for the Suzuki coupling reaction. The ligand systems **2a**,**b** and their related 2-(iminoethyl)-pyridines **3a**,**b** and a variety of metal complexes of ligands **3** were also prepared and characterised for comparison by X-ray diffraction.
(© Wiley-VCH Verlag GmbH & Co. KGaA, 69451 Weinheim, Germany, 2006)

## Introduction

Chelating ligand systems are of considerable importance in metal-catalysed organic reactions[1] and in polymerisation catalysis.[2] Among the various chelating ligand types, many salicylaldimine-derived bi- and multidentate ligands have been found to be very useful. The monoanionic bidentate systems **1**, which feature various types of substituent patterns at the central framework, have been employed extensively in homogeneous Ziegler–Natta-type polymerisation catalysis[3–5] as well as in asymmetric organic reactions,[6] and they form the basis of the many salen-type ligands whose metal complexes have found extensive catalytic uses.[7]

The neutral pyridine *N*-oxide aldimines or ketimines **2** (see Scheme 1) are the neutral analogues of the ubiquitous anionic ligand systems **1**. A variety of such examples and their metal complexes have been described so far[8–12] but overall much less is known about these interesting bidentate ligand systems than their phenolic counterparts, especially with a bulky alkyl substituent ($R^1$) in the 6-position. We have therefore prepared several examples of metal complexes of this class of neutral bidentate ligand systems **2** and compared their structural features with those of the related [2-(iminoethyl)pyridine]metal complex systems **3**.

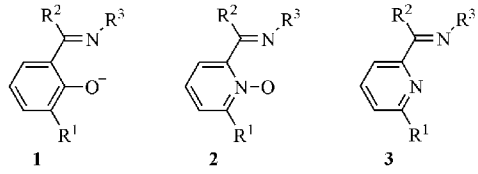


Scheme 1.

## Results and Discussion

### Preparation of the Chelating Ligand Systems

For this study two general lines of acetylpyridine ($R^2$ = $CH_3$) derived ligands were employed, namely the parent systems ($R^1$ = H) and the 6-isopropyl analogue ($R^1$ = *i*Pr). We also briefly investigated the corresponding *tert*-butyl system ($R^1$ = *t*Bu), but encountered some difficulties that will be described below. All the imine systems of this study were derived from 2,6-diisopropylaniline as the coupling component of the Schiff-base synthesis. 2-Acetylpyridine (**4**) was, thus, condensed with 2,6-diisopropylaniline to yield the Schiff-base product **3a** (see Scheme 2).[13] Oxidation of **4** with *m*-chloroperbenzoic acid in chloroform gave the cor-

[a] Organisch-Chemisches Institut der Universität Münster, Corrensstrasse 40, 48149 Münster, Germany
E-mail: erker@uni-muenster.de
Supporting information for this article is available on the WWW under http://www.eurjic.org or from the author.

 © 2006 Wiley-VCH Verlag GmbH & Co. KGaA, Weinheim 

responding 2-acetylpyridine *N*-oxide (**5a**),[14] which was then treated with diisopropylaniline to yield **2a**.

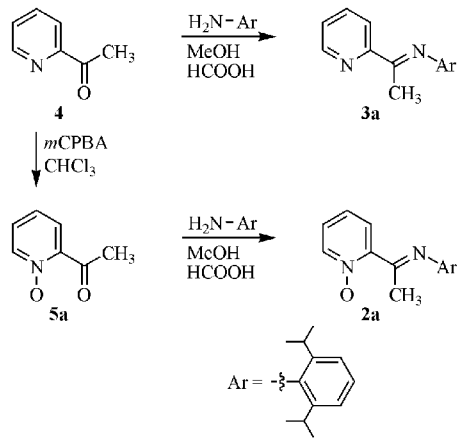


Scheme 2.

The synthesis of the 6-isopropyl and 6-*tert*-butyl derivatives of **2** and **3** started from 2-ethylpyridine (**6**, see Scheme 3). Deprotonation of **6** with *n*-butyllithium at –30 °C followed by treatment with methyl iodide at –50 °C furnished 2-isopropylpyridine (**7b**, 67%).[15] Subsequent α-deprotonation of **7b** was achieved by treatment with the stronger base potassium diisopropylamide (generated in situ from isopropylamine, KO*t*Bu and *n*BuLi) at –50 °C. Quenching with MeI at –75 °C then gave **7c** in 68% yield.[15] The 2-cyano substituent was introduced by a modified Reissert–Henze reaction.[16] For that purpose, compounds **7b** and **7c** were first converted into their respective pyridine *N*-oxides **8b** and **8c** by treatment with *m*-chloroperbenzoic acid in chloroform at 0 °C.[17] The selective CN introduction was achieved by treatment of compounds **8** with $Me_3SiCN$ in the presence of dimethylcarbamoyl chloride in $CH_2Cl_2$ at ambient temperature. Distillation gave the products **9b** (61%) and **9c** (65%) in good yield. The products **9** were then converted into the corresponding 2-acetyl-6-alkyl-pyridines **10b** (25%) and **10c** (36%) by treatment with methyllithium in diethyl ether (–25 °C), followed by aqueous workup and distillation. Subsequent treatment of compounds **10** with 2,6-diisopropylaniline (MeOH, catalysed by formic acid) eventually gave the 6-alkyl-substituted 2-(iminoethyl)pyridine ligands **3b** (R = *i*Pr) and **3c** (R = *t*Bu), respectively.

2-Acetyl-6-isopropylpyridine (**10b**) was converted into the corresponding pyridine *N*-oxide product **11b**. First attempts to achieve the selective oxidation by treatment with *m*-chloroperbenzoic acid were unsuccessful, and stronger oxidation conditions, such as 30% $H_2O_2$ at 80 °C in acetic acid for 20 h, were required to achieve the conversion of **10b** into **11b** (61% isolated). The *tert*-butyl-substituted analogue **10c** even proved inert under these forcing oxidation conditions and could not be converted into the corresponding *N*-oxide under the applied reaction conditions. Eventually, condensation of **11b** with 2,6-diisopropylaniline gave the *N*-aryl-2-(iminoethyl)-6-isopropylpyridine *N*-oxide system **2b**, which was used as a sterically more hindered chelate ligand in this study.

The chelate ligands **3a**, **3b** and **3c** and the pyridine *N*-oxide systems **2a** and **2b** were characterised by X-ray diffraction. Details of **3c** are given in the Supporting Information. The structures of the chelate ligand pairs **3a/2a** and **3b/2b** are depicted for comparison in Figures 1 and 2, respectively.

In the crystal, the ligand system **3a** features a close to planar central (iminoethyl)pyridine framework with an *s-trans* arrangement of the pyridyl and the imino subunits [dihedral angle $\theta 1$ = –177.1(1)° (see Table 1)]. The C7–N9 bond length [1.280(2) Å] is in the typical C=N double bond range,[18] which is (*E*)-configured in **3a**, i.e. the bulky pyridyl and 2,6-diisopropylphenyl substituents are oriented *trans* to each other. The plane of the 2,6-diisopropylphenyl

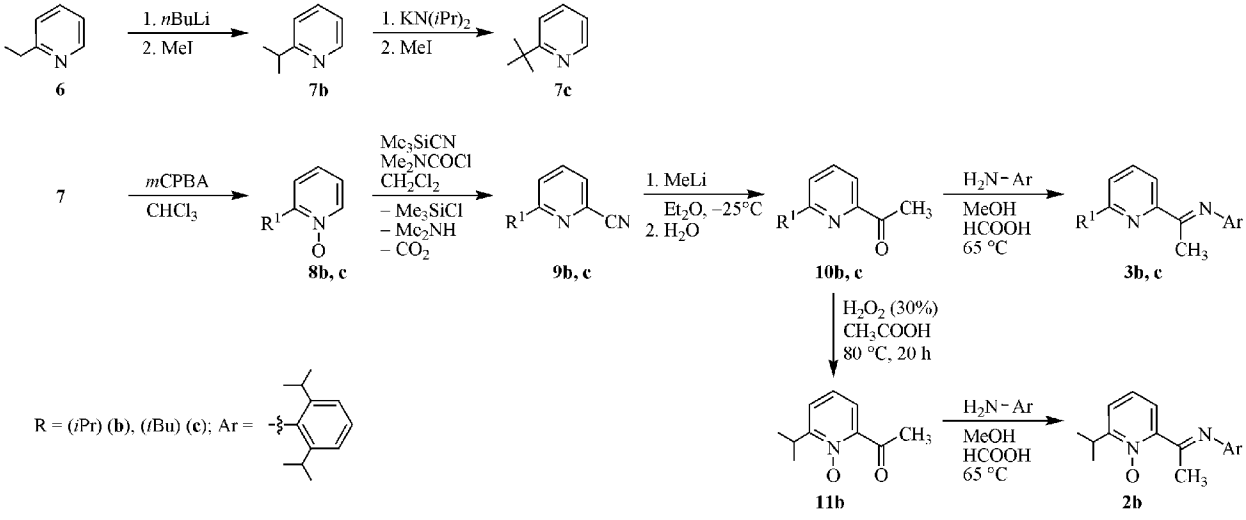


Scheme 3.

 © 2006 Wiley-VCH Verlag GmbH & Co. KGaA, Weinheim 

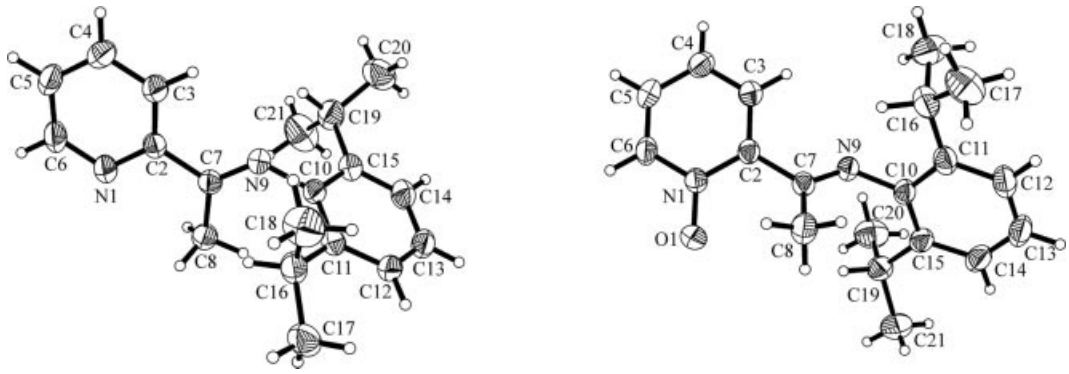


Figure 1. Comparison of the molecular structures of the ligand systems **3a** (left) and **2a** (right).

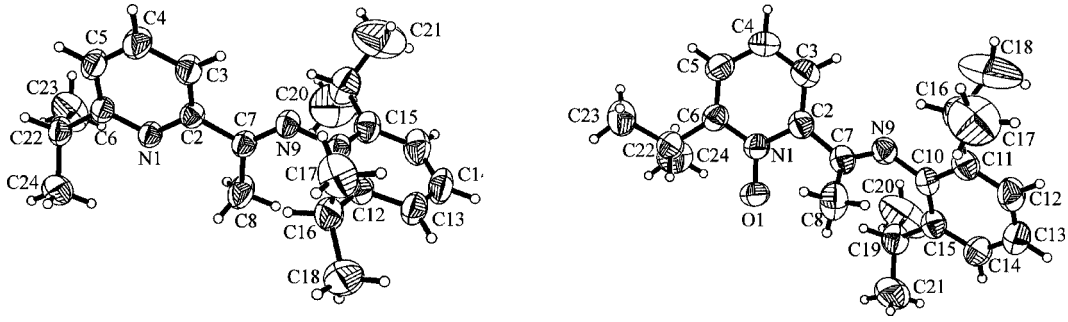


Figure 2. Comparison of the conformational arrangements of the chelating ligand systems **3b** (left) and **2b** (right).

Table 1. Selected structural parameters of the chelate ligands **2** and **3**.[a]

| | **3a** | **2a** | **3b** | **2b**[b] | |
|---|---|---|---|---|---|
| C7–N9 | 1.280(2) | 1.278(2) | 1.274(2) | 1.283(4) | 1.276(4) |
| C2–C7–N9–C10 [$\theta$1] | –177.1(1) | 174.3(1) | –179.0(1) | 177.4(3) | –177.7(2) |
| N1–C2–C7–N9 [$\theta$2] | –177.9(1) | 143.2(1) | 173.0(1) | 133.7(3) | –137.4(3) |
| C7–N9–C10–C15 (C11) [$\theta$3] | 104.0(2) | 93.1(2) | 98.0(2) | 88.1(3) | 97.2(4) |
| | –81.9(2) | –92.5(2) | –88.5(2) | –96.9(3) | –90.0(4) |
| pyridyl vs. aryl plane | 74.2 | 128.8 | 91.0 | 143.1 | 135.6 |

[a] Bond lengths in Å and angles in °. [b] Two independent molecules.

ring is rotated close to normal from the central C=N plane [$\theta$3 = 104.0(2)/–81.9(2)°].

The conformational arrangement of the corresponding *N*-aryl[2-(iminoethyl)]pyridine *N*-oxide system **2a** is related. The attachment of the oxygen atom to the pyridyl nitrogen atom [N1–O = 1.301(1) Å] causes the adjacent imino moiety to rotate away from the central plane by about 140° ($\theta$2, see Table 1 and Figure 1). This conformational arrangement appears to be the best compromise between competing repulsive interactions between the bulky =*N*-aryl group attached at the ($sp^2$) carbonyl carbon atom C7 or its $CH_3$ group, respectively, with the newly introduced N–O functionality. Again, the 2,6-diisopropylphenyl plane is oriented close to normal [$\theta$3 = 93.1(2)/–92.5(2)°] to the C=N plane in **2a**.

In the ligand system **3b** the bulky isopropyl substituent is attached to the pyridyl 6-position. The framework conformation in **3b** is *s-trans* [$\theta$1 = –179.0(1)°; see Table 1]. The central trisubstituted imino C=N double bond [1.274(2) Å] remains (*E*)-configured and the 2,6-diisopropylphenyl plane is close to normal to the C=N plane [$\theta$3 = 98.0(2)/–88.5(2)°; see Table 1].

In the pyridine *N*-oxide derivative **2b** the C=N double bond is again substantially rotated away from planarity. Actually, the observed dihedral angle $\theta$2 in **2b** [averaged absolute value 135.6(3)°] is very close to that observed in **2a** (see above and Table 1). Thus, compound **2b** has almost the same optimal rotational angle around the C2–C7 vector, which probably leads to an optimal compensation of the N–O vs. C7–$CH_3$ and C7–N9(Ar) steric interactions. Again, the 2,6-diisopropylphenyl substituent plane is oriented close to normal to the C=N substituent plane [averaged $\theta$3 = –93.1(4)°; see Table 1].

The ligand systems **2** and **3** seem to adopt similar conformational structures in solution. A perpendicular arrangement between the C=N and 2,6-diisopropylphenyl planes would create an axially prochiral subunit in all these compounds. This would be monitored by the occurrence of pairwise diastereotopic methyl groups of the isopropyl substituents of the *N*-aryl substituent. For **3b**, the *i*$Pr_2C_6H_3$

 © 2006 Wiley-VCH Verlag GmbH & Co. KGaA, Weinheim 

methyl resonances in the $^1$H NMR spectrum are, by chance, isochronous in $CDCl_3$ at ambient temperature, but they split upon cooling of the sample to –65 °C {$^1$H NMR: $\delta$ = 2.74 [sept, 2 H, C*H*$(CH_3)_{2ar}$], 1.12 and 1.10 [each d, 6 H, CH(C*H*$_3)_{2ar}$] ppm; $^{13}$C NMR: $\delta$ = 27.7 [*C*H$(CH_3)_{2ar}$], 23.1, 23.0 [CH(*C*H$_3)_2]_{ar}$ ppm}. The $^1$H NMR resonances of the remaining isopropyl group at C6 of the pyridyl ring occur at $\delta$ = 3.08 [sept, 1 H, C*H*$(CH_3)_{2py}$] and 1.32 [d, 6 H, CH(*C*H$_3)_{2py}$] ppm {$^{13}$C NMR: $\delta$ = 36.2 [*C*H$(CH_3)_{2py}$], 22.7 [CH(*C*H$_3)_{2py}$] ppm}.

The corresponding pyridine *N*-oxide derivative **2b** also shows a single CH(C*H*$_3)_{2py}$ $^1$H NMR resonance even at –60 °C in $CDCl_3$ [$\delta$ = 1.28 (d, 6 H) ppm; $^{13}$C: $\delta$ = 20.5 (25 °C) ppm]. In contrast, the CH$(CH_3)_{2ar}$ methyl groups of **2b** are diastereotopic at room temperature [$^1$H: $\delta$ = 1.23, 1.16 (each d, each 6 H) ppm; $^{13}$C: $\delta$ = 23.5, 22.9 ppm] which indicates that the rotation around the imino =N–C(aryl) vector is "frozen" on the NMR timescale under these conditions and that the *N*-aryl substituent plane is oriented substantially out of the N=C plane in solution, as was observed in this and the related systems in the crystal.

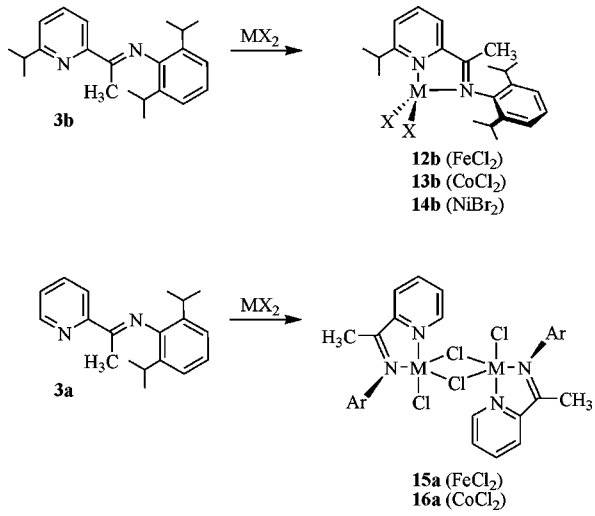


Scheme 4.

## Metal Complex Formation and Structural Characterisation

First, we treated the ligand system **3b** (R = *i*Pr) with $FeCl_2$, $CoCl_2$, and $NiBr_2$(dme). In clean reactions the corresponding 1:1 chelate complexes [(**3b**)$MX_2$] were obtained in high yields. Single crystals were obtained from all the three complexes **12b** [(**3b**)$FeCl_2$], **13b** [(**3b**)$CoCl_2$] and **14b** [(**3b**)$NiBr_2$], and their molecular structures in the solid state determined (see Table 2 and Scheme 4). Since the three compounds are structurally analogous, we will briefly describe only the nickel system **14b** (see Figure 3 for the structure). The structural data of **12b**, **13b** and **14b** are listed in Table 2. For additional information see the Supporting Information.

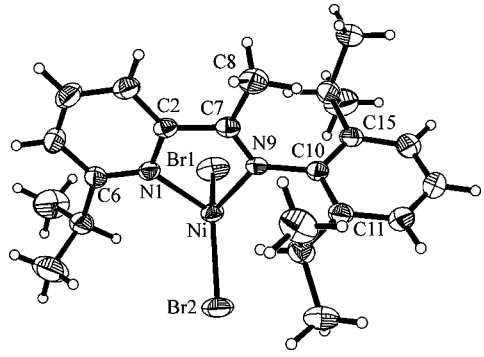


Figure 3. Molecular structure of the nickel chelate complex **14b**.

In complex **14b** the ligand system adopts a *cisoid* conformation [$\theta$(N1–C2–C7–N9) = 2.8(3)°] that allows both the nitrogen centres N1 and N9 to coordinate to the nickel atom. The C7–N9 bond length in the ligand system is not affected by the coordination and retains its value of

Table 2. Selected structural data of the [2-(iminoethyl)pyridine]metal complexes **12**–**16**.[a]

| | **12b** (Fe)[b] | **13b** (Co)[b] | **14b** (Ni)[c] | **15a** (Fe)[b] | **16a** (Co)[b] |
|---|---|---|---|---|---|
| C2–C7 | 1.497(5) | 1.484(5) | 1.474(4) | 1.483(11) | 1.482(2) |
| C7–N9 | 1.271(5) | 1.288(4) | 1.286(3) | 1.294(10) | 1.290(2) |
| M–N1 | 2.108(3) | 2.034(3) | 1.994(2) | 2.126(7) | 2.093(1) |
| M–N9 | 2.111(3) | 2.044(3) | 1.995(2) | 2.201(6) | 2.123(1) |
| M–Hal1 | 2.209(1) | 2.200(1) | 2.3577(5) | 2.385(2) | 2.3419(5) |
| M–Hal2 | 2.223(1) | 2.209(1) | 2.3169(5) | 2.278(3) | 2.2878(6) |
| M–Hal1* | – | – | – | 2.484(2) | 2.4589(5) |
| N1–M–N2 | 77.3(1) | 81.1(1) | 81.7(1) | 74.8(2) | 76.64(5) |
| Hal1–M–Hal2 | 118.68(5) | 113.78(5) | 123.64(2) | 105.3(1) | 103.42(2) |
| Hal1–M–Hal1* | – | – | – | 84.9(1) | 86.01(2) |
| C2–C7–N9–C10 | –179.0(3) | –178.6(3) | –178.0(2) | –175.4(7) | 175.2(1) |
| C7–N9–C10–C11 (C15) | –89.1(5) | –89.7(5) | 97.7(3) | –89.0(9) | 89.8(2) |
| | 94.3(5) | 94.5(4) | –84.0(3) | 90.3(9) | –88.8(2) |
| pyridyl vs. aryl plane | 93.1 | 85.9 | 99.7 | 98.6 | 97.9 |

[a] Bond lengths in Å; angles and dihedral angles in °. [b] Hal = Cl. [c] Hal = Br.

 © 2006 Wiley-VCH Verlag GmbH & Co. KGaA, Weinheim 

1.286(3) Å. The metal–nitrogen bond lengths amount to 1.994(2) Å (Ni–N1) and 1.995(2) Å (Ni–N9). In complex **14b** the nickel atom has a pseudo-tetrahedral coordination geometry with a small N1–Ni–N9 angle of 81.7(1)° inside the five-membered chelate ring and, consequently, a much larger complementary Br1–Ni–Br2 angle of 123.64(2) Å. Again, an (*E*)-trisubstituted C=N unit is found and the 2,6-diisopropylphenyl substituent at the imine nitrogen atom is rotated close to perpendicular to the plane of the central (iminoethyl)pyridine moiety (angle between the planes: 99.7°).

The less bulky parent ligand system **3a** also reacts readily with the metal dihalides $FeCl_2$ or $CoCl_2$. In both cases we were able to obtain single crystals and characterise the structures of the products (**15a** and **16a**, respectively) by X-ray diffraction. The coordination of the *cisoid* chelate ligand in **15a** and **16a** (see Scheme 4) is very similar to that in **12b** and **13b** (see Table 2). However, use of the less bulky ligand **3a** results in the formation of a chloro-bridged dimer.[19] In both **15a** and **16a** the coordination geometry of the central metal atom can best be described as distorted trigonal-bipyramidal with two equivalent half molecules in an overall $C_2$-symmetric framework. The pyridyl nitrogen atom (N1) and Cl1 mark the apical centres of the distorted trigonal bipyramid {**15a**: N1–Fe–Cl1 = 155.6(2)° [163.77(4)°]; the value in brackets is the corresponding value of the isostructural cobalt complex **16a**}. The angles between the three equatorial ligands amount to 126.0(2)° (N9–Fe–Cl1*) [122.86(4)°], 116.7(2)° (N9–Fe–Cl2) [114.03(4)°] and 115.5(1) (Cl1*–Fe–Cl2) [119.79(2)°], which amounts to a sum of the three bonding angles of 358.2° in the iron complex **15a** [356.68° in the cobalt complex **16a**]. Most angles between the apical and basal ligands are rather close to the expected value of 90° [Fe complex **15a**: between 84.1(2)° and 99.1(2)°; Co complex **16a**: between 83.18(4)° and 99.41(4)°] with the exception of the smaller chelate nitrogen angle [N1–Fe–N9 = 74.8(2)°; N1–Co–N9 = 76.64(5)°] and the correspondingly enlarged angle between the bridging halide ligands [Cl1–Fe–Cl2 = 105.3(1)°; Cl1–Co–Cl2 = 103.42(2)°]. The structure of the dimeric (chelate ligand) $FeCl_2$ complex **15a** is depicted in Figure 4 (for further details of the isostructural cobalt system **16a** see the Supporting Information).

The reaction of **3a** with [$NiBr_2$(dme)] in dichloromethane at room temperature takes a slightly different course. We isolated the 2:1 reaction product **17a** (see Scheme 5) of the composition $[(\mathbf{3a})_2NiBr]^+Br^-$ as a green-yellow solid.[20] The general trigonal-bipyramidal structural type of **17a** with the pyridyl nitrogen atoms was determined by X-ray diffraction but the quality of the X-ray crystal structure analysis of **17a** was too poor to allow for any detailed discussion.

Let us now turn to the reactions of the chelate pyridine *N*-oxide ligands with the metal halides. The reaction of **2a** with $FeCl_2$ did not give an (iminoethyl)pyridine *N*-oxide complex as one might have expected. Instead, it turned out that the *N*-oxide is reduced by part of the iron. Crystallisation of the crude reaction product furnished single crystals of the $Fe^{II}/Fe^{III}$ salt of the deoxygenated (iminoethyl)pyridine ligand $[(\mathbf{3a})_2FeCl]^+[FeCl_4]^-$ (**18a**; see Scheme 6 and Figure 5). The X-ray crystal structure analysis of **18a**, although of a rather poor quality, shows a distorted trigonal-bipyramidal coordination geometry around the $Fe^{II}$ centre in the cation (the $Fe^{III}$ centre in the $[FeCl_4]^-$ ion is tetrahedrally coordinated) with the pyridine nitrogen atoms oriented *trans* to each other at the apical positions [N1A–Fe1–N1B = 159.5(3)°] and a sum of the basal ligand angles [Cl1–Fe1–N9A = 117.2(2)°; Cl1–Fe–N9B = 117.8(2)°; N9A–Fe–N9B = 124.9(3)°] of 359.9°.

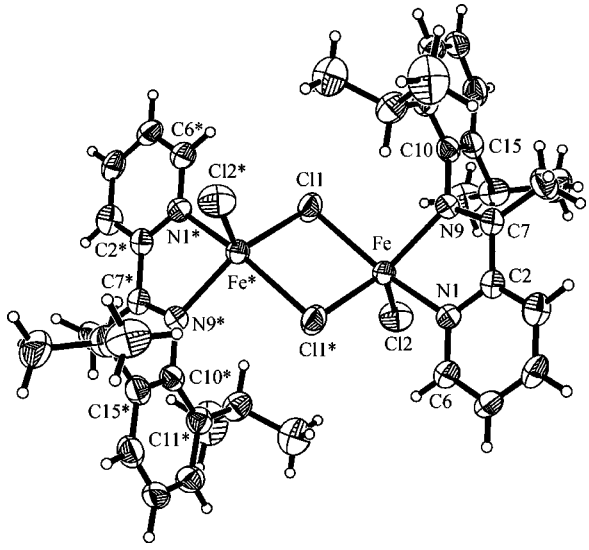


Figure 4. View of the molecular structure of the dimeric iron complex **15a**.

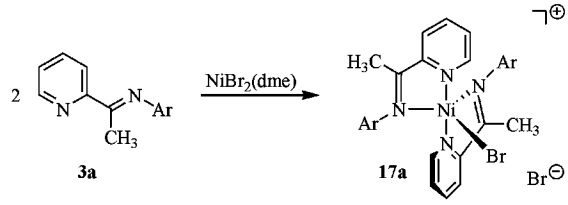


Scheme 5.

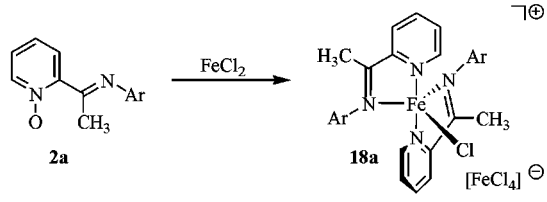


Scheme 6.

The reaction of the N,O-chelate ligand **2a** with $PdCl_2$ gave complex **19a** (see Scheme 7), which was isolated as a yellow solid in 75% yield. The X-ray crystal-structure analysis showed a six-membered chelate structure where both the pyridine *N*-oxide oxygen atom and the imino nitrogen atom are coordinated to the palladium atom [Pd–O1 = 2.029(1) Å; N9–Pd = 2.035(2) Å]. In complex **19a** both the N–O [1.343(2) Å] and the C7–N9 [1.284(2) Å] bond lengths are almost unchanged relative to the free ligand (see

 © 2006 Wiley-VCH Verlag GmbH & Co. KGaA, Weinheim 

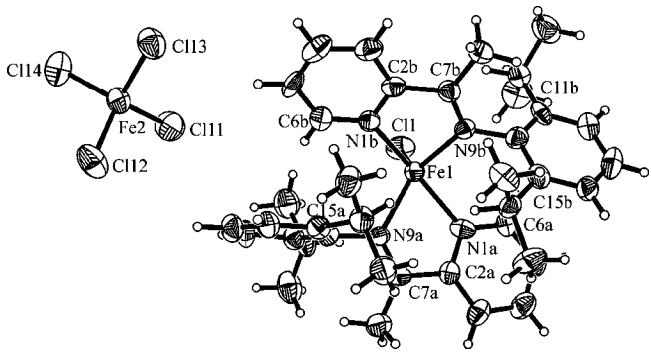


Figure 5. Molecular structure of the salt $[(\mathbf{3a})_2FeCl]^+[FeCl_4]^-$ (**18a**).

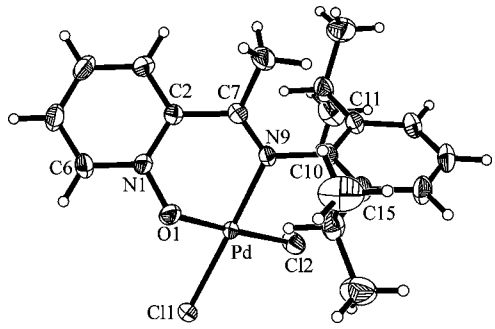


Figure 6. Molecular structure of palladium complex **19a**.

Table 3 and Table 1). The palladium atom in complex **19a** features a square-planar coordination geometry with Pd–Cl bond lengths of 2.2945(5) Å (Cl1) and 2.2678(5) Å (Cl2). The bond angles at Pd amount to 91.52(2)° (Cl1–Pd–Cl2), 90.46(4)° (Cl1–Pd–O1), 84.92(6)° (O1–Pd–N9) and 93.12(4)° (N9–Pd–Cl2) (sum of bonding angles at Pd: 360.02°). In contrast to the free ligand **2a**, the chelate core of complex **19a** is markedly rotated away from planarity, with central dihedral angles of 40.7(3)° (N9–C7–C2–N1) and –1.5(3)° (C7–C2–N1–O1). The six-membered core of complex **19a** features a twist-boat-like conformation (see Figure 6), and the 2,6-diisopropylphenyl substituent at the imine nitrogen centre N9 is rotated almost as far out of the adjacent imine C=N plane as in the free ligand **2a** [C7–N9–C10–C11 = –77.3(2)° in **19a** and –92.5(2)° in **2a**].

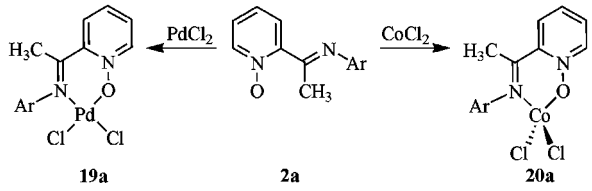


Scheme 7.

Complex **19a** is one of the few diamagnetic chelate systems obtained in this study, and could thus be characterised by NMR spectroscopy. Its most prominent feature is the observation of pair-wise diastereotopic methyl groups of the 2,6-diisopropylphenyl substituent at the C=N nitrogen atom [$^1$H NMR: $\delta$ = 1.59, 1.19 (each d, each 6 H) ppm; $^{13}$C: $\delta$ = 24.9, 23.8 ppm].

The [2-(*N*-aryliminoethyl)pyridine *N*-oxide]cobalt complex **20a** was obtained from the reaction of **2a** with $CoCl_2$ (see Scheme 7). The X-ray crystal structure analysis of **20a** features a pseudo-tetrahedral coordination geometry of the central transition metal atom. The intact chelate ligand is again N,O-coordinated, with the 2,6-diisopropylphenyl substituent oriented close to normal to the C=N plane (see Table 3 and Figure 7). The complex framework also features a twist-boat-type six-membered ring conformation with dihedral angles of –22.6(4)° (N1–C2–C7–N9) and 2.2(4)° (C7–C2–N1–O1).

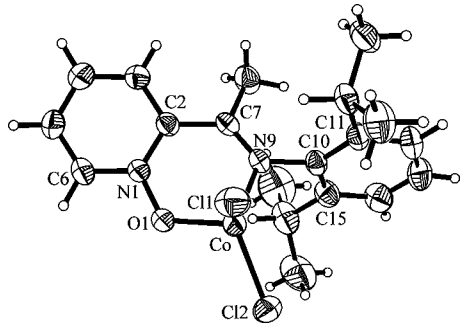


Figure 7. View of the molecular structure of the cobalt complex **20a**.

The reaction of the N,O-chelate ligand **2b** with $[NiBr_2(dme)]$ takes a different course. Again, a 1:1 addition product (**21b**, see Scheme 8) was obtained. Single crystals

Table 3. Selected structural data of the metal complexes **19**–**23**.[a]

| | **19a** (Pd) | **20a** (Co) | **21b** (Ni) | **21a** (Ni) | | **22a** (Zn) | | **23a** (Cu) |
|---|---|---|---|---|---|---|---|---|
| C2–C7 | 1.489(3) | 1.496(4) | 1.486(4) | 1.485(5) | 1.491(5)[b] | 1.499(6) | 1.500(6) | 1.490(4) |
| C7–N9 | 1.284(2) | 1.291(4) | 1.285(4) | 1.284(4) | 1.272(4)[b] | 1.282(5) | 1.285(6) | 1.281(4) |
| N1–O1 | 1.343(2) | 1.340(3) | 1.336(3) | 1.332(4) | 1.337(3)[b] | 1.340(5) | 1.332(5) | 1.340(3) |
| N9–M | 2.035(2) | 2.020(2) | 2.041(3) | 2.073(3) | – | 2.072(4) | 2.076(4) | 1.985(2) |
| O1–M | 2.029(1) | 1.957(2) | 2.005(2) | 2.049(2) | 2.055(2)[b] | 1.976(3) | 2.005(3) | 1.919(2) |
| C7–N9–M | 121.8(1) | 123.7(2) | 123.6(2) | 123.8(2) | – | 121.6(3) | 121.6(3) | 123.2(2) |
| N9–M–O1 | 84.92(6) | 87.84(9) | 82.9(1) | 81.7(1) | – | 84.3(1) | 83.7(1) | 87.07(9) |
| M–O1–N1 | 109.9(1) | 118.2(2) | 113.8(2) | 113.6(2) | – | 113.0(3) | 113.2(3) | 115.4(2) |
| C2–C7–N9–C10 | 175.9(2) | 174.4(2) | –175.3(3) | –179.3(4) | –176.6(3)[b] | –174.1(4) | 174.2(4) | –179.8(3) |
| C2–N1–O1–M | –54.9(2) | 40.8(4) | 57.6(3) | 53.5(4) | – | –52.3(5) | 50.4(5) | 49.0(3) |
| N1–C2–C7–N9 | 40.7(3) | –22.6(4) | –32.0(4) | –32.4(6) | –126.8(4)[b] | 26.8(7) | –26.9(7) | –29.7(4) |

[a] Bond lengths in Å and angles and dihedral angles in °. [b] κO-coordinated ligand **2a**.

 © 2006 Wiley-VCH Verlag GmbH & Co. KGaA, Weinheim 

were obtained from THF solution. In **21b** (see Figure 8) the (iminoethyl)pyridine *N*-oxide ligand coordinates to the nickel atom through both the oxygen atom and the imino nitrogen atom to form a favoured six-membered chelate ring. The ring conformation is twisted, with the core atoms N1–C2–C7–N9 deviating from coplanarity by about –32° (see Table 3). The corresponding dihedral angles amount to 57.6(3)° (C2–N1–O1–Ni), 5.9(4)° (C2–C7–N9–Ni), 31.8(2)° (C7–N9–Ni–O1) and –62.2(2)° (N1–O1–Ni–N9). The N1–O1 bond length in complex **21b** is 1.336(3) Å, which is similar to that found in the free ligand **2b**. The nickel atom in complex **21b** features a distorted trigonal-bipyramidal coordination geometry, with the pyridine *N*-oxide oxygen atom O1 [Ni–O1 = 2.005(2) Å] and the oxygen atom of a coordinated THF ligand [Ni–O25 = 2.160(2) Å] being at the apical positions [O1–Ni–O25 = 174.1(1)]. The imino-nitrogen atom N9 [Ni–N9 = 2.041(3) Å] and the pair of bromide ions [Ni–Br1 = 2.4407(6) Å; Ni–Br2 = 2.4173(6) Å] are oriented in the central plane [N9–Ni–Br1 = 96.17(7)°; N9–Ni–Br2 = 126.67(8)°; Br1–Ni–Br2 = 136.84(3)°]. The 2,6-diisopropylphenyl substituent at N2 is rotated almost normal to the C=N imine plane [C7–N9–C10–C11 = –94.3(4)°] as is the bulky $CHMe_2$ group at the α-position of the pyridine *N*-oxide ring.

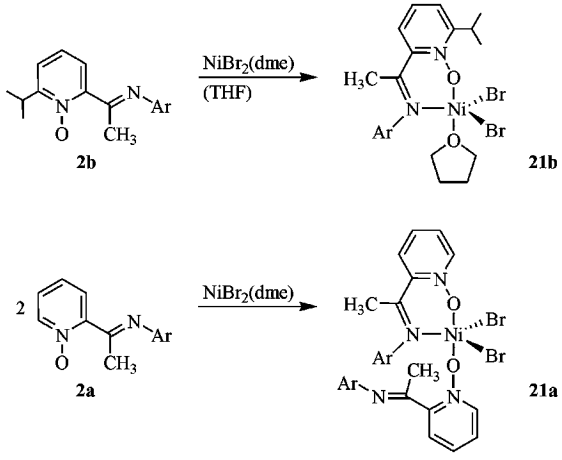


Scheme 8.

The reaction of the less bulky chelate pyridine *N*-oxide ligand **2a** with [$NiBr_2$(dme)] takes a similar course, except that a 2:1 adduct (**21a**, see Scheme 8 and Figure 9) was obtained after recrystallisation. The X-ray crystal-structure analysis of **21a** revealed the presence of a six-membered chelate ring that is very similar to the corresponding substructural unit in **21b** (see above and Table 3), but instead of the THF solvent the nickel atom in **21a** has picked up a second (iminoethyl)pyridine *N*-oxide ligand (**2a**) and is coordinated to it only through the N–O oxygen atom (κO) to complete its distorted trigonal-bipyramidal coordination sphere [Ni–O1a = 2.055(2) Å; N1a–O1a–Ni = 123.2(2)°]. The κO-coordinated ligand **2a** in **21a** features a conformation that is similar to that of the free ligand [N1a–C2a–C7a–N9a = –126.8(4)°].

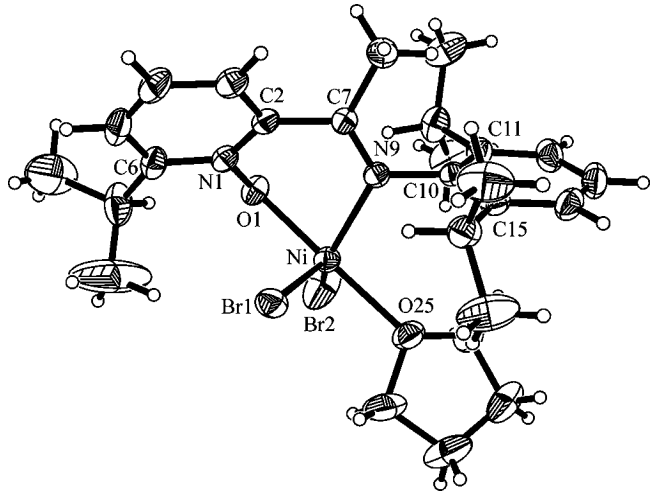


Figure 8. Molecular geometry of the nickel(II) complex **21b**.

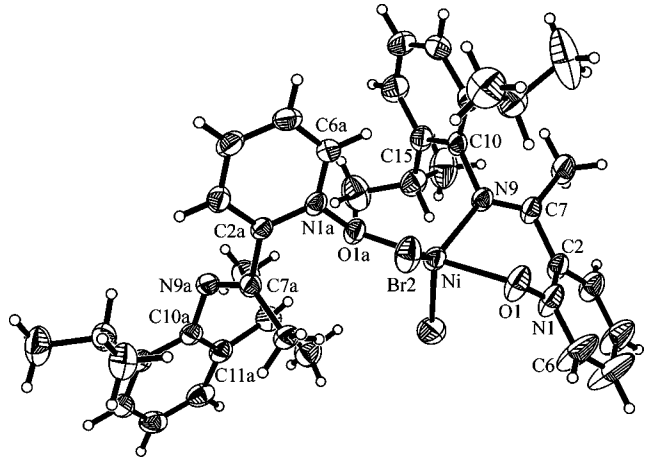


Figure 9. View of the molecular structure of complex **21a**.

In addition to the metal complexes described above, we also prepared a zinc and a copper complex of the unsubstituted N,O-ligand **2a** (see Scheme 9).

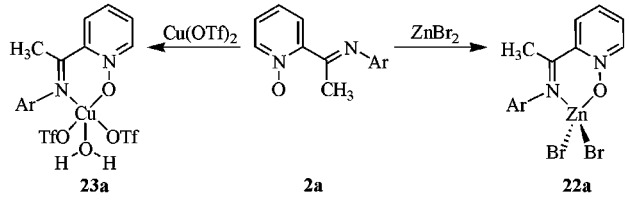


Scheme 9.

The reaction of ligand **2a** with $ZnBr_2$ in acetonitrile at room temperature yielded a bright yellow solid (**22a**). The molecular structure is depicted in Figure 10 and shows a monomeric complex with a four-coordinate zinc atom. The geometry around the metal centre can be described as distorted tetrahedral with an N9–Zn–O1 angle of 84.3(1)° and a Br1–Zn–Br2 angle of 121.60(4)°. Again, the six-membered metallacycle features a twist-boat-type conformation [dihedral angles C2–N1–O1–M = –52.3(5)° and N1–C2–C7–N9 = 26.8(7)°; all values for molecule A].

 © 2006 Wiley-VCH Verlag GmbH & Co. KGaA, Weinheim 

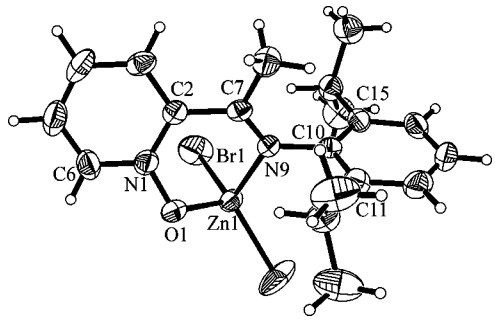


Figure 10. View of the molecular structure of complex **22a**.

Compound **23a** was obtained from the reaction of Cu(OTf)$_2$ with **2a** in dichloromethane (see Figure 11). In this case the metal centre is five-coordinate. The geometry can be regarded as distorted square-pyramidal, with the nitrogen atom of the imino bridge, the pyridine *N*-oxide oxygen atom, the oxygen atom of one triflate group and the oxygen atom of an additional water molecule as the four basal atoms [O2–Cu–N9 = 167.5(1)°; O1–Cu–O6 = 168.1(1)°]. The oxygen atom of the second triflate group occupies the axial coordination site.

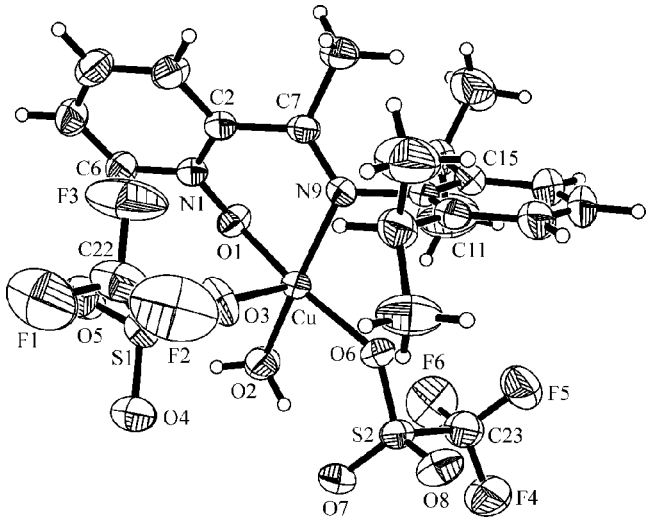


Figure 11. View of the molecular structure of complex **23a**.

We have only begun to investigate the chemistry of the (iminoethyl)pyridine *N*-oxide chelate metal complexes. In a first experiment, the (N,O-chelate)PdCl$_2$ system **19a** was employed as a catalyst in the Suzuki coupling reaction of bromobenzene with phenylboronic acid to yield biphenyl. With 3 mol-% of **19a** in the presence of the base $K_2CO_3$ (toluene, 80 °C, 8 h) a practically quantitative yield of the Ph-Ph coupling product was obtained, which is superior to the reaction catalysed by PdCl$_2$ alone in the absence of a supporting ligand, which gives only a 62% yield of biphenyl under these general reaction conditions. This makes it probably worthwhile to explore the catalytic potential of the [(iminoalkyl)pyridine *N*-oxide]metal complexes described in this article and related systems.

## Conclusion

We have shown that pyridine *N*-oxide systems can readily be obtained in a straightforward synthetic way. The systems **2a** and **2b** in many cases serve as rather stable chelate ligands, cleanly forming the respective κN,O-coordinated complexes with a variety of metal systems. Only in an exceptional case did we observe a redox reaction that resulted in loss of the pyridine *N*-oxide oxygen atom with concurrent formation of a corresponding (iminoethyl)pyridine chelate metal complex. The (iminoethyl)pyridine *N*-oxide complexes are structural analogues of the ubiquitous (salicylimino)metal complexes. However, the (iminoethyl)pyridine *N*-oxides are neutral ligands in contrast to their negatively charged salicylimino ligand analogues. Therefore, one might envision a variety of complementary use of these chelating ligand systems, both in coordination chemistry and catalysis.

## Experimental Section

**General:** All reactions involving air- or moisture-sensitive compounds were carried out under an inert gas using Schlenk-type glassware or in a glovebox. Solvents were dried and distilled prior to use. The following instruments were used for physical characterisation of the compounds: melting points: DSC 2010 TA-instruments; elemental analyses: Foss–Heraeus CHNO-Rapid; MS: Micromass Quattro LC-Z electrospray mass spectrometer; NMR: Bruker AC 200 P ($^1$H: 200 MHz; $^{13}$C: 50 MHz), ARX 300 ($^1$H: 300 MHz; $^{13}$C: 75 MHz), Varian UNITY plus NMR spectrometer ($^1$H: 600 MHz; $^{13}$C: 151 MHz). 2-Isopropylpyridine (**7b**),[15] 2-*tert*-butylpyridine (**7c**),[15] 2-acetylpyridine *N*-oxide (**5a**)[14] and (2,6-diisopropylphenyl)(1-pyridin-2-ylethylidene)amine (**3a**)[13] were synthesised according to methods published elsewhere. Compounds **8b** and **8c** were synthesised by a general procedure for the preparation of amine *N*-oxides.[17] Compounds **9b** and **9c** were synthesised according to a modified Reissert–Henze reaction.[16]

**X-ray Crystal Structure Determinations:** Data sets were collected with Enraf Nonius CAD4 and Nonius KappaCCD diffractometers, with Mo-$K_\alpha$ radiation, equipped with a rotating anode generator. Programs used: data collection EXPRESS (Nonius B.V., 1994) and COLLECT (Nonius B.V., 1998); data reduction MolEN (K. Fair, Enraf–Nonius B.V., 1990) and Denzo-SMN;[21] absorption correction for CCD data SORTAV[22] and Denzo;[23] structure solution SHELXS-97;[24] structure refinement SHELXL-97;[25] graphics XP (BrukerAXS, 2000). CCDC-277028 to -277044 contain the supplementary crystallographic data for this paper. These data can be obtained free of charge from The Cambridge Crystallographic Data Centre via www.ccdc.cam.ac.uk/data_request/cif.

**2-Isopropylpyridine *N*-Oxide (8b):** A solution of **7b** (70.0 g, 578 mmol) in chloroform (700 mL) was cooled to 0 °C and *m*-chloroperbenzoic acid (143 g, 578 mmol), dissolved in chloroform (400 mL), was added dropwise. The resulting mixture was warmed to ambient temperature within 3 h, then passed through a column of alkaline alumina. Evaporation of the solvent yielded the product as a yellow oil (63.0 g, 79%). $^1$H NMR (200 MHz, $CDCl_3$, 25 °C): $\delta$ = 8.19 (d, $^3J$ = 6.4 Hz, 1 H, 6-H), 7.18 (m, 2 H, 3-H/5-H), 7.12–7.01 (m, 1 H, 4-H), 3.74 [sept, $^3J$ = 6.8 Hz, 1 H, C*H*(CH$_3$)$_2$], 1.24 [d, $^3J$ = 6.9 Hz, 6 H, CH(C*H*$_3$)$_2$] ppm. $^{13}$C{$^1$H} NMR (75 MHz, $CDCl_3$, 25 °C): $\delta$ = 157.7 (C-2), 139.6 (C-6), 125.5 (C-5), 122.9 (C-4), 122.6 (C-3), 27.4 [*C*H(CH$_3$)$_2$], 20.1 [CH(*C*H$_3$)$_2$] ppm.

 © 2006 Wiley-VCH Verlag GmbH & Co. KGaA, Weinheim 

**2-*tert*-Butylpyridine *N*-Oxide (8c):** In an analogous procedure, reaction of **7c** (33.0 g, 244 mmol) in chloroform (750 mL) with *m*-chloroperbenzoic acid (60.2 g, 244 mmol) yielded **8c** as a yellow oil (29.0 g, 79%). $^1$H NMR (200 MHz, $CDCl_3$, 25 °C): $\delta$ = 8.15 (dd, $^3J$ = 6.1, $^4J$ = 1.8 Hz, 1 H, 6-H), 7.29 (dd, $^3J$ = 7.9, $^4J$ = 2.4 Hz, 1 H, 3-H), 7.15 (dt, $^3J$ = 7.9, $^4J$ = 1.8 Hz, 1 H, 4-H), 7.11–7.02 (m, 1 H, 5-H), 1.48 [s, 9 H, C(C$H_3$)$_3$] ppm. $^{13}$C{$^1$H} NMR (75 MHz, $CDCl_3$, 25 °C): $\delta$ = 157.9 (C-2), 141.6 (C-6), 125.3 (C-5), 123.5 (C-4), 123.4 (C-3), 36.1 [*C*(CH$_3$)$_3$], 26.8 [C(*C*H$_3$)$_3$] ppm.

**6-Isopropylpyridine-2-carbonitrile (9b):** Dimethylcarbamoyl chloride (52.7 mL, 574 mmol) was added dropwise to a solution of **8b** (62.3 g, 454 mmol) and trimethylsilyl cyanide (71.8 mL, 574 mmol) in dichloromethane (400 mL). The resulting mixture was stirred at room temperature for 2 d and the progress of the reaction was monitored by TLC (pentane/chloroform/triethylamine, 20:5:1). Then, a 10% aqueous $K_2CO_3$ solution was added and stirring continued for 15 min. The organic phase was separated and the aqueous layer extracted with dichloromethane. The combined organic layers were dried ($MgSO_4$), the solvent was evaporated and the crude product distilled to give the **9b** as a bright-yellow oil (40.2 g, 61%). $^1$H NMR (200 MHz, $CDCl_3$, 25 °C): $\delta$ = 7.71 (t, $^3J$ = 7.9 Hz, 1 H, 4-H), 7.47 (dd, $^3J$ = 7.9, $^4J$ = 1.0 Hz, 1 H, 3-H), 7.36 (dd, $^3J$ = 7.9, $^4J$ = 1.0 Hz, 1 H, 5-H), 3.06 [sept, $^3J$ = 7.0 Hz, 1 H, C*H*(CH$_3$)$_2$], 1.25 [d, $^3J$ = 7.0 Hz, 6 H, CH(C$H_3$)$_2$] ppm. $^{13}$C{$^1$H} NMR (75 MHz, $CDCl_3$, 25 °C): $\delta$ = 169.3 (C-6), 137.1 (C-4), 133.0 (C-2), 125.8 (C-3), 124.3 (C-5), 117.5 (*C*N), 36.2 [*C*H(CH$_3$)$_2$], 22.1 [CH(*C*H$_3$)$_2$] ppm.

**6-*tert*-Butylpyridine-2-carbonitrile (9c):**[26] Analogously to the preparation of **9b**, reaction of **8c** (29.0 g, 192 mmol), trimethylsilyl cyanide (30.4 mL, 243 mmol) and dimethylcarbamoyl chloride (22.3 mL, 243 mmol) in dichloromethane (200 mL) yielded **9c** as a bright-yellow oil (20.0 g, 65%). $^1$H NMR (200 MHz, $CDCl_3$, 25 °C): $\delta$ = 7.72 (t, $^3J$ = 7.9 Hz, 1 H, 4-H), 7.53 (dd, $^3J$ = 7.9, $^4J$ = 1.1 Hz, 1 H, 3-H), 7.46 (dd, $^3J$ = 7.9, $^4J$ = 1.1 Hz, 1 H, 5-H), 1.32 [s, 9 H, C(C$H_3$)$_3$] ppm. $^{13}$C{$^1$H} NMR (75 MHz, $CDCl_3$, 25 °C): $\delta$ = 171.4 (C-6), 137.0 (C-4), 132.7 (C-2), 125.3 (C-3), 122.7 (C-5), 117.7 (*C*N), 37.9 [*C*(CH$_3$)$_3$], 29.8 [C(*C*H$_3$)$_2$] ppm.

**2-Acetyl-6-isopropylpyridine (10b):** A solution of **9b** (38.0 g, 260 mmol) in diethyl ether (400 mL) was cooled to –25 °C and methyllithium (179 mL, 286 mmol, 1.6 M solution in diethyl ether) was added dropwise. The reaction mixture was warmed to ambient temperature within 2 h and then quenched with a mixture of aqueous ammonium chloride solution and hydrochloric acid. The organic phase was separated and the aqueous phase extracted with diethyl ether. The ethereal solution was dried ($Na_2SO_4$) and the solvent evaporated. Distillation yielded the product as a colourless oil (10.6 g, 25%). $^1$H NMR (200 MHz, $CDCl_3$, 25 °C): $\delta$ = 7.79 (dd, $^3J$ = 7.7, $^4J$ = 1.2 Hz, 1 H, 5-H), 7.67 (t, $^3J$ = 7.7 Hz, 1 H, 4-H), 7.28 (dd, $^3J$ = 7.7, $^4J$ = 1.2 Hz, 1 H, 3-H), 3.07 [sept, $^3J$ = 7.0 Hz, 1 H, C*H*(CH$_3$)$_2$], 2.68 (s, 3 H, COC$H_3$), 1.29 [d, $^3J$ = 7.0 Hz, 6 H, CH(C$H_3$)$_2$] ppm. $^{13}$C{$^1$H} NMR (75 MHz, $CDCl_3$, 25 °C): $\delta$ = 200.8 (*C*O), 166.6 (C-6), 153.0 (C-2), 136.8 (C-4), 124.2 (C-3), 118.6 (C-5), 36.0 [*C*H(CH$_3$)$_2$], 25.5 (CO*C*H$_3$), 22.4 [CH(*C*H$_3$)$_2$] ppm. $C_{10}H_{13}NO$ (163.22): calcd. C 73.59, H 8.03, N 8.58, found C 73.30, H 8.21, N 8.94.

**2-Acetyl-6-*tert*-butylpyridine (10c):** Analogously to the preparation of **10b**, **10c** was prepared from the reaction of **9c** (18.4 g, 115 mmol) with methyllithium (79.4 mL, 127 mmol, 1.6 M solution in diethyl ether) in diethyl ether (180 mL). After aqueous workup and distillation, the product was obtained as a colourless oil (7.33 g, 36%). $^1$H NMR (200 MHz, $CDCl_3$, 25 °C): $\delta$ = 7.79 (dd, $^3J$ = 7.7, $^4J$ = 1.3 Hz, 1 H, 3-H), 7.69 (t, $^3J$ = 7.7 Hz, 1 H, 4-H), 7.46 (dd, $^3J$ = 7.7, $^4J$ = 1.3 Hz, 1 H, 5-H), 2.69 (s, 3 H, COC$H_3$), 1.36 [s, 9 H, C(C$H_3$)$_3$] ppm. $^{13}$C{$^1$H} NMR (75 MHz, $CDCl_3$, 25 °C): $\delta$ = 201.0 (*C*O), 168.7 (C-6), 152.4 (C-2), 136.8 (C-4), 122.4 (C-5), 118.1 (C-3), 37.6 [*C*(CH$_3$)$_3$], 30.5 [C(*C*H$_3$)$_3$], 25.6 (CO*C*H$_3$) ppm. $C_{11}H_{15}NO$ (177.24): calcd. C 74.54, H 8.53, N 7.90; found C 74.30, H 8.64, N 7.85.

**2-Acetyl-6-isopropylpyridine *N*-Oxide (11b):** Compound **10b** (6.00 g, 36.8 mmol), dissolved in glacial acetic acid (25 mL), was treated with hydrogen peroxide solution (5.6 mL, 30%). The mixture was allowed to react at 70–80 °C for 10 h. Additional hydrogen peroxide solution (4.6 mL, 30%) was then added and the mixture was heated for another 10 h. After cooling to room temperature, the solvent was evaporated and the crude residue was treated with sodium carbonate solution. The aqueous phase was extracted with dichloromethane, the combined organic layers dried ($Na_2SO_4$) and the solvent evaporated. The product was obtained as a yellow oil (3.99 g, 61%). $^1$H NMR (200 MHz, $CDCl_3$, 25 °C): $\delta$ = 7.40 (dd, $^3J$ = 7.8, $^4J$ = 2.2 Hz, 1 H, 3-H), 7.30 (dd, $^3J$ = 7.8, $^4J$ = 2.2 Hz, 1 H, 5-H), 7.21 (t, $^3J$ = 7.8 Hz, 1 H, 4-H), 3.72 [sept, $^3J$ = 7.1 Hz, 1 H, C*H*(CH$_3$)$_2$], 2.71 (s, 3 H, COC$H_3$), 1.26 [d, $^3J$ = 7.1 Hz, 6 H, CH(C$H_3$)$_2$] ppm. $^{13}$C{$^1$H} NMR (75 MHz, $CDCl_3$, 25 °C): $\delta$ = 196.1 (*C*O), 158.6 (C-6), 147.5 (C-2), 124.9 (C-4), 124.3 (C-5), 123.4 (C-3), 30.2 (CO*C*H$_3$), 27.2 [*C*H(CH$_3$)$_2$], 20.1 [CH(*C*H$_3$)$_2$] ppm. $C_{10}H_{13}NO_2$ (179.22): calcd. C 67.02, H 7.31, N 7.82; found C 66.63, H 7.49, N 8.11.

**General Procedure for the Preparation of the Ketimines 3a, 3b, 2a, 2b:** A mixture of the appropriate 2-acetylpyridine compound (12 mmol), 2,6-diisopropylaniline (16 mmol), a catalytic amount of formic acid and sodium sulfate in methanol was refluxed for several hours. The progress of the reaction was monitored by TLC. After cooling to room temperature, the precipitate was removed by filtration, the solvent was evaporated and the crude product purified by column chromatography on silica gel. In most cases crystals suitable for the X-ray crystal structure analysis were grown from pentane at room temperature by means of solvent evaporation.

**(2,6-Diisopropylphenyl)[1-(pyridin-2-yl)ethylidene]amine (3a):** Formula $C_{19}H_{24}N_2$, $M$ = 280.40, light yellow crystal 0.50 × 0.30 × 0.10 mm, $a$ = 8.469(1), $b$ = 9.503(1), $c$ = 11.790(1) Å, $\alpha$ = 108.47(1), $\beta$ = 103.82(1), $\gamma$ = 100.68(1)°, $V$ = 838.1(2) Å$^3$, $\rho_{calcd.}$ = 1.111 g cm$^{-3}$, $\mu$ = 0.65 cm$^{-1}$, no absorption correction (0.968 ≤ $T$ ≤ 0.994), $Z$ = 2, triclinic, space group $P\bar{1}$ (no. 2), $\lambda$ = 0.71073 Å, $T$ = 198 K, $\omega$ and $\varphi$ scans, 5134 reflections collected (±$h$, ±$k$, ±$l$), [(sin$\theta$)/$\lambda$] = 0.62 Å$^{-1}$, 3372 independent ($R_{int}$ = 0.019) and 2651 observed reflections [$I \geq 2\sigma(I)$], 195 refined parameters, $R$ = 0.047, $wR^2$ = 0.124, max. residual electron density 0.18 (–0.16) e Å$^{-3}$, hydrogen atoms calculated and refined as riding atoms.

**(2,6-Diisopropylphenyl)[1-(6-isopropylpyridin-2-yl)ethylidene]amine (3b):** Reaction of 2-acetyl-6-isopropylpyridine (**10b**; 3.51 g, 21.5 mmol) with 2,6-diisopropylaniline (5.4 mL, 28.7 mmol) yielded a yellow solid (5.87 g, 85%) after column chromatography ($SiO_2$; pentane/ethyl acetate, 20:1). M.p. 81 °C. $^1$H NMR (600 MHz, $CDCl_3$, 25 °C): $\delta$ = 8.18 (br. d, 1 H, 3-H$_{py}$), 7.71 (t, $^3J$ = 7.7 Hz, 1 H, 4-H$_{py}$), 7.25 (d, $^3J$ = 7.7 Hz, 1 H, 5-H$_{py}$), 7.16 (m, 2 H, 3-/5-H$_{ar}$), 7.09 (m, 1 H, 4-H$_{ar}$), 3.12 [sept, $^3J$ = 6.9 Hz, 1 H, C*H*(CH$_3$)$_{2py}$], 2.77 [sept, $^3J$ = 6.9 Hz, 2 H, C*H*(CH$_3$)$_{2ar}$], 2.22 (s, 3 H, CNC$H_3$), 1.35 [d, $^3J$ = 6.9 Hz, 6 H, CH(C$H_3$)$_{2py}$], 1.15 [d, $^3J$ = 6.9 Hz, 12 H, CH(C$H_3$)$_{2ar}$] ppm. $^1$H NMR (600 MHz, $CDCl_3$, –65 °C): $\delta$ = 8.14 (d, $^3J$ = 7.6 Hz, 1 H, 3-H$_{py}$), 7.75 (t, $^3J$ = 7.6 Hz, 1 H, 4-H$_{py}$), 7.29 (d, $^3J$ = 7.6 Hz, 1 H, 5-H$_{py}$), 7.19 (m, 2 H, 3-/5-H$_{ar}$), 7.14 (m, 1 H, 4-H$_{ar}$), 3.08 [sept, $^3J$ = 6.7 Hz, 1 H, C*H*-(CH$_3$)$_{2py}$], 2.74 [sept, $^3J$ = 6.7 Hz, 2 H, C*H*(CH$_3$)$_{2ar}$], 2.22 (s, 3 H, CNC$H_3$), 1.32 [d, $^3J$ = 6.7 Hz, 6 H, CH(C$H_3$)$_{2py}$], 1.12 [d, $^3J$ =

 © 2006 Wiley-VCH Verlag GmbH & Co. KGaA, Weinheim 

6.7 Hz, 6 H, CH(C$H_3^A$C$H_3^B$)$_{ar}$], 1.10 [d, $^3J$ = 6.7 Hz, 6 H, CH(C$H_3^A$C$H_3^B$)$_{ar}$] ppm. $^{13}$C{$^1$H} NMR (150 MHz, $CDCl_3$, –65 °C): $\delta$ = 167.7 (*C*N), 165.9 (C-6$_{py}$), 154.7 (C-2$_{py}$), 145.9 (C-1$_{ar}$), 136.7 (C-4$_{py}$), 135.8 (C-2/–6$_{ar}$), 123.1 (C-4$_{ar}$), 122.7 (C-3/–5$_{ar}$), 121.7 (C-5$_{py}$), 118.2 (C-3$_{py}$), 36.2 [*C*H(CH$_3$)$_{2py}$], 27.7 [*C*H(CH$_3$)$_{2ar}$], 23.1 [CH(CH$_3^A$*C*H$_3^B$)$_{ar}$], 23.0 [CH(*C*H$_3^A$CH$_3^B$)$_{ar}$], 22.7 [CH(*C*H$_3$)$_{2py}$], 17.5 (CN*C*H$_3$) ppm. MS (ESI): *m*/*z* (%) = 345.3 (100) [M + Na]$^+$, 323 (12) [M + H]$^+$. $C_{22}H_{30}N_2$ (322.49): calcd. C 81.94, H 9.38, N 8.69; found C 81.75, H 9.32, N, 8.64.

**X-ray Crystal Structure Analysis of 3b:** Formula $C_{22}H_{30}N_2$, $M$ = 322.48, colourless crystal 0.45 × 0.30 × 0.20 mm, $a$ = 11.486(1), $b$ = 17.360(1), $c$ = 11.529(1) Å, $\beta$ = 117.34(1)°, $V$ = 2042.1(3) Å$^3$, $\rho_{calcd.}$ = 1.049 g cm$^{-3}$, $\mu$ = 4.59 cm$^{-1}$, no absorption correction (0.820 ≤ $T$ ≤ 0.914), $Z$ = 4, monoclinic, space group $P2_1/c$ (no. 14), $\lambda$ = 1.54178 Å, $T$ = 223 K, $\omega$ and $\varphi$ scans, 11145 reflections collected (±$h$, ±$k$, ±$l$), [(sin$\theta$)/$\lambda$] = 0.59 Å$^{-1}$, 3444 independent ($R_{int}$ = 0.022) and 2708 observed reflections [$I \geq 2\sigma(I)$], 225 refined parameters, $R$ = 0.046, $wR^2$ = 0.133, max. residual electron density 0.28 (–0.18) e Å$^{-3}$, hydrogen atoms calculated and refined as riding atoms.

**2-[1-(2,6-Diisopropylphenylimino)ethyl]pyridine *N*-Oxide (2a):** Reaction of 2-acetylpyridine *N*-oxide (5.77 g, 42.1 mmol) with 2,6-diisopropylaniline (10.6 mL, 56.0 mmol) yielded a yellow solid (8.36 g, 67%) after column chromatography ($SiO_2$; pentane/chloroform/triethylamine/methanol, 4:1:1:1). M.p. 80 °C. $^1$H NMR (600 MHz, $CDCl_3$, 25 °C): $\delta$ = 8.23 (m, $^3J$ = 6.4 Hz, 1 H, 6-H$_{py}$), 7.62 (dd, $^3J$ = 7.6, $^4J$ = 2.3 Hz, 1 H, 3-H$_{py}$), 7.35 (dt, $^3J$ = 7.6, $^4J$ = 1.3 Hz, 1 H, 4-H$_{py}$), 7.32 (ddd, $^3J$ = 7.6, $^3J$ = 6.4, $^4J$ = 2.3 Hz, 1 H, 5-H$_{py}$), 7.16 (m, 2 H, 3-/5-H$_{ar}$), 7.10 (m, 1 H, 4-H$_{ar}$), 2.88 [sept, $^3J$ = 6.8 Hz, 2 H, C*H*(CH$_3$)$_{2ar}$], 2.19 (s, 3 H, CNC*H*$_3$), 1.22 [d, $^3J$ = 6.8 Hz, 6 H, CH(C$H_3^A$CH$_3^B$)$_{ar}$], 1.16 [d, $^3J$ = 6.8 Hz, 6 H, CH(CH$_3^A$C$H_3^B$)$_{ar}$] ppm. $^1$H NMR (600 MHz, $CDCl_3$, –60 °C): $\delta$ = 8.27 (d, $^3J$ = 6.3 Hz, 1 H, 6-H$_{py}$), 7.66 (d, $^3J$ = 7.6 Hz, 1 H, 3-H$_{py}$), 7.46 (t, $^3J$ = 7.6 Hz, 1 H, 4-H$_{py}$), 7.41 (m, 1 H, 5-H$_{py}$), 7.19 (m, 2 H, 3-/5-H$_{ar}$), 7.16 (m, 1 H, 4-H$_{ar}$), 2.82 [sept, $^3J$ = 6.8 Hz, 2 H, C*H*(CH$_3$)$_{2ar}$], 2.17 (s, 3 H, CNC*H*$_3$), 1.19 [d, $^3J$ = 6.8 Hz, 6 H, CH(C$H_3^A$CH$_3^B$)$_{ar}$], 1.13 [d, $^3J$ = 6.8 Hz, 6 H, CH(CH$_3^A$C$H_3^B$)$_{ar}$] ppm. $^{13}$C{$^1$H} NMR (150 MHz, $CDCl_3$, 25 °C): $\delta$ = 164.9 (*C*N), 149.4 (C-2$_{py}$), 144.4 (C-1$_{ar}$), 140.1 (C-6$_{py}$), 136.1 (C-2/–6$_{ar}$), 128.0 (C-4$_{py}$), 126.9 (C-5$_{py}$), 126.1 (C-3$_{py}$), 124.3 (C-4$_{ar}$), 123.1 (C-3/–5$_{ar}$), 28.1 [*C*H(CH$_3$)$_{2ar}$], 23.4 [CH(CH$_3^A$*C*H$_3^B$)$_{ar}$], 22.9 [CH(*C*H$_3^A$CH$_3^B$)$_{ar}$], 19.8 (CN*C*H$_3$) ppm. MS (ESI): *m*/*z* (%) = 319 (100) [M + Na]$^+$, 297 (85) [M + H]$^+$. $C_{19}H_{24}N_2O$ (296.41): calcd. C 76.99, H 8.16, N 9.45; found C 76.87, H 8.10, N 9.37.

**X-ray Crystal Structure Analysis of 2a:** Formula $C_{19}H_{24}N_2O$, $M$ = 296.40, yellow crystal 0.35 × 0.25 × 0.15 mm, $a$ = 8.698(1), $b$ = 8.800(1), $c$ = 11.502(1) Å, $\alpha$ = 103.05(1), $\beta$ = 95.07(1), $\gamma$ = 97.15(1)°, $V$ = 844.8(2) Å$^3$, $\rho_{calcd.}$ = 1.165 g cm$^{-3}$, $\mu$ = 5.62 cm$^{-1}$, empirical absorption correction (0.828 ≤ $T$ ≤ 0.920), $Z$ = 2, triclinic, space group $P\bar{1}$ (no. 2), $\lambda$ = 1.54178 Å, $T$ = 223 K, $\omega/2\theta$ scans, 3610 reflections collected (±$h$, ±$k$, -$l$), [(sin$\theta$)/$\lambda$] = 0.62 Å$^{-1}$, 3433 independent ($R_{int}$ = 0.023) and 2840 observed reflections [$I \geq 2\sigma(I)$], 205 refined parameters, $R$ = 0.043, $wR^2$ = 0.126, max. residual electron density 0.20 (–0.20) e Å$^{-3}$, hydrogen atoms calculated and refined as riding atoms.

**2-[1-(2,6-Diisopropylphenylimino)ethyl]-6-isopropylpyridine *N*-Oxide (2b):** Reaction of 2-acetyl-6-isopropylpyridine *N*-oxide (3.21 g, 17.9 mmol) with 2,6-diisopropylaniline (4.5 mL, 23.9 mmol) yielded, after column chromatography ($SiO_2$; pentane/chloroform/methanol, 20:3:1), 2.47 g (41%) of a yellow solid. M.p. 117 °C. $^1$H NMR (600 MHz, $CDCl_3$, 25 °C): $\delta$ = 7.46 (br. m, 1 H, 3-H$_{py}$), 7.31 (m, 2 H, 4-/5-H$_{py}$), 7.16 (m, 2 H, 3-/5-H$_{ar}$), 7.10 (m, 1 H, 4-H$_{ar}$), 3.85 [sept, $^3J$ = 6.9 Hz, 1 H, C*H*(CH$_3$)$_{2py}$], 2.92 [sept, $^3J$ = 6.9 Hz, 2 H, C*H*(CH$_3$)$_{2ar}$], 2.17 (s, 3 H, CNC*H*$_3$), 1.31 [d, $^3J$ = 6.9 Hz, 6 H, CH(C*H*$_3$)$_{2py}$], 1.23 [d, $^3J$ = 6.9 Hz, 6 H, CH(C$H_3^A$CH$_3^B$)$_{ar}$], 1.16 [d, $^3J$ = 6.9 Hz, 6 H, CH(CH$_3^A$C$H_3^B$)$_{ar}$] ppm. $^1$H NMR (600 MHz, $CDCl_3$, –60 °C): $\delta$ = 7.46 (dd, $^3J$ = 7.7, $^4J$ = 2.1 Hz, 1 H, 3-H$_{py}$), 7.41 (t, $^3J$ = 7.7 Hz, 1 H, 4-H$_{py}$), 7.37 (dd, $^3J$ = 7.7, $^4J$ = 2.1 Hz, 1 H, 5-H$_{py}$), 7.19 (m, 2 H, 3-/5-H$_{ar}$), 7.15 (m, 1 H, 4-H$_{ar}$), 3.84 [sept, $^3J$ = 6.8 Hz, 1 H, C*H*(CH$_3$)$_{2py}$], 2.87 [sept, $^3J$ = 6.8 Hz, 2 H, C*H*(CH$_3$)$_{2ar}$], 2.15 (s, 3 H, CNC*H*$_3$), 1.28 [d, $^3J$ = 6.8 Hz, 6 H, CH(C*H*$_3$)$_{2py}$], 1.19 [d, $^3J$ = 6.8 Hz, 6 H, CH(C$H_3^A$CH$_3^B$)$_{ar}$], 1.14 [d, $^3J$ = 6.8 Hz, 6 H, CH(CH$_3^A$C$H_3^B$)$_{ar}$] ppm. $^{13}$C{$^1$H} NMR (150 MHz, $CDCl_3$, 25 °C): $\delta$ = 165.8 (*C*N), 158.3 (C-6$_{py}$), 149.5 (C-2$_{py}$), 144.2 (C-1$_{ar}$), 136.3 (C-2/–6$_{ar}$), 125.4 (C-4$_{py}$), 124.2 (C-4$_{ar}$), 123.2 (C-3$_{py}$), 123.1 (C-3/–5$_{ar}$, C-5$_{py}$), 28.0 [*C*H(CH$_3$)$_{2ar}$], 27.2 [*C*H(CH$_3$)$_{2py}$], 23.5 [CH(CH$_3^A$*C*H$_3^B$)$_{ar}$], 22.9 [CH(*C*H$_3^A$CH$_3^B$)$_{ar}$], 20.5 [CH(*C*H$_3$)$_{2py}$], 19.9 (CN*C*H$_3$) ppm. MS (ESI): *m*/*z* (%) = 361 (45) [M + Na]$^+$, 339 (100) [M + H]$^+$. $C_{22}H_{30}N_2O$ (338.49): calcd. C 78.06, H 8.93, N 8.28; found C 77.92, H 9.05, N 8.16.

**X-ray Crystal Structure Analysis of 2b:** Formula $C_{22}H_{30}N_2O$, $M$ = 338.48, colourless crystal 0.40 × 0.25 × 0.20 mm, $a$ = 8.534(1), $b$ = 14.593(1), $c$ = 16.546(1) Å, $\beta$ = 92.64(1)°, $V$ = 2058.4(3) Å$^3$, $\rho_{calcd.}$ = 1.092 g cm$^{-3}$, $\mu$ = 5.14 cm$^{-1}$, empirical absorption correction (0.821 ≤ $T$ ≤ 0.904), $Z$ = 4, monoclinic, space group $P2_1$ (no. 4), $\lambda$ = 1.54178 Å, $T$ = 293 K, $\omega/2\theta$ scans, 4517 reflections collected (±$h$, –$k$, +$l$), [(sin$\theta$)/$\lambda$] = 0.62 Å$^{-1}$, 4369 independent ($R_{int}$ = 0.035) and 3210 observed reflections [$I \geq 2\sigma(I)$], 466 refined parameters, $R$ = 0.045, $wR^2$ = 0.136, Flack parameter 0.0(4), max. residual electron density 0.21 (–0.16) e Å$^{-3}$, hydrogen atoms calculated and refined as riding atoms.

**General Procedure for the Preparation of Metal Complexes:** The metal precursor (1 mmol) was suspended in the appropriate solvent (20 mL), stirred, and a solution of the ligand (1 mmol) in the same solvent (10 mL) was added. The resulting mixture was stirred for several hours. For workup, the mixture was filtered, the solvent evaporated, the crude product washed with pentane and dried in vacuo. In most cases crystals suitable for X-ray analyses were grown from a concentrated solution of the complex in a mixture of acetonitrile/dichloromethane/THF layered with pentane.

**Reaction of Ligand 3b with $FeCl_2$; Synthesis of Compound 12b:** A suspension of anhydrous $FeCl_2$ (393 mg, 3.1 mmol) in THF was heated to 70 °C and a solution of **3b** (1.00 g, 3.1 mmol) in THF was added. The resulting mixture was stirred for 2 h. After workup and drying, the product was obtained as brown powder (1.22 g, 87%). MS (ESI): *m*/*z* (%) = 535.3 (100) [$FeCl_2$(**3b**) + $BF_4$]$^-$. $C_{22}H_{30}Cl_2FeN_2$ (449.24): calcd. C 58.82, H 6.73, N 6.24; found C 57.01, H 6.67, N, 5.71.

**X-ray Crystal Structure Analysis of 12b:** Formula $C_{22}H_{30}Cl_2FeN_2 \cdot C_4H_8O$, $M$ = 521.33, red crystal 0.30 × 0.25 × 0.15 mm, $a$ = 8.701(1), $b$ = 15.738(1), $c$ = 20.229(1) Å, $\beta$ = 97.33(1)°, $V$ = 2747.4(4) Å$^3$, $\rho_{calcd.}$ = 1.260 g cm$^{-3}$, $\mu$ = 7.63 cm$^{-1}$, empirical absorption correction (0.803 ≤ $T$ ≤ 0.894), $Z$ = 4, monoclinic, space group $P2_1/c$ (no. 14), $\lambda$ = 0.71073 Å, $T$ = 198 K, $\omega$ and $\varphi$ scans, 16643 reflections collected (±$h$, ±$k$, ±$l$), [(sin$\theta$)/$\lambda$] = 0.66 Å$^{-1}$, 6533 independent ($R_{int}$ = 0.047) and 4332 observed reflections [$I \geq 2\sigma(I)$], 282 refined parameters, $R$ = 0.069, $wR^2$ = 0.226, max. residual electron density 1.19 (–0.74) e Å$^{-3}$, solvent molecule disordered, refined with split positions, geometrical restraints, fixed occupancies (0.67:0.33) and one common isotropic displacement parameter, hydrogen atoms calculated and refined as riding atoms.

**Reaction of Ligand 3b with $CoCl_2$; Synthesis of Compound 13b:** Complex **13b** was prepared in an analogous procedure. Reaction

 © 2006 Wiley-VCH Verlag GmbH & Co. KGaA, Weinheim 

of $CoCl_2$ (402 mg, 3.1 mmol) and **3b** (1.00 g, 3.1 mmol) in THF yielded a green-blue powder (1.05 g, 74%). MS (ESI): *m*/*z* (%) = 451.1 (100) $[CoCl_2(\mathbf{3b})]^+$. $C_{22}H_{30}Cl_2CoN_2$ (452.33): calcd. C 58.42, H 6.69, N 6.19; found C 58.63, H 7.00, N 5.25.

**X-ray Crystal Structure Analysis of 13b:** Formula $C_{22}H_{30}Cl_2CoN_2{\cdot}0.5CH_2Cl_2{\cdot}0.5C_4H_8O$, $M$ = 530.83, turquoise crystal 0.40 × 0.05 × 0.05 mm, $a$ = 8.679(1), $b$ = 15.655(1), $c$ = 20.196(1) Å, $\beta$ = 97.93(1)°, $V$ = 2717.8(4) Å$^3$, $\rho_{calcd.}$ = 1.297 g cm$^{-3}$, $\mu$ = 9.42 cm$^{-1}$, empirical absorption correction (0.704 ≤ $T$ ≤ 0.954), $Z$ = 4, monoclinic, space group $P2_1/c$ (no. 14), $\lambda$ = 0.71073 Å, $T$ = 198 K, $\omega$ and $\varphi$ scans, 15372 reflections collected (±$h$, ±$k$, ±$l$), [(sin$\theta$)/$\lambda$] = 0.59 Å$^{-1}$, 4789 independent ($R_{int}$ = 0.091) and 2800 observed reflections [$I \geq 2\sigma(I)$], 323 refined parameters, $R$ = 0.056, $wR^2$ = 0.116, max. residual electron density 0.33 (–0.45) e Å$^{-3}$, solvent molecules sharing same side refined with split positons and fixed occupancies (0.5), hydrogen atoms calculated and refined as riding atoms.

**Reaction of Ligand 3b with $[NiBr_2(dme)]$; Synthesis of Compound 14b:** A suspension of $[NiBr_2(dme)]$ (948 mg, 3.1 mmol) in dichloromethane was treated with a solution of **3b** (1.0 g, 3.1 mmol) in dichloromethane. The resulting mixture was stirred at room temperature for 24 h. After workup, the product was isolated as a light-brown powder (1.19 g, 71%). MS (ESI) *m*/*z* (%) = 461.3 (83) $[NiBr(\mathbf{3b})]^+$, 323.4 (25) $[\mathbf{3b} + H]^+$, 189.1 (100). $C_{22}H_{30}Br_2N_2Ni$ (540.99): calcd. C 48.84, H 5.59, N 5.18; found C 48.81, H 5.51, N 5.04.

**X-ray Crystal Structure Analysis of 14b:** Formula $C_{22}H_{30}Br_2N_2Ni$, $M$ = 541.01, yellow crystal 0.50 × 0.30 × 0.08 mm, $a$ = 8.685(1), $b$ = 19.351(1), $c$ = 27.866(1) Å, $V$ = 4683.3(6) Å$^3$, $\rho_{calcd.}$ = 1.535 g cm$^{-3}$, $\mu$ = 42.50 cm$^{-1}$, empirical absorption correction (0.225 ≤ $T$ ≤ 0.727), $Z$ = 8, orthorhombic, space group $Pbca$ (no. 61), $\lambda$ = 0.71073 Å, $T$ = 198 K, $\omega$ and $\varphi$ scans, 10395 reflections collected (±$h$, ±$k$, ±$l$), [(sin$\theta$)/$\lambda$] = 0.66 Å$^{-1}$, 5573 independent ($R_{int}$ = 0.036) and 4039 observed reflections [$I \geq 2\sigma(I)$], 251 refined parameters, $R$ = 0.038, $wR^2$ = 0.079, max. residual electron density 0.91 (–0.89) e Å$^{-3}$, hydrogen atoms calculated and refined as riding atoms.

**Reaction of Ligand 3a with $FeCl_2$; Synthesis of Compound 15a:** Reaction of $FeCl_2$ (1.00 g, 7.89 mmol) in THF with **3a** (2.21 g, 7.89 mmol) at 80 °C yielded a black solid (1.99 g, 62%).

**X-ray Crystal Structure Analysis of 15a:** Formula $C_{19}H_{24}Cl_2FeN_2$, $M$ = 407.15, red crystal 0.30 × 0.25 × 0.15 mm, $a$ = 14.151(1), $b$ = 10.073(1), $c$ = 14.431(1) Å, $\beta$ = 109.97(1)°, $V$ = 1933.4(3) Å$^3$, $\rho_{calcd.}$ = 1.399 g cm$^{-3}$, $\mu$ = 10.59 cm$^{-1}$, empirical absorption correction (0.742 ≤ $T$ ≤ 0.857), $Z$ = 4, monoclinic, space group $P2_1/n$ (no. 14), $\lambda$ = 0.71073 Å, $T$ = 198 K, $\omega$ and $\varphi$ scans, 6709 reflections collected (±$h$, ±$k$, ±$l$), [(sin$\theta$)/$\lambda$] = 0.62 Å$^{-1}$, 3913 independent ($R_{int}$ = 0.043) and 2907 observed reflections [$I \geq 2\sigma(I)$], 222 refined parameters, $R$ = 0.096, $wR^2$ = 0.291, max. residual electron density 1.97 (–0.62) e Å$^{-3}$, the remaining electron density is located around $x$,0,$z$, all attempts to refine these in a chemically meaningful way failed, analysis only done to confirm the geometry of the complex, hydrogen atoms calculated and refined as riding atoms.

**Reaction of Ligand 3a with $CoCl_2$; Synthesis of Compound 16a:** In an analogous procedure, complex **16a** was obtained by treating $CoCl_2$ (1.0 g, 7.70 mmol) with compound **3a** (2.16 g, 7.70 mmol) in THF and collected as a green powder (2.10 g, 66%). MS (ESI): *m*/*z* (%) = 496.1 (100) $[CoCl_2(\mathbf{3a}) + BF_4]^-$. $C_{19}H_{24}Cl_2CoN_2$ (410.25): calcd. C 55.63, H 5.90, N 6.83; found C 56.96, H 6.90, N 5.10.

**X-ray Crystal Structure Analysis of 16a:** Formula $C_{19}H_{24}Cl_2CoN_2$, $M$ = 410.23, pink crystal 0.30 × 0.25 × 0.10 mm, $a$ = 14.132(1), $b$ = 10.132(1), $c$ = 14.308(1) Å, $\beta$ = 110.48(1)°, $V$ = 1919.2(3) Å$^3$, $\rho_{calcd.}$ = 1.420 g cm$^{-3}$, $\mu$ = 11.75 cm$^{-1}$, empirical absorption correction (0.719 ≤ $T$ ≤ 0.892), $Z$ = 4, monoclinic, space group $P2_1/n$ (no. 14), $\lambda$ = 0.71073 Å, $T$ = 198 K, $\omega$ and $\varphi$ scans, 21540 reflections collected (±$h$, ±$k$, ±$l$), [(sin$\theta$)/$\lambda$] = 0.66 Å$^{-1}$, 4559 independent ($R_{int}$ = 0.044) and 3700 observed reflections [$I \geq 2\sigma(I)$], 222 refined parameters, $R$ = 0.031, $wR^2$ = 0.070, max. residual electron density 0.30 (–0.32) e Å$^{-3}$, hydrogen atoms calculated and refined as riding atoms.

**Reaction of Ligand 3a with $[NiBr_2(dme)]$; Synthesis of Compound 17a:** A suspension of $[NiBr_2(dme)]$ (680 mg, 2.22 mmol) in dichloromethane was treated with a solution of **3a** (622 mg, 2.22 mmol) in dichloromethane. The resulting mixture was stirred at room temperature for 2 d, then another 300 mg of **3a** (1.07 mmol) was added, and stirring was continued for 2 d. After workup, compound **17a** was isolated as a green solid (1.46 g, 84%). MS (ESI): *m*/*z* (%) = 699.4 (100) $[NiBr(\mathbf{3a})_2]^+$. $C_{38}H_{48}Br_2N_4Ni$ (779.32): calcd. C 58.57, H 6.21, N 7.19; found C 57.46, H 6.48, N 6.82.

**Reaction of Ligand 2a with $FeCl_2$; Synthesis of Compound 18a:** The reaction of $FeCl_2$ (107 mg, 0.84 mmol) with **2a** (500 mg, 1.69 mmol) in THF at room temperature yielded a black powder (0.52 mmol, 62%). MS (ESI): *m*/*z* (%) = 651.4 (100) $[FeCl(\mathbf{3a})]^+$, 102.0 (45). $C_{38}H_{48}Cl_5Fe_2N_4$ (849.77): calcd. C 53.71, H 5.69, N 6.59; found C 53.02, H 5.78, N 6.58.

**X-ray Crystal Structure Analysis of 18a:** Formula $C_{38}H_{48}ClFeN_4{\cdot}FeCl_4$, $M$ = 849.76, red crystal 0.30 × 0.30 × 0.10 mm, $a$ = 8.835(1), $b$ = 15.414(1), $c$ = 15.138(1) Å, $\beta$ = 95.31(1)°, $V$ = 2052.7(3) Å$^3$, $\rho_{calc}$ = 1.375 g cm$^{-3}$, $\mu$ = 10.64 cm$^{-1}$, empirical absorption correction (0.741 ≤ $T$ ≤ 0.901), $Z$ = 2, monoclinic, space group $P2_1$ (no. 4), $\lambda$ = 0.71073 Å, $T$ = 198 K, $\omega$ and $\varphi$ scans, 17177 reflections collected (±$h$, ±$k$, ±$l$), [(sin$\theta$)/$\lambda$] = 0.59 Å$^{-1}$, 6886 independent ($R_{int}$ = 0.064) and 6040 observed reflections [$I \geq 2\sigma(I)$], 452 refined parameters, $R$ = 0.099, $wR^2$ = 0.267, Flack parameter 0.01(4), max. residual electron density 2.42 (–0.56) e Å$^{-3}$, very poor, partly amorphous crystal leads to an analysis of limited accuracy, hydrogen atoms calculated and refined as riding atoms.

**Reaction of Ligand 2a with $PdCl_2$; Synthesis of Compound 19a:** A suspension of $PdCl_2$ (500 mg, 2.82 mmol) in acetonitrile was treated with a solution of **2a** (836 mg, 2.82 mmol) in acetonitrile. After workup, the product was obtained as an orange solid (1.0 g, 75%). $^1$H NMR (600 MHz, $CH_3CN$, 25 °C): $\delta$ = 8.68 (dd, $^3J$ = 6.5, $^4J$ = 1.3 Hz, 1 H, 6-$H_{py}$), 8.18 (dd, $^3J$ = 8.0, $^4J$ = 1.8 Hz, 1 H, 3-$H_{py}$), 8.08 (dt, $^3J$ = 8.0, $^4J$ = 1.3 Hz, 1 H, 4-$H_{py}$), 7.82 (ddd, $^3J$ = 8.0, $^3J$ = 6.5, $^4J$ = 1.8 Hz, 1 H, 5-$H_{py}$), 7.33 (m, 2 H, 3-/5-$H_{ar}$), 7.28 (m, 1 H, 4-$H_{ar}$), 3.32 [sept, $^3J$ = 6.8 Hz, 2 H, C$H$(CH$_3$)$_{2ar}$], 2.23 (s, 3 H, CNC$H_3$), 1.59 [d, $^3J$ = 6.8 Hz, 6 H, CH(C$H_3^A$CH$_3^B$)$_{ar}$], 1.19 [d, $^3J$ = 6.8 Hz, 6 H, CH(CH$_3^A$C$H_3^B$)$_{ar}$] ppm. MS (ESI): *m*/*z* (%) = 561.0 (100) $[PdCl_2(\mathbf{2a}) + BF_4]^-$. $C_{19}H_{24}Cl_2N_2OPd$ (473.73): calcd. C 48.17, H 5.11, N 5.91; found C 47.94, H 5.49, N 5.97.

**X-ray Crystal Structure Analysis of 19a:** Formula $C_{19}H_{24}Cl_2N_2OPd{\cdot}C_2H_3N$, $M$ = 514.76, red crystal 0.50 × 0.40 × 0.30 mm, $a$ = 9.307(1), $b$ = 17.942(1), $c$ = 13.611(1) Å, $\beta$ = 97.51(1)°, $V$ = 2253.4(3) Å$^3$, $\rho_{calcd.}$ = 1.517 g cm$^{-3}$, $\mu$ = 10.77 cm$^{-1}$, empirical absorption correction (0.615 ≤ $T$ ≤ 0.738), $Z$ = 4, monoclinic, space group $P2_1/n$ (no. 14), $\lambda$ = 0.71073 Å, $T$ = 198 K, $\omega$ and $\varphi$ scans, 14417 reflections collected (±$h$, ±$k$, ±$l$), [(sin$\theta$)/$\lambda$] = 0.66 Å$^{-1}$, 5323 independent ($R_{int}$ = 0.034) and 5074 observed reflections [$I \geq 2\sigma(I)$], 259 refined parameters, $R$ = 0.026, $wR^2$ = 0.068, max. residual electron density 1.04 (–0.83) e Å$^{-3}$, hydrogen atoms calculated and refined as riding atoms.

 © 2006 Wiley-VCH Verlag GmbH & Co. KGaA, Weinheim 

**Reaction of Ligand 2a with $CoCl_2$; Synthesis of Compound 20a:** Reaction of $CoCl_2$ (1.0 g, 77 mol) with **2a** (2.28 g, 77 mmol) in THF yielded a blue powder (3.12 g, 95%). $C_{19}H_{24}Cl_2CoN_2O$ (426,25): calcd. C 53.54, H 5.68, N 6.57; found C 54.79, H 6.65, N 5.95.

**X-ray Crystal Structure Analysis of 20a:** Formula $C_{19}H_{24}Cl_2CoN_2O{\cdot}C_5H_{12}$, $M$ = 498.38, green crystal 0.60 × 0.10 × 0.05 mm, $a$ = 32.646(1), $b$ = 10.395(1), $c$ = 13.788(1) Å, $\beta$ = 93.73(1)°, $V$ = 4669.1(6) Å$^3$, $\rho_{calcd.}$ = 1.418 g cm$^{-3}$, $\mu$ = 9.83 cm$^{-1}$, empirical absorption correction (0.590 ≤ $T$ ≤ 0.953), $Z$ = 8, monoclinic, space group $C2/c$ (no. 15), $\lambda$ = 0.71073 Å, $T$ = 198 K, $\omega$ and $\varphi$ scans, 24564 reflections collected (±$h$, ±$k$, ±$l$), [(sin$\theta$)/$\lambda$] = 0.67 Å$^{-1}$, 5836 independent ($R_{int}$ = 0.054) and 3644 observed reflections [$I \geq 2\sigma(I)$], 251 refined parameters, $R$ = 0.052, $wR^2$ = 0.166, max. residual electron density 0.48 (–0.41) e Å$^{-3}$, solvent molecule refined as pentane with geometrical restraints, hydrogen atoms calculated and refined as riding atoms.

**Reaction of Ligand 2a with [$NiBr_2$(dme)]; Synthesis of Compound 21a:** A solution of the ligand **2a** (0.77 g, 26 mmol) in dichloromethane was added to a suspension of [$NiBr_2$(dme)] (1.0 g, 26 mmol) in dichloromethane. The resulting mixture was refluxed for 2 h. After workup, compound **21a** was obtained as a brown solid (1.17 g, 54%). MS (ESI): $m/z$ (%) = 731.3 (40) [NiBr(**2a**)$_2$]$^+$, 325.2 (80), 297.2 (100), 178.0 (70), 101.9 (70).

**X-ray Crystal Structure Analysis of 21a:** Formula $C_{38}H_{48}Br_2N_4NiO_2$, $M$ = 811.33, red crystal 0.35 × 0.30 × 0.20 mm, $a$ = 11.156(1), $b$ = 30.146(1), $c$ = 12.011(1) Å, $\beta$ = 109.81(1)°, $V$ = 3800.4(5) Å$^3$, $\rho_{calcd.}$ = 1.418 g cm$^{-3}$, $\mu$ = 26.50 cm$^{-1}$, empirical absorption correction (0.457 ≤ $T$ ≤ 0.619), $Z$ = 4, monoclinic, space group $P2_1/c$ (no. 14), $\lambda$ = 0.71073 Å, $T$ = 198 K, $\omega$ and $\varphi$ scans, 22711 reflections collected (±$h$, ±$k$, ±$l$), [(sin$\theta$)/$\lambda$] = 0.62 Å$^{-1}$, 7688 independent ($R_{int}$ = 0.059) and 4718 observed reflections [$I \geq 2\sigma(I)$], 434 refined parameters, $R$ = 0.047, $wR^2$ = 0.103, max. residual electron density 0.63 (–0.52) e Å$^{-3}$, hydrogen atoms calculated and refined as riding atoms.

**Reaction of Ligand 2b with [$NiBr_2$(dme)]; Synthesis of Compound 21b:** [$NiBr_2$(dme)] (453 mg, 1.48 mmol) was suspended in dichloromethane and **2b** (500 mg, 1.48 mmol) in dichloromethane was added. After workup compound **21b** was isolated as dark-brown solid (610 mg, 74%). MS (ESI) $m/z$ (%) = 477.3 (100) [NiBr(**2b**)]$^+$, 339.4 (61) [**2b** + H]$^+$. $C_{22}H_{30}Br_2N_2NiO$ (556.99): calcd. C 47.44, H 5.43, N 5.03; found C 48.02, H 5.40, N 4.83.

**X-ray Crystal Structure Analysis of 21b:** Formula $C_{26}H_{38}Br_2N_2NiO_2$, $M$ = 629.11, red crystal 0.75 × 0.15 × 0.10 mm, $a$ = 8.744(1), $b$ = 33.910(1), $c$ = 9.367(1) Å, $\beta$ = 95.39(1)°, $V$ = 2765.1(4) Å$^3$, $\rho_{calcd.}$ = 1.511 g cm$^{-3}$, $\mu$ = 36.16 cm$^{-1}$, empirical absorption correction (0.172 ≤ $T$ ≤ 0.714), $Z$ = 4, monoclinic, space group $P2_1/n$ (no. 14), $\lambda$ = 0.71073 Å, $T$ = 198 K, $\omega$ and $\varphi$ scans, 19041 reflections collected (±$h$, ±$k$, ±$l$), [(sin$\theta$)/$\lambda$] = 0.68 Å$^{-1}$, 6690 independent ($R_{int}$ = 0.054) and 5100 observed reflections [$I \geq 2\sigma(I)$], 305 refined parameters, $R$ = 0.045, $wR^2$ = 0.115, max. residual electron density 1.20 (–1.30) e Å$^{-3}$, hydrogen atoms calculated and refined as riding atoms.

**Reaction of Ligand 2a with $ZnBr_2$; Synthesis of Compound 22a:** Reaction of $ZnBr_2$ (0.76 g, 3.37 mmol) with ligand **2a** (1.0 g, 3.37 mmol) in acetonitrile yielded after workup a bright yellow powder (1.70 g, 97%).

**X-ray Crystal Structure Analysis of 22a:** Formula $C_{19}H_{24}Br_2N_2OZn{\cdot}0.5C_4H_8O$ $M$ = 557.64, colourless crystal 0.30 × 0.12 × 0.08 mm, $a$ = 15.943(1), $b$ = 10.254(1), $c$ = 28.396(1) Å, $\beta$ = 97.36(1)°, $V$ = 4603.9(6) Å$^3$, $\rho_{calcd.}$ = 1.609 g cm$^{-3}$, $\mu$ = 45.54 cm$^{-1}$, empirical absorption correction (0.342 ≤ $T$ ≤ 0.712), $Z$ = 8, monoclinic, space group $P2_1/c$ (no. 14), $\lambda$ = 0.71073 Å, $T$ = 198 K, $\omega$ and $\varphi$ scans, 29515 reflections collected (±$h$, ±$k$, ±$l$), [(sin$\theta$)/$\lambda$] = 0.68 Å$^{-1}$, 11531 independent ($R_{int}$ = 0.075) and 5668 observed reflections [$I \geq 2\sigma(I)$], 506 refined parameters, $R$ = 0.062, $wR^2$ = 0.144, max. residual electron density 1.34 (–1.25) e Å$^{-3}$, hydrogen atoms calculated and refined as riding atoms.

**Reaction of Ligand 2a with $Cu(OTf)_2$; Synthesis of Compound 23a:** $Cu(OTf)_2$ (1.0 g, 2.76 mmol) was treated with ligand **2a** (0.82 g, 2.76 mmol) at room temperature in dichloromethane. After workup a green powder was isolated (1.38 g, 76%).

**X-ray Crystal Structure Analysis of 23a:** Formula $C_{19}H_{24}CuN_2O(H_2O)(CF_3SO_3)_2{\cdot}CH_2Cl_2$, $M$ = 761.02, green crystal 0.40 × 0.15 × 0.05 mm, $a$ = 8.881(1), $b$ = 19.970(1), $c$ = 18.480(1) Å, $\beta$ = 97.77(1)°, $V$ = 3247.4(4) Å$^3$, $\rho_{calcd.}$ = 1.557 g cm$^{-3}$, $\mu$ = 10.44 cm$^{-1}$, empirical absorption correction (0.680 ≤ $T$ ≤ 0.950), $Z$ = 4, monoclinic, space group $P2_1/n$ (no. 14), $\lambda$ = 0.71073 Å, $T$ = 198 K, $\omega$ and $\varphi$ scans, 22468 reflections collected (±$h$, ±$k$, ±$l$), [(sin$\theta$)/$\lambda$] = 0.68 Å$^{-1}$, 8157 independent ($R_{int}$ = 0.052) and 5356 observed reflections [$I \geq 2\sigma(I)$], 399 refined parameters, $R$ = 0.052, $wR^2$ = 0.132, max. residual electron density 0.71 (–0.51) e Å$^{-3}$, hydrogen atoms at water from difference Fourier calculations, other calculated and all refined as riding atoms.

**Supporting Information** (see footnote on the first page of this article): X-ray crystal structure analyses of **3c**, **12b**, **13b** and **16a**, and additional spectroscopic information for **2a**,**b**, **3b**,**c** and **19a**.

## Acknowledgments

Financial support from the Fonds der Chemischen Industrie and the Deutsche Forschungsgemeinschaft is gratefully acknowledged. V. V. K. thanks the Alexander von Humboldt-Stiftung for a stipend.

[1] a) *Ferrocenes: Homogenous Catalysis, Organic Synthesis Materials Science* (Eds.: A. Togni, T. Hayashi), VCH, Weinheim, Germany, **1995**; b) T. P. Yoon, E. N. Jacobsen, *Science* **2003**, *299*, 1691–1693.

[2] For reviews see: a) G. J. P. Britovsek, V. C. Gibson, D. F. Wass, *Angew. Chem. Int. Ed.* **1999**, *38*, 428–447; b) S. D. Ittel, L. K. Johnson, M. Brookhart, *Chem. Rev.* **2000**, *100*, 1169–1203; c) V. C. Gibson, S. K. Spitzmesser, *Chem. Rev.* **2003**, *103*, 283–315; d) S. Park, Y. Han, S. K. Kim, J. Lee, H. K. Kim, Y. Do, *J. Organomet. Chem.* **2004**, *689*, 4263–4276.

[3] For representative examples see: a) M. Mitani, J. Mohri, Y. Yoshida, J. Saito, S. Ishii, K. Tsuru, S. Matsui, R. Furuyama, T. Nakano, H. Tanaka, S. Kojoh, T. Matsugi, N. Kashiwa, T. Fujita, *J. Am. Chem. Soc.* **2002**, *124*, 3327–3336; b) H. Makio, N. Kashiwa, T. Fujita, *Adv. Synth. Catal.* **2002**, *344*, 477–493; c) Y. Suzuki, H. Terao, T. Fujita, *Bull. Chem. Soc. Jpn.* **2003**, *76*, 1493–1517; d) M. Mitani, J. Saito, S.-I. Ishii, Y. Nakayama, H. Makio, N. Matsukawa, S. Matsui, J. Mohri, R. Furuyama, H. Terao, H. Bando, H. H. Tanaka, T. Fujita, *Chem. Rec.* **2004**, *4*, 137–158; e) H. Makio, T. Fujita, *Bull. Chem. Soc. Jpn.* **2005**, *78*, 52–66.

[4] a) P. A. Cameron, V. C. Gibson, C. Redshaw, J. A. Segal, M. D. Bruce, A. J. P. White, D. J. Williams, *Chem. Commun.* **1999**, *18*, 1883–1884; b) J. Strauch, T. H. Warren, G. Erker, R. Fröhlich, P. Saarenketo, *Inorg. Chim. Acta* **2000**, *300*, 810–821; c) D. J. Jones, V. C. Gibson, S. M. Green, P. J. Maddox, *Chem. Commun.* **2002**, *10*, 1038–1039; d) R. K. O'Reilly, V. C. Gibson, A. J. P. White, D. J. Williams, *J. Am. Chem. Soc.* **2003**, *125*, 8450–8451.

[5] a) C. Wang, S. Friedrich, T. R. Younkin, R. T. Li, R. H. Grubbs, D. A. Bansleben, M. W. Day, *Organometallics* **1998**,

 © 2006 Wiley-VCH Verlag GmbH & Co. KGaA, Weinheim 

*17*, 3149–3151; b) T. R. Younkin, E. F. Conner, J. I. Henderson, S. K. Friedrich, R. H. Grubbs, D. A. Bansleben, *Science* **2000**, *287*, 460–462.

[6] For representative examples see: a) B. M. Cole, K. D. Shimizu, C. A. Krueger, J. P. A. Harrity, M. L. Snapper, A. H. Hoveyda, *Angew. Chem. Int. Ed. Engl.* **1996**, *35*, 1668–1671; b) J. R. Porter, J. F. Traverse, A. H. Hoveyda, M. L. Snapper, *J. Am. Chem. Soc.* **2001**, *123*, 984–985; c) C. A. Luchaco-Cullis, H. Mizutani, K. E. Murphy, A. H. Hoveyda, *Angew. Chem. Int. Ed.* **2001**, *40*, 1456–1460; d) H. Deng, M. P. Isler, M. L. Snapper, A. H. Hoveyda, *Angew. Chem. Int. Ed.* **2002**, *41*, 1009–1012; e) K. E. Murphy, A. H. Hoveyda, *J. Am. Chem. Soc.* **2003**, *125*, 4690–4691; f) N. S. Josephsohn, M. L. Snapper, A. H. Hoveyda, *J. Am. Chem. Soc.* **2004**, *126*, 3734–3735.

[7] a) Reviews: *Comprehensive Asymmetric Catalysis I–III* (Eds.: E. N. Jacobsen, A. Pfaltz, H. Yamamoto), Springer, New York, **1999**; b) L. Canali, D. C. Sherrington, *Chem. Soc. Rev.* **1999**, *28*, 85–93; c) M. Bandini, P. G. Cozzi, A. Umani-Ronchi, *Pure Appl. Chem.* **2001**, *73*, 325–329; d) E. N. Jacobsen, *Acc. Chem. Res.* **2000**, *33*, 421–431; e) T. Katsuki, *Adv. Synth. Catal.* **2002**, *344*, 131–147; f) T. Katsuki, *Chem. Soc. Rev.* **2004**, *33*, 437–444; g) A. Fürstner, A. Leitner, M. Mendez, H. Krause, *J. Am. Chem. Soc.* **2002**, *124*, 13856–13863.

[8] For reviews of *N*-oxides see: a) N. M. Karayannis, *Coord. Chem. Rev.* **1973**, *11*, 93–159; b) A. Albini, *Synthesis* **1993**, 263–277; c) M. Nakajima, *J. Synth. Org. Chem. Jpn.* **2003**, *61*, 1081–1086; d) G. Chelucci, G. Murineddu, G. A. Pinna, *Tetrahedron: Asymmetry* **2004**, *15*, 1373–1389.

[9] For crystal structures of pyridine N-oxide aldimines see: a) Z. Jan, L. Qin, Y. Zhanfeng, Z. Cheng, D. Anbang, Z. Zhongyuan, *Gaodeng Xuexiao Huaxue Xuebao (Chin.) (Chem. J. Chin. Uni.)* **1989**, *10*, 1–5; b) L. Qin, W. Guo-Xiong, Z. Yan, Y. Zhan-Feng, Z. Cheng, Z. Zhong-Yuan, *Huaxue Xuebao (Chin.) (Acta Chim. Sinica)* **1989**, *47*, 1065; c) W. Guo-Xiong, L. Qin, Z. Cheng, *Jiegou Huaxue (Chin.) (Chin. J. Struct. Chem.)* **1989**, *8*, 278–282; d) D. C. Craig, D. J. Phillips, F. M. Z. Kaifi, *Inorg. Chim. Acta* **1989**, *161*, 247; e) Y. Zhanfeng, W. Guoxiong, Y. Ling, W. Fengshan, F. Yuguo, *Nanjing Daxue Xuebao, Ziran Kexue (Chin.) (J. Nanjing Univ., Nat. Sci.)* **1990**, *26*, 256–262; f) Y. Zang, Z. Yin, G. Wang, C. Zeng, A. Dai, Z. Zhou, *Inorg. Chem.* **1990**, *29*, 560–563; g) S. Gou, X. You, Z. Xu, K. Yu, Z. Zhou, *Polyhedron* **1990**, *9*, 2981–2985; h) Z. Zhongyuan, Y. Zhanfeng, Z. Yan, W. Guoxiong, Z. Cheng, D. Anbang, *Wuli Huaxue Xuebao (Chin.) (Acta Phys.-Chim. Sin.)* **1990**, *6*, 556–561; i) S.-H. Gou, X.-Z. You, Z. Xu, S.-X. Liu, C.-C. Lin, *Acta Crystallogr., Sect. C* **1991**, *47*, 708–711; j) S. H. Gou, Z. Xu, X. Z. You, K. B. Yu, *Chin. Chem. Lett.* **1991**, *2*, 801; k) Z. Zhou, K. Yu, S. Gou, X. You, Z. Xu, *Polyhedron* **1991**, *10*, 37–40; l) S. Gou, X. You, Z. Xu, Z. Zhou, K. Yu, *Polyhedron* **1991**, *10*, 1363–1366; m) Z. Xu, E. C. Alyea, G. Ferguson, M. C. Jennings, *Polyhedron* **1991**, *10*, 1625–1629; n) S. Gou, X. You, Z. Xu, Z. Zhou, K. Yu, *Polyhedron* **1991**, *10*, 2659–2663; o) S.-P. Yan, Z.-H. Jiang, D.-Z. Liao, G.-L. Wang, R.-J. Wang, H.-G. Wang, X.-K. Yao, *Gaodeng Xuexiao Huaxue Xuebao (Chin.) (Chem. J. Chin. Uni.)* **1992**, *13*, 1355–1357; p) S.-P. Yan, G.-L. Wang, H.-G. Wang, *Jiegou Huaxue (Chin.) (Chin. J. Struct. Chem.)* **1992**, *11*, 160–162; q) S. Gou, X. You, K. Yu, J. Lu, *Inorg. Chem.* **1993**, *32*, 1883–1887; r) C. Aili, W. Fengshan, Y. Ying, *Jilin Daxue Ziran Kex. Xue. (Chin.) (Acta Sci. Nat. Univ. Jil.)* **1994**, *5*, 81–82; s) G. Yuqui, C. Chenggang, H. Xiaofeng, *Synth. React. Inorg. Met.-Org. Chem.* **1994**, *24*, 877; t) A. B. Blake, E. Sinn, A. Yavari, B. Moubaraki, K. S. Murray, *Inorg. Chim. Acta* **1995**, *229*, 281–290; u) L. Xiaozeng, W. Genglin, L. Daizheng, Y. Shiping, J. Zonghui, W. Honggen, Y. Xinkan, *Polyhedron* **1995**, *14*, 511–514; v) R. E. Marsh, *Acta Crystallogr., Sect. B* **1997**, *53*, 317–322; w) Fariati, C. C. Craig, D. J. Phillips, *Inorg. Chim. Acta* **1998**, *268*, 135–140; x) M. Boča, P. Baran, R. Boča, G. Kickelbick, F. Renz, W. Linert, *Inorg. Chem. Commun.* **1999**, *2*, 188–190; y) G. C. Chiumia, D. C. Craig, D. J. Phillips, A. D. Rae, F. M. Z. Kaifi, *Inorg. Chim. Acta* **1999**, *285*, 297–300; z) B. Liu, R.-X. Hu, H. Liang, K.-B. Yu, *Jiegou Huaxue (Chin.) (Chin. J. Struct. Chem.)* **1999**, *18*, 414; aa) L. He, S. Gou, Q. Shi, M. Qian, C. Duan, *J. Chem. Cryst.* **1999**, *29*, 207–210; ab) G. Dyker, B. Hölzer, G. Henkel, *Tetrahedron: Asymmetry* **1999**, *10*, 3297–3307; ac) M. Boča, P. Baran, R. Boča, H. Fuess, G. Kickelbick, W. Linert, F. Renz, I. Svoboda, *Inorg. Chem.* **2000**, *39*, 3205–3212; ad) M. Gembicky, P. Baran, R. Boča, H. Fuess, I. Svoboda, M. Valko, *Inorg. Chim. Acta* **2000**, *305*, 75–82; ae) S. W. Ng, S.-Z. Hu, *Jiegou Huaxue (Chin.) (Chin. J. Struct. Chem.)* **2000**, *19*, 411–414; af) R. Boča, M. Nemečková, M. Vrbová, P. Baran, I. Svoboda, H. Fuess, *Polyhedron* **2000**, *19*, 835–839; ag) R.-X. Hu, Q. Yu, H. Liang, Z.-Y. Zhou, X.-G. Zhou, *Jiegou Huaxue (Chin.) (Chin. J. Struct. Chem.)* **2001**, *20*, 286; ah) H. Liang, X.-B. Chen, R.-X. Hu, Z.-F. Chen, K.-B. Yu, *Huaxue Xuebao (Chin.) (Acta Chim. Sinica)* **2002**, *60*, 939; ai) P. Baran, M. Boča, M. Breza, H. Elias, H. Fuess, V. Jorík, R. Klement, I. Svoboda, *Polyhedron* **2002**, *21*, 1561–1571; aj) H. Liang, Q. Yu, R.-X. Hu, Z.-Y. Zhou, X.-G. Zhou, *Transition Met. Chem.* **2002**, *27*, 454–457; ak) M. Boča, M. Valko, G. Kickelbick, M. Ďurík, W. Linert, *Inorg. Chim. Acta* **2003**, *349*, 111–122; al) P. Cheng, L. Z. Zhang, W.-M. Bu, J.-H. Peng, S.-P. Yan, D.-Z. Liao, Z.-H. Jiang, *Z. Anorg. Allg. Chem.* **2003**, *629*, 1996–1999.

[10] For crystal structures of pyridine *N*-oxide ketimines see ref.[9w] and: a) G. C. Chiumia, D. C. Craig, I. Phillips, D. J. Phillips, *Inorg. Chim. Acta* **1993**, *209*, 213–217; b) G. C. Chiumia, D. J. Phillips, A. D. Rae, *Inorg. Chim. Acta* **1995**, *238*, 197–201; c) T. Maekawa, S. Yamamoto, Y. Igata, S. Ikeda, T. Watanabe, M. Shiraishi, *Chem. Pharm. Bull.* **1997**, *45*, 1994; d) A. Murugkar, R. Bendre, A. Kumbhar, S. Padhye, R. Pritchard, C. A. McAuliffe, *Indian J. Chem. Sect. A* **1999**, *38*, 977; e) E. Bermejo, R. Carballo, A. Castineiras, R. Dominguez, C. Maichle-Mossmer, J. Strahle, D. X. West, *Polyhedron* **1999**, *18*, 3695–3702; f) E. Bermejo, A. Castineiras, R. Dominguez, R. Carballo, C. Maichle-Mössmer, J. Strähle, A. E. Liberta, D. X. West, *Z. Anorg. Allg. Chem.* **2000**, *626*, 878–884.

[11] See also: a) M. Hamana, B. Umezawa, Y. Goto, K. Noda, *Chem. Pharm. Bull.* **1960**, *8*, 692–697; b) M. Hamana, B. Umezawa, S. Nakashima, *Chem. Pharm. Bull.* **1962**, *10*, 961–968; c) G. R. Bedfor, A. R. Katritzk, H. M. Wues, *J. Chem. Soc.* **1963**, 4600–4602; d) M. Hamana, B. Umezawa, S. Nakashima, *Chem. Pharm. Bull.* **1962**, *10*, 969–974; e) G. Queguiner, P. Pastour, *Bull. Soc. Chim. Fr.* **1969**, *10*, 3655–3659; f) K. Kloc, J. Mlochowski, *Pol. J. Chem.* **1980**, *54*, 917–923; g) A. K. El-Shafei, K. M. Hassan, *Current Science* **1983**, *52*, 633–635; h) J. Mlochowski, E. Kubicz, K. Kloc, M. Mordarski, W. Peczynska, L. Syper, *Liebigs Ann. Chem.* **1988**, *5*, 455–464; i) Z. Yin, G. Wang, L. Ye, F. Wang, Y. Fan, *Nanjing Daxue Xuebao, Ziran Kexue* **1990**, *26*, 256–262; j) C. Zeng, Y. Zang, G. Wang, A. Dai, *Huaxue Xuebao* **1990**, *48*, 678–685; k) B. Wang, S. Zhang, D. Sun, Y. Liu, C. Zeng, *Wuji Huaxue Xuebao* **1993**, *9*, 244–248; l) H. Song, X. Wang, Y. Cong, H. Liang, *Guangxi Shifan Daxue Xuebao, Ziran Kexueban* **1997**, *15*, 56–60; m) Z. Chen, X. Wang, H. Liang, *Guangxi Shifan Daxue Xuebao, Ziran Kexueban* **1998**, *16*, 79–81; n) H.-H. Song, X.-J. Wang, Y.-L. Cong, H. Liang, *Hecheng Huaxue* **1998**, *6*, 188–190; o) Q. Yu, R.-X. Hu, *Guangxi Shifan Daxue Xuebao, Ziran Kexueban* **1999**, *17*, 68–70; p) M. Boča, D. Valigura, W. Linert, *Tetrahedron* **2000**, *56*, 441–446; q) Q. Yu, R.-X. Hu, H. Liang, *Guangxi Shifan Daxue Xuebao, Ziran Kexueban* **2001**, *19*, 63–66; r) Q. Yu, K. Chen, M. Y. Tan, *Pol. J. Chem.* **2003**, *77*, 917–921; s) M. Boča, G. Kickelbick, H. Fuess, *Chem. Pap.* **2004**, *58*, 145–147.

[12] *N*-oxide compounds: a) V. Derdau, S. Laschat, E. Hupe, W. A. König, I. Dix, P. G. Jones, *Eur. J. Inorg. Chem.* **1999**, 1001–1007; b) B. Tao, M. M.-C. Lo, G. C. Fu, *J. Am. Chem. Soc.* **2001**, *123*, 353–354; c) W.-L. Wong, W.-S. Lee, H.-L. Kwong, *Tetrahedron: Asymmetry* **2002**, *13*, 1485–1492.

[13] a) Described by: S. P. Meneghetti, P. J. Lutz, J. Kress, *Organometallics* **1999**, *18*, 2734–2737; b) T. V. Laine, U. Piironen, K.

 © 2006 Wiley-VCH Verlag GmbH & Co. KGaA, Weinheim 

Lappalainen, M. Klinga, E. Aitola, M. Leskelä, *J. Organomet. Chem.* **2000**, *606*, 112–124; c) C. Bianchini, H. M. Lee, G. Mantovani, A. Meli, W. Oberhauser, *New J. Chem.* **2002**, *4*, 387–397.
[14] K. Winterfeld, W. Zickel, *Arch. Pharm.* **1969**, *302*, 900–908.
[15] E. Pasquinet, P. Rocca, F. Marsais, A. Godard, G. Quéguiner, *Tetrahedron* **1998**, *54*, 8771–8782.
[16] W. K. Fife, *J. Org. Chem.* **1983**, *48*, 1375–1377.
[17] J. C. Cymerman, K. K. Purushothaman, *J. Org. Chem.* **1970**, *35*, 1721–1722.
[18] F. H. Allen, O. Kennard, D. G. Watson, *J. Chem. Soc., Perkin Trans. 2* **1987**, S1–S19.
[19] a) For an analogous dimeric Ni complex see: T. V. Laine, U. Piironen, K. Lappalainen, M. Klinga, E. Aitola, M. Leskelä, *J. Organomet. Chem.* **2000**, *606*, 112–124. b) For related dimeric structures, see for example: B. Le Gall, F. Conan, J.-M. Kerbaol, M. M. Kubicki, E. Vigier, Y. Le Mest, J. S. Pala, *Inorg. Chim. Acta* **2002**, *336*, 87; c) S. P. Meneghetti, P. J. Lutz, J. Kress, *Organometallics* **1999**, *18*, 2734–2737. d) For similar complexes, see: L. Gonsalvi, J. A. Gaunt, H. Adams, A. Castro, G. J. Sunley, A. Haynes, *Organometallics* **2003**, *22*, 1047–1054; e) C. Bianchini, G. Mantovani, A. Meli, F. Migliacci, *Organometallics* **2003**, *22*, 2545–2547.
[20] F. Li, G. P. A. Yap, S. L. Scott, S. I. Woo, *Transition Met. Chem.* **2001**, *26*, 271–275.
[21] Z. Otwinowski, W. Minor, *Methods Enzymol.* **1997**, *276*, 307–326.
[22] R. H. Blessing, *Acta Crystallogr., Sect A* **1995**, *51*, 33–37; R. H. Blessing, *J. Appl. Cryst.* **1997**, *30*, 421–426.
[23] Z. Otwinowski, D. Borek, W. Majewski, W. Minor, *Acta Crystallogr., Sect A* **2003**, *59*, 228–234.
[24] G. M. Sheldrick, *Acta Crystallogr., Sect A* **1990**, *46*, 467–473.
[25] G. M. Sheldrick, University of Göttingen, Germany, **1997**.
[26] G. Chelucci, S. Medici, A. Saba, *Tetrahedron: Asymmetry* **1999**, *10*, 543–550.

Received: July 20, 2005
Published Online: December 1, 2005

 © 2006 Wiley-VCH Verlag GmbH & Co. KGaA, Weinheim 

DOI: 10.1002/ejic.200500646

# Bis(stannyl)phosphanyl-Substituted Dichlorosilanes/Germanes − Potential Precursors for a Novel Strategy Toward P–Si/Ge Multiple Bonds?

**Marion Bender,[a] Edgar Niecke,*[a] Martin Nieger,[a] and Rudolf Pietschnig*[b]**

**Keywords:** Silicon / Tin / Phosphorus / Hyperconjugation

A general synthetic route to bis(stannyl)phosphanyl-substituted dichlorosilanes/germanes of the type R–$SiCl_2$–$P(SnMe_3)_2$ and R–$GeCl_2$–$P(SnMe_3)_2$ is reported. For R = Cp* (= 1,2,3,4,5-pentamethylcyclopentadienyl) crystal structures for the corresponding silane and germane could be obtained. These compounds are the first structurally characterized bis(stannyl)phosphanyl-substituted dichlorosilanes/germanes that due to their functionalities should be ideal precursors for the generation of unsaturated PSi and PGe units and possibly phosphasilynes and phosphagermynes.
(© Wiley-VCH Verlag GmbH & Co. KGaA, 69451 Weinheim, Germany, 2006)

## Introduction

After the recent success of preparing stable disilynes,[1–3] the synthesis of triple-bonded systems of silicon and germanium towards other elements remains one of the major challenges in main group chemistry. While examples for transition-metal complexed silylynes and germylynes have been reported,[4–6] triple bonds of silicon and germanium towards other main group elements have not to date been stabilized, despite theoretical predictions.[7,8] In this respect, 1,2-chlorosilane elimination has proven to be unsuccessful, while the analogous chlorostannane elimination has not been exploited for this purpose to date. This prompted us to investigate whether chlorostannane elimination might be a better alternative for generating unsaturated PSi and PGe units.

In this contribution we report on the synthesis and structural characterization of Cp*–$SiCl_2$–$P(SnMe_3)_2$ and Cp*–$GeCl_2$–$P(SnMe_3)_2$ (Cp* = 1,2,3,4,5-pentamethylcyclopentadienyl). They are the first structurally characterized bis(stannyl)phosphanyl-substituted dichlorosilanes/germanes. Owing to their functionalities, they should be ideal precursors for the generation of unsaturated PSi and PGe units and possibly phosphasilynes and phosphagermynes.

## Results and Discussion

To synthesize Cp*–$SiCl_2$–$P(SnMe_3)_2$ (**3a**) and Cp*–$GeCl_2$–$P(SnMe_3)_2$ (**4**), we started from the corresponding trichlorosilane Cp*–$SiCl_3$ (**1**) and trichlorogermane Cp*–$GeCl_3$ (**2**), respectively. In order to introduce the bis(stannyl)phosphanyl group we reacted **1** and **2** with tris(trimethylstannyl)phosphane $P[Sn(CH_3)_3]_3$ neat in the absence of any solvent. At elevated temperature the reaction proceeds under chlorotrimethylstannane elimination, which is continuously sublimed out of the reaction mixture. This approach is necessary to avoid further exchange reactions of the stannaphosphanes.[9,10] In both cases the desired products (**3a**) and (**4**) are obtained in high yield. In addition the related bis(stannyl)phosphanyl dichlorosilanes R-$SiCl_2$–$P(SnMe_3)_2$ [R = Mes (**3b**) (Mes = 2,4,6-trimethylphenyl), Tip (**3c**) (Tip = 2,4,6-triisopropylphenyl)] have been prepared which underlines the generality of this method (Scheme 1).

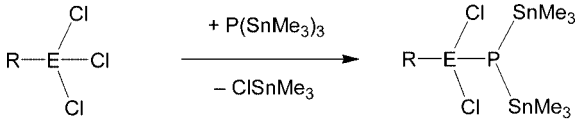


**1,2** **3,4**

Scheme 1. Synthesis of bis(stannyl)phosphanyl dichlorosilanes/germanes **3a**–**c** [E = Si; R = Cp* (**3a**), Mes (**3b**), Tip (**3c**)], **4** (E = Ge; R = Cp*) from **1** (E = Si) and **2** (E = Ge).

Compounds **3a**–**c** and **4** show an NMR signal in the high field region of the $^{31}P$ NMR spectra (Table 1), which is typical for stannylated phosphanes.[11] Due to the presence of the isotopes $^{117/119}Sn$ in the molecules, the $^1J_{P,Sn}$ coupling constants can be determined directly from the satellite transitions in these spectra. These coupling constants provide valuable information about the P–Sn bond situation which is significantly affected by the electronic behavior of the other substituents at the phosphorous atom. In principle, changing to a more electron-withdrawing substituent (R) should decrease the s-character of the P–Sn σ-bond in compounds of this constitution and therefore the $^1J_{P,Sn}$ coupling

[a] Institut für Anorganische Chemie, Rheinische Friedrich-Wilhelms-Universität Bonn,
Gerhard-Domagk-Str. 1, 53121 Bonn, Germany
[b] Institut für Chemie, Karl-Franzens-Universität Graz,
Schubertstraße 1, 8010 Graz, Austria
E-mail: rudolf.pietschnig@uni-graz.at

 © 2006 Wiley-VCH Verlag GmbH & Co. KGaA, Weinheim 

constants. Surprisingly at first sight, we observe just the opposite trend in our series of compounds (Table 1). In the same direction the $^{31}P$ NMR shift values were found to be shifted downfield. Similar observations have been made for other stannylphosphanes.[9–11] A notable feature is the relatively high $^{1}J_{P,Si}$ coupling constant observed in **3a**–**c**, which can be interpreted as an indication of strong electronic interaction within the silylphosphane unit. This is also supported by the short Si–P bond length found in the crystal structure of **3a**. Usually typical $^{1}J_{P,Si}$ values for silylphosphanes range between 16 and 53 Hz [exception $LiP(SiH_3)_2$, 256 Hz].[12] This strong electronic interaction within the silylphosphane unit can be understood assuming hyperconjugative interaction of occupied states at the phosphorus atom with vacant σ*-states derived from the Si–Cl bonds.[13,14] The decrease of $^{1}J_{P,Si}$ on going from **3a** to **3b**,**c** might be explained by the reduced phosphorus s-character of the P–Si bond due to an increase of the electron demand at the silicon atom. In line with these interpretations, the $^{31}P$ chemical shift of **4** appears at a lower field than that of **3a**, since germanium is more electronegative than silicon. Similarly, the formal $sp^2$ centers attached to silicon in **3b**,**c** should be more electron withdrawing than the formal $sp^3$ carbon atoms in **3a** resulting in a deshielding of the phosphorus center. Somewhat more subtle is the situation for the $^{1}J_{P,Sn}$ coupling constants for which an increase is observed with increasing electron demand at the E(IV) center. This trend is most likely a result of two counteracting tendencies. Again a higher electron demand on E(IV) should result in reduced phosphorus s-character of the P–Sn bond and therefore lower $^{1}J_{P,Sn}$ coupling constants. This however, is not observed, and therefore this effect is obviously not the dominant mechanism. The dominant effect leading to the observed increase of the $^{1}J_{P,Sn}$ coupling constants might, however, be attributed to the above-mentioned hyperconjugative interaction of occupied states at the phosphorus atom with vacant σ*-states derived from the Si–Cl bonds. Such occupied states could involve the σ-P–Sn bonds or alternatively the phosphorus lone pair. Increasing the electron demand on the E(IV) center should also increase this hyperconjugative interaction. Therefore, the simultaneous interaction of the phosphorus lone pair (predominant s-character) and the σ-P–Sn bonds with the σ*-states at the E(IV) atom might be responsible for an increase of the $^{1}J_{P,Sn}$ coupling that even overcompensates the decrease expected for more electron-withdrawing groups.

Table 1. Characteristic NMR spectroscopic data of **3a**–**c** and **4**.

| | $\delta(^{31}P)$ [ppm] | $^{1}J(P,^{117}Sn)$ [Hz] | $^{1}J(P,^{119}Sn)$ [Hz] | $^{1}J(P,Si)$ [Hz] |
|---|---|---|---|---|
| **3a** | –272.1 | 669.2 | 721.0 | 116.1 |
| **3b** | –242.5 | 681.2 | 713.4 | 99.0 |
| **3c** | –235.0 | 692.9 | 724.7 | 101.4 |
| **4** | –242.4 | 718.4 | 751.5 | – |

We were able to obtain single crystals of **3a** and **4** that were suitable for X-ray diffraction. The crystal structure analysis of **3a** confirms that one chlorine atom in **1** has been displaced by a bis(stannyl)phosphanyl group (Figure 1). The phosphorus atom shows a pyramidal coordination environment with an angular sum of 309.83(7)°. The silicon atom shows a slightly distorted tetrahedral environment with a Cl–Si–Cl angle of 100.6(1)° and a Cl(2)–Si–P angle of 114.31(9)°. The central Si–P bond is at 2.209(2) Å short compared to standard bond lengths (2.24–2.28 Å) and the sum of the covalence radii (2.28 Å).[15,16] Again this contraction can be understood assuming hyperconjugative interaction of occupied σ-states assigned to the P–Sn bond with vacant σ*-states derived from the Si–Cl bonds.[13,14] This interaction should be concomitant with an elongation of the Si–Cl bonds, which in fact is observed. The Si–Cl distances are at 2.078(2) and 2.080(2) Å longer than the standard bond length of 2.02 Å.[15] As a consequence of such hyperconjugative interaction also the Sn–P bond length should be affected. However, the values are at 2.505(1) and 2.510(1) Å for **3a** in the typical range for P–Sn single bonds.[23] The significant elongation of the Si–Cl bonds with no structural change of the P–Sn bonds might be an indication that the hyperconjugative interaction of the phosphorus lone pair with σ*-states derived from the Si–Cl bonds might in fact be more significant in this case. From a Newman projection along the Si–P bond, the eclipsed conformation becomes obvious (Figure 2). The lone pair of the phosphorus atom points towards the Cp* moiety. The almost perfect synperiplanar arrangement of the stannyl groups relative to the Cl atoms deviates only slightly, with dihedral angles Sn–P–Si–Cl of 0.2° and 7.4°. Within these planes the Sn···Cl distances are at 3.639 and 3.706 Å shorter than the sum of the van der Waals radii (Figure 3).[17]

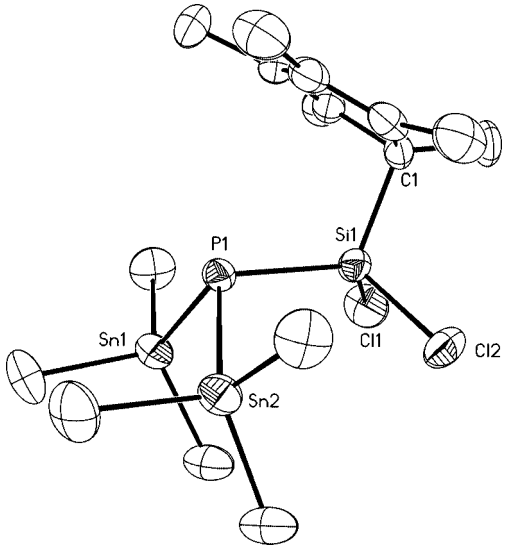


Figure 1. ORTEP plot of **3a** (thermal ellipsoids at 30% probability level).

A similar situation is found in the crystal structure of dichlorogermane **4** (Figure 4). The P–Ge distance is at 2.274(2) Å in the short range of single bond lengths observed for this element combination (2.30–2.36 Å).[18,19] Again, the substituents flanking this central bond show an eclipsed conformation concomitant with attractive Sn···Cl

 © 2006 Wiley-VCH Verlag GmbH & Co. KGaA, Weinheim 

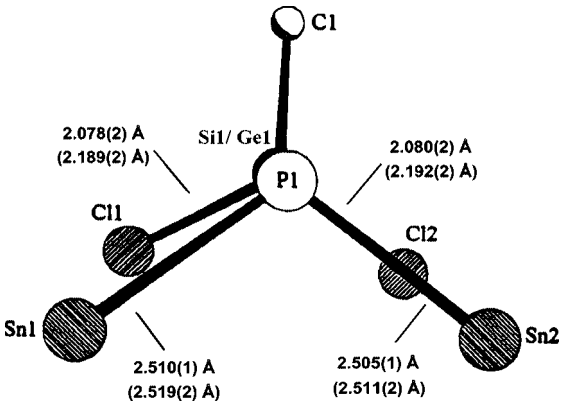


Figure 2. Newman projection and selected bond lengths of **3a** and **4** (in brackets).

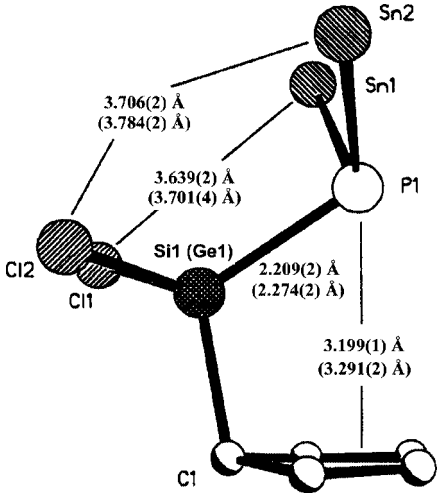


Figure 3. Relevant intramolecular distances of **3a** and **4** (in brackets).

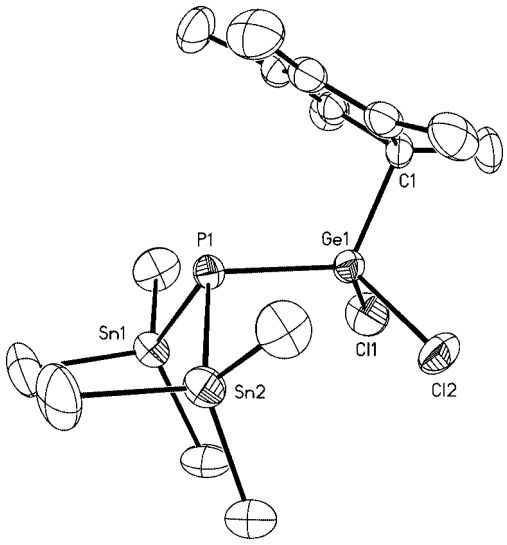


Figure 4. ORTEP plot of **4** (thermal ellipsoids at 30% probability level).

interaction. The Sn···Cl distances are at 3.701 and 3.784 Å close to those found in **3a**. The Ge–Cl distances show values of 2.189(2) and 2.192(2) Å. As in **3a**, the P–Sn distances in **4** show with values of 2.511(2) and 2.519(2) Å no peculiarities. The dihedral angles, by which the Sn–P–Ge–Cl planes differ from a perfect synperiplanar arrangement, are 1.1° and 6.2°.

In both structures the short Si–P or Ge–P bond lengths in addition to the attractive Sn···Cl interaction seem to underline the tendency of both molecules to eliminate chlorostannane. Interestingly in the mass spectra of **3a** and **4**, the molecular ions both lose one equivalent of chlorotrimethylstannane. The elimination of a second equivalent of chlorotrimethylstannane from the resulting phosphasilene and phosphagermene cations is not observed, however.

While solutions of these compounds in aprotic solvents are stable at room temperature, heating of **3a** or **4** as neat substances up to 200 °C leads to elimination of trimethylchlorostannane. During this process polymeric materials are formed which we have not been able to characterize yet. Preliminary results suggest that intermolecular condensation processes via chlorostannane elimination are favored over intramolecular elimination under these conditions.[20]

As outlined earlier, the structural and spectroscopic parameters of **3a**–**c** and **4** suggest significant hyperconjugative interaction in this type of molecules. To get further insight into the bonding situation we performed quantum chemical calculations on the germanium compound **4** which shows the largest hyperconjugative effect. As a result we find good agreement of the theoretical with the experimental structural data. Moreover, a population analysis provides evidence that bonding states at the phosphorus atom as well as the lone pair interact with σ*-states derived from the Ge–Cl bonds. The HOMO-1 of **4** is mainly located at the phosphorus atom but shows some mixing with the Ge–Cl bonds (Figure 5). Quite similar is the situation for the Cp*–centered HOMO-2 that also partially involves the phosphorus atom. In the HOMO-3 the antibonding Ge–Cl σ*-states mix with bonding Sn–P σ-states (Figure 6).

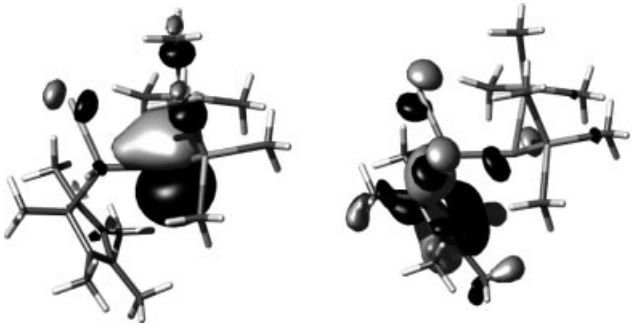

Figure 5. Surface plot of the HOMO-1 (left) and the HOMO-2 (right) in **4**.

In summary, we presented a general synthetic route to bis(stannyl)phosphanyl-substituted dichlorosilanes and germanes that should allow a novel approach towards the first

 © 2006 Wiley-VCH Verlag GmbH & Co. KGaA, Weinheim 

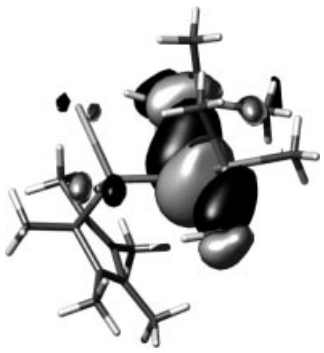

Figure 6. Surface plot of the HOMO-3 in **4**.

generation of hypothetical phosphasilylynes and phosphagermylynes. The molecular structures of two representative examples show substantial hyperconjugative interaction between the stannylphosphanyl and the chlorosilyl/germyl units, which are ideally preorganized for chlorostannane elimination.

## Experimental Section

All chemical experiments were performed under argon using standard Schlenk techniques or a glovebox. Solvents were dried with sodium/potassium alloy and stored under argon. $^{1}H$, $^{13}C$, $^{31}P$, $^{29}Si$, and $^{119}Sn$ NMR spectra were recorded with a Bruker AMX 300 at room temperature. Chemical shift values are given in ppm and were referenced to external standards. Mass spectra were measured on Kratos MS-50 and Masslab VG 12–250 spectrometers using the EI ionization technique. Compounds **1**, **2**, and $P(SnMe_3)_3$ were prepared according to published procedures.[21,22]

**Synthesis of 3a–c and 4:** Tris(trimethylstannyl)phosphane (1.05 g, 2 mmol) was placed in a sublimation apparatus together with an equimolar amount of the corresponding trichlorosilanes **1a**–**c** or trichlorogermane **2**. The mixture was heated to 150 °C until all the chlorotrimethylstannane sublimed off (approximately 1 h). The remaining residue was dissolved in pentane (10 mL) and stored at –20 °C. After 12 h, **3a**–**c** precipitated as colorless (**3a**) to slightly yellow (**3b**,**c**; **4**) crystalline solids in 95% (**3a**), 92% (**3b**), 94% (**3c**) and 95% (**4**) yield.

**3a:** M.p. 181 °C. $^{31}P$ NMR ($C_6D_6$): $\delta$ = –272.1 ($^{1}J_{P(119),Sn}$ = 721.0, $^{1}J_{P(117),Sn}$ = 669.2 Hz) ppm. $^{29}Si$ NMR ($C_6D_6$): $\delta$ = 33.1 (d, $^{1}J_{Si,P}$ = 116.1 Hz) ppm. $^{119}Sn$ NMR ($C_6D_6$): $\delta$ = 36.6 (d, $^{1}J_{Sn,P}$ = 721.0, $^{1}J_{Sn,C}$ = 320.4, $^{2}J_{Sn,Si}$ = 36.7, $^{2}J_{(119)Sn,(117)Sn}$ = 219.3 Hz) ppm. $^{1}H$ NMR ($C_6D_6$): $\delta$ = 1.90 (12 H), 1.85 (3 H), 0.44 (d, 18 H, $^{3}J_{H,P}$ = 2.39, $^{2}J_{H(119),Sn}$ = 54.9, $^{2}J_{H(117),Sn}$ = 52.7 Hz) ppm. $^{13}C$ NMR ($C_6D_6$): $\delta$ = 140.0, 134.5, 33.0 (d, $^{2}J_{C,P}$ = 12.0 Hz), 12.7, 12.2, –3.1 (d, $^{2}J_{C,P}$ = 7.6 Hz; $^{1}J_{C(119),Sn}$ = 320, $^{1}J_{C(117),Sn}$ = 305 Hz) ppm. MS (EI): *m*/*z* = 589.9510 ($\delta$ = 0.67 ppm dev.) $[M]^+$, 12%, 394 $[M – ClSn(CH_3)_3]^+$, 40%, 379 $[M – ClSn(CH_3)_3 – CH_3]^+$, 60%, 165 $[Sn(CH_3)_3]^+$, 100%, 135 $[Cp^*]^+$, 50%. $C_{16}H_{33}Cl_2PSiSn_2$ (592.82): calcd. C 32.42, H 5.61; found C 32.60, H 5.72.

**3b:** $^{31}P$ NMR ($C_6D_6$): $\delta$ = –242.5 ($^{1}J_{P(119),Sn}$ = 713.4, $^{1}J_{P(117),Sn}$ = 681.2 Hz) ppm. $^{29}Si$ NMR ($C_6D_6$): $\delta$ = 25.3 (d, $^{1}J_{Si,P}$ = 99.0 Hz) ppm. $^{13}C$ NMR ($C_6D_6$): $\delta$ = 156.0, 152.1, 147.6, 122.8, 25.6, 24.0, 7.9 (d, $^{2}J_{C,P}$ = 7.2 Hz) ppm. $C_{15}H_{29}Cl_2PSiSn_2$ (576.78): calcd. C 31.24, H 5.07; found C 31.38, H 5.18.

**3c:** $^{31}P$ NMR ($C_6D_6$): $\delta$ = –235.0 ($^{1}J_{P(119),Sn}$ = 724.7, $^{1}J_{P(117),Sn}$ = 692.9 Hz) ppm. $^{29}Si$ NMR ($C_6D_6$): $\delta$ = 24.4 (d, $^{1}J_{Si,P}$ = 101.4 Hz) ppm. $^{1}H$ NMR ($C_6D_6$): $\delta$ = 6.93 (s, 2 H), 4.13 (2 H, sept, $^{3}J_{H,H}$ = 6.9 Hz), 2.73 (1 H, sept, $^{3}J_{H,H}$ = 10.3 Hz), 1.23 (d, 12 H, $^{3}J_{HH}$ = 6.9 Hz), 1.17 (d, 6 H, $^{3}J_{H,H}$ = 10.3 Hz), 0.29 (d, 18 H, $^{3}J_{H,P}$ = 2.3 Hz) ppm. $^{13}C$ NMR ($C_6D_6$): $\delta$ = 155.9, 152.2, 129.7, 122.7, 34.6, 33.3, 25.6, 24.0, –4.1 (d, $^{2}J_{C,P}$ = 7.0 Hz) ppm. MS (EI): *m*/*z* = 662.0136 ($\delta$ = 2.6 ppm dev.) $[M]^+$, 50%, 447 $[M – ClSn(CH_3)_3 – CH_3]^+$, 70%, 278 $[TipSiPCH_4]^+$, 100%, 262 $[TipSiP]^+$, 5%. $C_{21}H_{41}Cl_2PSiSn_2$ (660.93): calcd. C 38.16, H 6.25; found C 38.34, H 6.36.

**4:** $^{31}P$ NMR ($C_6D_6$): $\delta$ = –242.4 ($^{1}J_{P(119),Sn}$ = 751.5, $^{1}J_{P(117),Sn}$ = 718.4 Hz) ppm. $^{1}H$ NMR ($C_6D_6$): $\delta$ = 1.94 (15 H), 0.50 (d, 18 H, $^{3}J_{H,P}$ = 2.5 Hz) ppm. $^{13}C$ NMR ($C_6D_6$): $\delta$ = 12.1 (m), –3.01 (d, $^{2}J_{C,P}$ = 7.5 Hz; $^{1}J_{C(119),Sn}$ = 160.9, $^{1}J_{C(117),Sn}$ = 153.6 Hz) ppm. MS (EI): *m*/*z* = 635.8953 ($\delta$ = 0.57 ppm dev.) $[M]^+$, 12%, 438 $[M – ClSn(CH_3)_3]^+$, 35%, 423 $[M – ClSn(CH_3)_3 – CH_3]^+$, 58%, 165 $[Sn(CH_3)_3]^+$, 100%. $C_{16}H_{33}Cl_2GePSn_2$ (637.34): calcd. C 30.15, H 5.22; found C 30.26, H 5.28.

**Crystallographic Details for 3a:** A colorless crystal of **3a** with dimensions 0.40 × 0.35 × 0.35 mm was sealed in a glass capillary. The measurements were performed with a Nicolet R3M diffractometer using graphite-monochromatized Mo-$K_a$ radiation at 273 K. A total of 4578 reflections were collected ($\Theta_{max}$ = 25.00°), from which 4383 were unique ($R_{int}$ = 0.0361), with 4380 having $I > 2\sigma(I)$. The structure was solved by direct methods and refined by full-matrix least-squares techniques against $F^2$ with SHELXTL-Plus[28]. The non-hydrogen atoms were refined with anisotropic displacement parameters without any constraints. For 210 parameters final *R* indices of *R* = 0.0573 and $wR_2$ = 0.1048 (*GOF* = 0.989) were obtained.

**Crystallographic Details for 4:** A yellow crystal of **4** with dimensions 0.55 × 0.55 × 0.25 mm was sealed in a glass capillary. The measurements were performed with a Nicolet R3M diffractometer using graphite-monochromatized Mo-$K_a$ radiation at 293 K. A total of 4549 reflections were collected ($\Theta_{max}$ = 25.00°), from which 4399 were unique ($R_{int}$ = 0.0780), with 4396 having $I > 2\sigma(I)$. The structure was solved by direct methods and refined by full-matrix least-squares techniques against $F^2$ with SHELX-97.[28] The non-hydrogen atoms were refined with anisotropic displacement parameters without any constraints. For 210 parameters final *R* indices of *R* = 0.0744 and $wR_2$ = 0.1174 (*GOF* = 0.946) were obtained (Table 2).

Table 2. Crystal data and structure refinement for **3a** and **4**.

| Reference | **3a** | **4** |
|---|---|---|
| Formula | $C_{16}H_{33}Cl_2PSiSn_2$ | $C_{16}H_{33}Cl_2GePSn_2$ |
| Formula weight | 592.8 | 637.3 |
| Temp. [K] | 293 | 293 |
| Wavelength | 0.71073 | 0.71073 |
| Crystal system | monoclinic | monoclinic |
| Space group | $P2_1/c$ | $P2_1/c$ |
| Unit cell dimensions | | |
| *a* [Å] | 10.004(3) | 10.027(2) |
| *b* [Å] | 14.326(2) | 14.325(2) |
| *c* [Å] | 17.908(3) | 17.916(3) |
| $\alpha$ [°] | 90 | 90 |
| $\beta$ [°] | 103.56(2) | 102.95(1) |
| $\gamma$ [°] | 90 | 90 |
| Volume [Å$^3$] | 2495.0(9) | 2508.0(1) |
| *Z* | 4 | 4 |
| Density (calcd.) [Mg/m$^3$] | 1.578 | 1.688 |
| $\mu$ [mm$^{-1}$] | 0.710 | 3.440 |
| Goodness-of-fit on $F^2$ | 0.989 | 0.946 |
| $R_1$ (obsd. data) | 0.0573 | 0.0744 |
| $wR_2$ (all data) | 0.1048 | 0.1174 |

 © 2006 Wiley-VCH Verlag GmbH & Co. KGaA, Weinheim 

CCDC-183386 (for **3a**) and -183388 (for **4**) contain the supplementary crystallographic data for this paper. These data can be obtained free of charge from The Cambridge Crystallographic Data Centre via www.ccdc.cam.ac.uk/data_request/cif.

**Computational Details:** Ab initio quantum chemical calculations were performed for compound **4** using the program Gaussian 03[23] on Hartree–Fock and DFT(B3LYP) level, employing a Dunning/Huzinaga full double zeta basis set on first row elements,[24] and Los Alamos ECP plus DZ on Na-Bi.[25–27] The harmonic vibrational frequencies and their infrared intensities for all of the optimized structures were evaluated by the B3LYP method to determine if a structure is a genuine minimum. Representations of the molecular orbitals are shown at a contour value of 0.04.

## Acknowledgments

R. P. is grateful for financial support from the Austrian Science Fund (FWF, project P17882-N11).

[1] A. Sekiguchi, R. Kinjo, M. Ichinohe, *Science* **2004**, *305*, 1755–1757.
[2] R. West, *Science* **2004**, *305*, 1724–1725.
[3] N. Wiberg, W. Niedermayer, G. Fischer, H. Nöth, M. Suter, *Eur. J. Inorg. Chem.* **2002**, 1066–1070.
[4] A. C. Filippou, P. Portius, A. I. Philippopoulos, *Organometallics* **2002**, *21*, 653–661.
[5] B. V. Mork, T. D. Tilley, *Angew. Chem. Int. Ed.* **2003**, *42*, 357–360.
[6] R. S. Simons, P. P. Power, *J. Am. Chem. Soc.* **1996**, *118*, 11966–11967.
[7] C.-H. Lai, M.-D. Su, S.-Y. Chu, *Inorg. Chem.* **2002**, *41*, 1320–1322.
[8] C.-H. Lai, S. Ming-Der, S.-Y. Chu, *J. Phys. Chem. B* **2002**, *106*, 575–579.
[9] H. Schumann, P. Schwabe, O. Stelzer, *Chem. Ber.* **1969**, *102*, 2900–2913.
[10] H. Schumann, H. J. Kroth, L. Rösch, *Z. Naturforsch., Teil B* **1974**, *29*, 608–610.
[11] H. Schumann, H. J. Kroth, *Z. Naturforsch. Teil B* **1977**, *32*, 876–879.
[12] H. Marsmann, "$^{29}$Si-NMR Spectroscopic Results" in *NMR Basic Principles and Progress, Oxygen-17 and Silicon-29* (Eds.: P. Diehl, E. Fluck, R. Kosfeld), Springer, Berlin, Heidelberg, New York, **1981**, pp. 65–235.
[13] A. J. Kos, P. v. R. Schleyer, *Tetrahedron* **1983**, *39*, 1141–1150.
[14] A. E. Reed, P. v. R. Schleyer, *J. Am. Chem. Soc.* **1990**, *112*, 1434–1445.
[15] P. Rademacher, *Strukturen Organischer Moleküle*, VCH, Weinheim, **1987**, p. 56.
[16] G. Becker, H. M. Hartmann, W. Schwarz, *Z. Anorg. Allg. Chem.* **1989**, *577*, 9–22.
[17] R. C. Weast, *Handbook of Chemistry and Physics*, CRC Press, Florida, **1983**.
[18] M. Regitz, O. J. Scherer, "Multiple Bonds and Low Coordination", in *Phosphorus Chemistry*, Thieme, Stuttgart, **1990**.
[19] K. M. Baines, W. G. Stibbs, *Coord. Chem. Rev.* **1995**, *145*, 157–200.
[20] Experiments to disfavor intermolecular elimination by dilution with high boiling solvents or by complexation prior to elimination are currently in progress.
[21] P. Jutzi, H. Saleske, D. Buehl, H. Grohe, *J. Organomet. Chem.* **1983**, *252*, 29–36.
[22] H. Schumann, L. Rösch, *Chem. Ber.* **1974**, *107*, 854–868.
[23] http://www.gaussian.com/.
[24] T. H. Dunning, Jr., P. J. Hay, *Modern Theoretical Chemistry* (Ed.: H. F. Schaefer III), Plenum, New York, **1977**, vol. 3, pp. 1–27.
[25] P. J. Hay, W. R. Wadt, *J. Chem. Phys.* **1985**, *82*, 270–283.
[26] W. R. Wadt, P. J. Hay, *J. Chem. Phys.* **1985**, *82*, 284–298.
[27] P. J. Hay, W. R. Wadt, *J. Chem. Phys.* **1985**, *82*, 299–310.
[28] G. M. Sheldrick, *Program for the Solution of Crystal Structures*, University of Göttingen, Germany, **1997**.

Received: July 20, 2005
Published Online: November 23, 2005

 © 2006 Wiley-VCH Verlag GmbH & Co. KGaA, Weinheim 

DOI: 10.1002/ejic.200500662

# From Molecular Double-Ladders to an Unprecedented Polycatenation: A Parallel Catenated 3D Network Containing Bicapped Keggin Polyoxometalate Clusters

**Zhenyu Shi,[a] Xiaojun Gu,[a] Jun Peng,*[a] Xia Yu,[a] and Enbo Wang[a]**

**Keywords:** Coordination polymers / Parallel catenation / Double ladders / Hydrothermal synthesis

A new three-dimensional coordination polymer, $\{Cu_3(4,4'\text{-bpy})_3(H_2O)[PMo_{12}O_{40}(VO)_2]\cdot 5H_2O\}_n$ (**1**) (4,4′-bpy = 4,4′-bipyridine), which represents the first example of 3D polycatenation generated by unprecedented parallel catenation of the 1D double ladders, has been hydrothermally synthesized.
(© Wiley-VCH Verlag GmbH & Co. KGaA, 69451 Weinheim, Germany, 2006)

## Introduction

Self-assembly of entangled network structures based upon the principle of crystal engineering has attracted much attention not only because of their promising potential applications in catalysis, ion exchange, photochemistry, and electromagnetism, but also because of their intriguing architectures and topologies.[1] Up to now, a number of entangled networks have been reported, however, the "true" engineering is still a great challenge because of the existence of numerous weak interactions in crystal packing. Recently, thanks to the work of Robson, Batten, Ciani and others,[1a,2] many entangled networks have been engineered under a strategy of "network approach". Success in producing such structures depends on understanding and controlling the topological and geometric relationships between molecular modules, along with the coordination characteristics of the metal ions. Of the many reported entangled network structures, those constructed from molecular ladder motifs are very attractive, while relatively rare.[1a] The main reason is probably attributed to the difficulty of obtaining T-shaped building blocks, which are essentially used to build up the ladder structures. So far two kinds of entanglement modes have been found in polycatenated ladders, namely, inclined catenation and parallel catenation (Scheme 1). Usually, inclined catenation of 1D ladders can generate 1D→2D and 1D→3D arrays,[3] while parallel catenation can produce 1D→1D, 1D→2D,[4] and 1D→3D arrays. To the best of our knowledge, no 3D polycatenation produced by parallel catenation of 1D ladders (1D→3D parallel) has been reported.

Scheme 1. Schematic representation of two kinds of entanglement modes of 1D molecular ladders: (top) inclined catenation, (bottom) parallel catenation.

Polyoxometalate (POM) clusters, known to have large sizes and interesting properties for medicine and nonlinear optics, are an outstanding class of linkers for the construction of interpenetrating networks.[1f] They have capabilities similar to those of organic ligands in linking metal centers, as evidenced in the recently reported literature.[5] Hence, directly utilizing POM clusters as linkers promises to be an appealing route to design new entangled network structures. Unfortunately, this strategy remains unexplored owing to the difficulties in choosing suitable POM clusters as a linker whose skeleton can be fully maintained during preparation. Our previous work has proved that bicapped Keggin POM clusters can function as rigid bidentate bridging ligands.[6] Thus, our synthetic strategy is to introduce two kinds of bidentate bridging ligands, i.e. Keggin clusters and 4,4′-bpy, as linkers into the metal centers with potential T-type coordination sites in order to construct new molecular ladders.

Herein, we report a new compound, $\{Cu_3(4,4'\text{-bpy})_3(H_2O)[PMo_{12}O_{40}(VO)_2]\cdot 5H_2O\}_n$ (**1**) (4,4′-bpy = 4,4′-bipyr-

[a] Institue of Polyoxometalate Chemistry, Department of Chemistry, Northeast Normal University,
Changchun, 130024, P. R. China
E-mail: jpeng@nenu.edu.cn or pjun56@yahoo.com
Supporting information for this article is available on the WWW under http://www.eurjic.org or from the author.

 © 2006 Wiley-VCH Verlag GmbH & Co. KgaA, Weinheim 

idine), which is based on a new motif 1D double ladder. The polycatenation of 1D double ladders in **1** gives a 3D polycatenation (1D→3D parallel). In comparison with other catenated ladders, **1** has several unique features: (i) a bicapped Keggin cluster $\{PMo_{12}O_{40}(VO)_2\}$ is utilized as a linker, (ii) the new motif, 1D double ladder, is introduced into an entangled system for the first time, and (iii) the 3D architecture is generated by unusual 1D→3D parallel catenation.

## Results and Discussion

The successful isolation of compound **1** relies on the exploitation of hydrothermal techniques and the choice of organic reductant species. So far hydrothermal synthesis has become a powerful method for the preparation of organic-inorganic hybrid materials because of its advantages over other methods (e.g., diffusion and sol-gel techniques), such as the effective use of inorganic and organic reagents with low solubility. Although in most cases the reaction mechanisms under hydrothermal conditions remain elusive and the control and prediction of crystal structures are very difficult, the architecture of the final product depends directly on the interplay of starting materials, pH value, reaction temperature, and pressure. Our interest is to construct new molecular ladders by using 4,4′-bpy and presynthesized Keggin clusters as linkers. Experiments demonstrated that triethylamine was crucial for obtaining compound **1**. Under hydrothermal conditions, triethylamine with moderate ability to reduce can activate the Keggin cluster by reducing $Mo^{VI}$ to $Mo^{V}$ without metal-exchange or decomposition. On the other hand, $Cu^{II}$ ions can also be reduced by it to $Cu^{I}$ ions with potential T-type coordination sites.[6c]

Single crystal X-ray diffraction reveals that **1** is a polycatenated 3D molecular double ladder. As shown in Figure 1, the 1D double ladder is composed of three crystallographically unique $Cu^{I}$ atoms as nodes linked by bicapped Keggin clusters $\{PMo_{12}O_{40}(VO)_2\}$ and 4,4′-bpy molecules. Each $Cu^{I}$ atom displays T-shaped trigonal geometry. Atoms Cu1 and Cu2 are coordinated by two nitrogen atoms from two 4,4′-bpy ligands and one oxygen atom from one {VO} group belonging to a $[PMo^{VI}_8Mo^{V}_4O_{40}(V^{IV}O)_2]^{3-}$ polyanion, while the Cu3 atom is coordinated by two nitrogen atoms from two 4,4′-bpy ligands and one oxygen atom from a water molecule. All the Cu2 atoms are joined together by 4,4′-bpy to form a middle rail of the double ladder. The alternate Cu1 and Cu3 atoms are also linked together by 4,4′-bpy to form the edge rails. The polyanion $[PMo^{VI}_8Mo^{V}_4O_{40}(V^{IV}O)_2]^{3-}$ functions as a rung of the double ladder, linking the two adjacent atoms Cu1 and Cu2 together. The structure of the polyanion $[PMo^{VI}_8Mo^{V}_4O_{40}(V^{IV}O)_2]^{3-}$, similar to that of $[PMo^{V}_6Mo^{VI}_6O_{40}(V^{IV}O)_2]^{5-}$,[7] can best be described as a bicapped Keggin structure that is essentially built on an α-Keggin core $\{PMo_{12}O_{40}\}$ capped by two{VO} units. The central atom P in the polyanion is located at the inversion center, which results in a disordered $PO_4$ tetrahedron, that is, the central atom P is surrounded by a cube of eight oxygen atoms, and each oxygen site is half-occupied. The valence sum calculations,[8] ESR and XPS spectra show that all the vanadium atoms are in the +4 oxidation state, while the four molybdenum atoms are in the +5 oxidation state, which confirms the molecular formula of **1**.

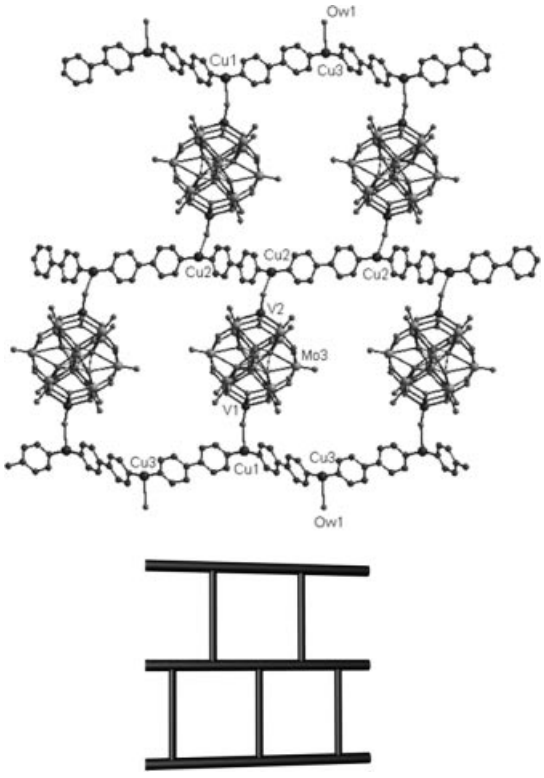


Figure 1. (top) View of part of the infinite 1D double ladder; (bottom) the schematic representation of the 1D double ladder.

In **1**, each rectangle (size ca. 17 × 14 Å) of the double ladder is penetrated by two other parallel double ladders that are staggered with each other (Figure 2). Although all the ladders run in the same direction (*b* axis), the staggered interpenetration by the parallel ladders increases the dimensionality of the whole polymeric system and thus leads to the 1D→3D expansion (Figure 3). To the best of our knowledge, among the few examples of polycatenated 3D molecular ladders (1D→3D), this is the first example of 3D structures generated by parallel catenation. Interpenetration in nature is a space-filling effect to produce a dense framework, but, surprisingly, the multiple catenation of the 1D double ladder does not occupy all the voids formed by one independent ladder. As shown in Figure S1 (Supporting Information), there are 1D channels running along the *c* axis direction that are filled by the guest water molecules. Hydrogen-bonding interactions between the ladders and clathrate water molecules generate a 3D complex supramolecular architecture (Figure S2).

Compared with recently reported Keggin-based compounds with 4,4′-bpy ligands, whose structures are very interesting but noninterpenetrated,[5] compound **1** is a polycatenated 3D molecular double ladder. The formation of such catenation may be ascribed to the bigger sizes of the rectangle grids.

 © 2006 Wiley-VCH Verlag GmbH & Co. KGaA, Weinheim

Figure 2. Schematic illustration of entanglement modes of the double ladder in compound **1**.

Figure 3. Schematic view of the 3D structure of compound **1** generated by parallel catenation of 1D double ladders.

The IR spectrum exhibits the characteristic peaks of the α-Keggin structure at 1060, 945, 860, and 775 $cm^{-1}$ in **1**, which are attributed to $\nu$(P–$O_a$), $\nu$(M–$O_t$), $\nu$(M–$O_b$–M), and $\nu$(M–$O_c$–M) (M = V or Mo). The peaks at 1640, 1515, and 1462 $cm^{-1}$ are characteristic of the 4,4′-bpy molecules. In the UV spectrum of **1**, there is a strong absorption peak at 206 nm and a weaker absorption band at 236 nm, which are consistent with the characteristic absorption bands of the Keggin skeleton. The EPR spectrum of **1** exhibits the $V^{IV}$ signal at 293 K with $g$ = 1.9704 (Figure S3). The XPS spectra give a peak at 516.2 eV for **1**, which is attributed to $V^{IV}$, and two overlapped peaks at 232.4 and 231.0 eV attributed to $Mo^{VI}$ and $Mo^{V}$, respectively (Figure S4). All of these results further confirm the structure analysis.

Thermogravimetric analysis in $N_2$ indicates three steps of weight loss. The first two stages of weight loss of 3.98% occur in the temperature range 45–320 °C and correspond to the release of the guest water molecules. The third weight loss of 17.51% occurs from 360 to 570 °C, because of the release of the 4,4′-bpy ligands (Figure S5).

In order to study the redox property of **1**, a **1**-bulk-modified carbon paste electrode (**1**-CPE) was fabricated as the working electrode because of its insolubility in water and most organic solvents. The cyclic voltammetric behavior of **1**-CPE was measured in an aqueous solution of NaCl and HCl (0.2 M, pH = 2.3). In the potential range from +600 to –350 mV, there are three pairs of reversible redox peaks, and the average peak potentials, $E_{1/2}$ = (Ecp + Eap)/2, are +370, +50, and –150 mV (Figure S6). Each pair of redox peaks can be ascribed to a two-electron process involving molybdenum.[9]

In conclusion, using the Keggin cluster and 4,4′-bpy ligand as linkers, we have successfully isolated the first example of polycatenated 3D molecular double ladders generated from parallel catenation. This method may lead to a new family of interpenetrated networks that can be obtained by using suitable POM clusters as linkers.

## Experimental Section

**Materials:** All reagents and solvents for syntheses were purchased commercially and used as received.

**Physical Methods:** Elemental analyses (C, H, and N) were performed with a PerkinElmer 2400 CHN Elemental Analyzer. P, Mo, V, and Cu were determined with a Leaman inductively coupled plasma (ICP) spectrometer. IR spectra were obtained with an Alpha Centaurt FT/IR spectrometer with KBr pellets in the 400–4000 $cm^{-1}$ region. XPS analyses were performed with a VG ESCALAB MK II spectrometer with a Mg-$K_\alpha$ (1253.6 eV) achromatic X-ray source. The vacuum inside the analysis chamber was maintained at $6.2 \times 10^{-6}$ Pa during analysis. The ESR spectrum was recorded with a Japanese JES-FE3AX spectrometer at room temperature. UV/Vis spectra were recorded with a 756 CRT UV/Vis spectrophotometer made in Shanghai, China. The TG analyses were performed with a Perkin–Elmer TGA7 instrument in flowing $N_2$ at a heating rate of 10 °C $min^{-1}$. Cyclic voltammograms were obtained with a CHI 660 electrochemical workstation at room temperature. Platinum gauze was used as the counter electrode and an Ag/AgCl was used as the reference electrode. A chemically bulk-modified carbon paste electrode (CPE) was used as the working electrode.

**Synthesis of $\{Cu_3(4,4'\text{-bpy})_3(H_2O)[PMo_{12}O_{40}(VO)_2]\cdot 5H_2O\}_n$ (1):** The starting materials $Cu(NO_3)_2\cdot 4H_2O$ (0.1298 g, 0.5 mmol), $H_3[PMo_{12}O_{40}]\cdot xH_2O$ (0.4658 g, 0.25 mmol), $NH_4VO_3$ (0.0585 g, 0.5 mmol), 4,4′-bpy (0.0961 g, 0.5 mmol), triethylamine (0.14 mL), and $H_2O$ (9 mL) were mixed together. The resulting suspension was stirred for 1 h, sealed in a Teflon-lined reactor, and heated at 160 °C for 72 h. Then the autoclave was cooled at 5 °C $h^{-1}$ to room temperature. Black prism crystals of compound **1** were filtered, washed with water, and dried at room temperature. Yield: 0.395 g (58% based on molybdenum). $C_{30}H_{36}Cu_3Mo_{12}N_6O_{48}PV_2$ (2723.46): calcd. C 13.23, H 1.33, Cu 7.00, Mo 42.27, N 3.08, P 1.14, V 3.74; found C 13.31, H 1.22, Cu 7.09, Mo 42.13, N 3.01, P 1.03, V 3.81. IR (KBr): 1640 (w), 1515 (m), 1462 (w), 1060 (w), 945 (m), 860 (w), 775 (m) $cm^{-1}$.

**Preparation of 1-CPE:** Graphite powder (90 mg) and **1** (15 mg) were mixed and ground together by an agate mortar and pestle to achieve an even, dry mixture. Nujol (0.12 mL) was added to the mixture and stirred with a glass rod. The homogenized mixture was then packed into a 1.2 mm inner diameter glass tube, and the surface was wiped with paper. Electrical contact was established with a copper rod through the back of the electrode.

**X-ray Crystallography:** Crystal data for the compound were collected with a Rigaku R-AXIS RAPID IP diffractometer, with Mo-$K_\alpha$ monochromated radiation ($\lambda$ = 0.71073 Å) at 293 K. The structure was solved by direct methods and refined by full-matrix least-squares on $F^2$ using the SHELXTL crystallographic software package.[10] The positions of the hydrogen atoms on carbon atoms were calculated theoretically. Crystal data: $C_{30}H_{36}Cu_3Mo_{12}N_6O_{48}PV_2$,

 © 2006 Wiley-VCH Verlag GmbH & Co. KGaA, Weinheim 

orthorhombic, *Pnma*, $M_r$ = 2723.46 g mol$^{-1}$, $a$ = 27.962(6), $b$ = 21.174(4), $c$ = 11.802(2) Å, $V$ = 6988(2) Å$^3$, $T$ = 293 K, $Z$ = 4, $D_c$ = 2.577 g cm$^{-3}$, $F$(000) = 5128, $\theta$ range 3.07–25.00°. A total of 47481 reflections were collected and 6009 were independent ($R_{int}$ = 0.0940). The final refinement including hydrogen atoms converged to $R$ = 0.0753, $wR$ = 0.1705.

CCDC-271165 contains the supplementary crystallographic data for this paper. These data can be obtained free of charge from The Cambridge Crystallographic Data Centre via www.ccdc.cam.ac.uk/data_request/cif.

**Supporting Information** (see footnote on the first page of this article): The detailed bond valence sum calculations and the figures illustrating the 3D structures, ESR, XPS, TG spectra, and electrochemical behavior of compound **1** are provided.

## Acknowledgments

This research was financially supported by the Nature Science Foundation of China (20271011).

[1] a) L. Carlucci, G. Ciani, D. M. Proserpio, *Coord. Chem. Rev.* **2003**, *246*, 247–289; b) R. Robson, *J. Chem. Soc. Dalton Trans.* **2000**, 3735–3744; c) M. Eddaoudi, J. Kim, N. Rosi, D. Vodak, J. Wacheter, M. O'Keeffe, O. M. Yaghi, *Science* **2002**, *295*, 469–472; d) M. A. Withersby, A. J. Blake, N. R. Champness, P. A. Cooke, P. Hubberstey, M. Schröder, *J. Am. Chem. Soc.* **2000**, *122*, 4044–4046; e) P. V. Ganesan, C. J. Kepert, *Chem. Commun.* **2004**, 2168–2169; f) J. Chen, S. F. Lu, R. M. Yu, Z. N. Chen, Z. X. Huang, C. Z. Lu, *Chem. Commun.* **2002**, 2640–2641; g) X. L. Wang, C. Qin, E. B. Wang, L. Xu, Z. M. Su, C. W. Hu, *Angew. Chem. Int. Ed.* **2004**, *43*, 5036–5040.

[2] a) S. R. Batten, R. Robson, *Angew. Chem. Int. Ed.* **1998**, *37*, 1460–1494; b) S. R. Batten, *CrystEngComm* **2001**, *18*, 1–7; c) V. A. Blatov, L. Carlucci, G. Ciani, D. M. Proserpio, *CrystEngComm* **2004**, *6*, 377–395.

[3] a) M. Fujita, O. Sasaki, K. Y. Watanabe, K. Ogura, K. Yamaguchi, *New J. Chem.* **1998**, *22*, 189–191; b) C. Y. Su, A. M. Goforth, M. D. Smith, H. C. Z. Loye, *Chem. Commun.* **2004**, 2158–2159; c) J. Tao, X. Yin, R. B. Huang, L. S. Zheng, *Inorg. Chem. Commun.* **2002**, *5*, 1000–1002; d) M. B. Zaman, K. Udachin, J. A. Ripmeester, M. D. Smith, H. C. Z. Loye, *Inorg. Chem.* **2005**, *44*, 5047–5059; e) M. Fujita, Y. J. Kwon, O. Sasaki, K. Yamaguchi, K. Ogura, *J. Am. Chem. Soc.* **1995**, *117*, 7287–7288.

[4] a) M. Maekawa, H. Konaka, Y. Suenaga, T. K. Sowa, M. Munkata, *J. Chem. Soc. Dalton Trans.* **2000**, 4160–4166; b) A. J. Blake, N. R. Champness, A. Khlobystov, D. A. Lemenovskii, W. S. Li, M. Schröder, *Chem. Commun.* **1997**, 2027–2028; c) L. Carlucci, G. Ciani, D. M. Proserpio, *Chem. Commun.* **1999**, 449–450.

[5] a) Y. Lu, E. B. Wang, J. Lu, C. W. Hu, L. Xu, *Cryst. Growth Des.* **2005**, *5*, 257–260; b) P. Q. Zheng, Y. P. Ren, L. S. Long, R. B. Huang, L. S. Zheng, *Inorg. Chem.* **2005**, *44*, 1190–1192.

[6] a) X. J. Gu, J. Peng, Z. Y. Shi, Y. H. Chen, Z. G. Han, E. B. Wang, J. F. Ma, N. H. Hu, *Inorg. Chim. Acta*, in press; b) Z. Y. Shi, X. J. Gu, J. Peng, Y. H. Chen, *J. Solid State Chem.* **2005**, 1988–1995; c) Z. Y. Shi, J. Peng, C. J. Gómez-García, X. J. Gu, *J. Solid State Chem.*, in press.

[7] Q. Chen, C. L. Hill, *Inorg. Chem.* **1996**, *35*, 2403–2405.

[8] I. D. Brown, D. Altermatt, *Acta Crystallogr. Sect. B* **1985**, *41*, 244–247.

[9] M. T. Pope, *Heteropoly and Isopoly Oxometalates*, Springer, Berlin, **1983**, p. 6 and p. 106.

[10] a) G. M. Sheldrick, *SHELXL 97, Program for Crystal Structure Refinement*, University of Göttingen, Germany, **1997**; b) G. M. Sheldrick, *SHELXL 97, Program for Crystal Structure Solution*, University of Göttingen, Germany, **1997**.

Received: July 25, 2005
Published Online: November 28, 2005

 © 2006 Wiley-VCH Verlag GmbH & Co. KGaA, Weinheim 

DOI: 10.1002/ejic.200500671

# Solid-State Luminescence and π-Stacking in Crystalline Uranyl Dipicolinates

**Jack M. Harrowfield,*[a] Noël Lugan,[b] Gholam H. Shahverdizadeh,[c] Ali A. Soudi,[c] and Pierre Thuéry[d]**

**Keywords:** Uranyl luminescence / Crystal structures / π-Stacking / Dipicolinates

Crystal structure determinations on the hydrated forms of the complexes $M_2UO_2(dipic)_2$, M = H, Rb, Cs, dipic = dipicolinate = pyridine-2,6-dicarboxylate, all of which show strong solid-state luminescence from the uranyl centre, have as a common feature extended π-stacking arrays of the dipicolinate ligands. Comparisons with related but non-luminescent complexes indicate that these stacking arrays may be associated with efficient energy transfer from the dipicolinate "antennae" to the uranyl unit.

(© Wiley-VCH Verlag GmbH & Co. KGaA, 69451 Weinheim, Germany, 2006)

## Introduction

Pyridine-2,6-dicarboxylic acid (dipicolinic acid, $dipicH_2$) is a widely employed and versatile complexing agent known to bind in its singly, doubly and even non-deprotonated and diester forms, often as mixed-ligand species.[1–5] Related ligands such as chelidamic acid (4-hydroxypyridine-2,6-dicarboxylic acid) and benzimidazole derivatives of dipicolinate also display interesting coordination properties.[6,7] Dipicolinic acid and its anions appear to bind well to all metals in the periodic table, though specific properties such as the strong luminescence of $Eu^{III}$ and $Tb^{III}$[8] and the biological activity of transition-metal complexes[3,9,10] have led to a strong focus in certain areas and to a relative neglect of actinide complexation. Nonetheless, in the specific case of the uranyl ion, a variety of species,[11–14] including the remarkable helical polymer, $[UO_2(dipic)(OH_2)]_n$,[15] has long been known and has recently been significantly expanded, principally through the characterisation of several binuclear complexes.[16] During a structural study, reported herein, of further members of the dipicolinate family, we noted that one property of these compounds that varies strikingly is their solid-state luminescence and hence we have attempted to rationalise this through an analysis of the different lattices.

[a] Laboratoire de Chimie Supramoléculaire, UMR 7006 du CNRS, Institut de Science et d' Ingénierie Supramoléculaires, 8 allée Gaspard Monge, 67083 Strasbourg, France
[b] Laboratoire de Chimie de Coordination du CNRS, UPR 8241 du CNRS,
205 route de Narbonne, 31077 Toulouse Cedex 04, France
[c] Department of Chemistry, University of Zanjan,
P. O. Box 49195, Zanjan, Iran
[d] CEA/Saclay, DSM/DRECAM/SCM, URA 331 du CNRS, Bât. 125,
91191 Gif-sur-Yvette, France
Supporting information for this article is available on the WWW under http://www.eurjic.org or from the author.

## Results and Discussion

A particularly useful technique for the production of crystals of rather insoluble metal complexes has proven to be the "branched tube" method[17] of diffusion along a thermal gradient.[18] In the extension of this procedure used here to uranyl complexes of dipicolinic acid, the product obtained from a mixture of reagents with a 1:2 ratio of $U^{VI}$/acid was found to be a mixture of crystalline materials, one of which was a complex containing the metal and ligand in this ratio but the other a 1:1 species. Both can also be obtained by direct reaction of $[UO_2(OH_2)_5]^{2+}$ with the appropriate ligand species in these different ratios in aqueous solution; the 1:2 complex appears to be of very low solubility and crystallising readily, whereas the 1:1 complex appears to be more soluble and deposits rather slowly. Structure determinations (Table 1) on crystals selected from the mixed product showed the 1:1 species, which crystallises as clusters of very fine, pale yellow needles, to be the known helical polymer, $[UO_2(dipic)(OH_2)]_n$,[15] and the 1:2 species, which crystallises as obviously greenish-yellow plates, to be $[UO_2(dipicH)_2]\cdot 4H_2O$. The dipicolinate units function as tridentate ligands in both cases, the uranium coordination environment being close to pentagonal bipyramidal $UNO_6$ in the 1:1 complex and close to hexagonal bipyramidal $UN_2O_6$ in the 1:2 complex.

The lattice of $[UO_2(dipicH)_2]\cdot 4H_2O$ is similar to that of $[NH(C_2H_5)_3]_2[UO_2(dipic)_2]\cdot 2H_2O$[16] (both crystals being monoclinic, space group *C*2/*c*, though they are not isomorphous) as is emphasised by a view down *c* (Figure 1). Hydrogen bonding in the lattice of the latter compound has been analysed in detail and the protons of the triethylammonium groups appear to form near-symmetrical bridges between the coordinated oxygen atoms of opposite dipicolinate units within the one complex unit. The complex can thus be considered to have a "pseudo-macrocyclic" form

 © 2006 Wiley-VCH Verlag GmbH & Co. KgaA, Weinheim 

Table 1. Crystal data and structure refinement details.

| | | | | |
|---|---|---|---|---|
| Empirical formula | $C_{14}H_{16}N_2O_{14}U$ | $C_7H_5NO_7U$ | $C_{14}H_{12}N_2O_{13}Rb_2U$ | $C_{14}H_{14}Cs_2N_2O_{14}U$ |
| Formula weight | 674.32 | 453.15 | 825.23 | 938.12 |
| $T$ [K] | 180(2) | 180(2) | 100(2) | 100(2) |
| Crystal system | monoclinic | hexagonal | monoclinic | triclinic |
| Space group | $C2/c$ | $P6_1$ | $C2/c$ | $P\bar{1}$ |
| $a$ [Å] | 18.5189(9) | 14.7245(7) | 19.1824(8) | 6.7725(3) |
| $b$ [Å] | 6.8384(3) | 14.7245(10) | 14.7980(6) | 8.4145(5) |
| $c$ [Å] | 15.4943(9) | 9.2583(9) | 7.5167(2) | 10.8428(7) |
| $\alpha$ [°] | 90 | 90 | 90 | 99.127(3) |
| $\beta$ [°] | 94.353(4) | 90 | 111.114(3) | 106.607(4) |
| $\gamma$ [°] | 90 | 120 | 90 | 110.102(3) |
| $V$ [Å$^3$] | 1956.53(17) | 1738.4(2) | 1990.45(13) | 532.93(6) |
| $Z$ | 4 | 6 | 4 | 1 |
| $D_{calcd.}$ [Mg·m$^{-3}$] | 2.289 | 2.597 | 2.754 | 2.923 |
| $\mu$(Mo-$K\alpha$) [mm$^{-1}$] | 8.375 | 14.024 | 13.089 | 11.057 |
| $F$(000) | 1272 | 1212 | 1520 | 426 |
| Crystal size [mm$^3$] | 0.26×0.24×0.10 | 0.64×0.09×0.07 | 0.17×0.11×0.09 | 0.15×0.12×0.06 |
| $\theta$ Range for data collection | 3.18–32.09 | 3.20–32.00 | 3.04–25.68 | 3.39–25.68 |
| Index ranges | $-26 \le h \le 27$ | $-21 \le h \le 21$ | $0 \le h \le 23$ | $0 \le h \le 8$ |
| | $-10 \le k \le 10$ | $-21 \le k \le 19$ | $0 \le k \le 18$ | $-10 \le k \le 9$ |
| | $-22 \le l \le 18$ | $-13 \le l \le 13$ | $-9 \le l \le 8$ | $-13 \le l \le 12$ |
| Reflections collected | 19458 | 18751 | 22423 | 16850 |
| Independent reflections | 3188 | 3833 | 1884 | 2020 |
| $R_{int}$ | 0.039 | 0.092 | 0.034 | 0.049 |
| Completeness to $\theta_{max}$ (%) | 92.9 | 97.6 | 99.8 | 99.8 |
| Absorption correction | analytical | semi-empirical | empirical | empirical |
| $T_{max.}/T_{min.}$ | 0.462/0.118 | 0.349/0.090 | 0.308/0.086 | 0.515/0.106 |
| Restraints/parameters | 0/142 | 1/145 | 0/147 | 0/151 |
| Goodness-of-fit on $F^2$ | 1.043 | 1.086 | 1.287 | 1.294 |
| $R_1/wR_2$ [$I > 2\sigma(I)$] | 0.023/0.054 | 0.039/0.089 | 0.026/0.103 | 0.028/0.121 |
| $R_1/wR_2$ (all data) | 0.025/0.055 | 0.045/0.092 | 0.028/0.104 | 0.028/0.121 |
| $\Delta\rho_{max.}/\Delta\rho_{min.}$ [e·Å$^{-3}$] | 0.98/–2.23 | 2.10/–1.68 | 0.93/–1.30 | 1.12/–0.88 |
| Flack parameter | | 0.01(2) | | |

somewhat like that well-known in $M^{II}$ complexes of the dimethylglyoxime monoanion.[19] In $[UO_2(dipicH)_2]\cdot 4H_2O$, while a water molecule bridges the coordinated oxygen atoms to give a similar form (Figure 2), in addition the residual acid protons appear to be located on the outer (uncoordinated) carboxylate oxygen atoms, O(3), and to be involved in H-bonding chains involving two water molecules and the confronting O(3′) atoms, defining another mode of formation of a "pseudo-macrocycle". The potentially more rigid resulting structure is associated with a closer approach to planarity of the $U(dipicH)_2$ unit, although it is both slightly bowed [N–U–N 174.05(8)°] and twisted into a chiral configuration, as is the case for the $U(dipic)_2$ unit in $[NH(C_2H_5)_3]_2[UO_2(dipic)_2]\cdot 2H_2O$, but there the bowing is more marked [N–U–N 165.21(10)°]. The H-bonded water molecule pairs which bridge complex ion units intramolecularly are also within H-bonding distances of carboxylate oxygen atoms of other complex units, so linking the lattice in at least two dimensions.

Perhaps significantly, H-bonding is not the only form of extended interaction apparent in the lattice. Parallel to $c$, the complex units can be considered to form undulating columns [for example, within the ovoid entities apparent in the view down $c$ (Figure 1)] in which there is considerable overlap of parallel dipicolinate rings of adjacent complexes of alternating chirality. This stacking[20,21] extends down $b$, so that there are two types of ring projections (Figure 3), describable as intra- and inter-ovoid, contributing to the formally infinite array. While projection of one ring onto its parallel neighbour in a given stack does not involve eclipsing of all atoms, there are numerous C···C contacts of <3.5 Å, associated in the case of the more strongly overlapped intra-ovoid array with an inter-centroid distance of 3.63 Å and a centroid offset of 1.35 Å. It is especially in this regard that the lattice differs from the remarkably beautiful lattice of $[UO_2(dipic)(OH_2)]_n$.[15] In the present redetermination of this structure, the crystal chosen was one in which the helical polymer units (Figure 4) present were all right-handed, with the pitch of the helices [9.26(1) Å] being such that projecting dipicolinate units are very remote. These helices interlock to some extent in a way which involves no short contacts between constituent atoms of the dipicolinate rings (shortest inter-centroid distance 5.54 Å), though there are some involving C and O of the carboxylate units. Instead, there is a rather short contact [3.04(1) Å] of one uranyl-$O$ to ring atom C2 [as well as UO···N of 3.09(1) Å]. Such uranyl group interactions are seen in other systems[22] and indeed in $[UO_2(dipicH)_2]\cdot 4H_2O$, there are longer UO···C(aromatic) approaches of 3.17(1) Å, though essentially in the plane of the ring.

Such points of difference between $[UO_2(dipicH)_2]\cdot 4H_2O$ and $[UO_2(dipic)(OH_2)]_n$ may be the cause of their marked difference in solid-state luminescence. Thus, 354 nm (Hg lamp) irradiation of $[UO_2(dipicH)_2]\cdot 4H_2O$ produces bright green luminescence characteristic of a uranyl centre[23] (and the greenish colour of the crystals under solar illumination

 © 2006 Wiley-VCH Verlag GmbH & Co. KGaA, Weinheim 

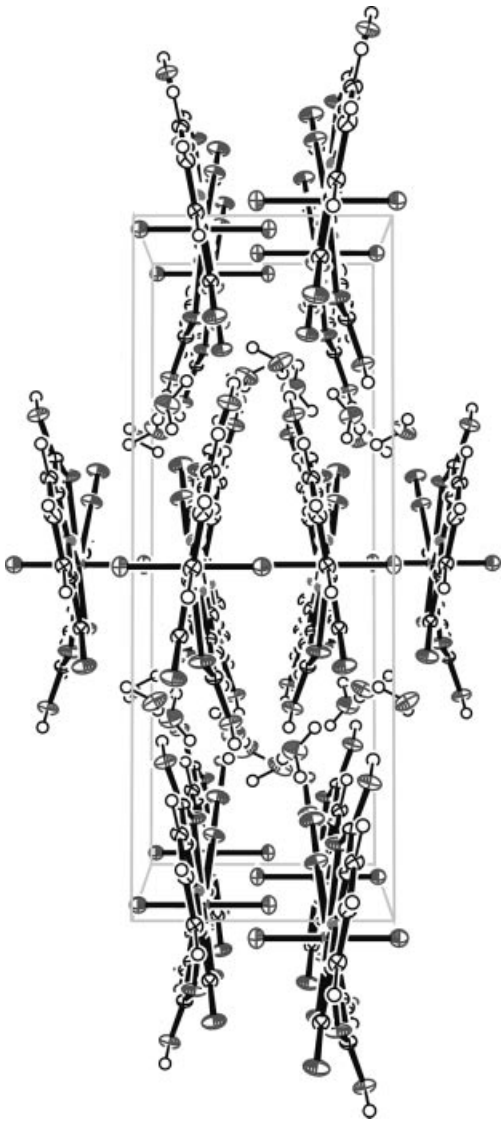

Figure 1. A view, down *c*, of the lattice of $[UO_2(dipicH)_2]\cdot 4H_2O$ which displays the columnar structures of ovoid cross-section present. Displacement ellipsoids are drawn at the 50% probability level. H atoms are shown with arbitrary radii of 0.1 Å.

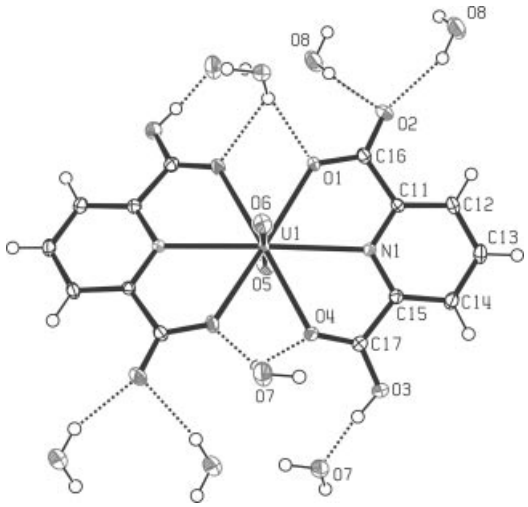


Figure 2. The hydrogen-bonding array present in the lattice of $[UO_2(dipicH)_2]\cdot 4H_2O$ (displacement ellipsoids at the 50% probability level).

may be explained as of the same origin), with the principal emission maxima at 487, 509, 532 and 558 nm (Figure 5) being a much closer match to those of hexagonal bipyramidal $U^{VI}$ as in $[UO_2(NO_3)_2(OH_2)_2]$[24] than to those of pentagonal bipyramidal $U^{VI}$ as in $[UO_2(OH_2)_5]^{2+}$[23]. $[UO_2(dipic)(OH_2)]_n$ is not luminescent by eye under the same conditions, though very weak luminescence, with maxima at 465, 490, 515 and 535 nm can be detected by use of a fluorimeter. Obviously, issues such as the presence of two dipicolinate ligands in the first and of a possibly electronically deactivating aqua ligand in the second (though even in the case of $[UO_2(OH_2)_5]^{2+}$, [23b] this does not seem to apply) must be considered, and then it is important to note that neither complex is strongly luminescent in aqueous solution. Further, deprotonation of $[UO_2(dipicH)_2]$ with $[NBu_4][OH]$ to produce a chloroform-soluble species, for which the electrospray mass spectrum (Supporting Information; for Supp. Inf. see also the footnote on the first page of this article) in this solvent shows a parent peak of the dianion, also results in loss of emission (thus excluding the possibility that the negligible luminescence in water is a consequence of deactivation by bound water after ligand hydrolysis), though evaporation of this solution produces a luminescent solid. Thus, even if dipicolinate units as "antennae" for energy absorption and transfer to the uranyl emissive state are only efficient when there are at least two per uranium atom, this efficiency must be associated with the solid-state structure. This is true also for $[NH(C_2H_5)_3]_2[UO_2(dipic)_2]\cdot 2H_2O$, which is luminescent as the solid,[25] again differing in this regard from several binuclear species having a single dipicolinate ligand per uranium.[16] In the lattices of these binuclear species, it is possible to discern parallel arrays of dipicolinate entities indicative of stacking interactions but, significantly, these all involve either relatively remote atom···atom contacts (>3.5 Å) or limited overlaps or pairwise interactions in one-dimensional arrays, unlike the extended two-dimensional arrays described above for $[UO_2(dipicH)_2]\cdot 4H_2O$ and which can also be discerned in $[NH(C_2H_5)_3]_2[UO_2(dipic)_2]\cdot 2H_2O$. [In the first complex, there are also O(carboxylate)···C(aromatic) contacts ca. 3.3 Å which produce a third dimension to the interactions between the aromatic entities.] In all the complexes presently discussed, there are UO···C(aromatic) contacts between 3.0 and 3.4 Å which vary in a way which seems unrelated to the luminescence properties of the solids. Thus, it would seem plausible that strong uranyl emission in these complexes is an indicator of extended stacking interactions with significant electronic consequences

An indication of the utility of the branched-tube method for crystal formation was provided in efforts to extend characterisation of the $M_2UO_2(dipic)_2$ family to the cases where M is an alkali metal cation. All (M = Li, Na, K, Rb, Cs) these compounds are of low water solubility and precipitate very rapidly as green, luminescent materials, of very similar

 © 2006 Wiley-VCH Verlag GmbH & Co. KGaA, Weinheim 

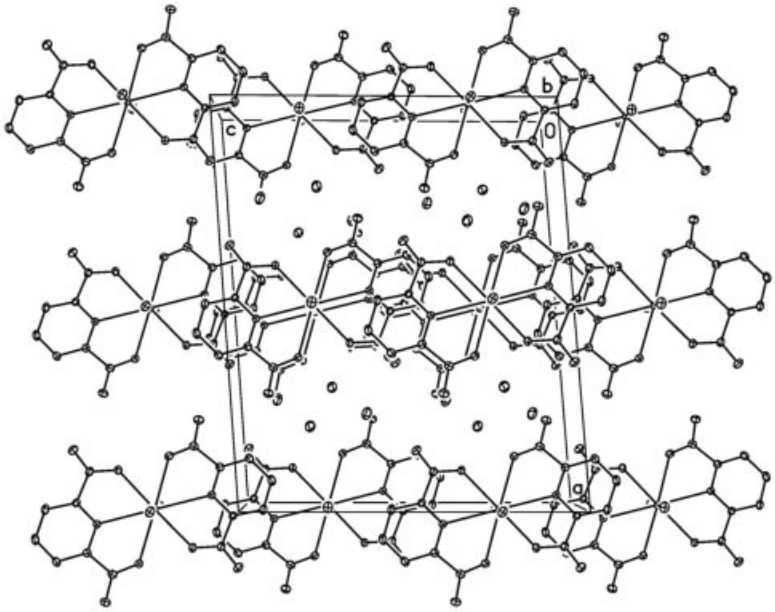


Figure 3. A view, perpendicular to the mean ring planes, showing the two types of dipicolinate stacks ("intra-" and "inter-ovoid") in the lattice of $[UO_2(dipicH)_2]\cdot 4H_2O$. The greater degree of ring overlap corresponds to the intra-ovoid stacks (displacement ellipsoids at the 50% probability level).

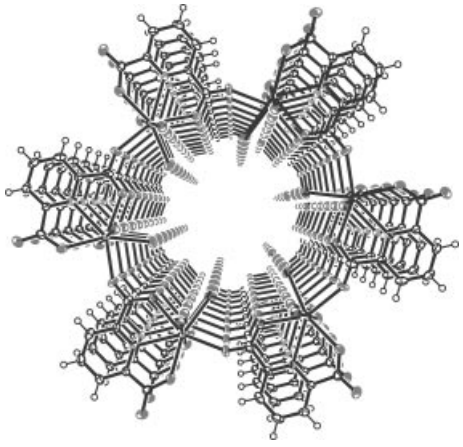

Figure 4. A view down the axis of one of the (right-handed) infinite helices present in the lattice of $[UO_2(dipic)(OH_2)]_n$ (displacement ellipsoids at the 50% probability level).

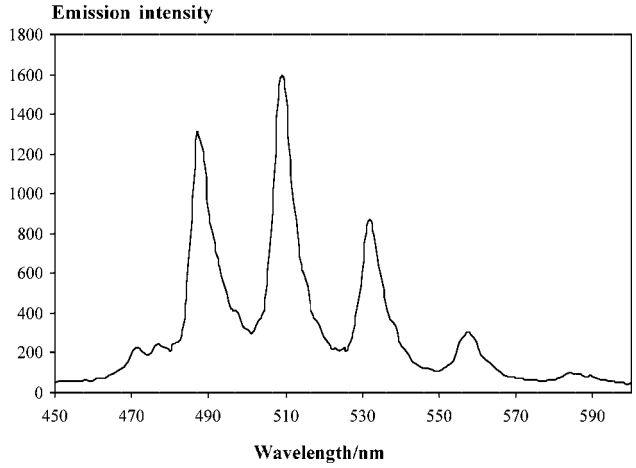


Figure 5. The room-temperature luminescence spectrum of powdered $[UO_2(dipicH)_2]\cdot 4H_2O$. Excitation wavelength 320 nm.

appearance to the M = H complex, when hot solutions are cooled. Despite numerous attempts at careful recrystallisation, the only members of this series obtained in a form suitable for X-ray structure determinations in this way were the Rb and Cs species (Table 1). While the Rb complex retains the same space group ($C2/c$) as the triethylammonium and proton compounds, the Cs complex crystallises in $P\bar{1}$, though this has only rather minor consequences in terms of the structure and self-interactions of the $U(dipic)_2$ entities. In both the Rb and Cs complexes, the $U(dipic)_2$ units are planar, with N–U–N 180° due to the location of the uranium atom on a symmetry centre. Perhaps as a reflection of this move to coplanarity, the U–N bond lengths (Table 2) are the longest of any in a uranyl dipicolinate. Their extension, however, is slight, and U–O bond lengths (Table 2) fall essentially within the range of those in other $U(dipic)_2$ species.

However, the Rb and Cs complexes do differ most obviously in the orientation of chains of the alkali metal atoms with respect to the array of $[UO_2(dipic)_2]^{2-}$ units. (Figure 6). Viewed down $c$, for example, both lattices can be regarded as containing sheets of uranium atoms lying parallel to [100], each U atom visible in the view down $c$ being the head of a column of such atoms lying parallel to $c$. Using the two shortest (and nearly equal) M···M separations [M = Rb, 4.0926(12) and 4.4260(12); M = Cs, 4.3109(9) and 4.9406(9) Å] to define association between M atoms, these can be considered to form zig-zag columns which, in the

 © 2006 Wiley-VCH Verlag GmbH & Co. KGaA, Weinheim 

Table 2. Selected bond lengths [Å] and angles [°].

| | | | | |
|---|---|---|---|---|
| $[UO_2(dipicH)_2]\cdot 4H_2O$[a] | U(1)–O(1) | 2.441(2) | O(1)–U(1)–N(1) | 60.77(7) |
| | U(1)–O(4) | 2.499(2) | N(1)–U(1)–O(4) | 60.42(7) |
| | U(1)–O(5) | 1.769(3) | O(1)–U(1)–O(4′) | 60.45(7) |
| | U(1)–O(6) | 1.782(3) | O(5)–U(1)–O(6) | 180 |
| | U(1)–N(1) | 2.641(2) | | |
| $[UO_2(dipic)(OH_2)]$[b] | U(1)–O(1) | 2.380(6) | O(1)–U(1)–N(1) | 63.30(19) |
| | U(1)–O(4) | 2.416(5) | N(1)–U(1)–O(4) | 63.66(19) |
| | U(1)–O(5) | 1.775(6) | O(4)–U(1)–O(7) | 73.9(2) |
| | U(1)–O(6) | 1.768(6) | O(7)–U(1)–O(3′) | 77.5(2) |
| | U(1)–O(7) | 2.423(6) | O(3′)–U(1)–O(1) | 81.9(2) |
| | U(1)–N(1) | 2.520(6) | O(5)–U(1)–O(6) | 178.4(3) |
| | U(1)–O(3′) | 2.340(6) | | |
| $[UO_2Rb_2(dipic)_2(H_2O)_3]$[c] | U–O(1) | 2.445(5) | O(1)–U–N(1) | 59.64(14) |
| | U–O(3) | 2.466(5) | N(1)–U–O(3) | 59.65(16) |
| | U–O(5) | 1.783(6) | O(1)–U–O(3′) | 60.72(15) |
| | U–N(1) | 2.657(5) | O(5)–U–O(5′) | 180 |
| | Rb–O(1) | 3.129(5) | Rb–O(5) | 3.035(6) |
| | Rb–O(2′′) | 3.046(4) | Rb–O(6) | 2.849(5) |
| | Rb–O(3′) | 3.006(5) | Rb–O(6$^{\$}$) | 2.914(5) |
| | Rb–O(4$^{\#}$) | 2.927(5) | Rb–O(7) | 2.813(5) |
| $[UO_2Cs_2(dipic)_2(H_2O)_4]$[d] | U–O(1) | 2.435(5) | O(1)–U–N(1) | 59.67(16) |
| | U–O(3) | 2.466(5) | N(1)–U–O(3) | 60.01(16) |
| | U–O(5) | 1.765(5) | O(1)–U–O(3′) | 60.33(15) |
| | U–N(1) | 2.669(6) | O(5)–U–O(5′) | 180 |
| | Cs–O(1) | 3.143(5) | Cs–O(6) | 3.211(5) |
| | Cs–O(2) | 3.439(5) | Cs–O(6$^{\$}$) | 3.390(5) |
| | Cs–O(2′′) | 3.115(5) | Cs–O(6′′) | 3.426(6) |
| | Cs–O(3′) | 3.207(5) | Cs–O(7) | 3.037(5) |
| | Cs–O(4$^{\#}$) | 3.307(5) | Cs–O(7*) | 3.399(6) |
| | Cs–O(4′) | 3.717(5) | | |

[a] Symmetry code: ′ for $-x-1, y, -z-1/2$. [b] Symmetry code: ′ for $y+1, -x+y+1, z-1/6$. [c] Symmetry codes: ′ for $1/2-x, 3/2-y, -z$; ′′ for $x, 1-y, z+1/2$; # for $x-1/2, 3/2-y, z-1/2$; $ for $-x, y, 1/2-z$. [d] Symmetry codes: ′ for $1-x, -y, -z$; ′′ for $2-x, 1-y, 1-z$; # for $1+x, y, 1+z$; $ for $3-x, 1-y, 1-z$; * for $2-x, -y, 1-z$.

case of M = Rb, lie along *c* and so define sheets for which the mean plane is parallel to those of the U atoms, i.e. to [100], whereas in the case of M = Cs these zig-zag columns lie parallel to *b*, forming undulating sheets with their mean planes parallel to [001]. An explanation of the difference in these alkali metal arrays may be that only Rb is involved in coordinative interaction with uranyl-*O* [Rb–O 3.035(6) Å]. As seems to be commonly the case with heavy and apparently weakly coordinating metals,[6,21,27–31] it is difficult to define a precise cutoff distance for interactions considered to be bonding but the coordination numbers of both Rb and Cs here appear to be high, involving *O*-donors only, with rather irregular geometry about the metals. Interestingly, the extreme M···O separations approach those of M···U, which, if they are correctly considered as contacts of closed-shell species of similar charge, would be regarded as involving negligible interactions, thus indicating that the extreme M···O contacts must also be of little significance.

In relation to development of the argument presently that uranyl luminescence in solid dipicolinate complexes may be associated with extended interactions of the dipicolinate "antennae", it is important to note that both the Rb and Cs complexes share with other luminescent uranyl dipicolinate species an essentially infinite stacked array of dipicolinates involving numerous relatively short C···C approaches (ca. 3.4 Å), corresponding in both compounds to a shortest centroid···centroid distance of 3.76 Å and centroid offsets of 1.37 and 1.62 Å for the Rb and Cs complexes, respectively. In the Rb complex, this stacking is apparent in the view down *c*, this axis being close to perpendicular to the mean ring planes, whereas in the Cs complex, it is a view down *a*, which exposes a similar array.

## Conclusions

If indeed it is true that stacking within the lattices of uranyl dipicolinates can produce efficient population of uranyl excited states, then these generally rather insoluble materials may have applications as solid photocatalysts, as recently described for some mixed U/Ag compounds also characterised by extended ligand stacking within the crystals.[26] Even more recently,[32] some uranyl complexes of isomeric (2,4- and 3,4-)pyridine dicarboxylates, though of different stoichiometry to the present materials, have also been described as luminescent due to uranyl centre emission. Though stacking of the pyridine units is extended in these solids, the ring atom separations are relatively large (ca. 3.7 Å) and the compounds are described as yellow, indicating that their luminescence is weak and that their polyuranate cores may not be as effective as $[UO_2(dipic)_2]^{2-}$ in creating lattices which may be considered to contain "antenna" units of the ligands. The stoichiometry of bis(dipicolinato)dioxouranium(VI) derivatives is obviously open to straightforward variations which may result in useful control of their photoreactivity and we are presently investiga-

 © 2006 Wiley-VCH Verlag GmbH & Co. KGaA, Weinheim 

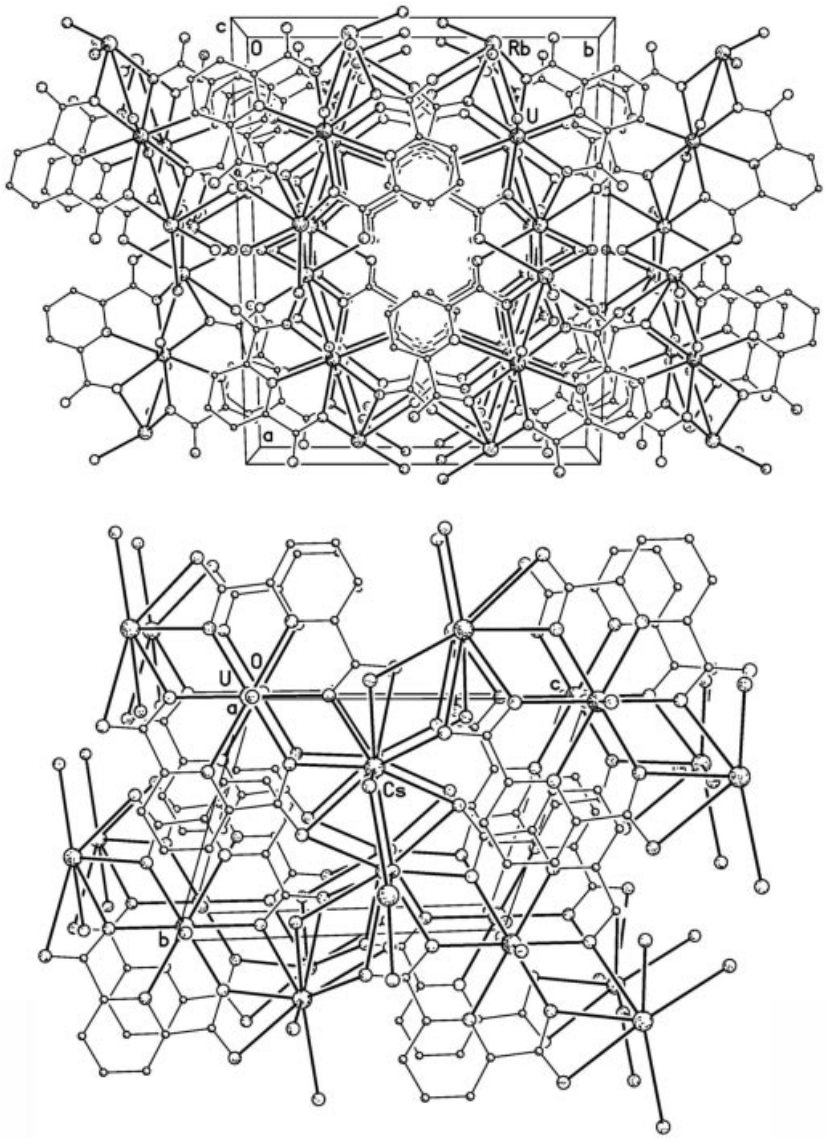


Figure 6. (top) The lattice of $[UO_2Rb_2(dipic)_2(H_2O)_3]$, viewed down *c*. (bottom) The lattice of $[UO_2Cs_2(dipic)_2(H_2O)_4]$, viewed down *a* (displacement ellipsoids at the 50% probability level).

ting lanthanide(III) species in which it appears possible to switch between uranyl and lanthanide ion luminescence.

## Experimental Section

**Synthesis:** $[UO_2(dipicH)_2]\cdot 4H_2O$ and $[UO_2(dipic)(OH_2)]$ (mixed): $[UO_2(O_2CCH_3)_2(OH_2)]\cdot H_2O$ (212 mg) and dipicolinic acid (167 mg) were placed in one arm of an inverted Y-tube ("branched tube"[17]) and the apparatus then carefully filled with water. The arm containing the partially soluble reactants was heated at 45 °C, with the other arm kept at ambient temperature. After 1 week, the cooler arm contained greenish-yellow plates mixed with clusters of pale yellow needles. Samples of both crystals were withdrawn for structure determinations, these showing the plates to be the new complex $[UO_2(dipicH)_2]\cdot 4H_2O$.

**$[UO_2(dipicH)_2]\cdot 4H_2O$:** A solution obtained by mixing dipicolinic acid (34 mg) and $Na_2CO_3$ (11 mg) in water (2 mL) and heating to 90 °C was mixed with a solution of $[UO_2(dmso)_5](ClO_4)_2$[22] (86 mg) in water (2 mL, 90 °C). The clear, pale yellow solution was allowed to stand at ambient temperature as plate-like crystals slowly deposited in essentially quantitative yield. After air-drying only, analysis of the sample was consistent with a higher degree of hydration than that of the single crystal taken for the structure determination. $[UO_2(dipicH)_2]\cdot 7H_2O$: calcd. C 23.09, H 3.04, N 3.85; found: C 22.9, H 2.8, N 3.5.

**$M_2UO_2(dipic)_2\cdot nH_2O$ (M = Li, Na, K, Rb, Cs):** Clear solutions, obtained by mixing dipicolinic acid ($2\cdot 10^{-4}$ mol) and $M_2CO_3$ ($2\cdot 10^{-4}$ mol) in water (2 mL) and heating at 90 °C until $CO_2$ evolution was complete, were mixed separately with solutions of $[UO_2(dmso)_2(NO_3)_2]$ ($10^{-4}$ mol; 55 mg) in hot (90 °C) water (2 mL). Cooling of the mixtures led to rapid and essentially quantitative

 © 2006 Wiley-VCH Verlag GmbH & Co. KGaA, Weinheim 

precipitation of microcrystalline greenish-yellow solids. Partial precipitation resulting when the initial solutions were allowed to slowly evaporate at 90 °C provided larger but still generally rather small crystals. On collection and washing with acetone, the crystals appeared to undergo some efflorescence, and analyses of the Rb and Cs compounds indicated a lower degree of hydration than found from the structure solutions. $Li_2UO_2(dipic)_2{\cdot}2H_2O$: calcd. C 25.86 (26.0); H 1.55 (2.0); N 4.31 (4.3); found C 26.0, H 2.0, N 4.3. $Na_2UO_2(dipic)_2$: calcd. C 26.02, H 0.94, N 4.33; found C 25.9, H 1.8, N 4.3. $K_2UO_2(dipic)_2{\cdot}1.5H_2O$: calcd. C 23.84, H 1.28, N 3.97; found C 23.9, H 2.0, N 3.9. $Rb_2UO_2(dipic)_2$: calcd. C 21.80, H 0.85, N 3.63; found C 21.8, H 1.3, N 3.5. $Cs_2UO_2(dipic)_2{\cdot}H_2O$: calcd. C 19.02, H 0.91, N 3.17; found C 19.4, H 1.3, N 2.9.

**Luminescence Measurements:** To obtain luminescence spectra for solid samples, the powdered complexes were pressed between two quartz plates with a spacing of ca. 0.1 mm. The plates were mounted in the normal cell holder of an AMINCO-Bowman Series 2 fluorimeter with the faces at 45° to the incident beam.

**Crystallography:** Intensities for both $[UO_2(dipicH)_2]{\cdot}4H_2O$ and $[UO_2(dipic)(OH_2)]$ were collected at 180(2) K with an Oxford Diffraction Xcalibur diffractometer using graphite-monochromated Mo-$K_\alpha$ radiation ($\lambda$ = 0.71073 Å). Cell refinement and data processing were performed using Crysalis RED.[33] All subsequent calculations were carried out using the WinGX system.[34] The structures were solved by using the SIR92 program,[35] which revealed in each instance the position of most of the non-hydrogen atoms. All remaining non-hydrogen atoms were located by the usual combination of full-matrix least-squares refinement and difference electron density syntheses by using the SHELXL97 program.[36] Atomic scattering factors were taken from the usual tabulations. Anomalous dispersion terms for U atoms were included in $F_c$. Analytical[37] ($[UO_2(dipicH)_2]{\cdot}4H_2O$) or semi-empirical[38] ($[UO_2(dipic)(OH_2)]$) absorption corrections were applied.

The data for $[UO_2Rb_2(dipic)_2(H_2O)_3]$ and $[UO_2Cs_2(dipic)_2(H_2O)_4]$ were collected at 100(2) K with a Nonius Kappa-CCD area detector diffractometer[39] using graphite-monochromated Mo-$K_\alpha$ radiation ($\lambda$ = 0.71073 Å). The data were processed with HKL2000.[40] The structures were solved by direct methods or Patterson map interpretation for the two compounds, respectively, with SHELXS-97 and subsequent Fourier-difference synthesis and refined by full-matrix least-squares on $F^2$ with SHELXL-97.[41] Absorption effects were corrected empirically with the program DELABS in PLATON.[42]

In all compounds, all non-hydrogen atoms were refined with anisotropic displacement parameters. Hydrogen atoms attached to the pyridine ring were introduced at idealised positions and were treated as "riding" atoms with C($sp^2$)–H = 0.93 Å and $U_{iso}$(H) = 1.2 times that of the parent atom. The hydrogen atoms of the water molecules (and hydroxy group when present) in the structures of $[UO_2(dipicH)_2]{\cdot}4H_2O$, $[UO_2Rb_2(dipic)_2(H_2O)_3]$ and $[UO_2Cs_2(dipic)_2(H_2O)_4]$ were located from Fourier-difference maps and their position was refined using a constrained model (O–H = 0.86 Å or left as found; $U_{iso}$ = 1.2 times that of the parent atom). The final Fourier-difference map for $[UO_2(dipic)(OH_2)]$ showed randomly distributed residual peaks all located in the vicinity of the U atom. No attempts were further made to locate the hydrogen atoms attached to the coordinated water molecule in this case. The molecular plots were drawn with ORTEP3[43] and SHELXTL.[41]

CCDC-279058 to -279061 contain the supplementary crystallographic data for this paper. These data can be obtained free of charge from The Cambridge Crystallographic Data Centre via www.ccdc.cam.ac.uk/data_request/cif.

**Supporting Information** (see footnote on the first page of this article): Solid-state luminescence spectra for $M_2UO_2(dipic)_2$, M = Li, Na, K, Rb, Cs, $NBu_4$; ESMS results for $[NBu_4]_2[UO_2(dipic)_2]$ in $CHCl_3$.


[1] P. A. Brayshaw, A. K. Hall, W. T. A. Harrison, J. M. Harrowfield, D. Pearce, T. M. Shand, B. W. Skelton, C. R. Whitaker, A. H. White, *Eur. J. Inorg. Chem.* **2005**, 1127–1141 and references cited therein.

[2] S. L. Jain, A. M. Z. Slawin, J. D. Woollins, P. Bhattacharyya, *Eur. J. Inorg. Chem.* **2005**, 721–726 and references cited therein.

[3] A. C. Gonzalez-Baró, E. E. Castellano, O. E. Piro, B. S. Parajón-Costa, *Polyhedron* **2005**, *24*, 49–55 and references cited therein.

[4] S. K. Ghosh, P. K. Bharadwaj, *Inorg. Chem.* **2004**, *43*, 2293–2298 and references cited therein.

[5] M. A. S. Goher, F. A. Mautner, A. K. Hafez, A. A. Youssef, *Polyhedron* **2003**, *22*, 515–520 and references cited therein.

[6] S. Burnet, A. K. Hall, J. M. Harrowfield, G. A. Koutsantonis, V. Sanford, D. Sauter, B. W. Skelton, A. H. White, *Supramol. Chem.* **2003**, *15*, 291–312.

[7] S. Floquet, M. Borkovec, G. Bernardinelli, A. Pinto, L.-A. Lenthold, G. Hopfgartner, D. Imbert, J.-C. G. Bünzli, C. Piguet, *Chem. Eur. J.* **2004**, *10*, 1091–1105.

[8] a) J. P. Riehl, F. S. Richardson, *Chem. Rev.* **1986**, *86*, 1–16; b) G. Muller, F. C. Muller, J. P. Riehl, *J. Alloys Compd.* **2004**, *380*, 79–83.

[9] C. Ma, C. Chen, Q. Liu, D. Liao, L. Li, *Eur. J. Inorg. Chem.* **2003**, 1227–1231.

[10] a) L. Yang, D. C. Crans, S. M. Miller, A. la Cour, O. P. Andersen, P. M. Koszynski, M. E. Godzala III, L. D. Austin, G. R. Willsky, *Inorg. Chem.* **2002**, *41*, 4859–4871; b) D. C. Crans, M. Mahroof-Tahir, M. D. Johnson, P. C. Wilkins, L. Yang, K. Robbins, A. Johnson, J. A. Alfano, M. E. Godzala III, L. D. Austin, G. R. Willsky, *Inorg. Chim. Acta* **2003**, *356*, 365–378.

[11] G. Marangoni, S. Degetto, R. Graziani, G. Bombieri, E. Forsellini, *J. Inorg. Nucl. Chem.* **1974**, *6*, 1787–1794.

[12] A. Cousson, J. Proust, E. N. Rizkalla, *Acta Crystallogr. Sect. C: Cryst. Struct. Commun.* **1991**, *47*, 2065–2069.

[13] A. Cousson, F. Nectoux, M. Pagès, E. N. Rizkalla, *Radiochim. Acta* **1993**, *61*, 177–180.

[14] Monothiocarboxylate derivative: M. P. Neu, M. T. Johnson, J. H. Matonic, B. L. Scott, *Acta Crystallogr. Sect. C: Cryst. Struct. Commun.* **2001**, *57*, 240–242.

[15] A. Immirzi, G. Bombieri, S. Degetto, G. Marangoni, *Acta Crystallogr., Sect. B: Struct. Sci* **1975**, *31*, 1023–1028.

[16] B. Masci, P. Thuéry, *Polyhedron* **2005**, *24*, 229–237.

[17] I. Wharf, T. Gramstad, M. Onyszchuk, *Can. J. Chem.* **1976**, *54*, 3430–3438.

[18] See, for example: G. A. Bowmaker, I. Bytheway, L. M. Engelhardt, J. M. Harrowfield, D. L. Kepert, H. Miyamae, J. M. Patrick, T. M. Shand, B. W. Skelton, A. A. Soudi, A. H. White, *Aust. J. Chem.* **1996**, *49*, 1026–1169.

[19] M. M. Bishop, A. H. W. Lee, L. F. Lindoy, P. Turner, B. W. Skelton, A. H. White, *J. Inclusion Phenom. Macrocyclic Chem.* **2005**, *17*, 37–45.

[20] C. Janiak, *Dalton Trans.* **2000**, 3885–3896.

[21] J. M. Harrowfield, G. S. Shahverdizadeh, A. A. Soudi, *Supramol. Chem.* **2003**, *15*, 367–373.

[22] J. M. Harrowfield, B. W. Skelton, A. H. White, *C. R. Chim.* **2005**, *8*, 169–180.

[23] a) H. D. Burrows, M. da G. Miguel, *Adv. Colloid Interface Sci.* **2001**, *89–90*, 495–496; b) S. J. Formosinho, H. D. Burrows, M. da G. Miguel, M. E. D. G. Azenha, I. M. Saraiva, A. C. D. N. Ribeiro, I. G. Khudyakov, R. G. Gasanov, M. Sarakha, *Photochem. Photobiol. Sci.* **2003**, *2*, 569–575.

[24] S. M. Fonseca, H. D. Burrows, M. da G. Miguel, M. Sarakha, M. Bolte, *Photochem. Photobiol. Sci.* **2004**, *3*, 317–321.

[25] B. Masci, personal communication.


 © 2006 Wiley-VCH Verlag GmbH & Co. KGaA, Weinheim 

[26] Z.-T. Yu, Z.-L. Liao, Y.-S. Jiang, G.-H. Li, J.-S. Chen, *Chem. Eur. J.* **2005**, *11*, 2642–2650.
[27] a) J. M. Harrowfield, B. W. Skelton, A. H. White, *Aust. J. Chem.* **1995**, *48*, 1311–1331; b) J. M. Harrowfield, R. P. Sharma, B. W. Skelton, A. H. White, *Aust. J. Chem.* **1998**, *51*, 707–722; J. M. Harrowfield, R. P. Sharma, B. W. Skelton, A. H. White, *Aust. J. Chem.* **1998**, *51*, 723–734; J. M. Harrowfield, R. P. Sharma, B. W. Skelton, A. H. White, *Aust. J. Chem.* **1998**, *51*, 735–746.
[28] L. Shimoni-Livny, J. P. Glusker, C. W. Bock, *Inorg. Chem.* **1998**, *37*, 1853–1867.
[29] Z. Asfari, J. M. Harrowfield, P. Thuéry, J. Vicens, *Supramol. Chem.* **2003**, *15*, 69–77.
[30] R. D. Hancock, J. H. Reibenspies, H. Maumela, *Inorg. Chem.* **2004**, *43*, 2981–2987.
[31] A. A. Soudi, F. Marandi, A. Ramazani, E. Ahmadi, A. Morsali, *C. R. Chim.* **2005**, *8*, 157–168.
[32] Y.-Z. Zheng, M.-L. Tong, X.-M. Chen, *Eur. J. Inorg. Chem.* **2005**, 4109–4117.
[33] *CrysAlis RED* (Version 1.171.24 beta), Oxford Diffraction Ltd., Oxford, United Kingdom, **2005**.
[34] L. J. Farrugia, *J. Appl. Crystallogr.* **1999**, *32*, 837–838.
[35] A. Altomare, G. Cascarano, C. Giacovazzo, A. Guagliardi, *J. Appl. Crystallogr.* **1993**, *26*, 343–350.
[36] SHELX97 [Includes SHELXS97, SHELXL97, CIFTAB]; *Programs for Crystal Structure Analysis* (Release 97–2). G. M. Sheldrick, Institute for inorganic chemistry, University of Göttingen, Göttingen, Germany, **1998**.
[37] N. W. Alcock, **1970**, *The Analytical Method for Absorption Correction* (Eds.: F. R Ahmed, S. R. Hall, C. P. Huber), Crystallographic Computing, Munksgaard, Copenhagen, pp. 271–278.
[38] R. H. Blessing, *Acta Crystallogr., Sect. A: Found. Crystallogr.* **1995**, *51*, 33–38.
[39] *Kappa-CCD Software*, Nonius BV, Delft, The Netherlands, **1998**.
[40] Z. Otwinowski, W. Minor, *Methods Enzymol.* **1997**, *276*, 307–326.
[41] G. M. Sheldrick, SHELXTL, Version 5.1, Bruker AXS Inc., Madison, WI, USA, **1999**.
[42] A. L. Spek, PLATON, University of Utrecht, The Netherlands, **2000**.
[43] L. J. Farrugia, *J. Appl. Crystallogr.* **1997**, *30*, 565.

Received: July 27, 2005
Published Online: December 1, 2005

 © 2006 Wiley-VCH Verlag GmbH & Co. KGaA, Weinheim 

DOI: 10.1002/ejic.200500682

# Hybrid Inorganic–Organic 1D and 2D Frameworks with $[As_6V_{15}O_{42}]^{6-}$ Polyoxoanions as Building Blocks

**Shou-Tian Zheng,[a] Yong-Mei Chen,[b] Jie Zhang,[a] Ji-Qing Xu,[c] and Guo-Yu Yang*[a,d]**

**Keywords:** Polyoxometalate / Vanadium / Arsenic

Three novel heteropolyoxovanadates, $[Ni(2,2'\text{-bpy})_3]_2[\{Ni(en)_2\}As_6V_{15}O_{42}(H_2O)]\cdot 9.5H_2O$ (**1**), $[Zn_2(dien)_3(H_2O)_2]_{1/2}\{[Zn_2(dien)_3]As_6V_{15}O_{42}(H_2O)\}\cdot 2H_2O$ (**2**), and $[Co(enMe)_2]_3[As_6V_{15}O_{42}(H_2O)]\cdot 2H_2O$ (**3**), were hydrothermally synthesized and characterized by single-crystal X-ray diffraction. Crystal data: **1**, monoclinic, $P2_1/n$, $a$ = 14.0324(9) Å, $b$ = 13.9900(8) Å, $c$ = 30.5785(19) Å, $\beta$ = 102.861(1)°, $Z$ = 2; **2**, monoclinic, $P2_1/c$, $a$ = 13.361(5) Å, $b$ = 23.979(8) Å, $c$ = 22.873(8) Å, $\beta$ = 102.459(4)°, $Z$ = 4; **3**, triclinic, $P\bar{1}$, $a$ = 13.2976(1) Å, $b$ = 15.0583(1) Å, $c$ = 20.1661(2) Å, $\alpha$ = 85.620(8)°, $\beta$ = 79.553(9)°, $\gamma$ = 65.087(9)°, $Z$ = 2. Compound **1** consists of 1D $[\{Ni(en)_2\}As_6V_{15}O_{42}(H_2O)]^{4-}$ chains and $[Ni(2,2'\text{-bpy})_3]^{2+}$ cations, in which the chain host has a molecular recognition ability for the chiral guest cations. Compound **2** is constructed from linking of the $[As_6V_{15}O_{42}]^{6-}$ polyoxoanions and novel dinuclear $[Zn_2(dien)_3]^{4+}$ cations into the first 1D helical As–V–O cluster chain. Compound **3** is the first 2D framework based on $[As_6V_{15}O_{42}]^{6-}$ polyoxoanions as building blocks.

(© Wiley-VCH Verlag GmbH & Co. KGaA, 69451 Weinheim, Germany, 2006)

## Introduction

Since the first polyoxometalates (POMs) were reported over 150 years ago, attention has been focused on their synthesis and various structural topologies, as well as their unexpected properties in such diverse fields as catalysis, materials science, and medicine.[1–3] To date, hundreds of POMs based on Mo–O clusters, V–O clusters, and W–O clusters and so on have been synthesized and described.[4,5] They provide a wide variety of robust structural motifs of different sizes and topologies ranging from closed cages and spherical shells to basket-, bowl-, barrel-, and belt-shaped structures. Those intriguing structures and potential applications attract more and more researchers and make the chemistry of POMs of continuous interest.[6] The preparation of extended structure solids with controllable and desirable properties and functions is of both fundamental and practical interest.[7] Now one of the challenging tasks in POM chemistry is to find some bridging units and then to link POM building units up into extended solid frameworks.[8,9] This approach is quite attractive and appears to hold the key to the development of rational approaches for tailor-made materials based on POMs with desirable features. During the past few years, a lot of research efforts have been focused on the application of secondary transition-metal complexes (TMCs) as bridging ligands linking POM clusters into 1-, 2-, and 3D networks under hydrothermal conditions.[10–13] Compounds $[\{Cu(enMe)_2\}_7\{V_{16}O_{38}(H_2O)\}_2]\cdot 4H_2O$[14] and $[Co(en)_2][Co(2,2'\text{-bpy})_2]_2[PMo_8V_8O_{44}]\cdot 4.5H_2O$[15] are recent examples. The former is made up of the hexadecavanadate clusters linked by the $[Cu(enMe)_2]^{2+}$ complex fragments into a rare 3D open framework, while the latter exhibited a novel 2D Mo–V–O polyoxometalate with two types of cobalt complex fragments as bridges. More recently, Khan et al. reported three novel 2D frameworks that consist of spherical $\{V_{18}O_{42}(X)\}$ shells linked by bridging $\{M(en)_2\}$ groups (X = $H_2O$, $Br^-$, $Cl^-$; M = Zn, Cd).[16]

An important subclass of the large POM family is As–V–O clusters with arsenic and vanadium in low oxidation states, which often act as cryptates encapsulating neutral molecules or anions. Since the first As–V–O cluster $K_6[As_6V_{15}O_{42}(H_2O)]\cdot 8H_2O$ was presented by Müller and Döring in 1988,[17] a number of As–V–O clusters have been synthesized,[18–27] such as $K_7[AsV_{14}O_{40}]\cdot 12H_2O$,[18] $Na_5[V_{12}As_8O_{40}(HCO_2)]\cdot 18H_2O$,[19] $[As_8V_{14}O_{42}(X)]^{6-}$ (X = $SO_3^{2-}$ or $SO_4^{2-}$),[20] $[N(Me)_4]_4[As_8V_{14}O_{42}(0.5H_2O)]$,[21] and $[NBu^n_4]_4[As_8V_6O_{26}]$.[23] However, most of them are discrete clusters; the linking of As–V–O clusters into extended

[a] State Key Laboratory of Structural Chemistry, Fujian Institute of Research on the Structure of Matter, Chinese Academy of Sciences,
Fuzhou, Fujian 350002, China
[b] Department of Applied Chemistry, Faculty of Science, Beijing University of Chemical Technology,
Beijing 100029, China
[c] State Key Laboratory of Inorganic Synthesis and Preparative Chemistry, Jilin University,
Changchun, Jilin 130023, China
[d] State Key Laboratory of Coordination Chemistry, Nanjing University,
Nanjing, Jiangsu 210093, China
Fax: +86-591-8371-0051
E-mail: ygy@ms.fjirsm.ac.cn

Supporting information for this article is available on the WWW under http://www.eurjic.org or from the author.

 © 2006 Wiley-VCH Verlag GmbH & Co. KgaA, Weinheim 

structures remains largely unexplored and a rewarding challenge. The aim of our work is to synthesize extended solids based on As–V–O clusters in the presence of TMCs. By this means, we recently successfully prepared a novel 2D sinusoidal layer structure constructed from $[As_8V_{14}O_{42}(SO_4)]^{6-}$ clusters and $[Ni(en)_2]^{2+}$ fragments.[28] As a part of continuing work in this system, here we describe the hydrothermal synthesis and structural characterization of the following three extended POMs based on $[As_6V_{15}O_{42}(H_2O)]^{6-}$ clusters as building blocks: $[Ni(2,2'\text{-bpy})_3]_2[\{Ni(en)_2\}As_6V_{15}O_{42}(H_2O)]\cdot 9.5H_2O$ (**1**), a 1D straight chain, $[Zn_2(dien)_3(H_2O)_2]_{1/2}\{[Zn_2(dien)_3]As_6V_{15}O_{42}(H_2O)\}\cdot 2H_2O$ (**2**), a 1D helical chain, and $[Co(enMe)_2]_3[As_6V_{15}O_{42}(H_2O)]\cdot 2H_2O$ (**3**), which is the first 2D $[As_6V_{15}O_{42}(H_2O)]^{6-}$ framework.

## Results and Discussion

Compounds **1**–**3** are made of the $[As_6V_{15}O_{42}(H_2O)]^{6-}$ ($As_6V_{15}$) clusters linked by corresponding TMCs into extended structures. The structure of the $As_6V_{15}$ anion, which has crystallographic $D_3$ symmetry, was first reported by Müller and Döring in $K_6[As_6V_{15}O_{42}(H_2O)]\cdot 8H_2O$.[17] It consists of fifteen $VO_5$ square pyramids and three handle-like $As_2O_5$ units. As shown inpart a of Figure 1, twelve $VO_5$ square pyramids form two triangles by sharing edges and sharing corners. In addition, another three $VO_5$ square pyramids and three $As_2O_5$ units are alternately joined together to form a ring (Figure 1, b). Then the two triangles are coordinated to each face the ring through sharing O

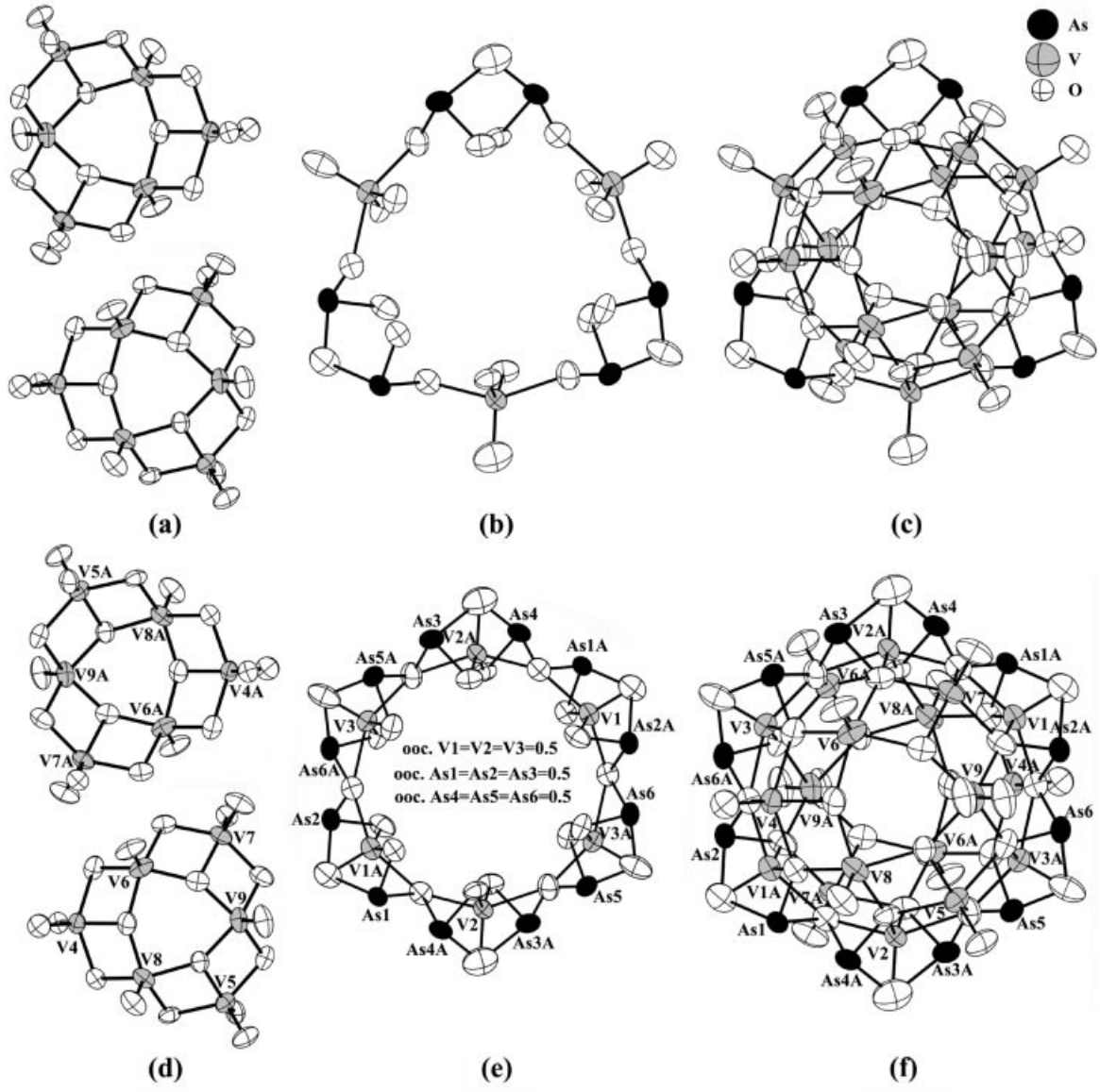


Figure 1. Structural contrast between normal $[As_6V_{15}O_{42}]^{6-}$ anion and disordered $[As_6V_{15}O_{42}]^{6-}$ anion in **1**. (a, b) Two $V_3$ triangles and one $As_6V_3$ ring in the normal $[As_6V_{15}O_{42}]^{6-}$ anion, respectively. (c) The normal $[As_6V_{15}O_{42}]^{6-}$ anion. (d, e) Two $V_3$ triangles and one disordered $As_6V_3$ ring in the disordered $[As_6V_{15}O_{42}]^{6-}$ anion in **1**. (f) The disordered $[As_6V_{15}O_{42}]^{6-}$ anion in **1**. (The thermal ellipsoids are shown at 50% probability.)

 © 2006 Wiley-VCH Verlag GmbH & Co. KGaA, Weinheim 

atoms, and form a ball-like $As_6V_{15}$ anion (Figure 1, c). In the structure of the $As_6V_{15}$ cluster in **1**, twelve $VO_5$ square pyramids form two identical triangles as described above (Figure 1, d). However, an interesting phenomenon is that the ring in the $As_6V_{15}$ anion of **1** was found to be disordered. As shown in Figure 1 (e), three positions occupied by $As_2O_5$ units are disordered over six positions with free refined occupancy of 0.5 for each position. At the same time, three positions occupied by $VO_5$ square pyramids are also disordered over six positions (V1, V2, V3, V1A, V2A, and V3A atoms) with free refined occupancy of 0.5 for each position. Then, similarly, the two triangles are coordinated to each face of the disordered ring through sharing O atoms, and form a disordered $As_6V_{15}$ anion (Figure 1, f). The structure of the disordered $As_6V_{15}$ anion in **1** can also be described as a well-known $\{V_{18}O_{42}\}$ rhombicuboctahedron[29] embedded with an arsenic ring (Figure S1). The $As_6V_{15}$ anion in **2** and **3** is essentially identical to that of the isolated cluster in $K_6[As_6V_{15}O_{42}(H_2O)]\cdot 8H_2O$[17] and is not disordered. In **1**–**3**, all V=O, V–O, and As–O bond lengths fall in the ranges 1.520(5)–1.631(6), 1.817(10)–2.107(9), and 1.748(6)–1.887(5) Å, respectively. On the basis of bond valence sum ($\Sigma_s$) calculations,[30] the oxidation states of all V atoms are +4 ($\Sigma_s$ = 4.04–4.48, **1**; $\Sigma_s$ = 4.02–4.15, **2**; $\Sigma_s$ = 4.03–4.16, **3**) and the As atoms are +3 ($\Sigma_s$ = 2.73–2.99, **1**; $\Sigma_s$ = 3.05–3.20, **2**; $\Sigma_s$ = 3.04–3.18, **3**). The oxidation states of the V atoms and the As atoms are consistent with the formulas of **1**–**3**. The EPR spectra of **1** and **2** at room temperature show the *g* values are 1.9591 and 1.9493, corresponding to the signal of $V^{4+}$, respectively. For **3**, no EPR signal of $V^{4+}$ was observed in **3** at room temperature. But at liquid nitrogen temperature, the EPR spectrum of **3** shows the *g* value is 1.9631, corresponding to the signal of $V^{4+}$.

The extended structure of **1** consists of disordered $As_6V_{15}$ sphere-like clusters. Each one is linked to two other neighboring clusters by two $[Ni2(en)_2]^{2+}$ bridges, generating a 1D straight chain of $[-As_6V_{15}-\mu_2\text{-}Ni2(en)_2-As_6V_{15}-]_\infty$ arrays (Figure 2). The bridging Ni2 atom shows an octahedron with four nitrogen donors of two en ligands [Ni2–N: 2.040(2)–2.061(18) Å] and two *trans* terminal oxo oxygen atoms coming from two adjacent $VO_5$ groups [Ni2–O: 2.199(11) Å, O–Ni2–O: 180(8)°]. An interesting feature is that another kind of TMC $[Ni1(2,2'\text{-bpy})_3]^{2+}$ rather than $[Ni(en)_3]^{2+}$ occupies the interchain regions as charge compensation. As shown in Figure 3, the $\{[Ni(en)_2]As_6V_{15}O_{42}(H_2O)\}^{4-}$ chains are aligned to the *b* axis and parallel packed beside each other along the *a* axis, generating a cluster anion layer along the *ab* plane, while the $[Ni(2,2'\text{-bpy})_3]^{2+}$ cations are exactly deposited between cluster anion layers

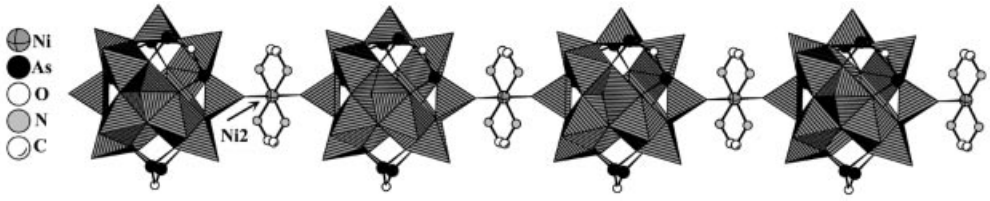


Figure 2. A view of the infinite straight chain in **1**. Half of the disordered atoms and H atoms were omitted for clarity.

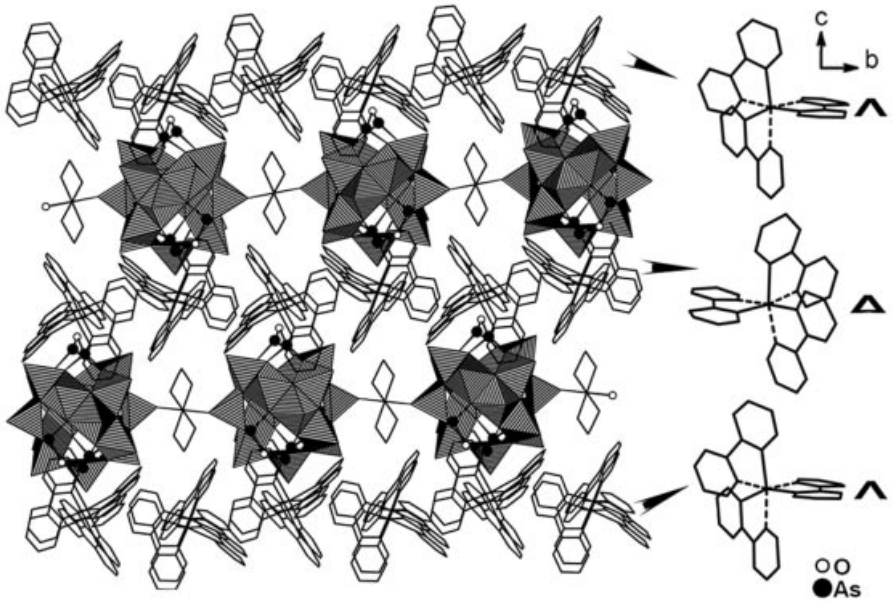


Figure 3. Packing diagrams of **1** along the *a* axis showing host chains have a molecular recognition ability for the guest metal complexes. All H atoms were omitted for clarity.

 © 2006 Wiley-VCH Verlag GmbH & Co. KGaA, Weinheim 

to form the cation layer along the *ab* plane. The $[Ni(2,2'\text{-bpy})_3]^{2+}$ cations in **1** present both Δ and Λ enantiomers. An unusual feature is that the Δ and Λ enantiomers of $[Ni(2,2'\text{-bpy})_3]^{2+}$ are separated orderly and deposited in alternate cluster anion layer regions, that is, the isolated $[Ni(2,2'\text{-bpy})_3]^{2+}$ cations are separated into Δ configuration layers and Λ configuration layers by cluster chain layers. The orderly separation of the enantiomers of $[Ni(2,2'\text{-bpy})_3]^{2+}$ indicates that the inorganic host has a molecular recognition ability for the guest TMCs.[31] Such a phenomenon is rarely reported in the POM system. The shortest inter-ring separation of 2,2′-bpy ligands along the *a* axis is 12.27 Å, hence, there is no notable π–π interaction in **1**.

POMs with helical or chiral structures are of particular interest.[32] For instance, a spiral-shaped chain has been described in $[H_2en]_2[\{Cu(en)(OH_2)\}Mo_5P_2O_{23}]\cdot 4H_2O$[33] and a double helical chain in $[(CH_3)_2NH_2]K_4[V_{10}O_{10}(H_2O)_2(OH)_4(PO_4)_7]\cdot 4H_2O$.[34] Single-crystal X-ray diffraction analysis revealed that compound **2** presents the first helical chain made of As–V–O clusters. As shown in Figure 4, the $As_6V_{15}$ clusters are connected to each other through novel $[(dien)Zn1(dien)Zn2(dien)]^{4+}$ dimeric cations by corner-sharing interactions of the type V=O–Zn1 to form an infinite 1D chain along the *b* axis, which arranged about a twofold screw axis and formed a left-hand helical array. Because compound **2** crystallizes in a centric space group $P2_1/c$, there are an equal number of right-handed (Figure S2) and left-handed helices (Figure 4) in the structure. As illustrated in Figure 5, it is interesting that the right-handed helical chains and the left-handed helical chains are aligned parallel to the *ab* plane to give right-handed helical chain layers and left-handed helical chain layers, respectively. Furthermore, these right-handed helical chain layers and left-handed helical chain layers are alternatively stacked along the *c* axis with another kind of novel dimeric cation, $[Zn_2(dien)_3(H_2O)_2]^{4+}$, occupying the interlayer regions (Figure 5, Figure 6). Hydrogen bonds play important roles in stabilizing the crystal structure of **2**. The isolated $[Zn_2(dien)_2(H_2O)_5]^{4+}$ cations link the chains through three pairs of hydrogen bonds [N10–O40a (a: $-x$, $y + 1/2$, $-z + 1/2$), 3.01(2) Å; N10–O37b (b: $-x$, $-y + 1$, $-z$), 3.25(3) Å; and N11–O41 3.02(2) Å, respectively] generating 2D networks along the *bc* plane, while $[Zn_2(dien)_3]^{4+}$ bridging cations interact with the chains along the *a* axis through strong hydrogen bonds [N···O: 2.835(10)–3.175(10) Å, listed in Table S1]. These hydrogen bonds force the structure of compound **2** to extend into a 3D supramolecular array.

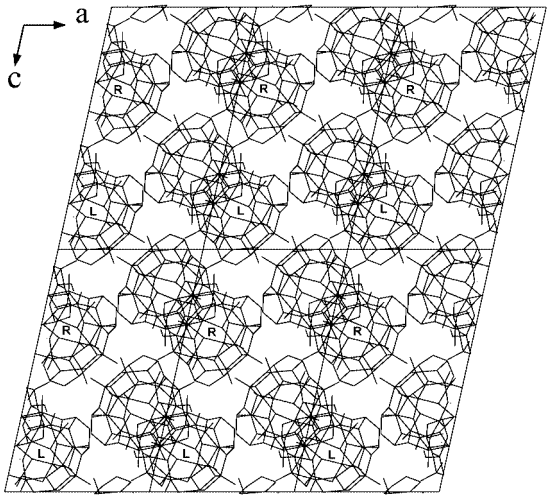


Figure 5. Packing diagram of **2** viewed along the *b* axis showing alternative right-hand and left-hand helical chain layers. All H atoms, water molecules, and isolated $[Zn_2(dien)_3(H_2O)_2]^{4+}$ cations are omitted for clarity.

The second unusual feature of **2** is that each Zn1(dien) bridging fragment hangs a $[Zn2(dien)]^{2+}$ complex linked through a tridentate dien ligand to form a novel dinuclear

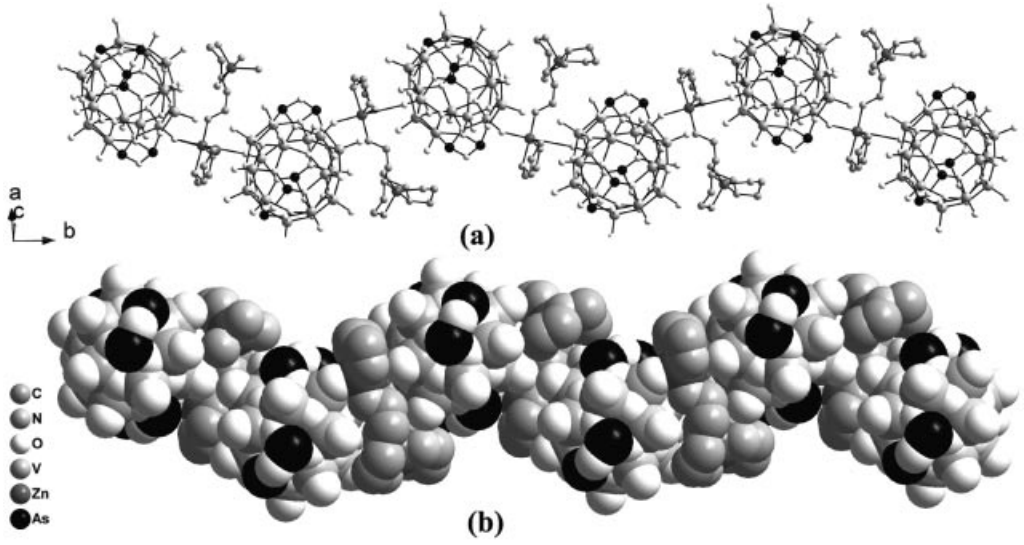


Figure 4. A ball-and-stick (a) and a space-filling (b) view of the left-hand helical chain of **2** showing the connectivity between the $[As_6V_{15}O_{42}(H_2O)]^{6-}$ clusters and $[Zn_2(dien)_3]^{4+}$ complexes and orientation of the chain. (Structure of right-hand helical chain of **2** can be seen in Figure S2.) All H atoms were omitted for clarity.

 © 2006 Wiley-VCH Verlag GmbH & Co. KGaA, Weinheim 

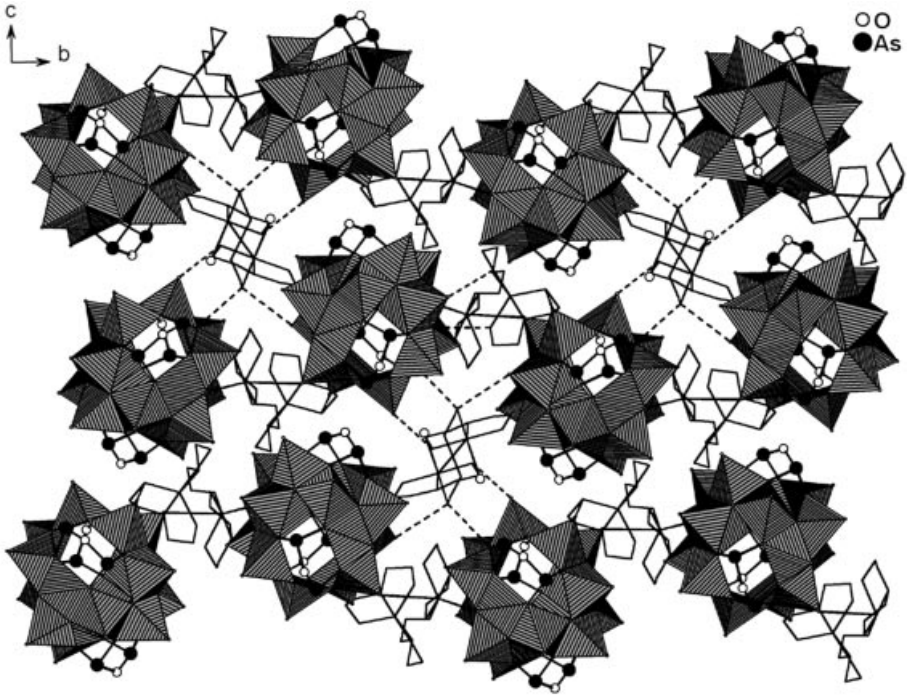


Figure 6. View of the 2D networks of **2** along the *a* axis showing the hydrogen bonds between helical chains and discrete $[Zn_2(dien)_3(H_2O)_2]^{4+}$ cations.

$[(dien)Zn1(dien)Zn2(dien)]^{4+}$ cation (Figure 7, b). Two N atoms of the bridging dien ligand coordinate to the Zn2 center, while the third N atom coordinates to the Zn1 center. Each Zn atom in dinuclear TMC is bound to two dien ligands in different coordination modes, respectively. Thus the Zn1 center is defined by four N donors from two dien ligands and two *trans* terminal oxo oxygen atoms from two adjacent arsenic–vanadium clusters to form a distorted octahedron [Zn1–N: 1.981(7)–2.155(9) Å; Zn1–O: 2.142(5) Å], whereas the five-coordinate Zn2 center is best described as a distorted trigonal bipyramidal configuration, with the atoms N5 and N8 occupying the axial positions [Zn2–N5: 2.265(8) Å; Zn2–N6: 2.049(6) Å; Zn2–N7: 2.081(7) Å; Zn2–N8: 2.187(7) Å; Zn2–N9: 2.017(9) Å]. Khan et al. has recently reported an unexpected binuclear $[Zn_2(en)_5]^{4+}$ cation (Figure 7, a) in compound $[Zn_2(en)_5][\{Zn(en)_2\}_2V_{18}O_{42}(H_2O)]\cdot 9H_2O$.[16] One striking difference between $[Zn_2(dien)_3]^{4+}$ and $[Zn_2(en)_5]^{4+}$ cations is that the former act as $\mu_2$-bridging units that link $As_6V_{15}$ clusters to form a 1D chain, while the latter just act as balance cations. Another distinct difference is that the $[Zn_2(en)_5]^{4+}$ cation is a centrosymmetric ion and the two zinc sites display the same coordination environments: distorted $ZnN_5$ trigonal bipyramidal configuration, while the $[Zn_2(dien)_3]^{4+}$ cation is a noncentral ion and two independent zinc sites display two kinds of different coordination environments: distorted $N_4Zn1O_2$ octahedron and distorted $Zn2N_5$ trigonal bipyramid. The average Zn–N distance (2.120 Å) in $[Zn_2(dien)_3]^{4+}$ is somewhat shorter than that of the $[Zn_2(en)_5]^{4+}$ cation (2.134 Å). The Zn1···Zn2 separation distance [6.492(7) Å] in the $[Zn_2(dien)_3]^{4+}$ cation is obviously shorter than that of the $[Zn_2(en)_5]^{4+}$ cation [7.592(2) Å].

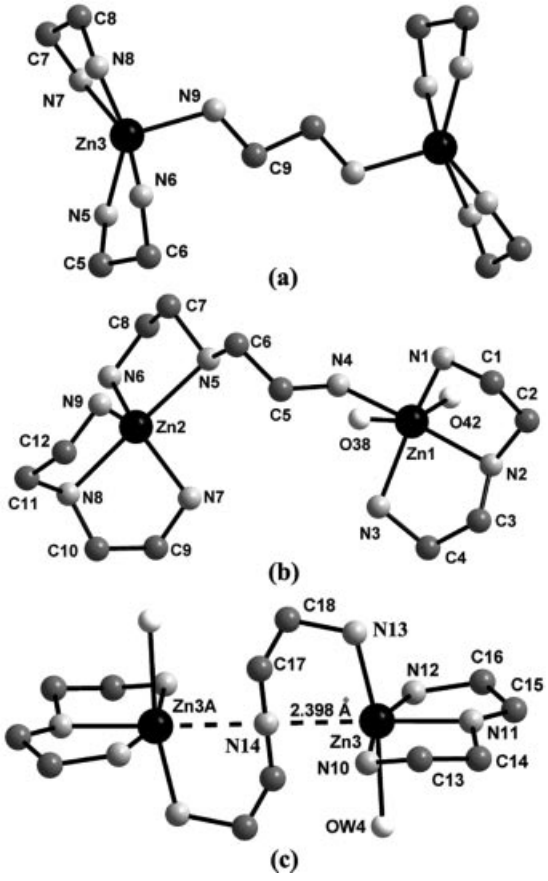


Figure 7. (a) Structure of binuclear TMC in ref.[16]. (b, c) Structures of binuclear TMCs in **2**, showing two unique coordination modes. All the H atoms are omitted for clarity.

 © 2006 Wiley-VCH Verlag GmbH & Co. KGaA, Weinheim 

The third unusual feature of **2** is that the structure contains another kind of novel isolated binuclear $[Zn_2(dien)_3(H_2O)_2]^{4+}$ cation providing charge compensation (Figure 7, c). The structure of the $[Zn_2(dien)_3(H_2O)_2]^{4+}$ cation can be described as two $[Zn(dien)(H_2O)]^{2+}$ moieties linked across an inversion center by a bridging dien ligand. The two terminal N13 and N13A atoms of bridging dien exhibit strong attachment to the Zn3 and Zn3A atoms, respectively, with Zn–N distances of 2.036(18) Å, while the middle N14 atom occupies the central site of the binuclear cation and exhibits weak attachment to both Zn3 and Zn3A atoms with Zn–N distances of 2.398(3) Å, which are much longer than the usual Zn–N values (about 1.90–2.20 Å) observed in many reported studies.[16,35,36] Such a coordination mode between the Zn atoms and the bridging dien ligand is peculiar. The Zn3–O distance [2.430(2) Å] and the bond valence sum[30] value (0.17) identify the O atom coordinated to the Zn3 center as $H_2O$ (denoted as OW4 in this paper). The Zn3···Zn3A separation distance [4.796(10) Å] is even shorter than that of Zn1···Zn2 [6.493(7) Å].

The solid architectures of **1** and **2** provide examples of a different way of connecting $As_6V_{15}$ clusters and TMCs groups. This suggests that further condensation of $As_6V_{15}$ clusters into higher dimensional solids through the linkage of TMCs groups could be feasible. Suitable modification of the synthetic conditions results in the successful crystallization of solid **3**, which is the first 2D $As_6V_{15}$ framework. As shown in Figure 8, the $As_6V_{15}$ cluster acts as a hexadentate ligand coordinating to six $Co^{2+}$ ions through the terminal oxo oxygen atoms with Co–O distances ranging from 2.180(6) to 2.278(6) Å, such that each $As_6V_{15}$ cluster is connected with six others through *trans*-{$Co(enMe)_2O_2$} groups to generate a 2D framework (Figure 9). Each Co atom in **3** acts as a bridge and is located at a distorted octahedral center, being coordinated by two O atoms from the arsenic–vanadium polyoxoanion and four N atoms from two enMe ligands with Co–N bond lengths ranging from 2.049(8) to 2.110(9) Å. These layers are stacked along the [1$\bar{1}$0] direction in AAAA sequence with an interlamellar separation of approximately 9.0 Å (see Figure S3 in the Supporting Information), forming *pseudo*-1D channels along the *c* axis, which are occupied by lattice water molecules and organic ligands (Figure S4).

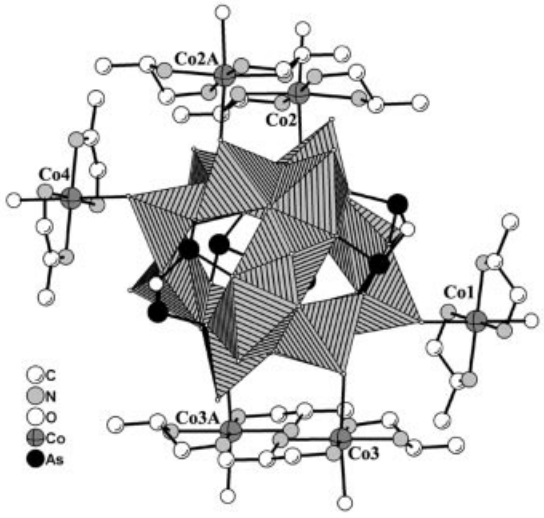


Figure 8. View of coordination mode of the $[As_6V_{15}O_{42}(H_2O)]^{6-}$ cluster in **3**.

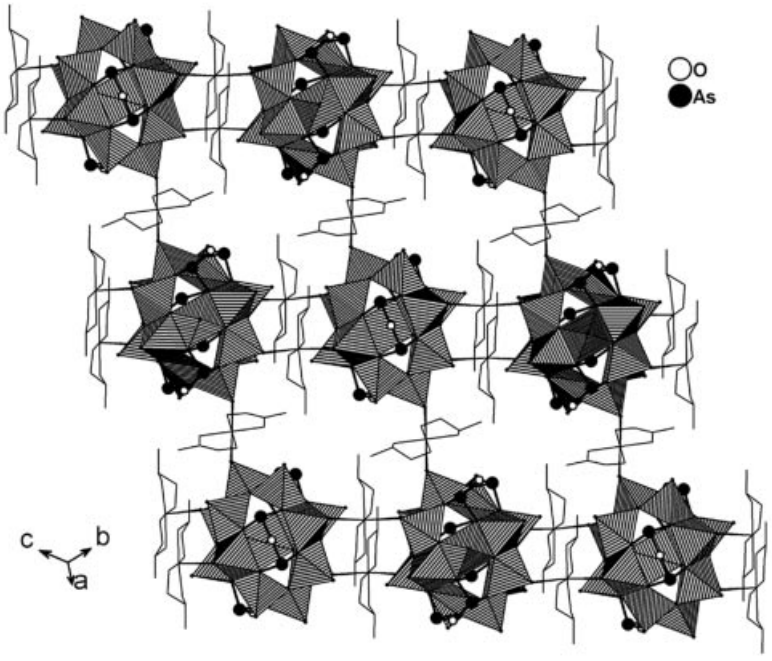


Figure 9. View of the 2D structure of **3** along the [111] direction. All the H atoms and water molecules are omitted for clarity.

 © 2006 Wiley-VCH Verlag GmbH & Co. KGaA, Weinheim 

The infrared spectrum of **1** exhibited features characteristics of $\nu$(M–O–M) (M = V or As) in the 480–800 $cm^{-1}$ regions. The strong bands at 983 can be assigned to the stretching vibrations of V=O bonds. The region of interest in determining the mode of 2,2′-pyridine binding and the bending bands of the $NH_2$ and $CH_2$ are from 1161–1599 $cm^{-1}$. The infrared spectrum of **2** shows the bending bands of the $NH_2$ and $CH_2$ present at around 1583, 1458, and 1362 $cm^{-1}$. While the strong peak 980 $cm^{-1}$ is attributed to the vibrations of V=O bands, a series of bands in the 480–760 $cm^{-1}$ region is characteristic of $\nu$(M–O–M) (M = V or As) and $\nu$(As–O). The infrared spectrum of **3** exhibits a number of absorption bands in the 1100–1600 $cm^{-1}$ region. Many of these bands are attributed to the fundamental vibration modes of enMe. The strong and sharp bands at 973 $cm^{-1}$ are assigned to the vibrations of V=O bands. Furthermore a broad band between 833 and 500 $cm^{-1}$ with maximum at 701 $cm^{-1}$ is attributed to asymmetric and symmetric {M–O–M} (M = V or As) stretching. These positions of the bands and their assignments of **1**–**3** are consistent with literature reports.[16,24,37]

The thermogravimetric analyses were carried out in flowing $N_2$ with a heating rate of 10 °C·$min^{-1}$ in the temperature range 30–1000 °C for compounds **1**–**3** (Figure 10). Three distinct weight-loss stages are observed on the TGA curve of compound **1**. The first stage, which occurs from 46 to 109 °C, is attributed to the loss of 10.5 water molecules; the observed weight loss (4.84%) is in agreement with the calculated value (5.71%). The remaining two stages occur between 156 and 847 °C, and are due to the loss of two en molecules and six 2,2′-bpy molecules, and the sublimation of three $As_2O_3$ molecules; the observed weight loss (49.68%) is consistent with the calculated value (49.89%). Assuming that the residue corresponds to $VO_2$ and NiO, the observed total weight loss (54.52%) is also in agreement with the calculated value (55.59%). The TG curve of **2** shows two major mass losses in the regions 46–132 °C and 178–776 °C. The first step corresponds to the loss of four water molecules (exp. 2.01%, calcd. 2.75%). The second huge mass loss can be assigned to the loss of 4.5 dien molecules and the sublimation of three $As_2O_3$ molecules (exp. 41.19%, calcd. 40.41%). Assuming that the residue corresponds to $VO_2$ and ZnO, the observed total weight loss (43.20%) is in good agreement with the calculated value (43.16%). The TG curve of **3** indicates that the weight loss of **1** cannot be completely divided into distinct stages. The whole stage, which occurs from 58 to 786 °C, is attributed to the loss of $H_2O$ and enMe, and the sublimation of $As_2O_3$. Assuming that the residue corresponds to $VO_2$ and CoO, the observed weight loss (43.29%) is in good agreement with the calculated value (42.74%).

The variable temperature magnetic susceptibilities of **1** and **2** were measured between 2 and 300 K. Figure 11 shows the magnetic behaviors of **1** and **2** in the form of the product $\chi_M T$ versus temperature, where $\chi_M$ is the molar magnetic susceptibility. The $\chi_M T$ value of complex **1** at 300 K is 3.33 $cm^3$·$mol^{-1}$·K, much smaller than the expected value (8.40 $cm^3$·$mol^{-1}$·K) for the fifteen uncoupled $S$ = 1/2 spins of $V^{4+}$ atoms (5.40 $cm^3$·$mol^{-1}$·K, $g$ = 1.9591 for $V^{4+}$ from EPR result) and three uncoupled $S$ = 1 spins of the $Ni^{2+}$ atoms (3.0 $cm^3$·$mol^{-1}$·K, $g$ = 2.0). Upon cooling, the $\chi_M T$ value decreases nearly linearly to 2.48 $cm^3$·$mol^{-1}$·K at 50 K, and then decreases rapidly from 50 K and reaches a minimum value of 1.74 $cm^3$·$mol^{-1}$·K at 2 K. Such magnetic behavior is characteristic of the combination of zero-field splitting of $Ni^{2+}$ in distorted octahedral environments and strong antiferromagnetic couplings between adjacent paramagnetic centers. The short V···V distance (≤ 3.006 Å) and structural disorder of $V^{4+}$ ions are probably mainly responsible for the strong magnetic interaction at high temperature.[38–40] For **2**, $\chi_M T$ at room temperature is 1.83 $cm^3$·$mol^{-1}$·K, which is also much lower than the value expected for 15 uncoupled electrons (5.34 $cm^3$·$mol^{-1}$·K, $g$ = 1.9493 for $V^{4+}$ from EPR result). As the temperature decreases, the $\chi_M T$ value decreases rapidly until 150 K to stabilize approximately at 1.08 $cm^3$·$mol^{-1}$·K. Below 25 K another faster decrease of $\chi_M T$ is observed, with about 0.47 $cm^3$·$mol^{-1}$·K at 2.0 K. Because the $Zn^{2+}$ ion is nonmagnetic, the magnetic behavior of **2** can be attributed to the exchange interactions between $V^{4+}$ ions in $[As_6V_{15}O_{42}]^{6-}$

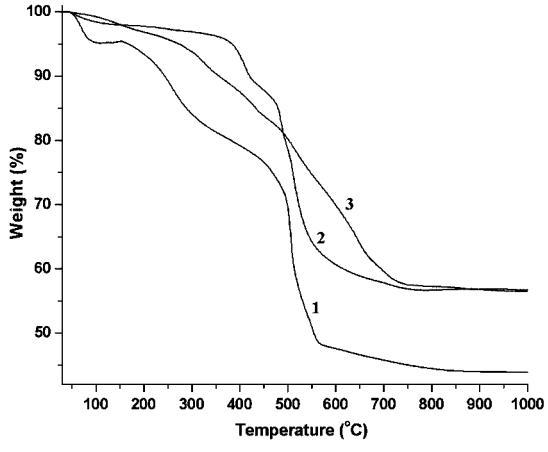


Figure 10. TGA curves of compounds **1**–**3**.

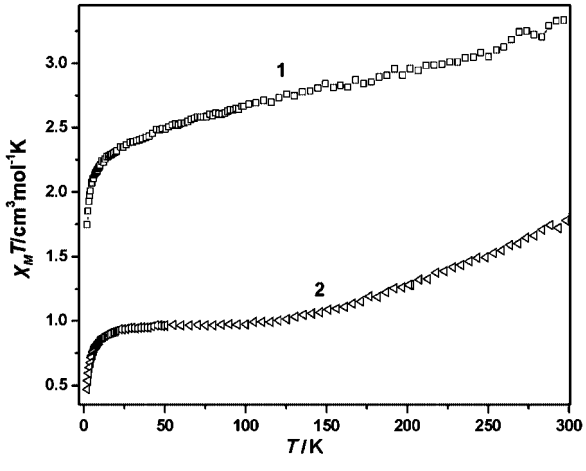


Figure 11. The temperature dependences of the product $\chi_M T$ for **1** and **2**.

 © 2006 Wiley-VCH Verlag GmbH & Co. KGaA, Weinheim 

polyoxoanions. The short neighboring V···V distances of V1···V3 (2.846 Å), V2···V4 (2.834 Å), V5···V6 (2.839 Å), V10···V11 (2.868 Å), V12···V13 (2.885 Å), and V14···V15 (2.882 Å) pairs with double O bridges lie in the range expected for strong antiferromagnetic coupling,[29,38–40] thus resulting in a low $\chi_M T$ value at high temperature. The remaining three vanadium ions are largely uncorrelated at high temperature. When temperature is lowered further, a weak antiferromagnetic coupling occurs between these three vanadium centers through the $[As_2O_5]^{4-}$ bridge, which corresponds to the second decrease below 25 K. The value (1.08 $cm^3 \cdot mol^{-1} \cdot K$) of the plateau of $\chi_M T$ in the range 150–25 K is in agreement with the calculated value for three uncoupled $V^{4+}$ ions.

The temperature dependences of $\chi_M T$ for **1** and **2** demonstrate the existence of strong antiferromagnetic coupling interactions, which are a common feature for most polyoxovanadate clusters.[29,41] Unfortunately, it is too difficult to fit the experimental magnetic data of these extended high-nuclearity heteropolymetallic spin systems using a suitable theoretical model.[42]

## Conclusions

In this paper, we have described three extended As–V–O compounds synthesized by a hydrothermal method, all constructed from $[As_6V_{15}O_{42}(H_2O)]^{6-}$ cluster units. These results emphasize the potential of $[As_6V_{15}O_{42}(H_2O)]^{6-}$ clusters as building blocks for constructing new materials and demonstrate that the hydrothermal techniques are a vital tool for the realization of materials design. Moreover, the construction of these new materials may facilitate the formation of unexpected species[16] such as the novel $[Zn_2(dien)_3]^{4+}$ and $[Zn_2(dien)_3(H_2O)_2]^{4+}$ cations observed during the course of this work. Linking discrete POMs to build solid-state materials is of great interest not only from a structural point of view, but also because they are potentially interesting for applications in different areas. Further research will concentrate on the suitable modification of the synthetic conditions to obtain 3D As–V–O cluster architecture, which has never been reported to date to the best of our knowledge and is a challenging task.

## Experimental Section

**General Remarks:** All reagents were purchased commercially and used without further purification. The contents of V, Ni, Zn, Co, and As were determined with an Utlima2 spectrometer. Elemental analyses (C, H, and N) were performed on an Elementar Vario III analyzer. IR spectra were recorded with an ABB Bomem MB102 spectrometer in KBr pellet. Thermal analyses were performed in a dynamic nitrogen atmosphere with a heating rate of 10 °C·min$^{-1}$, using a METTLER TGA/ SDTA851$^e$ thermal analyzer. EPR spectra were carried out on powder samples at X-band frequency with a Bruker ER-420 spectrometer at room temperature. Variable temperature susceptibility measurements were carried out in the temperature range 2–300 K at a magnetic field of 1 T on polycrystalline samples with a SQUID MPMS-7 magnetometer manufactured by Quantum Design. Background corrections for the sample holder assembly and diamagnetic components of the compound were applied.

**Synthesis of $[Ni(2,2'\text{-bpy})_3]_2[\{Ni(en)_2\}As_6V_{15}O_{42}(H_2O)]\cdot 9.5H_2O$ (1):** A mixture of $V_2O_5$ (0.30 g, 1.65 mmol), $As_2O_3$ (0.10 g, 0.51 mmol), $Ni(CH_3COO)_2\cdot 4H_2O$ (0.05 g, 0.20 mmol), 2,2′-bpy (0.05 g, 0.32 mmol), en (0.30 mL), and $H_2O$ (12 mL, 0.67 mol) was heated to 160 °C for 3 days and then cooled to room temperature. The product was isolated as brown blocks (0.473 g, 65.1% yield based on V). $C_{64}H_{85}As_6N_{16}Ni_3O_{52.50}V_{15}$ (3308.23): calcd. C 23.21, H 2.59, As 13.59, N 6.77, Ni 5.32, V 23.10; found C 22.96, H 2.71, As 13.16, N 6.58, Ni 5.09, V 22.94. IR (KBr) for **1**: $\tilde{\nu}$ = 1632 (m), 1599 (s), 1491 (w), 1471 (m), 1442 (s), 1318 (m), 1161 (w), 1020 (m), 983 (s), 778 (s), 754 (s), 738 (s), 633 (m), 488 (w), 464 (m) $cm^{-1}$.

**Synthesis of $[Zn_2(dien)_3(H_2O)_2]_{1/2}[\{Zn_2(dien)_3\}As_6V_{15}O_{42}(H_2O)]\cdot 2H_2O$ (2):** A mixture of $V_2O_5$ (0.20 g, 1.10 mmol), $As_2O_3$ (0.24 g, 1.21 mmol), dien (0.40 mL), $Zn(CH_3COO)_2\cdot 2H_2O$ (0.54 g, 2.10 mmol), and $H_2O$ (15 mL, 0.83 mol) was sealed in a Teflon-lined steel autoclave and heated to 160 °C for 3 days and then cooled to room temperature. The product was isolated as brown blocks (0.220 g, 57.3% yield based on V). $C_{18}H_{66.5}As_6N_{13.5}O_{46}V_{15}Zn_3$ (2618.08): calcd. C 8.25, H 2.56, As 17.17, N 7.22, V 29.19, Zn 7.49; found C 7.64, H 2.63, As 16.75, N 6.77, V 30.16, Zn 7.06. IR (KBr) for **2**: $\tilde{\nu}$ = 1583 (s), 1458 (m), 1386 (w), 1362 (w), 1326 (w), 1285 (w), 1144 (m), 1092 (m), 980 (s), 738 (s), 633 (s), 541 (m), 484 (m), 460 (m) $cm^{-1}$.

**Synthesis of $[Co(enMe)_2]_3[As_6V_{15}O_{42}(H_2O)]\cdot 2H_2O$ (3):** A mixture of $V_2O_5$ (0.55 g, 3.02 mmol), $As_2O_3$ (0.20 g, 1.01 mmol), $H_2C_2O_4\cdot 2H_2O$ (0.382 g, 3.04 mmol), enMe (0.30 mL), $CoSO_4\cdot 4H_2O$ (0.34 g, 1.50 mmol), and $H_2O$ (10 mL, 0.55 mol) was sealed in a Teflon-lined steel autoclave and heated to 160 °C for 6 days and then cooled to room temperature. The product was isolated as brown blocks (0.282 g, 27.3% yield based on V). $C_{18}H_{72}As_6Co_3N_{12}O_{45}V_{15}$ (2567.29): calcd. C 8.44, H 2.83, As 17.51, Co 6.89, N 6.55, V 29.76; found C 8.25, H 2.96, As 16.92, Co 6.80, N 6.38, V 29.05. IR (KBr) for **3**: $\tilde{\nu}$ = 1633 (m), 1578 (s), 1448 (m), 1300 (w), 1267 (m), 1081 (m), 1020 (s), 973 (s), 701 (s), 510 (s), 446 (m) $cm^{-1}$.

**X-ray Crystallography:** Crystal structure determinations by X-ray diffraction were performed with a Siemens SMART CCD diffractometer with graphite-monochromated Mo-$K_\alpha$ ($\lambda$ = 0.71073 Å) radiation in the $\omega$ scanning mode at room temperature. The program SADABS was used for the absorption correction. The structures were solved by the direct methods and refined by full-matrix least-squares on $F^2$. All calculations were performed using the SHELX97 program package. For **1**, in the cluster structure, three positions occupied by $As_2O_5$ dimers and three positions occupied by $VO_5$ square pyramids were disordered. Each of the six disordered positions was occupied either by an $As_2O_5$ dimer or a $VO_5$ square pyramid. The ratios $[As_2O_5]/[VO_5]$ were refined to 0.5:0.5 for all six disordered positions. The respective occupancies of those disordered As and V atoms were fixed finally according to the value of free refined occupancies. Although the final residuals ($R_1$ = 0.1122, $wR_2$ = 0.1967) were relatively large, the molecular anion and transition-metal complexes were well behaved, and there were no unusual temperature factors or excursions of electron density in these regions of the structure. The space group was unambiguous. For **2**, the Zn1 atom was disordered over two positions (Zn1 with SOF = 0.60 and Zn1A with SOF = 0.40). In addition, difference Fourier maps showed two significant regions (7.95 and 2.70 e·Å$^{-3}$) of electron density close to the Zn3 atom. A disordering effect of the Zn3 atom over three adjacent positions with occupancy of 0.57, 0.38, and 0.05 was therefore modeled. In each structure, hydrogen

 © 2006 Wiley-VCH Verlag GmbH & Co. KGaA, Weinheim 

Table 1. Crystallographic data for compounds **1**–**3**.

| Compound | **1** | **2** | **3** |
|---|---|---|---|
| Formula | $C_{64}H_{85}As_6N_{16}Ni_3O_{52.5}V_{15}$ | $C_{18}H_{66.5}As_6N_{13.5}O_{46}V_{15}Zn_3$ | $C_{18}H_{72}As_6Co_3N_{12}O_{45}V_{15}$ |
| $M_r$ | 3308.23 | 2618.08 | 2567.29 |
| Crystal system | monoclinic | monoclinic | triclinic |
| Space group | $P2_1/n$ | $P2_1/c$ | $P\bar{1}$ |
| Crystal size [mm] | $0.38\times0.22\times0.22$ | $0.20\times0.20\times0.20$ | $0.32\times0.40\times0.44$ |
| $a$ [Å] | 14.0324(9) | 13.361(5) | 13.2976(14) |
| $b$ [Å] | 13.9900(8) | 23.979(8) | 15.0583(12) |
| $c$ [Å] | 30.5785(19) | 22.873(8) | 20.1661(17) |
| $\alpha$ [°] | 90 | 90 | 85.620(8) |
| $\beta$ [°] | 102.861(1) | 102.459(4) | 79.553(9) |
| $\gamma$ [°] | 90 | 90 | 65.087(9) |
| $V$ [Å$^3$] | 5852.4(6) | 7155.7(4) | 3601.6(6) |
| $Z$ | 2 | 4 | 2 |
| $D_{calcd}$ [g·cm$^{-3}$] | 1.877 | 2.430 | 2.367 |
| $\mu$ [mm$^{-1}$] | 3.378 | 5.697 | 5.348 |
| Reflections collected | 16866 | 43070 | 18415 |
| Unique data ($R_{int}$) | 9624(0.0741) | 12225(0.0437) | 16313(0.0432) |
| $F$(000) | 3256 | 5080 | 2496 |
| $\theta$ range [°] | 2.00–25.08 | 2.49–25.03 | 1.71–27.50 |
| Goodness of fit | 1.087 | 1.075 | 0.992 |
| $R_1$, $wR_2$ [$I > 2\sigma(I)$][a] | 0.1122, 0.1967 | 0.0580, 0.1434 | 0.0649, 0.1279 |
| $\Delta\rho_{max}$, $\Delta\rho_{min}$ [e·Å$^{-3}$] | 1.622, –1.848 | 1.784, –1.343 | 1.767, –1.204 |

[a] $R_1 = \Sigma||F_o| - |F_c||/\Sigma|F_o|$; $wR_2 = \{\Sigma[w(F_o^2 - F_c^2)^2]/\Sigma[w(F_o^2)^2]\}^{1/2}$.

atoms of organic ligands were geometrically placed and refined using a riding model. These above-mentioned disordered atoms and several disordered C atoms (C31 and C32 in **1**, C6, C7, and C9 in **2**, and C12 in **3**) were refined isotropically; the other atoms were refined anisotropically. Experimental details for the structural determinations of **1**–**3** are presented in Table 1. Ranges of selected bond lengths of **1**–**3** are listed in Table 2.

Table 2. Ranges of some important bond lengths [Å] for compounds **1**–**3**.[a]

| | | | |
|---|---|---|---|
| **1** | | | |
| V=$O_t$ | 1.520(5)–1.624(11) | Ni1–N | 2.039(17)–2.110(15) |
| V–$O_b$ | 1.817(10)–2.107(9) | Ni2–N | 2.040(2)–2.061(18) |
| As–O | 1.767(5)–1.887(5) | Ni2–O | 2.199(11) |
| **2** | | | |
| V=$O_t$ | 1.600(5)–1.623(5) | Zn2–N | 2.017(9)–2.265(8) |
| V–$O_b$ | 1.913(4)–2.045(6) | Zn3–N | 2.021(16)–2.398(3) |
| As–O | 1.748(6)–1.811(6) | Zn1–O | 2.142(5) |
| Zn1–N | 1.981(7)–2.155(9) | Zn3–O | 2.430(2) |
| **3** | | | |
| V=$O_t$ | 1.590(6)–1.631(6) | Co4–N | 2.095(11)–2.102(11) |
| V–$O_b$ | 1.887(6)–2.042(7) | Co1–O | 2.180(6) |
| As–O | 1.750(6)–1.797(6) | Co2–O | 2.257(6)–2.278(6) |
| Co1–N | 2.097(8)–2.099(8) | Co3–O | 2.221(6)–2.263(6) |
| Co2–N | 2.049(8)–2.080(8) | Co4–O | 2.273(7) |
| Co3–N | 2.055(9)–2.110(9) | | |

[a] $O_t$, terminal oxygen atoms; $O_b$, oxygen atoms in basal plane of $VO_5$ pyramids.

CCDC-254404 (for **1**), -254405 (for **2**), and -259395 (for **3**) contain the supplementary crystallographic data for this paper. These data can be obtained free of charge from The Cambridge Crystallographic Data Centre via www.ccdc.cam.ac.uk/data_request/cif.

**Supporting Information:** Two Tables of hydrogen bonds of compounds **2** and **3**, and four additional plots for compounds **1**–**3**. This material is available free of charge via the Internet at http://www.eurjic.org or from the authors.

## Acknowledgments

This work was supported by the NNSF of China (Nos. 20271050/20473093), the Talents Program of Chinese Academy of Sciences, and the NSF of Fujian Province (Nos. E0510030/E0210029).

[1] D. E. Katsoulis, *Chem. Rev.* **1998**, *98*, 359–388.
[2] M. T. Pope, A. Müller, *Angew. Chem.* **1991**, *103*, 56–70; *Angew. Chem. Int. Ed. Engl.* **1991**, *30*, 34–48.
[3] A. Müller, F. Peters, M. T. Pope, D. Gatteschi, *Chem. Rev.* **1998**, *98*, 239–272.
[4] a) *Gmelin Handbuch der Anorganischen Chemie*, Verlag Chemie, Berlin, System No. 53 (Molybdän), **1935**; System No. 54 (Wolfram), **1933**; b) H. T. Evans Jr, *Perspect. Struct. Chem.* **1971**, *4*, 1–59; c) M. T. Pope, *Heteropoly and Isopoly Oxometalates*, Springer, Berlin, **1983**.
[5] a) V. W. Day, W. G. Klemperer, O. M. Yagi, *J. Am. Chem. Soc.* **1989**, *111*, 5959–5961; b) W. G. Klemperer, T. A. Marquart, O. M. Yagi, *Angew. Chem.* **1992**, *104*, 51–53; *Angew. Chem. Int. Ed. Engl.* **1992**, *31*, 49–51; c) G. K. Johnson, E. O. Schlemper, *J. Am. Chem. Soc.* **1978**, *100*, 3645–3646; d) M. I. Khan, J. Zubieta, *Angew. Chem.* **1994**, *106*, 784–786; *Angew. Chem. Int. Ed. Engl.* **1994**, *33*, 760–762; e) G. Huan, A. J. Jacobson, V. W. Day, *Angew. Chem.* **1991**, *103*, 426–427; *Angew. Chem. Int. Ed. Engl.* **1991**, *30*, 422–423.
[6] a) M. Piepenbrink, M. U. Triller, N. H. J. Gorman, B. Krebs, *Angew. Chem.* **2002**, *114*, 2633–2635; *Angew. Chem. Int. Ed.* **2002**, *41*, 2523–2525; b) M. I. Khan, S. Tabussum, R. J. Doedens, V. O. Golub, C. J. O'Connor, *Inorg. Chem.* **2004**, *43*, 5850–5859; c) K. Hegetschweiler, B. Morgenstern, J. Zubieta, P. J. Hagrman, N. Lima, R. Sessoli, F. Totti, *Angew. Chem.* **2004**, *116*, 3518–3521; *Angew. Chem. Int. Ed.* **2004**, *43*, 3436–3439; d) T. Whitfield, X. Wang, A. J. Jacobson, *Inorg. Chem.* **2003**, *42*, 3728–3733; e) X. M. Zhang, H. S. Hu, F. Q. Zhang, A. Prikhod′ko, S. Kuwata, P. Comba, *Chem. Commun.* **2004**, 2046–2047.
[7] E. Coronado, C. J. Gomez-Garcia, *Chem. Rev.* **1998**, *98*, 273–296.
[8] C. D. Wu, C. Z. Lu, H. H. Zhuang, J. S. Huang, *J. Am. Chem. Soc.* **2002**, *124*, 3836–3837.

 © 2006 Wiley-VCH Verlag GmbH & Co. KGaA, Weinheim 

[9] D. L. Long, H. Abbas, P. Kögerler, L. Cronin, *J. Am. Chem. Soc.* **2004**, *126*, 13880–13881.
[10] P. J. Hagrman, D. Hagrman, J. Zubieta, *Angew. Chem.* **1999**, *111*, 2798–2848; *Angew. Chem. Int. Ed.* **1999**, *38*, 2638–2684.
[11] J. Lu, E. H. Shen, M. Yuan, Y. G. Li, E. B. Wang, C. W. Hu, L. Xu, J. Peng, *Inorg. Chem.* **2003**, *42*, 6956–6958.
[12] J. R. D. DeBord, R. C. Haushalter, L. M. Meyer, D. J. Rose, P. J. Zapf, J. Zubieta, *Inorg. Chim. Acta* **1997**, *256*, 165–168.
[13] a) M. I. Khan, E. Yohannes, R. J. Doedens, *Angew. Chem.* **1999**, *111*, 1374–1376; *Angew. Chem. Int. Ed.* **1999**, *38*, 1292–1294; b) M. I. Khan, E. Yohannes, D. Powell, *Chem. Commun.* **1999**, 23–24.
[14] C. M. Liu, D. Q. Zhang, M. Xiong, D. B. Zhu, *Chem. Commun.* **2002**, 1416–1417.
[15] B. Z. Liu, S. X. Liu, *Chem. Commun.* **2002**, 2126–2127.
[16] M. I. Khan, E. Yohannes, R. J. Doedens, *Inorg. Chem.* **2003**, *42*, 3125–3129.
[17] A. Müller, J. Döring, *Angew. Chem.* **1988**, *100*, 1789–1789; *Angew. Chem. Int. Ed. Engl.* **1988**, *27*, 1721–1721.
[18] A. Müller, J. Döring, M. I. Khan, V. Wittneben, *Angew. Chem.* **1991**, *103*, 203–205; *Angew. Chem. Int. Ed. Engl.* **1991**, *30*, 210–212.
[19] A. Müller, J. Döring, H. Bögge, *J. Chem. Soc., Chem. Commun.* **1991**, 273–274.
[20] A. Müller, J. Döring, *Z. Anorg. Allg. Chem.* **1991**, *595*, 251–274.
[21] G. Huan, M. A. Greaney, A. J. Jacobson, *J. Chem. Soc., Chem. Commun.* **1991**, 260–261.
[22] G. Q. Huang, S. W. Zhang, Y. G. Wei, M. C. Shao, *Polyhedron* **1993**, *12*, 1483–1485.
[23] E. Dumas, C. Livage, S. Halut, G. Hervé, *Chem. Commun.* **1996**, 243–244.
[24] W.-M. Bu, G.-Y. Yang, L. Ye, J.-Q. Xu, Y.-G. Fan, *Chem. Lett.* **2000**, 462–463.
[25] J. Salta, Y. D. Chang, J. Zubieta, *J. Chem. Soc., Chem. Commun.* **1994**, 1039–1040.
[26] S.-T. Zheng, J. Zhang, G.-Y. Yang, *Eur. J. Inorg. Chem.* **2004**, 2004–2007.
[27] S.-T. Zheng, J. Zhang, G.-Y. Yang, *Inorg. Chem.* **2005**, *44*, 2426–2430.
[28] X.-B. Cui, J.-Q. Xu, Y. Li, Y.-H. Sun, G.-Y. Yang, *Eur. J. Inorg. Chem.* **2004**, 1051–1055.
[29] A. Müller, R. Sessoli, E. Krickemeyer, H. Bögge, J. Meyer, D. Gatteschi, L. Pardi, J. Westphal, K. Hovemeier, R. Rohlfing, J. Döring, F. Hellweg, C. Beugholt, M. Schmidtmann, *Inorg. Chem.* **1997**, *36*, 5239–5250.
[30] I. D. Brown, D. Altermatt, *Acta Crystallogr., Sect. B: Struct. Sci.* **1985**, *41*, 244–247.
[31] Y. Wang, J. Yu, Z. Shi, R. Xu, *Chem. Eur. J.* **2003**, *9*, 5048–5055.
[32] Z. Shi, S. H. Feng, S. Gao, L. R. Zhang, G.-Y. Yang, J. Hua, *Angew. Chem.* **2000**, *112*, 2415–2417; *Angew. Chem. Int. Ed.* **2000**, *39*, 2325–2327.
[33] J. J. Lu, Y. Xu, N. K. Goh, L. S. Chia, *Chem. Commun.* **1998**, 2733–2734.
[34] V. Soghomonian, Q. Chen, R. C. Haushalter, J. Zubieta, C. J. O'Connor, *Science* **1993**, *259*, 1596–1599.
[35] C. Lei, J. G. Mao, Y. Q. Sun, J. L. Song, *Inorg. Chem.* **2004**, *43*, 1964–1968.
[36] S. Natarajan, *Inorg. Chim. Acta* **2003**, *348*, 233–236.
[37] L. J. Zhang, X. L. Zhao, J. Q. Xu, T. G. Wang, *J. Chem. Soc., Dalton Trans.* **2002**, 3275–3276.
[38] T. Yamase, M. Suzuki, K. Ohtaka, *J. Chem. Soc., Dalton Trans.* **1997**, 2463–2472.
[39] D. Gatteschi, B. Tsukerblatt, A. L. Barra, L. C. Brunel, A. Müller, J. Döring, *Inorg. Chem.* **1993**, *32*, 2144–2147.
[40] A. L. Barra, D. Gatteschi, L. Pardi, A. Müller, J. Döring, *J. Am. Chem. Soc.* **1992**, *114*, 8509–8514.
[41] A. Müller, F. Peters, M. T. Pope, D. Gatteschi, *Chem. Rev.* **1998**, *98*, 239–271.
[42] O. Kahn, *Molecular Magnetism*, VCH, Weinheim, Germany, **1993**.

Received: July 29, 2005
Published Online: December 9, 2005

 © 2006 Wiley-VCH Verlag GmbH & Co. KGaA, Weinheim 

DOI: 10.1002/ejic.200500691

# Manganese Azides Based on Co-Ligands with a Flexible Tail: Diverse Structural and Magnetic Properties

Shi-Qiang Bai,[a] En-Qing Gao,[a,b] Zheng He,[a] Chen-Jie Fang,[a] Yan-Feng Yue,[a] and Chun-Hua Yan*[a]

**Keywords:** Azides / Coordination polymers / Ligand design / Magnetic properties / Manganese

Three azido-bridged coordination polymers, namely $[Mn(L^1)(N_3)_2]_n$ (**1**), $[Mn(L^2)(N_3)_2]_n$ (**2**), and $[Mn(L^3)(N_3)_2]_n$ (**3**) [$L^1$ = *N*-(2-pyridylmethylene)methylamine, $L^2$ = *N*-(2-pyridylmethylene)ethylamine, and $L^3$ = *N*-(2-pyridylmethylene)octylamine], have been synthesized with Schiff-base co-ligands with flexible tails, and their structures and magnetic properties characterized. Complex **1** is composed of one-dimensional, uniform chains with double end-on (EO) azido bridges, complex **2** consists of (6,3) net layers in which double EO azido-bridged dimers are interlinked by single end-to-end (EE) azido bridges, and complex **3** contains chains of $Mn^{II}$ ions bridged by alternating double EO and double EE azido bridges. Magnetically, **1** is a metamagnet built of ferromagnetic chains, **2** exhibits weak ferromagnetism due to spin canting, and **3** shows alternate ferro- and antiferromagnetic intrachain interactions.
(© Wiley-VCH Verlag GmbH & Co. KGaA, 69451 Weinheim, Germany, 2006)

## Introduction

Magnetic coordination polymers have attracted intense interest due not only to fundamental research into magnetic interactions but also the need for new molecule-based materials. Their magnetic properties depend on the nature of the interacting metal ions, and can be tuned by the nature of the bridging ligand and by the whole structural arrangement.[1] In recent years, an increasing number of azidomanganese(II) coordination polymers with different co-ligands have been reported that present a remarkable diversity in bridging topology, polymeric dimensionality, and bulk magnetic properties.[2–6] The main factors causing such diversity are the extreme versatilities of the azido ligating mode in bridging metal ions and in transmitting magnetic interactions. The azido bridge transmits mainly ferromagnetic (FM) interactions for the end-on (EO) binding mode and antiferromagnetic (AFM) interactions for the end-to-end (EE) mode.

Despite the large number of manganese azide complexes, no general correlation has been found so far between the properties of the co-ligand and the coordination mode of the azido bridge. Recently, we have reported a series of azidomanganese(II) complexes with didentate Schiff bases derived from 2-pyridylaldehyde and aniline derivatives, which exhibit similar one-dimensional (1D) structures with alternating double EO and double EE azido bridges despite the different substituents on the aniline moiety.[3i] Along this line, we decided to extend this study to similar didentate Schiff bases derived from aliphatic amines to investigate the correlation between the polymeric structures and the co-ligands. Here, we report the structural and magnetic properties of three new azidomanganese(II) complexes with didentate Schiff-base co-ligands derived from methylamine, ethylamine, and octylamine (Scheme 1). As will be shown, although they have the same $[Mn(L^i)(N_3)_2]_n$ stoichiometry, the structures vary from a 1D uniform chain with double EO azido bridges {$[Mn(L^1)(N_3)_2]_n$, **1**}, through a two-dimensional (2D) layer with double EO, and single EE azido bridges {$[Mn(L^2)(N_3)_2]_n$, **2**}, to a 1D chain with alternating double EO and double EE azido bridges {$[Mn(L^3)(N_3)_2]_n$, **3**} with increasing steric demand of the co-ligands $L^1$, $L^2$, and $L^3$, respectively. Consequently, these complexes exhibit different magnetic properties.

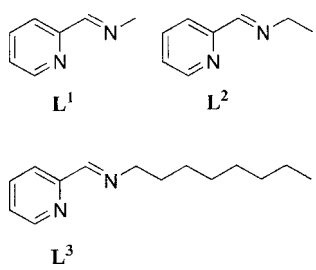


$L^1$ $L^2$

$L^3$

Scheme 1.

[a] State Key Lab of Rare Earth Materials Chemistry and Applications & PKU-HKU Joint Lab on Rare Earth Materials and Bioinorganic Chemistry, Peking University,
Beijing 100871, China
Fax: +86-10-6275-4179
E-mail: yan@pku.edu.cn
[b] Shanghai Key Lab of Green Chemistry and Chemical Processes, Department of Chemistry, East-China Normal University,
Shanghai 200062, China

 © 2006 Wiley-VCH Verlag GmbH & Co. KgaA, Weinheim InterScience 

## Results and Discussion

Complex **1** was prepared as crystals by slow interdiffusion between a methanol solution containing $Mn(ClO_4)_2 \cdot 6H_2O$ and $L^1$ and a methanol solution of $NaN_3$. Crystals of **2** and **3** were obtained by slow concentration of methanol solutions containing $Mn(ClO_4)_2 \cdot 6H_2O$, $NaN_3$, and the appropriate Schiff-base ligands.

### IR Spectra

The IR spectra of the three complexes display characteristic bands for the azido bridges and the C=N group. A sharp and strong band at 2067 $cm^{-1}$ in the spectrum of complex **1** is attributed to $\nu_{as}(N_3)$ in the EO mode. For complex **2**, a very strong band at 2067 $cm^{-1}$ with a small shoulder at the higher-frequency side indicates the presence of two different azido groups. Two sharp and strong bands at 2064 and 2095 $cm^{-1}$ indicate the presence of two different azido groups in complex **3**.[3a,7] The characteristic $\nu$(C=N) absorption of the Schiff-base ligands in these complexes appears at around 1595 $cm^{-1}$ as a medium-intensity band.

### X-ray Structures

Selected bond lengths and bond angles for the three complexes are summarized in Table 1. The three crystal structures exhibit different hydrogen-bonding patterns, and all the hydrogen-bonding parameters are given in Table 2.

Table 1. Selected bond lengths [Å] and angles [°] for complexes **1**–**3**.

| | | | |
|---|---|---|---|
| Complex **1**[a] | | | |
| Mn(1)–N(1) | 2.284(2) | Mn(2)–N(3) | 2.294(2) |
| Mn(1)–N(2) | 2.272(2) | Mn(2)–N(4) | 2.276(2) |
| Mn(1)–N(5) | 2.225(2) | Mn(2)–N(5) | 2.212(2) |
| Mn(1)–N(8) | 2.199(2) | Mn(2)–N(8) | 2.192(2) |
| Mn(1)–N(11) | 2.204(2) | Mn(2)–N(14) | 2.230(2) |
| Mn(1)–N(11A) | 2.221(2) | Mn(2)–N(14B) | 2.198(2) |
| N(8)–Mn(1)–N(5) | 78.06(8) | Mn(1)–N(11)–Mn(1A) | 103.96(9) |
| N(8)–Mn(2)–N(5) | 78.49(8) | Mn(2)–N(5)–Mn(1) | 100.85(9) |
| N(11)–Mn(1)–N(11A) | 76.04(9) | Mn(2)–N(8)–Mn(1) | 102.33(9) |
| N(14)–Mn(2)–N(14B) | 77.5(1) | Mn(2)–N(14)–Mn(2B) | 102.5(1) |
| Complex **2**[b] | | | |
| Mn(1)–N(1) | 2.299(4) | Mn(1)–N(6) | 2.172(3) |
| Mn(1)–N(2) | 2.276(4) | Mn(1)–N(3A) | 2.213(3) |
| Mn(1)–N(3) | 2.256(3) | Mn(1)–N(8B) | 2.209(4) |
| N(1)–Mn(1)–N(2) | 72.5(1) | N(6)–Mn(1)–N(8B) | 90.9(2) |
| N(3)–Mn(1)–N(3A) | 76.5(1) | Mn(1)–N(3)–Mn(1A) | 103.5(1) |
| Complex **3**[c] | | | |
| Mn(1)–N(1) | 2.287(1) | Mn(1)–N(6) | 2.190(1) |
| Mn(1)–N(2) | 2.277(1) | Mn(1)–N(5A) | 2.221(2) |
| Mn(1)–N(3) | 2.200(1) | Mn(1)–N(6B) | 2.245(1) |
| N(1)–Mn(1)–N(2) | 72.66(5) | N(6)–Mn(1)–N(6B) | 78.29(5) |
| N(3)–Mn(1)–N(5A) | 88.75(5) | Mn(1)–N(6)–Mn(1B) | 101.71(5) |

[a] Symmetry codes: A: $-x, -y, 2-z$; B: $1-x, -y, 2-z$. [b] Symmetry codes: A: $-x, 2-y, 1-z$; B: $0.5+x, 1.5-y, 1-z$. [c] Symmetry codes: A: $1-x, -y, -z$; B: $-x, -y, -z$.

Table 2. Hydrogen-bonding distances [Å] and angles [°] for complexes **1**–**3**.

| Complex | D–H···A[a] | D–H | D···A | H···A | ∠D–H···A |
|---|---|---|---|---|---|
| **1** | C8–H···N7B | 0.93 | 3.301 | 2.62 | 131 |
| | C3–H···N16C | 0.93 | 3.326 | 2.51 | 146 |
| | C6–H···N13D | 0.93 | 3.439 | 2.62 | 147 |
| | C13–H···N10E | 0.93 | 3.277 | 2.43 | 152 |
| **2** | C7–H···N7A | 0.97 | 3.418 | 2.47 | 164 |
| | C6–H···N5C | 0.93 | 3.352 | 2.56 | 143 |
| **3** | C7–H···N3B | 0.97 | 3.477 | 2.56 | 157 |
| | C6–H···N8C | 0.93 | 3.392 | 2.52 | 157 |

[a] Symmetry codes for **1**: B: $1-x, -y, 2-z$; C: $-x, -y, 1-z$; D: $x, 0.5-y, -0.5+z$; E: $x, -0.5-y, 0.5+z$. For **2**: A: $-x, 2-y, 1-z$; C: $0.5+x, y, 0.5-z$. For **3**: B: $-x, -y, -z$; C: $x, -1+y, z$.

Complex **1** contains neutral 1D chains constructed by double EO azido bridges linking $Mn^{II}$ ions along the *a* direction. The asymmetric unit consists of a binuclear unit involving two independent $Mn^{II}$ ions, each of which is octahedrally coordinated by six N atoms from a chelating $L^1$ and four azido ligands in the EO mode [Figure 1(a)]. The binuclear unit is further linked to its two neighbors through two pairs of double EO azido bridges, giving rise to a 1D chain with a Mn(2B)–Mn(2)–Mn(1)–Mn(1A) sequence with three different pairs of bridges between them [Figure 1(b)]. The Mn–N–Mn bridging angles in the centrosymmetric Mn(2B)···Mn(2) and Mn(1)···Mn(1A) pairs are 102.5(1)° and 103.96(9)°, respectively, and those for the noncentrosymmetric Mn(2)···Mn(1) pair are 100.85(9)° and 102.33(9)°. The three different Mn···Mn distances spanned by double EO azido bridges are in the range of 3.420 to 3.486 Å. All the azido ligands are essentially linear, with asymmetric N–N distances. In the lattice, a weak intrachain C–H···N hydrogen bond (Table 2) is formed between the pyridyl group (C8–H) of $L^1$ and the uncoordinated terminal nitrogen (N7) of the bridging EO azido ligands. Weak interchain C–H···N hydrogen bonds also exist between the azomethine and pyridyl C–H in $L^1$ and the uncoordinated terminal N atom of the bridging azido ligands [Figure 1(c)]. Neighboring pyridine rings from different chains are parallel to and overlap each other with an interplanar distance of 3.54 Å and a centroid–centroid distance of 4.00 Å; the displacement angle, as defined by Janiak, is about 27.7°.[8] These features indicate a weak π–π stacking interaction between neighboring chains. The nearest interchain Mn···Mn distance is 9.267 Å.

Complex **2** has a 2D layer structure constructed by binuclear units interconnected through single EE azido bridges. A perspective view of the binuclear unit of complex **2** is shown in Figure 2(a). Each $Mn^{II}$ ion is ligated by two N atoms from a chelating $L^2$ ligand and four azido N atoms, with Mn–N distances ranging from 2.172(3) to 2.299(4) Å. Two neighboring $Mn^{II}$ ions related by an inversion center are linked by double EO azido bridges, the Mn–N–Mn angle and the Mn···Mn distance being 103.5(1)° and 3.509 Å, respectively. Each binuclear unit is linked to four neighboring equivalent units through four single EE azido bridges to form a neutral 2D layer with a pseudo-honeycomb (6,3)

 © 2006 Wiley-VCH Verlag GmbH & Co. KGaA, Weinheim 

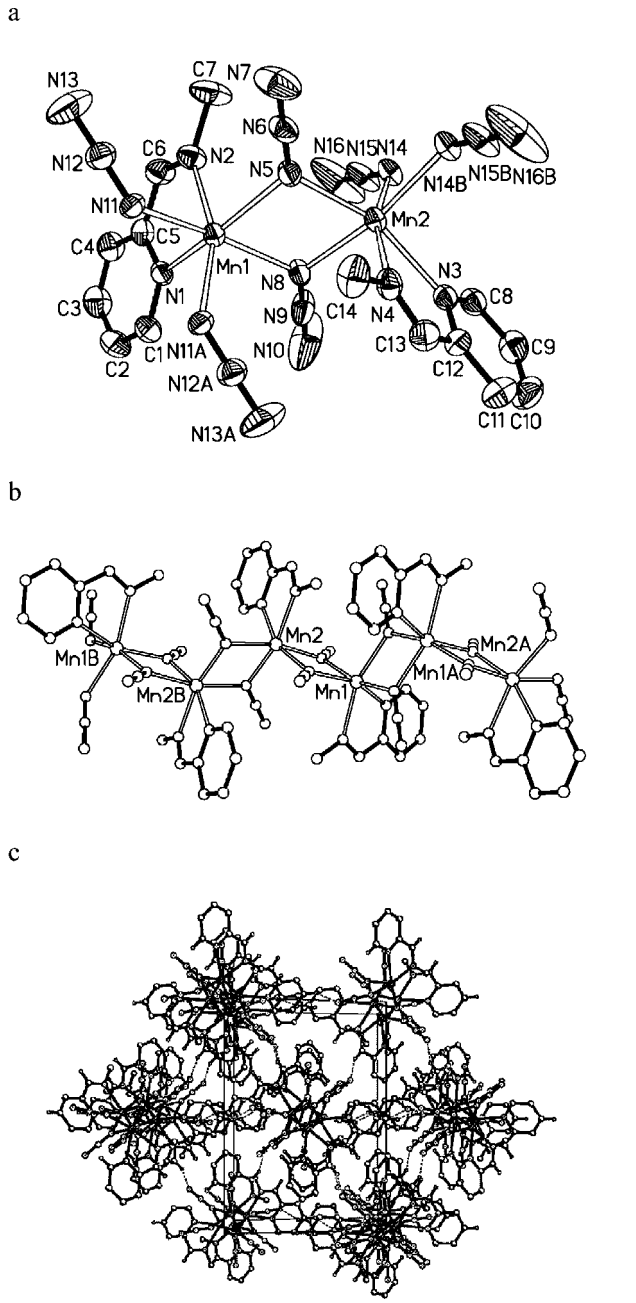


Figure 1. Thermal ellipsoid plot (30% probability), with atom-labeling scheme and H atoms omitted for clarity (a), chain plot (b), and packing of the chains along the *a* direction (c) in **1**.

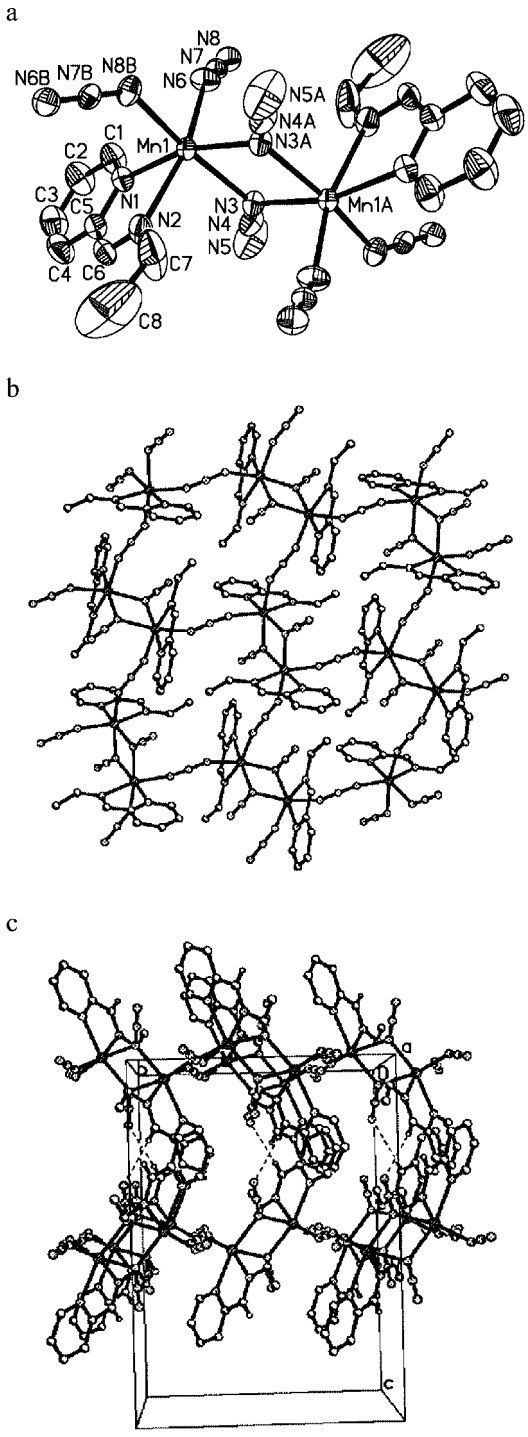


Figure 2. Thermal ellipsoid plot (30% probability), with atom-labeling scheme and H atoms omitted for clarity (a), 2D (6,3) net layer (b), and interactions of neighboring layers (c) in **2**.

topology [Figure 2(b)]. The neighboring $Mn_2N_2$ units are interrelated by a $2_1$ screw operation, with an acute dihedral angle (*a*) between their $Mn_2N_2$ planar rings (79.5°).

Just like the structures we reported previously,[4i] the structure can also be described as a layer consisting of EE azido-bridged Mn–$N_3$ helical chains interlinked by double EO azido bridges. The helical chain runs around a twofold screw axis along the *a* direction, and neighboring chains are related by inversion centers and hence have opposite chirality. Within the chain, the Mn–N–N angles are 146.0(3)° and 136.2(3)°, the N–Mn–N angle is 90.9(2)°, and the Mn–$N_3$–Mn torsion angle ($\tau$) is 7.1°. The Mn···Mn distance spanned by the EE azido bridge is 6.332 Å, and the helical pitch is 10.672 Å.

In the crystal packing, a weak intralayer C–H···N hydrogen bond (Table 2) is formed between the methylene C7–H

 © 2006 Wiley-VCH Verlag GmbH & Co. KGaA, Weinheim 

of $L^2$ and the N7 atom of the bridging EE azido ligand. Weak interlayer C–H···N hydrogen bonds also exist between the azomethine C–H of $L^2$ and the uncoordinated terminal nitrogen of the bridging EO azido ligand from neighboring layers [Figure 2(c)]. The 2D layers are stacked down the *c* direction, with the minimum interlayer Mn···Mn distance being 9.257 Å, which is significantly shorter than the distances found in most 2D Mn–azido systems. This short interlayer separation in **2** may be a consequence of deep complementary interdigitation between the consecutive layers. As can be seen from Figure 2(c), the pyridine groups of the $L^2$ ligands on each side of a layer extend deeply into the "empty" space of neighboring layers.

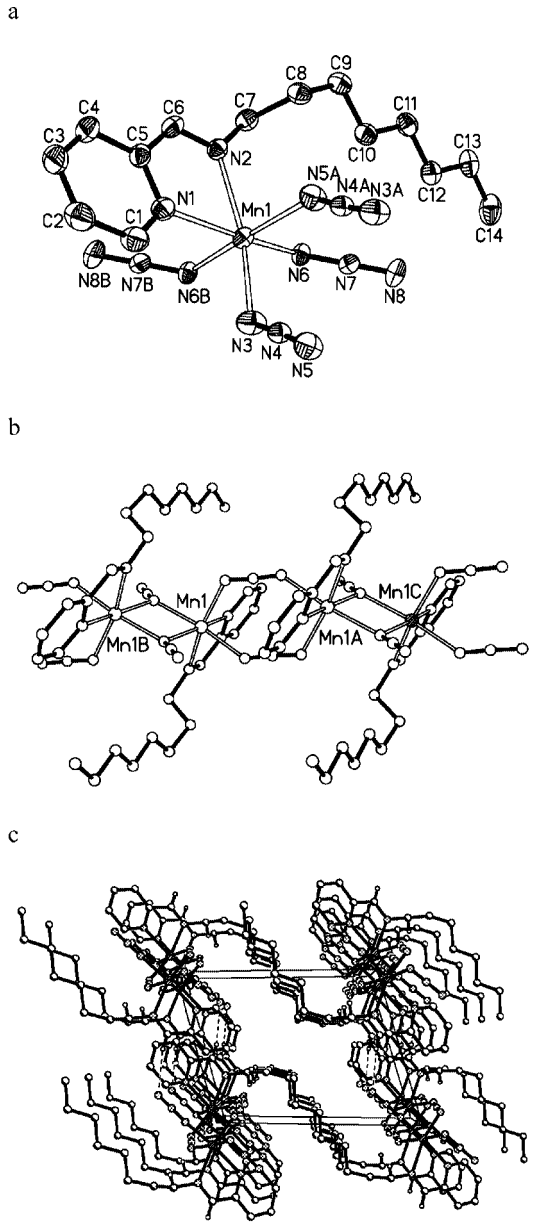


Figure 3. Thermal ellipsoid plot (30% probability), with atom-labeling scheme and H atoms omitted for clarity (a), chain plot (b) and packing of the chains along the *a* direction (c) in **3**.

In complex **3**, each $Mn^{II}$ center exhibits a distorted octahedral $MnN_6$ coordination sphere and is bonded by two EO and two EE azides with two N atoms from the chelate Schiff-base $L^3$ (Figure 3). Neighboring $Mn^{II}$ ions are linked alternately by double EO and double EE azido bridges to form an alternate chain running along the *a* direction. All the Mn–N distances are in the range of 2.190(1) to 2.287(1) Å. The small chelate angle [N1–Mn1–N2 = 72.66(5)°] indicates the severe distortion of the $Mn^{II}$ coordination geometry. The EO azido bridges possess asymmetric N–N distances, while the EE bridges are essentially symmetric. In the EO bridging moiety, the Mn1–N6–Mn1B angle and the Mn···Mn distance are 101.71(5)° and 3.440 Å, respectively. In the EE bridging moiety, the Mn–N–N angles are 126.1(1)° and 141.3(1)° and the Mn–$N_3$–Mn torsion angle is 15.9°. The dihedral angle between the (EE–$N_3$)$_2$ plane and the N5–Mn1–N3A plane is only 7.6°, thereby indicating a slight chair conformation for the Mn–(N$_3$)$_2$–Mn ring. The Mn···Mn distance separated by EE bridges is 5.466 Å.

In the crystal packing, a weak intrachain C–H···N hydrogen bond (Table 2) exists between the methylene C7–H of $L^3$ and the coordinated nitrogen (N3) of the bridging EE azido ligand. The azomethine C–H group of the $L^3$ also forms a weak interchain C–H···N hydrogen bond with the uncoordinated terminal N atom of the bridging EO azido ligands from neighboring chains along the *b* direction [Figure 3(c)]. The long tails of the $L^3$ ligands from neighboring chains interdigitate one another and separate the chains by 12.007 Å. Neighboring pyridine rings from different chains parallel and overlap each other with an interplanar distance of 3.52 Å and a centroid–centroid distance of 3.80 Å; the displacement angle is about 22.0°.[8] These features indicate weak π–π stacking interactions between neighboring chains. The minimum interchain Mn···Mn distance is 8.556 Å along the *b* direction.

## Magnetic Properties

### *Complex 1*

The magnetic susceptibility of **1** was measured at a field of 5 kOe in the temperature range 2–300 K [Figure 4(a)]. The temperature dependence of $\chi_M^{-1}$ above 21 K obeys the Curie–Weiss law with a positive Weiss constant ($\theta$ = 15.91 K), indicating an intrachain ferromagnetic interaction, as expected for the azido bridges in the double EO mode. The room-temperature $\chi_M T$ value is around 4.41 emu K mol$^{-1}$ per $Mn^{II}$ ion, which is close to the spin-only value (4.38 emu K mol$^{-1}$) for a high-spin $Mn^{II}$ ion. Upon cooling, $\chi_M T$ increases smoothly to a maximum at about 6 K, and then decreases rapidly. This may indicate an overall intrachain ferromagnetic interaction and an interchain antiferromagnetic interaction. The magnetic behavior of **1** was analyzed by fitting the experimental susceptibility to Fisher's calculation[9] for a classical or infinite spin chain, scaled to a real spin of 5/2.[10] The expression for

 © 2006 Wiley-VCH Verlag GmbH & Co. KGaA, Weinheim 

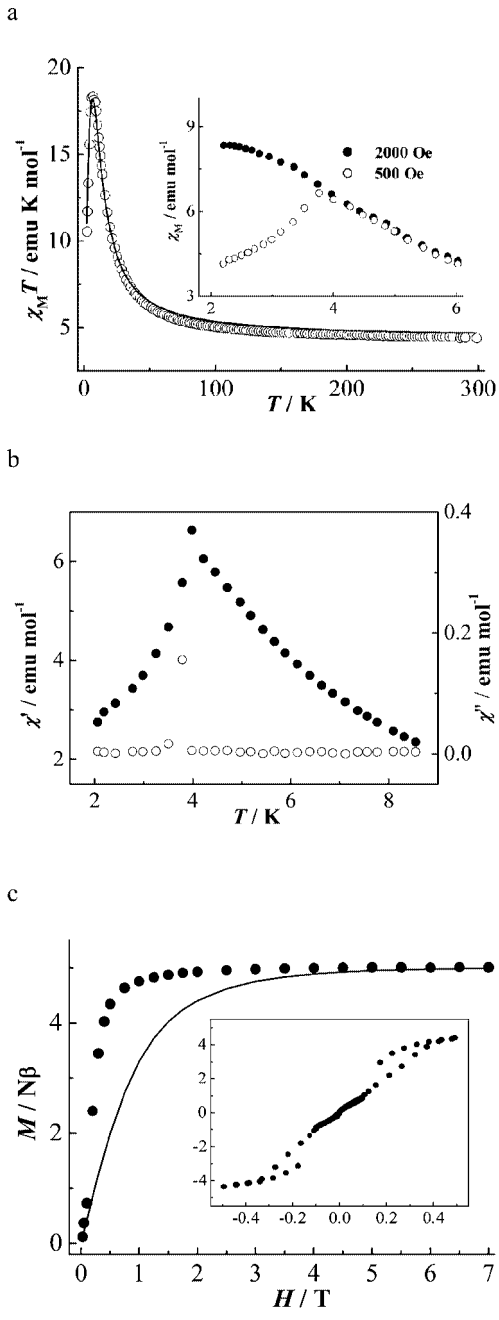


Figure 4. (a) $\chi_M T$ vs. $T$ plot of **1**. The solid line was plotted according to the fit parameters given in the text. Inset: fc magnetization curves at 500 and 2000 Oe. (b) Temperature-dependence of the ac magnetic susceptibility at zero applied dc field and an ac field of 2 Oe and 277 Hz. (c) Field dependence of the magnetization. The solid line was plotted according to the Brillouin function for an $S$ = 5/2 system with $g$ = 2. The inset is the hysteresis loop at 1.8 K.

the magnetic susceptibility is given by Equation (1), where $u = (T/T_o) - \coth(T_o/T)$ with $T_o = JS(S + 1)/k$.

$$\chi_{chain} = [Ng^2\beta^2S(S + 1)/(3kT)][(1 - u)/(1 + u)] \quad (1)$$

The $J$ parameter is based on the spin-Hamiltonian $H = -J\Sigma S_iS_{i+1}$. The interchain interaction ($zJ'$) was accounted for by the molecular-field approximation [Equation (2)].[14]

$$\chi_M = \chi_{chain}/[1 - (zJ'/Ng^2\beta^2)\chi_{chain}] \quad (2)$$

The best fit leads to $J$ = 2.54(2) cm$^{-1}$ and $zJ'$ = –0.41(5) cm$^{-1}$, with the $g$-value fixed at 2.0.

Although double EO azido bridges have been found in many metal azide complexes, chains with exclusive double EO azido bridges are still rare. One such compound, [Mn(2-bzpy)$(N_3)_2]_n$ (2-bzpy = 2-benzoylpyridine), which also exhibits ferromagnetic intrachain interactions, has been reported previously.[3d] Compared with EO azido-bridged complexes with similar structures, it has been suggested that the M–N–M bridging angle ($\theta$) is the main factor that controls the magnetic interaction between metal ions. The ferromagnetic intrachain interaction ($J$ = 2.54 cm$^{-1}$) for **1**, in which the bridging angles average to 102.4°, is stronger than that ($J$ = 0.8 cm$^{-1}$) for [Mn(2-bzpy)$(N_3)_2]_n$, in which the average bridging angle (100.5°) is smaller. This trend is consistent with the density functional calculations on model $Mn^{II}$ compounds performed by Ruiz et al.[12] This calculation predicts that a crossover between ferro- and antiferromagnetic interactions occurs at $\theta$ = 98°, and that the ferromagnetic interaction increases when the Mn–N–Mn bridging angle increases above 98°.[12]

To investigate further the magnetic behavior of **1**, field-cooled (fc) magnetization at different fields was measured and the plot is given in Figure 4(a, inset). At 500 Oe, the magnetization presents a maximum at around 3.7 K, suggesting the onset of 3D antiferromagnetic ordering among the ferromagnetic chains. However, the magnetization at 2 kOe shows no maximum and tends to saturate at lower temperature, thus indicating that the interchain antiferromagnetic interaction is overcome by the external field. These features are indicative of a metamagnet built of ferromagnetic chains. The temperature dependence of the ac magnetic susceptibility was also measured at zero dc field and confirmed the occurrence of the magnetic ordering, with $T_N$ = 3.9 K, at which both $\chi'$ (the in-phase component) and $\chi''$ (the out-of-phase component) reach maximum values [Figure 4(b)].

The metamagnetic behavior was confirmed by the field dependence of the magnetization, as shown in Figure 4(c). The sigmoid shape of the $M$ vs. $H$ curve at 1.8 K clearly indicates a field-induced transition from an antiferromagnetic to a ferromagnetic state, which is characteristic of a metamagnet. The critical field is about 2 kOe, estimated as the field at which a maximum $\partial M/\partial H$ value is reached. Upon increasing the field, the magnetization increases rapidly and saturates at 5.0 $N\beta$, and the saturation is much more rapid than that predicted by the Brillouin function. This definitely confirms the presence of ferromagnetic interactions. Hysteresis loop measurements revealed that **1** is a metamagnet with a typical crossover magnetic hysteresis [Figure 4(c, inset)].

In contrast to **1**, the previous compound [Mn(2-bzpy)$(N_3)_2]_n$ does not exhibit long-range magnetic ordering above 2 K. This may be due to its longer interchain Mn···Mn distance of 9.931 Å than that of **1** (9.267 Å), which weakens the interchain interactions.

 © 2006 Wiley-VCH Verlag GmbH & Co. KGaA, Weinheim 

### *Complex 2*

The magnetic susceptibility of **2** was measured in the range 2–300 K at 5 kOe and is shown as $\chi_M$ vs. $T$ and $\chi_M T$ vs. $T$ plots in Figure 5(a). The $\chi_M T$ value at 300 K is about 3.91 emu K mol$^{-1}$. Upon cooling, $\chi_M T$ decreases monotonically and vanishes when $T$ approaches zero, indicating an overall antiferromagnetic interaction. As the temperature is lowered, $\chi_M$ value increases first to a rounded maximum of 0.045 emu mol$^{-1}$ at about 36 K, then decreases to a minimum value of 0.044 emu mol$^{-1}$ at 21 K, and finally increases to 0.045 emu mol$^{-1}$ at 2 K. The behaviors above 20 K are typical of 1D and 2D $Mn^{II}$ complexes with dominant antiferromagnetic interactions, and the increase of $\chi_M$ below 20 K may be due to the presence of a spin-canted structure (see below).

To evaluate the magnetic interactions via the azido bridges in **2**, we used an approximate approach that has been used for similar compounds.[4e,4i] This approach treats the 2D layer as EE azido-bridged antiferromagnetic chains interacting ferromagnetically through the double EO azido bridges. Consequently, Equations (1) and (2) are applicable, where $J$ is the interaction through the EE azido bridge and z$J'$ is the interaction through the double EO azido bridges. The least-squares fit of the experimental data above 26 K to the above expressions led to $J$ = –4.85(4) cm$^{-1}$ and z$J'$ = 2.5(4) cm$^{-1}$ with $g$ = 2.0. These values are comparable to those for related compounds and confirm that the interactions mediated by the single EE and the double EO bridges are antiferro- and ferromagnetic, respectively. Selected structural and magnetic parameters for **2** and similar 2D $Mn^{II}$–azido complexes are collected in Table 3 for comparison. EHMO calculations have shown that the antiferromagnetic interactions through the single EE azido bridge should maximize as the Mn–N–N bond angle approaches 110° and the Mn–$N_3$–Mn torsion angle ($\tau$) approaches 0 or 180°.[4b] The data listed in Table 3 suggest that the influence of the torsion angle dominates in these systems: the strongest interaction is observed for compound **I**, in which the torsion angle is 180°, although the compound has the largest Mn–N–N angles. On the other hand, compound **III**, which has a torsion angle close to 90°, exhibits the lowest |$J$| value, although the Mn–N–N angles are the closest to 110°. Other compounds, including **2**, have in-between angles (the torsion angles are between 90 and 180 or 0°) and $J$ values. The interaction parameters of the double azido bridges for these complexes fall in the range 1.1–3.1 cm$^{-1}$, with the Mn–N–Mn angles in the narrow range of 100.8–103.5°. Apparently, the general trend whereby the ferromagnetic interaction increases with increasing bridging angle is not well followed: the largest $J$ value is obtained for the compound that has a relatively small angle (compound **II**, 101.9°), and the compound that has the largest angle exhibits a relatively small $J$ value (compound **2**, 2.5 cm$^{-1}$). This may be due to the

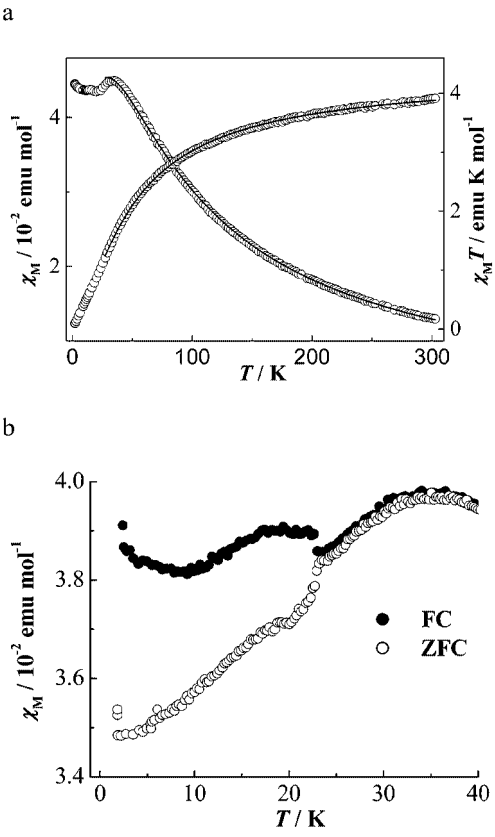


Figure 5. (a) $\chi_M$ and $\chi_M T$ vs. $T$ plots for **2**. The solid line was plotted according to the fit parameters given in the text. (b) zfc and fc magnetization at 200 Oe.

Table 3. Structural and magnetic parameters for double EO and single EE 2D $Mn^{II}$–azido complexes containing a (6,3) network.

| Complex[a] | $[Mn(dmbpy)(N_3)_2]_n$, **I** | $[Mn(2\text{-}bphz)(N_3)_2]_n$, **II** | $[Mn(mpci)(N_3)_2]_n$, **III** | $[Mn(4\text{-}Etpy)(N_3)_2]_n$, **IV** | $[Mn(L^2)(N_3)_2]_n$, **2** |
|---|---|---|---|---|---|
| $J_{EE}$ [cm$^{-1}$] | –5.4 | –5.1 | –4.6 | –5.3 | –4.85 |
| M–N–N [°][b] | 163.8, 153.9 | 158.1, 150.9 | 131.7, 132.3 | 150.3, 143.9 | 136.2(3), 146.0(3) |
| $\tau$ [°][c] | 180 | 21.5 | 92.4 | 17.6 | 7.1 |
| M···M(EE) [Å] | 6.611, 6.537 | 6.496 | 5.810 | 6.083 | 6.332 |
| $J_{EO}$ [cm$^{-1}$] | 1.7 | 3.1 | 1.1 | 2.9 | 2.5 |
| M–N–M [°][d] | 102.2 | 101.9 | 100.8 | 102.2 | 103.5(1) |
| M···M(EO) [Å] | 3.533 | 3.459 | 3.426 | 3.523 | 3.509 |
| $\alpha$ [°][e] | 0 | 78.9 | 83.7 | 86.7 | 79.5 |
| Canting | no | yes | yes | yes | yes |
| Ref. | [4e] | [4i] | [4i] | [4g] | this work |

[a] Dmbpy = 4,4′-dimethyl-2,2′-bipyridine; 2-bphz = 2-benzoylpyridine hydrazone; mpci = methyl pyrazinecarboximidate; 4-Etpy = 4-ethylpyridine; $L^2$ = *N*-(2-pyridylmethylene)ethylamine. [b] For the EE azido bridging moiety. [c] The M–N–N–N–M torsion angle. [d] For the EO azido bridging moiety. [e] The dihedral angle between the neighboring planar $Mn_2N_2$ rings.

 © 2006 Wiley-VCH Verlag GmbH & Co. KGaA, Weinheim 

operation of other factors such as Mn–N bond lengths and coordination environments, which should influence the magnetic orbitals around the metal center.

It has been shown that, except for compound **I** in Table 3, all the previous layered compounds with double EO and single EE bridges exhibit spin-canting behavior, which is consistent with the structural observation that the coordination polyhedra (or the double EO bridged $Mn_2N_2$ moieties) linked by the single EE azido bridges are slanted with respect to each other.[4b,4d,4g,4i] The absence of spin-canting in **I** has been related to the crystallographic centrosymmetry of the single EE azido bridges.[4e,4i] According to the structural data, **2** should exhibit a spin-canted structure. To confirm this point, the field-cooled and zero-field-cooled (zfc) magnetizations were measured at an applied field of 200 Oe [Figure 5(b)]. It is evident that the complex exhibits weak spontaneous magnetization below 22 K, which is characteristic of weak ferromagnets due to the spin-canting. Field-dependent magnetizations at 2 K were also measured, and the magnetization at 50 kOe is 0.46 $N\beta$, far below the saturation value expected for an $S = 5/2$ system (5.0 $N\beta$ with $g = 2.0$). No hysteresis was detected.

### *Complex 3*

The magnetic susceptibility of **3** was measured in the temperature range 2–300 K at 20 kOe. The $\chi_M$ and $\chi_M T$ vs. $T$ plots are shown in Figure 6. The experimental $\chi_M T$ value at 300 K is 3.63 emu K mol$^{-1}$. Upon cooling, the $\chi_M T$ product decreases monotonically, indicating a dominant antiferromagnetic interaction. The $\chi_M$ value increases monotonically, and a rapid increase below 17 K may be caused by the presence of a small amount of paramagnetic impurities.

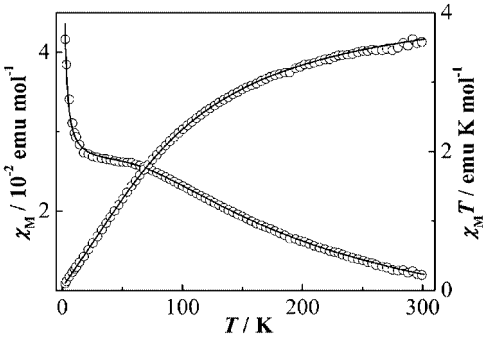


Figure 6. $\chi_M$ and $\chi_M T$ vs. $T$ plots of **3**. The solid line was plotted according to the fit parameters given in the text.

According to the structural data, complex **3** should possess alternating ferro- and antiferromagnetic interactions mediated by double EO and double EE azido bridges, respectively.[3a,3d,3i] To simulate the experimental magnetic behavior, we used a theoretical model proposed by Cortés et al. for alternating $S = 5/2$ chains.[3a] The nearest-neighbor exchange interactions are described by the spin-Hamiltonian given in Equation (3). The expression of the molar susceptibility is given by Equation (4).

$$H = -J_1\Sigma S_{2i}S_{2i+1} - J_2\Sigma S_{2i+1}S_{2i+2} \quad (3)$$

$$\chi_M = [Ng^2\beta^2S(S+1)/3kT]\{[(1+u_1+u_2+u_1u_2)/(1-u_1u_2)](1-\rho)+\rho\} \quad (4)$$

where $u_i = \coth[J_iS(S+1)/kT] - kT/[J_iS(S+1)]$ ($i = 1, 2$). In this expression we have included a $\rho$ parameter, which is related to the amount of paramagnetic impurities (presumably a monomeric $Mn^{II}$ complex), to account for the in-

Table 4. Structural and magnetic parameters for alternating double EE and double EO 1D $Mn^{II}$–azido complexes.

| Complex[a] | Mn–N–Mn [°] | $J_F$ [cm$^{-1}$] | $\delta$ [°] | $J_{AF}$ [cm$^{-1}$] | Ref. |
|---|---|---|---|---|---|
| $[Mn(bipy)(N_3)_2]_n$ | 101.0 | 9.6 | 22.7 | –11.9 | [3a] |
| $[Mn(3\text{-}bzpy)_2(N_3)_2]_n$ | 100.4 | 3.5 | 26.6 | –12.3 | [3d] |
| $[Mn(3\text{-}Et,4\text{-}Mepy)_2(N_3)_2]_n$ | 99.7 | 2.4 | 31.7 | –13.7 | [3c] |
| $[Mn(bpm)(N_3)_2]_n$ | 102.9 | **1.8** | 20.5 | **–7.3** | [3e] |
| | | (15.7)[b] | | (–63.7)[b] | [3e] |
| $[Mn(dpa)(N_3)_2]_n$ | 102.9 | **5.2** | 35.1 | **–6.1** | [3h] |
| | | (45.3)[b] | | (–53.3)[b] | [3h] |
| $[Mn(L1)(N_3)_2]_n$ | 99.6 | 3.8 | 9.8 | –15.4 | [3i] |
| $[Mn(L2)(N_3)_2]_n$ | 101.6 | 5.2 | – | –11.8 | [3i] |
| | 101.1 | | | | [3i] |
| $[Mn(L3)(N_3)_2]_n$ | 103.9 | 7.2 | 19.5 | –13.7 | [3i] |
| $[Mn(L4)(N_3)_2]_n$ | 100.6 | 4.1 | 9.8 | –13.3 | [3i] |
| $[Mn(L5)(N_3)_2]_n$ | 104.0 | 8.0 | 12.0 | –14.4 | [3i] |
| $[Mn(L)(N_3)_2]_n$ | 102.0 | 5.6 | 19.6 | –11.9 | [3j] |
| $[Mn(TaiEt)(N_3)_2]_n$ | 103.5 | 2.7 | 1.8 | –14.5 | [3k] |
| $\{[Mn(N_3)_2(3\text{-}Clpy)_2](3\text{-}Clpy)_{0.5}\}_n$ | 100.5 | 6.0 | 9.8 | –16.7 | [3n] |
| $[\{Mn(N_3)_2\}_2L']_n$ | 77.2 | 3.8 | 2.9 | –8.1 | [6e] |
| $[Mn(L^3)(N_3)_2]_n$ (**3**) | 101.7 | 1.6 | 7.6 | –13.9 | this work |

[a] Bipy = 2,2′-bipyridine; 3-bzpy = 3-benzoylpyridine; 3-Et,4-Mepy = 3-ethyl-4-methylpyridine; bpm = bis(pyrazol-1-yl)methane; dpa = 2,2′-dipyridylamine; L1 = *N*-phenyl-2-carbaldimine; L2 = *N*-(*p*-tolyl)-2-carbaldimine; L3 = *N*-(*m*-tolyl)-2-carbaldimine; L4 = *N*-(*p*-chlorophenyl)-2-carbaldimine; L5 = *N*-(*m*-chlorophenyl)-2-carbaldimine; L = 2-(pyrazol-1-ylmethyl)pyridine; TaiEt = 1-ethyl-2-(*p*-tolylazo)imidazole; 3-Clpy = 3-chloropyridine; L′ = 4,5-diazafluoren-9-one azine; $L^3$ = *N*-(2-pyridylmethylene)octylamine. [b] The recalculated values are indicated in bold and the values in parentheses are those reported in the references. After checking the data carefully, we believe that the $J$ values reported in refs.[3e,3h] are actually for $JS(S+1)$.

 © 2006 Wiley-VCH Verlag GmbH & Co. KGaA, Weinheim 

crease of $\chi_M$ below 17 K. The best fit of the experimental data led to $J_1$ = 1.6(2) cm$^{-1}$, $J_2$ = –13.9(1) cm$^{-1}$, and $\rho$ = 0.01 with $g$ fixed at 2.0. The $J_1$ and $J_2$ parameters verify the alternating ferro- and antiferromagnetic interactions, with the antiferromagnetic one dominating.

A chain structure with alternating double EO and double EE azido bridges is the most frequently encountered Mn–azido motif. In our previous work,[3i] this class of $Mn^{II}$ compounds follows the general trend that the ferromagnetic interaction through the double EO bridge increases with the Mn–N–Mn angle, and that the antiferromagnetic interaction through the double EE bridge decreases with the increase of the dihedral angle ($\delta$) between the $(N_3)_2$ plane and the N(EE azido)–Mn–N(EE azido) plane. Since then, several new compounds have been characterized structurally and magnetically. Relevant structural and magnetic data for the known compounds, along with **3**, are collected in Table 4 for comparison. As can be seen, the general trends, which have also been demonstrated by theoretical studies,[3a,12] are followed by most compounds, but it should be noted that there are some evident deviations. The most remarkable example is $[\{Mn(N_3)_2\}_2L']_n$, in which $Mn^{II}$ chains with alternating double EO and double EE azido bridges are linked into a 3D network by 4,5-diazafluoren-9-one azine (L′):[6e] the double EO bridge with a much smaller Mn–N–Mn angle (77°) than the AF–F crossover angle (98°) predicted by density functionl calculations mediates a ferromagnetic interaction, instead of antiferromagnetic interaction, and the double EE bridge with a very small $\delta$ angle (2.9°) mediates a relatively weak antiferromagnetic interaction. For **3** and $[Mn(TaiEt)(N_3)_2]_n$,[3k] the $J_{EO}$ values seem to be too small for their medium and large M–N–M angles, respectively. These deviations may be due to the influence of other structural parameters. Further pragmatic but laborious studies are therefore needed to get more accurate magneto-structural correlations.

## Conclusions

We have presented the syntheses, structures, and magnetic properties of three new azido-bridged $Mn^{II}$ coordination polymers with flexible tail co-ligands. With increasing steric demand of the co-ligands $L^1$, $L^2$, and $L^3$, the structures vary from a double EO azido-bridged uniform chain (**1**), through a double EO and single EE azido-bridged 2D layer (**2**), to a double EO and double EE azido-bridged alternate chain (**3**), respectively. Magnetically, **1** is a metamagnet built of ferromagnetic chains, **2** exhibits a weak ferromagnetism due to spin-canting, and **3** shows alternate ferro- and antiferromagnetic intrachain interactions. We are currently working with other flexible tail co-ligands by varying their substituents to get more information about the relationship between the final structures and the co-ligands and to study their magnetic behaviors towards the preparation of molecule-based magnetic materials.

## Experimental Section

**Materials and Physical Measurements:** All the starting chemicals were of A.R. grade and were used as received. The Schiff-base ligands $L^1$, $L^2$, and $L^3$ were prepared according to literature procedures.[13] Elemental analyses (C,H,N) were performed on an Elementar Vario EL analyzer. IR spectra were recorded with a Nicolet Magna-IR 750 spectrometer equipped with a Nic-Plan Microscope. Temperature- and field-dependent magnetic measurements were carried out on an Oxford MagLab 2000 magnetometer. Diamagnetic corrections were made with Pascal's constants.[14]

***Caution!*** *Azide and perchlorate complexes of metal ions are potentially explosive. Only a small amount of the materials should be prepared, and it should be handled with care.*

**$[Mn(L^1)(N_3)_2]_n$ (1):** A methanol solution (10 mL) containing $Mn(ClO_4)_2{\cdot}6H_2O$ (0.181 g, 0.5 mmol) and $L^1$ (0.061 g, 0.5 mmol), and a methanol solution (10 mL) of $NaN_3$ (0.065 g, 1.0 mmol) were added respectively to the two arms of an H-tube, then methanol was carefully added to both arms until the bridge of the tube was filled. Slow interdiffusion of the two solutions afforded yellow crystals of **1** after two weeks. Yield: 0.042 g (32%). $C_{14}H_{16}Mn_2N_{16}$ (518.31): calcd. C 32.45, H 3.11, N 43.24; found C 32.48, H 3.30, N 43.50. IR: $\tilde{\nu}$ = 2067 vs, 1595 m, 1441 m, 1334 m, 1305 m, 1283 m, 1014 m, 775 m cm$^{-1}$.

**$[Mn(L^2)(N_3)_2]_n$ (2):** A methanol solution (10 mL) of $Mn(ClO_4)_2{\cdot}6H_2O$ (0.181 g, 0.5 mmol) was added to a solution of $L^2$ (0.068 g, 0.5 mmol) in the same solvent. The mixture was stirred for 5 min, then a methanol (10 mL) solution of $NaN_3$ (0.065 g, 1 mmol) was added with continuous stirring. Slow evaporation of the resulting orange solution at room temperature yielded yellow crystals after two weeks. Yield: 0.080 g (59%). $C_8H_{10}MnN_8$ (273.18): calcd. C 35.18, H 3.69, N 41.02; found C 35.14, H 3.85, N 41.42. IR: $\tilde{\nu}$ = 2067 s, 1595 m, 1479 m, 1475 m, 1443 m, 1339 m, 1305 m, 1156 m, 1106 m, 1013 m, 779 m cm$^{-1}$.

**$[Mn(L^3)(N_3)_2]_n$ (3):** This complex was prepared in the same way as **2**, using $L^3$ instead of $L^2$. Yield: 0.043 g (24%). $C_{14}H_{22}MnN_8$ (357.34): calcd. C 47.06, H 6.21, N 31.36; found C 47.07, H 6.27, N 31.79. IR: $\tilde{\nu}$ = 2095 vs, 2064 vs, 1595 m, 1467 m, 1442 m, 1334 m, 1013 m, 775 m cm$^{-1}$.

**X-ray Crystallographic Study:** Diffraction intensity data for single crystals of **1**, **2**, and **3** were collected at room temperature on a Nonius Kappa CCD area detector equipped with graphite-mono-

Table 5. Summary of crystallographic data for complexes **1**–**3**.

| | **1** | **2** | **3** |
|---|---|---|---|
| Empirical formula | $C_{14}H_{16}Mn_2N_{16}$ | $C_8H_{10}MnN_8$ | $C_{14}H_{22}MnN_8$ |
| Formula mass | 518.31 | 273.18 | 357.34 |
| Crystal system | monoclinic | orthorhombic | triclinic |
| Space group | $P2_1/c$ | $Pbca$ | $P\bar{1}$ |
| $a$ [Å] | 12.016(2) | 10.6725(2) | 8.1436(2) |
| $b$ [Å] | 16.589(3) | 12.6390(3) | 9.4498(2) |
| $c$ [Å] | 11.867(2) | 17.6030(5) | 12.3898(4) |
| $\alpha$ [°] | 90 | 90 | 72.8132(9) |
| $\beta$ [°] | 103.51(3) | 90 | 76.3392(9) |
| $\gamma$ [°] | 90 | 90 | 82.161(1) |
| $V$ [Å$^3$] | 2300.0(8) | 2374.5(1) | 882.84(4) |
| $Z$ | 4 | 8 | 2 |
| $D_{calcd.}$ [g cm$^{-3}$] | 1.497 | 1.528 | 1.344 |
| $\mu$ [mm$^{-1}$] | 1.135 | 1.103 | 0.759 |
| $R_1$ [$I > 2\sigma(I)$] | 0.0352 | 0.0529 | 0.0328 |
| $wR_2$ (all data) | 0.0822 | 0.1663 | 0.0795 |
| GOF | 0.880 | 0.947 | 0.990 |

 © 2006 Wiley-VCH Verlag GmbH & Co. KGaA, Weinheim 

chromated Mo-$K_\alpha$ radiation ($\lambda$ = 0.71073 Å). Empirical absorption corrections were applied using the Sortav program.[15] The structures were solved by direct methods and refined by full-matrix least-squares on $F^2$ with anisotropic thermal parameters for all non-hydrogen atoms.[11] Hydrogen atoms were placed geometrically and refined isotropically. Pertinent crystallographic data and structure refinement parameters are summarized in Table 5.

CCDC-279815 (for **1**), -279816 (for **2**), and -279817 (for **3**) contain the supplementary crystallographic data for this paper. These data can be obtained free of charge from The Cambridge Crystallographic Data Center via www.ccdc.cam.ac.uk/data_request/cif.

## Acknowledgments

We acknowledge the NSFC (grant nos. 20221101, 20201009, and 20490210) and the Foundation of Science and Technology Development of Shanghai (03ZR14024) for financial support.

[1] a) O. Kahn, *Molecular Magnetism*, Wiley, New York, **1993**; b) *Molecular Magnets: Recent Highlights* (Eds.: W. Linert, M. Verdaguer), Springer, Wien, New York, **2003**.

[2] a) *Magnetism: Molecules to Materials* (Eds.: J. S. Miller, M. Drillon), Wiley VCH, Weinheim (Germany), **2001**; b) J. Ribas, A. Escuer, M. Monfort, R. Vicente, R. Cortés, L. Lezama, T. Rojo, *Coord. Chem. Rev.* **1999**, *193–195*, 1027–1068.

[3] a) R. Cortés, M. Drillon, X. Solans, L. Lezama, T. Rojo, *Inorg. Chem.* **1997**, *36*, 677–683; b) A. Escuer, R. Vicente, M. A. S. Goher, F. A. Mautner, *Inorg. Chem.* **1998**, *37*, 782–787; c) M. A. M. Abu-Youssef, A. Escuer, M. A. S. Goher, F. A. Mautner, R. Vicente, *Eur. J. Inorg. Chem.* **1999**, 687–691; d) M. A. M. Abu-Youssef, A. Escuer, D. Gatteschi, M. A. S. Goher, F. A. Mautner, R. Vicente, *Inorg. Chem.* **1999**, *38*, 5716–5723; e) L.-F. Tang, L. Zhang, L.-C. Li, P. Cheng, Z.-H. Wang, J.-T. Wang, *Inorg. Chem.* **1999**, *38*, 6326–6328; f) M. A. M. Abu-Youssef, A. Escuer, M. A. S. Goher, F. A. Mautner, G. J. Reiβ, R. Vicente, *Angew. Chem. Int. Ed.* **2000**, *39*, 1624–1626; g) M. A. M. Abu-Youssef, M. Drillon, A. Escuer, M. A. S. Goher, F. A. Mautner, R. Vicente, *Inorg. Chem.* **2000**, *39*, 5022–5027; h) M. Villanueva, J. L. Mesa, M. K. Urtiaga, R. Cortés, L. Lezama, M. I. Arriortua, T. Rojo, *Eur. J. Inorg. Chem.* **2001**, 1581–1586; i) E.-Q. Gao, S.-Q. Bai, Y.-F. Yue, Z.-M. Wang, C.-H. Yan, *Inorg. Chem.* **2003**, *42*, 3642–3649; j) E.-Q. Gao, S.-Q. Bai, C.-F. Wang, Y.-F. Yue, C.-H. Yan, *Inorg. Chem.* **2003**, *42*, 8456–8464; k) U. Ray, S. Jasimuddin, B. K. Ghosh, M. Monfort, J. Ribas, G. Mostafa, T.-H. Lu, C. Sinha, *Eur. J. Inorg. Chem.* **2004**, 250–259; l) J. Cano, Y. Journaux, M. A. S. Goher, M. A. M. Abu-Youssef, F. A. Mautner, G. J. Reiβ, A. Escuer, R. Vicente, *New J. Chem.* **2005**, *29*, 306–314; m) S. Deoghoria, S. K. Bera, B. Moulton, M. J. Zaworotko, J.-P. Tuchagues, G. Mostafa, T.-H. Lu, S. K. Chandra, *Polyhedron* **2005**, *24* 343–350; n) M. A. M. Abu-Youssef, A. Escuer, R. Vicente, F. A. Mautner, L. Öhrstrom, M. A. S. Goher, *Polyhedron* **2005**, *24*, 557–562.

[4] a) A. Escuer, R. Vicente, M. A. S. Goher, F. A. Mautner, *Inorg. Chem.* **1995**, *34*, 5707–5708; b) A. Escuer, R. Vicente, M. A. S. Goher, F. A. Mautner, *Inorg. Chem.* **1996**, *35*, 6386–6391; c) A. Escuer, R. Vicente, M. A. S. Goher, F. A. Mautner, *J. Chem. Soc., Dalton Trans.* **1997**, 4431–4434; d) A. Escuer, R. Vicente, M. A. S. Goher, F. A. Mautner, *Inorg. Chem.* **1997**, *36*, 3440–3446; e) Z. Shen, J.-L. Zuo, Z. Yu, Y. Zhang, J.-F. Bai, C.-M. Che, H.-K. Fun, J. J. Vittal, X.-Z. You, *J. Chem. Soc., Dalton Trans.* **1999**, 3393–3398; f) M. A. S. Goher, M. A. M. Abu-Youssef, F. A. Mautner, R. Vicente, A. Escuer, *Eur. J. Inorg. Chem.* **2000**, 1819–1823; g) A. Escuer, J. Cano, M. A. S. Goher, Y. Journaux, F. Lloret, F. A. Mautner, R. Vicente, *Inorg. Chem.* **2000**, *39*, 4688–4695; h) E.-Q. Gao, S.-Q. Bai, Z.-M. Wang, C.-H. Yan, *J. Am. Chem. Soc.* **2003**, *125*, 4984–4985; i) E.-Q. Gao, Y.-F. Yue, S.-Q. Bai, Z. He, S.-W. Zhang, C.-H. Yan, *Chem. Mater.* **2004**, *16*, 1590–1596; j) E.-Q. Gao, Y.-F. Yue, S.-Q. Bai, Z. He, C.-H. Yan, *J. Am. Chem. Soc.* **2004**, *126*, 1419–1429; k) A. Escuer, F. A. Mautner, M. A. S. Goher, M. A. M. Abu-Youssef, R. Vicente, *Chem. Commun.* **2005**, 605–607.

[5] a) F. A. Mautner, R. Cortés, L. Lezama, T. Rojo, *Angew. Chem. Int. Ed. Engl.* **1996**, *35*, 78–80; b) F. A. Mautner, S. Hanna, R. Cortés, L. Lezama, M. G. Barandika, T. Rojo, *Inorg. Chem.* **1999**, *38*, 4647–4652; c) M. A. S. Goher, J. Cano, Y. Journaux, M. A. M. Abu-Youssef, F. A. Mautner, A. Escuer, R. Vicente, *Chem. Eur. J.* **2000**, *6*, 778–784.

[6] a) G. De Munno, M. Julve, G. Viau, F. Lloret, J. Faus, D. Viterbo, *Angew. Chem. Int. Ed. Engl.* **1996**, *35*, 1807–1810; b) R. Cortés, L. Lezama, J. L. Pizarro, M. I. Arriortua, T. Rojo, *Angew. Chem. Int. Ed. Engl.* **1996**, *35*, 1810–1812; c) H.-Y. Shen, D.-Z. Liao, Z.-H. Jiang, S.-P. Yan, B.-W. Sun, G.-L. Wang, X.-K. Yao, H.-G. Wang, *Chem. Lett.* **1998**, 469–470; d) S. Martín, M. G. Barandika, L. Lezama, J. L. Pizarro, Z. E. Serna, J. I. Ruiz de Larramendi, M. I. Arriortua, T. Rojo, R. Cortés, *Inorg. Chem.* **2001**, *40*, 4109–4115; e) C.-M. Liu, S. Gao, D.-Q. Zhang, Y.-H. Huang, R.-G. Xiong, Z.-L. Liu, F.-C. Jiang, D.-B. Zhu, *Angew. Chem. Int. Ed.* **2004**, *43*, 990–994; f) E.-Q. Gao, Z.-M. Wang, C.-H. Yan, *Chem. Commun.* **2003**, 1748–1749; g) H.-L. Sun, S. Gao, B.-Q. Ma, G. Su, S. R. Batten, *Cryst. Growth Des.* **2005**, *5*, 269–277; h) A. K. Ghosh, D. Ghoshal, E. Zangrando, J. Ribas, N. Ray Chaudhuri, *Inorg. Chem.* **2005**, *44*, 1786–1793.

[7] S. S. Tandon, L. K. Thompson, M. E. Manuel, J. N. Bridson, *Inorg. Chem.* **1994**, *33*, 5555–5570.

[8] C. Janiak, *J. Chem. Soc., Dalton Trans.* **2000**, 3885–3896.

[9] M. E. Fisher, *Am. J. Phys.* **1964**, *32*, 343–346.

[10] R. Dingle, M. E. Lines, S. L. Holt, *Phys. Rev.* **1969**, *187*, 643–648.

[11] a) G. M. Sheldrick, *SHELXTL* Version 5.1. Bruker Analytical X-ray Instruments Inc., Madison, Wisconsin, USA, **1998**; b) G. M. Sheldrick, *SHELXL-97*, PC Version, University of Göttingen, Germany, **1997**.

[12] E. Ruiz, J. Cano, S. Alvarez, P. Alemany, *J. Am. Chem. Soc.* **1998**, *120*, 11122–11129.

[13] P. Bamfield, R. Price, R. G. J. Miller, *J. Chem. Soc., A* **1969**, 1447–1452.

[14] C. J. O'Connor, *Prog. Inorg. Chem.* **1982**, *29*, 203–283.

[15] a) R. H. Blessing, *Acta Crystallogr., Sect. A* **1995**, *51*, 33–38; b) R. H. Blessing, *J. Appl. Crystallogr.* **1997**, *30*, 421–426.

Received: August 2, 2005
Published Online: December 1, 2005

 © 2006 Wiley-VCH Verlag GmbH & Co. KGaA, Weinheim 

DOI: 10.1002/ejic.200500720

# Electronic Structure of Binary Phosphoric and Arsenic Triazides

Zeng Xiaoqing,[a,b] Wang Weigang,[a,b] Liu Fengyi,[a] Ge Maofa,*[a] Sun Zheng,[a] and Wang Dianxun*[a]

**Keywords:** Phosphorus / Arsenic / Triazides / Photoelectron spectroscopy / Ionization potentials

Two highly explosive binary triazides of the group 15 elements $P(N_3)_3$ and $As(N_3)_3$ have been obtained in the gas phase through the heterogeneous reaction of $PCl_3$ and $AsCl_3$, respectively with $AgN_3$ at room temperature. The electronic structures of both triazides have been characterized by photoelectron spectroscopy, combined with quantum chemical calculations. This represents the first electronic study of covalent triazides. The first experimental vertical ionization potentials for $P(N_3)_3$ and $As(N_3)_3$ are 9.74 and 9.98 eV, with the contribution primarily from the lone pairs of the azido moiety and the arsenic atom, respectively. The results indicate the relative "isolation" of azido moieties in triazides and less stability of these highly explosive compounds in comparison to monoazides and diazides.
(© Wiley-VCH Verlag GmbH & Co. KGaA, 69451 Weinheim, Germany, 2006)

## Introduction

The first synthesis of a covalent azide $HN_3$ was reported by Curtius more than 100 years ago.[1] However, the chemistry of covalent azides received little attention until the early 1960s, presumably because of their explosive nature and shock sensitivity.[2] Especially the synthesis, isolation, and structural characterization of high-energy compounds are an experimental challenge for chemists.[3] Binary azides of group 15 elements belong to this class of compounds, and little is known about their synthesis, structure, and properties.[4] For nitrogen azides, most studies are focused on theoretical predictions, such as the structures and stabilities of the azidamines $N(N_3)_3$ and $HN(N_3)_2$, the $N(N_3)_2^-$ anion, and the $N(N_3)_4^+$ cation.[5] However, the successful synthesis of the novel $N_5^+$ cation[6] by Christe et al. has greatly encouraged more research on polynitrogen compounds.[7] The binary phosphorus azides $P(N_3)_3$, $P(N_3)_4^+$, $P(N_3)_5$, $P(N_3)_6^-$, and $N_5^+[P(N_3)_6]^-$ have been characterized by vibrational methods and $^{31}P$ NMR spectroscopy, but no structural information is available.[8,9] For arsenic azides, much research has been devoted to the preparation and characterization of these compounds:[10] the first preparation of $As(N_3)_3$ and $As(N_3)_4^+$ was reported by Klapötke et al. in 1995;[10a,10c] the crystal structure of $As(N_3)_3$ was determined by Christe et al. in 2004;[11] and the crystal structure of $As(N_3)_6^-$ was determined by Klapötke et al. in 2000.[10c]

[a] State Key Laboratory for Structural Chemistry of Unstable and Stable Species, Institute of Chemistry, Chinese Academy of Sciences,
Beijing, 100080, China
Fax: +86-10-62559373
E-mail: gemaofa@iccas.ac.cn
[b] Graduate School of Chinese Academy of Sciences,
Beijing, 100039, China
Supporting information for this article is available on the WWW under http://www.eurjic.org or from the author.

The electronic and molecular structures of many azides (unstable molecules) have been studied with theoretical and spectroscopic methods.[12] Recently, photoelectron spectroscopy in combination with high-level quantum chemical calculations has been successfully performed for elucidating many interesting aspects of monoazides[13] and diazides.[14] The focus of these studies is the interaction taking place between the off-the-axis substituent group and the nearly linear $N_3$ moiety, as well as the interaction between the $N_3$ moieties. In 1994, Novak et al. studied the electronic structures of $(CF_3)_2AsN_3$ and $CF_3As(N_3)_2$.[15] However, reports on the electronic structure of triazide are rare because of their explosiveness. Herein, we report the experimental and calculated electronic structures of binary phosphorus and arsenic triazides.

## Results and Discussion

### Molecular Structures

Geometry optimizations were performed for $P(N_3)_3$ and $As(N_3)_3$ using the DFT method (B3LYP). All stationary points were verified as local minima by vibrational analysis. Three local minima were located for both triazides (see Figure 1 and Table 1). The relative energies for the stable conformers are listed in Table 2. Zero-point vibrational-energy corrections for these minima of $P(N_3)_3$ and $As(N_3)_3$ differ by less than 0.4 and 0.2 kcal mol$^{-1}$, respectively. The most stable structure at the B3LYP/6-311++G(3df) level is the conformer **b** with $C_s$ symmetry, in which two azido ligands adopt an approximate *gauche* orientation relative to the stereochemically active lone pair on the P/As atom, with the remaining azido ligand in an *anti* orientation. For $P(N_3)_3$,

 © 2006 Wiley-VCH Verlag GmbH & Co. KGaA, Weinheim 

the calculated P–N bond length, 1.73–1.74 Å, is slightly shorter than a typical P–N single bond with 1.76 Å,[16] while longer than a typical P=N double bond with 1.55 Å in iminophosphane (HP=NH).[17] Meanwhile, the azido moiety lies in an almost planar environment with the central P atom (see Table 1); this may provide an opportunity for interactions between the lone pair on the P atom with the three azido ligands to stabilize this conformer. The second most stable conformer of phosphorus triazide, **a**, with $C_3$ symmetry, is 1.46 kcal mol$^{-1}$ higher in energy than conformer **b** and has all three azido ligands in a *gauche* orientation. This energy gap may be the result of the interactions between the sterically active lone pair on the phosphorus atom and the three azido ligands. Finally, the least stable structure, **c** ($C_3$ symmetry), has all three azido ligands pointing away from the phosphorus lone-pair, and is 2.90 kcal mol$^{-1}$ higher in energy than conformer **b**. This structure was calculated to be a real local minimum at the B3LYP/6-311++G(d) level of theory,[18] however, the distances between N2 and N2′, and N3 and N3′ are 3.38 and 4.37 Å, respectively, which are much shorter than those in conformer **a** (4.41 and 6.21 Å, respectively). Also, the natural atomic population (NAO)[19] net charges calculated for this conformer are $Q_P$ = +1.11 e on phosphorus, $Q_{N1}$ = –0.68 e on the adjacent nitrogen atom, $Q_{N2}$ = +0.43 e on the second nitrogen atom, and $Q_{N3}$ = –0.12 e on the last nitrogen atom, indicating that the interactions between N1 and N1′, N2 and N2′, as well as N3 and N3′ might decrease the stability of this conformer.

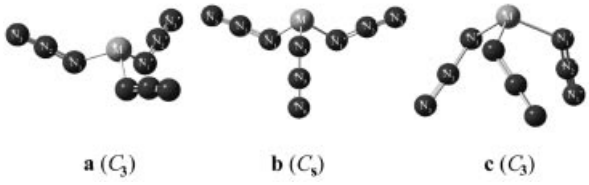


Figure 1. Local minima calculated for $M(N_3)_3$ (M = P, As) at the B3LYP/6-311++G(3df) level of theory. (The geometric parameters are given in Table 1.).

For $As(N_3)_3$, three similar stable conformers were located, with conformer **b** being the most stable structure. However, the most stable conformer previously reported by

Table 1. Calculated bond lengths [Å], bond angles [°], and torsion angles [°] for the local minima (**a**–**c**; see Figure 1) of $P(N_3)_3$ and $As(N_3)_3$ (given in parentheses) at B3LYP/6-311++G(3df) level.

| Conformer **a** $E$[a] = +1.46 kcal mol$^{-1}$ (2.06) | | Conformer **b** $E$ = 0.00 kcal mol$^{-1}$ (0.00) | |
|---|---|---|---|
| M–N1 | 1.732 (1.884) | M–N1 | 1.740 (1.888) |
| N1–N2 | 1.229 (1.229) | N1–N2 | 1.229 (1.229) |
| N2–N3 | 1.125 (1.128) | N2–N3 | 1.126 (1.128) |
| | | M–N4 | 1.730(1.889) |
| N1–M–N1′ | 96.5 (94.1) | N4–N5 | 1.234 (1.231) |
| N2–N1–M | 119.3 (117.6) | N5–N6 | 1.123 (1.126) |
| N3–N2–N1 | 174.3 (174.5) | | |
| N3–N2–N1–M | 176.9 (179.1) | N1–M–N1′ | 91.8 (88.2) |
| N2–N1–M–N1′ | 106.2 (96.7) | N2–N1–M | 119.2 (117.6) |
| Conformer **c** $E$ = +2.90 kcal mol$^{-1}$ (0.94) | | N3–N2–N1 | 174.4(174.4) |
| | | N1–M–N4 | 101.4(99.9) |
| M–N1 | 1.744 (1.898) | N5–N4–M | 121.3 (119.0) |
| N1–N2 | 1.228 (1.228) | N6–N5–N4 | 175.4 (175.7) |
| N2–N3 | 1.125 (1.127) | | |
| N1–M–N1′ | 101.8 (99.8) | N3–N2–N1–M | 178.4 (178.1) |
| N2–N1–M | 123.0 (120.1) | N2–N1–M–N1′ | 157.1 (166.7) |
| N3–N2–N1 | 175.8 (176.0) | N6–N5–N4–M | 180.0 (180.0) |
| | | N5–N4–M–N1 | 47.1 (45.0) |
| N3–N2–N1–M | 155.6 (169.0) | N2–N1–M–N4 | 100.9 (99.5) |
| N2–N1–M–N1′ | 95.1 (94.0) | | |

[a] Relative energy including ZPE corrections.

Table 2. Total energies (hartree) of conformers of $P(N_3)_3$ at different levels of theory, relative energies (kcal/mol) at the B3LYP/6-311++G(3df) level of theory, and the values for $As(N_3)_3$ at the B3LYP/6-311++G(3df) level of theory are given in parentheses.

| Conformer | B3LYP/6-31+G(d) | B3LYP/6-311++G(3df) | CCSD(T)/6-31G(d) | RE[a] |
|---|---|---|---|---|
| **a** | –833.9572663 | –834.1622444 (–2728.6537522) | –832.1959352 | 1.46 (2.06) |
| **b** | –833.9601526 | –834.1647579 (–2728.6572297) | –832.1995274 | 0.00 (0.00) |
| **c** | –833.9548009 | –834.1596547 (–2728.6554279) | –832.1953666 | 2.09 (0.94) |

[a] Relative energies with zero-point vibrational-energy corrections included.

 © 2006 Wiley-VCH Verlag GmbH & Co. KGaA, Weinheim 

using second-order perturbation theory (MP2), which had $C_1$ symmetry with two azido ligands adopting an *anti* orientation and the third azido ligand in a *gauche*-like orientation,[11] was calculated to be not a real local minimum at the B3LYP/6-311++G(3df) level of theory, and the relative energies for the two less stable conformers **a** and **c** here were calculated to be 2.06 and 0.94 kcal mol$^{-1}$ higher than conformer **b**, including the zero-point energy (ZPE) corrections.

### Photoelectron Spectroscopy

The He I photoelectron spectra of $P(N_3)_3$ and $As(N_3)_3$ are shown in Figure 2. Table 3 lists photoelectron spectroscopy (PES) experimental vertical ionization energies (IP in eV), theoretical vertical ionization energies ($E_v$ in eV), molecular orbital symmetries, and characters of outer valence shells for the most stable conformers by OVGF calculations for both triazides. The ionization potentials calculated for the other two stable conformers are also included. Because the three conformers with comparable energies are possible in some cases, first we should investigate whether the spectra can originate from a mixture of all three conformers or some of them dominate. However, in comparison to the calculated orbital energies, we limit our discussions to the analysis of the slightly more stable $C_s$-conformer **b** for $P(N_3)_3$ and $As(N_3)_3$.

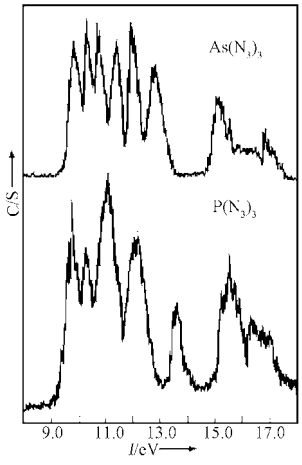


Figure 2. Full He I photoelectron spectra of $P(N_3)_3$ and $As(N_3)_3$.

#### *P(N$_3$)$_3$*

The photoelectron (PE) spectrum of $P(N_3)_3$ is much more complicated than that of $HN_3$,[20] owing to the participation of the phosphorus lone-pair. In the low ionization region (<15 eV) there are five bands with no obvious vibrational structure. From the calculated orbital characters shown in Table 3 and Figure 3, it can be easily concluded that all five bands originate from the removal of the lone pair on the phosphorus or the nitrogen atoms of the azido moieties. The first broad band centered at 9.74 eV matches well with the calculated value 9.81 eV, which is attributed to the ionization of lone pairs from the three azido moieties with almost equal contributions. Similar ionization processes also occur in other azides, such as $CH_3N_3$ (9.81 eV)[21] and $SO(N_3)_2$ (10.18 eV).[14] However, as we know, the removal of lone pair electrons or degenerate π orbital electrons leads to sharp peaks and lower ionization potentials in the PE spectrum of the molecule studied. This indicates that the peak caused by removing electrons from 25a′, with a calculated energy of 9.83 eV, overlaps with the peak caused by removing electrons from HOMO 14a′′. The calculated MO character of the second highest occupied orbital (SHOMO) 25a′ indicates that it has the dominant attribution from the P lone-pair (P3p) (Figure 3). The ionization of similar P lone-pairs actually happens in the low ionization region as well, such as $PH_3$ (10.59 eV)[22] and $(CH_3O)_3P$ (9.30 eV).[23] The second observed band with

Table 3. Experimental and calculated [ROVGF/6-311G(d)] ionization energies [eV].

| $IE_{exp.}$ | $IE_{calcd.}$ | | | Assignment |
|---|---|---|---|---|
| $P(N_3)_3$ | **a** ($C_3$) | **b** ($C_s$) | **c** ($C_3$) | |
| 9.74 | 9.34 | 9.81 | 9.58 | 14a′′ LpN3 [a] |
| | 10.14 | 9.83 | 10.44 | 25a′ P3p [b] |
| 10.37 | 10.77 | 10.43 | 11.66 | 24a′ LpN3 |
| 11.08 | 10.77 | 10.79 | 12.38 | 13a′′ LpN3 |
| | 11.75 | 11.93 | 12.76 | 12a′′ $\pi_{P\text{-}N4}$, $\sigma_{P\text{-}N1}$, $\sigma_{P\text{-}N1'}$ |
| 12.17 | 11.75 | 12.19 | 16.07 | 23a′ $\pi_{N1\text{-}P\text{-}N1'}$, $\pi_{N5\text{-}N6}$ |
| 13.59 | 14.47 | 13.82 | 16.34 | 22a′ P3p |
| 15.6 | 15.88 | 15.82 | 17.11 | 11a′′ $\sigma_{N1\text{-}N2\text{-}N3}$, $\sigma_{N1'\text{-}N2'\text{-}N3'}$ |
| $As(N_3)_3$ | | | | |
| 9.98 | 9.44 | 9.73 | 9.65 | 17a′′As4p [c] |
| | | 9.87 | | 31a′ LpN3 |
| 10.22 | 10.28 | 10.18 | 10.11 | 30a′ As4p, LpN3 |
| 10.7 | 10.31 | 10.36 | 11.17 | 16a′′ LpN3 |
| 11.43 | 11.39 | 11.61 | 11.17 | 15a′′ $\pi_{As\text{-}N4}$, $\sigma_{As\text{-}N1}$, $\sigma_{As\text{-}N1'}$ |
| 11.91 | 14.49 | 11.72 | 11.88 | 29a′ $\pi_{N1\text{-}As\text{-}N1'}$, $\pi_{N5\text{-}N6}$ |
| 12.95 | 15.64 | 13.99 | 13.2 | 28a′ As4p |
| 15.2 | 15.87 | 15.54 | 15.77 | 14a′′ $\sigma_{N1\text{-}N2\text{-}N3}$, $\sigma_{N1'\text{-}N2'\text{-}N3'}$ |

[a] Lp is the abbreviation of lone pair electrons. [b] 3p lone-pair on the phosphorus atom. [c] 4p lone-pair on the arsenious atom.

 © 2006 Wiley-VCH Verlag GmbH & Co. KGaA, Weinheim 

vertical ionization energy of 10.37 eV agrees well with the calculated value 10.43 eV for orbital 24a′, as can be seen in Figure 3; it has the character of nitrogen lone-pairs on the three azido moieties. The third kind of linear combination is embodied in the third broad band (11.08 eV), which ranges from 10.50 to 11.70 eV. Based on the calculated results and experimental intensity of this band, it is assigned to the removal of electrons from 13a′′ and 12a′′ orbitals. The $\pi_{P-N4}$ formed by the interaction of P3p with the N4 lone-pair is also attributed. The fourth band with experimental vertical ionization energy of 12.17 eV, corresponding to the calculated 12.19 eV for 23a′, has the character $\pi_{N1-P-N1'}$, $\pi_{N5-N6}$ (Figure 3). The next band with a vertical ionization of 13.59 eV corresponds to MO 22a′, which has the dominant character of the P3p lone-pairs. A similar band also occurs in $PH_3$ (13.6 eV).[22] The band centered near 15.6 eV in the high ionization region (>15.0 eV) is considered to be the ionization of electrons from several deep-shell orbitals in $P(N_3)_3$.

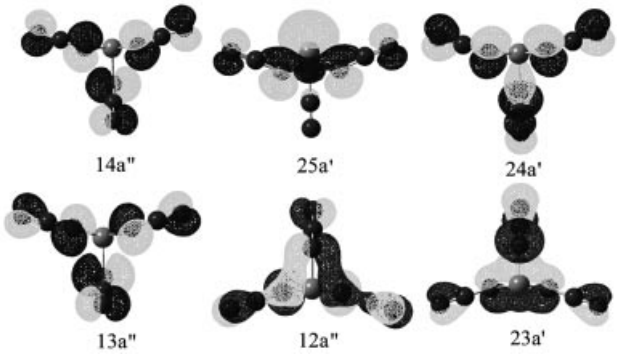


Figure 3. Characters of the six highest occupied molecular orbitals (HOMOs) of $C_s$: $P(N_3)_3$ (isovalue = 0.04).

### *As(N₃)₃*

The electronic structures of two arsenic azides $(CF_3)_2AsN_3$ and $CF_3As(N_3)_2$ have been reported previously.[15] The main interest in the analysis was the interactions taking place between the off-the-axis substituent and the linear (or nearly so) azido group. It was concluded that the larger bandwidth in their PE spectra may signify greater delocalization and bonding interaction between the azido moieties and the rest of the molecule. Compared with the PE spectra of the two above-mentioned azides, the bands in the PE spectrum of $As(N_3)_3$ are clearer and narrower in the low ionization region (<15.0 eV). The calculated MO characters (Figure 4) of this triazide reveal that the lone pair electrons on the azido moieties are more pronounced than in the monoazide and diazide, and imply weaker azido–azido interactions. These weaker interactions also lead to the lower stability of triazide.

In the low ionization region (<15.0 eV), six bands are clearly displayed. Because of the electronic similarity of phosphorus and arsenic, most outer valence shells for $As(N_3)_3$ are similar to that of $P(N_3)_3$. However, the HOMO in arsenic triazide is primarily the attribution of the 4p lone-pair from the As atom (As4p). The vertical ionization potential is 9.98 eV, which is slightly smaller than that of $(CF_3)_2AsN_3$ (10.40 eV) and $CF_3As(N_3)_2$ (10.23 eV),[15] and it corresponds to the calculated 9.73 eV for conformer **b**. Similar to the first band in the PE spectrum of $P(N_3)_3$, the ionization of electrons in the SHOMO 31a′ also happens in this region, with the contribution of the lone pair on nitrogen atoms of the three azido moieties being calculated as 9.87 eV. The second band at 10.22 eV originates not only from the lone pair of the nitrogen atoms on the azido ligands, but also the As4p lone-pair. The third band at 10.70 eV mainly comes from the ionization of the 16a′′ LPN3 (azido lone-pair) electron, and the fourth band at 11.43 eV should be from the 15a′′ $\pi_{As-N4}$, $\sigma_{As-N1}$, $\sigma_{As-N1'}$ (see Figure 4). In $P(N_3)_3$, the bands caused by removal of electrons from these two orbitals overlap. The main characters for the remaining two bands at 11.61 and 12.95 eV are similar to those of $P(N_3)_3$ (Figure 4). In the high ionization region (>15.0 eV), there also exist several broad bands, ranging from 15.00 to 17.50 eV, which might be the ionization of electrons from inner molecular orbitals.

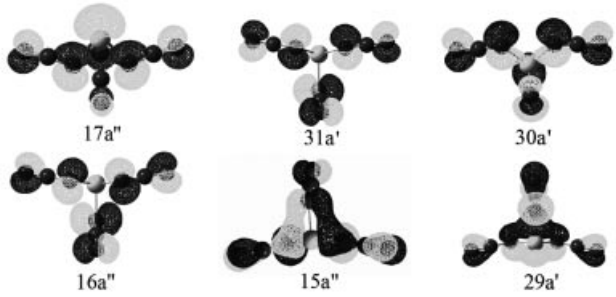


Figure 4. Characters of the six highest occupied molecular orbitals (HOMOs) of $C_s$: $As(N_3)_3$ (isovalue = 0.04).

## Conclusions

The electronic structures of two similar triazides, $P(N_3)_3$ and $As(N_3)_3$, were studied by means of PES and ab initio calculations. Three stable conformers for $P(N_3)_3$ and $As(N_3)_3$ were located at the B3LYP/6-311++G(3df) level of theory. It was found that the conformer **b** with $C_s$ symmetry is the most stable for both triazides. The first ionization potentials of these two stable conformers for $P(N_3)_3$ and $As(N_3)_3$ are 9.74 and 9.98 eV respectively, with the primary characters being the azido lone-pairs for $P(N_3)_3$ and the As4p lone-pairs for $As(N_3)_3$. The SHOMO for the two compounds mainly comes from the P3p lone-pair for $P(N_3)_3$, in comparison to the lone pairs of the azido group for $As(N_3)_3$. Another interesting aspect is that the PES bands for both triazides are almost all sharp without recognizable vibrational structure. And it is known that triazides are usually much less stable than the corresponding di- and mono- derivatives. The relative "isolation" of azido groups and less delocalization in triazides may account for this experimental fact.

 © 2006 Wiley-VCH Verlag GmbH & Co. KGaA, Weinheim 

## Experiment and Calculation

Recently, many azide-containing compounds have been successfully prepared and characterized,[13,14] and it was found that $AgN_3$ is an ideal precursor for the in situ preparation of highly explosive azides through the heterogeneous reactions with reactive halogen-containing molecules. $P(N_3)_3$ and $As(N_3)_3$ were prepared in a similar manner by the heterogeneous reactions of gaseous $PCl_3$ and $AsCl_3$ with $AgN_3$ at low pressure ($10^{-5}$ Torr). Both reactants were purchased from ACROS and distilled before the PES experiment, and their PE spectra were identical with those in the literature.[23,24] Solid $AgN_3$ was prepared as reported.[14] For efficient reaction, freshly prepared $AgN_3$ was loosely dispersed on the surface of quartz wool and filled the quartz inlet tube. After the vacuum reached $10^{-5}$ Torr, the vapor of the $PCl_3$ or $AsCl_3$ was passed through the solid $AgN_3$ at ambient temperature. The reactions [Equation (1) and Equation(2)] proceeded smoothly without the evolution of the possible decomposition product $N_2$. The He I PE spectra of $P(N_3)_3$ and $As(N_3)_3$ were recorded with a double-chamber machine[25] that was built specifically to detect transient species at a resolution of about 30 meV as indicated by the $Ar^+$ ($^2P_{3/2}$) photoelectron band. Experimental vertical ionization energies ($I_v$ in eV) were calibrated by simultaneous addition of a small amount of argon to the sample.

$$PCl_3\,(g) + 3AgN_3\,(s) \longrightarrow P(N_3)_3\,(g) + 3AgCl\,(s) \quad (1)$$

$$AsCl_3\,(g) + 3AgN_3\,(s) \longrightarrow As\,(N_3)_3\,(g) + 3AgCl\,(s) \quad (2)$$

Geometric optimizations of all possible conformers for phosphorus triazide were performed using density functional theory methods, and three stable conformers for each triazide were located. The calculations were carried out at the B3LYP level of theory with a 6-311++G(3df) basis set. The B3LYP is a hybrid functional method based on Becke's three-parameter nonlocal exchange functional,[26] with Lee et al.'s nonlocal correlation.[27] For the arsenic triazide, geometry optimization was carried out according to the reported stable conformers[11] at the same level of theory. To assign the PES bands of both triazides, OVGF calculations were performed for those three stable conformers of $P(N_3)_3$ and $As(N_3)_3$ using the 6-311G(d) basis set based on optimized structures. The vertical ionization energy ($E_v$) was calculated at the ab initio level according to Cederbaum's outer valence Green's function (OVGF) method,[28] which includes the effect of electron correlation and reorganization beyond the Hartree–Fock approximation. The self-energy part was expanded up to the third order, and contributions of higher orders were estimated by means of a renormalization procedure. All calculations were performed using the Gaussian 98 program.[29]

## Acknowledgments

This project was supported by the Chinese Academy of Sciences (Contract No: KJCX2-SW-H8 and Hundred talents fund) and the National Natural Science Foundation of China (Contract Nos: 20477047, 20473094, 50372071). Xiaoqing Zeng, Weigang Wang, and Fengyi Liu thank the Chinese Academy of Sciences for a scholarship during the period of this work.

[1] T. Curtius, *Ber. Dtsch. Chem. Ges.* **1890**, *23*, 3023–3033.
[2] C. Knapp, J. Passmore, *Angew. Chem. Int. Ed.* **2004**, *43*, 2–4.
[3] a) T. Grewer, *Thermal Hazards of Chemical Reactions, Industrial Safety Series 4*, Elsevier, Amsterdam, **1994**; b) *Bretherick's Handbook of Reactive Chemical Hazards*, 5th ed., Butterworth-Heinemann, Oxford, UK, **1995**.
[4] a) T. M. Klapötke, *Chem. Ber./Recueil* **1997**, *130*, 443–451; b) I. C. Tornieporth-Oetting, T. M. Klapötke, *Angew. Chem. Int. Ed. Engl.* **1995**, *34*, 511–520.
[5] a) H. H. Michels, J. A. Montgomery, K. O. Christe, D. A. Dixon, *J. Phys. Chem.* **1995**, *99*, 187–194; b) T. M. Klapötke, *Angew. Chem. Int. Ed.* **1999**, *38*, 2536–2538; c) T. M. Klapötke, A. Schulz, *Main Group Met. Chem.* **1997**, *20*, 325–338.
[6] K. O. Christe, W. W. Wilson, J. A. Sheehy, J. A. Boatz, *Angew. Chem. Int. Ed.* **1999**, *38*, 2004–2009.
[7] a) A. Vij, W. W. Wilson, V. Vij, F. S. Tham, J. A. Sheehy, K. O. Christe, *J. Am. Chem. Soc.* **2001**, *123*, 6308–6313; b) A. Hammerl, T. M. Klapötke, *Inorg. Chem.* **2002**, *41*, 906–912.
[8] a) W. Buder, A. Schmidt, *Z. Anorg. Allg. Chem.* **1975**, *415*, 263–267; b) A. Schmidt, *Chem. Ber.* **1970**, *103*, 3923–3927; c) P. Volgnandt, A. Schmidt, *Z. Anorg. Allg. Chem.* **1976**, *425*, 189–192; d) H. W. Roesky, *Angew. Chem. Int. Ed. Engl.* **1967**, *6*, 637; e) R. Haiges, S. Schneider, T. Schroer, K. O. Christe, *Angew. Chem. Int. Ed.* **2004**, *43*, 4919–4924.
[9] a) A. H. Cowley, F. Gabbai, R. Schluter, D. Atwood, *J. Am. Chem. Soc.* **1992**, *114*, 3142–3144; b) K. Karaghiosoff, T. M. Klapötke, B. Krumm, H. Nöth, T. Schütt, M. Suter, *Inorg. Chem.* **2002**, *41*, 170–179.
[10] a) T. M. Klapötke, P. Geissler, *J. Chem. Soc., Dalton Trans.* **1995**, 3365–3366; b) P. Geissler, T. M. Klapötke, H. J. Kroth, *Spectrochim. Acta, Part A* **1995**, *51*, 1075–1078; c) T. M. Klapötke, H. Nöth, T. Schütt, M. Warchhold, *Angew. Chem. Int. Ed.* **2000**, *39*, 2108–2109; d) T. M. Klapötke, T. Schütt, *J. Fluorine Chem.* **2001**, *109*, 151–162; e) T. M. Klapötke, H. Nöth, T. Schütt, M. Suter, *Eur. J. Inorg. Chem.* **2002**, 2511–2517.
[11] R. Haiges, A. Vij, J. A. Boatz, S. Schneider, T. Schroer, M. Gerken, K. O. Christe, *Chem. Eur. J.* **2004**, *10*, 508–517.
[12] a) M. Otto, S. D. Lotz, G. Frenking, *Inorg. Chem.* **1992**, *31*, 3647–3655; b) H. Bock, R. Dammel, *Angew. Chem. Int. Ed. Engl.* **1987**, *26*, 504–526.
[13] a) H. J. Che, H. M. Bi, Y. L. Zeng, L. P. Meng, S. J. Zheng, D. X. Wang, *ChemPhysChem* **2003**, *3*, 300–303; b) X. Q. Zeng, F. Y. Liu, Q. Sun, M. F. Ge, J. P. Zhang, X. C. Ai, L. P. Meng, S. J. Zheng, D. X. Wang, *Inorg. Chem.* **2004**, *43*, 4799–4801.
[14] T. M. Klapötke, B. Krumm, K. Polborn, *J. Am. Chem. Soc.* **2004**, *126*, 710–711.
[15] H. G. Ang, Y. W. Lee, I. Novak, *J. Phys. Chem.* **1994**, *98*, 12526–12529.
[16] a) E. Niecke, O. Altmeyer, M. Nieger, *J. Chem. Soc., Chem. Commun.* **1988**, 945–946; b) G. Fischer, S. Herler, P. Mayer, A. Schulz, A. Villinger, J. J. Weigand, *Inorg. Chem.* **2005**, *44*, 1740–1751.
[17] M. T. Nguyen, M. A. McGinn, A. F. Hegarty, *J. Am. Chem. Soc.* **1985**, *107*, 8029–8033.
[18] L. J. Wang, P. L. Warburton, P. G. Mezey, *J. Phys. Chem. A* **2005**, *109*, 1125–1130.
[19] a) E. D. Glendening, A. E. Reed, J. E. Carpenter, F. Weinhold, *NBO*, version 3.1; b) J. E. Carpenter, F. Weinhold, *J. Mol. Struct.: THEOCHEM* **1988**, *169*, 41–62; c) J. P. Foster, F. Weinhold, *J. Am. Chem. Soc.* **1980**, *102*, 7211–7218; d) A. E. Reed, F. Weinhold, *J. Chem. Phys.* **1983**, *78*, 4066–4073; e) A. E. Reed, R. B. Weinstock, F. Weinhold, *J. Chem. Phys.* **1985**, *83*, 735–746; f) A. E. Reed, P. v. R. Schleyer, *J. Am. Chem. Soc.* **1987**, *109*, 7362–7373; g) A. E. Reed, P. v. R. Schleyer, *Inorg. Chem.* **1988**, *27*, 3969–3987; h) F. Weinhold, J. E. Carpenter, *The Structure of Small Molecules and Ions*, Plenum Press, New York, **1988**, p. 227.
[20] T. Cvitas, L. Klasinc, *J. Chem. Soc., Faraday Trans.* **1976**, *72*, 1240–1244.
[21] H. Bock, R. Dammel, L. Horner, *Chem. Ber.* **1981**, *114*, 220–226.
[22] G. R. Branton, D. C. Frost, C. A. McDowell, I. A. Stenhouse, *Chem. Phys. Lett.* **1970**, *5*, 1–2.
[23] S. Chattorpadhyay, G. L. Findley, S. P. McGlynn, *J. Electron Spectrosc. Relat. Phenom.* **1981**, *24*, 27–36.

 © 2006 Wiley-VCH Verlag GmbH & Co. KGaA, Weinheim 

[24] T. H. Lee, J. W. Rabalais, *J. Chem. Phys.* **1974**, *60*, 1172–1176.
[25] a) J. Wang, Z. Sun, X. J. Zhu, X. J. Yang, M. F. Ge, D. X. Wang, *Angew. Chem. Int. Ed.* **2001**, *40*, 3055–3057; b) Y. M. Li, Z. M. Qiao, Q. Sun, J. C. Zhao, H. Y. Li, D. X. Wang, *Inorg. Chem.* **2003**, *42*, 8446–8448.
[26] A. D. Becke, *J. Chem. Phys.* **1993**, *98*, 5648–5652.
[27] C. Lee, W. Yang, R. G. Parr, *Phys. Rev. B* **1988**, *37*, 785–789.
[28] W. Von Niessen, J. Schirmer, L. S. Cederbaum, *Comput. Phys. Rep.* **1984**, *1*, 57–126.
[29] M. J. Frisch, G. W. Trucks, H. B. Schlegel, G. E. Scuseria, M. A. Robb, J. R. Cheeseman, V. G. Zakrzewski, J. A. Montgomery, Jr., R. E. Stratmann, J. C. Burant, S. Dapprich, J. M. Millam, A. D. Daniels, K. N. Kudin, M. C. Strain, O. Farkas, J. Tomasi, V. Barone, M. Cossi, R. Cammi, B. Mennucci, C. Pomelli, C. Adamo, S. Clifford, J. Ochterski, G. A. Petersson, P. Y. Ayala, Q. Cui, K. Morokuma, D. K. Malick, A. D. Rabuck, K. Raghavachari, J. B. Foresman, J. Cioslowski, J. V. Ortiz, B. B. Stefanov, G. Liu, A. Liashenko, P. Piskorz, I. Komaromi, R. Gomperts, R. L. Martin, D. J. Fox, T. Keith, M. A. Al-Laham, C. Y. Peng, A. Nanayakkara, C. Gonzalez, M. Challacombe, P. M. W. Gill, B. G. Johnson, W. Chen, M. W. Wong, J. L. Andres, M. Head-Gordon, E. S. Replogle, J. A. Pople, *Gaussian 98*, revision A.5, Gaussian, Inc., Pittsburgh, PA, **1998**.

Received: August 12, 2005
Published Online: December 9, 2005

 © 2006 Wiley-VCH Verlag GmbH & Co. KGaA, Weinheim 

DOI: 10.1002/ejic.200500745

# Synthesis, Characterization, and Electrochemical Properties of Novel Transition Metal–Fullerene Complexes Containing Di- and Tetraphosphane Ligands

**Li-Cheng Song,*[a] Fu-Hai Su,[a] Qing-Mei Hu,[a] Emanuela Grigiotti,[b] and Piero Zanello[b]**

**Keywords:** Electrochemistry / Fullerenes / Palladium / Phosphane ligands / Platinum

This paper reports the synthesis, characterization, and some properties of transition metal–fullerene complexes containing *trans*-1,1′-bis(diphenylphosphanyl)ethylene (dppet, *trans*-$Ph_2PCH{=}CHPPh_2$) and *N*,*N*,*N*′,*N*′-tetra(diphenylphosphanylmethyl)ethylene diamine (dppeda, $[(Ph_2PCH_2)_2NCH_2]_2$), including $[(\eta^2\text{-}C_{60}M)(dppet)_2]$ (M = Pt **1**, Pd **2**), $[(\eta^2\text{-}C_{60}M)(dppet)]_2$ (M = Pt **3**, Pd **4**), $[(\eta^2\text{-}C_{60}Pd)(\eta^2\text{-}C_{60}Pt)(dppet)_2]$ (**5**), $[(\eta^2\text{-}C_{60}Pd)(\eta^2\text{-}C_{70}Pd)(dppet)_2]$ (**6**), $[(\eta^2\text{-}C_{70}Pd)(dppet)]_2$ (**7**), $[(\eta^2\text{-}C_{60}M)(dppeda)]$ (M = Pt **8**, Pd **9**), and $[(\eta^2\text{-}C_{60}M)_2(dppeda)]$ (M = Pt **10**, Pd **11**). Interestingly, while complexes **1**, **2**, **8**, and **9** are the first examples of metallacyclopropafullerene diphosphane ligands containing fullerene cores, complexes **3**–**7**, **10**, and **11** are the first group 10 metal-containing, dumbbell-shaped bisfullerenes. All the complexes **1**–**11** were characterized by elemental analysis, spectroscopy, and, particularly for **4** and **5**, by X-ray crystallography and cyclic voltammetry. Pathways for the formation of **1**–**11** are suggested.
(© Wiley-VCH Verlag GmbH & Co. KGaA, 69451 Weinheim, Germany, 2006)

## Introduction

Since the isolation and characterization of the first transition metal–fullerene complex $[(\eta^2\text{-}C_{60})Pt(PPh_3)_2]$,[1] a large number of such complexes with unique structures and novel properties have been prepared and structurally characterized.[2–6] Previously, we have reported several series of transition metal–fullerene complexes that contain various phosphane ligands, such as $Ph_2PCH_2CH_2PPh_2$ (dppe),[7] 1,2-$(Ph_2P)_2C_6H_4$ (dppb),[8] DIOP,[9] $Ph_2PCH_2(CH_2OCH_2)_n\text{-}CH_2PPh_2$,[10] $[(\eta^5\text{-}Ph_2PC_5H_4)_2Fe]$ (dppf),[11] and $[(\eta^5\text{-}Ph_2PC_5H_4)_2Ru]$ (dppr).[12] Now, as a continuation of this research program, we report other types of transition metal–fullerene complexes that contain either the diphosphane ligand *trans*-1,1′-bis(diphenylphosphanyl)ethylene (dppet) or the tetraphosphane ligand *N*,*N*,*N*′,*N*′-tetra(diphenylphosphanylmethyl)ethylene diamine (dppeda). It should be noted that although some of the dppet-containing complexes were preliminarily reported in our recent communication,[13] this paper systematically describes both the dppet- and dppeda-containing fullerene complexes and includes new results, such as the crystal structure of $[(\eta^2\text{-}C_{60}Pd)(\eta^2\text{-}C_{60}Pt)(dppet)_2]$, the electrochemical properties of $[(\eta^2\text{-}C_{60}Pd)(dppet)]_2$ and $[(\eta^2\text{-}C_{60}Pd)(\eta^2\text{-}C_{60}Pt)(dppet)_2]$, as well as the synthesis and characterization of the dppet-containing [70]fullerene complexes $[(\eta^2\text{-}C_{60}Pd)(\eta^2\text{-}C_{70}Pd)(dppet)_2]$ and $[(\eta^2\text{-}C_{70}Pd)(dppet)]_2$ along with the dppeda-containing [60]fullerene complexes $[(\eta^2\text{-}C_{60}M)(dppeda)]$ and $[(\eta^2\text{-}C_{60}M)_2(dppeda)]$ (M = Pt, Pd).

[a] Department of Chemistry, State Key Laboratory of Elemento-Organic Chemistry, Nankai University,
Tianjin 300071, China
Fax: +86-22-2350-4853
E-mail: lcsong@nankai.edu.cn
[b] Dipartimento di Chimica dell' Università di Siena,
Via Aldo Moro, 53100 Siena, Italy

## Results and Discussion

### Synthesis and Characterization of Dppet-Containing Fullerene Complexes

A toluene solution of $C_{60}$ was treated with $[M(dba)_2]$ or $[Pt_2(dba)_3]$ (M = Pt, Pd; dba = dibenzylideneacetone) and dppet in a 1:1:2 molar ratio at room temperature to give the metallacyclopropa[60]fullerene complex $[(\eta^2\text{-}C_{60}Pt)(dppet)_2]$ (**1**) in 35–58% yield and complex $[(\eta^2\text{-}C_{60}Pd)(dppet)_2]$ (**2**) in 75% yield. The two different starting materials $[Pt(dba)_2]$ and $[Pt_2(dba)_3]$ can be used interchangeably, although $[Pt_2(dba)_3]$ is much more reactive than $[Pt(dba)_2]$, as judged by the rapidity of the development of the green color characteristic of product **1**, and when used in a slight excess this starting material gives the highest yield. Similarly, a toluene solution of $C_{60}$ was treated with $[Pt(dba)_2]$ and dppet in a 1:1:2 ratio or with $[Pd(dba)_2]$ and dppet in a 1:2:1 molar ratio at room temperature to give the homodinuclear bismetallacyclopropa[60]fullerene complexes $[(\eta^2\text{-}C_{60}M)(dppet)]_2$ (M = Pt **3**, Pd **4**) in 82% and 92% yields, respectively (Scheme 1).

We further found that treatment of a toluene solution of $C_{60}$ with $[Pd(dba)_2]$ and dppet in a 1:1:2 molar ratio at room temperature, followed by treatment with a mixture of $C_{60}$ and $[Pt_2(dba)_3]$ in a 2:1 molar ratio or $C_{70}$ and [Pd-

 © 2006 Wiley-VCH Verlag GmbH & Co. KGaA, Weinheim 

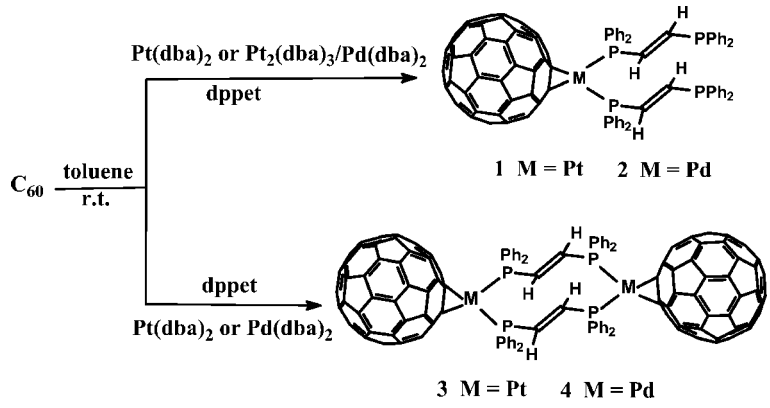


Scheme 1.

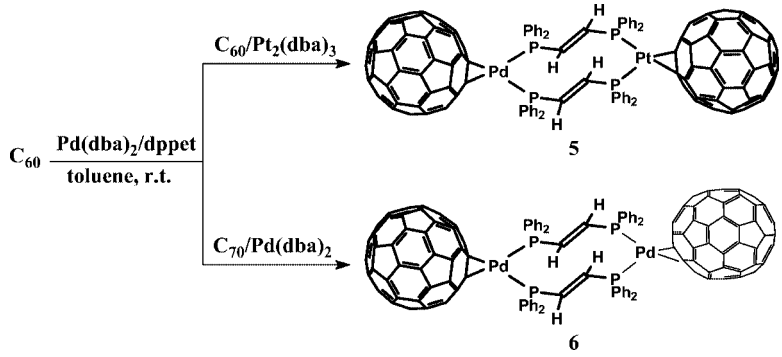


Scheme 2.

$(dba)_2$] in a 1:1 molar ratio, gave the heterodinuclear bismetallacyclopropa[60]fullerene complex [($\eta^2$-$C_{60}$Pd)($\eta^2$-$C_{60}$Pt)(dppet)$_2$] (**5**) and the homodinuclear bismetallacyclopropa[60]/[70]fullerene complex [($\eta^2$-$C_{60}$Pd)($\eta^2$-$C_{70}$Pd)(dppet)$_2$] (**6**) in 65% and 37% yields, respectively (Scheme 2).

Similarly, the homodinuclear bismetallacyclopropa[70]fullerene complex [($\eta^2$-$C_{70}$Pd)(dppet)]$_2$ (**7**) could be prepared by treatment of $C_{70}$ in toluene with [Pd(dba)$_2$] and dppet in a 1:1:2 molar ratio at room temperature in 44% yield (Scheme 3).

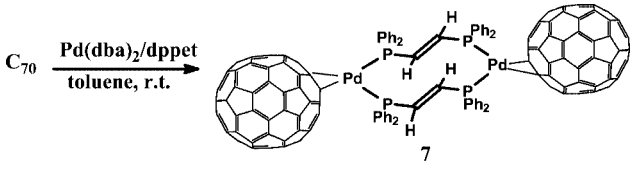


Scheme 3.

Interestingly, the above-mentioned dinuclear bisfullerene complexes **3**–**6** can be also prepared by another method in which the [60]fullerene-derived diphosphanes **1** and **2** were used as starting materials. Thus, treatment of **1** in toluene with $C_{60}$ and [Pt(dba)$_2$] in a 1:1:1 molar ratio at room temperature gave **3** in 59% yield, whereas treatment of **2** with $C_{60}$ and [Pd(dba)$_2$] under similar conditions gave **4** in 53% yield. In addition, while **2** reacts with $C_{60}$ and [Pt(dba)$_2$] in toluene at room temperature to produce the heterodinuclear bisfullerene **5** in 55% yield, the reaction of **2** with $C_{70}$ and [Pd(dba)$_2$] under similar conditions gives rise to the homodinuclear bisfullerene complex **6** in 38% yield.

It follows that the possible pathways for the formation of **1**–**7** might be as suggested in Scheme 4. That is: (i) **1** and **2** are produced by $\eta^1$-coordination of two molecules of dppet with the polymeric species [$C_{60}M_x$] (M = Pt, Pd; $x$ = 1) formed in situ from $C_{60}$ and [Pd(dba)$_2$], [Pt(dba)$_2$], or [$Pt_2$(dba)$_3$],[14,15] (ii) subsequent chelation of **1** as a bidentate ligand with [$C_{60}Pt_x$] gives **3**, (iii) subsequent chelation of **2** with [$C_{60}M_x$] affords **4** and **5**, and (iv) subsequent chelation of **2** with the polymeric species [$C_{70}Pd_x$] formed in situ from $C_{70}$ and [Pd(dba)$_2$][14,15] produces **6**. Apparently, **7** can be formed through similar elementary steps to those indicated in Scheme 4.

The dppet-containing fullerene complexes **1**–**7** were characterized by elemental analysis and spectroscopic methods. For example, the IR spectra of **1**–**5** display four absorption bands in the range 1434–513 cm$^{-1}$ for their $C_{60}$ cores,[16] whereas the IR spectrum of **6** exhibits nine absorption bands in the region 1433–456 cm$^{-1}$ for its $C_{60}$ and $C_{70}$ spheres,[16] and that of **7** shows nine absorption bands in the range 1432–457 cm$^{-1}$[16] for its $C_{70}$ cores. In addition, the $^{31}$P NMR spectra of **1** and **2** show one singlet and one triplet or two singlets at $\delta \approx -7$ and 20 ppm for their two identical uncoordinated P atoms and two identical coordinated P atoms, respectively, whereas the spectra of **3**–**7** display the corresponding signals for their four coordinated P atoms. That the chemical shifts of the coordinated P atoms

 © 2006 Wiley-VCH Verlag GmbH & Co. KGaA, Weinheim 

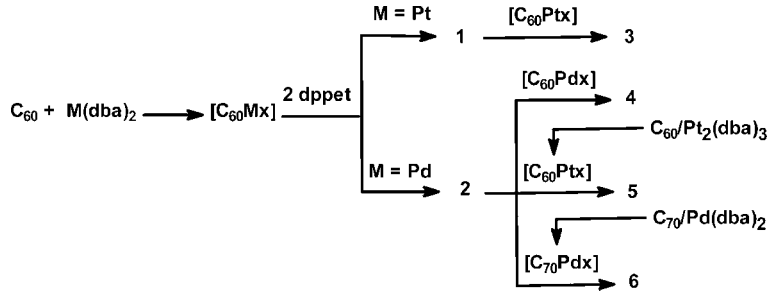


Scheme 4.

lie at much lower field relative to the corresponding free P atoms can be ascribed to transfer of electron density from the P atom to the metal center, which is consistent with other phosphane-coordinated fullerene complexes.[1,9,12] It is well-known that in single addition of a transition metal to fullerenes the $C_{60}$ ligand is bonded to the metal center in an $\eta^2$-fashion through its single C–C 6:6 bond, whereas the $C_{70}$ ligand is preferentially bonded to a metal center in an $\eta^2$-manner through one Ca–Cb 6:6 bond at the poles of the $C_{70}$ ligand.[3] Therefore, the structures of **1**–**7** are most likely as shown in Schemes 1, 2, and 3. The structures of **4** and **5** were unequivocally confirmed by X-ray crystal diffraction analysis.

### Crystal Structures of 4 and 5

The molecular structures of **4** and **5**, as determined by X-ray diffraction techniques, are presented in Figures 1 and 2, respectively; selected bond lengths and angles are given in Tables 1 and 2, respectively. The X-ray diffraction analysis

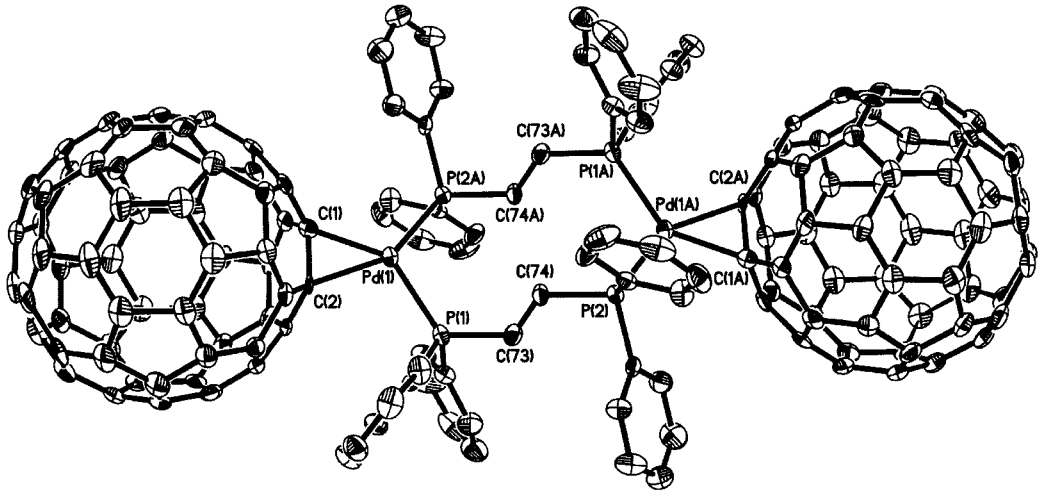


Figure 1. ORTEP drawing of **4** (30% thermal ellipsoids).

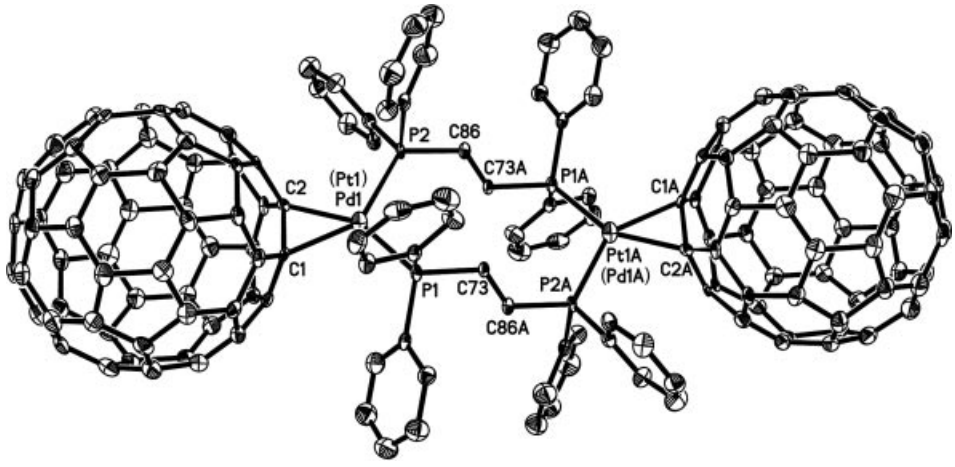


Figure 2. ORTEP drawing of **5** (30% thermal ellipsoids).

 © 2006 Wiley-VCH Verlag GmbH & Co. KGaA, Weinheim 

revealed that **4** (Figure 1) and **5** (Figure 2) are isostructural; they both consist of two $C_{60}$ spheres that are ligated to two metal centers of a ten-membered metallacycle in which two *trans*-dppet ligands are coordinated to Pd/Pd or Pd/Pt metal centers, respectively. It is worth pointing out that the Pd/Pt atoms in the structure of **5** are 50% disordered and therefore the geometric parameters associated with Pd/Pt atoms cannot be distinguished. In addition, the solvent molecules $C_6H_5Cl$ and $C_6H_5Me$ present in the crystal of **5** are also disordered, which might be responsible for the relatively high *R* value for the structure of **5**. Interestingly, **4** and **5** are the first structurally characterized group 10 metal-containing homo- and heterodinuclear fullerene complexes. The fullerene center-to-center separations of 16.869 Å for **4** and 16.807 Å for **5** are close to that of 16.559 Å in the dinuclear $Ir_2$ complex. However, the nonbonded metal-to-metal distances (6.83 Å for **4** and 6.82 Å for **5**) are much shorter than the corresponding intermetallic distance of 8.104 Å in the $Ir_2$ complex.[17] The two C–C double bonds [C(73)–C(74) = C(73A)–C(74A) = 1.290(14) Å for **4** and C(73)–C(86A) = C(73A)–C(86) = 1.26(2) Å for **5**] are slightly shorter than the common C–C double bond (1.34 Å). Each of the zero-valent metal centers has a square-planar geometry. For example, all the five atoms Pd(1), C(1), C(2), P(1), and P(2A) in **4** and Pt(1A), C(1A), C(2A), P(1A), and P(2A) in **5** are nearly coplanar, with a mean deviation of 0.0528 and 0.0483 Å, respectively. The $\eta^2$-coordinated 6:6 bonds [C(1)–C(2) = 1.473(14) Å for **4** and C(1)–C(2) = 1.50 (2) Å for **5**] are obviously longer than the other 58 uncoordinated 6:6 bonds in each $C_{60}$ sphere due to the metal-to-$C_{60}$ π back-donation.[5]

Table 1. Selected bond lengths [Å] and angles [°] for **4**.

| | | | |
|---|---|---|---|
| Pd(1)–C(1) | 2.137(11) | P(1)–C(73) | 1.826(11) |
| Pd(1)–C(2) | 2.130(9) | C(73)–C(74) | 1.290(14) |
| Pd(1)–P(1) | 2.326(3) | P(2)–C(74) | 1.820(10) |
| Pd(1)–P(2A) | 2.323(3) | C(1)–C(2) | 1.473(14) |
| C(2)–Pd(1)–C(1) | 40.4(4) | P(2A)–Pd(1)–P(1) | 109.06(10) |
| C(2)–Pd(1)–P(2A) | 147.0(3) | C(73)–P(1)–Pd(1) | 123.9(4) |
| C(1)–Pd(1)–P(2A) | 107.4(3) | C(74)–P(2)–Pd(1A) | 118.4(4) |
| C(2)–Pd(1)–P(1) | 101.8(3) | C(2)–C(1)–Pd(1) | 69.5(5) |
| C(1)–Pd(1)–P(1) | 141.9(3) | C(1)–C(2)–Pd(1) | 70.1(6) |

Table 2. Selected bond lengths [Å] and angles [°] for **5**.

| | | | |
|---|---|---|---|
| Pd(1)–C(1) | 2.169(17) | P(1)–C(73) | 1.822(17) |
| Pd(1)–C(2) | 2.115(17) | C(73)–C(86A) | 1.26(2) |
| Pd(1)–P(1) | 2.311(5) | C(86)–P(2) | 1.846(18) |
| Pd(1)–P(2) | 2.309(5) | C(1)–C(2) | 1.50(2) |
| C(2)–Pd(1)–C(1) | 41.1(6) | P(2)–Pd(1)–P(1) | 108.99(17) |
| C(2)–Pd(1)–P(2) | 101.7(4) | C(73)–P(1)–Pd(1) | 118.4(6) |
| C(1)–Pd(1)–P(2) | 142.5(4) | C(86)–P(2)–Pd(1) | 124.0(6) |
| C(2)–Pd(1)–P(1) | 147.6(4) | C(2)–C(1)–Pd(1) | 67.5(9) |
| C(1)–Pd(1)–P(1) | 107.1(4) | C(1)–C(2)–Pd(1) | 71.4(9) |

## Synthesis and Characterization of Dppeda-Containing Fullerene Complexes

More interestingly, the first examples of a tetraphosphane ligand-containing metallacyclopropafullerene complexes [($\eta^2$-$C_{60}$M)(dppeda)] (M = Pt **8**, Pd **9**) and bismetallacyclopropafullerene complexes [($\eta^2$-$C_{60}$M)$_2$(dppeda)] (M = Pt **10**, Pd **11**) were synthesized by treatment of a toluene solution of $C_{60}$ with [$Pt_2(dba)_3$] and the tetraphosphane ligand dppeda or with [$Pd(dba)_2$] and dppeda in 1:1:1 molar ratio at room temperature in ca. 26% and 45% yields, respectively (Scheme 5).

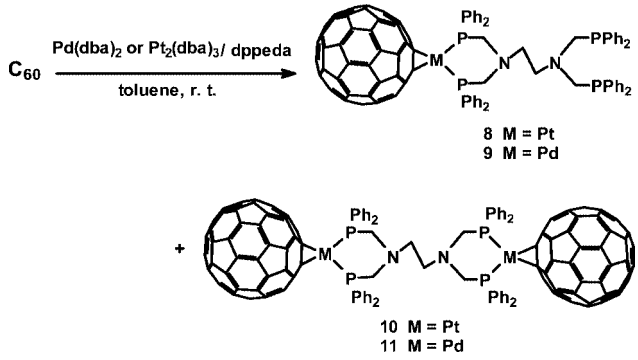


Scheme 5.

It is apparent that complexes **8**–**11** are produced through similar pathways to those mentioned above for the production of **1**–**7**. Complexes **8**–**11** are air-stable, green solids, which were characterized by elemental analysis and IR, $^1$H NMR, and $^{31}$P NMR spectroscopy. For example, the IR spectra of **8**–**11** show four absorption bands in the range 1434–526 cm$^{-1}$ characteristic of their $C_{60}$ spheres.[16] In addition, the $^{31}$P NMR spectra of **8** and **9** display one singlet and one triplet or two singlets at $\delta \approx -28$ and 6 ppm for their two identical uncoordinated P atoms and two identical coordinated P atoms, respectively, whereas the spectra of **10** and **11** exhibit one triplet and one singlet at $\delta \approx 6$ ppm for their four identical coordinated P atoms. In fact, the $^{31}$P NMR behavior of the tetraphosphane-containing complexes **8**–**11** is very similar to that of the diphosphane-containing complexes **1**–**7**, as well as that of the other phosphane-containing fullerene complexes.[1,9,12] Interestingly, while the $^1$H NMR spectrum of the free ligand dppeda shows one singlet at $\delta = 3.50$ ppm for its four $CH_2$ groups attached to P atoms and one singlet at $\delta = 2.88$ ppm for its two $CH_2$ groups attached to N atoms, the spectra of **8**–**11** display two broad singlets or multiplets at $\delta = 3.75$–3.35 ppm for their $CH_2$ groups attached to P atoms and one multiplet at $\delta = 2.45$–2.28 ppm for their $CH_2$ groups bound to N atoms.

## Electrochemical Study of 4 and 5

In order to ascertain if the presence of the p-π conjugated P–C=C–P structural units in the dppet ligands of the dinuclear bisfullerenes **3**–**7** could trigger inter-fullerene electronic communication, we examined the electrochemical behavior of the representative complexes **4** and **5**. Figure 3 shows the cyclic voltammetric profiles exhibited by complexes **4** and **5** in 1,2-dichlorobenzene solution.[18]

 © 2006 Wiley-VCH Verlag GmbH & Co. KGaA, Weinheim 

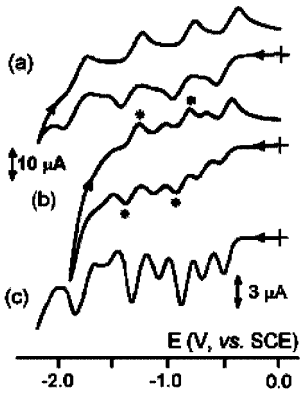


Figure 3. Cyclic voltammograms recorded at a platinum electrode in 1,2-$Cl_2C_6H_4$ solutions of (a) complex **4** ($1.1 \times 10^{-3}$ M) and (b) complex **5** ($1.1 \times 10^{-3}$ M). (c) Osteryoung square-wave voltammogram of **5** ($1.1 \times 10^{-3}$ M). $n$-$Bu_4NClO_4$ (0.2 M) supporting electrolyte. Scan rates: (a, b) 0.2 V $s^{-1}$; (c) 0.1 V $s^{-1}$.

As Figure 3a illustrates, the homodinuclear complex **4** exhibits four fullerene-centered reductions possessing features of chemical reversibility on the cyclic voltammetric timescale ($E°'$ = –0.48, –0.87, –1.34, and –1.85 V, vs. SCE). Controlled potential coulometry ($E_w$ = –0.65 V) proved that the first cathodic process involves two electrons per molecule, thus indicating that the stepwise addition of four electrons to each fullerene moiety proceeds simultaneously. As happens for most bisfullerene systems,[19] this suggests that no mutual electronic interaction exists between the two metallofullerene subunits. It should be noted that the mentioned processes take place at potential values essentially coincident with those of free fullerene. Cyclic voltammetry in chlorobenzene solution affords a quite similar profile ($E°'$ = –0.52, –0.93, and –1.46 V vs. SCE), but in such a solvent the difference with respect to free fullerene is better defined ($E°'$ = –0.49, –0.86, and –1.35 V, vs. SCE). Therefore, since the instantaneous complete decomposition of the original complex can be reasonably ruled out − the original green color of the solution ($\lambda_{max}$ = 602 and 656 nm) does not change with time − such an uncommon result can be likely accounted for by assuming that the cathodic shift induced by the $\eta^2$-coordinated C–C double bond of the [60]-fullerene, which is directly linked to the coordinating power of the metal ion, is just compensated by the anodic shift caused by the electron-withdrawing effects of the phosphane substituents.[19]

As Figure 3 (b) shows, a different reduction pattern is displayed by the heterodinuclear complex **5**. In fact, the sequential reductions appearing in correspondence of the preceding profile ($E°'$ = –0.49, –0.88, and –1.33 V, respectively) are followed by an interposed series of further cathodic steps ($E°'$ = –0.71, –1.08, and –1.6 V, respectively). Coulometric measurements showed that the first two processes involve one-electron additions (exhaustive electrolysis at $E_w$ = –0.75 V consumed 1.8 electrons per molecule). The fact that the height of the starred peak-systems is somewhat higher than that of the respective interposed peak-systems (as better seen from the square-wave voltammogram shown in Figure 3c) has to be attributed to slow release of free fullerene (two mols per mol of decomposed complex) following the concomitant addition of the first electron to each metallofullerene subunit, which is reflected in the high peak-height of the return peak associated with the first step. It seems that the appearance of separate sequential reductions in **5** has to be attributed to the higher coordination ability of Pt with respect to Pd towards fullerene, which renders the two metallofullerene subunits inequivalent, rather than the eventual presence of intramolecular electronic communication, as, in contrast, happens in [$Rh_6$-$(CO)_5$(dppm)(CNR)($\mu_3$-$\eta^2$,$\eta^2$,$\eta^2$-$C_{60}$)$_2$] (dppm = diphenylphosphanylmethane; R = $CH_2C_6H_5$).[20]

It follows that complexes **4** and **5** display no intramolecular electronic communication even though two p-π-conjugated P–C=C–P structural units are present in the sandwiched metallacycle. However, it can be expected that bismetallofullerenes having electronic communication could be obtained by variation of the spacer between the two metallofullerene subunits.

In summary, we have prepared the first diphosphane (dppet)- and tetraphosphane (dppeda)-containing transition metal–fullerene complexes **1**–**11** by simple and convenient synthetic methods in satisfactory yields. While complexes **1**, **2**, **8**, and **9** are diphosphane ligands with fullerene cores, complexes **3**–**7**, **10**, and **11** are bisfullerene complexes in which either a 10-membered metallacycle or two six-membered metallacycles are sandwiched between two fullerene spheres. Possible pathways for production of complexes **1**–**11** have been preliminarily proposed, and the crystal structures of **4** and **5** along with their electrochemical properties have been determined by X-ray diffraction and cyclic voltammetry. It is worth pointing out that in view of the widespread uses of phosphorus-donor ligands in transition metal chemistry,[21] the fullerene-containing diphosphane ligands **1**, **2**, **8**, and **9** can be expected to play an important role in the development of transition metal and fullerene chemistry.

## Experimental Section

**General:** All reactions were carried out under highly purified nitrogen using standard Schlenk or vacuum-line techniques. Toluene and hexane were distilled from Na/benzophenone ketyl. Other solvents were bubbled with nitrogen for at least 15 min before use. [$Pd(dba)_2$],[22] [$Pt(dba)_2$],[23] [$Pt_2(dba)_3$],[23] and [$(Ph_2PCH_2)_2NCH_2]_2$ (dppeda)[24] were prepared according to literature methods. $C_{60}$ (99.9%) and *trans*-$Ph_2PCH$=$CHPPh_2$ (dppet) were available commercially. $^1H$ and $^{31}P$ NMR spectra were recorded with a Bruker Avance 300 spectrometer, whereas IR spectra were taken on a Bio-Rad FTS 135 spectrophotometer. Elemental analysis was performed with an Elementar Vario EL analyzer. Melting points were determined on a Yanaco MP-500 apparatus.

**Preparation of [($\eta^2$-$C_{60}$Pt)(dppet)$_2$] (1):** A 100-mL, three-necked flask equipped with a magnetic stir-bar, a rubber septum, and a nitrogen inlet tube was charged with $C_{60}$ (0.072 g, 0.10 mmol), [$Pt(dba)_2$] (0.066 g, 0.10 mmol) or [$Pt_2(dba)_3$] (0.056 g, 0.10 mmol), and toluene (50 mL) to form a brown solution. *trans*-Dppet (0.078 g, 0.20 mmol) was added to this solution and then the mix-

 © 2006 Wiley-VCH Verlag GmbH & Co. KGaA, Weinheim 

ture was stirred at room temperature for 1.5 h. The resulting green mixture was filtered and the green filtrate was layered with 60 mL of hexane overnight to give a green precipitate. The precipitate was washed with hexane (2 × 5 mL) and diethyl ether (2 × 5 mL) sequentially, and then was dried in vacuo to afford 0.060 g (35%) of **1** from [Pt(dba)$_2$] or 0.098 g (58%) of **1** from [Pt$_2$(dba)$_3$] as a green solid. M.p. > 300 °C. $^1$H NMR (300 MHz, CS$_2$/CDCl$_3$): $\delta$ = 7.24–7.60 (m, 44 H, 8 C$_6$H$_5$ + 4 CH) ppm. $^{31}$P NMR (121.48 MHz, CS$_2$/CDCl$_3$, H$_3$PO$_4$): $\delta$ = –7.24 (s, 2 P, 2 PPh$_2$), 19.88 (t, $J_{Pt,P}$ = 3682 Hz, 2 P, 2 PPt) ppm. IR (KBr disk): $\tilde{\nu}$ = 1434 (s), 1184 (m), 577 (m), 524 (vs) (C$_{60}$), 1571 (m), 967 (m) (C=C) cm$^{-1}$. $C_{112}H_{44}P_4Pt$ (1708.6): calcd. C 78.73, H 2.60; found C 78.75, H 2.41.

**Preparation of [($\eta^2$-C$_{60}$Pd)(dppet)$_2$] (2):** The same procedure as that for the preparation of **1** was followed, but [Pd(dba)$_2$] (0.057 g, 0.10 mmol) was used instead of [Pt(dba)$_2$] or [Pt$_2$(dba)$_3$] to give 0.123 g (75%) of **2** as a green solid. M.p. > 300 °C. $^1$H NMR (300 MHz, CS$_2$/CDCl$_3$): $\delta$ = 7.09–7.63 (m, 44 H, 8 C$_6$H$_5$ + 4 CH) ppm. $^{31}$P NMR (121.48 MHz, CS$_2$/CDCl$_3$, H$_3$PO$_4$): $\delta$ = –7.48 (s, 2 P, 2 PPh$_2$), 20.21 (s, 2 P, 2 PPd) ppm. IR (KBr disk): $\tilde{\nu}$ = 1434 (s), 1183 (m), 578 (m), 513 (vs) (C$_{60}$), 1570 (m), 966 (m) (C=C) cm$^{-1}$. $C_{112}H_{44}P_4Pd$ (1619.9): calcd. C 83.04, H 2.74; found C 82.87, H 2.75.

**Preparation of [($\eta^2$-C$_{60}$Pt)(dppet)]$_2$ (3). Method (i):** The flask described above was charged with C$_{60}$ (0.072 g, 0.10 mmol), [Pt(dba)$_2$] (0.066 g, 0.10 mmol), *trans*-dppet (0.078 g, 0.20 mmol), and toluene (50 mL). The mixture was stirred at room temperature for 5 h to give a green precipitate. The precipitate was washed with toluene (2 × 10 mL), hexane (2 × 10 mL), and diethyl ether (2 × 10 mL), and finally dried in vacuo to afford 0.108 g (82%) of **3** as a dark-green solid. M.p. > 300 °C. $^1$H NMR (300 MHz, CS$_2$/CDCl$_3$): $\delta$ = 6.90–7.60 (m, 44 H, 8 C$_6$H$_5$ + 4 CH) ppm. $^{31}$P NMR (121.48 MHz, CS$_2$/CDCl$_3$, H$_3$PO$_4$): $\delta$ = 19.71 (t, $J_{Pt,P}$ = 3794 Hz, 4 P) ppm. IR (KBr disk): $\tilde{\nu}$ = 1434 (s), 1183 (m), 577 (m), 524 (vs) (C$_{60}$), 1571 (m), 969 (m) (C=C) cm$^{-1}$. $C_{172}H_{44}P_4Pt_2$ (2624.3): calcd. C 78.72, H 1.69; found C 78.71, H 1.70.

**Method (ii):** A mixture of diphosphane **1** (0.086 g, 0.05 mmol), C$_{60}$ (0.036 g, 0.05 mmol), and [Pt(dba)$_2$] (0.034 g, 0.05 mmol) in toluene (20 mL) was stirred at room temperature for 5 h to give a precipitate. The same workup as that in method (i) gave 0.078 g (59%) of **3**.

**Preparation of [($\eta^2$-C$_{60}$Pd)(dppet)]$_2$ (4). Method (i):** The flask described above was charged with C$_{60}$ (0.072 g, 0.10 mmol), [Pd(dba)$_2$] (0.114 g, 0.20 mmol), *trans*-dppet (0.039 g, 0.10 mmol), and toluene (50 mL). The mixture was stirred at room temperature for 5 h. The resulting mixture was filtered to give a green precipitate, which was purified by the same method used above for **3** to afford 0.112 g (92%) of **4** as a dark-green solid. M.p. > 300 °C. $^1$H NMR (300 MHz, CS$_2$/CDCl$_3$): $\delta$ = 7.20–7.66 (m, 44 H, 8 C$_6$H$_5$ + 4 CH) ppm. $^{31}$P NMR (121.48 MHz, CS$_2$/CDCl$_3$, H$_3$PO$_4$): $\delta$ = 20.22 (s, 4 P) ppm. IR (KBr disk): $\tilde{\nu}$ = 1432 (m), 1183 (m), 577 (m), 524 (vs) (C$_{60}$), 1571 (m), 964 (m) (C=C) cm$^{-1}$. $C_{172}H_{44}P_4Pd_2$ (2447.0): calcd. C 84.43, H 1.81; found C 84.16, H 2.00.

**Method (ii):** A mixture of diphosphane **2** (0.080 g, 0.05 mmol), C$_{60}$ (0.036 g, 0.05 mmol), and [Pd(dba)$_2$] (0.029 g, 0.05 mmol) in toluene (20 mL) was stirred at room temperature for 5 h to give a precipitate. The same workup as that in method (i) produced 0.064 g (53%) of **4**.

**Preparation of [($\eta^2$-C$_{60}$Pd)($\eta^2$-C$_{60}$Pt)(dppet)$_2$] (5). Method (i):** A mixture of C$_{60}$ (0.036 g, 0.05 mmol), [Pd(dba)$_2$] (0.029 g, 0.05 mmol), *trans*-dppet (0.039 g, 0.10 mmol), and toluene (25 mL) was stirred at room temperature for 1 h to give a green solution. C$_{60}$ (0.036 g, 0.05 mmol) and [Pt$_2$(dba)$_3$] (0.028 g, 0.025 mmol) were added to this solution. The new mixture was stirred at room temperature for 5 h to give a green precipitate. The precipitate was purified by the same method used for **3** to give 0.085 g (65%) of **5** as a green solid. M.p. > 300 °C. $^1$H NMR (300 MHz, CS$_2$/CDCl$_3$): $\delta$ = 7.08–7.60 (m, 44 H, 8 C$_6$H$_5$ + 4 CH) ppm. $^{31}$P NMR (121.48 MHz, CS$_2$/CDCl$_3$, H$_3$PO$_4$): $\delta$ = 19.79 (s, 2 P, 2 PPd), 20.12 (t, $J_{Pt,P}$ = 3848 Hz, 2 P, 2 PPt) ppm. IR (KBr disk): $\tilde{\nu}$ = 1434 (s), 1183 (m), 579 (m), 523 (vs) (C$_{60}$), 1571 (m), 967 (m) (C=C) cm$^{-1}$. $C_{172}H_{44}P_4PdPt$ (2535.6): calcd. C 81.47, H 1.75; found C 81.40, H 2.00.

**Method (ii):** A mixture of diphosphane **2** (0.080 g, 0.05 mmol), C$_{60}$ (0.036 g, 0.05 mmol), and [Pt(dba)$_2$] (0.034 g, 0.05 mmol) in toluene (20 mL) was stirred at room temperature for 5 h to give a precipitate. The same workup as that in method (i) afforded 0.070 g (55%) of **5**.

**Preparation of [($\eta^2$-C$_{60}$Pd)($\eta^2$-C$_{70}$Pd)(dppet)$_2$] (6). Method (i):** A mixture of C$_{60}$ (0.036 g, 0.05 mmol), [Pd(dba)$_2$] (0.029 g, 0.05 mmol), and *trans*-dppet (0.039 g, 0.10 mmol) in toluene (25 mL) was stirred at room temperature for 1 h to give a green solution. C$_{70}$ (0.042 g, 0.05 mmol) and [Pd(dba)$_2$] (0.029 g, 0.05 mmol) were then added to this solution. The new mixture was stirred at room temperature for 5 h to give a green precipitate. The precipitate was purified by the same method as that utilized for **3** to give 0.048 g (37%) of **6** as a brown solid. M.p. > 300 °C. $^1$H NMR (300 MHz, CS$_2$/CDCl$_3$): $\delta$ = 7.09–7.54 (m, 44 H, 8 C$_6$H$_5$ + 4 CH) ppm. $^{31}$P NMR (121.48 MHz, CS$_2$/CDCl$_3$, H$_3$PO$_4$): $\delta$ = 25.64–27.50 (m, 4 P) ppm. IR (KBr disk): $\tilde{\nu}$ = 1433 (s), 1183 (m), 576 (m), 510 (vs) (C$_{60}$), 1130 (w), 1097 (m), 793 (m), 673 (m), 640 (w), 456 (s) (C$_{70}$), 1569 (w), 967 (m) (C=C) cm$^{-1}$. $C_{182}H_{44}P_4Pd_2$ (2567.09): calcd. C 85.15, H 1.72; found C 84.95, H 1.88.

**Method (ii):** A mixture of diphosphane **2** (0.080 g, 0.05 mmol), C$_{70}$ (0.042 g, 0.05 mmol), and [Pd(dba)$_2$] (0.029 g, 0.05 mmol) in toluene (20 mL) was stirred at room temperature for 5 h. The same workup as that in method (i) afforded 0.049 g (38%) of **6**.

**Preparation of [($\eta^2$-C$_{70}$Pd)(dppet)]$_2$ (7):** A mixture of C$_{70}$ (0.042 g, 0.05 mmol), [Pd(dba)$_2$] (0.029 g, 0.05 mmol), and *trans*-dppet (0.039 g, 0.10 mmol) in toluene (25 mL) was stirred at room temperature for 1.5 h. The resulting mixture was filtered to give a brown precipitate, which was purified by the method used for purification of **3** to afford 0.023 g (44%) of **7** as a dark-green solid. M.p. > 300 °C. $^1$H NMR (300 MHz, CS$_2$/CDCl$_3$): $\delta$ = 7.15–7.67 (m, 44 H, 8 C$_6$H$_5$ + 4 CH) ppm. $^{31}$P NMR (121.48 MHz, CS$_2$/CDCl$_3$, H$_3$PO$_4$): $\delta$ = 21.15, 22.77 (2s, 4 P) ppm. IR (KBr disk): $\tilde{\nu}$ = 1432 (vs), 1129 (w), 1097 (m), 794 (m), 673 (s), 641 (w), 577 (m), 534 (s), 457 (s) (C$_{70}$), 1567 (m), 967 (m) (C=C) cm$^{-1}$. $C_{192}H_{44}P_4Pd_2$ (2687.2): calcd. C 85.82, H 1.65; found C 85.60, H 1.73.

**Preparation of [($\eta^2$-C$_{60}$Pt)(dppeda)] (8) and [($\eta^2$-C$_{60}$Pt)$_2$(dppeda)] (10):** A brown mixture of C$_{60}$ (0.036 g, 0.05 mmol) and [Pt$_2$(dba)$_3$] (0.028 g, 0.05 mmol) in toluene (25 mL) was stirred at room temperature for 15 min, and then dppeda (0.043 g, 0.05 mmol) was added to cause an immediate color change from brown to green. The green mixture was stirred at room temperature for 5 h and was then filtered to give a green filtrate and a green precipitate. Whereas the green filtrate was treated by a procedure similar to that used in the preparation of **1** to afford 0.025 g (28%) of **8**, the precipitate was purified by the method used for purification of **3** to afford 0.033 g (49%) of **10**.

**8:** Green solid. M.p. 300 °C (dec.). $^1$H NMR (300 MHz, CS$_2$/CDCl$_3$): $\delta$ = 2.37–2.45 (m, 4 H, NCH$_2$CH$_2$N), 3.35–3.47, 3.70–3.75 (2m, 8 H, 4 CH$_2$P), 7.27–7.74 (m, 40 H, 8 C$_6$H$_5$) ppm. $^{31}$P NMR

 © 2006 Wiley-VCH Verlag GmbH & Co. KGaA, Weinheim 

(121.48 MHz, $CS_2/CDCl_3$, $H_3PO_4$): $\delta$ = –27.68 (s, 2 P, 2 $PPh_2$), 6.67 (t, $J_{Pt,P}$ = 3575 Hz, 2 P, 2 PPt) ppm. IR (KBr disk): $\tilde{\nu}$ = 1434 (s), 1184 (m), 577 (m), 526 (vs) ($C_{60}$) $cm^{-1}$. $C_{114}H_{52}N_2P_4Pt$ (1768.7): calcd. C 77.42, H 2.96, N 1.58; found C 77.49, H 2.77, N 1.72.

**10:** Green solid. M.p. 290 °C (dec.). $^1H$ NMR (300 MHz, $CS_2/CDCl_3$): $\delta$ = 2.28–2.33 (m, 4 H, $NCH_2CH_2N$), 3.39–3.42, 3.71–3.75 (2m, 8 H, 4 $CH_2P$), 7.23–7.59 (m, 40 H, 8 $C_6H_5$) ppm. $^{31}P$ NMR (121.48 MHz, $CS_2/CDCl_3$): $\delta$ = 6.66 (t, $J_{Pt,P}$ = 3571 Hz, 4 P) ppm. IR (KBr disk): $\tilde{\nu}$ = 1434 (s), 1184 (m), 577 (m), 526 (vs) ($C_{60}$) $cm^{-1}$. $C_{174}H_{52}N_2P_4Pt_2$ (2684.4): calcd. C 77.85, H 1.95, N 1.04; found C 77.75, H 2.04, N 1.11.

**Preparation of [($\eta^2$-$C_{60}$Pd)(dppeda)] (9) and [($\eta^2$-$C_{60}$Pd)$_2$(dppeda)] (11):** Similar to the preparation of **8** and **10**, 0.021 g (25%) of **9** and 0.027 g (43%) of **11** were prepared from $C_{60}$ (0.036 g, 0.05 mmol), [Pd(dba)$_2$] (0.029 g, 0.05 mmol), dppeda (0.043 g, 0.05 mmol), and toluene (20 mL).

**9:** Green solid. M.p. 295 °C (dec.). $^1H$ NMR (300 MHz, $CS_2/CDCl_3$): $\delta$ = 2.30–2.34 (m, 4 H, $NCH_2CH_2N$), 3.54, 3.71 (2 br.s, 8 H, 4 $CH_2P$), 7.13–7.63 (m, 40 H, 8 $C_6H_5$) ppm. $^{31}P$ NMR (121.48 MHz, $CS_2/CDCl_3$): $\delta$ = –28.01 (s, 2 P, 2 $PPh_2$), 5.39 (s, 2 P, 2 PPd) ppm. IR (KBr disk): $\tilde{\nu}$ = 1434 (s), 1184 (m), 578 (m), 526 (vs) ($C_{60}$) $cm^{-1}$. $C_{114}H_{52}N_2P_4Pd$ (1680.00): calcd. C 81.50, H 3.12, N 1.67; found C 81.70, H 3.16, N 1.69.

**11:** Green solid. M.p. 280 °C (dec.). $^1H$ NMR (300 MHz, $CS_2/CDCl_3$): $\delta$ = 2.29–2.34 (m, 4 H, $NCH_2CH_2N$), 3.57, 3.72 (2 br.s, 8 H, 4 $CH_2P$), 7.09–7.65 (m, 40 H, 8 $C_6H_5$) ppm. $^{31}P$ NMR (121.48 MHz, $CS_2/CDCl_3$): $\delta$ = 5.55 (s, 4 P) ppm. IR (KBr disk): $\tilde{\nu}$ = 1434 (s), 1183 (m), 576 (m), 527 (vs) ($C_{60}$) $cm^{-1}$. $C_{174}H_{52}N_2P_4Pd_2$ (2507.1): calcd. C 83.36, H 2.09, N 1.12. found C 83.25, H, 2.08, N 1.15.

Table 3. Crystal data and structural refinements details for **4** and **5**.

| | **4** | **5** |
|---|---|---|
| Empirical formula | $C_{172}H_{44}P_4Pd_2{\cdot}3C_6H_5Cl{\cdot}0.5C_6H_5Me{\cdot}H_2O$ | $C_{172}H_{44}P_4PdPt{\cdot}3C_6H_5Cl{\cdot}C_6H_5Me$ |
| Formula mass | 2848.49 | 2965.23 |
| Crystal system | monoclinic | monoclinic |
| Space group | $P2_1/c$ | $P2_1/n$ |
| $a$ [Å] | 13.9731(13) | 13.941(7) |
| $b$ [Å] | 13.6933(13) | 13.638(7) |
| $c$ [Å] | 34.671(3) | 32.772(16) |
| $\alpha$ [°] | 90 | 90 |
| $\beta$ [°] | 109.149(5) | 94.634(10) |
| $\gamma$ [°] | 90 | 90 |
| $V$ [Å$^3$] | 6266.8(10) | 6210(5) |
| $Z$ | 2 | 2 |
| $D_{calcd.}$ [g cm$^{-3}$] | 1.510 | 1.586 |
| $\mu$ (Mo-$K_\alpha$) [mm$^{-1}$] | 0.469 | 1.454 |
| Crystal size [mm] | 0.26×0.20×0.16 | 0.32×0.20×0.16 |
| $F$(000) | 2874 | 2968 |
| $2\theta_{max}$ [°] | 45.00 | 50.00 |
| Unique reflections | 18461 | 30013 |
| Observed reflections | 8160 | 10922 |
| Index ranges | $-10 \le h \le 15$<br>$-14 \le k \le 11$<br>$-37 \le l \le 36$ | $-15 \le h \le 16$<br>$-15 \le k \le 16$<br>$-38 \le l \le 35$ |
| Goodness of fit on $F^2$ | 1.082 | 1.139 |
| $R$ | 0.0803 | 0.1544 |
| $Rw$ | 0.1855 | 0.3186 |
| Largest diff. peak and hole [e Å$^{-3}$] | 0.886 and –0.804 | 1.086 and –1.513 |

**X-ray Crystal Structure Determinations of 4 and 5:** Single-crystals of **4** and **5** suitable for X-ray diffraction analyses were obtained by slow diffusion of hexane into their $C_6H_5Cl/CS_2$ solutions at room temperature. A single crystal of **4** or **5** was glued to a glass fiber and mounted on a Bruker SMART 1000 automated diffractometer. Data were collected using graphite-monochromated Mo-$K_\alpha$ radiation ($\lambda$ = 0.71073 Å) at room temperature in the $\omega$–$2\theta$ scanning mode. Absorption corrections were performed using the SADABS method. The structures were solved by direct methods using the SHELXS-97 program[25] and refined by full-matrix least-squares techniques (SHELXL-97)[26] on $F^2$. Hydrogen atoms were located by a geometric method. All calculations were performed on a Bruker Smart computer. Details of the crystals, data collections, and structure refinements are summarized in Table 3. The calculations were performed using the TEXSAN crystallographic software package.[27]

CCDC-232273 (for **4**) and -232274 (for **5**) contain the supplementary crystallographic data for this paper. These data can be obtained free of charge from The Cambridge Crystallographic Data Centre via www.ccdc.cam.ac.uk/data_request/cif.

## Acknowledgments

We are grateful to the National Natural Science Foundation of China for financial support of this work. P. Zanello gratefully acknowledges financial support from the Università di Siena (PAR, 2003).

[1] P. J. Fagan, J. C. Calabrese, B. Malone, *Science* **1991**, *252*, 1160–1161.
[2] K. Lee, H. Song, J. T. Park, *Acc. Chem. Res.* **2003**, *36*, 78–86.
[3] A. L. Balch, M. M. Olmstead, *Chem. Rev.* **1998**, *98*, 2123–2165.
[4] J. R. Bowser, *Adv. Organomet. Chem.* **1994**, *36*, 57–94.
[5] P. J. Fagan, J. C. Calabrese, B. Malone, *Acc. Chem. Res.* **1992**, *25*, 134–142.
[6] See, for example: a) A. L. Balch, V. J. Catalano, J. W. Lee, M. M. Olmstead, *J. Am. Chem. Soc.* **1992**, *114*, 5455–5457; b) M. Sawamura, H. Iikura, E. Nakamura, *J. Am. Chem. Soc.* **1996**, *118*, 12850–12851; c) A. L. Balch, J. W. Lee, M. M. Olmstead, *Angew. Chem. Int. Ed. Engl.* **1992**, *31*, 1356–1358; d) I. J. Mavunkal, Y. Chi, S.-M. Peng, G.-H. Lee, *Organometallics* **1995**, *14*, 4454–4456; e) H.-F. Hsu, J. R. Shapley, *J. Am. Chem. Soc.* **1996**, *118*, 9192–9193; f) H. Song, K. Lee, J. T. Park, M.-G. Chio, *Organometallics* **1998**, *17*, 4477–4483; g) K. Lee, F.-F. Hsu, J. R. Shapley, *Organometallics* **1997**, *16*, 3876–3877; h) G. Lee, Y.-J. Cho, B. K. Park, K. Lee, J. T. Park, *J. Am. Chem. Soc.* **2003**, *125*, 13920–13921.
[7] L.-C. Song, Y.-H. Zhu, Q.-M. Hu, *Polyhedron* **1998**, *17*, 469–473.
[8] L.-C. Song, J.-T. Liu, Q.-M. Hu, L.-H. Weng, *Organometallics* **2000**, *19*, 1643–1647.
[9] L.-C. Song, P.-C. Liu, J.-T. Liu, F.-H. Su, G.-F. Wang, Q.-M. Hu, P. Zanello, F. Laschi, M. Fontani, *Eur. J. Inorg. Chem.* **2003**, 3201–3210.
[10] L.-C. Song, G.-A. Yu, H.-T. Wang, F.-H. Su, Q.-M. Hu, Y.-L. Song, Y.-C. Gao, *Eur. J. Inorg. Chem.* **2004**, 866–871.
[11] a) L.-C. Song, J.-T. Liu, Q.-M. Hu, G.-F. Wang, P. Zanello, M. Fontani, *Organometallics* **2000**, *19*, 5342–5351; b) L.-C. Song, G.-F. Wang, P.-C. Liu, Q.-M. Hu, *Organometallics* **2003**, *22*, 4593–4598.
[12] L.-C. Song, G.-A. Yu, F.-H. Su, Q.-M. Hu, *Organometallics* **2004**, *23*, 4192–4198.
[13] L.-C. Song, F.-H. Su, Q.-M. Hu, *J. Organomet. Chem.* **2005**, *690*, 1121–1124.
[14] H. Nagashima, A. Nakaoka, Y. Saito, M. Kato, T. Kawanishi, K. Itoh, *J. Chem. Soc., Chem. Commun.* **1992**, 377–379.

 © 2006 Wiley-VCH Verlag GmbH & Co. KGaA, Weinheim 

[15] H. Nagashima, Y. Kato, H. Yamaguchi, E. Kimura, T. Kawanishi, M. Kato, Y. Saito, M. Haga, K. Itoh, *Chem. Lett.* **1994**, 1207–1210.
[16] J. P. Hare, T. J. Dennis, H. W. Kroto, R. Taylor, A. W. Allaf, S. Balm, D. R. M. Walton, *J. Chem. Soc., Chem. Commun.* **1991**, 412–413.
[17] J. W. Lee, M. M. Olmstead, J. S. Vickery, A. L. Balch, *J. Cluster Sci.* **2000**, *11*, 67–77.
[18] The apparatus for electrochemical measurements has been described previously: E. Stulz, J. K. M. Sanders, M. Montalti, L. Prodi, N. Zaccheroni, F. Fabrizi de Biani, E. Grigiotti, P. Zanello, *Inorg. Chem.* **2002**, *41*, 5269–5275. 1,2-Dichlorobenzene and chlorobenzene (anhydrous, 99%), from Aldrich, and $n$Bu$_4$NClO$_4$ (electrochemical grade) supporting electrolyte, from Fluka, were used as supplied. In 1,2-dichlorobenzene solution, the one-electron oxidation of ferrocene occurs at +0.57 V vs. SCE.
[19] P. Zanello, *Inorganic Electrochemistry. Theory, Practice and Application*, RSC, **2003**, chapter 6, and references cited therein.
[20] K. Lee, H. Song, B. Kim, J. T. Park, S. Park, M.-G. Choi, *J. Am. Chem. Soc.* **2002**, *124*, 2872–2873.
[21] J. P. Collman, L. S. Hegedus, J. R. Norton, R. G. Finke, *Principles and Applications of Organotransition Metal Chemistry*, 2nd ed., University Science Books, Mill Valley, CA, **1987**.
[22] Y. Takahashi, T. Ito, S. Sakai, Y. Ishii, *J. Chem. Soc. D: Chem. Commun.* **1970**, 1065–1066.
[23] W. J. Cherwinski, B. F. G. Johnson, J. Lewis, *J. Chem. Soc., Dalton Trans.* **1974**, 1405–1409.
[24] S. O. Grim, L. J. Matienzo, *Tetrahedron Lett.* **1973**, *14*, 2951–2953.
[25] G. M. Sheldrick, *SHELXS-97, A Program for Crystal Structure Solution*; University of Göttingen, Germany, **1997**.
[26] G. M. Sheldrick, *SHELXL-97, A Program for Crystal Structure Refinement*; University of Göttingen, Germany, **1997**.
[27] *TEXSAN, Crystal Structure Analysis Package*, MSC/AFC Diffractometer Control Software, Molecular Structure Corporation Houston, MSC, 3200 Research Forest Drive, The Woodlands, Texas 77381, USA, **1992**.

Received: August 24, 2005
Published Online: December 9, 2005

 © 2006 Wiley-VCH Verlag GmbH & Co. KGaA, Weinheim 

DOI: 10.1002/ejic.200500748

# Synthesis and the Effect of a Peripheral *N*-Arylcarbazole Moiety on the Acid-Base and DNA Binding Properties of a Novel $Ru^{II}$ Complex

**Yuan-Yuan Lü,[a] Li-Hua Gao,[a,b] Mei-Jiao Han,[a] and Ke-Zhi Wang*[a]**

**Keywords:** Ruthenium / N ligands / DNA / Sensors / Luminescence / UV/Vis spectroscopy

A novel $Ru^{II}$ complex of $[Ru(bpy)_2(cpipH)](ClO_4)_2$ (where bpy = 2,2′-bipyridine, cpipH = 2-[4-(9*H*-carbazol-9-yl)phenyl]-1*H*-imidazol[4,5-*f*][1,10]phenanthroline) was synthesized. The binding of the complex to calf thymus DNA was investigated with UV/Vis absorption and luminescence titrations, steady-state emission quenching by $[Fe(CN)_6]^{4-}$, DNA competitive binding with ethidium bromide, and thermal denaturation. The pH effects on the UV/Vis absorption and emission spectra of the complex were also studied, and the ground- and excited-state ionization constants were derived. The results indicated that the complex intercalatively bound to the DNA, with an intrinsic binding constant of $(8.2 \pm 0.8) \times 10^5\ M^{-1}$ in buffered 50 mM NaCl, is stronger than the parent complex, $[Ru(bpy)_2(pip)]^{2+}$ (pip = 2-phenylimidazo[4,5-*f*][1,10]phenanthroline), and its excited states are 0.7–0.8 p$K_a$ units more basic than those of the ground states.
(© Wiley-VCH Verlag GmbH & Co. KGaA, 69451 Weinheim, Germany, 2006)

## Introduction

Over the past two decades ruthenium(II) polypyridyl complexes have attracted much attention with regard to DNA interaction studies because of their potential applications as nonradioactive structural probes of nucleic acids, in DNA cleaving, and as chemotherapeutic agents.[1,2] The results have shown that the subtle changes in the molecular structures of $Ru^{II}$ complexes might bring about substantial effects on binding modes, sites, and affinities, and provide a chance to explore valuable information on conformation- or site-specific DNA probes. The various factors of ligand planarity, the charge carried on the complex, enantioselectivity, the formation of intramolecular hydrogen bonding, and the hydrophobicity of ancillary ligands, etc., have been effectively explored, but the new $Ru^{II}$ complexes are still needed to establish the DNA binding property-structure relationships.[1,2] On the other hand, the $Ru^{II}$ complexes that append protonatable/deprotonatable groups, e.g. hydroxy, carboxyl and amino groups may respond sensitively to the changes in environmental pH, providing a chance to make pH sensing or switching molecular devices,[3] and to greatly modulate their biological functionalities.[4] The ruthenium(II) complexes containing imidazole groups have been well studied with respect to their interaction with DNA[5–8] or reversible acid-base interconversion.[6a,9–12] However, studies of the $Ru^{II}$ complexes with both the DNA-binding and acid-base interconversion properties remain relatively scarce. We have been interested in the syntheses and studies of the acid-base and DNA binding properties of both mononuclear and dinuclear imidazole-containing $Ru^{II}$ complexes.[6,13]

In this paper we wish to report on a novel $Ru^{II}$ complex, $[Ru(bpy)_2(cpipH)](ClO_4)_2$, in which cpipH was synthesized by grafting an *N*-substituted carbazole group to 2-phenylimidazo[4,5-*f*][1,10]phenanthroline (pip). Attention was paid to the effects of the peripheral carbazole group on the acid-base and DNA binding properties of this complex by comparison with the parent complex, $[Ru(bpy)_2(pip)]^{2+}$. 2,2′-Bipyridine (bpy) was chosen as the ancillary ligand for the complex since the "parent" complex $[Ru(bpy)_3]^{2+}$ was reported to bind extremely weakly to double-stranded DNA.[14] Hence, it is reasonable for us to examine the "inspected" ligand on the DNA binding properties of the complex. We demonstrate here the interesting findings regarding this novel $Ru^{II}$ complex, $[Ru(bpy)_2(cpipH)]^{2+}$, intercalated to the DNA with a binding constant of $(8.2 \pm 0.8) \times 10^5\ M^{-1}$ in buffered 50 mM NaCl, which is greater than that for $[Ru(bpy)_2(pip)]^{2+}$. The excited states of this new complex are 0.7–0.8 p$K_a$ units more basic than those of the ground states.

## Results and Discussion

### Synthesis and Common Spectral Characteristics

The synthetic route to the complex is summarized in Figure 1. CpipH was synthesized by coupling 1,10-phenanthroline-5,6-dione with 4-(carbazol-9-yl)benzaldehyde ac-

[a] Department of Chemistry and Key Laboratory of Radiopharmaceuticals, Ministry of Education, Beijing Normal University, Beijing 100875, China
Fax: +86-10-58802075
E-mail: kzwang@bnu.edu.cn
[b] School of Chemical and Environment Engineering, Beijing Technology and Business University, Beijing 100037, China

 © 2006 Wiley-VCH Verlag GmbH & Co. KGaA, Weinheim 

cording to protocols reported by Steck and Day.[15] The complex $[Ru(bpy)_2(cpipH)](ClO_4)_2$ was synthesized by direct reaction of $Ru(bpy)_2Cl_2{\cdot}2H_2O$ with cpipH in EtOH/$H_2O$ (4:1, v/v), and purified by column chromatography on silica gel with $CH_3CN/H_2O$/saturated aqueous $KNO_3$ (400:7:1, v/v/v) as eluent. The complex was obtained in satisfactory purity, which was verified by elemental analysis and $^1H$ NMR spectroscopy.

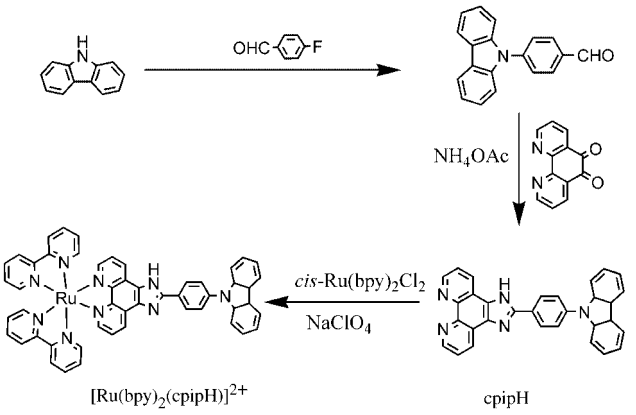


Figure 1. The synthetic route to the $Ru^{II}$ complex.

The complex, in aqueous solution, showed the lowest-energy metal-ligand charge transfer (MLCT) transition absorption band at 462 nm. The energy in the MLCT band increased in the order: $[Ru(bpy)_2(cpipH)]^{2+}$ (462 nm) < $[Ru(bpy)_2(pip)]^{2+}$ (458 nm) < $[Ru(bpy)_2(ip)]^{2+}$(455 nm).[5a] The high-energy absorption bands at 285 and 338 nm are attributed to the intraligand (IL) π-π* transition by comparison with those of $[Ru(bpy)_3]^{2+}$.[16] The order of energies in the IL bands parallels that of the MLCT bands: $[Ru(bpy)_2(cpipH)]^{2+}$ (285 nm) < $[Ru(bpy)_2(pip)]^{2+}$ (283 nm) < $[Ru(bpy)_2(ip)]^{2+}$(280 nm), indicating enhanced π delocalization upon grafting carbazole to $[Ru(bpy)_2(pip)]^{2+}$. The complex, in TRIS buffer at room temperature, was strongly emitting under visible light excitation at 465 nm with emission maxima occurring at 608 nm, which is characteristic of MLCT luminescence,[17] and is assigned to the $^3$MLCT [dπ(Ru) → π* (ligand)] state. An emission quantum yield for the complex in aerated $H_2O$ was determined to be 0.0497 by comparison with $[Ru(bpy)_3]^{2+}$ ($\varphi_{std}$ = 0.033) in aerated aqueous solution.[18,19] The MLCT emission maxima were bathochromically shifted on going from $[Ru(bpy)_2(cpipH)]^{2+}$ to $[Ru(bpy)_2(ip)]^{2+}$: $[Ru(bpy)_2(cpipH)]^{2+}$ ($\lambda_{em}$ = 608 nm) < $[Ru(bpy)_2(pip)]^{2+}$ ($\lambda_{em}$ = 615 nm) < $[Ru(bpy)_2(ip)]^{2+}$($\lambda_{em}$ = 625 nm).[5a]

## DNA-Binding Studies

### *UVIVis Spectra*

The electronic absorption spectra traces of the complex that was titrated with DNA are given in Figure 2. With increasing DNA concentrations, the hypochromisms for the bands at 285, 338 and 462 nm were found to be 54.2%, 37.3% and 23.7%, respectively, and the bathochromisms were found to be 4, 2 and 6 nm, respectively. The hypochromism of 23.7% for the MLCT band for the complex is larger than 15.5% for $[Ru(bpy)_2(ip)]^{2+}$ and 21.9% for $[Ru(bpy)_2(pip)]^{2+}$.[5a] The hypochromism observed for the IL transition of 54.2% (285 nm) for our complex appreciably prevailed over the 3.8% (280 nm) observed for $[Ru(bpy)_2(ip)]^{2+}$ and 20% (283 nm) for $[Ru(bpy)_2(pip)]^{2+}$.[5a] The spectroscopic changes suggest that the complex has a stronger interaction with DNA than $[Ru(bpy)_2(ip)]^{2+}$ and $[Ru(bpy)_2(pip)]^{2+}$.

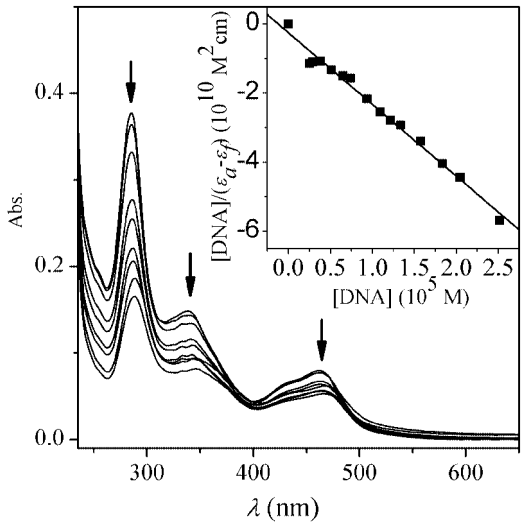


Figure 2. UV/Vis absorption spectra of the $Ru^{II}$ complex (4.6 μM), in the absence and presence of increasing concentrations of ct-DNA (0–25 μM).

To further illustrate the binding strength of the complex quantitatively, the intrinsic DNA binding constant of the complex was determined by monitoring the changes in absorbance at 285 nm with increasing concentrations of DNA, according to Equation (1),[20] where [DNA] is the concentration of DNA in base pairs; the apparent absorption coefficients $\varepsilon_a$, $\varepsilon_f$ and $\varepsilon_b$ correspond to the extinction coefficients at a given DNA concentration, the free complex in solution and the complex that is fully bound to DNA, respectively; and $K_b$ is given by the ratio of the slope to the intercept.

$$[DNA]/(\varepsilon_a - \varepsilon_f) = [DNA]/(\varepsilon_b - \varepsilon_f) + 1/K_b(\varepsilon_b - \varepsilon_f) \quad (1)$$

An intrinsic binding constant was derived to be $(8.2 \pm 0.8) \times 10^5$ M$^{-1}$ for $[Ru(bpy)_2(cpipH)]^{2+}$, and ca. twice that for $[Ru(bpy)_2(pip)]^{2+}$ ($4.7 \times 10^5$ M$^{-1}$).[20] The hypochromism ($H$%) and the intrinsic DNA binding constant of $[Ru(bpy)_2(cpipH)]^{2+}$ are compared with those reported for representative DNA intercalators in Table 1. The $K_b$ value of the complex is larger than those for most of the DNA intercalators collected in Table 1, while smaller than those for the strong DNA intercalators of Δ-$[Ru(phen)(dppz)]^{2+}$ ($3.2 \times 10^6$ M$^{-1}$), Λ-$[Ru(phen)(dppz)]^{2+}$ ($1.7 \times 10^6$ M$^{-1}$)[21] and $[Ru(bpy)_2(ebipcH_2)(bpy)_2Ru]^{2+}$ ($1.3 \times 10^6$ M$^{-1}$).[6a] The $H$% value listed in Table 1 for $[Ru(bpy)_2(cpipH)]^{2+}$ is even larger than those for the typical DNA intercalators mentioned above. The large hypochromism and clear red shifts, as well

 © 2006 Wiley-VCH Verlag GmbH & Co. KGaA, Weinheim 

Table 1. A comparison of DNA binding data for $[Ru(bpy)_2(cpipH)]^{2+}$ with those for analogous Ru(II) complexes.

| Complex[a] | Hypochromism[b] $H^b$/% ($\lambda_{max}$/nm) | $K_b \times 10^5$ [$M^{-1}$] | $R$[c] | Ref. |
|---|---|---|---|---|
| $[Ru(bpy)_2(ip)]^{2+}$ | 15.5 (455) | – | 0.25 | [5a] |
| $[Ru(bpy)_2(pip)]^{2+}$ | 21.9 (458) | 4.7 | 0.051 | [5a,20a] |
| $[Ru(bpy)_2(taptp)]^{2+}$ | 34.8 (248) | 1.7 | ≈0 | [20a] |
| $[Ru(bpy)_2(ipbp)]^{2+}$ | 17.4 (458) | 0.42 | 3.43 | [20b] |
| $[Ru(bpy)_2(cpipH)]^{2+}$ | 54.2 (285) | 8.2 | 0.0093 | this work |
| $[Ru(bpy)_2(ebipcH_2)(bpy)_2Ru]^{2+}$ | 36.6 (288) | 13.1 | ≈0 | [15] |
| $\Delta$-$[Ru(phen)_2(dppz)]^{2+}$ | 32.1 (372) | 32 | – | [21] |
| $\Lambda$-$[Ru(phen)_2(dppz)]^{2+}$ | 29.8 (372) | 17 | – | [21] |

[a] ip = imidazo[4,5-*f*][1,10]phenanthroline; pip = 2-phenylimidazo[4,5-*f*][1,10]phenanthroline; taptp = 4,5,9,18-tetraazaphenanthreno[9,10-*b*]triphenylene; ipbp = 3-(1*H*-imidazo[4,5-*f*][1,10] phenanthrolin-2-yl)-4*H*-1-benzopyran-4-one; $ebipcH_2$ = *N*-ethyl-4,7-bis([1,10]phenanthroline[5,6-*f*]imidazo-2-yl)carbazole; dppz = dipyrido[3,2-*a*:2′,3′-*c*]-phenazine. [b] The maximum hypochromism selected from the UV/Vis absorption peaks. [c] *R* is the ratio of the Stern–Volmer quenching constant by using $[Fe(CN)_6]^{4-}$ as the quencher, and obtained from the ratio of the presence of DNA to that obtained in the absence of DNA.

as a relatively large $K_b$ value observed for the interaction of the $Ru^{II}$ complex with the DNA, indicate that complex $[Ru(bpy)_2(cpipH)]^{2+}$ might bind to the DNA by intercalation.

### *Luminescence Studies*

Steady-state emission quenching experiments for the complex, using $[Fe(CN)_6]^{4-}$ as the quencher, further support the intercalation interaction. As illustrated in Figure 3, in the absence of DNA, the emission of $[Ru(bpy)_2(cpipH)]^{2+}$ is efficiently quenched by $[Fe(CN)_6]^{4-}$, resulting in a slope of 92.6 for a linear Stern–Volmer plot, but in the presence of DNA the slope of the quenching plot decreases remarkably to 0.49. The positively charged free complex ions should be readily quenched by $[Fe(CN)_6]^{4-}$, but when bound to DNA, the complex can be protected from the quencher because the highly negatively charged $[Fe(CN)_6]^{4-}$ would be repelled by the negative DNA phosphate backbone, hindering quenching of the emission of the bound complex. A ratio (*R*) of Stern–Volmer quenching constants, using $[Fe(CN)_6]^{4-}$ and obtained from the ratio of the presence of DNA to that of the absence of DNA, can be taken as a measure of the binding affinity. A large *R* value corresponds to a poorer protection and a weaker binding to DNA. As anticipitated, an *R* value of 0.0093 found for the complex we studied in this paper, is smaller than a value 0.051 reported for $[Ru(bpy)_2(pip)]^{2+}$, and 0.25 for $[Ru(bpy)_2(ip)]^{2+}$,[5a] providing further evidence that the binding affinity to the DNA is in the order of $[Ru(bpy)_2(cpipH)]^{2+} > [Ru(bpy)_2(pip)]^{2+} > [Ru(bpy)_2(ip)]^{2+}$,[5a] and the interaction mode between the complex and the DNA is intercalative.

The fluorescence of ethidium bromide (EB) itself in aqueous solution is very weak, but when it intercalates between adjacent DNA base pairs of double-stranded DNA ($K_b = 1.4 \times 10^6$ $M^{-1}$),[22] the fluorescence is greatly enhanced. If a second DNA intercalator is added to the EB–DNA system, it will compete with EB for the DNA binding site, and the fluorescence of the EB–DNA system will be quenched.[23,24] So, the quenching extent of fluorescence of the EB–DNA system can reflect the DNA binding strength of the second molecule. Otherwise, if the second added molecule is not a DNA intercalator, its addition will not

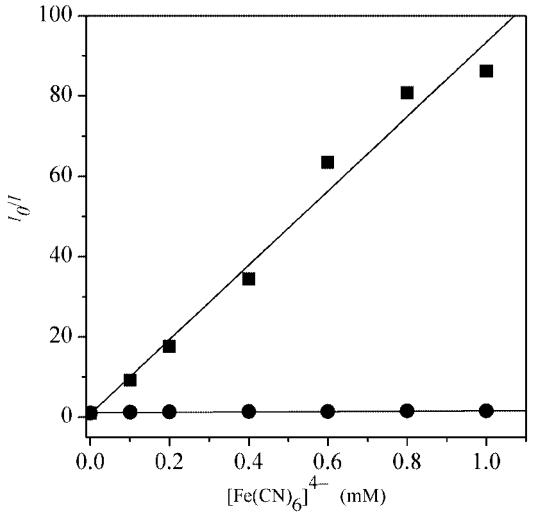


Figure 3. Emission quenching of the $Ru^{II}$ complex with increasing concentrations of $[Fe(CN)_6]^{4-}$ in the absence (■) and presence (●) of ct-DNA:[Ru] = 4.6 μM, [DNA]/[Ru] = 9.

cause the evident reduction in emission intensities of the EB–DNA system. The changes in the emission spectra of the EB–DNA system in the absence and presence of the complex are shown in Figure 4. The emission of the EB–DNA system was efficiently quenched by the complex, resulting in a linear Stern–Volmer plot according to Equation (2), where $I_0$ and $I$ represent the fluorescence intensities in the absence and presence of complex, respectively; $K$ is a linear Stern–Volmer quenching constant dependent on the ratio of the bound concentration of EB to the concentration of DNA; and $r$ is the ratio of the total concentration of the complex to that of DNA ([Ru]/[DNA]).

$$I_0/I = 1 + Kr \quad (2)$$

As shown in the inset of Figure 4, the Stern–Volmer plot has of a slope of $K = 6.17$, which is larger than 2.72 for $[Ru(dmp)_2(obpip)]^{2+}$ (dmp = 2,9-dimethyl-1,10-phenanthroline; obpip = 2-(2-bromophenyl)imidazo[4,5-*f*]-1,10-phenanthroline), and 5.98 for $[Ru(dmp)_2(pbip)]^{2+}$(pbip =2-(4-bromophenyl)imidazo[4,5-*f*]-1,10-phenanthroline),[25] but smaller than a *K* value of 19.3 for [Ru(bpy)-

 © 2006 Wiley-VCH Verlag GmbH & Co. KGaA, Weinheim 

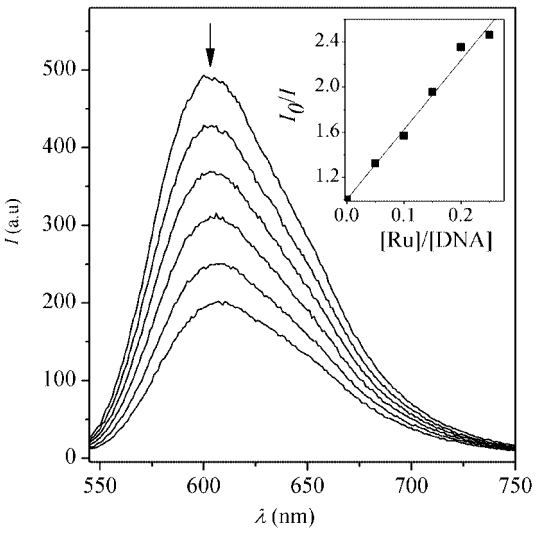


Figure 4. Emission quenching of the EB–DNA system with increasing concentration of the $Ru^{II}$ complex. [EB] = 20 μM, [DNA] = 100 μM, [Ru]:[DNA] = 0–0.25.

$(pp[2,3]p)_2]^{2+}$ (bpy = 2, 2′-bipyridine, pp[2,3]p = pyrido[2′,3′:5,6]pyrazino[2,3-*f*][1,10]phenanthroline), and 31.2 for $[Ru(phen)(pp[2,3]p)_2]^{2+}$ (phen = 1,10-phenanthroline).[13a] From the data in Figure 4, we also know that 50% of EB was replaced by $[Ru(bpy)_2(cpipH)]^{2+}$ from the DNA bound EB at a concentration ratio of [Ru]/[EB] ≈ 0.8. Hence, an apparent DNA binding constant of $1.8 \times 10^6$ M$^{-1}$ was derived [$K_b$(EB)/0.8].

### *Thermal Denaturation Studies*

The thermal melting study of the DNA is a technique used to evaluate the stability of a DNA double helix. When a complex intercalates into DNA base pairs, the base stacking will be more stable and hence the melting temperature of the double-stranded DNA will rise. So the DNA melting temperature ($T_m$) is useful in establishing the extent of intercalation.[26] The melting curves of ct-DNA in the absence and presence of the complex are presented in Figure 5. $T_m$ of ct-DNA was found to be 66.3 °C. In the presence of the complex at a concentration ratio [Ru]/[DNA] = 1:10, $T_m$ of ct-DNA was raised to 73.5 °C. The large increase of 7.2 °C in $T_m$ is comparable to that observed for a classical DNA intercalator.[22–29]

The DNA intrinsic binding constant at 73.5 °C can be obtained from the McGhee equation [Equation (3)], where $T_m^0$ is the melting temperature of ct-DNA alone, $T_m$ is the melting temperature in the presence of the $Ru^{II}$ complex, $\Delta H$ is the enthalpy of DNA (per base pair), $R$ is the gas constant, $K$ is the DNA binding constant at $T_m$, $L$ is the free complex concentration (approximated at the $T_m$ by the total complex concentration), and $n$ is the size of the binding site.

$$1/T_m^0 - 1/T_m = (R/\Delta H)\ln(1 + KL)^{1/n} \quad (3)$$

For the ct-DNA used in these studies, under identical solution conditions, a melting enthalpy of 6.9 kcal mol$^{-1}$ was determined by differential scanning calorimetry.[30]

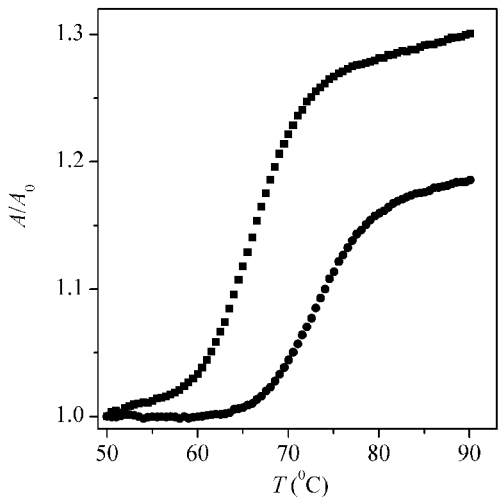


Figure 5. Melting curves of ct-DNA in the absence (■) and presence (●) of the $Ru^{II}$ complex. [Ru] = 5.8 μM, [DNA] = 58 μM.

And on the basis of the neighbor exclusion principle the $n$ value for the complex was assumed to be 2.0 base pairs. As a result $K$ was calculated to be $9.14 \times 10^4$ M$^{-1}$ at 73.5 °C. As the complex binds to ct-DNA, the changes in standard enthalpy, standard entropy and standard free energy can be determined according to Equations (4), (5), and (6), where $K_1$ and $K_2$ are the DNA intrinsic binding constants of the complex at temperature $T_1$ and $T_2$, respectively; $\Delta G°$, $\Delta H°$, and $\Delta S°$ are the corresponding standard free energy change, standard enthalpy change and standard entropy change, respectively.

$$\ln(K_1/K_2) = (\Delta H°/R)(T_1 - T_2)/T_1T_2 \quad (4)$$

$$\Delta G_T^\circ = -RT\ln K \quad (5)$$

$$\Delta G_T^\circ = \Delta H° - T\Delta S° \quad (6)$$

By substituting $K_1 = 8.21 \times 10^5$ M$^{-1}$ ($T_1$ = 298 K) and $K_2 = 9.14 \times 10^4$ M$^{-1}$ ($T_2$ = 346.5 $K$) into Equations (4)–(6), the values of $\Delta H°$, $\Delta G_{298}^\circ$ and $\Delta S°$ were found to be –38.9 kJ mol$^{-1}$, –33.8 kJ mol$^{-1}$ and –17.1 J mol$^{-1}$ K$^{-1}$ at 25 °C, respectively. The negative $\Delta G°$ value suggests that the energy of the adduct is lower than the sum of the energies of the free complex and DNA. The negative $\Delta H°$ suggests that the binding of the complex to DNA at 25 °C is exothermic and enthalpically driven.

## Spectrophotometric pH Titrations

### *UV/Vis Absorption Spectra*

As shown in Figure 6, $[Ru(bpy)_2(cpipH)]^{2+}$ underwent two successive deprotonation processes upon increasing the pH from –0.08 to 11.23. When the pH was increased from 0.10 to 3.73, the bands at 286 and 342 nm increased in intensity and an isosbestic point appeared at 360 nm. These spectral changes resulted from the dissociation of the proton on the protonated imidazole ring. The second depro-

 © 2006 Wiley-VCH Verlag GmbH & Co. KGaA, Weinheim 

tonation step, which takes place over the pH range of 7.00–10.45, is assigned to the deprotonation of the proton on the neutral imidazole ring, accompanying the following spectral features: the band at 342 nm and the wave valley at 490 nm increase, and the band at 286 nm is red-shifted from 286 nm to 289 nm without any changes in the intensities. The changes in absorbance at the fixed wavelengths as a function of pH are shown in the insets of Figure 6. Two ground-state ionization constants of $pK_{a1} = 0.31 \pm 0.06$, $pK_{a2} = 8.24 \pm 0.03$ were obtained by nonlinear sigmoidal fits of the data, shown in the insets of Figure 6(a) and Figure 6(b). As compared with the two ionization constants of the protonated imidazole ring on some representative $Ru^{II}$ analog complexes, the complex we studied in this paper is more acidic than $[Ru(bpy)_2(ip)]^{2+}$ ($pK_{ai}$ = 1.97, 10.46) and $[Ru(bpy)_2(ebipcH_2)(bpy)_2Ru]^{2+}$ {$ebipcH_2$ = *N*-ethyl-4,7-bis([1,10]phenanthroline[5,6-*f*]imidazo-2-yl)-carbazole} ($pK_{ai}$ = 4.16, 9.65).[6a,10]

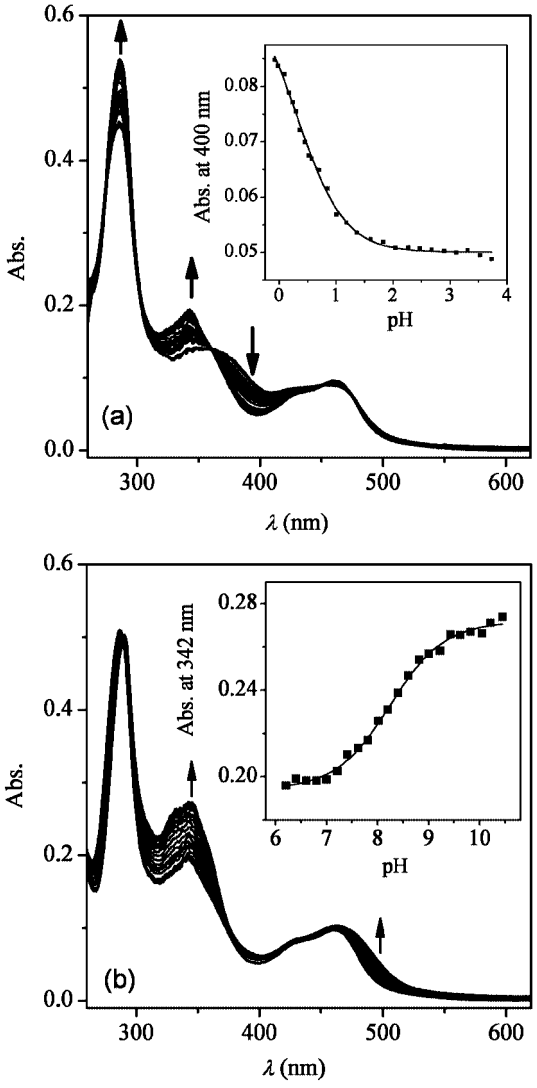


Figure 6. The changes of electronic absorption spectra of the $Ru^{II}$ complex upon raising the pH: (a) pH = –0.08 to 3.73; (b) pH = 6.21 to 10.45.

### *Luminescence Spectroscopic Studies*

As shown in Figure 7, the emission spectra of the complex are sensitive to pH. When the pH is increased from 0.10 to 3.31, the emission maxima are blue-shifted from 628 to 613 nm and the intensities decrease by about 13.9%. As the pH increases from 6.21 to 10.45, the emission maxima become red-shifted from 610 to 622 nm, and the intensities decrease by about 38.1%. The insets of Figure 7, which are the changes of relative emission intensities vs. pH, clearly show that the profiles consist of two sigmoidal curves of opposite gradients, indicative of two deprotonation processes. This is the same result as that described in the section on UV/Vis absorption spectral titrations. The protonation/deprotonation processes are summarized in Figure 8.

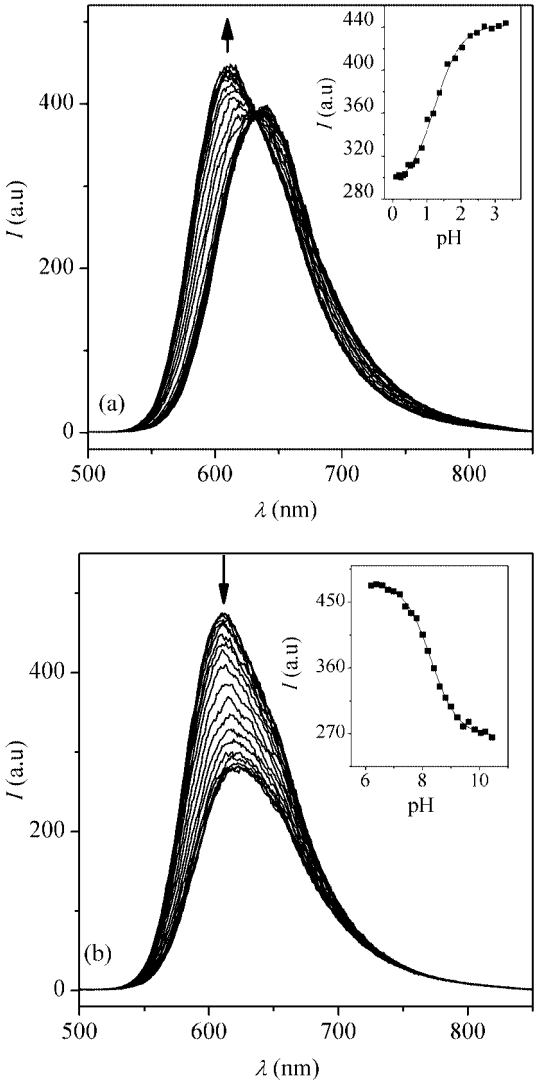


Figure 7. The changes in the emission spectra of the $Ru^{II}$ complex upon raising the pH: (a) pH = 0.10–3.31; (b) pH = 6.21–10.45.

Excited-state ionization constants, $pK_a^*$, could be roughly evaluated on the basis of the Förster cycle,[3] which thermodynamically correlates $pK_a^*$ with $pK_a$ according to

 © 2006 Wiley-VCH Verlag GmbH & Co. KGaA, Weinheim 

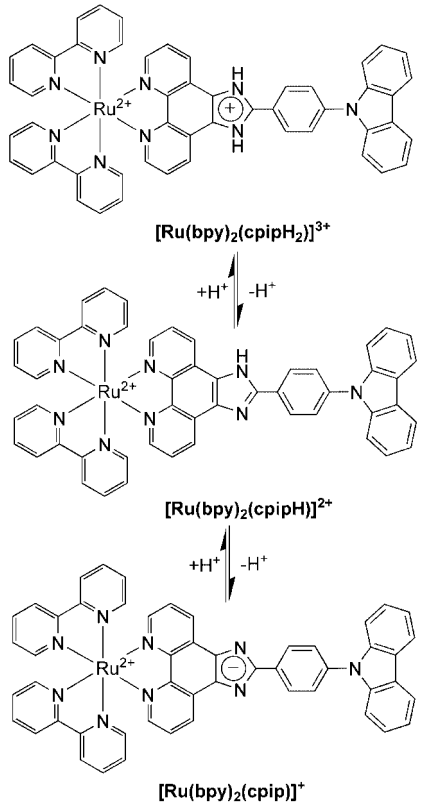


Figure 8. The acid–base equilibria of the $Ru^{II}$ complex.

Equation (7), where $\nu_B$ and $\nu_{HB}$ are pure 0–0 transitions in $cm^{-1}$ for the basic and acidic species, respectively.

$$pK_a^* = pK_a + (0.625/T)(\nu_B - \nu_{HB}) \quad (7)$$

In practice, $\nu_B$ and $\nu_{HB}$ are often difficult or even impossible to obtain. A good approximation is obtained by using the emission maxima for $\nu_B$ and $\nu_{HB}$, since protonation equilibrium is almost certainly established between the $^3$MLCT states.[18]

By using the emission band maxima from both the protonated and deprotonated forms of the ruthenium complex for $\nu_B$ and $\nu_{HB}$ in Equation (7), two $pK_a^*$ values of $pK_{a1}^* = 1.1 \pm 0.1$ and $pK_{a2}^* = 8.9 \pm 0.1$, were obtained. The excited state $pK_a^*$ values are 0.7–0.8 $pK_a$ units more basic than the respective ground-state ones, indicating that the excited electron was delocalized on the cpipH moiety rather than on that of the bpy moiety.

## Conclusions

In summary, a newly synthesized $Ru^{II}$ complex of $[Ru(bpy)_2(cpipH)](ClO_4)_2$ was demonstrated to be a DNA intercalator by evident hypochromism and clear bathochromic shifts of the band at 286 nm, and protection from emission quenching by $[Fe(CN)_6]^{4-}$ upon binding to the DNA, as well as comparable competitive binding to the DNA with the proven DNA intercalator EB and the large increase of 7.2 °C in the melting temperature of the double-stranded DNA at a concentration ratio [Ru]/[DNA] = 1:10. Its interesting DNA-binding and pH responsive spectroscopic properties make it attractive for applications involving molecular optical devices.

## Experimental Section

**Physical Measurements:** Elemental analyses were performed with a Vario EL elemental analyzer. Infrared spectra were measured with a Nicolet–Avatar 360 FT-IR spectrometer using KBr disks. $^1$H NMR spectra were obtained with a Bruker DRX-500 spectrometer. UV/Vis absorption spectra were determined with a GBC Cintra 10e UV/Vis spectrophotometer. Emission spectra were recorded with a Shimadzu RF-5301PC spectrofluorimeter. The interaction of the complex with DNA was conducted in buffer A (5 mM TRIS, 50 mM NaCl, pH = 7.1). A solution of ct-DNA gave ratios of UV absorbance at 260 and 280 nm of about 1.8–1.9:1 indicating that the DNA was sufficiently free of protein. The DNA per nucleotide was determined spectrophotometrically by assuming $\varepsilon_{260}$ = 6600 $M^{-1}cm^{-1}$. Thermal denaturation experiments of the DNA were performed on a GBC Cintra 10e UV/Vis spectrophotometer in Buffer B (1.5 mM $Na_2HPO_4$, 0.5 mM $NaH_2PO_4$, 1 mM $Na_2EDTA$). Using the thermal melting program, the temperature of the cell containing the cuvette was increased from 50 °C to 90 °C and the absorbance at 260 nm was measured every 0.5 °C. The data were smoothed at 0.5 °C intervals with a filter of 5, and the derivative of the resulting curve was taken at a data interval of 0.5 °C. The pH effects on the UV/Vis and emission spectra of the complex were carried out in DMF/Britton–Roberson buffer (4 mM $H_3BO_3$, 4 mM $H_3PO_4$, 4 mM $CH_3COOH$) (1:1, v/v).

**Materials:** 4-(Carbazol-9-yl)benzaldehyde,[31] 1,10-phenanthroline-5,6-dione[32] and *cis*-$Ru(bpy)_2Cl_2 \cdot 2H_2O$[33] were prepared according to literature methods.

**2-[4-(9*H*-Carbazol-9-yl)phenyl]-1*H*-imidazol[4,5-*f*][1,10]phenanthroline (cpipH):**[34] A solution of 1,10-phenanthroline-5,6-dione (0.21 g, 1 mmol), 4-(carbazol-9-yl)benzaldehyde (0.27 g, 1 mmol), and ammonium acetate (1.62 g, 21 mmol) dissolved in acetic acid (30 mL) was refluxed at 110 °C for 5 h under nitrogen. The solution was cooled to room temperature, and $H_2O$ (60 mL) was added. The suspension was then neutralized with concentrated aqueous ammonia. The yellow precipitate that formed was washed with water, dichloromethane and ethanol, and then dried at 100 °C in vacuo. Yield 0.185 g (40%). IR (KBr): $\tilde{\nu}_{max}$ = 3435 (s), 1610 (m), 1525 (m), 1482 (m), 1452 (s), 1352 (m), 739 (s), 720 (m) $cm^{-1}$. $^1$H NMR ([D$_6$]DMSO): $\delta$ = 13.95 (s, 1 H), 9.07 (s, 2 H), 8.98 (d, $J$ = 7.7 Hz, 2 H), 8.59 (d, $J$ = 8.4 Hz, 2 H), 8.30 (d, $J$ = 7.8 Hz, 2 H), 7.94 (d, $J$ = 8.4 Hz, 2 H), 7.88 (m, 2 H), 7.56 (d, $J$ = 8.2 Hz, 2 H), 7.50 (t, $J$ = 7.3 Hz, 2 H), 7.35 (t, $J$ = 7.2 Hz, 2 H) ppm. $C_{31}H_{19}N_5 \cdot 0.2C_2H_5OH$ (470.7): calcd. C 80.13, H 4.29, N 14.87; found C 81.90, H 4.61, N 14.63.

**Caution!** *All the perchlorate salts are potentially explosive and therefore should be handled in small quantities with care.*

**[Ru(bpy)$_2$(cpipH)](ClO$_4$)$_2$:** A mixture of *cis*-$[Ru(bpy)_2Cl_2] \cdot 2H_2O$ (0.052 g, 0.1 mmol), $cpipH \cdot 0.2C_2H_5OH$ (0.046 g, 0.98 mmol), ethanol (8 mL), and $H_2O$ (2 mL) was refluxed at 100 °C for 9 h under nitrogen. The solution was cooled to room temperature and was filtered to remove the insoluble substance. An orange precipitate was obtained by dropwise addition of a fourfold excessive of aqueous $NaClO_4$ solution. The product was purified by column chromatography on silica gel with $CH_3CN/H_2O$/saturated aqueous $KNO_3$ (400:7:1, v/v/v) as eluent followed by reprecipitation with aqueous $NaClO_4$ solution. Red crystals were obtained. Yield

 © 2006 Wiley-VCH Verlag GmbH & Co. KGaA, Weinheim 

0.064 g (60%). $C_{51}H_{35}Cl_2N_9O_8Ru$ (1073.9): calcd. C 57.04, H 3.28, N 11.92; found C 56.60, H 3.55, N 11.86. IR (KBr): $\tilde{\nu}_{max}$ = 3431 (s), 1624 (m), 1603 (m), 1479 (m), 1447 (s), 1359 (w), 1121 (s), 1090 (s), 754 (m), 726 (m), 623 (s) $cm^{-1}$. $^1H$ NMR ([D$_6$]DMSO): $\delta$ = 14.55 (s, 1 H), 9.15 (t, $J$ = 9.1 Hz, 2 H), 8.90 (d, $J$ = 8.2 Hz, 2 H), 8.87 (d, $J$ = 8.2 Hz, 2 H), 8.62 (d, $J$ = 8.4 Hz, 2 H), 8.32 (d, $J$ = 7.8 Hz, 2 H), 8.24 (t, $J$ = 7.9 Hz, 2 H), 8.13 (t, $J$ = 7.8 Hz, 2 H) 8.11 (d, $J$ = 5.2 Hz, 2 H), 8.02 (d, $J$ = 8.4 Hz, 2 H), 7.97 (m, 2 H), 7.87 (d, $J$ = 5.4 Hz, 2 H), 7.66 (s, 2 H), 7.60 (m, 4 H), 7.51 (t, $J$ = 7.6 Hz, 2 H), 7.37 (m, 4 H) ppm.

## Acknowledgments

We are grateful to the NSFC (20371008 and 90401007), and Beijing Natural Science Foundation (2052008) for their financial support of this work.

[1] B. Nordén, P. Lincoln, B. Akerman, E. Tuite, in *Met. Ions. Biol. Syst*. (Eds.: A. Sigel, H. Sigel), vol. 33, Dekker, New York, **1996**, p. 177–252.
[2] a) K. E. Erkkila, D. T. Odom, J. K. Barton, *Chem. Rev.* **1999**, *99*, 2777–2795; b) L. N. Ji, X. H. Zou, J. G. Liu, *Coord. Chem. Rev.* **2001**, *216–217*, 513–536; c) C. Metcalfe, J. A. Thomas, *Chem. Soc. Rev.* **2003**, *32*, 215–224; d) V. G. Vaidyanathan, B. U. Nair, *Dalton Trans.* **2005**, 2842–2848.
[3] J. G. Vos, *Polyhedron* **1992**, *11*, 2285–2299.
[4] a) C. S. Allardyce, P. J. Dyson, D. J. Ellis, S. L. Heath, *Chem. Commun.* **2001**, 1396–1397; b) D. Bashford, M. Karplus, *Biochemistry* **1990**, *29*, 10219–10225.
[5] a) J. Z. Wu, B. H. Ye, L. Wang, L. N. Ji, J. Y. Zhou, R. H. Li, Z. Y. Zhou, *J. Chem. Soc., Dalton Trans.* **1997**, 1395–1401; b) H. Chao, R. H. Li, B. H. Ye, H. Li, X. L. Feng, J. W. Cai, J. Y. Zhou, L. N. Ji, *J. Chem. Soc., Dalton Trans.* **1999**, 3711–3717.
[6] a) F. R. Liu, K. Z. Wang, G. Y. Bai, Y. A. Zhang, L. H. Gao, *Inorg. Chem.* **2004**, *43*, 1799–1806; b) G. Y. Bai, B. Dong, Y. Y. Lü, K. Z. Wang, L. P. Jin, L. H. Gao, *J. Inorg. Biochem.* **2004**, *98*, 2011–2015; c) G. Y. Bai, K. Z. Wang, Z. M. Duan, L. H. Gao, *J. Inorg. Biochem.* **2004**, *98*, 1017–1022; d) M. J. Han, K. Z. Wang, Y. Y. Lü, L. H. Gao, *Chem. J. Chin. Univ.* **2004**, *25*, 2221–2223 (in Chinese); e) S. D. Jiang, F. R. Liu, Y. A. Zhang, L. H. Gao, *Acta Chim. Sin.* **2005**, *63*, 783–786 (in Chinese).
[7] C. W. Jiang, *J. Inorg. Biochem.* **2004**, *98*, 1399–1404.
[8] M. Mariappan, B. G. Maiya, *Eur. J. Inorg. Chem.* **2005**, 2164–2173.
[9] a) M. A. Haga, T. Ano, K. Kano, S. Yamabe, *Inorg. Chem.* **1991**, *30*, 3843–3849; b) M. A. Haga, T. Ano, T. Ishizaki, K. Kano, K. Nozaki, T. J. Ohno, *J. Chem. Soc., Dalton Trans.* **1994**, 263–272; c) M. A. Haga, T. Takasugi, A. Tomie, M. Ishizuya, T. Yamada, M. D. Hossain, M. Inoue, *Dalton Trans.* **2003**, 2069–2079.
[10] B. W. Jing, T. Wu, C. H. Tai, M. H. Zhang, T. Shen, *Bull. Chem. Soc. Jpn.* **2000**, *73*, 1749–1755.
[11] a) M. A. Haga, *Inorg. Chim. Acta* **1983**, *75*, 29–35; b) M. A. Haga, A. Tsunemitu, *Inorg. Chim. Acta* **1989**, *164*, 137–142.
[12] K. Z. Wang, L. H. Gao, G. Y. Bai, L. P. Jin, *Inorg. Chem. Commun.* **2002**, *5*, 841–843.
[13] a) B. Y. Wu, L. H. Gao, Z. M. Duan, K. Z. Wang, *J. Inorg. Biochem.* **2005**, *99*, 1685–1691; b) B. Y. Wu, L. H. Gao, K. Z. Wang, *Chem. J. Chin. Univ.* **2005**, *26*, 1206–1209 (in Chinese).
[14] P. Lincoln, B. Nordén, *J. Phys. Chem. B* **1998**, *102*, 9583–9594.
[15] E. A. Steck, A. R. Day, *J. Am. Chem. Soc.* **1943**, *65*, 452–456.
[16] A. Juris, V. Balzani, F. Barigelletti, S. Campagna, P. Belser, A. von Zelewsky, *Coord. Chem. Rev.* **1988**, *84*, 85–277.
[17] K. Kalyanasundaram, *Coord. Chem. Rev.* **1982**, *46*, 159–244.
[18] G. Y. Zhang, Y. Wang, D. P. Rillema, *Inorg. Chem.* **1996**, *35*, 7118–7123.
[19] J. van Houten, R. J. Watts, *J. Am. Chem. Soc.* **1976**, *98*, 4853–4858.
[20] a) L. N. Ji, J. G. Liu, B. H. Ye, *Mater. Sci. Eng., C* **1999**, *10*, 51–57; b) Q. X. Zhen, B. H. Ye, Q. L. Zhang, J. G. Liu, H. Li, L. N. Ji, L. Wang, *J. Inorg. Biochem.* **1999**, *76*, 47–53; c) Y. J. Liu, H. Chao, J. H. Yao, H. Li, Y. X. Yuan, L. N. Ji, *Helv. Chim. Acta* **2004**, *87*, 3119–3130.
[21] I. Haq, P. Lincoln, D. Suh, B. Norden, B. Z. Chowdhry, J. B. Chaires, *J. Am. Chem. Soc.* **1995**, *117*, 4788–4796.
[22] J. B. LePecq, C. Paoletti, *J. Mol. Biol.* **1967**, *27*, 87–106.
[23] J. R. Lakowicz, G. Webber, *Biochemistry* **1973**, *12*, 4161–4170.
[24] B. C. Baguley, M. Lebret, *Biochemistry* **1984**, *23*, 937–943.
[25] H. Xu, K. C. Zheng, Y. Chen, Y. Z. Li, L. J. Lin, H. Li, P. X. Zhang, L. N. Ji, *Dalton Trans.* **2003**, 2260–2268.
[26] J. M. Kelly, A. B. Tossi, D. J. McConnell, C. OhUigin, *Nucleic Acids Res.* **1985**, *13*, 6017–6034.
[27] G. A. Neyhart, N. Grover, S. R. Smith, W. A. Kalsbeck, T. A. Fairley, M. Cory, H. H. Thorp, *J. Am. Chem. Soc.* **1993**, *115*, 4423–4428.
[28] R. B. Nair, E. S. Teng, S. L. Kirkland, C. J. Murphy, *Inorg. Chem.* **1998**, *37*, 139–141.
[29] R. C. Holmberg, H. H. Thorp, *Anal. Chem.* **2003**, *75*, 1851–1860.
[30] S. Satyanarayana, J. C. Dabrowiak, J. B. Chaires, *Biochemistry* **1993**, *32*, 2573–2584.
[31] X. M. Wang, Y. F. Zhou, W. T. Yu, C. Wang, Q. Fang, M. H. Jiang, H. Lei, H. Z. Wang, *J. Mater. Chem.* **2000**, *10*, 2698–2703.
[32] C. Hiort, P. Lincoln, B. Nordén, *J. Am. Chem. Soc.* **1993**, *115*, 3448–3454.
[33] B. P. Sullivan, D. J. Salmon, T. L. Meyer, *Inorg. Chem.* **1989**, *17*, 3334–3341.
[34] M. Guan, Z. Q. Bian, F. Y. Li, H. Xin, C. H. Huang, *New J. Chem.* **2003**, *27*, 1731–1734.

Received: August 25, 2005
Published Online: December 6, 2005

 © 2006 Wiley-VCH Verlag GmbH & Co. KGaA, Weinheim 

DOI: 10.1002/ejic.200500769

# Ionic Liquids: Synthesis and Characterisation of Triphenylphosphonium Tosylates

**Ludovic G. Bonnet[a] and Benson M. Kariuki*[a]**

**Keywords:** Structure elucidation / Ionic liquids / Solid-state structures / Melting points

Ionic liquids are currently attracting considerable interest from chemists, partly due to their potential as "green" alternatives to volatile molecular organic solvents. Phosphonium ionic liquids have received much less attention than ammonium salts in the past, but the situation is changing. The salts are applied in the liquid state but in this work, salts with higher melting points than is generally the case are investigated. They are solid at room temperature, thus enabling facile separation of liquid reaction products. Nine triphenylphosphonium tosylates have been prepared and characterised; their crystal structures have been determined and their melting points have been scrutinized, showing some sensitivity to the duration of drying. The structural information is expected to be invaluable in the understanding of the properties of the molten state.

(© Wiley-VCH Verlag GmbH & Co. KGaA, 69451 Weinheim, Germany, 2006)

## Introduction

Although ionic liquids were first described as long ago as 1914,[1] it is only relatively recently that they have received much attention from chemists.[2–5] The last few decades have witnessed increased application, initially as media for organic synthesis and later on with multiple uses. A number of properties make ionic liquids particularly suited to application as solvents; they have high thermal stability, low vapour pressure and the ability to dissolve a large range of inorganic, organic and polymeric materials. In addition, they have a wide liquid range and are relatively cheap and easy to prepare.

The terms "ionic liquid" and "room temperature ionic liquid" often refer to ionic salts with melting points below ca. 100 °C. Many ionic liquids studied to date fall within this category and, in particular, salts containing quaternary nitrogen cations have been investigated extensively. A number of phosphonium salts also fall within this low melting point class. A factor in the growing interest in these materials is their potential as "green" alternatives to molecular organic solvents; replacement of volatile organic solvents by ionic liquids, which are involatile, would significantly reduce their detrimental impact on the environment. This aspect will undoubtedly become increasingly important as the level of awareness and concern for the habitat intensifies.

Although phosphonium salts have attracted much less interest in the literature than quaternary nitrogen salts to date, their potential as ionic solvents has been recognized for a long time. For example, the first palladium-catalysed reaction in an ionic liquid was carbon–carbon coupling in tributylhexadecylphosphonium bromide.[6] Tetrabutylphosphonium halides (TBPHs) featured prominently in the earlier application of phosphonium salts as ionic solvents. One of the first reported uses of a phosphonium salt as a solvent in an organic reaction was of TBPHs in regioselective *o*-alkylation leading to an efficient and recyclable catalytic system.[7] Several years earlier, in 1981, TBPHs had been used in the ruthenium-catalysed hydrogenation of carbon monoxide to ethyleneglycol.[8] Hydroformylation of olefins in TBPHs and other quaternary phosphonium salts has also been demonstrated.[9,10] Interest in application as alternative solvents and co-catalysts continues to grow.[11]

In this investigation, we consider triphenylphosphonium salts with higher melting points than conventional ionic liquids, focusing exclusively on the tosylates shown in Scheme 1. The efficacy of some of the tosylates has already been demonstrated. The first reported use of a phosphonium molten salt with a tosylate counterion was as the solvent for catalytic hydroformylation of hex-1-ene to heptanal and 2-methylhexanal using **1**, **3**, **5** and **9**.[12] This established that alteration of the substituents in the cation could affect product distribution. Diels–Alder reactions of isoprene with methyl acrylate, but-3-en-2-one and acrylonitrile have also been performed in phosphonium tosylates, including **1**, **3**, **5** and **9**.[13] The results indicate that product selectivity varies with cation substituent and also that the solvents are more suitable for the reactions of oxygen-containing dienophiles than for nitrogenous ones, showing high regioselectivity. Phosphonium salts including **1** and **9** have also been reported to be good co-catalysts for the Baylis–Hillman reac-

[a] School of Chemistry, University of Birmingham, Edgbaston, Birmingham B15 2TT, UK
Fax: +44-121-414-4403
E-mail: B.M.Kariuki@bham.ac.uk

 © 2006 Wiley-VCH Verlag GmbH & Co. KgaA, Weinheim 

tion with the results showing that neither modification of the cation substituents nor a change in the anion has a major effect on the yield.[14] The tosylates have also been used in rhodium-catalysed transfer hydrogenation of acetophenone.[15]

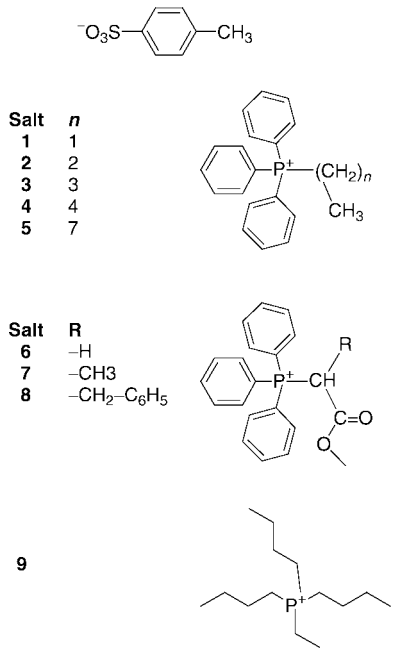


Scheme 1. The phosphonium tosylates under investigation.

In addition to the general properties of ionic liquids mentioned above, phosphonium salts have a number of other advantages. They can be prepared without halide contamination and therefore be used with no adverse effect on metal catalysts. They are also more thermally stable than quaternary nitrogen salts and thus can be applied under more demanding reaction conditions. The tosylates are relatively inexpensive, easily available, noncorrosive and are stable in air as well as in moisture. A high melting point has been found to be beneficial for the following reason. At the reaction temperature (above the melting point of the salt), the phosphonium salts act as solvents (for catalysts and reagents), allowing homogeneous conditions. On cooling, the salts crystallise out and trap the catalyst thereby enabling easy separation of liquid products. For example, in the hydroformylation,[12] Diels–Alder[13] and hydrogenation[15] reactions mentioned above, product separation involved filtration or decantation of the liquid organic product. The catalyst system or ionic solvent was subsequently reusable.

The growing interest in these materials as well as their potential as alternatives to other ionic and volatile organic solvents makes more fundamental research into their properties imperative. The properties of triphenylphosphonium salts can be affected by a change in the nature of both cation and anion; as a consequence, solvents can be tailor-made for a specific reaction by tuning their properties. For this to be achievable, the correlation between the physicochemical properties of the solvents and the molecular structure needs to be established.[4] This is a sizeable challenge as the number of available cations and anions is immense. Any investigation, therefore, needs to be performed systematically.

Melting points, which are an indication of the lower temperature limit of application of ionic solvents, can be related to the crystal structures and are looked at in some detail in this study. However, ionic salts are applied in the liquid state, where the challenge is to understand properties such as viscosity and ion diffusion. The more ordered crystalline state can provide important information (such as molecular geometry, intra- and intermolecular contacts) to assist in the process of beginning to understand and possibly model the properties of the liquid state. This is a realistic approach as shown by studies of imidazolium ionic liquids in which a correlation has been found between the structural properties of the solid state and those of the liquid state.[16–20] To the best of our knowledge, no structural information has been published for any triphenylphosphonium tosylates. An aim of this study has been to obtain this information, and to this end, the salts shown in Scheme 1 have been synthesised and characterised.

## Results and Discussion

### Melting Points

Melting points are invaluable in the characterisation of materials. In the case of ionic liquids, accurate melting points (along with boiling points and decomposition temperatures) are essential as they give an indication of the range of application. Melting points are also sensitive to the purity of the material – an important consideration as impurities may change the nature of ionic solvents. The melting points determined during this study are shown in Table 1. The "initial" values in the Table were obtained after sample preparation and some showed significant deviations from previously reported values. There were also some

Table 1. Melting points ($T_{mp}$) for the triphenylphosphonium tosylates.

| Salt | *n* | $T_{mp}$ [°C] | | |
|---|---|---|---|---|
| | | initial | after additional drying | literature |
| – | 0 | – | – | 137–139[21] |
| | | | | 147–149[22] |
| **1** | 1 | 118–120 | 139–141 | 94–95[12] |
| | | | | 82–83[21] |
| **2** | 2 | 142–143 | 143–145 | 141–143[21] |
| **3** | 3 | 130–131 | 132–134 | 116–117[12] |
| | | | | 139–140[21] |
| **4** | 4 | 120–122 | 123–125 | – |
| **5** | 7 | – | 129–131[a] | 70–71[12] |
| | | | | 70–78[21] |
| – | 9 | – | – | 94–96[23] |
| **6** | | 154–156 | 164–166 | – |
| **7** | | 173–175 | 175–176 | – |
| **8** | | – | – | – |
| **9** | | 74–76 | 74–75 | 81–83[12] |

[a] Solvate.

 © 2006 Wiley-VCH Verlag GmbH & Co. KGaA, Weinheim 

discrepancies between the various reports,[12,21–23] and hence further examination was undertaken.

The initial samples were rinsed using a volatile solvent and did not appear to be wet, but additional drying was found to raise the melting points significantly for some. The drying process was repeated until no further change was observed. Thus, for example, the melting point of **1** rose from 118–120 °C to 139–141 °C on storage under vacuum for several days and that of **6** increased from 154–156 °C to 164–166 °C under the same treatment. With the exception of **5**, which is a solvate, none of the analytical techniques indicated the presence of significant amounts of solvent in the initial samples and powder X-ray diffraction confirmed that no observable change in phase or crystallinity occurred during the drying process.

The final values of melting points obtained are also shown in Table 1. One literature value for **3** and that for **9** are significantly higher than the final values from this study, suggesting that even higher melting points might be obtained by further treatment. The final values from this study, along with the literature values for the *n*-alkyltriphenylphosphonium tosylates, are plotted in Figure 1. The need for reliable values is clearly illustrated by **1**. Going by the previously reported melting point, **1** falls within the conventional definition of ionic liquids (i.e. m.p. < 100 °C), whereas a considerably higher value has been obtained during this study. It is noted in passing, however, that **1**, **3** and **5** have been used at temperature as low as 80 °C, 40 °C and 60 °C[13] respectively although the melting points obtained for the pure phases are ca. 140 °C, 133 °C and 130 °C, respectively. This is attributable to the "impurity" effect of the reagents on the ionic solvents.

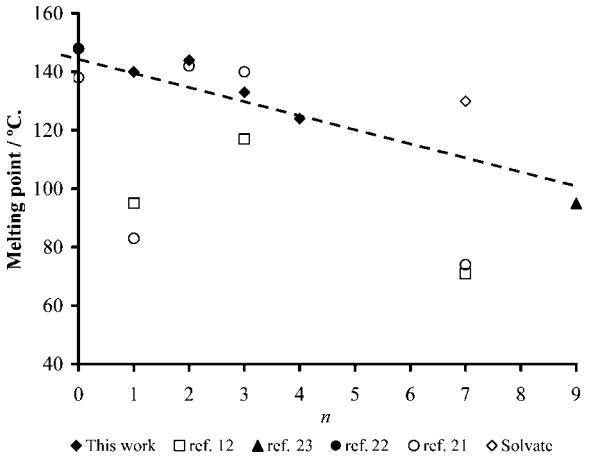


Figure 1. Melting points for the alkyltriphenylphosphonium tosylates.

Incorporation of solvent of crystallisation is clearly a consideration when selecting a salt for use as a solvent. Unlike the other samples investigated, the structure of **5** ($n$ = 7) included the solvent (dichloromethane). Two values have been reported previously for the melting point of **5**, and it is noteworthy that although they are close to each other, the range is quite large for one (8 °C). If an assumption is made that melting points decrease gradually with increasing $n$ for nonsolvated triphenylphosphonium tosylates (the dashed line in Figure 1), then a possible discrepancy is apparent for **5**, with the reported values falling well below that predicted.

The DSC results obtained indicate that endothermic processes occur at temperatures consistent with the melting

Table 2. Crystallographic data for the alkyltriphenylphosphonium tosylates.

| Salt | **1** | **2** | **3** | **4** | **5** |
|---|---|---|---|---|---|
| Formula | $C_{20}H_{20}P^+$ $C_7H_7O_3S^-$ | $C_{21}H_{22}P^+$ $C_7H_7O_3S^-$ | $C_{22}H_{24}P^+$ $C_7H_7O_3S^-$ | $C_{23}H_{26}P^+$ $C_7H_7O_3S^-$ | $C_{26}H_{32}P^+$ $C_7H_7O_3S^-$ $CH_2Cl_2$ |
| FW | 462.52 | 476.54 | 490.57 | 504.59 | 631.60 |
| $T$ [K] | 296 | 296 | 296 | 296 | 296 |
| $\lambda$ [Å] | 0.71069 | 0.71069 | 0.71069 | 1.54178 | 1.54178 |
| Crystal system | monoclinic | monoclinic | monoclinic | monoclinic | monoclinic |
| Space group | $P2_1/n$ | $P2_1/c$ | $P2_1/a$ | $P2_1/a$ | $P2_1/a$ |
| $a$ [Å] | 13.663(2) | 8.7830(8) | 12.672(1) | 12.6695(5) | 12.782(3) |
| $b$ [Å] | 12.695(2) | 16.244(2) | 17.227(2) | 17.2562(7) | 17.906(4) |
| $c$ [Å] | 13.811(2) | 17.643(2) | 12.451(2) | 12.6892(5) | 15.554(4) |
| $\beta$ [°] | 90.967(5) | 93.975(4) | 97.426(9) | 98.347(2) | 104.553(7) |
| $V$ [Å$^3$] | 2395.2(7) | 2511.0(4) | 2695.1(5) | 2744.82(19) | 3446(1) |
| $Z$ | 4 | 4 | 4 | 4 | 4 |
| $D_{calcd.}$ [Mg·m$^{-3}$] | 1.283 | 1.261 | 1.209 | 1.221 | 1.218 |
| $\mu$ [mm$^{-1}$] | 0.228 | 0.220 | 0.207 | 1.819 | 2.940 |
| $F$(000) | 976 | 1008 | 1040 | 1072 | 1336 |
| Crystal size [mm] | 0.50×0.15×0.10 | 0.50×0.15×0.10 | 0.10×0.08×0.01 | 0.34×0.10×0.04 | 0.24×0.12×0.06 |
| Total reflections | 13305 | 12967 | 12939 | 27287 | 8675 |
| Unique reflections | 4380 | 4319 | 4377 | 4917 | 2313 |
| $R_{int}$ | 0.042 | 0.034 | 0.065 | 0.096 | 0.094 |
| $S$ | 1.048 | 1.047 | 1.047 | 1.007 | 1.037 |
| $R_1$ [$I > 2\sigma(I)$] | 0.052 | 0.054 | 0.063 | 0.045 | 0.096 |
| $wR_p$ | 0.123 | 0.136 | 0.089 | 0.097 | 0.26 |

 © 2006 Wiley-VCH Verlag GmbH & Co. KGaA, Weinheim 

Table 3. Crystallographic data for the tosylates of triphenylphosphonium esters.

| Salt | **6** | **7** | **8** | **9** |
|---|---|---|---|---|
| Formula | $C_{21}H_{20}O_2P^+$ $C_7H_7O_3S^-$ | $C_{22}H_{22}O_2P^+$ $C_7H_7O_3S^-$ | $C_{28}H_{26}O_2P^+$ $C_7H_7O_3S^-$ | $C_{14}H_{32}P^+$ $C_7H_7O_3S^-$ |
| FW | 506.53 | 520.55 | 596.64 | 402.55 |
| $T$ [K] | 296 | 293 | 296 | 296 |
| $\lambda$ [Å] | 0.71069 | 0.71069 | 0.71069 | 0.71069 |
| Crystal system | monoclinic | orthorhombic | monoclinic | monoclinic |
| Space group | *Cc* | $P2_12_12_1$ | *Cc* | $P2_1/n$ |
| $a$ [Å] | 9.9121(9) | 13.048(1) | 17.752(2) | 8.137(3) |
| $b$ [Å] | 16.843(1) | 18.379(2) | 9.6829(7) | 13.249(6) |
| $c$ [Å] | 14.8464(9) | 10.9741(8) | 18.935(2) | 22.652(9) |
| $\beta$ / ° | 90.844(5) | – | 109.629(2) | 96.594(7) |
| $V$ [Å$^3$] | 2478.3(3) | 2631.8(3) | 3065.6(4) | 2426(2) |
| $Z$ | 4 | 4 | 4 | 4 |
| $D_{calcd.}$ [Mg·m$^{-3}$] | 1.358 | 1.314 | 1.293 | 1.102 |
| $\mu$ [mm$^{-1}$] | 0.233 | 0.221 | 0.199 | 0.215 |
| $F$(000) | 1064 | 1096 | 1256 | 880 |
| Crystal size [mm] | 0.30×0.20×0.02 | 0.40×0.10×0.05 | 0.50×0.40×0.40 | 0.40×0.30×0.10 |
| Total reflections | 7224 | 15070 | 9088 | 6127 |
| Unique reflections | 4006 | 4636 | 4630 | 2702 |
| $R_{int}$ | 0.072 | 0.047 | 0.030 | 0.103 |
| $S$ | 1.078 | 1.192 | 1.041 | 1.045 |
| $R_1$ [$I > 2\sigma(I)$] | 0.056 | 0.064 | 0.039 | 0.118 |
| $wR_p$ | 0.132 | 0.126 | 0.101 | 0.305 |
| $x$ (Flack) | 0.01(13) | –0.04(12) | 0.08(7) | – |

points. The peaks are sharp for the alkyltriphenyl compounds (**1**–**4** and **9**), and there is no indication of thermal instability within the timescale and temperature range of the experiment. These salts have high thermal stability, are tolerant toward air and are reusable as solvents.[12,13] On the other hand, DSC shows broader features in the cases of **5**–**7**; loss of the solvent is clearly a factor in **5**, whereas the results may be an indication of thermal transformation close to the melting point for the esters **6** and **7**.

## Structural Characterisation

Crystallographic data for **1**–**5** are shown in Table 2 and data for **6**–**9** are shown in Table 3. The asymmetric units are shown in Figure 2(a) to Figure 10(a).

### *Alkyltriphenylphosphonium Tosylates*

In the structure of **1**, tosylate ions are linked by C(3)–H(3)···O(2) interactions (with a H···O distance of 2.4 Å, a C–H···O angle of 170°) to form zigzag chains along the *b*-axis. These chains are arranged side-by-side to form sheets parallel to the (1,0,–1) plane, leading to a layered structure (Figure 2, b). In the structure, a number of edge-to-face interactions with "nonideal" geometry are observed. For example, an aromatic ring of the cation is the donor to two anion rings with planes at ca. 60° and 70° to it and both with CH···π(ring-plane) distances of ca. 3 Å. In the anion, the oxygen closest to the plane of the aromatic ring forms a torsion angle [O(3)–S(1)–C(1)–C(6)] of 16.9(3)°.

For **2**, the propyl chains of the cations are in *trans* conformation relative to the phosphorus atoms to which they are attached. In the crystal, the cations form channels, which run parallel to the *a*-axis and are occupied by pairs of anion chains (Figure 3, c). The two closest C–H···O contacts involve aryl hydrogen atoms [with angles C(26)–H(26B)···O(3) = 160.9(4)° and C(13)–H(13)···O(1) = 164.0(3)° and distances O(3)···H(26B) = 2.39(1) Å and O(1)···H(13) = 2.33(1) Å]. In the crystal structure, pairs of cations are linked by edge-to-face interactions involving all six

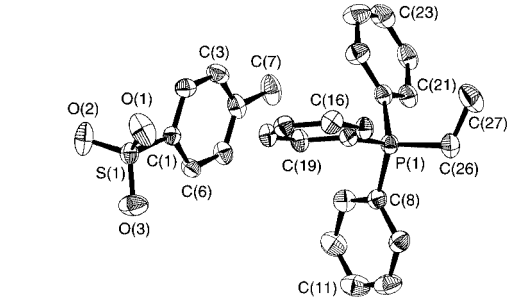


(a)

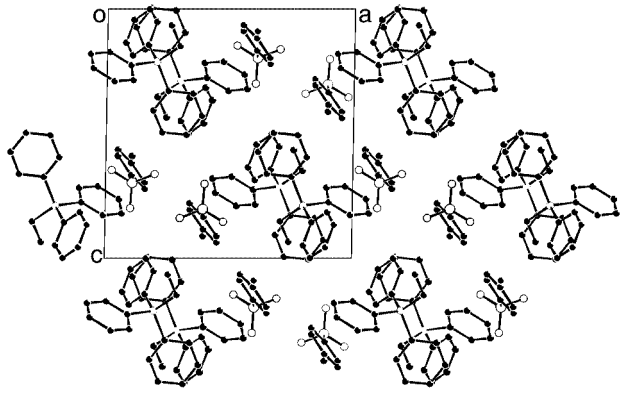


(b)

Figure 2. (a) The asymmetric unit and (b) the crystal structure of **1** viewed down the *b*-axis. Hydrogen atoms have been omitted for clarity.

 © 2006 Wiley-VCH Verlag GmbH & Co. KGaA, Weinheim 

phenyl rings as shown in Figure 3, (b) and, in addition, close CH···π contact occurs between a proton from a ring of the anion and one cation ring. For these interactions, the C–H···π(ring-plane) distances are in the 2.9–3.3 Å range. The oxygen closest to the plane of the aromatic ring of the anion forms a torsion angle O(2)–S(1)–C(1)–C(2) of –16.2(4)°.

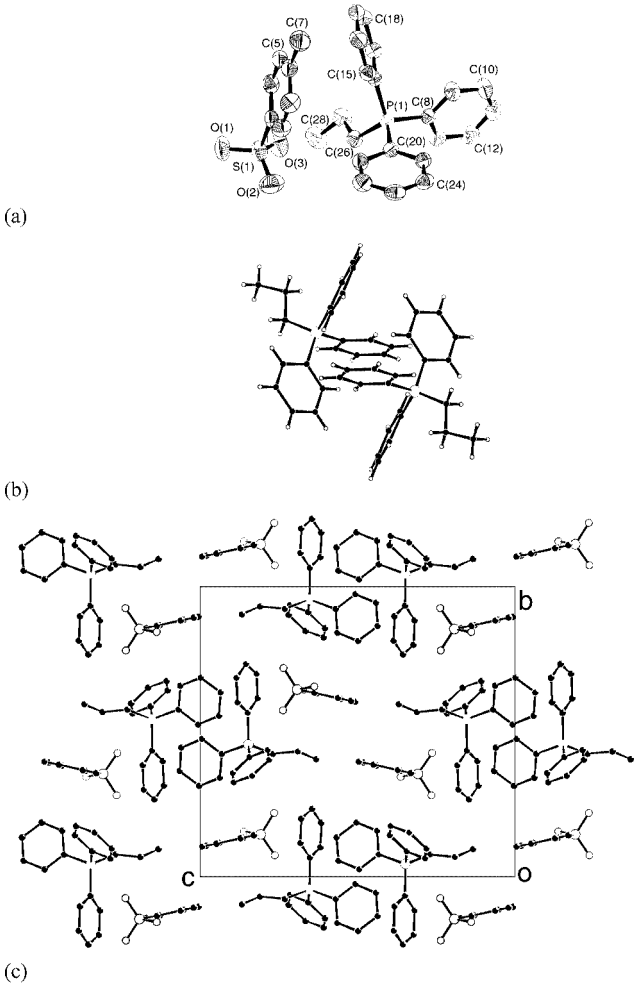


Figure 3. (a) The asymmetric unit, (b) a pair of cations and (c) the crystal structure of **2** viewed down the *a*-axis. Hydrogen atoms have been omitted from (a) and (c) for clarity.

The butyl chain in the crystal structure of **3** is also *all-trans* in conformation. In the structure (Figure 4, c), the tosylate anions are isolated from each other, with no direct contact between them. Pairs of symmetry related cations interact through edge-to-face contacts as shown in Figure 4, b. Each cation acts as both a donor and acceptor, with C–H···π(ring-centre) distance of ca. 2.64 Å. The two ions are also involved in π···π contact with a distance of ca. 3.5 Å between the planes of rings showing ca. 50% overlap. In the structure, a second type of π···π interaction occurs between phenyl rings of neighbouring cations with a separation distance of ca. 4.1 and an overlap of about 1/3 of a ring. The closest C–H···O contacts involve aryl–H and HC–H from the cation [with angles C(16)–H(16)···O(2) = 168.6(5)°, C(24)–H(24)···O(1) = 175.2(5)° and C(26)–H(26B)···O(1) = 173.4(4)° and contact distances O(2)···H(16) = 2.43(1) Å, O(1)···H(26B) = 2.29(1) Å, O(1)···H(24) = 2.37(1) Å]. The oxygen closest to the plane of the aromatic ring of the anion forms a torsion angle O(2)–S(1)–C(1)–C(2) of 12.8(4)°.

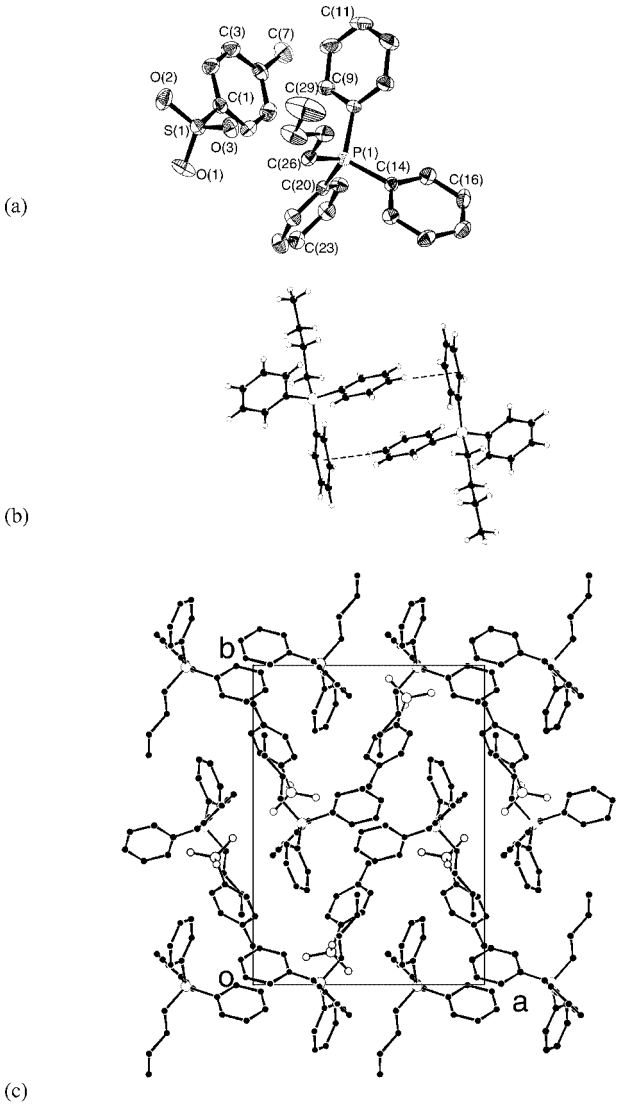


Figure 4. (a) The asymmetric unit of **3**, (b) a pair of cations with the dashed lines showing CH···π contacts and (c) the crystal structure viewed down the *c*-axis. Hydrogen atoms have been omitted from (a) and (c) for clarity.

In the structure of **4**, (Figure 5, c) the pentyl group of the cation is disordered with two components of 63% and 37% occupancy. For the major component, the chain adopts an all-*trans* conformation, except for the terminal methyl group which is *gauche*. As suggested by the similarity in the cell parameters and symmetry, the crystal structures of **3** and **4** are almost identical. Thus pairs of molecules interact in a manner similar to those discussed for **3**, with C–H···π(ring-centre) distance of ca. 2.67 Å and π···π contact interplanar distance of ca. 3.5 Å for rings showing 50% overlap (Figure 5, b). The separation between the planes of the pair of rings involved in the second type of π···π interaction (1/3 ring overlap) is also 4.1 Å. Aryl and $CH_2$

 © 2006 Wiley-VCH Verlag GmbH & Co. KGaA, Weinheim 

hydrogen atoms from the cation involved in the closest C–H···O contacts have CH···O distances: O(1)···H(19B) = 2.4(1) Å, O(1)···H(11) = 2.4(1) Å, O(2)···H(19A) = 2.4(1) Å and C–H···O angles: C(11)–H(11)···O(1) = 174.9(5)°, C(19)–H(19B)···O(1) = 170.6(5)°, C(19)–H(19A)···O(2) = 156.9(5)°. The oxygen closest to the plane of the aromatic ring of the anion forms a torsion angle O(3)–S(1)–C(24)–C(29) of 11.5(4)°.

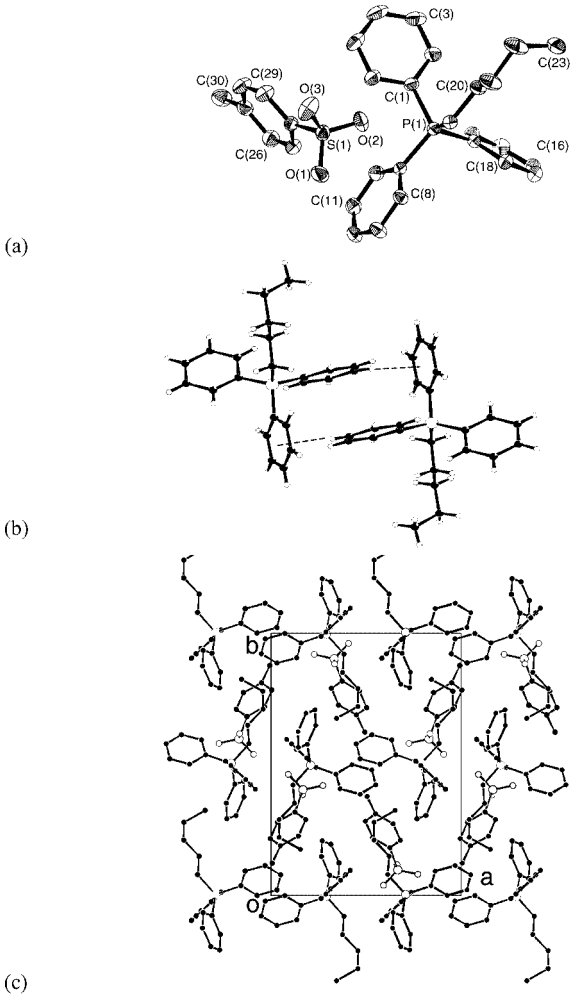


Figure 5. (a) The asymmetric unit of **4**, (b) a pair of cations with the dashed lines showing CH···π contacts and (c) the crystal structure viewed down the *c*-axis. Hydrogen atoms have been omitted from (a) and (c) for clarity.

Unlike the other salts, the crystals of **5** included the dichloromethane solvent (Figure 6, b). The structure consists of channels, parallel to the *a*-axis, which are occupied by the anions. The closest C–H···O contacts have distances: O(1)···H(26B) = 2.2(2) Å, O(1)···H(10) = 2.4(2) Å, O(2)···H(34A) = 2.4(2) Å and C–H···O angles: C(26)–H(26B)···O(1) = 178.7(9)°, C(10)–H(10)···O(1) = 176.0(9)°, C(34)–H(34A)···O(2) = 135.3(9)°. The oxygen closest to the plane of the aromatic ring of the anion forms a torsion angle O(2)–S(1)–C(1)–C(6) = 16.6(9)°. Interactions of π···π type also occur for a pair of cations (Figure 6, b), with an interplanar distance of ca. 3.5 Å for rings showing an overlap of ca. 1/3 of a ring. The rings involved are also donors in C–H···π interactions with –H···π distances of ca. 2.7 Å.

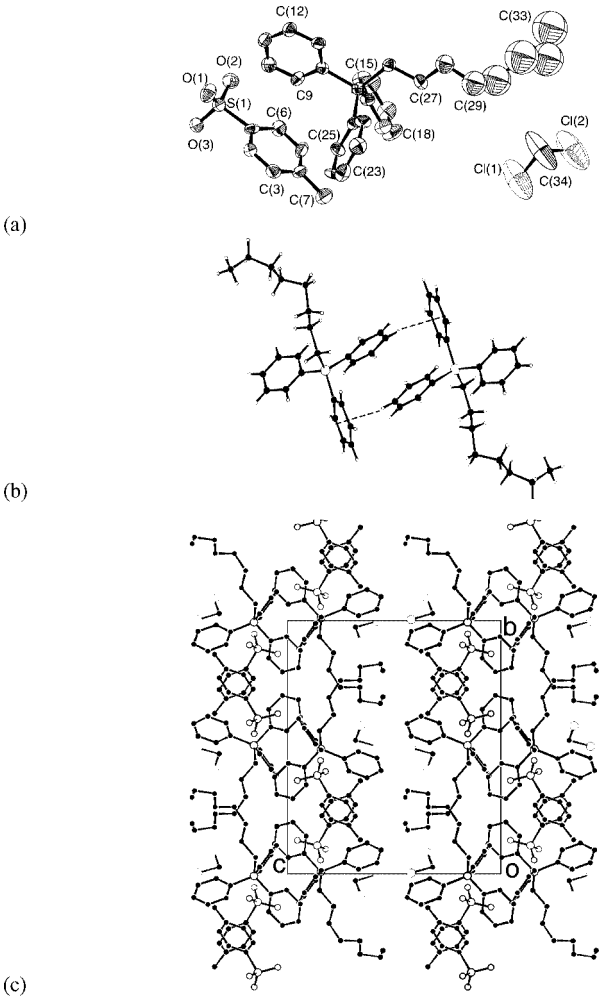


Figure 6. (a) The asymmetric unit, (b) a pair of cations with the dashed lines showing CH···π contacts and (c) the crystal structure of **5** viewed down the *a*-axis. Hydrogen atoms have been omitted from (a) and (c) for clarity.

### *Tosylates of Triphenylphosphonium Esters*

In the crystal structure of **6**, the cations form channels, parallel to the *a*-axis, which are occupied by straight chains of tosylate anions (Figure 7, b). A number of edge-to-face interactions are observed with the tosylate anion as the donor and the cation as the acceptor. However, the planes of the rings involved are not perpendicular. For example, a C–H···π(ring-plane) distance of 2.9 Å is observed between rings with planes oriented ca. 60° relative to each other. The closest CH···O contacts involve cation methylene groups and tosylate oxygen atoms, with distances O(1)···H(26A) = 2.24(1) Å, O(2)···H(26B) = 2.26(1) Å, and angles C(26)–H(26A)···O(1) = 153.3(6)°, and C(26)–H(26B)···O(2) = 164.6(6)°. The oxygen closest to the plane of the aromatic ring of the anion forms a torsion angle O(1)–S(1)–C(1)–C(6) is –19.4(6)°.

 © 2006 Wiley-VCH Verlag GmbH & Co. KGaA, Weinheim 

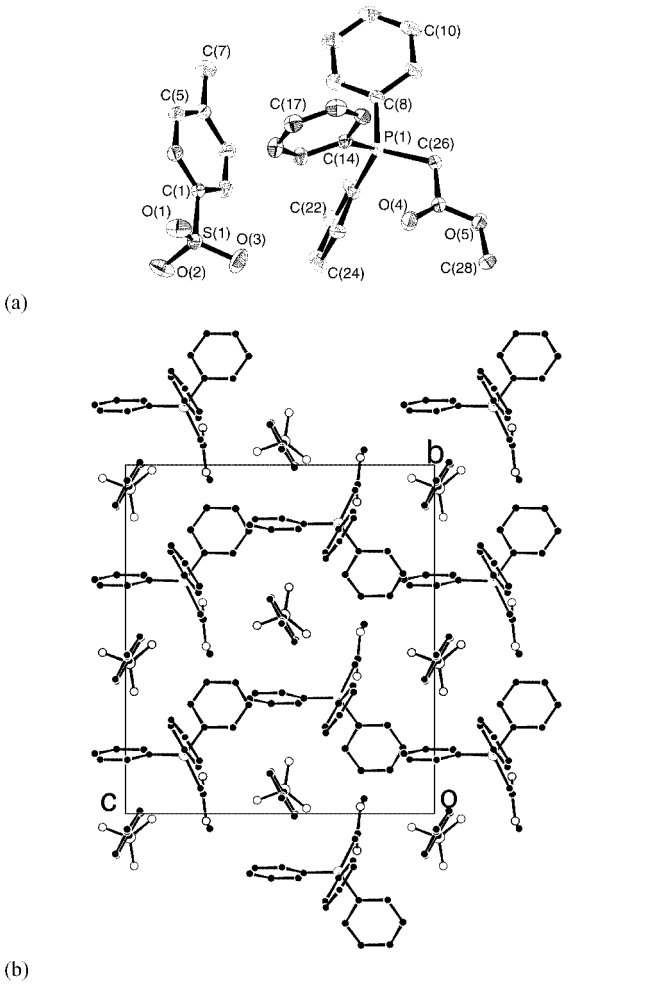


Figure 7. (a) The asymmetric unit and (b) the crystal structure of **6** viewed down the *a*-axis. Hydrogen atoms have been omitted for clarity.

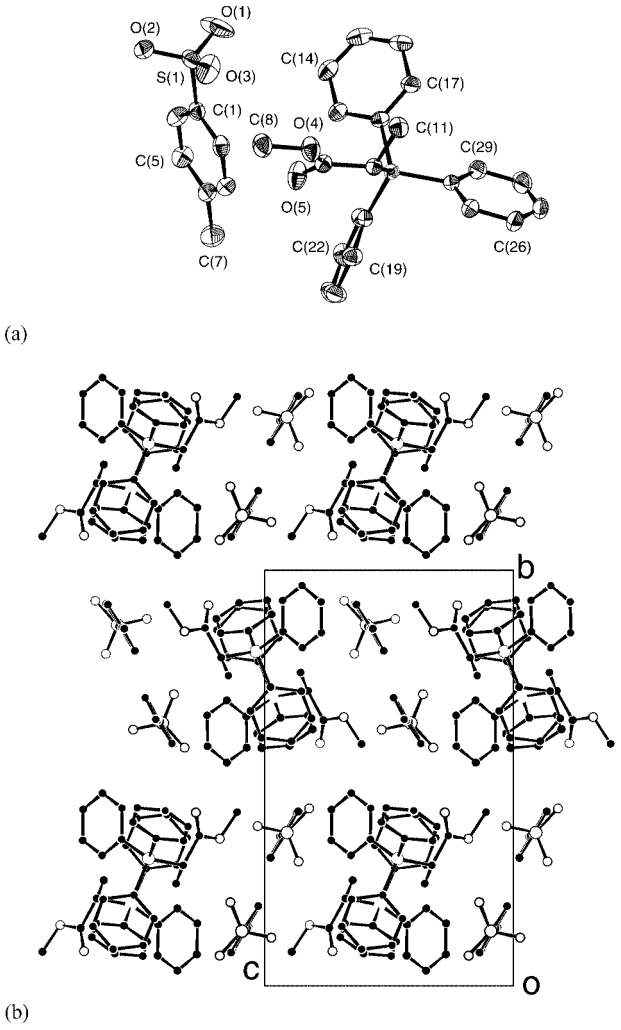


Figure 8. (a) The asymmetric unit and (b) the crystal structure of **7** viewed down the *a*-axis. Hydrogen atoms have been omitted for clarity.

In the crystal structure of **7**, the cations also form channels, running parallel to the *a*-axis (Figure 8, b), which are occupied by zigzag chains of tosylate anions. In the crystal structure, the closest C–H···π distance for an edge-to-face type of interaction involves a cation donor and anion acceptor with a distance of ca. 3.1 Å for rings oriented ca. 100° apart. The shortest C–H···O contact involves the tertiary proton of the cation and one tosylate oxygen with a distance O(2)···H(10) of 2.17(4) Å and angle C(10)–H(10)··· O(2) of 175(3)°. The oxygen closest to the plane of the aromatic ring of the anion forms a torsion angle O(3)–S(1)–C(1)–C(2) of –11.7(4)°.

The crystal structure of **8** (Figure 9, b) does not contain channels. The cations pack in layers, parallel to the *ab* plane, between which isolated anions are located. Edge-to-face interactions are found and involve one cation ring acting as donor to two rings of two neighbouring cations. The two acceptor rings are almost perpendicular to the donor ring, with a C–H···π(ring-plane) distance of ca. 3 Å. The shortest CH···O contact involves an aryl proton and a tosylate oxygen with a distance O(3)···H(17) of 2.40(1) Å and angle C(17)–H(17)···O(3) of 141.5(4)°. The oxygen closest to the plane of the aromatic ring of the anion forms a torsion angle O(2)–S(1)–C(1)–C(2) of –29.2(8)°.

### *Tributyl(ethyl)phosphonium Tosylate*

In the crystal structure of **9**, the methyl group of one butyl chain of the cation is disordered with two components of 60% and 40% occupancy. Considering just the major component, all the alkyl chains adopt *trans* conformation, apart from one, in which the methyl group is *gauche*. In the structure, the tosylate anions are isolated from each other, each being surrounded by cations. The structure can be visualised as being composed of sheets parallel to the *ab* (Figure 10, b), with intermolecular C–H···O contacts occurring within the sheets. The shortest CH···O contacts involve one tosylate oxygen with distances: O(1)···H(18A) = 2.4(3) Å, O(1)···H(12A) = 2.4(2) Å and angles: C(18)–H(18A)···O(1) = 173(1)°, C(12)–H(12A)···O(1) = 153(1)°. The oxygen closest to the plane of the aromatic ring of the anion forms a torsion angle O(1)–S(1)–C(1)–C(2) of –15.1(2)°.

 © 2006 Wiley-VCH Verlag GmbH & Co. KGaA, Weinheim 

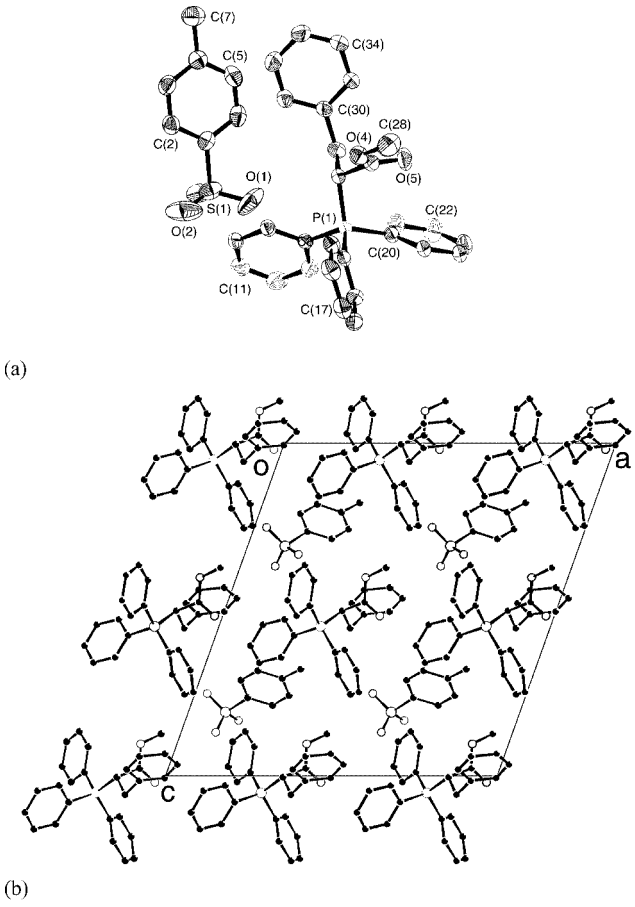


Figure 9. (a) The asymmetric unit and (b) the crystal structure of **8** viewed down the *b*-axis. Hydrogen atoms have been omitted for clarity.

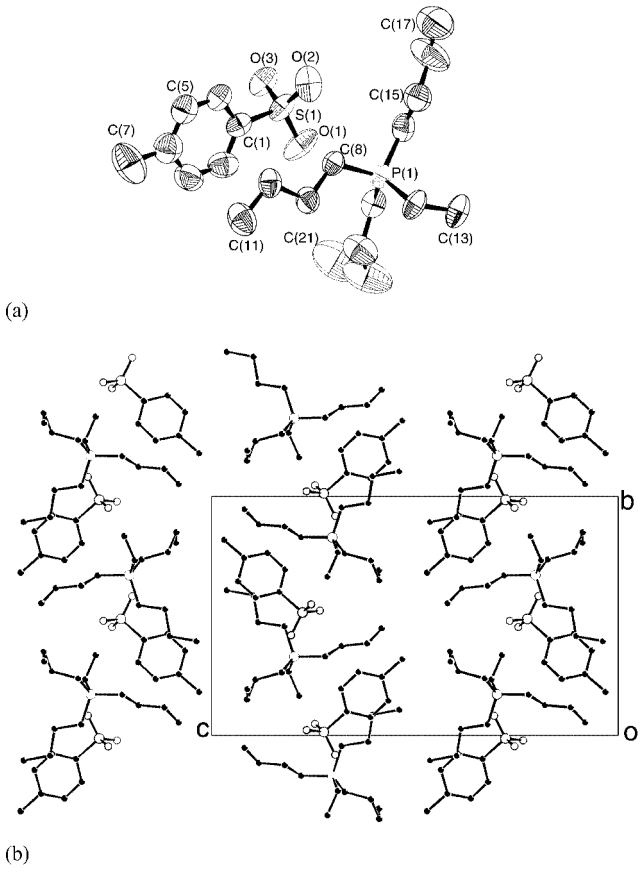


Figure 10. (a) The asymmetric unit and (b) the crystal structure of **9** viewed down the *a*-axis. Hydrogen atoms have been omitted for clarity.

## Conclusions

The observations made during this study show that some care needs to be exercised when determining and using the melting points of these materials. The values obtained suggest that minute amounts of solvent can have a significant effect on the melting points, a possible explanation for the inconsistencies in the previously reported values.

Being ionic, coulombic interactions obviously exist in all these materials. Another feature common to all nine salts is the absence of strong hydrogen-bond donors. There is thus no single strong directional interaction to influence crystal packing. Despite this, a number of structural patterns, which may be valuable when modelling their liquid properties, are evident. In the tosylate anion the angles between the ring and the plane through the C–S–O group containing the oxygen atom closest to the ring fall within the range 11–20° (except for **8** in which the angle is ca. 30°). Apart from **5**, none of the salts contains solvent of crystallisation, a desirable characteristic in ionic solvents. All structures (**1**–**9**) show some degree of C–H···O contact with the tosylate ion acting as the acceptor. In addition, ring edge-to-face C–H···π interactions of variable geometry are also observed (the exception in the C–H···π case is **9**, in which the cation has no phenyl groups). C–H···X interactions (e.g. with X = halide or π) are a recurring theme in the field of ionic liquids and have been described extensively for, for example, imidazolium salts.[16–20]

The cations in the *n*-alkyltriphenylphosphonium salts **1**–**5** tend to pack in pairs (with the exception of **1**, in which the short alkyl chain may allow more favourable alternative packing in the crystal). This motif involving pairs of $(phenyl)_3P$ groups is not unusual and has been observed in, for example, neutral triphenylphosphane oxides.[24] In the structures of **3**–**5**, the pairs of rings involved in C–H···π interactions are almost perpendicular, with interplanar angles of 86°, 85° and 81° respectively. The C–H···π distances (ca. 2.7 Å) in these three structures are also the shortest observed during this study and are similar to the average value obtained in a survey of organometallic materials (2.79 Å).[25] The donor rings in the ion pairs in **3**–**5** are also involved in π···π contacts, clearly leading to a stable motif. Although only a few structures have been determined, some clear differences are observed between the *n*-alkyl salts on the one hand and ester salts on the other. In the case of the esters, cation pairs are not observed and, in addition, the three structures are noncentrosymetric.

We believe that as in the case of imidazolium salts reported before, the structural information from this study will be important in future attempts to gain insight into the structural characteristics of ionic liquids of this type and

 © 2006 Wiley-VCH Verlag GmbH & Co. KGaA, Weinheim 

will aid in the understanding of the nature of interactions with solutes.

## Experimental Section

**Techniques:** NMR spectra were recorded with a Bruker AC-300 ($^1$H, 300 MHz; $^{13}$C, 75.5 MHz) and a Bruker AV-300 ($^1$H, 300 MHz; $^{13}$C, 75.5 MHz). Chemical shifts are described in parts per million (ppm) downfield shift from $SiMe_4$ and are reported consecutively as position ($\delta_H$ or $\delta_C$), multiplicity (s = singlet, d = doublet, t = triplet, q = quadruplet, m = multiplet, dd = doublet of doublet), coupling constant (*J*/Hz), relative integral and assignment. Proton NMR spectra were referenced to the chemical shift of residual proton signals ($CHCl_3$ $\delta$ = 7.27 ppm). Carbon spectra were referenced to a $^{13}$C resonance of the solvent ($CDCl_3$ $\delta$ = 77.16 ppm). $^{31}$P NMR spectra were referenced internally on $H_2PO_4$ 5%/$D_2O$ ($\delta$, 0.00). Mass spectra were recorded with a VG Zabspec spectrometer. LSIMS (ceasium ionisation) was performed using 3-nitrobenzyl alcohol as the matrix. DSC results for **1**–**7**, **9** were obtained using a Perkin–Elmer Pyris 1 instrument between 25 and 200 °C at a heating rate of 20°/min with nitrogen purge gas and aluminium sample pans.

Single crystals were obtained by slow diffusion of diethyl ether into a dichloromethane solution of the salt. Single-crystal diffraction data for **1**–**3**, **6**–**9** were recorded at ca. 296 K with a Rigaku R-axis II diffractometer equipped with a molybdenum rotating anode source and an image plate detector system. Data for **4** and **5** were recorded with a Bruker Smart 6000 diffractometer equipped with a CCD detector and a copper-tube source. Structures were solved and refined using SHELXL.[26] During final refinement, aromatic C–H atoms were riding on the atoms they are bonded to with a bond length of 0.93 Å. Powder diffraction data confirm that the crystal structures obtained are representative of the bulk samples, except for **8**, where the amount of crystalline material obtained was too small for powder diffraction.

CCDC-277854 to -277862 contain the supplementary crystallographic data for this paper. These data can be obtained free of charge from The Cambridge Crystallographic Data Centre via www.ccdc.cam.ac.uk/data_request/cif.

**Syntheses:** All manipulations were performed under argon using standard Schlenk techniques. All solvents were dried with the appropriate drying agent and distilled under dinitrogen: sodium benzophenone ketyl (diethyl ether, toluene) or calcium hydride (dichloromethane). Unless otherwise stated, all reagents were purchased from Aldrich, Acros or Lancaster and used as supplied. All the *p*-toluenesulfonates were obtained in good yield and high purity using known literature methods.[27]

The same method was used for all salts. Salts **1**–**5** were obtained by refluxing a 1:1 molar ratio solution of the alkyl *p*-toluenesulfonate (ca. 4 g) and triphenylphosphane (ca. 5 g) in toluene (ca. 50 mL) for 18 hours under argon. The solvent was then removed under reduced pressure and the residual was washed with diethyl ether. The resulting solid was recrystallised from dichloromethane/diethyl ether to a crystalline white solid.

The appropriate methoxycarbonylalkyl *p*-toluenesulfonate was used for **6** and **7**. The recrystallised product obtained for **6** had a pale brown colouration. For **8**, methyl 3-phenyl-2-(tolyl-4-sulfonyloxy)propionate was used and the solution was refluxed for 42 hours. The final recrystallised product was pale yellow in colour. A solution of ethyl *p*-toluenesulfonate and tributylphosphane was refluxed as described above to yield **9**.

**Ethyltriphenylphosphonium Tosylate (1):** Ethyl *p*-toluenesulfonate (3.8 g, 19.0 mmol) and triphenylphosphane (5.0 g, 19.1 mmol) afforded a crystalline white solid (8.1 g, 92%). M.p. 139–141 °C (ref.[21] 82–83 °C, ref.[12] 94–95 °C). FAB+: *m*/*z* (%) = 291 (100) $[M - C_7H_7SO_3]^+$, 753 (8) $[2M - C_7H_7SO_3]^+$. $^1$H NMR ($CDCl_3$, 300 MHz): $\delta$ = 1.34 (dt, $^3J_{H,H}$ = 7.4, $^3J_{P-H}$ = 20.1 Hz, 3 H, $CH_2CH_3$), 2.31 (s, 3 H, $CCH_3$), 3.60 (m, 2 H, $CH_2$), 7.08 (d, $^3J_{H,H}$ = 8.0 Hz, 2 H, $^{tosylate}$Ar-*H*), 7.63–7.79 (m, 17 H, Ar-*H*) ppm. $^{13}$C{$^1$H} NMR ($CDCl_3$, 75.5 MHz): $\delta$ = 5.6 (d, $^2J_{P,C}$ = 5.2 Hz, $CH_2CH_3$), 14.8 (d, $^1J_{P,C}$ = 52.3 Hz, $CH_2$), 20.3 ($CCH_3$), 116.8 (d, $^1J_{P,C}$ = 86.2 Hz, $^{phosphonium}$Ar-$C_{ipso}$), 125.1, 127.3 ($^{tosylate}$Ar-*C*H), 129.4, 129.5, 132.4, 132.5, 134.0 ($^{phosphonium}$Ar-*C*H), 137.6, 143.5 ($^{tosylate}$Ar-$C_{ipso}$) ppm. $^{31}$P NMR ($D_2O$, 121 MHz): $\delta$ = 26.3 ($^{phosphonium}P$) ppm.

**Triphenyl(propyl)phosphonium Tosylate (2):** Propyl *p*-toluenesulfonate (4.0 g, 18.7 mmol) and triphenylphosphane (4.9 g, 18.7 mmol) afford a crystalline white solid (8.4 g, 94%). M.p. 143–145 °C (ref.[21] 141–143 °C). FAB+: *m*/*z* (%) = 305 (100) $[M - C_7H_7SO_3]^+$, 781 (5) $[2M - C_7H_7SO_3]^+$. $^1$H NMR ($CDCl_3$, 300 MHz): $\delta$ = 1.18 (m, 3 H, $CH_2CH_3$), 1.61 (m, 2 H, $CH_2CH_3$), 2.33 (s, 3 H, $CCH_3$), 3.52 (m, 2 H, $PCH_2$), 7.04 (d, $^3J_{H,H}$ = 8.0 Hz, 2 H, $^{tosylate}$Ar-*H*), 7.62–7.84 (m, 17 H, Ar-*H*) ppm. $^{13}$C{$^1$H} NMR ($CDCl_3$, 75.5 MHz): $\delta$ = 14.7 (d, $^3J_{P,C}$ = 17.2 Hz, $CH_2CH_3$), 16.0 (d, $^2J_{P,C}$ = 4.0 Hz, $CH_2CH_3$), 20.9 ($CCH_3$), 23.1 (d, $^1J_{P,C}$ = 50.6 Hz, $PCH_2$), 117.9 (d, $^1J_{P,C}$ = 85.6 Hz, $^{phosphonium}$Ar-$C_{ipso}$), 125.8, 127.8 ($^{tosylate}$Ar-*C*H), 130.0, 130.2, 133.0, 133.2, 134.5 ($^{phosphonium}$Ar-*C*H), 137.8, 144.5 ($^{tosylate}$Ar-$C_{ipso}$) ppm. $^{31}$P NMR ($D_2O$, 121 MHz): $\delta$ = 23.9 ($^{phosphonium}P$) ppm.

***n*-Butyltriphenylphosphonium Tosylate (3):** *n*-Butyl *p*-toluenesulfonate (3.5 g, 15.3 mmol) and triphenylphosphane (4.0 g, 15.3 mmol) afforded a crystalline white solid (7.0 g, 93%). M.p. 132–134 °C (ref.[21] 139–140 °C, ref.[12] 116–117 °C). FAB+: *m*/*z* (%) = 319 (100) $[M - C_7H_7SO_3]^+$, 809 (11= $[2M - C_7H_7SO_3]^+$. $^1$H NMR ($CDCl_3$, 300 MHz): $\delta$ = 0.86 (t, $^3J_{H,H}$ = 7.1 Hz, 3 H, $CH_2CH_3$), 1.52 (m, 4 H, $CH_2CH_2CH_3$), 2.28 (s, 3 H, $CCH_3$), 3.50 (m, 2 H, $PCH_2$), 7.01 (d, $^3J_{H,H}$ = 7.9 Hz, 2 H, $^{tosylate}$Ar-*H*), 7.57–7.79 (m, 17 H, Ar-*H*) ppm. $^{13}$C{$^1$H} NMR ($CDCl_3$, 75.5 MHz): $\delta$ = 13.3 ($CH_2CH_3$), 20.9 ($CCH_3$), 21.3 (d, $^1J_{P,C}$ = 50.6 Hz, $PCH_2$), 23.2 (d, $^2J_{P,C}$ = 16.7 Hz, $PCH_2CH_2$), 24.5 (d, $^3J_{P,C}$ = 4.0 Hz, $CH_2CH_3$), 118.0 (d, $^1J_{P,C}$ = 85.6 Hz, $^{phosphonium}$Ar-$C_{ipso}$), 125.9, 127.8 ($^{tosylate}$Ar-*C*H), 130.1, 130.2, 133.1, 133.2, 134.6 ($^{phosphonium}$Ar-*C*H), 137.9, 144.5 ($^{tosylate}$Ar-$C_{ipso}$). $^{31}$P NMR ($D_2O$, 121 MHz): $\delta$ = 24.2 ($^{phosphonium}P$) ppm.

***n*-Pentyltriphenylphosphonium Tosylate (4):** *n*-Pentyl *p*-toluenesulfonate (3.8 g, 15.6 mmol) and triphenylphosphane (4.1 g, 15.6 mmol) afforded a crystalline white solid (6.9 g, 87%). M.p. 123–125 °C. FAB+: *m*/*z* (%) = 333 (100) $[M - C_7H_7SO_3]^+$, 837 (9) $[2M - C_7H_7SO_3]^+$. $^1$H NMR ($CDCl_3$, 300 MHz): $\delta$ = 0.76 (t, $^3J_{H,H}$ = 7.1 Hz, 3 H, $CH_2CH_3$), 1.24 (m, 2 H, $CH_2CH_3$), 1.53 (m, 4 H, $PCH_2CH_2CH_2CH_2$), 2.31 (s, 3 H, $CCH_3$), 3.61 (m, 2 H, $PCH_2$), 7.08 (d, $^3J_{H,H}$ = 8.0 Hz, 2 H, $^{tosylate}$Ar-*H*), 7.62–7.84 (m, 17 H, Ar-*H*) ppm. $^{13}$C{$^1$H} NMR ($CDCl_3$, 75.5 MHz): $\delta$ = 13.2 ($CH_2CH_3$), 20.8 ($CCH_3$), 21.3 (d, $^1J_{P,C}$ = 48.9 Hz, $PCH_2$), 21.6 ($CH_2CH_3$), 21.7 (d, $^3J_{P,C}$ = 4.6 Hz, $CH_2CH_2CH_3$), 31.8 (d, $^2J_{P,C}$ = 15.5 Hz, $PCH_2CH_2$), 117.9 (d, $^1J_{P,C}$ = 85.6 Hz, $^{phosphonium}$Ar-$C_{ipso}$), 125.7, 127.7 ($^{tosylate}$Ar-*C*H), 130.0, 130.1, 133.0, 133.1, 134.5 ($^{phosphonium}$Ar-*C*H), 137.8, 144.4 ($^{tosylate}$Ar-$C_{ipso}$) ppm. $^{31}$P NMR ($D_2O$, 121 MHz): $\delta$ = 24.1 ($^{phosphonium}P$) ppm.

***n*-Octyltriphenylphosphonium Tosylate (5):** *n*-Octyl *p*-toluenesulfonate (2.5 g, 8.8 mmol) and triphenylphosphane (2.3 g, 8.8 mmol) afforded a crystalline white solid (3.1 g, 65%). M.p. 129–131 °C, (ref.[12] 70–71 °C, ref.[21] 70–78 °C). FAB+: *m*/*z* (%) = 375 (100)

 © 2006 Wiley-VCH Verlag GmbH & Co. KGaA, Weinheim 

$[M - C_7H_7SO_3]^+$, 922 (6) $[2M - C_7H_7SO_3]^+$. $^1H$ NMR ($CDCl_3$, 300 MHz): $\delta$ = 0.79 (t, $^3J_{H,H}$ = 6.6 Hz, 3 H, $CH_2CH_3$), 1.11 (m, 8 H, $CH_2CH_3$), 1.48 (m, 4 H, $PCH_2CH_2CH_2CH_2$), 2.26 (s, 3 H, $CCH_3$), 3.46 (m, 2 H, $PCH_2$), 7.00 (d, $^3J_{H,H}$ = 8.1 Hz, 2 H, $^{tosylate}$Ar-*H*), 7.62–7.76 (m, 17 H, Ar-*H*) ppm. $^{13}C\{^1H\}$ NMR ($CDCl_3$, 75.5 MHz): $\delta$ = 13.6 ($CH_2CH_3$), 20.8 ($CCH_3$), 21.4 (d, $^1J_{P,C}$ = 50.6 Hz, $PCH_2$), 22.0, 28.4, 28.6 ($PCH_2CH_2CH_2CH_2CH_2$), 22.1 ($CH_2CH_3$), 29.8 (d, $^2J_{P,C}$ = 15.5 Hz, $PCH_2CH_2$), 31.2 ($CH_2CH_2CH_2CH_3$), 117.8 (d, $^1J_{P,C}$ = 85.6 Hz, $^{phosphonium}$Ar-$C_{ipso}$), 125.8, 127.7 ($^{tosylate}$Ar-*C*H), 129.9, 130.1, 133.0, 133.1, 134.5 ($^{phosphonium}$Ar-*C*H), 137.9, 144.1 ($^{tosylate}$Ar-$C_{ipso}$) ppm. $^{31}P$ NMR ($D_2O$, 121 MHz): $\delta$ = 24.3 ($^{phosphonium}P$) ppm.

**[(Methoxycarbonyl)methyl]triphenylphosphonium Tosylate (6):** (Methoxycarbonyl)methyl *p*-toluenesulfonate (2.9 g, 11.9 mmol) and triphenylphosphane (3.1 g, 11.9 mmol) afforded a crystalline pale brown solid (4.7 g, 78%). M.p. 164–166 °C. FAB+: *m*/*z* (%) = 335 (100) $[M - C_7H_7SO_3]^+$, 841 (9) $[2M - C_7H_7SO_3]^+$. $^1H$ NMR ($CDCl_3$, 300 MHz): $\delta$ = 2.32 (s, 3 H, $CCH_3$), 3.59 (s, 3 H, $OCH_3$), 5.30 (d, $^2J_{P-H}$ = 13.5 Hz, 2 H, $PCH_2$), 7.08 (d, $^3J_{H,H}$ = 8.0 Hz, 2 H, $^{tosylate}$Ar-*H*), 7.62–7.87 (m, 17 H, Ar-*H*) ppm. $^{13}C\{^1H\}$ NMR ($CDCl_3$, 75.5 MHz): $\delta$ = 21.2 ($CCH_3$), 31.3 (d, $^1J_{P,C}$ = 58.0 Hz, $PCH_2$), 53.2 ($OCH_3$), 117.9 (d, $^1J_{P,C}$ = 89.1 Hz, $^{phosphonium}$Ar-$C_{ipso}$), 126.1, 127.1 ($^{tosylate}$Ar-*C*H), 130.1, 130.3, 133.7, 133.8, 135.0 ($^{phosphonium}$Ar-*C*H), 138.3, 144.3 ($^{tosylate}$Ar-$C_{ipso}$), 165.3 (d, $^2J_{P,C}$ = 3.4 Hz, *C*O) ppm. $^{31}P$ NMR ($D_2O$, 121 MHz): $\delta$ = 20.8 ($^{phosphonium}P$) ppm.

**[1-(Methoxycarbonyl)ethyl]triphenylphosphonium Tosylate (7):** 1-(Methoxycarbonyl)ethyl *p*-toluenesulfonate (1.4 g, 5.4 mmol) and triphenylphosphane (1.42 g, 5.4 mmol) in toluene (50 mL) afforded crystalline white needles (1.8 g, 64%). M.p. 175–176 °C. FAB+: *m*/*z* (%) = 349 (100) $[M - C_7H_7SO_3]^+$, 869 (4) $[2M - C_7H_7SO_3]^+$. $^1H$ NMR ($CDCl_3$, 300 MHz): $\delta$ = 1.67 (dd, $^3J_{H,H}$ = 7.0, $^2J_{P-H}$ = 18.6 Hz, 3 H, $CHCH_3$), 2.33 (s, 3 H, $CCH_3$), 3.54 (s, 3 H, $OCH_3$), 6.36 (m, 1 H, $PCH$), 7.11 (d, $^3J_{H,H}$ = 7.7 Hz, 2 H, $^{tosylate}$Ar-*H*), 7.64–7.96 (m, 17 H, Ar-*H*) ppm. $^{13}C\{^1H\}$ NMR ($CDCl_3$, 75.5 MHz): $\delta$ = 13.0 (d, $^2J_{P,C}$ = 13.1 Hz, $CHCH_3$), 21.2 ($CCH_3$), 36.2 (d, $^1J_{P,C}$ = 48.2 Hz, $PCH$), 53.3 ($OCH_3$), 118.0 (d, $^1J_{P,C}$ = 79.7 Hz, $^{phosphonium}$Ar-$C_{ipso}$), 126.1, 128.2 ($^{tosylate}$Ar-*C*H), 130.0, 130.2, 134.0, 134.1, 134.7 ($^{phosphonium}$Ar-*C*H), 138.7, 144.5 ($^{tosylate}$Ar-$C_{ipso}$), 166.1 (d, $^2J_{P,C}$ = 3.2 Hz, *C*O). $^{31}P$ NMR ($D_2O$, 121 MHz): $\delta$ = 28.0 ($^{phosphonium}P$) ppm.

**[1-(Methoxycarbonyl)-2-phenylethyl]triphenylphosphonium Tosylate (8):** Methyl 3-phenyl-2-(tolyl-4-sulfonyloxy)propionate (0.5 g, 1.5 mmol) and triphenylphosphane (0.4 g, 1.5 mmol) in toluene (20 mL) afforded a crystalline pale yellow solid (0.5 g, 56%). The material was the most difficult to obtain and it was not possible to carry out full characterisation.

**Tributyl(ethyl)phosphonium Tosylate (9):** Ethyl *p*-toluenesulfonate (2.0 g, 10.0 mmol) and tributylphosphane (2.0 g, 10.0 mmol) in toluene (50 mL) afforded a crystalline white solid (3.7 g, 93%). M.p. 74–76 °C (ref.[12] 81–83 °C). FAB+: *m*/*z* (%) = 231 (100) $[M - C_7H_7SO_3]^+$. $^1H$ NMR ($CDCl_3$, 300 MHz): $\delta$ = 0.97 (m, 9 H, $CH_2CH_2CH_3$), 1.22 (m, 3 H, $PCH_2CH_3$), 1.46 (m, 12 H, $PCH_2CH_2CH_2$), 2.28 (m, 6 H, $PCH_2CH_2$), 2.31 (s, 3 H, $CCH_3$), 2.42 (m, 2 H, $PCH_2$), 7.10 (d, $^3J_{H,H}$ = 8.0 Hz, 2 H, $^{tosylate}$Ar-*H*), 7.78 (d, $^3J_{H,H}$ = 8.0 Hz, 2 H, $^{tosylate}$Ar-*H*) ppm. $^{13}C\{^1H\}$ NMR ($CDCl_3$, 75.5 MHz): $\delta$ = 5.1 (d, $^2J_{P,C}$ = 5.7 Hz, $CH_2CH_3$), 11.5 (d, $^1J_{P,C}$ = 48.9 Hz, $PCH_2CH_3$), 12.6 ($CH_2CH_2CH_3$), 17.2 (d, $^1J_{P,C}$ = 47.7 Hz, $PCH_2CH_2$), 20.4 ($CCH_3$), 22.7 (d, $^3J_{P,C}$ = 4.6 Hz, $CH_2CH_2CH_3$), 23.0 (d, $^2J_{P,C}$ = 15.5 Hz, $PCH_2CH_2$), 125.2, 127.5 ($^{tosylate}$Ar-*C*H), 137.8, 144.1 ($^{tosylate}$Ar-$C_{ipso}$) ppm. $^{31}P$ NMR ($D_2O$, 121 MHz): $\delta$ = 34.6 ($^{phosphonium}P$) ppm.

## Acknowledgments

The University of Birmingham is thanked for continued support.

[1] P. Walden, *Bull. Acad. Imp. Sci. St. Petersbourg* **1914**, 1800.
[2] R. D. Rogers, K. R. Seddon, in: *Ionic Liquids: Industrial Applications to Green Chemistry*, ACS Symposium Series 818, American Chemical Society, Washington, DC, **2002**.
[3] P. Wasserscheid, T. Welton (Eds.), *Ionic Liquids in Synthesis*, Wiley-VCH: Weinheim, **2003**.
[4] C. Chiappe, D. Pieraccini, *J. Phys. Org. Chem.* **2005**, *18*, 275–297.
[5] a) C. M. Gordon, *Appl. Catal., A* **2001**, *222*, 101–117; b) J. G. Huddleston, A. E. Visser, W. M. Reichert, H. D. Willauer, G. A. Broker, R. D. Rogers, *Green Chem.* **2001**, *3*, 156–164; c) R. Sheldon, *Chem. Commun. (Cambridge, U.K.)* **2001**, 2399–2407; d) T. Welton, *Chem. Rev. (Washington, DC, U.S.A.)* **1999**, *99*, 2071–2073; e) T. Welton, *Coord. Chem. Rev.* **2004**, *248*, 2459–2477; f) J. Dupont, R. F. de Souza, P. A. Z. Suarez, *Chem. Rev.* **2002**, *102*, 3667–3692.
[6] D. E. Kaufmann, M. Nouroozin, H. Henze, *Synlett* **1996**, 1091–1092.
[7] M. Badri, J. J. Brunet, R. Perron, *Tetrahedron Lett.* **1992**, *33*, 4435–4438.
[8] J. F. Knifton, *J. Am. Chem. Soc.* **1981**, *103*, 3959–3961.
[9] J. F. Knifton, *J. Mol. Catal.* **1987**, *43*, 65–77.
[10] J. F. Knifton, *J. Mol. Catal.* **1988**, *47*, 99–116.
[11] C. J. Bradaric, A. Downard, C. Kennedy, A. J. Robertson, Y. Zhou, *Green Chem.* **2003**, *5*, 143–152.
[12] N. Korodia, S. Guise, C. Newlands, J. Andersen, *Chem. Commun.* **1998**, 2341–2342.
[13] P. Ludley, N. Korodia, *Tetrahedron Lett.* **2001**, *42*, 2011–2014.
[14] C. L. Johnson, R. E. Donkor, W. Nawaz, N. Karodia, *Tetrahedron Lett.* **2004**, *45*, 7359–7361.
[15] C. Comyns, N. Karodia, S. Zeler, J. Andersen, *Catal. Lett.* **2000**, *67*, 113–115.
[16] J. Dupont, *J. Braz. Chem. Soc.* **2004**, *15*, 341–350.
[17] A. Elaiwi, P. B. Hitchcock, K. R. Seddon, N. Srinivasan, Y.-M. Tan, T. Welton, J. A. Zoraa, *J. Chem. Soc., Dalton Trans.* **1995**, 3467–3472.
[18] J. van den Broeke, M. Stam, M. Lutz, H. Kooijman, A. L. Spek, B.-J. Deelman, G. van Koten, *Eur. J. Inorg. Chem.* **2003**, 2798–2811.
[19] C. S. Consorti, P. A. Z. Suarez, R. F. de Souza, R. A. Burrow, D. H. Farrar, A. J. Lough, W. Loh, L. H. M. da Silva, J. Dupont, *J. Phys. Chem. B* **2005**, *109*, 4341–4349.
[20] , J. Dupont, P. A. Z. Suarez, R. F. de Souza, R. A. Burrow, J.-P. Kinkzinger, *Chem. Eur. J.* **2000**, *6*, 2377–2377.
[21] D. Klamann, P. Weyerstahl, *Ber.* **1964**, *97*, 2534–2538.
[22] D. E. Bugner, *J. Org. Chem* **1989**, *54*, 2580–2586.
[23] W. G. Dauben, J. M. Gerdes, R. A. Bunce, *J. Org. Chem.* **1984**, *49*, 4293–4295.
[24] P. Calcagno, B. M. Kariuki, S. Kitchin, J. M. A. Robinson, D. Philp, K. D. M. Harris, *Chem. Eur. J.* **2000**, *6*, 2338–2349.
[25] D. Braga, F. Grepioni, E. Tedesco, *Organometallics* **1998**, *17*, 2669–2672.
[26] G. M. Sheldrick, SHELXL. Program package for crystal structure determination. University of Göttingen, Germany.
[27] L. F Fieser, M. Fieser, in: *Reagents for Organic Synthesis*, Wiley, New York, **1967**.

Received: August 31, 2005
Published Online: November 9, 2005

 © 2006 Wiley-VCH Verlag GmbH & Co. KGaA, Weinheim 

DOI: 10.1002/ejic.200500794

# A Theoretical Study on $Pd^{II}$ Complexes Containing Hemilabile Pyrazole-Derived Ligands

**Albert Rimola,[a] Mariona Sodupe,*[a] Josep Ros,[a] and Josefina Pons*[a]**

**Keywords:** $Pd^{II}$ complexes / Pyrazole / Hemilabile ligands / Density functional theory

The properties of $Pd^{II}$ complexes containing hemilabile pyrazole-derived ligands (L) of the form BPz-$(CH_2)_x$-$A(CH_2)_yA(CH_2)_x$-PzB, with A being a donor atom and B a substituent group at the pyrazole ring, have been investigated through quantum-chemical calculations. The geometries of the $[PdLCl_2]$ and $[PdL]^{2+}$ complexes have been optimized and the reaction free energy of $[PdLCl_2] \rightarrow [PdL]^{2+} + 2\ Cl^-$ computed for 32 different ligands, using the hybrid B3LYP density functional method. The formation of the tetracoordinate $[PdL]^{2+}$ complexes is more favorable for the longer (eight- and nine-membered) chains than for the shorter (six- and seven-membered) ones. Moreover, results show the nature of the donor atom A influences significantly the formation of $[PdL]^{2+}$, the process becoming more favorable according to the order PH > NH > S > O. Finally, electron-donor substituents at the pyrazole ring enhance the formation of $[PdL]^{2+}$, whereas electron-acceptor groups hinder the process.
(© Wiley-VCH Verlag GmbH & Co. KGaA, 69451 Weinheim, Germany, 2006)

## Introduction

The study of hemilabile ligands has received an increasing interest in recent years. The main reason for this attention is the capability of hemilabile ligands to generate vacant coordination sites and to stabilize reaction intermediates which result in promising chemical properties. The relevance and utility of this concept gave rise to the publication of excellent reviews which cover all the aspects of these ligands.[1] The term "hemilabile" was first introduced by Jeffrey and Rauchfuss in 1979, and it refers to polidentate coordination ligands which possess at least one substitutionally labile donor function.[2] There are several examples in the literature about the influence of transition-metal complexes with hemilabile ligands in the activation of small molecules[3–6] and in the activity of homogeneous catalysis.[7–9] Furthermore, hemilability probably occurs also in other disciplines such as bioinorganic chemistry or surface phenomena. A very useful classification of hemilabile situations was reported by Braunstein and Naud in an excellent review.[10] According to these authors three general types of hemilability can be visualized (see Scheme 1). Hemilability of type I is found when the labile donor group coordinates and decoordinates spontaneously. In hemilability of type II there is an intramolecular competition between the donor groups in the same ligand (a) or between donor groups of two identical ligands (b). Finally, hemilability of type III refers to a situation where there is a competition between a labile donor center and an external solvent molecule. Although this phenomenon was first studied in mononuclear complexes, it has been expanded to dinuclear[11] and polynuclear ones, particularly to metal clusters.[12] It should be pointed out that, although homofunctional bidentate ligands such as $R_2N(CH_2)_nNR_2$ or $R_2P(CH_2)_nPR_2$ could coordinate in monodentate or bidentate forms, they are not considered hemilabile since their coordination mode depends on the metal center and the effects of the coordinated ligands. In fact, hybrid ligands containing very different do-

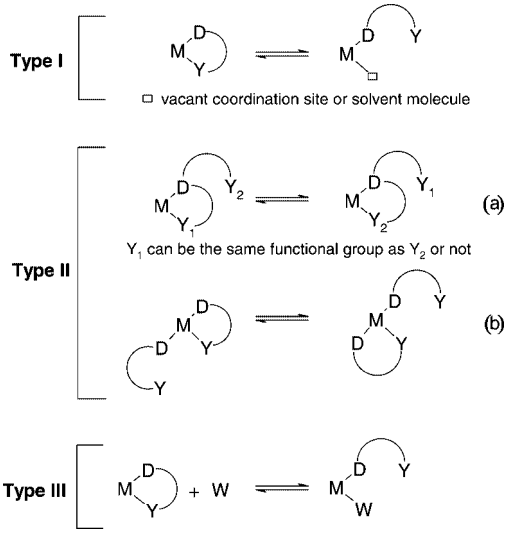


Scheme 1.

[a] Departament de Química, Universitat Autònoma de Barcelona, 08193 Bellaterra, Spain
E-mail: Mariona.Sodupe@uab.es
Josefina.Pons@uab.es
Supporting information for this article is available on the WWW under http://www.eurjic.org or from the author.

 © 2006 Wiley-VCH Verlag GmbH & Co. KgaA, Weinheim InterScience 

nor functions, such as hard and soft donor atoms, are the basis of most of hemilabile ligands.

Pyrazole-derived ligands are potential hemilabile ligands since steric and electronic properties of both the pyrazole and the ancillary donor groups can be easily tuned.[13] In recent years our research group has reported the synthesis, the characterization and the coordinating properties of pyrazolic ligands containing additional donor groups: N,N,[14] N,O,[15] N,P[16] and N,S.[17] NMR studies of complexes in solution have shown that some of them display hemilability; pyrazole is the stronger (inert) donor group, except in the case of N,P and N,S for which it can also behave as a labile group. Previous studies with Pz-$(CH_2)_x$S$(CH_2)_y$S$(CH_2)_x$-Pz tetradentate ligands and $Pd^{II}$ have shown that both N,N bicoordination and N,S,S,N tetracoordination are obtained and can be interconverted in solution (see Scheme 2).[17c] Moreover, the formation of the N,S,S,N coordinating mode in $Pd^{II}$ complexes appears to be controlled by the geometry imposed by the PdNNCS ring in such a manner that ligands Pz-$(CH_2)_x$S$(CH_2)_y$S$(CH_2)_x$-Pz with $x$ = 1 did not lead to the formation of the tetradentate coordination. However, the N,S,S,N complex was obtained for different lengths of the alkyl chain between S atoms ($y$ = 1, 2). This interesting observation can be visualized as a recognition phenomenon of the planar $Pd^{II}$ ion by the N,S,S,N ligand which would act as a chemical receptor. Given that the selective metal ion recognition plays a fundamental role in the search of chemical and biochemical sensors[18] the combination of both strong and weak donor centers found in the same pyrazole–thioether receptor might open new perspectives in the applications of hemilabile ligands. Some molecular recognition processes involving $Pd^{II}$ complexes were described in the literature.[19,20]

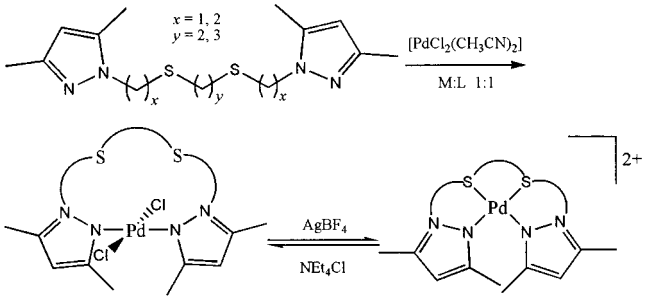


Scheme 2.

The main goal of this paper is to perform a comprehensive theoretical study on the properties of pyrazole-containing ligands (L) of the form BPz-$(CH_2)_x$A$(CH_2)_y$A$(CH_2)_x$-PzB, with A being a donor atom and B a substituent group at the pyrazole ring, through quantum-chemical calculations (Scheme 3). For that, we have optimized the geometry of the $[PdCl_2L]$ and $[PdL]^{2+}$ complexes and computed the reaction free energy of $[PdCl_2L] \rightarrow [PdL]^{2+} + 2\ Cl^-$, for 32 different ligands. This study has allowed us to analyze the influence of the number of $–CH_2–$ groups that join the two pyrazole rings, the nature of donor atoms directly bonded to Pd in the products, and the electronic effects induced by substituent groups at the pyrazole rings.

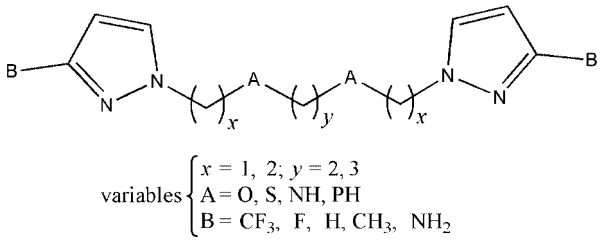


Scheme 3.

## Results and Discussion

As mentioned, the labile behavior of the ligands exposed in the introduction is given by the thioether groups, the inert groups being the pyrazole rings. This labile behavior varies depending on the number of $–CH_2–$ groups that join the two pyrazole rings (variables $x$ and $y$), but it can also be modified by other factors, such as the nature of the donor atom that is directly bonded to Pd in the products (variable A), and the electronic effects induced by substituent groups at the pyrazole rings (variable B). All these variables, labeled in Scheme 3, affect the electronic and the structural properties of the complexes and, consequently, the hemilabile equilibrium $[PdCl_2L] \rightleftarrows [PdL]^{2+} + 2\ Cl^-$. Free-energy calculations for this reaction with all ligands built with these variables show that there is a clear relationship between the energetic results and the structural factors.

### I. Chain Length

Ligands with different chain lengths have been built by changing the values of variables $x$ and $y$. We have considered six- ($x$ = 1, $y$ = 2), seven- ($x$ = 1, $y$ = 3), eight- ($x$ = 2, $y$ = 2), and nine-membered ($x$ = 2, $y$ = 3) chains. To make the discussion less tedious, hereafter, these systems will be referred to as hexane-, heptane-, octane-, and nonane-chain systems. In all cases, the other variables have been kept fixed to A = S and B = $CH_3$. Since the length of the chain mainly influences the geometry of the reaction products, only the optimized structures of $[PdL]^{2+}$ complexes are shown in Figure 1.

It can be observed that the bond lengths of the newly formed Pd–S bonds show significant deviations (about 0.06 Å) upon increasing the chain length. More importantly, the square-planar coordination of Pd in $[PdL]^{2+}$ can be significantly distorted depending on the length of the ligand. In particular, it is observed that hexane- and heptane-chain systems present N–Pd–N *cis* angles (102°–108°) that are much larger than the N–Pd–S *cis* ones (81°–82°), whereas in octane and nonane structures the computed N–Pd–N *cis* angles (90°–95°) are much closer to the N–Pd–S ones (88°–89°). On the other hand, the N–Pd–S *trans* angles tend to 180° and the deviation from planarity decreases[21]

 © 2006 Wiley-VCH Verlag GmbH & Co. KGaA, Weinheim 

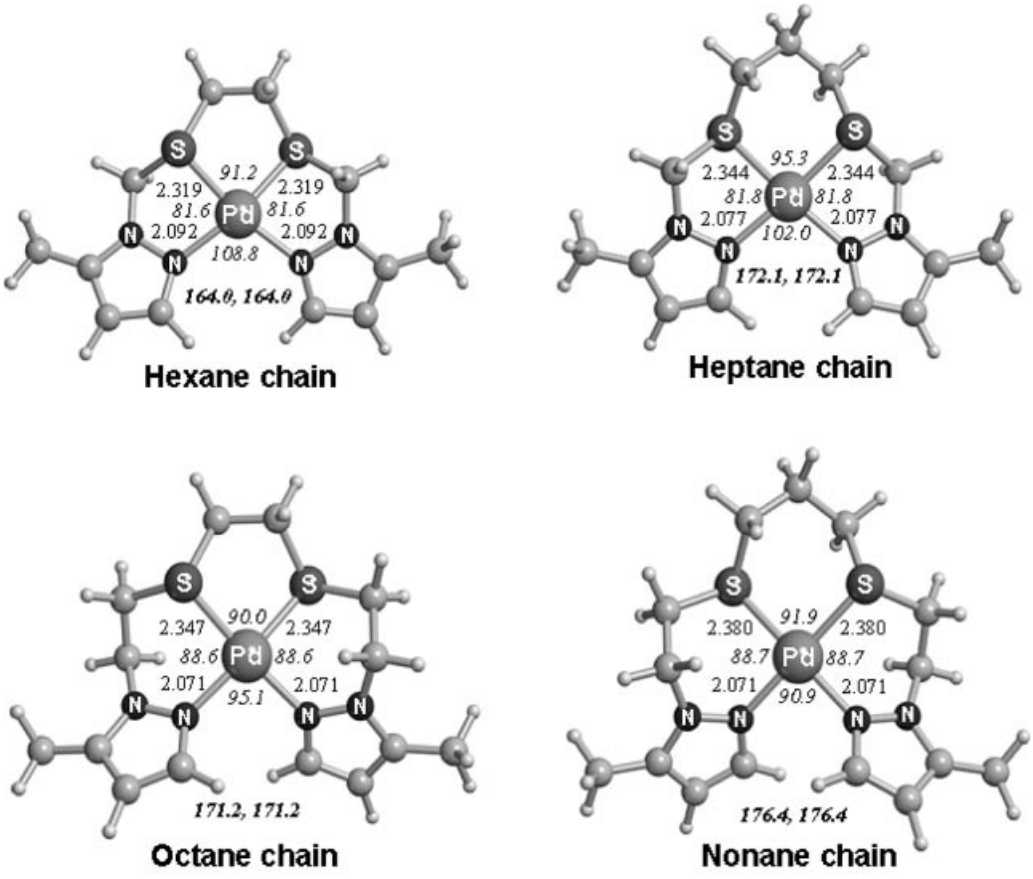


Figure 1. Main geometry parameters optimized at the B3LYP level. Distances are in Å and angles in degrees. Standard numbers correspond to distances, italic numbers to *cis* angles, and bold and italic numbers to *trans* angles.

as the chain length is increased. Therefore, we can conclude that, compared to the ideal square-planar geometry, products with six- and seven-membered chains are more distorted than those with eight- and nine-membered chains. This can be related to the type of rings formed in products. In the hexane-chain products, we obtain three five-membered rings, in the heptane-chain ones two five-membered rings and one six-membered ring, in the octane-chain complexes one five and two six-membered rings and, finally, in nonane-chain products all three rings are six-membered. These results seem to suggest that formation of five-membered rings introduce important strain in the complex that leads to quite distorted structures with respect to the ideal square-planar geometry. Computed structural parameters are in a good agreement with the crystallographic data of related complexes synthesized.[17c]

Reaction free energies have been calculated both in the gas phase and in solution. Calculations in solution have been performed using the conductor-like COSMO continuum model[27] with three different solvents: $CH_3OH$ ($\varepsilon$ = 32.63), acetone ($\varepsilon$ = 20.70), and $CH_2Cl_2$ ($\varepsilon$ = 8.93). Results are given in Figure 2. As expected, the computed free energy of the $[PdLCl_2] \rightarrow [PdL]^{2+} + 2\ Cl^-$ reaction is much smaller in solution than in the gas phase and decreases when the dielectric constant of the solvent increases due to the enhanced stability of the charged species. Nevertheless, in all cases the trends observed upon enlarging the chain length are the same; i.e the reaction is favored from the hexane- to the nonane-chain ligand, the reaction energy decreasing by 23–29 kcal/mol. Since product complexes are the ones that suffer larger structural changes due to the length of the chain, the reaction free energies are expected to be governed by the stability of the products. In principle, it is possible to distinguish two different groups: i) the six-

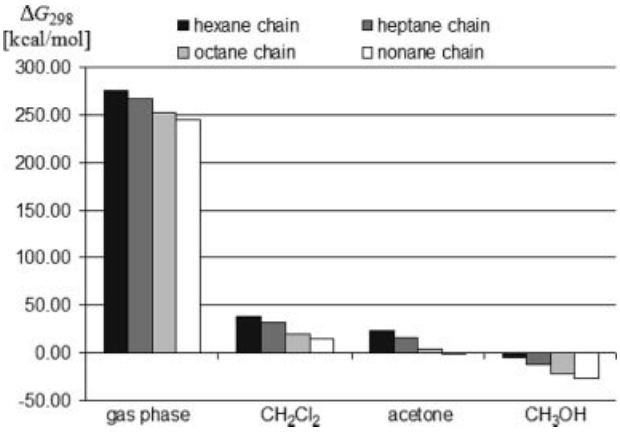


Figure 2. Computed reaction free energies ($\Delta G_{298}$) of $[PdLCl_2] \rightarrow [PdL]^{2+} + 2\ Cl^-$ in the gas phase and in solution. In kcal/mol. Effect of chain length.

 © 2006 Wiley-VCH Verlag GmbH & Co. KGaA, Weinheim 

and seven-membered chain complexes, and ii) the eight- and nine-membered ones, the reaction energies for the latter species being energetically more favorable. These two groups are the same observed when the structural factors were considered. So, there is a clear trend: the more distorted the products are, the more the equilibrium favors the reactants. These theoretical results agree with the experimental data which show that product complexes with octane- and nonane-chain ligands can be synthesized, whereas those with hexane- and heptane-chain ligands are not observed[17c].

### II. Donor Atom

The changes produced on the structural parameters have been analyzed for four different donor atoms A = O, S, NH, and PH. We have optimized all the structures built with the values $x$ = 1, 2; $y$ = 2, 3; and B = $CH_3$. Table 1 shows the optimized Pd–$N_{azine}$ and Pd–A distances, both for reactants and products.

For reactants, all Pd–$N_{azine}$ distances are similar (2.06–2.07 Å). This is not surprising considering that the chain length does not affect the Pd–NH interaction and that the donor atoms are not interacting with Pd in the reactant complexes [$PdLCl_2$]. In contrast, the Pd–$N_{azine}$ distances range from 2.01 to 2.15 Å in the product complexes $[PdL]^{2+}$. The longest Pd–$N_{azine}$ distances appear for species with PH, followed by those with S, NH, and finally O, which shows the shortest distance. Furthermore, for ligands with PH and S, the Pd–$N_{azine}$ bond lengths increase as the reaction proceeds, whereas for ligands with NH and O, these distances decrease. That is, the formation of the two new Pd–A bonds weakens the Pd–$N_{azine}$ interaction for A = PH and S and strengthens it for A = O and NH. The other structural parameters such as *cis* and *trans* angles are not affected by the effects of the different donor atoms.

In order to obtain a deeper insight into the hemilabile character of these ligands we have used Bader's theory of "Atoms in Molecules".[22] In this work we have computed the values of $\rho(r)$ (electron charge density at the bond critical point, bcp), the values of $\nabla^2\rho(r)$ (Laplacian of the electron charge density at the bcp that coincides with the sum of the three curvatures of the Hessian matrix), and the ratio $|\lambda_1/\lambda_3|$ ($\lambda_i$ being the curvatures of the Hessian matrix) at the Pd–$N_{azine}$ and Pd–A bcp. According to this theory, values of $\nabla^2\rho(r) < 0$ address regions where the charge density is concentrated. In contrast, regions in which $\nabla^2\rho(r) > 0$, the charge density is depleted. The ratio of $|\lambda_1/\lambda_3|$ is a measure of the covalency between two atoms. Ratios greater than unity indicate covalent or polar interactions, usually referred to as shared interactions. Ratios lower than 0.2 imply closed-shell interactions, such as those given in noble gas repulsive states, in ionic bonds, in hydrogen bonds, and in van der Waals molecules.[22b]

The $\rho(r)$ values at the Pd–$N_{azine}$ bcp, both in reactants and products, are shown in Figure 3. In agreement with the computed Pd–$N_{azine}$ distances, the computed electron density values in the reactants remain similar (between 0.093 and 0.096), regardless of the donor atom. However, in the products these values range from 0.111 to 0.081 and follow the sequence O > NH > S > PH. On the other hand, it can be observed in Figure 3 that when S is a donor atom, the electron density value at the Pd–$N_{azine}$ bcp is similar in reactants and products. Considering that in the reactants the Pd–$N_{azine}$ bond is in *trans* position with another Pd–$N_{azine}$ bond, and that in the products the Pd–$N_{azine}$ bonds are in *trans* position with the newly formed Pd–S bonds, this seems to suggest that the $N_{azine}$ and S donor atoms have a similar donor character and that the Pd–$N_{azine}$ and Pd–S bonds are similar in strength. For NH and O, the electron density values of Pd–$N_{azine}$ at the bond critical points increase as the reaction proceeds. Therefore, the $N_{azine}$ atoms exert a *trans* influence on NH and O donor atoms. In contrast, when PH acts as donor atom, the electron density values of Pd–$N_{azine}$ bond critical points decreases along the reaction because PH exerts a *trans* influ-

Table 1. Pd–$N_{azine}$ and Pd–A distances in [$PdLCl_2$] and $[PdL]^{2+}$. Distances are in Å.

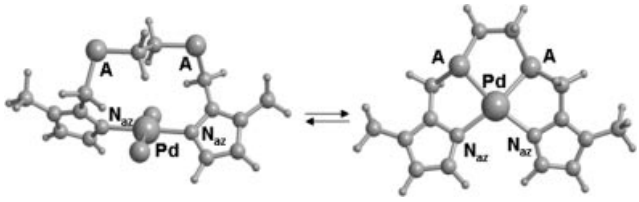


| | | Hexane chain | | Heptane chain | | Octane chain | | Nonane chain | |
|---|---|---|---|---|---|---|---|---|---|
| | | Reactant | Product | Reactant | Product | Reactant | Product | Reactant | Product |
| O | Pd–$N_{azine}$ | 2.063 | 2.030 | 2.065 | 2.019 | 2.061 | 2.014 | 2.062 | 2.024 |
| | Pd–A | | 2.060 | | 2.097 | | 2.096 | | 2.125 |
| N | Pd–$N_{azine}$ | 2.061 | 2.056 | 2.064 | 2.044 | 2.058 | 2.045 | 2.062 | 2.064 |
| | Pd–A | | 2.057 | | 2.096 | | 2.104 | | 2.113 |
| S | Pd–$N_{azine}$ | 2.069 | 2.092 | 2.066 | 2.077 | 2.058 | 2.071 | 2.061 | 2.071 |
| | Pd–A | | 2.319 | | 2.344 | | 2.353 | | 2.380 |
| P | Pd–$N_{azine}$ | 2.059 | 2.153 | 2.070 | 2.127 | 2.057 | 2.122 | 2.062 | 2.119 |
| | Pd–A | | 2.244 | | 2.264 | | 2.285 | | 2.308 |

 © 2006 Wiley-VCH Verlag GmbH & Co. KGaA, Weinheim 

ence on $N_{azine}$. According to these results, the strength of the Pd–A bonds seems to follow the order Pd–PH > Pd–S > Pd–NH > Pd–O.

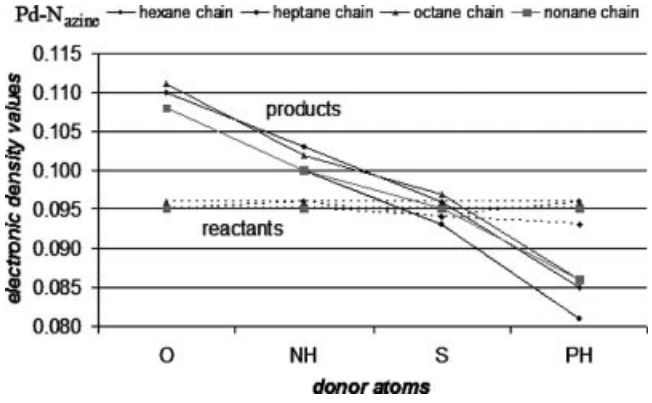


Figure 3. $\rho(r)$ density values at the Pd–$N_{azine}$ bond critical points in reactants, $PdLCl_2$, and products, $PdL^{2+}$. Effect of donor atoms.

The computed values of $\rho(r)$, $\nabla^2\rho(r)$, and $|\lambda_1/\lambda_3|$ at the Pd–$N_{azine}$ and Pd–A bond critical points as well as the net atomic charge of $Pd^{II}$ for nonane-chain products are summarized in Table 2. The fact that the values obtained for $\nabla^2\rho(r)$ at the bcp for Pd–$N_{azine}$ are positive and relatively large evidence a closed-shell interaction. This fact is reinforced by the values of $|\lambda_1/\lambda_3|$, which are lower than 0.2. Regarding the Pd–A bcp, it is worth to note an interesting tendency in the nature of the interaction. From the beginning to the end of the series O, NH, S, PH, the values of $\nabla^2\rho(r)$ decrease and the $|\lambda_1/\lambda_3|$ ratio increases. This fact means that the shared interaction between Pd and the donor atoms follows the order Pd–O < Pd–NH < Pd–S < Pd–PH. This tendency is confirmed by the values of the net atomic charge of Pd, which indicate that the charge transfer from the donor atoms to Pd increases according to the same order. These results agree with the trends observed by the *trans* influence. According to them one would expect that the formation of the new Pd–A bonds would become energetically more favorable as we go from O to NH, from NH to S, and from S to PH.

Table 2. Electron density, $\rho(r)$, Laplacian, $\nabla^2\rho(r)$ and $|\lambda_1/\lambda_3|$ values at the Pd–$N_{azine}$ and Pd–A bond critical points, and Pd net atomic charge.

| | Pd–$N_{azine}$ | | | Pd–A | | | Charge |
|---|---|---|---|---|---|---|---|
| | $\rho$ | $\nabla\rho^2$ | $\lambda_1/\lambda_3$ | $\rho$ | $\nabla\rho^2$ | $\lambda_1/\lambda_3$ | $q_{Pd}$ |
| O | 0.108 | 0.449 | 0.176 | 0.074 | 0.390 | 0.139 | 0.92 |
| N | 0.100 | 0.432 | 0.170 | 0.081 | 0.334 | 0.175 | 0.79 |
| S | 0.095 | 0.410 | 0.173 | 0.086 | 0.174 | 0.224 | 0.58 |
| P | 0.086 | 0.372 | 0.169 | 0.100 | 0.092 | 0.331 | 0.43 |

The computed reaction free energies of $[PdLCl_2] \rightarrow [PdL]^{2+} + 2\ Cl^-$ are given in Figure 4. We only report the values in the gas phase since both results in the gas phase and in solution follow the same trends (see above). It can be observed that the computed free energies do not follow the expected order as shown in Figure 4: $\Delta G(O) > \Delta G(S) > \Delta G(NH) > \Delta G(PH)$. That is, the reaction appears to be more favorable for ligands with NH than for those with S. To obtain a deeper insight into the reaction driving force, we have split the reaction energy ($\Delta E_{reaction}$) in two terms: i) the difference between the interaction energies in reactants and products ($\Delta E_{int}$) and ii) the reorganization energy ($\Delta E_{reorg}$) of the ligand. The interaction energy in the reactants ($E_{int(REACT)}$) corresponds to $E(PdLCl_2) - E(Pd^{II}) - E(L) - 2\ E(Cl^-)$, whereas that in the products ($E_{int(PROD)}$) is $E(PdL^{2+}) - E(Pd^{II}) - E(L)$. The term $\Delta E_{reorg}$ can be understood as the energy cost associated to the conformational change of the ligand along the reaction, and corresponds to the energy difference between single-point calculations of the ligand at the geometry of reactants and products. The values of these terms are shown in Table 3 for the nonane chains. Since $E_{int(REACT)}$ is quite constant for all systems and variations in $\Delta E_{reorg}$ are small, the main contribution on the reaction energy comes from $E_{int(PROD)}$, which follows the same trend of $\Delta E_{reaction}$ and $\Delta G_{298}$ (see Figure 4). It is worth noting that the largest reorganization energy is obtained for PH ligands. This is probably related to the higher barrier for inversion at P. Despite that, reactions with this donor atom are the most favored ones. The order obtained for the interaction energies in the products (PH > NH > S > O; in absolute values) is the same as that found for the interaction between $Pd^{II}$ and the smallest donor-atom-containing entities $H_2O$, $H_2S$, $NH_3$, and $PH_3$ (–141.6, –180.5, –192.1, and –211.8 kcal/mol, respectively) and arises from different factors: electrostatic interaction, metal–ligand repulsion, and charge transfer. As expected, population analysis indicates that the charge transfer from the ligand to Pd is larger for S and PH species than for O and NH ones. However, a point-charge model assuming a 2+ charge at the Pd position shows that the electrostatic stabilization is larger for $NH_3$ and $PH_3$ than for $H_2O$ and $H_2S$. As a consequence, the preference of $Pd^{II}$ to interact with donor atoms follows the order PH > NH > S > O. These results agree with the experimental fact that the inert groups of hemilabile ligands contain P atoms while the labile ones contain O atoms.[1]

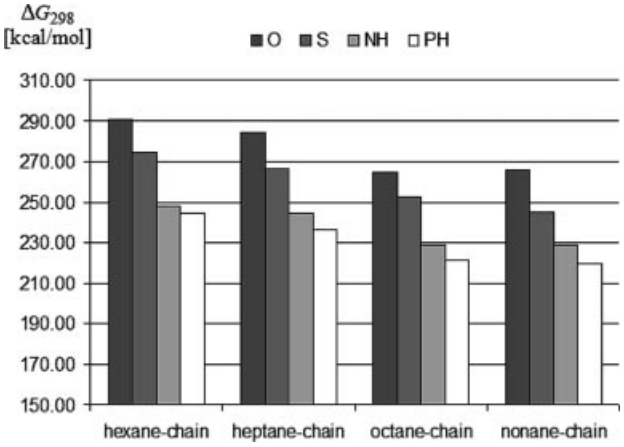


Figure 4. Computed reaction free energies ($\Delta G_{298}$) of $PdLCl_2 \rightarrow PdL^{2+} + 2\ Cl^-$ in the gas phase. In kcal/mol. Effect of donor atoms.

 © 2006 Wiley-VCH Verlag GmbH & Co. KGaA, Weinheim 

Table 3. Contribution of metal-ligand interaction energies and reorganization energy of the ligand to the $[PdLCl_2] \rightarrow [PdL]^{2+} + 2\ Cl^-$ reaction energy. In kcal/mol.

| | $E_{int(REACT)}$[a] | $E_{int(PROD)}$[b] | $\Delta E_{int}$[c] | $\Delta E_{reorg}$[d] | $\Delta E_{reaction}$ |
|---|---|---|---|---|---|
| O | –692.3 | –437.4 | 254.9 | 25.5 | 280.4 |
| S | –692.1 | –454.5 | 237.6 | 22.8 | 260.4 |
| N | –692.6 | –478.4 | 214.2 | 25.9 | 240.0 |
| P | –692.6 | –501.3 | 191.4 | 40.8 | 232.2 |

[a] $E_{int(REACT)} = E(PdLCl_2) - E(Pd^{II}) - E(L) - 2\ E(Cl^-)$. [b] $E_{int(PROD)} = E(PdL^{2+}) - E(Pd^{II}) - E(L)$. [c] $\Delta E_{int} = E_{int(PROD)} - E_{int(REACT)}$. [d] $\Delta E_{reorg} = E(L)_{PROD} - E(L)_{REACT}$.

### C. Ring Substituents

Substituents with different electronic properties (B = $CF_3$, F, H, $CH_3$, and $NH_2$) are introduced at position 5 of pyrazole rings in order to analyze their influence on the structural parameters of Pd complexes and on the $[PdLCl_2] \rightarrow [PdL]^{2+} + 2\ Cl^-$ reaction. Calculations have been performed for different chain lengths ($x$ = 1, 2 and $y$ = 2, 3) and assuming S as donor atom. Table 4 shows the optimized Pd–$N_{azine}$ bond lengths, both for reactants and products.

It can be observed that changing the substituent at the pyrazole ring does not induce a significant variation on the Pd–$N_{azine}$ bond length of the reactant complexes. This is due to the fact that ring pyrazoles are in the *trans* configuration, and thus the electronic effects of the substituents are mutually compensated. However, the Pd–$N_{azine}$ bond lengths in the products are longer when substituents have a global electron-withdrawing character. The contrary occurs if substituents have a global electron-donor character, the Pd–$N_{azine}$ distances becoming shorter. Nevertheless, the Pd–S bonds are not affected by the type of substituent.

We have also calculated the electron density values of the Pd–$N_{azine}$ bond critical points in the products, and the results are shown in Figure 5. The observed trends agree with the observed changes on the Pd–$N_{azine}$ distances; that is, products with electron-withdrawing substituents (and longer Pd–$N_{azine}$ bonds), present smaller electron density values at the bond critical points than product complexes with electron-donor substituents (and shorter Pd–$N_{azine}$ distances). Based on these results the variation on the Pd–$N_{azine}$ bond strength, due to the effects of substituents, is expected to follow the order $CH_3 > NH_2 > H > F > CF_3$.

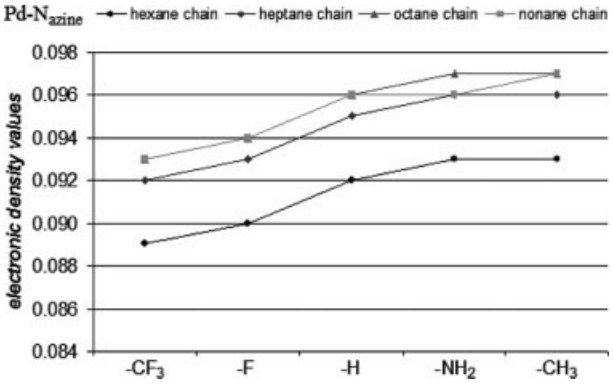


Figure 5. $\rho(r)$ density values at the Pd–$N_{azine}$ bond critical points in products, $[PdL]^{2+}$. Effect of ring substituent.

The induced structural and electronic changes will influence the stability of the products and consequently, the $[PdLCl_2] \rightarrow [PdL]^{2+} + 2\ Cl^-$ reaction energy. Gas-phase reaction free energies calculated for the different ligands considered are given in Figure 6. As expected, reactions are more favored when substituents have an electron-donor character, in agreement with the changes observed for the Pd–$N_{azine}$ bond lengths and electron density values at the bond critical point. However, the trends on Pd–$N_{azine}$ bond length or electron density values do not perfectly agree with the observed trends in reaction free energies. That is, whereas with $CH_3$ as substituent the Pd–$N_{azine}$ distances are shorter than with $NH_2$, the reaction is more favorable if the substituent is $NH_2$. This may be understood considering that, in addition to the σ-donor electronic character, $NH_2$ has a π-donor resonant character that enhances more the global stability of the products. It is worth noting that the reaction free energy can change by as much as 27–29 kcal/mol by introducing substituents of different character in the pyrazole ring.

Table 4. Pd–$N_{azine}$ distances in $[PdLCl_2]$ and $[PdL]^{2+}$. Distances are in Å.

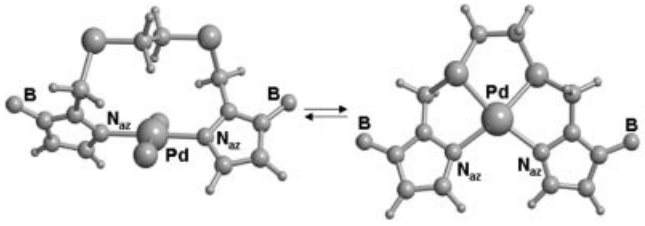


| | Hexane chain | | Heptane chain | | Octane chain | | Nonane chain | |
|---|---|---|---|---|---|---|---|---|
| B | Reactant | Product | Reactant | Product | Reactant | Product | Reactant | Product |
| $CF_3$ | 2.071 | 2.111 | 2.071 | 2.094 | 2.059 | 2.087 | 2.063 | 2.084 |
| F | 2.066 | 2.105 | 2.067 | 2.088 | 2.056 | 2.080 | 2.059 | 2.079 |
| H | 2.067 | 2.098 | 2.067 | 2.082 | 2.058 | 2.075 | 2.060 | 2.075 |
| $NH_2$ | 2.071 | 2.093 | 2.065 | 2.077 | 2.060 | 2.075 | 2.059 | 2.074 |
| $CH_3$ | 2.069 | 2.092 | 2.066 | 2.077 | 2.058 | 2.071 | 2.061 | 2.071 |

 © 2006 Wiley-VCH Verlag GmbH & Co. KGaA, Weinheim 

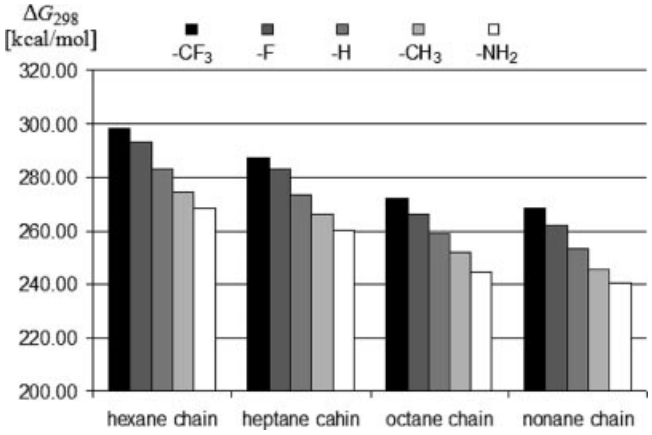


Figure 6. Computed reaction free energies ($\Delta G_{298}$) of $[PdLCl_2] \rightarrow [PdL]^{2+} + 2\ Cl^-$ in the gas phase. In kcal/mol. Effect of ring substituents.

## Conclusions

The properties of $Pd^{II}$ complexes containing pyrazole-derived hemilabile ligands BPz-$(CH_2)_x$A$(CH_2)_y$A$(CH_2)_x$-PzB (with $x$ = 1,2; $y$ = 2,3; A = O, NH, S and PH; and B = $CF_3$, F, H, $CH_3$, $NH_2$) have been investigated through quantum-chemical calculations. Optimal geometries for $[PdLCl_2]$ and $[PdL]^{2+}$ complexes and the reaction free energy of $[PdCl_2L] \rightarrow [PdL]^{2+} + 2\ Cl^-$ have been determined for 32 different ligands using the hybrid B3LYP density functional method. Compared to the ideal square-planar geometry, products with six- ($x$ = 1, $y$ = 2) and seven-membered ($x$ = 2, $y$ = 3) chains are more distorted than those with eight- ($x$ = 2, $y$ = 2) and nine-membered ($x$ = 2, $y$ = 3) chains. Thus, formation of tetracoordinate $[PdL]^{2+}$ complexes is more favorable for the longer chains. This is in agreement with the experimental results, which show that only octane and nonane ligand complexes can be isolated and characterized. Results for different donor atoms A show that the $[PdCl_2L] \rightarrow [PdL]^{2+} + 2\ Cl^-$ reaction is favoured according to the order PH > NH > S > O. This seems to contradict the electron density analysis which shows a larger $L \rightarrow Pd^{II}$ charge transfer for A = S than for A = NH. The reaction energy decomposition and point charge calculations show, however, that the electrostatic + polarization stabilizing term is larger when A = NH. Finally, the introduction of substituents at the pyrazole ring can modulate the strength of the Pd–$N_{azine}$ bond and modify the reaction energy, the electron-donor substituents enhancing the formation of $[PdL]^{2+}$.

## Theoretical Details

Molecular geometries were optimized using the non-local hybrid three-parameter B3LYP[23] density functional method with the Gaussian98 program package.[24] Frequency calculations were also performed to confirm that each stationary point is an actual minimum. For Pd we used the quasi-relativistic effective core potential (ECP) of Hay and Wadt[25] to represent the 28 innermost electrons of the palladium atom. The basis set used for the valence and outermost core orbitals is the standard double-ζ LANL2DZ set associated to the ECP. For atoms directly attached to the metal atom (Cl, $N_{azine}$, and the heteroatoms O, N, S, and P from the ligand chain) we used the 6-31++G(d,p) basis,[26] whereas the remaining atoms were described with the smaller 6-31G basis.[27] In order to analyze the influence of further enlarging the basis set on the $PdLCl_2 \rightarrow PdL^{2+} + 2\ Cl^-$ reaction energy, we have also performed (for a few cases) single-point calculations by adding an f function to the Pd basis,[28] and using the 6-311++G(2d,2p) basis sets for the atoms directly bonded to the metal center. Results showed that the reaction energies differ by less than 1 kcal/mol and thus, we expect computed reaction energies with the small basis set to be reasonably accurate. Thermodynamic corrections have been obtained by standard statistical methods, assuming the harmonic/rigid rotor approximation.[29] Solvent effects have been introduced using the Conductor-like Screening Model (COSMO) method,[30] by performing single-point calculations at the gas-phase-optimized geometries. Net atomic charges have been obtained using the natural population analysis (NPA) method of Weinhold et al.[31] while the topological properties of the electron density have been studied employing Bader's theory of "Atoms In Molecules" (AIM)[22] by means of the Xaim software.[32]

**Supporting Information** (see footnote on the first page of this article): Optimized geometries (Cartesian coordinates) of all considered $[PdLCl_2]$ and $[PdL]^{2+}$ complexes.

## Acknowledgments

Financial support from MCYT and FEDER (project BQU2002-04112-C02), DURSI (projects 2001SGR-00182 and 2001SGR-00290), and the use of the computational facilities of the Catalonia Supercomputer Center (CESCA) are gratefully acknowledged. M. S. A. R. is indebted to the Universitat Autònoma de Barcelona for a doctoral fellowship.

[1] For reviews on hemilabile ligands see: a) A. Bader, E. Lindner, *Coord. Chem. Rev.* **1991**, *108*, 27; b) E. Lindner, S. Pautz, M. Haustein, *Coord. Chem. Rev.* **1996**, *155*, 145; c) C. S. Slone, D. A. Weinberger, C. A. Mirkin, *Prog. Inorg. Chem.* **1999**, *48*, 233; d) P. Espinet, K. Soulantica, *Coord. Chem. Rev.* **1999**, *147*, 1; e) L. Pascale, N. Le Bris, H. des Abbayes, *Trends Organomet. Chem.***2002**, *4*, 131; f) U. Shubert, J. Pfeiffer, F. Stohr, D. Sturmayr, S. Thompson, *J. Organomet. Chem.* **2002**, *646*, 53; g) P. Braunstein, *J. Organomet. Chem.* **2004**, *689*, 3953.
[2] J. C. Jeffrey, T. B. Rauchfuss, *Inorg. Chem.* **1979**, *18*, 2658.
[3] E. Poverenov, M. Gandelman, L. J. W. Shimon, H. Rozenberg, Y. Ben-David, D. Milstein, *Organometallics* **2005**, *24*, 1082.
[4] M. Bassetti, P. Alvarez, J. Gimeno, E. Lastra, *Organometallics* **2004**, *23*, 5127.
[5] M. Bassetti, A. Capone, M. Salamone, *Organometallics* **2004**, *23*, 247.
[6] H. Werner, *Dalton Trans.* **2003**, 3829.
[7] J. Heinicke, M. Koehler, N. Peuleke, M. K. Kinderman, W. Keim, M. Koeckerling, *Organometallics* **2005**, *24*, 344.
[8] J. A. Brito, M. Gomez, G. Muller, H. Teruel, J. C. Clinet, E. Dunach, M. A. Maestro, *Eur. J. Inorg. Chem.* **2004**, 4278.
[9] M. Dieguez, O. Pamies, A. Ruiz, Y. Diaz, S. Castillon, C. Claver, *Coord. Chem. Rev.* **2004**, *248*, 2165.
[10] P. Braunstein, F. Naud, *Angew. Chem. Int. Ed.* **2001**, *40*, 680.
[11] P. Braunstein, M. Knorr, C. Stern, *Coord. Chem. Rev.* **1998**, *178–180*, 903.
[12] J. A. Cabeza, *Eur. J. Inorg. Chem.* **2002**, 1559.
[13] For reviews on pyrazole ligands see: a) S. Trofimenko, *Chem. Rev.* **1972**, *72*, 497; b) S. Trofimenko, *Prog. Inorg. Chem.* **1986**, *34*, 115; c) S. Trofimenko, *Chem. Rev.* **1993**, *93*, 943; d) G.

 © 2006 Wiley-VCH Verlag GmbH & Co. KGaA, Weinheim 

La Monica, G. A. Ardizzoia, *Prog. Inorg. Chem.* **1997**, *46*, 151; e) R. Mukherjee, *Coord. Chem. Rev.* **2000**, *203*, 151.
[14] a) G. Esquius, J. Pons, R. Yañez, J. Ros, *J. Organomet. Chem.* **2001**, *619*, 14; b) G. Esquius, J. Pons, R. Yañez, J. Ros, R. Mathieu, B. Donnadieu, N. Lugan, *Eur. J. Inorg. Chem.* **2002**, 2999; c) R. Mathieu, G. Esquius, N. Lugan, J. Pons, J. Ros, *Eur. J. Inorg. Chem.* **2001**, 2683; d) G. Aullon, G. Esquius, A. Lledos, F. Maseras, J. Pons, J. Ros, *Organometallics* **2004**, *23*, 5530.
[15] a) Boixassa, J. Pons, A. Virgili, X. Solans, M. Font-Bardia, J. Ros, *Inorg. Chim. Acta* **2002**, *340*, 49; b) A. Boixassa, J. Pons, X. Solans, M. Font-Bardia, J. Ros, *Inorg. Chim. Acta* **2003**, *346*, 151; c) A. Boixassa, J. Pons, X. Solans, M. Font-Bardia, J. Ros, *Inorg. Chim. Acta* **2003**, *355*, 254; d) A. Boixassa, J. Pons, X. Solans, M. Font-Bardia, J. Ros, *Inorg. Chim. Acta* **2003**, *357*, 733; e) A. Boixassa, J. Pons, J. Ros, R. Mathieu, N. Lugan, *J. Organomet. Chem.* **2003**, *682*, 233; f) A. Boixassa, J. Pons, X. Solans, M. Font-Bardia, J. Ros, *Inorg. Chim. Acta* **2004**, *357*, 827.
[16] a) R. Tribo, J. Pons, R. Yañez, J. F. Piniella, A. Alvarez-Larena, J. Ros, *Inorg. Chem. Commun.* **2000**, *3*, 545; b) R. Tribo, J. Ros, J. Pons, R. Yañez, A. Alvarez-Larena, J. F. Piniella, *J. Organomet. Chem.* **2003**, *676*, 38; c) G. Esquius, J. Pons, R. Yañez, J. Ros, R. Mathieu, N. Lugan, B. Donnadieu, *J. Organomet. Chem.* **2003**, *667*, 126.
[17] a) J. Garcia-Anton, J. Pons, X. Solans, M. Font-Bardia, J. Ros, *Eur. J. Inorg. Chem.* **2003**, 3952; b) J. Garcia-Anton, J. Pons, X. Solans, M. Font-Bardia, J. Ros, *Eur. J. Inorg. Chem.* **2003**, 2992; c) J. Garcia-Anton, J. Pons, X. Solans, M. Font-Bardia, J. Ros, *Eur. J. Inorg. Chem.* **2002**, 3319; d) J. Garcia-Anton, J. Pons, X. Solans, M. Font-Bardia, J. Ros, *Inorg. Chim. Acta* **2003**, *355*, 87; e) J. Garcia-Anton, J. Pons, X. Solans, M. Font-Bardia, J. Ros, *Inorg. Chim. Acta* **2004**, *357*, 571.
[18] J. W. Steed, J. L Atwood, in: *Supramolecular Chemistry*, Wiley & Sons Ltd., UK, **2000**.
[19] D. C. Smith, C. H. Lake, G. M. Gray, *Chem. Commun.* **1998**, 27771.
[20] A. Goshe, I. M. Steele, B. Bosnich, *Inorg. Chim. Acta* **2004**, *357*, 4544.
[21] The N–Pd–N–S dihedral angles decrease from 13° to 1° as we go from hexane- to nonane-chain ligands.
[22] a) R. F. Bader, in *Atoms in Molecules. A Quantum Theory*, University Oxford Press, Oxford, **1990**; b) R. F. Bader, *Chem. Rev.* **1991**, *91*, 893.
[23] a) A. D. Becke, *J. Chem. Phys.* **1993**, *98*, 5648; b) C. Lee, W. Yang, R. G. Parr, *Phys. Rev. B* **1998**, *37*, 785.
[24] M. J. Frisch, G. W. Trucks, H. B. Schlegel, G. E. Scuseria, M. A. Robb, J. R. Cheeseman, V. G. Zakrzewski, J. A. Montgomery, R. E. Stratmann, J. C. Burant, S. Dapprich, J. M. Millam, A. D. Daniels, K. N. Kudin, M. C. Strain, O. Farkas, J. Tomasi, V. Barone, M. Cossi, R. Cammi, B. Mennucci, C. Pomelli, C. Adamo, S. Clifford, J. Ochterski, G. A. Petersson, P. Y. Ayala, Q. Cui, K. Morokuma, D. K. Malick, A. D. Rabuck, K. Raghavachari, J. B. Foresman, J. Cioslowski, J. V. Ortiz, B. B. Stefanov, G. Liu, A. Liashenko, P. Piskorz, I. Komaromi, R. Gomperts, R. L. Martin, D. J. Fox, T. Keith, M. A. Al-Laham, C. Y. Peng, A. Nanayakkara, C. Gonzalez, M. Challacombe, P. M. W. Gill, B. G. Johnson, W. Chen, M. W. Wong, J. L. Andres, M. Head-Gordon, E. S. Replogle, J. A. Pople, *Gaussian 98*, Revision A.9 i A.11, Gaussian, Inc., Pittsburgh, PA, **1998**.
[25] P. J. Hay, W. R. Wadt, *J. Chem. Phys.* **1985**, *82*, 299.
[26] a) M. J. Frisch, J. A. Pople, J. S. Binkley, *J. Chem. Phys.* **1984**, *80*, 3265; b) T. Clark, J. Chandrasekhar, G. W. Spitznagel, P. v. R. Schleyer, *J. Comput. Chem.* **1983**, *4*, 294.
[27] W. J. Hehre, R. Ditchfield, J. A. Pople, *J. Chem. Phys.* **1972**, *56*, 2257.
[28] A. W. Ehlers, M. Böhme, S. Dapprich, A. Gobbi, A. Höllwarth, V. Jonas, K. F. Köhler, R. Stegmann, A. Veldkamp, G. Frenking, *Chem. Phys. Lett.* **1993**, *208*, 111.
[29] D. McQuarrie, in: *Statistical Mechanics*, Harper and Row, New York, **1986**.
[30] A. Klamt, G. Shürmann, *J. Chem. Soc., Perkin Trans. 2* **1993**, 799.
[31] F. Weinhold, J. E. Carpenter, in: *The Structure of Small Molecules and Ions*, Plenum, New York, **1988**.
[32] Xaim was developed by J. C. Ortiz and C. Bo, University of Rovira i Virgili, Tarragona, Spain. Xaim is available free from http:// www.quimica.urv.es/XAIM

Received: September 8, 2005
Published Online: November 21, 2005

 © 2006 Wiley-VCH Verlag GmbH & Co. KGaA, Weinheim 

DOI: 10.1002/ejic.200500823

# Cyclohexylbis(hydroxymethyl)phosphane: A Hydrophilic Phosphane Capable of Forming Novel Hydrogen-Bonding Networks

**Miriam Gonschorowsky,[b] Klaus Merz,[b] and Matthias Driess*[a]**

**Keywords:** (Hydroxymethyl)phosphanes / Phosphane conjugates / Phosphane sulfides / Hydrogen bonds

The cyclohexyl-substituted (hydroxymethyl)phosphane CyP-$(CH_2OH)_2$ (**1**) has been prepared by reaction of the corresponding primary phosphane $CyPH_2$ with aqueous formaldehyde. Compound **1** has been used as building block for the synthesis of new functionalized water-soluble phosphorus compounds. Thus, Mannich-type condensation of **1** with excess glycine affords the air-stable amino acid phosphane conjugate $CyP[CH_2N(H)CH_2COOH]_2$ (**2**). Simple oxidation of **1** with hydrogen peroxide and elemental sulfur leads to the crystalline chalcogenide derivatives $CyP(O)(CH_2OH)_2$ (**3**) and $CyP(S)(CH_2OH)_2$ (**4**). X-ray diffraction analyses of the latter revealed distinct intermolecular hydrogen bonding motifs and possess different types of hydrogen bond networks to each other due to the different proton acceptor ability of the chalcogen atom X of the P=X group (X = O, S): while the oxygen atom of the P=O moiety in **3** serves as proton acceptor, affording a P=O–HO bifurcated network, the sulfur atom of the P=S group denies hydrogen bonding interactions. In addition, the ligand ability of **1** has been studied towards Pt(+2) and Cu(+1) ions: Reaction of **1** with $Pt(COD)Cl_2$ (COD = cycloocta-1,5-diene) furnishes the air-stable complex *cis*-$[PtCl_2\{CyP(CH_2OH)_2\}_2]$ (**5**), while the crystalline dimeric Cu(+1) complex $[CuI\{CyP(CH_2OH)_2\}_2]_2$ (**6**) results from the reaction of CuI with two molar equivalents of **1**. The complex **6** shows a intermolecular hydrogen bonding pattern different from that of **1**, **3** and **4**, respectively. The new coordination compounds **5** and **6** represent metal-phosphane labelled alcohols which are promising building blocks for the synthesis of metal-based drugs.

(© Wiley-VCH Verlag GmbH & Co. KGaA, 69451 Weinheim, Germany, 2006)

## Introduction

(Hydroxymethyl)phosphanes $[P(CH_2OH)_xR_{3-x}$; R = H, alkyl, aryl; $x$ = 1, 2, 3] constitute an important class of functionalized hydrophilic phosphanes, which have gained considerable prominence in recent years. They are accessible by insertion of formaldehyde into the P–H bonds of secondary and primary phosphanes or $PH_3$ and combine the chemical properties of common organophosphane donor ligands with that of hydrophilic alcohols. In other words, such phosphanes are excellent precursors for the synthesis of a variety of water-soluble organic and organometallic phosphorus compounds. Since the P–$CH_2OH$ moieties can easily be re-transformed into P–H bonds by liberation of formaldehyde molecules, (hydroxymethyl)phosphanes can be considered as masked primary or secondary organophosphanes ($RPH_2$, $R_2PH$; R = alkyl, aryl) which are less sensitive against air but more water-soluble in contrast to the latter. Therefore (hydroxymethyl)phosphanes can participate in a number of chemical reactions, which are typical of $PH_3$ or organophosphanes, including oxidation reactions,[1,2] nucleophilic substitution and addition reactions to activated multiple bonds[1,3] or formation of phosphonium salts via nucleophilic addition to alkylhalides.[2] Another well established type of reactions of (hydroxymethyl)phosphanes represents the Mannich-type condensation with amino-functionalized compounds like amines,[4] amino acids[5] or enzymes,[6] which leads to the formation of (aminomethyl)phosphanes containing a >P–$CH_2$–N< moiety. As Henderson and co-workers have demonstrated, the Mannich-type condensation is, for example, a feasible method for the immobilization of phosphanes to amino-functionalized polymer supports[7] and also render covalent linkage of enzymes to insoluble supports by using multifunctional (hydroxymethyl)phosphanes like $P(CH_2OH)_3$ as coupling reagent.[6] Such immobilized supports are of high interest for the development of a new class of catalysts,[6] which may find diverse application, for imagine. In this context, metal complexes of phosphane-derived biomolecules[8] as well as the coordination chemistry of water-soluble (hydroxymethyl)phosphane ligands have attracted considerable interest in the last decade for the design and development of new water-soluble catalysts[9] or metal-based drugs.[8] (Hydroxymethyl)phosphane ligands, especially the parent system $P(CH_2OH)_3$, have been employed to synthesize stable water-soluble complexes with catalytic active metals (e.g. Rh and Ir)[10] – for their use in biphasic catalysis[11] –

[a] Institute of Chemistry: Metalorganics and Inorganic Materials, Technical University Berlin, Sekr. C2,
Strasse des 17. Juni 135, 10623 Berlin, Germany
Fax: +49-30-314-22168
E-mail: matthias.driess@tu-berlin.de
[b] Faculty of Chemistry, Inorganic Chemistry I, University Bochum,
Universitätsstrasse 150, 44801 Bochum, Germany

 © 2006 Wiley-VCH Verlag GmbH & Co. KgaA, Weinheim 

or with cytotoxic transition metals such as Pt and Au[12] for potential medical application. In addition, hydroxymethyl-functionalized phosphanes deserve not only attention as versatile phosphane ligands but also as versatile candidates for crystal engineering studies. Especially multifunctional bis(hydroxymethyl)phosphanes $RP(CH_2OH)_2$ and their chalcogenide derivatives $RP(X)(CH_2OH)_2$ (X = O, S) appear as potential building blocks for different hydrogen bonding pattern in solid state. However, there are only a few examples known, demonstrating that (hydroxymethyl) phosphanes and their chalcogenides[1] are able to form intermolecular hydrogen bonds. To our surprise, structural investigations are rather rare and only available for $(HOCH_2)_2P–CH_2CH_2–P(CH_2OH)_2$,[13] ferrocenyl (Fc)-substituted (hydroxymethyl)phosphanes,[2,14,15] and their derivatives $FcP(X)(CH_2OH)_2$ (X = O, S),[14,15] $FcCH_2P(S)(CH_2OH)_2$[2] and $FcCH(CH_3)P(S)(CH_2OH)_2$,[16] respectively. We report here the synthesis and characterization of a variety of new cyclohexyl-derived bis(hydroxymethyl) phosphane compounds. The versatile chemistry of the readily accessible phosphane $CyP(CH_2OH)_2$ (**1**) is demonstrated by several characteristic reactions, including Mannich-type condensation with glycine to form the amino acid phosphane conjugate **2** and simple oxidation reactions of the phosphorus atom with $H_2O_2$ and elemental sulfur, affording the new phosphane chalcogenides $CyP(X)(CH_2OH)_2$ (**3**) (X = O) and **4** (X = S), respectively. Additionally, initial studies on the coordination chemistry of ligand **1** were carried out towards Pt(+2) and Cu(+1) ions which lead to the new complexes **5** and **6** and represent metal-phosphane modified alcohols as potential precursors for metal-based drugs. In order to learn more about the molecular association of different bis(hydroxymethyl) phosphorus moieties with and without P=X functions (X = O, S) via hydrogen bonds, the structures of **1**, **3**, **4** and **6** were also established by X-ray diffraction analyses.

## Results and Discussion

### Synthesis and Characterization of 1–6

All reactions described in this work, that include the preparation of the starting compound $CyP(CH_2OH)_2$ (**1**) as well as the various syntheses performed with this precursor, are summarized in Scheme 1. A general procedure for the synthesis of hydroxymethyl-functionalized phosphanes involves hydrophosphanylation of the formyl group by addition of primary or secondary phosphanes to formaldehyde.[17] For the preparation of the title compound **1** we used $CyPH_2$[17] as starting material, which can easily be synthesized from commercially available and inexpensive chemicals. The formylation reaction of $CyPH_2$ with slight excess of aqueous formaldehyde solution (36.5%) at room temperature produced the bis(hydroxymethyl)phosphane (**1**) in almost quantitative yield (Scheme 1). The isolation of compound **1** can easily be achieved by removal of the solvent and excess formaldehyde in vacuo. The latter synthesis turned out to be much more efficient than the reported patent procedure,[18] by which **1** was obtained from the corresponding phosphonium salt by treatment with a base at 50 °C. However, no data concerning characterization of **1** were previously reported.

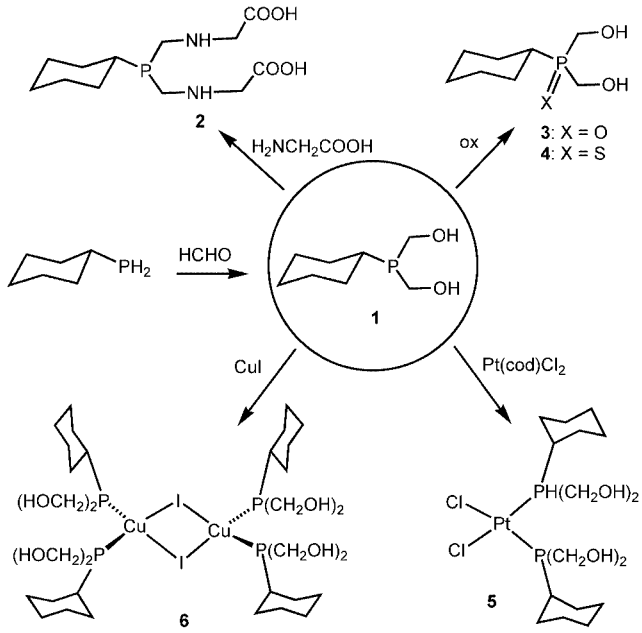


Scheme 1. Synthesis and reactions of $CyP(CH_2OH)_2$ **1**.

$CyP(CH_2OH)_2$ is an air-stable crystalline solid with an unpleasant odour, which is soluble in organic solvents as well as in water, due to its amphiphilic character. It was characterized by mass spectrometry, elemental analysis, NMR spectroscopy and X-ray diffraction analysis. The EI mass spectrum revealed the $[M]^+$ peak at $m/z$ = 176 (19%) and respective fragment ions due to the elimination of formaldehyde and decomposition of the cyclohexyl group. The $^{31}P$–NMR spectrum of **1** shows a broad singlet at $\delta$ = –11.4 ppm similar to the chemical shifts observed for related hydroxymethyl-functionalized phosphanes.[4] As expected, the $^1H$-NMR spectrum of **1** reveals that the $CH_2$ protons of the $PCH_2OH$ groups are chemically inequivalent (diastereotopic) and represent the AB part of an ABX spin system (A, B = $^1H$; X = $^{31}P$). The inequivalence of the methylene protons is caused by the pyramidally coordinated, prochiral phosphorus center. Simulation of the AB region of the $^1H$ NMR spectrum of **1** confirmed the observed eight-line pattern of higher order with partially overlapping signals for the $CH_2$ protons and their geminal coupling of $J_{AB}$ = 13 Hz and two different $^2J_{P,H}$ coupling constants of 5.4 (P,A) and 3.9 Hz (P,B), respectively (Figure 1). Similar coupling patterns were also observed for other bis(hydroxymethyl) phosphanes like cam-$P(CH_2OH)_2$ (cam = 8-camphanyl)[19] and $FcP(CH_2OH)_2$,[14] which exhibit bulky groups directly bonded to the phosphorus atom.

As suggested previously[15] the close proximity of these bulky groups may cause restricted rotation around the P–$CH_2$ and/or $CH_2$–O bonds. The ability of **1** to associate via hydrogen bonds was confirmed by an X-ray diffraction analysis, showing that the molecules constitute a two-di-

 © 2006 Wiley-VCH Verlag GmbH & Co. KGaA, Weinheim 

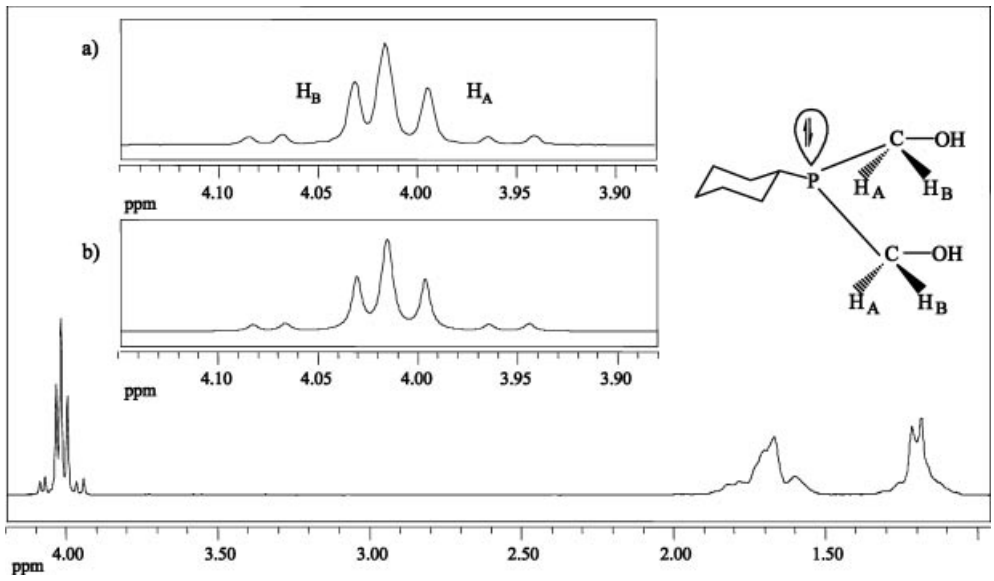


Figure 1. $^1$H NMR-spectrum of **1**; a) measured; b) simulated.[20]

mensional hydrogen bond network with the OH groups serving as proton donors and acceptors (see next section). The apparently activated OH group of the hydroxymethyl-functionalized phosphane **1** can be used to synthesize various new phosphorus ligands in biomedical applications. Since phosphanyl-containing amino acids or peptides represent new carrier ligands for the development of novel metal-containing drugs, the synthesis of bio-compatible phosphorus compounds is of increasing interest. A possible synthetic route to such systems offers the Mannich-type condensation of the OH groups in (hydroxymethyl)phosphanes with the $NH_2$ groups in amino acids and peptides, respectively.[5] In fact, the Mannich-type condensation of CyP-$(CH_2OH)_2$ with 3.5-fold excess of glycine in oxygen-free water/ethanol at room temperature affords the phosphane-glycine conjugate CyP$[CH_2N(H)CH_2COOH]_2$ (**2**), in which each hydroxymethyl group was reacted with one glycine molecule (Scheme 1). Addition of excess molar amounts of glycine was necessary in order to prevent disubstitution reactions at the nitrogen centers. The glycine-derived phosphane **2** was obtained as an air-stable, colorless crystalline solid, which is moderately soluble in water, but insoluble in organic solvents. Due to the expected protonation of the amino functions and deprotonation of the COOH groups, **2** shows excellent solubility in aqueous Brønstedt acids and bases. The new conjugate **2** was characterized by NMR spectroscopy and ESI mass spectrometry. Solutions of *N*-protonated **2** in $DCl/D_2O$ show one $^{31}$P NMR resonance signal at $\delta$ = –24.4 ppm, similar to the values observed for related amino acid-functionalized phosphanes in acidic solutions.[5] The $^1$H NMR spectrum exhibits two different sets of methylene protons: one for the methylene protons of the P–C*H*$_2$–N part and one for the $NH_2^+$–C*H*$_2$–COOH moiety. The first represents the AB part of an ABX spin system (A, B = $^1$H; X = $^{31}$P; $J_{AB}$ = 14.1, $^2J_{P,A}$ = 1.0 and $^2J_{P,B}$ = 2.2 Hz), while the other is an AB spin system without $^{31}$P coupling with a geminal A,B coupling of 17.2 Hz. In basic aqueous solutions ($NaOD/D_2O$), **2** is converted into the corresponding carboxylate with chemical equivalent methylene protons for the NH–$CH_2$–COO- moiety due to fast inversion of configuration at the nitrogen atom on the NMR time scale. However, this does not affect the AB pattern for the methylene protons of the P–$CH_2$–N moiety. The composition of **2** is proven by ESI mass spectrometry, recorded in negative mode, showing the $[M - H^+]$-ion peak at *m*/*z* = 289.3 as base-peak.

Oxidation of the phosphorus atom in **1** furnished the new crystalline chalcogenides CyP(X)$(CH_2OH)_2$ (**3**) (X = O) and (**4**) (X = S). The phosphane oxide **3** results by controlled oxidation of **1** with one equimolar amount of hydrogen peroxide in 81% yield (Scheme 1). The preparation of the phosphane sulfide homolog **4** was achieved in quantitative yield by stirring a solution of **1** in toluene with elemental sulfur at room temperature (Scheme 1). Both compounds are colorless crystalline solids, which are soluble in water and protic organic solvents like alcohols, but insoluble in apolar organic solvents in contrast to the parent phosphane **1**. The chalcogenides **3** and **4** were characterized by means of NMR spectroscopy and mass spectrometry. Their molecular structures were additionally confirmed by single-crystal X-ray diffraction analyses (see next section). As expected, the $^{31}$P NMR chemical shifts of **3** ($\delta$ = 55.7 ppm) and **4** ($\delta$ = 54.5 ppm) are quite similar to values of related phosphane chalcogenides,[2,15] which usually appear at relatively low field. The $^1$H NMR spectra of both compounds show unresolved overlapping multiplets for the methylene protons of the $PCH_2OH$ groups, which indicate the expected chemical inequivalence (AB part of an ABX spin system; A, B = $^1$H; X = $^{31}$P) of the latter. The $^{13}$C nucleus of the $PCH_2OH$ groups exhibits a doublet in the $^{13}C\{^1H\}$ NMR spectra of **3** and **4**, respectively, with characteristically large $^1J$(P,C) coupling constants (**3**: 75.6 Hz; **4**: 66.7 Hz) for phosphane chalcogenides.

 © 2006 Wiley-VCH Verlag GmbH & Co. KGaA, Weinheim 

In order to probe the coordination ability of **1**, the monodentate phosphane ligand was allowed to react with Pt(+2) and Cu(+1) compounds, since such metal complexes are of interest because of their important cytotoxic properties. In fact, the well established precursor $Pt(COD)Cl_2$ reacts with **1** in the molar ratio of 1:2 in dichloromethane at 25 °C, affording solely *cis*-$[PtCl_2\{CyP(CH_2OH)_2\}_2]$ (**5**) which can be isolated in 82% yield (Scheme 1). Complex **5** is an air-stable colorless crystalline solid, which is soluble in alcohols and moderate soluble in water. Its characterizations are based on multi-nuclear NMR spectroscopy, ESI-mass spectrometry and combustion analysis. Especially diagnostic is the $^{195}Pt\{^1H\}$ NMR spectrum of **5**, which shows one triplet at $\delta$ = –4523 ppm according to the coupling of the platinum nucleus with two chemically equivalent phosphorus atoms. The resulting $^1J_{Pt,P}$ coupling constant of 3490 Hz clearly indicates that the platinum atom has the *cis*-configuration.[21] This is evident by the fact that the corresponding *trans*-isomers of similar Pt complexes exhibit $^1J_{Pt,P}$ coupling constants which are around 1000 Hz lower than the values for *cis* complexes (e.g., *cis*-$[Pt\{P(CH_2OH)_3\}_2I_2]$: $^1J_{Pt,P}$ = 3227 Hz vs. *trans*-$[Pt\{P(CH_2OH)_3\}_2I_2]$: $^1J_{Pt,P}$ = 2162 Hz).[21] This trend can be simplified explained by the higher *trans*-influence of phosphorus compared to halide ligands, which weakens a Pt–P bond and hence lowers the Pt,P coupling constant. The $^{31}P$ NMR spectrum of complex **5** in $CD_3OD$ shows one resonance signal at $\delta$ = 15.8 ppm for the two equivalent phosphorus nuclei. Additionally, $^{195}Pt$-satellites can be observed, with the identical $^1J_{Pt,P}$ coupling constant as already observed in the corresponding $^{195}Pt$ NMR spectrum. In the $^{13}C\{^1H\}$ NMR spectrum of complex **5** two unresolved multiplets were observed at $\delta$ = 36.0 ppm and $\delta$ = 54.8 ppm. Due to potential coupling with the adjacent phosphorus and platinum nuclei these signals are assigned to the carbon atoms, which are directly bonded to the phosphorus (C1–Cy and $CH_2OH$). As expected and similar to the "free" ligand **1** and its chalcogenides **3** and **4**, the methylene protons of the $PCH_2OH$ groups of the complex **5** are chemically inequivalent. Thus, the $^1H$ NMR spectrum of **5** exhibits two broad multiplets at $\delta$ = 4.43 and 4.67 ppm for the inequivalent $CH_2$ protons, showing geminal coupling of 14 Hz and $^3J_{Pt,H}$ coupling constants of 18.6 Hz and 29.4 Hz, respectively, for the respective $^{195}Pt$-satellites. The ESI mass spectra show the characteristic peak for the $[M - Cl]^+$ ion at $m/z$ = 583.8 in positive mode and one for the $[M + Cl]^-$ ion peak at $m/z$ = 653.8 in negative mode, which are typical for related platinum chloride complexes (e.g. *cis*-$[PtCl_2\{P(FcCH_2)(CH_2OH)_2\}_2]$).[15]

Similar reaction of $CyP(CH_2OH)_2$ ligand **1** with CuI in molar ratio of 1:2 in dichloromethane at room temperature (Scheme 1) furnished air-stable, colorless crystals of **6**, which are soluble in alcohols and moderate soluble in water. According to an X-ray structure analysis, compound **6** forms a dimer with two iodo-bridges between the Cu atoms and the dimers are associated via hydrogen bonds in a different motif than **1**, **3** and **4** (see next section). Complex **6** was also characterized by NMR spectroscopy, mass spectrometry and elemental analysis. Its $^{31}P$ NMR spectrum in $CD_3OD$ shows one resonance signal at $\delta$ = –7.9 ppm for the four chemically equivalent phosphorus atoms which is broadened ($h_{1/2}$ ca. 25 Hz) due to the presence of the $^{63/65}Cu$-quadrupole nuclei. Broadening of the resonance signals is also observed in the $^1H$ NMR spectrum of **6** which limits stereochemical information. While ESI-MS investigations of **6** were in contrast to **5** unsuccessful, FAB mass spectromeric measurements revealed at least the fragmention $[Cu\{CyP(CH_2OH)_2\}_2]^+$ at $m/z$ = 415.2 as the largest fragment.

### X-ray Crystal Structure Determinations

Crystal structure elucidations were performed for the compounds **1**, **3**, **4** and **6**. Because hydroxymethyl-functionalized phosphorus compounds represent oligoalcohol molecules, they have a large tendency to associate via hydrogen bonding which makes them to versatile building blocks for the construction of new architectures by molecular recognition for crystal engineering. In fact, the compounds show a different variety of hydrogen bonding networks. Single crystals of **1** suitable for an X-ray diffraction analysis were grown in EtOH/$n$Bu$_2$O. (Table 1). However, the hydrogen-bonding network of **1** could not be analyzed by X-ray diffraction studies due to the moderate crystal quality. The compound crystallizes monoclinic with two independent molecules **1A** and **1B** in the unit cell (Figure 2). Their atomic distances and angles are practically identical and resemble the respective values observed for the related bis(hydroxymethyl) phosphanes $(Fc\text{-}P(CH_2OH)_2$,[15] $FcCH_2P(CH_2OH)_2$[2] or $(HOCH_2)_2P\text{–}CH_2CH_2\text{–}P(CH_2OH)_2$[13].

Table 1. Selected bond lengths [Å] and angles [°] for $CyP(CH_2OH)_2$ (**1**).

| Molecule **1A** | | Molecule **1B** | |
|---|---|---|---|
| lengths [Å] | | | |
| P(1)–C(7) | 1.879(1) | P(2)–C(14) | 1.896(9) |
| P(1)–C(15) | 1.778(9) | P(2)–C(12) | 1.790(9) |
| P(1)–C(13) | 1.778(6) | P(2)–C(3) | 1.770(5) |
| C(7)–O(4) | 1.355(9) | C(14)–O(1) | 1.362(1) |
| C(15)–O(3) | 1.389(4) | C(12)–O(2) | 1.333(2) |
| angles [°] | | | |
| C(7)–P(1)–C(15) | 98.3(6) | C(14)–P(2)–C(12) | 98.0(6) |
| C(7)–P(1)–C(13) | 102.2(6) | C(14)–P(2)–C(3) | 104.8(6) |
| C(15)–P(1)–C(13) | 101.1(6) | C(12)–P(2)–C(3) | 101.9(6) |
| P(1)–C(7)–O(4) | 116.0(9) | P(2)–C(14)–O(1) | 113.0(9) |
| P(1)–C(15)–O(3) | 110.3(8) | P(2)–C(12)–O(2) | 113.2(8) |
| O(1)···O(3) | 2.620 | | |
| O(3)···O(4) | 2.584 | | |
| O(4)···O(2) | 2.651 | | |

In contrast to the limited geometrical analysis of **1**, the crystal structure determinations of the phosphane derivatives $CyP(O)(CH_2OH)_2$ **3** and $CyP(S)(CH_2OH)_2$ **4** afforded better data sets (see Table 5) suitable for a topological analysis of the hydrogen-bonding networks. The latter revealed other types of hydrogen-bonding networks than that of the related ferrocenyl-substituted compounds $[FcP(X)(CH_2OH)_2$ (X = O, S),[15] $FcCH_2P(S)(CH_2OH)_2$,[2] and

 © 2006 Wiley-VCH Verlag GmbH & Co. KGaA, Weinheim 

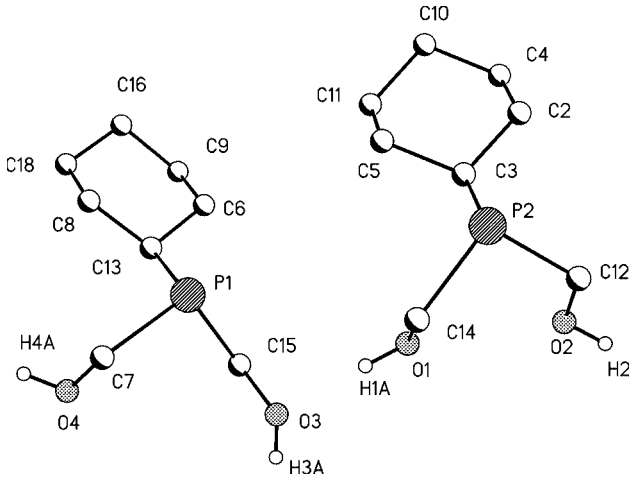


Figure 2. Molecular structure (without hydrogen atoms) of the two independent molecules of $CyP(CH_2OH)_2$ **1** in the unit cell.

$FcCH(CH_3)P(CH_2OH)_2$[16]] and presumably that of **1**. The molecular structures of compounds **3** and **4** are shown in the Figure 3 and Figure 6, respectively, while selected bond lengths and angles are given in the Table 2 and Table 3, respectively. The P–O bond length of 1.512 (4) Å in **3** is identical with that in $FcP(O)(CH_2OH)_2$ [1.510 (1) Å],[15] which represents the hitherto only known structure for this class of compounds. (Hydroxymethyl)phosphane oxides exhibit P=O groups which are favorable hydrogen-bond acceptors and therefore are predestined to form hydrogen bonds with proton donors like hydroxy groups. The hydrogen-bonding arrangement of compound **3** is shown in Figure 4, while Figure 5 depicts the crystal packing. In **3** each P=O group forms bifurcated hydrogen bonding interactions to the O–H groups of one neighboring molecule, with distances between hydrogen bonded oxygen atoms of 2.717 (6) Å for O(3)···O(1A) and 2.709 (6) Å for O(2)···O(1A), respectively. This leads to an arrangement of linked molecules via P=O···HO hydrogen bonds, where each molecule has solely two connected neighbors. As it is shown in the crystal packing of **3** (Figure 5), the one-dimensional chains are not linked to each other. The P=O···HO motif was also observed for the related compound $FcP(O)(CH_2OH)_2$.[15] but in contrast to **3**, $FcP(O)(CH_2OH)_2$ possesses a hydrogen-bonding network between three neighboring molecules, where each P=O unit forms hydrogen bonds to OH groups of different adjacent molecules.

As expected, the distances and angles around the P atom in the phosphane sulfide **4** (Table 3) are identical with that of the related compound $FcP(S)(CH_2OH)_2$.[7] The structure of **4** (Figures 6 and 7) shows a completely different hydrogen-bonding pattern compared to that of the oxide **3**. The hydrogen-bonding network and crystal packing of the sulfide **4** are presented in Figure 7 and Figure 8, respectively. Interestingly and in contrast to the oxygen atom in **3**, the sulfur atom in **4** is not involved in hydrogen-bonding. Hydrogen bonds are formed exclusively between the hydroxy groups, with each OH functionality acting as a donor in one and as an acceptor in another hydrogen bond. This

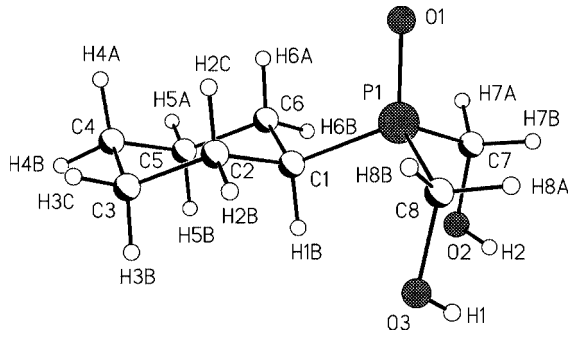


Figure 3. Molecular structure of $CyP(O)(CH_2OH)_2$ (**3**).

Table 2. Selected bond lengths [Å] and angles [°] for $CyP(O)(CH_2OH)_2$ (**3**).

| | | | |
|---|---|---|---|
| P(1)–C(8) | 1.808(6) | C(8)–P(1)–C(7) | 107.9(3) |
| P(1)–C(7) | 1.800(6) | C(8)–P(1)–C(1) | 107.2(3) |
| P(1)–C(1) | 1.795(6) | C(7)–P(1)–C(1) | 107.7(3) |
| P(1)–O(1) | 1.512(4) | C(8)–P(1)–O(1) | 109.8(2) |
| C(8)–O(3) | 1.422(6) | C(7)–P(1)–O(1) | 109.4(2) |
| C(7)–O(2) | 1.435(6) | C(1)–P(1)–O(1) | 114.6(2) |
| O(3)–H(1) | 0.71(5) | P(1)–C(8)–O(3) | 114.0(4) |
| O(2)–H(2) | 0.77(5) | P(1)–C(7)–O(2) | 113.4(4) |
| H(1)···O(1A) | 2.01(6) | C(8)–O(3)–H(1) | 108(5) |
| H(2)···O(1A) | 2.02(5) | C(7)–O(2)–H(2) | 90(4) |
| O(3)···O(1A) | 2.717(6) | O(3)–H(1)···O(1A) | 171(6) |
| O(2)···O(1A) | 2.709(6) | O(2)–H(2)···O(1A) | 149(5) |

Table 3. Selected bond lengths [Å] and angles [°] for $CyP(S)(CH_2OH)_2$ (**4**).

| | | | |
|---|---|---|---|
| P(1)–C(7) | 1.828(2) | C(7)–P(1)–C(8) | 103.6(1) |
| P(1)–C(8) | 1.833(2) | C(7)–P(1)–C(1) | 106.02(9) |
| P(1)–C(1) | 1.815(2) | C(8)–P(1)–C(1) | 104.27(9) |
| P(1)–S(1) | 1.954(8) | C(7)–P(1)–S(1) | 111.33(7) |
| C(7)–O(2) | 1.419(2) | C(8)–P(1)–S(1) | 113.84(7) |
| C(8)–O(1) | 1.415(3) | C(1)–P(1)–S(1) | 116.56(7) |
| O(2)–H(2) | 0.72(3) | P(1)–C(7)–O(2) | 112.5(1) |
| O(1)–H(1) | 0.77(2) | P(1)–C(8)–O(1) | 110.9(1) |
| H(1)···O(2) | 1.94(2) | C(7)–O(2)–H(2) | 112(2) |
| H(2)···O(1) | 1.98(3) | C(8)–O(1)–H(1) | 109.(3) |
| O(1)···O(2) | 2.686(2) | O(1)–H(1)···O(2) | 164(3) |
| O(2)···O(1) | 2.679(2) | O(2)–H(2)···O(1) | 168(3) |

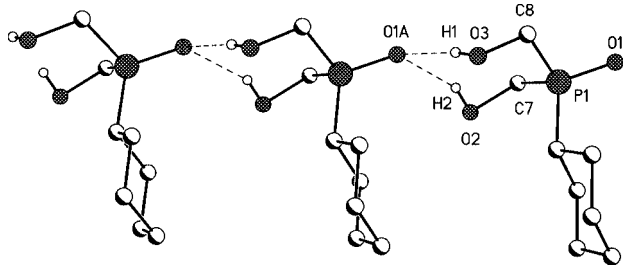


Figure 4. Intermolecular hydrogen bonds between **3** in the crystal.

leads to the formation of a two-dimensional hydrogen bonding network between three adjacent molecules, in which each molecule is crosslinked to four neighboring molecules.

Remarkably, the network of **4** with hydrogen bonded ten-membered rings is practically identical with that observed

 © 2006 Wiley-VCH Verlag GmbH & Co. KGaA, Weinheim 

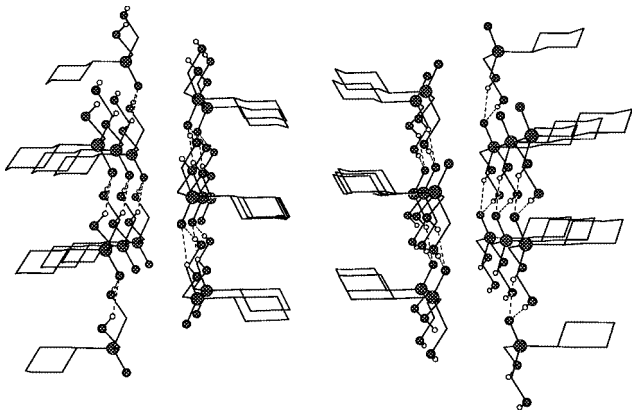

Figure 5. Crystal packing of $CyP(O)(CH_2OH)_2$ (**3**).

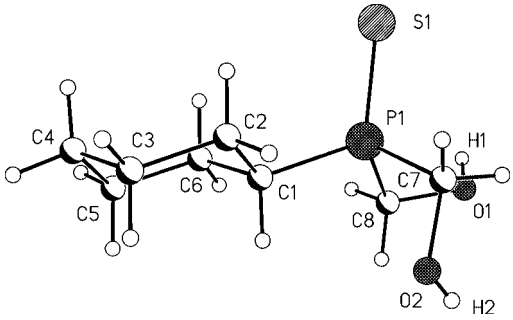


Figure 6. Molecular structure of $CyP(S)(CH_2OH)_2$ (**4**).

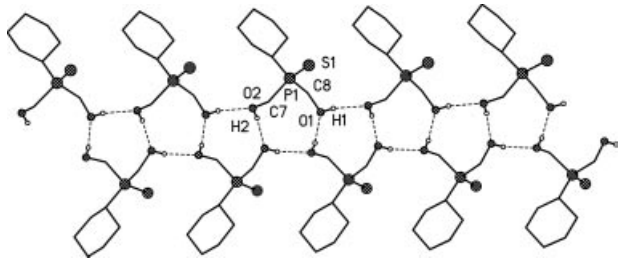


Figure 7. Two-dimensional network of **4** via hydrogen bonds.

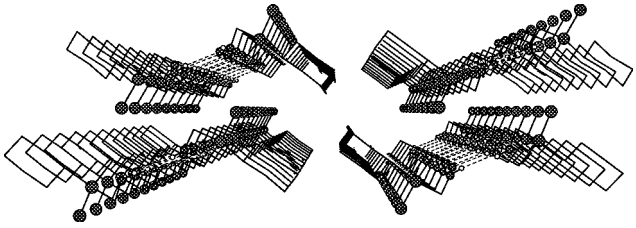

Figure 8. Crystal packing of $CyP(S)(CH_2OH)_2$ (**4**).

for the sulfur-free phosphane $FcP(CH_2OH)_2$[15] and reminiscent of that in the related sulfide $FcP(S)(CH_2OH)_2$.[15] In contrast to **4**, the hydrogen bonds in $FcP(S)(CH_2OH)_2$ are formed between three neighboring molecules with a network of alternating eight- and twelve-membered rings. However, in contrast to the sulfide **4** and $FcP(S)(CH_2OH)_2$, the structures of other related ferrocenyl-derived compounds $FcCH_2P(S)(CH_2OH)_2$[2] and $FcCH(CH_3)P(CH_2OH)_2$[16] show a hydrogen-bonding pattern with hydrogen bonds formed between the sulfur atom and hydroxy groups as well as between OH groups. The formation of O–H···S hydrogen bonds in $FcCH_2P(S)(CH_2OH)_2$ and $FcCH(CH_3)P(CH_2OH)_2$ on the one hand and the lack of O–H···S interactions in $FcP(S)(CH_2OH)_2$ and **4** on the other hand is rather peculiar. As already suggested previously,[15] the proximity of the bulky groups to the phosphorus centers in $FcP(S)(CH_2OH)_2$ and **4** may effectively shield the sulfur atoms and prevent hydrogen bonding interactions of the P=S group. Additionally, the sulfur atom of the P=S group is a much weaker hydrogen-bond acceptor compared to the P=O functionality.

As shown in the crystal packing diagrams of the compounds **3** (Figure 5) and **4** (Figure 8), the hydrophobic cyclohexyl groups have also an important influence on the aggregation behaviour of the molecules. Due to van der Waals interactions, the cyclohexyl groups are effectively stacked on each other, which leads to the formation of alternating hydrophobic and hydrophilic regions in the crystal packing.

The structural elucidation of the copper complex **6** revealed another new type of hydrogen-bonding network. The molecular structure and the hydrogen-bonding pattern of complex **6** are represented in the Figure 9 and Figure 10, respectively, while selected distances and angles are given in Table 4. The centrosymmetric complex **6** is a dimer and possesses two iodo-bridges in a planar $Cu_2I_2$ ring. There are other CuI–phosphane complexes known, having a four-membered $Cu_2I_2$ core and terminal coordinated monodentate phoshane ligands (e.g. $[CuI(PPh_2Me)_2]_2{\cdot}SO_2$,[22] $[CuI(PH_2Ph)_2]_2$[23] and $[CuI(PMe_3)_2]_2$[24]). Complex **6** represents the first example of a Cu(+1) complex containing functionalized monodentate phosphane ligands coordinated to a CuI dimer. The distances and angles of compound **6** are unexceptional and similar to that of $[CuI(PMe_3)_2]_2$.[24]

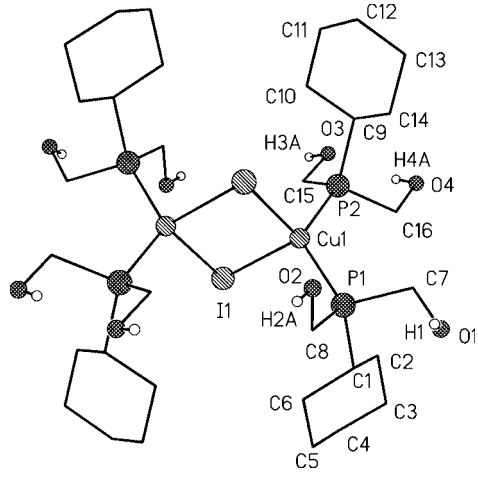


Figure 9. Molecular structure of $[CuI\{CyP(CH_2OH)_2\}_2]_2$ (**6**).

As expected, the crystal structure of **6** shows intermolecular hydrogen bonding interactions due to the presence of OH groups in the phosphane ligand. There exist two dif-

 © 2006 Wiley-VCH Verlag GmbH & Co. KGaA, Weinheim 

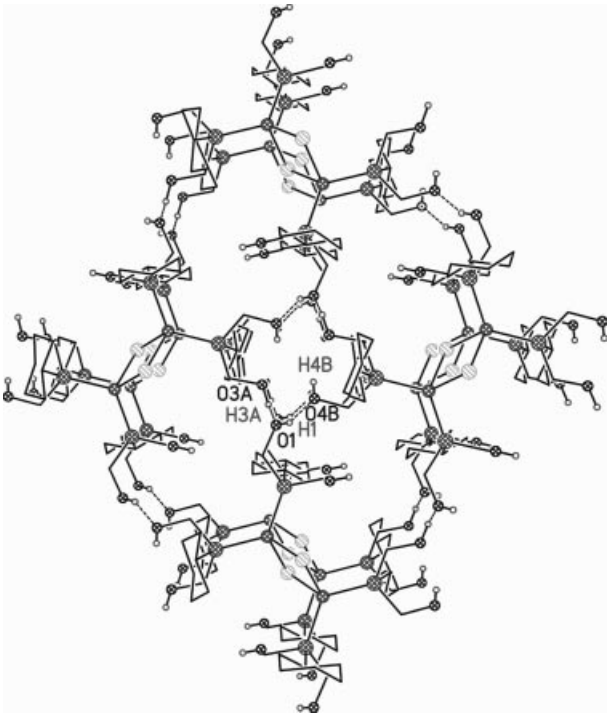


Figure 10. Hydrogen-bonding network in and crystal packing of $[CuI\{CyP(CH_2OH)_2\}_2]_2$ (**6**).

Table 4. Selected bond lengths [Å] and angles [°] of complex **6**.

| | | | |
|---|---|---|---|
| Cu(1)–I(1) | 2.716(4) | Cu(1)–I(1)–Cu′(1) | 78.5(1) |
| Cu(1)–I′(1) | 2.722(5) | I(1)–Cu(1)–I′(1) | 101.4(1) |
| Cu(1)–P(1) | 2.258(4) | P(1)–Cu(1)–P(2) | 123.45(7) |
| Cu(1)–P(2) | 2.257(4) | P(1)–Cu(1)–I(1) | 109.0(1) |
| P(1)–C(7) | 1.839(7) | P(1)–Cu(1)–I′(1) | 105.70(7) |
| P(1)–C(8) | 1.851(7) | P(2)–Cu(1)–I′(1) | 111.7(1) |
| P(1)–C(1) | 1.851(7) | P(2)–Cu(1)–I(1) | 103.3(1) |
| P(2)–C(15) | 1.843(7) | Cu(1)–P(1)–C(7) | 114.2(2) |
| P(2)–C(16) | 1.830(7) | Cu(1)–P(1)–C(8) | 115.0(2) |
| P(2)–C(9) | 1.838(7) | Cu(1)–P(2)–C(15) | 113.2(2) |
| C(7)–O(1) | 1.416(8) | Cu(1)–P(2)–C(16) | 112.2(2) |
| C(8)–O(2) | 1.412(8) | P(1)–C(7)–O(1) | 114.4(5) |
| C(15)–O(3) | 1.439(7) | P(1)–C(8)–O(2) | 112.7(4) |
| C(16)–O(4) | 1.449(8) | P(2)–C(15)–O(3) | 113.1(4) |
| | | P(2)–C(16)–O(4) | 114.0(4) |
| O(1)···O(4B) | 2.702(8) | O(1)–H(1)···O(4B) | 155.9(4) |
| O(3A)···O(1) | 2.684(8) | O(3A)–H(3A)···O(1) | 164.2(4) |

ferent types of intermolecular hydrogen bonds with the distances between the hydrogen bonded oxygen atoms O(1)···O(4B) of 2.702(8) Å and O(3A)···O(1) of 2.684(8) Å, respectively (Figure 10). The hydroxy group O(1)–H(1) of phosphane ligand 1 [with P(1)] acts as a donor in one hydrogen bond and as an acceptor in a second hydrogen bond with two adjacent molecules **6**. The hydroxy groups O(3)–H(3) and O(4)–H(4) of phosphane ligand 2 [with P(2)] are each involved in only one hydrogen bonding with two neighboring molecules. At least each dimer molecule is associated via six hydrogen bonds with four adjacent molecules, with the neighboring dimers are oriented about 90° to the observed molecule. This leads to the formation of two-dimensional networks, which are parallel stacked on each other.

## Conclusion

The amphiphilic cyclohexyl (hydroxymethyl)phosphane **1** is a valuable building block for designing novel hydrogen bonding networks. Using the versatile reactivity of phosphane **1** a variety of functionalized phosphorus compounds can be synthesized. Thus, Mannich-type condensation of **1** with glycine produced the air-stable amino acid functionalized phosphane **2**, and the crystalline derivatives **3** and **4** were prepared by simple oxidation reactions. The X-ray crystal structure diffraction analyses revealed completely different hydrogen bonding pattern for the oxide **3** and the sulfide **4**. While **3** shows intermolecular bifurcated hydrogen bonding interactions between the strong P=O acceptor and the O–H donor groups, the sulfur atom of **4** was not involved in any hydrogen bond. The hydrogen bonding network in **4** was exclusively formed by O–H···O–H interactions and was similar to that observed for the related phosphane $FcP(CH_2OH)_2$.[14,15] In addition, the coordination chemistry of **1** was studied which led to the air-stable complexes *cis*-$[PtCl_2\{CyP(CH_2OH)_2\}_2]$ (**5**) and $[CuI\{CyP(CH_2OH)_2\}_2]_2$ (**6**), respectively. The crystal structure of the latter revealed another new type of hydrogen-bonding network where one OH group of phosphane ligand 2 [with P(2)] is not involved in any hydrogen bond.

## Experimental Section

**General Remarks:** All manipulations were performed under dry and oxygen-free argon. Solvents were dried according to standard methods and saturated with argon or degassed, respectively. The NMR spectra were recorded on a Bruker Avance DPX 250 MHz spectrometer at room-temperature. Chemical shifts $\delta$ are given in ppm and were referenced against $Me_4Si$ ($^1H$, $^{13}C$; using residual protonated solvent peak or the carbon resonance, respectively), 85% $H_3PO_4$ ($^{31}P$) and $H_2PtCl_6$ in $D_2O$ ($^{195}Pt$). ESI-mass spectrometric analysis were performed in the positive and the negative mode using a Bruker Esquire 3000 instrument. The EI- and FAB-mass spectra were recorded at a VG instruments Autospec/EBEE spectrometer. Elemental analyses were carried out on a VarioEL (CHN) elemental analyzer. $CyPH_2$[25] and $PtCl_2(COD)$[26] were prepared according to published procedures. All other chemicals used as starting materials were obtained commercially and without further purification.

**Preparation of $CyP(CH_2OH)_2$ (1):** Aqueous formaldehyde (36.5%, 4.23 mL, 56.0 mmol) was placed in oxygen-free ethanol (10 mL) and purged with argon at room temperature for 30 min. Then a solution of $CyPH_2$ (2.60 g, 22.4 mmol) in 10 mL of oxygen-free ethanol was added dropwise and the mixture was stirred overnight at 25 °C. After removal of the solvent in vacuo the residual colorless solid is recrystallized from ethanol/di-*n*-butyl ether at –15 °C. Yield: 3.86 g, (98%). $C_8H_{17}O_2P$ (176.2): calcd. C 54.6, H 9.7; found C 54.4, H 10.1. $^1H$ NMR (250.13 MHz, $D_2O$): $\delta$ = 1.00–1.40 (m, 5 H, Cy), 1.44–1.98 (m, 6 H, Cy), 3.98 (dd, $^2J_{P,H}$ = 5.4, $^2J_{H,H}$ = 13.0 Hz, 2 H, $PCH_2$), 4.05 (dd, $^2J_{P,H}$ = 3.9, $^2J_{H,H}$ = 13.0 Hz, 2 H, $PCH_2$) ppm. $^{13}C$ NMR (62.90 MHz, $D_2O$): $\delta$ = 26.2 (s, C4-Cy),

 © 2006 Wiley-VCH Verlag GmbH & Co. KGaA, Weinheim 

26.4 (d, $^3J_{P,C}$ = 10.6 Hz, C3-, C5-Cy), 29.2 (d, $^2J_{P,C}$ = 12.0 Hz, C2-, C6-Cy), 29.4 (d, $^1J_{P,C}$ = 13.8 Hz, C1-Cy), 57.3 (d, $^1J_{P,C}$ = 10.4 Hz, $PCH_2$) ppm. $^{31}P$ NMR (101.25 MHz, $D_2O$): $\delta$ = –11.4 (br. s) ppm. EI-MS: *m/z* (%) = 176 [$M^+$ (19)], 146 [$M^+ - CH_2O$ (18)], 115 [$CyPH^+$ (17)], 83 [$Cy^+$ (70)], 55 [$C_4H_7^+$ (100)] 41 [$C_3H_5^+$ (74)].

**Preparation of $CyP[CH_2N(H)CH_2COOH]_2$ (2):** A solution of glycine (0.83 g, 11.38 mmol) in degassed water (3.5 mL) was added via a syringe to phosphane **1** (0.57 g, 3.24 mmol) in 1.5 mL oxygen-free ethanol and stirred overnight at 25 °C. The formed solid was filtered off and the filtrate evaporated giving the product as a colorless crystalline solid. Yield: 808 mg (86%). $^1H$ NMR (250.13 MHz, DCl/$D_2O$): $\delta$ = –0.92 to –0.80 (m, 5 H, Cy), –0.31 to –0.05 (m, 6 H, Cy), 1.61 (br. d, $^2J_{H,H}$ = 14.1 Hz, 2 H, $PCH_2$), 1.76 (dd, $^2J_{P,H}$ = 2.2, $^2J_{H,H}$ = 14.1 Hz, 2 H, $PCH_2$), 2.16 (d, $^2J_{H,H}$ = 17.2 Hz, 2 H, $CH_2COOH$), 2.20 (d, $^2J_{H,H}$ = 17.2 Hz, 2 H, $CH_2COOH$) ppm. $^{13}C$ NMR (62.90 MHz, DCl/$D_2O$): $\delta$ = 24.9 (s, C-4-Cy), 25.9 (d, $^3J_{P,C}$ = 11.3 Hz C-3-, C-5-Cy), 27.8 (d, $^2J_{P,C}$ = 10.8 Hz, C-2-,C-6-Cy), 32.8 (d, $^1J_{P,C}$ = 4.6 Hz, C-1-Cy), 43.6 (d, $^1J_{P,C}$ = 18.8 Hz, $PCH_2$), 48.4 (d, $^3J_{P,C}$ = 7.6 Hz, $CH_2COOH$), 168.0 (s, COOH) ppm. $^{31}P$ NMR (101.25 MHz, DCl/$D_2O$): $\delta$ = –24.4 (br. s) ppm. ESI-MS (negative mode): 289.3 [$M - H^+$].

**Preparation of $CyP(O)(CH_2OH)_2$ (3):** Aqueous hydrogen peroxide (0.3%, 6 mL) was added to a solution of compound **1** (100 mg, 0.568 mmol) in 20 mL methanol and stirred in air for 10 min. The solvent was removed at a rotor vapour, co-evaporated twice with water (2 × 10 mL) and washed with dry ether (10 mL). After drying in vacuo the product **3** was obtained as colorless crystalline solid. Yield: 87 mg (81%). $C_8H_{17}O_3P$ (192.2): calcd. C 50.0, H 8.9; found C 50.4, H 9.3. $^1H$ NMR (250.13 MHz, $D_2O$): $\delta$ = 1.10–1.41 (m, 4 H, Cy), 1.58 –1.85 (m, 6 H, Cy) 1.98 (m, 1 H, H1–Cy) 4.02 (m, 4 H, $PCH_2$) ppm. $^{13}C$ NMR (62.90 MHz, $D_2O$): $\delta$ = 24.4 (d, $^4J_{P,C}$ = 1 Hz, C-4-Cy), 25.7 (d, $^3J_{P,C}$ = 3.4 Hz, C3-, C-5-Cy), 25.9 (d, $^2J_{P,C}$ = 12.7 Hz, C-2,C-6-Cy), 32.2 (d, $^1J_{P,C}$ = 61.8 Hz, C-1 Cy), 54.8 (d, $^1J_{P,C}$ = 75.6 Hz, $PCH_2$) ppm. $^{31}P$ NMR (101.25 MHz, $D_2O$): $\delta$ = 55.7 (br. s) ppm. ESI-MS (negative mode): 191.3 [$M - H^+$].

**Preparation of $CyP(S)(CH_2OH)_2$ (4):** Elemental sulfur (86 mg, 2.670 mmol) was added to a solution of phosphane **1** (470 mg, 2.670 mmol) in 10 mL toluene at room temperature. While stirring for 30 min the sulfur disappeared and a colorless solid was formed. After evaporation of the solvent the residue was re-dissolved in ethanol (8 mL) and filtered. The solvent was again partly removed in vacuo and diethyl ether was added causing the product to precipitate. The solid was filtered off and dried in vacuo yielding **4** as a colorless crystalline solid. Yield: 555 mg (100%). $C_8H_{17}O_2SP$ (208.2): calcd. C 46.15, H 8.23; found C 45.9, H 8.15. $^1H$ NMR (250.13 MHz, $D_2O$): $\delta$ = 1.10–1.81 (m, 11 H, Cy), 4.18 (m, 4 H, $PCH_2$) ppm. $^{13}C$ NMR (62.90 MHz, $D_2O$): $\delta$ = 25.1 (s, C-4 Cy), 25.5 (d, $^3J_{P,C}$ = 3.8 Hz, C3-, C5-Cy), 26.5 (d, $^2J_{P,C}$ = 16.7 Hz, C-2,C-6 Cy), 32.8 (d, $^1J_{P,C}$ = 52.3 Hz, C-1Cy), 58.1 (d, $^1J_{P,C}$ = 66.7 Hz, $PCH_2$) ppm. $^{31}P$ NMR (101.25 MHz, $D_2O$): $\delta$ = 54.5 (s) ppm. EI-MS: *m/z* (%) = 208 [$M^+$ (69)], 178 [$M^+$-$CH_2O$ (9)], 127 [$M^+ - Cy + H$ (47)], 126 [$M^+ - Cy + 2H$ (38)], 108 [$M^+ - Cy - OH$ (100)], 83 [$Cy^+$ (39)], 78 [$HP(S)CH_2^+$ (84)], 55 [$C_4H_7^+$ (82)], 41 [$C_3H_5^+$ (70)].

**Preparation of *cis*-$[PtCl_2\{CyP(CH_2OH)_2\}_2]$ (5):** Phosphane **1** (218 mg, 1.236 mmol) and $Pt(COD)Cl_2$ (231 mg, 0.618 mmol) were dissolved in $CH_2Cl_2$ (10 mL) and stirred for 2 h at room temperature. After standing for another 4 h at 25 °C the formed solid was filtered off and dried in vacuo giving the product as a colorless crystalline solid, which may be recrystallized from hot methanol. Yield: 313 mg (82%). $C_{16}H_{34}Cl_2O_4P_2Pt$ (618.4): calcd. C 31.1, H 5.5; found C 31.2, H 5.8. $^1H$ NMR (250.13 MHz, [$D_4$]MeOH): $\delta$ = 1.21 –1.79 (m, 12 H, Cy-H3,–H4,–H5), 1.83 (br. m, 4 H, Cy-H2,-H6), 2.21 (br. m, 4 H, Cy-H2,-H6), 2.58 (br. m, 2 H, Cy-H1), 4.43 (m, $^2J_{H,H}$ = 14.0, $^2J_{P,H}$ = 0.8, $^3J_{Pt,H}$ = 18.6 Hz, 4 H, $PCH_2$), 4.67 (m, $^2J_{H,H}$ = 14.0, $^2J_{P,H}$ = 2.0, $^3J_{Pt,H}$ = 29.4 Hz, 4 H, $PCH_2$) ppm. $^{13}C$ NMR (62.90 MHz, [$D_4$]MeOH): $\delta$ = 26.2 (br. s, C-4 Cy), 27.2/27.4 (d, $^3J_{P,C}$ = 6.0 Hz, C-3, C-5 Cy), 29.8 (br. s, C2-,C6-Cy), 36.0 (m, C-1 Cy), 54.8 (m, $PCH_2$) ppm. $^{31}P$ NMR (101.25 MHz, [$D_4$]-MeOH): $\delta$ = 15.8 [s; Pt-satellites (d), $^1J_{Pt,P}$ = 3490 Hz] ppm.

Table 5. Crystallographic data for compounds **1**, **3**, **4** and **6**.

| | **1** | **3** | **4** | **6** |
|---|---|---|---|---|
| Empirical formula | $C_8H_{17}O_2P$ | $C_8H_{17}O_3P$ | $C_8H_{17}O_2PS$ | $C_8H_{17}Cu_2I_2O_8P_4$ |
| Formula mass | 179.19 | 192.19 | 208.25 | 1085.62 |
| Crystal system | monoclinic | monoclinic | monoclinic | monoclinic |
| Space group | *C*2/*c* | $P2_1/c$ | $P2_1/c$ | $P2_1/n$ |
| Cell constants | | | | |
| *a* [Å] | 34.28(2) | 6.613(3) | 15.882(5) | 9.48(2) |
| *b* [Å] | 5.161(4) | 31.132(16) | 6.4485(16) | 17.39(3) |
| *c* [Å] | 22.210(5) | 5.4195(19) | 11.102(3) | 13.99(2) |
| $\beta$ [°] | 110.21(2) | 114.014(14) | 108.740(5) | 107.81(8) |
| Volume [Å$^3$] | 3687(5) | 1019.2(8) | 1076.7(5) | 2196(7) |
| *Z* | 16 | 4 | 4 | 2 |
| Density (calculated) [Mg·m$^{-3}$] | 1.269 | 1.252 | 1.285 | 1.642 |
| Absorption coefficient [mm$^{-1}$] | 0.251 | 0.239 | 0.412 | 2.562 |
| Crystal size [mm] | 0.3 x0.2 × 0.2 | 0.3 × 0.2 × 0.1 | 0.2 × 0.1 × 0.1 | 0.3 × 0.2 × 0.2 |
| Theta range for data collection | 1.93 to 22.50 | 2.62 to 25.01 | 2.71 to 30.01 | 2.31 to 25.07 |
| Reflections collected | 2644 | 3799 | 5351 | 7412 |
| Independent reflections | 1974 ($R_{int}$ = 0.1165) | 1486 ($R_{int}$ = 0.0879) | 2730 ($R_{int}$ = 0.0309) | 3572 ($R_{int}$ = 0.0337) |
| Goodness-of-fit on $F^2$ | 1.069 | 1.033 | 1.028 | 1.028 |
| *R* indices [$I > 2\sigma(I)$] | $R_1$ = 0.1167, $wR_2$ = 0.2390 | $R_1$ = 0.0790, $wR_2$ = 0.1874 | $R_1$ = 0.0452, $wR_2$ = 0.1061 | $R_1$ = 0.0468, $wR_2$ = 0.1194 |
| *R* indices (all data) | $R_1$ = 0.2223, $wR_2$ = 0.2664 | $R_1$ = 0.1250, $wR_2$ = 0.2142 | $R_1$ = 0.0672, $wR_2$ = 0.1140 | $R_1$ = 0.0616, $wR_2$ = 0.1302 |
| Largest diff. peak/hole [e·Å$^{-3}$] | 0.474/–0.448 | 0.443/–0.518 | 0.438/–0.305 | 2.456/–0.850 |

 © 2006 Wiley-VCH Verlag GmbH & Co. KGaA, Weinheim 

$^{195}$PtNMR (53.52 MHz, [D$_4$]MeOH): $\delta$ = –4523 (t, $^1J_{Pt,P}$ = 3502 Hz) ppm. ESI-MS (positive mode): 583.8 [M – Cl]. ESI-MS (negative mode): 653.8 [M + Cl].

**Preparation of [CuI{CyP(CH$_2$OH)$_2$}$_2$]$_2$ (6):** A solution of phosphane **1** (107 mg, 0.61 mmol) in 3 mL of $CH_2Cl_2$ was added dropwise to a suspension of CuI (58 mg, 0. 305 mmol) in 3 mL of $CH_2Cl_2$ at room temperature. After stirring for 4 h at 25 °C the solvent was removed under reduced pressure and the solid re-dissolved in 2 mL hot degassed methanol. Colorless crystals of product **6** were formed during 1 day standing at 25°, which were filtered off and dried in vacuo. Yield: 152 mg (92%). $C_{32}H_{68}Cu_2I_2O_8P_4$ (1085.7): calcd. C 35.4, H 6.3; found C 34.9, H 6.0. $^1$H NMR (250.13 MHz, [D$_4$]MeOH): $\delta$ = 1.10–1.88 (m, 40 H, Cy), 2.01–2.20 (m, 4 H, 1-H Cy), 4.11 (br. s, 16 H, PCH$_2$) ppm. $^{31}$P NMR (101.25 MHz, [D$_4$]MeOH): $\delta$ = –7.97 (br. s, $w_{1/2}$ = 35 Hz) ppm. FAB-MS: *m*/*z* (%) = 415.2 [Cu{CyP(CH$_2$OH)$_2$}$_2^+$ (30)], 239.3 [CuCyP(CH$_2$OH)$_2^+$ (24)], 176.2 [CyP(CH$_2$OH)$_2^+$ (34)].

**X-ray Crystallographic Study:** Crystals of **1**, **3**, **4** and **6** were mounted on top of a thin glass fiber. Data were collected with a a Bruker-AXS SMART1000 diffractometer with graphite-monochromated Mo-*Kα* radiation ($\lambda$ = 0.71073 Å). The crystal data are summarized in Table 5. Structures were solved by direct methods (SHELX-97) and refined (SHELXL-97) by full-matrix least-squares methods. Except for **1**, the positions of the O–H hydrogen atoms were localized in the difference Fourier map and refined. All other hydrogen atoms were introduced at calculated positions (riding model), included in structure factor calculations, and not refined. CCDC-260936 to -260938 (for **3**, **4**, **6**) and -283461 (for **1**) contain the supplementary crystallographic data for this paper. These data can be obtained free of charge from The Cambridge Crystallographic Data Centre via www.ccdc.cam.ac.uk/data_request/cif.


[1] a) H. Hellmann, J. Bader, H. Birkner, O. Schuhmacher, *Justus Liebigs Ann. Chem.* **1962**, *659*, 49; b) N. J. Goodwin, W. Henderson, B. K. Nicholson, *Inorg. Chim. Acta* **2002**, *335*, 113–118.

[2] N. J. Goodwin, W. Henderson, B. K. Nicholson, J. K. Sarfo, J. Fawcett, D. R. Russell, *J. Chem. Soc., Dalton Trans.* **1997**, 4377.

[3] W. Vullo, *Ind. Eng. Chem. Prod. Res. Dev.* **1966**, *5*, 346.

[4] S. L. Vail, D. J. Daigle, A. W. Frank, *Text. Res. J.* **1982**, *52*, 738.

[5] D. E. Berning, K. V. Katti, C. L. Barnes, W. A. Volkert, *J. Am. Chem. Soc.* **1999**, *121*, 1658.

[6] W. Henderson, H. H. Petach, G. M. Olsen, *J. Chem. Soc., Chem. Commun.* **1994**, 2181.

[7] W. Henderson, G. M. Olsen, L. S. Bonnington, *J. Chem. Soc., Chem. Commun.* **1994**, 1863.

[8] K. V. Katti, H. Gali, C. J. Smith, D. E. Berning, *Acc. Chem. Res.* **1999**, *32*, 9.

[9] S. R. Gilbertson, X. W. Wang, *J. Org. Chem.* **1996**, *61*, 434.

[10] A. Fukuoka, W. Kosugi, F. Morishita, M. Hirano, L. McCaffrey, W. Henderson, S. Komiya, *Chem. Commun.* **1999**, 489.

[11] C. W. Kohlpainter, W. A. Herrmann, *Angew. Chem.* **1993**, *105*, 1588.

[12] N. J. Goodwin, W. Henderson, *Polyhedron* **1998**, *7*, 4071.

[13] G. F. Nieckarz, T. J. R. Weakley, W. K. Miller, D. K. Lyon, D. R. Tyler, *Inorg. Chem.* **1996**, *35*, 1721.

[14] S. R. Alley, W. Henderson, *Inorg. Chem. Commun.* **2001**, *4*, 741.

[15] W. Henderson, S. R. Alley, *J. Organomet. Chem.* **2002**, *658*, 181.

[16] T. V. V. Ramakrishna, A. J. Elias, A. Vij, *J. Organomet. Chem.* **2000**, *602*, 125.

[17] V. S. Reddy, K. V. Katti, C. L. Barnes, *Inorg. Chim. Acta* **1995**, *240*, 367.

[18] M. Grayson, *US Patent US 3243450*, **1966**.

[19] R. A. Berrigan, D. K. Russell, W. Henderson, M. T. Leach, B. K. Nicholson, G. Woodward, C. Harris, *New J. Chem.* **2001**, *25*, 322.

[20] J. C. Gómez, F. J. S. López, *Programm: MestReC 3.69* **1996–20**.

[21] J. W. Ellis, K. Harrison, P. A. T. Hoye, A. G. Orpen, P. G. Pringle, M. B. Smith, *Inorg. Chem.* **1992**, *31*, 3026.

[22] P. G. Eller, G. J. Kubas, R. R. Ryan, *Inorg. Chem.* **1977**, *16*, 2454.

[23] R. J. Batchelor, T. Birchall, R. Faggiani, *Can. J. Chem.* **1985**, *63*, 928.

[24] G. A. Bowmaker, R. D. Hart, B. E. Jones, B. W. Skelton, A. H. White, *J. Chem. Soc. Dalton Trans.* **1995**, 3063.

[25] R. Graf, *Chem. Ber.* **1952**, *85*, 9.

[26] J. X. McDermott, J. F. White, G. M. Whitesides, *J. Am. Chem. Soc.* **1976**, *98*, 6521.


Received: September 15, 2005
Published Online: Decenber 1, 2005

 © 2006 Wiley-VCH Verlag GmbH & Co. KGaA, Weinheim 

DOI: 10.1002/ejic.200500830

# Reaction of the Heteronuclear Cluster $[Cp^*IrRu_3(\mu\text{-}H)_2(CO)_{10}]$ with Alkynes: Stereoselective Binding

**Padmamalini Srinivasan[a] and Weng Kee Leong*[a]**

**Keywords:** Heterometallic complexes / Ruthenium / Iridium / Alkynes / Stereoselectivity

The reaction of the heteronuclear cluster $[Cp^*IrRu_3(\mu\text{-}H)_2(CO)_{10}]$ (**1**) with the symmetrical alkynes RCCR (R = Ph, Et) afforded the butterfly clusters $[Cp^*IrRu_3(CO)_9(RCCR)]$ (**2**) and the trinuclear clusters $[Cp^*IrRu_2(CO)_7(RCCR)]$ (**3**) and $[Ru_3(CO)_8(C_4R_4)]$ (**4**). The clusters **2** and **3** have the alkyne aligned parallel to an Ru–Ir bond. The reaction of **1** with unsymmetrical alkynes also afforded stereoselective binding of the alkyne such that the bulkier substituent was pointing away from the $Cp^*Ir$ moiety; with PhCCH, however, all three stereoisomers were obtained. With the bis-silylated alkynes (R = $SiMe_3$, $SiEt_3$), loss of one trialkylsilyl group occurred to give $[Cp^*IrRu_3(CO)_9(HCCR)]$ and $[Ru_3(CO)_9(\mu\text{-}H)(CCR)]$ (**5**).
(© Wiley-VCH Verlag GmbH & Co. KGaA, 69451 Weinheim, Germany, 2006)

## Introduction

Mixed-metal alkyne clusters have been of interest because of their catalytic potential in hydrogenation reactions,[1] as models for the carbon–carbon triple bond activation on metal surfaces and for chemisorption of small molecules on metal surfaces,[2] as well as precursors to bimetallic particles.[3] The reaction of tetrahedral clusters with alkynes often results in cluster opening to give "butterfly" structures,[4] where the $M_3M'$ skeleton takes the form of a butterfly and the alkyne $C_2$ unit binds to the metal framework in a $\mu_4$-$\eta^2$ fashion to form a quasi-octahedral $M_3M'C_2$ skeleton.[5] The total electron count for these clusters are best considered using the Wade's system, i.e., as octahedral $M_3M'C_2$ clusters, with each CR unit donating three electrons to the skeletal bonding. They are therefore 62-electron "electron precise" butterfly or 14-electron *closo* octahedral clusters;[6] use of the EAN rule predicts unsaturation, which is not in agreement with their reactivity and hence discouraged.[7]

Three isomers are possible for the $M_3M'C_2$ skeleton and for the coordinated alkynes (Figure 1). The alkyne can be disposed parallel to a heterometallic MM′ bond (a) or to a homometallic MM bond (b); these are related as hinge-apex isomers. The orientation of the alkyne with respect to the hinge bond can also be different, such as in (a) and (c), which are related as (*cis*,*trans*) alkyne isomers.

Most reactions of heterometallic tetrahedral clusters with alkynes afforded butterfly clusters exhibiting either hinge-apex or alkyne, or both types of isomerism. In some cases, however, the reactions were found to be highly stereoselective. For example, the reaction of $[CpMRu_3(CO)_{12}]^-$ (M = W, Mo), $[IrRu_3(\mu\text{-}H)(CO)_{13}]$ and $[IrRu_3(CO)_{13}]^-$ towards internal alkynes afforded ‖M–Ru (M = W, Mo and Ir) clusters with alkyne insertion into the Ru–Ru bond as the only product.[8] However, the reaction of $[CpMRu_3(CO)_{12}]^-$ (M = W, Mo) clusters with phenyl acetylene afforded ‖M–Ru *cis* and *trans* isomers,[8a] while the reaction of $[FeRu_3(\mu\text{-}H)_2(CO)_{13}]$ with alkynes afforded hinge-apex as well as alkyne isomers; isomerisation of the ‖Fe–Ru to the ‖Ru–Ru isomer occurred on heating.[9] In the reaction of $[Cp^*RhRu_3(\mu\text{-}H)_4(CO)_9]$ with alkynes, the isomer with the heterometal atom at the wingtip (‖Ru–Ru) was obtained as the only isomer, while the Cp analogue afforded both hinge-apex isomers (‖Rh–Ru and ‖Ru–Ru). However, it was observed that the ‖Rh–Ru isomer converted into the ‖Ru–Ru isomer during purification of the product on TLC plates.[10] In both the FeRu and RhRu systems, the reverse isomerisation was not facile. This suggested that for these two systems, the isomer with the heterometal atom in the hinge was the kinetically favored product and that with the heterometal atom in the wingtip was the thermodynamically more stable product.

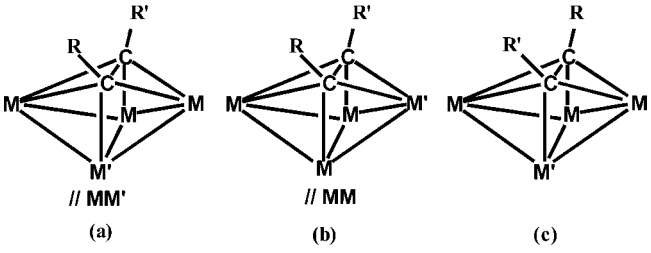


Figure 1. Isomers in $M_3M'C_2$ clusters.

Heterometallic clusters like the previously reported $[CpRhRu_3(\mu\text{-}H)_4(CO)_9]$ are attractive as they allow for the study of site selectivity in the binding of alkynes, particularly unsymmetrical alkynes; the Cp serves as a ligand which allows for stereoelectronic influence on the cluster.

[a] Department of Chemistry, National University of Singapore, Kent Ridge, Singapore 119260

 © 2006 Wiley-VCH Verlag GmbH & Co. KGaA, Weinheim 

However, this cluster was known to fragment readily under the reaction conditions,[10] and we thus sought to examine the reactivities of some heavier relatives, viz., $[Cp^*IrM_3(\mu\text{-}H)_2(CO)_{10}]$ [M = Ru (**1**) or Os], which we have recently synthesised,[24] in the hope that the third-row elements would lend stability to the cluster core. Our investigations with the cluster **1** are reported here.

## Results and Discussion

**Reactions of 1 with Alkynes:** The thermal reaction of **1**, with the symmetrical alkynes RCCR (R = Ph, Et) in hexane afforded a dark red solution from which three compounds, viz., $[Cp^*IrRu_3(CO)_9(RCCR)]$ (**2**), $[Cp^*IrRu_2(CO)_7(RCCR)]$ (**3**), and $[Ru_3(CO)_8(C_4R_4)]$ (**4**) were isolated (Scheme 1).

All the products have been completely characterised, including by single-crystal X-ray crystallographic studies. The clusters **4a** and **4b** have been reported previously,[11] including the X-ray crystal structure in the case of the former.[12] The ORTEP plots for **2a**, **3a** and **4b** are shown in Figure 2, Figure 3 and Figure 4, respectively. The alkyne butterfly clusters **2** have the alkyne C≡C bond parallel to an Ru–Ir hinge; their structural discussion will follow later.

The gross structural features of **4b** are very similar to those of **4a**.[11a] As has been observed there, the $Ru_3C_4$ unit is in an approximately pentagonal bipyramidal arrangement, the Ru–Ru bonds are rather short and attributable to the two bridging carbonyl groups, and the double bonds of the butadiene-1,4-diyl moiety are delocalised over the three C–C bonds although the central bond is marginally longer. However, the asymmetry observed in **4b** is statistically more significant than those observed in **4a** because of the lower e.s.d.s. Thus the two Ru–Ru bonds are different and the difference in bond lengths between the central C–C bond of the butadiene-1,4-diyl moiety compared to the other two is now statistically significant.

A common atomic numbering scheme and selected bond parameters for **3a** and **3b** are given in Table 1. Both the clusters **3** are $Ru_2Ir$ clusters with an electron count of 48; their structural features are similar. There is an asymmetrical carbonyl bridge, and the alkyne ligand is coordinated in a $\mu_3$-$\eta^2$ fashion over the $Ru_2Ir$ triangle, with the alkyne C–C bond parallel to the Ru–Ir bond bridged by the carbonyl. This type of bonding mode of an alkyne has been observed in a number of clusters.[13] The longest metal–metal bond

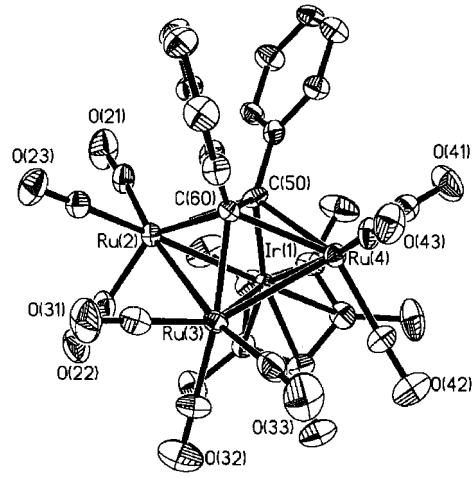


Figure 2. ORTEP diagram of **2a**. Thermal ellipsoids are drawn at the 50% probability level. The phenyl hydrogen atoms are omitted for clarity.

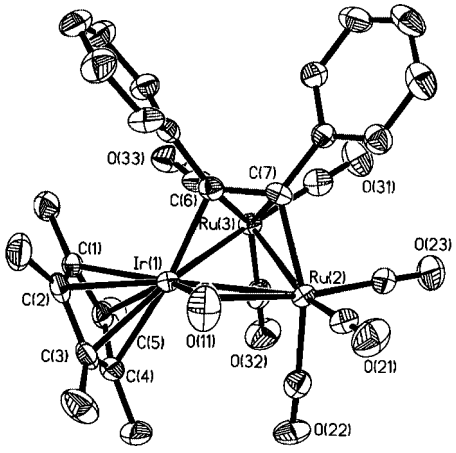


Figure 3. ORTEP diagram of **3a**. Thermal ellipsoids are drawn at 50% probability level. The phenyl hydrogen atoms are omitted for clarity.

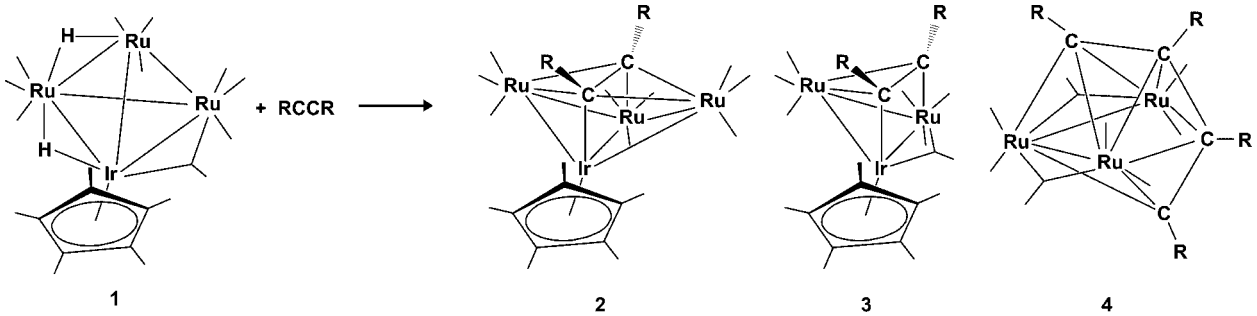


| | 2 | 3 | 4 |
|---|---|---|---|
| **a** R = Ph | 24% | 17% | 37% |
| **b** R = Et | 41% | 13% | 33% |

Scheme 1.

 © 2006 Wiley-VCH Verlag GmbH & Co. KGaA, Weinheim 

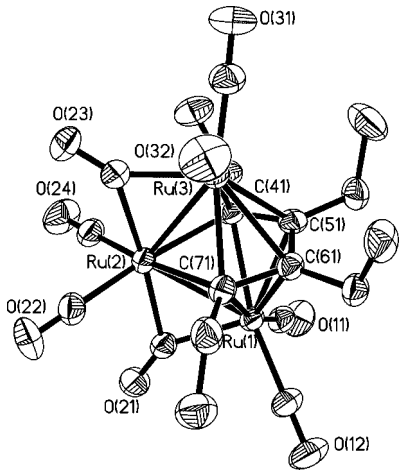


Figure 4. ORTEP diagram and selected bond parameters of **4b**. Thermal ellipsoids are drawn at 50% probability level. Organic hydrogen atoms are omitted for clarity. Ru(1)–Ru(2) = 2.6646(4) Å; Ru(2)–Ru(3) = 2.6741(4) Å; Ru(1)–C(41) = 2.275(3) Å; Ru(1)–C(51) = 2.297(3) Å; Ru(1)–C(61) = 2.300(3) Å; Ru(1)–C(71) = 2.317(3) Å; Ru(2)–C(41) = 2.192(3) Å; Ru(2)–C(71) = 2.188(3) Å; Ru(3)–C(41) = 2.315(3) Å; Ru(3)–C(51) = 2.363(3) Å; Ru(3)–C(61) = 2.352(3) Å; Ru(3)–C(71) = 2.252(3) Å; C(41)–C(51) = 1.440(5) Å; C(51)–C(61) = 1.479(5) Å; C(61)–C(71) = 1.444(5) Å; Ru(1)–Ru(2)–Ru(3) = 88.967(11)°.

is Ir(1)–Ru(2), which is bridged by the carbonyl and is also parallel to the alkyne C–C bond; this bond is significantly longer than the other two. The alkyne C–C bond lengths at ca. 1.40 Å have clearly lost their triple bond character; the bond order is less than two.[14]

Table 1. Common atomic numbering scheme and selected bond parameters for **3a** and **3b**.

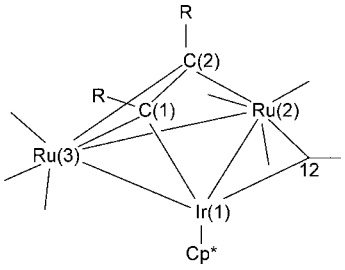


| | **3a** (R = Ph) | **3b** (R = Et) |
|---|---|---|
| Bond lengths [Å] | | |
| Ir(1)–Ru(2) | 2.7977(5) | 2.8034(5) |
| Ir(1)–Ru(3) | 2.7091(5) | 2.7022(5) |
| Ru(2)–Ru(3) | 2.6852(6) | 2.6892(7) |
| Ir(1)–C(1) | 2.090(6) | 2.067(6) |
| Ru(2)–C(2) | 2.116(5) | 2.094(7) |
| Ru(3)–C(1) | 2.196(5) | 2.196(6) |
| Ru(3)–C(2) | 2.250(5) | 2.214(6) |
| Ir(1)–C(12) | 1.880(6) | 1.893(7) |
| Ru(2)–C(12) | 2.422(6) | 2.362(7) |
| C(1)–C(2) | 1.393(8) | 1.402(9) |
| C(12)–O(12) | 1.160(7) | 1.164(8) |
| Bond angles [°] | | |
| Ru(2)Ir(1)Ru(3) | 58.342(14) | 58.443(16) |
| Ir(1)Ru(2)Ru(3) | 59.178(14) | 58.896(15) |
| Ir(1)Ru(3)Ru(2) | 62.481(15) | 62.660(16) |
| Ir(1)C(12)O(12) | 153.0(5) | 150.6(6) |
| Ru(2)C(12)O(12) | 126.9(5) | 127.8(5) |

The yields of the clusters **3** increased at the expense of that for clusters **2** when the reaction time was prolonged. This suggested that **3** were derived from the butterfly alkyne clusters **2**. This was also supported by the observation that thermolyses of **2a** and **2b** afforded **3a** and **3b**, respectively. Furthermore, we have also found that the UV photolyses of solutions of **2** yielded **3**. Thus the butterfly alkyne clusters were not very stable at high temperatures or under photolytic conditions, and were prone to undergo fragmentation to yield the stable triangular clusters. However, neither thermolysis nor photolysis yielded the triruthenium clusters **4**, which indicated that **2** were not the precursors. Similarly, we have found that $[Cp^*Ir(CO)_2]$ did not react with **4a** or **4b** under thermolytic or photolytic conditions. Thus the formation of clusters **4** involved a different pathway from that leading to **2** and **3**.

The reaction of **1** with the unsymmetrical alkynes *t*BuCCMe, 1-hexyne and $Me_3SiCCH$, however, gave only very low yields of the alkyne butterfly clusters **2** (Scheme 2). The reaction with 1-hexyne was particularly poor, and the amount of material obtained was very little, although the IR spectral profile suggested that it had a similar structure to **2c**.[15] For $Me_3SiCCH$, the known triruthenium cluster $[Ru_3(CO)_9(\mu\text{-}H)(C_2SiMe_3)]$ (**5a**) was also obtained.[16] With the exception of **2d**, the molecular structures of all the products have been determined by single-crystal X-ray crystallographic studies, albeit that for **5a** has already been reported.[17,18] The ORTEP plot for **2c** is shown in Figure 5, and it shows that the C≡C bond of the alkyne is again parallel to an Ru–Ir hinge, and the less bulky group of the alkyne is *cis* to the Cp*Ir. The $^1$H NMR spectrum of **2c** did not show the presence of isomers. Hence the binding of the unsymmetrical alkyne appeared to be highly stereoselective. Monitoring of the reaction using infrared spectroscopy showed that strong peaks attributable to $[Cp^*Ir(CO)_2]$ were formed, suggesting fragmentation of the cluster.

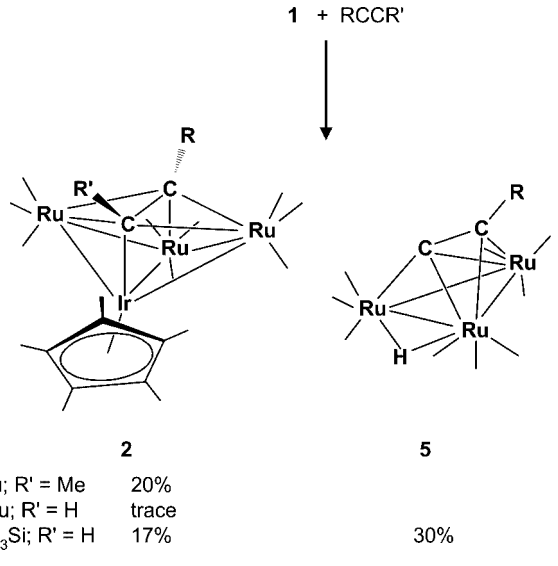


Scheme 2.

 © 2006 Wiley-VCH Verlag GmbH & Co. KGaA, Weinheim 

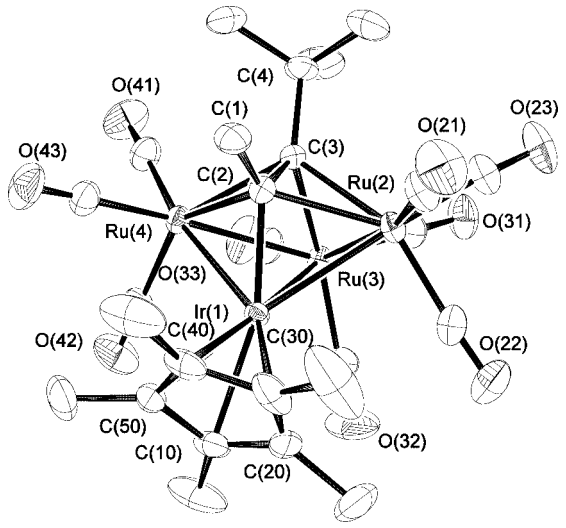


Figure 5. ORTEP diagram of **2c**. Thermal ellipsoids are drawn at 50% probability level. Organic hydrogen atoms are omitted for clarity.

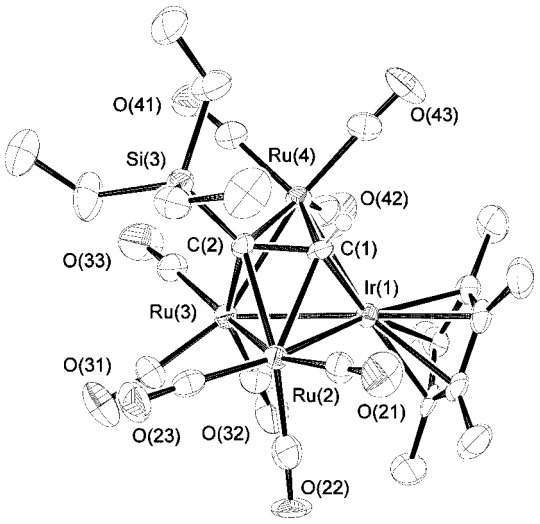


Figure 6. ORTEP diagram of **2f**. Thermal ellipsoids are drawn at 50% probability level. Organic hydrogen aotms are omitted for clarity.

Somewhat surprisingly, the thermal reaction of **1** with the bis-silylated alkynes $R_3SiCCSiR_3$ (R = Me, Et) in hexane afforded two products which were analogous (or identical for R = Me) to those for $Me_3SiCCH$ (Scheme 3). The identity of the clusters **2e** and **2f** have been confirmed by complete characterisation, including by single-crystal X-ray crystallographic studies; the ORTEP plot for **2f** is shown in Figure 6.

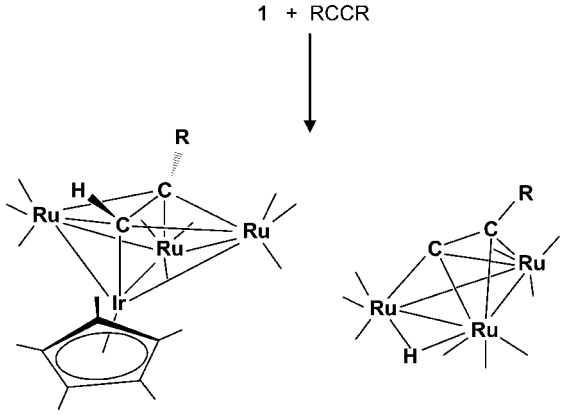


Scheme 3.

The replacement of one trialkylsilyl group by hydrogen was also clearly supported by the $^1$H NMR and FAB MS data; the singlets at $\delta \approx 10.5$ ppm corresponded to the alkenic hydrogen atoms on the alkynes and were in agreement with similar compounds reported in the literature.[18] Monitoring of the reaction with $Me_3SiCCSiMe_3$ by $^1$H NMR spectroscopy showed that the trimethylsilyl group was lost during the reaction and not during workup. GC analysis of an aliquot of the crude reaction mixture suggested that the trimethylsilyl group was lost as octamethyltrisiloxane, which suggested that the hydrogen may have originated from trace amounts of water. However, the desilylation product was observed in almost similar yields even when the reaction was carried out with thoroughly dried solvents and glassware. Since [Cp*Ir(CO)$_2$] is known to bring about C–H activation of hydrocarbons, it is also possible that the Cp*Ir(CO) fragment in these clusters may be responsible for the hydride exchange with $SiMe_3$ group.

Desilylation has been reported by Schneider and co-workers in their attempt to synthesize Fe–Ni heteronuclear clusters by the vaporisation of nickel atoms into a solution of (bistrimethylsilyl)acetylene and [Fe(CO)$_5$]; the reaction had unexpectedly afforded the cluster [Fe$_3$(CO)$_9$(μ-H)(C≡CSiMe$_3$)], and it was suggested that cleavage might have occurred during chromatographic work-up.[19] Vahrenkamp and co-workers have also reported desilylation in the reaction of [RuCo$_2$(CO)$_{11}$] with $Me_3SiC{\equiv}CMe$. The initial product, [RuCo$_2$(CO)$_9$(μ$_3$-$Me_3SiC{\equiv}CMe$)], formed in the reaction underwent subsequent desilylation to give [RuCo$_2$(CO)$_9$(μ$_3$-HC≡CMe)].[20]

In contrast to the highly stereoselective reactions with the other unsymmetrical alkynes above, the reaction of **1** with phenylacetylene afforded three isomeric alkyne butterfly clusters as red crystalline products (Scheme 4). The major product, obtained in 28% yield, was identified as [Cp*IrRu$_3$(CO)$_9$(PhCCH)] (**2g$_3$**); it has been characterised spectroscopically and analytically, as well as by a single-crystal X-ray structure analysis. The ORTEP plot of **2g$_3$** is shown in Figure 7, and it shows that the alkyne C≡C bond is parallel to an Ru–Ru hinge. The other two products were obtained in very low yields. A single-crystal X-ray structural study on **2g$_2$** showed it to be a hinge-apex isomer of **2g$_3$** in which the bulkier Ph group of the alkyne is oriented *cis* to the Cp*Ir; the ORTEP plot for **2g$_2$** is shown in Figure 8. The IR spectrum of the third product, **2g$_1$**, shows a

 © 2006 Wiley-VCH Verlag GmbH & Co. KGaA, Weinheim 

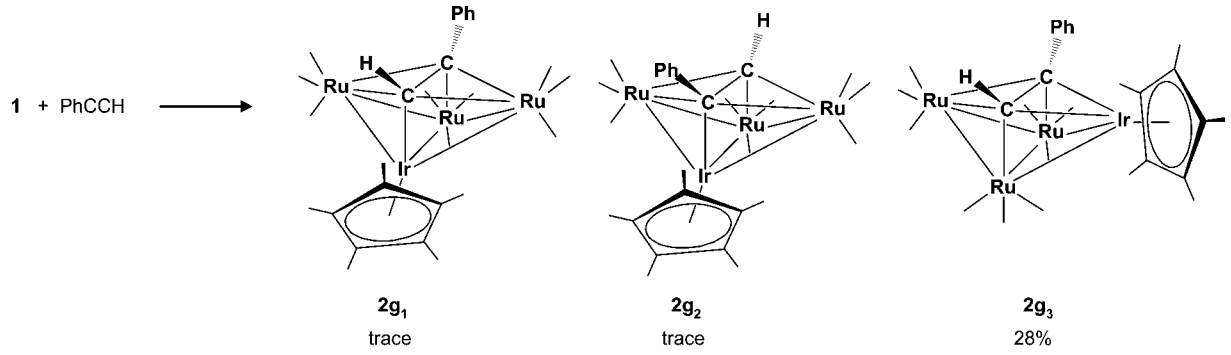


Scheme 4.

pattern similar to that of **2a**–**f**. The $^1$H NMR characteristics are consistent with the assumption of a cluster-bound PhCCH. The multiplet between $\delta$ = 7.00 and 7.77 ppm is due to aromatic protons, the singlet at $\delta$ = 1.82 ppm can be assigned to Cp* methyl protons, and the singlet at $\delta$ = 10.58 ppm corresponds to the alkyne C–H. The MS is also consistent with structures like those observed for $\mathbf{2g_2}$ and $\mathbf{2g_3}$. Based on these spectroscopic characteristics it was thus tentatively identified as a third isomer in which the alkyne C≡C bond is parallel to an Ru–Ir hinge, and the bulkier Ph group of the alkyne is *trans* to the Cp*Ir, i.e., similar to **2c**–**f**.

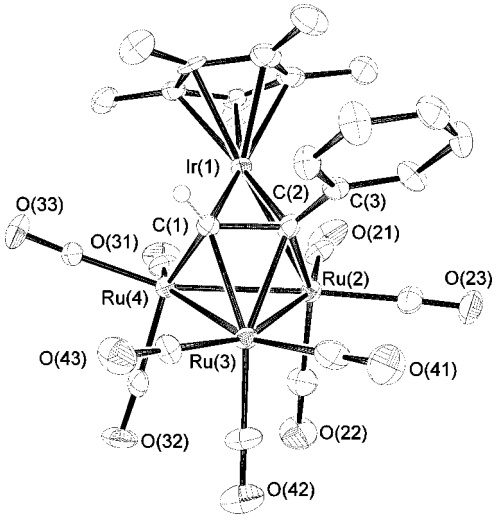


Figure 7. ORTEP diagram of $\mathbf{2g_3}$. Thermal ellipsoids are drawn at 50% probability level. Organic hydrogen atoms are omitted for clarity.

In the reaction of **1** with internal alkynes, only the ‖Ru–Ir isomers were observed; prolonged heating of this isomer did not lead to isomerisation but to cluster fragmentation instead. In contrast, the reaction with phenylacetylene yielded the ‖Ru–Ru isomer $\mathbf{2g_3}$ as the major product; the ‖Ru–Ir *cis* and ‖Ru–Ir *trans* isomers were obtained as minor products. It was observed by IR spectroscopy that a solution of $\mathbf{2g_3}$ converted slowly to $\mathbf{2g_1}$ and $2g_2$ on standing. Likewise, monitoring of a deuterated benzene solution of

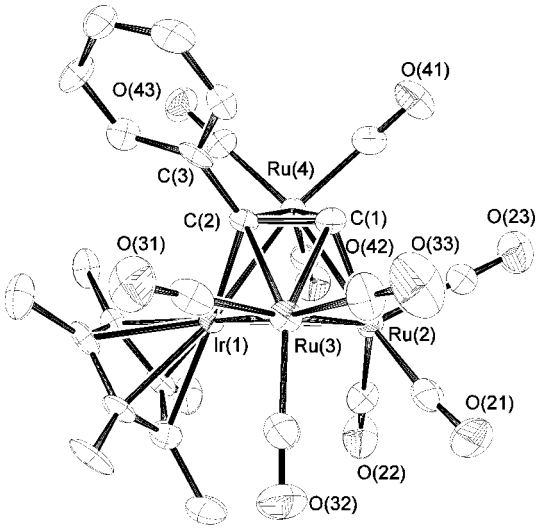


Figure 8. ORTEP diagram of $\mathbf{2g_2}$. Thermal ellipsoids are drawn at 50% probability level. Organic hydrogen atoms are omitted for clarity.

$\mathbf{2g_3}$ by $^1$H NMR at ambient temperature indicated the slow formation of two new singlets at $\delta$ = 1.82 and 1.87 ppm, assignable to the Cp* signals of $\mathbf{2g_1}$ and $\mathbf{2g_2}$, respectively, as well as singlets at $\delta$ = 10.58 and 11.37 ppm, due to the respective C–H protons of the phenylacetylene. However, complete conversion to either $\mathbf{2g_1}$ or $\mathbf{2g_2}$ was not observed even after a month. Prolonged heating of $\mathbf{2g_3}$ finally afforded a 1.2:1.0:5.4 equilibrium mixture of $\mathbf{2g_1}$/$\mathbf{2g_2}$/$\mathbf{2g_3}$. This indicated clearly that the equilibrium lies towards the ‖Ru–Ru isomer $\mathbf{2g_3}$, i.e., that it was the thermodynamically most stable isomer. This is in agreement with the earlier observations on the $[FeRu_3(\mu\text{-}H)_2(CO)_{13}]$ and $[Cp/Cp^*RhRu_3(\mu\text{-}H)_4(CO)_9]$ systems.[9,10]

As a natural extension from the above reactions with alkynes, we attempted the reaction of **1** with 1-hexene to see if cluster-olefin complexes may be prepared, but none could be isolated. Instead, we found that the cluster-catalysed isomerisation of 1-hexene gave a mixture of 2- and 3-hexenes. However, we have monitored the reaction by $^1$H NMR spectroscopy and found that complete isomerisation was not achieved even after many hours.

 © 2006 Wiley-VCH Verlag GmbH & Co. KGaA, Weinheim 

### Structural Discussions on 2

The clusters **2** have been studied crystallographically; selected bond parameters using a common atomic numbering scheme were presented in Table 2. With the exception of **2g$_3$**, the alkyne is disposed parallel to the hinge heterometallic bond, with the torsion angle between the carbon–carbon backbone and the Ir(1)–Ru(3) edge close to 0° [torsion angles ranging between –0.7 to 1.9°]. This hinge Ir–Ru bond is also the longest of the metal–metal bonds, as has been generally found in $M_4C_2$ butterfly clusters.[21] The Ir–Ru bond lengths in general are, however, comparable to Ir–Ru bond lengths reported in the literature [Ir–Ru = 2.4972–2.9882 Å].[22] Also evident is the loss of multiple-bond character in the alkyne C–C bond; this length is surprisingly consistent across the different clusters, averaging 1.45 Å and with the range of values well within the experimental errors, despite the variation in substituents. However, there is a clear trend that the alkyne is closer to the iridium than to the ruthenium, as has been observed for clusters **3** above; this is consistent with the difference in the metal–metal bond lengths of [Ir$_4$(CO)$_{12}$] and [Ru$_3$(CO)$_{12}$] (mean of 2.693 and 2.853 Å, respectively).[23] The effect of asymmetry in the alkyne is also evident in the $M_{wingtip}$–$C_{alkyne}$ bond lengths; the M–C distance to the $C_{alkyne}$ carrying the bulkier substituent is longer than that to the $C_{alkyne}$ carrying the less bulky group. This difference ranges from 0.04 to 0.08 Å, with the exception of **2c**, while for the symmetrical alkynes **2a** and **2b**, the difference in this bond length is less than 0.03 Å. The effect of asymmetry in the alkyne is also apparent in **2g$_3$**.

## Conclusions

The cluster [Cp*IrRu$_3$(μ-H)$_2$(CO)$_{10}$] reacts with alkynes under thermal activation to yield butterfly clusters of the general formulae [Cp*IrRu$_3$(CO)$_9$(RCCR′)], but with substantial cluster fragmentation. The reactions did not proceed under photochemical or chemical activation with TMNO (trimethylamine *N*-oxide). However, the thermal activation also led to cluster fragmentation to [Cp*Ir(CO)$_2$] and alkyne substituted triruthenium clusters such as **4** and **5**, or the iridium-diruthenium clusters **3**. The yields of these decomposition products can be quite high; over 50% in the case of the combined yields of **3a** and **4a**, and accounted for the observed low yields of the clusters **2**.

The binding of the alkyne also appears to be highly stereoselective, with a general preference towards the stereoisomer in which the alkyne is aligned parallel to an Ru–Ir hinge, and with the bulkier substituent oriented away from the Cp*Ir moiety in the case of unsymmetrical alkynes. A notable exception is observed in the case of phenylacetylene, for which all three possible isomers are observed to be in equilibrium, with the isomer in which the alkyne is aligned parallel to an Ru–Ru hinge being the thermodynamically most stable.

Our results thus represent a map of the possibility of stereoselective binding of alkynes in such heteronuclear clusters. The high stereoselectivity exhibited in some cases suggests that such clusters may be useful in the stereocontrol of reactions with alkynes, and our future work will be directed towards that.

Table 2. Common atomic numbering scheme and selected bond lengths [Å] for **2a**–**c**, **2e**, **2f**, **2g$_2$** and **2g$_3$**.

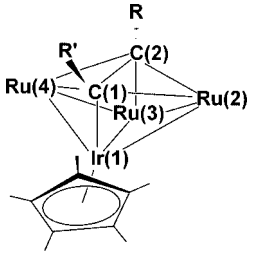


| | **2a** R = R′ = Ph | **2b** R = R′ = Et | **2c** R = *t*Bu R′ = Me | **2e** R = $SiMe_3$ R′ = H | **2f** R = $SiEt_3$ R′ = H | **2g$_2$** R = H R′ = Ph | **2g$_3$**[a] R = Ph R′ = H |
|---|---|---|---|---|---|---|---|
| Ir(1)–Ru(2) | 2.6858(5) | 2.6542(3) | 2.6699(3) | 2.6734(4) | 2.6836(8) | 2.6545(10) | 2.7360(8) |
| Ir(1)–Ru(3) | 2.7997(5) | 2.8019(3) | 2.8078(3) | 2.7964(3) | 2.7864(8) | 2.7865(11) | 2.7890(9) |
| Ir(1)–Ru(4) | 2.6435(5) | 2.6594(3) | 2.6456(3) | 2.6840(4) | 2.6845(8) | 2.6980(10) | 2.7380(10) |
| Ru(2)–Ru(3) | 2.7011(7) | 2.6979(4) | 2.6903(4) | 2.7054(4) | 2.7033(10) | 2.7266(14) | 2.7136(7) |
| Ru(3)–Ru(4) | 2.7075(7) | 2.6921(4) | 2.6947(4) | 2.7132(5) | 2.6987(11) | 2.7071(13) | 2.7571(9) |
| Ir(1)–C(1) | 2.059(6) | 2.057(3) | 2.053(3) | 2.023(4) | 2.026(9) | 2.047(11) | 2.163(10) |
| Ru(2)–C(1) | 2.258(6) | 2.270(3) | 2.246(3) | 2.202(4) | 2.197(9) | 2.236(11) | 2.147(10) |
| Ru(4)–C(1) | 2.261(6) | 2.242(3) | 2.286(3) | 2.186(4) | 2.203(9) | 2.240(11) | 2.237(10) |
| Ru(2)–C(2) | 2.230(5) | 2.260(3) | 2.312(3) | 2.241(4) | 2.257(9) | 2.220(12) | 2.103(8) |
| Ru(4)–C(2) | 2.265(6) | 2.254(3) | 2.296(3) | 2.259(4) | 2.255(9) | 2.214(11) | 2.203(9) |
| Ru(3)–C(2) | 2.170(6) | 2.184(3) | 2.224(3) | 2.178(4) | 2.203(9) | 2.139(12) | 2.148(9) |
| C(1)–C(2) | 1.470(8) | 1.458(5) | 1.457(5) | 1.454(5) | 1.444(2) | 1.477(16) | 1.477(13) |

[a] For **2g$_3$**, interchange Ir(1) with Ru(2).

 © 2006 Wiley-VCH Verlag GmbH & Co. KGaA, Weinheim 

## Experimental Section

All reactions were carried out using standard Schlenk techniques under nitrogen. Solvents used in reactions were of AR grade, and were dried, distilled and kept under argon in flasks fitted with Teflon valves prior to use. The products were generally separated by thin-layer chromatography (TLC), using plates coated with silica gel 60 F254 of 0.25 mm or 0.5 mm thickness and extracted with hexane or dichloromethane. Infrared spectra were recorded as hexane solutions unless otherwise stated with a Bio-Rad FTS 165 FTIR spectrometer at a resolution of 1 $cm^{-1}$ using a solution cell with NaCl windows of path length 0.1 mm. NMR spectra were acquired with a Bruker ACF 300 MHz as $CDCl_3$ solutions unless otherwise stated. Chemical shifts reported are referenced to residual protons of the solvent. Mass spectra were collected using the Fast Atom Bombardment (FAB) technique and were carried out with a Finnigan MAT95XL-T mass spectrometer normally with 3-nitrobenzyl alcohol matrix at the National University of Singapore mass spectrometry laboratory. Microanalyses were carried out by the microanalytical laboratory at the National University of Singapore. GC analyses were carried out with an Agilent GC-MS consisting of a GC 6890 MS 5973 equipped with an HP-1 column (300 mm × 0.25 mm × 0.25 μm). In photochemical reactions, UV irradiation was performed with a Hanovia 450 W UV lamp ($\lambda_{max}$ = 254 nm). The cluster **1** was prepared according to published procedures.[24]

**Reaction of 1 with Alkynes:** In a typical reaction, cluster **1** (10.0 mg, 10.0 μmol), PhCCPh (2.5 mg, 10 μmol) and hexane (20 mL) were placed in a Carius tube fitted with a teflon valve, and the solution degassed by three freeze-pump-thaw cycles. The reaction was then heated in an oil-bath at 90 °C for 6 h. After removal of the solvent and volatiles under reduced pressure, the residue was redissolved in a minimum volume of dichloromethane and chromatographed on silica-gel TLC plates with 100% hexane as eluent. The analytical and spectroscopic data for the products are given in Table 3. Diffraction quality crystals were grown from hexane by slow cooling.

**Thermolysis of 2a and 2b:** Cluster **2a** (6.7 mg, 6.0 μmol) and hexane (20 mL) were placed in a Carius tube fitted with a Teflon valve, and the reaction mixture degassed by three freeze-pump-thaw cycles. The mixture was then heated at 90 °C for 7 h. Chromatographic separation of the mixture on silica-gel TLC plates using hexane as eluent afforded three bands. These were, in order of elution, unreacted **2a** (2.0 mg, 30%), **3a** (2.5 mg, 40%), and **1** (0.5 mg, 8%), identified by their IR spectra.

Heating **2b** (8.4 mg, 8.0 μmol) under the same conditions followed by a similar work-up afforded **2b** (3.3 mg, 40%), **3b** (2.4 mg, 35%), and **1** (0.6 mg, 7%).

**Photolysis of 2a and 2b:** A hexane solution of **2a** (6 mg, 6.0 μmol) was photolysed in a quartz Carius tube under UV light for 7 h. Chromatographic separation of the mixture on silica-gel TLC

Table 3. Spectroscopic and analytical data for the reaction products.

| | IR, $\nu_{(CO)}$ [$cm^{-1}$] | $^1$H NMR, $\delta$ [ppm] | Elemental analysis calculated (found) | MS, $M^+$ found (calculated) |
|---|---|---|---|---|
| **2a** | 2067 m, 2046 vs, 2023 s, 1994 s, 1973 m | 7.13–6.85 (m, 10 H, Ph), 2.07 (s, 15 H, Cp*) | C 37.32 (37.59), H 2.36 (2.04) | 1060.8 (1060.9) |
| **2b** | 2062 m, 2038 vs, 2018 s, 1988 s, 1971 m | ($C_6D_6$) 2.85 (q, $^3J_{HH}$ = 7.4 Hz, 2 H, $CH_3CH_2CCCH_2CH_3$), 2.61 (q, $^3J_{HH}$ = 7.4 Hz, 2 H, $CH_3CH_2CCCH_2CH_3$), 1.76 (s, 15 H, Cp*), 1.21 (t, $^3J_{HH}$ = 7.4 Hz, 3 H, $CH_3CH_2CCCH_2CH_3$), 0.97 (t, $^3J_{HH}$ = 7.4 Hz, 3 H, $CH_3CH_2CCCH_2CH_3$) | C 31.09 (31.25), H 2.59 (2.51) | 964.8 (964.9) |
| **2c** | 2060 m, 2037 vs, 2027 (sh), 2015 s, 1986 s, 1968 m | 2.73 (s, 3 H, $CH_3$), 2.08 (s, 15 H, Cp*), 1.45 (s, 9 H, *t*Bu) | C 31.87(32.33), H 2.69 (1.98) | 980.9 (978.9) |
| **2e** | 2064 m, 2041 vs, 2016 s, 1991 s, 1973 m | 10.53 (s, 1 H, ≡CH), 2.07 (s, 15 H, Cp*), 0.25 (s, 9 H, $SiMe_3$) | C 29.36 (29.54), H 2.55 (2.44) | 979.5 (980.9) |
| **2f** | 2062 m, 2039 vs, 2015 s, 1989 s, 1972 m | ($C_6D_6$) 10.51 (s, 1 H, ≡CH), 1.72 (s, 15 H, Cp*), 1.09 (q, 6 H, $CH_2$), 0.92 (t, 9 H, $CH_3$) | C 32.18 (31.70), H 3.05 (3.16) | 1023.6 (1023.0) |
| **2g$_1$** | 2070 m, 2048 vs, 2024 vs, 1996 s, 1960 w | ($C_6D_6$) 10.58 (s, 1 H, ≡CH), 7.00–7.77 (m, 5 H, Ph), 1.82 (s, 15 H, Cp*) | low yield | 987.7920 (987.7945) |
| **2g$_2$** | 2069 vs, 2048 vs, 2036 s, 2024 s, 2016 m, 1995 s | ($C_6D_6$) 11.37 (s, 1 H, ≡CH), 7.00–7.77 (m, 5 H, Ph), 1.87 (s, 15 H, Cp*) | low yield | 987.7908 (987.7945) |
| **2g$_3$** | 2071 vs, 2048 vw, 2031 vs, 2019 vs, 2001 m, 1991 m, 1981 w, 1973 mw, 1960 m, 1950 w | ($C_6D_6$) 9.44 (s, 1 H, ≡CH), 7.75–6.60 (m, 5 H, Ph), 1.16 (s, 15 H, Cp*) | C 32.93 (33.04), H 2.15 (2.09) | 986.0 (987.8) |
| **3a** | 2065 s, 2032 vs, 1992 m, 1963 m, 1846 br. | 7.12–6.88 (m, 10 H, Ph), 1.87 (s, 15 H, Cp*) | C 41.19 (40.71), H 2.79 (2.71) | 905.8 (903.9) |
| **3b** | 2060 s, 2027 vs, 1989 vs, 1962 m, 1834 br. | ($C_6D_6$) 2.65 (dq, $^3J_{HaHc}$ = $^3J_{HbHc}$ = 7.4 Hz, 2 H, $CH_{3c}CH_aH_bCCCH_{a'}H_{b'}CH_{3c'}$), 2.47 (dq, $CH_{3c}CH_aH_bCCCH_{a'}H_{b'}CH_{3c'}$, $^3J_{Ha'Hc'}$ = 7.4 Hz, 1 H), 2.27 (dq, $^3J_{Hb'Hc'}$ = 7.4 Hz, 1 H, $CH_{3c}CH_aH_bCCCH_{a'}H_{b'}CH_{3c'}$), 1.67 (s, 15 H, Cp*), 1.24 (t, $^3J_{HH}$ = 7.4 Hz, 3 H, $CH_{3c}CH_aH_bCCCH_{a'}H_{b'}CH_{3c'}$), 1.15 (t, $^3J_{HH}$ = 7.4 Hz, 3 H, $CH_{3c}CH_aH_bCCCH_{a'}H_{b'}CH_{3c'}$) | C 34.20 (34.45), H 3.12 (2.99) | 807.9 (807.8) |

 © 2006 Wiley-VCH Verlag GmbH & Co. KGaA, Weinheim 

Table 4. Crystal and refinement data for **2a**–**c**, **2e** and **2f**.

| Compound | **2a** | **2b** | **2c** | **2e** | **2f** |
|---|---|---|---|---|---|
| Empirical formula | $C_{33}H_{25}IrO_9Ru_3$ | $C_{25}H_{25}IrO_9Ru_3$ | $C_{26}H_{27}IrO_9Ru_3$ | $C_{24}H_{25}IrO_9Ru_3Si$ | $C_{27}H_{31}IrO_9Ru_3Si$ |
| Formula mass | 1060.94 | 964.86 | 978.89 | 980.94 | 1023.02 |
| Crystal system | monoclinic | monoclinic | monoclinic | monoclinic | orthorhombic |
| Space group | $P2_1/c$ | $P2_1/n$ | $P2_1/n$ | $P2_1/c$ | $Pbca$ |
| Unit cell dimensions [Å, °] | $a$ = 14.0776(5) | $a$ = 9.6671(4) | $a$ = 10.7358(3) | $a$ = 9.3772(4) | $a$ = 16.5440(7) |
| | $b$ = 9.6907(3) | $b$ = 15.1800(7) | $b$ = 14.8779(4) | $b$ = 15.5636(7) | $b$ = 17.7258(8) |
| | $c$ = 23.9906(9) | $c$ = 19.4979(9) | $c$ = 18.1779(5) | $c$ = 20.0285(9) | $c$ = 21.6281(9) |
| | $\alpha$ = 90 | $\alpha$ = 90 | $\alpha$ = 90 | $\alpha$ = 90 | $\alpha$ = 90 |
| | $\beta$ = 92.603(2) | $\beta$ = 99.6300(10) | $\beta$ = 92.2750(10) | $\beta$ = 93.4090(10) | $\beta$ = 90 |
| | $\gamma$ = 90 | $\gamma$ = 90 | $\gamma$ = 90 | $\gamma$ = 90 | $\gamma$ = 90 |
| Volume [Å$^3$] | 3269.5(2) | 2820.9(2) | 2901.20(14) | 2917.8(2) | 6342.6(5) |
| $Z$ | 4 | 4 | 4 | 4 | 8 |
| $\rho_{calcd.}$ [Mg/m$^3$] | 2.155 | 2.272 | 2.241 | 2.233 | 2.143 |
| Absorption coefficient [mm$^{-1}$] | 5.470 | 6.326 | 6.153 | 6.157 | 5.670 |
| $F$(000) | 2016 | 1824 | 1856 | 1856 | 3904 |
| Crystal size [mm] | 0.22 × 0.16 × 0.10 | 0.32 × 0.24 × 0.20 | 0.34 × 0.26 × 0.14 | 0.30 × 0.22 × 0.08 | 0.12 × 0.04 × 0.01 |
| $\theta$ range for data collection [°] | 2.18–26.37 | 2.12–26.37 | 2.17–30.01 | 2.04–29.55 | 2.25–26.37 |
| Reflections collected | 25711 | 41944 | 24638 | 22671 | 49894 |
| Independent reflections | 6683 [$R$(int) = 0.0444] | 5761 [$R$(int) = 0.0303] | 8188 [$R$(int) = 0.0277] | 7440 [$R$(int) = 0.0326] | 6478 [$R$(int) = 0.1287] |
| Data/restraints/parameters | 6683/0/420 | 5761/0/350 | 8188/0/361 | 7440/0/355 | 6478/0/381 |
| Goodness-of-fit on $F_2$ | 1.107 | 1.090 | 1.050 | 1.036 | 1.034 |
| Final $R$ indices [$I > 2\sigma(I)$] | $R_1$ = 0.0399, | $R_1$ = 0.0213, | $R_1$ = 0.0277, | $R_1$ = 0.0307, | $R_1$ = 0.0504, |
| | $wR_2$ = 0.0842 | $wR_2$ = 0.0520 | $wR_2$ = 0.0621 | $wR_2$ = 0.0645 | $wR_2$ = 0.0870 |
| $R$ indices (all data) | $R_1$ = 0.0460, | $R_1$ = 0.0231, | $R_1$ = 0.0318, | $R_1$ = 0.0363, | $R_1$ = 0.0898, |
| | $wR_2$ = 0.0867 | $wR_2$ = 0.0528 | $wR_2$ = 0.0637 | $wR_2$ = 0.0666 | $wR_2$ = 0.0996 |
| Largest diff. peak/hole [e·Å$^{-3}$] | 1.836/–0.755 | 1.141/–0.575 | 1.570/–0.847 | 1.127/–0.796 | 1.276/–0.871 |

Table 5. Crystal and refinement data for **2g$_2$**, **2g$_3$**, **3a**, **3b** and **4b**.

| Compound | **2g$_2$** | **2g$_3$** | **3a** | **3b** | **4b** |
|---|---|---|---|---|---|
| Empirical formula | $C_{27}H_{21}IrO_9Ru_3$ | $C_{27}H_{21}IrO_9Ru_3$ | $C_{31}H_{25}IrO_7Ru_2$ | $C_{23}H_{25}IrO_7Ru_2$ | $C_{20}H_{20}O_8Ru_3$ |
| Formula mass | 984.85 | 984.85 | 903.85 | 807.77 | 691.57 |
| Crystal system | monoclinic | monoclinic | monoclinic | orthorhombic | monoclinic |
| Space group | $P2_1/c$ | Cc | $P2_1/n$ | $Pbca$ | $P2_1/n$ |
| Unit cell dimensions [Å, °] | $a$ = 16.2320(8) | $a$ = 19.9566(11) | $a$ = 10.0663(3) | $a$ = 9.9869(3) | $a$ = 9.7768(5) |
| | $b$ = 13.0498(7) | $b$ = 9.9529(4) | $b$ = 19.1058(6) | $b$ = 16.0665(4) | $b$ = 18.1206(9) |
| | $c$ = 13.5375(7) | $c$ = 16.6241(7) | $c$ = 15.2570(6) | $c$ = 30.8922(8) | $c$ = 12.9616(6) |
| | $\alpha$ = 90 | $\alpha$ = 90 | $\alpha$ = 90 | $\alpha$ = 90 | $\alpha$ = 90 |
| | $\beta$ = 90.843(2) | $\beta$ = 119.6740(10) | $\beta$ = 97.0130(10) | $\beta$ = 90 | $\beta$ = 93.1270(10) |
| | $\gamma$ = 90 | $\gamma$ = 90 | $\gamma$ = 90 | $\gamma$ = 90 | $\gamma$ = 90 |
| Volume [Å$^3$] | 2867.3(3) | 2868.9(2) | 2912.34(17) | 4956.8(2) | 2292.88(19) |
| $Z$ | 4 | 4 | 4 | 8 | 4 |
| $\rho_{calcd.}$ [Mg/m$^3$] | 2.281 | 2.280 | 2.061 | 2.165 | 2.003 |
| Absorption coefficient [mm$^{-1}$] | 6.227 | 6.223 | 5.628 | 6.599 | 1.993 |
| $F$(000) | 1856 | 1856 | 1728 | 3072 | 1344 |
| Crystal size [mm] | 0.13 × 0.12 × 0.02 | 0.20 × 0.08 × 0.06 | 0.22 × 0.10 × 0.08 | 0.18 × 0.16 × 0.02 | 0.34 × 0.24 × 0.04 |
| $\theta$ range for data collection [°] | 2.00–26.37 | 2.35–28.28 | 2.13–24.71 | 2.49–26.37 | 2.25–26.37 |
| Reflections collected | 36509 | 42704 | 23408 | 40378 | 31805 |
| Independent reflections | 5864 [$R$(int) = 0.0848] | 3553 [$R$(int) = 0.0777] | 4960 [$R$(int) = 0.0449] | 5060 [$R$(int) = 0.0593] | 4682 [$R$(int) = 0.0335] |
| Data/restraints/parameters | 5864/1/370 | 3553/8/369 | 4960/0/375 | 5060/0/305 | 4682/0/284 |
| Goodness-of-fit on $F_2$ | 1.386 | 0.929 | 1.064 | 1.195 | 1.128 |
| Final $R$ indices [$I > 2\sigma(I)$] | $R_1$ = 0.0733, | $R_1$ = 0.0297, | $R_1$ = 0.0333, | $R_1$ = 0.0405, | $R_1$ = 0.0298, |
| | $wR_2$ = 0.1350 | $wR_2$ = 0.0810 | $wR_2$ = 0.0746 | $wR_2$ = 0.0776 | $wR_2$ = 0.0722 |
| $R$ indices (all data) | $R_1$ = 0.0826, | $R_1$ = 0.0302, | $R_1$ = 0.0374, | $R_1$ = 0.0487, | $R_1$ = 0.0330, |
| | $wR_2$ = 0.1383 | $wR_2$ = 0.0817 | $wR_2$ = 0.0765 | $wR_2$ = 0.0803 | $wR_2$ = 0.0739 |
| Largest diff. peak/hole [e·Å$^{-3}$] | 2.152/ –2.267 | 1.623/–1.490 | 2.138/–0.488 | 1.214/–1.151 | 1.041/–0.341 |

plates using hexane as eluent afforded **2a** (2.3 mg, 40%), **3a** (2 mg, 30%), and **1** (0.4 mg, 6%).

Irradiation of **2b** (8.5 mg, 9.0 μmol) under the same conditions, followed by a similar work-up, afforded **2b** (3.4 mg, 40%), **3b** (2.5 mg, 38%), and **1** (0.5 mg, 6%).

**Reaction of 1 with 1-Hexene:** Cluster **1**, (5 mg, 5.0 μmol) and 1-hexene (10 μL, 80 μmol) in deuterated toluene (0.5 mL) were stirred in an NMR tube and the reaction monitored by $^1$H NMR over a period of 7 h. Signals due to a mixture of 2- and 3-hexene were observed in the $^1$H NMR spectrum, suggesting isomerisation of the

 © 2006 Wiley-VCH Verlag GmbH & Co. KGaA, Weinheim 

alkene. The infrared spectrum of the reaction mixture showed that cluster **1** remained mainly unchanged.

**X-Ray Crystal Structure Determinations:** Crystals were mounted on quartz fibres. X-ray data were collected with a Bruker AXS APEX system, using Mo-$K_\alpha$ radiation, at 223 K with the SMART suite of programs.[25] Data were processed and corrected for Lorentz and polarisation effects with SAINT,[26] and for absorption effects with SADABS.[27] Structural solution and refinement were carried out with the SHELXTL suite of programs.[28] Crystal and refinement data are summarised in Table 4 and Table 5.

The structures were solved by direct methods to locate the heavy atoms, followed by difference maps for the light, non-hydrogen atoms. All non-hydrogen atoms were generally given anisotropic displacement parameters in the final model. Organic hydrogen atoms were placed in calculated positions and refined with a riding model. Compound $\mathbf{2g_3}$ was refined as a racemic twin.

CCDC-283339 to -283350 contain the supplementary crystallographic data for this paper. These data can be obtained free of charge from The Cambridge Crystallographic Data Centre via www.ccdc.cam.ac.uk/data_request/cif.

## Acknowledgments

This work was supported by the National University of Singapore (Research Grant No. R143-000-190-112) and one of us (P. S.) thanks the University for a Research Scholarship.

[1] R. D. Adams, F. A. Cotton, *Catalysis by Di- and Polynuclear Metal Cluster Complexes*, Wiley: New York, **1998**.
[2] a) E. Sappa, A. Tiripicchio, P. Braunstein, *Chem. Rev.* **1983**, *83*, 203; b) N. T. Allison, J. R. Fritch, K. P. C. Vollhardt, E. C. Walborsky, *J. Am. Chem. Soc.* **1983**, *105*, 1384; c) A. D. Clauss, J. R. Shapley, C. N. Wilker, R. Hoffmann, *Organometallics* **1984**, *3*, 619; d) E. Roland, H. Vahrenkamp, *Organometallics* **1983**, *2*, 183; e) E. L. Muetterties, *Angew. Chem. Int. Ed. Engl.* **1978**, *90*, 577; f) E. L. Muetterties, T. N. Rhodin, E. Band, C. F. Bruker, W. R. Pretzer, *Chem. Rev.* **1979**, *79*, 91.
[3] A. Choualeb, P. Braunstein, J. Rose, R. Welter, *Inorg. Chem.* **2004**, *43*, 57.
[4] E. Sappa, A. Tiripicchio, A. J. Carty, G. E. Toogood, *Prog. Inorg. Chem.* **1987**, *35*, 437.
[5] a) E. W. Abel, F. G. A. Stone, G. Wilkinson, *Comprehensive Organometallic Chemistry II*, 1st ed., Pergamon: Oxford, New York, **1995**; b) L. F. Dahl, D. L. Smith, *J. Am. Chem. Soc.* **1962**, *84*, 2450; c) R. J. Haines, N. D. C. T. Steen, M. Laing, P. Sommerville, *J. Organomet. Chem.* **1980**, *198*, C72.
[6] K. Wade, *Adv. Inorg. Chem. Radiochem.* **1976**, *18*, 1.
[7] J. A. Cabeza, P. García-Alvarez, E. Pérez-Carreño, *Organometallics* **2005**, *24*, 2000.
[8] a) M. Cazanoue, N. Lugan, J. J. Bonnet, R. Mathieu, *Organometallics* **1988**, *7*, 2480; b) V. Ferrand, G. Süss-Fink, A. Neels, H. Stoeckli-Evans, *J. Chem. Soc., Dalton Trans.* **1998**, 3825; c) V. Ferrand, G. Süss-Fink, A. Neels, H. Stoeckli-Evans, *Eur. J. Inorg. Chem.* **1999**, 853.
[9] J. R. Fox, W. L. Gladfelter, G. L. Geoffroy, I. Tavanaiepour, S. Abdel-Mequid, V. W. Day, *Inorg. Chem.* **1981**, *20*, 3230.
[10] J. L. Le Grand, W. E. Lindsell, K. J. McCullough, C. H. McIntosh, A. G. Meiklejohn, *J. Chem. Soc., Dalton Trans.* **1992**, 1089.
[11] a) M. V. Capparelli, Y. De Sanctis, A. J. Arce, *Acta Crystallogr. Sect. C: Cryst. Struct. Commun.* **1995**, *51*, 1819; b) S. Aime, L. Milone, D. Osella, M. Valle, *J. Chem. Res. Synop.* **1978**, 77.
[12] Crystal data for **5a**: $P2_1/c$, $a$ = 9.5075(4) Å; $b$ = 18.5955(9) Å; $c$ = 18.3912(8) Å; $\beta$ = 95.457(2)°. Ref.[11a] $P2_1/c$, $a$ = 9.556(3) Å, $b$ = 18.694(4) Å, $c$ = 18.465(2) Å, $\beta$ = 95.77(1)°.
[13] For examples see: a) P. Braunstein, J. Rose, O. Bars, *J. Organomet. Chem.* **1983**, *252*, C101; b) E. Roland, H. Vahrenkamp, *Organometallics* **1983**, *2*, 1048; c) E. Sappa, A. Tiripicchio, M. T. Camellini, *J. Organomet. Chem.* **1981**, *213*, 175; d) L. Busetto, M. Green, J. A. K. Howard, B. Hessner, J. C. Jeffery, R. M. Mills, F. G. A. Stone, P. Woodward, *J. Chem. Soc., Dalton Trans.* **1981**, 1101.
[14] M. Smith, J. March, *March's Advanced Organic Chemistry: Reactions, Mechanisms and Structure*, 5th ed., John Wiley & Sons: New York, Singapore, **2001**.
[15] $\nu_{CO}$ (hex): 2064 m, 2042 vs, 2028 (sh), 2019 s, 1991 s, 1974 m $cm^{-1}$.
[16] A. J. Edwards, N. E. Leadbeater, J. Lewis, P. R. Raithby, *J. Chem. Soc., Dalton Trans.* **1995**, 3785.
[17] Crystal data: space group $P\bar{1}$; $a$ = 9.0738(7) Å; $b$ = 9.1688(7) Å; $c$ = 13.0136(9) Å; $\alpha$ = 93.546(1)°; $\beta$ = 107.152(1)°; $\gamma$ = 97.881(1)°. Lit. values: $P\bar{1}$, $a$ = 9.1554(10) Å; $b$ = 9.2373(10) Å; $c$ = 13.1229(10) Å; $\alpha$ = 92.135(10)°; $\beta$ = 106.738(10)°; $\gamma$ = 98.483(10)°.
[18] F. J. Zuno-Cruz, A. L. Carrasco, M. J. Rosales-Hoz, *Polyhedron* **2002**, *21*, 1105.
[19] J. J. Schneider, M. Nolte, C. Krueger, *J. Organomet. Chem.* **1991**, *403*, C4.
[20] H. Bantel, A. K. Powell, H. Vahrenkamp, *Chem. Ber.* **1990**, *123*, 661.
[21] a) S. Haak, G. Süss-Fink, A. Neels, H. Stoeckli-Evans, *Polyhedron* **1999**, *18*, 1675; b) G. Süss-Fink, S. Haak, V. Ferrand, H. Stoeckli-Evans, *J. Chem. Soc., Dalton Trans.* **1997**, 3861.
[22] a) A. Fumagalli, M. C. Malatesta, M. Vallario, G. Ciani, M. Moret, A. Sironi, *J. Cluster Sci.* **2001**, *12*, 187; b) H. C. Bottcher, M. Graf, K. Merzweiler, C. Wagner, *Polyhedron* **2000**, *19*, 2593; c) G. Süss-Fink, S. Haak, V. Ferrand, H. Stoeckli-Evans, *J. Mol. Catal. A* **1999**, *143*, 163; d) J. R. Galsworthy, C. E. Housecroft, D. M. Matthews, R. Ostrander, A. L. Rheingold, *J. Chem. Soc., Dalton Trans.* **1994**, 69; e) L. Y. Hsu, W. L. Hsu, D. A. McCarthy, J. A. Krause, J. H. Chung, S. G. Shore, *J. Organomet. Chem.* **1992**, *426*, 121.
[23] a) M. R. Churchill, J. P. Hutchinson, *Inorg. Chem.* **1978**, *17*, 3528; b) V. J. Johnston, F. W. B. Einstein, R. K. Pomeroy, *Organometallics* **1988**, *7*, 1867; c) M. R. Churchill, F. J. Hollander, J. P. Hutchinson, *Inorg. Chem.* **1977**, *16*, 2655.
[24] P. Srinivasan, W. K. Leong, *J. Organomet. Chem.*, manuscript accepted.
[25] SMART version 5.628, Bruker AXS Inc., Madison, Wisconsin, USA, **2001**.
[26] SAINT+ version 6.22a, Bruker AXS Inc., Madison, Wisconsin, USA, **2001**.
[27] G. M. Sheldrick, SADABS, **1996**.
[28] SHELXTL version 5.1, Bruker AXS Inc., Madison, Wisconsin, USA, **1997**.

Received: September 16, 2005
Published Online: November 15, 2005

 © 2006 Wiley-VCH Verlag GmbH & Co. KGaA, Weinheim 

DOI: 10.1002/ejic.200500849

# Fluorinated β-Diketones for the Extraction of Lanthanide Ions: Photophysical Properties and Hydration Numbers of Their $Eu^{III}$ Complexes

**Anne-Sophie Chauvin,[a] Frédéric Gumy,[a] Izuru Matsubayashi,[b] Yuko Hasegawa,*[b] and Jean-Claude G. Bünzli*[a]**

**Keywords:** Lanthanide / Luminescence / β-diketonate / Hydration number / Extraction

Tris(β-diketonato)europium(III) with a series of variably fluorinated ligands derived from 3,5-heptanedione were synthesised with the aim of determining their hydration state under extraction conditions. The number of coordinated water molecules was determined by measuring the lifetime of the $Eu(^5D_0)$ excited level in water and deuterated water. The hydration gain ($\Delta q = q - q_0$) after shaking chloroform solutions during 10 min with 0.1 M $NaClO_4$ aqueous solutions depends on the fluorination extent of the diketonates: fluorination of one methyl group leads to a decrease in $\Delta q$ of ca. 0.5 unit, while fluorination of one ethyl group results in a decrease of ca. 1.3 units. Highly fluorinated complexes (i.e with hexafluoroacetylacetonate and related ligands) display a hydration number close to one while poorly fluorinated compounds (or nonfluorinated ones, such as the acetylacetonate complex) have a hydration state close to two. Photophysical properties of the $Eu^{III}$ β-diketonates are also described and the synthesis of the fluorinated β-diketones is re-investigated and discussed in details.

(© Wiley-VCH Verlag GmbH & Co. KGaA, 69451 Weinheim, Germany, 2006)

## Introduction

Tris and tetrakis (β-diketonato)lanthanides(III) are the most widely studied complexes of the 4f-element series because of their potential use in several applications,[1] from NMR shift reagents to electroluminescent materials for light-emitting diodes, trace analysis, and separation/extraction systems.[2,3] Lanthanide β-diketonates are easily synthesised from the parent β-diketones, they possess large thermodynamic stability and, in addition, some of them are commercially available. The introduction of fluorine substituents on β-diketones produces large changes in the properties of the resulting $Ln^{III}$ complexes. For instance, while the separation factor between $La^{III}$ or $Pr^{III}$ and $Lu^{III}$ by solvent extraction drops from almost $4{\cdot}10^7$[4] with acetylacetone (Hacac) to 3000[5,6] with 2-thenoyltrifluoroacetone (Htta), and less than 100 with hexafluoroacetylacetone (Hhfa),[7] the complexes become more volatile and can be used to separate trivalent lanthanide ions by gas chromatography.[8,9] Moreover, due to the heavy atom effect,[10] which facilitates intersystem crossing, the metal-centred luminescent properties are enhanced, for instance in the case of $Sm^{III}$ and $Eu^{III}$ electroluminescent devices.[11] As a consequence, ternary complexes of the tris(β-diketonato)$Ln^{III}$ with tta and 1,10 phenanthroline are routinely used to produce luminescent resins[12] and liquid crystals.[13]

The stability of lanthanide β-diketonates in aqueous solutions decreases with fluorination since the electron-withdrawing effect of the fluorine atoms reduces the charge density on the oxygen atoms. This decrease in stability could influence the extraction and separation efficiency of lanthanides with β-diketones. The relationship between extractability and stability of aqueous complexes is presently investigated in one of our laboratories.[7] On the other hand, synergistic extraction of lanthanides(III) with β-diketonate and a Lewis base improves the extractability and also depends on the fluorination of β-diketonates. For instance, in $CHCl_3$ [$Eu(acac)_3$] forms a 1:1 ternary complex with tributylphosphate (tbp) having $\log\beta_1 = 1.90$, while trifluoroacetonate (tfa) forms both 1:1 and 1:2 ternary complexes with $\log\beta_1$ and $\log\beta_2$ equal to 3.32 and 4.64, respectively, where $\beta_n = [EuA_3(tbp)_n]_O/[EuA_3]_O[tbp]^n_O$ with A = β-diketonate ion while the subscript O indicates concentrations in the organic solvent.[14] Similarly, benzoylacetonate forms only the 1:1 adduct ($\log\beta_1 = 1.60$) but benzoyltrifluoroacetonate leads to both 1:1 and 1:2 ternary complexes ($\log\beta_1 = 3.64$ and $\log\beta_2 = 5.28$).[14]

Two opposite effects will compete as far as the hydration state of the tris(β-diketonates) is concerned: the smaller complexation power of the fluorinated ligands is expected to foster interaction with water whereas the presence of the fluorine substituents will create a protective, repulsive shell around the metal centre. We determine here the hydration state $q$ of the europium β-diketonates with the fluorinated ligands depicted in Scheme 1, using the luminescent lifetime method, to unravel the relationship between $q$ and the extent of fluorination. We also re-investigate the synthesis of

[a] École Polytechnique Fédérale de Lausanne (EPFL), Laboratory of Lanthanide Supramolecular Chemistry, BCH 1405, 1015 Lausanne, Switzerland
[b] Department of Chemistry, Faculty of Science, Science University of Tokyo, 1-3, Kagurazaka, Shinjuku-ku, Tokyo 162-8601, Japan

 © 2006 Wiley-VCH Verlag GmbH & Co. KgaA, Weinheim 

the fluorinated β-diketones since published literature procedures are sometimes imprecisely described. The acronyms used here for β-diketonates (see Scheme 1) are relative to partially fluorinated methyl (acac, hfa) or ethyl groups ($F_5H_3$, $F_5H_5$, $F_5F_5$, $F_3H_5$, $F_3F_5$); β-diketones are indicated by an additional H in front of the acronym.

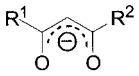

acac : $R^1 = R^2 = CH_3$

hfa : $R^1 = R^2 = CF_3$

$F_5H_3$ : $R^1 = C_2F_5$ $R^2 = CH_3$

$H_5H_5$ : $R^1 = R^2 = C_2H_5$

$F_5H_5$ : $R^1 = C_2F_5$ $R^2 = C_2H_5$

$F_5F_5$ : $R^1 = R^2 = C_2F_5$

$F_3H_5$ : $R^1 = CH_2CF_3$ $R^2 = C_2H_5$

$F_3F_5$ : $R^1 = CH_2CF_3$ $R^2 = C_2F_5$

Scheme 1. Ligands used in this study. Acronyms refer to the number of fluorine atoms present in the β-diketonates.

## Results and Discussion

### Syntheses of the Ligands

Two different pathways can be envisaged for the synthesis of fluorinated β-diketones. The most common synthetic route consists in methoxide-mediated acylation of the appropriate ketones with fluorinated esters (route I, see Scheme 2), for which the yields are generally good because fluorinated esters have electrophilic carbonyl moieties that are highly reactive in Claisen condensations. On the other hand, there are few reported examples of the condensation of alkyl perfluoroalkyl ketones with nonfluorinated esters under basic conditions (route II, see Scheme 2), due to the lack of reactivity or even the decomposition of the reactants. The presence of fluorine atoms is known to reduce intermolecular interactions (van der Waals forces and hydrogen bonding) and therefore fluorinated β-diketones are highly volatile (as well as their complexes, used in the chromatographic separation of lanthanides).[1,8] As a consequence, special care has to be exercised during the synthesis and subsequent isolation of the fluorinated β-diketones which are easily lost by co-evaporation with the solvent: several ketones form azeotropes with the reaction solvent [for example $H(F_3F_5)$ or $H(F_5F_5)$, either in ether, THF, or hexane] or extraction solvent ($CHCl_3$) after acidic treatment. Surprisingly, experimental details pertaining to the synthesis of some of the ligands used in this study could not be found in the literature, even though complexes have been isolated. In other cases, the reported synthesis could not be reproduced and/or the starting materials used are no more commercially available. For instance, the synthesis of $H(F_5F_5)$ reported in the literature simply refers to that of 1,1,1,2,2,3,3-heptafluoro-7,7-dimethyl-4,6-octanedione H(fod), without any experimental detail nor characterisation of the final $H(F_5F_5)$ product.[15] For these reasons and because lanthanide β-diketonates are presently stirring a renewed interest,[1,12,13] we discuss in detail the synthesis of all the ligands described in Scheme 1.

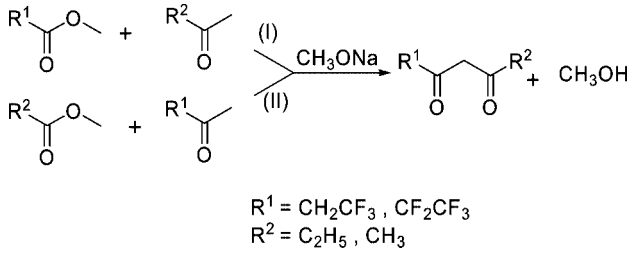


Scheme 2. Pathways for the synthesis of fluorinated β-diketones.

S. N. Misra et al. have reported the synthesis of 1,1,1-trifluorohexane-2,4-dione, $H(F_3H_5)_5$, in hexane and its subsequent isolation by distillation.[16] We found, however, that an azeotropic mixture forms upon carrying out the reaction in hexane or ether. Therefore, this ligand was isolated as its sodium salt. Further treatment to convert it into its neutral form was unsuccessful. After a methanolic solution of the sodium salt was passed through an ion exchange column (Amberlite 120), subsequent distillation yielded a colourless oily liquid. Although the latter displayed $^{19}F$ NMR signals, elemental analysis showed it to contain only 5% of carbon. 1,1,1,2,2-Pentafluoro-3,5-heptanedione $H(F_5H_5)$ was synthesised by addition of the enolate of 2-butanone to methyl pentafluoropropionate (route I). To ensure that all the 2-butanone was converted under its enolate form, more than two equivalents of base were added; otherwise, the 2-butanone enolate reacts with the fluorinated ketone, the enolate ion of which is formed preferentially if only one equivalent of base is added.[17,18] The synthesis can be conducted either in ether or in THF, but a higher yield is obtained with the former solvent. Moore et al.[19] reported an analogous synthesis, in which the ketone was added to a mixture of sodium methoxide and methyl pentafluoropropionate. However, the product was only characterised by IR so that we report its full analytical data. Two reports describe the isolation of the hydrated form of 1,1,1,2,2,6,6,7,7,7-decafluoro-3,5-heptanedione, $H(F_5F_5)$, by distillation.[20,21] Again, we observed the formation of azeotropic mixtures when ether or $CH_2Cl_2$ were used as solvents, as mentioned for $H(F_3H_5)$. As a consequence, this ligand has been isolated as its sodium salt. Alternatively, for large scale synthesis, removal of $H(F_5F_5)$ from the reaction mixture can be achieved by complexation with $Cu^{II}$, the metal being then released under acidic conditions and the ligand purified by distillation.[22] The synthesis of 1,1,1,2,2,7,7,7-octafluoro-3,5-heptanedione, $H(F_3F_5)$, was the most troublesome. First attempts using either route I or II were unsuccessful, the product being only isolated in trace amounts. In case of route I, this possibly arises from

 © 2006 Wiley-VCH Verlag GmbH & Co. KGaA, Weinheim 

the low boiling point of the starting ketone $CF_3CH_2COCH_3$ (41 °C), which can be easily evaporated from the reaction mixture either by the $N_2$ flux used to keep the conditions anhydrous or because deprotonation of this ketone is exothermic, which favours evaporation. The reaction was consequently conducted in presence of an excess of ketone and in a sealed tube. Finally, it was found that treating the resulting sodium salt $Na(F_3F_5)$ with sulfuric acid led to a partial decomposition of the product into $CF_3CF_2COCH_2COCH_3$. Therefore, $F_3F_5$ was also isolated in the form of its sodium salt $Na(F_3F_5)$. The yield of the reaction remains low, although it can be somewhat improved by using diethyl ether as solvent instead of hexane (37 vs. 25%, respectively).

The absence of spectroscopic feature, such as the single carbonyl vibration band in the spectral range 1740–1780 $cm^{-1}$, the $^1H$ NMR signal in the range 5.6–6.2 ppm arising from the CH=C proton, and the $^{13}C$ NMR resonances occurring for both *C*=CO and *C*=O, point to all the ligands, except $Na(F_3F_5)$, being exclusively under the enol form. This was expected in view of the presence of the electron-withdrawing $CF_2$ and $CF_3$ groups:[23] indeed, literature data based on $^1H$ NMR evidences show that the only detected form for β-diketones with more than four fluorine atoms is the enol isomer. A noticeable exception is 1,1,1,5,5,5-hexafluoro-3-(trifluoromethyl)pentane-2,4-dione, which is reported to exist under its keto form.[24] In our case, $Na(F_3F_5)$, which features a nonfluorinated α-carbon, has structural similarity with the latter compound. An enol-ketone equilibrium was found, displaced in favour of the enol form, 70%. The occurrence of the keto form for these two diketones is however difficult to explain.

## Syntheses of the Complexes

The neutral ligand was deprotonated (alternatively, its sodium salt was used) and the resulting β-diketonate easily reacted with europium acetate, giving in most cases a solid or a viscous oil which could be recrystallised either in methanol or in a mixture of methanol and water. The complexes were characterised by elemental analyses and in most cases they were found to be mono- or di-hydrated. Since the β-diketonates are hygroscopic, all the solutions for the luminescence studies were prepared in a glove-box and care was taken to keep them free of water. In the case of $EuF_3H_5$, the microanalysis was not reproducible, with a very low proportion of carbon (less than 10 percent), which is probably due to the high volatility of the β-diketone. For the same reasons, care had to be taken when preparing the $10^{-5}$ M solutions to avoid evaporation of the compound upon weighting. The tris(β-diketonates) were all studied in chloroform, the usual extraction solvent, for comparison reasons.

## Photophysical Properties

Absorption data for some of the ligands (in chloroform), their sodium salts (in water) and their $Eu^{III}$ complexes (in chloroform) are reported in Table 1. The ligands, except $H(F_5H_3)$, and the sodium salts feature one main absorption band located in the range 32500–39000 $cm^{-1}$ which is assigned to π→π* transitions. According to calculations performed with the CAChe Pro 6.0 program package for Microsoft Windows® (Fujitsu Ltd., 2000–2002), the enol forms should yield π→π* transitions located at lower energy than the bands arising from the keto form (> 40000 $cm^{-1}$). In addition, $Na(F_5H_3)$ displays a shoulder at 26620 $cm^{-1}$. For the neutral ligands, shifts of the maximum of the main absorption band seem to depend on two factors, the length of the alkyl substituent and the extent of fluorination. For instance, $H(F_5H_5)$ has one more carbon atom compared with $H(F_5H_3)$, and the resulting inductive effect materialises in a bathochromic shift of ca. –3250 $cm^{-1}$. On the other hand, fluorination induces hypsochromic shifts: +2670 $cm^{-1}$ for the replacement of the two methyl groups of acac by trifluoromethyl groups in hfa, while fluorination of an ethyl group of $H(H_5H_5)$ leads to a small shift of +490 $cm^{-1}$ only. These trends are inverted for the sodium salts in water. A small hypsochromic shift (+550 $cm^{-1}$) occurs in going from $Na(F_5H_3)$ to $Na(F_5H_5)$ while fluorination leads to bathochromic shifts: –1560 $cm^{-1}$ between Na(acac) and Na(hfa), –400 $cm^{-1}$ and –2180 $cm^{-1}$ in going from $Na(H_5H_5)$ to $Na(F_5H_5)$ and $Na(F_5F_5)$, respectively. Substitution of the ethyl group in $Na(F_3H_5)$ by a pentafluoroethyl group in $Na(F_3F_5)$ unexpectedly results in quite a large energy shift (–2890 $cm^{-1}$). Even larger red

Table 1. Ligand-centred absorption of the ligands and their $[Eu(L)_3]\cdot(H_2O)_n$ ($n$ = 0–3.8) complexes. Molar absorption coefficients (log $\varepsilon$) are reported within parentheses.

| | $E$ / $cm^{-1}$ | | $E$ / $cm^{-1}$ | | $E$ / $cm^{-1}$ |
|---|---|---|---|---|---|
| Hacac $[H(H_3H_3)]$[a] | 33690 (4.4) | Na(acac)[b] | 34700 (4.3) | | |
| Hhfa $[H(F_3F_3)]$[a] | 36360 (5.0) | Na(hfa)[b] | 33140 (4.4) | $Eu(hfa)_3$[a] | 32895 (4.4), sh 30490 (4.1) |
| $H(F_5H_3)$[a] | 38460 (4.8), 26 620 (sh, 4.4) | $Na(F_5H_3)$[b] | 33700 (4.4) | $Eu(F_5H_3)_3$[a] | 39215 (4.4), sh 30960 (4.0), 26380 (3.6), 25380 (3.4) |
| $H(H_5H_5)$[a] | 34720 (4.8) | $Na(H_5H_5)$[b] | 34650 (4.3) | $Eu(H_5H_5)_3$[a] | 36365 (4.2) |
| $H(F_5H_5)$[a] | 35210 (4.8) | $Na(F_5H_5)$[b] | 34250 (5.4) | $Eu(F_5H_5)_3$[a] | 34130 (4.4) |
| | | $Na(F_5F_5)$[b] | 32470 (4.8) | $Eu(F_5F_5)_3$[a] | 32787 (4.6), sh 30400 (4.3) |
| | | $Na(F_3H_5)$[b] | 39250 (4.4) | $Eu(F_3H_5)_3$[a] | 38 000 (4.4), sh 30900 (4.0) |
| | | $Na(F_3F_5)$[b] | 36360 (4.7) | $Eu(F_3F_5)_3$[a] | 34485 (4.5), sh 30760 (4.1) |

[a] In chloroform. [b] In water.

 © 2006 Wiley-VCH Verlag GmbH & Co. KGaA, Weinheim 

shifts are observed when fluorinating the methylene group in $Na(F_3H_5)$ to yield $Na(F_5H_5)$, –5000 $cm^{-1}$ or in $Na(F_3F_5)$ to generate $Na(F_5F_5)$, –3890 $cm^{-1}$. Upon complexation with trivalent europium, both batho- and hypso-chromic shifts are seen with respect to the de-protonated ligands (Figure 1). The coordinated ligands are under their enol form, as ascertained by IR data. In addition to the shift undergone by the main absorption band, most of the $Eu^{III}$ complexes display a shoulder located at smaller energy, in the range 30400–30900 $cm^{-1}$.

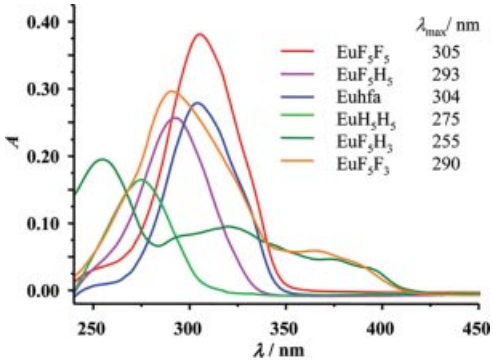


Figure 1. UV/Vis absorption spectra of europium complexes $10^{-5}$ M in chloroform.

Excitation of $Eu^{III}$ β-diketonates either into the f-f or ligand-centred absorption bands at room temperature results in a line-like emission characteristic of the $Eu(^5D_0)$ level. At lower temperature (77 K) and upon enforcement of a time delay, no broad emission band corresponding to a triplet state of the ligand is seen, thus reflecting an efficient ligand-to-metal energy transfer. Spectra are very similar whatever the ligand is, pointing to a similar structure for all the complexes; the $^5D_0 \rightarrow {}^7F_1$ emission band is comprised of three regularly spaced components, indicative of a low symmetry of the metal ion environment in solution. Two typical spectra are presented in Figure 2 and relative intensities of the $^5D_0 \rightarrow {}^7F_J$ transitions ($J$ = 1–4), are compared in Table 2.

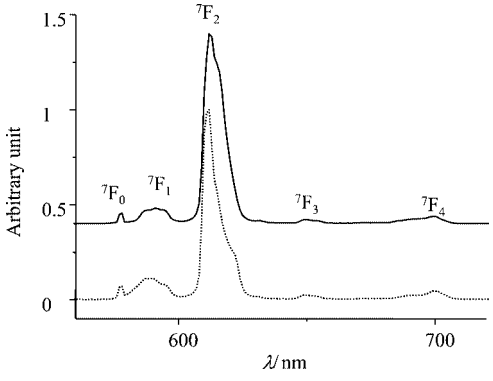


Figure 2. Luminescence spectra of $Eu(F_5F_5)_3$ (black line) and $Eu(F_5H_5)_3$ (dotted line) $10^{-5}$ M in $CHCl_3$, at 295 K, without time delay, with excitation at 32785 $cm^{-1}$ and 31130 $cm^{-1}$, respectively.

Table 2. Intensities of the $^5D_0 \rightarrow {}^7F_J$ transitions, relative to the magnetic dipole $^5D_0 \rightarrow {}^7F_1$ transition and measured at 295 K on $10^{-5}$ M solutions of the Eu complexes in $CHCl_3$.

| | $^7F_0$ | $^7F_1$ | $^7F_2$ | $^7F_3$ | $^7F_4$ |
|---|---|---|---|---|---|
| $Eu(hfa)_3$ | 0.11 | 1.00 | 17.50 | 0.48 | 1.58 |
| $Eu(F_5H_3)_3$ | 0.28 | 1.00 | 14.98 | 0.47 | 1.86 |
| $Eu(H_5H_5)_3$ | 0.15 | 1.00 | 11.87 | 0.63 | 2.43 |
| $Eu(F_5H_5)_3$ | 0.06 | 1.00 | 10.20 | 0.35 | 1.48 |
| $Eu(F_5F_5)_3$ | 0.11 | 1.00 | 16.29 | 0.42 | 1.85 |
| $Eu(F_5H_3)_3$ | 0.12 | 1.00 | 18.25 | 0.55 | 1.82 |
| $Eu(F_5F_3)_3$ | 0.05 | 1.00 | 13.23 | 0.47 | 1.95 |

### Hydration Numbers in Water-Saturated Chloroform

In solvent extraction systems, the aqueous solutions containing the lanthanide ions are mixed with a nonmiscible organic solvent, e.g. chloroform containing the organic ligand. Therefore the organic phase is saturated with water which interacts directly with the europium complex, affecting the hydration number of the extracted species.[25,26] In order to determine the efficiency of the β-diketonate complexes towards extraction of $Eu^{III}$, the number of water molecules present in the first coordination sphere, $q$, has been determined under extraction conditions (see Exp. Section). Results are listed in Table 3. To make sure that the calculated $q$ values are connected with the extraction process, hydration of the complexes was also measured before putting the chloroform solution in contact with the aqueous solution ($q_0$). In all cases, the hydration $q_0$ was found to be less than 1.

The hydration gains ($q - q_0$) upon shaking the solutions during ten minutes with the aqueous solution of sodium perchlorate are plotted vs. the number of fluorine atoms in Figure 3. As expected, ligands bearing fluorine atoms pro-

Table 3. Lifetimes of the $Eu(^5D_0)$ level and hydration numbers $q$ of the β-diketonate complexes $10^{-5}$ M in water-saturated chloroform.

| | $\tau_{H_2O}$ [ms][a] | $k_{H_2O}$ [$ms^{-1}$] | $\tau_{D_2O}$ [ms][a] | $k_{D_2O}$ [$ms^{-1}$] | $q \pm 0.1$ | $q_0 \pm 0.1$[b] |
|---|---|---|---|---|---|---|
| $Eu(hfa)_3$ | 0.365 ± 0.006 | 2.74 | 0.78 ± 0.06 | 1.28 | 1.3 | 0.7 |
| $Eu(F_5H_3)_3$ | 0.48 ± 0.04 | 2.08 | 1.30 ± 0.30 | 0.77 | 1.1 | 0.0 |
| $Eu(H_5H_5)_3$ | 0.28 ± 0.05 | 3.57 | 0.57 ± 0.06 | 1.75 | 1.7 | 0.0 |
| $Eu(F_5H_5)_3$ | 0.40 ± 0.01 | 2.50 | 1.08 ± 0.01 | 0.93 | 1.4 | 1.0 |
| $Eu(F_5F_5)_3$ | 0.41 ± 0.01 | 2.44 | 0.82 ± 0.07 | 1.22 | 1.0 | 0.8 |
| $Eu(F_3H_5)_3$ | 0.33 ± 0.01 | 3.03 | 0.83 ± 0.08 | 1.20 | 1.7 | 0.5 |
| $Eu(F_3F_5)_3$ | 0.43 ± 0.03 | 2.33 | 0.83 ± 0.07 | 1.20 | 0.9 | 0.3 |

[a] Average of data obtained by monitoring the $^5D_0 \rightarrow {}^7F_2$ and $^5D_0 \rightarrow {}^7F_4$ transitions. [b] $q_0$ Is the hydration number in the chloroform solution (before mixing with the aqueous solution).

 © 2006 Wiley-VCH Verlag GmbH & Co. KGaA, Weinheim 

vide complexes with a smaller increase in the number of coordinated water molecules than, for instance, $H_5H_5$. The data reported in Figure 3 allow us to differentiate three types of compounds. The first series comprises the complexes with ligands having one completely hydrogenated ethyl substituent, $H_5H_5$, $F_3H_5$ and $F_5H_5$. Fluorination of the methyl group corresponds to a decrease of 0.5 in ($q$ – $q_0$) and complete fluorination of the ethyl substituent to a decrease of 1.3. A similar behaviour is seen in the second series, having one completely fluorinated ethyl substituent, with a decrease in ($q$ – $q_0$) of 0.4 between the complexes with $F_3F_5$ and $F_5F_5$. In the last series, with hfa and $F_5H_3$, $q$ – $q_0$ = –0.5. Altogether, the highest fluorinated complex with $F_5F_5$ tends to remain non hydrated ($\Delta q = 0.2 \pm 0.2$) while the nonfluorinated compound with $H_5H_5$ tends to acquire two water molecules ($\Delta q = 1.7 \pm 0.1$), in line with the usual composition [$Ln(L)_3 \cdot 2H_2O$] exhibited by lanthanide tris(β-diketonates).[1] However, larger hydration numbers have sometimes been reported, for instance for [$Ln(tta)_3$] and [$Ln(pta)_3$] (pta: pivaloyltrifluoroacetone) in $CHCl_3$,[27] and for [$Eu(tta)_3$] in benzene ($q$ = 3).[28] The water uptake does not vary linearly with the number of fluorine atoms and steric effects also play an important role, as seen for the complexes with hfa and $F_5H_3$ which display a larger hydration increase upon shaking the chloroform solution with aqueous sodium perchlorate than the other complexes with ligands bearing two $C_2$ substituents.

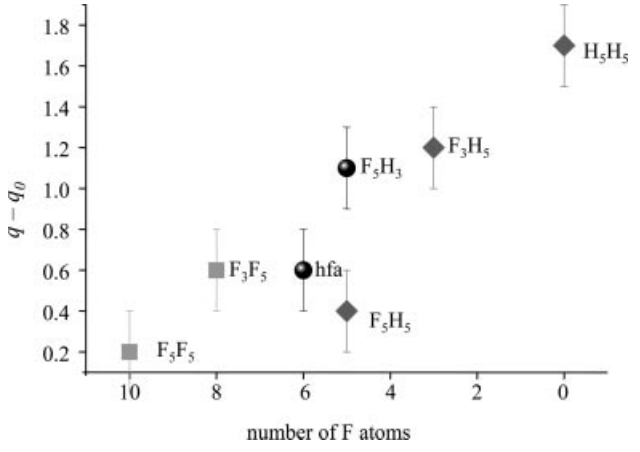


Figure 3. Increase in the number of water molecules in the inner coordination sphere ($q$ – $q_0$) of the europium tris(β-diketonates) upon shaking the solution with aqueous $NaClO_4$.

Furthermore, 1,10-phenanthroline was added to the solutions after the extraction processes, and the lifetimes were measured again: the corresponding $q$ values were in the range 0–0.1. In the case of $Eu(H_5H_5)_3$, further mixing of the phenanthroline-containing solution with aqueous sodium perchlorate resulted in a $q$ value equal to 0.3, confirming the strength of the *o*-phen-Eu interaction.

## Conclusion

From the results reported in this paper, the extent of β–diketone fluorination changes the ratio between the keto and enol forms. Increasing fluorination favours the presence of the keto form in organic solvent. It may be one of the reasons why more fluorinated β-diketones form more stable ternary complexes with Lewis bases in organic solvents. On the other hand, the hydration number of the "extracted" species in $CHCl_3$ decreases with fluorination, which seems to be in contradiction with the previous statement. Our understanding is that fluorine substituents form a repulsive shell around the metal centre reducing, via potentially strong F···H bonds, the metal–water interaction.

## Experimental Section

**Synthesis and Characterisations:** Starting materials were purchased from Narchem, Apollo Scientific, Acros, or Fluka and were of analytical grade. Reactions were conducted under inert atmosphere with standard Schlenk and dry box techniques. Tetrahydrofuran and diethyl ether were freshly distilled from sodium and benzophenone, respectively. Elemental analyses were performed by Dr. Eder. (Microchemical Laboratory, University of Geneva). When fluorinated compounds were analyzed, $CeO_2$ was added to the samples to avoid evaporation and to improve burning conditions; the ratio of oxygen introduced into the burner was also increased. $^1H$ NMR and $^{13}C$ NMR spectra were recorded on a Bruker Avance DRX 400 spectrometer at 298 K and their assignment was based on $^1H$ coupling. Chemical shifts are given in part par million with respect to TMS. $^{19}F$ NMR spectra were recorded at 298 K on a Bruker AV 200 MHz. ES-MS spectra of $10^{-5}$–$10^{-4}$ M solutions in acetonitrile or MeOH/$H_2O$ were obtained with a Finningan SSQ 710C spectrometer using a capillary temperature of 200 °C, an acceleration potential of 4.5 kV and an ion spray voltage of 4.6 kV. The instrument was calibrated using the horse myoglobin standard and the analyses were conducted in positive mode. Analyses by MALDI-Tof MS were performed in the positive ion mode on an Axima CFR plus mass spectrometer (Kratos, Manchester, UK) equipped with a 337 nm nitrogen laser and pulsed extraction. Analyses were carried out in the reflectron mode at a mass range of $m/z$ = 600–3000 with an accelerating voltage of 20 kV. The instrument was externally calibrated with a mixture of Angiotensin II and ACTH (18–39). The resulting compounds were loaded onto the target plate by mixing 1μL of sample solution with the same volume of a matrix solution (10 mg/mL α-cyano-4-hydroxycinnammic acid in 50% 0.1% TFA plus 50% acetonitrile) and left to dry in the drying box at room temperature. Electron impact ionisation spectra were recorded on a Nermag R10–10C mass spectrometer with an ionisation potential of 70 V. IR spectra were recorded in ATR mode with a Perkin–Elmer FT-IR Spectrum One spectrometer fitted with a universal ATR sampling accessory featuring a diamond/ZnSe crystal. UV/Vis absorption spectra were measured on a Perkin–Elmer Lambda 900 spectrometer using quartz Suprasil® cells of 0.1 and 1 cm path length.

Low-resolution luminescence data (spectra and lifetimes) were recorded at room temperature (298 ± 0.1 K) with a Fluorolog FL3–22 spectrometer from Horiba-Jobin–Yvon-Spex using 1-cm path length quartz Suprasil® cells. The temperature was kept constant by using a FL-1027 thermostated cell holder. Emission and excitation spectra were corrected for the instrumental function. The complexes were dissolved in $CHCl_3$ or $CDCl_3$, the concentration being adjusted to $1 \cdot 10^{-5}$ M. Phosphorescence lifetimes of frozen solutions at 77 K in quartz capillaries or in 1-cm Suprasil® cells were determined with the instrument in time-resolved mode. Solutions for the

 © 2006 Wiley-VCH Verlag GmbH & Co. KGaA, Weinheim 

determination of the number of coordinated water molecules were prepared as follows. The organic $CHCl_3$ phase containing the Eu β-diketonate (3.3 mL, $10^{-5}$ M) was mixed with the aqueous phase (0.1 M $NaClO_4$, 0.1 mL) and stirred during 10 minutes before extraction (this span of time is necessary to get a constant lifetime value). A similar solution in $CDCl_3/D_2O$ was prepared in parallel in a glove-box to avoid moisture contamination. The solutions were then centrifuged and the organic phase was recovered and further analysed by luminescence enforcing a 0.03–0.05 ms delay to avoid interference with fluorescence emission from the ligand. Lifetimes were determined upon ligand excitation and monitoring the $^5D_0 \rightarrow {}^7F_2$ and the $^5D_0 \rightarrow {}^7F_4$ transitions; they are the average of at least three independent measurements. All luminescence decays proved to be single exponential and were analysed using Origin 7.0®. The number of coordinated water molecules was determined by using Horrock's equation $q = 1.11\ (\Delta k\ -0.31)$.[29]

**Syntheses of the Ligands:** 1,1,1,5,5,5-Hexafluoropentane-2,4-dione H(hfa), and heptane-3,5-dione $H(H_5H_5)$ were commercial products (Aldrich).

**Synthesis of 5,5,6,6,6-Pentafluorohexane-2,4-dione $H(F_5H_3)$:** Sodium methoxide (2.16 g, 39 mmol) was suspended in hexane (10 mL). Methyl pentafluoropropionate (1.78 g, 10 mmol) was added with stirring and cooling to 0 °C. After further stirring during 1 h under $N_2$, acetone (0.4 g, 7 mmol) was added dropwise which resulted in an orange solution. The mixture was further stirred during 3 days, then the solution was cooled to 0 °C and sulfuric acid (7.0 mL, 6.0 M) was slowly added. Two phases formed, which were separated, the hexane phase being orange. The aqueous phase was washed 5 times with hexane and the combined organic phases were dried with $Na_2SO_4$ before distillation of the solvent. The residue was further distilled to give the desired product as pale oil (580 mg, yield: 40%). IR ($cm^{-1}$, ATR): $\tilde{\nu}$ = 738, 798, 845, 942, 1019, 1117, 1166, 1198, 1329 (aliphatic C–F), 1411, 1440, 1596, 1653, (C=C), 1745 (C=O), 2854, 2963, 3130 ($sp^3$ C–H). $^1H$ NMR (400 MHz, $CDCl_3$): $\delta_H$ = 3.77 (s, 3 H, $–CH_3$), 6.14 (s, 1 H, –CH) ppm. $^{13}C$ NMR (400 MHz, $CDCl_3$): $\delta_H$ = 44.9 ($–CH_3$), 99.0 (–CH=C), 110–130 ($CF_x$), 166 (C=O) 176.0 (C=C–O) ppm. $^{19}F$ NMR (200 MHz, $CDCl_3$): $\delta_F$ = –82.08 (3F, $-CF_3$), –123.40 (2F, $–CF_2$) ppm. Maldi-MS (negative mode): *m/z* = 203.55 $[(F_5H_3)^-$, calcd. 203.01]. CI-MS ($CHCl_3$): *m/z* = 84 $[CH_3COCHC^+(OH)]$, 119 $[CF_3CF_2^+]$, 189 $[CF_3CF_2COCHC^+(OH)]$. $C_6H_5F_5O_2 \cdot 0.3H_2O$ (209.4): calcd. C 34.40, H 2.69; found C 34.34, H 2.67.

**Sodium Salt of 1,1,1-Trifluoro-3,5-heptanedione $Na(F_3H_5)$:** Sodium methoxide (0.78 g, 15 mmol) was dissolved in diethyl ether (2 mL) and introduced into a tube equipped with a magnetic stirrer. Propanoic acid methyl ester (0.62 g, 7.00 mmol) was added with stirring and the solution was cooled to 0 °C. 4,4,4-Trifluorobutane-2-one (1.06 g, 8.4 mmol) was added dropwise to the stirred mixture and an orange solution resulted. The tube was sealed and the mixture was further stirred during 3 days. The ether was removed by rotary evaporation and a deep orange residue was obtained (570 mg, yield: 36%). IR ($cm^{-1}$, ATR): $\tilde{\nu}$ = 668, 742 815, 912 1039, 1133, 1144, 1200, 1257, 1320, 1361 (aliphatic C–F), 1378, 1408, 1437, 1530, 1633, (C=C), 1712 (C=O), 2840, 2956, 2997 ($sp^3$ C–H). $^1H$ NMR (400 MHz, $CDCl_3$ + DCl 0.1 M, 10 μL): $\delta_H$ = 0.96 (s, 3 H, $–CH_3$), 2.28 (q, 2 H, $–CH_3CH_2$), 3.57 (s, 2 H, $–CF_3CH_2$), 5.67 (s, 1 H, –CH), 8.33 (s, OH) ppm. $^{19}F$ NMR (200 MHz, $D_2O$): $\delta_F$ = –121.0 ppm. Maldi-MS (negative mode, 34 mV): *m/z* = 181.44 $[(F_3H_5)^-$, calcd. 181.14].

**1,1,1,2,2-Pentafluoro-3,5-heptanedione ($F_5H_5$):** Sodium methoxide (1.98 g, 33 mmol) was suspended in diethyl ether (40 mL). 2-Butanone (1.08 g, 15 mmol) was added to the mixture which was stirred during 1 h under $N_2$ at room temp., whereupon a white slurry resulted. A solution of methyl pentafluoropropionate (1.60 g, 9 mmol) in diethyl ether (25 mL) was added whilst stirring, which resulted in the formation of a pale pink slurry. The mixture was further stirred during 16 h, then sulfuric acid (100 mL, 1.5 M) was slowly added whilst stirring and the ether phase turned orange. The aqueous phase was extracted with freshly distilled diethyl ether (4× 100 mL), and the resulting organic phases were dried with $Na_2SO_4$. The solvent was partially removed and the product was purified by distillation at 133 °C to give a colourless yellow liquid (880 mg, yield 45%). IR ($cm^{-1}$, ATR): $\tilde{\nu}$ = 738, 815, 889, 984, 1021, 1064, 1120, 1168, 1203, 1329, 1384 (aliphatic C–F) 1417, 1459, 1594, (C=C), 1779, (C=O) 2890, 2988, 2949 ($sp^3$ C–H). $^1H$ NMR (400 MHz, $CDCl_3$): $\delta_H$ = 1.20 (t, 3 H, *J* = 7.6 Hz, $–CH_3$), 2.55 (q, 2 H, *J* = 7.6 Hz, $–CH_2$), 5.99 (s, 1 H, –CH) ppm. $^{13}C$ NMR (400 MHz, $CDCl_3$): $\delta_C$ = 9.55 ($–CH_3$), 32.19 ($–CH_2$), 80–130 ($–CF_x$),176–180 (C=C–O, –CH=C), 199.0 (C=O) ppm. $^{19}F$ NMR (200 MHz, DMSO): $\delta_F$ = –81.4, –81.6 ($–CF_3$), –120.0, –122.3 ($–CF_2$) ppm. CI-MS ($CHCl_3$): *m/z* = 99 $[CH_3CH_2COCHC(OH)]^+$, 119 $[CF_3CF_2]^+$, 189 $[CF_3CF_2COCHC(OH)]^+$, 218.46 $[(F_5H_5 + H)^+$, calcd. 218.04]. $C_7H_7F_5O_2 \cdot 0.3H_2O$ (223.4): calcd. C 37.62, H 3.43; found C 37.82, H 3.43.

**Sodium Salt of 1,1,1,2,2,7,7,7-Octafluoro-3,5-heptanedione $Na(F_3F_5)$:** Sodium methoxide (0.78 g, 15.4 mmol) was placed with diethyl ether (2 mL) in a tube containing a magnetic stirrer. Methyl pentafluoropropionate (1.25 g, 7.00 mmol) was added with stirring and cooling to 0 °C. 4,4,4-Trifluorobutane-2-one (1.06 g, 8.40 mmol) was added to the stirred mixture dropwise and an orange solution resulted. After sealing the tube, the mixture was further stirred during 3 days. The ether was removed by rotary evaporation and an orange residue was obtained (756 mg, yield: 37%). IR ($cm^{-1}$, ATR, as Na salt): $\tilde{\nu}$ = 742, 813, 874, 924, 943, 959, 994, 1040, 1066, 1113, 1032, 1149, 1174, 1208, 1265, 1319, 1362 (aliphatic C–F), 1407, 1438, 1600, 1669, 1713, 1743 (C=O), 2958, 3008 ($sp^3$ C–H) ppm. $^1H$ NMR (400 MHz, $D_2O$): $\delta_H$ = 2.34 (s, 2 H, $CH_2COCH_2CF_3$), 3.70 (s, 2 H, $CH_2COCH_2CF_3$), 4.02 (s, 2 H, $CH_2CF_3$), 5.88 (s, 1 H, CH=C) ppm. $^{19}F$ NMR (200 MHz, DMSO): $\delta_F$ = –81.14 ($–CF_3$), –82.32 ($–CF_3$), –119.71 ($–CF_2$) ppm. Maldi-MS (positive mode): *m/z* = 252.4 $[(NaF_3F_5 – NaF)^+$, calcd. 252.00]; 294.1 $[(NaF_3F_5)^+$, calcd. 293.99].

**Sodium Salt of 1,1,1,2,2,6,6,7,7,7-Decafluoro-3,5-heptanedione $Na(F_5F_5)$:** Sodium methoxide (0.76 g, 14.2 mmol) was suspended in diethyl ether (40 mL). 3,3,4,4,4-Pentafluorobutane-2-one (1.13 g, 7.00 mmol) was added and the mixture was stirred at room temp. during 1 h under $N_2$ atmosphere, whereupon a colourless solution resulted. A solution of methyl pentafluoropropionate (1.25 g, 7.00 mmol) in diethyl ether (10 mL) was added whilst stirring, which resulted in a pale orange solution. After further stirring during 16 h the mixture turned orange. The ether was removed by distillation and a brown residue was obtained together with an oily liquid. The latter was removed and the residue was washed 5 times with dichloromethane. The resulting brown powder was dried under vacuum (960 mg, yield 42%). IR ($cm^{-1}$, ATR, Na salt): 736, 821, 922, 1019, 1103, 1139, 1165, 1192, 1322, 1368 (aliphatic C–F), 1427, 1521, 1582, 1661, (C=O), 2967 ($sp^3$ C–H). $^1H$ NMR (400 MHz, $CDCl_3$ + DCl 0.1 M, 10 μL): $\delta_H$ = 5.03 (s, 1 H, –CH). $^{13}C$ NMR (400 MHz, $D_2O$): $\delta_C$ = 90.0 (–CH=C), 110–130 (broad bands due to coupling with $^{19}F$), 170–175 (C=O), 177.00 (C=C–O) ppm. $^{19}F$ NMR (200 MHz, DMSO): $\delta_F$ = –80.81 ($–CF_3$), –81.17 ($–CF_3$), –117.71 ($–CF_2$), –121.14 ($–CF_2$) ppm. Maldi-MS (negative mode): *m/z* = 307.59 $[(F_5F_5 + H)^-$, calcd. 307.08].

**Synthesis of the Europium Complexes:** Europium acetate solutions were prepared just before being used, by dissolution of europium

 © 2006 Wiley-VCH Verlag GmbH & Co. KGaA, Weinheim 

oxide (0.16 g, 0.45 mmol) in $CH_3COOH$ (3 mL, 0.9 M). After stirring during 1 h, the solutions were filtered and the resulting filtrate cooled to 0 °C.

**Tris(hexafluoroacetonato)europium(III), $Eu(hfa)_3·3H_2O$:** A solution of hfa (0.30 g, 1.44 mmol) in methanol (3 mL) was added dropwise at 0 °C to the europium acetate solution. After stirring overnight, a white yellow precipitate formed, which was removed by filtration, and recrystallised from methanol, giving $Eu(hfa)_3·3H_2O$ (280 mg, yield: 70%) as a pale yellow solid. IR ($cm^{-1}$, ATR): $\tilde{\nu}$ = 659, 677, 742, 772, 804, 855, 956, 1011, 1104, 1133, 1194, 1211, 1252, 1351 (aliphatic C–F), 1464, 1532, 1561, 1613, 1650, (C=O), 2968 ($sp^3$ C–H), 3160, 3314, 3642 (O–H). $^{19}F$ NMR (200 MHz, DMSO): $\delta_F$ = –75.35 (–$CF_3$) ppm. $C_{15}H_3EuF_{18}O_6·3H_2O·0.5MeOH$ (843.99): calcd. C 22.08, H 1.32; found C 22.07, H 1.68.

**Tris(3,5-heptanedionato)europium(III), $Eu(H_5H_5)_3·2H_2O$:** A solution of $H_5H_5$ (0.19 g, 1.44 mmol) in methanol (3 mL) was added dropwise to at 0 °C to the europium acetate solution. After a few minutes, a precipitate formed. The pH of the mixture, which was 4, was then adjusted at 6.5 by addition of NaOH 1 M. After stirring overnight, the mixture was filtered. The resulting precipitate was recrystallised from methanol yielding $Eu(H_5H_5)_3·2H_2O$ as white yellow powder (160 mg, yield: 60%). IR ($cm^{-1}$, ATR): $\tilde{\nu}$ = 759, 806, 854, 898, 947, 980, 1005, 1068, 1175 (C=O), 1219, 1243, 1306, 1330 (=C–O), 1371, 1398, 1511 (C=C), 1587, (C=O), 2877, 2936, 2968 ($sp^3$ C–H), 3079, 3346, 3576 (O–H). $C_{21}H_{33}EuO_6·2H_2O$ (570.17): calcd. C 44.29, H 6.55; found C 44.79, H 6.59.

**Tris(1,1,1,2,2-pentafluoro-3,5-heptanedionato)europium(III), $Eu(F_5H_5)_3·3.8H_2O$:** A solution of $F_5H_5$ (0.31 g, 1.44 mmol) in methanol (5 mL) was added dropwise at 0 °C to the europium acetate solution. After stirring overnight, a white powder was filtered and recrystallised from methanol to provide $Eu(F_5H_5)_3·3.8H_2O$ (185 mg, yield 44%). IR ($cm^{-1}$, ATR): $\tilde{\nu}$ = 679, 721, 753, 811, 943, 1021, 1067, 1133, 1157, 1191, 1325 (aliphatic C–F), 1408, 1461, 1512, 1627 (C=O), 2983 ($sp^3$ C–H), 3301 (O–H). $^{19}F$ NMR (200 MHz, DMSO): $\delta_F$ = –82.46 (–$CF_3$), –82.75 (–$CF_3$), –125.76 (–$CF_2$), –125.95 (–$CF_2$) ppm. $C_{21}H_{24}EuF_{15}O_6·3.8H_2O$ (894.53): calcd. C 28.93, H 2.96; found C 28.95, H 2.81.

**Tris(1,1,1,2,2,6,6,7,7,7-decafluoro-3,5-heptanedionato)europium(III), $Eu(F_5F_5)_3·2H_2O$:** The sodium salt of $F_5F_5$ (0.3 g, 0.91 mmol) was introduced into a flask in which water (10 mL) and methanol (1 mL) were added and the solution warmed at 60 °C until complete dissolution. The europium acetate solution was then added dropwise, which induced a precipitate. After stirring overnight, the mixture was filtered and the filtrate recrystallised from methanol to give $Eu(F_5F_5)_3·2H_2O$ (140 mg, yield: 43%). IR ($cm^{-1}$, ATR): $\tilde{\nu}$ = 658, 744, 766, 796, 924, 1027, 1121, 1145, 1175, 1195, 1289, 1327 (aliphatic C–F), 1476, 1520, 1542 (C=C), 1646 (C=O), 3388 (O–H). $^{19}F$ NMR (200 MHz): $\delta_F$ = –78.49 (–$CF_3$), –82.52 (–$CF_3$), –121.13 (–$CF_2$) ppm. $C_{21}H_3EuF_{30}O_6·2H_2O$ (1109.19): calcd. for C 22.74, H 0.64; found C 22.96, H 0.44.

**Tris(5,5,6,6,6-pentafluoro-2,4-hexanedionato)europium(III), $Eu(F_5H_3)_3$:** A solution of 5,5,6,6,6-pentafluoro-2,4-hexanedione (0.3 g, 1.44 mmol) in methanol (5 mL) was added dropwise at 0 °C to the europium acetate solution. A white precipitate formed and, after stirring overnight, methanol was removed to give a yellow oily residue which was recrystallised from methanol/water (50:50 v/v) to give $Eu(F_5H_3)_3$ (153 mg, yield: 42%). IR ($cm^{-1}$, ATR): $\tilde{\nu}$ = 738, 798, 845, 942, 1019, 1118, 1166, 1198, 1329 (aliphatic C–F), 1411, 1440, 1596, 1653 (C=C), 1745 (C=O), 2854, 2963 ($sp^3$ C–H), 3130 (O–H). $^{19}F$ NMR (200 MHz, $CDCl_3$): $\delta_F$ = –82.90 (–$CF_3$), –126.96 (–$CF_2$) ppm. $C_{18}H_{12}EuF_{15}O_6$ (761.96): calcd. for C 28.67, H 1.84; found C 28.40, H 1.59.

**Tris(1,1,1,2,2,7,7,7-octafluoro-3,5-heptanedionato)europium(III), $Eu(F_3F_5)_3$:** The sodium salt of $F_3F_5$ (0.2 g, 0.67 mmol) was dissolved in a mixture water (5 mL) and methanol (1 mL). The europium acetate solution was then added dropwise at 0 °C. After stirring overnight, the product was extracted with 3 × 20 mL of dichloromethane then the solvent was removed to give a solid which was recrystallised from water/methanol (50:50 v/v) to provide a pale yellow compound (80 mg, yield: 37%). IR ($cm^{-1}$, ATR): $\tilde{\nu}$ = 681, 743, 771, 789, 844, 872, 896, 960, 998, 1024, 1049, 1067, 1084, 1120, 1156, 1185, 1206, 1267, 1328, 1370, (aliphatic C–F), 1439, 1521, 1576, 1626, 1664 (C=C), 1732 (C=O), 2854, 2958, 3003 ($sp^3$ C–H). $^{19}F$ NMR (200 MHz, $CDCl_3$): $\delta_F$ = –81.36 (–$CF_3$), –82.72 (–$CF_3$), –119.78 (–$CF_2$) ppm.

**Tris(1,1,1-trifluoro-3,5-heptanedionato)europium(III), $Eu(F_3H_5)_3$:** This compound was synthesised similarly to $Eu(F_3F_5)_3$, but starting from the sodium salt of $F_3H_5$ (0.3 g, 0.97 mmol). $Eu(F_3H_5)_3$ was obtained as a pale yellow solid (92 mg, yield: 38%). IR ($cm^{-1}$, ATR, as Na salt): $\tilde{\nu}$ = 753, 833, 869, 945, 989, 1114, 1167, 1210, 1249, 1278, 1325, 1389 (aliphatic C–F), 1427, 1498, 1630, 1699, 1725, 1748 (C=O), 2968, 3037 ($sp^3$ C–H). $^{19}F$ NMR (200 MHz, DMSO): $\delta_F$ = –121.9 (–$CF_3$) ppm.


[1] K. Binnemans, in: *Handbook on the Physics and Chemistry of Rare Earths* (Eds.: K. A. Gschneidner Jr., J.-C. G. Bünzli, V. K. Pecharsky), Elsevier, Amsterdam, **2005**, vol. 35, chapter 225.
[2] S. Umetani, Y. Kawase, H. Takahara, Q. T. H. Le, M. Matsui, *J. Chem. Soc., Chem. Commun.* **1993**, 78.
[3] Y. Meguro, Y. Kitatsuji, T. Kimura, Z. Yoshida, *J. Alloys Comp.* **1998**, *271*, 790.
[4] J. Alstad, J. H. Augustson, L. Farbu, *J. Inorg. Nucl. Chem.* **1974**, *36*, 899.
[5] Y. Albinsson, A. Mahmood, M. Majdan, J. Rydberg, *Radiochim. Acta* **1989**, *48*, 49.
[6] Y. Albinsson, *Acta Chem. Scand.* **1989**, *43*, 919.
[7] A. Oga, K. Yamaoka, K. Itano, Y. Hasegawa, *Bunseki Kagaku* **2004**, *53*, 1199.
[8] R. E. Sievers, J. E. Sadlowski, *Science* **1978**, *201*, 217.
[9] J. W. Mitchell, C. V. Banks, *Anal. Chim. Acta* **1971**, *57*, 415.
[10] J.-C. G. Bünzli, C. Piguet, *Chem. Soc. Rev.* **2005**, 1048.
[11] J. Yu, L. Zhou, H. Zhang, Y. Zheng, H. Li, R. Deng, Z. Peng, Z. Li, *Inorg. Chem.* **2005**, *44*, 1611.
[12] P. Lenaerts, K. Driesen, R. Van Deun, K. Binnemans, *Chem. Mater.* **2005**, *17*, 2148.
[13] L. Puntus, K. J. Schenk, J.-C. G. Bünzli, *Eur. J. Inorg. Chem.* **2005**, 4739.
[14] T. Sekine, M. Ono, *Bull. Chem. Soc. Jpn.* **1965**, *38*, 2087.
[15] C. S. Springer Jr., D. W. Meek, R. E. Sievers, *Inorg. Chem.* **1967**, *6*, 1105.
[16] S. N. Misra, W. N. Cabalfin, *Chem. Scr.* **1989**, *29*, 75.
[17] A.-S. Chauvin, S. Gras, J.-C. G. Bünzli, *Org. Biomol. Chem.* **2003**, *1*, 737.
[18] M. Kawatsura, J. F. Hartwig, *J. Am. Chem. Soc.* **1999**, *121*, 1473.
[19] R. A. Moore, R. Levine, *J. Org. Chem.* **1964**, *29*, 1439.
[20] C. A. Burgett, J. S. Fritz, *Anal. Chem.* **1972**, *44*, 1738.
[21] W. G. Scribner, *Anal. Chem.* **1969**, *41*, 44.
[22] C. A. Burgett, **1975**, US patent, US3867418.
[23] J. L. Burdett, M. T. Rogers, *J. Am. Chem. Soc.* **1964**, *86*, 2105.
[24] K. I. Pashkevich, V. I. Saloutin, I. Y. A. Postovskii, *Russ. Chem. Rev.* **1981**, *50*, 325.
[25] Y. Hasegawa, K. Nakaya, I. Matsubayashi, *Bull. Chem. Soc. Jpn.* **2001**, *74*, 1879.
[26] I. Matsubayashi, E. Ishiwata, T. Shionoya, Y. Hasegawa, *Talanta* **2004**, *63*, 625–633.


 © 2006 Wiley-VCH Verlag GmbH & Co. KGaA, Weinheim 

[27] Y. Hasegawa, E. Ishiwata, T. Ohnishi, G. R. Choppin, *Anal. Chem.* **1999**, *71*, 5060; Y. Hasegawa, M. Miratsu, T. Kondo, *Inorg. Chim. Acta* **2000**, *303*, 291.
[28] S. Lis, J. N. Matur, G. R. Choppin, *Solvent Extr. Ion Exch.* **1991**, *9*, 637.
[29] R. M. Supkowski, W. DeWitt Horrocks Jr., *Inorg. Chim. Acta* **2002**, *340*, 44.

Received: September 23, 2005
Published Online: December 5, 2005

 © 2006 Wiley-VCH Verlag GmbH & Co. KGaA, Weinheim 

DOI: 10.1002/ejic.200500568

# Syntheses, Crystal Structures and Magnetic Properties of Carboxylato-Bridged Polymeric Networks of $Mn^{II}$

**Subal Chandra Manna,[a] Ennio Zangrando,[b] Michael G. B. Drew,[c] Joan Ribas,*[d] and Nirmalendu Ray Chaudhuri*[a]**

**Keywords:** Manganese(II) / Carboxylate / Crystal structure / Magnetic behavior

Three new carboxylato-bridged polymeric networks of $Mn^{II}$ having molecular formula $[Mn(ox)(dpyo)]_n$ (**1**), $\{[Mn_2(mal)_2(bpee)(H_2O)_2]\cdot 0.5(bpee)\cdot 0.5(CH_3OH)\}_n$ (**2**) and $\{[Mn_3(btc)_2(2,2'\text{-bipy})_2(H_2O)_6]\cdot 4H_2O\}_n$ (**3**) [dpyo, 4,4′-bipyridine *N*,*N*′-dioxide; bpee, *trans*-1,2 bis(4-pyridyl)ethylene; 2,2′-bipy, 2,2′-bipyridine; ox = oxalate dianion; mal = malonate dianion; btc = 1,3,5-benzenetricarboxylate trianion] have been synthesized and characterized by single-crystal X-ray diffraction studies and low temperature magnetic measurements. Structure determination of complex **1** reveals a covalent bonded 2D network containing bischelating oxalate and bridging dpyo; complex **2** is a covalent bonded 3D polymeric architecture, formed by bridging malonate and bpee ligands, resulting in an open framework with channels filled by uncoordinated disordered bpee and methanol molecules. Whereas complex **3**, comprising btc anions bound to three metal centers, is a 1D chain which further extends its dimensionality to 3D via π-π and H-bonding interactions. Low temperature magnetic measurements reveal the existence of weak antiferromagnetic interaction in all these complexes.
(© Wiley-VCH Verlag GmbH & Co. KGaA, 69451 Weinheim, Germany, 2006)

## Introduction

Metal-organic frameworks (MOFs) containing paramagnetic metal ions represent a new class of materials for their intriguing network topologies and for their potential applications in the area of catalysis, separation, sorption, sensors, but also as electronic and magnetic devices.[1,2] Moreover, such MOFs have compositional/structural diversities which may be tuned by the suitable choice of ligands as well as metal ions. Thus, the construction of target molecules with the properties mentioned above is a challenge for synthetic chemists.[3] To achieve the desired networks, various carboxylates have been used due to their wide variety of coordination modes,[4] resulting in efficient superexchange pathways. Several groups as well as our labs[5–8] reported the syntheses and characterizations of a large number of carboxylato-bridged multidimensional networks. Oxalate, malonate, succinate, fumarate, maleate, terephthalate, 1,3,5-benzenetricarboxylate etc. are among the more employed carboxylates to build up the framework. Moreover, combination of nitrogen donor co-/bridging- ligands i.e. pyrazine, piperazine, 1,2-bis(4-pyridyl)ethane, 4,4′-trimethylenedipyridine, 4,4′-bipyridyl disulphide, hexamethylenetetramine etc. with carboxylates may enhance the dimensionality of the molecular frameworks.[7] But evaluation of magnetic interaction of these coordination polymers as a function of geometry and electronic configuration of the individual metal ion is the most important issue in the current research.[9,10] Manganese-carboxylates are well recognized from the magnetic point of view[11,12] as these systems often possess a large number of unpaired electrons. Literature survey reveals[13] that there are several manganese-containing networks showing single molecular magnetism, ability of individual molecules to function as magnetizable magnets in the absence of an external magnetic field and with no long-range ordering from intermolecular interactions. Due to these novel properties, increasing attention has been devoted to the construction of manganese–carboxylate frameworks in order to assess the correlation between structure and magnetism.

While manganese–oxalate frameworks are rare,[14] there are some reports[15] on the molecular-based magnets formed by bimetallic three-dimensional oxalate networks. On the other hand, there are some reports by our group using malonate,[6] showing antiferromagnetic coupling only, besides interesting networks. Our studies till date did not investigate the effect of coligand on the magnetic property in the manganese-malonate frameworks. In addition, metal carboxylates, alone and in combination with nitrogen donor

[a] Department of Inorganic Chemistry, Indian Association for the Cultivation of Science,
Kolkata 700032, India
Fax: +91-33-2473-2805
E-mail: icnrc@iacs.res.in
[b] Dipartimento di Scienze Chimiche, University of Trieste, 34127 Trieste, Italy
[c] Department of Chemistry, The University of Reading, Whiteknights, Reading RG6 6AD, UK
[d] Departament de Química Inorgànica. Universitat de Barcelona, Diagonal, 647, 08028 Barcelona, Spain
E-mail: joan.ribas@qi.ub.es
Supporting information for this article is available on the WWW under http://www.eurjic.org or from the author.

 © 2006 Wiley-VCH Verlag GmbH & Co. KgaA, Weinheim 

coligands, are of particular interest for the possibility to form open-framework structures[4b] besides the existence of magnetic interactions. The above mentioned facts have driven us to pursue the design and syntheses of manganese–carboxylates varying the carboxylate anion as well as the coligand.

The present contribution reports the syntheses, crystal structures and low-temperature magnetic measurements of three new carboxylato-bridged polymeric architectures of manganese(II) using three different carboxylates, $[Mn(ox)(dpyo)]_n$ (**1**), $\{[Mn_2(mal)_2(bpee)(H_2O)_2]\cdot 0.5(bpee)\cdot 0.5(CH_3OH)\}_n$ (**2**) and $\{[Mn_3(btc)_2(2,2'\text{-bipy})_2(H_2O)_6]\cdot 4H_2O\}_n$(**3**) [dpyo = 4,4′-bipyridine *N*,*N*′-dioxide; bpee = *trans*-1,2-bis(4-pyridyl)ethylene; 2,2′-bipy = 2,2′-bipyridine; ox = oxalate dianion; mal = malonate dianion; btc = 1,3,5-benzenetricarboxylate trianion].

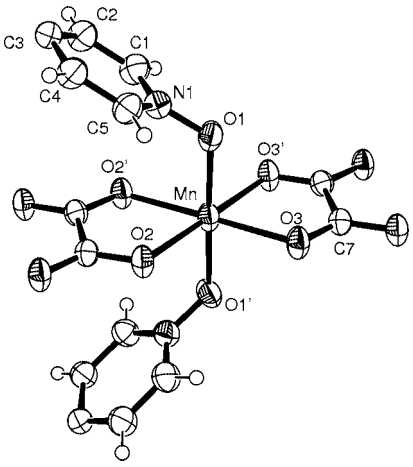


Figure 2. ORTEP drawing of the manganese coordination sphere in complex **1**. The metal is located on a twofold axis passing in between the oxalate C–C bond.

## Results and Discussion

### Description of the Structures

#### *Complex 1*

The X-ray diffraction analysis of complex **1** displays a 2D layered structure of composition $[Mn(ox)(dpyo)]_n$, as depicted in Figure 1. In the framework of (4,4) topology, the manganese ions occupy the 4-connecting nodes while double chelating oxalate and dpyo ligands form the rhomboid grid, with the latter spacers arranged in a herringbone pattern with respect to the –Mn–ox– arrays. The metals are separated by 5.657(2) Å (axis b) along the oxalate and by 12.537(3) Å through the dpyo linkers. Each manganese(II) center is arranged on a twofold axis and the coordination sphere comprises of *trans*-located dpyo oxygen atoms and four oxalate donors in the equatorial plane (Figure 2). All the Mn–O bond lengths are comparable in length within their e.s.d.'s. (Table 1). The dpyo ligand, positioned on a center of symmetry, presents coplanar pyridine rings and is connected to the metal with a N(1)–O(1)–Mn angle of 119.8(2)°.

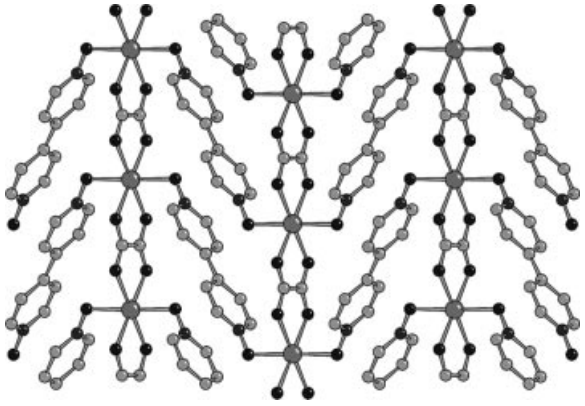

Figure 1. Ball and stick drawing of the 2D sheet of complex **1**.

Table 1. Selected coordination bond lengths [Å] and angles [°] of complex **1**.

| | | | |
|---|---|---|---|
| Mn–O(3) | 2.175(2) | Mn–O(2) | 2.185(2) |
| Mn–O(1) | 2.180(2) | O(1)–N(1) | 1.332(4) |
| O(2)–Mn–O(2′) | 75.64(11) | O(3)–Mn–O(1) | 87.63(9) |
| O(3′)–Mn–O(3) | 77.40(12) | O(3)–Mn–O(2) | 103.48(8) |
| O(1)–Mn–O(1′) | 178.60(14) | O(3)–Mn–O(2′) | 179.12(9) |
| O(1)–Mn–O(2) | 88.81(9) | C(7)–O(2)–Mn | 115.70(19) |
| O(1′)–Mn–O(2) | 92.30(9) | C(7′)–O(3)–Mn | 113.49(19) |
| O(3′)–Mn–O(1) | 91.28(9) | N(1)–O(1)–Mn | 119.8(2) |

The packing shows well-separated layers and the shortest intermetallic distance is 7.648(2) Å. The shortest contact of 3.315(4) is detected between C(1) and O(2) that can be interpreted as a CH···O interaction.

#### *Complex 2*

The structure of **2** reveals covalently bonded $[Mn(mal)(H_2O)]_n$ layers connected by bpee ligands to form a 3D polymer (Figure 3 and Figure 4). The malonate anion, in its frequently found coordination mode[6,16,17] acts as a chelating and a bis(monodentate) ligand towards three metal ions. A selection of bond lengths and angles is reported in Table 2, and the metal coordination sphere with atom labeling Scheme is shown in Figure 5. The octahedral coordination geometry of the metal atom consists of four planar equatorial carboxylate oxygen atoms [range of Mn–O bond lengths of 2.165(3)–2.183(3) Å], while the axial positions are occupied by a water molecule and a bpee nitrogen donor with slightly longer bond lengths [Mn–O(1w) 2.263(3), Mn–N(21) 2.297(3) Å, Table 2].

In the (4,4) square grid (Figure 3) of side dimensions 5.419 × 5.614 Å (Mn–Mn distances), the coordinated water molecule forms two intra-layer hydrogen bonds with oxygen atoms of the neighboring chelating anions [O(1w)–O(17) 2.719(5) Å, O(1w)–O(11) 2.748(4) Å].

 © 2006 Wiley-VCH Verlag GmbH & Co. KGaA, Weinheim 

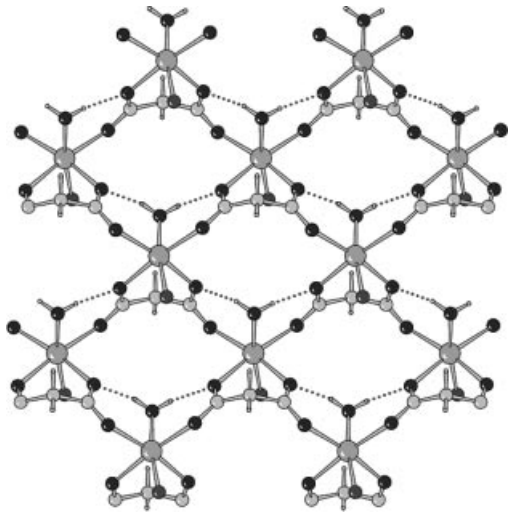

Figure 3. Corrugated $[Mn(H_2O)(mal)]_n$ layers in complex **2** down axis *b* (only nitrogen donor of bpee shown, dotted lines indicate H-bonds).

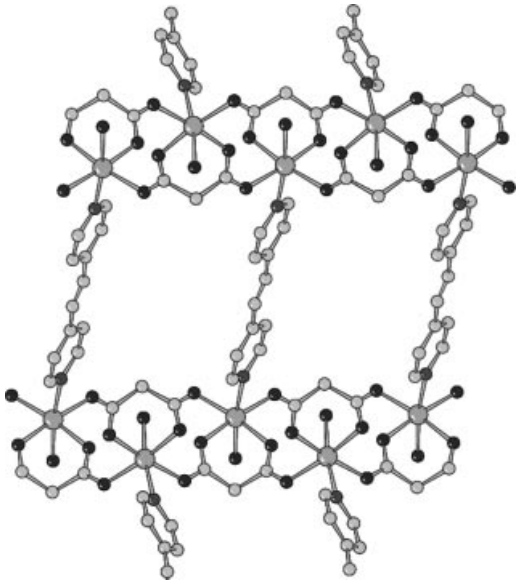

Figure 4. 3D crystal packing of complex **2** viewed down axis *a* showing layers connected by bpee ligands.

Table 2. Selected coordination bond lengths [Å] and angles [°] of complex **2**.

| | | | |
|---|---|---|---|
| Mn–O(13) | 2.165(3) | Mn–O(11) | 2.183(3) |
| Mn–O(16) | 2.172(3) | Mn–O(1w) | 2.263(3) |
| Mn–O(17) | 2.173(3) | Mn–N(21) | 2.297(3) |
| O(13)–Mn–O(16) | 99.24(12) | O(13)–Mn–N(21) | 86.28(12) |
| O(13)–Mn–O(17) | 90.15(12) | O(16)–Mn–N(21) | 93.51(12) |
| O(16)–Mn–O(17) | 170.60(11) | O(17)–Mn–N(21) | 86.81(13) |
| O(13)–Mn–O(11) | 173.19(12) | O(11)–Mn–N(21) | 91.99(13) |
| O(16)–Mn–O(11) | 87.43(12) | O(1w)–Mn–N(21) | 172.13(13) |
| O(17)–Mn–O(11) | 83.17(11) | C(12)–O(11)–Mn | 127.9(2) |
| O(13)–Mn–O(1w) | 88.59(11) | C(15)–O(17)–Mn | 128.1(2) |
| O(16)–Mn–O(1w) | 93.19(12) | C(12)–O(13′′)–Mn′′ | 132.6(3) |
| O(17)–Mn–O(1w) | 87.25(12) | C(15)–O(16′)–Mn′ | 127.6(3) |
| O(11)–Mn–O(1w) | 92.41(12) | | |

Symmetry operations: (′) ½ + *x*, ½ – *y*, ½ + *z*, (′′) ½ + *x*, ½ – *y*, ½ – *z*

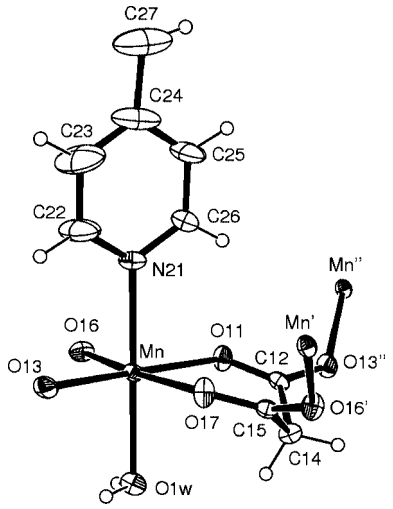


Figure 5. ORTEP drawing showing the coordination pattern of malonate anion in complex **2**.

The present structure is close comparable to those detected in analogous derivatives $[Mn_2(mal)_2(4,4\text{-bipy})(H_2O)_2]_n$,[6a] and $[Mn_2(mal)_2(hmt)(H_2O)_2]_n$,[6b] where $[Mn(mal)(H_2O)]_n$ layers are connected by 4,4′-bipy and hmt spacers, respectively. However, in the present complex **2**, the sheets are separated by 11.944 Å (half *b* axis), a longer value than that measured in closer packed layers of the 4,4′-bipy and hmt derivatives (9.386 and 8.029 Å, respectively). The intermetallic distance spaced by the bpee ligand is 14.052 Å, which is evidently longer than the value of 11.727 Å found in the 4,4′-bipy derivative.

A view of the packing along axis *a* evidences channels, accounting for 26.2% of the unit cell,[18] that are filled by disordered uncoordinated bpee and methanol molecules.

### *Complex 3*

Complex **3**, of composition $[Mn_3(btc)_2(bipy)_2(H_2O)_6]\cdot 4(H_2O)$, forms a ladder-like ribbon built up of $Mn(H_2O)(bipy)$ and $Mn(H_2O)_4$ units bridged by btc anions as depicted in Figure 6. Of the two crystallographically independent manganese ions, Mn(1) possesses a distorted trigonal bipyramid coordination geometry (Figure 7). The equatorial plane encloses bipy nitrogen N(2) and btc oxygen donors O(2), O(4) [coordination distances of 2.289(8), 2.203(6), 2.204(6) Å, respectively], while bipy N(1) and aqua O(1w) are located at the axial sites [Mn(1)–N(1) = 2.242(9), Mn(1)–O(1w) = 2.132(7) Å]. However, oxygens O(1) and O(3) from different btc carboxylate groups at longer distance [Mn–O of 2.513(6), 2.528(6) Å] appear also to interact with the metal. This epta coordination pattern observed for Mn(1) is not novel, and, among other structures, it was reported in various Mn(EDTA) derivatives.[19] On the other hand, Mn(2) is located on a center of symmetry and attains the usual octahedral coordination geometry through four aqua ligands [Mn–$OH_2$ of 2.189(7),

 © 2006 Wiley-VCH Verlag GmbH & Co. KGaA, Weinheim 

2.206(8) Å] and two btc oxygens [Mn–O 2.156(6) Å]. A selection of coordination bond lengths and angles is reported in Table 3. Thus each btc ligand bridges three metal ions and the $Mn_3$ triangle have dimensions 10.096(4) Å along the Mn(1)–Mn(1) edge, 8.594(3) and 10.450(3) Å for the Mn(1)–Mn(2) edges. All the atoms of btc are coplanar within ± 0.14 Å, and the max deviation of metal ions from the best-fit-plane through the dianion is displayed by Mn(2) (Figure 6), being displaced by 0.34 Å. The distance measured between the btc centroids forming the (btc)-$Mn(H_2O)_4$-(btc) rungs of the stairlike chain is 11.59 Å.

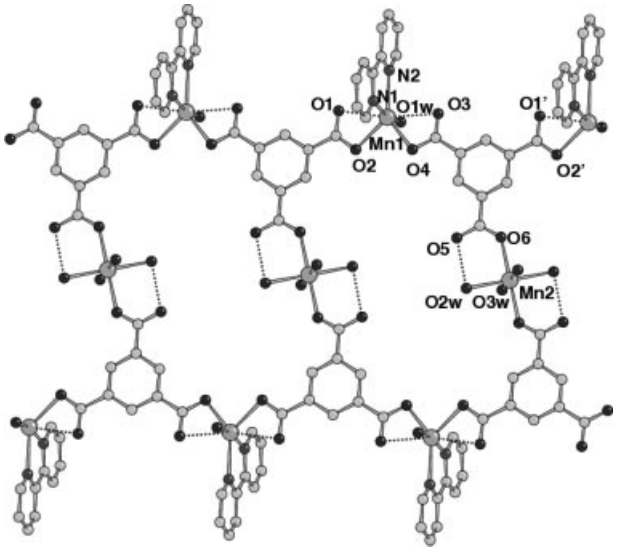


Figure 6. Double-stranded chain of complex **3** viewed down axis *c*. O(2w) forms an intrachain hydrogen bond, dotted lines Mn(1)–O(1) and Mn(1)–O(3) represent long coordination distances.

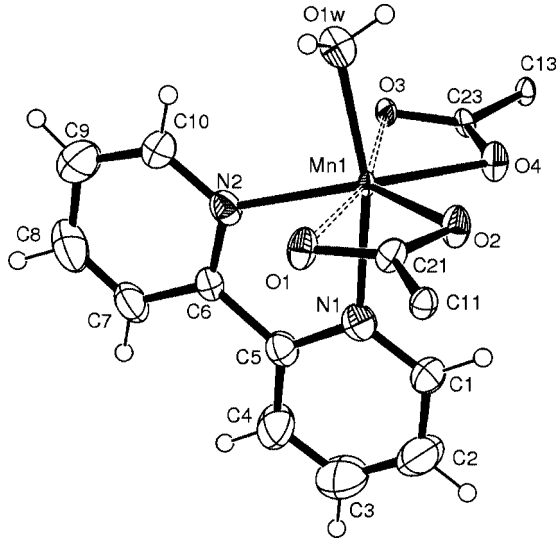


Figure 7. Detail of the coordination sphere of Mn(1) ion in complex **3** (ORTEP drawing, 40% probability level).

Table 3. Selected coordination bond lengths [Å] and angles [°] of complex **3**.

| | | | |
|---|---|---|---|
| Mn(1)–N(1) | 2.242(9) | Mn(1)–O(1) | 2.528(6) |
| Mn(1)–N(2) | 2.289(8) | Mn(1)–O(3) | 2.513(6) |
| Mn(1)–O(1w) | 2.132(7) | Mn(2)–O(2w) | 2.189(7) |
| Mn(1)–O(2) | 2.203(6) | Mn(2)–O(3w) | 2.206(8) |
| Mn(1)–O(4) | 2.204(6) | Mn(2)–O(6) | 2.156(6) |
| N(1)–Mn(1)–N(2) | 72.1(3) | O(2)–Mn(1)–O(3) | 137.5(2) |
| O(1w)–Mn(1)–N(1) | 165.6(3) | N(1)–Mn(1)–O(3) | 96.6(2) |
| O(2)–Mn(1)–N(1) | 93.0(3) | N(2)–Mn(1)–O(3) | 84.3(2) |
| O(4)–Mn(1)–N(1) | 92.1(3) | O(6)–Mn(2)–O(6′) | 180.0 |
| O(1w)–Mn(1)–N(2) | 93.6(3) | O(3w)–Mn(2)–O(3w) | 180.0 |
| O(2)–Mn(1)–N(2) | 137.7(2) | O(2w)–Mn(2)–O(2w′) | 180.0 |
| O(4)–Mn(1)–N(2) | 135.2(3) | O(6)–Mn(2)–O(2w) | 89.0(2) |
| O(1w)–Mn(1)–O(2) | 96.9(3) | O(6′)–Mn(2)–O(2w) | 91.0(2) |
| O(1w)–Mn(1)–O(4) | 99.4(3) | O(6)–Mn(2)–O(3w) | 88.4(3) |
| O(2)–Mn(1)–O(4) | 83.1(2) | O(6′)–Mn(2)–O(3w) | 91.6(3) |
| O(2)–Mn(1)–O(1) | 55.3(2) | O(2w)–Mn(2)–O(3w) | 87.4(3) |
| O(4)–Mn(1)–O(3) | 55.3(2) | O(2w′)–Mn(2)–O(3w) | 92.6(3) |
| O(3)–Mn(1)–O(1) | 165.73(19) | C(21)–O(1)–Mn(1) | 84.1(5) |
| O(1w)–Mn(1)–O(1) | 89.4(2) | C(21)–O(2)–Mn(1) | 98.9(5) |
| O(4)–Mn(1)–O(1) | 138.3(2) | C(23)–O(3)–Mn(1) | 84.3(4) |
| N(1)–Mn(1)–O(1) | 87.8(3) | C(23)–O(4)–Mn(1) | 98.5(5) |
| N(2)–Mn(1)–O(1) | 84.1(2) | C(25)–O(6)–Mn(2) | 130.8(5) |
| O(1w)–Mn(1)–O(3) | 83.0(2) | | |

In the crystal packing the 1D chains are connected by a H-bonding Scheme that occurs among coordinated and lattice water molecules with carboxylate groups (Table 4). The shortest interchain Mn–Mn distance is 6.306(2) Å. The framework is locked through π-π interactions between the peripheral bipyridine ligands (Figure 8), enhancing the dimensionality of the complex to 3D. The $[Mn_3(btc)_2(bipy)_2(H_2O)_6]$ framework shows an accessible porosity that accounts for 20.4% of the unit cell volume (Platon program[18]): this space is occupied by lattice water molecules (four per metal unit). The present compound is isomorphous with that of cobalt derivative,[8k] where the uncoordinated water molecules were found disordered over different locations.

Table 4. Hydrogen bonding in complex **3**.

| D–H | *d*(D–H) | *d*(H–A) | ∠ D–H–A | *d*(D–A) | *A*[a] |
|---|---|---|---|---|---|
| O1w–H1 | 0.846 | 1.888 | 158.22 | 2.692(9) | O5 [–*x* + 1, –*y* + 2, –*z* + 1] |
| O1w–H2 | 0.838 | 1.994 | 154.91 | 2.776(12) | O4w [*x* + 1, *y*, *z*] |
| O2w–H1 | 0.851 | 2.048 | 145.75 | 2.793(9) | O5 [–*x* + 1, –*y* + 2, –*z* + 1] |
| O2w–H2 | 0.844 | 2.126 | 130.31 | 2.748(9) | O3 [–*x* + 1, –*y* + 1, –*z* + 1] |
| O3w–H1 | 0.849 | 1.977 | 147.18 | 2.730(10) | O1 |
| O3w–H2 | 0.855 | 2.042 | 150.78 | 2.820(14) | O5w [–*x* + 1, –*y* + 1, –*z* + 2] |

[a] The acceptor atoms O4w, O5w are lattice water molecules for which hydrogen atoms were not located.

 © 2006 Wiley-VCH Verlag GmbH & Co. KGaA, Weinheim 

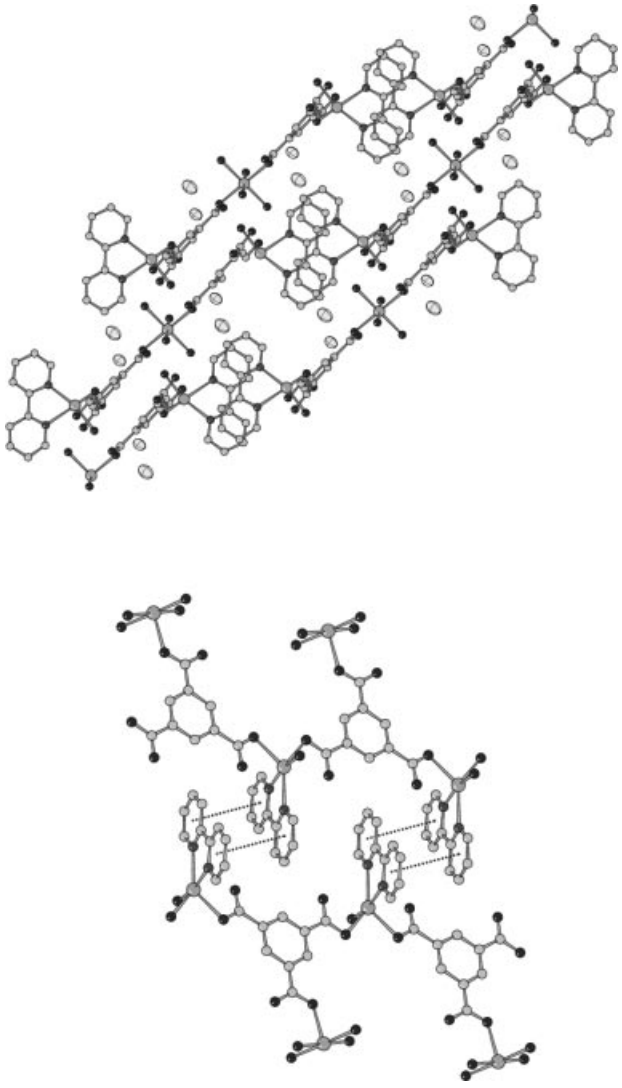

Figure 8. Top: packing diagram down axis *a* of complex **3** showing the π-π interactions between bipy ligands (ellipsoids represent lattice water oxygens). Bottom: detail of adjacent polymers with stacking bipy.

## Magnetic Properties

### *Complex 1*

Although the structure is two-dimensional, from a magnetic point of view the system can be considered as one-dimensional owing to the long Mn–Mn distance created by the linker dpyo, for which we can assume a negligible overlap between the magnetic orbitals of the $Mn^{II}$ ions.

The temperature dependence of $\chi_M T$ ($\chi_M$ being the magnetic susceptibility for one $Mn^{II}$ ion) for complex **1** is shown in Figure 9 (from 300 K to 2 K). At 300 K $\chi_M$ is 0.018 $cm^3$ $mol^{-1}$, and decreasing the temperature the $\chi_M$ value increases in a monotonous form up to 0.13 $cm^3$ $mol^{-1}$ at 18 K, where the curve presents a maximum, and then decreases to 0.09 $cm^3$ $mol^{-1}$ at 2 K. The value of $\chi_M T$ at 300 K is 4.6 $cm^3$ $mol^{-1}$ K, which is as expected for an "isolated" $Mn^{II}$ ion (Figure 9). Decreasing the temperature $\chi_M T$ gradually decreases reaching 0.2 $cm^3$ $mol^{-1}$ K at 2.00 K. The shape of these curves is characteristic of the occurrence of antiferromagnetic interactions between the $Mn^{II}$ centers and the presence of a maximum in the $\chi_M$ curve (Figure 9) indicates that the AF coupling is not negligible. The plot of the reduced magnetization ($M/N\beta$) at 2 K from 0 to 5 T is also indicative of the antiferromagnetic coupling (Figure 9, inset). The curve reaches the value of 1.2 $N\beta$, instead of 5.0 for an isolated $S = 2.5$ ion at 2 K, assuming $g = 2.00$. The X-band powder EPR spectrum at room temperature gives an isotropic signal centered at $g = 2.00$, typical for manganese(II) ions (Figure 1S).

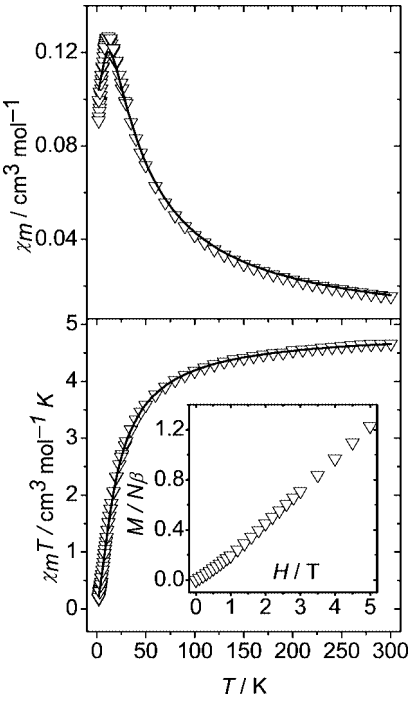


Figure 9. Plots of $\chi_M$ and $\chi_M T$ vs. T for complex **1**. Solid lines represent the best fit by using the expression cited in the text. Inset: plot of the reduced magnetization at 2 K.

This kind of magnetism for one-dimensional $Mn^{II}$ system has been theoretically studied mainly by Fisher.[20] His approach allows to analyze the magnetic data by means of an analytical expression assuming an infinite number of classical spins ($S = 5/2$).[20] The best fit was obtained for $J = -1.89 \pm 0.01$ $cm^{-1}$, $g = 2.00 \pm 0.004$ and $R = 5.4 \times 10^{-5}$ ($R$ is the agreement factor defined as $\Sigma_i[(\chi_M T)_{obs} - (\chi_M T)_{calc}]^2 / \Sigma_i[(\chi_M T)_{obs}]^2$). The value of $g = 2.00$ perfectly agrees with that expected for a manganese(II) ion ($S = 5/2$).

Scarce $J$ data for manganese ions bridged by the oxalate ligand have been reported. In an excellent paper of Glerup et al.,[14] comparing the coupling in μ-oxalate complexes with manganese, iron, cobalt, and nickel, the mean value of $J$ for three different Mn–oxalato complexes is –2.14 $cm^{-1}$, analogous to that found in complex **1**.

### *Complex 2*

Before describing the features of complex **2**, we would like to recall that carboxylate functionality is among the most widely used bridging groups for designing polynuclear

 © 2006 Wiley-VCH Verlag GmbH & Co. KGaA, Weinheim 

complexes with interesting magnetic properties. Its versatility as a linker is illustrated by the variety of its coordination modes while acting as a bridge,[21] the most common being indicated as *syn-syn*, *syn-anti* and *anti-anti*. Usually the exchange coupling through the carboxylate moiety is highly dependent on the conformation of the bridge between the interacting metal centers.[22] The *syn-anti* bridge for carboxylate ligands appears to be a rather common binding mode for $Mn^{II}$ complexes,[23] and a little is known about the magnetic properties of such complexes. In general, these bridges induce much smaller $J$ values because of the expanded metallic core and the mismatch in the orientation of magnetic orbitals.[23] The magnetic properties for *syn-anti* $Mn^{II}$-carboxylato bridged complexes have been studied for some two-dimensional polymers such as $[Mn(MCPA)_2(H_2O)_2]_n$ (MCPA = 2-methyl-4-chlorophenoxyacetic acid),[24] for some one-dimensional polymers such as $[Mn(\mu\text{-}3\text{-}ClPhCOO)_2(2,2'\text{-bipy})_2]_n{\cdot}nH_2O$,[25] with two *syn-anti* carboxylate bridges and for discrete $Mn^{II}$ homodinuclear complexes involving either only one *syn-anti* carboxylate bridge, $[Mn(2,2'\text{-bipy})_2(H_2O)_2(Me_2NCH_2COO)](ClO_4)$[26] or two *syn-anti* carboxylate bridges, $[Mn_2(\mu\text{-}PhCOO)_2(2,2'\text{-bipy})_4](ClO_4)_2$.[25] The antiferromagnetic coupling is always very small. In the presence of two carboxylate bridges[25] the coupling parameter $J$ is slightly greater than that derived for a single bridge.[25,26] All these exchange coupling constants are of the same order (between –0.5 and –2 $cm^{-1}$).

The temperature dependence of $\chi_M T$ ($\chi_M$ being the magnetic susceptibility for one $Mn^{II}$ ion) for complex **2** is shown in Figure 10 (top; from 300 K to 2 K). At 300 K $\chi_M$ is 0.0012 $cm^3\ mol^{-1}$ (Figure 2S) and it increases in a monotonous form to 0.65 $cm^3\ mol^{-1}$ at 2 K as the temperature is lowered. At 300 K $\chi_M T$ is 4.35 $cm^3\ mol^{-1}$ K, a value which is as expected for an "isolated" $Mn^{II}$ ion. $\chi_M T$ is almost invariable up to 100 K and gradually decreases on cooling to reach the value of 1.3 $cm^3\ mol^{-1}$ K at 2.00 K. The shape of these curves is characteristic of the occurrence of weak antiferromagnetic interactions between the $Mn^{II}$ centers. The lack of a maximum in the $\chi_M$ curve (Figure 2S) indicates that the AF coupling is very small. The plot or the reduced magnetization ($M/N\beta$) at 2 K from 0 to 5 T is also indicative of small antiferromagnetic coupling (Figure 10, bottom). The curve reaches the value of 4.7 $N\beta$, but the shape is different from the Brillouin function for an isolated $S = 2.5$ ion at 2 K, assuming $g = 2.00$.

Taking into account the structure of **2** in which Mn(mal) layers are linked together by the long bpee ligands, the susceptibility data were fitted by the expansion series of Lines[27] for a $S = 5/2$ antiferromagnetic quadratic layer, based on the exchange Hamiltonian $H = -\Sigma_{nn} J S_i S_j$, where $\Sigma_{nn}$ runs over all pairs of nearest-neighbor spins $i$ and $j$, Equation (1).

$$Ng^2\beta^2/\chi|J| = 3\theta + (\Sigma C_n/\theta^{n-1}) \quad (1)$$

$\theta = kT/|J|S(S+1)$, $C_1 = 4$, $C_2 = 1.448$, $C_3 = 0.228$, $C_4 = 0.262$, $C_5 = 0.119$, $C_6 = 0.017$ and $N$, $g$ and $\beta$ in Equation (1) have their usual meanings. The best fit is obtained for the superexchange parameters $J = -0.20 \pm 0.02$ $cm^{-1}$ and $g = 2.00 \pm 0.003$ (Figure 10) with $R = 2.6 \times 10^{-4}$.

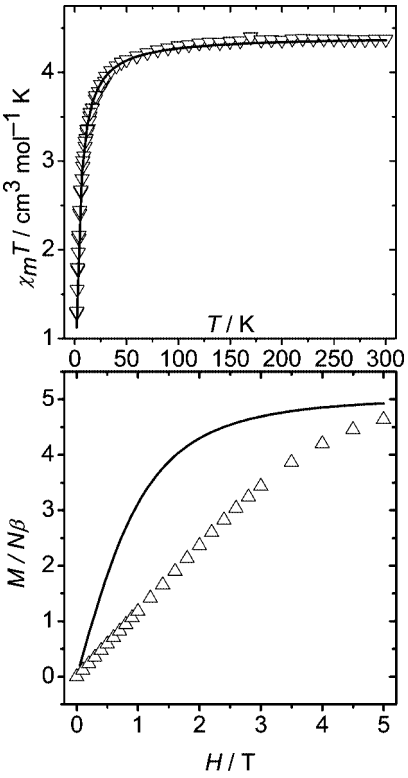


Figure 10. Top: plot of the $\chi_M T$ vs. $T$ for complex **2**. Solid line represents the fit with the expression given in the text. Bottom: plot of the reduced magnetization at 2 K. Solid line represents the Brillouin function for $S = 2.5$ and $g = 2.00$.

The magnetic properties of **2** may be compared with those observed of other two-dimensional manganese(II) systems showing low antiferromagnetic coupling and for which possible antiferromagnetic ordering is not yet achieved at the lowest limit of the measurement temperature. For example, in $[\{Mn(SCN)_2(EtOH)_2\}_2]$,[27b] the superexchange parameter $J$ was reported to be –1.22 $cm^{-1}$ and the low-temperature EPR spectra show an increase in the line width at low temperature, but the susceptibility plot does not show important deviations from the theoretical two-dimensional susceptibility plot even not at low temperature. Room temperature X-band EPR spectrum (Figure 3S) shows an isotropic signal centered at $g = 2.00$, typical for manganese(II) ions.

### *Complex 3*

Plot of $\chi_M T$ vs. $T$ for complex **3** is shown in Figure 11 (top). At 300 K $\chi_M T$ starts at 4.36 $cm^3\ mol^{-1}$ K, which is the typical value for one isolated $Mn^{II}$ ion ($g = 2.00$). This value is almost constant up to 50 K, then it decreases rapidly to 3.62 $cm^3\ mol^{-1}$ K at 2 K, a trend indicative of very weak antiferromagnetic coupling among the manganese(II) ions. The reduced magnetization curve ($M/N\beta$) vs. $H$ at 2 K corroborates this very weak antiferromagnetic coupling. The experimental data are slightly smaller than those corresponding to the Brillouin function for $S = 5/2$

 © 2006 Wiley-VCH Verlag GmbH & Co. KGaA, Weinheim 

and $g$ = 2.00 (Figure 11, bottom). This almost negligible antiferromagnetic coupling is due to the extended benzenetricarboxyalate bridging ligand, which cannot create any significant coupling.[28]

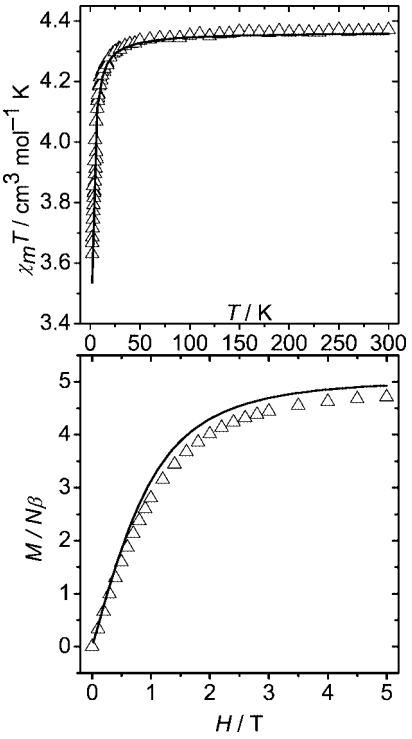


Figure 11. Top: plot of $\chi_M T$ vs. $T$ for complex **3** with the best fit calculation represented by the solid line. Bottom: plot of the reduced magnetization vs. $H$ at 2 K. Solid line corresponds to the Brillouin function for $g$ = 2.00.

The magnetic fit for complex **3** is impracticable, due to its intrinsic complication. Considering the structure as a pseudo-one-dimensional $Mn^{II}$ systems ($S$ = 5/2) it is possible to try to fit the experimental susceptibility data by using the formula given by Fisher for a model with classical spin.[20,22] The best fit parameters were $J$ = –0.05 cm$^{-1}$, $g$ = 2.00 and $R = 1.8 \times 10^{-3}$. However, $J$ value must be taken cautiously, being the one-dimensionality only a drastic estimate, and thus the Fisher's formula would not be completely valid. Furthermore, the asymmetry of one of the manganese ions could give a $g$ value different from 2.00, likely indicative that the hypothesis of the $g$ = 2.00 in the reduced magnetization is not fully accurate, and the AF coupling is even lower than –0.05 cm$^{-1}$. The X-band powder EPR spectrum at room temperature shows an isotropic signal centered at $g$ = 2.00. (Figure 4S).

### Thermal Analysis

Complex **1** upon heating does not show any mass change up to 300 °C and on further heating its frame work gradually collapses. The thermogravimetric analysis of complex **2** shows desolvation within the temperature range of 70–200 °C (Figure 5S). The behavior suggests the loss of lattice methanol and dehydration of coordinated water molecules (vide infra) takes place in sequence without showing any intermediate species. This also corroborates the involvement of H-bonding between the malonate oxygens and water molecules. The lattice bpee cannot leave the system upon heating up to 200 °C, then the framework of the complex collapses. On the other hand complex **3**, that comprises of ten water molecules per trinuclear unit, loses water in multi steps upon heating (Figure 6S). The first step (60–125 °C) accounts for the release of four guest water as well as two coordinated water molecules. This upon further heating starts to lose coordinated water molecules showing a non isolable intermediate at ca. 200 °C and then the framework appears to collapse on continuation of heating. Through careful heating we have been able to isolate the intermediate, $[Mn_3(btc)_2(2,2'\text{-bipy})_2(H_2O)_4]$ (**3a**) which reverts on exposure to humid atmosphere (≈ 70%) for 2–3 hours. The formation of **3a** is not unlikely as elimination of one water molecule from each terminal metal center results in a six coordinated geometry for Mn(1) (see Figure 7), but further elimination of coordinated water molecules leads to an unstable system and to the collapse of the metal organic framework. Thus the thermal analyses of these three complexes hint that the MOF of **1** is thermally more stable than those of **2** and **3**.

## Conclusions

In this paper we have presented the syntheses, the crystal structures, variable temperature magnetic studies and thermal behaviors of three carboxylato-bridged polymeric networks of manganese(II). The above discussion shows that the use of different carboxylates, namely oxalate, malonate and 1,3,5-benzenetricarboxylate, in combination with neutral coligands, dpyo, bpee, and 2,2′-bipy, has made feasible the construction of coordination polymers of different dimensionality. Complexes **2** and **3** are 3D open frameworks, the former contains channels filled up by disordered uncoordinated bpee and methanol and the latter is achieved through π-π and H-bonding interactions. On the other hand, complex **1** is a covalent bonded 2D network.

## Experimental Section

**Materials:** High purity manganese chloride tetrahydrate; 4,4′-bipyridyl *N*,*N*′-dioxide; 2,2′-bipyridine and *trans*-1,2-bis(4-pyridyl)ethylene were purchased from Aldrich chemical Company. All other chemicals used were of analytical grade.

**Physical Measurements:** Elemental analyses (carbon, hydrogen and nitrogen) were performed using a Perkin–Elmer elemental analyzer. IR spectra (4000–600 cm$^{-1}$) were taken in KBr pellets using a Jasco FT-IR (model 300E). The magnetic measurements were carried out on polycrystalline samples with a Quantum Design MPMS SQUID magnetometer (applied field 0.1 T) working in the temperature range 300–2 K. Diamagnetic corrections were estimated from Pascal's tables. EPR spectra were recorded on powder samples at X-band frequency with a BRUKER 300E automatic spectrometer, varying the temperature between 4–300 K. Thermal analysis were done on a Pyris Diamond system.

 © 2006 Wiley-VCH Verlag GmbH & Co. KGaA, Weinheim 

Table 5. Crystal data and refinements details of complexes **1**, **2** and **3**.

| | **1** | **2** | **3** |
|---|---|---|---|
| Formula | $C_{12}H_8MnN_2O_6$ | $C_{24.50}H_{25}Mn_2N_3O_{10.50}$ | $C_{38}H_{42}Mn_3N_4O_{22}$ |
| $M_r$ [g mol$^{-1}$] | 331.14 | 639.35 | 1071.58 |
| Crystal system | monoclinic | monoclinic | triclinic |
| Space group | $C2/c$ | $P2_1/n$ | $P\bar{1}$ |
| $a$ [Å] | 14.231(3) | 7.413(4) | 10.096(4) |
| $b$ [Å] | 5.657(2) | 23.889(5) | 10.756(4) |
| $c$ [Å] | 15.189(3) | 7.467(4) | 12.167(5) |
| α [°] | | | 74.097(10) |
| β [°] | 94.59(2) | 92.224(10) | 76.083(10) |
| γ [°] | | | 81.210(10) |
| Volume [Å$^3$] | 1218.9(6) | 1321.3(10) | 1228.0(8) |
| $Z$ | 4 | 2 | 1 |
| $D_{calcd.}$ [g cm$^{-3}$] | 1.805 | 1.607 | 1.449 |
| μ, Mo-$K_\alpha$ [mm$^{-1}$] | 1.115 | 1.020 | 0.840 |
| $\theta_{max}$ [°] | 26.41 | 25.73 | 26.21 |
| Reflections collected | 5256 | 7634 | 6091 |
| Unique reflections | 1187 | 2338 | 3560 |
| $R_{int}$ | 0.0710 | 0.0314 | 0.0418 |
| Refined parameters | 96 | 223 | 323 |
| Goodness of fit ($F^2$) | 0.923 | 1.129 | 1.082 |
| $R_1$ [$I > 2\sigma(I)$][a] | 0.0365 | 0.0529 | 0.0983 |
| $wR_2$[a] | 0.0823 | 0.1225 | 0.2602 |

[a] $R_1(F_o) = \Sigma \, ||F_o| - |F_c||/\Sigma|F_o|$, $wR_2(F_o^2) = [\Sigma w(F_o^2 - F_c^2)^2/\Sigma w(F_o^2)^2]^{1/2}$.

**Crystallographic Data Collection and Refinement:** Crystal data and details of data collections and refinements for the structures reported are summarized in Table 5. Diffraction data set of complex **1** was carried out on a Nonius DIP-1030H system with Mo-$K_\alpha$ radiation. For complexes **2** and **3**, reflections were collected on a STOE four–circle diffractometer equipped with MAR–research image plate system and Mo-$K_\alpha$ radiation. Cell refinement, indexing and scaling of the data sets were carried out using Denzo and Scalepack,[29] and XDS.[30] All the structures were solved by Patterson and Fourier analyses[31] and refined by the full-matrix least-squares method based on $F^2$ with all observed reflections.[31] Two lattice water molecules were detected in the ΔF map of complex **3**. Disordered peaks in the electron-density map of complex **2** were interpreted as a bpee ligand and a methanol (both arranged over a center of symmetry), each accounting for 0.25 molecule per metal unit. The contribution of H atoms at calculated positions were included in the final cycles of refinement, except those of lattice water and disordered molecules. All the calculations were performed using the WinGX System 1.64.05.[32]

**[Mn(ox)(dpyo)]$_n$ (1):** A methanolic solution (10 mL) of 4,4′-bipyridine *N*,*N*′-dioxide (1 mmol, 0.188 g) was added dropwise to an aqueous solution (5 mL) of $MnCl_2{\cdot}4H_2O$ (1 mmol, 0.197 g) with constant stirring for 10 min. To the resulting reaction mixture an aqueous solution of disodium oxalate (1 mmol, 0.134 g) was added whilst stirring condition. After 30 minutes a bright red compound separated. Single crystals suitable for X-ray analysis were obtained by diffusing a methanolic solution (10 mL) of $MnCl_2{\cdot}4H_2O$ and 4,4′-bipyridine *N*,*N*′-dioxide on an aqueous solution (10 mL) of disodium oxalate in a tube. Bright red crystals deposited at the junction of two solutions after one week. Yield: 80%. $C_{12}H_8MnN_2O_6$ (331.14): C 43.48, H 2.41, N 8.45; found C 43.47, H 2.42, N 8.46. IR: $\tilde{\nu}$ = 3114 (w), 3085 (w), 2929 (vw), 1619 (vs), 1468 (s), 1222 (s), 1176 (w), 844 (w), 792 (vw), 553 (vw) cm$^{-1}$.

**{[Mn$_2$(mal)$_2$(bpee)(H$_2$O)$_2$]·0.5(bpee)·0.5(CH$_3$OH)}$_n$ (2):** An aqueous solution (5 mL) of disodium malonate (1 mmol, 0.148 g) was added to an aqueous solution (5 mL) of $MnCl_2{\cdot}4H_2O$ (1 mmol, 0.197 g) whilst stirring condition. To this reaction mixture a methanolic solution (10 mL) of *trans*-1,2-bis(4-pyridyl)ethylene (1 mmol, 0.182 g) was added. The resultant reaction mixture was stirred for 1 h and filtered. The filtrate was kept in a desiccator ($CaCl_2$) and after a few days bright yellow single crystals of X-ray diffraction quality were obtained. Yield 75%. $C_{24.50}H_{25}Mn_2N_3O_{10.50}$ (639.35): C 45.98, H 3.91, N 6.56; found C 46.01, H 3.90, N 6.57. IR: $\tilde{\nu}$ = 3436-3190 (s, v br), 1675 (w), 1611 (vs), 1558 (vs), 1467 (w), 1436 (s), 1372 (vs), 1314 (w), 1104 (w), 1016 (w), 830 (w), 761 (s), 731 (s), 628 (w), 542 (w) cm$^{-1}$.

**{[Mn$_3$(btc)$_2$(2,2′-bipy)$_2$(H$_2$O)$_6$]·4H$_2$O}$_n$ (3):** An aqueous solution (5 mL) of $MnCl_2{\cdot}4H_2O$ (1 mmol, 0.197 g) was added to a methanolic solution of (10 mL) of 2,2′-bipyridine (1 mmol, 0.156 g) dropwise whilst stirring condition. The resultant yellow colored solution was mixed to an aqueous solution (5 mL) of btc (0.66 mmol, 0.184 g) and stirred for 1 h and filtered. The filtrate was kept in a desiccator ($CaCl_2$). After one week bright yellow crystals suitable for X-ray diffraction were obtained. Yield 70%. $C_{38}H_{42}Mn_3N_4O_{22}$ (1071.58): C 42.55, H 3.91, N 5.22, found C 42.57, H 3.93, N 5.20. IR: $\tilde{\nu}$ = 3475–3025 (s, v br) 1671 (w), 1611 (vs), 1557 (vs), 1437 (s), 1372 (s), 1314 (w), 1247 (w), 1157 (w), 1016 (w), 932 (w), 761 (s), 731 (s), 650 (w), 541 (w) cm$^{-1}$.

CCDC-276231, -276232 and -276233 (for complexes **1**, **2** and **3**, respectively) contain the supplementary crystallographic data for this paper. These data can be obtained free of charge from The Cambridge Crystallographic Data Centre via www.ccdc.cam.ac.uk/data_request/cif.

**Supporting Information** (for details see the footnote on the first page of this article): X-band EPR spectra for complexes **1**–**3**, the $\chi_M$ plot vs. T for **2**, and the thermogravimetric analysis of **2** and **3** (Figures 1S–6S).

## Acknowledgments

N. R. C. thanks Council of Scientific and Industrial Research, New Delhi, and J.R. thanks Spanish Government for financial support (BQU2003/00539).

 © 2006 Wiley-VCH Verlag GmbH & Co. KGaA, Weinheim 

[1] a) H. K. Chae, D. Y. Siberio-Perez, J. Kim, Y. B. Go, M. Eddaoudi, A. J. Matzger, M. O'Keeffe, O. M. Yaghi, *Nature* **2004**, *427*, 523; b) A. I. Skoulidas, *J. Am. Chem. Soc.* **2004**, *126*, 1356; c) N. L. Rosi, J. Eckert, M. Eddaoudi, D. T. Vodak, J. Kim, M. O'Keeffe, O. M. Yaghi, *Science* **2003**, *300*, 1127; d) M.-L. Tong, S. Kitagawa, H.-C. Chang, M. Ohba, *Chem. Commun.* **2004**, 418; e) S. C. Zimmerman, M. S. Wendland, N. A. Rakow, I. Zharov, K. S. Suslick, *Nature* **2002**, *418*, 399; f) A. Katz, M. E. Davis, *Nature* **2000**, *403*, 286; g) X.-J. Zheng, L.-C. Li, S. Gao, L.-P. Jin, *Polyhedron* **2004**, *23*, 1257; h) M. Tominaga, S. Tashiro, M. Aoyagi, M. Fujita, *Chem. Commun.* **2002**, 2038; i) K. Biradha, M. Fujita, *Angew. Chem. Int. Ed.* **2002**, *41*, 3392; j) O. R. Evans, W. Lin, *Acc. Chem. Res.* **2002**, *35*, 511.

[2] a) D. W. Bruce, D. O'Hare. *Inorganic Materials*, Eds. John Wiley & Sons New York **1992**; b) R. D. Willet, D. Gatteschi, O. Kahn. *Magneto Structural Correlations in Exchange Coupled System* Eds. NATO ATI Series C140; Reidal: Dordrecht, The Netherlands **1985**; c) B. Multon, M. J. Zaworotko, *Chem. Rev.* **2001**, *101*, 1629; d) P. J. Hagrman, D. Hagrman, J. Zubieta, *Angew. Chem. Int. Ed.* **1999**, *38*, 2638; e) R. Robson, *J. Chem. Soc., Dalton Trans.* **2000**, 3735; f) W. Su, M. Hong, J. Weng, R. Cao, S. Lu, *Angew. Chem. Int. Ed.* **2000**, *39*, 2911; g) D. Gatteschi, O. Kahn, J. Miller, *Molecular Magnetic Materials* Eds. Nato ASI Series EI98; Kluwer. Dordrecht, The Netherlands, **1991**; h) O. M. Yaghi, G. Li, H. Li, *Nature* **1995**, *378*, 703; i) K. Marouka, N. Murase, H. Yamamoto, *J. Org. Chem.* **1993**, *58*, 2938; j) C. Chen, K. S. Suslick, *Coord. Chem. Rev.* **1993**, *128*, 293 and references cited therein; k) O. C. Montelro, H. I. S. Noguelra, T. Trindade, *Chem. Mater.* **2001**, *13*, 2103; l) A. J. Waddon, E. B. Coughlin, *Chem. Mater.* **2003**, *15*, 4555; m) M. Kondo, Y. Irie, Y. Shimizu, M. Miyazawa, H. Kawaguchi, A. Nakamura, T. Naito, K. Maeda, H. Uchida, *Inorg. Chem.* **2004**, *43*, 6139; n) S. C. Johannessen, R. G. Brisbois, *J. Am. Chem. Soc.* **2001**, *123*, 3818; o) J.-W. Park, E. L. Thomas, *J. Am. Chem. Soc.* **2002**, *124*, 515.

[3] a) Y. Cui, O. R. Evans, H. L. Ngo, P. S. White, W. Lin, *Angew. Chem. Int. Ed.* **2002**, *41*, 1159; b) D. K. Chand, K. Biradha, M. Fujita, S. Sakamoto, K. Yamaguchi, *Chem. Commun.* **2002**, 2486; c) L. Pan, X. Y. Huang, J. Li, Y. Wu, N. Zheng, *Angew. Chem. Int. Ed.* **2000**, *39*, 527; d) S. Takamizawa, E.-I. Nakata, H. Yokoyama, K. Mochizuki, W. Mori, *Angew. Chem. Int. Ed.* **2003**, *42*, 4331; e) J. Y. Lu, A. M. Babb, *Chem. Commun.* **2002**, 1340.

[4] a) L. Dubois, D.-F. Xiang, X.-S. Tan, J. Pécaut, P. Jones, S. Baudron, L. L. Pape, J.-M. Latour, C. Baffert, S. Chardon-Noblat, M.-N. Collomb, A. Deronzier, *Inorg. Chem.* **2003**, *42*, 750; b) C. N. R. Rao, S. Natarajan, R. Vaidhyanathan, *Angew. Chem. Int. Ed.* **2004**, *43*, 1466.

[5] a) S. Konar, P. S. Mukherjee, E. Zangrando, F. Lloret, N. Ray Chaudhuri, *Angew. Chem. Int. Ed.* **2002**, *41*, 1561; b) P. S. Mukherjee, T. K. Maji, G. Mostafa, J. Ribas, M. S. E. Fallah, N. Ray Chaudhuri, *Inorg. Chem.* **2001**, *40*, 928; c) S. Konar, E. Zangrando, N. Ray Chaudhuri, *Inorg. Chim. Acta* **2003**, *355*, 264.

[6] a) T. K. Maji, S. Sain, G. Mostafa, T.-H. Lu, J. Ribas, M. Monfort, N. Ray Chaudhuri, *Inorg. Chem.* **2003**, *42*, 709; b) S. Konar, S. C. Manna, E. Zangrando, T. Mallah, J. Ribas, N. Ray Chaudhuri, *Eur. J. Inorg. Chem.* **2004**, 4202; c) S. Sain, T. K. Maji, G. Mostafa, T.-H. Lu, N. Ray Chaudhuri, *Inorg. Chim. Acta* **2003**, *351*, 12.

[7] a) S. Sain, T. K. Maji, G. Mostafa, T.-H. Lu, N. Ray Chaudhuri, *New J. Chem.* **2003**, *27*, 185; b) S. Dalai, P. S. Mukherjee, E. Zangrando, F. Lloret, N. Ray Chaudhuri, *J. Chem. Soc., Dalton Trans.* **2002**, 822; c) S. Konar, P. S. Mukherjee, M. G. B. Drew, J. Ribas, N. Ray Chaudhuri, *Inorg. Chem.* **2003**, *42*, 2545; d) P. S. Mukherjee, S. Konar, E. Zangrando, T. Mallah, J. Ribas, N. Ray Chaudhuri, *Inorg. Chem.* **2003**, *42*, 2695; e) S. Konar, E. Zangrando, M. G. B. Drew, J. Ribas, N. Ray Chaudhuri, *Dalton Trans.* **2004**, 260.

[8] a) E. G. Bakalbassis, M. Korabik, A. Michailides, J. Mrozinski, C. Raptopoulou, S. Skoulika, A. Terzis, D. Tsaousis, *J. Chem. Soc., Dalton Trans.* **2001**, 850; b) C. Livage, C. Egger, M. Nogues, G. Férey, *J. Mater. Chem.* **1998**, *8*, 2743; c) C. Livage, C. Egger, G. Férey, *Chem. Mater.* **1999**, *11*, 1546; d) L.-S. Long, X.-M. Chen, M.-L. Tong, Z.-G. Sun, Y.-P. Ren, R.-B. Huang, L.-S. Zheng, *J. Chem. Soc., Dalton Trans.* **2001**, 2888; e) M.-X. Li, G.-Y. Xie, S.-L. Jin, Y.-D. Gu, M.-Q. Li, J. Liu, Z. Xu, X.-Z. You, *Polyhedron* **1996**, *15*, 535; f) J. J. Girerd, M. Verdaguer, *Inorg. Chem.* **1980**, *19*, 274; g) M. Julve, M. Verdaguer, A. Gleizes, M. Philoche-Lavisalles, O. Kahn, *Inorg. Chem.* **1984**, *23*, 3808; h) M. Julve, J. Faus, M. Verdaguer, A. Gleizes, *J. Am. Chem. Soc.* **1984**, *106*, 3808; i) L. Deakin, A. M. Ariff, J. S. Miller, *Inorg. Chem.* **1999**, *38*, 5072; j) M.-F. S. Lo, S.-Y. S. Chui, I. D. Willams, L. Y. Shek, Z. Lin, X. X. Zang, G. H. Wen, *J. Am. Chem. Soc.* **2000**, *122*, 6293; k) M. J. Plater, M. R. St. J. Foreman, E. Coronado, C. J. Gómez-García, A. M. Z. Slawin, *J. Chem. Soc., Dalton Trans.* **1999**, 4209.

[9] a) *Magneto Structural Correlations in Exchange Coupled Systems* (Eds.: R. D. Willet, D. Gatteschi, O. Kahn); NATO ASI Series C140; Reidel: Dordrecht, The Netherlands, **1985**.

[10] a) C. Janiak, *Dalton Trans.* **2003**, 2781; b) C.-T. Chen, K. S. Suslick, *Coord. Chem. Rev.* **1993**, *128*, 293; c) O. Kahn, J. Larionova, L. Ouahab, *Chem. Commun.* **1999**, 945; d) J. Cernak, M. Orendac, I. Potocnak, J. Chomic, A. Orendacova, J. Skorsepa, A. Feher, *Coord. Chem. Rev.* **2002**, *224*, 51; e) O. Sato, I. Iyoda, A. Fujishima, K. Hashimoto, *Science* **1996**, *271*, 49; f) T. Mallah, S. Thiebaut, M. Verdaguer, P. Veillet, *Science* **1993**, *262*, 1554.

[11] G. Christou, D. Gatteschi, D. N. Hendrickson, R. Sessoli, *MRS Bull.* **2000**, *25*, 66.

[12] G. Aromí, S. M. J. Aubin, M. A. Bolcar, G. Christou, H. J. Eppley, K. Folting, D. N. Hendrickson, J. C. Huffman, R. C. Squire, H.-L. Tsai, S. Wang, M. W. Wemple, *Polyhedron* **1998**, *17*, 3005.

[13] a) R. Sessoli, D. Gatteschi, A. Caneschi, M. A. Novak, *Nature* **1993**, *365*, 141; b) G. Christou, in: *Magnetism: A Supramolecular Function* (Ed.: O. Kahn); NATO Series; Kluwer: Dordrecht, The Netherlands, **1996**; pp. 383–410; c) R. Sessoli, H.-L. Tsai, A. R. Schake, S. Wang, J. B. Vincent, K. Folting, D. Gatteschi, G. Christou, D. N. Hendrickson, *J. Am. Chem. Soc.* **1993**, *115*, 1804.

[14] J. Glerup, P. A. Goodson, D. J. Hodgson, K. Michelsen, *Inorg. Chem.* **1995**, *34*, 6255.

[15] a) E. Coronado, J. R. Galán-Mascarós, C. J. Gómez-García, J. M. Martínez-Agudo, *Inorg. Chem.* **2001**, *40*, 113; b) E. Coronado, J. R. Galán-Mascarós, C. J. Gómez-García, E. Martínez-Ferrero, S. V. Smaalen, *Inorg. Chem.* **2004**, *43*, 4808; c) A. Alberola, E. Coronado, J. R. Galán-Mascarós, C. Giménez-Saiz, C. J. Gómez-García, *J. Am. Chem. Soc.* **2003**, *125*, 10774.

[16] P. Lightfoot, A. Snedden, *J. Chem. Soc., Dalton Trans.* **1999**, 3549.

[17] T. Lis, J. Matuszewski, *Acta Crystallogr., Sect. B* **1979**, *35*, 2212.

[18] A. L. Spek, *Acta Crystallogr., Sect. A* **1990**, *46*, C34.

[19] a) S. Richards, B. Pedersen, J. V. Silverton, J. L. Hoard, *Inorg. Chem.* **1964**, *3*, 27; b) X. Solans, S. Gali, M. Font-Altaba, J. Oliva, J. Herrera, *Afinidad* **1988**, *45*, 243.

[20] M. E. Fisher, *Am. J. Phys.* **1964**, *32*, 343.

[21] C. Oldham, in: *Comprehensive Coordination Chemistry*; (Eds.: G. Wilkinson, R. D. Gillard, J. A. McCleverty); Pergamon Press: Oxford, **1987**; Vol. 2, p. 435.

[22] O. Kahn, *Molecular Magnetism*, VCH, New York, **1993**.

[23] C. Policar, F. Lambert, M. Cesario, I. Morgenstern-Badarau, *Eur. J. Inorg. Chem.* **1999**, 2201 and references cited therein.

[24] V. Tangoulis, G. Psomas, C. Dendrinou-Samara, C. P. Raptopoulou, A. Terzis, D. P. Kessissoglou, *Inorg. Chem.* **1996**, *35*, 7655.

[25] B. Albela, M. Corbella, J. Ribas, I. Castro, J. Sletten, H. Stoeckli-Evans, *Inorg. Chem.* **1998**, *37*, 788.


 © 2006 Wiley-VCH Verlag GmbH & Co. KGaA, Weinheim 

[26] X. M. Xen, Y. X. Tong, Z. T. Xu, T. C. W. Mak, *J. Chem. Soc., Dalton Trans.* **1995**, 4001.
[27] a) M. E. Lines, *J. Phys. Chem. Solids* **1970**, *31*, 101; b) A. Escuer, R. Vicente, M. A. S. Goher, F. A. Mautner, *J. Chem. Soc., Dalton Trans.* **1997**, 4431 and references cited therein.
[28] H. J. Choi, M. P. Suh, *J. Am. Chem. Soc.* **1998**, *120*, 10622.
[29] Z. Otwinowski, W. Minor, "Processing of X-ray Diffraction Data Collected, in: Oscillation Mode", Methods in Enzymology, Volume 276: Macromolecular Crystallography (Eds.: C. W. Carter, Jr., R. M. Sweet) **1997**, part A, p. 307–326, Academic Press.
[30] W. Kabsch, *J. Appl. Cryst.* **1988**, *21*, 916.
[31] SHELX 97 Programs for Crystal Structure Analysis (Release 97–2). G. M. Sheldrick, University of Göttingen, Germany, **1998**.
[32] L. J. Farrugia, *J. Appl. Crystallogr.* **1999**, *32*, 837.

Received: June 27, 2005
Published Online: November 7, 2005

 © 2006 Wiley-VCH Verlag GmbH & Co. KGaA, Weinheim 

EurJIC
European Journal of Inorganic Chemistry

Issue 3/2006

Pages 493–680

*Papers available ahead of print in Early View at www.interscience.wiley.com*

*Earliest available Table of Contents:*
*Automatically, free of charge by e-mail through*
*www.interscience.wiley.com/alerts*

## COVER PICTURE

**The cover picture shows** the self-assembly of a tetranuclear $Co^{III}$ metallacycle from the reaction of a bis(benzene-*o*-dithiolato) ligand and $Co^{II}$ after aerial oxidation. Two differently coordinated metal centres (*syn* and *anti*) are observed in the metallacycle even though a ligand with two identical donor sites has been used. This unusual structural motif is formed in order to avoid strong steric interactions between the *ortho*-sulfur atoms, which would result in a hypothetical dinuclear complex. Details are discussed in the article by F. E. Hahn et al. on p. 535ff.

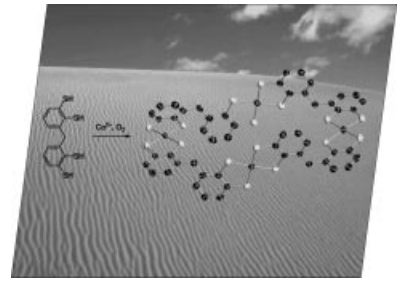

## MICROREVIEW

**Contents**

**507** **M. Makha, A. Purich, C. L. Raston,* A. N. Sobolev**

Structural Diversity of Host–Guest and Intercalation Complexes of Fullerene $C_{60}$

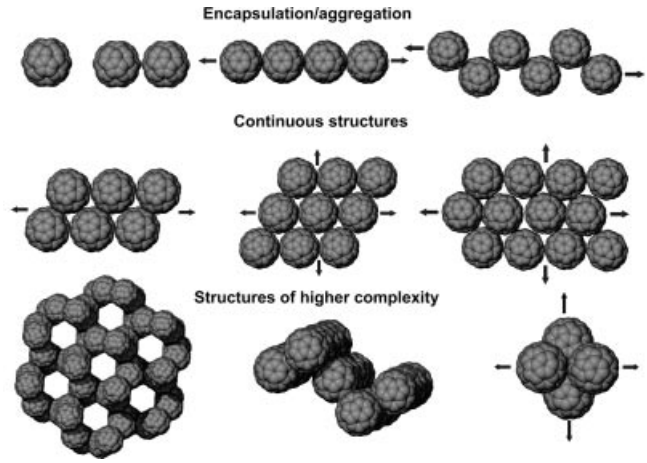


**Keywords:** Fullerenes / Crystal structures / Packing models / Host–guest interactions

 © 2006 Wiley-VCH Verlag GmbH & Co. KGaA, Weinheim 

# SHORT COMMUNICATIONS


**519** **J. Ma, X. Liu,* X. Cao, S. Feng, M. E. Fleet**

Bundle of Nanobelts Up to 4 cm in Length: One-Step Synthesis and Preparation of Titanium Trisulfide ($TiS_3$) Nanomaterials

**Keywords:** One dimensional / Nanostructures / Layered compounds / Titanium / Sulfides / CVT / One-step synthesis

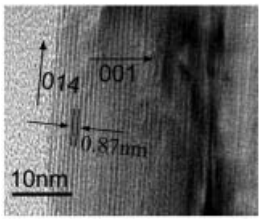


**523** **D. Shamir, I. Zilbermann,* E. Maimon, A. I. Shames, H. Cohen, D. Meyerstein***

Pyrophosphate and ATP as Stabilizing Ligands for High-Valent Nickel Complexes

**Keywords:** ATP / Cyclam / High-valent transition metal complexes

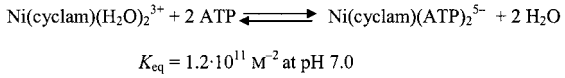


**526** **M. Wu, D. Yuan, L. Han, B. Wu, Y. Xu, M. Hong***

Inclusion of Metal Complexes into Cavities of 2D Coordination Networks Built from *p*-Sulfonatothiacalix[4]arene Tetranuclear Clusters

**Keywords:** *p*-Sulfonatothiacalix[4]arene / Supramolecular chemistry / Coordination polymer / Inclusion

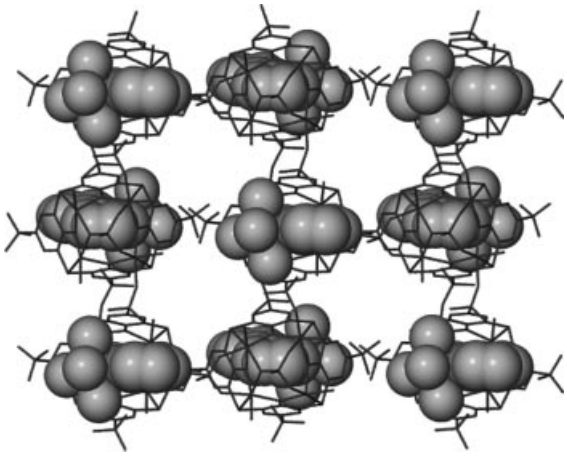

**531** **M. Sarkar, K. Biradha***

Entrapment of a Hexamer of Nitrobenzene Molecules between the Layers of (4,4)-Coordination Networks Containing Intra-β-Sheet Hydrogen Bonds

**Keywords:** Coordination networks / Hydrogen bonds / Aggregation / Host-guest systems

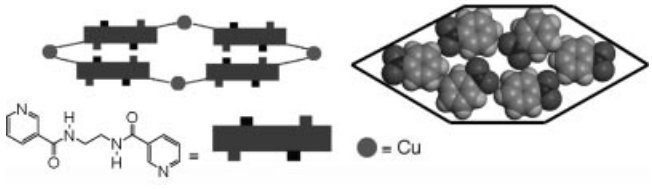



# FULL PAPERS


**535** **F. E. Hahn,* T. Kreickmann, T. Pape**

Self-Assembly of a Tetranuclear $Co^{III}$-Metallacycle from the Reaction of a Bis(benzene-*o*-dithiolato) Ligand with $Co^{II}$ and Subsequent Aerial Oxidation

**Keywords:** Cobalt / S ligands / Metallacycles / Self-assembly

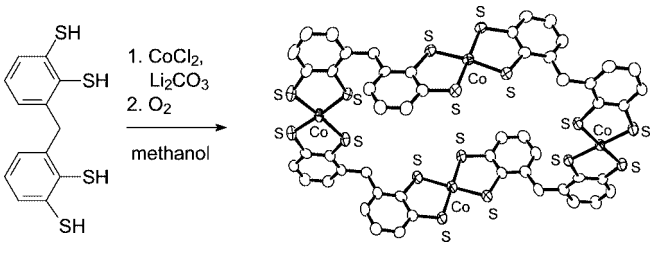



 © 2006 Wiley-VCH Verlag GmbH & Co. KGaA, Weinheim 

**540** **J. Cugny, H. W. Schmalle, T. Fox, O. Blacque, M. Alfonso, H. Berke***

Hydride Transfer Reactivity of $Mo(L)(H)(depe)_2$ (L = N, $NBEt_3$)

**Keywords:** Hydride complexes / Hydride transfer reaction / Insertion reaction / Nitride complexes / Phosphane complexes / Molybdenum

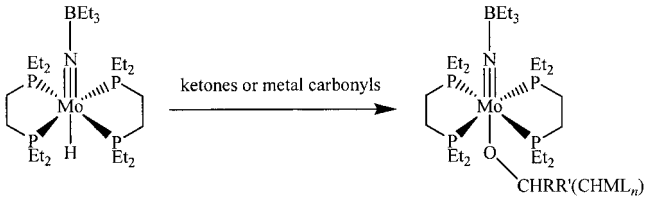


**553** **Y. V. Mironov, V. E. Fedorov,* H. Bang, S.-J. Kim***

The First Coordination Polymers Based on Octahedral Hexahydroxo Rhenium Cluster Complexes $[Re_6Q_8(OH)_6]^{4-}$ (Q = S, Se) and Alkaline Earth Metal Cations

**Keywords:** Rhenium / Synthesis / Luminescent properties / Cluster compounds

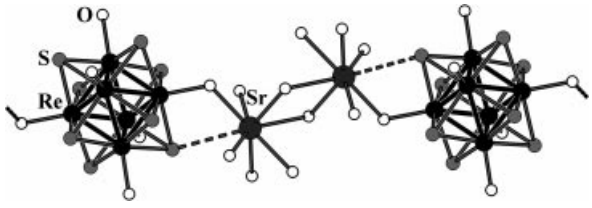


**558** **T. Mochida,* R. Torigoe, T. Koinuma, C. Asano, T. Satou, K. Koike, T. Nikaido**

Platinum-Group Chelate Complexes with 9-Hydroxyphenalenone Derivatives: Synthesis, Structures, Spectroscopic Properties and Cytotoxic Activities

**Keywords:** Platinum / Rhodium / Palladium / O ligands / Metal−metal interactions

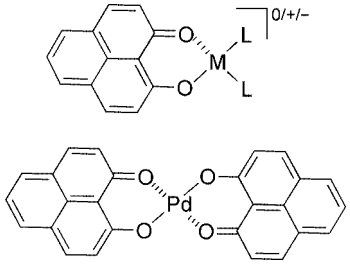


**566** **A. Goswami, Y. Nie, T. Oeser, W. Siebert***

Reactivity of Carboranylacetylenes towards Cobalt Complexes

**Keywords:** Carboranes / Carboranylacetylenes / Cobalt / (Cyclobutadiene)cobalt complexes / (Cyclopentadienone)cobalt complexes

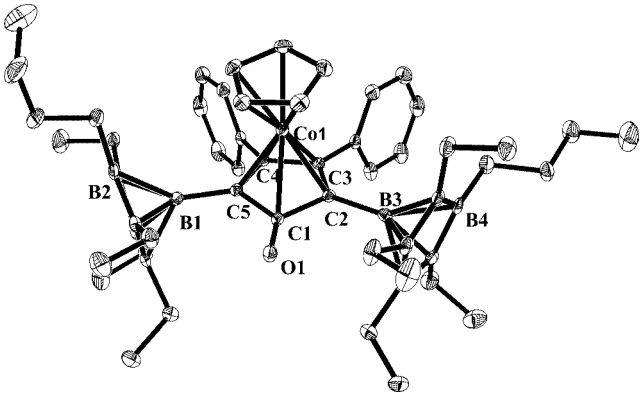


 © 2006 Wiley-VCH Verlag GmbH & Co. KGaA, Weinheim 

**573** **M. H. Klingele, P. D. W. Boyd, B. Moubaraki, K. S. Murray, S. Brooker***

Probing the Dinucleating Behaviour of a Di-Bidentate Ligand: Synthesis and Characterisation of Some Di- and Mononuclear Cobalt(II), Nickel(II), Copper(II) and Zinc(II) Complexes of 3,5-Bis(2-pyridyl)-4-(1*H*-pyrrol-1-yl)-4*H*-1,2,4-triazole

**Keywords:** 1,2,4-Triazoles / Bridging ligands / N ligands / Copper complexes / Cobalt complexes / Nickel complexes / Zinc complexes / Magnetic properties

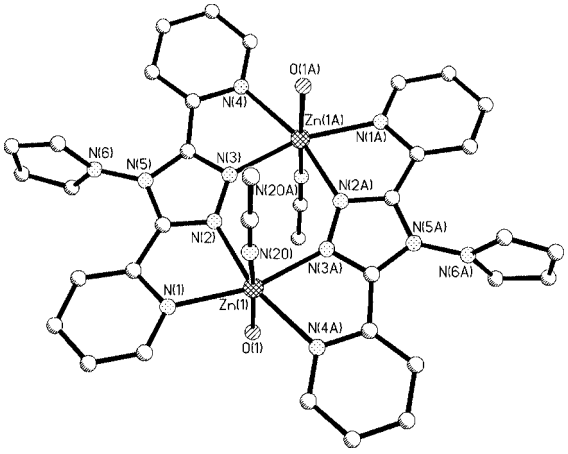


**590** **C. Makedonas, C. A. Mitsopoulou***

An Investigation of the Reactivity of [(diimine)-(dithiolato)M] Complexes Using the Fukui Functions Concept

**Keywords:** Density functional calculations / Fukui indices / Oxidation / S ligands / Schiff bases / Stacking interactions

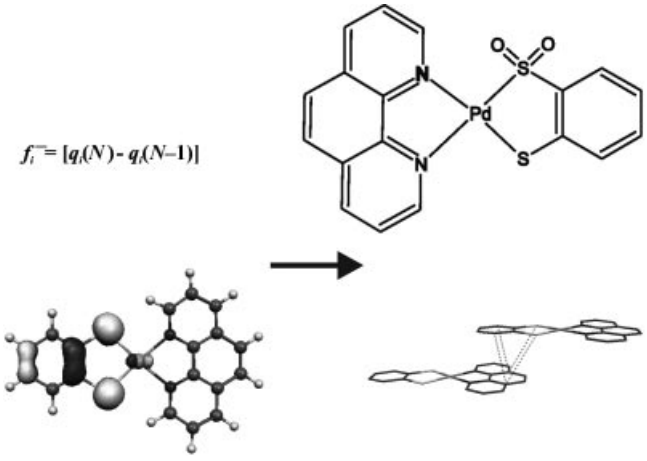


**599** **D. Cuervo, J. Díez, M. P. Gamasa,* J. Gimeno, P. Paredes**

Novel Carbonyliridium and -rhodium Complexes Containing 2,6-Bis[(4′*S*)-4′-isopropyloxazolin-2′-yl]pyridine (*i*Pr-pybox) and 2,6-Bis[(4′*R*)-4′-phenyloxazolin-2′-yl]pyridine (Ph-pybox) Ligands

**Keywords:** Carbonyl complexes / Homogeneous catalysis / Iridium / N ligands / Rhodium

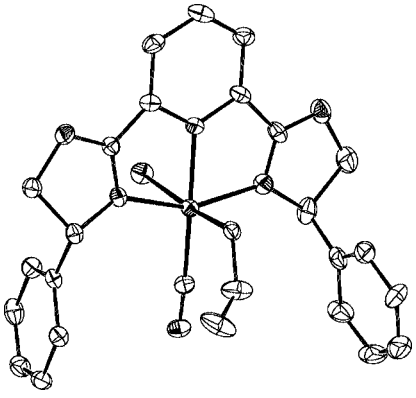

**609** **R. Koschabek, R. Gleiter,* F. Rominger**

Synthesis and Properties of Cryptands with a Thioether Bridge and π-Donors − Silver(I) and Copper(I)-Complexes

**Keywords:** Cage compounds / Alkynes / Silver / Copper

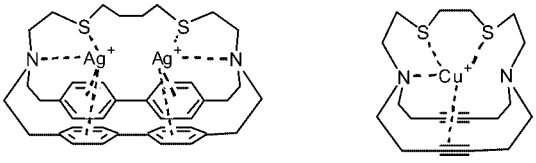



 © 2006 Wiley-VCH Verlag GmbH & Co. KGaA, Weinheim 

**621** **A. Kunze, R. Gleiter,* F. Rominger**

A Prime Example of Hard-Hard and Soft-Soft Interactions: Complexes between 4,7-Dioxa-1,10-diazabicyclo[8.6.6]docosa-13,19-diyne and $Li^+$, $Na^+$, $Cu^+$, $Ag^+$, $Cd^{2+}$, $Hg^{2+}$

**Keywords:** Cage compounds / Alkynes / Metal complexes

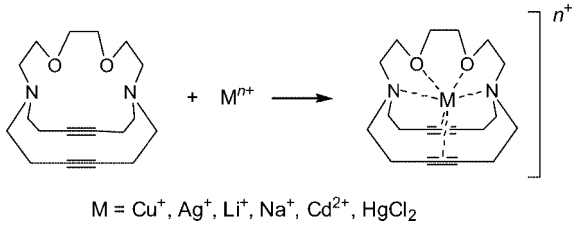


**628** **X. Ma, K. Starke, C. Schulzke,* H.-G. Schmidt, M. Noltemeyer**

Structural, Electrochemical, and Theoretical Investigations of New Thio- and Selenoether Complexes of Molybdenum and Tungsten

**Keywords:** Bioinorganic chemistry / Molybdenum / Tungsten / Ligand effects / Redox chemistry

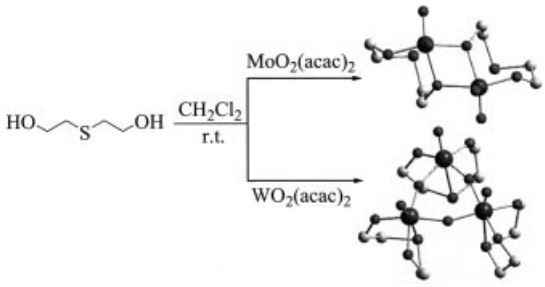


**638** **A. Doménech,* F. J. Torres, E. Ruiz de Sola, J. Alarcón**

Electrochemical Detection of High Oxidation States of Chromium(IV and V) in Chromium-Doped Cassiterite and Tin-Sphene Ceramic Pigmenting Systems

**Keywords:** Chromium / High oxidation states / Voltammetry / Cassiterite / Tin-sphene

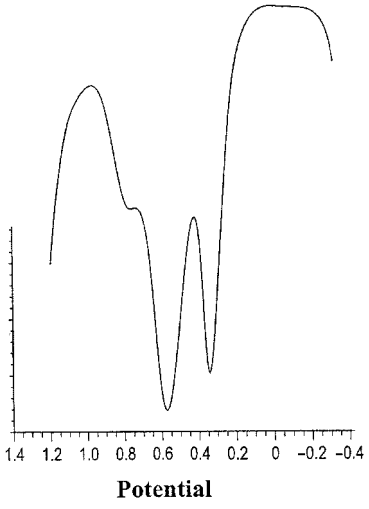


**649** **K.-H. Chang, H.-L. Sung, Y.-C. Lin***

Reactions of Furylruthenium Complexes with Oxygen and Trimethylsilyl Azide

**Keywords:** Ruthenium / Furyl ligand / Oxygen

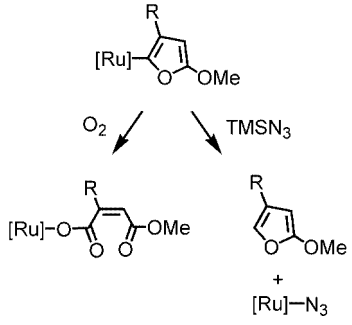


**656** **I. Correia, A. Dornyei, F. Avecilla, T. Kiss,* J. Costa Pessoa***

X-ray Crystal Structure and Characterization in Aqueous Solution of {*N*,*N*′-Ethylenebis-(pyridoxylaminato)}zinc(II)

**Keywords:** N,O ligands / Speciation / Structure elucidation / Zinc

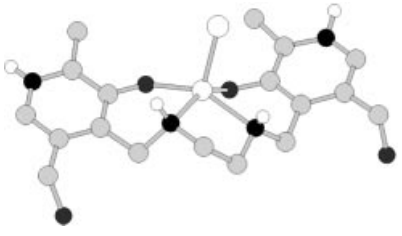


 © 2006 Wiley-VCH Verlag GmbH & Co. KGaA, Weinheim 

**663** **S. Y. Ng, L. Y. Goh,* L. L. Koh, W. K. Leong*, G. K. Tan, S. Ye, Y. Zhu**

Heterobimetallic Ruthenium-Cobalt Complexes Containing the Pentamethylcyclopentadienyl or Indenyl Ligand

**Keywords:** Heterometallic complexes / Ruthenium / Cobalt / Phosphanes / Indenyl

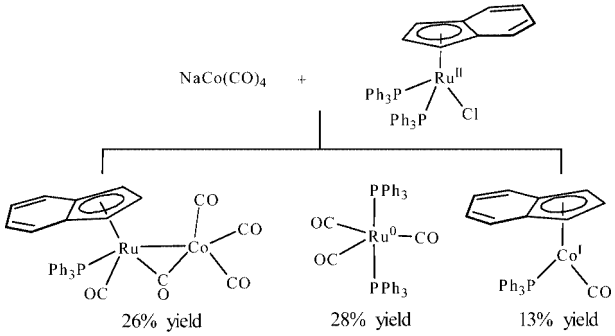


**671** **M. Merkofer, A. Domazou, T. Nauser, W. H. Koppenol***

Dissociation of CP20 from Iron(II)(cp20)$_3$: A Pulse Radiolysis Study

**Keywords:** Iron / Chelates / Reduction / Electron transfer / Kinetics

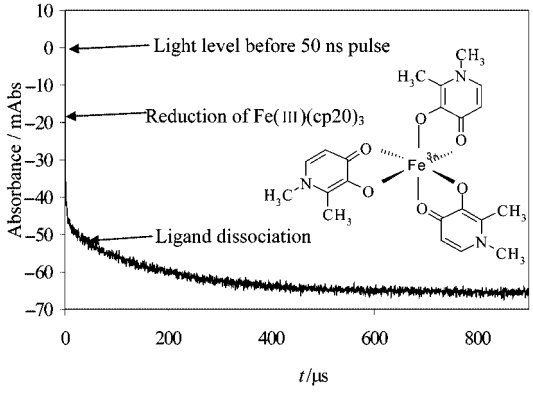


## CORRECTION

**676** **W. Niu, E. H. Wong, G. R. Weisman,* Y. Peng, C. J. Anderson, L. N. Zakharov, J. A. Golen, A. L. Rheingold**

Structural and Dynamic Studies of Zinc, Gallium, and Cadmium Complexes of a Dicarboxylate Pendant-Armed Cross-Bridged Cyclen

**Keywords:** Zinc / Gallium / Cadmium / Cyclen / Cross-bridged ligand / Pendant arms

 © 2006 Wiley-VCH Verlag GmbH & Co. KGaA, Weinheim 

DOI: 10.1002/ejic.200500768

# Structural Diversity of Host–Guest and Intercalation Complexes of Fullerene $C_{60}$

**Mohamed Makha,[a] Ariaan Purich,[a] Colin L. Raston,*[a] and Alexandre N. Sobolev[a]**

**Keywords:** Fullerenes / Crystal structures / Packing models / Host–guest interactions

Pristine fullerene $C_{60}$ has a *fcc* structure. Crystallisation of the fullerene in a variety of solvents can lead to inclusion complexes, as well as discrete host–guest complexes in the presence of cavitands and porphyrins, and related molecules. The complexes retain varying degrees of fullerene···fullerene interactions at the van der Waals limit, except in a limited number of cases where the fullerenes are completely shrouded by one or more included/host molecule. Analysis of the fullerene···fullerene interactions in these complexes reveals a diverse structural arrangement of the fullerenes. They can be organised into dimers, single linear columns or zigzag chains, double columns, spectacular fivefold Z-shaped columnar arrays, hexagonal close-packed layers, corrugated sheets, honeycomb motifs, non-close-packed layers and complex three-dimensional networks. Disorder of the fullerenes in the solid state is common, although structures with close-packed planar arrangements of $C_{60}$ molecules and/or with symmetry matching between the host molecule and the fullerene (two-, three- and fivefold symmetry) tend to have less disorder of the fullerene.
(© Wiley-VCH Verlag GmbH & Co. KGaA, 69451 Weinheim, Germany, 2006)

## Introduction

Icosahedral fullerene $C_{60}$ readily forms intercalation complexes affording materials that contain small molecules such as haloforms[1,2] through to larger molecules like ferrocene,[3] curved- or bowl-shaped receptor molecules including modified calixarenes,[4] cyclotriveratrylene and related molecules,[5] porphyrins and metal macrocycles.[6] Some of these complexes have the fullerene completely shrouded by other molecules whereby the structures are devoid of fullerene···fullerene interactions, although most of them have fullerene···fullerene interactions to varying degrees. Herein, we analyse the structures of these complexes that were previously established using X-ray diffraction techniques, focusing on the nature of the fullerene···fullerene interactions (closest contacts), on any geometrical alignment of the polyhedral faces from adjacent fullerenes and on any disorder of the fullerenes. Such aspects of the structures are often overlooked or oversimplified despite their fundamental importance in developing the supramolecular chemistry of $C_{60}$ and, ultimately, in devising ways of controlling the interplay of $C_{60}$ molecules as a paradigm in crystal engineering in building up new materials with novel function. Indeed, the supramolecular chemistry of fullerenes has been used to control the interplay of fullerenes in the solid state, and fullerenes have been covalently linked under high pressure and temperature[7] and advances have been made in the building up of arrays of $C_{60}$ that involve complexation with calix[5]arene.[8] Typically, the structure determination of fullerene complexes is carried out at ca. 150 K with no distinction between dynamic or static disorder.

General aspects of the supramolecular chemistry of fullerenes feature in various review articles;[9] these reviews include aspects of chemically modified $C_{60}$, which is beyond the scope of this review, although it is noteworthy that there have been some spectacular findings. The organization of the potassium salt of a pentasubstituted fullerene into ≈17-nm spherical bilayer vesicles,[10] the assembling of fullerenes on surfaces,[11] the binding of porphyrins[12] and assembling of 64 $C_{60}^-$ anions on the surface a dendrimer with terminal ferricinium moieties[13] are particular noteworthy. Dendrimers can also bind fullerenes within their internal cavities;[14] these include porphyrin-containing systems.[15] In addition, self-assembly processes can stabilise nanoparticles of fullerenes, such as a diblock polymer shrouding, which involves approximately $10^{10}$ fullerene molecules.[16] Fuller-

[a] School of Biomedical, Biomolecular and Chemical Sciences, University of Western Australia,
Crawley, WA 6009, Australia
Fax: +618-6488-1005
E-mail: clraston@chem.uwa.edu.au

**MICROREVIEWS:** This feature introduces the readers to the authors' research through a concise overview of the selected topic. Reference to important work from others in the field is included.

 © 2006 Wiley-VCH Verlag GmbH & Co. KGaA, Weinheim 

enes can also be taken up in the pores of mesoporous silica, with aggregation of the fullerenes in the presence of cavitand molecules. This process is the basis of a qualitative test for host–guest chemistry between the fullerene and cavitands in solution,[17] and confinement of the fullerene can be used to form hydrated $C_{60}$ at 350 °C, i.e. by controlling the synthesis in a confined space.[18] Fullerenes, including metallofullerenes such as $Sm@C_{82}$,[19] and $C_{60}O$ can also be drawn inside carbon nanotubes.

The formation of inclusion complexes of $C_{60}$ with small molecules such as solvent molecules has limited scope in building up new arrays since the relatively large fullerene molecules can still interact with several fullerenes, and fullerene···fullerene interactions dominate the extended structure. Inclusion complexes involving larger molecules tend to have less fullerene···fullerene interactions because the molecules can cover a larger part of the surface of the fullerene. The limiting case is when the fullerene is completely shrouded by other molecules, and clearly the greater the attraction between other molecules and the electron deficient $C_{60}$, the less likelihood of multiple fullerene···fullerene interactions or any such interactions. Optimising the complementarity of curvature and size of $C_{60}$ with host molecules such as bowl-shaped cavitands and saddle-shaped molecules has been used to good effect in forming assemblies of host–guest complexes as part of extended structures with fullerene···fullerene interactions, although the origins of such work relate to the use of cavitand molecules as a means of purifying the fullerene through host–guest/molecular-recognition chemistry.[4]

Matching the curvature of $C_{60}$ with that of potential host molecules is not an essential strategy for forming complexes, since planar porphyrins readily form complexes in the solid state with spheroidal fullerenes, often with the structures possessing fullerene···fullerene interactions.[20] In addition, the choice of solvent can effect the formation of host–guest complexes, tipping the balance from complexation to complexation with aggregation of the fullerenes through to little or no complexation. Even the presence of $C_{70}$ can affect the nature of the host–guest complex of $C_{60}$ with a host molecule.[23] Figure 1 summarises the main types of "host" molecules that have been used for the for-

*Dr. Mohamed Makha completed his BSc at the University Mohammed V (Morocco) and then gained a government scholarship to China for a Chinese literature diploma and a Masters degree in industrial chemistry. He also was awarded a Monash University postgraduate scholarship and completed his Ph.D. in 2001 under the supervision of Prof. Colin Raston. He then embarked on a postdoctoral fellowship at the University of Leeds (UK), and since 2004 he has been appointed to the University of Western Australia following his ARC Australian Postdoctoral Fellowship Award. His research interests are centred on macrocyclic chemistry, green chemistry, biopolymers and nanomaterials.*

*Ariaan Purich was born in Perth, Australia in 1984. She is currently completing a double degree in Science and Engineering at the University of Western Australia. She completed the science component of her degree in 2004, majoring in Chemistry. As her third year project, she researched the relationship between fullerene $C_{60}$ arrangements within different compounds and the distances between these fullerene molecules. She enjoys skiing, bungee jumping and going to the beach. Ariaan is currently completing the engineering component of her degree, majoring in Environmental Engineering.*

*Professor Colin Raston is an Australian Research Council Professorial Fellow at the University of Western Australia, being appointed to the University in 2003. He completed a Ph. D. under the guidance of Professor Allan White, and after postdoctoral studies with Professor Michael Lappert at the University of Sussex, he was appointed as Lecturer at the University of Western Australia (1981) then to the Chair of Chemistry at Griffith University (1988), being awarded a DSc there in 1993, Monash University (1995) and Leeds (2001). His research interests cover aspects of nanochemistry, supramolecular chemistry, crystal engineering and green chemistry.*

*Dr. Alexandre N. Sobolev has M.Sc. and Ph.D. degrees (1972, 1988) in "small-molecule" crystallography from the Laboratory of Crystal Chemistry and Structure Analysis at the L. Karpov Physico-Chemical Research Institute, Moscow. He moved to the University of Western Australia in 1992 to participate in advanced projects involving structural studies on a number of series of chemical compounds in various areas. Currently, the emphasis has been on the crystal chemistry of the macromolecular complexes.*

 © 2006 Wiley-VCH Verlag GmbH & Co. KGaA, Weinheim 

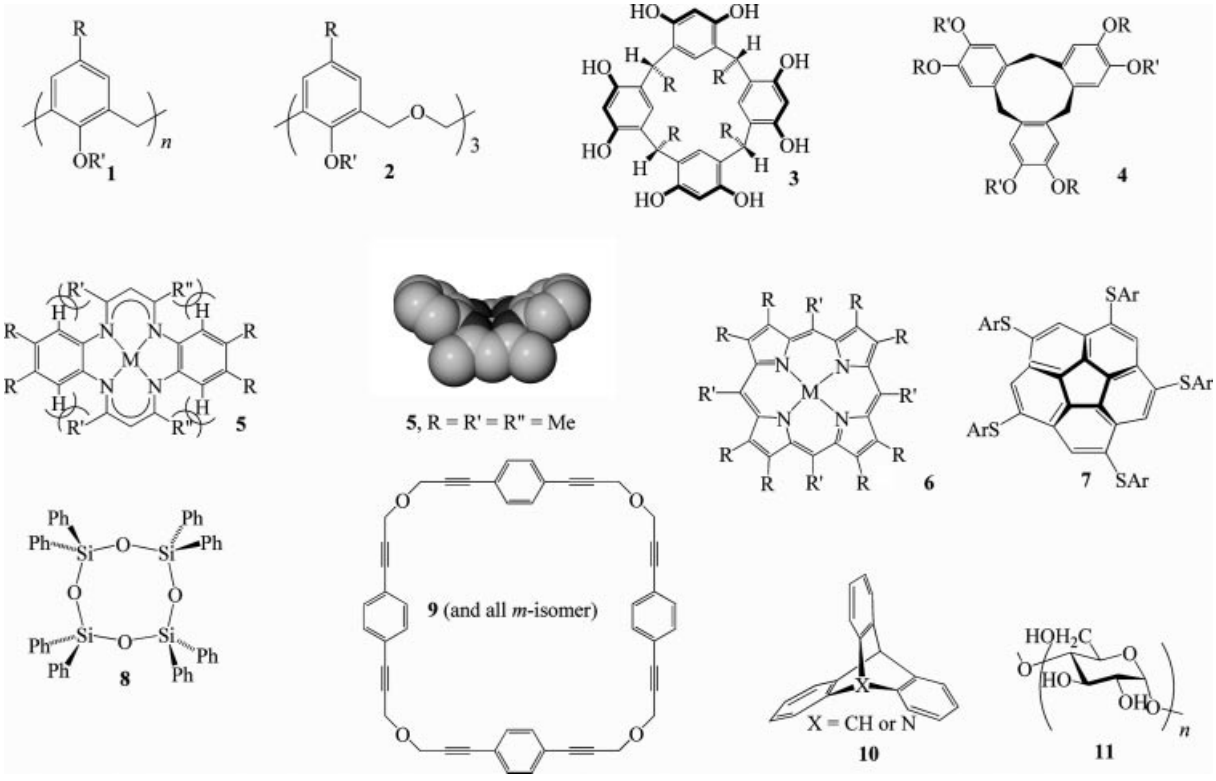


Figure 1. Types of molecules that form complexes with fullerenes with a specific example for **5** shown in space filling.

mation of complexes of $C_{60}$ and includes cavitands **1**–**4**, **7**[21] and **9**,[22] saddle-shaped molecules **5**, porphyrins **6**, siloxanes **8**, curved-faced tryptophanes **10**,[23] and β- and γ-cyclodextrins ($n$ = 7, 8) **11**, although not all of these lead to crystalline material and structure authentication by using diffraction data. When complexation is not prevalent, the addition of other synthons can be effective. For example, group 1 ions bind to modified calixarenes (R′ = ester), resulting in the complexation of $C_{60}$.[24] Seemingly, most molecules with aromatic-ring systems and electron-rich moieties can form complexes with $C_{60}$, including benzene and extended aromatic systems and tetrathiafulvalenes,[25] but the conditions to effect complexation can vary.

While the solid-state structures of many fullerene host–guest complexes of $C_{60}$ have been determined, the focus of the structures has usually been on the nature of the host–guest interplay, often with little regard to the nature of the extended structure dealing with fullerene···fullerene interactions and to the nexus to the structure of *fcc* $C_{60}$. In analysing the extended structures, the indicator for fullerene···fullerene interactions is any centroid-to-centroid distance that is close to 10.0 Å (the van der Waals limit of

Table 1. Structural types for the arrangement of $C_{60}$ molecules in the solid state.

| Structural types | Number of examples | Number of structures with ordered $C_{60}$ | Number of fullerenes with close contacts | Closest centroid···centroid fullerene distances [Å] |
|---|---|---|---|---|
| Pure $C_{60}$[26] | 8 | 0 | 12 | 9.940 |
| Encapsulated/Isolated fullerenes[27] | 37 | 8 | 0 | – |
| Dimers[28] | 7 | 1 | 2 | 9.93–10.20 |
| Single, linear columns[29] | 6 | 1 | 2 | 9.90–10.10 |
| Zigzag chains[30] | 11 | 3 | 3 | 9.90–10.20 |
| Double columns[31] | 4 | 0 | 4 | 9.90–10.00 |
| Fivefold Z-shaped columns[32] | 1 | 0 | 4–6 | 9.90 |
| Close-packed layers[33] | 10 | 5 | 6 | 9.80–10.30 |
| Nonclose-packed layers[34] | 6 | 4 | 6 | 9.80–10.30 |
| Corrugated sheets[35] | 11 | 8 | 5 | 9.90–10.30 |
| Honeycomb motif[36] | 6 | 0 | 4 | 9.90–10.00 |
| 3D continuous networks[37] | 23 | 10 | 4–6 | 9.90–10.20 |
| Total[a] | 126 | 40 | 60 | |

[a] Note that there are also twelve compounds in the appendix for which the structure is unknown because of lack of coordinate data or extreme disorder, and accordingly, are not included in the Table.

 © 2006 Wiley-VCH Verlag GmbH & Co. KGaA, Weinheim 

the fullerene). Fullerene $C_{60}$ molecules can be positioned with different combinations of five- and six-membered rings facing each other, an edge facing a ring face, or two edges facing each other. The type of positioning affects the closest carbon-to-carbon distance – and to a certain extent the centroid···centroid distance. In general, for fullerene molecules at the van der Waals limit, the closest carbon-to-carbon distances are between 3.1–3.4 Å, depending on how the fullerene molecules are oriented. Thus, analysing different $C_{60}$ arrangements also involves considering the state of order/disorder of the fullerenes. Table 1 summarises the salient information, including the number of compounds that exhibit a particular arrangement of $C_{60}$ molecules, the proportion of each arrangement in which $C_{60}$ is ordered and the proportion of each arrangement in which fullerene centroid···centroid distances are $<10.30$ Å. While this is slightly beyond the van der Waals limit, it nevertheless is a guide for the packing of the fullerenes in building up continuous structures.

## The Extreme Cases – Pristine *fcc* and Encapsulated $C_{60}$

In pure *fcc* $C_{60}$ (Figure 2), the centroid···centroid distance is 9.94 Å, and this is a reference point to compare centroid···centroid distances with complexes of the fullerene. Pure $C_{60}$ contains disordered molecules, which is not surprising given the spheroidal nature of the fullerene in the absence of any directional contacts beyond the 12 fullerene···fullerene interactions for each fullerene.[26]

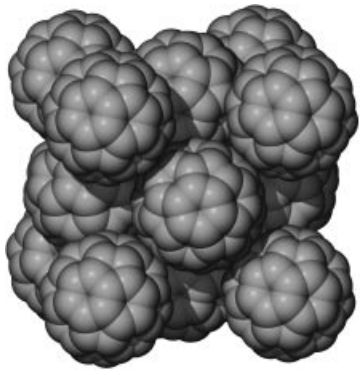

Figure 2. Space filling *fcc* for pristine $C_{60}$.[26]

In some complexes, each $C_{60}$ molecule is completely encapsulated with no intimate contact with other $C_{60}$ molecules, for example, in complexes of calix[5]arenes with *p*-substituted pendant arms (phenyl or benzyl) in which two calixarenes shroud each fullerene. For calix[5]arenes, the complementarity of size and shape of the fullerene with the cavity defined by the phenol moieties is striking. Calix[5]arene with H atoms in the *p*-positions can also form a complex in which two calixarenes interact with a central fullerene, but there is still enough room on the surface of the fullerene to allow close contacts with other fullerenes. This is part of a one-dimensional array of five columns of close-packed fullerenes in a Z-shaped array (see below).[8] This is a spectacular example of a simple change in substitution of calixarene that dramatically changes the nature of the complex.

*p*-Benzylcalix[5]arenes **1** form a 2:1 complex with $C_{60}$ in which the fullerene is shrouded by two staggered *trans* host molecules in the cone conformation with dangling benzyl groups [Figure 3(a)].[38,39] Interestingly, the symmetry axis of the calixarene is aligned with a $C_5$ symmetry-element of $C_{60}$. However, in the case of the related $C_{60}$ complex of *p*-phenylcalix[5]arene,[40] the rigid extended arms interdigitate in one hemisphere of the 2:1 supermolecule such that symmetry matching for both calixarenes is not possible, and the "confused" fullerene is now completely disordered.[40] Other authenticated structures in which $C_{60}$ is encapsulated by two calix[5]arenes such that there are no interfullerene contacts include a calix[5]arene complex with three methyl and two iodo groups (1,3-disposition) in the *p*-positions of the upper rim.[41]

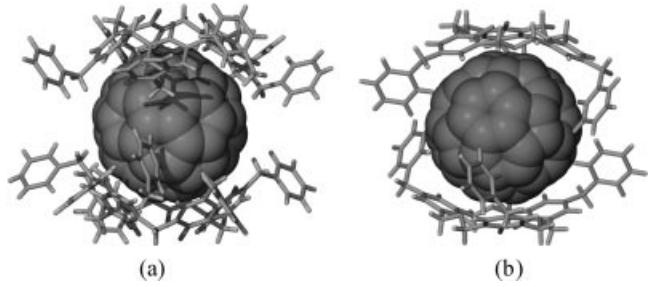


Figure 3. Encapsulation of single fullerene $C_{60}$. Structure of (a) [$C_{60}$⊂{*p*-benzylcalix[5]arene}$_2$] and (b) [$C_{60}$⊂{*p*-benzyloxacalix[3]arene}$_2$].[38]

Oxacalix[3]arenes **2** also have complementarity of curvature with $C_{60}$, and *p*-benzyloxacalix[3]arene similarly forms a 2:1 complex in which two calixarenes shroud the fullerene. Here, a $C_3$ symmetry-axis of $C_{60}$ lines up with the symmetry axis of the two host molecules in the *trans* arrangement, i.e. the fullerene is not disordered at the temperature at which the diffraction data were acquired, ca. 173 K.[38] The benzyl groups are edge-on to the fullerene, with C–H···fullerene interactions [Figure 3(b)], rather than face-on for π···π interactions, or the benzyl groups are directed away from the fullerene such as in the structure of the analogous *p*-benzylcalix[5]arene complex.[38] Clearly, symmetry matching is a worthwhile endeavour to afford ordered fullerene molecules in the solid state, at least at low temperature (ca. 173 K).

## Dimeric Arrangement of $C_{60}$ Molecules

In a few cases, $C_{60}$ molecules are confined as pairs at the van der Waals limit (9.93–10.20 Å).[28] Only one compound has ordered fullerenes at the temperature of the X-ray diffraction studies. A striking feature of the 1:1 *p*-bromohomooxocalix[3]arene $C_{60}$ complex is the relatively small

 © 2006 Wiley-VCH Verlag GmbH & Co. KGaA, Weinheim 

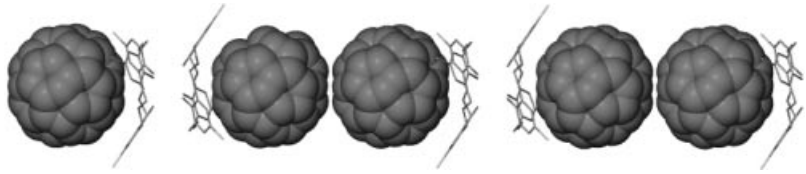

Figure 4. Inclusion complex $C_{60}$ as van der Waals dimers sandwiched by two *p*-bromo-homooxocalix[3]arene molecules.[43]

calixarene that disrupts the interfullerene interactions. Isolated pairs of fullerenes have π···π interactions with the calixarenes, with distances between the centroids within the pairs of fullerenes of 9.93 Å. The cup shape of the calixarene and possible polarization effects from the bromine substituents presumably impact on the overall structure, which consists of the stacking of the dimeric columns as represented by the top view projection with no other fullerene···fullerene close contact other than that of the dimers, Figure 4.[43] While a trimeric aggregate of $C_{60}$ molecules have been proposed for the structure of the 1:1 complex of $C_{60}$ with *p*-*t*Bu-calix[8]arene,[42] its solid-state structure authentication remains elusive, and the same can be said of higher arrays. For the dimeric arrangement, there are only a couple of structures in which the fullerene molecules are ordered.

## Single Linear Columns

A common arrangement of $C_{60}$ molecules is as single linear columns with each fullerene in close contact to two fullerenes and the dihedral angle set at 180°. All structures have disordered fullerene molecules, and the fullerenes are at the van der Waals limit (10.1 Å) (Figure 5).[44]

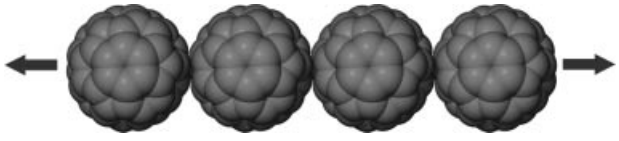

Figure 5. Single column arrays of $C_{60}$ found in the structure of bis(1,3,5-triphenylbenzene)chlorobenzene clathrate; fullerene centroid-to-centroid distances: 10.10 Å.[44]

## Zigzag Chains

$C_{60}$ molecules can be organised into continuous zigzag chains, with varying $C_{60}$–$C_{60}$ close contacts (9.90–10.20 Å). These chains are similar to linear columns, but with the $C_{60}$ molecules offset with respect to each other and with the dihedral angle <180°. The dihedral angle ranges from 118 to 172° thus presenting the intermediate structures between linear-chains and double-column arrangements. There are more zigzag-chain structures than linear-column structures of $C_{60}$, and the proportion of ordered structures is much higher (Table 1). It is interesting that the zigzag chains (and corrugated sheets, see below) contain higher proportions of $C_{60}$ centroid-to-centroid distances that are at the lower end of the van der Waals limits than linear columns and planar layers. This suggests that the zigzag arrangement of fullerenes encourages fullerene···fullerene interactions more than the linear counterparts.

The 1:1 complex between $C_{60}$ and CTV (cyclotriveratrylene; **4**, R = R′ = Me), and the recent structure of the 1:1 complex of calix[5]arene and $C_{60}$ (Figure 6), form zigzag structures. It is interesting to note that the CTV complex forms in toluene in the presence of a saturated solution of CTV (approximately 20-fold excess of CTV relative to the fullerene), whereas a fivefold excess of CTV gives a 3:2 complex that is rich in $C_{60}$ and the fullerenes are arranged in close-packed, hexagonal sheets (see below).

## Double Columns (Close Packed)

A few examples of $C_{60}$ complexes crystallising with the fullerenes arranged into two close-packed columns have been authenticated. This is the limiting case for zigzag chains in which the dihedral angle between the fullerenes is 60° and each fullerene is in close contact with four other

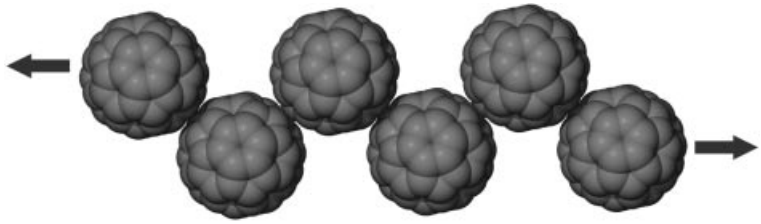

Figure 6. Zigzag fullerene arrangement in the structure of [$C_{60}${calix[5]arene}]; fullerene centroid-to-centroid distances: 10.03 Å.[8]

 © 2006 Wiley-VCH Verlag GmbH & Co. KGaA, Weinheim 

fullerenes rather than with two (Figure 7). All of the complexes have some level of disorder, and the fullerene arrangement is depicted for the siloxane/$C_{60}$-fullerene complex in which each fullerene is surrounded by four others with centroid···centroid distances of 9.85–10.10 Å.[45]

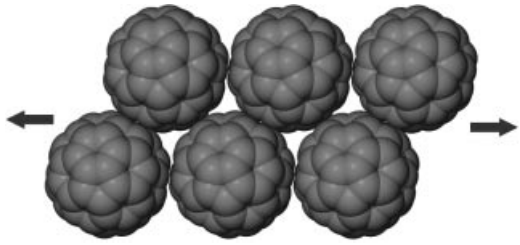

Figure 7. The double-columnar array in a siloxane/$C_{60}$-fullerene complex; centroid···centroid distances: 9.85–10.1 Å.[45]

## Fivefold Z-Shaped Columns (Close Packed)

Calix[5]arene **1**, $n$ = 5, R = R′ = H, forms a unique complicated complex with $C_{60}$, $[(C_{60})_5\{\text{calix[5]arene}\}_4]$,[32] in which the fullerenes assemble into five columns in a Z-arrangement [Figure 8(a)], which are surrounded by a sheath of calixarenes. The fullerenes are close packed in the columns with three different fullerene environments [Figure 8(b)]: (i) those on the outer columns, and each fullerene is in contact with four other fullerenes (cf. the environment the fullerene in the double-column arrangement, Figure 7), (ii) those in the two nearest columns of the bend of the "Z" shape, where the fullerenes have six close contacts, and (iii) the central column where each fullerene also has six close fullerenes, albeit now in a flat hexagonal arrangement. On the basis of analytical data, prior to the structure determination, the complex was thought to be a 1:1 complex rather than a 5:4 complex, and in this context, care needs to be exercised in establishing the stoichiometry of fullerene host–guest complexes in the absence of structural elucidation. Moreover, the presence of other fullerenes, and other globular molecules in solution, dramatically changes the nature of the complex that crystallises from solution. In the presence of $C_{70}$, which is the other major fullerene in fullerite, a 1:1 calixarene: $C_{60}$ complex forms (see above).[8] Remarkably no $C_{70}$ is incorporated into the structure, but it still predetermines the nature of the $C_{60}$ complex formed. This is despite the solution binding constants that favour $C_{70}$ complexation over that of $C_{60}$, and thus crystal packing forces must be more important. The same 1:1 complex involving $C_{60}$ also forms in the presence of $C_{84}$ and 1,2-dicarborane ($1,2\text{-}C_2B_{10}H_{12}$), an icosahedral molecule, which in the absence of $C_{60}$ is drawn into the cavity of the calixarene.[46]

## Close-Packed Layers

The structure of these 2D arrays takes on some aspects of the structure of *fcc* for pure $C_{60}$. Hexagonal close packing of the fullerene molecules occurs in several structures with fullerene···fullerene centroid-to-centroid distances of 10.0–10.2 Å (Figure 9). In comparison to other $C_{60}$ arrangements, the proportion of structures in this category is relatively low, despite the fact that hexagonal close packing is a common arrangement for two-dimensional arrays of spheroidal moieties. Within these structures, the $C_{60}$ molecules tend to be ordered, and in some cases, this relates to the interplay of the fullerenes with inclusion/host molecules on either side of the hexagonal arrays, as in the complex with CTV (see below).[47]

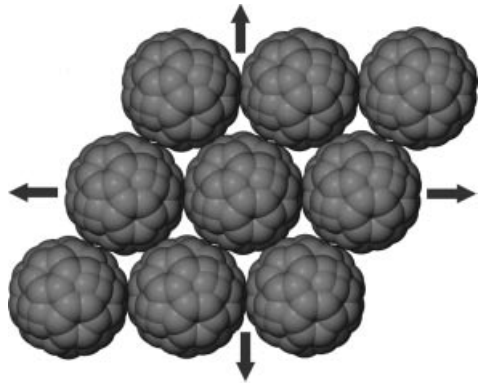

Figure 9. Hexagonal close-packed $C_{60}$ fullerenes in $(C_{60})_{1.5}$(CTV); centroid-to-centroid distances: 10.00 –10.2 Å.[47]

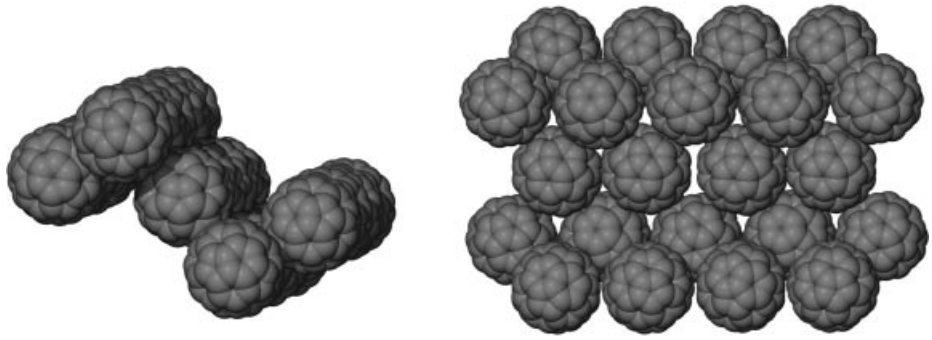

(a) (b)

Figure 8. (a) Projection of the fivefold Z-shaped arrangement of fullerenes in $[(C_{60})_5\{\text{calix[5]arene}\}_4]$, and (b) the projection normal to this; closest centroid-to-centroid distances: 9.88 Å.[32]

 © 2006 Wiley-VCH Verlag GmbH & Co. KGaA, Weinheim 

Complexation of $C_{60}$ in toluene solutions of CTV (**4**, R = R′ = Me) results in polymeric structures in the solid state, with either a fullerene-rich phase $(C_{60})_{1.5}$(CTV) or a 1:1 phase $(C_{60})$(CTV)[47,48] (Figure 9); both complexes were studied electrochemically (solution and solid state). The structures are dominated by fullerene···fullerene interactions, and each CTV has a $C_{60}$ that is associated within the cavity of the CTV as a "ball and socket" nanostructure. For $(C_{60})_{1.5}$(CTV), the fullerenes collectively comprise a two-dimensional, close-packed array with half of the fullerenes devoid of CTV (Figure 9).[47] Disorder is found for the fullerenes that are not capped by CTV, while the fullerenes included in the cavity of CTV are stabilised and show order. Solvated host–guest species of (CTV)$(C_{60})$ are formed first in solution, and this results in the polarisation of the fullerene that promotes aggregation, which is evident by a resonant interfullerene transition band as 475 nm. Interestingly, $C_{70}$ does not form an isolable complex with CTV, yet remarkably in the presence of 1,2-dicarborane, a ternary complex forms, with each fullerene in the cavity of a CTV molecule and with each of these supermolecules linked by bifurcated H-bonding to two carborane molecules, thus forming a helical arrangement. Therefore, additional synthons can encourage host–guest chemistry.[49]

## Corrugated Sheets

$C_{60}$ molecules can also form corrugated sheets in a manner that is similar to layering. In this arrangement, the $C_{60}$ molecules form layers, but these layers are not planar. From a side-on view, these sheets look like zigzag arrangements. Corrugated sheets are also a common arrangement for $C_{60}$ molecules, and a very high proportion of the compounds that exhibit this structure exhibit fullerene···fullerene close contacts, and this fact indicates that these molecules are at the van der Waals limits. Hence, it can be concluded that when $C_{60}$ molecules are arranged in corrugated layers, as opposed to planar layers, close contact between the fullerenes is encouraged. Corrugated-sheet structures also have a high proportion of ordered compounds.

Non-aromatic macrocycles **5** have two divergent concave surfaces in a saddle-shape arrangement that arises from the otherwise unfavourable interactions between the methyl groups and the adjacent H-atoms on the aromatic rings. This arrangement can act as a divergent heterotopic receptor towards $C_{60}$. In the structure of $(C_{60})$Ni(TMTAA) (**5**, R = H, R′ = R′′ = Me), two host molecules shroud the fullerene such that a fullerene is in the saddle of one Ni(TMTAA) molecule with the methyl groups directed towards it and in the opposite saddle of another Ni(TMTAA) molecule; the overall host–guest contacts form a continuous zigzag array in which the fullerenes form a corrugated two-dimensional sheet (Figure 10).[50] $Cu^{II}$ and $Zn^{II}$ TMTAA molecules bind $C_{60}$ in a similar fashion and are isostructural with the $Ni^{II}$ analogue. OMTAA (**5**, R = Me) forms a 1:1 complex with $C_{60}$ in which the extended supramolecular array is based on linear chains of close-contact $C_{60}$ molecules and on linear chains of π-stacked alternating molecules of $C_{60}$ and Ni(OMTAA) in which the adjacent chains run in opposite directions and thus cancel out the dipole moments. The same macrocycle forms a 1:1 complex with $C_{70}$, which is isostructural with the $C_{60}$ complex of Ni(TMTAA). In all of these $Ni^{II}$ macrocyclic structures, there are no significant contacts between the metal centres and the fullerenes. As in other systems, there is evidence for the formation of 1:1 solvated supermolecules in solution, which then go on to form micelle-like species.[50] The unsymmetrical macrocycle **5** (R = H, R′ = Me, R′′ = Ph) also forms a 1:1 complex with $C_{60}$.[51]

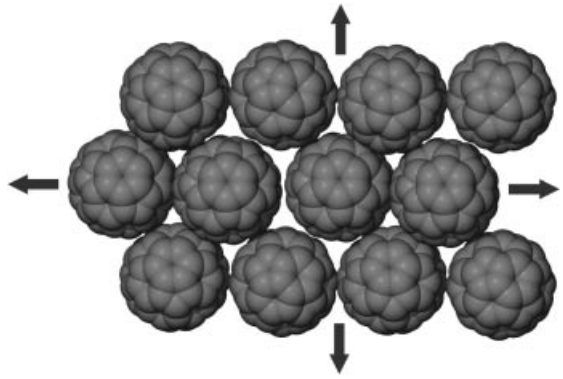

Figure 10. The corrugated array of fullerenes in the Ni(TMTAA)/$C_{60}$ complex; centroid-to-centroid distances: 9.99 to10.07 Å.[50]

## Honeycomb Motif

An unusual arrangement of the $C_{60}$ molecules is one in which the fullerene molecules form a honeycomb motif as shown in Figure 11.[52] Few compounds exhibit this type of arrangement, and in most cases, these structures have disordered fullerenes.[36]

Figure 11. The honeycomb arrangement of $C_{60}$ molecules in 5,10,15,20-tetraphenylporphyrin bis($C_{60}$-fullerene) benzene solvate; centroid-to-centroid distances: 9.98 Å.[52]

## 3D Continuous Networks of $C_{60}$

The arrangement of fullerenes in fullerene-$C_{60}$ complexes can have continuous three-dimensional networks. Some are

 © 2006 Wiley-VCH Verlag GmbH & Co. KGaA, Weinheim 

simply analogues of the *fcc* packing of pristine $C_{60}$. Indeed, the simplest structure is one in which the *fcc* packing is maintained and small molecules are included in the interstices, for example ethene (Figure 12).[53] For larger molecules, other arrangements are possible. Alternatively, other close-packed arrangements can result, notably *bcc* packing found in the ethane complex.[53]

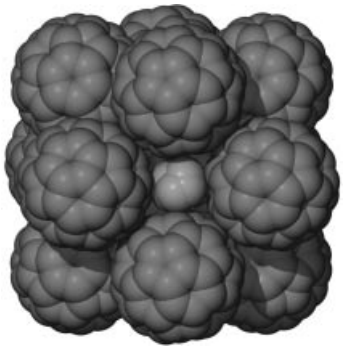

Figure 12. The *fcc* arrangement in the ethene inclusion complex with $C_{60}$; centroid-to-centroid distances: 10.03 Å.[53]

Other continuous three-dimensional arrangements are more complex, often, with more included molecules, for example, the carbon disulfide complex $C_{60}{\cdot}1.5CS_2$ (Figure 13).[54]

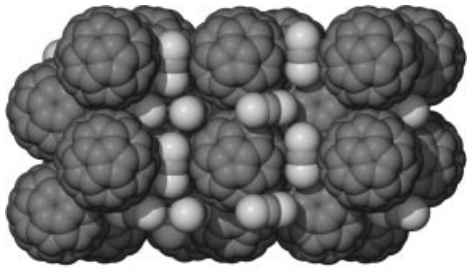

Figure 13. Continuous array in the $C_{60}$-fullerene carbon disulfide solvate ($C_{60}{\cdot}1.5CS_2$); closest centroid-to-centroid distances: 9.96 Å.[54]

From Table 1, it is evident that three-dimensional arrangements are more prevalent and by their very nature have more interfullerene contacts at the van der Waals limits. Intersecting sheets of fullerenes with moderately sized molecules creating channels are possible; this is exemplified by the structures in Figure 14.[55]

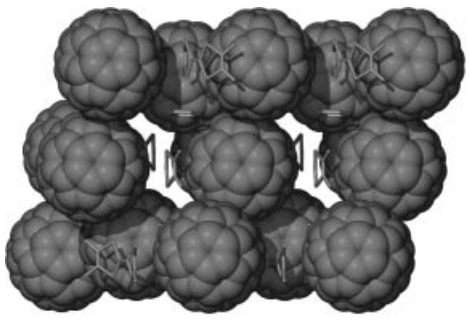

Figure 14. Structure of $C_{60}$-fullerene/tetramethyltetraselenafulvalene benzene solvate; centroid-to-centroid distances: 9.80 Å.[55]

## Higher Complexity Structural Motifs

The structures here are based on complexes containing large host/included molecules. The fullerene rich calix[6]arene complexes, $(C_{60}/C_{70})_2$calix[6]arene, have been structurally authenticated as isomorphous complexes,[56] and exhibit the calixarene in a double-cone conformation and a fullerene perched in each of the shallow cavities – this arrangement resembles the jaws of a pincer acting on two adjacent cage molecules; the extended structures have continuous three-dimensional interplay of the fullerenes that is close to the van der Waals limit. In the case of the $C_{70}$ complex, the principle axis of the fullerene is aligned such that the end of the fullerene that is close to this axis, where the curvature of the cage is similar to that of $C_{60}$, resides in the cavity.

Calix[4]arenes and Calix[4]resorcinarenes have cavities that are too small to accommodate fullerenes. Nevertheless, some calix[4]arenes have been shown to form stable crystalline complexes with $C_{60}$ with the fullerene *exo* to the calixarene cavity, and include: (i) *p*-phenyl-calix[4]arene, which has a toluene molecule in the cavity; the overall structure is dominated by fullerene–fullerene and *exo*-calixarene–fullerene interactions,[57] (ii) *p*-bromo-calix[4]arene propyl ether – the structure shows very close interfullerene contacts in a columnar structure, which most likely results in opposing induced dipoles from the unidirectionally aligned calixarenes,[58] and (iii) *p*-iodo-calix[4]arene benzyl ether – the fullerenes are ordered without appreciable interfullerene interactions.[59] There is also calix[4]resorcinarene **3** (R = $CH_2CH_2Ph$), which has a molecular capsule derived from head-to-head hydrogen bonding of two resorcinarene and propan-2-ol molecules – the fullerenes are also arranged in columns.[60] Biscalix[4]resorcinare is effective in binding $C_{60}$ (cf. biscalixarenes, Figure 4),[61] and calix[4]resorcinarenes (**3**) that bear dithiocarbamate groups between the oxo groups, with R = alkyl chains and with methylene groups between adjacent oxo groups form torus-shaped complexes that comprise three calixarenes with divalent cadmium and zinc ions, which effectively bind $C_{60}$.[62]

The fourfold symmetry of calixarenes and resorcinarenes relates to complexation of siloxane **8** with $C_{60}$ in toluene.[49,59,60] Here, the fullerenes are arranged in double-columnar arrays and are shrouded by edge-on siloxanes – the siloxanes are interlocked by one of the phenyl groups of one molecule residing in the cavity of another.

Bulky groups incorporated into porphyrin **6** [R = H, R′ = $C_6H_3$-3,5-($t$Bu)$_2$] result in a 1:1 complex with $C_{60}$, but there is a fullerene on either side of the porphyrin such that the continuous structure has the fullerene encapsulated.[63]

## Conclusion and Prospects

Structural analysis reveals a diverse range of structures; in some cases, these structures appear regularly, whilst others are represented by a single example. Even with prior knowledge on the composition of fullerene $C_{60}$ complexes, it is difficult to predict the arrangement of fullerenes given the inherently weak interactions between the components

 © 2006 Wiley-VCH Verlag GmbH & Co. KGaA, Weinheim 

and the delicate balance between fullerene···fullerene interactions and host···fullerene interactions. Predicting the outcome of crystallization with respect to host/guest ratios and the arrangement between the components is even more problematic, and this is compounded by the effect of other solutes on the complexes formed that are still not an integral part of the structure. Greater structural diversity is anticipated along with higher complexity of the structures, although full characterization of such complexes using diffraction data will be a major challenge. Compounds in which the $C_{60}$ molecules are arranged in planar layers contain the highest levels of order of the fullerenes, and, in general, structures in which there is symmetry matching between the host and the fullerene reduces the disorder of the fullerene at low temperature. Arrays of fullerenes can be completely shrouded by a sheath of host molecules. The reverse is possible whereby the "host molecules" can reside in channels formed by a continuous array of fullerenes at the van der Waals limit. Clearly designing host molecules to bind fullerenes in cavities is now well established, but unless the fullerene is completely shrouded by host molecules, predicting the interplay of the fullerenes has serious limitations.

## Acknowledgments

We thank the Australian Research Council for support of this work.

[1] M. Jansen, G. Waidmann, *Z. Anorg. Allg. Chem.* **1995**, *621*, 14.
[2] R. E. Dinnebier, O. Gunnarsson, H. Brumm, E. Koch, P. W. Stephens, A. Huq, M. Jansen, *Science* **2002**, *296*, 109.
[3] J. D. Crane, P. B. Hitchcock, H. W. Kroto, R. Taylor, D. R. M. Walton, *J. Chem. Soc., Chem. Commun.* **1992**, 1764.
[4] J. L. Atwood, G. A. Koutsantonis, C. L. Raston, *Nature* **1994**, *368*, 229; J. L. Atwood, L. J. Barbour, C. L. Raston, *Cryst. Growth Des.* **2002**, *2*, 3; T. Haino, Y. Yamanaka, H. Araki, Y. Fukazawa, *Chem. Commun.* **2002**, 402; J. Wang, S. G. Bodige, W. H. Watson, C. D. Gutsche, *J. Org. Chem.* **2000**, *65*, 8260.
[5] J. L. Atwood, M. J. Barnes, M. G. Gardiner, C. L. Raston, *Chem. Commun.* **1996**, 1449; J. L. Atwood, M. J. Barnes, R. S. Burkhalter, P. C. Junk, J. W. Steed, C. L. Raston, *J. Am. Chem. Soc.* **1994**, *116*, 10346; D. Felder, B. Heinrich, D. Guillon, J.-F. Nicoud, J.-F. Nierengarten, *Chem. Eur. J.* **2000**, *6*, 3501; H. Matsubara, S. Oguri, K. Asano, K. Yamamoto, *Chem. Lett.* **1999**, 431.
[6] T. Ishii, N. Aizawa, R. Kanehama, M. Yamashita, K. Sugiura, H. Miyasaka, *Coord. Chem. Rev.* **2002**, *226*, 113; A. L. Balch, M. M. Olmstead, *Coord. Chem. Rev.* **1999**, *185–186*, 601.
[7] D. Sun, C. A. Reed, *Chem. Commun.* **2000**, 2391–2392.
[8] J. L. Atwood, L. J. Barbour, M. W. Heaven, C. L. Raston, *Angew. Chem. Int. Ed.* **2003**, *42*, 3257.
[9] C. L. Raston, "Complexation of Fullerenes", in *Comprehensive Supramolecular Chemistry* (Eds.: J. L. Atwood, J. E. D. Davies, D. D. Macnicol, F. Vögtle), Pergamon, Oxford, **1996**, vol. 1, 777–787; M. J. Hardie, C. L. Raston, *Chem. Commun.* **1999**, 1153–1163; T. Ishii, N. Aizawa, R. Kanehama, M. Yamashita, K. Sugiura, H. Miyasaka, *Coord. Chem. Rev.* **2002**, *226*, 113–124; F. Diederich, M. Gomez-Lopez, *Chem. Soc. Rev.* **1999**, *28*, 263–277; D. V. Konarev, R. N. Lyubovskaya, N. V. Drichko, *J. Mater. Chem.* **2000**, *10*, 803.
[10] S. Zhou, C. Burger, B. Chu, M. Sawamura, N. Nagahama, M. Toganoh, U. E. Hackler, H. Isobe, E. Nakamura, *Science* **2001**, *291*, 1944–1946.
[11] D. M. Guldi, N. Martin, *J. Mater. Chem.* **2002**, *12*, 1978–1992.
[12] D. V. Konarev, S. S. Khasanov, A. Otsuka, Y. Yoshida, G. Saito, *J. Am. Chem. Soc.* **2002**, *124*, 7648–7649.
[13] J. Ruiz, C. Pradet, F. Varret, D. Astruc, *Chem. Commun.* **2002**, 1108–1109.
[14] J. P. Majoral, A. M. Caminade, *Chem. Rev.* **1999**, *99*, 845–880; J. F. Nierengarten, L. Oswald, J. F. Eckert, J. F. Nicoud, N. Armaroli, *Tetrahedron Lett.* **1999**, *40*, 5681–5684.
[15] M. Ayabe, A. Ikeda, Y. Kubo, M. Takeuchi, S. Shinkai, *Angew. Chem. Int. Ed.* **2002**, *41*, 2790–2792; M. Kimura, Y. Saito, K. Hanabusa, H. Shiral, N. Kobayashi, *J. Am. Chem. Soc.* **2002**, *124*, 5274–5275.
[16] S. A. Jenekhe, X. L. Chen, *Science* **1998**, *279*, 1903–1906.
[17] M. J. Hardie, C. L. Raston, *Chem. Commun.* **1999**, 1153–1163.
[18] K. Moller, T. Bein, *Chem. Mater.* **1998**, *10*, 2950–2963.
[19] T. Okazaki, K. Suenaga, K. Hirahara, S. Banow, S. Iijima, H. Shinohara, *J. Am. Chem. Soc.* **2001**, *123*, 9673–9674.
[20] D. Sun, F. S. Tham, C. A. Reed, L. Chaker, P. D. W. Boyd, *J. Am. Chem. Soc.* **2002**, *124*, 6604.
[21] S. Mizyed, P. E. Georghiou, M. Bancu, B. Cuadra, A. K. Rai, P. Cheng, L. T. Scott, *J. Am. Chem. Soc.* **2001**, *123*, 12770–12774.
[22] Y. Yamaguchi, S. Kobayashi, N. Amita, T. Wakamiya, *Tetrahedron Lett.* **2002**, *43*, 3277–3280.
[23] E. M. Veen, P. M. Postma, H. T. Jonkman, A. L. Spek, B. L. Feringa, *Chem. Commun.* **1999**, 1709–1710.
[24] A. Ikeda, Y. Suzuki, M. Yoshimura, S. Shinkai, *Tetrahedron* **1998**, *54*, 2497–2508.
[25] D. V. Konarev, A. Y. Kovalevsky, P. Coppens, R. N. Lyubovskaya, *Chem. Commun.* **2000**, 2358–2359.
[26] H.-B. Burgi, E. Blanc, D. Schwarzenbach, S. Liu, Y.-J. Lu, M. M. Kappes, J. A. Ibers, *Angew. Chem. Int. Ed. Engl.* **1992**, *31*, 640.
[27] T. Ishii, N. Aizawa, R. Kanehama, M. Yamashita, H. Matsuzaka, T. Kodama, K. Kikuchi, I. kemoto, *Inorg. Chim. Acta* **2001**, *317*, 81; H. Matsubara, A. Hasegawa, K. Shiwaku, K. Asano, M. Uno, S. Takahashi, K. Yamamoto, *Chem. Lett.* **1998**, 923; S. Mizyed, M. Ashram, D. O. Miller, P. E. Georghiou, *J. Chem. Soc., Perkin Trans. 2* **2001**, 1916; D. V. Soldatov, P. R. Diamente, C. I. Ratcliffe, J. A. Ripmeester, *Inorg. Chem.* **2001**, *40*, 5660; M. M. Olmstead, D. A. Costa, K. Maitra, B. C. Noll, S. L. Phillips, P. M. Van Calcar, A. L. Balch, *J. Am. Chem. Soc.* **1999**, *121*, 7090; J. L. Atwood, L. J. Barbour, P. J. Nichols, C. L. Raston, C. A. Sandoval, *Chem. Eur. J.* **1999**, *5*, 990; A. L. Balch, M. M. Olmstead, *Coord. Chem. Rev.* **1999**, *1858*, 601; J. Wang, S. G. Bodige, W. H. Watson, C. D. Gutsche, *J. Org. Chem.* **2000**, *65*, 8260; D. V. Konarev, A. Y. Kovalevsky, X. Li, I. S. Neretin, A. L. Litvinov, N. V. Drichko, Y. L. Slovokhotov, P. Coppens, R. N. Lyubovskaya, *Inorg. Chem.* **2002**, *41*, 3638; T. Ishii, N. Aizawa, M. Yamashita, H. Matsuzaka, T. Kodama, K. Kikuchi, I. Ikemoto, Y. Iwasa, *J. Chem. Soc., Dalton Trans.* **2000**, 4407; E. Blanc, R. Restori, D. Schwarzenbach, H.-B. Burgi, M. Fortsch, P. Venugopalan, O. Ermer, *Acta Crystallogr., Sect. B: Struct. Sci.* **2000**, *56*, 1003; T. Ishii, R. Kanehama, N. Aizawa, M. Yamashita, H. Matsuzaka, K. Sugiura, H. Miyasaka, T. Kodama, K. Kikuchi, I. Ikemoto, H. Tanaka, K. Marumoto, S. Kuroda, *J. Chem. Soc., Dalton Trans.* **2001**, 2975; T. Haino, M. Yanase, Y. Fukazawa, *Angew. Chem. Int. Ed. Engl.* **1997**, *36*, 259; V. V. Kveder, E. A. Steinman, B. Z. Narymbetov, S. S. Khasanov, L. P. Rozenberg, R. P. Shibaeva, A. V. Bazhenov, A. V. Gorbunov, M. Y. Maksimuk, D. V. Konarev, R. N. Lyubovskaya, Yu. A. Ossipyan, *Chem. Phys.* **1997**, *216*, 407; M. Jansen, G. Waidmann, *Z. Anorg. Allg. Chem.* **1995**, *621*, 14; K. N. Rose, L. J. Barbour, G. W. Orr, J. L. Atwood, *Chem. Commun.* **1998**, 407; D. H. Hochmuth, S. L. J. Michel, A. J. P. White, D. J. Williams, A. G. M. Barrett, B. M. Hoffman, *Eur. J. Inorg. Chem.* **2000**,

 © 2006 Wiley-VCH Verlag GmbH & Co. KGaA, Weinheim 

593; M. Fedurco, M. M. Olmstead, W. R. Fawcett, *Inorg. Chem.* **1995**, *34*, 390; N. G. Spitsina, V. V. Gritsenko, O. A. D'yachenko, B. B. Safoklov, Y. M. Shul'ga, E. B. Yagubskii, *Izv. Akad. Nauk SSSR, Ser. Khim.(Russ.) (Russ. Chem. Bull.)* **2000**, 365; A. L. Balch, K. Maitra, M. M. Olmstead, Private Communication, **2000**; A. Arrais, E. Diana, R. Gobetto, M. Milanesio, D. Viterbo, P. L. Stanghellini, *Eur. J. Inorg. Chem.* **2003**, 1186; L. J. Barbour, G. W. Orr, J. L. Atwood, *Chem. Commun.* **1997**, 1439; M. Makha, M. J. Hardie, C. L. Raston, *Chem. Commun.* **2002**, 1446.

[28] A. L. Litvinov, D. V. Konarev, R. N. Lyubovskaya, B. P. Tarasov, I. S. Neretin, Yu. L. Slovokhotov, *Synth. Met.* **200**1, *121*, 1119; T. Haino, M. Yanase, Y. Fukazawa, *Tetrahedron Lett.* **1997**, *38*, 3739; K. Tsubaki, K. Tanaka, T. Kinoshita, K. Fuji, *Chem. Commun.* **1998**, 895; D. Sun, F. S. Tham, C. A. Reed, L. Chaker, P. D. W. Boyd, *J. Am. Chem. Soc.* **2002**, *124*, 6604; P. D. W. Boyd, M. C. Hodgson, C. E. F. Rickard, A. G. Oliver, L. Chaker, P. J. Brothers, R. D. Bolskar, F. S. Tham, C. A. Reed, *J. Am. Chem. Soc.* **1999**, *121*, 10487; D. V. Konarev, A. Yu. Kovalevsky, X. Li, I. S. Neretin, A. L. Litvinov, N. V. Drichko, Y. L. Slovokhotov, P. Coppens, R. N. Lyubovskaya, *Inorg. Chem.* **2002**, *41*, 3638; T. Haino, M. Yanase, Y. Fukazawa, *Tetrahedron Lett.* **1997**, *38*, 3739.

[29] E. M. Veen, P. M. Postma, H. T. Jonkman, A. L. Spek, B. L. Feringa, *Chem. Commun.* **1999**, 1709; L. J. Barbour, G. W. Orr, J. L. Atwood, *Chem. Commun.* **1998**, 1901; A. L. Litvinov, D. V. Konarev, A. Y. Kovalevsky, I. S. Neretin, Yu. L. Slovokhotov, P. Coppens, R. N. Lyubovskaya, *CrystEngComm* **2002**, *4*, 618; L. Golic, R. Blinc, P. Cevc, D. Arcon, D. Mihailovic, A. Omerzu, P. Venturini, *Proc. 10th Int. Winter. Electron Prop. Novel Mater.* **1996**, 531; B. Narymbetov, H. Kobayashi, M. Tokumoto, A. Omerzu, D. Mihailovic, *Chem. Commun.* **1999**, 1511; K. Tanaka, M. R. Caira, *J. Chem. Res.* **2002**, 642; D. M. Eichhorn, S. Yang, W. Jarrell, T. F. Baumann, L. S. Beall, A. J. P. White, D. J. Williams, A. G. M. Barrett, B. M. Hoffman, *Chem. Commun.* **1995**, 1703.

[30] M. M. Olmstead, D. A. Costa, K. Maitra, B. C. Noll, S. L. Phillips, P. M. Van Calcar, A. L. Balch, *J. Am. Chem. Soc.* **1999**, *121*, 7090; D. H. Hochmuth, S. L. J. Michel, A. J. P. White, D. J. Williams, A. G. M. Barrett, B. M. Hoffman, *Eur. J. Inorg. Chem.* **2000**, 593; J. L. Atwood, M. J. Barnes, M. G. Gardiner, C. L. Raston, *Chem. Commun.* **1996**, 1449; D. V. Konarev, I. S. Neretin, Y. L. Slovokhotov, E. I. Yudanova, N. V. Drichko, Y. M. Shul'ga, B. P. Tarasov, L. L. Gumanov, A. S. Batsanov, J. A. K. Howard, R. N. Lyubovskay, *Chem. Eur. J.* **2001**, *7*, 2605; H. M. Lee, M. M. Olmstead, T. Suetsuna, H. Shimotani, N. Dragoe, R. J. Cross, K. Kitazawa, A. L. Balch, *Chem. Commun.* **2002**, 1352; S. I. Troyanov, E. Kemnitz, *Zh. Neorg. Khim. (Russ.) (Russ. J. Inorg. Chem.)* **2001**, *46*, 1704; O. A. D'yachenko, S. V. Konovalikhin, *Koord. Khim. (Russ.) (Coord. Chem.)* **1998**, *24*, 700; D. V. Konarev, I. S. Neretin, Y. L. Slovokhotov, E. I. Yudanova, N. V. Drichko, Y. M. Shul'ga, B. P. Tarasov, L. L. Gumanov, A. S. Batsanov, J. A. K. Howard, R. N. Lyubovskay, *Chem. Eur. J.* **2001**, *7*, 2605; B. Z. Narymbetov, S. S. Khasanov, L. V. Zorina, L. P. Rozenberg, R. P. Shibaeva, D. V. Konarev, R. N. Lyubovskaya, *Kristallografiya (Russ.) (Crystallogr. Rep.)* **1997**, *42*, 851.

[31] I. E. Grey, M. J. Hardie, T. J. Ness, C. L. Raston, *Chem. Commun.* **1999**, 1139; M. M. Olmstead, A. S. Ginwalla, B. C. Noll, D. S. Tinti, A. L. Balch, *J. Am. Chem. Soc.* **1996**, *118*, 7737; A. Izuoka, T. Tachikawa, T. Sugawara, Y. Saito, H. Shinohara, *Chem. Lett.* **1992**, 1049; A. Izuoka, T. Tachikawa, T. Sugawara, Y. Suzuki, M. Konno, Y. Saito, H. Shinohara, *Chem. Commun.* **1992**, 1472.

[32] J. L. Atwood, L. J. Barbour, C. L. Raston, *Cryst. Growth Des.* **2002**, *2*, 3.

[33] M. V. Korobov, A. L. Mirakian, N. V. Avramenko, E. F. Valeev, I. S. Neretin, Y. L. Slovokhotov, A. L. Smith, G. Oloffson, R. S. Ruoff, *J. Phys. Chem. B* **1998**, *102*, 3712; A. L. Litvinov, D. V. Konarev, A. Y. Kovalevsky, I. S. Neretin, Y. L. Slovokhotov, P. Coppens, R. N. Lyubovskaya, *CrystEngComm* **2002**, *4*, 618; U. Geiser, S. Kalyan Kumar, B. M. Savall, S. S. Harried, K. D. Carlson, P. R. Mobley, H. Wang, J. M. Williams, R. E. Botto, W. Liang, M.-H. Whangbo, *Chem. Mater.* **1992**, *4*, 1077; S. V. Konovalikhin, O. A. D'yachenko, G. V. Shilov, N. G. Spitsina, K. V. Van, E. B. Yagubskii, *Izv. Akad. Nauk SSSR, Ser. Khim. (Russ.) (Russ. Chem. Bull.)* **1997**, 1480; R. E. Marsh, M. Kapon, S. Hu, F. H. Herbstein, *Acta Crystallogr., Sect. B: Struct. Sci.* **2002**, *58*, 62; D. V. Konarev, A. Yu. Kovalevsky, P. Coppens, R. N. Lyubovskaya, *Chem. Commun.* **2000**, 2357; E. M. Veen, P. M. Postma, H. T. Jonkman, A. L. Spek, B. L. Feringa, *Chem. Commun.* **1999**, 1709; D. V. Konarev, E. F. Valeev, Y. L. Slovokhotov, Y. M. Shul'ga, R. N. Lyubovskaya, *J. Chem. Res.* **1997**, *442*, 2647.

[34] A. M. Bond, W. Miao, C. L. Raston, T. J. Ness, M. J. Barnes, J. L. Atwood, *J. Phys. Chem. B* **2001**, *105*, 1687; J. D. Crane, P. B. Hitchcock, H. W. Kroto, R. Taylor, D. R. M. Walton, *Chem. Commun.* **1992**, 1764; N. G. Spitsyna, S. V. Konovalikhin, A. S. Lobach, G. V. Shilov, O. A. D'yachenko, *Izv. Akad. Nauk SSSR, Ser. Khim. (Russ.) (Russ. Chem. Bull.)* **1999**, 2298; V. A. Nadtochenko, V. V. Gritsenko, O. A. Dyachenko, G. V. Shilov, A. P. Moravsky, *Izv. Akad. Nauk SSSR, Ser. Khim. (Russ.) (Russ. Chem. Bull.)* **1996**, 1285.

[35] T. Ishii, N. Aizawa, R. Kanehama, M. Yamashita, H. Matsuzaka, T. Kodama, K. Kikuchi, I. Ikemoto, *Inorg. Chim. Acta* **2001**, *317*, 81; A. L. Litvinov, D. V. Konarev, A. Y. Kovalevsky, I. S. Neretin, Y. L. Slovokhotov, P. Coppens, R. N. Lyubovskaya, *CrystEngComm* **2002**, *4*, 618; G. Waidmann, M. Jansen, *Z. Naturforsch. B: Chem. Sci.* **1998**, *53*, 161; T. Ishii, N. Aizawa, M. Yamashita, H. Matsuzaka, T. Kodama, K. Kikuchi, I. Ikemoto, Y. Iwasa, *J. Chem. Soc., Dalton Trans.* **2000**, 4407; R. Schwenninger, J. Schlogl, J. Maynollo, K. Gruber, P. Ochsenbein, H.-B. Burgi, R. Konrat, B. Krautler, *Chem. Eur. J.* **2001**, *7*, 2676; N. G. Spitsina, V. V. Gritsenko, M. G. Kaplunov, O. A. D'yachenko, E. G. Yagubsky, *Izv. Akad. Nauk SSSR, Ser. Khim. (Russ.) (Russ. Chem. Bull.)* **2001**, 1354; P. C. Andrews, J. L. Atwood, L. J. Barbour, P. D. Croucher, P. J. Nichols, N. O. Smith, B. W. Skelton, A. H. White, C. L. Raston, *J. Chem. Soc., Dalton Trans.* **1999**, 2927.

[36] D. V. Konarev, I. S. Neretin, Y. L. Slovokhotov, E. I. Yudanova, N. V. Drichko, Y. M. Shul'ga, B. P. Tarasov, L. L. Gumanov, A. S. Batsanov, J. A. K. Howard, R. N. Lyubovskaya, *Chem. Eur. J.* **2001**, *7*, 2605; E. M. Veen, P. M. Postma, H. T. Jonkman, A. L. Spek, B. L. Feringa, *Chem. Commun.* **1999**, 1709; M. F. Meidine, P. B. Hitchcock, H. W. Kroto, R. Taylor, D. R. M. Walton, *Chem. Commun.* **1992**, 1534; A. L. Balch, J. W. Lee, B. C. Noll, M. M. Olmstead, *Chem. Commun.* **1993**, 56; H. B. Burgi, R. Restori, D. Schwarzenbach, A. L. Balch, J. W. Lee, B. C. Noll, M. M. Olmstead, *Chem. Mater.* **1994**, *6*, 1325.

[37] P. R. Birkett, C. Christides, P. B. Hitchcock, H. W. Kroto, K. Prassides, R. Taylor, D. R. M. Walton, *J. Chem. Soc., Perkin Trans. 2* **1993**, 1407; A. O'Neil, C. Wilson, J. M. Webster, F. J. Allison, J. A. K. Howard, M. Poliakoff, *Angew. Chem. Int. Ed.* **2002**, *41*, 3796; A. Penicaud, O. Y. Carreon, A. Perrier, D. J. Watkin, C. Coulon, *J. Mater. Chem.* **2002**, *12*, 913; J. C. A. Boeyens, M. Ramm, D. Zobel, P. Luger, *S. Afr. J. Chem.* **1997**, *50*, 28; M. M. Olmstead, F. Jiang, A. L. Balch, *Chem. Commun.* **2000**, 483; A. I. Kotov, S. V. Konovalikhin, R. V. Pisarev, G. V. Shilov, O. A. Dyachenko, E. B. Yagubskii, *Mendeleev Commun.* **1994**, 180; A. Penicaud, K. Boubekeur, A. I. Kotov, E. B. Yagubskii, *Acta Crystallogr., Sect. B: Struct. Sci.* **2000**, *56*, 497; S. Margadonna, E. Aslanis, W. Z. Li, K. Prassides, A. N. Fitch, T. C. Hansen, *Chem. Mater.* **2000**, *12*, 2736; M. Ramm, P. Luger, W. Duczek, J. C. A. Boyens, *Cryst. Res. Technol.* **1996**, *31*, 43; W. Bensch, H. Werner, H. Bartl, R. Schlogl, *J. Chem. Soc., Faraday Trans.* **1994**, *90*, 2791; L. I. Buravov, O. A. D'yachenko, S. V. Konovalikhin, N. D. Kushch, I. P. Lavrent'ev, N. G. Spitsyna, G. V. Shilov, E. B. Yagubskii, *Izv. Akad. Nauk SSSR, Ser. Khim. (Russ.) (Russ. Chem. Bull.)* **1994**, 262;

 © 2006 Wiley-VCH Verlag GmbH & Co. KGaA, Weinheim 

G. Roth, P. Adelmann, *Appl. Phys. A: Solids and Surfaces* **1993**, *56*, 169; P. D. Croucher, P. J. Nichols, C. L. Raston, *J. Chem. Soc., Dalton Trans.* **1999**, 279; A. Izuoka, T. Tachikawa, T. Sugawara, Y. Suzuki, M. Konno, Y. Saito, H. Shinohara, *Chem. Commun.* **1992**, 1472; K. Tsubaki, K. Tanaka, T. Kinoshita, K. Fuji, *Chem. Commun.* **1998**, 895.

[38] J. L. Atwood, L. J. Barbour, P. J. Nichols, C. L. Raston, C. A. Sandoval, *Chem. Eur. J.* **1999**, *5*, 990.

[39] A. M. Bond, W. Miao, C. L. Raston, C. A. Sandoval, *J. Phys. Chem. B.* **2000**, *104*, 8129–8137.

[40] M. Makha, M. J. Hardie, C. L. Raston, *Chem. Commun.* **2002**, 1446–1447.

[41] T. Haino, M. Yanase, Y. Fukuzawa, *Angew. Chem. Int. Ed. Engl.* **1997**, *36*, 259–260; T. Haino, M. Yanase, Y. Fukazawa, *Tetrahedron Lett.* **1997**, *38*, 3739–3742.

[42] C. L. Raston, J. L. Atwood, P. J. Nichols, I. B. N. Sudria, *Chem. Commun.* **1996**, *23*, 2615–2616.

[43] K. Tsubaki, K. Tanaka, T. Kinoshita, K. Fuji, *Chem. Commun.* **1998**, 895.

[44] A. L. Litvinov, D. V. Konarev, A. Yu. Kovalevsky, I. S. Neretin, Yu. L. Slovokhotov, P. Coppens, R. N. Lyubovskaya, *CrystEngComm* **2002**, *4*, 618.

[45] I. E. Grey, M. J. Hardie, T. J. Ness, C. L. Raston, *Chem. Commun.* **1999**, 1139.

[46] M. J. Hardie, C. L. Raston, *Chem. Commun.* **1999**, 1153–1163.

[47] A. M. Bond, W. Miao, C. L. Raston, T. J. Ness, M. J. Barnes, J. L. Atwood, *J. Phys. Chem. B* **2001**, *105*, 1687–1695.

[48] J. L. Atwood, M. J. Barnes, M. G. Gardiner, C. L. Raston, *Chem. Commun.* **1996**, 1449–1450.

[49] M. J. Hardie, P. D. Godfrey, C. L. Raston, *Chem. Eur. J.* **1999**, *5*, 1828–1833.

[50] P. C. Andrews, J. L. Atwood, L. J. Barbour, P. J. Nichols, C. L. Raston, *Chem. Eur. J.* **1998**, *4*, 1384.

[51] D. V. Soldatov, P. R. Diamente, C. I. Ratcliffe, J. A. Ripmeester, *Inorg. Chem.* **2001**, *40*, 5660.

[52] D. V. Konarev, I. S. Neretin, Y. L. Slovokhotov, E. I. Yudanova, N. V. Drichko, Y. M. Shul'ga, B. P. Tarasov, L. L. Gumanov, A. S. Batsanov, J. A. K. Howard, R. N. Lyubovskaya, *Chem. Eur. J.* **2001**, *7*, 2605.

[53] A. O'Neil, C. Wilson, J. M. Webster, F. J. Allison, J. A. K. Howard, M. Poliakoff, *Angew. Chem. Int. Ed.* **2002**, *41*, 3796.

[54] M. M. Olmstead, F. Jiang, A. L. Balch, *Chem. Commun.* **2000**, 483.

[55] O. A. D'yachenko, S. V. Konovalikhin, *Koord. Khim. (Russ.) (Coord. Chem.)* **1998**, *24*, 700.

[56] J. L. Atwood, L. J. Barbour, C. L. Raston, I. B. N. Sudria, *Angew. Chem. Int. Ed. Engl.* **1998**, *37*, 981.

[57] S. Mizyed, P. R. Tremaine, P. E. Georghiou, *J. Chem. Soc., Perkin Trans. 2* **2001**, 3–6.

[58] L. J. Barbour, G. W. Orr, J. L. Atwood, *Chem. Commun.* **1998**, 1901–1902.

[59] J. Barbour, G. W. Orr, J. L. Atwood, *Chem. Commun.* **1997**, 1439–1440.

[60] K. N. Rose, L. J. Barbour, G. W. Orr, J. L. Atwood, *Chem. Commun.* **1998**, 407.

[61] Y. Wan, O. Mitkin, L. Barnhurst, A. Kurchan, A. Kutateladze, *Org. Lett.* **2000**, *2*, 3817–3819.

[62] G. D. Fox, M. G. B. Drew, E. J. S. Wilkinson, P. D. Beer, *Chem. Commun.* **2000**, 391–392.

[63] D. V. Konarev, I. S. Neretin, Y. L. Slovokhotov, E. I. Yudanova, N. V. Drichko, Y. M. Shul'ga, B. P. Tarasov, L. L. Gumanov, A. S. Batsanov, J. A. K. Howard, R. N. Lyubovskay, *Chem. Eur. J.* **2001**, *7*, 2605.

Received: August 31, 2005
Published Online: December 27, 2005

 © 2006 Wiley-VCH Verlag GmbH & Co. KGaA, Weinheim 

DOI: 10.1002/ejic.200500805

# Bundle of Nanobelts Up to 4 cm in Length: One-Step Synthesis and Preparation of Titanium Trisulfide ($TiS_3$) Nanomaterials

**Jingjing Ma,[a] Xiaoyang Liu,*[a] Xuejing Cao,[a] Shouhua Feng,[a] and Michael E. Fleet[b]**

**Keywords:** One dimensional / Nanostructures / Layered compounds / Titanium / Sulfides / CVT / One-step synthesis

One-dimensional (1D) titanium trisulfide ($TiS_3$) nanobelt bundles up to 4 cm in length have been successfully synthesized through an easy and common chemical vapor transition (CVT) process. The as-synthesized samples were characterized by X-ray powder diffraction (XRD), polarized light microscopy, scanning electron microscopy (SEM), and transmission electron microscopy (TEM). All microscopic observations indicated a belt-like morphology. Powder XRD patterns showed that $TiS_3$ crystallized in the monoclinic system with $a = 4.958(1)$ Å, $b = 3.393(1)$ Å, $c = 8.793(3)$ Å and $\beta = 97.27(5)°$. TEM images revealed a nanostructure with an interplanar spacing of 0.87 nm. The ED pattern and HRTEM images confirmed the [014] elongated direction and the [001] dilated direction of the bundle of $TiS_3$ nanobelts. Its tensile strength (TS) was further examined with a universal testing machine with 20 N as the biggest strength: the maximum stress and the break strain were 111.027 MPa and 97.1 %, respectively. Because the $TiS_3$ nanocrystals are up to 4 cm in length and flexible enough to be cut into small pieces, they should be used directly in electrical and electronic applications. Also, these nanomaterials are synthesized and prepared by a simple one-step process.
(© Wiley-VCH Verlag GmbH & Co. KGaA, 69451 Weinheim, Germany, 2006)

## I. Introduction

Recently, there is a growing interest in the synthesis, characterization, and application of one-dimensional (1D) nanomaterials such as nanobelts, nanowires, etc. because of their low dimensionality and high aspect ratio, as well as their unusual physical properties. The synthesis and functionality of 1D nanomaterials have become one of the most highly energized research areas. During the past two decades, various sulfide nanomaterials have been synthesized.[1–12] However, the preparation of sulfide nanobelts remains poorly studied, and only a few successful examples have been reported. For example, ZnS nanobelts with wurtzite structure have been prepared by simple thermal evaporation of ZnS powder in the presence of Au catalysts at 970 °C.[13] PbS nanobelts have been successfully synthesized in the mixed solution of $PbCl_2$ and $Na_2S_2O_3$.[14]

Titanium trisulfide $TiS_3$ is of interest to us because of its potential application in CuO-based cathodes of non-aqueous alkali metal batteries. Measurements of the electrical conductivity and the Hall coefficient at 15–300 K and of the thermal EMF at 80–400 K indicate that $TiS_3$ is semiconducting with extrinsic n-type conductivity. The mobility of the carriers is approximately 30 $cm^2/V$ at room temperature, and increases up to approximately 100 $cm^2/V$ at 100 K, and then drops at lower temperatures.[15] Thin films of $TiS_3$ have been prepared by thermal chemical vapor deposition (CVD), by reacting $TiCl_4$ and a series of sulfur sources,[16] but the nanoscale synthesis of $TiS_3$ has few successful results reported. Only Dong-Kyun Seo synthesized the $TiS_3$ material in the same size with $TiO_2$ powder and the mixtures of boron and sulfur as starting materials by a solid-gas metathetical reaction,[17] but there was neither SEM nor TEM image to indicate its nanosize. Furthermore, the boron powder could not adsorb all the oxygen completely during this oxidation–deoxidization process, and the remained $TiO_2$ would reduce the purity of the sample, some other peaks of the mixture from its XRD pattern also confirmed that.

It is well known that the synthesis and preparation generally require two separate steps in the fabrication of functional materials, e.g., firstly the phase is obtained in powder form using different synthesis methods, and then the powder product is processed into different functional forms according to specific applications, with hot pressing being the most common method used to work the powders. However, for nanomaterials, the particle size increases when the nanopowders are hot-pressed, which results in the loss of physical properties associated with the small-size effect (high specific surface area, surface conductivity, etc.). The retention of small particle size while processing the powders into different shapes is a very important issue in the field of nanomaterials. We presently report the synthesis and preparation of high-purity $TiS_3$ with nanobelt structure by an easy and

[a] State Key Laboratory of Inorganic Synthesis and Preparative Chemistry, College of Chemistry, Jilin University,
2699 Qianjin Street, Changchun, 130012, P. R. China
Fax: +86-431-5168316
E-mail: liuxy@jlu.edu.cn
[b] Department of Earth Sciences, University of Western Ontario, London, Ontario N6A 5B7, Canada

 © 2006 Wiley-VCH Verlag GmbH & Co. KGaA, Weinheim 

common one-step CVT process, which yields a product that can be used directly in electrical and electronic applications.

## II. Results and Discussion

The products were characterized by X-ray diffraction (XRD, with a SIEMENS D5005 diffractometer with a graphite monochromator), scanning electron microscopy (SEM JEOL.LTD JSM-6700F), transmission electron microscopy (TEM, Jeol Ltd., JEM-3010), polarized-light microscopy (Olympus BX51), universal testing machine (Shimadzu AG-I).

The XRD pattern of the bulk samples (e.g., Figure 1) was consistent with pure $TiS_3$ (JCPDS No. 36–1337). The product crystallized in the monoclinic system with $a$ = 4.958(1) Å, $b$ = 3.393(1) Å, $c$ = 8.793(3) Å and $\beta$ = 97.27(5)°. The structure calculations were optimized by least-squares refinement. The diffraction peaks were sharp and strong, confirming that the products were well crystallized. This XRD pattern also proved that the [001] direction should be the direction of growth of $TiS_3$ nanobelts bundle either elongated direction or dilated direction. Using polarized-light microscopy, the $TiS_3$ crystals were seen to be dark grey with a metallic shine and belt-like habit (Figure 2). The nanocrystals were up to 4 cm in length and, thus, apparently suitable without further treatment as functional material in electrical devices. Figure 2 (c and d) reveal a layered structure in agreement with the strong preferred orientation indicated by the bulk XRD pattern (Figure 1) and the habit of $TiS_3$ crystals deduced in previous studies.[18,19]

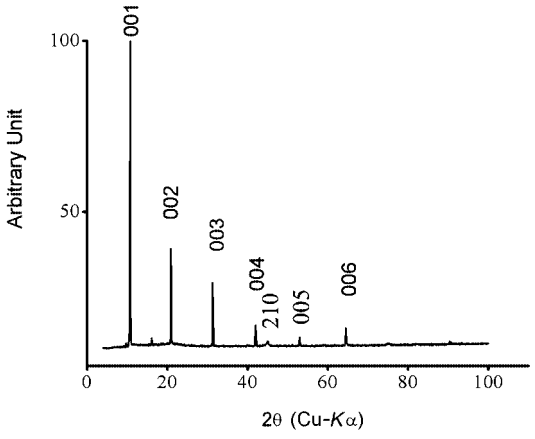


Figure 1. Bulk XRD pattern of the bundle of $TiS_3$ nanobelts. The numbers above the peaks are the Miller indices for the monoclinic structure.

The morphology of the nanobelt crystals was further investigated by SEM. A typical SEM image of the $TiS_3$ products (Figure 3, a) shows smooth laminar crystal faces and a layered structure. Figure 3 (b, c and d), shows a more massive habit with individual $TiS_3$ nanobelts up to 100 μm in length.

TEM images (Figure 4) provide further insight into the morphology of these materials. $TiS_3$ nanobelts with length

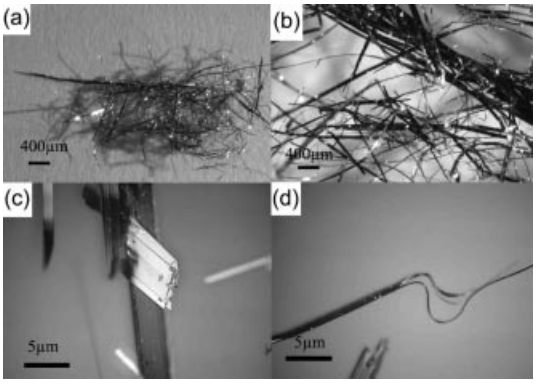


Figure 2. The appearance of the bundle of $TiS_3$ nanobelts in polarized-light microscopy (Olympus BX51). a) and b) show the dark grey belt-like appearance. c) and d) reveal the layered microstructure.

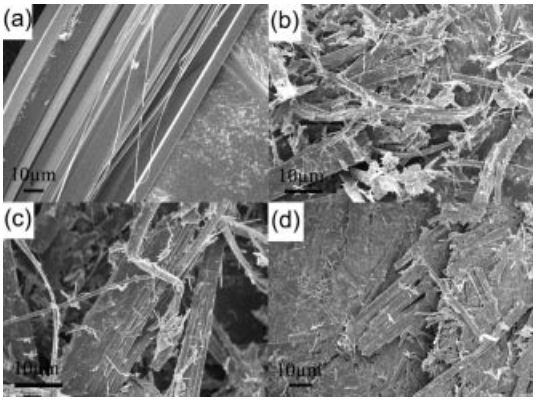


Figure 3. Low-magnification SEM images of $TiS_3$ nanobelt bundles synthesized by a simple CVT process of Ti and S at 600 °C; a) is taken from the centre of a $TiS_3$ nanobelt bundle; b) shows the typical appearance of $TiS_3$ nanobelt bundles; c) and d) show details of massive nanobelts.

up to 4 cm were first comminuted by grinding in ethanol, then the mixed solution was pulsed by ultrasonic cleaner for ca. 10 min. In order to sample the smallest size fraction of $TiS_3$ crystals, the clear solution on top of the sedimented column was pipetted onto a holey carbon grid, and the ethanol allowed to evaporate. Typical TEM images at low magnification (Figure 4, a and b) show that the ground crystal products are nanobelts, and that the yield of nanobelts is quite high (>95%). The selected-area electron diffraction pattern taken from a single $TiS_3$ nanobelt confirms the single-crystal nature of the sample and can be indexed on a monoclinic unit cell, consistent with the powder XRD results presented above (JCPDS No. 36–1337). The [014] direction of the ED pattern is parallel to the elongated axis of the belt, showing that the elongated growth might occur along the [014] direction. Furthermore, the [001] direction of the ED pattern is parallel to the dilated axis of the belt, showing that the dilated growth might occur along the [001] direction which corresponds to the XRD result. High-resolution TEM images (Figure 4, c and d) show that the nanobelts are single crystals and free of dislocations and defects.

 © 2006 Wiley-VCH Verlag GmbH & Co. KGaA, Weinheim 

From Figure 4 (c), we can see that the nanobelts are structurally uniform with an interplanar spacing of 0.87 nm; it should be elongated along the [014] direction and dilated along the [210] direction which is consonant with the ED pattern. The $TiS_3$ nanobelts were not sensitive to electron beam irradiation during the HRTEM investigation.

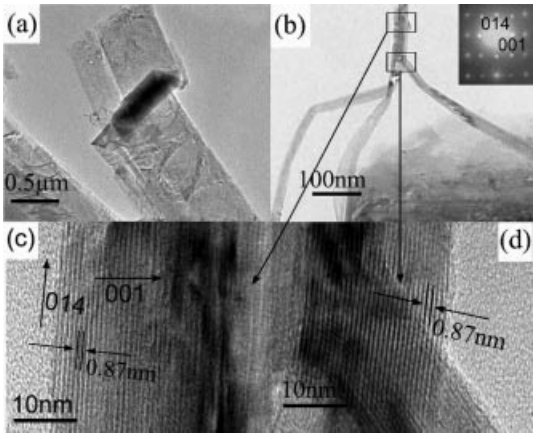


Figure 4. TEM and HRTEM images of the $TiS_3$ nanobelts revealing details of their geometry; a) and b) are images of several overlapped $TiS_3$ nanobelts, (inset) The corresponding electron diffraction pattern confirms the single-crystal nature of the sample and can be indexed to a monoclinic unit cell consistent with the XRD results presented above; c) and d) are HRTEM images of a $TiS_3$ nanobelt, showing that the nanobelts are single crystals and free from dislocations and defects, also, the nanobelts are structurally uniform with an interplanar spacing about 0.87 nm.

Figure 5 shows that in the structure of monoclinic titanium trisulfide $TiS_3$, two of the three S atoms per formula unit are present as a single-bonded disulfide ion ($S_2^{2-}$; S–S = 2.04 Å), and the third S atom is formally sulfide ($S^{2-}$).[16] The Ti atom is in irregular eightfold coordination with S atoms. Six shorter Ti–S distances (2.45 to 2.49 Å) form $TiS_6$ trigonal prisms, which are linked through shared faces into an infinite chain parallel to the *b*-axis, that makes the structure quasi one-dimensional. Neighboring chains are offset by *b*/2 and connected laterally by longer Ti–S bonds (2.63 and 2.64 Å) into sheets parallel to the crystal face (001). Individual (001) sheets are bounded above and below by a layer of disulfide groups, and held together in the resulting two-dimensional structure by only van der Waals' forces. Extensive bulk and powder XRD[16,18] (Figure 1) and microfocus single-crystal XRD[18] show that the acicular (needle-shaped) and blade- or belt-like crystals of $TiS_3$ are elongated in a gradient direction, and that the layer surface (i.e., the prominent growth surface) is (001), which is also concluded from HRTEM images and ED pattern. In addition, the $TiS_3$ nanobelts bundle can be broken into 1D needles, having a parting or cleavage parallel to the (100) direction. This parting is believed to be responsible for the belt-like morphology of the nanocrystals shown in Figure 2 (d) and Figure 4, and requires the severing of the long (2.63 and 2.64 Å) Ti–S bonds. Thus, the broad surface of the nanobelts (Figure 4, a) is a cleavage or parting surface populated by broken bonds, although the strong bonds of the monoclinic $TiS_3$ structure remain in tact. The nanobelts tend to separate into 1D needles by cleavage along (001), which requires the breaking of the weak van der Waals' bonds. On the basis of this orientational relationship, one would expect that the lattice fringes of Figure 4 (c and d) should correspond to the interlayer spacing $d_{001}$ (0.8706 nm). The 1D $TiS_3$ needles should get widen layer by layer along the [100] direction which is consistent with the HRTEM results.

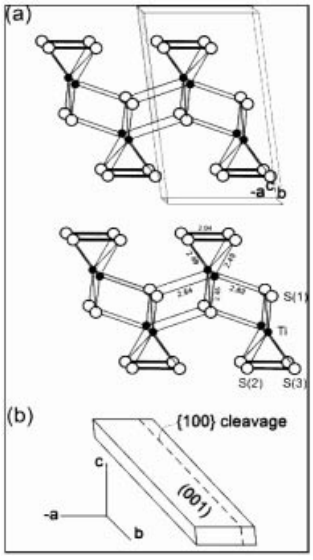


Figure 5. Structure of titanium trisulfide $TiS_3$; (a) monoclinic structure of titanium trisulfide $TiS_3$ shows that the Ti atom is in irregular eightfold coordination with S atoms. Six shorter Ti–S distances (2.45 to 2.49 Å) form $TiS_6$ trigonal prisms, which are linked by shared faces into an infinite chain parallel to the *b*-axis, making the structure quasi one-dimensional; (b) schematic pattern of the layer structure of titanium trisulfide ($TiS_3$) shows that the crystals of $TiS_3$ are elongated in the *b*-axis direction and that the layer surface is (001). Also, the crystals have a cleavage parallel to (100).

In order to prove that these bundles of $TiS_3$ are not extremely fragile, we use an universal testing machine with 20 N as the biggest strength to examine the tensile strength of this material. Figure 6 showed that the maximum stress was 111.027 MPa, the break strain 97.1% and the average stress 100–110 MPa. The maximum stress value of a bundle of $TiS_3$ is nearly the same with that of aluminum (≈ 100 MPa),[20] and much higher than those of some widely used engineering plastics such as PVC (≈ 25 MPa), poly(propylene) (25.48 MPa)[21] and poly(vinyl acetate) (29.4 MPa),[21] even some films used in conducting application. For example, a poly(*p*-phenylene) (PPP) film was electrochemically deposited onto a stainless steel electrode surface by direct oxidation of benzene in $BF_3$–diethyl ether solution at an applied potential of 1.7 V (vs. Ag/AgCl), and the as-grown PPP film had a tensile strength of 53.9–63.7 MPa;[22] a crystalline polythiophene (Pth) film was electrochemically deposited onto a nickel substrate from freshly distilled $BF_3$–diethyl ether (BFEE) solution containing 15 mM thiophene, and the crystalline film had a tensile

 © 2006 Wiley-VCH Verlag GmbH & Co. KGaA, Weinheim 

strength of 73.5–83.3 MPa.[23] So we believe these $TiS_3$ nanobelts bundles should be flexible enough to be used in applications directly.

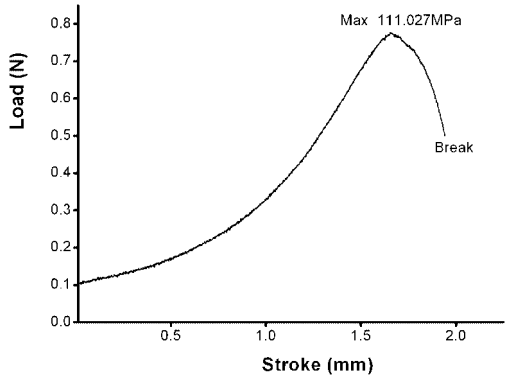


Figure 6. Tensile strength (TS) of the $TiS_3$ nanobelts bundle.

## III. Conclusions

Nanobelt crystals of $TiS_3$ with sufficient length (≈ 4 cm) and tensile strength (the average stress is 100–110 MPa) to be used directly in electrical devices without further treatment have been produced by a one-step reaction process. The successful synthesis of $TiS_3$ nanobelts encourages us to investigate the synthesis and preparation of other nanostructured metal sulfides by this easy and common CVT method, which does not require the use of organic (organic sulfur, organometallic) reagents. For the synthetic process, reaction temperature and length of the quartz-glass tube are of great importance. Therefore, establishing these parameters and the relationship between them are key points to the synthesis of metal sulfides with nanostructures. Moreover, the $TiS_3$ semiconductor nanobelts are expected to present more novel physical properties and applications in practice, and further research is now in progress in our laboratory.

## IV. Experimental Section

$TiS_3$ nanobelt crystals were prepared by the direct reaction of titanium and sulfur within evacuated sealed quartz-glass tubes with a diameter of 10 mm and a length of 130 mm. In order to ensure the purity of the sample, titanium sponge (99.7%; Alfa Aesar) and sulfur sublimate (99.99%; Aldrich) instead of oxides were used as the titanium and sulfur sources, respectively. Charges, consisting of about 1 g of starting composition in the stoichiometric proportion of $TiS_3$, were loaded in a quartz-glass tube closed at one end using a long-stemmed funnel. Then the tube with the starting materials was evacuated and sealed, and heated in a horizontal-tube furnace. The synthesis was achieved by establishing a temperature gradient of 80–100 °C along the tube with the starting mixture at the hot end. $TiS_3$ fibers were obtained at the cool end when charges were heated at 600 °C for 15 days. When the temperature was set below 600 °C, the sulfur did not react completely with titanium, and an excess amount of it was deposited at the cool end. Temperatures above 600 °C tended to produce unwanted powder and crystals of $TiS_2$: $TiS_3$ undergoes peritectic decomposition (to $TiS_2$ + native sulfur) at 632 °C, 8.95 atm. The optimum reaction duration was 15 days.

## Acknowledgments

This work was supported by the Natural Sciences Foundation of China (No. 20471022) and the Natural Sciences and Engineering Research Council of Canada.

[1] X. Duan, Y. Huang, R. Agarwal, C. M. Lieber, *Nature* **2003**, *421*, 241–245.
[2] C. H. Ye, G. W. Meng, Z. Jiang, Y. H. Wang, G. Z. Wang, L. D. Zhang, *J. Am. Chem. Soc.* **2002**, *124*, 15180–15181.
[3] C. Chen, W. Gao, Z. Qin, W. Hu, M. Qu, *J. Appl. Phys.* **1991**, *70*, 6277–6279.
[4] C. Chen, M. Qu, W. Hu, X. Zhang, F. Lin, H. Hu, *J. Appl. Phys.* **1991**, *69*, 6114–6116.
[5] D. M. Pasquariello, R. Kershaw, J. D. Passaretti, K. Dwight, A. Wold, *Inorg. Chem.* **1984**, *23*, 872–874.
[6] Y. D. Li, X. L. Li, R. R. He, *J. Am. Chem. Soc.* **2002**, *124*, 1411–1416.
[7] Margolin, R. Rosentsveig, A. Albu-Yaron, R. Popovitz-Biro, R. Teme, *J. Mater. Chem.* **2004**, *14*, 617–624.
[8] K. Oshima, M. Yokoyama, H. Hinode, M. Wakihara, M. Taniguchi, *J. Solid State Chem.* **1986**, *65*, 392–395.
[9] C. Sourisseau, S. P. Gwet, P. Gard, Y. Mathey, *J. Solid State Chem.* **1988**, *72*, 257–271.
[10] P. Gard, F. Cruege, C. Sourisseau, O. Gorochov, *J. Raman Spectrosc.* **1986**, *17*, 283–288.
[11] Y. D. Li, J. P. Ge, *Chem. Commun.* **2003**, 2498–2499.
[12] X. B. Cao, L. Y. Li, Y. Xie, *J. Colloid Interface Sci.* **2004**, *273*, 175–180.
[13] H. Liang, Y. Shimizu, T. Sasaki, H. Umehara, N. Koshizaki, *J. Phys. Chem. B* **2004**, *108*, 9728–9733.
[14] S. M. Zhou, X. H. Zhang, X. M. Meng, X. Fan, S. T. Lee, S. K. Wu, *J. Solid State Chem.* **2005**, *178*, 399–403.
[15] E. Finkman, B. Fisher, *Solid State Commun.* **1984**, *50*, 25–28.
[16] H. S. W. Chang, D. M. Schleich, *J. Solid State Chem.* **1992**, *100*, 62–70.
[17] L. M. Wu, D. K. Seo, *J. Am. Chem. Soc.* **2004**, *126*, 4676–4681.
[18] S. Furuseth, L. Bratts, A. Kjekshus, *Acta Chem. Scand. A* **1975**, *29*, 623–631.
[19] M. E. Fleet, S. L. Harmer, X. Y. Liu, H. W. Nesbitt, *Surface Sci.* **2005**, *584*, 133–145.
[20] G. Q. Shi, C. Li, Y. Q. Liang, *Adv. Mater.* **1999**, *11*, 1145–1146.
[21] J. Brandup, E. H. Immergut (Ed.), *Polymer Handbook*, John Wiley & Sons, New York, **1975**, p.V-23, V-51.
[22] C. Li, G. Q. Shi, Y. Q. Liang, W. Ye, Z. L. Sha, *Polymer* **1997**, *38*, 5023–5026.
[23] C. Li, G. Q. Shi, Y. Q. Liang, Z. L. Sha, *Polymer* **1997**, *38*, 6421–6422.

Received: September 13, 2005
Published Online: December 27, 2005

 © 2006 Wiley-VCH Verlag GmbH & Co. KGaA, Weinheim 

DOI: 10.1002/ejic.200500891

# Pyrophosphate and ATP as Stabilizing Ligands for High-Valent Nickel Complexes

**Dror Shamir,[a] Israel Zilbermann,*[a,b] Eric Maimon,[a,b] Alexander I. Shames,[d] Haim Cohen,[a,c] and Dan Meyerstein*[a,c]**

**Keywords:** ATP / Cyclam / High-valent transition metal complexes

ATP stabilizes trivalent nickel complexes which suggests that another plausible role of ATP in biological systems is the stabilization of high-valent transition metal complexes.

(© Wiley-VCH Verlag GmbH & Co. KGaA, 69451 Weinheim, Germany, 2006)

Anionic ligands, which are hard acids e.g. $SO_4^{2-}$ or $CH_3CO_2^-$, are known to stabilize, through axial coordination, $Ni^{III}$ complexes with tetraazamacrocyclic ligands, e.g. (cyclam)$Ni^{III}$ (cyclam = 1,4,8,11-tetraazacyclotetradecane).[1–4] Thus, good stabilizing anionic ligands are needed in order to synthesize stable high-valent nickel complexes. It has been observed that phosphate[4] and its derivatives are good axial ligands and therefore the effect of $P_2O_7^{4-}$ as a ligand was studied. The electrochemical results (CV) of the oxidation of $Ni^{II}L^{2+}$ in the presence of pyrophosphate on a glassy carbon electrode (Figure 1) point out that pyrophosphate forms a very stable complex; the formation constant of the pyrophosphate complex $Ni^{III}L(P_2O_7)_2^{5-}$ at pH = 7.0 is calculated from the intercept of the line in the inset of Figure 1 (Nernst equation) to be $K_{eq} = 9.6\cdot10^{10}$ M$^{-2}$ {the stability constants were calculated using the total concentration of pyrophosphate in the solution, relative to $E_{1/2}[NiL(H_2O)_2^{3+}/NiL^{2+}]$ at pH = 2.0[4b]}. One obtains $E_{1/2}$ = 0.44 V (vs. SCE), for the $Ni^{III/II}L$ couple in solutions containing 0.016 M pyrophosphate (as p$K_{a4}$ of $H_4P_2O_7$ is 8.66, it is reasonable to assume that at pH = 7.0, due to the inductive effect of the central $Ni^{III}$ ion,[4] the ligand is $P_2O_7^{4-}$). The electrochemical results are independent of the presence of dioxygen in the solution. Furthermore, the cyclic voltammogram at pH = 3.0, consists of two pseudo-reversible oxidation waves (Figure 1). The first wave is the oxidation of divalent nickel to trivalent nickel (one-electron oxidation) and the second wave might be attributed to the oxidation of trivalent nickel to tetravalent nickel. In order to characterize the electrochemical oxidation product, preparative electrolysis at 640 mV (vs. SCE) was performed and the resulting oxidized complex was characterized by EPR. The results point out that it is indeed a trivalent nickel complex (the measured $g$ values are typical for trivalent (cyclam)nickel: $g_\perp$ = 2.220; $g_\parallel$ = 2.022; $g_{av}$ = 2.154, at 200 K).[5] In order to determine whether an $Ni^{IV}$ complex is formed during the second oxidation wave, a second preparative electrolysis (vs. SCE) was performed by applying a controlled voltage of 800 mV to a solution containing $Ni^{III}L(P_2O_7)_2^{5-}$, and the resulting oxidized solution was characterized by EPR. However, formation of tetravalent (cyclam)nickel was not observed, probably due to the fast decomposition of the unstable $Ni^{IV}$ complex. A similar result was obtained when a CV experiment was performed using the electrolyzed solution, beginning the cycle at +0.9 V. The electrochemical results were corroborated by pulse radiolysis experiments which show that $Ni^{IV}L(P_2O_7)_n^{4-4n}$ ($n$ = 1 or 2) can be formed, but indeed is short-lived. The reaction of $Ni^{III}L(P_2O_7)_2^{5-}$ with the $N_3^{\cdot}$ radical, which is an outer-sphere oxidizing agent[6] with $E^0$ = 1.3 vs. NHE,[6] was studied by pulse radiolysis: $Ni^{III}L(P_2O_7)_2^{5-}$ was prepared by oxidation of $Ni^{II}L^{2+}$ with $Na_2S_2O_8$ at pH = 3.0[7] in a solution containing 0.016 M $Na_4P_2O_7$. To this solution 0.1 M $NaN_3$ was added, which did not affect the spectrum of the $Ni^{III}L(P_2O_7)_2^{5-}$ complex. Upon exposure to ionizing radiation, $N_3^{\cdot}$ radicals were formed accoding to Equations (1), (2) and (3) in less then 5 μs.

$$H_2O \xrightarrow{e^-,\,\gamma} {}^{\cdot}OH,\ H^{\cdot},\ e^-_{aq},\ H_2,\ H_2O_2,\ H_3O^+,\ OH^-$$
$$G({}^{\cdot}OH) = 2.65;\ G(H^{\cdot}) = 0.60;\ G(e^-_{aq}) = 2.65;\ G(H_2) = 0.45;\ G(H_2O_2) = 0.75[8] \quad (1)$$

$$e^-_{aq} + N_2O + H_2O \rightarrow {}^{\cdot}OH + OH^- + N_2;\ k = 9.1\cdot10^9\ M^{-1}s^{-1}[9] \quad (2)$$

$${}^{\cdot}OH + N_3^- \rightarrow {}^{\cdot}N_3;\ k = 1.0\cdot10^{10}\ M^{-1}s^{-1}[10] \quad (3)$$

The reaction of $^{\cdot}N_3$ with $Ni^{III}L(P_2O_7)_2^{5-}$ results in the formation of an intermediate with a strong absorption band shifted to the red (450 nm relative to that of $Ni^{III}L$-

[a] Chemistry Department, Ben-Gurion University of the Negev, Beer-Sheva, Israel
[b] Chemistry Department, Nuclear Research Centre Negev, Beer-Sheva, Israel
[c] Biological Chemistry Department, College of Judea and Samaria, Ariel, Israel
[d] Department of Physics, Ben-Gurion University of the Negev, Beer-Sheva, Israel

 © 2006 Wiley-VCH Verlag GmbH & Co. KGaA, Weinheim 

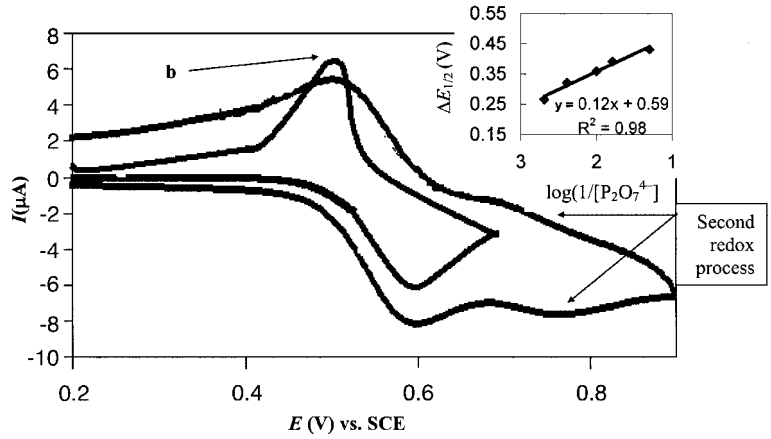


Figure 1. Electrochemical oxidations of $Ni^{II}L^{2+}$ in the presence of $Na_4P_2O_7$. Solution composition: 0.1 M $NaClO_4$, pH = 3.0, 0.001 M $Ni^{II}L^{2+}$, 0.016 M pyrophosphate, scan rate 50 mV/s; b: the same performed only for the 1st oxidation wave. Inset: Dependence of $\Delta E_{1/2}$ on log (1/[$P_2O_7^{4-}$]), where $\Delta E_{1/2}$ is the difference between $E_{1/2}$ for $NiL^{2+}$ in the absence of $P_2O_7^{4-}$ and the measured $E_{1/2}$.

$(P_2O_7)_2^{5-}$ at 380 nm; Figure 2), which plausibly represents the $Ni^{IV}L$ complex. The kinetics of formation of the intermediate obey a pseudo-first-order rate law, i.e. the observed rate is proportional to $[Ni^{III}L(P_2O_7)_2^{5-}]$. The rate of the reaction is independent of (i) $[N_3^-]$, (ii) $[N_2O]$, (iii) pH in the range 6–11 and wavelength, and the rate constant is $k\{LNi^{III}(P_2O_7)_2^{5-} + N_3^{\cdot}\} = (3.1 \pm 0.4) \times 10^8\ M^{-1}\,s^{-1}$. Thus, it is suggested that the reaction observed occurs between the trivalent nickel complex and the azide radical to produce the tetravalent nickel complex according to Equation (4).

$$[LNi^{III}(P_2O_7)_2]^{5-} + N_3^{\cdot} \rightarrow [LNi^{IV}(P_2O_7)_2]^{4-} + N_3^- \quad (4)$$

The formation of the transient is followed by three time-separated processes which obey first-order rate laws. The first two are probably isomerisation processes, with rate constants of ca. $2 \cdot 10^3$ and 90 $s^{-1}$ respectively; similar rates were reported for the isomerisation reactions of $Ni^{III}L$ complexes.[1] The third reaction is the decomposition of the tetravalent complex in which the absorption spectrum due to the transient disappears. The suggestion that the transient is $[LNi^{IV}(P_2O_7)_2]^{4-}$ is corroborated by its long life time (Figure 2). The rate of decomposition of the transient is ca. 0.25 $s^{-1}$ and is nearly independent on pH, in the range $6 < pH < 10$, complex concentration and the presence of dioxygen; all these properties point out that the transient formed is not a ligand-based radical.

As $P_2O_7^{4-}$ was found to stabilize the $Ni^{III}L$ complexes, it was decided to study the effect of ATP as a ligand, which might form the stable complex $Ni^{III}L(ATP)_2^{5-}$. It is indeed observed that ATP reacts with $Ni^{III}L(H_2O)_2^{3+}$ to form a stable $Ni^{III}L(ATP)_2^{5-}$ complex. From the electrochemical results (Figure 3), which point out that ATP forms a very stable complex, one calculates the formation constant of the ATP complex $Ni^{III}L(ATP)_2^{5-}$ to be $K_{eq} = 1.2 \cdot 10^{11}\ M^{-2}$ and $E_{1/2} = 0.41$ V (vs. SCE) for the $Ni^{III/II}L$ couple in solutions containing 0.016 M ATP (the stability constants were calculated using the total concentration of ATP in the solution). As expected, the electrochemical results also point out that the cathodic shift (compared to $Ni^{II}L$) at pH = 7.0 is higher than that at pH = 5.0 ($K_{eq} = 2.0 \cdot 10^8\ M^{-2}$ and $E_{1/2} = 0.51$ V

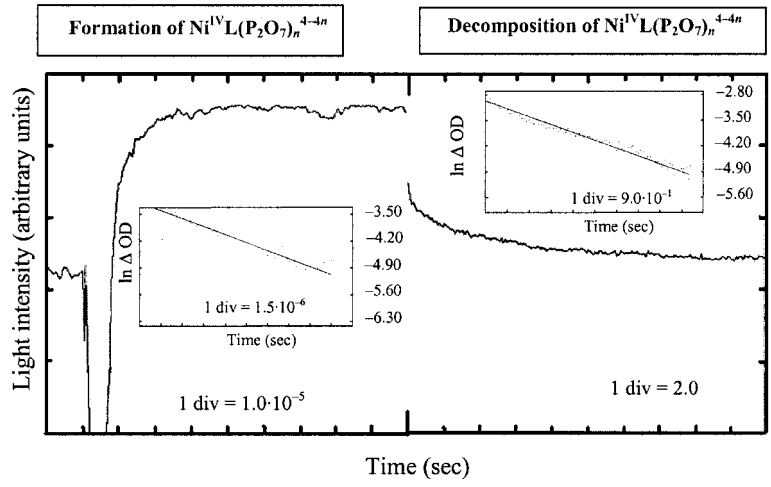


Figure 2. Pulse radiolysis of $Ni^{III}L^{2+}$ in the presence of $Na_4P_2O_7$. Solution composition: $4 \cdot 10^{-4}$ M $Ni^{III}L(SO_4)_2^-$, 0.1 M pyrophosphate, 0.02 M $NaN_3$, pH = 8.0; $\lambda_{max}$ = 450 nm.

 © 2006 Wiley-VCH Verlag GmbH & Co. KGaA, Weinheim 

for the $Ni^{III/II}L$ couple in solutions containing 0.016 M ATP at pH = 5.0). This pH effect is attributed to the $pK_a$ values of ATP ($pK_{a1}$ = 1.77; $pK_{a2}$ = 3.96; $pK_{a3}$ = 6.24).[11] Preparative electrolysis of a solution containing $Ni^{II}L$ in the presence of ATP at 420 mV (vs. SCE) yields an $Ni^{III}L(ATP)_2^{5-}$ complex which is stable for hours in Ar- or air-saturated solutions (as in the $P_2O_7^{4-}$ system it is assumed that due to the inductive effect of the central $Ni^{III}$ ion the ligand is $ATP^{4-}$). The EPR spectrum at 200 K ($g_\perp$ = 2.209; $g_\parallel$ = 2.025; $g_{av}$ = 2.148, 200 K) is in agreement with this assignment. However, the electrochemical oxidation of $Ni^{II}L^{2+}$ in aerated solutions containing ATP is an irreversible process (Figure 3). This observation suggests that the $Ni^{III}L(ATP)_2^{5-}$ complex formed is synergistically oxidized by the electrode and by $O_2$ causing a decomposition of the complex. The results demonstrate that pyrophosphate and ATP stabilize high-valent transition metal complexes. Thus, it is reasonable to suggest that another role of ATP in biological systems is the stabilization of high-valent transition metal complexes, e.g. $Fe^{III}$ and $Mn^{III}$.

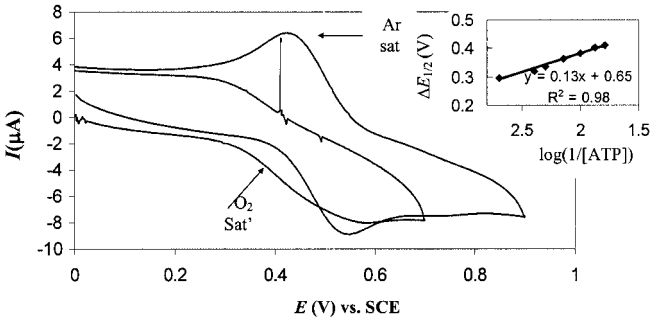


Figure 3. Electrochemistry of $Ni^{II}L^{2+}$ in the presence of ATP. Solution composition: 0.1 M $NaClO_4$, pH = 6.0; a: Ar-saturated; 0.01 M ATP, 0.001 M $Ni^{II}L^{2+}$; b: $O_2$-saturated; 0.01 M ATP, 0.001 M $Ni^{II}L^{2+}$; scan rate 50 mV/s. Inset: Dependence of $\Delta E_{1/2}$ on log (1/[ATP]), where $\Delta E_{1/2}$ is the difference between $E_{1/2}$ for $NiL^{2+}$ in the absence of ATP and the measured $E_{1/2}$.

## Acknowledgments

This study was supported in part by a grant from the Budgeting and Planning Committee of The Council of Higher Education and the Israel Atomic Energy Commission. D. M. wishes to express his thanks to Mrs. Irene Evens for her ongoing interest and support.

[1] I. Zilbermann, E. Maimon, H. Cohen, D. Meyerstein, *Chem. Rev.* **2005**, *105*, 2609.
[2] I. Zilbermann, A. Meshulam, H. Cohen, D. Meyerstein, *Inorg. Chim. Acta* **1993**, *206*, 127.
[3] A. G. Lappin, A. McAuley, *Adv. Inorg. Chem.* **1988**, *32*, 241.
[4] a) E. Zeigerson, I. Bar, J. Bernstein, L. J. Kirchenbaum, D. Meyerstein, *Inorg. Chem.* **1982**, *21*, 73; b) I. Zilbermann, Ph. D. Thesis, Ben-Gurion University of the Negev, **1995**: $K[NiL(HPO_4)_2]^- = 5.8 \cdot 10^8$ M$^{-2}$.
[5] R. I. Haines, A. McAuley, *Coord. Chem. Rev.* **1981**, *39*, 77.
[6] B. J. Parsons, Z. Zhar, S. Navartman, *J. Chem. Soc., Faraday Trans.* **1995**, *91*, 3133.
[7] E. Zeigerson, G. Ginzburg, L. J. Kirschenbaum, D. Meyerstein, *J. Electroanal. Chem.* **1981**, *127*, 113.
[8] M. S. Matheson, L. M. Dorfman, *Pulse Radiolsis*, M.I.T. Press, Cambridge, MA, USA, **1969**.
[9] G. V. Buxton, C. L. Greenstock, W. P. Helman, A. B. Ross, *J. Phys. Chem. Ref.* **1988**, *17*, 513.
[10] Z. B. Alfassi, S. R. Schuler, *J. Phys. Chem.* **1985**, *89*, 3359.
[11] *Standard Critical Stability Constants of Metal Complexes Database*, NIST Standard Reference Date, Gaithersburg, MD, USA.

Received: October 6, 2005
Published Online: December 21, 2005

 © 2006 Wiley-VCH Verlag GmbH & Co. KGaA, Weinheim 

DOI: 10.1002/ejic.200500863

# Inclusion of Metal Complexes into Cavities of 2D Coordination Networks Built from *p*-Sulfonatothiacalix[4]arene Tetranuclear Clusters

**Mingyan Wu,[a] Daqiang Yuan,[a] Lei Han,[a] Benlai Wu,[a] Yanqing Xu,[a] and Maochun Hong*[a]**

**Keywords:** *p*-Sulfonatothiacalix[4]arene / Supramolecular chemistry / Coordination polymer / Inclusion

Reactions of the *p*-sulfonatothiacalix[4]arene salt ($Na_4H_4TCAS$) and $MSO_4$ (M = Co, Cu) in the presence of 2,2′-bipyrazine (2,2′-bpz) generated 2D coordination networks formed by tetranuclear cluster subunits, namely $\{[Co(2,2'\text{-bpz})(H_2O)_4]^{2+}\subset[Co_4(TCAS)(\mu_4\text{-}SO_4)(H_2O)_4]^{2-}\cdot 10.75H_2O\}_n$ (**1**) and $\{[Cu(2,2'\text{-bpz})(H_2O)_3]^{2+}\subset[Cu_4(TCAS)(\mu_4\text{-}SO_4)(H_2O)_4]^{2-}\cdot 16H_2O\}_n$ (**2**). X-ray diffraction analyses reveal that both these complexes include metal–2,2′-bipyrazine complexes into the hydrophobic cavities of *p*-sulfonatothiacalix[4]arenes as guests through supramolecular interactions. (© Wiley-VCH Verlag GmbH & Co. KGaA, 69451 Weinheim, Germany, 2006)

## Introduction

Recently, both the fields of host–guest chemistry and coordination polymers have seen rapid progress and continue to receive wide attention in the chemical sciences.[1,2] The overlapping of these two diverse fields occurs when host molecules are employed as building blocks to construct coordination polymers.[3] The incorporation of host molecules into coordination frameworks, which have well-documented inclusion properties, brings out a number of special aspects not necessarily achievable with conventional ligands, such as multiple inclusion behaviors, unusual topologies, and a vast range of intermolecular interactions. In addition, the coordination polymers formed from host molecules may lead to the development of useful chemoselective materials. Water-soluble calixarenes, which show a wide variety of inclusion properties and coordination abilities to both main-group and transition-metal ions,[4–5] are potentially versatile synthons for the syntheses of coordination polymers. Though there are several examples of coordination polymers constructed from water-soluble calixarenes exhibiting the inclusion of large guest molecules, such as [2.2.2]cryptand and crown ether,[3a,3b] coordination polymers of calixarenes incorporating transition-metal complexes as guests are rarely reported.[3g] Recently, *p*-sulfonatothiacalix[4]arene (TCAS), a new member of the calixarene family, has attracted considerable interest in the broad field of supramolecular chemistry.[6] Like its classic counterpart *p*-sulfonatocalix[4]arene (CAS), *p*-sulfonatothiacalix[4]arene possesses strongly hydrophilic upper and lower rims and a strongly hydrophobic conelike cavity that is bound by four phenyl rings. It can change its conformation from $C_{4v}$ to a cleftlike $C_{2v}$ symmetry while keeping a cone conformation to better accommodate many kinds of ionic and neutral guests. However, the introduction of four sulfur atoms into the calix[4]arene skeleton leads to at least two significant changes. Firstly, the electron-rich cavity of thiacalix[4]arene is larger than that of the classic calix[4]arene. Thus, regardless of electron-density effects, *p*-sulfonatothiacalix[4]arene shows a higher inclusion ability to encapsulate aromatic moieties than classic calix[4]arene, which suggests that the size of the cavity is more important in determining the inclusion ability.[7] Secondly, *p*-sulfonatothiacalix[4]arene can bind metal ions not only at the upper and lower rims but also at the linker positions,[8] which makes it a good candidate for constructing polymers. As reported previously, it tends to form tetranuclear bivalent anions with transition metal ions, capture small guests such as water and the pyridinium cation in its hydrophobic pocket, and further extend its structure through metal–sulfonate oxygen bonds into a 2D layer.[9] Based on the above discussion, we reason that divalent metal complexes with aromatic ligands such as 2,2′-bipyrazine are likely to be incorporated into the 2D cavities of thiacalixarenes for the balance of the charge and interactions with aromatic rings,[10] as shown in Scheme 1. Herein, we wish to report two coordination polymers derived from *p*-sulfonatothiacalix[4]arenes, 2,2′-bipyrazine (2,2′-bpz), and $MSO_4$ (M = Co, Cu), namely, $\{[Co(2,2'\text{-bpz})(H_2O)_4]^{2+}\subset[Co_4(TCAS)(\mu_4\text{-}SO_4)(H_2O)_4]^{2-}\cdot 10.75H_2O\}_n$

[a] State Key Laboratory of Structural Chemistry, Fujian Institute of Research on the Structure of Matter, Chinese Academy of Sciences,
Fuzhou, Fujian, China
Fax: + 86-591-8379-4946
E-mail: mailto:hmc@ms.fjirsm.ac.cn

Supporting information for this article is available on the WWW under http://www.eurjic.org or from the author.

 © 2006 Wiley-VCH Verlag GmbH & Co. KGaA, Weinheim 

(**1**) and $\{[Cu(2,2'\text{-bpz})(H_2O)_3]^{2+}\subset[Cu_4(TCAS)(\mu_4\text{-}SO_4)(H_2O)_4]^{2-}\cdot 16H_2O\}_n$ (**2**), with an unusual incorporation of the metal–2,2′-bpz complexes into the cavities of the *p*-sulfonatothiacalix[4]arenes.

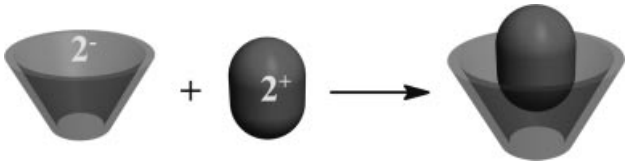


Scheme 1. Schematic representation of the incorporation of the divalent metal complex with aromatic ligands into the bivalent anionic cavity of the *p*-sulfonatothiacalix[4]arene.

## Results and Discussion

Crystals of complexes **1** and **2** suitable for X-ray diffraction were obtained by slow diffusion of an MeOH solution of 2,2′-bpz into an aqueous solution of $Na_4H_4TCAS$ and $CoSO_4$, and $Na_4H_4TCAS$ and $CuSO_4$, respectively. Complexes **1** and **2** crystallize in space group *C*2/*c* and $P2_1/c$, respectively. They display a very similar structure of a 2D, up–down bilayer arrangement built from $[M_4(TCAS)(\mu_4\text{-}SO_4)]^{2-}$(M = Co for **1**, Cu for **2**) subunits, with inclusion of metal–2,2′-bpz cations into the cavities of the *p*-sulfonatothiacalix[4]arenes as counterions.

In the bowl-like anion subunit, a trapezoid-like tetranuclear cluster is sandwiched between one TCAS unit and one sulfate ligand (Figure 1). The fully deprotonated $TCAS^{8-}$ unit maintains a conventional cone conformation and utilizes its phenoxy groups as $\mu_2$-phenoxy bridges to bind four $M^{II}$ ions. The average $M\text{–}O_{(phenoxy)}$ distances are 2.105 Å in **1** and 2.072 Å in **2**. Interestingly, at the lower rim of $TCAS^{8-}$, the $SO_4^{2-}$ anion binds to the four $M^{II}$ ions in a rare tridentate coordination mode to complete the base of the bowl.[9] Two oxygen atoms of the sulfate anion ligate to two metal centers and one acts as a bridge linking the other two metal centres. All of the four cobalt(II) ions in **1** and three of the copper(II) ions (Cu1, Cu2, Cu3) in **2** are in an $O_5S$ octahedral geometry. The oxygen atoms from aqua ligands and the sulfonate groups of adjacent *p*-sulfonatothiacalix[4]arenes complete the six-coordination spheres. Exceptionally, in **2**, Cu4 is in an $O_4S$ square-pyramidal geometry, with an aqua ligand in the equatorial plane. Notably, each $[M_4(TCAS)(\mu_4\text{-}SO_4)]^{2-}$ subunit acts as a three-connector and extends the structure of **1** or **2** into an interesting molecular brick-wall architecture (Scheme 2). Though the aggregation of the tetranuclear clusters in both complexes is directed by the coordination of the sulfonate groups of

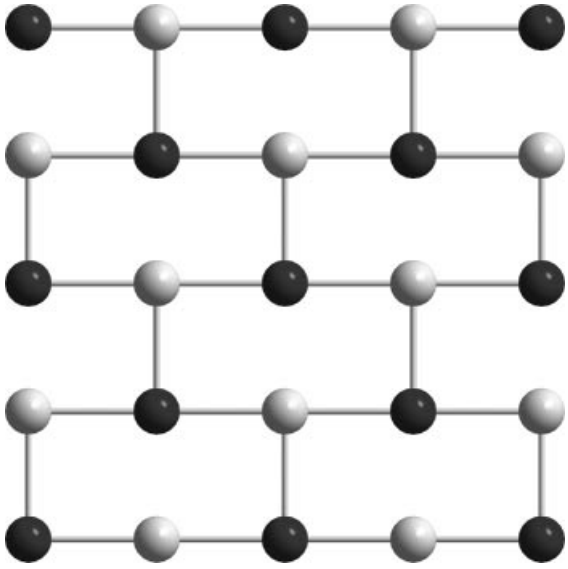

Scheme 2. Schematic representation of the brick-wall networks of **1** and **2**.

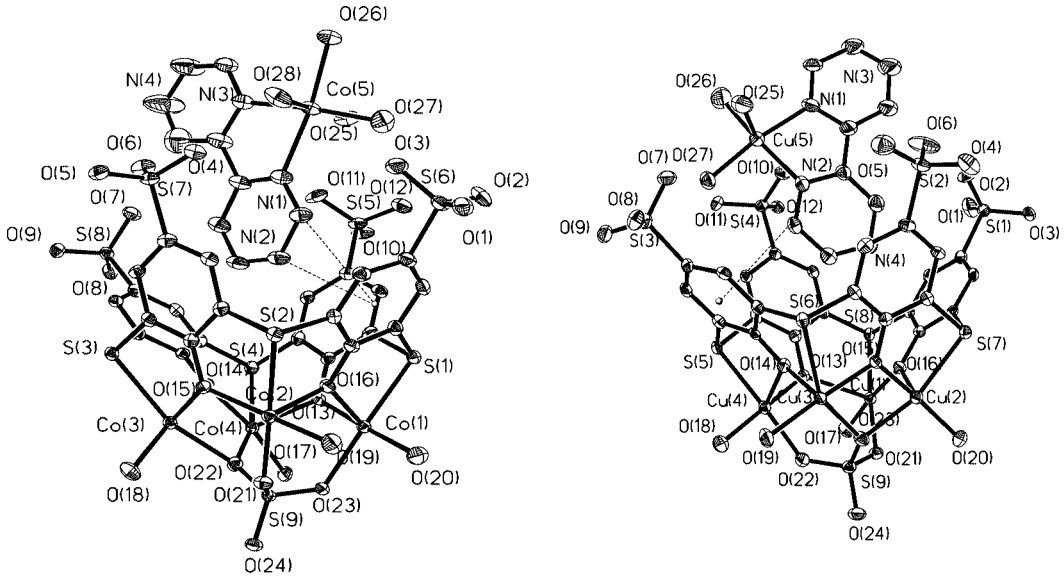


Figure 1. The X-ray asymmetric units of **1** (left) and **2** (right). Hydrogen atoms and solvent molecules omitted for clarity.

 © 2006 Wiley-VCH Verlag GmbH & Co. KGaA, Weinheim 

$TCAS^{8-}$, there is a slight difference in the coordination modes. In **1**, two sulfonate groups monodentately link the subunits into an infinite chain along the crystallographic *b* axis (Figure 2). Along the crystallographic *a* axis, two sulfonate groups adopt an O,O′-$\eta^1$:$\eta^1$:$\mu_2$ bridging bidentate mode to connect the two adjacent linear chains into an up–down bilayer structure (Figure 2). In **2**, one sulfonate group adopts an O,O′-$\eta^1$:$\eta^1$:$\mu_2$ bridging bidentate mode (Figure 3) to join the subunits into an infinite chain along the crystallographic *b* axis. Along the crystallographic *c* axis, two sulfonate groups bind in a monodentate coordination mode and act as chain linkers (Figure 3). Along the third crystallographic axis (*c* axis for **1**, *a* axis for **2**), the layers lie directly above one another to give 1D channels. Large numbers of lattice water molecules (10.75 and 16 in the asymmetric units of **1** and **2**, respectively) fill the channels and interstices between the layers (Figure S1 and Figure S2 in the Supporting Information).

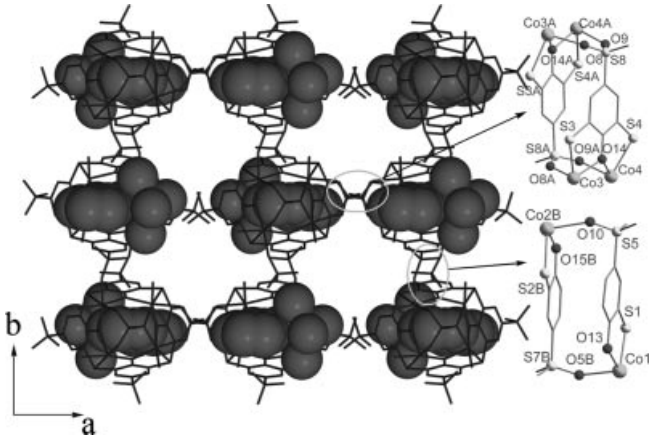


Figure 2. The extended structure of **1** with the incorporation of cobalt–2,2′-bpz cations into the cavities of *p*-sulfonatothiacalix[4]-arenes.

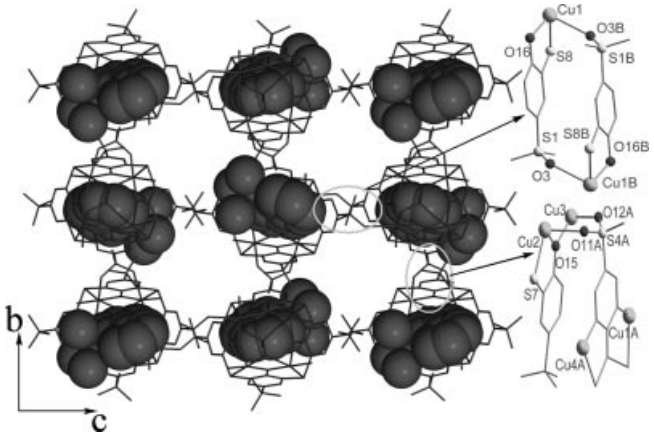


Figure 3. The extended structure of **2** with the incorporation of copper–2,2′-bpz cations into the cavities of *p*-sulfonatothiacalix[4]-arenes.

Despite being fixed by the four metal centers and the $SO_4^{2-}$ anion at the lower rim, the *p*-sulfonatothiacalix[4]arene shows versatility in displaying various conformations and splays its opposite aromatic rings into a cleftlike $C_{2v}$ symmetry to accommodate the guest. Comparatively, the separation distance between the opposite phenyl ring centroids of each *p*-sulfonatothiacalix[4]arene in **1** is much larger (7.5 Å) than that of **2** (6.2 Å). Accordingly, the dihedral angles between the aromatic rings and the plane of the phenolic oxygen atoms are 137.9° (in **1**) and 136.9° (in **2**), which are larger than that of the corresponding coordination polymer that encapsulates the pyridinium cation (133.8°).[9a] The metal–2,2′-bpz cation, as expected, is precariously held in the shallow hydrophobic pocket of the $TCAS^{8-}$ anion as the counterion (Figure 1) by cooperative supramolecular interactions. In **1**, the $[Co(2,2'\text{-bpz})(H_2O)_4]^{2+}$ moiety is held by two CH···π interactions, one involving a *meta* pyridyl hydrogen atom and a phenyl ring of the *p*-sulfonatothiacalix[4]arene with a C–H···Ar centroid distance of 2.926 Å, and the other involving a *para* pyridyl hydrogen atom and the same phenyl ring of the *p*-sulfonatothiacalix[4]arene with a C–H···Ar centroid distance of 3.164 Å, as shown in Figure 1 left. However, in **2**, the $[Cu(2,2'\text{-bpz})(H_2O)_3]^{2+}$ cation uses one of its *meta* pyridyl hydrogen atoms to form a CH···π interaction with a phenyl ring of the *p*-sulfonatothiacalix[4]arene, with a C–H···Ar centroid distance of 2.700 Å (Figure 1 right). Additionally, other intermolecular interactions such as electrostatic attractions, hydrophobic–hydrophobic interactions, and hydrogen bonding may also play important roles in the recognition process between metal–2,2′-bpz cations and $TCAS^{8-}$ anions. The closest O···O separations of the aqua ligands in the metal–2,2′-bpz cations and the oxygen atoms of the sulfonate groups are 2.703 Å in **1** and 2.705 Å in **2**, which shows rather strong hydrogen-bonding interactions between the hosts and guests.

In summary, we have successfully synthesized two tetranuclear cluster coordination polymers, which both include metal–2,2′-bpz complexes as guests through a combination of supramolecular interactions. It further demonstrates that *p*-sulfonatothiacalix[4]arene is a good host molecule with the flexibility to accommodate a range of guests through self-adjustment and that it is a good ligand to construct coordination polymers. Because of the thermal stability of the skeleton, the layer coordination networks built from tetranuclear clusters may prove to be of high interest in separation/absorption applications.[11] Further research is under way and systematic results will be reported later.

## Experimental Section

**Syntheses of Complexes 1 and 2:** A solution of 2,2′-bipyrazine (8 mg, 0.05 mmol) in $CH_3OH$ (4 $cm^3$) was carefully layered on a solution of $Na_4H_4TCAS$ (45 mg, 0.05 mmol) and $CoSO_4{\cdot}6H_2O$ (66 mg, 0.25 mmol) or $CuSO_4{\cdot}5H_2O$ (63 mg, 0.25 mmol) in water (4 $cm^3$, pH = 3.8) using an $H_2O/CH_3OH$ (3 $cm^3$) buffer. Over a period of about three weeks, red (**1**) or orange (**2**) prism crystals formed, which were suitable for X-ray diffraction analyses. Yield: 26 mg for **1** (30.67%, based on $Na_4H_4TCAS$) or 24 mg for **2** (26.95%, based on $Na_4H_4TCAS$). **1**, $C_{32}H_{51.50}Co_5N_4O_{38.75}S_9$ (1695.46): calcd. C 22.67, H 3.06, N 3.30; found C 22.81, H 2.98,

 © 2006 Wiley-VCH Verlag GmbH & Co. KGaA, Weinheim 

N 3.36%. **2**, $C_{32}H_{46}Cu_5N_4O_{43}S_9$ (1780.97): calcd. C 21.58, H 2.60, N 3.15; found C 21.69, H 2.53, N 3.19%.

**X-ray Structure Determination:** Crystal data for **1**: $C_{32}H_{51.50}Co_5N_4O_{38.75}S_9$ (1695.46), monoclinic, space group *C*2/*c*, $T$ = 173(2) K, $a$ = 22.764(4), $b$ = 18.334(4), $c$ = 30.170(6) Å, $\beta$ = 95.057 (7), $V$ = 12543(4) Å$^3$, $Z$ = 8, $d_{calcd.}$ = 1.796 Mg m$^{-3}$, $F$(000) = 6884, $\mu$ (Mo-$K_\alpha$) = 1.695 mm$^{-1}$, red, 0.20 × 0.13 × 0.06 mm, $\theta$ range 3.05–27.49°, 46748 reflections collected, 14025 unique ($R_{int}$ = 0.0381). Final *GooF* = 1.074, $R_1$ = 0.0546, $wR_2$ = 0.1301, $R$ indices based on 12226 reflections with $I > 2\sigma(I)$ (refinement on $F^2$), 838 parameters, $(\Delta\rho)_{max}$ = 1.802, $(\Delta\rho)_{min}$ = –0.767 e/Å$^{-3}$. Crystal data for **2**: $C_{32}H_{46}Cu_5N_4O_{43}S_9$ (1780.97), monoclinic, space group $P2_1/c$, $T$ = 173(2) K, $a$ = 14.981(3), $b$ = 18.407(4), $c$ = 23.447(5) Å, $\beta$ = 100.571(2), $V$ = 6356(2) Å$^3$, $Z$ = 4, $d_{calcd.}$ = 1.861 Mg m$^{-3}$, $F$ (000) = 3596, $\mu$ = 2.049 mm$^{-1}$, orange, 0.40 × 0.15 × 0.60 mm, $\theta$ range 2.32–27.48°, 47791 reflections collected, 14314 unique ($R_{int}$ = 0.0457), Final *GooF* = 1.161, $R_1$ = 0.0659, $wR_2$ = 0.1342, $R$ indices based on 12550 reflections with $I > 2\sigma(I)$ (refinement on $F^2$), 895 parameters, $(\Delta\rho)_{max}$ = 1.495, $(\Delta\rho)_{min}$ = –0.848 e/Å$^{-3}$. Data collections for the two compounds were performed with a Rigaku Mercury-CCD diffractometer with graphite-monochromated Mo-*K*α radiation ($\lambda$ = 0.71073 Å). The data sets were collected at 173(2) K ($\omega$-scan mode). The structures of the two compounds were solved by direct methods and refined by full-matrix least-squares techniques with the *SHELXTL*-97 program package.[12] All non-hydrogen atoms were refined anisotropically except for several disordered solvent molecules. The organic hydrogen atoms were located at geometrically calculated positions and refined using a riding model [C–H = 0.95 Å $U_{iso}$(H) = 1.2$U_{eq}$(C)]. The hydrogen atoms on the water molecules were located in difference density maps and were refined as riding using the instruction AFIX 3,[12] and no attempt was made to locate the hydrogen atoms of disorder water molecules.

CCDC-266331 and CCDC-266330 (for **1** and **2**, respectively) contain the supplementary crystallographic data for this paper. These data can be obtained free of charge from The Cambridge Crystallographic Data Centre via www.ccdc.cam.ac.uk/data_request/cif.

**Supporting Information:** (see footnote on the first page of this article). Figure S1 – Lattice water molecules occupying the channels and the interstices between the layers in **1**, and Figure S2 – Lattice water molecules occupying the channels and the interstices between the layers in **2**.

## Acknowledgments

We are grateful for the financial support from NSFC (No. 20231020), Natural Foundation of Fujian Province. Many thanks to Professor Xiaotai Wang for the modifications suggested for this paper.

[1] a) J. W. Steed, J. L. Atwood, *Supramolecular Chemistry*, John Wiley & Sons Ltd. Chichester, **2000**; b) Z. Asfari, V. Bohmer, *Calixarenes 2001*, Kluwer Academic Publications, Dordrecht, **2001**; c) L. Mandolini, R. Ungaro, *Calixarenes in Action*, Imperial College Press, London, **2000**; d) E. Arunkumar, C. C. Forbes, B. D. Smith, *Eur. J. Org. Chem.* **2005**, 4051–4059; e) C. H. Huang, D. M. Bassani, *Eur. J. Org. Chem.* **2005**, 4041–4050.

[2] a) C. Janiak, *Dalton Trans.* **2003**, 2781–2804; b) S. L. James, *Chem. Soc. Rev.* **2003**, *32*, 276–288; c) R. Robson, *J. Chem. Soc., Dalton Trans.* **2000**, 3735–3744; d) A. J. Blake, N. R. Champness, P. Hubberstey, W. S. Li, M. Schroder, M. A. Withersby, *Coord. Chem. Rev.* **1999**, *183*, 117–138.

[3] a) S. J. Dalgarno, C. L. Raston, *Chem. Commun.* **2002**, 2216–2217; b) H. R. Webb, M. J. Hardie, C. L. Raston, *Chem. Eur. J.* **2001**, *7*, 3616–3620; c) M. J. Hardie, C. J. Sumby, *Inorg. Chem.* **2004**, *43*, 6872–6874; d) H. Akdas, E. Graf, M. W. Hosseini, A. D. Cian, J. M. Harrowfield, *Chem. Commun.* **2000**, 2219–2220; e) L. Pan, X. Y. Huang, H. N. Phan, T. J. Emge, J. Li, X. T. Wang, *Inorg. Chem.* **2004**, *43*, 6878–6880; f) L. Carlucci, G. Ciani, D. M. Proserpio, F. Porta, *Angew. Chem. Int. Ed.* **2003**, *42*, 317–322; g) S. J. Dalgarno, M. J. Hardie, J. E. Warren, C. L. Raston, *Dalton Trans.* **2004**, 2413–2416.

[4] a) G. W. Orr, L. J. Barbour, J. L. Atwood, *Science* **1999**, *285*, 1049–1052; b) J. L. Atwood, L. J. Barbour, S. J. Dalgarno, M. J. Hardie, C. L. Raston, H. R. Webb, *J. Am. Chem. Soc.* **2004**, *126*, 13170–13171; c) S. J. Dalgarno, M. J. Hardie, M. Makha, C. L. Raston, *Chem. Eur. J.* **2001**, *7*, 2834–2839; d) T. Ness, P. J. Nichols, C. L. Raston, *Eur. J. Inorg. Chem.* **2001**, 1993–1997; e) S. J. Dalgarno, M. J. Hardie, M. Makha, C. L. Raston, *Chem. Eur. J.* **2003**, *9*, 2834–2839; f) J. L. Atwood, L. J. Barbour, M. J. Hardie, C. L. Raston, *Coord. Chem. Rev.* **2001**, *222*, 3–32.

[5] a) A. W. Coleman, S. Bott, G. S. D. Morley, C. M. Means, K. D. Robinson, H. Zhang, J. L. Atwood, *Angew. Chem. Int. Ed. Engl.* **1988**, *27*, 1361–1362; b) S. G. Bott, A. W. Coleman, J. L. Atwood, *J. Am. Chem. Soc.* **1988**, *110*, 610–611; c) J. L. Atwood, G. W. Orr, F. Hamada, R. L. Vincent, S. G. Bott, K. D. Robinson, *J. Am. Chem. Soc.* **1991**, *113*, 2760–2761; d) J. W. Steed, C. P. Johnson, C. L. Barnes, R. K. Juneja, J. L. Atwood, S. Reilly, R. L. Hollis, P. H. Smith, D. L. Clark, *J. Am. Chem. Soc.* **1995**, *117*, 11426–11433; e) A. Drljaca, M. J. Hardie, T. J. Ness, C. L. Raston, *Eur. J. Inorg. Chem.* **2000**, 2221–2229.

[6] a) Q. L. Guo, W. X. Zhu, S. L. Ma, S. J. Dong, M. Q. Xu, *Polyhedron* **2004**, *23*, 1461–1466; b) Q. L. Guo, W. X. Zhu, S. L. Ma, D. Q. Yuan, S. J. Dong, M. Q. Xu, *J. Mol. Struct.* **2004**, *690*, 63–68; c) B. Wanno, W. Sang-aroon, T. Tuntulani, B. Polpoka, V. Ruangpornvisuti, *J. Mol. Struct. (Theochem.)* **2003**, *629*, 137–150; d) T. Horiuchi, N. Iki, H. Oka, S. Miyano, *Bull. Chem. Soc. Jpn.* **2002**, *75*, 2615–2619; e) P. Lhotak, *Eur. J. Org. Chem.* **2004**, 1675–1692; f) Y. Liu, H. Wang, H. Y. Zhang, L. H. Wang, *Cryst. Growth Des.* **2005**, *5*, 231–235.

[7] N. Kon, N. Iki, S. Miyano, *Org. Biomol. Chem.* **2003**, *1*, 751–755.

[8] a) N. Iki, N. Morohashi, C. Kabuto, S. Miyano, *Chem. Lett.* **1999**, 219–220; b) G. Mislin, E. Graf, M. W. Hosseini, A. Bilyk, A. K. Hall, J. M. Harrowfield, B. W. Skelton, A. H. White, *Chem. Commun.* **1999**, 373–374; c) A. Bilyk, A. K. Hall, J. M. Harrowfield, M. W. Hosseini, G. Mislin, B. W. Skelton, C. Taylor, A. H. White, *Eur. J. Inorg. Chem.* **2000**, 823–826; d) H. Akdas, E. Graf, M. W. Hosseini, A. D. Cian, A. Bilyk, B. W. Skelton, G. A. Koutsantonis, I. Murray, J. M. Harrowfield, A. H. White, *Chem. Commun.* **2002**, 1042–1043; e) A. Bilyk, A. K. Hall, J. M. Harrowfield, M. W. Hosseini, B. W. Skelton, A. H. White, *Aust. J. Chem.* **2000**, *53*, 895–898.

[9] a) D. Q. Yuan, Y. Q. Xu, M. C. Hong, W. H. Bi, Y. F. Zhou, X. Li, *Eur. J. Inorg. Chem.* **2005**, 1182–1187; b) Q. L. Guo, W. X. Zhu, S. Gao, S. L. Ma, S. J. Dong, M. Q. Xu, *Inorg. Chem. Commun.* **2004**, *7*, 467–470.

[10] a) P. J. Nichols, C. L. Raston, J. W. Steed, *Chem. Commun.* **2001**, 1062–1063; b) Y. Liu, D. S. Guo, H. Y. Zhang, *J. Mol. Struct.* **2005**, *734*, 241–245; c) A. R. Mustafina, V. V. Skripacheva, A. T. Gubaidullin, S. K. Latipov, A. V. Toropchina, V. V. Yanilkin, S. E. Solovieva, I. S. Antipin, A. I. Konovalov, *Inorg. Chem.* **2005**, *44*, 4017–4023; d) M. Makha, C. L. Raston, A. N. Sobolev, A. H. White, *Chem. Commun.* **2004**, 1066–1067; e) Y. Liu, D. S. Guo, E. C. Yang, H. Y. Zhang, Y. L. Zhao, *Eur. J. Org. Chem.* **2005**, 162–170.

[11] a) J. L. Atwood, L. J. Barbour, A. Jerga, *Science* **2002**, *296*, 2367–2369; b) J. L. Atwood, L. J. Barbour, A. Jerga, *Angew. Chem. Int. Ed.* **2004**, *43*, 2948–2950; c) J. L. Atwood, L. J.

 © 2006 Wiley-VCH Verlag GmbH & Co. KGaA, Weinheim 

Barbour, P. K. Thallapally, T. B. Wirsig, *Chem. Commun.* **2005**, 51–53.
[12] a) G. M. Sheldrick, *SHELXS97, Program for the Solution of Crystal Structure*, **1997**, University of Göttingen, Germany; b) G. M. Sheldrick, *SHELXL97, Program for the Solution of Crystal Structure*, **1997**, University of Göttingen, Germany.
Received: September 26, 2005
Published Online: December 16, 2005

 © 2006 Wiley-VCH Verlag GmbH & Co. KGaA, Weinheim 

DOI: 10.1002/ejic.200500924

# Entrapment of a Hexamer of Nitrobenzene Molecules between the Layers of (4,4)-Coordination Networks Containing Intra-β-Sheet Hydrogen Bonds

**Madhushree Sarkar[a] and Kumar Biradha*[a]**

**Keywords:** Coordination networks/ Hydrogen bonds/ Aggregation / Host-guest systems

Two *exo*-bidentate pyridyl ligands containing diamides as spacers were shown to form non-interpenetrated 2D-coordination networks of (4,4)-geometry upon treatment with $Cu(NO_3)_2$ and NaSCN. The crystal structures reveal that both structures contain intralayer β-sheet hydrogen bonds. In one of these structures nitrobenzene occupies 60 % of the crystal volume included between the coordination networks. The nitrobenzene molecules form a layer which has the hexameric C–H···O hydrogen bonded aggregate as a basic building block.
(© Wiley-VCH Verlag GmbH & Co. KGaA, 69451 Weinheim, Germany, 2006)

The design and syntheses of novel coordination networks is currently an interesting area of research in chemistry as it offers novel materials with functional properties.[1] One of the interesting aspects of coordination networks is that they offer intriguing possibilities for the inclusion and aggregation of guest molecules. The exploration of the geometry of such aggregates of small molecules in different surroundings is the most significant aspect as it helps in delineating and updating the principles of crystal engineering and supramolecular chemistry. The structure and characteristic properties of those aggregates are distinctly different from the properties of the parent molecules.[2] There are several instances in which weak intermolecular interactions have led to the formation of a variety of aggregations of small molecules in different surroundings.[2] We report here the C–H···O hydrogen-bonded hexameric aggregate of nitrobenzene that is trapped between the layers of a (4,4)-metal-organic network formed by $Cu^{II}$ and bis(3-pyridylcarboxamido)ethane (**1**). Ligand **1** contains two pyridine moieties for the formation of extended coordination networks, an alkyl moiety for providing the flexibility and two amide moieties for the formation of N–H···O hydrogen bonds.[3] Recently, ligand **1** was shown by us to form doubly interpenetrated and non-interpenetrated (4,4)-coordination networks upon reaction with CuI.[4] In both cases the networks are propagated by CuI clusters, secondary building units, and are joined together by β-sheet hydrogen bonds. Here we report another interesting variation of a (4,4)-network which is formed by the reaction of ligand **1** with $Cu(SCN)_2$. The salient feature of the network is that the β-sheet hydrogen bonds exist within the layer of the (4,4)-network but not between the layers. As a result, the (4,4)-networks have no cavities and the aromatic guest molecules are included between the layers. The Cambridge Structural Database (CSD)[5] analysis on nitrobenzene complexes reveals that the C–H···O hydrogen-bonded nitrobenzene aggregate observed here is unique and unprecedented.

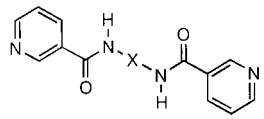


**1**: X= -$CH_2$-$CH_2$- **2**: X= -$C_6H_4$-

The careful layering of an MeOH solution of $Cu(NO_3)_2$ and NaSCN onto a nitrobenzene solution of ligand **1** resulted in single crystals of complex $\{Cu(\mathbf{1})_2(SCN)_2 \cdot 6(\text{nitrobenzene})\}_n$ (**3**). An X-ray structure analysis reveals that complex **3** exhibits a (4,4)-coordination network and includes six nitrobenzene molecules per metal atom. The asymmetric unit of **3** contains a Cu atom with half occupancy (on inversion center), two half units of **1**, one SCN anion and three nitrobenzene molecules. Furthermore, the Cu atom has a highly distorted octahedral geometry as four units of **1** occupy the equatorial positions [Cu–N: 2.048(5) Å and 2.642(5) Å] and two SCN [Cu–N: 1.953(5) Å] anions occupy the axial positions. Each loop of the (4,4)-network has a rhomboidal shape with two Cu–Cu diagonal distances of 31.2 and 10 Å (Figure 1a). The ligands in the sheet recognize each other through β-sheet hydrogen bonds [N–H···O: 2.989(7) Å, 164°; 2.933(7) Å, 157°] and edge-to-edge aromatic C–H···π interactions. The interlayer separation between the coordination networks is as high as 11 Å as one layer of nitrobenzene molecules occupies the space between the layers (Figure 1b).

[a] Department of Chemistry, Indian Institute of Technology, Kharagpur 721302, West Bengal, India
Fax: +91-3222-282252
E-mail: kbiradha@chem.iitkgp.ernet.in
Supporting information for this article is available on the WWW under http://www.eurjic.org or from the author.

 © 2006 Wiley-VCH Verlag GmbH & Co. KGaA, Weinheim 

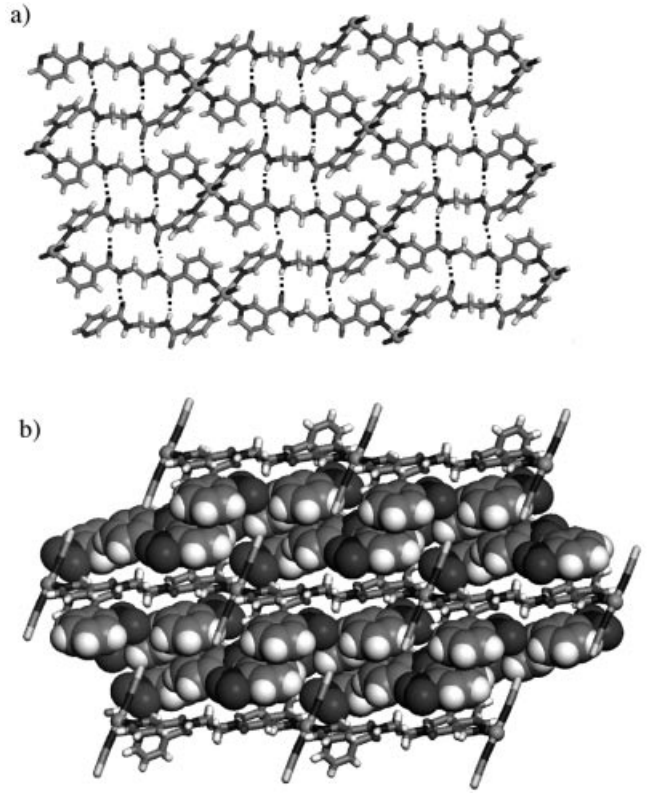


Figure 1. a) (4,4)-Network in the crystal structure of **3**. Note the intralayer β-sheet hydrogen bonds; b) entrapment of a nitrobenzene layer between (4,4)-coordination networks (view along the short diagonal).

The layer of nitrobenzene consists of C–H···O hydrogen-bonded hexameric aggregates of nitrobenzene molecules (Figure 2a). In the aggregate all the molecules lie in a plane and interact with each other through six C–H···O hydrogen bonds [C···O, C–H···O: 3.221(12) Å, 144°; 3.340(18) Å, 132°; 3.303(15) Å, 129°]. Furthermore, the aggregate has a distorted hexagon shape with the length and width dimensions of 25.8 and 11.4 Å, respectively. These aggregates stack on each other in a slipped fashion through aromatic π–π interactions to form a layer which interacts with the host framework through C–H···O hydrogen bonds and aromatic interactions (Figure 2b).

The repetition of the reaction by using other aromatic guests such as benzene, xylene, toluene, naphthalene and benzoic acid in place of nitrobenzene resulted in precipitates but not single crystals. Furthermore, the change of spacers from ethyl to butyl/hexyl/octyl did also not result in single-crystal formation. However, use of bromobenzene instead of nitrobenzene resulted in single crystals in very low yield (5%) which are very unstable for data collection.[6]

In **3**, nitrobenzene occupies as much as 61% of the unit-cell volume. The analysis of the CSD shows that this aggregate is the first of its kind among the 135 nitrobenzene solvates that are present in the database. However, the structural motif **I**, which is part of the aggregate, was found to exist in 23 structures out of the 4607 structures of the nitroaromatic derivatives.

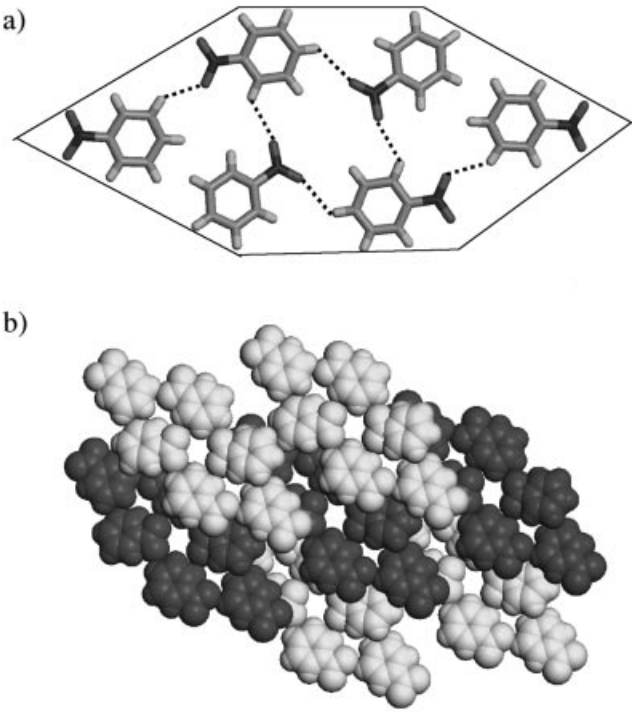


Figure 2. a) C–H···O hydrogen-bonded hexameric aggregate of nitrobenzene molecules; b) layer of hexameric aggregates formed through π–π interactions.

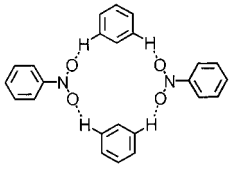

**I**

In TGA, a gradual weight loss (8%) of **3** occurred from 50–96 °C which may correspond to the loss of one of the nitrobenzene molecules bound by only one C–H···O hydrogen bond in the hexamer. From 90–141 °C, 40% weight loss occurred which corresponds to five nitrobenzene molecules. The network is stable up to 260 °C. Guest exchange reactions were tried by immersing crystals of **3** in benzene, toluene or naphthalene in $CHCl_3$. TLC of these crystals indicated the absence of nitrobenzene. From the elemental and powder X-ray diffraction analysis of the immersed crystals, it can be concluded that the nitrobenzene molecules are expelled, but the new guest molecules are not included. The TGA plots and XRPD spectra are included in the Supporting Information.

Ligand **2** was then considered as it has a phenyl spacer which makes the host network self-sufficient to interact with neighboring layers. The layering of an MeOH solution of $Cu(NO_3)_2$ and NaSCN onto a nitrobenzene solution of ligand **2** resulted in single crystals of the complex $\{Cu(\mathbf{2})_2(SCN)_2\}$ (**4**). The X-ray diffraction analysis revealed that complex **4** also contains a (4,4)-network similar to **3**. The unit-cell contents are the same as for **3** but without nitrobenzene molecules, and the coordination geometry of the

 © 2006 Wiley-VCH Verlag GmbH & Co. KGaA, Weinheim 

Cu atom is a distorted octahedron [Cu–N: 2.060(4), 2.494(4) Å; Cu–NCS: 1.965(4) Å]. Within the (4,4)-network the ligands recognize each other through β-sheet hydrogen bonds [N–H···O: 2.924(5) Å, 150°; 3.154(5) Å, 152°] as well as aromatic edge-to-face interactions which form between the phenyl spacers and also between the pyridyl groups of adjacent ligands (Figure 3). The Cu atoms in the network are joined together by ligand **2** with a distance of 17.272 Å and each loop has a rhomboidal shape with diagonal-to-diagonal distances of 33.7 and 10.5 Å. These layers stack on each other with an interlayer separation of 5.2 Å which suggests strong aromatic edge-to-face interactions between the layers. The use of other solvents, such as $CHCl_3$ or toluene, in place of nitrobenzene also resulted in single crystals of complex **4**, which indicates that the crystallization of complex **4** does not depend on the nature of the solvents. These reactions emphasize the fact that the host–host (aromatic) interactions are robust enough to allow crystal formation of complex **4**.

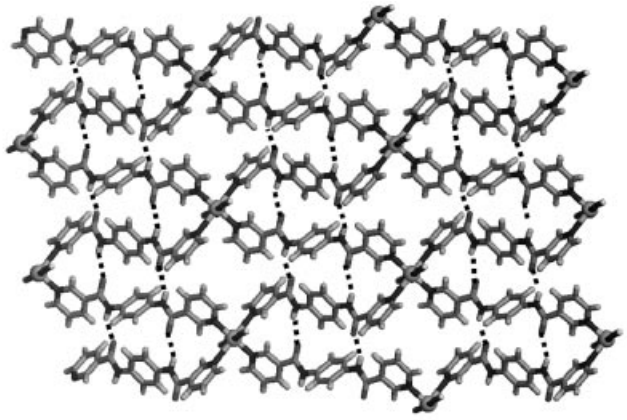

Figure 3. (4,4)-Coordination network of crystal structure **4**. Note the intralayer β-sheet hydrogen bonds and edge-to-face aromatic interactions between the ligands.

## Experimental Section

**General:** FTIR spectra were recorded with an NEXUS-870 instrument, Thermo Nicolet Corporation. UV/Vis spectra were recorded with a Shimadzu UV-1601. Elemental analyses were obtained with a Perkin Elmer instrument, series II, CHNS/O analyzer 2400. TGA data were recorded with a Perkin Elmer instrument, Pyris Diamond TG/DTA (air). Powder XRD data were recorded with a Philips PW 1710 diffractometer.

**Synthesis of Complex 3:** Methanol (1.0 mL) was layered onto a nitrobenzene (5.0 mL) solution of *N*,*N*′-bis(3-pyridinecarboxamido)-1,2-ethane (**1**) (40.0 mg, 0.148 mmol). Onto this solution was layered a $Cu(SCN)_2$ solution, which was obtained by mixing a methanolic solution (0.5 mL) of $Cu(NO_3)_2$ (17.8 mg, 0.074 mmol) and a methanolic solution (0.5 mL) of NaSCN (11.9 mg, 0.148 mmol). Green crystals formed in 70% yield (300 mg) after 3–4 d. $C_{66}H_{58}CuN_{16}O_{16}S_2$ (1458.94): calcd. C 54.33, H 3.97, N 15.35; found C 53.48, H 3.71, N 15.02. IR: $\tilde{\nu}$ = 3317 (N–H stretch), 3071 (aromatic C–H stretch), 2064 (thiocyanate CN stretch), 1632 (amide C=O stretch), 1601(amide II), 1519 (asym. N–O stretch), 1342 (sym. N–O stretch), 849.46 (C–N stretch) $cm^{-1}$. UV: $\lambda_{max}$ ($\varepsilon$) = 205.67 (816097), 260.27 (616248 $dm^3 mol^{-1} cm^{-1}$) nm.

**Synthesis of Complex 4:** A methanolic solution of $Cu(SCN)_2$, formed by addition of an MeOH (0.5 mL) solution of $Cu(NO_3)_2$ (15.2 mg, 0.063 mmol) to an MeOH (0.5 mL) solution of NaSCN (10.2 mg, 0.126 mmol), was carefully layered onto an ethanol (1 mL)/$CHCl_3$ (5.0 mL) solution (6 mL) of 1,4-bis(3-pyridinecarboxamido)benzene (**2**) (40.0 mg, 0.126 mmol). Light-green crystals formed in 20% yield (40.8 mg) after a week. $C_{38}H_{28}CuN_{10}O_4S_2$ (816.36): calcd. C 55.9, H 3.4, N 17.1; found C 55.0, H 2.9, N 16.8. IR: $\tilde{\nu}$ = 3326 (N–H stretch), 3066 (aromatic C–H stretch), 2068 (thiocyanate, CN), 1645 (C=O stretch), 1610 (amide) $cm^{-1}$. UV: $\lambda_{max}$ ($\varepsilon$) = 204 (45314), 295.71 (27043 $dm^3 mol^{-1} cm^{-1}$) nm.

**X-ray Structure Analysis of Complexes 3 and 4:** The single-crystal data sets were collected at room temperature for both complexes with a Bruker-Nonius Mach3 CAD4 X-ray diffractometer using graphite-monochromated Mo-$K_\alpha$ radiation ($\lambda$ = 0.71073 Å) in the ω-scan mode. The crystals of complex **3** were immersed in oil and covered with glue in order to prevent loss of guest molecules. The structure was solved by direct methods and refined by least-squares methods on $F^2$ using SHELX-97.[7] Non-hydrogen atoms were refined anisotropically and hydrogen atoms were fixed at calculated positions and refined using a riding model. In complex **4**, the S atom of the NCS anion was disordered over two sites and hence the occupancies were refined (61 and 39%). Crystal data for **3**: Triclinic, $P\bar{1}$, $a$ = 9.967(2), $b$ = 12.950(3), $c$ = 14.945(3) Å, $\alpha$ = 106.90(3), $\beta$ = 102.94(3), $\gamma$ = 102.11, $V$ = 1718.9(6) $Å^3$, $Z$ = 1, $D_{calcd.}$ = 1.409 $g cm^{-3}$, 3111 reflections out of 5858 unique reflections with $I > 2\sigma(I)$, 1.50° < $\theta$ < 25.06°, final $R$ values: $R_1$ = 0.0778, $wR_2$ = 0.1724. Crystal data for **4**: Triclinic, $P\bar{1}$, $a$ = 8.259(2), $b$ = 9.613(2), $c$ = 12.656(3) Å, $\alpha$ = 85.70(3), $\beta$ = 74.66(3), $\gamma$ = 71.18, $V$ = 917.1(3) $Å^3$, $Z$ = 1, $D_{calcd.}$ = 1.478 $g cm^{-3}$, 2292 reflections out of 3231 unique reflections with $I > 2\sigma(I)$, 1.67° < $\theta$ < 25.00°, final $R$ values: $R_1$ = 0.0522, $wR_2$ = 0.1177. CCDC-286845 (**3**) and -286846 (**4**), contain the supplementary crystallographic data for this paper. These data can be obtained free of charge from The Cambridge Crystallographic Data Centre via www.ccdc.cam.ac.uk/data_request/cif.

**Supporting Information** (see footnote on the first page of this article): Preparative procedures for **1**–**4**, TGA measurement of **3**, powder spectra of guest-exchanged materials of **3**, ORTEP drawings of **3** and **4**, and IR and UV spectra of complexes and ligands.

## Acknowledgments

We gratefully acknowledge financial support from the Department of Science and Technology (DST) and DST-FIST for the single-crystal X-ray facility. M. S. thanks CSIR for a research fellowship.

[1] a) G. R. Desiraju, *Crystal Engineering: The Design of Organic Solids*, Elsevier, Amsterdam, **1989**; b) G. R. Desiraju, *Angew. Chem. Int. Ed. Engl.* **1995**, *34*, 2311; c) J. Bernstein, R. E. Davis, L. Shimoni, N.-L. Chang, *Angew. Chem. Int. Ed. Engl.* **1995**, *34*, 1555; d) C. B. Aakeröy, *Acta Crystallogr., Sect. B* **1997**, *53*, 569; e) Y. Aoyama, *Topp. Curr. Chem.* **1998**, *198*, 131; f) M. J. Zaworotko, *Chem. Commun.* **2001**, 1; g) K. T. Holman, A. M. Pivovar, J. A. Swift, M. D. Ward, *Acc. Chem. Res.* **2001**, *34*, 107; h) C. B. Aakeröy, A. M. Beatty, B. A. Helfrich, *Angew. Chem. Int. Ed.* **2001**, *40*, 3240; i) G. R. Desiraju, *Acc. Chem. Res.* **2002**, *35*, 565; j) K. Biradha, *CrystEngCommun.* **2003**, *5*, 274.

[2] a) D. J. Cram, J. M. Cram, *Container Molecules and Their Guests*, Royal Society of Chemistry, Cambridge, U. K., **1994**;

 © 2006 Wiley-VCH Verlag GmbH & Co. KGaA, Weinheim 

b) J.-M. Lehn, *Supramolecular Chemistry: Concept and perspectives*, VCH, Weinheim, **1995**; c) M. M. Conn, J. Rebek, Jr., *Chem. Rev.* **1997**, *97*, 1647; d) M. Fujita, K. Umemoto, M. Yoshizawa, N. Fujita, T. Kusukawa, K. Biradha, *Chem. Commun.* **2001**, 509; e) K. Biradha, M. J. Zaworotko, *J. Am. Chem. Soc.* **1998**, *120*, 6431.

[3] a) S. Muthu, J. H. K. Yip, J. J. Vittal, *J. Chem. Soc., Dalton Trans.* **2001**, 3577; b) S. Muthu, J. H. K. Yip, J. J. Vittal, *J. Chem. Soc., Dalton Trans.* **2002**, 4561; c) C.-H. Ge, X.-D. Zhang, P. Zhang, W. Guan, F. Guo, Q.-T. Liu, *Polyhedron* **2003**, *22*, 3493.

[4] a) M. Sarkar, K. Biradha, *Chem. Commun.* **2005**, 2229; b) M. Sarkar, K. Biradha, *Cryst Growth Des.* **2005**, ASAP article.

[5] F. H. Allen, O. Kennard, *Chem. Des. Automation News* **1993**, *8*, 31.

[6] $C_{30}H_{28}CuN_{10}O_4S_2$ (719.5): calcd. C 50.03, H 3.83, N 19.45; found C 48.83, H 3.64, N 18.39.

[7] G. M. Sheldrick, *SHELX-97, Program for the Solution and Refinement of Crystal Structures*, University of Göttingen, Göttingen, Germany, **1997**.

Received: October 19, 2005
Published Online: December 22, 2005

 © 2006 Wiley-VCH Verlag GmbH & Co. KGaA, Weinheim 

DOI: 10.1002/ejic.200500862

# Self-Assembly of a Tetranuclear $Co^{III}$-Metallacycle from the Reaction of a Bis(benzene-*o*-dithiolato) Ligand with $Co^{II}$ and Subsequent Aerial Oxidation

**F. Ekkehardt Hahn,*[a] Thorsten Kreickmann,[a,b] and Tania Pape[a]**

**Keywords:** Cobalt / S ligands / Metallacycles / Self-assembly

The bis(benzene-*o*-dithiol) ligand [$(HS)_2$-2,3-$C_6H_3$–$CH_2$–$C_6H_3$-2,3-$(SH)_2$] ($H_4$-**1**) reacts, after deprotonation with $Li_2CO_3$, with $CoCl_2{\cdot}6H_2O$. Aerial oxidation in methanol gives the tetranuclear metallacycle $Li_4[Co_4(\mathbf{1})_4]$. The X-ray structure analysis of $(PNP)_4[Co_4(\mathbf{1})_4]$ (**7**) reveals a cyclic structure in which each of the bis(benzene-*o*-dithiolato) ligands forms a bridge between two cobalt centers. Two differently coordinated cobalt atoms (*syn* and *anti*) are observed in the tetranuclear complex.

(© Wiley-VCH Verlag GmbH & Co. KGaA, 69451 Weinheim, Germany, 2006)

## Introduction

The combination of polydentate organic ligands and transition metals has led to supramolecular complexes.[1] Metal-directed self-assembly has been used to form different supramolecular architectures like helicates,[2] boxes,[3] squares,[4] molecular containers,[5] and other structural motifs.[6] Among those, metal helicates have attracted special interest owing to their presence in nature.[2] The first triple-stranded helicate $[Fe_2(RA)_3]$ (RA = rhodotorulic acid), containing exclusively oxygen donor functions from hydroxamate groups, was isolated and characterized by Raymond et al.[7] The early helicate chemistry, however, was dominated by nitrogen donor ligands like oligobipyridines.[2,8] Later, triple-stranded helical complexes with catecholato donor groups were prepared.[2,9] The coordination chemistry of dicatechol ligands has been reviewed.[10] Double-stranded helical structures built from ligands with an unsymmetrical spacer (directional ligands) have been reported.[11] Even the triple-stranded helicate of a catecholato/aminophenolato ligand has been described.[12]

Much less is known about helicates containing benzene-*o*-dithiolato or other dithiolene donor groups. We have described a method for the *o*-functionalization of benzene-1,2-dithiol, which gives 2,3-dimercaptobenzoic acid[13] or 2,3-dimercaptobenzyl alcohol.[14] These building blocks were used to synthesize bis(benzene-*o*-dithiol) ligands of type **A**,[15,16] **B**,[16] and the benzene-*o*-dithiol/catechol ligand **C**[17] (Scheme 1). Non-helical mono- and dinuclear complexes have been obtained with ligands **A** and **B**, while ligand **C** reacts with $Ti^{IV}$ to give a triple-stranded helicate with a parallel ligand orientation.

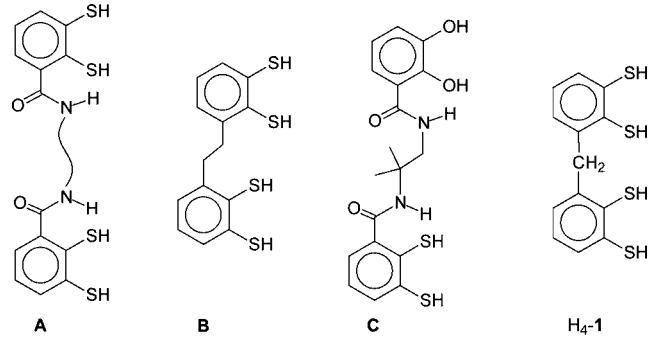


Scheme 1. Ligands containing the benzene-*o*-dithiol donor group.

However, no dinuclear triple-stranded helicates have been obtained so far from bis(benzene-*o*-dithiol) ligands such as **A** and **B**. Albrecht et al. have shown that methylene-bridged dicatecholato[18] and catecholato/aminophenolato[12] ligands are capable of forming triple-stranded helicates with $Ti^{IV}$ and $Ga^{III}$. In our search for helicates built exclusively from sulfur donors, we have therefore prepared the novel methylene-bridged bis(benzene-*o*-dithiol) ligand $H_4$-**1** (Scheme 1). Here we present the preparation of ligand $H_4$-**1** and its coordination chemistry with $Co^{III}$.

## Results and Discussion

Ligand $H_4$-**1** was prepared as depicted in Scheme 2. 1,2-Bis(isopropylmercapto)benzene (**2**) was synthesized as described previously.[14,16] Deprotonation of **2** with *n*BuLi/TMEDA in hexane yielded the organolithium compound **3**. Compound **3** was not isolated but immediately transformed into 2,3-bis(isopropylmercapto)benzaldehyde (**4**) by reaction with *N*,*N*-dimethylformamide followed by an acidic

[a] Institut für Anorganische und Analytische Chemie, Westfälische Wilhelms-Universität Münster,
Wilhelm Klemm Straße 8, 48149 Münster, Germany
Fax: + 49-251-833-3108
E-mail: fehahn@uni-muenster.de
[b] NRW Graduate School of Chemistry,
Münster, Germany

 © 2006 Wiley-VCH Verlag GmbH & Co. KGaA, Weinheim 

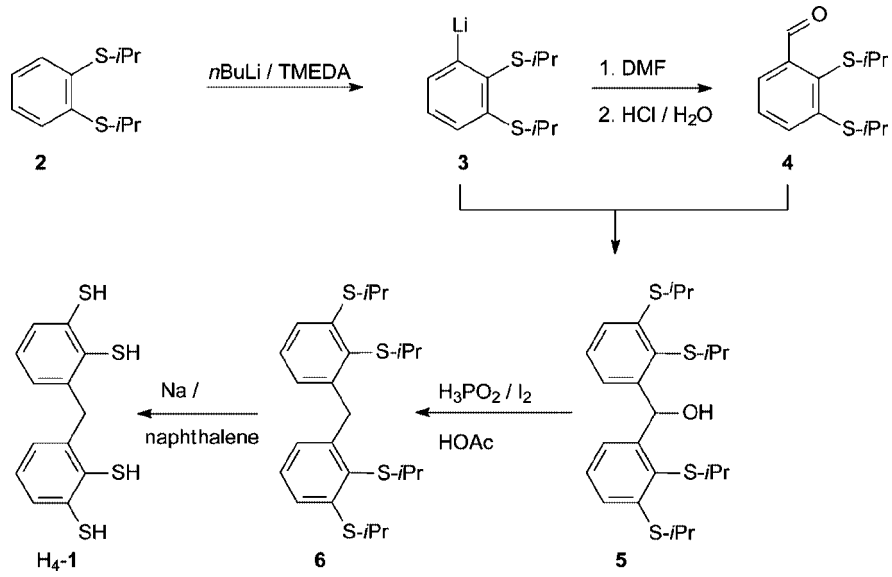


Scheme 2. Synthesis of the bis(benzene-*o*-dithiol) ligand $H_4$-**1**.

workup. Reaction of equimolar amounts of **3** and **4** in hexane yielded the alcohol **5** after acidification. Alcohol **5** was deoxygenated with hypophosphorous acid in the presence of a catalytic amount of iodine in acetic acid.[19] Removal of the *S*-protection groups in ligand precursor **6** with sodium/naphthalene in THF liberated ligand $H_4$-**1**, which was isolated after hydrolysis in approximately 85% yield (relative to **2**).

Reaction of equimolar amounts of $H_4$-**1** and $CoCl_2 \cdot 6H_2O$ in methanol at ambient temperature in the presence of two equivalents of $Li_2CO_3$ yielded a brown solution. We assume that this solution contained $Co^{II}$ complexes with benzene-*o*-dithiolato ligands. Upon aerial oxidation, the brown solution immediately turned deep blue, which indicates the formation of a $Co^{III}$–benzene-*o*-dithiolato complex. Addition of PNPCl [$PNP^+$ = bis(triphenylphosphoranylidene)ammonium] led to the precipitation of a blue solid, which was isolated and dried. The composition of the blue solid was established by ESI mass spectroscopy (Figure 1, negative ions). No peaks for a double-stranded complex of composition $[Co_2(\mathbf{1})_2]^{4-}$ are observed. Instead, three peaks are found at *m*/*z* = 351, 648, and 1241. These are assigned to the ions $[Co_4(\mathbf{1})_4]^{4-}$, $\{(PNP)[Co_4(\mathbf{1})_4]\}^{3-}$, and $\{(PNP)_2[Co_4(\mathbf{1})_4]\}^{2-}$. These assignments were corroborated by matching isotope patterns. Thus, the reaction of ligand $H_4$-**1** with $CoCl_2$ followed by aerial oxidation and precipitation with PNPCl does not yield a dinuclear complex, as was expected, but instead a tetranuclear complex of composition $(PNP)_4[Co_4(\mathbf{1})_4]$ (**7**).

To establish the molecular structure of the $[Co_4(\mathbf{1})_4]^{4-}$ anion, crystals suitable for an X-ray analysis were grown by slow vapour diffusion of pentane into a solution of **7** in dichloromethane. The molecular structure of tetraanion $[Co_4(\mathbf{1})_4]^{4-}$ is shown in Figure 2. The complex anion contains four $[Co(S_2C_6H_3R)_2]$ units arranged in a cyclic fashion. Each $\mathbf{1}^{4-}$ ligand bridges two cobalt atoms. Each of the cobalt atoms is coordinated by two benzene-*o*-dithiolato

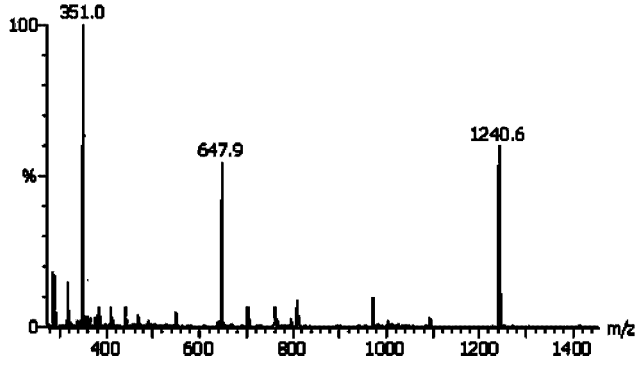


Figure 1. ESI mass spectrum (negative ions) of $(PNP)_4[Co_4(\mathbf{1})_4]$ (**7**).

units from different ligands in a square-planar fashion. The Co–S and C–S distances in **7** are normal and match those reported for the mononuclear complex $(AsPh_3Me)[Co(S_2C_6H_3CH_3)_2]$.[20] Cobalt(III) complexes with electron-poor benzene-*o*-dithiolato ligands [$S_2C_6Cl_4$ or $S_2C_6H_2(CN)_2$] have been reported to dimerize.[21] In such dimers the $[Co(bdt)_2]^-$ (bdt = substituted benzene-*o*-dithiolate) units lie parallel to one another such that the cobalt atom of each $[Co(bdt)_2]^-$ unit is directly opposite a sulfur atom belonging to the second unit. This arrangement leads to the formation of two new Co–S bonds and a tetragonal-pyramidal coordination environment for each cobalt atom.

No such extra Co–S interactions are observed in the anion $[Co_4(\mathbf{1})_4]^{4-}$. The $[Co_4(\mathbf{1})_4]^{4-}$ anions are well separated in the solid state, and no intramolecular Co–Co (shortest separation about 9 Å) and Co–S (shortest separation about 7 Å) or intermolecular Co–Co (shortest separation longer than 9 Å) and Co–S (shortest separation longer than 7 Å) contacts are found.

In contrast to the recently reported dinuclear nickel complex with an ethylene bridged bis(benzene-*o*-dithiolato) ligand (Scheme 1, **B**),[16] the tetranuclear complex $(PNP)_4$-

 © 2006 Wiley-VCH Verlag GmbH & Co. KGaA, Weinheim 

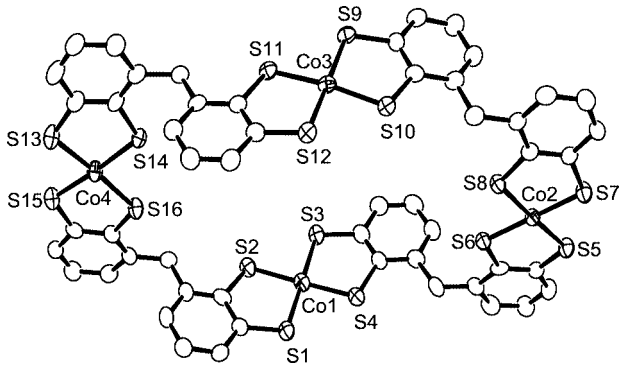


Figure 2. Molecular structure of the $[Co_4(\mathbf{1})_4]^{4-}$ anion of **7**. Hydrogen atoms and cations have been omitted for clarity. Selected ranges for bond lengths [Å] and bond angles [°]: Co–S 2.157(2)–2.176(2), C–S 1.746(6)–1.769(6), S–Co–S (intra ligand) 91.08(7)–91.84(7), Co–S–C 104.4(2)–105.9(2).

$[Co_4(\mathbf{1})_4]$ contains two metal centers with a slightly different coordination environment. Two cobalt atoms (Co1 and Co3) are coordinated by benzene-*o*-dithiolato units and the alkyl substituents are arranged in *anti* positions, while the other two cobalt atoms (Co2 and Co4) are coordinated by benzene-*o*-dithiolato units that have their alkyl substituents arranged in a *syn* fashion. This leads to two different $C_2$ axes along the two metal–metal connection lines Co1–Co3 and Co2–Co4 (Figure 3). The distances between the equivalent cobalt atoms are 9.661 Å (Co1–Co3) and 15.933 Å (Co2–Co4). A large internal cavity is formed by this arrangement. Two benzene rings of the $PNP^+$ cations partly fill this cavity without any interaction with the metallacycle. Complex **7** is, to the best of our knowledge, the first metallosupramolecular assembly that contains two differently coordinated metal centers even though a ligand with two identical donor sites has been used.

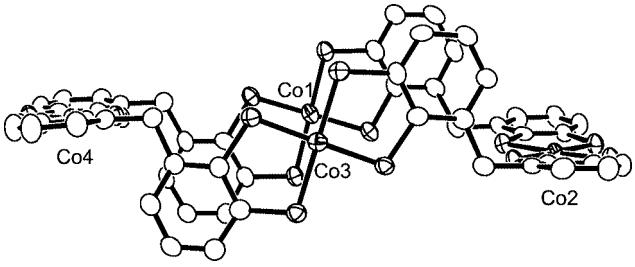


Figure 3. View along the Co1–Co3 axis showing the *syn* (Co2, Co4) and *anti* (Co1, Co3) arrangement of the substituted benzene-*o*-dithiolato ligands.

Although a tetranuclear complex $[Co_4(\mathbf{1})_4]^{4-}$ is entropically less favorable than two dinuclear complexes $[Co_2(\mathbf{1})_2]^{2-}$, the larger compound is exclusively formed. We believe that this occurs because of a strong steric interaction between the two sulfur atoms in the 2-positions of the aromatic rings that would occur in a hypothetical dinuclear complex $[Co_2(\mathbf{1})_2]^{2-}$ (Scheme 3, left). Albrecht et al. prepared a dicatechol ligand, with the same topology as $H_4$-**1**, that forms a dinuclear triple-stranded helicate with $Ti^{IV}$ (Scheme 3, right).[18] In this complex, no repulsion between the oxygen atoms in the 2-positions is observed (intraligand O···O distance 2.85 Å). In addition, possible repulsion between these oxygen atoms is also compensated by coordination to hard lithium cations. This coordination is not possible and was not observed with the soft sulfur donor atoms. In a hypothetical dinuclear complex with benzene-*o*-dithiol ligands, steric interaction between the sulfur atoms in the 2-position would occur owing to the longer C–S bonds (1.76 Å versus 1.35 Å for the C–O bonds) and the larger intraring C–C–S angles (119° versus 114° for the C–C–O angles). On the basis of these parameters, the S···S distance in a dinuclear complex $[Co_2(\mathbf{1})_2]^{2-}$ would be around 2.2 Å, which is far too short for a nonbonding interaction (typically S–S bond lengths are 2.0 Å). Consequently, strong repulsion between the sulfur atoms must occur in the hypothetical $[Co_2(\mathbf{1})_2]^{2-}$ complex in which two cobalt atoms are coordinated in a square-planar fashion by two $CH_2$-bridged bdt ligands. In order to avoid this unfavourable repulsion, one benzene-*o*-dithiolato group of each $\mathbf{1}^{4-}$ ligand is rotated by about 90° around the Ar–$CH_2$ axis, which, in turn, leads to the formation of the tetranuclear metallacycle.

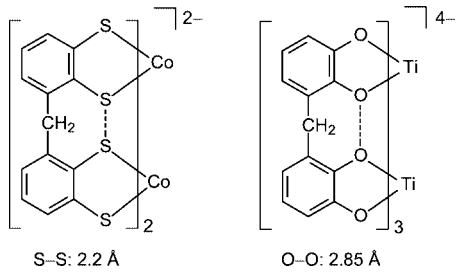


Scheme 3. Hypothetical complex $[Co_2(\mathbf{1})_2]^{2-}$ (left) and triple-stranded helicate (right).

## Experimental Section

If not stated otherwise, all manipulations were carried out under dry argon by using standard Schlenk techniques. Hexane, tetrahydrofurane, and *N*,*N*,*N*′,*N*′-tetramethylethylenediamine (TMEDA) were freshly distilled from sodium/benzophenone prior to use. The starting material 1,2-bis(isopropylmercapto)benzene (**2**) was prepared as described before.[16]

**2,3-Bis(isopropylmercapto)benzaldehyde (4):** A sample of *n*-butyllithium (12.16 mL of a 2.5 M solution in hexane) was added dropwise to a solution of TMEDA (4.56 mL, 30.4 mmol) and 1,2-bis(isopropylmercapto)benzene (**2**, 6.9 g, 30.4 mmol) in hexane (100 mL) at 0 °C. After 30 min, the ice bath was removed, and the stirring was continued for 3 h at ambient temperature, which resulted in the formation of an off-white slurry. Dry *N*,*N*-dimethylformamide (3.53 mL, 45.6 mmol) was added, and the solution was stirred for 12 h. Water (100 mL) and hydrochloric acid (37%, 20 mL) were added, and the aqueous solution was extracted with diethyl ether (3 × 50 mL). The combined organic layers were dried with $MgSO_4$, and the solvent was removed in vacuo. Column chromatography ($SiO_2$, $Et_2O$/petroleum ether, 1:3) gave a yellow oil (7.33 g, 28.8 mmol, 95%). $^1H$ NMR ($CDCl_3$, 300.1 MHz): $\delta$ = 10.8 (s, HC=O), 7.67 (dd, 1 H, Ar-H), 7.49–7.35 (m, 2 H, Ar-H), 3.54–3.32 (m, 2 H, SCH), 1.39 (d, $^3J$ = 7.0 Hz, 6 H, $CH_3$), 1.23 (d, $^3J$ = 7.0 Hz, 6 H, $CH_3$) ppm. $^{13}C$ NMR ($CDCl_3$, 75.5 MHz): $\delta$ = 193.4

 © 2006 Wiley-VCH Verlag GmbH & Co. KGaA, Weinheim 

(C=O), 146.5, 139.7, 136.4, 131.4, 129.2, 124.3 (Ar-C), 40.9 (SCH), 36.0 (SCH), 23.0 ($CH_3$), 22.6 ($CH_3$) ppm. GC/MS (EI, 70 eV): *m/z* (%) = 254 (66) $[M]^+$, 211 (10) $[M - C_3H_7]^+$, 179 (5) $[M - SC_3H_7]^+$, 41 (100) $[C_3H_5]$. $C_{13}H_{18}OS_2$ (254.40): calcd. C 61.38, H 7.13, S 25.20; found C 61.47, H 7.36, S 24.87.

**Bis[2,3-bis(isopropylmercapto)phenyl]methanol (5):** A sample of *n*-butyllithium (3.00 mL of a 2.5 M solution in hexane) was added dropwise to a solution of TMEDA (1.15 mL, 7.50 mmol) and 1,2-bis(isopropylmercapto)benzene **2** (1.7 g, 7.50 mmol) in hexane (30 mL) at 0 °C. After 30 min, the ice bath was removed, and the stirring was continued for 3 h at ambient temperature, which resulted in the formation of an off-white slurry. 2,3-Bis(isopropylmercapto)benzaldehyde (**4**, 1.91 g, 7.50 mmol) dissolved in hexane (10 mL) was added dropwise, and the solution was stirred for 12 h. Acidification with hydrochloric acid (37%) yielded a yellow precipitate, which was isolated by filtration, washed with hexane, and dried in vacuo to give **5** as a white powder (3.46 g, 7.20 mmol, 96%). $^1$H NMR ($CDCl_3$, 300.1 MHz): $\delta$ = 7.26–7.18 (m, 4 H, Ar-H), 7.01 (s, 1 H, C*H*–OH), 7.00 (dd, 2 H, Ar-H), 3.66 (sept, 2 H, SCH), 3.50 (sept, 2 H, SCH), 1.37 (d, 12 H, $CH_3$), 1.24 (d, 12 H, $CH_3$) ppm. $^{13}$C NMR ($CDCl_3$, 75.5 MHz): $\delta$ = 148.3, 144.9, 131.4, 128.7, 126.3, 124.5 (Ar-C), 72.0 (CH–OH), 39.1 (SCH), 36.1 (SCH), 25.5 ($CH_3$), 25.1 ($CH_3$) ppm. IR (KBr): $\tilde{\nu}$ = 3457 (br., O–H), 3050 (s, Ar-H), 2960, 2923, 2863 (s, $CHMe_2$), 1557 (m, Ar-C=C), 1443 (s, CH) $cm^{-1}$. MS (EI, 70 eV): *m/z* (%) = 480 (64) $[M]^+$, 437 (73) $[M - C_3H_7]^+$, 405 (100) $[M - SC_3H_7]^+$. $C_{25}H_{36}OS_4$ (480.16): calcd. C 62.45, H 7.55, S 26.68; found C 62.51, H 7.47, S 26.44.

**Bis[2,3-bis(isopropylmercapto)phenyl]methane (6):** Iodine (80 mg, 0.31 mmol) and bis[2,3-bis(isopropylmercapto)phenyl]methanol (**5**, 1.50 g, 3.10 mmol) were dissolved in concentrated acetic acid (60 mL). Hypophosphorous acid (1.60 mL, 50% solution by weight in water) was added, and the solution was stirred at 60 °C for 24 h. Water (100 mL) was added at ambient temperature, and the aqueous phase was extracted with hexane (3 × 50 mL). The combined organic layers were washed with saturated $NaHCO_3$ solution (2 × 20 mL) and dried with $MgSO_4$, and the solvent was removed in vacuo. Column chromatography ($SiO_2$, $Et_2O$/hexane, 1:5) gave **6** as a white powder (1.41 g, 3.04 mmol, 98%). $^1$H NMR ($CDCl_3$, 300.1): $\delta$ = 7.20–7.15 (m, 4 H, Ar-H), 6.80–6.75 (dd, 2 H, Ar-H), 4.72 (s, 2 H, $CH_2$), 3.54 (m, 4 H, SCH), 1.45 (d, 12 H, $CH_3$), 1.30 (d, 12 H, $CH_3$) ppm. $^{13}$C NMR ($CDCl_3$, 75.5 MHz): $\delta$ = 149.1, 147.4, 134.3, 130.9, 128.6, 126.6 (Ar-C), 42.5 ($CH_2$), 41.3 (SCH), 38.1 (SCH), 25.5 ($CH_3$), 25.1 ($CH_3$) ppm. IR (KBr): $\tilde{\nu}$ = 3048 (Ar-H), 2960, 2923, 2863 (s, $CHMe_2$), 1443 (s, $CH_2$) $cm^{-1}$. MS (EI, 70 eV): *m/z* (%) = 464 (8) $[M]^+$, 421 (5) $[M - C_3H_7]^+$, 389 (100) $[M - SC_3H_7]^+$, 357 (53) $[M - S_2C_3H_7]^+$. $C_{25}H_{36}S_4$ (464.17): calcd. C 64.60, H 7.81, S 27.59; found C 64.47, H 7.87, S 27.72.

**Bis(2,3-dimercaptophenyl)methane ($H_4$-1):** Compound **6** (3.80 g, 8.19 mmol) and naphthalene (5.20 g, 41.0 mmol) were dissolved in tetrahydrofurane (80 mL), and pieces of sodium (1.90 g, 82 mmol) were added. The mixture was stirred for 12 h at ambient temperature, and degassed methanol (15 mL) was then added dropwise. After 10 min, the solvent was removed in vacuo, and the residue was dissolved in degassed water (30 mL). The aqueous phase was washed with degassed diethyl ether (3 × 20 mL), filtered, and acidified with hydrochloric acid (37%). The product was extracted with dichloromethane (3 × 20 mL), the combined organic layers were dried with $MgSO_4$, and the solvent was removed in vacuo to give $H_4$-**1** as an off-white powder (2.33 g, 7.78 mmol, 96%). $^1$H NMR ($CDCl_3$, 300.1 MHz): $\delta$ = 7.34 (dd, $^3J$ = 7.9, $^4J$ = 1.3 Hz, 2 H, Ar-H), 7.00 (t, $^3J$ = 7.9 Hz, 2 H, Ar-H), 6.78 (dd, $^3J$ = 7.9, $^4J$ = 1.3 Hz, 2 H, Ar-H), 4.18 (s, 2 H, $CH_2$), 3.84 (s, 2 H, SH), 3.81 (s, 2 H, SH) ppm. $^{13}$C NMR ($CDCl_3$, 75.5 MHz): $\delta$ = 141.5, 134.7, 133.2, 131.5, 129.7, 128.3 (Ar-C), 43.3 ($CH_2$) ppm. IR (KBr): $\tilde{\nu}$ = 3050 (s, Ar-H), 2894 (m, C–H), 2525 (m, S–H), 1443, 717 (C–H) $cm^{-1}$. MS (EI, 70 eV): *m/z* (%) = 296 (76) $[M]^+$, 263 (85) $[M - SH]^+$, 230 (100) $[M - 2SH]^+$, 197 (47) $[M - 3SH]^+$. $C_{13}H_{12}S_4$ (295.98): calcd. C 52.67, H 4.08, S 43.25; found C 53.22, H 3.88, S 43.82.

**$(PNP)_4[Co_4(1)_4]$ (7):** A solution of $H_4$-**1** (50 mg, 0.169 mmol) and $Li_2CO_3$ (25 mg, 0.34 mmol) in methanol (10 mL) was added to a solution of $CoCl_2 \cdot 6H_2O$ (40 mg, 0.169 mmol) in methanol (10 mL). The mixture was stirred for 12 h, exposed to air for 10 min, and filtered. Addition of bis(triphenylphosphoranylidene)ammonium chloride (PNPCl) (97 mg, 0.169 mmol) to the filtrate gave a blue precipitate of **7**, which was isolated by filtration, washed with methanol, and dried in vacuo (110 mg, 0.031 mmol, 74%). MS (ESI, negative ions): *m/z* (%) = 351.0 $[Co_4(\mathbf{1})_4]^{4-}$, 648 $[(Co_4(\mathbf{1})_4)^{4-} + PNP^+]^{3-}$, 1241 $[(Co_4(\mathbf{1})_4)^{4-} + 2\,PNP^+]^{2-}$. $C_{196}H_{152}N_4P_8S_{16}Co_4$ (3559.7): calcd. C 66.13, H 4.30, N 1.57, S 14.41; found C 65.77, H 4.42, N 1.48, S 14.28.

**X-ray Crystallographic Study of 7:** A suitable crystal of **7** (0.15 × 0.10 × 0.08 mm) was mounted on a Bruker AXS APEX diffractometer equipped with a rotating molybdenum anode ($\lambda$ = 0.71073 Å), cooling device, and graphite monochromator. $(PNP)_4[Co_4(\mathbf{1})_4]$, $C_{196}H_{152}N_4P_8S_{16}Co_4$, $M$ = 3559.7, triclinic $P\bar{1}$, $a$ = 18.473(7), $b$ = 19.797(7), $c$ = 24.497(9) Å, $\alpha$ = 80.724(7), $\beta$ = 89.026(7), $\gamma$ = 79.787(7)°, $V$ = 8701(6) Å$^3$, $Z$ = 2, $\rho_{calcd.}$ = 1.359 g $cm^{-3}$, $\mu$ = 0.696 $mm^{-1}$. 54025 Structure factors ($-19 \le h \le 19$, $-21 \le k \le 21$, $-26 \le l \le 26$, $2\theta$ range 2.1–55.0°) were collected at 123(2) K. An empirical absorption correction was applied ($T_{min}$ = 0.903, $T_{max}$ = 0.947) before merging gave 22725 unique intensities ($R_{int}$ = 0.069). Structure solution with SHELXS[22] and subsequent refinement of 2053 parameters against $F^2$ of 22725 unique intensities [13118 observed intensities $I > 2\sigma(I)$] using SHELXL[23] with anisotropic thermal parameters for all non-hydrogen atoms. Hydrogen atoms were added to the structure model on calculated positions. Final residues $R$ = 0.0591, $wR$ = 0.1186. CCDC-284858 contains the supplementary crystallographic data for this paper. These data can be obtained free of charge from The Cambridge Crystallographic Data Centre via www.ccdc.cam.ac.uk/data_request/cif.

## Acknowledgments

This work was financially supported by the Deutsche Forschungsgemeinschaft and the NRW International Graduate School of Chemistry.

[1] J.-M. Lehn, *Supramolecular Chemistry: Concepts and Perspectives*, VCH, Weinheim, **1995**.
[2] a) C. Piguet, G. Bernardinelli, G. Hopfgartner, *Chem. Rev.* **1997**, *97*, 2005–2062; b) M. Albrecht, *Chem. Rev.* **2001**, *101*, 3457–3497.
[3] a) P. Baxter, J.-M. Lehn, A. DeCian, J. Fischer, *Angew. Chem.* **1993**, *105*, 92–95; *Angew. Chem. Int. Ed. Engl.* **1993**, *32*, 69–72; b) E. Leize, A. Van Dorsselaer, R. Krämer, J.-M. Lehn, *J. Chem. Soc., Chem. Commun.* **1993**, 990–993.
[4] F. Würthner, C.-C. You, C. R. Saha-Möller, *Chem. Soc. Rev.* **2004**, *33*, 133–146.
[5] a) C. J. Jones, *Chem. Soc. Rev.* **1998**, *27*, 289–299; b) X. Sun, D. W. Johnson, D. L. Caulder, K. N. Raymond, E. H. Wong, *J. Am. Chem. Soc.* **2001**, *123*, 2752–2763; c) C. Brückner, R. E. Powers, K. N. Raymond, *Angew. Chem.* **1998**, *110*, 1937–1940; *Angew. Chem. Int. Ed.* **1998**, *37*, 1837–1839; d) D. L. Caulder, R. E. Powers, T. N. Parac, K. N. Raymond, *Angew. Chem.*

 © 2006 Wiley-VCH Verlag GmbH & Co. KGaA, Weinheim 

**1998**, *110*, 1940–1943; *Angew. Chem. Int. Ed.* **1998**, *37*, 1840–1843; e) T. Beissel, R. E. Powers, K. N. Raymond, *Angew. Chem.* **1996**, *108*, 1166–1168; *Angew. Chem. Int. Ed. Engl.* **1996**, *35*, 1084–1086; f) D. Fiedler, R. G. Bergman, K. N. Raymond, *Angew. Chem.* **2004**, *116*, 6916–6919; *Angew. Chem. Int. Ed.* **2004**, *43*, 6748–6751.

[6] a) G. F. Swiegers, T. J. Malefetse, *Chem. Rev.* **2000**, *100*, 3483–3537; b) C. A. Schalley, A. Lützen, M. Albrecht, *Chem. Eur. J.* **2004**, *10*, 1072–1080.

[7] a) C. J. Carrano, K. N. Raymond, *J. Am. Chem. Soc.* **1978**, *100*, 5371–5374; b) C. J. Carrano, S. R. Cooper, K. N. Raymond, *J. Am. Chem. Soc.* **1979**, *101*, 599–604; c) R. C. Scarrow, D. L. White, K. N. Raymond, *J. Am. Chem. Soc.* **1985**, *107*, 6540–6546.

[8] a) J.-M. Lehn, A. Rigault, J. Siegel, J. Harrowfield, B. Chevrier, D. Moras, *Proc. Natl. Acad. Sci. USA* **1987**, *84*, 2565–2569; b) R. Krämer, J.-M. Lehn, A. Marquis-Rigault, *Proc. Natl. Acad. Sci. USA* **1993**, *90*, 5394–5398; c) R. Krämer, J.-M. Lehn, A. De Cian, J. Fischer, *Angew. Chem.* **1993**, *105*, 764–767; *Angew. Chem. Int. Ed. Engl.* **1993**, *32*, 703–706; d) E. C. Constable, F. Heirtzler, M. Neuburger, M. Zehnder, *J. Am. Chem. Soc.* **1997**, *119*, 5606–5617.

[9] a) B. Kersting, M. Meyer, R. E. Powers, K. N. Raymond, *J. Am. Chem. Soc.* **1996**, *118*, 7221–7222; b) D. L. Caulder, K. N. Raymond, *Angew. Chem.* **1997**, *109*, 1508–1510; *Angew. Chem. Int. Ed. Engl.* **1997**, *36*, 1440–1442; c) M. Albrecht, S. Kotila, *Angew. Chem.* **1995**, *107*, 2285–2287; *Angew. Chem. Int. Ed. Engl.* **1995**, *34*, 2134–12136; d) M. Albrecht, *Synthesis* **1996**, 230–236; e) E. J. Enemark, T. D. P. Stack, *Angew. Chem.* **1995**, *107*, 1082–1084; *Angew. Chem. Int. Ed. Engl.* **1995**, *34*, 996–998; f) E. J. Enemark, T. D. P. Stack, *Angew. Chem.* **1998**, *110*, 977–981; *Angew. Chem. Int. Ed. Engl.* **1998**, *37*, 932–935.

[10] M. Albrecht, *Chem. Soc. Rev.* **1998**, *27*, 281–287.

[11] a) M. J. Hannon, S. Bunce, A. J. Clarke, N. W. Alcock, *Angew. Chem.* **1999**, *111*, 1353–1355; *Angew. Chem. Int. Ed.* **1999**, *38*, 1277–1278; b) M. Albrecht, M. Napp, M. Schneider, P. Weis, R. Fröhlich, *Chem. Commun.* **2001**, 409–410; c) M. Albrecht, M. Napp, M. Schneider, P. Weis, R. Fröhlich, *Chem. Eur. J.* **2001**, *7*, 3966–3975.

[12] M. Albrecht, R. Fröhlich, *J. Am. Chem. Soc.* **1997**, *119*, 1656–1661.

[13] F. E. Hahn, W. W. Seidel, *Angew. Chem.* **1995**, *107*, 2938–2941; *Angew. Chem. Int. Ed. Engl.* **1995**, *34*, 2700–2703.

[14] H. V. Huynh, W. W. Seidel, T. Lügger, R. Fröhlich, B. Wibbeling, F. E. Hahn, *Z. Naturforsch. Teil B* **2002**, *57*, 1401–1408.

[15] a) W. W. Seidel, F. E. Hahn, T. Lügger, *Inorg. Chem.* **1998**, *37*, 6587–6596; b) W. W. Seidel, F. E. Hahn, *J. Chem. Soc., Dalton Trans.* **1999**, 2237–2241.

[16] H. V. Huynh, C. Schulze Isfort, W. W. Seidel, T. Lügger, R. Fröhlich, O. Kataeva, F. E. Hahn, *Chem. Eur. J.* **2002**, *8*, 1327–1335.

[17] F. E. Hahn, C. Schulze Isfort, T. Pape, *Angew. Chem.* **2004**, *116*, 4911–4915; *Angew. Chem. Int. Ed.* **2004**, *43*, 4807–4810.

[18] M. Albrecht, S. Kotila, *Chem. Commun.* **1996**, 2309–2310.

[19] P. E. Gordon, A. J. Fry, *Tetrahedron Lett.* **2001**, *42*, 831–833.

[20] R. Eisenberg, Z. Dori, H. B. Gray, J. A. Ibers, *Inorg. Chem.* **1968**, *7*, 741–748.

[21] a) M. J. Baker-Hawkes, Z. Dori, R. Eisenberg, H. B. Gray, *J. Am. Chem. Soc.* **1968**, *90*, 4253–4259; b) H. Alves, D. Simao, I. Cordeiro Santos, V. Gama, R. Teives Henriques, H. Novais, M. Almeida, *Eur. J. Inorg. Chem.* **2004**, 1318–1329.

[22] G. M. Sheldrick, *SHELXS-97*, *Acta Crystallogr., Sect A: Found. Crystallogr.* **1990**, *46*, 467–473.

[23] G. M. Sheldrick, SHELXL-97, University of Göttingen, Germany, **1997**.

Received: September 26, 2005
Published Online: December 16, 2005

 © 2006 Wiley-VCH Verlag GmbH & Co. KGaA, Weinheim 

DOI: 10.1002/ejic.200500721

# Hydride Transfer Reactivity of $Mo(L)(H)(depe)_2$ (L = N, $NBEt_3$)

**Johan Cugny,[a] Helmut W. Schmalle,[a] Thomas Fox,[a] Olivier Blacque,[a] Montserrat Alfonso,[a] and Heinz Berke*[a]**

**Keywords:** Hydride complexes / Hydride transfer reaction / Insertion reaction / Nitride complexes / Phosphane complexes / Molybdenum

Starting from $Mo(N_2)_2(depe)_2$ (**1**), the nitrido complex Mo(N)$(N_3)(depe)_2$ (**2**) was obtained by the reaction of **1** with $Me_3SiN_3$. Subsequent reaction of **2** with HCl in $CH_3OH$ afforded the cationic imido chloride **3**, which could be converted into the nitrido chloride **4** with sodium bis(trimethylsilyl)amide. From **3** and **4** the hydrido complexes of the type Mo(H)(L)$(depe)_2$ [L = N (**7**), $NBEt_3$ (**8**)] were obtained by the reaction with the hydride reagents $LiBH_4$ and $NaHBEt_3$. The hydridic character of the $L_nM$–H bond of **8** was determined by DQCC measurements (bond ionicity $i$ = 81%). Hydride reactivity studies were carried out on **7** and **8**; however, only **8** underwent hydride transfer reactions. **8** reacted with 4,4′-dichlorobenzophenone and acetophenone to afford the corresponding alkoxide complexes Mo$(NBEt_3)$(OCHRR′)$(depe)_2$ [R, R′ = $C_6H_4Cl$ (**10**); R = Me, R′ = Ph (**11**)]. The high propensity of **8** to undergo carbonyl insertion was documented further by reactions with $CO_2$ and carbonylmetal compounds. Conversion with $CO_2$ led to formation of the formato complex Mo(N$BEt_3$)(OCHO)$(depe)_2$ (**9**) and reactions with $Fe(CO)_5$ and $Re_2(CO)_{10}$ resulted in the formation of Mo[(μ-OCH)Fe$(CO)_4$]$(NBEt_3)(depe)_2$ (**12**) and Mo[(μ-OCH)$Re_2(CO)_9$]$(NBEt_3)$(depe)$_2$ (**13**). X-ray diffraction studies were carried out on **1**–**4**, **6**, **8**–**10** and **12**–**14**.

(© Wiley-VCH Verlag GmbH & Co. KGaA, 69451 Weinheim, Germany, 2006)

## Introduction

For various homogeneous catalyses the activation of $L_nM$–H bonds[1–13] (M = transition metal) plays a decisive role. Insertion reactions of these bonds with unsaturated molecules are strongly dependent on the ancillary ligand sphere.[14] An increasing number of strongly σ-donating *cis*-phosphane substituents are expected to enhance the electron density on the metal center and on the hydrido ligand.[15] The ligand *trans* to the hydrido ligand is attributed a crucial *trans* influence. In a DFT study[16] the three complexes $LW(H)(dmpe)_2$ with L = NO, CH and N were compared and analyzed according to their various *trans* influences. The $L_nM$–H bond strength was found to decrease in the order NO > CH > N suggesting in this order increasing hydride transfer activity.

The nitrido ligand ($N^{3-}$)[21–23] is regarded as a strong *trans*-influence ligand and a very strong π-donor; similar in this property may only be the isoelectronic oxo ligand. A combined experimental and theoretical study[24] has compared the Cr–L bonds with L = $O_{oxo}$, $N_{nitrido}$ and $C_{carbyne}$. From a natural bond orbital analysis, bond lengths and topological analyses of the total electron density, the bond order and the total binding interaction of this multiple bond is in the order Cr–N > Cr–O > Cr–C. The nitrido moiety is therefore expected to display an additional nucleophilic behaviour for early and middle transition metal complexes in high oxidation states.[25] The reactivity patterns of related hydrido complexes with *trans* ligands L = NO and CMes were reported earlier so that it remains to study the influence of the nitrido ligand.[14,17–20]

We describe here the synthesis of molecules based on nitrido ligands such as $Mo(H)(L)(depe)_2$ (L = N and $NBEt_3$) and we present also reactivity studies carried out with the $Mo(H)(NBEt_3)(depe)_2$ complex.

## Results and Discussion

### Hydrido Nitrido Complexes

A common route to access nitrido complexes consists of the decomposition of (azido)metal complexes. The synthetic route described in this paper was thus largely inspired by the initial work of Chatt and Dilworth[26] with some modifications developed in the group of Pickett.[27] For the synthesis of $Mo(N_2)_2(depe)_2$ (**1**) we applied the procedure described by George and Noble[28] which utilizes the reduction of $MoCl_5$ with sodium amalgam followed by the addition of the phosphane ligand under dinitrogen. The bis(dinitrogen) species **1** was obtained in 69% yield and characterized by an X-ray diffraction study (crystallographic data for **1** in the Supporting Information). The de-

[a] Anorganisch-Chemisches Institut der Universität Zürich, Winterthurerstrasse 190, 8057 Zürich, Switzerland
E-mail: hberke@aci.unizh.ch

Supporting information for this article is available on the WWW under http://www.eurjic.org or from the author.

 InterScience © 2006 Wiley-VCH Verlag GmbH & Co. KGaA, Weinheim 

sired nitrido function was formed by treatment of **1** with trimethylsilyl azide[29,30] to yield the known compound Mo(N)(N$_3$)(depe)$_2$ (**2**). The imido derivative [Mo(Cl)(NH)(depe)$_2$][Cl] (**3**) was then produced by protonation of **2**, dissolved in methanol, with a small amount of aqueous concentrated hydrochloric acid in $CH_3OH$.

Suitable crystals of **2** and **3** for X-ray diffraction studies were grown from a saturated THF solution at –30 °C (crystallographic data for both complexes are available in the Supporting Information).

According to literature[26,31,32] the imido group can be deprotonated by a suitable base. In this study sodium bis(trimethylsilyl)amide in toluene was used, which prevents side reactions and leads to higher yields[32] of the nitrido species Mo(Cl)(N)(depe)$_2$ (**4**) (Scheme 1).

The structure of **4** was additionally confirmed by an X-ray diffraction analysis (Figure 1) using a single crystal obtained by cooling of a saturated toluene solution to –30 °C. Three independent molecules were found in the asymmetric unit. For all of which a pseudooctahedral geometry was observed with the two depe ligands in equatorial and the chloride ion and nitrido group in *trans* positions. The average of the Mo–N bonds of 1.699(5) Å is slightly shorter than those observed in similar (R$_2$P–CH$_2$–CH$_2$–PR$_2$)$_2$(X)-Mo≡N complexes [1.79(2) Å for R = Ph, X = N–N≡N,[33] 1.704(6) Å for R = Ph, X = N≡C–C(CN)=C(O)(CH$_3$)[34] and 1.704(3) Å for R = Ph, X = N≡C–C(H)=C(O)(Ph)[35]] which confirms the triple bond character of this unit. The *trans* influence of the nitride group is demonstrated by a long Mo–Cl distance [average value 2.772(2) Å], which is by more than 0.3 Å longer in comparison with the unweighted mean value of 2.410 Å reported in the literature.[36]

The preparation of two types of hydrido nitrido complexes was achieved. Starting from **3**, the borohydride Mo($\eta^1$-HBH$_3$)(NBH$_3$)(depe)$_2$ (**5**) was obtained when an excess of LiBH$_4$ in THF was applied. The $^1$H NMR spectrum of **5** in [D$_8$]THF revealed a broad quadruplet at $\delta$ = –2.90 ppm with a characteristic $^{11}$B coupling ($^1J_{HB}$ = 88 Hz), which was assigned to the protons of the tetrahydroborate moiety. The $^{11}$B NMR spectrum furthermore showed a quadruplet at $\delta$ = –15.9 ppm ($^1J_{HB}$ = 82 Hz) for the BH$_3$ unit on the nitrido group, and a quintuplet at $\delta$ = –44.6 ppm ($^1J_{HB}$ = 82 Hz) for the BH$_4$ unit. Presumably, the reaction to **5** proceeded via the intermediate Mo(Cl)(NBH$_3$)(depe)$_2$ (**6**), since the reaction of **3** with just 1 equiv. of LiBH$_4$ indeed yields **6**. In the $^1$H NMR spectrum a broad signal appeared at $\delta$ = 2.4 ppm, which was attributed to the NBH$_3$ moiety. The $^{11}$B NMR spectrum of **6** revealed one quadruplet at $\delta$ = –13.5 ppm for the NBH$_3$ unit and its $^{31}$P{$^1$H} NMR spectrum displayed a singlet at $\delta$ = 49.0 ppm indicating the presence of the four chemically equivalent phosphorus nuclei. A unique crystal of **6** suitable for an X-ray diffraction analysis was obtained from a saturated THF solution at –30 °C. Figure 2 shows the molecular

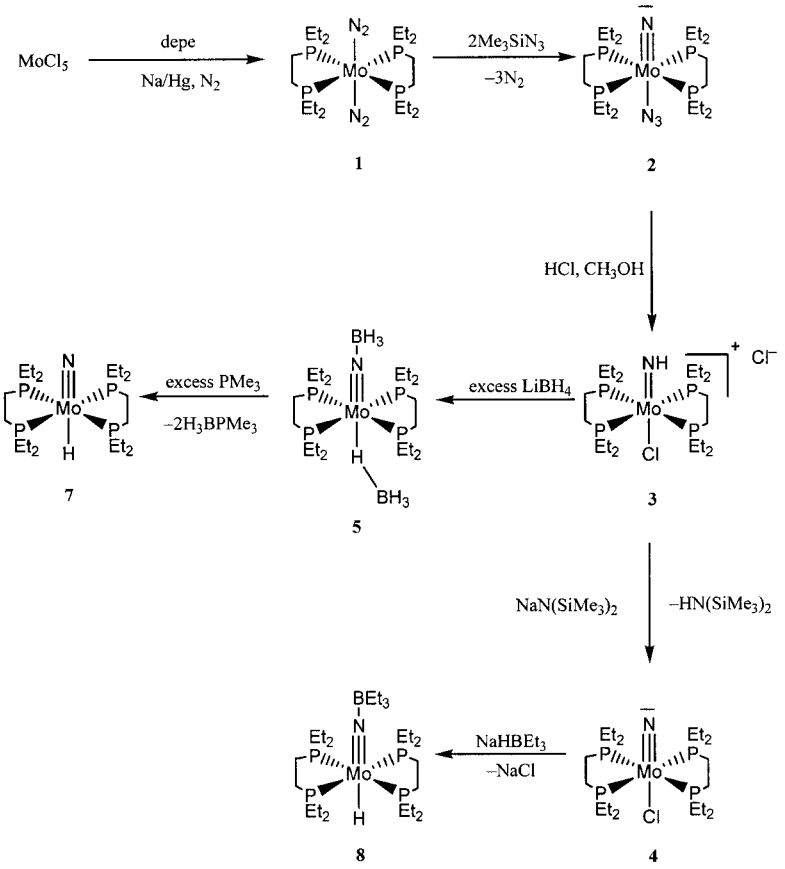


Scheme 1.

 © 2006 Wiley-VCH Verlag GmbH & Co. KGaA, Weinheim 

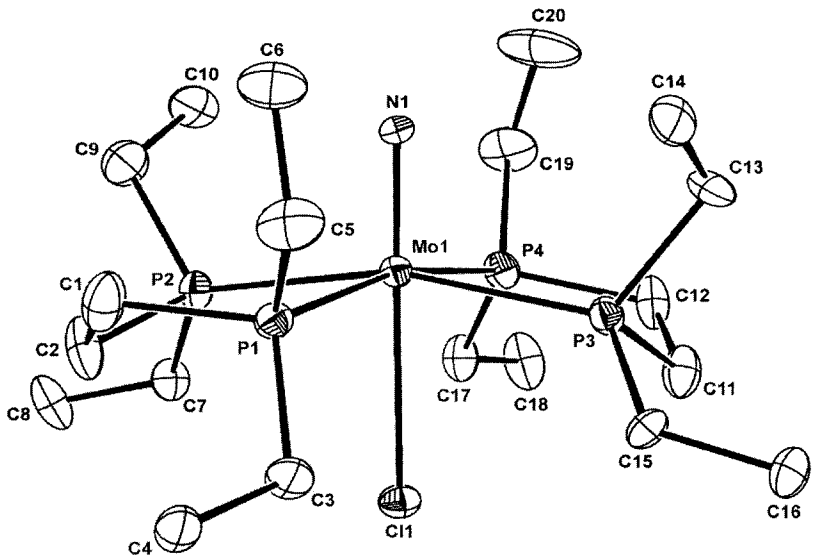


Figure 1. Molecular structure of **4**; only one of the three independent molecules is shown. Selected bond lengths [Å] and angles [°]: Mo1–N1 1.690(5), Mo1–Cl1 2.7901(19), N1–Mo1–Cl1 177.6(2) (molecule 1), Mo2–N2 1.684(5), Mo2–Cl2 2.7406(17), N2–Mo2–Cl2 175.06(18) (molecule 2) and Mo3–N3 1.722(5), Mo3–Cl3 2.7859(19), N3–Mo3–Cl3 174.23(19) (molecule 3). The displacement ellipsoids are of 20% probability and all hydrogen atoms have been omitted for clarity.

structure of **6**. Disorder was recognized between the $NBH_3$ and Cl groups, which prevented an accurate comparison of the bond parameters of **4** and **6**. On a rough scale, however, a significantly shorter Mo–Cl bond of 2.621(2) Å seems to be present in **6**, which speaks for a weaker *trans* influence of the $NBH_3$ unit in **6** with respect to that of the nitrido group in **4**.

Treatment of the borohydride species **5** with an excess of $PMe_3$ in toluene at 120 °C for 11 d resulted in the formation of the desired hydride Mo(H)(N)(depe)$_2$ (**7**). The $^1$H NMR spectrum of **7** in $C_6D_6$ displayed at room temperature, among other resonances, that of the hydrido ligand as a quintuplet at $\delta$ = –5.99 ppm ($^2J_{HP}$ = 30 Hz). The $^{31}$P{$^1$H} NMR spectrum reveals a singlet at $\delta$ = 80.6 ppm.

The $NBEt_3$-substituted hydrido complex **8** was obtained from the nitrido chloride **4** by treatment with a slight excess of the hydride reagent $NaHBEt_3$ in THF at room temperature for 15 h. Due to the considerable basicity of the ter-

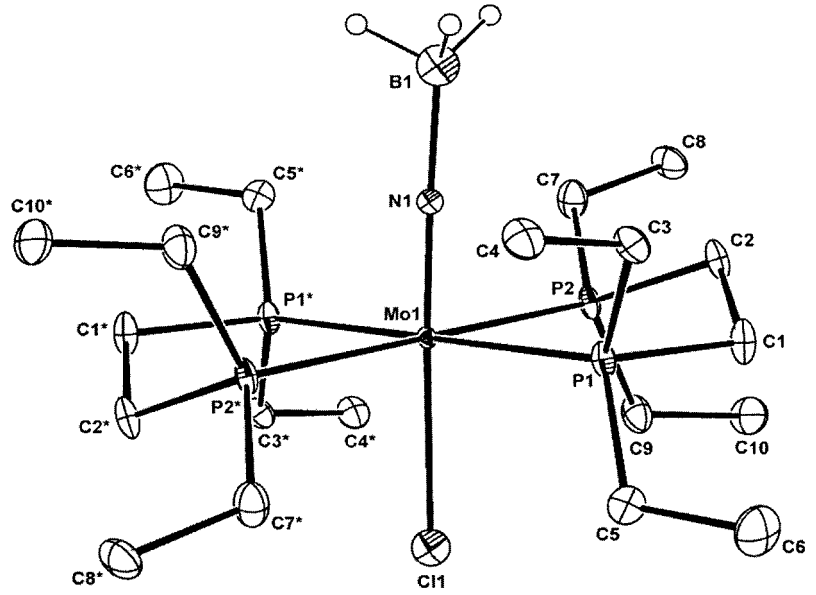


Figure 2. Molecular structure of **6** (ellipsoids are drawn at the 30% probability level). Selected bond lengths [Å] and angles [°]: Mo1–N1 1.656(4), Mo1–Cl1 2.621(2), N1–B1 1.62(1); N1–Mo1–Cl1 177.49(13), B1–N1–Mo1 177.9(4). The molybdenum center lies on a special position (inversion center) and half of the molecule is reproduced by the symmetry operation 1 – *x*, 1 – *y*, 1 – *z* (the symmetry-related atoms are labeled with an asterisk). The hydrogen atoms of the $BH_3$ group have been refined with soft B–H distance restraints. The $NBH_3$/Cl disorder and selected hydrogen atoms have been omitted for clarity.

 © 2006 Wiley-VCH Verlag GmbH & Co. KGaA, Weinheim 

minal nitrido group the "leftover" $BEt_3$ moiety is scavenged after $H^-$ transfer to the Mo center. The $^1H$ NMR spectrum of **8** shows a characteristic resonance for the hydrido ligand as a quintuplet at $\delta$ = –6.23 ppm ($^2J_{HP}$ = 36 Hz). The presence of the *N*-bound $BEt_3$ group was confirmed by a $CH_2$ resonance in the $^1H$ NMR spectrum appearing as a 1:3:3:1 quadruplet at $\delta$ = 0.86 ppm ($^3J_{HH}$ = 8 Hz) and a triplet for the Me groups at $\delta$ = 1.36 ppm ($^3J_{HH}$ = 8 Hz). In the $^{13}C$ NMR spectrum the signal of the $CH_2$ groups of the $BEt_3$ moiety could not be detected. Their chemical shift at $\delta$ = 18.9 ppm could only be extracted from a C–H correlation spectrum of **8**.

The molecular structure of **8** was confirmed by an X-ray diffraction analysis. It exhibits pseudooctahedral coordination of the Mo center with the two depe ligands in equatorial positions and the hydrido ligand and the $NBH_3$ group *trans* to each other (Figure 3). The hydride atom was found in the difference electron density map. It could be refined isotropically (0.022 Å$^2$). The Mo–H bond length of 1.85(2) Å compares well with that observed for the Mo(H)(CO)(NO)(PMe$_3$)$_3$ complex [1.84(3) Å].[19] The Mo–N bond of 1.7571(14) is longer than in **4** [1.698(5) Å], presumably due to the attached $BEt_3$ group which apparently reduces the strength of the metal–nitrogen triple bond.

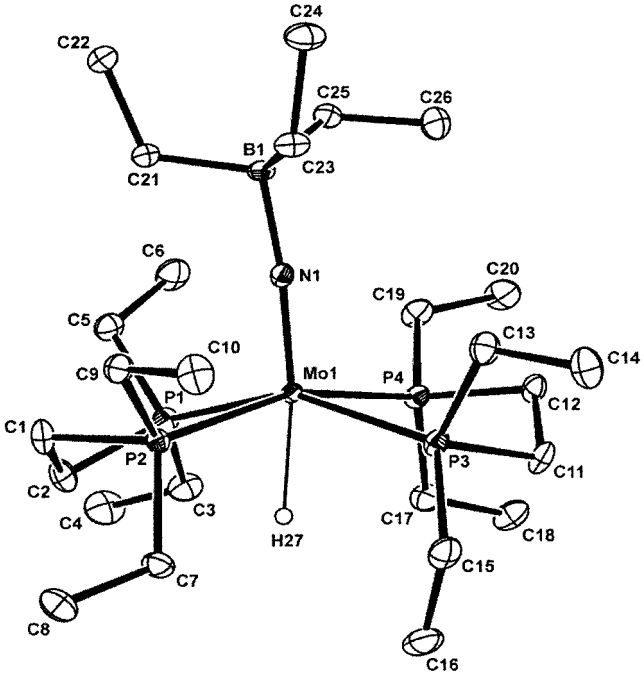


Figure 3. Molecular structure of **8** (ellipsoids are drawn at the 30% probability level). Selected bond lengths [Å] and angles [°]: Mo1–N1 1.7571(14), Mo1–H27 1.85(2), N1–B1 1.568(2), N1–Mo1–H27 171.2(7), B1–N1–Mo1 173.69(14). All hydrogen atoms have been omitted for clarity, except the hydrido atom H27 for which the positional parameters were freely refined.

### Hydridic Character of the *trans*-Mo(H)(NBEt$_3$)(depe)$_2$ Complex 8

Different approaches to classify the L$_n$M–H bond in terms of its hydridic character are based either on kinetic or thermodynamic studies of hydride transfer reactions. Cheng and Bullock[37] determined kinetic hydridicities by the reaction of L$_n$M–H bonds (M = transition metal) with the trityl cation. The work of Sarker and Bruno[38] rely on the equilibration of both types of species to establish a thermodynamic scale of hydridicities. Bond ionicities may also be taken as an indicator for the hydridic character of the L$_n$M–H bond. We used $^2H$ NMR spectroscopy to determine the deuterium quadrupole coupling constant (DQCC) of the D nucleus by measuring the temperature-dependent $T_{1min}$ relaxation time in [H$_8$]toluene[39,40] and also by calculation of the DQCC from the "Pake doublet" appearing in the static solid-state NMR spectrum, preferably at low temperatures. For these experiments the deuterium derivative Mo(D)(NBEt$_3$)(depe)$_2$ (**8a**) had to be prepared using LiDBEt$_3$ instead of NaHBEt$_3$. According to the $T_{1min}$ method, the DQCC of the deuteride **8a** was calculated to be 43 ± 1 kHz. The ionicity of the Mo–D(H) is thus 81.0 ± 0.4% and stresses the strong polarity of the Mo–D bond in **8a**. This bond ionicity belongs to the largest ionicities reported for transition metal hydrides.[41] From the solid-state $^2H$ NMR spectra a Δ value of the "Pake doublet" of 31.1 kHz is obtained, from which the DQCC was calculated to be 42 ± 1 kHz corresponding to a bond ionicity of 81.7 ± 0.5% very close to the value obtained by the $T_{1min}$ method.

### Hydride Transfer Reactions of Mo(H)(N)(depe)$_2$ (7) and *trans*-Mo(H)(NBEt$_3$)(depe)$_2$ (8)

Very much to our surprise, the hydride **7** turned out to be very unreactive. It did not react with ketones or carbonylmetal compounds and produced a mixture of unidentified products in the presence of $CO_2$. The reason for this is yet unclear, especially in view of the fact that the very related derivative **8**, distinguished from **7** by an additional Lewis acid bound to the nitrido ligand, showed various hydride transfer reactions.

The Mo–H bond of **8** was shown to be highly polarized and at least in a kinetic sense this complex seemed to be prone to undergo hydride transfer reactions, i.e. insertions with a wide variety of unsaturated compounds such as $CO_2$,[42–48] ketones and carbonylmetal compounds (Scheme 2). Reaction of **8** with an excess of $CO_2$ (450 mbar at –196 °C) in [D$_8$]toluene indeed proceeded smoothly at room temeperature. The reaction was complete after a few minutes and the *O*-formate product Mo(OCHO)(NBEt$_3$)(depe)$_2$ (**9**) was isolated in 70% yield as analytically pure yellow crystals after recrystallisation from diethyl ether solution. The formate group of **9** displayed a singlet resonance at $\delta$ = 8.04 ppm in the $^1H$ NMR spectrum and a singlet resonance at $\delta$ = 166.0 ppm in the $^{13}C$ NMR spectrum. The IR spectrum of **9** revealed two intense bands at 1611 and 1320 cm$^{-1}$ for the formate ligand, in accordance with other $\eta^1$-formate complexes reported in the literature.[49,50] The structure of **9** was finally confirmed by an X-ray diffraction analysis (Figure 4).

 © 2006 Wiley-VCH Verlag GmbH & Co. KGaA, Weinheim 

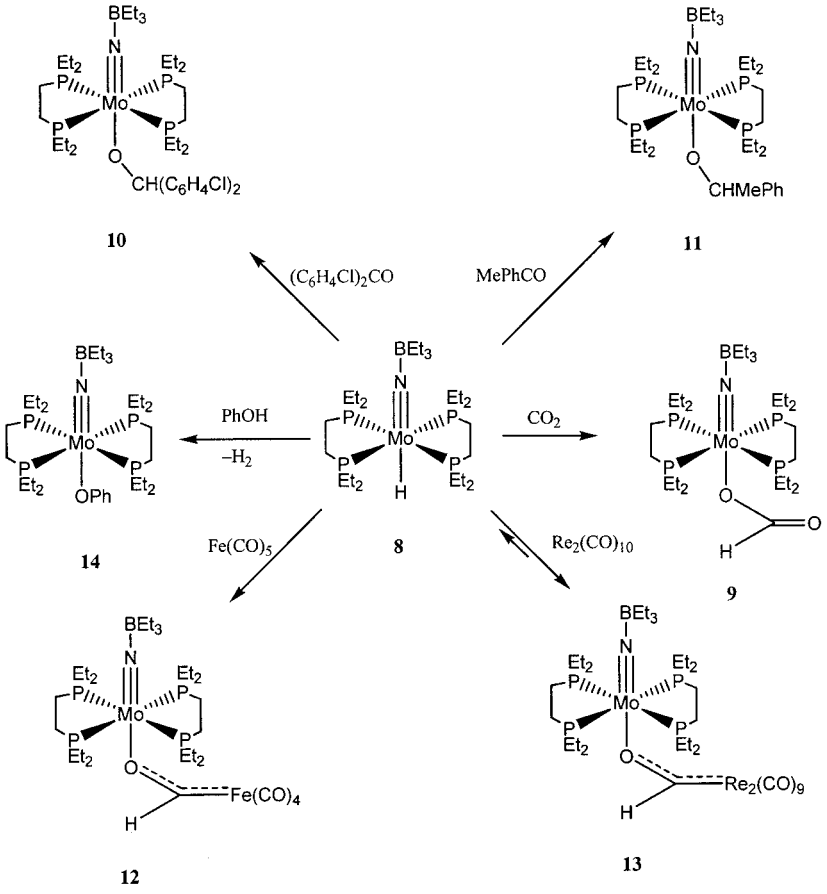


Scheme 2.

The molybdenum centre adopts a pseudooctahedral geometry, with the $NBEt_3$ moiety and the $\eta^1$-formato ligand *trans* to each other. The structure revealed an Mo–O bond length of 2.214(2) Å.[18,50,51] The Mo–N and N–B bond lengths of 1.713(3) Å and 1.609(5) Å, respectively, are similar to those of **10** and **14**.

Reactions of **8** with 4,4′-dichlorobenzophenone and acetophenone were completed at 60 °C in 1 d and at room temperature in 3 d, respectively, to afford the corresponding alkoxide complexes *trans*-$Mo(OCHRR')(NBEt_3)(depe)_2$ [R = R′ = *p*-$C_6H_4Cl$ (**10**); R = Ph, R′ = Me (**11**)]. 4,4′-Dichlorobenzophenone was chosen as a model reagent for disubstituted aromatic ketones, because of difficulties faced in the reaction of **8** with the parent benzophenone where two products were obtained, which could not be separated. In the $^1H$ NMR spectrum compound **10** shows a singlet at $\delta$ = 4.68 ppm and a characteristic signal at $\delta$ = 83.1 ppm in the $^{13}C$ NMR spectrum, both being attributed to the Mo–OCH moiety. In a similar manner, the OCH moiety of complex **11** was identified by a quadruplet at $\delta$ = 4.11 ppm ($^3J_{HH}$ = 6.3 Hz) in the $^1H$ NMR spectrum and by a singlet at $\delta$ = 75.1 ppm in the $^{13}C$ NMR spectrum. Single crystals of **10** suitable for X-ray diffraction analysis were obtained by cooling a concentrated solution of **10** in diethyl ether to –30 °C.

As shown in Figure 5, the molybdenum center of **10** exhibits a pseudooctahedral coordination environment similar to that of the complexes mentioned before. This structure shows an Mo–O bond length of 2.1781(16) Å, in the range of those reported in related structures.[19,52] The Mo1–N1 bond length of 1.733(2) Å falls into the range of those observed for **8** and **9**, while the N1–B1 bond length of 1.612(4) is similar to that in **9**.

The insertion of CO into an activated $L_nM$–H bond could result in the formation of a formyl species. This reaction has been proposed to be a key step in the homogeneous hydrogenation of CO. However, the direct product of CO insertion into an $L_nM$–H bond to give a metal-bound formyl group has only rarely been observed,[53–57] because in most cases this step is thermodynamically not favourable. Despite this, metal-bound CO was found to insert into strongly polar $L_nM$–H bonds. Insertion of **8** with $Fe(CO)_5$ and $Re_2(CO)_{10}$ was thus attempted affording the μ-formyl complexes *trans*-$Mo[(\mu\text{-}OCH)Fe(CO)_4](NBEt_3)(depe)_2$ (**12**) and *trans*-$Mo[(\mu\text{-}OCH)Re_2(CO)_9](NBEt_3)(depe)_2$ (**13**). Compound **12** was isolated as yellow crystals after recrystallisation from a saturated toluene solution. In contrast to the reaction with $Fe(CO)_5$, the reaction with $Re_2(CO)_{10}$ in toluene reaches an equilibrium after 2 d which is strongly shifted to the formyl side. Analytically pure

 © 2006 Wiley-VCH Verlag GmbH & Co. KGaA, Weinheim 

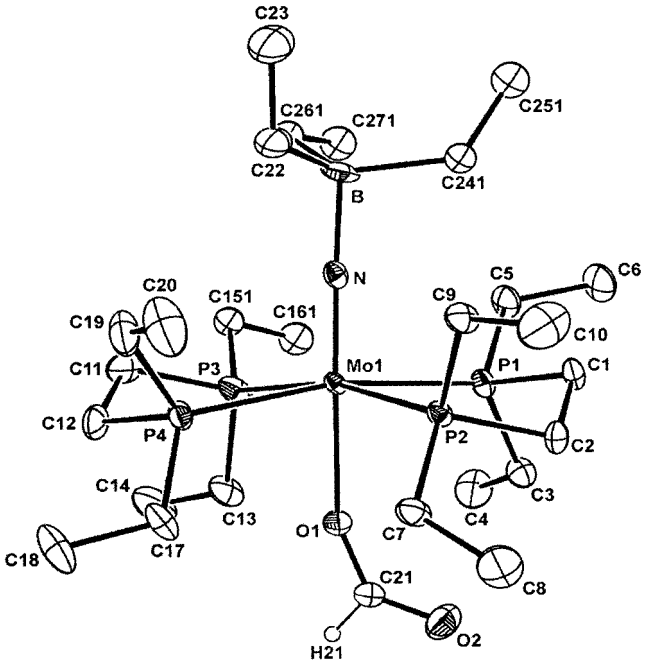


Figure 4. Molecular structure of **9** (ellipsoids are drawn at the 30% probability level). Selected bond lengths [Å] and angles [°]: Mo1–N 1.713(3), Mo1–O1 2.214(2), N–B 1.609(5), O1–C21 1.234(4), Mo1–*N*–B 177.5(3), N–Mo1–O1 179.07(13), Mo1–O1–C21 157.6(3). Selected hydrogen atoms and the disordered ethyl groups on the phosphorus atom P3 and on the boron atom have been omitted for clarity.

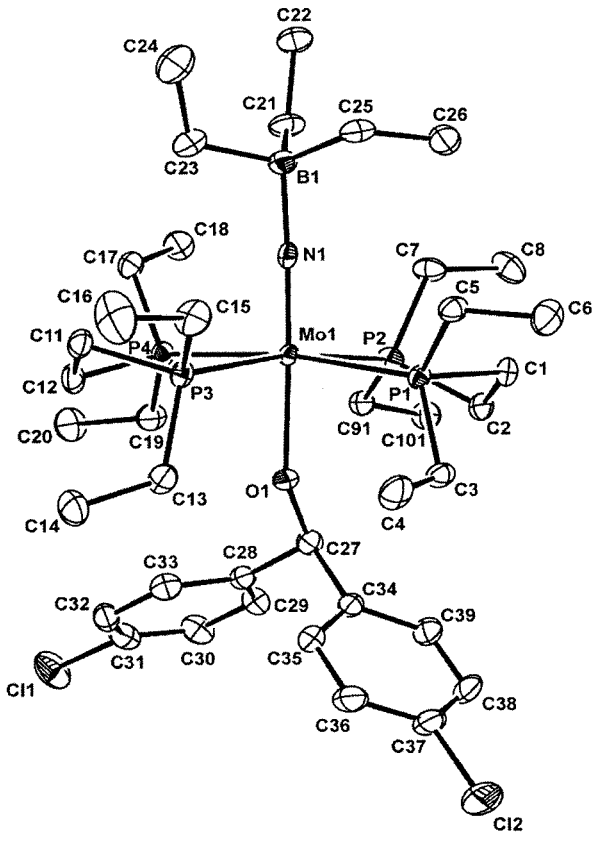


Figure 5. Molecular structure of **10** (ellipsoids are drawn at the 30% probability level). Selected bond lengths [Å] and angles [°]: Mo1–N1 1.732(2), N1–B1 1.612(4), Mo1–O1 2.1781(16), Mo1–N1–B1 177.1(2), N1–Mo1–O1 177.39(8), Mo1–O1–C27 147.98(16). All hydrogen atoms and the disordered ethyl group of the phosphorus atom P2 have been omitted for clarity.

orange crystals of **13** were obtained by crystallization from toluene. Among other resonances, the $^1$H NMR spectra of **12** and **13** show characteristic $H_{formyl}$ signals at $\delta$ = 13.78 ppm and at $\delta$ = 14.91 ppm in a typical chemical shift region reported for similar complexes.[14,17,19,52] The $^{31}$P NMR spectrum displays a singlet for the four equivalent phosphorus nuclei at $\delta$ = 52.2 ppm and at $\delta$ = 54.4 ppm for **12** and **13**, respectively. In the low-field region the $^{13}$C NMR spectra consist of a broad signal for the $C_{formyl}$ atom at $\delta$ = 293.2 ppm and $\delta$ = 289.5 ppm for **12** and **13**, respectively. In the IR spectrum of **12** the ν(CO) bands of the $Fe(CO)_4$ moiety appear at 2020, 1966 and 1870 cm$^{-1}$ and in the IR spectrum of **13** seven bands at 2094, 2070, 2025, 2007, 1969, 1935 and 1902 cm$^{-1}$ are found, which were assigned to the ν(CO) vibrations of the $Re_2(CO)_9$ unit.

The X-ray structures of **12** and **13** are presented in Figures 6 and 7. Both coordination geometries around the Mo centers possess a distorted octahedral arrangement. The μ-formyl bond lengths in **12** [1.219(3) Å] and **13** [1.250(4) Å] are noticeably different, with a longer separation in the rhenium complex **13** indicating a stronger π-donation of the $Re_2(CO)_9$ fragment.

The potential for hydrogenations using **8** was tested by the reaction of the hydride with acetone in the presence of a proton donor (PhOH) simulating a stoichiometric "ionic hydrogenation". The reaction of **8** with the phenol alone was so fast that instantaneous formation of $H_2$ and the phenoxy complex **14** was observed (signal at $\delta$ = 4.45 ppm in the $^1$H NMR spectrum). A crystal of **14** suitable for an X-ray analysis was obtained from a saturated diethyl ether solution at –30 °C. The molecular structure of **14** shows the molybdenum atom in pseudo-octahedral environment with the phenoxy[58] group and the $Et_3BN$ ligand *trans*-disposed to each other (Figure 8).

The hydrogenation of cyclohexene was also attempted using **8** without the presence of an acidic substrate. A Young NMR tube was pressurized with 1700 mbar $H_2$ in the presence of complex **8** (1%). After 12 d at 110 °C, 94% of the cyclohexene was found to be hydrogenated to cyclohexane. The $^1$H NMR spectrum of the reaction mixture showed that the typical signals of the cyclohexene starting material ($\delta$ = 5.59, 1.85, 1.46 ppm) decreased, while the characteristic resonance for cyclohexane ($\delta$ = 1.34 ppm) appeared. The presence of the cyclohexane was further confirmed by GC-MS. However, **8** could not be recovered. The $^{31}$P NMR showed the presence of the free depe phosphane ($\delta$ = –17.9 ppm) among several unidentified signals indicating that **8** is a precursor to the irreversibly formed catalytically active species, which presumably coordinates only one depe ligand.

 © 2006 Wiley-VCH Verlag GmbH & Co. KGaA, Weinheim 

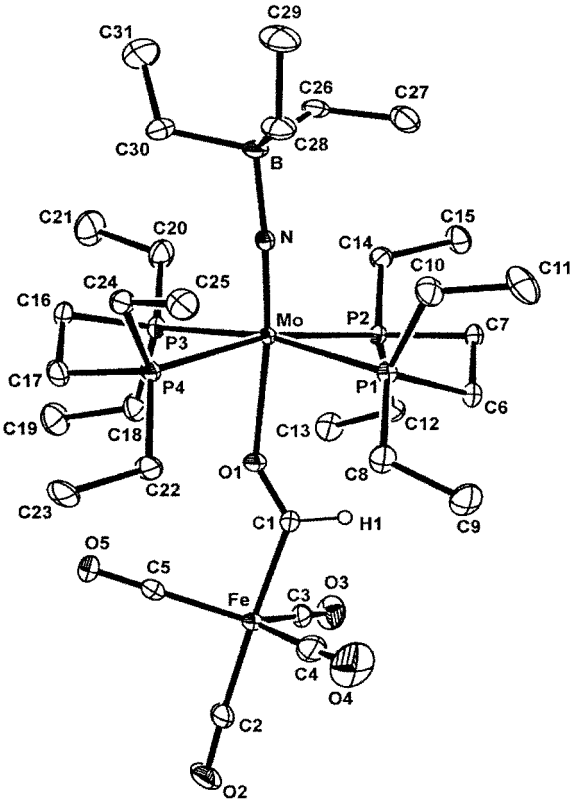


Figure 6. Molecular structure of **12** (ellipsoids are drawn at the 30% probability level). Selected bond lengths [Å] and angles [°]: Mo–N 1.717(2), Mo–O1 2.3044(17), N–B 1.615(4), C–O 1.219(3), Fe–C 1.933(3), Mo–O1–C1 145.10(18), Fe–C1–O1 132.0(2), N–Mo–O1 173.27(9), Mo–N–B 175.7(2). All hydrogen atoms, except H1, and the co-crystallized solvent molecule of toluene have been omitted for clarity.

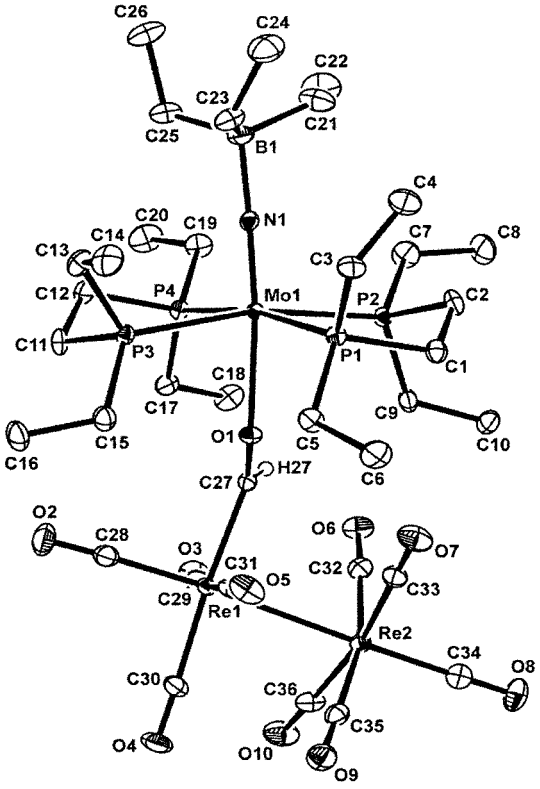


Figure 7. Molecular structure of **13** (ellipsoids are drawn at the 40% probability level). Selected bond lengths [Å] and angles [°]: Mo1–N1 1.712(3), Mo1–O1 2.350(2), N1–B1 1.625(5), C27–O1 1.250(4), Re1–C27 2.137(4), Re1–Re2 3.0511(3), Mo1–O1–C27 139.4(2), Re1–C27–O1 130.6(3), C27–Re1–Re2 91.26(10), N1–Mo1–O1 173.63(12), Mo1–N1–B1 176.0(3). All hydrogen atoms, except H27, have been omitted for clarity.

## Conclusion

Two transition metal hydride complexes of the type $Mo(H)(L)(depe)_2$ [L = N (**7**), $NBEt_3$ (**8**)] were prepared. Since a high propensity for insertion reactions was found for **8**, but not for **7**, hydridicity and reactivity of **8** were investigated in detail. Even though this difference in chemical behaviour is yet unexplained, it indicates that slight alterations in the coordination sphere may cause rather pronounced reactivity changes of the $L_nM$–H bond; an important circumstance for any hydride tuning efforts.

## Experimental Section

**General:** Reagent grade benzene, toluene, pentane, diethyl ether and tetrahydrofuran were dried and distilled from sodium benzophenone ketyl prior to use. MeOH was dried and distilled from Mg. Literature procedures were used to prepare the following compounds: 1,2-bis(diethylphosphanyl)ethane (depe)[59] and $PMe_3$.[60] Other reagents were purchased and used without further purification. All the manipulations were carried out under nitrogen using Schlenk techniques or a dry glovebox. IR spectra were obtained with a Bio-Rad FTS-45 instrument and Raman spectra were obtained with a Renishaw Labram Raman spectrometer. Mass spectra were obtained with a Finnigan-MAT-8400 spectrometer. Gas chromatography-mass spectra (GC-MS) were recorded with a Varian-Chrompack CP-3800 gas chromatograph equipped with a Saturn 2000 electron impact mass spectrometer (EI-MS). The samples were carried by an He flow through a CP-SIL 8 CB-MS FS 30 × 25 (.25) column; flow: 1 mL/ min, split: 100:1, EI: 70 eV, isothermal method at 30 °C. NMR spectra were measured with a Varian Mercury 200 spectrometer at 81.0 MHz for $^{31}P\{^1H\}$, with a Varian Gemini 300 spectrometer at 300.1 MHz for $^1H$, 121.5 MHz for $^{31}P\{^1H\}$, 75.4 MHz for $^{13}C\{^1H\}$ and 96.2 MHz for $^{11}B\{^1H\}$ and with a Bruker-DRX-500 spectrometer at 500.2 MHz for $^1H$, 202.5 MHz for $^{31}P\{^1H\}$, 125.8 MHz for $^{13}C\{^1H\}$, 36.2 MHz for $^{14}N$ and 32.5 MHz for $^{95}Mo$. Chemical shifts for $^1H$ and $^{13}C$ are given in ppm relatively to TMS ($SiMe_4$), the $^{31}P\{^1H\}$ NMR spectra were referenced to 98% external $H_3PO_4$, $^{11}B$ relative to $Et_2O{\cdot}BF_3$, $^{14}N$ relative to $CH_3NO_2$ and $^{95}Mo$ relative to $MoO_4^{2-}$. Elemental analyses: Leco CHN(S)-932 instrument.

**Preparation of *trans*-$Mo(N_2)_2(depe)_2$ (1):** Ligand depe (0.744 g, 3.61 mmol) was added dropwise to 20 mL of a THF suspension of 1% Na amalgam under nitrogen. Then sublimed $MoCl_5$ (0.410 g, 1.5 mmol) was added and the brown solution was stirred for 18 h. The solution was filtered twice through Celite which was then rinsed with toluene. The solvent was removed under vacuum and the resulting precipitate dissolved in 30 mL of toluene. The solution was filtered further twice through Celite, and brought to a volume of 12 mL under vacuum; 24 mL of MeOH was added to precipitate the product at –30 °C within 15 h. The orange needles were filtered off, washed with MeOH and then dried under vacuum. Yield of **1**:

 © 2006 Wiley-VCH Verlag GmbH & Co. KGaA, Weinheim 

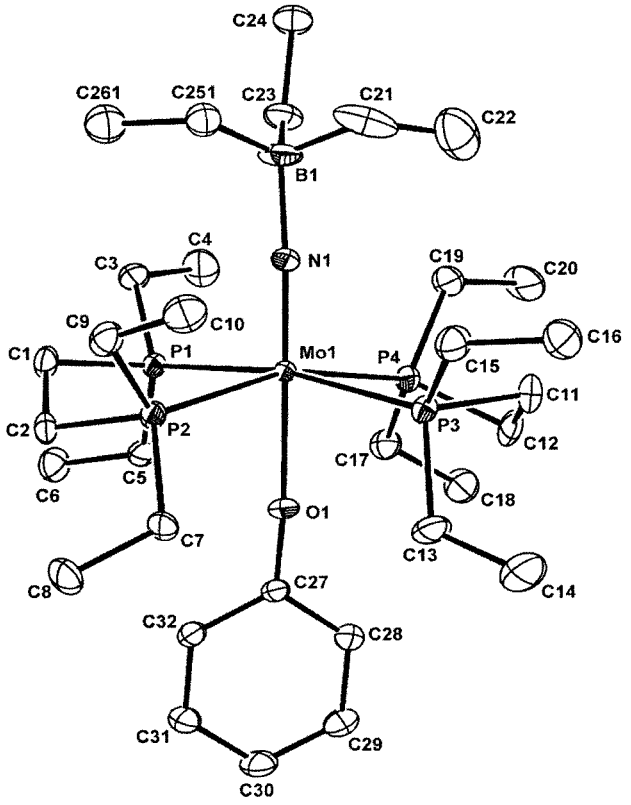


Figure 8. Molecular structure of **14** (ellipsoids are drawn at the 30% probability level). Selected bond lengths [Å] and angles [°]: Mo1–N1 1.719(2), Mo1–O1 2.1656(18), N1–B1 1.603(4), Mo1–O1–C27 175.43(19), N1–Mo1–O1 178.05(10), Mo1–N1–B1 176.8(2). All hydrogen atoms and the disordered ethyl group on the boron atom have been omitted for clarity.

0.592 mg, 1.04 mmol, 69%. $^1$H NMR ($C_6D_6$, 298 K, 300.1 MHz): $\delta$ = 1.83 (m, 16 H, PC$H_2$CH$_3$), 1.35 [m, 8 H, P(C$H_2$)$_2$P], 1.09 (m, 24 H, PCH$_2$C$H_3$) ppm. $^{31}$P{$^1$H} NMR ($C_6D_6$, 298 K, 121.5 MHz): $\delta$ = 56.7 (s) ppm. $^{13}$C{$^1$H} NMR ($C_6D_6$, 298 K, 75.4 MHz): $\delta$ = 23.7 [m, P(*C*H$_2$)$_2$P], 21.4 (m, P*C*H$_2$CH$_3$), 8.7 (m, PCH$_2$*C*H$_3$) ppm. IR (KBr): $\tilde{\nu}$ = 1921 [$\nu_{asym}$(N$_2$)] cm$^{-1}$. Raman: $\tilde{\nu}$ = 1997 [$\nu_{sym}$(N$_2$)] cm$^{-1}$. $C_{20}H_{48}MoN_4P_4$ (564.45): calcd. C 42.56, H 8.57, N 9.93; found C 42.86, H 8.44, N 9.88.

**Preparation of *trans*-Mo(N)(N$_3$)(depe)$_2$ (2):** Complex **1** (0.507 mg, 0.90 mmol) was dissolved in 30 mL of THF in a round-bottomed flask and trimethylsilyl azide (0.32 mL, 2.43 mmol) was added. The mixture was refluxed for at least 1 h. The reddish solution was filtered through Celite and concentrated under vacuum. The solid was rinsed with pentane and dried under vacuum to afford a brown solid. Yield of **2**: 0.449 mg, 0.79 mmol, 88%. $^1$H NMR ($C_6D_6$, 293 K, 300.1 MHz): $\delta$ = 2.11–1.73 (m, 16 H, PC$H_2$CH$_3$), 1.52 [br. m, 4 H, P(CH$_2$)$_2$P], 1.36 [br. m, 4 H, P(CH$_2$)$_2$P], 1.20 (m, 12 H, PCH$_2$C$H_3$), 1.02 (m, 12 H, PCH$_2$C$H_3$) ppm. $^{31}$P{$^1$H} NMR ($C_6D_6$, 293 K, 121.5 MHz): $\delta$ = 59.2 (br. s) ppm. $^{13}$C{$^1$H} NMR ($C_6D_6$, 293 K, 75.4 MHz): $\delta$ = 22.2 [m, P(*C*H$_2$)$_2$P], 21.8 (m, P*C*H$_2$CH$_3$), 19.0 (m, P*C*H$_2$CH$_3$), 8.5 (s, PCH$_2$*C*H$_3$), 7.5 (s, PCH$_2$*C*H$_3$) ppm. IR (ATR): $\tilde{\nu}$ = 2022 [$\nu_{asym}$(N$_3$)], 977 [$\nu$(Mo≡N)] cm$^{-1}$. Raman: $\tilde{\nu}$ = 1342 [$\nu_{sym}$(N$_3$)] cm$^{-1}$. $C_{20}H_{48}MoN_4P_4$ (564.45): calcd. C 42.56, H 8.57, N 9.93; found C 42.92, H 8.45, N 9.56.

**Preparation of *trans*-[Mo(Cl)(NH)(depe)$_2$][Cl] (3):** Compound **2** (0.412 g, 0.73 mmol) was dissolved in 15 mL of MeOH and a few drops of 32% aqueous HCl were added. A darkening of the red solution was observed. The solution was stirred for 15 min and then the solvent was removed under vacuum. The precipitate was dissolved in THF, the solution filtered through Celite, concentrated under vacuum, and the residue washed three times with pentane and dried under vacuum to yield a red powder. Yield of **3**: 349 mg, 0.59 mmol, 80%. $^1$H NMR ([D$_8$]THF, 295 K, 500.2 MHz): $\delta$ = 2.07 (m, 16 H, PC$H_2$CH$_3$), 1.92 [br. m, 8 H, P(C$H_2$)$_2$P], 1.21 (m, 24 H, PCH$_2$C$H_3$) ppm. $^{31}$P{$^1$H} NMR ([D$_8$]THF, 295 K, 202.5 MHz): $\delta$ = 47.5 (s) ppm. $^{13}$C{$^1$H} NMR ([D$_8$]THF, 295 K, 125.8 MHz): $\delta$ = 23.2 [m, P(*C*H$_2$)$_2$P], 19.0 (m, P*C*H$_2$CH$_3$), 8.3 (s, PCH$_2$*C*H$_3$) ppm. $C_{20}H_{49}Cl_2MoNP_4$ (594.35): calcd. C 40.42, H 8.31, N 2.36; found C 40.03, H 7.97, N 2.07.

**Preparation of *trans*-Mo(Cl)(N)(depe)$_2$ (4):** Compound **3** (203.6 mg, 0.34 mmol) was suspended in 15 mL of toluene and a 0.6 M solution of NaN(SiMe$_3$)$_2$ in toluene (1.14 mL, 0.68 mmol) was added. The precipitate was dissolved and the solution stirred overnight. The brown solution was filtered through Celite and concentrated under vacuum. Then **4** was extracted with pentane and the solution concentrated under vacuum to yield a brown powder. Yield of **4**: 123.5 mg, 0.22 mmol, 64%. $^1$H NMR ($C_6D_6$, 293 K, 500.2 MHz): $\delta$ = 2.38 (m, 4 H, PC$H_2$CH$_3$), 1.88 (m, 4 H, PC$H_2$CH$_3$), 1.80 (m, 4 H, PC$H_2$CH$_3$), 1.75 (m, 4 H, PC$H_2$CH$_3$), 1.64 [br. m, 4 H, P(C$H_2$)$_2$P], 1.41 [br. m, 4 H, P(C$H_2$)$_2$P], 1.27 (m, 12 H, PCH$_2$C$H_3$), 1.04 (m, 12 H, PCH$_2$C$H_3$) ppm. $^{31}$P{$^1$H} NMR ($C_6D_6$, 293 K, 121.5 MHz): $\delta$ = 56.0 (s) ppm. $^{13}$C{$^1$H} NMR ($C_6D_6$, 293 K, 125.8 MHz): $\delta$ = 22.4 [m, P(*C*H$_2$)$_2$P], 21.7 (m, P*C*H$_2$CH$_3$), 19.4 (m, P*C*H$_2$CH$_3$), 9.0 (s, PCH$_2$*C*H$_3$), 7.8 (s, PCH$_2$*C*H$_3$) ppm. IR (KBr): $\tilde{\nu}$ = 984 [$\nu$(Mo≡N)] cm$^{-1}$. Raman: $\tilde{\nu}$ = 915 [$\nu$(Mo≡N)] cm$^{-1}$. MS (EI): *m*/*z* = 560 [M$^+$], 353 [M$^+$ – 1 depe]. $C_{20}H_{48}ClMoNP_4$ (557.88): calcd. C 43.06, H 8.67, N 2.51; found C 43.35, H 8.53, N 2.63.

**Preparation of *trans*-Mo($\eta^1$-HBH$_3$)(NBH$_3$)(depe)$_2$ (5):** Complex **3** (1.0192 g, 1.71 mmol) was mixed with LiBH$_4$ (28.8 mg, 8.59 mmol), dissolved in 50 mL of THF. Evolution of gas, assumed to be H$_2$, was observed and the mixture was stirred overnight. The solution was filtered through Celite and concentrated under vacuum. The precipitate was dissolved in toluene, the solution filtered through Celite twice and concentrated under vacuum to afford a brown powder. Yield of **5**: 502 mg, 0.91 mmol, 53%. $^1$H NMR ([D$_8$]THF, 293 K, 500.2 MHz): $\delta$ = 2.17–1.93 (m, 16 H, PC$H_2$CH$_3$), 1.83 [br. m, 8 H, P(C$H_2$)$_2$P], 1.44 (br., 3 H, B$H_3$), 1.25 (m, 12 H, PCH$_2$C$H_3$), 1.18 (m, 12 H, PCH$_2$C$H_3$), –2.9 (q, 4 H, *H*B$H_3$, $^1J_{HB}$ = 82 Hz) ppm. $^{31}$P{$^1$H} NMR ([D$_8$]THF, 293 K, 202.5 MHz): $\delta$ = 47.0 (s) ppm. $^{13}$C{$^1$H} NMR ([D$_8$]THF, 293 K, 125.8 MHz): $\delta$ = 22.5 [m, P(*C*H$_2$)$_2$P], 19.8 (m, P*C*H$_2$CH$_3$), 19.4 (m, P*C*H$_2$CH$_3$), 9.1 (s, PCH$_2$*C*H$_3$), 8.6 (s, PCH$_2$*C*H$_3$) ppm. $^{11}$B NMR ([D$_8$]THF, 293 K, 160.5 MHz): $\delta$ = –15.9 (q, 1 B, N*B*H$_3$, $^1J_{HB}$ = 88 Hz), –44.62 (quint, 1 B, H*B*H$_3$, $^1J_{HB}$ = 82 Hz) ppm. IR (ATR): $\tilde{\nu}$ = 2290 [$\nu$(B–H)] cm$^{-1}$. $C_{20}H_{55}B_2MoNP_4$ (551.11): calcd. C 43.59, H 10.06, N 2.54; found C 43.27, H 10.35, N 2.24.

**Preparation of *trans*-Mo(Cl)(NBH$_3$)(depe)$_2$ (6):** Compound **3** (50.7 mg, 0.085 mmol) was mixed with LiBH$_4$ (1.85 mg, 0.085 mmol), dissolved in 15 mL of THF. H$_2$ gas evolution was observed and the mixture was stirred overnight. The solution was filtered through Celite and concentrated under vacuum; the precipitate was dissolved in toluene, the solution filtered twice again through Celite and concentrated under vacuum to yield a yellow powder. Yield of **6**: 39.2 mg, 0.069 mmol, 80%. $^1$H NMR ($C_6D_6$, 293 K, 300.1 MHz): $\delta$ = 2.4 (q, 3 H, B$H_3$, $^1J_{HB}$ = 85 Hz), 2.17–1.93 (m, 16 H, PC$H_2$CH$_3$), 1.83 [br. m, 8 H, P(C$H_2$)$_2$P], 1.18 (m, 12 H, PCH$_2$C$H_3$), 0.95 (m, 12 H, PCH$_2$C$H_3$) ppm. $^{31}$P{$^1$H} NMR ($C_6D_6$, 293 K, 121.5 MHz): $\delta$ = 49.0 (s) ppm. $^{13}$C{$^1$H} NMR ($C_6D_6$, 293 K, 75.4 MHz): $\delta$ = 21.7 [m, P(*C*H$_2$)$_2$P], 19.3 (m, P*C*H$_2$CH$_3$),

 © 2006 Wiley-VCH Verlag GmbH & Co. KGaA, Weinheim 

18.1 (m, P*C*H$_2$CH$_3$), 9.1 (s, PCH$_2$*C*H$_3$), 8.2 (s, PCH$_2$*C*H$_3$) ppm. $^{11}$B NMR ([H$_8$]THF, 293 K, 96.2 MHz): $\delta$ = –13.5 (q, 1 B, N*B*H$_3$, $^1J_{HB}$ = 95 Hz) ppm. IR (ATR): $\tilde{\nu}$ = 2287 [ν(B–H)] cm$^{-1}$. $C_{20}H_{51}BClMoNP_4$ (571.72): calcd. C 42.01, H 8.99, N 2.45; found C 41.88, H 8.95, N 2.23.

**Preparation of *trans*-Mo(H)(N)(depe)$_2$ (7):** A mixture of **5** (502 mg, 0.91 mmol) with an excess of PMe$_3$ (1.41 mL, 13.6 mmol) was dissolved in 40 mL of toluene in an autoclave. The autoclave was placed in an oil bath at 120 °C for 11 d. The solution was concentrated under vacuum; **7** was extracted into pentane, the solution filtered through Celite and concentrated under vacuum to yield a red oil. Yield of **7**: 347.5 mg, 0.66 mmol, 73%. $^1$H NMR (C$_6$D$_6$, 293 K, 500.2 MHz): $\delta$ = 1.54 [br. m, 24 H, P(C*H*$_2$)$_2$P, PC*H*$_2$CH$_3$], 1.14 (br. m, 24 H, PCH$_2$C*H*$_3$), –5.99 (quint, 1 H, Mo–*H*, $^2J_{PH}$ = 30 Hz) ppm. $^{31}$P{$^1$H} NMR (C$_6$D$_6$, 293 K, 202.5 MHz): $\delta$ = 80.6 (s, $^1J_{PMo}$ = 102 Hz) ppm. $^{13}$C{$^1$H} NMR (C$_6$D$_6$, 293 K, 125.8 MHz): $\delta$ = 28.2 [br., P*C*H$_2$CH$_3$, P(*C*H$_2$)$_2$P], 9.3 (br., PCH$_2$*C*H$_3$) ppm. $^{14}$N{$^1$H} NMR (C$_6$D$_6$, 293 K, 36.2 MHz): $\delta$ = –71.6 (s) ppm. $^{95}$Mo NMR (C$_6$D$_6$, 293 K, 32.5 MHz): $\delta$ = –2062 (quint, $^1J_{PMo}$ = 102 Hz) ppm. MS (EI): *m*/*z* = 526 [M$^+$]. $C_{20}H_{49}MoNP_4$ (523.4): calcd. C 45.89, H 9.44, N 2.68; found C 45.66, H 9.62, N 2.71.

**Preparation of *trans*-Mo(H)(NBEt$_3$)(depe)$_2$ (8):** Complex **4** (291.8 mg, 0.52 mmol) was dissolved in THF (40 mL) and a 1 M solution of NaHBEt$_3$ in THF (0.54 mL, 0.54 mmol) was added. The reaction mixture was stirred at room temperature for 1 d. The solvent was removed under vacuum and the precipitate was extracted into pentane, the solution filtered through Celite and concentrated under vacuum. The crude product was recrystallised from a saturated diethyl ether solution by cooling to –30 °C to afford yellow-orange crystals. Yield of **8**: 385.5 mg, 0.48 mmol, 92%. $^1$H NMR (C$_6$D$_6$, 293 K, 500.2 MHz): $\delta$ = 2.18 (br. m, 8 H, PC*H*$_2$CH$_3$), 1.65 (br. m, 4 H, PC*H*$_2$CH$_3$), 1.48 [br. m, 4 H, P(C*H*$_2$)$_2$P], 1.37 [br. m, 4 H, P(C*H*$_2$)$_2$P], 1.36 (t, 9 H, BCH$_2$C*H*$_3$, $^3J_{HH}$ = 7.5 Hz), 1.25 (br. m, 4 H, PC*H*$_2$CH$_3$), 1.17 (m, 12 H, PCH$_2$C*H*$_3$), 0.77 (m, 12 H, PCH$_2$C*H*$_3$), 0.68 (q, 6 H, BC*H*$_2$CH$_3$, $^3J_{HH}$ = 7.5 Hz), –6.23 (quint, 1 H, Mo–*H*, $^2J_{PH}$ = 36 Hz) ppm. $^{31}$P{$^1$H} NMR (C$_6$D$_6$, 293 K, 202.5 MHz): $\delta$ = 65.5 (s) ppm. $^{13}$C{$^1$H} NMR (C$_6$D$_6$, 293 K, 125.8 MHz): $\delta$ = 24.8 (m, P*C*H$_2$CH$_3$), 23.6 [m, P(*C*H$_2$)$_2$P], 23.5 (m, P*C*H$_2$CH$_3$), 18.9 (br., B*C*H$_2$CH$_3$), 12.7 (s, BCH$_2$*C*H$_3$), 9.2 (s, PCH$_2$*C*H$_3$), 8.1 (s, PCH$_2$*C*H$_3$) ppm. $^{11}$B{$^1$H} NMR (C$_6$D$_6$, 293 K, 160.5 MHz): $\delta$ = –1.7 (s, 1 B, N*B*Et$_3$) ppm. IR (ATR): $\tilde{\nu}$ = 1417 [ν(Mo–H)] cm$^{-1}$. $C_{26}H_{64}BMoNP_4$ (621.43): calcd. C 50.25, H 10.38, N 2.25; found C 50.18, H 10.49, N 2.22.

**Preparation of *trans*-Mo(D)(NBEt$_3$)(depe)$_2$ (8a):** Complex **8a** was obtained by an analogous procedure as for **8**, using LiDBEt$_3$ instead of NaHBEt$_3$. $^2$H NMR ([H$_8$]toluene, 293 K, 76.79 MHz): $\delta$ = –6.51 (br.) ppm. $^{31}$P{$^1$H} NMR ([H$_8$]toluene, 293 K, 202.5 MHz): $\delta$ = 65.1 (t, $^2J_{PD}$ = 5.4 Hz) ppm.

**Preparation of *trans*-Mo[$^1$η-OC(O)H](NBEt$_3$)(depe)$_2$ (9):** The hydrido complex **8** (42.4 mg, 0.068 mmol) was dissolved in 0.5 mL of [D$_8$]toluene in a Young NMR tube, which was put under 450 mbar of CO$_2$ at 77 K. The reaction mixture was warmed to room temperature. The solution became light orange and after 30 min the solvent and the excess of CO$_2$ were removed under vacuum. The compound was extracted into Et$_2$O and the solution filtered through Celite. Recrystallisation from Et$_2$O at –30 °C afforded yellow crystals. Yield of **9**: 31.9 mg, 0.048 mmol, 70%. $^1$H NMR (C$_6$D$_6$, 293 K, 300.1 MHz): $\delta$ = 8.04 (s, 1 H, OC*H*O), 2.2 [br. m, 4 H, P(CH$_2$)$_2$P], 2.10 (br. m, 8 H, PC*H*$_2$CH$_3$), 1.64 [br. m, 4 H, P(CH$_2$)$_2$P], 1.51 (br. m, 8 H, PC*H*$_2$CH$_3$), 1.19 (t, 9 H, BCH$_2$C*H*$_3$, $^3J_{HH}$ = 7.3 Hz), 1.11 (m, 12 H, PCH$_2$C*H*$_3$), 0.87 (m, 12 H, PCH$_2$C*H*$_3$), 0.55 (q, 6 H, BC*H*$_2$CH$_3$, $^3J_{HH}$ = 7.3 Hz) ppm. $^{31}$P{$^1$H} NMR (C$_6$D$_6$, 293 K, 121.5 MHz): $\delta$ = 52.3 (s) ppm. $^{13}$C{$^1$H} NMR (C$_6$D$_6$, 293 K, 125.8 MHz): $\delta$ = 166.0 (s, O*C*HO), 21.6 [m, P(*C*H$_2$)$_2$P], 21.4 (m, P*C*H$_2$CH$_3$), 19.5(br., B*C*H$_2$CH$_3$), 18.0 (m, P*C*H$_2$CH$_3$), 12.6 (s, BCH$_2$*C*H$_3$), 9.3 (s, PCH$_2$*C*H$_3$), 7.9 (s, PCH$_2$*C*H$_3$) ppm. $^{11}$B{$^1$H} NMR (C$_6$D$_6$, 293 K, 96.2 MHz): $\delta$ = 0.3 (br., 1 B, N*B*Et$_3$) ppm. IR (ATR): $\tilde{\nu}$ = 1611 [$\nu_{asym}$(COO)], 1320 [$\nu_{sym}$(COO)] cm$^{-1}$. $C_{27}H_{64}BMoNP_4O_2$ (665.44): calcd. C 48.73, H 9.69, N 2.11; found C 48.91, H 9.75, N 2.15.

**Preparation of *trans*-Mo[$^1$η-OCH(PhCl)$_2$](NBEt$_3$)(depe)$_2$ (10):** 15.4 mg (0.061 mmol, 1.1 equiv.) of 4,4′-dichlorobenzophenone was added to a [D$_8$]toluene solution (0.7 mL) of Mo(H)(NBEt$_3$)-(depe)$_2$ (34 mg, 0.055 mmol). After 1 d at 60 °C, the solvent was removed under vacuum to afford a light orange powder. The precipitate was washed with pentane and then the product was extracted with diethyl ether. Crystallization from diethyl ether at –30 °C gave yellow single crystals. Yield of **10**: 37.9 mg, 0.043 mmol, 80%. $^1$H NMR ([D$_8$]toluene, 293 K, 500.2 MHz): $\delta$ = 6.92 (d, 4 H, Ph, $^3J_{HH}$ = 8.4 Hz), 6.78 (d, 4 H, Ph, $^3J_{HH}$ = 8.4 Hz), 4.68 (s, C*H*O), 2.12–2.00 [br., 8 H, P(C*H*$_2$)$_2$P], 1.48 (br., 8 H, PC*H*$_2$CH$_3$), 1.29 (br., 8 H, PC*H*$_2$CH$_3$), 1.06 (m, 12 H, PCH$_2$C*H*$_3$), 1.04 [t, 9 H, B(CH$_2$C*H*$_3$)$_3$, $^3J_{HH}$ = 7.7 Hz], 0.79 (m, 12 H, PCH$_2$C*H*$_3$), 0.35 [q, 6 H, B(C*H*$_2$CH$_3$)$_3$, $^3J_{HH}$ = 7.4 Hz] ppm. $^{31}$P{$^1$H} NMR ([D$_8$]toluene, 293 K, 121.5 MHz): $\delta$ = 48.15 (s, 4 P) ppm. $^{13}$C{$^1$H} NMR ([D$_8$]toluene, 293 K, 125,8 MHz): $\delta$ = 150.8 (s, *i*-Ph), 131.5 (s, *p*-Ph), 129.0 (t, Ph), 128.0 (t, Ph), 83.1 (s, O*C*H), 21.8–21.6 [m, P(*C*H$_2$)$_2$P and P*C*H$_2$CH$_3$], 20.9–20.1 [br., B(*C*H$_2$CH$_3$)$_3$], 19.9 (P*C*H$_2$CH$_3$), 12.9 [s, B(CH$_2$*C*H$_3$)$_3$], 9.1 (s, PCH$_2$*C*H$_3$), 8.4 (s, PCH$_2$*C*H$_3$) ppm. $^{11}$B NMR ([D$_8$]toluene, 293 K, 96.2 MHz): $\delta$ = 3.5 [br., *B*(C*H*$_2$CH$_3$)$_3$] ppm. $C_{39}H_{72}BCl_2MoNOP_4$ (872.54): calcd. C 53.68, H 8.32, N 1.61; found C 53.67, H 8.36, N 1,63.

**Preparation of *trans*-Mo[$^1$η-OCH(Me)Ph](NBEt$_3$)(depe)$_2$ (11):** Complex **8** (36.8 mg, 0.059 mmol) was dissolved in 0.5 mL of C$_6$D$_6$ in a Young NMR tube. Then acetophenone (6.9 μL, 0.059 mmol) was added by a micro-syringe. After 3 d of standing at room temperature, the solution was concentrated under vacuum and the solid was dissolved in diethyl ether, the solution filtered through Celite and put in a refrigerator at –30 °C where yellow crystals were obtained. Yield of **11**: 40.5 mg, 0.054 mmol, 92%. $^1$H NMR (C$_6$D$_6$, 293 K, 300.1 MHz): $\delta$ = 7.11–6.97 (m, 5 H, Ph), 4.11 [q, 1 H, OC*H*(Me)Ph, $^3J_{HH}$ = 6.3 Hz], 2.20 (br. m, 8 H, PC*H*$_2$Me), 1.75 [br. m, 4 H, P(CH$_2$)$_2$P], 1.60–1.54 (br. m, 8 H, PC*H*$_2$Me), 1.38 [br. m, 4 H, P(CH$_2$)$_2$P], 1.25 (t, 9 H, BCH$_2$C*H*$_3$, $^3J_{HH}$ = 7.5 Hz), 1.18 (m, 12 H, PCH$_2$C*H*$_3$), 0.96 (d, 3 H, OCHC*H*$_3$Ph, $^3J_{HH}$ = 6 Hz), 0.92 (m, 12 H, PCH$_2$C*H*$_3$), 0.52 (q, 6 H, BC*H*$_2$Me, $^3J_{HH}$ = 7.5 Hz) ppm. $^{31}$P{$^1$H} NMR (C$_6$D$_6$, 293 K, 121.5 MHz): $\delta$ = 48.1 (s) ppm. $^{13}$C{$^1$H} NMR (C$_6$D$_6$, 293 K, 125.8 MHz): $\delta$ = 128.0–126.7 (m, Ph), 75.1 (s, O*C*HMePh), 30.3 [s, OCH(*C*H$_3$)Ph], 21.8 [m, P(*C*H$_2$)$_2$P], 21.4 (m, PC*H*$_2$CH$_3$), 19.9 (br., B*C*H$_2$Me), 17.3–17.6 (m, PC*H*$_2$Me), 13.1 (s, BCH$_2$*C*H$_3$), 9.5 (s, PCH$_2$*C*H$_3$), 8.2 (s, PCH$_2$*C*H$_3$) ppm. $^{11}$B{$^1$H} NMR (C$_6$D$_6$, 293 K, 96.2 MHz): $\delta$ = –2.5 (s, 1 B, N*B*Et$_3$) ppm. $C_{34}H_{72}BMoNP_4O$ (741.58): calcd. C 55.07, H 9.79, N 1.89; found C 55.25, H 10.01, N 1.90.

**Preparation of *trans*-Mo(NBEt$_3$)[(μ-OCH)Fe(CO)$_4$](depe)$_2$ (12):** 6.74 μL (0.05 mmol) of pentacarbonyliron was added to a [D$_8$]toluene solution (0.7 mL) of hydride **8** (13 mg, 0.05 mmol). After 30 min at room temperature, the solution was filtered through Celite and the solvent was removed under vacuum to afford a light orange powder. Then the product was extracted with toluene. Crystallization from toluene at –30 °C gave yellow single crystals. Yield of **12**: 35.7 mg, 0.044 mmol, 88%. $^1$H NMR ([D$_8$]toluene,

 © 2006 Wiley-VCH Verlag GmbH & Co. KGaA, Weinheim 

293 K, 500.2 MHz): $\delta$ = 13.78 (s, C*H*O), 1.90–1.66 [br., 10 H, P(C$H_2$)$_2$P and PC$H_2$CH$_3$], 1.65–1.44 (br., 8 H, PC$H_2$CH$_3$), 1.47–1.34 [br., 10 H, P(C$H_2$)$_2$P and PC$H_2$CH$_3$], 1.02 (m, 12 H, PCH$_2$C$H_3$), 0.98 [t, 9 H, B(CH$_2$C$H_3$)$_3$, $^3J_{HH}$ = 7.8 Hz], 0.91 (m, 12 H, PCH$_2$C$H_3$), 0.34 [q, 6 H, B(C$H_2$CH$_3$)$_3$, $^3J_{HH}$ = 7.7 Hz] ppm. $^{31}$P{$^1$H} NMR ([D$_8$]toluene, 293 K, 81.0 MHz): $\delta$ = 52.2 (s) ppm. $^{13}$C{$^1$H} NMR ([D$_8$]toluene, 293 K, 125 MHz): $\delta$ = 293.2 (br., O*C*H), 219.2 [s, Fe(*C*O)$_4$], 21.9 [br., P(*C*H$_2$)$_2$P and P*C*H$_2$CH$_3$], 19.1 [br., B(*C*H$_2$CH$_3$)$_3$], 18.4 (m, P*C*H$_2$CH$_3$), 12.4 [s, B(CH$_2$*C*H$_3$)$_3$], 8.7 (s, PCH$_2$*C*H$_3$), 7.7 (s, PCH$_2$*C*H$_3$) ppm. $^{11}$B NMR ([D$_8$]toluene, 293 K, 96.2 MHz): $\delta$ = 1.9 [br., *B*(CH$_2$CH$_3$)$_3$] ppm. IR (ATR): $\tilde{\nu}$ = 2020, 1966, 1870 {$\nu$[Fe(CO)$_4$]} cm$^{-1}$. $C_{31}H_{64}BFeMoNO_5P_4$ (817.33): calcd. C 45.55, H 7.89, N 1.71; found C 45.19, H 8.04, N 1.91.

**Preparation of *trans*-Mo(NBEt$_3$)[(μ-OCH)Re$_2$(CO)$_9$](depe)$_2$ (13):** 1.06 equiv. (50.9 mg, 0.078 mmol) of Re$_2$(CO)$_{10}$ was added to a [D$_8$]-toluene solution (0.7 mL) of complex **8** (45.6 mg, 0.073 mmol). The reaction proceeded smoothly at room temperature and seemed to reach equilibrium after 2 d. The solvent was removed under vacuum and the excess of hydride was extracted with pentane. Crystallization from toluene at –30 °C gave orange single crystals. Yield of **13**: 82.5 mg, 0.065 mmol, 88%. $^1$H NMR ([D$_8$]toluene, 293 K, 300.1 MHz): $\delta$ = 14.91 (s, C*H*O), 1.92–1.82 [br., 10 H, P(C$H_2$)$_2$P and PC$H_2$CH$_3$], 1.65–1.44 (br., 8 H, PC$H_2$CH$_3$), 1.47–1.38 [br., 10 H, P(C$H_2$)$_2$P and PC$H_2$CH$_3$], 1.02 (m, 12 H, PCH$_2$C$H_3$), 0.95 [t, 9 H, B(CH$_2$C$H_3$)$_3$, $^3J_{HH}$ = 7.8 Hz], 0.88 (m, 12 H, PCH$_2$C$H_3$), 0.55 [q, 6 H, B(C$H_2$CH$_3$)$_3$, $^3J_{HH}$ = 7.5 Hz] ppm. $^{31}$P{$^1$H}NMR ([D$_8$]toluene, 293 K, 121.5 MHz): $\delta$ = 54.4 (s) ppm. $^{13}$C{$^1$H} NMR ([D$_8$]toluene, 293 K, 75.5 MHz): $\delta$ = 289.5 (br., O*C*H), 196.2 [s, Re(*C*O)$_9$], 21.8 [m, P(*C*H$_2$)$_2$P and P*C*H$_2$CH$_3$], 19.3 [br., B(*C*H$_2$CH$_3$)$_3$], 18.3 (m, P*C*H$_2$CH$_3$), 11.4 [s, B(CH$_2$*C*H$_3$)$_3$], 8.9 (s, PCH$_2$*C*H$_3$), 7.6 (s, PCH$_2$*C*H$_3$) ppm. $^{11}$B NMR ([D$_8$]toluene, 293 K, 96.2 MHz): $\delta$ = 2.0 [br., *B*(CH$_2$CH$_3$)$_3$] ppm. IR (ATR): $\tilde{\nu}$ = 2094, 2070, 2025, 2007, 1969, 1935, 1902 {$\nu$[Re$_2$(CO)$_9$]} cm$^{-1}$. $C_{36}H_{64}BMoNO_{10}P_4Re_2$ (1273.95): calcd. C 33.94, H 5.06, N 1.10; found C 34.23, H 5.22, N 1.12.

**Preparation of *trans*-Mo(OPh)(NBEt$_3$)(depe)$_2$ (14):** Complex **8** (34 mg, 0.055 mmol) was dissolved in 0.4 mL of [D$_8$]toluene in a Young NMR tube and phenol (6 mg, 0.064 mmol) was added. The reaction occurred instantaneously. The solvent was removed under vacuum and the residue was extracted into diethyl ether and the solution filtered through Celite. The product **14** crystallized from diethyl ether at –30 °C to afford yellow crystals. Yield of **14**: 24 mg, 0.034 mmol, 61%. $^1$H NMR (C$_6$D$_6$, 293 K, 300.1 MHz): $\delta$ = 7.08 (d, 2 H, *m*-Ph, $^1J_{HH}$ = 7.5 Hz), 6.54 (t, 1 H, *p*-Ph, $^1J_{HH}$ = 7.8 Hz), 5.91 (d, 2 H, *o*-Ph, $^1J_{HH}$ = 8.1 Hz), 2.23 (br. m, 4 H, PC$H_2$CH$_3$), 2.14 (br. m, 4 H, PC$H_2$CH$_3$), 1.70 (br. m, 4 H, PC$H_2$CH$_3$), 1.63 [br. m, 8 H, P(CH$_2$)$_2$P], 1.38 (br. m, 4 H, PC$H_2$CH$_3$), 1.22 (t, 9 H, BCH$_2$C$H_3$, $^3J_{HH}$ = 7.5 Hz), 1.18 (m, 12 H, PCH$_2$C$H_3$), 0.83 (m, 12 H, PCH$_2$C$H_3$), 0.55 (q, 6 H, BC$H_2$CH$_3$, $^3J_{HH}$ = 7.5 Hz) ppm. $^{31}$P{$^1$H} NMR (C$_6$D$_6$, 293 K, 121.5 MHz): $\delta$ = 52.4 (s) ppm. $^{13}$C{$^1$H} NMR (C$_6$D$_6$, 293 K, 125.8 MHz): $\delta$ = 129.0 (s, *m*-Ph), 119.5 (s, *o*-Ph), 114.0 (s, *p*-Ph), 21.8 [m, P(*C*H$_2$)$_2$P], 21.5 (m, PC$H_2$CH$_3$), 19.5 (br., BC$H_2$CH$_3$), 17.3 (m, PC$H_2$CH$_3$), 12.9 (s, BCH$_2$C$H_3$), 9.6 (s, PCH$_2$C$H_3$), 7.8 (s, PCH$_2$C$H_3$) ppm. $^{11}$B{$^1$H} NMR (C$_6$D$_6$, 293 K, 96.2 MHz): $\delta$ = –0.9 (br., 1 B, N*B*Et$_3$) ppm. IR (ATR, 22 °C): $\tilde{\nu}$ = 1309 [$\nu$(OPh)] cm$^{-1}$. $C_{32}H_{68}BMoNP_4O$ (713.53): calcd. C 53.86, H 9.61, N 1.96; found C 53.71, H 9.33, N 1.84.

**Attempt of Stoichiometric "Ionic Hydrogenation" of Acetone by 8 in the Presence of Phenol:** Compound **8** (6.3 mg, 0.01 mmol) was dissolved in 0.4 mL of [D$_8$]THF in a Young NMR tube. Then 0.73 μL of acetone (0.58 mg, 0.01 mmol) and PhOH (1 mg, 0.01 mmol) were added. Formation of complex **14** was detected by NMR spectroscopy. A product of hydrogenation could not be observed.

**Hydrogenation of Cyclohexene:** To a [D$_8$]toluene solution (0.7 mL) of Mo(H)(NBEt$_3$)(depe)$_2$ (**8**) (3.8 mg, 0.006 mmol) was added 66 μL (0.65 mmol) of cyclohexene in a Young NMR tube. The reaction mixture was degassed in 3 freeze-pump-thaw cycles. H$_2$ (1400 mbar) was applied at 77 K. The catalytic reaction was carried out at 110 °C. After 24 h, cyclohexane (8%) could be detected spectroscopically. In the $^{31}$P NMR spectrum characteristic signals of the free phosphane ligand were observed. After an additional period of 31 h, the amount of cyclohexane was 25% and it had hardly changed after 45 h. Another flush of H$_2$ (1739 mbar) was then introduced at 77 K to the solution mixture. After 9 d at 110 °C, the amount of cyclohexane had reached 94%. Cyclohexane: $^1$H NMR ([D$_8$]toluene, 300 MHz, 20 °C): $\delta$ = 1.34 (s, 6 H). GC-MS: $t_r$ = 1.63 min; $m/z$ = 83 [M$^+$].

**X-ray Crystal Structure Analyses:** Crystallographic data for compounds **4**, **6**, **8**–**10** and **12**–**14** are collected in Tables 1 and 2. All crystals were embedded in polybutene oil within a glove box, mounted on glass fibers and fixed by a cold N$_2$ stream of an Oxford Cryogenic System at the diffractometer. Measurement temperatures of 153(2) K for compound **6**, 173(2) K for compound **4** and 183(2) K for the remaining compounds were used. An imaging plate detector system (Stoe IPDS) with graphite-monochromated Mo-$K_\alpha$ radiation ($\lambda$ = 0.71073 Å) was used for the exposure of 222, 176, 200, 182, 200, 236, 300 and 187 images at constant times of 3.5, 3.0, 1.6, 8.0, 4.0, 6.0, 4.0 and 3.0 min per image.[61] The crystal-to-image distances were set to 50 mm for **6**, **8**, **9**, **10**, **12** and **14**, to 64 mm for **13** and to 70 mm for **4**; φ-rotation (for **6** and **8**) and φ-oscillation modes (for **4**, **9**, **10**, **12**, **13** and **14**) were necessary for the increments of 1.7 and 1.1° or of 0.9, 1.0, 1.0, 1.1, 0.7 and 1.0° per exposure in each case. The intensities were integrated by using a dynamic peak profile analysis, and an estimated mosaic spread (EMS) check was performed to prevent overlapping intensities. For the cell parameter refinements, 7998 (**4**, **12** and **14**), 8000 (**8** and **9**) and 8001 reflections[61] (**6**, **10** and **13**) were selected out of the whole limiting spheres with intensities $I > 6\sigma(I)$. A total of 59134, 12588, 43658, 37490, 53007, 33565, 43402 and 23754 reflections were collected, of which 16225, 3869, 9585, 10353, 12539, 11856, 10343 and 11186 were unique after performing absorption correction and data reduction ($R_{int}$ = 16.02, 5.62, 8.57, 11.06, 8.70, 7.43, 4.99 and 8.77%). A total of 12, 10, 10, 11, 12, 12, 10 and 15 indexed crystal faces were used for the numerical absorption corrections.[62] The structures were solved with the merged unique data set after checking for correct space groups. The Patterson method was used to solve the crystal structures by applying the software options of the program SHELXS-97.[63] The structure refinements were performed with the program SHELXL-97.[63] The programs PLATON[64] and PLUTON[65] were used to check the results of the X-ray analyses. The crystal structure of compound **4** showed a superstructure with three independent complexes in the asymmetric unit of the monoclinic cell (space group $P2_1/c$). A complete check with PLATON[64] did not suggest a higher symmetry system or space group. Compound **6** crystallized in the centrosymmetric triclinic space group $P\bar{1}$. The Mo atoms of the structure lie on centers of inversion; thus, only half of the molecule had to be refined. As a consequence, a disorder between the NBH$_3$ and Cl ligands was observed. The hydrogen atoms of the BH$_3$ group were located by difference electron density calculations. The geometry of the BH$_3$ group has been corrected by using B–H and H···H distance restraints and the coordinates of the H atoms were finally fixed dur-

 © 2006 Wiley-VCH Verlag GmbH & Co. KGaA, Weinheim 

Table 1. Crystallographic details of **4**, **6**, **8** and **9**.

| | **4** | **6** | **8** | **9** |
|---|---|---|---|---|
| Empirical formula | $C_{20}H_{48}ClMoNP_4$ | $C_{20}H_{51}BClMoNP_4$ | $C_{26}H_{64}BMoNP_4$ | $C_{27}H_{64}BMoNO_2P_4$ |
| Color | orange | yellow | yellow | yellow |
| $M_r$ [g mol$^{-1}$] | 557.86 | 571.70 | 621.41 | 665.42 |
| Crystal size [mm] | 0.21 × 0.20 × 0.13 | 0.17 × 0.15 × 0.07 | 0.44 × 0.34 × 0.08 | 0.27 × 0.13 × 0.10 |
| $T$ [K] | 173(2) | 153(2) | 183(2) | 183(2) |
| $\lambda$(Mo-$K_\alpha$) [Å] | 0.71073 | 0.71073 | 0.71073 | 0.71073 |
| Crystal system | monoclinic | triclinic | monoclinic | monoclinic |
| Space group | $P2_1/c$ (14) | $P\bar{1}$ (2) | $P2_1/n$ (14) | $P2_1/n$ (14) |
| $a$ [Å] | 23.4140(13) | 8.2157(8) | 10.4337(8) | 9.4820(11) |
| $b$ [Å] | 13.7435(7) | 8.9506(9) | 18.3864(10) | 20.5582(19) |
| $c$ [Å] | 26.0626(13) | 10.1080(10) | 17.6487(15) | 17.946(2) |
| α [°] | 90 | 94.918(12) | 90 | 90 |
| $\beta$ [°] | 90.727(6) | 98.569(12) | 96.230(10) | 97.262(13) |
| $\gamma$ [°] | 90 | 103.428(11) | 90 | 90 |
| $V$ [Å$^3$] | 8386.0(8) | 709.29(12) | 3365.7(4) | 3470.2(6) |
| $Z$ | 12 | 1 | 4 | 4 |
| $\rho_{calcd.}$ [g·cm$^{-3}$] | 1.326 | 1.338 | 1.226 | 1.274 |
| $\mu$ [mm$^{-1}$] | 0.801 | 0.790 | 0.595 | 0.586 |
| $F$(000) | 3528 | 302 | 1336 | 1424 |
| Transmission range | 0.850–0.903 | 0.877–0.947 | 0.747–0.945 | 0.891–0.960 |
| 2$\theta$ range [°] | $2.15 < 2\theta < 25.91$ | $2.59 < 2\theta < 30.32$ | $2.63 < 2\theta < 30.45$ | $2.49 < 2\theta < 30.38$ |
| Measured reflections | 59134 | 12588 | 43658 | 37490 |
| Unique reflections | 16225 | 2351 | 9585 | 10353 |
| $I > 2\sigma(I)$ reflections | 4924 | 2086 | 6777 | 5128 |
| Parameters | 740 | 131 | 312 | 330 |
| Goodness-of-fit (for $F^2$) | 0.500 | 0.992 | 0.842 | 0.742 |
| $R_1[I > 2\sigma(I)]$, $R_1$(all data)[a] | 0.0401, 0.1508 | 0.0263, 0.0311 | 0.0302, 0.0461 | 0.0453, 0.1103 |
| $wR_2[I > 2\sigma(I)]$, $wR_2$(all data)[a] | 0.0590, 0.0760 | 0.0664, 0.0675 | 0.0667, 0.0695 | 0.0907, 0.1033 |
| $\Delta\rho_{max/min}$ | 0.451/–0.541 | 0.300/–0.656 | 0.596/–1.086 | 0.859/–1.204 |

[a] $R_1 = \Sigma(F_o - F_c)/\Sigma F_o$; $wR_2 = \{\Sigma w(F_o^2 - F_c^2)^2/\Sigma w(F_o^2)^2\}^{1/2}$.

Table 2. Crystallographic details of **10**, **12**, **13** and **14**.

| | **10** | **12** | **13** | **14** |
|---|---|---|---|---|
| Empirical formula | $C_{39}H_{72}BCl_2MoNOP_4$ | $C_{31}H_{64}BFeMoNO_5P_4$, $0.5C_7H_8$ | $C_{36}H_{64}BMoNO_{10}P_4Re_2$ | $C_{32}H_{68}BMoNOP_4$ |
| Color | yellow | yellow | orange | yellow |
| $M_r$ [g mol$^{-1}$] | 872.51 | 863.38 | 1273.91 | 713.50 |
| Crystal size [mm] | 0.23 × 0.21 × 0.07 | 0.15 × 0.13 × 0.10 | 0.17 × 0.15 × 0.08 | 0.36 × 0.31 × 0.11 |
| $T$ [K] | 183(2) | 183(2) | 183(2) | 183(2) |
| $\lambda$(Mo-$K_\alpha$) [Å] | 0.71073 | 0.71073 | 0.71073 | 0.71073 |
| Crystal system | monoclinic | triclinic | monoclinic | monoclinic |
| Space group | $P2_1/n$ (14) | $P\bar{1}$ (2) | $P2_1/n$ (14) | $P2_1/n$ (14) |
| $a$ [Å] | 13.6170(14) | 10.9338(15) | 11.8594(8) | 10.2952(11) |
| $b$ [Å] | 19.5423(17) | 11.2735(17) | 12.1646(7) | 19.6339(19) |
| $c$ [Å] | 16.8397(14) | 19.924(3) | 32.705(3) | 18.6052(17) |
| α [°] | 90 | 96.882(17) | 90 | 90 |
| $\beta$ [°] | 91.283(11) | 94.450(17) | 98.271(9) | 91.236(12) |
| $\gamma$ [°] | 90 | 116.307(15) | 90 | 90 |
| $V$ [Å$^3$] | 4480.0(7) | 2162.0(5) | 4669.0(5) | 3759.9(6) |
| $Z$ | 4 | 2 | 4 | 4 |
| $\rho_{calcd.}$ [g·cm$^{-3}$] | 1.294 | 1.326 | 1.812 | 1.260 |
| $\mu$ [mm$^{-1}$] | 0.585 | 0.810 | 5.624 | 0.544 |
| $F$(000) | 1848 | 910 | 2496 | 1528 |
| Transmission range | 0.883–0.962 | 0.886–0.936 | 0.662–0.422 | 0.848–0.936 |
| 2$\theta$ range [°] | $2.82 < 2\theta < 30.39$ | $2.73 < 2\theta < 30.37$ | $2.09 < 2\theta < 27.21$ | $2.47 < 2\theta < 30.42$ |
| Measured reflections | 53007 | 33565 | 43402 | 41417 |
| Unique reflections | 12539 | 11856 | 10343 | 11186 |
| $I > 2\sigma(I)$ reflections | 5568 | 6234 | 8139 | 6042 |
| Parameters | 451 | 423 | 507 | 367 |
| Goodness-of-fit (for $F^2$) | 0.617 | 0.682 | 0.879 | 0.753 |
| $R_1[I > 2\sigma(I)]$, $R_1$(all data)[a] | 0.0344, 0.0996 | 0.0356, 0.0897 | 0.0225, 0.0314 | 0.0395, 0.0857 |
| $wR_2[I > 2\sigma(I)]$, $wR_2$(all data)[a] | 0.0562, 0.0649 | 0.0558, 0.0631 | 0.0530, 0.0541 | 0.0840, 0.0917 |
| $\Delta\rho_{max/min}$ | 0.588/–0.992 | 0.718/–0.921 | 0.708/–0.849 | 1.083/–0.912 |

[a] $R_1 = \Sigma(F_o - F_c)/\Sigma F_o$; $wR_2 = \{\Sigma w(F_o^2 - F_c^2)^2/\Sigma w(F_o^2)^2\}^{1/2}$.

 © 2006 Wiley-VCH Verlag GmbH & Co. KGaA, Weinheim 

ing the last refinement. For compound **8** the position of the hydride atom H27 was also located by difference electron density calculations but all its parameters were freely refined while the other positions of hydrogen atoms were calculated after each refinement cycle. Compound **9** crystallized in the centrosymmetric monoclinic space group $P2_1/n$. Large anisotropic displacement parameters were observed for two ethyl groups on the boron atom and for one ethyl group on the phosphorus atom P3. The disorder refinement for these ethyl groups done with distance restraints improved significantly the result, the atomic splitting was kept and the corresponding carbon atoms were refined isotropically. For compound **10** one ethyl group on the phosphorus atom P2 was treated for disorder and isotropically refined. Compound **12** crystallized in the triclinic space group $P\bar{1}$. One toluene solvent molecule cocrystallized with the structure and is located near a center of inversion leading to a disorder. Many FREE instructions were necessary to calculate the positions of H atoms of the disordered toluene, and the corresponding carbon atoms were refined isotropically. One ethyl group on the boron atom B1 in compound **14** was found to be positionally disordered. All structures in this paper crystallize in centrosymmetric triclinic or monoclinic space groups, except the structure of **2** given in the Supporting Information. CCDC-280778 to -280788 and CCDC-249319 (for **1**–**4**, **6**, **8**–**10** and **12**–**14**) contain the supplementary crystallographic data for this paper. These data can be obtained free of charge from The Cambridge Crystallographic Data Centre via www.ccdc.cam.ac.uk/data_request/cif.

**Supporting Information** (see footnote on the first page of this article): ORTEP representations and crystallographic details of compounds **1**, **2** and **3**.

## Acknowledgments

Funding from the Swiss National Science Foundation (SNSF) and from the University of Zürich is gratefully acknowledged.

[1] W. Hieber, F. Leutert, *Naturwissenschaften* **1931**, *19*, 360.
[2] W. Hieber, H. Schulten, *Z. Anorg. Allg. Chem.* **1937**, *29*, 232.
[3] J. P. Collman, L. S. Hegedus, J. R. Norton, R. G. Finke, *Principles and Applications of Organotransition Metal Chemistry*, University Science Book, Mill Valley, California, **1987**.
[4] J. Chatt, *Science* **1968**, *160*, 723.
[5] G. W. Parshall, *Homogemeous Catalysis*, John Wiley & Sons, New York, **1980**.
[6] S. S. Kristjansdottir, J. K. Norton, *Transition Metal Hydrides* (Ed.: A. Dedieu), VCH Publishers Inc., New York, **1992**.
[7] R. L. Sweany, J. W. Owens, *J. Organomet. Chem.* **1983**, *255*, 327.
[8] H. W. Chen, W. L. Jolly, J. Kopf, T. H. Lee, *J. Am. Chem. Soc.* **1979**, *101*, 2607.
[9] D. K. Seo, G. Papoian, R. Hoffmann, *Int. J. Quantum Chem.* **2000**, *77*, 408.
[10] T. A. Albright, J. K. Burdett, M. H. Whangboo, in *Orbital Interaction in Chemistry*, Wiley, New York, **1985**.
[11] J. A. M. Simoes, J. L. Beauchamp, *Chem. Rev.* **1990**, *90*, 629.
[12] P. J. Chirik, M. W. Day, J. E. Bercaw, *Organometallics* **1999**, *18*, 1873.
[13] J. H. Gilchrist, J. E. Bercaw, *J. Am. Chem. Soc.* **1996**, *118*, 12021.
[14] J. Höck, H. Jacobsen, H. W. Schmalle, G. R. J. Artus, T. Fox, J. I. Amor, F. Bath, H. Berke, *Organometallics* **2001**, *20*, 1533.
[15] A. A. H. van der Zeijden, H. Berke, *Helv. Chim. Acta* **1992**, *75*, 513.
[16] H. Jacobsen, H. Berke, *J. Chem. Soc., Dalton Trans.* **2002**, 3117.
[17] F. Furno, T. Fox, M. Alfonso, H. Berke, *Eur. J. Inorg. Chem.* **2001**, 1559.
[18] F. Furno, T. Fox, H. W. Schmalle, H. Berke, *Organometallics* **2000**, *19*, 3620.
[19] F. P. Liang, H. Jacobsen, H. W. Schmalle, T. Fox, H. Berke, *Organometallics* **2000**, *19*, 1950.
[20] F. P. Liang, H. W. Schmalle, T. Fox, H. Berke, *Organometallics* **2003**, *22*, 3382.
[21] K. Dehnicke, J. Strähle, *Angew. Chem. Int. Ed. Engl.* **1981**, *20*, 413.
[22] K. Dehnicke, J. Strähle, *Angew. Chem. Int. Ed. Engl.* **1992**, *31*, 955.
[23] W. P. Griffith, *Coord. Chem. Rev.* **1972**, *8*, 369.
[24] C. C. Wang, T. H. Tang, Y. Wang, *J. Phys. Chem. A* **2000**, *104*, 9566.
[25] R. A. Eikey, M. M. Abu-Omar, *Coord. Chem. Rev.* **2003**, *243*, 83.
[26] J. Chatt, J. R. Dilworth, *J. Indian Chem. Soc.* **1977**, *54*, 13.
[27] D. L. Hughes, M. Y. Mohammed, C. J. Pickett, *J. Chem. Soc., Dalton Trans.* **1990**, 2013.
[28] T. A. George, M. E. Noble, *Inorg. Chem.* **1978**, *17*, 1678.
[29] P. C. Bevan, J. Chatt, J. R. Dilworth, R. A. Henderson, G. J. Leigh, *J. Chem. Soc., Dalton Trans.* **1982**, 821.
[30] J. Chatt, G. J. Leigh, R. A. Head, C. J. Pickett, *J. Chem. Soc., Dalton Trans.* **1978**, 1638.
[31] R. A. Henderson, *J. Chem. Soc., Dalton Trans.* **1983**, 51.
[32] R. A. Henderson, G. Davies, J. R. Dilworth, R. N. F. Thorneley, *J. Chem. Soc., Dalton Trans.* **1981**, 40.
[33] J. R. Dilworth, P. L. Dahlstrom, J. R. Hyde, J. Zubieta, *Inorg. Chim. Acta* **1983**, *71*, 21.
[34] Y. Tanabe, H. Seino, Y. Ishii, M. Hidai, *J. Am. Chem. Soc.* **2000**, *122*, 1690.
[35] H. Seino, Y. Tanabe, Y. Ishii, M. Hidai, *Inorg. Chim. Acta* **1998**, *280*, 163.
[36] A. G. Orpen, L. Brammer, F. H. Allen, O. Kennard, D. G. Watson, R. Taylor, *J. Chem. Soc., Dalton Trans.* **1989**, S1.
[37] T. Y. Cheng, B. S. Brunschwig, R. M. Bullock, *J. Am. Chem. Soc.* **1998**, *120*, 13121.
[38] N. Sarker, J. W. Bruno, *J. Am. Chem. Soc.* **1999**, *121*, 2174.
[39] D. G. Gusev, D. Nietlispach, A. B. Vymenits, V. I. Bakhmutov, H. Berke, *Inorg. Chem.* **1993**, *32*, 3270.
[40] D. Nietlispach, V. I. Bakhmutov, H. Berke, *J. Am. Chem. Soc.* **1993**, *115*, 9191.
[41] H. Jacobsen, H. Berke, in *Recent Advances in Hydride Chemistry* (Eds.: R. Poli, P. M.), Elsevier, Amsterdam, **2001**, p. 89.
[42] G. L. Hillhouse, B. L. Haymore, *Inorg. Chem.* **1987**, *26*, 1876.
[43] M. G. Mason, J. A. Ibers, *J. Am. Chem. Soc.* **1982**, *104*, 5153.
[44] P. Kundel, H. Berke, *J. Organomet. Chem.* **1988**, *339*, 297.
[45] D. J. Darensbourg, R. A. Kudaroski, *Adv. Organomet. Chem.* **1983**, *22*, 129.
[46] A. R. Cutler, P. K. Hanna, J. C. Vites, *Chem. Rev.* **1988**, *88*, 1363.
[47] W. Leitner, *Angew. Chem. Int. Ed. Engl.* **1995**, *34*, 2207.
[48] K. Toyohara, H. Nagao, T. Mizukawa, K. Tanaka, *Inorg. Chem.* **1995**, *34*, 5399.
[49] J. C. Tsai, K. M. Nicholas, *J. Am. Chem. Soc.* **1992**, *114*, 5117.
[50] L. K. Fong, J. R. Fox, N. J. Cooper, *Organometallics* **1987**, *6*, 223.
[51] M. K. Whittlesey, R. N. Perutz, M. H. Moore, *Organometallics* **1996**, *15*, 5166.
[52] Z. Chen, H. W. Schmalle, T. Fox, H. Berke, *Dalton Trans.* **2005**, 580.
[53] W. A. Herrmann, *Angew. Chem. Int. Ed. Engl.* **1982**, *21*, 117.
[54] J. A. Gladysz, *Adv. Organomet. Chem.* **1982**, *20*, 1.
[55] U. Burckhardt, T. D. Tilley, *J. Am. Chem. Soc.* **1999**, *121*, 6328.
[56] R. L. Miller, R. Toreki, R. E. Lapointe, P. T. Wolczanski, G. D. Vanduyne, D. C. Roe, *J. Am. Chem. Soc.* **1993**, *115*, 5570.
[57] G. Süssfink, G. Meister, *Adv. Organomet. Chem.* **1993**, *35*, 41.
[58] R. J. Morris, G. S. Girolami, *Inorg. Chem.* **1990**, *29*, 4167.

 © 2006 Wiley-VCH Verlag GmbH & Co. KGaA, Weinheim 

[59] R. J. Burt, J. Chatt, W. Hussain, G. J. Leigh, *J. Organomet. Chem.* **1979**, *182*, 203.
[60] M. L. Luetkens, A. P. Sattelberger, H. H. Murray, J. D. Basil, J. P. Fackler, R. A. Jones, D. E. Heaton, *Inorg. Synth.* **1989**, *26*, 7.
[61] *STOE-IPDS Software package*, Version 2.92/1999, STOE & Cie, GmbH, Darmstadt, Germany, **1999**.
[62] P. Coppens, L. Leiserowitz, D. Rabinovich, *Acta Crystallogr.* **1965**, *18*, 1035.
[63] G. M. Sheldrick, *SHELX97, Programs for crystal structure analysis*, University of Göttingen, Germany, **1997**.
[64] A. L. Spek, *Acta Crystallogr., Sect. A* **1990**, *46*, C34.
[65] A. L. Spek, *PLUTON-91, A computer program for the graphical representation of crystallographic models*, University of Utrecht, The Netherlands, **1991**.

Received: August 12, 2005
Published Online: December 13, 2005

 © 2006 Wiley-VCH Verlag GmbH & Co. KGaA, Weinheim 

DOI: 10.1002/ejic.200500738

# The First Coordination Polymers Based on Octahedral Hexahydroxo Rhenium Cluster Complexes $[Re_6Q_8(OH)_6]^{4-}$ (Q = S, Se) and Alkaline Earth Metal Cations

**Yuri V. Mironov,[a,b] Vladimir E. Fedorov,*[a] Hyunjin Bang,[b] and Sung-Jin Kim*[b]**

**Keywords:** Rhenium / Synthesis / Luminescent properties / Cluster compounds

Seven novel octahedral cluster compounds $[\{Mg(H_2O)_5\}_2Re_6S_8(OH)_6]\cdot 6H_2O$ (**1**), $[\{Ca(H_2O)_3\}_2Re_6S_8(OH)_6]$ (**2**), $[\{Ca(H_2O)_3\}_2Re_6Se_8(OH)_6]$ (**3**), $[\{Sr_2(H_2O)_{10}\}Re_6S_8(OH)_6]\cdot 6H_2O$ (**4**), $[\{Sr_2(H_2O)_{10}\}Re_6Se_8(OH)_6]\cdot 6H_2O$ (**5**), $[\{Ba_2(H_2O)_8\}Re_6S_8(OH)_6]$ (**6**), and $[\{Ba_2(H_2O)_8\}Re_6Se_8(OH)_6]$ (**7**) were prepared by the direct reaction of $K_4[Re_6S_8(OH)_6]\cdot 8H_2O$ and $K_4[Re_6Se_8(OH)_6]\cdot 8H_2O$ with the cations of the elements of main group II. All compounds have been characterized by single crystal X-ray diffraction. Compound **1** has a discrete molecular structure, compounds **4** and **5** have a one-dimensional chain structure, and compounds **2**, **3**, **6**, and **7** crystallize in two different types of two-dimensional layered structure. This sulfur containing series has been characterized by luminescent spectroscopy.
(© Wiley-VCH Verlag GmbH & Co. KGaA, 69451 Weinheim, Germany, 2006)

## Introduction

Octahedral rhenium clusters present an attractive class of structural and functional building blocks for the design of solids including coordination polymers and supramolecular constructions.[1] Coordination polymer compounds based on rhenium chalcohalide[2] and chalcogenide[3] clusters have been known for a long time. Others were obtained quite recently. One of the most developed building blocks is the octahedral rhenium chalcogenide cluster complexes of general formula $Re_6Q_8L_6$ where Q = S, Se, Te and L = an acido ligand or an organic donor group. There are two groups of terminal ligand, L, that are suitable for inclusion in such complexes with the appropriate partners. Firstly, there is the ambidentate CN ligand; in this case the $[Re_6Q_8(CN)_6]^{4-/3-}$ building blocks act with the transition or post-transition metals forming cyano-bridged inorganic polymeric structures.[4] Secondly, it is possible to use specific organic molecules that can function as a bidentate-bridge, and in this case mixed organic/inorganic polymers are formed.[5]

Very recently[6] two novel cluster complexes $K_4[Re_6Q_8(OH)_6]\cdot 8H_2O$ (Q = S, Se) were synthesized and characterized. In a preceding contribution, we presented the cluster anions $[Re_6Q_8(OH)_6]^{4-}$ as promising new building blocks for the construction of coordination polymers. In the present work a series of crystalline solids **1**–**7** are prepared by the direct reaction of $K_4[Re_6S_8(OH)_6]\cdot 8H_2O$ and $K_4[Re_6Se_8(OH)_6]\cdot 8H_2O$ with the cations of the elements of main group II.

$[\{Mg(H_2O)_5\}_2Re_6S_8(OH)_6]\cdot 6H_2O$ (**1**)
$[\{Ca(H_2O)_3\}_2Re_6S_8(OH)_6]$ (**2**)
$[\{Ca(H_2O)_3\}_2Re_6Se_8(OH)_6]$ (**3**)
$[\{Sr_2(H_2O)_{10}\}Re_6S_8(OH)_6]\cdot 6H_2O$ (**4**)
$[\{Sr_2(H_2O)_{10}\}Re_6Se_8(OH)_6]\cdot 6H_2O$ (**5**)
$[\{Ba_2(H_2O)_8\}Re_6S_8(OH)_6]$ (**6**)
$[\{Ba_2(H_2O)_8\}Re_6Se_8(OH)_6]$ (**7**)

Simple synthetic methods produce these complexes on a large scale. All seven structures were elucidated by single-crystal X-ray diffraction. Compound **1** has a discrete molecular structure, and compounds **4** and **5** are isostructural and form a one-dimensional chain structure. Compounds **2** is isostructural with **3**, and **6** is isostructural with **7**; these compounds form two types of two-dimensional layered structure.

To date, only the ionic alkaline earth aqua complexes $[Ca(H_2O)_7][Re_6Q_6Cl_8]\cdot 3H_2O$ (Q = S, Se), $[Ca(H_2O)_8][Re_6S_6Cl_8]$, and $Mg(H_2O)_6[Re_6S_6Cl_8]\cdot 2H_2O$ have been reported.[7]

## Results

### Structures

Compounds **1**–**7** contain hexahydroxo cluster anions $[Re_6Q_8(OH)_6]^{4-}$ (Q = S or Se) coordinated to $M^{2+}$ cations, where M = Mg, Ca, Sr, Ba. The structures of the $[Re_6-$

[a] Nikolaev Institute of Inorganic Chemistry, Siberian Branch of the Russian Academy of Sciences,
3, Acad. Lavrentiev pr., 630090 Novosibirsk, Russia
Fax: +7-383-3309489,
E-mail: yuri@che.nsk.su
[b] Department of Chemistry, Ewha Womans University,
Seoul 120-750, Korea
E-mail: sjkim@ewha.ac.kr

 © 2006 Wiley-VCH Verlag GmbH & Co. KGaA, Weinheim 

$Q_8(OH)_6]^{4-}$ (Q = S, Se) cluster anions are similar to those observed in the starting materials, and to the well known octahedral complexes of type $[Re_6Q_8L_6]^{4-}$ with L = $Cl^-$, $Br^-$, $I^-$, $CN^-$. The $Re_6$ octahedron that resides inside a cube of $Q_8$ (S, Se) forms a system of Re–Re and Re–($\mu_3$-Q) bonds. Six terminal $OH^-$ ligands are coordinated to the Re atoms with Re–O bond lengths in the following ranges: 2.090(6)–2.093(6) Å (**1**), 2.100(4) Å (**2**), 2.124(3) Å (**3**), 2.077(7)–2.096(6) Å (**4**), 2.080(6)–2.110(5) Å (**5**), 2.059(9)–2.093(11) Å (**6**) and 2.083(7)–2.100(8) Å (**7**). The structures of complexes with $M^{2+}$ demonstrate a strong dependence on the atomic size of the metal used.

Compound **1** has a discrete molecular structure (Figure 1) where the cluster anion $[Re_6S_8(OH)_6]^{4-}$ is coordinated to by two aqua cationic $[Mg(H_2O)_5]^{2+}$ complexes in a *trans* arrangement about the OH bridges. In this way each Mg atom is coordinated to by 5 water molecules, with Mg–O distances in the range of 2.052(7)–2.216(7) Å, and by the O atom of the OH ligand of the cluster anion. The Mg–O(OH) distance is equal to 2.046(7) Å, and the ∠Re–O–Mg is equal to 138.0(3)°.

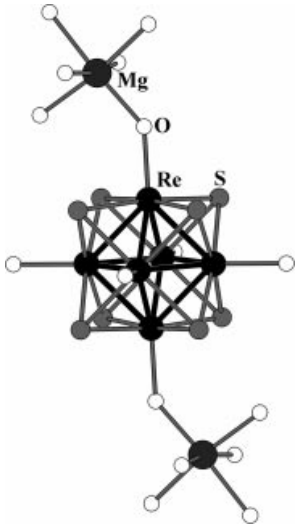


Figure 1. Structure of molecular complex $[\{Mg(H_2O)_5\}_2Re_6S_8(OH)_6]$ in (**1**).

Compounds **2** and **3** have a two-dimensional layered structure (Figure 2). Each Ca atom of compounds **2** and **3** is coordinated to by three water molecule O atoms with Ca–O distances of 2.377(5) Å, and by three O atoms from the OH ligands of three different cluster anions with Ca–O distances of 2.338(4) Å. This results in the formation of the *fac*-isomer. Whereas each Ca atom is coordinated to by three cluster anions, and each cluster anion is coordinated to by six Ca atoms giving a Ca/cluster anion ratio of 2:1. Interlayer distances are in the range excepted for hydrogen bonds between the O atoms of the water molecules coordinated to the Ca atoms and the O atoms of the OH groups of the cluster anions in an adjacent layer (2.745 Å in **2** and 2.804 Å in **3**).

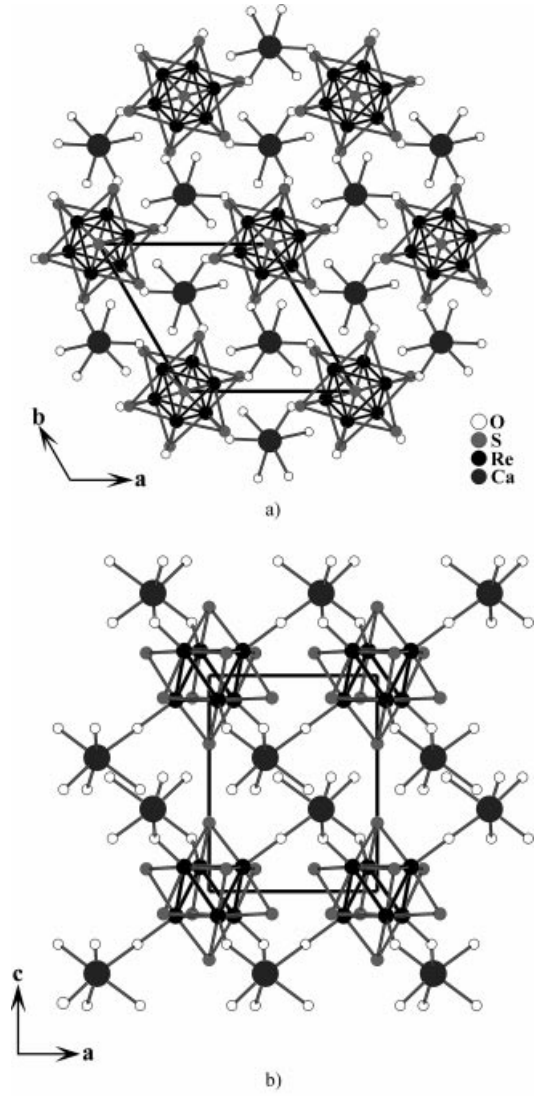


Figure 2. Structure of $[\{Ca(H_2O)_3\}_2Re_6S_8(OH)_6]$ (**2**): a) view along the *c*-axes; b) view along the *b*-axes.

Compounds **4** and **5** form one-dimensional chain-like structures (Figure 3). In these compounds cluster anions are bonded by cationic dimers $[Sr_2(H_2O)_{10}]^{4+}$. Two Sr atoms are bridged by two water molecules to form a dimer with an Sr–Sr separation of 4.3140(19) Å in **4** and 4.3016(16) in **5** and Sr–O distances of 2.675(8) Å and 2.680(8) Å in **4** and 2.666(6) Å and 2.686(7) Å in **5**. Additionally each Sr atom is coordinated to by 4 terminal water molecules (Sr–O distances are in the ranges of 2.555(8)– 2.603(9) Å in **4** and 2.551(7)–2.622(7) Å in **5**) and two O atoms of the OH ligands of the cluster anion [Re–O(OH) distances equal 2.532(7) Å in **4** and 2.547(6) Å in **5**]. Each Sr atom is connected to the Q atom of the cluster anion with Sr–Q distances equal to 3.260(3) Å (**4**) and 3.3649(12) Å (**5**).

In compounds **6** and **7** (Figure 4) the Ba atoms also form dimers but of a different type to the Sr dimers: two O atoms of the OH ligands of the cluster anions bridge the Ba atoms. The Ba–Ba distances in these compounds are equal to

 © 2006 Wiley-VCH Verlag GmbH & Co. KGaA, Weinheim 

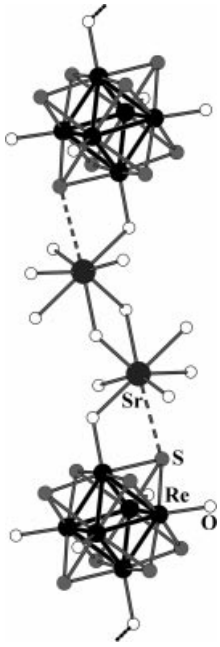


Figure 3. Structure of fragment of the $[\{Sr_2(H_2O)_{10}\}Re_6S_8(OH)_6]_n$ chain in (**4**).

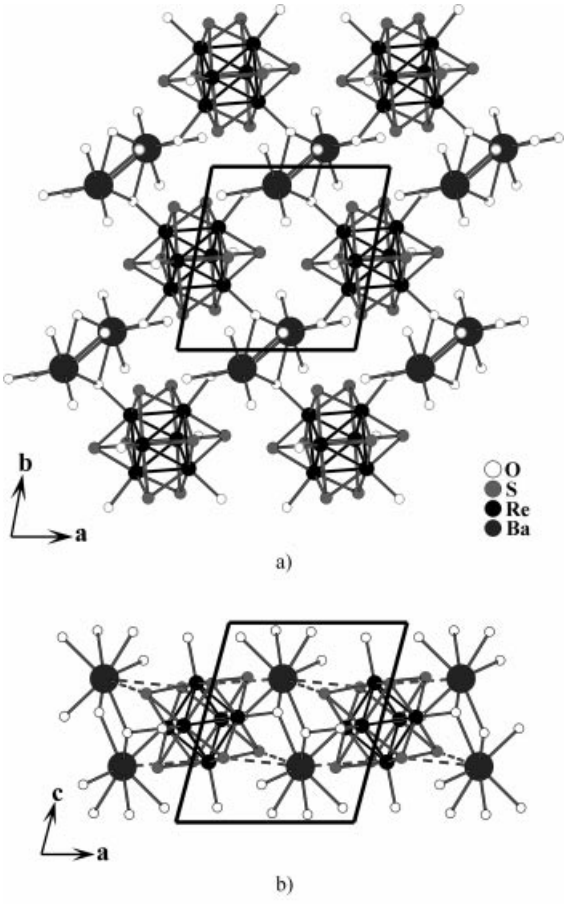


Figure 4. Structure of $[\{Ba_2(H_2O)_8\}Re_6S_8(OH)_6]$ (**6**): a) view along the *c*-axes; b) view along the *b*-axes.

4.352(2) Å in **6** and 4.4016(16) Å in **7**, the Ba–O distances for the bridged OH ligands are equal to 2.724(10) Å and 2.795(11) Å for **6**, 2.708(7) Å and 2.799(7) Å for **7**. Additionally each Ba atom is coordinated to by four water molecule O atoms [Ba–O distances are in range of 2.761(12)–2.86(3) Å (**6**) and 2.809(12)–2.92(2) Å (**7**)], and one atom of a OH ligand of a cluster anion [Ba–O distances are equal to 2.648(11) Å in **6** and 2.632(8) Å in **7**]. The coordination spheres of the Ba atoms are expanded by three Q atoms of the cluster core [Ba–S distances in **6** are 3.537(4), 3.660(3) and 3.878(4) Å, and the Ba–Se distances in **7** are 3.5715(14), 3.7457(13) and 3.7883(14) Å]. In this way each Ba dimer is coordinated to four cluster anions resulting in the formation of two-dimensional layered structures. Finally, in compounds **6** and **7** four OH ligands coordinated to the Ba atoms are associated with the anion clusters, whereas the other two are terminal and are in a *trans* arrangement about the dimer unit. The terminal OH groups are hydrogen bonded to the O atoms of water molecules coordinated to Ba atoms in an adjacent layer causing close packing of the layers. The closest interlayer distances are $O(H_2O)$–O(OH) = 2.748 Å in **6** and 2.813 Å in **7**.

Thus, the coordination numbers of the metal atoms in these compounds vary from 6 for Mg and Ca to 8 for Sr, and 10 for Ba.

### Luminescence

The luminescent properties of the starting cluster compound $K_4[Re_6S_8(OH)_6]\cdot 8H_2O$ and the thio complexes **1**, **2**, **4**, **6** were studied. All compounds show similar behavior; for example, upon excitation at 440 nm, the solid sulfur containing samples $K_4[Re_6S_8(OH)_6]\cdot 8H_2O$ and **1**, **2**, **4** and **6** displayed photoluminescence maxima at 618, 621, 618, 619 and 625 nm, respectively (Figure 5). These results are consistent with those previously reported for sulfide rhenium clusters.[5f,6] Figure 6 shows a comparison of the emission spectra for the rhenium sulfide (**2**) and selenide (**3**) cluster compounds. The emission maximum of the selenide

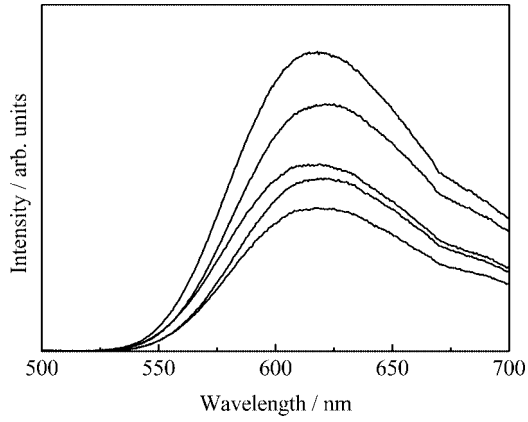


Figure 5. Solid-state emission ($\lambda_{exc}$ = 440 nm) spectra of the compounds $K_4[Re_6S_8(OH)_6]\cdot 8H_2O$ and **1**, **2**, **4**, **6** (from top to bottom). The maxima are observed at 618, 621, 618, 619 and 625 nm.

 © 2006 Wiley-VCH Verlag GmbH & Co. KGaA, Weinheim 

cluster is shifted by about 40 nm to a longer wavelength relative to the sulfide cluster, which is consistent with previous reports.[5f,8]

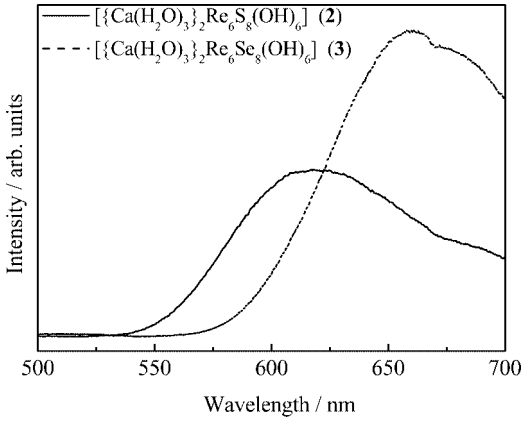


Figure 6. Solid-state emission ($\lambda_{exc}$ = 440 nm) spectra of compounds $[\{Ca(H_2O)_3\}_2Re_6S_8(OH)_6]$ (**2**) and $[\{Ca(H_2O)_3\}_2Re_6Se_8(OH)_6]$ (**3**). The maxima are observed at 619 and 659 nm.

## Experimental Section

$K_4[Re_6S_8(OH)_6]\cdot 8H_2O$ and $K_4[Re_6Se_8(OH)_6]\cdot 8H_2O$ were prepared as previously described.[6] All other reagents were commercially available products of reagent grade quality, and were used as obtained. All experiments were not performed under controlled atmospheric conditions.

All compounds were obtained in 70–90% yield by mixing an aqueous solution of $K_4[Re_6Q_8(OH)_6]\cdot 8H_2O$ with the chloride or nitrate salt of the corresponding metal. Crystals of compound **1** were obtained in the presence of 1,3,5-trioxane. The formation of compounds **2**–**5** may be forced by adding a few drops of DMF to the reaction mixture.

**Luminescence Measurements:** The emission spectra of solid samples of **1**, **2**, **3**, **4**, **6** were recorded in the wavelength range of 500 nm to 700 nm using a UV-Spectrofluorimeter equipped with a ORIEL 77200 monochromator and a Hamamatsu R928 PMT detector. The Xe lamp (ORIEL photomax, 75 W) was used as a light source, which emitted intense and relatively stable radiation in a continuous range of 200 nm to 800 nm. The excitation slit width was 1.56 mm, and the emission slit width was 60 μm.

**X-ray Crystallography:** Single crystal X-ray diffraction data were collected on $[\{Mg(H_2O)_5\}_2Re_6S_8(OH)_6]$ (**1**), $[\{Ca(H_2O)_3\}_2Re_6Q_8(OH)_6]$ where Q = S (**2**), Se (**3**), $[\{Sr_2(H_2O)_{10}\}Re_6Q_8(OH)_6]$ where Q = S (**4**), Se (**5**), and $[\{Ba_2(H_2O)_8\}Re_6Q_8(OH)_6]$ where Q = S (**6**), Se (**7**). Data were collected with graphite-monochromated Mo-$K_\alpha$ radiation ($\lambda$ = 0.71073 Å) at 170 K (**1**, **3**) and 293 K (**2**, **4**, **5**, **6**, **7**) with a Bruker Smart APEX CCD diffractometer with the operating program SMART. A face-indexed absorption correction was performed numerically with the use of XPREP. The program SADABS was then employed to perform incident beam and decay corrections. All structures were solved by direct methods and refined (full-matrix least-squares on $F^2$) with the SHELX-97 program suite.[9]

**$[\{Mg(H_2O)_5\}_2Re_6S_8(OH)_6]\cdot 6H_2O$ (1):** ($M$ = 1812.60), crystal size 0.28 × 0.06 × 0.05 mm, triclinic space group $P\bar{1}$, $a$ = 8.4986(18) Å, $b$ = 8.6593(19) Å, $c$ = 10.920(2) Å, $\alpha$ = 78.179(4)°, $\beta$ = 85.273(3)°, $\gamma$ = 76.809(3)°, $V$ = 765.3(3) Å$^3$, $Z$ = 1, $\rho_{calcd.}$ = 3.933 g cm$^{-3}$, $\mu$ = 24.294 mm$^{-1}$, 1.91 < $\theta$ < 28.22°, $T$ = 173(2) K. Reflections: 4799 collected, 3406 unique ($R_{int}$ = 0.0229), 2893 observed [$I > 2\sigma(I)$]; 173 parameters refined with $R$ = 0.0333 [$I > 2\sigma(I)$], $wR_2$ = 0.0882 (all data), GOF = 0.996, residual electron density: +2.814 e Å$^3$, –2.745 e Å$^3$.

**$[\{Ca(H_2O)_3\}_2Re_6S_8(OH)_6]$ (2):** ($M$ = 1663.98), crystal size 0.16 × 0.14 × 0.026 mm, trigonal space group $P\bar{3}$, $a$ = 8.3359(8) Å, $c$ = 9.3100(18) Å, $V$ = 560.25(13) Å$^3$, $Z$ = 1, $\rho_{calcd.}$ = 4.932 g cm$^{-3}$, $\mu$ = 33.527 mm$^{-1}$, 2.19 < $\theta$ < 28.03°, $T$ = 293(2) K. Reflections: 3450 collected, 904 unique ($R_{int}$ = 0.0394), 832 observed [$I > 2\sigma(I)$]; 56 parameters refined with $R$ = 0.0246 [$I > 2\sigma(I)$], $wR_2$ = 0.0608 (all data), GOF = 1.046, residual electron density: +3.390 e Å$^3$, –1.795 e Å$^3$.

**$[\{Ca(H_2O)_3\}_2Re_6Se_8(OH)_6]$ (3):** ($M$ = 2039.18), crystal size 0.28 × 0.20 × 0.01 mm, trigonal space group $P\bar{3}$, $a$ = 8.4729(6) Å, $c$ = 9.4353(14) Å, $V$ = 586.61(11) Å$^3$, $Z$ = 1, $\rho_{calcd.}$ = 5.772 g cm$^{-3}$, $\mu$ = 43.719 mm$^{-1}$, 2.78 < $\theta$ < 28.13°, $T$ = 293(2) K. Reflections: 3667 collected, 927 unique ($R_{int}$ = 0.0288), 859 observed [$I > 2\sigma(I)$]; 44 parameters refined with $R$ = 0.0222 [$I > 2\sigma(I)$], $wR_2$ = 0.0572 (all data), GOF = 1.13, residual electron density: +1.551 e Å$^3$, –1.616 e Å$^3$.

**$[\{Sr_2(H_2O)_{10}\}Re_6S_8(OH)_6]\cdot 6H_2O$ (4):** ($M$ = 1939.22), crystal size 0.26 × 0.20 × 0.16 mm, triclinic space group $P\bar{1}$, $a$ = 8.7027(12) Å, $b$ = 9.2442(13) Å, $c$ = 10.8666(15) Å, $\alpha$ = 87.545(2)°, $\beta$ = 74.635(2)°, $\gamma$ = 73.721(2)°, $V$ = 808.70(19) Å$^3$, $Z$ = 1, $\rho_{calcd.}$ = 3.982 g cm$^{-3}$, $\mu$ = 26.214 mm$^{-1}$, 1.94 < $\theta$ < 28.25°, $T$ = 293(2) K. Reflections: 5077 collected, 3587 unique ($R_{int}$ = 0.0271), 3192 observed [$I > 2\sigma(I)$]; 173 parameters refined with $R$ = 0.0386 [$I > 2\sigma(I)$], $wR_2$ = 0.1085 (all data), GOF = 1.057, residual electron density: +4.172 e Å$^3$, –3.669 e Å$^3$.

**$[\{Sr_2(H_2O)_{10}\}Re_6Se_8(OH)_6]\cdot 6H_2O$ (5):** ($M$ = 2314.42), crystal size 0.26 × 0.14 × 0.02 mm, triclinic space group $P\bar{1}$, $a$ = 8.8380(13) Å, $b$ = 9.3615(13) Å, $c$ = 11.0489(16) Å, $\alpha$ = 86.906(2)°, $\beta$ = 73.821(2)°, $\gamma$ = 72.735(2)°, $V$ = 838.0(2) Å$^3$, $Z$ = 1, $\rho_{calcd.}$ = 4.586 g cm$^{-3}$, $\mu$ = 33.488 mm$^{-1}$, 2.28 < $\theta$ < 28.26°, $T$ = 293(2) K. Reflections: 5255 collected, 3732 unique ($R_{int}$ = 0.0199), 2981 observed [$I > 2\sigma(I)$]; 173 parameters refined with $R$ = 0.0317 [$I > 2\sigma(I)$], $wR_2$ = 0.0935 (all data), GOF = 1.069, residual electron density: +2.536 e Å$^3$, –1.956 e Å$^3$.

**$[\{Ba_2(H_2O)_8\}Re_6S_8(OH)_6]$ (6):** ($M$ = 1894.54), crystal size 0.18 × 0.03 × 0.02 mm, triclinic space group $P\bar{1}$, $a$ = 8.2413(14) Å, $b$ = 8.4332(15) Å, $c$ = 9.4651(17) Å, $\alpha$ = 81.879(3) , $\beta$ = 74.242(3) , $\gamma$ = 77.937(3) , $V$ = 616.63(19) Å$^3$, $Z$ = 1, $\rho_{calcd.}$ = 5.102 g cm$^{-3}$, $\mu$ = 33.185 mm$^{-1}$, 2.24 < $\theta$ < 28.24°, $T$ = 293(2) K. Reflections: 3898 collected, 2757 unique ($R_{int}$ = 0.0253), 2166 observed [$I > 2\sigma(I)$]; 137 parameters refined with $R$ = 0.0426 [$I > 2\sigma(I)$], $wR_2$ = 0.1139 (all data), GOF = 1.008, residual electron density: +4.294 e Å$^3$, –3.040 e Å$^3$.

**$[\{Ba_2(H_2O)_8\}Re_6Se_8(OH)_6]$ (7):** ($M$ = 2269.74), crystal size 0.30 × 0.03 × 0.02 mm, triclinic space group $P\bar{1}$, $a$ = 8.4020(12) Å, $b$ = 8.5735(12) Å, $c$ = 9.6420(14) Å, $\alpha$ = 81.049(3)°, $\beta$ = 73.639(2)°, $\gamma$ = 77.308(2)°, $V$ = 646.88(16) Å$^3$, $Z$ = 1, $\rho_{calcd.}$ = 5.826 g cm$^{-3}$, $\mu$ = 42.241 mm$^{-1}$, 2.21 < $\theta$ < 28.26°, $T$ = 293(2) K. Reflections: 4076 collected, 2882 unique ($R_{int}$ = 0.0279), 2225 observed [$I > 2\sigma(I)$]; 137 parameters refined with $R$ = 0.0340 [$I > 2\sigma(I)$], $wR_2$ = 0.0879 (all data), GOF = 0.957, residual electron density: +2.288 e Å$^3$, –1.875 e Å$^3$.

 © 2006 Wiley-VCH Verlag GmbH & Co. KGaA, Weinheim 

Further details of the crystal structure investigations may be obtained from the Fachinformationszentrum Karlsruhe, 76344 Eggenstein-Leopoldshafen, Germany, on quoting the depository CSD number filenames 415688–415694 (for **1**–**7**).

## Acknowledgments

This work was supported by the Russian Foundation for Basic Research (grants 05-03-32123, 05-03-08090) and the SRC program of the Korea Science and Engineering Foundation (KOSEF) through the Center for Intelligent Nano-Bio Materials at Ewha Womans University (grant: R11-2005-008-00000-0).

[1] a) Y. V. Mironov, V. E. Fedorov, *J. Struct. Chem.* **1999**, *40*, 959–974; b) J.-C. P. Gabriel, K. Boubekeur, S. Uriel, P. Batail, *Chem. Rev.* **2001**, *101*, 2037–2066; c) H. D. Selby, B. K. Roland, Z. Zheng, *Acc. Chem. Res.* **2003**, *36*, 933–944.

[2] L. Leduc, A. Perrin, M. Sergent, *Acta Crystallogr. Sect. C* **1983**, *39*, 1503–1506.

[3] M. Spangenberg, W. Bronger, *Angew. Chem. Int. Ed. Engl.* **1978**, *17*, 368–369.

[4] a) N. G. Naumov, A. V. Virovets, V. E. Fedorov, *J. Struct. Chem.* **2000**, *41*, 499–520; b) V. E. Fedorov, N. G. Naumov, Y. V. Mironov, A. V. Virovets, S. B. Artemkina, K. A. Brylev, S. S. Yarovoi, O. A. Efremova, U. H. Peak, *J. Struct. Chem.* **2002**, *43*, 669–684; c) Y. V. Mironov, V. E. Fedorov, I. Ijjaali, J. A. Ibers, *Inorg. Chem.* **2001**, *40*, 6320–6323; d) K. A. Brylev, Y. V. Mironov, N. G. Naumov, V. E. Fedorov, J. A. Ibers, *Inorg. Chem.* **2004**, *43*, 4833–4838; e) Y. Kim, S.-M. Park, W. Nam, S.-J. Kim, *Chem. Commun.* **2001**, 1470–1471; f) S.-M. Park, Y. Kim, S.-J. Kim, *Eur. J. Inorg. Chem.* **2003**, 4117–4121.

[5] a) B. K. Roland, H. D. Selby, J. R. Cole, Z. Zheng, *Dalton Trans.* **2003**, 4307–4312; b) H. D. Selby, B. K. Roland, M. D. Carducci, Z. Zheng, *Inorg. Chem.* **2003**, *42*, 1656–1662; c) B. K. Roland, H. D. Selby, M. D. Carducci, Z. Zheng, *J. Am. Chem. Soc.* **2002**, *124*, 3222–3223; d) Z.-N. Chen, T. Yoshimura, M. Abe, K. Tsuge, Y. Sasaki, S. Ishizaka, H.-B. Kim, N. Kitamura, *Chem. Eur. J.* **2001**, *7*, 4447–4455; e) A. Itasaka, M. Abe, T. Yoshimura, K. Tsuge, M. Suzuki, T. Imamura, Y. Sasaki, *Angew. Chem. Int. Ed.* **2002**, *41*, 463–466; f) Y. V. Mironov, M. A. Shestopalov, K. A. Brylev, S. S. Yarovoi, G. V. Romanenko, V. E. Fedorov, H. Spies, H.-J. Pietzsch, H. Stephan, G. Geipel, G. Bernhard, W. Kraus, *Eur. J. Inorg. Chem.* **2005**, 657–661.

[6] S. S. Yarovoi, Y. V. Mironov, D. Y. Naumov, Y. V. Gatilov, S. G. Kozlova, S.-J. Kim, V. E. Fedorov, *Eur. J. Inorg. Chem.* **2005**, 3945–3949.

[7] S. Uriel, K. Boubekeur, J.-C. Gabriel, P. Batail, J. Orduna, *Bull. Soc. Chim. Fr.* **1996**, *133*, 783–794.

[8] a) Z.-N. Chen, T. Yoshimura, M. Abe, Y. Sasaki, S. Ishizaka, H.-B. Kim, N. Kitamura, *Angew. Chem. Int. Ed.* **2001**, *40*, 239–242; b) T. G. Gray, C. M. Rudzinski, E. E. Meyer, D. G. Nocera, R. H. Holm, *J. Am. Chem. Soc.* **2003**, *125*, 4755–4770; c) R. Arratia-Perez, L. Hernandez-Acevedo, *J. Chem. Phys.* **1999**, *111*, 168–172; d) R. Arratia-Perez, L. Hernandez-Acevedo, *J. Chem. Phys.* **2003**, *118*, 7425 –7430.

[9] a) G. M. Sheldrick, SHELXS-97, *Program for Crystal Structure Solution*, Göttingen; b) G. M. Sheldrick, SHELXL-97, *Program for Crystal Structure Refinement*, Göttingen.

Received: August 19, 2005
Published Online: December 13, 2005

 © 2006 Wiley-VCH Verlag GmbH & Co. KGaA, Weinheim 

DOI: 10.1002/ejic.200500778

# Platinum-Group Chelate Complexes with 9-Hydroxyphenalenone Derivatives: Synthesis, Structures, Spectroscopic Properties and Cytotoxic Activities

Tomoyuki Mochida,*[a,b] Reiko Torigoe,[a] Takeo Koinuma,[a] Chika Asano,[a] Tadaaki Satou,[c] Kazuo Koike,[c] and Tamotsu Nikaido[c]

**Keywords:** Platinum / Rhodium / Palladium / O ligands / Metal–metal interactions

The following platinum-group chelate complexes with 5-R-9-hydroxyphenalenone ($L^1$: R = H; $L^2$: R = Me; $L^3$: R = Pr) have been prepared: $[Rh^I(L)(CO)_2]$ (**1a**: L = $L^1$; **1b**: L = $L^2$; **1c**: L = $L^3$), $[Pd^{II}(L)_2]$ (**2a**: L = $L^2$; **2b**: L = $L^3$), $[Pt^{II}(L^1)(NH_3)_2](NO_3)$ (**3**), and $(Bu_4N)[Pt^{II}(L^1)(Cl)_2]$ (**4**). Compounds **1a** and **1b** are different colors in the solid state: yellow and deep red, respectively. X-ray analysis revealed that **1a** has a regular π–π stacking structure while **1b** has a dimer-like arrangement with a $Rh^I$–$Rh^I$ distance of 3.2336(6) Å. Both solids were luminescent at 77 K. Compounds **2a** and **2b** are planar extended π-conjugated complexes, which exhibit two-dimensional stacking modes in the crystal. The solid-state structure of complex **3** is hydrogen-bonded in a polar arrangement. The cytotoxic activities of **1a**, **3**, and **4**, evaluated in vitro against HL60 human acute myeloid leukemia cell lines, were comparable to that of cisplatin.
(© Wiley-VCH Verlag GmbH & Co. KGaA, 69451 Weinheim, Germany, 2006)

## Introduction

Platinum-group metal complexes with various ligands have attracted growing attention in recent decades because of their unique photochemical[1] and electronic properties.[2] Here we report the use of hydroxyphenalenone as an extended π-conjugated ligand to explore a novel type of complex. The phenalenyl system is an odd-alternant hydrocarbon,[3,4] the unique properties of which have been widely investigated. Haddon has reported the interesting properties of spiro-biphenalenyl radicals, which exhibit electronic-switching phenomena in the solid state.[5] Several transition-metal complexes of phenalenyl derivatives have been reported: a neutral palladium complex with a $\eta^3$-phenalenyl ligand was prepared by Nakasuji,[6] and some transition-metal complexes with phenalenone-related ligands were prepared in the 1970s.[7,8] More recently, metal chelate complexes with 9-hydroxyphenalenones have been prepared, including aluminum complexes for multilayer light-emitting devices[9] and a luminescent europium complex.[10] However, no examples of phenalenone chelate complexes with platinum-group metals have been reported. We are interested in the antitumor potential of such complexes because their planar π-conjugated nature might allow intercalation into DNA to enhance cytotoxic activity.

In this study, we prepared chelate complexes of platinum-group metals with 9-hydroxyphenalenone ($HL^1$), its 5-methyl derivative ($HL^2$), and a 5-propyl derivative ($HL^3$) (Scheme 1). Use of the 5-alkyl derivatives improved the solubility of the complexes. We also tried, unsuccessfully, to prepare a 5-*tert*-butyl ligand by a Friedel–Crafts or similar condensation reaction. Here we report the preparation and properties of $[Rh^I(L)(CO)_2]$ (**1a**: L = $L^1$; **1b**: L = $L^2$; **1c**: L = $L^3$), $[Pd^{II}(L)_2]$ (**2a**: L = $L^2$; **2b**: L = $L^3$), $[Pt^{II}(L^1)(NH_3)_2](NO_3)$ (**3**), and $(Bu_4N)[Pt^{II}(L^1)(Cl)_2]$ (**4**). The molecular structures were confirmed crystallographically, and the remarkable difference in color between **1a** and **1b** was rationalized in terms of metal–metal interactions. Furthermore, the cytotoxic activities of **1a**, **3**, and **4** against human acute myeloid leukemia cells were evaluated.

## Results and Discussion

### Preparation and Spectroscopic Properties

Reaction of the 9-hydroxyphenalenone derivatives ($HL^1$, $HL^2$, and $HL^3$) with various metal sources in the presence of base produced chelate complexes (Scheme 1). We prepared the neutral complexes **1a**–**c** and **2a**–**b**, the anionic complex **3**, and the cationic complex **4** using methods analogous to the known preparations of chelate complexes of platinum-group metals with acetylacetonate derivatives.[11–15] We could not obtain platinum analogs of **2**; similar procedures afforded uncharacterizable black precipi-

[a] Department of Chemistry, Faculty of Science, Toho University, Miyama, Funabashi, Chiba 274-8510, Japan
Fax: +81-47-472-4406
E-mail: mochida@chem.sci.toho-u.ac.jp
[b] Research Center for Materials with Integrated Properties, Toho University,
Miyama, Funabashi, Chiba 274-8510, Japan
[c] Department of Pharmacognosy, Faculty of Pharmaceutical Sciences, Toho University,
Miyama, Funabashi, Chiba 274-8510, Japan
Supporting information for this article is available on the WWW under http://www.eurjic.org or from the author.

 © 2006 Wiley-VCH Verlag GmbH & Co. KGaA, Weinheim 

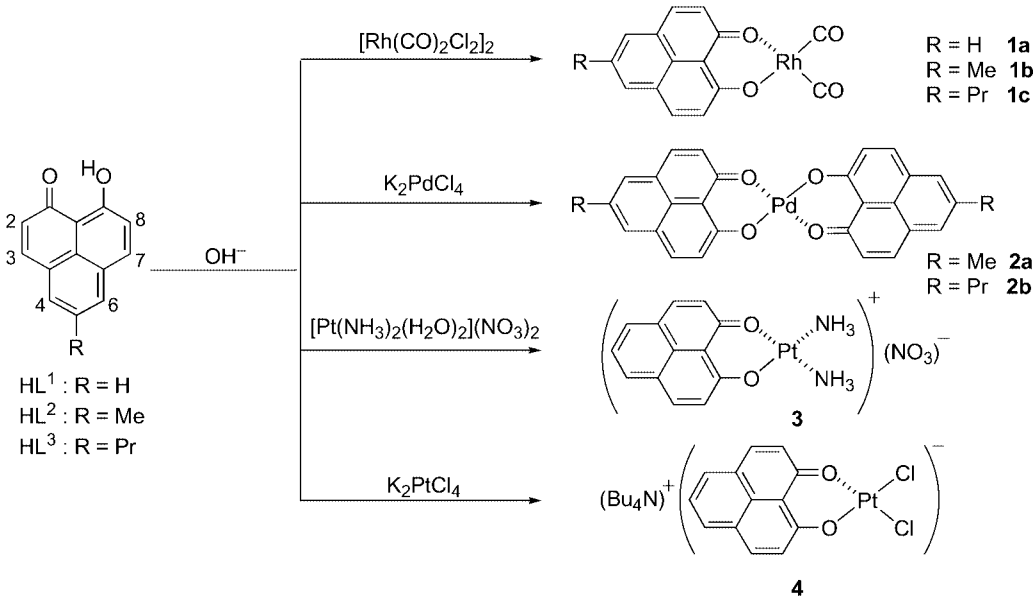


Scheme 1.

tates. Attempted syntheses of Magnus-type complexes using **3** and **4** failed.

The $^1$H NMR spectroscopic data for compounds **1**–**4** are listed in Table 1 alongside the infrared stretching frequencies of C=O and other characteristic vibrations. In **1a**–**c** and **2b**, the signals for $H^2$ and $H^4$ exhibited downfield shifts, while $H^3$ was shifted upfield relative to their free ligand values. In **3** and **4**, the ring protons showed slight upfield shifts. The ligand C=O stretching bands were observed at frequencies slightly lower than those of the free ligand. In DMF solution, the lowest energy UV/Vis absorption bands for $HL^1$, $HL^2$, and $HL^3$ appeared at $\lambda_{max}$ = 449, 449, and 438 nm, respectively. The lowest energy absorption bands for the metal complexes were found at lower energies than those of the ligands: $\lambda_{max}$ = 498 (**2a**), 497 (**2b**), 477 (**3**), and 461 nm (**4**) in DMF, and at around $\lambda_{max}$ = 460 nm for **1a**–**c** in dichloromethane. Compounds **1a**–**c** decomposed[16] when heated in DMF or DMSO.

In the following sections, the structures and solid-state properties of the individual complexes are described. Crystal data, data collection parameters, and analysis statistics are listed in Table 2, and selected bond lengths and bond angles given in Table 3. ORTEP[17] drawings of the molecular structures of **1a**, **2a**, **3**, and **4**, as well as the packing diagrams of **2b** and **4**, have been deposited as supporting information.

### [Rh$^I$(L$^1$)(CO)$_2$] (1a) and [Rh$^I$(L$^2$)(CO)$_2$] (1b)

The rhodium ion in these complexes is coordinated by the phenalenone ligand and two CO ligands in a square planar arrangement. The molecular geometries of **1a** and

Table 1. $^1$H NMR chemical shifts [ppm] and IR stretching frequencies [cm$^{-1}$] for ligands and complexes **1**–**4**.

| Comp. | $^1$H NMR[a] Solvent | H2, H8 ($J_{H,H}$) | H3, H7 ($J_{H,H}$) | H4, H6 ($J_{H,H}$) | R ($J_{H,H}$) | IR[b] $\nu$(C=O) |
|---|---|---|---|---|---|---|
| $HL^1$ | $CDCl_3$ | 7.19 (9.16 Hz) | 8.11 (9.80 Hz) | 8.03 (9.16 Hz) | 7.61 [R = H] (7.64 Hz) | 1585, 1633 |
| $HL^1$ | [D$_6$]DMSO | 7.24 (9.16 Hz) | 8.41 (9.16 Hz) | 8.30 (7.32 Hz) | 7.74 [R = H] (7.64 Hz) | |
| **1a** | $CDCl_3$ | 7.33 (9.16 Hz) | 8.08 (9.16 Hz) | 8.06 (7.32 Hz) | 7.61 [R = H] (7.62 Hz) | 1577, 1625, 1999,[d] 2068[d] |
| **3** | [D$_6$]DMSO | 7.23 (9.16 Hz) | 8.45 (9.16 Hz) | 8.45 (9.16 Hz) | 7.71 [R = H] (7.32 Hz) | 1579, 1628, 3246,[e] 1385[f] |
| **4** | [D$_6$]DMSO | 7.05 (9.16 Hz) | 8.32 (9.80 Hz) | 8.36 (7.92 Hz) | 7.66 [R = H] (7.32 Hz) | 1579, 1628 |
| $HL^2$ | $CDCl_3$ | 7.16 (9.16 Hz) | 8.04 (9.16 Hz) | 7.84 | 2.61 [R = $CH_3$] | 1598, 1636 |
| **1b** | $CDCl_3$ | 7.31 (9.16 Hz) | 8.02 (9.16 Hz) | 7.88 | 2.62 [R = $CH_3$] | 1592, 1630, 1992,[d] 2061[d] |
| **2a** | [D$_7$]DMF[c] | 7.35 (9.16 Hz) | 8.20 (9.16 Hz) | 7.77 | 2.61 [R = $CH_3$] | 1594, 1630 |
| $HL^3$ | $CDCl_3$ | 7.16 (9.76 Hz) | 8.06 (9.16 Hz) | 7.84 | 0.99–2.86 [R = Pr] | 1597, 1633 |
| **1c** | $CDCl_3$ | 7.31 (9.16 Hz) | 8.04 (9.16 Hz) | 7.88 | 0.99–2.89 [R = Pr] | 1593, 1631, 2004,[d] 2067[d] |
| **2b** | $CDCl_3$ | 7.45 (9.16 Hz) | 7.93 (9.76 Hz) | 7.85 | 0.98–2.86 [R = Pr] | 1591, 1629 |

[a] Numbering of hydrogen is shown in Scheme 1. [b] KBr pellet. [c] Measured at 70 °C. [d] C≡O stretch. [e] N–H stretch. [f] N–O stretch.

 © 2006 Wiley-VCH Verlag GmbH & Co. KGaA, Weinheim 

Table 2. Crystallographic parameters for **1**–**4**.

| | **1a** | **1b** | **2a** | **2b** | **3** | **4** |
|---|---|---|---|---|---|---|
| Empirical formula | $C_{15}H_7O_4Rh$ | $C_{16}H_9O_4Rh$ | $C_{28}H_{18}O_4Pd$ | $C_{32}H_{26}O_4Pd$ | $C_{13}H_{13}N_3O_5Pt$ | $C_{29}H_{43}Cl_2NO_2Pt$ |
| Formula weight | 354.12 | 368.14 | 524.85 | 580.93 | 486.35 | 703.66 |
| Crystal dimensions [mm] | 0.5×0.25×0.25 | 0.1×0.02×0.9 | 0.2×0.13×0.04 | 0.4×0.1×0.08 | 0.5×0.25×0.25 | 0.4×0.3×0.3 |
| Crystal system | monoclinic | monoclinic | monoclinic | monoclinic | monoclinic | monoclinic |
| *a* [Å] | 9.9623(13) | 9.1960(15) | 7.4391(7) | 7.5663(7) | 11.525(2) | 16.366(7) |
| *b* [Å] | 4.5870(6) | 10.0050(16) | 8.5785(8) | 9.7649(10) | 5.916(1) | 8.732(3) |
| *c* [Å] | 14.3155(18) | 15.178(2) | 16.005(2) | 16.4833(16) | 10.528(2) | 22.127(9) |
| *β* [°] | 107.070(2) | 107.407(3) | 91.882(2) | 100.641(2) | 89.17(1) | 116.303(6) |
| *V* [Å$^3$] | 625.36(14) | 1332.5(4) | 1020.8(2) | 1196.9(2) | 717.8(2) | 2834.8(18) |
| Space group | $P2_1$ (#4) | $P2_1/n$ (#14) | $P2_1/c$ (#14) | $P2_1/c$ (#14) | $Pc$ (#7) | $Cc$ (#9) |
| *Z* | 2 | 4 | 2 | 2 | 2 | 4 |
| $D_{calcd.}$ [g cm$^{-3}$] | 1.881 | 1.835 | 1.707 | 1.612 | 2.250 | 1.649 |
| $\mu$ [mm$^{-1}$] | 1.374 | 1.294 | 0.946 | 0.814 | 9.763 | 5.145 |
| *F*(000) | 348 | 728 | 528 | 592 | 460 | 1408 |
| No. of reflections | 4634 | 9597 | 7661 | 8649 | 5363 | 12885 |
| No. of observations | 2768 | 3285 | 1837 | 2943 | 4714 | 5244 |
| Diffractometer | Bruker APEX | Bruker APEX | Bruker APEX | Bruker APEX | Rigaku Mercury | Rigaku Mercury |
| Radiation | Mo-$K_\alpha$ | Mo-$K_\alpha$ | Mo-$K_\alpha$ | Mo-$K_\alpha$ | Mo-$K_\alpha$ | Mo-$K_\alpha$ |
| Refl./param. ratio | 15.29 | 17.20 | 11.48 | 17.31 | 24.62 | 9.87 |
| Temperature [K] | 293 | 293 | 293 | 293 | 293 | 120 |
| $R_1$, $R_w$[a] | 0.0486, 0.1190 | 0.037; 0.069 | 0.030; 0.072 | 0.0353; 0.0775 | 0.046; 0.136 | 0.058; 0.147 |
| Goodness of fit | 1.01 | 1.05 | 1.11 | 1.06 | 1.14 | 1.01 |

[a] $R_1 = \Sigma||F_o| - |F_c||/\Sigma|F_o|$; $R_w = [\Sigma w(F_o^2 - F_c^2)^2/\Sigma w(F_o^2)^2]^{1/2}$.

**1b** were almost identical; the structure of **1b**, determined by X-ray crystallography, is shown in Figure 1. Comparing the intramolecular bond lengths of these complexes with those of [Rh$^I$(acac)(CO)$_2$] (acac = acetylacetone)[13] shows that the Rh–O and C≡O distances are shorter in the phenalenone complexes (by about 0.04 and 0.1 Å, respectively), while the Rh–C(CO) distances are longer (by about 0.09 Å). This suggests that the bonds between Rh and the chelating ligand are somewhat stronger in the phenalenone complexes.

The packing diagram of **1a** is shown in Figure 2. The crystal structure has a polar space group ($P2_1$), in which the molecules are arranged in a column along the stacking (*b*) axis. There is no intermolecular metal–metal bonding: the intermolecular Rh···Rh distance is 4.587 Å. The packing of **1b** is different from that of **1a** and is shown in Figure 3. An intermolecular Rh–Rh interaction [Rh–Rh: 3.2336(6) Å] forms dimers, which have a staggered configuration. In the crystal, the long molecular axes are located within the *a*–*c* plane, and interdimer face-to-face stacking interactions form columns along the *b* axis. The molecules in adjacent columns are arranged such that their long axes are orthogonal.

It is known that d$^8$ metal complexes can associate through metal–metal interactions in the solid state.[2a,18] In [Rh$^I$(acac)(CO)$_2$],[13] the molecules form one-dimensional arrays with Rh···Rh distances of 3.26 Å. The Rh–Rh distance in **1b** is comparable to that in Rh$^I$ 1D chain complexes and bridged dinuclear Rh$^I$ complexes.[19–21]

Solutions of **1a** and **1b** were yellow and exhibited almost identical absorption spectra, but **1b** formed intense deep red crystals while **1a** remained yellow in the crystalline state. Similar structure-dependent color change has been observed previously in some platinum complexes.[22] Figure 4 (a) and (b) show the absorption and emission spectra of powder samples of **1a** and **1b**, respectively. Solid lines represent room temperature absorption spectra, obtained by applying a Kubelka–Munk conversion to reflectance spectra. The absorption edge of **1a** appears at around 500 nm while that for **1b** appears at around 600 nm; the lower energy of **1b**'s absorption is consistent with its intense color. The broken lines in Figure 4 represent the emission spectra at 77 K. Compound **1a** exhibited red emission, with two bands at $\lambda_{max}$ = 600 nm and $\lambda_{max}$ = 648 nm. Compound **1b** exhibited a weak, broad band at $\lambda_{max}$ = 658 nm. These complexes were emissive at 77 K but not room temperature, and not in solution.

The low-energy absorption in **1b** is a consequence of metal–metal interactions. DFT calculations were carried out using the crystallographically determined geometries of **1a** and **1b**, and the frontier orbitals are plotted in Figure 5. In **1a**, the HOMO (–6.22 eV) and LUMO (–2.69 eV) are of predominantly ligand character with only a small contribution from the metal d orbitals. The d orbitals' contribution is more significant for the HOMO and therefore the lowest energy excitation is predominantly π–π* mixed with an MLCT character. In contrast to **1a**, the HOMO of **1b** (–5.48 eV) consists of metal d$z^2$ orbitals; the d–d interaction raises the energy level of the Rh$^I$–Rh$^I$ σ-antibonding orbital above that of the ligand orbital. The LUMO (–2.53 eV) is a ligand-based orbital. Therefore, the intense color of **1b** is attributed to MLCT. Electronic absorptions from metal-centered ($4d_{z^2}$ to $5p_z$) transitions in binuclear rhodium complexes are mostly found between 550 and 600 nm,[20] but the transition in **1b** is of a different character because the conjugation of the ligand lowers the π* level. The crystal structure of **1c** could not be determined but its yellow color suggests that it has no metal–metal interactions.

 © 2006 Wiley-VCH Verlag GmbH & Co. KGaA, Weinheim 

Table 3. Selected bond lengths [Å] and bond angles [°] with estimated standard deviations in parentheses.

| | | | |
|---|---|---|---|
| **1a** | | | |
| Rh–O1 | 2.008(5) | Rh–O2 | 2.007(5) |
| Rh–C14 | 1.848(8) | Rh–C15 | 1.845(8) |
| O1–C1 | 1.285(8) | O2–C3 | 1.285(8) |
| C1–C2 | 1.434(8) | C1–C12 | 1.417(10) |
| C2–C3 | 1.428(8) | C3–C4 | 1.431(9) |
| C14–O4[a] | 1.125(10) | C15–O3[a] | 1.129(10) |
| O1–Rh–O2 | 88.8(2) | C14–Rh–C15 | 88.2(4) |
| O1–Rh–C14 | 92.1(3) | O2–Rh–C15 | 91.0(3) |
| C1–O1–Rh | 128.9(4) | C3–O2–Rh | 129.1(4) |
| C2–C1–O1 | 125.2(6) | C2–C3–O2 | 125.1(6) |
| **1b** | | | |
| Rh–O1 | 2.018(2) | Rh–O2 | 2.021(2) |
| Rh–C15 | 1.846(3) | Rh–C16 | 1.839(3) |
| O1–C1 | 1.290(3) | O2–C3 | 1.284(3) |
| C1–C2 | 1.431(3) | C1–C12 | 1.433(3) |
| C2–C3 | 1.425(3) | C3–C4 | 1.439(3) |
| C15–O4[a] | 1.136(3) | C16–O3[a] | 1.133(6) |
| O1–Rh–O2 | 89.00(6) | C15–Rh–C16 | 87.7(1) |
| O1–Rh–C15 | 91.97(9) | O2–Rh–C16 | 91.34(9) |
| C1–O1–Rh | 128.0(1) | C3–O2–Rh | 128.6(1) |
| C2–C1–O1 | 125.9(2) | C2–C3–O2 | 125.6(2) |
| **2a** | | | |
| Pd–O1 | 1.960(2) | Pd–O2 | 1.978(2) |
| O1–C1 | 1.293(4) | O2–C3 | 1.284(3) |
| C1–C2 | 1.421(4) | C1–C12 | 1.434(4) |
| C2–C3 | 1.440(4) | C3–C4 | 1.437(4) |
| O1–Pd–O2 | 93.38(8) | Pd–O1–C1 | 125.4(2) |
| Pd–O2–C3 | 125.4(2) | O1–C1–C2 | 126.6(3) |
| O2–C3–C2 | 126.1(3) | C1–C2–C3 | 122.9(3) |
| O1–C1–C12 | 114.8(3) | O2–C3–C4 | 115.6(3) |
| **2b** | | | |
| Pd–O1 | 1.965(1) | Pd–O2 | 1.972(1) |
| O1–C1 | 1.284(2) | O2–C3 | 1.289(2) |
| C1–C2 | 1.437(2) | C1–C12 | 1.432(3) |
| C2–C3 | 1.427(2) | C3–C4 | 1434(3) |
| O1–Pd–O2 | 93.67(6) | Pd–O1–C1 | 125.4(1) |
| Pd–O2–C3 | 125.2(1) | O1–C1–C2 | 126.1(2) |
| O2–C3–C2 | 126.1(2) | C1–C2–C3 | 123.4(2) |
| O1–C1–C12 | 115.5(2) | O2–C3–C4 | 115.3(2) |
| **3** | | | |
| Pt–N1 | 2.020(9) | Pt–N2 | 2.025(10) |
| Pt–O1 | 1.962(7) | Pt–O2 | 1.998(8) |
| O1–C1 | 1.31(1) | O2–C3 | 1.31(1) |
| C1–C2 | 1.42(1) | C2–C3 | 1.42(1) |
| C3–C4 | 1.43(1) | C1–C12 | 1.42(1) |
| N1–Pt–N2 | 92.3(3) | O1–Pt–O2 | 94.3(3) |
| O1–Pt–N1 | 86.6(3) | O2–Pt–N2 | 86.9(4) |
| C1–O1–Pt | 124.1(6) | C3–O2–Pt | 123.8(6) |
| C2–C1–O1 | 126.6(9) | C2–C3–O2 | 125.9(9) |
| **4** | | | |
| Pt–Cl1 | 2.284(5) | Pt–Cl2 | 2.300(5) |
| Pt–O1 | 1.961(13) | Pt–O2 | 1.975(10) |
| O1–C1 | 1.29(2) | O2–C3 | 1.30(2) |
| C1–C2 | 1.42(2) | C2–C3 | 1.44(2) |
| C3–C4 | 1.44(2) | C1–C12 | 1.46(2) |
| Cl1–Pt–Cl2 | 91.8(2) | O1–Pt–O2 | 93.7(5) |
| O1–Pt–Cl1 | 87.9(4) | O2–Pt–Cl2 | 86.8(3) |
| C1–O1–Pt | 125.5(10) | C3–O2–Pt | 124.5(8) |
| C2–C1–O1 | 126.5(13) | C2–C3–O2 | 126.2(11) |

[a] Carbonyl groups (C≡O).

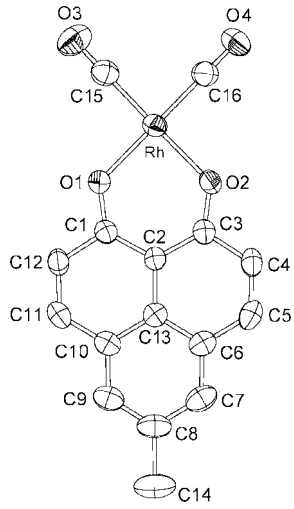


Figure 1. ORTEP drawing of the molecular structure of **1b** with the atom-numbering scheme. The counterions are omitted. Displacement ellipsoids are shown at the 50% probability level. The numbering of the phenalenyl moiety is the same in the other complexes.

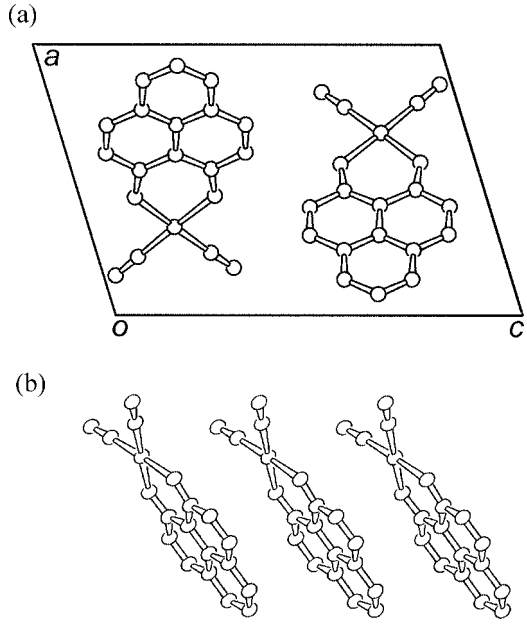


Figure 2. (a) Packing diagram of **1a** viewed along the *b* axis. (b) Stacking arrangement of **1a**.

Mononuclear $Rh^I$ complexes are known to emit from MLCT or π–π* intraligand excited states.[23] The emission from **1a** is assigned to vibronic progressions from the π–π* excited state mixed with some MLCT character. Consistent with this, a long emission lifetime of 2.0 ms was observed for this band. Solid $[Rh^I(acac)_2(CO)_2]$ also exhibits weak π–π* emission as a structured band in the 430–530 region.[16] Dinuclear $Rh^I$ complexes often exhibit a strong red emission between 650 and 850 nm because of metal–metal interactions,[21] but, in the case of **1b**, the emission was very weak. This might be a consequence of the highly conjugated nature of the ligand.

 © 2006 Wiley-VCH Verlag GmbH & Co. KGaA, Weinheim 

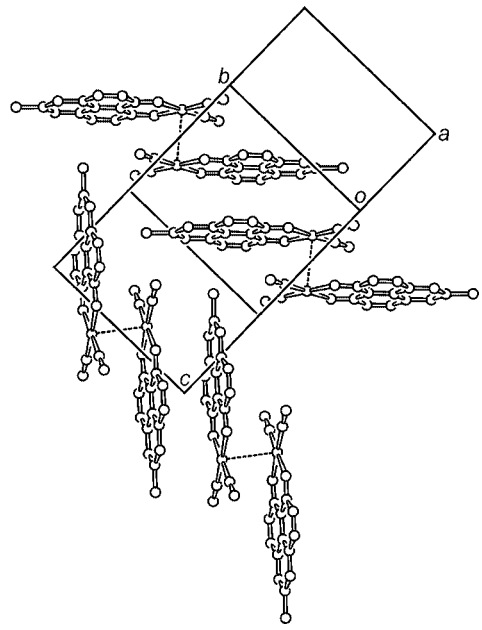


Figure 3. Packing diagram of **1b**. The hydrogen atoms are omitted for clarity. The dashed lines represent Rh–Rh interactions.

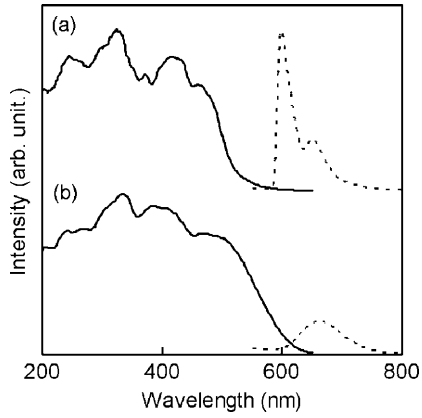


Figure 4. UV/Vis absorption spectra at room temperature (solid lines) and emission spectra at 77 K (dashed lines) for solid samples of (a) **1a** and (b) **1b**.

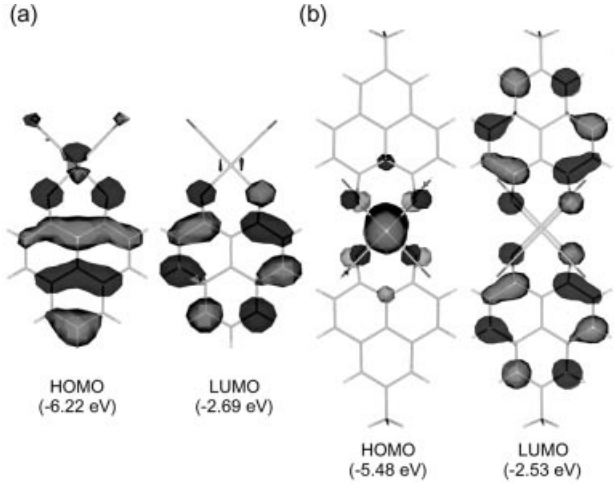


Figure 5. Frontier orbitals for (a) **1a** and (b) **1b** (dimer) derived from DFT calculations.

### $[Pd^{II}(L^2)_2]$ (2a) and $[Pd^{II}(L^3)_2]$ (2b)

The molecular structures of **2a** and **2b**, determined by X-ray crystallography, are almost identical. The coordination of the palladium atom in each case is square planar, forming an extended π-conjugated planar complex. The Pd–O distances are comparable to those in the chelate complex $[Pd(acac)_2]$.[12] The packing diagram of **2a** is shown in Figure 6 (a), and the structure of **2b** is almost identical, except that the *b* axis is elongated (by 1.2 Å) because of the longer

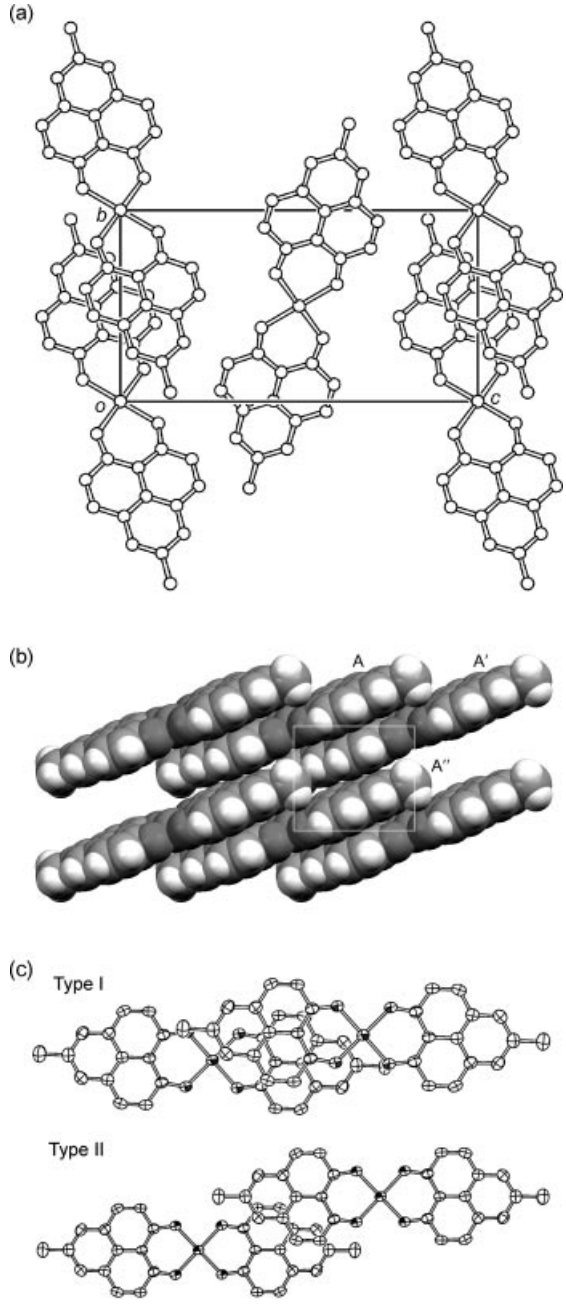


Figure 6. (a) Packing diagram of **2a** viewed along the *a* axis. The hydrogen atoms are omitted for clarity. (b) Space-filling representation of the sheet structure of **2a** within the *ab* plane. (c) ORTEP drawing of the overlapping modes of **2a**, viewed along the molecular plane.

 © 2006 Wiley-VCH Verlag GmbH & Co. KGaA, Weinheim 

alkyl group. The packing diagram of **2b** has been deposited as supporting information. In both crystals, the palladium atoms are located on the origin of the crystal lattice, and the closest distances between palladium atoms are equal to the *a* axis length: 7.439 Å for **2a** and 7.566 Å for **2b**. The complexes form two-dimensional layered structures, consisting of stacking of the planar molecules along the *a* axis. The layered structure of **2a** is shown in Figure 6 (b) as a space-filling model. There are two stacking modes, as shown in Figure 6 (c): type I stacking is formed between molecules A and A′ in Figure 6 (b), the symmetry code for A′ being $x$, $1 + y$, $z$, and type II stacking is formed between molecules A′ and A′′, the symmetry code for A′′ being $1 + x$, $1 + y$, $z$. The overlap between phenalenyl rings is larger for type I than type II. The stacking modes of **2a** and **2b** are similar, although the overlap of stacking type II is slightly more significant in **2b**, which results in stronger intermolecular interactions. It is interesting to note that the stacking structures of these complexes resemble those of polycyclic aromatic compounds.

### $[Pt^{II}(L^1)(NH_3)_2](NO_3)$ (3) and $(Bu_4N)[Pt^{II}(L^1)(Cl)_2]$ (4)

Complex **3** shows an approximate $C_{2v}$ structure. The distances C(1)–C(2), C(2)–C(3), and C(3)–C(4) are about 1.42 Å, and Pt–O(1) and Pt–O(2) are about 1.96 Å. These bond lengths are similar to the corresponding distances in the chelate compounds $[Pt(acac)_2]$[24] and $[PtCl_2(acac)]$.[14] Figure 7 shows the packing diagram. This complex has a layered structure, with hydrogen-bonded sheets and hydrophobic phenalenone layers arranged alternately along the *a* axis. The two ammine ligands are involved in intermolecular hydrogen bonding with the nitrate counteranions (N–H···O distances: 2.89 and 3.03 Å) to form a two-dimensional zigzag hydrogen-bond network within the *b*–*c* plane. Within the phenalenone layer, the aromatic rings have a herring-bone-like arrangement. Furthermore, this crystal has a polar space group (*Pc*), which is associated with a hydrogen-bond-assisted arrangement of the phenalenone complex, as seen in Figure 7. The face-to-face distance between the neighboring phenalenone planes along the *b* axis is 4.5 Å. The intermolecular distance between the neighboring platinum atoms is 5.9 Å; no direct metal–metal interactions are observed.

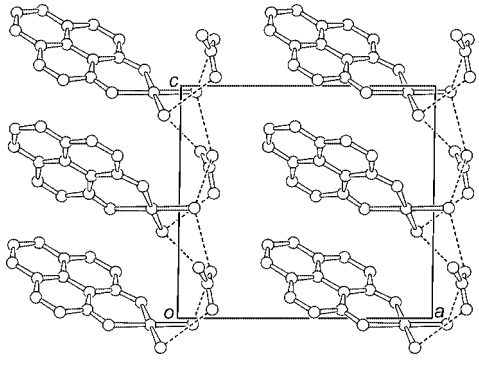


Figure 7. Packing diagram of **3** viewed along the *b* axis. The hydrogen atoms are omitted for clarity. The dashed lines represent hydrogen bonds.

In complex **4**, the lengths of the C–C and Pt–O bonds are almost the same as those found in **3**. The Pt–Cl distances are about 2.30 Å, which is comparable to the value found in $[PtCl_2(acac)]$.[14] The tetrabutyl ammonium cation and phenalenone complex anion are paired and arranged alternately in the crystal. The distance between neighboring platinum atoms is 8.73 Å; again, there were no metal–metal interactions. The molecular structure and packing diagram of **4** are deposited as Supporting Information.

### Cytotoxic Activities

Antitumor activity, as typified by cisplatin (*cis*-$[PtCl_2(NH_3)_2]$), is an important feature of platinum-group metal complexes.[25] In this study, we have evaluated the cytotoxic activities of **1a**, **3**, and **4** against human acute myeloid leukemia (HL60) cells. The concentration of the metal complexes giving a growth inhibition of 50% ($IC_{50}$) was evaluated in vitro by the MTT assay. The $IC_{50}$ values (estimated standard deviations) for **1a**, **3**, and **4** were 3.12 (0.37), 1.69 (0.51), and 3.62 (0.46) μmol/L, respectively. The observed activities were of the same order, although **3** seems to be somewhat more active than the others. Under the same experimental conditions, the $IC_{50}$ for cisplatin was 3.16 (0.50) μmol/L (control for **1a**) and 2.19 (0.59) μmol/L (control for **3** and **4**). Thus, the present compounds have the same order of cytotoxic activity as cisplatin. However, the activity is possibly due to the ligand, and, therefore, the cytotoxicity of 9-hydroxyphenalenone needs to be evaluated for discussion of the cytotoxicity of the metal complexes.

## Conclusions

We have prepared a series of platinum-group metal complexes with hydroxyphenalenone derivatives and investigated their structures, properties, and cytotoxic activities. In the solid state, the colors of the rhodium complexes **1a** and **1b** are very different; we attribute the intense color of the latter to metal–metal interactions. These compounds were emissive at 77 K in the solid state, but the highly conjugated ligands might not be favorable for emission. In the crystals of these rhodium complexes, change of ligand led to a different packing arrangement, but no corresponding change in packing was seen in the palladium complexes **2a** and **2b**. Complexes **2a** and **2b** exhibited interesting packing arrangements. No metal–metal interactions were seen in these complexes, but incorporation of a sterically hindered substituent at the 5-position of the ligand might lead to a staggered molecular arrangement and shortened metal–metal distances. The rhodium and platinum complexes exhibit noteworthy cytotoxic activity. Future research into phenalenone complexes might focus on the construction of one-dimensional complexes with metal–metal interactions, and, furthermore, use a redoxed ligand (that is, a phenalenyl radical), which could interact with the one-dimensional electronic system.

 © 2006 Wiley-VCH Verlag GmbH & Co. KGaA, Weinheim 

## Experimental Section

**General Remarks:** NMR spectra were recorded with a JEOL JNM-ECL-400 spectrometer. Infrared spectra were recorded as KBr pellets on a JASCO FTIR 230 spectrometer. UV/Vis spectra were recorded with a JASCO V-570 UV/Vis/NIR spectrometer. Solid-state electronic absorption spectra were measured with the same spectrometer equipped with an integrating sphere for diffuse reflectance spectroscopy, Kubelka–Munk conversion being applied to the resultant spectra. Emission spectra were recorded with a JASCO FP-6500 spectrometer. DFT calculations were performed with Gaussian 98[26] software at the B3LYP level using a Lanl2DZ basis set.

**Cytotoxic Studies:** The direct growth-inhibition effects of **1a**, **3**, and **4** were examined in vitro against HL60 human acute myeloid leukemia cells. These cells were obtained from the RIKEN Cell Bank, Japan. The HL60 cells were washed and suspended in the culture medium at a concentration of $3 \times 10^4$ cells/mL, and this suspension was incubated in 5% $CO_2$/air for 24 h at 37 °C. To this suspension was added the metal complex dissolved in ethanol and water. Cisplatin was used as control. These cells were further incubated for 72 h, and cell growth evaluated using a modified 3-(4,5-dimethylthiazol-2-yl)-2,5-diphenyltetrazolium bromide (MTT) reduction assay.[27] After termination of the cell culture, MTT in phosphate-buffered saline was added to each well and incubated for 4 h in 5% $CO_2$/air at 37 °C. After adding DMSO, the plates were examined using a microplate reader at 550 nm.

**X-ray Crystallographic Study:** X-ray diffraction data for single crystals were collected on a Rigaku Mercury or a Bruker APEX CCD diffractometer using Mo-$K_\alpha$ radiation ($\lambda$ = 0.71073 Å). The structures were solved by the direct method (SHELXS 97[28]) and expanded using Fourier techniques. The non-hydrogen atoms were refined anisotropically. Hydrogen atoms were inserted at the calculated positions and allowed to ride on their respective parent atoms.

CCDC-259428 (for **1a**), -259427 (for **1b**), -259429 (for **2a**), -259430 (for **2b**), -259431 (for **3**), and -259432 (for **4**) contain the supplementary crystallographic data for this paper. These data can be obtained free of charge from The Cambridge Crystallographic Data Centre via www.ccdc.cam.ac.uk/data_request/cif.

**Ligands:** The syntheses of 9-hydroxyphenalenone ($HL^1$) and 9-hydroxy-5-methylphenalenone ($HL^2$) were carried out according to published methods,[29] and 9-hydroxy-5-propylphenalenone ($HL^3$) was prepared from 6-methoxy-2-propylnaphthalene[30] in the same way as $HL^2$. The crude product was purified by sublimation under vacuum followed by recrystallization from hexane to give a yield of 44%.

**$[Rh^I(L^1)(CO)_2]$ (1a):** To a stirred DMF solution (1 mL) of $[Rh(CO)_2Cl]_2$ (15 mg, $3.9 \times 10^{-5}$ mol), which was cooled in an ice bath, 9-hydroxyphenalenone ($HL^1$) (16 mg, $8.1 \times 10^{-5}$ mol) was added, dissolved in a methanol solution of potassium hydroxide ($9.3 \times 10^{-5}$ mol). A lustrous red powder precipitated immediately, which was collected by filtration, washed with dichloromethane, and dried under vacuum to afford a yellow powder; 57% yield (16 mg). Yellow plate-like crystals suitable for X-ray crystallography were obtained by recrystallization from dichloromethane/pentane. $\lambda_{max}$/nm (DMF): 266, 352, 368, 428, 452. $C_{15}H_7O_4Rh$ (354.11): calcd. C 50.88, H 1.99; found: C 50.62, H 2.13.

**$[Rh^I(L^2)(CO)_2]$ (1b):** This compound was prepared in the same way as **1a**, using 15 mg ($8.5 \times 10^{-5}$ mol) of 9-hydroxy-5-methylphenalenone ($HL^2$). Red powder, 84% yield (24 mg). Red needle-like crystals suitable for X-ray crystallography were obtained by recrystallization from dichloromethane/hexane. $\lambda_{max}$/nm (DMF): 266, 356, 372, 436, 462. $C_{32}H_{18}O_8Rh_2$ (736.26): calcd. C 52.20, H 2.46; found C 51.92, H 2.60.

**$[Rh^I(L^3)(CO)_2]$ (1c):** This compound was prepared in the same way as **1a**, using $[Rh(CO)_2Cl_2]$ (22 mg, ($5.7 \times 10^{-5}$ mol), 9-hydroxy-5-propylphenalenone ($HL^2$) (26 mg, $1.1 \times 10^{-4}$ mol), and potassium hydroxide in methanol ($1.0 \times 10^{-4}$ mol), and stirring for 30 min. A yellow powder was obtained in a quantitative yield. $\lambda_{max}$/nm ($CH_2Cl_2$): 369, 435, 462. $C_{18}H_{13}O_4Rh$ (396.18): calcd. C 54.57, H 3.31; found C 54.75, H 3.56.

**$[Pd^{II}(L^2)_2]$ (2a):** 9-Hydroxy-5-methylphenalenone ($HL^2$) (22 mg, $1.1 \times 10^{-4}$ mol) and a methanol solution of potassium hydroxide ($1.6 \times 10^{-4}$ mol) were added to a stirred aqueous solution (1 mL) of $K_2PdCl_4$ (15 mg, $4.6 \times 10^{-5}$ mol). An orange precipitate was generated immediately, which was collected by filtration, washed with dichloromethane, and dried under vacuum. Orange needles, 92% yield (22 mg). Single crystals suitable for X-ray crystallography were obtained by slow cooling of a hot DMF solution. $\lambda_{max}$/nm (DMF): 367, 385, 498. $C_{28}H_{18}O_4Pd$ (524.82): calcd. C 64.07, H 3.46; found C 62.13, H 3.62.

**$[Pd^{II}(L^3)_2]$ (2b):** This compound was prepared in the same way as **2a**, using $K_2PdCl_4$ (16 mg, $4.8 \times 10^{-5}$ mol), 9-hydroxy-5-propylphenalenone ($HL^3$) (22 mg, $9.2 \times 10^{-5}$ mol), and potassium hydroxide ($1.2 \times 10^{-4}$ mol), and heating for 30 min at 50 °C. Red-orange powder, 80% yield (22 mg). Single crystals were obtained by recrystallization from DMF. $\lambda_{max}$/nm (DMF): 271, 369, 384, 466, 497. $C_{32}H_{26}O_4Pd$ (580.93): calcd. C 66.16, H 4.51; found C 65.94, H 4.59.

**$[Pt^{II}(L^1)(NH_3)_2](NO_3)$ (3):** Silver nitrate (44 mg, $2.6 \times 10^{-4}$ mol) was added to a solution of *cis*-$Pt(NH_3)_2Cl_2$ (40 mg, $1.3 \times 10^{-4}$ mol) in methanol/water (1:3 v/v, 1 mL) . This solution was stirred in the dark at 60 °C for 3 h, and then the AgCl was removed by filtration (Celite plug). 9-Hydroxyphenalenone ($HL^1$) (26 mg, $1.3 \times 10^{-4}$ mol) and a methanol solution of potassium hydroxide ($1.3 \times 10^{-4}$ mol) were added to this solution of *cis*-$[Pt(NH_3)_2(H_2O)_2](NO_3)_2$. After stirring for 3 h at 60 °C, the solvent was removed by vacuum evaporation. Orange powder, 54% yield (31 mg). Orange needle-like crystals suitable for X-ray crystallography were obtained by recrystallization from DMF/diethyl ether. $\lambda_{max}$/nm (DMF): 378, 395, 452, 477. $C_{13}H_{13}N_3O_5Pt$ (486.36): calcd. C 32.11, H 2.69, N 8.64; found C 31.95, H 2.72, N 8.71.

**$(Bu_4N)[Pt^{II}(L^1)(Cl)_2]$ (4):** A 10% tetrabutylammonium hydroxide/methanol solution (250 mg, $9.6 \times 10^{-4}$ mol) was added to a stirred methanol solution (0.3 mL) of 9-hydroxyphenalenone ($HL^1$) (9.7 mg, $4.9 \times 10^{-5}$ mol). This solution was transferred to a test tube, and a methanol solution (2 mL) of $K_2PtCl_4$ (20 mg, $4.8 \times 10^{-5}$ mol) and 18-crown-6 (60 mg, $2.3 \times 10^{-5}$ mol) was layered over the solution and allowed to react slowly by diffusion. Over a few days, the color of the solution changed from orange to red, and a black powder was gradually deposited. The powder was removed by filtration, and the filtrate concentrated to a small volume on a rotary evaporator. After adding a small amount of water, the solution was cooled in an ice bath for about 1 h. A red powder precipitated, which was collected by filtration, washed with dichloromethane, and dried under vacuum. Red powder, 26% yield (8.8 mg). Needle-like crystals suitable for X-ray crystallography were obtained by recrystallization from DMF/diethyl ether. $\lambda_{max}$/nm (DMF): 350, 414, 438, 461. $C_{29}H_{43}Cl_2NO_2Pt$ (703.64): calcd. C 49.50, H 6.16, N 1.99; found C 48.95, H 6.07, N 2.06.

**Supporting Information:** (see footnote on the first page of this article) ORTEP drawings of the molecular structures of **1a**, **2a**, **3**, and **4**, and packing diagrams of **2b** and **4** are provided.

 © 2006 Wiley-VCH Verlag GmbH & Co. KGaA, Weinheim 

## Acknowledgments

This work was financially supported by "High-Tech Research Center" Project 2005–2009 from MEXT (Ministry of Education, Culture, Sports, Science and Technology). We thank Dr. Mikio Ueda (Toho University) for helpful suggestions on the preparations, Mr. Kazuya Okazawa (Toho University) for crystallographic analyses, and Ms. Ayako Morishima (JASCO Corp.) for measuring emission spectra. We also thank the Japan Science and Technology Agency for the loan of experimental equipment. Mr. Masaru Nakama (Warpstream, Tokyo) is also acknowledged for providing Web-DB systems. This work was performed using the facilities of the Institute for Solid State Physics at the University of Tokyo.

[1] a) V. W.-W. Yam, C.-K. Hui, K. M.-C. Wong, N. Zhu, K.-K. Cheung, *Organometallics* **2002**, *21*, 4326–4334, and references cited therein; b) J. Brooks, Y. Babayan, S. Lamansky, P. I. Djurovich, I. Tsyba, R. Ban, M. E. Thompson, *Inorg. Chem.* **2002**, *41*, 3055–3066, and references cited therein; c) A. J. Lees, *Chem. Rev.* **1987**, *87*, 711–743; d) D. M. Roundhill, *Photochemistry and Photophysics of Metal Complexes*, Plenum Press, New York, **1994**; e) M. Hissler, J. E. McGarrah, W. B. Connick, D. K. Geiger, S. D. Cummings, R. Eisenberg, *Coord. Chem. Rev.* **2000**, *208*, 115–137; f) A. Vogler, H. Kunkely, *Top. Curr. Chem.* **2001**, *213*, 143–182; g) G. L. Geoffroy, M. S. Wrighton, *Organometallic Photochemistry*, Academic Press, New York, **1979**.

[2] a) *Extended Linear Chain Compounds* (Ed.: J. S. Miller), vols. 1–3, Plenum Press, New York, **1982**–**1983**; b) K. Sakai, M. Takeshita, Y. Tanaka, T. Ue, M. Yanagisawa, M. Kosaka, T. Tsubomura, M. Ato, T. Nakano, *J. Am. Chem. Soc.* **1998**, *120*, 11353–11363; c) M. E. Prater, L. E. Pence, R. Clérac, G. M. Finniss, C. Campana, P. A. Senzier, D. Jérome, E. Canadell, K. R. Dunbar, *J. Am. Chem. Soc.* **1999**, *121*, 8005–8016; d) M. Kato, A. Omura, A. Toshikawa, S. Kishi, Y. Sugimoto, *Angew. Chem. Int. Ed.* **2002**, *41*, 3183–3185; e) H. Kishida, H. Matsuzaki, H. Okamoto, T. Manabe, M. Yamashita, Y. Taguchi, Y. Tokura, *Nature* **2000**, *405*, 929–932.

[3] R. C. Haddon, *Nature* **1975**, *256*, 394–396.

[4] K. Goto, T. Kubo, K. Yamamoto, K. Nakasuji, K. Sato, D. Shiomi, T. Takui, M. Kubota, T. Kobayashi, K. Yakushi, J. Ouyang, *J. Am. Chem. Soc.* **1999**, *121*, 1619–1620.

[5] a) M. E. Etkis, X. Chi, A. W. Cordes, R. C. Haddon, *Science* **2002**, *296*, 1443–1445; b) X. Chi, M. E. Itkis, K. Kirschbaum, A. A. Pinkerton, R. T. Oakley, A. W. Cordes, R. C. Haddon, *J. Am. Chem. Soc.* **2001**, *123*, 4041–4048.

[6] K. Nakasuji, M. Yamaguchi, I. Murata, *Chem. Lett.* **1983**, 1489–1490.

[7] a) R. Neidlein, Z. Behzadi, *Chem. Ztg.* **1976**, *100*, 388–389; b) R. Neidlein, Z. Behzadi, *Chem. Ztg.* **1978**, *102*, 150–152.

[8] Y. Demura, T. Kawato, H. Kanatomi, I. Murase, *Bull. Chem. Soc. Jpn.* **1975**, *48*, 2820–2824.

[9] R. C. Haddon, United States Patent, **2002**, 6,428,912.

[10] R. V. Deun, P. Nockemann, P. Fias, K. V. Hecke, L. V. Meervelt, K. Binnemans, *Chem. Commun.* **2005**, 590–592.

[11] a) A. Werner, *Ber. Dtsch. Chem. Ges.* **1901**, *34*, 2584–2593; b) G. T. Behnke, K. Nakamoto, *Inorg. Chem.* **1967**, *6*, 433–440.

[12] S. Okeya, S. Ooi, K. Matsumoto, Y. Nakamura, S. Kawaguchi, *Bull. Chem. Soc. Jpn.* **1981**, *54*, 1085–1095.

[13] N. A. Bailey, E. Coates, G. B. Robertson, F. Bonati, R. Ugo, *J. Chem. Soc., Chem. Commun.* **1967**, 1041–1042.

[14] G. T. Behnke, K. Nakamoto, *Inorg. Chem.* **1967**, *6*, 433–440.

[15] J. Conradie, G. J. Lamprecht, S. Otto, J. C. Swarts, *Inorg. Chim. Acta* **2002**, *328*, 191–203.

[16] N. Dunwoody, S.-S. Sun, A. J. Lees, *Inorg. Chem.* **2000**, *39*, 4442–4451.

[17] ORTEP-3 for Windows, L. J. Farrugia, *J. Appl. Crystallogr.* **1997**, *30*, 565.

[18] J. S. Miller, A. J. Epstein, *Prog. Inorg. Chem.* **1976**, *20*, 1–151.

[19] a) J. Real, J. C. Bayón, F. J. Lahoz, J. A. López, *J. Chem. Soc., Chem. Commun.* **1989**, 1889–1890; b) C. W. Lange, M. Földeàki, V. I. Nevodchikov, V. K. Cherkasov, G. A. Abakumov, C. G. Pierpont, *J. Am. Chem. Soc.* **1992**, *114*, 4220–4222.

[20] a) O. Gerlits, A. U. Kovalevsky, P. Coppens, *Dalton Trans.* **2004**, 3955–3962; b) M. Inga, S. Kenney, J. W. Kenney, G. A. Crosby, *Organometallics* **1986**, *5*, 230–234; c) K. R. Mann, N. S. Lewis, R. M. Williams, H. B. Gray, J. G. Gordon II, *Inorg. Chem.* **1978**, *17*, 828–834; d) A. L. Balch, *J. Am. Chem. Soc.* **1976**, *98*, 8049–8054.

[21] a) C.-M. Che, W.-M. Lee, H.-L. Kwong, V. W.-W. Yam, K.-C. Cho, *J. Chem. Soc., Dalton Trans.* **1990**, 1717–1722; b) V. M. Miskowski, G. L. Nobinger, D. S. Kliger, G. S. Hammond, N. S. Lewis, K. R. Mann, H. B. Gray, *J. Am. Chem. Soc.* **1978**, *100*, 485–488; c) K. R. Mann, J. A. Thich, R. A. Bell, C. L. Coyle, H. B. Gray, *Inorg. Chem.* **1980**, *19*, 2462–2468; d) S. J. Milder, R. A. Goldbeck, D. S. Kliger, H. B. Gray, *J. Am. Chem. Soc.* **1980**, *102*, 6761–6764; e) W. A. Fordyce, G. A. Crosby, *J. Am. Chem. Soc.* **1982**, *104*, 985–988.

[22] C.-M. Che, L.-Y. He, C.-K. Poon, T. C. W. Mak, *Inorg. Chem.* **1989**, *28*, 3081–3083.

[23] G. L. Geoffroy, M. S. Wrighton, G. S. Hammond, H. B. Gray, *J. Am. Chem. Soc.* **1974**, *96*, 3105–3108.

[24] M. Katoh, K. Miki, Y. Kai, N. Tanaka, N. Kasai, *Bull. Chem. Soc. Jpn.* **1981**, *54*, 611–612.

[25] a) J. Reedijk, *Chem. Rev.* **1999**, *99*, 2499–2510; b) R. R. Jamieson, S. J. Lippard, *Chem. Rev.* **1999**, *99*, 2467–2498; c) B. Rosenberg, L. Van Camp, J. E. Trosko, V. H. Mansour, *Nature* **1969**, *222*, 385–386.

[26] *Gaussian 98, Revision A.11*, M. J. Frisch, G. W. Trucks, H. B. Schlegel, G. E. Scuseria, M. A. Robb, J. R. Cheeseman, V. G. Zakrzewski, J. A. Montgomery, Jr., R. E. Stratmann, J. C. Burant, S. Dapprich, J. M. Millam, A. D. Daniels, K. N. Kudin, M. C. Strain, O. Farkas, J. Tomasi, V. Barone, M. Cossi, R. Cammi, B. Mennucci, C. Pomelli, C. Adamo, S. Clifford, J. Ochterski, G. A. Petersson, P. Y. Ayala, Q. Cui, K. Morokuma, P. Salvador, J. J. Dannenberg, D. K. Malick, A. D. Rabuck, K. Raghavachari, J. B. Foresman, J. Cioslowski, J. V. Ortiz, A. G. Baboul, B. B. Stefanov, G. Liu, A. Liashenko, P. Piskorz, I. Komaromi, R. Gomperts, R. L. Martin, D. J. Fox, T. Keith, M. A. Al-Laham, C. Y. Peng, A. Nanayakkara, M. Challacombe, P. M. W. Gill, B. Johnson, W. Chen, M. W. Wong, J. L. Andres, C. Gonzalez, M. Head-Gordon, E. S. Replogle, J. A. Pople, Gaussian, Inc., Pittsburgh, **2001**.

[27] J. M. Sargent, C. G. Taylor, *Br. J. Cancer* **1989**, *60*, 206–210.

[28] G. M. Sheldrick, *Program for the Solution for Crystal Structures*, University of Göttingen, Germany, **1997**.

[29] R. C. Haddon, R. Rayford, A. M. Hirani, *J. Org. Chem.* **1981**, *46*, 4587–4588.

[30] N. G. Buu-Hoi, D. Labit, *J. Org. Chem.* **1957**, *22*, 912–914.

Received: September 3, 2005
Published Online: December 13, 2005

 © 2006 Wiley-VCH Verlag GmbH & Co. KGaA, Weinheim 

DOI: 10.1002/ejic.200500787

# Reactivity of Carboranylacetylenes towards Cobalt Complexes

**Avijit Goswami,[a] Yong Nie,[a] Thomas Oeser,[b] and Walter Siebert*[a]**

*Dedicated to Professor Herbert Schumann on the occasion of his 70th birthday*

**Keywords:** Carboranes / Carboranylacetylenes / Cobalt / (Cyclobutadiene)cobalt complexes / (Cyclopentadienone)cobalt complexes

The reaction of 1,6-diiodo-$C_4B_2$ *nido*-carborane derivative **1** with $RC_2Li$ (R = Me, SPh) yields the corresponding carboranylacetylenes **2b**,**c**. Treatment of the $PPh_2$-substituted *nido*-carborane **3a** with $PhC_2ZnCl$ in the presence of a catalytic amount of $Pd(PPh_3)_4$ leads to the known basal-substituted *nido*-carboranylacetylene **2a**. The synthesis of apical-substituted compound **4b** is achieved by the substitution of **3b** by a $Pd^0$-catalyzed Nigishi-type cross-coupling reaction; the basal boron atom is blocked by the *n*-butyl group. The 1,3-dicarboranyl-substituted ($\eta^4$-cyclobutadiene)cobalt complexes **5a**,**c** are obtained from the reactions of **2a**,**c** with stoichiometric amounts of $CpCo(C_2H_4)_2$. The 1,6-dialkynyl carborane **6** reacts regioselectively at the basal acetylene group with a stoichiometric amount of $CpCo(CO)_2$ to give 1,3-dicarboranyl-substituted (cyclobutadiene)cobalt complex **7**. The dicarboranyl-substituted (cyclopentadienone)cobalt complex **8** is formed by the reaction of compound **4b** with $CpCo(CO)_2$. The new compounds are characterized by NMR spectroscopy, mass spectrometry, and by X-ray crystal structure analyses for **5a** and **8**.
(© Wiley-VCH Verlag GmbH & Co. KGaA, 69451 Weinheim, Germany, 2006)

## Introduction

Over the past decades numerous functionalized carboranes were synthesized,[1] and their properties have been extensively investigated by both theoretical[2] and experimental analyses.[3] A large number of carborane derivatives are used in medicinal and pharmaceutical applications.[4] The reactivity of carboranylacetylenes towards transition-metal complexes has received relatively little attention. In 1973, Hawthorne et al.[5] reported the first generation of 1,2,4-tris(*closo*-1,2-$C_2B_{10}H_{11}$-1-yl)benzene by the reaction of 1-ethynyl-1,2-carborane with a catalytic amount of bis(acrylonitrile)nickel(0). Michl et al.[6] presented a convenient route to synthesize tris(1,12-carboranyl)-substituted benzene derivatives by a palladium-catalyzed cross-coupling of three 1,12-dicarba-*closo*-dodecaboranyl units to a 1,3,5-trihalobenzene. In 1982, a series of σ-1-*ortho*- and σ-1-*meta*-carboranylacetylenides of copper, silver, palladium, platinum, and iron were synthesized by Zakharkin and his coworkers.[7] In 2003, Grimes[8] published an account on cluster formation between a 1,3,5-tris(carboranylacetylene)benzene and $Co_2(CO)_8$. Very recently, we reported cobalt-mediated dimerization reactions of apically alkynyl-substituted *closo*-$C_2B_5$ carboranes with cobalt complexes.[9] While the inherent scope and reaction efficiencies are found to be limited, the study introduces the attractive prospect that small alkynyl-substituted carboranes might be utilized for metal-mediated dimerization reactions. Here we report the synthesis of functionalized *nido*-$C_4B_2$ carboranes and the reactions of some of the alkynyl-substituted derivatives with cobalt complexes.

## Results and Discussion

### Preparation and Characterization of $C_4B_2$ *nido*-Carboranylacetylenes 2b,c

Because of the easy accessibility and high stability of the peralkylated 2,3,4,5-tetracarba-*nido*-hexaboranes(6)[10] (in comparison with the parent $C_4B_2H_6$[11]), their reactivity has drawn special attention.[12,13] To investigate substitution reactions of $C_4B_2$ *nido*-carboranes, functional groups other than alkyl or aryl groups are needed at the boron atom(s). Wrackmeyer et al.[12] and more recently our group[14] noticed that nucleophilic substitutions proceeded smoothly at the basal boron atom to give the corresponding carboranes with organyl, stannyl, diphenylphosphanyl, N-bonded (μ-NS)$Fe_2(CO)_6$ groups, as well as with the [$CpFe(CO)_2$] group. However, even the presence of an excess of nucleo-

[a] Anorganisch-Chemisches Institut der Universität Heidelberg, Im Neuenheimer Feld 270, 69120 Heidelberg, Germany
Fax: +49-6221-54-5609
E-mail: walter.siebert@urz.uni-heidelberg.de
[b] Organisch-Chemisches Institut der Universität Heidelberg, Im Neuenheimer Feld 270, 69120 Heidelberg, Germany
E-mail: oeser@uni-hd.de

 InterScience © 2006 Wiley-VCH Verlag GmbH & Co. KGaA, Weinheim 

phile was not enough to achieve substitution at the apical boron atom.[12,14]

Analogously, nucleophilic substitution reactions of 2,3,4,5-tetraethyl-1,6-diiodo-2,3,4,5-tetracarba-*nido*-hexaborane(6) (**1**) with $RC_2Li$ (R = Me, SPh) led to the corresponding basal-substituted carborane derivatives **2b**,**c** in high yields (Scheme 1). In agreement with the findings of Wrackmeyer et al.[12] and our recent results,[14] an excess of lithium acetylides did not effect additional substitution at the apical boron atom. Compounds **2b**,**c** (light yellow oils) were characterized by $^1$H-, $^{13}$C-, and $^{11}$B NMR spectroscopy, as well as by mass spectrometry. The *nido*-$C_4B_2$ framework is retained, and little difference is found in the $^1$H- and $^{13}$C NMR spectra in comparison to that of compound **1**. In the $^{11}$B NMR spectra of **2b**,**c** the basal boron atoms give signals at $\delta$ = 10–12 ppm, which are only slightly shifted downfield from that of **1** ($\delta$ = 5.5 ppm), while the shifts of the signals for the apical boron atoms are the same as that of the starting carborane **1** ($\delta$ = –52.7 ppm).

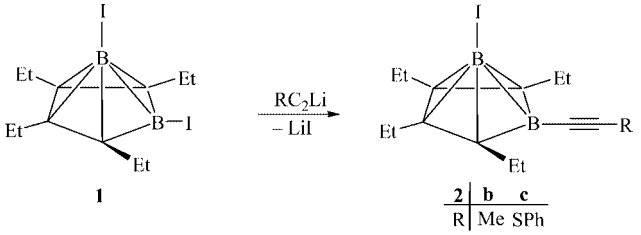


Scheme 1.

The $^1$H NMR spectrum of **2b** exhibits the signals ($\delta$ = 1.2–2.4 ppm) for the ethyl groups, in addition to the methyl resonance ($\delta$ = 1.98 ppm). In the $^{13}$C NMR spectrum, a signal ($\delta$ = 112.4 ppm) is found for the skeletal carbon atoms nonadjacent to the basal boron atom, whereas the signals for the boron-bound carbon atoms and for the acetylene carbon atoms are not observed. Similarly, the $^1$H NMR spectrum of **2c** shows the signals ($\delta$ = 1.3–2.4 ppm) for the ethyl groups along with the multiplets ($\delta$ = 7.2–7.6 ppm) for the aryl protons. The $^{13}$C NMR spectrum features a signal at $\delta$ = 113.0 ppm for the skeletal carbon atoms nonadjacent to the basal boron atom; however, the signals for the boron-bound carbon atoms and the acetylene carbon atoms are not detected. EI-MS data confirm the identity of carboranes **2b**,**c** through the appearance of the molecular ion peaks with the correct isotopic pattern.

### Substitution Reactions at the Apical Boron Atom of 3a

In most of the cases, the apical boron–halogen bonds are found to be inert;[12,14] however, substitution reactions can be achieved by $Pd^0$-catalyzed Nigishi-type cross-coupling reactions.[15] Analogously, an attempt to prepare the carborane **4a** by the reaction of **3a** with $PhC_2ZnCl$ in the presence of a catalytic amount of $Pd(PPh_3)_4$ was not successful, as the known carborane **2a**[14] was obtained by the substitution of $PPh_2$ at the basal boron atom (Scheme 2).

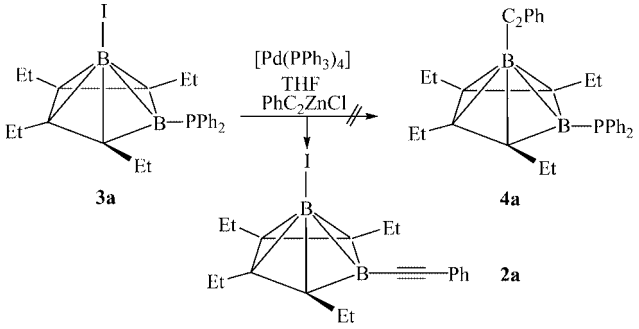


Scheme 2.

On the other hand, treatment of compound **3b** with $PhC_2ZnCl$ in the presence of a catalytic amount of $Pd(PPh_3)_4$ led to the expected carborane **4b** in moderate yield (Scheme 3). Compound **4b** (yellow oil) was characterized by $^1$H-, $^{13}$C-, and $^{11}$B NMR spectroscopy, as well as by mass spectrometry. The $^{11}$B NMR signal of the substituted apical boron atom is shifted only slightly downfield to $\delta$ = –50.5 ppm, whereas the chemical shift for the basal boron atom remains the same as that for **3b** ($\delta$ = 19 ppm). In the EI mass spectrum of **4b**, the molecular ion peak appears at *m*/*z* = 344 with the expected isotopic distribution.

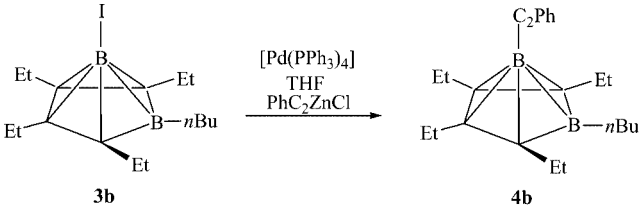


Scheme 3.

### Formation of Bis(carboranyl)cyclobutadiene Cobalt Complexes 5 and 7

No reaction was observed between carboranylacetylene derivatives **2** with catalytic and stoichiometric amounts of $CpCo(CO)_2$ in refluxing toluene for several days, as monitored by $^{11}$B NMR spectroscopy. However, adding $CpCo(C_2H_4)_2$ to the reaction mixture and refluxing for an additional two days, followed by column chromatography afforded the 1,3-dicarboranyl-substituted $CpCo(\eta^4$-cyclobutadiene) complexes **5a**,**c** (Scheme 4). No reaction was observed with **2d**,**e**.

The *trans*-1,3-isomers are sterically favored, as confirmed by the solid-state structure of **5a**. However, several known complexes have *cis*-bis(trimethylsilyl)cyclobutadiene ligands.[16] The stereochemistry problem was resolved unequivocally by the analysis of the major peaks in the mass spectra with respect to the degradation of the cyclobutadiene ring. In general, three different acetylene molecules are released from the molecular ion of the *cis* isomer, whereas only one acetylene molecule is released from the *trans* isomer.[17] Here, in both of **5a** and **5c**, only a single acetylene molecule was released from the molecular ion. Therefore,

 © 2006 Wiley-VCH Verlag GmbH & Co. KGaA, Weinheim 

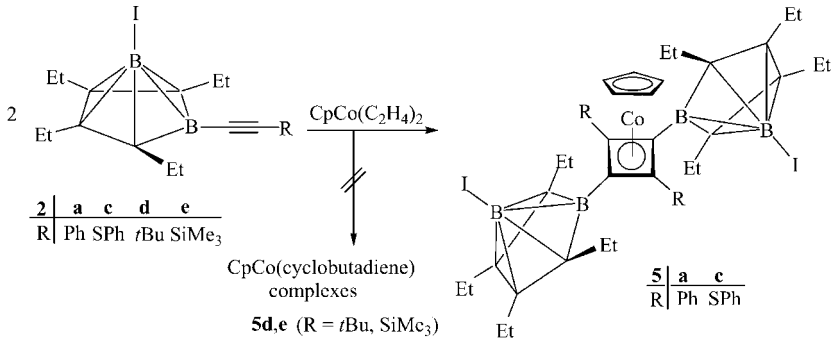


Scheme 4.

the mass spectra clearly provide evidence for *trans* isomers. The $^{11}$B NMR signals of **5a**,**c** for the basal boron atoms are shifted downfield to $\delta$ = 18 ppm, while the chemical shifts for the apical boron atoms remain the same as those for in the starting carboranes ($\delta$ = –52 ppm). The $^{1}$H NMR spectra of **5a**,**c** show the multiplets ($\delta$ = 7.1–7.6 ppm) for the aryl hydrogen atoms in addition to the Cp resonances ($\delta$ = 4.95 and 5.10 ppm). In the $^{13}$C NMR spectra, the signals ($\delta$ = 84–86 ppm) for the Cp–C are observed, but the signals for the four quaternary carbon atoms of the cyclobutadiene ring are not found.

The structure of **5a** was characterized by performing a single-crystal X-ray diffraction analysis. Two independent molecules were found in the asymmetric unit with very similar distances and angles; the structure of one molecule is shown in Figure 1. It reveals almost equal C–C bond lengths within the cyclobutadiene ring, and none of the phenyl groups lie in the $C_4$ plane. The conformation is highly influenced by the bulky $C_4B_2$ *nido*-carboranyl groups, which are oriented away from the metal center.

Regioselective reactivity of the carboranylacetylene derivative **6**[14] towards cobalt complexes $CpCoL_2$ (L = CO, $C_2H_4$) was observed. In the reactions of $CpCoL_2$ with the $C_4B_2$ *nido*-carborane **6** containing two acetylene moieties at the boron atoms, only the basal boron-substituted acetylene unit undergoes cyclobutadiene ring formation to give **7** (Scheme 5). The $^{11}$B NMR spectrum of complex **7** exhibits signals at $\delta$ = 15 and –50.4 ppm; the latter value for the apical boron atom is shifted slightly downfield relative to that of the starting carborane **6**. The mass spectrum shows the molecular ion peak with the expected isotopic pattern.

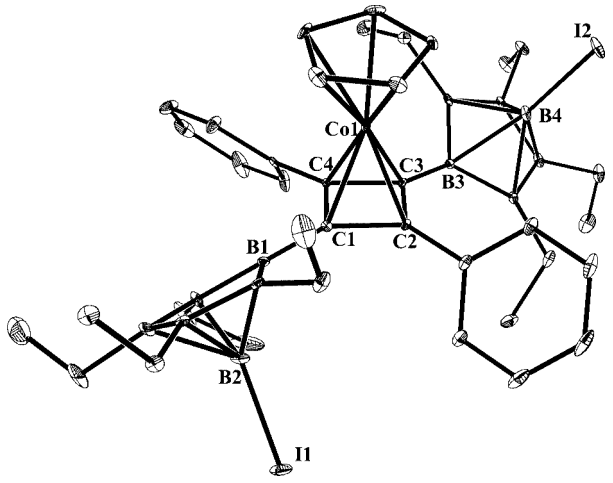


Figure 1. Molecular structure of **5a** in the solid state; hydrogen atoms are omitted for clarity; selected bond lengths [Å] and bond angles [°]: C1–B1 1.559(6), C3–B3 1.549(6), C1–C2 1.471(5), C2–C3 1.480(5), C3–C4 1.465(5), C4–C1 1.466(5), B2–I1 2.131(5), B4–I2 2.114(5), B1–B2 1.943(6), B3–B4 1.820(6), C1–C2–C3 91.2(3), C2–C3–C4 88.2(3), C3–C4–C1 92.0(3), C4–C1–C2 88.5(3), B1–B2–I1 144.5(3), B3–B4–I2 141.6(3). Only one of the two independent molecules is shown to provide a better overview.

### ($\eta^5$-Cyclopentadienyl)($\eta^4$-2,5-bis-carboranyl)(cyclopentadienone)cobalt Complex 8

To investigate the reactivity of the apical boron-bound acetylene group, the carboranylacetylene derivative **4b** was prepared (see earlier), in which the basal boron atom is blocked by the *n*-butyl group. Interestingly, the reaction of compound **4b** with a stoichiometric amount of CpCo-

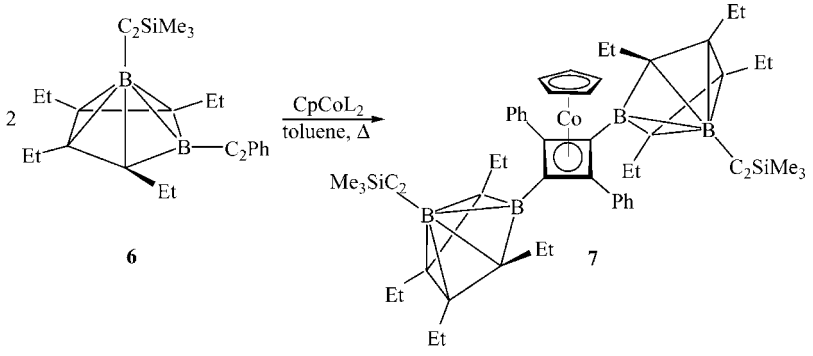


Scheme 5.

 © 2006 Wiley-VCH Verlag GmbH & Co. KGaA, Weinheim 

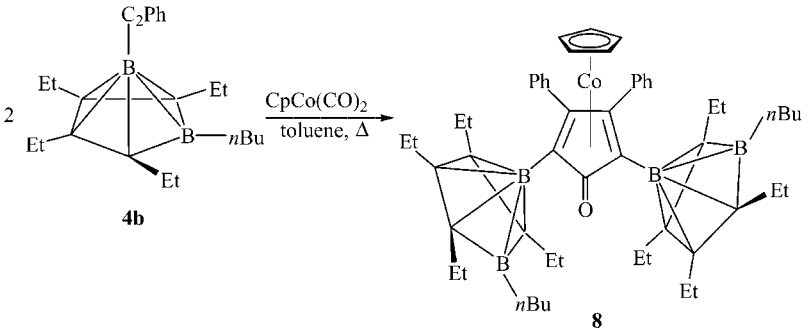


Scheme 6.

$(CO)_2$ led to the 2,5-dicarboranyl-substituted ($\eta^4$-cyclocyclopentadienone)cobalt complex **8** in good yield (Scheme 6). It was characterized by $^1$H-, $^{13}$C-, and $^{11}$B NMR spectroscopy, mass spectrometry, and X-ray crystal structure analysis. As expected, the $^{11}$B NMR signal of the apical boron atom is shifted downfield to $\delta$ = –44.4 ppm. The $^1$H NMR spectrum of **8** shows a singlet at $\delta$ = 4.95 ppm for $C_5H_5$, in addition to the phenyl group resonances ($\delta$ = 6.90–7.63 ppm). In the $^{13}$C NMR spectrum, the signals for the Cp–C and carbonyl groups are observed at $\delta$ = 81.7 and 188.1 ppm, respectively, while the signals for the cyclopentadienone ring are not found. The IR spectrum of **8** shows a band at $\tilde{\nu}$ = 1593 cm$^{-1}$, and the appearance of the molecular ion peak with the correct isotopic distribution in the EI-MS data confirms the identity.

The solid-state structure of **8** was characterized by performing a single-crystal X-ray diffraction analysis (Figure 2). Four molecules of **8** crystallized with one hexane molecule. As expected,[18] the structure reveals that the bulky carboranyl groups are bound to α-carbon atoms of the cyclopentadienone ring to reduce the steric strain.

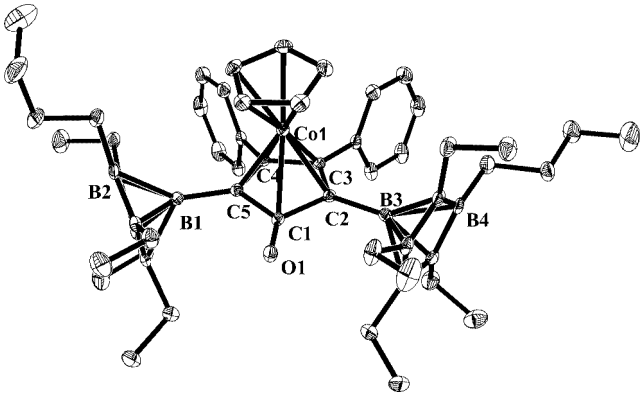


Figure 2. Molecular structure of **8** in the solid state; hydrogen atoms are omitted for clarity; selected bond lengths [Å] and bond angles [°]: C5–B1 1.549(5), C2–B3 1.560(5), C1–C2 1.490(5), C2–C3 1.427(5), C3–C4 1.452(5), C4–C5 1.447(5), C5–C1 1.488(5), C1–O1 1.241(4), B1–B2 1.878(6), B3–B4 1.851(6), C1–C2–C3 108.0(3), C2–C3–C4 108.6(3), C3–C4–C5 109.3(3), C4–C5–C1 106.7(3), C5–C1–C2 106.3(3), O1–C1–C5 126.5(3), O1–C1–C2 126.9(3).

## Conclusions

The reactions of carboranylacetylenes with catalytic and stoichiometric amounts of cobalt complexes $CpCoL_2$ (L = CO, $C_2H_4$) have been studied. Reactions in the presence of catalytic amounts of $[CpCoL_2]$ with carboranylacetylenes **2**, **4b**, and **6** do not lead to benzene derivatives, which can be explained on steric grounds. The ($\eta^4$-1,3-dicarboranylcyclobutadiene)cobalt complexes **5a**,**c** are formed by the reactions of **2a**,**c** with stoichiometric amounts of $CpCo(C_2H_4)_2$. Regioselective reactions occur between $CpCoL_2$ and the $C_4B_2$ *nido*-carborane **6**. Only the basal-substituted borylacetylene moiety of compound **6** is involved in cyclobutadiene ring formation, whereas the apical-substituted borylacetylene unit remains unreacted. The reaction of carboranylacetylene **4b**, carrying an *n*-butyl group at the basal boron atom, with $CpCo(CO)_2$ leads to the (cyclopentadienone)cobalt complex **8**. The cobalt complexes **5**, **7**, and **8** are stable at room temperature and are resistant to light, oxygen, and moisture.

## Experimental Section

**General:** All reactions were performed under nitrogen using standard Schlenk techniques. Solvents were dried with the appropriate drying agents and distilled under nitrogen. Glassware was dried with a heat gun under high vacuum. $^1$H-, $^{13}$C- and $^{11}$B NMR spectra were recorded with a Bruker AC 200 spectrometer. $^1$H- and $^{13}$C NMR spectra were referenced to $(CH_3)_4Si$, and $^{11}$B NMR spectra were referenced to $F_3B{\cdot}OEt_2$. IR spectra were recorded with a Bruker IFS 28 FT spectrometer. Mass spectra were obtained with Finnigan MAT 8230 plus spectrometers using the EI technique. Melting points (uncorrected) were obtained with a Büchi apparatus, using capillaries that were filled under nitrogen and sealed. The *nido*-carboranes **1**,[19] **2a**,**d**,**e**,[14] **3a**,[14] **6**,[14] and $CpCo(C_2H_4)_2$[20] were prepared according to literature procedures. $CpCo(CO)_2$ was purchased from Aldrich®.

**General Procedure for Basal Boron-Substituted Carboranylacetylenes 2b,c**

An appropriate solution of lithium acetylide in hexane (30 mL) was cooled to –40 °C and added by syringe to a solution of the *nido*-carborane **1** in hexane (20 mL) at –78 °C. The mixture was warmed to room temp. and stirred for 2 d. After filtration, the light yellow solution was dried in vacuo to give a yellow oil.

**2,3,4,5-Tetraethyl-1-iodo-6-methylethynyl-2,3,4,5-tetracarba-*nido*-hexaborane(6) (2b):** Starting materials: compound **1** (0.9 g, 2.05 mmol) and $MeC_2Li$ (0.23 g, 5.0 mmol). Yield: 0.5 g (69%), yellow oil. $^1$H NMR (200.1 MHz, $CDCl_3$): $\delta$ = 1.25 (t, $^3J_{H,H}$ = 7.6 Hz, 12 H, $CH_2CH_3$), 1.98 (s, 3 H, Me), 2.22 (m, 8 H, $CH_2CH_3$) ppm. $^{13}$C NMR (50.3 MHz, $CDCl_3$): $\delta$ = 13.4, 14.3 ($CH_2CH_3$), 18.2

 © 2006 Wiley-VCH Verlag GmbH & Co. KGaA, Weinheim 

(Me), 18.1, 19.6 ($CH_2CH_3$), 112.4 (skeletal carbon atoms nonadjacent to the basal boron) ppm; skeletal carbon atoms adjacent to the basal boron and alkynyl carbon atoms were not observed. $^{11}B$ NMR (64.2 MHz, $CDCl_3$): $\delta$ = 10 (br., $B_{basal}$), 52.7 (s, $B_{apical}$) ppm. MS (EI, 70 eV): *m*/*z* (%) = 352 (100) [$M^+$], 225 (20) [$M^+$ – I]. MS (HR-EI, 70 eV): *m*/*z* (%) = 352.1031 (100) [$M^+$], $^{12}C_{15}{}^{1}H_{23}{}^{11}B_2{}^{127}I$: 352.1030; $\Delta$mmu = 0.1.

**2,3,4,5-Tetraethyl-1-iodo-6-phenylthioethynyl-2,3,4,5-tetracarba-*nido*-hexaborane(6) (2c):** Starting materials: compound **1** (0.9 g, 2.05 mmol) and $PhSC_2Li$ (0.7 g, 5.0 mmol). Yield: 0.65 g (71%), yellow oil. $^1H$ NMR (200.1 MHz, $CDCl_3$): $\delta$ = 1.29, 1.31 (t, $^3J_{H,H}$ = 7.5 Hz, 2×6 H, $CH_3$), 2.05, 2.38 (m, 2×4 H, $CH_2$), 7.22–7.61 (m, 5 H, SPh) ppm. $^{13}C$ NMR (50.3 MHz, $CDCl_3$): $\delta$ = 13.5, 14.6 ($CH_3$), 18.5, 19.9 ($CH_2$), 113.0 (skeletal carbon atoms nonadjacent to the basal boron), 127.6, 128.1, 131.7 (SPh) ppm; skeletal carbon atoms adjacent to the basal boron and alkynyl carbon atoms were not observed. $^{11}B$ NMR (64.2 MHz, $CDCl_3$): $\delta$ = 12 (br., $B_{basal}$), –52.7 (s, $B_{apical}$) ppm. MS (EI, 70 eV): *m*/*z* (%) = 446 (100) [$M^+$], 319 (10) [$M^+$ – I]. MS (HR-EI, 70 eV): *m*/*z* (%) = 446.0922 (58) [$M^+$], $^{12}C_{20}{}^{1}H_{25}{}^{11}B_2{}^{127}I^{32}S$: 446.0908; $\Delta$mmu = 1.4.

**6-Butyl-2,3,4,5-tetraethyl-1-iodo-2,3,4,5-tetracarba-*nido*-hexaborane(6) (3b):** A solution of *n*BuLi (1.7 mL, 4.2 mmol) was very slowly added to a solution of *nido*-carborane **1** (0.92 g, 2.1 mmol) in hexane (50 mL) at –78 °C. The mixture was warmed to room temp. and was stirred for 20 h. After filtration, the slightly yellow filtrate was dried in vacuo and distilled at 43 °C/0.04 mbar to give a yellow oil. Yield: 0.70 g (90%). $^1H$ NMR (200.1 MHz, $CDCl_3$): $\delta$ = 0.89, 1.45, 1.95 (m, 9 H, *n*Bu), 1.19, 1.40 (t, 2×6 H, $CH_2CH_3$), 2.08, 2.36 (m, 2×4 H, $CH_2CH_3$) ppm. $^{13}C$ NMR (50.3 MHz, $CDCl_3$): $\delta$ = 13.7, 14.2 ($CH_3$), 18.5, 19.0 ($CH_2$), 16.0, 17.6, 25.9, 26.6 (*n*Bu), 112.9 (skeletal carbon atoms nonadjacent to the basal boron) ppm. $^{11}B$ NMR (64.2 MHz, $CDCl_3$): $\delta$ = 19 (br., $B_{basal}$), –52.6 (s, $B_{apical}$) ppm. MS (EI, 70 eV): *m*/*z* (%) = 370 (100) [$M^+$], 243 (10) [$M^+$ – I].

**Attempt to Prepare 2,3,4,5-Tetraethyl-1-phenylethnyl-6-diphenylphosphanyl-*nido*-carborane (4a):** To lithium phenylacetlylide (0.54 g, 5.0 mmol) in THF (15 mL) at room temp. was added $ZnCl_2$ (0.68 g, 5.0 mmol), and the solution was stirred for 3 h. The solution was then added to a mixture of **3a** (1.24 g, 2.5 mmol) and $Pd(PPh_3)_4$ (0.04 g, 0.034 mmol), and the resulting yellow mixture was heated at reflux for 10 d. The solvent was removed under high vacuum, the black residue was extracted with hexane (2×20 mL) and filtered. The yellow filtrate was dried in vacuo to give a yellow viscous oil. Yield: 0.51 g (49%) **2a**. NMR and mass spectroscopic data were in agreement with the previously reported result.[19]

**6-Butyl-2,3,4,5-tetraethyl-1-phenylethynyl-2,3,4,5-tetracarba-*nido*-hexaborane(6) (4b):** To lithium phenylacetlylide (0.54 g, 5.0 mmol) in THF (30 mL) at room temp. was added $ZnCl_2$ (0.68 g, 5.0 mmol), and the solution was stirred for 3 h. The solution was then added to a mixture of **3b** (0.85 g, 2.3 mmol) and $Pd(PPh_3)_4$ (0.04 g, 0.034 mmol) in THF (30 mL). The resulting yellow mixture was heated at reflux for 6 d. After evaporation of the solvent, the black residue was extracted with hexane (2×20 mL) and filtered. The yellow filtrate was dried in vacuo to give a yellow oil. Yield: 0.5 g (63%). $^1H$ NMR (200.1 MHz, $CDCl_3$): $\delta$ = 0.95, 1.52, 2.02 (m, 9 H, *n*Bu), 1.19, 1.25 (t, 2×6 H, $CH_2CH_3$), 2.10, 2.45 (m, 2×4 H, $CH_2CH_3$), 7.22–7.35 (m, 5 H, Ph) ppm. $^{13}C$ NMR (50.3 MHz, $CDCl_3$): $\delta$ = 14.1, 15.4, 22.6, 26.3 (*n*Bu), 17.4, 18.5 ($CH_3$), 29.7, 30.5 ($CH_2$), 112.1 (skeletal carbon atoms nonadjacent to the basal boron), 127.7, 128.0, 131.9 (Ph) ppm. $^{11}B$ NMR (64.2 MHz, $CDCl_3$): $\delta$ = 20 (br., $B_{basal}$), –50.5 (s, $B_{apical}$) ppm. MS (EI, 70 eV): *m*/*z* (%) = 344 (100) [$M^+$].

**General Procedure for Cobalt Complexes 5a,c**

To an appropriate solution of carboranylacetylene in toluene was added a portion of $CpCo(CO)_2$ at room temp. The deep-red mixture was heated at reflux and monitored by $^{11}B$ NMR spectroscopy, indicating that no reaction took place. After 4 d, one portion of $CpCo(C_2H_4)_2$ was added, and the resulting mixture was again heated at 120 °C for another 2 d. After completion of the reaction, the solvent was removed to dryness, and the crude product was purified by column chromatography on silica gel to give two fractions. Using hexane as the eluant, unreacted $CpCo(CO)_2$ and $CpCo(C_2H_4)_2$ were obtained. The second fraction (toluene) contained the corresponding (cyclobutadiene)cobalt complex.

**{η⁴-Bis[2,3,4,5-tetraethyl-1-iodo-2,3,4,5-tetracarba-*nido*-hexaboranyl]diphenyl(cyclobutadiene)}(η⁵-cyclopentadienyl)cobalt(I) (5a):** Starting materials: compound **2a** (0.50 g, 1.2 mmol), $CpCo(CO)_2$ (0.10 g, 0.6 mmol), and $CpCo(C_2H_4)_2$ (0.10 g, 0.6 mmol). Yield: 0.40 g (76%), yellow crystals, m.p. 124–125 °C. Compound **5a** was recrystallized from a solution of toluene at –20 °C. $^1H$ NMR (200.1 MHz, $CDCl_3$): $\delta$ = 1.3 (m, 24 H, $CH_3$), 2.3 (m, 16 H, $CH_2$), 5.10 (s, 5 H, Cp–H), 7.25, 7.55 (m, 10 H, Ph) ppm. $^{13}C$ NMR (50.3 MHz, $CDCl_3$): $\delta$ = 13.4, 14.3 ($CH_3$), 18.4, 19.8 ($CH_2$), 84.5 (Cp–C), 113.0 (skeletal carbon atoms nonadjacent to the basal boron), 127.6, 128.0, 131.7 (Ph) ppm; quaternary carbon atoms were not found. $^{11}B$NMR (64.2 MHz, $CDCl_3$): $\delta$ = 18 (br., $B_{basal}$), –52.0 (s, $B_{apical}$) ppm. MS (EI, 70 eV): *m*/*z* (%) = 952 (100) [$M^+$], 538 (10) [$M^+$ – $Et_4C_4B_2I(C_2Ph)$]. MS (HR-EI, 70 eV): *m*/*z* = 952.2087 [$M^+$], $^{12}C_{45}{}^{1}H_{55}{}^{11}B_4{}^{59}Co^{127}I_2$: 952.2097; $\Delta$mmu = –1.0.

**{η⁴-Bis[2,3,4,5-tetraethyl-1-iodo-2,3,4,5-tetracarba-*nido*-hexaboranyl]diphenylthio(cyclobutadiene)}(η⁵-cyclopentadienyl)cobalt(I) (5c):** Starting materials: compound **2c** (0.40 g, 1.2 mmol), $CpCo(CO)_2$ (0.10 g, 0.6 mmol), and $CpCo(C_2H_4)_2$ (0.10 g, 0.6 mmol). Yield: 0.25 g (54%), brown-red oil. $^1H$ NMR (200.1 MHz, $CDCl_3$): $\delta$ = 1.26, 1.35 (t, 2×12 H, $CH_3$), 2.10, 2.35 (m, 2×8 H, $CH_2$), 4.95 (s, 5 H, Cp–H), 7.15–7.55 (m, 10 H, SPh) ppm. $^{13}C$ NMR (50.3 MHz, $CDCl_3$): $\delta$ = 13.6, 15.7 ($CH_3$), 19.1, 19.7 ($CH_2$), 85.4 (Cp–C), 115.5 (skeletal carbon atoms nonadjacent to the basal boron), 125.0, 128.8, 131.0 (SPh) ppm; skeletal carbon atoms adjacent to the basal boron and quaternary carbon atoms were not found. $^{11}B$NMR (64.2 MHz, $CDCl_3$): $\delta$ = 18 (br., $B_{basal}$), –52.1 (s, $B_{apical}$) ppm. MS (EI, 70 eV): *m*/*z* (%) = 1016 (70) [$M^+$], 570 (5) [$M^+$ – $Et_4C_4B_2I(C_2SPh)$]. MS (HR-EI, 70 eV): *m*/*z* = 1016.1550 [$M^+$], $^{12}C_{45}{}^{1}H_{55}{}^{11}B_4{}^{59}Co^{127}I_2{}^{32}S_2$: 1016.1538; $\Delta$mmu = 1.2.

**CpCo[Bis(carboranyl)cyclobutadiene] (7):** To a solution of **6** (0.053 g, 0.14 mmol) in toluene (8 mL) was added a portion of $CpCo(CO)_2$ (0.04 g, 0.22 mmol) at room temp. The deep-red reaction mixture was heated at reflux for 9 d. The brown reaction mixture was cooled and filtered through a pad of sea sand; the yellow-brown filtrate was dried in vacuo to give a brown oil. Yield: 0.056 g (89%). $^{11}B$ NMR (64.2 MHz, $CDCl_3$): $\delta$ = 15 (br, $B_{basal}$), –50.4 (s, $B_{apical}$) ppm. MS (EI, 70 eV): *m*/*z* (%) = 892 (100) [$M^+$]. MS (HR-EI, 70 eV): *m*/*z* = 892.4999 [$M^+$], $^{12}C_{55}{}^{1}H_{73}{}^{11}B_4{}^{59}Co^{28}Si_2$: 892.4955; $\Delta$mmu = 4.4.

**(η⁵-Cyclopentadienyl)(η⁴-2,5-bis-carboranyl-3,4-diphenylcyclopentadienone)cobalt(I) (8):** Carboranylacetylene **4b** (0.45 g, 1.3 mmol) and (η⁵-cyclopentadienyl)(dicarbonyl)cobalt(I) (0.11 g, 0.65 mmol) were dissolved in toluene (30 mL). The resulting dark-red mixture was stirred at 120 °C for 3 d. After cooling, the solvent was removed under high vacuum, and the black residue was purified by column chromatography ($SiO_2$, hexane). Cobalt complex **8** was recrystallized from a solution of hexane at –20 °C. Yield: 0.4 g (73%), brown solid, m.p. 133–136 °C. $^1H$ NMR (200.1 MHz, $CDCl_3$): $\delta$ = 1.20 (m, 2×12 H, $CH_2CH_3$), 0.90, 1.85, 2.12 (m, 2×9

 © 2006 Wiley-VCH Verlag GmbH & Co. KGaA, Weinheim 

Table 1. Crystal data and structure refinement for **5a** and **8**.

| | **5a** | **8** |
|---|---|---|
| Empirical formula | $C_{45}H_{55}B_4CoI_2$ | $C_{55}C_{54}H_{73}B_4CoO + ¼\ C_6H_{14}$ |
| Formula weight | 951.86 | 861.84 |
| Crystal system | monoclinic | triclinic |
| Space group | $P2_1/c$ | $P\bar{1}$ |
| $a$ [Å] | 18.045(1) | 11.0954(2) |
| $b$ [Å] | 27.847(2) | 13.7519(3) |
| $c$ [Å] | 17.133(1) | 18.9481(4) |
| $\alpha$ [°] | 90 | 108.757(1) |
| $\beta$ [°] | 93.395(2) | 103.617(1) |
| $\gamma$ [°] | 90 | 94.669(1) |
| Volume [Å$^3$] | 8594(1) | 2621.6(1) |
| $Z$ | 8 | 2 |
| Calcd. density [g/cm$^3$] | 1.47 | 1.09 |
| $\mu$ [mm$^{-1}$] | 1.87 | 0.36 |
| $F$(000) | 3824 | 929 |
| Crystal size [mm] | 0.29×0.09×0.08 | 0.3×0.16×0.06 |
| $\Theta_{max}$ [°] | 28.3 | 22.0 |
| Index ranges | –24/24, –36/37, 22/22 | –11/11, –14/14, –19/19 |
| Reflections: | | |
| Collected | 87065 | 17190 |
| Independent ($R_{int}$) | 21131(0.051) | 6392 (0.042) |
| Observed [$I > 2\sigma I$] | 18167 | 4865 |
| Parameters | 953 | 574 |
| Goodness-of-fit on $F^2$ | 1.24 | 1.02 |
| $R_1$ [$I > 2\sigma I$] | 0.064 | 0.048 |
| $wR_2$ [$I > 2\sigma I$] | 0.101 | 0.129 |
| $T$ [K] | 100(2) | 200(2) |
| Residual electron density [e/A$^3$] | 2.42/–2.17 | 0.76/–0.29 |

H, *n*Bu), 2.10, 2.35 (m, 2×8 H, $CH_2$), 4.95 (s, 5 H, Cp–H), 6.90, 7.45, 7.63 (m, 2×5 H, Ph) ppm. $^{13}$C NMR (50.3 MHz, $CDCl_3$): $\delta$ = 14.1, 14.9 ($CH_3$), 19.3, 19.9 ($CH_2$), 17.1, 19.5, 21.2, 25.3 (*n*Bu), 81.7 (Cp–C), 113.5 (skeletal carbon atoms nonadjacent to the basal boron), 126.9, 128.8, 132.0 (Ph), 188.1 (CO) ppm; skeletal carbon atoms adjacent to the basal boron and quaternary carbon atoms were not found. $^{11}$BNMR (64.2 MHz, $CDCl_3$): $\delta$ = 18 (br., $B_{basal}$), –44.4 (s, $B_{apical}$) ppm. IR (hexane): $\tilde{\nu}$ = 1593 (s) cm$^{-1}$. MS (EI, 70 eV): *m*/*z* (%) = 840 (50) [M$^+$], 812 (100) [M$^+$ – CO]. MS (HR-EI, 70 eV): *m*/*z* = 840.5334 [M$^+$], $^{12}C_{54}{}^1H_{73}{}^{11}B_4{}^{59}Co^{16}O$: 840.5365; $\Delta$mmu = –3.1.

**X-ray Crystal Structure Determinations of 5a and 8:** Crystal data and details of the structure determinations are listed in Table 1. Reflections were collected with Bruker SMART APEX (**5a**) and Bruker-AXS SMART 1000 (**8**) diffractometers (Mo-$K_\alpha$ radiation, $\lambda$ = 0.71073 Å, graphite monochromator, $\omega$-scan). Empirical absorption corrections were applied. The structure was solved by direct methods and refined by least-square methods based on $F^2$ with all measured reflections (SHELXTL 6.12).[21] All non-hydrogen atoms were refined anisotropically. CCDC-276980 (**5a**) and CCDC-276981 (**8**) contain the supplementary crystallographic data for this paper. These data can be obtained free of charge from The Cambridge Crystallographic Data Centre via www.ccdc.cam.ac.uk/data_request/cif.

## Acknowledgments

This work was supported by the Deutsche Forschungsgemeinschaft (SFB 623) and the Fonds der Chemischen Industrie.

[1] a) D. S. Matteson, *J. Organomet. Chem.* **1973**, *58*, 1–48; b) R. N. Grimes, *Pure Appl. Chem.* **1974**, *39*, 455–474; c) M. S. Gaunt, A. G. Massey, *Educ. Chem.* **1974**, *11*, 118–121; d) E. V. Leonova, *Uspekhi Khimii* **1980**, 283–326; e) V. V. Korshak, S. A. Pavlova, P. N. Gribkova, T. N. Balykova, *Acta Polymerica* **1981**, *32*, 61–74; f) K. Wade, H. M. Colquhoun, M. G. Davidson, M. A. Fox, W. R. Gill, P. L. Herbertson, T. G. Hibbert, J. A. H. Macbride, R. J. Peace, G. P. Rivers, *Royal Soc., Chem.* **1997**, *201*, 289–296; g) R. N. Grimes, *Pure Appl. Chem.* **2003**, *75*, 1211–1218; h) W. Siebert, C.-J. Maier, A. Maier, P. Greiwe, M. J. Bayer, M. Hoffmann, H. Pritzkow, *Pure Appl. Chem.* **2003**, *75*, 1277–1286; i) Z. Xie, *Pure Appl. Chem.* **2003**, *75*, 1335–1341; j) P. A. Jelliss, *Organomet. Chem.* **2004**, *31*, 112–129; k) G.-X. Jin, *Coord. Chem. Rev.* **2004**, *248*, 587–602.

[2] A. Berndt, M. Hoffmann, W. Siebert, B. Wrackmeyer in *Molecular Clusters of the Main Group Elements* (Eds.: D. Driess, H. Nöth), Wiley, **2004**, pp. 267–309.

[3] a) A. R. Oki, H. Zhang, N. S. Hosmane, H. Ro, W. E. Hatfield, *J. Am. Chem. Soc.* **1991**, *113*, 8531–8532; b) W. Haubold, W. Keller, G. Sawitzki, *Angew. Chem.* **1988**, *100*, 958–959; *Angew. Chem. Int. Ed. Engl.* **1988**, *27*, 925; c) A. E. Goeta, J. A. K. Howard, A. K. Hughes, A. L. Johnson, K. Wade, *Chem. Commun.* **1998**, 1713–1714; d) J. M. Russell, H. Sabat, R. N. Grimes, *Organometallics* **2002**, *21*, 4113–4128; e) N. S. Hosmane, J. A. Maguier, *Eur. J. Inorg. Chem.* **2003**, 3989–3999; f) R. N. Grimes, *J. Chem. Educ.* **2004**, *81*, 657–672.

[4] a) J. F. Valliant, K. J. Guenther, A. S. King, P. Morel, P. Schaffer, O. O. Sogbein, K. A. Stephenson, *Coord. Chem. Rev.* **2002**, *232*, 173–230; b) V. Tolmachev, S. Sjöberg, *Collect. Czech. Chem. Commun.* **2002**, *67*, 913–915.

[5] K. P. Callahan, M. F. Hawthorne, *J. Am. Chem. Soc.* **1973**, *95*, 4574–4580.

[6] U. Schöberl, T. F. Magnera, R. M. Harrison, F. Fleischer, J. L. Pflug, P. F. H. Schwab, X. Meng, D. Lipiak, B. C. Noll, V. S. Allured, T. Rudalevige, S. Lee, J. Michl, *J. Am. Chem. Soc.* **1997**, *119*, 3907–3917.

[7] L. I. Zakharkin, A. I. Kovredov, V. A. Ol'shevskaya, *Seriya Khim.* **1982**, *3*, 673–675.

 © 2006 Wiley-VCH Verlag GmbH & Co. KGaA, Weinheim 

[8] H. Yao, M. Sabat, R. N. Grimes, *Organometallics* **2003**, *22*, 2581–2593.
[9] Y. Nie, A. Goswami, W. Siebert, *Z. Naturforsch.* **2005**, *60b*, 1–6.
[10] a) P. Binger, *Tetrahedron Lett.* **1966**, *7*, 2675–2680; b) P. Binger, *Angew. Chem.* **1968**, *80*, 288–289; *Angew. Chem. Int. Ed. Engl.* **1968**, *7*, 286; c) R. Köster, M. A. Grassberger, *Angew. Chem.* **1967**, *79*, 197–252; *Angew. Chem. Int. Ed. Engl.* **1967**, *6*, 218–240; d) L. Killian, B. Wrackmeyer, *J. Organomet. Chem.* **1977**, *132*, 213–221; e) H. O. Berger, H. Nöth, B. Wrackmeyer, *Chem. Ber.* **1979**, *112*, 2884–2893.
[11] a) T. P. Onak, G. T. F. Wong, *J. Am. Chem. Soc.* **1970**, *92*, 5226; b) V. R. Miller, R. N. Grimes, *Inorg. Chem.* **1972**, *11*, 862–865.
[12] a) B. Wrackmeyer, G. Kehr, *J. Organomet. Chem.* **1995**, *501*, 87–93; b) B. Wrackmeyer, A. Glöckle, *Z. Naturforsch.* **1996**, *51b*, 859–864; c) B. Wrackmeyer, A. Glöckle, *Main Group Metal Chem.* **1997**, *20*, 181–189; d) B. Wrackmeyer, G. Kehr, A. Glöckle, *Phosphorus, Sulfur Silicon Relat. Elem.* **1997**, *131*, 25–35; e) M. Herberhold, U. Bertholdt, W. Milius, A. Glöckle, B. Wrackmeyer, *Chem. Commun.* **1996**, 1219–1220.
[13] C. Balzereit, H. J. Winkler, W. Massa, A. Berndt, *Angew. Chem.* **1994**, *106*, 1579–1581; *Angew. Chem. Int. Ed. Engl.* **1994**, *33*, 1487–1489.
[14] Y. Nie, H. Pritzkow, W. Siebert, *Eur. J. Inorg. Chem.* **2004**, 2425–2433.
[15] E.-I. Negishi, L. Anastasia, *Chem. Rev.* **2003**, *103*, 1979–2017.
[16] a) E. R. F. Gesing, K. P. C. Vollhardt, *J. Organomet. Chem.* **1981**, *217*, 105–118; b) J. R. Fritch, K. P. C. Vollhardt, *J. Am. Chem. Soc.* **1978**, *100*, 3643–3644.
[17] H. Sakurai, J. Hayashi, *J. Organomet. Chem.* **1972**, *39*, 365–370.
[18] J. H. Hardesty, J. B. Koerner, T. A. Albright, G. Y. Lee, *J. Am. Chem. Soc.* **1999**, *121*, 6055–6067.
[19] Y. Nie, S. Schwiegk, H. Pritzkow, W. Siebert, *Eur. J. Inorg. Chem.* **2004**, 1630–1638.
[20] a) K. Jonas, E. Deffense, D. Habermann, *Angew. Chem.* **1983**, *95*, 729; *Angew. Chem. Int. Ed. Engl.* **1983**, *22*, 716; b) J. K. Cammack, S. Jalisatgi, A. J. Matzger, A. Negron, K. P. C. Vollhardt, *J. Org. Chem.* **1996**, *61*, 4798–4800.
[21] *SHELXTL 6.12*, Bruker AXS, Madison, WI, USA, **2001**.

Received: September 6, 2005
Published Online: December 16, 2005

 © 2006 Wiley-VCH Verlag GmbH & Co. KGaA, Weinheim 

DOI: 10.1002/ejic.200500972

# Probing the Dinucleating Behaviour of a Bis-Bidentate Ligand: Synthesis and Characterisation of Some Di- and Mononuclear Cobalt(II), Nickel(II), Copper(II) and Zinc(II) Complexes of 3,5-Di(2-pyridyl)-4-(1*H*-pyrrol-1-yl)-4*H*-1,2,4-triazole

**Marco H. Klingele,[a] Peter D. W. Boyd,[b] Boujemaa Moubaraki,[c] Keith S. Murray,[c] and Sally Brooker*[a]**

**Keywords:** 1,2,4-Triazoles / Bridging ligands / N ligands / Copper complexes / Cobalt complexes / Nickel complexes / Zinc complexes / Magnetic properties

As a probe of the dinucleating ability of the known but little studied bis-bidentate ligand 3,5-di(2-pyridyl)-4-(1*H*-pyrrol-1-yl)-4*H*-1,2,4-triazole (pldpt) its reactivity towards $MX_2{\cdot}6H_2O$ (M = $Co^{II}$, $Ni^{II}$ and $Zn^{II}$; X = $ClO_4^-$ and $BF_4^-$) as well as $Cu(ClO_4)_2{\cdot}6H_2O$, in a 1:1 metal-to-ligand molar ratio in MeCN, has been investigated. In the case of $Co^{II}$, $Ni^{II}$ and $Zn^{II}$, these reactions gave dinuclear complexes $M^{II}_2(pldpt)_2X_4(MeCN)_m(H_2O)_n$, whereas for $Cu^{II}$ initially the mononuclear complex $[Cu^{II}(pldpt)_2(ClO_4)_2]$ was isolated, followed by the dinuclear complex $[Cu^{II}_2(pldpt)_2(MeCN)_2(H_2O)_2](ClO_4)_4$. The use of the strongly polar aprotic co-solvent DMF resulted in the partial breakdown of the initial dinuclear entities in the case of $Co^{II}$ and $Ni^{II}$ but not in the case of $Zn^{II}$. In all five of the structurally characterised dinuclear complexes the $(N',N^1,N^2,N'')_2$ double-bridging coordination mode is realised with distorted octahedral $N_4Y_2$-coordinated metal centres (Y = DMF, $H_2O$ or MeCN). The two mononuclear complexes feature the common *trans*-$(N',N^1)_2$ coordination mode with axial DMF or $ClO_4^-$ co-ligands. The near-perpendicular orientation [82.4(3)–88.8(1)°] of the π-electron-rich 4-(1*H*-pyrrol-1-yl) substituent with respect to the triazole ring of pldpt, observed in all of these structures, means that no π-interactions are expected between these rings so any electronic interaction is likely to be small. Whether a di- or mononuclear complex of pldpt forms is therefore primarily determined by a number of other factors, including the reaction stoichiometry, the nature of the counterions and the solvent, as well as the relative solubility of the various possible products. Clearly the nature of the $N^4$ substituent can have a major impact on the last of these factors. Magnetic studies carried out on the dinuclear complexes revealed that the triazole bridges mediate relatively weak antiferromagnetic coupling between the two metal centres.

(© Wiley-VCH Verlag GmbH & Co. KGaA, 69451 Weinheim, Germany, 2006)

## Introduction

The utilisation of 1,2,4-triazole derivatives as bridging ligands in transition-metal complexes is currently of considerable interest.[1–3] The 4-substituted 3,5-di(2-pyridyl)-4*H*-1,2,4-triazoles are bis-bidentate so they are potentially dinucleating ligands that should be capable of bridging two metal ions by means of the $N_2$ unit of the central triazole ring.[2] Quite a large range of such ligands have been used for the preparation of transition-metal complexes (Figure 1). In the resulting di- and mononuclear complexes a variety of coordination modes have been observed of which the dinuclear $(N',N^1,N^2,N'')_2$ double bridging and the mononuclear $(N',N^1)_2$ coordination mode are the most common and most important ones (Figure 2).[2] For octahedral complexes featuring the latter mode, the *trans* type is frequently encountered. Here, the pyridine–triazole moieties of the two ligands are coordinated to the metal centre in a common plane with axially *trans*-positioned co-ligands. In contrast, there is only one example in the literature where the isomeric *cis* type is realised.[4]

Within this ligand class the reactivity of 4-amino-3,5-di(2-pyridyl)-4*H*-1,2,4-triazole ($NH_2$dpt, **2**) (Figure 1) towards transition-metal salts and the properties of the resulting di- and mononuclear complexes have been studied quite extensively over the last 20 years.[5–29] From an electronic point of view the presence of the strongly electron-donating amino group on $N^4$ should facilitate the formation of dinuclear complexes of this ligand. However, of this family only two dinuclear complexes, namely $[Ni^{II}_2(NH_2dpt)_2(H_2O)_2Cl_2]Cl_2{\cdot}4H_2O$[5] and $[Cu^{II}_2(NH_2dpt)(H_2O)_4(SO_4)_2]{\cdot}H_2O$,[12] have been structurally characterised

[a] Department of Chemistry, University of Otago, P. O. Box 56, Dunedin, New Zealand
Fax: +64-3-479-7906
E-mail: sbrooker@alkali.otago.ac.nz
[b] Department of Chemistry, The University of Auckland, Private Bag 92019, Auckland, New Zealand
[c] School of Chemistry, Building 23, Monash University, Clayton, Victoria 3800, Australia
Supporting information for this article is available on the WWW under http://www.eurjic.org or from the author.

 © 2006 Wiley-VCH Verlag GmbH & Co. KGaA, Weinheim 

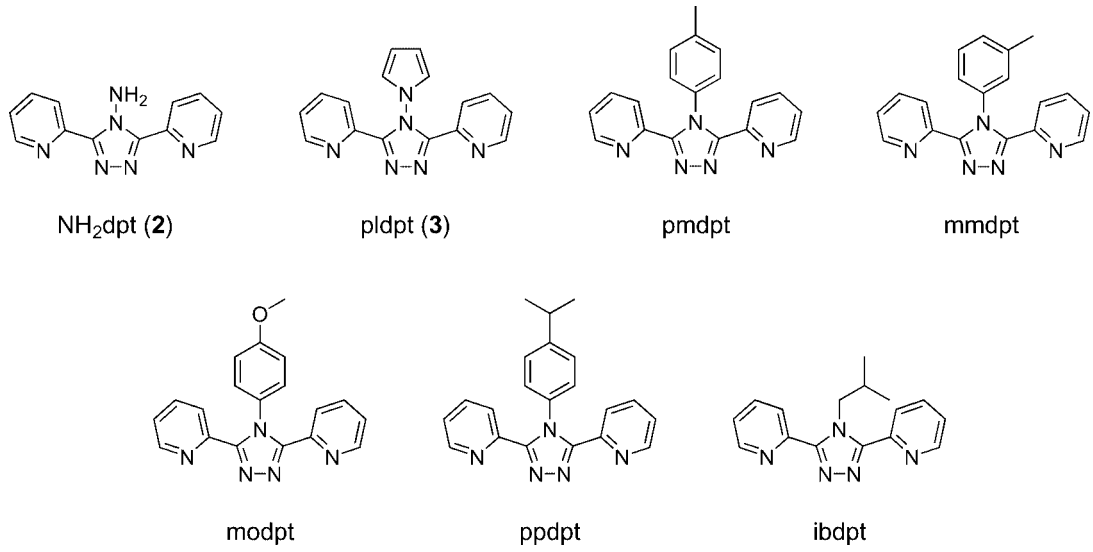


Figure 1. Structural drawings of the 4-substituted 3,5-di(2-pyridyl)-4*H*-1,2,4-triazoles that have been employed to date as ligands in coordination compounds.

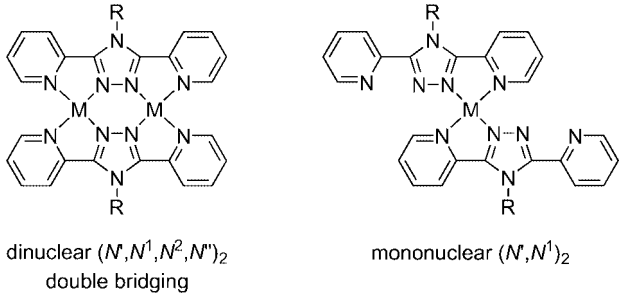


Figure 2. Schematic representation of the two most common coordination modes of 4-substituted 3,5-di(2-pyridyl)-4*H*-1,2,4-triazoles. In the actual complexes the metal centres can bind additional co-ligands according to the respective coordination geometries.

to date. 4-Isobutyl-3,5-di(2-pyridyl)-4*H*-1,2,4-triazole (ibdpt)[30] (Figure 1), with its electron-donating alkyl substituent on $N^4$, has also been found to afford both di- and mononuclear complexes.[31–33] In contrast, the 4-aryl-3,5-di(2-pyridyl)-4*H*-1,2,4-triazoles have almost exclusively produced mononuclear complexes to date, in some cases despite the reaction being carried out with a metal-to-ligand molar ratio of 1:1.[4,34–42] The first, and so far the only, dinuclear complex of a 4-aryl-3,5-di(2-pyridyl)-4*H*-1,2,4-triazole, namely a dinuclear silver(I) complex of 4-(4-isopropylphenyl)-3,5-di(2-pyridyl)-4*H*-1,2,4-triazole (ppdpt) (Figure 1) obtained from MeCN employing a 1:1 metal-to-ligand molar ratio, was reported very recently.[43] Given that in these complexes the aryl substituents on $N^4$ form angles of about 68–84° with the triazole ring, no significant π-interactions are expected between them. Therefore, any electronic effect that the aryl substituent on $N^4$ might exert on the triazole ring must occur through the σ-bond framework so is likely to be small. There is only one report in the literature dealing with 3,5-di(2-pyridyl)-4-(1*H*-pyrrol-1-yl)-4*H*-1,2,4-triazole (pldpt, **3**) (Figure 1) and it describes the structural characterisation of the dinuclear complex $[Co^{II}_2(pldpt)_2(H_2O)_4]Cl_4{\cdot}2MeOH{\cdot}2H_2O$, which was formed from the 1:1 reaction of $CoCl_2{\cdot}6H_2O$ and pldpt (**3**) in MeOH/$H_2O$, 4:1.[44]

Overall it appears that the factors which combine to determine the nature of the products of such a complexation reaction, in particular whether a di- or mononuclear complex is formed as the main product, include the reaction stoichiometry, the choice of the counterions and the solvent used, as well as the influence of the $N^4$ substituent on the electronic structure and conformation of the respective ligand and on the relative solubility of the various possible product complexes. Systematic studies aimed at investigating the relative importance of these factors are currently lacking but clearly desirable so we are beginning to address this as part of our ongoing studies which are directed towards the synthesis and characterisation of dinuclear 1,2,4-triazole-bridged complexes of such ligands,[2,3,30,32,33,45–51] with a particular interest in iron(II) complexes.[52] Given that to date dinuclear 1,2,4-triazole-bridged complexes are far less common than the corresponding mononuclear complexes, here we target the controlled formation of further examples of dinuclear complexes of pldpt (**3**) by employing a metal-to-ligand molar ratio of 1:1 in the complexation reactions and varying the solvents and counterions.

## Results and Discussion

### Ligand Synthesis

Following the classic two-step procedure of Geldard and Lions,[53] the condensation of 2-pyridinecarbonitrile with $N_2H_4{\cdot}H_2O$ gave 3,6-di(2-pyridyl)-1,4-dihydro-1,2,4,5-tetrazine (**1**) in 58% yield (Scheme 1). The subsequent rearrangement of the dihydrotetrazine **1** in 2 M HCl afforded $NH_2$dpt (**2**) in 84% yield.[53] Alternatively, $NH_2$dpt (**2**) could be obtained directly from the two reactants by em-

 © 2006 Wiley-VCH Verlag GmbH & Co. KGaA, Weinheim 

ploying the one-pot procedure described by Lagrenée and co-workers (Scheme 1).[54] However, it was found that the reaction was much slower than reported and difficult to drive to completion. The initial product thus obtained had to be recrystallised at least twice in order to obtain pure material. This caused the final yield of $NH_2$dpt (**2**) to drop significantly and the two-step procedure of Geldard and Lions[53] was therefore preferred. The reaction of $NH_2$dpt (**2**) with 2,5-dimethoxytetrahydrofuran[55,56] in AcOH/1,4-dioxane (1:1) readily gave pldpt (**3**) in 77% yield.[44] Compounds **1**–**3** were fully characterised by spectroscopic methods. In addition, pldpt (**3**) was characterised by single-crystal X-ray diffraction (Figures S1 and S2).

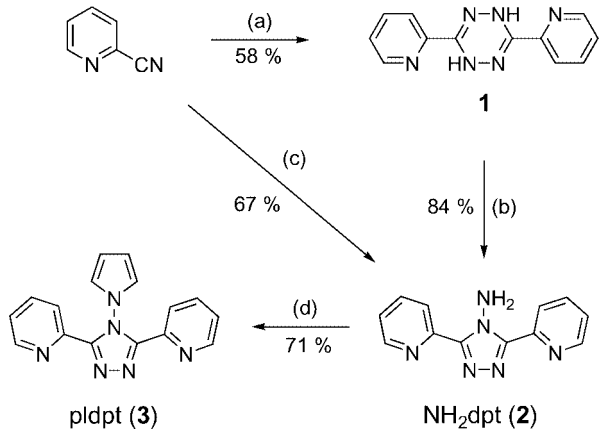


Scheme 1. Synthesis of 3,5-di(2-pyridyl)-4-(1*H*-pyrrol-1-yl)-4*H*-1,2,4-triazole (pldpt, **3**). Reagents and conditions: (a) $N_2H_4{\cdot}H_2O$, reflux; (b) 2 M HCl, reflux; (c) $N_2H_4{\cdot}H_2O$, $N_2H_4{\cdot}H_2SO_4$, 1,2-ethandiol, 130 °C; (d) 2,5-dimethoxytetrahydrofuran, AcOH, 1,4-dioxane, reflux.

There has been some confusion about the exact nature of the dihydrotetrazine intermediates arising from the condensation of nitriles with hydrazine. Especially in the older literature, including leading reviews on tetrazines and their dihydro derivatives[57–59] as well as one on a related topic,[60] these compounds are mostly considered to be the 1,2-tautomers. However, at least in the case of the condensation of 2-pyridinecarbonitrile with $N_2H_4{\cdot}H_2O$, it has now been proven unequivocally by two independent research groups on the basis of single-crystal X-ray diffraction that the product of this reaction is in fact the 1,4-tautomer.[61,62]

### Synthesis of the Cobalt(II) Complexes

According to the literature, the reaction of pldpt (**3**) with $CoCl_2{\cdot}6H_2O$ in a 1:1 molar ratio in MeOH/$H_2O$ (4:1) gives, on slow evaporation of the reaction mixture, orange crystals of $[Co^{II}_2(pldpt)_2(H_2O)_4]Cl_4{\cdot}2MeOH{\cdot}2H_2O$ in 60–70% yield.[44] Following this procedure as closely as possible, the synthesis of this material was attempted. However, instead of orange crystals, irregular beige crystals started to separate from the orange-brown solution after a few days. Over the course of four weeks the solution was allowed to evaporate almost completely forming even more of the beige material. On filtration and drying, the beige crystalline material became dull which indicated the loss of some solvent. Visual examination of the resulting solid under a microscope showed that it contained a few tiny orange prisms, presumably of $[Co^{II}_2(pldpt)_2(H_2O)_4]Cl_4{\cdot}2MeOH{\cdot}2H_2O$. The small amount of orange product was separated physically from the bulk beige material but since it could not be obtained in sufficient amounts for an elemental analysis its presumed identity could not be verified. The elemental analysis of the beige solid was in good agreement with a mononuclear 1:2 complex with a composition of $Co^{II}(pldpt)_2Cl_2$(solvent). These findings are in marked contrast to the results reported by Mandal and co-workers.[44]

In the hope of getting a well-defined and less soluble solid product directly from the reaction mixture the reaction was subsequently carried out in neat EtOH instead of MeOH/$H_2O$ (4:1). Thus, the reaction of pldpt (**3**) with $CoCl_2{\cdot}6H_2O$ in a 1:1 molar ratio at reflux resulted in the initial formation of a blue solid. After 15 minutes the reaction mixture was cooled and stirring the resulting suspension at room temperature for 24 hours caused the solid to turn pink, presumably due to slow co-ligand exchange of a kinetic product to form a thermodynamically more stable product. The elemental analysis of this pink solid was in good agreement with a dinuclear 2:2 complex with a composition of $Co^{II}_2(pldpt)_2Cl_4$(solvent). This material proved to be insoluble in all organic solvents, including DMF, $MeNO_2$ and DMSO, and could only be dissolved in $H_2O$. However, since all attempts to obtain a crystalline material from $H_2O$ were unsuccessful, further purification and characterisation was not possible.

As a result of these disappointing findings using $CoCl_2{\cdot}6H_2O$ the coordination behaviour of pldpt (**3**) towards $Co(ClO_4)_2{\cdot}6H_2O$ was investigated next, in the hope of obtaining a solid product straight from the reaction mixture that would exhibit better solubility in organic solvents, thus allowing purification and proper characterisation. In order to achieve the formation of a dinuclear 2:2 complex, $Co(ClO_4)_2{\cdot}6H_2O$ was treated with pldpt (**3**) in a 1:1 molar ratio in MeCN. The resulting orange solid, which separated from the reaction mixture in ca. 90% yield, gave an elemental analysis in good agreement with a dinuclear 2:2 complex with a composition of $Co^{II}_2(pldpt)_2(ClO_4)_4(MeCN)_m(H_2O)_n$ (**4**). The solvent content of this material varied widely from batch to batch and the drying of samples at 60 °C in vacuo (CAUTION!) for several days similarly resulted in the formation of materials of variable solvent content. While complex **4** was only very sparingly soluble in MeCN, the addition of a little DMF led to dissolution. Vapour diffusion of $Et_2O$ into a solution of complex **4** in MeCN/DMF (10:1) resulted in the formation of two different kinds of crystalline materials, namely orange prisms and yellow blocks, in variable relative amounts. Both species were studied by single-crystal X-ray diffraction. Thus, the orange crystals were identified as the dinuclear complex $[Co^{II}_2(pldpt)_2(DMF)_2(H_2O)_2](ClO_4)_4{\cdot}0.5Et_2O$ (**5**) (Figure 3) whereas the yellow crystals were found to be of the mononuclear complex $[Co^{II}(pldpt)_2(DMF)_2](ClO_4)_2$ (**6**) (Figure 4). These findings suggest that in the presence of DMF

 © 2006 Wiley-VCH Verlag GmbH & Co. KGaA, Weinheim 

the initial dinuclear complex **4** is unstable, resulting in the formation of a mixture of di- and mononuclear species, complexes **5** and **6**, respectively.

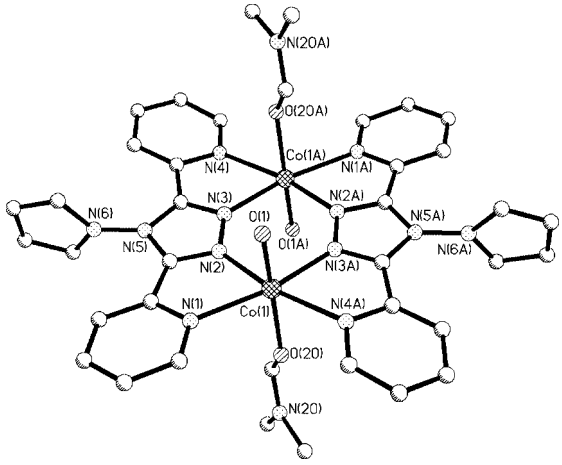


Figure 3. View of the molecular structure of the cation of $[Co^{II}_2(pldpt)_2(H_2O)_2(DMF)_2](ClO_4)_4{\cdot}0.5Et_2O$ (**5**). Hydrogen atoms have been omitted for clarity. Symmetry operation used to generate equivalent atoms: (A) $-x + 1, -y + 1, -z + 2$.

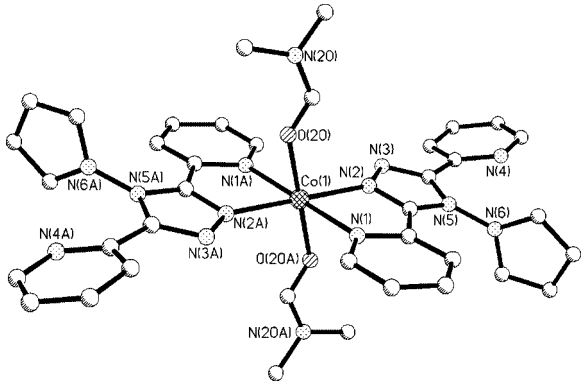


Figure 4. View of the molecular structure of the cation of $[Co^{II}(pldpt)_2(DMF)_2](ClO_4)_2$ (**6**). Hydrogen atoms have been omitted for clarity. Symmetry operation used to generate equivalent atoms: (A) $-x + 1, -y, -z$.

Faced with the need to use DMF as a co-solvent in order to dissolve the $ClO_4^-$ complex **4** and the resulting formation of a mixture of species of different nuclearities, the synthesis of the $BF_4^-$ analogue was carried out as this material was expected to exhibit better solubility in MeCN and therefore might not require the use of DMF. Thus, reacting $Co(BF_4)_2{\cdot}6H_2O$ with pldpt (**3**) in a 1:1 molar ratio in MeCN afforded a pale orange powder, in ca. 80% yield, which had a composition of $Co^{II}_2(pldpt)_2(BF_4)_4(MeCN)_m(H_2O)_n$ (**7**). As found earlier for the $ClO_4^-$ analogue **4**, the solvent content of the material was variable and prolonged heating in vacuo afforded only partially desolvated materials of variable compositions. As anticipated, this complex could be readily redissolved in MeCN. Vapour diffusion of $Et_2O$ into the MeCN mother liquor, or into a solution of complex **7** in MeCN, gave only one crystalline species which was identified as $[Co^{II}_2(pldpt)_2(MeCN)_2(H_2O)_2](BF_4)_4$ (**8**) (Figure S3) by single-crystal X-ray diffraction. Thus, in MeCN alone the initial dinuclear complex **7** is stable and is not broken down into a mixture of di- and mononuclear species.

### Synthesis of the Nickel(II) Complexes

In parallel with the attempted synthesis of $[Co^{II}_2(pldpt)_2(H_2O)_4]Cl_4{\cdot}2MeOH{\cdot}2H_2O$[44] the reaction of pldpt (**3**) with $NiCl_2{\cdot}6H_2O$ in a 1:1 molar ratio under analogous conditions was examined. The slow evaporation of the olive-green MeOH/$H_2O$ (4:1) reaction mixture over the course of six weeks produced a mixture of a greenish crystalline solid and blue prisms in an estimated 3:1 ratio. As the physical separation of the two materials was practically impossible no analytical data for either of the compounds could be obtained. However, it is quite likely that, by analogy to the experiment employing $CoCl_2{\cdot}6H_2O$ described above, a mixture of di- and mononuclear compounds was formed. Carrying out the reaction of pldpt (**3**) with $NiCl_2{\cdot}6H_2O$ in a 1:1 molar ratio in EtOH instead of MeOH/$H_2O$ (4:1) gave a pale green solid which was subsequently identified, on the basis of its elemental analysis, as a dinuclear 2:2 complex with a composition of $Ni^{II}_2(pldpt)_2Cl_4$(solvent). This material showed the same low solubility in organic solvents as the cobalt(II) analogue and this prevented its purification and further characterisation.

The reaction of pldpt (**3**) with $Ni(ClO_4)_2{\cdot}6H_2O$ in a 1:1 molar ratio in MeCN afforded $Ni^{II}_2(pldpt)_2(ClO_4)_4(MeCN)_m(H_2O)_n$ (**9**) as a pale violet powder in ca. 80% yield. The solvent content of the initial powder was very variable. Once again prolonged heating in vacuo (CAUTION!) afforded materials of variable solvent content. As with the cobalt(II) analogue **4** the addition of a little DMF was necessary to dissolve the powder in MeCN. Vapour diffusion of $Et_2O$ into a solution of complex **9** in MeCN/DMF (10:1) afforded an inseparable mixture of blue fern-like crystals and pink buttons, none of which were suitable for single-crystal X-ray diffraction studies. Here too, the use of DMF as a co-solvent has resulted in the formation of two different, presumably di- and mononuclear, species.

Employing $Ni(BF_4)_2{\cdot}6H_2O$ instead of the $ClO_4^-$ salt in the 1:1 reaction with pldpt (**3**) in MeCN gave $Ni^{II}_2(pldpt)_2(BF_4)_4(MeCN)_m(H_2O)_n$ (**10**) as a pale violet powder in ca. 40% yield and variable degrees of solvation. It could not be obtained in solvent-free form. As for the cobalt(II) analogues, this $BF_4^-$ complex exhibited good solubility in neat MeCN, unlike its $ClO_4^-$ analogue **9**. Vapour diffusion of $Et_2O$ into a solution of complex **10** in MeCN or into the MeCN mother liquor of the initial powder afforded purple-blue prisms of $[Ni^{II}_2(pldpt)_2(MeCN)_4](BF_4)_4{\cdot}2MeCN$ (**11**) (Figure S4). Only one crystal type was observed so once again the initial dinuclear complex **10** is stable in MeCN.

### Synthesis of the Copper(II) Complexes

The reaction of $Cu(ClO_4)_2{\cdot}6H_2O$ with pldpt (**3**) in a 1:1 molar ratio in MeCN gave a sea-green solution from which

 © 2006 Wiley-VCH Verlag GmbH & Co. KGaA, Weinheim 

a blue powder separated after a few hours. This solid was identified as the mononuclear 1:2 complex $[Cu^{II}(pldpt)_2(ClO_4)_2]$ (**12**) on the basis of its elemental analysis. Thus, the yield was subsequently calculated as 59%. Complex **12** could be readily dissolved in MeCN to give a blue solution. Vapour diffusion of $Et_2O$ into this solution afforded blue single crystals of $[Cu^{II}(pldpt)_2(ClO_4)_2]\cdot 2DMF$ (**13**) (Figure 5). While the origin of the DMF solvates in complex **13** could not be determined with absolute certainty it is likely that the glassware used was contaminated with DMF.

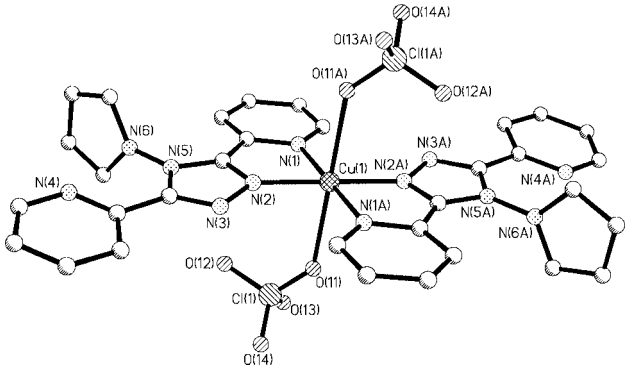


Figure 5. View of the molecular structure of $[Cu^{II}(pldpt)_2(ClO_4)_2]\cdot 2DMF$ (**13**). Hydrogen atoms have been omitted for clarity. The DMF solvates are not shown. Symmetry operation used to generate equivalent atoms: (A) $-x, -y, -z + 1$.

Interestingly, the mother liquor remaining after filtering off the blue mononuclear complex **12**, now significantly enriched in $Cu^{2+}$ ions relative to pldpt (**3**), retained its sea-green colour, suggesting the presence of a different species in solution. Subjecting this sea-green solution to vapour diffusion of $Et_2O$ produced a small quantity of large green blocks. Single-crystal X-ray diffraction studies of these crystals revealed their dinuclear nature and led to the formulation of $[Cu^{II}_2(pldpt)_2(MeCN)_2(H_2O)_2](ClO_4)_4$ (**14**) (Figure 6).

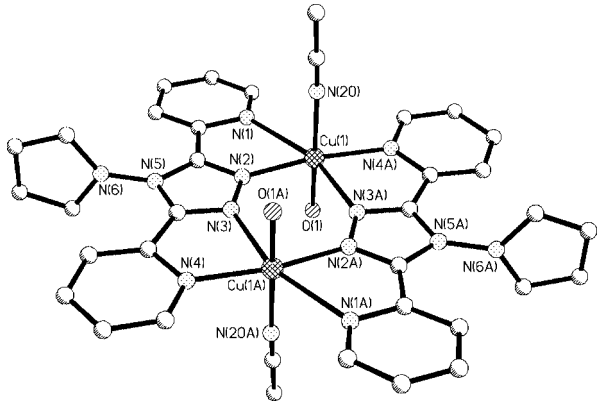


Figure 6. View of the molecular structure of the cation of $[Cu^{II}_2(pldpt)_2(H_2O)_2(MeCN)_2](ClO_4)_4$ (**14**). Hydrogen atoms have been omitted for clarity. Symmetry operation used to generate equivalent atoms: (A) $-x + 2, -y + 1, -z + 1$.

It is noteworthy that of all the $ClO_4^-$ complexes of pldpt (**3**) only the copper(II) complexes were readily soluble in neat MeCN. In addition, while in all other cases the initial precipitates consisted of dinuclear species, in the case of $Cu(ClO_4)_2\cdot 6H_2O$ the mononuclear complex $[Cu^{II}(pldpt)_2(ClO_4)_2]$ (**12**) was the initial solid product despite the 1:1 metal-to-ligand molar ratio employed in the reaction.

### Synthesis of the Zinc(II) Complexes

The reaction of pldpt (**3**) with $Zn(ClO_4)_2\cdot 6H_2O$ in a 1:1 molar ratio in MeCN afforded $Zn^{II}_2(pldpt)_2(ClO_4)_4(MeCN)_m(H_2O)_n$ (**15**) as a colourless powder in ca. 80% yield. The solvent content of this material was variable and it could not be obtained in a solvent-free form even by heating it in vacuo (CAUTION!) for several days. Recrystallisation by vapour diffusion of $Et_2O$ into a MeCN/DMF (10:1) solution of complex **15** gave colourless blocks and visually only one crystal type could be detected. Numerous attempts to grow single crystals by this method were made but only once could a poor X-ray data set be collected and this indicated that the crystals were of a dinuclear product. However, due to the very poor quality of the data, a complete analysis of the structure was not possible. Consistent with these findings, the elemental analysis of complex **15** clearly confirmed the 2:2 stoichiometry of this complex and the symmetrical NMR spectra obtained in $[D_7]$DMF were also in agreement with the presence of only one species, specifically one with a symmetrical dinuclear architecture (see below). It is interesting to note that this dinuclear zinc(II) $ClO_4^-$ complex does not form an equilibrium with a mononuclear species when it is dissolved in DMF as, if it did, this should be observed in the NMR spectra. This contrasts with the behaviour of the dinuclear cobalt(II) and nickel(II) $ClO_4^-$ analogues, complexes **4** and **9**, respectively, which on recrystallisation from solutions containing DMF form mixtures of di- and mononuclear solid products. The relative amounts of these products present in solution are unknown.

In order to access better single crystals, our attention shifted from using the $ClO_4^-$ salt to using the $BF_4^-$ salt. Under the same conditions as employed for the preparation of the analogous $BF_4^-$ complexes of cobalt(II) and nickel(II), complexes **7** and **10**, respectively, $Zn^{II}_2(pldpt)_2(BF_4)_4(MeCN)_m(H_2O)_n$ (**16**) was obtained from pldpt (**3**) and $Zn(BF_4)_2\cdot 6H_2O$, in ca. 60% yield, as a colourless powder. As with all complexes of pldpt (**3**) synthesised in this work, the solvent content of complex **16** varied considerably from batch to batch and the drying of samples at 60 °C in vacuo for several days again resulted in materials of variable solvent content. Vapour diffusion of $Et_2O$ into a solution of complex **16** in MeCN, or into its MeCN mother liquor, gave colourless blocks which were identified by single-crystal X-ray diffraction as the dinuclear complex $[Zn^{II}_2(pldpt)_2(MeCN)_2(H_2O)_2](BF_4)_4$ (**17**) (Figure S5).

### Description of the Structures

Single crystals of pldpt (**3**), in the form of colourless blocks, were obtained by slow evaporation of a solution of

 © 2006 Wiley-VCH Verlag GmbH & Co. KGaA, Weinheim 

the compound in EtOH. There are two crystallographically independent molecules in the asymmetric unit (Figures S1 and S2). The most noteworthy feature of this structure is the dissimilar orientation of the pairs of pyridine rings in the two molecules. While in the first molecule the pyridine nitrogen atoms point in opposite directions, both pyridine nitrogen atoms in the second molecule point away from the $N_2$ unit of the central five-membered heterocyclic ring. For the related ligand 2,5-di(2-pyridyl)-1,3,4-thiadiazole the latter conformation was recently calculated to be energetically favoured over the other two local minima forms with one or both pyridine nitrogen atoms pointing towards the $N_2$ unit.[63] Indeed, an orientation of the pyridine rings with the nitrogen atoms pointing away from the $N_2$ unit of the central triazole ring is the only one previously observed in 4-substituted 3,5-di(2-pyridyl)-4*H*-1,2,4-triazoles[30,37,64–73] and it is also the one usually adopted by non-coordinating pyridine rings in mononuclear 2:1 complexes incorporating such ligands.[2] There are, in fact, only very few examples of complexes in the literature where the non-coordinated pyridine ring is reported to point away from the $N^4$ substituent.[13,40,42] The reason for the adoption of this unusual conformation for one of the two crystallographically independent molecules of pldpt (**3**) is difficult to pinpoint but presumably arises from a complex combination of weak π–π and other packing effects. The conformation of the N(1)- and N(4)-pyridine rings was established by the differences in electron density for the two possible sites of the nitrogen atoms within the rings. This assignment was further supported by the fact that a hydrogen atom could only be located from the difference map at one of the two possible sites within the respective rings. Refinement of the structure with the alternative orientations was tried but was found to fit less well with the data.

In the dinuclear orange complex $[Co^{II}_2(pldpt)_2(DMF)_2(H_2O)_2](ClO_4)_4\cdot 0.5Et_2O$ (**5**) (Figure 3) the $(N',N^1,N^2,N'')_2$ double-bridging coordination mode (Figure 2) is realised. The two cobalt centres are 4.273(2) Å apart (Table 1) and in a distorted octahedral environment with a DMF and a $H_2O$ molecule as axial co-ligands completing the coordination sphere (Table 2 and Table 3). While in this complex the normal situation of longer Co–$N_{pyr}$ distances [2.235(5) and 2.244(5) Å] than Co–$N_{trz}$ distances [2.085(5) and 2.098(4) Å] is again observed, the former are slightly longer than the corresponding distances observed in dinuclear cobalt(II) complexes of the related ligand 4-isobutyl-3,5-di(2-pyridyl)-4*H*-1,2,4-triazole (ibdpt)[32] and also slightly longer than those in the mononuclear complex $[Co^{II}(pldpt)_2(DMF)_2](ClO_4)_2$ (**6**) and the dinuclear complex $[Co^{II}_2(pldpt)_2(MeCN)_2(H_2O)_2](BF_4)_4$ (**8**) described below. Within

Table 1. Metal···metal distances [Å] in dinuclear complexes of 4-substituted 3,5-di(2-pyridyl)-4*H*-1,2,4-triazoles.

| Complex | M···M[a] | Reference |
|---|---|---|
| $[Co^{II}_2(pldpt)_2(H_2O)_4]Cl_4\cdot 2MeOH\cdot 2H_2O$ | 4.226(2) | [44] |
| $[Co^{II}_2(ibdpt)_2(MeCN)_2(H_2O)_2](ClO_4)_4$ (red-orange polymorph) | 4.1481(7) | [32] |
| $[Co^{II}_2(ibdpt)_2(MeCN)_2(H_2O)_2](ClO_4)_4$ (yellow-orange polymorph) | 4.1722(4) | [32] |
| $[Co^{II}_2(pldpt)_2(DMF)_2(H_2O)_2](ClO_4)_4\cdot 0.5Et_2O$ (**5**) | 4.273(2) | this work |
| $[Co^{II}_2(pldpt)_2(MeCN)_2(H_2O)_2](BF_4)_4$ (**8**) | 4.2660(4) | this work |
| $[Ni^{II}_2(NH_2dpt)_2(H_2O)_2Cl_2]Cl_2\cdot 4H_2O$ | 4.1348(3) | [5] |
| $[Ni^{II}_2(ibdpt)_2(MeCN)_4](ClO_4)_4$ | 4.1107(9) | [32] |
| $[Ni^{II}_2(pldpt)_2(MeCN)_4](BF_4)_4\cdot 2MeCN$ (**11**) | 4.170(1) | this work |
| $[Cu^{II}_2(NH_2dpt)(H_2O)_4(SO_4)_2]\cdot H_2O$ | 4.415(1) | [12] |
| $[Cu^{II}_2(ibdpt)_2(MeCN)_2(ClO_4)_2](ClO_4)_2\cdot 2MeCN$ | 4.0701(10) | [32] |
| $[Cu^{II}_2(pldpt)_2(MeCN)_2(H_2O)_2](ClO_4)_4$ (**14**) | 4.3140(5) [4.0861(9)] | this work |
| $[Zn^{II}_2(pldpt)_2(MeCN)_2(H_2O)_2](BF_4)_4$ (**17**) | 4.455(2) | this work |
| $[Ag^{I}_2(ppdpt)_2](ClO_4)_2\cdot MeCN$ | 4.367(4) | [43] |

[a] Values in square brackets refer to the second molecule within the asymmetric unit.

Table 2. Selected distances [Å] for $[Co^{II}_2(pldpt)_2(DMF)_2(H_2O)_2](ClO_4)_4\cdot 0.5Et_2O$ (**5**), $[Co^{II}(pldpt)_2(DMF)_2](ClO_4)_2$ (**6**), $[Co^{II}_2(pldpt)_2(MeCN)_2(H_2O)_2](BF_4)_4$ (**8**), $[Ni^{II}_2(pldpt)_2(MeCN)_4](BF_4)_4\cdot 2MeCN$ (**11**), $[Cu^{II}(pldpt)_2(ClO_4)_2]\cdot 2DMF$ (**13**), $[Cu^{II}_2(pldpt)_2(MeCN)_2(H_2O)_2](ClO_4)_4$ (**14**) and $[Zn^{II}_2(pldpt)_2(MeCN)_2(H_2O)_2](BF_4)_4$ (**17**).

| | **5** | **6** | **8** | **13** |
|---|---|---|---|---|
| M–$N_{pyr}$ | Co(1)–N(1) 2.235(5)<br>Co(1)–N(4A) 2.244(5) | Co(1)–N(1) 2.190(3) | Co(1)–N(1) 2.1876(12)<br>Co(1)–N(4A) 2.2188(12) | Cu(1)–N(1) 2.034(2) |
| M–$N_{trz}$ | Co(1)–N(2) 2.085(5)<br>Co(1)–N(3A) 2.098(4) | Co(1)–N(2) 2.210(3) | Co(1)–N(2) 2.0976(12)<br>Co(1)–N(3A) 2.0769(12) | Cu(1)–N(2) 1.979(2) |
| M–X | Co(1)–O(1) 2.052(4)<br>Co(1)–O(20) 2.028(4) | Co(1)–O(20) 1.994(3) | Co(1)–N(20) 2.0876(12)<br>Co(1)–O(1) 2.0464(11) | Cu(1)–O(11) 2.470(2) |
| | **11** | | **14** | **17** |
| M–$N_{pyr}$ | Ni(1)–N(1) 2.184(2)<br>Ni(1)–N(7) 2.149(2) | Ni(2)–N(4) 2.165(2)<br>Ni(2)–N(10) 2.171(2) | Cu(1)–N(1) 2.5170(18)<br>Cu(1)–N(4A) 2.0264(17) | Zn(1)–N(1) 2.173(4)<br>Zn(1)–N(4A) 2.227(4) |
| M–$N_{trz}$ | Ni(1)–N(2) 2.026(2)<br>Ni(1)–N(8) 2.038(2) | Ni(2)–N(3) 2.042(2)<br>Ni(2)–N(9) 2.023(2) | Cu(1)–N(2) 1.9908(17)<br>Cu(1)–N(3A) 2.2564(17) | Zn(1)–N(2) 2.164(4)<br>Zn(1)–N(3A) 2.119(4) |
| M–X | Ni(1)–N(40) 2.025(2)<br>Ni(1)–N(50) 2.031(2) | Ni(2)–N(60) 2.038(2)<br>Ni(2)–N(70) 2.034(2) | Cu(1)–N(20) 2.0024(19)<br>Cu(1)–O(1) 2.0029(16) | Zn(1)–N(20) 2.127(4)<br>Zn(1)–O(1) 2.103(4) |

 © 2006 Wiley-VCH Verlag GmbH & Co. KGaA, Weinheim 

Table 3. Selected angles [°] for $[Co^{II}_2(pldpt)_2(DMF)_2(H_2O)_2](ClO_4)_4 \cdot 0.5Et_2O$ (**5**), $[Co^{II}(pldpt)_2(DMF)_2](ClO_4)_2$ (**6**), $[Co^{II}_2(pldpt)_2(MeCN)_2(H_2O)_2](BF_4)_4$ (**8**), $[Ni^{II}_2(pldpt)_2(MeCN)_4](BF_4)_4 \cdot 2MeCN$ (**11**), $[Cu^{II}(pldpt)_2(ClO_4)_2] \cdot 2DMF$ (**13**), $[Cu^{II}_2(pldpt)_2(MeCN)_2(H_2O)_2](ClO_4)_4$ (**14**) and $[Zn^{II}_2(pldpt)_2(MeCN)_2(H_2O)_2](BF_4)_4$ (**17**).

| **5** | | **6** | | **8** | |
|---|---|---|---|---|---|
| N(1)–Co(1)–N(2) | 74.21(18) | N(1)–Co(1)–N(2) | 82.10(12) | N(1)–Co(1)–N(2) | 75.13(4) |
| N(1)–Co(1)–N(3A) | 166.98(18) | N(1)–Co(1)–N(1A) | 180 | N(1)–Co(1)–N(3A) | 166.95(5) |
| N(1)–Co(1)–N(4A) | 119.19(18) | N(1)–Co(1)–N(2A) | 97.90(12) | N(1)–Co(1)–N(4A) | 118.12(4) |
| N(1)–Co(1)–O(1) | 86.61(17) | N(1)–Co(1)–O(20) | 93.21(12) | N(1)–Co(1)–N(20) | 87.89(4) |
| N(1)–Co(1)–O(20) | 86.62(18) | N(1)–Co(1)–O(20A) | 86.79(12) | N(1)–Co(1)–O(1) | 86.60(4) |
| N(2)–Co(1)–N(3A) | 92.78(17) | N(2)–Co(1)–N(2A) | 180 | N(2)–Co(1)–N(3A) | 91.98(4) |
| N(2)–Co(1)–N(4A) | 166.46(16) | N(2)–Co(1)–O(20) | 107.24(11) | N(2)–Co(1)–N(4A) | 166.41(4) |
| N(2)–Co(1)–O(1) | 94.53(17) | N(2)–Co(1)–O(20A) | 72.76(11) | N(2)–Co(1)–N(20) | 93.56(5) |
| N(2)–Co(1)–O(20) | 99.46(18) | O(20)–Co(1)–O(20A) | 180 | N(2)–Co(1)–O(1) | 93.90(5) |
| N(3A)–Co(1)–N(4A) | 73.82(17) | | | N(3A)–Co(1)–N(4A) | 74.86(4) |
| N(3A)–Co(1)–O(1) | 94.32(16) | | | N(3A)–Co(1)–N(20) | 90.97(5) |
| N(3A)–Co(1)–O(20) | 95.98(17) | | | N(3A)–Co(1)–O(1) | 96.46(5) |
| N(4A)–Co(1)–O(1) | 88.53(16) | | | N(4A)–Co(1)–N(20) | 90.12(5) |
| N(4A)–Co(1)–O(20) | 80.44(17) | | | N(4A)–Co(1)–O(1) | 84.39(5) |
| O(1)–Co(1)–O(20) | 162.17(18) | | | N(20)–Co(1)–O(1) | 169.28(5) |
| **11** | | | | | |
| N(1)–Ni(1)–N(2) | 76.21(9) | N(3)–Ni(2)–N(4) | 76.25(9) | | |
| N(1)–Ni(1)–N(7) | 115.16(9) | N(3)–Ni(2)–N(9) | 92.58(9) | | |
| N(1)–Ni(1)–N(8) | 168.53(9) | N(3)–Ni(2)–N(10) | 168.75(9) | | |
| N(1)–Ni(1)–N(40) | 88.80(9) | N(3)–Ni(2)–N(60) | 91.21(9) | | |
| N(1)–Ni(1)–N(50) | 87.74(9) | N(3)–Ni(2)–N(70) | 90.09(9) | | |
| N(2)–Ni(1)–N(7) | 168.52(9) | N(4)–Ni(2)–N(9) | 168.67(9) | | |
| N(2)–Ni(1)–N(8) | 92.34(9) | N(4)–Ni(2)–N(10) | 114.89(9) | | |
| N(2)–Ni(1)–N(40) | 91.94(9) | N(4)–Ni(2)–N(60) | 87.54(9) | | |
| N(2)–Ni(1)–N(50) | 91.49(9) | N(4)–Ni(2)–N(70) | 91.29(9) | | |
| N(7)–Ni(1)–N(8) | 76.30(9) | N(9)–Ni(2)–N(10) | 76.32(9) | | |
| N(7)–Ni(1)–N(40) | 86.97(9) | N(9)–Ni(2)–N(60) | 90.83(9) | | |
| N(7)–Ni(1)–N(50) | 90.53(9) | N(9)–Ni(2)–N(70) | 90.64(9) | | |
| N(8)–Ni(1)–N(40) | 92.44(9) | N(10)–Ni(2)–N(60) | 90.84(9) | | |
| N(8)–Ni(1)–N(50) | 91.82(9) | N(10)–Ni(2)–N(70) | 88.18(9) | | |
| N(40)–Ni(1)–N(50) | 174.42(9) | N(60)–Ni(2)–N(70) | 177.99(9) | | |
| **13** | | **14** | | **17** | |
| N(1)–Cu(1)–N(2) | 80.85(9) | N(1)–Cu(1)–N(2) | 70.77(6) | N(1)–Zn(1)–N(2) | 75.47(14) |
| N(1)–Cu(1)–N(1A) | 180 | N(1)–Cu(1)–N(3A) | 162.04(6) | N(1)–Zn(1)–N(3A) | 163.75(14) |
| N(1)–Cu(1)–N(2A) | 99.15(9) | N(1)–Cu(1)–N(4A) | 120.03(7) | N(1)–Zn(1)–N(4A) | 121.33(14) |
| N(1)–Cu(1)–O(11) | 94.20(8) | N(1)–Cu(1)–N(20) | 90.40(7) | N(1)–Zn(1)–N(20) | 88.94(14) |
| N(1)–Cu(1)–O(11A) | 85.80(8) | N(1)–Cu(1)–O(1) | 81.71(7) | N(1)–Zn(1)–O(1) | 86.17(15) |
| N(2)–Cu(1)–N(2A) | 180 | N(2)–Cu(1)–N(3A) | 91.86(6) | N(2)–Zn(1)–N(3A) | 88.35(14) |
| N(2)–Cu(1)–O(11) | 86.33(8) | N(2)–Cu(1)–N(4A) | 169.17(7) | N(2)–Zn(1)–N(4A) | 162.70(14) |
| N(2)–Cu(1)–O(11A) | 93.67(8) | N(2)–Cu(1)–N(20) | 90.53(7) | N(2)–Zn(1)–N(20) | 93.64(14) |
| O(11)–Cu(1)–O(11A) | 180 | N(2)–Cu(1)–O(1) | 94.59(7) | N(2)–Zn(1)–O(1) | 93.69(14) |
| | | N(3A)–Cu(1)–N(4A) | 77.31(7) | N(3A)–Zn(1)–N(4A) | 74.91(14) |
| | | N(3A)–Cu(1)–N(20) | 94.39(7) | N(3A)–Zn(1)–N(20) | 90.66(15) |
| | | N(3A)–Cu(1)–O(1) | 95.61(7) | N(3A)–Zn(1)–O(1) | 96.50(14) |
| | | N(4A)–Cu(1)–N(20) | 90.21(7) | N(4A)–Zn(1)–N(20) | 90.96(14) |
| | | N(4A)–Cu(1)–O(1) | 86.68(7) | N(4A)–Zn(1)–O(1) | 84.06(14) |
| | | N(20)–Cu(1)–O(1) | 168.60(7) | N(20)–Zn(1)–O(1) | 169.89(14) |

the pyridine–triazole–pyridine moiety of complex **5** the N(4)-pyridine ring shows the largest twist, being inclined by 10.4(3)° relative to the triazole mean plane. The pyrrole ring intersects with the triazole mean plane at an angle of 82.4(3)° (Table 4). There are hydrogen bonds between the $H_2O$ co-ligand and the two $ClO_4^-$ counterions [O(1)···O(11) 2.78 and O(1)···O(21) 2.84 Å].

The mononuclear yellow complex $[Co^{II}(pldpt)_2(DMF)_2](ClO_4)_2$ (**6**) (Figure 4) features the common *trans*-($N'$,$N^1$)$_2$ coordination mode (Figure 2). The coordination sphere about the cobalt centre is a strongly distorted octahedron with two DMF molecules in the axial positions (Table 2 and Table 3). In this complex the Co–$N_{pyr}$ distances are actually shorter than the Co–$N_{trz}$ distances [2.189(3) and 2.209(3) Å, respectively], albeit only slightly, which is a geometrical feature that has not been observed previously in complexes of any 4-substituted 3,5-di(2-pyridyl)-4*H*-1,2,4-triazole. In complexes of this ligand type the M–$N_{pyr}$ distances are usually longer, often significantly, than the M–$N_{trz}$ distances.[2] In addition, both the Co–$N_{pyr}$ and the Co–$N_{trz}$ distances are unusually long compared to those observed in related systems [2.102(4)–2.147(3) and 2.052(4)–2.124(2) Å, respectively].[36,37,42] As is normal, the nitrogen atom of the non-coordinated pyridine ring points towards

 © 2006 Wiley-VCH Verlag GmbH & Co. KGaA, Weinheim 

Table 4. Angles [°] between the mean planes of central triazole ring and the attached pyridine and pyrrole rings in 3,5-di(2-pyridyl)-4-(1*H*-pyrrol-1-yl)-4*H*-1,2,4-triazole (pldpt, **3**) and its complexes.

| Compound | N(1)-pyridine[a] | N(4)-pyridine[a] | N(6)-pyrrole[a] |
|---|---|---|---|
| pldpt (**3**) | 31.1(1) [17.9(1)] | 36.8(1) [29.2(1)] | 82.4(1) [81.9(1)] |
| $[Co^{II}_2(pldpt)_2(DMF)_2(H_2O)_2](ClO_4)_4 \cdot 0.5Et_2O$ (**5**) | 6.7(4) | 10.4(3) | 82.4(3) |
| $[Co^{II}(pldpt)_2(DMF)_2](ClO_4)_2$ (**6**) | 6.2(2) | 24.7(2) | 87.4(1) |
| $[Co^{II}_2(pldpt)_2(MeCN)_2(H_2O)_2](BF_4)_4$ (**8**) | 4.7(1) | 5.6(1) | 88.2(1) |
| $[Ni^{II}_2(pldpt)_2(MeCN)_4](BF_4)_4 \cdot 2MeCN$ (**11**) | 7.7(2) | 4.1(2) | 88.0(1) |
| $[Cu^{II}(pldpt)_2(ClO_4)_2] \cdot 2DMF$ (**13**) | 3.8(2) | 8.2(1) | 85.3(1) |
| $[Cu^{II}_2(pldpt)_2(MeCN)_2(H_2O)_2](ClO_4)_4$ (**14**) | 4.4(1) | 4.7(1) | 88.8(1) |
| $[Zn^{II}_2(pldpt)_2(MeCN)_2(H_2O)_2](BF_4)_4$ (**17**) | 5.2(3) | 5.5(3) | 88.4(2) |

[a] Values in square brackets refer to the N(7)-pyridine, N(10)-pyridine and N(12)-pyrrole rings of the second ligand molecule within the asymmetric unit.

the pyrrole ring which intersects with the triazole mean plane at an angle of 87.4(1)°. The N(1)- and N(4)-pyridine rings are tilted by 6.1(2)° and 24.7(2)°, respectively, relative to the triazole mean plane (Table 4).

The overall architecture of the dinuclear orange complex $[Co^{II}_2(pldpt)_2(MeCN)_2(H_2O)_2](BF_4)_4$ (**8**) (Figure S3) is very similar to that of the corresponding $ClO_4^-$ complex **5** described above. Here, the $(N',N^1,N^2,N'')_2$ double-bridging coordination mode (Figure 2) is realised with a MeCN molecule being the second axial co-ligand, instead of DMF, in addition to the $H_2O$ molecule which forms hydrogen bonds to the two $BF_4^-$ counterions [O(1)···F(11) 2.72 and O(1)···F(21) 2.73 Å]. The usual situation of longer Co–$N_{pyr}$ distances [2.1876(12) and 2.2188(12) Å] than Co–$N_{trz}$ distances [2.0769(12) and 2.0976(12) Å] is again observed (Table 2 and Table 3). The distance between the two cobalt centres of 4.2660(4) Å is almost identical to the value observed for the $ClO_4^-$ complex **5** (Table 1). The pyridine–triazole–pyridine moiety is almost perfectly planar [4.7(1) and 5.6(1)°] while the pyrrole ring is practically perpendicular [88.2(1)°] to the triazole mean plane (Table 4).

The dinuclear $(N',N^1,N^2,N'')_2$ double-bridging coordination mode (Figure 2) is also featured in the purple-blue complex $[Ni^{II}_2(pldpt)_2(MeCN)_4](BF_4)_4 \cdot 2MeCN$ (**11**) (Figure S4). Here, each of the two nickel centres binds two MeCN co-ligands in the axial positions resulting in distorted octahedral $N_6$ coordination environments (Table 2 and Table 3). The distance of 4.170(1) Å between the two nickel centres is somewhat larger than the distances observed in other nickel(II) complexes of related ligands (Table 1).[5,32] The Ni–$N_{pyr}$ and Ni–$N_{trz}$ distances of 2.149(2)–2.184(2) and 2.023(2)–2.042(2) Å, respectively, in complex **11** are in the same range as those observed in related complexes.[5,32] The four Ni–$N_{MeCN}$ distances are all very similar and within the range of 2.025(2)–2.038(2) Å. In both ligand molecules the pyridine–triazole–pyridine moiety is almost flat [7.7(2) and 4.1(2)°] while the respective pyrrole rings are virtually perpendicular [88.0(1)°] to the triazole mean plane (Table 4).

The copper centre in $[Cu^{II}(pldpt)_2(ClO_4)_2] \cdot 2DMF$ (**13**) (Figure 5) is octahedrally $N_4O_2$ coordinated with two molecules of pldpt (**3**) occupying the equatorial positions and two $ClO_4^-$ ions being bound axially, giving rise to the *trans*-$(N',N^1)_2$ coordination mode (Figure 2). Thus, the overall architecture of complex **13** is the same as in $[Cu^{II}(pyppt)_2(ClO_4)_2] \cdot MeCN$,[49] $[Cu^{II}(ibdpt)_2(ClO_4)_2]$[32] and $[Cu^{II}(pmdpt)_2(ClO_4)_2]$[41] with the Cu–$N_{pyr}$, Cu–$N_{trz}$ and Cu–O distances [2.034(2), 1.979(2) and 2.470(2) Å, respectively] (Table 2 and Table 3) having very similar values as the corresponding distances observed in these related complexes [2.038(3)–2.045(2), 1.962(3)–1.989(2) and 2.466(3)–2.471(3) Å, respectively]. Both the coordinated and the non-coordinated pyridine rings show only slight deviations from planarity [3.8(2) and 8.2(1)°, respectively] with respect to the triazole mean plane. The pyrrole ring is almost perpendicular [85.3(1)°] to the triazole mean plane (Table 4).

In all of the previous structures of dinuclear complexes of 4-substituted 3,5-di(2-pyridyl)-4*H*-1,2,4-triazoles featuring the dinuclear $(N',N^1,N^2,N'')_2$ double-bridging coordination mode (Figure 2), described in this paper and elsewhere,[5,32,43,44] the two ligand molecules have been found to be in practically perfect alignment with each other, i.e. with the four nitrogen atoms of the bridging $N_2$ units of the two triazole moieties forming a rectangle. In contrast, in $[Cu^{II}_2(pldpt)_2(MeCN)_2(H_2O)_2](ClO_4)_4$ (**14**) (Figure 6) the two ligand molecules are offset sideways from one another, i.e. with the four nitrogen atoms of the bridging $N_2$ units of the two triazole moieties forming a parallelogram with acute angles of about 78°, resulting in a pronounced tetragonal distortion of the copper(II) centres. The consequences with regard to the distances between the two equivalent copper centres and their donor atoms are quite dramatic. The Cu–$N_{pyr}$ and Cu–$N_{trz}$ distances in complex **14** are the longest observed for any complex of a ligand featuring the bidentate pyridine–triazole moiety. The two Cu–$N_{pyr}$ distances are markedly different from each other [2.5170(18) and 2.0264(17) Å] as are the two Cu–$N_{trz}$ distances [1.9908(17) and 2.2564(17) Å] (Table 2 and Table 3). These geometrical features are a manifestation of an unsymmetrical Jahn–Teller elongation of the distorted $CuN_5O$ coordination octahedron along the N(1)–Cu(1)–N(3A) axis [Cu(1)–N(1) 2.5170(18) and Cu(1)–N(3A) 2.2564(17) Å]. The Cu(1)–N(20) and the Cu(1)–O(1) distances between the metal centre and the axial MeCN and $H_2O$ co-ligands, respectively, are practically identical [2.0024(19) and 2.0029(16) Å]. In contrast, in $[Cu^{II}(pldpt)_2(ClO_4)_2] \cdot 2DMF$ (**13**) (see above) as well as in analogous copper(II) complexes of related ligands the Jahn–Teller elongation of the

 © 2006 Wiley-VCH Verlag GmbH & Co. KGaA, Weinheim 

coordination octahedron occurs along the $X_{axial}$–Cu–$X_{axial}$ axis and is symmetrical. The distance of 4.3140(5) Å between the two copper centres in complex **14** is in between the corresponding distances observed in $[Cu^{II}_2(NH_2dpt)(H_2O)_4(SO_4)_2]\cdot H_2O$[12] and $[Cu^{II}_2(ibdpt)_2(MeCN)_2(ClO_4)_2](ClO_4)_2\cdot 2MeCN$[32] (Table 1). The axial $H_2O$ co-ligand is involved in hydrogen bonding to the two $ClO_4^-$ counterions [O(1)···O(11) 2.78 and O(1)···O(21) 2.81 Å]. Here too, the pyridine–triazole–pyridine moiety is nearly planar [4.4(1) and 4.7(1)°], with the pyrrole ring intersecting the triazole mean plane almost at 88.8(1)° (Table 4).

The molecular structure of $[Zn^{II}_2(pldpt)_2(MeCN)_2(H_2O)_2](BF_4)_4$ (**17**) (Figure S5) is basically the same as that of the cobalt(II) analogue $[Co^{II}_2(pldpt)_2(MeCN)_2(H_2O)_2](BF_4)_4$ (**8**) (Figure S3). Complex **17** is the first dinuclear zinc(II) complex of any 4-substituted 3,5-di(2-pyridyl)-4*H*-1,2,4-triazole to be synthesised and structurally characterised. The two zinc centres are separated by 4.455(2) Å (Table 1) and the pyridine–triazole–pyridine moiety shows only a slight deviation from planarity [5.2(3) and 5.5(3)°], while the pyrrole ring is almost perpendicular [88.4(2)°] to the triazole mean plane (Table 4). The complex adopts the dinuclear $(N',N^1,N^2,N'')_2$ double-bridging coordination mode (Figure 2). Here too, the two ligand molecules are somewhat shifted sideways relative to each other resulting in a slight tetragonal distortion of the system which is manifested in the relatively large variation of the Zn–$N_{pyr}$ and Zn–$N_{trz}$ distances [2.173(4)–2.227(4) and 2.119(4)–2.164(4) Å, respectively] (Table 2 and Table 3). The $H_2O$ co-ligand forms hydrogen bonds to the two $BF_4^-$ counterions [O(1)···F(11) 2.75 and O(1)···F(21) 2.77 Å].

In all of the complexes of pldpt (**3**) synthesised and structurally characterised in the course of this work the mean planes of the central triazole ring and the π-electron-rich pyrrole ring of the ligand are not co-planar but rather intersect at almost right angles [82.4(3)–88.8(1)°] (Table 4). This precludes an electronic interaction occurring between them by a π-pathway. Therefore, if there is any transmission of electron density between these two heterocyclic rings it must occur across the σ-bond between them. Consequently, it is likely to be small.

## Mass Spectrometry

ESI mass spectra were recorded in MeCN for all of the initial powdery complexes. In all of the spectra the parent peak was assigned to the species $[(pldpt) + H]^+$. The spectra of the dinuclear $ClO_4^-$ complexes **4**, **9** and **15** showed, almost exclusively, peaks that were assigned to mononuclear species, including the fragments $[M(pldpt)_3]^{2+}$ at $m/z$ = 461.7 (M = $Co^{II}$), 461.1 (M = $Ni^{II}$) and 464.3 (M = $Zn^{II}$), respectively, with a metal-to-ligand molar ratio of 1:3 which has not been observed for complexes of any 4-substituted 3,5-di(2-pyridyl)-4*H*-1,2,4-triazole in the solid state so far. As the only peaks assignable to dinuclear species, the three spectra also had in common peaks for the fragments $[M_2(pldpt)_2(ClO_4)_3]^+$ at $m/z$ = 993.3 (M = $Co^{II}$), 991.2 (M = $Ni^{II}$) and 1003.1 (M = $Zn^{II}$), respectively.

Despite their good solubility in MeCN, and the fact that only one dinuclear solid state species was formed in each case on crystallisation, the ESI mass spectra of the $BF_4^-$ complexes **7**, **10** and **16** were not particularly informative and showed only about half the number of assignable peaks that the analogous $ClO_4^-$ complexes had. As was the case with the $ClO_4^-$ analogues, the spectra of complexes **7**, **10** and **16** all had peaks for the fragments $[M(pldpt)_3]^{2+}$ in common, while no peaks corresponding to dinuclear species were observed for these compounds.

The ESI mass spectrum of $[Cu^{II}(pldpt)_2(ClO_4)_2]$ (**12**) was in full agreement with the other analytical data of this complex, albeit that most of the peaks were assigned to copper(I) rather than copper(II) species, the former arising from reduction of the metal centre under the conditions of the experiment.

## NMR Spectroscopy

The $^1H$ NMR spectrum of the dinuclear zinc(II) $ClO_4^-$ complex **15** in [$D_7$]DMF showed only six signals in the aromatic region, which was in agreement with only one species being present (Figure S6). This confirmed that this complex does not exist in an equilibrium with mononuclear species in DMF solution but retains its symmetrical dinuclear architecture in this solvent, in contrast to the recrystallisation behaviour of the analogous cobalt(II) and nickel(II) complexes **4** and **9**, respectively, in the presence of this solvent. Five of the signals were well resolved and only the signal at $\delta$ = 7.55 ppm, which was assigned to 3-Py*H*, was broad. While the other five signals were shifted downfield, as could be expected upon coordination, by 0.12–0.23 ppm relative to the signals of free pldpt (**3**) in [$D_7$]DMF, the signal for 3-Py*H* was shifted upfield by 0.40 ppm, thus swapping places with the signal for 5-Py*H*. The single-crystal X-ray structure analysis of the analogous $BF_4^-$ complex **17** shows that the pyrrole ring is, as expected on steric grounds, almost perpendicular to the two pyridine rings and the triazole ring in the solid state. The significant upfield shift of the signal for 3-Py*H* observed in the $^1H$ NMR spectra of both the $ClO_4^-$ complex **15** and the $BF_4^-$ complex **16** (see below) in [$D_7$]DMF indicates that the same relative orientation is adopted in solution, as this proton appears to be interacting with the π-electron system of the adjacent pyrrole ring. As outlined above, the normal conformation of the pyridine rings in non-coordinated 4-substituted 3,5-di(2-pyridyl)-4*H*-1,2,4-triazoles is the one where the nitrogen atoms of the pyridine rings point towards the face of the pyrrole ring, i.e. the pyrrole ring is almost at a right angle to the triazole ring in all of the structurally characterised compounds, whereas on coordination in a dinuclear complex the pyridine rings are held the other way round due to the binding of the metal ions, so the 3-Py*H* protons now point towards the face of the pyrrole ring. For complex **17** the two independent distances between the 3-Py*H* and

 © 2006 Wiley-VCH Verlag GmbH & Co. KGaA, Weinheim 

the centroid of the pyrrole ring are 3.02 and 3.66 Å in the solid state. Finally, given that in the dinuclear complex the coordinated pyridine and triazole rings are expected to be approximately co-planar, these NMR spectroscopic data in [$D_7$]DMF are consistent with the triazole and pyrrole rings being almost perpendicular to one another, precluding an electronic interaction occurring between them by a π-pathway and indicating that any electronic interactions occur via the N–N σ-bond.

The $^{13}C$ NMR spectrum of the dinuclear zinc(II) $ClO_4^-$ complex **15** in [$D_7$]DMF, which was very similar to the corresponding spectrum of pldpt (**3**) with all of the signals being shifted only slightly (Figure S7), was also consistent with the formulation of a dinuclear solution species and with only one species being present in DMF solution.

As expected, the NMR spectra, recorded in [$D_7$]DMF, of the dinuclear zinc(II) $BF_4^-$ complex **16**, which upon recrystallisation from MeCN/$Et_2O$ afforded the structurally characterised dinuclear complex **17** (see above), were practically identical to those observed for the analogous $ClO_4^-$ complex **15**. Attempts were also made to record NMR spectra of complex **16** in [$D_3$]MeCN for comparison but for unknown reasons this failed and useful spectral information could not be obtained using this solvent.

### Conductivity Measurements

The molar conductivities of the $ClO_4^-$ complexes **4**, **9** and **15** were determined in DMF. The values obtained (260, 300 and 255 $\Omega^{-1}\cdot cm^2\cdot mol^{-1}$, respectively) are in agreement with the expected value of about 240–300 $\Omega^{-1}\cdot cm^2\cdot mol^{-1}$ for a 4:1 electrolyte in this solvent.[74] For the $BF_4^-$ complexes **7**, **10** and **16** the corresponding values, determined in DMF, were found to be 280, 250 and 270 $\Omega^{-1}\cdot cm^2\cdot mol^{-1}$, respectively, which are also within the expected range. Likewise, the molar conductivities of complexes **7**, **10** and **16** in MeCN (480, 470 and 475 $\Omega^{-1}\cdot cm^2\cdot mol^{-1}$, respectively) were found to be in good agreement with the expected value of about 420–500 $\Omega^{-1}\cdot cm^2\cdot mol^{-1}$ for 4:1 electrolytes in this solvent.[74] The molar conductivity of the mononuclear copper(II) complex **12** was determined as 245 $\Omega^{-1}\cdot cm^2\cdot mol^{-1}$ in MeCN. This value agrees well with that expected for a 2:1 electrolyte in MeCN (220–300 $\Omega^{-1}\cdot cm^2\cdot mol^{-1}$ ).[74]

### Magnetic Studies

Magnetic measurements were carried out on powder samples of the two dinuclear cobalt complexes $Co^{II}_2(pldpt)_2(ClO_4)_4(MeCN)_m(H_2O)_n$ (**4**) and $Co^{II}_2(pldpt)_2(BF_4)_4(MeCN)_m(H_2O)_n$ (**7**) as well as of the two dinuclear nickel complexes $Ni^{II}_2(pldpt)_2(ClO_4)_4(MeCN)_m(H_2O)_n$ (**9**) and $Ni^{II}_2(pldpt)_2(BF_4)_4(MeCN)_m(H_2O)_n$ (**10**), revealing in each case weak antiferromagnetic coupling between the metal centres (Table 6).

The dinuclear cobalt(II) complexes **4** and **7** exhibited almost identical magnetic behaviour despite the different counterions, thus indicating that the nature of the latter has practically no influence on the magnetism of these compounds. Similarly, the magnetic behaviour of different samples of the same compound was found to be independent within experimental error from the actual solvent content. The magnetic moments for complexes **4** (Figure 5) and **7** (Figure S7) at room temperature were 4.50 and 4.29 $\mu_B$ per cobalt(II) centre, respectively, and thus somewhat higher than for spin-only $d^7$ high-spin systems as a result of spin-orbit coupling and ligand field splitting effects acting on the $^4T_{1g}$ single ion states. For both complexes the fitted curves for the temperature dependence of the molar magnetic susceptibility showed a maximum, at $T$ = 13 K with $\chi_m$ = 0.06806 $cm^3\cdot mol^{-1}$ for complex **4** (Figure 7) and with

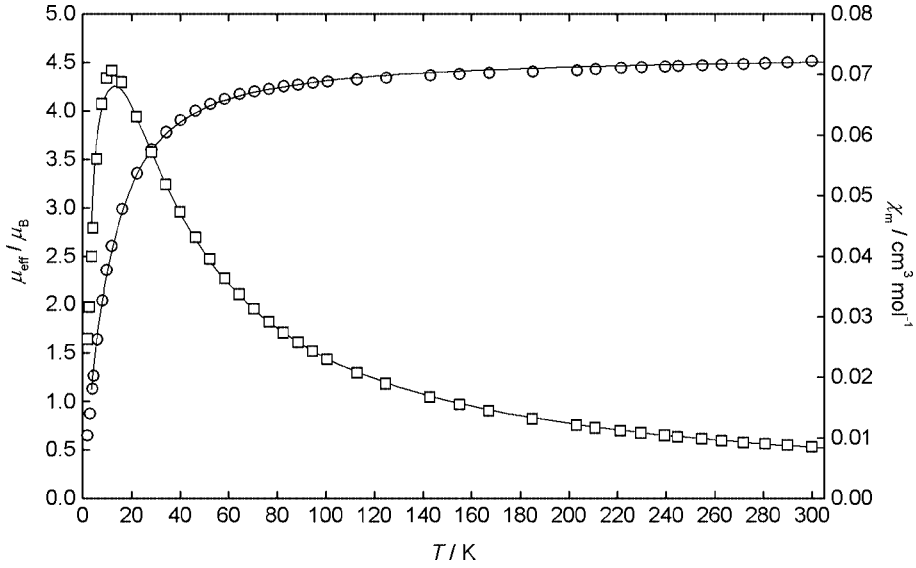


Figure 7. Temperature dependence of the effective magnetic moment $\mu_{eff}$ (○) and the molar magnetic susceptibility $\chi_m$ (□) per cobalt(II) centre for $Co^{II}_2(pldpt)_2(ClO_4)_4(MeCN)_m(H_2O)_n$ (**4**) ($m$ = 1, $n$ = 0). The solid lines represent the best fit using the parameters given in Table 5.

 © 2006 Wiley-VCH Verlag GmbH & Co. KGaA, Weinheim 

$\chi_m$ = 0.06166 cm$^3$·mol$^{-1}$ for complex **7** (Figure S8), a feature typical for antiferromagnetic exchange coupling. The magnetic data were fitted well by an $S$ = 3/2 dimer model of the spin-only Heisenberg–Van Vleck type ($-2J\mathbf{S_1}\cdot\mathbf{S_2}$)[75] indicating that orbital degeneracy had largely been removed. The best fit parameters are given in Table 5. The magnitude of the coupling between the two cobalt(II) centres in the $ClO_4^-$ complex **4** ($J$ = –3.1 cm$^{-1}$) and the $BF_4^-$ complex **7** ($J$ = –3.1 cm$^{-1}$) was similar to the corresponding value observed for $[Co^{II}_2(TsPMAT)_2](BF_4)_4\cdot 4H_2O$ ($J$ = –3.3 cm$^{-1}$)[51] and was only slightly less than that reported for related complexes of other 4-substituted 3,5-di(2-pyridyl)-4*H*-1,2,4-triazoles.[5,32]

Table 5. Magnetic data for $Co^{II}_2(pldpt)_2(ClO_4)_4(MeCN)_m(H_2O)_n$ (**4**), $Co^{II}_2(pldpt)_2(BF_4)_4(MeCN)_m(H_2O)_n$ (**7**), $Ni^{II}_2(pldpt)_2(ClO_4)_4(MeCN)_m(H_2O)_n$ (**9**) and $Ni^{II}_2(pldpt)_2(BF_4)_4(MeCN)_m(H_2O)_n$ (**10**).

| Complex | $m$ | $n$ | $J$ [cm$^{-1}$] | $g$ | *TIP* [cm$^3$·mol$^{-1}$] | Monomer [%] |
|---|---|---|---|---|---|---|
| **4** | 1 | 0 | –3.1 | 2.36 | 60·10$^{-6}$ | 0.1 |
| **7** | 1 | 2 | –3.1 | 2.25 | 65·10$^{-6}$ | 0.4 |
| **9** | 0 | 0 | –8.8 | 2.05 | 0 | 0.5 |
| **10** | 0 | 4 | –7.8 | 2.15 | 65·10$^{-6}$ | 0.5 |

The room temperature effective magnetic moment of 2.82 $\mu_B$ per nickel(II) centre for the $ClO_4^-$ complex **9** (Figure 8) was reduced from the typical uncoupled value of ca. 3.1 $\mu_B$ thus indicating that antiferromagnetic coupling was occurring. For the $BF_4^-$ complex **10** the corresponding value was 3.00 $\mu_B$ (Figure S9) and hence the nickel(II) centres are less strongly coupled than in complex **9**. The fitted curves for the temperature dependence of the molar magnetic susceptibility of complexes **9** (Figure 8) and **10** (Figure S9) had maxima at $T$ = 26 K with $\chi_m$ = 0.01639 cm$^3$·mol$^{-1}$ and $T$ = 22 K with $\chi_m$ = 0.02058 cm$^3$·mol$^{-1}$, respectively. The antiferromagnetic coupling between the two nickel(II) centres in the $ClO_4^-$ complex **9** was somewhat larger than in the $BF_4^-$ complex **10**, the coupling constants being –8.8 and –7.8 cm$^{-1}$, respectively. Here too, the magnetic behaviour of different samples of the same compound was found to be independent within experimental error from the actual solvent content. As with the cobalt(II) complexes of this ligand described above, the antiferromagnetic coupling in complexes **9** and **10** was less than that observed in related nickel(II) complexes of other 4-substituted 3,5-di(2-pyridyl)-4*H*-1,2,4-triazoles.[5,32]

## Conclusion

The coordination behaviour of the known ligand pldpt (**3**)[44] towards the first-row transition-metal ions $Co^{2+}$, $Ni^{2+}$, $Cu^{2+}$ and $Zn^{2+}$ in reactions with a metal-to-ligand molar ratio of 1:1 has been investigated in detail for the first time. From these studies it is clear that this ligand can act as a bis-bidentate chelator and thus form dinuclear complexes but it has also been revealed that its dinuclear complexes can be labile in solution depending on the solvent used. Although in most cases the initial precipitates are dinuclear, equilibria between di- and mononuclear species can occur in solution, depending on the metal salt and the solvent employed. Thus, for example, the strongly polar aprotic solvent DMF causes the dinuclear cobalt(II) and nickel(II) $ClO_4^-$ complexes **4** and **9**, respectively, to break up to some extent giving rise to mixtures of di- and mononuclear species, while the corresponding dinuclear zinc(II) $ClO_4^-$ complex **15** appears to be perfectly stable in this solvent. In contrast, from solutions of the analogous $BF_4^-$ complexes **7**, **10** and **16** in the less polar solvent MeCN only dinuclear species are isolated.

Given that our primary interest in pldpt (**3**) was to use it to prepare and study further examples of, prior to our re-

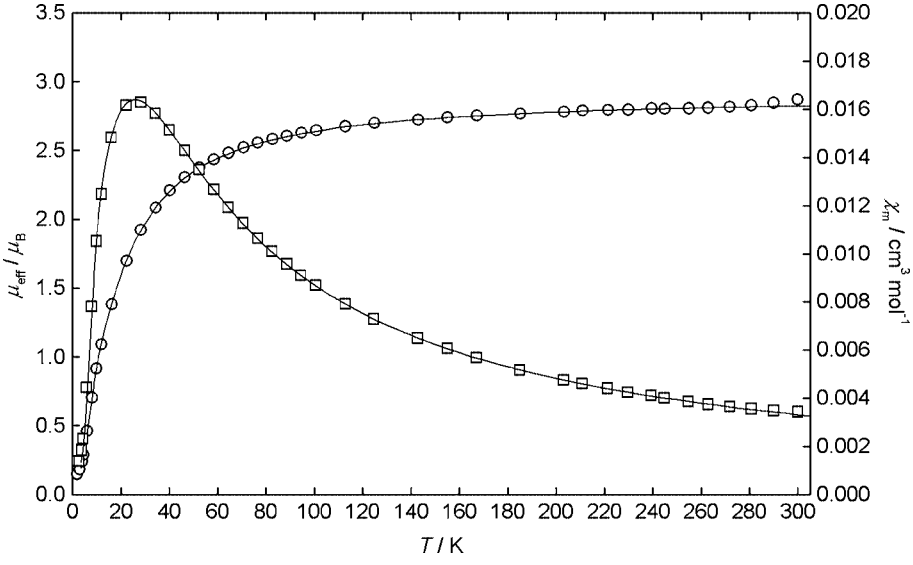


Figure 8. Temperature dependence of the effective magnetic moment $\mu_{eff}$ (○) and the molar magnetic susceptibility $\chi_m$ (□) per nickel(II) centre for $Ni^{II}_2(pldpt)_2(ClO_4)_4(MeCN)_m(H_2O)_n$ (**9**) ($m$ = 0, $n$ = 0). The solid lines represent the best fit using the parameters given in Table 5.

 © 2006 Wiley-VCH Verlag GmbH & Co. KGaA, Weinheim 

search, rarely observed, discrete dinuclear complexes of 4-substituted-3,5-di(2-pyridyl)-4*H*-1,2,4-triazoles, the deliberate preparation of mononuclear complexes employing metal-to-ligand molar ratios of 1:2 or 1:3 was not attempted in the course of this particular study. However, such studies are currently being carried out as an integral component of our ongoing investigation into the iron(II) coordination chemistry of pldpt (**3**) and related ligands.[52]

The enhanced dinucleating ability of pldpt (**3**), as compared to the 4-aryl-3,5-di(2-pyridyl)-4*H*-1,2,4-triazoles, is attributed largely to the effect of the 4-(1*H*-pyrrol-1-yl) group on the relative solubility of the various possible products in the solvents employed. The X-ray crystallographic data, and the NMR spectroscopic data for the zinc(II) complex **15**, indicate that the electronic effect of this particular substituent is probably quite small because the potentially strong π-donation from the pyrrole ring is switched off due to the near-perpendicular orientation of the pyrrole ring relative to the triazole ring, leaving only the effects transmitted by the σ-pathway, which are likely to be weak. These findings are consistent with the suggestion that the substituent on $N^4$ in 4-substituted 3,5-di(2-pyridyl)-4*H*-1,2,4-triazoles influences the ability of such a ligand to form only mononuclear or both di- and mononuclear complexes by a complex mixture of factors, the most important of which, in the case of pldpt (**3**), appears to be its effect on the relative solubility of the various possible products in the solvents employed during the preparation and/or the recrystallisation of the complexes, although in other cases subtle electronic effects may also be at work.[2,31,32,52]

Magnetic studies carried out on the dinuclear cobalt(II) complexes **4** and **7** and the dinuclear nickel(II) complexes **9** and **10** have shown that the two central triazole bridges provided by pldpt (**3**) mediate weak antiferromagnetic exchange coupling between the two metal centres of these complexes. With a view to systematically accessing families of spin crossover systems, the exploration of the coordination behaviour of pldpt (**3**), and related ligands, towards iron(II) salts in 1:1, 1:2 and 1:3 metal-to-ligand molar ratios, in a variety of solvents, is well underway and the results of this study will be reported in due course.[52]

## Experimental Section

**General Remarks:** All solvents used for reactions were laboratory reagent grade while UV/Vis/NIR and conductivity measurements were carried out in HPLC-grade solvents. All chemicals were purchased from Aldrich and used as received. Elemental analyses were carried out by the Campbell Microanalytical Laboratory at the University of Otago. Melting points were determined with a Gallenkamp melting point apparatus in open-glass capillaries and are uncorrected. $^1$H and $^{13}$C NMR spectra were recorded with a Varian INOVA-500 spectrometer at 25 °C. Chemical shifts are given relative to TMS using the residual solvent signals as secondary reference ($CDCl_3$: $\delta_H$ = 7.26 ppm, $\delta_C$ = 77.16 ppm; [$D_7$]DMF: $\delta_H$ = 8.02 ppm, $\delta_C$ = 163.15 ppm). Peak assignments were made on the basis of chemical shifts, integration patterns and coupling constants as well as two-dimensional correlation experiments where necessary. IR spectra were recorded in the range 4000–400 cm$^{-1}$ with a Perkin–Elmer Spectrum BX FT-IR spectrophotometer. UV/Vis/NIR spectra were recorded with a Varian CARY 500 Scan UV/Vis/NIR spectrophotometer in the range 200–1400 nm. Conductivity measurements were carried out at 25 °C using a Suntex SC-170 conductivity meter. ESI mass spectra of organic compounds were run on a Shimadzu LCMS-QP8000α spectrometer while spectra of complexes were run on a MicroMass LCT spectrometer. For all compounds MeCN was used as the solvent. Magnetic data were recorded in the range 300–4.2 K using a Quantum Design MPMS5 SQUID magnetometer with an applied field of 1 T.

***Caution:*** *While no problems were encountered in the course of this work, reactions involving $N_2H_4{\cdot}H_2O$ may form potentially explosive mixtures so must be carried out with extreme caution. Similarly, $ClO_4^-$ salts are potentially explosive so should be handled with appropriate care.*

**3,6-Di(2-pyridyl)-1,4-dihydro-1,2,4,5-tetrazine (1):** A heterogeneous mixture of 2-pyridinecarbonitrile (20.8 g, 0.20 mol) and $N_2H_4{\cdot}H_2O$ (50 mL) was refluxed for 2 hours during which time the mixture became homogeneous, turned orange and a solid separated from the solution with heavy foaming. After cooling, all volatiles were evaporated under reduced pressure and the orange solid thus obtained was dried in vacuo. Recrystallisation from pyridine gave 13.8 g (58%) of analytically pure 3,6-di(2-pyridyl)-1,4-dihydro-1,2,4,5-tetrazine (**1**) as bright orange needles. M.p. 191–193 °C. $C_{12}H_{10}N_6$ (238.25): calcd. C 60.50, H 4.23, N 35.27; found C 60.50, H 4.14, N 35.33. $^1$H NMR (500 MHz, $CDCl_3$, ppm): $\delta$ = 7.34 [ddd, $^3J_{4,5}$ = 7.7 Hz, $^3J_{5,6}$ = 4.8 Hz, $^4J_{3,5}$ = 1.2 Hz, 2 H, 2×5-Py*H*], 7.74 [dt, $^3J_{3,4}$ = $^3J_{4,5}$ = 7.7 Hz, $^4J_{4,6}$ = 1.8 Hz, 2 H, 2×4-Py*H*], 8.05 [ddd, $^3J_{3,4}$ = 7.7 Hz, $^4J_{3,5}$ = 1.2 Hz, $^5J_{3,6}$ = 0.9 Hz, 2 H, 2×3-Py*H*], 8.54–8.59 [m, 4 H, 2×6-Py*H* and 2×PyCN*H*]. $^{13}$C{$^1$H} NMR (125 MHz, $CDCl_3$, ppm): $\delta$ = 121.41 [2×3-Py*C*], 124.97 [2×5-Py*C*], 136.83 [2×4-Py*C*], 146.75 [2×N*C*NH], 147.65 [2×2-Py*C*], 148.51 [2×6-Py*C*]. IR (KBr): $\tilde{\nu}$ = 3343, 3296, 3058, 1588, 1564, 1470, 1446, 1387, 1288, 1251, 1155, 1117, 1089, 1077, 1041, 995, 981, 903, 885, 795, 787, 771, 745, 720, 677, 667, 655, 622, 490 cm$^{-1}$. ESI-MS (pos., MeCN): *m*/*z* = 239 [M + H]$^+$, 261 [M + Na]$^+$, 277 [M + K]$^+$.

**4-Amino-3,5-di(2-pyridyl)-4*H*-1,2,4-triazole ($NH_2$dpt, 2):** 3,6-Di(2-pyridyl)-1,4-dihydro-1,2,4,5-tetrazine (**1**) (11.9 g, 50.0 mmol) was dissolved in 2 M HCl (100 mL) and the dark brown solution was refluxed for 30 minutes. After cooling, the resulting golden solution was basified to pH ≈ 9 by dropwise addition of concd. $NH_3$ resulting in the formation of a voluminous colourless precipitate. The solid was filtered off, washed with $H_2O$ and dried in vacuo. Recrystallisation from $H_2O$/EtOH (1:1) gave 10.1 g (84%) of analytically pure $NH_2$dpt (**2**) as colourless needles. Alternatively, a mixture of 2-pyridinecarbonitrile (10.4 g, 0.10 mol), $N_2H_4{\cdot}H_2SO_4$ (13.0 g, 0.10 mol) and $N_2H_4{\cdot}H_2O$ (15.0 g, 0.30 mol) in 1,2-ethanediol (50 mL) was heated at 130 °C for 24 hours. An orange solid that soon separated from the solution with heavy foaming redissolved almost completely over time. On cooling to room temperature, the reaction mixture solidified to give an almost colourless solid contaminated with some orange material. $H_2O$ (100 mL) was added, the resulting slurry was filtered and the crude product was washed with water and dried in vacuo. Recrystallisation from $H_2O$/EtOH (1:1) gave 8.06 g (67%) of crude $NH_2$dpt (**2**) as a yellowish solid. This material could be used in the next step without further purification. Analytically pure material was obtained as colourless needles only after at least one more recrystallisation from $H_2O$/EtOH (1:1). M.p. 185–187 °C. $C_{12}H_{10}N_6$ (238.25): calcd. C 60.50, H 4.23, N 35.27; found C 60.35, H 4.10, N 35.00. $^1$H NMR (500 MHz, $CDCl_3$, ppm): $\delta$ = 7.36 [ddd, $^3J_{4,5}$ = 7.7 Hz, $^3J_{5,6}$ =

 © 2006 Wiley-VCH Verlag GmbH & Co. KGaA, Weinheim 

4.8 Hz, $^4J_{3,5}$ = 1.2 Hz, 2 H, 2×5-Py*H*], 7.86 [dt, $^3J_{3,4}$ = $^3J_{4,5}$ = 7.7 Hz, $^4J_{4,6}$ = 1.8 Hz, 2 H, 2×4-Py*H*], 8.38 [ddd, $^3J_{3,4}$ = 7.7 Hz, $^4J_{3,5}$ = 1.2 Hz, $^5J_{3,6}$ = 0.9 Hz, 2 H, 2×3-Py*H*], 8.49 [br. s, 2 H, TzN$H_2$], 8.65 [ddd, $^3J_{5,6}$ = 4.8 Hz, $^4J_{4,6}$ = 1.8 Hz, $^5J_{3,6}$ = 0.9 Hz, 2 H, 2×6-Py*H*]. $^{13}C\{^1H\}$ NMR (125 MHz, $CDCl_3$, ppm): $\delta$ = 122.97 [2×3-Py*C*], 124.11 [2×5-Py*C*], 137.41 [2×4-Py*C*], 147.82 [3- and 5-Tz*C*], 148.10 [2×2-Py*C*], 148.43 [2×6-Py*C*]. IR (KBr): $\tilde{\nu}$ = 3421, 3293, 1588, 1566, 1545, 1465, 1432, 1412, 1390, 1318, 1273, 1249, 1148, 1093, 1074, 1041, 998, 968, 912, 795, 787, 737, 693, 677, 623, 586, 489 $cm^{-1}$. ESI-MS (pos., MeCN): *m*/*z* = 239 $[M + H]^+$, 261 $[M + Na]^+$, 277 $[M + K]^+$.

**3,5-Di(2-pyridyl)-4-(1*H*-pyrrol-1-yl)-4*H*-1,2,4-triazole (pldpt, 3):** A mixture of $NH_2$dpt (**2**) (4.77 g, 20 mmol) and 2,5-dimethoxytetrahydrofuran (3.30 g, 25.0 mmol) in 1,4-dioxane (20 mL) and acetic acid (20 mL) was refluxed for 24 hours. After cooling, all volatiles were removed in vacuo to give a dark crystalline solid. This was taken up in $CH_2Cl_2$ (50 mL) and the mixture was filtered through a short column of silica gel. The filtrate was evaporated under reduced pressure and the yellowish solid thus obtained was dried in vacuo. Recrystallisation from EtOH gave 4.46 g (77%) of analytically pure pldpt (**3**) as colourless needles. M.p. 199–201 °C. $C_{16}H_{12}N_6$ (288.31): calcd. C 66.66, H 4.20, N 29.15; found C 66.90, H 3.96, N 29.22. $^1H$ NMR (500 MHz, $CDCl_3$, ppm): $\delta$ = 6.22 [t, $^3J$ = 2.4 Hz, 2 H, 3- and 4-Pl*H*], 6.86 [t, $^3J$ = 2.4 Hz, 2 H, 2- and 5-Pl*H*], 7.30 [ddd, $^3J_{4,5}$ = 7.7 Hz, $^3J_{5,6}$ = 4.8 Hz, $^4J_{3,5}$ = 1.2 Hz, 2 H, 2×5-Py*H*], 7.75 [dt, $^3J_{3,4}$ = $^3J_{4,5}$ = 7.7 Hz, $^4J_{4,6}$ = 1.8 Hz, 2 H, 2×4-Py*H*], 7.84 [ddd, $^3J_{3,4}$ = 7.7 Hz, $^4J_{3,5}$ = 1.2 Hz, $^5J_{3,6}$ = 0.9 Hz, 2 H, 2×3-Py*H*], 8.52 [ddd, $^3J_{5,6}$ = 4.8 Hz, $^4J_{4,6}$ = 1.8 Hz, $^5J_{3,6}$ = 0.9 Hz, 2 H, 2×6-Py*H*]. $^1H$ NMR (500 MHz, [$D_7$]DMF, ppm): $\delta$ = 6.12 [t, $^3J$ = 2.4 Hz, 2 H, 3- and 4-Pl*H*], 7.20 [t, $^3J$ = 2.4 Hz, 2 H, 2- and 5-Pl*H*], 7.51 [ddd, $^3J_{4,5}$ = 7.7 Hz, $^3J_{5,6}$ = 4.8 Hz, $^4J_{3,5}$ = 1.2 Hz, 2 H, 2×5-Py*H*], 7.95 [ddd, $^3J_{3,4}$ = 7.7 Hz, $^4J_{3,5}$ = 1.2 Hz, $^5J_{3,6}$ = 0.9 Hz, 2 H, 2×3-Py*H*], 8.00 [dt, $^3J_{3,4}$ = $^3J_{4,5}$ = 7.7 Hz, $^4J_{4,6}$ = 1.8 Hz, 2 H, 2×4-Py*H*], 8.54 [ddd, $^3J_{5,6}$ = 4.8 Hz, $^4J_{4,6}$ = 1.8 Hz, $^5J_{3,6}$ = 0.9 Hz, 2 H, 2×6-Py*H*]. $^{13}C\{^1H\}$ NMR (125 MHz, $CDCl_3$, ppm): $\delta$ = 108.44 [3- and 4-Pl*C*], 122.34 [2- and 5-Pl*C*], 123.54 [2×3-Py*C*], 124.90 [2×5-Py*C*], 136.84 [2×4-Py*C*], 145.33 [2×2-Py*C*], 149.93 [2×6-Py*C*], 153.16 [3- and 5-Tz*C*]. $^{13}C\{^1H\}$ NMR (125 MHz, [$D_7$]DMF, ppm): $\delta$ = 108.51 [3- and 4-Pl*C*], 124.02 [2- and 5-Pl*C*], 124.74 [2×3-Py*C*], 126.16 [2×5-Py*C*], 138.21 [2×4-Py*C*], 146.69 [2×2-Py*C*], 150.79 [2×6-Py*C*], 154.15 [3- and 5-Tz*C*]. IR (KBr): $\tilde{\nu}$ = 3118, 1587, 1569, 1533, 1465, 1443, 1435, 1423, 1332, 1281, 1246, 1181, 1150, 1088, 1069, 1044, 1010, 992, 963, 912, 790, 736, 729, 710, 703, 633, 619, 608, 524, 489 $cm^{-1}$. ESI-MS (pos., MeCN): *m*/*z* = 289 $[M + H]^+$, 311 $[M + Na]^+$, 327 $[M + K]^+$. UV/Vis/NIR (MeCN): $\lambda_{max}$ ($\varepsilon$/L·mol$^{-1}$·cm$^{-1}$) = 251 (14600), 281 nm (18500).

**Reaction of pldpt (3) with $CoCl_2·6H_2O$ (Method A):** A pinkish-red solution of $CoCl_2·6H_2O$ (238 mg, 1.00 mmol) in $H_2O$ (5 mL) was added to a colourless solution of pldpt (**3**) (288 mg, 1.00 mmol) in MeOH (20 mL) dropwise at room temperature and the resulting orange-brown solution was stirred for 30 minutes. Slow evaporation over the course of 4 weeks led to the formation of a large quantity of a beige solid and a few tiny orange prisms. The solid products were filtered off and washed with MeOH. Drying in vacuo gave $Co^{II}(pldpt)_2Cl_2(H_2O)_{1.5}$. $C_{32}H_{27}Cl_2CoN_{12}O_{1.5}$ (733.49): calcd. C 52.40, H 3.71, N 22.92, Cl 9.67; found C 52.36, H 3.49, N 23.17, Cl 9.66.

**Reaction of pldpt (3) with $CoCl_2·6H_2O$ (Method B):** A deep blue solution of $CoCl_2·6H_2O$ (238 mg, 1.00 mmol) in EtOH (5 mL) was added to a colourless refluxing solution of pldpt (**3**) (288 mg, 1.00 mmol) in EtOH (20 mL). A blue solid formed almost immediately. The resulting suspension was refluxed for another 15 minutes and was then stirred at room temperature for 24 hours. The solid was filtered off and washed with EtOH. Drying in vacuo gave 388 mg (ca. 90%) of $Co^{II}_2(pldpt)_2Cl_4(H_2O)$ as a pink powder. $C_{32}H_{26}Cl_4Co_2N_{12}O$ (854.32): calcd. C 44.99, H 3.07, N 19.67; found C 45.38, H 3.05, N 19.51.

**Reaction of pldpt (3) with $Co(ClO_4)_2·6H_2O$:** An orange solution of $Co(ClO_4)_2·6H_2O$ (366 mg, 1.00 mmol) in MeCN (5 mL) was added to a colourless refluxing solution of pldpt (**3**) (288 mg, 1.00 mmol) in MeCN (20 mL). An orange solid formed almost immediately. The resulting suspension was cooled to room temperature and the solid was filtered off and washed with MeCN. Drying in vacuo gave 555 mg (ca. 90%) of $Co^{II}_2(pldpt)_2(ClO_4)_4(MeCN)_m(H_2O)_n$ (**4**) as a pale orange powder. The solvent content of the initial products varied considerably from batch to batch. Heating of the powders at 60 °C in vacuo for several days similarly afforded materials of variable solvent content. A sample analysing as $Co^{II}_2(pldpt)_2(ClO_4)_4(MeCN)$ was used for characterisation purposes. $C_{34}H_{27}Cl_4Co_2N_{13}O_{16}$ (1133.34): calcd. C 36.03, H 2.40, N 16.07; found C 36.08, H 2.54, N 16.26. IR (KBr): $\tilde{\nu}$ = 1611, 1544, 1517, 1473, 1439, 1405, 1354, 1302, 1263, 1188, 1113, 1074, 1012, 931, 911, 794, 746, 725, 701, 654, 635, 625 $cm^{-1}$. ESI-MS (pos., MeCN): *m*/*z* = 235.1 $[Co(pldpt)(MeCN)_3]^{2+}$, 289.1 $[(pldpt)H]^+$, 338.1 $[Co(pldpt)_2(MeCN)]^{2+}$, 446.0 $[Co(pldpt)(ClO_4)]^+$, 461.7 $[Co(pldpt)_3]^{2+}$, 487.0 $[Co(pldpt)(MeCN)(ClO_4)]^+$, 577.4 $[(pldpt)_2H]^+$, 734.3 $[Co(pldpt)_2(ClO_4)]^+$, 993.3 $[Co_2(pldpt)_2(ClO_4)_3]^+$. Molar conductivity (DMF): $\Lambda_m$ = 260 $\Omega^{-1}$·cm$^2$·mol$^{-1}$. Vapour diffusion of $Et_2O$ into an orange solution of complex **4** in MeCN/DMF (10:1) afforded orange crystals of $[Co^{II}_2(pldpt)_2(H_2O)_2(DMF)_2](ClO_4)_4·0.5Et_2O$ (**5**) and yellow crystals of $[Co^{II}(pldpt)_2(DMF)_2](ClO_4)_2$ (**6**).

**Reaction of pldpt (3) with $Co(BF_4)_2·6H_2O$:** An orange solution of $Co(BF_4)_2·6H_2O$ (341 mg, 1.00 mmol) in MeCN (5 mL) was added to a colourless refluxing solution of pldpt (**3**) (288 mg, 1.00 mmol) in MeCN (20 mL). The resulting orange solution was refluxed for 10 minutes and was then stirred at room temperature for another 4 hours during which time an orange precipitate formed. The solid was filtered off and washed with MeCN. Drying in vacuo gave 465 mg (ca. 80%) of $Co^{II}_2(pldpt)_2(BF_4)_4(MeCN)_m(H_2O)_n$ (**7**) as a pale orange powder. The solvent content of the initial products varied considerably from batch to batch. Heating of the powders at 60 °C in vacuo for several days similarly afforded materials of variable solvent content. A sample analysing as $Co^{II}_2(pldpt)_2(BF_4)_4(MeCN)(H_2O)_2$ was used for characterisation purposes. $C_{34}H_{31}B_4Co_2F_{16}N_{13}O_2$ (1118.79): calcd. C 36.50, H 2.79, N 16.28; found C 36.37, H 2.75, N 16.17. IR (KBr): $\tilde{\nu}$ = 1610, 1577, 1545, 1518, 1474, 1440, 1402, 1356, 1297, 1263, 1189, 1073, 911, 862, 796, 765, 749, 727, 705, 655, 636, 563, 533, 521, 436, 414 $cm^{-1}$. ESI-MS (pos., MeCN): *m*/*z* = 289.1 $[(pldpt)H]^+$, 317.6 $[Co(pldpt)_2]^{2+}$, 338.1 $[Co(pldpt)_2(MeCN)]^{2+}$, 461.7 $[Co(pldpt)_3]^{2+}$, 722.3 $[Co(pldpt)_2(BF_4)]^+$. UV/Vis/NIR (MeCN): $\lambda_{max}$ ($\varepsilon$/L·mol$^{-1}$·cm$^{-1}$) = 252 (25200), 291 (37000), 481 (46), 1022 nm (12). Molar conductivity (MeCN): $\Lambda_m$ = 480 $\Omega^{-1}$·cm$^2$·mol$^{-1}$. Molar conductivity (DMF): $\Lambda_m$ = 280 $\Omega^{-1}$·cm$^2$·mol$^{-1}$. Vapour diffusion of $Et_2O$ into the orange MeCN mother liquor or an orange solution of complex **7** in MeCN afforded orange crystals of $[Co^{II}_2(pldpt)_2(MeCN)_2(H_2O)_2](BF_4)_4$ (**8**).

**Reaction of pldpt (3) with $NiCl_2·6H_2O$ (Method A):** A grass green solution of $NiCl_2·6H_2O$ (238 mg, 1.00 mmol) in $H_2O$ (5 mL) was added to a colourless solution of pldpt (**3**) (288 mg, 1.00 mmol) in MeOH (20 mL) dropwise at room temperature and the resulting olive-green solution was stirred for 30 minutes. Slow evaporation over the course of 6 weeks led to the formation of an inseparable

 © 2006 Wiley-VCH Verlag GmbH & Co. KGaA, Weinheim 

mixture of a greenish crystalline solid and blue prisms in an estimated 3:1 ratio. These were not easily separable so no analytical data were obtained for either of the products.

**Reaction of pldpt (3) with $NiCl_2{\cdot}6H_2O$ (Method B):** A grass green solution of $NiCl_2{\cdot}6H_2O$ (238 mg, 1.00 mmol) in EtOH (5 mL) was added to a colourless solution of pldpt (**3**) (288 mg, 1.00 mmol) in EtOH (20 mL) dropwise at room temperature. The resulting green solution was stirred at room temperature for 4 hours during which time a green precipitate formed. The solid was filtered off and washed with EtOH. Drying in vacuo gave 275 mg (ca. 60%) of $Ni^{II}_2(pldpt)_2Cl_4(H_2O)_3$ as a very pale green powder. $C_{32}H_{30}Cl_4Ni_2N_{12}O_3$ (889.86): calcd. C 43.19, H 3.40, N 18.89; found C 43.62, H 3.28, N 18.74.

**Reaction of pldpt (3) with $Ni(ClO_4)_2{\cdot}6H_2O$:** A blue solution of $Ni(ClO_4)_2{\cdot}6H_2O$ (366 mg, 1.00 mmol) in MeCN (5 mL) was added to a colourless refluxing solution of pldpt (**3**) (288 mg, 1.00 mmol) in MeCN (20 mL). A purple solid formed almost immediately. The resulting suspension was cooled to room temperature and the solid was filtered off and washed with MeCN. Drying in vacuo gave 475 mg (ca. 80%) of $Ni^{II}_2(pldpt)_2(ClO_4)_4(MeCN)_m(H_2O)_n$ (**9**) as a pale violet powder. The solvent content of the initial products varied considerably from batch to batch. Heating of the powders at 60 °C in vacuo for several days similarly afforded materials of variable solvent content. A sample analysing as $Ni^{II}_2(pldpt)_2(ClO_4)_4$ was used for characterisation purposes. $C_{32}H_{24}Cl_4Ni_2N_{12}O_{16}$ (1091.81): calcd. C 35.20, H 2.22, N 15.39; found C 35.18, H 2.53, N 15.59. IR (KBr): $\tilde{\nu}$ = 1612, 1548, 1526, 1517, 1474, 1440, 1410, 1355, 1304, 1265, 1195, 1114, 1074, 1025, 1012, 931, 911, 793, 747, 725, 700, 659, 636, 625 $cm^{-1}$. ESI-MS (pos., MeCN): *m/z* = 214.1 $[Ni(pldpt)(MeCN)_2]^{2+}$, 234.6 $[Ni(pldpt)(MeCN)_3]^{2+}$, 255.1 $[Ni(pldpt)(MeCN)_4]^{2+}$, 289.1 $[(pldpt)H]^+$, 317.1 $[Ni(pldpt)_2]^{2+}$, 337.7 $[Ni(pldpt)_2(MeCN)]^{2+}$, 358.2 $[Ni(pldpt)_2(MeCN)_2]^{2+}$, 445.0 $[Ni(pldpt)(ClO_4)]^+$, 461.1 $[Ni(pldpt)_3]^{2+}$, 486.0 $[Ni(pldpt)(MeCN)(ClO_4)]^+$, 527.1 $[Ni(pldpt)(MeCN)_2(ClO_4)]^+$, 568.2 $[Ni(pldpt)(MeCN)_3(ClO_4)]^+$, 577.4 $[(pldpt)_2H]^+$, 733.2 $[Ni(pldpt)_2(ClO_4)]^+$, 991.2 $[Ni_2(pldpt)_2(ClO_4)_3]^+$. Molar conductivity (DMF): $\Lambda_m$ = 300 $\Omega^{-1}{\cdot}cm^2{\cdot}mol^{-1}$.

**Reaction of pldpt (3) with $Ni(BF_4)_2{\cdot}6H_2O$:** A blue solution of $Ni(BF_4)_2{\cdot}6H_2O$ (340 mg, 1.00 mmol) in MeCN (5 mL) was added to a colourless refluxing solution of pldpt (**3**) (288 mg, 1.00 mmol) in MeCN (20 mL). The resulting purple solution was refluxed for 10 minutes and was then stirred at room temperature for another 4 hours during which time a purple precipitate formed. The solid was filtered off and washed with MeCN. Drying in vacuo gave 215 mg (ca. 40%) of $Ni^{II}_2(pldpt)_2(BF_4)_4(MeCN)_m(H_2O)_n$ (**10**) as a pale violet powder. The solvent content of the initial products varied considerably from batch to batch. Heating of the powders at 60 °C in vacuo for several days similarly afforded materials of variable solvent content. A sample analysing as $Ni^{II}_2(pldpt)_2(BF_4)_4(H_2O)_4$ was used for characterisation purposes. $C_{32}H_{32}B_4F_{16}N_{12}Ni_2O_4$ (1113.28): calcd. C 34.52, H 2.90, N 15.10; found C 34.55, H 2.70, N 15.09. IR (KBr): $\tilde{\nu}$ = 1612, 1578, 1549, 1521, 1475, 1441, 1410, 1356, 1300, 1265, 1190, 1073, 911, 796, 750, 727, 705, 694, 659, 637, 564, 533, 522, 439, 415 $cm^{-1}$. ESI-MS (pos., MeCN): *m/z* = 289.1 $[(pldpt)H]^+$, 317.1 $[Ni(pldpt)_2]^{2+}$, 337.6 $[Ni(pldpt)_2(MeCN)]^{2+}$, 358.1 $[Ni(pldpt)_2(MeCN)_2]^{2+}$, 461.1 $[Ni(pldpt)_3]^{2+}$, 721.3 $[Ni(pldpt)_2(BF_4)]^+$. UV/Vis/NIR (MeCN): $\lambda_{max}$ ($\varepsilon$/L·mol$^{-1}$·cm$^{-1}$) = 238 (24400), 295 (36400), ca. 530 sh (ca. 70), 866 nm (40). Molar conductivity (MeCN): $\Lambda_m$ = 470 $\Omega^{-1}{\cdot}cm^2{\cdot}mol^{-1}$. Molar conductivity (DMF): $\Lambda_m$ = 250 $\Omega^{-1}{\cdot}cm^2{\cdot}mol^{-1}$. Vapour diffusion of $Et_2O$ into the purple MeCN mother liquor or a purple solution of complex **10** in MeCN afforded purple crystals of $[Ni^{II}_2(pldpt)_2(MeCN)_4](BF_4)_4{\cdot}2MeCN$ (**11**).

**Reaction of pldpt (3) with $Cu(ClO_4)_2{\cdot}6H_2O$:** A blue solution of $Cu(ClO_4)_2{\cdot}6H_2O$ (371 mg, 1.00 mmol) in MeCN (5 mL) was added to a colourless refluxing solution of pldpt (**3**) (288 mg, 1.00 mmol) in MeCN (20 mL). The resulting green solution was refluxed for 10 minutes and was then stirred at room temperature for another 4 hours during which time a blue precipitate formed. The solid was filtered off and washed with a minimum amount of MeCN. Drying in vacuo gave 249 mg (59%) of $[Cu^{II}(pldpt)_2(ClO_4)_2]$ (**12**) as a blue powder. $C_{32}H_{24}Cl_2CuN_{12}O_8$ (839.07): calcd. C 45.81, H 2.88, N 20.03; found C 45.52, H 2.78, N 20.05. IR (KBr): $\tilde{\nu}$ = 1614, 1588, 1571, 1554, 1533, 1513, 1485, 1456, 1434, 1340, 1311, 1272, 1193, 1105, 1023, 991, 929, 913, 793, 750, 742, 722, 698, 645, 622, 568, 495 $cm^{-1}$. ESI-MS (pos., MeCN): *m/z* = 289.1 $[(pldpt)H]^+$, 319.6 $[Cu(pldpt)_2]^{2+}$, 340.1 $[Cu(pldpt)_2(MeCN)]^{2+}$, 351.0 $[Cu(pldpt)]^+$, 369.1 $[Cu(pldpt)(H_2O)]^+$, 392.1 $[Cu(pldpt)(MeCN)]^+$, 639.2 $[Cu(pldpt)_2]^+$, 738.2 $[Cu(pldpt)_2(ClO_4)]^+$. UV/Vis/NIR (MeCN): $\lambda_{max}$ ($\varepsilon$/L·mol$^{-1}$·cm$^{-1}$) = 242 (35000), 295 (33500), 659 nm (90). Molar conductivity (MeCN): $\Lambda_m$ = 245 $\Omega^{-1}{\cdot}cm^2{\cdot}mol^{-1}$. Vapour diffusion of $Et_2O$ into a blue solution of complex **12** in MeCN gave blue crystals of $[Cu^{II}(pldpt)_2(ClO_4)_2]{\cdot}2DMF$ (**13**) while vapour diffusion of $Et_2O$ into the green MeCN mother liquor afforded green crystals of $[Cu^{II}_2(pldpt)_2(H_2O)_2(MeCN)_2](ClO_4)_4$ (**14**). The occurrence of the DMF solvates in complex **13** was probably due to the use of contaminated glassware.

**Reaction of pldpt (3) with $Zn(ClO_4)_2{\cdot}6H_2O$:** A colourless solution of $Zn(ClO_4)_2{\cdot}6H_2O$ (372 mg, 1.00 mmol) in MeCN (5 mL) was added to a colourless refluxing solution of pldpt (**3**) (288 mg, 1.00 mmol) in MeCN (20 mL). A colourless solid formed almost immediately. The resulting suspension was cooled to room temperature and the solid was filtered off and washed with MeCN. Drying in vacuo gave 470 mg (ca. 80%) of $Zn^{II}_2(pldpt)_2(ClO_4)_4(MeCN)_m(H_2O)_n$ (**15**) as a colourless powder. The solvent content of the initial products varied considerably from batch to batch. Heating of the powders at 60 °C in vacuo for several days similarly afforded materials of variable solvent content. A sample analysing as $Zn^{II}_2(pldpt)_2(ClO_4)_4(H_2O)_4$ was used for characterisation purposes. $C_{32}H_{32}Cl_4N_{12}O_{20}Zn_2$ (1177.25): calcd. C 32.65, H 2.74, N 14.28; found C 32.28, H 2.59, N 14.30. $^1H$ NMR (500 MHz, [D$_7$]-DMF, ppm): $\delta$ = 6.35 [t, $^3J$ = 2.4 Hz, 4 H, 2×3- and 4-Pl*H*], 7.37 [t, $^3J$ = 2.4 Hz, 4 H, 2×2- and 5-Pl*H*], 7.55 [br. s, 4 H, 4×3-Py*H*], 7.69 [ddd, $^3J_{4,5}$ = 7.7 Hz, $^3J_{5,6}$ = 4.8 Hz, $^4J_{3,5}$ = 1.2 Hz, 4 H, 4×5-Py*H*], 8.12 [dt, $^3J_{3,4}$ = $^3J_{4,5}$ = 7.7 Hz, $^4J_{4,6}$ = 1.8 Hz, 4 H, 4×4-Py*H*], 8.68 [ddd, $^3J_{5,6}$ = 4.8 Hz, $^4J_{4,6}$ = 1.8 Hz, $^5J_{3,6}$ = 0.9 Hz, 4 H, 4×6-Py*H*]. $^{13}C\{^1H\}$ NMR (125 MHz, [D$_7$]DMF, ppm): $\delta$ = 109.91 [2×3- and 4-Pl*C*], 123.38 [2×2- and 5-Pl*C*], 124.08 [4×3-Py*C*], 127.49 [4×5-Py*C*], 139.61 [4×4-Py*C*], 144.25 [4×2-Py*C*], 150.95 [4×6-Py*C*], 154.01 [2×3- and 5-Tz*C*]. IR (KBr): $\tilde{\nu}$ = 1611, 1546, 1525, 1517, 1476, 1441, 1354, 1306, 1297, 1264, 1192, 1117, 1089, 1014, 930, 911, 795, 748, 724, 703, 653, 636, 625 $cm^{-1}$. ESI-MS (pos., MeCN): *m/z* = 217.1 $[Zn(pldpt)(MeCN)_2]^{2+}$, 237.6 $[Zn(pldpt)(MeCN)_3]^{2+}$, 289.1 $[(pldpt)H]^+$, 320.1 $[Zn(pldpt)_2]^{2+}$, 340.7 $[Zn(pldpt)_2(MeCN)]^{2+}$, 451.1 $[Zn(pldpt)(ClO_4)]^+$, 464.3 $[Zn(pldpt)_3]^{2+}$, 492.2 $[Zn(pldpt)(MeCN)(ClO_4)]^+$, 577.4 $[(pldpt)_2H]^+$, 739.3 $[Zn(pldpt)_2(ClO_4)]^+$, 1003.1 $[Zn_2(pldpt)_2(ClO_4)_3]^+$. Molar conductivity (DMF): $\Lambda_m$ = 255 $\Omega^{-1}{\cdot}cm^2{\cdot}mol^{-1}$ .

**Reaction of pldpt (3) with $Zn(BF_4)_2{\cdot}6H_2O$:** A colourless solution of $Zn(BF_4)_2{\cdot}6H_2O$ (347 mg, 1.00 mmol) in MeCN (5 mL) was added to a colourless refluxing solution of pldpt (**3**) (288 mg, 1.00 mmol) in MeCN (20 mL). The resulting colourless solution was refluxed for 10 minutes and was then stirred at room temperature for an-

 © 2006 Wiley-VCH Verlag GmbH & Co. KGaA, Weinheim 

Table 6. Crystallographic data for 3,5-di(2-pyridyl)-4-(1*H*-pyrrol-1-yl)-4*H*-1,2,4-triazole (pldpt, **3**), $[Co^{II}_2(pldpt)_2(DMF)_2(H_2O)_2](ClO_4)_4 \cdot 0.5Et_2O$ (**5**), $[Co^{II}(pldpt)_2(DMF)_2](ClO_4)_2$ (**6**), $[Co^{II}_2(pldpt)_2(MeCN)_2(H_2O)_2](BF_4)_4$ (**8**), $[Ni^{II}_2(pldpt)_2(MeCN)_4](BF_4)_4 \cdot 2MeCN$ (**11**), $[Cu^{II}(pldpt)_2(ClO_4)_2] \cdot 2DMF$ (**13**), $[Cu^{II}_2(pldpt)_2(MeCN)_2(H_2O)_2](ClO_4)_4$ (**14**) and $[Zn^{II}_2(pldpt)_2(MeCN)_2(H_2O)_2](BF_4)_4$ (**17**).

| | **3** | **5** | **6** | **8** |
|---|---|---|---|---|
| Empirical formula | $C_{16}H_{12}N_6$ | $C_{40}H_{47}Cl_4Co_2N_{14}O_{20.5}$ | $C_{38}H_{38}Cl_2CoN_{14}O_{10}$ | $C_{36}H_{34}B_4Co_2F_{16}N_{14}O_2$ |
| Formula weight [g mol$^{-1}$] | 288.32 | 1311.58 | 980.65 | 1159.87 |
| Crystal system | monoclinic | triclinic | monoclinic | triclinic |
| Space group | $P2_1$ | $P\bar{1}$ | $P2_1/c$ | $P\bar{1}$ |
| $a$ [Å] | 10.0461(2) | 10.349(2) | 8.8443(1) | 9.9087(3) |
| $b$ [Å] | 7.3951(2) | 12.680(3) | 13.3043(2) | 10.3844(4) |
| $c$ [Å] | 19.1277(5) | 13.065(3) | 18.2462(2) | 11.8599(4) |
| $\alpha$ [°] | 90 | 76.62(3) | 90 | 76.834(1) |
| $\beta$ [°] | 103.000(1) | 88.30(3) | 82.518(1) | 74.254(1) |
| $\gamma$ [°] | 90 | 72.46(3) | 90 | 85.140(1) |
| $V$ [Å$^3$] | 1384.61(6) | 1588.9(5) | 2128.70(5) | 1143.33(7) |
| $Z$ | 4 | 1 | 2 | 1 |
| $\rho_{calcd.}$ [g cm$^{-3}$] | 1.383 | 1.371 | 1.530 | 1.685 |
| $\mu$ [mm$^{-1}$] | 0.089 | 0.765 | 0.604 | 0.844 |
| Temperature [K] | 83(2) | 200(2) | 200(2) | 83(2) |
| $F$(000) | 600 | 671 | 1010 | 582 |
| Crystal colour and shape | colourless block | orange prism | yellow block | orange prism |
| Crystal size [mm$^3$] | 0.50 × 0.50 × 0.36 | 0.34 × 0.32 × 0.30 | 0.36 × 0.12 × 0.10 | 0.40 × 0.22 × 0.18 |
| $\Theta_{min.}/\Theta_{max.}$ [°] | 2.08/25.63 | 1.60/26.45 | 1.90/31.07 | 1.83/27.13 |
| $h$ | –12 → 12 | –12 → 12 | –11 → 11 | –12 → 12 |
| $k$ | –7 → 9 | –15 → 15 | –17 → 17 | –12 → 13 |
| $l$ | –21 → 23 | –16 → 16 | –23 → 23 | 0 → 15 |
| Reflections collected | 7900 | 11447 | 20754 | 11760 |
| Independent reflections | 4140 [$R$(int) = 0.0109] | 6364 [$R$(int) = 0.0741] | 4677 [$R$(int) = 0.0632] | 4996 [$R$(int) = 0.0156] |
| Completeness to $\Theta_{max.}$ [%] | 99.6 | 97.3 | 68.5 | 98.6 |
| Data/restraints/parameter | 4140/1/397 | 6364/10/421 | 4677/0/295 | 4996/0/343 |
| GOF | 1.055 | 1.023 | 1.067 | 1.026 |
| $R_1/wR_2$ [$I > 2\sigma(I)$] | 0.0242/0.0610 | 0.0902/0.2579 | 0.0677/0.1622 | 0.0245/0.0597 |
| $R_1/wR_2$ (all data) | 0.0249/0.0613 | 0.1204/0.2926 | 0.1035/0.1818 | 0.0286/0.0618 |
| Absolute structure factor | –0.2(11) | | | |
| Max. peak/hole [e·Å$^{-3}$] | 0.156/–0.189 | 1.316/–1.049 | 0.511/–0.712 | 0.349/–0.357 |

| | **11** | **13** | **14** | **17** |
|---|---|---|---|---|
| Empirical formula | $C_{44}H_{42}B_4F_{16}N_{18}Ni_2$ | $C_{38}H_{38}Cl_2CuN_{14}O_{10}$ | $C_{36}H_{34}Cl_4Cu_2N_{14}O_{18}$ | $C_{36}H_{34}B_4F_{16}N_{14}O_2Zn_2$ |
| Formula weight [g mol$^{-1}$] | 1287.62 | 985.26 | 1219.65 | 1172.76 |
| Crystal system | triclinic | monoclinic | triclinic | triclinic |
| Space group | $P\bar{1}$ | $P2_1/n$ | $P\bar{1}$ | $P\bar{1}$ |
| $a$ [Å] | 12.621(5) | 8.584(5) | 9.8490(1) | 9.981(5) |
| $b$ [Å] | 13.122(5) | 18.854(5) | 10.4408(1) | 10.458(5) |
| $c$ [Å] | 18.940(5) | 13.105(5) | 12.1340(2) | 11.968(5) |
| $\alpha$ [°] | 76.283(5) | 90 | 76.178(1) | 76.824(5) |
| $\beta$ [°] | 76.145(5) | 98.793(5) | 74.267(1) | 74.183(5) |
| $\gamma$ [°] | 62.922(5) | 90 | 84.505(1) | 85.209(5) |
| $V$ [Å$^3$] | 2681.7(16) | 2096.0(16) | 1165.62(3) | 1170.0(9) |
| $Z$ | 2 | 2 | 1 | 1 |
| $\rho_{calcd.}$ [g cm$^{-3}$] | 1.595 | 1.561 | 1.738 | 1.664 |
| $\mu$ [mm$^{-1}$] | 0.811 | 0.725 | 1.233 | 1.141 |
| Temperature [K] | 83(2) | 83(2) | 83(2) | 83(2) |
| $F$(000) | 1304 | 1014 | 618 | 588 |
| Crystal colour and shape | purple-blue prism | blue needle | green block | colourless plate |
| Crystal size [mm$^3$] | 0.32 × 0.18 × 0.18 | 0.21 × 0.16 × 0.12 | 0.48 × 0.34 × 0.28 | 0.30 × 0.25 × 0.12 |
| $\Theta_{min.}/\Theta_{max.}$ [°] | 1.12/27.25 | 1.91/25.72 | 1.79/27.15 | 1.81/25.63 |
| $h$ | –15 → 16 | –10 → 10 | –12 → 12 | –12 → 12 |
| $k$ | –16 → 16 | –23 → 22 | –12 → 13 | –12 → 12 |
| $l$ | –24 → 24 | –15 → 15 | 0 → 15 | –14 → 14 |
| Reflections collected | 27141 | 18555 | 11913 | 10501 |
| Independent reflections | 11701 [$R$(int) = 0.0445] | 3987 [$R$(int) = 0.0475] | 5077 [$R$(int) = 0.0225] | 4334 [$R$(int) = 0.0771] |
| Completeness to $\Theta_{max.}$ [%] | 97.4 | 99.8 | 98.0 | 98.2 |
| Data/restraints/parameters | 11701/0/763 | 3987/0/297 | 5077/0/343 | 4334/0/343 |
| GOF | 1.077 | 1.132 | 1.047 | 0.975 |
| $R_1/wR_2$ [$I > 2\sigma(I)$] | 0.0485/0.1070 | 0.0405/0.0815 | 0.0333/0.0875 | 0.0622/0.1561 |
| $R_1/wR_2$ (all data) | 0.0716/0.1200 | 0.0537/0.0884 | 0.0379/0.0911 | 0.0826/0.1663 |
| Absolute structure factor | | | | |
| Max. peak/hole [e·Å$^{-3}$] | 0.906/–0.662 | 0.352/–0.401 | 0.820/–0.868 | 1.647/–1.462 |

 © 2006 Wiley-VCH Verlag GmbH & Co. KGaA, Weinheim 

other 4 hours during which time a colourless precipitate formed. The solid was filtered off and washed with MeCN. Drying in vacuo gave 345 mg (ca. 60%) of $Zn^{II}_2(pldpt)_2(BF_4)_4(MeCN)_m(H_2O)_n$ (**16**) as a colourless powder. The solvent content of the initial products varied considerably from batch to batch. Heating of the powders at 60 °C in vacuo for several days similarly afforded materials of variable solvent content. A sample analysing as $Zn^{II}_2(pldpt)_2(BF_4)_4(H_2O)_2$ was used for characterisation purposes. $C_{32}H_{28}B_4F_{16}N_{12}O_2Zn_2$ (1090.63): calcd. C 35.24, H 2.59, N 15.41; found C 35.13, H 2.58, N 15.33. IR (KBr): $\tilde{\nu}$ = 1609, 1576, 1546, 1526, 1518, 1477, 1442, 1400, 1355, 1298, 1264, 1192, 1073, 911, 862, 797, 766, 750, 727, 706, 653, 640, 563, 533, 522, 436, 412 $cm^{-1}$). ESI-MS (pos., MeCN): *m/z* = 289.1 $[(pldpt)H]^+$, 320.1 $[Zn(pldpt)_2]^{2+}$, 340.6 $[Zn(pldpt)_2(MeCN)]^{2+}$, 464.2 $[Zn(pldpt)_3]^{2+}$, 727.2 $[Zn(pldpt)_2(BF_4)]^+$. Molar conductivity (MeCN): $\Lambda_m$ = 475 $\Omega^{-1}\cdot cm^2\cdot mol^{-1}$. Molar conductivity (DMF): $\Lambda_m$ = 270 $\Omega^{-1}\cdot cm^2\cdot mol^{-1}$. Vapour diffusion of $Et_2O$ into the colourless MeCN mother liquor or a colourless solution of complex **16** in MeCN afforded colourless crystals of $[Zn^{II}_2(pldpt)_2(MeCN)_2(H_2O)_2](BF_4)_4$ (**17**).

**X-ray Crystallography:** X-ray data (Table 6) were collected with a Bruker SMART CCD area detector using graphite-monochromated Mo-$K_\alpha$ radiation ($\lambda$ = 0.71073 Å). The structures were solved by direct methods with SIR-92[76] or SHELXS-97[77,78] and refined against $F^2$ using all data by full-matrix least-squares techniques with SHELXL-97.[79] All non-hydrogen atoms were refined anistropically. All hydrogen atoms, except H(101) and H(102) of the axial $H_2O$ co-ligands in complexes **5**, **8**, **14** and **17**, were placed at calculated positions using a riding model with thermal parameters 1.2 times the equivalent isotropic thermal parameter of the atom to which they were bonded. The hydrogen atoms of the $H_2O$ co-ligands in complexes **8**, **14** and **17** were located from the difference maps and allowed to refine freely. For complex **5** they were placed in calculated positions and subsequently fixed in their respective positions with thermal parameters 1.2 times the equivalent isotropic thermal parameter of the atom to which they were bonded. Further details of the refinement of the structures and the modelling of the disordered $ClO_4^-$ counterions and $Et_2O$ solvate in complex **5** can be found in the respective CIF files. CCDC-277057 (for **3**), -277058 (for **5**), -277059 (for **6**), -277060 (for **8**), -277061 (for **11**), -277062 (for **13**), -277063 (for **14**) and -277064 (for **17**) contain the supplementary crystallographic data for this paper. These data can be obtained free of charge from The Cambridge Crystallographic Data Centre via www.ccdc.cam.ac.uk/data_request/cif.

**Supporting Information** (see also the footnote on the first page of this article): A PDF file (six pages) with supporting information for this article is available on the WWW under http://www.eurjic.org or from the authors. It contains a view of the asymmetric unit of ligand **3** (Figure S1), an overlay of the two crystallographically independent molecules within the asymmetric unit of ligand **3** (Figure S2), views of the molecular structures of the cations of complexes **8**, **11** and **17** (Figure S3, S4 and S5, respectively), comparisons of the $^1H$ and $^{13}C$ NMR spectra, respectively, of ligand **3** and complex **15** (Figures S6 and S7, respectively) and the curves for the molar magnetic susceptibilities and effective magnetic moments of complexes **7** and **10** over the range 300–4.2 K (Figures S8 and S9, respectively).

## Acknowledgments

This work was supported by grants from the University of Otago (including a University of Otago Postgraduate Scholarship to MHK and a Bridging Grant) and the Australian Research Council (Discovery Grant). The authors are grateful to Ms. T. Groutso and Prof. G. R. Clark (University of Auckland) for collecting some of the X-ray data, to Mr. B. M. Clark (University of Canterbury) for recording the ESI mass spectra of the complexes reported in this paper and to Mr. R. M. Hellyer (University of Otago) for his help. Prof. G. B. Jameson (Massey University), Prof. W. T. Robinson (University of Canterbury) as well as Dr. D. S. Larsen, Dr. J. Klingele (née Hausmann) and Dr. C. D. Brandt (University of Otago) are thanked for helpful discussions.

[1] J. G. Haasnoot, *Coord. Chem. Rev.* **2000**, *200–202*, 131–185.
[2] M. H. Klingele, S. Brooker, *Coord. Chem. Rev.* **2003**, *241*, 119–132.
[3] U. Beckmann, S. Brooker, *Coord. Chem. Rev.* **2003**, *245*, 17–29.
[4] D. Zhu, Y. Xu, Z. Yu, Z. Guo, H. Sang, T. Liu, X. You, *Chem. Mater.* **2002**, *14*, 838–843.
[5] F. J. Keij, R. A. G. de Graaff, J. G. Haasnoot, J. Reedijk, *J. Chem. Soc., Dalton Trans.* **1984**, 2093–2097.
[6] M. P. García, J. A. Manero, L. A. Oro, M. C. Apreda, F. H. Cano, C. Foces-Foces, J. G. Haasnoot, R. Prins, J. Reedijk, *Inorg. Chim. Acta* **1986**, *122*, 235–241.
[7] C. Faulmann, P. J. van Koningsbruggen, R. A. G. de Graaff, J. G. Haasnoot, J. Reedijk, *Acta Crystallogr., Sect. C* **1990**, *46*, 2357–2360.
[8] J. P. Cornelissen, J. H. van Diemen, L. R. Groeneveld, J. G. Haasnoot, A. L. Spek, J. Reedijk, *Inorg. Chem.* **1992**, *31*, 198–202.
[9] G. Giuffrida, V. Ricevuto, G. Guglielmo, S. Campagna, M. Ciano, *Inorg. Chim. Acta* **1992**, *194*, 23–29.
[10] A. L. Rheingold, P. Saisuwan, N. C. Thomas, *Inorg. Chim. Acta* **1993**, *214*, 41–45.
[11] G. Calogero, G. Giuffrida, S. Serroni, V. Ricevuto, S. Campagna, *Inorg. Chem.* **1995**, *34*, 541–545.
[12] P. J. van Koningsbruggen, D. Gatteschi, R. A. G. de Graaff, J. G. Haasnoot, J. Reedijk, C. Zanchini, *Inorg. Chem.* **1995**, *34*, 5175–5182.
[13] U. Hartmann, H. Vahrenkamp, *Inorg. Chim. Acta* **1995**, *239*, 13–17.
[14] P. J. Kunkeler, P. J. van Koningsbruggen, J. P. Cornelissen, A. N. van der Horst, A. M. van der Kraan, A. L. Spek, J. G. Haasnoot, J. Reedijk, *J. Am. Chem. Soc.* **1996**, *118*, 2190–2197.
[15] G. Di Marco, M. Lanza, M. Pieruccini, S. Campagna, *Adv. Mater.* **1996**, *8*, 576–580.
[16] A. J. Jircitano, S. O. Sommerer, K. A. Abboud, *Acta Crystallogr., Sect. C* **1997**, *53*, 434–436.
[17] P. J. van Koningsbruggen, K. Goubitz, J. G. Haasnoot, J. Reedijk, *Inorg. Chim. Acta* **1998**, *268*, 37–42.
[18] N. Moliner, M. C. Muñoz, P. J. van Koningsbruggen, J. A. Real, *Inorg. Chim. Acta* **1998**, *274*, 1–6.
[19] G. Di Marco, M. Lanza, A. Mamo, I. Stefio, C. Di Pietro, G. Romeo, S. Campagna, *Anal. Chem.* **1998**, *70*, 5019–5023.
[20] N. Moliner, M. C. Muñoz, S. Létard, J.-F. Létard, X. Solans, R. Burriel, M. Castro, O. Kahn, J. A. Real, *Inorg. Chim. Acta* **1999**, *291*, 279–288.
[21] J.-F. Létard, L. Capes, G. Chastanet, N. Moliner, S. Létard, J.-A. Real, O. Kahn, *Chem. Phys. Lett.* **1999**, *313*, 115–120.
[22] N. Moliner, A. B. Gaspar, M. C. Muñoz, V. Niel, J. Cano, J. A. Real, *Inorg. Chem.* **2001**, *40*, 3986–3991.
[23] A. B. Gaspar, M. C. Muñoz, N. Moliner, V. Ksenofontov, G. Levchenko, P. Gütlich, J. A. Real, *Monatsh. Chem.* **2003**, *134*, 285–294.
[24] M. Shakir, S. Parveen, N. Begum, Y. Azim, *Polyhedron* **2003**, *22*, 3181–3186.
[25] G. S. Matouzenko, A. Bousseksou, S. A. Borshch, M. Perrin, S. Zein, L. Salmon, G. Molnar, S. Lecocq, *Inorg. Chem.* **2004**, *43*, 227–236.

 © 2006 Wiley-VCH Verlag GmbH & Co. KGaA, Weinheim 

[26] M. Shakir, S. Parveen, N. Begum, P. Chingsubam, *Transition Met. Chem.* **2004**, *29*, 196–199.
[27] P. Gütlich, A. B. Gaspar, V. Ksenofontov, Y. Garcia, *J. Phys. Condens. Matter* **2004**, *16*, S1087–S1108.
[28] H. M. Burke, J. F. Gallagher, M. T. Indelli, J. G. Vos, *Inorg. Chim. Acta* **2004**, *357*, 2989–3000.
[29] U. García-Couceiro, O. Castillo, A. Luque, G. Beobide, P. Román, *Acta Crystallogr., Sect. E* **2004**, *60*, m720–m722.
[30] M. H. Klingele, S. Brooker, *Eur. J. Org. Chem.* **2004**, 3422–3434.
[31] M. H. Klingele, PhD Thesis, University of Otago (New Zealand), **2004**.
[32] M. H. Klingele, P. D. W. Boyd, B. Moubaraki, K. S. Murray, S. Brooker, *Eur. J. Inorg. Chem.* **2005**, 910–918.
[33] M. H. Klingele, P. D. W. Boyd, S. Brooker, manuscript in preparation.
[34] S.-C. Shao, D.-R. Zhu, X.-H. Zhu, X.-Z. You, S. S. S. Raj, H.-K. Fun, *Acta Crystallogr., Sect. C* **1999**, *55*, 1412–1413.
[35] S. C. Shao, D. R. Zhu, T. W. Wang, Y. Zhang, S. S. S. Raj, H. K. Fun, *Chin. Chem. Lett.* **2000**, *11*, 93–94.
[36] D. Zhu, Y. Song, Y. Liu, Y. Xu, Y. Zhang, X. You, *Transition Met. Chem.* **2000**, *25*, 589–593.
[37] D.-R. Zhu, Y. Song, Y. Xu, Y. Zhang, S. S. S. Raj, H.-K. Fun, X.-Z. You, *Polyhedron* **2000**, *19*, 2019–2025.
[38] D. Zhu, Y. Xu, Y. Mei, Y. Shi, C. Tu, X. You, *J. Mol. Struct.* **2001**, *559*, 119–125.
[39] D.-R. Zhu, T.-W. Wang, S.-L. Zhong, Y. Xu, X.-Z. You, *Chin. J. Inorg. Chem.* **2004**, *20*, 508–512.
[40] S.-C. Shao, Z.-D. Liu, H.-L. Zhu, *Acta Crystallogr., Sect. E* **2004**, *60*, m1815–m1816.
[41] S.-P. Zhang, Z.-D. Liu, J.-L. Ma, S. Yang, S.-C. Shao, *Acta Crystallogr., Sect. E* **2005**, *61*, m423–m424.
[42] S.-P. Zhang, S.-C. Shao, Z.-D. Liu, H.-L. Zhu, *Acta Crystallogr., Sect. E* **2005**, *61*, m799–m800.
[43] S.-C. Shao, Z.-L. You, S.-P. Zhang, H.-L. Zhu, S. W. Ng, *Acta Crystallogr., Sect. E* **2005**, *61*, m265–m267.
[44] S. K. Mandal, H. J. Clase, J. N. Bridson, S. Ray, *Inorg. Chim. Acta* **1993**, *209*, 1–4.
[45] U. Beckmann, S. Brooker, C. V. Depree, J. D. Ewing, B. Moubaraki, K. S. Murray, *Dalton Trans.* **2003**, 1308–1313.
[46] U. Beckmann, J. D. Ewing, S. Brooker, *Chem. Commun.* **2003**, 1690–1691.
[47] C. V. Depree, U. Beckmann, K. Heslop, S. Brooker, *Dalton Trans.* **2003**, 3071–3081.
[48] M. H. Klingele, S. Brooker, *Inorg. Chim. Acta* **2004**, *357*, 1598–1602.
[49] M. H. Klingele, S. Brooker, *Inorg. Chim. Acta* **2004**, *357*, 3413–3417.
[50] M. H. Klingele, B. Moubaraki, J. D. Cashion, K. S. Murray, S. Brooker, *Chem. Commun.* **2005**, 987–989.
[51] M. H. Klingele, B. Moubaraki, K. S. Murray, S. Brooker, *Chem. Eur. J.* **2005**, *11*, 6962–6973.
[52] J. A. Kitchen, C. D. Brandt, M. Weitzer, B. Moubaraki, K. S. Murray, S. Brooker, unpublished results.
[53] J. F. Geldard, F. Lions, *J. Org. Chem.* **1965**, *30*, 318–319.
[54] F. Bentiss, M. Lagrenée, M. Traisnel, B. Mernari, H. Elattari, *J. Heterocycl. Chem.* **1999**, *36*, 149–152.
[55] N. Elming, N. Clauson-Kaas, *Acta Chem. Scand.* **1952**, *6*, 867–874.
[56] H.-P. Husson, J. Royer, in: *Encyclopedia of Reagents for Organic Synthesis*, (Ed.: L. A. Paquette), Wiley, Chichester, **1995**, vol. 3, pp. 1982–1983.
[57] P. F. Wiley, *Chem. Heterocycl. Compd.* **1956**, *10*, 179–249.
[58] V. P. Wystrach, in: *Heterocyclic Compounds* (Ed.: R. C. Elderfield), Wiley, New York, **1967**, vol. 8, pp. 105–161.
[59] P. F. Wiley, *Chem. Heterocycl. Compd.* **1978**, *33*, 1073–1283.
[60] D. G. Neilson, R. Roger, J. W. M. Heatlie, L. R. Newlands, *Chem. Rev.* **1970**, *70*, 151–170.
[61] M. R. Caira, R. G. F. Giles, L. R. Nassimbeni, G. M. Sheldrick, R. G. Hazell, *Acta Crystallogr, Sect. B* **1976**, *32*, 1467–1469.
[62] L.-S. Liou, P.-S. Chen, C.-H. Sun, J.-C. Wang, *Acta Crystallogr., Sect. C* **1996**, *52*, 1841–1843.
[63] F. Bentiss, M. Lagrenée, H. Vezin, J.-P. Wignacourt, E. M. Holt, *Polyhedron* **2004**, *23*, 1903–1907.
[64] Z. Wang, Z. Bai, J. Yang, K. Okamoto, X. You, *Acta Crystallogr., Sect. C* **1998**, *54*, 438–439.
[65] W. Chen, Z. X. Wang, F. F. Jian, Z. P. Bai, X. Z. You, *Acta Crystallogr., Sect. C* **1998**, *54*, 851–852.
[66] H.-K. Fun, K. Chinnakali, S. Shao, D. Zhu, X. Z. You, *Acta Crystallogr., Sect. C* **1999**, *55*, 770–772.
[67] D.-R. Zhu, Y. Xu, Y. Zhang, T.-W. Wang, X.-Z. You, *Acta Crystallogr., Sect. C* **2000**, *56*, 895–896.
[68] S.-C. Shao, H.-J. Liu, S.-P. Zhang, S. Yang, F.-Y. Hao, C.-P. Li, H.-L. Zhu, *Acta Crystallogr., Sect. E* **2004**, *60*, o722–o723.
[69] S.-P. Zhang, H.-J. Liu, S.-C. Shao, Y. Zhang, D.-G. Shun, S. Yang, H.-L. Zhu, *Acta Crystallogr., Sect. E* **2004**, *60*, o1113–o1114.
[70] S.-C. Shao, S. Yang, S.-P. Zhang, D.-Q. Wang, H.-L. Zhu, *Z. Kristallogr. New Cryst. Struct.* **2004**, *219*, 257–258.
[71] S.-C. Shao, S. Yang, S.-P. Zhang, D.-Q. Wang, H.-L. Zhu, *Z. Kristallogr. New Cryst. Struct.* **2004**, *219*, 259–260.
[72] S.-P. Zhang, Z.-L. You, S.-C. Shao, H.-L. Zhu, *Acta Crystallogr., Sect. E* **2005**, *61*, o8–o9.
[73] S.-P. Zhang, Z.-L. You, S.-C. Shao, H.-L. Zhu, *Acta Crystallogr., Sect. E* **2005**, *61*, o27–o28.
[74] W. J. Geary, *Coord. Chem. Rev.* **1971**, *7*, 81–122.
[75] O. Kahn, *Molecular Magnetism*, VCH, Weinheim, **1993**.
[76] A. Altomare, G. Cascarano, C. Giacovazzo, A. Guagliardi, M. C. Burla, G. Polidori, M. Camalli, *J. Appl. Crystallogr.* **1994**, *27*, 435.
[77] G. M. Sheldrick, *Acta Crystallogr., Sect. A* **1990**, *46*, 467–473.
[78] G. M. Sheldrick, *Methods Enzymol.* **1997**, *276*, 628–641.
[79] G. M. Sheldrick, T. R. Schneider, *Methods Enzymol.* **1997**, *277*, 319–343.

Received: November 2, 2005
Published Online: December 21, 2005

 © 2006 Wiley-VCH Verlag GmbH & Co. KGaA, Weinheim 

DOI: 10.1002/ejic.200500664

# An Investigation of the Reactivity of [(diimine)(dithiolato)M] Complexes Using the Fukui Functions Concept

**Christodoulos Makedonas[a] and Christiana A. Mitsopoulou*[a]**

**Keywords:** Density functional calculations / Fukui indices / Oxidation / S ligands / Schiff bases / Stacking interactions

Fukui functions are widely used when investigating the reactivity of organic molecules, but rarely with metal complexes. Here, we investigate the reactivity of [(diimine)(dithiolato)M] complexes with different types of reagents and upon oxidation employing this concept. Mixed-ligand complexes of this type have a peculiar electronic description due to the mixed-metal-ligand-to-ligand charge-transfer band, which is why they are considered as very promising candidates for non-linear optical (NLO) materials and molecular photochemical devices (MPD). As a result, their reactivity is of crucial importance for their potential applications. The obtained results of $f^+$ and $f^-$ for the neutral [(diimine)(dithiolato)M] complexes (M = Pd, Ni and Pt) not only predict that the sulfur atom is the preferable active site for electrophilic attack but also reveal the different tunability of these complexes when they are subjected to an oxidation process, in agreement with experimental results. Under the framework of the Fukui indices we also provide an alternative explanation for crystal packing that could find widespread application.

(© Wiley-VCH Verlag GmbH & Co. KGaA, 69451 Weinheim, Germany, 2006)

## 1. Introduction

The concept of reactivity is a milestone in the investigation of chemical phenomena. Electron density plays a fundamental role in understanding chemical reactivity as it explains the attack of reagent on the basis of electrostatic interactions. However, it seems that things are not as simple as that as electron density by itself does not provide an answer to every question that arises. The reason for this is the influence of the approaching reagent. Small changes in the electron-density distribution and how susceptible this is to these changes are also of importance. In recent years, much attention has been paid to the insights that density functional theory (DFT) can give into chemical reactivity. Global reactivity parameters such as electronegativity ($\chi$), hardness ($\eta$) and the electrophilicity index ($\omega$), accompanied by local indices like the local softness and the Fukui function [$f(\mathbf{r})$], have been introduced in the chemical literature[1–3] and have eventually obtained legitimacy within DFT.[4] The latter was proposed by Parr and Yang[5–8] and represents one of the most effective tools of conceptual DFT for the investigation of molecular reaction sites. This model is frequently employed for the interpretation of factors and trends that influence the tunability of organic molecules, but is more rarely used in the case of transition-metal complexes.[9] Here it is the main tool in our effort to gain insight into the reactivity of [(diimine)(dithiolato)M]-type complexes.

[a] Inorganic Chemistry Laboratory, Department of Chemistry, National and Kapodistrian University of Athens, Panepistimiopolis, Zografou 15771, Greece
E-mail: cmitsop@chem.uoa.gr

Over the last three decades [(diimine)(dithiolato)M] complexes of group VIII metals have attracted the attention of numerous researchers because of their unique properties, which include solution luminescence, solvatochromism, large molecular hyperpolarizabilities, and large excited-state oxidation potentials.[10–29] Due to these properties, they are considered as very promising candidates for non-linear optical (NLO) materials and molecular photochemical devices (MPD), especially in view of their peculiar electronic structure. This specific structure is dominated by the presence of two different unsaturated chelating ligands in the same molecule, one of which is a good π*-donor (the dithiolato ligand) and the other a good π*-acceptor (the diimine). Moreover, the intense solvatochromic band in the low-energy region of their electronic spectra is considered to involve the highest occupied molecular orbital (HOMO) and the lowest unoccupied molecular orbital (LUMO), the former of which is a mixture of metal and dithiolato orbitals and the latter is a π*-orbital of the diimine. This transition has been assigned as a "mixed-metal-ligand-to-ligand charge-transfer" (MMLL′CT) transition on the basis of both experimental[15] and theoretical[28,29] work. The square-planar geometry of these complexes permits one to tailor their properties for potential applications as photosensitizers or photocatalysts by designing both the diimine and dithiolato ligands appropriately.

On the other hand, [(diimine)(dithiolato)M] complexes are known to be susceptible to oxidation, either photochemically or chemically induced. The first contributions to this field were provided by Vogler,[19] Srivastava,[20–22] and Schanze.[23] In 1997, Connick and Gray reported the com-

 © 2006 Wiley-VCH Verlag GmbH & Co. KGaA, Weinheim 

plete structural and spectroscopic characterization of the photooxidation products of [Pt(bpy)(bdt)] (bpy = 2,2′-bipyridine, bdt = 1,2-benzenedithiolate); they identified both a monosulfinate and a disulfinate complex depending on the oxidation conditions.[24] Later, Cocker and Bachman reported that the related Pd complex has a similar tunability, while the reactivity of the nickel analogue is substantially different. In the latter case they managed to isolate an octahedral disulfonate complex and a dimetallic one, suggesting that the mechanistic pathway for their production is not simply the result of differences in the electronic structure of Ni compounds. They attributed it to the ability of nickel to adopt an octahedral coordination and to the relative stability of metal–oxygen bonds for first-row transition metals.[25,26] Matsubashi and co-workers,[27] in order to increase the electrical conductivity of these compounds, have performed halogen doping experiments and proposed that partial oxidation occurred on the sulfur ligand, a suggestion that is also supported by Tang.[17] Other compounds of the same class with ligands such as bme-daco [*N*,*N*′-bis(2-sulfanylethyl)-1,5-diazacyclooctane] are known to be easily thermally or photochemically oxidized.[30] Furthermore, these complexes also undergo electrophilic substitution reactions, as recently demonstrated by Chen.[18]

Here we have employed density functional techniques[4] in order to obtain insight into the oxidation of [(diimine)(dithiolato)M] complexes and to address the reactivity factors of these compounds through the local hard–soft acid–base principle (HSAB) and the Fukui functions.[1–8] For this purpose, the complexes [Pd(phen)(bdt)] (**1**), [Pd(bpy)(bdt)] (**2**), [Ni(bpy)(bdt)] (**3**), [Pt(bpy)(bdt)] (**4**), [Pt(bpy)(edt)] (**5**), and [Pt(bpy)(mnt)] (**6**) have been taken under consideration.

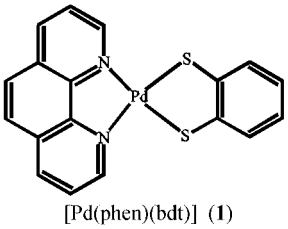


[Pd(phen)(bdt)] (**1**)

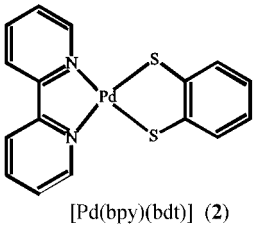


[Pd(bpy)(bdt)] (**2**)

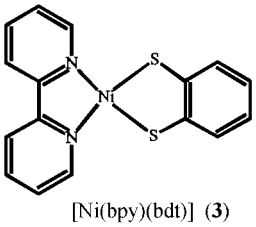


[Ni(bpy)(bdt)] (**3**)

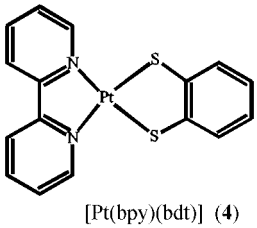


[Pt(bpy)(bdt)] (**4**)

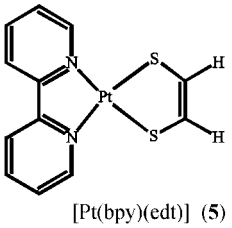


[Pt(bpy)(edt)] (**5**)

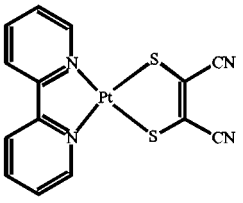


[Pt(bpy)(mnt)] (**6**)

The main part of this report is organized as follows: a brief description of the background theory is given in Section 2. The theoretical results are critically analyzed and compared with experimental ones in Section 3. This section is subdivided into three subsections. In Section 3.1 both theoretical and experimental structural data are compared in order to test the correctness of our calculations. The local softness parameters $f^+$ and $f^-$ are compared to locate the preferable electrophilic and nucleophilic sites, respectively, in these complexes in Section 3.2. Moreover, differences in the local softness descriptors induced by changing both the central metal and the ligands are discussed and compared to experimental results. They are also used to evaluate intermolecular reactivity sequences. The importance of local softness parameters for explaining the molecular stacking in the crystal lattice is shown for the first time in Section 3.3.

## 2. Theoretical Background

By definition, the Fukui function is given by the functional derivative of the chemical potential with respect to a change in the external potential. Alternatively, because of the Maxwell relations, it is identical to the change in electron density upon a change in the number of electrons and can be written as

$$f(\vec{r}) = \left(\frac{\delta \mu}{\delta v(\vec{r})}\right)_N = \left(\frac{\partial \rho(\vec{r})}{\partial N}\right)_{v(\vec{r})} \quad (1)$$

where $\mu$ is the chemical potential, $v(\mathbf{r})$ is the external potential, and the derivative must be taken at a constant number of electrons. An important feature of the Fukui function is that it integrates to unity.

The physical meaning of $f(\mathbf{r})$ is implied directly by its definition as $[\delta\mu/\delta v(\mathbf{r})]_N$: it measures how sensitive a system's chemical potential is to an external perturbation at a particular point. Moreover, local softness is given by[31]

$$S(\vec{r}) = \left(\frac{\partial \rho(\vec{r})}{\partial \mu}\right)_{v(\vec{r})} = \left(\frac{\partial \rho(\vec{r})}{\partial N}\right)_{v(\vec{r})}\left(\frac{\partial N}{\partial \mu}\right)_{v(\vec{r})} = f(\vec{r})S \quad (2)$$

From the above equation it is obvious that the Fukui function provides the same information for the system under study as the local softness, and can be used instead of it in deriving the relative site reactivity in a molecule. This implies that the regions of a molecule where the Fukui function is large are chemically softer than those with a small value of the function, and by invoking the HSAB principle in a local sense one may establish the tunability of different sites with respect to different reagents.[32]

Application of a *finite difference* approximation to Equation (1) leads to the following working equations, known as condensed Fukui functions according to Yang and Mortier[8]

$$f_i^+ = -[q_i(N+1) - q_i(N)], \text{ for nucleophilic attack} \quad (3a)$$

$$f_i^- = -[q_i(N) - q_i(N-1)], \text{ for electrophilic attack} \quad (3b)$$

 © 2006 Wiley-VCH Verlag GmbH & Co. KGaA, Weinheim 

$f_i^0 = -\{\frac{1}{2}[q_i(N+1) - q_i(N-1)]\}$, for radical attack (3c)

where $q_i$ is the partial charge of atom $i$, extracted from a Mulliken gross population analysis,[33] in a compound with $N-1$, $N$, and $N+1$ electrons, calculated in the ground-state geometry of the $N$-electron system, while the negative sign obeys the convention of negative electron charge.

Alternatively, employing a Mulliken population based approach to the *frozen core* approximation[2,5] we derive

$$f_i^- \approx \sum_{a\in i}^{AO} |c_{aHOMO}|^2 + \sum_{b\neq a}^{AO} |c_{bHOMO} \times c_{aHOMO}| S_{ab} \quad \text{for electrophilic attack} \quad (4a)$$

$$f_i^+ \approx \sum_{a\in i}^{AO} |c_{aLUMO}|^2 + \sum_{b\neq a}^{AO} |c_{bLUMO} \times c_{aLUMO}| S_{ab} \quad \text{for nucleophilic attack} \quad (4b)$$

$f_i^0 \approx \frac{1}{2}[f_i^+ + f_i^-]$, for radical attack (4c)

where HOMO and LUMO are the frontier orbitals. Apart from Mulliken population analysis (MPA), there are also other partitioning schemes for the electronic density, such as natural bond orbital analysis and Hirshfield analysis. In fact, Roy et al.[34–38] have shown that the latter is more reliable than MPA for calculating local reactivity descriptors and also produces nonnegative condensed Fukui function values. A lot of other work on nonnegative Fukui functions has been reported,[39–41] and it can be concluded that the Fukui function itself can be negative, although condensed Fukui functions cannot be negative, except in certain cases.

Equations (4a–4c) indicate the relationship between Fukui indicators and molecular orbitals.[7] In a sense, a nucleophilic reaction could be considered as involving the HOMO of the nucleophile and the LUMO of the electrophile. One of the major benefits of using the Fukui functions instead of the frontier orbitals − Equations (3a–3c) instead of Equations (4a–4c) − is that Fukui functions include the effects of orbital relaxation, which is very important.[42–44]

## 3. Results and Discussion

### 3.1. Molecular Structure

The six complexes under study have a square-planar geometry with almost $C_{2v}$ molecular symmetry. They were selected as suitable candidates for investigation of the influence induced by the different contributing fragments to the molecule's reactivity. Compounds **1** and **2** were selected, because 1,10-phenanthroline and 2,2′-bipyridine, along with their substituted derivatives, are the most widely used diimines in synthesis. Complexes **4**, **5**, and **6** were used to study the role of the dithiolate by choosing substituents with different π*-accepting ability. More precisely, CN is a better π*-accepting group than H, while benzenedithiolate is a widely used aromatic ligand. Finally, the series **2**–**4** was employed in order to incorporate the role of the metal in our analysis. For this purpose two ligands with medium π*-accepting and π*-donating ability, namely bpy and $bdt^{2-}$, respectively, were selected.

Their structures were fully optimized at the B3LYP/SDD/6-311+G* level of theory. A comparison between the theoretically derived bond lengths and angles and the crystallographically extracted ones is presented in Table 1, where it can be seen that, apart from the calculated M–X bonds, which are systematically overestimated by 0.04 Å, something that is anticipated,[46] all the other structural parameters are in good agreement with the crystallographic data. Based on these facts the overall agreement between theory and experiment is judged as satisfactory. It is noteworthy that the M–N bonds are longer than those observed in bis(diimine) compounds, while the M–S distances are shorter than those of the related bis(dithiolenes). This trend is a direct consequence of a significant *trans* influence, with $d_{C-S}$ and $d_{C-N}$ being in the area of C–S($sp^2$) and N–C($sp^2$), respectively. An extensive analysis of the compounds' electronic structure has been presented elsewhere[28,47] and will not be discussed further here.

### 3.2. Searching Reactivity Sites

We begin our analysis with the palladium complexes **1** and **2** by investigating the diimine's role. Employing the condensed Fukui functions formalism under the *finite difference* approximation we derived the values for $f_i^+$, $f_i^-$, and $f_i^0$. These values are presented in Figures 1 and 2 along with the numbering of the corresponding atoms. Inspection of the two figures shows that the most reactive sites of the molecules upon electrophilic attack are the sulfur atoms in both cases.

Table 1. Comparison of selected calculated bond lengths [Å] and angles [°] for **1**–**6** with experimental values from X-ray analysis.

| | M | M–N[a] | M–S[a] | C–S[a] | C=N[a] | C=C$^{dithiol\cdot}$ | C=C$^{diim\cdot}$ | $\varphi_{diim.}$ | $\varphi_{dithiol.}$ |
|---|---|---|---|---|---|---|---|---|---|
| **1**[28] | Exp. | 2.096(8) | 2.261(3) | 1.787(10) | 1.368(12) | 1.376(13) | 1.437(13) | 80.2(3) | 89.17(10) |
| | Calcd. | 2.128 | 2.283 | 1.775 | 1.364 | 1.401 | 1.434 | 78.69 | 88.49 |
| **2**[25] | Exp. | 2.071(2) | 2.245(1) | 1.762(2) | 1.353(3) | 1.396(3) | 1.474(3) | 79.41(6) | 88.67(2) |
| | Calcd. | 2.120 | 2.286 | 1.774 | 1.358 | 1.401 | 1.476 | 77.85 | 88.16 |
| **3**[25] | Exp. | 1.937(2) | 2.144(3) | 1.755(3) | 1.358(3) | 1.395(3) | 1.472(3) | 83.31(8) | 90.18(3) |
| | Calcd. | 1.970 | 2.178 | 1.765 | 1.358 | 1.401 | 1.467 | 82.26 | 90.18 |
| **4**[24] | Exp. | 2.050(5) | 2.248(2) | 1.761(6) | 1.367(8) | 1.373(8) | 1.464(8) | 80.1(2) | 89.0(1) |
| | Calcd. | 2.095 | 2.299 | 1.771 | 1.363 | 1.402 | 1.466 | 78.00 | 88.26 |
| **5**[45] | Exp. | 2.049(4) | 2.250(1) | 1.743(7) | 1.362(7) | 1.346(14) | 1.469(10) | 79.26(16) | 88.67(6) |
| | Calcd. | 2.092 | 2.302 | 1.754 | 1.365 | 1.341 | 1.462 | 78.10 | 88.05 |
| **6** | Calcd. | 2.099 | 2.296 | 1.759 | 1.362 | 1.365 | 1.469 | 78.04 | 88.44 |

[a] Average of two distances.

 © 2006 Wiley-VCH Verlag GmbH & Co. KGaA, Weinheim 

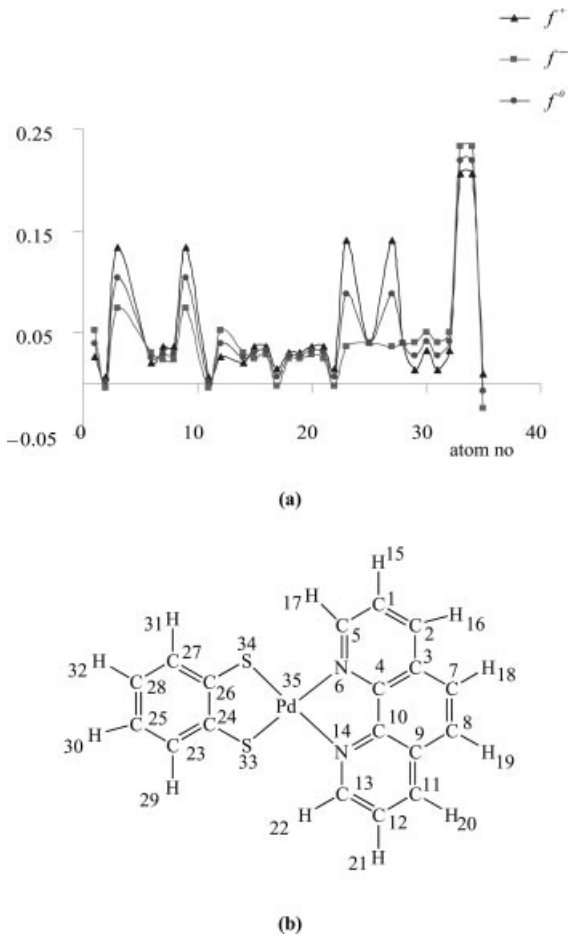


Figure 1. Condensed Fukui indices for **1** as derived from the *finite difference* approximation (a) and the atom numbering system (b).

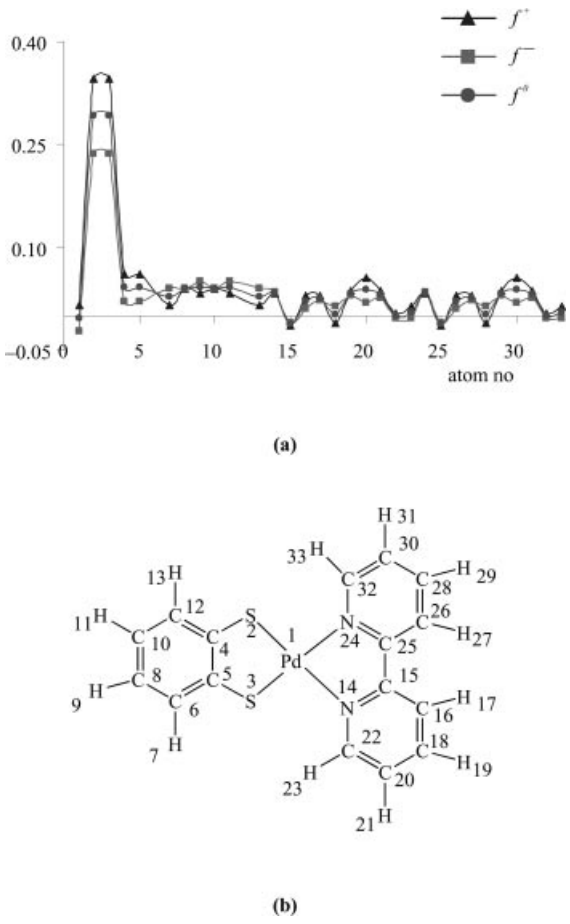


Figure 2. Condensed Fukui indices for **2** as derived from the *finite difference* approximation (a) and the atom numbering system (b).

Moreover, the sulfur atoms tend to react similarly during a radical attack, according to the $f^0$ values. In the phenanthroline compound **1** the reactive sites could also be the diimine's C1/C12 and C3/C9 atoms, although to a considerably lower degree. On the other hand, things change when discussion comes to $f^+$. The most reactive atoms are bdt's C23/C27 and phenanthroline's C3/C9 atoms in **1**. Of course, based on the relative nucleophilicity ($s_k^-/s_k^+$) and electrophilicity ($s_k^+/s_k^-$) introduced by Roy et al.,[48] we could accurately locate the preferable site for electrophilic and nucleophilic attack, respectively, and distinguish these carbon atoms. The reactive sites in **2** would also be dithiolate's C4/C5 and bpy's C20/C30. In other words, selection of the diimine as a bipyridine or phenanthroline derivative would not affect the complexes' reactivity towards an electrophile, but would certainly do so in the case of nucleophiles. The reason for this different reactivity is due to the nature of these attacks. In the case of the $f_i^+$ index, for example, one more electron is added to the system and the latter has to partition the excess of charge. Complex **1** can easily accommodate an extra electron through extended resonance of the phen's three condensed aromatic rings. Complex **2** can also accommodate an extra electron because of the presence of the two aromatic rings (bpy), but this is less effective than with phen rings. On the contrary, an electron subtraction from an almost identical HOMO (if the situation warranted, for example when an electrophile approaches S atoms), is expected to have a similar effect in both cases. In other words, although the HOMO has the same nature in both complexes, the LUMO is different since it is mainly present on diimine rings (phen vs. bpy).

Complex **2** would also be more reactive than **1** in the case of radical attack. Taking all these results into account, we conclude that, despite the similarity of the frontier orbitals of **1** and **2**, as was shown previously by us,[28] the two complexes are not expected to show an identical reactivity. Since most experimental results in this field have their origin in an electrophilic attack type of reaction or oxidation, in the next section we will try to shed light on their thermodynamics. Proceeding in a similar manner, we examine the dithiolate's role during electrophilic attack (Figure 3). In Figure 3(b) the numbering scheme concerns **4** but is also the same for **5** and **6** along with the following additions. Contributions from the dithiolate protons in **5** are represented by positions 31 and 32, while the nitrile carbon and nitrogen atoms in **6** are labeled as sites 10 and 11, and 31 and 32, respectively.

 © 2006 Wiley-VCH Verlag GmbH & Co. KGaA, Weinheim 

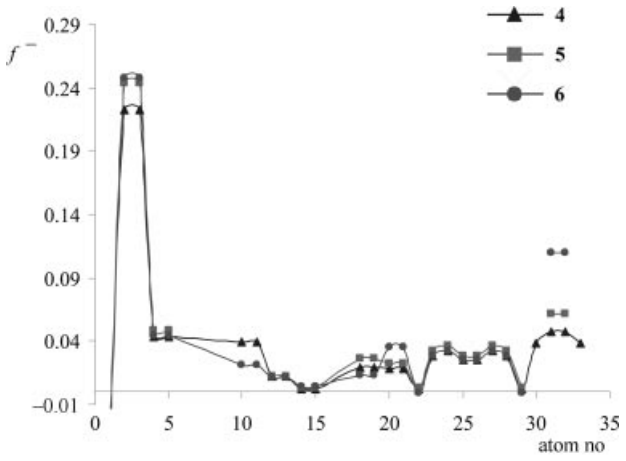


(a)

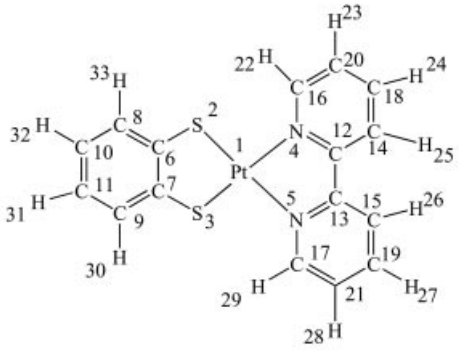


(b)

Figure 3. Condensed Fukui indices $f_i^-$ for **4**, **5**, and **6** as derived from the *finite difference* approximation (a), along with the atom numbering system (b).

Figure 3 shows that electron-accepting groups on the dithiolate moiety increase the sulfur atom's softness towards electrophilic reagents in keeping with the observed softness of the sulfur atoms in the series **6** > **5** > **4** (or mnt > edt > bdt). Moreover, in the case of **6**, the nitrogen atoms of the CN groups seem to be an additional reactive site on the molecule. As a result, 1,2-dithiolates with strong electron-accepting groups as substituents are considered to be more reactive towards soft electrophiles or photochemically/chemically induced oxidation than those having donor groups, while the presence of a π*-delocalized system on the S ligand reduces its reactivity.

Complexes **2**–**4** provide a great opportunity for demonstrating the role of the metal from the Fukui functions (Figure 4). We prefer to elaborate the Fukui function in this series in terms of the *frozen core* instead of the *finite difference* approximation due to the fact that metal atoms in the case of the latter give a value slightly below zero as a result of the following partitioning scheme (MPA). Thus, $q_i(N-1)$ is found to have a higher value than $q_i(N)$ and when these are replaced in Equation (3b) a negative $f_i^-$ value is obtained.

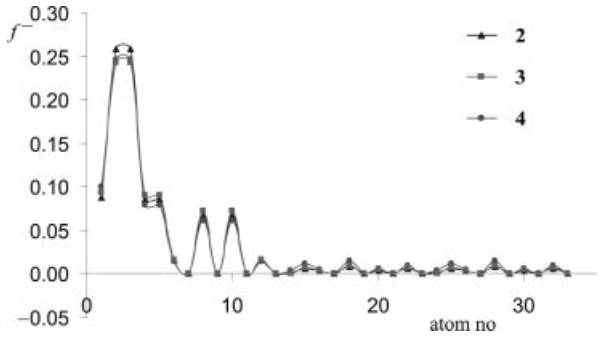


Figure 4. Condensed Fukui indices for **2**–**4** as derived from the *frozen core* approximation. The numbering system is the same as in Figure 2(b).

In a previous paper,[28] based on spectroscopic and mainly on DFT and TDDFT results, we clarified that the main, highly solvatochromic band in these complexes' visible spectra arises from a mixed-metal-ligand-to-ligand charge transfer despite the relatively low metal contribution in the frontier orbitals. Moreover, we have suggested that the metal atom is not just the right connector between the two conductors but its role is essential for the reactivity of this class of compounds. In order to test the validity of this suggestion, we examined the reactivity of **2**–**4** towards a common reagent ($O_2$) in combination with Fukui indices. Before we proceed to the analysis of experimental results, however, the bonding picture of these compounds should be given. First of all, recalling results from Table 5 in ref.[28] we can see that the HOMO is mainly localized on the dithiolato ligand (85.4% for **2**, 84.2% for **3**, and 81.1% for **4**), whereas the metal contribution is 8.8%, 9.3%, and 10.0% for **2**, **3**, and **4**, respectively.

The HOMO is the orbital where any oxidation process or electrophilic attack should take place. A closer inspection reveals that it originates from the antibonding combination of the metal's $d_{xz}$ orbital with the dithiolate's $4b_1$ out-of-plane HOMO localized mainly on sulfur's $3p_z$ (51.7% for **2**, 48.6% for **3**, and 49.1% for **4**), whereas the diimine's contribution arises from the $4b_1$ LUMO of bipyridine. Hence, the dithiolate, which is a strong π-donor, interacts in an antibonding way with the metal's $t_{2g}$ (under a pure $O_h$ geometry) orbital. This interaction is valid since both orbitals lie relatively close in energy, and the stronger the interaction the higher the HOMO lies. On the other hand, the metal back-donates electron density to the diimine, which is a good π-acceptor. As the metal–dithiolate interaction increases, back-donation becomes more effective. Taking the whole picture into consideration, it is clear that the metal's involvement in the HOMO increases as a direct consequence of a more effective interaction with the $bdt^{2-}$ moiety, the nucleophilicity of whose sulfur atoms also rises (the HOMO in all cases is largely a sulfur-based orbital). Grapperhaus et al. have referred to a relative bonding situation using the term π-repulsion.[47] Moreover, since the above description of the HOMO is, by definition, consistent with the characteristics of the Fukui function $f^-$, according to the *frozen core* approximation, it is clear that the driving

 © 2006 Wiley-VCH Verlag GmbH & Co. KGaA, Weinheim 

force of the reaction with an electrophilic reagent is maximized in **4** (thermodynamic criterion), according to the series **4** > **3** > **2** (Pt > Ni > Pd). On the other hand, as the sulfur contribution to the HOMO is lower for Ni compounds (48.6% vs. 51.7% for Pd), an electrophilic attack on it could elongate the Ni–S bond and break it. Thus, the sulfur atom is not favorable for electrophilic attack (Figure 4).

On the basis of the points mentioned above, and in order to test our results, we elaborated Bachman and Gray's excellent oxidation experiments.[24–26] Our analysis showed that the sulfur atoms in platinum complex **4** are more nucleophilic and thus more reactive, while the metal's larger contribution to the HOMO raises its energy and makes it more easily oxidized with more stable oxidation products (vide supra). Comparing the reported oxidation potentials for **2** (25 mV)[24] and **4** (165 mV),[25] we conclude that the first two results are correct. Moreover, the similarity of the $f^-$ index (Figure 4) for both **2** and **4** indicates that both complexes yield the same product upon oxidation. Indeed, oxidation takes place for both Pd and Pt complexes (Scheme 1).[25]

The reactivity of the nickel analogue **3** is substantially different, according to the $f^-$ function (based on finite difference approximation). Indeed, the sulfur atoms do not appear to be the unique active sites in this complex as the Ni atom and the C atoms of the bdt and bpy moieties also take part in the oxidation. In addition to these results, we must take into consideration that $Ni^{II}$ can also form complexes with octahedral or trigonal-bipyramidal structures, whereas $Pd^{II}$ and $Pt^{II}$ cannot. The observed photochemical oxidation of **3** to give a mixture of octahedral disulfonate complex **8** and a dimetallic complex **9** is in agreement with this (Scheme 2).[25]

We have shown that the most reactive sites in [(diimine)-(dithiolato)M] complexes from an electronic point of view are the sulfur atoms, although the site preferences for each type of attack differ. Thus, an electrophilic attack should occur from the upper (or lower) side of the molecule while a nucleophilic substitution should occur from the side (Figures 5 and 6). Based on these diagrams we can select the appropriate ligands in order to proceed stereochemically or

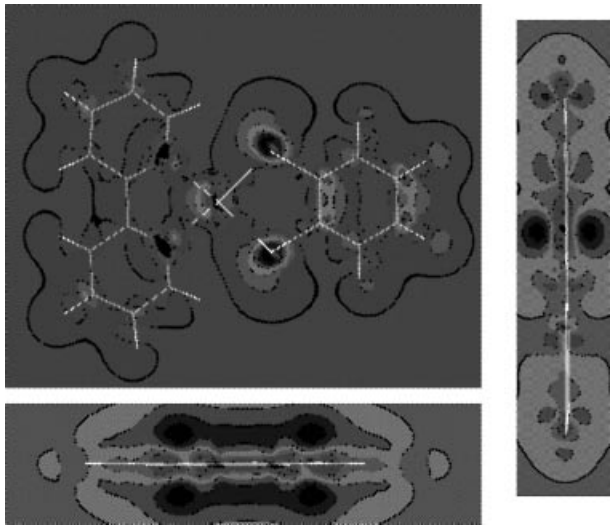

Figure 5. Projections of the difference in electron density between the neutral and the cationic form of **2**.

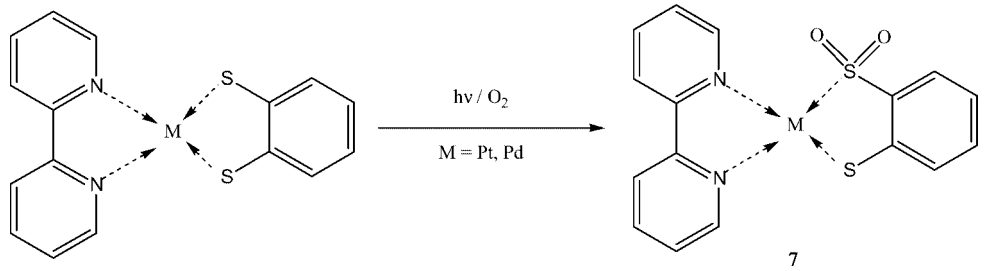


Scheme 1.

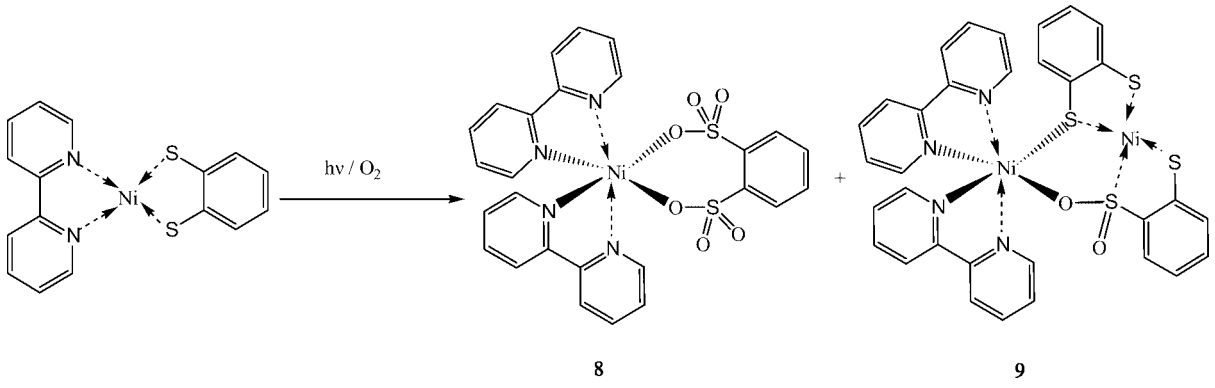


Scheme 2.

 © 2006 Wiley-VCH Verlag GmbH & Co. KGaA, Weinheim 

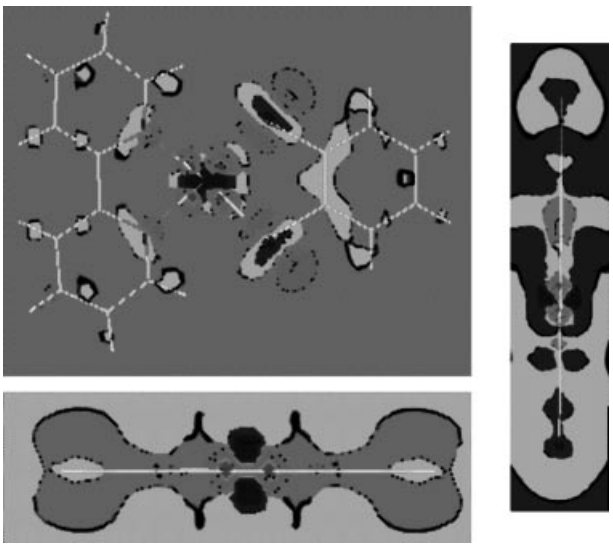

Figure 6. Projections of the difference in electron density between the anionic and the neutral form of **2**.

stop a certain type of substitution reaction. An experimental proof of the above discussion would be the complexes' interaction with electrophiles. Chen et al. in their fine paper[18] have shown that a series of platinum complexes analogous to **4** can act as ligands to unsaturated [bis(diphenylphosphanyl)methane]$Ag^{I}$ and -$Au^{I}$ compounds, yielding heterotrinuclear complexes of the type $Pt^{II}Au^{I}_2$ or $Pt^{II}Ag^{I}_2$. The formation of this class of compounds, and especially their structure, can be understood from the Fukui functions in Figures 3 and 5. Both $Au^{I}$ and $Ag^{I}$ are soft, and their soft–soft interaction with mixed (diimine)(dithiolato) complexes will take place from the upper side of the molecule at the sulfur atom to yield compound **10**.

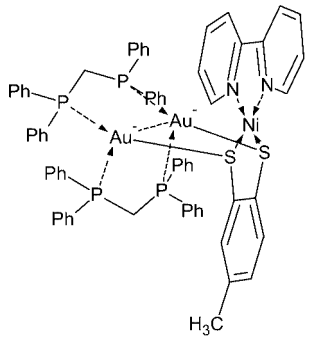


**10**

### 3.3. Crystal Packing Under the Prism of Soft–Soft Interactions

Until now crystal packing has been explained mainly in terms of π–π interactions, hydrogen bonding, and intermolecular metal–ligand interactions. We report here an alternative explanation of stacking in terms of the Fukui functions (vide supra). Our working hypothesis starts from the assumption that in a molecule with distinct electrophilic and nucleophilic atoms or areas it is very likely that these atoms/areas interact and play a major role in the formation of the complexes' lattice. Complex **1** crystallizes in the $P2_1/c$ space group,[28] and slight intermolecular interactions seem to be present in the crystal (Figure 7).

If packing is examined in terms of Fukui function indices for **1**, as computed under the *finite difference* approximation (vide supra), S33/S34–C3/C9 and C3/C9–C23/C29 interactions of the electrophile–nucleophile type are expected. The latter provides a reasonable explanation for the relative position of each molecule in the crystal lattice and simultaneously implies that soft–soft interactions define the molecules' stacking. In a forthcoming paper the validity of this working hypothesis will be tested both experimentally and theoretically for a series of analogous Ni, Pd, and Pt complexes.[49]

## 4. Conclusions

In this study we have tested the usefulness of condensed Fukui functions in locating the preferred sites (atoms) for nucleophilic and electrophilic attack in a metal complex and predicting/explaining the products (even the minor ones) obtained during a reaction. The studied cases are referred especially to the addition of oxygen and other electrophiles such as unsaturated complexes of $Ag^{I}$ or $Au^{I}$ to mixed (diimine)(dithiolato) complexes.

For this purpose, the condensed Fukui indices were determined to characterize the nucleophile (and electrophile) sites in [(diimine)(dithiolato)M] complexes (M = Ni, Pd, and Pt). The former were calculated by two approximations well established in the literature, namely *frozen core* and *finite difference*. In general, we have found a good agreement between the results obtained for the condensed Fukui indices of [(diimine)(dithiolato)M] complexes and the experimental results of electrophilic attack and oxidation. In every case, except Ni complexes, the electrophilic attack occurs at a unique atomic site – the sulfur atom. Different reactive sites upon changing the central metal are reflected

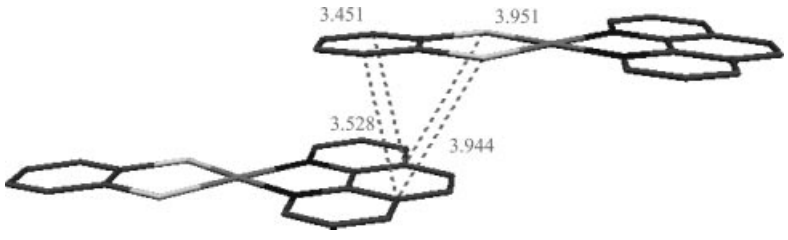


Figure 7. Packing of two molecules in molecular crystals of **1**.

 © 2006 Wiley-VCH Verlag GmbH & Co. KGaA, Weinheim 

in the differences products obtained, in accordance with experimental results. Moreover, the nucleophilicity of the sulfur atoms has been shown to increase in the series phen ≈ bpy, mnt > edt > bdt and Pt > Ni > Pd. There is total agreement between the condensed Fukui function indices and the existence of different products obtained upon oxidative addition to mixed (diimine)(dithiolato) complexes. Moreover, the Fukui indicators provide the correct intermolecular reactivity sequence of these complexes, which is not always attainable when comparing only the frontier orbitals. Last but not least, a different approach from π-stacking theory for crystal packing of these complexes is proposed based on Fukui indices and soft–soft interactions. This idea could be applied generally and could be the main reason for the different ways of molecular stacking in a crystal lattice, even within the same class of compounds, although the validity of this hypothesis has yet to be verified.

## 5. Experimental Section

### 5.1. Computational Details

Ground-state electronic structure calculations of all compounds under study were performed using density functional theory (DFT) [4] methods employing the GAUSSIAN 98/03 software package.[50] The functional used throughout this study is the B3LYP, which consists of a nonlocal hybrid exchange functional as defined by Becke's three-parameter equation[51] and the nonlocal Lee–Yang–Parr correlation functional.[52] The ground-state geometries were obtained in the gas phase by full geometry optimization, starting from structural data, regularized in order to satisfy the $C_{2v}$ symmetry. The VeryTight option was used in all cases, which demands tighter convergence criteria than the default ones, while numerical integration was performed using the UltraFine option, which requests a pruned (99,590) grid. The optimum structures located as stationary points on the potential-energy surfaces were verified by the absence of imaginary frequencies. The derived wavefunctions were found to be free of internal instabilities.

The basis set used for all nonmetal atoms was the well-known valence triple-ζ 6-311+G*.[53,54] The quasi-relativistic Stuttgardt–Dresden effective core potential of the type ECP10MDF, ECP28MWB, and ECP60MWB was used for Ni, Pd, and Pt, respectively.[55] The core potentials were complemented by the relative valence basis sets.[55] For all other calculations related to the properties' investigation an additional diffuse and polarization function was added to the hydrogen atoms. Percentage compositions of molecular orbitals from the three contributing fragments (metal, dithiolate, diimine) and condensed Fukui functions according to the *frozen core* approximation were calculated using the AOMix program.[56,57] The graphics presented here were drawn with the aid of GaussView[58] and Molekel.[59]

## Acknowledgments

We acknowledge the EPEAEK "Pythagoras I" and the Administration of Education of Greece for financial support.

[1] P. W. Ayers, M. Levy, *Theor. Chem. Acc.* **2000**, *103*, 353.
[2] P. Geerlings, F. De Proft, W. Langenaeker, *Chem. Rev.* **2003**, *103*, 1793.
[3] P. W. Ayers, J. S. M. Anderson, L. J. Bartolotti, *Int. J. Quantum Chem.* **2005**, *101*, 520.
[4] R. G. Parr, W. Yang, *Density Functional Theory of Atoms and Molecules*, Oxford University Press, Oxford, **1989**.
[5] R. G. Parr, W. Yang, *J. Am. Chem. Soc.* **1984**, *106*, 4049.
[6] W. Yang, R. G. Parr, R. Pucci, *J. Chem. Phys.* **1984**, *81*, 2862.
[7] K. Fukui, *Science* **1982**, *218*, 747.
[8] W. Yang, W. J. Mortier, *J. Am. Chem. Soc.* **1986**, *108*, 5708.
[9] A. Ríos-Escudero, I. Costamagna, G. J. Cárdenas-Jirón, *J. Phys. Chem. A* **2004**, *108*, 7253.
[10] T. R. Miller, I. G. Dance, *J. Am. Chem. Soc.* **1973**, *95*, 6970.
[11] M. Hissler, I. E. McGarrah, W. B. Connick, D. K. Geiger, S. D. Cummings, R. Eisenberg, *Coord. Chem. Rev.* **2000**, *208*, 115.
[12] W. Paw, S. D. Cummings, M. A. Mansour, W. B. Connick, D. K. Geiger, R. Eisenberg, *Coord. Chem. Rev.* **1998**, *171*, 125.
[13] S. D. Cummings, L.-T. Cheng, R. Eisenberg, *Chem. Mater.* **1997**, *9*, 440.
[14] S. D. Cummings, R. Eisenberg, *J. Am. Chem. Soc.* **1996**, *118*, 1949.
[15] S. D. Cummings, R. Eisenberg, *Inorg. Chem.* **1995**, *34*, 2007.
[16] C.-T. Chen, S.-Y. Liao, K.-J. Lin, C.-H. Chen, T.-Y. J. Lin, *Inorg. Chem.* **1999**, *38*, 2734.
[17] Z. Hao, Z. Tang, Q. Shi, *Inorg. Chim. Acta* **1999**, *284*, 112.
[18] Y.-D. Chen, Y.-H. Qin, L.-Y. Zhang, L.-X. Shi, Z.-N. Chen, *Inorg. Chem.* **2004**, *43*, 1197.
[19] A. Vogler, H. Kunkely, *J. Am. Chem. Soc.* **1981**, *103*, 1559.
[20] K. H. Puthraya, T. S. Srivastava, *Polyhedron* **1985**, *4*, 1579.
[21] S. Shukla, S. S. Kamath, T. S. Srivastava, *J. Photochem. Photobiol., A* **1989**, *50*, 199.
[22] A. K. Paul, R. Venkatesan, T. S. Srivastava, *J. Photochem. Photobiol., A* **1991**, *56*, 399.
[23] Y. Zhang, K. D. Ley, K. S. Schanze, *Inorg. Chem.* **1996**, *35*, 7102.
[24] W. B. Connick, H. B. Gray, *J. Am. Chem. Soc.* **1997**, *119*, 11620.
[25] T. M. Cocker, R. E. Bachman, *Inorg. Chem.* **2001**, *40*, 1550.
[26] T. M. Cocker, R. E. Bachman, *Chem. Commun.* **1999**, 875.
[27] K. Kubo, M. Nakano, H. Tamura, G.-E. Matsubayashi, *Inorg. Chim. Acta* **2002**, *336*, 120.
[28] C. Makedonas, C. A. Mitsopoulou, F. J. Lahoz, A. I. Balana, *Inorg. Chem.* **2003**, *42*, 8853.
[29] C. Makedonas, C. A. Mitsopoulou, *Spectrochim. Acta A*., in press.
[30] V. E. Kaasjager, E. Bouwman, S. Gorter, J. Reedijk, C. A. Grapperhaus, J. H. Reibenspies, J. J. Smee, M. Y. Darensbourg, A. Derecskei-Kovacs, L. M. Thomson, *Inorg. Chem.* **2002**, *41*, 1837.
[31] W. Yang, R. G. Parr, *Proc. Natl. Acad. Sci·USA* **1985**, *82*, 6723.
[32] F. Méndez, J. L. Gázquez, *J. Am. Chem. Soc.* **1994**, *116*, 9298.
[33] R. S. Mülliken, *J. Chem. Phys.* **1955**, *23*, 1833.
[34] R. K. Roy, S. Pal, K. Hirao, *J. Chem. Phys.* **1999**, *110*, 8236.
[35] R. K. Roy, K. Hirao, S. Pal, *J. Chem. Phys.* **2000**, *113*, 1372.
[36] R. K. Roy, N. Tajima, K. Hirao, *J. Phys. Chem. A* **2001**, *105*, 2117.
[37] R. K. Roy, *J. Phys. Chem. A* **2003**, *107*, 397.
[38] R. K. Roy, *J. Phys. Chem. A* **2003**, *107*, 10428.
[39] F. A. Bullat, E. Chamorro, P. Fuentealba, A. Toro-Labbe, *J. Phys. Chem. A* **2004**, *108*, 342.
[40] P. Bultinck, R. Carbo-Dorca, *J. Math. Chem.* **2003**, *34*, 67.
[41] P. Bultinck, R. Carbo-Dorca, W. Langenaeker, *J. Chem. Phys.* **2003**, *118*, 4349.
[42] W. Langenaeker, K. Demel, P. Geerlings, *J. Mol. Struct.: Theochem* **1991**, *80*, 329.
[43] L. J. Bartolotti, P. W. Ayers, *J. Phys. Chem. A* **2005**, *109*, 1146.
[44] K. Flurchick, L. Bartolotti, *J. Mol. Graphics Modell.* **1995**, *13*, 10.
[45] C. E. Keefer, R. D. Bereman, S. T. Purrington, B. W. Knight, P. D. Boyle, *Inorg. Chem.* **1999**, *38*, 2294.

 © 2006 Wiley-VCH Verlag GmbH & Co. KGaA, Weinheim 

[46] W. Koch, M. C. Holthausen, *A Chemist's Guide to Density Functional Theory*, 2nd ed., Wiley-VCH Verlag GmbH, Weinheim, **2001**.
[47] C. A. Grapperhaus, C. S. Mullins, P. M. Koziowski, M. S. Mashuta, *Inorg. Chem.* **2004**, *43*, 2859.
[48] R. K. Roy, S. Krishnamuri, P. Geerlings, S. Pal, *J. Phys. Chem. A* **1998**, *102*, 3746.
[49] C. Macedonas, G. Lappa, F. Lahoz, C.-A. Mitsopoulou, *paper in preparation*.
[50] M. J. Frisch, G. W. Trucks, H. B. Schlegel, G. E. Scuseria, M. A. Robb, J. R. Cheeseman, V. G. Zakrzewski, J. A. Montgomery, Jr.,; R. E. Stratmann, J. C. Burant, S. Dapprich, J. M. Millam, A. D. Daniels, K. N. Kudin, M. C. Strain, O. Farkas, J. Tomasi, V. Barone, M. Cossi, R. Cammi, B. Mennucci, C. Pomelli, C. Adamo, S. Clifford, J. Ochterski, G. A. Petersson, P. Y. Ayala, Q. Cui, K. Morokuma, D. K. Malick, A. D. Rabuck, K. Raghavachari, J. B. Foresman, J. Cioslowski, J. V. Ortiz, A. G. Baboul, B. B. Stefanov, G. Liu, A. Liashenko, P. Piskorz, I. Komaromi, R. Gomperts, R. L. Martin, D. J. Fox, T. Keith, M. A. Al-Laham, C. Y. Peng, A. Nanayakkara, M. Challacombe, P. M. W. Gill, B. Johnson, W. Chen, M. W. Wong, J. L. Andres, C. Gonzalez, M. Head-Gordon, E. S. Replogle, J. A. Pople, *Gaussian 98*, revision A.9, Gaussian, Inc., Pittsburgh, PA, **1998**.
[51] A. D. Becke, *J. Chem. Phys.* **1993**, *98*, 5648.
[52] C. Lee, W. Yang, R. G. Parr, *Phys. Rev. B* **1988**, *37*, 785.
[53] A. D. McLean, G. S. Chandler, *J. Chem. Phys.* **1980**, *72*, 5639.
[54] R. Krishnan, J. S. Binkley, R. Seeyer, J. A. Pople, *J. Chem. Phys.* **1980**, *72*, 650.
[55] D. Andrae, U. Haeussermann, M. Dolg, H. Stoll, H. Preuss, *Theor. Chim. Acta* **1990**, *77*, 123–141.
[56] S. I. Gorelsky, *AOMix progam*, revisions 4.7 and 5.1, http://www.sg-chem.net/aomix.
[57] S. I. Gorelsky, A. B. P. Lever, *J. Organomet. Chem.* **2001**, *635*, 187.
[58] *GaussView*, 2.00, Gaussian, Inc., **2000**.
[59] P. Flükiger, H. P. Lüthi, S. Portman, J. Weber, *MOLEKEL*, version 4.3, Swiss Center for Scientific Computing, Manno, Switzerland, **2000**–**2002**.

Received: July 25, 2005
Published Online: December 13, 2005

 © 2006 Wiley-VCH Verlag GmbH & Co. KGaA, Weinheim 

DOI: 10.1002/ejic.200500680

# Novel Carbonyliridium and -rhodium Complexes Containing 2,6-Bis[(4′*S*)-4′-isopropyloxazolin-2′-yl]pyridine (*i*Pr-pybox) and 2,6-Bis[(4′*R*)-4′-phenyloxazolin-2′-yl]pyridine (Ph-pybox) Ligands

**Darío Cuervo,[a] Josefina Díez,[a] M. Pilar Gamasa,*[a] José Gimeno,[a] and Paloma Paredes[a]**

**Keywords:** Carbonyl complexes / Homogeneous catalysis / Iridium / N ligands / Rhodium

The iridium(I) complexes [Ir(CO)(κ$^3$-*N*,*N*,*N*-R-pybox)][$PF_6$] [R-pybox = (*S*,*S*)-*i*Pr-pybox (**1**), (*R*,*R*)-Ph-pybox (**2**)] have been prepared by reaction of their precursor complexes [Ir(η$^2$-$C_2H_4$)$_2$(κ$^3$-*N*,*N*,*N*-R-pybox)][$PF_6$] (R = *i*Pr or Ph) with carbon monoxide. The analogous carbonylrhodium(I) complexes [Rh(CO)(κ$^3$-*N*,*N*,*N*-R-pybox)][$PF_6$] [R-pybox = (*S*,*S*)-*i*Pr-pybox (**3**), (*R*,*R*)-Ph-pybox (**4**)] have been synthesised by reaction of [Rh(μ-Cl)(η$^2$-$C_2H_4$)$_2$]$_2$, carbon monoxide, R-pybox and $NaPF_6$. Complexes **1**–**4** undergo oxidative addition reactions with iodine and $CH_3I$ leading, with high stereoselectivity, to the complexes [MI(X)(CO)(κ$^3$-*N*,*N*,*N*-R-pybox)][$PF_6$] [M = Ir, R = *i*Pr, X = I (**5**); M = Rh, R = *i*Pr, X = I (**6**); M = Rh, R = Ph, X = I (**7**); M = Ir, R = *i*Pr, X = $CH_3$ (**8**); M = Ir, R = Ph, X = $CH_3$ (**9**); M = Rh, R = *i*Pr, X = $CH_3$ (**10**); M = Rh, R = Ph, X = $CH_3$ (**11**)]. The treatment of complexes **1** and **2** with HCl, allyl chloride or acyl chloride results, in most cases, in the stereoselective formation of the iridium(III) complexes [IrHCl(CO)(κ$^3$-*N*,*N*,*N*-R-pybox)][$PF_6$] [R = *i*Pr (**12**), Ph (**13**)], [IrCl(η$^1$-$CH_2CH{=}CH_2$)(CO)(κ$^3$-*N*,*N*,*N*-R-pybox)][$PF_6$] [R = *i*Pr (**14**), Ph (**15**)] or [IrCl{η$^1$-C(O)$CH_3$}(CO)(κ$^3$-*N*,*N*,*N*-R-pybox)][$PF_6$] [R = *i*Pr (**16**), Ph (**17**)], respectively. The structures of derivatives **10** and **15** have been determined by single-crystal X-ray diffraction analysis. The catalytic activity of monocarbonylrhodium(I) and -iridium(I) complexes **1** and **3** in the hydrosilylation and dehydrosilylation of acetophenone with diphenylsilane has also been examined.
(© Wiley-VCH Verlag GmbH & Co. KGaA, 69451 Weinheim, Germany, 2006)

## Introduction

In the last few years the enantiopure, tridentate nitrogen ligands R-pybox [R-pybox = 2,6-bis(4′-R-oxazolin-2′-yl)-pyridine; R = *i*Pr, Ph, *t*Bu, etc.] have been shown to be efficient chiral ancillary ligands in transition-metal-catalysed asymmetric synthesis. A recent and specific survey discusses the state-of-the-art of this field.[1]

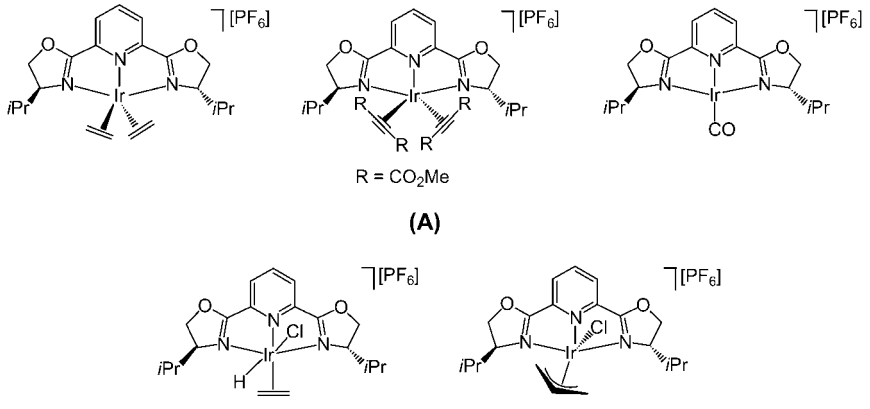


Despite the importance of iridium complexes in catalytic processes, as far as we know only a few examples of asymmetric catalysis using [IrCl(cod)]$_2$/pybox mixtures as the catalyst have been described. Thus, a reductive aldol reaction catalysed by [IrCl(cod)]$_2$/indane-pybox[2] and a regio- and enantioselective allylic substitution catalysed by mix-

[a] Instituto Universitario de Química Organometálica "Enrique Moles" (Unidad Asociada al CSIC), Departamento de Química Orgánica e Inorgánica, Facultad de Química, Universidad de Oviedo,
33071 Oviedo, Spain
Fax: +34-985-103-446
E-mail: pgb@uniovi.es

 © 2006 Wiley-VCH Verlag GmbH & Co. KGaA, Weinheim 

tures of $[IrCl(cod)]_2$/phenyl-pybox and nitrogen nucleophiles such as oximes, amines and hydroxylamines, have been reported recently.[3,4] Moreover, we have just described the preparation of the first (pybox)iridium complexes,[5] namely diolefin-, dialkyne- and monocarbonyliridium(I) complexes (**A**) as well as hydrido(olefin)- and $\eta^3$-allyliridium(III) derivatives (**B**). In light of these recent results, we decided it would be interesting to explore the synthesis of (pybox)-iridium complexes in order to understand their properties and eventually apply them in asymmetric catalysis. Therefore, we report here the synthesis of novel carbonyliridium(I) and -iridium(III) complexes containing the enantiopure (*S*,*S*)-*i*Pr-pybox and (*R*,*R*)-Ph-pybox ligands. This paper also deals with the synthesis of the analogous carbonylrhodium complexes, a type of systems that are scarcely found in the literature.[6] Moreover, the monocarbonyl(*i*Pr-pybox)rhodium(I) and -iridium(I) complexes have been tested as catalysts in the asymmetric hydrosilylation of acetophenone with diphenylsilane.

stirring a mixture of $[Rh(\mu\text{-}Cl)(\eta^2\text{-}C_2H_4)_2]_2$ (1 equiv.), R-pybox (2 equiv.) and $NaPF_6$ (3 equiv.) in dichloromethane/methanol (4:1) under CO at room temperature for 1 h. The monocarbonyl complexes $[Rh(CO)(\kappa^3\text{-}N,N,N\text{-R-pybox})][PF_6]$ were isolated as air-stable solids in high yields [R = *i*Pr (**3**), 91%; R = Ph (**4**), 84%; Scheme 2]. The preparation of complexes **1** and **3** has been reported previously.[5,6]

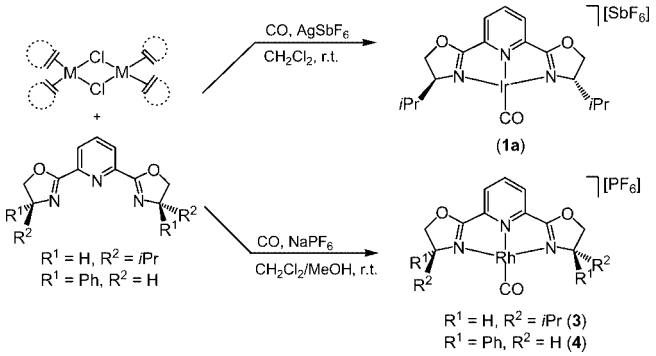


Scheme 2.

## Results and Discussion

### Synthesis of the Complexes $[M(CO)(\kappa^3\text{-}N,N,N\text{-R-pybox})][PF_6]$ [M = Ir, R = *i*Pr (1), Ph (2); M = Rh, R = *i*Pr (3), Ph (4)]

The reaction of complexes $[Ir(\eta^2\text{-}C_2H_4)_2(\kappa^3\text{-}N,N,N\text{-R-pybox})][PF_6]$ (R = *i*Pr[5] or Ph) with carbon monoxide (1 atm) in dichloromethane at room temperature results in the replacement of two ethylene molecules and the formation of the complexes $[Ir(CO)(\kappa^3\text{-}N,N,N\text{-R-pybox})][PF_6]$ [R = *i*Pr (**1**), Ph (**2**)], which were isolated as air-stable solids in excellent yields (96% and 94%, respectively; Scheme 1). Complexes **1** and **2** can be obtained in higher purity if a flow of nitrogen is slowly bubbled through the dichloromethane solution during the reaction over 50 min and before work-up. The IR spectra in the ν(CO) region show, along the reaction course, the initial formation of a non-isolated dicarbonyl complex intermediate [ν(CO) = 2088, 2021 $cm^{-1}$], which leads to the 16-electron monocarbonyl complexes when the reaction mixture is worked up [ν(CO) = 1989 (**1**), 1996 (**2**) $cm^{-1}$].

Complex **1** was also isolated as the hexafluoroantimonate derivative $[Ir(CO)\{\kappa^3\text{-}N,N,N\text{-}(S,S)\text{-}i\text{Pr-pybox}\}][SbF_6]$ (**1a**) after treatment of $[Ir(\mu\text{-}Cl)(\eta^2\text{-}C_8H_{14})_2]_2$ ($C_8H_{14}$ = cyclooctene) with *i*Pr-pybox (2 equiv.), CO (1 atm) and $AgSbF_6$ (4 equiv.) in $CH_2Cl_2$ at room temperature. Similarly, the analogous rhodium complexes were prepared by

The analytical and spectroscopic data [IR and $^1H$, $^{13}C\{^1H\}$ NMR] for complexes **1**–**4** support the proposed formulations (see Experimental Section for details). In particular: (a) the NMR spectroscopic data are consistent with the $C_2$-symmetric structure of the compounds, (b) a low-field singlet or doublet signal in the $^{13}C\{^1H\}$ NMR spectra [$\delta$ = 182.3 (**1**), 173.8 (**2**), 191.7 (d, $J_{C,Rh}$ = 76.3 Hz; **3**), 189.9 (d, $J_{C,Rh}$ = 76.3 Hz; **4**) ppm] confirms the presence of the carbonyl group, (c) the IR spectra of $CH_2Cl_2$ solutions show a strong ν(CO) absorption band in the ranges of 1996–1989 $cm^{-1}$ (for **1** and **2**) and 2014–2001 $cm^{-1}$ (for **3** and **4**).

Since oxidative addition is one of the most typical reactions of square-planar iridium(I) and rhodium(I) complexes, a comparative study of such a process for the cationic monocarbonyliridium(I) and -rhodium(I) complexes **1**–**4** was performed.

### Synthesis of the Complexes $[MI_2(CO)(\kappa^3\text{-}N,N,N\text{-R-pybox})][PF_6]$ [M = Ir, R = *i*Pr (5); M = Rh, R = *i*Pr (6), Ph (7)]

The reaction of equimolar amounts of $[M(CO)(\kappa^3\text{-}N,N,N\text{-R-pybox})][PF_6]$ (M = Ir, R = *i*Pr; M = Rh, R = *i*Pr, Ph) and iodine in dichloromethane at room temperature

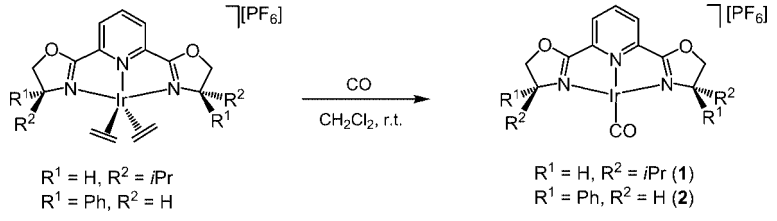


Scheme 1.

 © 2006 Wiley-VCH Verlag GmbH & Co. KGaA, Weinheim 

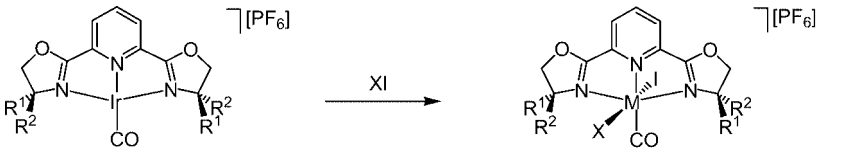


**1–4**

$R^1$ = H, $R^2$ = *i*Pr, X = I, M = Ir (**5**), Rh (**6**)
$R^1$ = Ph, $R^2$ = H, X = I, M = Rh (**7**)
$R^1$ = H, $R^2$ = *i*Pr, X = $CH_3$, M = Ir (**8**), Rh (**10**)
$R^1$ = Ph, $R^2$ = H, X = $CH_3$, M = Ir (**9**), Rh (**11**)

Scheme 3.

gives stereoselectively the complexes $[IrI_2(CO)\{\kappa^3\text{-}N,N,N\text{-}(S,S)\text{-}i\text{Pr-pybox}\}][PF_6]$ (**5**) and $[RhI_2(CO)(\kappa^3\text{-}N,N,N\text{-R-pybox})][PF_6]$ [R = *i*Pr (**6**),[6] Ph (**7**)] by oxidative addition (Scheme 3). Complexes **5**–**7** were isolated as air-stable, garnet (**5**) or orange-brown (**6**, **7**) solids in high yields (83–89%) and were characterised by elemental analyses and NMR spectroscopy (see Experimental Section for details). In particular, it must be noted that: (a) $CH_2Cl_2$ solutions of complexes **5**–**7** show the ν(CO) absorption as a strong band in the range of 2125–2092 $cm^{-1}$, which is at higher energy than that found for the rhodium(I) and iridium(I) precursors **1**–**4** (2014–1989 $cm^{-1}$), in accordance with the higher effective oxidation state of the metal atom in complexes **5**–**7**; (b) the NMR spectroscopic data for **5**–**7** are consistent with the presence of the $C_2$ symmetry axis shown by the precursor complexes, thus indicating that the iodine atoms are in a *trans* arrangement;[7] (c) a low-field signal in the $^{13}C\{^1H\}$ NMR spectra due to the carbonyl group is observed as a singlet at $\delta$ = 157.8 ppm for **5** or as a doublet at $\delta$ = 177.9–177.2 ppm ($J_{C,Rh}$ = 55.1–53.4 Hz) for **6** and **7**.

### Synthesis of the Complexes $[MI(CH_3)(CO)(\kappa^3\text{-}N,N,N\text{-R-pybox})][PF_6]$ [M = Ir, R = *i*Pr (8), Ph (9); M = Rh, R = *i*Pr (10), Ph (11)]

The room-temperature reaction of complexes **1** and **2** with methyl iodide (1:10 molar ratio) in dichloromethane leads to the formation of the complexes $[IrI(CH_3)(CO)(\kappa^3\text{-}N,N,N\text{-R-pybox})][PF_6]$ [R = *i*Pr (**8**), Ph (**9**); Scheme 3]. However, the synthesis of analogous rhodium complexes $[RhI(CH_3)(CO)(\kappa^3\text{-}N,N,N\text{-R-pybox})][PF_6]$ [R = *i*Pr (**10**),[6] Ph (**11**)] requires the rhodium complexes **3** and **4** to be heated at 30 °C in neat $CH_3I$. Complexes **8**–**11** were isolated from the reaction mixture as yellow solids in high yields [up to 90% (**8**, **9**) and 70–80% (**10**, **11**)] and were characterised by elemental analyses and NMR spectroscopy (see Experimental Section for details). In particular: (a) the presence of the methyl group is confirmed in the $^1H$ NMR spectra by a singlet or doublet ($^2J_{H,Rh}$ = 1.5–1.7 Hz) in the range of $\delta$ = 1.40–0.73 ppm; (b) this methyl carbon atom resonates in the $^{13}C\{^1H\}$ NMR spectra at high field as a singlet or doublet [$\delta$ = –9.5 (**8**), –10.9 (**9**), 10.3 ($J_{C,Rh}$ = 18.3 Hz; **10**), 9.3 ($J_{C,Rh}$ = 17.2 Hz; **11**) ppm], while the carbonyl carbon atom appears at low field as either a singlet or a doublet at $\delta$ = 166.8–165.1 and 185.5–184.0 ppm ($J_{C,Rh}$ = 60.4–59.8 Hz) for the iridium and rhodium complexes, respectively.

Even though the synthesis of complexes **9**–**11** is completely stereoselective, the reaction of complex **1** with $CH_3I$ gives rise to the complex **8** along with a minor amount of another diastereoisomer (*de* = 80%) according to the $^1H$ NMR spectrum of the crude reaction mixture. Since the NMR and IR spectroscopic data of complexes **9**–**11** did not allow us to unambiguously determine their stereochemistry, an X-ray crystal structure analysis was performed for complex **10**, which shows the expected octahedral coordination of the rhodium atom as well as a *trans* orientation for the methyl and iodo ligands. Selected bond lengths and angles are collected in Figure 1 (see also ref.[6] for further structural data). We assume that complexes **8** (major isomer), **9** and **11** have the same stereochemistry.

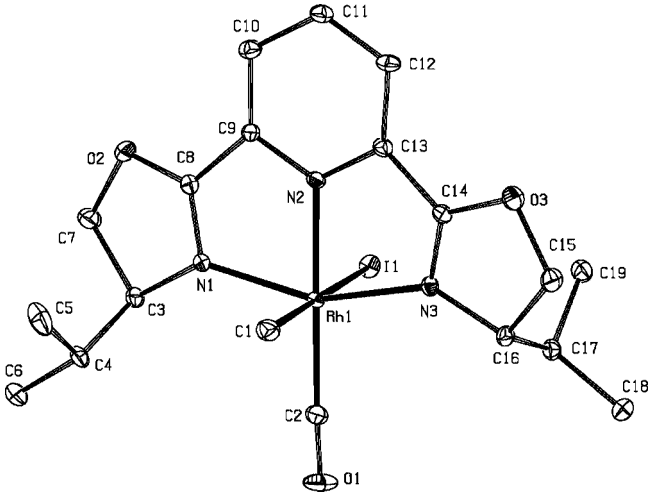


Figure 1. ORTEP-type view of the molecular structure of the cation of $[RhI(CH_3)(CO)\{\kappa^3\text{-}N,N,N\text{-}(S,S)\text{-}i\text{Pr-pybox}\}][PF_6]$ (**10**) drawn at the 10% probability level. Hydrogen atoms have been omitted for clarity. Selected bond lengths [Å] and angles [°]: Rh–N(1) 2.059(5), Rh–N(2) 1.994(5), Rh–N(3) 2.056(5), Rh–C(1) 2.120(8), Rh–C(2) 1.900(7), Rh–I 2.7759(14), C(2)–O(1) 1.113(10); N(3)–Rh–N(1) 156.5(2).

As we have described above, monocarbonylrhodium(I) and -iridium(I) complexes **1**–**4** undergo oxidative addition reaction with iodine and $CH_3I$. However, monocarbonyliridium(I) complexes **1** and **2** also react under mild reaction conditions with HCl and allyl and acyl chloride to give the

 © 2006 Wiley-VCH Verlag GmbH & Co. KGaA, Weinheim 

iridium(III) complexes **12**–**17**, whereas the rhodium complexes **3** and **4** remain unchanged under similar or stronger conditions ($CH_2Cl_2$ or refluxing MeOH). This behaviour is in accordance with the well-known higher stability of iridium(III) complexes in comparison with that of rhodium(III) complexes.[8]

### Synthesis of the Complexes [IrHCl(CO)(κ³-*N*,*N*,*N*-R-pybox)][$PF_6$] [R = *i*Pr (12), Ph (13)]

We are particularly interested in the synthesis of hydrido complexes as they are extensively found as intermediates in both stoichiometric and catalytic processes. The treatment of a solution of complexes **1** and **2** in dichloromethane with a solution of HCl in diethyl ether at room temperature gives stereoselectively the complexes [IrClH(CO){κ³-*N*,*N*,*N*-(*S*,*S*)-R-pybox}][$PF_6$] [R = *i*Pr (**12**), Ph (**13**)], which were isolated as air-stable, yellow solids (92–94% yield; Scheme 4). Complexes **12** and **13** were characterised by elemental analysis and NMR spectroscopy (see Experimental Section for details). The most significant features of the spectroscopic data are: (a) the characteristic ν(Ir–H) and ν(CO) IR absorptions at 2180–2164 and 2083–2075 $cm^{-1}$, respectively, (b) the high-field singlet for the hydrido ligand in the $^1H$ NMR spectra at $\delta$ = –19.25 (**12**) and –19.73 (**13**) ppm, and (c) the low-field singlet for the carbonyl carbon atom in the $^{13}C\{^1H\}$ NMR spectra at $\delta$ = 165.6 (**12**) and 163.0 (**13**) ppm. The NMR and IR spectroscopic data are consistent with three possible stereoisomers. Unfortunately, all attempts to crystallise complexes **12** or **13** from a number of solvents were unsuccessful, therefore an X-ray analysis could not be performed. We assume that the hydrido and chloro ligands are *trans* to each other, in a similar stereochemical environment to that found for complexes **10** and **15** (see below), whose structures were determined by X-ray diffraction analysis.

### Synthesis of the Complexes [IrCl(η¹-$CH_2CH{=}CH_2$)(CO)(κ³-*N*,*N*,*N*-R-pybox)][$PF_6$] [R = *i*Pr (14), Ph (15)] and [IrCl{η¹-$C(O)CH_3$}(CO)(κ³-*N*,*N*,*N*-R-pybox)][$PF_6$] [R = *i*Pr (16), Ph (17)]

The oxidative addition of allyl chloride and acyl chloride to complexes **1** and **2** was also performed. Thus, the reaction of **1** and **2** with allyl chloride (3 equiv.) and acyl chloride (1 equiv.) in dichloromethane at room temperature produces the allyl- and acyliridium(III) complexes **14**/**15** and **16**/**17**, respectively (Scheme 4). These complexes were isolated as air-stable, yellow solids in 85–91% yield. Their analytic and spectroscopic data (IR and $^1H$, $^{13}C\{^1H\}$ NMR) support the proposed formulations (see Experimental Section for details). In particular, the following can be pointed out: (a) the IR spectra of **16** and **17** show the expected ν(COMe) absorptions of the acyl group at 1677–1669 $cm^{-1}$, (b) the $^1H$ and $^{13}C$ NMR resonances of the allyl group in complexes **14** and **15** are in accordance with the σ-coordination mode [$^{13}C\{^1H\}$ NMR spectra show the expected resonances in the ranges $\delta$ = 5.9–5.7 (s) and 112.9–112.1 (s) ppm for the $C_\alpha$ and $C_\gamma$ nuclei, respectively, of the η¹-allyl group], (c) the low-field singlet signals for the carbonyl carbon nuclei of the acyl and carbonyl ligands in the $^{13}C\{^1H\}$ NMR spectra appear in the range $\delta$ = 196.9–196.0 and 165.9–164.1 ppm, respectively.

The stereochemistry of complex **15** was confirmed by a single-crystal X-ray analysis. An ORTEP view of the molecular structure is shown in Figure 2. Selected bond lengths and angles are collected in Table 1.The structure exhibits a distorted octahedral geometry around the iridium atom which is bonded to the three nitrogen atoms of the Ph-pybox ligand, a chlorine atom, a carbon monoxide molecule and an η¹-allyl group (Figure 2). The chlorine atom and the allyl group are located in a *trans* disposition. The Ir–N(1) [2.032(8) Å], Ir–N(2) [2.014(8) Å] and Ir–N(3) [2.024(10) Å] distances as well as the N–Ir–N [77.0(3)°, 78.6(4)° and

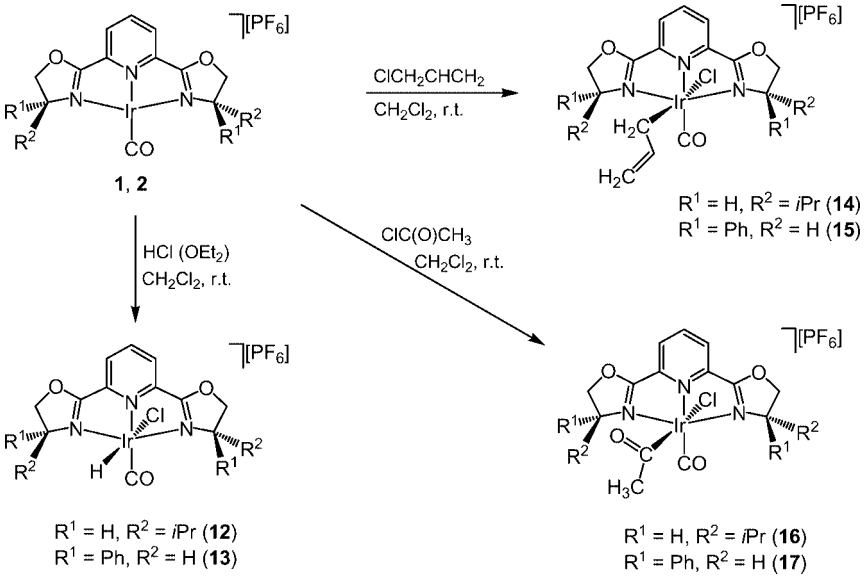


Scheme 4.

 © 2006 Wiley-VCH Verlag GmbH & Co. KGaA, Weinheim 

155.6(4)°] bond angles fall in the range observed for the related complexes [Ir($\eta^2$-$C_2H_4$)$_2$\{$\kappa^3$-*N*,*N*,*N*-(*S*,*S*)-*i*Pr-pybox\}][$PF_6$][5] and [IrCl($\eta^3$-$C_3H_5$)\{$\kappa^3$-*N*,*N*,*N*-(*S*,*S*)-*i*Pr-pybox\}][$PF_6$].[5] The Ir–allyl distances [Ir–C(1) = 2.118(11), C(1)–C(2) = 1.427(13) and C(2)–C(3) = 1.223(17) Å] are slightly shorter than those found for other σ-allyliridium(III) complexes such as [Ir($\eta^1$-$CH_2CH{=}CH_2$)$_3$($PP_2$)] [$PP_2$ = $PhP(CH_2CH_2PPh_2)_2$; Ir–C(1) = 2.208(4)–2.186(4), C(1)–C(2) = 1.488(6)–1.463(6) and C(2)–C(3) = 1.319(6)–1.253(9) Å].[9] Finally, the C–O bond length of the CO ligand in complex **15** [1.117(13) Å] is comparable to that found in the case of the carbonylrhodium complex **10** [C(2)–O(1) = 1.113(10) Å]. In conclusion, both complexes **10** and **15** present the same stereochemistry, with the CO ligand *trans* to the pyridine nitrogen atom of the pybox ligand (see Figures 1 and 2).

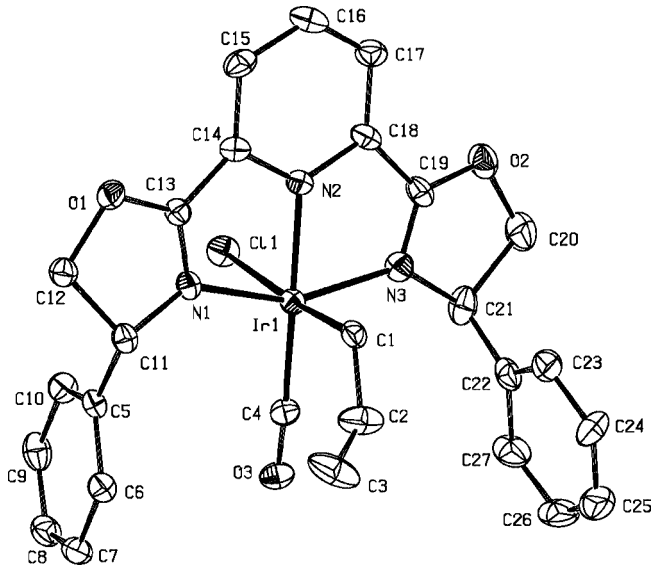


Figure 2. ORTEP-type view of the molecular structure of the cation of [IrCl($\eta^1$-$CH_2CH{=}CH_2$)(CO)\{$\kappa^3$-*N*,*N*,*N*-(*S*,*S*)-*i*Pr-pybox\}][$PF_6$] (**15**) drawn at the 10% probability level. Hydrogen atoms have been omitted for clarity.

Table 1. Selected bond lengths [Å] and angles [°] for complex **15**.

| | |
|---|---|
| Ir–Cl | 2.470(3) |
| Ir–N(1) | 2.032(8) |
| Ir–N(2) | 2.014(8) |
| Ir–N(3) | 2.024(10) |
| Ir–C(1) | 2.118(11) |
| Ir–C(4) | 1.882(11) |
| C(1)–C(2) | 1.427(13) |
| C(2)–C(3) | 1.223(17) |
| C(4)–O(3) | 1.117(13) |
| N(1)–Ir–N(3) | 155.6(4) |
| N(1)–Ir–N(2) | 77.0(3) |
| N(2)–Ir–N(3) | 78.6(4) |
| N(1)–Ir–C(4) | 103.1(4) |
| N(3)–Ir–C(4) | 101.3(5) |
| N(2)–Ir–C(4) | 178.7(4) |
| N(1)–Ir–C(1) | 87.9(4) |
| N(3)–Ir–C(1) | 92.0(4) |
| N(2)–Ir–C(1) | 89.1(4) |
| Ir–C(1)–C(2) | 116.2(8) |
| C(1)–C(2)–C(3) | 138(2) |
| C(4)–Ir–C(1) | 92.2(4) |
| Cl–Ir–C(1) | 175.2(3) |
| N(1)–Ir–Cl | 91.6(2) |
| N(2)–Ir–Cl | 86.2(3) |
| N(3)–Ir–Cl | 86.6(3) |
| O(3)–C(4)–Ir(1) | 174.6(10) |

We have recently reported the synthesis of the complex [IrCl($\eta^3$-$C_3H_5$)\{$\kappa^3$-*N*,*N*,*N*-(*S*,*S*)-*i*Pr-pybox\}][$PF_6$][5] by treatment of the complex [Ir($\eta^2$-$C_2H_4$)$_2$\{$\kappa^3$-*N*,*N*,*N*-(*S*,*S*)-*i*Pr-pybox\}][$PF_6$] with allyl chloride in acetone at room temperature. The reaction presumably involves the formation of an intermediate monoolefiniridium(III) complex with the allyl group having a monodentate coordination. However, complexes **14** and **15** are stable in the sense that they do not evolve into the corresponding $\eta^3$-allyl complexes [IrCl($\eta^3$-$C_3H_5$)($\kappa^3$-*N*,*N*,*N*-*R*-pybox)][$PF_6$] (R = *i*Pr, Ph) by loss of carbon monoxide.

### Hydrosilylation of Acetophenone

The rhodium(III) complexes [$RhCl_3$(R-pybox)] (R = *i*Pr, *s*Bu, *t*Bu, etc.) were first used as catalyst precursors by Nishiyama and co-workers in the enantioselective synthesis of secondary alcohols by the asymmetric reduction of ketones with diphenylsilane.[10] (Scheme 5). They assumed the formation of a rhodium(I) complex as the active species in situ by reduction of the precatalyst in the presence of $AgBF_4$ and diphenylsilane.

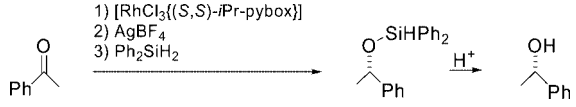


Scheme 5.

We became interested to know the behaviour of the cationic carbonyliridium(I) and -rhodium(I) complexes reported here since neither the previous reduction of the precatalyst nor the use of $AgBF_4$ as additive would be necessary. Therefore, the catalytic activity of the complexes [M(CO)\{$\kappa^3$-*N*,*N*,*N*-(*S*,*S*)-*i*Pr-pybox\}][$PF_6$] [M = Ir (**1**), Rh (**3**)] in the hydrosilylation/reduction of acetophenone was investigated (Scheme 6 and Table 2).

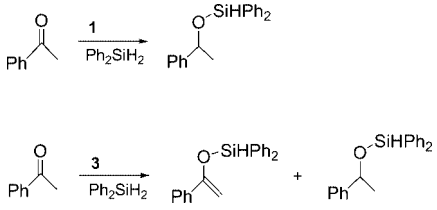


Scheme 6.

[Ir(CO)\{$\kappa^3$-*N*,*N*,*N*-(*S*,*S*)-*i*Pr-pybox\}][$PF_6$] (**1**) was found to be catalytically active, with complete conversion of the ketone into the corresponding silyl ether at room temperature after 72 h of reaction (Table 2, entry 1). However, the desilylation of the product led to racemic 1-phenylethanol, which means that the reduction takes place without asym-

 © 2006 Wiley-VCH Verlag GmbH & Co. KGaA, Weinheim 

Table 2. Hydrosilylation of acetophenone catalysed by complexes **1** and **3**.[a]

| Entry | Catalyst | *i*Pr-pybox | *T* [°C] | *t* [h] | Conversion [%][b] | Silyl ether [%][b] | Silyl enol ether [%][b] |
|---|---|---|---|---|---|---|---|
| 1 | **1** | – | 18 | 72 | 99 | 99 | – |
| 2 | **3** | 4 equiv. | 0 | 4 | 100 | 16 | 84 |
| 3 | **3** | – | 0 | 3 | 100 | 30 | 70 |
| 4 | **3** | 4 equiv. | 18 | 1 | 100 | 9 | 91 |
| 5 | **3** | – | 18 | 0.5 | 100 | 10 | 90 |

[a] The reactions were carried out under conditions similar to those reported in the literature.[11] Details of the procedure are given in the Experimental Section. [b] The values in the last three columns were calculated by integration of signals in the $^1$H NMR spectra.

metric induction. At first sight, this fact can be understood if the *i*Pr-pybox ligand decoordinates before the active species is formed, otherwise some degree of induction should have been observed. This result contrasts with those obtained with the rhodium(I) complex [Rh(CO){κ$^3$-*N*,*N*,*N*-(*S*,*S*)-*i*Pr-pybox}][$PF_6$] (**3**; Table 2, entries 2–5), since variable mixtures of the expected diphenylsilyl ether (as racemate) and diphenylsilylenol ether are obtained when the reaction is run either at 0 °C or at room temperature (Scheme 6). The latter product results from the reductive O–Si coupling between diphenylsilane and the enol tautomer of the ketone. In all cases the conversion is quantitative and the diphenylsilyl enol ether is the major reaction product. We also found that the best selectivity in favour of the silyl enol ether is achieved at room temperature (Table 2, Entries 4 and 5 vs. 2 and 3) and that no excess of ligand is required at that temperature (Entries 4 and 5). A dehydrogenative silylation of ketones with a bifunctional organosilane catalysed by a mixture of the chiral or achiral complexes derived from [$RhCl_3$(pybox)] and AgOTf was reported in 1993 by Nishiyama.[11] Representative examples of the transition-metal-catalysed dehydrogenative silylation of ketones with hydrosilanes have been reported.[12]

In conclusion, acetophenone is easily and quantitatively transformed into its corresponding diphenylsilyl enol ether, at room temperature, with very high selectivity (9:1) in the presence of 1.0 mol% of [Rh(CO){κ$^3$-*N*,*N*,*N*-(*S*,*S*)-*i*Pr-pybox}][$PF_6$]. Silyl enol ethers are reagents of enormous interest in organic synthesis that take part in numerous organic transformations.[13]

## Conclusions

In summary, the synthesis of monocarbonyl derivatives [M(CO)(κ$^3$-*N*,*N*,*N*-R-pybox)][$PF_6$] (M = Rh, Ir) containing the enantiopure (*S*,*S*)-*i*Pr-pybox and (*R*,*R*)-Ph-pybox ligands has been reported. This paper also deals with the synthesis of new organometallic iridium(III) and rhodium(III) complexes by stereoselective oxidative addition reactions. The catalytic activity of the complexes [M(CO){κ$^3$-*N*,*N*,*N*-(*S*,*S*)-*i*Pr-pybox}][$PF_6$] (M = Rh, Ir) in the hydrosilylation of acetophenone has been examined. In particular, the complex [Rh(CO){κ$^3$-*N*,*N*,*N*-(*S*,*S*)-*i*Pr-pybox}][$PF_6$] has been demonstrated to be a very efficient catalyst for the dehydro-*O*-silylation of acetophenone to give the silyl enol ether PhC(OSiH$Ph_2$)=$CH_2$ as the major product.

## Experimental Section

**General:** All reactions were performed under dry nitrogen using vacuum-line and standard Schlenk techniques. All reagents were obtained from commercial suppliers and used without further purification. Solvents were dried by standard methods and distilled under nitrogen before use. The complexes [Ir(η$^2$-$C_2H_4$)$_2${κ$^3$-*N*,*N*,*N*-(*S*,*S*)-*i*Pr-pybox}][$PF_6$], [Ir(μ-Cl)(η$^2$-$C_8H_{14}$)$_2$]$_2$ ($C_8H_{14}$ = cyclooctene) and [Rh(μ-Cl)(η$^2$-$C_2H_4$)$_2$]$_2$ were prepared according to previously reported methods.[5,14] Infrared spectra were recorded with a Perkin–Elmer FT 1720-X or Paragon 1000 spectrometer. The conductivities were measured at room temperature, for approx. $5\times10^{-4}$ M acetone solutions, with a Jenway PCM3 conductimeter. The C, H and N analyses were carried out with a Perkin–Elmer 240-B microanalyzer. Mass spectra (FAB) were determined with a VG-Autospec mass spectrometer, operating in the positive mode; 3-nitrobenzyl alcohol (NBA) was used as the matrix. NMR spectra were recorded with a Bruker AC300 (DPX-300 or AV-300) instrument at 300 MHz ($^1$H) or 75.4 MHz ($^{13}$C) or a Bruker AMX-400 instrument at 400 MHz ($^1$H) or 100.6 MHz ($^{13}$C), using $SiMe_4$ as standard. DEPT experiments were carried out for most of the complexes.

**Synthesis of [Ir(η$^2$-$C_2H_4$)$_2${κ$^3$-*N*,*N*,*N*-(*R*,*R*)-Ph-pybox}][$PF_6$]:** A flow of ethylene was slowly bubbled at room temperature into a suspension of [Ir(μ-Cl)(coe)$_2$]$_2$ (0.448 g, 0.5 mmol) in 5 mL of methanol. After the solution colour became yellow, Ph-pybox (0.369 g, 1 mmol) was added and the mixture stirred at –40 °C for 40 min. $NaPF_6$ (0.248 g, 1.45 mmol) was added to the resulting red solution and the mixture stirred at –40 °C for 45 min. Diethyl ether was then added (ca. 100 mL) and the resulting red solid was washed with cold diethyl ether (3 × 5 mL) and then vacuum-dried (89% yield). Yield: 89% (0.064 g). Colour: red. $C_{27}H_{27}F_6IrN_3O_2P$ (762.70): calcd. C 42.52, H 3.57, N 5.51; found C 41.32, H 3.40, N 5.34. FAB-MS: *m*/*z* = 590 [$M^+ - C_2H_4$], 562 [$M^+ - 2\ C_2H_4$]. IR (KBr): $\tilde{\nu}$ = 840 ($PF_6^-$) cm$^{-1}$. Conductivity (acetone, 20 °C): 129 Ω$^{-1}$ cm$^2$ mol$^{-1}$. $^1$H NMR (300 MHz, $CD_2Cl_2$, 20 °C): $\delta$ = 8.17 (s, 3 H, $C_5H_3N$), 7.40, 7.09 (2 × m, 10 H, CH*Ph*), 5.23 (m, 2 H, $OCH_2$ or C*H*Ph), 4.81 (m, 2 H, $OCH_2$ or C*H*Ph), 4.47 (m, 2 H, $OCH_2$ or C*H*Ph), 2.33 (br., 4 H, $C_2H_4$), 1.97 (br., 4 H, $C_2H_4$) ppm. $^{13}$C{$^1$H} NMR (75.48 MHz, $CD_2Cl_2$, 20 °C): $\delta$ = 170.09 (s, OCN), 145.66 (s, $C^{2,6}$ $C_5H_3N$), 136.60 (s, $C^4$H $C_5H_3N$), 130.31, 129.66, 128.30, 126.52 (s, $C^{3,5}$H $C_5H_3N$ and Ph), 79.27 (s, $OCH_2$), 66.99 (s, *C*HPh), 32.97 (s, $C_2H_4$) ppm.

**Synthesis of Complexes [Ir(CO)(κ$^3$-*N*,*N*,*N*-R-pybox)][X] [X = $PF_6$, R = *i*Pr (1), Ph (2); X = $SbF_6$, R = *i*Pr (1a)]. Method A:** A solution of [Ir(η$^2$-$C_2H_4$)$_2$(κ$^3$-*N*,*N*,*N*-R-pybox)][$PF_6$] (R = *i*Pr or Ph) (0.1 mmol) in dichloromethane (10 mL) was stirred at room temperature under CO for 5 min. The resulting solution was then concentrated to about 3 mL and the residue diluted with 30 mL of diethyl ether to yield a dark solid, which was washed with diethyl ether (3 × 5 mL) and vacuum-dried. Complexes **1** and **2** were obtained in higher purity if a flow of nitrogen was slowly bubbled into the dichloromethane solution over 50 min and the mixture worked up as above. **Method B:** A solution of [Ir(μ-Cl)(η$^2$-$C_8H_{14}$)$_2$]$_2$ (0.036 g, 0.04 mmol) in dichloromethane (10 mL) was stirred at room temperature under CO for 5 min. *i*Pr-pybox (0.024 g, 0.08 mmol) and $AgSbF_6$ (0.052 g, 0.15 mmol) were then added and the mixture was stirred in the dark for 4 h. The suspen-

 © 2006 Wiley-VCH Verlag GmbH & Co. KGaA, Weinheim 

sion was filtered through kieselguhr and the resulting solution was then concentrated to about 3 mL. Addition of hexane (30 mL) yielded a dark solid, which was washed with hexane (3 × 5 mL) and vacuum-dried. **1:** Yield: 96% (0.064 g). Colour: dark green. $C_{18}H_{23}F_6IrN_3O_3P$ (666.58): calcd. C 32.43, H 3.48, N 6.30; found C 31.85, H 3.13, N 5.81. IR (KBr): $\tilde{\nu}$ = 1968 (CO), 840 ($PF_6^-$) $cm^{-1}$. IR ($CH_2Cl_2$): $\tilde{\nu}$ = 1989 (CO) $cm^{-1}$. Conductivity (acetone, 20 °C): 123 $\Omega^{-1}cm^2mol^{-1}$. $^1H$ NMR (300 MHz, [D$_6$]acetone, 20 °C): $\delta$ = 8.36 [t, $J_{H,H}$ = 8.0 Hz, 1 H, H$^4$ $C_5H_3N$), 8.17 (d, $J_{H,H}$ = 8.0 Hz, 2 H, H$^{3,5}$ $C_5H_3N$), 5.16 (m, 4 H, $OCH_2$), 4.48 (m, 2 H, C*H*iPr), 2.22 (m, 2 H, C*H*Me$_2$), 1.06 (d, $J_{H,H}$ = 7.1 Hz, 6 H, CH*Me*$_2$), 0.98 (d, $J_{H,H}$ = 6.8 Hz, 6 H, CH*Me*$_2$) ppm. $^{13}C\{^1H\}$ NMR (75.48 MHz, [D$_6$]acetone, 20 °C): $\delta$ = 182.3 (s, CO), 172.0 (s, OCN), 149.0 (s, C$^4$H C$^{2,6}$ $C_5H_3N$), 125.4 (s, C$^{3,5}$H $C_5H_3N$), 74.5 (s, $OCH_2$), 71.7 (s, *C*HiPr), 31.1 (s, *C*HMe$_2$), 18.3 (s, CH*Me*$_2$), 14.5 (s, CH*Me*$_2$) ppm. **2:** Yield: 94% (0.069 g). Colour: garnet. $C_{24}H_{19}F_6IrN_3O_3P$ (734.62): calcd. C 39.24, H 2.61, N 5.72; found C 38.57, H 2.45, N 5.34. IR (KBr): $\tilde{\nu}$ = 1978 (CO), 842 ($PF_6^-$) $cm^{-1}$. IR ($CH_2Cl_2$): $\tilde{\nu}$ = 1996 (CO) $cm^{-1}$. Conductivity (acetone, 20 °C): 117 $\Omega^{-1}cm^2mol^{-1}$. $^1H$ NMR (300 MHz, [D$_6$]acetone, 20 °C): $\delta$ = 8.41 (m, 1 H, H$^4$ $C_5H_3N$), 8.28 (d, $J_{H,H}$ = 8.5 Hz, 2 H, H$^{3,5}$ $C_5H_3N$), 7.43 (m, 10 H, CH*Ph*), 5.63 (m, 2 H, $OCH_2$), 5.48 (m, 2 H, $OCH_2$), 5.04 (m, 2 H, C*H*Ph) ppm. $^{13}C\{^1H\}$ NMR (75.48 MHz, [D$_6$]acetone, 20 °C) $\delta$ = 173.8 (s, CO), 166.1 (s, OCN), 143.5 (s, C$^{2,6}$ $C_5H_3N$), 140.0 (s, C$^4$H $C_5H_3N$), 132.0 (s, *ipso*-Ph), 123.6, 123.4, 122.7 (s, Ph), 118.9 (s, C$^{3,5}$H $C_5H_3N$), 74.7 (s, $OCH_2$), 65.0 (s, *C*HPh) ppm. **1a:** Colour: very dark green. $C_{18}H_{23}F_6IrN_3O_3Sb$ (757.36): calcd. C 28.55, H 3.06, N 5.55; found C 29.06, H 3.06, N 5.20. IR (KBr): $\tilde{\nu}$ = 1973 (CO), 659 ($SbF_6^-$) $cm^{-1}$. IR ($CH_2Cl_2$): $\tilde{\nu}$ = 1989 (CO) $cm^{-1}$. Conductivity (acetone, 20 °C): 130 $\Omega^{-1}cm^2mol^{-1}$. $^1H$ NMR (300 MHz, [D$_6$]acetone, 20 °C): $\delta$ = 8.36 (t, $J_{H,H}$ = 8.0 Hz, 1 H, H$^4$ $C_5H_3N$), 8.16 (d, $J_{H,H}$ = 8.0 Hz, 2 H, H$^{3,5}$ $C_5H_3N$), 5.16 (m, 4 H, $OCH_2$), 4.47 (m, 2 H, C*H*iPr), 2.24 (m, 2 H, C*H*Me$_2$), 1.07 (d, $J_{H,H}$ = 7.2 Hz, 6 H, CH*Me*$_2$), 0.99 (d, $J_{H,H}$ = 6.9 Hz, 6 H, CH*Me*$_2$) ppm.

**Synthesis of Complexes [Rh(CO)(κ$^3$-*N*,*N*,*N*-R-pybox)][PF$_6$] [R = *i*Pr (3), Ph (4)]:** A solution of the corresponding pybox ligand (1.028 mmol), [Rh(μ-Cl)(η$^2$-$C_2H_4$)$_2$]$_2$ (0.200 g, 0.514 mmol) and $NaPF_6$ (0.259 g, 1.542 mmol) in dichloromethane (20 mL)/methanol (5 mL) was stirred at room temperature under CO for 1 h. The solvent was then removed under reduced pressure and the solid residue was extracted with dichloromethane and filtered. The resulting solution was then concentrated to about 3 mL and 30 mL of diethyl ether added to yield a solid, which was washed with diethyl ether (2 × 30 mL) and vacuum-dried. **3:** Yield: 91% (0.542 g). Colour: garnet $C_{18}H_{23}F_6N_3O_3PRh$ (577.26): calcd. C 37.45, H 4.01, N 7.28; found C 37.81, H 3.96, N 7.02. FAB-MS: *m*/*z* = 432 [M$^+$], 404 [M$^+$ – CO]. IR (KBr): $\tilde{\nu}$ = 1981 (CO), 840 ($PF_6^-$) $cm^{-1}$. IR ($CH_2Cl_2$): $\tilde{\nu}$ = 2001 (CO) $cm^{-1}$. Conductivity (acetone, 20 °C): 118 $\Omega^{-1}cm^2mol^{-1}$. $^1H$ NMR (300 MHz, [D$_6$]acetone, 20 °C): $\delta$ = 8.50 (t, $J_{H,H}$ = 8.2 Hz, 1 H, H$^4$ $C_5H_3N$), 8.16 (d, $J_{H,H}$ = 8.2 Hz, 2 H, H$^{3,5}$ $C_5H_3N$), 5.14–4.99 (m, 4 H, $OCH_2$), 4.36 (m, 2 H, C*H*iPr), 2.16 (m, 2 H, C*H*Me$_2$), 1.05 (d, $J_{H,H}$ = 6.8 Hz, 6 H, CH*Me*$_2$), 0.98 (d, $J_{H,H}$ = 6.8 Hz, 6 H, CH*Me*$_2$) ppm. $^{13}C\{^1H\}$ NMR (75.48 MHz, [D$_6$]acetone, 20 °C): $\delta$ = 191.7 (d, $J_{C,Rh}$ = 76.3 Hz, CO), 168.1 (s, OCN), 146.3 (s, C$^4$H $C_5H_3N$), 144.5 (s, C$^{2,6}$ $C_5H_3N$), 125.9 (s, C$^{3,5}$H $C_5H_3N$), 73.7 and 70.1 (s, $OCH_2$ and *C*HiPr), 30.9 (s, *C*HMe$_2$), 18.1 (s, CH*Me*$_2$) 14.5 (s, CH*Me*$_2$) ppm. **4:** Yield: 84% (0.557 g). Colour: green. $C_{24}H_{19}F_6N_3O_3PRh$ (645.30): calcd. C 44.67, H 2.96, N 6.51; found C 43.74, H 2.60, N 6.10. FAB-MS: *m*/*z* = 500 [M$^+$], 472 [M$^+$ – CO]. IR (KBr): $\tilde{\nu}$ = 1997 (CO), 840 ($PF_6^-$) $cm^{-1}$. IR ($CH_2Cl_2$): $\tilde{\nu}$ = 2014 (CO) $cm^{-1}$. Conductivity (acetone, 20 °C): 130 $\Omega^{-1}cm^2mol^{-1}$. $^1H$ NMR (300 MHz, [D$_6$]acetone, 20 °C): $\delta$ = 8.52 (t, $J_{H,H}$ = 8.0 Hz, 1 H, H$^4$ $C_5H_3N$), 8.23 (d, $J_{H,H}$ = 8.0 Hz, 2 H, H$^{3,5}$ $C_5H_3N$), 7.43 (m, 10 H, Ph), 5.47 (m, 4 H, $OCH_2$), 4.93 (pt, $J_{H,H}$ = 8.6 Hz, 2 H, C*H*Ph) ppm. $^{13}C\{^1H\}$ NMR (75.48 MHz, [D$_6$]acetone, 20 °C): $\delta$ = 189.9 (d, $J_{C,Rh}$ = 76.3 Hz, CO), 168.8 (s, OCN), 147.2 and 144.4 (s, Ph and C$^{2,6}$ $C_5H_3N$), 139.0 (s, C$^4$H $C_5H_3N$), 129.8, 129.7, 128.9, 126.2 (s, Ph and C$^{3,5}$H $C_5H_3N$), 80.6 (s, $OCH_2$), 69.9 (s, *C*HPh) ppm.

**Synthesis of Complex *trans*-[IrI$_2$(CO){κ$^3$-*N*,*N*,*N*-(*S*,*S*)-*i*Pr-pybox}][PF$_6$] (5):** $I_2$ (0.076 g, 0.30 mmol) was added to a solution of complex **1** (0.100 g, 0.15 mmol) in 10 mL of dichloromethane. Upon addition of iodine, the black solution turned red. The solution was stirred at room temperature for 5 min. The volume was then reduced to about 3 mL and 30 mL of diethyl ether was added to yield an orange solid, which was washed with diethyl ether (2 × 20 mL) and dried under reduced pressure. Yield: 85% (0.125 g). Colour: garnet. $C_{18}H_{23}F_6I_2IrN_3O_3P$ (920.39): calcd. C 23.49, H 2.52, N 4.57; found C 24.28, H 2.68, N 4.51. IR (KBr): $\tilde{\nu}$ = 2102 (CO), 845 ($PF_6^-$) $cm^{-1}$. IR ($CH_2Cl_2$): $\tilde{\nu}$ = 2092 (CO) $cm^{-1}$. Conductivity (acetone, 20 °C): 128 $\Omega^{-1}cm^2mol^{-1}$. $^1H$ NMR (300 MHz, [D$_6$]acetone, 20 °C): $\delta$ = 8.90 (m, 1 H, H$^4$ $C_5H_3N$), 8.74 (d, $J_{H,H}$ = 8.0 Hz, 2 H, H$^{3,5}$ $C_5H_3N$), 5.37 (m, 4 H, $OCH_2$), 4.64 (m, 2 H, C*H*iPr), 2.28 (m, 2 H, C*H*Me$_2$), 1.17 (d, $J_{H,H}$ = 7.0 Hz, 6 H, CH*Me*$_2$), 1.13 (d, $J_{H,H}$ = 6.6 Hz, 6 H, CH*Me*$_2$) ppm. $^{13}C\{^1H\}$ NMR (75.48 MHz, [D$_6$]acetone, 20 °C): $\delta$ = 170.9 (s, OCN), 157.8 (s, CO), 145.9 (s, C$^4$H $C_5H_3N$), 143.9 (s, C$^{2,6}$ $C_5H_3N$), 130.8 (s, C$^{3,5}$H $C_5H_3N$), 75.3 (s, $OCH_2$), 71.3 (s, *C*HiPr), 30.4 (s, *C*HMe$_2$), 18.5 (s, CH*Me*$_2$), 15.8 (s, CH*Me*$_2$) ppm.

**Synthesis of Complexes *trans*-[RhI$_2$(CO)(κ$^3$-*N*,*N*,*N*-R-pybox)][PF$_6$] [R = *i*Pr (6), Ph (7)]:** $I_2$ (0.044 g, 0.173 mmol) was added to a solution of complex **3** or **4** (0.173 mmol) in 10 mL of dichloromethane or THF. The green solution turned orange. After 5 min, the volume was reduced to about 2 mL and 30 mL of diethyl ether added, yielding an orange-brown solid which was washed with diethyl ether (2 × 20 mL) and vacuum-dried. **6:** Yield: 89% (0.129 g). Colour: orange-brown. $C_{18}H_{23}F_6I_2N_3O_3PRh$ (831.07): calcd. C 26.01, H 2.79, N 5.06; found C 25.58, H 2.86, N 5.34. IR (KBr): $\tilde{\nu}$ = 2110 (CO), 840 ($PF_6^-$) $cm^{-1}$. IR ($CH_2Cl_2$): $\tilde{\nu}$ = 2112 (CO) $cm^{-1}$. Conductivity (acetone, 20 °C): 122 $\Omega^{-1}cm^2mol^{-1}$. $^1H$ NMR (300 MHz, $CD_2Cl_2$, 20 °C): $\delta$ = 8.73 (t, $J_{H,H}$ = 8.1 Hz, 1 H, H$^4$ $C_5H_3N$), 8.41 (d, $J_{H,H}$ = 8.1 Hz, 2 H, H$^{3,5}$ $C_5H_3N$), 5.12–4.97 (m, 4 H, $OCH_2$), 4.39 (m, 2 H, C*H*iPr), 2.17 (m, 2 H, C*H*Me$_2$), 1.08 (d, $J_{H,H}$ = 6.5 Hz, 6 H, CH*Me*$_2$), 1.06 (d, $J_{H,H}$ = 6.2 Hz, 6 H, CH*Me*$_2$) ppm. $^{13}C\{^1H\}$ NMR (75.48 MHz, $CD_2Cl_2$, 20 °C): $\delta$ = 177.9 (d, $J_{C,Rh}$ = 53.4 Hz, CO), 167.4 (s, OCN), 145.1 and 144.6 (2 × s, C$^4$H and C$^{2,6}$ $C_5H_3N$), 130.1 (s, C$^{3,5}$H $C_5H_3N$), 74.5 and 71.0 (s, $OCH_2$ and *C*HiPr), 30.2 (s, *C*HMe$_2$), 15.9 (s, CH*Me*$_2$), 14.3 (s, CH*Me*$_2$) ppm. **7:** Yield: 83% (0.129 g). Colour: orange-brown. $C_{24}H_{19}F_6I_2N_3O_3PRh$ (899.10): calcd. C 32.06, H 2.13, N 4.67; found C 32.83, H 2.33, N 4.10. IR (KBr): $\tilde{\nu}$ = 2125 (CO), 840 ($PF_6^-$) $cm^{-1}$. IR ($CH_2Cl_2$): $\tilde{\nu}$ = 2125 (CO) $cm^{-1}$. Conductivity (acetone, 20 °C): 127 $\Omega^{-1}cm^2mol^{-1}$. $^1H$ NMR (300 MHz, [D$_6$]acetone, 20 °C): $\delta$ = 8.52 (t, $J_{H,H}$ = 7.8 Hz, 1 H, H$^4$ $C_5H_3N$), 8.23 (d, $J_{H,H}$ = 7.8 Hz, 2 H, H$^{3,5}$ $C_5H_3N$), 7.43 (m, 10 H, Ph), 5.47 (m, 4 H, $OCH_2$), 5.30 (m, 2 H, C*H*Ph) ppm. $^{13}C\{^1H\}$ NMR (75.48 MHz, [D$_6$]acetone, 20 °C): $\delta$ = 177.2 (d, $J_{C,Rh}$ = 55.1 Hz, CO), 168.3 (s, OCN), 146.0 and 145.7 (2 × s, C$^{2,6}$H $C_5H_3N$), 134.4 (s, C$^4$H $C_5H_3N$), 131.1–128.8 (Ph and C$^{3,5}$H $C_5H_3N$), 80.7 (s, $OCH_2$), 70.9 (s, *C*HPh) ppm.

**Synthesis of Complexes [Ir(CH$_3$)I(CO)(κ$^3$-*N*,*N*,*N*-R-pybox)][PF$_6$] [R = *i*Pr (8), Ph (9)]:** Iodomethane (0.093 mL, 1.5 mmol) was added to a solution of complex **1** or **2** (0.15 mmol) in 10 mL of dichloromethane. The solution was stirred at room temperature. The re-

 © 2006 Wiley-VCH Verlag GmbH & Co. KGaA, Weinheim 

sulting orange solution was then concentrated to about 3 mL and 30 mL of a mixture of diethyl ether and hexane (1:1) was added to yield a yellow solid, which was washed with diethyl ether (3 × 5 mL) and dried under reduced pressure. **8:** Reaction time: 1 h. Yield: 93% (0.113 g). Colour: yellow. FAB-MS: *m*/*z* = 664 [$M^+$]. IR (KBr): $\tilde{\nu}$ = 2076 (CO), 840 ($PF_6^-$) $cm^{-1}$. IR ($CH_2Cl_2$): $\tilde{\nu}$ = 2069 (CO) $cm^{-1}$. Conductivity (acetone, 20 °C): 125 $\Omega^{-1}cm^2mol^{-1}$. $^1H$ NMR (300 MHz, [D$_6$]acetone, 20 °C): $\delta$ = 8.79 (t, $J_{H,H}$ = 8.1 Hz, 1 H, $H^4$ $C_5H_3N$), 8.56 (m, 2 H, $H^{3,5}$ $C_5H_3N$), 5.35 (m, 4 H, $OCH_2$), 4.66 (m, 2 H, C*H*i*Pr*), 2.27 (m, 2 H, C*H*Me$_2$), 1.13 (m, 9 H, CH*Me*$_2$), 1.11 (s, 3 H, IrMe), 1.02 (d, $J_{H,H}$ = 6.7 Hz, 3 H, CH*Me*$_2$) ppm. $^{13}C\{^1H\}$ NMR (75.48 MHz, [D$_6$]acetone, 20 °C, major isomer): $\delta$ = 170.8 (s, OCN), 170.3 (s, OCN), 166.8 (s, CO), 145.0 (s, $C^4H$ $C_5H_3N$), 144.8 (s, $C^{2,6}$ $C_5H_3N$), 144.0 (s, $C^{2,6}$ $C_5H_3N$), 130.0 (s, $C^{3,5}H$ $C_5H_3N$), 129.8 (s, $C^{3,5}H$ $C_5H_3N$), 75.2 (s, *C*H*i*Pr), 75.1 (s, *C*H*i*Pr), 71.9 (s, $OCH_2$), 71.1 (s, $OCH_2$), 30.7 (s, *C*HMe$_2$), 30.4 (s, *C*HMe$_2$), 19.2 (s, CH*Me*$_2$), 19.0 (s, CH*Me*$_2$), 16.4 (s, CH*Me*$_2$), 15.5 (s, CH*Me*$_2$), –9.5 (s, IrMe) ppm. **9:** Reaction time: 20 min. Yield: 94% (0.123 g). Colour: yellow. $C_{25}H_{22}F_6IIrN_3O_3P$ (876.56): calcd. C 34.26, H 2.53, N 4.79; found C 34.54, H 2.51, N 4.72. IR (KBr): $\tilde{\nu}$ = 2067 (CO), 842 ($PF_6^-$) $cm^{-1}$. IR ($CH_2Cl_2$): $\tilde{\nu}$ = 2075 (CO) $cm^{-1}$. Conductivity (acetone, 20 °C): 119 $\Omega^{-1}cm^2mol^{-1}$. $^1H$ NMR (300 MHz, [D$_6$]acetone, 20 °C): $\delta$ = 8.84 (m, 1 H, $H^4$ $C_5H_3N$), 8.65 (m, 2 H, $H^{3,5}$ $C_5H_3N$), 7.70–7.30 (2 × m, 10 H, CH*Ph*), 5.80 (m, 2 H, $OCH_2$), 5.62 (m, 2 H, $OCH_2$), 5.31 (m, 2 H, C*H*Ph), 0.73 (s, 3 H, IrMe) ppm. $^{13}C\{^1H\}$ NMR (50.32 MHz, [D$_6$]acetone, 20 °C): $\delta$ = 170.5 (s, OCN), 170.3 (s, OCN), 165.1 (s, CO), 144.7 (s, $C^4H$ $C_5H_3N$), 135.8 (s, $C^{2,6}$ $C_5H_3N$), 135.0 (s, $C^{2,6}$ $C_5H_3N$), 131.1, 130.7, 130.3, 129.7, 129.7 (s, $C^{3,5}H$ $C_5H_3N$, Ph), 80.5 (s, $OCH_2$), 80.3 (s, $OCH_2$), 71.0 (s, *C*HPh), 70.7 (s, *C*HPh), –10.9 (s, IrMe) ppm.

**Synthesis of Complexes [Rh(CH$_3$)I(CO)(κ$^3$-*N*,*N*,*N*-R-pybox)][PF$_6$] [R = *i*Pr (10), Ph (11)]:** A suspension of [Rh(CO)(κ$^3$-*N*,*N*,*N*-R-pybox)][$PF_6$] (0.346 mmol) in $CH_3I$ (5 mL) was stirred at 30 °C for 5 min. The excess of reagent was then removed under reduced pressure and the resulting solid residue was dissolved in dichloromethane (5 mL) and subjected to silica gel column chromatography. Elution with a dichloromethane/methanol mixture gave a yellow band from which complexes **10** and **11** were isolated as yellow solids after solvent removal. **10:** Eluted with dichloromethane/methanol (10:1). Yield: 80% (0.201 g). Colour: yellow. $C_{19}H_{26}F_6IN_3O_3PRh$ (719.20): calcd. C 31.73, H 3.64, N 5.84; found C 31.72, H 3.14, N 6.52. IR (KBr): $\tilde{\nu}$ = 2096 (CO), 843 ($PF_6^-$) $cm^{-1}$. Conductivity (acetone, 20 °C): 110 $\Omega^{-1}cm^2mol^{-1}$. $^1H$ NMR (300 MHz, $CD_2Cl_2$, 20 °C): $\delta$ = 8.58 (t, $J_{H,H}$ = 8.0 Hz, 1 H, $H^4$ $C_5H_3N$), 8.25 (m, 2 H, $H^{3,5}$ $C_5H_3N$), 5.12–4.87 (m, 4 H, $OCH_2$), 4.57 (m, 1 H, C*H*i*Pr*), 4.28 (m, 1 H, C*H*i*Pr*), 2.23 (m, 1 H, C*H*Me$_2$), 2.10 (m, 1 H, C*H*Me$_2$), 1.40 (d, $^2J_{H,Rh}$ = 1.5 Hz, 3 H, RhMe), 1.05–0.93 (m, 12 H, CH*Me*$_2$) ppm. $^{13}C\{^1H\}$ NMR (75.48 MHz, [D$_6$]acetone, 20 °C): $\delta$ = 185.5 (d, $J_{C,Rh}$ = 59.8 Hz, CO), 167.6 (s, OCN), 167.3 (s, OCN), 145.1, 144.4 and 144.3 (s, $C^4H$ and $C^{2,6}$ $C_5H_3N$), 129.8 (s, $C^{3,5}H$ $C_5H_3N$), 129.6 (s, $C^{3,5}H$ $C_5H_3N$), 74.8, 74.7, 70.9 and 70.3 (s, $OCH_2$ and *C*H*i*Pr), 19.2 (s, CH*Me*$_2$), 19.0 (s, CH*Me*$_2$), 16.2 (s, CH*Me*$_2$), 15.4 (s, CH*Me*$_2$), 10.3 (d, $J_{C,Rh}$ = 18.3 Hz, RhMe) ppm. **11:** Eluted with dichloromethane/methanol (50:1). Yield: 74% (0.202 g). Colour: yellow. $C_{25}H_{22}F_6IN_3O_3PRh$ (787.23): calcd. C 38.14, H 2.82, N 5.34; found C 38.99, H 2.61, N 5.46. IR (KBr): $\tilde{\nu}$ = 2099 (CO), 842 ($PF_6^-$) $cm^{-1}$. Conductivity (acetone, 20 °C): 128 $\Omega^{-1}cm^2mol^{-1}$. $^1H$ NMR (300 MHz, [D$_6$]acetone, 20 °C): $\delta$ = 8.90 (t, $J_{H,H}$ = 8.0 Hz, 1 H, $H^4$ $C_5H_3N$), 8.66 (m, 2 H, $H^{3,5}$ $C_5H_3N$), 7.53 (m, 10 H, Ph), 5.65 (m, 4 H, $OCH_2$), 5.19 (m, 2 H, C*H*Ph), 1.18 (d, $^2J_{H,Rh}$ = 1.7 Hz, 3 H, RhMe) ppm. $^{13}C\{^1H\}$ NMR (75.48 MHz, [D$_6$]acetone, 20 °C): $\delta$ = 184.0 (d, $J_{C,Rh}$ = 60.4 Hz, CO), 167.7 (s, OCN), 167.3 (s, OCN), 145.6, 145.1 and 144.5 (s, Ph and $C^{2,6}$ $C_5H_3N$), 136.2 and 135.4 (s, Ph and $C^4H$ $C_5H_3N$), 131.1–129.7 (Ph and $C^{3,5}H$ $C_5H_3N$), 80.6 (s, $OCH_2$), 80.6 (s, $OCH_2$), 70.3 (s, *C*HPh), 69.9 (s, *C*HPh), 9.3 (d, $J_{C,Rh}$ = 17.2 Hz, RhMe) ppm.

**Synthesis of Complexes [IrClH(CO)(κ$^3$-*N*,*N*,*N*-R-pybox)][PF$_6$] [R = *i*Pr (12), Ph (13)]:** A solution of HCl in diethyl ether (1 M, 0.1 mL, 0.1 mmol) was added to a solution of complex **1** or **2** (0.1 mmol) in 10 mL of dichloromethane at room temperature and the reaction mixture was stirred. A diethyl ether/hexane (1:1) mixture was added and the resulting yellow solid washed with the same mixture (2 × 5 mL) and then vacuum-dried. **12:** Reaction time: 50 min. Yield: 92% (0.071 g). Colour: yellow. FAB-MS: *m*/*z* = 558 [$M^+$], 530 [$M^+$ – CO]. IR (KBr): $\tilde{\nu}$ = 2180 (Ir–H), 2063 (CO), 842 ($PF_6^-$) $cm^{-1}$. IR ($CH_2Cl_2$): $\tilde{\nu}$ = 2075 (CO) $cm^{-1}$. Conductivity (acetone, 20 °C): 124 $\Omega^{-1}cm^2mol^{-1}$. $^1H$ NMR (300 MHz, [D$_6$]acetone, 20 °C): $\delta$ = 8.82 (t, $J_{H,H}$ = 8.0 Hz, 1 H, $H^4$ $C_5H_3N$), 8.54 (d, $J_{H,H}$ = 8.0 Hz, 2 H, $H^{3,5}$ $C_5H_3N$), 5.34 (m, 4 H, $OCH_2$), 4.63 (m, 2 H, C*H*i*Pr*), 2.26 (m, 2 H, C*H*Me$_2$), 1.12 (d, $J_{H,H}$ = 6.8 Hz, 9 H, CH*Me*$_2$), 0.96 (d, $J_{H,H}$ = 6.8 Hz, 3 H, CH*Me*$_2$), –19.25 (s, 1 H, IrH) ppm. $^{13}C\{^1H\}$ NMR (75.48 MHz, [D$_6$]acetone, 20 °C): $\delta$ = 171.8 (s, OCN), 171.1 (s, OCN), 165.6 (s, CO), 145.6 (s, $C^4H$ $C_5H_3N$), 145.1 (s, $C^{2,6}$ $C_5H_3N$), 129.3 (s, $C^{3,5}H$ $C_5H_3N$), 75.1 (s, $OCH_2$), 74.7 (s, $OCH_2$), 72.4 (s, *C*H*i*Pr), 70.2 (s, *C*H*i*Pr), 31.2 (s, *C*HMe$_2$), 30.7 (s, *C*HMe$_2$), 18.7 (s, CH*Me*$_2$), 18.3 (s, CH*Me*$_2$), 15.8 (s, CH*Me*$_2$), 14.3 (s, CH*Me*$_2$) ppm. **13:** Reaction time: 5 min. Yield: 94% (0.073 g). Colour: yellow. $C_{24}H_{20}ClF_6IrN_3O_3P$ (771.30): calcd. C 37.38, H 2.61, N 5.45; found C 36.70, H 2.60, N 5.11. IR (KBr): $\tilde{\nu}$ = 2164 (Ir–H), 2074 (CO), 843 ($PF_6^-$) $cm^{-1}$. IR ($CH_2Cl_2$): $\tilde{\nu}$ = 2083 (CO) $cm^{-1}$. Conductivity (acetone, 20 °C): 123 $\Omega^{-1}cm^2mol^{-1}$. $^1H$ NMR (300 MHz, [D$_6$]acetone, 20 °C): $\delta$ = 8.84 (m, 1 H, $H^4$ $C_5H_3N$), 8.61 (m, 2 H, $H^{3,5}$ $C_5H_3N$), 7.63–7.45 (m, 10 H, Ph), 5.80, 5.56, 5.20 (m, 6 H, $OCH_2$, C*H*Ph), –19.73 (s, 1 H, IrH) ppm. $^{13}C\{^1H\}$ NMR (75.48 MHz, [D$_6$]acetone, 20 °C): $\delta$ = 171.5 (s, OCN), 171.1 (s, OCN), 163.0 (s, CO), 146.0 (s, $C^{2,6}$ $C_5H_3N$), 145.6 (s, $C^{2,6}$ $C_5H_3N$), 145.2 (s, $C^4H$ $C_5H_3N$), 136.6 (s, *ipso*-Ph), 135.4 (s, *ipso*-Ph), 130.4, 130.2, 130.1, 129.4, 129.3, 128.9, 128.9 (s, $C^{3,5}H$ $C_5H_3N$, Ph), 80.7 (s, $OCH_2$), 74.7 (s, $OCH_2$), 71.9 (s, *C*HPh), 70.1 (s, *C*HPh) ppm.

**Synthesis of Complexes [IrCl(η$^1$-$CH_2CH{=}CH_2$)(CO)(κ$^3$-*N*,*N*,*N*-R-pybox)][PF$_6$] [R = *i*Pr (14), Ph (15)]:** Allyl chloride (0.025 mL, 0.30 mmol) was added to a solution of complex **1** or **2** (0.1 mmol) in 10 mL of dichloromethane. The solution was stirred at room temperature. The resulting yellow solution was then concentrated to about 3 mL and 30 mL of a mixture of diethyl ether and hexane (1:3) was added to yield a yellow solid, which was washed with the same solvent mixture (3 × 5 mL) and dried under reduced pressure. **14:** Reaction time: 1 h. Yield: 85% (0.063 g). Colour: yellow. $C_{21}H_{28}ClF_6IrN_3O_3P$ (743.11): calcd. C 33.94, H 3.80, N 5.65; found C 34.05, H 3.99, N 5.77. IR (KBr): $\tilde{\nu}$ = 2079 (CO), 846 ($PF_6^-$) $cm^{-1}$. IR ($CH_2Cl_2$): $\tilde{\nu}$ = 2070 (CO) $cm^{-1}$. Conductivity (acetone, 20 °C): 126 $\Omega^{-1}cm^2mol^{-1}$. $^1H$ NMR (300 MHz, [D$_6$]acetone, 20 °C): $\delta$ = 8.78 (t, $J_{H,H}$ = 8.0 Hz, 1 H, $H^4$ $C_5H_3N$), 8.53 (d, $J_{H,H}$ = 8.0 Hz, 1 H, $H^{3,5}$ $C_5H_3N$), 8.52 (d, $J_{H,H}$ = 8.0 Hz, 1 H, $H^{3,5}$ $C_5H_3N$), 5.84 (m, 1 H, *H*C=$CH_2$), 5.32 (m, 4 H, $OCH_2$), 4.87 (m, 1 H, HC=C*H*$_2$), 4.81 (m, 1 H, HC=C*H*$_2$), 4.64 (m, 1 H, C*H*i*Pr*), 4.56 (m, 1 H, C*H*i*Pr*), 3.18 (m, 1 H, $IrCH_2$), 2.34 (m, 1 H, $IrCH_2$), 2.28 (m, 2 H, C*H*Me$_2$), 1.16 (d, $J_{H,H}$ = 7.0 Hz, 3 H, CH*Me*$_2$), 1.11 (d, $J_{H,H}$ = 7.0 Hz, 3 H, CH*Me*$_2$), 1.09 (d, $J_{H,H}$ = 6.7 Hz, 3 H, CH*Me*$_2$), 1.07 (d, $J_{H,H}$ = 6.7 Hz, 3 H, CH*Me*$_2$) ppm. $^{13}C\{^1H\}$ NMR (75.48 MHz, [D$_6$]acetone, 20 °C): $\delta$ = 171.7 (s, OCN), 171.0 (s, OCN), 165.9 (s, CO), 145.7 (s, $C^4H$ $C_5H_3N$ or H*C*=$CH_2$ allyl), 145.0 (s, $C^{2,6}$ $C_5H_3N$), 144.3 (s, $C^{2,6}$ $C_5H_3N$), 142.9 (s, $C^4H$ $C_5H_3N$ or H*C*=$CH_2$ allyl), 129.8 (s, $C^{3,5}H$ $C_5H_3N$), 112.9 (s, HC=*C*$H_2$ allyl), 75.8 (s, $OCH_2$), 75.1 (s, $OCH_2$), 71.7 (s, *C*H*i*Pr), 71.0 (s,

 © 2006 Wiley-VCH Verlag GmbH & Co. KGaA, Weinheim 

*C*H*i*Pr), 31.2 (s, *C*HMe$_2$), 30.4 (s, *C*HMe$_2$), 19.3 (s, CH*Me*$_2$), 18.6 (s, CH*Me*$_2$), 15.8 (s, CH*Me*$_2$), 15.6 (s, CH*Me*$_2$), 5.9 (s, IrCH$_2$) ppm. **15:** Reaction time: 15 min. Yield: 89% (0.072 g). Colour: yellow. $C_{27}H_{24}ClF_6IrN_3O_3P$ (811.14): calcd. C 39.98, H 2.98, N 5.18; found C 39.22, H 3.16, N 5.12. FAB-MS: *m*/*z* = 666 [M$^+$]. IR (KBr): $\tilde{\nu}$ = 2069 (CO), 842 (PF$_6^-$) cm$^{-1}$. IR (CH$_2$Cl$_2$): $\tilde{\nu}$ = 2077 (CO) cm$^{-1}$. Conductivity (acetone, 20 °C): 127 Ω$^{-1}$ cm$^2$ mol$^{-1}$. $^1$H NMR (300 MHz, [D$_6$]acetone, 20 °C): $\delta$ = 8.85 (t, $J_{H,H}$ = 8.0 Hz, 1 H, H$^4$ C$_5$H$_3$N), 8.64 (d, $J_{H,H}$ = 8.0 Hz, 2 H, H$^{3,5}$ C$_5$H$_3$N), 7.70–7.40 (4m, 10 H, Ph), 5.83 (m, 2 H, OCH$_2$, C*H*Ph), 5.65 (m, 1 H, C*H*Ph), 5.40 (m, 3 H, OCH$_2$, *H*C=CH$_2$ allyl), 5.19 (m, 1 H, OCH$_2$), 4.64 (m, 2 H, HC=C*H*$_2$ allyl), 2.57 (m, 1 H, IrCH$_2$), 2.10 (m, 1 H, IrCH$_2$) ppm. $^{13}$C{$^1$H} NMR (75.48 MHz, [D$_6$]acetone, 20 °C): $\delta$ = 171.6 (s, OCN), 171.1 (s, OCN), 164.1 (s, CO), 145.7 (s, C$^4$H C$_5$H$_3$N or H*C*=CH$_2$ allyl), 145.4 (s, C$^{2,6}$ C$_5$H$_3$N), 145.3 (s, C$^{2,6}$ C$_5$H$_3$N), 143.6 (s, C$^4$H C$_5$H$_3$N or H*C*=CH$_2$ allyl), 135.9 (s, *ipso*-Ph), 135.4 (s, *ipso*-Ph), 131.1, 130.6, 130.4, 130.2, 129.8, 129.7 (s, Ph, C$^{3,5}$H C$_5$H$_3$N), 112.1 (s, HC=*C*H$_2$ allyl), 81.0 (s, OCH$_2$), 80.8 (s, OCH$_2$), 70.8 (s, *C*HPh), 70.2 (s, *C*HPh), 5.8 (s, IrCH$_2$) ppm.

**Synthesis of Complexes [IrCl{η$^1$-C(O)CH$_3$}(CO)(κ$^3$-*N*,*N*,*N*-R-pybox)][PF$_6$] [R = *i*Pr (16), Ph (17)]:** Acetyl chloride (0.007 mL, 0.1 mmol) was added to a solution of complex **1** or **2** (0.1 mmol) in 10 mL of dichloromethane. The solution was stirred at room temperature. The resulting yellow solution was then concentrated to about 3 mL and 30 mL of diethyl ether was added to yield a yellow solid, which was washed with diethyl ether (3 × 5 mL) and dried under reduced pressure. **16:** Reaction time: 40 min. Yield: 86% (0.065 g). Colour: yellow. FAB-MS: *m*/*z* = 600 [M$^+$]. IR (KBr): $\tilde{\nu}$ = 2086 (CO), 1677 (COMe), 842 (PF$_6^-$) cm$^{-1}$. IR (CH$_2$Cl$_2$): $\tilde{\nu}$ = 2079 (CO) cm$^{-1}$. Conductivity (acetone, 20 °C): 120 Ω$^{-1}$ cm$^2$ mol$^{-1}$. $^1$H NMR (300 MHz, [D$_6$]acetone, 20 °C): $\delta$ = 8.89 (t, $J_{H,H}$ = 8.0 Hz, 1 H, H$^4$ C$_5$H$_3$N), 8.63 (d, $J_{H,H}$ = 8.1 Hz, 1 H, H$^{3,5}$ C$_5$H$_3$N), 8.54 (d, $J_{H,H}$ = 8.1 Hz, 1 H, H$^{3,5}$ C$_5$H$_3$N), 5.35 (m, 4 H, OCH$_2$), 4.90 (m, 1 H, C*H*i*P*r), 4.56 (m, 1 H, C*H*i*P*r), 2.62 (s, 3 H, COMe), 2.41 (m, 1 H, C*H*Me$_2$), 2.23 (m, 1 H, C*H*Me$_2$), 1.13 (m, 9 H, CH*Me*$_2$), 0.88 (d, $J_{H,H}$ = 6.8 Hz, 3 H, CH*Me*$_2$) ppm. $^{13}$C{$^1$H} NMR (75.48 MHz, [D$_6$]acetone, 20 °C, major isomer): $\delta$ = 196.9 (s, *C*OMe), 172.1 (s, OCN), 171.9 (s, OCN), 164.9 (s, CO), 146.3 (s, C$^4$H C$_5$H$_3$N), 144.8 (s, C$^{2,6}$ C$_5$H$_3$N), 144.4 (s, C$^{2,6}$ C$_5$H$_3$N), 130.2 (s, C$^{3,5}$H C$_5$H$_3$N), 129.5 (s, C$^{3,5}$H C$_5$H$_3$N), 75.4 (s, OCH$_2$), 75.1 (s, OCH$_2$), 71.6 (s, *C*H*i*Pr), 71.1 (s, *C*H*i*Pr), 46.2 (s, CO*Me*), 31.3 (s, *C*HMe$_2$), 30.4 (s, *C*HMe$_2$), 19.1 (s, CH*Me*$_2$), 18.8 (s, CH*Me*$_2$), 15.6 (s, CH*Me*$_2$), 14.6 (s, CH*Me*$_2$) ppm. **17:** Reaction time: 10 min. Yield: 91% (0.074 g). Colour: yellow. $C_{26}H_{22}ClF_6IrN_3O_4P$ (813.12): calcd. C 38.41, H 2.73, N 5.17; found C 37.97, H 2.60, N 4.98. IR (KBr): $\tilde{\nu}$ = 2080 (CO), 1669 (COMe), 844 (PF$_6^-$) cm$^{-1}$. IR (CH$_2$Cl$_2$): $\tilde{\nu}$ = 2087 (CO) cm$^{-1}$. Conductivity (acetone, 20 °C): 123 Ω$^{-1}$ cm$^2$ mol$^{-1}$. $^1$H NMR (300 MHz, [D$_6$]acetone, 20 °C): $\delta$ = 8.93 (t, $J_{H,H}$ = 8.0 Hz, 1 H, H$^4$ C$_5$H$_3$N), 8.71 (d, $J_{H,H}$ = 8.0 Hz, 1 H, H$^{3,5}$ C$_5$H$_3$N), 8.62 (d, $J_{H,H}$ = 8.0 Hz, 1 H, H$^{3,5}$ C$_5$H$_3$N), 7.80–7.40 (m, 10 H, CH*Ph*), 5.85 (3 H), 5,53 (1 H), 5.42 (1 H), 5.21 (1 H) (4 × m, OCH$_2$, C*H*Ph), 1.92 (s, 3 H, COMe) ppm. $^{13}$C{$^1$H} NMR (75.48 MHz, [D$_6$]acetone, 20 °C): $\delta$ = 195.9 (s, *C*OMe), 172.3 (s, OCN), 171.4 (s, OCN), 163.3 (s, CO), 146.1 (s, C$^4$H C$_5$H$_3$N), 145.2 (s, C$^{2,6}$ C$_5$H$_3$N), 145.1 (s, C$^{2,6}$ C$_5$H$_3$N), 135.6 (s, *ipso*-Ph), 135.1 (s, *ipso*-Ph), 131.0, 130.7, 130.6, 130.2, 130.2, 130.1, 129.7, 129.4 (s, C$^{3,5}$H C$_5$H$_3$N, Ph), 81.0 (s, OCH$_2$), 80.7 (s, OCH$_2$), 71.0 (s, *C*HPh), 70.4 (s, *C*HPh), 46.1 (s, CO*Me*) ppm.

**General Procedure for Catalytic Reactions:** A 10-mL flask was charged with the complex catalyst (0.04 mmol, 1.0 mol%), *i*Pr-pybox (when applicable; 0.16 mmol, 4.0 mol%) and acetophenone (4.00 mmol) under dry nitrogen. After cooling to –10 °C, $Ph_2SiH_2$ (6.4 mmol) was added dropwise. The reaction mixture was warmed to the reaction temperature and stirred until completion of the reaction. The disappearance of acetophenone was monitored by TLC. Before the aqueous workup, an aliquot was taken and examined by $^1$H NMR spectroscopy. The workup of the reaction mixture was carried out as described by Nishiyama.[10] The enantiomeric excess was determined, after hydrolysis, by GC analysis with a Supelco β-DEX 120 chiral capillary column.

**X-ray Structure Determination of 15:** Single crystals suitable for an X-ray study were obtained by slow diffusion of diethyl ether into a solution of complex **15** in dichloromethane. An orange, prismatic single crystal (0.50 × 0.25 × 0.17 mm), orthorhombic, space group $P2_12_12_1$ (determined from systematic absences) was used. Diffraction data were recorded at 293(2) K with a Nonius Kappa CCD single-crystal diffractometer, using Cu-$K_\alpha$ radiation (λ = 1.5418 Å). The crystal–detector distance was fixed at 29 mm, and a total of 2432 frames were collected using the oscillation method, with 2° oscillation and a 60 s exposure time per frame. The data-collection strategy was calculated with the program Collect.[15] Data reduction and cell refinement were performed using the programs HKL Denzo and Scalepack.[16] Unit-cell dimensions were determined from 7669 reflections. Unit-cell parameters: $a$ = 13.0003(8), $b$ = 13.4939(9), $c$ = 17.8850(8) Å, $V$ = 3137.5(3) Å$^3$, $Z$ = 4, $D_{calcd.}$ = 1.717 g cm$^{-3}$. Absorption coefficient: $\mu$ = 10.121 mm$^{-1}$. A total of 50428 reflections were collected, with 5662 independent reflections ($R_{int}$ = 0.087). Data completeness was 98.7%. The software package WINGX was used for space-group determination, structure solution and refinement.[17] The structure was solved by Patterson interpretation and phase expansion using DIRDIF.[18] An empirical absorption correction was applied using XABS2.[19] (Ratio of minimum to maximum apparent transmission: 0.164460.) Isotropic least-squares refinement on $F^2$ was carried out using SHELXL-97.[20] During the final stages of the refinements, all positional parameters and the anisotropic temperature factors of all the non-H atoms were refined. The H atoms were placed geometrically and their coordinates were refined riding on their parent atoms. The final cycle of full-matrix least-squares refinement based on 5662 reflections and 379 parameters converged to a final value of $R_1$ [$F^2 > 2\sigma(F^2)$] = 0.0607, $wR_2$ [$F^2 > 2\sigma(F^2)$] = 0.1580, $R_1$ ($F^2$) = 0.0656, $wR_2$ ($F^2$) = 0.1631. The absolute structure parameter was found to be 0.053(19). The function minimised was $[(\Sigma wF_o^2 - F_c^2)/\Sigma w(F_o^2)]^{1/2}$, where $w = 1/[\sigma^2(F_o^2) + (0.1216P)^2]$ with $\sigma(F_o^2)$ from counting statistics and $P = [\mathrm{Max}(F_o^2,0) + 2F_c^2]/3$. Atomic scattering factors were taken from the International Tables for X-ray Crystallography.[21] Final difference electron density maps showed no features outside the range +1.135 to –0.764 e Å$^{-3}$. Geometrical calculations were made with PARST.[22] The crystallographic plots were made with PLATON.[23] CCDC-278506 (**15**) contains the supplementary crystallographic data for this paper. These data can be obtained free of charge from The Cambridge Crystallographic Data Centre via www.ccdc.cam.ac.uk/data_request/cif.

## Acknowledgments

This work was supported by the Ministerio de Ciencia y Tecnología of Spain (project BQU2003-00255) and FICYT (project PR-01-GE-4). P. P. thanks the Ministerio de Educación y Cultura (MEC) of Spain for the award of a PhD grant.

[1] G. Desimoni, G. Faita, P. Quadrelli, *Chem. Rev.* **2003**, *103*, 3119–3154.
[2] C.-X. Zhao, M. O. Duffey, S. J. Taylor, J. P. Morken, *Org. Lett.* **2001**, *3*, 1829–1831.

 © 2006 Wiley-VCH Verlag GmbH & Co. KGaA, Weinheim 

[3] H. Miyabe, A. Matsumura, K. Moriyama, Y. Takemoto, *Org. Lett.* **2004**, *6*, 4631–4634.
[4] H. Miyabe, K. Yoshida, M. Yamauchi, Y. Takemoto, *J. Org. Chem.* **2005**, *70*, 2148–2153.
[5] J. Díez, M. P. Gamasa, J. Gimeno, P. Paredes, *Organometallics* **2005**, *24*, 1799–1802.
[6] D. Cuervo, J. Díez, M. P. Gamasa, S. García-Granda, J. Gimeno, *Inorg. Chem.* **2002**, *41*, 4999–5001.
[7] The $^{1}H$ and $^{13}C\{^{1}H\}$ NMR signals for the pybox ligands provide an unequivocal structural elucidation in *cis*- or *trans*-dihalogen octahedral complexes containing pybox ligands. See, for example, *cis*- and *trans*-[$RuCl_2$(L)(Ph-pybox)] (L = phosphane): a) D. Cuervo, M. P. Gamasa, J. Gimeno, *Chem. Eur. J.* **2004**, *10*, 425–432; and *cis*-[$RhCl_2$(L)(*i*Pr-pybox)] (L = alkenyl, acyl): b) D. Cuervo, J. Díez, M. P. Gamasa, J. Gimeno, *Organometallics* **2005**, *24*, 5529–5537.
[8] F. A. Cotton, G. Wilkinson, C. A. Murillo, M. Bochmann, *Advanced Inorganic Chemistry*, 6th ed., Wiley & Sons, New York, **1999**.
[9] K. D. John, K. V. Salazar, B. L. Scott, R. T. Baker, A. P. Sattelberger, *Chem. Commun.* **2000**, 581–582.
[10] a) H. Nishiyama, H. Sakaguchi, T. Nakamura, M. Horihata, M. Kondo, K. Itoh, *Organometallics* **1989**, *8*, 846–848; b) H. Nishiyama, M. Kondo, T. Nakamura, K. Itoh, *Organometallics* **1991**, *10*, 500–508.
[11] H. Nagashima, T. Ueda, H. Nishiyama, K. Itoh, *Chem. Lett.* **1993**, 347–350.
[12] For recent examples see: a) F. Ozawa, M. Yoshifuji, *C. R. Chim.* **2004**, *7*, 747–754; b) F. Ozawa, S. Yamamoto, S. Kawagishi, M. Hiraoka, S. Ikeda, T. Minami, S. Ito, M. Yoshifuji, *Chem. Lett.* **2001**, 972–973; c) M. Igarashi, Y. Sugihara, T. Fuchikami, *Tetrahedron Lett.* **1999**, *40*, 711–714.
[13] See for example: a) K. C. Nicolaou, D. L. F. Gray, T. Montagnon, S. T. Harrison, *Angew. Chem. Int. Ed.* **2002**, *41*, 996–1000; b) T. Ool, R. Goto, K. Maruoka, *J. Am. Chem. Soc.* **2003**, *125*, 10494–10495; c) P. Langer, G. Bose, *Angew. Chem. Int. Ed.* **2003**, *42*, 4033–4036.
[14] a) A. van der Ent, A. L. Onderdelinden, *Inorg. Synth.* **1973**, *14*, 92–95; b) R. E. Cramer, J. A. McCleverty, J. Bray, *Inorg. Synth.* **1991**, *28*, 86.
[15] Collect, Nonius BV, Delft, The Netherlands **1997**–**2000**.
[16] Z. Otwinowski, W. Minor, *Methods Enzymol.* **1997**, *276*, 307–326.
[17] L. J. Farrugia, *J. Appl. Crystallogr.* **1999**, *32*, 837–838.
[18] P. T. Beurskens, G. Admiraal, G. Beurskens, W. P. Bosman, S. García-Granda, R. O. Gould, J. M. M. Smits, C. Smykalla, *The DIRDIF Program System*;, Technical Report of the Crystallographic Laboratory, University of Nijmegen, Nijmegen, The Netherlands, **1999**.
[19] S. Parkin, B. Moezzi, H. Hope, *J. Appl. Crystallogr.* **1995**, *28*, 53–56.
[20] G. M.Sheldrick, *SHELXL-97, Program for the Refinement of Crystal Structures*, University of Göttingen, Germany, **1997**.
[21] *International Tables for X-ray Crystallography*, Kynoch Press, Birmingham, U. K. **1974**, vol. IV (present distributor: Kluwer Academic Publishers, Dordrecht, The Netherlands).
[22] M. Nardelli, *Comput. Chem.* **1983**, *7*, 95–98.
[23] A. L. Spek, *PLATON, A Multipurpose Crystallographic Tool*, University of Utrecht, The Netherlands, **2005**.

Received: July 28, 2005
Published Online: December 20, 2005

 © 2006 Wiley-VCH Verlag GmbH & Co. KGaA, Weinheim 

DOI: 10.1002/ejic.200500685

# Synthesis and Properties of Cryptands with a Thioether Bridge and π-Donors – Silver(I) and Copper(I)-Complexes

René Koschabek,[a] Rolf Gleiter,*[a] and Frank Rominger[a]

**Keywords:** Cage compounds / Alkynes / Silver / Copper

The syntheses of seven bridgehead diazabicycloalkanes are reported. The bridges are represented by either a thioether chain and two 3-hexyne units (**4** and **6**–**8**), one selenoether chain and two 3-hexyne units (**5**), or one dithioether chain and two 4,4′-diethylbiphenyl units (**9**, **10**). X-ray investigations reveal for **4**–**10** the *in*/*in* conformation at the bridgehead nitrogen atoms. Reactions with $Cu^{I}$ triflate yield the endohedral $Cu^{I}$ complexes of **4**–**6**. Endohedral complexes of **6**, **7**, and **10** were isolated with silver triflate. X-ray investigations and spectroscopic studies on the metal complexes reveal interactions between the metal ion and the nitrogen-, chalcogen-, and π-units. In addition to the bicyclic systems **4**–**10** we synthesized the tripodal systems **28**–**33** in a one-pot reaction. In the cases of **28** and **33** we were able to isolate the corresponding $Ag^{I}$ complexes. X-ray studies show an interaction between the metal ion and the nitrogen atom and one double bond of each of the three adjacent phenyl rings.

(© Wiley-VCH Verlag GmbH & Co. KGaA, 69451 Weinheim, Germany, 2006)

## Introduction

After the seminal papers of Pedersen[1] on crown ethers and Lehn et al.[2] on cryptands these types of compounds were in the focus of chemists. Quite some time had to pass until crown thioethers participated in this development[3] because safe and high-yield routes to these species were lacking. Advances in synthetic methodology[4] and safe and general, high-yield routes[5] resulted in strong activity in this field.[5] Reports on the corresponding podands[6] and cryptands[7] with thioether bridges such as **1** are sparse, probably because a method that provides them in high yields is still missing.

The starting point of the research reported in this manuscript was a simple one-pot synthesis of the bridgehead diazabicycloalkanes **2** and **3**[8,9] with alkyne and phenyl units in the bridges (Figure 1). The two species were able to form isolable complexes with $Cu^{+}$ and $Ag^{+}$ (**2**) and $Ag^{+}$ (**3**), respectively. In both cases the metal ion does not only interact with the nitrogen atoms but also with the π-units. In order to extend the variety of ligands for transition metals it was of interest to have easy access to bicyclic ligands with at least one thioether bridge and further alkyne or phenyl ligands. In this paper we report a one-pot synthesis of the bicyclic cryptands **4**–**10** and their complexing properties with silver and/or copper(I) ions.

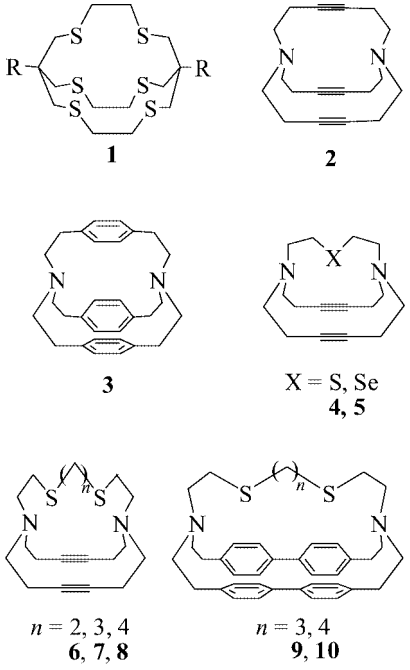


Figure 1. Bicyclic cryptands **1**–**10**.

## Results

### (a) Synthesis and Structures of 4–8

To synthesize our target molecules we adopted a one-pot synthesis developed for bridgehead diazabicycloalkanes.[10] The preparation of **4**–**8** was achieved in a three-component cyclization from an α,ω-diamine (**11**) and an α,ω-dibromide

[a] Organisch-Chemisches Institut, Universität Heidelberg, Im Neuenheimer Feld 270, 69120 Heidelberg, Germany
Fax: +49-6221-544205
E-mail: Rolf.Gleiter@urz.uni-heidelberg.de

 © 2006 Wiley-VCH Verlag GmbH & Co. KGaA, Weinheim 

(**12**) as shown in Scheme 1. The components were heated in acetonitrile under reflux. The yields varied between 33% (**5**) and 53% (**7**). From the starting materials 1,5-diamino-3-thiapentane (**13**),[11] 1,5-diamino-3-selenapentane (**14**),[12] 1,8-diamino-3,6-dithiaoctane (**15**),[13] as well as 1,6-dibromohex-3-yne (**16**)[14] were prepared according to literature procedures.

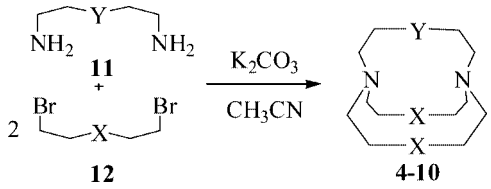


Scheme 1.

The synthesis of 1,9-diamino-3,7-dithianonane (**17**) and 1,10-diamino-3,8-dithiadecane (**18**) followed those procedures[13] used for **13**–**15** and is summarized in Scheme 2. The dianions of the α,ω-dithiols **19** and **20** were reacted with *N*-(2-bromoethyl)phthalimide (**21**) to the α,ω-diphthalimidodithianes **22** and **23**. The protecting groups were removed by heating of **22** and **23**, respectively, with hydrazine in ethanol to afford **17** and **18** in good yields.

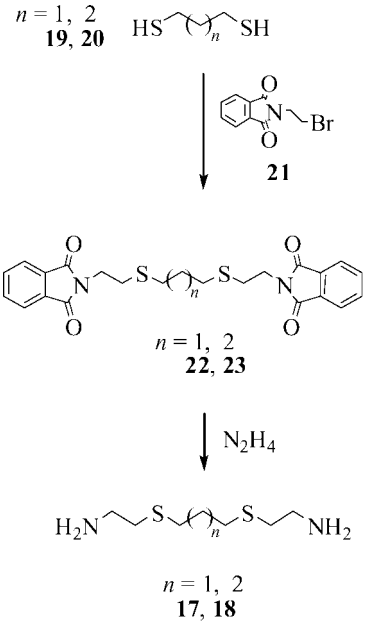


Scheme 2.

The preparation of 4,4′-bis(2-hydroxyethyl)biphenyl (**25**) (Scheme 3) was described in the literature from biphenyl and ethylene oxide under Lewis acid catalysis.[15] This procedure gave us a mixture of the 4-(2-hydroxyethyl)biphenyl and **25** which was difficult to separate. Therefore, a different path as shown in Scheme 3 was used. The starting point was the commercially available 4,4′-dibromobiphenyl (**24**), which was treated with an excess of *n*-butyllithium and ethylene oxide to afford **25** in 92% yield. The diol **25** was converted via the dimesylate **26** into the dibromide **27** in a straight forward way (Scheme 3).

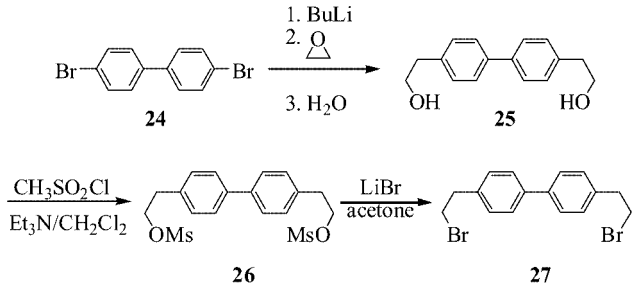


Scheme 3.

With regard to the silver(I) complexes of **3**, **9**, and **10** we also prepared the tripodal systems **28**–**33** listed in Figure 2. The synthesis follows that given in Scheme 1 by applying a one-pot reaction of (2-bromoethyl)benzene[15] or 4-(2-bromoethyl)biphenyl[16] with the corresponding amines such as (2-aminoethyl)benzene which was commercially available, 4-(2-aminoethyl)biphenyl,[17] or 1-aminobut-3-yne.[18,19] The components were heated in acetonitrile under reflux with an excess of potassium carbonate.

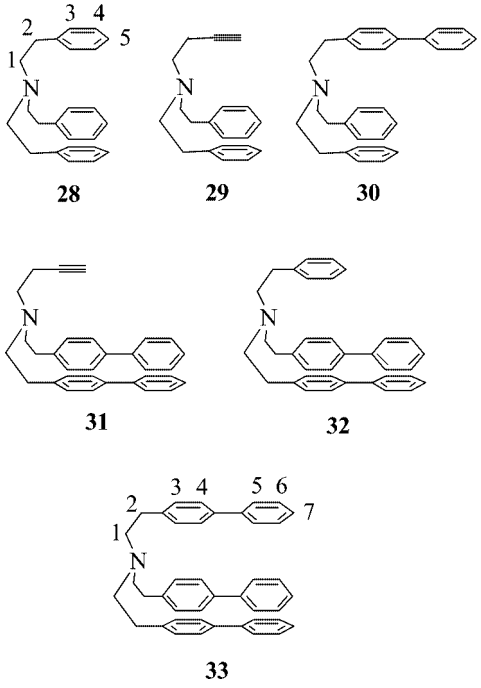


Figure 2. Tripodal systems **28**–**33**.

### (b) Spectroscopic and Structural Properties

In Table 1 we list the $^{13}C$ chemical shift of the sp centers of **4**–**8** as well as the wave numbers for the C,C stretching mode of the triple bonds derived by Raman spectroscopy. It is seen that the $\delta$ values for the sp centers vary only slightly between 79.5 and 81 ppm indicating hardly any strain in these systems. This view is supported by the wave numbers for the stretching vibration of the triple bonds. For **7** and **8** we encountered dynamic processes in the $^1H$ NMR spectra which led to a line broadening at room temperature.

 © 2006 Wiley-VCH Verlag GmbH & Co. KGaA, Weinheim 

Table 1. Comparison of the chemical shift of the sp carbon atoms ($\delta$) and the alkyne wave numbers of **4**–**8**.

| Compound | **4** | **5** | **6** | **7** | **8** |
|---|---|---|---|---|---|
| $\delta$(sp) [ppm] | 80.6[b] | 80.6[b] | 79.5[a] | 79.9[a] | 80.2[a] |
| $\tilde{\nu}$ [cm$^{-1}$][c] | 2228 | 2227 | 2236 | 2231 | 2237 |
| | 2291 | 2289 | 2300 | 2293 | 2297 |

[a] $CDCl_3$. [b] $CD_2Cl_2$. [c] Raman spectroscopic data.

For **4**–**10** we grew single crystals which allowed a comparison of the geometrical parameters. In Figure 3 we show the structures of **4**, **6**, **7**, and **10**. In all cases we find the *in*/*in* conformation at the bridgehead positions. A single nearly planar nitrogen atom is only seen in **4**. The heteroatoms of the bridges point outwards and do not seem very well suited for the complexation of a cation in the inside of the cages. In Table 2 we list the distances between the bridgeheads (N···N), the sum of the bonding angles ($\Sigma_{\omega N}$), and the distance between the centers of the π-systems, either triple bonds (**4**–**8**) or aromatic rings (**9**, **10**). In the latter case each biphenyl ring provides two centers. It is interesting to note that the N···N distance of **4** is larger than that of **5**. We ascribe this difference to the larger C–S–C angle (99°) of **4** as compared to the C–Se–C angle (97°) of **5**. In all cases the triple bonds are not oriented parallel to each other. In the biphenyl-bridged cages the N···N distances amount to nearly 10 Å.

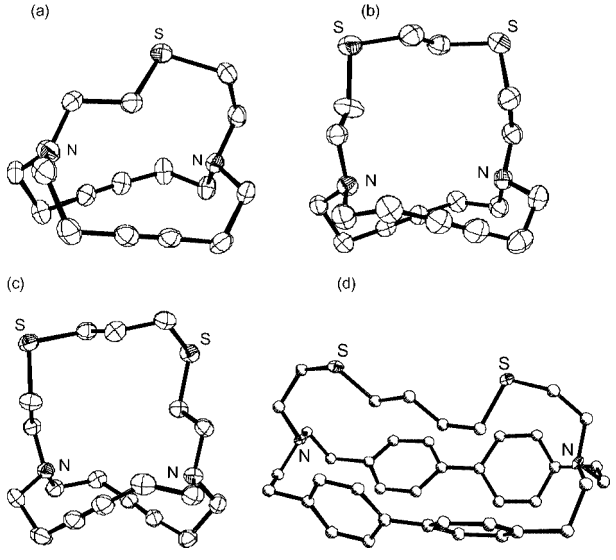


Figure 3. Molecular structures of **4** (a), **6** (b), **7** (c) and **10** (d).

Table 2. Selected distances and angles (degrees) of **4**–**10**.

| Compound | **4** | **5** | | **6**[d] | **7** | **8** | **9** | **10** |
|---|---|---|---|---|---|---|---|---|
| N···N [Å] | 4.72 | 4.31 | 4.87 | 4.79 | 4.90 | 5.20 | 9.79 | 9.94 |
| ($\Sigma_{\omega N}$)[a] | 344 | (329)[c] | 342 | 335 | 338 | 343 | 328 | 328 |
| | 357 | 343 | 342 | 336 | 342 | 344 | 343 | 330 |
| π···π | 3.84 | 4.30 | 3.87 | 4.17 | 3.92 | 3.77 | | |
| (sp)(Å)[b] | | | | | | | | |

[a] Sum of the C–N–C angles at nitrogen centers. [b] Transannular distances between centers of π-systems. [c] Unreliable due to partial disorder. [d] Two independent molecules in the unit cell.

### (c) Formation of Metal Complexes

The reactions of **28** and **33** with silver triflate afforded the 1:1 complexes. For **29**, **30**, and **32** the corresponding 1:1 silver complexed ions were only detected in the mass spectrum (FAB+). In Figure 4 we show the molecular structures of **28**·$Ag^+$ and **33**·$Ag^+$ in a front and side view. In **28**·$Ag^+$ the distance between the nitrogen center and silver atom amounts to 2.41 Å. This distance is closer than that found in the silver complex of **3** (2.47 Å).[10] The interaction between the silver ion and the aromatic rings is evident from the change of the NMR shifts. In the uncomplexed species (**28**) the protons at the $sp^3$ centers (positions 1 and 2 in **28**) show two close lying multiplets at 2.75–2.81 and 2.84–2.90 ppm. Similarly, the aromatic protons resonate at 7.21–7.24 and 7.32 ppm. In the silver complex the $CH_2$ protons give rise to two pronounced triplets at $\delta$ = 2.70 and 2.94 ppm. In the aromatic region two protons of each $C_6H_5$ ring give rise to a doublet at $\delta$ = 6.84 ppm. These spectroscopic data are in line with the observation that the silver ion shows a much closer contact with the *ortho* carbon atoms (position 3 in **28**) of the benzene rings as compared to the other $sp^2$ centers. For the three phenyl rings in **28**·$Ag^+$ we observe a tilting of the aromatic rings in a conrotatory fashion parallel to the $C_3$ axis. This brings one carbon atom per ring close to the metal center. The distance between these carbon atoms of the phenyl rings and the metal ion (average 2.47 Å, see Table 3) are similar to that found for various silver complexes of [2.2.2]- and [2.2.1]cyclophanes.[20–25] For **33**·$Ag^+$ we observe in the $^1$H NMR spectrum two triplets at $\delta$ = 2.83 and 2.99 ppm for the hydrogen atoms at centers 1 and 2 (see Figure 2). Six of the aromatic hydrogen atoms are shifted towards higher field due to the complexation and give rise to a doublet at $\delta$ = 6.96 ppm. The other 21 aromatic hydrogen atoms show up at 7.35–7.44 ppm. These results suggest a similar situation for the silver atom as in **28**·$Ag^+$. Indeed, the molecular structure of **33**·$Ag^+$ reveals that the metal ion is situated close to the nitrogen atom. The N–$Ag^+$ distance amounts to 2.37 Å (Table 3). The view along the N···Ag axis of **33**·$Ag^+$ shows that the aromatic rings are twisted in a conrotatory way similar to that found in **28**·$Ag^+$. This orientation allows a closer interaction between the metal atom and C3 than to the other $sp^2$ centers (average 2.43 Å, Table 3).

For **4**–**10** we infer from the downfield shift of the signals for the aliphatic hydrogen atoms in the $^1$H NMR spectra and from the mass spectrometric data the inclusion of silver and/or copper(I) ions into the cavities of these species. In all cases except for **9** this result was confirmed by the isolation of single crystals which allowed a detailed study of the molecular structure. For **4** and **5** we were able to isolate only complexes with copper(I) triflate. The reaction of **6** with silver or copper triflate gave complexes with one metal ion in the cavity. For all the other cryptates, only silver complexes could be characterized. In the case of **10** even two silver ions were incorporated in the cavity. In Figure 5 we show the molecular structures of **4**·$Cu(CF_3SO_3)$, **8**·$Ag(CF_3SO_3)$, and **10**·$2[Ag(CF_3SO_3)_2]$.

 © 2006 Wiley-VCH Verlag GmbH & Co. KGaA, Weinheim 

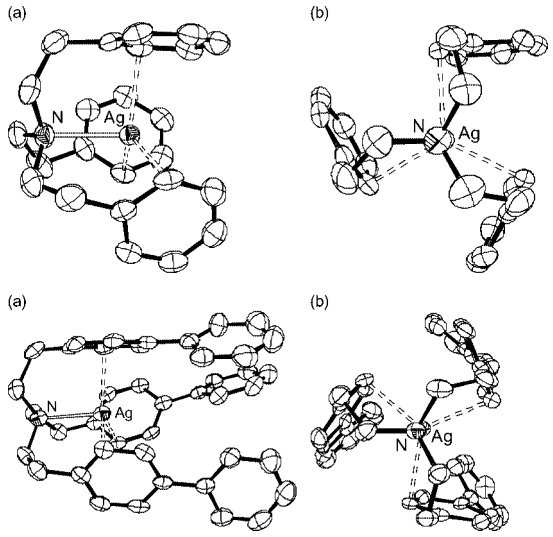


Figure 4. Molecular structures of **28**·$Ag^+$ (top) and **33**·$Ag^+$ in a front view (a) and a view along the N–Ag axis (b).

Table 3. Selected distances [Å] of $Ag^I$ triflates of **28** and **33**.

| | **28**·$Ag^+$ | **33**·$Ag^+$ |
|---|---|---|
| N···Ag | 2.409 | 2.371 |
| π···Ag | 2.47[a,b] | 2.43[a,b] |
| π···π | 3.72[a,b] | 3.72[a,b] |

[a] Average value. [b] Closest atom of $C_6$ units.

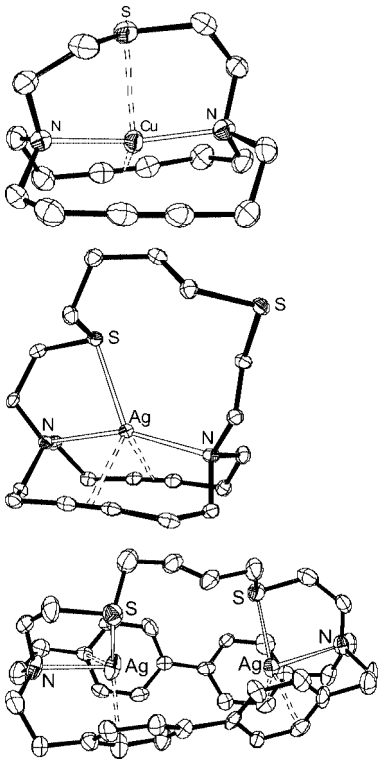


Figure 5. Molecular structures of **4**·$Cu^+$ (top), **8**·$Ag^+$ and **10**·2($Ag^+$) (bottom).

In Table 4 we collected the most relevant distances and angles of the metal complexes of **4**–**8** and **10**. The copper complex of **4** shows a considerable change in the conformation of the ligand. The N···N distance is substantially shortened from 4.72 Å (free ligand) to 4.20 Å (complex) (see Figure 3 and Figure 5). As a result of this change the triple bonds are oriented almost parallel and the chalcogen center of the bridge is turned towards the metal. This change allows almost equal distances to both nitrogen centers (2.10 and 2.16 Å) but close contact to only one triple bond (2.13 Å), whereas the distance to the other (2.71 Å) is considerably longer. The copper–nitrogen distances are expanded with regard to copper(I) amine complexes (average value 2.18 Å)[26] but comparable to those reported for **2**·$Cu^+$ (2.11 Å).[9] The distance Cu–S (2.52 Å) is longer than those reported in other thioether-$Cu^I$ complexes (2.25–2.30 Å).[27]

The molecular structure of **5**·$Cu^+$ is isomorphous to that of **4**·$Cu^+$. The N···N distance in the complex (4.21 Å) is about as long as that in **4**·$Cu^+$ (4.20 Å). The same holds for the N–Cu distances and the N–M–N angle, 160.5° in **4**·$Cu^+$ and 161.6° for **5**·$Cu^+$. Also both triple bonds are almost oriented parallel to each other in contrast to the free ligand. The selenium atom is bent sideways to interact with the copper ion (Cu–Se = 2.62 Å). The complex shows one close contact to one triple bond (2.16 Å) only.

Table 4. Selected distances [Å] and angles (degrees) of $Ag^I$ or $Cu^I$ triflates of **4**–**8** and **10**.

| Compound | **4**·$Cu^+$ | **5**·$Cu^+$ | **6**·$Ag^+$ | **6**·$Cu^+$ | **7**·$Ag^+$ | **8**·$Ag^+$ | **10**·2($Ag^+$) |
|---|---|---|---|---|---|---|---|
| N···N | 4.200 | 4.209 | 4.830 | 5.077 | 5.129 | 4.739 | 9.951 |
| N···M | 2.101 | 2.098 | 2.435 | 2.150 | 2.646 | 2.368 | 2.429 |
| | 2.160 | 2.166 | 2.450 | 3.150 | 2.678 | 2.468 | 2.444 |
| X···M[a] | 2.520 | 2.620 | 2.757 | 2.275 | 2.754 | 2.574 | 2.500 |
| | | | 2.876 | 2.562 | 2.773 | 5.043 | 2.564 |
| M···π | 2.134 | 2.157 | 2.609 | 2.093 | 2.640 | 2.656 | 2.53[b,d,e] |
| | 2.705 | 2.733 | 2.664 | 3.015 | 2.721 | 2.745 | 2.47[c,d,e] |
| N···M···N[f] | 160.5 | 161.6 | 197.3 | 214.0 | 211.6 | 203.2 | |
| π···π | 4.335 | 4.363 | 4.286 | 3.751 | 4.011 | 4.304 | 3.611[d,e] |
| $\tilde{\nu}_{(C\equiv C)}$ [$cm^{-1}$][g] | | | | | 2206 | 2204 | |
| | | | | | 2281 | 2266 | |

[a] X = S for **4**, **7**–**9**, **11**; X = Se for **5**; X = O for **6**. [b] Average value for Ag1. [c] Average value for Ag2. [d] Average value. [e] Closest atom of $C_6$ units. [f] For comparison with the other structures we define the N–metal–N angle as greater than 180° if the metal deviates from the N···N axis in the direction of the thioether bridge and smaller than 180° if it deviates towards the π-system. [g] Raman spectroscopic data.

 © 2006 Wiley-VCH Verlag GmbH & Co. KGaA, Weinheim 

The molecular structures of **6**·$Ag^+$ and **6**·$Cu^+$ are shown in Figure 6. In the case of **6**·$Ag^+$ we are not dealing with a purely endohedral complex between ligand and metal. The unit cell does not only show the endohedral metal ion but also exohedral metal ions between the thioether groups (see Figure 6) that lead to a coordination polymer. In the endohedral complex the metal ion deviates from the N···N axis in the direction of the thioether bridge N···Ag···N (197.3°). This deviation is due to a interaction between the silver ion and the sulfur centers. The Ag···S distances found (Table 4; 2.76 Å and 2.88 Å) compare well with other thioether–silver distances.[28,29] The distances between the exohedral silver centers and the thioether groups amount to 2.49 Å and 2.50 Å. The average Ag···N distance (2.45 Å) is longer than the one reported for **2**·Ag (2.31 Å).[8] The distances between the endohedral silver ions and the triple bonds (2.61, 2.66 Å) are still within the reach of a weak metal–π-bond. Raman studies on **6**·$Ag^+$ failed due to a fast decomposition of the complex during the Raman experiment. Our studies show that the large silver ion prefers a coordination number of 6.

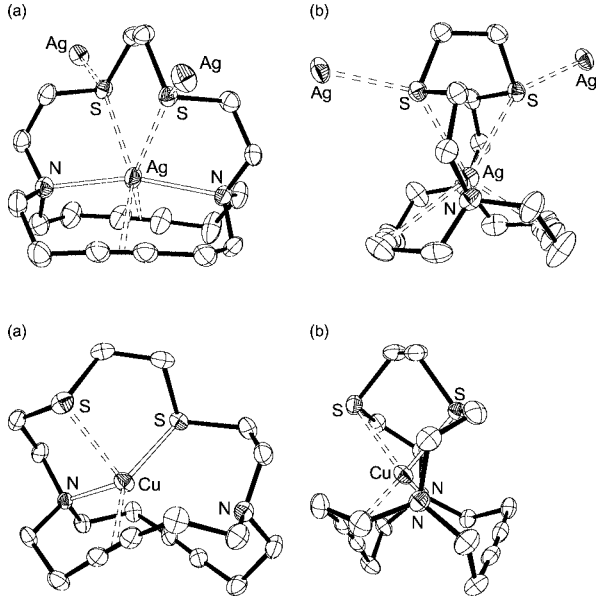


Figure 6. Molecular structure of **6**·$Ag^+$ (top) and **6**·$Cu^+$ (bottom) in a front view (a) and a view along the N–N axis (b). The hydrogen atoms are omitted for the sake of clarity.

The structure of **6**·$Cu^+$ (Figure 6) is remarkably different from that of **6**·$Ag^+$. The position of the metal is shifted towards one nitrogen center and one triple bond. The distance to the nitrogen center amounts to 2.15 Å and to the triple bond to 2.09 Å. The distances to the second nitrogen center and to the second triple bond in **6**·$Cu^+$ exceed 3 Å (Table 4). As a consequence both triple bonds in **6**·$Cu^+$ are not oriented parallel (Figure 6). Furthermore, the metal ion coordinates to both thioether groups (2.28, 2.56 Å). This establishes a coordination number of 4 for the metal in **6**·$Cu^+$.

The inclusion of $Ag^I$ in the cavity of **7** does not change the tilting of the triple bonds, but changes the conformation of the 3,7-dithiononane bridge in so far as the sulfur centers are turned inward to interact with the metal ion. The N···N distance is even increased as compared to the free ligand. The silver ion is shifted considerably out of the N···N axis towards the sulfur atoms (N–Ag–N angle 211.6°). In line with this, the distances between the triple bonds and the silver ion amount to 2.64 and 2.72 Å. These values are about 0.2 Å larger than those reported for **2**·$Ag^+$.[9] In the case of **7**·$Ag^+$ it was possible to measure the wave number for the stretching vibration of the triple bond ($\tilde{\nu}$ = 2281 and 2206 $cm^{-1}$). These values are shifted towards lower energy as compared to the free ligand ($\tilde{\nu}$ = 2293 and 2231 $cm^{-1}$) which is evidence for an interaction between the metal and the triple bonds. The distances between the sulfur centers and the metal atom amount to 2.75 and 2.77 Å. These values are close to those reported for thioether-silver distances (2.6–2.8 Å).[28,29]

The molecular structure of **8**·$Ag^+$ (Figure 5) is quite different from that of **7**·$Ag^+$ in so far as only one sulfur atom of the flexible dithia bridge interacts with the silver center. The other sulfur atom points outwards. The Ag–S distance (2.57 Å) is rather close compared to the other values. The N···N distance is shortened by about 0.5 Å compared to the uncomplexed system. The N–Ag distances (2.37 and 2.47 Å) are much shorter than for **7**·$Ag^+$ (see Table 4) and the two triple bonds are oriented parallel to each other. The interaction between the silver ion and the triple bonds is evident not only from the distances (2.66 and 2.75 Å) but also in the lowering of the wave numbers for the stretching vibration ($\tilde{\nu}$ = 2266 and 2204 $cm^{-1}$) as compared to **8** ($\tilde{\nu}$ = 2297 and 2237 $cm^{-1}$). The reaction of **9** with silver(I) triflate afforded a 1:1 complex as evidenced by HR-FAB$^+$ data. The comparison between the $^1$H NMR spectroscopic data of **9**·$Ag^+$ with those of **9** shows a downfield shift of the signals for the protons.

The reaction of **10** with silver(I) triflate afforded single crystals which could be investigated by means of the X-ray technique. It turned out that the cavity of **10** is large enough to house two silver ions (Figure 5). The incorporation of the two metal ions causes only a small change in the length of the cavity but a large one in the conformation of the thioether chain. The sulfur atoms are now turned inwards (see also Figure 3). The distance between the two silver ions in **10**·2($Ag^+$) was found to be 5.18 Å. This value is clearly larger than the sum of the van der Waals radii of $Ag^+$ (3.1–3.2 Å).[30,31] The average distance to the nitrogen atoms was found to be 2.44 Å which compares well with those recorded for **6**·$Ag^+$ and **8**·$Ag^+$ (Table 4). A closer look at the Ag···phenyl interaction reveals a situation very similar to that encountered for **28**·$Ag^+$and **33**·$Ag^+$ as well as for various [2.2.2] and [2.2.1]cyclophanes.[20–25] One carbon atom per ring is much closer to the silver ion than the other $sp^2$ centers. For three phenyl rings this is a *ortho* carbon (average distance 2.48 Å), only in one case is the silver ion closest to the *ipso*-carbon (2.50 Å). This coordination does not affect the planarity of the aromatic rings. The Ag–S distance of 2.50 Å is similar to that found in **8**·$Ag^+$ and shorter than in **6**·$Ag^+$ and **7**·$Ag^+$ (see Figure 6).

 © 2006 Wiley-VCH Verlag GmbH & Co. KGaA, Weinheim 

## Concluding Remarks

Our main goal to find a simple procedure for the preparation of N-bridgehead diazabicyclo-cages with one thioether bridge and π units in the other two was achieved. Like in crown thioethers the sulfur atoms adopt the exodentate orientation. However, when a metal ion was in the cavity this unfavorable position was changed to a more favorable one, mostly to the endodentate one. The prepared cage systems afforded endohedral complexes with silver or copper ions. It could be shown that the metal ions try to interact with a maximum of *n*-donors (N, S, Se) and π-donors (triple bonds or phenyl rings).

## Experimental Section

**General Methods:** All melting points are uncorrected. Elemental analyses were carried out by the Mikroanalytisches Laboratorium der Universität Heidelberg. UV/Vis absorption data were recorded with a Hewlett-Packard HP 8452A Diode Array-spectrometer, IR spectra were recorded with a Bruker Vector 22 FT-IR instrument. The NMR spectra were measured with a Bruker WH 300 or Avance 500 spectrometer ($^1$H NMR at 300 or 500 MHz and $^{13}$C NMR at 75 or 125 MHz), using the solvent as an internal standard ($\delta$). FAB mass spectra refer to data from a JEOL JMS-700 instrument. As matrix for the FAB experiments, *m*-nitrobenzyl alcohol was used. All reactions were carried out in dried glassware under argon using dried and oxygen-free solvents. Starting materials were prepared according to literature procedures. From the starting materials 1,5-diamino-3-thiapentane,[11] 1,5-diamino-3-selenapentane,[12] 1,8-diamino-3,6-dithiaoctane,[13] 1,6-dibromohex-3-yne,[14] (2-bromoethyl)benzene,[15] 4-(2-bromoethyl)biphenyl,[16] 4-(2-aminoethyl)biphenyl[17], and 1-aminobut-3-yne[18,19] were prepared according to literature procedures. 2-Aminoethylbenzene and 4,4′dibromobiphenyl were commercially available.

**X-ray Crystallographic Study:** Data were collected with a Bruker Smart CCD diffractometer at 200 K for **4**, **6**, **7**, **4**·$Cu^+$, **5**·$Cu^+$, **6**·$Cu^+$, **6**·$Ag^+$, **7**·$Ag^+$, **10**·2($Ag^+$), **28**·$Ag^+$, **33**·$Ag^+$, and with a Bruker APEX diffractometer at 100 K for **5**, **8**, **9**, **10**, and **8**·$Ag^+$. Mo-$K_\alpha$ radiation was used in all cases and the intensities were corrected for Lorentz, polarization, and absorption effects. Relevant crystal and data collection parameters are given in Tables 5, 6, 7, 8 and 9. The structures were solved by direct methods and refined against $F^2$ with a full-matrix least square algorithm by using the SHELXTL software package.[32] Hydrogen atoms were refined isotropically for **8**, in all other cases they were considered at calculated positions and refined using appropriate riding models. In **10**, **10**·2($Ag^+$), and **6**·$Ag^+$ some solvent molecules or anions had to be treated as disordered, in **4**·$Cu^+$ and **5**·$Cu^+$ on one side of the cage the three methylene groups next to the nitrogen atom occur in two alternative positions, in **9** an ethylene unit of the thioether bridge is affected by disorder. In **4**·$Cu^+$ and **5**·$Cu^+$ the copper position is not fully occupied. The charge balance is maintained by partial replacement of the metal ion by a proton, which could be refined isotropically with an occupation of about 30% in both cases. CCDC-279304 (for **4**), -279305 (for **5**), -279306 (for **6**), -279307 (for **7**), -279308 (for **8**), -279309 (for **9**), -279310 (for **10**), -279311 (for **4**·$Cu^+$), -279312 (for **5**·$Cu^+$), -279313 (for **6**·$Cu^+$), -279314 (for **6**·$Ag^+$), -279315 (for **7**·$Ag^+$), -279316 (for **8**·$Ag^+$), -279317 [for **10**·2($Ag^+$)], -279318 (for **28**·$Ag^+$), and -279319 (for **33**·$Ag^+$) contain the supplementary crystallographic data for this paper. These data can be obtained free of charge from The Cambridge Crystallographic Data Centre via www.ccdc.cam.ac.uk/data_request/cif.

**1,9-Diphthalimido-3,7-dithiononane (22):** To a solution of 1,3-propane dithiole (4.2 g, 39 mmol) in dry toluene (250 mL) cooled to –30 °C, was added dropwise *n*BuLi in hexane (51 mL). After 30 min

Table 5. Crystal data and structural refinement for **4**–**7**.

| | **4** | **5** | **6** | **7** |
|---|---|---|---|---|
| Empirical formula | $C_{16}H_{24}N_2S$ | $C_{16}H_{24}N_2Se$ | $C_{18}H_{28}N_2S_2$ | $C_{19}H_{30}N_2S_2$ |
| Formula weight [g/mol] | 276.43 | 323.33 | 336.54 | 350.57 |
| Temperature [K] | 200(2) | 200(2) | 200(2) | 200(2) |
| Crystal system | monoclinic | triclinic | triclinic | monoclinic |
| Space group | $P2_1/c$ | $P\bar{1}$ | $P\bar{1}$ | $P2_1/c$ |
| $Z$ | 4 | 2 | 4 | 4 |
| $a$ | 13.9024(4) | 8.7619(9) | 9.5652(2) | 13.6724(2) |
| $b$ | 12.1766(4) | 9.3813(10) | 13.0918(3) | 9.6549(1) |
| $c$ | 9.4685(3) | 10.0202(11) | 15.9324(3) | 15.3467(2) |
| $\alpha$ | 90 | 74.661(2) | 102.849 (1) | 90 |
| $\beta$ | 107.952(1) | 79.285(2) | 93.051(1) | 102.995(1) |
| $\gamma$ | 90 | 84.656(2) | 100.820(1) | 90 |
| $V$ [Å$^3$] | 1524.83(8) | 779.61(14) | 1901.9(7) | 1973.97(4) |
| $D_{calcd.}$ [g/cm$^3$] | 1.204 | 1.377 | 1.176 | 1.180 |
| Abs. coeff. [mm$^{-1}$] | 0.202 | 2.398 | 0.279 | 0.272 |
| Max. / min. transmission | 0.97 / 0.95 | 0.80 / 0.67 | 0.95 / 0.73 | 0.97 / 0.92 |
| Crystal shape | polyhedron | polyhedron | polyhedron | polyhedron |
| Crystal size [mm$^3$] | 0.24×0.16×0.14 | 0.18×0.11×0.10 | 0.37×0.29×0.24 | 0.30×0.20×0.10 |
| $\Theta$ range [°] | 1.54 to 26.36 | 2.14 to 28.38 | 1.84 to 27.44 | 1.53 to 27.49 |
| Reflections collected | 14360 | 8130 | 19809 | 19923 |
| Indep. reflections [$R$(int)] | 3112 (0.0428) | 3870 (0.0344) | 8624 (0.0255) | 4535 (0.0356) |
| Obsd. reflections [$I > 2\sigma(I)$] | 2310 | 2878 | 6308 | 3568 |
| Data / restraints / parameters | 3112 / 0 / 172 | 3870 / 74 / 191 | 8624 / 0 / 397 | 4535 / 0 / 208 |
| GOF($F^2$) | 1.02 | 1.04 | 1.07 | 1.04 |
| $R(F)$ | 0.037 | 0.045 | 0.039 | 0.033 |
| $R_w(F^2)$ | 0.083 | 0.103 | 0.097 | 0.078 |
| $(\Delta\rho)_{max}$, $(\Delta\rho)_{min}$ [e·Å$^{-3}$] | 0.18 and –0.25 | 0.60 and –0.51 | 0.39 and –0.44 | 0.22 and –0.23 |

 © 2006 Wiley-VCH Verlag GmbH & Co. KGaA, Weinheim 

Table 6. Crystal data and structural refinement for **8**–**10**.

| | **8** | **9** | **10** |
|---|---|---|---|
| Empirical formula | $C_{20}H_{32}N_2S_2$ | $C_{39}H_{46}N_2S_2$ | $C_{40}H_{48}N_2S_2{\cdot}1.5\ CH_2Cl_2$ |
| Formula weight | 364.60 | 606.90 | 748.31 |
| Temperature [K] | 100(2) | 200(2) | 100(2) |
| Crystal system | monoclinic | monoclinic | orthorhombic |
| Space group | $P2_1/n$ | $P2_1/c$ | $P2_12_12$ |
| $Z$ | 4 | 4 | 4 |
| $a$ | 7.2802(6) | 14.392(2) | 14.648(2) |
| $b$ | 14.149(1) | 16.697(2) | 29.035(4) |
| $c$ | 19.870(2) | 15.492(2) | 8.950(1) |
| $\alpha$ | 90 | 90 | 90 |
| $\beta$ | 93.587(2) | 117.506(3) | 90 |
| $\gamma$ | 90 | 90 | 90 |
| $V$ [Å$^3$] | 2042.7(3) | 3301.9(7) | 3806.6(9) |
| $D_{calcd.}$ [g/cm$^3$] | 1.186 | 1.22 | 1.306 |
| Abs. coeff. [mm$^{-1}$] | 0.265 | 0.19 | 0.383 |
| Max. / min. transmission | 0.98 / 0.92 | 0.99 / 0.93 | 0.98 / 0.89 |
| Crystal shape | irregular | irregular | irregular |
| Crystal size [mm$^3$] | 0.30×0.07×0.07 | 0.38×0.07×0.04 | 0.32×0.26×0.06 |
| $\Theta$ range [°] | 1.77 to 24.71 | 2.01 to 21.97 | 1.56 to 28.32 |
| Reflections collected | 15874 | 19853 | 39939 |
| Indep. reflections [$R$(int)] | 3486 (0.0789) | 4021 (0.0725) | 9449 (0.1470) |
| Obsd. reflections [$I > 2\sigma(I)$] | 2937 | 3227 | 6525 |
| Data / restraints / parameters | 3486 / 0 / 345 | 4021 / 0 / 574 | 9449 / 12 / 436 |
| GOF($F^2$) | 1.25 | 1.19 | 1.10 |
| $R(F)$ | 0.071 | 0.058 | 0.134 |
| $R_w(F^2)$ | 0.122 | 0.104 | 0.311 |
| $(\Delta\rho)_{max}$, $(\Delta\rho)_{min}$ [e·Å$^{-3}$] | 0.37 and –0.33 | 0.20 and –0.20 | 0.83 and –0.71 |

Table 7. Crystal data and structural refinement for **6**·$Ag^+$, **7**·$Ag^+$, and **8**·$Ag^+$.

| | **6**·$Ag^+$ | **7**·$Ag^+$ | **8**·$Ag^+$ |
|---|---|---|---|
| Empirical formula | $C_{20}H_{28}Ag_2F_6N_2O_6S_4$ | $C_{20}H_{30}AgF_3N_2O_3S_3$ | $C_{21}H_{32}AgF_3N_2O_3S_3$ |
| Formula weight | 850.42 | 607.51 | 621.54 |
| Temperature [K] | 200(2) | 200(2) | 200(2) |
| Crystal system | monoclinic | monoclinic | triclinic |
| Space group | $P2_1/c$ | $P2_1/c$ | $P\bar{1}$ |
| $Z$ | 4 | 4 | 2 |
| $a$ | 11.3822(1) | 10.5359(1) | 9.846(1) |
| $b$ | 13.6579(1) | 15.1706(3) | 9.918(1) |
| $c$ | 19.1305(1) | 15.0937(3) | 13.103(1) |
| $\alpha$ | 90 | 90 | 96.383(2) |
| $\beta$ | 93.208(1) | 93.805(1) | 106.648(2) |
| $\gamma$ | 90 | 90 | 92.734(29) |
| $V$ [Å$^3$] | 2969.31(4) | 2407.20(7) | 1214.0(2) |
| $D_{calcd.}$ [g/cm$^3$] | 1.902 | 1.676 | 1.700 |
| Abs. coeff. [mm$^{-1}$] | 1.676 | 1.146 | 1.138 |
| Max. / min. transmission | 0.7638 / 0.5538 | 0.89 / 0.80 | 0.97 / 0.83 |
| Crystal shape | polyhedron | polyhedron | irregular |
| Crystal size [mm$^3$] | 0.40×0.21×0.17 | 0.20×0.12×0.10 | 0.17×0.17×0.03 |
| $\Theta$ range [°] | 1.79 to 27.48 | 1.91 to 27.46 | 1.64 to 28.36 |
| Reflections collected | 30222 | 16273 | 12638 |
| Indep. reflections [$R$(int)] | 6807 | 5420 | 5974 |
| | 0.0253 | 0.0422 | 0.0314 |
| Obsd. reflections [$I > 2\sigma(I)$] | 5876 | 3979 | 4803 |
| Data / restraints / parameters | 6807 / 91 / 434 | 5420 / 0 / 289 | 5974 / 0 / 426 |
| GOF($F^2$) | 1.07 | 1.03 | 1.00 |
| $R(F)$ | 0.025 | 0.032 | 0.034 |
| $R_w(F^2)$ | 0.061 | 0.068 | 0.068 |
| $(\Delta\rho)_{max}$, $(\Delta\rho)_{min}$ [e·Å$^{-3}$] | 0.89 and –0.82 | 0.52 and –0.77 | 1.06 and –0.89 |

of mechanical stirring at –30 °C a solution of *N*-2-bromoethylphthalimid (20 g, 78.7 mmol) in dry toluene (250 mL) was added dropwise over a period of 1 h so that the temperature was maintained below 0 °C. After mechanical stirring overnight at room temperature the suspension was finally refluxed for 1 h. To workup water (100 mL) was added and the organic layer was washed a further 2× with water. After drying with magnesium sulfate and removal of the solvent, pure **22** (13.2 g, 75%) was obtained by crystallization from acetone as a white solid, m.p. 106 °C. $^1$H NMR (500 MHz, $C_6D_6$): $\delta$ = 1.59 (q, $^3J$ = 7.1 Hz, 2 H, $CH_2$), 2.36 (t, $^3J$

 © 2006 Wiley-VCH Verlag GmbH & Co. KGaA, Weinheim 

Table 8. Crystal data and structural refinement for **10·2(Ag$^+$)**, **28·Ag$^+$**, and **33·Ag$^+$**.

| | **10·2(Ag$^+$)** | **28·Ag$^+$** | **33·Ag$^+$** |
|---|---|---|---|
| Empirical formula | $C_{42}H_{48}Ag_2F_6N_2O_{6.5}S_4$ | $C_{26}H_{29}AgCl_2F_3NO_3S$ | $C_{44}H_{41}AgCl_2F_3NO_3S$ |
| Formula weight | 1142.80 | 671.33 | 899.61 |
| Temperature [K] | 200(2) | 200(2) | 200(2) |
| Crystal system | monoclinic | orthorhombic | monoclinic |
| Space group | *C*2 | $P2_12_12_1$ | *Cc* |
| *Z* | 4 | 4 | 4 |
| *a* | 49.5268(10) | 13.6160(2) | 30.3342(5) |
| *b* | 8.3859(2) | 13.8719(2) | 9.0243(2) |
| *c* | 11.1401(1) | 14.8042(3) | 15.2387(3) |
| *α* | 90 | 90 | 90 |
| *β* | 102.566(1) | 90 | 103.637(1) |
| *γ* | 90 | 90 | 90 |
| *V* [Å$^3$] | 4516.32(15) | 2796.21(8) | 4053.92(14) |
| $D_{calcd.}$ [g/cm$^3$] | 1.681 | 1.595 | 1.474 |
| Abs. coeff. [mm$^{-1}$] | 1.127 | 1.035 | 0.735 |
| Max. / min. transmission | 0.96 / 0.81 | 0.95 / 0.62 | 0.96 / 0.77 |
| Crystal shape | polyhedron | polyhedron | polyhedron |
| Crystal size [mm$^3$] | 0.20 × 0.04 × 0.04 | 0.52 × 0.28 × 0.05 | 0.38 × 0.24 × 0.06 |
| *Θ* range [°] | 0.84 to 22.99 | 2.01 to 24.09 | 1.38 to 25.34 |
| Reflections collected | 16130 | 22138 | 17041 |
| Indep. reflections [*R*(int)] | 6290 (0.0591) | 4431 (0.0493) | 7344 (0.0484) |
| Obsd. reflections [$I>2\sigma(I)$] | 4918 | 3867 | 5788 |
| Data / restraints / parameters | 6290 / 264 / 637 | 4431 / 0 / 334 | 7344 / 2 / 496 |
| GOF ($F^2$) | 1.04 | 1.02 | 0.99 |
| *R* (*F*) | 0.042 | 0.031 | 0.040 |
| $R_w(F^2)$ | 0.076 | 0.064 | 0.062 |
| $(\Delta\rho)_{max}$, $(\Delta\rho)_{min}$ [e·Å$^{-3}$] | 0.63 and –0.44 | 0.49 and –0.36 | 0.42 and –0.47 |

Table 9. Crystal data and structural refinement for **4·Cu$^+$**, **5·Cu$^+$**, and **6·Cu$^+$**.

| | **4·Cu$^+$** | **5·Cu$^+$** | **6·Cu$^+$** |
|---|---|---|---|
| Empirical formula | $C_{17}H_{24}CuF_3N_2O_3S_2$ | $C_{17}H_{24}CuF_3N_2O_3SSe$ | $C_{19}H_{28}CuF_3N_2O_3S_3$ |
| Formula weight | 489.04 | 535.94 | 549.15 |
| Temperature [K] | 200(2) | 201(2) | 200(2) |
| Crystal system | monoclinic | monoclinic | monoclinic |
| Space group | $P2_1/c$ | $P2_1/c$ | $P2_1$ |
| *Z* | 4 | 4 | 2 |
| *a* | 9.7328(1) | 9.7680(1) | 9.0166(1) |
| *b* | 10.5468(2) | 10.6242(2) | 9.7697(1) |
| *c* | 18.9631(3) | 18.9135(1) | 13.6670(2) |
| *α* | 90 | 90 | 90 |
| *β* | 93.159(1) | 92.897(1) | 108.306(1) |
| *γ* | 90 | 90 | 90 |
| *V* [Å$^3$] | 1943.60(5) | 1960.28 | 1142.99(2) |
| $D_{calcd.}$ [g/cm$^3$] | 1.671 | 1.816 | 1.596 |
| Abs. coeff. [mm$^{-1}$] | 1.388 | 3.127 | 1.278 |
| Max. / min. transmission | 0.77 / 0.67 | 0.71 / 0.41 | 0.88 / 0.57 |
| Crystal shape | polyhedron | polyhedron | polyhedron |
| Crystal size [mm$^3$] | 0.32 × 0.30 × 0.20 | 0.36 × 0.24 × 0.12 | 0.49 × 0.29 × 0.10 |
| *Θ* range [°] | 2.10 to 27.47 | 2.09 to 27.48 | 1.57 to 27.48 |
| Reflections collected | 19753 | 19922 | 11787 |
| Indep. reflections [*R*(int)] | 4451 (0.0283) | 4494 (0.0298) | 5192 (0.0227) |
| Obsd. reflections [$I > 2\sigma(I)$] | 3799 | 3961 | 4853 |
| Data / restraints / parameters | 4451 / 92 / 285 | 4494 / 92 / 285 | 5192 / 1 / 280 |
| GOF ($F^2$) | 1.04 | 1.05 | 1.04 |
| *R* (*F*) | 0.027 | 0.024 | 0.025 |
| $R_w(F^2)$ | 0.068 | 0.055 | 0.064 |
| $(\Delta\rho)_{max}$, $(\Delta\rho)_{min}$ [e·Å$^{-3}$] | 0.34 and –0.42 | 0.28 and –0.35 | 0.35 and –0.41 |

= 7.2 Hz, 4 H, C$H_2$), 2.55 (t, $^3J$ = 7.0 Hz, 4 H, C$H_2$), 3.60 (t, $^3J$ = 7.0 Hz, 4 H, C$H_2$), 6.81–6.85 (m, 4 H, C$_{ar}H$), 7.36–7.41 (m, 4 H, C$_{ar}H$) ppm. $^{13}$C NMR (125 MHz, $C_6D_6$): $\delta$ = 29.2 (s, *C*H$_2$), 30.0 (s, *C*H$_2$), 30.4 (s, *C*H$_2$), 37.2 (s, *C*H$_2$), 123.1 (t, *C*$_{ar}$), 132.6 (q, *C*$_{ar}$), 133.6 (t, *C*$_{ar}$), 167.9 (q, *C*O) ppm. IR (KBr): $\tilde{\nu}$ = 3459, 3053, 2964, 2929, 2850, 1773, 1714, 1465, 1449, 1442, 1419 cm$^{-1}$. UV/Vis ($CH_2Cl_2$): $\lambda_{max}$ (lg $\varepsilon$) = 294 (4.5) nm. HRMS (FAB) calcd. for $C_{23}H_{22}N_2O_4S_2$, 455.1099; found 455.1073. $C_{23}H_{22}N_2O_4S_2$ (455.11): calcd. C 60.77, H 4.88, N 6.16, S 14.11; found C 60.49, H 4.96, N 6.13, S 14.08.

 © 2006 Wiley-VCH Verlag GmbH & Co. KGaA, Weinheim 

**1,10-Diphthalimido-3,8-dithiodecane (23):** To a solution of 1,3-propanedithiol (4.8 g, 39 mmol) in dry toluene (250 mL), cooled to –30 °C was added dropwise *n*BuLi in hexane (51 mL). After 30 min of mechanical stirring at –30 °C a solution of *N*-2-bromoethylphthalimide (20 g, 78.7 mmol) in dry toluene (250 mL) was added dropwise over a period of 1 h so that the temperature was maintained below 0 °C. After mechanical stirring overnight at room temperature the suspension was finally refluxed for 1 h. To workup water (100 mL) was added and the organic layer was washed further 2× with water. After drying with magnesium sulfate and removal of the solvent, pure **23** (12.1 g, 66%) was obtained by crystallization from acetone as a white solid, m.p. 100 °C. $^1$H NMR (500 MHz, $C_6D_6$): $\delta$ = 1.39 (s, 4 H, C$H_2$), 2.27 (s, 4 H, C$H_2$), 2.57 (t, $^3J$ = 7.1 Hz, 4 H, C$H_2$), 3.62 (t, $^3J$ = 7.0 Hz, 4 H, C$H_2$), 6.82–6.86 (m, 4 H, $C_{ar}H$), 7.38–7.42 (m, 4 H, $C_{ar}H$) ppm. $^{13}$C NMR (125 MHz, $C_6D_6$): $\delta$ = 28.6 (s, *C*H$_2$), 30.1 (s, *C*H$_2$), 31.2 (s, *C*H$_2$), 37.2 (s, *C*H$_2$), 123.1 (t, $C_{ar}$), 132.6 (q, $C_{ar}$), 133.6 (t, $C_{ar}$), 167.9 (q, *C*O) ppm. IR (KBr): $\tilde{\nu}$ = 3460, 3102, 3048, 3018, 2945, 2923, 2865, 1774, 1699, 1613, 1578, 1464, 1433, 1417 cm$^{-1}$. UV/Vis ($CH_2Cl_2$): $\lambda_{max}$ (lg $\varepsilon$) = 294 (3.5) nm. HRMS (FAB) calcd. for $C_{24}H_{24}N_2O_4S_2$ 469.1256; found 469.1263. $C_{24}H_{24}N_2O_4S_2$ (469.13): calcd. C 61.52, H 5.16, N 5.98, S 13.68; found C 61.26, H 5.15, N 6.01, S 13.56.

**1,9-Diamino-3,7-dithiononane·Dihydrochloride (17·2HCl):** To a solution of **22** (13.2 g, 29.1 mmol) in dry ethanol (50 mL) was added dropwise a solution of hydrazine (3.1 g, 61.1 mmol) in water (5 mL). After temporary clearance of the solution a solid precipitate commenced to separate. The whole mixture was heated at reflux for 2 h then concentrated hydrochloric acid (12 mL) was added slowly and the obtained clear solution was stirred for a further 30 min. The alcohol was removed by evaporation and the suspension was dissolved in water. The solid was filtered off and washed with water. The water was removed by evaporation and the raw material was crystallized from methanol to obtain **17·2HCl** (7.5 g, 96%) as a white solid, m.p. 192 °C. $^1$H NMR (300 MHz, $CD_3OD$): $\delta$ = 1.86–1.96 (m, 2 H, C$H_2$), 2.72 (t, $^3J$ = 7.1 Hz, 4 H, C$H_2$), 2.86 (t, $^3J$ = 6.9 Hz, 4 H, C$H_2$), 3.16 (t, $^3J$ = 6.7 Hz, 4 H, C$H_2$), 4.84 (s, 6 H, N$H_3$Cl) ppm. $^{13}$C NMR (75 MHz, $CD_3OD$): $\delta$ = 29.7 (s, *C*H$_2$), 30.3 (s, *C*H$_2$), 31.1 (s, *C*H$_2$), 40.2 (s, *C*H$_2$) ppm. IR (KBr): $\tilde{\nu}$ = 3440, 3023, 2040, 1718, 1628, 1459, 1412 cm$^{-1}$. $C_7H_{20}Cl_2N_2S_2$ (267.29): calcd. C 31.46, H 7.54, N 10.48, S 23.99, Cl 26.53; found C 31.61, H 7.52, Cl 26.42, N 10.34, S 23.71.

**1,10-Diamino-3,8-dithiodecane·Dihydrochloride (18·2HCl):** To a solution of **23** (5.5 g, 11.7 mmol) in dry ethanol (25 mL) was added dropwise a solution of hydrazine (1.23 g, 24.6 mmol) in water (2 mL). After temporary clearance of the solution a solid precipitate commenced to separate. The whole mixture was heated at reflux for 2 h then concentrated hydrochloric acid (12 mL) was added slowly and the obtained clear solution was stirred for further 30 min. The alcohol was removed by evaporation and the suspension was dissolved in water. The solid was filtered off and washed with water. The water was removed by evaporation and the raw material was crystallized from methanol to obtain **18·2HCl** (2.7 g, 83%) as a white solid, m.p. 203 °C. $^1$H NMR (300 MHz, $CD_3OD$): $\delta$ = 1.71–1.76 (m, 4 H, C$H_2$), 2.63 (t, $^3J$ = 7.1 Hz, 4 H, C$H_2$), 2.83 (t, $^3J$ = 6.9 Hz, 4 H, C$H_2$), 3.15 (t, $^3J$ = 6.8 Hz, 4 H, C$H_2$), 4.83 (s, 6 H, N$H_3$Cl) ppm. $^{13}$C NMR (75 MHz, $CD_3OD$): $\delta$ = 29.4 (s, *C*H$_2$), 29.7 (s, *C*H$_2$), 31.9 (s, *C*H$_2$), 40.0 (s, *C*H$_2$) ppm. IR (KBr): $\tilde{\nu}$ = 3440, 2999, 2045, 2059, 1582, 1508, 1463 cm$^{-1}$. $C_8H_{22}Cl_2N_2S_2$ (281.31): calcd. C 34.16, H 7.88, N 9.96, S 22.79, Cl 25.21; found C 34.31, H 7.85, Cl 25.27, N 9.90, S 22.83.

**4,4′-Bis(2-hydroxyethyl)biphenyl (25):** To a suspension of 4,4′-dibromobiphenyl (30.00 g, 96 mmol) in dry hexane (1200 mL) was added a solution of 10 M *n*BuLi in hexane (42 mL, 420 mmol). The mixture was heated at reflux for 12 h. To this suspension dry THF (500 mL) was added and cooled to –40 °C. Subsequently ethylene oxide (31 mL, 617 mmol) was added. After 36 h of mechanical stirring at –35 °C water (500 mL) was added. Subsequently the mixture was stirred for a further 30 min. The white precipitate was then filtered off and dried with silica gel and finally crystallized from hexane to yield **25** (21 g, 92%), m.p. 183 °C. $^1$H NMR (500 MHz, $CD_2Cl_2$): $\delta$ = 1.45 (t, $^3J$ = 5.8 Hz, 2 H, OH), 2.87 (t, $^3J$ = 6.6 Hz, 4 H, C$H_2$), 3.85 (t, $^3J$ = 6.6 Hz, 4 H, C$H_2$), 7.29 (d, $^3J$ = 8.1 Hz, 4 H, $C_{ar}H$), 7.53 (d, $^3J$ = 8.1 Hz, 4 H, $C_{ar}H$) ppm. $^{13}$C NMR (125 MHz, $CD_2Cl_2$): $\delta$ = 38.8 (s, *C*H$_2$), 63.44 (s, *C*H$_2$), 126.9 (t, $C_{ar}$), 129.4 (t, $C_{ar}$), 137.9 (q, $C_{ar}$), 138.9 (q, $C_{ar}$) ppm. IR (KBr): $\tilde{\nu}$ = 3420, 3030, 2942, 2878, 2049, 1911, 1633, 1500, 1476 cm$^{-1}$. UV/Vis ($CH_2Cl_2$): $\lambda_{max}$ (lg $\varepsilon$) = 258 (4.3) nm. HRMS (FAB) calcd. for $C_{16}H_{18}O_2$ 242.1307; found 242.1323. $C_{16}H_{18}O_2$ (242.13): calcd. C 79.31, H 7.49; found C 79.17, H 7.31.

**4,4′-Bis(2-methylsulfonylethyl)biphenyl (26):** To a solution of **25** (21.4 g, 88.3 mmol) in dichloromethane (350 mL) was added by cooling to –20 °C triethylamine (28.8 g, 285 mmol). Subsequently methanesulfonyl chloride (24.5 g, 213.8 mmol) was added to the mixture at such a rate that the temperature was maintained below –10 °C. After the addition was completed the suspension was stirred for 2 h. For workup water (100 mL) was added and the organic layer was washed with 10% hydrogen chloride solution, followed by saturated sodium hydrogen carbonate solution and again by saturated sodium chloride solution and water. The organic layer was dried with magnesium sulfate and the solvent evaporated. Purification by column chromatography (alumina; cyclohexane/ethyl acetate, 4:1) afforded **26** (29.0 g, 82%) as a white solid, m.p. 82 °C. $^1$H NMR (300 MHz, $CD_2Cl_2$): $\delta$ = 2.87 (s, 6 H, C$H_3$), 3.09 (t, $^3J$ = 6.8 Hz, 4 H, C$H_2$), 4.43 (t, $^3J$ = 6.8 Hz, 4 H, C$H_2$), 7.32 (d, $^3J$ = 8.2 Hz, 4 H, $C_{ar}H$), 7.56 (d, $^3J$ = 8.2 Hz, 4 H, $C_{ar}H$) ppm. $^{13}$C NMR (75 MHz, $CD_2Cl_2$): $\delta$ = 35.6 (s, *C*H$_2$), 37.6 (*C*H$_3$), 70.9 (s, *C*H$_2$), 127.5 (t, $C_{ar}$), 129.9 (t, $C_{ar}$), 136.2 (q, $C_{ar}$), 139.7 (q, $C_{ar}$) ppm. IR (KBr):$\tilde{\nu}$ = 3434, 3027, 2942, 1913, 1500, 1428, 1401 cm$^{-1}$. UV/Vis ($CH_2Cl_2$): $\lambda_{max}$ (lg $\varepsilon$) = 258 (4.4) nm. HRMS (FAB) calcd. for $C_{18}H_{22}O_6S_2$ 398.0858; found 398.0850. $C_{18}H_{22}O_6S_2$ (398.09): calcd. C 54.25, H 5.56, S 16.09; found C 54.61, H 5.54, S 15.85.

**4,4′-Bis(2-bromoethyl)biphenyl (27):** A solution of **26** (20 g, 50.2 mmol) in acetone (800 mL) was refluxed with LiBr (26 g, 301.1 mmol) overnight. Water was added to dissolve the precipitated salt and the acetone was removed by evaporation. The aqueous layer was extracted 5× with dichloromethane, and the combined organic layers were dried with magnesium sulfate. After evaporation of the solvent pure **27** (14.3 g, 81%) was obtained by column chromatography (alumina; hexane/diethyl ether, 5:1) as a white solid, m.p. 107 °C. $^1$H NMR (500 MHz, $CD_2Cl_2$): $\delta$ = 3.20 (t, $^3J$ = 7.5 Hz, 4 H, C$H_2$), 3.63 (t, $^3J$ = 7.4 Hz, 4 H, C$H_2$), 7.30 (d, $^3J$ = 8.1 Hz, 4 H, $C_{ar}H$), 7.56 (d, $^3J$ = 8.2 Hz, 4 H, $C_{ar}H$) ppm. $^{13}$C NMR (125 MHz, $CD_2Cl_2$): $\delta$ = 33.5 (s, *C*H$_2$), 39.2 (s, *C*H$_2$), 127.3 (t, $C_{ar}$), 129.5 (t, $C_{ar}$), 138.4 (q, $C_{ar}$), 139.6 (q, $C_{ar}$) ppm. IR (KBr): $\tilde{\nu}$ = 3444, 3052, 3026, 2959, 2930, 2051, 1633, 1493, 1447 cm$^{-1}$. UV/Vis ($CH_2Cl_2$): $\lambda_{max}$ (lg $\varepsilon$) = 260 (4.4) nm. HRMS (FAB) calcd. for $C_{16}H_{16}Br_2$ 367.9599; found 367.9607. $C_{16}H_{16}Br_2$ (367.96): calcd. C 52.21, H 4.38, Br 43.41; found C 52.35, H 4.44, Br 43.19.

**General Procedure for the Condensation of Primary Amines with Terminal Bromo Compounds to the Tertiary Amines 28–33:** A primary amine (5 mmol) and a terminal bromo-compound (10 mmol) were added together to a suspension of finely powdered potassium

 © 2006 Wiley-VCH Verlag GmbH & Co. KGaA, Weinheim 

carbonate (4.9 g, 35 mmol) in acetonitrile (200 mL). The mixture was stirred intensively and refluxed for 2 d until the starting material was consumed. The mixture was filtered and the solvent evaporated. The residue was purified by column chromatography on alumina.

**Tris(2-phenylethyl)amine (28):** 945 mg (58%); m.p. 31 °C; cyclohexane/ethyl acetate, 50:1. $^1$H NMR (300 MHz, $CD_2Cl_2$): $\delta$ = 2.75–2.81 (m, 6 H, C$H_2$), 2.84–2.90 (m, 6 H, C$H_2$), 7.21–7.24 (m, 9 H, $C_{ar}H$), 7.32 (t, $^3J$ = 7.2 Hz, 6 H, $C_{ar}H$) ppm. $^{13}$C NMR (75 MHz, $CD_2Cl_2$): $\delta$ = 34.2 (s, $CH_2$), 56.4 (s, $CH_2$), 126.2 (t, $C_{ar}$), 128.7 (t, $C_{ar}$), 129.2 (t, $C_{ar}$), 141.4 (q, $C_{ar}$) ppm. IR (KBr): $\tilde{\nu}$ = 3480, 3086, 3028, 2957, 2933, 2864, 2798, 1946, 1873, 1809, 1751, 1600, 1491, 1452 cm$^{-1}$. UV/Vis ($CH_2Cl_2$): $\lambda_{max}$ (lg $\varepsilon$) = 258 (3.0) nm. HRMS (FAB) calcd. for $C_{24}H_{28}N$ 330.2221; found 330.2207. $C_{24}H_{27}N$ (330.22): calcd. C 87.49, H 8.26, N 4.25; found C 87.44, H 8.22, N 4.40.

**(But-3-ynyl)bis(2-phenylethyl)amine (29):** 305 mg (22%) colorless liquid; hexane/diethyl ether, 10:1. $^1$H NMR (300 MHz, $CD_2Cl_2$): $\delta$ = 2.01 (m, 1 H, ≡C$H$), 2.30 (m, 2 H, C$H_2$), 2.72–2.84 (m, 10 H, C$H_2$), 7.15–7.21 (m, 4 H, $C_{ar}H$), 7.25–7.31 (m, 6 H, $C_{ar}H$) ppm. $^{13}$C NMR (75 MHz, $CD_2Cl_2$): $\delta$ = 17.7 (s, $CH_2$), 34.4 (s, $CH_2$), 53.2 (s, $CH_2$), 56.3 (s, $CH_2$), 69.1 (t, ≡$CH$), 83.6 (q, ≡$C$), 126.3 (t, $C_{ar}$), 128.7 (t, $C_{ar}$), 129.2 (t, $C_{ar}$), 141.2 (q, $C_{ar}$) ppm. IR (KBr): $\tilde{\nu}$ = 3294, 3026, 2948, 2860, 2812, 2117, 1946, 1868, 1805, 1742, 1602, 1496, 1453 cm$^{-1}$. UV/Vis ($CH_2Cl_2$): $\lambda_{max}$ (lg $\varepsilon$) = 260 (2.5) nm. HRMS (FAB) calcd. for $C_{20}H_{23}N$ 278.1909; found 278.1918. $C_{20}H_{23}N$ (278.19): calcd. C 86.59, H 8.36, N 5.05; found C 86.64, H 8.33, N 5.27.

**[2-(Biphenyl-4-yl)ethyl]bis(2-phenylethyl)amine (30):** 940 mg (47%); m.p. 54 °C; hexane/diethyl ether, 10:1. $^1$H NMR (500 MHz, $CD_2Cl_2$): $\delta$ = 2.74–2.87 (m, 12 H, C$H_2$), 7.18 (d, $^3J$ = 8.0 Hz, 6 H, $C_{ar}H$), 7.26 (m, 6 H, $C_{ar}H$), 7.31–7.34 (m, 1 H, $C_{ar}H$), 7.43 (t, $^3J$ = 7.7 Hz, 2 H, $C_{ar}H$), 7.53 (d, $^3J$ = 8.0 Hz, 2 H, $C_{ar}H$), 7.60 (d, $^3J$ = 7.5 Hz, 2 H, $C_{ar}H$) ppm. $^{13}$C NMR (125 MHz, $CD_2Cl_2$): $\delta$ = 33.7 (s, $CH_2$), 34.1 (s, $CH_2$), 56.1 (s, $CH_2$), 56.2 (s, $CH_2$), 126.1 (t, $C_{ar}$), 127.2 (t, $C_{ar}$), 127.2 (t, $C_{ar}$), 127.3 (t, $C_{ar}$), 128.5 (t, $C_{ar}$), 129.0 (t, $C_{ar}$), 129.1 (t, $C_{ar}$), 129.6 (t, $C_{ar}$), 139.0 (q, $C_{ar}$), 140.5 (q, $C_{ar}$), 141.3 (q, $C_{ar}$) ppm. IR (KBr): $\tilde{\nu}$ = 3025, 2946, 1597, 1495, 1486, 1453 cm$^{-1}$. UV/Vis ($CH_2Cl_2$): $\lambda_{max}$ (lg $\varepsilon$) = 256 (4.4) nm. HRMS (EI+) calcd. for $C_{30}H_{31}N$ 405.2457; found 405.2448. $C_{30}H_{31}N$ (405.24): calcd. C 88.84, H 7.70, N 3.45; found C 88.44, H 7.84, N 3.57.

**Bis[2-(biphenyl-4-yl)ethyl]but-3-ynylamine (31):** 553 mg (25%) colorless oil; hexane/diethyl ether, 10:1. $^1$H NMR: (500 MHz, $CD_2Cl_2$): $\delta$ = 2.04 (t, $^4J$ = 2.6 Hz, 1 H, ≡C$H$), 2.37 (dt, $^3J$ = 4.8, $^4J$ = 2.6 Hz, 2 H, C≡CC$H_2$), 2.82–2.87 (m, 10 H, C$H_2$), 7.29 (d, $^3J$ = 8.1 Hz, 4 H, $C_{ar}H$), 7.34 (pt, $^3J$ = 7.4 Hz, 2 H, $C_{ar}H$), 7.44 (pt, $^3J$ = 7.7 Hz, 4 H, $C_{ar}H$), 7.54 (d, $^3J$ = 8.1 Hz, 4 H, $C_{ar}H$), 7.61 (d, $^3J$ = 7.2 Hz, 4 H) ppm. $^{13}$C NMR: (125 MHz, $CD_2Cl_2$): $\delta$ = 17.6 (s, $CH_2$), 33.9 (s, $CH_2$), 53.10 (s, $CH_2$), 56.1 (s, $CH_2$), 69.10 (t, ≡$CH$), 83.6 (q, ≡$C$), 127.2 (t, $C_{ar}$), 127.3 (t, $C_{ar}$), 127.4 (t, $C_{ar}$), 129.1 (t, $C_{ar}$), 129.6 (t, $C_{ar}$), 139.1 (q, $C_{ar}$), 140.3 (q, $C_{ar}$), 141.3 (q, $C_{ar}$) ppm. IR (KBr): $\tilde{\nu}$ = 3441, 3307, 3055, 3026, 1487, 1449, 1407 cm$^{-1}$. UV/Vis ($CH_2Cl_2$): $\lambda_{max}$ (lg $\varepsilon$) = 258 (4.6) nm. HRMS (FAB) calcd. for $C_{32}H_{31}N$ 430.2534; found 430.2534. $C_{32}H_{31}N$ (430.25): calcd. C 89.47, H 7.27, N 3.26; found C 89.08, H 7.25, N 3.32.

**Bis[2-(biphenyl-4-yl)ethyl](2-phenylethyl)amine (32):** 566 mg (56%); m.p. 82 °C; hexane/diethyl ether, 10:1. $^1$H NMR (300 MHz, $CD_2Cl_2$): $\delta$ = 2.78–2.92 (m, 12 H, C$H_2$), 7.20 (d, $^3J$ = 7.6 Hz, 3 H, $C_{ar}H$), 7.26 (d, $^3J$ = 8.2 Hz, 6 H, $C_{ar}H$), 7.31–7.36 (m, 2 H, $C_{ar}H$),7.44 (t, $^3J$ = 8.0 Hz, 4 H, $C_{ar}H$), 7.53 (d, $^3J$ = 8.2 Hz, 4 H, $C_{ar}H$), 7.60 (d, $^3J$ = 8.5 Hz, 4 H, $C_{ar}H$) ppm. $^{13}$C NMR (75 MHz, $CD_2Cl_2$): $\delta$ = 33.9 (s, $CH_2$), 34.2 (s, $CH_2$), 56.2 (s, $CH_2$), 56.3 (s, $CH_2$), 126.2 (t, $C_{ar}$), 127.3 (t, $C_{ar}$), 127.3 (t, $C_{ar}$), 127.5 (t, $C_{ar}$), 128.7 (t, $C_{ar}$), 129.1 (t, $C_{ar}$), 129.2 (t, $C_{ar}$), 129.7 (t, $C_{ar}$), 135.4 (q, $C_{ar}$), 139.1 (q, $C_{ar}$), 140.6 (q, $C_{ar}$), 141.4 (q, $C_{ar}$) ppm. IR (KBr): $\tilde{\nu}$ = 3440, 3057, 3027, 2943, 2859, 2808, 1486, 1452, 1408 cm$^{-1}$. UV/Vis ($CH_2Cl_2$): $\lambda_{max}$ (lg $\varepsilon$) = 258 (4.6) nm. HRMS (FAB) calcd. for $C_{36}H_{36}N$ 482.2848; found 482.2881. $C_{36}H_{35}N$ (482.28): calcd. C 89.77, H 7.32, N 2.91; found C 89.54, H 7.39, N 3.03.

**Tris[2-(biphenyl-4-yl)ethyl]amine (33):** 405 mg (15%); m.p. 75 °C; hexane/diethyl ether, 20:1. $^1$H NMR: (300 MHz, $CD_2Cl_2$): $\delta$ = 2.79–2.85 (m, 6 H, C$H_2$), 2.88–2.93 (m, 6 H, C$H_2$), 7.26 (d, $^3J$ = 8.1 Hz, 6 H, $C_{ar}H$), 7.30–7.35 (m, 3 H, $C_{ar}H$), 7.43 (t, $^3J$ = 7.5 Hz, 6 H, $C_{ar}H$), 7.52 (d, $^3J$ = 8.1 Hz, 6 H, $C_{ar}H$), 7.59 (d, $^3J$ = 7.6 Hz, 6 H, $C_{ar}H$) ppm. $^{13}$C NMR (75 MHz, $CD_2Cl_2$): $\delta$ = 33.8 (s, $CH_2$), 56.2 (s, $CH_2$), 127.3 (t, $C_{ar}$), 127.3 (t, $C_{ar}$), 127.4 (t, $C_{ar}$), 129.1 (t, $C_{ar}$), 129.7 (t, $C_{ar}$), 139.0 (q, $C_{ar}$), 140.6 (q, $C_{ar}$), 141.4 (q, $C_{ar}$) ppm. IR (KBr): $\tilde{\nu}$ = 3440, 3027, 2924, 2854, 1486, 1461, 1450 cm$^{-1}$. UV/Vis ($CH_2Cl_2$): $\lambda_{max}$ (lg $\varepsilon$) = 258 (4.7) nm. HRMS (FAB) calcd. for $C_{42}H_{40}N$ 558.3160; found 558.3134. $C_{42}H_{39}N$ (558.32): calcd. C 90.44, H 7.05, N 2.51; found C 90.09, H 7.32, N 2.65.

**General Procedure for the Cyclization of α,ω-Diamines with 1,6-Dibromo-3-hexyne (16) to the Bicyclic Diynes 4–8:** 1,6-Dibromo-3-hexyne (**17**) (1.5 g, 6.25 mmol) and the corresponding α,ω-diamines (2 mmol) were added together to a suspension of finely powdered potassium carbonate (4.5 g, 33 mmol) in acetonitrile (125 mL). The mixture was stirred intensively and refluxed for 3 d until the starting material was consumed. The mixture was filtered and the solvent evaporated. The residue was purified by column chromatography on alumina.

**4-Thia-1,7-diazabicyclo[5.6.6]nonadeca-10,16-diyne (4):** Yield: 227 mg of **4** (41%), column chromatography with cyclohexane/ethyl acetate, 20:1, m.p. 69 °C. $^1$H NMR (500 MHz, $CD_2Cl_2$): $\delta$ = 2.24–2.35 (m, 8 H, C$H_2$), 2.52–2.56 (m, 8 H, C$H_2$), 2.76 (t, $^3J$ = 6.0 Hz, 4 H, C$H_2$), 2.98 (t, $^3J$ = 6.0 Hz, 4 H, C$H_2$) ppm. $^{13}$C NMR (125 MHz, $CD_2Cl_2$): $\delta$ = 19.5 (s, $CH_2$), 30.6 (s, $CH_2$), 53.4 (s, $CH_2$), 56.5 (s, $CH_2$), 80.6 (q, $C_{alkyne}$) ppm. IR (KBr): $\tilde{\nu}$ = 3447, 2900, 2835, 2801, 2781, 2731, 1449, 1432 cm$^{-1}$. Raman: $\tilde{\nu}$ = 2228, 2291 cm$^{-1}$. HRMS (FAB) calcd. for $C_{16}H_{25}N_2S$ 277.1738; found 277.1731. $C_{16}H_{24}N_2S$ (272.17): calcd. C 69.52, H 8.75, N 10.13, S 11.60; found C 69.31, H 8.77, N 10.04, S 11.43.

**4-Selena-1,7-diazabicyclo[5.6.6]nonadeca-10,16-diyne (5):** Yield: 212 mg of **5** (33%), column chromatography with cyclohexane/ethyl acetate, 20:1, m.p. 107 °C. $^1$H NMR (300 MHz, $CD_2Cl_2$): $\delta$ = 2.26–2.33 (m, 8 H, C$H_2$), 2.52–2.56 (m, 8 H, C$H_2$), 2.89 (t, $^3J$ = 6.1 Hz, 4 H, C$H_2$), 3.01 (t, $^3J$ = 6.1 Hz, 4 H, C$H_2$) ppm. $^{13}$C NMR (75 MHz, $CD_2Cl_2$): $\delta$ = 19.5 (s, $CH_2$), 22.2 (s, $CH_2$), 53.3 (s, $CH_2$), 57.4 (s, $CH_2$), 80.6 (q, $C_{alkyne}$) ppm. IR: (KBr): $\tilde{\nu}$ = 3445, 2951, 2903, 2790, 2728, 1453, 1428 cm$^{-1}$. Raman: $\tilde{\nu}$ = 22278, 22891 cm$^{-1}$. HRMS (FAB) calcd. for $C_{16}H_{25}N_2{}^{82}Se$ 327.1184; found 327.1144. $C_{16}H_{24}N_2Se$ (327.12): calcd. C 59.43, H 7.48, N 8.66; found C 59.28, H 7.55, N 8.58.

**4,7-Dithia-1,10-diazabicyclo[8.6.6]docosa-13,19-diyne (6):** Yield: 291 mg of **6** (43%), column chromatography with cyclohexane/ethyl acetate, 50:1, m.p. 134 °C. $^1$H NMR (300 MHz, $CD_2Cl_2$): $\delta$ = 2.26 (mt, 8 H, C$H_2$), 2.44–2.48 (m, 8 H, C$H_2$), 2.61–2.65 (m, 8 H, C$H_2$), 2.74 (s, 4 H, SC$H_2$C$H_2$S) ppm. $^{13}$C NMR (75 MHz, $CDCl_3$): $\delta$ = 18.7 (s, $CH_2$), 30.4 (s, $CH_2$), 31.8 (s, $CH_2$), 53.2 (s, $CH_2$), 54.3 (s, $CH_2$), 79. 5 (q, $C_{alkyne}$) ppm. IR (KBr): $\tilde{\nu}$ = 3440, 2956, 2900, 2801, 2730, 1630, 1455, 1421 cm$^{-1}$. Raman: $\tilde{\nu}$ = 22368, 2300 cm$^{-1}$. HRMS (FAB) calcd. for $C_{18}H_{29}N_2S_2$ 337.1772; found 337.1735.

 © 2006 Wiley-VCH Verlag GmbH & Co. KGaA, Weinheim 

$C_{18}H_{28}N_2S_2$ (337.18): calcd. C 64.24, H 8.39, N 8.32, S 19.05; found C 64.25, H 8.33, N 8.26, S 19.21.

**4,8-Dithia-1,11-diazabicyclo[9.6.6]tricosa-14,20-diyne (7):** Yield 360 mg of **7** (53%), column chromatography with cyclohexane/ethyl acetate, 50:1, m.p. 89 °C. $^1$H NMR (300 MHz, $CDCl_3$): $\delta$ = 1.91–2.00 (q, $^3J$ = 7.1 Hz, 2 H, C$H_2$), 2.29 (br. s, 8 H, C$H_2$), 2.57 (br. s, 12 H, C$H_2$), 2.71 (t, $^3J$ = 7.0 Hz, 8 H, SC$H_2$CH$_2$C$H_2$S) ppm. $^{13}$C NMR (75 MHz, $CDCl_3$): $\delta$ = 19.3 (s, *C*H$_2$), 28.2 (s, *C*H$_2$), 29.2 (s, *C*H$_2$), 30.0 (s, *C*H$_2$), 53.7 (s, *C*H$_2$), 54.5 (s, *C*H$_2$), 79.9 (q, $C_{alkyne}$) ppm. IR (KBr): $\tilde{\nu}$ = 3446, 2943, 2924, 2901, 2821, 2745, 2725, 1458, 1434, 1424 cm$^{-1}$. Raman: $\tilde{\nu}$ = 2231, 2293 cm$^{-1}$. HRMS (FAB) calcd. for $C_{19}H_{31}N_2S_2$ 351.1928; found 351.1920. $C_{19}H_{30}N_2S_2$ (351.19): calcd. C 65.09, H 8.62, N 7.99, S 18.29; found C 64.71, H 8.52, N 7.94, S 18.38.

**4,9-Dithia-1,12-diazabicyclo[10.6.6]tetracosa-15,21-diyne (8):** Yield: 275 mg of **8** (39%), column chromatography with cyclohexane/ethyl acetate, 50:1, m.p. 72 °C. $^1$H NMR (300 MHz, $CDCl_3$): $\delta$ = 1.79–1.83 (m, 4 H, C$H_2$), 2.32 (s, 8 H, C$H_2$), 2.62–2.70 (m, 20 H, C$H_2$) ppm. $^{13}$C NMR (75 MHz, $CDCl_3$): $\delta$ = 19.3 (s, *C*H$_2$), 28.7 (s, *C*H$_2$), 31.0 (s, *C*H$_2$), 31.8 (s, *C*H$_2$), 53.89 (s, *C*H$_2$), 55.4 (s, *C*H$_2$), 80.2 (q, $C_{alkyne}$) ppm. IR (KBr): $\tilde{\nu}$ = 3440, 2939, 2900, 2819, 2744, 1628, 1456, 1422, 1422 cm$^{-1}$. Raman: $\tilde{\nu}$ = 2237, 2297 cm$^{-1}$. HRMS (FAB) calcd. for $C_{20}H_{32}N_2S_2$ 365.2095; found 365.2056. $C_{20}H_{32}N_2S_2$ (365.21): calcd. C 65.88, H 8.85, N 7.68, S 17.59; found C 65.70, H 8.84, N 7.65, S 17.30.

**General Procedure for the Cyclization of α,ω-Diamines with 4,4′-Bis(2-bromoethyl)biphenyl (27):** To the bicyclic compounds **9** and **10** 4,4′-bis(2-dibromoethyl)biphenyl (**27**) (6.7 g, 10 mmol) and the diamines **17** and **18** (4 mmol), respectively, were added together to a suspension of finely powdered potassium carbonate (8.5 g, 61 mmol) in acetonitrile (400 mL). The mixture was stirred intensively and refluxed for 5 d until the starting material was consumed. The mixture was filtered and the solvent evaporated. The residue was purified by column chromatography on alumina.

**4,8-Dithia-14,15,20,21-tetrabenzena-1,11-diazabicyclo[9.6.6]tricosaphane (9):** 476 mg (20%); hexane/diethyl ether, 20:1, m.p. 180 °C (decomp.). $^1$H NMR (500 MHz, $CD_2Cl_2$): $\delta$ = 0.49–0.54 (q, $^3J$ = 7.4 Hz, 2 H, SCH$_2$C$H_2$), 1.13 (t, $^3J$ = 7.1 Hz, 4 H, C$H_2$), 1.30 (t, $^3J$ = 7.4 Hz, 4 H, SC$H_2$CH$_2$C$H_2$S), 2.21 (t, $^3J$ = 7.1 Hz, 4 H, C$H_2$), 2.51–2.55 (m, 4 H, C$H_2$), 2.72–2.77 (m, 4 H, C$H_2$), 2.89–2.94 (m, 4 H, C$H_2$), 2.97–3.02 (m, 4 H, C$H_2$), 7.22 (d, $^3J$ = 8.1 Hz, 8 H, $C_{ar}H$), 7.45 (d, $^3J$ = 8.1 Hz, 8 H, $C_{ar}H$) ppm. $^{13}$C NMR (125 MHz, $CD_2Cl_2$): $\delta$ = 30.6 (s, *C*H$_2$), 30.8 (s, *C*H$_2$), 31.9 (s, *C*H$_2$), 33.6 (s, *C*H$_2$), 53.7 (s, *C*H$_2$), 53.9 (s, *C*H$_2$), 126.3 (t, $C_{ar}$), 130.5 (t, $C_{ar}$), 138.3 (q, $C_{ar}$), 139.5 (t, $C_{ar}$) ppm. IR (KBr): $\tilde{\nu}$ = 3439, 2910, 2849, 2788, 1733, 1499, 1457, 1422 cm$^{-1}$. UV/Vis ($CH_2Cl_2$): $\lambda_{max}$ (lg $\varepsilon$) = 260 (4.8) nm. HRMS (FAB) calcd. for $C_{39}H_{47}N_2S_2$ 607.3181; found 607.3166. $C_{39}H_{46}N_2S_2$ (607.32): calcd. C 77.18, H 7.64, N 4.62, S 10.57; found C 77.04, H 7.65, N 4.65, S 10.77.

**4,9-Dithia-15,16,21,22-tetrabenzena-1,12-diazabicyclo[10.6.6]tetracosaphane (10):** Yield: 384 mg of **10** (16%), column chromatography with hexane/diethyl ether, 10:1, m.p. 189 °C (decomp.). $^1$H NMR (500 MHz, $CD_2Cl_2$): $\delta$ = 0.67 (m, 4 H, SCH$_2$C$H_2$), 1.53–1.54 (pd, $^3J$ = 8.9 Hz, 4 H, C$H_2$), 1.70 (t, $^3J$ = 6.6 Hz, 4 H, C$H_2$), 2.36 (t, $^3J$ = 6.6 Hz, 4 H, C$H_2$), 2.54–2.59 (m, 4 H, C$H_2$), 2.73–2.78 (m, 4 H, C$H_2$), 2.87–2.94 (m, 8 H, C$H_2$), 7.16 (d, $^3J$ = 8.0 Hz, 8 H, $C_{ar}H$), 7.32 (d, $^3J$ = 8.0 Hz, 8 H, $C_{ar}H$) ppm. $^{13}$C NMR (125 MHz, $CD_2Cl_2$): $\delta$ = 30.0 (s, *C*H$_2$), 31.0 (s, *C*H$_2$), 31.1 (s, *C*H$_2$), 33.1 (s, *C*H$_2$), 54.2 (s, *C*H$_2$), 55.2 (s, *C*H$_2$), 126.5 (t, $C_{ar}$), 130.2 (t, $C_{ar}$), 138.6 (q, $C_{ar}$), 139.3 (q, $C_{ar}$) ppm. IR (KBr): $\tilde{\nu}$ = 3440, 3022, 2963, 2908, 2855, 2783, 2729, 1738, 1632, 1500, 1456, 1448, 1402 cm$^{-1}$. UV/Vis ($CH_2Cl_2$): $\lambda_{max}$ (lg $\varepsilon$) = 258 (4.5) nm. HRMS (FAB) calcd. for $C_{40}H_{49}N_2S_2$ 621.3337; found 621.3317. $C_{40}H_{48}N_2S_2$ (621.33): calcd. C 77.37, H 7.79, N 4.51, S 10.33; found C 77.01, H 7.75, N 4.60, S 10.43.

**General Procedure for the Synthesis of Copper(I) Complexes [4·Cu$^+$][$CF_3SO_3$] and [5·Cu$^+$][$CF_3SO_3$]:** To a solution of the copper(I) triflate toluene complex (61 mg, 0.2 mmol) in anhydrous dichloromethane (5 mL) was added in the absence of light a solution of the corresponding cryptand (0.1 mmol) in anhydrous dichloromethane (5 mL). After stirring for 1 h the mixture was filtered and evaporation of the solvent gave the corresponding copper(I) complex in quantitative yield.

**Complex [4·Cu$^+$][$CF_3SO_3^-$]:** $^1$H NMR (500 MHz, $CD_2Cl_2$): $\delta$ = 2.71 (t, $^3J$ = 5.6 Hz, 8 H, C$H_2$), 2.69–2.72 (m, 4 H, C$H_2$), 2.75–2.77 (m, 4 H, C$H_2$), 2.84–2.88 (m, 4 H, C$H_2$), 2.95 (s, 4 H, C$H_2$) ppm. $^{13}$C NMR (125 MHz, $CD_2Cl_2$): $\delta$ = 19.8 (s, *C*H$_2$), 30.9 (s, *C*H$_2$), 37.8 (s, *C*H$_2$), 54.2 (s, *C*H$_2$), 55. 5 (q, OTf$^-$), 80.2 (q, $C_{alkyne}$) ppm. IR (KBr): $\tilde{\nu}$ = 3444, 2924, 2906, 2839, 1634, 1457, 1426 cm$^{-1}$. Raman: $\tilde{\nu}$ = 2231 cm$^{-1}$. HRMS (FAB) calcd. for $C_{16}H_{24}CuN_2S$ 341.0939; found 341.0938.

**Complex [5·Cu$^+$][$CF_3SO_3^-$]:** $^1$H NMR (500 MHz, $CD_2Cl_2$): $\delta$ = 2.64 (t, $^3J$ = 6.0 Hz, 8 H, C$H_2$), 2.71–2.78 (m, 8 H, C$H_2$), 2.86–2.91 (m, $^3J$ = 6.0 Hz, 4 H, C$H_2$), 2.98 (t, $^3J$ = 5.3 Hz, 4 H, C$H_2$), 2.95 (s, 4 H, C$H_2$) ppm. $^{13}$C NMR (125 MHz, $CD_2Cl_2$): $\delta$ = 18.9 (s, *C*H$_2$), 30.9 (s, *C*H$_2$), 53.9 (s, *C*H$_2$), 56.4 (s, *C*H$_2$), 80.0 (q, $C_{alkyne}$) ppm. IR (KBr): $\tilde{\nu}$ = 3441, 2922, 2868, 1630, 1460, 1427 cm$^{-1}$. HRMS (FAB) calcd. for $C_{16}H_{24}CuN_2Se$ 387.0400; found 387.0406.

**General Procedure for the Synthesis of Silver Complexes [6·Ag$^+$][$CF_3SO_3^-$], [10·2(Ag$^+$)][$CF_3SO_3^-$]$_2$, [28·Ag$^+$][$CF_3SO_3^-$], and [33·Ag$^+$][$CF_3SO_3^-$]:** To a solution of silver triflate (53 mg, 0.2 mmol) in anhydrous dichloromethane (5 mL) was added in the absence of light a solution of the corresponding cryptand (0.1 mmol) in anhydrous dichloromethane (5 mL). After stirring for 1 h the mixture was filtered and evaporation of the solvent gave the corresponding silver complex in quantitative yield.

**Complex [6·Ag$^+$][$CF_3SO_3^-$]:** $^1$H NMR (300 MHz, $CD_2Cl_2$): $\delta$ = 2.46–2.61 (m, 16 H, C$H_2$), 2.69–2.73 (m, 4 H, C$H_2$), 2.77–2.81 (m, 4 H, C$H_2$), 2.93 (s, 4 H, SC$H_2$C$H_2$S) ppm. $^{13}$C NMR (75 MHz, $CD_2Cl_2$): $\delta$ = 18.6 (s, *C*H$_2$), 29.3 (s, *C*H$_2$), 30.7 (s, *C*H$_2$), 53.0 (s, *C*H$_2$), 53.1 (s, *C*H$_2$), 79.3 (q, $C_{alkyne}$) ppm. IR (KBr): $\tilde{\nu}$ = 3444, 2963, 2920, 2849, 1461, 1434 cm$^{-1}$. HRMS (FAB) calcd. For $C_{18}H_{28}AgN_2S_2$ 445.0741; found 445.0701.

**Complex [7·Ag$^+$][$CF_3SO_3^-$]:** $^1$H NMR (300 MHz, $CD_2Cl_2$): $\delta$ = 1.79 (t, $^3J$ = 6.6 Hz, 4 H, C$H_2$), 2.13–2.22 (m, 2 H, C$H_2$), 2.47–2.54 (m, 8 H, C$H_2$), 2.61 (m, 4 H, C$H_2$), 2.74 (t, $^3J$ = 5.5 Hz, 4 H, C$H_2$), 2.86–2.93 (m, 8 H, C$H_2$), 2.63–3.68 (m, 4 H, C$H_2$) ppm. $^{13}$C NMR (75 MHz, $CD_2Cl_2$): $\delta$ = 19.4 (s, *C*H$_2$), 25.9 (s, *C*H$_2$), 31.6 (s, *C*H$_2$), 32.3 (s, *C*H$_2$), 53.3 (s, *C*H$_2$), 53.7 (s, *C*H$_2$), 68.0 (q, OTf$^-$), 79.7 (q, $C_{alkyne}$) ppm. IR (KBr): $\tilde{\nu}$ = 3441, 2963, 2916, 2840, 2823, 1629, 1459, 1446, 1433, 1418 cm$^{-1}$. Raman: $\tilde{\nu}$ = 2206, 2281 cm$^{-1}$. HRMS (FAB) calcd. for $C_{19}H_{30}AgN_2S_2$ 459.0898; found 459.0888.

**Complex [8·Ag$^+$][$CF_3SO_3^-$]:** $^1$H NMR (500 MHz, $CD_2Cl_2$): $\delta$ = 1.92 (s, 4 H, C$H_2$), 2.53–2.66 (m, 16 H, C$H_2$), 2.76 (t, $^3J$ = 6.5 Hz, 4 H, C$H_2$), 2.91 (s, 4 H, C$H_2$), 2.98 (t, $^3J$ = 6.5 Hz, 4 H, C$H_2$) ppm. $^{13}$C NMR (125 MHz, $CD_2Cl_2$): $\delta$ = 18.5 (s, *C*H$_2$), 26.4 (s, *C*H$_2$), 31.4 (s, *C*H$_2$), 32.2 (s, *C*H$_2$), 53.4 (s, *C*H$_2$), 60.9 (q, OTf$^-$), 78.9 (q, $C_{alkyne}$) ppm. IR (KBr):$\tilde{\nu}$ = 3443, 2924, 2846, 1629, 1457, 1439 cm$^{-1}$. HRMS (FAB) calcd. for $C_{20}H_{32}AgN_2S_2$ 471.1058; found 471.1075.

**Complex [9·Ag$^+$][$CF_3SO_3^-$]:** $^1$H NMR (500 MHz, $CD_2Cl_2$): $\delta$ = 0.77 (s, 2 H, C$H_2$), 1.63 (s, 4 H, C$H_2$), 2.27 (t, $^3J$ = 6.8 Hz, 4 H, C$H_2$),

 © 2006 Wiley-VCH Verlag GmbH & Co. KGaA, Weinheim 

2.62–2.67 (m, 4 H, C$H_2$), 2.84–2.89 (m, 4 H, C$H_2$), 3.00–3.05 (m, 4 H, C$H_2$), 3.11–3.17 (m, 4 H, C$H_2$), 7.39 (d, $^3J$ = 7.6 Hz, 8 H, $C_{ar}H$), 7.55 (d, $^3J$ = 7.6 Hz, 8 H, $C_{ar}H$) ppm. IR: (KBr): $\tilde{\nu}$ = 3449, 3022, 2941, 2915, 2795, 2736, 1626, 1499, 1450, 1425, 1407 cm$^{-1}$. UV/Vis ($CH_2Cl_2$): $\lambda_{max}$ (lg $\varepsilon$) = 270 (3.4) nm. HRMS (FAB) calcd. for $C_{39}H_{46}AgN_2S_2$ 715.2150; found 715.2158.

**Complex [10·2(Ag$^+$)][CF$_3$SO$_3^-$]$_2$:** $^1$H NMR (300 MHz, $CD_2Cl_2$): $\delta$ = 1.01 (s, 4 H, C$H_2$), 2.44 (s, 4 H, C$H_2$), 2.51 (br. s, 4 H, C$H_2$), 2.75 (br. s, 4 H, C$H_2$), 2.80–2.88 (m, 4 H, C$H_2$), 2.95–3.05 (m, 4 H, C$H_2$), 3.09–3.21 (m, 8 H, C$H_2$), 7.56 (d, $^3J$ = 7.8 Hz, 8 H, $C_{ar}H$), 7.68 (d, $^3J$ = 7.1 Hz, 8 H, $C_{ar}H$) ppm. $^{13}$C NMR (75 MHz, $CD_2Cl_2$): $\delta$ = 27.4 (s, *C*H$_2$), 31.8 (s, *C*H$_2$), 33.3 (s, *C*H$_2$), 34.6 (s, *C*H$_2$), 49.6 (s, *C*H$_2$), 53.7 (s, *C*H$_2$), 54.1 (s, *C*H$_2$), 54.4 (s, *C*H$_2$), 67.9 (q, OTf$^-$), 124.7 (t, $C_{ar}$), 125.8 (t, $C_{ar}$), 127.3 (t, $C_{ar}$), 138.0 (q, $C_{ar}$), 139.0 (q, $C_{ar}$) ppm. IR (KBr): $\tilde{\nu}$ = 3444, 2926, 2792, 1627, 1500, 1451 cm$^{-1}$. HRMS (FAB) calcd. for $C_{40}H_{47}Ag_2N_2S_2$ 835.1279; found 835.1303. $C_{42}H_{48}Ag_2F_6N_2O_6S_4$ (863.88): calcd. C 44.54, H 4.26, N 2.47; found C 44.84, H 4.60, N 2.57.

**Complex [28·Ag$^+$][CF$_3$SO$_3^-$]:** Colorless crystals, soluble in dichloromethane or chloroform, m.p. 145 °C (decomp.). $^1$H NMR (500 MHz, $CD_2Cl_2$): $\delta$ = 2.70 (t, $^3J$ = 6.0 Hz, 6 H, C$H_2$), 2.94 (t, $^3J$ = 6.0 Hz, 6 H, C$H_2$), 6.84 (d, $^3J$ = 7.0 Hz, 6 H, $C_{ar}H$), 7.30–7.37 (m, 9 H, $C_{ar}H$) ppm. $^{13}$C NMR (125 MHz, $CD_2Cl_2$): $\delta$ = 33.0 (s, $CH_2$), 57.6 (s, $CH_2$), 124.2 (t, $C_{ar}$), 127.7 (t, $C_{ar}$), 130.6 (t, $C_{ar}$), 139.2 (q, $C_{ar}$) ppm. IR (KBr): $\tilde{\nu}$ = 3441, 3085, 3061, 3026, 2951, 2861, 2799, 1627, 1603, 1495, 1453 cm$^{-1}$. HRMS (FAB) calcd. for $C_{24}H_{27}{}^{109}AgN$ 438.1191; found 438.1229. $C_{25}H_{27}AgF_3NO_3S$ (586.42)·0.75 $CH_2Cl_2$: calcd. C 47.57, H 4.42, N 2.15, S 4.93; found C 47.50, H 4.42, N 2.31, S 5.10.

**Complex [33·Ag$^+$][CF$_3$SO$_3^-$]:** Colorless, light-sensitive crystals, soluble in dichloromethane or chloroform, m.p. 173 °C (decomp.). $^1$H NMR (500 MHz, $CD_2Cl_2$): $\delta$ = 2.83 (t, $^3J$ = 5.8 Hz, 6 H, $CH_2$), 2.99 (t, $^3J$ = 5.8 Hz, 6 H, $CH_2$), 6.96 (d, $^3J$ = 7.9 Hz, 6 H, $C_{ar}H$), 7.43 (d, $^3J$ = 8.0 Hz, 6 H, $C_{ar}H$) ppm. $^{13}$C NMR (125 MHz, $CD_2Cl_2$): $\delta$ = 32.4 (s, $CH_2$), 57.1 (s, $CH_2$), 124.6 (t, $C_{ar}$), 126.9 (t, $C_{ar}$), 127.9 (t, $C_{ar}$), 128.7 (t, $C_{ar}$), 129.6 (t, $C_{ar}$), 138.1 (q, $C_{ar}$), 138.6 (q, $C_{ar}$), 140.2 (q, $C_{ar}$) ppm. IR (KBr): $\tilde{\nu}$ = 3441, 3028, 2929, 1625, 1519, 1487, 1458, 1407 cm$^{-1}$. HRMS (FAB) calcd. for $C_{43}H_{39}{}^{109}AgN$ 666.2130; found 666.2112. $C_{43}H_{29}AgF_3NO_3S$ (804.64): calcd. C 63.39, H 4.82, N 1.71, S 3.94; found C 63.28, H 4.89, N 2.04, S 4.28.

## Acknowledgments

We are grateful to the Deutsche Forschungsgemeinschaft and the Fonds der Chemischen Industrie for financial support. We thank Mrs. P. Krämer for typing and graphical work.

[1] a) C. J. Pedersen, *J. Am. Chem. Soc.* **1967**, *89*, 2495–2496; b) C. J. Pedersen, *J. Am. Chem. Soc.* **1967**, *89*, 7017–7036.
[2] a) B. Dietrich, J.-M. Lehn, J. P. Sauvage, *Tetrahedron Lett.* **1969**, *10*, 2885–2888; b) B. Dietrich, J.-M. Lehn, J. P. Sauvage, *Tetrahedron Lett.* **1969**, *10*, 2889–2892.
[3] Reviews: a) R. M. Kellogg, in *Crown Compounds* (Ed.: S. R. Cooper), VCH, Weinheim, **1992**, 261–284; b) S. R. Cooper, in *Crown Compounds* (Ed.: S. R. Cooper), VCH, Weinheim, **1992**, 285–302; c) S. R. Cooper, S. C. Rawle, *Struct. Bonding* **1990**, *72*, 1–72; d) W. Levason, G. Reid, in *Comprehensive Coordination Chemistry II* (Eds.: J. A. McCleverty, T. J. Meyer), Elsevier, Amsterdam, **2004**, vol. 1, 399–410.
[4] L. A. Ochrymowycz, C.-P. Mak, J. D. Michna, *J. Org. Chem.* **1974**, *39*, 2079–2084.
[5] a) J. Buter, R. M. Kellogg, *J. Chem. Soc., Chem. Commun.* **1980**, 466–467; b) J. Buter, R. M. Kellogg, *J. Org. Chem.* **1981**, *46*, 4481–4485.
[6] a) C. M. Thorne, S. C. Rawle, G. Admans, S. R. Cooper, *Inorg. Chem.* **1986**, *25*, 3848–3850; b) F. Vögtle, E. Weber, *Angew. Chem.* **1974**, *86*, 896–898; *Angew. Chem. Int. Ed. Engl.* **1974**, *13*, 814–816.
[7] a) P. Osvath, A. M. Sargeson, B. W. Skelton, A. H. White, *J. Chem. Soc., Chem. Commun.* **1991**, 1036–1038; b) B. Dietrich, J. M. Lehn, J. P. Sauvage, *J. Chem. Soc. Chem. Commun.* **1970**, 1055–1056; c) R. A. Pascal, Jr., J. Spergel, D. Van Engen, *Tetrahedron Lett.* **1986**, *27*, 4099–4102; d) M. Mascal, J.-L. Kerdelhué, A. J. Blake, P. A. Cooke, *Angew. Chem.* **1999**, *111*, 2094–2096; *Angew. Chem. Int. Ed.* **1999**, *38*, 1968–1971.
[8] A. Kunze, R. Gleiter, F. Rominger, *Chem. Commun.* **1999**, 171–172.
[9] A. Kunze, S. Bethke, R. Gleiter, F. Rominger, *Org. Lett.* **2000**, *2*, 609–612.
[10] V. Wolfart, R. Gleiter, H. Irngartinger, T. Oeser, C. Krieger, *Eur. J. Org. Chem.* **1998**, 2803–2809.
[11] G. G. Hermann, A. M. Goeminne, Z. Eeckhaut, *J. Coord. Chem.* **1979**, *9*, 1–5.
[12] V. Srivastava, R. Batheja, A. K. Singh, *J. Organomet. Chem.* **1994**, *484*, 93–96.
[13] H. R. Ing, R. H. F. Manske, *J. Chem. Soc.* **1926**, 2348–2351.
[14] M. Brudermüller, H. Musso, A. Wagner, *Chem. Ber.* **1988**, *121*, 2239–2244.
[15] M. K. W. Choi, H. S. He, P. H. Toy, *J. Org. Chem.* **2003**, *68*, 9831–9834.
[16] M. Kawasaki, M. Goto, S. Kawabata, T. Kometani, *Tetrahedron: Asymmetry* **2001**, *12*, 585–596.
[17] J. W. Dankwardt, *Angew. Chem.* **2004**, *116*, 2482–2486; *Angew. Chem. Int. Ed.* **2004**, *43*, 2428–2432.
[18] D. Pérez, G. Burés, E. Guitián, L. Castedo, *J. Org. Chem.* **1996**, *61*, 1650–1654.
[19] C. Qioa, H.-B. Jeon, L. M. Sayre, *J. Am. Chem. Soc.* **2004**, *126*, 8038–8045.
[20] J. L. Pierre, P. Baret, P. Chautemps, M. Armand, *J. Am. Chem. Soc.* **1981**, *103*, 2986–2988.
[21] T. Lahtinen, E. Wegelius, K. Airola, E. Kolehmainen, K. Rissanen, *J. Prakt. Chem.* **1999**, *341*, 237–244.
[22] T. Lahtinen, E. Wegelius, K. Rissanen, *New J. Chem.* **2001**, *25*, 905–911.
[23] F. R. Heirtzler, H. Hopf, P. G. Jones, P. Bubenitschek, *Tetrahedron Lett.* **1995**, *36*, 1239–1242; F. R. Heirtzler, H. Hopf, P. G. Jones, J. Bubentschik, V. Lehne, *J. Org. Chem.* **1993**, *58*, 2781–2784; P. G. Jones, P. Bubentschik, S. Heirtzler, *Acta Crystallogr., Sect. C* **1996**, *52*, 1380–1384; P. G. Jones, F. R. Heirtzler, H. Hopf, *Acta Crystallogr., Sect. C* **1996**, *52*, 1384–1388.
[24] J. E. Gano, G. Subramaniam, R. Birnbaum, *J. Org. Chem.* **1990**, *55*, 4760–4763.
[25] A. Garcia Martinez, J. Osio Barcina, M. del Rosario Colorado Heras, A. de Fresno Cerezo, M. del Rosario Torres Salvador, *Chem. Eur. J.* **2003**, *9*, 1157–1165.
[26] F. H. Allen, *Acta Crystallogr., Sect. B* **2002**, *58*, 380–388.
[27] M. M. Bernardo, M. J. Heeg, R. R. Schroeder, L. A. Ochrymowycz, D. B. Rorabacher, *Inorg. Chem.* **1992**, *31*, 191–198.
[28] A. J. Blake, R. O. Gould, A. J. Holder, T. I. Hyde, M. Schröder, *Polyhedron* **1989**, *8*, 513–518.
[29] T. Tsuchiya, T. Shimizu, K. Hirabayashi, N. Kamigata, *J. Org. Chem.* **2002**, *67*, 6632–6637.
[30] G. W. Eastland, M. A. Mazid, D. R. Russell, M. C. R. Symons, *J. Chem. Soc., Dalton Trans.* **1980**, 1682–1687.
[31] P. Pyykkö, *Chem. Rev.* **1997**, *97*, 597–636.
[32] G. M. Sheldrick, *SHELXTL*, Bruker Analytical X-ray Division, Madison, Wisconsin, **1997**.

Received: July 29, 2005
Published Online: December 13, 2005

 © 2006 Wiley-VCH Verlag GmbH & Co. KGaA, Weinheim 

DOI: 10.1002/ejic.200500684

# A Prime Example of Hard-Hard and Soft-Soft Interactions: Complexes between 4,7-Dioxa-1,10-diazabicyclo[8.6.6]docosa-13,19-diyne and $Li^+$, $Na^+$, $Cu^+$, $Ag^+$, $Cd^{2+}$, $Hg^{2+}$

**Andreas Kunze,[a,b] Rolf Gleiter,*[a] and Frank Rominger[a]**

**Keywords:** Cage compounds / Alkynes / Metal complexes

The crystal structures of 4,7-dioxa-1,10-diazabicyclo[8.6.6]-docosa-13,19-diyne (**7**), its *N*,*N*′-dioxide derivative **10** and the complexes of **7** with $LiClO_4$, $NaNO_3$, $Cu^I$ and $Ag^I$ triflate, $Cd(NO_3)_2$, and $HgCl_2$ were investigated. The $Li^+$ and $Na^+$ ions reveal a strong interaction between the ether bridge and the nitrogen atoms of **7**. The $Cu^I$ ion prefers an interaction between the nitrogen centers and the alkyne units whereas the $Ag^I$ ion interacts with the hard oxygen and nitrogen centers as well as with the alkyne units. The reaction of $HgCl_2$ with **7** in the presence of water afforded a molecule which could be looked at as the intermediate of a mercury-catalyzed addition of water to the triple bonds.
(© Wiley-VCH Verlag GmbH & Co. KGaA, 69451 Weinheim, Germany, 2006)

## Introduction

Some time ago we found that 1,8-diazabicyclo[6.6.6]-eicosa-4,11,17-triyne (**1**) provided a flexible cage structure with the *in*/*in* conformation of the bridgehead lone-pairs.[1] This and the triple bonds in the bridges were responsible for including copper(I) and silver(I) ions inside the cage.[1b] In the preceding paper we reported the synthesis and properties of diazacryptands which can be derived from **1** by replacing one 3-hexyne unit of the bridge by a tether with thioether functions (see Figure 1), the cage systems **2**–**6**.[2]

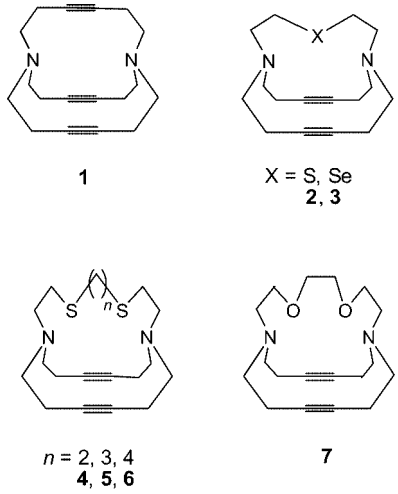


Figure 1. Bicyclic cryptands **1**–**7**.

[a] Organisch-Chemisches Institut der Universität Heidelberg, Im Neuenheimer Feld, 270, 69120 Heidelberg, Germany
Fax: +49-6221-544205
E-mail: Rolf.Gleiter@urz.uni-heidelberg.de
[b] CarboGen AG
Schachenallee 29, 5001 Aarau, Switzerland

The investigations of **2**–**6** afforded a series of endohedral copper(I) and silver(I) complexes when the reaction was carried out with copper(I) and silver(I) triflates. In the resulting complexes the soft metal ion interacted with the soft alkyne and chalcogen units as well as with the nitrogen centers. A comparison among the cryptands **2**–**6** revealed that the geometrical requirements for a metal heteroatom and metal–alkyne interaction were optimal in **4**. These results led us to synthesize the title compound **7** as a cryptand, because the compound should be able to host soft as well as hard ions according to the HSAB concept.[3,4]

## Results

The synthesis of **7** was achieved by a one-pot reaction with two equivalents of 1,6-dibromohex-3-yne (**8**)[5] and one equivalent of 1,8-diamino-3,6-dioxaoctane (**9**). Both components were heated in acetonitrile with a surplus of ground potassium carbonate to afford **7** in 40% yield (Scheme 1). The rather high yield of this three-component reaction we ascribe to a fixation of **9** by a potassium ion in a conformation where an intramolecular ring closure is favored over an intermolecular one.[6,7] The yields with lithium carbonate and cesium carbonate turned out to be much less than with potassium carbonate.

The structure of **7** was confirmed by X-ray investigations on single crystals. The results revealed the *in*/*in* conformation for both nitrogen atoms.[8,9] The molecule adopts noncrystallographic $C_2$ symmetry. The two triple bonds are inclined towards each other by 55°. The intramolecular distance of the nitrogen atoms amounts to 5.49 Å which is longer than in **4** (4.87 Å). The molecular structure of **7** is shown in Figure 2. The oxygen atoms of the ether bridge

 © 2006 Wiley-VCH Verlag GmbH & Co. KGaA, Weinheim 

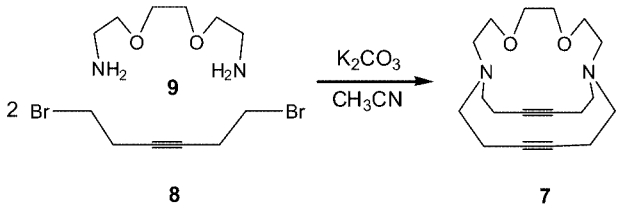


Scheme 1.

point outwards. The longer ether bridge as compared to the 3-hexyne bridge in **1** gives **7** more flexibility. This shows up when **7** is oxidized with hydroperoxide. The resulting *N*,*N*′-oxide **10** now adopts the *out*/*out* conformation at the bridgeheads (Scheme 2, Figure 2). The N–O groups are tilted by 46° relative to the N···N axis and the ether oxygen atoms point inside the cavity.

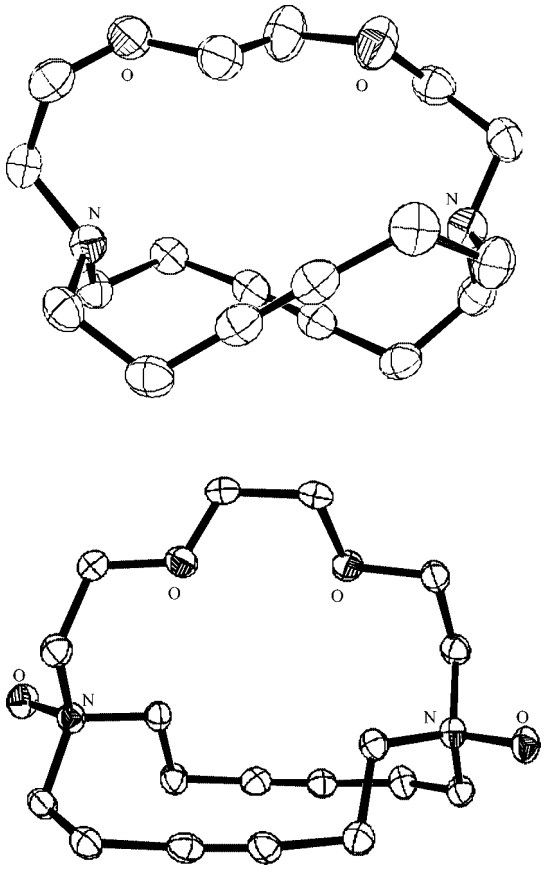

Figure 2. Molecular structures of **7** (top) and **10**.

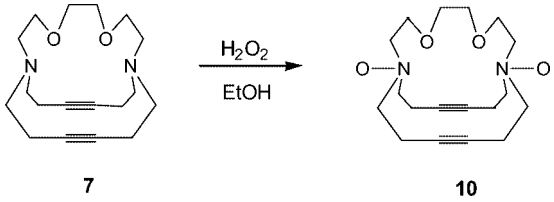


Scheme 2.

To probe the complexation properties of **7** we reacted this ligand with silver(I) and copper(I) triflates in dichloromethane and with lithium perchlorate, sodium nitrate, and cadmium nitrate in methanol. In all five experiments we obtained a colorless crystalline powder which allowed us to grow single crystals for X-ray investigations.

In Table 1 we list the most relevant distances and angles of the metal complexes of **7**. In Figure 3 we show a side view of the molecular structures. It is seen that the small copper ion prefers a close contact with the nitrogen centers and the triple bonds. No contact with the oxygen atom can be observed. As a consequence the N···N distance is shortened to 4.12 Å as compared to the 5.49 Å of the free ligand. The distances between the copper ion and the center of the triple bonds amount to 2.34 and 2.55 Å. These values are larger than the copper alkyne distances reported for copper–alkyne complexes[10,11] (1.87–2.00 Å) but similar to those found in the copper complex of **1** (2.46–2.57 Å).[1b] We also notice a lowering of the stretching frequencies found for the triple bonds in the Raman spectrum for [**7**·Cu]$^+$ as compared to **7**. A criterion for the preference of the alkyne units over the oxygen centers is the N–Cu–N angle of 170.6°.[12]

Table 1. Most relevant distances, angles, and wave numbers in the $Ag^+$, $Cu^+$, $Li^+$, $Na^+$, and $Cd^{2+}$ cryptates with **7**. The distances are given in Å and the angles in degrees.[12]

| Compound | [**7**•Cu]$^+$ | [**7**•Ag]$^+$ | [**7**•Li]$^+$ | [**7**•Na]$^+$ | [**7**•Cd]$^{2+}$ | **7** |
|---|---|---|---|---|---|---|
| N···N | 4.116 | 4.827 | 4.337 | 4.930 | 4.678 | 5.485 |
| N···M | 2.063 | 2.423 | 2.211 | 2.585 | 2.417 | |
| | 2.066 | 2.468 | 2.212 | 2.590 | 2.408 | |
| O···M | 3.227 | 2.639 | 2.080 | 2.389 | 2.409 | |
| | 3.634 | 2.716 | 2.095 | 2.412 | 2.459 | |
| π···M | 2.342 | 2.640 | 2.676 | 2.733 | 2.775 | |
| | 2.545 | 2.650 | 2.744 | 2.977 | 2.611 | |
| M···$ONO_2^-$ | | | | 2.425 | 2.263 | |
| N···M···N[10] | 170.6 | 198.5 | 202.6 | 215.4 | 208.4 | |
| $\tilde{\nu}$ C≡C[a] Raman | 2268 | | 2285 | 2284 | 2282 | 2293 |
| | 2230 | 2273 | | | | |
| | | | 2228 | 2225 | 2226 | 2227 |
| | 2203 | 2207 | | | | |

[a] $cm^{-1}$.

The larger silver ion prefers a coordination with N, O, and the triple bonds. The flexible ether chain in **7** has now changed its conformation in such a way that the oxygen centers point inside the cavity. The N···N distance is longer than in the copper complex (Table 1) and the N–Ag–N angle amounts to 198.5°.[12] The distance between the silver ion and the center of the triple bonds amounts to 2.64–2.65 Å. This value is longer than that reported for cyclic alkynes (2.33 Å)[10,13] and also longer than that reported for [**1**·Ag]$^+$ (2.44–2.51 Å). The N–Ag distances (2.42, 2.47 Å) are somewhat longer with regard to the value found for **1** (2.31 Å) but rather expanded compared to values reported for homoleptic two coordinated silver(I) amine complexes

 © 2006 Wiley-VCH Verlag GmbH & Co. KGaA, Weinheim 

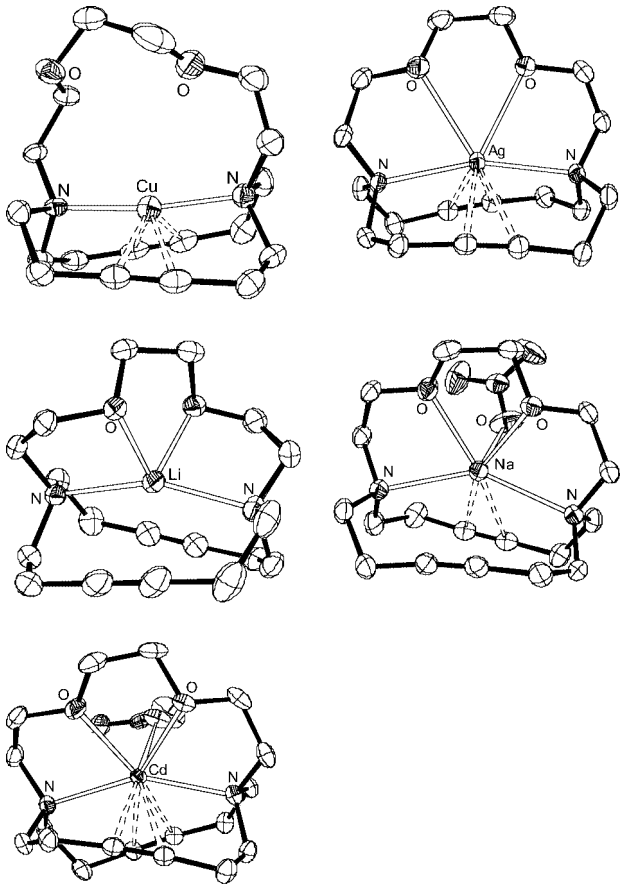


Figure 3. Molecular structures of the $Cu^+$, $Ag^+$, $Li^+$, $Na^+$, and $Cd^{2+}$ complexes of **7**. In the cases of the $Na^+$ and $Cd^{2+}$ complexes the coordinated nitrate anion is shown.

e.g. $Ag(NH_3)_2NO_3$ (2.12 Å).[14] The silver-alkyne interaction in [**7**·Ag]$^+$ also shows up in a lowering of the wave number of the stretching vibration of the triple bond (Table 1). The Ag–O–distance (2.64–2.72 Å) is close to that reported for other silver-ether complexes (average value 2.59 Å).[15] The complex [**7**·Ag]$^+$ is rather stable. We could not detect any precipitate of silver iodide when we reacted [**7**·Ag]$^+$ with iodide ions. Such an absence of precipitation was also reported for [**1**·Ag]$^+$ and silver salts of aza-bridged macrocycles.[16]

The lithium ion prefers to coordinate with the nitrogen and oxygen centers. This shows up in the short Li–O (2.09 Å) and Li–N (2.21 Å) distances and a N–Li–N angle of 202.6°. The measured Li–O and Li–N distances are close to those reported for lithium crown ether complexes (average value Li–O = 2.02 Å, Li–N = 2.07 Å).[15] We also do not find any significant change for the stretching vibration of the triple bond in [**7**·Li]$^+$. The sodium ion prefers a coordination sphere with six donor groups: The two ether oxygen atoms (Na–O = 2.39, 2.41 Å), the two nitrogen atoms (Na–N = 2.59 Å), one oxygen atom from the nitrate anion (Na–O = 2.43 Å) and one alkyne unit ($Na^+$ to the center of triple bond = 2.73 Å). This latter interaction hardly has any influence on the stretching vibration of the triple bond. The recorded Na–O and Na–N distances are close to those found in sodium crown ether complexes (average value Na–O = 2.47 Å, Na–N = 2.59 Å).[15] The even larger $Cd^{2+}$ ion adopts a coordination number of seven by interacting with all donor units. The N–Cd–N angle of 208.4° shows that the N,O coordination is preferred over the interaction with the triple bonds. The latter at most weakly influences the stretching vibration of the triple bonds (Table 1). The complex [**7**·Cd]$^{2+}$ shows a significant low field shift of the resonances for the $CH_2$ protons as compared to **7** by 0.2–0.4 ppm. Like in the sodium complex the metal in [**7**·Cd]$^{2+}$ coordinates with one oxygen center of the nitrate anion (Cd–O = 2.23 Å).

The reaction of a solution of **7** in methanol with $HgCl_2$ yielded first a colorless precipitate which was insoluble in all common solvents. In analogy to a protocol described by Pickardt and Kühn[17] we carefully added to an aqueous solution of $HgCl_2$ a solution of the ligand **7** in methanol in such a way that the two solutions formed two layers. After one month crystals appeared between the two phases. Unfortunately, the crystals were insoluble in common solvents. The mass spectrum revealed that we are dealing with an adduct of **7** with two equivalents of water, three mercury cations, and two chloride anions. The IR spectrum revealed two intensive peaks in the CO region. Fortunately, the isolated material, **11**, contained single crystals which allowed a diffraction experiment. In Figure 4 we show a side view and a view along the N···N axis of **11**. The molecule contains one central mercury atom bound to the two nitrogen centers, to two carbon atoms adjacent to the CO groups and to the two oxygen atoms of the ether bridge (Scheme 3). To the former sp centers, adjacent to the CO groups two further HgCl units are attached which point outwards. The distances between the central mercury atom and the ether oxygen atoms amount to 2.87 and 2.97 Å. These values are somewhat longer than that reported for the mean distance between $Hg^{2+}$ and ether (2.83 Å).[15] The Hg–N distances (2.61 and 2.62 Å) are also longer than the mean value reported in the literature (2.35 Å).[15] Of interest are the short bonds between both Hg centers and the carbon atoms in the α position to the CO groups. For the central mercury we find Hg–C distances of 2.22 and 2.17 Å. For the HgCl groups the C–Hg distances are even shorter (2.08 and 2.11 Å). We ascribe the longer C–Hg bond for the central metal to the donor effects of the oxygen and nitrogen atoms. The low stretching frequencies recorded for the CO groups (1601, 1551 $cm^{-1}$) point to a delocalization of the formal negative charge at the carbon atoms in the α positions to the CO groups. We find a distance between the central and the peripheral mercury atoms of 3.29 and 3.39 Å. This points to a $d^{10}$–$d^{10}$ interaction between the metals due to relativistic effects.[18]

Of special interest is the regioselectivity of the twofold oxymercuration of **7** to **11** which occurred under preservation of the $C_2$ axis of the molecule. We ascribe this observation to the twisted arrangement of the alkyne units in **7**. To rationalize the regioselectivity we assume that the inclusion of a $Hg^{2+}$ ion into the cavity slows down the interchange between the enantiomeric twist conformations of **7**

 © 2006 Wiley-VCH Verlag GmbH & Co. KGaA, Weinheim 

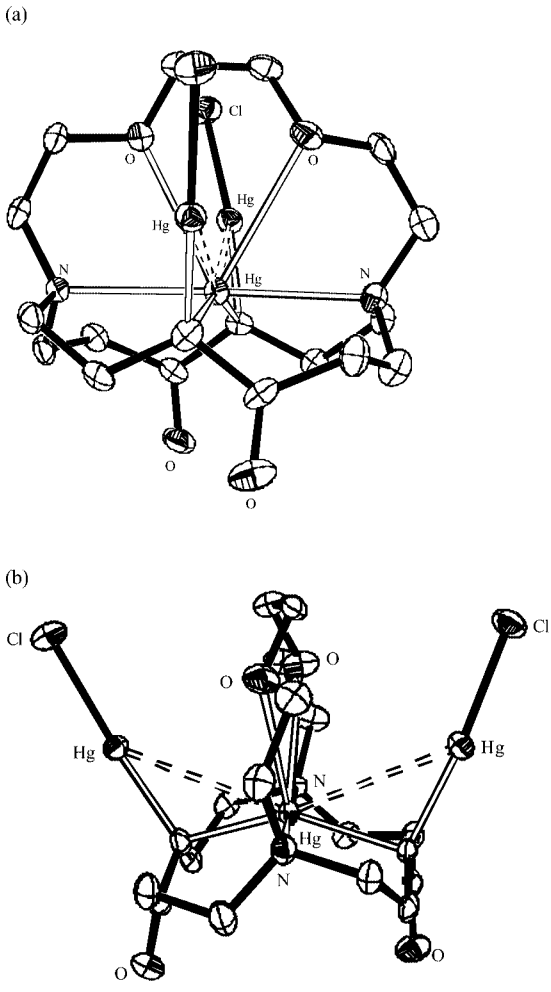


Figure 4. Molecular structure of the product **11** obtained by the reaction of **7** with $HgCl_2$ in the presence of water.

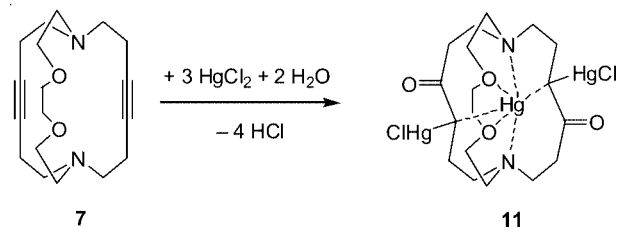


Scheme 3.

(Scheme 4). The coordination of the $Hg^{2+}$ with the ether bridge forces the metal closer to one sp center of one triple bond than to the other (**A**, **A***). Supported by water molecules an *endo*-mercuration starts (**B**) followed by the addition of water (**C**) and *exo*-mercuration of the vinyl alcohol to **D**. In connection with the proposed mechanism in Scheme 4 it is interesting to note that we found single crystals with both enantiomers of the product.

## Concluding Remarks

The replacement of one 3-hexyne unit in **1** by the 3,6-dioxaoctane unit gives the resulting cryptand **7** more flexibility and more coordination possibilities. The higher flexibility is also demonstrated by the oxidation of **7** to **10**. A look at the five structures in Figure 2 shows that the hard ions ($Li^+$, $Na^+$, and to some extent $Cd^{2+}$) prefer the complexation with the hard centers (O, N). The soft ion $Cu^+$ prefers the nitrogen centers and the triple bonds. The larger silver ion adopts a coordination number of six. Only in the cases of the $Cu^+$ and the $Ag^+$ complexes is the stretching vibration of the triple bonds altered significantly. In the cryptates shown in Figure 3 the ions are less shielded than in the cryptates of **1**, this is shown in the $Na^+$ and $Cd^{2+}$ salts where the corresponding anion is coordinated.

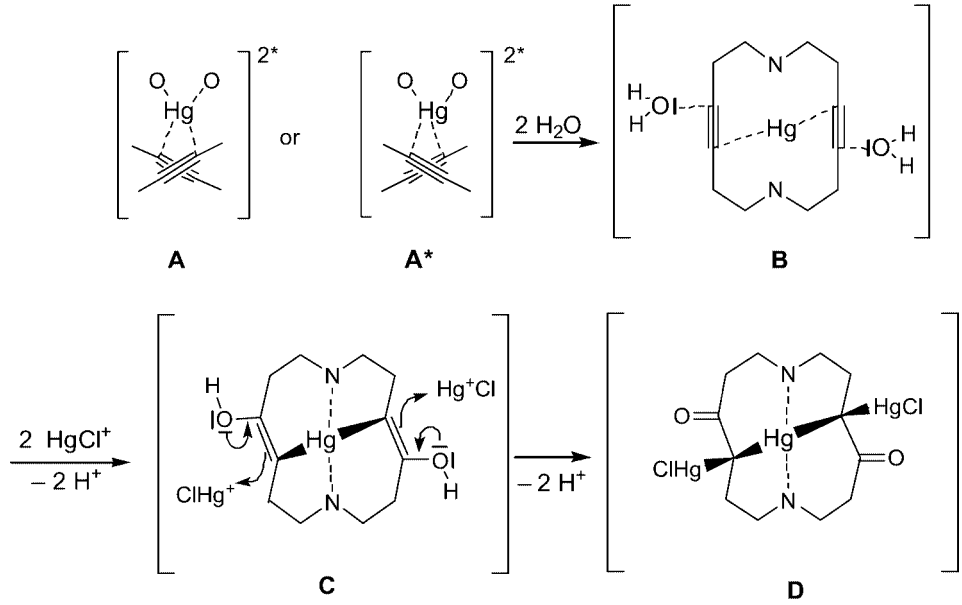


Scheme 4.

 © 2006 Wiley-VCH Verlag GmbH & Co. KGaA, Weinheim 

## Experimental Section

**General Methods:** All melting points are uncorrected. Elemental analyses were carried out by the Mikroanalytisches Laboratorium der Universität Heidelberg. UV/Vis absorption spectra were recorded with a Hewlett–Packard HP 8452A Diode-Array spectrometer, IR spectra were recorded with a Bruker Vector 22 FT-IR instrument. The NMR spectra were measured with a Bruker WH 300 or Avance 500 spectrometer ($^1$H NMR at 300 MHz or 500 MHz and $^{13}$C NMR at 75 or 125 MHz) using the solvent as an internal standard ($\delta$). FAB mass spectra refer to data from a JEOL JMS-700 instrument. As matrix for the FAB experiments *m*-nitrobenzyl alcohol was used. All reactions were carried out in dried glassware under argon using dried and oxygen-free solvents. Compound **8** was prepared according to literature procedure[5] and **9** as well as the inorganic salts were commercially available.

**X-ray Crystallographic Study:** Data were collected with a Bruker Smart CCD diffractometer at 200 K for **7**, **10**, **11**, [**7**·Cu]$^+$, [**7**·Ag]$^+$, [**7**·Na]$^+$ and with a Nonius CAD 4 diffractometer at 293 K for [**7**·Li]$^+$ and 223 K for [**7**·Cd]$^{2+}$. Mo-$K_\alpha$ radiation was used in all cases and the intensities were corrected for Lorentz, polarization, and absorption effects. The structures were solved by direct methods and refined against $F^2$ with a full-matrix least square algorithm by using the SHELXTL software package.[19] Relevant crystal and data collection parameters are given in Tables 2 and 3. Hydrogen atoms were refined isotropically for **7** and [**7**·Li]$^+$ and in all other cases they were considered at calculated positions and refined using appropriate riding models. In the case of **10**, **11**, [**7**·Li]$^+$, and [**7**·Cd]$^{2+}$ some solvent molecules or anions had to be treated as disordered, in [**7**·Cu]$^+$ disorder was observed in parts of the complex cation itself. On one side of the cage the three methylene groups next to the nitrogen atom occur in two alternative positions, also the ether bridge is partially affected by disorder. CCDC-277362 (for **7**), -277363 (for **10**), -277364 (for **11**), -277365 {for [**7**·Cu]($CF_3SO_3$)}, -277366 {for [**7**·Ag]($CF_3SO_3$)}, -277367 {for [**7**·Li]($CLO_4$)}, -277368 {for [**7**·Na]($NO_3$)}, and -277369 {for [**7**·Cd]($NO_3$)$_2$} contain the supplementary crystallographic data for this paper. These data can be obtained free of charge from The Cambridge Crystallographic Data Centre via www.ccdc.cam.ac.uk/data_request/cif.

**4,7-Dioxa-1,10-diazabicyclo[8.6.6]docosa-13,19-diyne (7):** To a suspension of finely ground dry potassium carbonate (16 g) in dry acetonitrile (500 mL) was added 1,6-dibromo-3-hexyne (**8**) (6.3 g, 26.2 mmol) and 1,8-diamino-3,6-dioxaoctane (**9**) (1.3 g, 8,3 mmol) and it was refluxed for 4 d. After cooling of the mixture the residual potassium carbonate was filtered off and the solvent was removed in vacuo. The raw material of the reaction was chromatographed on ALOX III using cyclohexane/ethyl acetate (1:1) as the solvent. The product was recrystallized from ethyl acetate to yield colorless crystals (1.1 g, 43%) with a m.p. of 68 °C. $^1$H NMR (500 MHz, $CD_3OD$): $\delta$ = 2.26 (m, 8 H, C$H_2$–C≡), 2.43–2.52 (m, 12 H, C$H_2$–N), 3.63 (m, 4 H, C$H_2$–O), 3.78 (s, 4 H, O–C$H_2$–C$H_2$–O) ppm. $^{13}$C NMR (125 MHz, $CD_3OD$): $\delta$ = 20.0 (*C*H$_2$–C≡), 55.7 (4, *C*H$_2$–N), 58.0 (2, *C*H$_2$–N), 71.5 (*C*H$_2$–O), 72.1 (O–*C*H$_2$–*C*H$_2$–O), 80.5 (*C*≡C) ppm. IR (KBr): $\tilde{\nu}$ = 2937, 2903, 2803, 2740, 1459, 1334, 1291 cm$^{-1}$. Raman (neat): $\tilde{\nu}$ = 2957, 2903, 2821, 2292, 2227, 1457, 1419 cm$^{-1}$. $C_{18}H_{28}N_2O_2$ (304.43): calcd. C 71.02, H 9.27, N 9.20; found C 71.23, H 9.21, N 9.27.

**4,7-Dioxa-1,10-diazabicyclo[8.6.6]docosa-13,19-diyne *N*,*N*′-Dioxide (10):** To a solution of **7** (37 mg, 0.1 mmol) in ethanol (5 mL) was added hydrogen peroxide (1 mL, 30%) solution in water at room temperature. After stirring for 6 d a colorless precipitate was found. After separation and recrystallization from methanol/water colorless crystals were obtained (23 mg, 60%), m.p. 145 °C (decomp). $^1$H NMR (300 MHz, $CD_3OD$): $\delta$ = 2.79 (m, 8 H, C$H_2$–C≡), 3.61–3.93 (m, 16 H, C$H_2$), 3.65 (s, 4 H, O–C$H_2$–C$H_2$–O) ppm. $^{13}$C NMR (75 MHz, $CD_3OD$): $\delta$ = 15.8 (*C*H$_2$–C≡), 65.9 (N–*C*H$_2$–*C*H$_2$–C≡), 66.1 (N–*C*H$_2$–*C*H$_2$–O), 71.5 (*C*H$_2$–O), 81.2 (*C*≡*C*) ppm. IR (KBr): $\tilde{\nu}$ = 2924, 1435, 1351, 1246 cm$^{-1}$. HRMS (FAB$^+$) $C_{18}H_{29}N_2O_4$ calcd. 337.2127; found 337.2132.

**4,7-Dioxa-1,10-diazabicyclo[8.6.6]docosa-13,19-diyne (7) Complex with Silver Triflate:** In a Schlenk tube a solution of **7** (50 mg, 0.16 mmol) and silver(I) triflate (43 mg, 0.17 mmol) in dry dichloromethane (6 mL) was stirred for 3 h at room temperature under argon. The silver triflate complex (90 mg, 100%) of **7** was isolated in quantitative yield as a colorless powder, m.p. 165 °C (decomp.). $^1$H NMR (300 MHz, $CDCl_3$): $\delta$ = 2.46–2.59 (m, 16 H, N–C$H_2$–C$H_2$–C≡), 2.69 (t, $^3J$ = 4.8 Hz, 4 H, C$H_2$–N), 3.56 (t, $^3J$ = 4.8 Hz, 4 H, N–C$H_2$–C$H_2$–O), 3.66 (s, 4 H, O–C$H_2$–C$H_2$–O) ppm. $^{13}$C NMR (75 MHz, $CDCl_3$): $\delta$ = 17.9 (*C*H$_2$–C≡), 53.7 (N–*C*H$_2$–CH$_2$–C≡), 55.2 (*C*H$_2$–N), 66.5 (N–CH$_2$–*C*H$_2$–O), 69.8 (O–*C*H$_2$–*C*H$_2$–O), 78.2 (C≡C) ppm. IR (KBr): $\tilde{\nu}$ = 2963, 2904, 1453, 1363 cm$^{-1}$. Raman (neat): $\tilde{\nu}$ = 2910, 2859, 2273, 2207, 1452, 1335 cm$^{-1}$. HRMS (FAB$^+$) $C_{18}H_{28}{}^{109}AgN_2O_2$: calcd. 413.1198, found: 413.1221. $C_{18}H_{28}{}^{107}AgN_2O_2$: calcd. 411.1201, found: 411.1212. $C_{19}H_{28}AgF_3N_2O_5S$ (561.37): calcd. C 40.65, H 5.03; found C 40.65, H 5.33.

**4,7-Dioxa-1,10-diazabicyclo[8.6.6]docosa-13,19-diyne (7) Complex with Cu$^I$ Triflate:** A solution of **7** (30 mg, 0.1 mmol) and the benzene complex of Cu$^I$ triflate (27 mg, 0.1 mmol) in dry dichloromethane (10 mL) was stirred under argon for 3 h at room temperature. Filtration of the precipitate yielded a colorless powder (43 mg, 85%), m.p. 127 °C (decomp.). $^1$H NMR (500 MHz, $CD_2Cl_2$): $\delta$ = 2.66 (t, $^3J$ = 5.4 Hz, 8 H, C$H_2$–C≡), 2.73–2.84 (m, 12 H, C$H_2$–N), 3.71 (s, 4 H, O–C$H_2$–C$H_2$–O), 3.83 (t, $^3J$ = 5.0 Hz, 4 H, C$H_2$–O) ppm. $^{13}$C NMR (125 MHz, $CD_2Cl_2$): $\delta$ = 18.3 (*C*H$_2$–C≡), 55.6 (N–*C*H$_2$–CH$_2$–C≡), 55.7 (*C*H$_2$–N), 68.2 (*C*H$_2$–O), 69.7 (O–*C*H$_2$–*C*H$_2$–O), 80.7 (C≡C) ppm. IR (KBr): $\tilde{\nu}$ = 3108, 2962, 2870, 1453 cm$^{-1}$. Raman (neat): $\tilde{\nu}$ = 2922, 2874, 2268, 2229, 2202, 1454 cm$^{-1}$. HRMS (FAB$^+$) $C_{18}H_{28}{}^{65}CuN_2O_2$: calcd. 369.1429; found 369.1419. $C_{18}H_{28}{}^{63}CuN_2O_2$: calcd. 367.1446; found 367.1430.

**4,7-Dioxa-1,10-diazabicyclo[8.6.6]docosa-13,19-diyne (7) Complex with Lithium Perchlorate:** A solution of **7** (50 mg, 0.16 mmol) and lithium perchlorate (15 mg) in dry methanol (5 mL) was stirred for 3 h at room temperature. After removal of the solvent the residue was washed with toluene to yield **7**·$LiClO_4$ (42 mg, 63%) as colorless crystals, m.p. 160 °C (decomp.). $^1$H NMR (300 MHz, $CD_3OD$): $\delta$ = 2.33 (m, 8 H, C$H_2$–C≡), 2.51 (m, 8 H, N–C$H_2$–CH$_2$–C≡), 2.56 (t, $^3J$ = 5.2 Hz, 4 H, N–C$H_2$–CH$_2$–O), 3.66 (t, $^3J$ = 5.2 Hz, 4 H, N–CH$_2$–C$H_2$–O), 3.78 (s, 4 H, O–C$H_2$–C$H_2$–O) ppm. $^{13}$C NMR (75 MHz, $CD_3OD$): $\delta$ = 19.8 (*C*H$_2$–C≡), 55.5 (N–*C*H$_2$–CH$_2$–C≡), 57.4 (N–*C*H$_2$–CH$_2$–O), 70.6 (N–CH$_2$–*C*H$_2$–O), 71.2 (O–*C*H$_2$–*C*H$_2$–O), 80.7 (C≡C) ppm. IR (KBr): $\tilde{\nu}$ = 2930, 2848, 2020, 1464, 1350 cm$^{-1}$. Raman (neat): $\tilde{\nu}$ = 2931, 2861, 2285, 2228, 1445, 1342 cm$^{-1}$. HRMS (FAB$^+$) $C_{18}H_{26}LiN_2O_2$: calcd. 311.2311; found 311.2305. $C_{18}H_{28}ClLiN_2O_6$ (410.82): calcd. C 52.61, H 6.87, N 6.82; found C 52.44, H 7.19, N 6.70.

**4,7-Dioxa-1,10-diazabicyclo[8.6.6]docosa-13,19-diyne (7) Complex with Sodium Nitrate:** A solution of **7** (50 mg, 0.16 mmol) and $NaNO_3$ (14 mg, 0.17 mmol) in dry methanol (5 mL) was stirred at room temperature for 12 h. After removal of the solvent in vacuo the residue was washed with toluene to yield **7**·$NaNO_3$ (42 mg, 66%) as colorless crystals, m.p. 165 °C (decomp.). $^1$H NMR

 © 2006 Wiley-VCH Verlag GmbH & Co. KGaA, Weinheim 

Table 2. Crystallographic data and details of the refinement procedure of **7**, **10**, and **11**.

| | **7** | **10** | **11** |
|---|---|---|---|
| Empirical formula | $C_{18}H_{28}N_2O_2$ | $C_{18}H_{38}N_2O_9$ | $C_{18}H_{28}Cl_2Hg_3N_2O_5$·solvent |
| Formula mass [g/mol] | 304.42 | 426.50 | 1034.12 |
| Crystal size [mm] | 0.44×0.32×0.22 | 0.53×0.19×0.03 | 0.40×0.21×0.05 |
| Crystal shape | irregular | polyhedron | polyhedron |
| Crystal system | triclinic | triclinic | orthorhombic |
| Space groups | $P\bar{1}$ | $P\bar{1}$ | $P2_12_12$ |
| $a$ [Å] | 7.5002(4) | 8.7957(7) | 14.7875(3) |
| $b$ [Å] | 7.9180(4) | 10.6449(9) | 17.1697(4) |
| $c$ [Å] | 15.0480(7) | 13.343(1) | 9.5715(2) |
| $\alpha$ [°] | 83.627(1) | 109.444(1) | 90.00 |
| $\beta$ [°] | 82.697(1) | 108.163(1) | 90.00 |
| $\gamma$ [°] | 79.153(1) | 94.862(1) | 90.00 |
| $V$ [Å$^3$] | 867.08(8) | 1094.3(2) | 2430.17(9) |
| $D_{calcd.}$ [g/cm$^3$] | 1.166 | 1.294 | 2.826 |
| $Z$ | 2 | 2 | 4 |
| $\mu$ [mm$^{-1}$] | 0.076 | 0.103 | 19.157 |
| $\Theta_{min}/\Theta_{max}$ | 1.37/25.49 | 1.74/25.55 | 1.82/27.49 |
| $T_{min}/T_{max}$ | 0.77/0.97 | 0.83/1.00 | 0.17/0.46 |
| Reflections collected | 6530 | 8210 | 25114 |
| Reflections unique | 2910 | 3657 | 5586 |
| Refleections observed | 2504 | 2605 | 5376 |
| Parameter | 311 | 302 | 282 |
| $R(F)$ | 0.034 | 0.054 | 0.030 |
| $R\omega$ ($F^2$) | 0.084 | 0.134 | 0.076 |
| $S$ (GOF) on $F^2$ | 1.05 | 1.04 | 1.10 |
| $\Delta\rho_{max}$ [e·Å$^{-3}$]/$\Delta\rho_{min}$ [e·Å$^{-3}$] | 0.15/–0.18 | 1.24/–0.20 | 1.69/–1.89 |

Table 3. Crystallographic data and details of the refinement procedure of the complexes of **7** with $Cu(CF_3SO_3)$, $Ag(CF_3SO_3)$, $LiClO_4$, $NaNO_3$, and $Cd(NO_3)_2$.

| | **7**·$Cu(CF_3SO_3)$ | **7**·$Ag(CF_3SO_3)$ | **7**·$LiClO_4$ | **7**·$NaNO_3$ | **7**·$Cd(NO_3)_2$ |
|---|---|---|---|---|---|
| Empirical formula | $C_{19}H_{28}CuF_3N_2O_5S$ | $C_{19}H_{28}AgF_3N_2O_5S$ | $C_{18}H_{28}LiN_2O_2$·$ClO_4$ | $C_{18}H_{30}NaN_3O_6$ | $C_{18}H_{28}CdN_4O_9$ |
| Formula mass [g/mol] | 517.03 | 561.36 | 410.81 | 407.44 | 556.8 |
| Crystal size [mm] | 0.27×0.12×0.08 | 0.40×0.14×0.06 | 0.40×0.30×0.30 | 0.47×0.30×0.13 | 0.40×0.30×0.01 |
| Crystal shape | polyhedron | polyhedron | needle | polyhedron | polyhedron |
| Crystal system | triclinic | triclinic | monoclinic | orthorhombic | monoclinic |
| Space groups | $P\bar{1}$ | $P\bar{1}$ | $P2_1/n$ | $Pbca$ | $P2_1/n$ |
| $a$ [Å] | 8.3241(2) | 8.1915(2) | 10.296(2) | 12.7864(3) | 7.710(3) |
| $b$ [Å] | 10.3173(2) | 11.3557(4) | 15.813(4) | 16.2833(2) | 20.505(5) |
| $c$ [Å] | 12.9635(1) | 12.6963(4) | 13.143(4) | 19.4195(4) | 14.290(4) |
| $\alpha$ [°] | 84.318(1) | 107.740(1) | 108.67(2) | 90.00 | 90.00 |
| $\beta$ [°] | 85.480(1) | 99.277(1) | 85.480(1) | 90.00 | 101.88(3) |
| $\gamma$ [°] | 84.264(1) | 91.324(1) | 90.00 | 90.00 | 90.00 |
| $V$ [Å$^3$] | 1099.64(3) | 1106.86(6) | 2027.2(9) | 4043.2(1) | 2211(1) |
| $D_{calcd.}$ [g/cm$^3$] | 1.56 | 1.68 | 1.35 | 1.34 | 1.67 |
| $Z$ | 2 | 2 | 4 | 8 | 4 |
| $\mu$ [mm$^{-1}$] | 1.147 | 1.063 | 0.23 | 0.118 | 1.04 |
| $\Theta_{min}/\Theta_{max}$ | 1.58/25.55 | 1.71/25.53 | 2.1/28.0 | 2.10/25.50 | 2.5/28.0 |
| $T_{min}/T_{max}$ | 0.81/0.93 | 0.77/0.94 | 0.93/0.96 | 0.82/0.92 | 0.59/0.76 |
| Reflections collected | 8325 | 8352 | 5144 | 28230 | 5698 |
| Reflections unique | 3698 | 3708 | 4886 | 3585 | 5319 |
| Reflections observed | 2814 | 3434 | 2883 | 2693 | 4226 |
| Parameter | 327 | 280 | 398 | 261 | 337 |
| GOF ($F^2$) | 1.02 | 1.05 | 1.03 | 1.03 | 1.02 |
| $R(F)$ | 0.040 | 0.021 | 0.049 | 0.033 | 0.037 |
| $R\omega$ ($F^2$) | 0.096 | 0.052 | 0.133 | 0.083 | 0.083 |
| $\Delta\rho_{max}$ [e·Å$^{-3}$]/$\Delta\rho_{min}$ [e·Å$^{-3}$] | 0.45/–0.41 | 0.53/–0.44 | 0.41/–0.32 | 0.33/–0.20 | 0.51/–0.63 |

(500 MHz, $CD_3OD$): $\delta$ = 2.51 (m, 16 H, N–C$H_2$–C$H_2$–C≡), 2.70 (t, $^3J$ = 5.1 Hz, 4 H, N–C$H_2$), 3.67 (t, $^3J$ = 5.1 Hz, 4 H, C$H_2$–O), 3.70 (s, 4 H, O–C$H_2$–C$H_2$–O) ppm. $^{13}$C NMR (125 MHz, $CD_3OD$): $\delta$ = 18.8 (*C*H$_2$–C≡), 54.0 (N–*C*H$_2$–CH$_2$–C≡), 57.4 (N–*C*H$_2$–CH$_2$–O), 67.7 (N–CH$_2$–*C*H$_2$–O), 70.0 (O–*C*H$_2$–CH$_2$–O), 80.7 (C≡C) ppm. IR (KBr): $\tilde{\nu}$ = 2963, 2914, 2877, 2835, 1456 cm$^{-1}$. Raman (neat): $\tilde{\nu}$ = 2965, 2918, 2883, 2838, 2284, 2225, 1456 cm$^{-1}$. HRMS (FAB$^+$) $C_{18}H_{28}NaN_2O_2$: calcd. 327.2048; found 327.2051. $C_{18}H_{28}NaN_3O_5$ (389.43): calcd. C 55.52, H 7.25, N 10.79; found C 55.23, H 7.42, N 10.42.

 © 2006 Wiley-VCH Verlag GmbH & Co. KGaA, Weinheim 

**4,7-Dioxa-1,10-diazabicyclo[8.6.6]docosa-13,19-diyne (7) Complex with Cadmium Nitrate:** A solution of **7** (15 mg, 0.05 mmol) and $Cd(NO_3)_2 \cdot 4H_2O$ (15 mg, 0.05 mmol) in methanol (6 mL) was stirred for 24 h at room temperature. After removal of the solvent a colorless crystalline material (27 mg, 100%) could be isolated which could be recrystallized from methanol and dichloromethane, m.p. 130 °C (decomp.). $^1$H NMR (500 MHz, $CD_3OD$): $\delta$ = 2.83 (m, 16 H, N–C$H_2$–C$H_2$–C≡), 3.12 (s, 4 H, N–C$H_2$), 3.89 (m, 4 H, C$H_2$–O), 3.92 (s, 4 H, O–C$H_2$–C$H_2$–O) ppm. $^{13}$C NMR (125 MHz, $CD_3OD$): $\delta$ = 18.8 (*C*$H_2$–C≡), 53.5 (N–*C*$H_2$–CH$_2$–C≡), 58.4 (N–*C*$H_2$–CH$_2$–O), 66.6 (N–CH$_2$–*C*$H_2$–O), 69.5 (O–*C*$H_2$–*C*$H_2$–O), 84.0 (C≡C) ppm. IR (KBr): $\tilde{\nu}$ = 2931, 2887, 2362, 1664 cm$^{-1}$. Raman (neat): $\tilde{\nu}$ = 2925, 2827, 2282, 2226, 1457 cm$^{-1}$. HRMS (FAB$^+$) $C_{18}H_{28}{}^{114}CdN_3O_5$: calcd. 480.1063; found 480.1080. $C_{18}H_{28}{}^{113}CdN_3O_5$: calcd. 479.1073; found 479.1095. $C_{18}H_{28}{}^{112}CdN_3O_5$: calcd. 478.1056; found 478.1082. Elemental analysis of the dichloride $C_{18}H_{28}CdCl_2N_2O_2$ (487.74): calcd. C 44.33, H 5.79, N 5.74; found C 44.19, H 6.01, N 5.83.

**Reaction of 4,7-Dioxa-1,10-diazabicyclo[8.6.6]docosa-13,19-diyne (7) with $HgCl_2$ to Yield 11:** To an aqueous solution of $HgCl_2$ (13 mg, 0.05 mmol) in water (3 mL) was added a solution of **7** (15 mg, 0.05 mmol) in methanol (3 mL) in such a way that the two solutions did not mix. After one month at room temperature we isolated colorless crystals (15 mg, 91%) which were insoluble in all common solvents, m.p. 158 °C. MS (FAB$^+$): *m*/*z* (%) = 1032 (23) [M + Na]$^+$, 1010 (84) [M + H]$^+$. The calculated isotopic pattern was identical with the obtained one. IR (KBr): $\tilde{\nu}$ = 2832, 1601, 1551, 1455, 1332, 1248, 1179, 1098, 1018 cm$^{-1}$.

## Acknowledgments

The work was supported by the Deutsche Forschungsgemeinschaft, the Fonds der Chemischen Industrie, and the State of Baden-Württemberg.

[1] a) V. Wolfart, R. Gleiter, H. Irngartinger, T. Oeser, C. Krieger, *Eur. J. Org. Chem.* **1998**, 2803–2809; b) A. Kunze, R. Gleiter, F. Rominger, *Chem. Commun.* **1999**, 171–172.
[2] R. Koschabek, R. Gleiter, F. Rominger, *Eur. J. Inorg. Chem.* **2006**, 609–620; preceding article.
[3] a) R. G. Pearson, *J. Am. Chem. Soc.* **1963**, *85*, 3533–3539; b) R. G. Pearson, J. Songstad, *J. Am. Chem. Soc.* **1967**, *89*, 1827–1836; c) R. G. Pearson, *Inorg. Chem. Acta* **1995**, *240*, 93–98.
[4] a) R. G. Pearson, *Hard and Soft Acids and Bases*, Dowden, Hutchinson & Ross, Stroudsburg, **1973**; b) T. L. Ho, *Chem. Rev.* **1975**, *75*, 1–20.
[5] M. Brudermüller, H. Musso, A. Wagner, *Chem. Ber.* **1988**, *121*, 2239–2244.
[6] R. N. Greene, *Tetrahedron Lett.* **1972**, *18*, 1793–1796.
[7] B. Dietrich, P. Viont, J. M. Lehn, *Macrocyclic Chemistry*, VCH, Weinheim, **1993**.
[8] H. E. Simmons, C. H. Park, *J. Am. Chem. Soc.* **1968**, *90*, 2428–2429; C. H. Park, H. E. Simmons, *J. Am. Chem. Soc.* **1968**, *90*, 2429–2431.
[9] R. W. Alder, S. P. East, *Chem. Rev.* **1996**, *96*, 2097–2111 and references cited therein.
[10] R. Gleiter, M. Karcher, D. Kratz, M. L. Ziegler, B. Nuber, *Chem. Ber.* **1990**, *123*, 1461–1468.
[11] G. Gröger, U. Behrens, F. Olbrich, *Organometallics* **2000**, *19*, 3354–3360.
[12] For comparison with the other structures we define the N-metal–N angle as greater than 180° if the metal deviates from the N···N axis in the direction of the ether bridge and smaller than 180° if it deviates towards the alkyne units.
[13] P. Schulte, U. Behrens, *J. Organomet. Chem.* **1998**, *563*, 235–249.
[14] T. Yamaguchi, O. Lindquist, *Acta Chem. Scand.* **1983**, *A37*, 685–689.
[15] F. H. Allen, *Acta Crystallogr., Sect. B* **2002**, *58*, 380–388.
[16] H. Takomura, N. Kon, K. Tani, K. Takehara, J. Kimoto, T. Shinmyozu, T. Inazu, *J. Chem. Soc., Perkin Trans. 1* **1997**, 239–246.
[17] J. Pickardt, B. Kühn, *Z. Naturforsch.* **1994**, *49*, 1031–1035.
[18] P. Pyykkö, *Chem. Rev.* **1997**, *97*, 597–636 and references cited therein.
[19] G. M. Sheldrick, *SHELXTL*, Bruker Analytical X-ray Division, Madison, Wisconsin, **1997**.

Received: July 29, 2005
Published Online: December 13, 2005

 © 2006 Wiley-VCH Verlag GmbH & Co. KGaA, Weinheim 

DOI: 10.1002/ejic.200500698

# Structural, Electrochemical, and Theoretical Investigations of New Thio- and Selenoether Complexes of Molybdenum and Tungsten

Xiaoli Ma,[a] Kerstin Starke,[a] Carola Schulzke,*[a] Hans-Georg Schmidt,[a] and Mathias Noltemeyer[a]

**Keywords:** Bioinorganic chemistry / Molybdenum / Tungsten / Ligand effects / Redox chemistry

Molybdenum and tungsten complexes with tridentate bis-anionic ligands ($^{-}OC_2H_4XC_2H_4O^{-}$, X = S, Se) were synthesized and analyzed electrochemically. Crystal structures of $[\{MoO_2[O(CH_2)_2S(CH_2)_2O]\}_2]$ and $[\{WO_2[O(CH_2)_2S(CH_2)_2O]\}_3]$ were obtained. For these two complexes as well as for the virtual molybdenum trimer and the tungsten dimer, DFT calculations were performed in order to better understand the formation of two significantly different complexes for molybdenum and tungsten with the same ligand and by the same preparation method. The compound $WO_2Cl_2[MeS(CH_2)_2SMe]$ was synthesized and characterized by crystal structure analysis. A structural and electrochemical comparison of this compound with the recently published analogous molybdenum compound and the dme analogs of molybdenum and tungsten were undertaken. All these data were used to evaluate the structural and electronic influences of replacing molybdenum by tungsten and of varying the ligand atoms (O/S/Se) from the point of view of the different coordination spheres of the molybdopterin-dependent oxygen-atom-transfer enzymes.
(© Wiley-VCH Verlag GmbH & Co. KGaA, 69451 Weinheim, Germany, 2006)

## Introduction

Molybdenum as well as tungsten can be found at the active sites of the molybdopterin-containing oxygen-atom-transfer enzymes (OATs),[1] which catalyze oxygen transfer by two-electron redox reactions. This is not surprising because of the chemical similarity of the two metals. The distribution of the metals is quite interesting; molybdenum is found mainly in mesophilic organisms while tungsten is found mainly in thermophilic and hyperthermophilic microorganisms, and it is not known until today whether this distribution was developed for reasons of supply,[2,3] stability,[2,4] or reactivity[5] (i.e. redox potential). Therefore, the comparison of the characteristics of corresponding molybdenum and tungsten compounds remains a vital field of research.

Another interesting diversity of these enzymes is that, in the DMSO reductase family[6] (molybdenum enzymes with two molybdopterin ligands), the metal is bound to the peptide moiety through either serine (O),[7] cysteine (S),[8] selenocysteine (Se),[9] or aspartate (O, mono- or bidentate).[10] The amino acid ligands are supposed to play a role in stabilizing the enzyme–substrate complexes. It is still not known whether the different types of amino acid ligands are used purposefully or merely accidentally. The coordination of selenocysteine as well as the coordination of sulfur atoms to tungsten were also established, although far fewer structures of tungsten-containing OATs are available.[11,12]

High-valent metal complexes with thioether or selenoether ligands that represent hard–soft metal–ligand combinations are relatively rare mainly because these compounds are rather unstable.[13]

Even though molybdenum(VI) and tungsten(VI) can be considered as moderately hard, only a handful of thioether or selenoether complexes of these metals are known.[14–17]

In spite of the assumption that these kinds of complexes with $Mo^{VI}$ and $W^{VI}$ may not be easy to prepare and handle, we tried to synthesize and characterize a small variety of these compounds with additional alkoxy functions at the ligands for enhanced stability. In the synthesis we focused on the simple replacement of acetylacetonate ligands in $MO_2(acac)_2$ (M = Mo, W) by alkali salts of alkoxylates containing a thio- or selenoether function. We had two reasons for this: (i) In this way we would obtain complexes that mimic the active sites of the OATs where the coordination sphere of the metal consists only of oxygen and sulfur or selenium, respectively, and where one oxo ligand is present with an oxidation state of +6 for the metal. (ii) We would also obtain complexes that enable us to compare the influences of molybdenum versus tungsten and sulfur versus selenium with regard to their redox properties. Although in the enzymes the sulfur atom is bound as the thiolate or sulfido ligand and the selenium as the selenate ligand, the investigation of the ether variants of these ligand atoms could give some insight into their influence. The focus here

[a] Institut f. Anorganische Chemie, Universität Göttingen, Tammannstr. 4, 37077 Göttingen, Germany
Fax: +49-551-393373
E-mail: carola.schulzke@chem.uni-goettingen.de
Supporting information for this article is available on the WWW under http://www.eurjic.org or from the author.

 © 2006 Wiley-VCH Verlag GmbH & Co. KGaA, Weinheim 

was to evaluate atom-dependent structural and redox potential changes that might offer a clue as to whether the different types of OATs having different coordinated amino acids, were developed for fine tuning of the redox potential, for their structural influence, or just by chance.

We also synthesized the compound $WO_2Cl_2[MeS(CH_2)_2SMe]$, which is analogous to a recently published molybdenum compound.[14] The compounds $MO_2Cl_2(dme)$ are well-established for both metals.[18,19] Therefore, with this new compound a thorough structural and electrochemical investigation of these compounds and a comparison between oxygen and sulfur coordination as well as a comparison between molybdenum and tungsten compounds could be undertaken. The results are presented here.

## Results and Discussion

### Synthesis and Structural Analysis

$WO_2Cl_2[MeS(CH_2)_2SMe]$ (**1**) was synthesized by an analogous method to the published preparation of $MoO_2Cl_2[MeS(CH_2)_2SMe]$[14] (Scheme 1). The starting material ($WO_2Cl_2$) was prepared in situ from $WOCl_4$.

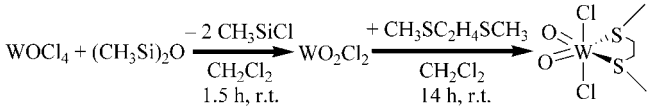


Scheme 1. Preparation of $WO_2Cl_2(CH_3SC_2H_4SCH_3)$ (**1**).

The structures of $MoO_2Cl_2[MeS(CH_2)_2SMe]$[14] and $WO_2Cl_2[MeS(CH_2)_2SMe]$ (**1**) (see Figure 1) are almost identical, and the largest differences occur for the metal–chlorine bond length (0.05 Å) and the O=M=O angle (1°) (see Table 1). Both compounds crystallize in the same crystal system (hexagonal) and space group ($P6_1$).

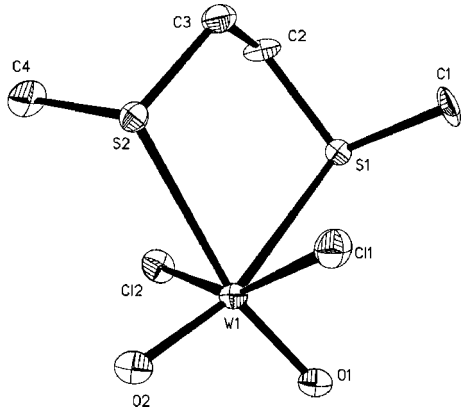


Figure 1. View of the structure of $WO_2Cl_2[MeS(CH_2)_2SMe]$ (**1**) (with numbering Scheme). Hydrogen atoms are not shown. Ellipsoids are drawn at 50% probability.

This is also true for the compounds $MoO_2Cl_2(dme)$[18] and $WO_2Cl_2(dme)$,[19] where the largest difference for a bond length is that for the M–O(ether) bond of 0.04 Å, and the difference for the O(ether)–M–O(ether) angle is 0.4°, which is the largest difference for an angle. Nevertheless, it has to be noted that the value for the Cl–Mo–Cl angle is not mentioned in the respective publication.[18] Again, both compounds crystallize in the same crystal system (monoclinic) and space group ($P2_1/n$).

The differences observed as a result of a comparison of ether and thioether ligands are of course larger, but only for those values that are derived directly from the different radii of the oxygen and sulfur atoms. The difference in the metal–ether/thioether bond is 0.49 Å for the molybdenum complexes and 0.50 Å for the tungsten complexes. The values for the O/S–M–O/S angles differ by 6.5° for the molybdenum and by 6.9° for the tungsten compound, where the angles for the thioether ligands are wider. All other distances and angles involving the metal center are only slightly influenced; the largest difference for a bond length was 0.05 Å for the Mo–Cl bond and the largest difference for an angle was 2.5° for the Cl–W–Cl angle.

This is an indication that the electronic influence of replacing oxygen ligand atoms by sulfur ligand atoms is only very small. Otherwise we would have observed larger differences, especially in the parameters for the ligand atoms that are in a *trans* position to the ether/thioether functions (oxo ligands in all four cases).

The compounds $[\{MoO_2[O(CH_2)_2S(CH_2)_2O]\}_2]$ (**2**), $[\{WO_2[O(CH_2)_2S(CH_2)_2O]\}_3]$ (**3**), and $[\{WO_2[O(CH_2)_2Se(CH_2)_2O]\}_n]$ (**4**) were all prepared by the same method (Scheme 2). The ligand and the $MO_2(acac)_2$ precursor were combined in a $CH_2Cl_2$ solution, stirred at room temperature for one to two days, and filtered. The compounds were isolated from the filtrate by crystallization or drying in vacuo. The yields range from a rather good 60% for the tungsten selenoether (**4**) compound (obtained by drying) to only 32% for the tungsten thioether compound (**3**). Because we were unable to obtain crystals of the tungsten selenium compound, $^{77}Se$ NMR spectroscopy was performed on the complex ($\delta$ = 100.22 ppm) as well as on the ligand ($\delta$ = 68.23 ppm), in addition to the usual characterization methods. In both spectra, we observed only one signal that was shifted to higher frequencies/lower field in the complex, which indicates that a metal–selenium bond was indeed formed.[20]

Suitable crystals of the molybdenum and tungsten thioether compounds were analyzed by X-ray crystallography with quite interesting results (see Figure 2 and Figure 3).

The molybdenum complex with the thioether ligand has a dimeric structure in which the two molybdenum atoms are bridged by one alkoxylate function of each of the two thioether ligands. The tungsten, on the other hand, forms a trimeric structure in which one of the former oxo ligands of each metal bridges two tungsten atoms, forming a six-membered ring. In both structures, the metal achieves a slightly distorted octahedral coordination geometry through the two different kinds of aggregation, although the molybdenum is explicitly only bound to five ligand atoms with rather long metal–sulfur distances. Instead of the usual distance between the metal (molybdenum or tungsten) and sulfur atoms of a thioether ligand, which is in the range of 2.45 to 2.77 Å,[14,21] we found distances of 2.93

 © 2006 Wiley-VCH Verlag GmbH & Co. KGaA, Weinheim 

Table 1. Selected bond lengths and angles for the molybdenum and tungsten complexes with bidentate ether and thioether ligands.

| | $WO_2Cl_2(MeSC_2H_4SMe)$ (**1**) | $MoO_2Cl_2(MeSC_2H_4SMe)$[a] | $WO_2Cl_2(dme)$[b] | $MoO_2Cl_2(dme)$[c] |
|---|---|---|---|---|
| M=O [Å] | 1.716 | 1.691 | 1.690 | 1.667 |
| | 1.716 | 1.699 | 1.690 | 1.673 |
| M–Cl [Å] | 2.333 | 2.345 | 2.344 | 2.347 |
| | 2.337 | 2.385 | 2.344 | 2.340 |
| M–O/S [Å] | 2.748 | 2.759 | 2.253 | 2.289 |
| | 2.752 | 2.771 | 2.292 | 2.281 |
| O=M=O [°] | 105.3 | 106.3 | 105.1 | 105.0 |
| O/S–M–O/S [°] | 77.4 | 77.3 | 70.5 | 70.9 |
| Cl–M–Cl [°] | 155.1 | 154.4 | 157.6 | – |

[a] Ref.[14] [b] Ref.[19] [c] Ref.[18]

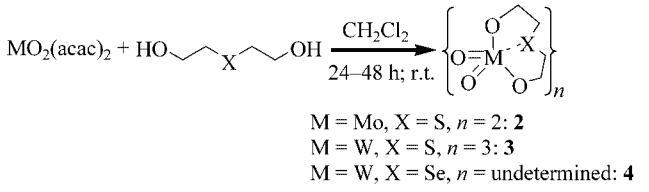


M = Mo, X = S, *n* = 2: **2**
M = W, X = S, *n* = 3: **3**
M = W, X = Se, *n* = undetermined: **4**

Scheme 2. Preparation of $[\{MoO_2[O(CH_2)_2S(CH_2)_2O]\}_2]$ (**2**), $[\{WO_2[O(CH_2)_2S(CH_2)_2O]\}_3]$ (**3**), and $[\{WO_2[O(CH_2)_2Se(CH_2)_2O]\}_n]$ (**4**). No X-ray structural analysis was possible for **4** and *n* could not be determined.

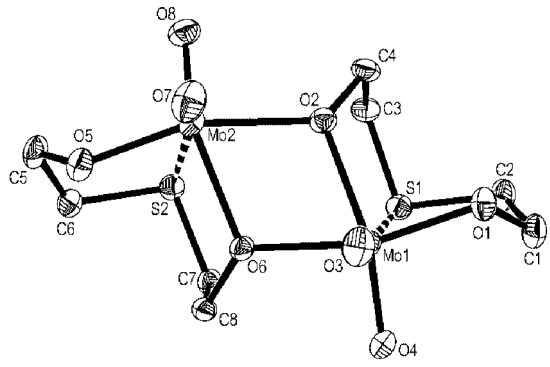


Figure 2. View of the structure of $[\{MoO_2[O(CH_2)_2S(CH_2)_2O]\}_2]$ (**2**) (with numbering scheme). Hydrogen atoms are not shown. Ellipsoids are drawn at 50% probability.

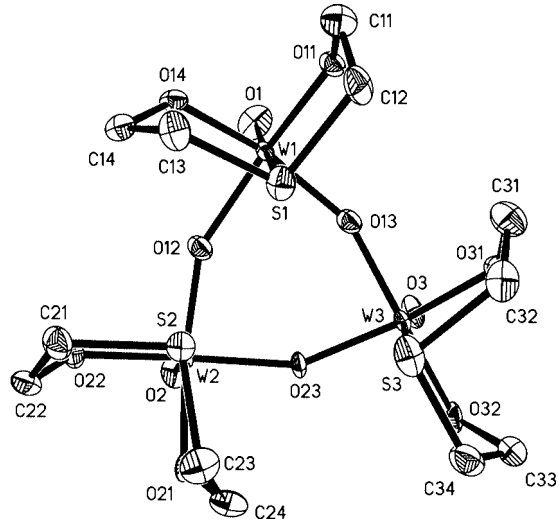


Figure 3. View of the structure of $[\{WO_2[O(CH_2)_2S(CH_2)_2O]\}_3]\cdot CH_2Cl_2$ (**3**·$CH_2Cl_2$) (with numbering scheme). Hydrogen atoms and solvent are not shown. Ellipsoids are drawn at 50% probability.

and 3.00 Å, indicating only weak bonds, if bonds at all. The tungsten–sulfur distances are shorter (2.79, 2.81, and 2.83 Å), even though the central metal is slightly larger, and these interactions can be considered bonds.

In spite of the fact that five-ring complexes with thio- or selenoether functions are supposed to be stable,[14] the expected molybdenum–sulfur bond with this ligand is not explicitly formed. The reaction of the OSO ligand with $MoO_2(acac)_2$ results in a compound that instead of forming two stable five-ring units, somehow rather resembles an eight-ring complex. In contrast, a certain monomeric molybdenum complex with the analogous ligand that contains an ether function instead of the thioether function is known to exhibit an oxygen(ether)–metal bond even though the distance is longer than usual.[22] This is not completely surprising for these kinds of ligands although the analogous cobalt complexes, with ligands where the alkoxylate and the ether/thioether functions are bridged by phenyl rings, show the reverse behavior. With the ether function, no bond is formed between the metal and oxygen atoms, whereas with the thioether function, there is a bond between the cobalt and sulfur atoms.[23]

Unfortunately, the crystals of **3** were racemic twins, and the structure could only be solved in an acentric space group. The crystallographic problem encountered was one reason for performing DFT calculations on this compound. The results of the DFT calculations confirmed those of the structural analysis with some differences especially in the bond lengths between the metal and sulfur atoms (see Table 2). In general, the distances obtained from X-ray analysis are shorter than the calculated ones, with the only exception of the metal–oxo distances, which are slightly longer. With these two data sets (X-ray data and DFT data) for **3**, we are now able to discuss the structural parameters of compound **3** as well as of compound **2** with some certainty, despite the crystallographic problems concerning the structure of **3**.

In compound **2** the metal is pseudo-octahedrally coordinated. The thioethers form only very weak bonds, if at all, to the molybdenum atoms (interatomic distances: 2.931, 3.002 Å). The molybdenum atoms are positioned above (0.3647 and 0.3664 Å) the plane that consists of three alkox-

 © 2006 Wiley-VCH Verlag GmbH & Co. KGaA, Weinheim 

Table 2. Selected bond lengths and angles obtained from an X-ray structural analysis of $[\{MoO_2[O(CH_2)_2S(CH_2)_2O]\}_2]$ (**2**) and $[\{WO_2[O(CH_2)_2S(CH_2)_2O]\}_3]$ (**3**) and from DFT calculations for $[\{WO_2[O(CH_2)_2S(CH_2)_2O]\}_3]$ (**3**).

| | $[\{MoO_2(OSO)\}_2]$ (**2**)[a] X-ray | $[\{WO_2(OSO)\}_3]$ (**3**)[a] X-ray | $[\{WO_2(OSO)\}_3]$ (**3**)[a] DFT |
|---|---|---|---|
| M=O [Å] | 1.6916(19), 1.6912(19) | 1.707(12) | 1.7060 |
| | 1.6926(19), 1.6982(18) | 1.712(11) | 1.7062 |
| | | 1.734(11) | 1.7076 |
| M–S [Å] | 2.931(4), 3.002(5) | 2.793(4), 2.812(4), 2.827(4), | 3.1220, 3.1286, 3.2135 |
| $M–O_{alkoxy}$ [Å] | 1.8973(18) | 1.865(10), 1.889(10) | 1.9544, 2.0095 |
| | 1.8973(18) | 1.888(10), 1.897(11) | 1.9350, 1.9461 |
| | | 1.862(10), 1.880(10) | 1.9274, 1.9377 |
| $M–O_{bridge}$ | 2.0718(17), 2.1410(17) | 1.870(10), 1.944(8) | 1.9206, 1.9407 |
| | 2.0940(17), 2.1484(18) | 1.853(8), 1.937(7) | 1.9112, 1.9358 |
| | | 1.885(10), 1.905(10) | 1.9143, 1.9487 |
| O=M=O [°] | 106.65(9), 108.19(10) | | |
| $O_{bridge}–M–O_{bridge}$ [°] | 70.04(7), 69.49(7) | 85.2(4), 85.4(3), 84.9(4) | 86.32, 86.11, 84.26 |
| $M–O_{bridge}–M$ [°] | 105.72(7), 106.24(7) | 150.7(5), 153.7(5), 153.6(4) | 139.693, 150.67, 151.89 |
| $O_{alkoxy}–M–O_{alkoxy}$ [°] | 90.34(7), 90.99(7) | 90.5(4), 86.4(4), 94.1(4) | 85.94, 86.91, 92.29 |
| S–M=O [°] | 167.52(7), 165.71(7) | 172.7(4), 170.9(4), 170.3(4) | 164.76, 164.22, 167.00 |
| C–S–C [°] | 100.70(13), 101.76(13) | 100.9(8), 100.7(8), 101.1(8) | 100.88, 102.20, 102.54 |

[a] OSO = $^{-}OC_2H_4SC_2H_4O^{-}$.

ylate groups and one oxo function in the direction of the second oxo ligand at each molybdenum atom, which is coordinated *trans* to the thioether sulfur. Within the $Mo_2O_2$ ring, the angles at the metal atom are smaller than 90°, whereas the angles at the oxygen atom are larger. The tridentate ligands and the oxo ligands that are coordinated *trans* to the sulfur atoms are positioned on different sides of the $Mo_2O_2$ ring. The two oxo functions, as well as the two tridentate ligands, are on the same side of this ring, although one could assume that the *trans* form would be sterically less demanding.

Compound **3** is analogous to the published tungsten trimer, but phenyl rings bridge the alkoxylate and thioether functions instead of ethyl groups.[24] In the published complex, two of the tridentate ligands and one oxo function are positioned on one side of the W1–W2–W3 plane, whereas the remaining two oxo functions and one tridentate ligand are on the opposite side. For compound **3**, all oxo functions are positioned on the same side of the W1–W2–W3 plane and all tridentate ligands on the opposite side. From the structural analysis, we obtained metal–oxo distances that were longer, and metal–sulfur and metal–oxygen distances that were shorter than the parameters obtained from DFT calculations. The significantly longer metal–sulfur distances in the theoretical investigations were also observed for compound **2** (compare Table 2 and Table 3). Therefore, we think that the structural analysis gives a more accurate value for this parameter than the DFT calculations. In compound **3**, the metal is again coordinated in a pseudo-octahedral geometry that is slightly less distorted than that of compound **2**. The tungsten–sulfur distances (2.79, 2.81, and 2.83 Å) are shorter than the molybdenum–sulfur distances in compound **2**. The oxo ligand is bound *trans* to the sulfur atom with a short distance of 1.71 to 1.73 Å. In this way, the ligand that is most tightly bound to tungsten is in a *trans* position to the ligand that is most weakly bound to the metal, which is the most stable geometry. All other metal–oxygen distances to the alkoxylate functions as well as to the bridging oxygen atoms are within the usual range of 1.86 to 1.95 Å for oxygen–tungsten single bonds. The tungsten atoms are positioned slightly above the equatorial plane (two bridging oxygen atoms, two alkoxylate functions) in the direction of the oxo ligands by 0.04 to 0.36 Å.

## DFT Calculations

DFT calculations were not only performed to confirm the results of the X-ray crystal structure analysis for compound **3**, but also to understand the formation of surprisingly different complexes for molybdenum and tungsten with the same ligand and by the same preparation method. The most important differences between the two structures can be summarized shortly as follows: (i) a trimeric structure for the tungsten compound versus a dimeric structure for the molybdenum compound; (ii) former oxo ligands as bridging atoms for the tungsten compound versus alkoxylate functions of the thioether ligand for the molybdenum compound.

We performed calculations on both of the observed structures for the two metals in order to better understand the different behavior of molybdenum and tungsten regarding the formation of the two significantly different complexes. The important parameters obtained from DFT calculations are summarized in Table 3.

The most significant differences between the molybdenum and the tungsten compounds are as follows: The metal-to-bridging-oxygen distances for the trimer are much more unsymmetrical for the molybdenum than for the tungsten compound. It seems that the molybdenum center is somehow reluctant to share one of its oxo ligands with another molybdenum atom and to form a single bond instead of a double bond to the respective oxygen atom. The double-bond character of the metal–oxygen interaction is certainly more conserved in the molybdenum than in the tungsten trimer. In the dimer as well as in the trimer the molybdenum–oxo bonds are shorter than the tungsten–oxo bonds. All this is an indication that the molybdenum–oxo

 © 2006 Wiley-VCH Verlag GmbH & Co. KGaA, Weinheim 

Table 3. Selected bond lengths and angles obtained from DFT calculations for the molybdenum dimer **2** and trimer and for the tungsten dimer and trimer **3**.

| | [{$MoO_2$(OSO)}$_2$] (**2**)[a] | [{$MoO_2$(OSO)}$_3$][a] | [{$WO_2$(OSO)}$_2$][a] | [{$WO_2$(OSO)}$_3$] (**3**)[a] |
|---|---|---|---|---|
| M=O [Å] | 1.7127, 1.7295 | 1.6988 | 1.7189, 1.7344 | 1.7060 |
| | 1.7124, 1.7294 | 1.7014 | 1.7185, 1.7343 | 1.7078 |
| | | 1.7035 | | 1.7098 |
| M–S [Å] | 3.3557, 3.4079 | 3.1567/3.2187/3.2778 | 3.2903, 3.3594 | 3.1220, 3.1486, 3.2135 |
| M–$O_{alkoxy}$ [Å] | 1.9227 | 1.9421, 1.9505 | 1.9116 | 1.9348, 1.9409 |
| | 1.9232 | 1.9411, 1.9561 | 1.9119 | 1.9333, 1.9445 |
| | | 1.9299, 1.9410 | | 1.9221, 1.9325 |
| M–$O_{bridge}$ | 2.1265, 2.1363 | 1.8872/1.9723 | 2.1122, 2.1390 | 1.8988, 1.9453 |
| | 2.1273, 2.1349 | 1.8876/1.9710 | 2.1116, 2.1346 | 1.9010, 1.9441 |
| | | 1.9168/1.9695 | | 1.9295, 1.9440 |
| O=M=O [°] | 108.05, 108.09 | | 107.22, 107.36 | |
| $O_{bridge}$–M–$O_{bridge}$ [°] | 68.35, 68.39 | 86.76, 87.91, 93.68 | 67.87, 67.96 | 83.10, 85.88, 91.71 |
| M–$O_{bridge}$–M [°] | 110.26, 110.28 | 142.35, 150.89, 156.09 | 110.95, 111.10 | 142.99, 150.15, 155.62 |
| S–M=O [°] | 163.47, 164.36 | 163.79, 164.03, 166.84 | 163.27, 164.32 | 164.23, 164.76, 167.00 |
| S–M–$O_{equatorial}$ [°] | 76.32 | 77.46 | 68.45 | 77.73 |
| C–S–C [°] | 101.29, 101.33 | 100.75, 100.79, 102.26 | 101.15, 101.21 | 100.72, 100.95, 102.08 |
| HOMO LUMO gap [eV] | 0.144 | 0.127 | 0.175 | 0.157 |

[a] OSO = $^-OC_2H_4SC_2H_4O^-$.

bond is stronger than the tungsten–oxo bond, as would be expected when taking the hard–soft interactions into account.

The metal–sulfur distances provide a further clue to the differing behavior of the two metals in reaction with the same ligand. It has to be noted that, although these calculated parameters are the ones that differ most from the X-ray structural parameters, at least the trend seems to be represented correctly. The metal–sulfur distances for the dimer as well as for the trimer are shorter for the tungsten than for the molybdenum compound, and the metal–sulfur distances for the trimers are shorter than the distances for the dimers. The octahedral geometry is less distorted for the tungsten trimer than for the tungsten dimer, providing more space for the sixth ligand, the sulfur atom. Even though the metal–sulfur distances in all four cases are significantly longer than for a regular metal–thioether bond, the observed parameters show that the trimer provides a coordination geometry that enhances the formation of a metal–sulfur bond much more than the dimer does. We also have to keep in mind that the actual metal–sulfur distances, at least for the two compounds that were analyzed by X-ray diffraction, are much shorter than those provided by the DFT calculations. We conclude from all of this that molybdenum forms the dimeric structure, because it is able to keep both of the doubly bonded oxo ligands, and that tungsten forms the trimeric structure because it is able to form a stronger metal–sulfur interaction. This behavior is confirmed by the fact that with similar ligand sets, only a tungsten trimer,[24] where terminal oxo ligands are converted into bridging oxo ligands, and molybdenum monomers[22] and dimers,[25] where the oxo ligands are retained as doubly bonded, are obtained and structurally characterized.

Again, this shows that molybdenum forms stronger interactions with oxygen than tungsten but weaker interactions with sulfur.

## Electrochemical Results

In order to evaluate the influence of the metal and of the ligand atoms (S versus Se) on the redox properties, compounds **2**, **3**, and **4** were investigated by differential pulse voltammetry (DPV). This method was chosen over cyclic voltammetry because all compounds, but especially compound **4**, were only slightly soluble in acetonitrile, and the signals of the redox processes in the cyclic voltammograms were rather weak (see Figure 4), whereas in the oxidative as well as in the reductive DPVs all transitions were sharp and sufficiently intense and therefore easily detected (Figure 5). The peak positions given in Table 4 were determined from both the reductive and the oxidative DPVs as an average. For each of the compounds [**2** (MoS), **3** (WS), **4** (WSe)], two reversible transitions were observed in the differential pulse voltammograms for the redox processes $M^{IV} \leftrightarrow M^{V}$ and $M^{V} \leftrightarrow M^{VI}$ (see Figure 4). As expected, the redox processes $M^{VI} \leftrightarrow M^{V}$ and $M^{V} \leftrightarrow M^{IV}$ for the molybdenum compound are at a higher voltage than those for the respective tungsten compound, and those for the tungsten–selenium compound are at a higher voltage than those for the tungsten–sulfur compound. A third redox process was found at a rather high voltage for all three compounds. It showed irreversible behavior in the cyclic voltammograms, but a slightly shifted transition was also observed in the reductive DPV (see Figure 5). This leads to the conclusion that the third redox process is due to a structural reorganization of the molecule, where the oxidation occurs much more readily than the reduction. Because the oxidation probably takes place at the sulfur/selenium atom, the metal–sulfur/metal–selenium bond must dissolve, and therefore a reorganization of the molecule is necessary. We assume that the reduction at the sulfur/selenium atom involves a more demanding structural reorganization than the oxidation process. Therefore, reduction occurs much more slowly, and it could not

 © 2006 Wiley-VCH Verlag GmbH & Co. KGaA, Weinheim 

Table 4. Redox potentials for the molybdenum and tungsten compounds with the tridentate thioether/selenoether alkoxylate ligands for the $M^{IV}\leftrightarrow M^{V}$ and $M^{V}\leftrightarrow M^{VI}$ transitions and for the oxidation at the ligand atom as obtained from DPV investigations referenced internally vs. ferrocene/ferrocenium.

| Compound | $E_{1/2}$ $M^{IV}\leftrightarrow M^{V}$ vs. $Fc/Fc^{+}$ [V] | $E_{1/2}$ $M^{V}\leftrightarrow M^{VI}$ vs. $Fc/Fc^{+}$ [V] | $E_{1/2}$ ($[MO_2(OXO)]\leftrightarrow[MO_2(OXO)]^{+}$) vs. $Fc/Fc^{+}$ [V] |
|---|---|---|---|
| $[\{MoO_2(OSO)\}_2]$ (**2**)[a] | –0.93 | 0.31 | 1.49 |
| $[\{WO_2(OSO)\}_3]$ (**3**)[a] | –1.41 | –0.07 | 1.24 |
| $[\{WO_2(OSeO)_n\}$ (**4**)[b] | –1.37 | –0.02 | 0.96 |

[a] OSO = $^{-}OC_2H_4SC_2H_4^{-}$. [b] OSeO = $^{-}OC_2H_4SeC_2H_4^{-}$.

be observed in the CV but in the much slower DPV recording. Interestingly, the third transition for compound **4** (WSe) is at a significantly lower voltage than the transition for compound **3** (WS), reversing the observed behavior for the two transitions taking place at the metal atom with more positive potentials for **4** (WSe) than for **3** (WS). This is another indication that this redox process does indeed take place at the ligand atom. Here, the oxidation of selenium is easier to achieve than that of sulfur, as would be expected by taking the sizes of the two atoms and the metallic character of the selenium atom into account.

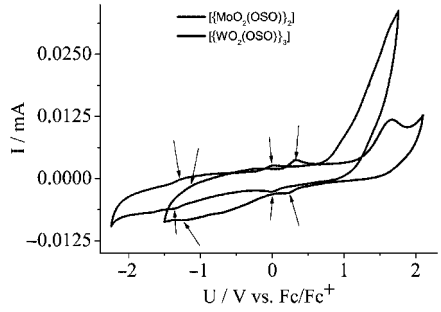


Figure 4. Cyclic voltammograms of compounds $[\{MoO_2[O(CH_2)_2S(CH_2)_2O]\}_2]$ (**2**) and $[\{WO_2[O(CH_2)_2S(CH_2)_2O]\}_3]$ (**3**) referenced vs. ferrocene/ferrocenium showing two reversible redox processes (indicated by arrows) and an irreversible oxidation (of very poor intensity for **3**). The current values of **3** were multiplied by a factor of 4 in order to fit all the data into one graph.

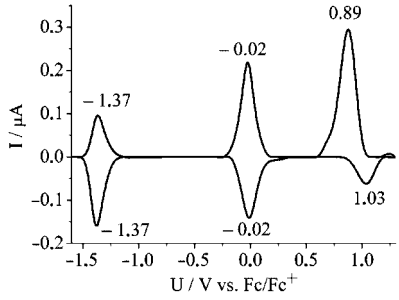


Figure 5. Reductive and oxidative differential pulse voltammograms of compound **4** referenced vs. ferrocene/ferrocenium. The plots were generated using the automatic baseline correction function of the Gepris software.

The redox potentials of compounds $MoO_2Cl_2$(dme),[18] $WO_2Cl_2$(dme),[19] $MoO_2Cl_2[MeS(CH_2)_2SMe]$,[14] and $WO_2Cl_2[MeS(CH_2)_2SMe]$ (**1**) were also compared (see Table 5). Here, we used cyclic voltammetry and observed quasi-reversible behavior for all compounds for the $M^{V}\leftrightarrow M^{VI}$ transition. In the range –1.0 to –1.5 V, an irreversible reduction occurs in all cases probably because of the loss of one oxo ligand accompanying the reduction to $M^{IV}$. The formation of this new species led to the emergence of new signals in the voltammograms. We therefore only compared the potentials of the quasi-reversible process assigned to the $M^{V}\leftrightarrow M^{VI}$ transition. Figures showing a long-range cyclic voltammogram (including the irreversible reduction and ligand-centered quasi-reversible oxidation) of $MoO_2Cl_2$(dme), a short-range cyclic voltammogram of $MoO_2Cl_2(MeSC_2H_4SMe)$, and a long-range cyclic voltammogram of $WO_2Cl_2$(dme) with the internal reference ferrocene can be found in the Supporting Information.

Table 5. Redox potentials for the molybdenum and tungsten compounds with the bidentate ether/thioether ligands for the $M^{V}\leftrightarrow M^{VI}$ redox processes referenced internally vs. ferrocene/ferrocenium.

| Compound | $E_{1/2}$ $M^{V}\leftrightarrow M^{VI}$ vs. $Fc/Fc^{+}$ [V] |
|---|---|
| $MoO_2Cl_2$(dme) | –0.17 |
| $MoO_2Cl_2(MeSC_2H_4SMe)$ | –0.15 |
| $WO_2Cl_2$(dme) | –0.34 |
| $WO_2Cl_2(MeSC_2H_4SMe)$ (**1**) | –0.28 |

Again, the molybdenum compounds have potentials that are higher than their tungsten analogs, and the complexes with sulfur ligand atoms have potentials that are higher than their counterparts with oxygen ligand atoms. The latter differences are again smaller (between 20 and 60 mV) than the differences between molybdenum and tungsten compounds, which are about three times larger (between 130 and 170 mV). Since the bonds between metal and sulfur atoms exhibit π–π-interactions, it can be noted that the differences between the redox potentials of the molybdenum and tungsten thioether complexes are smaller than those between the complexes with the oxygen ligand atoms.

Again, changing the metal atoms has a much more significant influence on the redox potentials than changing the ligand atoms.

## Concluding Remarks

We have seen that molybdenum and tungsten form almost identical complexes with the bidentate ether and thioether ligands. The metal atom does not affect the structure of the complexes, though it has an influence on the stability of the complexes because of a difference in the strength of orbital overlap. For the oxygen-atom-transfer enzymes, where only mono- or bidentate ligands are present, a geo-

 © 2006 Wiley-VCH Verlag GmbH & Co. KGaA, Weinheim 

metrical or steric influence as a result of changing the metal atom can be excluded.

Changing the ligand atoms does not result in any significant structural alterations, with the only exception of the metal-to-ether/thioether-ligand-atom bond length and angle, but these differences are merely a result of the different radii of the ligand atoms. There was no indication of a significant electronic influence of changing the ligand atoms (oxygen versus sulfur) on the metal, except that the potentials of the molybdenum and tungsten complexes were closer together with sulfur ligation than with oxygen ligation.

With the tridentate bisanionic ligands, molybdenum and tungsten form rather different complexes, the former giving a dimeric and the latter a trimeric complex. Interestingly, the thioether function forms no explicit bond with the molydenum, whereas the analogous ether ligand does form a bond with this metal atom (no analogous compound was published for tungsten).[22]

We conclude from this that the structural influence of the ligand atom plays a vital role in structurally demanding ligands (tridentate) but not in those with a simpler geometry (bidentate or monodentate).

This may be because the hard–soft interactions between the ether/thioether function of the ligands and the metal center favor the oxygen–molybdenum combination over the sulfur–molybdenum combination. Molybdenum prefers O-functional ligands although it has been said that the bond strength of ether functions to metals increases within the group of the chalcogens.[21] Interestingly, in nature the ligand–metal combinations that are less favorable than others from this point of view occur at the active sites of the OATs: for instance the coordination of thiolate (cysteine) to molybdenum at the active site of the DMSO reductase of *Desulfovibrio desulfuricans*[8] or the coordination of serine to tungsten in the aldehyde oxidoreductase of *Pyrococcus furiosus*.[11]

The influence of the metal on the redox potential is, as expected, such that the molybdenum complexes have more positive redox potentials than the analogous tungsten complexes in all cases. With regard to the enzymes, this means that in all cases one metal is better suited for the catalyzed reaction with the substrate, while with the other metal the active site is more easily regenerated. For a given enzyme, there is always an advantage as well as a disadvantage in using either of the two metals, molybdenum or tungsten. If the redox potential is important for the choice of the metal, the basis of this choice would be a difference in the redox behavior of the two metals at different temperatures[26] rather than their relative redox potentials at room temperature.

The influence of the ligand atoms on the redox potentials is small but of consequence; the sulfur ligands cause more positive redox potentials than the oxygen ligands, and the selenium ligands cause more positive potentials than the sulfur ligands. However, the observed differences are smaller than those that result from changing the metal atoms.

The fact that there are two molybdenum cofactors that both catalyze the reduction of DMSO but contain molybdenum coordinated to cysteine in one case (*Desulfovibrio desulfuricans*)[8] and to serine in the other case (*Rhodobacter spharoides*)[7a,7b] is another indication that the use of different amino acids as ligands to the active sites is probably not an answer to the substrate demands on the redox potentials of the enzymes.

In addition, there does not seem to be any correspondence between the atom that is oxidized or reduced and the coordinated amino acid. Carbon can be oxidized by active sites that have selenocysteine (formate dehydrogenase from *E. coli*) or serine (aldehyde oxidoreductase from *P. furiosus*)[11] coordination. As mentioned above, sulfur can be oxidized by active sites that have serine or cysteine coordination, and nitrogen can be reduced by active sites that have cysteine (nitrate reductase from *E. coli*)[27] or aspartate (nitrate reductase from *Paracoccus pantotrophus*)[10] coordination, to name only a few examples.

The only parameters that are significantly influenced by changing the ligand atoms and which are not compromised by being part of a multidentate ligand system within the enzymes are the length and the strength of the metal–amino acid bond. If there is a reason for using different amino acid ligands, it is probably the ability to stabilize the active-site–substrate complex during turnover of the enzymatic reaction in cooperation with the peptide side chain residues close to the active site. A substantial effect of the coordinated amino acid on the enzymatic reaction by itself seems to be unlikely.

To finally answer the question about the reason for using different amino acid ligands at the active sites of the OATs, two strategies are to be followed. One is to synthesize model compounds for the enzyme–substrate complexes and to evaluate the ability of different amino acid ligands to stabilize these complexes with different substrates. The other is to undertake theoretical investigations of the intermediate states of the active sites, taking into account the influence of the peptide side chain on the stabilizing effect of the coordinated amino acid. These are challenging tasks for the future.

## Experimental Section

**Materials:** $MoO_2Cl_2(dme)$,[18] $WO_2Cl_2(dme)$,[19] $MoO_2Cl_2[MeS(CH_2)_2SMe]$,[14] $WOCl_4$,[28] $Me(SCH_2CH_2S)Me$,[29] $WO_2(acac)_2$[30] and bis(2-hydroxyethyl)selenide[31] were prepared as described in the literature. $MoO_2(acac)_2$ and bis(2-hydroxyethyl) sulfide are commercially available and were used as received. Reagent-grade solvents were dried and distilled prior to use. All manipulations were performed under dry and oxygen-free conditions in nitrogen using Schlenk line techniques.

### Syntheses

**$WO_2Cl_2(MeSCH_2CH_2SMe)$ (1):** Liquid $(Me_3Si)_2O$ (0.341 g, 2.10 mmol) was added to a suspension of freshly sublimed $WOCl_4$ (0.68 g, 2.00 mmol) in $CH_2Cl_2$ (20 mL). The orange crystals were

 © 2006 Wiley-VCH Verlag GmbH & Co. KGaA, Weinheim 

slowly consumed to give a yellow solution. After stirring for approximately 1.5 h at room temp., a light yellow solid precipitate was obtained. A solution of $MeSCH_2CH_2SMe$ (0.366 g, 3.00 mmol) in $CH_2Cl_2$ (10 mL) was added, and the reaction mixture was stirred overnight and filtered to remove the brownish precipitate. The clear yellow filtrate was concentrated at room temp. in vacuo until the solid began to precipitate. After keeping this solution at 4 °C overnight colorless crystals were obtained. The crystals were collected on a filter, washed once with diethyl ether (5 mL), and dried in vacuo. Yield: 0.53 g, 65%. M.p. 128–130 °C. $C_4H_{10}Cl_2S_2O_2W$ (407.90): calcd. C 11.75, H 2.46; found C 11.95, H 2.54. IR (KBr): $\tilde{\nu}$ = 3013 (m), 2966 (m), 2933 (m), 1868 (w), 1618 (w), 1424 (m), 1326 (w), 1259 (s), 1179 (w), 1145 (w), 1099 (m), 1028 (m), 956 (vs), 917 (vs), 883 (s), 841 (s), 803 (s), 646 (s), 444 (w), 363 (m), 344 (vs) $cm^{-1}$. EI-MS (70 eV): *m/z* (%) = 409 (1) $[M^+]$, 288 (100) $[WO_2Cl_2]^+$, 251 (49) $[WO_2Cl]^+$, 255 (12) $[WCl_2]^+$.

**$[\{MoO_2[O(CH_2)_2S(CH_2)_2O]\}_2]$ (2):** Bis(2-hydroxyethyl) sulfide (0.25 g, 2.05 mmol) was added to a stirred solution of $MoO_2(acac)_2$ (0.65 g, 2.00 mmol) in $CH_2Cl_2$ (20 mL) at room temp. The reaction mixture was stirred for 24 h. A small amount of white precipitate was filtered off, and the solvent was removed in vacuo. The residue was extracted with *n*-hexane (20 mL) and stored at room temp. for several days to yield colorless crystals. Yield: 0.10 g, 41%. M.p. 190 °C. $C_8H_{16}O_8S_2Mo_2$ (499.84): calcd. C 19.36, H 3.25; found C 19.61, H 3.26. IR (KBr): $\tilde{\nu}$ = 1460 (m) 1415 (m), 1403 (m), 1368 (s), 1305 (w), 1277 (m), 1263 (m), 1218 (w), 1181 (w), 1069 (s, $\nu_{Mo=O}$), 1041 (s), 1025 (s), 997 (m), 936 (m), 910 (m), 802 (s), 723 (m), 694 (w), 651 (w), 571 (m), 530 (m), 475 (m), 396 (m), 360 (s) $cm^{-1}$. $^1$HNMR ($CDCl_3$, 200 MHz): $\delta$ = 2.31 (t), 3.36 (t) ppm. EI-MS (70 eV): *m/z* (%) = 248 (11) $[\{MoO_2[O(CH_2)_2S(CH_2)_2O]\}^+]$, 216 (40) $[\{Mo[O(CH_2)_2S(CH_2)_2O]\}^+]$.

**$[\{WO_2[O(CH_2)_2S(CH_2)_2O]\}_3]$ (3):** Bis(2-hydroxyethyl) sulfide (0.12 g, 1.00 mmol) was added to a stirred solution of $WO_2(acac)_2$ (0.41 g, 1.00 mmol) in $CH_2Cl_2$ (20 mL) at room temp. The reaction mixture was stirred for 24 h. The white precipitate was filtered off, and the clear filtrate was concentrated under reduced pressure until the solution was saturated. The solution was stored overnight at room temp. to yield colorless crystals. Yield: 0.11 g, 32%. M.p. 240 °C (dec.). $C_{12}H_{24}O_{12}S_3W_3$ (1007.90): calcd. C 14.30, H 2.40; found C 14.51, H 2.50. IR (KBr): $\tilde{\nu}$ = 1464 (vs), 1378 (vs), 1306 (w), 1262 (w),1261 (w), 1170 (w),1153 (w),1091 (m), 1066 (m, $\nu_{W=O}$), 1033 (m), 962 (w), 935 (w), 858 (w), 838 (w), 801 (m), 722 (m), 657 (w) $cm^{-1}$. EI-MS (70 eV): *m/z* (%) = 352 (33) $[\{WO_3[O(CH_2)_2S(CH_2)_2O]\}^+]$, 337 (100) $[\{WO_2[O(CH_2)_2S(CH_2)_2O]\}^+]$.

**$[\{WO_2[O(CH_2)_2Se(CH_2)_2O]\}_n]$ (4):** A solution of bis(2-hydroxyethyl)selenide (0.17 g, 1.00 mmol) in $CH_2Cl_2$ (5 mL) was added to a stirred solution of $WO_2(acac)_2$ (0.41 g, 1.00 mmol) in $CH_2Cl_2$ (20 mL) at room temp. The reaction mixture was stirred for 2 d. The green solution turned yellow, and a small amount of yellow precipitate formed. The precipitate was filtered off, and ether was added to the filtrate to precipitate the product. The yellow product was collected by filtration and washed with diethyl ether twice. The compound was dried in vacuo. Yield: 0.23 g, 60%. M.p. 210 °C. $C_4H_8O_4SeW$ (383.91): calcd. C 12.55, H 2.11; found C 12.63, H 2.18. IR (KBr): $\tilde{\nu}$ = 1527 (w), 1459 (m), 1400 (m), 1377 (m), 1261 (vs), 1094 (vs, $\nu_{W=O}$), 1020 (vs), 962 (w), 939 (w), 863 (w), 800 (vs), 722 (w), 703 (w), 668 (w), 583 (w), 533 (w), 472 (w) $cm^{-1}$. $^1$HNMR ([D$_6$]DMSO, 300 MHz): $\delta$ = 2.60 (t), 3.56 (t) ppm. $^{13}$CNMR ([D$_6$]-DMSO, 300 MHz): $\delta$ = 26.14 (s), 61.62 (s) ppm. $^{77}$Se NMR ([D$_6$]-DMSO, 500 MHz): $\delta$ = 100.22 (s) ppm. EI-MS (70 eV): *m/z* (%) = 355 (50) $[M^+ - CH_2CH_2]$.

### Electrochemistry

Electrochemical measurements were performed with an AUTOLAB PGSTAT12 potentiostat/galvanostat with a glassy carbon working electrode, a platinum wire reference electrode, and a platinum wire auxiliary electrode, in acetonitrile solutions within a glove box under argon. The supporting electrolyte was $Bu_4NPF_6$ (0.1 M) used as received from Fluka. Acetonitrile used for the electrochemistry was predried with $CaCl_2$, dried by reflux over $CaH_2$ for 2 d, and distilled onto freshly regenerated molecular sieves A3. Referencing was done internally using the ferrocene/ferrocenium couple. The temperature during the measurements was controlled with a Julabo refrigerated/heating circulator FP50-MV at 25 °C. The solutions were prepared within a glove box by dissolving the $Bu_4NPF_6$ electrolyte ($10^{-3}$ mol) and the compounds ($10^{-6}$ mol) in acetonitrile (10 mL) to give $10^{-4}$ M solutions. For reasons of poor solubility, compound **4** could only be prepared as an approximately $0.5 \times 10^{-5}$ M solution.

### Other Physical Measurements

Melting points were obtained in sealed capillaries with a Büchi B 540 instrument and were not corrected. Elemental analyses were performed with a Heraeus CHN-O-Rapid elemental analyzer. Infrared spectra were recorded as KBr pellets with a Bio-Rad Digilab FTS-7 spectrometer from 4000 to 300 $cm^{-1}$. NMR spectra were recorded with Bruker Avance 200, AM 300 and Bruker Avance 500 NMR spectrometers and referenced to the chemical shifts of the deuterated solvent. All NMR-grade solvents were dried prior to use. The chemical shifts are reported in ppm; external reference $SiMe_4$ for $^1$H and $^{13}$C nuclei, and $SeMe_2$ for $^{77}$Se nuclei. Mass spectra were obtained with a Finnigan MAT system 8230 or Varian MAT CH5 instrument by EI-MS methods.

### X-ray Crystallography

Data for crystal structures of compounds **1**, **2**, and **3** were collected with a Stoe–Siemens–Huber four-circle diffractometer coupled to a Siemens CCD area detector with graphite-monochromated Mo-$K_\alpha$ radiation ($\lambda$ = 0.71073 Å). All structures were solved by direct methods (SHELXS-97)[32] and refined with all data by full-matrix least-squares methods on $F^2$.[33] All non-hydrogen atoms were refined anisotropically. The hydrogen atoms were included at geometrically calculated positions and refined using a riding model. Parameters of the X-ray crystallography are summarized in Table 6. CCDC-280029 (**1**), CCDC-280030 (**2**), and CCDC-280028 (**3**) contain the supplementary crystallographic data for this paper. These data can be obtained free of charge from The Cambridge Crystallographic Data Centre via www.ccdc.cam.ac.uk/data_request/cif.

### DFT Calculations

All calculations have been carried out with the Gaussian G03[34] program package using the implemented DFT variant B3LYP[35,36] (Becke three-parameter exchange functional B3 and the Lee–Yang–Parr correlation functional LYP). A basis consisting of the well-established small core ECP[37] (for Mo and W), 3-21g[38] (for carbon and hydrogen) and following a proposal by K. Peterson,[39,40] a modified 6-31G basis including double diffuse functions [6-31G(d′, p′)] to give a suitable description of the lone pairs on oxygen and sulfur were used.

All structures were fully optimized without employing any symmetry constraints. The starting geometries were taken from experimental data. Analytical frequency calculations were performed to verify these structures as local minima.

**Supporting Information** (see footnote on the first page of this article): Cyclic voltammograms of $MoO_2Cl_2$(dme), $MoO_2$-

 © 2006 Wiley-VCH Verlag GmbH & Co. KGaA, Weinheim 

Table 6. Crystallographic parameters.

| | $WO_2Cl_2(MeSC_2H_4SMe)$ (**1**) | $[\{MoO_2(OSO)\}_2]$ (**2**)[a] | $[\{WO_2(OSO)\}_3]\cdot CH_2Cl_2$ (**3**)[a] |
|---|---|---|---|
| Formula | $C_4H_{10}Cl_2O_2S_2W$ | $C_8H_{16}Mo_2O_8S_2$ | $C_{13}H_{25}Cl_2O_{12}S_3W_3$ |
| $M$ [g/mol] | 408.99 | 496.21 | 1091.96 |
| Crystal system | hexagonal | monoclinic | monoclinic |
| Space group | $P6(5)$ | $P21/n$ | $P2(1)$ |
| $a$ [Å] | 7.3222(3) | 9.4839(7) | 11.615(2) |
| $b$ [Å] | 7.3222(3) | 12.4405(7) | 7.8739(16) |
| $c$ [Å] | 33.3889(17) | 12.8003(7) | 14.4620(3) |
| $\alpha$ [°] | 90 | 90 | 90 |
| $\beta$ [°] | 90 | 101.567(4) | 111.81(3) |
| $\gamma$ [°] | 120 | 90 | 90 |
| $V$ [Å$^3$] | 1550.30(12) | 1479.56(14) | 1228.0(4) |
| $Z$ | 6 | 4 | 2 |
| $\mu$ [cm$^{-1}$] | 120.5 | 20.08 | 145.45 |
| Reflections collected | 15469 | 22121 | 12796 |
| Independent reflections | 1757 | 2554 | 4153 |
| Completeness of $\theta$ [°] | 99.4% (24.80°) | 99.7% (24.84°) | 97.6% (24.94°) |
| $R_1[I_0 > 2\sigma(I_0)]$ | 0.0247 | 0.0180 | 0.0350 |
| $wR_2[I_0 > 2\sigma(I_0)]$ | 0.0535 | 0.0442 | 0.0904 |
| $R_1$[all data] | 0.0260 | 0.0228 | 0.0403 |
| $wR_2$[all data] | 0.0538 | 0.0451 | 0.0957 |

$R_1 = \Sigma||F_o| - |F_c||/\Sigma|F_o|$; $wR_2 = [\Sigma_w(F_o^2 - F_c^2)^2/\Sigma wF_{oi}^4]^{1/2}$

[a] (OSO) = $^-OC_2H_4SC_2H_4O^-$.

$Cl_2(MeSC_2H_4SMe)$ and $WO_2Cl_2$(dme), and the complete list of data obtained from DFT calculations.

## Acknowledgments

Financial support from the Institut für Anorganische Chemie, University Goettingen, is gratefully acknowledged.

[1] J. H. Enemark, J. J. A. Cooney, *Chem. Rev.* **2004**, *104*, 1175–1200.
[2] M. K. Johnson, D. C. Rees, M. W. W. Adams, *Chem. Rev.* **1996**, *96*, 2817–2840, DOI: 10.1021/cr950063d.
[3] S. K. Das, D. Biswas, R. Maiti, S. Sarkar, *J. Am. Chem. Soc.* **1996**, *118*, 1387–1397, DOI: 10.1021/ja9511580.
[4] J. Bernholc, E. I. Stiefel, *Inorg. Chem.* **1985**, *24*, 1323–1330.
[5] H. Oku, N. Ueyama, A. Nakamura, *Chem. Lett.* **1996**, 1131–1132.
[6] R. Hille, *Chem. Rev.* **1996**, *96*, 2757–2816, DOI: 10.1021/cr950061t.
[7] a) H. Schindelin, C. Kisker, J. Hilton, K. V. Rajagopalan, D. C. Rees, *Science* **1996**, *272*, 1615–1621; b) G. N. George, J. Hilton, K. V. Rajagopalan, *J. Am. Chem. Soc.* **1996**, *118*, 1113–1117; c) G. N. George, J. Hilton, C. Temple, R. C. Prince, K. V. Rajagopalan, *J. Am. Chem. Soc.* **1999**, *121*, 1256–1266.
[8] J. M. Dias, M. E. Than, A. Humm, R. Huber, G. P. Bourenkov, H. D. Bartunik, S. Bursakov, J. Calvete, J. Caldeira, C. Carveiro, J. J. G. Moura, I. Moura, M. J. Romão, *Structure* **1999**, *7*, 65–79.
[9] J. C. Boyington, V. N. Gladyshev, S. V. Khangulov, T. C. Stadtman, P. D. Sun, *Science* **1997**, *275*, 1305–1308.
[10] M. G. Bertero, R. A. Rothery, M. Palak, C. Hou, D. Lim, F. Blasco, J. H. Weiner, N. C. J. Strynadka, *Nat. Struct. Mol. Biol.* **2003**, *10*, 681–687.
[11] a) M. K. Chan, S. Mukund, A. Kletzin, M. W. W. Adams, D. C. Rees, *Science* **1995**, *267*, 1463–1469; b) Y. Hu, S. Faham, R. Roy, M. W. W. Adams, D. C. Rees, *J. Mol. Biol.* **1999**, *286*, 899–914.
[12] a) H. Raaijmakers, S. Maciera, J. M. Dias, S. Texeira, S. Bursakov, R. Huber, J. J. G. Moura, I. Moura, M. J. Romão, *Structure* **2002**, *10*, 1261–1272; b) H. Raaijmakers, S. Texeira, J. M. Dias, M. J. Almendra, C. D. Brondino, I. Moura, J. J. G. Moura, M. J. Romão, *J. Biol. Inorg. Chem.* **2001**, *6*, 398–404.
[13] R. Hart, W. Levason, B. Patel, G. Reid, *J. Chem. Soc., Dalton Trans.* **2002**, 3153–3159.
[14] M. D. Brown, M. B. Hursthouse, W. Levason, R. Ratnani, G. Reid, *Dalton Trans.* **2004**, 2487–2491.
[15] D. Sevdic, L. Fekete, *Inorg. Chim. Acta* **1982**, *57*, 111–117.
[16] P. M. Boorman, M. Islip, M. M. Reimer, K. J. Reimer, *J. Chem. Soc., Dalton Trans.* **1972**, 890–893.
[17] P. Berges, W. Hinrichs, A. Holzmann, J. Wiese, G. Klar, *J. Chem. Research (S)* **1986**, 10–11.
[18] B. Kamenar, M. Penavić, B. Kopar-Ćolig, B. Marković, *Inorg. Chim. Acta* **1982**, *65*, L245–L247.
[19] K. Dreisch, C. Andersson, C. Stålhandske, *Polyhedron* **1991**, *10*, 2417–2421.
[20] E. G. Hope, W. Levason, *Coord. Chem. Rev.* **1993**, *122*, 109–170.
[21] S. G. Murray, F. H. Hartley, *Chem. Rev.* **1981**, *81*, 365–414.
[22] A. J. Wilson, B. R. Penfold, C. J. Wilkins, *Acta Crystallogr. C: Cryst. Struct. Commun.* **1983**, *39*, 329–330.
[23] H. Müller, A. Holzmann, W. Hinrichs, G. Z. Klar, *Z. Naturforsch. Teil B* **1982**, *37*, 341–347.
[24] P. Berges, W. Hinrichs, A. Holzmann, J. Wiese, G. Klar, *J. Chem. Research (S)* **1986**, 10–11.
[25] V. McKee, C. J. Wilkins, *J. Chem. Soc., Dalton Trans.* **1987**, 523–528.
[26] C. Schulzke, *Dalton Trans.* **2005**, 713–720.
[27] C. S. Butler, J. M. Charnock, C. D. Garner, A. J. Thomson, S. J. Ferguson, B. C. Berks, D. J. Richardson, *Biochem. J.* **2000**, *352*, 859–864.
[28] V. C. Gibson, T. P. Kee, A. Shaw, *Polyhedron* **1990**, *9*, 2293–2298.
[29] O. V. Alekminskaya, N. V. Russavskaya, N. A. Korchevin, E. N. Deryagina, *Russ. J. Gen. Chem.* **2002**, *72*, 75–78.
[30] S.-B. Yu, R. H. Holm, *Inorg. Chem.* **1989**, *28*, 4385–4391.
[31] X. Hu, Z. Tian, Y. Chen, X. Lu, *Synth. Commun.* **2000**, *30*, 523–529.
[32] SHELXS-97, Programs for Structure Solution: G. M. Sheldrick, *Acta Crystallogr., Sect. A* **1990**, *46*, 467–473.
[33] G. M. Sheldrick, *SHELXL-97, Programs for Crystal Structure Refinement*, University of Göttingen, Germany, **1997**.

 © 2006 Wiley-VCH Verlag GmbH & Co. KGaA, Weinheim 

[34] M. J. Frisch, G. W. Trucks, H. B. Schlegel, G. E. Scuseria, M. A. Robb, J. R. Cheeseman, J. A. Montgomery, Jr., T. Vreven, K. N. Kudin, J. C. Burant, J. M. Millam, S. S. Iyengar, J. Tomasi, V. Barone, B. Mennucci, M. Cossi, G. Scalmani, N. Rega, G. A. Petersson, H. Nakatsuji, M. Hada, M. Ehara, K. Toyota, R. Fukuda, J. Hasegawa, M. Ishida, T. Nakajima, Y. Honda, O. Kitao, H. Nakai, M. Klene, X. Li, J. E. Knox, H. P. Hratchian, J. B. Cross, C. Adamo, J. Jaramillo, R. Gomperts, R. E. Stratmann, O. Yazyev, A. J. Austin, R. Cammi, C. Pomelli, J. W. Ochterski, P. Y. Ayala, K. Morokuma, G. A. Voth, P. Salvador, J. J. Dannenberg, V. G. Zakrzewski, S. Dapprich, A. D. Daniels, M. C. Strain, O. Farkas, D. K. Malick, A. D. Rabuck, K. Raghavachari, J. B. Foresman, J. V. Ortiz, Q. Cui, A. G. Baboul, S. Clifford, J. Cioslowski, B. B. Stefanov, G. Liu, A. Liashenko, P. Piskorz, I. Komaromi, R. L. Martin, D. J. Fox, T. Keith, M. A. Al-Laham, C. Y. Peng, A. Nanayakkara, M. Challacombe, P. M. W. Gill, B. Johnson, W. Chen, M. W. Wong, C. Gonzalez, and J. A. Pople, *Gaussian 03, Revision B.04*, Gaussian, Inc., Pittsburgh, PA, **2003**.
[35] C. Lee, W. Yang, R. G. Parr, *Phys. Rev. B* **1988**, *37*, 785–789.
[36] B. Miehlich, A. Savin, H. Stoll, H. Preuss, *Chem. Phys. Lett.* **1989**, *157*, 200–206.
[37] T. R. Cundari, W. J. Stevens, *J. Chem. Phys.* **1993**, *98*, 5555–5565.
[38] K. D. Dobbs, W. J. Hehre, *J. Comput. Chem.* **1987**, *8*, 880–893.
[39] G. A. Petersson, M. A. Al-Laham, *J. Chem. Phys.* **1991**, *94*, 6081–6090.
[40] G. A. Petersson, A. Bennett, T. G. Tensfeldt, M. A. Al-Laham, W. A. Shirley, J. Mantzaris, *J. Chem. Phys.* **1988**, *89*, 2193–2218.

Received: August 3, 2005
Published Online: December 9, 2005

 © 2006 Wiley-VCH Verlag GmbH & Co. KGaA, Weinheim 

DOI: 10.1002/ejic.200500775

# Electrochemical Detection of High Oxidation States of Chromium(IV and V) in Chromium-Doped Cassiterite and Tin-Sphene Ceramic Pigmenting Systems

**Antonio Doménech,*[a] Francisco Jose Torres,[b] Esther Ruiz de Sola,[b] and Javier Alarcón[b]**

**Keywords:** Chromium / High oxidation states / Voltammetry / Cassiterite / Tin-sphene

Solid-state electrochemistry is applied to detect the presence of chromium centres with high oxidation states in chromium-doped cassiterite and tin-sphene ceramic pigmenting systems. Voltammetric data indicate that $Cr^{V}$ and $Cr^{IV}$ centres with different coordinative arrangements exist in the studied materials, and yield proton-assisted reduction processes at +0.95, +0.42 AgCl/Ag in contact with 0.50 M $H_2SO_4$. Electrochemical measurements are correlated with spectroscopic data. The $Cr^{IV}$ and $Cr^{V}$ metal ions display a significant light-driven electrocatalytic effect on the oxidation of 1,4-dihydrobenzoquinone and $Fe(CN)_6^{4-}$ ions that involves the formation of surface-confined adducts.
(© Wiley-VCH Verlag GmbH & Co. KGaA, 69451 Weinheim, Germany, 2006)

## Introduction

Ceramic pigments are formed by crystalline phases containing cromophore cations. These materials are dispersed in particulate form in the bulk ceramic body or in the outer glassy layer on the ceramic support. During the thermal processing of ceramic materials, these particulate components must be stable at the high temperatures reached and must be inert to the chemical action of other components of the ceramic body, i.e. other crystalline phases and/or glassy phases.

Purple and pink chromium-containing, tin-based ceramic pigments have been widely used in the industry for years. Two of the main crystalline structures included in this group of ceramic pigments are cassiterite ($SnO_2$) and sphene or malayaite ($CaSnSiO_5$), which produce the purple and pink colours, respectively. As is well known, cassiterite has a rutile-type structure, while sphene possesses a titanite-type structure.

The preparation and characterisation of these two types of chromium-containing pigments have been widely studied by different authors for the past decades.[1,2] Different preparation procedures have been used in order to facilitate the kinetics of the reaction, which lead to the Cr-doped cassiterite or sphene particulate materials.[3–5] Microstructural features such as morphology, shape and size of the crystals, as well as important characteristics of particulate materials, have also been investigated extensively.[6,7]

The crystallochemistry of cassiterite and sphene structures indicates that the chromium cations in both structures are in octahedral sites, replacing the $Sn^{IV}$ centres. There is agreement amongst various authors on this point. However, the controversy on the chemical states of the doped chromium cation exists for some time now.[6–11] Thus, Ren et al.,[8] on the basis of electron spin resonance spectroscopy, reflectance spectroscopy and magnetic susceptibility measurements, claimed that the violet colour of the Cr-$SnO_2$ pigment is caused by the simultaneous presence of $Cr^{IV}$ and $Cr^{III}$ ions, the former as a $Cr^{IV}$-$SnO_2$ solid solution and the latter as $Cr_2O_3$. López-Navarrete et al.[6–8] reached the same conclusion from X-ray photoelectron, diffuse reflectance and magnetic susceptibility data. More recently, these authors concluded that in Cr-doped sphene structures most of the tetravalent chromium cations form a solid solution with the sphene lattice by mostly substituting the $Sn^{IV}$ cations in the isolated octahedral positions, while a very small amount of $Cr^{IV}$ also substitutes the tetrahedral $Si^{IV}$ ions. In contrast, Pavlov et al.,[10] from electronic absorption spectroscopy studies, concluded that the chromium cation is in the oxidation state +3 in Cr-$SnO_2$, while in the Cr-doped sphene there is an additional band in the near-IR part of the spectrum (around 1200 nm), which can be attributed to $Cr^{IV}$.

Recently, Julián et al.,[11] using a wet synthetic route, indicated that the violet colour in the Cr-$SnO_2$ pigmenting system is mainly produced by $Cr^{III}$ and/or $Cr^{IV}$ ions incorporated in the cassiterite structure. On the basis of electron spin resonance spectroscopy data, these authors concluded that different amounts of $Cr^{V}$, $Cr^{IV}$ and $Cr^{III}$ ions are present in chromium-doped cassiterite.

From the above reports it seems possible that in both ceramic-pigmenting systems, the chromium cation can be present in several oxidation states. However, it can also be

[a] Departament de Química Analítica, Universitat de València, Dr. Moliner, 50, 46100 Burjassot (València), Spain
E-mail: antonio.domenech@uv.es
[b] Departament de Química Inorgànica. Universitat de València, Dr. Moliner, 50, 46100 Burjassot (València) Spain
Supporting information for this article is available on the WWW under http://www.eurjic.org or from the author.

 © 2006 Wiley-VCH Verlag GmbH & Co. KGaA, Weinheim 

concluded that it is quite difficult to establish unambiguously the presence of these oxidation states of chromium in both host lattices from spectroscopic and magnetic techniques. Furthermore, the small amount of chromium in such materials makes it even more difficult to check the presence of $Cr^{IV}$ or even $Cr^{V}$ cations. Therefore, it would be interesting to use an experimental technique with enough sensitivity to distinguish between the different oxidation states of chromium in the Cr-doped cassiterite and Cr-doped sphene ceramic pigments. The coexistence of metal ions in different oxidation states is of interest in a wide variety of contexts. In particular, the simultaneous presence of $Cr^{III}$ and $Cr^{IV}$ in porous chromium-containing α-tin phosphate[12] and silica optical fibres[13] has been reported recently.

Over the last years the voltammetry of microparticles has emerged as a powerful technique to obtain chemical information on doped materials. Therefore, in this paper the possible presence of high oxidation states of chromium in the studied materials will be investigated by square wave voltammetry upon attachment of solid samples to paraffin-impregnated graphite electrodes (PIGEs). This follows the methodology of the voltammetry of microparticles approach, an increasingly growing research field for which extensive reviews are available.[14,15] The voltammetry of tin oxide microparticles and related compounds has not been described in detail in spite of the wide range of applications of tin oxide electrodes.[16] Recently, Scholz et al. described the electrochemistry of natural and synthetic tin sulfosalts using the voltammetry of microparticles methodology.[17] This scheme has previously been applied for studying the electrochemistry of $SnO_2$ and Sn-rich glazed ceramics.[18] Studies on nanosized $SnO_2$ particles dispersed on graphite electrodes,[19] nanocrystalline tin oxide electrodes[20] and modification of the film of $SnO_2$ nanocrystallites with organic reagents,[21] all devoted to the detection of selected analytes, have also been reported. The electrochemical dissolution of chromium oxides, spinels, and chromites has been studied by Blesa et al.[22–24] and Grygar et al.[25–27] Other reports on the solid-state electrochemistry of chromium concern chromium(II), hexacyanochromate(III),[28] some organic Cr complexes[29] and chromium oxide films deposited on stainless steel.[30] However, no detailed studies on the presence of high oxidation states of chromium have been reported.

The electrochemical reduction of chromate and dichromate in solution is complicated by adsorption processes.[31] Three reduction waves appear at acidic pH values for the electrochemical pathway involving any $Cr^{IV}$ intermediate species.[32] However, intermediate $Cr^{V}$ species have been electrochemically characterised in the oxidation of oxalic acid by chromic acid at pH 1.[33]

We report here on a solid-state electrochemical study devoted to the determination of the possible presence of high oxidation states of chromium in chromium-doped cassiterite and chromium-doped tin-sphene. For this purpose, solid samples were attached to paraffin-impregnated graphite electrodes in contact with electrolytic solutions of aqueous $H_2SO_4$ or $HClO_4$, and $NaClO_4$. Cyclic and square wave voltammetry were used as detection modes. The latter technique is of particular interest because of its high sensitivity and immunity to capacitive effects.[34] In an attempt to correlate voltammetric and spectroscopic data, the electrocatalytic effect of chromium-doped materials on the oxidation of hexacyanoferrate(II) ions and 1,4-dihydrobenzoquinone in aqueous solution has been studied. Apart from its applications in chemical sensing and electrosynthesis, such catalytic processes can be used as amplifiers of the electrochemical properties of the catalytic centres, as illustrated by prior data on vanadium-doped zirconias and cobalt-containing cordierite materials.[35–37]

## Results and Discussion

### Characterisation of Chromium-containing Cassiterite and Sphene

X-ray diffraction patterns of the ceramic pigmenting systems, based on cassiterite and sphene structures, are supplied in the Supporting Information. The formation of a crystalline phase with a sphene structure is displayed in samples M-1 to M-4, after thermal treatment at 1300 °C and a 2-h holding time. In accordance with the JCPD card number 70-0437, all peaks can be associated with the main crystalline phase. It is worth noting that a small amount of $SnO_2$ is still present in the sample of M-2. For samples M-5 and M-6, the only crystalline phase detected is that of the cassiterite structure (JCPD card number 41-1445).

The diffuse reflectance spectra of both types of samples, i.e. cassiterite- and sphene-based structures, are shown in Figure 1. For the Cr-sphene specimens, two bands around 540 nm and 1200 nm are detected. The first one is attributed to the $^4A_{2g}$–$^4T_{2g}$ spin-allowed transition of the $Cr^{III}$ ion with octahedral coordination,[10] as well as to the $Cr^{IV}$ centres.[9,38] The band in the near-infrared part of the spectrum, centred at 1200 nm, is assigned to $^3A_2$–$^3T_1$ transitions of $Cr^{IV}$ in tetrahedral surroundings.[9,39] The sphene structure can be described as composed of chains of corner-sharing $SnO_6$ octahedra running parallel to the cell edges that are cross-linked by silicate tetrahedra to form a $SnOSiO_4$ framework that accommodates $Ca^{2+}$ in irregular hepta-coordinated polyhedra. Here, López-Navarrete et al.[9] recently suggested that $Cr^{IV}$ replaced the partially octahedral $Sn^{IV}$ and tetrahedral $Si^{IV}$ sites.

The spectra of the chromium-containing cassiterite consist of a strong band at 560 nm and a weak band at 740 nm, which are attributed to $Cr^{III}$ with octahedral coordination. However, the first band has also been ascribed to $Cr^{IV}$ ions with octahedral symmetry.[9] In contrast to the Cr-sphene-based materials, in the cassiterite-derived materials there is no band around 1200 nm. The reason for the absence of the band associated with the $Cr^{IV}$ ions with tetrahedral coordination is that there are no available tetrahedral sites in this structure.

The investigation by FESEM of the final ceramic pigments indicates that the particles that have formed have a

 © 2006 Wiley-VCH Verlag GmbH & Co. KGaA, Weinheim 

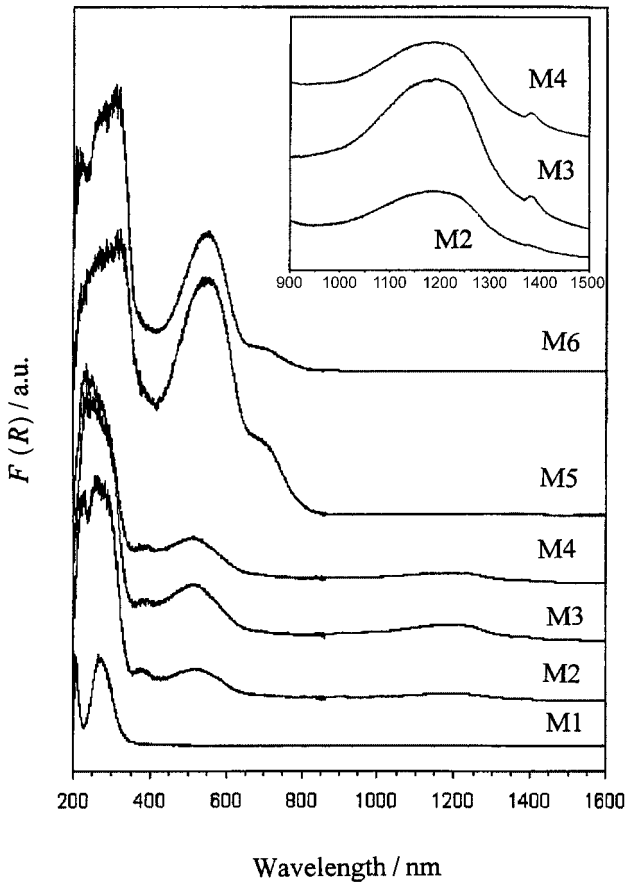


Figure 1. UV/Vis spectra of specimens thermally treated at final temperatures for 2 h: M-1 at 1400 °C and M-5 and M-6 at 1300 °C.

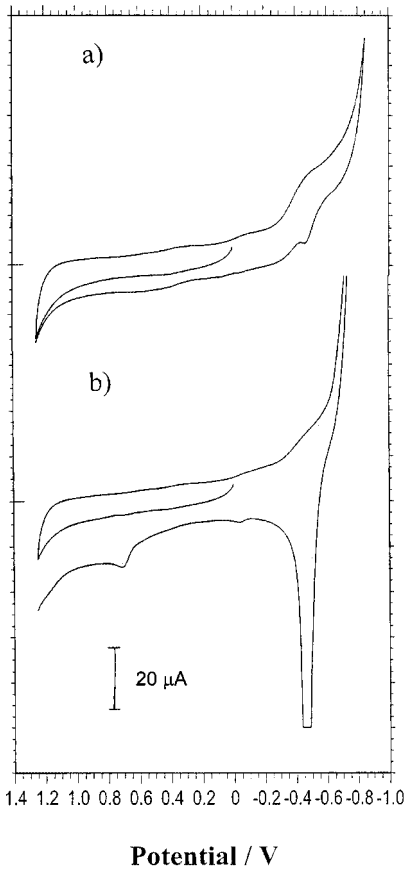


Figure 2. CVs of PIGEs modified by: (a) M-2, and (b) M-5, immersed in 0.50 M $H_2SO_4$. Potential scan rate 50 mV $s^{-1}$.

well-defined morphology. Micrographs of samples of M-4 and M-6 are shown in the Supporting Information. The discrete particles are prismatic and their sizes are smaller than 2 μm long and 0.5 μm wide.

### Electrochemical Study of Prepared Materials

The electrochemistry of the studied materials is, in principle, dominated by tin-centred processes. This can be seen in Figure 2, in which the cyclic voltammograms (CVs) of: (a) M-2 and (b) M-5 in 0.50 M $H_2SO_4$ are shown. Such voltammograms are essentially identical to those recorded for sphene and cassiterite, respectively. For M-2 a reduction peak at –0.55 V vs. AgCl/Ag appears, followed by a prominent reduction current increasing from –0.70 V. In the reverse scan, a weak anodic peak near –0.50 V appears. The response of M-5 was similar, but here a prominent cathodic current appears at –0.55 V, while in the subsequent anodic scan a well-defined tall peak at –0.50 V is recorded. This corresponds, as described in detail elsewhere,[18] to the stripping oxidation of Sn to $Sn^{2+}$ in solution, thus denoting that the prior cathodic step results in the formation of a deposit of Sn metal. In the positive region of potentials, a weak anodic peak near +0.5 V is also recorded.

Sn-centred electrochemical processes can be described in terms of the reduction of $Sn^{IV}$ via the stepwise formation of solid $Sn^{II}$ to Sn metal. These electrochemical processes can be represented for cassiterite as:

$$SnO_2(s) + 2\ H^+ + 2e^- \rightarrow x\ SnO(s) + (1 - x)\ Sn^{2+}(aq) + H_2O \quad (1)$$

$$SnO(s) + 2\ H^+ + 2e^- \rightarrow Sn(s) + H_2O \quad (2)$$

$$Sn^{2+}(aq) + 2\ e^- \rightarrow Sn(s) \quad (3)$$

(s) denotes the solid phases.

On scanning the potential in the positive direction, after a reductive step, the metal deposits generated electrochemically are oxidized to $Sn^{2+}$ ions and $SnO^{2+}$ in the solution phase:

$$Sn(s) \rightarrow Sn^{2+}(aq) + 2\ e^- \quad (4)$$

$$Sn^{2+}(aq) + H_2O \rightarrow SnO^{2+}(aq) + 2\ H^+ + 2\ e^- \quad (5)$$

this last step is responsible for the oxidation signal at +0.5 V.

Chromium-centred processes were studied for sample-modified PIGEs upon immersion into an electrolytic solution of $H_2SO_4$ or $HClO_4$, and $NaClO_4$. To prevent the appearance of tin-centred electrochemical processes, potentials between 0.0 and +1450 mV were routinely used. The response of $Cr_2O_3$, taken as a reference in this potential

 © 2006 Wiley-VCH Verlag GmbH & Co. KGaA, Weinheim 

range, is illustrated by the square wave voltammograms (SQWVs) in Figure 3. On scanning the potential in the positive direction, a prominent oxidation wave (I) is recorded at +1340 mV (Figure 3, a). This peak shows well-defined anodic and cathodic components of the square wave current, thus suggesting a quasi-reversible behaviour.[34] Following Grygar et al.,[25–27] this wave corresponds to the oxidative dissolution process:

$$Cr_2O_3(s) + 4\ H_2O \rightarrow Cr_2O_7^{2-} + 8\ H^+ + 6\ e^- \quad (6)$$

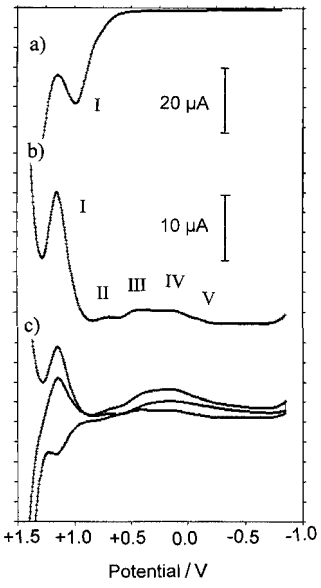


Figure 3. SQWV of $Cr_2O_3$ in contact with 0.10 M $HClO_4$ and 0.15 M $NaClO_4$. (a) potential scan initiated at –0.25 V in the positive direction; (b) potential scan initiated at +1.45 V in the negative direction; (c) id. with separate plots for the forward, backward and current increment vs. potential. Potential step increment 4 mV; square wave amplitude 25 mV; frequency 15 Hz.

On scanning the potential from +1450 mV in the negative direction, a peak near +1240 mV appears (I), followed by overlapping peaks at +700, +430, +250 and 0 mV (labelled as II, III, IV and V, respectively), as depicted in Figure 3 (b). The peak at +1240 mV corresponds to the oxidation of $Cr_2O_3$, as represented by Equation (6), and also appears when the potential is scanned in the positive direction because square wave voltammetry provides simultaneous inspection of both oxidation and reduction processes. Peaks II–V decrease rapidly until they disappear altogether when the potential scan is initiated at potentials below +950 mV, a potential for which no significant oxidative dissolution of $Cr_2O_3$ takes place; thus this denotes that such electrochemical processes are due to chromium species in solution generated during the electrochemical oxidation of chromium oxide.

The peak potential of I shifts positively on increasing the square wave frequency, *f*, while peaks II, III and IV remain essentially independent of *f* in the frequency range between 5 and 200 Hz [$E_p$(I) = +1140 ± 20 + (68 ± 2)log *f* (*N* = 9, *r* = 0.994)]. In this frequency range, peak V shifts to negative potentials on increasing the square wave frequency [$E_p$(V) = +145 ± 5 – (65 ± 5)log *f* (*N* = 9, *r* = 0.991)]. Interestingly, separate plots of the anodic and cathodic contributions to the square wave current, measured at the start and end of potential pulses, provided well-defined anodic and cathodic components for the peak at +1215 mV. However, peaks II–V exhibit only cathodic contributions as can be seen in Figure 3 (c): this denotes that these are essentially irreversible reduction processes.[34] These processes can be attributed to the stepwise reduction of $Cr_2O_7^{2-}$ ions in solution generated in the oxidative dissolution of $Cr_2O_3$. Electrochemical reduction of dichromate to $Cr^{III}$ and $Cr^{II}$ involves the formation of $Cr^{V}$ and $Cr^{IV}$ intermediates by processes II and III, but $Cr^{IV}$ is thermodynamically unstable in solution and disproportionates into $Cr^{III}$ and $Cr^{VI}$:[22]

$$6\ Cr^{IV} \rightarrow 4\ Cr^{3+} + Cr_2O_7^{2-} \quad (7)$$

Peak II is therefore enhanced with respect to peak III.

SQWVs of the studied materials exhibited some significant differences compared with those of $Cr_2O_3$. To clearly discriminate from the chromium-centred processes, in all cases, the SQWV of cassiterite and sphene was subtracted from that of the corresponding chromium-doped material. Thus, as shown in Figure 4 for: (a) M-2, and (b) M-5, the peak I appears at potentials that are more positive than that for $Cr_2O_3$ (+1290 mV) and is lowered. For samples M-2, M-3 and M-4 (Figure 4, a), an additional well-defined peak at +970 mV (VI) appears that precedes the separated peaks at +420 (VII), –30 (VIII) and –420 mV (IX). The peak VII exhibits a tall profile, suggesting that it corresponds to different electrochemical processes from those recorded for $Cr_2O_3$ at similar potentials. For samples M-5 and M-6 (see Figure 4, b), the peak VI is well developed and enhanced with respect to peaks VII, VIII and IX. Remarkably, peaks VI, VII, VIII and IX are enhanced on decreasing the frequency, a property typical of electrochemical processes involving solid phases.

Peaks VIII and IX shift to negative potentials on increasing the frequency [$E_p$(VIII) = 40 ± 5 – (60 ± 3)log *f* (*N* = 7, *r* = 0.997); $E_p$(IX) = –275 ± 5 – (99 ± 6)log *f* (*N* = 9, *r* = 0.992)], while peaks VI and VII remain essentially independent of frequency. On initiating the potential scan at +1050 mV, i.e. at a potential at which no significant oxidative dissolution of chromium centres occurs, peaks VI–IX appear with no significant decrease when compared with voltammograms initiated at +1450 mV. The above features are in contrast with those of the SQWV of $Cr_2O_3$ – peaks III–V decrease significantly on lowering the starting potential below +1250 mV.

The differences between $Cr_2O_3$ and the studied materials can be seen in Figure 5 in which the charge passed through processes III and VII ($q_{III}$, $q_{VII}$), calculated as the area under the voltammetric peak, is plotted as a function of the starting potential of the SQWVs, $E_i$. For chromium oxide, a fast decrease of $q_{III}$ with decreasing $E_i$ is obtained, whereas for the studied materials $q_{III}$ becomes insensitive to changes in $E_i$ at starting potentials below +950 mV.

 © 2006 Wiley-VCH Verlag GmbH & Co. KGaA, Weinheim 

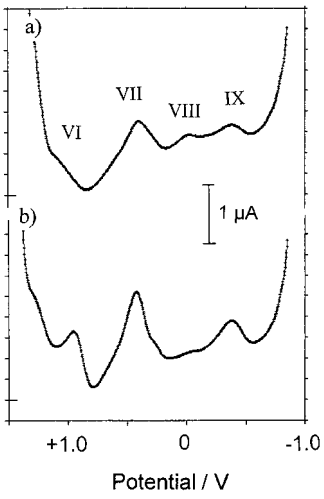


Figure 4. Semi-derivative convolution of SQWVs of : (a) M-2, and (b) M-5 immersed into 0.10 M $HClO_4$ and 0.15 M $NaClO_4$ after subtracting the SQWV of sphene and cassiterite, respectively. Potential scan initiated at +1.45 V in the negative direction. Potential step increment 4 mV; square wave amplitude 25 mV; frequency 5 Hz.

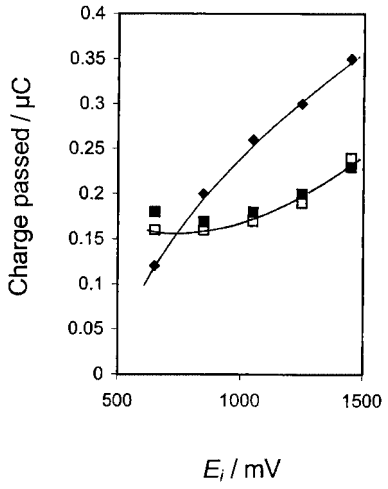


Figure 5. Variation of the charge passed during the electrochemical process III/VII with the starting potential of the SQWVs for diamonds: $Cr_2O_3$; squares: M-3; solid squares: M-6. Electrolyte: 0.10 M $HClO_4$ and 0.15 M $NaClO_4$. Potential step increment 4 mV; square wave amplitude 25 mV; frequency 5 Hz.

In the pH range between 1.5 and 4.0, peaks VII and IX shift to negative potentials on increasing the pH. For M-5, SQWVs with a potential step increment of 4 mV, a square wave amplitude of 25 mV and a frequency of 15 Hz produced: $E_p$(VII) = 585 ± 5 – (97 ± 6)pH ($N$ = 7; $r$ = 0.993); $E_p$(IX) = –255 ± 5 – (78 ± 6)pH ($N$ = 7, $r$ = 0.992). Peaks VI and VIII are essentially pH independent.

The voltammetric profile of peaks VI and VII is significantly different from that of peaks II–V recorded for $Cr_2O_3$. Remarkably, the peaks VI and VII exhibit well-developed anodic and cathodic components of the square wave current, as can be seen in Figure 6 for M-5. Here, peaks VIII and IX behave irreversibly.

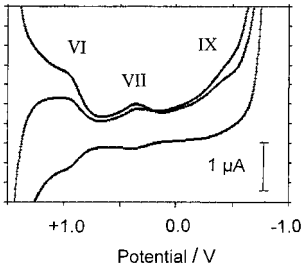


Figure 6. Separate forward, backward and current increment vs. potential graphs for the SQWVs of M-3 immersed in 0.10 M $HClO_4$ and 0.15 M $NaClO_4$. Potential scan initiated at +1.45 V in the negative direction. Potential step increment 4 mV; square wave amplitude 25 mV; frequency 15 Hz.

On comparing the SQWVs in Figure 6 with those depicted in Figure 3 (c), corresponding to $Cr_2O_3$, one can appreciate a notable increase in the reversibility of the electrochemical processes of VI and VII of the studied materials in contrast with the processes II–IV recorded for chromium oxide.

Additionally, peak VII is significantly enhanced in chromium-doped materials relative to peak I, while peaks II and IV disappear. Since it is not possible to control the exact amount of material transferred to the electrode, the quotients between the peak currents were used for comparing the voltammetric response of the studied materials with that of $Cr_2O_3$. Thus, the quotient between the peak currents of VII and I for chromium-doped materials, $i_p$(VII)/$i_p$(I), is larger than the $i_p$(III)/$i_p$(I) ratio determined for chromium(III) oxide. Interestingly, the $i_p$(VII)/$i_p$(I) ratio for M-3 increases abruptly at low frequencies, as can be seen in Figure 5. This behaviour is in contrast with that observed for $Cr_2O_3$. Here, as shown in Figure 7, the $i_p$(III)/$i_p$(I) ratio increases slowly on decreasing the frequency. For all chromium-doped cassiterites and chromium-doped sphenes, the $i_p$(VII)/$i_p$(I) ratio increases on increasing the chromium content. Pertinent peak potential data are summarised in Table 1.

All these data suggest that an amount of high oxidation states of chromium exists in the studied materials. Accordingly, the response of such materials results from the superimposition of solution processes initiated in the oxidative dissolution of $Cr^{III}$, which is similar to those described for $Cr_2O_3$, and a solid-state pathway starting from the reduction of chromium centres that exist in high oxidation states of the solids. Then, peak VI can be attributed to the reduction of $Cr^{V}$ centres mainly existing in chromium-doped cassiterite, while the peak VII, which prevails in chromium-doped sphenes, is attributable to the reduction of pristine $Cr^{IV}$ centres. In view of the possible presence of $Cr^{IV}$ centres in two different coordinations, peaks VII and VIII can be associated with the reduction of differently coordinated $Cr^{IV}$ units. This assignment is consistent with prior data showing the existence of site-characteristic voltammetric responses in vanadium-doped zircon,[35] zirconia[36] and cobalt cordierites[37] and appears to be in agreement with spectral data (vide infra). In this scheme, pro-

 © 2006 Wiley-VCH Verlag GmbH & Co. KGaA, Weinheim 

Table 1. Peak potential and peak current data for $Cr_2O_3$ and chromium-doped materials from SQWVs recorded at sample-modified PIGEs in contact with $H_2SO_4$ and 0.15 M $NaClO_4$, pH = 1.7. Potential step increment 4 mV; square wave amplitude 25 mV; frequency 15 Hz.

| Modifier | $E_p$ (I) [mV] | $E_p$(VI) [mV] | $E_p$(II) [mV] | $E_p$(III) [mV] | $E_p$(VII) [mV] | $E_p$(IV) [mV] | $i_p$(VII)/$i_p$(I) | $i_p$(III)/$i_p$(I) | $i_p$(III′)/$i_p$(I) |
|---|---|---|---|---|---|---|---|---|---|
| $Cr_2O_3$ | +1215 | – | +700 | +480 | – | +230 | – | 0.39 | – |
| M-2 | +1300 | +970 | – | – | +420 | – | 0.25 | – | 0.44 |
| M-3 | +1305 | +970 | – | – | +410 | – | 0.64 | – | 0.56 |
| M-4 | +1305 | +995 | – | – | +405 | – | 0.26 | – | 0.48 |
| M-5 | +1320 | +990 | – | – | +420 | – | 0.22 | – | 0.40 |
| M-6 | +1305 | +985 | – | – | +400 | – | 0.23 | – | 0.42 |

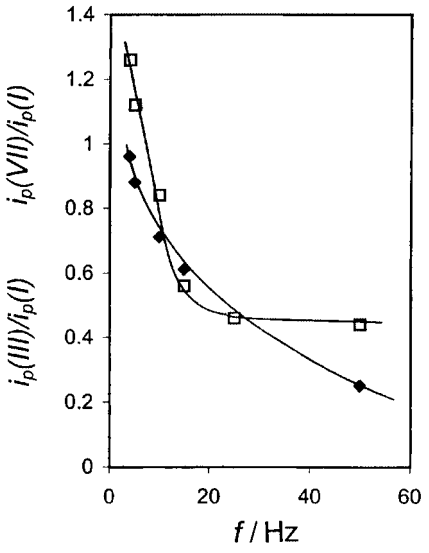


Figure 7. Variation with the square wave frequency of: $i_p$(VI)/$i_p$(I) ratio for M-6 (squares) and the $i_p$(III)/$i_p$(I) ratio for $Cr_2O_3$ (rhombs). (From SQWVs of sample-modified PIGEs immersed in 0.10 M $HClO_4$ and 0.15 M $NaClO_4$). Potential step increment 4 mV; square wave amplitude 25 mV.

cesses VI–VIII can be described in terms of solid-state redox reactions yielding $Cr^{IV}$ and $Cr^{III}$ centres. Under the experimental conditions employed here, both processes behave reversibly in such a way that proton transfer does not affect the overall reaction rate.

### Electrochemical Pathway

This reaction scheme can, in principle, be related to the model of Lovric, Scholz, Oldham and co-workers for describing the electrochemistry of insulating solids.[40–43] Redox conductivity occurs by electron hopping between adjacent redox centres and by the exchange of ions or protons with the electrolyte, as a consequence of the gradient of the electrochemical potential in the particle.

In the studied cases, the propagation of the redox reaction through the solid microparticle requires the presence of appropriate redox-active centres on the surface of the particles and free access of protons or electrolyte ions from the supporting electrolyte. The foregoing considerations also apply for the fast charge transfer observed for organic complexes of Cr,[44] metallocenes[45] and organic compounds.[46]

Subsequent reduction of the $Cr^{IV}$ centres to $Cr^{III}$ centres involves two irreversible proton-assisted reduction processes that probably result in the formation of $Cr^{III}$ centres in the solid phase (peak VII) and in solution through the processes VIII–IX.

It should be noted that in this solid-state pathway the $Cr^{IV}$ oxidation state is stabilised with respect to disproportionation, as denoted by the appearance of the well-resolved, separated peak III′.

Following a scheme similar to that previously postulated for vanadium-doped zirconias,[37] formation of $Cr^{V}$ centres may be described in terms of a process involving the insertion of OH groups and lattice distortion. Formally this can be represented as:

$$Sn_{1-x}Cr^{III}{}_xO_{2-x/2} + 2y\ OH^- \rightarrow Sn_{1-x}Cr^{III}{}_{x-y}Cr^{V}{}_yO_{2-x/2}(OH)_{2y} + 2y\ e^- \quad (8)$$

This picture is, in principle, consistent with the reaction schemes proposed for the oxidative dissolution of chromium oxides by oxometallates. According to Blesa et al., the reaction with oxometallates proceeds by oxygen transfer from the oxidant to surface $Cr^{III}$ sites and is mediated by the oxo bridge Cr–O–M.[21–23] Then, peak VI at +970 mV can be attributed to the reduction of $Cr^{V}$ surface centres to $Cr^{IV}$ centres. To describe this kind of electrode process, it is assumed that a fraction of the total $Cr^{V}$ centres is reduced to $Cr^{IV}$ ones with concomitant loss of $OH^-$ groups to ensure charge conservation and provide minor lattice distortion. Tentatively, this process can be represented by the redox reaction:

$$Sn_{1-x}Cr^{III}{}_{x-y}Cr^{V}{}_yO_{2-x/2}(OH)_{2y} + y\ e^- \rightarrow Sn_{1-x}Cr^{III}{}_{x-y}Cr^{IV}{}_yO_{2-x/2}(OH)_y + y\ OH^- \quad (9)$$

$Cr^{IV}$ centres are subsequently reduced to $Cr^{III}$ centres. Following the above criteria, this reduction process (peak VII at +420 mV) can be formulated for cassiterite as:

$$Sn_{1-x}Cr^{III}{}_{x-y}Cr^{IV}{}_yO_{2-x/2}(OH)_y + y\ e^- \rightarrow Sn_{1-x}Cr^{III}{}_{x-y}Cr^{IV}{}_yO_{2-x/2} + y\ OH^- \quad (10)$$

Reduction of the $Cr^{IV}$ centres in sphene probably involves two different processes that correspond to the octahedral $Cr^{IV}$ centres substituting for $Sn^{IV}$ and tetrahedral $Cr^{IV}$ centres substituting for $Si^{IV}$. Such electrode processes

 © 2006 Wiley-VCH Verlag GmbH & Co. KGaA, Weinheim 

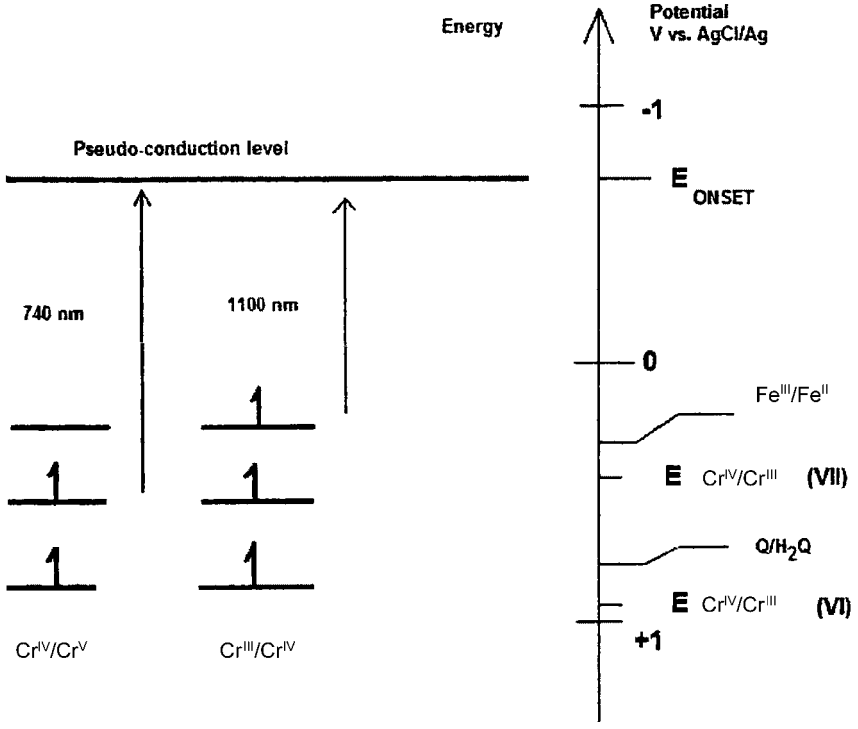


Figure 8. Energy/redox potential diagram for correlating spectrophotometric and electrochemical data in Cr-doped cassiterite and Cr-doped sphene.

can correspond to peak VIII and eventually can form $Cr^{3+}$ ions in solution:

$$CaSn_{1-x}Cr^{III}_{x-y}Cr^{V}_{y}SiO_{5-x/2}(OH)_y + y\ H^+ + y\ e^- \rightarrow CaSn_{1-x}Cr^{III}_{x}SiO_{5-x/2} + y\ H_2O \quad (11)$$

Finally, the peak IX can be attributed to the reduction of $Cr^{3+}$ to $Cr^{2+}$ in the solution phase.

## Correlation Between Spectral and Electrochemical Data

Correlation between electrochemical and spectroscopic data in solids usually focuses on the determination of the bandgap energy and the electrochemical HOMO and LUMO energies ($E^{HOMO}$, $E^{LUMO}$), corresponding to the estimated position of the upper edge of the valence band (HOMO) and the lower edge of the conduction band (LUMO).[47] In our case, spectral properties of chromium centres can be correlated with formal electrode potentials on the basis of energy diagrams of the 3d energy states of $Cr^{III}$, $Cr^{IV}$, and $Cr^{V}$ proposed by Sakai et al.,[48] and Moretti and Michel-Calendini[49] with respect to the cluster valence edge of chromium-doped $BaTiO_3$ and to those recently calculated by Long et al.[50] for describing the spectra of $Cr^{III}$-doped $LaSc_3(BO_3)_4$, by Torchia et al.[51] for $Cr^{III}$ ions in $LiNbO_3$, by Kammoun[52] for $Cr^{IV}$ ions in $LiAlO_2$ and by Herren et al.[53] for $Cr^{V}$ in chromium-doped $SiO_2$ glass.

From this one can attribute energies of 2.06, 0.98 and 0.36 eV to the $Cr^{III}$ ($^4A_2$ state), $Cr^{IV}$ ($^3T_1$) and $Cr^{V}$ ($^2T_2$) centres in octahedral coordination, respectively, relative to the valence band edge corresponding to the O 2p $t_{1g}$ level relevant to the $MO_6$ cluster. Term energies for crystal field transitions are: $Cr^{III}$ ($^4A_2 \rightarrow {}^4T_1$, $^4T_2$) 2.10 eV; $Cr^{IV}$ ($^3T_1 \rightarrow {}^1T_2$) 1.26 eV; $Cr^{V}$ ($^2T_2 \rightarrow {}^2E_2$) 2.60 eV.[50–53] Formal electrode potentials are correlated with the vacuum level by assuming that the normal hydrogen electrode is 4.4 eV below the vacuum level.[54,55] Accordingly, the AgCl/Ag electrode will be 4.6 eV below the vacuum level. The corresponding energy diagram is shown in Figure 8. The upper edge of the valence band can in principle be approached by the voltammetric onset potential obtained from the intersection of the two tangents drawn at the rising current and the baseline charging current of the curves for the oxidation process.[56,57] The onset potential taken from the rising background current in Figure 4 was +1.43 V. Examination of the energy diagram in Figure 8 reveals that formal electrode potentials for the $Cr^{V}/Cr^{IV}$ and $Cr^{IV}/Cr^{III}$ couples are close to the vacuum energy levels for $Cr^{V}$ and $Cr^{IV}$ ions, respectively.

## Electrocatalytic Processes

As already reported,[36,37] inorganic materials doped with electroactive species can exert a significant catalytic effect on selected electrochemical processes. Thus, Figure 9 shows a comparison of the CVs recorded in a 0.50 mM $K_4Fe(CN)_6$ and a 0.50 M $H_2SO_4$ solution at: (a) bare PIGE, (b) M-3 under dark conditions and (c) M-3 under Vis-IR illumination. As can be seen in Figure 9 (a), at the unmodified PIGE, the CVs of $Fe(CN)_6^{4-}$ solutions exhibit a well-defined reversible couple at peak potentials of +445 (anodic) and +335 mV (cathodic). For electrodes modified with chromium-doped materials under "dark" conditions, the

 © 2006 Wiley-VCH Verlag GmbH & Co. KGaA, Weinheim 

anodic portion of the CV becomes significantly modified. As can be seen in Figure 9 (b), an additional peak at +620 mV appears coupled with a weak cathodic signal near +580 mV and the overall peak current is enhanced. For samples M-2, M-3 and M-4, this response changes upon illumination. As can be seen in Figure 9 (c) for M-3, the current is depleted, while the peak at +620 mV vanishes. However, for samples M-5 and M-6 the catalytic effect remains insensitive to illumination with visible light.

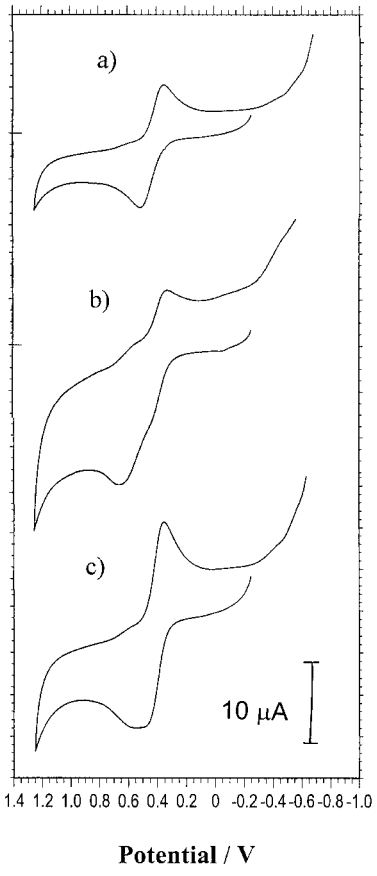


Figure 9. CVs recorded in a 0.50 mM $K_4Fe(CN)_6$ and 0.50 M $H_2SO_4$ solution at: a) bare PIGE; b) M-3-modified electrode under dark conditions, and c) M-3-modified electrode under illumination. Potential scan rate 50 mV $s^{-1}$.

The anodic peak at +620 mV can be attributed to the modifier-mediated oxidation of $Fe(CN)_6^{4-}$. In view of the close proximity of the potentials for the $Fe(CN)_6^{3-}/Fe(CN)_6^{4-}$, $Cr^V/Cr^{IV}$ and $Cr^{IV}/Cr^{III}$ couples, the catalytic effect can, in principle, be attributed to both $Cr^V$ and $Cr^{IV}$ centres, in agreement with the theory for mediated electrocatalysis.[58] The observed voltammetric profile can be interpreted in terms of the formation of a surface (chromium centre)–$Fe(CN)_6^{4-}$ adduct and the superimposition of the currents for the nonmediated (peak at +440 mV) and mediated (peak at +620 mV) oxidation of $Fe(CN)_6^{4-}$.

This is consistent with the variation with the frequency of the SQWVs illustrated in Figure 10 for M-4 in contact with 0.50 mM $K_4Fe(CN)_6$ and 0.50 M $H_2SO_4$. The peak at +620 mV is enhanced as the frequency decreases, in agreement with the assignment of this peak to the oxidation of a surface-confined species.

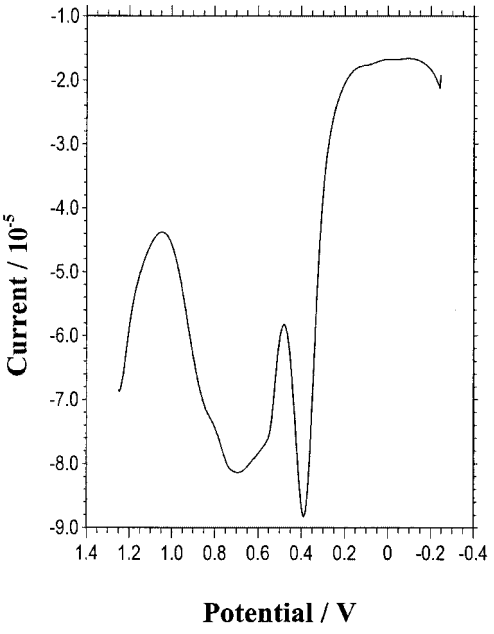


Figure 10. SQWV of a 0.50 mM $K_4Fe(CN)_6$ and 0.50 M $H_2SO_4$ solution at an M-4-modified electrode under dark conditions. Potential step increment 4 mV; square wave amplitude 25 mV; frequency 25 Hz.

The decrease in the catalytic ability of samples M-2, M-3 and M-4 under illumination can be rationalised on the basis of previously discussed spectroscopic data assuming that $Cr^{IV}$ centres act as catalytic sites, as suggested by the close vicinity of its redox potential (+420 mV) and that of the $Fe(CN)_6^{3-}/Fe(CN)_6^{4-}$ couple (+390 mV). Upon illumination, there is excitation of $Cr^{IV}$ centres that is equivalent, in agreement with literature data,[50,53] to a negative potential shift of 1.03 V of the $Cr^{IV}/Cr^{III}$ couple, as schematised in Figure 8. These features result in a significant decrease in the catalytic ability of chromium centres, which is reflected in the lowering of the peak current.

Comparable features were obtained for the electrocatalyis of 1,4-dihydrobenzoquinone ($H_2Q$) oxidation, illustrated in Figure 11 for a 0.40 mM solution of $H_2Q$ in 0.50 M $H_2SO_4$. As depicted in Figure 11 (a), at a bare graphite electrode, two overlapping anodic peaks appear at +700 and +850 mV, corresponding, in agreement with extensive literature on the electrochemistry of $H_2Q$, to the stepwise oxidation of hydroquinone to quinone:[59,60]

$$H_2Q \rightarrow Q + 2\,H^+ + 2\,e^- \quad (12)$$

As shown in Figure 11 (b) for M-6, the current for $H_2Q$ oxidation is enhanced at electrodes modified with Cr-doped cassiterite under dark conditions. Again, the catalytic effect decreases upon illumination with visible light, as can be seen in Figure 11 (c). Remarkably, the catalytic effect is almost entirely absent for Cr-doped sphene samples. Such electrochemical data can again be interpreted with the help of the energy/redox potential diagram in Figure 8. Here, the

 © 2006 Wiley-VCH Verlag GmbH & Co. KGaA, Weinheim 

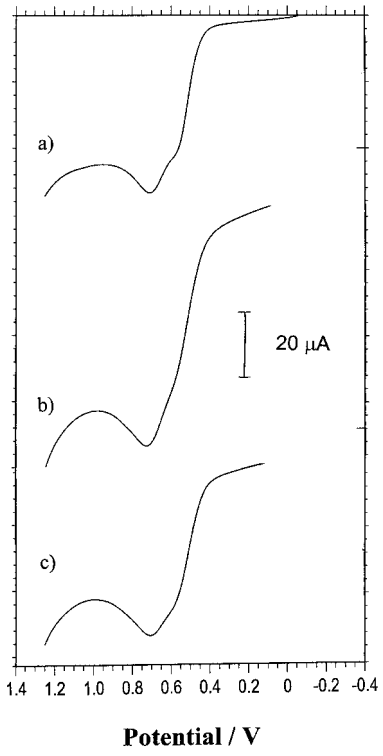


Figure 11. LSVs of a 0.40 mM solution of 1,4-dihydrobenzoquinone in 0.50 M $H_2SO_4$ at: a) bare PIGE; b) M-6 under dark conditions; and c) M-6 under illumination. Potential scan rate 20 mV $s^{-1}$.

formal potential of the $Cr^V/Cr^{IV}$ couple (+970 mV) is close to the redox potential for $H_2Q$ oxidation (+850 mV), thus suggesting that the $Cr^V$ species in Cr-doped cassiterite are now catalytically active. Excitation of $Cr^V$ centres upon illumination involves a gain in energy of 2.60 eV,[48,53] equivalent to a significant negative shift of the potential of the $Cr^V/Cr^{IV}$. Accordingly, illumination produces a significant decrease in the catalytic ability of $Cr^V$ centres in chromium-doped cassiterite.

## Final Considerations

Solid-state electrochemical data suggest that $Cr^V$ and $Cr^{IV}$ centres exist in chromium-doped cassiterite and sphene materials. The well-defined reduction of $Cr^V$ centres to $Cr^{IV}$ ones occurs at +0.97 mV for Cr-doped $SnO_2$. The oxidation state $Cr^{IV}$ prevails in Cr-doped sphene, where the solid-state $Cr^{IV}$ to $Cr^{III}$ reduction takes place at +420 mV.

$Cr^{IV}$ centres produce a significant catalytic effect on the electrochemical oxidation of $Fe(CN)_6^{4-}$ ions in acidic aqueous media. For chromium-doped sphenes the electrocatalytic effect decreases upon visible light irradiation. Electrochemical and spectroscopic data are consistent with an electrocatalytic pathway involving the formation of a surface-confined $Cr^{IV}$–hexacyanoferrate(II) adduct. Similarly, the oxidation of 1,4-dihydrobenzoquinone is catalysed by Cr-doped sphene, but the catalytic effect decreases upon illumination. This electrocatalytic effect can be associated with the presence of $Cr^V$ in such materials.

All these results illustrate the capabilities of the voltammetry of microparticles for providing chemical information on doped materials.

## Experimental Section

### Preparation and Characterisation of Specimens

We have used two methods of synthesis in order to show the industrial preparation of these ceramic pigmenting systems. The undoped and Cr-doped sphene were prepared by a sol-gel technique used previously.[5] The prepared samples contain an amount of chromium that replace the Sn cations, and in order to preserve the electroneutrality the divalent calcium cation was replaced by neodymium or ytrium trivalent cations. The prepared samples of the undoped $CaSnSiO_5$, $Ca_{0.95}Nd_{0.05}Sn_{0.95}Cr_{0.05}SiO_5$ and $Ca_{0.95}Y_{0.05}Sn_{0.95}Cr_{0.05}SiO_5$, are referred to as M-1, M-2 and M-3, respectively. An additional sample was prepared by replacing some of the silicium cations by aluminium cations, $Ca_{0.90}Y_{0.10}Sn_{0.95}Cr_{0.05}Si_{0.95}Al_{0.05}O_5$, and is referred to as M-4. Tetraethylorthosilicate (TEOS), $CaCl_2{\cdot}2H_2O$, $CrCl_3{\cdot}6H_2O$, and $Y^{III}$ acetate (from Merck), $SnCl_2$ (from Aldrich) and $Nd(NO_3)_3{\cdot}6H_2O$ (from Rhône–Poulenc) were used as reagents. Gels were prepared by refluxing an ethanolic solution containing the required amounts of cation salts and TEOS at 70 °C. The TEOS/$H_2O$/ethanol molar ratio in the final solution was 1:12:20. The obtained gel was further dried at 120 °C.

The Cr-doped $SnO_2$ samples were prepared by a wet method that is similar to that described previously.[2] Samples with stoichiometry $Cr_xSn_{1-x}O_2$ ($x$ = 0.05 and 0.1, referred to as M-5 and M-6) were prepared from $Cr(NO_3)_3{\cdot}6H_2O$ and $SnO_2$ (from Merck). First, the required amount of chromium nitrate was dissolved in distilled water. $SnO_2$ was then added to the above, and the final concentration of the solution was 0.05 mol·$dm^{-3}$. The obtained dispersion was heated whilst stirring until the water was removed. Further drying of the powdered sample was performed at 120 °C. Dried gels were thermally treated at several temperatures from 800 to 1300 °C with 2 h holding time.

$H_2SO_4$, $HClO_4$ (Panreac) and $NaClO_4$ (Merck) were used for electrolyte preparation. $SnO_2$ (Fluka) and $Cr_2O_3$ (Fluka) were used as reference materials. Electrocatalytic experiments were performed in solutions of $K_4Fe(CN)_6$ (Carlo Erba) and 1,4-dihydrobenzoquinone (Fluka).

### Characterisation Techniques

The structural and microstructural features of the final pigmenting systems were examined using different techniques. X-ray diffraction analysis (Model D-500, Siemens, Karlsruhe, Germany) was performed using a graphite-monochromated Cu-$K_a$ radiation. The diffractometer had two 1° divergence slits, the scatter and receiving slits were 1° and 0.05°, respectively.

UV/Vis spectra of the specimens (Model Lambda 9, Perkin–Elmer, Norwalk, Connecticut, U.S.A.) were obtained using the diffuse reflectance technique in the range of 200 to 1000 nm using a $BaSO_4$ plate as the reflectance standard. The absorbance was represented by the emission function, $F(R) = (1 - R)^2/2R$, where $R$ is reflectance.

The microstructure of the final powdered samples was observed by field emission scanning electron microscopy at 30 kV (Model S-4100, Hitachi Ltd., Tokyo, Japan). To check the quality of the observation, some of the samples were etched with a diluted HF solution for 10 s and subsequently washed with distilled water.

 © 2006 Wiley-VCH Verlag GmbH & Co. KGaA, Weinheim 

**Modified Electrode Preparation and Electrochemical Techniques**

Paraffin-impregnated graphite electrodes (PIGEs) consist of cylindrical rods of graphite, with a diameter of 5 mm, which are impregnated under vacuum by paraffin. Preparation details are described in ref.[1]

To prepare sample-modified PIGEs, 0.1–1 mg of the material was powdered in an agate mortar and pestle, and placed on a glazed porcelain tile to form a spot of finely distributed material and then abrasively transferred to the surface of a PIGE by rubbing the electrode over that spot of sample.

Electrochemical experiments were performed at 298 K in a three-electrode cell under argon using a AgCl (3 M NaCl)/Ag reference electrode and a platinum-wire auxiliary electrode. Linear potential scan, cyclic and square wave voltammograms were obtained with BAS CV 50 W and CH I420 instruments. Unless stated, SQWVs were recorded by initiating the potential scan either at +0.85 and –0.85 V using a potential step increment of 4 mV and varying the square wave amplitude between 20 and 200 mV and the frequency between 2 and 200 Hz. Eventually semi-derivative convolution of data was performed in order to increase peak resolution.

Electrocatalytic experiments were performed in $K_4Fe(CN)_6$ solutions in two ways: (a) under dark conditions, confining the cell within the BAS CE-2 box, and (b) upon exposing the cell to direct illumination with conventional VIS and IR lamps located in azimuthal positions with respect to the electrochemical cell.

**Supporting Information:** (see footnote on the first page of this article). X-ray diffraction patterns of specimens thermally treated at final temperatures for 2 h: M1 at 1400 °C and M-5 and M-6 at 1300 °C; and field emission scanning electron microscopy micrographs of specimens thermally heated at 1300 °C.


[1] D. V. Shangani, G. R. Abrams, P. J. Smith, *Trans. J. Br. Ceram. Soc.* **1981**, *80*, 210–214.
[2] P. Escribano, C. Guillem, J. Alarcón, *Am. Ceram. Soc. Bull.* **1984**, *63*, 1492–1494.
[3] I. Ou-benmmou, H. Ahamdane, M. A. El idrisi, F. Bensamka, A. Mosset, M. L. El Idrisi, J. C. Jumas, *J. Eur. Ceram. Soc.* **2000**, *20*, 2159–2163.
[4] M. Muthuraman, K. C. Patil, *Mater. Res. Bull.* **1998**, *33*, 655–661.
[5] L. Ferrer, M. Sales, J. Alarcón, *Third Euro-Ceramics* **1993**, *2*, 935–938.
[6] E. Lopez-Navarrete, M. Ocaña, *J. Eur. Ceram. Soc.* **2002**, *22*, 353–359.
[7] E. Lopez-Navarrete, A. R. González-Elipe, M. Ocaña, *Ceram. Int.* **2003**, *29*, 385–392.
[8] F. Ren, S. Ishida, N. Takeuchi, K. Fujiyoshi, *Am. Ceram. Soc. Bull.* **1992**, *71*, 759–764.
[9] E. López-Navarrete, A. Caballero, V. M. Orera, F. J. Lázaro, M. Ocaña, *Acta Materialia* **2003**, *51*, 2371–2381.
[10] R. S. Pavlov, V. B. Marzá, J. B. Carda, *J. Mater. Chem.* **2002**, *12*, 2825–2832.
[11] B. Julián, H. Beltrán, E. Cordoncillo, P. Escribano, J. V. Folgado, V. Vallet-Regí, R. P. Del Real, *Eur. J. Inorg. Chem.* **2000**, *10*, 2694–2700.
[12] P. Maireles-Torres, P. Oliveira-Pastor, E. Rodríguez-Castellón, A. Jiménez-López, A. A. G. Tomlinson, *J. Solid State Chem.* **1991**, *94*, 368–380.
[13] V. Felice, B. Dussardier, J. K. Jones, G. Monnom, D. B. Ostrowsky, *Optical Mater.* **2001**, *16*, 269–277.
[14] F. Scholz, B. Meyer, *Electroanalytical Chemistry, A Series of Advances* (Eds.: A. J. Bard, I. Rubinstein), Marcel Dekker, New York, **1998**, *20*, p. 1.
[15] T. Grygar, F. Marken, U. Schröder, F. Scholz, *Collect. Czech. Chem. Commun.* **2002**, *67*, 163–208.
[16] H. A. Laitinen, *Denki Kagaku* **1976**, *44*, 626–631.
[17] S. Zhang, B. Meyer, G. Moh, F. Scholz, *Electroanalysis* **1995**, *7*, 319–328.
[18] A. Doménech, M. T. Doménech, M. T. *Electroanalysis*, in press.
[19] J. Liu, Z. H. Wang, Y. M. Wang, G. A. Luo, H. W. Sun, *Chinese Chem. Lett.* **2002**, *13*, 765–768.
[20] W. Y. Wang, C. M. Wang, *J. Chin. Chem. Soc.* **2000**, *47*, 405–414.
[21] D. Liu, P. V. Kamat, *J. Electrochem. Soc.* **1995**, *142*, 835–839.
[22] M. A. Blesa, P. J. Morando, A. E. Regazzoni, *Chemical dissolution of metal oxides.* CRC Press, Boca Raton, **1994**.
[23] L. G. Rodenas, P. J. Morando, M. A. Blesa, S. Duhalde, C. Saragovi, *Can. J. Chem.* **1993**, *71*, 771–778.
[24] L. G. Rodenas, M. Chocrón, P. J. Morando, M. A. Blesa, *Can. J. Chem.* **1996**, *74*, 103–106.
[25] T. Grygar, *J. Electroanal. Chem.* **1996**, *405*, 117–125.
[26] T. Grygar, *J. Solid State Electrochem.* **1998**, *2*, 127–136.
[27] T. Grygar, P. Bezdicka, *J. Solid State Electrochem.* **1998**, *3*, 31–38.
[28] A. Dostal, U. Schröder, F. Scholz, *Inorg. Chem.* **1995**, *34*, 1711–1717.
[29] A. M. Bond, R. Colton, F. Daniels, D. R. Fernando, F. Marken, Y. Nagaosa, R. F. M. Van Steveninck, J. N. Walter, *J. Am. Chem. Soc.* **1993**, *115*, 9556–9562.
[30] M. J. Carmezim, A. M. Simoes, M. O. Figueiredo, M. Da Cunha Belo, *Corros. Sci.* **2002**, *44*, 451–465.
[31] G. Horanyi, *J. Electroanal. Chem.* **1991**, *306*, 287–290.
[32] R. Bardykina, A. I. Falicheva, *Elektrokhimiya* **1987**, *23*, 1080–1086.
[33] J. M. Eckert, R. J. Judd, P. A. Lay, *Inorg. Chem.* **1987**, *26*, 2189–2191.
[34] M. Lovric, in *Electroanalytical Methods* (Ed.: F. Scholz), Springer, Berlin, **2002**, p. 111.
[35] A. Doménech, J. Alarcón, *J. Solid State Electrochem.* **2002**, *6*, 443–450.
[36] A. Doménech, F. J. Torres, J. Alarcón, *Electrochim. Acta* **2004**, *49*, 4623–4632.
[37] A. Doménech, F. J. Torres, J. Alarcón, *J. Solid State Electrochem.* **2004**, *8*, 127–137.
[38] A. M. Heyns, P. M. Harden, *J. Phys. Chem. Solids* **1999**, *60*, 277–284.
[39] A. Belletti, R. Borromei, L. Oleari, *Inorg. Chim. Acta* **1995**, *235*, 349–355.
[40] M. Lovric, F. Scholz, *J. Solid State Electrochem.* **1997**, *1*, 108–113.
[41] M. Lovric, F. Scholz, *J. Solid State Electrochem.* **1999**, *3*, 172–175.
[42] K. B. Oldham, *J. Solid State Electrochem.* **1998**, *2*, 367–377.
[43] U. Schröder, K. B. Oldham, J. C. Myland, P. J. Mahon, F. Scholz, *J. Solid State Electrochem.* **2000**, *4*, 314–324.
[44] A. M. Bond, F. Marken, *J. Electroanal. Chem.* **1994**, *372*, 125–135.
[45] A. M. Bond, J. B. Cooper, F. Marken, D. M. Way, *J. Electroanal. Chem.* **1995**, *396*, 407–418.
[46] S. Komorsky-Lovric, *J. Solid State Electrochem.* **1997**, *1*, 94–99.
[47] F. P. Koffyberg, F. A. Benko, *J. Appl. Phys.* **1982**, *53*, 1173–1177.
[48] P. Moretti, F. M. Michel-Calendini, *Phys. Rev. B* **1987**, *36*, 3522–3527.
[49] N. Sakai, Y. Ebina, K. Takada, T. Sasaki, *J. Am. Chem. Soc.* **2004**, *126*, 5851–5858.
[50] X. Long, Z. Lin, Z. Hu, G. Wang, *Chem. Phys. Lett.* **2004**, *392*, 192–195.
[51] G. A. Torchia, O. Martínez-Matos, P. Vaveliuk, J. O. Tocho, *Solid State Commun.* **2003**, *127*, 535–539.
[52] S. Kammoun, *J. Lumin.* **2004**, *106*, 205–210.
[53] M. Herren, H. Nishiuchi, M. Morita, *J. Chem. Phys.* **1994**, *101*, 4461–4462.


 © 2006 Wiley-VCH Verlag GmbH & Co. KGaA, Weinheim 

[54] S. Trasatti, *Pure Appl. Chem.* **1986**, *58*, 955–966.
[55] T. Kida, G. Guan, Y. Minami, T. Ma, A. Yoshida, *J. Mater. Chem.* **2003**, *13*, 1186–1191.
[56] Z.-K. Chen, W. Huang, L.-H. Wang, E.-T. Kang, B. J. Chen, C. S. Lee, S. T. Lee, *Macromolecules* **2000**, *33*, 9015–9025.
[57] M. S. Liu, X. Jiang, S. Liu, P. Herguth, A. K.-Y. Jen, *Macromolecules* **2002**, *35*, 3532–3538.
[58] C. P. Andrieux, J. M. Dumas-Bouchiat, J. M. Savéant, *J. Electroanal. Chem.* **1982**, *131*, 1–35.
[59] D. Garreau, P. Hapiot, J. M. Savéant, *J. Electroanal. Chem.* **1990**, *281*, 73–83.
[60] D. H. Evans, *Chem. Rev.* **1990**, *90*, 739–751.
Received: September 1, 2005
Published Online: December 13, 2005

 © 2006 Wiley-VCH Verlag GmbH & Co. KGaA, Weinheim 

DOI: 10.1002/ejic.200500621

# Reactions of Furylruthenium Complexes with Oxygen and Trimethylsilyl Azide

**Ku-Hsien Chang,[a] Hui-Ling Sung,[a] and Ying-Chih Lin*[a]**

**Keywords:** Ruthenium / Furyl ligand / Oxygen

The reaction of the (α-alkoxyfuryl)ruthenium complexes **4** with oxygen opens the five-membered furyl ring to give the addition product [Ru]$O_2$CCR=CHC$O_2$$CH_3$, (**5**, [Ru] = Cp($PPh_3$)$_2$Ru). Further reactions of **5** with $CH_3I$ and with organic acid gave $CH_3O_2$CCR=CHC$O_2$$CH_3$, (**6**), and $HO_2$CCR=CHC$O_2$$CH_3$, (**7**), respectively. The reaction of **4** with $TMSN_3$ [TMS = $(CH_3)_3$Si] gives the ruthenium azide [Ru]–$N_3$ and α-alkoxyfuran, which is readily hydrolyzed to lactone in acidic medium. Treatment of the cyclopropenylruthenium complex **11b** containing a methyl crotonate group with $TMSN_3$ affords the five-membered-ring triazole and [Ru]–CN. In this reaction cleavage of the C=C double bond of the three-membered ring could be caused by consecutive additions of $TMSN_3$ to olefinic carbon atoms of intermediates formed during the reaction.

(© Wiley-VCH Verlag GmbH & Co. KGaA, 69451 Weinheim, Germany, 2006)

## Introduction

Chemistry of organometallic ruthenium complexes plays important role in many catalytic reactions, such as asymmetric hydrogenation,[1] olefin metathesis[2] and polymerization.[3] Metal-mediated processes in many instances make possible certain reactions, which are not feasible without the involvement of metal ions. It is therefore important to better understand how an organic moiety attached on the metal undergoes chemical transformation. We previously reported the synthesis of cyclopropenyl complexes of ruthenium through a deprotonation reaction of vinylidene complexes.[4] The same approach could also be used for the synthesis of metal-coordinated azirinyl complexes from metal isocyanide complexes.[5] Highly strained organic cyclopropene and azirine compounds are synthetically useful.[6] Participation of *d* orbital of Ru metal may stabilize this highly strained organic moiety consisting of a three-membered ring thus making these complexes readily accessible for further exploitation for the preparation of organic molecules. For example, reactions of various cyclopropenylruthenium complexes with $TMSN_3$ gave a number of tetrazole and triazole compounds depending on the substituents on the three-membered ring.[7] And the reactions of azirinylruthenium complexes with aldehyde or acetone gave oxazolinyl complexes.[6] The previously reported regiochemistry of the carbon–carbon bond formation in the photoreaction of organic azirine with carbonyl group is reversed.[8]

Interestingly, upon deprotonation of vinylidene complexes containing an ester group at Cγ of the vinylidene ligand, we observed formation of furyl complexes as thermodynamic products. The corresponding cyclopropenyl complex was also observed as a kinetic product. It is known that organic cyclopropenyl ketones in the presence of metal halides could be converted to furans.[9] D′yakonov and his co-workers also reported that the reaction of ethyl diazoacetate with 1-phenylpropyne give cyclopropene ester and 2-ethoxyfuran.[10] The former compound underwent photolysis to give the latter one, which yielded diethyl ester upon air oxidation.[11] Synthesis and reactions of a few transition-metal furyl complexes have been reported. Iridium hydride complex containing σ-furyl ligand can be obtained by the reaction of metal cyclooctadienyl complex with furan.[12] The metal furyl complex reacted with *tert*-butylacetylene by insertion of the alkyne into the Ir–C bond to form an vinyl iridium hydride complex.[13] Furyl tungsten complexes are obtained by the reaction of propargyl tungsten complexes with aldehydes. This furyl ligand is easily dissociated from the metal fragment and further reacts with Grignard reagent.[14]

Trimethylsilyl azide and sodium azide were used widely in organic or organometallic reactions.[15] Organic azides react with alkenes or alkynes giving triazoline or triazole compounds through a [3+2] cycloaddition.[16] However, for efficient [3+2] cycloaddition to give triazoles, the presence of an electron-withdrawing group is needed either at the alkyne or at the azide part. Coupling reaction between azide, such as $TMSN_3$, with simple alkyne and allyl carbonates catalyzed by $Pd^0$/$Cu^I$ was reported by Yamamoto and his co-workers[17] as an efficient method for the synthesis of triazoles. The azide reagent is also commonly used in the synthesis of metal complexes with N-heterocyclic ligand. A number of N-coordinated Fe tetrazole derivatives were obtained by the reaction of sodium azide with the coordinated CN of the N-coordinated iron nitrile complex. The mechanism probably involves nucleophilic attack of the azide

[a] Department of Chemistry, National Taiwan University, Taipei, Taiwan 106, Republic of China

 © 2006 Wiley-VCH Verlag GmbH & Co. KGaA, Weinheim InterScience 

anion to the carbon atom of the coordinated nitrile followed by cyclization.[18] The reaction of furyl metal complexes with $TMSN_3$ was not investigated before. Herein we report reactions of the furylruthenium complex with oxygen and $TMSN_3$ and the reaction of the cyclopropenylruthenium complex containing a crotonate group with $TMSN_3$ is also reported.

## Results and Discussion

**Preparation of Furyl Complexes:** The reaction of the vinylidene complex **2a** containing a 1-cyclohexenyl group at $C_\beta$ and an ester group at $C_\gamma$ with $n$Bu$_4$NOH in acetone yields the furyl complex **4a** as the thermodynamic product (Scheme 1). The reaction proceeds through protonation at $C_\gamma$ followed by an intramolecular cyclization first giving the three-membered cyclopropenyl complex **3a** as the kinetic product with a small amount of **4a** within 0.5 h. Conversion of **3a** to **4a** is completed within 3 h. The $^{31}$P NMR spectrum of **4a** displays a singlet resonance at $\delta$ = 50.6 ppm, however, the $^{31}$P NMR spectrum of the kinetic product **3a** displays a two-doublet pattern at $\delta$ = 52.5, 48.5 ppm with $J_{P-P}$ = 36.4 Hz indicating the presence of a stereogenic carbon center at the cyclopropenyl ligand. As shown in Scheme 1, the furylruthenium complex **4b** was also prepared by deprotonation of the vinylidene complex **2b** containing a phenyl substituent.[4b] Deprotonation reaction of dinuclear vinylideneruthenium complexes containing an ester substituent at C$\gamma$ gave the dinuclear bisfuryl complexes.[4e] Organic furan adds to [Ir(COD)(PMe$_3$)$_3$]Cl to yield a furyl iridium hydride complex.[12]

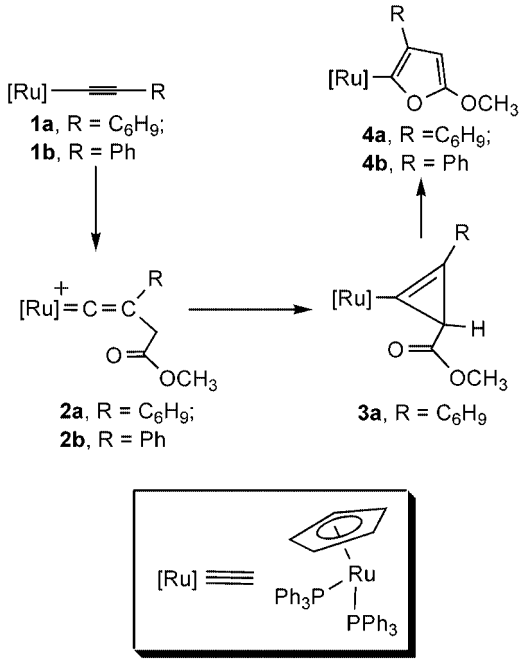


Scheme 1.

**Reaction of 4 with Oxygen:** Exposure of complex **4a** as a solid in air for two weeks generates the oxygen addition product [Ru]O$_2$CC(C$_6$H$_9$)=CHCO$_2$CH$_3$, (**5a**) in almost quantitative yield. The reaction is faster in solution but is accompanied with extensive decomposition. Under the same reaction condition, exposure of complex **4b** also yields the analogous oxygen addition product **5b** (Scheme 2).

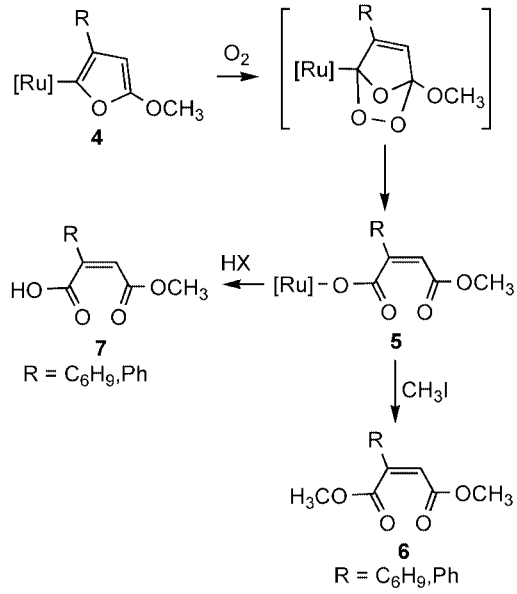


Scheme 2.

In the $^1$H NMR spectrum of **5a** two singlet resonances at $\delta$ = 5.53 and 4.79 ppm are assigned to the olefinic proton and the Cp group, respectively. The $^{31}$P NMR spectrum of **5a** in $CDCl_3$ displays a singlet resonance at $\delta$ = 39.5 ppm. In the $^{13}$C NMR spectrum the resonance at $\delta$ = 174.2 ppm is assigned to the O-coordinated $CO_2$ group and the resonance at $\delta$ = 166.9 ppm is assigned to the $CO_2$ group of the terminal ester.

Furan is known to react with singlet oxygen.[19] It has been reported by Scarpati and her co-workers that photosensitized oxidation of various substituted furans under strictly anhydrous conditions at about –15 °C generated in quantitative yields the *endo*-peroxides, which decomposed at room temperature in the absence of solvent and moisture. However, at 4 °C the *endo*-peroxide in nitromethane was converted into the oxiranes.[20] These *endo*-peroxides could also react with diethyl sulfide at 0 °C yielding diones, which further react with *tert*-butyl hydroperoxide in the presence of triethylamine to give oxiranes. On the basis of these reports, we propose that the reaction of the furylruthenium complex with $O_2$ could proceed through the formation of the *endo*-peroxide intermediate with subsequent ruthenium migration to oxygen accompanied with cleavage of both C–O and O–O bonds affording complex **5a** (Scheme 2). The reaction could occur in both solid and liquid state without prior formation of singlet oxygen.[19] The *endo*-peroxide intermediate was not observed in our system. This facile reaction could possibly be assisted by the participation of the *d* orbital of the ruthenium metal and/or the presence of the neighboring methoxy group.[11]

Further reaction of **5a** with $CH_3I$ generates metal iodide [Ru]–I and the diester **6a** containing a 1-cyclohexenyl sub-

 © 2006 Wiley-VCH Verlag GmbH & Co. KGaA, Weinheim 

stituent[21] by cleavage of the Ru–O bond (Scheme 2). The reaction was carried out at 50 °C and the organic product **6a** was extracted with diethyl ether and was identified by NMR spectroscopy. In the $^1$H NMR spectrum of **6a**, two singlet resonances at $\delta$ = 3.88 and 3.71 ppm with the ratio 1:1 are assigned to two $OCH_3$ groups. Analogous, the diester compound **6b** can also be obtained from the reaction of **5b** with $CH_3I$. Compound **6b** was previously obtained from the reaction of phenylacetylene with alcohol at room temperature under atmospheric pressure of carbon monoxide in the presence of Pd catalyst.[22] The reaction of **5** with protic acid breaks the Ru–O bond and yields compound **7**, which was identified by NMR and high-resolution mass spectroscopy.

**Reactions of $TMSN_3$ with Furylruthenium Complexes:** Reactions of $TMSN_3$ with furylruthenium complexes **4a** and **4b** give the metal-free α-alkoxyfuran **8**, (**8a**, R = $C_6H_9$; **8b**, R = Ph), respectively, and the ruthenium azide complex [Ru]–$N_3$[7a] in high yield (Scheme 3). In the $^1$H NMR spectrum of **8a**, the doublet resonance at $\delta$ = 5.25 with $^4J_{H,H}$ = 1.2 Hz is assigned to the olefinic hydrogen. In the 2D-NMR COSY spectrum, this resonance is found to correlate with the resonance at $\delta$ = 6.78 ppm (overlapped with those of phenyl hydrogen) assignable to the other olefinic proton on the furyl ring. Hydrolysis of α-alkoxyfuran **8b** in acidic condition gave organic the lactone 4-phenyl-2(5*H*)-furanone (**9b**) in quantitative yield. The $^1$H NMR spectrum of **9b** displays a triplet resonance at $\delta$ = 6.36 ppm and a doublet resonance at $\delta$ = 5.22 ppm with a ratio of 1:2 with $^4J_{H,H}$ = 1.8 Hz. Hydrolysis of alkoxyfuran to lactone has been reported.[23] Comparison of spectroscopic data with those of the authentic sample[24] confirms the structure of **9b**.

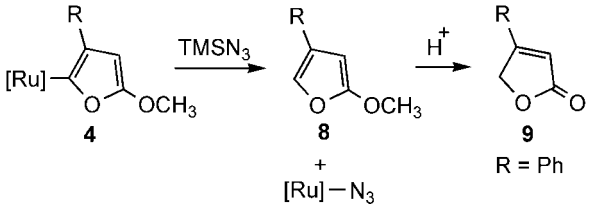


Scheme 3.

The reaction of $TMSN_3$ with the cyclopropenylruthenium complex[7] caused opening of the three-membered ring, but the reaction of **4** with $TMSN_3$ brought about cleavage of the M–C bond. This could be explained as follows: Organic cyclopropene is highly strained with the estimated strain energy well over 50 kcal/mol.[25] However, the cyclopropenyl ligand can be stabilized by coordination to a transition metal through back-bonding from the metal *d* orbital to $C_\alpha$. We previously reported solid-state structure of several cyclopropenylruthenium complexes.[4] From single-crystal X-ray diffraction studies, Ru–C bond lengths are in the range of 2.0345–2.0482 Å for these complexes, which are consistently shorter than that of a typical Ru–C($sp^2$) single bond [bond length 2.0637–2.09012 Å].[26] This might indicate that the Ru–C bond in cyclopropenyl-Ru complex could be slightly stronger than a regular Ru–C single bond indicating some degree of back-bonding from the metal moiety. In contrast, furan compounds have less ring strain. It thus requires less or even no back-bonding of the metal *d* electron for the coordination of the relatively more stable furyl group. Thus, unlike the M–C bond in cyclopropenyl complex, the M–C bond in furyl metal complexes is relatively weak and cleavage of the bond was observed in the reaction with $TMSN_3$.

**Synthesis and Reactions of Vinylidene Complex Containing Crotonate Group:** Because the five-membered ring furyl complex was readily prepared from the vinylidene complex containing a terminal ester group, it would be interesting to carry out deprotonation reaction of the vinylidene complex containing a crotonate group, which als possess a terminal ester group. A seven-membered ring ligand is expected to be obtained. We prepared the cationic vinylidene complex {[Ru]=C=C(R)$CH_2$CH=CH–$CO_2CH_3$][Br]} (R = $C_6H_9$, **10a**; R = Ph, **10b**) containing a terminal methyl crotonate group at $C_\beta$ in high yield by the treatment of [Ru]–C≡C–R ([Ru] = $Cp(PPh_3)_2Ru$, R = $C_6H_9$, **1a**; R = Ph, **1b**) with $BrCH_2CH$=$CHCO_2CH_3$. These cationic pink vinylideneruthenium complexes are stable in air and soluble in polar solvent but insoluble in ether and hexane. Spectroscopic data of **10a** displays of a deshielded $C_\alpha$ resonance as a triplet at $\delta$ = 351.8 ppm with $J_{P-C}$ = 15.4 Hz in the $^{13}$C NMR spectrum and a singlet $^{31}$P NMR resonance at $\delta$ = 42.3 ppm in $CDCl_3$ at room temperature. Complex **10b** was isolated in 88% yield. In the $^{13}$C NMR spectrum of **10b**, resonances at $\delta$ = 153.9 and 144.7 are assigned to the olefinic carbon atoms of the crotonate group and the corresponding $^1$H NMR resonances appear at $\delta$ = 6.71 and 5.62 ppm, assigned from the 2D HMQC spectrum.

However, in the deprotonation of the vinylidene complex containing a crotonate group only the cyclopropenyl complex was obtained. The reaction of **10b** with $n$Bu$_4$NOH gives the three-membered ring cyclopropenyl complex **11b**, (Scheme 4). The $^{31}$P NMR spectrum of **11b** displays two-doublet resonances at $\delta$ = 52.2 and 48.9 ppm with $J_{P-P}$ = 36.1 Hz due to the presence of a stereogenic carbon center at the three-membered ring. In the $^1$H NMR spectrum of **11b** the doublet resonance at $\delta$ = 2.62 with $J_{H,H}$ = 9.62 Hz is assigned to the CH group of the three-membered ring indicating the presence of a CH group of the adjacent double bond. However, deprotonation of the vinylidene complex **10a** containing a 1-cyclohexenyl group gave several unidentifiable decomposition products, no cyclopropenyl complex was observed. Conjugate double bond of the cyclopropenyl and 1-cyclohexenyl groups could possibly lower the degree of back donation from the metal, thus destabilizing the compound.

The reaction of the cyclopropenylruthenium complex **11b** containing a methyl crotonate substituent with excess of $TMSN_3$ resulted in formation of a five-membered triazolate ring organic product **12** (Scheme 4) and [Ru]–CN.[27] The organic product **12** was collected by extraction of the reaction mixture with hexane and was identified by $^1$H NMR spectrum and high-resolution mass spectrum. In the $^1$H NMR spectrum of compound **12**, the resonance at $\delta$ = 3.31

 © 2006 Wiley-VCH Verlag GmbH & Co. KGaA, Weinheim 

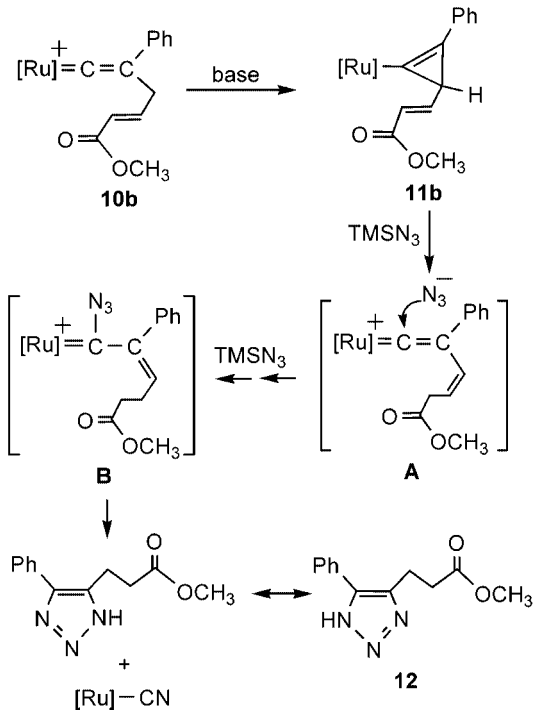


Scheme 4.

ppm is assigned to the $OCH_3$ group, and two triplet resonances at $\delta$ = 3.07 and 2.71 ppm with $^3J_{H,H}$ = 7.39 Hz are assigned to two neighboring $CH_2$ groups. Tautomerism of the triazole compound **12** might occur to yield two possible structures shown in Scheme 4.

The reaction of **11b** with $TMSN_3$ results in cleavage of the C=C double bond of the cyclopropenyl ring yielding [Ru]–CN and **12**. A possible reaction sequence is depicted in Scheme 4. The reaction may start with an addition of a TMS group to the double bond of the methyl crotonate group. This is accompanied with opening of the three-membered ring resulting in the formation of a cationic vinylidene intermediate followed by hydrolysis of TMS to afford **A** (Scheme 4). Then addition of the azide anion at $C_\alpha$ accompanied with addition of the second TMS group at $C_\delta$ followed by hydrolysis of the TMS group gave **B**. The single-bond character of the $C_\alpha$–$C_\beta$ in **B** may facilitate its cleavage. Loss of $N_2$ and a [3+2] cycloaddition of the $C_\beta$–$C_\gamma$ double bond with $N_3^-$ give the triazole **12** and [Ru]–CN. This result is the same as that observed for the reaction of $TMSN_3$ with cyclopropenyl complex containing a vinyl group.[7]

Recently, synthesis of organic tetrazolates complexes using transition-metal complexes as catalysts has received much attention.[28] The three-component coupling reaction using organic cyano compounds, allyl methyl carbonate, and trimethylsilyl azide catalyzed by a palladium complex gave various 2-allyltetrazoles in good yields. Tetrazolate complexes of palladium have also been prepared by nucleophilic attack of azide anion at the carbon atom of the coordinated nitrile followed by cycloaddition reaction.[17]

## Concluding Remarks

The reactions of furyl and cyclopropenylruthenium complexes with $O_2$ and $TMSN_3$ are investigated. While the cyclopropenyl complex with an ester substituent undergoes tautomerization to give the furyl complex, the methyl crotonate cyclopropenyl complex is inert toward such a transformation. The reaction of furyl metal complex with oxygen through *endo*-peroxide requires no assistance of photo-irradiation. Cleavage of the Ru–C bond was observed in the reaction of $TMSN_3$ with the furylruthenium complex. Reaction of $TMSN_3$ with the cyclopropenylruthenium complex containing a methyl crotonate substituent yielded ruthenium cyanide and organic triazole. The reaction causes cleavage of the C=C double bond of the three-membered ring.

## Experimental Section

**General Procedures:** All manipulations were performed under nitrogen using vacuum-line, dry box, and standard Schlenk techniques. $CH_3CN$ and $CH_2Cl_2$ were distilled from $CaH_2$ and diethyl ether and THF from Na/ketyl. All other solvents and reagents were of reagent grade and were used without further purification. NMR spectra were recorded with Bruker DMX-500, AM-300 and AC-200 (FT-NMR spectrometers at room temperature unless states otherwise) and were reported in units of $\delta$ with residual protons in the solvent as a standard ($CDCl_3$, δ = 7.24 ppm; $C_6D_6$, δ = 7.15 ppm; $C_2D_6CO$, δ = 2.04 ppm). FAB mass spectra were recorded with a JEOL SX-102A spectrometer. Vinylidene complexes ([Ru]=C=C(R)$CH_2CO_2CH$, R = $C_6H_9$, **2a**; R = Ph, **2b**) and furyl complexes **4** (R = $C_6H_9$, **4a**; R = Ph, **4b**) were prepared following the method reported in the literature.[4b] Elemental analyses were carried out at the Regional Center of Analytical Instrument located at the National Taiwan University.

**Synthesis of Vinylidene Complexes with Ester Group [Ru]=C=C($C_6H_9$)$CH_2CO_2CH_3$][Br] (2a):** To a $CH_2Cl_2$ (20.0 mL) solution of [Ru]C≡C$C_6H_9$[4b] (200 mg, 0.25 mmol) (**1b**), $BrCH_2CO_2CH_3$ (0.12 mL, 1.25 mmol) was added under nitrogen. The resulting solution was stirred at room temperature for 18 h, then, the solvent was concentrated to about 5 mL. This mixture was slowly added to 60 mL of vigorously stirred diethyl ether. The light-orange precipitate thus formed was filtered off and washed with diethyl ether and hexane and dried under vacuum to give the product **2a** (172 mg, 79% yield). Spectroscopic data for **2a** are as follows: $^1$H NMR (300 MHz, $CDCl_3$, 25 °C): $\delta$ = 7.42–6.95 (m, 30 H, Ph), 5.77 (br., 1 H, CH of $C_6H_9$), 5.22 (s, 5 H, Cp), 3.69 (s, 3 H, $OCH_3$), 2.69 (s, 2 H, $CH_2$), 2.14, 1.88, 1.68, 1.49 (br., 8 H, 4 $CH_2$ of $C_6H_9$) ppm. $^{31}$P{$^1$H} NMR (121.6 MHz, $CDCl_3$, 25 °C): $\delta$ = 42.1 (s) ppm. $^{13}$C NMR (75.4 MHz, $CDCl_3$, 25 °C): $\delta$ = 351.5 ($C_\alpha$, $J_{C,P}$ = 15.0 Hz), 171.8 ($CO_2$), 134–128.4 (Ph), 125.6 ($C_\beta$), 94.5 (Cp), 52.2 ($OCH_3$), 28.8 ($CH_2$), 27.5, 26.0, 22.7, 21.6 ($CH_2$ of $C_6H_9$) ppm. MS FAB: *m*/*z* = 869.0 [$M^+$ – Br], 606.9 [$M^+$ – Br, $PPh_3$], 428.8 [$M^+$ – Br, $PPh_3$, $C_2(C_6H_9)CH_2CO_2CH_3$], 345.1 [$M^+$ – Br, 2$PPh_3$]. $C_{52}H_{49}BrO_2P_2Ru$ (948.88): calcd. C 65.82 H, 5.20; found C 66.17, H 5.36.

**Synthesis of 4a:** To a solution of **2a** (100 mg, 0.11 mmol) in 5 mL of acetone was added a solution of $n$Bu$_4$NOH (0.2 mL, 0.2 mmol) under nitrogen. The mixture was stirred at room temperature for 4 h yielding a light yellow microcrystalline precipitate. The product was filtered off and washed with 2×5 mL of acetone, 2×5 mL of

 © 2006 Wiley-VCH Verlag GmbH & Co. KGaA, Weinheim 

$CH_3CN$, then dried under vacuum and was identified as **4a** (74 mg, 74% yield). Spectroscopic data for **4a** are as follows: $^1H$ NMR (300 MHz, $C_6D_6$, 25 °C): $\delta$ = 7.43–6.96 (m, 30 H, Ph), 5.99 (br., 1 H, CH of $C_6H_9$), 5.12 (s, 1 H, CH), 4.50 (s, 5 H, Cp), 2.97 (s, 3 H, $OCH_3$), 2.46, 2.29, 1.86, 1.78 (br., 8 H, 4 $CH_2$ of $C_6H_9$) ppm. $^{31}P\{^1H\}$ NMR (121.6 MHz, $C_6D_6$, 25 °C): $\delta$ = 50.6 (s) ppm. $^{13}C$ NMR (75.4 MHz, $C_6D_6$, 25 °C): $\delta$ = 164.9 (CO), 141.4 (t, $J_{C,P}$ = 18.8 Hz, $C_\alpha$), 139.7–127.8 (Ph), 124.5 (=CH), 85.5 ($C_\gamma$), 84.9 (Cp), 57.9 ($OCH_3$), 32.2, 26.3, 24.5, 23.4 ($CH_2$ of $C_6H_9$) ppm. MS FAB: *m*/*z* = 869.4 [$M^+$ + 1]. $C_{52}H_{48}O_2P_2Ru$ (867.97): calcd. C 71.96, H 5.57; found C 71.83, H 5.48.

**Observation of 3a:** To a solution of **2a** (100 mg, 0.12 mmol) in 5 mL of acetone was added a solution of $n$Bu$_4$NOH (0.3 mL, 0.3 mmol, 1 M in $CH_3OH$) under nitrogen at room temperature. $H_2O$ was added to the mixture immediately and yielded the light yellow microcrystalline precipitate. The product was filtered off and washed with 2×5 mL of $CH_3CN$, then dried under vacuum and identified as **3a** (89 mg, 89% yield). Complex **3a** is not stable at room temperature. By monitoring the $^{31}P$ NMR spectrum, **3a** was found as a pure product at the initial stage, spectroscopic data of **3a** was obtained within 3 min. Then the product **4a** was observed. Spectroscopic data for **3a** are as follows: $^1H$ NMR (300 MHz, $C_6D_6$, 25 °C): $\delta$ = 7.44–6.94 (m, 30 H, Ph), 5.65 (br., 1 H, CH of $C_6H_9$), 4.65 (s, 5 H, Cp), 3.74 (s, 3 H, $OCH_3$), 2.47 (s, 1 H, CH), 2.50–1.24 (br., 8 H, 4 $CH_2$ of $C_6H_9$) ppm. $^{31}P\{^1H\}$ NMR (121.6 MHz, $C_6D_6$, 25 °C): $\delta$ = 52.5, 48.5 (AX, $J_{P-P}$ = 36.4 Hz) ppm.

**Synthesis of [Ru]$O_2CC(C_6H_9)$=$CHCO_2CH_3$ (5a):** Complex **4a** (0.20 g, 0.23 mmol) was exposed to air for 5 days at room temperature, and the light yellow powder became deep yellow. The product was identified as **5a** (0.20 g, 99% yield). Spectroscopic data for **5a** are as follows: $^1H$ NMR (300 MHz, $C_6D_6$, 25 °C): $\delta$ = 7.64–6.96 (m, 30 H, Ph), 5.79 (br., 1 H, CH of $C_6H_9$), 5.53 (s, 1 H, CH), 4.79 (s, 5 H, Cp), 3.51 (s, 3 H, $OCH_3$), 1.99, 1.45, 1.26, 1.01 (br., 8 H, 4 $CH_2$ of $C_6H_9$) ppm. $^{31}P\{^1H\}$ NMR (121.6 MHz, $C_6D_6$, 25 °C): $\delta$ = 39.5 (s) ppm. $^{13}C$ NMR (75.4 MHz, $C_6D_6$, 25 °C): $\delta$ = 174.2 ($RuO_2C$), 166.9 ($CO_2CH_3$), 160.3 ($CC_6H_9$), 139.6–127.4 (Ph), 107.2 (CH), 80.2 (Cp), 50.6 ($CH_3$), 26.7, 25.4, 23.1, 22.2 ($CH_2$ of $C_6H_9$) ppm. MS FAB: *m*/*z* = 901 [$M^+$ + 1], 869 [$M^+$ + 1 – $O_2$], 719.2 [$M^+$ + CO – $O_2CC(C_6H_9)$=$CHCO_2CH_3$], 691.1 [$M^+$ – $O_2CC(C_6H_9)$=$CHCO_2CH_3$], 638 [$M^+$ + 1 – $PPh_3$], 429.0 [$M^+$ – $PPh_3$, $O_2CC(C_6H_9)$=$CHCO_2CH_3$]. $C_{52}H_{48}O_4P_2Ru$ (899.97): calcd. C 69.40, H 5.38; found C 69.28, H 5.22.

**Synthesis of [Ru]$O_2CC(Ph)$=$CHCO_2CH_3$ (5b):** Complex **4b** (0.20 g, 0.23 mmol) was exposed to air for 10 days at room temperature, and the orange powder became yellow. The $^{31}P$ NMR was used to confirm complete transformation. The yellow product was identified as **5b**, and the yield is almost quantitative (0.21 g, 99% yield). Spectroscopic data of **5b** are as follows: $^1H$ NMR (300 MHz, $CDCl_3$, 25 °C): $\delta$ = 7.40–6.93 (m, 35 H, Ph), 5.76 (s, 1 H, CH), 4.44 (s, 5 H, Cp), 3.63 (s, 3 H, $OCH_3$) ppm. $^{31}P\{^1H\}$ NMR (121.6 MHz, $CDCl_3$, 25 °C): $\delta$ = 40.85 (s) ppm. $^{13}C$ NMR (75.4 MHz, $CDCl_3$, 25 °C): $\delta$ = 174.0 ($RuO_2C$), 166.0 ($CO_2CH_3$), 157.3 ($CPh$), 138.2–25.2 (Ph), 111.9 (CH), 78.6 (Cp), 51.1 ($CH_3$) ppm. MS FAB: *m*/*z* = 896.1 [$M^+$], 719.2 [$M^+$ + CO, $O_2CC(Ph)$=$CHCO_2CH_3$], 691.2 [$M^+$ – $O_2CC(Ph)$=$CHCO_2CH_3$], 634.1 [$M^+$ – $PPh_3$]. $C_{52}H_{44}O_4P_2Ru$ (895.93): calcd. C 69.70, H 4.95; found C 69.56, H 4.82.

**Reaction of 5 with $CH_3I$:** To a solution of complex **5a** (100 mg, 0.11 mmol) in $CDCl_3$ prepared under $N_2$ in a NMR tube, 36 μL (0.58 mmol) of $CH_3I$ was added. The reaction was carried out at 50 °C for 3–4 h. The solvent was removed under vacuum. The organic product along with excess $CH_3I$ was extracted with diethyl ether. The solvent and $CH_3I$ were removed under vacuum. The organic product is identified as **6a** (21 mg, 85% yield). The organometallic product was identified as [Ru]–I[29] (82 mg, 92% yield). **6a:** $^1H$ NMR (300 MHz, $CDCl_3$, 25 °C): $\delta$ = 5.08 (br., 1 H, CH of $C_6H_9$), 5.77 (s, 1 H, =CH), 3.88 (s, 3 H, $OCH_3$), 3.71 (s, 3 H, $OCH_3$), 2.21–1.59 (br., 8 H, 4 $CH_2$ of $C_6H_9$) ppm. MS (EI): *m*/*z* = 224 [$M^+$]. High-resolution MS for $C_{12}H_{16}O_4$: calcd. 224.2567; found 224.2563. The same procedure was used for the reaction of **5b** (100 mg, 0.11 mmol) with $CH_3I$ (36 μL, 0.58 mmol), and the product extracted with diethyl ether was identified as **6b** in 89% yield (21 mg). The organometallic product was identified as [Ru]–I (84 mg, 94% yield). **6b:** $^1H$ NMR (300 MHz, $CDCl_3$, 25 °C): $\delta$ = 7.25–7.18 (m, 5 H, Ph), 6.29 (s, 1 H, CH), 3.92 (s, 3 H, $CH_3$), 3.76 (s, 3 H, $CH_3$) ppm. $^{13}C$ NMR (75.4 MHz, $CDCl_3$, 25 °C): $\delta$ = 168.3, 165.4 (two $COCH_3$), 149.0 ($CPh$), 133.1–126.8 (Ph), 117.0 (CH), 52.7, 52.0 (two $CH_3$) ppm. High-resolution MS for $C_{12}H_{12}O_4$: calcd. 220.0736; found 220.0732.

**Reaction of 5 with Protic Acid:** To a solution of complex **5a** (100 mg, 0.10 mmol) in $CDCl_3$ prepared under $N_2$ in an NMR tube, hydrochloric acid (50 μL of aqueous 37% HCl, 0.6 mmol) was added. The reaction is complete within about 4 h at room temperature. The solvent was removed under vacuum. The organic product was extracted with diethyl ether and identified as **7a** (18 mg, 86% yield). The organometallic product was identified as [Ru]–Cl (73 mg, 92% yield). The solvent and HCl were removed under vacuum at 60 °C. **7a:** $^1H$ NMR (300 MHz, $CDCl_3$, 25 °C): $\delta$ = 6.82 (s, 1 H, CH), 6.30 (br., 1 H, CH of $C_6H_9$), 3.73 (s, 3 H, $OCH_3$), 2.22–1.58 (br., 8 H, 4 $CH_2$ of $C_6H_9$) ppm. MS (EI): 210 [$M^+$]. The same procedure was used for the reaction of **5b** (100 mg, 0.11 mmol) with acid, and the product extracted with diethyl ether was identified as **7b** (17 mg, 90% yield). The organometallic product was identified as [Ru]–Cl (65 mg, 90% yield). **7b:** $^1H$ NMR (300 MHz, $CDCl_3$, 25 °C): $\delta$ = 7.25–7.01 (m, 5 H, Ph), 6.28 (s, 1 H, CH), 3.76 (s, 3 H, $CH_3$) ppm. $^{13}C$ NMR (75.4 MHz, $CDCl_3$, 25 °C): $\delta$ = 170.6 ($CO_2H$), 165.5 ($CO_2CH_3$), 148.8 ($CPh$), 133.3–126.8 (Ph), 116.8 (CH), 52.0 ($CH_3$) ppm. MS (EI): *m*/*z* = 174 [$M^+$ – $CH_3OH$]. The HCl could be replaced with trifluoroacetic acid or acetic acid yielding **7** and [Ru]–$OCOCF_3$[30] or [Ru]–$OCOCH_3$,[30] respectively. Both reactions completed in 36 h. Trifluoroacetic acid and acetic acid could be removed under vacuum without heating.

**Reaction of 4a with $TMSN_3$:** A solution of **4a** (100 mg, 0.12 mmol) in THF (10 mL) was treated with $TMSN_3$ (0.07 mL, 0.54 mmol). The resulting solution was stirred at room temperature for 1 h then the solvent was removed under vacuum. The mixture was added to a stirred diethyl ether. Orange precipitates thus formed were filtered off and washed with diethyl ether. The organometallic product was identified as [Ru]–$N_3$ (79 mg, 90% yield). The organic product was collected by extraction with ether and purified by chromatography, then, the solvent was removed under vacuum to give **8a**, (19 mg, 90% yield). **8a:** $^1H$ NMR (300 MHz, $C_6D_6$ 25 °C): $\delta$ = 6.78 (d, $^4J_{H,H}$ = 1.2 Hz, 1 H, CH), 5.88 (br., 1 H, CH of $C_6H_9$), 5.25 (d, $^4J_{H,H}$ = 1.2 Hz, 1 H, CH), 3.79 (s, 3 H, $OCH_3$), 2.16–1.58 (br., 8 H, 4 $CH_2$ of $C_6H_9$) ppm. MS (EI): *m*/*z* = 178 [$M^+$].

**Reaction of 4b with $TMSN_3$:** To a flask containing compound **4b** (0.20 g, 0.23 mmol) in THF (10 mL), $TMSN_3$ (0.20 mL, 1.49 mmol) was added. The solution was stirred at room temperature for 2 h, then the solvent was removed under vacuum. The yellow solid was washed with hexane and identified as [Ru]–$N_3$ (0.16 g, 95% yield). The organic product was extracted with hexane and was found to contain some triphenylphosphane oxide. The pure organic product was obtained by eluting the mixture with diethyl ether on a silica gel column and solvent was removed on a

 © 2006 Wiley-VCH Verlag GmbH & Co. KGaA, Weinheim 

rotary evaporator. The organic product was identified as compound **8b** (34 mg, 91% yield). **[Ru]–$N_3$:** $^1$H NMR (300 MHz, $C_6D_6$ 25 °C): $\delta$ = 7.32–7.08 (m, 30 H, Ph), 4.18 (s, 5 H, Cp) ppm. $^{31}P\{^1H\}$ NMR (121.6 MHz, $CDCl_3$, 25 °C): $\delta$ = 41.8 (s) ppm. **8b:** $^1$H NMR (300 MHz, $C_6D_6$, 25 °C): $\delta$ = 7.30–7.10 (m, 5 H, Ph), 6.96 (d, 1 H, CH, $^4J_{H,H}$ = 1.3 Hz), 5.24 (d, 1 H, CH, $^4J_{H,H}$ = 1.3 Hz), 3.23 (s, 3 H, $CH_3$) ppm. High-resolution MS for $C_{11}H_{10}O_2$: calcd. 174.0681; found 174.0691. **Isolation of 9b:** Transformation of **8b** to **9b** under acidic condition was monitored by NMR in $CDCl_3$. Addition of HCl (37%, 9.2 μL) to the solution of **8b** (19 mg, 0.11 mmol) caused the formation of **9b** (16 mg, 95% yield) in about 30 min. **9b:** $^1$H NMR (300 MHz, $CDCl_3$, 25 °C): $\delta$ = 7.48 (s, 5 H, Ph), 6.36 (t, $J_{H,H}$ = 1.8 Hz, 1 H, CH), 5.22 (d, $J_{H,H}$ = 1.8 Hz, 2 H, $CH_2$) ppm. $^{13}$C NMR (75.4 MHz, $CDCl_3$, 25 °C): $\delta$ = 173.9 (OC), 163.9 (*C*Ph), 131.8–129.6 (Ph), 113.0 (CH), 71.0 ($CH_2$) ppm. High-resolution MS for $C_{10}H_8O_2$: calcd. 160.0524; found 160.0521.

**Synthesis of Vinylidene Complexes with Methyl Crotonate:** To a Schlenk flask charged with [Ru]C≡C$C_6H_9$ (**1a**) (200 mg, 0.25 mmol) in $CH_2Cl_2$ (20 mL), $BrCH_2CH{=}CHCO_2CH_3$ (0.15 mL, 1.25 mmol) was added under nitrogen. The mixture was stirred at room temperature for 6 h, then the solution was concentrated to about 5 mL and added dropwise to 60 mL of a vigorously stirred diethyl ether. The pink precipitate thus formed was filtered off, and washed with diethyl ether and hexane. The product was identified as [Ru]=C=C($C_6H_9$)$CH_2CH{=}CHCO_2CH_3$][Br] (**10a**) (179 mg, 85% yield). **10a:** $^1$H NMR (300 MHz, $CDCl_3$, 25 °C): $\delta$ = 7.41–6.99 (m, 30 H, Ph), 6.71, 6.68 (dt, $J_{H,H}$ = 10.0, 6.4 Hz, 1 H, C*H*=C), 5.73 (br., 1 H, CH of $C_6H_9$), 5.70 (d, $J_{H,H}$ = 10.0 Hz, 1 H, =C*H*), 5.11 (s, 5 H, Cp), 3.76 (s, 3 H, $OCH_3$), 2.73 (d, $J_{H,H}$ = 6.4 Hz, 2 H, $CH_2$), 2.16, 1.71, 1.52, 1.49 (br., 8 H, 4 $CH_2$ of $C_6H_9$) ppm. $^{31}P\{^1H\}$ NMR (121.6 MHz, $CDCl_3$, 25 °C): $\delta$ = 42.3 (s) ppm. $^{13}$C NMR (75.4 MHz, $CDCl_3$, 25 °C): $\delta$ = 351.8 ($C_\alpha$, $J_{C,P}$ = 15.4 Hz), 166.4 ($CO_2$), 145.8, 122.3 (C=C), 134.3–128.0 (Ph), 130.1 (CH of $C_6H_9$), 125.1 ($C_\beta$), 94.2 (Cp), 51.5 ($OCH_3$), 27.3, 25.8, 22.6, 21.5 ($CH_2$ of $C_6H_9$), 25.4 ($CH_2$) ppm. MS FAB: *m*/*z* = 895.4 [$M^+$ – Br], 633.2 [$M^+$ – Br, $PPh_3$], 429.0 [$M^+$ – Br, $PPh_3$, $C_2(C_6H_9)$-$CH_2CH{=}CHCO_2CH_3$], 371.1 [$M^+$ – Br, 2$PPh_3$]. $C_{54}H_{51}BrO_2P_2Ru$ (974.92): calcd. C 66.53, H 5.27; found C 66.27, H 5.19. To a solution of [Ru]C≡CPh[4b] (**1b**) (200 mg, 0.25 mmol) in $CH_2Cl_2$ (20 mL), $BrCH_2CH{=}CHCO_2CH_3$ (0.15 mL, 1.25 mmol) was added under nitrogen. The mixture was stirred at room temperature for 6 h, then the volume was reduced to about 5 mL. Addition of the mixture dropwise into 60 mL of a vigorously stirred diethyl ether caused a pink-red solid to precipitate out. The precipitate thus formed was filtered off and washed with diethyl ether and hexane and dried under reduced pressure to yield the product [Ru]=C=C(Ph)$CH_2CH{=}CHCO_2CH_3$][Br] (**10b**) (197 mg, 88% yield). **10b:** $^1$H NMR (300 MHz, $CDCl_3$, 25 °C): $\delta$ = 7.41–6.80 (m, 35 H, Ph), 6.71, 6.68 (dt, $J_{H,H}$ = 15.4, 6.58 Hz, 1 H, C*H*=C), 5.62 (d, $J_{H,H}$ = 15.4 Hz, 1 H, =C*H*), 5.11 (s, 5 H, Cp), 3.70 (s, 3 H, $CH_3$), 3.07 (d, $J_{H,H}$ = 6.58 Hz, 2 H, $CH_2$) ppm. $^{31}P\{^1H\}$ NMR (121.6 MHz, $CDCl_3$, 25 °C): $\delta$ = 41.9 (s) ppm. $^{13}$C NMR (75.4 MHz, $CDCl_3$, 25 °C): $\delta$ = 347.8 ($C_\alpha$, $J_{C,P}$ = 14.7 Hz), 166.4 ($CO_2$), 153.9, 144.7 (C=C), 134.7–126.7 (Ph), 123.0 ($C_\beta$), 94.4 (Cp), 51.6 ($OCH_3$), 29.2 ($CH_2$) ppm. MS FAB: *m*/*z* = 891.1 [$M^+$ – Br], 629.3 [$M^+$ – Br, $PPh_3$], 429.1 [$M^+$ – Br, $PPh_3$, $C_2$(Ph)$CH_2CH{=}CHCO_2CH_3$]. $C_{54}H_{47}BrO_2P_2Ru$ (1050.79): calcd. C 66.80, H 4.88; found C 66.72, H 4.82.

**Synthesis of 11b:** To a solution of **10b** (200 mg, 0.22 mmol) in 5 mL of acetone was added a 1 M solution of $n$$Bu_4NOH$ (0.3 mL, 0.3 mmol, in $CH_3OH$). The mixture was stirred for 1 h yielding the light yellow microcrystalline precipitate which was filtered off and washed with 2×5 mL of $CH_3CN$, dried under vacuum. The product was analytically pure and was identified as **11b** in 72% yield. (140 mg) Spectroscopic data for **11b** are as follows: $^1$H NMR (300 MHz, $C_6D_6$, 25 °C): $\delta$ = 7.91 (q, $J_{H,H}$ = 15.1, 9.62 Hz, 1 H, C*H*=), 7.39–6.90 (m, 35 H, Ph), 6.67 (d, $J_{H,H}$ = 15.1 Hz, 1 H, =C*H*), 4.56 (s, 5 H, Cp), 3.62 (s, 3 H, $CH_3$), 2.62 (d, $J_{H,H}$ = 9.62 Hz, 1 H, CH) ppm. $^{31}P\{^1H\}$ NMR (121.6 MHz, $C_6D_6$, 25 °C): $\delta$ = 52.2, 48.9 (AX, $J_{P-P}$ = 36.1 Hz) ppm. $^{13}$C NMR (75.4 MHz, $C_6D_6$, 25 °C): $\delta$ = 169.1 (CH=), 168.3 (C=O), 140.2–125.8 (Ph), 112.6 (=CH), 86.4 (Cp), 50.2 ($OCH_3$), 36.7 (CH) ppm. MS FAB: *m*/*z* = 891.4 [$M^+$ + 1], 629.3 [$M^+$ + 1, $PPh_3$], 429.1 [$M^+$ + 1 – $PPh_3$, =C=C(Ph)$CH_2CH{=}CHCO_2CH_3$]. $C_{54}H_{46}O_2P_2Ru$ (899.97): calcd. C 72.88, H 5.21; found C 72.63, H 5.12.

**Reaction of 11b with $TMSN_3$:** To a Schlenk flask charged with complex **11b** (50 mg, 0.06 mmol) was added THF (10 mL) under nitrogen. The resulting yellow solution was stirred and $TMSN_3$ (0.1 mL, 0.75 mmol) was added. The mixture was stirred at room temperature for 4 h, then the solution was concentrated to about 3 mL, and slowly added to 20 mL of a stirred hexane solution. The orange precipitate thus formed was filtered off, and washed with diethyl ether. The product was identified as [Ru]–CN (39 mg, 90%). The organic product was extracted with hexane, then the extract was filtered through silical gel. Solvent of the filtrate was removed under vacuum and the product was identified as **12** (12 mg, 88% yield). **[Ru]–CN:** $^1$H NMR (300 MHz, $C_6D_6$, 25 °C): $\delta$ = 7.81–6.96 (m, 30 H, Ph), 4.45 (s, 5 H, Cp) ppm. $^{31}P\{^1H\}$ NMR (121.6 MHz, $C_6D_6$, 25 °C): $\delta$ = 50.38 (s) ppm. **12:** $^1$H NMR (300 MHz, $C_6D_6$, 25 °C): $\delta$ = 7.81–6.96 (m, 5 H, Ph), 3.31 (s, 3 H, $OCH_3$), 3.07 (t, 2 H, $CH_2$, $^3J_{H,H}$ = 7.39 Hz), 2.71 (t, 2 H, $CH_2$, $^3J_{H,H}$ = 7.39 Hz) ppm. $^1$H NMR (300 MHz, $CDCl_3$, 25 °C): $\delta$ = 7.67–7.06 (m, 5 H, Ph), 3.67 (s, 3 H, $OCH_3$), 3.19 (t, 2 H, $CH_2$, $^3J_{H,H}$ = 7.39 Hz), 2.80 (t, 2 H, $CH_2$, $^3J_{H,H}$ = 7.39 Hz) ppm. $^{13}$C NMR (75.4 MHz, $CDCl_3$, 25 °C): $\delta$ = 173.9 (CO), 134.1–128.0 (Ph), 52.4 ($OCH_3$), 33.1 ($CH_2O$), 21.1 ($CH_2$) ppm. MS (EI): *m*/*z* = 230 [$M^+$]

## Acknowledgments

We thank the National Science Council of Taiwan, R.O.C. for financial support of this work.

[1] a) F. Pezet, J. C. Daran, I. Sasaki, H. Ait-Haddou, G. G. A. Balavoine, *Organometallics* **2000**, *19*, 4008–4015; b) m. J. Burk, W. Hems, D. Herzberg, C. Malan, A. Zanotti-Gerosa, *Org. Lett.* **2000**, *2*, 4173–4176; c) D. A. Alonso, S. J. M. Nordin, P. Roth, T. Tarnai, P. G. Andersson, M. Thommen, U. Pittelkow, *J. Org. Chem.* **2000**, *65*, 3116–3122; d) M. Yamakawa, H. Ito, R. Noyori, *J. Am. Chem. Soc.* **2000**, *122*, 1466–1478; e) B. M. Trost, F. D. Toste, A. B. Pinkerton, *Chem. Rev.* **2001**, *101*, 2067–2096; f) M. Kitamura, M. Tsukamoto, Y. Bessho, M. Yoshimura, U. Kobs, M. Widhalm, R. Noyori, *J. Am. Chem. Soc.* **2002**, *124*, 6649–6667; g) S. N. Ringelberg, A. Meetsma, S. I. Troyanov, B. Hessen, J. H. Teuben, *Organometallics* **2002**, *21*, 1759–1765; h) J. H. Xie, L. X. Wang, Y. Fu, S. F. Zhu, B.-M. Fan, H. F. Duan, Q. L. Zhou, *J. Am. Chem. Soc.* **2003**, *125*, 4404–4405.

[2] a) W. D. Cotter, L. Barbour, K. L. McNamara, R. Hechter, R. J. Lachicotte, *J. Am. Chem. Soc.* **1998**, *120*, 11016–11017; b) M. H. Chisholm, S. T. Haubrich, J. C. Huffman, W. E. Streib, *J. Am. Chem. Soc.* **1997**, *119*, 1634–1647; c) T. Itoh, K. Mitsukura, N. Ishida, K. Uneyama, *Org. Lett.* **2000**, *2*, 1431–1434; d) T. L. Choi, C. W. Lee, A. K. Chatterjee, R. H. Grubbs, *J. Am. Chem. Soc.* **2001**, *123*, 10417–10418; e) L. Jafarpour, S. P. Nolan, *Organometallics* **2000**, *19*, 2055–2057; f) Y. M. Ahn, K. Yang, G. I. Georg, *Org. Lett.* **2001**, *3*, 1411–1413; g) M. S. Sanford, M. Ulman, R. H. Grubbs, *J. Am. Chem. Soc.* **2001**, *123*, 749–750; h) A. E. Sutton, B. A. Seigal, D. F. Finnegan, M. L.

 © 2006 Wiley-VCH Verlag GmbH & Co. KGaA, Weinheim 

Snapper, *J. Am. Chem. Soc.* **2002**, *124*, 13390–13391; i) S. Fomine, S. M. Vargas, M. A. Tlenkopatchev, *Organometallics* **2003**, *22*, 93–99.
[3] a) J. E. Mcalvin, C. L. Fraser, *Macromolecules* **1999**, *32*, 6925–6932; b) P. S. Wolfe, K. B. Wagener, *Macromolecules* **1999**, *32*, 7961–7967; c) M. Kamigaito, Y. Watanabe, T. Ando, M. Sawamoto, *J. Am. Chem. Soc.* **2002**, *124*, 9994–9995; d) S. Hamasaki, M. Kamigaito, M. Sawamoto, *Macromolecules* **2002**, *35*, 2934–2940; e) L. Delaude, A. Demonceau, A. F. Noels, *Macromolecules* **2003**, *36*, 1446–1456; f) C. Bianchini, G. Mantovani, A. Meli, F. Migliacci, F. Laschi, *Organometallics* **2003**, *22*, 2545–2547.
[4] a) P. C. Ting, Y. C. Lin, M. C. Cheng, Y. Wang, *Organometallics* **1994**, *13*, 2150–2152; b) P. C. Ting, Y. C. Lin, G. H. Lee, M. C. Cheng, Y. Wang, *J. Am. Chem. Soc.* **1996**, *118*, 6433–6444; c) Y. H. Lo, Y. C. Lin, G. H. Lee, Y. Wang, *Organometallics* **1999**, *18*, 982–988; d) C. W. Chang, Y. C. Lin, G. H. Lee, Y. Wang, *Organometallics* **2000**, *19*, 3211–3219; e) Huang, C. C. Lin, Y. C. Huang, S. L. Liu, Y. H. Wang, *Organometallics* **2003**, *22*, 1512–1518.
[5] J. Y. Yang, Y. H. Lo, S. L. Huang, Y. C. Lin, *Organometallics* **2001**, *20*, 3621–3623.
[6] a) M. Nakamura, N. Isobe, E. Nakamura, *Chem. Rev.* **2003**, *103*, 1295–1326; b) I. Nakamura, G. B. Bajracharya, Y. J. Yamamoto, *Org. Chem.* **2003**, *68*, 2297–2299; c) L. Liao, J. M. Fox, *J. Am. Chem. Soc.* **2002**, *124*, 14322–14323; d) P. W. Jennings, L. L. Johnson, *Chem. Rev.* **1994**, *94*, 2241–2290.
[7] a) K. H. Chang, Y. C. Lin, *Chem. Commun.* **1998**, 1441–1442; b) K. H. Chang, Y. C. Lin, Y. H. Liu, Y. J. Wang, *J. Chem. Soc., Dalton Trans. Chem. Soc., Dalton Trans.* **2001**, *21*, 3154–3159.
[8] A. Padwa, *Acc. Chem. Res.* **1976**, *9*, 371–378.
[9] S. M. Ma, J. L. Zhang, *J. Am. Chem. Soc.* **2003**, *125*, 12386–12387.
[10] a) I. A. D′yakonov, M. I. Komendantov, *Zh. Obshch. Khim.* **1961**, *31*, 681–683; b) I. A. D′yakonov, M. I. Komendantov, *Zh. Obshch. Khim.* **1961**, *31*, 3483–3485.
[11] J. A. Pincock, A. A. Moutokapa, *Can. J. Chem.* **1977**, *55*, 979–985.
[12] H. E. Selnau, J. S. Merola, *Organometallics* **1993**, *12*, 1583–1591.
[13] H. E. Selnau, J. S. Merola, *Organometallics* **1993**, *12*, 3800–3801.
[14] a) K. W. Liang, W. T. Li, S. M. Peng, S. L. Wang, R. S. Liu, *J. Am. Chem. Soc.* **1997**, *119*, 4404–4412; b) H. G. Shu, L. H. Shiu, S. H. Wang, S. L. Wang, G. H. Lee, S. M. Peng, R. S. Liu, *J. Am. Chem. Soc.* **1996**, *118*, 530–540.
[15] a) Z. P. Demko, K. B. Sharpless, *J. Org. Chem.* **2001**, *66*, 7945–7950; b) E. D. Soli, P. J. DeShong, *Org. Chem.* **1999**, *64*, 9724–9726; c) A. Dondoni, M. C. Scherrmann, A. Marra, J. L. Delépine, *J. Org. Chem.* **1994**, *59*, 7517–7520; d) R. M. Moriarty, R. K. Vaid, T. E. Hopkin, B. K. Vaid, A. Tuncay, *Tetrahedron Lett.* **1989**, *30*, 3019–3022; e) P. Magnus, J. Lacour, *J. Am. Chem. Soc.* **1992**, *114*, 3993–3994; f) Y. Kita, H. Tohma, M. Inagaki, K. Hatanaka, T. Yakura, *Tetrahedron Lett.* **1991**, *32*, 4321–4324.
[16] a) R. H. Wiley, K. F. Hussung, J. Moffat, *J. Org. Chem.* **1956**, *21*, 190–192; b) R. J. D. Pasquale, C. D. Padgett, R. W. Rosser, *J. Org. Chem.* **1975**, *40*, 810–811; c) S. Kamijo, T. Jin, Z. Huo, Y. Yamamoto, *Tetrahedron Lett.* **2002**, *43*, 9707–9710; d) R. Shintani, G. C. Fu, *J. Am. Chem. Soc.* **2003**, *125*, 10778–10779; e) W. Carruthers, *Cycloaddition Reaction in Organic Synthesis Pergamon*, Oxford, **1990**, p. 269; f) C. W. Tornøe, C. Christensen, M. Meldal, *J. Org. Chem.* **2002**, *67*, 3057–3064; g) K. V. Gothelf, K. A. Jørgensen, *Chem. Rev.* **1998**, *98*, 863–910; h) G. L′abbé, *Chem. Rev.* **1969**, *69*, 345–363.
[17] a) S. Kamijo, T. Jin, Z. Huo, Y. Yamamoto, *J. Am. Chem. Soc.* **2003**, *125*, 7786–7787; b) S. Kamijo, Y. Yamamoto, *Angew. Chem. Int. Ed.* **2002**, *41*, 3230–3233; c) S. Kamijo, T. Jin, Y. Yamamoto, *J. Am. Chem. Soc.* **2001**, *123*, 9453–9454; d) S. Kamijo, T. Jin, Y. Yamamoto, *J. Org. Chem.* **2002**, *67*, 7413–7417.
[18] A. Palazzi, S. Stagni, S. Bordoni, M. Monari, S. Selva, *Organometallics* **2002**, *21*, 3774–3781.
[19] a) M. L. Graziano, M. R. Iesce, *Synthesis* **1984**, 64–66; b) M. L. Graziano, M. R. Iesce, R. Scarpati, *Synthesis* **1984**, 66–68.
[20] a) M. L. Graziano, M. R. Iesce, S. Chiosi, R. Scarpati, *J. Chem. Soc., Perkin Trans. 1.* **1983**, 2071–2074; b) M. L. Graziano, M. R. Iesce, B. Carli, R. Scarpati, *Synthesis* **1983**, 125–126; c) M. L. Graziano, M. R. Iesce, R. Scarpati, *Chem. Soc., Perkin Trans. 1.* **1982**, 2007–2012; d) M. L. Graziano, M. R. Iesce, B. Carli, R. Scarpati, *Synthesis* **1982**, 736–738; e) M. L. Graziano, M. R. Iesce, R. Scarpati, *J. Chem. Soc., Perkin Trans. 1.* **1980**, 1955–1959.
[21] K. C. Brannock, R. D. Burpitt, V. Goodlett, W. J. G. Thweatt, *J. Org. Chem.* **1964**, *29*, 813–817.
[22] a) B. Gabriele, G. Salerno, M. Costa, G. P. Chiusoli, *J. Organomet. Chem.* **1995**, *503*, 21–28; b) R. C. Larock, K. Narayanan, S. S. Hershberger, *J. Org. Chem.* **1983**, *48*, 4377–4380.
[23] B. T. Donovan-Merkert, J. Malik, L. V. Gray, J. M. O'Connor, B. S. Fong, M. C. Chen, *Organometallics* **1998**, *17*, 1007–1009.
[24] a) N. B. Carter, R. Mabon, A. M. E. Richecoeur, J. B. Sweeney, *Tetrahedron* **2002**, *58*, 9117–9129; b) J. Wu, Q. Zhu, L. Wang, R. Fathi, Z. Yang, *J. Org. Chem.* **2003**, *68*, 670–673.
[25] I. R. Likhotvorik, D. W. Brown, M. Jones Jr., *J. Am. Chem. Soc.* **1994**, *116*, 6175–6178.
[26] a) A. Romero, A. Santo, A. Vegas, *Organometallics* **1988**, *7*, 1988–1993; b) N. W. Alcock, A. F. Hill, R. P. Melling, *Organometallics* **1991**, *10*, 3898–3903.
[27] W. M. Laidlaw, R. G. Denning, *J. Organomet. Chem.* **1993**, *463*, 199–204.
[28] a) M. Alterman, A. Hallberg, *J. Org. Chem.* **2000**, *65*, 7984–7989; b) R. A. Batey, D. A. Powell, *Org. Lett.* **2000**, *2*, 3237–3240; c) Z. P. Demko, K. Sharpless, *Org. Lett.* **2001**, *3*, 4091–4094; d) Z. P. Demko, K. B. Sharpless, *J. Org. Chem.* **2001**, *66*, 7945–7950; e) P. D. Zachary, K. B. Sharpless, *Angew. Chem. Int. Ed.* **2002**, *41*, 2110–2113; f) P. D. Zachary, K. B. Sharpless, *Angew. Chem. Int. Ed.* **2002**, *41*, 2113–2116.
[29] T. Wilczewski, B. M. Ochenska, J. F. Biernat, *J. Organomet. Chem.* **1981**, *215*, 87–96.
[30] H. Werner, T. Braun, T. Daniel, O. Gevert, M. Schulz, *J. Organomet. Chem.* **1997**, *541*, 127–141.

Received: July 13, 2005
Published Online: November 17, 2005

 © 2006 Wiley-VCH Verlag GmbH & Co. KGaA, Weinheim 

DOI: 10.1002/ejic.200500623

# X-ray Crystal Structure and Characterization in Aqueous Solution of {*N*,*N*′-Ethylenebis(pyridoxylaminato)}zinc(II)

**Isabel Correia,[a] Agnes Dornyei,[b] Fernando Avecilla,[c] Tamás Kiss,*[b] and João Costa Pessoa*[a]**

**Keywords:** N,O ligands / Speciation / Structure elucidation / Zinc

The complexation of $Zn^{II}$ with $H_2Rpyr_2en$ [$H_2Rpyr_2en$ = *N*,*N*′-ethylenebis(pyridoxylaminato)] in aqueous solution has been studied by pH potentiometry and $^1H$ NMR spectroscopy. Complex formation constants are determined and binding modes proposed. Complex formation starts at around pH 4, and several species with a 1:1 ligand-to-metal ratio with different protonation states form up to pH 12. Only above pH 10 does a hydrolytic species $[ZnLH_{-1}]^-$ become important. The crystal and molecular structures of $[ZnCl(H_2Rpyr_2en)]^+Cl^-\cdot 1.5H_2O$ (**1**) have been determined by X-ray diffraction. The coordination of the $H_2Rpyr_2en$ ligand involves the two phenolate-O and two amine-N atoms in a distorted square-pyramidal geometry. The two pyridine-N atoms are protonated, and a $Cl^-$ atom completes the coordination sphere. Upon coordination, both N-amine atoms of $H_2Rpyr_2en$ become stereogenic centres, and in both molecules of the unit cell of **1** one of the N-amine donors has an (*R*)-configuration, and the other an (*S*)-configuration.
(© Wiley-VCH Verlag GmbH & Co. KGaA, 69451 Weinheim, Germany, 2006)

## Introduction

$Sal_2en$-type ligands are known to coordinate several metal ions in different oxidation states and are among the most studied/important ligand systems used in asymmetric catalysis.[1–3] Their reduced derivatives (frequently named tetrahydrosalen or salan ligands),[4] are much less studied and exhibit different structural and chemical properties: the presence of an amine backbone (instead of an imine) results in a more flexible structure that is also more resistant to hydrolysis of the C–N bond. Moreover, the N-amine atoms become stereogenic centres upon coordination, and this may lead to complexes that give a higher enantiomeric excess when used in catalysis.

Despite the interest of zinc $sal_2en$ complexes as models of the active site of carbonic anhydrase and other zinc-containing enzymes,[4–6] they are not easily obtained. Their low solubility in most common solvents is another drawback, and only a few complexes have been characterized by X-ray diffraction. The $Zn^{II}$ ion in these complexes is either five-coordinate with a square-pyramidal geometry[6,7] or has a dinuclear structure.[8] Singer et al.[6] have characterized two mononuclear zinc complexes with $sal_2en$-type SB's (SB = Schiff base) containing a solvent molecule in a fifth coordination position. When using a reduced derivative they obtained a dinuclear arrangement with a trigonal-bipyramidal geometry around the metal ion.

We recently[9] reported the synthesis and characterization of the SB *N*,*N*′-ethylenebis(pyridoxylideneiminato) ($pyr_2en$) and of its reduced derivative *N*,*N*′-ethylenebis(pyridoxylaminato) ($H_2Rpyr_2en$; structure depicted in Scheme 1). Both compounds are vitamin $B_6$ analogues and are water-soluble, and several vanadium-based $Rpyr_2en$ complexes have been prepared and characterized.[9,10] Two molecular structures were obtained for the dioxovanadium(v) complexes[9,10] with $H_2Rpyr_2en$, which emphasises the flexibility of the ligand when coordinated to the metal ion.

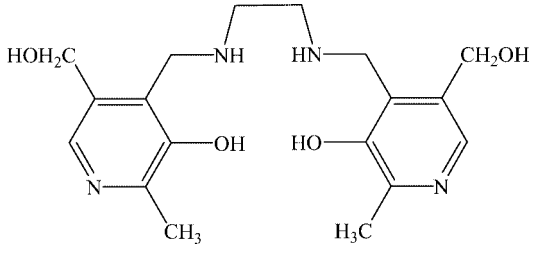


Scheme 1. Formula of $H_2Rpyr_2en$ ($H_2L$), which is a water-soluble compound. It may be considered as two pyridoxamine molecules linked by an ethylene bridge. In its fully protonated form the molecule corresponds to $H_6L^{4+}$, and in its totally deprotonated form to $L^{2-}$. As a ligand it may coordinate through the two amine-N and two phenolate-O atoms, either with both pyridine-N atoms protonated ($H_2L$), monoprotonated ($HL^-$), or deprotonated ($L^{2-}$).

Several vanadium complexes have been shown to be insulin mimetics,[11–13] namely vanadium–$Rpyr_2en$ com-

[a] Centro Química Estrutural, Instituto Superior Técnico, Av. Rovisco Pais, 1049-001, Lisbon, Portugal
[b] Department of Inorganic and Analytical Chemistry, Biocoordination Chemistry Research Group of the Hungarian Academy of Sciences, University of Szeged, PO Box 440, 6701 Szeged, Hungary
[c] Departamento de Química Fundamental, Universidade da Coruña, Campus de A Zapateira, 15071 A Coruña, Spain

 © 2006 Wiley-VCH Verlag GmbH & Co. KGaA, Weinheim 

plexes.[9,10,14,15] Zinc–Rpyr$_2$en complexes may also be good candidates as insulin mimetics,[16] and in this work we report the preparation of $Zn^{II}$–$H_2$Rpyr$_2$en complexes and the characterisation of $[ZnCl(H_2Rpyr_2en)]^+Cl^-\cdot 1.5H_2O$ (**1**) by X-ray diffraction. The molecular structure of **1** shows that the $H_2$Rpyr$_2$en ligand is tetracoordinated in a distorted square-pyramidal geometry, with a chlorine atom completing the coordination sphere. The aqueous solution behaviour of the $Zn^{II}$ + $H_2$Rpyr$_2$en system has been studied by pH-potentiometry and $^1$H NMR spectroscopy.

## Results and Discussion

### Synthesis and Characterization

A white solid, which was characterized by elemental analysis and $^1$H NMR and IR spectroscopy, was obtained from an aqueous solution containing $H_2$Rpyr$_2$en and $ZnCl_2$ (1:1) at pH 9.5. The elemental analysis results are consistent with the formulation $Zn(Rpyr_2en)\cdot 5H_2O$. All $^1$H NMR peaks of the compound dissolved in $D_2O$ at pH 7.6 are broad, and only the peaks assigned to $CH_2N$ clearly show two resonances (see Exp. Sect.).

Colourless crystals of $[ZnCl(H_2Rpyr_2en)]^+Cl^-\cdot 1.5H_2O$ (**1**) were obtained from an alcoholic solution containing zinc acetate, $H_2$Rpyr$_2$en and $Cl^-$ (from HCl, which was used to set the pH) and characterized by single-crystal X-ray diffraction. Figure 1 shows an ORTEP diagram with the atom labelling scheme, and Table 1 contains selected bond lengths and angles. The molecule is cationic, with both pyridine N-atoms protonated, and the $H_2$Rpyr$_2$en ligand is tetracoordinated through the two $O_{phenolate}$ and the two $N_{amine}$ atoms. A chloride in the axial position completes the coordination sphere of the metal. The molecule is not planar, but presents a shape similar to an open umbrella. The geometry that best describes the metal centre is square-pyramidal, with the $H_2$Rpyr$_2$en donor atoms occupying the basal plane and the $Cl^-$ the apical position. The flexibility of the ligand can be analysed in terms of the deformation of the $N_2O_2$ plane and the displacement of the zinc ion from it. The rms deviation of the four donor atoms O(1)–N(1)–N(2)–O(2) from planarity is 0.0140(16) Å; the central Zn(1) ion lies 0.5105(17) Å above the plane. These values indicate that there is a significant deformation of the coordination plane, which is greater than in other Zn–sal$_2$en complexes.[5,17] The Zn–$O_{phenolate}$ bond lengths are within the normal range for this type of bonds,[6,18,19] as are the Zn–$N_{amine}$ and Zn–Cl bonds.[6,20,21] Overall, the complex has one positive charge and the counterion is a chloride, which is 7.76 Å away from the zinc centre. The C–O bond lengths are normal for phenolate-O atoms coordinated to zinc (1.318 and 1.296 Å),[18,19] and the C–N distances (1.480–1.483 Å) are typical of single bonds.[6,20] There are no important changes in the C–$N_{amine}$ bond lengths upon coordination to the zinc ion − they increase by less than 0.012 Å − but the C–$O_{phenolate}$ bonds decrease by more than 0.03 Å (0.061 Å for one of them).[9]

Both pyridoxal rings are approximately planar, with rms deviations from the plane of the six atoms of 0.0183(27) and 0.0114(28) Å. The ligand is quite flexible, this being evidenced, for example, by the torsion angles between N(1)–C(2)–C(1)–N(2), C(4)–C(3)–N(1)–C(2) and C(11)–C(10)–N(2)–C(1), which are 57.7(5)°, 168.9(3)° and 176.3(5)°, respectively. Some relevant H-bonds in the crystal packing (see Figure 2) are included in Table 1.

Comparing this structure with that reported for $[Zn^{II}(pyridoxamine)_2(H_2O)_2](NO_3)_2$,[22] several differences become clear, namely i) that the pyridoxamine complex corresponds to an octahedral geometry, and ii) the Zn–$N_{amine}$ bond lengths are shorter than the Zn–O bonds, which is probably due to the different coordination number and to the higher steric requirement in the Zn–$H_2$Rpyr$_2$en complex.

The IR spectra of the Zn–$H_2$Rpyr$_2$en complexes in the powder and crystalline forms are similar. They are quite complex in the 2600–3500 cm$^{-1}$ range, which contains several bands assigned to stretching (symmetrical and asym-

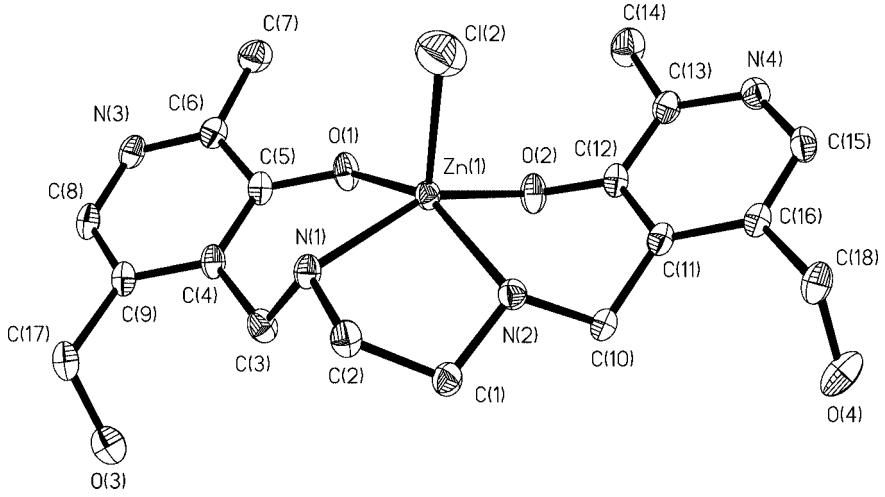


Figure 1. ORTEP diagram of $[ZnCl(H_2Rpyr_2en)]^+Cl^-\cdot 1.5H_2O$ (**1**) showing the atom labelling scheme. The ligand coordinates through the two amine-N and two phenolate-O atoms, with both pyridine-N atoms protonated. The thermal ellipsoids are drawn at 30% probability level. The hydrogen atoms and water molecules are not included, namely those bound to the pyridine N atoms N(3) and N(4).

 © 2006 Wiley-VCH Verlag GmbH & Co. KGaA, Weinheim 

Table 1. Selected bond lengths [Å], angles [°] and hydrogen-bonds parameters for $[ZnCl(H_2Rpyr_2en)]^+Cl^-\cdot 1.5H_2O$ (**1**).

| Bond lengths [Å] | | Angles [°] | | A···H–D | A–D [Å] | A···H–D [°] | Symmetry code |
|---|---|---|---|---|---|---|---|
| Zn(1)–O(1) | 1.976(3) | O(1)–Zn(1)–O(2) | 88.96(11) | Cl(1)···H–N(4) | 3.078(4) | 164(5) | |
| Zn(1)–O(2) | 2.026(3) | O(1)–Zn(1)–N(1) | 88.00(11) | Cl(1)···H–O(4) | 3.120(4) | 161(6) | $x+1, y, z$ |
| Zn(1)–N(1) | 2.167(3) | O(2)–Zn(1)–N(1) | 150.66(13) | O(3)–H···O(1) | 2.735(4) | 149(5) | $-x, -y+2, -z+2$ |
| Zn(1)–N(2) | 2.159(4) | O(1)–Zn(1)–N(2) | 151.80(13) | O(3)–H···O(2) | 3.203(4) | 124(5) | $-x, -y+2, -z+2$ |
| Zn(1)–Cl(2) | 2.2282(18) | O(2)–Zn(1)–N(2) | 88.16(12) | O(3)–H···O(1W) | 2.794(5) | 166(7) | $x-1, y, z$ |
| O(1)–C(5) | 1.318(4) | N(1)–Zn(1)–N(2) | 81.00(12) | O(1W)–H···N(3) | 2.760(5) | 165.9(8) | |
| O2–C(12) | 1.296(5) | O(1)–Zn(1)–Cl(2) | 106.38(10) | | | | |
| N(2)–C(1) | 1.464(5) | O(2)–Zn(1)–Cl(2) | 104.37(10) | | | | |
| N(2)–C(10) | 1.480(5) | N(1)–Zn(1)–Cl(2) | 104.48(10) | | | | |
| N(1)–C(2) | 1.478(5) | N(2)–Zn(1)–Cl(2) | 101.51(10) | | | | |
| N(1)–C(3) | 1.483(5) | | | | | | |

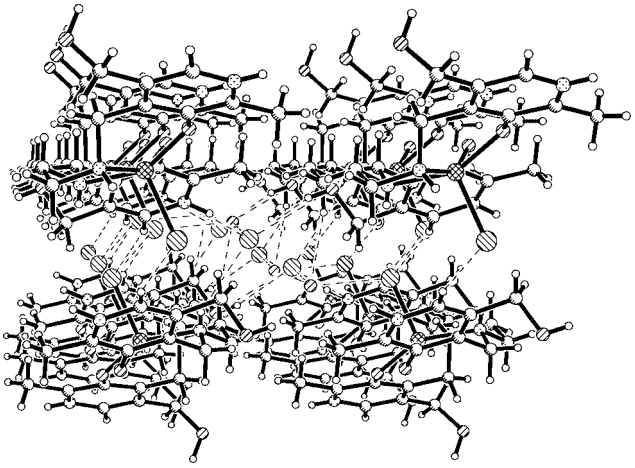

Figure 2. Crystal packing of the $[ZnCl(H_2Rpyr_2en)]^+Cl^-\cdot 1.5H_2O$ molecules, showing the hydrogen-bonding network.

metrical) of the hydrogen-bonded $CH_2O$–H groups of the pyridoxal ring and water molecules.[23,24] The $\nu$(N–H) absorption, which is present in the ligand spectrum at 3286 $cm^{-1}$,[9] appears at 3210 and 3261 $cm^{-1}$ in the crystal and powder complexes, respectively, in agreement with the coordination through the amine-N atoms. The $\nu(C–O)_{phenolate}$ absorptions are in the expected range for this type of compounds at 1294 and 1296 $cm^{-1}$, respectively.[23,24] The two $\nu(N_{pyridine}–H)$ absorptions appear at 3317 and 3340 $cm^{-1}$ in the spectrum of the crystal.

We found[9] that two main types of isomers, which correspond to different energies, form in solution for the $V^{IV}O$– and $V^VO_2$–$H_2Rpyr_2en$ complexes. For the $V^{IV}O$ complexes, two types of binding modes can form, one with the two N-amines and two O-phenolates as equatorial donors, and the other with one of these donor atoms in an axial position, the fourth equatorial donor atom now being an O atom from a water ligand. The two types of isomers give distinct peaks in the EPR spectrum (for the $V^{IV}O$ complexes), and for the $V^VO_2$ complexes two broad $^{51}V$ NMR resonances and two distinct $^1H$ NMR peaks are observed for all H-atoms. If similar isomers were to form in solution for the $Zn^{II}$–$H_2Rpyr_2en$ system (see Scheme 2, type I and type II isomers), we would also expect the observation of distinct $^1H$ NMR resonances for the H-atoms of the isomers with either one O-phenolate (type IIA) or one N-amine (type IIB) in an axial position. However, this is not the case (see below), therefore only one type of isomer forms, namely the one with a binding mode similar to that found for **1**, but with no apical $Cl^-$ donor atom, i.e. type I in Scheme 2. For similar complexes with $[V^{IV}O\{R(SO_3\text{-sal})_2en\}]$ ($SO_3$-sal = salicylaldehyde-5-sulfonate), we have also observed that the isomers with one equatorial $H_2O$ ligand essentially do not form.[10]

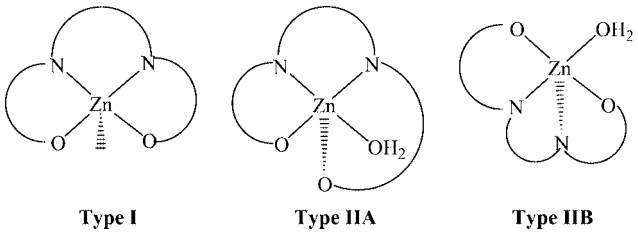


Scheme 2. Schematic representation of the main types of isomeric complexes that may form in solution.

As the coordinated N-amine atoms of $H_2Rpyr_2en$ are stereogenic centres, two main types of stereoisomeric complexes may form for the type I binding mode, namely those with both N-amine donors either *R* or *S*, and those with one *S* and one *R*. As found for the $V^{IV}O$– and $V^VO_2$–$H_2Rpyr_2en$ complexes,[9] we could expect that for the $Zn^{II}$–$H_2Rpyr_2en$ system these isomeric complexes also correspond to approximately similar energy. In the $^1H$ NMR spectra of **1** the peaks are relatively broad, and only in the case of the $CH_2NH$ resonances are separate peaks observed.

## Speciation Studies

### *pH-Potentiometry*

The acid–base behaviour of $H_2Rpyr_2en$ and its complex formation with $V^{IV}O$ and $V^V$ have been reported previously.[9] The study of the $Zn^{II}$–$H_2Rpyr_2en$ system by pH-potentiometry and $^1H$ NMR spectroscopy is presented here. The pH-metric titration curves were measured between pH 2.2 and 11.7, and the evaluation was made by considering a model similar to that obtained for the $V^{IV}O$ system, which corresponds to the best model fitting the experimental data. The formation constants are listed in

 © 2006 Wiley-VCH Verlag GmbH & Co. KGaA, Weinheim 

Table 2 and a species-distribution diagram is depicted in Figure 3.

Table 2. Protonation (p*K*) and $Zn^{II}$ complex ($M_pL_qH_r$) formation constants (log *β*) with $H_2Rpyr_2en$ at $I$ = 0.2 M (KCl) and 25 °C.[a]

| | log *β* | p*K* |
|---|---|---|
| $H_6L^{4+}$ | 38.46 | 2.20 |
| $H_5L^{3+}$ | 36.26 | 3.01 |
| $H_4L^{2+}$ | 33.25 | 5.96 |
| $H_3L^{+}$ | 27.29 | 7.66 |
| $H_2L$ | 19.63 | 9.13 |
| $HL^{-}$ | 10.50 | 10.50 |
| $[ZnLH_2]^{2+}$ | 27.08 (1) | 7.44 |
| $[ZnLH]^{+}$ | 19.64 (2) | 8.11 |
| ZnL | 11.53 (2) | 10.80 |
| $[ZnLH_{-1}]^{-}$ | 0.72 (2) | |
| No. of points | 481 | |
| Fitting[b] [mL] | $5.61 \times 10^{-3}$ | |

[a] Three times the standard deviation is reported in parentheses. [b] The average difference between the calculated and the experimental titration curves, expressed in millilitres of titrant. The total initial volumes were 25 mL.

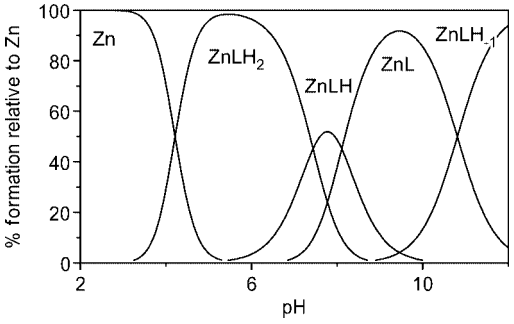


Figure 3. Species-distribution diagram for the complexes formed in the $Zn^{II}$–$H_2Rpyr_2en$ system; $C_{Zn}$ = 2.0 mM and L/M = 2.

Analysis of the potentiometric data with the PSEQUAD program[25] showed the presence of only 1:1 complexes of different protonation states ($[ZnLH_2]^{2+}$, $[ZnLH]^{+}$, [ZnL] and $[ZnLH_{-1}]^{-}$) in the pH range studied. Coordination starts at around pH 4 with the displacement of four protons from the ligand to form $[ZnLH_2]^{2+}$. Further deprotonation, now involving the pyridine-N atoms, results in the progressive formation of $[ZnLH]^{+}$ and [ZnL]. Above pH 10 a hydrolytic species, $[ZnLH_{-1}]^{-}$, becomes important. Upon comparison with the $V^{IV}O$–, $Ni^{II}$– and $Cu^{II}$–$H_2Rpyr_2en$ systems,[9,26] the proton displacement constants ($K$*), which refer to the process $H_6L + M^{2+} \rightleftharpoons MLH_2^{2+} + 4H^{+}$ [$K$*($CuLH_2^{2+}$) = –3.24; $K$*($V^{IV}OLH_2^{2+}$) = –5.63; $K$*($NiLH_2^{2+}$) = –10.08; $K$*($ZnLH_2^{2+}$) = –11.38], give the stability order $Cu^{II} > V^{IV}O > Ni^{II} > Zn^{II}$.

Complexation of $Zn^{II}$ with a hexadentate diacetic acid derivative of $H_2Rpyr_2en$, namely PLED (*N*,*N*′-dipyridoxyethylenediamine-*N*,*N*′-diacetic acid),[27–29] presents a similar speciation, although with a higher stability for the complex formed {$K$*($ZnLH_2$) = –5.33 [$T$ = 25 °C, $I$ = 0.1 M (NaCl)]} due to the hexadentate coordination of the ligand.[29]

### *$^1$H NMR Spectroscopic Studies*

The acid–base properties and the protonation scheme of $Rpyr_2en^{2-}$ have been studied by $^1$H NMR spectroscopy and pH-potentiometry previously.[9] The formation of H bonds between the phenolic and the amino groups is favourable as the phenolic protons are quite acidic and are even more acidic than those of pyridoxamine.[9] Figure 4 shows the ligand, the atom labelling scheme used in the $^1$H NMR spectra and the pH-dependence of the chemical shifts for solutions containing a total $Zn^{II}$ concentration ($C_{Zn}$) of 4 mM and a ligand-to-metal (L/M) ratio of 2.

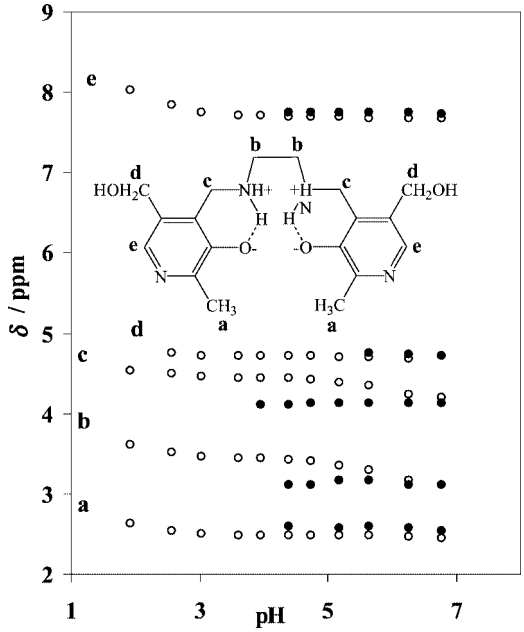


Figure 4. pH-dependence of the chemical shifts ($\delta$ in ppm) of the ligand protons in the absence (open circles) and the presence of $Zn^{II}$ ion (L/M = 2, full circles); $C_{ligand}$ = 8 mM. The $H_2Rpyr_2en$ molecule and the proton-labelling scheme are also depicted in the figure.

The complex formation of $H_2Rpyr_2en$ with $Zn^{II}$ was also studied by $^1$H NMR spectroscopy by measuring spectra at room temperature for L/M ratios of 1 and 2, with $C_{Zn}$ = 4 mM. Below pH 4 no complexes could be detected in solution, all peaks being directly assignable to the free ligand. At a pH of around 4, however, where complex formation starts (see Figure 3), the peaks broaden, then new, slightly shifted peaks appear for all protons (see Figure 5), i.e. separate peaks can be ascribed to protons in the free and the complexed ligand, suggesting an exchange that is somewhat slower than the NMR timescale. The peaks of protons **a**, **e** and **d** in the complexes are slightly deshielded relative to the ligand, while protons **b** and **c** are shielded. Precipitation occurs above pH 7. This is probably due to the higher concentrations used in the $^1$H NMR titrations. Moreover, while in the pH-metric titrations the equilibrium was reached very rapidly, in the $^1$H NMR titrations a few minutes were required to stabilize the pH readings.

Due to the presence of the amine bonds (instead of imine as in $sal_2en$-type ligands) $H_2Rpyr_2en$ is a more flexible molecule and its coordination does not yield similarly symmetrical complexes. As mentioned above, the coordinated amine-N atoms of $H_2Rpyr_2en$ are stereogenic centres, and for binding mode I (Scheme 2) several stereoisomers may

 © 2006 Wiley-VCH Verlag GmbH & Co. KGaA, Weinheim 

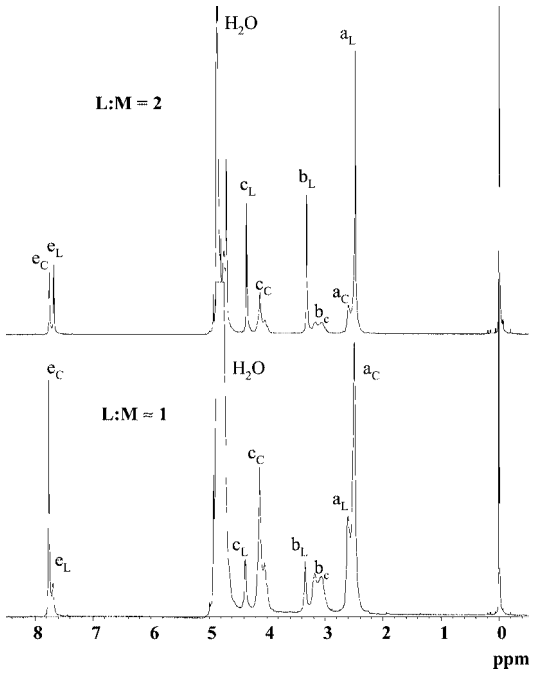


Figure 5. $^1$H NMR spectra for solutions containing $Zn^{II}$ ($C_{Zn}$ = 4 mM) and $H_2Rpyr_2en$ at pH 5.47. The approximate L/M ratios and the peak assignments are indicated. See Figure 4 for the proton-labelling scheme. The subscripts L and C mean free and coordinated ligand, respectively. For the spectrum shown at L/M ≈ 1, a small excess of ligand is present.

form as both amine donors may be either *R* or *S*, or both *S*, or both *R* (three isomers for $ZnLH_2$ and ZnL stoichiometries and four for the ZnLH stoichiometry).

This is probably the reason why two peaks are observed for the protons of the $CH_2CH_2$ and $CH_2N$ groups in the coordinated ligand. The intensity ratios of these peaks are not clear as some are broader than others, and they strongly overlap, but from the NMR spectra the intramolecular non-equivalence of these protons is clear.

Overall, and despite some different experimental conditions (e.g. ionic strength, equilibrium time and concentrations), the spectroscopic results confirm the pH-metric data obtained for the $Zn^{II}$–$H_2Rpyr_2en$ system.

## Conclusions

The coordination of $Zn^{II}$ to $H_2Rpyr_2en$ has been investigated. The complexes have moderate solubility in aqueous solution. The compound $[ZnCl(H_2Rpyr_2en)]^+Cl^-\cdot 1.5H_2O$ (**1**) has been characterized by single-crystal X-ray diffraction, thereby confirming the flexibility of the reduced Schiff base as compared with the Schiff base $pyr_2en$. In the molecular structure of **1**, one of the coordinated amine-N atoms has an (*S*)-configuration and the other an (*R*)-configuration. All combinations of these configurations presumably occur in solution, and in the $^1$H NMR spectra either broader peaks and/or two distinct resonances are observed for the hydrogen atoms of the coordinated ligand, namely for the H atoms of the $CH_2NCH_2CH_2NCH_2$ moiety. The $H_2Rpyr_2en$ ligand in **1** is coordinated through the two phenolate-O and amine-N atoms in a distorted square-pyramidal geometry. To the best of our knowledge this is the first example of a monomeric $Zn^{II}$–reduced salen-type SB that does not dimerize. The solution studies have revealed the high stability of the $Zn^{II}$ complexes formed, although they are less stable than those formed by $H_2Rpyr_2en$ with $Cu^{II}$, $Ni^{II}$ or $V^{IV}O$. Vanadium and copper complexes with chiral $sal_2an$ type ligands are presently being tested for catalytic asymmetric synthesis. The additional stereogenic centres formed upon coordination of the N-amine donors may favour higher enantiomeric excesses in some of these catalytic systems.

## Experimental Section

**$H_2Rpyr_2en$:** The synthesis of this ligand has been reported previously.[9]

**$[Zn(Rpyr_2en)]\cdot 5H_2O$:** $H_2Rpyr_2en$ (66mg, 0.18 mmol) was dissolved in 10 mL of $H_2O$ containing a few drops of 1 M HCl. $ZnCl_2$ (10.2 mL of a 0.0156 M solution) was added and the pH adjusted to 9.5 with 1 M KOH. The solution was stirred for one hour, and a white precipitate was removed by filtration, washed with ethanol and diethyl ether and dried under vacuum. $C_{18}H_{24}N_4O_4Zn\cdot 5H_2O$ (515.9): calcd. C 41.91, H, 6.64, N 10.86; found C 42.2, H 7.0, N 10.7. $^1$H NMR (300 MHz, $D_2O$, 25 °C, pH 7.63): $\delta$ = 7.67 (s, 2 H, $CH_{arom}$), 4.66 (s, 4 H, $CH_2OH$), 4.02 (d, $J$ = 0.1 Hz, 4 H, $CH_2N$), 3.09 (s, 4 H, $CH_2CH_2$), 2.38 (s, 6 H, $CH_3$) ppm.

**Crystals of $[ZnCl(H_2Rpyr_2en)]^+Cl^-\cdot 1.5H_2O$ (1):** $H_2Rpyr_2en$ (0.20 g, 0.55 mmol) was dissolved in a mixture of ethanol and water (1:1, 5 mL) containing a few drops of 1 M NaOH, and $Zn(CH_3COO)_2\cdot 2H_2O$ (0.12 g) dissolved in 5 mL of water was slowly added. The pH was adjusted to 7 by addition of a 1 M HCl solution. The mixture was then refluxed at 70 °C for 2 h. No precipitation was observed and the solution was cooled and kept at about 5 °C. After about one month colourless crystals were collected for single-crystal X-ray analysis.

**X-ray Crystal Structure Determinations:** X-ray data were collected on a Bruker SMART 1000 CCD diffractometer by the $\varphi$–$\omega$ scan method at room temperature. Reflections were measured for a hemisphere of data with frames covering 0.3° in $\omega$. Of the 7285 reflections measured, all of which were corrected for Lorentz and polarization effects and for absorption by semi-empirical methods based on symmetry-equivalent and repeated reflections, 3949 independent reflections exceeded the significance level $|F|/\sigma(|F|) > 4.0$. Complex scattering factors were taken from the program package SHELXTL.[30] The structure was solved by direct methods and refined by full-matrix least-squares methods on $F^2$. The hydrogen atoms were left to refine freely, except the hydrogen atoms H3, H7A, H7B, H7C, H14A, H14B and H14C, which were included in calculated positions and refined in a riding mode. Refinement converged with allowance for thermal anisotropy of all non-hydrogen atoms. Crystal data and details on data collection and refinement are summarized in Table 3.

CCDC-276399 (for **1**) contains the supplementary crystallographic data for this paper. These data can be obtained free of charge from the Cambridge Crystallographic Data Centre via www.ccdc.cam.ac.uk/data_request/cif.

 © 2006 Wiley-VCH Verlag GmbH & Co. KGaA, Weinheim 

Table 3. Crystal data collection and refinement parameters.

| | |
|---|---|
| Formula | $C_{18}H_{29}Cl_2N_4O_{5.5}Zn$ |
| $M$ | 525.72 |
| Crystal system | triclinic |
| Space group | $P\bar{1}$ |
| $T$ [K] | 298(2) |
| $a$ [Å] | 9.1208(10) |
| $b$ [Å] | 10.0030(12) |
| $c$ [Å] | 12.3033(14) |
| $\alpha$ [°] | 82.629(2) |
| $\beta$ [°] | 88.885(2) |
| $\gamma$ [°] | 89.296(2) |
| $F_{000}$ | 546 |
| $Z$ | 2 |
| $D_{calcd.}$ [g cm$^{-3}$] | 1.569 |
| $\mu$ [mm$^{-1}$] | 1.383 |
| $R_{int}$ | 0.0209 |
| No. measured reflections | 7285 |
| No. observed reflections | 3949 |
| $R_1$ | 0.0522 |
| $wR_2$ (all data) | 0.1516 |
| Largest diff. peak and hole [e Å$^{-3}$] | 0.421 and –1.492 |

**Physical and Spectroscopic Studies:** IR spectra were recorded with a BioRad FTS 3000 MX FTIR spectrometer. $^1$H NMR spectra were recorded with a Varian Unity 300 spectrometer at a probe temperature of about 25 °C.

**pH-metric Titration:** Protonation and formation constants were determined by pH-metric titration of 25-mL samples. The ionic strength was adjusted to 0.2 M with KCl and the temperature was 25.0 ± 0.1 °C. The ligand concentrations were 0.002 or 0.004 M and the L/M ratios varied from 1 to 4. Titrations were normally carried out from pH 2.2 up to 11.7, with carbonate-free KOH solution of known concentration (ca. 0.2 M) under purified argon. The $Zn^{II}$ stock solution was prepared by dissolving ZnO of *puriss.* quality in excess HCl solution. The $Zn^{II}$ content was determined gravimetrically from the oxinate. The free-acid content was measured by pH-potentiometry. An automatic titration set including a Dosimat 665 autoburette, an Orion 710A precision digital pH-meter and an IBM-compatible computer was used. A Metrohm 6.0234.100 semi-micro combined glass electrode was calibrated for hydrogen-ion concentration as described earlier.[31] The p$K_w$ calculated from strong acid–strong base titration was 13.755 ± 0.010. The concentration stability constants, $\beta_{pqr} = [M_pL_qH_r]/[M]_p[L]_q[H]_r$, were calculated with the aid of the computer program PSEQUAD.[25] When referring to stoichiometries of species present in solution, the normal $M_pL_qH_r$ notation is used, where L = $Rpyr_2en^{2-}$.

**$^1$H NMR Spectroscopy:** All NMR samples were prepared at room temperature immediately before recording the spectra. A quantity of $ZnCl_2$ aqueous solution of known concentration (ca. 0.02 M) was evaporated to dryness and $D_2O$ added and evaporated at least three times to replace the H by D. The samples were prepared in $D_2O$ (99.995% D) by weighing the appropriate amount of ligand and $Zn^{II}$ to give the desired concentration and L/M ratio. The pD values of these solutions were adjusted with DCl and $CO_2$-free NaOD solutions and measured with a Thermo Orion 420A+ pH-meter with a Mettler Toledo U402-M3-S7/200 combined electrode. The microelectrode was previously calibrated with standard buffered aqueous solutions, and the pH was measured directly in the NMR tubes. The pH-meter readings were converted into pD by using the equation pD = pH + 0.40.[32] Two sets of experiments were performed as a function of pH, with metal-ion concentrations of 4 mM and L/M ratios of 1 and 2. The $^1$H NMR chemical shifts were referenced relative to DSS (sodium 2,2-dimethyl-2-silapentane-5-sulfonate) at $\delta$ = 0 ppm. The signal intensities of the NMR resonances were obtained using the program NUTS.[33]

## Acknowledgments

We would like to thank the Fundação para a Ciência e Tecnologia (FCT), POCTI (POCTI/QUI/56949/2004), the Hungarian National Research Fund (OTKA T49417/2005), the Hungarian Academy of Sciences, the bilateral Portugal–Hungary Intergovernmental Cooperation Programme, the University of A Coruña and Portugal–Spain Cooperation Programme E-56/2005 for financial support.

[1] P. G. Cozzi, *Chem. Soc. Rev.* **2004**, *33*, 410–421.
[2] T. Achard, Y. N. Belokon, J. A. Fuentes, M. North, T. Parsons, *Tetrahedron* **2004**, *60*, 5919–5930.
[3] E. N. Jacobsen, *Acc. Chem. Res.* **2000**, *33*, 421–431.
[4] D. A. Atwood, *Coord. Chem. Rev.* **1997**, *165*, 267–296.
[5] E. Szlyk, A. Wojtczak, A. Surdykowski, M. Gozdzikiewicz, *Inorg. Chim. Acta* **2005**, *358*, 467–475.
[6] A. L. Singer, D. A. Atwood, *Inorg. Chim. Acta* **1998**, *277*, 157–162.
[7] G. A. Morris, H. Zhou, C. L. Stern, S. T. Nguyen, *Inorg. Chem.* **2001**, *40*, 3222–3227.
[8] J. S. Matalobos, A. M. Garcýa-Deibe, M. Fondo, D. Navarro, M. R. Bermejo, *Inorg. Chem. Commun.* **2004**, *7*, 311–314.
[9] I. Correia, J. Costa Pessoa, M. T. Duarte, R. T. Henriques, M. F. M. Piedade, L. F. Veiros, T. Jackush, A. Dornyei, T. Kiss, M. M. C. A. Castro, C. F. G. C. Geraldes, F. Avecilla, *Chem. Eur. J.* **2004**, *10*, 2301–2317.
[10] I. Correia, J. Costa Pessoa, M. T. Duarte, M. F. M. Piedade, T. Jackush, T. Kiss, M. M. C. A. Castro, C. F. G. C. Geraldes, F. Avecilla, *Eur. J. Inorg. Chem.* **2005**, 732–744.
[11] K. H. Thompson, J. H. McNeill, C. Orvig, *Chem. Rev.* **1999**, *99*, 2561–2571.
[12] C. Orvig, K. H. Thompson, *Coord. Chem. Rev.* **2001**, *219–221*, 1033–1053.
[13] H. Sakurai, H. Yasui, Y. Adachi, *Expert Opin. Invest. Drugs* **2003**, *12*, 1189–1203.
[14] T. C. Delgado, I. Tomaz, I. Correia, J. Costa Pessoa, J. G. Jones, C. F. G. C. Geraldes, M. M. C. A. Castro, *J. Inorg. Biochem.*, manuscript accepted.
[15] D. Rehder, J. Costa Pessoa, C. F. G. C. Geraldes, M. M. C. A. Castro, T. Kabanos, T. Kiss, B. Meier, G. Micera, L. Pettersson, M. Rangel, A. Salifoglou, I. Turel, D. Wang, *J. Biol. Inorg. Chem.* **2002**, *7*, 384–396.
[16] H. Sakurai, Y. Kojima, Y. Yoshikawa, K. Kawabe, H. Yasui, *Coord. Chem. Rev.* **2002**, *226*, 187–198.
[17] J. Reglinski, S. Morris, D. E. Stevenson, *Polyhedron* **2002**, *21*, 2175–2182.
[18] M. A. Torzilli, S. Colquhoun, D. Doucet, R. H. Beer, *Polyhedron* **2002**, *21*, 697–704.
[19] A. Garcia-Raso, J. J. Fiol, A. López-Zafra, I. Mata, E. Espinosa, E. Molins, *Polyhedron* **2000**, *19*, 673–680.
[20] S. Gourbatsis, S. P. Perlepes, I. S. Butler, N. Hadjiliadis, *Polyhedron* **1999**, *18*, 2369–2375.
[21] C. López, A. Caubet, S. Pérez, R. Bosque, X. Solans, M. Font-Bardía, *Polyhedron* **2002**, *21*, 2361–2367.
[22] D. M. Thompson, W. Balenovich, H. M. Hornich, M. F. Richardson, *Inorg. Chim. Acta* **1980**, *46*, 199–203.
[23] D. H. Williams, I. Fleming, in *Spectroscopic Methods in Organic Chemistry*, 5th edn. McGraw-Hill, London, **1995**; p. 42–49.
[24] K. Nakamoto, in *Infrared and Raman Spectra of Inorganic Compounds*, 5th edn., **1997**; p. 73–271.
[25] L. Zekany, I. Nagypal, in *Computational Methods for the Determination of Stability Constants* (Ed.: D. Leggett), Plenum, New York, **1985**.

 © 2006 Wiley-VCH Verlag GmbH & Co. KGaA, Weinheim 

[26] I. Correia, A. Dornyei, T. Jackush, F. Avecilla, T. Kiss, J. Costa Pessoa, manuscript in preparation.
[27] C. H. Taliaferro, R. J. Motekaitis, A. E. Martell, *Inorg. Chem.* **1984**, *23*, 1188–1192.
[28] C. H. Taliaferro, A. E. Martell, *Inorg. Chem.* **1985**, *24*, 2408–2413.
[29] S. M. Rocklage, S. H. Sheffer, W. P. Cacheris, S. C. Quay, F. E. Hahn, K. N. Raymond, *Inorg. Chem.* **1988**, *27*, 3530–3534.
[30] G. M. Sheldrick, *SHELXTL Bruker Analytical X-ray system*, version release 5.1; Madison, WI: **1997**.
[31] R. D. Gillard, J. Costa Pessoa, T. Gajda, T. Kiss, S. M. Luz, J. J. G. Moura, I. Tomaz, J. P. Telo, I. Török, *J. Chem. Soc., Dalton Trans.* **1998**, 3587.
[32] P. K. Glasoe, F. A. Long, *J. Phys. Chem.* **1960**, *64*, 188–190.
[33] NUTS-NMR spectroscopic data processing software, version pro; Acorn NMR: **1999**.

Received: July 13, 2005
Published Online: December 13, 2005

 © 2006 Wiley-VCH Verlag GmbH & Co. KGaA, Weinheim 

DOI: 10.1002/ejic.200500785

# Heterobimetallic Ruthenium-Cobalt Complexes Containing the Pentamethylcyclopentadienyl or Indenyl Ligand

**Sin Yee Ng,[a] Lai Yoong Goh,*[a] Lip Lin Koh,[a] Weng Kee Leong*[a] Geok Kheng Tan,[a] Suming Ye,[b] and Yinghuai Zhu[b]**

**Keywords:** Heterometallic complexes / Ruthenium / Cobalt / Phosphanes / Indenyl

The salt elimination reaction between $NaCo(CO)_4$ and the ruthenium complexes LRu(diphos)Cl and [(Ind)$Ru(CO)_2Cl$] afforded the Ru–Co bimetallic complexes [$LRu(\mu\text{-}CO)_2(\mu\text{-}diphos)Co(CO)_2$] [L = $C_5Me_5$ ($Cp^*$), diphos = $Ph_2P(CH_2)_nPPh_2$, **3a**: $n$ = 1 , or **3b**: $n$ = 2; **3**: L = $C_9H_7$ (Ind), diphos = $Ph_2PCH_2PPh_2$ ] and [(Ind)$Ru(CO)_2Co(CO)_4$] (**3d**), respectively, in high yields. However, the same reaction with the monophosphane analogue, [(Ind)$Ru(PPh_3)_2Cl$], gave the heterobimetallic complex [(Ind)$Ru(PPh_3)(CO)(\mu\text{-}CO)Co(CO)_3$] (**3e**) in fair yield, together with redox-initiated derivatives $Ru(PPh_3)_2(CO)_3$ (**4e**) and [(Ind)$Co(CO)(PPh_3)$] (**6e**). A similar redox process in the reaction of the dppf analogue, [(Ind)Ru(dppf)Cl] (dppf = 1,1′-diphenylphosphanylferrocene) gave [Ru(dppf)$(CO)_3$] (**4f**) and [(Ind)$Co(CO)_2$] (**6f**), together with a complex salt [(Ind)Ru(dppf)(CO)][$Co(CO_4)$] [**5f·Co(CO)$_4$**].

(© Wiley-VCH Verlag GmbH & Co. KGaA, 69451 Weinheim, Germany, 2006)

## Introduction

There has been much research activity on the employment of heterobimetallic complexes in catalysis.[1] The prime motivation for this has been the possibility of cooperative reactivity of adjacent heterometallic centres, which may impart new reactivity patterns significantly different from those of the homobimetallic complexes. Early reports of the superb catalytic efficacy of mixtures of cobalt and ruthenium compounds,[2] and later of ruthenium-cobalt heterobimetallic complexes,[2e] in methanol homologation, had spurred a surge in synthetic and reactivity studies of these complexes.[3,4] When supported on silica, they have also been found to be effective catalysts in hydroformylation.[5]

Synthetic routes to metal–metal bonded heterobimetallic complexes are very well documented;[6] one of the most commonly employed being the displacement of a halide ligand by an anionic metal fragment such as $[Co(CO)_4]^-$. Nevertheless, ruthenium-cobalt heterobimetallic complexes containing a half-sandwich ruthenium moiety have been relatively less studied. Ligands such as cyclopentadienyl (Cp) or Cp* often confer stability on the complexes, and when derivatised can effect changes in properties at the metal centre. The indenyl ligand is of much interest on account of its "indenyl effect", which is primarily a reflection of the ligand's ability to undergo $\eta^5 \leftrightarrow \eta^3$ ring slippage, thereby creating a vacant site on the metal centre without any ligand dissociation. Most of the reported compounds of this class were isolated in low yields, e.g., [(*p*-cymene)Ru$(CO)(\mu_2\text{-}PPh_2)Co(CO)_3$] (30% yield),[3d] [$CpRu(CO)_2$-$Co(CO)_4$] (10% yield),[3a] [$CpRu(PPh_3)_2Co(CO)_4$] (28% yield),[2e] and [$CpRuCo(CO)_3$(R-DAB)] (R = *i*Pr, *t*Bu, DAB = 1,4-diaza-1,3-butadiene) (10% yield).[3f] However, Matsuzaka et al. managed to isolate [$Cp^*Ru(CO)_2(\mu_2\text{-}CO)$-$Co(CO)_3$] in high yield (86%);[3h,7] subsequent substitution by dppm, *t*BuNC and alkynes (HC≡CTol, HC≡$CCO_2$Me) in the presence of $Me_3NO{\cdot}2H_2O$ gave very high yields of the substituted products.

In this paper, we present results from the reactions of various Cp* and Ind complexes of ruthenium with $NaCo(CO)_4$ (**1**), which gave in addition to the anticipated Ru–Co metal–metal bonded complexes, derivatives arising from redox pathways.

## Results and Discussion

Salt elimination reactions between $NaCo(CO)_4$ (**1**), and the ruthenium complexes LRu(diphos)Cl (**2**) [L = Cp*, diphos = $Ph_2P(CH_2)_nPPh_2$, **2a**: $n$ = 1 , or **2b**: $n$ = 2; **2c**: L = Ind, diphos = $Ph_2PCH_2PPh_2$], at room temperature afforded Ru–Co bimetallic complexes [$LRu(\mu\text{-}CO)_2(\mu\text{-}diphos)$-$Co(CO)_2$] (**3**), in 78–85% yields (Scheme 1). The displacement of the halide ligand by the anionic metal fragment $[Co(CO)_4]^-$ is accompanied by the bridging of the diphosphane and two carbonyl ligands across the Ru–Co bond. We note that while [(Ind)$Ru(CO)_2Cl$] (**2d**) reacted with **1** to give the metal–metal bonded complex **3d**, $Cp^*Ru(CO)_2Cl$

[a] Department of Chemistry, National University of Singapore, 3 Science Drive 3, Singapore 117543
[b] Institute of Chemical and Engineering Sciences, 1 Pesek Road, Jurong Island, Singapore 627833

 © 2006 Wiley-VCH Verlag GmbH & Co. KGaA, Weinheim 

(**2d**′) gave a monocarbonyl-bridged complex **3e**′ (the prime refers to previously reported complexes), which could be decarbonylated to produce **3a** (Scheme 2).[3h]

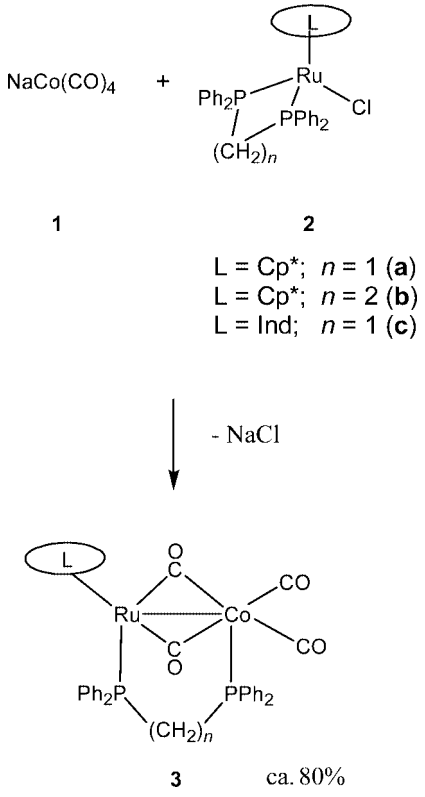


Scheme 1.

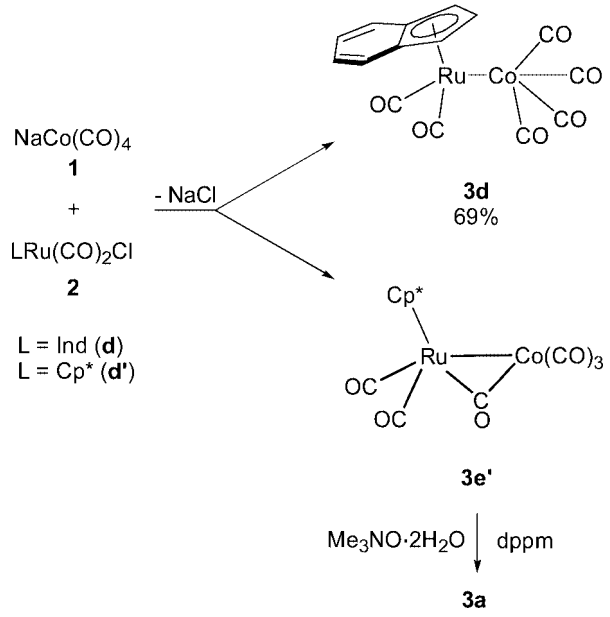


Scheme 2.

The complexes **3a**–**c** exhibited the expected resonances for the diphosphanes and Cp* or indenyl ligands in their $^1$H NMR spectra. Their $^{31}$P{$^1$H} NMR spectra all showed a sharp doublet and a broad doublet at lower field; the latter due to quadrupolar coupling to the cobalt. The IR spectra indicated the presence of both terminal and bridging carbonyls. Complex **3c** has also been characterized by a single-crystal X-ray structural study (Figure 1); that for **3a** has already been reported.[3h] Their molecular structures are very similar in that both comprise a bimetallic complex in which the ruthenium and cobalt atoms are connected by a metal–metal bond, two bridging CO ligands and a bridging diphos ligand. The Ru–Co bond length in **3c** is shorter than that in **3a** [2.6474(4) and 2.677(2) Å, respectively] and probably reflects the weaker indenyl-ruthenium compared to the Cp*–ruthenium interaction; stronger interaction in the latter would be expected to lengthen the metal–metal bond via a *trans* influence. The metal–phosphane bond lengths in both **3a** and **3c** are shorter to cobalt than to ruthenium [Ru(1)–P(3) = 2.3048(6) Å and Co(2)–P(4) = 2.2199(7) Å for **3c**]; these are comparable to the Co–P bond length of 2.175(1) Å in $Co_2(CO)_6(PMe_3)_2$,[8] and the Ru–P bond length of 2.385 Å in $\{Ru_2(CO)_4(PMe_3)_2(\mu\text{-}O_2CCH_2CO_2)\}_2$,[9] and suggest that the difference is due to the different formal oxidation states [Co(0) vs. Ru$^{I}$] since ruthenium and cobalt have the same covalent radii (1.26 Å). However, the reverse situation seems to be the case with regard to the bridging carbonyls.

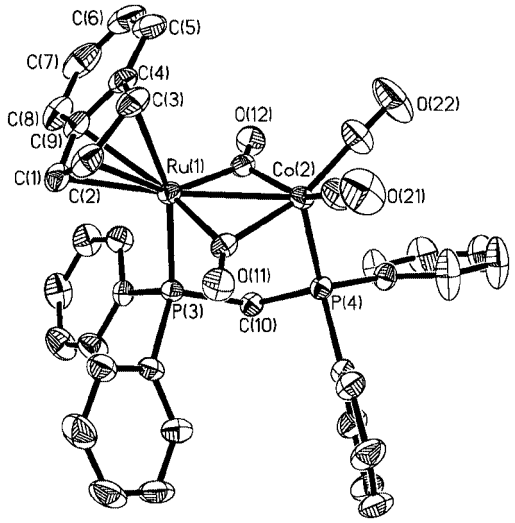


Figure 1. ORTEP diagram (50% probability thermal ellipsoids, hydrogen atoms omitted) and selected bond lengths [Å] and angles [°] of **3c**. Ru(1)–Co(2) = 2.6474(4); Ru(1)–P(3) = 2.3048(6); Co(2)–P(4) = 2.2199(7); Ru(1)–C(11) = 1.947(3); Ru(1)–C(12) = 1.962(3); Co(2)–C(22) = 1.772(3); Co(2)–C(21) = 1.776(3); Co(2)–C(12) = 2.002(3); Co(2)–C(11) = 2.021(3); O(11)–C(11) = 1.170(3); O(12)–C(12) = 1.182(3); O(21)–C(21) = 1.144(4); O(22)–C(22) = 1.130(4); P(3)–Ru(1)–Co(2) = 92.116(18); P(4)–Co(2)–Ru(1) = 99.16(2); Ru(1)–C(11)–Co(2) = 83.69(10); Ru(1)–C(12)–Co(2) = 83.80(10).

The IR spectrum of [(Ind)Ru(CO)$_2$Co(CO)$_4$] (**3d**) showed clearly the absence of any bridging carbonyl ligand, in contrast to that for the Cp* analogue **3e**′. This may be attributed to the greater electron donating ability of Cp* compared to Ind,[3h] and hence the tendency for the carbonyl ligands to bridge. This tendency is further enhanced by phosphane substitution at the metal centres, as observed in **3a**–**3c**.

 © 2006 Wiley-VCH Verlag GmbH & Co. KGaA, Weinheim 

The analogous reaction of the monophosphane-substituted derivative [(Ind)Ru($PPh_3$)$_2$Cl] (**2e**), however, was more complex (Scheme 3). In addition to the expected heterobimetallic product [(Ind)Ru($PPh_3$)(CO)($\mu_2$-CO)Co(CO)$_3$] (**3e**), there were the mononuclear complexes Ru($PPh_3$)$_2$-(CO)$_3$ (**4e**), and [(Ind)Co(CO)($PPh_3$)] (**6e**). These three compounds have been characterized completely, including by single-crystal X-ray crystallographic studies which confirmed that exchange of CO and $PPh_3$ ligands had occurred between the metal centres. The structure of **4e** determined here in the form of its $CH_2Cl_2$ solvate is essentially similar to that of its THF solvate reported previously.[10] The molecular structures of **3e** and **6e** are shown in Figure 2 and Figure 3, respectively.

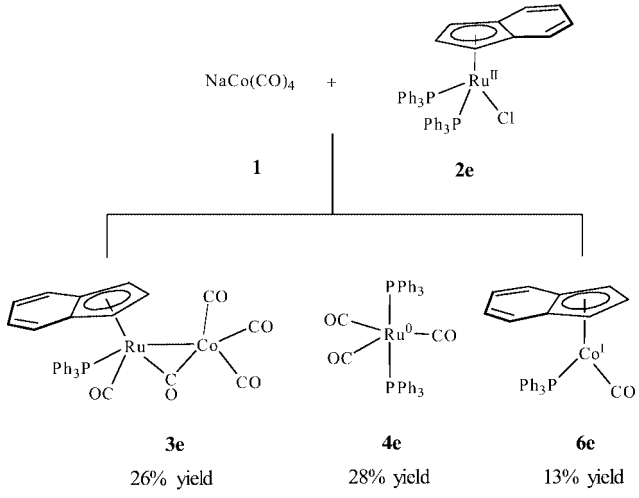


Scheme 3.

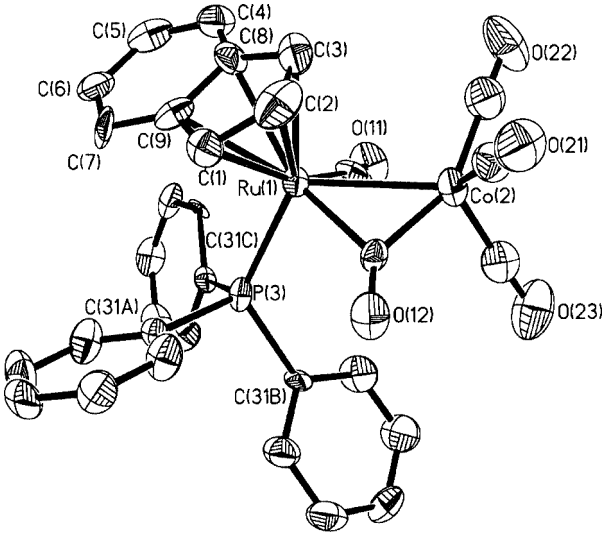


Figure 2. ORTEP diagram of **3e** (50% probability thermal ellipsoids, hydrogen atoms omitted).

There is no known Cp or Cp* analogue to **3e**. However, it is interesting to compare its structure with those of the previously reported Cp* parent carbonyl [Cp*Ru(CO)$_2$($\mu$-CO)Co(CO)$_3$] (**3e′**) and its isocyanide derivative [Cp*Ru(CNBu$^t$)(CO)($\mu$-CO)Co(CO)$_3$] (**3f′**);[3h] a common

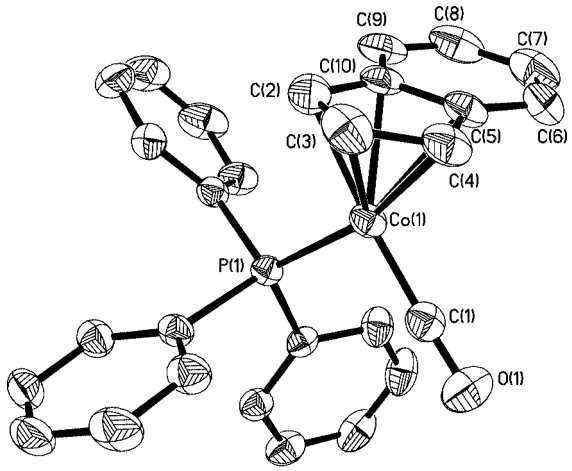


Figure 3. ORTEP diagram (50% probability thermal ellipsoids, hydrogen atoms omitted) and selected bond lengths [Å] and angles [°] of **6e**. Co(1)–C(1) = 1.711(3); Co(1)–P(1) = 2.1459(7); O(1)–C(1) = 1.156(3); C(1)–Co(1)–P(1) = 95.39(9); O(1)–C(1)–Co(1) = 176.3(3).

atomic numbering scheme and selected bond parameters are collected in Table 1. The overall structural features of the three compounds are the same, comprising of a single carbonyl bridging the Ru–Co bond, a terminal carbonyl on the ruthenium, and three on the cobalt. As in the case of **3c**, the Ru–Co bond length for **3e** is significantly shorter than in either of the Cp* analogues [2.677(2) vs. 2.7445(6) and 2.735(4) Å in **3e**, **3e′** and **3f′**, respectively]. The bridging carbonyl is obviously skewed towards the cobalt in all three compounds, as in the case of **3c**. Although there appears to be only one bridging carbonyl in these three compounds, in contrast to two for **3a** and **3c**, the carbonyl which should have made up the second bridging carbonyl [CO(11)] is actually semi-bridging [$\angle$Ru–C(11)–O(11) $\approx$ 167–169°, compared with $\angle$Co–C–O $\approx$ 173–179°].[11] This can be attributed to the presence of an electron-donating phosphorus on cobalt in the case of **3a** and **3c**, which increased electron density on the cobalt and hence the propensity towards bridging carbonyl.[12]

The molecular structure of **6e** is similar to those of known cyclopentadienyl analogues such as [CpCo(CO)$_2$],[13] and [Cp*Co(CO)$_2$],[14] and substituted indenyl analogues such as [($\eta^5$-C$_9$H$_3$Me$_4$)Rh(CO)$_2$],[15] and [($\eta^5$-C$_9$H$_6$CHPh$_2$)-Rh(CO)(P*i*Pr$_3$)].[16] The indenyl ligand is coordinated unsymmetrically to the Co centre, as indicated by the longer bond lengths (by $\approx$ 0.1 Å) from the metal to the bridgehead carbons than to the other three carbons of the five-membered ring. The values of the slip-fold parameters: slip distortion, $\Delta$ = 0.12(3) Å; hinge angle, HA = 5.6°; and fold angle, FA = 5.3°, are in agreement with $\eta^5$ coordination of the indenyl.[15,17]

The presence of the complexes **4e** and **6e** indicated that ligand exchange and redox reaction between the ruthenium and cobalt precursors had occurred. While the oxidation state of Ru has been reduced from +2 to 0 in **4e**, that for Co has been increased from –1 to +1 in **6e**; the ruthenium complex has also lost its indenyl and phosphane ligands in

 © 2006 Wiley-VCH Verlag GmbH & Co. KGaA, Weinheim 

Table 1. Common atomic numbering scheme and selected bond parameters for **3e**, **3e′** and **3f′**.

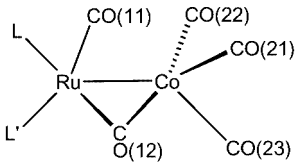


L = Ind; L' = $PPh_3$ **3e**
L = Cp*; L' = CO **3e'**
L = Cp*; L' = CN*t*Bu **3f'**

| Bond lengths [Å] or angles [°] | **3e** | **3e′** | **3f′** |
|---|---|---|---|
| Ru–Co | 2.677(2) | 2.7445(6) | 2.735(4) |
| Ru–L[a] | 2.319(4) | 1.890(4) | 1.94(3) |
| Ru–C(11) | 1.929(14) | 1.899(4) | 1.92(3) |
| Ru–C(12) | 2.030(12) | 2.206(3) | 2.10(3) |
| Co–C(12) | 1.877(14) | 1.817(4) | 1.83(3) |
| C(11)–O(11) | 1.105(16) | 1.136(4) | 1.11(3) |
| C(12)–O(12) | 1.186(16) | 1.174(4) | 1.20(3) |
| Co–Ru–L[a] | 115.12(11) | 103.7(1) | 101.7(8) |
| Ru–C(11)–O(11) | 167.2(15) | 168.6(3) | 168(2) |
| Ru–C(12)–O(12) | 135.5(11) | 126.0(3) | 127(2) |
| Co–C(12)–O(12) | 138.0(11) | 148.5(3) | 145(3) |

[a] Refers to centroid of the five-membered ring.

exchange for three carbonyls. This result was in sharp contrast with the reported chemistry of the Cp analogue, for which the heterobimetallic complex, viz., $[CpRu(PPh_3)_2Co(CO)_4]$ was isolated in low yield from the reaction of $[CpRu(PPh_3)_2Cl]$ with $TlCo(CO)_4$, but on switching from the $Tl^+$ to the $Na^+$ salt, the complex salt $[CpRu(PPh_3)_2(CO)][Co(CO)_4]$ was isolated instead.[3e] Neither the displacement of $PPh_3$ by CO, nor the redox products that we have observed, were reported in these reactions.

Similar redox chemistry was also observed in the case of [(Ind)Ru(dppf)Cl] (**2f**). However, the heterobimetallic complex was not isolated and instead the complex salt [(Ind)-Ru(dppf)(CO)][$Co(CO_4)$] (**5f·[Co(CO)$_4$]**) was obtained, together with the $Ru^0$ complex $[Ru(dppf)(CO)_3]$ (**4f**) and the known $Co^I$ complex $[(Ind)Co(CO)_2]$ (**6f**) (Scheme 4).[18] The IR spectrum of **4f** exhibited three CO stretching bands (2007, 1924 and 1896 $cm^{-1}$), as opposed to one (1896 $cm^{-1}$) for **4e**. This indicated that they have different symmetries, as was confirmed by an X-ray crystallographic study on **4f** (Figure 4). Complex **4f** adopts a distorted trigonal bipyramidal geometry at the ruthenium atom. The two phosphorus atoms of the diphos occupy an axial [P(1)] and an equatorial position [P(2)].

However, the $^{31}P$ NMR spectrum of **4f** showed only a singlet at $\delta$ = 40.8 ppm, implying fluxionality, as may be expected for a five-coordinate complex. Complex **5f·[Co(CO)$_4$]** was characterized spectroscopically and analytically. Its IR spectrum showed two carbonyl stretches at 1972 and 1889 $cm^{-1}$; very similar to the values for $[CpRu(PPh_3)_2(CO)][Co(CO)_4]$ ($\tilde{\nu}_{CO}$ = 1978 and 1872 $cm^{-1}$).[3e] The cation showed up as a molecular ion in the positive mode of the FAB-MS at *m*/*z* 799, together with fragments corresponding to subsequent loss of a CO and an indenyl ligand, while the anion appeared in the negative mode at *m*/*z* 171.

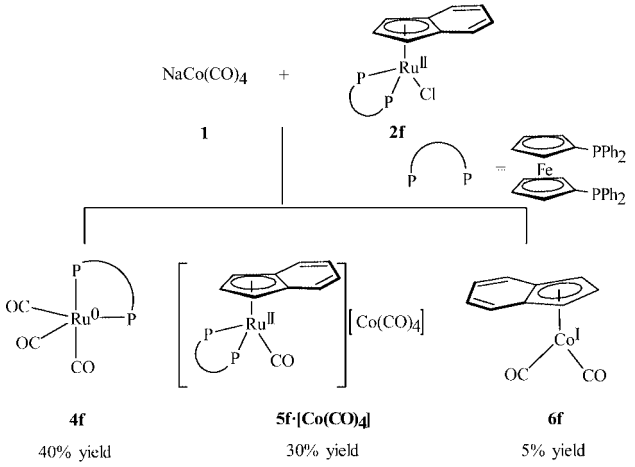


Scheme 4.

The failure to form the heterobimetallic complex at all in this case was intriguing. We have found that the halide ligand in **2f** could not be substituted by CO in a direct reaction to form [(Ind)Ru(dppf)(CO)]Cl (**5f·Cl**); a mixture of products which were not characterized was obtained instead. However, stirring **2f** under 1 atm of CO and in the presence of $NaPF_6$ afforded **5f·PF$_6$** in high yield; the same product could also be obtained from the reaction of the solvated complex $[(Ind)Ru(dppf)(NCCH_3)]PF_6$ (**7**) with 1 atm of CO (Scheme 5). We therefore believe that in the reaction between **2f** and **1**, the $Cl^-$ ligand was abstracted and this was replaced by the coordination of CO originating from the decomposition of $[Co(CO)_4]^-$. It is this coordination of CO to the Ru centre which inhibits formation of a Ru–Co bond, presumably because of the reduced electrophilicity.

 © 2006 Wiley-VCH Verlag GmbH & Co. KGaA, Weinheim 

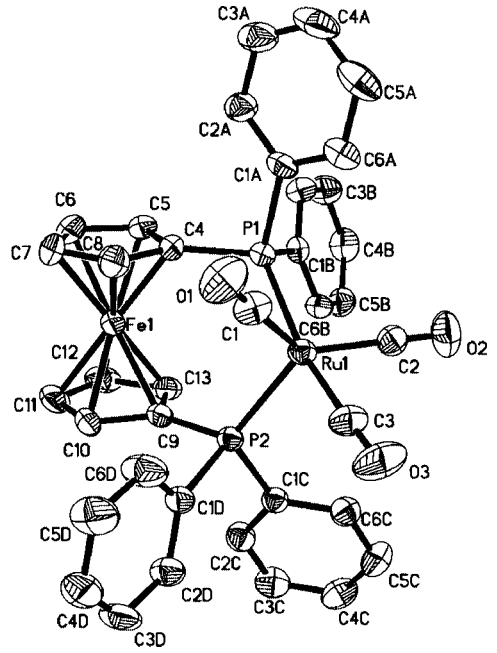


Figure 4. ORTEP diagram (50% probability thermal ellipsoids, hydrogen atoms omitted) and selected bond lengths [Å] and angles [°] of **4f**. Ru(1)–C(3) = 1.899(4); Ru(1)–C(1) = 1.902(4); Ru(1)–C(2) = 1.912(4); Ru(1)–P(1) = 2.3737(9); Ru(1)–P(2) = 2.3957(9); O(1)–C(1) = 1.150(4); O(2)–C(2) = 1.148(4); O(3)–C(3) = 1.133(4); C(3)–Ru(1)–C(1) = 88.53(16); C(3)–Ru(1)–C(2) = 87.62(16); C(1)–Ru(1)–C(2) = 135.35(16); C(3)–Ru(1)–P(1) = 168.31(12); C(1)–Ru(1)–P(1) = 86.86(12); C(2)–Ru(1)–P(1) = 88.12(11); C(3)–Ru(1)–P(2) = 94.04(12); C(1)–Ru(1)–P(2) = 110.63(12); C(2)–Ru(1)–P(2) = 114.01(12); P(1)–Ru(1)–P(2) = 97.63(3).

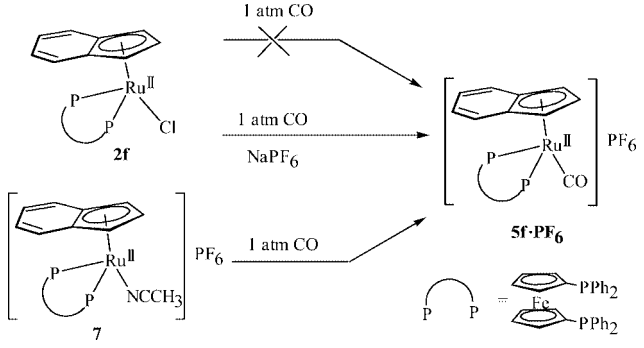


Scheme 5.

## Concluding Remarks

The results above clearly show that the salt elimination reaction between $NaCo(CO)_4$ and Cp* or indenyl ruthenium chloride complexes do not always lead simply to a heterobimetallic species. The nature of the products depends on the nature of the ligands on ruthenium; in some cases, there are redox processes involved. Unfortunately, no clear trend is discernible yet as to when redox processes can become important although it would appear that a suitable diphosphane that can bridge across the heterometallic metal–metal bond is important for stabilization of the heterobimetallic product.

## Experimental Section

**General Procedures:** All reactions were performed under dry nitrogen using Schlenk techniques or under argon in a Braun Labmaster 130 glovebox. Chromatographic separations were performed inside the glovebox. $^1H$, $^{31}P\{^1H\}$ and $^{13}C\{^1H\}$ NMR spectra were recorded with a Bruker ACF300 NMR spectrometer, with chemical shifts referenced to residual non-deuterio solvent and external $H_3PO_4$, respectively. IR spectra were obtained as either KBr pellets or as a solution with a Shimadzu Prestige-21 FTIR-8400S spectrometer. Mass spectra were obtained with either a Finnigan MAT95XL-T (FAB) or a Finnigan MAT LCQ (ESI) spectrometer. All elemental analyses were performed by the Microanalytical Laboratory in NUS. The complexes **1**[19] and **2a**–**f**,[20] were prepared according to published methods. All other reagents are commercially available and used without further purification. All solvents were distilled from standard drying agents before use.

**Reaction of $NaCo(CO)_4$ with [Cp*Ru{$Ph_2P(CH_2)_nPPh_2$}Cl] ($n$ = 1, 2):** To a THF (10 mL) solution of [Cp*Ru($Ph_2PCH_2PPh_2$)Cl] (**2a**) (100 mg, 0.15 mmol) was added a solution of $NaCo(CO)_4$ (**1**) in THF (1 equiv. in 5 mL) by cannula transfer, and the solution was refluxed for 40 h. The solvent was then removed in vacuo and the resulting residue extracted with $CH_2Cl_2$. Removal of the solvent gave an orange-red solid which was recrystallized from THF/hexane to afford [Cp*Ru(μ-$CO)_2$(μ-$Ph_2PCH_2PPh_2$)$Co(CO)_2$] (**3a**) as red crystals. Yield 102 mg (85%). IR (KBr, $cm^{-1}$): $\tilde{\nu}_{CO}$ = 1973 s, 1913 s, 1784 w, 1721 s (lit. values:[3h] (THF) $\tilde{\nu}_{CO}$ = 1985 s, 1923 s, 1728 m). $^1H$ NMR (300 MHz, $CDCl_3$): $\delta$ = 1.60 (s, 15 H, Cp*), 2.14 (t, 2 H, $PCH_2P$), 7.20–7.37 (m, 20 H, Ph) ppm. $^{31}P\{^1H\}$ NMR: $\delta$ = 55.8 (d, $^2J_{PP}$ = 103 Hz, Ru–P), 43.5 (br. s, Co–P) ppm. MS (ESI): $m/z$ (%) = 791 $[M]^+$, 677 $[M - Co(CO)_2]^+$. $C_{39}H_{37}CoO_4P_2Ru$: C 59.2, H 4.7; formula mass 791.67; found C 59.2, H 5.2. The residue from a similar reaction between **1** and [Cp*Ru{$Ph_2P(CH_2)_2PPh_2$}Cl] (**2b**) was dissolved in a minimum volume of THF for chromatographic separation on silica gel. The main fraction (eluent: hexane/THF, 5.5:1, v/v) gave [Cp*Ru(μ-$CO)_2${μ-$Ph_2P(CH_2)_2PPh_2$}$Co(CO)_2$] (**3b**) as an orange-red solid. Yield 94 mg (78%). IR (KBr, $cm^{-1}$): $\tilde{\nu}_{CO}$ = 1978 s, 1920 s, 1771 w, 1722 s. $^1H$ NMR (300 MHz, $CDCl_3$): $\delta$ = 1.60 (s, 15 H, Cp*), 2.04, 1.84 (m, 4 H, $PCH_2CH_2P$), 7.19–7.68 (m, 20 H, Ph) ppm. $^{31}P\{^1H\}$ NMR: $\delta$ = 45 (s, Ru–P), 34.6 (br. s, Co–P) ppm. MS (ESI): $m/z$ (%) = 806 $[M]^+$, 778 [M – CO], 691 $[M - Co(CO)_2]^+$. $C_{40}H_{39}CoO_4P_2Ru$: calcd. C 59.6, H 4.9; formula mass 805.70; found C 59.9, H 5.2.

**Reaction of 1 with [(Ind)Ru($Ph_2PCH_2PPh_2$)Cl]:** To a THF (10 mL) solution of [(Ind)Ru($Ph_2PCH_2PPh_2$)Cl] (**2c**) (100 mg, 0.13 mmol) was added **1** (1 equiv.) and the solution was stirred at room temp. for 24 h. The solvent was removed under reduced pressure, and the residue was first washed with hexane, followed by extraction with toluene. The toluene extract was concentrated and loaded onto a silica gel column prepared in *n*-hexane. Elution with toluene gave a reddish brown band as the major eluate which afforded [(Ind)Ru(μ-$CO)_2$(μ-$Ph_2PCH_2PPh_2$)$Co(CO)_2$] (**3c**). Yield 97 mg (80%). IR ($CH_2Cl_2$, $cm^{-1}$): $\tilde{\nu}_{CO}$ = 1997 s, 1944 s, 1739 s. $^1H$ NMR (300 MHz, $C_6D_6$): $\delta$ = 2.03 [t, $J$ = 9.06 Hz, 2 H, $CH_2(PPh_2)_2$], 5.18–5.20 (m, 3 H, η$^5$-$C_9H_7$), 6.64–6.67, 6.89–7.01, 7.10–7.14, 7.30–7.36 [m, 24 H, $CH_2(PPh_2)_2$ and η$^5$-$C_9H_7$] ppm. $^{31}P\{^1H\}$ NMR: $\delta$ = 44.4 (br. d, $^2J_{PP}$ = 109 Hz, Co–P), 59.3 (d, $^2J_{PP}$ = 109 Hz, Ru–P) ppm. MS ($FAB^+$): $m/z$ (%) = 716 $[M - 2CO]^+$, 657 $[M - 2CO - Co]^+$, 629 $[M - 3CO - Co]^+$, 601 $[M - 4CO - Co]^+$. $C_{38}H_{29}CoO_4P_2Ru$: calcd. C 59.2, H 3.8; formula mass 771.60; found C 59.6, H 3.4.

For the reaction with [(Ind)$Ru(CO)_2$Cl] (**2d**) (30 mg, 0.098 mmol), the hexane extract was concentrated and cooled to –30 °C for 1 day

 © 2006 Wiley-VCH Verlag GmbH & Co. KGaA, Weinheim 

to give [(Ind)Ru(CO)$_2$Co(CO)$_4$] (**3d**) (30 mg, 69%) as dark red crystals.

**For 3d:** IR (hexane, cm$^{-1}$): $\tilde{\nu}_{CO}$ = 2067 m, 2022 s, 1986 m, br., 1963 w, br., 1955 w, br. $^1$H NMR (300 MHz, $C_6D_6$): $\delta$ = 4.60 (t, $^3J_{HH}$ = 3.3 Hz, 1 H, $\eta^5$-$C_9H_7$), 4.81 (d, 2 H, $\eta^5$-$C_9H_7$), 6.79 (s, 4 H, $\eta^5$-$C_9H_7$) ppm. $^{13}$C NMR (75 MHz, $C_6D_6$): $\delta$ = 76.5 (s, C1,3), 91.5 (s, C2), 111.1 (s, C8,9), 124.2 and 129.8 (s, C4–7), 204.3 (CO) ppm. MS (FAB$^+$): *m/z* (%) = 444 [M]$^+$, 388 [M – 2CO]$^+$, 360 [M – 3CO]$^+$, 332 [M – 4CO]$^+$. $C_{15}H_7CoO_6Ru$: calcd. C 40.7, H 1.6; formula mass 443.22; found C 40.8, H 1.5.

For the reaction with [(Ind)Ru(PPh$_3$)$_2$Cl] (**2e**), the toluene extract was concentrated and chromatographed on a silica gel column. Elution gave four fractions: (i) A yellow eluate with hexane/toluene (4:1, v/v) yielded [(Ind)Co(CO)(PPh$_3$)] (**6e**) (8 mg, 13%) as air-sensitive dark red crystals after recrystallization from $CH_2Cl_2$/hexane; (ii) an orange-yellow eluate (severe tailing) with hexane/toluene (3:1, v/v) gave [Ru(PPh$_3$)$_2$(CO)$_3$] (**4e**) after several recrystallizations from toluene/hexane (1:4, v/v) (26 mg, 28%); (iii) a reddish brown eluate with hexane/toluene (1:1, v/v) yielded [(Ind)-Ru(PPh$_3$)(CO)($\mu_2$-CO)Co(CO)$_3$] (**3e**) (23 mg, 26%); and (iv) a red eluate with toluene/THF (1:1, v/v) afforded unreacted **2e** (20 mg, 20%).

**For 3e:** IR ($CH_2Cl_2$, cm$^{-1}$): $\tilde{\nu}_{CO}$ = 1975 s, 1920 s, 1744 m. $^1$H NMR (300 MHz, $C_6D_6$): $\delta$ = 4.98 (s, 3 H, $\eta^5$-$C_9H_7$), 6.57–6.93 (m, 4 H, $\eta^5$-$C_9H_7$), 7.03–7.72 (m, 15 H, PPh$_3$) ppm. $^{31}$P{$^1$H} NMR: $\delta$ = 48.6 (s, PPh$_3$) ppm. MS (FAB$^+$): *m/z* (%) = 566 [M – 4CO]$^+$, 535 [M – Co – 3CO]$^+$, 479 [M – Co – 5CO]$^+$. $C_{32}H_{22}CoFeO_5P{\cdot}2C_6H_5CH_3$: calcd. C 64.4, H 4.0; formula mass 816.56; found C 64.1, H 4.2. The presence of toluene solvent has been confirmed by $^1$H NMR spectroscopy.

**For 4e:** IR ($CH_2Cl_2$, cm$^{-1}$): $\tilde{\nu}_{CO}$ = 1896 s (lit. values:[10b] (THF) $\tilde{\nu}_{CO}$ = 1900 s). $^1$H NMR (300 MHz, $C_6D_6$): $\delta$ = 6.96–7.05 (m, 18 H, PPh$_3$), 7.87–7.93 (m, 12 H, PPh$_3$) ppm. $^{31}$P{$^1$H}NMR: $\delta$ = 55.9 (s, PPh$_3$) ppm.

**For 6e:** IR (KBr, cm$^{-1}$): $\tilde{\nu}_{CO}$ = 1922 s. $^1$H NMR (300 MHz, $C_6D_6$): $\delta$ = 4.61 (s, 2 H, $\eta^5$-$C_9H_7$), 5.67 (t, $^3J_{HH}$ = 3.3 Hz, 1 H, $\eta^5$-$C_9H_7$), 6.74–6.78 (4-lines m, 2 H, $\eta^5$-$C_9H_7$), 6.94–6.97, 6.98–7.01, 7.41–7.48 (each m, total 17 H, PPh$_3$ and $\eta^5$-$C_9H_7$) ppm. $^{31}$P NMR: $\delta$ = 65.6 (br. s, PPh$_3$) ppm. ESI$^+$-MS: 667 [2M – PPh$_3$]$^+$, 405 [2M – 2PPh$_3$]$^+$. $C_{28}H_{22}CoOP{\cdot}\frac{1}{8}CH_2Cl_2$: calcd. C 71.0, H 4.7; formula mass 475.00; found C 70.5, H 4.5. The presence of dichloromethane solvent has been confirmed by $^1$H NMR spectroscopy.

For the reaction with [(Ind)Ru(dppf)Cl] (**2f**), extraction with toluene was followed by extraction with $CH_3CN$. The toluene extract was concentrated and chromatographed on a silica gel column. Elution with hexane/toluene (2:1, v/v) gave a yellow eluate of [(Ind)-Co(CO)$_2$] (**6f**). Yield 4 mg (5%). IR ($CH_2Cl_2$): $\tilde{\nu}_{CO}$ = 2027 and 1970 cm$^{-1}$; lit. values ($CH_2Cl_2$):[18] 2030, 1970. Further elution with hexane/toluene (4:3, v/v) afforded an orange-yellow eluate which gave [Ru(dppf)(CO)$_3$] **4f** after several recrystallizations from toluene/hexane (1:4, v/v). Yield 37 mg (40%). The $CH_3CN$ extract gave [(Ind)Ru(dppf)(CO)][Co(CO$_4$)] (**5f·[Co(CO)$_4$]**) as a dark brown oil. Yield 36 mg (30%).

**For 4f:** IR ($CH_2Cl_2$, cm$^{-1}$): $\tilde{\nu}_{CO}$ = 2007 s, 1924 m, 1896 s. $^1$H NMR (300 MHz, $C_6D_6$): 4.27 (s, 4 H, $C_5H_4$), 4.28 (s, 4 H, $C_5H_4$), 7.02–7.88 (m, 20 H, Ph) ppm. $^{31}$P{$^1$H} NMR: $\delta$ = 40.8 (s, dppf) ppm. MS (FAB$^+$): *m/z* (%) = 740 [M]$^+$, 712 [M – CO]$^+$, 684 [M – 2CO]$^+$, 655 [M – 3CO]$^+$. $C_{37}H_{28}FeO_3P_2Ru$: calcd. C 59.9, H 3.8; formula mass 739.49; found C 60.1, H 3.8.

**For 5f·[Co(CO)$_4$]:** IR ($CH_2Cl_2$): $\tilde{\nu}_{CO}$ = 1972 m, 1889 s cm$^{-1}$. $^1$H NMR (300 MHz, $CD_3CN$): $\delta$ = 4.37 (s, 2 H, $C_5H_4$), 4.46 (s, 2 H, $C_5H_4$), 4.57 (s, 2 H, $C_5H_4$), 4.61 (s, 2 H, $C_5H_4$), 5.25 (s, 3 H, $\eta^5$-$C_9H_7$), 6.77–7.06 (m, 4 H, $\eta^5$-$C_9H_7$), 7.18–7.71 (m, 20 H, Ph) ppm. $^{31}$P{$^1$H}: $\delta$ = 54.8 (s, dppf) ppm. FAB$^+$-MS: *m/z* 799 [M]$^+$, 771 [M –

Table 2. Crystal and refinement data for **3c**, **3e**, **4e**, **4f** and **6e**.

| Compound | **3c** | **3e** | **4e** | **4f** | **6e** |
|---|---|---|---|---|---|
| Empirical formula | $C_{38}H_{29}CoO_4P_2Ru{\cdot}CH_2Cl_2$ | $C_{32}H_{22}CoO_5PRu$ | $C_{39}H_{30}O_3P_2Ru{\cdot}CH_2Cl_2$ | $C_{37}H_{28}FeO_3P_2Ru$ | $C_{28}H_{22}CoOP$ |
| Formula weight | 856.48 | 677.47 | 794.57 | 739.45 | 464.36 |
| Crystal system | monoclinic | orthorhombic | triclinic | monoclinic | monoclinic |
| Space group | $P2_1/c$ | $P2_12_12_1$ | $P\bar{1}$ | $P2_1/c$ | $P2_1/c$ |
| *a* [Å] | 10.5588(5) | 11.898(2) | 9.9667(6) | 9.7242(6) | 9.1150(5) |
| *b* [Å] | 16.9898(8) | 15.098(3) | 13.6718(8) | 16.2461(10) | 25.7691(15) |
| *c* [Å] | 20.1273(9) | 15.376(3) | 15.4090(9) | 19.9335(12) | 10.4250(6) |
| $\alpha$ [°] | 90 | 90 | 63.7400(10) | 90 | 90 |
| $\beta$ [°] | 94.3280(10) | 90 | 87.6650(10) | 95.082(2) | 115.9190(10) |
| $\gamma$ [°] | 90 | 90 | 74.4430(10) | 90 | 90 |
| Volume [Å$^3$] | 3600.4(3) | 2762.2(9) | 1806.60(18) | 3136.7(3) | 2202.4(2) |
| *Z* | 4 | 4 | 2 | 4 | 4 |
| Density (calculated) [Mg/m$^3$] | 1.580 | 1.629 | 1.461 | 1.566 | 1.400 |
| Absorption coefficient [mm$^{-1}$] | 1.158 | 1.246 | 0.708 | 1.083 | 0.870 |
| *F*(000) | 1728 | 1360 | 808 | 1496 | 960 |
| Crystal size [mm] | 0.36 × 0.32 × 0.20 | 0.25 × 0.08 × 0.07 | 0.20 × 0.16 × 0.14 | 0.30 × 0.12 × 0.09 | 0.30 × 0.10 × 0.08 |
| $\theta$ range for data collection [°] | 2.28 to 30.01 | 2.18 to 26.37 | 2.34 to 27.50 | 1.62 to 27.50 | 1.58 to 27.50 |
| Reflections collected | 33154 | 20635 | 23823 | 18602 | 15374 |
| Independent reflections | 10167 [*R*(int) = 0.0303] | 3171 [*R*(int) = 0.1020] | 8273 [*R*(int) = 0.0430] | 7202 [*R*(int) = 0.0443] | 5057 [*R*(int) = 0.0375] |
| Max. and min. transmission | 0.8014 and 0.6806 | 0.9178 and 0.7458 | 0.9074 and 0.8714 | 0.9088 and 0.7371 | 0.9337 and 0.7804 |
| Data / restraints / parameters | 10167 / 7 / 451 | 3171 / 30 / 361 | 8273 / 6 / 455 | 7202 / 0 / 397 | 5057 / 0 / 280 |
| Goodness-of-fit on $F^2$ | 1.070 | 1.333 | 1.101 | 1.037 | 1.114 |
| Final *R* indices [$I > 2\sigma(I)$] | $R_1$ = 0.0392, $wR_2$ = 0.1029 | $R_1$ = 0.0889, $wR_2$ = 0.1779 | $R_1$ = 0.0534, $wR_2$ = 0.1258 | $R_1$ = 0.0468, $wR_2$ = 0.1018 | $R_1$ = 0.0521, $wR_2$ = 0.1088 |
| *R* indices (all data) | $R_1$ = 0.0498, $wR_2$ = 0.1154 | $R_1$ = 0.0964, $wR_2$ = 0.1807 | $R_1$ = 0.0636, $wR_2$ = 0.1311 | $R_1$ = 0.0646, $wR_2$ = 0.1087 | $R_1$ = 0.0694, $wR_2$ = 0.1152 |
| Largest diff. peak / hole [e·Å$^{-3}$] | 0.942 / –0.492 | 1.958 / –1.437 | 1.158 / –0.813 | 0.682 / –0.337 | 0.654 / –0.236 |

 © 2006 Wiley-VCH Verlag GmbH & Co. KGaA, Weinheim 

$CO]^+$, 655 $[M - CO - Ind]^+$. MS ($FAB^-$): *m/z* (%) = 171 $[Co(CO)_4]^-$. MS (HR-$FAB^+$): *m/z* (%) = 799.0562 (found), 799.0562 (calcd.).

**Synthesis of [(Ind)Ru(dppf)(CO)]$PF_6$**

**Method A:** $NaPF_6$ (5 mg, 0.03 mmol) was added to a solution of **2f** (20 mg, 0.02 mmol) in THF (10 mL). The mixture was subjected to three freeze-pump-thaw cycles, then CO (1 atm) was bubbled through the solution for about 10 min. The reaction mixture was stirred at room temp. for 24 h, during which the colour of the solution changed from red to yellow. The mixture was filtered and concentrated to ca. 2 mL. Addition of ether (5 mL) followed by cooling at –30 °C for 1 d gave [(Ind)Ru(dppf)(CO)]$PF_6$ (**5f·$PF_6$**). Yield 20 mg (85%).

**Method B:** A solution of **7** (20 mg, 0.02 mmol) in THF (10 mL) was degassed by three freeze-pump-thaw cycles, and then saturated with CO (1 atm; bubbling for ca. 10 min). The reaction mixture was stirred at room temp. for 24 h, filtered and then concentrated to ca. 2 mL. Addition of ether (5 mL) followed by cooling at –30 °C for 1 day gave **5f·$PF_6$**. Yield 17 mg (86%). IR (THF, $cm^{-1}$): $\tilde{\nu}_{CO}$ = 1973 s. $^1H$ NMR (300 MHz, $CD_3CN$): $\delta$ = 4.37 (s, 2 H, $C_5H_4$), 4.46 (s, 2 H, $C_5H_4$), 4.57 (s, 2 H, $C_5H_4$), 4.61 (s, 2 H, $C_5H_4$), 5.24 (s, 3 H, $\eta^5$-$C_9H_7$), 6.76–7.06 (m, 4 H, $\eta^5$-$C_9H_7$), 7.18–7.71 (m, 20 H, Ph) ppm. $^{31}P\{^1H\}$ NMR: $\delta$ = 54.8 (s, dppf), –142.9 (sept, $PF_6$) ppm. MS ($FAB^+$): *m/z* (%) = 799 $[M]^+$, 771 $[M - CO]^+$, 655 $[M - CO - Ind]^+$. MS ($FAB^-$): *m/z* (%) = 145 $[PF_6]^-$. $C_{44}H_{35}F_6FeOP_3Ru$: calcd. C 56.0, H 3.7; formula mass 943.59; found C 56.0, H 3.7.

**Crystal Structure Determinations:** Crystals were grown from dichloromethane/hexane solutions and mounted on quartz fibres. X-ray data were collected with a Bruker AXS APEX system, using Mo-$K_a$ radiation, with the SMART suite of programs.[21] Data were processed and corrected for Lorentz and polarisation effects with SAINT,[22] and for absorption effects with SADABS.[23] Structural solution and refinement were carried out with the SHELXTL suite of programs.[24] Crystal and refinement data are summarised in Table 2. The structures were solved by direct methods or Patterson maps to locate the heavy atoms, followed by difference maps for the light, non-hydrogen atoms. All non-hydrogen atoms were generally given anisotropic displacement parameters in the final model (except for the carbon atoms of the disordered solvate in **4e**). Clusters **3c** and **4e** had one $CH_2Cl_2$ solvate molecule each, which exhibited disorder over two sites. For **3c**, the site occupancies were 0.75 and 0.25; for **4e**, these were 0.9 and 0.1. Appropriate restraints were placed on the atomic anisotropic parameters and bond and interatomic distances.

CCDC 283009–283013 contain the supplementary crystallographic data for this paper. These data can be obtained free of charge from The Cambridge Crystallographic Data Centre via www.ccdc.cam.ac.uk/data_request/cif.

## Acknowledgments

This work was supported by an A*STAR grant (Research Grant No. 012 101 0035) and one of us (S. Y. N.) thanks the University for a Research Scholarship. Contribution from Dr. J. Zhang in the earlier part of this work is also acknowledged.

[1] a) P. Braunstein, E. W. Rose in *Comprehensive Organometallic Chemistry II* (Eds.: J. Abel, F. G. A. Stone, G. Wilkinson), Elsevier, Oxford, **1995**, vol. 10, p. 351; b) R. D. Adams, F. A. Cotton (Eds.), *Catalysis by Di and Polynuclear Metal Cluster Complexes*, Wiley-VCH, Weinheim, **1998**; c) P. Braunstein, I. Rose in *Chemical Bonds: Better Ways to Make Them and Break Them* (Ed.: I. Bernal), Elsevier, Amsterdam, **1989**, p. 89; d) G. Süss-Fink, G. Meister, *Adv. Organomet. Chem.* **1993**, *35*, 41.

[2] a) W. R. Pretzer, T. P. Kobylinski, J. E. Bozik (Gulf Research and Development Company), U. S. Patents 4133966, **1979** and 4239924, **1980**; b) R. Fiato (Union Carbide Corporation), U. S. Patent 4253987, **1980**; c) British Petroleum, Ltd, British Patent 2036739, **1980**; d) G. Doyle (Exxon Research & Engineering Company), U. S. Patent 4348541, **1982**; e) G. Doyle, *J. Mol. Catal.* **1983**, *18*, 251; f) M. Hidai, M. Orisaku, M. Ue, Y. Koyasu, T. Kodoma, Y. Uchida, *Organometallics* **1983**, *2*, 292; g) K. Watanabe, K. Kudo, N. Sugita, *Bull. Chem. Soc. Jpn.* **1985**, *58*, 2029; h) E. Santacesaria, M. Di Serio, *J. Mol. Catal.* **1990**, *58*, 43; i) K. Tominaga, Y. Sasaki, T. Watanabe, M. Saito, *Stud. Surf. Sci. Catal.* **1998**, *114*, 495.

[3] a) A. R. Manning, *J. Chem. Soc. (A)* **1971**, 2321; b) R. Regragui, P. H. Dixneuf, *J. Organomet. Chem.* **1982**, *239*, C12; c) H. C. Foley, W. C. Finch, C. G. Plerpont, G. L. Geoffroy, *Organometallics* **1982**, *1*, 1379; d) R. Regragui, P. H. Dixneuf, N. J. Taylor, A. J. Carty, *Organometallics* **1984**, *3*, 1020; e) G. Doyle, D. V. Engen, *J. Organomet. Chem.* **1985**, *280*, 253; f) R. Zoet, G. van Koten, A. L. J. van der Panne, P. Versloot, C. H. Stam, K. Vrieze, *Inorg. Chim. Acta* **1988**, *149*, 177; g) M. R. Gagné, J. Takats, *Organometallics* **1988**, *7*, 561; h) H. Matsuzaka, K. Ichikawa, T. Ishioka, H. Sato, T. Okubo, T. Ishii, M. Yamashita, S. Kondo, M. Kitagawa, *J. Organomet. Chem.* **2000**, *596*, 121.

[4] a) R. Regragui, P. H. Dixneuf, N. J. Taylor, A. J. Carty, *Organometallics* **1984**, *3*, 814; b) R. Regragui, P. H. Dixneuf, N. J. Taylor, A. J. Carty, *Organometallics* **1986**, *5*, 1; c) S. Guesmi, P. H. Dixneuf, G. Süss-Fink, N. J. Taylor, A. J. Carty, *Organometallics* **1989**, *8*, 307; d) J. N. L. Dennett, J. Jacke, G. Nilsson, A. Rosborough, M. J. Ferguson, M. Wang, R. McDonald, J. Takats, *Organometallics* **2004**, *23*, 4478.

[5] a) L. Tang, M. Huang, Y. Jiang, *Reactive Polymers* **1994**, *23*, 119; b) S. Guan, M. Huang, Y. Jiang, *Chinese J. Polymer Sci.* **1993**, *11*, 103; c) H. Zong, W. Tang, Z. Chen, Y. Jiang, *Chinese J. Polymer Sci.* **1991**, *9*, 171; d) Q. Tang, H. Zong, Z. Chen, Y. Jiang, *Chinese J. Polymer Sci.* **1991**, *9*, 39; e) S. Cao, M. Huang, Y. Jiang, *Polym. Bull.* **1988**, *19*, 353.

[6] a) D. W. Stephan, *Coord. Chem. Rev.* **1989**, *95*, 41; b) N. Wheatley, P. Kalck, *Chem. Rev.* **1999**, *99*, 3379; c) E. W. Adams in *Comprehensive Organometallic Chemistry II* (Eds.: R. D. Abel, F. G. A. Stone, G. Wilkinson), Elsevier, Oxford, **1995**, vol. 10, p. 1; d) E. W. Chetcuti in *Comprehensive Organometallic Chemistry II* (Eds.: M. J. Abel, F. G. A. Stone, G. Wilkinson), Elsevier, Oxford, **1995**, vol. 10, p. 24.

[7] H. Matsuzaka, K. Ichikawa, T. Ishii, M. Kondo, S. Kitagawa, *Chem. Lett.* **1998**, 1175.

[8] R. A. Jones, M. H. Seeberger, A. L. Stuart, B. R. Whittlesey, T. C. Wright, *Acta Crystallogr. Sect. C: Cryst. Struct. Commun.* **1986**, *42*, 399.

[9] K.-B. Shiu, H.-C. Lee, G.-H. Lee, Y. Wang, *Organometallics* **2002**, *21*, 4013.

[10] a) F. Dahan, S. Sabo, B. Chaudret, *Acta Crystallogr. C: Cryst. Struct. Commun.* **1984**, *40*, 786; b) E. M. Gordon, R. Eisenberg, *J. Mol. Catal.* **1988**, *45*, 57.

[11] R. H. Crabtree, M. Lavin, *Inorg. Chem.* **1986**, *25*, 805.

[12] P. J. Dyson, J. S. McIndoe, *Transition Metal Carbonyl Cluster Chemistry*, Gordon and Breach, Amsterdam, **2000**.

[13] M. Y. Antipin, Y. T. Struchkov, A. N. Chernega, M. F. Meidine, J. F. Nixon, *J. Organomet. Chem.* **1992**, *436*, 79.

[14] L. R. Byers, L. F. Dahl, *Inorg. Chem.* **1980**, *19*, 277.

[15] A. K. Kakkar, N. J. Taylor, T. B. Marder, J. K. She, N. Hallinan, F. Basolo, *Inorg. Chim. Acta* **1992**, *198–200*, 219.

[16] E. Bleuel, O. Gevert, M. Laubender, H. Werner, *Organometallics* **2000**, *19*, 3109.

[17] M. J. Calhorda, L. F. Veiros, *Coord. Chem. Rev.* **1999**, *185–186*, 37 and references cited therein.

 © 2006 Wiley-VCH Verlag GmbH & Co. KGaA, Weinheim 

[18] A. Salzer, C. Täschler, *J. Organomet. Chem.* **1985**, *294*, 261.
[19] W. F. Edgell, J. Lyford, *Inorg. Chem.* **1970**, *9*, 1932.
[20] a) M. I. Bruce, B. G. Ellis, P. J. Low, B. W. Skelton, A. H. White, *Organometallics* **2003**, *22*, 3184; b) L. A. Oro, M. A. Ciriano, M. Campo, C. Foces-Foces, F. H. Cano, *J. Organomet. Chem.* **1985**, *289*, 117; c) M. P. Gamasa, J. Gimeno, C. Gonzelz-Bernardo, B. M. Martí-Vaca, D. Monti, M. Bassetti, *Organometallics* **1996**, *15*, 302; d) S. Y. Ng, Y. Zhu, W. K. Leong, R. Webster, L. Y. Goh, manuscript in preparation.
[21] *SMART* version 5.628, Bruker AXS Inc., Madison, Wisconsin, USA, **2001**.
[22] *SAINT*+ version 6.22a, Bruker AXS Inc., Madison, Wisconsin, USA, **2001**.
[23] G. W. Sheldrick, *SADABS*, University of Göttingen, **1996**.
[24] G. W. Sheldrick, *SHELXTL*, Bruker Analytical Instruments, Madison, Version 5.1, **1997**.

Received: September 6, 2005
Published Online: December 13, 2005

 © 2006 Wiley-VCH Verlag GmbH & Co. KGaA, Weinheim 

DOI: 10.1002/ejic.200500821

# Dissociation of CP20 from Iron(II)(cp20)$_3$: A Pulse Radiolysis Study

**Martin Merkofer,[a] Anastasia Domazou,[a] Thomas Nauser,[a] and Willem H. Koppenol*[a]**

**Keywords:** Iron / Chelates / Reduction / Electron transfer / Kinetics

Deferiprone (CP20), a hydroxypyridine-4-one, is used in iron-chelation therapy. For the iron(III)-/(II)(cp20)$_3$ couple, a standard electrode potential of –620 mV was measured by cyclic voltammetry [Templeton et al., *Inorg. Chim. Acta* **1996**, *245*, 199; Merkofer et al., *Helv. Chim. Acta* **2004**, *87*, 3021]. On the basis of this value and the overall stability constant for the equilibrium of iron(III) and three CP20 molecules, ligand dissociation ought to take place after reduction of the iron(III)(cp20)$_3$ complex. By pulse radiolysis, we show that hydrated electrons reduce the iron(III)(cp20)$_3$ complex with a rate constant of $k = (6.4 \pm 0.3) \times 10^{10}$ M$^{-1}$ s$^{-1}$, and that the iron(II)(cp20)$_3$ complex aquates rapidly. The dissociation of the first two CP20 molecules takes place within a few μs after the pulse. The dissociation rate constant for the last CP20 ligand is $(8 \pm 1) \times 10^3$ s$^{-1}$. The observation of a dissociation illustrates that, under dilute conditions, iron(II) is not fully complexed by CP20 and could potentially participate in redox cycling to produce oxyradicals. The $CO_2^{\bullet-}$ radical does not reduce iron(III)(cp20)$_3$, which indicates that this complex reacts, as expected, very slowly with inner-sphere reductants.

(© Wiley-VCH Verlag GmbH & Co. KGaA, 69451 Weinheim, Germany, 2006)

## Introduction

Iron is essential to life. It is used, transported and stored by specific proteins such as haem proteins, transferrin and ferritin. When, for various reasons, iron is released from these proteins or excessively absorbed from food, it can participate in redox cycling that generates toxic oxyradicals.[1,2]

The bidentate chelating agent CP20 (1,2-dimethyl-3-hydroxypyrid-4(1*H*)-one, also known as deferiprone or L1, Scheme 1) is effective at facilitating iron removal from iron-overload patients when administered orally.[3] It forms five-membered chelate rings in which the metal is coordinated by two vicinal oxygen atoms. This chelating agent is an alternative to the well-established desferrioxamine, which requires intravenous administration. Another orally active drug, tridentate ICL670 (4-[3,5-bis(2-hydroxyphenyl)-1*H*-1,2,4-triazol-1-yl]benzoic acid), is under development.[4] It is generally assumed that these chelating agents are not toxic when the standard electrode potentials of the iron(III)/iron(II) couples are such that they cannot be reduced by ascorbate or oxidised by hydrogen peroxide, that is, below $E°'(Asc^{\bullet-},H^+/HAsc^-) = +282$ mV[5] or above $E°'(H_2O_2,H^+/HO^{\bullet},H_2O) = +370$ mV, respectively. The latter value is based on Gibbs energies of formation of the hydroxyl radical and hydrogen peroxide determined by Schwarz and Dodson[6] and Kern,[7] respectively. This is the case for the electrode potential of the iron(III)-/iron(II)(cp20)$_3$ couple, –620 mV at pH = 11. However, the in vivo conditions are far removed from those of the standard state: the concentration of iron–CP20 complexes is only in the micromolar range, and the pH is much lower than 11. By cyclic voltammetry, we could show that, under dilute conditions, the electrode potentials shift to more positive values, which may occur as a result of dissociation of ligands from iron(II).[8] Indeed, binding data derived from electrode potentials indicate that iron(II) complexes of CP20 are not fully formed at physiological pH and low iron concentration, even when CP20 is present in fivefold excess. We show here by pulse radiolysis that, indeed, the proposed ligand dissociation[8] occurs after rapid reduction of iron(III)(cp20)$_3$ by hydrated electrons.

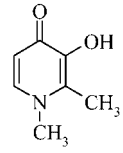


CP20 (L1)

Scheme 1.

## Results

### Distribution Diagram of the Iron(II)–(CP20) and Iron(III)–(CP20) Complexes

Speciation diagrams for the iron(II)–(CP20) and iron(III)–(CP20) complexes at 20 μM iron, 100 μM CP20 and pH = 7.2 are shown in Figure 1A and Figure 1B, respectively. As the binding constants $\beta_1$ and $\beta_2$ are not known for iron(II), we assumed that the ratios $\beta_3/\beta_2$ and $\beta_3/\beta_1$ for iron(II) are

[a] Laboratorium für Anorganische Chemie, Departement Chemie und Angewandte Biowissenschaften, ETH Hönggerberg, 8093 Zürich, Switzerland
E-mail: koppenol@inorg.chem.ethz.ch

 © 2006 Wiley-VCH Verlag GmbH & Co. KGaA, Weinheim InterScience 

similar to those of iron(III). The data for Figure 1A and Figure 1B were obtained from the literature.[8] While iron(III) tightly binds three CP20 ligands at pH = 7 and higher, iron(II) does not. In fact, not even the 1:1 complex of iron(II) and CP20 is fully formed at pH = 7.

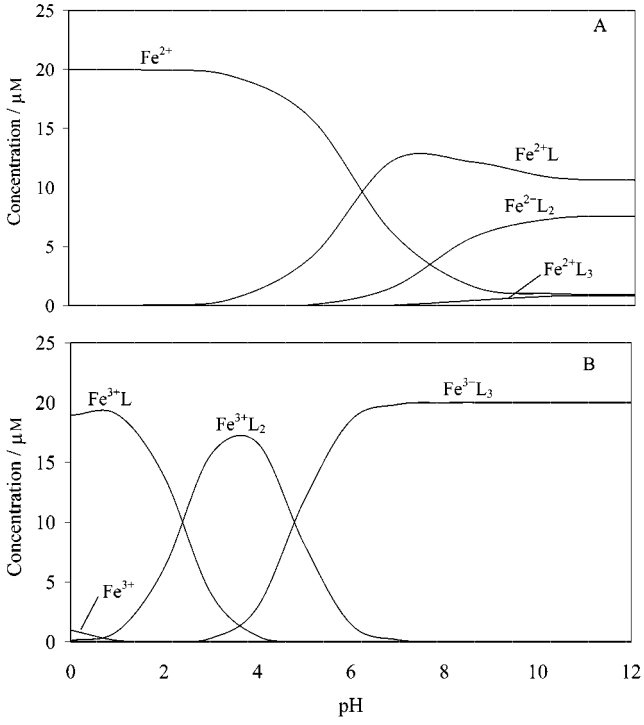


Figure 1. Iron(II) (**A**) and iron(III) (**B**) speciation in the presence of CP20. [CP20] = 100 μM, [$Fe^{2+}$] and [$Fe^{3+}$] = 20 μM. While iron(III) tightly binds three CP20 ligands at pH = 7 and higher, iron(II) does not. The p$K_a$ value used for CP20 is 9.76.[20]

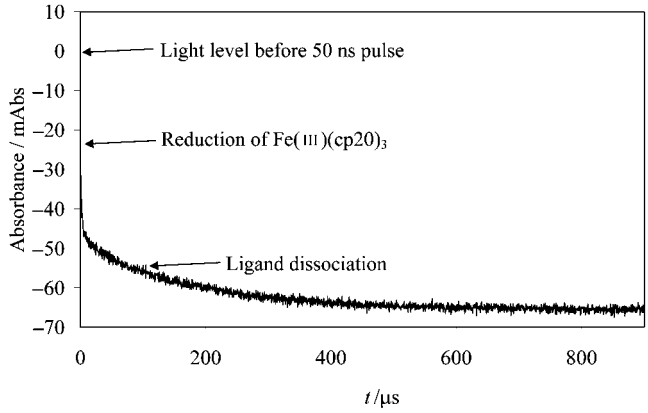


Figure 2. Reduction of $Fe^{III}(cp20)_3$ (100 μM) with hydrated electrons (14 μM) at 450 nm. Reaction conditions: phosphate buffer (5 mM) with *tert*-butyl alcohol (0.1 M) at pH = 7.2 and room temperature. Following rapid reduction, a slower process is observed that is ascribed to ligand dissociation. The reduction with hydrated electrons proceeds quantitatively.

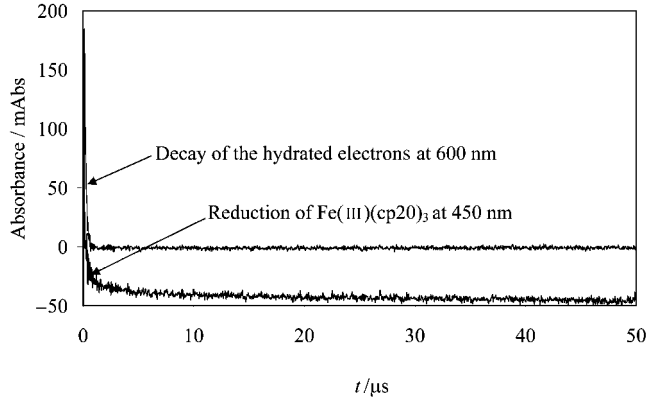


Figure 3. Reduction of $Fe^{III}(cp20)_3$ (100 μM) with hydrated electrons (12 μM) at 450 nm and decay of the hydrated electrons at 600 nm. Reaction conditions: phosphate buffer (5 mM) with *tert*-butyl alcohol (0.1 M) at pH = 7.2 and room temperature. The decay of the hydrated electrons at 600 nm shows the same time-dependence as the fast decay at 450 nm.

### Reduction of the Iron(III)(cp20)$_3$ Complex by $e^-_{aq}$ and $CO_2^{\cdot-}$

Rapid reduction of iron(III)(cp20)$_3$ (100 μM) by hydrated electrons (14 μM) leads to decreases in absorption at 450 nm. The fastest is finished within one μs and the slowest within one ms (Figure 2 and Figure 3). Reduction proceeds quantitatively (Figure 2), based on an extinction coefficient of 4600 $M^{-1}cm^{-1}$ for the iron(III)(cp20)$_3$ complex at 450 nm.[8] These processes are not caused by the presence of *tert*-butyl alcohol (data not shown). The rate of decay of hydrated electrons measured at 600 nm is identical to the rate of the fast process at 450 nm (Figure 3). This rate is first-order in iron(III)(cp20)$_3$ (Figure 4), from which a rate constant of $(6.4 \pm 0.3) \times 10^{10}$ $M^{-1}s^{-1}$ is calculated. The rate of decay of the hydrated electrons measured at 600 nm indicates that the reduction is over within one μs. The change in absorbance at 450 nm during 1 and 3 μs is interpreted as a result of the sequential dissociation of two CP20 ligands. The slow absorbance change after that process, which fits to a single exponential, is attributed to the dissociation of the last ligand, as described in Equation (1). The reaction is strictly first-order, with a reaction rate constant of $(8 \pm 1) \times 10^3$ $s^{-1}$.

$$[Fe^{II}(cp20)]^+ \rightarrow Fe^{2+} + CP20^- \quad (1)$$

Mechanistically, the observed first-order reaction might also be represented by Equation (2) at constant pH.

$$H^+ + [Fe^{II}(cp20)]^+ \rightarrow [Fe^{II}(Hcp20)]^{2+} \rightarrow Fe^{2+} + Hcp20 \quad (2)$$

However, control experiments at pH = 8.6 showed that the rate of reaction is independent of pH; therefore, reaction 2 is not relevant.

Identical results to those with *tert*-butyl alcohol were obtained when methanol was used as a hydroxyl-radical scavenger. Interestingly, dioxocarbonate(·1–), a strong reductant $E°$ ($CO_2/CO_2^{\cdot-}$) = –1.9 V,[9] did not reduce iron(III)(cp20)$_3$ to any detectable degree.

 © 2006 Wiley-VCH Verlag GmbH & Co. KGaA, Weinheim 

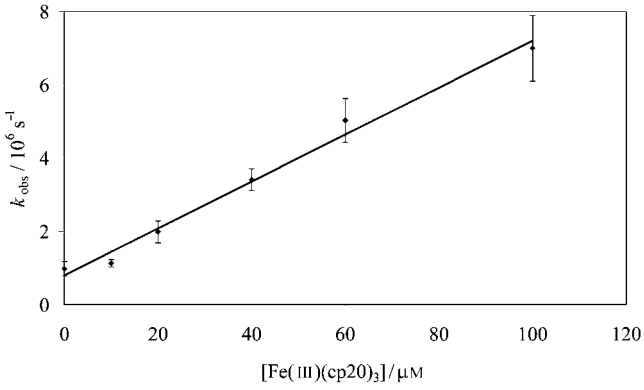


Figure 4. First-order rate constants at various concentrations of $Fe^{III}(cp20)_3$. The reactions with hydrated electrons (5 μM) were carried out at pH = 7.2 and room temperature. The reduction of iron(III)(cp20)$_3$ is linearly dependent on the complex concentration. The bimolecular rate constant is $k = (6.4 \pm 0.3) \times 10^{10}$ $M^{-1} s^{-1}$.

### Oxidation of Iron(II) by Hydrogen Peroxide in the Presence of CP20

The absorbance change of this oxidation, per reducing equivalent, should equal that for the reduction of iron(III)-(cp20)$_3$ by hydrated electrons. To calculate a difference spectrum for the iron(II)- and the iron(III)(cp20) complexes, we mixed a solution of iron(II) (20 μM) and CP20 (100 μM) with hydrogen peroxide (200 μM) at pH = 7.2 and 15 °C (Figure 5). At this temperature, the reaction becomes slower, and the signal-to-noise ratio of the time-dependent spectrum improves. Between 350 and 550 nm, the absorption increase per hydrogen peroxide matches the absorption decrease per hydrated electron in this range, as shown in Figure 6. The hydroxyl radical or oxoiron(IV) formed in the Fenton reaction is scavenged by the Tris buffer. The resulting Tris radical is not expected to re-reduce iron(III)-(cp20)$_3$. Because the iron(II)(cp20) complex can reduce water, it is impossible to prepare solutions of the pure complex: Under anaerobic conditions, in gas-tight syringes as well as in a flask purged with argon, the colour of the iron(II)(cp20) solution changes from light green to light orange within several minutes, indicating the formation of

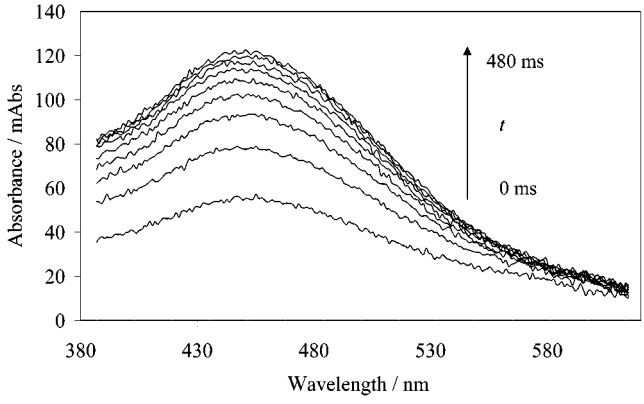


Figure 5. Time-dependent spectrum of the reaction of iron(II) (20 μM) and CP20 (100 μM) with hydrogen peroxide (200 μM) at pH = 7.2 and 15 °C. Formation of the iron(III)(cp20)$_3$ complex.

the iron(III) complex. At high pH values, this process is slower. Hegetschweiler and coworkers[10] reported that the iron(II)–ICL670 complex behaves similarly.

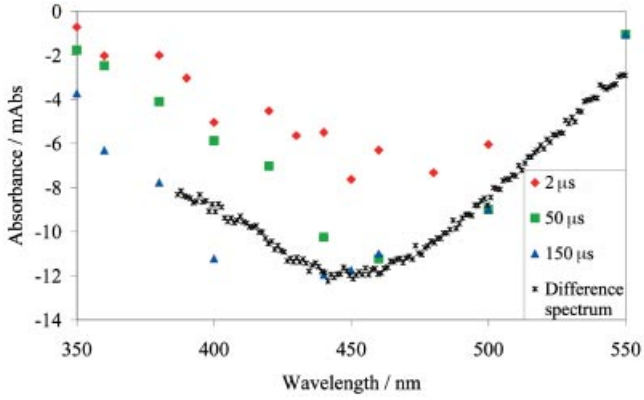


Figure 6. Time-dependent spectra measured by pulse radiolysis (diamonds, squares and triangles) of the reaction of iron(III) (33 μM) and CP20 (100 μM) with hydrated electrons (3.4 μM) at pH = 7.2 and room temperature. The small crosses indicate the difference spectrum of the iron(II)- and the iron(III)(cp20) complex measured by stopped-flow spectroscopy (see text). Per redox equivalent, the final difference spectrum from the pulse radiolysis is equal to that obtained by the stopped-flow technique.

## Discussion

As revealed by the speciation diagrams and as substantiated by kinetics experiments, CP20 stabilises iron(III), but not iron(II), very well. The first-order rate constant for the dissociation of the last CP20 molecule from iron(II) is of the same order of magnitude, $10^4$ $s^{-1}$, as that for the dissociation of a pyridine ligand from a ferriprotoporphyrin in chloroform.[11] CP20 is a bidentate ligand with two hard, oxygen coordination atoms, whereas pyridine is a monodentate ligand with a soft donor atom that stabilises iron(II), which leads to similar stability constants and similar dissociation rate constants. To the best of our knowledge, no other dissociation rates of ligands similar to hydroxypyridinones have been reported in the literature. The solvent-exchange rates for water ($k = 4.4 \times 10^6$ $s^{-1}$),[12] methanol ($k = 5 \times 10^4$ $s^{-1}$)[13] and acetonitrile ($k = 6.6 \times 10^5$ $s^{-1}$)[14] on iron(II) are higher. Given the speciation diagram (Figure 1A), the observed dissociation process involves all three ligands. After dissociation of CP20 from iron(II), monodentate ligands, such as water, bind to the metal ion and exchange much faster than CP20. Consequently, the probability that hydrogen peroxide coordinates to the metal centre and undergoes a Fenton reaction is increased.[15]

It is to be emphasised that the dissociation rate constant is independent of pH, and, therefore, does not result from protonation of the coordinated CP20 ligands. The spectral changes underline that the observed process is also not a dissociation of CP20 from iron(III), because this would result in a red shift, rather than the observed blue shift, of the spectrum.[8]

 © 2006 Wiley-VCH Verlag GmbH & Co. KGaA, Weinheim 

The reduction of the iron(III)(cp20)$_3$ complex by hydrated electrons is most likely a diffusion-controlled process. Reduction is possible with hydrated electrons, but not with dioxocarbonate(·1–) radicals, although from a comparison of the electrode potential of the iron(III)-/iron(II)(cp20)$_3$ couple (–0.62 V)[8] with that of the carbon dioxide/dioxocarbonate(·1–) couple (–1.90 V), it is clear that reduction is thermodynamically very favourable. This result shows that it is difficult to reduce the iron(III)(cp20)$_3$ complex with an inner-sphere reductant, because accessibility of the metal centre is sterically hindered by the large CP20 ligands. In a pulse radiolysis study of 2-pyridone, Moorthy et al.[16] could reduce the ligand with hydrated electrons, but not with dioxocarbonate(·1–) radicals. They concluded that an electrode potential smaller than –1.90 V is required to reduce 2-pyridone. On the basis of these and our observations, we conclude that the iron(III) is not directly accessible and is reduced via the ligand.

Reoxidation of iron(II) by hydrogen peroxide formed during the irradiation was not detected. This is understandable: if 10 μM iron(II) is produced, 2.5 μM hydrogen peroxide is also formed. Given a reaction rate constant of $10^4$ M$^{-1}$ s$^{-1}$ for the Fenton reaction, the pseudo-first-order rate constant would be ca. $10^{-2}$ s$^{-1}$.

We have shown that reduction by hydrated electrons is followed by ligand dissociation. One might now ask what would happen with more physiologically relevant reductants. El-Jammal and Templeton[17] proposed on the basis of their electrochemical measurements that reduction of iron(III) takes place after dissociation of the complex. We assess here the thermodynamics of two scenarios: first reduction followed by dissociation, and then the opposite. The standard electrode potential of the iron(III)-/iron(II)-(cp20)$_3$ couple is –0.62 V, and reduction by an electron donor with an electrode potential near 0 V "costs" ca. 58 kJ mol$^{-1}$. This process is then followed by favourable ligand dissociation. The dissociation of one CP20 ligand from the iron(III)(cp20)$_3$ complex requires less energy, about 53 kJ mol$^{-1}$, based on the difference between $\beta_3$ and $\beta_2$. In dilute solutions, this Gibbs energy decreases considerably, which makes the "ligand dissociation first" scenario more favourable. Therefore, for biologically relevant conditions, we agree with the proposal of El-Jammal and Templeton.[17]

Iron(II) complexes of other hydroxypyridinones and of ICL670 are also unlikely to be formed, given the similarly low electrode potentials.[8] Previously, a chelating agent with an electrode potential for its iron(III)/iron(II) complex of ca. –470 mV or lower, such as that of iron(III)-/iron(II) desferrioxamine,[18] was considered nontoxic. This hexadentate ligand binds iron(II) well at high dilution, in contrast to bi- and tridentate chelating agents. Iron complexes with bidentate chelating agents are more sensitive to dissociation upon dilution, which causes their electrode potentials to shift to more positive values.[8] Considering that the "free" iron concentration in vivo is about 10 times lower than that used here, one can conclude that CP20 does not bind iron(II) under physiological conditions. Recently, we showed that the electrode potentials of the iron(III)/iron(II) complexes with CP20 and ICL670 are near –150 mV under physiological conditions, and that superoxide is unable to reduce these complexes when they are fully formed. For complexes with less than three CP20 or two ICL670 molecules, reduction is thermodynamically feasible.[8] Electrode potentials of other reducing agents will be discussed in a future communication.

## Experimental Section

All chemicals used were of analytical reagent grade or higher. $Fe(NO_3)_3 \cdot 9H_2O$ was the source of $Fe^{III}$. Hydrogen peroxide stock solutions were prepared from Merck Analyzed Reagent 30% hydrogen peroxide. Water was purified with a Millipore Milli-Q unit fed with deionised water.

For pulse radiolysis, a Febetron 705 (Titan Systems Corp., San Leandro, CA, USA) 2.3-MeV accelerator with a pulse width (full width at half maximum) of <50 ns was used as the radiation source. The optical system consisted of a 75W Xe arc lamp (Hamamatsu, Schüpfen, Switzerland), a 1-cm quartz cell (Hellma GmbH & Co KG, Müllheim, Germany) and an Acton SP300 monochromator (Roper Scientific, Ottobrunn, Germany). For signal detection, there were two options: (1) a R928 photomultiplier (Hamamatsu, Japan) with a DHPCA-200 amplifier (Femto Messtechnik GmbH, Berlin, Germany) and a DL7100 digital storage oscilloscope (Yokogawa Electric Corporation, Tokyo, Japan) for kinetics traces or (2) a Princeton Instruments PI-MAX 512T gateable ICCD-camera (Roper Scientific) for time-resolved spectra. The dose per pulse used was 7–65 Gy, which corresponds to hydrated electron concentrations of 1.8–17 μM.[19] Dosimetry was carried out with thiocyanate.

The primary products from the radiolysis of water are $H^+_{aq}$, $e^-_{aq}$, $HO^\cdot$, $H^\cdot$, $H_2$ and $H_2O_2$. We used *tert*-butyl alcohol (0.1 M) or methanol (0.1 M) as scavengers for $HO^\cdot$ and $H^\cdot$ radicals to produce the fairly unreactive 2-hydroxy-2-methylpropyl- and hydroxymethyl radicals.[19] Solutions for experiments with hydrated electrons contained phosphate buffer (5 mM) and *tert*-butyl alcohol (0.1 M) or methanol (0.1 M), and were evacuated and saturated with argon at least five times.

The dioxocarbonate(·1–) radical was generated by reactions represented by Equation (3) and Equation (4). These solutions were saturated with dinitrogen monoxide (24 mM) and contained formate (50 mM, pH = 8.6).

$$e^-_{aq} + N_2O \rightarrow HO^\cdot + HO^- + N_2 \quad (3)$$

$$HCOO^- + HO^\cdot \rightarrow CO_2^{\cdot-} + H_2O \quad (4)$$

The kinetics of the reduction of the iron(III)(cp20)$_3$ complex and the ligand dissociation were recorded at 450 nm. The decay of the hydrated electrons was followed at 600 nm.

Stopped-flow experiments were obtained with an OLIS stopped-flow instrument (Bogart, GA, USA) equipped with an OLIS RSM 1000 rapid-scanning monochromator set to collect up to 1000 spectra per second. Solutions for the stopped-flow experiments were prepared in Tris buffer (0.1 M), and evacuated and saturated with argon at least five times before addition of iron(II). Hydrochloric acid was used to adjust the pH. The hydrogen peroxide solution was purged with argon for at least 30 min.

 © 2006 Wiley-VCH Verlag GmbH & Co. KGaA, Weinheim 

Species-distribution diagrams were calculated with the SPEC program (R. Kissner, ETHZ). In SPEC, which was designed to calculate the species distribution in solution equilibria from known formation constants and total concentrations, the Newton–Raphson algorithm is used to solve the system of nonlinear partition equations ("tangential method").

## Acknowledgments

This work was supported by the ETH Zürich, Swiss National Science Foundation, and the BBW (01.0397), in support of EU (QLK1-CT-2002–00444).

[1] R. Crichton, *Inorganic Biochemistry of Iron Metabolism*, John Wiley & Sons, Chichester, **2001**, pp. 235–257.
[2] R. J. Bergeron, J. S. McManis, J. Wiegand, W. R. Weimar, G. M. Brittenham, in *Iron Chelators: New Development Strategies* (Eds.: D. G. Badman, R. J. Bergeron, G. M. Brittenham), The Saratoga Group, Ponte Verda Beach, FL, **2000**, pp. 253–292.
[3] R. C. Hider, Z. D. Liu, *Curr. Med. Chem.* **2003**, *10*, 1051–1064.
[4] H. Nick, P. Acklin, R. Lattmann, P. Buehlmayer, S. Hauffe, J. Schupp, D. Alberti, *Curr. Med. Chem.* **2003**, *10*, 1065–1076.
[5] M. H. Williams, J. K. Yandell, *Aust. J. Chem.* **1982**, *35*, 1133–1144.
[6] H. A. Schwarz, R. W. Dodson, *J. Phys. Chem.* **1984**, *88*, 3643–3647.
[7] M. H. Kern, *J. Am. Chem. Soc.* **1954**, *76*, 4208–4214.
[8] M. Merkofer, R. Kissner, R. C. Hider, W. H. Koppenol, *Helv. Chim. Acta* **2004**, *87*, 3021–3034.
[9] H. A. Schwarz, R. W. Dodson, *J. Phys. Chem.* **1989**, *93*, 409–414.
[10] S. Steinhauser, U. Heinz, M. Bartholomä, T. Weyhermüller, H. Nick, K. Hegetschweiler, *Eur. J. Inorg. Chem.* **2004**, 4177–4192.
[11] E. von Goldammer, H. Zorn, *Biophys. Chem.* **1975**, *3*, 249–254.
[12] Y. Ducommun, K. E. Newman, A. Merbach, *Inorg. Chem.* **1980**, *19*, 3696–3703.
[13] F. W. Breivogel, Jr., *J. Chem. Phys.* **1969**, *51*, 445–448.
[14] M. J. Sisley, Y. Yano, T. W. Swaddle, *Inorg. Chem.* **1982**, *21*, 1141–1145.
[15] E. Graf, J. R. Mahoney, R. G. Bryant, J. W. Eaton, *J. Biol. Chem.* **1984**, *259*, 3620–3624.
[16] D. B. Naik, P. N. Moorthy, *Proc. Indian Acad. Sci. (Chem. Sci.)* **1991**, *103*, 667–675.
[17] A. El-Jammal, D. M. Templeton, *Inorg. Chim. Acta* **1996**, *245*, 199–207.
[18] K. N. Raymond, G. Müller, B. F. Matzanke, in *Structural Chemistry* (Ed.: F. L. Boschke), Springer-Verlag, Berlin, **1984**, pp. 49–97.
[19] G. V. Buxton, C. L. Greenstock, W. P. Helman, A. B. Ross, *J. Phys. Chem. Ref. Data* **1988**, *17*, 513–886.
[20] R. J. Motekaitis, A. E. Martell, *Inorg. Chim. Acta* **1991**, *183*, 71–80.

Received: September 15, 2005
Published Online: December 20, 2005

 © 2006 Wiley-VCH Verlag GmbH & Co. KGaA, Weinheim 

DOI: 10.1002/ejic.200501090

# Structural and Dynamic Studies of Zinc, Gallium, and Cadmium Complexes of a Dicarboxylate Pendant-Armed Cross-Bridged Cyclen

**Weijun Niu,[a] Edward H. Wong,*[a] Gary R. Weisman,*[a] Yijie Peng,[a] Carolyn J. Anderson,[b] Lev N. Zakharov,[c] James A. Golen,[c][‡] and Arnold L. Rheingold[c]**

**Keywords:** Zinc / Gallium / Cadmium / Cyclen / Cross-bridged ligand / Pendant arms

*Inadvertently, the wrong X-ray structure was reported[1] for the Zn-CB-DO2A complex. Instead, the structural data for a related zinc complex was actually presented. The first paragraph of the section X-ray Structural Data and Figure 5 on page 3312, Table 1 on page 3313, the last two sentences of the paragraph [Zn·**1**](NaClO$_4$)$_{1.5}$ and Table 3 on page 3314, and the paragraph X-ray Crystallography on page 3315 should be replaced as follows (in addition, a corrected X-ray CIF file was deposited with the CCDC):*

## X-ray Structural Data

The core structure of the zinc complex [Zn·**1**] is shown in Figure 5. The $Zn^{II}$ cation is fully enveloped within the *cis*-$N_4O_2$ donor set of the cross-bridged ligand in a distorted octahedral geometry. The axial N(3)–Zn(1)–N(4) angle of 156.97(11) [158.36(10)]° (structural data for a second independent molecule are given in brackets) is substantially away from linearity, showing that the $Zn^{II}$ is distended from the cross-bridged cyclen cavity. Previous structural data of zinc complexes of the cross-bridged cyclen and its derivatives have also shown this distention from the ligand cavity with axial N–Zn–N angles between 148 and 159°.[16–18] Another manifestation of these distortions can also be seen in their longer axial N–Zn bonds (2.17–2.26 Å), similar to the average of 2.19 Å found in [Zn·**1**]. All Zn–N and Zn–O bond lengths are within a relatively narrow range of 2.03–2.20 Å. Selected bond lengths and angles are shown in Table 1. An X-ray structure of a DOTA complex of zinc(II) featuring a related *cis*-$N_4O_2$ ligand coordination mode has been reported.[19] This has an axial N–Zn–N angle of 153.9°, an axial Zn–N distance of 2.232 Å, an equatorial Zn–N distance of 2.171 Å, and a shorter Zn–O distance of 2.037 Å. However, without the cross-bridging ethylene, the equatorial N–Zn–N angle is opened up to 107.8° [compared to the 83.6(1)° for N(1)–Zn(1)–N(2) here]. Also, the coordinated carboxylate pendant arms are on the equatorial macrocyclic nitrogen atoms rather than the axial ones and this DOTA structure is thus close to $C_{2v}$ symmetry.

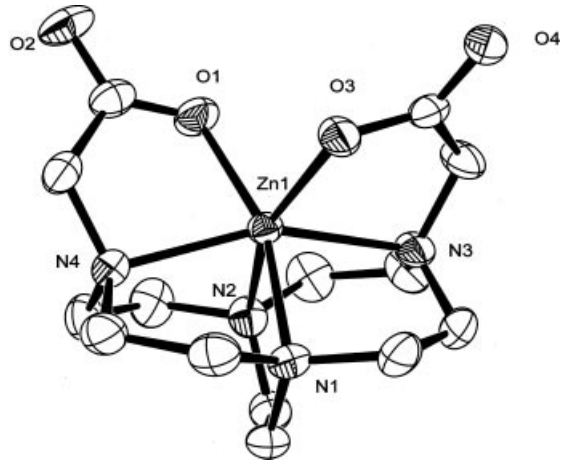


Figure 5. Molecular structure of Zn-CB-DO2A·NaClO$_4$; hydrogen atoms and sodium perchlorate have been omitted for clarity.

X-ray quality crystals were grown by ether diffusion into a sample dissolved in methanol solution. These have a composition of [Zn·**1**](NaClO$_4$)(CH$_3$OH)(H$_2$O).

**X-ray Crystallography:** Diffraction intensity data were collected with Bruker Smart Apex CCD ([Zn·**1**]) and Siemens P4 CCD ([Ga·**1**]NO$_3$) diffractometers. Crystal data collection and refinement parameters are given in Table 3. The structures were solved using direct methods, completed by subsequent difference Fourier syntheses, and refined by full-matrix least-squares procedures on $F^2$. SADABS absorption corrections were applied to [Ga·**1**]NO$_3$ data ($T_{min}/T_{max}$ = 0.724). In both structures all non-hydrogen

[a] Department of Chemistry, University of New Hampshire, Durham, New Hampshire 03824, USA
Fax: +1-603-862-4278
E-mail: ehw@cisunix.unh.edu
gary.weisman@unh.edu
[b] Mallinckrodt Institute of Radiology, Washington University, School of Medicine,
St. Louis, MO 63110, USA
Fax: +1-314-362-9940
E-mail: AndersonCJ@mir.wustl.edu
[c] Department of Chemistry and Biochemistry, University of California,
San Diego, La Jolla, California 92093, USA
E-mail: arnrhein@chem.ucsd.edu
[‡] On leave from the Department of Chemistry and Biochemistry, University of Massachusetts Dartmouth,
North Dartmouth, Massachusetts 02747, USA


© 2006 Wiley-VCH Verlag GmbH & Co. KGaA, Weinheim

Table 1. Selected bond lengths [Å] and bond angles [°] for [Zn·**1**] (values for two symmetry-independent molecules are given).

| | | | |
|---|---|---|---|
| Zn(1)–O(1) | 2.032(3) | O(1)–Zn(1)–O(3) | 89.58(11) |
| Zn(1)–O(3) | 2.047(2) | O(1)–Zn(1)–N(1) | 159.24(11) |
| Zn(1)–N(1) | 2.130(3) | O(1)–Zn(1)–N(2) | 98.80(12) |
| Zn(1)–N(2) | 2.116(3) | N(1)–Zn(1)–N(2) | 83.60(12) |
| Zn(1)–N(3) | 2.193(3) | N(3)–Zn(1)–N(4) | 156.97(11) |
| Zn(1)–N(4) | 2.195(3) | N(1)–Zn(1)–N(3) | 83.08(12) |
| | | | |
| Zn(2)–O(5) | 2.058(2) | O(5)–Zn(2)–O(7) | 89.55(9) |
| Zn(2)–O(7) | 2.040(2) | O(5)–Zn(2)–N(5) | 160.24(10) |
| Zn(2)–N(5) | 2.123(3) | O(5)–Zn(2)–N(6) | 96.84(10) |
| Zn(2)–N(6) | 2.126(3) | N(5)–Zn(2)–N(6) | 84.03(11) |
| Zn(2)–N(7) | 2.172(3) | N(5)–Zn(2)–N(7) | 83.76(10) |
| Zn(2)–N(8) | 2.182(3) | N(7)–Zn(2)–N(8) | 158.36(10) |

Table 3. Crystallographic data for [Zn·**1**] and [Ga·**1**]$NO_3$.

| | [Zn·**1**] | [Ga·**1**]$NO_3$ |
|---|---|---|
| Empirical formula | $C_{30}H_{48}Cl_2N_8Na_2O_{20}Zn_2$ | $C_{14}H_{24}GaN_5O_7$ |
| Formula mass | 1088.38 | 444.10 |
| Crystal system, space group | monoclinic, $P2_1/c$ | orthorhombic, $P2_12_12_1$ |
| $a$ [Å] | 8.8197(6) | 8.7107(7) |
| $b$ [Å] | 17.2311(13) | 12.5119(10) |
| $c$ [Å] | 29.841(2) | 7.5586(6) |
| $\alpha$ [°] | 90.0 | 90.0 |
| $\beta$ [°] | 96.319(2) | 90.0 |
| $\gamma$ [°] | 90.0 | 90.0 |
| $V$ [Å$^3$] | 4507.4(6) | 823.79(11) |
| $Z$ | 4 | 2 |
| $T$ [K] | 218(2) | 218(2) |
| $\lambda$ [Å] | 0.71073 (Mo-$K_\alpha$) | 0.71073 (Mo-$K_\alpha$) |
| $\rho_{calcd.}$ [g·cm$^{-3}$] | 1.604 | 1.790 |
| $\mu$ [mm$^{-1}$] | 1.286 | 1.724 |
| Measured reflections | 33251 | 6004 |
| Independent reflections | 10841 ($R_{int}$=0.0352) | 1967 ($R_{int}$=0.0260) |
| $R^{[a]}$, $R^{[b]}(\omega F^2)$ (obsd. data) | 0.0514, 0.1415 | 0.0231, 0.0553 |
| $R^{[a]}$, $R^{[b]}(\omega F^2)$ (all data) | 0.0638, 0.1495 | 0.0244, 0.0557 |
| *GOF* | 1.027 | 1.006 |

[a] $R = \Sigma||F_o| - |F_c||/\Sigma|F_o|$. [b] $R(\omega F^2) = \{\Sigma[\omega(F_o^2 - F_c^2)^2]/\Sigma[\omega(F_o^2)^2]\}^{1/2}$; $\omega = 1/[\sigma^2(F_o^2) + (aP)^2 + bP]$, $P = [2F_c^2 + \max(F_o,0)]/3$.

atoms were refined with anisotropic displacement coefficients. Hydrogen atoms were treated as idealized contributions. The Flack parameter for [Ga·**1**]$NO_3$ is 0.014(11). All software and sources of scattering factors are contained in the SHELXTL (5.10) program package (G. Sheldrick, Bruker XRD, Madison, WI, USA). CCDC-291598 ([Zn·**1**]) and -229394 ([Ga·**1**]$NO_3$) contain the supplementary crystallographic data for this paper. These data can be obtained free of charge at www.ccdc.uk/conts/retrieving.html [or from the Cambridge Crystallographic Data Centre, 12 Union Road, Cambridge CB2 1EZ, UK; Fax: +44-1223-336-033; E-mail: deposit@ccdc.cam.ac.uk].

[1] W. Niu, E. H. Wong, G. R. Weisman, Y. Peng, C. J. Anderson, L. N. Zakharov, J. A. Golen, A. L. Rheingold, *Eur. J. Inorg. Chem.* **2004**, 3310–3315.

Received: December 6, 2005
*The Authors*

 © 2006 Wiley-VCH Verlag GmbH & Co. KGaA, Weinheim 

EurJIC
European Journal of Inorganic Chemistry

Issue 4/2006

Pages 681–872

*Papers available ahead of print in Early View at www.interscience.wiley.com*

*Earliest available Table of Contents:*
*Automatically, free of charge by e-mail through*
*www.interscience.wiley.com/alerts*

## COVER PICTURE

**The cover picture shows** the Mn12 single-molecule magnet (SMM), which has a 3-thiophenecarboxylate ligand and is formed by the ligand substitution reaction of Mn12-ac with 16 equiv. of 3-thiophenecarboxylic acid in toluene. The reaction of Mn12-ac with 17 equiv. of 3-thiophenecarboxylic acid affords a different Mn12 SMM that shows a more distorted structure and has a faster relaxation rate. The Mn12 SMM is strongly anchored on the gold surface through the sulfur atoms of the thiophenyl group. The Mn12 molecular film on Au(111) was characterized by XPS, STM, and AFM. Further details are discussed in the article by J. Kim et al. on p. 711 ff.

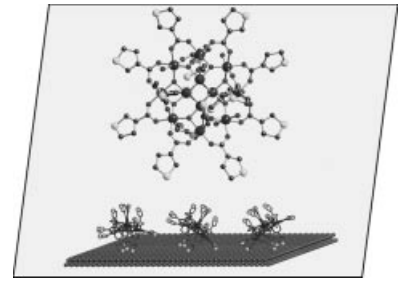

## MICROREVIEW

**Contents**

**695** **A. Riisager,* R. Fehrmann, M. Haumann,* P. Wasserscheid**

Supported Ionic Liquid Phase (SILP) Catalysis: An Innovative Concept for Homogeneous Catalysis in Continuous Fixed-Bed Reactors

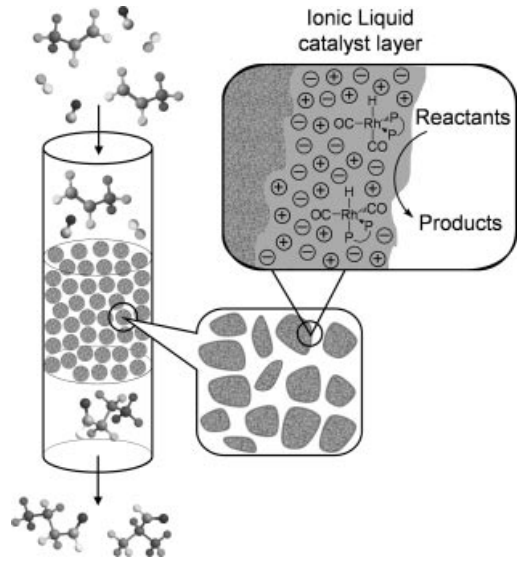


**Keywords:** Ionic liquids / Supported catalysts / Immobilisation / Homogeneous catalysis / Hydroformylation

 © 2006 Wiley-VCH Verlag GmbH & Co. KGaA, Weinheim 

## SHORT COMMUNICATION


**707** **A. Otero,* J. Fernández-Baeza,* A. Antiñolo, J. Tejeda, A. Lara-Sánchez, L. Sánchez-Barba, M. Sánchez-Molina, S. Franco, I. López-Solera, A. M. Rodríguez**

A Simple and Efficient Synthetic Route to Enantiopure Scorpionate Ligands

**Keywords:** Scorpionate ligands / Chiral ligands / Lithium / Titanium


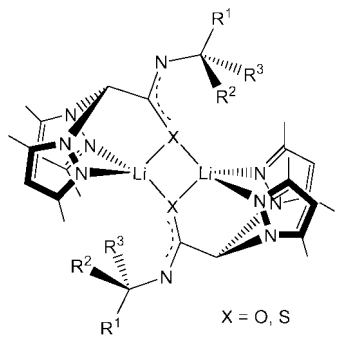


## FULL PAPERS


**711** **J. M. Lim, Y. Do, J. Kim***

Molecular Structures and Magnetism of $Mn_{12}$ Nanomagnets Containing the 3-Thiophenecarboxylate Ligand

**Keywords:** Single-molecule magnet / $Mn_{12}$ complex / Molecular structure / Magnetic properties / Molecular films


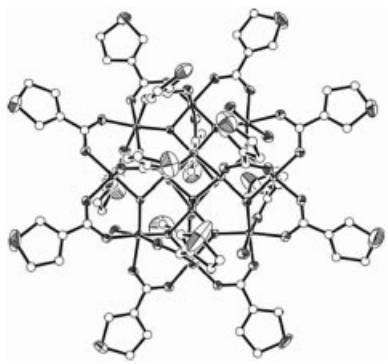


**718** **H. Jang, C.-H. Shin, B.-J. Jung, D. Kim, H.-K. Shim,* Y. Do***

Synthesis and Characterization of Dinuclear Europium Complexes Showing Pure Red Electroluminescence

**Keywords:** Electroluminescence / Europium / Dinuclear complexes / 2,2′-Bipyrimidine


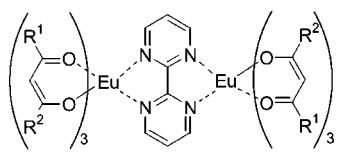



**726** **F. L. Sousa, M. Pillinger, R. A. Sá Ferreira, C. M. Granadeiro, A. M. V. Cavaleiro, J. Rocha, L. D. Carlos, T. Trindade, H. I. S. Nogueira***

Luminescent Polyoxotungstoeuropate Anion-Pillared Layered Double Hydroxides

**Keywords:** Layered double hydroxides / Layered compounds / Polyoxometalates / Host−guest systems / Luminescence


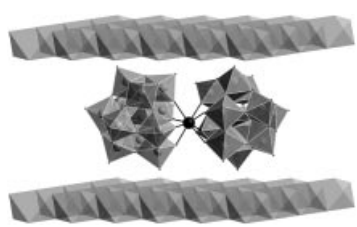

**735** **M. Mehring,* D. Mansfeld, B. Costisella, M. Schürmann**

The First Metal-Oxo Cluster Containing Lithium and Bismuth

**Keywords:** Bismuth / Lithium / Silanolate / Alkoxide / Metal-oxo cluster

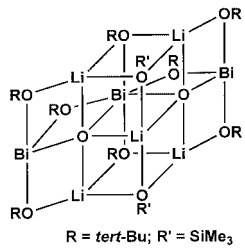


**740** **M. Ravera, C. Cassino, S. Baracco, D. Osella***

New Insights into the Redox Chemistry of Ruthenium Metallopharmaceuticals: The Electrochemical Behaviour of [LH][*trans*-$Ru^{III}Cl_4L_2$] (L = imidazole or indazole) Complexes

**Keywords:** Antitumor agents / Electrochemistry / Redox chemistry / Ruthenium

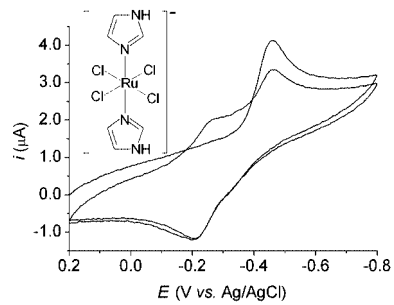


**747** **A. A. Trifonov,* D. M. Lyubov, E. A. Fedorova, G. K. Fukin, H. Schumann, S. Mühle, M. Hummert, M. N. Bochkarev**

Chloro, Alkyl and Aryl Complexes of Rare Earth Metals Supported by Bulky Tetrasubstituted Guanidinate Ligands

**Keywords:** Alkyl complexes / Aryl complexes / Guanidinates / N ligands / Rare Earths

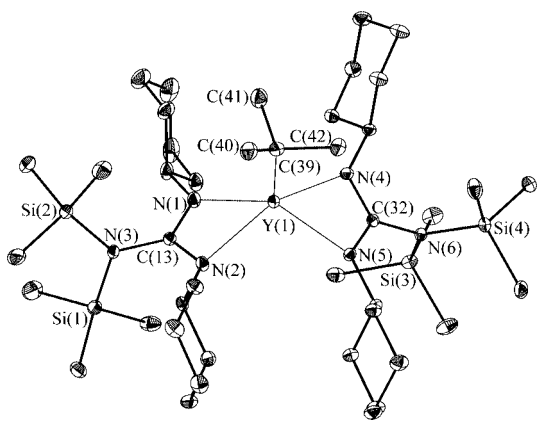


**757** **F. Demirhan,* B. Çağatay, D. Demir, M. Baya, J.-C. Daran, R. Poli***

Reduction of [$Cp^*_2Mo_2O_5$] in Aqueous Medium: Structure and Properties of a Triangular Mixed Oxo-Hydroxo-Bridged Product, [$Cp^*_3Mo_3(\mu\text{-}O)_2(\mu\text{-}OH)_4](X)_2$ (X = $CF_3CO_2$ or $CF_3SO_3$)

**Keywords:** Bridging ligands / Hydrogen bonding / Metal−metal interactions / Molybdenum / Oxo ligands

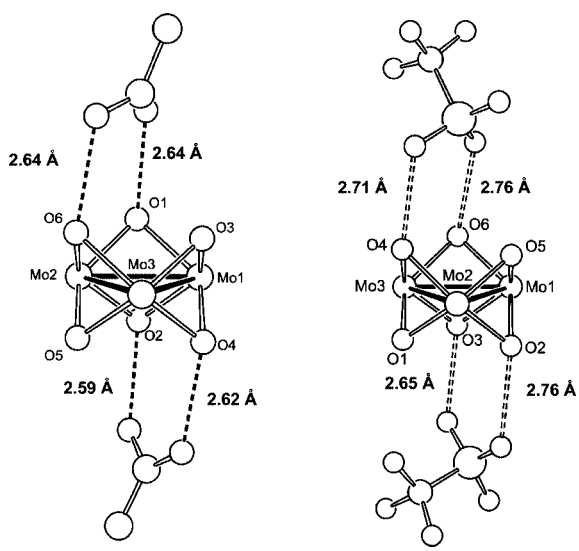



 © 2006 Wiley-VCH Verlag GmbH & Co. KGaA, Weinheim 

**765** **G. Marangoni,* B. Pitteri, G. Annibale, M. Bortoluzzi**

Ring Opening and Displacement by Chloride of the Bidentate Chelate Ligand from Dichloro-[pyridine-2-(α-methoxymethanolato)]gold(III) − A Kinetic and Mechanistic Study

**Keywords:** Chelate displacement / Gold / Kinetics / Reaction mechanism

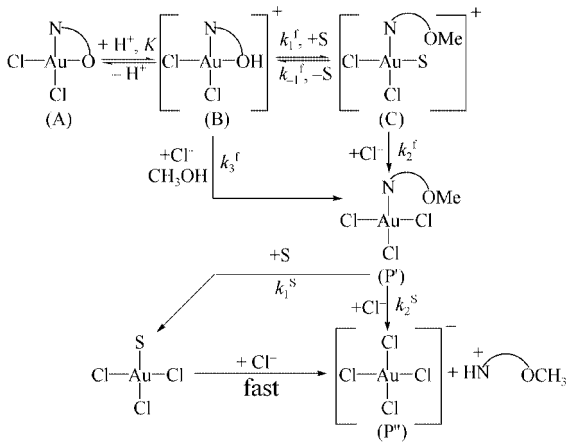


**772** **D. M. D'Alessandro, P. H. Dinolfo, J. T. Hupp, P. C. Junk, F. R. Keene***

The Effective Electron-Transfer Distance in Dinuclear Ruthenium Complexes Containing the Unsymmetrical Bridging Ligand 3,5-Bis(2-pyridyl)-1,2,4-triazolate

**Keywords:** Electron transfer / Mixed-valent compounds / Through-bond interactions / Dinuclear / Stereochemistry / Stark spectroscopy / Ruthenium

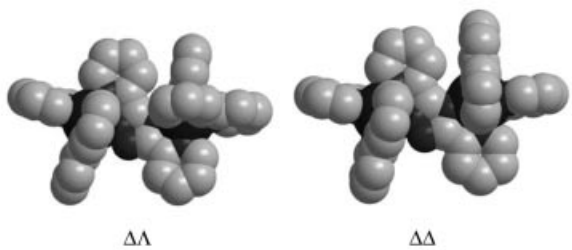


**784** **M. Barboiu, M. Ruben, G. Blasen, N. Kyritsakas, E. Chacko, M. Dutta, O. Radekovich, K. Lenton, D. J. R. Brook,* J.-M. Lehn***

Self-Assembly, Structure and Solution Dynamics of Tetranuclear $Zn^{2+}$ Hydrazone [2×2] Grid-Type Complexes

**Keywords:** Self-assembly / Grid-type complexes / Hydrazone ligands / Zinc / Supramolecular chemistry

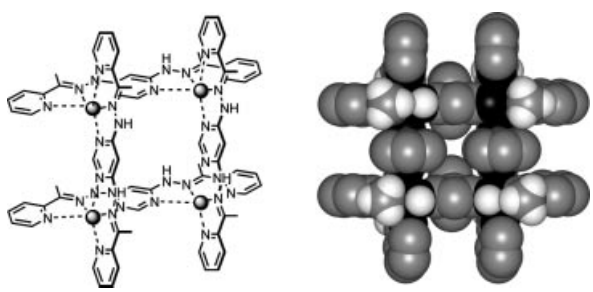

**793** **E. Jaime, J. Weston***

Mechanism of the MeOH/$H_2O$ Substitution in a Series of Biomimetic Bimetallo Zinc-Based $H_3O_2$ Complexes

**Keywords:** Density functional calculations / Enzyme models / Metalloenzymes / $H_3O_2$ bridges / Zinc

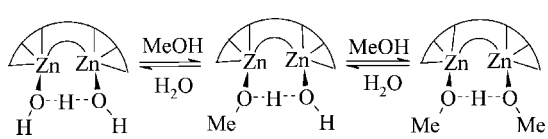



 © 2006 Wiley-VCH Verlag GmbH & Co. KGaA, Weinheim 

**802** **E. Martinez-Ferrero, K. Boubekeur, F. Ribot***

Carboxylate-Containing Tin(IV) Isopropoxides: Synthesis and Characterization of $[Sn(OiPr)_2(O_2CR)_2]_2$ [R = $(CH_3)CCH_2$, $C_6H_5$, $CH_3$]

**Keywords:** Carboxylate ligands / Organic−inorganic hybrid composites / NMR spectroscopy / Solgel processes / Tin

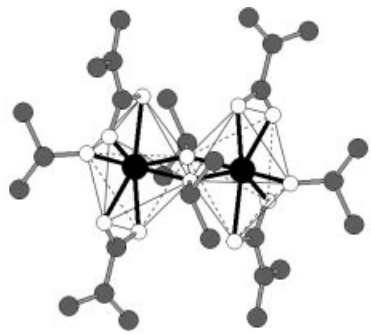

**808** **W.-P. Leung,* K.-H. Chong, Y.-S. Wu, C.-W. So, H.-S. Chan, T. C. W. Mak**

Synthesis of Chalcogeno[3-(pyrid-2-yl)-1-aza-allyl]germanium Complexes

**Keywords:** Chalcogens / Germanium / N ligands

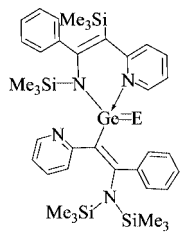


E = S **(3)**, Se **(4)**

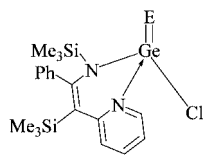


E = S **(5)**, Se **(6)**

**813** **K. P. Rao, K. Vidyasagar***

Synthesis and X-ray Crystal Structures of the New, Three-Dimensional Ethylenediphosphonates $[A\{HO_3P(CH_2)_2PO_3H_2\}]$ (A = Alkali Metal, Tl, or $NH_4$): Solid Brönsted Acids That Exhibit Topotactic Intercalation and Deintercalation of Ammonia

**Keywords:** Intercalation / Organic−inorganic hybrid composites / Phosphonates / X-ray diffraction

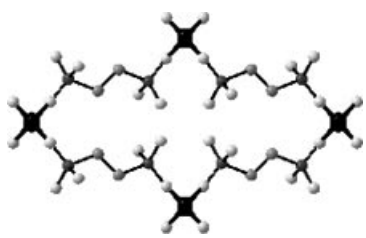

**820** **C.-C. Wang,* C.-H. Yang, G.-H. Lee**

Hydrothermal Synthesis and Structural Characterization of Two pH-Controlled Cd−Squarate Coordination Frameworks, $[Cd_2(C_4O_4)_{2.5}(H_2O)_4]\cdot(dpaH)\cdot1.5(H_2O)$ and $[Cd(C_4O_4)(dpa)(OH_2)]$ (dpa = 2,2′-dipyridylamine)

**Keywords:** Hydrothermal synthesis / Self-assembly / Hydrogen bonds / Squarate / Cadmium

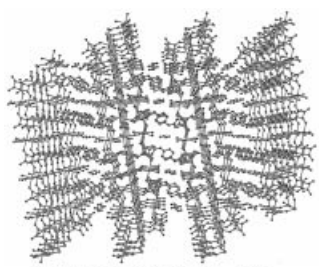

$[Cd_2(C_4O_4)_{2.5}(H_2O)_4](dpaH)$ **1**

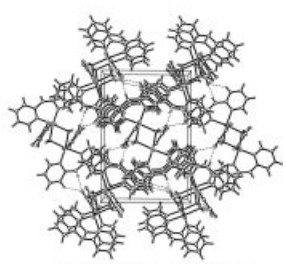

$[Cd(dpa)(C_4O_4)(H_2O)]$ **2**


 © 2006 Wiley-VCH Verlag GmbH & Co. KGaA, Weinheim 

**827** **I. L. Fedushkin,* V. M. Makarov, E. C. E. Rosenthal, G. K. Fukin**

Single-Electron-Transfer Reactions of α-Diimine dpp-BIAN and Its Magnesium Complex (dpp-BIAN)$^{2-}$Mg$^{2+}$(THF)$_3$

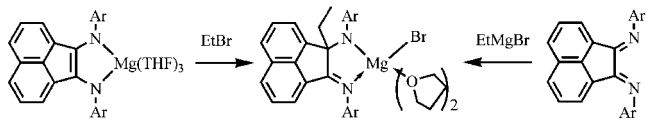


**Keywords:** Magnesium / N-ligands / Single-electron transfer

**833** **F. Mohr, L. R. Falvello, M. Laguna***

Synthesis, Structural Characterisation and Reactions of Some Vinylgold(I) Phosphane Complexes

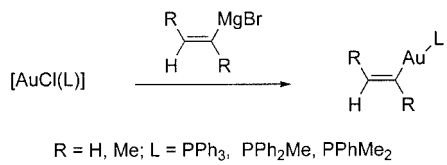


R = H, Me; L = $PPh_3$, $PPh_2Me$, $PPhMe_2$

**Keywords:** Gold / Vinyl ligands / Phosphane ligands

**839** **D. Jaramillo, D. P. Buck, J. G. Collins, R. R. Fenton, F. H. Stootman, N. J. Wheate, J. R. Aldrich-Wright***

Synthesis, Characterisation and Biological Activity of Chiral Platinum(II) Complexes

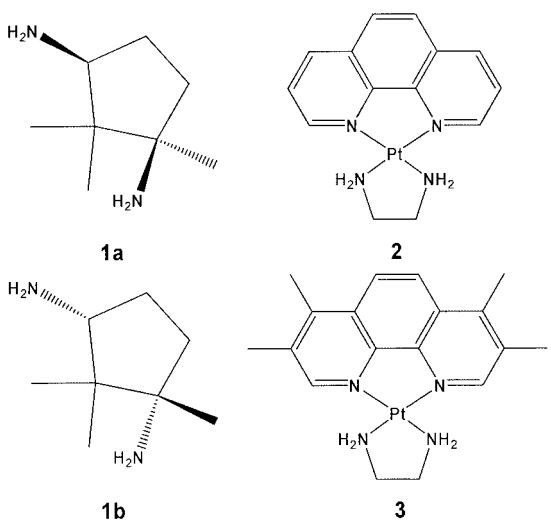


**Keywords:** Platinum / Chiral / Intercalator / Cancer / L1210 / Induced circular dichroism

**850** **I. Mayer, G. S. Nunes, H. E. Toma, K. Araki***

Steric and Catalytic Effects in Tetraruthenated Manganese Porphyrins

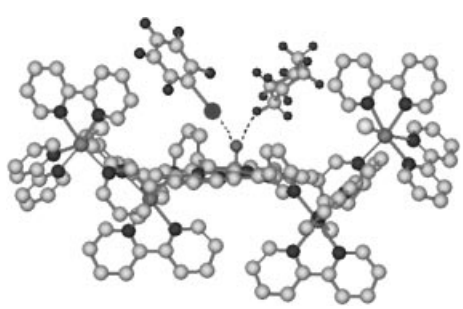

**Keywords:** Electrochemistry / Manganese / Porphyrinoids / Sensors / Supramolecular chemistry


 © 2006 Wiley-VCH Verlag GmbH & Co. KGaA, Weinheim 

**857** **M. Malessa, J. Heck,* J. Kopf, M. H. Garcia**

Polar Cofacially Fixed Sandwich Complexes: Do They Demonstrate Second Harmonic Generation (SHG)?

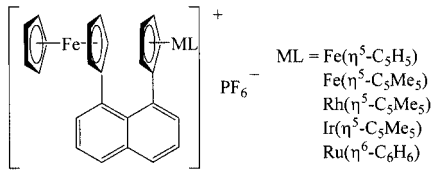


**Keywords:** Heterometallic complexes / Sandwich complexes / Donor−acceptor systems / Nonlinear optics / Through-space interaction

 © 2006 Wiley-VCH Verlag GmbH & Co. KGaA, Weinheim 

DOI: 10.1002/ejic.200500872

# Supported Ionic Liquid Phase (SILP) Catalysis: An Innovative Concept for Homogeneous Catalysis in Continuous Fixed-Bed Reactors

**Anders Riisager,*[a] Rasmus Fehrmann,[a] Marco Haumann,*[b] and Peter Wasserscheid[b]**

**Keywords:** Ionic liquids / Supported catalysts / Immobilisation / Homogeneous catalysis / Hydroformylation

Applications of ionic liquids to replace conventional solvents in homogeneous transition-metal catalysis have increased significantly during the last decade. Biphasic ionic liquid/organic liquid systems offer advantages with regard to product separation, catalyst stability, and recycling but utilise in the case of fast chemical reactions only a small amount of expensive ionic liquid and catalyst. The novel Supported Ionic Liquid Phase (SILP) catalysis concept overcomes these drawbacks and allows the use of fixed-bed reactors for continuous reactions. In this Microreview the SILP catalysis concept is surveyed by presenting results for the continuous gas-phase hydroformylation of propene, as a reaction example.
(© Wiley-VCH Verlag GmbH & Co. KGaA, 69451 Weinheim, Germany, 2006)

## Introduction

In the last decade, ionic liquids have been studied extensively as alternative solvents for homogeneous catalysis.[1] Their ionic nature, nonvolatility, and thermal stability make them highly suitable for biphasic ionic liquid/organic liquid transition-metal catalysis.[2] The almost unlimited combinations of cation and anion allow the synthesis of tailor-made ionic liquids that can stabilise the catalytic species.[3] Moreover, appropriate ionic liquids can enhance substrate solubility while possessing low product solubility, and thus facilitate simple product separation and complete catalyst recovery.[4]

Biphasic ionic liquid/organic liquid systems generally require a large amount of ionic liquid. On the basis of economic considerations this is unattractive since ionic liquids remain relatively expensive even though they are now commercially available.[5] In addition, the high viscosity of ionic liquids can induce mass transfer limitations if the chemical reaction is fast, causing only a minor part of the ionic liquid and precious transition metal catalyst dissolved therein to take part in the catalysed reaction. This problem can, however, to some extent be circumvented by intense stirring to create smaller droplets with a larger reaction surface. This, on the other hand, necessitates a high energy input due to the viscosity of the ionic liquid and makes continuous processes economically unviable. Thus, in contrast to the conventional ionic liquid/organic liquid biphasic systems, an ideal catalyst system would consist of a bulk catalyst phase having the size of the diffusion layer, which allows all the available metal complexes and ionic liquid to be involved in the catalytic reaction. Additionally, solid catalyst systems would allow application of continuous-flow-operated fixed-bed processing.

A "heterogenised" type of homogeneous ionic liquid catalyst system, described as Supported Ionic Liquid Phase (SILP) catalysts, has recently been introduced and examined by us and other research groups for hydroformylation[6,7] (Rh-catalysed), carbonylation[8] (Rh-catalysed), hydrogenation[9] (Rh-catalysed), Heck reactions[10] (Pd-catalysed), hydroaminations[11] (Rh-, Pd-, and Zn-catalysed) and epoxidation[12] (W-catalysed). In these SILP systems, a thin film of ionic liquid containing the homogeneous catalyst is immobilised on the surface of a high-area, porous support material, as depicted in Figure 1.

In SILP catalysts the combination of high solvent polarity combined with nonvolatility [in contrast to water in Supported Aqueous Phase (SAP) catalysis], ensures that the catalytic species remain dissolved also in continuously operated reactions. Furthermore, the combination facilitates separation of the catalyst phase from the organic product

[a] Department of Chemistry and Center for Sustainable and Green Chemistry, Technical University of Denmark, Building 207,
2800 Kgs. Lyngby, Denmark
Fax: +45-4525-2235
E-mail: ar@kemi.dtu.dk
[b] Lehrstuhl für Chemische Reaktionstechnik (CRT), Universität Erlangen-Nürnberg,
Egerlandstrasse 3, 91058 Erlangen, Germany
Fax: +49-9131-8527421
E-mail: haumann@crt.cbi.uni-erlangen.de

**MICROREVIEWS:** This feature introduces the readers to the authors' research through a concise overview of the selected topic. Reference to important work from others in the field is included.

 © 2006 Wiley-VCH Verlag GmbH & Co. KGaA, Weinheim 

phase in contrast to many traditional organic liquid Supported Liquid Phase (SLP) catalysts. In addition, the high dispersion of the ionic liquid/catalyst solution on the support surface results in a very efficient use of ionic liquid, reducing the necessary amount of the precious catalyst and the ionic liquid required. Consequently, SILP catalyst systems offer significant advantages compared to biphasic catalysis in organic liquid/ionic liquid mixtures and to current SLP and SAP catalyst systems.

Despite the important advantages mentioned above it should be realised, however, that the use of SILP catalysts in most cases is limited to gas-phase applications. For liquid-phase reactions even a minor ionic liquid solubility in a liquid feedstock/product mixture can be sufficient to remove the catalyst from the carrier over time in both continuously operated or batch processes upon catalyst recycling (due to the very small amount of ionic liquid on the support). Even worse, the thin immobilised catalyst layer can physically be removed from the support by mechanical forces, for example, by a convective liquid flow.

One of the first examples of liquid SILP catalysis, where the problems of leaching became evident, was reported by Mehnert and co-workers on the hydroformylation of 1-hexene in batch autoclave mode.[6] They immobilised the ionic liquid 1-butyl-3-methylimidazolium hexafluorophosphate ([BMIM][$PF_6$]) by covalent bonding (through pendant silyl groups) to the chemically modified surface of a silica gel. Two monodentate phosphane ligands, tris(*m*-sulfonylphenyl)phosphane trisodium salt (TPPTS) and tris(*m*-sulfonylphenyl)phosphane tris(1-butyl-3-methylimidazolium) salt (TPPTI) were used for ligand modification of the rhodium precursor Rh(acac)$(CO)_2$. The activity of the obtained Rh/SILP catalysts was almost three times higher than for comparable biphasic systems and was attributed to a higher rhodium concentration at the large reaction interface. However, at higher conversions significant rhodium leaching occurred accompanied by significant depletion of the supported ionic liquid layer. Recently, Rh–TPPTS/SILP catalysts have also been prepared by immobilising the complexes in the ionic liquids [BMIM][$PF_6$], [BMIM][$BF_4$], and

*Anders Riisager was born in Glostrup, Denmark in 1973. He finished his Master studies in chemistry at the University of Copenhagen in 1999 with a thesis on metal-templated amino acid synthesis. In the same year he started his Ph.D. on immobilisation of biphasic hydroformylation catalyst systems by use of SAP and SILP methodologies at the Interdisciplinary Research Center for Catalysis (ICAT) and Department of Chemistry at the Technical University of Denmark with Prof. Rasmus Fehrmann. In the period 2002–2005 he continued the work on SILP catalysis and examined other phase-separable ionic liquid systems in a postdoctoral research project with the group of Prof. Peter Wasserscheid at RWTH Aachen (later University of Erlangen-Nürnberg), Germany. Currently he is employed as Assistant Professor at the Department of Chemistry, Technical University of Denmark, where his main research interests are focused on further developments of the concept of supported ionic liquid phase catalysis.*

*Rasmus Fehrmann was born in Denmark in 1948. He studied Chemical Engineering at the Technical University of Denmark (DTU), where he received his master degree (M.Sc. Eng.) in 1973 and his Ph.D. degree in 1976 at the Department of Chemistry. In 1977 and 1979 he was awarded candidate and senior scholarships, respectively, from DTU and during the years 1981–1985 he held postdoctoral positions at the Institute of Catalysis, Novosibirsk (Russia), Université de Provence, Marseille (France), and University of Patras (Greece) in addition to periods at the Department of Chemistry, DTU, where he has been Associate Professor since 1986. In 1997 he was visiting professor at Georgia Institute of Technology (USA), and since 2000 he has been a member of the Danish National Committee for Chemistry. Administratively, he has been a member of the board and assistant head of the Department of Chemistry, DTU, since 1987. His main research interests have been in the field of inorganic molten salt chemistry, complex formation in ionic media and, with increasing importance, also within the areas of molten salt catalysis, environmental catalysis, and catalysis in ionic liquids with emphasis on performance and mechanistic understanding of industrial catalysts and model systems.*

*Marco Haumann was born 1969 in Dortmund, Germany. After preliminary studies in mechanical engineering in Dortmund he moved to TU Berlin where he studied chemistry until 1998. He finished his Ph.D. thesis in the group of Prof. Schomäcker on hydroformylation in microemulsions in 2001. In 2002 he started a postdoctoral research project funded by Sasol Technology, Pty, Ltd. at the University of Cape Town (Prof. John R. Moss) aiming at the synthesis of novel cobalt-based catalysts. At the end of 2002 he moved to Rand Afrikaans University in Johannesburg (Prof. Andre Roodt) to study the mechanism of cobalt phosphite catalysed hydroformylation. Since 12/2003 he has been employed as a research assistant in the group of Prof. Peter Wasserscheid. His main research interests are in the field of homogeneous catalyst immobilisation using the Supported Ionic Liquid Phase (SILP) concept and reaction engineering aspects of this innovative technology.*

*Peter Wasserscheid was born 1970 in Würzburg, Germany. He studied chemistry at the RWTH Aachen from 4/1991 till 3/1995. After his Ph.D. thesis with Prof. Willi Keim (10/1995–5/1998) he worked as an industrial post-doc for four months at BP/Sunbury, GB. Returning to RWTH Aachen, he carried out his Habilitation (08/1998–10/2002) at the Institute of Technical and Macromolecular Chemistry (ITMC) entitled "Ionic liquids – a new Solvent Concept for Catalysis". Since 10/2003 Peter Wasserscheid has been full professor for Chemical Reaction Engineering at the University of Erlangen-Nürnberg, Germany. He has been awarded several research prizes including the Carl-Zerbe award of DGMK (2000), the DECHEMA award of the Max-Buchner Forschungsstiftung (2001), and the "Innovation award of the German Industry" (with Solvent Innovation GmbH, Cologne) (2003). Together with Tom Welton he edited the monograph "Ionic Liquids in Synthesis" (Wiley-VCH, 2003). His main research interests are in the field of ionic liquid chemistry and in the application of advanced materials in continuous catalytic processes.*

 © 2006 Wiley-VCH Verlag GmbH & Co. KGaA, Weinheim 

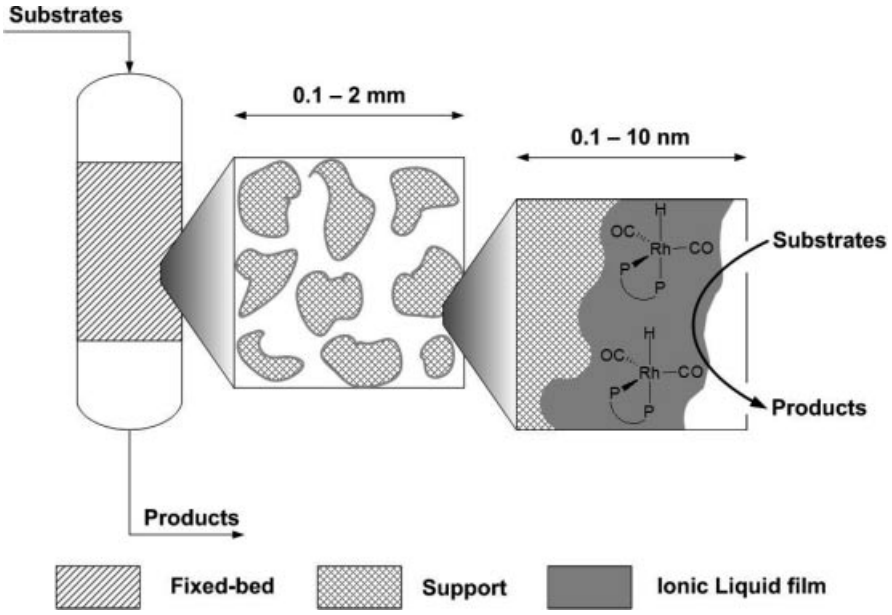


Figure 1. Schematic illustration of Supported Ionic Liquid Phase (SILP) catalysts for fixed-bed reactor technology.

tetramethylguanidinium lactate (TMGL) supported on mesoporous MCM-41.[13] The catalytic performance of these catalysts was investigated in hydroformylation of different alkenes ($C_6$ to $C_{12}$), and the SILP catalysts were further characterised by various methods. $^{31}P$ NMR spectroscopic data revealed that the Rh–TPPTS complex formation in the SILP system occurred in a similar way to that in an aqueous solution, clearly indicating the homogeneous nature of Rh/SILP catalyst systems. Using the specific combination of TMGL ionic liquid and MCM-41 support the leaching problem was here claimed to be negligible, most likely because of the slightly coordinating ability of the ionic liquid to the rhodium atom. Notable, however, in none of the above examples has a combination of good catalyst durability and high product selectivity towards linear aldehyde been demonstrated.

In this Microreview the advantages of SILP catalysis are exemplified for the Rh-phosphane catalysed, continuous gas-phase hydroformylation of propene. The Rh/SILP catalysts employed in the study contained 1-butyl-3-methylimidazolium-based ionic liquids and the phosphane ligands shown in Scheme 1. The involved ligands comprised both mono- and bisphosphanes modified with ionic groups. All the Rh(phosphane)/SILP systems, which can be stored under argon over several months, were prepared using impregnation by dissolving appropriate amounts of catalyst precursor, ligand, and ionic liquid in dried methanol, followed

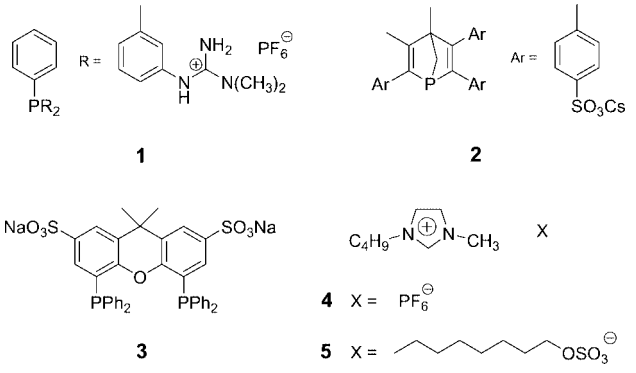


Scheme 1. Phosphane ligands and ionic liquids applied in the study.

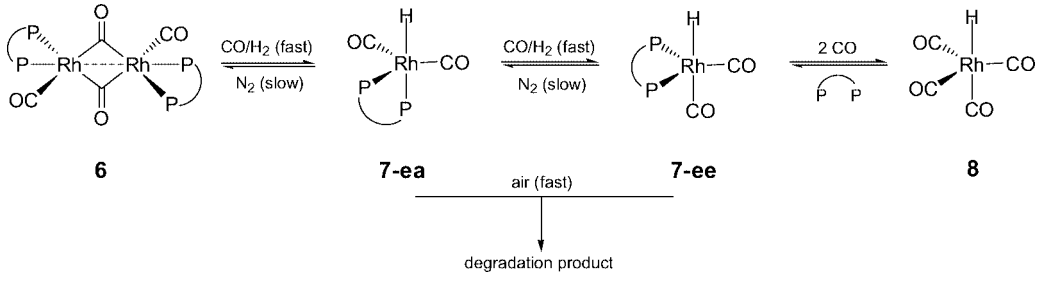


Scheme 2. Reaction scheme for Rh(**3**) complexes.

 © 2006 Wiley-VCH Verlag GmbH & Co. KGaA, Weinheim 

by addition of dried support material and removal of methanol in vacuo (details about materials and methods are described in previous reports[7,14,15]). The catalysts are characterised by the nature of the support, the ionic liquid loading *α* (ratio ionic liquid volume/support pore volume), the rhodium content (mass ratio rhodium/support) and the molar ligand/rhodium ratio (L/Rh).

The $[Rh(\mu\text{-}CO)(\mathbf{3})(CO)]_2$ precursor **6** (see Scheme 2), dissolved in ionic liquid [BMIM][$PF_6$], has been investigated by van Leeuwen et al. in the hydroformylation of 1-octene.[16] In-situ high-pressure IR and NMR studies indicated that the formation of the active catalyst complex **7** occurred in a similar fashion to the formation in organic solvents.[17] Beside these studies, detailed mechanistic understanding of homogeneous catalysis in ionic liquids is still scarce.[18]

## Catalyst Composition Studies

### Variation of Support Material

As a first approach, different commercially available porous, high-area supports were used to prepare Rh(phosphane)/SILP catalyst systems containing the same type of ionic liquid and ligand content.[14] Table 1 compiles the support characteristics and Figure 2 shows the performance of the Rh(**3**)/SILP catalysts with regard to activity (turn-over frequency, TOF) and aldehyde selectivity (% *n*-butanal).

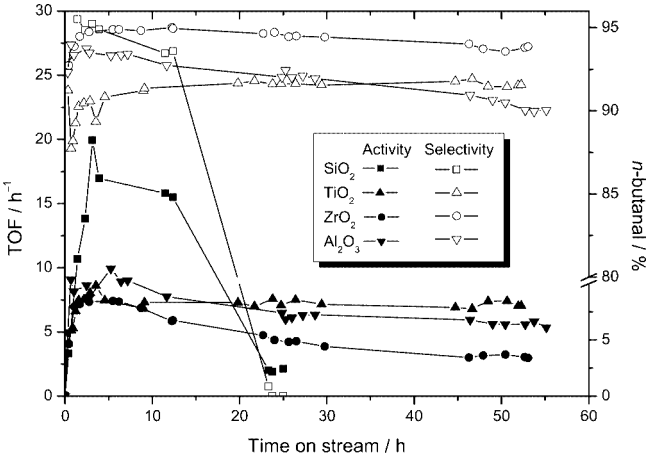


Figure 2. Propene hydroformylation activities and selectivities of Rh(**3**)/SILP catalyst systems.

Among the examined catalysts, the Rh(phosphane)/$SiO_2$/SILP catalysts revealed the highest initial activity (TOF = 21 $h^{-1}$) and selectivity (95% *n*-butanal), but deactivated almost completely within 24 h on stream ending up with very low activity and only half the initial selectivity. The Rh(phosphane)/$Al_2O_3$/SILP and Rh(phosphane)/$ZrO_2$/SILP catalysts had both a lower initial activity and selectivity than the $SiO_2$-based system but deactivated only slightly at prolonged reaction (55 h). The most stable system examined was the Rh(phosphane)/$TiO_2$/SILP catalyst which maintained the initial (but rather poor) performance over 55 h, showing no sign of deactivation. It should be noted that the ionic liquid loading differed for the various systems which made the comparison of the absolute catalyst activities difficult. Though, a trend appeared to be that higher pore volume of the support had a more pronounced effect on the initial activity of the resultant catalyst than the BET surface area. The use of supports with both low pore volume and BET area (i.e. $Al_2O_3$ and $ZrO_2$) apparently resulted in the least active SILP catalysts.

The different SILP catalysts were analysed by FT-IR prior to and after reaction. After short-term reactions, all SILP catalysts revealed CO stretching bands at ν(CO) ≈ 1998 and 1940 $cm^{-1}$, corresponding to the presence of catalytically active $[HRh(\mathbf{3})(CO)_2]$ complexes (examples are shown in Figure 3 for $TiO_2$ catalysts). However, only the FT-IR spectra of the used Rh(phosphane)/$TiO_2$/SILP cata-

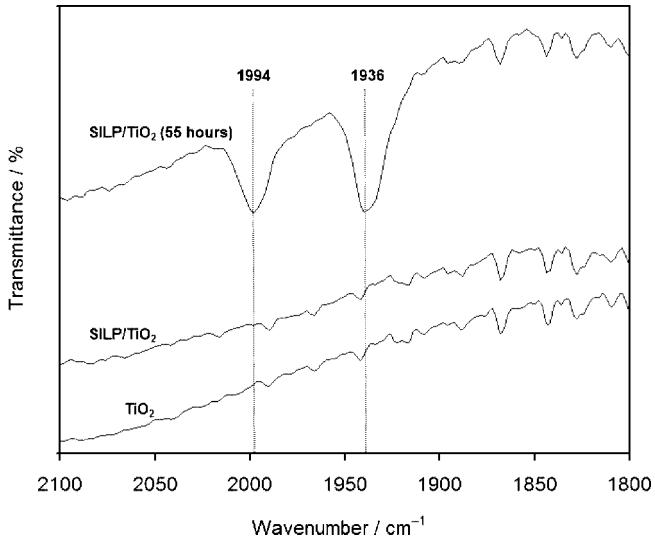


Figure 3. FT-IR spectra of $TiO_2$-based Rh(**3**)/SILP catalyst system.

Table 1. Support material used for SILP-catalysed hydroformylation of propene.[a]

| | $SiO_2$ | $Al_2O_3$ | $TiO_2$ | $ZrO_2$[b] |
|---|---|---|---|---|
| Supplier | Merck | Merck | Millennium Co. | MEL Chemicals |
| Trade name | Silica gel 100 | Alumina 90 neutral | TIONA-G5 anatase | MELCAT XZO-882 |
| BET area [$m^2 \cdot g^{-1}$] | 298 | 103 | 309 | 100 |
| Pore volume [$cm^3 \cdot g^{-1}$] | 1.02 | 0.25 | 0.37 | 0.13 |
| Mean pore diameter [Å] | 137 | 98 | 47 | 50 |
| Particle size [μm] | 63–200 | 63–200 | n/a | 15[c] |

[a] The BET surface areas, pore volumes, and pore diameters were determined by nitrogen adsorption/desorption experiments and are reproduced from ref.[14] [b] Obtained by calcination of $Zr(OH)_4 \cdot xH_2O$ (500 °C, 15 h). [c] Corresponds to the 50% fractile.

 © 2006 Wiley-VCH Verlag GmbH & Co. KGaA, Weinheim 

lyst exhibited bands at ν(CO) = 1994 and 1936 $cm^{-1}$ after 55 h on-stream. In contrast, the analogous CO bands for the Rh(phosphane)/$SiO_2$/SILP catalyst gradually disappeared after only 4 h in use and were not present after 55 h of reaction.

For all SILP catalysts additional bands in the 1700–2100 $cm^{-1}$ region corresponding to bridging CO ligands, indicative of formation of inactive dimer or cluster compounds, were not observed. Hence, it was concluded that the deactivation was caused by a support effect. Because of the highest initial catalyst activity and selectivity, $SiO_2$ was used as the support material in all further experiments.

### Variation of Ligand and Ionic Liquid

In homogeneous hydroformylation with rhodium–phosphane catalysts the nature of the involved ligands are known to have a large influence on the catalytic performance of the resultant catalyst.[19] Generally, this is attributed to a combination of electronic and steric factors induced by the ligands to the metal atom thereby altering its coordination chemistry.

The effect of the phosphane ligand and of the ligand content (i.e. L/Rh ratio) contained in the SILP catalysts were evaluated by determining the catalytic performance of SILP catalysts containing the different ligands **1**–**3** (see Scheme 1).[7] These ligands are based on triphenylphosphane, bridged phosphinane (both monodentate), and diphenyl-xantphos (bidentate) backbones, respectively. The obtained results are summarised in Table 2.

Table 2. Catalytic performance of Rh(L)/$SiO_2$/SILP systems with different types of ligand and L/Rh ratios.

| Entry | L | L/Rh | $\alpha$[a] | TOF [$h^{-1}$] | *n*/iso | *n*-Butanal [%] |
|---|---|---|---|---|---|---|
| 1 | – | – | 0.76 | 0.0 | – | – |
| 2 | **1** | 2.9 | 0.00 | 55.5 | 0.9 | 47.4 |
| 3 | **1** | 2.9 | 0.33 | 3.7 | 1.0 | 50.0 |
| 4 | **1** | 2.9 | 0.78 | 20.6 | 0.9 | 47.4 |
| 5 | **1** | 2.9 | 1.00 | 16.8 | 1.0 | 50.0 |
| 6 | **2** | 2.9 | 0.00 | 114.8 | 1.0 | 50.0 |
| 7 | **2** | 2.9 | 0.30 | 6.9 | 0.9 | 47.4 |
| 8 | **2** | 2.9 | 0.78 | 38.0 | 0.9 | 47.4 |
| 9 | **2** | 2.9 | 1.00 | 30.5 | 0.9 | 47.4 |
| 10 | **2** | 11.3 | 0.05 | 88.4 | 2.0 | 66.7 |
| 11 | **2** | 11.3 | 0.15 | 79.4 | 1.3 | 56.5 |
| 12 | **2** | 21.4 | 0.00 | 45.8 | 2.8 | 73.8 |
| 13 | **2** | 21.3 | 0.05 | 28.2 | 2.6 | 72.2 |
| 14 | **3** | 2.5 | 0.00 | 37.4 | 1.7 | 63.0 |
| 15 | **3** | 2.4 | 0.17 | 1.5 | 1.8 | 64.0 |
| 16 | **3** | 2.5 | 0.49 | 5.1 | 2.0 | 66.4 |
| 17 | **3** | 10.2 | 0.00 | 40.8 | 16.9 | 94.4 |
| 18 | **3** | 10.0 | 0.08 | 37.0 | 23.3 | 95.9 |
| 19 | **3** | 10.0 | 0.18 | 34.9 | 22.6 | 95.8 |
| 20 | **3** | 10.0 | 0.52 | 25.4 | 22.0 | 95.6 |
| 21 | **3** | 20.0 | 0.20 | 16.7 | 23.7 | 96.0 |
| 22[b] | – | – | 0.51 | 0.2 | 1.0 | 50.0 |
| 23[b] | **3** | 2.5 | 0.52 | 6.4 | 1.9 | 65.4 |
| 24[b] | **3** | 10.0 | 0.50 | 17.9 | 18.6 | 94.9 |

[a] Ionic liquid loading, $\alpha$ = ratio of ionic liquid volume to support pore volume. [b] Ionic liquid = [BMIM][*n*-$C_8H_{17}O$–$SO_3$]. All other catalysts were based on [BMIM][$PF_6$].

For the monophosphane catalysts the obtained selectivities were significantly lower than for analogous bis(phosphane) catalysts, as expected, with only 47–74% linear aldehyde being formed compared to typically 94–96% for the Rh(**3**) catalyst at identical catalyst composition. Furthermore, an increase in mono(phosphane) ligand content generally resulted in less active but more selective SILP catalysts (e.g. Entries 10 and 13). The effect on the selectivity was, however, less pronounced at very large excess of ligand, i.e. with L/Rh ratio of 21.4 (Entry 13), but remained significantly negative for the activity. Thus, the optimal L/Rh ratio for the mono(phosphane) **2** catalysts was found to be around 10.

The same ligand content trend observed for the catalysts based on ligands **1** or **2** was also observed for the catalysts containing the bidentate ligand **3** (Entries 15, 19, and 21). Additionally, for the Rh(**3**) catalysts with low L/Rh ratios of 2.5 the activity was found to be high only for the ionic-liquid-free system (Entry 14), while selectivities towards linear aldehyde were low in all reactions regardless of ionic liquid loading (Entries 14–16). This catalytic behaviour differed from the one observed with Rh(**3**) catalyst solutions in ionic liquid/organic and aqueous/organic biphasic systems, where catalysts having L/Rh ratios of 5 yielded product linearity > 97%.[20] Increasing the L/Rh ratio to 10 and 20 resulted in high linearities of 94.4–96.0%, similar to the ones for biphasic catalysis. Furthermore, for L/Rh ratios of 10 the activities were reasonably high with TOFs between 25 and 41 $h^{-1}$, depending on the liquid loading (Entries 17–20). Here the optimal L/Rh ratio was also found to be 10, indicating a support–ligand interaction which reduced the effective ligand excess for all three types of ligand-based catalysts. All consecutive experiments were carried out using ligand **3** with an L/Rh ratio of 10.

With respect to the ionic liquid in the catalysts, the ionic liquid [BMIM][$PF_6$] itself was not catalytically active in the hydroformylation (Entry 1), as expected. The degree of pore filling, indicated by the ionic liquid loading ($\alpha$), had, however, a significant effect on the activity of all three catalyst systems applied, revealing a decreasing activity with increasing liquid loading. Thus, for the mono(phosphane) ligand systems the highest initial activity was obtained in the absence of ionic liquid (Entries 2, 6, and 12), which might be attributed to the formation of surface-bound rhodium species exhibiting high activities and to the absence of any mass-transport-limiting factors in these purely heterogeneous catalysts. However, for catalysts with $\alpha$ values about 0.3 (Entries 3 and 7) exceptionally low activities were obtained for ligands **1** and **2**, the reason for this being at present not clear. For Rh(**3**) catalysts the highest initial activity was also obtained in the absence of ionic liquid (Entry 17). Moreover, a linear dependence between the decrease in activity and the ionic liquid loading could be correlated with results from nitrogen absorption studies, where the catalyst pore volume was found to decrease proportionally with the different ionic liquid loadings.[21]

In contrast to the ionic liquid content, the nature of the ionic liquid anion had essentially no influence on the SILP

 © 2006 Wiley-VCH Verlag GmbH & Co. KGaA, Weinheim 

catalyst performance. Thus, upon replacing [BMIM][$PF_6$] with the halogen-free ionic liquid [BMIM][$n$-$C_8H_{17}O$–$SO_3$] similar activities and selectivities were observed (Entries 16 and 23, and 20 and 24). Hence, in consecutive experiments catalysts containing [BMIM][$n$-$C_8H_{17}O$–$SO_3$] were applied, and the ionic liquid loading was maintained at $\alpha = 0.1$ in order to achieve high pore volume and large reaction surface area.

## Catalyst Stability Studies

### Support Pretreatment

From the results obtained in the catalyst composition studies (see above) it became obvious that ligand–support interactions probably were responsible for catalyst instability. In the case of titania catalysts, where the support contained practically no Brønsted acidic sites, long catalyst lifetimes beyond 50 h of reaction were achieved, whereas catalysts based on more Brønsted-acidic silica gel support deactivated relatively fast, indicated by loss of both activity and selectivity. In order to examine the effect of the support acidity, acidic sites on the silica gel support were reduced before use by thermal dehydroxylation of the support (500 °C, 15 h). Subsequently, using dehydroxylated silica catalysts with L/Rh ratio of 10 and ionic liquid loadings of $\alpha = 0.1$, the SILP catalyst systems proved stable over 60 h, as shown in Figure 4 for an Rh(**3**) catalyst.[15]

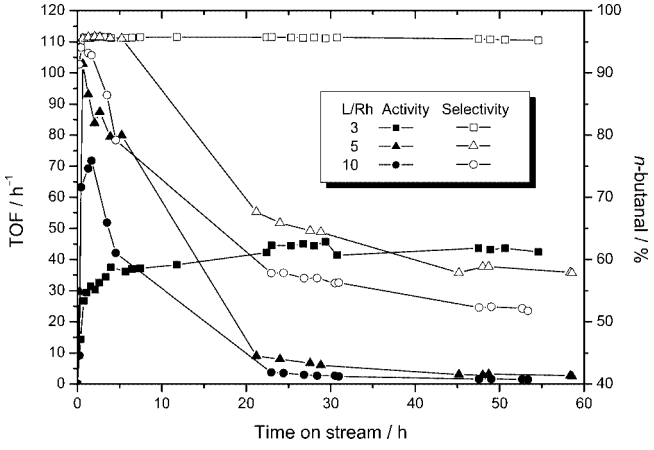


Figure 4. Propene hydroformylation activity and selectivity of Rh(**3**) silica-based SILP catalysts ($\alpha = 0.1$) as a function of **3**/Rh ratios.

The catalytic performance and catalyst stability, however, still proved to be significantly influenced by the ligand excess, as also shown in Figure 4. Rh(**3**) catalysts having low ligand contents (**3**/Rh ratios of 3 and 5) were initially very active compared to the catalyst with **3**/Rh ratio of 10 but less selective, and deactivated furthermore within the first 24 h of reaction resulting in very low catalytic performance (TOF = 4–5 $h^{-1}$, $n$/iso ratio = 1–1.3). In contrast, catalysts with a high ligand content (**3**/Rh ratios ≥ 10) retained the initial catalytic performance with significantly higher activity (TOF = 44 $h^{-1}$) and selectivity ($n$/iso ratio > 20) during prolonged (60 h) reactions. These results clearly indicated that a large excess of ligand was required to obtain a stable SILP catalytic system. Even after the thermal pretreatment, which induced a considerable removal of acidic surface sites, support–ligand reactions apparently still lowered the amount of effective ligand excess necessary for complex formation.

Beside the ligand content, the amount of ionic liquid also influenced the catalytic performance of catalysts based on the pretreated silica support, clearly signifying the importance of the ionic liquid solvent. Thus, varying the amount of ionic liquid loading ($\alpha = 0$–$0.5$), the catalyst systems containing no ionic liquid deactivated rapidly; only 30% of the initial activity and selectivity remained after 60 h of reaction time. The deactivation could be explained by surface diffusion of ligand **3** from the initially Rh-coordinated active state to the stronger surface-bonded state, in which the metal atom was less coordinated to the ligand but possibly more strongly coordinated to the support and thus less active and selective. Evidently, the Rh(**3**)/SILP catalysts required a certain amount of ionic liquid solvent; not only to provide a high selectivity but also to retain long-term stability during continuous processes.

Further, since the hydroformylation product selectivity with respect to aldehydes is known to depend on the available amount of ligand for coordination,[22] the simultaneous decrease in selectivity along with activity indicated that deactivation was closely related to a gradual degradation and removal of ligand from the catalyst complex system. The presence of surface–ligand interaction in the pretreated Rh(**3**) catalyst (**3**/Rh = 10) was confirmed by solid-state MAS $^{31}P$ NMR spectra recorded prior to reaction, as shown in Figure 5. Here, signals corresponding to free ligand ($\delta$ = –13 ppm, 27%), surface-bonded ligand ($\delta$ = –21 ppm, 54%), and complexed ligand ($\delta$ = 31 ppm, 19%) were found.[15]

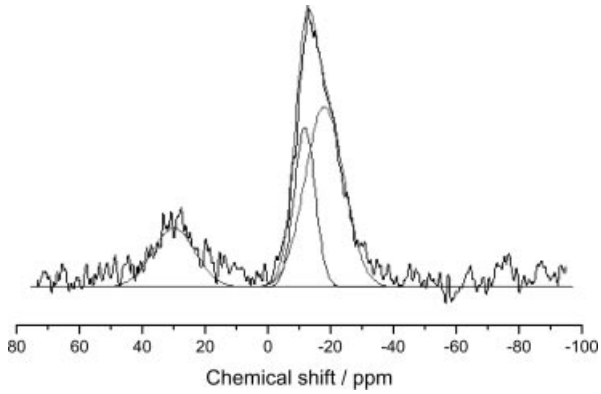


Figure 5. MAS $^{31}P$ NMR spectra and deconvoluted spectra of prepared Rh(**3**)/$SiO_2$/SILP catalyst (**3**/Rh ratio = 10). $\delta_1$ = –21 ppm, 54%, support-bonded **3**; $\delta_2$ = –13 ppm, 27%, **3**; $\delta_3$ = 31 ppm, 19%, complex-bonded **3**.

Additional explanation of the observed catalytic results was obtained from in-situ FT-IR measurements of complex formation at 100 °C and atmospheric pressure. In Figure 6 the FT-IR spectra of the catalyst with **3**/Rh = 10 under (a)

 © 2006 Wiley-VCH Verlag GmbH & Co. KGaA, Weinheim 

nitrogen, (b) after 15 min, and (c) 30 min exposure to syngas ($CO/H_2$ = 1:1) are shown. They indicate the relatively fast transformation (Scheme 2) from the pale-red dimeric complex [Rh(μ-CO)(**3**)(CO)]$_2$ (**6**) [$\nu$(CO) = 1990 (br.) cm$^{-1}$], which is a nonactive, stable state of the catalyst, to the light-yellow precatalytic monomeric HRh(CO)$_2$(**3**) ea- and ee-isomeric complexes **7-ea** [ν(CO) = 1994, 1948 cm$^{-1}$] and **7-ee** [ν(CO) = 2035 (w), 1964 cm$^{-1}$], which co-exist in dynamic equilibrium.[15]

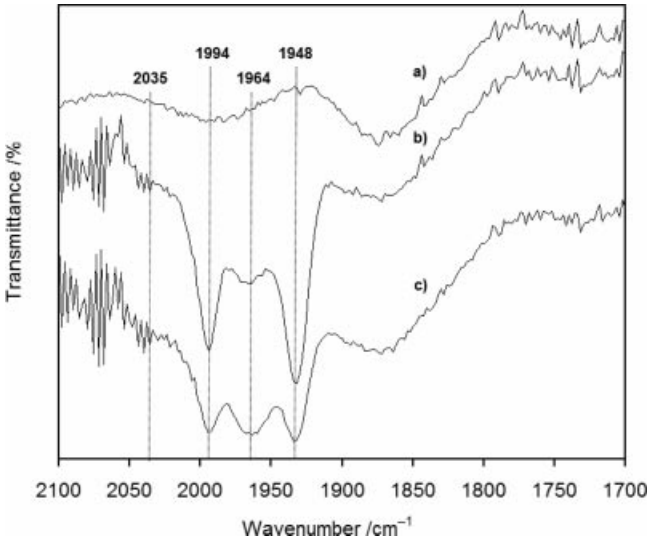


Figure 6. Part of FT-IR spectra of Rh(**3**)/$SiO_2$/SILP catalysts (**3**/Rh = 10, $\alpha$ = 0.5) at 100 °C after (a) 15 min nitrogen exposure, (b) 15 min syngas exposure, and (c) 30 min syngas exposure.

Re-exposure of the **7-ea/7-ee** isomeric mixture to inert gas slowly regenerated the dimer **6** reversibly, while air treatment presumably led to irreversible complex degradation and oxidation of excess ligand. The degradation product was dark yellow and had a broad CO band at ν(CO) = 1972 cm$^{-1}$. Importantly, the complex formation in the Rh(**3**)/$SiO_2$/SILP catalysts having **3**/Rh ratio of ≥ 10 were very similar to what previously has been reported for Rh(**3**) and analogous Rh(xanthene-based ligand) systems in ionic liquids[16] and organic solvents,[23] as shown in Table 3. Thus, it seemed reasonable to conclude that the Rh(**3**) complex was formed in the ionic liquid film and that the examined SILP hydroformylation reactions were indeed of purely homogeneous nature.[15]

In the FT-IR spectra recorded of the analogous catalysts with **3**/Rh ratios of 3 and 5, the degradation product was (in sharp contrast to the catalysts with high ligand content) irreversibly formed independent of the gas treatment, and was significantly more pronounced for catalysts with **3**/Rh = 3 than for catalysts having **3**/Rh = 5. This clearly suggested that an insufficient excess of ligand **3** was present in these systems with low ligand content to maintain the equilibrium between the modified hydrido complex **7** and the unmodified hydrido complex **8** in favour of complex **7**, as shown in Scheme 2. This was in excellent accordance with the relative catalyst selectivities and stabilities measured, since the unmodified hydrido complex provided low selectivity (*n*/iso ratio ≈ 2) and facilitated formation of inactive clusters at the modest CO partial pressure applied. Hence, it seemed unambiguously justified that the SILP catalyst stability was directly connected to the complex degradation reaction, which additionally seemed to be correlated to the amount of accessible ligand available for complex formation in the systems.

The content of acidic support OH groups (mostly Brønsted sites) contained in the partly dehydroxylated silica support was evaluated by ammonia temperature-programmed desorption (TPD) to be 69 μmol OH/g support, corresponding to 26% of the original content present in the untreated support. This was in relatively good agreement with the remaining fraction of 35% Si–OH groups (Q3, $\delta$ ≈ 100 ppm) relative to Si–O–Si groups (Q4, $\delta$ ≈ 111 ppm) measured by solid-state MAS $^{29}$Si NMR spectroscopy for analogous samples. Therefore, it seemed reasonable to assume that the applied pretreatment decreased the amount of acidic support OH groups only by dehydroxylation of surface silanol groups thereby causing no significant structural changes of the support. This was further affirmed by the identical $T_{max}$ values obtained for ammonia desorption (i.e. desorption sites are identical), and by the practically unchanged BET surface area and pore volume after dehydroxylation.

As a consequence, it should therefore be anticipated that highly stable SILP catalysts could only be obtained in those cases where the ligand content was sufficient to compensate the loss induced by the surface bonding as shown in Table 4. This was in excellent agreement with the experimental data from the catalytic reactions, thus clearly showing that the relative content of acidic support OH groups most probably was the key factor determining the long-term stability for silica-support-based Rh(phosphane)/SILP catalysts.[15]

Table 4. Effective L/Rh ratios in SILP-catalysed hydroformylation using pretreated silica.

| L/Rh | $c_{L,eff}$ [μmol g$^{-1}$] | free L [%] | $(L/Rh)_{eff}$ |
|---|---|---|---|
| 3 | 58 | 0 | <1 |
| 5 | 97 | 30 | 1.5 |
| 10 | 194 | 65 | 6.5 |

Table 3. Comparison of IR $\nu$(CO) bands in HRh(CO)$_2$(L) complexes in different systems.

| Complex system | Solvent | ν(CO) ea isomer [cm$^{-1}$] | ν(CO) ee isomer [cm$^{-1}$] | Ref. |
|---|---|---|---|---|
| Rh(**3**)/$SiO_2$/SILP | [BMIM][*n*-$C_8H_{17}O$–$SO_3$] | 1994, 1948 | 2035(w), 1964 | [15] |
| HRh(CO)$_2$(**3**) | [BMIM][$PF_6$] | 1985, 1935 | 2032, 1967 | [16] |
| HRh(CO)$_2$(xantphos) | benzene | 1991, 1941 | 2036, 1969 | [23] |
| HRh(CO)$_2$(thixantphos) | cyclohexane | 1999, 1953 | 2040, 1977 | [23] |

 © 2006 Wiley-VCH Verlag GmbH & Co. KGaA, Weinheim 

### Deactivation/Reactivation Assessment

All the stability measurements of the Rh(**3**)/SILP catalyst discussed so far were initially studied at 100 °C and 10 bar syngas pressure ($H_2$/CO = 1:1) over a period of up to 36 h. This time on-stream was further extended to 180 h to test the long-term stability of the Rh(**3**) dehydroxylated catalyst system.[24]

In the extended reaction period the selectivity towards linear butanal remained constant around 95% (*n*/iso = 19), whereas the TOFs slightly decreased over time, corresponding to a total loss in activity of 17% or 0.1% per hour. Since the selectivity remained unchanged it was excluded that deactivation was caused by catalyst decomposition, as observed in the previous studies when using low L/Rh ratios.[7,14,15] ICP (inductively coupled plasma) analyses of the exit gas streams condensed by liquid nitrogen further established the rhodium contents to be below the detection limit of 3 ppm. Instead, the formation of high-boiling side-products, dissolving in the ionic liquid layer during reaction causing a lowering in the effective rhodium concentration, was suspected to be the reason of the slow activity decrease measured. Furthermore, the film thickness might be increased and smaller pores flooded, which would lead to a lower reaction surface. To confirm this hypothesis, the gas flow was temporary stopped after 180 h on-stream and the reaction setup evacuated for 10 min at 100 °C. When the experiment was continued after this procedure, the activity had indeed increased by 80% from initially 60 to 108 $h^{-1}$. Within the next 20 h of reaction the TOFs decreased again from 108 $h^{-1}$ to 76 $h^{-1}$ and the selectivity was re-established at 95% *n*-butanal. A second vacuum period of 10 min resulted in improved TOFs, as depicted in Figure 7. In both cases the observed "overshooting" of the activity directly after evacuation might be caused by either simultaneous removal of CO ligand of the Rh complex leading to higher activity or a rearrangement of the active surface due to sudden evaporation of dissolved heavies. In the first case a lower selectivity would be expected which was indeed observed directly after the evacuation. Thereafter, the catalyst solution was resaturated with CO gas and both the activity and the selectivity approached the initial levels.

The findings from the evacuation experiment confirmed the interpretation that the observed slight deactivation over time was not due to catalyst decomposition, as an accompanying decrease in activity and selectivity otherwise would have been observed. Instead, we expected the formation of 2-ethylhexanal and 2-ethylhexanol to be of relevance, as traces of these high-boiling side products were observed at particular high conversions.

To support this interpretation the deactivated catalyst was removed from the reactor and the pale yellow catalyst particles placed in two round-bottomed flasks containing cyclohexane and ethanol, respectively. Immediately, the ethanol solution became orange whereas the cyclohexane solution remained colourless, indicating that the ethanol wash led to removal of the ionic catalyst phase from the support while the cyclohexane wash did not. Both solutions were subsequently analysed by means of GC-MS (ethanol solution after distillation and separation of nonvolatile ionic liquid fragments), where content of small amounts of by-products 1-butanol, 2-ethylhexanal, and 2-ethylhexanol were confirmed, as expected. Additionally, IR analysis of both used and unused Rh/SILP catalysts was carried out. The used catalyst showed an absorbance band at 1730 $cm^{-1}$ (corresponding to the C=O stretching frequency) clearly indicating the presence of aldehydes in the catalyst.

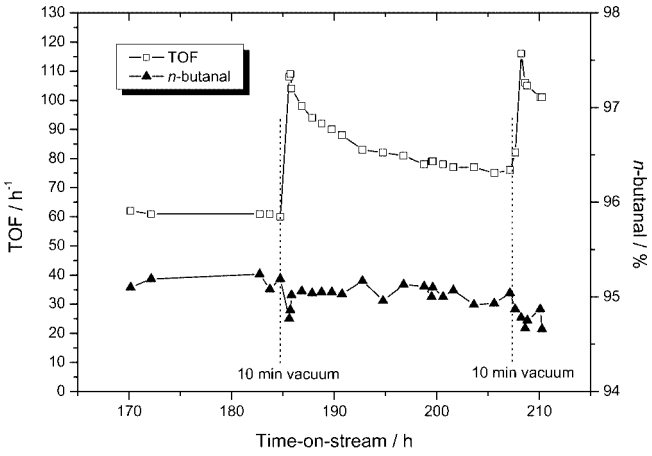


Figure 7. Reactivation of Rh(**3**)/$SiO_2$/SILP catalyst by consecutive application of vacuum. 100 °C, 10 bar syngas.

## Kinetic Studies

Long-term stability and kinetic experiments have been conducted in order to further prove the findings from the catalyst composition studies with Rh(**3**) catalysts. For these studies a continuous reactor setup equipped with online gas chromatography, described in detail previously, has been applied.[24] The general rate law for the hydroformylation of propene was assumed to be

$$r = k \cdot p^{n}_{\text{propene}} \cdot p^{x}_{\text{H}_2} \cdot p^{y}_{\text{CO}}$$

### Differential, Integral, and Arrhenius Analysis

In the first kinetic experiments the substrate concentration was varied by changing the propene partial pressure $p_{\text{propene}}$ in the feed gas (at constant total pressure) between 0.9 and 3.2 bar at temperatures in the range of 65–140 °C. In Figure 8 the obtained results are compiled.

As expected, the highest catalyst activities (corresponding to TOFs of about 500 $h^{-1}$) and the lowest selectivities (down to 88% linearity) were obtained at high propene partial pressure and high temperature. However, the activities at 140 °C were not as high as expected assuming a normal Arrhenius temperature dependence, which was attributed to the formation of high-boiling by-products dissolved in the ionic liquid layer, thus lowering the effective catalyst concentration (see "deactivation/reactivation assessment"). The rate constants *k* were derived from differential analyses of the data, and the reaction with respect to propene partial

 © 2006 Wiley-VCH Verlag GmbH & Co. KGaA, Weinheim 

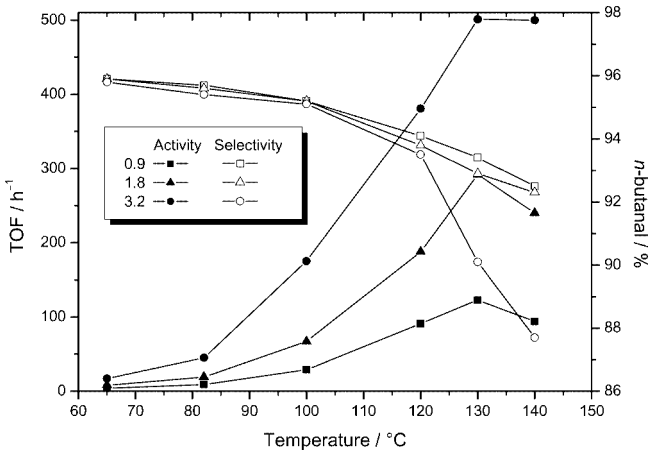


Figure 8. Activity and selectivity in Rh(**3**)/$SiO_2$/SILP-catalysed propene hydroformylation as a function of temperature and propene partial pressure.

pressure was determined to be of first order (i.e. $n = 1$). This dependency was similar to traditional organic and aqueous (phosphane)Rh-catalysed hydroformylation systems.[19]

At a constant propene partial pressure of 2.1 bar the residence time inside the catalyst bed was varied by altering the total reactant flow, as shown in Figure 9.

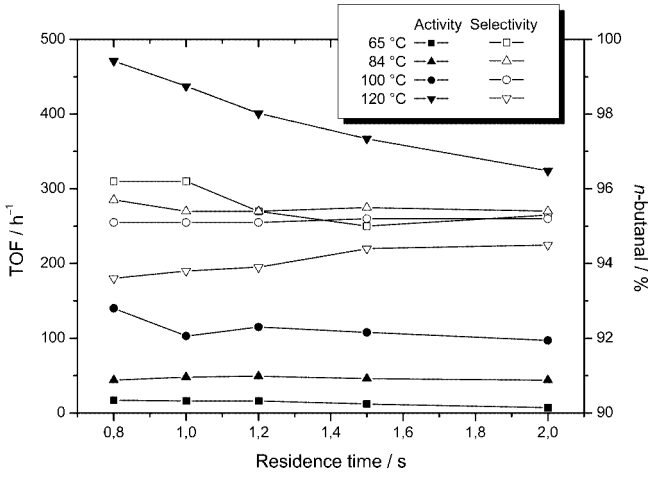


Figure 9. Activity and selectivity in Rh(**3**)/$SiO_2$/SILP-catalysed propene hydroformylation as a function of residence time.

The selectivity for the desired linear aldehyde was only influenced by temperature and not by residence time. Shorter residence times generally resulted in lower conversions, as expected. However, under nondifferential conditions at higher conversions the observed TOFs decreased slightly with longer residence times, due to lower mean levels of propene present in the reactor. An integral analysis of the data revealed the rate constants $k$ for the temperature range between 65 and 120 °C.

From the independent propene pressure and residence time experiments the activation energy was calculated from Arrhenius plots to be $63.3 \pm 2.1$ kJ·mol$^{-1}$. This value indicated that the Rh(**3**)/$SiO_2$/SILP catalyst was operating under kinetically controlled reaction conditions and added further proof to the homogeneous nature of the Rh/SILP catalyst as confirmed by spectroscopic studies (vide supra). In Table 5 the result obtained with the Rh(**3**)/SILP catalyst is compared with results for other rhodium-catalysed hydroformylations using sulfonated ligands in aqueous media and supported aqueous media.

Table 5. Comparison of results for Rh(**3**)/$SiO_2$/SILP hydroformylation with literature results.

| Substrate | Catalyst | $E_A$ [kJ·mol$^{-1}$] | Solvent | Support | Ref. |
|---|---|---|---|---|---|
| Propene | $HRh(CO)_2$(**3**) | 63.2 | IL[a] | $SiO_2$ | [20] |
| Propene | $HRh(CO)(L)_3$[b] | 77.0 | water | – | [21] |
| 1-Octene | $HRh(CO)(L)_3$[b] | 65.9 | water | – | [22] |
| 1-Octene | $HRh(CO)(L)_3$[b] | 71.0 | water | $SiO_2$ | [23] |
| Linalool | $HRh(CO)(L)_3$[b] | 60.7 | water | $SiO_2$ | [24] |
| 1-Dodecene | $HRh(CO)(L)_3$[b] | 72.8/70.9[c] | water[d] | – | [25] |

[a] Ionic liquid = [BMIM][$n$-$C_8H_{17}O$–$SO_3$]. [b] L = TPPTS. [c] Two different algorithms were used for data analysis. [d] CTAB (cetyltrimethylammonium bromide) surfactant used.

The activation energy of propene using Rh/SILP catalysts is slightly lower than the one determined by Mao et al. for $HRh(CO)(TPPTS)_3$ in water,[25] while the activation energy compared with $HRh(CO)(TPPTS)_3$ in supported aqueous phase (SAP) catalysis of higher alkenes[26–29] is in good agreement. This comparison provides additional evidence that the Rh/SILP catalyst truly acts as a homogeneous catalyst in the ionic liquid film immobilised on the silica.

### Variation in Syngas Composition and Total Pressure

In order to further assess the effect of parametrical changes to the Rh(**3**)/SILP hydroformylation system, the ratio between the partial pressures of hydrogen and carbon monoxide ($p_{H_2}/p_{CO}$ ratio) has been varied between 0.25 and 4 (at constant total pressure) in reactions performed at 65 and 100 °C.[24] Increasing the hydrogen partial pressure had a profound effect on the catalyst activity for both temperatures, as depicted in Figure 10.

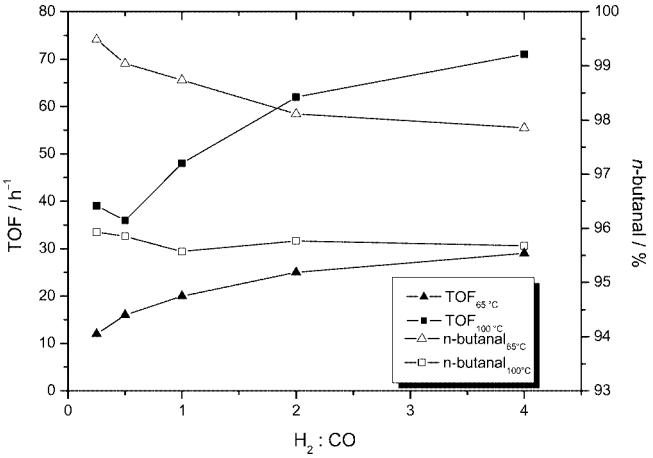


Figure 10. Activity of Rh(**3**)/$SiO_2$/SILP catalyst at different syngas compositions ($H_2$/CO ratios) and temperatures. 10 bar syngas pressure.

 © 2006 Wiley-VCH Verlag GmbH & Co. KGaA, Weinheim 

The positive effect of a high relative hydrogen pressure is well known in homogeneous hydroformylation[30] and can be derived from the generally accepted Wilkinson mechanism for ligand-modified rhodium catalysis,[31] in which the pre-equilibrium between dimer **6** and monomer **7** is shifted towards the active monomer **7** at higher partial pressures of hydrogen. Furthermore, the observed negative influence of high carbon monoxide partial pressures was also in accordance with this mechanism, in which the formation of catalytically active species requires the loss of CO during the cycle.[30,32] Thus, these findings provided further verification of the homogeneous nature of the Rh/SILP catalyst system.

At 100 °C the catalyst selectivity for *n*-butanal was practically independent of the $H_2$/CO ratio (< 0.5% variation), while the syngas ratio significantly influenced the selectivity at the lower temperature of 65 °C providing high selectivity of about 98% with an $H_2$/CO ratio of 4. Moreover, at 65 °C with a large excess of CO gas ($H_2$/CO = 0.25) *n*-butanal was formed exclusively with 99.5% selectivity (*n*/iso = 193). Such high selectivity has not previously been reported for Rh(**3**) catalyst systems in either homogeneous or biphasic reaction systems, normally performed in batch autoclaves. These results indicate the high potential of the SILP concept for obtaining a better mechanistic understanding in homogeneous catalysis, as exceptionally low steady-state conversions (impossible to realise in batch mode) can be adjusted in fixed-bed reactors. Additionally, the fixed-bed SILP catalytic concept allows a variety of reaction parameters to be altered over a broad range by using only small amounts of precious catalyst.

At a reaction temperature of 100 °C, the effect of the total syngas pressure $p_{total}$ on the catalyst performance was further examined by changing the pressure between 10 and 30 bar at fixed $p_{H_2}/p_{CO}$ pressure ratios.[24] From these pressure variations the reaction order with respect to hydrogen was determined to be $x = 0.4$ and the reaction order with respect to carbon monoxide to be $y = -0.4$. The selectivity remained nearly unchanged around 93% *n*-butanal for all experiments. By combining the obtained pressure dependencies for all of the three gases involved the general rate law for the propene hydroformylation using Rh(**3**)/$SiO_2$/SILP catalysts could therefore been established as

$$r = k \cdot p^{1}_{propene} \cdot p^{0.4}_{H_2} \cdot p^{-0.4}_{CO}$$

## Effect of Carbon Dioxide Cofeeding

Carbon dioxide gas is known to have high solubilities in most ionic liquids, lowering their viscosity and thus enhancing the diffusion of other gases.[33] In recent publications, the effect of super- and sub-critical $CO_2$ on hydrogen and oxygen solubilities has been reported.[34] In order to study the effect of $CO_2$ addition on the SILP-catalysed hydroformylation of propene, inert gas helium was replaced by a $CO_2$ cofeed corresponding to partial pressures between 1.8 and 36.4 bar.

From the results in Table 6 it became obvious that $CO_2$ indeed had a positive effect on the performance of the SILP catalyst. The initial activity obtained using helium could be increased by 2% at 1.8 bar $CO_2$ gas up to 35.1% at 36.4 bar $CO_2$ pressure. In contrast, the initial selectivity was not influenced by the $CO_2$ addition and remained constant around 94.5% throughout the experiments, and hydrogenation by-products could not be detected by GC analysis.

## Concluding Remarks

In this Microreview, we have described important progress in the very promising field of SILP catalysis, exemplified by the hydroformylation of propene. The long-term stability of Rh(**3**)/[BMIM][*n*-$C_8H_{17}O$–$SO_3$] catalysts supported on partly dehydroxylated silica was demonstrated, and clear spectroscopic evidence for the homogeneous nature of the catalysis in the supported ionic liquid layer was presented. Moreover, the prerequisite for obtaining active, highly selective, and Rh(**3**)/SILP hydroformylation catalysts with long-term stability was established to involve both the presence of an ionic liquid solvent and the content of a relatively large excess of phosphane ligand to compensate for some detrimental surface activity. The activation energy of 63.3 ± 2.1 kJ·mol$^{-1}$ added evidence that the catalyst was indeed homogeneous, i.e. a complex dissolved in an ionic liquid film on a support. Furthermore, the Rh/SILP catalyst performed similarly to a homogeneous catalyst with regard to variation in syngas composition. The presented work further confirms the high technical potential of the SILP catalysis concept as it allows the combination of homogeneous catalysis and its advantages with heterogeneous, fixed-bed technology. In this way, the SILP concept might provide a better mechanistic understanding of homogeneous catalysis (with only a small amount of precious catalyst) as reaction studies may be carried out at steady-state conversions unattainable by traditional batch reactions.

In perspective, we believe that the knowledge gained in this work could accelerate significantly the successful development of new SILP catalysts and future SILP catalysis

Table 6. Rh(**3**)/$SiO_2$/SILP catalyst performance in propene hydroformylation with $CO_2$ cofeed.

| $p_{He}$ [bar] | TOF [h$^{-1}$] | *n*-Butanal [%] | $p_{CO_2}$ [bar] | TOF [h$^{-1}$] | *n*-Butanal [%] | Δ(TOF)[a] [%] | Δ(*n*-Butanal)[b] [%] |
|---|---|---|---|---|---|---|---|
| 1.8 | 15.9 | 94.8 | 1.8 | 16.2 | 94.0 | 2.0 | 0.9 |
| 7.3 | 20.4 | 94.8 | 7.3 | 21.6 | 94.2 | 6.1 | 0.6 |
| 13.6 | 25.9 | 95.1 | 13.6 | 28.1 | 94.5 | 8.3 | 0.7 |
| 36.4 | 34.9 | 94.7 | 36.4 | 46.7 | 94.6 | 35.1 | 0.1 |

[a] $\Delta = [(TOF_{CO_2} - TOF_{He})/TOF_{He}] \cdot 100\%$. [b] $\Delta = [(n\text{-Butanal}_{CO_2} - n\text{-Butanal}_{He})/n\text{-Butanal}_{He}] \cdot 100\%$.

 © 2006 Wiley-VCH Verlag GmbH & Co. KGaA, Weinheim 

applications (e.g. other C–C couplings, hydrogenations etc.). Here, advent of task-specific ionic liquids (TSILs)[35] may also provide new opportunities for catalyst immobilisation and stabilisation in the ionic phase. From our work it becomes quite obvious that the combination of well-defined catalyst complexes, nonvolatile ionic liquids and solid, porous supports offers much more than traditional supported liquid-phase catalysis[36] using water or organic solvents which clearly suffers from evaporation of the supported solvent.[37] We therefore anticipate that the SILP catalysis concept may be able to contribute significantly to future developments aiming for highly selective, heterogenised homogeneous catalysts.

## Acknowledgments

This work was supported by the framework "Smart ligands – smart solvents" of ConNeCat financed by the German Federal Ministry for Education and Research (BMBF). Financial support by the Deutsche Forschungsgemeinschaft, DFG (M. H.), the Danish Research Council for Technology and Production, FTP, and the Villum Kann Rasmussen Foundation (A. R.) is gratefully acknowledged. The authors thank H. Gerhard, B. S. K. Gorle, B. Melcher, and C. Ernst, University of Erlangen-Nürnberg, and U. Maymann and A. Kustov, Technical University of Denmark, for their contributions in connection with analyses and SILP catalyst preparation. Furthermore, O. B. Lapina, Boreskov Institute of Catalysis (Novosibirsk, Russia) and G. Henze, University of Dortmund, are acknowledged for performing MAS NMR measurements and ICP analyses, respectively.

[1] a) J. D. Holbrey, K. R. Seddon, *Clean Prod. Proc.***1999**, *1*, 223; b) T. Welton, *Chem. Rev.* **1999**, *99*, 2071; c) J. Dupont, C. S. Consorti, J. Spencer, *J. Braz. Chem. Soc.* **2000**, *11*, 337; d) R. Sheldon, *Chem. Commun.* **2001**, 2399; e) H. Olivier-Bourbigou, L. Magna, *J. Mol. Catal. A: Chem.* **2002**, *182–183*, 419; f) O. Stenzel, H. G. Raubenheimer, C. Esterhysen, *J. Chem. Soc., Dalton Trans.* **2002**, 1132; g) H. Zhao, S. V. Malhotra, *Aldrichim. Acta* **2002**, *35*, 75.

[2] a) P. Wasserscheid, W. Keim, *Angew. Chem. Int. Ed.* **2000**, *39*, 3772; b) C. M. Gordon, *Appl. Catal., A* **2001**, *222*, 101; c) P. J. Dyson, *Transition Met. Chem.* **2002**, *27*, 353; d) D. Zhao, M. Wu, Y. Kou, E. Min, *Catal. Today* **2002**, *74*, 157; e) J. Dupont, R. F. de Souza, P. A. Z. Suarez, *Chem. Rev.* **2002**, *102*, 3667.

[3] a) P. Wasserscheid, H. Waffenschmidt, P. Machnitzki, K. W. Kottsieper, O. Stetzler, *Chem. Commun.* **2001**, 451; b) F. Favre, H. Olivier-Bourbigou, D. Commereuc, L. Saussine, *Chem. Commun.* **2001**, 1360; c) P. Wasserscheid, T. Welton (Eds.), *Ionic Liquids in Synthesis*, Wiley-VCH, Weinheim, Germany, **2003**.

[4] P. Wasserscheid, M. Eichmann, *Catal. Today* **2001**, *66*, 309.

[5] Selection of ionic liquid suppliers: a) Acros Organics (www.acros.com); b) Fluka (www.fluka.com); c) Merck (www.merck.com); d) Sigma–Aldrich (www.sigma-aldrich.com); e) Solvent Innovation (www.solvent-innovation.com); f) Strem (www.strem.com); g) Wako (www.wako-chem.co.jp).

[6] C. P. Mehnert, R. A. Cook, N. C. Dispenziere, M. Afeworki, *J. Am. Chem. Soc.* **2002**, *124*, 12932.

[7] a) A. Riisager, K. M. Eriksen, P. Wasserscheid, R. Fehrmann, *Catal. Lett.* **2003**, *90*, 149; b) A. Riisager, P. Wasserscheid, R. van Hal, R. Fehrmann, *J. Catal.* **2003**, *219*, 252.

[8] a) A. Riisager, B. Jørgensen, P. Wasserscheid, R. Fehrmann, *Chem. Commun.*, in press. b) A. Riisager, R. Fehrmann, *Patent Application 2005/00735*, **2005** (assigned to DTU).

[9] a) C. P. Mehnert, E. J. Mozeleski, R. A. Cook, *Chem. Commun.* **2002**, 3010; b) A. Wolfson, I. F. J. Vankelecom, P. A. Jacobs, *Tetrahedron Lett.* **2003**, *44*, 1195.

[10] H. Hagiwara, Y. Sugawara, K. Isobe, T. Hoshi, T. Suzuki, *Org. Lett.* **2004**, *6*, 2325.

[11] S. Breitenlechner, M. Fleck, T. E. Müller, A. Suppan, *J. Mol. Catal. A: Chem.* **2004**, *214*, 175.

[12] K. Yamaguchi, C. Yoshida, S. Uchida, N. Mizuno, *J. Am. Chem. Soc.* **2005**, *127*, 530.

[13] a) Y. Yang, H. Lin, C. Deng, J. She, Y. Yuan, *Chem. Lett.* **2005**, *34*, 220; b) Y. Yang, C. Deng, Y. Yuan, *J. Catal.* **2005**, *232*, 108.

[14] A. Riisager, R. Fehrmann, P. Wasserscheid, R. van Hal in *Ionic Liquids IIIB: Fundamentals, Progress, Challenges, and Opportunities – Transformations and Processes* (Eds.: R. D. Rogers, K. R. Seddon), ACS Symposium Series, **2005**, vol. 902, chapter 23, p. 334.

[15] A. Riisager, R. Fehrmann, S. Flicker, R. van Hal, M. Haumann, P. Wasserscheid, *Angew. Chem. Int. Ed.* **2005**, *44*, 185.

[16] S. M. Silva, R. P. J. Bronger, Z. Freixa, J. Dupont, P. W. N. M. van Leeuwen, *New J. Chem.* **2003**, *27*, 1294.

[17] a) L. A. van der Veen, P. C. J. Kamer, P. W. N. M. van Leeuwen, *Organometallics* **1999**, *18*, 4765; b) L. A. van der Veen, M. D. K. Boele, F. R. Bregman, P. C. J. Kamer, P. W. N. M. van Leeuwen, K. Goubitz, J. Fraanje, H. Schenk, C. Bo, *J. Am. Chem. Soc.* **1998**, *120*, 11616; c) L. A. van der Veen, P. H. Keeven, G. C. Schoemaker, J. N. H. Reek, P. C. J. Kamer, P. W. N. M. van Leeuwen, M. Lutz, A. L. Spek, *Organometallics* **2000**, *19*, 872.

[18] P. Wasserscheid, "Transition Metal Catalysis in Ionic Liquids", in *Ionic Liquids in Synthesis* (Eds.: P. Wasserscheid, T. Welton), Wiley-VCH, Weinheim, Germany, **2003**.

[19] P. W. N. M. van Leeuwen, C. Claver (Eds.), *Rhodium Catalyzed Hydroformylation, Catalysis by Metal Complexes Series*, Springer, Heidelberg, **2000**.

[20] M. Schreuder Goedheijt, P. C. J. Kamer, P. W. N. M. van Leeuwen, *J. Mol. Catal. A: Chem.* **1998**, *134*, 243.

[21] A. Riisager, M. Haumann, unpublished results.

[22] C. D. Frohning, C. W. Kohlpaintner, "Synthesis Gas Chemistry", in *Applied Homogeneous Catalysis with Organometallic Compounds* (Eds.: B. Cornils, W. A. Herrmann), Wiley-VCH, Weinheim, **1996**.

[23] a) L. A. van der Veen, M. D. K. Boele, F. R. Bregman, P. C. J. Kamer, P. W. N. M. van Leeuwen, K. Goubitz, J. Fraanje, H. Schenk, C. Bo, *J. Am. Chem. Soc.* **1998**, *120*, 11616; b) L. A. van der Veen, P. H. Keeven, G. C. Schoemaker, J. N. H. Reek, P. C. J. Kamer, P. W. N. M. van Leeuwen, M. Lutz, A. L. Spek, *Organometallics* **2000**, *19*, 872.

[24] A. Riisager, R. Fehrmann, M. Haumann, B. S. K. Gorle, P. Wasserscheid, *Ind. Eng. Chem. Res.* **2005**, *44*, 9853.

[25] C. Yang, Z. S. Mao, Y. Wang, J. Chen, *Catal. Today* **2002**, *74*, 111.

[26] R. M. Desphande, P. Purwanto, H. Delmas, R. V. Chaudhari, *Ind. Eng. Chem. Res.* **1996**, *35*, 3927.

[27] U. J. Jáuregui-Haza, E. Pardillo-Fontdevila, P. Kalck, *Catal. Today* **2003**, *79–80*, 409.

[28] M. Benaissa, U. J. Jáuregui-Haza, I. Nikovc, A. M. Wilhelm, H. Delmas, *Catal. Today* **2003**, *79–80*, 419.

[29] Y. Zhang, Z. S. Mao, J. Chen, *Catal. Today* **2002**, *74*, 23.

[30] a) G. Gregorio, G. Montrasi, M. Tampieri, P. Cavalieri dÓro, G. Pagani, A. Andreetta, *Chim. Ind. (Milan)* **1980**, *62*, 389; b) P. Cavalieri d'Oro, L. Raimondi, G. Pagani, G. Montrasi, G. Gregorio, A. Andreetta, *Chim. Ind. (Milan)* **1980**, *62*, 572.

[31] a) J. F. Young, J. A. Osborn, F. A. Jardine, G. Wilkinson, *J. Chem. Soc., Chem. Commun. (London)* **1965**, 131; b) D. Evans, J. A. Osborn, G. Wilkinson, *J. Chem. Soc. A* **1968**, 3133; c) D. Evans, G. Yagupsky, G. Wilkinson, *J. Chem. Soc. A* **1968**, 2660.

[32] S. S. Divekar, R. M. Desphande, R. V. Chaudhari, *Catal. Lett.* **1993**, *21*, 191.

 © 2006 Wiley-VCH Verlag GmbH & Co. KGaA, Weinheim 

[33] a) L. A. Blanchard, Z. Gu, J. F. Brennecke, *J. Phys. Chem. B* **2001**, *105*, 2437; b) J. L. Anthony, E. J. Maginn, J. F. Brennecke, *J. Phys. Chem. B* **2002**, *106*, 7315.
[34] a) M. Solinas, A. Pfaltz, P. G. Cozzi, W. Leitner, *J. Am. Chem. Soc.* **2004**, *126*, 16142; b) D. G. Hert, J. L. Anderson, S. N. V. K. Aki, J. F. Brennecke, *Chem. Commun.* **2005**, 2603.
[35] J. H. Davis Jr., *Chem. Lett.* **2004**, *33*, 1072.
[36] K. T. Wan, M. E. Davis, *Nature* **1994**, *370*, 449.
[37] A. Beckmann, F. J. Keil, *Chem. Eng. Sci.* **2003**, *58*, 841.
Received: September 28, 2005
Published Online: January 19, 2006

 © 2006 Wiley-VCH Verlag GmbH & Co. KGaA, Weinheim 

DOI: 10.1002/ejic.200501054

# A Simple and Efficient Synthetic Route to Enantiopure Scorpionate Ligands

**Antonio Otero,*[a] Juan Fernández-Baeza,*[a] Antonio Antiñolo,[a] Juan Tejeda,[a] Agustín Lara-Sánchez,[a] Luis Sánchez-Barba,[a] Margarita Sánchez-Molina,[a] Sonia Franco,[a] Isabel López-Solera,[a] and Ana M. Rodríguez[a]**

**Keywords:** Scorpionate ligands / Chiral ligands / Lithium / Titanium

A simple and efficient synthetic route for the preparation of enantiopure scorpionate ligands is described that allows the optimization and rapid access to ligands with diverse chiral environments.

(© Wiley-VCH Verlag GmbH & Co. KGaA, 69451 Weinheim, Germany, 2006)

## Introduction

The traditional approach to asymmetric catalysis with metal-based catalysts is an iterative operation that revolves around the synthesis of chiral ligands of high enantiopurity.[1] Once the chiral ligands have been bound to the metal centers, the new catalysts are examined to determine their enantioselectivities and activities. The results of these studies are evaluated, and the next generation of ligands is designed. In this process, the key to efficient reaction optimization is often rapid access to numerous catalysts with diverse chiral environments. Unfortunately, the synthesis of enantiopure ligands can be an arduous task, severely hampering the optimization of the asymmetric process.[2]

During the last decade, our research group has been interested in the synthesis of new "heteroscorpionate" ligands[3] with pyrazole rings. These new ligands are related to the tris(pyrazol-1-yl)methane system,[4] but in this case one of the pyrazole groups is replaced by a carboxylate, dithiocarboxylate, methoxy, or cyclopentadienyl[5] group. We recently reported a racemic example of a bis(pyrazol-1-yl)acetate tripod ligand in which the chirality originates from the two different pyrazolyl donor groups bound to the methoxyacetate moiety.[6] More recently, Burzlaff et al.[7] prepared two enantiopure NNO acetate–scorpionate ligands in which the chirality originates from pyrazolyl groups; the process involved three synthetic steps. We present here a simple, versatile, and efficient synthetic route for the preparation of enantiopure scorpionate ligands in one step by an insertion reaction of a commercial, enantiopure isocyanate or isothiocyanate into a conventional bis(pyrazol-1-yl)methane. This approach extends our method for the insertion of carbon dioxide into the bridging carbon atom to other types of heterocumulenes. We have prepared the first amidate and thioamidate lithium compounds as a new class of enantiopure scorpionate ligands. These ligand systems can be optimized by modifications in both the bis(pyrazol-1-yl)methane and the isocyanate or isothiocyanate moieties to give diverse chiral environments. Titanium complexes have been prepared with these types of chiral ligands.

## Results and Discussion

Deprotonation at the methylene group of bis(3,5-dimethylpyrazol-1-yl)methane (bdmpzm)[8] with *n*BuLi, followed by reaction with achiral and chiral isocyanates [e.g., *tert*-butyl isocyanate and (*S*)-(–)-α-methylbenzyl isocyanate] and isothiocyanates [e.g., *tert*-butyl isothiocyanate and (*S*)-(–)-1-phenylpropyl isothiocyanate] yielded the lithium compounds $[Li(tbpam)]_2$ (**1**) [tbpam = *N*-*tert*-butyl-2,2-bis(3,5-dimethylpyrazol-1-yl)acetamidate], $[Li(S\text{-}mbbpam)]_2$ (**2**) [S-mbbpam = (*S*)-(–)-*N*-α-methylbenzyl-2,2-bis(3,5-dimethylpyrazol-1-yl)acetamidate], $[Li(tbptam)]_2$ (**3**) [tbptam = *N*-*tert*-butyl-2,2-bis(3,5-dimethylpyrazol-1-yl)thioacetamidate], and $[Li(S\text{-}ppbptam)]_2$ (**4**) [S-ppbptam = (*S*)-(–)-*N*-1-phenylpropyl-2,2-bis(3,5-dimethylpyrazol-1-yl)thioacetamidate], which were isolated as white or yellow solids in good yield (85%) after the appropriate work-up (see Scheme 1).

The mass spectra (FAB) of **1**–**4** indicate a dinuclear formulation. The $^1H$ and $^{13}C\text{-}\{H\}$ NMR spectra of **1** and **3** (achiral compounds) show a single set of resonances for the pyrazole rings, indicating that the two pyrazole rings are equivalent. However, the $^1H$ and $^{13}C\text{-}\{H\}$ NMR spectra of complexes **2** and **4** (chiral compounds) exhibit two resonances for each of the $H^4$, $Me^3$, and $Me^5$ pyrazole protons, indicating that the two pyrazole rings are nonequivalent.

[a] Departamento de Química Inorgánica, Orgánica y Bioquímica, Universidad de Castilla-La Mancha, Campus Universitario, 13071-Ciudad Real, Spain
Fax: +34-926-255318
E-mail: juan.fbaeza@uclm.es
antonio.otero@uclm.es

Supporting information for this article is available on the WWW under http://www.eurjic.org or from the author.

 © 2006 Wiley-VCH Verlag GmbH & Co. KGaA, Weinheim 

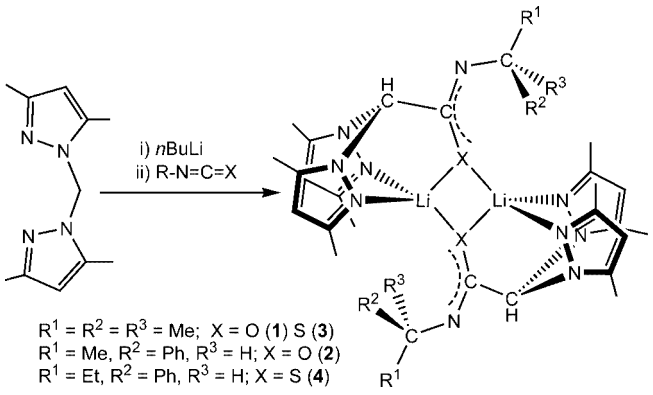


Scheme 1. Synthesis of lithium compounds **1**–**4**.

These results agree with a proposed tetrahedral arrangement for the lithium atoms with a $\kappa^3$-NNE-coordination (E = O or S) for the heteroscorpionate ligand, where the oxygen or the sulfur atom of the scorpionate ligands bridge the two lithium atoms (see Scheme 1). In this arrangement, when $R^1 = R^2 = R^3$ (achiral compounds), there is a symmetry plane that contains the lithium atoms, the bridging carbon atoms of the pyrazolyl rings, and the amidate or thioamidate fragments. However, when $R^1 \neq R^2 \neq R^3$, this symmetry plane does not exist, and the pyrazole rings are nonequivalent. This structural arrangement was corroborated by an X-ray crystal structure determination for **1** (see Figure 1).[9] The geometry around the Li atom can be described as a distorted tetrahedron with a "heteroscorpionate" ligand that acts in a tridentate fashion (two coordinated pyrazole rings and an oxygen atom from the amidate fragment bridge the lithium atoms). The dimeric aggregate is based on $Li_2O_2$ four-membered rings, which have previously been observed in other lithium compounds containing, for example, anionic tris(imidazol-2-yl)phosphanes,[10] boroxides,[11] aryloxides,[12] or ester enolate[13] ligands. However, it should be noted that compounds with this type of metallacycle containing a scorpionate ligand have not been reported in the literature. The corresponding Li–O bond lengths are essentially the same as in the lithium compounds mentioned above, although notable asymmetry is present within the amidate bridge [Li(1)–O(1) = 1.946(8) Å; Li(1)–O(2) = 1.825(8) Å; Li(2)–O(1) = 1.860(8) Å; Li(2)–O(2) = 1.978(7) Å]. Thus, the four-membered ring is approximately a square that is slightly folded about the Li···Li and O···O diagonal (21.0° and 24.4°, respectively), the Li···Li diagonal being much shorter than the O···O diagonal.

The C(12)–O(1) and C(12)–N(5) bond lengths [1.290(5) and 1.287(5) Å] or C(28)–O(2) and C(28)–N(10) bond lengths [1.291(5) and 1.271(5) Å] indicate the existence of a delocalized O–C–N bond in both amidate fragments of the heteroscorpionate ligands, which presents a Z-geometry for the C=N bonds. The absence of a response in the $^1$H NOESY-1D experiment from the *tert*-butyl group upon irradiating the methyne bringing group confirms this geometry in solution. In the chiral complexes **2** and **4**, we confirmed the presence of one enantiomer in solution by the addition of a chiral shift reagent, namely (*R*)-(–)-(9-anthryl)-2,2,2-trifluoroethanol. The addition of this compound did not modify the $^1$H NMR spectra of either compound. However, addition of the shift reagent to a racemic mixture of complex **2** gave rise to the appearance of two signals for each proton in the $^1$H NMR spectra, resulting from the two diastereoisomers of the corresponding two enantiomers. In addition, the specific rotations of **2** and **4** were examined by optical polarimetry. Preliminary studies also show that this type of isocyanate and isothiocyanate can be inserted into other types of bis(pyrazol-1-yl)methane.

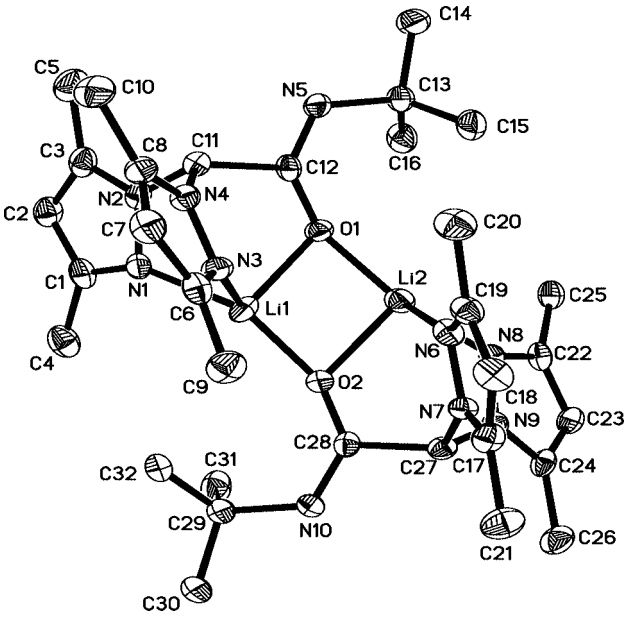


Figure 1. ORTEP diagram of **1** with 30% probability ellipsoids. Selected bond lengths [Å] and angles [°]: Li(1)–O(1), 1.946(8); Li(1)–O(2), 1.825(8); Li(2)–O(1), 1.860(8); Li(2)–O(2), 1.978(7); Li(1)–N(1), 2.063(8); Li(1)–N(3), 2.017(8); C(12)–O(1), 1.290(5); C(12)–N(5), 1.287(5); C(28)–O(2), 1.291(5); C(28)–N(10), 1.271(5); O(1)–Li(1)–O(2), 98.5(4); Li(1)–O(1)–Li(2), 80.4(3); O(1)–Li(2)–O(2), 96.1(3); Li(1)–O(2)–Li(2), 80.5(3).

These lithium compounds have been used for the synthesis of new titanium complexes. Thus, **2** and **3** reacted with $[TiCl_4(THF)_2]$ to give the complexes $[TiCl_3$(S-mbbpamH)]Cl (**5**) [S-mbbpamH = (*S*)-(–)-*N*-α-methylbenzyl-2,2-bis(3,5-dimethylpyrazol-1-yl)acetamide] and $[TiCl_3$(tbptamH)]Cl (**6**) [tbptamH = *N*-*tert*-butyl-2,2-bis(3,5-dimethylpyrazol-1-yl)thioacetamide] (see Scheme 2). Although the reactions were carried out under rigorously anhydrous experimental conditions, the presence of adventitious HCl proceeding from $TiCl_4$ in the reaction mixture during the work-up procedure was probably responsible for the protonation of the acetamidate or thioacetamide moieties and their transformation into carboxamide[14] or thiocarboxamide moieties, respectively. However, the character of the enantiopure scorpionate ligand in complex **5** is not modified. The $^1$H and $^{13}$C{H}-NMR spectra of **5** and **6** exhibit two singlets and one singlet, respectively for each of the $H^4$, $Me^3$ and $Me^5$ pyrazole protons. An X-ray crystal structure analysis was carried out for complex **6** (see Figure 2).[9] The titanium

 © 2006 Wiley-VCH Verlag GmbH & Co. KGaA, Weinheim 

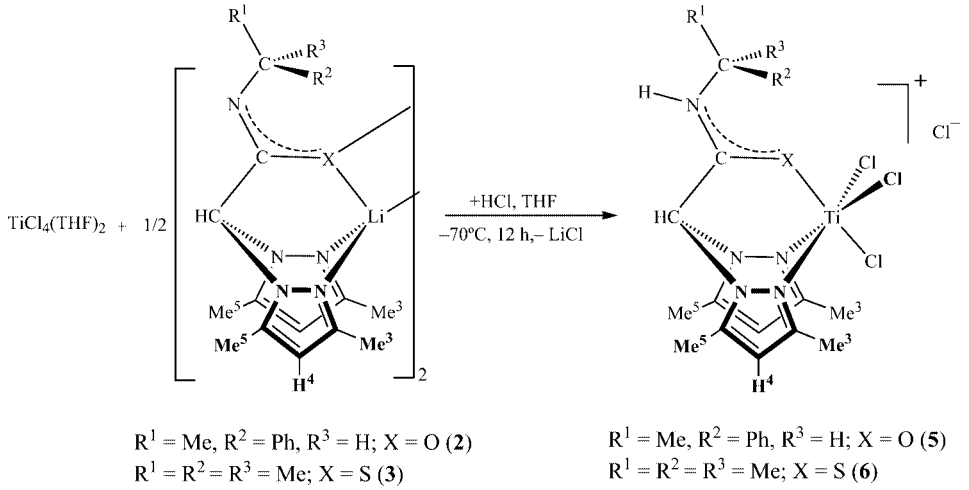


Scheme 2. Synthesis of titanium complexes **5** and **6**.

center has a distorted octahedral environment with a major distortion in the N(3)–Ti(1)–Cl(2) angle, which has a value of 166.1(2)°. In addition, the specific rotation of **5** was examined by optical polarimetry.

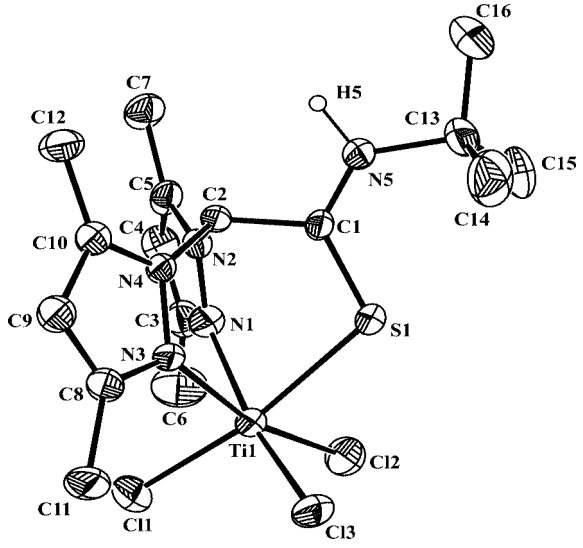


Figure 2. ORTEP diagram of **6** with 30% probability ellipsoids. Selected bond lengths (Å) and angles [°]: Ti(1)–N(3), 2.144(7); Ti(1)–N(1), 2.192(7); Ti(1)–Cl(3), 2.217(3); Ti(1)–Cl(1), 2.231(3); Ti(1)–Cl(2), 2.243(3); Ti(1)–S(1), 2.500(3); S(1)–C(1), 1.672(8); N(5)–C(1), 1.31(1); N(3)–Ti(1)–Cl(2), 166.1(2); N(1)–Ti(1)–Cl(3), 167.1(2); Cl(1)–Ti(1)–S(1), 170.5(1); N(5)–C(1)–S(1), 126.3(6).

In conclusion, we present here a simple and efficient synthetic route for the preparation of enantiopure scorpionate ligands. This approach will allow the optimization and rapid access to numerous ligands with diverse chiral environments by modification of the bis(pyrazol-1-yl)methane as well as the enantiopure isocyanate and isothiocyanate fragments. In addition, these lithium compounds are excellent reagents for the introduction of these ligands into transition-metal complexes.

## Experimental Section

All reactions were performed using standard Schlenk-tube techniques under dry nitrogen. Solvents were distilled from appropriate drying agents and degassed before use. Microanalyses were carried out with a Perkin–Elmer 2400 CHN analyzer. Mass spectra were recorded with a VG Autospec instrument using the FAB technique and nitrobenzyl alcohol as matrix. $^{1}$H- and $^{13}$C NMR spectra were recorded with a Varian Inova FT-500 spectrometer and referenced to the residual deuterated solvent. Optical rotations were determined with a Perkin–Elmer 241 MC polarimeter at the sodium D line, equipped with a quartz cell of 1.00-dm path length. Experimental procedures and characterization data for compounds **1**–**6** are given in the Supporting Information.

**Supporting Information** (see footnote on the first page of this article): Spectroscopic data and experimental procedures for compounds **1**–**6**.

## Acknowledgments

This work was financially supported by the Dirección General de Enseñanza Superior e Investigación Científica, Spain (Grant. No. BQU2002-04638-CO2-02) and the Junta de Comunidades de Castilla-La Mancha (Grant. No. PAC-02-003, GC-02-010 and PAI-02-016). We would like to thank Dr. B. Rodríguez and V. Hornillos from Instituto de Química Orgánica (CSIC) for assistance with the optical polarimetry experiments.

[1] a) I. Ojima (Ed.), *Catalytic Asymmetric Synthesis* 2nd ed., Wiley-VCH, New York, **2000**; b) E. N. Jacobsen, A. Pfaltz, H. Yamamoto, *Comprehensive Asymmetric Catalysis*, Springer, Berlin, **1999**, vol. 1–3; c) R. Noyori, *Asymmetric Catalysis in Organic Synthesis*, John Wiley & Sons, New York, **1994**.

[2] J. Seyden-Penne, *Chiral Auxiliaries and Ligands in Asymmetric Synthesis*, John Wiley & Sons, New York, **1995**.

[3] a) S. Trofimenko, *Scorpionates. The Coordination Chemistry of Polypyrazolylborate Ligands*, Imperial College Press, London, **1999**; b) A. Otero, J. Fernández-Baeza, A. Antiñolo, J. Tejeda, A. Lara-Sánchez, *Dalton Trans.* **2004**, 1499 (perspective article).

[4] a) J. Fernández-Baeza, F. A. Jalón, A. Otero, M. E. Rodrigo, *J. Chem. Soc., Dalton Trans.* **1995**, 1015; b) A. Antiñolo, F.

 © 2006 Wiley-VCH Verlag GmbH & Co. KGaA, Weinheim 

Carrillo-Hermosilla, E. Diez-Barra, J. Fernández-Baeza, M. Fernández-Lopez, A. Lara-Sánchez, A. Moreno, A. Otero, A. M. Rodríguez, J. Tejeda, *J. Chem. Soc., Dalton Trans.* **1998**, 3737.

[5] A. Otero, J. Fernández-Baeza, A. Antiñolo, J. Tejeda, A. Lara-Sánchez, L. Sánchez-Barba, A. M. Rodríguez, M. A. Maestro, *J. Am. Chem. Soc.* **2004**, *126*, 1330.

[6] A. Otero, J. Fernández-Baeza, A. Antiñolo, J. Tejeda, A. Lara-Sánchez, L. Sánchez-Barba, M. T. Expósito, A. M. Rodríguez, *Dalton Trans.* **2003**, 1614.

[7] a) I. Hegelmann, N. Burzlaff, *Eur. J. Inorg. Chem.* **2003**, 409; b) L. Peters, N. Burzlaff, *Polyhedron* **2004**, *23*, 245.

[8] a) J. Sebastian, P. Sala, J. Del Mazo, M. Sancho, C. Ochoa, J. Elguero, J. P. Fayet, M. C. Vertut, *J. Heterocyc. Chem.* **1982**, *19*, 1141; b) E. Díez-Barra, A. de la Hoz, A. Sánchez-Migallon, J. Tejeda, *J. Chem. Soc., Perkin Trans. 1* **1993**, 1079.

[9] Crystallographic data for **1**: $C_{32}H_{48}Li_2N_{10}O_2$·THF, orthorhombic, $P2_12_12_1$, $a$ = 11.567(1), $b$ = 17.538 (1), $c$ = 19.568 (1) Å; $V$ = 3969.7 (5) Å$^3$; $Z$ = 4; $D_{calcd.}$ = 1.156 g/cm$^3$; $\lambda$ (Mo-$K_\alpha$) = 0.71073 Å; $\mu$ (Mo-$K_\alpha$) = 0.075 mm$^{-1}$; 100(2) K; $R$ = 0.0447; $R_w$ = 0.1134. Crystallographic data for **6**: $[C_{16}H_{25}Cl_3N_5STi]$-Cl·0.5$CH_2Cl_2$·0.25$C_6H_{14}$, monoclinic, $C2/c$, $a$ = 37.375(5), $b$ = 9.892 (3), $c$ = 30.905 (3) Å; $V$ = 11326 (4) Å$^3$; $Z$ = 16; $D_{calcd.}$ = 1.345 g/cm$^3$; $\lambda$ (Mo-$K_\alpha$) = 0.71073 Å; $\mu$(Mo-$K_\alpha$) = 0.862 mm$^{-1}$; 230(2) K; $R$ = 0.0839, $R_w$ = 0.2532. The $R$ factors obtained are high because of the poor quality of the crystals. CCDC-277594 (**1**) and CCDC-277595 (**6**) contain the supplementary crystallographic data for this paper. These data can be obtained free of charge from The Cambridge Crystallographic Data Centre via www.ccdc.cam.ac.uk/data_request/cif.

[10] M. Enders, O. Fritz, H. Pritzkow, *Z. Anorg. Allg. Chem.* **2004**, *630*, 1501.

[11] S. C. Cole, M. P. Coles, P. B. Hitchcock, *Organometallics* **2004**, *23*, 5159.

[12] T. J. Boyle, D. M. Pedrotty, T. M. Alam, S. C. Vick, M. A. Rodriguez, *Inorg. Chem.* **2000**, *39*, 5133.

[13] D. Seebach, R. Amstutz, T. Laube, W. B. Schweizer, J. D. Dunitz, *J. Am. Chem. Soc.* **1985**, *107*, 5403.

[14] a) N. Niklas, O. Walter, R. Alsfasser, *Eur. J. Inorg. Chem.* **2000**, 1723; b) N. Niklas, O. Walter, F. Hampel, R. Alsfasser, *J. Chem. Soc., Dalton Trans.* **2002**, 3367.

Received: November 25, 2005
Published Online: January 19, 2006

 © 2006 Wiley-VCH Verlag GmbH & Co. KGaA, Weinheim 

DOI: 10.1002/ejic.200500727

# Molecular Structures and Magnetism of $Mn_{12}$ Nanomagnets Containing the 3-Thiophenecarboxylate Ligand

**Jin Mook Lim,[b] Youngkyu Do,[b] and Jinkwon Kim*[a]**

**Keywords:** Single-molecule magnet / $Mn_{12}$ complex / Molecular structure / Magnetic properties / Molecular films

The new $Mn_{12}$ single-molecule magnets containing thiophenyl ligands, $[Mn_{12}O_{12}(O_2CC_4H_3S)_{16}(HO_2CC_4H_3S)(H_2O)_2]\cdot 5CH_2Cl_2$(**1**) and $[Mn_{12}O_{12}(O_2CC_4H_3S)_{16}(H_2O)_4]\cdot 6CH_2Cl_2\cdot 2H_2O$ (**2**), have been synthesized by ligand-substitution reactions of 3-thiophenecarboxylic acid and $[Mn_{12}O_{12}(O_2CCH_3)_{16}(H_2O)_4]$ and investigated by magnetic measurements with a SQUID magnetometer. The X-ray analysis of **1** shows five-coordination geometry around the $Mn^{III}$ ion due to the unusual coordination of 3-thiophenecarboxylic acid to the $Mn^{III}$ ion. Compound **1** displays two different rates of magnetization relaxation, which are faster than that of compound **2** because of structural distortion in the $Mn_{12}$ complex of **1**. Magnetic susceptibility measurements on **1** and **2** give the following parameters: $U_{eff}$ (the faster relaxation form of **1**) = 51.81 K, $1/\tau_0 = 1.90\cdot 10^8\ s^{-1}$; $U_{eff}$ (the slower relaxation form of **1**) = 66.44 K, $1/\tau_0 = 1.50\cdot 10^8\ s^{-1}$; $U_{eff}$(**2**) = 67.09 K, $1/\tau_0 = 1.32\cdot 10^8\ s^{-1}$.

(© Wiley-VCH Verlag GmbH & Co. KGaA, 69451 Weinheim, Germany, 2006)

## Introduction

Single-molecule magnets (SMMs) have been the subject of intensive investigation in the last years.[1] SMM behavior was first observed in $[Mn_{12}O_{12}(OAc)_{16}(H_2O)_4]$ ($Mn_{12}Ac$) in 1993.[2,3] SMMs display stepwise magnetization hysteresis loops below the blocking temperature due to a very slow magnetization relaxation rate as well as a resonant quantum tunneling of magnetization. SMMs also exhibit quantum phase interference. Therefore, SMMs are regarded as the elementary units in ultimate high-density magnetic storage[4] and in the design of quantum computers.[5,6] One the other hand, recent research reports showed that molecular clusters possessing quantized magnetic properties may provide powerful new systems for single-molecule transistors.[7,8]

Investigating individual molecules is essential for realizing the proposed application of SMMs. An approach to accomplishing this goal is to deposit SMMs on a suitable substrate and use scanning probe microscopy (SPM) to sense individual molecules. Various types of SPM techniques, such as scanning tunneling microscopy (STM), atomic force microscopy (AFM), and magnetic force microscopy (MFM) can be employed to verify the electronic, mechanical, and magnetic characterization of the molecules. Recently, various attempts have been made in preparation and SPM characterization: Langmuir–Blodgett (LB) films of $Mn_{12}$ clusters,[9] MFM study on $Mn_{12}$ complexes embedded in a polycarbonate matrix,[10] STM study of $[Mn_{12}O_{12}\{16\text{-(hydrothio)hexanecanoate}\}_{16}(H_2O)_4]$ organized on a gold surface,[11] stamp assisted deposition and patterning,[12] the preparation of monolayer and multilayer films on functionalized surfaces,[13] and study of molecular ordering and magnetism of $[Mn_{12}O_{12}(t\text{BuCO}_2)_{16}(H_2O)_4]$ on a gold surface.[14] Very recently, grafting of $Mn_{12}$ complexes on a Si surface have been reported.[15,16] However, the methodology for depositing SMMs with monolayer or submonolayer coverage on a useful substrate such as silicon or gold is not yet well established, and the direct measurement of the characteristics of individual molecules of SMMs is still in the beginning stage. Therefore, we designed a new $Mn_{12}$ complex with surface-adhesive functional groups in peripheral ligands to give molecular monolayers on a gold surface. Here we report the synthesis, structure, and magnetic properties of $Mn_{12}$ complexes containing the thiophenyl group, $[Mn_{12}O_{12}(O_2CC_4H_3S)_{16}(HO_2CC_4H_3S)(H_2O)_2]\cdot 5CH_2Cl_2$ (**1**) and $[Mn_{12}O_{12}(O_2CC_4H_3S)_{16}(H_2O)_4]\cdot 6CH_2Cl_2\cdot 2H_2O$ (**2**).

## Results and Discussion

### Synthesis

The ligand-substitution reaction of $Mn_{12}Ac$ with 3-thiophenecarboxylic acid has been carried out by a modified azeotropic distillation method.[17] Most ligand-substitution reactions have been performed with a large excess of RCOOH. However, in our modified method, only a stoichiometric amount of 3-thiophenecarboxylic acid was al-

[a] Department of Chemistry, Kongju National University, 182 Shinkwan, Kongju, Chungnam 314-701, Korea
Fax: + 82-41-850-8479
E-mail: jkim@kongju.ac.kr
[b] Department of Chemistry, School of Molecular Science BK21 and Center for Molecular Design and Synthesis, KAIST, 373-1 Guseong-dong, Yuseong-gu, Daejeon 305-701, Korea

 © 2006 Wiley-VCH Verlag GmbH & Co. KGaA, Weinheim 

lowed to react with $Mn_{12}Ac$. The solubility of $Mn_{12}Ac$ is very poor in dichloromethane. Nevertheless, as $Mn_{12}Ac$ reacts with 3-thiophenecarboxylic acid, the color of the solution darkens, indicating that the ligand-substitution reaction proceeds. To complete the substitution reaction, toluene was added to the reaction mixture and evaporated to remove acetic acid as the toluene azeotrope. The reaction of $Mn_{12}Ac$ with 17 equiv. of 3-thiophenecarboxylic acid gives complex **1**, whereas complex **2** is obtained by a reaction with 16 equiv. 3-thiophenecarboxylic acid. Complex **1** has a 3-thiophenecarboxylic acid as terminal coordination ligand which can be substituted by a water molecule. Complex **1** is converted to complex **2** by recrystallization in wet $CH_2Cl_2$/hexane mixed solvent.

### Molecular Structures

An ORTEP diagram of $[Mn_{12}O_{12}(O_2CC_4H_3S)_{16}(HO_2CC_4H_3S)(H_2O)_2]$ is shown in Figure 1. Selected bond parameters are listed in Table 1 and Table 2. Complex **1** has unusual molecular structure compared with other normal $Mn_{12}$–carboxylate species. $Mn_{12}$–carboxylate complexes usually have sixteen carboxylates as peripheral bridging ligands which bridge the outer-ring $Mn^{III}$ atoms to both the inner $Mn^{IV}$ and the other outer-ring $Mn^{III}$ atoms. Four water molecules are coordinated to the outer-ring $Mn^{III}$ atoms. Complex **1** has sixteen 3-thiophenecarboxylates as peripheral bridging ligands, but it abnormally has one 3-thiophenecarboxylic acid and only two water molecules as terminal coordination ligands to $Mn^{III}$ ions. As a result of the coordination of 3-thiophenecarboxylic acid, the $Mn^{III}$ ion (Mn6) has highly distorted five-coordination geometry. The octahedral $Mn^{III}$–O bonds of $[Mn_{12}O_{12}]$ complexes are tetragonally elongated because of a Jahn–Teller distortion. An elongation axis is usually parallel to the molecular $C_2$ axis. However, there is no such elongation at Mn6 because of its five-coordination geometry. The longest $Mn^{III}$–O bond length around Mn6 is 2.067(7) Å, which is significantly shorter than the axially elongated $Mn^{III}$–O bond lengths (2.096–2.218 Å) of the six-coordinate $Mn^{III}$ atoms. Bond angles of O7–Mn6–O38 and O14–Mn6–O38 are 101.4(3)° and 92.8(3)°, respectively. Examples of five-coordinate $Mn^{III}$ atoms in $Mn_{12}$ complexes are quite rare and only observed previously in $[Mn_{12}O_{12}(O_2CEt)_{16}(H_2O)_3]$.[18] The two water molecules are located on the two Mn atoms (Mn8 and Mn12) to complete octahedral coordination.

The structure of complex **2** is quite similar in many respects to the previously characterized $Mn_{12}$ complexes. Complex **2** has normal $[Mn_{12}O_{12}]^{16+}$ core structure, as shown in Figure 2 and Figure 3, possessing four water ligands bound to three Mn centers (Mn8, Mn10, Mn12) with a 1:1:2 arrangement. All Jahn–Teller elongation axes of eight $Mn^{III}$ centers of both complexes are oriented approximately in the axial direction.

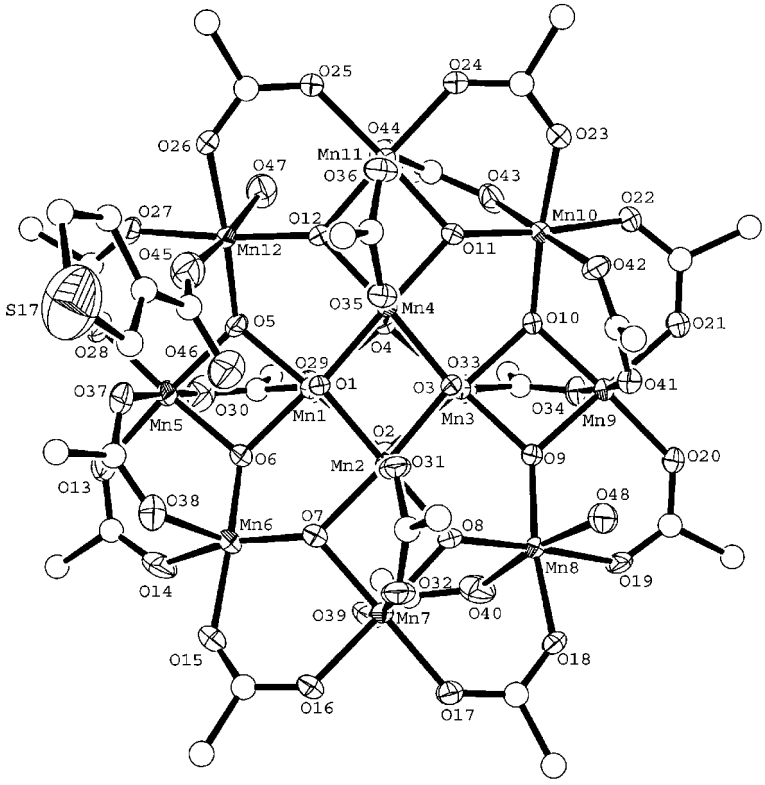


Figure 1. ORTEP representation of the $Mn_{12}$ complex of **1** showing 50% probability ellipsoids. For clarity, thiophenyl groups of the 3-thiophenecarboxylate bridging ligands are omitted.

 © 2006 Wiley-VCH Verlag GmbH & Co. KGaA, Weinheim 

Table 1. Selected bond lengths [Å] in **1**.

| A | B | Bond length | A | B | Bond length |
|---|---|---|---|---|---|
| Mn(1) | O(1) | 1.919(6) | Mn(1) | O(2) | 1.898(5) |
| Mn(1) | O(4) | 1.903(5) | Mn(1) | O(5) | 1.877(5) |
| Mn(1) | O(6) | 1.870(6) | Mn(1) | O(29) | 1.908(7) |
| Mn(2) | O(1) | 1.924(5) | Mn(2) | O(2) | 1.906(6) |
| Mn(2) | O(3) | 1.931(5) | Mn(2) | O(7) | 1.889(6) |
| Mn(2) | O(8) | 1.853(5) | Mn(2) | O(31) | 1.900(6) |
| Mn(3) | O(2) | 1.912(5) | Mn(3) | O(3) | 1.897(6) |
| Mn(3) | O(4) | 1.921(5) | Mn(3) | O(9) | 1.867(5) |
| Mn(3) | O(10) | 1.864(5) | Mn(3) | O(33) | 1.920(6) |
| Mn(4) | O(1) | 1.938(5) | Mn(4) | O(3) | 1.903(5) |
| Mn(4) | O(4) | 1.908(6) | Mn(4) | O(11) | 1.850(5) |
| Mn(4) | O(12) | 1.860(5) | Mn(4) | O(35) | 1.903(6) |
| Mn(5) | O(5) | 1.905(6) | Mn(5) | O(6) | 1.899(6) |
| Mn(5) | O(13) | 1.957(7) | Mn(5) | O(28) | 1.927(6) |
| Mn(5) | O(30) | 2.181(8) | Mn(5) | O(37) | 2.096(8) |
| Mn(6) | O(6) | 1.859(6) | Mn(6) | O(7) | 1.893(6) |
| Mn(6) | O(14) | 1.943(8) | Mn(6) | O(15) | 1.926(7) |
| Mn(6) | O(38) | 2.067(7) | Mn(7) | O(7) | 1.915(6) |
| Mn(7) | O(8) | 1.895(6) | Mn(7) | O(16) | 1.951(6) |
| Mn(7) | O(17) | 1.951(6) | Mn(7) | O(32) | 2.196(7) |
| Mn(7) | O(39) | 2.135(7) | Mn(8) | O(8) | 1.898(6) |
| Mn(8) | O(9) | 1.873(5) | Mn(8) | O(18) | 1.944(6) |
| Mn(8) | O(19) | 1.963(6) | Mn(8) | O(40) | 2.111(7) |
| Mn(8) | O(48) | 2.218(7) | Mn(9) | O(9) | 1.898(5) |
| Mn(9) | O(10) | 1.887(5) | Mn(9) | O(20) | 1.932(6) |
| Mn(9) | O(21) | 1.945(6) | Mn(9) | O(34) | 2.174(7) |
| Mn(9) | O(41) | 2.168(7) | Mn(10) | O(10) | 1.877(6) |
| Mn(10) | O(11) | 1.911(5) | Mn(10) | O(22) | 1.980(6) |
| Mn(10) | O(23) | 1.936(6) | Mn(10) | O(42) | 2.135(7) |
| Mn(10) | O(43) | 2.189(6) | Mn(11) | O(11) | 1.892(5) |
| Mn(11) | O(12) | 1.890(5) | Mn(11) | O(24) | 1.945(6) |
| Mn(11) | O(25) | 1.945(6) | Mn(11) | O(36) | 2.208(6) |
| Mn(11) | O(44) | 2.178(7) | Mn(12) | O(5) | 1.887(6) |
| Mn(12) | O(12) | 1.880(6) | Mn(12) | O(27) | 1.938(6) |
| Mn(12) | O(26) | 1.941(6) | Mn(12) | O(45) | 2.198(8) |
| Mn(12) | O(47) | 2.216(7) | | | |

Table 2. Selected bond lengths [Å] in **2**.

| A | B | Bond length | A | B | Bond length |
|---|---|---|---|---|---|
| Mn(1) | O(1) | 1.904(5) | Mn(1) | O(2) | 1.932(5) |
| Mn(1) | O(4) | 1.925(5) | Mn(1) | O(5) | 1.892(5) |
| Mn(1) | O(6) | 1.852(5) | Mn(1) | O(29) | 1.911(5) |
| Mn(2) | O(1) | 1.920(5) | Mn(2) | O(2) | 1.901(5) |
| Mn(2) | O(3) | 1.926(5) | Mn(2) | O(7) | 1.873(5) |
| Mn(2) | O(8) | 1.864(5) | Mn(2) | O(31) | 1.912(5) |
| Mn(3) | O(2) | 1.925(5) | Mn(3) | O(3) | 1.911(5) |
| Mn(3) | O(4) | 1.929(5) | Mn(3) | O(9) | 1.886(5) |
| Mn(3) | O(10) | 1.868(5) | Mn(3) | O(33) | 1.932(5) |
| Mn(4) | O(1) | 1.926(5) | Mn(4) | O(3) | 1.904(5) |
| Mn(4) | O(4) | 1.899(5) | Mn(4) | O(11) | 1.887(5) |
| Mn(4) | O(12) | 1.870(5) | Mn(4) | O(35) | 1.936(5) |
| Mn(5) | O(5) | 1.920(5) | Mn(5) | O(6) | 1.878(5) |
| Mn(5) | O(13) | 1.932(5) | Mn(5) | O(28) | 1.945(6) |
| Mn(5) | O(30) | 2.216(6) | Mn(5) | O(37) | 2.204(6) |
| Mn(6) | O(6) | 1.890(5) | Mn(6) | O(7) | 1.929(5) |
| Mn(6) | O(14) | 1.983(6) | Mn(6) | O(15) | 1.976(5) |
| Mn(6) | O(38) | 2.117(6) | Mn(6) | O(40) | 2.104(6) |
| Mn(7) | O(7) | 1.895(5) | Mn(7) | O(8) | 1.888(5) |
| Mn(7) | O(16) | 1.944(5) | Mn(7) | O(17) | 1.941(5) |
| Mn(7) | O(32) | 2.226(6) | Mn(7) | O(39) | 2.198(6) |
| Mn(8) | O(8) | 1.890(5) | Mn(8) | O(9) | 1.899(5) |
| Mn(8) | O(18) | 1.972(5) | Mn(8) | O(19) | 1.966(5) |
| Mn(8) | O(42) | 2.101(6) | Mn(8) | O(47) | 2.227(6) |
| Mn(9) | O(9) | 1.902(5) | Mn(9) | O(10) | 1.880(5) |
| Mn(9) | O(20) | 1.926(5) | Mn(9) | O(21) | 1.938(5) |
| Mn(9) | O(34) | 2.237(6) | Mn(9) | O(41) | 2.199(5) |
| Mn(10) | O(10) | 1.889(5) | Mn(10) | O(11) | 1.902(5) |
| Mn(10) | O(22) | 1.944(5) | Mn(10) | O(23) | 1.977(5) |
| Mn(10) | O(43) | 2.119(6) | Mn(10) | O(48) | 2.216(6) |
| Mn(11) | O(11) | 1.905(5) | Mn(11) | O(12) | 1.879(5) |
| Mn(11) | O(24) | 1.919(5) | Mn(11) | O(25) | 1.941(5) |
| Mn(11) | O(36) | 2.222(6) | Mn(11) | O(44) | 2.219(5) |
| Mn(12) | O(5) | 1.888(5) | Mn(12) | O(12) | 1.873(5) |
| Mn(12) | O(26) | 1.978(6) | Mn(12) | O(27) | 1.941(6) |
| Mn(12) | O(45) | 2.204(6) | Mn(12) | O(46) | 2.192(6) |

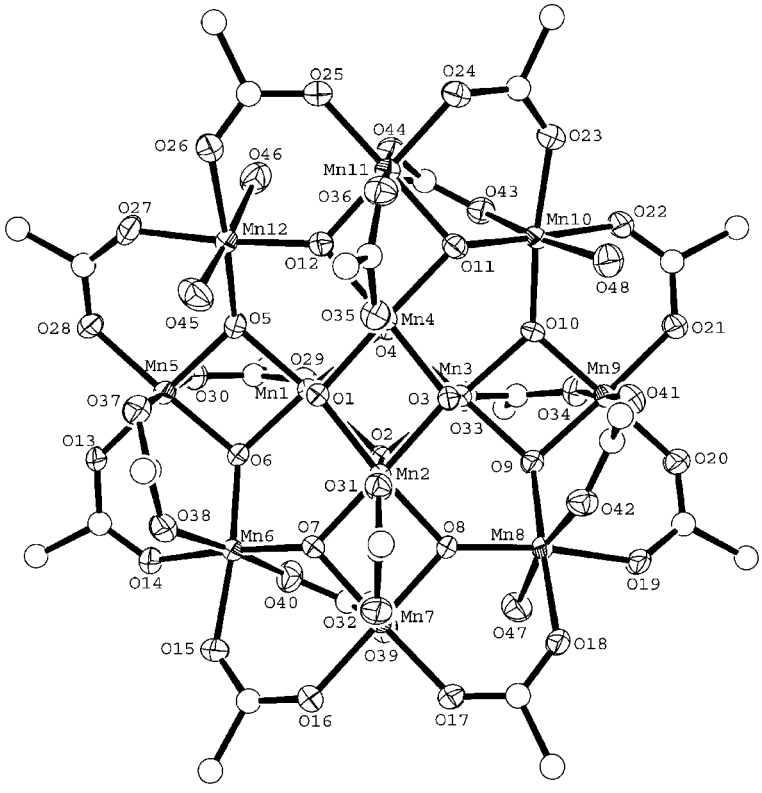


Figure 2. ORTEP representation of the $Mn_{12}$ complex of **2** showing 50% probability ellipsoids. For clarity, thiophenyl groups of the 3-thiophenecarboxylate bridging ligands are omitted.

 © 2006 Wiley-VCH Verlag GmbH & Co. KGaA, Weinheim 

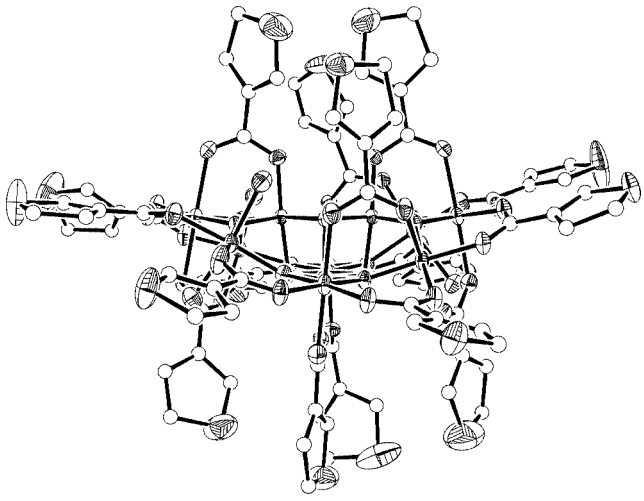

Figure 3. Side view of complex **2**.

### Magnetic Properties

Out-of-phase ac magnetic susceptibility ($\chi_M''$) measurements were carried out in the region of 2 to 10 K at zero dc field. As shown in Figure 4, frequency-dependent $\chi_M''$ peaks in the 4–7 K region of **1** are less symmetric compared with those of **2**, and the shoulders in the 3–6 K region indicate a chemical species having a faster relaxation rate of quantum tunneling of magnetization.

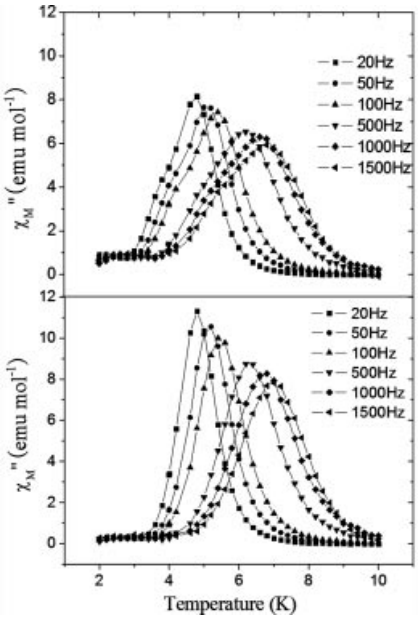


Figure 4. Comparison of out-of phase ac susceptibility signals of **1** (top) and **2** (bottom).

Magnetization relaxation rates ($1/\tau$) and effective anisotropy energy barriers were calculated from the theoretical Equation (1) given by

$$\ln(1/\tau) = -U_{eff}/kT + \ln(1/\tau_0) \quad (1)$$

where $U_{eff}$ is the effective anisotropy energy barrier, $k$ is the Boltzmann constant, and $T$ is the temperature. Magnetic relaxation times ($\tau$) are obtained from the relationship $\omega\tau = 1$ at the maxima of the $\chi_M''$ vs. $T$ plots. Peak maxima are accurately determined by fitting the peaks to a Lorentzian function. Figure 5 displays deconvolution of out-of-phase ac susceptibilities of **1** at 20 Hz. A least-squares fit (Figure 6) of ac susceptibility relaxation data to Equation (1) for faster-relaxation and slower-relaxation forms of **1** as well as **2** gives the following parameters: $U_{eff}$ (the faster-relaxation form of **1**) = 51.81 K; $1/\tau_0 = 1.90 \cdot 10^8$ s$^{-1}$, $U_{eff}$ (the slower-relaxation form of **1**) = 66.44 K; $1/\tau_0 = 1.50 \cdot 10^8$ s$^{-1}$, $U_{eff}$(**2**) = 67.09 K, $1/\tau_0 = 1.32 \cdot 10^8$ s$^{-1}$.

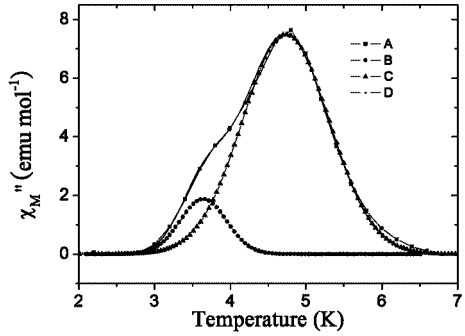


Figure 5. Deconvolution of ac susceptibilities of **1** at 20 Hz. A: original plot, B: deconvoluted low-temperature form, C: deconvoluted high-temperature form, D: sum of B and C.

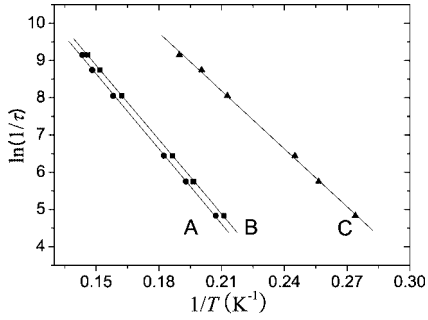


Figure 6. Arrhenius Plots of the natural logarithm of relaxation rate, $\ln(1/\tau)$ vs. inverse temperature for **1** and **2**. A: **2**, B: high temperature form of **1**, C: low temperature form of **1**.

The relaxation rate of the $Mn_{12}$ SMM is dependent on the structural distortion of the $Mn_{12}$ species because the rate of tunneling is determined by transverse magnetic fields (either outside or inside the molecule) or by transverse higher-order zero-field interaction terms.[19] Dislocations should be an external source of spin tunneling in $Mn_{12}$ crystals.[20] Jahn–Teller isomerism[21] is proposed as an internal source causing the tunneling rate of the $Mn_{12}$ species to increase. An example of Jahn–Teller isomerism can be given by mentioning the compounds $[Mn_{12}O_{12}(O_2CC_6H_4Me\text{-}4)_{16}(H_2O)_4]\cdot HO_2CC_6H_4Me\text{-}4$[19] and $[Mn_{12}O_{12}(O_2CPh\text{-}4\text{-}SMe)_{16}(H_2O)_4]\cdot 7CH_2Cl_2$,[17c] which have an equatorially elongated axis and predominantly a $\chi_M''$ peak in the region 2–4 K. Solvent molecules in the crystal lattice, which might be an external factor influencing the rate of tunneling, also affect the tunneling rate. For example, different tunneling rates were observed in the $Mn_{12}$–propionate complexes $[Mn_{12}O_{12}(O_2CCH_2CH_2Cl)_{16}(H_2O)_4]\cdot 0.5CH_2Cl_2\cdot 2H_2O$ and

 © 2006 Wiley-VCH Verlag GmbH & Co. KGaA, Weinheim 

$[Mn_{12}O_{12}(O_2CCH_2CH_2Cl)_{16}(H_2O)_4]\cdot CH_2ClCH_2CO_2H$.[22] As shown in Figure 6, the rate of quantum tunneling in the magnetization of **1** is a little bit faster than that of **2** because of the unusual five-coordination around the Mn6 ion as well as the ligation of 3-thiophenecarboxylates in complex **1**. Such structural distortions can be regarded as an internal source that increases the rate of quantum tunneling.

Hysteresis loops for **1** (filled squares) and **2** (open circles) at 2 K are shown in Figure 7 (left). Small plateaus for both complexes are observed in the hysteresis loops because of quantum tunneling of magnetization (QTM). To clarify the positions of QTM, plots of $dM/dH$ vs. $H$ are drawn in Figure 7 (right). QTM occurs at the field of each peak. Plots of reduced magnetization ($M/N\mu_B$) as a function of $H/T$, where $N$ is Avogadro's number and $\mu_B$ is the Bohr magneton, were also obtained for compounds **1** and **2**. The data were fitted to the basic thermodynamic expression given in Equation (2), which takes the full power of the average of the magnetization into account:[23]

$$M = -\frac{N}{4\pi}\int_0^{2\pi}\int_0^{\pi}\frac{\sum_p (dE_p/dH)\exp(-E_p/k_BT)}{\sum_p \exp(-E_p/k_BT)} \times \sin\theta d\theta d\phi \quad (2)$$

In Equation (2), $k_B$ is the Boltzmann constant and $E_p$ is the eigenenergy obtained by diagonalization of the spin Hamiltonian matrix, including axial zero-field splitting and Zeeman interactions. The plots of reduced magnetization ($M/N\mu_B$) vs. $H/T$ fitted well with $S = 10$, $g = 1.84$, and $D = 0.61$ K for **1** and $S = 10$, $g = 1.86$, and $D = 0.65$ K for **2**.

The sulfur atoms of **2** are directed toward the outside and are able to form strong bonds to the gold surface. A molecular thin film of **2** was prepared by immersing atomically flat gold substrates in a 0.1 mM solution of **2** in toluene for more than 5 minutes. The atomically flat gold substrates were prepared by electron-beam evaporation of gold on mica at 300 °C and subsequent annealing at 500 °C for 30 minutes. XPS analysis was performed to determine the composition and the chemical state of the film of compound **2** on Au(111). A survey spectrum clearly displays the photoelectron peaks for manganese, sulfur, oxygen, carbon, and gold. Figure 8 shows the high-resolution spectrum of the Mn 2p region for the Mn12 film. The Mn $2p_{1/2}$ and $2p_{3/2}$ and peaks are observed at 654 eV and 642 eV, respectively, and are consistent with the values observed with the Mn12–ac crystal.[24] The surface morphology of the film has been investigated by STM and AFM.[25,26] These studies indicate that the thiophenyl group can be used to anchor the $Mn_{12}$ complex to the Au surface and demonstrate that individual molecules can be addressed and their physical properties can be investigated by using the SPM techniques. We plan to conduct an STM experiment at low temperatures of the SMM at the molecular level and eventually devise a strategy for the application of the SMM to quantum devices.

## Conclusions

The syntheses and X-ray structures of $[Mn_{12}O_{12}(O_2CC_4H_3S)_{16}(HO_2CC_4H_3S)(H_2O)_2]\cdot 5CH_2Cl_2$ (**1**) and $[Mn_{12}O_{12}(O_2CC_4H_3S)_{16}(H_2O)_4]\cdot 6CH_2Cl_2\cdot 2H_2O$ (**2**) are reported. There is a distorted five-coordination site due to the very unusual coordination of 3-thiophenecarboxylic acid as a terminal ligand in complex **1**. Complex **2** has normal coordination geometry. Such an internal structure distortion of **1** causes faster relaxation of magnetization in **1** relative to **2**. A molecular thin film of the Mn12 SMM has been successfully fabricated by using complex **2**. The molecules

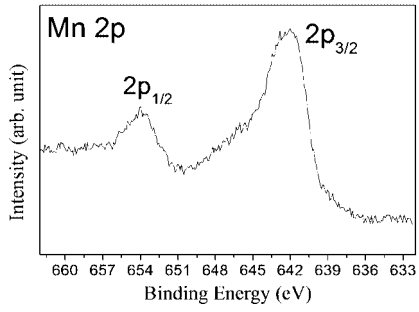


Figure 8. Photoelectron spectrum of Mn 2p core-level obtained from the film of compound **2** on Au(111) surface.

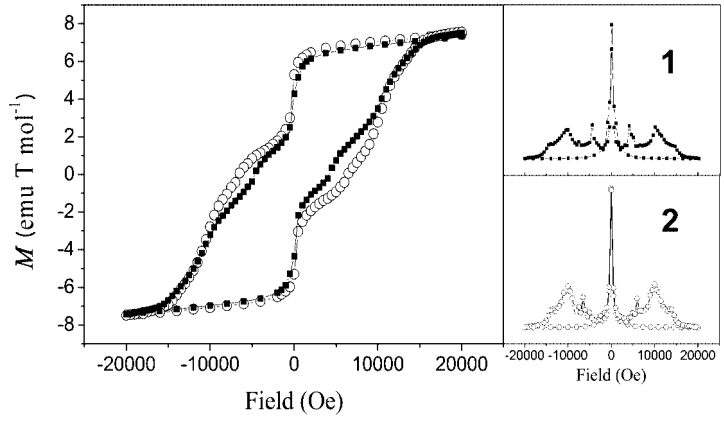


Figure 7. Hysteresis loops (left) and $dM/dH$ plots (right) of **1** (■) and **2** (○) at 2 K.

 © 2006 Wiley-VCH Verlag GmbH & Co. KGaA, Weinheim 

of **2** are anchored on a gold surface strongly through sulfur atoms of 3-thiophenecarboxylate ligands.

## Experimental Section

**General Remarks:** $Mn_{12}Ac$ was prepared according to a published procedure.[27] All reagents and solvents were purchased from commercial sources and used as received.

**Physical Measurements:** Elemental analyses were carried out by the Analytical Laboratory of the Korea Basic Science Institute, Seoul. Infrared spectra were recorded with a Perkin–Elmer 16 PC spectrophotometer. Variable-temperature magnetic susceptibility measurements were carried out on powder samples of complex **1** and complex **2** using a Quantum Design MPMS*XL* susceptometer well equipped with a 50-kG magnet. The samples were introduced into the XPS chamber by means of a load lock system. The base pressure was $1 \cdot 10^{-10}$ Torr. All XPS spectra were recorded with a VG Scientific ESCALAB MK II spectrometer using an Al-$K_\alpha$ source run at 15 kV and 10 mA. The binding energy scale was calibrated to 284.6 eV for the main C 1s peak. Each sample was analyzed at a 90° angle relative to the electron analyzer. The ac field range was $1 \cdot 10^{-4}$ to 5 Oe, oscillating at a frequency in the range $5 \cdot 10^{-4}$ to 1512 Hz. The sets of ac susceptibility data were collected for the powdered, microcrystalline sample in an ac field of 3.0 Oe, oscillating in the 20–1500 Hz range. The samples were aligned in eicosane with an applied dc field of 5 T at a temperature above the melting point of eicosane for 15 min. Corrections for the diamagnetism of the complexes were estimated using Pascal's constants, and magnetic data were corrected for diamagnetic contributions of the sample holder.

**Synthesis of Complex 1:** A slurry of $Mn_{12}Ac$ (206 mg, 0.1 mmol) in dichloromethane (30 ml) was stirred with 3-thiophenecarboxylic acid (230 mg, 1.8 mmol) for 4 h at room temperature to give a dark blown solution. Azeotropic distillation with toluene (20 ml) was performed six times to completely remove the released acetic acid, and the resultant dark brown solid was dissolved in dichloromethane and filtered. The filtrate was allowed to diffuse with pentane vapor. After a week, black crystals of **1** were collected by filtration and washed with hexane. FTIR data: 1561(s), 1522(s), 1439(s), 1358(s), 1319(s), 1208(w), 1120(w), 1073(w), 940(w), 873(w), 833(W), 754(s), 702(m), 658(m), 628(m), 517(m) $cm^{-1}$. $C_{90}H_{66}Cl_{10}Mn_{12}O_{48}S_{17}$ (3474.23): calcd. C 33.48, H 1.85, S 17.87; found C 33.41, H 1.95, S 18.21.

**Synthesis of Complex 2:** Complex **2** was synthesized in the same manner as complex **1** except that 16 equiv. 3-thiophenecarboxylic acid (215 mg, 1.8 mmol) was treated with $Mn_{12}Ac$ (205 mg, 0.1 mmol) in dichloromethane (30 mL). After several azeotropic distillations, the dark brown product was recrystalized from dichloromethane/hexane to give complex **2**. $C_{86}H_{72}Cl_{12}Mn_{12}O_{50}S_{16}$ (3503.08): calcd. C 32.10, H 2.02, S 17.14; found C 31.78, H 2.11, S 17.26.

**Crystal Structure Determination:** Reflection data were collected with a Bruker SMART CCD diffractometer using monochromated Mo-$K_\alpha$ ($\lambda$ = 0.71073 Å) radiation. The data were integrated and scaled using the SAINT software package.[28] Collected data were corrected for absorbance by using SADABS[28] based upon the Laue symmetry using equivalent reflections. Structures ware solved by the direct method and refined by least-squares calculations with the SHELXL-PLUS 5.05 software package.[29] The non-hydrogen atoms were refined anisotropically, and the geometrically restrained hydrogen atoms were treated using an appropriate riding model. A summary of the crystallographic parameters and data is given in Table 3. The proposed models include disorders of the thiophene rings and solvent molecules.

CCDC-280093 and CCDC-280094 contain the supplementary crystallographic data for this paper. These data can be obtained free of charge from The Cambridge Crystallographic Data Centre via www.ccdc.cam.ac.uk/data_request/cif.

## Acknowledgments

This work was supported by the NRL program of the Ministry of Science and Technology, Korea.

[1] D. Gatteschi, R. Sessoli, *Angew. Chem. Int. Ed.* **2003**, *42*, 268.
[2] R. Sessoli, D. Gatteschi, A. Caneschi, M. A. Novak, *Nature* **1993**, *365*, 141.
[3] R. Sessoli, H.-L. Tsai, A. R. Schake, S. Wang, J. B. Vincent, K. Folting, D. Gatteschi, G. Christou, D. N. Hendrickson, *J. Am. Chem. Soc.* **1993**, *115*, 1804.

Table 3. Details of crystallographic data collection for **1** and **2**.

| | **1** | **2** |
|---|---|---|
| Chemical formula | $C_{90}H_{66}Cl_{10}Mn_{12}O_{48}S_{17}$ | $C_{86}H_{72}Cl_{12}Mn_{12}O_{50}S_{16}$ |
| Chemical formula weight | 3474.23 | 3503.08 |
| Space group | $P\bar{1}$ | $P\bar{1}$ |
| $a$ [Å] | 17.552(1) | 15.993(1) |
| $b$ [Å] | 17.936(1) | 16.396(1) |
| $c$ [Å] | 23.957(2) | 25.628(2) |
| $\alpha$ [°] | 78.790(2) | 79.748(1) |
| $\beta$ [°] | 76.300(2) | 85.147(1) |
| $\gamma$ [°] | 64.885(2) | 80.856(1) |
| $V$ [Å$^3$] | 6596.9(9) | 6517.9(7) |
| $Z$ | 2 | 2 |
| $\rho_{calcd.}$ [g cm$^{-3}$] | 1.749 | 1.785 |
| $\mu$ [mm$^{-1}$] | 1.658 | 1.704 |
| No. of unique reflections | 28359 | 28387 |
| No. of observed reflections | 13369 [$I_o > 2\sigma(I_o)$] | 18224 [$I_o > 2\sigma(I_o)$] |
| $2\theta_{max}$ [°] | 56 | 56 |
| No. of parameters refined | 1696 | 1603 |
| $R(F)$, $wR(F_2)$ | 0.0861, 0.2503 | 0.0883, 0.2645 |
| GOF | 0.968 | 1.023 |

 © 2006 Wiley-VCH Verlag GmbH & Co. KGaA, Weinheim 

[4] L. Krusin-Elbaum, T. Shibauchi, B. Argyle, L. Gignac, D. Weller, *Nature* **2001**, *410*, 444.
[5] J. Tejada, E. M. Chudnovsky, E. del Barco, J. M. Hernandez, T. P. Spiller, *Nanotechnology* **2001**, *12*, 181.
[6] B. Zhou, R. Tao, S.-Q. Shen, J.-Q. Liang, *Phys. Rev. A* **2002**, *66*, 010301(R).
[7] G.-H. Kim, T.-S. Kim, *Phys. Rev. Lett.* **2004**, *92*, 137203.
[8] W. Liang, M. P. Shores, M. Bockrath, J. R. Long, H. Park, *Nature* **2002**, *417*, 725.
[9] M. Clemente-León, H. Soyer, E. Coronado, C. Mingotaud, C. J. Gómez-García, P. Delhaès, *Angew. Chem. Int. Ed.* **1998**, *37*, 2841.
[10] D. Ruiz-Molina, M. Mas-Torrent, J. Gomez, A. I. Balana, N. Domingo, J. Tejada, M. T. Martinez, C. Rovira, J. Veciana, *Adv. Mater.* **2003**, *15*, 42.
[11] A. Cornia, A. C. Fabretti, M. Pacchioni, L. Zobbi, D. Bonacchi, A. Caneschi, D. Gatteschi, R. Biagi, U. Del Pennino, V. De Renzi, L. Gurevich, H. S. J. Van der Zant, *Angew. Chem. Int. Ed.* **2003**, *42*, 1645.
[12] M. Cavallini, F. Biscarini, J. Gomez-Segura, D. Ruiz, J. Veciana, *Nano Lett.* **2003**, *3*, 1527.
[13] J. S. Steckel, N. S. Persky, C. R. Martinez, C. L. Barnes, E. A. Fry, J. Kulkarni, J. D. Burgess, R. B. Pacheco, S. L. Stoll, *Nano Lett.* **2004**, *4*, 399.
[14] A. Naitabdi, J.-P. Bucher, P. Gerbier, P. Rabu, M. Drillon, *Adv. Mater.* **2005**, *17*, 1612.
[15] G. G. Condorelli, A. Motta, I. L. Fragalà, F. Giannazzo, V. Raineri, A. Caneschi, D. Gatteschi, *Angew. Chem. Int. Ed.* **2004**, *43*, 4081.
[16] B. Fleury, L. Catala, V. Huc, C. David, W. Z. Zhong, P. Jegou, L. Baraton, S. Palacin, P.-A. Albouy, T. Mallah, *Chem. Commun.* **2005**, 2002.
[17] a) H. J. Eppley, H.-L. Tsai, N. de Vries, K. Folting, G. Christou, D. N. Hendrickson, *J. Am. Chem. Soc.* **1995**, *117*, 301; b) W. Jeon, M. K. Jin, Y. Kim, D.-Y. Jung, B. J. Suh, S. Yoon, *Bull. Korean Chem. Soc.* **2004**, *25*, 1036; c) J. M. Lim, Y. Do, J. Kim, *Bull. Korean Chem. Soc.* **2005**, *26*, in press.
[18] H. J. Eppley, H.-L. Tsai, N. de Vries, K. Folting, G. Christou, D. N. Hendrickson, *J. Am. Chem. Soc.* **1995**, *117*, 301.
[19] Z. Sun, D. Ruiz, E. Rumberger, C. D. Incarvito, K. Folting, A. L. Rheingold, G. Christou, D. N. Hendrickson, *Inorg. Chem.* **1998**, *37*, 4758.
[20] D. A. Garanin, E. M. Chudnovsky, *Phys. Rev. B* **2002**, *65*, 94423.
[21] S. M. J. Aubin, Z. Sun, H. J. Eppley, E. M. Rumberger, I. A. Guzei, K. Folting, P. K. Gantzel, A. L. Rheingold, G. Christou, D. N. Hendrickson, *Inorg. Chem.* **2001**, *40*, 2127.
[22] C.-D. Park, S. W. Rhee, Y. Kim, W. Jeon, D.-Y. Jung, D. Kim, Y. Do, H.-C. Ri, *Bull. Korean Chem. Soc.* **2001**, *22*, 453.
[23] V. Vermaas, W. L. Groeneveld, *Chem. Phys. Lett.* **1974**, *27*, 583.
[24] J.-S. Kang, J. H. Kim, Y. J. Km, W. S. Jeon, D.-Y. Jung, S. W. Han, K. H. Kim, K. J. Kim, B. S. Kim, *J. Korean Phys. Soc.* **2002**, *40*, L402.
[25] B. J. Kim, B. J. Suh, S. Yoon, S. H. Phark, Z. G. Khim, J. Kim, J. M. Lim, Y. Do, *J. Korean Phys. Soc.* **2004**, *45*, 1593.
[26] S. Phark, Z. G. Khim, B. J. Kim, B. J. Suh, S. Yoon, J. Kim, J. M. Lim, Y. Do, *Jpn. J. Appl. Phys., Part 1* **2004**, *43*, 8273.
[27] T. Lis, *Acta Crystallogr. Sect. B: Struct. Sci.* **1980**, *36*, 2042.
[28] Bruker AXS: Madison, WI, **1997**.
[29] R. H. Blessing, *Acta Crystallogr., Sect. A: Found. Crystallogr.* **1995**, *51*, 33.

Received: August 16, 2005
Published Online: January 3, 2006

 © 2006 Wiley-VCH Verlag GmbH & Co. KGaA, Weinheim 

DOI: 10.1002/ejic.200500438

# Synthesis and Characterization of Dinuclear Europium Complexes Showing Pure Red Electroluminescence

Hyosook Jang,[a] Chang-Hwan Shin,[a] Byung-Jun Jung,[b] Do-hyeon Kim,[a] Hong-Ku Shim,*[b] and Youngkyu Do*[a]

**Keywords:** Electroluminescence / Europium / Dinuclear complexes / 2,2′-Bipyrimidine

Two dinuclear $Eu^{III}$ complexes have been synthesized by employing β-diketones and 2,2′-bipyrimidine (bpm) as sensitizing ligands for the Eu ion and a bridging ligand, respectively, and characterized by various means including single-crystal X-ray crystallography. The use of dibenzoylmethane (dbm) and trifluorothenoylacetone (tta) as β-diketones gave $[Eu_2(dbm)_6(bpm)]$ (**1**) and $[Eu_2(tta)_6(bpm)]$ (**2**). Both show strong intermolecular π–π interactions that may be responsible for their high melting points. The analysis of the absorption, excitation, and emission spectra of the dinuclear complexes along with a comparison with analogous mononuclear complexes containing the same β-diketone ligands and 1,10-phenanthroline (phen) suggests that the dinuclear complexes follow the luminescence mechanism of general $Ln^{III}$ complexes. An EL device with the structure ITO/PEDOT/PVK + PBD + **1** 10 wt.-%/LiF/Al shows pure red emission with an efficiency similar to those of mononuclear complexes.

(© Wiley-VCH Verlag GmbH & Co. KGaA, 69451 Weinheim, Germany, 2006)

## Introduction

Luminescent metal complexes are attractive due to their potential applications in the development of organic light-emitting diodes (OLEDs),[1] sensors,[2] and molecular optoelectronic devices.[3] In particular, various metal complexes for OLEDs have been intensively studied and developed;[4,5] typical examples are lanthanide complexes.[5] Electroluminescent (EL) lanthanide complexes have the advantages of extremely narrow emission spectra and the possibility of high EL efficiency caused by the intramolecular energy transfer that consists of the absorption of energy by organic ligands, intersystem crossing into a triplet state of the organic ligands, and energy transfer to the central lanthanide cation.[5] Among lanthanide complexes, $Eu^{III}$ complexes are of particular interested because of their red emission. However, europium systems still require improvement in color purity, carrier-transporting, and thermal stability for practical use.

Although a number of mononuclear lanthanide complexes have been used in OLEDs,[5] examples of electroluminescent dinuclear lanthanide systems are very rare and to date $[Tb_2(acac\text{-}azain)_4(\mu\text{-}acac\text{-}azain)_2]$ [acac-azain = 1-(*N*-7-azaindolyl)-1,3-butanedionato], a green emitter in electroluminescent devices, is the only reported system.[6] Other dinuclear lanthanide complexes based on pyridylamine ligands ($Eu^{III}$, $Tb^{III}$, and $Dy^{III}$),[7] diketonate ligands ($Eu^{III}$, $Nd^{III}$, and $Sm^{III}$),[8] calix[8]arene ($Eu^{III}$),[9] and N,N,O donor ligands ($Sm^{III}$, $Eu^{III}$, $Tb^{III}$, and $Dy^{III}$;[10a] $La^{III}$–$Lu^{III}$[10b]) are known to display photoluminescence. It should also be noted that the lanthanide complexes $[Eu_xTb_{1-x}(acac)_3(phen)]$ ($x$ = 0–1)[11] employed in white-

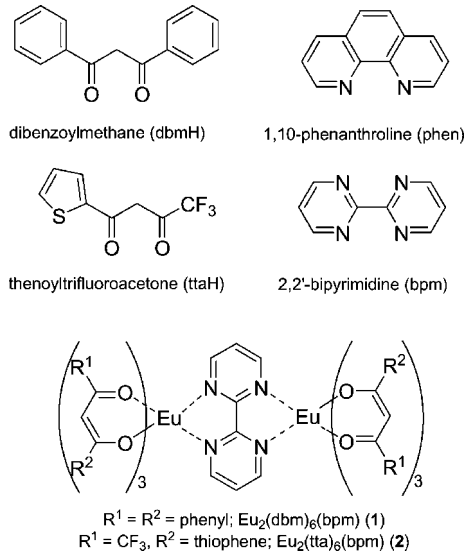


Figure 1. Molecular structures and abbreviations of the materials.

[a] Department of Chemistry, School of Molecular Science-BK21 and Center for Molecular Design and Synthesis, Korea Advanced Institute of Science and Technology,
Daejeon, 305-701, Republic of Korea
Fax: +82-42-869-2810
E-mail: ykdo@kaist.ac.kr
[b] Department of Chemistry, School of Molecular Science-BK21 and Center for Advanced Functional Polymers, Korea Advanced Institute of Science and Technology,
Daejeon, 305-701, Republic of Korea
E-mail: hkshim@kaist.ac.kr

Supporting information for this article is available on the WWW under http://www.eurjic.org or from the author.


© 2006 Wiley-VCH Verlag GmbH & Co. KGaA, Weinheim

light-emitting OLEDs have been claimed to be dinuclear systems, although in the absence of characterization data it is difficult to consider them as legitimate dinuclear systems. To lessen the scarcity of electroluminescent dinuclear lanthanide system, we have designed and synthesized a set of dinuclear $Eu^{III}$ complexes based on 2,2′-bipyrimidine (bpm) as a bridging ligand and β-diketones (L) as sensitizing ligands (Figure 1). We reported here the details of the synthesis, structures, and luminescence characteristics of $[Eu_2L_6(bpm)]$ [L = dibenzoylmethane (dbm) **1** and thenoyltrifluoroacetone (tta) **2**].

## Results and Discussion

### Syntheses and Structures

The dinuclear $Eu^{III}$ complexes $[Eu_2L_6(bpm)]$ (L = dbm, tta) were prepared in moderate yields by the reaction of $EuCl_3·6H_2O$, the corresponding β-diketone ligand, and bpm in a 2:6:1 molar ratio and fully characterized by various means. The use of $EuCl_3·6H_2O$, β-diketone ligand, and bpm in 1:3:1 molar ratio, a stoichiometric ratio for the as-yet-unknown mononuclear complex $[EuL_3(bpm)]$, also resulted in the formation of the corresponding dinuclear species. It is interesting to note that this reaction chemistry of $Eu^{III}$ was not similarly applied to diamagnetic $La^{III}$ since the analogous reaction systems with $LaCl_3·7H_2O$ gave mononuclear $[LaL_3(bpm)]$, as judged by $^1H$ NMR spectroscopy. The unavailability of mononuclear $[EuL_3(bpm)]$ led us to select the known complexes $[EuL_3(phen)]$[12] (L = dbm **3** and tta **4**) as closely corresponding mononuclear systems for comparison purposes. (Figure 1) The dinuclear $Eu^{III}$ complexes were initially isolated as solvates $[Eu_2L_6(bpm)]·2(solvent)$ (solvent = $Et_2O$ for **1** and THF for **2**) but the desolvated forms, confirmed by TGA and elemental analysis, were used for measurement purpose except the single-crystal X-ray diffraction studies. They are soluble in common organic solvents and **1** shows better solubility than **2**. Their solubility is similar to that of the corresponding mononuclear complexes **3** and **4**. They are air-stable both in the solid state and in solution. The thermal stability of the dinuclear systems, estimated by the temperature $T_{d5}$ causing 5% weight loss, is also similar to that of the corresponding mononuclear compounds, although the dinuclear species tend to have higher melting points than the mononuclear complexes.

The molecular structures of **1**·$2Et_2O$ and **2**·2THF are depicted in Figures 2 and 3, respectively. Selected bond lengths and angles are summarized in Tables 1 and 2. Compound **1** has two eight-coordinate $Eu^{III}$ sites that are separated by 7.011 Å and symmetrically related by an inversion center lying on the planar bpm moiety. The coordination sphere of each Eu center in **1** can be best described as a distorted square antiprism (Figure 4, a). The average Eu–O bond length is 2.343 Å and the average Eu–N bond length

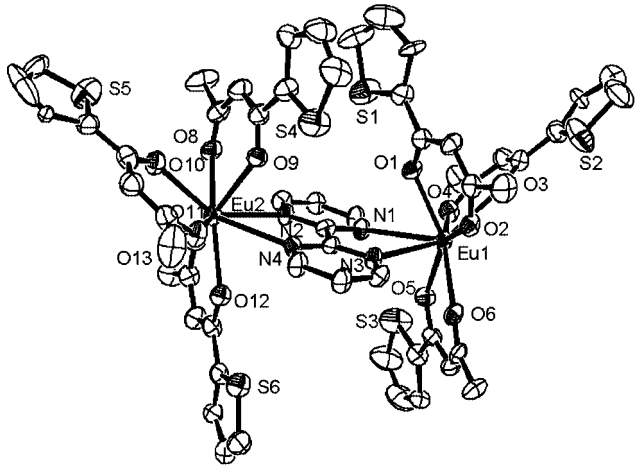


Figure 3. Molecular structure of **2**·2THF. Thermal ellipsoids are drawn at the 30% probability level. The hydrogen and fluorine atoms and tetrahydrofuran molecules have been omitted for clarity.

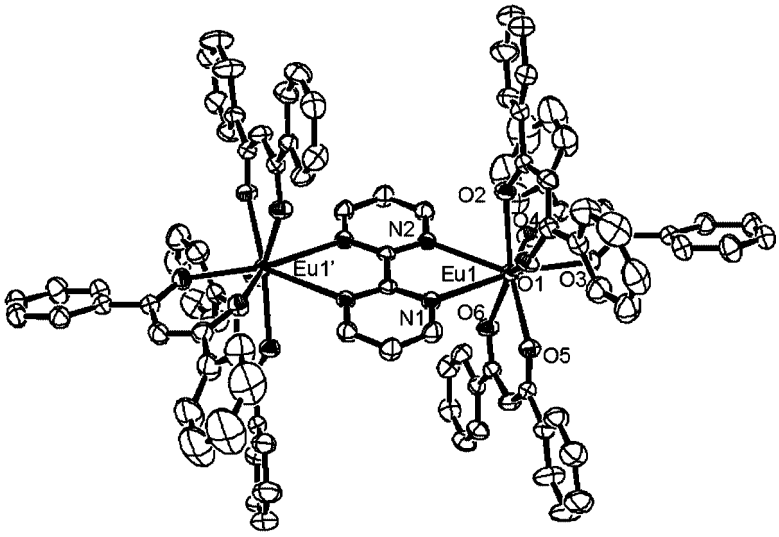


Figure 2. Molecular structure of **1**·$2Et_2O$. Thermal ellipsoids are drawn at the 30% probability level. The hydrogen atoms and diethyl ether molecules have been omitted for clarity.

 © 2006 Wiley-VCH Verlag GmbH & Co. KGaA, Weinheim 

Table 2. Selected bond lengths [Å] and angles [°] for **2**·2THF.

| | | | | | |
|---|---|---|---|---|---|
| Eu(1)–O(1) | 2.404(7) | Eu(1)–O(2) | 2.382(7) | Eu(1)–O(3) | 2.447(8) |
| Eu(1)–O(4) | 2.373(8) | Eu(1)–O(5) | 2.381(7) | Eu(1)–O(6) | 2.433(8) |
| Eu(1)–O(7) | 2.525(8) | Eu(1)–N(1) | 2.699(8) | Eu(1)–N(3) | 2.679(9) |
| Eu(2)–O(8) | 2.399(8) | Eu(2)–O(9) | 2.370(8) | Eu(2)–O(10) | 2.392(8) |
| Eu(2)–O(11) | 2.354(8) | Eu(2)–O(12) | 2.382(8) | Eu(2)–O(13) | 2.406(8) |
| Eu(2)–O(14) | 2.612(9) | Eu(2)–N(2) | 2.664(9) | Eu(2)–N(4) | 2.703(8) |
| O(1)–Eu(1)–O(2) | 73.0(2) | O(1)–Eu(1)–O(3) | 72.6(3) | O(1)–Eu(1)–O(4) | 86.4(3) |
| O(1)–Eu(1)–O(5) | 135.6(2) | O(1)–Eu(1)–O(6) | 135.1(3) | O(1)–Eu(1)–O(7) | 140.6(3) |
| O(2)–Eu(1)–O(3) | 70.6(3) | O(2)–Eu(1)–O(4) | 139.3(3) | O(2)–Eu(1)–O(5) | 144.5(3) |
| O(2)–Eu(1)–O(6) | 73.8(3) | O(2)–Eu(1)–O(7) | 92.1(3) | O(3)–Eu(1)–O(4) | 69.9(3) |
| O(3)–Eu(1)–O(5) | 130.5(3) | O(3)–Eu(1)–O(6) | 122.2(3) | O(3)–Eu(1)–O(7) | 68.0(3) |
| O(4)–Eu(1)–O(5) | 72.8(3) | O(4)–Eu(1)–O(6) | 137.9(3) | O(4)–Eu(1)–O(7) | 81.9(3) |
| O(5)–Eu(1)–O(6) | 70.7(2) | O(5)–Eu(1)–O(7) | 75.6(3) | O(6)–Eu(1)–O(7) | 69.4(3) |
| O(1)–Eu(1)–O(1) | 66.8(3) | N(1)–Eu(1)–O(2) | 125.4(3) | N(1)–Eu(1)–O(3) | 125.9(3) |
| N(1)–Eu(1)–O(4) | 73.3(3) | N(1)–Eu(1)–O(5) | 69.8(3) | N(1)–Eu(1)–O(6) | 111.8(3) |
| N(1)–Eu(1)–O(7) | 142.0(3) | N(3)–Eu(1)–O(1) | 72.4(3) | N(3)–Eu(1)–O(2) | 73.5(3) |
| N(3)–Eu(1)–O(3) | 135.5(3) | N(3)–Eu(1)–O(4) | 133.4(3) | N(3)–Eu(1)–O(5) | 93.9(3) |
| N(3)–Eu(1)–O(6) | 69.8(3) | N(3)–Eu(1)–O(7) | 139.1(3) | N(1)–Eu(1)–N(3) | 60.2(3) |
| O(8)–Eu(2)–O(9) | 71.9(3) | O(8)–Eu(2)–O(10) | 69.9(3) | O(8)–Eu(2)–O(11) | 136.7(3) |
| O(8)–Eu(2)–O(12) | 143.0(3) | O(8)–Eu(2)–O(13) | 73.6(3) | O(8)–Eu(2)–O(14) | 107.7(3) |
| O(9)–Eu(2)–O(10) | 77.4(3) | O(9)–Eu(2)–O(11) | 80.5(3) | O(9)–Eu(2)–O(12) | 131.9(2) |
| O(9)–Eu(2)–O(13) | 139.4(3) | O(9)–Eu(2)–O(14) | 141.7(3) | O(10)–Eu(2)–O(11) | 71.9(3) |
| O(10)–Eu(2)–O(12) | 134.9(3) | O(10)–Eu(2)–O(13) | 109.7(3) | O(10)–Eu(2)–O(14) | 67.3(3) |
| O(11)–Eu(2)–O(12) | 79.9(3) | O(11)–Eu(2)–O(13) | 140.0(3) | O(11)–Eu(2)–O(14) | 74.9(3) |
| O(12)–Eu(2)–O(13) | 71.8(3) | O(12)–Eu(2)–O(14) | 71.9(3) | O(13)–Eu(2)–O(14) | 69.9(3) |
| N(2)–Eu(2)–O(8) | 71.6(3) | N(2)–Eu(2)–O(9) | 78.3(3) | N(2)–Eu(2)–O(10) | 139.2(3) |
| N(2)–Eu(2)–O(11) | 134.5(3) | N(2)–Eu(2)–O(12) | 85.2(3) | N(2)–Eu(2)–O(13) | 71.1(3) |
| N(2)–Eu(2)–O(14) | 139.2(3) | N(4)–Eu(2)–O(8) | 120.9(3) | N(4)–Eu(2)–O(9) | 66.4(3) |
| N(4)–Eu(2)–O(10) | 133.6(3) | N(4)–Eu(2)–O(11) | 74.1(3) | N(4)–Eu(2)–O(12) | 66.1(3) |
| N(4)–Eu(2)–N(13) | 116.7(3) | N(4)–Eu(2)–O(14) | 131.0(3) | N(2)–Eu(2)–N(4) | 60.6(3) |

is 2.677 Å. In the case of the analogous mononuclear complex **3**, the average Eu–O and Eu–N lengths are 2.355 and 2.642 Å, respectively.[13] The crystal of **1**·2$Et_2O$ contains moderate bimolecular π–π interactions between the phenyl rings of the dbm ligands, with an average π–π interaction distance of 3.765 Å, as shown in Figure 5. The stacking interactions are only present between the dimeric pairs.

Table 1. Selected bond lengths [Å] and angles [°] for **1**·2$Et_2O$.

| | | | |
|---|---|---|---|
| Eu(1)–O(1) | 2.335(2) | Eu(1)–O(5) | 2.338(2) |
| Eu(1)–O(4) | 2.354(2) | Eu(1)–N(2) | 2.675(3) |
| Eu(1)–N(1) | 2.679(3) | Eu(1)–O(3) | 2.329(2) |
| Eu(1)–O(2) | 2.363(2) | Eu(1)–O(6) | 2.338(2) |
| O(1)–Eu(1)–O(2) | 71.65(8) | O(1)–Eu(1)–O(3) | 9.79(9) |
| O(1)–Eu(1)–O(4) | 138.50(8) | O(1)–Eu(1)–O(5) | 74.56(8) |
| O(1)–Eu(1)–O(6) | 143.25(8) | O(2)–Eu(1)–O(3) | 85.78(9) |
| O(2)–Eu(1)–O(4) | 76.11(9) | O(2)–Eu(1)–O(5) | 146.00(9) |
| O(2)–Eu(1)–O(6) | 142.18(9) | O(3)–Eu(1)–O(4) | 72.37(9) |
| O(3)–Eu(1)–O(5) | 84.78(9) | O(3)–Eu(1)–O(6) | 110.01(9) |
| O(4)–Eu(1)–O(5) | 130.88(9) | O(4)–Eu(1)–O(6) | 76.54(9) |
| O(5)–Eu(1)–O(6) | 71.37(8) | N(1)–Eu(1)–O(1) | 74.47(8) |
| N(1)–Eu(1)–O(2) | 7.96(8) | N(1)–Eu(1)–O(3) | 151.22(9) |
| N(1)–Eu(1)–O(4) | 136.30(9) | N(1)–Eu(1)–O(5) | 76.22(9) |
| N(1)–Eu(1)–O(6) | 84.35(9) | N(2)–Eu(1)–O(1) | 115.10(9) |
| N(2)–Eu(1)–O(2) | 71.39(8) | N(2)–Eu(1)–O(3) | 145.45(8) |
| N(2)–Eu(1)–O(4) | 77.09(9) | N(2)–Eu(1)–O(5) | 128.33(8) |
| N(2)–Eu(1)–O(6) | 77.41(8) | N(1)–Eu(1)–N(2) | 60.41(8) |

For compound **2**, the Eu–Eu, average Eu–O, and average Eu–N distances are similar to those in **1** (6.993, 2.394, 2.687 Å, respectively), although the coordination sphere of a distorted hendecahedron (square bicapped trigonal prism; Figure 4, b)[14] for **2** is different from that for **1**. The two pyrimidine rings on the bpm ligand deviate slightly from planarity by 6.3°. The crystal of **2**·2THF exhibits two types of moderate π–π interactions, as shown in Figure 6: one is an intramolecular π–π interaction between the closer thiophene rings in a molecule and the other is a bimolecular π–π interaction between the thiophene rings of neighboring molecules. The average π–π interaction distances are 3.861 and 3.892 Å, respectively, and the stacking interactions are not extended into a one-dimensional array but are isolated between the dimeric pairs, as in **1**. We consider that these bimolecular π–π interactions, as well as the high molecular weight, might be responsible for the lack of sublimability of **1**·2$Et_2O$ and **2**·2THF.

The dinuclear entities of **1** and **2** are considered to remain unchanged in solution. Their electrospray mass spectra (see Exp. Sect. and Figure S1 in the Supporting Information) contain peaks centered at *m/z* = 1577 and 1568 assignable to $[(dbm)_3Eu(bpm)Eu(dbm)_2]^+$ and $[(tta)_3Eu(bpm)Eu(tta)_2]^+$, respectively, thereby demonstrating the formation of dinuclear species as well as the existence of the coordinated β-diketone sensitizing (dbm or tta) and bridging (bpm) ligands in solution. Additional efforts to probe the solution structures of paramagnetic lanthanide complexes **1** and **2** by recording the $^1H$ NMR spectra of the diamagnetic analogues to avoid the line-broadening effect associated with paramagnetism[8] were hampered by the dissimilar reactivity of $Eu^{III}$ and $La^{III}$ mentioned above.

 © 2006 Wiley-VCH Verlag GmbH & Co. KGaA, Weinheim 

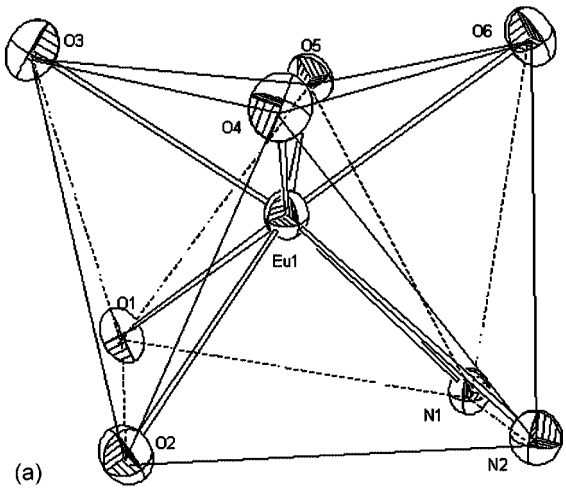


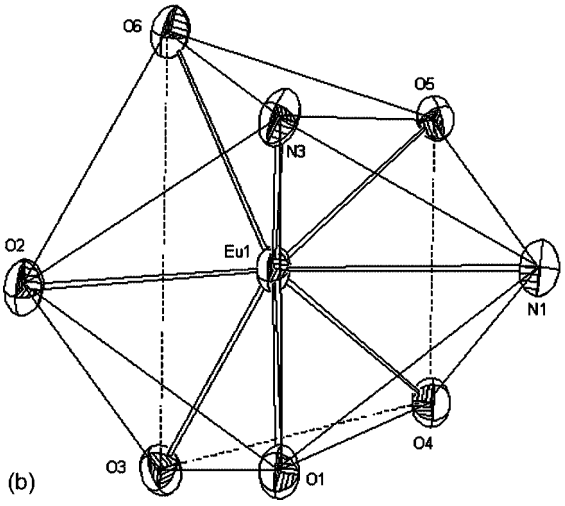


Figure 4. Coordination spheres of **1** (a) and **2** (b).

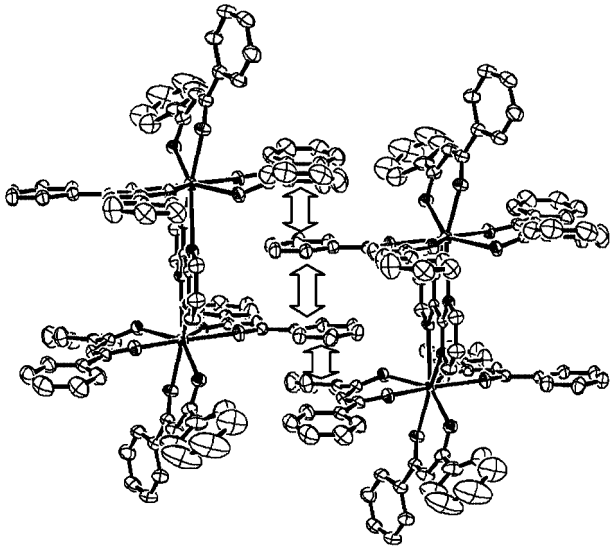

Figure 5. π-Stacked dimer in **1**·2$Et_2O$.

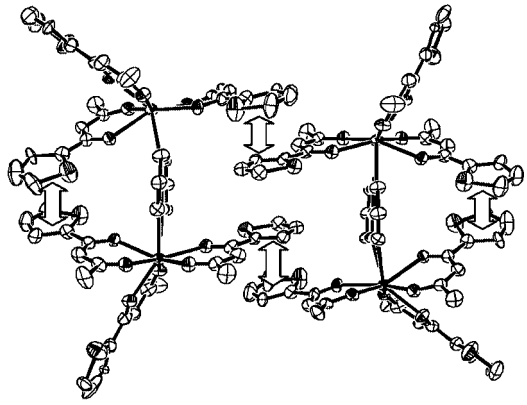

Figure 6. π-Stacked dimer in **2**·2THF.

### Absorption and Photoluminescence Properties

The UV/Vis absorption spectra and the normalized PL spectra of the dinuclear europium complexes **1** and **2** and their closely corresponding mononuclear complexes **3** and **4**, in chloroform, are illustrated in Figures 7 and 8, respectively. A close inspection of Figure 7 and the spectroscopic data summarized in Table 3 reveal that the electronic excitation spectra of all the europium complexes are similar and contain features similar to those of the uncoordinated β-diketone ligands (dbmH and ttaH) regardless of the nuclearity. The strong absorption around 350 nm is attributed to the $\pi \rightarrow \pi^*$ transition of the β-diketone ligands.[15] The excitation spectra also show features similar to the absorption spectra of the Eu complexes and are red-shifted by about 30 nm (see Table 3 and Table S2 in the Supporting Information), thus indicating the indirect excitation by energy transfer from the ligand to the $Eu^{III}$ ion.[8b,10a] Hence, we expect that the dinuclear complexes have the same luminescence mechanism mentioned in the Introduction. In fact, compounds **1**–**4** show very similar normalized PL spectra. All the complexes exhibit five peaks at 580, 591, 612, 651, and 692 nm corresponding to the $^5D_0 \rightarrow {}^7F_J$ ($J$ = 0–4) transitions of the $Eu^{3+}$ ion, respectively.[16] However, the full width at half maximum (FWHM) of the most intense $^5D_0 \rightarrow {}^7F_2$ transition at 612 nm in **1** and **2** is broader than that of **3** and **4**. We consider that the broadening of this hyper-

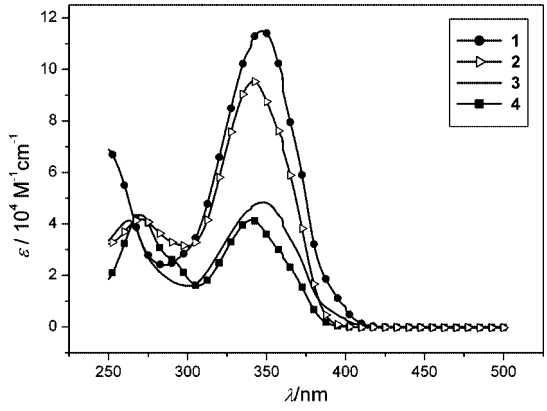


Figure 7. UV/Vis absorption spectra of **1**–**4** in chloroform solution.

 © 2006 Wiley-VCH Verlag GmbH & Co. KGaA, Weinheim 

sensitive transition arises from the fluxionality of the larger bimetallic complexes in solution compared to monometallic species.

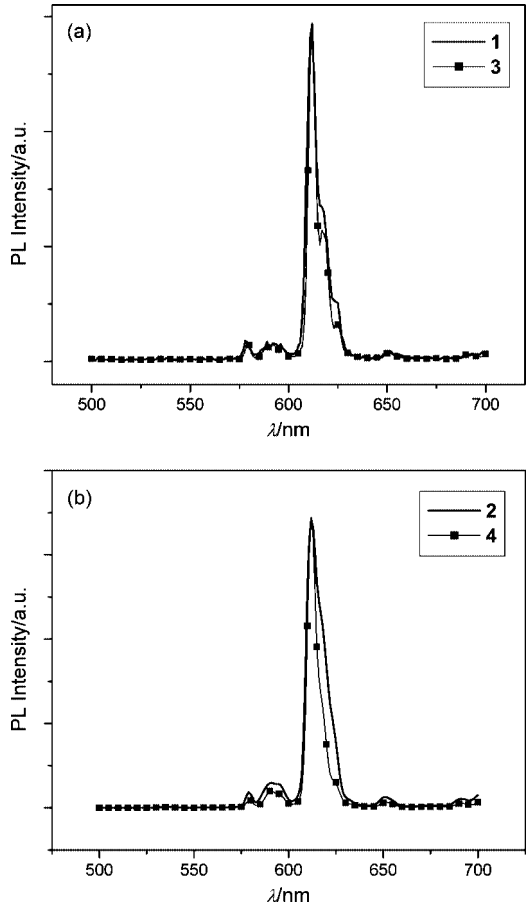


Figure 8. Normalized PL spectra of (a) dbm-containing complexes (**1**, **3**) and (b) tta-containing complexes (**2**, **4**) in chloroform solution.

The PL quantum efficiency of **1**–**4** measured in very dilute solutions of nearly the same optical density[17] decreases in the order **4** > **2** >> **1** ≈ **3** (Table 3). In addition, the europium complexes **1**, **3** containing the tta ligand show a higher efficiency than those (**2**, **4**) containing a dbm ligand due to the inductive effect of the thiophene and the fluorine substituent.[18]

The absorption and emission characteristics of **1**–**4** doped (4, 5, and 10 wt.-%) in PVK/PBD (7:3) films were also investigated. PVK, which has a good hole-transporting ability, was employed since its emission partially overlaps with the absorption spectra of the four Eu complexes. PBD is known to be a good electron-transporting and hole-blocking material and is widely used in polymer LEDs.[19] The 7:3 ratio of PVK/PBD was employed since the same mixed system has been used to fabricate white-light-emitting organic electroluminescent devices[19b] and the use of a large amount of discrete PBD would result in poor film quality. The UV/Vis spectra of the films are almost equal to that of a blank PVK/PBD host film. The minimum doping concentration at which red luminescence of $Eu^{3+}$ appears without the occurrence of PVK/PBD host emission is 10 wt.-% for **1**–**3** and 5 wt.-% for **4**. In addition, the shape of the film PL spectrum of each compound is similar to that of the solution PL spectrum. Therefore, a 7:3 PVK/PBD mixture is a good host for these dinuclear systems.

## Electroluminescent Properties

The EL devices were fabricated with a structure ITO/PEDOT (30 nm)/PVK + PBD + Eu complex (≈80 nm)/LiF (1 nm)/Al (100 nm). Chloroform and 1,2-dichloroethane (DCE) solutions were tested for spin-coating, and the DCE solution was chosen because of the better quality of its films. However, the films of tta-based complexes **2** and **4** were still of poor quality and many pin-holes and dark spots were formed immediately when the devices were operated, thus hampering the fabrication of stable EL devices with these complexes. On the other hand, dbm-containing complexes **1** and **3** show good film quality and stable red light emission. The EL spectra of **1**- and **3**-based devices (in Figure 9) resemble their PL spectra, thus the emission originates from $Eu^{3+}$ and differs only in the intensity at 593 and 625 nm. Nonetheless, **1** emits pure red light with the CIE color coordinate (0.66, 0.34) while **3** emits red-orange light with the CIE color coordinate (0.65, 0.33). The CIE color coordinate of NTSC pure red is (0.67, 0.33). Generally, in the blended system the CIE color coordinate is known to vary as the current density increases[6,20] but the extent of such a change in **1** is much smaller than in **3**, as shown in Figure 10. The EL device with **1** has a turn-on voltage ($V_T$) of 12 V, a maximum brightness ($L_{max}$) of 25.4 cd m$^{-2}$ at 16 V (Figure 11), and a quantum efficiency ($\eta_{EL}$) of 0.021% at 11 V. The EL characteristics of the **3**-

Table 3. Spectroscopic properties in $CHCl_3$ solution.

| Complex | $\lambda_{abs}$ [nm] ($\varepsilon$ [$10^4$ M$^{-1}$ cm$^{-1}$]) | $\lambda_{ex}$ [nm] | $\lambda_{em}$ [nm] ($\eta$)[a] | FWHM [nm] |
|---|---|---|---|---|
| **1** | 347 (11.5), 250 (6.9) | 388 | 612 (0.0016) | 7 |
| **2** | 341 (9.5), 271 (4.2) | 379, 289, 254 | 612 (0.0624) | 11 |
| **3** | 348 (4.8), 263 (4.1) | 388, 286(w)[b] | 612 (0.0029) | 5 |
| **4** | 340 (4.2), 270 (4.3) | 373, 312, 289, 252 | 612 (0.105) | 6 |
| dbmH | 346, 257 | – | – | – |
| ttaH | 350, 264 | – | – | – |
| bpm | 250 | – | – | – |
| phen | 265 | – | – | – |

[a] PL quantum efficiency was determined in $CH_2Cl_2$ solution by using quinine sulfate dihydrate in 1 N $H_2SO_4$ solution ($\eta$ = 0.55) as a standard.[16] [b] w: weak.

 © 2006 Wiley-VCH Verlag GmbH & Co. KGaA, Weinheim 

based device are similar to those of the **1**-based device, with $V_T$ = 12 V, $L_{max}$ = 30.2 cd m$^{-2}$ at 14 V, and $\eta_{EL}$ = 0.012 at 11 V (see Figure S3 in the Supporting Information).

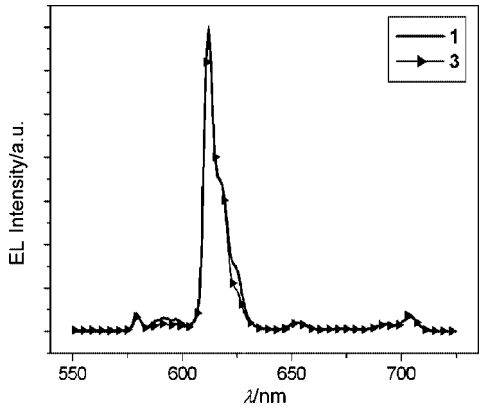


Figure 9. Comparison with normalized EL spectra of **1**- and **3**-based devices.

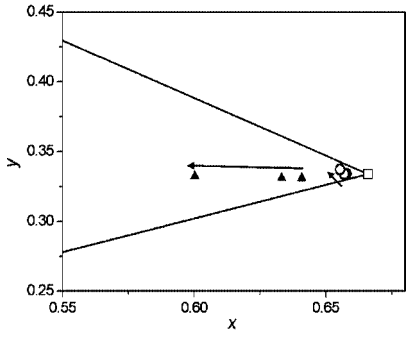


Figure 10. CIE color coordinates of **1**- (○) and **3**-based devices (▲) at a current density of 10, 20, and 100 mA cm$^{-2}$ and the NTSC pure red (□).

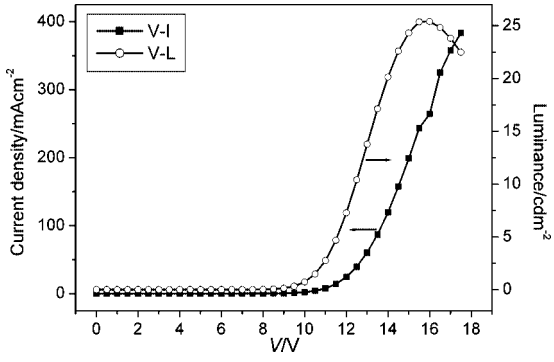


Figure 11. I-V-L characteristics of the **1**-based device.

## Conclusions

Two new dinuclear $Eu^{III}$ complexes with formula $[Eu_2L_6(bpm)]$ have been synthesized and fully characterized. Single-crystal X-ray diffraction analyses reveal their dimeric structures formed due to intermolecular π–π interactions, which seem to contribute to the lack of sublimability to some degree. It seems that the solution PL efficiency depends more on the β-diketone sensitizing ligand than the nuclearity or the bridging ligand. The dinuclear compounds are also considered to follow the luminescence mechanism adopted in mononuclear lanthanide complexes. $[Eu_2(dbm)_6(bpm)]$ (**1**) readily forms a polymer EL device ITO/PEDOT (30 nm)/PVK + PBD + Eu complex (≈80 nm)/LiF (1 nm)/Al (100 nm) that produces pure red EL. Overall, the dinuclear system shows similar thermal stability, improved EL color purity, and comparable EL efficiency with respect to the corresponding mononuclear system. Nonetheless, in order to further confirm the concept of dinuclear europium systems in developing pure red EL materials, a synthetic route to sublimable dinuclear europium complexes needs to be developed. A search for ligand systems that can not only block the formation of intermolecular π–π interactions but also have good carrier-transporting ability is in progress.

## Experimental Section

**Materials:** The experiments were carried out using standard Schlenk techniques. THF and *n*-hexane were distilled from Na-K alloy, diethyl ether ($Et_2O$) from Na-benzophenone ketyl, and $CH_2Cl_2$ from $CaH_2$. Ethanol and other reagents were used without any further purification after purchase from Hayman (ethanol), Aldrich (dbmH, ttaH, phen, $EuCl_3·6H_2O$), and Lancaster (bpm). $[Eu(dbm)_3(phen)]$ (**3**) and $[Eu(tta)_3(phen)]$ (**4**) were prepared according to a literature procedure,[12b] purified from THF/*n*-hexane and dried at 110 °C at $10^{-5}$ Torr for 6 h. Chemicals for EL devices were purchased from Aldrich [poly(9-vinylcarbazole) (PVK), 2-(4-biphenylyl)-5-(4-*tert*-butylphenyl)-1,3,4-oxadiazole (PBD), LiF, Al, and anhydrous 1,2-dichloroethane (DCE)] and Bayer [poly(styrenesulfonate)-doped poly(3,4-ethylenedioxythiophene) (PEDOT)] and used without further purification.

**Synthesis of $[Eu_2(dbm)_6(bpm)]$ (1):** Aqueous NaOH solution (3.0 mL, 1.0 M) and then, rapidly, an aqueous solution of $EuCl_3·6H_2O$ (0.37 g, 1.0 mmol) were added to a 30-mL ethanol solution of dbmH (0.67 g, 3.0 mmol) and bpm (0.079 g, 0.50 mmol) in a two-necked flask. The reaction mixture was refluxed at 60 °C for 12 h and cooled to ambient temperature to give a yellow precipitate, which was filtered off and washed with water and ethanol. The resulting solid was air-dried and recrystallized from a $CH_2Cl_2$/$Et_2O$ solution as yellow crystals of **1**·2$Et_2O$. The solvate $Et_2O$ molecules in the crystals were removed at 110 °C under a vacuum of $10^{-5}$ Torr for 6 h after grinding. Yield: 1.1 g (59%). M.p. 240–242 °C. $T_{d5}$ = 300 °C. IR (KBr): $\tilde{\nu}$ = 444, 511, 609, 656, 670, 687, 719, 940, 1070, 1218, 1310, 1408, 1458, 1478, 1522, 1547, 1595 cm$^{-1}$. $C_{98}H_{72}Eu_2N_4O_{12}$ (1802.4): calcd. C 65.33, H 4.03, N 3.11; found C 64.88, H 4.02, N 3.12. MS (ESI): *m*/*z* = 159 [bpm + H]$^+$, 225 [dbmH + H]$^+$, 756 $[(dbm)_2Eu(bpm)]^+$, 822 $[(dbm)_3Eu + H]^+$, 914 $[(dbm)_2Eu(bpm)_2]^+$, 980 $[(dbm)_3Eu(bpm) + H]^+$, 1048 $[(dbm)_4Eu + 2H]^+$, 1577 $[(dbm)_3Eu(bpm)Eu(dbm)_2]^+$.

**Synthesis of $[Eu_2(tta)_6(bpm)]$ (2):** This complex was synthesized by an analogous method to **1** but with 3.0 mmol (0.67 g) of ttaH. Recrystallization from THF/*n*-hexane afforded light-yellow crystals of **2**·2THF. The solvate THF molecules in the crystals were removed at 110 °C under a vacuum of $10^{-5}$ Torr for 6 h after grinding. Yield: 1.1 g (59%). M.p. 268–270 °C. $T_{d5}$ = 305 °C. IR (KBr): $\tilde{\nu}$ = 499, 582, 641, 683, 759, 793, 935, 1061, 1143, 1187, 1231, 1251, 1308, 1354, 1413, 1459, 1509, 1540, 1580, 1600 cm$^{-1}$.

 © 2006 Wiley-VCH Verlag GmbH & Co. KGaA, Weinheim 

Table 4. Crystallographic data for **1**·2$Et_2O$ and **2**·2THF.

| | **1**·2$Et_2O$ | **2**·2THF |
|---|---|---|
| Formula | $C_{49}H_{36}EuN_2O_6$·($C_4H_{10}O$) | $C_{56}H_{30}Eu_2F_{18}N_4O_{12}S_6$·($C_8H_{16}O_2$) |
| $M$ | 974.88 | 1933.33 |
| Crystal system | monoclinic | triclinic |
| Space group | $P2_{1/n}$ | $P\bar{1}$ |
| $a$ [Å] | 10.9094(13) | 10.198(2) |
| $b$ [Å] | 23.016(3) | 18.211(4) |
| $c$ [Å] | 19.176(2) | 23.169(5) |
| $\alpha$ [°] | 90 | 102.378(4) |
| $\beta$ [°] | 99.202(2) | 102.121(4) |
| $\gamma$ [°] | 90 | 100.233(4) |
| $V$ [Å$^3$] | 4752.9(10) | 3995.7(15) |
| $Z$ | 4 | 2 |
| $D_{calc}$ [g cm$^{-3}$] | 1.362 | 1.607 |
| $\mu$ [mm$^{-1}$] | 1.372 | 1.813 |
| No. of reflections measured | 55647 | 46354 |
| No. of reflections used ($R_{int}$) | 11275 (0.0518) | 18300 (0.0851) |
| Final $R$ [$I > 2\sigma(I)$] $R_1$,[a] $wR_2$[b] | 0.0337, 0.0690 | 0.0763, 0.2085 |
| Goodness of fit on $F^2$ | 0.930 | 0.960 |

[a] $R_1 = \Sigma||F_0| - |F_c||/\Sigma|F_0|$. [b] $wR_2 = [\Sigma\{w(F_0^2 - F_c^2)^2\}/\Sigma\{w(F_0^2)\}^2]^{1/2}$, where $w = 1/[\sigma^2(F_0^2) + (xP)^2 + yP]$ and $P = (F_0^2 + 2F_c^2)/3$.

$C_{56}H_{30}Eu_2F_{18}N_4O_{12}S_6$ (1789.8): calcd. C 37.59, H 1.69, N 3.13; found C 37.72, H 1.58, N 3.21. MS (ESI): $m/z$ = 159 [bpm + H]$^+$, 181 [bpm + Na]$^+$, 752 [$(tta)_2Eu(bpm)$]$^+$, 910 [$(tta)_2Eu(bpm)_2$]$^+$, 1522 [$(tta)_2Eu(bpm)_2Eu(tta)_2$ + OH$^-$]$^+$, 1568 [$(tta)_3Eu(bpm)$-$Eu(tta)_2$]$^+$.

**X-ray Crystallography:** Suitable crystals of **1**·2$Et_2O$ and **2**·2THF were obtained by diffusion of $Et_2O$ into a $CH_2Cl_2$ solution and *n*-hexane into a THF solution, respectively. Reflection data were collected on a Bruker 1 K SMART CCD-based diffractometer with graphite-monochromated Mo-$K_\alpha$ radiation ($\lambda$ = 0.71073 Å) at 293 K. A hemisphere of reflection data was collected as $\omega$ scan frames with a width of 0.3° per frame and an exposure time of 10 s per frame. Cell parameters were determined and refined with the SMART program.[21] Data reductions were performed with SAINT,[22] which corrects for Lorentz polarization effects; no corrections for crystal decay were required. Empirical absorption corrections were applied with SADABS.[23] The structures of the compounds were solved by direct methods and refined by full-matrix least-squares methods using the SHELXTL program package with anisotropic thermal parameters for all non-hydrogen atoms. Hydrogen atoms were placed at their geometrically calculated positions and refined riding on the corresponding carbon atoms with isotropic thermal parameters. Crystal data for both systems are summarized in Table 4.

CCDC-250346 (for **1**) and -250347 (for **2**) contain the supplementary crystallographic data for this paper. These data can be obtained free of charge from The Cambridge Crystallographic Data Center via www.ccdc.cam.ac.uk/data_request/cif.

**Instrumentation:** Infrared spectra were obtained from KBr pellets with a Bruker EQUINOX-55 spectrometer. Elemental analyses were performed on an EA1110-FISONS (CE Instruments) by the Environmental Analysis Laboratory at KAIST. Electrospray mass spectra were measured on a Mariner instrument at the Korea Basic Science Institute. Melting points were determined on an Electrothermal IA 9100 apparatus. Thermogravimetric analyses (TGA) were carried out under a nitrogen atmosphere at a heating rate of 10 °C min$^{-1}$ with a Dupont 9900 Analyzer. UV/Vis spectra were obtained with a Jasco V-530 spectrophotometer. PL spectra and PL quantum efficiency were recorded with a Spex Fluorog-3 luminescence spectrometer. Excitation spectra were obtained with a Perkin–Elmer LS 50B luminescence spectrometer.

**Fabrication of EL Devices:** The configuration of the EL device was ITO/PEDOT/emitting layer (EML)/LiF/Al. PEDOT, used as a hole-injection layer, was spin-coated onto a pre-cleaned ITO/glass substrate at a spin speed of 1500 rpm for 60 s. Then, a layer of Eu complex-doped PVK/PBD (7:3) was fabricated by spin-coating from their 1,2-dichloroethane solutions (10–11 mg mL$^{-1}$) at 1250 rpm for 60 s. The film thickness of the EML was determined with a TENCOR alpha-step 500 profiler and was approximately 80 nm. LiF (1 nm) and Al (100 nm) were deposited on top of the EML using the vacuum-evaporation method at a pressure of $10^{-6}$ Torr. EL spectra were obtained with a Minolta CS-1000. The current–voltage and luminance–voltage characteristics were recorded with a current–voltage source (Keithley 238) and a luminescence detector (Minolta LS-100), respectively. All EL measurements were carried out at room temperature under an ambient atmosphere.

## Acknowledgments

The authors gratefully acknowledge financial support from the Korea Science and Engineering Foundation (R02-2002-000-00057-0), CMDS, MOCIE, and the BK 21 Project.

[1] a) S. Miyata, H. S. Nalwa, *Organic Electroluminescent Materials and Devices*, Gordon and Breach Publishers, The Netherlands, **1997**; b) D. M. Roundhill, J. P. Fackler, *Optoelectronic Properties of Inorganic Compounds*, Plenum Press, New York, **1999**; c) U. Mitschke, P. Bauerle, *J. Mater. Chem.* **2000**, *10*, 1471; d) L. S. Hung, C. H. Chen, *Mater. Sci. Eng., R* **2002**, *39*, 143.

[2] a) E. Cariati, J. Bourassa, P. C. Ford, *Chem. Commun.* **1998**, 1623; b) M. Montalti, L. Prodi, N. Zaccheroni, L. Charbonniere, L. Douce, R. Ziessel, *J. Am. Chem. Soc.* **2001**, *123*, 12694; c) V. W.-W. Yam, S.-K. Yip, L.-H. Yuan, K.-L. Cheung, N. Zhu, K.-K. Cheung, *Organometallics* **2003**, *22*, 2630; d) K. K.-W. Lo, C.-K. Chung, T. K.-W. Lee, L.-H. Lui, K. H.-K. Tsang, N. Zhu, *Inorg. Chem.* **2003**, *42*, 6886.

[3] a) L. Fabbrizzi, F. Foti, M. Licchelli, P. M. Maccarini, D. Sacchi, M. Zema, *Chem. Eur. J.* **2002**, *8*, 4965; b) M. Hissler, J. E. McGarrah, W. B. Connick, D. B. Geiger, S. D. Cummings, R. Eisenberg, *Coord. Chem. Rev.* **2000**, *208*, 115.

[4] a) Y. Hamada, *IEEE Trans. Elec. Dev.* **1997**, *44*, 1208; b) C. H. Chen, J. Shi, *Coord. Chem. Rev.* **1998**, *171*, 161; c) S. Wang,

 © 2006 Wiley-VCH Verlag GmbH & Co. KGaA, Weinheim 

*Coord. Chem. Rev.* **2001**, *215*, 79; d) C. W. Tang, S. A. VanSlyke, *Appl. Phys. Lett.* **1987**, *51*, 913; e) S. Lamansky, P. Djurovich, D. Murphy, F. Abdel-Razzaq, H.-E. Lee, C. Adachi, P. E. Burrows, S. R. Forrest, M. E. Thompson, *J. Am. Chem. Soc.* **2001**, *123*, 4304.

[5] a) J. Kido, Y. Okamoto, *Chem. Rev.* **2002**, *102*, 2357 and references cited therein; b) M. D. McGehee, T. Bergstedt, C. Zhang, A. P. Saab, M. B. O'Regem, G. C. Bazan, V. I. Srdanov, A. J. Heeger, *Adv. Mater.* **1999**, *11*, 1349; c) G. Yu, Y. Liu, X. Wu, D. Zhu, H. Li, L. Jin, M. Wang, *Chem. Mater.* **2000**, *12*, 2537; d) X. Jiang, A. K.-Y. Jen, D. Huang, G. D. Phelan, T. M. Londergan, L. R. Dalton, *Synth. Met.* **2002**, *125*, 331; e) M. Sun, H. Xin, K.-Z. Wang, Y.-A. Zhang, L.-P. Jin, C.-H. Huang, *Chem. Commun.* **2003**, 702; f) F. Liang, Q. Zhou, Y. Cheng, L. Wang, D. Ma, X. Jing, F. Wang, *Chem. Mater.* **2003**, *15*, 1935; g) P.-P. Sun, J.-P. Duan, H.-T. Shih, C.-H. Cheng, *Appl. Phys. Lett.* **2002**, *81*, 792.

[6] a) Y. Wang, D. Song, C. Seward, Y. Tao, S. Wang, *Inorg. Chem.* **2002**, *41*, 5187.

[7] W.-Y. Yang, L. Chen, S. Wang, *Inorg. Chem.* **2001**, *40*, 507.

[8] a) M. M. Castaño-Briones, A. P. Bassett, L. L. Meason, P. R. Ashton, Z. Pikramenou, *Chem. Commun.* **2004**, 2832; b) A. P. Bassett, S. W. Magennis, P. B. Glover, D. J. Lewis, N. Spencer, S. Parsons, R. M. Williams, L. De Cola, Z. Pikramenou, *J. Am. Chem. Soc.* **2004**, *126*, 9413.

[9] J.-C. G. Bünzli, F. Besançon, *Phys. Chem. Chem. Phys.* **2005**, *7*, 2191.

[10] a) V. Patroniak, P. N. W. Baxter, J.-M. Lehn, Z. Hnatejko, M. Kubicki, *Eur. J. Inorg. Chem.* **2004**, 2379; b) K. Zeckert, J. Hamacek, J.-P. Rivera, S. Floquet, A. Pinto, M. Borkovec, C. Piquet, *J. Am. Chem. Soc.* **2004**, *126*, 11589.

[11] D. Zhao, W. Li, Z. Hong, X. Liu, C. Liang, D. Zhao, *J. Lumin.* **1999**, *82*, 105.

[12] a) J. Kido, H. Hayase, K. Hongawa, K. Nagai, K. Okuyama, *Appl. Phys. Lett.* **1994**, *65*, 2124; b) T. Sano, M. Fujita, T. Fujii, Y. Hamada, K. Shibata, K. Kuroki, *Jpn. J. Appl. Phys.* **1995**, *34*, 1883.

[13] a) M. O. Ahmed, J.-L. Liao, X. Chen, S.-A. Chen, J. H. Kaldis, *Acta Crystallogr., Sect. E* **2003**, *59*, m29; b) Y. Jian, H. Xian, Z. Zhong-Yuan, L. Li, *J. Struct. Chem.* **1989**, *8*, 187.

[14] a) C. W. Haigh, *Polyhedron* **1996**, *15*, 605; b) S. J. Lippard, *Prog. Inorg. Chem.* **1967**, *8*, 109.

[15] a) N. J. Turro, *Modern Molecular Photochemistry*, University Science Books, Herndon, USA, **1991**, p.77; b) J.-C. G. Bünzli, E. Moret, V. Foiret, K. J. Schenk, W. Mingzhao, J. Linpei, *J. Alloys Compd.* **1994**, *207/208*, 107.

[16] L. Huang, K.-Z. Wang, C.-H. Huang, F.-Y. Li, Y.-Y. Huang, *J. Mater. Chem.* **2001**, *11*, 790.

[17] a) G. E. Hardy, W. C. Kaska, B. P. Chandra, J. I. Zink, *J. Am. Chem. Soc.* **1981**, *103*, 1074; b) H. S. Joshi, R. Jamishidi, Y. Tor, *Angew. Chem. Int. Ed.* **1999**, *38*, 2722.

[18] a) C. N. R. Rao, J. R. Ferraro, *Spectroscopy in Inorganic Chemistry*, vol. 2, Academic Press, New York, USA, **1971**; b) J. Yuan, K. Matsumoto, *Anal. Sci.* **1996**, *12*, 31.

[19] a) S. Miyata, H. S. Nalwa, *Organic Electroluminescent Materials and Devices*, Gordon and Breach Publishers, The Netherlands, **1997**, p. 203; b) J. Kido, H. Shionoya, K. Nagai, *Appl. Phys. Lett.* **1995**, *67*, 2281.

[20] a) J. Wang, R. Wang, J. Yang, Z. Zheng, M. D. Carducci, T. Cayou, N. Peyghambarian, G. E. Jabbour, *J. Am. Chem. Soc.* **2001**, *123*, 6179; b) H. Heil, J. Steiger, R. Schmechel, H. von Seggern, *J. Appl. Phys.* **2001**, *90*, 535.

[21] *SMART*, *Version 5.0, Data collection software*, Bruker AXS, Inc., Madison, WI, USA, **1998**.

[22] *SAINT*, *Version 5.0, Data integration software*, Bruker AXS, Inc., Madison, WI, USA, **1998**.

[23] G. M. Sheldrick, *SADABS*, *Program for absorption correction with the Bruker SMART system*, University of Göttingen, Germany, **1996**.

Received: May 16, 2005
Published Online: December 20, 2005

 © 2006 Wiley-VCH Verlag GmbH & Co. KGaA, Weinheim 

DOI: 10.1002/ejic.200500518

# Luminescent Polyoxotungstoeuropate Anion-Pillared Layered Double Hydroxides

**Filipa L. Sousa,[a] Martyn Pillinger,[a] Rute A. Sá Ferreira,[b] Carlos M. Granadeiro,[a] Ana M. V. Cavaleiro,[a] João Rocha,[a] Luís D. Carlos,[b] Tito Trindade,[a] and Helena I. S. Nogueira*[a]**

**Keywords:** Layered double hydroxides / Layered compounds / Polyoxometalates / Host–guest systems / Luminescence

Novel luminescent polyoxometalate anion-pillared layered double hydroxides (LDHs) were prepared by aqueous ion exchange of a Zn–Al LDH precursor in nitrate form with the europium-containing polyoxotungstate anions $[EuW_{10}O_{36}]^{9-}$, $[Eu(BW_{11}O_{39})(H_2O)_3]^{6-}$ and $[Eu(PW_{11}O_{39})_2]^{11-}$. The host–guest interaction has a strong influence on the nature of the final intercalated species, as evidenced by elemental analysis, powder X-ray diffraction (XRD), infra-red (IR) and Raman spectroscopy, solid state magic-angle spinning (MAS) $^{11}B$ and $^{31}P$ NMR spectroscopy, and photoluminescence spectroscopy.

(© Wiley-VCH Verlag GmbH & Co. KGaA, 69451 Weinheim, Germany, 2006)

## Introduction

Layered double hydroxides are an important class of ionic lamellar solids with the general formula $[M^{2+}_{1-x}M^{3+}_{x}(OH)_2](A^{m-})_{x/m}\cdot nH_2O$ ($M^{2+}$ = $Mg^{2+}$, $Zn^{2+}$, $Ni^{2+}$ etc., $M^{3+}$ = $Al^{3+}$, $Cr^{3+}$, $Ga^{3+}$ etc).[1] The positively charged layers, containing divalent and trivalent cations in octahedral positions, are separated by charge balancing anions and water molecules. The water molecules are connected to both the metal hydroxide layers and the interlayer anions through extensive hydrogen bonding. A range of organic or inorganic guests may be incorporated into LDHs by either ion exchange, direct synthesis or hydrothermal reconstruction of calcined precursors.[2,3] In particular, intercalation chemistry has been explored with the aim of introducing catalytically active sites and photo- and electroactive species. Many different types of metal coordination compounds and oxometalates have been immobilized in LDHs, including phthalocyanines, cyanocomplexes, oxalate complexes and polyoxometalates (POMs).[4]

The first report of LDHs containing polyoxometalates concerned their use as exhaust gas and hydrocarbon conversion catalysts.[5] Since then, a variety of iso- and heteropolyanions with different nuclearities and structures (Keggin, Dawson, Preyssler, Finke) have been incorporated into the interlayer space of these materials.[6–18] Two factors assume considerable importance for the successful intercalation of polyoxometalates into an LDH compound. First, the heteropoly species should carry sufficient charge in order to be spatially capable of compensating the host layer charge. Ideally, the charge should be higher than that necessary in order to increase the lateral separation of the anions in the interlayer and afford a material with microporosity. The second consideration is that the intercalated anion should be resistant to hydrolytic decomposition over the pH domain of stability of the LDH.

In recent years, heteropolyoxometalates incorporating lanthanide ions have excited interest because of their luminescence properties and potential use in lasers and luminescent materials.[19–23] As a result, the preparation of hybrid materials containing these species is now being investigated.[24–32] Francesconi and co-workers recently described Mg–Al LDHs intercalated by luminescent polyoxometalate anions with Dawson-like $[Eu(H_2O)_3(\alpha_2\text{-}P_2W_{17}O_{61})]^{7-}$ and Keggin-like $[Eu_2(H_2O)_2(PW_{11}O_{39})]^{4-}$ structures.[32] In the present work, new polyoxotungstoeuropate anion-pillared layered double hydroxides were prepared by anion exchange reactions of a Zn–Al LDH precursor in nitrate form. Reaction of the wet precursor with the species $[EuW_{10}O_{36}]^{9-}$, $[Eu(BW_{11}O_{39})(H_2O)_3]^{6-}$ and $[Eu(PW_{11}O_{39})_2]^{11-}$ gave the final materials, which were characterized by powder X-ray diffraction, solid state NMR ($^{11}B$, $^{27}Al$, $^{31}P$), infrared and Raman spectroscopy. The luminescence properties of the pillared LDHs were investigated in detail and are compared with those of the precursor polyoxotungstoeuropate anions.

## Results and Discussion

### Synthesis of Polyoxotungstate Anion-Pillared Layered Double Hydroxides

The layered double hydroxide starting material, denoted as $ZnAl[NO_3^-]$, was prepared using a standard coprecipi-

[a] Department of Chemistry, CICECO, University of Aveiro, 3810-193 Aveiro, Portugal
E-mail: helena@dq.ua.pt
[b] Department of Physics, CICECO, University of Aveiro, 3810-193 Aveiro, Portugal

 © 2006 Wiley-VCH Verlag GmbH & Co. KGaA, Weinheim 

Table 1. Representative reaction conditions and observed gallery heights for polyoxotungstoeuropate anion-pillared layered double hydroxides.

| Sample | $n_P$[a] [mmol] | $C_P$[b] [mol dm$^{-3}$] | $T$ [°C] | $G$[c] [Å] |
|---|---|---|---|---|
| ZnAl[$EuW_{10}O_{36}^{9-}$] | 0.479 | 0.019 | 70 | 4.8 |
| ZnAl[$Eu(BW_{11}O_{39})(H_2O)_n^{6-}$] | 0.175 | 0.017 | 60 | 9.6 |
| ZnAl[$Eu(PW_{11}O_{39})_2^{11-}$] | 0.392 | 0.012 | 60 | 9.8 |

[a] Number of moles of polyoxometalate treated with precursor slurry containing 0.25 g clay material. [b] Polyoxometalate concentration. [c] Gallery height, calculated by subtracting the layer thickness (4.8 Å) from the $d_{(003)}$ spacing.

tation method with special attention paid to the avoidance of carbonate interference. Anion-exchange reactions were then carried out on an aqueous slurry of ZnAl[$NO_3^-$] with the polyoxotungstoeuropate anions [$EuW_{10}O_{36}$]$^{9-}$, [$Eu(BW_{11}O_{39})(H_2O)_3$]$^{6-}$ and [$Eu(PW_{11}O_{39})_2$]$^{11-}$ (Table 1). Analysis of the final polyoxotungstoeuropate anion-pillared layered double hydroxides was performed by ICP-AES and the metal atom ratios are presented in Table 2. The Zn/Al ratio was about 1.7 ($x$ = 0.37) for all of the materials and therefore unchanged compared with that for the ZnAl[$NO_3^-$] precursor. Polyoxometalate ($A^{m-}$) loadings were calculated for [$Zn_{1-x}Al_x(OH)_2$]($A^{m-}$)$_{x/m}$ as a percentage of the theoretical maximum calculated from the ICP-determined mol fractions of aluminium.

Table 2. Metal atom ratios determined by ICP-AES for the polyoxotungstoeuropate anion-pillared layered double hydroxides.

| Sample | Zn | Al | W | Eu | $L$[a] |
|---|---|---|---|---|---|
| ZnAl[$EuW_{10}O_{36}^{9-}$] | 1.73 | 1.00 | 1.02 | 0.09 | 92 |
| ZnAl[$Eu(BW_{11}O_{39})(H_2O)_n^{6-}$] | 1.68 | 1.00 | 1.44 | 0.13 | 79 |
| ZnAl[$Eu(PW_{11}O_{39})_2^{11-}$] | 1.77 | 1.00 | 1.26 | 0.05 | 63 |

[a] Polyoxometalate ($A^{m-}$) loadings as a percentage of the theoretical maximum calculated for [$Zn_{1-x}Al_x(OH)_2$]($A^{m-}$)$_{x/m}$ from the ICP-determined mol fractions of aluminium. The calculations assume that the only incorporated polyoxoanions are as indicated in the sample abbreviations.

### Powder X-ray Diffraction

Figure 1 shows the powder XRD patterns obtained for the ZnAl[$NO_3^-$] starting material and the pillared derivatives. Successful ion exchange of nitrate ions for POMs was revealed by the absence of reflections due to the starting material and the appearance of several new equally spaced (00$l$) harmonics with the (003) reflection having shifted to lower 2$\theta$ values. As is often observed for LDH-POM intercalates,[17] the first-order peaks for the pillared phases have very low intensity. This may be related to the high X-ray scattering power of the interlayer, out of phase with the brucite-like layer.[33] The positions of the (003) reflections are confirmed by the presence of the peaks at about 7.25 (006), 4.85 (009), 3.60 (0012) and 2.90 (0015) Å for the phases with $d_{(003)} \approx$ 14.5 Å [traces (c) and (d)], and 4.86 (006) and 3.26 (009) Å for the phase with $d_{(003)} \approx$ 9.6 Å [trace (b)]. The patterns also contain large and asymmetric (*hkl*) reflections in the 33–50° (2$\theta$) range. This is characteristic of some disorder in the periodicity of the layers, such as a turbostratic effect or an intergrowth of the rhombohedral and hexagonal polytypes.[34] Table 1 gives the gallery heights, calculated by subtracting the layer thickness (4.8 Å) from the $d_{(003)}$ spacing, for materials dried under reduced pressure in a vacuum desiccator. The anions [$Eu(BW_{11}O_{39})(H_2O)_3$]$^{6-}$ and [$Eu(PW_{11}O_{39})_2$]$^{11-}$ afforded pillared derivatives with a gallery height of about 10 Å. This layer separation is typical of LDHs pillared by Keggin-type or related structures and is consistent with a guest orientation in which the $C_2$ axis of the oxygen framework is perpendicular to the brucite-like layers.[8,11,12,18] The positions and relative intensities of the (00$l$) reflections in traces (c) and (d) are entirely in agreement with results reported in the literature for related compounds, for example a $Zn_2Al$-LDH pillared by [$\alpha$-$H_2W_{12}O_{40}$]$^{6-}$ anions.[8] A surprising result was obtained for the LDH-POM ZnAl[$EuW_{10}O_{36}^{9-}$]. The basal spacing of about 9.6 Å is only slightly larger than that measured for the precursor ZnAl[$NO_3^-$] (8.94 Å). In the sodium tetrastrontium salt $NaSr_4[EuW_{10}O_{36}]\cdot 34.5H_2O$ the structure of the decatungstoeuropate anion consists of two $W_5O_{18}^{6-}$ units (derived from the hexatungstate $W_6O_{19}^{2-}$

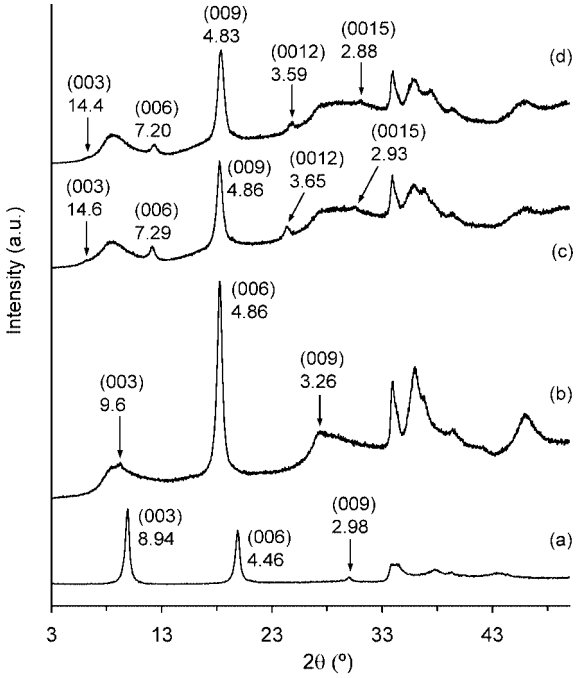


Figure 1. Powder XRD patterns for the LDH intercalates ZnAl[$NO_3^-$] (a), ZnAl[$EuW_{10}O_{36}^{9-}$] (b), ZnAl[$Eu(PW_{11}O_{39})_2^{11-}$] (c) and ZnAl[$Eu(BW_{11}O_{39})(H_2O)_n^{6-}$] (d). Values adjacent to the diffraction peaks are $d$ spacings in Å for several 00$l$ harmonics.

 © 2006 Wiley-VCH Verlag GmbH & Co. KGaA, Weinheim 

by removal of one W=O group) linked by the europium ion.[35] The four former bridging oxygen atoms from each $W_5O_{18}^{6-}$ unit form a square antiprism around Eu. The shortest dimension of the $[EuW_{10}O_{36}]^{9-}$ anion is about 10 Å (including van der Waals radii for the oxygen atoms). A basal spacing of at least 14.8 Å would therefore be expected for an LDH intercalate containing this anion. The observed basal spacing is much shorter and is in fact only compatible with the presence of two oxygen-atom layers in the interslab space. For example, a very similar powder XRD pattern was reported by Vaysse et al. for a NiCo LDH intercalated by $W_2O_7^{2-}$ anions.[36] All of the diffraction patterns for the exchanged products contain a broad and asymmetric peak at $2\theta$ = 5–11°. This is a common feature for LDH-POM composites and is often attributed to a quasi-crystalline $M^{2+}/M^{3+}$ salt of the POM formed in low quantities,[11] although alternative origins have also been claimed.[37]

### Infrared and Raman Spectroscopy

The infrared and Raman spectra of the polyoxotungstoeuropate anion-pillared layered double hydroxides showed that the exchange of nitrate anions for polyoxotungstate anions was almost complete (by the absence in the infrared spectra of the nitrate $\nu_3$ absorption band at 1384 $cm^{-1}$, or in one case just a very weak IR band present) and also that there was no carbonate present in these materials (by the absence in the infrared spectra of the carbonate $\nu_3$ absorption band at 1370 $cm^{-1}$). The intercalation of polyoxoanions into the layered double hydroxide was clearly shown by the presence in the infrared and Raman spectra of several bands in the range 700–1200 $cm^{-1}$, on top of the lattice vibrations of the host (Figure 2, Table 3), assigned to X–O stretch (X = B or P), the terminal W=O stretch (918–989 $cm^{-1}$), and the W–O–W corner or edge-shared stretching modes (700–900 $cm^{-1}$).[38,39] For ZnAl[$Eu(PW_{11}O_{39})_2^{11-}$] and ZnAl[$Eu(BW_{11}O_{39})(H_2O)_n^{6-}$] the similarity of the guest vibrations to those for the corresponding polyoxotungstoeuropate salts indicates that the structures of the core lacunary anions, i.e. $PW_{11}O_{39}^{7-}$ and $BW_{11}O_{39}^{9-}$, were unaffected by the ion-exchange reaction. In contrast, the bands

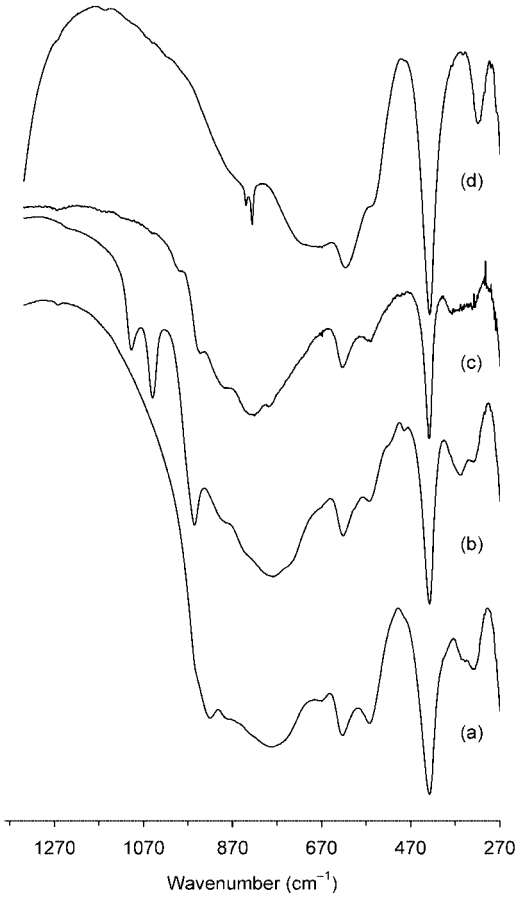


Figure 2. Infrared spectra (transmission mode) for the LDH intercalates ZnAl[$EuW_{10}O_{36}^{9-}$] (a), ZnAl[$Eu(PW_{11}O_{39})_2^{11-}$] (b), ZnAl[$Eu(BW_{11}O_{39})(H_2O)_n^{6-}$] (c) and ZnAl[$NO_3^-$] (d).

Table 3. Vibrational data for the polyoxotungstoeuropate anions and the respective anion-pillared layered double hydroxides.[a]

| Sample | Clay lattice and nitrate vibrations [$cm^{-1}$] | Polyoxoanion stretching frequency assignment [$cm^{-1}$] X–O (X = B or P) | W=$O_{terminal}$ | W–O–$W_{corner-shared}$ | W–O–$W_{edge-shared}$ |
|---|---|---|---|---|---|
| ZnAl[$NO_3^-$] | 1623 m, 1383 vs, 621 s, 560 s, 427 s | | | | |
| $Na_9[EuW_{10}O_{36}]$ | | | 932 vs | | 841 vs, 707 s |
| | | | *968* vs, *946* vs | | *891 s*, *842 w* |
| ZnAl[$EuW_{10}O_{36}^{9-}$] | 1624 m, 624 s, 561 s, 427 vs | | 918 s | | 883 m, 784 s |
| | | | *963 sh*, *941* vs | | *863 m* |
| $K_5H[Eu(BW_{11}O_{39})(H_2O)_3]$ | | | 943 s | 883 s | 830 vs, 790 s, 758 m |
| | | *909 m* | *972* vs | *874 m* | *820 w* |
| ZnAl[$Eu(BW_{11}O_{39})(H_2O)_n^{6-}$] | 1623 m, 1384 w, 623 s, 560 m, 429 vs | | 943 m | 887 s | 820 vs, 789 s |
| | | *900 sh* | *969* vs | *867 m* | |
| $K_{11}[Eu(PW_{11}O_{39})_2]$ | | 1102 s, 1048 s | 952 vs | 892 s | 824 s, 773 vs, 732 s |
| | | | *987* vs, *973 s* | *895 m*, *867 m* | |
| ZnAl[$Eu(PW_{11}O_{39})_2^{11-}$] | 1624 m, 621 s, 564 m, 427 vs | 1098 m, 1049 s | 955 s | 882 m | 830 sh, 779 vs, 730 sh |
| | | | *989* vs, *973* vs | *898 sh*, *867 sh* | |

[a] Infrared and Raman (in *italics*) data: vs, very strong; s, strong; m, medium; w, weak; sh, shoulder.

 © 2006 Wiley-VCH Verlag GmbH & Co. KGaA, Weinheim 

attributed to the guest species in ZnAl[$EuW_{10}O_{36}^{9-}$] are significantly different from those exhibited by solid $Na_9[EuW_{10}O_{36}]$, for example the W=O stretch for the guest species is shifted by 14 $cm^{-1}$ and the W–O–W stretching modes present a set of maxima at wavenumbers that are different from those for $Na_9[EuW_{10}O_{36}]$. These changes indicate that the intercalated species have a different structure, in agreement with the powder XRD data and the photoluminescence results discussed below.

### $^{11}B$, $^{27}Al$ and $^{31}P$ MAS NMR

Figure 3 shows the $^{11}B$ MAS NMR spectrum of the pillared LDH ZnAl[$Eu(BW_{11}O_{39})(H_2O)_n^{6-}$]. The spectrum consists of one main peak (with a broad low frequency shoulder) centred at $\delta$ = –6.8 ppm, with a full-width at half-maximum (fwhm) of about 580 Hz. For comparison, the potassium salt $K_5[\alpha\text{-}BW_{12}O_{40}]$ displays a single sharp (fwhm 15 Hz) and symmetric resonance at $\delta$ = –7.4 ppm, while the spectrum of lacunary $K_{6.5}Na_{1.5}[HBW_{11}O_{39}]$ (fwhm 130 Hz) consists of a second-order quadrupole powder pattern, showing that boron is in a distorted tetrahedral coordination.[31,40] The corresponding lanthanopolyoxotungstoborate salt, $K_5H[Eu(BW_{11}O_{39})(H_2O)_3]$, gives rise to a much broader peak (fwhm 440 Hz) at 0.1 ppm (Figure 3).[31] As described in ref.[31], the broadening of the resonance as compared with the monovacant Keggin polyoxotungstoborate is due to insertion of the europium ion into the polyoxoanion. Hence, the observation of the broad resonance at $\delta$ = –6.8 ppm in the $^{11}B$ MAS NMR spectrum of the pillared LDH ZnAl[$Eu(BW_{11}O_{39})(H_2O)_n^{6-}$] suggests that the coordination of the europium ions to the polyoxotungstoborate was maintained after intercalation into the LDH host. Taking into account the results from powder XRD, elemental analysis (which gave the W/Eu molar ratio as 11.1), vibrational spectroscopy and photoluminescence studies (see below), we propose that the resonance at $\delta$ = –6.8 ppm is due to intercalated monomeric 1:1 [$Eu(BW_{11}O_{39})(H_2O)_n]^{6-}$ anions. The crystal structure of the potassium salt, $K_5H[Eu(BW_{11}O_{39})(H_2O)_3]$, is unknown, but by comparison with the analogous $Ce^{3+}$ compound it is likely that a polymeric structure exists in the solid-state, comprising Keggin-type anions bridged by $Eu^{3+}$ cations.[41] The difference in the chemical shifts for the pillared LDH ($\delta$ = –6.8 ppm) and the potassium salt ($\delta$ = 0.1 ppm) may therefore be attributed to the dissociation of the polymer into the monomeric building blocks, and the intercalation of these species into the host LDH. In support of this, it has previously been shown that polymeric lanthanopolyoxotungstosilicates dissociate in aqueous solution.[42] As mentioned above, the peak at $\delta$ = –6.8 ppm in the $^{11}B$ MAS NMR spectrum of the pillared LDH has a weaker low frequency shoulder. This may be due to a small amount of an insoluble $K^+/Zn^{2+}/Al^{3+}$ salt of the POM $[Eu(BW_{11}O_{39})(H_2O)_3]^{6-}$ (related with the broad peak at $2\theta$ = 5–11° in the powder XRD pattern).

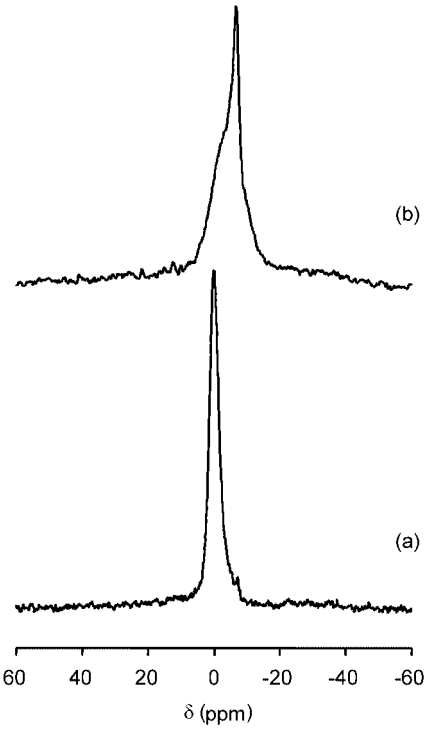


Figure 3. $^{11}B$ MAS NMR spectra of (a) $K_5H[Eu(BW_{11}O_{39})(H_2O)_3]$ and (b) ZnAl[$Eu(BW_{11}O_{39})(H_2O)_n^{6-}$].

The $^{31}P$ MAS NMR spectrum of solid $K_{11}[Eu(PW_{11}O_{39})_2]$ presents a peak centred at 0.3 ppm with a high frequency shoulder at $\delta$ = –1.5 ppm (not shown). The presence of two peaks is probably due to slight asymmetry in the structure with respect to the two $\{PW_{11}O_{39}\}$ moieties.[43] An aqueous solution of this potassium salt exhibits one resonance at $\delta$ = –0.3 ppm, suggesting that the 1:2 structure is stable in solution and that the two phosphorus atoms are equivalent.[43] A complicated $^{31}P$ MAS NMR spectrum was obtained for the pillared LDH ZnAl[$Eu(PW_{11}O_{39})_2^{11-}$], comprising several overlapping peaks between ca. 5 and –12 ppm (Figure 4). Spectral deconvolution gave four main components at –12.2, –10.1, –2.5 and 2.1 ppm in 1.0:1.0:5.3:1.9 intensity ratios. A much weaker peak was also found at $\delta$ = –7.7 ppm with a relative integration of 0.2. The major signal at $\delta$ = –2.5 ppm is assigned to intercalated $[Eu(PW_{11}O_{39})_2]^{11-}$ anions. The two overlapping peaks at –12.2 and –10.1 ppm are attributed to uncoordinated $[PW_{11}O_{39}]^{7-}$ anions in slightly different environments, and the peak at ca. 2.1 ppm is assigned to co-intercalated 1:1 $[Eu(PW_{11}O_{39})(H_2O)_n]^{4-}$ anions.[43] If we exclude the weak resonance at $\delta$ = –7.7 ppm (which, at present, we are unable to assign) and assume that there are no other tungsten or europium-containing species present, the peak area integrated intensities allow a value of 22.3 to be estimated for the overall W/Eu molar ratio. This is in reasonable agreement with the value of 25 found by elemental analysis.

All compounds were also characterized by $^{27}Al$ MAS NMR spectroscopy. The spectra for the precursor ZnAl[$NO_3^-$] and ZnAl[POM] samples present a sharp reso-

 © 2006 Wiley-VCH Verlag GmbH & Co. KGaA, Weinheim 

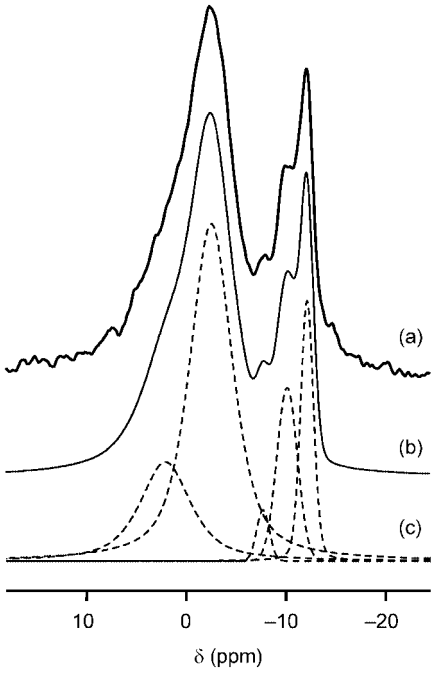


Figure 4. Experimental (a) and simulated (b) $^{31}P$ MAS NMR spectra of $ZnAl[Eu(PW_{11}O_{39})_2^{11-}]$. The individual peaks for the deconvolution are also shown (c).

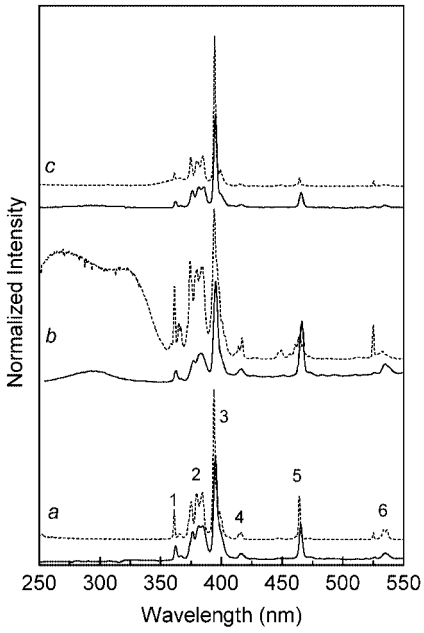


Figure 5. Room-temperature excitation spectra monitored around 612 nm of the polyoxotungstoeuropates (dotted lines) and the corresponding layered double hydroxide intercalates (solid lines): (a) $K_5H[Eu(BW_{11}O_{39})(H_2O)_3]$, $ZnAl[Eu(BW_{11}O_{39})(H_2O)_n^{6-}]$, (b) $Na_9[EuW_{10}O_{36}]$, $ZnAl[EuW_{10}O_{36}^{9-}]$, (c) $K_{11}[Eu(PW_{11}O_{39})_2]\cdot nH_2O$, $ZnAl[Eu(PW_{11}O_{39})_2^{11-}]$.

nance centred at 14.5–15.6 ppm that indicates the presence of octahedral aluminium only.[44]

### Photoluminescence

Figure 5 shows the room-temperature photoluminescence excitation (PLE) spectra of the europium-containing polyoxotungstate materials monitored within the $^5D_0 \rightarrow {}^7F_2$ lines. The spectra are mainly composed of a series of straight lines ascribed to intra-$4f^6$ transitions. Only the spectrum of $Na_9[EuW_{10}O_{36}]$ presents a large broad band in the UV spectral region with two main peaks around 270 and 320 nm. The origin of the PLE components may be related to ligand-to-europium charge-transfer (LMCT) transitions resulting from the interaction between the europium ion and the POM, in particular LMCT states associated with O → Eu and O →W transitions as already reported for other polyoxometalates containing $Eu^{3+}$ ions.[31,45,46] The higher intensity of the $Eu^{3+}$ straight lines indicate that the $Eu^{3+}$ ions are excited via direct excitation into the intra-$4f^6$ levels, and only for $Na_9[EuW_{10}O_{36}]$ is the sensitized process comparable with direct excitation into the $Eu^{3+}$ levels.

The incorporation of the europium-containing polyoxotungstate into the Zn–Al LDH (to give the material designated as $ZnAl[EuW_{10}O_{36}^{9-}]$) induces the appearance of a low-intensity band centred around 292 nm. For the other two LDH compounds the intensity of this band is negligible. The higher intensity of the $Eu^{3+}$ lines for all of the ion-exchanged LDH materials indicates that the excitation occurs essentially via direct lanthanide excitation, rather than by an efficient sensitized process involving the lanthanide ion ligands.

The changes induced in the $Eu^{3+}$ local structures due to intercalation of the polyoxotungstate anions in the LDH host were further investigated by comparison of the respective emission (PL) spectra. The spectra shown in Figure 6 were obtained for different excitation wavelengths, selected according to the excitation spectra in Figure 5, namely direct excitation into the $Eu^{3+}$ intra-$4f^6$ levels ($^5L_6$, 395 nm), and within the UV band, at 320 nm for $K_{11}[Eu(PW_{11}O_{39})_2]\cdot nH_2O$ and 292 nm for the LDH materials. We will first consider the emission features of the polyoxotungstate salts. All of the spectra display the well-known $Eu^{3+}$ orange-red emission ascribed to transitions between the first excited state $^5D_0$ and the $^7F_{0-4}$ levels of the ground multiplet. No emission from the ligands could be detected. The profile of the PL lines, namely the energy, fwhm and number of components, depends on the sample, confirming that the $Eu^{3+}$ local environments in the three compounds are different. For $K_5H[Eu(BW_{11}O_{39})(H_2O)_3]$ and $K_{11}[Eu(PW_{11}O_{39})_2]\cdot nH_2O$, the higher number of Stark components, in particular for the $^5D_0 \rightarrow {}^7F_{1,2}$ transitions (3 and 4 lines, respectively), suggests that the metal ion local structure is characterized by a low symmetry group without an inversion centre according to the higher intensity of the $^5D_0 \rightarrow {}^7F_2$ transition. The spectrum of $Na_9[EuW_{10}O_{36}]$ has already been reported.[45] The compound prepared by us revealed a different spectrum with singular features, in particular the absence of the $^5D_0 \rightarrow {}^7F_0$ transition and an abnormally high intensity for the $^5D_0 \rightarrow {}^7F_4$ transition. A deeper investigation of these singular emission features lies

 © 2006 Wiley-VCH Verlag GmbH & Co. KGaA, Weinheim 

beyond the scope of the present manuscript and will be discussed in a forthcoming study. For all of the polyoxotungstates, upon changing the excitation wavelength, no major variations are observed in the energy, fwhm and number of emission lines, suggesting that all of the metal ions occupy the same average local coordination site within each polyoxotungstate. This conclusion is further supported by the analyses of the decay curves monitored within the $^5D_0 \rightarrow {}^7F_2$ transition for an excitation wavelength around 395 nm. The decay curves are well reproduced by a single exponential function from which the $^5D_0$ lifetime was extracted (Table 4). For the $[EuW_{10}O_{36}]^{9-}$ anion the decay curve was also monitored for an excitation wavelength within the large broad band in the PLE spectrum, revealing a $^5D_0$ lifetime value similar to that obtained for direct excitation in the $^5L_6$ $Eu^{3+}$ level.

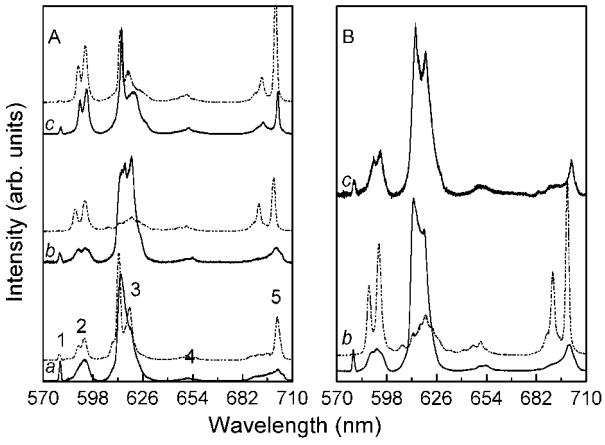


Figure 6. Room-temperature emission spectra of the polyoxotungstoeuropates (dotted lines) and the corresponding layered double hydroxide intercalates (solid lines): (a) $K_5H[Eu(BW_{11}O_{39})(H_2O)_3]$, $ZnAl[Eu(BW_{11}O_{39})(H_2O)_n^{6-}]$, (b) $Na_9[EuW_{10}O_{36}]$, $ZnAl[EuW_{10}O_{36}^{9-}]$, (c) $K_{11}[Eu(PW_{11}O_{39})_2]{\cdot}nH_2O$, $ZnAl[Eu(PW_{11}O_{39})_2^{11-}]$, excited around A: 395 nm and B: 292–320 nm.

Table 4. $^5D_0$ lifetimes, $\tau$, monitored around 611 nm at different excitation wavelengths (292 and 395 nm) for the polyoxotungstoeuropate anions and the respective anion-pillared layered double hydroxides.

| Sample | $\tau$ [ms] 292 nm | 395 nm |
|---|---|---|
| $ZnAl[Eu(BW_{11}O_{39})(H_2O)_n^{6-}]$ | 0.260 ± 0.002 | 0.255 ± 0.002 |
| $[Eu(BW_{11}O_{39})(H_2O)_3]^{6-}$ | – | 0.302 ± 0.001 |
| $ZnAl[EuW_{10}O_{36}^{9-}]$ | 0.347 ± 0.003 | 0.289 ± 0.001 |
| $[EuW_{10}O_{36}]^{9-}$ | 2.976 ± 0.002 | 2.929 ± 0.005 |
| $ZnAl[Eu(PW_{11}O_{39})_2^{11-}]$ | 0.324 ± 0.002 and 2.950 ± 0.118 | 0.326 ± 0.003 and 3.050 ± 0.038 |
| $[Eu(PW_{11}O_{39})_2]^{11-}$ | – | 2.084 ± 0.002 |

The emission spectra of the LDH-POM intercalates obtained by direct excitation into the lanthanide ion levels resemble those of the precursor polyoxotungstoeuropate salts with the exception of $ZnAl[EuW_{10}O_{36}^{9-}]$, which presents an inversion of the relative intensities of the $^5D_0 \rightarrow {}^7F_{1,2}$ transitions, indicating that the $Eu^{3+}$ local coordination site in the ion-exchanged material is different from that in $Na_9[EuW_{10}O_{36}]$, in particular the local symmetry group around the metal ion lost the inversion centre after incorporation in the LDH. This is consistent with the results from powder XRD and vibrational spectroscopy. For the remaining polyoxotungstates, minor changes were measured in the PL spectra. For $ZnAl[Eu(PW_{11}O_{39})_2^{11-}]$, an increase was observed in the relative intensity of the $^5D_0 \rightarrow {}^7F_4$ transition, while for $ZnAl[Eu(BW_{11}O_{39})(H_2O)_n^{6-}]$ an enlargement of the emission lines was detected. These minor changes in the PL spectra are compatible with changes in the $Eu^{3+}$ second coordination shell, induced by the LDH incorporation. However, upon decreasing the excitation wavelength to 292 nm, major changes in the PL profile were recorded, in particular for $ZnAl[EuW_{10}O_{36}^{9-}]$ and $ZnAl[Eu(PW_{11}O_{39})_2^{11-}]$, which must be related with the presence of another $Eu^{3+}$ local site that was not observed in the precursor. This metal ion local coordination site must be related with the appearance of the large broad band in the PLE spectra. The spectrum of $ZnAl[Eu(BW_{11}O_{39})(H_2O)_n^{6-}]$ with an excitation wavelength of 292 nm was omitted from Figure 6 (see part B) because it resembles that obtained at 395 nm, thus strongly suggesting a single $Eu^{3+}$ environment. At this point it should be noted that the PL results for this material do not preclude the existence of a minor second phase comprising a quasi-crystalline $K^+/Zn^{2+}/Al^{3+}$ salt of the POM $[Eu(BW_{11}O_{39})(H_2O)_n]^{6-}$, the existence of which is indicated by the powder XRD and $^{11}B$ MAS NMR results.

In order to further investigate the number of distinct $Eu^{3+}$ local coordination sites in each material the PL and the lifetimes of the $^5D_0$ excited state were acquired at low-temperature for the same excitation wavelengths used to record the room-temperature emission. The number of $Eu^{3+}$ local coordination sites can be inferred through the analysis of the energy and fwhm of the $^5D_0 \rightarrow {}^7F_0$ transition, estimated by deconvoluting the spectrum assuming a Gaussian function. The analysis of the energy and fwhm of the $^5D_0 \rightarrow {}^7F_0$ transition is quite important, since this transition occurs between nondegenerated levels and its energy is usually correlated with the sum of the nephelauxetic effects arising from the $Eu^{3+}$ first neighbours.[47] The existence of more than one line or the variation of its energy and fwhm upon variation of the excitation wavelength suggest the presence of more than one $Eu^{3+}$ local coordination site. Figure 7 shows the low temperature PL spectra for the three LDH-POM samples.

For $ZnAl[Eu(BW_{11}O_{39})(H_2O)_n^{6-}]$ the data collected at low temperature support the conclusion drawn from the room temperature PL spectra, i.e. that the europium ions occupy the same average local coordination site, since the spectra obtained under different excitation wavelengths are essentially the same. Moreover, the energy and fwhm of the $^5D_0 \rightarrow {}^7F_0$ transition is independent of the selected excitation wavelength (Table 5). The nature of this local environment must involve a low site symmetry group without

 © 2006 Wiley-VCH Verlag GmbH & Co. KGaA, Weinheim 

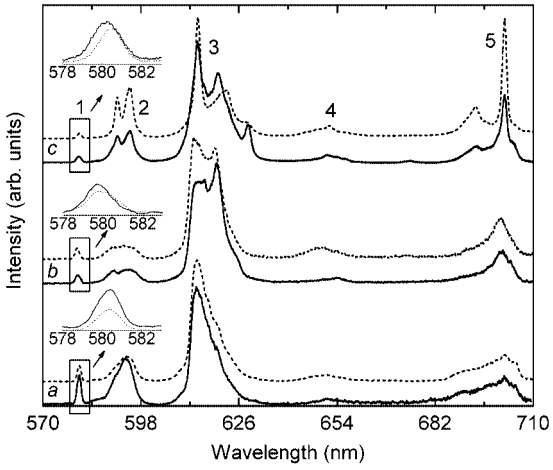


Figure 7. Emission spectra (10 K) for the LDH intercalates ZnAl-$[Eu(BW_{11}O_{39})(H_2O)_n^{6-}]$ (a), $ZnAl[EuW_{10}O_{36}^{9-}]$ (b) and ZnAl-$[Eu(PW_{11}O_{39})_2^{11-}]$ (c) excited at 292 (solid line) and 395 nm (dotted line). (1), (2), (3), (4) and (5) denote the $^5D_0 \rightarrow {}^7F_{0-2}$ transitions, respectively.

inversion centre according to the number of components for the $^5D_0 \rightarrow {}^7F_{0-2}$ transitions (1, 3 and 4, respectively) and the higher intensity of the $^5D_0 \rightarrow {}^7F_2$ lines, respectively.

For the other two LDH-POM samples, changes are observed in the number, energy, fwhm and relative intensity of the $^5D_0 \rightarrow {}^7F_{0-2}$ components as the excitation wavelength increases from 292 to 395 nm. Increasing the excitation wavelength for $ZnAl[EuW_{10}O_{36}^{9-}]$ induces a reduction of the fwhm and a blue-shift of the $^5D_0 \rightarrow {}^7F_0$ transition, suggesting the presence of more than one type of first coordination sphere for the europium ions. Moreover, changes are also observed in the energy and relative intensity of components for the remaining transitions. The presence of at least two distinct local coordination sites for the $Eu^{3+}$ cations is also apparent for $ZnAl[Eu(PW_{11}O_{39})_2^{11-}]$. Upon varying the excitation wavelength from 262 to 395 nm the fwhm and the energy of the $^5D_0 \rightarrow {}^7F_0$ transition decrease. An increase in the relative intensity of the $^5D_0 \rightarrow {}^7F_1$ transition and a decrease in the intensity of the $^5D_0 \rightarrow {}^7F_2$ transition are also detected. These results support the interpretation of the $^{31}P$ MAS NMR spectrum, that is, the co-intercalation of $[Eu(PW_{11}O_{39})_2]^{11-}$ and $[Eu(PW_{11}O_{39})(H_2O)_n]^{4-}$ anions.

The $^5D_0$ lifetime was measured at low temperature using two different excitation wavelengths (292 and 395 nm) and a monitoring wavelength around the more intense line of the $^5D_0 \rightarrow {}^7F_2$ transition (not shown). Regardless of the selected excitation wavelength, the experimental data for $ZnAl[Eu(BW_{11}O_{39})(H_2O)_n^{6-}]$ are well reproduced by a single exponential function, revealing a lifetime value of $0.255 \pm 0.002$ ms (Table 4), which further confirms the existence of a single $Eu^{3+}$ coordination site in this material. For $ZnAl[EuW_{10}O_{36}^{9-}]$, the decay curve is also well reproduced by a single exponential, but different lifetime values of $0.347 \pm 0.003$ and $0.289 \pm 0.001$ were obtained for excitation wavelengths around 292 and 395 nm, respectively (Table 5). The decay curves for $ZnAl[Eu(PW_{11}O_{39})_2^{11-}]$ revealed a two-exponential behaviour for the two selected excitation wavelengths, indicating lifetime values of $0.324 \pm 0.002$ and $2.950 \pm 0.118$ ms.

We can estimate the efficiency, $q$, of the $^5D_0$ $Eu^{3+}$ excited state. Assuming that only nonradiative and radiative processes are essentially involved in the depopulation of the $^5D_0$ state, $q$ can be defined as shown in Equation (1)

$$q = \frac{k_r}{k_r + k_{nr}} \quad (1)$$

where $k_r$ and $k_{nr}$ are the radiative and the nonradiative transition probabilities, respectively.

The emission intensity, $I$, taken as the integrated intensity $S$ of the emission curves, for the $^5D_0 \rightarrow {}^7F_{0-4}$ transitions, is expressed by Equation (2)

$$I_{i \rightarrow j} = \hbar w_{i \rightarrow j} A_{i \rightarrow j} N_i \equiv S_{i \rightarrow j} \quad (2)$$

where $i$ and $j$ represent the initial ($^5D_0$) and final ($^7F_{0-4}$) levels, respectively, $\hbar w_{i \rightarrow j}$ is the transition energy, $A_{i \rightarrow j}$ corresponds to Einstein's coefficient of spontaneous emission and $N_i$ is the population of the $^5D_0$ emitting level.[47b] The radiative contribution may be calculated from the relative intensities of the $^5D_0 \rightarrow {}^7F_{0-4}$. The branching ratio for the $^5D_0 \rightarrow {}^7F_{5,6}$ transitions must be neglected as they are not observed experimentally. Their influence on the depopulation of the $^5D_0$ excited state can therefore be ignored. Since the $^5D_0 \rightarrow {}^7F_1$ transition can be considered as a reference, due to its dipolar magnetic nature, $k_r$ can be calculated as shown in Equation (3)

$$k_r = A_{0 \rightarrow 1} \frac{\hbar\omega_{0 \rightarrow 1}}{S_{0 \rightarrow 1}} \sum_{J=0}^{4} \frac{S_{0-J}}{\hbar\omega_{0-J}} \quad (3)$$

where $A_{0-1}$ is Einstein's coefficient of spontaneous emission between the $^5D_0$ and the $^7F_1$ Stark levels. The $^5D_0 \rightarrow {}^7F_1$ transition does not depend on the local ligand field seen by $Eu^{3+}$ ions and, thus, may be used as a reference for the

Table 5. Energy, $E$, [$cm^{-1}$] and fwhm [$cm^{-1}$] of the $^5D_0 \rightarrow {}^7F_0$ transition at different excitation wavelengths (292 and 395 nm) for the anion-pillared layered double hydroxides.

| Sample | 292 nm $E$ | fwhm | 395 nm $E$ | fwhm |
|---|---|---|---|---|
| $ZnAl[Eu(BW_{11}O_{39})(H_2O)_n^{6-}]$ | $17231.4 \pm 0.5$ | $33 \pm 1$ | $17231.1 \pm 0.1$ | $34 \pm 1$ |
| $ZnAl[EuW_{10}O_{36}^{9-}]$ | $17242.2 \pm 0.4$ | $42 \pm 1$ | $17247.5 \pm 0.4$ | $36 \pm 1$ |
| $ZnAl[Eu(PW_{11}O_{39})_2^{11-}]$ | 17234.4 | $42 \pm 1$ | $17228.4 \pm 0.2$ | $36 \pm 1$ |

 © 2006 Wiley-VCH Verlag GmbH & Co. KGaA, Weinheim 

Table 6. Quantum efficiency, $q$ [%], experimental, $k_{exp}$ [ms$^{-1}$], radiative, $k_r$ [ms$^{-1}$], and the nonradiative, $k_{nr}$ [ms$^{-1}$], transition probabilities of the $^5D_0$ level for the polyoxotungstoeuropate salts and the LDH intercalate ZnAl[Eu(BW$_{11}$O$_{39}$)(H$_2$O)$_n$$^{6-}$].

| | $[Eu(PW_{11}O_{39})_2]^{11-}$ | $[EuW_{10}O_{36}]^{9-}$ | $[Eu(BW_{11}O_{39})(H_2O)_3]^{6-}$ | ZnAl[Eu(BW$_{11}$O$_{39}$)(H$_2$O)$_n$$^{6-}$] |
|---|---|---|---|---|
| $k_{exp}$ | 0.480 | 0.353 | 3.309 | 3.922 |
| $k_r$ | 0.153 | 0.139 | 0.260 | 0.298 |
| $k_{nr}$ | 0.326 | 0.215 | 3.049 | 3.623 |
| $q$ | 32.0 | 39.2 | 7.9 | 7.6 |

whole spectrum; in vacuo $A_{0-1}$ = 14.65 s$^{-1}$.[48] An effective refractive index of 1.5 was used. It was not possible to evaluate the $q$ value for the LDH intercalates ZnAl-[EuW$_{10}$O$_{36}$$^{9-}$] and ZnAl[Eu(PW$_{11}$O$_{39}$)$_2$$^{11-}$], due to the presence of more than one local coordination site for the metal ions. Since it was not possible to selectively excite the emission ascribed to each $Eu^{3+}$ ion, the emission intensity, $I$, cannot be determined independently, thus preventing any $^5D_0$ quantum efficiency calculations.

The quantum efficiency value for the compound K$_5$H[Eu(BW$_{11}$O$_{39}$)(H$_2$O)$_3$] is lower than those for the other two polyoxotungstoeuropate salts, essentially due to a higher nonradiative transition probability, that may be due to a higher number of coordinated water molecules (Table 6). Although the radiative transition probability for the LDH intercalate ZnAl[Eu(BW$_{11}$O$_{39}$)(H$_2$O)$_3$$^{6-}$] is higher, there is also an increase in the nonradiative transition probability, contributing to a slight decrease of the overall $^5D_0$ quantum efficiency.

## Conclusions

A new family of luminescent materials has been prepared by treatment of a Zn–Al layered double hydroxide in nitrate form with different polyoxotungstoeuropate anions. The photoluminescence studies, in conjunction with elemental analysis, powder XRD, IR and Raman spectroscopy, and solid state MAS NMR, allow us to construct a detailed picture of the possible nature of the intercalated anions. After ion exchange with an aqueous solution of K$_5$H[Eu(BW$_{11}$O$_{39}$)(H$_2$O)$_3$], powder XRD, elemental analysis for W and Eu, vibrational and $^{11}$B MAS NMR spectroscopy strongly indicate that the guest species in the resultant material, ZnAl[Eu(BW$_{11}$O$_{39}$)(H$_2$O)$_n$$^{6-}$], are monomeric 1:1 [Eu(BW$_{11}$O$_{39}$)(H$_2$O)$_n$]$^{6-}$ anions, which give rise to a gallery height of about 10 Å. The photoluminescence data acquired at room temperature and also at low temperature confirm the existence of a single $Eu^{3+}$ coordination site in this material. Overall, the room-temperature excitation and emission spectra for the pillared LDH are not very different from those for the potassium salt, K$_5$H[Eu(BW$_{11}$O$_{39}$)(H$_2$O)$_3$]. Slight differences were, however, observed in the lifetimes and transition probabilities of the $^5D_0$ level. Ion exchange of the starting LDH compound with a solution of K$_{11}$-[Eu(PW$_{11}$O$_{39}$)$_2$] also gave a pillared derivative with a gallery height close to 10 Å. The photoluminescence data for this material show the presence of at least two distinct local coordination sites for the $Eu^{3+}$ cations, which supports the interpretation of the $^{31}$P MAS NMR spectrum, that is, the assignment of two of the peaks to co-intercalated 2:1 [Eu(PW$_{11}$O$_{39}$)$_2$]$^{11-}$ and 1:1 [Eu(PW$_{11}$O$_{39}$)(H$_2$O)$_n$]$^{4-}$ anions. The $^{31}$P MAS NMR spectrum also indicates the presence of uncoordinated [PW$_{11}$O$_{39}$]$^{7-}$ anions. All three of these species could conceivably give rise to pillared LDHs with gallery heights around 10 Å. Deconvolution of the $^{31}$P MAS NMR spectrum showed that the 2:1 Eu-containing anion was the major species present. These results show that, regardless of the initial polyoxometalate species in solution, the nature of the final intercalated species can be different, presumably due to the strong host–guest interaction(s). This was especially evident for the anion [EuW$_{10}$O$_{36}$]$^{9-}$, which gave rise to a material containing intercalated anions with a quite different and, as yet, unknown structure. The observed basal spacing was only compatible with the presence of anions smaller than the decatungstometalate species, and the photoluminescence studies reveal the presence of more than one first coordination sphere for the lanthanide ions.

## Experimental Section

**Reagents and Materials:** Commercial materials were of reagent grade or better and used without further purification. Literature methods were used to prepare sodium or potassium salts of the polyoxotungstoeuropate anions [EuW$_{10}$O$_{36}$]$^{9-}$,[49] [Eu(BW$_{11}$O$_{39}$)(H$_2$O)$_3$]$^{6-}$,[31] and [Eu(PW$_{11}$O$_{39}$)$_2$]$^{11-}$.[50] The Zn–Al LDH starting material, ZnAl[NO$_3^-$], was prepared as described previously.[12]

**Synthesis of Polyoxotungstoeuropate Anion-Pillared Layered Double Hydroxides:** Anion-exchange reactions with a series of europium-containing polyoxotungstate anions were carried out on an aqueous slurry of ZnAl[NO$_3^-$], using the method described by Evans et al. (Table 1).[12] A typical reaction scale was 12.5 cm$^3$ and involved dropwise addition of an aqueous solution of the polyoxometalate (up to 100% in excess over that theoretically required for complete exchange) to the ZnAl[NO$_3^-$] slurry. The mixtures were then stirred for 3 to 5 h in the temperature range of 60–70 °C (Table 1). Yields for approximately 0.25 g precursor clay: ZnAl[EuW$_{10}$O$_{36}$$^{9-}$], 0.36 g; ZnAl[Eu(BW$_{11}$O$_{39}$)(H$_2$O)$_3$$^{6-}$], 0.42 g; ZnAl[Eu(PW$_{11}$O$_{39}$)$_2$$^{11-}$], 0.30 g.

**Instrumentation:** The Zn, Al, Eu, W and P contents were measured by Inductively Coupled Plasma-Atomic Emission Spectrometry (ICP-AES, Analytical Laboratories, University of Aveiro). FT-IR spectra were collected from KBr pellets (Aldrich, 99%+, FT-IR grade) with a Mattson 7000 FT-IR spectrometer. FT-Raman spectra were recorded with a Bruker RFS100/S FT-Raman spectrometer (Nd:YAG laser, 1064 nm excitation). $^{11}$B, $^{27}$Al and $^{31}$P MAS NMR spectra were recorded with a Bruker Avance 400 spectrometer at, respectively, 128.37, 104.26 and 161.97 MHz, using spinning rates of 14 kHz. The $^{31}$P MAS NMR spectra were recorded with

 © 2006 Wiley-VCH Verlag GmbH & Co. KGaA, Weinheim 

45° pulses and 50 s recycle delays. The $^{27}Al$ MAS NMR spectra were recorded with 9° pulses and 1 s recycle delays. The $^{11}B$ MAS NMR spectra were recorded with 15° pulses and 5 s recycle delays. Chemical shifts are quoted in ppm from $BF_3{\cdot}O(C_2H_5)_2$ ($^{11}B$), $Al(H_2O)_6^{3+}$ ($^{27}Al$) and 85% $H_3PO_4$ ($^{31}P$). Powder XRD data were collected at room temperature with a Philips X′pert diffractometer operating at 40 kV and 50 mA using Cu-$K_\alpha$ radiation. The diffractometer was equipped with a curved graphite monochromator, in a Bragg–Brentano *para*-focusing optics configuration. The ZnAl[$NO_3^-$] sample was step-scanned in 0.05° 2$\theta$ steps with a counting time of 1 s per step. For the other samples, a step size of 0.02° 2$\theta$ was used with a counting time of 16 s per step. The room-temperature emission and excitation spectra of the LDHs were recorded using a Jobin Yvon-Spex spectrometer (HR, 460) coupled to a R928 Hamamatsu photomultiplier. A Xe arc lamp (150 mW) coupled to a Jobin Yvon monochromator (TRIAX 180) was used as the excitation source. All of the spectra were corrected for the response of the detector. The room-temperature photoluminescence of the POMs and the spectra and lifetimes recorded at low-temperature (10 K) were detected with a modular double grating excitation spectrofluorimeter with a TRIAX 320 emission monochromator (Fluorolog-3, Jobin Yvon-Spex) coupled to a R928 Hamamatsu photomultiplier, in the front face acquisition mode. All of the photoluminescence spectra were corrected for optics and detection spectral response.

## Acknowledgments

We are grateful to the Fundação para a Ciência e a Tecnologia (FCT, Portugal) for their general financial support under the POCTI program (supported by FEDER).

[1] V. Rives (Ed.), *Layered Double Hydroxides: Present and Future*, Nova Science Publishers, Inc., New York, **2001**.
[2] A. I. Khan, D. O'Hare, *J. Mater. Chem.* **2002**, *12*, 3191.
[3] S. P. Newman, W. Jones, *New J. Chem.* **1998**, *22*, 105.
[4] V. Rives, M. A. Ulibarri, *Coord. Chem. Rev.* **1999**, *181*, 61.
[5] G. M. Woltermann, *US Pat.*, 4 454 244, **1984**.
[6] T. Kwon, G. A. Tsigdinos, T. J. Pinnavaia, *J. Am. Chem. Soc.* **1988**, *110*, 3653.
[7] M. A. Drezdon, *Inorg. Chem.* **1988**, *27*, 4628.
[8] T. Kwon, T. J. Pinnavaia, *Chem. Mater.* **1989**, *1*, 381.
[9] E. D. Dimotakis, T. J. Pinnavaia, *Inorg. Chem.* **1990**, *29*, 2393.
[10] J. Wang, Y. Tian, R.-C. Wang, A. Clearfield, *Chem. Mater.* **1992**, *4*, 1276.
[11] E. Narita, P. D. Kaviratna, T. J. Pinnavaia, *J. Chem. Soc. Chem. Commun.* **1993**, 60.
[12] J. Evans, M. Pillinger, J. Zhang, *J. Chem. Soc. Dalton Trans.* **1996**, 2963.
[13] S. K. Yun, T. J. Pinnavaia, *Inorg. Chem.* **1996**, *35*, 6853.
[14] E. A. Gardner, S. K. Yun, T. Kwon, T. J. Pinnavaia, *Appl. Clay Sci.* **1998**, *13*, 479.
[15] M. R. Weir, R. A. Kydd, *Inorg. Chem.* **1998**, *37*, 5619.
[16] C. Barriga, W. Jones, P. Malet, V. Rives, M. A. Ulibarri, *Inorg. Chem.* **1998**, *37*, 1812.
[17] H. Nijs, M. de Bock, E. F. Vansant, *J. Porous Mater.* **1999**, *6*, 101.
[18] Y. Guo, D. Li, C. Hu, Y. Wang, E. Wang, *Int. J. Inorg. Mater.* **2001**, *3*, 347.
[19] T. Yamase, M. Sugeta, *J. Chem. Soc. Dalton Trans.* **1993**, 759.
[20] T. Yamase, T. Kobayashi, M. Sugeta, H. Naruke, *J. Phys. Chem. A* **1997**, *101*, 5046.
[21] J. Bartis, M. Dankova, J. J. Lessmann, Q. Luo, W. D. Horrocks, L. C. Francesconi, *Inorg. Chem.* **1999**, *38*, 1042.
[22] Q. Luo, R. C. Howell, J. Bartis, M. Dankova, W. D. Horrocks, A. L. Rheingold, L. C. Francesconi, *Inorg. Chem.* **2002**, *41*, 6112.
[23] C. Zhang, R. C. Howell, K. B. Scotland, F. G. Perez, L. Todaro, L. C. Francesconi, *Inorg. Chem.* **2004**, *43*, 7691.
[24] W. Xu, Q. Luo, H. Wang, L. C. Francesconi, R. E. Stark, D. L. Akins, *J. Phys. Chem. B* **2003**, *107*, 497.
[25] L. Xu, H. Zhang, E. Wang, D. G. Kurth, Z. Li, *J. Mater. Chem.* **2002**, *12*, 654.
[26] Y. Wang, X. Wang, C. Hu, C. Shi, *J. Mater. Chem.* **2002**, *12*, 703.
[27] J. Wang, H. Wang, F. Liu, L. Fu, H. Zhang, *J. Lumin.* **2003**, *101*, 63.
[28] H. Y. Zhang, L. Xu, E. B. Wang, M. Jiang, A. G. Wu, Z. Li, *Mater. Lett.* **2003**, *57*, 1417.
[29] W. Bu, L. Wu, X. Zhang, A.-C. Tang, *J. Phys. Chem. B* **2003**, *107*, 13425.
[30] H. Ma, J. Peng, Z. Han, Y. Feng, E. Wang, *Thin Solid Films* **2004**, *446*, 161.
[31] F. L. Sousa, A. C. A. S. Ferreira, R. A. Sá Ferreira, A. M. V. Cavaleiro, L. D. Carlos, H. I. S. Nogueira, J. Rocha, T. Trindade, *J. Nanosci. Nanotechnol.* **2004**, *4*, 214.
[32] C. Zhang, R. C. Howell, W. Xu, Q.-H. Luo, D. L. Akins, L. C. Francesconi, *Technical Proceedings of the 2003 Nanotechnology Conference and Trade Show*, vol. 3, pp. 235–238.
[33] J. J. Bravo-Suárez, E. A. Páez-Mozo, S. T. Oyama, *Chem. Mater.* **2004**, *16*, 1214.
[34] M. Bellotto, B. Rebours, O. Clause, J. Lynch, D. Bazin, E. Elkaïm, *J. Phys. Chem.* **1996**, *100*, 8527.
[35] T. Yamase, T. Ozeki, K. Ueda, *Acta Crystallogr. Sect. C: Cryst. Struct. Commun.* **1993**, *49*, 1572.
[36] C. Vaysse, L. Guerlou-Demourgues, A. Demourgues, F. Lazartigues, D. Fertier, C. Delmas, *J. Mater. Chem.* **2002**, *12*, 1035.
[37] M. del Arco, D. Carriazo, S. Gutiérrez, C. Martín, V. Rives, *Inorg. Chem.* **2004**, *43*, 375, and references therein.
[38] C. Rocchiccioli-Deltcheff, M. Fournier, R. Franck, R. Thouvenot, *Inorg. Chem.* **1983**, *22*, 207.
[39] A. M. V. Cavaleiro, J. D. Pedrosa de Jesus, H. I. S. Nogueira, *Metal Clusters in Chemistry* (Eds.: P. Braunstein, L. A. Oro, P. Raithby), Wiley-VCH, Weinheim, **1999**, vol. 1, pp. 444–458.
[40] A. R. Couto, C. N. Trovão, J. Rocha, A. M. V. Cavaleiro, J. D. Pedrosa de Jesus, *J. Chem. Soc. Dalton Trans.* **1994**, 2585.
[41] F. L. Sousa, F. A. A. Paz, C. M. C. E. Granadeiro, A. M. V. Cavaleiro, J. Rocha, J. Klinowski, H. I. S. Nogueira, *Inorg. Chem. Commun.* **2005**, *8*, 924.
[42] M. Sadakane, M. H. Dickman, M. T. Pope, *Angew. Chem. Int. Ed.* **2000**, *39*, 2914.
[43] W. P. Griffith, N. Morley-Smith, H. I. S. Nogueira, A. G. F. Shoair, M. Suriaatmaja, A. J. P. White, D. J. Williams, *J. Organomet. Chem.* **2000**, *607*, 146.
[44] S. Gago, M. Pillinger, A. A. Valente, T. M. Santos, J. Rocha, I. S. Gonçalves, *Inorg. Chem.* **2004**, *43*, 5422, and references therein.
[45] M. Sugeta, T. Yamase, *Bull. Chem. Soc. Jpn.* **1993**, *66*, 444.
[46] R. Ballardinni, Q. G. Mulazzani, M. Venturini, F. Bolletta, B. Balzani, *Inorg. Chem.* **1984**, *23*, 300.
[47] a) L. D. Carlos, R. A. Sá Ferreira, V. de Zea Bermudez, C. Molina, L. A. Bueno, S. J. L. Ribeiro, *Phys. Rev. B* **1999**, *60*, 10042; b) L. D. Carlos, Y. Messaddeq, H. F. Brito, R. A. Sá Ferreira, V. de Zea Bermudez, S. J. L. Ribeiro, *Adv. Mater.* **2000**, *12*, 594; c) R. A. Sá Ferreira, L. D. Carlos, R. R. Goncalves, S. J. L. Ribeiro, V. de Zea Bermudez, *Chem. Mater.* **2001**, *13*, 2991.
[48] M. H. V. Werts, R. T. F. Jukes, J. W. Verhoeven, *Phys. Chem. Chem. Phys.* **2002**, *4*, 1542.
[49] R. D. Peacock, T. J. R. Weakley, *J. Chem. Soc. (A)* **1971**, 1836.
[50] N. Haraguchi, Y. Okaue, T. Isobe, Y. Matsuda, *Inorg. Chem.* **1994**, *33*, 1015.

Received: June 9, 2005
Published Online: December 20, 2005

 © 2006 Wiley-VCH Verlag GmbH & Co. KGaA, Weinheim 

DOI: 10.1002/ejic.200500629

# The First Metal-Oxo Cluster Containing Lithium and Bismuth

**Michael Mehring,*[a] Dirk Mansfeld,[a] Burkhard Costisella,[a] and Markus Schürmann[a]**

**Keywords:** Bismuth / Lithium / Silanolate / Alkoxide / Metal-oxo cluster

The reaction of $[Bi(OtBu)_3]$ with $LiOSiMe_3$ gave the heterobimetallic bismuth-oxo cluster $[Bi_3Li_5(\mu_5\text{-}O)_2(\mu_3\text{-}OSiMe_3)_2(\mu_3\text{-}OtBu)_2(\mu_2\text{-}OtBu)_6]$ (**1**) after elimination of $Me_3SiOSiMe_3$. The cage compound **1** is the first example of a mixed-metal alkoxide/siloxide composed of lithium and bismuth. Crystals of **1**·2 $C_7H_8$ and **1**·1.5 THF suitable for X-ray single crystal structure analysis were obtained by crystallisation from toluene and THF, respectively. Both solvates crystallise in the orthorhombic space group *Pmmn* with $Z = 2$. The lattice constants are $a = 16.267(3)$ Å, $b = 17.126(3)$ Å and $c = 12.155(2)$ Å (**1**·2 $C_7H_8$) and $a = 16.353(2)$ Å, $b = 17.156(1)$ Å and $c = 12.256(1)$ Å (**1**·1.5 THF). In both compounds the solvent molecules occupy channels along the *c*-axis. The basic molecular unit is best described as a face-sharing double cubane $[Bi\text{-}Li_5(\mu_4\text{-}O)_2(\mu_3\text{-}OSiMe_3)_2(\mu_3\text{-}OtBu)_2]$ which is coordinated by two $[Bi(OtBu)_3]$ molecules. The compound is kinetically labile in solution and readily decomposes in 1,1,2,2-tetrachloroethane with elimination of 1,1,2-trichloroethylene.
(© Wiley-VCH Verlag GmbH & Co. KGaA, 69451 Weinheim, Germany, 2006)

## Introduction

Heterometallic bismuth-oxo compounds including element combinations such as Bi/Mo/O,[1,2] Bi/Ti/O,[3] Bi/Sr/Ta/O[4] as well as Bi/V/O[5] have found various applications as ferroelectric devices, oxide ion conductors, non-toxic pigments, catalysts and catalyst models. We are interested in novel precursors for bismuth-containing materials and therefore we have started to systematically explore the chemistry of bismuth silanolates[6] which has been scarcely reported before.[7,8] The synthesis of one of the most promising precursors, $[Bi(OSiMe_3)_3]$, was published in 1968 starting from $BiCl_3$ and $NaOSiMe_3$.[8] Our attempts to reproduce the synthetic procedure did not result in the pure bismuth tris(trimethylsilanolate). We always observed sodium contamination of the final material and isolated several heterobimetallic sodium bismuth-oxo clusters.[9] The formation of such heterobimetallic cage compounds composed of bismuth and sodium is not surprising given the similar ionic radii [$r(Bi^{3+}) = 117$ pm; $r(Na^+) = 116$ pm; coordination number CN = 6],[10] and the rich and variable coordination chemistry of both atom types. Indeed, several such heterobimetallic alkoxides composed of sodium and bismuth were synthesized previously.[11,12] In addition, heterobimetallic bismuth alkoxides including metals such as potassium,[12] barium,[13] vanadium,[14] titanium,[15] molybdenum,[2,16] and terbium[17] were reported. Mixed-metal carboxylates/alkoxides are also known for some transition metals.[18] However, to the best of our knowledge no heterobimetallic alkoxide containing lithium as the lightest metal atom [$r(Li^+) = 73$ pm; CN = 4][10] and bismuth, the heaviest stable element of the periodic table, was reported before. The only cage compound we are aware of is $[Li_2Bi_2(NtBu)_2(thf)_2]$.[19] Notably, the reaction of $[Bi(OtBu)_3]$ with $NaOtBu$ and $KOtBu$ was reported to give $[Bi_2Na_4O(OtBu)_8]$ and $[BiK(OtBu)_4]$, respectively, whereas no reaction was observed with $LiOtBu$.[12] This prompted us to look at the reaction of $[Bi(OtBu)_3]$ with $LiOSiMe_3$ as an alternative method for the synthesis of $[Bi(OSiMe_3)_3]$ by ligand exchange.

## Results and Discussion

The metathesis reaction of $[Bi(OtBu)_3]$ with $LiOSiMe_3$ was expected to provide the bismuth silanolate $[Bi(OSiMe_3)_3]$. However, the reaction according to Equation (1) gave the heterometallic bismuth-oxo cluster $[Bi_3Li_5(\mu_5\text{-}O)_2(\mu_3\text{-}OSiMe_3)_2(\mu_3\text{-}OtBu)_2(\mu_2\text{-}OtBu)_6]$ (**1**) (Figure 1) with high yield (> 90%). Both GC-MS and $^{29}Si$ NMR of the reaction solution from which compound **1** had been filtered off revealed the formation of $Me_3SiOSiMe_3$. Apparently, the trimethylsiloxy groups are the source for the $\mu_5$-oxygen atoms in compound **1**. Similarly, we did ob-

$$3\,[Bi(OtBu)_3] + 6\,LiOSiMe_3 \xrightarrow[-\,LiOtBu\;-\,2\,Me_3SiOSiMe_3]{THF} [Bi_3Li_5O_2(OSiMe_3)_2(OtBu)_8]$$

**1** (1)

[a] Universität Dortmund, Anorganische Chemie II,
44221 Dortmund, Germany
Fax: +49-231-755-5048
E-mail: michael.mehring@uni-dortmund.de
Supporting information for this article is available on the WWW under http://www.eurjic.org or from the author.

 © 2006 Wiley-VCH Verlag GmbH & Co. KGaA, Weinheim 

serve recently that $Me_3SiOSiMe_3$ is eliminated by the reaction of $BiCl_3$ with $NaOSiMe_3$ and also upon thermally induced decomposition of $[Bi(OSiMe_3)_3]$.[9,20] Notably, elimination of di-*tert*-butyl ether was reported to take place upon reaction of $[Bi(OtBu)_3]$ with $NaOtBu$ but not with $LiOtBu$.[12]

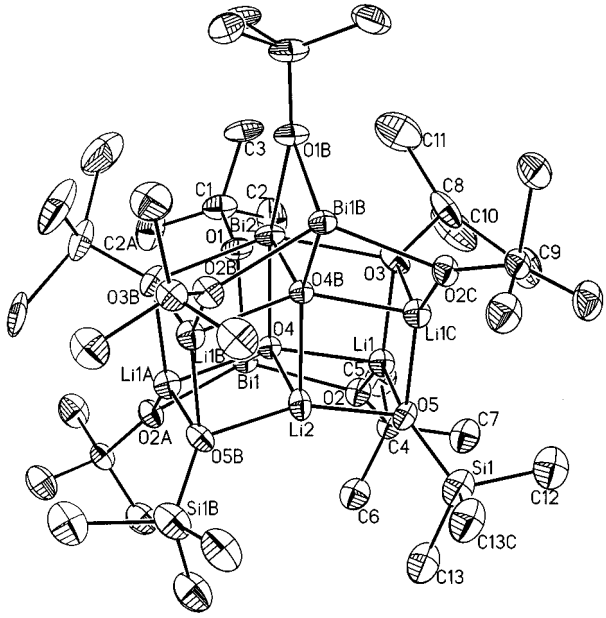


Figure 1. View of the molecular structure of $[Bi_3Li_5(\mu_5\text{-}O)_2(\mu_3\text{-}OSiMe_3)_2(\mu_3\text{-}OtBu)_2(\mu_2\text{-}OtBu)_6]$ (**1**) showing the atom numbering scheme (ORTEP drawing with 30% probability ellipsoids). Selected bond lenghts [Å] and angles [°] associated with Li (for Bi see also Figure 3): Li(1)–O(2) 1.865(13), Li(1)–O(3) 1.992(13), Li(1)–O(4) 2.087(12), Li(1)–O(5) 1.925(12), Li(2)–O(5) 1.897(8), Li(2)–O(4) 2.10(2); O(2)–Li(1)–O(3) 128.3(7), O(2)–Li(1)–O(4) 86.5(5), O(2)–Li(1)–O(5) 133.7(7), O(3)–Li(1)–O(4) 86.9(5), O(3)–Li(1)–O(5) 97.9(5), O(4)–Li(1)–O(5) 98.7(6), O(4)–Li(2)–O(4B) 84(1), O(4)–Li(2)–O(5) 99.1(5), O(5)–Li(2)–O(5B) 155(2), Li(1)–O(4)–Li(2) 76.6(4), Li(1)–O(5)–Li(2) 85.6(7), Li(1)–O(3)–Li(1C) 80.3(7), Li(1)–O(3)–Bi(2) 96.5(4), Li(2)–O(4)–Bi(2) 97.5(5), Li(2)–O(4)–Bi(1) 144.1(5), Bi(1)–O(1)–Bi(2) 96.9(2), Bi(1)–O(4)–Bi(2) 118.4(3). Symmetry operations used to generate equivalent atoms: A = $-x$ + 1/2, $y$, $z$; B = $-x$ + 1/2, $-y$ + 3/2, $z$; C = $x$, $-y$ + 3/2, $z$.

The molecular structure of compound **1** is best described to consist of the face-sharing double-cubane $[BiLi_5(\mu_4\text{-}O)_2(\mu_3\text{-}OSiMe_3)_2(\mu_3\text{-}OtBu)_2]$ and two $[Bi(OtBu)_3]$ molecules which are coordinated to the heterocubane through their oxygen atoms as well as the bismuth atoms (Figure 2). The incorporation of the large bismuth atom results in distortions from an ideal face-centred double cubane structure.

As a result of the high symmetry of compound **1** only two distinct lithium and bismuth atoms, respectively, are observed. Both lithium atoms are coordinated to four oxygen atoms and adopt a coordination geometry, which is best described as distorted trigonal bipyramid with one vertex being unoccupied. For Li(1) this vertex is in axial and for Li(2) it is in equatorial position. Slight differences in the Li–O bond lengths are observed depending on the bridging mode of the oxygen atoms. The shortest Li–O bond lengths are observed for $\mu_2$-$OtBu$ [Li(1)–O(2) 1.865(13) Å] followed

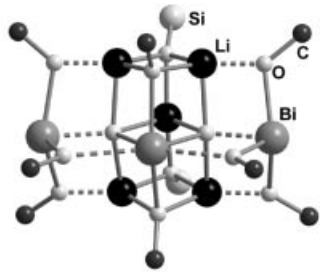


Figure 2. Ball and stick model of the face sharing double-cubane $[BiLi_5(\mu_4\text{-}O)_2(\mu_3\text{-}OSiMe_3)_2(\mu_3\text{-}OtBu)_2]$ coordinated by $[Bi(OtBu)_3]$. Methyl groups omitted for clarity. The dimensions of the spheres do not correlate with the effective ionic radii of the atoms.

by $\mu_3$-$OSiMe_3$/$\mu_3$-$OtBu$ [Li(1)–O(3) 1.992(13) Å, Li(1)–O(5) 1.925(12) Å, Li(2)–O(5) 1.897(8) Å] and $\mu_5$-O [Li(1)–O(4) 2.087(12) Å, Li(2)–O(4) 2.10(2) Å]. Irregular coordination polyhedra are observed for both bismuth atoms. The coordination geometry at Bi(1) might be described as a distorted *pseudo*-trigonal bipyramid $BiO_4X$ with the lone pair X occupying an axial position (Figure 3). The Bi–O bond lengths are in the range 2.087(6)–2.242(5) Å with the shortest bond lengths found in axial position. As a result of the stereochemical activity of the lone pair the torsion angle Bi(1)–O(1)–O(2A)–O(2) amounts to 22°. A [4+2]-coordination is observed for Bi(2) with a short Bi–O bond length of 2.087(6) Å for Bi(1)–O(4), a bond length of 2.331(7) Å for Bi(2)–O(3) and a longer bismuth–oxygen distance of 2.683(7) Å for Bi(2)···O(1). In first approximation the polyhedron might be described as strongly distorted *pseudo*-pentagonal bipyramid $BiO_6X$ with a stereochemically active lone pair occupying a position within the pentagonal plane. Consequently, the O(3)–Bi(2)–O(3B) angle decreases from 180° to 146.4(3)° and the O(1)–Bi(2)–O(1B) angle increases from 144° to 146.0(3)°.

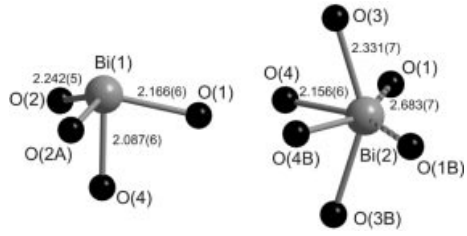


Figure 3. View of the bismuth–oxygen polyhedra observed for Bi(1) and Bi(2) including distances given in Å. Selected O–Bi–O angles [°]: O(1)–Bi(1)–O(2) 108.9(1), O(1)–Bi(1)–O(4) 78.3(2), O(2)–Bi(1)–O(2A) 128.6(2), O(2)–Bi(1)–O(4) 77.5(1); O(1)–Bi(2)–O(1B) 146.0(3), O(1)–Bi(2)–O(3) 94.9(1), O(1)–Bi(2)–O(4) 66.4(2), O(3)–Bi(2)–O(3B) 146.4(3), O(3)–Bi(2)–O(4) 77.3(1), O(4)–Bi(2)–O(1B) 147.6(2), O(4)–Bi(2)–O(4B) 81.3(3). Symmetry operations used to generate equivalent atoms: $A$ = $-x$ + 1/2, $y$, $z$; $B$ = $-x$ + 1/2, $-y$ + 3/2, $z$.

The heterometallic bismuth-oxo cluster crystallises from both toluene and THF in form of the solvates **1**·2 $C_7H_8$ and **1**·1.5 THF, respectively. In the solid state the metal-oxo clusters, which have a brick-like shape with approximate dimensions of $12 \times 11 \times 11$ Å$^3$ (atom to atom distance), arrange in such a way that channels along the *c-axis* are

 © 2006 Wiley-VCH Verlag GmbH & Co. KGaA, Weinheim 

formed. Solvent molecules occupy these channels. In Figure 4 a packing diagram of **1**·2 $C_7H_8$ leaving the voids unoccupied is shown. The diameter of the channels amounts to approximately 6 Å (atom to atom distance). The THF solvate **1**·1.5 THF shows similar crystallographic data.

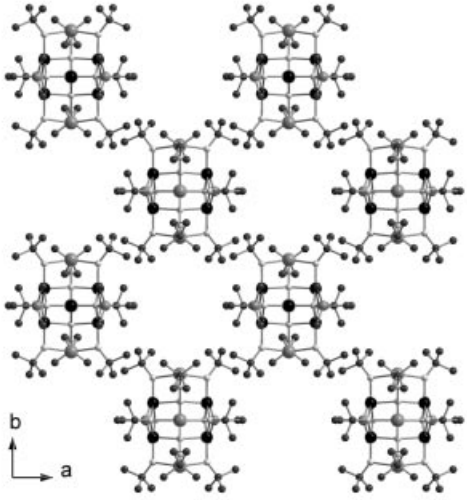


Figure 4. Packing diagram of **1**·2$C_7H_8$ in the solid state. The solvent molecules which occupy the channels along the *c*-axis are removed for clarity.

The moisture-sensitive compound dissolves in solvents such as $CD_2Cl_2$, $C_2D_2Cl_4$, $CCl_4$, toluene and THF at room temperature, but its solubility is significantly decreased at lower temperature. The $^1$H NMR spectrum of a [$D_6$]toluene solution of **1** is rather complex and shows a vast number of signals which are grouped in the regions (a): $\delta$ = 0.22–0.52 ppm and (b): $\delta$ = 1.05–1.67 ppm with an overall integral ratio of approximately 1:4 (see Figure S1 in the Supporting Information). Similarly, complex $^1$H NMR spectra are observed in other solvents such as 1,1,2,2-tetrachlorethane and $CCl_4$. These spectra are not compatible with the structure of compound **1** observed in the solid state. Thus we conclude that in solution the metal-oxo cluster is kinetically labile and gives a mixture of metal (oxo)alkoxides. This hypothesis is further supported by a comparison of the IR spectra of the solid material **1** and its saturated $CCl_4$ solution (Figure S2). Decomposition of compound **1** in 1,1,2,2-[$D_2$]tetrachloroethane under base-catalysed elimination of DCl to give [D]-1,1,2-trichloroethylene was observed at room temperature overnight. Heating of a 1,1,2,2-tetrachlorethane solution significantly enhances this process and a colourless solid containing chloride and bismuth was obtained.[21] In contrast compound **1** is stable in $CCl_4$ and heating a toluene solution of **1**·1.5 THF at reflux and subsequent crystallisation at –20 °C gave single crystals of the toluene solvate **1**·2 $C_7H_8$.

## Conclusion

In contrast to heterometallic sodium/bismuth oxoalkoxides and oxosilanolates those of lithium were not reported so far. We anticipated that formation of lithium derivatives is less likely as a result of the great difference of the ionic radii of lithium and bismuth. However, metathesis reaction of [Bi(O*t*Bu)$_3$] with $LiOSiMe_3$ gave the novel heterometallic metal-oxo cluster [$Bi_3Li_5(\mu_5\text{-}O)_2(\mu_3\text{-}OSiMe_3)_2(\mu_3\text{-}O$*t*$Bu)_2(\mu_2\text{-}O$*t*$Bu)_6$] (**1**) instead of [Bi(OSiMe$_3$)$_3$]. Formation of the metal-oxo cluster **1** proceeds through elimination of $Me_3SiOSiMe_3$. It should be noted that our attempts to prepare [Bi(OSiMe$_3$)$_3$] by salt elimination using $BiCl_3$ and $MOSiMe_3$ (M = Li, Na, K) also failed.[9] Apparently, the ready formation of $Me_3SiOSiMe_3$ makes the salt metathesis unfavourable for the synthesis of bismuth tris(trimethylsilanolate) even with the small lithium cation. However, heterometallic bismuth compounds might be suitable precursors for novel mixed metal oxide materials prepared through mild non-aqueous procedures.

## Experimental Section

**General Remarks:** Solvents were distilled from appropriate drying agents prior to use (THF, $Et_2O$ and toluene from sodium; $C_2D_2Cl_4$, $CD_2Cl_2$ and $CCl_4$ from $CaH_2$). All manipulations were carried out under argon using the Schlenk-type technique. [Bi(O*t*Bu)$_3$][22] and $LiOSiMe_3$[23] were prepared according to literature procedures. Elemental analyses were performed on a LECO-CHNS-932 analyser. The deviation from the calculated values results from the moisture sensitivity of the compound. NMR experiments were performed using a Bruker DPX 300, DRX 400 and DRX 500. Chemical shifts $\delta$ are given in ppm and were referenced against $Me_4Si$ ($^1$H, $^{29}$Si). The $^{29}$Si NMR of the reaction solution was recorded with a $D_2O$ capillary as external lock reference. NMR experiments were carried out in sealed NMR tubes. IR spectra were obtained from a Bruker FTIR IFS 28 spectrometer. The IR spectra were run as Nujol mulls and absorption bands assigned to the compound are listed in the range 400–1500 cm$^{-1}$. Decomposition of compound **1** in 1,1,2,2-tetrachloroethane to give 1,1,2-trichloroethylene and a colourless solid (**A**) was observed. GC-MS (Perkin–Elmer Turbomass Gold) of the supernatant solution revealed the formation of 1,1,2-trichloroethylene and *t*BuOH. The amount of 1,1,2-trichloroethylene was negligible in freshly distilled 1,1,2,2-tetrachlorethane. According to an EDX analysis (Hitachi FEG S 4500) the inhomogeneous solid material (**A**) contains Bi and Cl with a ratio in the range 1:2.8–4.8.

**[$Bi_3Li_5(\mu_5$-O)$_2(\mu_3$-OSiMe$_3)_2(\mu_3$-O*t*Bu)$_2(\mu_2$-O*t*Bu)$_6$] (1):** A solution of $LiOSiMe_3$ (15.36 g, 0.16 mmol) in 200 mL $Et_2O$ was added to a solution of [Bi(O*t*Bu)$_3$] (22.84 g, 0.05 mmol) in 250 mL THF at room temperature and the reaction mixture was stirred overnight to give a cloudy yellow solution. After filtration the amount of solvent was reduced to approximately 100 mL and fractional crystallisation at –20 °C gave colorless crystals of **1**·1.5 THF. The $^{29}$Si NMR of the supernatant solution showed a signal at 7.4 ppm assigned to $Me_3SiOSiMe_3$ and a second signal at 9.9 ppm assigned to $LiOSiMe_3$. The combined crystalline fractions (24.99 g, 92% based on Bi) were dried in vacuo to remove the THF and to leave a colourless amorphous solid. Comparison of the IR spectra of the single crystals **1**·1.5 THF and the amorphous material **1** indicates removal of the guest molecules THF without collapse of the molecular structure (see Supporting Information). Single crystals suitable for X-ray crystallography were obtained from both THF and toluene by dissolution of the amorphous material and subsequent crystallisation at –20 °C. Analytical data of **1**: $C_{38}H_{90}Bi_3Li_5O_{12}Si_2$ (1456.93): calcd. C 31.3, H 6.2; found C 30.7, H 6.7. $^1$H NMR

 © 2006 Wiley-VCH Verlag GmbH & Co. KGaA, Weinheim 

(500.13 MHz, $C_2D_2Cl_4$): $\delta$ = 0.02–0.06 ($OSiMe_3$), 1.22–1.28 (O*t*Bu), 1.36–1.40 ppm (O*t*Bu). $^1H$ NMR (400.13 MHz, [$D_8$]toluene): $\delta$ = 0.22–0.52 ($OSiMe_3$), 1.05–1.67 (O*t*Bu). $^{29}Si$ NMR (79.49 MHz, $CD_2Cl_2$): $\delta$ = –3.8, –3.9, –4.2 ppm (major signal), –4.3, –4.6. IR $\tilde{\nu}$ = 1357 (s), 1241 (m), 1229 (m), 1191 (s), 1020 (s), 984 (s), 941 (s), 918 (m), 828 (m), 752 (w), 742 (w), 639 (w), 576 (m), 546 (m), 528 (m), 480 (w), 463 (w), 445 $cm^{-1}$ (w).

**X-ray Crystallography:** Intensity data for the colorless crystal **1**·2$C_7H_8$ were collected with a Nonius KappaCCD diffractometer with graphite-monochromated Mo-$K_\alpha$ radiation at 173 K. The data collection covered almost the whole sphere of reciprocal space with three sets at different $\kappa$-angles and 307 frames via $\omega$-rotation ($\Delta/\omega$ = 1°) at two times 75 s per frame. The crystal–detector distance was 3.4 cm. Crystal decay was monitored by repeating the initial frames at the end of data collection. Analyzing the duplicate reflections there was no indication for any decay. The structure was solved by direct methods SHELXS97[24] and successive difference Fourier syntheses. Refinement applied full-matrix least-squares methods SHELXL97.[25] The H atoms were placed in geometrically calculated positions using a riding model with $U_{iso}$ constrained at 1.2 times $U_{eq}$ of the carrier C atom for non-methyl and 1.5 times $U_{eq}$ of the carrier C atom for methyl groups. Atomic scattering factors for neutral atoms and real and imaginary dispersion terms were taken from the International Tables for X-ray Crystallography. An absorption correction was applied with a multi-scan method using SCALEPACK[26] ($T_{min}$ = 0.385, $T_{max}$ = 0.572). Disorder was found for two *tert*-butyl groups. The methyl group C3 (0.25, *y*, *z*) is disordered over two position and refined on a normal position with an occupancy of 0.5. Three methyl groups (C9–C11) on special position (*x*, 0.75, *z*) were refined with occupancies of 0.2 (C9), 0.9 (C10), and 0.4 (C11). All atoms of the solvent molecules toluene were isotropically refined with an occupancy of 0.25. Further details are listed in Table 1.

Table 1. Crystallographic data for $[Bi_3Li_5(\mu_5\text{-}O)_2(\mu_3\text{-}OSiMe_3)_2(\mu_3\text{-}OtBu)_2(\mu_2\text{-}OtBu)_6]$·2$C_7H_8$ (**1**·2$C_7H_8$).

| Compound | **1**·2$C_7H_8$ |
|---|---|
| Empirical formula | $C_{52}H_{106}Bi_3Li_5O_{12}Si_2$ |
| Formula weight | 1641.19 |
| Crystal system | orthorhombic |
| Space group | *Pmmn* |
| *a* [Å] | 16.267(3) |
| *b* [Å] | 17.126(3) |
| *c* [Å] | 12.155(2) |
| Volume [Å$^3$] | 3386(1) |
| *Z* | 2 |
| $\rho_{calcd.}$ [g $cm^{-3}$] | 1.610 |
| Absorption coefficient [$mm^{-1}$] | 7.860 |
| Crystal size [mm] | 0.15 × 0.12 × 0.08 |
| Theta range for data collection [°] | 3.94 to 27.45 |
| Reflections collected | 11338 |
| Independent reflections | 4110 [$R_{int}$ = 0.038] |
| Goodness-of-fit on $F_2$ | 0.938 |
| $R$ [$I > 2\sigma(I)$] | 0.0277 |
| $wR_2$ (all data) | 0.0661 |
| Largest diff. peak and hole [e·Å$^{-3}$] | 1.140/–1.209 |

CCDC-273897 (for **1**·2$C_7H_8$) and -288998 (for **1**·1.5THF) contain the supplementary crystallographic data for this paper. These data can be obtained free of charge from The Cambridge Crystallographic Data Centre via www.ccdc.cam.ac.uk/data_request/cif.

**Supporting Information** (for details see the footnote on the first page of this article): Figure S1: NMR spectra of $[Bi_3Li_5(\mu_5\text{-}O)_2(\mu_3\text{-}OSiMe_3)_2(\mu_3\text{-}OtBu)_2(\mu_2\text{-}OtBu)_6]$ (**1**). Figure S2: IR spectra of $[Bi_3Li_5(\mu_5\text{-}O)_2(\mu_3\text{-}OSiMe_3)_2(\mu_3\text{-}OtBu)_2(\mu_2\text{-}OtBu)_6]$ (**1**).

## Acknowledgments

We acknowledge the Deutsche Forschungsgemeinschaft, the Fonds der Chemischen Industrie, the Fachbereich Chemie of Dortmund University (Grant for young scientists) and Professor Dr. K. Jurkschat for support of this work.

[1] a) C. Limberg, *Angew. Chem.* **2003**, *115*, 6112–6136; *Angew. Chem. Int. Ed.* **2003**, *42*, 5932–5954; b) R. K. Grasselli, J. D. Burrington, *Adv. Catal.* **1981**, *30*, 133–163; c) A. M. Beale, G. Sankar, *Chem. Mater.* **2003**, *15*, 146–153; d) A. Castro, P. Begue, B. Jimenez, J. Ricote, R. Jimenez, J. Galy, *Chem. Mater.* **2003**, *15*, 3395–3401; e) T. A. Hanna, *Coord. Chem. Rev.* **2004**, *248*, 429–440; f) S. Roggan, C. Limberg, B. Ziemer, M. Brandt, *Angew. Chem.* **2005**, *117*, 1303–1307; *Angew. Chem. Int. Ed.* **2005**, *44*, 5259–5262.

[2] C. Limberg, M. Hunger, W. Habicht, E. Kaifer, *Inorg. Chem.* **2002**, *41*, 3359–3365.

[3] a) B. H. Park, B. S. Kang, S. D. Bu, T. W. Noh, J. Lee, W. Jo, *Nature* **1999**, *401*, 682–684; b) M. Schuisky, K. Kukli, M. Ritala, A. Harsta, M. Leskelä, *Chem. Vap. Deposition* **2000**, *6*, 139–145; c) W. F. Su, Y. T. Lu, *Mater. Chem. Phys.* **2003**, *80*, 632–637; d) Y. Kageyama, T. Yoshida, Y. Mitsushima, K. Suzuki, K. Kato, *Integr. Ferroelectr.* **2001**, *36*, 173–181.

[4] a) C. A. Paz de Araujo, J. D. Cuchiaro, L. D. McMillan, M. C. Scott, J. F. Scott, *Nature* **1995**, *374*, 627–629; b) Y. Tsunoda, W. Sugimoto, Y. Sugahara, *Chem. Mater.* **2003**, *15*, 632–635; c) Y. Tsunoda, M. Shirata, W. Sugimoto, Z. Liu, O. Terasaki, K. Kuroda, Y. Sugahara, *Inorg. Chem.* **2001**, *40*, 5768–5771.

[5] a) H. M. Smith (Ed.), *High Performance Pigments*, Wiley-VCH, Weinheim, **2001**; b) A. Kudo, K. Omori, H. Kato, *J. Am. Chem. Soc.* **1999**, *121*, 11459–11467.

[6] a) D. Mansfeld, M. Mehring, M. Schürmann, *Z. Anorg. Allg. Chem.* **2004**, *630*, 1795–1797; b) D. Mansfeld, M. Mehring, M. Schürmann, *Angew. Chem.* **2005**, *117*, 250–254; *Angew. Chem. Int. Ed.* **2005**, *44*, 245–249; c) M. Mehring, D. Mansfeld, S. Paalasmaa, M. Schürmann, *Chem. Eur. J.*; DOI: 10.1002/chem.200500857.

[7] a) K. W. Terry, K. Su, T. D. Tilley, A. L. Rheingold, *Polyhedron* **1998**, *17*, 891–897; b) M.-C. Massiani, R. Papiernik, L. G. Hubert-Pfalzgraf, J.-C. Daran, *Polyhedron* **1991**, *10*, 437–445.

[8] H. Schmidbaur, M. Bergfeld, *Z. Anorg. Allg. Chem.* **1968**, *363*, 84–88.

[9] a) M. Mehring, D. Mansfeld, C. Nolde, M. Schürmann, in: *Organosilicon Chemistry VI - From Molecules to Materials,* **2005**, 233–239 (Eds.: N. Auner, J. Weis), Wiley-VCH; b) M. Mehring, S. Paalasmaa, M. Schürmann, *Eur. J. Inorg. Chem.* **2005**, 4891–4901.

[10] a) R. D. Shannon, C. T. Prewitt, *Acta Crystallogr., Sect. B* **1969**, *25*, 925–946; b) R. D. Shannon, *Acta Crystallogr., Sect. A* **1976**, *32*, 751–767.

[11] a) C. M. Jones, M. D. Burkart, K. H. Whitmire, *J. Chem. Soc., Chem. Commun.* **1992**, 1638–1639; b) J. L. Jolas, S. Hoppe, K. H. Whitmire, *Inorg. Chem.* **1997**, *36*, 3335–3340; c) K. H. Whitmire, S. Hoppe, O. Sydora, J. L. Jolas, C. M. Jones, *Inorg. Chem.* **2000**, *39*, 85–97.

[12] M. Veith, E.-C. Yu, V. Huch, *Chem. Eur. J.* **1995**, *1*, 26–32.

[13] S. Parola, R. Papiernik, L. G. Hubert-Pfalzgraf, C. Bois, *J. Chem. Soc., Dalton Trans.* **1998**, 737–739.

[14] J. W. Pell, W. C. Davis, H. C. zur Loye, *Inorg. Chem.* **1996**, *35*, 5754–5755.

[15] S. Parola, R. Papiernik, L. G. Hubert-Pfalzgraf, S. Jagner, M. Hakansson, *J. Chem. Soc., Dalton Trans.* **1997**, 4631–4635.

[16] a) M. Hunger, C. Limberg, P. Kircher, *Angew. Chem.* **1999**, *111*, 1171–1174; *Angew. Chem. Int. Ed.* **1999**, *38*, 1105–1108; b) M.

 © 2006 Wiley-VCH Verlag GmbH & Co. KGaA, Weinheim 

Hunger, C. Limberg, P. Kircher, *Organometallics* **2000**, *19*, 1044–1050.
[17] R. E. Bachman, K. H. Whitmire, J. H. Thurston, A. Gulea, O. Stavila, V. Stavila, *Inorg. Chim. Acta* **2003**, *346*, 249–255.
[18] a) J. H. Thurston, A. Kumar, C. Hofmann, K. H. Whitmire, *Inorg. Chem.* **2004**, *43*, 8427–8436; b) J. H. Thurston, T. O. Ely, D. Trahan, K. H. Whitmire, *Chem. Mater.* **2003**, *15*, 4407–4416; c) J. H. Thurston, K. H. Whitmire, *Inorg. Chem.* **2003**, *42*, 2014–2023.
[19] A. J. Edwards, M. A. Beswick, J. R. Galsworthy, M. A. Paver, P. R. Raithby, M. A. Rennie, C. A. Russell, K. L. Verhorevoort, D. S. Wright, *Inorg. Chim. Acta* **1996**, *248*, 9–14.
[20] S. Paalasmaa, D. Mansfeld, M. Schürmann, M. Mehring, *Z. Anorg. Allg. Chem.* **2005**, *631*, 2433–2438.
[21] The base-catalysed elimination of HCl from 1,1,2,2-tetrachloroethane to give 1,1,2-trichloroethylene is well known. Whereas $[Bi(OtBu)_3]$ reacts sluggishly even at higher temperature the mixed metal-oxo cluster **1** as well as $[Li(OSiMe_3)]$ readily induce the decomposition of 1,1,2,2-tetrachloroethane; a) L. Metz, *J. Prakt. Chem.* **1932**, *135*, 142–144; b) S. G. Sastry, *Chem. Zentralblatt* **1916**, *87*, 306–307; c) E. Müller, K. Ehrmann, *Ber. Dtsch. Chem. Ges.* **1936**, *69*, 2207–2210.
[22] W. J. Evans, J. J. H. Hain, J. W. Ziller, *J. Chem. Soc., Chem. Commun.* **1989**, 1628–1629.
[23] S. Sieburth, W. Mu, *J. Org. Chem.* **1993**, *58*, 7584–7586.
[24] G. M. Sheldrick, *Acta Crystallogr. Sect. A* **1990**, *46*, 467–473.
[25] G. M. Sheldrick, *University of Göttingen* **1997**.
[26] Z. Otwinowski, W. Minor, in *Macromolecular Crystallography* (Eds.: C. W. Carter, Jr., R. M. Sweet), Academic Press, New York, **1997**, part A, vol. 276, 307–326.

Received: July 15, 2005
Published Online: December 22, 2005

 © 2006 Wiley-VCH Verlag GmbH & Co. KGaA, Weinheim 

DOI: 10.1002/ejic.200500634

# New Insights into the Redox Chemistry of Ruthenium Metallopharmaceuticals: The Electrochemical Behaviour of [LH][*trans*-$Ru^{III}Cl_4L_2$] (L = imidazole or indazole) Complexes

**Mauro Ravera,[a] Claudio Cassino,[a] Sara Baracco,[a] and Domenico Osella*[a]**

**Keywords:** Antitumor agents / Electrochemistry / Redox chemistry / Ruthenium

Here we report the findings from a study on the electrochemical behaviour of two $Ru^{III}$ complexes [LH][*trans*-$Ru^{III}Cl_4L_2$] (L = imidazole, ICR, or indazole, IndCR) in aqueous solution at different pH values. An electrochemically reversible and chemically quasi-reversible one-electron reduction is observed for both compounds. Despite the similarity of the structures, the fate of the electrogenerated $Ru^{II}$ species is different; in the case of ICR, imidazole, followed by a chloride ion, is released as the consequence of the reduction, while for IndCR two subsequent water for chloride substitutions take place. Our measurements suggests that the $Ru^{III}$ complexes under study may serve as pro-drugs, being activated by reduction in a suitable aqueous environment and, therefore, binding biomolecules more rapidly.
(© Wiley-VCH Verlag GmbH & Co. KGaA, 69451 Weinheim, Germany, 2006)

## Introduction

Three $Pt^{II}$ compounds, commercially known as cisplatin, carboplatin, and oxaliplatin, are currently the most widely used anticancer agents. Notwithstanding the widespread applications of platinum anticancer drugs, there is still a great need for the development of novel metal-based compounds with additional features.

The search for "nonclassical" metal antitumor drugs has long stimulated investigations into the field of non-platinum metal drugs. Non-platinum active compounds are likely to have different mechanisms of action, biodistribution and toxicity from those of platinum drugs, and might therefore be active against human malignancies that are resistant, or have acquired resistance, to the latter agents. They may also show reduced host toxicity. Ruthenium seems to be the most promising among the several metals investigated.[1,2]

Among the different metal complexes, [ImH][*trans*-$RuCl_4$(dmso-S)(Im)] (NAMI-A, where Im = imidazole) was selected because of its very good antimetastatic activity; from 1999 to 2002 it was introduced into clinical trials.[3] Two similar complexes, containing imidazole (Im) and indazole (Ind) as ligands, namely [ImH][*trans*-$RuCl_4Im_2$], ICR, and [IndH][*trans*-$RuCl_4Ind_2$], IndCR, showed excellent antitumour activity in various animal models.[4] In particular, IndCR entered phase I clinical trials in 2003 as an anticancer drug which is very active against colon carcinomas and in metastases (Figure 1).[2]

[a] Dipartimento di Scienze dell'Ambiente e della Vita, Università del Piemonte Orientale "Amedeo Avogadro",
Spalto Marengo 33, 15100 Alessandria, Italy
Fax: +39-0131-287416
E-mail: domenico.osella@mfn.unipmn.it

Despite the large number of works published, the mechanism of action of ruthenium complexes is still largely unknown. Given that $Ru^{III}$ complexes are kinetically more inert than the corresponding $Ru^{II}$ derivatives, an "activation by reduction" mechanism has been proposed to explain the biological activity of some ruthenium derivatives.[5,6] According to this hypothesis, NAMI-A is considered to be a *pro-drug*, a compound that is converted in the body through reductive metabolism to the $Ru^{II}$ pharmacologically active species. This reactive intermediate should link the biological target after rapid dissociation of some of its ligands. Solid tumours create hypoxic (reducing) regions because they grow faster than the tissue can generate new blood vessels to supply enough oxygen.[7] Nontoxic drugs which can only be "activated" in hypoxic regions (*hypoxia-activated prodrugs*) therefore offer the promise of a specific systemic treatment against solid tumours, including metastases. For this reason, the $Ru^{III}/Ru^{II}$ electron transfer reaction is particularly interesting.

Aquation of the imidazole (NAMI-A[8] and ICR[9]) and indazole (IndCR[10]) complexes leads mainly to mono- and diaqua complexes, at different time scales. The initial transformation into a monoaqua complex seems to play a crucial role for further biological activity, since reactions with biological substrates are much faster in "aged" solutions of ICR than in "fresh" solutions. Further hydrolysis products are unknown, but could be μ-oxo complexes. Formation of such di- or polynuclear Ru complexes is pH-dependent, as hydrolysis proceeds faster at higher pH, leading to precipitation. Recently, we reported a detailed electrochemical study on NAMI-A indicating the structural and chemical consequences stemming from the easy $Ru^{III}/Ru^{II}$ electron

 © 2006 Wiley-VCH Verlag GmbH & Co. KGaA, Weinheim 

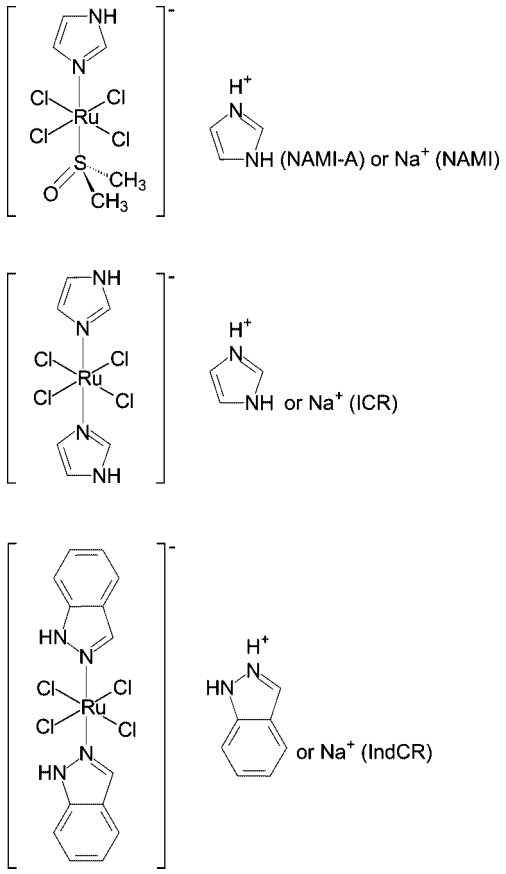


Figure 1. Sketch of compounds NAMI-A, ICR and IndCR.

## Results and Discussion

### Electrochemical Behaviour of ICR [ImH][*trans*-$Ru^{III}Cl_4Im_2$] (Im = imidazole)

As illustrated in Figure 2, the cyclic voltammetric (CV) response of an aqueous solution of $[Ru^{III}Cl_4Im_2]^-$ (1.0 mM Ru complex in 0.1 M $NaClO_4$, pH 4.0) at a glassy carbon (GC) electrode reveals a coulometrically checked (see below) one-electron reduction (peak A) coupled to chemical complications, as testified by the appearance of peak C in the back scan at $\Delta E_p$ = 260 mV.

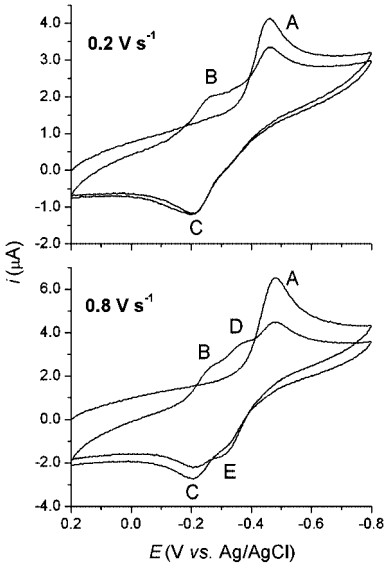


Figure 2. CV response of a 1.0 mM aqueous solution of $[Ru^{III}Cl_4Im_2]^-$ (0.1 M $NaClO_4$, pH 4.0), at a GC electrode, scan rate = 0.2 (top) and 0.8 (bottom) V $s^{-1}$.

transfer in aqueous solution.[11] Surprisingly, the reduction in acidic solutions (pH 6.0) generates the transient $Ru^{II}$ homologue, which quickly undergoes substitution of Im by a water molecule affording $[Ru^{II}(H_2O)Cl_4(DMSO)]^{2-}$, followed after a longer period by the substitution of one chloride ligand by a water molecule affording the ultimate product $[Ru^{II}(H_2O)_2Cl_3(DMSO)]^-$. At physiological pH (7.4), only the substitution of two chlorides by water is observed, just in the longer period of the electrolysis time scale. The hypoxic and acidic environment present in a tumoral tissue may favour the $Ru^{III}/Ru^{II}$ reduction and the subsequent Im hydrolysis, thereby promoting a unique means of activation of such a metallic drug in tumour tissue.

A thorough study of the electrochemical behaviour of the title compounds in aqueous solution has not yet been published. A few remarks were made by Sadler et al.[9] and, very recently, a seminal electrochemical study in organic solvents (DMF and DMSO) was published by Keppler et al.[12] In order to shed light on the redox properties of antitumour ruthenium complexes and their possible activation by reduction in experimental conditions nearer to the physiological ones, we show here a voltammetric, coulometric, and NMR study on ICR and IndCR in water at different pH values.

When a double cycle CV experiment is performed, the cathodic counterpart of the oxidation C (peak B) is observed, indicating that the peak system B/C is related to a stable species produced after the reduction occurring at peak A. In the scan rate ($v$) range 0.05–5.00 V $s^{-1}$, no return peak associated to peak A is observed. At a $v > 0.8$ V $s^{-1}$ a third peak system (D/E) appears between A and B/C. This new couple is chemically quasi-reversible and electrochemically reversible. For peak systems A and B/C, the current functions $i_p$ vs. $v^{1/2}$ and $i_p$ vs. concentration plots are linear through the origin, supporting the absence of adsorption phenomena. Table 1 summarizes the CV data.

All these observations are consistent with an ECE mechanism: the chemical reaction following reduction A produces further electroactive species.[13,14]

In order to substantiate the identity of such intermediates, the CV response of $[Ru^{III}Cl_4Im_2]^-$ was compared with that of two possible candidates, namely $[Ru^{III}(H_2O)Cl_3Im_2]$ and $[Ru^{III}(H_2O)Cl_4Im]^-$ (obtained on standing $[Ru^{III}Cl_5Im]^{2-}$ in water, see Experimental Section). Since $[Ru^{III}(H_2O)Cl_3Im_2]$ is stable only under acidic conditions (pH < 4.0),[15] an accurate comparison was feasible only with such pH values. Figure 3 shows the overlap of the three CVs. All three complexes display a similar ECE behaviour, with the final

 © 2006 Wiley-VCH Verlag GmbH & Co. KGaA, Weinheim 

Table 1. Relevant electrochemical data for $[Ru^{III}Cl_4Im_2]^-$ and its aquated compounds.

| | $E_p$(A) (V vs. Ag/AgCl at 0.2 V $s^{-1}$) | $E°'$(B/C) (V vs. Ag/AgCl) | $E°'$(D/E) (V vs. Ag/AgCl) |
|---|---|---|---|
| $[Ru^{III}Cl_4Im_2]^-$ | –0.46 | –0.24 | –0.34 (at $v$>0.8 V $s^{-1}$) |
| $[Ru^{III}(H_2O)Cl_3Im_2]$ | – | –0.24 | –0.34 |
| $[Ru^{III}(H_2O)Cl_4Im]^-$ | –0.44 | –0.23 | – |

redox couple (peaks B/C) located at the same potential, while the first reduction (A) is obviously located at different values.

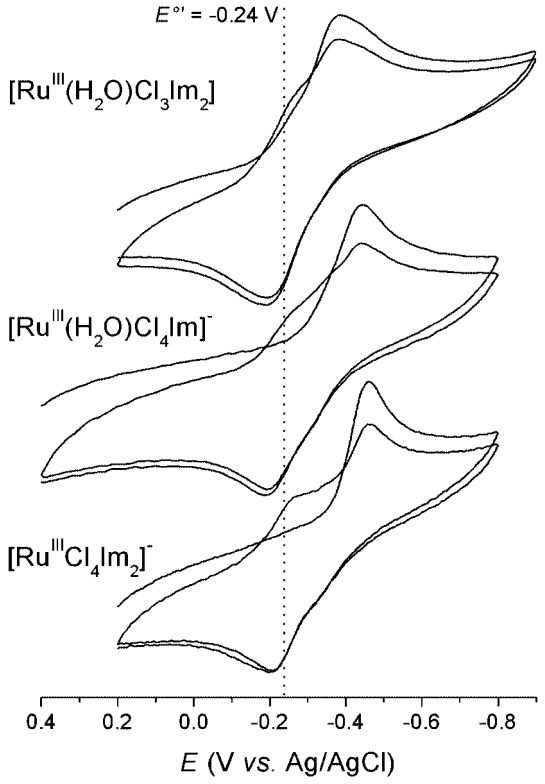


Figure 3. CV response of 1.0 mM aqueous solutions of $[Ru^{III}(H_2O)Cl_3Im_2]$ (top), $[Ru^{III}(H_2O)Cl_4Im]^-$ (middle), and $[Ru^{III}Cl_4Im_2]^-$ (bottom) (0.1 M $NaClO_4$, pH 4.0), at a GC electrode, scan rate = 0.2 V $s^{-1}$.

We propose the diaqua $[Ru^{III}(H_2O)_2Cl_3Im]$ as the final product of the ECE sequence, as it is the only intermediate that could reasonably be obtained from all three complexes. In the case of $[Ru^{III}Cl_4Im_2]^-$ the intermediate $[Ru^{III}(H_2O)Cl_3Im_2]$ is clearly present at $v > 0.8$ V $s^{-1}$ (Figure 2). The same behaviour and the same CVs are also observed in phosphate buffer (PB) at pH 6.0; for this reason, we can extend the mechanism of reaction (Figure 4) to this pH value as well.

Bulk electrolysis of an aqueous, acidic solution (pH 4.0 and 6.0) of $[Ru^{III}Cl_4Im_2]^-$ ($E_w$ = –0.60 V) consumes 1 mol of electrons per mol of complex, producing a change in colour from deep orange to lemon yellow, indicative of the formation of a $Ru^{II}$ species. In the longer electrolysis time scale, the Im/water and $Cl^-$/water exchanges occur completely so that the $E°'$ of the final species correspond to that of the B/C peak couple. The overall bulk electrolysis

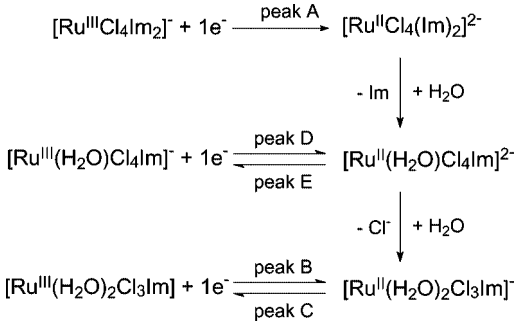


Figure 4. Proposed reaction scheme for the reduction of ICR.

behaviour is confirmed by the chemical reduction with reduced glutathione (GSH) followed by CV tests; the results show that the diaqua complex is obtained during the reaction (30 min), although some decomposition occurs (ca. 20%).

In neutral solution (0.1 M PB, pH 7.4) the general trend is maintained. However, there is a moderate shift in $E_p$(A) and a strong shift in $E°'$(B/C). Indeed, $E_p$(A) changes from –0.46 to –0.49 V by passing from pH 4.0 to 7.4, while $E°'$(B/C) shifts from –0.24 to –0.37 V in the same pH range. This may be due to the less efficient protonation of the leaving $ImH^+$ (peak A), and to the partial formation of hydroxylated aqua species (peaks B/C). Given that the A and B/C signals partially overlap, the peak couple D/E is also completely obscured at high $v$. The similarity of the behaviour at pH 7.4 of the two $Ru^{III}$ complexes with that at acidic pH values confirms the stepwise loss of Im and chloride with replacement by the water after the initial reduction step in the pH range 4.0–7.4.

## Chemical Reduction of ICR Followed by NMR Spectroscopy

In order to confirm the assignment of the species produced at different pH values, chemical reductions with GSH were followed by $^1H$ NMR spectroscopy. To avoid the interference of the imidazolium countercation, all experiments were performed with ICR sodium salt. The oxidation of glutathione to glutathione disulfide (GSSG) is a two-electron reaction (2 GSH → GSSG + $2e^-$ + 2 $H^+$). In order to increase the reaction speed, an ICR sodium salt/GSH ratio of 1:2 was used (37 °C, NMR measured after 15 min); the resulting mixture exhibited no broadening of the internal standard peak [referenced to the water-soluble silane 3-(trimethylsilyl)-1-propanesulfonic acid sodium salt, DSS] due to the presence of paramagnetic species as residual ICR ($Ru^{III}$ $d^5$) or glutathyil radical intermediate.

 © 2006 Wiley-VCH Verlag GmbH & Co. KGaA, Weinheim 

The reduction carried out on a 10 mM solution of ICR in 0.1 M acetate buffer (pH 4.0), and PB (pH 6.0 and 7.4), parallels that reported by Keppler et al.[16] (Figure 5). Two sets of signals are observed; the first corresponds to the free imidazole (A), while the second is typical of a coordinated imidazole (B). Pattern A increases with time, while pattern B decreases as the result of the reduction of the complex to the corresponding $Ru^{II}$ analogue and the following Im/$H_2O$ exchange. All these observations are consistent with the electrochemical data in which the substitution of Im by a water molecule in the reduced dianion $[Ru^{II}Cl_4Im_2]^{2-}$ (not observed in NMR) produces $[Ru^{II}(H_2O)Cl_4Im]^{2-}$ and/or $[Ru^{II}(H_2O)_2Cl_3Im]^-$ (pattern B). At longer reaction times, the reduced species is completely destroyed (only pattern A is observed).

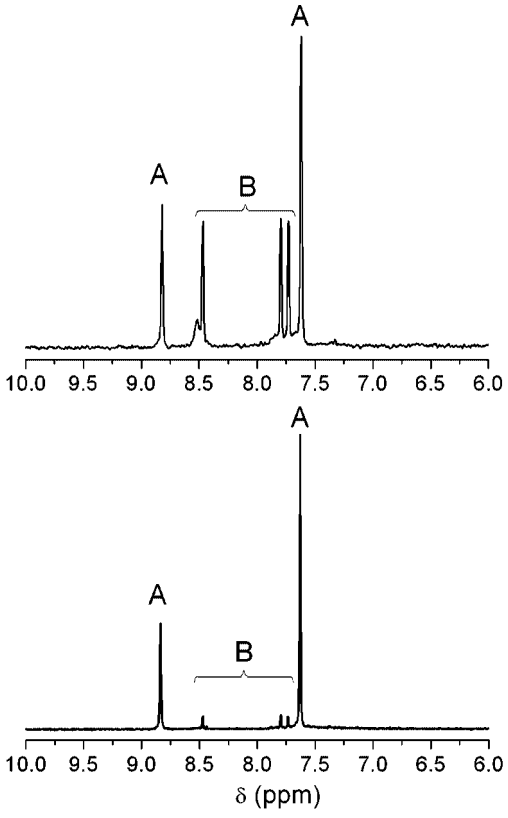


Figure 5. Expanded 6.0–10.0 ppm resonance region of the $^1H$ NMR spectrum of ICR (10 mM in 0.1 M phosphate buffer, pH 6.0) recorded 15 min (top) and 1 h (bottom) after the addition of glutathione (20 mM) at 37 °C.

### Electrochemical Behaviour of IndCR Sodium Salt [Na][*trans*-$Ru^{III}Cl_4Ind_2$] (Ind = indazole)

Since the indazolium salt of IndCR is barely soluble in water, all experiments were performed with the sodium salt.

Figure 6 shows the CV response of an aqueous solution of $[Ru^{III}Cl_4Ind_2]^-$ (1.0 mM Ru complex in 0.1 M $NaClO_4$, pH 4.0, water solution) at a GC electrode. The coulometrically checked one-electron reduction (peak-system F/G) is followed by chemical complications, as testified by the appearance of peak J in the back scan. In the scan rate range 0.05–5.00 V $s^{-1}$, the diagnostic electrochemical features are:

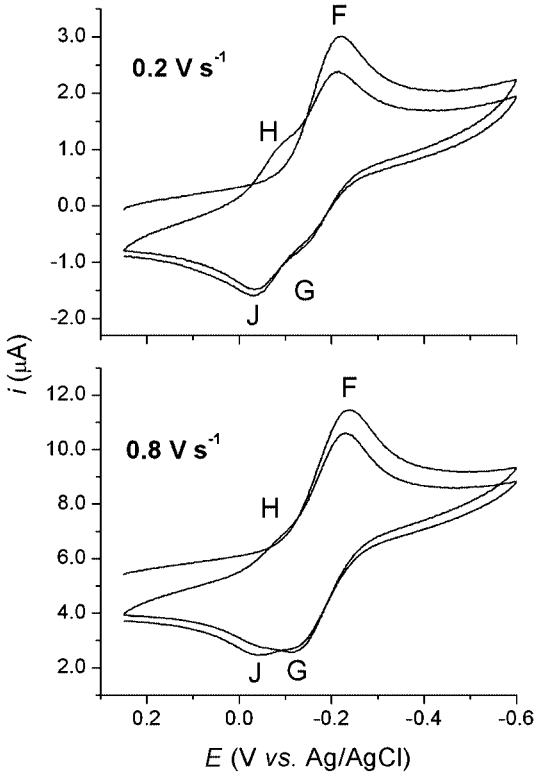


Figure 6. CV response of a 1.0 mM aqueous solution of $[Ru^{III}Cl_4Ind_2]^-$ (0.1 M $NaClO_4$, pH 4.0), at a GC electrode, scan rate: 0.2 (top) and 0.8 (bottom) V $s^{-1}$.

i. The current ratio $i_{p,a}(G)/i_{p,c}(F)$ is 0.3 at 0.05 V $s^{-1}$ and progressively increases with $v$ until it reaches unity at 1.5 V $s^{-1}$;
ii. The peak-to-peak separation $\Delta E_p = E_{p,a} - E_{p,c}$ remains practically constant (80 mV) by increasing $v$ in the range of $v$ where peak G is present ($v > 0.8$ V $s^{-1}$);
iii. The formal electrode potential $E°' = (E_{p,c} + E_{p,a})/2$ is equal to –0.160 V vs. Ag/AgCl ($v > 0.8$ V $s^{-1}$);
iv. The plots of $i_p$ vs. $v^{1/2}$ and $i_p$ vs. concentration are linear through the origin, indicating the absence of any adsorption process.

Also in this case, when a double cycle CV experiment is performed, the cathodic counterpart of the oxidation J (peak H) is observed. This couple is located at –0.072 V vs. Ag/AgCl, and shows electrochemical parameters similar to that of the F/G system.

After increasing the pH to 6.0 and 7.4, all the peaks remain at the same potential except peak H, which slightly shifts under peak F. The overall electrochemical behaviour is compatible with an ECE mechanism.

Bulk electrolysis of an aqueous, acidic solution (pH 4.0) of $[Ru^{III}Cl_4Ind_2]^-$ ($E_w$ = –0.35 V) consumes 1 mol of electrons per mol of complex, yielding the usual $Ru^{II}$ yellow lemon solution. Despite strong decomposition, after 0.5 Faradays, the two peak couples F/G and H/J are still present. After 1 Faraday, only a new species at $E°'$ = +0.065 V vs. Ag/AgCl is present (peaks K/L, Figure 7). At

 © 2006 Wiley-VCH Verlag GmbH & Co. KGaA, Weinheim 

pH 6.0 only a species at $E°' = -0.065$ V, compatible with the H/J system, is present, while at pH 7.4 the decomposition is so high that after 45 min of electrolysis the complex is fully decomposed. The chemical reduction with GSH parallels the above-reported results.

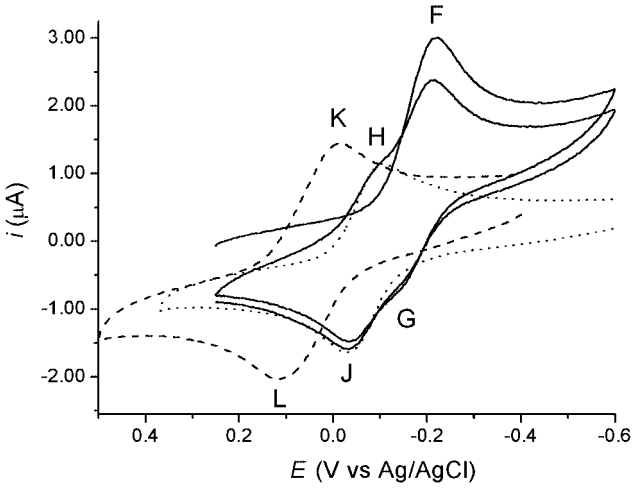


Figure 7. CVs performed before electrolysis (solid line), after 1 F in 0.1 M acetate buffer (pH 4.0, dashed line) and after 1 F in 0.1 M phosphate buffer (pH 6.0, dotted line).

### Chemical Reduction of IndCR Followed by NMR Spectroscopy

The reduction carried out with GSH ([IndCR] = 10 mM, IndCR/GSH ratio 1:2, 37 °C, NMR measured after 15 min) in 0.1 M acetate buffer (pH 4.0), and PB (pH 6.0, Figure 8) shows a similar pattern of peaks. Free indazole is not present throughout the experiment. If we consider only the set of signals at ca. 9 ppm (in particular, the singlet due to the proton in position 3; this signal is the most easily characterized), the fate of the chemically generated $Ru^{II}$ species is unambiguous: the singlet at $\delta = 9.06$ ppm (peak C) decreases until it disappears after 1 h, while another singlet at $\delta = 8.97$ ppm (peak D) increases as well. After 30 min, a new singlet at $\delta = 8.92$ ppm (peak E) starts to increase. At pH 6.0, peak C′ ($\delta = 8.96$ ppm) represents the only species present at the beginning of the experiment. After 30 min, peak D′ ($\delta = 8.92$ ppm) begins to increase. After 2 h a 1:1 ratio is reached, and after 4 h peak D′ is about twice as high.

By combining the experimental results obtained in CV and NMR, we can propose the reaction pattern reported in Figure 9. The reduction of IndCR produces the dianion $[Ru^{II}Cl_4Ind_2]^{2-}$. This species is more stable than the corresponding $[Ru^{II}Cl_4Im_2]^{2-}$, and slowly exchanges stepwise two $Cl^-$ for water. At pH 6.0 this exchange is inhibited, so that only the first step is observed both in NMR and bulk electrolysis. Surprisingly, in this case, the "traditional" $Cl^-$,$Cl^-$/$2H_2O$ substitution takes place, while in ICR the Im,$Cl^-$/$2H_2O$ substitution, as observed also for NAMI-A in acidic conditions, is the predominant reaction.

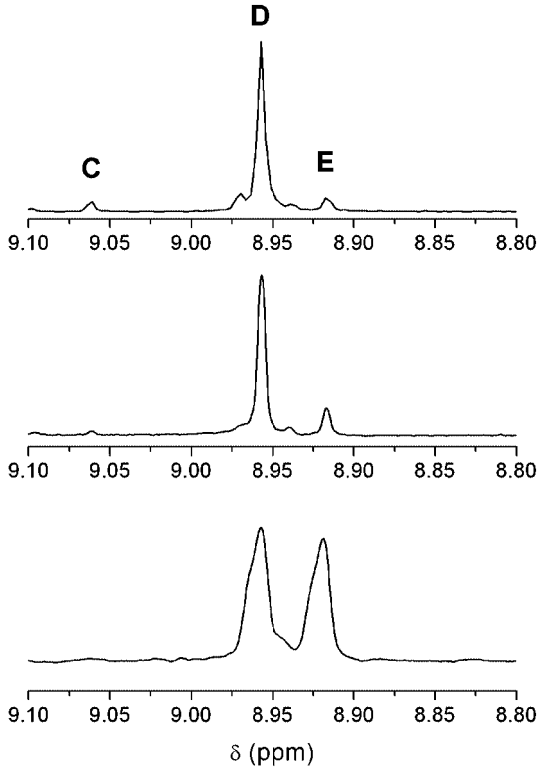


Figure 8. Expanded 8.80–9.10 ppm resonance region of the $^1H$ NMR spectrum of IndCR (10 mM in 0.1 M acetate buffer, pH 4.0) recorded 15 min (top), 1 h (middle), and 2 h (bottom) after the addition of glutathione (20 mM).

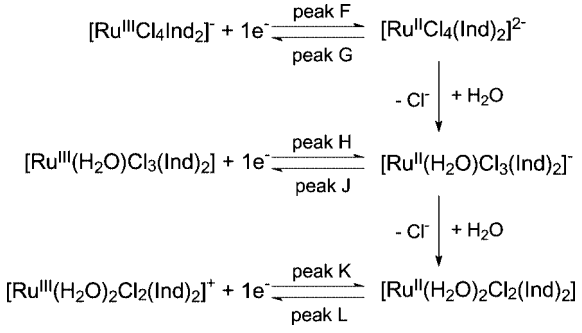


Figure 9. Proposed reaction scheme for the reduction of IndCR.

## Conclusions

We have reported on a study of the electrochemical behaviour of the two $Ru^{III}$ complexes [LH][*trans*-$RuCl_4L_2$] (L = imidazole, ICR, or indazole, IndCR) in aqueous solution at different pH values. An electrochemically reversible and partially chemically reversible one-electron reduction is observed for both compounds. Despite the similarity of the structure, the fate of the electrogenerated $Ru^{II}$ species is different; in the case of ICR, imidazole, followed by a chloride ion, is released as the consequence of the reduction, while in IndCR $Cl^-$,$Cl^-$/$2H_2O$ substitution takes place. The chemical complications following the electron transfer in IndCR are also independent of pH, and act only on the kinetic aspect of the substitutions. It is noteworthy that, while the acti-

 © 2006 Wiley-VCH Verlag GmbH & Co. KGaA, Weinheim 

vation of the $Ru^{III}$ homologues occurs in a time interval of hours,[9] that of the reduced species takes place in less than one hour. The differences in the chemical behaviour of the electrogenerated $Ru^{II}$ species may be imputable to the different basicity of Im ($pK_a$ = 7.11) and Ind ($pK_a$ = 1.25).[17] In fact, the propensity toward protonation of the axial ligand L (where L is Im or Ind) influences the formation of $[LH]^+$ and, hence, its detachment from the complex. As reported in the Introduction, we found precedents for this in a recent study on the electrochemical behaviour of NAMI-A:[11] Furthermore, as reduction of $Ru^{III}$ to $Ru^{II}$ fills the dπ orbitals, an axial ligand such as Ind, having a higher electronic delocalization than Im by virtue of annulation, could partially act as a π-acceptor and, thus, increase the Ru–L bond stability.

There are many redox couples in a cell that maintain the redox environment, with the glutathione disulfide/reduced glutathione (GSSG/2GSH) being the most abundant.[18] In proliferating cells, the reduction potential is about –0.24 V vs. NHE (i.e. –0.44 V vs. Ag/AgCl).[19] According to the $E°'(Ru^{III}/Ru^{II})$ measured, the biological reduction process of ICR and IndCR is thus possible. The $Ru^{II}$ species show a lower stability with respect to the $Ru^{III}$ counterpart and thus the chemical reactions following the electron transfer may produce more reactive intermediates. The combination of electrochemical and NMR measurements shed light on the overall mechanism, suggesting that $Ru^{III}$ complexes may serve as prodrugs, which may be activated by reduction in vivo to coordinate more rapidly to biomolecules. The low $O_2$ content in tumour cells (hypoxic environment) should favour the reduction to $Ru^{II}$, which is generally more active than $Ru^{III}$ enforcing the "activation by reduction" hypothesis.

## Experimental Section

Complexes $Na[RuCl_4Im_2]$[16] and $[ImH][RuCl_4Im_2]$,[20] (Im = imidazole), and $Na[RuCl_4Ind_2]$ (Ind = indazole)[21] were obtained following published procedures. Their aquated products ($[Ru(H_2O)Cl_4Im]^-$[22] and $[Ru(H_2O)Cl_3Im_2]$[15]) were obtained directly in solution according to data in the literature. The identity and the purity of all species were checked using the usual techniques. All salts were analytical grade and used as received. Deionized water was obtained through a Milli-Q (18 MΩ) deionizing system and was used for the preparation of all solutions. $^1H$ NMR spectra were measured in $D_2O$ with a JEOL Eclipse Plus spectrometer operating at 400 MHz. Proton chemical shifts were reported in parts per million (ppm) referenced to residual solvent proton resonance (i.e. HDO 4.8 ppm) or silane standard 3-(trimethylsilyl)-1-propanesulfonic acid sodium salt (DSS).

Electrochemical experiments were performed using an EG&G PAR 273 electrochemical analyser interfaced to a personal computer, employing PAR M270 electrochemical software. A standard three-electrode cell was designed to allow the tip of the reference electrode to closely approach the working electrode. The reference electrode was silver/silver chloride (Ag/AgCl), containing saturated, aqueous KCl. Its stability was checked using the $[Fe(CN)_6]^{3-}/[Fe(CN)_6]^{4-}$ redox couple. The Ag/AgCl reference electrode was stable with a precision of ±5 mV. The working electrode was a glassy carbon disk (diameter 0.1 cm) sealed in epoxy resin. The solid electrodes were polished with alumina followed by diamond paste, then washed with distilled water and dried. This process yielded a reproducible surface for all experiments. Positive-feedback iR compensation was applied routinely. All electrochemical measurements were carried out under nitrogen in water; solutions were 1.0 mM with respect to the compounds under study and 0.1 M with respect to the supporting electrolyte. The temperature of the solution was kept constant (20 ± 1 °C), by circulation of a thermostatted water/ethanol mixture through a jacketed cell.

The reduced species were produced in quantitative yield by bulk electrolysis. This was carried out in a conventional two-compartment glass cell with porous glass separation. A Pt basket was used as the cathode at a potential ca. 100–150 mV more negative than the formal potential $E°'$, a Pt wire was used as the anode, and Ag/AgCl was the reference electrode. Nitrogen was continuously bubbled through the solution during electrolysis. In all cases, transformation of $Ru^{III}$ to $Ru^{II}$ was checked by current integration and by in situ CV.

## Acknowledgments

S.B. thanks the Consorzio CIRCMSB (Bari, Italy) for a grant. Johnson Matthey (Reading, UK) is gratefully acknowledged for a generous loan of $RuCl_3$. This research was carried out within the framework of the European Cooperation COST D20 action (Metal compounds in the treatment of cancer and viral diseases) and COST B16 action (Multidrug resistance reversal). The help of Dr. Silvia Gemme in the synthesis and electrochemical characterization of Ru complexes is also acknowledged. We are indebted to Dr. Laura McLean for her assistance in writing this manuscript.

[1] M. J. Clarke, *Coord. Chem. Rev.* **2003**, *236*, 209–233.
[2] M. Galanski, V. B. Arion, M. A. Jakupec, B. K. Keppler, *Curr. Pharm. Des.* **2003**, *9*, 2078–2089.
[3] E. Alessio, G. Mestroni, A. Bergamo, G. Sava, *Curr. Top. Med. Chem.* **2004**, *4*, 1525–1535.
[4] M. J. Clarke, *Coord. Chem. Rev.* **2002**, *232*, 69–93.
[5] M. J. Clarke in *Metal Ions in Biological Systems* (Ed.: H. Siegel), Marcel Dekker Inc., New York, **1980**, pp. 231–283.
[6] G. Mestroni, E. Alessio, G. Sava, S. Pacor, M. Coluccia in *Metal Complexes in Cancer Chemotherapy* (Ed.: B. K. Keppler), VCH Verlagsgesellschaft, Weinheim (Germany), **1993**, pp. 157–185.
[7] J. M. Brown, A. J. Giaccia, *Cancer Res.* **1998**, *58*, 1405–1416.
[8] G. Sava, E. Alessio, A. Bergamo, G. Mestroni, "Metallopharmaceuticals I DNA Interactions", in *Topics in Biological Inorganic Chemistry* (Eds.: M. J. Clarke, P. J. Sadler), Springer, Berlin, **1999**, vol. 1, pp. 144–169.
[9] O. M. Ni Dhubhghaill, W. R. Hagen, B. K. Keppler, K. G. Lipponer, P. J. Sadler, *J. Chem. Soc., Dalton Trans.* **1994**, 3305–3310.
[10] T. Pieper, W. Peti, B. K. Keppler, *Met.-Based Drugs* **2000**, *7*, 225–232.
[11] M. Ravera, S. Baracco, C. Cassino, P. Zanello, D. Osella, *Dalton Trans.* **2004**, 2347–2351.
[12] E. Reisner, V. B. Arion, M. F. C. Guedes da Silva, R. Lichtenecker, A. Eichinger, B. K. Keppler, V. Y. Kukushkin, A. J. L. Pombeiro, *Inorg. Chem.* **2004**, *43*, 7083–7093.
[13] A. J. Bard, L. R. Faulkner, *Electrochemical Methods. Fundamentals and Applications*, 2nd ed., Wiley, New York, **2001**.
[14] P. Zanello, *Inorganic Electrochemistry. Theory, Practice and Application*, Royal Society of Chemistry, London, **2003**.
[15] J. Chatlas, R. van Eldik, B. K. Keppler, *Inorg. Chim. Acta* **1995**, *233*, 59–63.

 © 2006 Wiley-VCH Verlag GmbH & Co. KGaA, Weinheim 

[16] M. Hartmann, K. G. Lipponer, B. K. Keppler, *Inorg. Chim. Acta* **1998**, *267*, 137–141.
[17] J. Catalan, R. M. Claramunt, J. Elguero, J. Laynez, M. Menendez, F. Anvia, J. H. Quian, M. Taagepera, R. W. Taft, *J. Am. Chem. Soc.* **1988**, *110*, 4105–4111.
[18] C. V. Smith, D. P. Jones, T. M. Guenthner, L. H. Lash, B. H. Lauterburg, *Toxicol. Appl. Pharmacol.* **1996**, *140*, 1–12.
[19] F. Q. Schafer, G. R. Buettner, *Free Radical Biol. Med.* **2001**, *30*, 1191–1212.
[20] B. K. Keppler, W. Rupp, U. M. Juhl, H. Endres, R. Niebl, W. Balzer, *Inorg. Chem.* **1987**, *26*, 4366–4370.
[21] W. Peti, T. Pieper, M. Sommer, B. K. Keppler, G. Giester, *Eur. J. Inorg. Chem.* **1999**, 1551–1555.
[22] C. Anderson, A. L. Beauchamp, *Inorg. Chem.* **1995**, *34*, 6065–6073.

Received: July 18, 2005
Published Online: December 22, 2005

 © 2006 Wiley-VCH Verlag GmbH & Co. KGaA, Weinheim 

DOI: 10.1002/ejic.200500641

# Chloro, Alkyl and Aryl Complexes of Rare Earth Metals Supported by Bulky Tetrasubstituted Guanidinate Ligands

**Alexander A. Trifonov,*[a] Dmitrii M. Lyubov,[a] Elena A. Fedorova,[a] Georgy K. Fukin,[a] Herbert Schumann,[b] Stefan Mühle,[b] Markus Hummert,[b] and Mikhail N. Bochkarev[a]**

**Keywords:** Alkyl complexes / Aryl complexes / Guanidinates / N ligands / Rare Earths

The reactions of anhydrous $LnCl_3$ (Ln = Y, Nd, Sm, Lu) with two equiv. of sodium *N*,*N*′-dicyclohexyl-*N*′′-bis(trimethylsilyl)guanidinate Na[$(Me_3Si)_2NC(NCy)_2$], obtained from Na[$N(SiMe_3)_2$] and the 1,3-dicyclohexyl-substituted carbodiimide CyN=C=NCy in THF, yield the monochloro bis(guanidinate) tetrahydrofuranate complexes [$(Me_3Si)_2NC(NCy)_2]_2$LnCl(THF) [Ln = Y (**1**), Nd (**2**), Sm (**3**) and Lu (**4**)]. The analogous reactions of $YCl_3$ and $LuCl_3$ with the lithium guanidinate [$Li(Et_2O)$][$(Me_3Si)_2NC(NCy)_2$] afford the bis(guanidinate) "ate" complexes [$(Me_3Si)_2NC(NCy)_2]_2$Ln(μ-Cl)$_2$Li(THF)$_2$ [Ln = Y (**5**) and Lu (**6**)]. Treatment of **5** with dimethoxyethane results in the formation of [$(Me_3Si)_2NC(NCy)_2]_2$Y(μ-Cl)$_2$Li(DME) (**7**). The carbyl complexes [$(Me_3Si)_2NC(NCy)_2]_2$Y-*t*Bu] (**8**), [$(Me_3Si)_2NC(NCy)_2]_2$Y(μ-Me)$_2$Li(TMEDA) (**10**) and [$(Me_3Si)_2NC(NCy)_2]_2$YPh(THF) (**13**) were obtained by interaction of complex **1** with RLi (R = *t*Bu, Me or Ph). The molecular structures of **1**, **6**, **7**, **8** and the side product [Li(TMEDA)]-[$(Me_3Si)_2NC(NCy)_2$] have been determined by single-crystal X-ray analyses. Agostic interactions between the yttrium atom and the *tert*-butyl group in complex **8** in the solid state as well as in solution have been substantiated by $^{13}C$ NMR spectroscopy and X-ray analysis.
(© Wiley-VCH Verlag GmbH & Co. KGaA, 69451 Weinheim, Germany, 2006)

## Introduction

The organometallic chemistry of the rare earth metals has made considerable progress in the course of the past two decades and has been generally dominated by the synthesis of cyclopentadienyl sandwich and half-sandwich complexes.[1] These complexes have been and remain of special interest because of their potential as catalysts in a wide range of transformations of unsaturated substrates.[2] Recently, research activity has been directed to the substitution of the cyclopentadienyl ligands by other coordinating systems in order to obtain complexes with modified structures and reactivities. To this end, many research groups have focused their work on "harder", mono-anionic polydentate N- and/or O- coordinating ligands providing enough steric bulk to prevent further coordination of Lewis bases, dimerisation or ligand redistribution reactions but still possessing high reactivity.[3] Ligand frameworks containing electronegative nitrogen atoms as donor atoms have turned out to be the most promising ligands since they show a high affinity for the hard Lewis acidic atoms of the rare earths metals[4] combined with structural diversity. Guanidinate anions $[R_2NC(NR'_2)]^-$ are isoelectronic with the cyclopentadienyl anion and have been widely used as supporting ligands for non-transition and d-block transition metals[5] and also, in recent years, for rare earth metals.[6] Based on their anionic character, the facile modification of their electronic and steric properties by variation of the substituents at the nitrogen atoms and their flexible coordination behavior, tetrasubstituted guanidinate anions are very attractive ligand systems for the synthesis of kinetically stable, low-coordinate rare earth metal complexes. We have already used the guanidinate anion $[(Me_3Si)_2NC(N\mathit{i}Pr)_2]^-$ for the successful synthesis of the hydrido complex {[$(Me_3Si)_2$-$NC(N\mathit{i}Pr)_2]_2$Lu(μ-H)}$_2$ which was found to be an active catalyst for the polymerisation of ethylene, propylene and styrene.[7] Here we report on the synthesis, properties and structures of some chloro, alkyl and aryl derivatives of bis(guanidinate)-coordinated complexes of some rare earth metals.

[a] G. A. Razuvaev Institute of Organometallic Chemistry of Russian Academy of Sciences,
Tropinina 49, 603950 Nizhny Novgorod GSP-445, Russia
Fax: +7-8312-127-497
E-mail: trif@imoc.sinn.ru
[b] Institut für Chemie der Technischen Universität Berlin,
Straße des 17. Juni 135, 10623 Berlin, Germany
Fax: +49-30-3142-2168
E-mail: schumann@chem.tu-berlin.de

## Results and Discussion

In order to prepare low-coordinate organometallic complexes of rare earth metals which would be predicted to be resistant towards dimerisation, ligand redistribution and further coordination by Lewis bases, we used the bulky guanidinate ligand $[(Me_3Si)_2NC(NCy)_2]^-$ bearing cyclohexyl groups at the coordinating nitrogen atoms. The respective sodium and lithium guanidinates are available by treatment of Na[$N(SiMe_3)_2$] or [$Li(Et_2O)$][$N(SiMe_3)_2$] with 1,3-dicy-

 © 2006 Wiley-VCH Verlag GmbH & Co. KGaA, Weinheim 

clohexylcarbodiimide, CyN=C=NCy, in THF and can be isolated in a pure state.[6a] Addition of anhydrous $LnCl_3$ (Ln = Y, Nd, Sm, Lu) to freshly prepared THF solutions of the sodium guanidinate (1:2 mol ratio) at room temperature allows the isolation of the monomeric crystalline lanthanide bis(guanidinate) chlorides $[(Me_3Si)_2NC(NCy)_2]_2$-LnCl(THF) [Ln = Y (**1**), Nd (**2**), Sm (**3**) and Lu (**4**)] from the respective solution in yields of 60 to 80% (Scheme 1).

The reactions of $YCl_3$ and $LuCl_3$ with the lithium salt $[Li(Et_2O)][(Me_3Si)_2NC(NCy)_2]$ instead of the sodium analogue afford the monomeric "ate" complexes $[(Me_3Si)_2$-$NC(NCy)_2]_2Ln(\mu\text{-}Cl)_2Li(THF)_2$ [Ln = Y (**5**), Lu (**6**)] in yields of 74 and 70%, respectively (Scheme 2). In contrast, the metathesis of $YCl_3$ with $[Li(Et_2O)][(Me_3Si)_2NC(N\textit{i}Pr)_2]$ containing less steric demanding isopropyl instead of cyclohexyl groups results in the formation of the dimeric complex $\{[(Me_3Si)_2NC(N\textit{i}Pr)_2]_2Y(\mu\text{-}Cl)\}_2$.[6b,6e] Furthermore, treatment of **5** with dimethoxyethane results in replacement of the two THF ligands coordinated to the lithium atom by a DME molecule producing $[(Me_3Si)_2NC(NCy)_2]_2Y(\mu\text{-}Cl)_2$-Li(DME) (**7**). Though $LaCl_3$ clearly reacts with sodium or lithium *N*,*N*′-dicyclohexyl-*N*′′-bis(trimethylsilyl)guanidinate under comparable reaction conditions, no THF-soluble lanthanum complex could be isolated.

The colourless (**1**, **4**, **5** to **7**), pale blue (**2**) or pale yellow (**3**) crystalline complexes are moisture- and air-sensitive. In an inert atmosphere they can be stored without decomposition at room temperature. They are soluble in ethers and aromatic hydrocarbons and moderately soluble in hexane and pentane but it should be added that the solubilities of the monochloro bis(guanidinate) complexes **1** to **4** are noticeably higher than those of the related "ate" complexes **5** and **6**.

The $^1H$ and $^{13}C$ NMR spectra of the diamagnetic complexes **1**, **4**, **5**, **6** and **7** in [D$_6$]benzene at 20 °C show the expected sets of resonances due to the guanidinate moiety and the coordinated THF and DME molecules. The $^1H$ NMR signals of the THF methylene protons in **1**, **4**, **5** and **6** appear as broad singlets reflecting the labile coordination. Crystals suitable for single-crystal X-ray diffraction studies of **1**, **6** and **7** were obtained from hexane solutions by slow evaporation of the solvent at room temperature (**1** and **7**) or by cooling the solution to –20 °C (**6**). The molecular structures of **1**, **6** and **7** are depicted in Figure 1, Figure 2 and Figure 3, respectively. The crystal and structural refinement data are listed in Table 1.

Complex **1** crystallises as the monomeric hexane solvate $[(Me_3Si)_2NC(NCy)_2]_2YCl(THF)(C_6H_{14})_{1/2}$ in the monoclinic space group $P2_1/c$ with four molecules in the unit cell. The molecular structure shows the yttrium atom hexacoordinated by two chelating guanidinate anions, one chlorine atom and one THF molecule (Figure 1).

The distances Y–N(1,2) [2.387(5), 2.327(5) Å] and Y–N(4,5) [2.377(4), 2.344(5) Å] as well as the distances

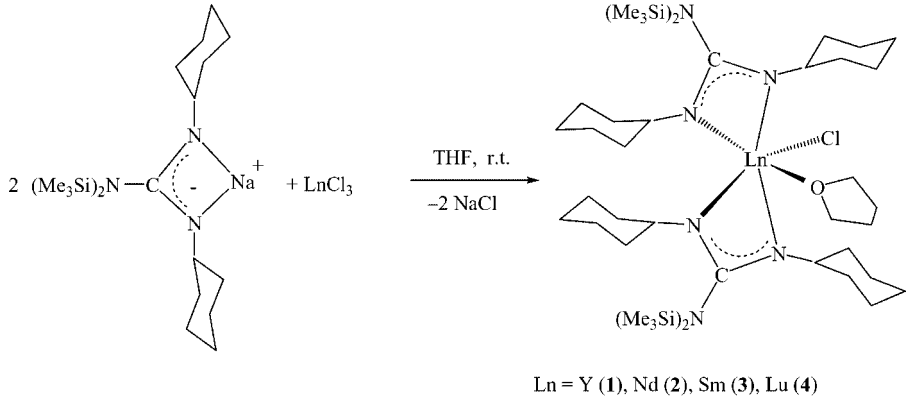


Scheme 1.

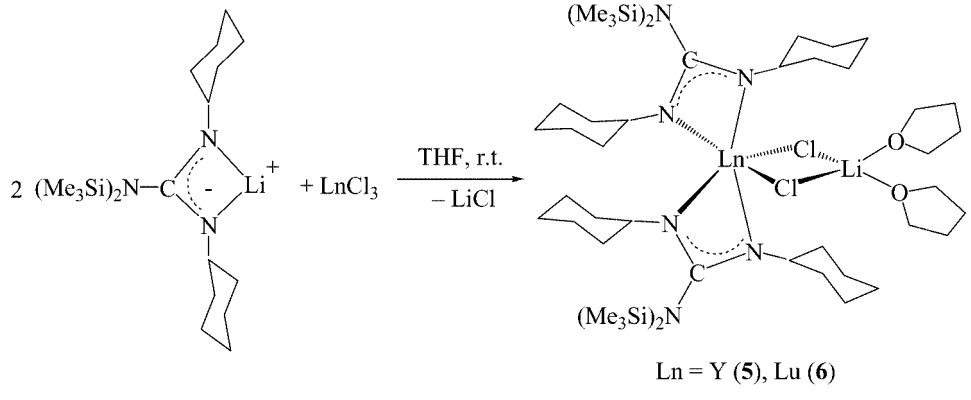


Scheme 2.

 © 2006 Wiley-VCH Verlag GmbH & Co. KGaA, Weinheim 

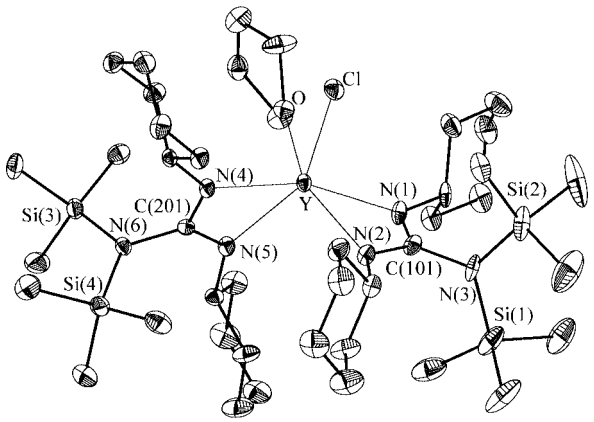


Figure 1. ORTEP diagram (30% probability thermal ellipsoids) of $[(Me_3Si)_2NC(NCy)_2]_2YCl(THF)$ (**1**) showing the non-hydrogen atom numbering scheme. Hydrogen atoms are omitted for clarity. Selected bond lengths [Å] and angles [°]: Y–N(1) 2.387(5), Y–N(2) 2.327(5), Y–N(4) 2.377(4), Y–N(5) 2.344(5), Y–C1 2.584(2), Y–O 2.406(4), C(101)–N(1) 1.335(8), C(101)–N(2) 1.332(7), C(101)–N(3) 1.442(7), C(201)–N(4) 1.314(8), C(201)–N(5) 1.348(7), C(201)–N(6) 1.451(7); N(1)–Y–N(2) 56.87(17), N(4)–Y–N(5) 56.84(17), N(1)–C(101)-N(2) 114.7(5), N(4)–C(201)–N(5) 115.2(5), O–Y–Cl 84.55(11).

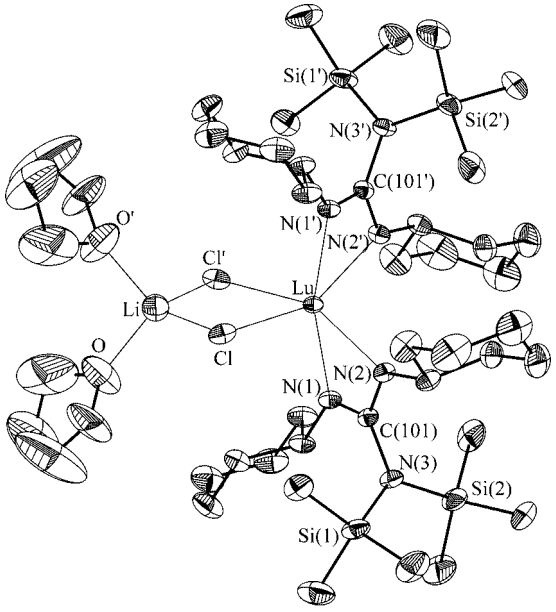


Figure 2. ORTEP diagram (30% probability thermal ellipsoids) of $[(Me_3Si)_2NC(NCy)_2]_2Lu(\mu\text{-}Cl)_2Li(THF)_2$ (**6**) showing the non-hydrogen atom numbering scheme. Hydrogen atoms are omitted for clarity. Selected bond lengths [Å] and angles [°]: Lu–N(1) 2.320(5), Lu–N(2) 2.291(5), Lu–Cl 2.7468(17), Li–Cl 2.304(14), Li–O 1.932(16), C(101)–N(1) 1.316(7), C(101)–N(2) 1.339(7), C(101)–N(3) 1.439(7); N(1)–Lu–N(2) 57.74(7), N(1)–Lu–N(2)′ 109.49(17), N(1)′–Lu–N(2)′ 57.74(17), N(1)–C(101)–N(2) 114.0(5), C(101)–Lu–C(101A) 130.3(2), Cl–Lu–Cl′ 83.90(6), Cl–Li–Cl′ 105.7(9). Symmetry operation: $-x$, $y$, to $-z + 0.5$.

C(101)–N(1,2) [1.335(8), 1.332(7) Å] and C(201)–N(4,5) [1.314(8), 1.348(7) Å] in the guanidinate ligands differ only slightly from each other, thus indicating electron delocalisation within the anionic NCN units. The considerably longer distances C(101)–N(3) [1.442(7) Å] and C(201)–N(6) [1.451(7) Å] indicate that the $N(SiMe_3)_2$ moiety does not take part in the conjugation. The opposite orientation of the $N(SiMe_3)_2$ and cyclohexyl groups relative to the NCN planes corresponds to the minimisation of their mutual steric repulsion. The dihedral angles between the planes formed by the SiNSi and the NCN fragments as well as between the mean plane of the cyclohexyl groups and the plane of the NCN fragment are close to 90° (89.7 and 82.9, and 73.8 and 96.6°, respectively).

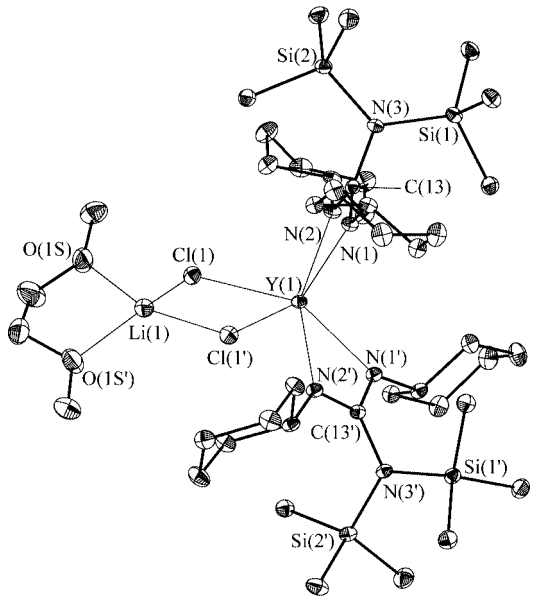


Figure 3. ORTEP diagram (30% probability thermal ellipsoids) of $[(Me_3Si)_2NC(NCy)_2]_2Y(\mu\text{-}Cl)_2Li(DME)$ (**7**) showing the non-hydrogen atom numbering scheme. Hydrogen atoms are omitted for clarity. Selected bond lengths [Å] and angles [°]: Y(1)–N(1) 2.3517(10), Y(1)–N(2) 2.3566(10), Y(1)–Cl(1) 2.6693(3), Li(1)–Cl(1) 1.2311(2), Li(1)–O(1S′) 1.980(3), N(1)–C(13) 1.3304(14), N(2)–C(13) 1.3325(15), N(3)–C(13) 1.4377(16); N(1)–Y(1)–N(2) 56.80(3), Cl(1)–Y(1)–Cl(1′) 82.106(14), N(1)–C(13)–N(2) 114.47(11), C(13)–Y(1)–C(13′) 125.77(5), O(1S′)–Li(1)–O(1S) 81.14(14), Cl(1′)–Li(1)–Cl(1) 98.70. Symmetry operation: $-x$, $y$, to $-z + 0.5$.

Complex **6** crystallises in the monoclinic space group *C*2/*c* with four molecules in the unit cell. The lutetium atom is hexacoordinated by the four nitrogen atoms of the two bidentate guanidinate ligands and by two chlorine atoms. The two chlorine atoms form bridges to the lithium atom which is in turn coordinated to two THF molecules (Figure 2).

As in the molecular structure of **1**, the small differences between the Lu–N(1,2) distances [2.320(5), 2.291(5) Å] and the C(101)–N(1,2) distances [1.316(7), 1.339(7) Å] indicate electron delocalisation within the anionic NCN fragments. The lengths of the lutetium-nitrogen bonds are very close to those in the related lutetium complex $[(Me_3Si)_2NC(N\textit{i}Pr)_2]_2Lu(\mu\text{-}Cl)_2Li(THF)_2$ [2.285(1)–2.346(1) Å] containing less sterically demanding isopropyl-substituted guanidinate ligands[7] and to the lengths of the Lu–N bonds in $[Li(THF)_4][(C_5H_5)_2Lu(NPh_2)_2]$ [2.290(7), 2.293(7) Å][8] but are much shorter than the coordinate N→Lu bonds in $(\eta^8\text{-}C_8H_8)Lu[o\text{-}C_6H_4CH_2N(CH_3)_2](THF)$ [2.479(6) Å][9] and

 © 2006 Wiley-VCH Verlag GmbH & Co. KGaA, Weinheim 

Table 1. Crystallographic data and structure refinement details for **1**, **6**, **7**, **8** and **11**.

| | **1** | **6** | **7** | **8** | **11** |
|---|---|---|---|---|---|
| Empirical formula | $C_{45}H_{95}ClLiN_6OSi_4Y$ | $C_{46}H_{96}Cl_2LiLuN_6O_2Si_4$ | $C_{42}H_{90}Cl_2LiN_6O_2Si_4Y$ | $C_{42}H_{89}N_6Si_4Y$ | $C_{25}H_{56}LiN_5Si_2$ |
| Formula mass | 972.99 | 1130.46 | 990.31 | 879.46 | 489.87 |
| $T$ [K] | 173(2) | 173(2) | 100(2) | 100(2) | 100(2) |
| Crystal system | monoclinic | monoclinic | monoclinic | monoclinic | monoclinic |
| Space group | $P2_1/c$ (No. 14) | $C2/c$ (No.15) | $C2/c$ (No. 15) | $P2_1/c$ (No. 14) | $P2_1/c$ (No. 14) |
| $a$ [Å] | 17.9072(3) | 26.4406(9) | 24.6189(13) | 13.9177(11) | 17.583(3) |
| $b$ [Å] | 11.5050(1) | 13.6217(4) | 13.9815(7) | 18.2575(15) | 10.6598(16) |
| $c$ [Å] | 27.7509(4) | 19.1255(4) | 17.7688(9) | 20.0347(16) | 17.615(3) |
| $\alpha$ [°] | 90 | 90 | 90 | 90 | 90 |
| $\beta$ [°] | 100.082(1) | 119.992(1) | 116.150(1) | 92.452(2) | 106.652(2) |
| $\gamma$ [°] | 90 | 90 | 90 | 90 | 90 |
| $V$ [Å$^3$] | 5629.02(13) | 5966.0(3) | 5490.1(5) | 5086.2(7) | 3163.3(8) |
| $Z$ | 4 | 4 | 4 | 4 | 4 |
| Density (calcd.) [g cm$^{-3}$] | 1.148 | 1.259 | 1.198 | 1.149 | 1.029 |
| $\mu$ [mm$^{-1}$] | 1.204 | 1.862 | 1.284 | 1.274 | 0.132 |
| $T_{max.}/T_{min.}$ | 0.7590/0.3488 | 0.8448/0.6565 | 0.7151/0.5440 | 0.8832/0.7497 | 0.9491/0.9430 |
| $F(000)$ | 2108 | 2376 | 2128 | 1912 | 1088 |
| Crystal size [mm] | 0.45×0.22×0.16 | 0.38×0.22×0.15 | 0.54×0.49×0.28 | 0.24×0.16×0.10 | 0.45×0.40×0.40 |
| $\theta$ range [°] | 1.15–27.50 | 1.74–27.50 | 1.72–24.50 | 1.84–29.08 | 1.94–25.00 |
| Completeness to $\theta$ [%] | 99.7 | 99.4 | 99.7 | 99.2 | 99.9 |
| | $-22 \le h \le 23$ | $-34 \le h \le 34$ | $-27 \le h \le 28$ | $-18 \le h \le 18$ | $-20 \le h \le 20$ |
| Index ranges | $-14 \le k \le 12$ | $-14 \le k \le 17$ | $-16 \le k \le 9$ | $-24 \le k \le 24$ | $-12 \le k \le 12$ |
| | $-36 \le l \le 33$ | $-24 \le l \le 24$ | $-20 \le l \le 20$ | $-26 \le l \le 27$ | $-20 \le l \le 20$ |
| Reflections collected | 40939 | 21775 | 14137 | 53204 | 24254 |
| Independent reflections | 12878 [$R_{int}$ = 0.2185] | 6830 [$R_{int}$ = 0.0712] | 4568 [$R_{int}$ = 0.0186] | 13505 [$R_{int}$ = 0.0600] | 5559 [$R_{int}$ = 0.0302] |
| Data/restraints/parameters | 12878/0/536 | 6830/2/297 | 4568/7/445 | 13505/0/834 | 5559/0/522 |
| Goodness-of-fit on $F^2$ | 0.979 | 1.112 | 1.052 | 0.997 | 1.062 |
| $R$ indices [$I > 2\sigma(I)$] | $R_1$ = 0.0949, | $R_1$ = 0.0598, | $R_1$ = 0.0268, | $R_1$ = 0.0444, | $R_1$ = 0.0414, |
| | $wR_2$ = 0.1499 | $wR_2$ = 0.1428 | $wR_2$ = 0.0671 | $wR_2$ = 0.0925 | $wR_2$ = 0.1123 |
| $R$ indices (all data) | $R_1$ = 0.2331, | $R_1$ = 0.0753, | $R_1$ = 0.0311, | $R_1$ = 0.0772, | $R_1$ = 0.0505, |
| | $wR_2$ = 0.1996 | $wR_2$ = 0.1518 | $wR_2$ = 0.0687 | $wR_2$ = 0.1038 | $wR_2$ = 0.1177 |
| Largest diff. peak/hole [e Å$^{-3}$] | 0.483/–0.783 | 2.634/–0.767 | 0.420/–0.279 | 1.422/–0.612 | 0.889/–0.259 |

Lu[*o*-$C_6H_4CH_2N(CH_3)_2]_3$ [2.468(6), 2.478(5) and 2.588(5) Å].[10] Since the silylamine nitrogen is not involved in the conjugation, the (Si)N–C bond is substantially longer [1.439(7) Å] than the C–N(1,2) bonds. The bridging Lu–Cl distances in **6** [both 2.747(2) Å] are longer than the terminal Lu–Cl distances in $[(Me_3Si)_2NC(NiPr)_2]_2Lu(\mu\text{-}Cl)_2Li(THF)_2$ [2.600(1) and 2.622(1) Å][7] and $(tBu_2C_5H_3)_2Lu(\mu\text{-}Cl)_2Li$(TMEDA) [2.60(1) Å][11] which can be attributed to the stronger steric repulsions of the bulkier cyclohexyl groups and the THF molecules coordinated to the lithium atom. The angle C(101)–Lu–C(101A) [130.3(2)°], defined as a bite angle, is slightly smaller than the corresponding angle in $[(Me_3Si)_2NC(NiPr)_2]_2Lu(\mu\text{-}Cl)_2Li(THF)_2$ [132.30(6)°][7] but larger than the centroid-metal-centroid angle in $(tBu_2C_5H_3)_2Lu(\mu\text{-}Cl)_2Li$(TMEDA) [127.9(1)°].[11]

Complex **7** crystallises in the monoclinic space group *C*2/*c*. The unit cell contains four molecules and the coordination environment of the yttrium atom (Figure 3) is analogous to that of the lutetium atom in **6**. The Y–N(1,2) distances [2.352(1), 2.357(1) Å] differ only very slightly and are in the range of the corresponding distances for the related yttrium guanidinate and amidinate complexes $\{[(Me_3Si)_2NC(NiPr)_2]_2Y(\mu\text{-}Cl)\}_2$ [2.326(4)–2.388(4) Å],[6b] $\{[PhC(NSiMe_3)_2]_2Y(\mu\text{-}H)\}_2$ [2.327(3)–2.389(3) Å][12a] and $[PhC(NSiMe_3)_2]_2Y(\mu\text{-}Cl)_2Li$(TMEDA) [2.334(2)–2.373(2) Å].[13] The Y–Cl distances [2.669(1) Å] are slightly longer than those in the metallocene type "ate" complexes $Cp^*_2Y(\mu\text{-}Cl)_2Li(THF)_2$ [2.646(2), 2.655(2) Å][14] and $[(1,3\text{-}Me_3Si)_2C_5H_3]_2Y(\mu\text{-}Cl)_2Li(THF)_2$ [2.626(1), 2.631(1) Å][15] but shorter than the Y–Cl bonds in the dimeric complex $\{[(Me_3Si)_2NC(NiPr)_2]_2Y(\mu\text{-}Cl)\}_2$ [2.7128(15), 2.7166(15) Å].[12b] The bite angle C(13)–Y(1)–C(13′) [125.77(5)°] is substantially smaller than that in **6** [130.3(2)°]. As expected, the distance of the yttrium atom to the bridging Cl atoms [2.6693(3) Å] is significantly longer than to the terminal Cl atom in **1** [2.584(2) Å].

Complex **1** turned out to be suitable for alkylation and arylation reactions. The alkylation with *t*BuLi, carried out in hexane at 0 °C, affords the THF-free complex $[(Me_3Si)_2NC(NCy)_2]_2Y$–*t*Bu (**8**) (Scheme 3) which was isolated as colourless crystals in a yield of 52%. $^1$H NMR spectroscopic monitoring of the course of the reaction revealed that **8** is actually formed quantitatively. However, its isolation in a crystalline state is hampered by its very high solubility in hexane and pentane. The NMR spectra of **8**, recorded in [D$_6$]benzene at ambient temperature, conditions under which the complex is stable for at least the three days over which measurements were made, show three remarkable features: 1) The $^1$H NMR signal of the methyl protons of the *tert*-butyl group appears as a broadened singlet at $\delta$ = 1.48 ppm and the corresponding carbon atoms cause the appearance of two $^{13}C\{^1H\}$ NMR signals at $\delta$ = 30.6 and 30.7 ppm which can be interpreted as a doublet with a coupling constant $^2J_{Y,C}$ = 2.3 Hz. The tertiary carbon atom

 © 2006 Wiley-VCH Verlag GmbH & Co. KGaA, Weinheim 

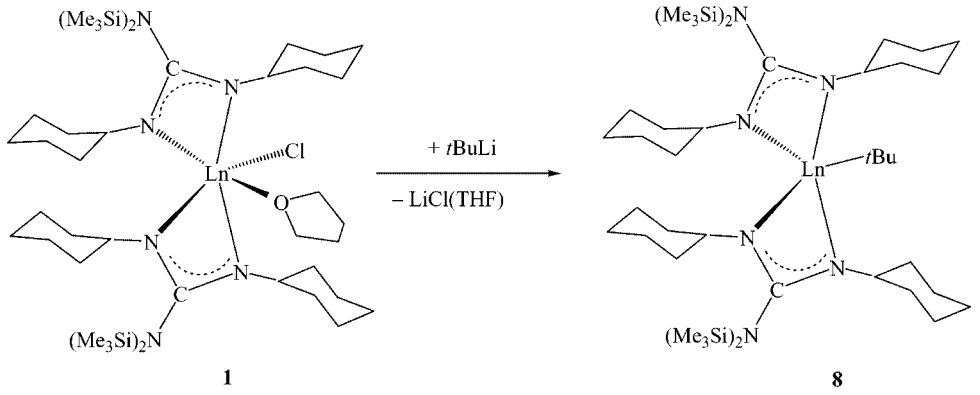


Scheme 3.

of the *tert*-butyl group bonded to the yttrium atom gives rise to a $^{13}C\{^1H\}$ NMR doublet at $\delta$ = 37.5 ppm with a coupling constant $^1J_{Y,C}$ = 56 Hz. 2) The methine protons of the four cyclohexyl groups appear as two broad multiplet signals at $\delta$ = 3.45 and 3.63 ppm with an intensity ratio of 1:3 which collapse to a very broad multiplet at $\delta$ = 3.54 ppm in the $^1H$ NMR spectrum in [D$_8$]toluene below –10 °C. The methine carbon atoms display a $^{13}C\{^1H\}$ NMR signal at $\delta$ = 55.2 ppm and their methylene carbon atoms show a single set of five signals at 24.9, 25.9, 26.1, 26.2 and 26.4 ppm. These observations indicate non-equivalence of the guanidinate ligands apparently resulting from the steric repulsion of the bulky *t*Bu and cyclohexyl groups. 3) The methylsilyl protons give rise to three singlet signals at $\delta$ = 0.28, 0.32 and 0.36 ppm in an intensity ratio of 1:3:2 at room temperature and in [D$_8$]toluene below –10 °C. They correspond to the three $^{13}C\{^1H\}$ NMR signals of the methylsilyl carbon atoms at 2.3, 2.4 and 2.8 ppm. The different shielding of the $CH_3$(Si) groups is not clear. It may be caused by restricted rotation of the N(SiMe$_3$)$_2$ units due to the neighbourhood of the bulky cyclohexyl moieties.

Crystals of **8** suitable for X-ray diffraction studies were obtained by prolonged cooling of concentrated hexane solutions to –30 °C. The molecular structure of **8** is shown in Figure 4 and the crystal and structure refinement data are listed in Table 1.

The coordination sphere of the yttrium atom is composed of the four nitrogen atoms of the two bidentate guanidinate ligands and the tertiary carbon atom of the *tert*-butyl group resulting in a formal coordination number of 5 for yttrium, a lower number than for other organo-yttrium compounds.[1] The most striking feature in the structure of **8** is the strongly distorted geometry of the *t*Bu ligand. The angles C(41)–C(39)–Y(1) [91.71(16)°] and C(42)–C(39)–Y(1) [98.99(16)°] are substantially smaller and the angle C(40)–C(39)–Y(1) [135.62(17)°] is much larger than the value expected for an sp$^3$ hybridised carbon atom, thus leading to rather close contacts between yttrium and the methyl carbon atoms C(41) [2.877(3) Å] and C(42) [3.038(3) Å] and the hydrogens belonging to them. The distance Y(1)–C(40) remains very long [3.639(3) Å] and indicates the absence of an interaction between the methyl group and yttrium. Despite the fact that the C–C distances

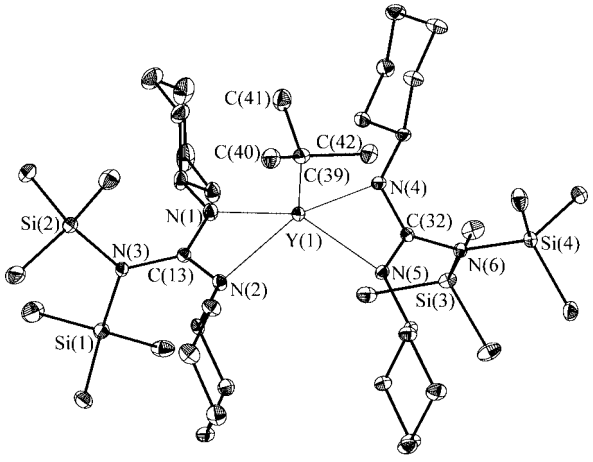


Figure 4. ORTEP diagram (30% probability thermal ellipsoids) of [(Me$_3$Si)$_2$NC(NCy)$_2$]$_2$Y–*t*Bu (**8**) showing the non-hydrogen atom numbering scheme. Hydrogen atoms are omitted for clarity. Selected bond lengths [Å] and angles [°]: Y(1)–N(1) 2.3360(19), Y(1)–N(2) 2.3545(17), Y(1)–N(4) 2.3990(17), Y(1)–N(5) 2.3167(17), Y(1)–C(39) 2.399(2), N(1)–C(13) 1.338(3), N(2)–C(13) 1.333(3), N(3)–C(13) 1.432(3), N(4)–C(32) 1.334(3), N(5)–C(32) 1.341(3), N(6)–C(32) 1.429(3), C(39)–C(40) 1.515(4), C(39)–C(41) 1.518(4), C(39)–C(42) 1.527(3); N(1)–Y(1)–N(2) 57.05(6), N(4)–Y(1)–N(5) 57.14(6), N(1)–C(13)–N(2) 114.03(19), N(4)–C(32)–N(5) 115.03(18), C(39)–Y(1)–C(13) 112.08(7), C(39)–Y(1)–C(32) 116.23(7), C(40)–C(39)–Y(1) 135.62(17), C(41)–C(39)–Y(1) 91.71(16), C(42)–C(39)–Y(1) 98.99(16).

within the *tert*-butyl group do not change considerably [C(39–C(40) = 1.515(4), C(39)–C(41) = 1.518(4) and C(39)–C(42) = 1.527(2) Å] we suggest that agostic interactions are present in **8**. To evaluate qualitatively the hindrance of the *t*Bu group to rotation around the Y(1)–C(39) bond, the MOLDRAW program[17] was used to estimate the changes in the energies of non-bonding interactions as a function of the torsion angle N(5)–Y(1)–C(39)–C(42). As shown in Figure 5, the minimum energy corresponds exactly to a torsion angle of 22.5° estimated for **8** from its molecular structure. In this case, even the shortest intramolecular distances between the carbon atoms C(40) and C(42) and the carbon atoms of the cyclohexyl and the SiMe$_3$ groups are rather long ranging from 3.653 to 4.122 Å, thus excluding steric hindrance. According to the diagram the first and, at the same time, the highest maximum of energy corresponds to

 © 2006 Wiley-VCH Verlag GmbH & Co. KGaA, Weinheim 

a torsion angle of between 163.0 and 172.1°. Such an orientation of the *tert*-butyl group would cause a short contact of 2.700 Å between the C(41) methyl carbon atom and the C(8) methylene carbon atom of the cyclohexyl ring thus provoking steric repulsion. In the case of a torsion angle of 242.8–252.8° corresponding to the second maximum, the shortest intramolecular contact of 2.800 Å would be between the C(42) methyl carbon atom and the C(8) methylene carbon atom of the cyclohexyl moiety. In the last two cases, the distances to the methyl carbon atoms of the $SiMe_3$ groups are in the range of van der Waals contacts. These data clearly show that the hindrance to rotation of the *t*Bu group is caused by agostic interactions with the yttrium atom. At this point it should be noted that $[(Me_3Si)_2NC(NiPr)_2]_2Y$–*t*Bu, containing the less steric demanding *i*Pr groups, shows no signs of agostic interactions. In this compound the Y–C bond [2.332(9) Å][6b] is noticeably shorter than that in **8** [2.399(2) Å] and in other *N*,*N*- and *N*,*O*-coordinated alkyl yttrium complexes.[16] The bonding situation within the four-membered metallocycles in **8** is different from that in **7**. Whereas in complex **7** both guanidinate ligands are bonded to the metal atom in a symmetric fashion, the Y–N distances in **8** range from 2.3167(17) to 2.3990(17) Å. The very small differences in the bond lengths within the coordinating NCN fragments in **8** [C(13)–N(1) = 1.338(3), C(13)–N(2) = 1.333(3), C(32)–N(4) = 1.334(3) and C(32)–N(5) = 1.341(3) Å] are indicative of delocalised π systems.

Analogous to the synthesis of **8**, we treated equimolar amounts of **1** and MeLi in order to obtain the corresponding methyl yttrium complex. In fact, the NMR-scale reaction carried out in [$D_8$]toluene at 0 °C occurred with formation of $[(Me_3Si)_2NC(NCy)_2]_2YMe$ (**9**) as indicated by the appearance of a broad signal at –0.36 ppm in the $^1$H NMR spectrum which could be assigned to the protons of the yttrium bonded methyl group. However, the compound was no longer formed when the reaction was carried out on a preparative scale in hexane at 0 °C. On the other hand, the reaction of **1** with two equiv. of MeLi in hexane at 0 °C and in the presence of TMEDA afforded the corresponding "ate" complex $[(Me_3Si)_2NC(NCy)_2]_2Y(\mu\text{-}Me)_2Li(TMEDA)$ (**10**) as a colourless microcrystalline solid in 61% yield. As

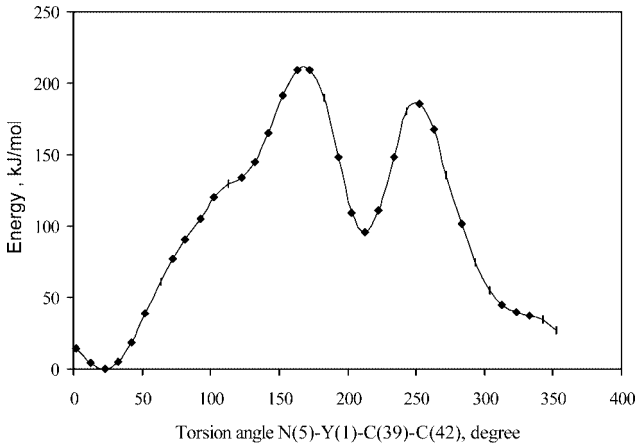


Figure 5. Energy diagram of the non-bonding interactions in complex **8** as function of the torsion angle N(5)–Y(1)–C(39)–C(42).

a side product, lithium guanidinate $[Li(TMEDA)][(Me_3Si)_2NC(NCy)_2]$ (**11**) was isolated in a yield of 7%.

The moisture- and air-sensitive complex **10** is soluble in THF and toluene and moderately soluble in hexane. [$D_6$]benzene solutions of **10** are stable at room temperature for several days. The NMR spectra of **10** recorded in [$D_6$]benzene show a broad $^1$H singlet signal at –0.51 ppm and a broad $^{13}C\{^1H\}$ resonance at $\delta$ = 11.6 ppm with no resolved yttrium coupling for the yttrium bonded methyl groups. These chemical shift values are very close to those reported for the related methyl complexes $[(Me_3Si)_2NC(NiPr)_2]_2Y(\mu\text{-}Me)_2Li(TMEDA)$[6b] and $[PhC(NSiMe_3)_2]_2Y(\mu\text{-}Me)_2Li(TMEDA)$[12a,12b] but are noticeably lower-field compared with those of the metallocene type complexes such as $Cp^*_2Y(\mu\text{-}Me)_2Li(OEt_2)$.[12c] The guanidinate fragments give rise to a single set of signals indicating the equivalence of both ligands.

The lithium guanidinate $[Li(TMEDA)][(Me_3Si)_2NC(NCy)_2]$ (**11**), formed as a side product, was characterised by $^1$H and $^{13}$C NMR spectroscopy as well as by an X-ray structure analysis. An ORTEP drawing of its molecular structure is shown in Figure 6 and the crystal and structure refinement data are listed in Table 1. Unlike $[\{(Me_3Si)_2NC(NCy)_2\}Li]_2$[18] obtained from the reaction of ether-free

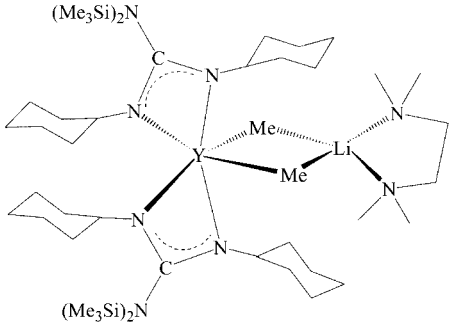


**10**

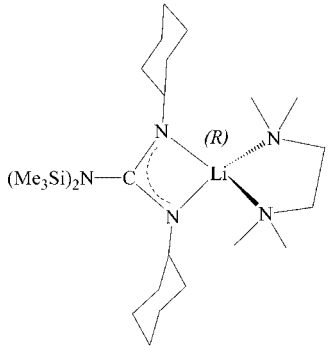


**11**

 © 2006 Wiley-VCH Verlag GmbH & Co. KGaA, Weinheim 

$Li[N(SiMe_3)_2]$ with CyN=C=NCy in toluene, complex **11** was found to be monomeric in the solid state.

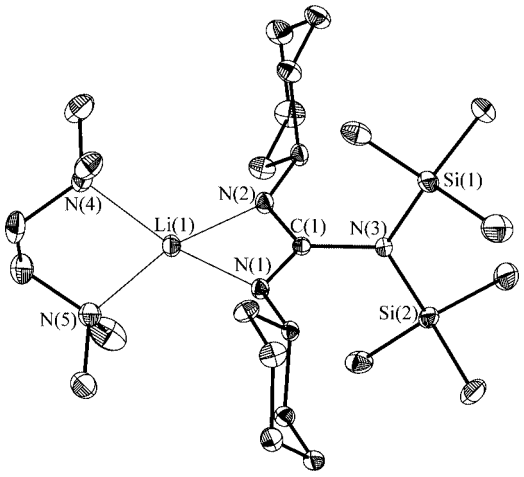


Figure 6. ORTEP diagram (30% probability thermal ellipsoids) of $[Li(TMEDA)][(Me_3Si)_2NC(NCy)_2]$ (**11**) showing the non-hydrogen atom numbering scheme. Hydrogen atoms are omitted for clarity. Selected bond lengths [Å] and angles [°]: Li(1)–N(1) 1.969(3), Li(1)–N(2) 1.971(3), Li(1)–N(4) 2.110(3), Li(1)–N(5) 2.089(3), N(1)–C(1) 1.3258(19), N(2)–C(1) 1.3217(19), N(3)–C(1) 1.4655(19); N(1)–Li(1)–N(2) 69.46(10), N(5)–Li(1)–N(4) 87.01(11).

At first, the reaction of **1** with $LiCH_2SiMe_3$ was carried out in an NMR tube in [D$_8$]toluene at 0 °C and the $^1$H NMR spectrum confirmed the formation of the alkylated product $[(Me_3Si)_2NC(NCy)_2]_2YCH_2SiMe_3$ (**12**) by the appearance of a characteristic doublet signal at –0.16 ppm with a coupling constant $^2J_{Y,H}$ = 3.0 Hz for the yttrium bonded methylene group. However, the reaction carried out on a preparative scale in hexane yielded an inseparable mixture of **12** and compounds which are most likely thermal decomposition products since the signal of TMS was detected in the $^1$H NMR spectrum of the reaction mixture.

The guanidinate supported phenyl yttrium derivative $[(Me_3Si)_2NC(NCy)_2]_2YPh(THF)$ (**13**) was synthesised by treatment of **1** with equimolar amounts of phenyllithium in THF (Scheme 4) and was isolated as a colourless microcrystalline solid in 61% yield. It is soluble in ethers, toluene and hexane. Under NMR conditions ([D$_6$]benzene solution, room temperature, inert atmosphere, sealed tube) it is stable for several days but decomposes immediately in the presence of air or moisture. The $^1$H NMR spectrum of **13** shows a complex multiplet in the region of 7.20–7.45 ppm for the five phenyl protons and two broad multiplets of equal intensity at $\delta$ = 3.24 and 3.55 ppm for the methine protons of the cyclohexyl groups. The methine carbon atoms give rise to two $^{13}C\{^1H\}$ singlet signals at $\delta$ = 54.8 and 56.9 ppm. The presence of the coordinated THF molecule is apparent from two broad $^1$H singlet signals at $\delta$ = 1.79 and 3.75 ppm and two $^{13}C\{^1H\}$ resonances at $\delta$ = 25.2 and 68.7 ppm.

## Conclusions

The *N*,*N*′-dicyclohexyl-*N*′′-bis(trimethylsilyl)-substituted guanidinate anion is a suitable ligand for the synthesis of stable monomeric monochloro and "ate" complexes of yttrium, neodymium, samarium and lutetium. Alkyl and phenyl complexes of yttrium with very low coordination numbers stabilised by this guanidinate ligand have been synthesised and characterised. Agostic interactions between yttrium and the methyl groups of the *tert*-butyl ligand in $[(Me_3Si)_2NC(NCy)_2]_2Y$–*t*Bu (**8**) in the solid state as well as in solution have been confirmed by X-ray structural analysis and NMR spectroscopy.

## Experimental Section

All experiments were performed in evacuated tubes using standard Schlenk techniques with rigorous exclusion of traces of moisture and air. After drying over KOH, THF was purified by distillation from sodium/benzophenone ketyl. Hexane and toluene were dried by distillation from sodium/triglyme and benzophenone ketyl prior to use. [D$_6$]benzene was dried with sodium and condensed in vacuo into the NMR tubes prior to use. *N*,*N*′-dicyclohexylcarbodiimide and *t*BuLi were purchased from Acros. Anhydrous $LuCl_3$,[19] $[Li(Et_2O)][N(SiMe_3)_2]$[20] and $Na[N(SiMe_3)_2]$[21] were prepared according to literature procedures. All other commercially available chemicals were used after appropriate purification. NMR spectra were recorded on a Bruker DPX 200 spectrometer ($^1$H, 200 MHz; $^{13}$C, 50 MHz). Chemical shifts for $^1$H and $^{13}$C spectra were referenced internally using the residual solvent resonances and are reported relative to TMS. IR spectra were recorded as Nujol mulls on a Specord M80 instrument. Lanthanide metal analyses were carried out by complexometric titration. The C,H elemental analyses were carried out by the microanalytical laboratory of the IOMC.

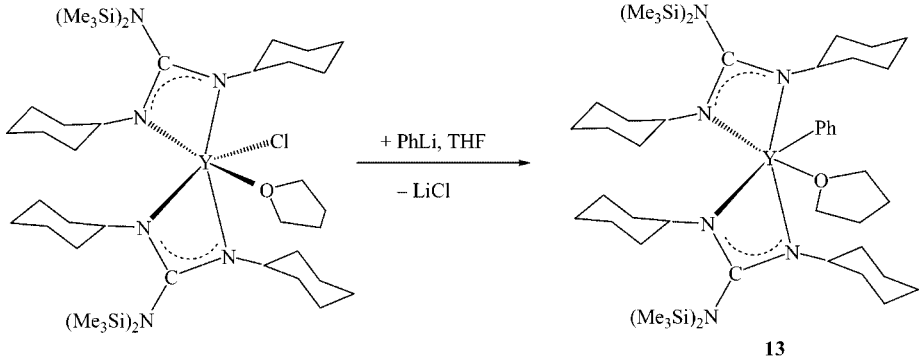


Scheme 4.

 © 2006 Wiley-VCH Verlag GmbH & Co. KGaA, Weinheim 

**Synthesis of [(Me$_3$Si)$_2$NC(NCy)$_2$]$_2$YCl(THF) (1):** To a solution of Na[N(SiMe$_3$)$_2$] (1.00 g, 5.45 mmol) in THF (30 mL) was added CyN=C=NCy (1.12 g, 5.45 mmol) slowly at 20 °C and after 45 min stirring $YCl_3$ (0.53 g, 2.72 mmol) was added. The reaction mixture was stirred for further 12 h and the NaCl formed was filtered off and from the clear solution and the solvent was evaporated in vacuo. The remaining solid was extracted twice with toluene (2 × 20 mL). After filtration of the toluene extracts, the toluene was evaporated in vacuo. The remaining off-white solid was dissolved in hexane (30 mL). The resultant solution was slowly concentrated at room temperature to a quarter of its volume and was then cooled to –30 °C. The crystalline precipitate formed overnight was washed with cold hexane and then dried in vacuo at room temperature for 40 min yielding **1** (1.67 g, 66%) as a colourless crystalline solid. $C_{42}H_{88}ClN_6OSi_4Y$ (929.2): calcd. C 54.28, H 9.47, Y 9.56; found C 53.83, H, 9.12, Y 9.83. $^1$H NMR (200 MHz, [D$_6$]benzene): $\delta$ = 0.43 [s, 36 H, Si(CH$_3$)$_3$], 1.12–1.88 (br. m, 44 H, CH$_2$/Cy, β-CH$_2$/THF), 3.29 (br. m, 4 H, CH/Cy), 3.94 (br. s, 4 H, α-CH$_2$/THF) ppm. $^{13}$C{$^1$H} NMR (50 MHz, [D$_6$]benzene): δ = 3.1 (N[Si(CH$_3$)$_3$]$_2$), 25.4 (β-CH$_2$/THF), 23.1, 26.3, 26.6, 31.9, 37.4 (CH$_2$/Cy), 55.1 (CH/Cy), 70.1 (α-CH$_2$/THF), 169.1 (CN$_3$) ppm. IR (Nujol, KBr): $\tilde{\nu}$ = 1620 (s), 1320 (m), 1240 (s), 1270 (m), 1200 (m), 1150 (m), 1100 (m), 1050(m), 950 (s), 930 (s), 860 (m), 830 (s) cm$^{-1}$.

**Synthesis of [(Me$_3$Si)$_2$NC(NCy)$_2$]$_2$NdCl(THF) (2):** Complex **2** was synthesised following the standard procedure described for **1** from Na[N(SiMe$_3$)$_2$] (1.80 g, 9.81 mmol), CyN=C=NCy (2.02 g, 9.81 mmol) and $NdCl_3$ (1.22 g, 4.90 mmol) in THF (30 mL). Complex **2** was isolated as a pale blue crystalline solid (1.67 g, 79%). $C_{42}H_{88}ClN_6NdOSi_4$ (984.6): calcd. C 51.23, H 8.93, Nd 14.64; found C 50.80, H 9.28, Nd 14.48. IR (Nujol, KBr): $\tilde{\nu}$ = 1620 (s), 1330 (m), 1290 (m), 1240 (s), 1160 (s), 1120 (s), 1050 (m), 990 (s), 950 (s), 930 (s), 850 (s), 830 (s) cm$^{-1}$.

**Synthesis of [(Me$_3$Si)$_2$NC(NCy)$_2$]$_2$SmCl(THF) (3):** Complex **3** was synthesised following the standard procedure described for **1** from Na[N(SiMe$_3$)$_2$] (1.00 g, 5.45 mmol), CyN=C=NCy (1.12 g, 5.45 mmol) and $SmCl_3$ (0.7 g, 2.72 mmol) in THF (30 mL). Complex **3** was isolated as a pale yellow crystalline solid (1.50 g, 56%). $C_{42}H_{88}ClN_6OSi_4Sm$ (990.6): calcd. C 50.92, H 8.88, Sm 17.17; found C 50.61, H, 8.49, Sm 17.51. IR (Nujol, KBr): $\tilde{\nu}$ = 1620 (s), 1335 (m), 1290 (s), 1240 (s), 1170 (m), 1120 (m), 1060 (m), 990 (s), 930 (s), 930 (s), 850 (s), 830 (s) cm$^{-1}$.

**Synthesis of [(Me$_3$Si)$_2$NC(NCy)$_2$]$_2$LuCl(THF) (4):** Complex **4** was synthesised following the standard procedure described for **1** from Na[N(SiMe$_3$)$_2$] (1.35 g, 7.36 mmol), CyN=C=NCy (1.51 g, 7.36 mmol) and $LuCl_3$ (1.03 g, 3.68 mmol) in THF (30 mL). Complex **4** was isolated as a colourless crystalline solid (1.67 g, 69%). $C_{42}H_{88}ClLuN_6OSi_4$ (1015.3): calcd. C 49.68, H 8.66, Lu 17.23; found C 49.30, H, 8.16, Lu 17.58. $^1$H NMR (200 MHz, [D$_6$]benzene): $\delta$ = 0.35 [s, 36 H, Si(CH$_3$)$_3$], 1.01–2.09 (br. m, 44 H, CH$_2$/Cy, β-CH$_2$/THF), 3.15 (br. m, 4 H, CH/Cy), 3.61 (br. s, 4 H, α-CH$_2$/THF) ppm. $^{13}$C{$^1$H} NMR (50 MHz, [D$_6$]benzene): $\delta$ = 2.8 (N[Si(CH$_3$)$_3$]$_2$), 25.7 (β-CH$_2$/THF), 22.8, 23.1, 25.1, 29.4, 31.2 (CH$_2$/Cy), 55.7 (CH/Cy), 68.1 (α-CH$_2$/THF), 169.6 (CN$_3$) ppm. IR (Nujol, KBr): $\tilde{\nu}$ = 1640 (m), 1305 (m), 1260 (s), 1250 (s), 1200 (m), 1150 (m), 1050 (s), 970 (m), 950 (s), 860 (s), 840 (s) cm$^{-1}$.

**Synthesis of [(Me$_3$Si)$_2$NC(NCy)$_2$]$_2$Y(μ-Cl)$_2$Li(THF)$_2$ (5):** Complex **5** was synthesised following the standard procedure described for **1** from [Li(Et$_2$O)][N(SiMe$_3$)$_2$] (1.28 g, 5.30 mmol), CyN=C=NCy (1.09 g, 5.30 mmol) and $YCl_3$ (0.52 g, 2.65 mmol) in THF (30 mL). Complex **5** was isolated as colourless crystalline solid (2.03 g, 74%). $C_{46}H_{96}Cl_2LiN_6O_2Si_4Y$ (1043.7): calcd. C 52.93, H 9.19, Y 8.51; found C 52.57, H, 8.81, Y 8.23. $^1$H NMR (200 MHz, [D$_6$]benzene): $\delta$ = 0.37 [s, 36 H, Si(CH$_3$)$_3$], 1.30–2.03 (br. m, 48 H, CH$_2$/Cy, β-CH$_2$/THF), 3.41 (br. m, 4 H, CH/Cy), 3.79 (br. s, 8 H, α-CH$_2$/THF) ppm. $^{13}$C{$^1$H} NMR (50 MHz, [D$_6$]benzene): $\delta$ = 2.8 (N[Si(CH$_3$)$_3$]$_2$), 25.2 (β-CH$_2$/THF), 26.1, 26.4, 37.1 (CH$_2$/Cy), 54.8 (CH/Cy), 71.0 (α-CH$_2$/THF), 169.0 (CN$_3$) ppm. IR (Nujol, KBr): $\tilde{\nu}$ = 1620 (m), 1340 (m), 1290 (m), 1240 (s), 1210 (m), 1100 (m), 1060 (m), 970 (m), 950 (s), 860 (m), 830 (s) cm$^{-1}$.

**Synthesis of [(Me$_3$Si)$_2$NC(NCy)$_2$]$_2$Lu(μ-Cl)$_2$Li(THF)$_2$ (6):** Complex **6** was synthesised following the standard procedure described for **1** from [Li(Et$_2$O)][N(SiMe$_3$)$_2$] (1.56 g, 6.49 mmol), CyN=C=NCy (1.34 g, 6.49 mmol) and $LuCl_3$ (0.91 g, 3.24 mmol) in THF (30 mL). Complex **6** was isolated as colourless crystalline solid (2.54 g, 70%). $C_{46}H_{96}Cl_2LiLuN_6O_2Si_4$ (1129.8): calcd. C 48.90, H 8.49, Lu 15.48; found C 48.48, H, 8.10, Lu 15.31. $^1$H NMR (200 MHz, [D$_6$]benzene): $\delta$ = 0.38 [s, 36 H, Si(CH$_3$)$_3$], 1.21–2.11 (br. m, 48 H, CH$_2$/Cy, β-CH$_2$/THF), 3.56 (br. m, 4 H, CH/Cy), 3.75 (br. s, 8 H, α-CH$_2$/THF) ppm. $^{13}$C{$^1$H} NMR (50 MHz, [D$_6$]-benzene): $\delta$ = 2.9 (N[Si(CH$_3$)$_3$]$_2$), 25.4 (β-CH$_2$/THF), 14.1, 22.8, 26.0, 26.3, 36.9, (CH$_2$/Cy), 54.9 (CH/Cy), 68.8 (α-CH$_2$/THF), 171.2 (CN$_3$) ppm. IR (Nujol, KBr): $\tilde{\nu}$ = 1630 (m), 1350 (m), 1300 (m), 1250 (s), 1210 (m), 1100 (m), 1050 (s), 950 (s), 920 (s), 870 (m), 830 (s) cm$^{-1}$.

**Synthesis of [(Me$_3$Si)$_2$NC(NCy)$_2$]$_2$Y(μ-Cl)$_2$Li(DME) (7):** Complex **5** (1.10 g, 1.05 mmol) was dissolved in DME (10 mL). Volatiles were evaporated in vacuo and the solid residue was recrystallised from hexane. Complex **7** was isolated as a colourless crystalline solid (0.77 g, 74%). $C_{42}H_{90}Cl_2LiN_6O_2Si_4Y$ (989.7): calcd. C 50.97, H 9.09, Y 8.98; found C 50.60, H, 8.71, Y 8.51. $^1$H NMR (200 MHz, [D$_6$]benzene): $\delta$ = 0.23 [s, 36 H, Si(CH$_3$)$_3$], 1.42–2.02 (br. m, 40 H, CH$_2$/Cy), 2.79 (s, 4 H, CH$_2$/DME), 3.15 (s, 6 H, CH$_3$/DME), 3.46 (br. m, 4 H, CH/Cy) ppm. $^{13}$C{$^1$H} NMR (50 MHz, [D$_6$]benzene): $\delta$ = 2.8 (N[Si(CH$_3$)$_3$]$_2$), 26.1, 26.2, 26.4, 33.4, 37.2 (CH$_2$/Cy), 54.8 (CH/Cy), 58.8 (OCH$_3$/DME), 70.2 (CH$_2$/DME), 168.6 (CN$_3$) ppm. IR (Nujol, KBr): $\tilde{\nu}$ = 1640 (s), 1320 (m), 1260 (s), 1240 (s), 1100 (w), 1060 (m), 950 (s), 880 (m), 830 (s) cm$^{-1}$.

**Synthesis of [(Me$_3$Si)$_2$NC(NCy)$_2$]$_2$Y–*t*Bu (8):** To a solution of **1** (0.82 g, 0.88 mmol) in hexane (20 mL) was added a solution of *t*BuLi in hexane (0.58 mL, 1.5 M solution, 0.88 mmol) slowly at 0 °C and the reaction mixture was stirred for 1 h. The mixture was then warmed to room temperature and was stirred again for 1 h. The pale-yellow solution was filtered and concentrated in vacuo to approximately a quarter of its initial volume. The concentrated solution was cooled to –30 °C and kept at that temperature overnight. The mother liquor was then decanted from the precipitate formed. The latter was washed with cold hexane and was dried in vacuo at room temperature for 30 min yielding **8** as colourless crystals (0.40 g, 52%). $C_{42}H_{89}N_6Si_4Y$ (879.4): calcd. C 57.36, H 10.12, Y 10.10; found C 56.99, H, 9.81, Y 9.79. $^1$H NMR (200 MHz, [D$_6$]-benzene): $\delta$ = 0.28, 0.32, 0.36 [3 s, 36 H, Si(CH$_3$)$_3$], 1.48 [s, 9 H, C(CH$_3$)$_3$], 1.27–2.04 (br. m, 40 H, CH$_2$/Cy), 3.45, 3.63 (2 br. m, 4 H, CH/Cy) ppm. $^{13}$C{$^1$H} NMR (50 MHz, [D$_6$]benzene): $\delta$ = 2.3, 2.4, 2.8 (N[Si(CH$_3$)$_3$]$_2$), 24.9, 25.9, 26.1, 26.2, 26.4 (CH$_2$/Cy), 30.65 [d, $^2J$ = 2.3 Hz, C(*C*H$_3$)$_3$], 37.5 [d, $^1J_{Y,C}$ = 56 Hz, *C*(CH$_3$)$_3$], 55.2 (CH/Cy), 168.7 (CN$_3$) ppm. IR (Nujol, KBr): $\tilde{\nu}$ = 1620 (s), 1330 (m), 1220 (s), 1260 (m), 1205 (m), 1150 (m), 950 (s), 930 (s), 830 (s) cm$^{-1}$.

**NMR Tube Synthesis of [(Me$_3$Si)$_2$NC(NCy)$_2$]$_2$YMe (9):** A solution of MeLi in diethyl ether (0.028 mL, 1.6 M, 0.0448 mmol) was added to a solution of **1** (41.62 mg, 0.0448 mmol) in [D$_8$]toluene (2 mL) in an NMR tube at 0 °C which was then sealed. The reaction mixture was warmed to room temperature, shaken for 30 min and then left for 45 min to allow the LiCl to settle. $^1$H NMR (200 MHz,

 © 2006 Wiley-VCH Verlag GmbH & Co. KGaA, Weinheim 

[$D_6$]benzene): $\delta$ = –0.36 (br. s, 3 H, $YCH_3$), 0.46, 0.47 [s, 36 H, $NSi(CH_3)_3$], 1.32–2.03 (br. m, 40 H, $CH_2$/Cy), 3.47, 3.95 (br. m, together 4 H, CH/Cy) ppm.

**Synthesis of [$(Me_3Si)_2NC(NCy)_2]_2Y(\mu$-Me)$_2$Li(TMEDA) (10):** To a solution of **1** (0.97 g, 1.04 mmol) in hexane (20 mL) were added TMEDA (0.24 g, 2.08 mmol) and a solution of MeLi in diethyl ether (1.3 mL, 1.6 M solution, 2.08 mmol) slowly at 0 °C. The reaction mixture was stirred for 45 min and was then warmed to room temperature and again stirred for 1.5 h. The pale-yellow solution was filtered and concentrated in vacuo to approximately half of its initial volume. When the precipitation of crystals started, the solution was cooled to –10 °C and kept at that temperature for 2 h. The mother liquor was decanted and the small amount of colourless crystals was washed with cold hexane, dried in vacuo at room temperature for 15 min and identified as the side product **11** (0.07 g, 7%). The decanted mother liquor was concentrated to the half of its initial volume, cooled to –30 °C and left at that temperature for one week. The crystalline solid formed was separated by decantation, washed with cold hexane and dried in vacuo leaving colourless crystals of **10** (0.40 g, 61%). $C_{46}H_{102}LiN_8Si_4Y$ (974.7): calcd. C 56.68, H 10.46, Y 9.12; found C 56.31, H, 10.02, Y 9.33. $^1$H NMR (200 MHz, [$D_6$]benzene): $\delta$ = –0.51 (br. s, 6 H, $\mu$-$CH_3$), 0.53 [s, 36 H, $Si(CH_3)_3$], 1.32–2.00 [br. m, 44 H, $CH_2$/Cy, $(NCH_2)_2$], 2.12 [s, 12 H, $N(CH_3)_2$], 3.58 (br. m, 4 H, CH/Cy). $^{13}$C{$^1$H} NMR (50 MHz, [$D_6$]benzene): $\delta$ = 3.1 ($N[Si(CH_3)_3]_2$), 11.6 (br., $\mu$-$CH_3$), 14.3, 23.0, 26.6, 26.7, 31.2 ($CH_2$/Cy), 46.2 ($[N(CH_3)_2]_2$), 55.2 (CH/Cy), 57.6 ($NCH_2$), 167.6 ($CN_3$) ppm. **11**: $C_{25}H_{56}LiN_5Si_2$ (489.8): calcd. C 61.29, H 11.43; found C 61.56, H, 11.81. $^1$H NMR (200 MHz, [$D_6$]benzene): $\delta$ = 0.31 [s, 18 H, $Si(CH_3)_3$], 1.15–2.00 [br. m, 24 H, $CH_2$/Cy, $(NCH_2)_2$], 2.15 [s, 12 H, $N(CH_3)_2$], 3.42 (m, 4 H, CH/Cy). $^{13}$C{$^1$H} NMR (50 MHz, [$D_6$]-benzene): $\delta$ = 3.0 ($N[Si(CH_3)_3]_2$), 26.6, 26.7, 31.2 ($CH_2$/Cy), 46.6 [$N(CH_3)$], 54.8 (CH/Cy), 57.4 ($NCH_2$), 165.3 ($CN_3$) ppm.

**NMR Tube Synthesis of [$(Me_3Si)_2NC(NCy)_2]_2YCH_2SiMe_3$ (12):** In an inert atmosphere, compound **1** (36.00 mg, 0.0387 mmol), $LiCH_2SiMe_3$ (3.64 mg, 0.0387 mmol) and [$D_8$]toluene (2 mL) were mixed in an NMR tube at 0 °C which was then sealed. The reaction mixture was warmed to room temperature, shaken for 30 min then left for 30 min for the LiCl to settle. The spectroscopic investigation of the solution product indicated the formation of **12**: $^1$H NMR (200 MHz, [$D_8$]toluene): $\delta$ = –0.16 (d, $^2J_{Y,H}$ = 3.0 Hz, 2 H, $YCH_2$), 0.37 [s, 36 H, $NSi(CH_3)_3$], 0.52 [s, 9 H, $CH_2Si(CH_3)_3$], 1.24–2.00 (br. m, 40 H, $CH_2$/Cy), 3.46 (br. m, 4 H, CH/Cy) ppm.

**Synthesis of [$(Me_3Si)_2NC(NCy)_2]_2YPh(THF)$ (13):** A solution of phenyllithium (0.10 g, 1.20 mmol) in THF (10 mL) was slowly added at 0 °C to a solution of **1** (1.12 g, 1.20 mmol) in THF (20 mL) and the reaction mixture was stirred for 2 h. After warming to room temperature the solvent was evaporated in vacuo. The remaining off-white solid was extracted with hexane (40 mL). The extract was filtered and concentrated to a quarter of its initial volume, cooled to –30 °C and left at that temperature for one week. The crystalline solid formed was separated from the mother liquor by decantation, washed with cold hexane and dried in vacuo at room temperature for 20 min leaving colourless crystals of **13** (0.66 g, 61%). $C_{48}H_{93}N_6OSi_4Y$ (970.8): calcd. C 59.38, H 9.57, Y 9.15; found C 59.00, H, 9.19, Y 9.41. $^1$H NMR (200 MHz, [$D_6$]-benzene): $\delta$ = 0.53 [s, 36 H, $Si(CH_3)_3$], 1.33–2.10 (br. m, 44 H, $CH_2$/Cy, $\beta$-$CH_2$/THF), 3.24, 3.55 (br. m, 4 H, CH/Cy), 3.75 (br. s, 4 H, $\alpha$-$CH_2$/THF), 7.20–7.45 (m, 5 H, Ar) ppm. $^{13}$C{$^1$H} NMR (50 MHz, [$D_6$]benzene): $\delta$ = 3.4 ($N[Si(CH_3)_3]_2$), 25.2 ($\beta$-$CH_2$/THF), 22.8, 25.8, 26.4, 26.9, 37.2 ($CH_2$/Cy), 54.8, 56.9 (CH/Cy), 68.7 ($\alpha$-$CH_2$/THF), 127.1, 127.6, 128.0, 137.2 (Ar), 169.4 ($CN_3$), 177.8 (d, $^1J_{Y,C}$ = 51 Hz, *ipso*-C, Ar) ppm.

**X-ray Crystallographic Study:** The crystal data and details of data collection are given in Table 1. X-ray data were collected on a Siemens SMART CCD diffractometer (graphite-monochromated Mo-$K_\alpha$ radiation, $\lambda$ = 0.71073 Å, $\omega$-scan technique) with an area-detector at –100 °C. The intensity data were integrated with the SAINT program.[22] SADABS[23] was used to perform area-detector scaling and absorption corrections. The structures were solved by direct methods and were refined on $F^2$ using all reflections with SHELXTL.[24] All non-hydrogen atoms were refined anisotropically. The hydrogen atoms of the THF ligands in **1** and **6** were placed in calculated positions and refined in the "riding-model". All other hydrogen atoms in **1** and **6** as well as in **7**, **8** and **11** were found from the Fourier syntheses and refined isotropically. CCDC-281699 (for **1**), -281698 (for **6**), -281697 (for **7**), -281695 (for **8**) and -281696 (for **11**) contain the supplementary crystallographic data for this paper. These data can be obtained free of charge from The Cambridge Crystallographic Data Centre via www.ccdc.cam.ac.uk/data_request/cif.

## Acknowledgments

This work was supported by the Russian Foundation for Basic Research (Grant No. 05–03–32390), the Fonds der Chemischen Industrie and the Deutsche Forschungsgemeinschaft (Graduiertenkolleg "Synthetische, mechanistische und reaktionstechnische Aspekte von Metallkatalysatoren"). We gratefully acknowledge Dr. Yu. A. Kurskii for recording the NMR spectra.

[1] a) M. N. Bochkarev, L. N. Zakharov, G. N. Kalinina, *Organoderivatives of Rare Earth Elements*; Kluwer Academic Publishers, Dordrecht, **1995**; b) H. Schumann, J. A. Meese-Marktscheffel, L. Esser, *Chem. Rev.* **1995**, *95*, 865–893; c) S. Arndt, J. Okuda, *Chem. Rev.* **2002**, *102*, 1953–1976; d) J. Okuda, *Dalton Trans.* **2003**, 2367–2378.

[2] a) Z. Hou, Y. Wakatsuki, *Coord. Chem. Rev.* **2002**, *231*, 1–22; b) Y. Nakayama, H. Yasuda, *J. Organomet. Chem.* **2004**, *689*, 4489–4498; c) H. Yasuda, *J. Organomet. Chem.* **2002**, *647*, 128–138; d) G. A. Molander, J. A. C. Romero, *Chem. Rev.* **2002**, *102*, 2161–2185; e) G. A. Molander, E. C. Dowdy, *Top. Organomet. Chem.* **1999**, *2*, 119–155; f) T. E. Mueller, M. Beller, *Chem. Rev.* **1998**, *98*, 675–703; g) S. Hong, T. J. Marks, *Acc. Chem. Res.* **2004**, *37*, 673–686; h) M. R. Douglass, C. L. Stern, T. J. Marks, *J. Am. Chem. Soc.* **2001**, *123*, 10221–10238; i) A. M. Kawaoka, M. R. Douglass, T. J. Marks, *Organometallics* **2003**, *22*, 4630–4632; j) K. N. Harrison, T. J. Marks, *J. Am. Chem. Soc.* **1992**, *114*, 9220–9221; k) E. A. Bijpost, R. Duchateau, J. H. Teuben, *J. Mol. Catal. A* **1995**, *95*, 121–128.

[3] a) F. T. Edelmann, D. M. M. Freckmann, H. Schumann, *Chem. Rev.* **2002**, *102*, 1851–1896; b) W. E. Piers, D. J. H. Emslie, *Coord. Chem. Rev.* **2002**, *233–234*, 131–155; c) P. Mountford, B. D. Ward, *Chem. Commun.* **2003**, 1797–1803; d) H. Kawaguchi, T. Matsuo, *J. Organomet. Chem.* **2004**, *689*, 4228–4243.

[4] a) R. Anwander, *Top. Curr. Chem.* **1996**, *179*, 34–112; b) R. Kempe, *Angew. Chem.* **2000**, *112*, 478–504; *Angew. Chem. Int. Ed.* **2000**, *39*, 468–493.

[5] P. J. Bailey, S. Pace, *Coord. Chem. Rev.* **2001**, *214*, 91–141.

[6] a) Y. Zhou, G. P. A. Yap, D. S. Richeson, *Organometallics* **1998**, *17*, 4387–4391; b) Z. Lu, G. P. Yap, D. S. Richeson, *Organometallics* **2001**, *20*, 706–712; c) G. R. Giesbrecht, G. D. Whitener, J. Arnold, *J. Chem. Soc., Dalton Trans.* **2001**, 923–927; d) Y. Luo, Y. Yao, Q. Shen, K. Yu, L. Weng, *Eur. J. Inorg. Chem.* **2003**, 318–323; e) Y. Yao, Y. Luo, J. Chen, Z. Zhang, Y. Zhang, Q. Shen, *J. Organomet. Chem.* **2003**, *679*, 229–237; f) C. Jing-Lei, Y. Ying-Ming, L. Yun-Jie, Z. Li-Ying, Z. Yong, S. Qi, *J. Organomet. Chem.* **2004**, *689*, 1019–1024; g) J. Zhang, R. Cai,

 © 2006 Wiley-VCH Verlag GmbH & Co. KGaA, Weinheim 

L. Weng, X. Zhou, *J. Organomet. Chem.* **2003**, *672*, 94–99; h) J. Zhang, R. Cai, L. Weng, X. Zhou, *Organometallics* **2004**, *23*, 3303–3308; i) X. Pang, H. Sun, Y. Zhang, Q. Shen, H. Zhang, *Eur. J. Inorg. Chem.* **2005**, 1487–1491.
[7] A. A. Trifonov, E. A. Fedorova, G. K. Fukin, M. N. Bochkarev, *Eur. J. Inorg. Chem.* **2004**, 4396–4401.
[8] H. Schumann, E. Palamidis, J. Loebel, *J. Organomet. Chem.* **1990**, *390*, 45–52.
[9] A. L. Wayda, R. D. Rogers, *Organometallics* **1985**, *4*, 1440–1444.
[10] A. L. Wayda, J. L. Atwood, W. E. Hunter, *Organometallics* **1984**, *3*, 939–941.
[11] V. K. Belsky, S. Y. Knyazhansky, B. M. Bulychev, G. L. Soloveitchik, *Metalloorgan. Khim.* **1989**, *2*, 754–756.
[12] a) R. Duchateau, C. T. van Wee, A. Meetsma, P. van Duijnen, J. H. Teuben, *Organometallics* **1996**, *15*, 2279–2290; b) R. Duchateau, A. Meetsma, J. H. Teuben, *Organometallics* **1996**, *15*, 1656–1661; c) K. H. den Haan, Y. Wielstra, J. J. W. Eshuis, J. H. Teuben, *J. Organomet. Chem.* **1987**, *323*, 181–192.
[13] K. B. Aubrecht, K. Chang, M. A. Hillmyer, W. B. Tolman, *J. Polym. Sci., Part A: Polym. Chem.* **2001**, *39*, 284–293.
[14] W. J. Evans, T. J. Boyle, J. W. Ziller, *Inorg. Chem.* **1992**, *31*, 1120–1122.
[15] M. Westerhausen, S. Schneiderbauer, N. Makropoulos, M. Warchhold, H. Nöth, H. Piotrowski, K. Karaghiosoff, *Organometallics* **2002**, *21*, 4335–4341.
[16] a) A. G. Avent, F. G. N. Cloke, B. R. Elvidge, P. B. Hitchcock, *Dalton Trans.* **2004**, 1083–1096; b) L. Lee, D. J. Berg, G. W. Bushnell, *Organometallics* **1995**, *14*, 8–10; c) L. Lee, D. J. Berg, F. W. Einstein, R. J. Batchelor, *Organometallics* **1997**, *16*, 1819–1821; d) D. D. Graf, W. M. Davis, R. R. Schrock, *Organometallics* **1998**, *17*, 5820–5824.
[17] a) P. Ugliengo, D. Viterbo, G. Borzani, *J. Appl. Crystallogr.* **1988**, *21*, 75–84; b) P. Ugliengo, G. Borzani, D. Viterbo, *Z. Kristallogr.* **1988**, *185*, 712–718; c) P. Ugliengo, G. Borzani, G. Chiari, *Z. Kristallogr.* **1993**, *209*, 9–16.
[18] G. R. Giesbrecht, A. Shafir, J. Arnold, *J. Chem. Soc., Dalton Trans.* **1999**, 3601–3604.
[19] M. D. Taylor, C. P. Carter, *J. Inorg. Nucl. Chem.* **1962**, *24*, 387–393.
[20] L. E. Manzer, *Inorg. Chem.* **1978**, *17*, 1552–1558.
[21] Z. S. Novikova, S. N. Zdorova, V. N. Kardner, N. F. Lutzenko, *Zh. Obsh. Khim.* **1976**, *46*, 575–578.
[22] Bruker, SAINTPlus Data Reduction and Correction Program v. 6.02a, Bruker AXS, Madison, Wisconsin, USA, **2000**.
[23] G. M. Sheldrick, SADABS v.2.01, Bruker/Siemens Area Detector Absorption Correction Program, Bruker AXS, Madison, Wisconsin, USA, **1998**.
[24] G. M. Sheldrick, SHELXTL v. 6.12, Structure Determination Software Suite, Bruker AXS, Madison, Wisconsin, USA, **2000**.

Received: July 19, 2005
Published Online: December 16, 2005

 © 2006 Wiley-VCH Verlag GmbH & Co. KGaA, Weinheim 

DOI: 10.1002/ejic.200500665

# Reduction of $[Cp^*_2Mo_2O_5]$ in Aqueous Medium: Structure and Properties of a Triangular Mixed Oxo-Hydroxo-Bridged Product, $[Cp^*_3Mo_3(\mu\text{-}O)_2(\mu\text{-}OH)_4](X)_2$ (X = $CF_3CO_2$ or $CF_3SO_3$)

**Funda Demirhan,*[a] Bahar Çağatay,[a] Deniz Demir,[a] Miguel Baya,[b] Jean-Claude Daran,[b] and Rinaldo Poli*[b]**

**Keywords:** Bridging ligands / Hydrogen bonding / Metal–metal interactions / Molybdenum / Oxo ligands

The reduction of $[Cp^*_2Mo_2O_5]$ with Zn in a MeOH/$H_2O$ solution acidified with either $CF_3COOH$ or $CF_3SO_3H$ leads to the formation of the $[Cp^*_3Mo_3(\mu\text{-}O)_2(\mu\text{-}OH)_4]^{2+}$ ion as its trifluoroacetate or trifluoromethanesulfonate salt. The structure of the compound was confirmed by X-ray analyses. The anions establish hydrogen-bonding interactions with all four bridging OH groups. Density functional calculations afford bonding parameters in close agreement with the observed structure and indicate that the cluster is best described as a valence-delocalized $Mo_3^{13+}$ species. The five metal electrons are distributed among an *a*-type ($z^2$) orbital, which accounts for most of the metal–metal attraction, and two essentially metal–metal nonbonding *e*-type (*xy*) orbitals with a slight Mo-(μ-O) π*-type contribution. Because of the $C_2$ symmetry, the latter orbitals are not degenerate. The calculations show that the unpaired electron is located in a molecular orbital with equal contribution from two Mo atoms, in agreement with the experimental observation of coupling of the unpaired electron to two Mo atoms in the isotropic EPR spectrum.

(© Wiley-VCH Verlag GmbH & Co. KGaA, 69451 Weinheim, Germany, 2006)

## Introduction

We have recently initiated a research program aimed at developing the chemistry of high-oxidation-state organometallic compounds in water, in the spirit of "green" chemistry[1–3] and with the long term goal of exploring the catalytic and electrocatalytic potential of organometallic compounds in water.[4,5] Unlike low-valent organometallic systems, which are generally supported by water-soluble modified phosphane or cyclopentadienyl ligands,[6–8] high-oxidation-state complexes are supported by oxo ligands, which makes them soluble in water by virtue of hydrogen bonding and protonation equilibria that yield charged hydroxo and aqua complexes. Although oxo-supported high-oxidation-state organometallic complexes are now well established and have interesting catalytic properties,[9,10] their systematic investigation in water has received little attention. We further argue that the greater metal electronegativity in these higher oxidation states confers a higher degree of covalency to the metal–carbon bonds with odd-electron carbon ligands (i.e. alkyls, allyls, cyclopentadienyls, etc.), which consequently may become quite resistant toward hydrolytic decomposition. For a redox-active metal, reduction of a high-oxidation-state oxo complex should favor the generation of aqua ligands and open the way to the generation of open coordination sites for substrate activation and catalytic and electrocatalytic applications.[11]

We have so far focused our attention on the speciation[12] and electrochemical behavior[13,14] of $[Cp^*_2Mo_2O_5]$. The Cp*–Mo bond in this complex is quite hydrolytically stable and is split only quite slowly at very low pH.[15] We have obtained novel oxo-supported complexes, the nature of which seems to depend intimately on the nature of the acid used, by chemical reduction with zinc in an acidic MeOH/$H_2O$ mixed solvent medium. For instance, with acetic acid we isolated the dinuclear $Mo^{IV}$ complex $[Cp^*_2Mo_2(\mu\text{-}O)_2(\mu\text{-}O_2CCH_3)_2]$ (**I**),[16] whereas with $CF_3COOH$ under the same conditions (mixed MeOH/$H_2O$ solvent, Zn as reducing agent) we obtained the $Mo^V$ trinuclear complex $[Cp^*_3Mo_3(\mu_3\text{-}O)(\mu\text{-}O)_3(\mu\text{-}O_2CCF_3)_3]^+$ (**II**) as a salt of the $Zn_2(O_2CCF_3)_6^{2-}$ dianion.[17] The formation of these compounds demonstrates that the removal of water ligands (from the expected protonation of oxo ligands, following the reduction process) generates vacant positions that are filled by the anions of the acids used. In previous contributions,[11,18] we have mentioned that another product may also be crystallized from the reaction mixture obtained by reduction in the presence of $CF_3COOH$, depending on the solvent and conditions used for the crystallization. This is another triangular cluster to which the formula $[Cp^*_3Mo_3(\mu\text{-}OH)_x(\mu\text{-}O)_{6-x}]^{2+}$ was assigned on the basis of an X-ray structural analysis. However, this product could

[a] Celal Bayar University, Faculty of Sciences & Liberal Arts, Department of Chemistry,
45030, Muradiye-Manisa, Turkey
[b] Laboratoire de Chimie de Coordination, UPR CNRS 8241,
205 Route de Narbonne, 31077 Toulouse Cedex, France
Fax: +33-561-553-003
E-mail: poli@lcc-toulouse.fr

 © 2006 Wiley-VCH Verlag GmbH & Co. KGaA, Weinheim 

not be properly characterized because of severe disorder problems in the cation as well as in the $CF_3COO^-$ anion. This situation did not even allow the unambiguous identification of the *x* value (number of hydrogen atoms on the bridging oxygen atoms), and thus of the number of electrons in the cluster. We have now repeated the same reaction with a related strong acid, $CF_3SO_3H$, and crystallized the corresponding product. We report here the structure of these compounds and a description of their properties.

## Results

### Structure of the Trifluoroacetate Salt

The general procedure for the reduction of $[Cp^*_2Mo_2O_5]$, i.e. zinc reduction in a water-methanol solution acidified by $CF_3COOH$, has been described previously.[19] Numerous subsequent syntheses and crystallization of the resulting product consistently gave the same kind of crystals, which were always affected by the initially observed severe disorder problem (see above).[20] Interestingly, the same product (as revealed by the EPR study, vide infra) was also obtained in the presence of other weaker acids, in an attempt to obtain other kinds of carboxylate derivatives analogous to the previously reported $[Cp^*_2Mo_2(\mu\text{-}O)_2(\mu\text{-}O_2CCH_3)_2]$, when working at the same low pH.[16] This observation attests to the thermodynamic stability of this product.

Although badly disordered, the structure of the trifluoroacetate salt serves to identify the structural motif and to set the stage for the discussion of this compound. A view of the central $Mo_3O_6$ core, including the interaction with the two $CF_3CO_2$ anions, is shown in Figure 1 (a). The three Mo atoms form a nearly ideal equilateral triangle (vide infra), each edge of which is symmetrically bridged by two oxygen atoms, with one above and one below the $Mo_3$ plane. Thus, the three O atoms above the metal plane, and the three below, define two additional approximately equilateral triangles that are parallel to, and staggered with respect to, the $Mo_3$ triangle. The two anions are located above and below the $Mo_3$ plane and establish hydrogen-bonding interactions with the bridging O atoms, which desymmetrize the triangle. Both bridging O atoms of one particular $Mo_3$ edge (namely Mo1–Mo2 in Figure 1, a) are engaged in hydrogen bonding, each with an O atom of a different trifluoroacetate anion. The second O atom of each $CF_3COO^-$ anion interacts with a bridging O atom of a different edge (O4 bridges Mo1–Mo3 and O6 bridges Mo2–Mo3). The four O···O distances, in the range 2.59–2.64 Å, unambiguously show the presence of four OH groups. However, the quality of the structure is not sufficient to establish whether the two remaining bridging O atoms carry additional H atoms or not. Although of low quality, the structure of the trifluoroacetate salt indicates that the unique Mo1–Mo2 distance is slightly longer (2.797 Å) than the other two (Mo1–Mo3 2.786 Å; Mo2–Mo3 2.785 Å). It is important to stress that the spectroscopic and magnetic properties are insufficient to make an unambiguous choice because both an $(OH)_4(O)_2$ and a $(OH)_6$ structure correspond to an odd number of electrons (paramagnetic). Thus, they would not be easily distinguishable by EPR spectroscopy. They are likewise difficult to distinguish by infrared spectroscopy.

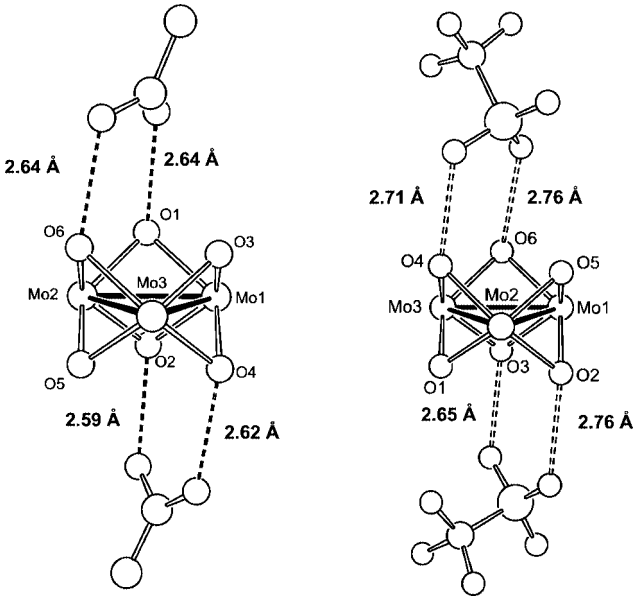


Figure 1. An ORTEP view of the central $Mo_3O_6$ core of $[Cp^*_3Mo_3(\mu\text{-}O)_2(\mu\text{-}OH)_4]^{2+}$ in the acetate (left, the disordered F atoms are not shown) and trifluoromethanesulfonate salts (right), showing the hydrogen-bonding interactions with the two anions.

### Structure of the Trifluoromethanesulfonate Salt

The reduction process described in the previous section was repeated in the presence of triflic acid, with two objectives in mind. First, the different anion may allow a less problematic crystal-structure determination. Second, and most important, the triflate anion has three equivalent oxygen atoms available for hydrogen bonding. Therefore, should the two additional bridging functions that are not involved in hydrogen bonding with the trifluoroacetate anions (i.e. O3 and O5 in Figure 1, a) also bear hydrogen atoms, the triflate ions would be expected to establish an interaction with them. Conversely, the lack of such interactions may be taken as a strong indication against the presence of H atoms in these positions.

Complex $[Cp^*_3Mo_3(\mu\text{-}O)_2(\mu\text{-}OH)_4](CF_3SO_3)_2$ crystallizes under the same experimental conditions that lead to the crystallization of its trifluoroacetate congener. The compound dissolves readily in chlorinated solvents (dichloromethane, chloroform) and has identical EPR properties to those of the trifluoroacetate salt (vide infra). It is important to note that the crude product also gave NMR resonances that could be attributed to the Cp* protons of one or more diamagnetic products. However, a sample of carefully cleaned single crystals from the batch used for the X-ray structural analysis yielded NMR-silent $CDCl_3$ solutions.

The single-crystal X-ray analysis gave an orthorhombic unit cell and the structure was solved in the *Pbca* space

 © 2006 Wiley-VCH Verlag GmbH & Co. KGaA, Weinheim 

group. A peculiar twinning problem prevented refinement of the data to very low residuals (see Experimental Section). However, the structure was apparently not complicated by interstitial solvent, nor by disorder. The strongest residual peak and hole in the last difference Fourier map were reasonably low and without any chemical significance. A view of the $[Cp^*_3Mo_3(\mu\text{-}O)_2(\mu\text{-}OH)_4]^{2+}$ cation is shown in Figure 2.

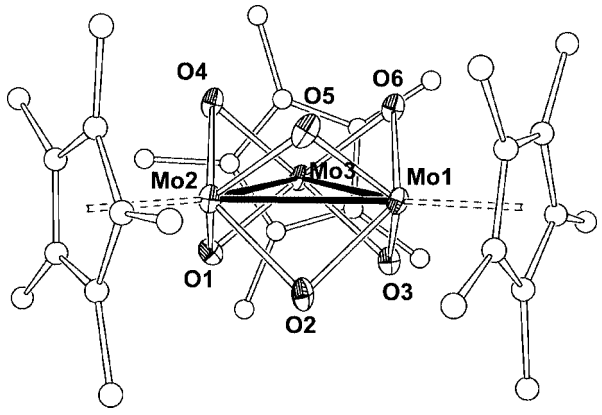


Figure 2. An ORTEP view of the $[Cp^*_3Mo_3(\mu\text{-}O)_2(\mu\text{-}OH)_4]^{2+}$ ion from the structure of the trifluoromethanesulfonate salt. For clarity, the hydrogen atoms of the Cp* ligands are not shown and the ellipsoids of the Cp* C atoms are replaced by spheres of arbitrary radius. The ellipsoids of the Mo and O atoms are shown at the 30% probability level.

The relative arrangement of the ions in the structure is shown in Figure 1 (b). Like in the related trifluoroacetate salt, only two of the three bridging groups on each triangular face establish hydrogen bonds with the oxygen atoms of the $CF_3SO_3$ anions. The third O atom of each trifluoromethanesulfonate anion does not point toward the third bridging O atom. Specifically, the $CF_3SO_3$ anion located on the same side occupied by the bridging O1, O2, and O3 atoms places the third $SO_3$ oxygen atom away from (*exo*), and the $CF_3$ group on the same side as (*endo*), the triangle of the bridging O atoms. One $CF_3$ fluorine atom is in proximity of atom O1, but the F···O distance (3.22 Å) is too long to envisage a hydrogen bond (sum of van der Waals radii of F and O: 2.75 Å). The second $CF_3SO_3$ anion, which is located on the same side as O4, O5 and O6 from the $Mo_3$ triangle, places the third O atom *endo* and the $CF_3$ group *exo*, but the anion is tilted in such a way as to place the third O atom at 4.02 Å from O5, clearly indicating a repulsive interaction (sum of van der Waals radii of the two O atoms: 2.80 Å). This evidence allows us to propose the molecular formula of the dicationic trimetallic cluster as having four bridging hydroxo and two bridging oxo groups. Although the structure of the trifluoroacetate salt (vide supra) is much less precisely determined than that of the trifluoromethanesulfonate salt, a comparison of the hydrogen bonded O···O contacts shows that these are tighter with the former anion and looser with the latter one, in agreement with their relative basicity.

Although the structure has no crystallographically imposed symmetry, the trimetallic dication possesses an approximate $C_2$ local symmetry, with the pseudo-symmetry axis passing through the Mo2 atom and the middle of the Mo1–Mo3 bond. We shall refer to all averaged bonding parameters by using the symbol Mo for the unique atom Mo2 and the symbol Mo′ for the two pseudo-symmetry related Mo1 and Mo3 atoms. The unique Mo′–Mo′ bond is marginally, but significantly, longer than the two Mo–Mo′ bonds, possibly as a consequence of the different nature of the bridging groups. Indeed, the bridging Mo–(μ-O) and Mo′–(μ-O) bonds are significantly shorter than the corresponding Mo–(μ-OH) and Mo′–(μ-OH) bonds. The alternative interpretation of assigning a greater oxidation state (+5) to the Mo atom and a lower one (+4) to the Mo′ atoms seems excluded by the density functional calculations (vide infra). There is no significant difference, neither between the Mo–(μ-O) and Mo′–(μ-O) bonds [average 1.95(1) Å] nor between the Mo–(μ-OH) and Mo′–(μ-OH) bonds [average 2.05(1) Å], in agreement with an insignificant difference in metal ionic radius between Mo and Mo′. This analysis further serves to confirm the interpretation of atoms O1 and O5 as (μ-O) rather than (μ-OH) groups. The Mo–Mo distances are slightly longer than those found in related triangular $[Cp^*_3Mo_3(\mu\text{-}O)_6]$-type clusters, e.g. 2.730(13) Å in $[Cp^*_4Mo_5O_{11}]$ (where the central $[Cp^*_3Mo_3(\mu\text{-}O)_6]^-$ unit is capped by a $[Cp^*Mo^{VI}O_2(\mu\text{-}O)Mo^{VI}O_2]^+$ fragment),[21] and 2.744(9) Å in $[Cp^*_6Mo_8O_{16}]$ (where two equivalent $[Cp^*_3Mo_3(\mu\text{-}O)_6]^-$ units are bridged by a $[Mo^V_2O_2(\mu\text{-}O)_2]^{2+}$ fragment).[22] They are identical, on the other hand, to the average distance reported for $[Cp^*_3Mo_3(\mu\text{-}OH)_n(\mu\text{-}O)_{6-n}]Cl_2$ [2.78(3) Å]. The latter structure, however, was poorly defined because of solvent disorder.[21]

### Mass Spectrometric Characterization

Both salts (trifluoroacetate and triflate) were investigated by electrospray mass spectrometry (positive mode) in mixed $H_2O$/MeOH solvents. In both cases the spectrum shows the presence of trinuclear species and the absence of mono- and dinuclear species. For the trifluoroacetate salt, the major envelope is satisfactorily simulated on the basis of the formula $[Cp^*_3Mo_3(\mu\text{-}O)_5(\mu\text{-}OMe)]^+$ (see Figure 3). This shows that, under the conditions of the electrospray MS experiment, the dication readily loses one proton and exchanges the residual bridging OH group with the methanol solvent. The shape of the simulated envelope matches very closely the experimental one, but the major peak *m*/*z* value leaves a doubt as to the exact number of protons. This question was resolved by the additional experiments that will be presented in later sections. The minor envelope (Figure 3, c) corresponds to the formula ($[Cp^*_3Mo_3(\mu\text{–}O)_5(\mu\text{-}OMe)]^+$ + $CF_3COOH$ + MeOH) and therefore gives direct evidence for the presence of the trifluoroacetate anion. This envelope overlaps with a weaker peak distribution at higher *m*/*z* values, which could correspond to further addition of a water molecule. A parallel FAB (NBA matrix) spectrometric analysis shows the absence of solvent association phenom-

 © 2006 Wiley-VCH Verlag GmbH & Co. KGaA, Weinheim 

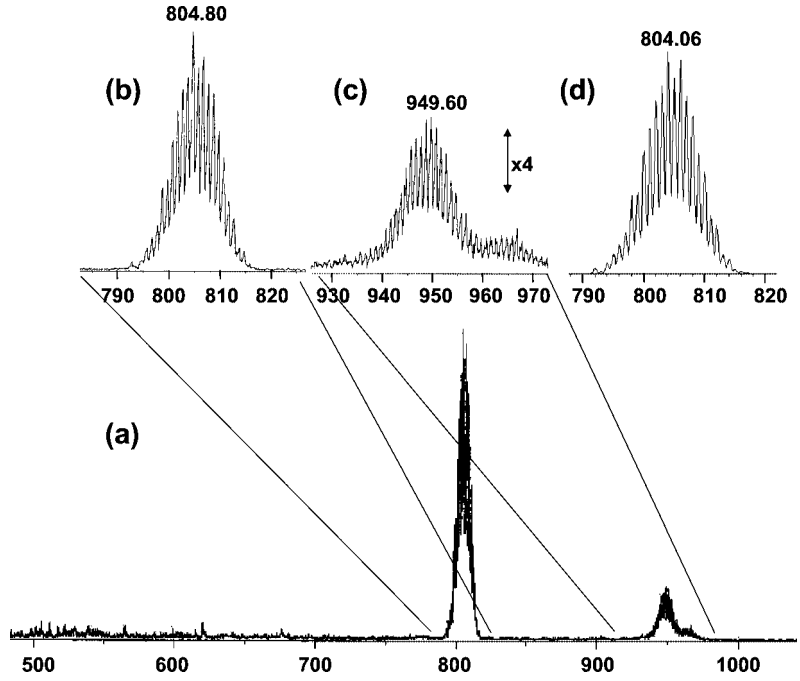


Figure 3. (a) Electrospray mass spectrum (positive mode) of $[Cp^*_3Mo_3(\mu\text{-}O)_4(\mu\text{-}OH)_2](O_2CF_3)_2$ in MeOH. Portions of this spectrum are shown in (b) and (c), and a simulation of the envelope corresponding to the $[Cp^*_3Mo_3(\mu\text{-}O)_5(\mu\text{-}OMe)]^+$ ion is given in (d).

ena. However, the spectrum is more complex because of reduction and fragmentation of the trinuclear unit. The highest peak distributions observed correspond to $[Cp^*_3Mo_3O_4(OH)_2]$ (massif centered around $m/z$ = 791) and $[Cp^*_3Mo_3O_4(OH)]$ (massif centered around $m/z$ = 774).

The spectrum of the triflate salt is closely related to that of the trifluoroacetate analogue. The major envelope, centered around $m/z$ = 804, is identical to that observed for the trifluoroacetate analogue (the major peak is found at $m/z$ = 804.25 in this case), whereas the smaller envelope at higher $m/z$ values is centered at 1036.35, corresponding to $([Cp^*_3Mo_3(\mu\text{-}O)_5(\mu\text{-}OMe)]^+ + CF_3SO_3H + 2\,MeOH + H_2O)$. Thus, this mass spectrum also gives direct evidence for the presence of the triflate counterion.

## EPR Spectroscopic Properties

Solutions of the complex $[Cp^*_3Mo_3(\mu\text{-}O)_2(\mu\text{-}OH)_4]^{2+}$ (either salt) in dichloromethane exhibit a relatively sharp EPR spectrum at room temperature (see Figure 4), whereas the compounds are NMR-silent in $CDCl_3$. The absence of an NMR spectrum is consistent with the odd-electron nature of the cluster. The observation of an isotropic EPR spectrum at relatively high temperature, on the other hand, clearly indicates that the system must have a single unpaired electron ($S$ = ½) in a nondegenerate orbital. An accurate analysis of the Mo hyperfine coupling pattern helps us determine the localization of the unpaired electron. As Figure 4 shows, simulations were carried out using hyperfine coupling constant, shape, and line-broadening parameters from the experimental spectrum, but assuming coupling to either one, two, or all three cluster Mo atoms. The height and shape of the satellite peaks, relative to the central resonance and especially relative to each other, unambiguously identify the spectrum as involving coupling to two equivalent Mo nuclei. Unfortunately, the relative broadness of the spectrum conceals the outer peaks of the 1:2:3:4:5:6:5:4:3:2:1 envelope (6.25% overall intensity), which is generated by the isotopomers having two $I$ = 5/2 Mo nuclei. The spectrum was also recorded at temperatures down to 210 K in an attempt to improve the spectral resolution, but no significant change was noted.

## Magnetic Susceptibility

The compound exhibits a simple Curie behavior consistent with the presence of a single unpaired electron. Measurements carried out in the 6–60 K range show a linear $\chi^{-1}$ vs. $T$ plot, with a negligible value for the Curie temperature (–0.38 K; see Figure 5).

The corresponding effective magnetic moment, which is approximately temperature independent, averages 1.66 $\mu_B$ after correction for the ligands' diamagnetism. This is rather close to the expected spin-only value for one unpaired electron (1.73 $\mu_B$). This result is consistent with the EPR spectrum and confirms that the latter is representative of the bulk sample.

## Density Funtional Calculations

In order to further confirm the assignment of the chemical composition and electronic structure, we carried out a theoretical study. Before describing the computational results, it is useful to qualitatively analyze the electronic struc-

 © 2006 Wiley-VCH Verlag GmbH & Co. KGaA, Weinheim 

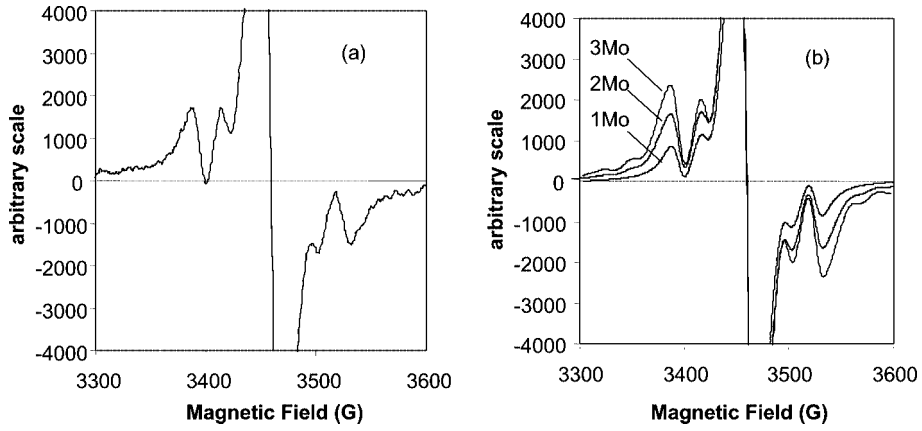


Figure 4. EPR spectrum of $[Cp^*_3Mo_3(\mu\text{-}O)_2(\mu\text{-}OH)_4](CF_3SO_3)_2$ in $CH_2Cl_2$ solution. (a) Experimental spectrum. (b) Simulated spectra with coupling to one, two, and three equivalent Mo nuclei (simulation parameters: Gaussian line shape, linewidth: 18 G). All spectra are scaled to the same peak-to-peak height for the central resonance.

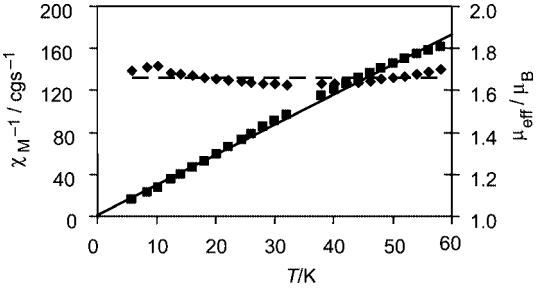


Figure 5. Magnetic properties (molar magnetic susceptibility, $\chi_M$, and effective magnetic moment, $\mu_{eff}$) of $[Cp^*_3Mo_3(\mu\text{-}O)_2(\mu\text{-}OH)_4](CF_3SO_3)_2$.

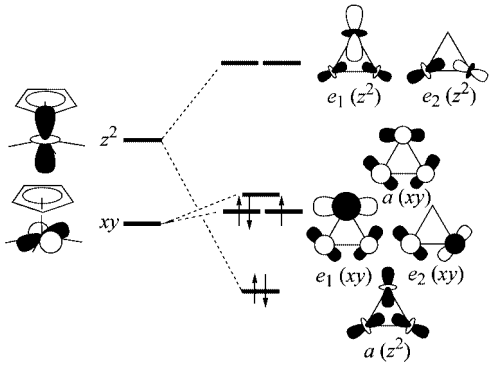


Scheme 1.

ture on the basis of first principles and relevant previous knowledge.[21,23,24] The cluster may be viewed as resulting from the assembly of three "four-legged piano stools" of the $Cp^*MoO_4$ type, whose electronic structure is well known,[25,26] as shown in Scheme 1. Taking a $D_{3h}$-symmetrical structure with six identical bridging ligands as a first approximation, it is possible to envisage that the interaction of the $z^2$-type orbitals will lead to one bonding (of type *a*) and two degenerate antibonding (of type *e*) combinations, and that the interaction of the *xy*-type orbitals will equally lead to one *a*-type bonding and two degenerate antibonding *e*-type combinations. As the overlap between the *xy* orbitals is much weaker, the energy of the MOs resulting from these orbitals will be less perturbed from that of the starting fragment orbitals. However, as well documented for other bridging systems, π* mixing with the bridging ligands' lone pairs should destabilize the *xy* orbital combinations.[27] It is easily predictable that this destabilization should be strongest for the symmetric (*a*-type) orbital, as shown in Scheme 1. The asymmetric nature of the bridging ligands (four OH and two O), however, is expected to alter this scheme, particularly by removing the degeneracy of the *e*-type combinations.

The DFT-optimized geometry agrees quite well with the experimental geometry (see Table 1). The minor variations could partly be attributed to the different environment (hydrogen-bonded, solid-state structure with the $CF_3SO_3$ anion for the experimental geometry, free, "gas-phase" dication for the DFT-optimized one); and partly to the well-known overestimation of bond lengths by DFT. In particular, it is comforting to see the same trend of Mo–O bond lengths [Mo-(μ-O) < Mo-(μ-OH)] in the optimized and experimental parameters, once again confirming the structural assignment.

The calculated electronic structure (Figure 6) confirms the qualitative expectations. The bonding $a(z^2)$ orbital is located just above the group of the six MOs describing the three double-sided Mo–Cp* π interactions. Above it, we find the pair of $e(xy)$ orbitals, which contains three electrons. The calculation converges with two electrons in the $e_1$-type orbital and one in the $e_2$-type orbital, whose degeneracy (in the ideal $C_3$ symmetry) is substantially split by the different nature of the bridging groups (O vs. OH). It is rewarding to see that the unpaired electron, according to the calculations, chooses to reside in the orbital from the *e* set that has the nodal plane parallel to the $C_2$ symmetry axis ($e_2$), rather than in the orbital with the nodal plane perpendicular to it ($e_1$). The half-occupied orbital has contributions only from the two Mo′ atoms and a symmetry-imposed zero contribution from the Mo atom, in perfect

 © 2006 Wiley-VCH Verlag GmbH & Co. KGaA, Weinheim 

Table 1. Selected bond lengths [Å] and angles [°] for $[Cp^*_3Mo_3(\mu\text{-}O)_2(\mu\text{-}OH)_4]^{2+}$: observed (from the X-ray structure of the $CF_3SO_3$ salt) and DFT-optimized (gas-phase).

| Distance[a,b] | Experimental | DFT-optimized |
|---|---|---|
| Mo–Mo′ | 2.7854(13), 2.7820(13) | 2.859, 2.876 |
| Mo′–Mo′ | 2.8244(12) | 2.946 |
| Mo–(μ-O) | 1.946(8), 1.959(8) | 1.979, 1.987 |
| Mo–(μ-OH) | 2.041(8), 2.061(7) | 2.108, 2.110 |
| Mo′–(μ-O) | 1.949(8), 1.956(8) | 1.938, 1.943 |
| Mo′–(μ-OH) | 2.048(8), 2.053(7), 2.055(8) | 2.090, 2.094, 2.097 |
| | 2.049(8), 2.028(8), 2.053(8) | 2.099, 2.106, 2.108 |
| Mo–CNT | 2.0145(9) | 2.082 |
| Mo′–CNT | 2.0058(9), 2.0168(9) | 2.079, 2.080 |

| Angle[a,b] | Experimental | DFT-optimized |
|---|---|---|
| Mo′–Mo–Mo′ | 60.97(3) | 61.92 |
| Mo–Mo′–Mo′ | 59.46(3), 59.57(3) | 58.91, 59.16 |
| Mo–(μ-O)–Mo′ | 91.0(3), 90.9(3) | 93.61, 93.83 |
| Mo–(μ-OH)–Mo′ | 85.1(3), 85.9(3) | 85.96, 85.97 |
| Mo′–(μ-OH)–Mo′ | 87.5(3), 87.0(3) | 88.93, 88.94 |
| CNT–Mo–(μ-O) | 112.7 (2), 114.7(2) | 114.04, 116.94 |
| CNT–Mo–(μ-OH) | 112.2(2), 112.7(2) | 113.22, 113.92 |
| CNT–Mo′–(μ-O) | 113.4(2), 113.9(2) | 113.01, 113.92 |
| CNT–Mo′–(μ-OH) | 110.8(2), 113.4(2), 115.1(2) | 112.94, 115.54, 117.05 |
| | 111.7(2), 114.8(2), 115.0(2) | 112.99, 115.30, 117.88 |

[a] Mo indicates the unique atom with a $[Cp^*Mo(O)_2(OH)_2]$ coordination environment and Mo′ indicates the two symmetry-related atoms with a $[Cp^*Mo(O)(OH)_3]$ coordination environment. [b] CNT indicates the ring centroid of the pentamethylcyclopentadienyl ligand.

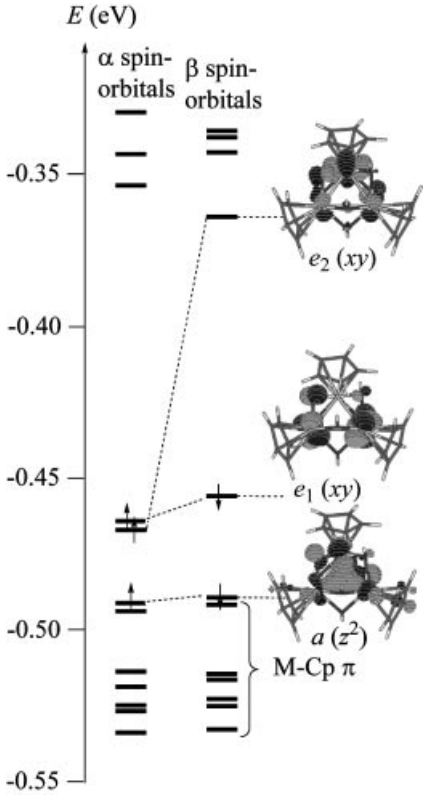


Figure 6. Electronic structure of the $[Cp^*_3Mo_3(\mu\text{-}O)_2(\mu\text{-}OH)_4]^{2+}$ cluster as resulting from a gas-phase DFT calculation. The shape of the spin-orbitals connected by a dashed line is essentially identical (only one for each pair is shown).

agreement with the result of the EPR analysis above. Furthermore, the DFT calculation suggests that the cluster is completely valence-delocalized. Indeed, the computed natural charge[28] is very similar on atoms Mo (+1.075) and Mo′ (+1.100 and 1.101), and so is the computed Mulliken spin density (–0.820, 0.849, and 0.847, respectively). We note that the mean value of $S^2$ from the spin-unrestricted calculation is high (see Computational Details), suggesting the mixing of an excited $[a(z^2)]^2[e_1(xy)]^1[a_2(xy)]^1[a(xy)]^1$ configuration into the ground state. However, according to the result of the EPR experiment, this contribution must be negligible for the real system because the isotropic resonance is relatively sharp at room temperature and unaffected by cooling.

A somewhat related triangular $Mo_3$ cluster, $[Mo_3CuS_4(H_2O)_{10}]^{4+}$, which was described as having a $Cu^I$ ion and a $Mo_3^{11+}$ core,[29] has an electronic structure similar to that described here, although there are two additional electrons, thereby also involving occupation of the *a*(xy)-type orbitals. In that case, the experimental observation of electronic coupling to a single Mo nucleus in the EPR spectrum was interpreted as resulting from a valence-trapped $Mo^{IV}Mo^{IV}Mo^{III}$ structure, the unpaired electron being mostly localized on the $Mo^{III}$ center, although the calculations (at the EHMO level) indicated a delocalized shape for the MOs similar to that reported here.

## Discussion

It is useful to compare the salts reported here with a closely related one reported by Bottomley et al., namely $[Cp^*_3Mo_3(\mu\text{-}O)_{6-n}(\mu\text{-}OH)_n]^{2+}(Cl^-)_2$.[21] This compound was obtained by a synthetic strategy closely related to ours (zinc reduction of $[Cp^*MoO_2Cl]$ in $CHCl_3$ in the presence of concentrated HCl). The X-ray structure presented for this compound was affected by severe disorder, thus preventing the unambiguous determination of the number of bridging OH groups, as for the trifluoroacetate complex reported here. We have already pointed out above that the reported Mo–Mo distances for the dichloride salt are very similar to those reported here for the $[Cp^*_3Mo_3(\mu\text{-}O)_2(\mu\text{-}OH)_4]^{2+}$-$(CF_3SO_3^-)_2$ salt. For $[Cp^*_3Mo_3(\mu\text{-}O)_{6-n}(\mu\text{-}OH)_n]^{2+}(Cl^-)_2$, the authors proposed 5 as the most likely *n* value, but also suggested the presence of a redox disproportionation equilibrium in solution that involves other species characterized by *n* = 4 and *n* = 6. This suggestion was based on magnetic, EPR, and NMR observations. In particular, the EPR spectrum was assigned to the *n* = 6 species, whereas two NMR resonances − a sharp one and a broad one − were assigned to the diamagnetic *n* = 5 species and to the paramagnetic *n* = 4 species, respectively. The room-temperature isotropic EPR spectrum reported for solutions of the dichloride salt seems very similar to that of the trifluoromethanesulfonate

 © 2006 Wiley-VCH Verlag GmbH & Co. KGaA, Weinheim 

and trifluoroacetate salts reported here, but it was interpreted in that case as arising from coupling to three equivalent Mo nuclei. An argument given in favor of the above scheme is the fact that the $n = 4$ species could not yield an observable isotropic EPR spectrum, given the expected $(e)^3$ electronic configuration.[21] Our DFT calculation, however, shows that the asymmetry associated with the distribution of the two μ-O and four μ-OH groups splits this orbital degeneracy significantly. The trifluoromethanesulfonate and trifluoroacetate salts reported here (at least batches of clean single crystals) do not show any sharp or even broadened NMR signal that could be assigned to the Cp* ligand in a diamagnetic or paramagnetic compound. All evidence, therefore, points to the fact that the trifluoromethanesulfonate salt reported here maintains its identity as a single compound in solution.

Another useful comparison involves compounds $[Cp^*_4Mo_5O_{11}]$[21] and $[Cp^*_6Mo_8O_{16}]$,[22] both of which are described as containing a central $[Cp^*_3Mo_3(\mu\text{-}O)_6]^-$ unit (vide supra). In this unit, there are only four cluster electrons ($Mo_3^{IV,V,V}$) and the structures are stabilized by capping one triangular $O_3$ face with either $Mo^V$ or $Mo^{VI}$ ions. Therefore, it seems possible that the salts of $[Cp^*_3Mo_3(\mu\text{-}O)_2(\mu\text{-}OH)_4]^{2+}$ exhibit interesting electrochemical properties, which may be dependent on pH and/or on the presence of other metal ions.

## Conclusion

We have shown in this paper that the zinc reduction of $[Cp^*_2Mo_2O_5]$ in an acidic aqueous environment leads to the triangular $[Cp^*_3Mo_3(\mu\text{-}O)_2(\mu\text{-}OH)_4]^{2+}$ cluster, containing a paramagnetic (five-electron) trimetallic core. The spectroscopic evidence points to a solution structure identical to the solid-state structure, with the unpaired electron located in a delocalized molecular orbital that has atomic orbital participation from only two Mo atoms. A study of the redox properties and acid/base properties of this system, followed by an investigation of its chemical reactivity, are now in progress and will be reported in due course.

## Experimental Section

**General Methods:** All preparations and manipulations were carried out with Schlenk techniques under an oxygen-free argon atmosphere. All glassware was oven-dried at 120 °C. Solvents were dried by standard procedures and distilled under dinitrogen prior to use. EPR spectra were measured with an Elexsys E500 Bruker spectrometer (X-band) equipped with both a frequency meter and a gaussmeter. Magnetic susceptibility measurements were carried out with a MPMS5 QUANTUM DESIGN magnetometer. Mass spectra were recorded with a NERMAG R10-10 instrument. The starting compound $[Cp^*_2Mo_2O_5]$ was prepared as described in the literature.[19]

**Synthesis and Crystallization of $[Cp^*_3Mo_3(\mu\text{-}O)_2(\mu\text{-}OH)_4](CF_3SO_3)_2$:** Metallic zinc (20 mesh, 0.48 g, 7.38 mmol) was added to a solution of $[Cp^*_2Mo_2O_5]$ (0.05 g, 0.092 mmol) in MeOH/$H_2O$ (1:1, 6 mL) after acidification with concentrated $CF_3SO_3H$ (10 drops). The mixture was stirred under argon at room temperature for two days, during which time it changed from a clear, yellow solution to a green suspension. The mixture was filtered and the solid was dried in vacuo. The solid was extracted with THF and, after filtration, addition of *n*-hexane yielded a green precipitate (0.021 g, 31.3%). A single crystal for the X-ray analysis was obtained by diffusion of *n*-hexane into a green $CH_2Cl_2$ solution at room temperature.

$C_{32}H_{49}F_6Mo_3O_{12}S_2{\cdot}2CH_2Cl_2$ (1261.53): calcd. C 32.37, H 4.23; found C 32.92, H 3.65. EPR ($CH_2Cl_2$): $g = 1.962$, $a_{Mo} = 26.2$ G. Average $\mu_{eff}$ in the 6–60 K range: 1.66 $\mu_B$ (diamagnetic correction: $-7.91 \times 10^{-4}$ cgs).

**X-ray Analyses:** Single crystals of $[Cp^*_3Mo_3(\mu\text{-}O)_2(\mu\text{-}OH)_4](X)_2$ (X = $CF_3CO_2$, $CF_3SO_3$) were mounted under inert perfluoropolyether at the tip of a glass fiber and cooled in the cryostream of an Oxford-Diffraction XCALIBUR CCD diffractometer. Data were collected using monochromatic Mo-$K_\alpha$ radiation ($\lambda = 0.71073$). The structures were solved by direct methods (SIR97[30]) and refined by least-squares procedures on $F^2$ using SHELXL-97.[31] Although the model could be easily defined by direct methods for both structures, its refinement appeared to be very poor, with large elongated ellipsoids for the Cp* and rather high $R$ and $wR_2$ values. The $CF_3CO_2$ salt did not lead to a successful refinement, so this structure is not further commented. For the $CF_3SO_3$ salt, the elongated ellipsoids suggest a free rotation of the Cp ring around the Mo–Cp* centroid axis. However, all attempts to refine a disordered Cp* model failed. The occurrence of a twinned structure by pseudo merohedry, considering a monoclinic cell, was also attempted but again without improvement of the refinement. Refinement in a noncentrosymmetric space group did not improve the result either. Careful examination of the reciprocal space revealed that the crystal used was certainly not single but an attempt to integrate using different domains failed. There is, however, no doubt about the reality of the model, as confirmed by different analytical methods. All H atoms attached to carbon were introduced in the calculation in idealized positions and treated as riding models. Owing to the poor quality of the refinement, the H atom attached to the hydroxy groups could not be located. The drawings were produced with the help of ORTEP32.[32] The structures were solved by direct methods (SIR97)[30] and refined by least-squares procedures on $F^2$ using SHELXL-97.[31] All H atoms attached to carbon were introduced in calculation in idealized positions and treated as riding models. The drawing of the molecules was realized with the help of ORTEP32.[32] The crystal data and refinement parameters are shown in Table 2 and selected geometric parameters are collected in Table 1.

**Computational Details:** The DFT calculation was carried out on a model system where the Cp* ligands were replaced by the simpler Cp rings. The starting geometry was based on the crystallographically determined structure of the triflate salt and no symmetry restrictions were imposed. The geometry was fully optimized and the resulting minimum of the potential energy surface (PES) was verified by the positive value of all second derivatives of the energy. The calculation, which used the spin-unrestricted formulation, was performed using the B3LYP three-parameter hybrid density functional method of Becke,[33] as implemented in the Gaussian03 suite of programs.[34] The basis sets used for the geometry optimizations are the standard 6-31G** for C, H, and P atoms, and the standard LANL2DZ basis set, which includes the Hay and Wadt effective core potentials (ECP),[35] for the metal atoms. The value of $<S^2>$ resulting from the calculation is 1.39 (0.81 after annihilation). This shows that there is significant spin contamination, indicating mixing with low-lying excited states. The correspondence between the resulting Kohn–Sham spin-orbitals was verified by producing contour plots with the aid of the program MOLDEN.[36]

 © 2006 Wiley-VCH Verlag GmbH & Co. KGaA, Weinheim 

Table 2. Crystal data and refinement parameters for $[Cp^*_3Mo_3(\mu\text{-}O)_2(\mu\text{-}OH)_4](CF_3SO_3)_2$.

| | |
|---|---|
| Empirical formula | $C_{32}H_{35}F_6Mo_3O_{12}S_2$ |
| Formula weight | 1087.62 |
| Temperature | 180(2) K |
| Wavelength | 0.71073 Å |
| Crystal system | orthorhombic |
| Space group | *Pbca* |
| Unit-cell dimensions | $a$ = 15.5156(6) Å |
| | $b$ = 16.8899(7) Å |
| | $c$ = 31.0271(12) Å |
| | $\alpha$ = 90° |
| | $\beta$ = 90° |
| | $\gamma$ = 90° |
| Volume | 8130.9(6) Å$^3$ |
| $Z$ | 8 |
| Density (calculated) | 1.777 Mg m$^{-3}$ |
| Absorption coefficient | 1.098 mm$^{-1}$ |
| $F$(000) | 4360 |
| Crystal size | 0.24 × 0.12 × 0.077 mm$^3$ |
| Theta range for data collection | 2.82 to 26.37° |
| Index ranges | $-19 \le h \le 19$ |
| | $-18 \le k \le 21$ |
| | $-38 \le l \le 38$ |
| Reflections collected | 59030 |
| Independent reflections | 8302 [$R$(int) = 0.0997] |
| Completeness to $\theta$ = 26.37° | 99.8% |
| Absorption correction | Semi-empirical from equivalents |
| Max. and min. transmission | 0.9623 and 0.7409 |
| Refinement method | Full-matrix least-squares on $F^2$ |
| Data / restraints / parameters | 8302 / 0 / 487 |
| Goodness-of-fit on $F^2$ | 1.088 |
| Final $R$ indices [$I > 2\sigma(I)$] | $R_1$ = 0.1145, $wR_2$ = 0.2423 |
| $R$ indices (all data) | $R_1$ = 0.1279, $wR_2$ = 0.2495 |
| Largest diff. peak and hole | 2.867 and –3.776 e Å$^{-3}$ |

## Acknowledgments

This research was supported by the CNRS in France and by TUBITAK in Turkey. Supplemental travel support by a bilateral CNRS-TUBITAK (TBAG-U/62-102T211) program is also gratefully acknowledged. In addition, R.P. acknowledges support from the European Commission through the Research Training Network "AQUACHEM" (contract No. MRTN-CT-2003-503864), the COST D29 program (working group 0009-03) and CINES for a grant of free computing time. F.D. thanks the University of Celal Bayar (FEF, 2002/101) for a research grant. We thank Alain Mari for assistance with the EPR and magnetic susceptibility measurements and analyses.

[1] T. Chan, L. Li, Y. Yang, W. Lu, *ACS Symp. Ser.* **2002**, *819*, 166–177.
[2] F. Joó, *Acc. Chem. Res.* **2002**, *35*, 738–745.
[3] I. T. Horvath, *Acc. Chem. Res.* **2002**, *35*, 685.
[4] D. Sinou, *Topic in Current Chemistry* **1999**, *206*, 41–59.
[5] D. Sinou, *Adv. Synth. Catal.* **2002**, *344*, 221–237.
[6] P. Kalck, F. Monteil, *Adv. Organomet. Chem.* **1992**, *34*, 219–284.
[7] B. E. Hanson, *Coord. Chem. Rev.* **1999**, *186*, 795–807.
[8] C. Muller, D. Vos, P. Jutzi, *J. Organomet. Chem.* **2000**, *600*, 127–143.
[9] W. A. Herrmann, E. Herdtweck, M. Flöel, J. Kulpe, U. Küsthardt, J. Okuda, *Polyhedron* **1987**, *6*, 1165–1182.
[10] W. A. Herrmann, *Comments Inorg. Chem.* **1988**, *7*, 73–107.
[11] R. Poli, *Chem. Eur. J.* **2004**, *10*, 332–341.
[12] E. Collange, J. Garcia, R. Poli, *New J. Chem.* **2002**, *26*, 1249–1256.
[13] J. Gun, A. Modestov, O. Lev, D. Saurenz, M. A. Vorotyntsev, R. Poli, *Eur. J. Inorg. Chem.* **2003**, 482–492.
[14] J. Gun, A. Modestov, O. Lev, R. Poli, *Eur. J. Inorg. Chem.* **2003**, 2264–2272.
[15] E. Collange, L. Metteau, P. Richard, R. Poli, *Polyhedron* **2004**, *23*, 2605–2610.
[16] F. Demirhan, P. Richard, R. Poli, *Inorg. Chim. Acta* **2003**, *347*, 61–66.
[17] F. Demirhan, J. Gun, O. Lev, A. Modestov, R. Poli, P. Richard, *J. Chem. Soc., Dalton Trans.* **2002**, 2109–2111.
[18] E. Collange, F. Demirhan, J. Gun, O. Lev, A. Modestov, R. Poli, P. Richard, D. Saurenz, in *Perspectives in Organometallic Chemistry* (Eds.: C. G. Screttas, B. R. Steele), Royal Society of Chemistry, London, **2003**, vol. 287, pp. 167–182.
[19] D. Saurenz, F. Demirhan, P. Richard, R. Poli, H. Sitzmann, *Eur. J. Inorg. Chem.* **2002**, 1415–1424.
[20] Crystal data for compound $[Cp^*_3Mo_3(\mu\text{-}O)_2(\mu\text{-}OH)_4](CF_3CO_2)_2$: monoclinic, $P2_1/c$, $a$ = 15.537(2) Å, 15.195(1) Å, 16.763(2) Å, β = 94.46(1)..
[21] F. Bottomley, J. Chen, K. F. Preston, R. C. Thompson, *J. Am. Chem. Soc.* **1994**, *116*, 7989–7995.
[22] J. R. Harper, A. L. Rheingold, *J. Am. Chem. Soc.* **1990**, *112*, 4037–4038.
[23] P. Hofmann, N. Roesch, H. R. Schmidt, *Inorg. Chem.* **1986**, *25*, 4470–4478.
[24] F. Bottomley, S. Karslioglu, *Organometallics* **1992**, *11*, 326–337.
[25] P. Kubácek, R. Hoffmann, Z. Havlas, *Organometallics* **1982**, *1*, 180–188.
[26] T. A. Albright, J. K. Burdett, M. H. Whangbo, *Orbital Interactions in Chemistry*, John Wiley & Sons, New York, **1985**.
[27] F. Abugideiri, J. C. Fettinger, R. Poli, *Inorg. Chim. Acta* **1995**, *229*, 445–454.
[28] A. E. Reed, L. A. Curtiss, F. Weinhold, *Chem. Rev.* **1988**, *88*, 899–926.
[29] R. Miyamoto, S. Kawata, M. Iwaizumi, H. Akashi, T. Shibahara, *Inorg. Chem.* **1997**, *36*, 542–546.
[30] A. Altomare, M. Burla, M. Camalli, G. Cascarano, C. Giacovazzo, A. Guagliardi, A. Moliterni, G. Polidori, R. Spagna, *J. Appl. Crystallogr.* **1999**, *32*, 115–119.
[31] G. M. Sheldrick, *SHELXL97. Program for Crystal Structure refinement*, University of Göttingen, Germany, **1997**.
[32] L. J. Farrugia, *J. Appl. Crystallogr.* **1997**, *30*, 565.
[33] A. D. Becke, *J. Chem. Phys.* **1993**, *98*, 5648–5652.
[34] M. J. Frisch, G. W. Trucks, H. B. Schlegel, G. E. Scuseria, M. A. Robb, J. R. Cheeseman, J. Montgomery, J. A., T. Vreven, K. N. Kudin, J. C. Burant, J. M. Millam, S. S. Iyengar, J. Tomasi, V. Barone, B. Mennucci, M. Cossi, G. Scalmani, N. Rega, G. A. Petersson, H. Nakatsuji, M. Hada, M. Ehara, K. Toyota, R. Fukuda, J. Hasegawa, M. Ishida, T. Nakajima, Y. Honda, O. Kitao, H. Nakai, M. Klene, X. Li, J. E. Knox, H. P. Hratchian, J. B. Cross, C. Adamo, J. Jaramillo, R. Gomperts, R. E. Stratmann, O. Yazyev, A. J. Austin, R. Cammi, C. Pomelli, J. W. Ochterski, P. Y. Ayala, K. Morokuma, G. A. Voth, P. Salvador, J. J. Dannenberg, V. G. Zakrzewski, S. Dapprich, A. D. Daniels, M. C. Strain, O. Farkas, D. K. Malick, A. D. Rabuck, K. Raghavachari, J. B. Foresman, J. V. Ortiz, Q. Cui, A. G. Baboul, S. Clifford, J. Cioslowski, B. B. Stefanov, G. Liu, A. Liashenko, P. Piskorz, I. Komaromi, R. L. Martin, D. J. Fox, T. Keith, M. A. Al-Laham, C. Y. Peng, A. Nanayakkara, M. Challacombe, P. M. W. Gill, B. Johnson, W. Chen, M. W. Wong, C. Gonzalez, J. A. Pople, *Gaussian 03, Revision B.04*, Gaussian, Inc., Pittsburgh PA, **2003**.
[35] P. J. Hay, W. R. Wadt, *J. Chem. Phys.* **1985**, *82*, 270–283.
[36] G. Schaftenaar, *Molden v3.2*, CAOS/CAMM Center Nijmegen, Toernooiveld, Nijmegen, The Netherlands, **1991**.

Received: July 25, 2005
Published Online: December 22, 2005

 © 2006 Wiley-VCH Verlag GmbH & Co. KGaA, Weinheim 

DOI: 10.1002/ejic.200500749

# Ring Opening and Displacement by Chloride of the Bidentate Chelate Ligand from Dichloro[pyridine-2-(α-methoxymethanolato)]gold(III) – A Kinetic and Mechanistic Study

**Giampaolo Marangoni,*[a] Bruno Pitteri,[a] Giuliano Annibale,[a] and Marco Bortoluzzi[a]**

**Keywords:** Chelate displacement / Gold / Kinetics / Reaction mechanism

The kinetics of ring opening and displacement of the bidentate chelate ligand from dichloro[pyridine-2-(α-methoxymethanolato)]gold(III) [Au(N–O)$Cl_2$] (**1**) have been studied spectrophotometrically in methanol/water (95:5, v/v) at 25 °C and constant ionic strength ($I$ = 1 mol dm$^{-3}$, $LiClO_4$). In the presence of LiCl and perchloric acid the reaction consists of a pre-equilibrium protonation of the coordinated oxygen followed first by ring opening at oxygen accompanied by the entry of chloride or solvent and fast acetalisation of the hemiacetalic form of the ligand to give [$AuCl_3$(N–OMe)], and then by displacement of the *N*-bonded ligand to give [$AuCl_4$]$^-$. The ligand is not displaced in the absence of chloride and no reaction is observed in the presence of chloride alone.

(© Wiley-VCH Verlag GmbH & Co. KGaA, 69451 Weinheim, Germany, 2006)

## Introduction

The lability of oxygen-donor ligands in the substitution reactions at square planar tetra-coordinate $Pt^{II}$, $Pd^{II}$ and $Au^{III}$ complexes depends very greatly upon their nature, ranging from the highly labile coordinated water to the very inert hydroxide.[1] Unfortunately, the lack of suitable substrates of $Au^{III}$, because of the synthetic difficulties involved in preparing appropriate complexes with monodentate oxygen ligands, has hampered any extensive study in this field. One way to overcome the problem is to incorporate the oxygen donor in a bi- or multidentate ligand so providing the required ease of preparation and stability. Very recently, gold(III) complexes of the type [Au(N–O)$Cl_2$] (N–O = pyridine-2-methanolato,[2] substituted pyridine-2-carboxylato[3]) have been reported to be excellent catalysts in organic synthesis. Some years ago we reported the preparation of dichloro(pyridine-2-carboxylato)gold(III) and dichloro(pyridine-2-methanolato)gold(III) neutral complexes and we studied the replacement of N–O bidentate ligands by chloride in acidic solutions.[4,5] In the first case it was shown that the chelate ring opened at nitrogen and the carboxylate group was displaced in a slower subsequent step. In the second case, because the change in the 2-substituent from $CO_2^-$ to $CH_2O^-$ increases the basicity of the nitrogen by more than three orders of magnitude and hence decreases the lability of the Au–N bond by about two orders of magnitude, and the bond to the alkoxide oxygen is considerably more labile to direct chloride substitution than the bond to carboxylate, the reaction sequence is reversed, ring opening at oxygen occurring in the first stage of the reaction.

In a recent study dealing with the interaction of pyridine-2-carbaldehyde (2CHO–py) with [$AuCl_4^-$] in water we found[6] that the initially formed *N*-coordinated [$AuCl_3$(2-CHO–py)] complex adds a molecule of $H_2O$ to the aldehydic group to form the corresponding diolic derivative which, by elimination of HCl, gives rise to *O*-chelation at the metal centre. Successive treatment with alcohols affords the corresponding N–O-chelated hemiacetalic complexes [(I), Scheme 1]. On the other hand, when the reaction be-

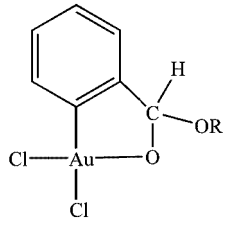


**I**: R = -H, -$CH_2CH_3$, -$CH_2CF_3$

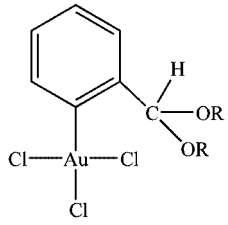


**II**: R = -$CH_3$, -$CH_2CH_3$, -$CH_2CH_2CH_3$, -$CH_2CH_2CH_2CH_3$

Scheme 1.

[a] Department of Chemistry, Cà Foscari University of Venice, Calle Larga S. Marta 2137, 30123 Venice, Italy

 © 2006 Wiley-VCH Verlag GmbH & Co. KGaA, Weinheim InterScience 

tween pyridine-2-carbaldehyde and [$AuCl_4^-$] is carried out in alcohols at 60 °C, the *N*-coordinated acetal complexes trichloro(pyridine-2-carbaldehyde dialkyl acetal)gold(III) are directly formed [(II), Scheme 1]. Some of the complexes of both the series have been characterised by X-ray diffractometry.[6]

As an extension of that work, we have now prepared the analogous neutral dichloro[pyridine-2-(α-methoxymethanolato)]gold(III) (**1**), [Au(N–O)$Cl_2$], and have studied the displacement of the new type of N–O chelate ligand by chloride in acidic methanol containing 5% water.

## Results

The electronic spectrum in the wavelength range 250–370 nm of a $1 \times 10^{-4}$ mol dm$^{-3}$ solution of [Au(N–O)$Cl_2$] (**1**) in methanol/water (95:5 v/v) in the presence of a large excess of LiCl to suppress any solvolysis is shown in Figure 1 (curve *a*). This spectrum does not change over long periods of time.

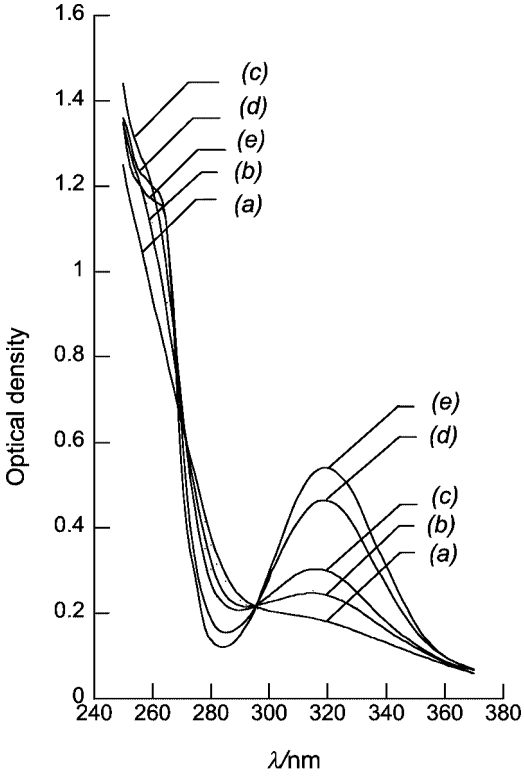


Figure 1. Electronic spectra of $1.0 \times 10^{-4}$ mol dm$^{-3}$ solutions of **1** in methanol/water (95:5 v/v) at 25 °C under the different experimental conditions reported in the text.

In the absence of lithium chloride, addition of perchloric acid to a solution of **1** of the same concentration causes a relatively fast change of the spectrum with time to finally give the spectrum represented by curve *b*. Successive addition of 1:1 LiCl gives rise to a rapid change of the spectrum *b* to that of curve *c*, which is identical to that of the trichloro(pyridine-2-carbaldehyde dimethyl acetal)gold(III) (**2**) measured under the same experimental conditions. Further addition of excess LiCl results in a slower reaction, which leads to the displacement of the 2-substituted pyridine ligand and formation of [$AuCl_4$]$^-$ with a well-maintained isosbestic point at 296 nm until the end of the reaction (curves *d*, *e*). When an excess of both LiCl and perchloric acid is added to a solution of **1**, the change of absorbance with time at 320 nm indicates a two-stage reaction, the second stage being identical to that described above.

Table 1. Observed rate constants: for the first stage ($k_{obs}^f$), for the second stage ($k_{obs}^s$) of the reaction,[a] and in the presence of perchloric acid alone ($k'_{obs}^f$).

| [$H^+$] [mol dm$^{-3}$] | $10^3$ [$Cl^-$] [mol dm$^{-3}$] | $10^2$ $k_{obs}^f$ [s$^{-1}$] | $10^4$ $k_{obs}^s$ [s$^{-1}$] | $10^3$ $k'_{obs}^f$ [s$^{-1}$] |
|---|---|---|---|---|
| 0.15 | | | | 3.69 |
| 0.2 | | | | 4.47 |
| 0.25 | | | | 5.64 |
| 0.3 | | | | 6.40 |
| 0.4 | | | | 7.60 |
| 0.5 | | | | 9.33 |
| 0.05 | 1.0 | 0.29 | | |
| 0.05 | 2.0 | 0.72 | | |
| 0.05 | 4.0 | 1.22 | | |
| 0.05 | 6.0 | 1.82 | | |
| 0.05 | 8.0 | 2.40 | | |
| 0.05 | 10 | 3.0 | | |
| 0.05 | 12 | 3.70 | | |
| 0.1 | 1.0 | 0.96 | | |
| 0.1 | 2.0 | 1.67 | | |
| 0.1 | 4.0 | 2.85 | | |
| 0.1 | 6.0 | 4.05 | | |
| 0.1 | 8.0 | 5.11 | | |
| 0.1 | 10 | 6.40 | | |
| 0.1 | 12 | 7.58 | | |
| 0.15 | 1.0 | 1.56 | 0.99 | |
| 0.15 | 2.0 | 2.30 | 1.85 | |
| 0.15 | 3.0 | 3.20 | 2.56 | |
| 0.15 | 4.0 | 4.05 | 2.91 | |
| 0.15 | 5.0 | 4.61 | 3.90 | |
| 0.15 | 6.0 | 5.30 | | |
| 0.15 | 7.0 | 6.14 | 5.40 | |
| 0.15 | 8.0 | 6.89 | 6.20 | |
| 0.15 | 9.0 | 7.60 | | |
| 0.15 | 10 | 8.40 | 7.93 | |
| 0.2 | 1.0 | 2.50 | | |
| 0.2 | 2.0 | 3.51 | | |
| 0.2 | 3.0 | 4.82 | | |
| 0.2 | 4.0 | 5.82 | | |
| 0.2 | 5.0 | 6.61 | | |
| 0.2 | 6.0 | 7.82 | | |
| 0.2 | 7.0 | 8.90 | | |
| 0.2 | 8.0 | 9.85 | | |
| 0.2 | 9.0 | 11.4 | | |
| 0.2 | 10 | 12.55 | | |
| 0.3 | 1.0 | 3.22 | | |
| 0.3 | 2.0 | 4.84 | | |
| 0.3 | 3.0 | 6.0 | | |
| 0.3 | 4.0 | 7.48 | | |
| 0.3 | 5.0 | 9.01 | | |
| 0.4 | 1.0 | 3.57 | | |
| 0.4 | 2.0 | 5.30 | | |
| 0.4 | 3.0 | 7.60 | | |
| 0.4 | 4.0 | 9.10 | | |
| 0.4 | 5.0 | 10.38 | | |

[a] $I$ = 1 mol dm$^{-3}$, $LiClO_4$, [substrate] = $1 \times 10^{-4}$ mol dm$^{-3}$, 25 °C, MeOH/$H_2O$ (95:5 v/v); rate constants were accurate to within 5%.

 © 2006 Wiley-VCH Verlag GmbH & Co. KGaA, Weinheim 

### Kinetics

The kinetics were evaluated from the change in absorbance at a fixed wavelength (320 nm) where both stages lead to an increase of absorbance and as the two rate constants differed by at least ten, their separate evaluation presented no problem. Values of the rate constants for the first, $k_{obs}^{f}$, and second, $k_{obs}^{s}$, stages of the reaction in the presence of both LiCl and perchloric acid under pseudo-first-order conditions, as well as in the presence of perchloric acid alone, are collected in Table 1. Rate constants were accurate to within 5%.

At constant $[H^+]$, $k_{obs}^{f}$ varies with $[Cl^-]$ such that a plot of $k_{obs}^{f}$ versus $[Cl^-]$ is linear with a finite intercept (Figure 2), according to Equation (1).

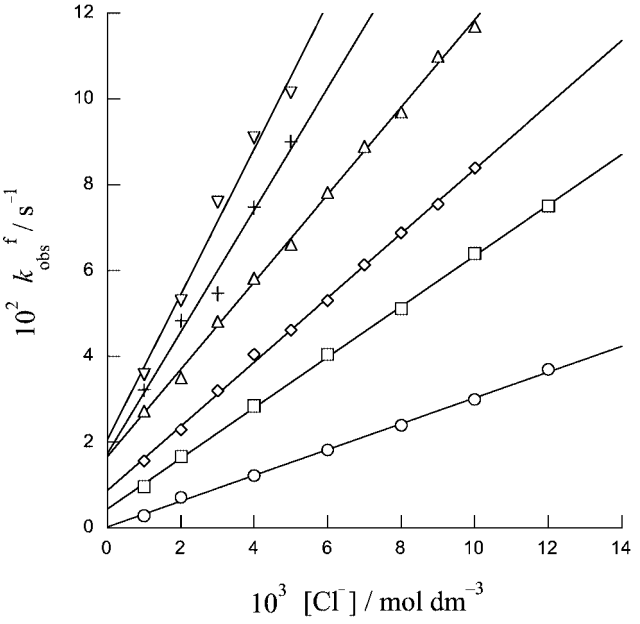


Figure 2. Plots of $k_{obs}^{f}$ vs $[Cl^-]$ for the reaction between [Au(N–O)$Cl_2$] (**1**) and chloride at $[H^+]$ = 0.05 (○), 0.1 (□), 0.15 (◊), 0.2 (△), 0.3 (+), 0.4 (▽) mol dm$^{-3}$.

$$k_{obs}^{f} = i + s[Cl^-] \quad (1)$$

Both $i$ and $s$ depend upon $[H^+]$ as shown in Figure 2 and Table 2.

Table 2. Values of parameters $i$ and $s$ at constant added acid.

| $[H^+]$ [mol dm$^{-3}$] | $i$ [s$^{-1}$] | $s$ [mol$^{-1}$ dm$^3$ s$^{-1}$] |
|---|---|---|
| 0.4 | $(1.9\pm0.3)\times10^{-2}$ | 17.4±0.1 |
| 0.3 | $(1.8\pm0.1)\times10^{-2}$ | 14.2±0.4 |
| 0.2 | $(1.3\pm0.1)\times10^{-2}$ | 10.9±0.2 |
| 0.15 | $(0.87\pm0.05)\times10^{-2}$ | 7.52±0.08 |
| 0.1 | $(0.43\pm0.04)\times10^{-2}$ | 5.95±0.06 |
| 0.05 | $(0.03\pm0.04)\times10^{-2}$ | 3.01±0.05 |

The dependence of $s$ upon $[H^+]$ shows a tendency to slow negative deviations as $[H^+]$ progressively increases, but a plot of $s^{-1}$ against $[H^+]^{-1}$ is linear (Figure 3) with intercept $c = (1.8\pm0.5)\times10^{-2}$ s$^{-1}$ and slope $d = (1.6\pm0.5)\times10^{-2}$ mol dm$^{-3}$ s$^{-1}$, from which the empirical Equation (2) can be derived.

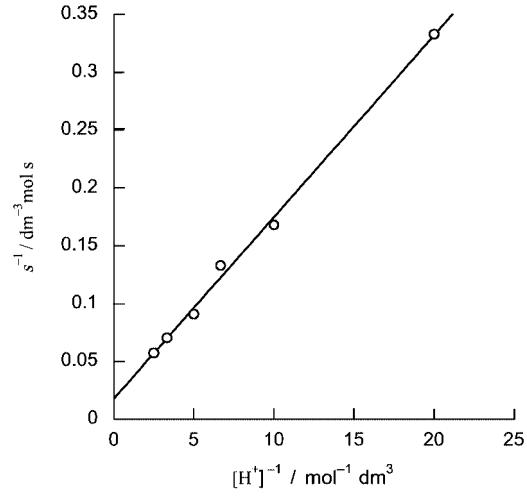


Figure 3. Linear dependence of $s^{-1}$ on $[H^+]^{-1}$. Data from Table 2.

$$s = \frac{[H^+]}{c[H^+] + d} \quad (2)$$

Owing to the large uncertainty in the values of $i$, its dependence on $[H^+]$ was better determined on studying the reaction in the absence of added LiCl. The values of the relative rate constants ($k'_{obs}{}^{f} \equiv i$) are collected in Table 1. $k'_{obs}{}^{f}$ increases as $[H^+]$ increases but appears to reach a limiting value at the higher $[H^+]$ concentrations. A plot of $(k'_{obs}{}^{f})^{-1}$ against $[H^+]^{-1}$ is linear in the range of examined $[H^+]$ (Figure 4) with intercept $e = (40\pm6)$ s and gradient $f = (35\pm1)$ mol dm$^{-3}$ s$^{-1}$.

These results are in agreement with Equation (3).

$$k'_{obs}{}^{f} = \frac{[H^+]}{e[H^+] + f} \quad (3)$$

On substituting Equations (3) and (2) into Equation (1), the experimental rate law for the first step of the reaction

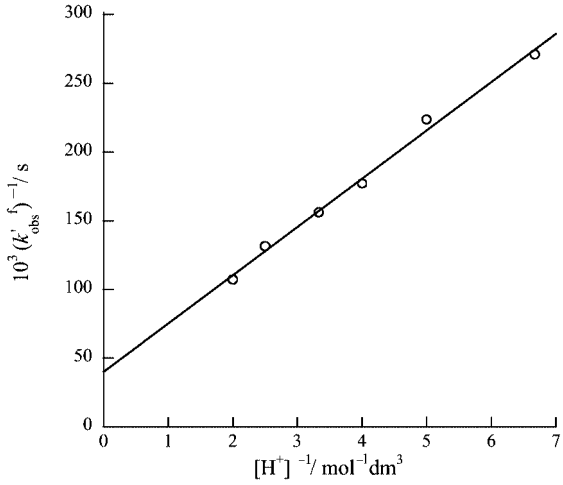


Figure 4. Plot of $(k'_{obs}{}^{f})^{-1}$ against $[H^+]^{-1}$ in the absence of added chloride.

 © 2006 Wiley-VCH Verlag GmbH & Co. KGaA, Weinheim 

takes the form of Equation (4) which can be rearranged as Equation (5) with $e/f$ ($1.14 \pm 0.05$ mol$^{-1}$ dm$^3$) = $c/d$ ($1.1 \pm 0.4$ mol$^{-1}$ dm$^3$) within the limit of the experimental error and an average value of $1.12 \pm 0.03$.

$$k_{obs}^{f} = \frac{[H^+]}{e[H^+] + f} + \frac{[H^+][Cl^-]}{c[H^+] + d} \quad (4)$$

$$k_{obs}^{f} = \frac{\frac{1}{f}[H^+]}{1 + \frac{e}{f}[H^+]} + \frac{\frac{1}{d}[H^+][Cl^-]}{1 + \frac{c}{d}[H^+]} \quad (5)$$

The rate constants for the displacement of the *N*-coordinated pyridine ligand, $k_{obs}^{s}$ (Table 1), are independent from [H$^+$] and obey the usual relationship Equation (6) with $g = (2 \pm 1) \times 10^{-4}$ s$^{-1}$ and $h = (7.6 \pm 0.2) \times 10^{-2}$ mol$^{-1}$ dm$^3$ s$^{-1}$ (Figure 5).

$$k_{obs}^{s} = g + h[Cl^-] \quad (6)$$

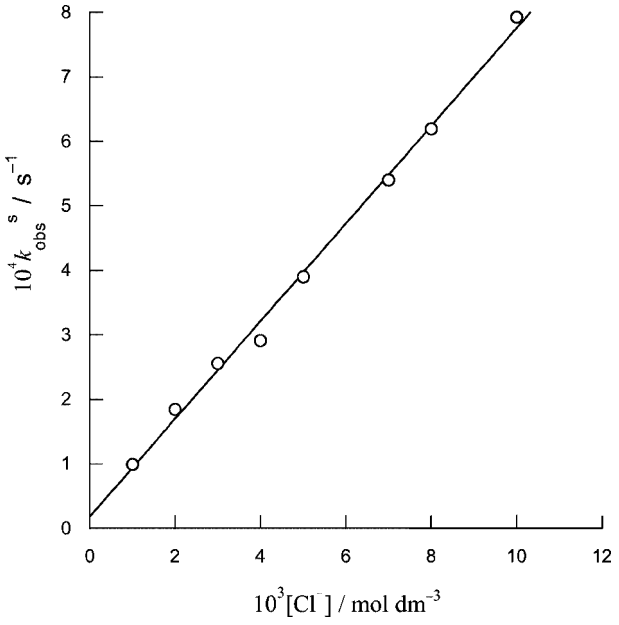


Figure 5. Plot of $k_{obs}^{s}$ against [Cl$^-$]. Data from Table 1.

## Discussion

The spectroscopic evidence together with the kinetic results are fully consistent with the reaction depicted in Scheme 2.

The reaction observed in the presence of $HClO_4$ alone is described as a fast protonation pre-equilibrium A⇌B followed by a slow reversible reaction to give the solvato species C (spectrum *b* in Figure 1). C is formulated as the acetalic species, assuming that acetylation of the hemiacetalic group is a fast process in acidic media (see below). Addition of an equimolar amount of LiCl rapidly affords the anation product P′ (spectrum *c* in Figure 1). The same species can also be formed directly from B by reaction with Cl$^-$. In the presence of higher [Cl$^-$], such as those used under pseudo-first-order conditions, displacement of the *N*-coordinated ligand through two parallel reactions, solvolysis and direct chloride substitution, occurs to give the final product P′′. This latter process corresponds to the second stage of the reaction observed in the kinetic runs, better followed in the presence of chloride ions in acidic solution. The derived rate law, $k_{obs}^{s} = k_1^{s} + k_2^{s}$[Cl$^-$] typical for the displacement of *N*-bonded pyridines is obeyed,[7] with a solvolytic rate constant $k_1^{s} = (2 \pm 1) \times 10^{-4}$ s$^{-1}$ and the second-order rate constant $k_2^{s} = (7.6 \pm 0.2) \times 10^{-2}$ mol$^{-1}$ dm$^3$ s$^{-1}$ nearly equal, within the limit of experimental error, to that relative to the displacement of the *N*-coordinated dimethyl acetal ligand from the trichloro(pyridine-2-carbaldehyde dimethyl acetal) gold(III) complex (**2**), [$k_2 = (7.875 \pm 0.003) \times 10^{-2}$ mol$^{-1}$ dm$^3$ s$^{-1}$], kinetically measured under the same experimental conditions, as well as to those found for the displacement of the strictly related pyridine-2-methanol ($k_2 = 7.58 \times 10^{-2}$ mol$^{-1}$ dm$^3$ s$^{-1}$) and 2-methoxymethylpyridine ($k_2 = 7.93 \times 10^{-2}$ mol$^{-1}$ dm$^3$ s$^{-1}$).[5] Values of $k_{obs}$ for the displacement of the ligand from the trichloro(pyridine-2-carbaldehyde dimethyl acetal)gold(III) complex (**2**) and the derived rate constants are reported in Table 3.

The close resemblance of the electronic spectra of the intermediate formed at the end of the first stage of the reaction and that of complex **2**, as well as the values of their second-order rate constants quoted above for the final displacement of the ligand, strongly support the conclusion that the hemiacetalic form of the chelated ligand, once protonated and then O-opened, undergoes a rapid process of acetalisation in the presence of the solvent MeOH under acidic conditions to give the derived *N*-coordinated dimethyl acetal as the true leaving 2-substituted pyridine in the second stage of the reaction. This behaviour is in agreement with the instability of the hemiacetals of the free organic carbaldehydes[8] that, under comparable experimental conditions, react with alcohols to rapidly give the corresponding acetals. This conclusion has been fully confirmed by the series of $^1$H NMR experiments reported in Figure 6.

When dichloro[pyridine-2-(α-methoxymethanolato)]gold(III) (**1**) in $CD_3NO_2$ [integrated proton ratio C–H ($\delta$ = 5.45 ppm)/O–$CH_3$ ($\delta$ = 3.56 ppm) of 1:3] (spectrum **A**) is added to methanol and DCl [molar ratio 5:1 and 1:1 with respect to the concentration of complex **1** ($2.56 \times 10^{-2}$ mol dm$^{-3}$)] its spectrum rapidly changes (spectrum **B**) to that of an authentic sample of the trichloro(pyridine-2-carbaldehyde dimethyl acetal)gold(III) (**2**) in $CD_3NO_2$ at a similar concentration ($2.34 \times 10^{-2}$ mol dm$^{-3}$ (spectrum **C**), both of them showing an integrated proton

 © 2006 Wiley-VCH Verlag GmbH & Co. KGaA, Weinheim 

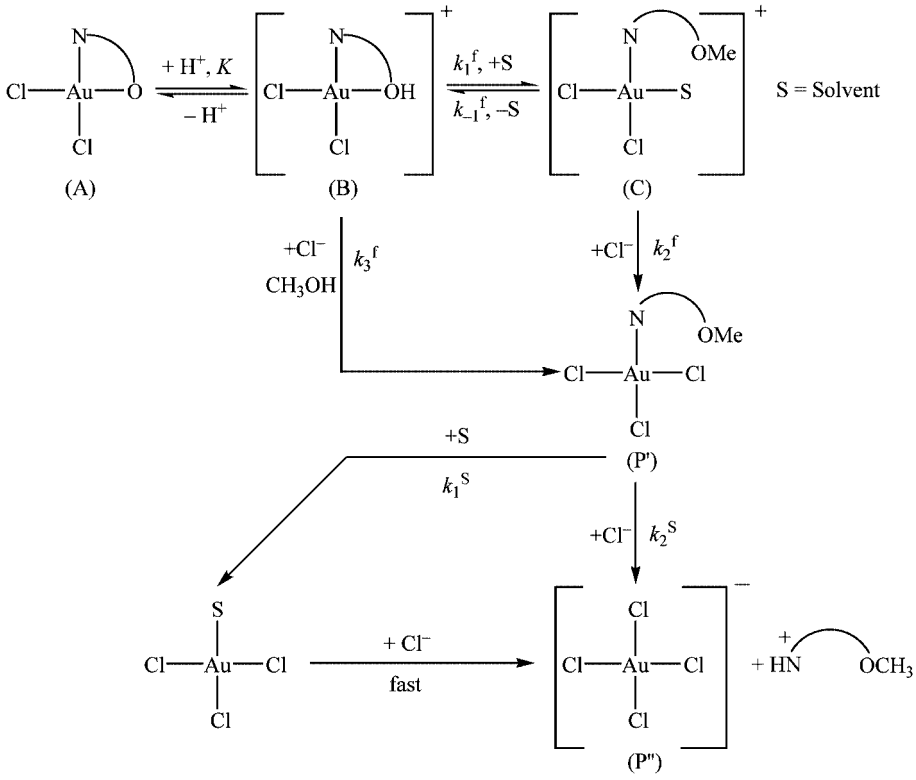


Scheme 2. $K$ = 1.12 ± 0.03 dm$^3$ mol$^{-1}$, $k_3^f$ = 56 ± 17 dm$^3$ mol$^{-1}$ s$^{-1}$, $k_1^f$ = 0.025 ± 0.001 s$^{-1}$, $k_1^s$ = (2 ± 1) × 10$^{-4}$ s$^{-1}$, $k_2^s$ = (7.6 ± 0.2) × 10$^{-2}$ dm$^3$ mol$^{-1}$ s$^{-1}$.

Table 3. Observed rate constants ($k_{obs}$) and derived rate constants ($k_1$ and $k_2$) for the reaction [Au(N–OMe)Cl$_3$] + Cl$^-$ → [AuCl$_4$]$^-$ + $^+$HN–OMe at 25 °C in MeOH/H$_2$O (95:5 v/v).

| [Cl$^-$] [mol dm$^{-3}$] | 10$^3$ $k_{obs}$ [s$^{-1}$] | $k_1$ [s$^{-1}$] | $k_2$ [mol$^{-1}$ dm$^{-3}$ s$^{-1}$] |
|---|---|---|---|
| 0.01 | 0.84 | | |
| 0.02 | 1.68 | | |
| 0.03 | 2.44 | (5 ± 3) × 10$^{-5}$ | (7.875±0.003) × 10$^{-2}$ |
| 0.04 | 3.13 | | |
| 0.08 | 6.34 | | |
| 0.1 | 7.96 | | |

ratio C–H ($\delta$ = 6.15 ppm)/O–CH$_3$ ($\delta$ = 3.66 ppm) of 1:6. Further addition of DCl [molar ratio 10:1 with respect to the concentration of complex **1**] allows the reaction to go to completion with release of the ligand in the form of the *N*-protonated pyridine-2-carbaldehyde dimethyl acetal [integrated proton ratio C–H ($\delta$ = 6.02 ppm)/O–CH$_3$ ($\delta$ = 3.64 ppm) of 1:6], as comes from a comparison of its spectrum (spectrum **D**) with the spectrum of the released ligand from **2** under the same experimental conditions (spectrum **E**). Spectrum **B** shows also the presence of some free *N*-protonated pyridine-2-carbaldehyde dimethyl acetal as a result of the incoming development of the second stage of the reaction.

From the reaction in Scheme 2, on assuming species C as a steady-state intermediate {d$C$/d$t$ = 0 which implies that ($k_{-1}^f$ + $k_2^f$[Cl$^-$]) >> $k_1^f$}, the following dependence of $k_{obs}^f$ on [H$^+$] and [Cl$^-$] is derived [Equation (7)].

Because under our experimental conditions in the presence of [H$^+$] ≥ 0.05 mol dm$^{-3}$ alone, the reaction is completely shifted towards the solvato species C, the condition $k_{-1}^f$ << $k_1^f$ must hold and hence, in the presence of Cl$^-$, the condition $k_2^f$[Cl$^-$] >> $k_{-1}^f$ must be satisfied. Under these conditions Equation (7) reduces to Equation (8).

Equation (8) is identical to the empirical Equation (5) if $k_1^f K$ = 1/f, $K$ = e/f, $k_3^f K$ = 1/d, from which the values of the equilibrium constant ($K$ = 1.12 ± 0.03 dm$^3$ mol$^{-1}$) and of the rate constants ($k_3^f$ = 56 ± 17 dm$^3$ mol$^{-1}$ s$^{-1}$, $k_1^f$ = 0.025 ± 0.001 s$^{-1}$) can be calculated. These values together with the rate constants for the second stage of the reaction ($k_1^s$ and $k_2^s$) are also reported in Scheme 2.

A point that deserves to be underlined is the different reactivity of complex **1** with respect to that of the previously studied dichloro(pyridine-2-methanolato)gold(III)[5] as regards the reaction with Cl$^-$ in the absence of acid. In the first case no reaction takes place, whereas in the second case the reaction goes to completion with ring opening at oxygen followed by substitution of the pyridine ligand. This different behaviour, which implies a stronger Au–O bond in complex **1**, would suggest a remarkable effect on the reactivity as a result of the replacement of a hydrogen atom with a methoxy group, possibly related to their different inductive effects. Accordingly, both the values of the protonation constant ($K$ = 1.12 mol$^{-1}$ dm$^3$) and the rate con-

 © 2006 Wiley-VCH Verlag GmbH & Co. KGaA, Weinheim 

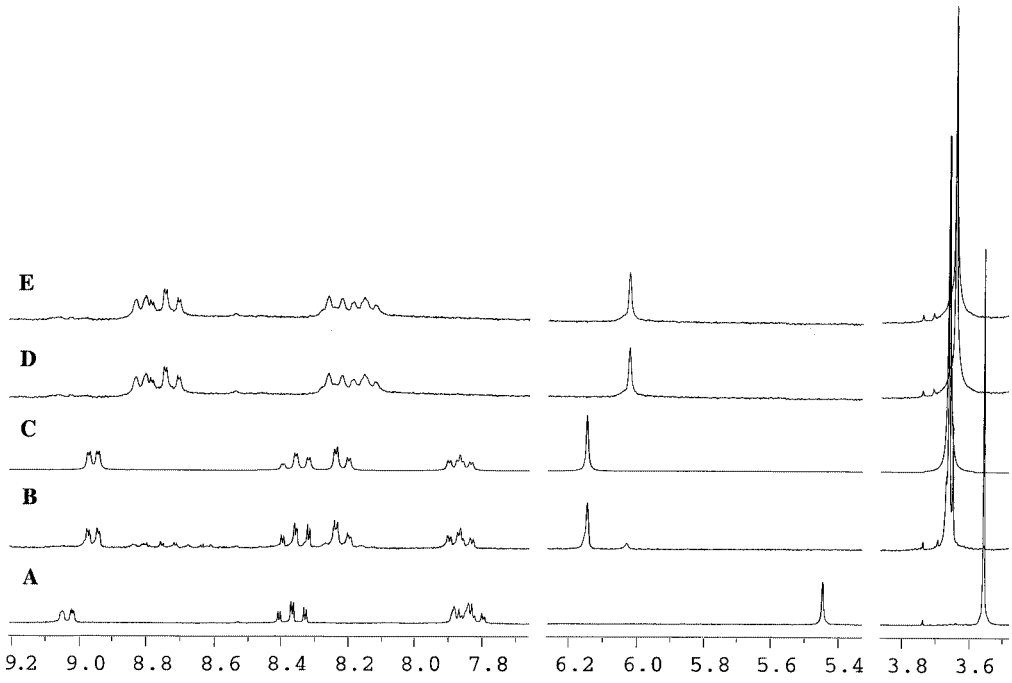


Figure 6. $^1$H NMR spectrum of **1** in $CD_3NO_2$ (spectrum **A**); spectrum of **1** in methanol and DCl [molar ratio 5:1 and 1:1 with respect to the concentration of the complex] (spectrum **B**); spectrum of an authentic sample of **2** in $CD_3NO_2$ (spectrum **C**); spectrum of the released ligand at the end of the reaction in the presence of methanol and an excess of DCl [molar ratio 5:1 and 10:1 with respect to the concentration of complex (**1**)] (spectrum **D**); spectrum of the released ligand from **2** under the same experimental conditions (spectrum **E**).

$$k_{obs}^{f} = \frac{K[H^+]}{1+K[H^+]}\left(\frac{k_1^{f}k_2^{f}[Cl^-]}{k_{-1}^{f}+k_2^{f}[Cl^-]}+k_3^{f}[Cl^-]\right) \quad (7)$$

$$k_{obs}^{f} = \frac{k_1^{f}K[H^+]}{1+K[H^+]}+\frac{k_3^{f}K[H^+][Cl^-]}{1+K[H^+]} \quad (8)$$

stant relative to the ring opening of the protonated species ($k_3^{f}$ = 56 mol$^{-1}$ dm$^3$ s$^{-1}$) for the hemiacetalic complex (**1**) are lower than the corresponding constants for the complex with pyridine-2-methanol ($K$ = 9.7 mol$^{-1}$ dm$^3$, $k$ = 126 mol$^{-1}$ dm$^3$ s$^{-1}$).[5]

The second stage of the reaction, that is the displacement of the 2-substituted pyridine by $Cl^-$ from the species P′, can be compared with other reactions of this sort as it is known that the second-order rate constant for the reaction with chloride depends upon the basicity of the leaving pyridine, according to the linear relationship $\log k_2 = a(pK_a) + C$ ($pK_a$ is that of the protonated base in water at 25 °C) and is independent from steric hindrance of the ring substituents.[7] In the mixture methanol/water (95:5, v/v) this relationship is also obeyed and the values of $a$ and $C$, already measured, are –0.67 and 2.81 respectively.[9] A $k_2^{s}$ value of $7.6\times10^{-2}$ mol$^{-1}$ dm$^3$ s$^{-1}$ leads therefore to a $pK_a$ of 5.86 for the leaving pyridine-2-carbaldehyde dimethyl acetal, which closely compares to those of pyridine-2-methanol and 2-(methoxymethyl)pyridine, as they both have a $pK_a$ value of 5.6.[5]

## Concluding Remarks

The kinetics of ring opening and displacement of the bidentate chelate ligand from dichloro[pyridine-2-(α-methoxymethanolato)]gold(III), [Au(N–O)$Cl_2$] (**1**) have been studied spectrophotometrically in methanol/water (95:5 v/v). Because of the relative inertness of the Au–alkoxide oxygen bond, complex **1** does not react with chloride alone. In the presence of LiCl and perchloric acid the reaction proceeds through a pre-equilibrium protonation of the coordinated oxygen followed first by ring opening at oxygen accompanied by the entry of chloride or solvent and then by displacement of the *N*-bonded ligand to give $[AuCl_4]^-$. However, once opened the hemiacetalic *N*-coordinated ligand is rapidly transformed in the corresponding 2-(pyridinecarbaldehyde dimethyl acetal), which is the true leaving ligand, to be displaced in the second stage of the reaction as a 2-substituted pyridine with a $pK_a$ value of 5.86.

## Experimental Section

**Materials:** Pyridine-2-carbaldehyde (Aldrich) was vacuum distilled and stored at 4 °C. Potassium tetrachloroaurate(III) dihydrate, the inorganic salts and the solvents were reagent grade products (Aldrich) used without further purification.

**Instruments:** UV/Vis spectra and kinetics were recorded with a Perkin–Elmer Lambda 5 spectrophotometer. IR spectra (4000–500 cm$^{-1}$, KBr disks; 600–50 cm$^{-1}$, polyethylene pellets) were collected with a Nicolet Magna FTIR 750 spectrometer. $^1$H NMR spectra in high purity $CD_3NO_2$ (Aldrich) were obtained with a Bruker AC 200 spectrometer. Chemical shifts (ppm) were internally

 © 2006 Wiley-VCH Verlag GmbH & Co. KGaA, Weinheim 

referenced to the residual undeuterated solvent resonances and related to tetramethylsilane ($\delta$ = 0 ppm). Conductivity measurements were carried out in dmf with a CDM 83 Radiometer Copenhagen conductivity meter and a CDC 334 immersion cell. Elemental analyses were performed by the Microanalytical Laboratory of the University of Padua.

**Synthesis of Complexes 1 and 2 and of the Ligand Released at the End of the Process (3)**

**Dichloro[pyridine-2-(α-methoxymethanolato)]gold(III) (1):** [Spectrum A in Figure 6] This complex was prepared following the same procedure as for the ethoxy species previously reported[4] using methanol instead of ethanol as a solvent. Yield (80%). $C_7H_8AuCl_2NO_2$ (406.02): calcd. C 20.71, H 1.99, Cl 17.46, N 3.45; found C 20.64, H 1.72, Cl 17.32, N 3.46. $^1$H NMR (200 MHz, $CD_3NO_2$, 25 °C): $\delta$ = 9.04 (d, $^3J_{HH}$ = 5.2 Hz, 1 H, py-$H_6$), 8.37 (td, $^3J_{HH}$ = 7.6, $^4J_{HH}$ = 1.4 Hz, 1 H, py-$H_4$), 7.92–7.77 (m, 2 H, py-$H_{3,5}$), 5.45 (s, 1 H, CH), 3.56 (s, 3 H, $OCH_3$) ppm. Selected IR bands: 1609 ($\nu_{C=N}$), 1079 ($\nu_{O-CH_3}$), 370, 349 ($\nu_{Au-Cl}$) cm$^{-1}$. $\Lambda_M$(dmf) = 2.7 Ω$^{-1}$ cm$^2$ mol$^{-1}$.

**Trichloro(pyridine-2-carbaldehyde dimethyl acetal)gold(III) (2):** [Spectra B, C in Figure 6] The complex was prepared as previously reported.[6] Yield (75%). $C_8H_{11}AuCl_3NO_2$ (456.51): calcd. C 21.05, H 2.43, Cl 23.30, N 3.07; found C 20.94, H 2.39, Cl 23.61, N 3.10. $^1$H NMR (200 MHz, $CD_3NO_2$, 25 °C): $\delta$ = 8.96 (d, $^3J_{HH}$ = 6.0 Hz, 1 H, py-$H_6$), 8.36 (td, $^3J_{HH}$ = 7.9, $^4J_{HH}$ = 1.4 Hz, 1 H, py-$H_4$), 8.22 (dd, $^3J_{HH}$ = 7.9, $^4J_{HH}$ = 1.8 Hz, 1 H, py-$H_3$); 7.87 (ddd, $^3J_{HH}$ = 6.0, $^3J_{HH}$ = 7.9, $^4J_{HH}$ = 1.8 Hz 1 H, py-$H_5$), 6.15 (s, 1 H, CH), 3.66 (s, 6 H, $OMe_2$) ppm. Selected IR bands: 1611 ($\nu_{C=N}$), 1098 ($\nu_{O-CH_3}$), 366, 349 ($\nu_{Au-Cl}$) cm$^{-1}$. $\Lambda_M$(dmf) = 2.3 Ω$^{-1}$ cm$^2$ mol$^{-1}$.

**2-CH(OMe)$_2$py·HCl (3):** [Spectra D, E in Figure 6] $^1$H NMR (200 MHz, $CD_3NO_2$, 25 °C): $\delta$ = 8.81 (d, $^3J_{HH}$ = 6.0 Hz, 1 H, py-$H_6$), 8.75 (td, $^3J_{HH}$ = 7.9, $^4J_{HH}$ = 1.6 Hz, 1 H, py-$H_4$), 8.30–8.08 (m, 2 H, py-$H_3$+$H_5$), 6.91 (br, 1 H, NH), 6.02 (s, 1 H, CH), 3.64 (s, 6 H, $OMe_2$) ppm.

**Kinetics:** The reactions were followed spectrophotometrically by measuring the changing absorbance at a suitable wavelength as a function of time. They were initiated by adding 10–20 μL of a 0.015 mol dm$^{-3}$ dimethylformamide (dmf) solution of **1** or **2** to a methanol/water (95:5 v/v) solution (3 cm$^3$) of the appropriate reagent, either $HClO_4$ or $HClO_4$, and LiCl, previously brought to the reaction temperature (25 °C) in the thermostatted cell in the spectrophotometer. All reactions were carried out at constant ionic strength ($I$ = 1.0 mol dm$^{-3}$, $LiClO_4$). Pseudo-first-order rate constants ($k_{obs}$/s$^{-1}$) were obtained either from the gradients of plots of $\log(D_t - D_\infty)$ versus time or from a nonlinear least-squares fit of experimental data to the equation $D_t = D_\infty + [D_0 - D_\infty \exp(-k_{obs}t)]$, where $D_0$, $D_\infty$ and $k_{obs}$ are the parameters to be optimised ($D_0$ is absorbance after mixing of reactants, $D_\infty$ is absorbance at completion of reaction). Rate constants were accurate within 5%.

## Acknowledgments

We thank the Cà Foscari University of Venice for financial support (Ateneo fund 2004).

[1] F. Basolo, R. G. Pearson, *Mechanisms of Inorganic Reactions*, 3rd ed., Wiley, New York, **1967**, p. 384.
[2] A. S. K. Hashmi, M. Rudolph, J. P. Weyrauch, M. Wölfle, W. Frey, J. W. Bats, *Angew. Chem. Int. Ed.* **2005**, *44*, 2798–2801.
[3] A. S. K. Hashmi, J. P. Weyrauch, M. Rudolph, E. Kurpejovic, *Angew. Chem. Int. Ed.* **2004**, *43*, 6545–6547.
[4] G. Annibale, L. Canovese, L. Cattalini, G. Marangoni, G. Michelon, M. L. Tobe, *J. Chem. Soc., Dalton Trans.* **1984**, 1641–1646.
[5] L. Canovese, L. Cattalini, G. Marangoni, M. L. Tobe, *J. Chem. Soc., Dalton Trans.* **1985**, 731–735.
[6] V. Bertolasi, G. Annibale, G. Marangoni, G. Paolucci, B. Pitteri, *J. Coord. Chem.* **2003**, 397–406.
[7] L. Cattalini, M. L. Tobe, *Inorg. Chem.* **1966**, *5*, 1145–1150.
[8] J. March, *Advanced Organic Chemistry. Reactions, Mechanisms, and Structure*, 3rd ed., Wiley, New York, **1985**, p. 790.
[9] L. Cattalini, G. Chessa, G. Marangoni, B. Pitteri, M. L. Tobe, *J. Chem. Soc., Dalton Trans.* **1985**, 2091–2094.

Received: August 25, 2005
Published Online: December 28, 2005

 © 2006 Wiley-VCH Verlag GmbH & Co. KGaA, Weinheim 

DOI: 10.1002/ejic.200500916

# The Effective Electron-Transfer Distance in Dinuclear Ruthenium Complexes Containing the Unsymmetrical Bridging Ligand 3,5-Bis(2-pyridyl)-1,2,4-triazolate

**Deanna M. D'Alessandro,[a] Peter H. Dinolfo,[b] Joseph T. Hupp,[b] Peter C. Junk,[c][‡] and F. Richard Keene*[a]**

**Keywords:** Electron transfer / Mixed-valent compounds / Through-bond interactions / Dinuclear / Stereochemistry / Stark spectroscopy / Ruthenium

Electroabsorption (Stark effect) measurements on the intervalence charge-transfer (IVCT) transitions in the diastereoisomers of $[\{Ru(bpy)_2\}_2(\mu\text{-}bpt^-)]^{4+}$ [bpy = 2,2′-bipyridine, $bpt^-$ = 3,5-bis(2-pyridyl)-1,2,4-triazolate] in *n*-butyronitrile glass at 77 K reveal effective charge-transfer distances of 5.92 ± 0.03 Å for the ΔΛ/ΛΔ form and 5.44 ± 0.04 Å for the ΔΔ/ΛΛ form. These values correspond to approximately 95 and 88 %, respectively, of the geometrical metal–metal distance of 6.185(10) Å, obtained from the X-ray crystal structure of the cation in the related complex (ΔΛ)-$[\{Ru(Me_2bpy)_2\}_2(\mu\text{-}bpt^-)](PF_6)_3$. The results are consistent with a localized Class II classification for the mixed-valence systems $[\{Ru(pp)_2\}_2(\mu\text{-}bpt^-)]^{4+}$, where pp = bpy, $Me_2bpy$ = 4,4′-dimethyl-2,2′-bipyridine.
(© Wiley-VCH Verlag GmbH & Co. KGaA, 69451 Weinheim, Germany, 2006)

## Introduction

Dinuclear polypyridyl complexes of ruthenium and osmium based on di-bidentate polypyridyl bridging ligands have been the subject of extensive research efforts over the past two decades, as part of rapid advances in metallosupramolecular chemistry. Bridging ligands provide the linkage between the metal centers in polymetallic assemblies and control the distances and relative orientations of the components, as well as the inter-component electron- and energy-transfer processes.[1–8]

The anion of 3,5-bis(2-pyridyl)-1,2,4-triazole (shown in Figure 1) is a particularly interesting bridging ligand, as it carries a negative charge and exhibits a high σ-donor and low π-acceptor ability.[9] As a consequence, $bpt^-$ constitutes a member of a relatively small class of bridging ligands, which mediate the electronic coupling between the metal centers (denoted by $M^1$ and $M^2$ in Figure 1) by a hole-transfer mechanism. Because these ligands possess electron-rich high-lying π* orbitals, the decisive factor in the metal–metal coupling is the energy gap between the highest-occupied molecular orbitals (HOMOs) of the bridge and the metal-based dπ orbitals, as shown in Figure 2.[6]

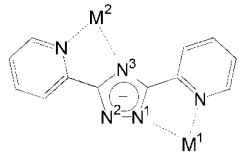


Figure 1. The 3,5-bis(2-pyridyl)-1,2,4-triazolate ($bpt^-$) bridging ligand. $M^1$ and $M^2$ denote the metal centers coordinated at the $N^1$ and $N^3$ sites, respectively.

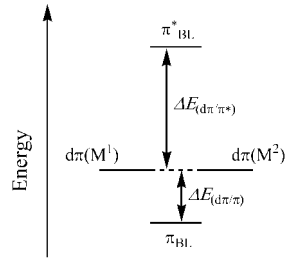


Figure 2. Schematic energy level diagrams for superexchange-assisted electronic coupling by a *hole-transfer* mechanism.[6] $M^1$ and $M^2$ denote the metal centers and BL denotes the bridging ligand.

The coupling between $M^1$ and $M^2$ can involve direct contributions from a "through-space" mechanism, and/or indirect contributions from a "through-bond" superexchange process where the bridging ligand mediates the donor-ac-

[a] School of Pharmacy and Molecular Sciences, James Cook University,
Townsville, Queensland 4811, Australia
Fax: +61-7-4781-6078
E-mail: Richard.Keene@jcu.edu.au
[b] Department of Chemistry, Northwestern University,
211 Sheridan Road, Evanston, IL 60208-3113, USA
[c] School of Pharmacy and Molecular Sciences, James Cook University,
Townsville, Queensland 4811, Australia
[‡] Present address: Department of Chemistry, Monash University, Clayton, Victoria 3800, Australia
Supporting information for this article is available on the WWW under http://www.eurjic.org or from the author.


© 2006 Wiley-VCH Verlag GmbH & Co. KGaA, Weinheim

ceptor coupling. In the latter case, the superexchange theory[10] provides a conceptual framework for bridging ligand effects in intramolecular electron transfer.[5,6] The parameters, which are effective to describe the through-bond interaction are the overlap between the frontier orbitals of the metals, $d\pi(M^1)$ and $d\pi(M^2)$, and the bridging ligand ($\pi_{BL}$ and $\pi_{BL}^*$), and the electronic interactions between the atoms of the bridge connecting the frontier units to one another.

In dinuclear complexes incorporating bpt⁻, the coordination environments of the two metal centers are chemically distinct due to the enhanced σ-donor ability of the $N^1$ (≡ $N^2$) position of the triazolate ring relative to the $N^3$ position.[11] As a consequence, a "redox asymmetry" (denoted by $\Delta E_0$) exists between the inequivalent coordination sites.[12,13]

The classical theory developed by Hush[14,15] provides a conceptual framework for the contribution of redox asymmetry effects to the electron-transfer barrier through the analysis of the intervalence charge-transfer (IVCT) transitions generated in the mixed-valence forms of dinuclear complexes. In accordance with Equation (1), the energy ($\nu_{max}$) of an IVCT band, which is typically observed in the near-infrared (NIR) region of the absorption spectrum of the mixed-valence complex, is given in terms of the redox asymmetry and the Franck-Condon reorganizational energy contributions. The latter are composed of an inner-sphere component ($\lambda_i$) due to bond length and angle rearrangement, and also an outer-sphere component ($\lambda_o$) due to solvent and anion rearrangement in the secondary coordination sphere.[14,15]

$$\nu_{max} = = \lambda_i + \lambda_o + \Delta E_0 \quad (1)$$

In recent work from our laboratory, comparisons between the characteristics of the IVCT transitions, generated by the mixed-valence forms of the diastereoisomers, (ΔΛ/ΛΔ)- and (ΔΔ/ΛΛ)-[{Ru(bpy)$_2$}$_2$(μ-BL)]$^{n+}$ (BL = a range of bis-bidentate polypyridyl bridging ligands) have revealed a stereochemical dependence of the IVCT energies, intensities and bandwidths. The origins of such dependencies have been ascribed to redox asymmetry contributions to Equation 1) due to stereochemically-directed structural distortions[16] and ion-pairing interactions,[17] as well as the outer-sphere reorganizational contributions due to spatially-directed solvent interactions.[18] The present work broadens our investigation into the use of stereoisomers as probes for the factors that govern the electron-transfer barrier through the characterization of the IVCT transitions in the ΔΛ/ΛΔ and ΔΔ/ΛΛ diastereoisomers of [{Ru(pp)$_2$}$_2$(μ-bpt⁻)]$^{4+}$ (pp = bpy, Me$_2$bpy), shown in Figure 3. Electroabsorption (Stark effect) measurements on the IVCT bands of the diastereoisomers of [{Ru(bpy)$_2$}$_2$(μ-bpt⁻)]$^{4+}$ provide a measure of the *effective* charge-transfer distances, which may be shortened relative to the geometric metal–metal distances due to electronic delocalization, self-polarization and other effects.[19–23] Whereas Browne and co-workers[24] concluded that the stereoisomeric identity of the ΔΛ, ΛΔ, ΔΔ and ΛΛ forms of [{Ru(bpy)$_2$}$_2$(μ-bpt⁻)]$^{3+}$ had no influence on the photophysical properties of the complexes either at 77 K or room temperature, the influence of stereochemical effects on the IVCT properties of the systems were not addressed. Previous studies have, however, reported the redox and spectroscopic characteristics,[9,11,12,25–27] resonance Raman spectra[28] and photophysical behavior[9,29] of stereoisomeric mixtures of the homo- and hetero-dinuclear complexes of ruthenium, osmium, rhodium and iridium incorporating bpt⁻ and its protonated analog, Hbpt.

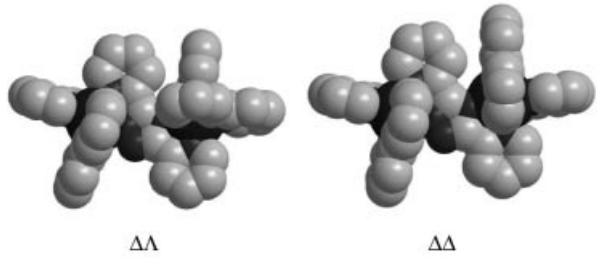


Figure 3. Schematic representations of (ΛΔ)- and (ΔΔ)-[{Ru(bpy)$_2$}$_2$(μ-bpt⁻)]$^{3+}$; hydrogen atoms are omitted for clarity.

It must be noted that due to the inequivalence of the metal coordination sites, the ΔΛ/ΛΔ form comprises a pair of geometric isomers. No attempt was made to separate the geometric forms in the present report.

The understanding of the fundamental stereochemical effects on the IVCT transitions in dinuclear complexes has important implications for the elucidation of spatial influences on electron migration in natural processes such as photosynthesis. Because the unsymmetrical component in bpt⁻ may be exploited to facilitate vectorial electron- and energy-transfer processes in polynuclear complexes, which form the basis of novel molecular-scale devices,[9,11,12,24,25,27–40] stereochemical effects may also offer a novel means of "fine-tuning" the metal–metal interactions.

## Results and Discussion

**Diastereoisomer Synthesis, Separation and Structural Characterization:** The complex [{Ru(bpy)$_2$}$_2$(μ-bpt⁻)]$^{3+}$ has been synthesized previously by the reaction of [Ru(bpy)$_2$Cl$_2$]·2H$_2$O with bpt in ethanol/water (2:1) under reflux.[11,33] In the present case, an alternative microwave-assisted methodology was employed[16,41–44] which produced equivalent or increased reaction yields of the dinuclear species compared with the thermal method; however, there was a significant reduction in the reaction times.

The chromatographic separation of the diastereoisomers of [{Ru(bpy)$_2$}$_2$(μ-bpt⁻)]$^{3+}$ by a semi-preparative HPLC technique has been reported previously;[24] in the present report, the separation was achieved using a cation-exchange chromatographic procedure with SP Sephadex C-25 as the support and aqueous solutions of sodium toluene-4-sulfonate as the eluent. The band 1 and 2 eluates were determined to be the ΔΛ/ΛΔ and ΔΔ/ΛΛ diastereoisomers, respectively. Interestingly, the two forms exhibited different colors on the column, with the ΔΛ/ΛΔ form displaying a

 © 2006 Wiley-VCH Verlag GmbH & Co. KGaA, Weinheim 

red, and the ΔΔ/ΛΛ form displaying an orange coloration. During the procedure, a small amount of smearing was observed as the complex passed down the column. This was attributed to the presence of an uncoordinated nitrogen atom on the triazole ring of the bpt⁻ bridging ligand. Measurements on the pH dependence of the absorption spectrum of $[\{Ru(bpy)_2\}_2(\mu\text{-bpt}^-)]^{3+}$ by Hage et al.[11] revealed a p$K_a$ of $-0.6 \pm 0.3$ for the complex in aqueous solution. This suggests that the protonation of the free nitrogen atom under the conditions employed in the chromatographic separation is unlikely.

Because poor microanalysis figures were obtained, the characterization and purity assessment of the diastereoisomers were based on the NMR spectra and electrochemical data. Incomplete combustion may in part account for these unsatisfactory figures;[45] however, the occlusion of variable numbers of solvent molecules and counter-anions may also be a factor. Such difficulties have previously been noted for dinuclear complexes of ruthenium(II).[46]

The $^1$H numbering schemes for the ligands in $[\{Ru(bpy)_2\}_2(\mu\text{-bpt}^-)]^{4+}$ are shown in Figure S1 (Supporting Information; see footnote on the first page of this article) and the assignments of the spectra were performed with the assistance of $^1$H COSY spectra.[47] The coordinated bpy ligands exhibited the expected coupling constant values[48] ($J_{3,4}$ = 8, $J_{3,5}$ = 1.5, $J_{4,5}$ = 8, $J_{4,6}$ = 1.5 Hz and $J_{5,6}$ = 5 Hz) and coupling patterns based on the symmetry requirements of the complexes.

The assignment of the $^1$H resonances associated with individual terminal ligands was based on the differential anisotropic effects of the two ligands above (and below) the plane of the bridging ligand. Because an analysis of the $^1$H NMR spectra of the diastereoisomers of $[\{Ru(bpy)_2\}_2(\mu\text{-bpt}^-)]^{3+}$ have been reported previously,[11] the assignments for the diastereoisomers of $[\{Ru(pp)_2\}_2(\mu\text{-bpt}^-)]^{3+}$ in the present investigation are listed in the Experimental Section only.

### Structural Considerations: X-Ray Crystallography

A limited number of crystal structures have been reported of dinuclear ruthenium complexes incorporating polypyridyl ligands. Of the three examples of dinuclear species containing unsymmetrical bridging ligands,[12,49] two have contained the bpt⁻ bridging ligand. In both cases, the crystals were obtained in the ΔΛ/ΛΔ form during an attempt to separate the diastereoisomers of the complexes through fractional crystallization. Accordingly, the single crystals of $(\Delta\Lambda/\Lambda\Delta)$-$[\{Ru(Me_2bpy)_2\}_2(\mu\text{-bpt}^-)](PF_6)_3$ obtained in the present investigation represent the first example of the selective isolation of one of the components containing an unsymmetrical bridging ligand *prior* to crystal growth.

Figure 4 shows the X-ray crystal structure for the cation in $(\Delta\Lambda/\Lambda\Delta)$-$[\{Ru(Me_2bpy)_2\}_2(\mu\text{-bpt}^-)](PF_6)_3$. The complex crystallises in the triclinic space group $P\bar{1}$ with two dinuclear cations in the unit cell. A summary of the crystal data and refinement are provided in Table S1 (Supporting Information). The ruthenium–nitrogen distances of 2.026(10)–2.109(10) Å correlate with those published for previous structures.[12,50–52] The Ru(2)–N(1) distance of 2.004(9) Å is significantly shorter than the Ru(1)–N(3) distance of 2.109(10) Å, which is consistent with the enhanced σ-donor ability of the N(1) site of the triazolate ring compared with the N(3) site.[9,11,12,27,33] The bond lengths and angles of the terminal $Me_2$bpy ligands are in the normal range for complexes incorporating $[Ru(Me_2bpy)_2]^{2+}$ and $[Ru(bpy)_2]^{2+}$ moieties.[12,50–52] The "bite-angles" of the terminal chelating ligands vary between 78.1(5)° and 79.4(5)°, which is typical for bipyridine-like ligands.[12,50–52]

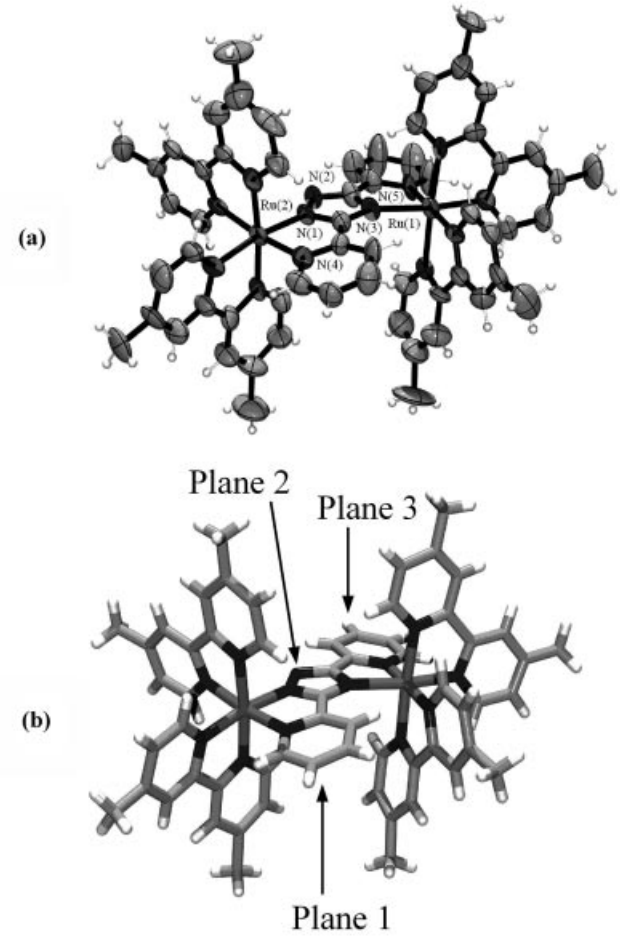


Figure 4. (a) Partial atom labelling, and (b) designation of the planes for the cation in $(\Delta\Lambda/\Lambda\Delta)$-$[\{Ru(Me_2bpy)_2\}_2(\mu\text{-bpt}^-)](PF_6)_3$.

As shown in Figure 4 (b), the dihedral angles between the least-squares plane of the triazolate ring (plane 2) and the planes of the two pyridine rings (planes 1 and 3) are 10.8(5)° and 8.63(5)°, respectively, indicating a considerable deviation from planarity of the bpt⁻ ligand after the coordination of two $[Ru(Me_2bpy)_2]^{2+}$ moieties. This distortion appears to arise from steric crowding between the methyl groups oriented perpendicular to the "long axis" of the bridge. The methyl groups located "above" the plane of the bridging ligand induce a curvature in the bridge, which re-

 © 2006 Wiley-VCH Verlag GmbH & Co. KGaA, Weinheim 

sults in the pyridyl groups bending downwards away from the normal bridging plane. In the representation of the ΔΔ/ΛΛ diastereoisomer shown in Figure 3, one might anticipate less structural distortion relative to the ΔΛ/ΛΔ form, as the potentially unfavorable interactions between the methyl groups are avoided due to the parallel orientation of the terminal ligands above (and below) the bridging plane. The Ru(1)···Ru(2) separation is 6.185(10) Å.

### Electrochemical and UV/Vis/NIR Spectral Characterization

The redox potentials for the $E_{ox1}$ ([5+/4+]; i.e. $Ru^{III}$–$Ru^{II}$/$Ru^{II}$–$Ru^{II}$) and $E_{ox2}$ ([6+/5+]; i.e. $Ru^{III}$–$Ru^{III}$/$Ru^{III}$–$Ru^{II}$) couples for (ΔΛ/ΛΔ)- and (ΔΔ/ΛΛ)-$[\{Ru(pp)_2\}_2(\mu\text{-bpt}^-)]^{4+}$ (pp = bpy, $Me_2$bpy) were investigated by cyclic and differential pulse voltammetry in acetonitrile containing 0.1 M $[(n\text{-}C_4H_9)_4N]PF_6$, and are reported in Table 1. $\Delta E_{ox}$ defines the potential difference between the [6+/5+] and [5+/4+] couples. The full electrochemical characteristics of the diastereoisomers $[\{Ru(bpy)_2\}_2(\mu\text{-bpt}^-)]^{4+}$ in 0.1 M $[(n\text{-}C_4H_9)_4N]PF_6$ and 0.02 M $[(n\text{-}C_4H_9)_4N]\{B(C_6F_5)_4\}$ electrolytes have been reported previously.[53]

Table 1. Electrochemical data (in mV relative to the $Fc^+/Fc^0$ couple) and comproportionation constants ($K_c$) for $[\{Ru(pp)_2\}_2(\mu\text{-bpt}^-)]^{3+}$ in 0.1 M $[(n\text{-}C_4H_9)_4N]PF_6/CH_3CN$.

| Complex | $K_c$[a] ($\times 10^{-5}$) | $\Delta E_{ox}$[b] | $E_{ox2}$ | $E_{ox1}$ |
|---|---|---|---|---|
| (ΔΛ/ΛΔ)-$[\{Ru(bpy)_2\}_2(\mu\text{-bpt}^-)]^{3+}$ | 1.88 | 312 | 992 | 680 |
| (ΔΔ/ΛΛ)-$[\{Ru(bpy)_2\}_2(\mu\text{-bpt}^-)]^{3+}$ | 1.61 | 308 | 992 | 684 |
| (ΔΛ/ΛΔ)-$[\{Ru(Me_2bpy)_2\}_2(\mu\text{-bpt}^-)]^{3+}$ | 5.58 | 340 | 927 | 587 |
| (ΔΔ/ΛΛ)-$[\{Ru(Me_2bpy)_2\}_2(\mu\text{-bpt}^-)]^{3+}$ | 3.78 | 330 | 902 | 572 |

[a] $K_c$ values are given by $K_c = \exp(\Delta E_{ox}F/RT)$ where $F/RT$ = 38.92 $V^{-1}$ at 298 K. [b] $\Delta E_{ox} = E_{ox2} - E_{ox1}$. Potentials are quoted ±3 mV.

The dinuclear systems are each characterized by two reversible one-electron redox processes corresponding to successive oxidation of the metal centers, in addition to multiple reversible ligand-based reductions in the cathodic region. The effect of terminal ligand variation on the redox couples is consistent with the trends observed for the mononuclear complexes $[Ru(pp)_3]^{2+}$ (pp = bpy, $Me_2$bpy);[54] the stronger σ-donor ability of $Me_2$bpy relative to bpy results in a less anodic potential for the first oxidation in the diastereoisomers of $[\{Ru(Me_2bpy)_2\}_2(\mu\text{-bpt}^-)]^{3+}$.

The separation between the two metal-centered oxidations is larger for the diastereoisomers incorporating the $Me_2$bpy terminal ligands relative to those incorporating bpy ligands, and small differences are observed between the diastereoisomeric forms of the same complex. As an increase in delocalization leads to a decrease in the magnitude of $\Delta E_{ox}$ for electron-rich bridging ligands such as $bpt^-$,[2] the results suggest that delocalization is enhanced for the bpy-based diastereoisomers. It should be noted, however, that these differences cannot be solely ascribed to variations in the extent of electronic delocalization, as the magnitude of $\Delta E_{ox}$ also reflects contributions from ion-pairing interactions,[53] solvation energies and statistical factors.[4,55]

### Electronic Spectroscopy and Spectroelectrochemistry

The UV/Vis/NIR spectroscopic data for the un-oxidized (+3), mixed-valence (+4) and fully-oxidized (+5) forms of (ΔΛ/ΛΔ)- and (ΔΔ/ΛΛ)-$[\{Ru(pp)_2\}_2(\mu\text{-bpt}^-)]^{n+}$ for the range 3050-30000 $cm^{-1}$ are characterized by a combination of overlapping $d\pi(Ru^{II}) \rightarrow \pi^*$(pp, $bpt^-$) singlet metal-to-ligand ($^1$MLCT) transitions. The lowest energy-absorption band is assigned as a $d\pi(Ru^{II}) \rightarrow \pi^*$(pp) transition.

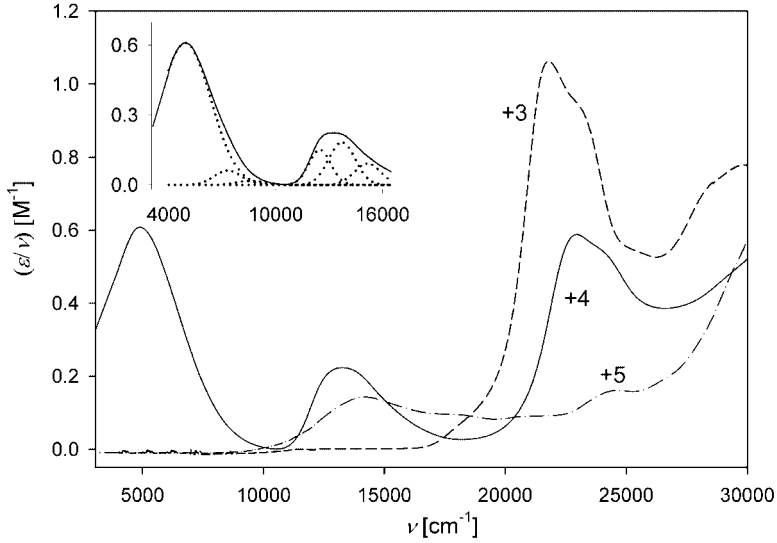


Figure 5. UV/Vis/NIR spectra of the reduced absorption spectra, ($\varepsilon/\nu$) vs. $\nu$, of (ΔΛ/ΛΔ)-$[\{Ru(bpy)_2\}_2(\mu\text{-bpt}^-)]^{n+}$; $n$ = 3 (------), 4 (——), 5 (–·–·–·) in 0.1 M $[(n\text{-}C_4H_9)_4N]PF_6/CH_3CN$ at –35 °C. The inset shows the bands obtained by Gaussian deconvolution of the NIR spectra (·····).

 © 2006 Wiley-VCH Verlag GmbH & Co. KGaA, Weinheim 

Table 2. UV/Vis/NIR spectroscopic data of the reduced absorption spectra ($\varepsilon/\nu$ vs. $\nu$) for the mono- and dinuclear complexes in 0.1 M [($n$-$C_4H_9)_4N]PF_6/CH_3CN$ at –35 °C.[a] The NIR spectroscopic data are indicated in bold type.[a]

| Complex | $n$ | $\nu_{max}$ [$cm^{-1}$] {$(\varepsilon/\nu)_{max}$ [$M^{-1}$]}[a] | |
|---|---|---|---|
| | | bpy | Me2bpy |
| $(\Delta\Lambda/\Lambda\Delta)$-[{Ru(pp)$_2$}$_2$(μ-bpt$^-$)]$^{n+}$ | 3 | 21810 (1.063) | 21720 (1.015) |
| | | sh 23090 (0.9332) | sh 22880 (0.9136) |
| | 4 | **4930 (0.6094)** | **4730 (0.5517)** |
| | | 13210 (0.2340) | 13720 (0.1890) |
| | | 22930 (0.6034) | 22820 (0.6364) |
| | | sh 24000 (0.5620) | sh 23750 (0.6048) |
| | 5 | 14190 (0.1428) | 14710 (0.1218) |
| | | 24650 (0.1634) | 22610 (0.2124) |
| $(\Delta\Delta/\Lambda\Lambda)$-[{Ru(pp)$_2$}$_2$(μ-bpt$^-$)]$^{n+}$ | 3 | 21880 (1.044) | 21780 (1.031) |
| | | sh 23930 (0.9332) | sh 22980 (0.9220) |
| | | 29200 (0.7611) | 29410 (0.7204) |
| | 4 | **5030 (0.5043)** | **4920 (0.5542)** |
| | | 13450 (0.2170) | 13790 (0.1848) |
| | | 22920 (0.5750) | 22780 (0.6232) |
| | 5 | 14340 (0.1563) | 14890 (0.1302) |
| | | 22710 (0.2218) | 22710 (0.2320) |
| [Ru(bpy)$_2$(bpt$^-$)]$^{n+}$ | 1 | 21830 (0.5022) | |
| | | 23240 (0.4758) | |
| | | sh 25720 (0.3517) | |
| | 2 | 12930 (0.1449) | |
| | | 21490 (0.1408) | |

[a] $\nu_{max}$ ±10/$cm^{-1}$ and $(\varepsilon/\nu)_{max}$ ±0.001/$M^{-1}$; sh = shoulder band.

The UV/Vis/NIR spectra for $(\Delta\Lambda/\Lambda\Delta)$-[{Ru(pp)$_2$}$_2$(μ-bpt$^-$)]$^{n+}$ ($n$ = 3, 4, 5) at –35 °C are shown in Figure 5, and the full details of the spectroscopic data for the series of complexes are reported in Table 2. Spectroelectrochemical generation of the +4 and +5 forms of the diastereoisomers revealed stable isosbestic points in the spectral progressions accompanying both oxidation processes. The $^1$MLCT absorption bands decreased in intensity on one-electron oxidation and collapsed on further oxidation to the +5 species. The formation of the mixed-valence complex was also characterized by the appearance of two new bands in the regions 5000–5500 $cm^{-1}$ and 13000–14500 $cm^{-1}$. The former was assigned as an IVCT band and disappeared on further oxidation to the +5 state. The band at 13000–14500 $cm^{-1}$ experienced a slight blue-shift on oxidation to the +5 state, and was assigned as a $\pi(bpy) \rightarrow d\pi(Ru^{III})$ ligand-to-metal charge-transfer (LMCT) transition, consistent with the LMCT transition at 12930 $cm^{-1}$ in [Ru(bpy)$_2$(bpt$^-$)]$^{2+}$ (see Table 2 and Figure S2 in the Supporting Information). As shown in the inset in Figure 5, the LMCT transition is composed of three underlying Gaussian-shaped transitions, which may arise due to the non-equivalence of the Ru centers bound to the $N^1$ and $N^3$ coordination sites in bpt$^-$ (Figure 1).

### Intervalence Charge Transfer

An overlay of the NIR spectra of the diastereoisomers of the mixed-valence systems [{Ru(pp)$_2$}$_2$(μ-bpt$^-$)]$^{4+}$ is shown in Figure 6, and the results of the IVCT band maxima $\nu_{max}$, molar absorption coefficients $(\varepsilon/\nu)_{max}$ and bandwidths $\Delta\nu_{1/2}$ derived from the deconvolution procedure are summarized in Table 3.

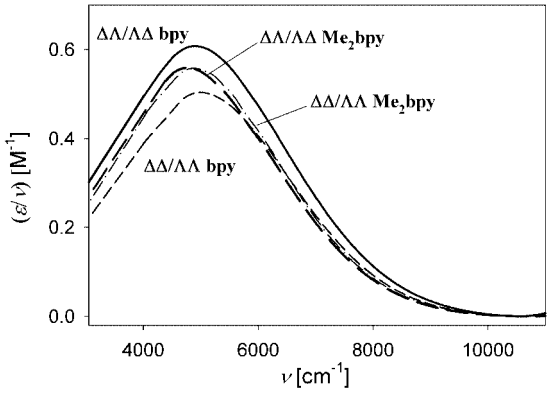


Figure 6. Overlay of the IVCT bands for the diastereoisomers of [{Ru(bpy)$_2$}$_2$(μ-bpt$^-$)]$^{4+}$ ($\Delta\Lambda/\Lambda\Delta$ and $\Delta\Delta/\Lambda\Lambda$) and [{Ru(Me$_2$bpy)$_2$}$_2$-(μ-bpt$^-$)]$^{4+}$ ($\Delta\Lambda/\Lambda\Delta$ and $\Delta\Delta/\Lambda\Lambda$) in 0.1 M [($n$-$C_4H_9)_4N]PF_6/CH_3CN$ at –35 °C.

Whereas the IVCT properties for [{Ru(bpy)$_2$}$_2$(μ-bpt$^-$)]$^{4+}$ (as a diastereoisomeric mixture) have been discussed previously,[11,12,38,56] the influence of the inherent stereochemical identity of the systems on their intramolecular electron-transfer properties had not been addressed. In the present investigation, the diastereoisomers of [{Ru(pp)$_2$}$_2$(μ-BL)]$^{4+}$ (pp = bpy, Me$_2$bpy) are seen to exhibit Gaussian-shaped IVCT bands. Because the lower energy side of the bands was obscured by the detector limit, the electronic coupling parameters ($H_{ab}$) were determined from Equation (2).[57,58] For simplicity (and due to a lack of detailed information) the issue of multiple overlapping intervalence bands was ignored in estimating $H_{ab}$. The zeroth-order moments ($M_0$) of the IVCT bands [see Equation (i) below and Exp. Sect.] were obtained by doubling the band area on the high-en-

 © 2006 Wiley-VCH Verlag GmbH & Co. KGaA, Weinheim 

Table 3. Characteristics of the IVCT bands for the dinuclear mixed-valence complexes in 0.1 M $[(n\text{-}C_4H_9)_4N]PF_6/CH_3CN$ at –35 °C. Parameters for overall envelope are shown in bold type: details of deconvoluted bands are in normal type.[a]

| Complex | $\nu_{max}$ [$cm^{-1}$] | $(\varepsilon/\nu)_{max}$ [$M^{-1}$] | $\Delta\nu_{1/2}$ [$cm^{-1}$] | $\Delta\nu_{1/2}°$ [$cm^{-1}$] | $M_0$ [$M^{-1}$] | $\lvert\mu_{12}\rvert$ [e·Å] | $H_{ab}$ [$cm^{-1}$] |
|---|---|---|---|---|---|---|---|
| (ΔΛ/ΛΔ)-[{Ru(bpy)$_2$}$_2$(μ-bpt$^-$)]$^{4+}$ | **4930** | **0.6094** | **3780** | 2754 | 2473 | 1.024 | 817 |
| | 4930 | 0.6094 | 3770 | | 2350 | | |
| | 7315 | 0.0623 | 1808 | | 120 | | |
| | 8617 | 0.0177 | 1920 | | 36.2 | | |
| | 12486 | 0.1508 | 1450 | | 233 | | |
| | 13728 | 0.1835 | 1760 | | 344 | | |
| | 15164 | 0.0912 | 1770 | | 165 | | |
| | 16528 | 0.0376 | 1500 | | 29.1 | | |
| (ΔΔ/ΛΛ)-[{Ru(bpy)$_2$}$_2$(μ-bpt$^-$)]$^{4+}$ | **5030** | **0.5043** | **3660** | 2786 | 1985 | 0.9178 | 746 |
| | 5030 | 0.0504 | 3450 | | 1870 | | |
| | 7630 | 0.0437 | 2266 | | 105 | | |
| | 12658 | 0.1523 | 1617 | | 262 | | |
| | 14010 | 0.1584 | 1710 | | 288 | | |
| | 15434 | 0.0808 | 1566 | | 127 | | |
| | 16490 | 0.0354 | 1104 | | 21.2 | | |
| (ΔΛ/ΛΔ)-[{Ru(Me$_2$bpy)$_2$}$_2$(μ-bpt$^-$)]$^{4+}$ | **4730** | **0.5517** | **3776** | 2686 | 2275 | 0.9826 | 750 |
| | 4730 | 0.5517 | 3640 | | 2010 | | |
| | 6517 | 0.0672 | 1772 | | 127 | | |
| | 7550 | 0.0601 | 2345 | | 149.9 | | |
| | 12945 | 0.1381 | 1582 | | 232 | | |
| | 14269 | 0.1477 | 1678 | | 264 | | |
| | 15590 | 0.0649 | 1468 | | 101 | | |
| | 16688 | 0.0271 | 1492 | | 43.0 | | |
| (ΔΔ/ΛΛ)-[{Ru(Me$_2$bpy)$_2$}$_2$(μ-bpt$^-$)]$^{4+}$ | **4920** | **0.5542** | **3553** | 2750 | 2140 | 0.9530 | 758 |
| | 4920 | 0.5542 | 3320 | | 1970 | | |
| | 6883 | 0.0276 | 1320 | | 38.8 | | |
| | 7935 | 0.0378 | 2080 | | 83.6 | | |
| | 12957 | 0.1399 | 1633 | | 243 | | |
| | 14260 | 0.1393 | 1670 | | 248 | | |
| | 15690 | 0.0834 | 1802 | | 160 | | |
| | 17070 | 0.0270 | 1405 | | 40.3 | | |

[a] The errors in the observed parameters are ±10 $cm^{-1}$ for $\nu_{max}$, $M^1$ and $\Delta\nu_{1/2}$, ±0.001 $M^{-1}$ for $(\varepsilon/\nu)_{max}$, ±5 $M^{-1}$ for $M_0$ and ±0.001 e·Å for $|\mu_{12}|$.

ergy half of the bands, and the transition moments, $|\mu_{12}|$, were subsequently determined from Equation (ii) (see Exp. Sect.). For all complexes, $r_{ab}$ was initially equated with the through-space geometrical distance between the metal centers,[59] which was estimated as 6.185(10) Å from the X-ray crystal structure of (ΔΛ/ΛΔ)-[{Ru(Me$_2$bpy)$_2$}$_2$(μ-bpt$^-$)]$^{3+}$.

$$H_{ab} = \frac{|\mu_{12}|}{e r_{ab}} \nu_{max} \quad (2)$$

The IVCT manifolds were fitted by a Gaussian-shaped band, which reproduced the maximum energy and intensity, as shown by the deconvolution for (ΔΛ/ΛΔ)-[{Ru(bpy)$_2$}$_2$-(μ-bpt$^-$)]$^{4+}$ in the inset in Figure 5. Additional minor Gaussian-shaped bands were required to reproduce the bandwidth on the high-energy side. From a classical two-state analysis[60] of the IVCT transitions, the predicted bandwidth is given by Equation (3), where $16RT\ln 2$ = 1836 $cm^{-1}$ at 238 K. $\Delta E_0$ represents the energy difference induced by the unsymmetrical coordination environment, and has been estimated as 800 $cm^{-1}$ from electrochemical measurements on the two isomers of [Ru(bpy)$_2$(pyridyltriazole)]$^{2+}$.[12,13]

$$\Delta\nu_{1/2}° = [16\,RT\ln 2(\lambda - \Delta E_0)]^{1/2} \quad (3)$$

On the basis of the broad bandwidths compared with the theoretical bandwidths in Table 3, the complexes may be classified as localized Class II systems within the Robin and Day classification scheme.[61]

As electronic coupling decreases the *effective* electron-transfer distance relative to the geometrical metal–metal separation, the $H_{ab}$ values presented in Table 3 represent lower limits for the electronic coupling parameter. The *effective* electron transfer distance was determined from Stark effect spectroscopy on the IVCT transitions.[19]

## The *Effective* Electron-Transfer Distance: Stark Absorption Spectroscopy

Stark absorption spectra were obtained for the diastereoisomers of [{Ru(bpy)$_2$}$_2$(μ-bpt$^-$)]$^{4+}$ in *n*-butyronitrile glass at 77 K and a field strength $F_{ext}$ of 4.0 MV·$cm^{-1}$. The quantitative Liptay analysis[62] of the Stark response[63–65] yielded the dipole moment change ($|\Delta\mu_{12}|$), the angle between the transition moment and the dipole moment change ($\xi$), the difference polarisability ($\Delta\alpha$), and the magnitude of the trace of the difference polarisability Tr($\Delta\alpha$). The results for the absorption $A(\nu)$ vs. $\nu$ and Stark absorption $\Delta A(\nu)$ vs. $\nu$ spectra for the diastereoisomers are pre-

 © 2006 Wiley-VCH Verlag GmbH & Co. KGaA, Weinheim 

sented in Table 4. The spectra for (ΔΛ/ΛΔ)-[{Ru(bpy)$_2$}$_2$(μ-bpt$^-$)]$^{4+}$ are shown in Figure 7, where panel (a) shows the unperturbed absorption spectrum, and panels (b) and (c) show the first- and second-derivatives of the absorption spectrum, respectively. The Stark spectrum and the best fit to the spectrum are shown in panel (d). The corresponding spectra for (ΔΔ/ΛΛ)-[{Ru(bpy)$_2$}$_2$(μ-bpt$^-$)]$^{4+}$ are shown in Figure S3 (Supporting Information).

The most notable features of the Stark signals in the range 3050–15000 cm$^{-1}$ are the presence of strong second-derivative components for the IVCT transition [Figure 7 (i)] and the two lowest-energy components of the LMCT manifold [Figure 7 (ii)]. As shown in Table 4, the energies of the absorption bands at 77 K are blue-shifted relative to those reported in Table 2 at 238 K (–35 °C). Whereas the IVCT band retains a Gaussian-shaped appearance at both temperatures, the bandwidth is relatively narrower in *n*-butyronitrile glass. On the basis of the classical analysis,[59] the IVCT band characteristics at 77 K are consistent with the localized (Class II) classification for the mixed-valence species, consistent with the findings from the UV/Vis/NIR spectroelectrochemical studies at 238 K.

The results for the parameters obtained from the Liptay analysis of the IVCT and LMCT bands [Equations (iii) and (iv), Exp. Sect.] are reported in Table 4. The IVCT bands in the ΔΛ/ΛΔ and ΔΔ/ΛΛ diastereoisomers exhibit dipole moment changes of 5.92 ± 0.03 e·Å and 5.44 ± 0.04 e·Å, respectively. From Equations (4) and (5), diabatic distances ($r_{ab}$) of 6.26 ± 0.03 Å and 5.74 ± 0.04 Å were obtained for the ΔΛ/ΛΔ and ΔΔ/ΛΛ forms, respectively, using the $|\mu_{12}|$ values reported in Table 3.[58]

$$r_{ab} = [(r_{12})^2 + (|\mu_{12}|)^2]^{1/2} \quad (4)$$

$$\text{where } r_{12} = |\Delta\mu_{12}|/e \quad (5)$$

Notably, the adiabatic charge-transfer distances for both diastereoisomers and the diabatic charge-transfer distance for the ΔΔ/ΛΛ form are shorter than the geometrical metal–metal separation ($r_{geo}$), which is estimated as 6.185(10) Å from the crystal structure of the (ΔΛ/ΛΔ)-[{Ru(Me$_2$bpy)$_2$}$_2$(μ-bpt$^-$)]$^{3+}$ cation. The diabatic distance for (ΔΛ/ΛΔ)-[{Ru(bpy)$_2$}$_2$(μ-bpt$^-$)]$^{3+}$ is approximately identical to the geometrical separation. From Equation (6), $\Delta q$ represents the actual amount of charge transferred in the IVCT process, and is necessarily less than *e* (unit electronic charge). The quantity $(1 - \Delta q)/2$ can be identified with the amount of charge, which has been transferred prior to intervalence excitation. The adiabatic description reveals partial delocalization as a reduction in $r_{12}$ (the *effective* charge-transfer distance) relative to $r_{ab}$ (the true distance), whereas the diabatic description reveals delocalization as a reduction in the amount of charge ($\Delta q$) actually transferred. In the present case, $\Delta q$ is estimated as ca. 95% for both diastereoisomeric forms.

$$er_{12} = (\Delta q)r_{ab} \quad (6)$$

Accordingly, the $H_{ab}$ parameters for the ΔΛ/ΛΔ and ΔΔ/ΛΛ forms are re-evaluated as 773 and 707 cm$^{-1}$, respectively, from Equation (2) using the $r_{ab}$ values derived from the Stark analysis. These values are in close agreement to the estimates of 817 and 746 cm$^{-1}$ (respectively) obtained from the application of Hush theory to the IVCT absorption bands, when the geometric metal–metal separation was employed rather than $r_{ab}$.[60] The results confirm the localized assignment for the systems.

Interestingly, the two dominant underlying transitions of the LMCT manifold in the region 12000–15000 cm$^{-1}$ are well resolved at 77 K. As shown in Table 4, the LMCT transitions are characterized by dipole moment changes, which are significantly smaller than those for the IVCT transitions. It should be noted that the parameters obtained from spectral deconvolution of the LMCT manifold were somewhat arbitrary as the bands were assumed to be Gaussian-shaped. Accordingly, the apparent large differences in the Liptay parameters obtained for the first and second LMCT components should be interpreted cautiously.

As the uncertainties in the Stark-derived parameters reported in Table 4 reflect the errors obtained from the fitting procedure, the absolute error is likely to be considerably higher. The actual magnitudes will incorporate the uncertainties in the deconvolution and concentration, as well as the assumption of a value of 1.3 for the local field correction factor (*f*). The actual value of the latter depends on effects arising from the solvent, chromophore and counterion concentrations, which may also differ between the diastereoisomers. The shortcomings of the experimental and theoretical analysis of electroabsorption data have been discussed in detail previously by Boxer and co-workers.[66–69]

Table 4. Absorption and electroabsorption properties of the IVCT bands for the diastereoisomers of [{Ru(bpy)$_2$}$_2$(μ-bpt$^-$)]$^{4+}$ in *n*-butyronitrile glass at 77 K and a field strength of 4.0 MVcm$^{-1}$.[a]

| Diastereoisomer | $\nu_{max}$ [cm$^{-1}$] | $\Delta\nu_{1/2}$ [cm$^{-1}$] | $\|\Delta\mu_{12}\|$ [e·Å] | $\|\Delta\mu_{12}\|$ [D] | $\Xi$ [b] [°] | Tr($\Delta\alpha$) [Å$^3$] | $\Delta\alpha$ [Å$^3$] |
|---|---|---|---|---|---|---|---|
| (ΔΛ/ΛΔ) | 5660 | 2980 | 5.92(3) | 28.2(2) | 0 | 8103(100) | 6787(70) |
| | 12546 | 1180 | 1.30(2) | 6.19(2) | 0 | –139(20) | –516(50) |
| | 13742 | 1354 | 2.44(1) | 11.6(1) | 0 | 632(30) | 1135(50) |
| (ΔΔ/ΛΛ) | 5530 | 2815 | 5.44(4) | 25.9(2) | 0 | 3755(50) | 3579(30) |
| | 12470 | 1210 | 1.20(2) | 5.72(3) | 0 | 740(10) | 761(150) |
| | 13760 | 1640 | 2.38(3) | 11.3(2) | 0 | 606(50) | 1755(200) |

[a] The errors in the observed and calculated parameters (not tabulated) are ±10 cm$^{-1}$ for $\nu_{max}$ and $\Delta\nu_{1/2}$, ±2° for $\xi$, and ±10 Å$^3$ for Tr($\Delta\alpha$) and $\Delta\alpha$. [b] The zero values for $\xi$ indicate that the direction of charge displacement in the excited state is aligned with the transition moment.

 © 2006 Wiley-VCH Verlag GmbH & Co. KGaA, Weinheim 

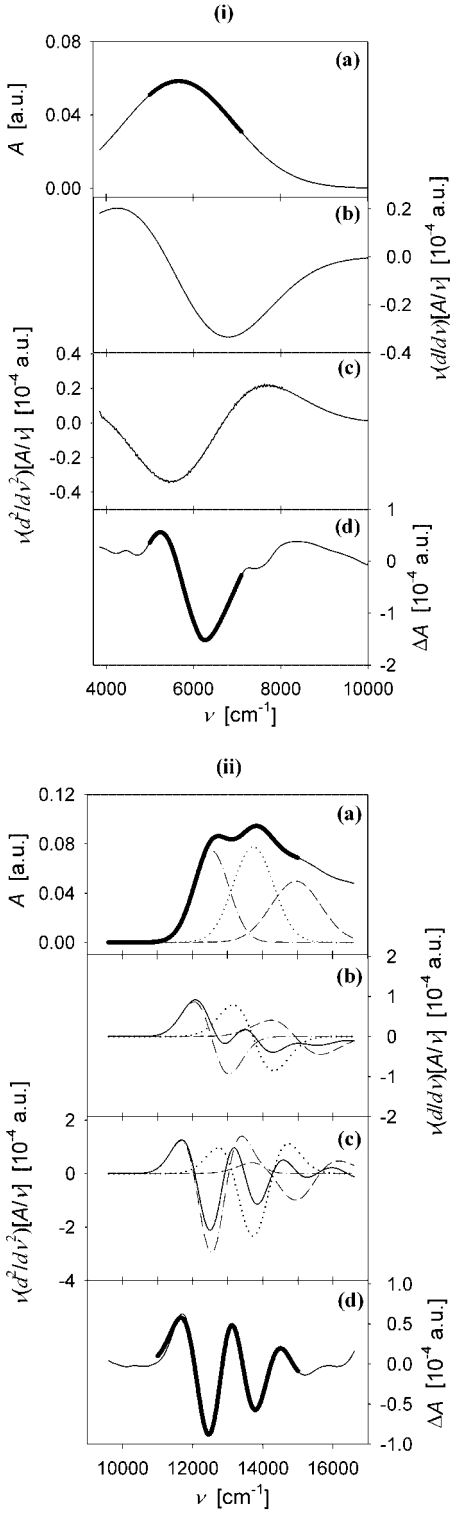


Figure 7. Liptay analysis of the Stark absorption spectra ($A$ vs. $\nu$) of the **(i)** IVCT and **(ii)** LMCT transitions for (ΔΛ/ΛΔ)-[{Ru(bpy)$_2$}$_2$(μ-bpt$^-$)]$^{4+}$ in *n*-butyronitrile glass at 77 K, with a field strength of 4.0 MV·cm$^{-1}$. (a) Unperturbed absorption spectrum with the bands obtained by Gaussian deconvolution and energy weighted first (b) and second (c) derivatives of the absorption spectrum. (d) Measured (– – –) and fitted (——) Stark signals ($\Delta A$ vs. $\nu$) at 45°. The deconvoluted components are (–•–•–), (------) and (·····).

### The Mechanism of Electronic Coupling

The intra-metal coupling in complexes incorporating anionic bridging ligands such as bpt$^-$ is facilitated by a hole-transfer superexchange mechanism, utilising the high-lying π(bpt$^-$) HOMOs of the ligand.[11,12,38,56] The situation is depicted schematically in Figure 8, where the ground state of the mixed-valence system is depicted in part (a), and the hole-transfer virtual state in (b).

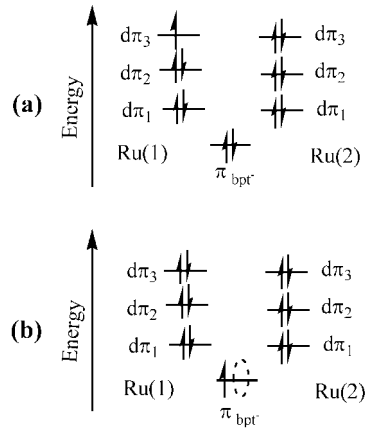


Figure 8. Schematic energy level diagram for the hole-transfer superexchange mechanism. Ground state (a) and (b) hole-transfer virtual state of the mixed-valence system [{Ru(bpy)$_2$}$_2$(μ-bpt$^-$)]$^{3+}$ showing the composition of the three Ru(dπ) orbitals and the bpt$^-$ HOMO. The dotted oval represents the position of the hole on the bridging ligand.

While the σ-donor ability of N$^1$ site is greater than that of the N$^3$ site, the Ru center coordinated to N$^1$, denoted by Ru(1), is relatively more stabilized and undergoes oxidation prior to the Ru center coordinated to the N$^3$ site, denoted by Ru(2). As a consequence, the IVCT transition corresponds to the vectorial charge-transfer transition Ru(2) → Ru(1).

The similarity in the parameters of the IVCT transitions for the complexes incorporating the bpy and Me$_2$bpy terminal ligands demonstrates that terminal ligand variation has a minor influence on the extent of metal–metal interaction.

### Stereochemical Consequences on Electron Transfer

In addition to differences between the complexes incorporating the bpy and Me$_2$bpy terminal ligands, measurable differences are observed in the IVCT parameters between the diastereoisomeric forms of the same complex. Whereas the origins of the stereochemical dependence of the IVCT properties is uncertain, previous studies have revealed the presence of differential solvent and anion interactions with the diastereoisomers,[16,18] in addition to differential stereochemically-induced structural distortions in the bridging ligands.[16,17] In the present case, the crystal structure of the cation in (ΔΛ/ΛΔ)-[{Ru(Me$_2$bpy)$_2$}$_2$(μ-bpt$^-$)]$^{3+}$ reveals a slight curvature of the bridging ligand due to steric crowd-

 © 2006 Wiley-VCH Verlag GmbH & Co. KGaA, Weinheim 

ing between the methyl groups on the terminal ligands. However, this minor distortion is expected to be similar for the corresponding ΔΔ/ΛΛ form, and should be negligible for both diastereoisomers of the complex incorporating the terminal bpy ligands, as described above. The stereochemical dependence of the IVCT parameters is therefore likely to arise from differential solvent and anion interactions with the two forms. Indeed, a recent report has demonstrated that differential anion interactions with the diastereoisomers of $[\{Ru(bpy)_2\}_2(\mu\text{-}bpt^-)]^{4+}$ lead to differences in the electrochemical potentials of the metal-based redox processes in the presence of the strongly ion-pairing electrolyte $[(n\text{-}C_4H_9)_4]PF_6$ (employed in the present study) and the weakly ion-pairing electrolyte $[(n\text{-}C_4H_9)_4]\{B(C_6F_5)_4\}$.[53,70]

## Conclusions

The synthesis and chromatographic separation of the diastereoisomeric forms of the complexes $[\{Ru(pp)_2\}_2(\mu\text{-}bpt^-)]^{3+}$ (pp = bpy, $Me_2$bpy) has permitted an investigation of the dependence of the IVCT properties of their mixed-valence forms on the stereochemical relationship of the metal centers. The *effective* metal–metal charge-transfer distances in the complexes incorporating the bpy terminal ligands were determined as 5.92 ± 0.03 Å for the ΔΛ/ΛΔ form, and 5.44 ± 0.04 Å for the ΔΔ/ΛΛ form, from Stark effect spectroscopy. These distances correspond to approximately 95 and 88%, respectively, of the geometrical metal–metal distance of 6.185(10) Å, obtained from the X-ray crystal structure of the cation in (ΔΛ/ΛΔ)-$[\{Ru(Me_2bpy)_2\}_2(\mu\text{-}bpt^-)](PF_6)_3$. A classical analysis of the results from the IVCT absorption and electroabsorption spectra are consistent with a localized Class II classification for the mixed-valence systems.

## Experimental Section

**Materials:** Potassium hexafluorophosphate ($KPF_6$; Aldrich, 98%), ammonium hexafluorophosphate ($NH_4PF_6$; Aldrich, 99.99%), nitrosonium hexafluorophosphate ($NOPF_6$ stored under Ar; Alfa Aesar, 96%), ethylene glycol (Ajax, 95%), sodium toluene-4-sulfonate (Aldrich, 98%), DOWEX® 1×8, 50–100 mesh (Aldrich) anion-exchange resin and laboratory reagent solvents were used as received. Tetra-*n*-butylammonium hexafluorophosphate ($[(n\text{-}C_4H_9)_4N]PF_6$; Fluka, 99+%) was dried in vacuo at 60 °C prior to use and ferrocene (Fc; BDH) was purified by sublimation prior to use. SP Sephadex C-25 (Amersham Pharmacia Biotech), and silica gel (200–400 mesh, 60 Å, Aldrich) were employed for the chromatographic separation and purification of ruthenium complexes. Acetonitrile ($CH_3CN$; Aldrich, 99.9+%) was distilled from over $CaH_2$ prior to use and *n*-butyronitrile (Aldrich, 99+%) was used as received.

**General:** 1D and 2D $^1H$ NMR spectra were collected with a Varian Mercury 300 MHz spectrometer. $^1H$ NMR chemical shifts for all complexes are reported relative to 99.9% [$D_3$]acetonitrile [$CD_3CN$, Cambridge Isotope Laboratories (CIL)] at $\delta$ = 1.93 ppm. $^1H$ NMR assignments were performed with the assistance of COSY experiments to identify each pyridine ring system.

**Electrochemistry:** Electrochemical measurements were performed under argon using a Bioanalytical Systems (BAS) 100A Electrochemical Analyser. Cyclic (CV) and differential pulse (DPV) voltammograms were recorded in a standard three-electrode cell using a glassy carbon or platinum button working electrode, a platinum wire auxiliary electrode and an Ag/AgCl reference electrode (0.1 M $[(n\text{-}C_4H_9)_4N]PF_6$ in $CH_3CN$). Ferrocene was added as an internal standard on completion of each experiment; the ferrocene/ferrocenium couple ($Fc^+/Fc^0$) occurred at +550 mV vs. Ag/AgCl. Solutions contained 0.1 M $[(n\text{-}C_4H_9)_4N]PF_6$ as electrolyte. Cyclic voltammetry was performed with a sweep rate of 100 $mVs^{-1}$; differential pulse voltammetry was conducted with a sweep rate of 4 $mVs^{-1}$ and a pulse amplitude, width and period of 50 mV, 60 ms and 1 s, respectively. All potentials are reported ±3 mV.

**UV/Vis/NIR Spectroelectrochemistry:** UV/Vis/NIR spectroelectrochemistry was performed using a CARY 5E spectrophotometer interfaced to Varian WinUV software. The absorption spectra of the electrogenerated mixed-valence species were obtained in situ by the use of a cryostatted Optically Semi-Transparent Thin-Layer Electrosynthetic (OSTLE) cell.[71] An account of the procedure employed in the spectroelectrochemical measurements has been detailed previously.[72] Solutions for the spectroelectrochemial experiments contained 0.1 M $[(n\text{-}C_4H_9)_4N]PF_6$ supporting electrolyte in $CH_3CN$ and the complex (ca. $1\cdot10^{-3}$ M).

The analysis and spectral deconvolution of the data were performed as described in a previous report.[17] The IVCT spectra were scaled as $\int\varepsilon(\nu)/\nu\cdot d\nu$[14,73] and deconvolution of the NIR transitions was performed using the curve-fitting subroutine implemented within the GRAMS32 commercial software package.[72] On the basis of the reproducibility of the parameters obtained from the deconvolutions, the uncertainties in the energies $\nu_{max}$, intensities $(\varepsilon/\nu)_{max}$ and bandwidths $\Delta\nu_{1/2}$ were estimated as ±10 $cm^{-1}$, ±0.001 $M^{-1}$ and ±10 $cm^{-1}$, respectively. The transition moment $|\mu_{12}|$ in e·Å is defined by Equation (ii) where the zeroth-moment, $M_0$, represents the area under the band of the reduced absorption spectrum.

$$M_0 = \int_{\nu_1}^{\nu_2} f(\nu)d\nu \quad \text{(i)}$$

$$|\mu_{12}| = 0.0206\ \text{Å} \times M_0^{1/2} \quad \text{(ii)}$$

**Stark Absorption Spectroscopy:** Detailed accounts of the instrumentation, sample preparation and analysis have been reported previously.[63,64] In a typical experiment, the un-oxidized complex (ca. 5 mg) was dissolved in *n*-butyronitrile (1 mL) and the mixed-valence species was generated by chemical oxidation with $NOPF_6$ (saturated solution in *n*-butyronitrile, 1 mL).

Stark absorption measurements were performed in a dual liquid-nitrogen immersion cryostat (Janis Research Corporation) at 77 K.[74] The electroabsorption cell consisted of two indium-tin oxide (ITO) coated quartz slides (Delta Technologies) separated by 100 μm Kapton spacers (DuPont). Electroabsorption measurements were performed at 77 K and a field strength of 4.0 MV·$cm^{-1}$ using a CARY-14 spectrophotometer featuring OLIS control software. Dry nitrogen gas was blown over the dewar windows to prevent fogging. Electroabsorption measurements over the range 3850–12500 $cm^{-1}$ were recorded with a photovoltaic HgCdTe detector that was thermoelectrically cooled to –40 °C (Judson Technologies), and a DE110 Silicon photodiode for measurements over the range 9090–20000 $cm^{-1}$.

 © 2006 Wiley-VCH Verlag GmbH & Co. KGaA, Weinheim 

The analysis of the data was performed according to the method of Liptay,[47] as described in detail elsewhere.[63–65] Each Stark spectrum, obtained from duplicate experiments at two angles (90° and 45°), was fitted to a linear combination of the zeroth-, first- and second-derivatives of the absorption spectrum (at 77 K) to yield values for the coefficients, $A_\chi$, $B_\chi$ and $C_\chi$ in Equation (iii).

$$\Delta A(\nu) = \left\{ A_\chi A(\nu) + \frac{B_\chi \nu}{15hc}\frac{d[A(\nu)/\nu]}{d\nu} + \frac{C_\chi \nu}{30h^2c^2}\frac{d^2[A(\nu)/\nu]}{d\nu^2} \right\} \mathbf{F}_{\text{int}}{}^2 \quad \text{(iii)}$$

Here, $\chi$ is the experimental angle between $\mathbf{F}_{ext}$ and the polarization of the incident light, $h$ is Planck's constant, and $c$ is the speed of light in a vacuum. $\mathbf{F}_{int}$ represents the internal electric field experienced by the chromophore, and is given by $f \times \mathbf{F}_{ext}$, where $f$ is the local-field correction factor (typically assumed to be 1.3 for organic solvents[19]). The coefficients $A_\chi$, $B_\chi$ and $C_\chi$ provide information on changes in the transition dipole moment, and the excited state/ground-state polarisability and dipole moment differences, respectively, according to Equation (iv).

$$A_\chi = \frac{\langle \alpha_m \rangle}{3} + \tfrac{1}{30}(3\cos^2\chi - 1)[3\langle \beta_m \rangle - 2\langle \alpha_m \rangle]$$

$$B_\chi = \tfrac{5}{2}\mathrm{Tr}(\Delta\alpha) + (3\cos^2\chi - 1)[\tfrac{3}{2}\hat{\mathbf{g}}\cdot\Delta\alpha\cdot\hat{\mathbf{g}} - \tfrac{1}{2}\mathrm{Tr}(\Delta\alpha)]$$

$$C_\chi = |\mu_v|^2\,[5 + (3\cos^2\xi - 1)(3\cos^2\chi - 1)] \quad \text{(iv)}$$

In these Equations, $\langle a_m \rangle$ and $\langle \beta_m \rangle$ are the scalar functions of the transition-moment polarisability and hyperpolarisability tensors, $\mathrm{Tr}(\Delta a)$ is the trace of the polarisability change between the ground and excited electronic states, $\hat{\mathbf{g}}\cdot\Delta\alpha\cdot\hat{\mathbf{g}}$ is the polarisability change along the transition moment ($\hat{\mathbf{g}}$ is the unit vector), $|\mu v|$ is the vector change in dipole moment (its sign is not determined), and $\xi$ is the angle between the transition dipole moment and change in dipole moment vectors.[21] Measurement of Stark spectra at two or more values of $\chi$ (incident angle of polarized light in relation to the electric field) are fitted to a sum of the zeroth-, first- and second-derivatives of the absorption spectrum to yield values for the molecular parameters according to Equation (iv).

While the Liptay treatment interprets first-derivative (*i.e.* $B_\chi$) contributions in Equations (iii) and (iv) in terms of polarisability changes, for the special case of symmetrical mixed-valence systems significant non-Liptay contributions due to field-induced changes in degenerate ground-state populations can be expected. For simplicity, we report $B_\chi$ only in terms of apparent polarisability changes.[75]

### Synthetic Procedures

3,5-Bis(2-pyridyl)-1,2,4-triazole (Hbpt)[11,76] and *cis*-$[Ru(pp)_2Cl_2]\cdot 2H_2O$ (pp = bpy, $Me_2bpy$)[77] were prepared according to the literature methods.

**$[\{Ru(bpy)_2\}_2(\mu\text{-bpt}^-)](PF_6)_3$:** A suspension of Hbpt (21 mg, 0.094 mmol) in ethylene glycol (10 mL) was heated in a modified microwave oven (Model R-2V55; 600 W, 2450 MHz) on medium-high power[41] for 20 s to complete dissolution. *cis*-$[Ru(bpy)_2Cl_2]\cdot 2H_2O$ (100 mg, 0.207 mmol) was added and the mixture heated at reflux for a further 8 min during which time the solution attained a red-orange coloration. The mixture was diluted with water (ca. 50 mL) and the dinuclear product was separated from the crude mixture by a gradient elution procedure on SP Sephadex C-25 support using aqueous 0.1–0.5 M NaCl. A band of mononuclear material eluted first (0.2 M NaCl), followed by the desired orange product (0.4 M NaCl), which was precipitated as the $PF_6^-$ salt by addition of a saturated aqueous solution of $KPF_6$. The solid was isolated by vacuum filtration and washed with diethyl ether (3·10 mL). Yield: 93 mg (66%). The separation of the diastereoisomers was achieved by cation-exchange chromatography on SP Sephadex C-25 support (dimensions 96 cm length, 1.6 cm diameter). The complex (ca. 100 mg) was loaded onto the column in aqueous solution (as the $Cl^-$ form, obtained by stirring an aqueous suspension of the complex with DOWEX® 1×8 anion exchange resin) and eluted with 0.15 M sodium toluene-4-sulfonate solution.[41] The diastereoisomers separated after passing through an effective column length of 1.5 m. The two bands were collected, and the products were precipitated by the addition of a saturated aqueous $KPF_6$ solution. The solids were isolated by vacuum filtration and washed with diethyl ether (3×10 mL).

Rigorous purification methods were employed prior to characterization because of the potentially strong associations between the complex cations and the anions present in the eluents employed for the chromatographic separations.[41,46] Each product was dissolved in a minimum volume of acetone and loaded onto a short column of silica gel (dimensions: 2 cm diameter, 4 cm length), washed with acetone, water and acetone and then eluted with acetone containing 5% $NH_4PF_6$. Addition of water and removal of the acetone under reduced pressure afforded a product of suitable purity for the physical measurements. Band 1 and band 2 exhibited different NMR spectra, with the former identified as the ΔΛ/ΛΔ and the latter as the ΔΔ/ΛΛ diastereoisomers. $^1$H NMR ($CD_3CN$): $\delta$ (**Band 1; ΔΛ/ΛΔ**) = 6.40 (dd, $J$ = 8, 1.5 Hz, 1 H, H3 bpt$^-$), 6.82 (dd, $J$ = 8, 1.5 Hz, 1 H, H3′ bpt$^-$), 6.92 (t, $J$ = 8, 5 Hz, 1 H, H5 bpt$^-$), 7.00 (dd, $J$ = 8, 8 Hz, 1 H, H4 bpt$^-$), 7.04 (dd, $J$ = 8, 8 Hz, 1 H, H4′ bpt$^-$), 7.12 (t, $J$ = 8, 5 Hz, 1 H, H5 bpy), 7.23 (t, $J$ = 8, 5 Hz, 3 H, H5 bpy), 7.27 (t, $J$ = 8, 5 Hz, 1 H, H5 bpy), 7.33 (t, $J$ = 8, 5 Hz, 2 H, H5 bpy), 7.53 (dd, $J$ = 5, 1.5 Hz, 1 H, H6 bpt$^-$), 7.56 (t, $J$ = 8, 5 Hz, 1 H, H5 bpy), 7.63 (dd, $J$ = 5, 1.5 Hz, 1 H, H6 bpy), 7.66 (dd, $J$ = 5, 1.5 Hz, 1 H, H6 bpy), 7.74 (dd, $J$ = 5, 1.5 Hz, 1 H, H6 bpy), 7.76 (dd, $J$ = 5, 1.5 Hz, 1 H, H6 bpy), 7.79 (t, $J$ = 8, 5 Hz, 1 H, H5′ bpt$^-$), 7.81 (dd, $J$ = 5, 1.5 Hz, 1 H, H6 bpy), 7.85 (dd, $J$ = 8, 8 Hz, 2 H, H4 bpy), 7.88 (dd, $J$ = 5, 1.5 Hz, 1 H, H6 bpy), 7.89 (dd, $J$ = 8, 8 Hz, 3 H, H4 bpy), 7.94 (dd, $J$ = 8, 8 Hz, 2 H, H4 bpy), 7.98 (dd, $J$ = 5, 1.5 Hz, 2 H, H6 bpy), 8.01 (dd, $J$ = 8, 8 Hz, 1 H, H4 bpy), 8.33 (dd, $J$ = 8, 1.5 Hz, 1 H, H3 bpy), 8.36 (dd, $J$ = 8, 1.5 Hz, 1 H, H3 bpy), 8.43 (dd, $J$ = 8, 1.5 Hz, 1 H, H3 bpy), 8.44 (dd, $J$ = 5, 1.5 Hz, 1 H, H6′ bpt$^-$), 8.45 (dd, $J$ = 8, 1.5 Hz, 1 H, H3 bpy), 8.48 (dd, $J$ = 8, 1.5 Hz, 2 H, H3 bpy), 8.52 (dd, $J$ = 8, 1.5 Hz, 2 H, H3 bpy); $\delta$ (**Band 2; ΔΔ/ΛΛ**) = 6.54 (dd, $J$ = 8, 1.5 Hz, 1 H, H3 bpt$^-$), 6.98 (dd, $J$ = 8, 1.5 Hz, 1 H, H3′ bpt$^-$), 6.86 (t, $J$ = 8, 5 Hz, 1 H, H5 bpt$^-$), 7.06 (dd, $J$ = 8, 8 Hz, 1 H, H4 bpt$^-$), 7.42 (dd, $J$ = 8, 8 Hz, 1 H, H4′ bpt$^-$), 7.44 (dd, $J$ = 5, 1.5 Hz, 1 H, H6 bpt$^-$), 7.89 (t, $J$ = 8, 5 Hz, 1 H, H5′ bpt$^-$), 8.38 (dd, $J$ = 5, 1.5 Hz, 1 H, H6′ bpt$^-$), 7.31 (dd, $J$ = 5, 1.5 Hz, 1 H, H6 bpy), 7.38 (dd, $J$ = 5, 1.5 Hz, 1 H, H6 bpy), 6.90-7.20 (5 H, H5 bpy), 7.89 (dd, $J$ = 8, 8 Hz, 1 H, H4 bpy), 7.92 (dd, $J$ = 8, 8 Hz, 1 H, H4 bpy), 7.70-8.00 (5 H, H4 bpy), 7.70-8.00 (5 H, H6 bpy), 7.98 (dd, $J$ = 5, 1.5 Hz, 1 H, H6 bpy), 8.13 (dd, $J$ = 5, 1.5 Hz, 1 H, H6 bpy), 8.54 (dd, $J$ = 8, 1.5 Hz, 1 H, H3 bpy), 8.60 (dd, $J$ = 8, 1.5 Hz, 1 H, H3 bpy), 8.30-8.60 ($J$ = 8, 1.5 Hz, 5 H, H3 bpy) ppm.

**$[\{Ru(Me_2bpy)_2\}_2(\mu\text{-bpt}^-)](PF_6)_3$:** This compound was prepared from Hbpt (19 mg, 0.084 mmol) and $[Ru(Me_2bpy)_2Cl_2]\cdot 2H_2O$ (100 mg, 0.18 mmol) by a procedure analogous to that detailed above for $[\{Ru(bpy)_2\}_2(\mu\text{-bpt}^-)](PF_6)_3$. Yield: 107 mg (67%). The separation of the diastereoisomers was achieved by cation-exchange chromatography on SP Sephadex C-25 support using 0.15 M so-

 © 2006 Wiley-VCH Verlag GmbH & Co. KGaA, Weinheim 

dium toluene-4-sulfonate solution as the eluent. Band 1 and band 2 exhibited different NMR spectra, with the former identified as the ΔΛ/ΛΔ and the latter as the ΔΔ/ΛΛ diastereoisomers. $^1$H NMR ($CD_3CN$): $\delta$ (**Band 1; ΔΛ/ΛΔ**) = 2.45 (s, 6 H, $CH_3$), 2.48 (s, 6 H, $CH_3$), 2.51 (s, 6 H, $CH_3$), 2.57 (s, 6 H, $CH_3$), 6.38 (dd, $J$ = 8, 1.5 Hz, 1 H, H3 bpt$^-$), 6.81 (dd, $J$ = 8, 1.5 Hz, 1 H, H3′ bpt$^-$), 6.90 (t, $J$ = 8, 5 Hz, 1 H, H5 bpt$^-$), 7.02 (dd, $J$ = 8, 8 Hz, 1 H, H4 bpt$^-$), 7.06 (dd, $J$ = 8, 8 Hz, 1 H, H4′ bpt$^-$), 7.05 (d, $J$ = 6 Hz, 1 H, H5 $Me_2$bpy), 7.23 (d, $J$ = 6 Hz, 3 H, H5 $Me_2$bpy), 7.23 (d, $J$ = 6 Hz, 1 H, H5 $Me_2$bpy), 7.29 (d, $J$ = 6 Hz, 2 H, H5 $Me_2$bpy), 7.51 (dd, $J$ = 5, 1.5 Hz, 1 H, H6 bpt$^-$), 7.52 (d, $J$ = 6 Hz, 1 H, H5 $Me_2$bpy), 7.59 (d, $J$ = 6 Hz, 1 H, H6 $Me_2$bpy), 7.63 (d, $J$ = 6 Hz, 1 H, H6 $Me_2$bpy), 7.70 (d, $J$ = 6 Hz, 1 H, H6 $Me_2$bpy), 7.71 (d, $J$ = 6 Hz, 1 H, H6 $Me_2$bpy), 7.76 (t, $J$ = 8, 5 Hz, 1 H, H5′ bpt$^-$), 7.77 (d, $J$ = 6 Hz, 1 H, H6 $Me_2$bpy), 7.83 (d, $J$ = 6 Hz, 1 H, H6 $Me_2$bpy), 7.95 (d, $J$ = 6 Hz, 2 H, H6 $Me_2$bpy), 8.27 (s, 1 H, H3 $Me_2$bpy), 8.33 (s, 1 H, H3 $Me_2$bpy), 8.40 (s, 1 H, H3 $Me_2$bpy), 8.41 (dd, $J$ = 5, 1.5 Hz, 1 H, H6′ bpt$^-$), 8.37 (s, 1 H, H3 $Me_2$bpy), 8.46 (s, 2 H, H3 $Me_2$bpy), 8.49 (s, 2 H, H3 $Me_2$bpy); $\delta$ (**Band 2; ΔΔ/ΛΛ**) = 2.47 (s, 12 H, $CH_3$), 2.50 (s, 6 H, $CH_3$), 2.53 (s, 6 H, $CH_3$), 6.51 (dd, $J$ = 8, 1.5 Hz, 1 H, H3 bpt$^-$), 6.95 (dd, $J$ = 8, 1.5 Hz, 1 H, H3′ bpt$^-$), 6.81 (t, $J$ = 8, 5 Hz, 1 H, H5 bpt$^-$), 7.39 (dd, $J$ = 8, 8 Hz,1 H, H4′ bpt$^-$), 7.42 (dd, $J$ = 5, 1.5 Hz, 1 H, H6 bpt$^-$), 7.85 (t, $J$ = 8, 5 Hz, 1 H, H5′ bpt$^-$), 8.32 (dd, $J$ = 5, 1.5 Hz, 1 H, H6′ bpt$^-$), 7.26 (d, $J$ = 6 Hz, 1 H, H6 $Me_2$bpy), 7.35 (d, $J$ = 6 Hz, 1 H, H6 $Me_2$bpy), 6.80-7.15 (5 H, H5 $Me_2$bpy), 7.63-7.95 (5 H, H6 $Me_2$bpy), 7.94 (d, $J$ = 6 Hz, 1 H, H6 $Me_2$bpy), 8.07 (d, $J$ = 6 Hz, 1 H, H6 $Me_2$bpy), 8.51 (s, 1 H, H3 $Me_2$bpy), 8.57 (s, 1 H, H3 $Me_2$bpy), 8.22-8.55 (5 H, H3 $Me_2$bpy) ppm.

**X-ray Crystallography:** Single crystals of (ΔΛ/ΛΔ)-[{Ru($Me_2$bpy)$_2$}$_2$(μ-bpt$^-$)]($PF_6$)$_3$ were obtained by dissolution of ca. 1 mmol of the complex in acetone/water (1:1, 2 mL). Slow evaporation of the solution at room temperature yielded dark red rod-shaped crystals suitable for X-ray determination. The collection and refinement of X-ray data was performed in the Advanced Analytical Centre at James Cook University. Hemispheres of data were collected (capillary sealed specimens) at room temperature with a Bruker SMART CCD diffractometer using the omega scan mode. A summary of the data collection and refinement details is provided in Table S1 of the Supporting Information. Data sets were corrected for absorption using the program SADABS.[78] The solution and refinement for all structures was carried out using SHELXL-97[79] utilising the graphical interface X-Seed.[80] Crystallographic data (excluding structure factors) for the structure reported in this paper have been deposited with the Cambridge Crystallographic Data Centre as supplementary publication no. CCDC-286553 contains the supplementary crystallographic data for this paper. These data can be obtained free of charge from The Cambridge Crystallographic Data Centre via www.ccdc.cam.ac.uk/data_request/cif.

**Supporting Information** (for details see the footnote on the first page of this article): Proton numbering schemes for NMR characterization (Figure S1), spectroelectrochemical progression for [Ru(bpy)$_2$(bpt$^-$)]$^{+/2+}$ (Figure S2) and Stark absorption spectra for (ΔΔ/ΛΛ)-[{Ru(bpy)$_2$}$_2$(μ-bpt$^-$)]$^{3+}$ (Figure S3).

## Acknowledgments

This work was supported by the Australian Research Council. Stark effect measurements were conducted at Northwestern University and DMD gratefully acknowledges the financial support of grants from Professor Joe Hupp and the JCU Doctoral Research Scheme for travel to Northwestern University. JTH gratefully acknowledges support from the Basic Energy Sciences Program, Office of Science, U.S. Dept. of Energy under grant No. DE-FG02-8713808.

[1] V. Balzani, A. Juris, M. Venturi, S. Campagna, S. Serroni, *Chem. Rev.* **1996**, *96*, 759–833.
[2] K. Kalyanasundaram, M. K. Nazeeruddin, *Inorg. Chim. Acta* **1994**, *226*, 213–230.
[3] M. D. Ward, *Chem. Soc. Rev.* **1995**, *24*, 121–134.
[4] D. E. Richardson, H. Taube, *J. Am. Chem. Soc.* **1983**, *105*, 40–51.
[5] D. E. Richardson, H. Taube, *Coord. Chem. Rev.* **1984**, *60*, 107–129.
[6] G. Giuffrida, S. Campagna, *Coord. Chem. Rev.* **1994**, *135*, 517–531.
[7] M. D. Newton, *Chem. Rev.* **1991**, *91*, 767–792.
[8] C. G. Garcia, J. F. de Lima, N. Y. M. Iha, *Coord. Chem. Rev.* **2000**, *196*, 219–247.
[9] F. Barigelletti, L. De Cola, V. Balzani, R. Hage, J. G. Haasnoot, J. Reedijk, J. G. Vos, *Inorg. Chem.* **1991**, *30*, 641–645.
[10] H. M. McConnell, *J. Chem. Phys.* **1961**, *35*, 508–515.
[11] R. Hage, A. H. J. Dijkhuis, J. G. Haasnoot, R. Prins, J. Reedijk, B. E. Buchanan, J. G. Vos, *Inorg. Chem.* **1988**, *27*, 2185–2189.
[12] R. Hage, J. G. Haasnoot, H. A. Nieuwenhuis, J. Reedijk, D. J. A. De Ridder, J. G. Vos, *J. Am. Chem. Soc.* **1990**, *112*, 9245–9251.
[13] B. E. Buchanan, R. Wang, J. G. Vos, R. Hage, J. P. Haasnoot, J. Reedijk, *Inorg. Chem.* **1990**, *29*, 3263–3265.
[14] N. S. Hush, *Prog. Inorg. Chem.* **1967**, *8*, 391–444.
[15] N. S. Hush, *Electrochim. Acta* **1968**, *13*, 1005–1023.
[16] D. M. D'Alessandro, L. S. Kelso, F. R. Keene, *Inorg. Chem.* **2001**, *40*, 6841–6844.
[17] D. M. D'Alessandro, P. C. Junk, F. R. Keene, *Supramol. Chem.* **2005**, in press.
[18] D. M. D'Alessandro, F. R. Keene, *Chem. Phys.* **2005**, in press.
[19] G. U. Bublitz, S. G. Boxer, *Annu. Rev. Phys. Chem.* **1997**, *48*, 213–242.
[20] B. S. Brunschwig, C. Creutz, N. Sutin, *Coord. Chem. Rev.* **1998**, *177*, 61–79.
[21] K. A. Walters, *Comprehensive Coord. Chem. II* **2003**, *2*, 303–313.
[22] A. Ferretti, *Coord. Chem. Rev.* **2003**, *238–239*, 127–141.
[23] F. W. Vance, R. D. Williams, J. T. Hupp, *Int. Rev. Phys. Chem.* **1998**, *17*, 307–329.
[24] W. R. Browne, C. M. O'Connor, C. Villani, J. G. Vos, *Inorg. Chem.* **2001**, *40*, 5461–5464.
[25] R. Hage, *Coord. Chem. Rev.* **1991**, *111*, 161–166.
[26] B. E. Buchanan, J. G. Vos, M. Kaneko, W. J. M. van der Putten, J. M. Kelly, R. Hage, R. A. G. de Graaff, J. G. Haasnoot, J. Reedijk, *J. Chem. Soc., Dalton Trans.* **1990**, 2425–2431.
[27] J. H. van Diemen, R. Hage, J. G. Haasnoot, H. E. B. Lempers, J. Reedijk, J. G. Vos, L. De Cola, F. Barigelletti, V. Balzani, *Inorg. Chem.* **1992**, *31*, 3518–3522.
[28] R. Hage, J. G. Haasnot, D. J. Stufkens, T. L. Snoeck, J. G. Vos, J. Reedijk, *Inorg. Chem.* **1989**, *28*, 1413–1414.
[29] L. De Cola, F. Barigelletti, V. Balzani, R. Hage, J. G. Haasnoot, J. Reedijk, J. G. Vos, *Chem. Phys. Lett.* **1991**, *178*, 491–496.
[30] W. R. Browne, C. M. O'Connor, H. P. Hughes, R. Hage, O. Walter, M. Doering, J. F. Gallagher, J. G. Vos, *J. Chem. Soc., Dalton Trans.* **2002**, 4048–4054.
[31] G. Giuffrida, G. Calogero, G. Guglielmo, V. Ricevuto, S. Campagna, *Inorg. Chim. Acta* **1996**, *251*, 255–264.
[32] G. Giuffrida, G. Calogero, V. Ricevuto, S. Campagna, *Inorg. Chem.* **1995**, *34*, 1957–1960.
[33] H. P. Hughes, D. Martin, S. Bell, J. J. McGarvey, J. G. Vos, *Inorg. Chem.* **1993**, *32*, 4402–4408.

 © 2006 Wiley-VCH Verlag GmbH & Co. KGaA, Weinheim 

[34] G. Giuffrida, G. Calogero, G. Guglielmo, V. Ricevuto, M. Ciano, S. Campagna, *Inorg. Chem.* **1993**, *32*, 1179–1183.
[35] G. Giuffrida, V. Ricevuto, G. Guglielmo, S. Campagna, M. Ciano, *Inorg. Chim. Acta* **1992**, *194*, 23–29.
[36] R. Sahai, D. P. Rillema, R. Shaver, S. Van Wellendael, D. C. Jackman, M. Boldaji, *Inorg. Chem.* **1989**, *28*, 1022–1028.
[37] F. Barigelletti, L. De Cola, V. Balzani, R. Hage, J. G. Haasnoot, J. Reedijk, J. G. Vos, *Inorg. Chem.* **1989**, *28*, 4344–4350.
[38] C. Di Pietro, S. Serroni, S. Campagna, M. T. Gandolfi, R. Ballardini, S. Fanni, W. R. Browne, J. G. Vos, *Inorg. Chem.* **2002**, *41*, 2871–2878.
[39] A. C. Lees, C. J. Kleverlaan, C. A. Bignozzi, J. G. Vos, *Inorg. Chem.* **2001**, *40*, 5343–5349.
[40] K. F. Mongey, J. G. Vos, B. D. MacCraith, C. M. McDonagh, *Coord. Chem. Rev.* **1999**, *185–186*, 417–429.
[41] N. C. Fletcher, P. C. Junk, D. A. Reitsma, F. R. Keene, *J. Chem. Soc., Dalton Trans.* **1998**, 133–138.
[42] L. S. Kelso, PhD Thesis, James Cook University, Townsville, Australia, **2000**.
[43] B. D. Yeomans, L. S. Kelso, P. A. Tregloan, F. R. Keene, *Eur. J. Inorg. Chem.* **2001**, 239–246.
[44] T. J. Rutherford, O. Van Gijte, A. Kirsch-De Mesmaeker, F. R. Keene, *Inorg. Chem.* **1997**, *36*, 4465–4474.
[45] P. A. Adcock, F. R. Keene, R. S. Smythe, M. R. Snow, *Inorg. Chem.* **1984**, *23*, 2336–2343.
[46] N. C. Fletcher, F. R. Keene, *J. Chem. Soc., Dalton Trans.* **1999**, 683–689.
[47] X. Hua, PhD Thesis, University of Fribourg, Fribourg, Switzerland, **1993**.
[48] E. C. Constable, J. Lewis, *Inorg. Chim. Acta* **1983**, *70*, 251–253.
[49] V. Balzani, D. A. Bardwell, F. Barigelletti, F. L. Cleary, M. Guardigli, J. C. Jeffery, T. Sovrani, M. D. Ward, *J. Chem. Soc., Dalton Trans. J. Chem. Soc., Dalton Trans* **1995**, 3601–3608.
[50] R. Hage, J. P. Turkenburg, R. A. G. de Graaff, J. G. Haasnoot, J. Reedijk, *Acta Crystallogr., Sect. A Acta Crystallogr.* **1989**, *45*, 381–383.
[51] D. P. Rillema, D. G. Taghdiri, D. S. Jones, C. D. Keller, L. A. Worl, T. J. Meyer, H. A. Levy, *Inorg. Chem.* **1987**, *26*, 578–585.
[52] D. P. Rillema, D. S. Jones, H. A. Levy, *J. Chem. Soc., Chem. Commun.* **1979**, 849–851.
[53] D. M. D'Alessandro, F. R. Keene, *Dalton Trans.* **2004**, 3950–3954.
[54] A. Juris, S. Barigelletti, S. Campagna, V. Balzani, P. Belser, A. von Zelewsky, *Coord. Chem. Rev.* **1988**, *84*, 85–277.
[55] K. A. Goldsby, T. J. Meyer, *Inorg. Chem.* **1984**, *23*, 3002–3010.
[56] R. Hage, J. G. Haasnoot, J. Reedijk, R. Wang, J. G. Vos, *Inorg. Chem.* **1991**, *30*, 3263–3269–3275.
[57] C. Creutz, M. D. Newton, N. Sutin, *J. Photochem. Photobiol., A* **1994**, *82*, 47–59.
[58] R. J. Cave, M. D. Newton, *Chem. Phys. Lett.* **1996**, *249*, 15–19.
[59] K. D. Demadis, C. M. Hartshorn, T. J. Meyer, *Chem. Rev.* **2001**, *101*, 2655–2685.
[60] N. S. Hush, *Coord. Chem. Rev.* **1985**, *64*, 135–157.
[61] M. B. Robin, P. Day, *Adv. Inorg. Chem. Radiochem.* **1967**, *10*, 247–403.
[62] W. Liptay, *Angew. Chem. Int. Ed. Engl.* **1969**, *8*, 177–188.
[63] L. Karki, J. T. Hupp, *Inorg. Chem.* **1997**, *36*, 3318–3321.
[64] P. H. Dinolfo, J. T. Hupp, *J. Am. Chem. Soc.* **2004**, *126*, 16814–16819.
[65] Y. G. K. Shin, B. S. Brunschwig, C. Creutz, N. Sutin, *J. Phys. Chem.* **1996**, *100*, 8157–8169.
[66] D. H. Oh, M. Sano, S. G. Boxer, *J. Am. Chem. Soc.* **1991**, *113*, 6880–6890.
[67] G. U. Bublitz, S. G. Boxer, *J. Am. Chem. Soc.* **1998**, *120*, 3988–3992.
[68] Y. G. K. Shin, B. S. Brunschwig, C. Creutz, N. Sutin, *J. Phys. Chem.* **1996**, *100*, 8157–8169.
[69] Y. G. K. Shin, B. S. Brunschwig, C. Creutz, N. Sutin, *J. Am. Chem. Soc.* **1995**, *117*, 8668–8669.
[70] R. LeSuer, W. E. Geiger, *Angew. Chem. Int. Ed.* **2000**, *39*, 248–250.
[71] C. M. Duff, G. A. Heath, *Inorg. Chem.* **1991**, *30*, 2528–2535.
[72] D. M. D'Alessandro, F. R. Keene, *Chem. Eur. J.* **2005**, *11*, 3679–3688.
[73] J. R. Reimers, N. S. Hush, *Inorg. Chem.* **1990**, *29*, 3686–3697.
[74] S. S. Andrews, S. G. Boxer, *Rev. Sci. Instrum.* **2000**, *71*, 3567–3569.
[75] T. P. Treynor, S. G. Boxer, *J. Phys. Chem. A* **2004**, *108*, 1764–1778.
[76] J. F. Geldard, F. Lions, *J. Org. Chem.* **1965**, *30*, 318–319.
[77] T. Togano, N. Nagao, M. Tsuchida, H. Kumakura, K. Hisamatsu, F. S. Howell, M. Mukaida, *Inorg. Chim. Acta* **1992**, *195*, 221–225.
[78] R. H. Blessing, *Acta Crystallogr., Sect. A* **1995**, *51*, 33–38.
[79] G. M. Sheldrick, SHELXL-97, University of Göttingen, Göttingen, Germany, **1997**.
[80] L. J. Barbour, *J. Supramol. Chem.* **2001**, *1*, 189–191.

Received: October 17, 2005
Published Online: December 20, 2005

 © 2006 Wiley-VCH Verlag GmbH & Co. KGaA, Weinheim 

DOI: 10.1002/ejic.200500963

# Self-Assembly, Structure and Solution Dynamics of Tetranuclear $Zn^{2+}$ Hydrazone [2×2] Grid-Type Complexes

**Mihail Barboiu,[a,b] Mario Ruben,[c] Georges Blasen,[a] Nathalie Kyritsakas,[d] Elizabeth Chacko,[e] Manisha Dutta,[e] Olga Radekovich,[e] Kimberly Lenton,[e] David J. R. Brook,*[e][‡] and Jean-Marie Lehn*[a]**

**Keywords:** Self-assembly / Grid-type complexes / Hydrazone ligands / Zinc / Supramolecular chemistry

We describe the self-assembly processes as well as the structural and physico-chemical properties of $[2\times2]Zn^{2+}_4$ grid complexes involving the bis-tridentate ligands **7**–**12**, based on bis(hydrazone)pyrimidine complexation subunits and octahedrally coordinated $Zn^{2+}$ ions. The NMR spectroscopic data and the X-ray crystal structure results indicate that in solution and in the solid state the complexes **13**–**18** adopt a very compact arrangement providing stable [2×2] hydrazone-grid arrays. The π–π stacking between the phenyl ring and the hydrazone units of the perpendicular ligands in the complexes induces a perfect orthogonal arrangement suitable for applications in self-organized metallosupramolecular systems. Zinc complexes provide an opportunity to study the acid–base chemistry without the added effects due to paramagnetism or redox chemistry. The intermediate protonated grids undergo relatively rapid proton exchange on the NMR timescale, the presence of a sharp pyrimidine proton resonance suggesting that there is significant delocalization of the negative charge along the backbone of the ligand. Rotation of the phenyl ring is observed. It involves probably a mechanism in which one of the ligands partially dissociates allowing the initially intercalated phenyl group to rotate, before recoordination of the terminal pyridine.

(© Wiley-VCH Verlag GmbH & Co. KGaA, 69451 Weinheim, Germany, 2006)

## Introduction

During the last decade, intense investigations have been carried out on the spontaneous generation of various types of supramolecular inorganic architectures, both as touchstone for the design of self-organization processes and as devices for nanotechnology.[1] The first complexes of [2×2] grid-type architecture employed bipyridine- and terpyridine-like binding subunits and respectively tetrahedrally ($Cu^+$ and $Ag^+$)[2a,2b,2f] and octahedrally ($Co^{2+}$, $Ni^{2+}$, $Zn^{2+}$)[2c–2f] coordinated metal ions. The latter in particular present remarkable electronic,[2d,3] magnetic,[4] and photophysical[7a] properties. The success in the formation of the [2×2] grid-type complexes as well as their interesting physical properties stimulated us to extend our investigations towards grids based on ligands for octahedrally coordinating metal ions, that would be synthetically more accessible than the earlier pyridine–pyrimidine sequences.[5]

The hydrazone unit is a suitable isomorphic analog of a pyridine group and is easily generated by hydrazine–carbonyl condensation. It has been implemented as a useful and simple method for the formation of molecular strands presenting extended helical architectures.[6] The *transoid*,*transoid* form of the free ligand is converted into the *cisoid,cisoid* form, corresponding to a terpyridine-type complexation site, on metal–ion binding (Scheme 1).

Thus, hydrazone-containing ligands were shown to yield [2×2] grid complexes presenting novel physical (optical,[7a] electrochemical,[7b,7c] magnetic[7d]) properties.

Based on these premises, we report here a study of the generation of several tetranuclear $[2\times2]Zn^{2+}_4$ grid-type complexes using such bis(hydrazone)pyrimidine ligands. It confirms their value as a synthetic alternative to the previously used pyridine–pyrimidine sequence and markedly simplifies the methodology for the synthesis of grid complexes based on octahedrally coordinated transition-metal ions.

We describe the self-assembly processes as well as the structural and physico-chemical properties of $[2\times2]Zn^{2+}_4$ grid complexes involving bis-tridentate ligands **7**–**12**, based on bis-hydrazone-pyrimidine complexation subunits and octahedrally coordinated $Zn^{2+}$ ions.

[a] Laboratoire de Chimie Supramoléculaire, ISIS, Université Louis Pasteur, CNRS UMR 7006,
8, allée Gaspard Monge, BP 70028, 67083 Strasbourg, France
[b] Institut Européen des Membranes - IEM-CNRS 5635,
Place Eugène Bataillon, CC 047, 34095 Montpellier, France
[c] Institute of Nanotechnology, FZ-Karlsruhe,
P. O. Box 3640, 76021 Karlsruhe, Germany
[d] Laboratoire de Cristallochimie, Institut Le Bel, Université Louis Pasteur,
4, rue Blaise Pascal, 67000 Strasbourg, France
[e] Department of Chemistry and Biochemistry, University of Detroit Mercy,
P. O. Box 19900 Detroit, MI 48219, USA
[‡] Current address: Department of Chemistry, Santa Clara University,
500 El Camino Real, Santa Clara CA 95053, USA

 © 2006 Wiley-VCH Verlag GmbH & Co. KGaA, Weinheim 

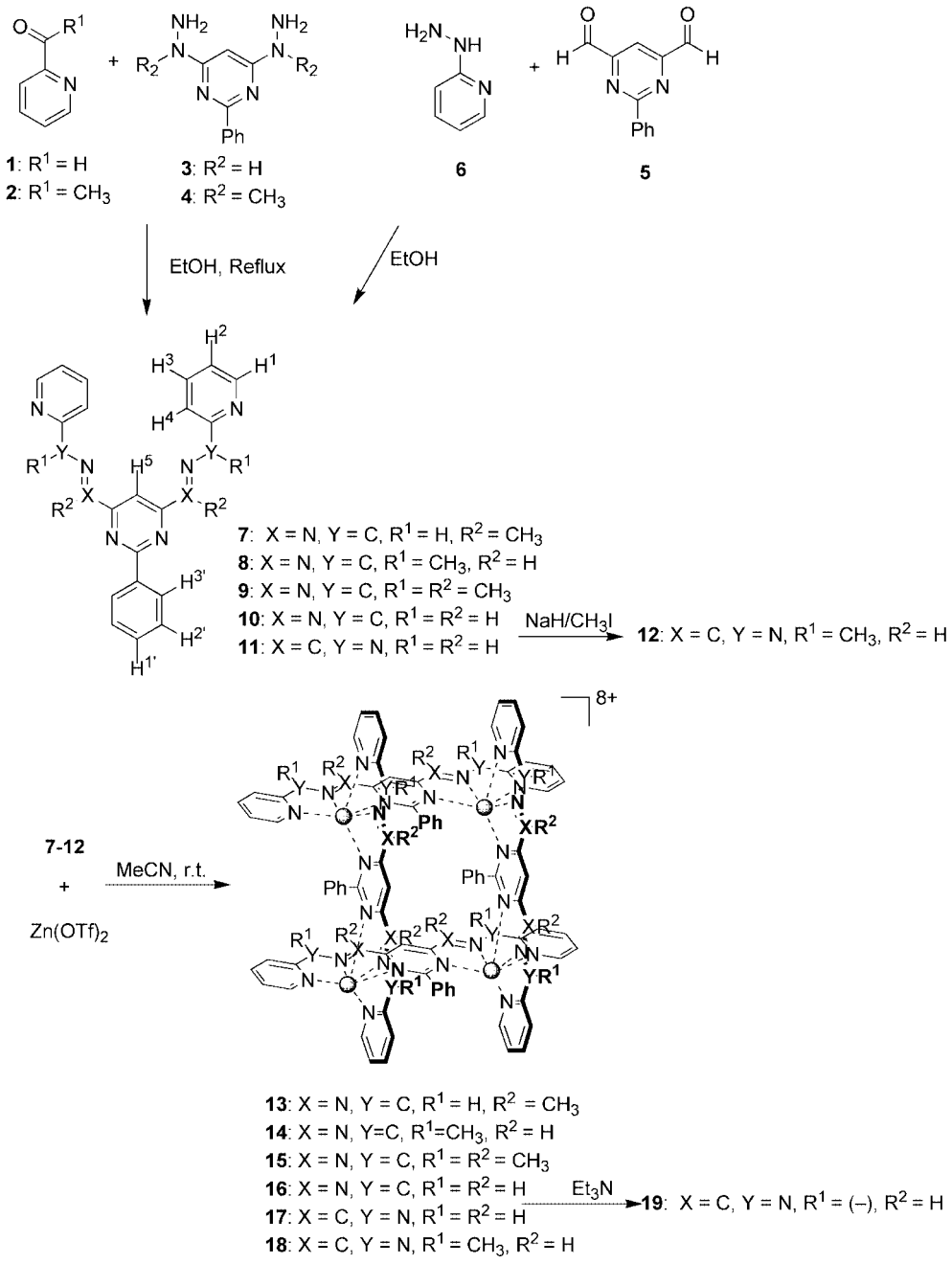


Scheme 1. Synthesis of the ligands **7**–**12** and of the $[2\times2]Zn^{2+}{}_4$ grid-type complexes **13**–**18**.

## Results and Discussions

### Synthesis and Characterization of Ligands 7–12 and of the $[2\times2]Zn^{2+}{}_4$ Grid-Type Complexes 13–18

The synthesis of the ligands **7**–**12** is outlined in Scheme 1.

The ligands **7**–**10** were obtained by the condensation of two equivalents of 2-pyridinecarboxaldehyde (**1**), or of 2-acetylpyridine (**2**), with one equivalent of dihydrazinopyrimidine (**3**) or of (dimethylhydrazino)pyrimidine (**4**) in ethanol. These ligands precipitate from the reaction mixture in ca. 90% yield as pure compounds. The NMR and ESI-MS spectra were in agreement with the proposed formula. Ligand **11** was obtained by the analogous condensation of the pyrimidinedicarbaldehyde **5** with 2-hydrazinopyridine (**6**). Ligand **12** was obtained through methylation of **11** in THF with $NaH/CH_3I$.

The grid-type complexes **13**–**18** resulted from spontaneous self-assembly of the ligands **7**–**12** with $Zn(CF_3SO_3)_2$ in acetonitrile (Scheme 1) at room temperature, followed by crystallization with diisopropyl ether or diethyl ether. The compounds **13**–**18** were characterized by NMR spectroscopy, positive ESI mass spectrometry, elemental analysis and in the case of **13**–**15** by single-crystal X-ray diffraction.

 © 2006 Wiley-VCH Verlag GmbH & Co. KGaA, Weinheim 

### Crystal Structure of the Complexes 13–15

Layering a 1:1 solution of the ligands **7**–**10** and $Zn(CF_3SO_3)_2$ in acetonitrile onto benzene resulted in the development of light-yellow prismatic crystals of grid-type Zn complexes **13**–**15**, which were investigated by X-ray crystallography.

In all these structures the complexes present a $[2\times2]Zn^{2+}{}_4$ grid-type architecture in which four metal ions form a square and lie close to an average common plane (Figure 1). In the case of complex **16** the overall quality of the crystal structure data is too low, and crystals of better quality are required for improving the structural data.

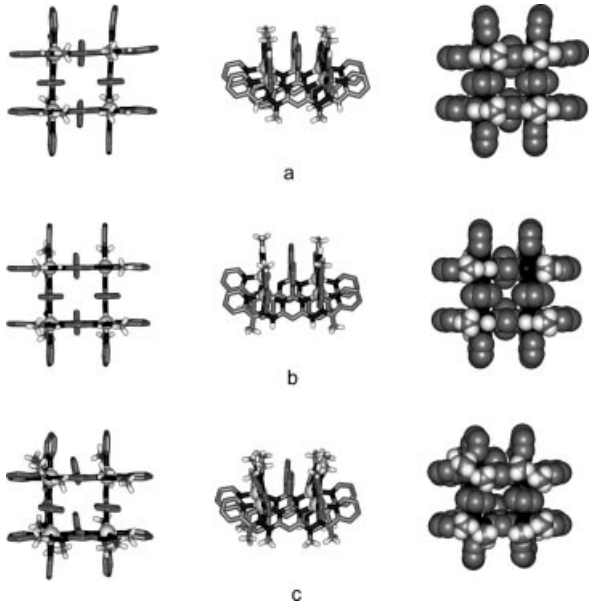


Figure 1. Crystal structure of the [2×2] $Zn_4^{2+}$ grid complexes: a) **13**, b) **14**, c) **15**: top view (left), side view in stick representation (center) and space-filling representation (right) The $Zn^{2+}$ ions are shown as spheres.

In the complexes **13**–**15** the $Zn^{2+}$ ions display a distorted octahedral coordination. The Zn–Zn distances lie in the range of 6.37–6.60 Å and the average inner angle between three Zn atoms of about 90°. The average Zn–N bonds are 2.17 Å for the pyridine nitrogen atoms, 2.20 Å for the pyrimidine nitrogen atoms and 2.14 Å for the hydrazone nitrogen atoms.

The average distance between two parallel ligands is 6.50 Å, and the average distance between the $–R^1C=N–NR^2–$ moiety of one ligand and the phenyl ring of the orthogonal one is 3.25 Å, indicating van der Waals contact and a strong π–π stacking. The almost parallel insertion of the phenyl substituent between two ligands, leads to an overall geometry of the $[2\times2]Zn^{2+}{}_4$ grid complexes **13** (Figure 1, a) and **14** (Figure 1, b) close to regular square. In the case of **15** (Figure 1, c) the steric interactions due to the close contacts (C–C distance of 2.95 Å) of the methyl substituents of the hydrazone moiety, are found to cause a distorted geometry, bending the planes of the ligands. The pinching angle provides information about the shape of complexes, smaller values being correlated with increased linearity of the ligand in the complex. It is smaller for **13**–**15** (16.5°) than for the analogous terpyridine grid-type[2e] (19.3°) and rack-type[8] (19.6°) $Zn^{2+}$ complexes.

### $^1$H NMR Spectra

The $^1$H NMR spectra of the ligands **7**–**12** are consistent with the presence of a *transoid*,*transoid* conformation along the connecting NC–CN bonds in both hydrazone pyridine functionalities. This conformation was further confirmed by intermolecular NOE interactions between the $H^4$ protons of external pyridines and the $H^5$ proton of internal pyrimidine, and between the protons of the $R^1$ (H or Me) and $R^2$ (H or Me) substituents of the hydrazone units.

The metal complexation leads to changes in $^1$H NMR spectra with large modifications in the chemical shifts of the protons of the ligands **7**–**12**. The metal–ion binding converts the wrapped *transoid*,*transoid* form of the free ligand to the linear *cisoid*,*cisoid* form, corresponding to a terpyridine-type complexation site (Scheme 1). This has been confirmed by a ROESY NMR experiment, where NOE interactions between $H^4$ and $R^1$ = H or Me as well as between $H^5$ and $R^2$ = H or Me are observed for the complexes **13**–**18**. The major changes observed in the NMR spectra on complexation reside in the strong shielding ($\Delta\delta$ = –1.66–3.34) of the phenyl protons when the zinc complexes **13**–**18** are formed (Table 1). Moreover, the *o*,*o′* and *m*,*m′* protons of the phenyl ring, which are equivalent in the ligands **7**–**12**, become non-equivalent in the complexes **13**–**17**, suggesting that in solution the grid-type-Zn complexes adopt a very compact structure where the phenyl rings of the two ligands on one face of the grid structure insert between the two ligands on the other face, blocking the rotation around the phenyl–pyrimidine C–C bonds, as seen in the parent grids.[2c] The phenyl insertion has been confirmed by a ROESY NMR experiment, where NOE interactions between $R^1$ and $H^{2'o}$, between $R^2$ and $H^{3'}$ and between $H^5$ and $H^{2'i}$ are observed for the complexes **9**–**12**.

The well-resolved NMR spectra of these species provide an opportunity to investigate the deprotonation of the hydrazone NH protons in these molecules. The hydrazones in the analogous complex $Zn(papy)_2$ are significantly more acidic as a result of metal complexation;[9] similar effects, with accompanying optical changes, have been reported for grids containing a hydrazone N–H group.[7a] Addition of eight equivalents of triethylamine to acetonitrile solutions of **18** results in the precipitation of the neutral complex **19** as gold-colored crystals. This deprotonation reaction can be monitored by titration with triethylamine and monitoring with $^1$H NMR spectroscopy (Figure 2).

The chemical shift of the ethyl $CH_2$ group is consistent with the nearly complete protonation of the triethylamine throughout the titration, confirming the high acidity of these complexes. Early in the titration, the exchange coupling to the ammonium NH proton is clearly resolved, indicating that proton-exchange processes are confined to the grid complex; however, as the titration proceeds, loss of this

 © 2006 Wiley-VCH Verlag GmbH & Co. KGaA, Weinheim 

Table 1. Chemical shifts[a] and chemical shift differences for $^1H$ NMR signals of the ligands **7**–**12** (in $CDCl_3$) and Zn grid-type complexes (in $CD_3CN$).[b]

| Compound | $H^{1'i}$ | $H^{1'o}$ | $H^{2'i}$ | $H^{2'o}$ | $H^{3'}$ | $H^1$ | $H^2$ | $H^3$ | $H^4$ | $H^5$ | $R^1$ | $R^2$ |
|---|---|---|---|---|---|---|---|---|---|---|---|---|
| **7** | 8.48 | 8.48 | 7.48 | 7.48 | 7.5 | 8.63 | 7.32 | 7.82 | 8.21 | 7.84 | 7.99 | 3.84 |
| **13** | 5.44 | 6.49 | 7.18 | 7.78 | 8.01 | 7.6 | 7.25 | 7.87 | 7.65 | 6.84 | 7.98 | 3.67 |
| $\Delta\delta$ | –3.04 | –1.99 | –0.3 | 0.3 | 0.5 | –0.98 | –0.07 | 0.05 | –0.61 | –1 | –0.01 | –0.17 |
| **8** | 8.36 | 8.36 | 7.46 | 7.46 | 7.46 | 8.68 | 7.25 | 7.76 | 8.24 | 8.39 | 2.48 | 8.42 |
| **14** | 5.51 | 6.48 | 7.07 | 7.8 | 8.05 | 7.66 | 7.27 | 7.9 | 7.79 | 6.74 | 2.4 | 10.97 |
| $\Delta\delta$ | –2.85 | –1.88 | –0.39 | 0.34 | 0.59 | –1.02 | 0.02 | 0.14 | –0.45 | –1.65 | –0.08 | 2.55 |
| **9** | 8.52 | 8.52 | 7.48 | 7.48 | 7.51 | 8.63 | 7.3 | 7.58 | 8.17 | 6.35 | 2.52 | 3.6 |
| **15** | 5.18 | 6.56 | 7.03 | 7.72 | 7.96 | 7.37 | 7.06 | 7.88 | 7.6 | 6.6 | 2.57 | 3.8 |
| $\Delta\delta$ | –3.34 | –1.96 | –0.45 | 0.24 | 0.45 | –1.26 | –0.24 | 0.3 | –0.57 | 0.25 | 0.05 | 0.2 |
| **10** | 7.48 | 7.48 | 7.32 | 7.32 | 7.34 | 8.69 | 7.42 | 7.68 | 8.18 | 6.89 | 7.96 | 9.87 |
| **16** | 5.82 | 5.92 | 7.49 | 7.49 | 8.19 | 7.39 | 6.84 | 7.75 | 6.97 | 7.89 | 8.09 | 12.09 |
| $\Delta\delta$ | –1.66 | –1.56 | 0.17 | 0.17 | 0.85 | –1.3 | –0.58 | 0.07 | –1.21 | 1 | 0.13 | 2.22 |
| **11**[c] | 8.42 | 8.42 | 7.55 | 7.55 | 7.55 | 8.21 | 6.91 | 7.78 | 7.42 | 8.17 | 11.62 | 8.11 |
| **17** | 5.84 | 5.92 | 7.45 | 7.45 | 8.14 | 7.39 | 6.83 | 7.75 | 6.98 | 8.07 | 11.8 | 7.88 |
| $\Delta\delta$ | –2.58 | –2.5 | –0.1 | –0.1 | 0.59 | –0.82 | –0.08 | –0.03 | –0.44 | –0.1 | 0.18 | –0.23 |
| **12** | 8.50 | 8.50 | 7.49 | 7.49 | 7.49 | 8.28 | 6.89 | 7.65 | 7.85 | 8.33 | 3.74 | 7.72 |
| **18** | 5.81 | 5.89 | 7.34 | 7.53 | 8.16 | 7.34 | 6.93 | 7.86 | 7.29 | 8.14 | 3.51 | 7.86 |
| $\Delta\delta$ | –2.69 | –2.61 | –0.15 | 0.04 | 0.67 | –0.94 | 0.04 | 0.21 | –0.56 | –0.19 | –0.23 | 0.14 |

[a] Chemical shifts for ligands **7**–**10** and complexes **13**–**16** were recorded at 500 MHz, chemical shifts for ligands **11**–**12** and complexes **17**–**18** were recorded at 300 MHz. [b] *i* and *o* designate the inner and outer *ortho* and *meta* protons, respectively, on the phenyl substituent. [c] 1H NMR spectrum of **11** was recorded in $[D_6]$DMSO.

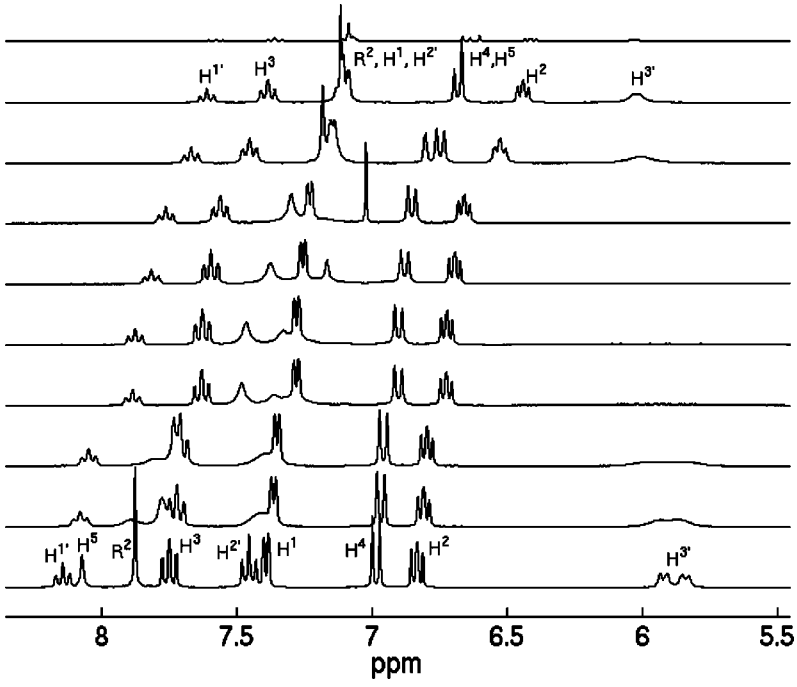


Figure 2. $^1H$ NMR of grid complex **17** with triethylamine in $[D_3]$acetonitrile. From bottom to top, the ratio $Et_3N$/**17** is 0.0, 0.7, 1.0, 2.5, 2.8, 3.5, 4.1, 5.0, 6.4, 7.9. The intensity of the last spectrum is reduced as a result of precipitation of the neutral complex.

resolution indicates rapid exchange of protons between the ammonium ion and the grid. During the titration, the $^1H$ NMR spectrum of the ligand undergoes a general upfield shift consistent with an increasing electron density on the ligand. The overall spectrum is remarkably simple indicating a rapid exchange of protons between sites on the grid, though significant broadening of some of the grid complex protons occurs. In particular, the imine and pyrimidine protons ($R^2$, $H^5$) show significant broadening consistent with deprotonation of the hydrazone N–H sites. Whereas the imine protons remain broadened until near the end of the titration, the pyrimidine proton appears as a sharp singlet around $Et_3N$/**18** ratios of 4:1 (i.e. deprotonation of half of the acidic NH sites). This is consistent with each ligand being deprotonated once before any are deprotonated a second time; with each ligand singly deprotonated, proton exchange does not significantly change the environment of the pyrimidine proton. More remarkable is the behavior of the phenyl *ortho* and *meta* protons, which rapidly broaden upon addition of traces of base. Halfway through the titration

 © 2006 Wiley-VCH Verlag GmbH & Co. KGaA, Weinheim 

these protons are barely visible as a broad rise in the baseline. The resonances only reappear toward the end of the titration but no longer show clear 'inner' and 'outer' peaks, which suggests a dynamic mechanism that allows rotation of the phenyl ring.

This is further supported by variable-temperature NMR studies of the neutral complex **19** in chloroform (Figure 3). While at room temperature the inner and outer phenyl protons are equivalent, lowering the temperature results in broadening of this resonance. Resolved inner and outer phenyl proton resonances were not observed for this complex above the freezing point of the solvent.

Repeating the titration in [$D_6$]DMSO results in significantly different observations (Figure 4). Initially, NMR indicates that the grid complex **18** is completely dissociated in [$D_6$]DMSO; the $^1$H NMR spectrum indicates only free ligand. Addition of $Et_3N$, however, results in loss of the free ligand and eventual formation of the neutral grid **19** upon

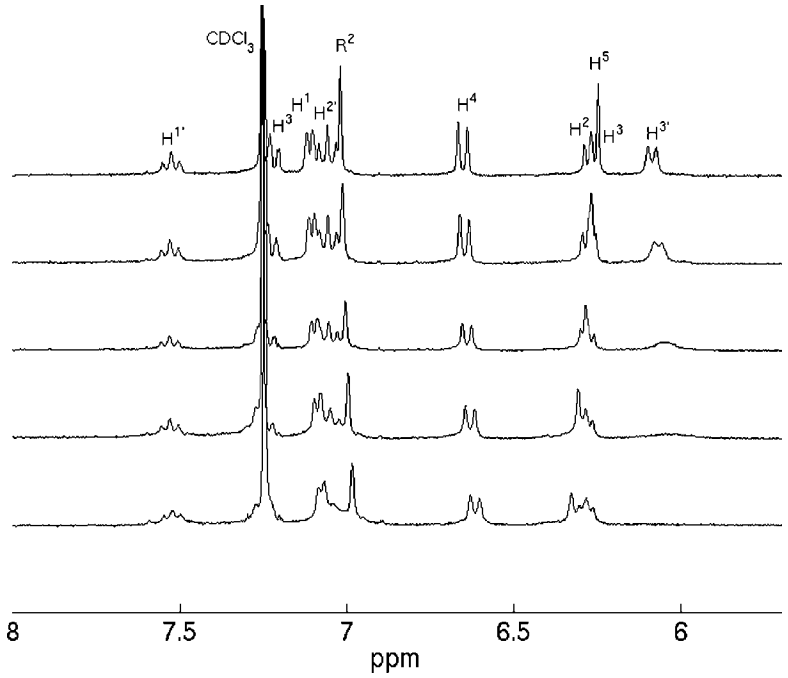


Figure 3. $^1$H NMR of neutral grid complex **19** in $CDCl_3$ at (top to bottom) 40 °C, 20 °C, 0 °C, –20 °C, –40 °C.

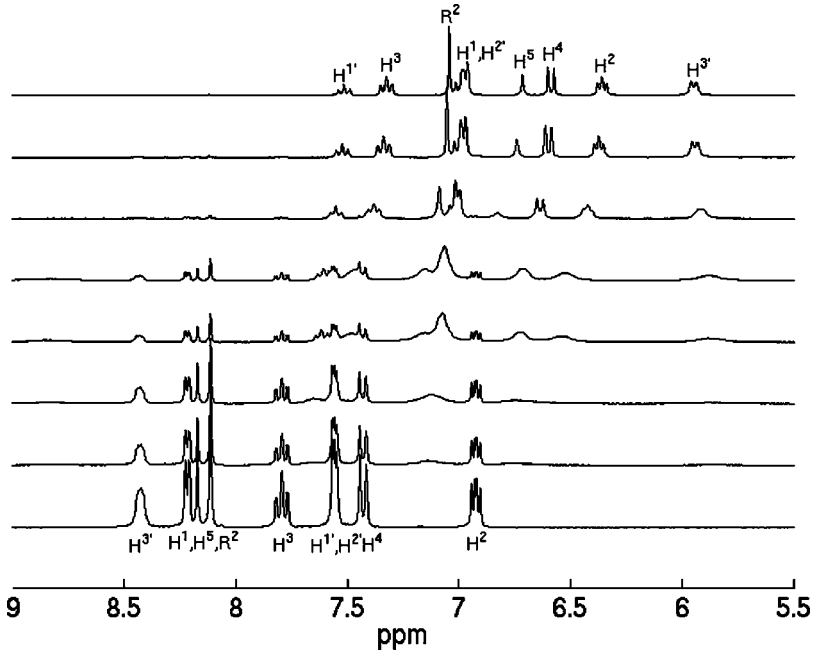


Figure 4. $^1$H NMR of grid complex **17** with triethylamine in [$D_6$]DMSO. From bottom to top, the ratio $Et_3N$/**17** is 0.0, 1.0, 2.0, 4.3, 5.0, 6.8, 9.3, 11.9.

 © 2006 Wiley-VCH Verlag GmbH & Co. KGaA, Weinheim 

addition of a full eight equivalents of base. That this is the only species in solution was confirmed by electrospray mass spectrometry. It is noteworthy that the coordinated ligand initially appears as very broad resonances in the $^1$H NMR spectrum, again indicative of dynamic processes, but upon completion of the titration a sharp spectrum is observed. Furthermore re-assembly of the grid is fast; the equilibration time allowed for collection of the data in Figure 4 was only that required to load and shim the sample and no further spectral changes were observed upon standing for 5–10 min.

## Discussion

The introduction of hydrazone links into the backbone of grid-forming ligands offers a means to modulate their properties and assembly through pH. The change in oxidation potential of protonated vs. unprotonated cobalt complexes has already been used to control the regioselective assembly of heterometallic cobalt grids.[7b] Zinc complexes provide an opportunity to study this acid–base chemistry without the added effects due to paramagnetism or redox chemistry. Any information on the pattern of deprotonation will give some information about the interactions within the grid complex. The quantitative protonation of triethylamine early in the titration clearly indicates the acidity of these complexes. Though the intermediate protonated grids undergo relatively rapid proton exchange on the NMR timescale, the presence of a sharp pyrimidine proton resonance at $Et_3N$/grid ratios of 4:1 indicates that not all of these are equally populated, and the ligands are all deprotonated once before they are further deprotonated. This suggests that there is significant delocalization of the negative charge along the backbone of the ligand. The intercalated phenyl ring could yield more information about the preferred tautomers; however, this is complicated by the presence of a dynamic process that allows interchange of inner and outer phenyl protons.

Rotation of the phenyl ring in a pyridine-type grid complex is a phenomenon that has not been previously observed. Examination of models suggests that simple phenyl rotation is unlikely because the cavity is too constrained; more likely is a mechanism in which one of the ligands partially dissociates allowing the initially intercalated phenyl group to rotate. In such a mechanism, the enhanced donor strength of the hydrazone anion ligand would increase the electron density on the metal ion and allow dissociation of one of the terminal pyridyl nitrogen atoms. The flexibility of the resulting five-coordinate metal-ion center would allow rotation of the phenyl ring before recoordination of the pyridine. The effect of the increased ligand donor strength accounts for the initially paradoxical observation of greater complex stability combined with greater flexibility observed in DMSO.

The NMR spectroscopic data and the X-ray crystal structure results suggest that in solution and in the solid state the complexes **13**–**18** adopt a very compact arrangement providing stable [2×2] hydrazone-grid arrays. The π–π stacking between the phenyl ring and the hydrazone units of the perpendicular ligands in the complexes induces a perfect orthogonal arrangement suitable for applications in self-organized metallosupramolecular systems.

## Experimental Section

**General:** Compounds **1** and **2** were obtained from commercial suppliers and used without purification. Compounds **3**, **4** and **5** were prepared according to the procedures described in the literature.[10] $^1$H NMR, COSY and ROESY correlation measurements were recorded with an ARX 500 MHz Bruker spectrometer or a JEOL Eclipse+ 300 MHz spectrometer in $CDCl_3$, [$D_6$]DMSO and $CD_3CN$, with the use of the residual solvent peak as reference. Mass spectrometric studies were performed in the positive ion mode with a quadrupole mass spectrometer (Micromass, Platform II) or an ion trap mass spectrometer (Agilent 1100 series). Samples were dissolved in acetonitrile and were continuously introduced into the mass spectrometer at a flow rate of 10 mL/min by using either a Waters 616HPLC pump or a syringe pump. The temperature (60 °C), and the extraction cone voltage ($V_c$ = 5–10 V) was usually set to avoid fragmentations. The microanalyses were carried out at Service de Microanalyses, Institut Charles Sadron, Strasbourg.

**General Procedure for the Synthesis of the Ligands 7–12:** Two equivalents of 2-pyridinecarboxaldehyde **1** or of 2-acetylpyridine **2** with one equivalent of dihydrazinopyrimidine **3** or of di-methylhydrazinopyrimidine **4** were refluxed in ethanol for 3 h. The resulting precipitates were filtered and washed with ethanol to give **7**–**12** as analytically pure compounds.

**4,6-Bis{[*N*-methyl-*N*′-(pyridin-2-yl)methylidene]hydrazino}-2-phenylpyrimidine (7):** $^1$H NMR ($CDCl_3$, ppm): $\delta$ = 8.63 (d, $J$ = 3.6 Hz, 2 H, $H^1$), 8.49 (m, 4 H, $H^{2'}$), 8.21 (d, $J$ = 3.6 Hz, 2 H, $H^4$), 7.99 (s, 2 H, $R^1$ = H), 7.84 (s, 1 H, $H^5$), 7.82 (dt, $J$ = 7.6 Hz, 2 H, $H^3$), 7.50 (m, 2 H, $H^{4'}$), 7.48 (m, 4 H, $H^{3'}$), 7.32 (dt, $J$ = 7.6 Hz, 2 H, $H^2$), 3.84 (s, 6 H, $R^2$ = $CH_3$); assignments made on the basis of the COSY and the ROESY spectra. $^{13}$C NMR ($CDCl_3$, ppm): $\delta$ = 42.4, 88.9, 124.1, 125.9, 127.0, 128.5, 129.0, 135.8, 149.9, 152.5, 154.7 163.8, 170.7. ES-MS: $m/z$ (%) = 423.5 (100) $[M + H]^+$. $C_{24}H_{22}N_8$ (422.5): calcd. C 68.23, H 5.26, N, 26.52; found C 66.49, H 5.36, N 27.10.

**2-Phenyl-4,6-bis{[1-(pyridin-2-yl)ethylidene]hydrazino}pyrimidine (8):** $^1$H NMR ($CDCl_3$, ppm): $\delta$ = 8.68 (d, $J$ = 3.6 Hz, 2 H, $H^1$), 8.42 (s, 2 H, $R^1$ = H), 8.39 (s, 1 H, $H^5$), 8.36 (m, 4 H, $H^{1'}$), 8.24 (d, $J$ = 3.6 Hz, 2 H, $H^4$), 7.76 (dt, $J$ = 7.6 Hz, 2 H, $H^3$), 7.46 (m, 6 H, $H^{2'}$, $H^{3'}$), 7.25 (dt, $J$ = 7.6 Hz, 2 H, $H^2$), 2.48 (s, 6 H, $R^1$ = $CH_3$); assignments made on the basis of the COSY and the ROESY spectra. $^{13}$C NMR ($CDCl_3$, ppm): $\delta$ = 12.4, 88.9, 124.1, 126.4, 127.0, 128.5, 129.3, 134.8, 149.9, 152.5, 155.6, 164.6, 170.2. ES-MS: $m/z$ (%) = 423.5 (100) $[M + H]^+$. $C_{24}H_{22}N_8$ (422.5): calcd. C 68.23, H 5.26, N, 26.52; found C 66.45, H 5.56, N 26.53.

**4,6-Bis{[*N*-methyl-*N*′-[1-(pyridin-2-yl)ethylidene]hydrazino}-2-phenylpyrimidine (9):** $^1$H NMR ($CDCl_3$, ppm): $\delta$ = 8.63 (d, $J$ = 3.6 Hz, 2 H, $H^1$), 8.52 (m, 4 H, $H^{1'}$), 8.17 (d, $J$ = 3.6 Hz, 2 H, $H^4$), 7.58 (dt, $J$ = 3.6 Hz, 2 H, $H^3$), 7.51 (m, 2 H), 7.48 (m, 4 H), 7.30 (dt, $J$ = 7.6 Hz, 2 H, $H^2$), 6.35 (s, 1 H, $H^5$), 3.60 (s, 6 H, $R^2$ = $CH_3$), 2.52 (s, 6 H, $R^1$ = $CH_3$); assignments made on the basis of the COSY and the ROESY spectra. $^{13}$C NMR ($CDCl_3$, ppm): $\delta$ = 12.8, 42.4, 88.9, 124.1, 125.9, 127.0, 128.5, 129.0, 135.8, 149.9, 152.5, 155.6 163.8, 170.7. ES-MS: $m/z$ (%) = 451.5 (100) $[M + H]^+$. $C_{26}H_{26}N_8$

 © 2006 Wiley-VCH Verlag GmbH & Co. KGaA, Weinheim 

(450.3): calcd. C 69.31, H 5.82, N, 24.87; found C 70.48, H 5.63, N 29.35.

**2-Phenyl-4,6-bis{[(pyridin-2-yl)methylidene]hydrazino}pyrimidine (10):** $^1$H NMR ($CDCl_3$, ppm): $\delta$ = 9.87 (s, 2 H, $R^2$ = H), 8.69 (d, $J$ = 3.6 Hz, 2 H, $H^1$), 8.18 (d, $J$ = 3.6 Hz, 2 H, $H^4$), 7.96 (s, 2 H, $R^1$ = H), 7.68 (dt, $J$ = 7.6 Hz, 2 H, $H^3$), 7.48 (m, 4 H, $H^{1'}$), 7.42 (dt, $J$ = 7.6 Hz, 2 H, $H^2$), 7.32–7.34 (m, 6 H), 6.89 (s, 1 H, $H^5$); assignments made on the basis of the COSY and the ROESY spectra. $^{13}$C NMR ($CDCl_3$, ppm): $\delta$ = 12.8, 42.4, 88.9, 124.1, 125.9, 127.0, 128.5, 129.0, 135.8, 149.9, 152.5, 155.6 163.8, 170.7. ES-MS: $m/z$ (%) = 395.5 (100) $[M + H]^+$. $C_{22}H_{18}N_8$ (394.5): calcd. C 66.99, H 4.60, N, 28.41; found C 67.34, H 4.89, N 27.86.

**2-Phenylpyrimidine-4,6-dicarbaldehyde Bis[(pyridin-2-yl)hydrazone] (11):** To a solution of 2-phenylpyrimidine-4,6-dicarbaldehyde (0.201 g, 0.95 mmol) in ethanol (15 mL) was added a solution of 2-hydrazinopyridine (0.206 g) in ethanol (2 mL). A yellow precipitate of **11** formed after about 30 s. The solution was allowed to stand overnight after which the precipitate was removed by filtration, recrystallized from tetrahydrofuran and dried in air to give 0.370 g of the product (99%).$^1$H NMR ([D$_6$]DMSO, ppm): $\delta$ = 11.62(s, 1 H, NH, exchanges w $D_2O$, $R^1$ = H), 8.42 (m, 2 H, $H^{1'}$), 8.21 (d, $J$ = 4.11 Hz, 2 H, $H^1$) 8.17 (s, 1 H, $H^5$), 8.11 (s, 2 H, $R^2$ = H), 7.78 (dd, $J$ = 7.4 Hz, $J$ = 8.2 Hz, 2 H, $H^3$), 7.55 (m, 3 H, $H^{2'}$, $H^{3'}$) 7.42 (d, $J$ = 8.2 Hz, 2 H, $H^4$), 6.91 (dd, $J$ = 7.4 Hz, $J$ = 4.1 Hz, 2 H, $H^2$). $^{13}$C NMR ([D$_6$]DMSO, ppm): $\delta$ = 107.5, 107.6, 117.1, 128.4, 129.2, 131.5, 137.6, 137.7, 139.0, 148.5, 156.7, 161.9, 164.2. IR (NaCl plate): $\tilde{\nu}$ = 1640, 1561, 1439, 751 cm$^{-1}$. ES-MS: $m/z$ (%) = 395 (100) $[M - H]^+$. $C_{22}H_{18}N_8$ (394.5): calcd. C 66.99, H 4.60, N, 28.41; found C 66.12, H 4.71, N 27.50.

**2-Phenylpyrimidine-4,6-dicarbaldehyde Bis[*N*-methyl-*N*-(pyridin-2-yl)hydrazone] (12):** Excess sodium hydride (60% dispersion in mineral oil) was added to a solution of **11** (419 mg) in tetrahydrofuran. The yellow solution rapidly turned dark blue-purple. To this solution was added excess methyl iodide, and the solution was stirred for 30 minutes during which the color dispersed to give a yellow solution. The solution was filtered and evaporated, and the residue washed with hexane to give 435 mg (97%) of **12**. $^1$H NMR ($CDCl_3$, ppm): $\delta$ = 3.74 (s, 6 H, $R^1$ = $CH_3$) 6.89 (ddd, $J$ = 1.0, $J$ = 5.0, $J$ = 7.0 Hz, 2 H, $H^2$), 7.49 (m, 3 H, phenyl) 7.65 (ddd, $J$ = 1.8, $J$ = 7.0, $J$ = 8.6 Hz, 2 H, $H^3$), 7.72 (s, 2 H, $R^2$) 7.85(d, $J$ = 8.6 Hz, 2 H, $H^4$), 8.28 (ddd, $J$ = 1.0, $J$ = 1.8, $J$ = 1.8 Hz, 2 H, $H^1$), 8.33 (s, 1 H, $H^5$), 8.5 (m, phenyl). $^{13}$C NMR ($CDCl_3$, ppm): $\delta$ = 30.03, 107.75, 110.44, 128.26, 128.61, 130.57, 132.98, 137.62, 138.01, 147.23, 157.21, 162.19. IR (NaCl plate): $\tilde{\nu}$ = 1624 cm$^{-1}$ (C=N). ES-MS: $m/z$ (%) = 423 (50) $[M + H]^+$, 421 (100), 242 (100). $C_{24}H_{22}N_8$ (422.5): calcd. C 68.23, H 5.25, N, 26.52; found C 67.04, H 5.35, N 25.57.

**General Procedure for the Formation of the [2×2]$Zn^{2+}_4$ Grid-Type Complexes 13–18:** An equimolar mixture of $Zn(CF_3SO_3)_2$ and of the ligands **7**–**12** in acetonitrile was stirred at room temperature for 5 h. The complexes were obtained by crystallization with diisopropyl ether or diethyl ether.

**Complex [$7_4Zn_4$]$(CF_3SO_3)_8$ (13):** $^1$H NMR ($CDCl_3$, ppm): $\delta$ = 8.01 (t, $J$ = 7.6, 2 H, $H^{3'}$), 7.98 (s, 2 H, $R^1$ = H), 7.87 (dt, $J$ = 7.6 Hz, 2 H, $H^3$), 7.78 (dt, $J$ = 7.6 Hz, 2 H, $H^{2'o}$), 7.65 (d, $J$ = 3.6 Hz, 2 H, $H^1$), 7.60 (d, $J$ = 3.6 Hz, 2 H, $H^4$), 7.25 (dt, $J$ = 7.6 Hz, 2 H, $H^2$), 7.18 (dt, $J$ = 7.6 Hz, 2 H, $H^{2'i}$), 6.84 (s, 1 H, $H^5$), 6.49 (d, $J$ = 7.3 Hz, 2 H, $H^{1'o}$), 5.44 (d, $J$ = 7.3 Hz, 2 H, $H^{1'i}$), 3.67 (s, 6 H, $R^2$ = $CH_3$); assignments made on the basis of the COSY and the ROESY spectra. ES-MS: $m/z$ (%) = 637 (100) [(**7**$_4$Zn$_4$)$(CF_3SO_3)_4]^{4+}$.

**Complex [$8_4Zn_4$]$(CF_3SO_3)_8$ (14):** $^1$H NMR ($CDCl_3$, ppm): $\delta$ = 10.97 (s, 2 H, $R^2$ = H), 8.05 (t, $J$ = 7.6 Hz, 2 H, $H^{3'}$), 7.76 (dt, $J$ = 7.6 Hz, 2 H, $H^3$), 7.80 (dt, $J$ = 7.6 Hz, 2 H, $H^{2'o}$), 7.79 (d, $J$ = 3.6 Hz, 2 H, $H^4$), 7.66 (d, $J$ = 3.6 Hz, 2 H, $H^1$), 7.27 (dt, $J$ = 7.6 Hz, 2 H, $H^2$), 7.07 (dt, $J$ = 7.6 Hz, 2 H, $H^{2'i}$), 6.74 (s, 1 H, $H^5$), 6.48 (d, $J$ = 7.3 Hz, 2 H, $H^{1'o}$), 5.51 (d, $J$ = 7.3 Hz, 2 H, $H^{1'i}$), 2.40 (s, 6 H, $R^1$ = $CH_3$); assignments made on the basis of the COSY and the ROESY spectra. ES-MS: $m/z$ (%) = 637 (100) [(**8**$_4$Zn$_4$)$(CF_3SO_3)_4]^{4+}$.

**Complex [$9_4Zn_4$]$(CF_3SO_3)_8$ (15):** $^1$H NMR ($CDCl_3$, ppm): $\delta$ = 7.96 (t, $J$ = 7.6 Hz, 2 H, $H^{3'}$), 7.88 (dt, $J$ = 7.6 Hz, 2 H, $H^3$), 7.72 (dt, $J$ = 7.6 Hz, 2 H, $H^{2'o}$), 7.60 (d, $J$ = 3.6 Hz, 2 H, $H^4$), 7.37 (d, $J$ = 3.6 Hz, 2 H, $H^1$), 7.06 (dt, $J$ = 7.6 Hz, 2 H, $H^2$), 7.03 (dt, $J$ = 7.6 Hz, 2 H, $H^{2'i}$), 6.60 (s, 1 H, $H^5$), 6.56 (d, $J$ = 7.3 Hz, 2 H, $H^{1'o}$), 5.18 (d, $J$ = 7.3 Hz, 2 H, $H^{1'i}$), 3.80 (s, 6 H, $R^2$ = $CH_3$) 2.57 (s, 6 H, $R^1$ = $CH_3$); assignments made on the basis of the COSY and the ROESY spectra. ES-MS: $m/z$ (%) = 669.5 (100) [(**9**$_4$Zn$_4$)-$(CF_3SO_3)_4]^{4+}$.

**Complex [$10_4Zn_4$]$(CF_3SO_3)_8$ (16):** $^1$H NMR ($CDCl_3$, ppm): $\delta$ = 12.09 (s, 6 H, $R^2$ = H) 8.19 (t, $J$ = 7.6 Hz, 2 H, $H^{3'}$), 8.09 (s, 6 H, $R^1$ = H), 7.89 (s, 1 H, $H^5$), 7.75 (dt, $J$ = 7.6 Hz, 2 H, $H^3$), 7.49 (dt, $J$ = 7.6 Hz, 2 H, $H^{2'}$), 7.39 (d, $J$ = 3.6 Hz, 2 H, $H^1$), 6.97 (d, $J$ = 3.6 Hz, 2 H, $H^4$), 6.84 (dt, $J$ = 7.6 Hz, 2 H, $H^2$), 5.92 (d, $J$ = 7.3 Hz, 2 H, $H^{1'o}$), 5.82 (d, $J$ = 7.3 Hz, 2 H, $H^{1'i}$); assignments made on the basis of the COSY and the ROESY spectra. ES-MS: $m/z$ (%) = 610 (100) [(**10**$_4$Zn$_4$)$(CF_3SO_3)_4]^{4+}$.

**Complex [$11_4Zn_4$]$(CF_3SO_3)_8$ (17):** Ligand **11** (38 mg, 0.1 mmol) and $Zn(OTf)_2$ (38 mg, 0.11 mmol) gave after recrystallization from acetonitrile/diethyl ether, 48 mg (63%) of greenish yellow crystals $^1$H NMR ($CD_3CN$, ppm): $\delta$ = 11.80 (s, 8 H, $R^2$ = H) 8.14 (t, $J$ = 7.6 Hz, 8 H, $H^{3'}$), 8.07 (s, 4 H, $H^5$), 7.88 (s, 8 H, $R^1$ = H), 7.75 (ddd, $J$ = 1.6, 7.4, 8.2, Hz 2 H, $H^3$), 7.45 (t, $J$ = 7.7 Hz, 2 H, $H^{2'}$), 7.39 (dd, $J$ = 0.8 Hz, 5.5, 2 H, $H^1$), 6.98 (d, $J$ = 8.5 Hz, 2 H, $H^4$), 6.83 (td, $J$ = 0.8 Hz, 1.6, 5.5, 2 H, $H^2$), 5.92 (d, $J$ = 7.1 Hz, 2 H, $H^{1'o}$), 5.84 (d, $J$ = 7.1 Hz, 2 H, $H^{1'i}$); assignments made on the basis of the COSY and the ROESY spectra. $^{13}$C NMR ([D$_3$]acetonitrile, ppm): $\delta$ = 166.1, 157.8, 148.9, 146.1, 142.8, 135.8, 134.0, 131.0, 129.0, 127.1, 123.1, 123.0, 121.0, 120.5, 111.9. ES-MS: $m/z$ (%) = 545 (100) 395 (45). **11**$_4$Zn$_4$$(CF_3SO_3)_8$ (3031.8): calcd. C 38.03, H 2.39, N, 14.78; found C 37.13, H 2.37, N 14.51.

**Complex [$12_4Zn_4$]$(CF_3SO_3)_8$ (18):** Ligand **12** (42 mg, 0.1 mmol) and $Zn(OTf)_2$ (38 mg, 0.1 mmol) gave after recrystallization from acetonitrile/diethyl ether, 55 mg (68%) of orange crystals with $^1$H NMR ($CD_3CN$, ppm): $\delta$ = 8.16 (t, $J$ = 7.6 Hz, 4 H, $H^{3'}$), 8.14 (s, 8 H, $H^5$), 7.86 (m, 16 H, $R^1$ = H, $H^3$), 7.53 (t, $J$ = 7.4 Hz, 4 H, $H^{2'o}$), 7.34 (m, 12 H, $H^1$,$H^{2'i}$), 7.29 (d, $J$ = 8.5 Hz, 8 H, $H^4$), 6.93 (dd, $J$ = 6.7 Hz, 5.4, 8 H, $H^2$), 5.89 (d, $J$ = 7.4 Hz, 4 H, $H^{1'o}$), 5.81 (d, $J$ = 7.7 Hz, 4 H, $H^{1'i}$), 3.51 (s, 24 H, $R^2$ = $CH_3$). $^{13}$C NMR (ppm): $\delta$ = 165.8, 157.9, 149.5, 146.8, 143.2, 135.1, 133.8, 130.2, 129.7, 129.0, 127.7, 123.8, 122.0, 121.1, 111.7, 34.0; assignments made on the basis of the COSY and the ROESY spectra. ES-MS: $m/z$ (%) mass envelope at 637 (100) [(**12**$_4$Zn$_4$)$(CF_3SO_3)_4]^{4+}$: calcd. C 39.73, H 2.82, N 14.26; found C 37.83 H 2.54 N 13.46

**Complex [$11^{2-}_4Zn_4$] (19) Method 1:** 2-Phenylpyrimidine-4,6-dicarbaldehyde bis[(pyridin-2-yl)hydrazone], (0.11 g, 0.28 mmol) was suspended in EtOH (20 mL), and a solution of anhydrous $ZnCl_2$ (0.04 g ) in EtOH (1 mL) was added. After stirring 5 min, the dark brown solution was made basic by the addition of 2 equiv. NaOH whereupon the mixture turned blue-purple. Evaporation left a dark purple-bronze solid that was purified by dissolution in THF, filtration and evaporation of the filtrate. The residue was recrystallized from water/EtOH to give small, golden, pyramidal crystals (85 mg, 66%)

**Method 2:** Complex **17** (20 mg) was dissolved in acetonitrile (2 mL) and excess triethylamine (10 μL) was added. The solution immedi-

 © 2006 Wiley-VCH Verlag GmbH & Co. KGaA, Weinheim 

ately turned dark blue and small golden crystals of complex **19** began to precipitate. After standing for 15 h, these were removed by filtration and dried to give 3.9 mg (33%). Spectral properties of both products were identical. $^1$H NMR ([D$_6$]DMSO, ppm): $\delta$ = 5.96 (d, $J$ = 7.7 Hz, 8 H), 6.32 (t, $J$ = 5.8 Hz, 8 H), 6.56 (d, $J$ = 8.2 Hz, 8 H), 6.64 (s, 4 H), ≈ 6.95 (m, 16 H), 7.02 (s, 8 H), 7.29 (ddd, 8 H, $J$ = 8.2, 7.1, 2.0 Hz), 7.49 (t, $J$ = 7.3 Hz, 4 H). $^1$H NMR ($CDCl_3$, 40 °C, ppm) d 6.09 (d, $J$ = 7.2 Hz, 8 H), 6.246 (s, 4 H), 6.27 (t, $J$ = 6.3 Hz, 8 H), 6.65 (d, $J$ = 8.3 Hz, 8 H), 7.02 (s, 8 H), 7.06 (t, 8 H, $J$ = 7.2 Hz), 7.11 (d, $J$ = 5.2 Hz, 8 H), 7.23 (m, 8 H), 7.52 (t, $J$ = 7.4 Hz, 4 H). $^{13}$C NMR (25 °C, [D$_6$]DMSO, ppm): $\delta$ = 165.13, 162.04, 156.88, 143.83, 139.28, 138.02, 129.04 (broad), 128.48 (broad), 128.16, 125.36, 123.79, 117.16, 115.51. $^{13}$C NMR ($CDCl_3$, 40 °C, ppm): $\delta$ = 165.48, 161.74, 156.92, 144.00, 138.51, 138.21, 128.67, 128.05, 125.64, 123.35, 117.06, 115.45, 110.40. IR (NaCl plate): $\tilde{\nu}$ = 1587, 1548, 1513, 1476, 1458, 1412, 1334, 1295, 1269, 1236, 1113, 1093, 984 cm$^{-1}$; ES-MS (solution in DMSO/NaCl): $m/z$(%) = 1831 [(**11**$^{2-}{}_4$Zn$_4$)H]$^+$, 1855 [(**11**$^{2-}{}_4$Zn$_4$)Na]$^+$. (**11**$^{2-}{}_4$Zn$_4$)·10H$_2$O: calcd. C 52.55, H 4.21, N 22.28; found C 52.86, H 4.02, N 21.88.

**Crystal Structure Determinations:** X-ray diffraction data for compounds **13**–**15** were collected with a Nonius Kappa charge-coupled device (CCD) diffractometer with a graphite-monochromatized Mo-$K_\alpha$ radiation ($\lambda$ = 0.71073 Å). $\varphi$ scans at 173 K, at the Laboratoire de Cristallochimie, Université Louis Pasteur, Strasbourg. The structures of the compounds **13**–**15** were determined using direct methods and refined (based on $F_2$ using all independent data) by full-matrix least-square methods (SHELXTL 97). Data were reduced by using the Bruker SAINT software. Hydrogen atoms were included at calculated positions by using a riding model. Single crystals of **13**–**15** were grown from acetonitrile/benzene. Crystals were placed in oil and a single crystal was selected, mounted on a glass fiber and placed in a low-temperature $N_2$ stream. The structure of **2-H** and **2-DH** were determined using direct methods and refined (based on $F_2$ using all independent data) by full-matrix least-square methods (SHELXTL 97). Hydrogen atoms were included at calculated positions by using a riding model.

**Complex [5$_4$Zn$_4$](CF$_3$SO$_3$)$_8$ (13):** Yellow single crystal of (**7**$_4$Zn$_4$)(CF$_3$SO$_3$)$_8$ (**13**), ($C_{120}H_{112}F_{24}N_{40}O_{24}S_8Zn_4$) of dimension 0.18×0.16×0.14 mm. The structure contains four grid complexes together with thirty two triflate anions and thirty two acetonitrile molecules. The unit cell was monoclinic with a space group of $C2/c$. Cell dimensions: $a$ = 27.5875(4) Å, $b$ = 26.9243(4) Å, $c$ = 20.1356(3) Å, $\alpha = \gamma$ = 90°, $\beta$ = 92.759(5)°, $V$ = 14938.9(4) Å$^3$ and $Z$ = 8 (FW is 7072, $\rho$ = 1.54 g cm$^{-3}$). Reflections were collected from 2.5° ≤ $\theta$ ≤ 27.48° for a total of 17483 of which 9423 were unique having $I > 3\sigma(I)$; number of parameters is 931. Final $R$ factors were $R_1$ = 0.103 (based on observed data), $wR_2$ = 0.121 (based on all data), GOF = 1.303, maximum residual electron density is 1.406 e·Å$^{-3}$.

**Complex [6$_4$Zn$_4$](CF$_3$SO$_3$)$_8$ (14):** Single yellow crystals of (**8**$_4$Zn$_4$)(CF$_3$SO$_3$)$_8$ (**14**), ($C_{120}H_{112}F_{24}N_{40}O_{24}S_8Zn_4$) of dimension 0.08×0.08×0.08 mm. The structure contains eight grid complexes together with sixty four triflate anions, thirty two acetonitrile molecules and thirty two water molecules. The unit cell was tetragonal with a space group of $P42/n$. Cell dimensions: $a$ = 17.9114(3) Å, $b$ = 17.9114(3) Å, $c$ = 22.7093(4) Å, $\alpha = \gamma = \beta$ = 90°, $V$ = 7285.6(2) Å$^3$ and $Z$ = 8 (FW is 3440, $\rho$ = 1.54 g cm$^{-3}$). Reflections were collected from 2.5° ≤ $\theta$ ≤ 27.48° for a total of 15477 of which 3415 were unique having $I > 3\sigma(I)$; number of parameters is 428. Final $R$ factors were $R_1$ = 0.087 (based on observed data), $wR_2$ = 0.107 (based on all data), GOF = 1.280, maximum residual electron density is 1.269 e·Å$^{-3}$.

**Complex [7$_4$Zn$_4$](CF$_3$SO$_3$)$_8$ (15):** Single yellow crystals of (**9**$_4$Zn$_4$)(CF$_3$SO$_3$)$_8$ (**15**), ($C_{136}H_{145}F_{24}N_{38}O_{28}S_8Zn_4$) of dimension 0.16×0.13×0.10 mm. The structure contains two grid complexes together with sixteen triflate anions, twelve acetonitrile molecules, three benzene molecules, two ethanol molecules and four water molecules. The unit cell was triclinic with a space group of $P\bar{1}$. Cell dimensions: $a$ = 18.212(2) Å, $b$ = 20.4537(2) Å, $c$ = 23.5718(4) Å, $\alpha$ = 99.242(5)°, $\beta$ = 1000.793(5)°, $\gamma$ = 103.058(5)°, $V$ = 82112(2) Å$^3$ and $Z$ = 2 (FW is 3830, $\rho$ = 1.51 g cm$^{-3}$). Reflections were collected from 2.5° ≤ $\theta$ ≤ 27.48° for a total of 64440 of which 14197 were unique having $I > 3\sigma(I)$; number of parameters is 1987. Final $R$ factors were $R_1$ = 0.072 (based on observed data), $wR_2$ = 0.097 (based on all data), GOF = 1.598, maximum residual electron density is 1.558 e·Å$^{-3}$.

CCDC-288070 to -288072 contain the supplementary crystallographic data for this paper. These data can be obtained free of charge from The Cambridge Crystallographic Data Centre via www.ccdc.cam.ac.uk/data_request/cif.

## Acknowledgments

Funding for this work was provided by the Petroleum Research Fund (Award 39923-B1 to D. J. R. B.) and the National Science Foundation for purchase of NMR (DUE-ILI-9851311) and Electrospray MS (Award MRI-CHE0116181 to D. J. R. B.) spectrometers. This research was partly supported by the CNRS and the Collège de France (post-doctoral fellowship to M. B.).

[1] a) J.-M. Lehn, *Supramolecular Chemistry-Concepts and Perspectives*, VCH, Weinheim, **1995**, 124–138; b) J.-M. Lehn, *Science* **2002**, *295*, 2400–2403; c) J.-M. Lehn, *Proc. Natl. Acad. Sci. USA* **2002**, *99*, 4763–4768; d) S. Leininger, B. Olenyuk, P. J. Stang, *Chem. Rev.* **2000**, *100*, 853–908; e) G. F. Swiegers, T. F. Malfetese, *Chem. Rev.* **2000**, *100*, 3483–3538; f) B. J. Holliday, C. A. Mirkin, *Angew. Chem. Int. Ed.* **2001**, *40*, 2022–2043; g) S. R. Seidel, P. J. Stang, *Acc. Chem. Res.* **2002**, *35*, 972–983; h) M. Fujita, K. Umemoto, M. Yoshizawa, N. Fujita, T. Kusukawa, K. Biradha, *Chem. Commun.* **2001**, 509–518.

[2] a) M.-T. Youinou, N. Rahmouni, J. Ficher, J. A. Osborn, *Angew. Chem.* **1992**, *104*, 771–773; *Angew. Chem. Int. Ed. Engl.* **1992**, *31*, 733–735; b) P. N. W. Baxter, J.-M. Lehn, J. Ficher, M.-T. Youinou, *Angew. Chem.* **1994**, *106*, 2432–2434; *Angew. Chem. Int. Ed. Engl.* **1994**, *33*, 2284–2487; c) G. S. Hanan, D. Volkmer, U. S. Schubert, J.-M. Lehn, G. Baum, D. Fenske, *Angew. Chem.* **1997**, *109*, 1929–1931; *Angew. Chem. Int. Ed. Engl.* **1997**, *36*, 1842–1844; d) G. S. Hanan, Ph. D. thesis, Université Louis Pasteur, Strasbourg, 1995; e) D. M. Bassani, J.-M. Lehn, K. Fromm, D. Fenske, *Angew. Chem.* **1998**, *110*, 2534–2537; *Angew. Chem. Int. Ed. Engl.* **1998**, *37*, 2364–2367; f) J. Rojo, F. J. Romero-Salguero, J.-M. Lehn, G. Baum, D. Fenske, *Eur. J. Inorg. Chem. Eur. J. Inorg. Chem* **1999**, *9*, 1421–1428; g) M. Ruben, J. Rojo, F. J. Romero-Salguero, L. H. Uppadine, J.-M. Lehn, *Angew. Chem.* **2004**, *116*, 3728–3747; *Angew. Chem. Int. Ed.* **2004**, *43*, 3644–3662; h) G. S. Hanan, D. Volkmer, J.-M. Lehn, *Can. J. Chem.* **2004**, *82*, 1428–1434.

[3] a) M. Ruben, E. Breuning, J.-P. Gisselbrecht, J.-M. Lehn, *Angew. Chem.* **2000**, *112*, 4312–4315; *Angew. Chem. Int. Ed.* **2000**, *39*, 4139–4142; b) M. Ruben, E. Breuning, M. Barboiu, J.-P. Gisselbrecht, J.-M. Lehn, *Chem. Eur. J.* **2003**, *9*, 291–299.

[4] a) E. Breuning, M. Ruben, J.-M. Lehn, F. Renz, V. Ksenofotov, P. Gütlich, E. Wengelius, K. Rissanen, *Angew. Chem.* **2000**, *112*, 2563–2566; *Angew. Chem. Int. Ed.* **2000**, *39*, 2504–2507; b) M. Ruben, E. Breuning, J.-M. Lehn, V. Ksenofontov, F. Renz, P. Gütlich, G. B. M. Vaughan, *Chem. Eur. J.* **2003**, *9*, 4422–4429; c) M. Ruben, U. Ziener, J.-M. Lehn, V. Ksenofon-

 © 2006 Wiley-VCH Verlag GmbH & Co. KGaA, Weinheim 

tov, P. Gütlich, G. B. M. Vaughan, *Chem. Eur. J.* **2005**, *11*, 94–100.
[5] a) D. M. Bassani, J.-M. Lehn, *Bull. Soc. Chim. Fr.* **1997**, *134*, 897–906; b) M. Ohkita, J.-M. Lehn, G. Baum, D. Fenske, *Chem. Eur. J.* **1999**, *12*, 3471–3481.
[6] a) K. M. Gardinier, R. G. Khoury, J.-M. Lehn, *Chem. Eur. J.* **2000**, *6*, 4124–4131; b) J.-L. Schmitt, A.-M. Stadler, N. Kyritsakas, J.-M. Lehn, *Helv. Chim. Acta* **2003**, *86*, 1598–1624.
[7] a) M. Ruben, J.-M. Lehn, G. Vaughan, *Chem. Commun.* **2003**, 1338–1339; b) L. H. Uppadine, J. M. Lehn, *Angew. Chem. Int. Ed.* **2004**, *43*, 240; c) L. H. Uppadine, J. P. Gisselbrecht, J. M. Lehn, *Chem. Commun.* **2004**, 718; d) J. Nitschke, J.-M. Lehn, unpublished work.
[8] M. Barboiu, J.-M. Lehn, unpublished work.
[9] R. W. Green, P. S. Hallman, F. Lions, *Inorg. Chem.* **1964**, *3*, 376.
[10] J. L. Schmitt, A. M. Stadler, N. Kyritsakas, J. M. Lehn, *Helv. Chim. Acta* **2003**, *86*, 1598–1624.

Received: October 28, 2005
Published Online: December 27, 2005

 © 2006 Wiley-VCH Verlag GmbH & Co. KGaA, Weinheim 

DOI: 10.1002/ejic.200500450

# Mechanism of the MeOH/$H_2O$ Substitution in a Series of Biomimetic Bimetallo Zinc-Based $H_3O_2$ Complexes

**Elke Jaime[a] and Jennie Weston*[a]**

**Keywords:** Density functional calculations / Enzyme models / Metalloenzymes / $H_3O_2$ bridges / Zinc

Small bimetallo biomimetic zinc-based compounds containing a bridging μ-OH functionality can be easily hydrated to yield complexes containing an intramolecular Zn–$H_3O_2$–Zn bridge. Because such bridges are intrinsically more nucleophilic than the corresponding μ-OH functionality, this effectively activates the complex. The Zn–$H_3O_2$–Zn unit is labile, and one can successively substitute the "water" and the "hydroxide" in the bridge for methanol and methoxide to form metal-bound HO–H–OMe and MeO–H–OMe functionalities. We have performed an extensive density functional investigation of this substitution mechanism for a series of bimetallo zinc complexes which have been synthesised and investigated by F. Meyer et al. There are two mechanisms for water/methanol exchange – an addition–elimination and a direct exchange mechanism. If the metal ions are coordinatively unsaturated, and their ligand sphere does not sterically hinder the approach of the methanol, both pathways compete with each other. For coordinatively saturated bimetallo complexes with larger ligand spheres, only the direct exchange mechanism is possible. Regardless of the mechanism operating, the exchange is facile and is controlled by the relative thermodynamic stability of the intermediates.
(© Wiley-VCH Verlag GmbH & Co. KGaA, 69451 Weinheim, Germany, 2006)

## Introduction

Binuclear metallo-hydrolases have been recognised as a wide class of enzymes which contain two divalent metal ions in close proximity to each other (3.5–4.5 Å apart) in the active site, that work together in a cocatalytic manner to activate various organic substrates for hydrolysis.[1] The resting state of these enzymes often contains a μ-hydroxide bridge where a deprotonated water molecule is shared between the ions.[1] This μ-OH linkage can be relatively easily hydrated to form an intramolecular M–$H_3O_2$–M functionality. This is not surprising because $H_3O_2^-$ anions are quite stable in the gas phase[2] and can even be crystallised as isolated $H_3O_2^-$ anions in the solid state.[3] In the meantime, small inorganic complexes containing such $H_3O_2$ linkages have been reported for most of the first-row transition-metal ions (V,[4] Cr,[5,6] Fe,[7] Co,[6,8] Ni,[9,10] Cu[10] and Zn[11]), as well as for Mo,[12] W[12] and Ru.[13] In several cases, F. Meyer et al. have shown that it is possible to *selectively* obtain the μ-OH or the M–$H_3O_2$–M form by fine-tuning the ligand environment.[9b,14] In addition, one can replace the μ-OH and/or the $H_3O_2$ functionality with other ligands; for example fluoride,[15] chloride,[16] nitriles,[9d] N=C=O,[9e] carboxylates,[9e,9f] urea,[9a,9b] or $N_3^-$.[17]

The pyrazolate dinucleating ligand **1a** developed by F. Meyer et al. leads to the urease biomimetic $\mathbf{1_{Ni}a}$ in the presence of nickel ions.[9a] The M–$H_3O_2$–M functionality in $\mathbf{1_{Ni}a}$ is rather labile, as extensive kinetic studies have shown (Scheme 1).[9a] If $\mathbf{1_{Ni}a}$ is dissolved in absolute methanol, a rapid ligand exchange occurs and a $CH_3O$–H–$OCH_3$ bridged species $\mathbf{1_{Ni}c}$ can be isolated.[9a] In methanol/water mixtures, an equilibrium between three different species ($\mathbf{1_{Ni}a}$, $\mathbf{1_{Ni}b}$ and $\mathbf{1_{Ni}c}$) occurs. At low water concentrations (0.1 M) the predominate species is $\mathbf{1_{Ni}b}$ which can be independently isolated.[18] Raising the $H_2O$ concentration to 2 M shifts the equilibrium to favour $\mathbf{1_{Ni}a}$.[9a]

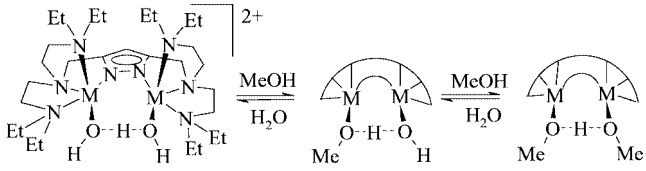


Scheme 1. Methanol substitution in the $H_3O_2$ bridge of a binuclear urease biomimetic developed by F. Meyer et al.

Meyer's pyrazolate ligand **1a** can also be used to obtain the corresponding zinc ($\mathbf{1_{Zn}a}$)[18] and cobalt ($\mathbf{1_{Co}a}$)[19] "$H_3O_2$" complexes; both of which are possible functional models for binuclear phosphatases and/or peptidases. As for the nickel complex $\mathbf{1_{Ni}a}$, the M–$H_3O_2$–M functionality

[a] Institut für Organische Chemie und Makromolekulare Chemie of the Friedrich-Schiller University,
Humboldtstrasse 10, 07743 Jena, Germany
Fax: +49-3641-948212
E-mail: c9weje@uni-jena.de
Supporting information for this article is available on the WWW under http://www.eurjic.org or from the author.

 © 2006 Wiley-VCH Verlag GmbH & Co. KGaA, Weinheim 

in $\mathbf{1}_{Zn}\mathbf{a}$ and $\mathbf{1}_{Co}\mathbf{a}$ is relatively labile and can be successively exchanged with methanol in the same manner as illustrated in Scheme 1.[18,19]

Many mononuclear zinc complexes (biomimetics for carbonic anhydrase,[20] for example) contain a metal-bound hydroxide ligand. Although the p$K_a$ value of water (15.7) and methanol (15.1) are very similar, the Zn–OH form usually predominates in methanolic solutions, rather than the corresponding M–$OCH_3$ form.[21] In contrast to this, F. Meyer et al. have clearly demonstrated that, for the binuclear analogues, it is possible to select which form is present ($\mathbf{1}_{M}\mathbf{a}$, $\mathbf{1}_{M}\mathbf{b}$ or $\mathbf{1}_{M}\mathbf{c}$) by carefully controlling the reaction conditions.[18,19] This could possibly open new synthetic applications for functional binuclear biomimetica, and we have therefore, in co-operation with the research group of F. Meyer, recently become interested in the mechanism of this water/methanol exchange reaction.

There are fundamentally two possible mechanisms for the substitution of water bound in a bimetallo $H_3O_2$ linkage; both of which we considered in this study – an addition–elimination and a direct exchange mechanism. In the addition–elimination variant, the methanol first binds to one of the metal ions and, in a second step, displaces the water in the $H_3O_2$ bridge. Such an addition–elimination mechanism requires a free binding position at the metal ion, thus implicating a certain coordinative flexibility for the transition-metal ions involved. In the second variant, the methanol directly attacks the $H_3O_2$ bridge and replaces water through a direct exchange mechanism.

## Results and Discussion

### Model Systems

We selected three different model systems for study – a very simple carboxylate-bridged complex $\mathbf{2}_{Zn}\mathbf{a}$ (Scheme 2) which simulates the active site of many hydrolases containing two tetrahedrally coordinated metal ions held together by a bridging carboxylate ligand.[1] Compound $\mathbf{2}_{Zn}\mathbf{a}$ is small enough to investigate the hypersurface of these substitution reactions in detail. We then investigated the effect of the ligand sphere and the metal coordination geometry on the fundamental mechanism by means of Meyer's pyrazolate ligand-based complex $\mathbf{1}_{Zn}\mathbf{a}$,[18,19] and substituting the *N*-ethyl groups for *N*-methyl in order to reduce the calculational demand somewhat. This resulted in the model system $\mathbf{3}_{Zn}\mathbf{a}$. Increasing the complexity of the system, we then substituted the amino arms by pyridyl arms to yield the complex $\mathbf{4}_{Zn}\mathbf{a}$, which has also been reported by Meyer et al. to undergo reversible substitution by MeOH according to Scheme 1.[19] Both models $\mathbf{3}_{Zn}\mathbf{a}$ and $\mathbf{4}_{Zn}\mathbf{a}$ contain pentacoordinate metal ions. A comparison of all three of these models should allow us to determine how steric and electronic effects originating from the ligand sphere affects the intrinsic substitution mechanism(s). In all models, the ligand environments are symmetric for both metal cations. In the case of an asymmetric environment, the $H_3O_2$ functionality becomes polarised (as we have recently demonstrated for a computational model of the active site of bovine lens leucine aminopeptidase[22]) and one would need to investigate which "water" would be initially substituted. We selected zinc, because many of the natural systems are zinc-based hydrolases[1] and now report our findings in the present article. In continuance of our investigations, we are now calculating the cobalt analogues because many mechanistic investigations employ $Co^{2+}$-substituted enzymes due to the spectroscopic silence of $Zn^{2+}$.[23] It is quite often assumed that the mode of action of the $Co^{2+}$-substituted analogue parallels that of the natural $Zn^{2+}$-system – an assumption which we are now beginning to investigate in detail for these model compounds.

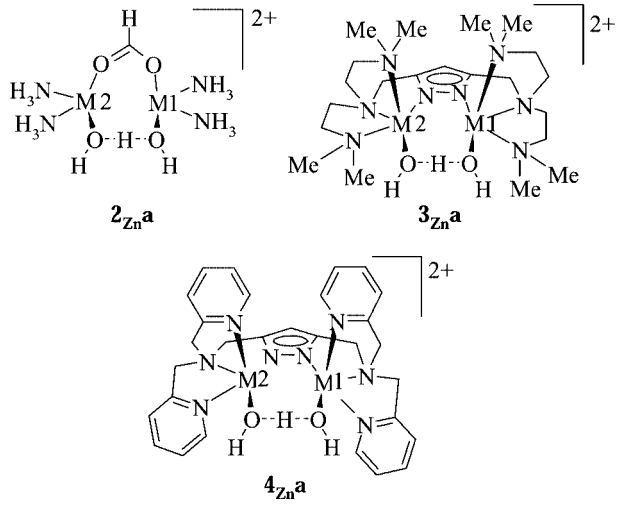


$\mathbf{2}_{Zn}\mathbf{a}$ $\mathbf{3}_{Zn}\mathbf{a}$

$\mathbf{4}_{Zn}\mathbf{a}$

Scheme 2. Model compounds selected for study.

### Substitution Mechanism

Extensive calculations on the smallest model system $\mathbf{2}_{Zn}\mathbf{a}$ revealed that the hypersurface for the second methanol substitution is fundamentally the same as for the first. The following discussion therefore focuses on the mechanism of the first methanol/water exchange which is illustrated in Scheme 3 and Figure 1. The structures of the intermediates/transition structures involved in the second substitution can be found in the supporting information (Scheme S1 in the Supporting Information, for details see the footnote on the first page of this article).

As a methanol approaches the $H_3O_2$ bridge in compound $\mathbf{2}_{Zn}\mathbf{a}$, it interacts with the bridge to form a hydrogen-bonded initial encounter complex $\mathbf{2}_{Zn}\mathbf{E1}$. The methanolic oxygen is within electrostatic range (contact) of Zn1. In addition, the methanolic proton just barely "sees" the O2 in the $H_3O_2$ bridge. Each of these two rather weak electrostatic contacts is capable of opening up a different substitution pathway. If the MeOH swings up over transition structure $\mathbf{2}_{Zn}\mathbf{T1}$ and binds to Zn1 to generate the stable intermediate $\mathbf{2}_{Zn}\mathbf{1}$, a two-step addition–elimination mechanism is accessed. Addition of the MeOH triggers a conformational change from a tetrahedral to a trigonal bipyramidal binding situation at Zn1. This is a very low energy process with

 © 2006 Wiley-VCH Verlag GmbH & Co. KGaA, Weinheim 

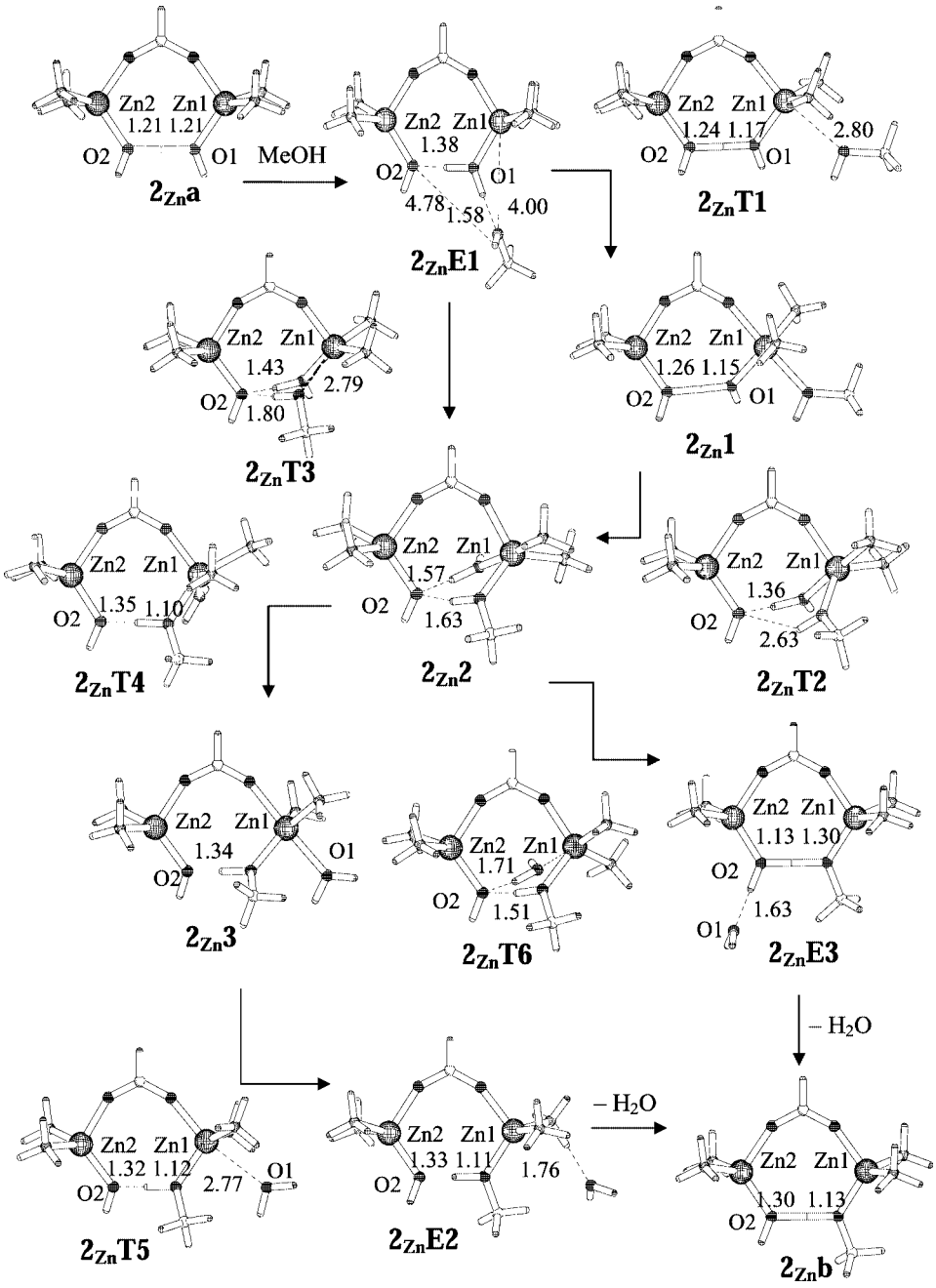


Scheme 3. Mechanism of the first $H_2O$/MeOH substitution in the model complex $\mathbf{2}_{Zn}$.

an activation barrier of only 3.3 kcal/mol respective to the encounter complex $\mathbf{2}_{Zn}$**E1** (Table 1). The differential coordination of the metal ions slightly polarises the $H_3O_2$ bridge in the direction of a Zn1-bound hydroxide and a Zn2-bound water in $\mathbf{2}_{Zn}$**1**. The barrier for hydrogen transfer is extremely low (less than 1 kcal/mol) and the hydrogen can easily move between both oxygen atoms in the bridge. In the second step of this addition–elimination pathway, a pseudorotation on Zn1 over the transition structure $\mathbf{2}_{Zn}$**T2** swings the MeOH into the plane of the bridge which begins to disrupt the $H_3O_2$ functionality. This coupled process exhibits a somewhat higher barrier (6.6 kcal/mol respective to $\mathbf{2}_{Zn}$**1**). The barrier is approximately additive, because 2–3 kcal/mol are needed for the pseudorotation and 3–4 kcal/mol for bridge distortion. In the course of this process, the methanolic proton builds a strong hydrogen bond to O2 which transfers the bridging hydrogen to O1. The stable intermediate $\mathbf{2}_{Zn}$**2** is generated, in which the MeOH and the (formerly bridging) water are now both bound in a lateral manner to Zn1 and a hydroxide (O2) is localised on Zn2.

In an alternative mechanism, intermediate $\mathbf{2}_{Zn}$**2** can be accessed in a one-step manner from the initial encounter complex $\mathbf{2}_{Zn}$**E1**. In this second pathway, the MeOH swings towards the $H_3O_2$ bridge over transition structure $\mathbf{2}_{Zn}$**T3** and inserts itself between the metal ions. In the absence of steric effects originating from the ligand sphere, the effective

 © 2006 Wiley-VCH Verlag GmbH & Co. KGaA, Weinheim 

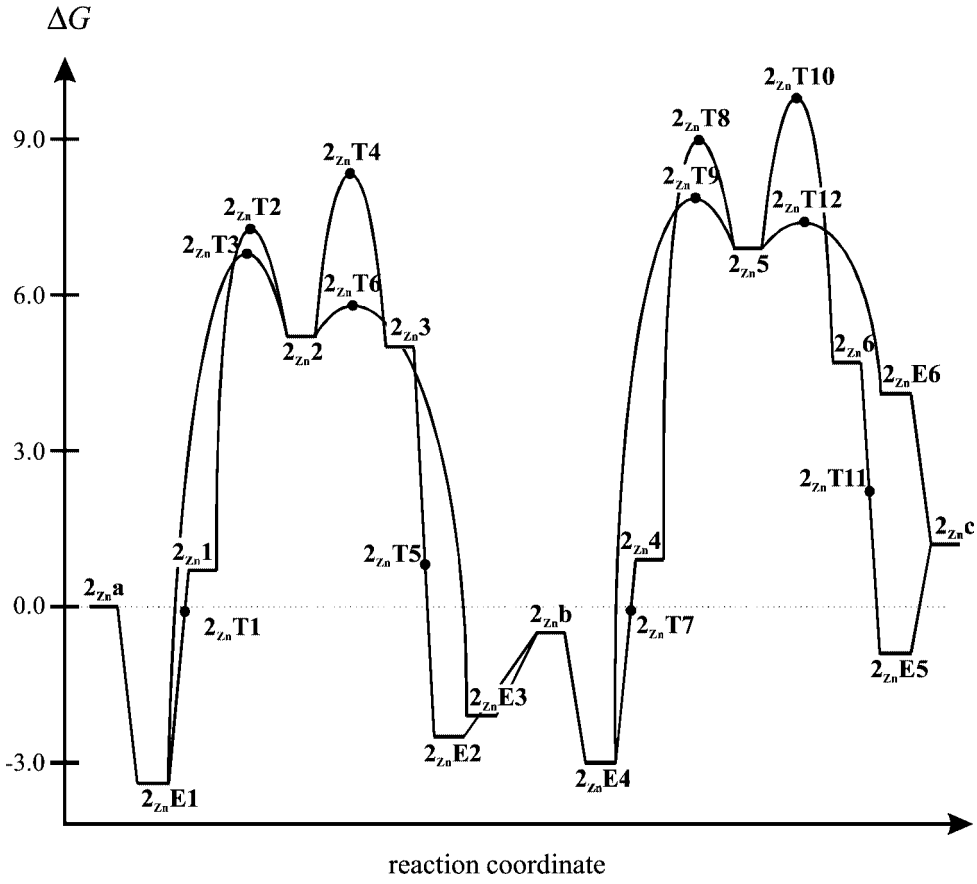


Figure 1. Energy diagram of water/methanol substitution in $\mathbf{2_{Zn}}$. Calculated at the B3LYP/aug–cc–pVTZ level of theory and given relative to $\mathbf{2_{Zn}a}$ and a free methanol.

Table 1. Relative energies (Gibb's free energies of reaction) for methanol/water exchange in the model complexes $\mathbf{2_{Zn}}$. Calculated at the B3LYP/aug-cc-pVTZ level of theory and given in kcal/mol relative to $\mathbf{2_{Zn}a}$ and a free methanol.

| First substitution | $\Delta G$ | Second substitution | $\Delta G$ |
|---|---|---|---|
| $\mathbf{2_{Zn}a}$ | 0.0 | $\mathbf{2_{Zn}b}$ | –0.5 |
| $\mathbf{2_{Zn}E1}$ | –3.4 | $\mathbf{2_{Zn}E4}$ | –3.0 |
| $\mathbf{2_{Zn}T1}$ | –0.1 | $\mathbf{2_{Zn}T7}$ | –0.1 |
| $\mathbf{2_{Zn}1}$ | 0.7 | $\mathbf{2_{Zn}4}$ | 0.9 |
| $\mathbf{2_{Zn}T2}$ | 7.3 | $\mathbf{2_{Zn}T8}$ | 9.0 |
| $\mathbf{2_{Zn}T3}$ | 6.8 | $\mathbf{2_{Zn}T9}$ | 7.9 |
| $\mathbf{2_{Zn}2}$ | 5.2 | $\mathbf{2_{Zn}5}$ | 6.9 |
| $\mathbf{2_{Zn}T4}$ | 8.3 | $\mathbf{2_{Zn}T10}$ | 9.8 |
| $\mathbf{2_{Zn}3}$ | 5.0 | $\mathbf{2_{Zn}6}$ | 4.7 |
| $\mathbf{2_{Zn}T5}$ | 0.8 | $\mathbf{2_{Zn}T11}$ | 2.2 |
| $\mathbf{2_{Zn}E2}$ | –2.5 | $\mathbf{2_{Zn}E5}$ | –0.9 |
| $\mathbf{2_{Zn}T6}$ | 5.8 | $\mathbf{2_{Zn}T12}$ | 7.4 |
| $\mathbf{2_{Zn}E3}$ | –2.1 | $\mathbf{2_{Zn}E6}$ | 4.1 |
| $\mathbf{2_{Zn}b}$ | –0.5 | $\mathbf{2_{Zn}c}$ | 1.2 |

barriers for both processes are very similar and an equilibrium between both pathways can be expected.

Complex $\mathbf{2_{Zn}2}$ now expels the Zn1-bound water. This can again occur through either a two-step or a one-step mechanism. In the first possibility, a pseudorotation at Zn1 over transition structure $\mathbf{2_{Zn}T4}$ pulls the water down and away from its bridging position. A stable HO–H–OMe bridged species $\mathbf{2_{Zn}3}$ results which contains a pentacoordinate zinc. The activation barrier (relative to intermediate $\mathbf{2_{Zn}2}$) for this pseudorotation is with 3.1 kcal/mol again quite low. The zinc ion in $\mathbf{2_{Zn}3}$ then regains its original tetrahedral geometry by kicking out the axial water over transition structure $\mathbf{2_{Zn}T5}$. As the water leaves, it first builds an encounter complex $\mathbf{2_{Zn}E2}$ in which the departing water forms a hydrogen bond to one of the ammonia ligands before it finally departs to yield $\mathbf{2_{Zn}b}$ in which one of the waters has been substituted by methanol.

Alternatively, $\mathbf{2_{Zn}2}$ can expel the water over a one-step mechanism. The water departs over $\mathbf{2_{Zn}T6}$ in a lateral manner and simply swings down to build an encounter complex $\mathbf{2_{Zn}E3}$ before finally departing. The monosubstituted complex $\mathbf{2_{Zn}b}$ is characterised by a slightly asymmetric O–H–O bridge in which the shared hydrogen is more tightly bound to the methanol than the hydroxide.

The mechanism for substitution by a second methanol is almost identical to that calculated for the first substitution and is therefore illustrated in the supporting information (Scheme S1). An incoming methanol interacts with the hydroxide in the HO–H–OMe bridge of $\mathbf{2_{Zn}b}$ to build an initial encounter complex identical to $\mathbf{2_{Zn}E3}$. A stable intermediate analogue to $\mathbf{2_{Zn}2}$ is then generated either over a two-step metal-based addition–elimination or a one-step direct insertion mechanism. A water is then eliminated through

 © 2006 Wiley-VCH Verlag GmbH & Co. KGaA, Weinheim 

an analogous one- or two-step mechanism, which finally generates the bisubstituted product $\mathbf{2_{Zn}c}$ containing a symmetric MeO–H–OMe bridge.

As to be expected from the structural/mechanistic similarities calculated for both hypersurfaces (see Scheme 3 and Scheme S1 in the Supporting Information), the energetics of the first and the second substitution are very similar. All barriers are quite low (less than 10 kcal/mol), indicating that these processes are controlled by thermodynamic equilibrium processes. Throughout the course of these substitutions, the metal–metal distance remains with an average value of 4.57 Å quite constant.

The coordinational hypersurface is quite flat with pseudorotation barriers of only ca. 2–4 kcal/mol, thus facilitating an easy change in the coordination number. This is, in the case of zinc, not unusual[24] and is probably one of the reasons why nature often preferentially selects zinc over other transition-metal ions in the active site of multinuclear hydrolases.[1] Preliminary calculations (substitution of $Co^{2+}$ for $Zn^{2+}$ in model **2**) indicate that $Co^{2+}$ ions in binuclear systems also possess a flexible coordination sphere – and the mechanism for $H_2O$/methanol substitution is nearly independent of the identity of the metal ion.[25]

**Ligand-Sphere Effects**

We then turned our attention to the sterically more demanding system $\mathbf{3_{Zn}a}$ (Scheme 2) in which both metal ions are pentacoordinate. After extensive calculations, we conclude that the steric bulk of the ligands prevents an easy expansion to an octahedral coordination sphere. We did not succeed in finding a single stable intermediate with an axial Zn–OHMe coordination analogue to the species $\mathbf{2_{Zn}1}$ (Scheme 3). The hypersurface is thus considerably simplified because only a one-step, direct substitution mechanism is possible. Although bulky, the ligand environment allows the methanol to approach the $H_3O_2$ bridge in $\mathbf{3_{Zn}a}$ from beneath, and an initial hydrogen-bound encounter complex $\mathbf{3_{Zn}E1}$ is formed (Scheme 4). The methanol then swings in to interact with Zn1 (which undergoes a partial pseudorotation), thus disrupting the $H_3O_2$ bridge. In the transition structure $\mathbf{3_{Zn}T1}$, the MeOH and the (formerly bridging) water are now bound to Zn1, which is octahedrally coordinated, and a hydroxide is localised on Zn2. Steric constraints of the ligand environment stiffens the coordination sphere of Zn1 and destabilises $\mathbf{3_{Zn}T1}$, thus leading to a much larger barrier for the substitution (17.1 kcal/mol;

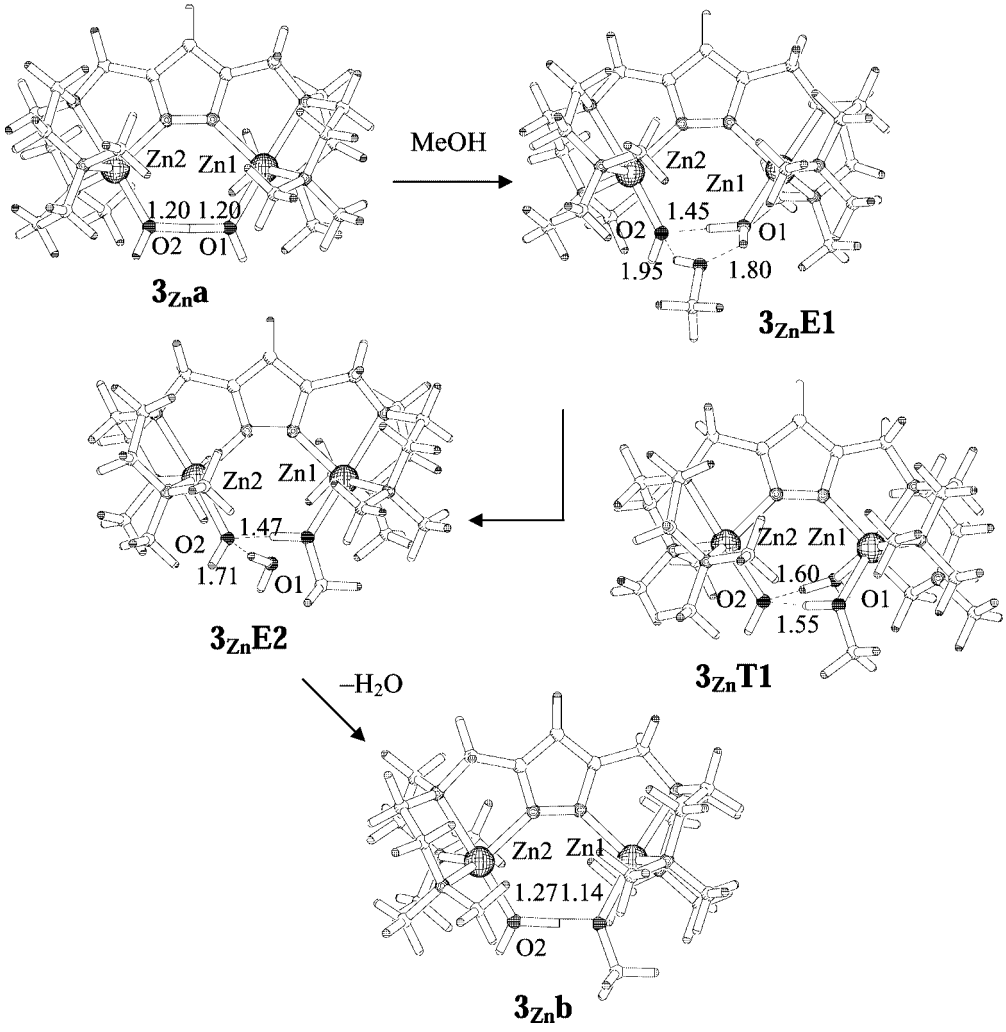


Scheme 4. Mechanism of the first $H_2O$/MeOH substitution in model complex $\mathbf{3_{Zn}}$.

 © 2006 Wiley-VCH Verlag GmbH & Co. KGaA, Weinheim 

Table 2) than for the flexible model $\mathbf{2_{Zn}}$ (for which the corresponding structure $\mathbf{2_{Zn}2}$ is a stable intermediate). The complex $\mathbf{3_{Zn}T1}$ then eliminates the water which retains electrostatic contact with O2 and departs over a second encounter complex $\mathbf{3_{Zn}E2}$. The mechanism for introducing a second MeOH into the bridge to generate $\mathbf{3_{Zn}c}$ is completely analogue. The intermediates/transition structure for this second step can be found in Scheme S2 (Supporting Information).

Table 2. Relative energies (Gibb's free energies of reaction) for methanol/water exchange in the model complexes $\mathbf{3_{Zn}}$ and $\mathbf{4_{Zn}}$. Calculated at the B3LYP/lanl2dz level of theory and given in kcal/mol relative to $\mathbf{3_{Zn}a}$ or $\mathbf{4_{Zn}a}$ and a free methanol.

| | $\Delta G$ | | $\Delta G$ |
|---|---|---|---|
| $\mathbf{3_{Zn}a}$ | 0 | $\mathbf{4_{Zn}a}$ | 0 |
| $\mathbf{3_{Zn}E1}$ | 0 | $\mathbf{4_{Zn}E1}$ | –4.7 |
| $\mathbf{3_{Zn}T1}$ | 17.1 | $\mathbf{4_{Zn}T1}$ | 10.5 |
| $\mathbf{3_{Zn}E2}$ | 7.1 | $\mathbf{4_{Zn}1}$ | 5.8 |
| $\mathbf{3_{Zn}b}$ | 4.8 | $\mathbf{4_{Zn}T2}$ | 7.7 |
| $\mathbf{3_{Zn}E3}$ | 9.0 | $\mathbf{4_{Zn}E2}$ | –1.2 |
| $\mathbf{3_{Zn}T2}$ | 23.6 | $\mathbf{4_{Zn}b}$ | 3.3 |
| $\mathbf{3_{Zn}E4}$ | 13.8 | $\mathbf{4_{Zn}E3}$ | –1.1 |
| $\mathbf{3_{Zn}c}$ | 10.4 | $\mathbf{4_{Zn}T3}$ | 15.2 |
| | | $\mathbf{4_{Zn}2}$ | 10.4 |
| | | $\mathbf{4_{Zn}T4}$ | 11.8 |
| | | $\mathbf{4_{Zn}E4}$ | 8.6 |
| | | $\mathbf{4_{Zn}c}$ | 6.9 |

The hypersurface is illustrated in Figure 2. Methanol exchange is an endothermic process and the intermediates $\mathbf{3_{Zn}b}$ (HO–H–OMe bridge) and $\mathbf{3_{Zn}c}$ (MeO–H–OMe) are 4.8 and 10.4 kcal/mol respectively less stable than the $H_3O_2$ form $\mathbf{3_{Zn}a}$. Although steric constraints have considerably increased the barriers ($\mathbf{3_{Zn}T1}$ = 17.1; $\mathbf{3_{Zn}T2}$ = 23.6 kcal/mol), they are still low enough to enable an equilibrium between the three species to take place under experimental conditions. It is therefore not surprising, that the bisubstituted form **c** can only be isolated from absolute methanol. The barrier for the second addition is higher than for the first, which corresponds well with the fact that the monosubstituted form **b** is preferred in water/methanol mixtures.[18,19]

The largest system we investigated is $\mathbf{4_{Zn}a}$ which contains *N*-pyridyl arms (Scheme 2). The methanol prefers to directly attack the $H_3O_2$ bridge in much the same manner as calculated for the system $\mathbf{3_{Zn}}$. An initial encounter complex $\mathbf{4_{Zn}E1}$ is formed, which then undergoes a metal-assisted insertion over $\mathbf{4_{Zn}T1}$ (Scheme 5). The *N*-pyridyl arms are not as rigid as the *N*-methyl arms in model $\mathbf{3_{Zn}}$ (the flat aromatic rings can swing out and away from the $H_3O_2$ functionality much better than the bulky *N*-methyl groups). The substitution barrier of $\mathbf{4_{Zn}T1}$ (10.5 kcal/mol) therefore lies considerably below that calculated for $\mathbf{3_{Zn}}$ (17.1 kcal/mol). Because of this increased flexibility, the hypersurface (Scheme 5 and Figure 2) is somewhat more complicated than for the model $\mathbf{3_{Zn}}$. There is enough room to comfortably bind both the MeOH and the water in a lateral manner to Zn1, and a stable intermediate $\mathbf{4_{Zn}1}$ results, which can be directly compared to $\mathbf{2_{Zn}2}$ calculated for the most flexible model system. The water molecule then leaves the coordination sphere of the zinc ions via the transition structure $\mathbf{4_{Zn}T2}$ to first generate the encounter complex $\mathbf{4_{Zn}E2}$ and finally the stable mixed bridged species $\mathbf{4_{Zn}b}$. As for all other models, the mechanism for the second substitution is identical to the first and is illustrated in the supporting information (Scheme S3).

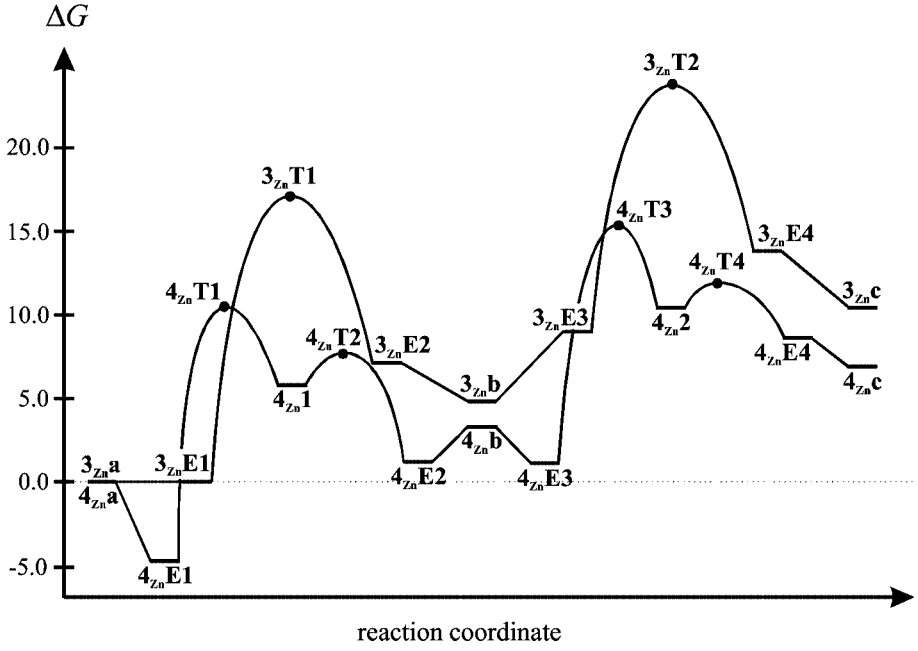


Figure 2. Energy diagram of water/methanol substitution in $\mathbf{3_{Zn}}$ and $\mathbf{4_{Zn}}$. Calculated at the B3LYP/lanl2dz level of theory and given relative to $\mathbf{3_{Zn}a}$ or $\mathbf{4_{Zn}a}$ and a free methanol.

 © 2006 Wiley-VCH Verlag GmbH & Co. KGaA, Weinheim 

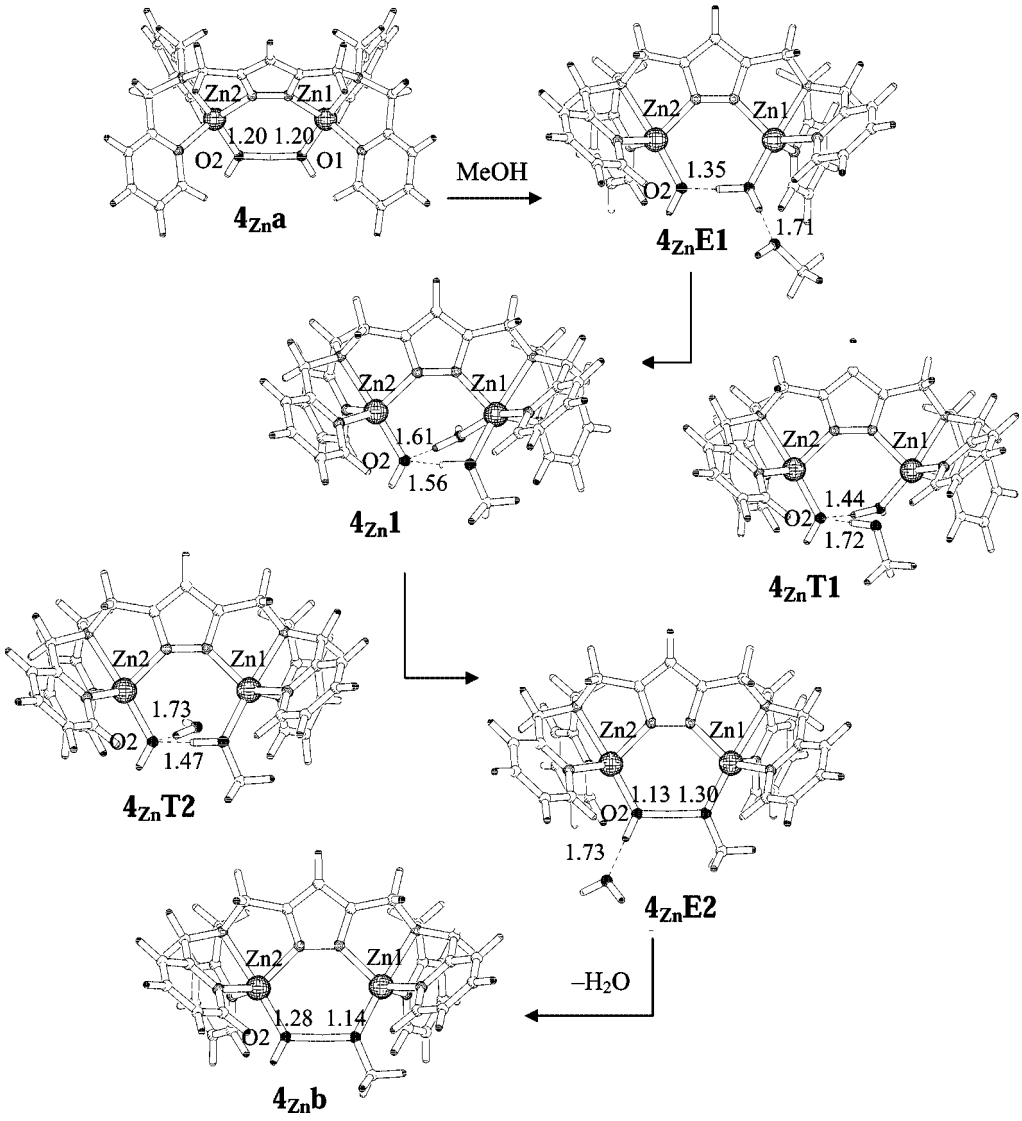


Scheme 5. Mechanism of the first $H_2O$/MeOH substitution in model complex $\mathbf{4_{Zn}}$.

**Relative Nucleophilicity**

Biomimetic complexes containing metallated A–O–H–O–B bridges (A, B = H and/or alkyl) are potentially quite interesting for synthetic applications because the refunctionalisation of simple esters, amides, phosphates, etc. under "biological" (mild) conditions is synthetically more valuable than their simple hydrolysis. We therefore addressed two final questions of interest – which functionality, the "hydroxide" or the "methoxide" in the bridge, will be the reacting nucleophile?

Due to the ionic nature of the Zn–O interactions, the oxygen atoms possess two lone electron pairs (the O–H–O three-centred bond and the OH/Me bonds are covalent in nature). One lone pair (sp-hybridised) is involved in the ionic bond and thus oriented towards the zinc cation. The orbital of the remaining lone pair is approximately p in character and is the only lone pair available (and properly oriented) for nucleophilic attack on an incoming substrate. The energy of this p-type orbital can be expected to be one of the major factors determining the nucleophilicity. The higher it lies, the easier will be an attack on the $\pi_{C=O}$* orbital of a substrate.

NBO (natural bond orbital) analyses (Table 3) show small but clear trends in the p-orbital energies as a function of increasing substitution by methanol. These trends are independent of the model (ligand sphere) selected. The "$H_3O_2$" species $\mathbf{X_{Zn}a}$ can clearly be expected to be the least and the "methoxide" species $\mathbf{X_{Zn}c}$ the most nucleophilic. It is quite interesting that, for mixed bridges ($\mathbf{X_{Zn}b}$), the calculations predict that the "hydroxide" will always be slightly (average difference of 0.2 eV in their orbital energies) more nucleophilic than the "methoxide". This means that practical applications (refunctionalisation instead of hydrolysis) will probably have to be carried out under non-aqueous conditions. The atomic charges (q) on oxygen in

 © 2006 Wiley-VCH Verlag GmbH & Co. KGaA, Weinheim 

Table 3. NBO atomic charges $q$ and the energy $\varepsilon$ (eV) of the nucleophilic lone electron pair (p-orbital) on oxygen.

| | | $q$[a] | $\varepsilon$ [eV][a] | | | $q$[b] | $\varepsilon$ [eV][b] | | | $q$[b] | $\varepsilon$ [eV][b] |
|---|---|---|---|---|---|---|---|---|---|---|---|
| $\mathbf{2_{Zn}a}$ | $O_{wat}$ | –1.17 | –15.0 | $\mathbf{3_{Zn}a}$ | $O_{wat}$ | –1.20 | –13.1 | $\mathbf{4_{Zn}a}$ | $O_{wat}$ | –1.20 | –12.8 |
| $\mathbf{2_{Zn}b}$ | $O_{wat}$ | –1.21 | –14.8 | $\mathbf{3_{Zn}b}$ | $O_{wat}$ | –1.23 | –13.0 | $\mathbf{4_{Zn}b}$ | $O_{wat}$ | –1.23 | –12.6 |
| | $O_{Me}$ | –0.95 | –14.5 | | $O_{Me}$ | –0.98 | –12.8 | | $O_{Me}$ | –0.99 | –12.4 |
| $\mathbf{2_{Zn}c}$ | $O_{Me}$ | –0.98 | –14.4 | $\mathbf{3_{Zn}c}$ | $O_{Me}$ | –1.01 | –12.6 | $\mathbf{4_{Zn}c}$ | $O_{Me}$ | –1.01 | –12.3 |

[a] Calculated using B3LYP/aug-cc-pVTZ wavefunctions. [b] Calculated using B3LYP/lanl2dz wavefunctions.

the bridges also show small but clear trends – opposing those calculated for the orbital energies. The oxygen atoms in the "$H_3O_2$" species $\mathbf{X_{Zn}a}$ are more negatively charged (average of 0.19 e) than those in the "methoxide" compounds $\mathbf{X_{Zn}c}$. This is due to the well known inductive effect of C–H bonds (partial delocalization of the negative charge on oxygen through hyperconjugation) and is a reason why charges should not be used to judge relative nucleophilicities.

## Conclusion

Extensive DFT calculations on a series of model complexes have provided mechanistic details for the experimentally observed replacement of water molecules by methanol (and other alcohols) in metallated M–$H_3O_2$–M functionalities. This replacement can occur through two fundamentally different substitution mechanisms – an addition–elimination, controlled by the metal ions, and a direct exchange mechanism in which the metal ions function as templates. If the ligand sphere in the bimetallo complex is flexible and there are free coordination holes on the metal ions, these mechanisms compete with each other. In the case of "stiff" ligands and a higher coordination number at the central ions, only the direct exchange mechanism is feasible. Stiffening the ligand sphere leads to an increase in the energy barrier for substitution. However, this effect is not enough to effectively hinder substitution under experimental conditions, and one can expect a thermodynamic equilibrium between all three possible intermediates ($H_3O_2$, HOHOMe and MeOHOMe bridges) to occur. A "methoxide" in such a bridge is fundamentally more nucleophilic than an "hydroxide". The "$H_3O_2$" form $\mathbf{X_{Zn}a}$ is clearly less nucleophilic than the "methoxide" form $\mathbf{X_{Zn}c}$. However, the "hydroxide" in a mixed species $\mathbf{X_{Zn}b}$ is more nucleophilic than the "methanol" component; a fact which will have experimental consequences.

## Computational Section

The calculations reported in this article were performed with the gradient-corrected, hybrid B3LYP[26] density functional using the Gaussian98[27] program package. In the case of the smallest model system $\mathbf{2_{Zn}}$, H, C, N and O were described with the very large correlation consistent aug-cc-pVTZ basis set.[28] The SDD basis[29] was employed for the central $Zn^{2+}$ ions. The size of the larger models $\mathbf{3_{Zn}}$ and $\mathbf{4_{Zn}}$ limited our computational investigations to the smaller lanl2dz basis set (D95[30] basis for the first row atoms and the Los Alamos effective core potential plus DZ was used for $Zn^{2+}$[31]). We found this smaller basis set to deliver qualitatively and quantitatively approximately the same results as the much larger aug-cc-pVTZ basis. All species found on the hypersurface were characterised as energetical minima or transition structures by vibrational analyses at the B3LYP/aug-cc-pVTZ or B3LYP/lanl2dz level of theory. Default convergence criteria were used and no symmetry was employed in any of the calculations. All relative stabilities reported are gas phase Gibb's free energies that contain standard thermochemical (298 K) and vibrational corrections. Natural bond orbital (NBO[32]) analyses were carried out using B3LYP/aug-cc-pVTZ (model $\mathbf{2_{Zn}}$) or B3LYP/lanl2dz wavefunctions (models $\mathbf{3_{Zn}}$ and $\mathbf{4_{Zn}}$) using NBO version 5.0[33] as patched into Gaussian98.

The mechanism for substitution by a second methanol is almost identical to that calculated for the first substitution for all model complexes ($\mathbf{2_{Zn}}$, $\mathbf{3_{Zn}}$ and $\mathbf{4_{Zn}}$) and is therefore illustrated in the supporting information, Schemes S1, S2 and S3 (see footnote on the first page of this article).

## Acknowledgments

Financial support by the Deutsche Forschungsgemeinschaft (Sonderforschungsbereich 436, Jena, Germany) and by the Thüringer Ministerium für Wissenschaft, Forschung und Kultur (Erfurt, Germany) is gratefully acknowledged. Special thanks goes to Franc Meyer and his research group for providing us with unpublished solid-state structures and for stimulating discussions.

[1] a) W. T. Lowther, B. W. Matthews, *Chem. Rev.* **2002**, *102*, 4581–4607; b) D. E. Wilcox, *Chem. Rev.* **1996**, *96*, 2435–2458; c) N. Sträter, W. N. Lipscomb, T. Klabunde, B. Krebs, *Angew. Chem. Int. Ed. Engl.* **1996**, *35*, 2024–2055; *Angew. Chem.* **1996**, *108*, 2158–2191; d) W. N. Lipscomb, N. Sträter, *Chem. Rev.* **1996**, *96*, 2375–2433.

[2] a) E. A. Price, W. H. Robertson, E. G. Diken, G. H. Weddle, M. A. Johnson, *Chem. Phys. Lett.* **2002**, *366*, 412–416; b) X. Huang, B. J. Braams, S. Carter, J. M. Bowman, *J. Am. Chem. Soc.* **2004**, *126*, 5042–5043; c) W. H. Robertson, E. G. Diken, E. A. Price, J. W. Shin, M. A. Johnson, *Science* **2003**, *299*, 1367–1372; d) H. J. Deyerl, A. K. Luong, T. G. Clements, R. E. Continetti, *Faraday Discuss.* **2000**, *115*, 147–160; e) D. W. Arnold, C. Xu, D. M. Neumark, *J. Chem. Phys.* **1995**, *102*, 6088–6099; f) See also literature mentioned above.

[3] a) M. Schmidt, A. Schier, J. Riede, H. Schmidbaur, *Inorg. Chem.* **1998**, *37*, 3452–3453; b) K. Abu-Dari, K. N. Raymond, D. P. Freyberg, *J. Am. Chem. Soc.* **1979**, *101*, 3688–3689.

[4] M. Kosugi, S. Hikichi, M. Akita, Y. Moro-oka, *Inorg. Chem.* **1999**, *38*, 2567–2578.

[5] a) P. A. Goodson, J. Glerup, D. J. Hodgson, N. B. Jensen, K. Michelsen, *J. Chem. Soc., Dalton Trans.* **2001**, 2783–2790; b) M. Ardon, A. Bino, K. Michelsen, E. Pedersen, R. C. Thompson, *Inorg. Chem.* **1997**, *36*, 4147–4150; c) A. G. McKenna, W. T. Pennington, J. C. Fanning, *Inorg. Chim. Acta* **1991**, *183*, 127–129; d) M. Ardon, B. Magyar, *J. Am. Chem. Soc.* **1984**, *106*, 3359–3360.

[6] A. Ardon, A. Bino, *Inorg. Chem.* **1985**, *24*, 1342–1347.

 © 2006 Wiley-VCH Verlag GmbH & Co. KGaA, Weinheim 

[7] a) L. Lopes, J. de Laat, B. Legube, *Inorg. Chem.* **2002**, *41*, 2505–2517; b) S. Poussereau, G. Blondin, G. Chottard, J. Guilhem, L. Tchertanov, E. Rivière, J. J. Girerd, *Eur. J. Inorg. Chem.* **2001**, 1057–1062; c) E. C. Wilkinson, Y. H. Dong, L. Que Jr, *J. Am. Chem. Soc.* **1994**, *116*, 8394–8395.
[8] a) M. Ghiladi, J. T. Gomez, A. Hazell, P. Kofod, J. Lumtscher, C. J. McKenzie, *Dalton Trans.* **2003**, 1320–1325; b) W. G. Jackson, *Inorg. React. Mech.* **2002**, *4*, 111–124.
[9] a) S. V. Kryatov, E. V. Rybak-Akimova, F. Meyer, H. Pritzkow, *Eur. J. Inorg. Chem.* **2003**, 1581–1590; b) S. Buchler, F. Meyer, E. Kaifer, H. Pritzkow, *Inorg. Chim. Acta* **2002**, *337*, 371–386; c) H. Adams, S. Clunas, D. E. Fenton, *Chem. Commun.* **2002**, 418–419; d) F. Meyer, I. Hyla-Kryspin, E. Kaifer, P. Kircher, *Eur. J. Inorg. Chem.* **2000**, 771–781; e) F. Meyer, E. Kaifer, P. Kircher, K. Heinze, H. Pritzkow, *Chem. Eur. J.* **1999**, *5*, 1617–1630; f) F. Meyer, H. Pritzkow, *Chem. Commun.* **1998**, 1555–1556.
[10] L. Siegfried, T. A. Kaden, F. Meyer, P. Kircher, H. Pritzkow, *J. Chem. Soc., Dalton Trans.* **2001**, 2310–2315.
[11] a) F. Meyer, P. Rutsch, *Chem. Commun.* **1998**, 1037–1038; b) M. Ruf, K. Weis, H. Vahrenkamp, *J. Am. Chem. Soc.* **1996**, *118*, 9288–9294.
[12] a) R. D. Lorentz, A. Bino, J. E. Penner-Hahn, *J. Am. Chem. Soc.* **1986**, *108*, 8116–8117; b) A. Bino, D. Gibson, *J. Am. Chem. Soc.* **1982**, *104*, 4383–4388; c) A. Bino, D. Gibson, *J. Am. Chem. Soc.* **1981**, *103*, 6741–6742.
[13] a) Y. Takahashi, S. Hikichi, Y. Moro-oka, M. Akita, *Polyhedron* **2004**, *23*, 225–234; b) T. Hirano, M. Kuroda, N. Takeda, M. Hayashi, M. Mukaida, T. Oi, H. Nagao, *J. Chem. Soc., Dalton Trans.* **2002**, 2158–2162.
[14] a) B. Bauer-Siebenlist, F. Meyer, E. Farkas, D. Vidovic, S. Dechert, *Chem. Eur. J.* **2005**, 4349–4360; b) J. Ackermann, F. Meyer, E. Kaifer, H. Pritzkow, *Chem. Eur. J.* **2002**, *8*, 247–258.
[15] a) J. Ackermann, F. Meyer, H. Pritzkow, *Inorg. Chim. Acta* **2004**, *357*, 3703–3711; b) F. Meyer, K. Heinze, B. Nuber, L. Zsolnai, *J. Chem. Soc., Dalton Trans.* **1998**, 207–213.
[16] F. Meyer, S. Beyreuther, K. Heinze, L. Zsolnai, *Chem. Ber./Recueil* **1997**, *130*, 605–613.
[17] G. Leibeling, S. Demeshko, B. Bauer-Siebenlist, F. Meyer, H. Pritzkow, *Eur. J. Inorg. Chem.* **2004**, 2413–2420.
[18] B. Bauer-Siebenlist, F. Meyer, E. Farkas, D. Vidovic, J. A. Cuesta-Seijo, R. Herbst-Irmer, H. Pritzkow, *Inorg. Chem.* **2004**, *43*, 4189–4202.
[19] F. Meyer, unpublished results.
[20] a) G. Parkin, *Chem. Rev.* **2004**, *104*, 699–767; b) A. Bottoni, C. Z. Lanza, G. P. Miscione, D. Spinelli, *J. Am. Chem. Soc.* **2004**, *126*, 1542–1550; c) H. Brombacher, H. Vahrenkamp, *Inorg. Chem.* **2004**, *43*, 6042–6049; d) E. Kimura, *Acc. Chem. Res.* **2001**, *34*, 171–179; e) M. Mauksch, M. Bräuer, J. Weston, E. Anders, *ChemBioChem* **2001**, *2*, 190–198; f) this represents only a small fraction of publications dealing with this topic; please see the references in the above mentioned literature for more information.
[21] a) H. Brombacher, H. Vahrenkamp, *Inorg. Chem.* **2004**, *43*, 6043–6049; 6054–6060; b) L. Cronin, P. H. Walton, *Chem. Commun.* **2003**, 1572–1573; c) P. C. Kunz, G. J. Reiß, W. Frank, W. Kläui, *Eur. J. Inorg. Chem.* **2003**, 3945–3951; d) C. Bergquist, T. Fillebeen, M. M. Morlok, G. Parkin, *J. Am. Chem. Soc.* **2003**, *125*, 6189–6199; e) D. K. Garner, S. B. Fitch, L. H. McAlexander, L. M. Bezold, A. M. Arif, L. M. Berreau, *J. Am. Chem. Soc.* **2002**, *124*, 9970–9971; f) C. Berquist, H. Storrie, L. Koutcher, B. M. Bridgewater, R. A. Friesner, G. Parkin, *J. Am. Chem. Soc.* **2000**, *122*, 12651–12658; g) C. Berquist, G. Parkin, *Inorg. Chem.* **1999**, *38*, 422–423; h) E. Kimura, M. Shionoya, A. Hoshino, T. Ikeda, Y. Yamada, *J. Am. Chem. Soc.* **1992**, *114*, 10134–10137; i) This represents only a small fraction of the newer results on this topic; please see the references in the above mentioned literature for more information.
[22] S. Erhardt, E. Jaime, J. Weston, *J. Am. Chem. Soc.* **2005**, *127*, 3654–3655.
[23] R. C. Holz, *Coord. Chem. Rev.* **2002**, *232*, 5–26.
[24] C. W. Bock, A. K. Katz, J. P. Glusker, *J. Am. Chem. Soc.* **1995**, *117*, 3754–3765.
[25] E. Jaime, J. Weston, manuscript in preparation.
[26] a) A. D. Becke, *J. Chem. Phys.* **1993**, *98*, 5648–5652; b) C. Lee, W. Yang, R. G. Parr, *Phys. Rev. B.* **1988**, *37*, 785–789.
[27] M. J. Frisch, G. W. Trucks, H. B. Schlegel, G. E. Scuseria, M. A. Robb, J. R. Cheeseman, V. G. Zakrzewski, J. A. Montgomery, R. E. Stratmann, J. C. Burant, S. Dapprich, J. M. Millam, A. D. Daniels, K. N. Kudin, M. C. Strain, O. Farkas, J. Tomasi, V. Barone, M. Cossi, R. Cammi, B. Mennucci, C. Pomelli, C. Adamo, S. Clifford, J. Ochterski, G. A. Petersson, P. Y. Ayala, Q. Cui, K. Morokuma, N. Rega, P. Salvador, J. J. Dannenberg, D. K. Malick, A. D. Rabuck, K. Raghavachari, J. B. Foresman, J. Cioslowski, J. V. Ortiz, A. G. Baboul, B. B. Stefanov, G. Liu, A. Liashenko, P. Piskorz, I. Komaromi, R. Gomperts, R. L. Martin, D. J. Fox, T. Keith, M. A. Al-Laham, C. Y. Peng, A. Nanayakkara, M. Challacombe, P. M. W. Gill, B. Johnson, W. Chen, M. W. Wong, J. L. Andres, C. Gonzalez, M. Head-Gordon, E. S. Replogle, J. A. Pople, *Gaussian 98*, Revision A.11.4, Gaussian Inc., Pittsburgh, PA, **1998**.
[28] a) E. R. Davidson, *Chem. Phys. Lett.* **1996**, *260*, 514–518; b) R. A. Kendall, T. H. Dunning Jr, R. J. Harrison, *J. Chem. Phys.* **1992**, *96*, 6796–6806.
[29] J. M. L. Martin, A. Sundermann, *J. Chem. Phys.* **2001**, *114*, 3408–3420.
[30] T. H. Dunning Jr, P. J. Hay, in: *Modern Theoretical Chemistry* (Ed.: H. F. Schaefer III), Plenum, New York, **1976**, vol. 3, 1–28.
[31] a) P. J. Hay, W. R. Wadt, *J. Chem. Phys.* **1985**, *82*, 270–283; b) W. R. Wadt, P. J. Hay, *J. Chem. Phys.* **1985**, *82*, 284–298; c) P. J. Hay, W. R. Wadt, *J. Chem. Phys.* **1985**, *82*, 299–310.
[32] a) A. E. Reed, L. A. Curtis, F. Weinhold, *Chem. Rev.* **1988**, *88*, 899–926; b) A. E. Reed, L. R. B. Weinstock, F. Weinhold, *J. Chem. Phys.* **1985**, *83*, 735–746; c) A. E. Reed, F. Weinhold, *J. Chem. Phys.* **1983**, *78*, 4066–4073.
[33] E. D. Glendening, J. K. Badenhoop, A. E. Reed, J. E. Carpenter, J. A. Bohmann, C. M. Morales, F. Weinhold, **2001**, *NBO 5.0*, Theoretical Chemistry Institute; University of Wisconsin, Madison, WI USA; http://www.chem.wisc.edu/~nbo5/.

Received: May 18, 2005
Published Online: December 20, 2005

 © 2006 Wiley-VCH Verlag GmbH & Co. KGaA, Weinheim 

DOI: 10.1002/ejic.200500570

# Carboxylate-Containing Tin(IV) Isopropoxides: Synthesis and Characterization of $[Sn(OiPr)_2(O_2CR)_2]_2$ [R = $(CH_3)CCH_2$, $C_6H_5$, $CH_3$]

**Eugenia Martinez-Ferrero,[a] Kamal Boubekeur,[b] and François Ribot*[a]**

**Keywords:** Carboxylate ligands / Organic–inorganic hybrid composites / NMR spectroscopy / Sol–gel processes / Tin

Tin(IV) isopropoxide solvate has been modified by treatment with methacrylic, benzoic and acetic acid. For carboxylate to tin ratios ranging from 1.4 to 2, a dimer, namely $[Sn(\mu_2\text{-}OiPr)(OiPr)(O_2CR)_2]_2$ [R = $(CH_3)CCH_2$, $C_6H_5$, $CH_3$], is isolated. Its structure, as determined by X-ray diffraction on the methacrylate derivative, is based on two seven-coordinate tin atoms, terminal and bridging isopropoxy ligands, and purely chelating carboxylates. These compounds have also been characterized by $^{119}Sn$, $^{1}H$, and $^{13}C$ solution NMR and $^{119}Sn$ CP-MAS NMR spectroscopy. The possible use of this dimer as a precursor for carboxylate-modified tin–oxo clusters has been tested.
(© Wiley-VCH Verlag GmbH & Co. KGaA, 69451 Weinheim, Germany, 2006)

## Introduction

Hybrid organic–inorganic materials are excellent candidates for the design of new functional materials.[1] One approach to them relies on the chemical modification of metal alkoxides by suitable organic ligands,[2] which, in addition to providing a chemical link between the organic and inorganic components, control the reactivity of these precursors during the sol–gel process. The reaction of metal alkoxides with carboxylic acids, β-diketones, or related compounds is also often the first step in the synthesis of metal–oxo clusters of well-defined structure that can be used as versatile building blocks in the preparation of hybrid organic–inorganic materials.[3] Among the various modifying carboxylates used in the area of hybrid materials, the most extensively studied are probably methacrylate and acrylate, as they can be easily polymerized. A large number of modified transition metal–oxo clusters have been reported with these ligands[4–6] and polymerized with various co-monomers (e.g. methacrylic acid, methyl methacrylate) to yield materials with enhanced properties compared to those of the parent polymers.[7]

Methacrylic acid modified tin(IV) alkoxides have already been used to prepare tin dioxide thin films (with or without antimony doping).[8] The films were obtained by UV-induced free radical polymerization of the organic modifiers and the results showed that the direct photo-patterning process increases the conductivity of the films. The photo-patterned organo–metal polymer structures could, furthermore, be thermally decomposed into the corresponding metal oxides at elevated temperatures. However, these previous studies did not give any information about the structure of the methacrylate-modified tin(IV) alkoxides. Moreover, if compounds containing C–Sn bonds are excluded, there are only a few reports of tin(IV)–alkoxo clusters.[9] All this prompted us to look at the compounds formed by treating tin(IV) isopropoxide solvate with different carboxylic acids.

The work presented here reports the modification of tin(IV) isopropoxide solvate by methacrylic, benzoic, and acetic acids. The compounds $[Sn(OiPr)_2(O_2CR)_2]_2$ [R = $(CH_3)CCH_2$, $C_6H_5$, $CH_3$] were characterized by NMR spectroscopy ($^{119}Sn$, $^{1}H$, and $^{13}C$) and the X-ray structure of the methacrylate derivative was determined. The possibility of obtaining defined oxo clusters from this modified alkoxide was also tested.

## Results and Discussion

Crystals of $[Sn(OiPr)_2(OMc)_2]_2$ (**1**) were obtained with carboxylate to tin ratios ranging from 1.4 to 2 (see Experimental Section). According to previously reported data on the influence of the solvent in the preparation of mixed metal–oxo clusters,[9c,10] two different solvents, i.e. toluene and THF, were tested. No influence was found, and the same compounds were obtained with both solvents.

The structure of this complex was elucidated by single-crystal X-ray diffraction (Figure 1 and Table 1). The molecular unit corresponds to a centrosymmetric dimer containing two bridging isopropoxy groups. Each tin atom is also coordinated by two chelating carboxylate molecules. The remaining isopropoxy groups are terminal, resulting in an overall coordination number of seven for tin. The geometry around each tin atom is well described by a pentagonal

[a] Chimie de la Matière Condensée de Paris (UMR, 7574), Université Pierre et Marie Curie,
4 Place Jussieu, 75252 Paris cedex 05, France
E-mail: fri@ccr.jussieu.fr
[b] Chimie Inorganique et Matériaux Moléculaires (UMR, 7071), Université Pierre et Marie Curie,
4 Place Jussieu, 75252 Paris cedex 05, France

 © 2006 Wiley-VCH Verlag GmbH & Co. KGaA, Weinheim 

bipyramid, where O5 and O6 occupy the apical positions. The Sn–O bond lengths of the isopropoxy ligands are similar to those found in $[Sn(OiPr)_4{\cdot}HOiPr]_2$,[11a] and $[Sn(OiPr)_3(acac)]_2$,[11b] and are longer for the bridging groups [2.0601(5) and 2.0939(12) Å] than for the terminal ones [1.9549(16) Å]. The bridging isopropoxy ligands are planar, the sum of the angles about O6 being 360.0°. The angle at the oxygen atom of the in-plane terminal alkoxy is smaller in compound **1** [Sn1–O5–C9 = 119.21(12)°] than in $[Sn(OiPr)_4{\cdot}HOiPr]_2$ (139° and 160°)[11a] but similar to the ones observed in $[Sn(OiPr)_3(acac)]_2$ (122.0° and 124.4°)[11b] and $[Sn(OtBu)_4]$ (124.1° and 125.0°).[11a] These values of around 120° are expected for alkoxy ligands not involved in π-donation to the metal center. The carboxylate ligands are purely chelating and fairly symmetrical, with Sn–O bond lengths ranging from 2.1764(14) to 2.2465(15) Å. The charge of each carboxylate moiety is equally delocalized over the two oxygen atoms as the C–O bond lengths are almost identical [from 1.260(2) to 1.275(3) Å].

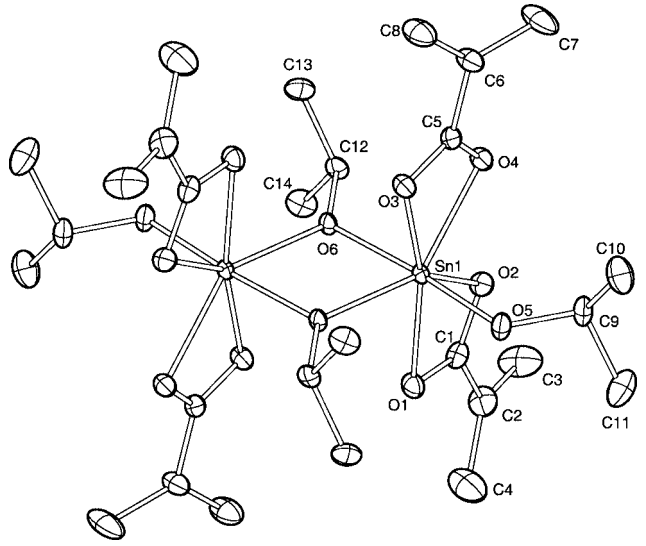


Figure 1. DIAMOND drawing of $[Sn(\mu_2\text{-}OiPr)(OiPr)(OMc)_2]_2$ showing the atom-labeling scheme. Atomic thermal ellipsoids are drawn at 50% probability and H atoms have been omitted for clarity.

Table 1. Selected interatomic distances [Å] and angles [°] for compound **1**.

| | | | |
|---|---|---|---|
| Sn1–O1 | 2.2465(15) | Sn1–O5 | 1.9549(16) |
| Sn1–O2 | 2.1764(14) | Sn1–O6 | 2.0601(15) |
| Sn1–O3 | 2.2113(15) | Sn1–O6[a] | 2.0939(12) |
| Sn1–O4 | 2.1987(14) | Sn1···Sn1[a] | 3.3370(3) |
| O5–Sn1–O6 | 174.11(5) | O5–Sn1–O4 | 94.89(5) |
| O1–Sn1–O2 | 58.87(5) | O5–Sn1–O6[a] | 101.06(6) |
| O2–Sn1–O4 | 79.83(5) | O6–Sn1–O1 | 91.79(5) |
| O3–Sn1–O4 | 59.12(5) | O6–Sn1–O2 | 88.25(5) |
| O3–Sn1–O6[a] | 81.21(5) | O6–Sn1–O3 | 88.86(5) |
| O1–Sn1–O6[a] | 82.00(5) | O6–Sn1–O4 | 89.01(5) |
| O5–Sn1–O1 | 88.20(6) | O6–Sn1–O6[a] | 73.11(6) |
| O5–Sn1–O2 | 96.78(6) | Sn1–O6–Sn1[a] | 106.89(6) |
| O5–Sn1–O3 | 89.35(6) | | |

[a] Symmetry operation: $-x, -y, -z$.

To assess the purity of the crystalline precipitate the $^{119}$Sn solid-state NMR (CP-MAS) spectrum of compound **1** was recorded (Figure 2). It displays a single, sharp, isotropic resonance, at $\delta$ = –759 ppm, with an anisotropy ($\zeta$) and asymmetry ($\eta$) equal to 325 ppm and 0, respectively. The observation of a single resonance is in agreement with the presence of a unique tin environment in the crystal structure. Moreover, the axial (or nearly axial)[12] character of the chemical shielding tensor is in line with the pentagonal bipyramid coordination polyhedron.

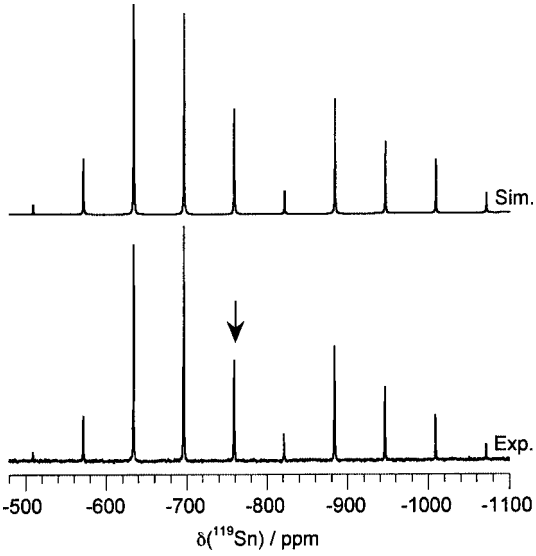


Figure 2. $^{119}$Sn CP-MAS NMR spectrum (111.9 MHz, $\nu_{MAS}$ = 7000 Hz) of $[Sn(OiPr)_2(OMc)_2]_2$ with its simulation (the arrow points to the isotropic chemical shift).

To the best of our knowledge there are very few reports of crystalline compounds in which a tin atom exhibits a sevenfold coordination based only on oxygen atoms ($SnO_7$ environment),[13] and no $^{119}$Sn NMR spectroscopic data have been reported for these compounds. For comparison, the $^{119}$Sn solid-state NMR (CP-MAS) spectrum of $[Sn(OiPr)_4{\cdot}HOiPr]_2$ was also recorded. It exhibits an isotropic chemical shift of $\delta$ = –654 ppm ($\zeta$ = 103 ppm and $\eta$ = 0.65) for its unique $SnO_6$ environment. The $^{119}$Sn NMR isotropic chemical shift of tin dioxide, in which tin is also six-coordinate, has been reported to be $\delta$ = –603 ppm.[14] For $SnO_8$ environments, there is a series of tin tetracarboxylates, the $^{119}$Sn NMR chemical shifts of which have been reported to lie in the range $\delta$ = –840 to –860 ppm,[15] and two tetrakis(*N*,*N*-dialkylcarbamato-*O*,*O'*)tin(IV) complexes, with $^{119}$Sn NMR chemical shifts of around $\delta$ = –925 ppm.[16] In conclusion, according to the general rules whereby an increase of one oxygen atom at tin causes a low-frequency shift of about 100 to 150 ppm,[17] the $^{119}$Sn NMR isotropic chemical shift observed for compound **1**, i.e. $\delta$ = –759 ppm, indeed falls in the expected range for a seven-coordinate tin atom surrounded only by oxygen atoms.

The $^{119}$Sn solution NMR spectrum of compound **1** shows a single narrow line at $\delta$ = –754.7 ppm, in very good agreement with the solid-state isotropic chemical shift and the heptacoordinate nature of tin. Moreover, this line exhibits a set of satellites the intensity and magnitude of which are consistent with a dimer and a two-bond $^{119}$Sn-$^{117}$Sn

 © 2006 Wiley-VCH Verlag GmbH & Co. KGaA, Weinheim 

coupling constant. All these features indicate unambiguously that the molecular structure observed for compound **1** in the solid state is maintained in solution.

The $^{1}H$ and $^{13}C$ solution NMR spectra of compound **1**, at room temperature, indicate the presence of one type of methacrylate and two types of isopropoxy groups (2:1:1 ratio), in perfect agreement with the dimeric structure. The intensities of the $^{13}C$-$^{119/117}Sn$ coupling satellites for the methyne carbon of the isopropoxy groups account for about 19 and 35% of the resonances located at $\delta$ = 66.8 and 74.1 ppm, respectively. As a bridging alkoxy sees two tin atoms and a terminal alkoxy only one, the $^{13}C$ resonance at $\delta$ = 66.8 ppm can be assigned to the terminal isopropoxy groups while the one at $\delta$ = 74.1 ppm is assigned to the bridging ligands. This result shows that in compound **1**, the magnitudes of the $^{2}J_{^{13}C\text{-}^{119}Sn}$ coupling constants follow the rule observed for tin(IV) tetraalkoxide, i.e. they are larger for terminal alkoxides (ca. 40 Hz) than for doubly bridging alkoxides (ca. 20 Hz).[18] With these first assignments and with the help of 2D NMR experiments ($^{1}H$-$^{1}H$ COSY and $^{1}H$-$^{13}C$ HMQC), the $^{1}H$ and $^{13}C$ resonances of compound **1** have been fully attributed (Table 2). The $^{3}J_{^{1}H\text{-}^{119}Sn}$ coupling constants of the isopropoxy ligands appear to follow the same order as $^{2}J_{^{13}C\text{-}^{119}Sn}$ in that they are larger for a terminal than for a bridging alkoxy. These features likely arise from the longer Sn–O bond of a bridging alkoxy compared to a terminal one. The observation of several $^{n}J_{^{1}H\text{-}^{119}Sn}$ and $^{n}J_{^{13}C\text{-}^{119}Sn}$ scalar couplings, which, moreover, are different for the terminal and bridging isopropoxy groups, indicates that the exchange of ligands (isopropoxy or methacrylate) between different dimers and the exchange of terminal and bridging isopropoxy groups within the same dimer is either absent or very slow (slower than 1/*J*).

Table 2. $^{1}H$ and $^{13}C$ NMR spectroscopic data for $[Sn(OiPr)_2(OMc)_2]_2$.[a]

| $\delta(^{1}H)$/mult./integr./[$^{n}J_{^{1}H\text{-}^{119}Sn}$] | $\delta(^{13}C)$ [$^{n}J_{^{13}C\text{-}^{119}Sn}$] | Assignment |
|---|---|---|
| 1.35/d/12 H | 27.4 [48][b] | $OCH(CH_3)_2$ |
| 1.63/d/12 H | 24.2 | $\mu_2$-$OCH(CH_3)_2$ |
| 1.92/s/12 H | 18.7 | $O_2CC(CH_3)=CH_2$ |
| 4.49/sept/2 H/[90][b] | 66.8 [52][c] | $OCH(CH_3)_2$ |
| 5.27/sept/2 H/[70][b] | 74.1 [16][c] | $\mu_2$-$OCH(CH_3)_2$ |
| 5.29[d]/d/4 H and 6.37[e]/d/4 H | 128.1 | $O_2CC(CH_3)=CH_2$ |
| – | 135.0 [32][b] | $O_2CC(CH_3)=CH_2$ |
| – | 179.0 [25][c] | $O_2CC(CH_3)=CH_2$ |

[a] $\delta$ in ppm, *J* in Hz. [b] *n* = 3. [c] *n* = 2. [d] *cis*-$CH_3$. [e] *trans*-$CH_3$.

Syntheses were also performed with acetic or benzoic acid instead of methacrylic acid under the same conditions as for compound **1** (see Experimental Section). Transparent crystals were obtained with both acids and characterized by multinuclear NMR spectroscopy. Solution NMR ($^{119}Sn$, $^{1}H$, and $^{13}C$) clearly indicated that the same dimer is formed $[Sn(\mu_2\text{-}OiPr)(OiPr)(O_2CR)_2]_2$ (R = $CH_3$ or $C_6H_5$). Solid-state $^{119}Sn$ NMR (CP-MAS) spectra were also recorded for the benzoate (compound **2**) and acetate (compound **3**) derivatives. The spectra exhibit a single, sharp, isotropic resonance ($\delta$ = –757.3 and –759.5 ppm for **2** and **3**, respectively) very similar to the one reported for compound **1** and assigned to seven-coordinate tin atoms. Analysis of the spinning side-band manifolds for both compounds yields the same results, i.e. $\zeta$ = 280 ppm and $\eta$ = 0.0. As for compound **1**, the unique tin site of compounds **2** and **3** exhibits an axial environment. The tin shielding anisotropy is slightly smaller for compounds **2** and **3** than for **1**. This feature likely indicates that the tin environment in the acetate and benzoate derivatives is less distorted than in the methacrylate derivative.

Experiments with a carboxylate to tin ratio of 1 were also performed with acetic and benzoic acid. Clear solutions were obtained in toluene or THF and characterized by $^{119}Sn$ NMR spectroscopy (Figure 3). For benzoic acid (in THF), the $^{119}Sn$ NMR spectrum shows two main resonances of equal intensity (46% for each) at $\delta$ = –662.7 and –683.4 ppm, both with coupling satellites, the magnitude (180 Hz) and the intensity (17%)[19] of which are consistent with two nonequivalent tin atoms bridged by two alkoxy groups. The spectrum also shows minor resonances between $\delta$ = –632 and –654 ppm (8% for all). For acetic acid (in toluene), there are also two main resonances of equal intensity ($\delta$ = –664.9 and –687.5 ppm, 48% each), but their width prevented us from measuring the tin–tin scalar coupling which, however, could exist. The remaining 4% of tin atoms are located in a single minor resonance at $\delta$ = –645.3 ppm that could be assigned to tin isopropoxide solvate.[18] Bearing in mind that the tin starting material and the compound formed with two carboxylates per tin atoms are both dimers, it is reasonable to hypothesize that the major species formed with only one carboxylate per tin is also a dimer. Such a dimer has to be made of two nonequivalent six-coordinate tin atoms. Such a feature could arise from a molecular structure based on two edge-sharing octahedra {as in $[Sn(OiPr)\cdot HOiPr]_2$}[11a] with a chelating carboxylate on each tin (carboxylate/Sn = 1) but without any symmetry operation between the two carboxylates. Another possibility would be a dimer built by chelation, through two bridging isopropoxy ligands, of $[Sn(OiPr)_4]$ by $[Sn(OiPr)_2(O_2CR)_2]$. One tin atom would be coordinated by four terminal and two bridging isopropoxy groups, while the other would be coordinated by two chelating carboxylates and two bridging isopropoxy ligands. At this stage, there is no reason to prefer one possibility over the other.

Attempts were made to isolate the major compound by crystallization at low temperature or solvent evaporation and recrystallization. None of them were successful, but the $^{119}Sn$ NMR spectrum ($CDCl_3$) of the dried benzoate sample indicates a modification of the tin speciation. The peaks at $\delta$ = –662.8 and –683.2 ppm, assigned to a dimer, now account for only around 36% each, while two of the minor peaks, located at $\delta$ = –643.9 and –655.1 ppm increase to about 22 and 6%, respectively. The $^{1}H$ and $^{13}C$ spectra of the same sample reveal complex patterns made up of many different benzoates (at least six from the $^{13}C$ carbonyl signals at around $\delta$ = 172 ppm) and isopropoxy groups (at least ten from the $^{13}C$ methyne signals between $\delta$ = 77 and 65 ppm).

 © 2006 Wiley-VCH Verlag GmbH & Co. KGaA, Weinheim 

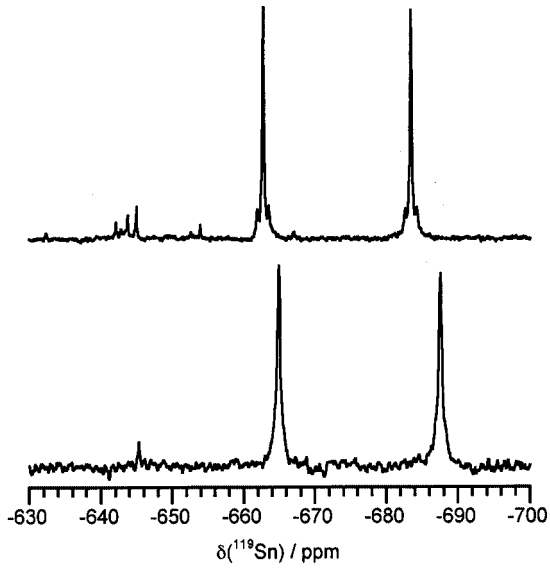


Figure 3. $^{119}$Sn NMR spectra (111.9 MHz) of $[Sn(OiPr)_4{\cdot}HOiPr]_2$ with 2 equiv. of benzoic acid in THF (top) and 2 equiv. of acetic acid in toluene (bottom).

Crystals of compounds **1**, **2**, and **3**, which exhibit a carboxylate to tin ratio of 2, can be precipitated for initial ratios smaller than 2. Therefore, some tin-containing species must remain in solution. Their nature was studied in the case of the benzoate derivative only. Compound **2** was prepared, in toluene, with a benzoic acid to tin ratio of 1.5 and the $^{119}$Sn NMR spectrum was recorded for the solution once the crystals of **2** had been removed. The spectrum exhibits the same resonances as those described for an experiment with a benzoic acid to tin ratio of 1.0. It also shows a small peak at around $\delta$ = –751 ppm that can be assigned to compound **2**. In conclusion, the tin-containing species that remain in solution correspond mainly to the dimer made of two nonequivalent tin atoms and discussed above.

The formation of carboxylate-modified metal–oxo clusters upon treatment of metal alkoxides with carboxylic acids generally results from esterification reactions[20,21] that can take place between free acid and released alcohol molecules, which results in the slow generation of water in situ for the controlled hydrolysis and condensation of the remaining alkoxy groups, or between a bonded carboxylate and a bonded alkoxy group, which yields an M–O–M link and an ester directly. Studies performed on titanium oxoacetate clusters have demonstrated that a very small increase of the AcOH/Ti ratio favors the formation of more condensed species. However, extreme conditions (e.g. solvothermal synthesis) might be needed in order to force the esterification process.[22] For instance, $[SnO(OtBu)(OAc)]_6$, a tin(IV) carboxylate oxo cluster, can only be obtained by refluxing $[Sn(OtBu)_4]$ and $[Sn(OAc)_4]$ in toluene, a noncoordinating solvent.[9c] We tried several approaches to the possible formation of well-defined methacrylate-modified tin–oxo clusters with compound **1** as precursor. Solvothermal treatment or refluxing compound **1** in different solvents (THF, DMF, toluene) gave gels or clear solutions. The $^{119}$Sn NMR spectra of the latter did not indicate any new resonance that could be associated with the formation of new, well-defined molecular species. Direct addition of various amounts of water to compound **1** always yielded transparent gels that are insoluble in organic solvents or turbid solutions that did not show any significant signals in the solution NMR spectra that could be linked back to a well-defined methacrylate-modified tin–oxo clusters.

In an alternative approach to prepare well-defined, methacrylate-modified tin–oxo clusters, syntheses were performed with higher McOH/Sn molar ratios, i.e. 5 and 10. In both cases a white precipitate was obtained. These precipitates are soluble in $CDCl_3$ but their $^{119}$Sn NMR spectra are silent and their $^1$H NMR spectra show only the presence of methacrylate ligands. The absence of any well-defined $^{119}$Sn NMR resonance might be attributed to the formation of ill-defined oxo polymers,[23] either by esterification or parasitic hydrolysis, but in any case indicates clearly that this alternative approach is not more successful for preparing well-defined, methacrylate-modified tin–oxo clusters.

## Conclusions

The behavior of tin(IV) isopropoxide towards the addition of different carboxylic acids (methacrylic, benzoic, and acetic) has been studied. The nature of the carboxylic acid does not affect the final result. Moreover, the solvent (i.e. toluene or tetrahydrofuran) does not seem to play any major role either. Thus, the main parameter is the carboxylate to metal molar ratio. For a ratio of 1, a dimer based on hexacoordinate tin atoms is likely formed but its exact structure remain unknown. For ratios between 1.4 and 2 the compound $[Sn(\mu_2\text{-}OiPr)(OiPr)(O_2CR)_2]_2$ [R = $(CH_3)CCH_2$, $C_6H_5$, and $CH_3$], based on heptacoordinate tin atoms, is isolated. Ratios higher than 2 do not seem to yield well-defined oxo species, as for titanium or zirconium,[21] but probably result in the formation of ill-defined polymeric species.

Studies with other tin(IV) alkoxides are in progress to check the influence of the nature of the alkoxide ligand on the carboxylate substitution reactions.

## Experimental Section

**Synthesis:** All the reactions were carried under inert atmosphere using Schlenk tubes and vacuum-line techniques. The compound $[Sn(OiPr)_4{\cdot}HOiPr]_2$ was prepared by isopropanolysis of $[Sn(OtBu)_4]$, which was obtained according to literature methods and purified by vacuum distillation.[24] The reactions between tin(IV) isopropoxide solvate and carboxylic acids were performed in toluene or tetrahydrofuran (THF) as tin(IV) isopropoxide solvate shows little solubility in its parent alcohol (2-propanol).

**$[Sn(OiPr)_2(OMc)_2]_2$ (OMc = methacrylate) (1):** A solution of methacrylic acid (1.22 g, 14.2 mmol) in THF (4.6 mL) was added to $[Sn(OiPr)_4{\cdot}HOiPr]_2$ (3.03 g, 3.7 mmol, McOH/Sn = 1.94). The resulting clear solution was kept at –18 °C after stirring. Crystals of **1** were obtained after one week. For $^1$H and $^{13}$C NMR ($C_6D_6$,

 © 2006 Wiley-VCH Verlag GmbH & Co. KGaA, Weinheim 

25 °C) data see Table 2. $^{119}$Sn NMR ($C_6D_6$, 25 °C): $\delta$ = –754.7 ppm ($^2J_{^{119}Sn,^{117}Sn}$ = 190 Hz, with satellites corresponding to 7.3% of the total intensity). Yield: 76.7% (2.28 g). Compound **1** is highly soluble in chloroform, dichloromethane, and benzene. It is poorly soluble in acetonitrile, DMSO, and 2-propanol.

**[Sn(O*i*Pr)$_2$(O$_2$CC$_6$H$_5$)$_2$]$_2$ (2):** A similar compound was obtained by replacing methacrylic acid with benzoic acid. A solution of benzoic acid (0.91 g, 7.5 mmol) in THF (6 mL) was added to [Sn(O*i*Pr)$_4$·HO*i*Pr]$_2$ (2.00 g, 2.4 mmol, $C_6H_5CO_2H$/Sn = 1.55). $^1$H NMR ($CDCl_3$, 25 °C): $\delta$ = 8.22 (d, 8 H, *o*-$C_6H_5CO_2$), 7.67 (m, 4 H, *p*-$C_6H_5CO_2$), 7.49 (m, 8 H, *m*-$C_6H_5CO_2$), 5.10 [sept, $^3J_{^1H\text{-}^{119/117}Sn}$ = 70 Hz, 2 H, OC*H*(CH$_3$)$_2$], 4.18 [sept, $^3J_{^1H\text{-}^{119/117}Sn}$ = 90 Hz, 2 H, OC*H*(CH$_3$)$_2$], 1.37 [d, 12 H, OCH(C*H*$_3$)$_2$], 1.08 [d, 12 H, OCH(C*H*$_3$)$_2$] ppm. $^{13}$C NMR ($CDCl_3$, 25 °C): $\delta$ = 178.0 [$^2J_{^{13}C\text{-}^{119/117}Sn}$ = 26 Hz, $C_6H_5CO_2$], 134.0 (*p*-$C_6H_5CO_2$), 131.5 (*o*-$C_6H_5CO_2$), 128.5 (*m*-$C_6H_5CO_2$), 127.9 ($^3J_{^{13}C\text{-}^{119/117}Sn}$ = 33 Hz, *i*-$C_6H_5CO_2$), 74.2 [$^2J_{^{13}C\text{-}^{119/117}Sn}$ = 17 Hz, $\mu_2$-OCH(CH$_3$)$_2$], 66.5 [$^2J_{^{13}C\text{-}^{119/117}Sn}$ = 54 Hz, OCH(CH$_3$)$_2$], 27.0 [$^3J_{^{13}C\text{-}^{119/117}Sn}$ = 48 Hz, OCH(*C*H$_3$)$_2$], 24.0 [$\mu_2$-OCH(*C*H$_3$)$_2$] ppm. $^{119}$Sn NMR ($CDCl_3$, 25 °C): $\delta$ = –751.3 ppm ($^2J_{^{119}Sn,^{117}Sn}$ = 180 Hz, with satellites corresponding to 8.7% of the total intensity). Yield: 58.9% (1.354 g).[25] Compound **2** is highly soluble in chloroform, dichloromethane, and benzene. It is poorly soluble in acetonitrile, DMSO, and 2-propanol.

**[Sn(O*i*Pr)$_2$(O$_2$CCH$_3$)$_2$]$_2$ (3):** A similar compound was obtained by replacing methacrylic acid by acetic acid. A solution of acetic acid (0.44 g, 7.4 mmol) in toluene (3 mL) was added to [Sn(O*i*Pr)$_4$·HO*i*Pr]$_2$ (2.00 g, 2.4 mmol, $CH_3CO_2H$/Sn = 1.53). $^1$H NMR ($CDCl_3$, 25 °C): $\delta$ = 4.72 [sept, $^3J_{^1H\text{-}^{119/117}Sn}$ = 70 Hz, 2 H, OC*H*(CH$_3$)$_2$], 4.10 [sept, $^3J_{^1H\text{-}^{119/117}Sn}$ = 90 Hz, 2 H, OC*H*(CH$_3$)$_2$], 2.18 (s, 12 H, O$_2$CC*H*$_3$) 1.35 [d, 12 H, OCH(C*H*$_3$)$_2$], 1.14 [d, 12 H, OCH(C*H*$_3$)$_2$] ppm. $^{13}$C NMR ($CDCl_3$, 25 °C): $\delta$ = 183.6 ($^2J_{^{13}C\text{-}^{119/117}Sn}$ = 26 Hz, $CH_3CO_2$), 73.8 [$^2J_{^{13}C\text{-}^{119/117}Sn}$ = 16 Hz, $\mu_2$-OCH(CH$_3$)$_2$], 66.4 [$^2J_{^{13}C\text{-}^{119/117}Sn}$ = 52 Hz, OCH(CH$_3$)$_2$], 27.0 [$^3J_{^{13}C\text{-}^{119/117}Sn}$ = 47 Hz, OCH(*C*H$_3$)$_2$], 24.0 [$\mu_2$-OCH(*C*H$_3$)$_2$], 18.3 ($^3J_{^{13}C\text{-}^{119/117}Sn}$ = 32 Hz, *C*H$_3$CO$_2$) ppm. $^{119}$Sn NMR ($CDCl_3$, 25 °C): $\delta$ = –748.4 ppm ($^2J_{^{119}Sn,^{117}Sn}$ = 190 Hz, with satellites corresponding to about 8% of the total intensity). Yield: 24.4% (0.418 g).[25] Compound **3** is highly soluble in chloroform, dichloromethane, benzene and poorly soluble in acetonitrile, DMSO, and 2-propanol.

**Chemical Analyses:** Despite numerous attempts, including sampling under inert atmosphere, chemical analyses matching reasonably well the expected results could not be obtained due to a too high sensitivity of the sample to moisture. However, the $^{119}$Sn solid-state and solution NMR ($^{119}$Sn, $^1$H, and $^{13}$C) spectra indicate that the samples are pure.

**NMR Spectroscopy:** $^1$H, $^{13}$C, and $^{119}$Sn solution NMR experiments were performed on a Bruker AC300 spectrometer (300.13, 75.47, and 111.92 MHz for $^1$H, $^{13}$C, and $^{119}$Sn, respectively). $CDCl_3$ and $C_6D_6$ were used as solvent and internal lock. $^1$H and $^{13}$C chemical shifts are quoted relative to TMS, using the solvent or its protonated impurities as secondary internal reference ($^1$H: $\delta$ = 7.26 and 7.16 ppm for $CHCl_3$ and $C_6HD_5$, respectively; $^{13}$C: $\delta$ = 77.16 and 128.06 ppm for $CDCl_3$ and $C_6D_6$, respectively).[26] The $^{119}$Sn chemical shifts are quoted relative to external tetramethyltin ($\delta$ = 0 ppm). To avoid the loss of quantitativity that can arise from the Nuclear Overhauser effect, $^{119}$Sn-{$^1$H} spectra were obtained with an inverse gated decoupling sequence (pulse of about 30°, recycling delay set to 2 s for an acquisition/decoupling time of 0.18 s). $^1$H-$^1$H COSY and $^1$H-$^{13}$C HMQC experiments were performed on a Bruker Avance 400 spectrometer (400.13 and 100.61 MHz for $^1$H and $^{13}$C, respectively).

$^{119}$Sn solid-state NMR (CP-MAS) spectra were recorded at room temperature on a Bruker Avance 300 spectrometer (111.92 MHz for $^{119}$Sn) equipped with a 4-mm locked Bruker probe. The chemical shifts are quoted relative to tetramethyltin ($\delta$ = 0 ppm) using tetracyclohexyltin ($\delta$ = –97.35 ppm) as a secondary external reference. At least two different MAS speeds were used to locate the isotropic chemical shifts unambiguously. The contact time was 3 ms and the recycling delay 3 s. The chemical shielding tensor analyses were performed according to Herzfeld and Berger[27] using the software "dm2004".[28] The results are reported as the isotropic chemical shift ($\delta_{iso}$), the anisotropy ($\zeta = \sigma_{33} - \sigma_{iso}$), and the asymmetry ($\eta = |\sigma_{22} - \sigma_{11}|/|\zeta|$), with $\delta_{iso} = -(\sigma_{11} + \sigma_{22} + \sigma_{33})/3 = -\sigma_{iso}$ and the principal components of the tensor labeled according to $|\sigma_{33} - \sigma_{iso}| > |\sigma_{11} - \sigma_{iso}| > |\sigma_{22} - \sigma_{iso}|$.

**Crystal Structure Determination:** A single crystal of the moisture-sensitive compound **1** was selected, rapidly mounted on a glass fiber, and transferred into a cold nitrogen gas stream. Diffraction data were collected on a Nonius KappaCCD diffractometer at 123 K. Unit-cell parameters determination, data collection, and integration were carried out with the Nonius EVAL-14 suite of programs.[29] The data were corrected for absorption by a multi-scan method.[30] The structure was solved by direct methods with SHELXS-86,[31] refined by full-matrix least-squares on $F^2$ and completed with SHELXL-97.[32] Graphics were produced with DIAMOND.[33] All non-H atoms were refined with anisotropic displacement parameters and H atoms were simply introduced at calculated positions (riding model).

$C_{28}H_{48}O_{12}Sn_2$, $M$ = 814.04, monoclinic, $a$ = 11.1180(10), $b$ = 11.1316(10), $c$ = 14.3234(13) Å, $\beta$ = 101.36°, $V$ = 1737.9(3) Å$^3$, $T$ = 123(2) K, $P2_1/n$, $Z$ = 2, $d_{calcd.}$ = 1.556 g cm$^{-3}$, $\lambda$(Mo-$K_\alpha$) = 0.71073, $\mu$(Mo-$K_\alpha$) = 1.492 mm$^{-1}$, 28539 reflections measured, 6040 unique ($R_{int}$ = 0.0791) which were used in all calculations. The final $wR(F)^2$ was 0.0770 (all data).

CCDC-256335 contains the supplementary crystallographic data for this paper. These data can be obtained free of charge from The Cambridge Crystallographic Data Center via www.ccdc.cam.ac.uk/data_request/cif.

## Acknowledgments

This work was supported in part by the European Community's Human Potential Program under contract HPRN-CT-2002-00306 (NBB Hybrids). E.M.-F. thanks the European Community for financial support [HPRN-CT-2002-00306 (NBB Hybrids)]. Ms. Marie-Nöelle Rager is gratefully acknowledged for her kind and valuable help in recording and processing the 2D NMR spectra.

[1] *Functional Hybrid Materials* (Eds.: C. Sanchez, P. Gómez-Romero), Wiley-VCH Verlag, Weinheim, Germany, **2004**.
[2] a) C. Sanchez, F. Ribot, *New J. Chem.* **1994**, *18*, 1007–1047; b) U. Schubert, *J. Chem. Soc., Dalton Trans.* **1996**, 3343–3348.
[3] a) C. Sanchez, G. J. de A. A. Soler-Illia, F. Ribot, T. Lalot, C. R. Mayer, V. Cabuil, *Chem. Mater.* **2001**, *13*, 3061–3083; b) F. Ribot, C. Sanchez, *Comments Inorg. Chem.* **1999**, *20*, 327–371.
[4] a) U. Schubert, E. Arpac, W. Glaubitt, A. Helmerich, C. Chau, *Chem. Mater.* **1992**, *4*, 291–295; b) G. Kickelbick, U. Schubert, *Eur. J. Inorg. Chem.* **1998**, 159–161; c) G. Kickelbick, U. Schubert, *Chem. Ber./Recueil* **1997**, *130*, 473–477.
[5] L. G. Hubert-Pfalzgraf, V. Abada, S. Halut, J. Roziere, *Polyhedron* **1997**, *16*, 581–585.
[6] a) B. Moraru, G. Kickelbick, U. Schubert, *Eur. J. Inorg. Chem.* **2001**, 1295–1301; b) M. Jupa, G. Kiclelbick, U. Schubert, *Eur. J. Inorg. Chem.* **2004**, *9*, 1835–1839.

 © 2006 Wiley-VCH Verlag GmbH & Co. KGaA, Weinheim 

[7] a) B. Moraru, N. Hüsing, G. Kickelbick, U. Schubert, P. Fratzl, H. Peterlik, *Chem. Mater.* **2002**, *14*, 2732–2740; b) G. Kickelbick, M. P. Feth, H. Bertagnolli, M. Puchberger, D. Holzinger, S. Gross, *J. Chem. Soc., Dalton Trans.* **2002**, 3892–3898; c) S. Gross, V. Di Noto, U. Schubert, *J. Non-Cryst. Solids* **2003**, *322*, 154–159; d) V. Torma, N. Husing, H. Peterlik, U. Schubert, *C. R. Chimie* **2004**, *7*, 495–502; e) U. Schubert, T. Völkel, N. Moszner, *Chem. Mater.* **2001**, *13*, 3811–3812.
[8] a) T. Kololuoma, A. H. O. Kärkkäinen, J. T. Rantala, *Thin Solid Films* **2002**, *408*, 128–131; b) T. Kololuoma, L.-S. Johansson, J. M. Campbell, A. Tolonen, M. Halttunen, T. Haatainen, J. T. Rantala, *Chem. Mater.* **2002**, *14*, 4443–4447; c) T. Kololuoma, A. H. O. Kärkkäinen, A. Tolonen, J. T. Rantala, *Thin Solid Films* **2003**, *440*, 184–189.
[9] a) H. Reuter, M. Kremser, *Z. Anorg. Allg. Chem.* **1992**, *615*, 137–142; b) M. Verdenelli, S. Parola, L. G. Hubert-Pfalzgraf, S. Lecocq, *Polyhedron* **2000**, *19*, 2069–2075; c) J. Caruso, M. J. Hampden-Smith, A. L. Rheingold, G. Yap, *J. Chem. Soc., Chem. Commun.* **1995**, 157–158.
[10] a) J. Caruso, M. J. Hampden-Smith, E. N. Duesler, *J. Chem. Soc., Chem. Commun.* **1995**, 1041–1042; b) J. Caruso, C. Roger, F. Schwertfeger, M. J. Hampden-Smith, A. L. Rheingold, G. Yap, *Inorg. Chem.* **1995**, *34*, 449–453.
[11] a) M. J. Hampden-Smith, T. A. Wark, A. Rheingold, J. C. Huffman, *Can. J. Chem.* **1991**, *69*, 121–129; b) C. D. Chandler, G. D. Fallon, A. J. Koplick, B. O. West, *Aust. J. Chem.* **1987**, *40*, 1427–1439.
[12] P. Amornsakchai, D. C. Apperley, R. K. Harris, P. Hodgkinson, P. C. Waterfield, *Solid State Nucl. Magn. Reson.* **2004**, *26*, 160–171.
[13] a) G. J. Kruger, E. L. J. Breet, R. van Eldik, *Inorg. Chim. Acta* **1976**, *19*, 151; b) N. W. Alcock, V. L. Tracy, *J. Chem. Soc., Dalton Trans.* **1976**, 2246; c) M. C. Barret, M. F. Mahon, K. C. Molloy, P. Wright, *Main Group Met. Chem.* **2000**, *23*, 663–671; d) J. J. Park, D. M. Collins, J. L. Hoard, *J. Am. Chem. Soc.* **1970**, *92*, 3636.
[14] C. Cossement, J. Darville, J.-M. Gilles, J. B. Nagy, C. Fernandez, J.-P. Amoureux, *Magn. Reson. Chem.* **1992**, *30*, 263–270.
[15] S. Nagabrahmanandachari, K. C. Kumar Swamy, *Ind. J. Chem., Sect. A* **1995**, *34*, 658–660.
[16] a) G. A. Horley, M. F. Mahon, K. C. Molloy, P. W. Haycock, C. P. Myers, *Inorg. Chem.* **2002**, *41*, 5052–5058; b) L. Abis, D. B. Dell'Amico, F. Calderazzo, R. Caminiti, F. Garbassi, S. Ianelli, G. Pelizzi, P. Robino, A. Tomei, *J. Mol. Catal., A: Chem.* **1996**, *108*, L113–L117.
[17] a) R. K. Harris, J. D. Kennedy, W. McFarlane, *NMR and the Periodic Table*, Academic Press, London **1978**, p. 348; b) B. Wrackmeyer, *Ann. Rep. NMR Spectrosc.* **1985**, *16*, 73–186.
[18] M. J. Hampden-Smith, T. A. Wark, C. J. Brinker, *Coord. Chem. Rev.* **1992**, *112*, 81–116.
[19] This value matches fairly well the sum of the natural abundances of $^{119}$Sn and $^{117}$Sn (16.2%).
[20] N. Steunou, F. Robert, K. Boubekeur, F. Ribot, C. Sanchez, *Inorg. Chim. Acta* **1998**, *279*, 144–151.
[21] G. Kickelbick, U. Schubert, *Mat. Res. Soc., Symp. Proc.* **1998**, *519*, 401–406.
[22] a) N. Steunou, F. Ribot, K. Boubekeur, J. Maquet, C. Sanchez, *New J. Chem.* **1999**, *23*, 1079–1086; b) N. Steunou, C. Sanchez, S. Forster, C. Goltner, M. Antonietti, P. Florian, *Ceram. Trans.* **2001**, *123*, 49–71.
[23] C. Eychenne-Baron, F. Ribot, N. Steunou, C. Sanchez, F. Fayon, M. Biesemans, J. C. Martins, R. Willem, *Organometallics* **2000**, *19*, 1940–1949.
[24] I. M. Thomas, U. S. Pat. 3,946,056, **1976**.
[25] These yields are expressed relative to the amount of starting tin isopropoxide solvate. However, as the carboxylic acid to tin ratio is lower than 2, the maximum achievable yield is lower than 100%.
[26] H. E. Gottlieb, V. Kotlyar, A. Nudelman, *J. Org. Chem.* **1997**, *62*, 7512–7515.
[27] J. Herzfeld, A. E. Berger, *J. Chem. Phys.* **1980**, *73*, 6021–6030.
[28] a) D. Massiot, F. Fayon, M. Capron, I. King, S. Le Calvé, B. Alonso, J.-O. Durand, B. Bujoli, Z. Gan, G. Hoatson, *Magn. Reson. Chem.* **2002**, *40*, 70–76; b) http://crmht-europe.cnrs-orleans.fr/dmfit/help/dmfit.htm.
[29] A. J. M. Duisenberg, L. M. J. Kroon-Batenburg, A. M. M. Schreurs, *J. Appl. Crystallogr.* **2003**, *36*, 220–229.
[30] R. H. Blessing, *Acta Crystallogr., Sect. A* **1995**, *51*, 33–38.
[31] G. M. Sheldrick, *SHELXS-86*, Computer program for structure solution, University of Göttingen, Germany, **1986**.
[32] G. M. Sheldrick, *SHELXL-97*, Computer program for structure refinement, University of Göttingen, Germany, **1997**.
[33] K. Brandenburg, M. Berndt, *Diamond™*, Crystal Impact GbR, Bonn, Germany, **1999**.

Received: June 27, 2005
Published Online: December 27, 2005

 © 2006 Wiley-VCH Verlag GmbH & Co. KGaA, Weinheim 

DOI: 10.1002/ejic.200500717

# Synthesis of Chalcogeno[3-(pyrid-2-yl)-1-azaallyl]germanium Complexes

**Wing-Por Leung,*[a] Kim-Hung Chong,[a] Yuen-Sze Wu,[a] Cheuk-Wai So,[a] Hoi-Shan Chan,[a] and Thomas C. W. Mak[a]**

**Keywords:** Chalcogens / Germanium / N ligands

The reaction of [Ge{C($C_5H_4$N-2)C(Ph)N($SiMe_3$)$_2$}{N($SiMe_3$)C(Ph)C($SiMe_3$)($C_5H_4$N-2)}] (**1**) and [Ge{N($SiMe_3$)C(Ph)C($SiMe_3$)($C_5H_4$N-2)}Cl] (**2**) with stoichiometric amounts of elemental chalcogens in toluene affords [Ge(E){C($C_5H_4$N-2)C(Ph)N($SiMe_3$)$_2$}{N($SiMe_3$)C(Ph)C($SiMe_3$)($C_5H_4$N-2)}] [E = S (**3**), Se (**4**)] and [Ge(E){N($SiMe_3$)C(Ph)C($SiMe_3$)($C_5H_4$N-2)}Cl] [E = S (**5**), Se (**6**)], respectively. Compounds **3**–**6** were characterized by X-ray analysis.
(© Wiley-VCH Verlag GmbH & Co. KGaA, 69451 Weinheim, Germany, 2006)

## Introduction

Compounds containing a double bond between group 14 and 16 elements are considered to be unstable due to the weak pπ–pπ bonding.[1] Nevertheless, stable chalcogenogermane and -stannane (>M=E) (M = Ge, Sn; E = S, Se, Te) complexes have been isolated in the past few years.[2] These compounds are either base-stabilized or stabilized by sterically bulky protecting group. For example, [{$\eta^4$-$Me_8$taa}M=E] (M = Ge, Sn; E = S, Se; $\eta^4$-$Me_8$taa = octamethyldibenzotetraaza[14]annulene),[3] [(Tbt)(Tip)Ge=E] {Tbt = 2,4,6-tris[bis(trimethylsilyl)methyl]phenyl; Tip = 2,4,6-triisopropylphenyl; E = S, Se, Te},[4] and [$R^N_2$M=E] [$R^N$ = CPh($SiMe_3$)$C_5H_4$N-2; M = Ge; E = S, Se, Te; $R^N$ = CH($SiMe_3$)$C_9H_6$N-8; M = Sn; E = S, Se, Te][5] have been reported. In contrast, chalcogeno group 14 metal halide complexes [RM(E)X] are rare, and to date only the complexes [{HC(CMeNAr)$_2$}Ge(E)X] (Ar = 2,6-*i*$Pr_2C_6H_3$, Ph; E = S, Se; X = F, Cl) have been prepared and structurally characterized.[6]

Recently, we have reported the synthesis of [Ge{C($C_5H_4$N-2)C(Ph)N($SiMe_3$)$_2$}{N($SiMe_3$)C(Ph)C($SiMe_3$)($C_5H_4$N-2)}] and [Ge{N($SiMe_3$)C(Ph)C($SiMe_3$)($C_5H_4$N-2)}Cl] from the reaction of $GeCl_2$·dioxane with the [3-(pyrid-2-yl)-1-azaallyl]lithium complex [Li{N($SiMe_3$)C(Ph)C(R)($C_5H_4$N-2)}]$_2$.[7] Herein, we report the synthesis of chalcogenogermanium complexes from the direct reaction of these complexes with elemental chalcogens.

## Results and Discussion

The reaction of [Ge{C($C_5H_4$N-2)C(Ph)N($SiMe_3$)$_2$}{N($SiMe_3$)C(Ph)C($SiMe_3$)($C_5H_4$N-2)}] (**1**) with a stoichiometric amount of elemental chalcogen in toluene afforded the thermally stable germanethione **3** and -selone **4** (Scheme 1). Similarly, treatment of [Ge{N($SiMe_3$)C(Ph)C($SiMe_3$)($C_5H_4$N-2)}Cl] (**2**) with an equimolar amount of elemental chalcogen in toluene gave the thermally stable complexes [Ge(E){N($SiMe_3$)C(Ph)C($SiMe_3$)($C_5H_4$N-2)}Cl] [E = S (**5**), Se (**6**)] (Scheme 2).

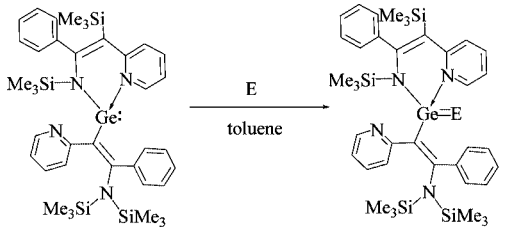


**1** E = S (**3**), Se (**4**)

Scheme 1.

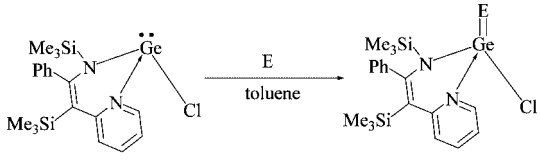


**2** E = S (**5**), Se (**6**)

Scheme 2.

Compounds **3**–**6** are yellow, crystalline solids that are soluble in $Et_2O$, toluene, and THF and sparingly soluble in hydrocarbon solvents. The $^{13}$C NMR spectra of **3** and **4** display three sharp singlets assignable to the three types of $SiMe_3$ groups, consistent with the solid-state structure. The $^1$H and $^{13}$C NMR spectra of **5** and **6** show a similar pattern and display one set of signals due to the 3-(pyrid-2-yl)-1-azaallyl ligand.

[a] Department of Chemistry, The Chinese University of Hong Kong,
Shatin, New Territories, Hong Kong, China
E-mail: kevinleung@cuhk.edu.hk


© 2006 Wiley-VCH Verlag GmbH & Co. KGaA, Weinheim

The $^{77}Se$ NMR spectrum of **4** displays a singlet at $\delta$ = –28.63 ppm, whereas the $^{77}Se$ NMR spectrum of **6** displays a singlet at $\delta$ = –266.21 ppm, which is similar to that found for [{HC(CMeNAr)$_2$}Ge(Se)Cl] (Ar = 2,6-*i*Pr$_2$C$_6$H$_3$; $\delta$ = –228 ppm). The values for **4** and **6** lie between those of [Ge{(NSiMe$_3$)$_2$}$_2$(μ-Se)]$_2$ ($\delta$ = –476.0 ppm)[8] and [(Tbt)(Tip)Ge=Se] ($\delta$ = 940 ppm).[4b] We suggest that **4** and **6** exist as intermediates between the resonance forms **A** and **B** in solution (Scheme 3).

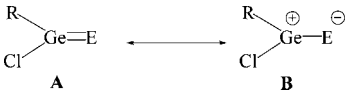


Scheme 3.

The molecular structures, with the atom-numbering schemes, of compounds **3** and **6** are shown in Figures 1 and 2, respectively. Selected bond lengths and angles of complexes **3/4** and **5/6** are listed in Tables 1 and 2, respectively.

Compounds **3** and **4** are isostructural. The germanium center is bonded to an [2-(pyrid-2-yl)ethenyl]amido-*N*,*N*′ chelate and an η$^1$-alkenyl ligand in a tetrahedral geometry, with the chalcogen atom occupying the axial position. Compounds **5** and **6** are also isostructural, and the geometry around the germanium center is also tetrahedral.

The Ge–S distance of 2.094(8) Å in **3** is similar to that of 2.11 Å in [{η$^4$-Me$_8$taa}Ge=S][3a] and 2.063(3) Å in [(Tbt)(Tip)Ge=S],[4a] and the Ge–S distance of 2.056(2) Å in **5** is comparable to that of 2.053(6) Å in [{HC(CMeNAr)$_2$}Ge(S)Cl] (Ar = 2,6-*i*Pr$_2$C$_6$H$_3$).[6a] The Ge–S distances in **3** and **5** are close to the calculated value for a Ge=S bond (2.06 Å).[9] This suggests that the resonance structure **A** contributes more than the resonance **B** (Scheme 3) in compounds **3** and **5**.

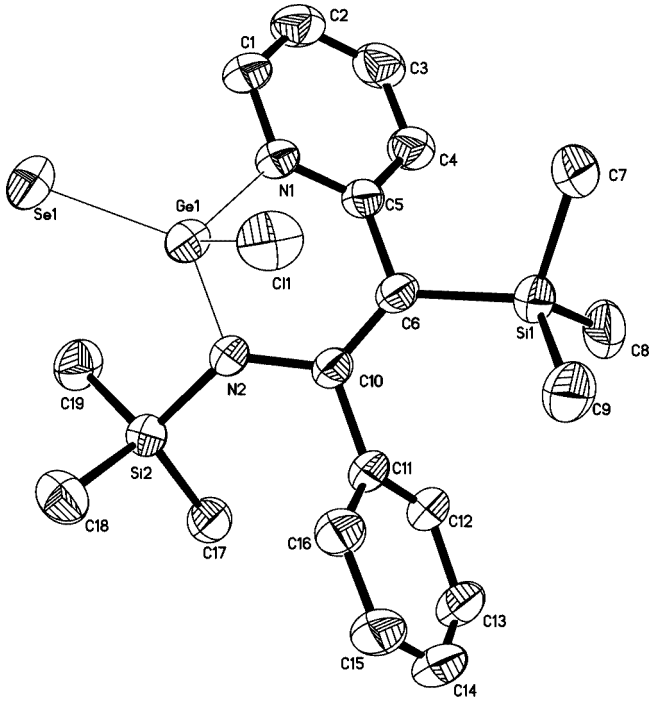


Figure 2. Molecular structure of **6**.

The Ge–Se distance of 2.223(9) Å in **4** is similar to that of 2.247(7) Å in [{C(SiMe$_3$)$_2$C$_5$H$_4$N-2}$_2$Ge=Se][10] and 2.247(1) Å in [{η$^4$-Me$_8$taa}Ge=Se],[3a] and the Ge–Se distance of 2.191(1) Å in **6** is comparable to that of 2.210(1) Å in [{HC(CMeNPh)$_2$}Ge(Se)Cl].[6b] The Ge–Se bond length in **4** lies between the calculated values for a Ge–Se single (2.39 Å) and double bond (2.19 Å), suggesting that the type of Ge–Se bonding in **4** lies somewhere between the reso-

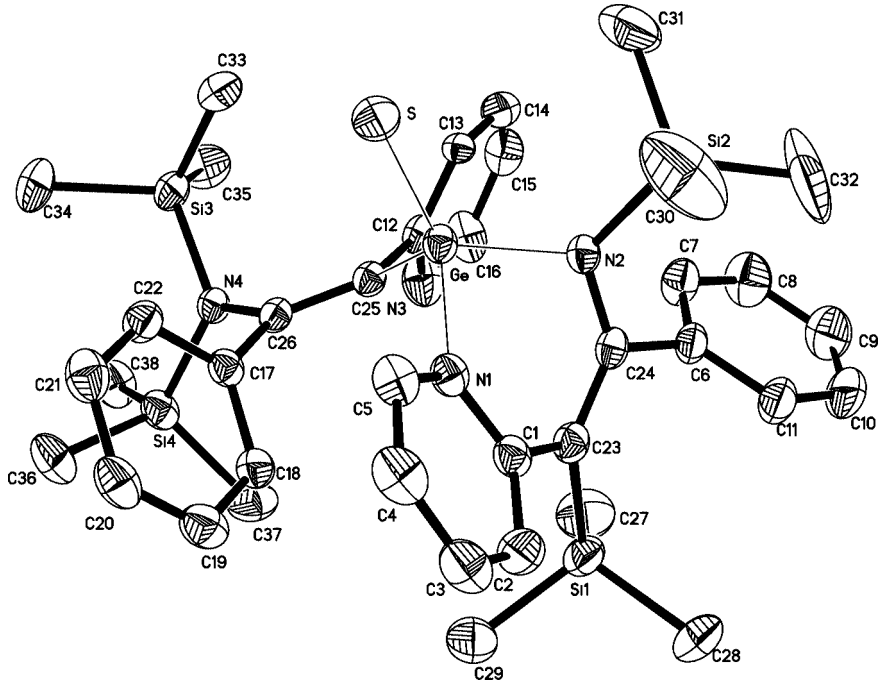


Figure 1. Molecular structure of **3**.

 © 2006 Wiley-VCH Verlag GmbH & Co. KGaA, Weinheim 

Table 1. Selected bond lengths [Å] and angles [°] for compounds **3** and **4**.

| | **3** | | |
|---|---|---|---|
| Ge–S | 2.094(8) | Ge–N(2) | 1.878(17) |
| Ge–N(1) | 1.999(17) | Ge–C(25) | 1.969(19) |
| C(25)–C(26) | 1.349(3) | N(4)–C(26) | 1.435(2) |
| N(4)–Si(4) | 1.768(18) | Si(3)–N(4) | 1.764(18) |
| C(12)–C(25) | 1.482(3) | C(17)–C(26) | 1.498(3) |
| N(1)–C(1) | 1.357(3) | C(1)–C(23) | 1.466(3) |
| C(23)–C(24) | 1.382(3) | N(2)–C(24) | 1.388(3) |
| Si(1)–C(23) | 1.902(2) | Si(2)–N(2) | 1.778(7) |
| N(2)–Ge–C(25) | 108.4(8) | N(2)–Ge–N(1) | 89.0(7) |
| C(25)–Ge–N(1) | 109.1(8) | N(2)–Ge–S | 121.2(6) |
| C(25)–Ge–S | 117.8(6) | N(1)–Ge–S | 106.9(6) |
| C(1)–N(1)–Ge | 118.8(1) | N(1)–C(1)–C(23) | 121.2(2) |
| C(24)–C(23)–C(1) | 124.3(2) | N(4)–C(26)–C(17) | 114.3(2) |
| C(25)–C(26)–N(4) | 124.3(2) | C(26)–N(4)–Si(3) | 119.0(2) |
| | **4** | | |
| Ge–Se | 2.223(9) | Ge–N(2) | 1.873(3) |
| Ge–N(1) | 1.996(3) | Ge–C(23) | 1.976(4) |
| N(2)–C(26) | 1.402(6) | C(25)–C(26) | 1.399(6) |
| C(5)–C(25) | 1.465(7) | N(1)–C(5) | 1.365(6) |
| C(18)–C(23) | 1.502(5) | C(23)–C(24) | 1.345(5) |
| C(12)–C(24) | 1.490(6) | N(4)–C(24) | 1.441(4) |
| Si(2)–N(4) | 1.757(4) | Si(1)–N(4) | 1.767(3) |
| Si(3)–N(2) | 1.762(4) | Si(4)–C(25) | 1.894(5) |
| C(6)–C(26) | 1.490(6) | | |
| N(2)–Ge–C(23) | 109.7(2) | N(2)–Ge–N(1) | 88.9(1) |
| C(23)–Ge–N(1) | 109.0 (2) | N(2)–Ge–Se | 120.6(1) |
| C(23)–Ge–Se | 116.6(1) | N(1)–Ge–Se | 108.0(1) |
| C(18)–C(23)–Ge | 111.4(3) | C(24)–C(23)–C(18) | 124.1(3) |
| C(23)–C(24)–C(12) | 120.5(3) | N(4)–C(24)–C(12) | 114.9(3) |
| C(24)–N(4)–Si(1) | 118.3(3) | Si(2)–N(4)–Si(1) | 122.1(2) |
| C(24)–C(23)–Ge | 122.3(3) | C(26)–N(2)–Ge | 113.3(3) |
| C(26)–N(2)–Si(3) | 122.8(2) | Si(3)–N(2)–Ge | 121.8(2) |
| C(25)–C(26)–C(6) | 118.5(4) | C(25)–C(26)–N(2) | 125.2(4) |
| C(26)–C(25)–C(5) | 117.6(4) | N(1)–C(5)–C(25) | 120.6(4) |

Table 2. Selected bond lengths [Å] and angles [°] for compounds **5** and **6**.

| | [Ge(E){N(SiMe$_3$)C(Ph)C(SiMe$_3$)(C$_5$H$_4$N-2)}Cl] | |
|---|---|---|
| | E = S (**5**) | E = Se (**6**) |
| Ge(1)–E(1) | 2.056(2) | 2.191(1) |
| Ge(1)–Cl(1) | 2.180(2) | 2.179(2) |
| Ge(1)–N(2) | 1.840(4) | 1.823(5) |
| N(2)–C(10) | 1.392(6) | 1.410(7) |
| C(6)–C(10) | 1.388(7) | 1.362(7) |
| C(5)–C(6) | 1.475(8) | 1.465(7) |
| C(5)–N(1) | 1.345(7) | 1.357(8) |
| N(1)–Ge(1) | 1.952(5) | 1.947(5) |
| N(1)–Ge(1)–N(2) | 94.0(2) | 94.5(2) |
| E(1)–Ge(1)–Cl(1) | 116.1(8) | 116.1(8) |
| N(2)–Ge(1)–E(1) | 124.5(1) | 125.8(1) |
| N(2)–Ge(1)–Cl(1) | 103.5(2) | 103.1(2) |
| Ge(1)–N(2)–C(10) | 113.3(3) | 112.9(3) |
| N(2)–C(10)–C(6) | 124.5(5) | 124.2(5) |
| C(10)–C(6)–C(5) | 120.0(5) | 120.1(5) |
| C(5)–N(1)–Ge(1) | 119.0(4) | 117.9(3) |
| N(1)–Ge(1)–Cl(1) | 99.2(2) | 99.7(2) |
| N(1)–Ge(1)–E(1) | 114.9(2) | 112.9(1) |

nance structures **A** and **B**. The short Ge–Se distance in **6** indicates a double bond between germanium and selenium in the solid state.

The Ge–Cl distances of 2.180(2) Å in **5** and 2.179(2) Å in **6** are shorter than that of 2.283(9) Å in **2**. Similarly, the Ge–N$_{amide}$ distances [1.878(17) (**3**), 1.873(3) (**4**), 1.840(4) (**5**), 1.823(5) Å (**6**)] are shorter than those in the corresponding parent complexes [1.942(17) (**1**), 1.920(2) Å (**2**)].[7] This is because the germanium center in **3**–**6** has a higher oxidation state.

## Conclusions

A series of chalcogeno[2-(pyrid-2-yl)-1-azaallyl]germanium complexes has been synthesized, namely [Ge(E)-{C(C$_5$H$_4$N-2)C(Ph)N(SiMe$_3$)$_2$}{N(SiMe$_3$)C(Ph)C(SiMe$_3$)-(C$_5$H$_4$N-2)}] [E = S (**3**), Se (**4**)] and [Ge(E){N(SiMe$_3$)C(Ph)-C(SiMe$_3$)(C$_5$H$_4$N-2)}Cl] [E = S (**5**), Se (**6**)]. The Ge–E bond lengths in compounds **3**–**6** are indicative of a formal double bond or a Ge–E σ-bond with significant ionic character.[6a,6b]

## Experimental Section

**General Remarks:** All manipulations were carried out under dinitrogen by standard Schlenk techniques. Solvents were dried with, and distilled from, $CaH_2$ (hexane) and/or Na ($Et_2O$, toluene and THF). Anhydrous S and Se were purchased from Aldrich Chemicals and used without further purification. [Ge{C(C$_5$H$_4$N-2)C(Ph)-N(SiMe$_3$)$_2$}{N(SiMe$_3$)C(Ph)C(SiMe$_3$)(C$_5$H$_4$N-2)}] (**1**) and [Ge{N(SiMe$_3$)C(Ph)C(SiMe$_3$)-(C$_5$H$_4$N-2)}Cl] (**2**) were prepared according to literature procedures.[7] The $^1$H, $^{13}$C, and $^{77}$Se NMR spectra were recorded with Bruker WM-300 or Varian 400 instruments. All spectra were recorded in [D$_8$]THF, and the chemical shifts are given relative to SiMe$_4$ ($^1$H, $^{13}$C) or Se$_2$Me$_2$ ($^{77}$Se).

**[{N(SiMe$_3$)C(Ph)C(SiMe$_3$)(C$_5$H$_4$N-2)}{C(C$_5$H$_4$N-2)C(Ph)N(SiMe$_3$)$_2$}Ge=S] (3):** A solution of **1** (0.73 g, 0.97 mmol) in toluene (30 mL) was added slowly to a suspension of sulfur (0.03 g, 0.97 mmol) in toluene (25 mL) at 0 °C. The yellow mixture was warmed to room temperature and stirred at room temperature for 16 h. The precipitate was filtered and the filtrate was concentrated to yield yellow crystals of **3**. Yield: 0.23 g (30%); m.p. 222–226 °C (dec.). C$_{38}$H$_{54}$GeN$_4$SSi$_4$ (783.9): calcd. C 58.22, H 6.94, N 7.14; found C 58.12, H 7.03, N 7.29. $^1$H NMR (300 MHz, [D$_8$]THF, 25 °C): $\delta$ = –0.40 (s, SiMe$_3$, 9 H), –0.12 (s, SiMe$_3$, 9 H), –0.06 (s, SiMe$_3$, 9 H), –0.03 (s, SiMe$_3$, 9 H), 6.70 (t, $J$ = 6.5 Hz, py, 1 H), 7.21–7.32 (m, Ph, 5 H), 7.34–7.37 (m, py, 1 H), 7.40–7.47 (m, Ph, 5 H), 7.61–7.65 (m, py, 1 H), 7.77–7.79 (m, py, 1 H), 8.35 (d, $J$ = 5.7 Hz, py, 1 H), 8.47 (d, $J$ = 4.5 Hz, py, 1 H), 8.53 (d, $J$ = 4.8 Hz, py, 1 H), 8.78 (d, $J$ = 6 Hz, py, 1 H) ppm. $^{13}$C{$^1$H} NMR (300 MHz, [D$_8$]THF, 25 °C): $\delta$ = 1.76, 2.23, 2.76 (SiMe$_3$), 94.46 (*C*SiMe$_3$), 111.70, 119.02, 125.05, 128.49, 130.81, 132.08, 133.10, 134.44, 137.29, 140.76, 143.45, 145.18, 146.21, 147.81, 151.83, 157.03, 160.04, 162.42 (Ph and py), 163.95 (py*C*Ge), 164.26, 165.64 (N*C*Ph) ppm.

**[{N(SiMe$_3$)C(Ph)C(SiMe$_3$)(C$_5$H$_4$N-2)}{C(C$_5$H$_4$N-2)C(Ph)N(SiMe$_3$)$_2$}Ge=Se] (4):** A solution of **1** (0.75 g, 1.00 mmol) in toluene (15 mL) was added to a stirred suspension of selenium powder (0.08 g, 1.00 mmol) in toluene (15 mL) at 0 °C. The resultant yellowish-orange solution was warmed to room temperature and stirred for 18 h. Unreacted selenium powder was removed by filtration. The filtrate was concentrated and stored at –30 °C. Compound **4** was obtained as yellow crystals. Yield: 0.50 g (60%); m.p.

 © 2006 Wiley-VCH Verlag GmbH & Co. KGaA, Weinheim 

Table 3. Crystallographic data for compounds **3**–**6**.

| | **3** | **4** | **5** | **6** |
|---|---|---|---|---|
| Empirical formula | $C_{38}H_{54}GeN_4SSi_4$ | $C_{38}H_{54}GeN_4Si_4Se$ | $C_{19}H_{27}ClGeN_2SSi_2$ | $C_{19}H_{27}ClGeN_2Si_2Se$ |
| Formula mass | 783.86 | 832.78 | 479.71 | 526.61 |
| Color | yellow | yellow | yellow | yellow |
| Crystal system | triclinic | triclinic | monoclinic | triclinic |
| Space group | $P\bar{1}$ | $P\bar{1}$ | $C2/c$ | $P\bar{1}$ |
| $a$ [Å] | 11.290(2) | 11.380(2) | 33.234(3) | 6.7285(13) |
| $b$ [Å] | 12.724(3) | 12.722(3) | 6.5646(3) | 11.154(2) |
| $c$ [Å] | 15.977(3) | 16.049(3) | 21.5209(3) | 16.577(3) |
| $\alpha$ [°] | 77.49(3) | 77.12(3) | 90 | 86.17(3) |
| $\beta$ [°] | 89.89(3) | 89.53(3) | 90.750(2) | 88.45(3) |
| $\gamma$ [°] | 72.51(3) | 72.42(3) | 90 | 76.08(3) |
| $V$ [Å$^3$] | 2132.1(7) | 2154.9(7) | 4694.8(6) | 1204.8(4) |
| $Z$ | 2 | 2 | 8 | 2 |
| $d_{calcd.}$ [g cm$^{-3}$] | 1.221 | 1.283 | 1.357 | 1.452 |
| $\mu$ [mm$^{-1}$] | 0.910 | 1.697 | 1.616 | 2.998 |
| $F(000)$ | 828 | 868 | 1984 | 532 |
| Crystal size [mm] | 0.48 × 0.46 × 0.38 | 0.30 × 0.21 × 0.13 | 0.50 × 0.40 × 0.20 | 0.50 × 0.40 × 0.30 |
| $2\theta$ range [°] | 2.13–24.99 | 1.73–25.00 | 1.23–28.72 | 1.23–25.60 |
| Index range | $-13 \le h \le 12$ | $-13 \le h \le 13$ | $-38 \le h \le 44$ | $-7 \le h \le 7$ |
| | $-15 \le k \le 0$ | $-14 \le k \le 15$ | $-8 \le k \le 8$ | $-13 \le k \le 0$ |
| | $-18 \le l \le 18$ | $0 \le l \le 19$ | $-27 \le l \le 29$ | $-20 \le l \le 19$ |
| No. of reflections collected | 7488 | 4741 | 16056 | 3778 |
| No. of independent reflections | 5814 | 3833 | 6019 | 3778 |
| $R1$, $wR2$ [$I > 2\sigma(I)$] | 0.0496, 0.1366 | 0.0771, 0.1983 | 0.0668, 0.1534 | 0.0722, 0.1955 |
| $R1$, $wR2$ (all data) | 0.0739, 0.1495 | 0.0972, 0.2149 | 0.1606, 0.2041 | 0.0771, 0.2043 |
| Goodness of fit ($F^2$) | 1.025 | 1.067 | 0.949 | 1.082 |
| No. of data/restraints/parameters | 7488/0/434 | 4741/0/447 | 6019/0/235 | 3778/0/235 |
| Largest difference peaks [e Å$^{-3}$] | 0.582/–0.703 | 0.910/–0.610 | 1.169/–0.582 | 1.029/–1.399 |

233–236 °C (dec.). $C_{38}H_{54}GeN_4Si_4Se$ (830.8): calcd. C 54.94, H 6.55, N 6.75; found C 55.07, H 6.63, N 6.94. $^1$H NMR (300 MHz, [D$_8$]THF, 25 °C): $\delta$ = –0.30 (s, SiMe$_3$, 9 H), –0.21 (s, SiMe$_3$, 9 H), –0.17 (s, SiMe$_3$, 9 H), 0.00 (s, SiMe$_3$, 9 H), 6.87–6.90 (m, py, 1 H), 6.91–6.94 (m, py, 1 H), 7.05–7.14 (m, Ph, 5 H), 7.16–7.18 (m, py, 1 H), 7.25–7.27 (m, py, 1 H), 7.33–7.38 (m, Ph, 5 H), 7.48–7.52 (m, py, 1 H), 7.67 (t, $J$ = 6.9 Hz, py, 1 H), 7.98 (d, $J$ = 4.8 Hz, py, 1 H), 8.27 (d, $J$ = 3.9 Hz, py, 1 H) ppm. $^{13}$C{$^1$H} NMR (300 MHz, [D$_8$]THF, 25 °C): $\delta$ = 2.31, 2.77, 2.86 (SiMe$_3$), 114.60 (*C*SiMe$_3$), 118.94, 119.46, 124.54, 124.69, 127.60, 127.95, 128.33, 129.08, 130.99, 131.59, 135.63, 137.93, 144.30, 145.67, 147.59, 148.31, 150.69, 153.95 (Ph and py), 156.32 (py*C*Ge), 167.06, 171.49 (N*C*Ph) ppm. $^{77}$Se NMR (400 MHz, [D$_8$]THF, 25 °C): $\delta$ = –28.63 ppm.

**[Ge(S){N(SiMe$_3$)C(Ph)C(SiMe$_3$)(C$_5$H$_4$N-2)}Cl] (5):** A solution of **2** (0.48 g, 1.07 mmol) in toluene (15 mL) was added to a stirred suspension of sulfur powder (0.035 g, 1.09 mmol) in toluene (15 mL) at 0 °C. The resultant yellowish-orange solution was warmed to room temperature and stirred for 18 h. The precipitate was filtered and the filtrate was concentrated to yield yellow crystals of **5**. Yield: 0.28 g (54%); m.p. 250–252 °C. $C_{19}H_{27}ClGeN_2SSi_2$ (479.7): calcd. C 47.63, H 5.68, N 5.85; found C 47.36, H 5.10, N 5.85. $^1$H NMR (300 MHz, [D$_8$]THF, 25 °C): $\delta$ = –0.14 (s, SiMe$_3$, 9 H), 0.00 (s, SiMe$_3$, 9 H), 7.42–7.49 (m, 1 H, 5-py), 7.49–7.69 (m, 5 H, Ph), 7.75–7.78 (m, 1 H, 3-py), 8.25–8.26 (m, 1 H, 4-py), 9.26–9.28 (m, 1 H, 6-py) ppm. $^{13}$C{$^1$H} NMR (300 MHz, [D$_8$]THF, 25 °C): $\delta$ = 1.80, 3.11 (SiMe$_3$), 116.01 (*C*SiMe$_3$), 123.73, 128.65, 129.46, 131.48, 131.89, 132.14, 142.11, 144.80, 157.63 (Ph and py), 164.83 (N*C*Ph) ppm.

**[Ge(Se){N(SiMe$_3$)C(Ph)C(SiMe$_3$)(C$_5$H$_4$N-2)}Cl] (6):** A solution of **2** (0.50 g, 1.12 mmol) in toluene (15 mL) was added to a stirred suspension of selenium powder (0.089 g, 1.13 mmol) in toluene (15 mL) at 0 °C. The resultant yellowish-orange solution was warmed to room temperature and stirred for 18 h. The precipitate was filtered and the filtrate was added to 5 mL of $CH_2Cl_2$ and concentrated to yield yellow crystals of **5**. Yield: 0.35 g (60%); m.p. 198–200 °C. $C_{19}H_{27}ClGeN_2Si_2Se\bullet1/2CH_2Cl_2$ (569.1): calcd. C 41.15, H 4.96, N 4.96; found C 41.41, H 5.17, N 5.17. $^1$H NMR (300 MHz, [D$_8$]THF, 25 °C): $\delta$ = –0.15 (s, SiMe$_3$, 9 H), –0.01 (s, SiMe$_3$, 9 H), 7.42–7.52 (m, 1 H, 5-py), 7.58–7.72 (m, 5 H, Ph), 7.75–7.77 (m, 1 H, 3-py), 8.24–8.25 (m, 1 H, 4-py), 9.34–9.36 (m, 1 H, 6-py) ppm. $^{13}$C{$^1$H} NMR (300 MHz, [D$_8$]THF, 25 °C): $\delta$ = 1.74, 3.47 (SiMe$_3$), 116.47 (*C*SiMe$_3$), 122.70, 127.50, 128.63, 129.52, 131.48, 132.19, 142.73, 144.83, 157.28 (Ph and py), 164.65 (N*C*Ph) ppm. $^{77}$Se NMR (400 MHz, [D$_8$]THF, 25 °C): $\delta$ = –266.21 ppm.

**X-ray Crystallographic Study:** Single crystals were sealed in Lindemann glass capillaries under nitrogen. X-ray data of **3**–**6** were collected with a Rigaku R-AXIS II imaging plate using graphite-monochromated Mo-$K_\alpha$ radiation ($\lambda$ = 0.71073 Å) from a rotating-anode generator operating at 50 kV and 90 mA. Crystal data for **3**–**6** are summarized in Table 3. The structures were solved by direct phase determination using the computer program SHELXTL-PC[11] with a PC 486 and refined by full-matrix least-squares with anisotropic thermal parameters for the non-hydrogen atoms. Hydrogen atoms were introduced in their idealized positions and included in structure factor calculations with assigned isotropic temperature factor calculations. CCDC-292827 (**3**), -292825 (**4**) -292826 (**5**), and -292824 (**6**) contain the supplementary crystallographic data for this paper. These data can be obtained free of charge from The Cambridge Crystallographic Data Center via www.ccdc.cam.ac.uk/data_request/cif.

## Acknowledgments

This work was supported by the Hong Kong Research Grants Council (project no. CUHK 4265-00P).

 © 2006 Wiley-VCH Verlag GmbH & Co. KGaA, Weinheim 

[1] J. Barrau, J. Escudié, J. Satgé, *J. Chem. Rev.* **1990**, *90*, 283.
[2] For selected reviews and examples of chalcogenones, see: a) P. P. Power, *Chem. Rev.* **1999**, *99*, 3463; b) N. Tokitoh, R. Okazaki, *Adv. Organomet. Chem.* **2001**, *47*, 121; c) R. Okazaki, N. Tokitoh, *Acc. Chem. Res.* **2000**, *33*, 625; d) M. Veith, S. Becker, V. Huch, *Angew. Chem. Int. Ed. Engl.* **1989**, *28*, 1237; e) S. R. Foley, C. Bensimon, D. S. Richeson, *J. Am. Chem. Soc.* **1997**, *119*, 10359; f) T. Matsumoto, N. Tokitoh, R. Okazaki, *J. Am. Chem. Soc.* **1999**, *121*, 8811; g) N. Tokitoh, M. Saito, R. Okazaki, *J. Am. Chem. Soc.* **1993**, *115*, 2065; h) Y. Matsuhashi, N. Tokitoh, R. Okazaki, M. Goto, *Organometallics* **1993**, *12*, 2573.
[3] a) M. C. Kuchta, G. Parkin, *J. Chem. Soc., Chem. Commun.* **1994**, 1351; b) M. C. Kuchta, G. Parkin, *J. Am. Chem. Soc.* **1994**, *116*, 8372.
[4] a) N. Tokitoh, T. Matsumoto, K. Manmaru, R. Okazaki, *J. Am. Chem. Soc.* **1993**, *115*, 8855; b) T. Matsumoto, N. Tokitoh, R. Okazaki, *Angew. Chem. Int. Ed. Engl.* **1994**, *33*, 2316; c) N. Tokitoh, T. Matsumoto, R. Okazaki, *J. Am. Chem. Soc.* **1997**, *119*, 2337.
[5] a) W.-P. Leung, W.-H. Kwok, Z.-Y. Zhou, T. C. W. Mak, *Organometallics* **2000**, *19*, 296; b) W.-P. Leung, W.-H. Kwok, L. T. C. Law, Z.-Y. Zhou, T. C. W. Mak, *Chem. Commun.* **1996**, 505.
[6] a) Y. Ding, Q. Ma, H. W. Roesky, I. Usón, M. Noltemeyer, H. G. Schmidt, *Dalton Trans.* **2003**, 1094; b) Y. Ding, Q. Ma, I. Usón, H. W. Roesky, M. Noltemeyer, H. G. Schmidt, *J. Am. Chem. Soc.* **2002**, *124*, 8542; c) I. Saur, G. Rima, H. Gornitzka, K. Miqueu, J. Barrau, *Organometallics* **2003**, *22*, 1106.
[7] W.-P. Leung, C.-W. So, Y.-S. Wu, H.-W. Li, *Eur. J. Inorg. Chem.* **2005**, *3*, 513.
[8] P. B. Hitchcock, E. Jang, M. F. Lappert, *J. Chem. Soc., Dalton Trans.* **1995**, 3179.
[9] L. Pauling *The Nature of The Chemical Bond*, 3rd ed., Cornell University Press, Ithaca, N.Y., **1960**, p. 224.
[10] G. Ossig, A. Meller, C. Brönneke, O. Müller, M. Schäfer, R. Herbst-Irmer, *Organometallics* **1997**, *16*, 2116.
[11] G. M. Sheldrick, in *Crystallographic Computing 3: Data Collection, Structure Determination, Proteins, and Databases* (Eds.: G. M. Sheldrick, C. Kruger, R. Goddard), Oxford University Press, New York, **1985**, p. 175.

Received: August 11, 2005
Published Online: December 27, 2005

 © 2006 Wiley-VCH Verlag GmbH & Co. KGaA, Weinheim 

DOI: 10.1002/ejic.200500730

# Synthesis and X-ray Crystal Structures of the New, Three-Dimensional Ethylenediphosphonates [A{$HO_3P(CH_2)_2PO_3H_2$}] (A = Alkali Metal, Tl, or $NH_4$): Solid Brönsted Acids That Exhibit Topotactic Intercalation and Deintercalation of Ammonia

**Koya Prabhakara Rao[a] and Kanamaluru Vidyasagar*[a]**

**Keywords:** Intercalation / Organic–inorganic hybrid composites / Phosphonates / X-ray diffraction

Seven new ethylenediphosphonates with the formula [A{$HO_3P(CH_2)_2PO_3H_2$}] [A = Li (**1**), Na (**2**), K (**3**), Rb (**4**), Cs (**5**), Tl (**6**), and $NH_4$ (**7**)], have been synthesized and characterized by single-crystal X-ray diffraction, infrared spectroscopy, and thermal studies. They have four types of three-dimensional structures, with variations in the coordination of the $A^+$ ions. All of them are solid Brönsted acids that undergo room-temperature, acid–base intercalation reactions with ammonia.

(© Wiley-VCH Verlag GmbH & Co. KGaA, 69451 Weinheim, Germany, 2006)

## Introduction

Metal organophosphonates are a class of organic–inorganic hybrid materials in which the organophosphonate groups are covalently bonded to the metal inorganic backbone. In the recent past, there has been a renewed interest and activity in the research area of metal organophosphonates,[1–6] mainly due to their varied compositions, structural diversity, and potential applications,[7–11] for example, as sorbents, ion-exchangers, sensors, and catalysts. The expansion of metal organophosphonate chemistry includes phosphonates[12–15] and diphosphonates[16–18] of s-, p-, d- and f-block metals, and the structures reported for these compounds can be broadly classified into two categories, namely zero-dimensional types, such as mononuclear and complex molecular clusters, and extended framework types like one-, two-, and open three-dimensional networks. Low-dimensional structures such as chains and layers are mostly observed for compounds of the second type due to the segregation of hydrophobic regions of the organic moieties from the rest of the framework.

The solid-state chemistry of diphosphonates[16–18] is an emerging area of research, and several investigations concerning the synthesis, structures, and properties of di-, tri-, and tetravalent metal diphosphonates with extended frameworks,[16–18] such as $(VO)_2[CH_2(PO_3)_2]\cdot 4H_2O$, $[Ti_3O_2(H_2O)_2(O_3PCH_2PO_3)_2]\cdot(H_2O)_2$, $[Al_2\{(O_3PCH_2CH_2PO_3)\}(H_2O)_2F_2]\cdot H_2O$, $[Al_2\{(O_3PC_2H_4PO_3)_{1-x}(HPO_3)_{2x}\}(H_2O)_2F_2]\cdot H_2O$ ($0 \leq x \leq 0.32$), $[Al_2(OH)_2(H_2O)_2(O_3PCH_2CH_2PO_3)]$, $[Ga_2\{(O_3PCH_2CH_2PO_3)\}(H_2O)_2F_2]\cdot 2H_2O$, $[Sb_2\{O(O_3PCH_2PO_3H)\}]$, $[Ni_4(O_3PCH_2PO_3)_2]\cdot(H_2O)_n$ ($n$ = 3, 2, 0), $[Cr_2\{O_3P\text{-}(CH_2)_2\text{-}PO_3\}_2]\cdot 3H_2O$, $[Cu_2\{(O_3PCH_2CH_2PO_3)(H_2O)_2\}]$, $[Cu_2\{(O_3PC_3H_6PO_3)(H_2O)_2\}]\cdot H_2O$, $[Cu_2\{(O_3PC_4H_8PO_3)(H_2O)_2\}]\cdot 2H_2O$, $[Cu_2\{(O_3PC_5H_{10}PO_3)(H_2O)_2\}]\cdot 2.8H_2O$, $[Zn_2\{(O_3PCH_2CH_2PO_3)_2(H_2O)\}]$, $[Zn_2\{(O_3PC_3H_6PO_3)\}]$, $[Co_2(O_3PCH_2PO_3)]\cdot H_2O$, $[Fe_2\{(O_3PCH_2CH_2PO_3)\}]$, and $[Fe_2\{(O_3PCH_2CH_2PO_3)\}]\cdot 2H_2O$, have been reported. These examples illustrate the structural diversity and the compositional variations, with different ratios of metal to diphosphonates, inclusion of $F^-$, $O^{2-}$, and/or $H_2O$ in the coordination sphere of the metals, and di-, tri-, and tetraanionic forms of diphosphonic acids with different alkyl chain lengths. One noteworthy feature of all these alkyl diphosphonates is their insolubility in water, which enables their isolation as precipitates from aqueous solutions.

Among the many diphosphonates reported, there are only a few reports[18] of compounds with a metal to diphosphonic acid ratio of 1:1. These include $[Ti\{O_3P(CH_2)_nPO_3\}]$ ($n$ = 2, 3), $[LnH\{O_3P(CH_2)_nPO_3\}]$ ($n$ = 1–3), $[Sb\{O_3P(CH_2)_nPO_3H\}]$ ($n$ = 2, 3), and $[Sn(HO_3PCH_2PO_3H)]$. These tri- and divalent metal compounds contain $(HO_3PCH_2PO_3H)^{2-}$ and $(HO_3PCH_2PO_3)^{3-}$ anions and are, therefore, potential solid Brönsted acids. However, there are no reports of the intercalation properties of these diphosphonates. It is in this context that 1:1 diphosphonates of monovalent metals, [A{$HO_3P(CH_2)_nPO_3H_2$}], are envisaged to be strong, solid Brönsted acids that can undergo intercalation with bases. Only two monovalent metal diphosphonates, namely $[Ag_4\{O_3P(CH_2)_2PO_3\}]$ and [Na{$HO_3PCH_2PO_3H_2$}], have been reported[19] so far. We have recently synthe-

[a] Department of Chemistry,
Indian Institute of Technology Madras,
Chennai, 600036, India
E-mail: kvsagar@iitm.ac.in

Supporting information for this article is available on the WWW under http://www.eurjic.org or from the author.

 © 2006 Wiley-VCH Verlag GmbH & Co. KGaA, Weinheim 

sized[20] seven new, low-dimensional 1:2 phenylphosphonates of monovalent metals, $[A(HO_3PPh)(H_2O_3PPh)]$ (A = Li, Na, K, Rb, Cs, $NH_4$, and Tl). These solid Brönsted acids undergo intercalation of amines and ammonia and, in a few cases, to the largest extent ever known. In view of these observations, we have undertaken a study of 1:1 metal alkyl diphosphonates of alkali and thallium metals and ammonium. We report here the successful synthesis, characterization, and ammonia-intercalation of the new, water-soluble ethylene diphosphonates $[A\{HO_3P(CH_2)_2PO_3H_2\}]$ [A = Li (**1**), Na (**2**), K (**3**), Rb (**4**), Cs (**5**), Tl (**6**), and $NH_4$ (**7**)].

## Results and Discussion

### X-ray Diffraction and Crystal Structures

The observed powder XRD patterns for all the seven structurally characterized $[A\{HO_3P(CH_2)_2PO_3H_2\}]$ compounds agree with those simulated with the LAZY-PULVERIX program[21] on the basis of single-crystal X-ray structures, thus indicating the single-phase nature of the samples. However, the observed relative intensities of some of the reflections are different from those calculated due to the preferential orientation of the crystallites. The crystal structures of ethylenediphosphonates **1**–**7** can be broadly classified into four structural types, namely those of compounds **1**, **2**, **3**, and **7**. From the point of view of A-P-O frameworks the sodium compound is two-dimensional, whereas the others are all one-dimensional compounds. However, these frameworks are connected three-dimensionally by the ethylene moiety.

$[Li\{HO_3P(CH_2)_2PO_3H_2\}]$ (**1**) contains half of one unit formula in the asymmetric unit. The lithium atom sits on a twofold axis and is tetrahedrally bonded to four O(1) atoms, which are near the inversion center 4b. Each $LiO(1)_4$ tetrahedron shares two edges with two such tetrahedra to form "$LiO_2$" chains parallel to the *c*-axis (Figure 1). O(1) is bonded to two Li atoms, and each diphosphonate, in turn, is bonded to four Li atoms, linking two such "$LiO_2$"chains. The ethylenediphosphonate groups connect these chains three-dimensionally. The four phosphonate moieties of different diphosphonates are positioned near the inversion center 4a such that O(3)–H(3) forms a hydrogen bond with O(2) and the other acidic hydrogen atom, H(2), at the inversion center is between two O(2) atoms, as shown in the encircled region of Figure 1. This unique region of space could be conceived as being porous. To the best of our knowledge this is the first lithium diphosphonate.

$[Na\{HO_3P(CH_2)_2PO_3H_2\}]$ (**2**) contains two formula units in the asymmetric unit. The two crystallographically distinct sodium atoms, Na1 and Na2, are confined approximately to the *xy* planes at $z \approx ¼$ and ¾ and octahedrally coordinated to ten of twelve crystallographically distinct oxygen atoms [O(1)–O(12)]. Only O(8) and O(11) are not bonded to sodium atoms. These two $NaO_6$ octahedra share the O(7)–O(10) edge to form a $Na_2O_{10}$ unit, which is linked to ten phosphonate moieties of five diphosphonates (Figure 2). Thus, the diphosphonates connect $Na_2O_{10}$ units in

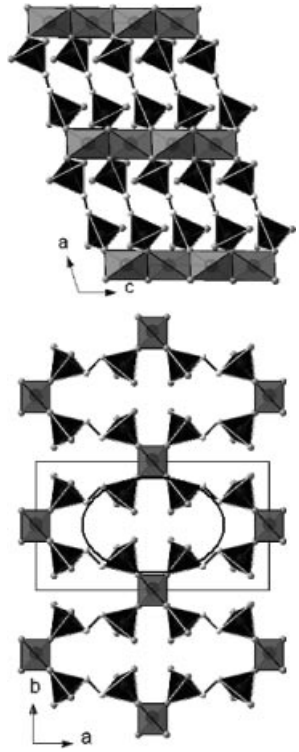


Figure 1. Polyhedral representation of the unit cell of $[Li\{HO_3P(CH_2)_2PO_3H_2\}]$ (**1**) viewed along the *b*-axis (top) and the *c*-axis (bottom).

the same plane as well as those in the adjacent planes, leading to a layered–pillared structure (Figure 2). The two diphosphonates are distinct in that one is bonded to six sodium atoms whereas the other is bonded to only four.

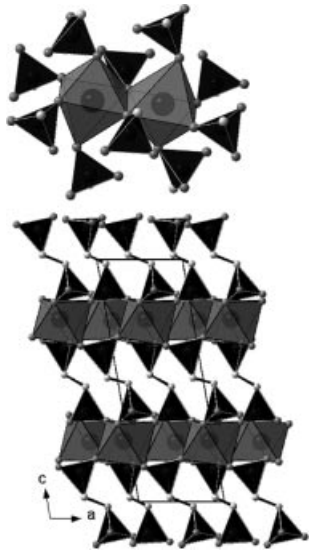


Figure 2. Polyhedral representation of the $Na_2O_{10}$ bi-octahedral unit with phosphonate moieties (top) and unit cell of $[Na\{HO_3P(CH_2)_2PO_3H_2\}]$ (**2**) viewed along the *b*-axis (bottom).

$[K\{HO_3P(CH_2)_2PO_3H_2\}]$ (**3**) has one formula unit in the asymmetric unit. The potassium atoms are confined approximately to the *xz* planes at $y \approx ¼$ and ¾ and coordinated dodecahedrally to oxygen atoms O(1)–O(6) of the di-

 © 2006 Wiley-VCH Verlag GmbH & Co. KGaA, Weinheim 

phosphonate, with the maximum value of the K–O bond length being 3.073(2) Å. Each $KO_8$ dodecahedron shares two O(1)–O(4) edges with two such polyhedra to form "$KO_6$" chains parallel to the *c*-axis (Figure 3). These chains are linked to one another three-dimensionally by diphosphonate moieties through the O(5) atoms. Thus, this compound is three-dimensional in nature. The diphosphonate is coordinated to five potassium atoms. Similarly, each potassium atom is bonded to five phosphonate moieties of different diphosphonates: three of them are bonded in a bidentate fashion and other two in a monodentate fashion. O(3)–H(3) and O(6)–H(6) form hydrogen bonds with O(1) and O(4), respectively. H(2) and H(5), at two inversion centers, represent two disordered positions of the other acidic hydrogen atom and are located, respectively, between the O(2) and O(5) atoms. These structural features are present in the similar three-dimensional rubidium (**4**), cesium (**5**), and thallium (**6**) compounds as well.

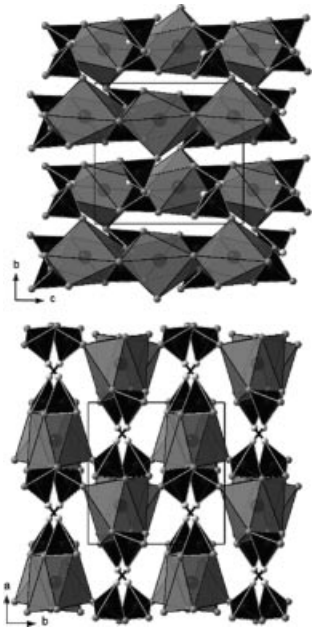

Figure 3. Polyhedral representation of the unit cell of $[K\{HO_3P(CH_2)_2PO_3H_2\}]$ (**3**) viewed along the *a*-axis (top) and the *c*-axis (bottom).

The rubidium (**4**) and cesium (**5**) compounds have the same positional parameters and contain half a formula unit in their asymmetric units. The metal atoms sit on twofold axes and are dodecahedrally coordinated to the O(1)–O(3) atoms of a diphosphonate moiety. The maximum values of the Rb–O and Cs–O bond lengths are 3.199(3) and 3.431(3) Å, respectively. Each $AO_8$ dodecahedron shares two O(1)–O(1′) edges with two such polyhedra to form "$AO_6$" chains parallel to [101]. These chains are linked to one another three-dimensionally, by diphosphonate moieties, through the O(1) atoms. Unlike cesium, which is bonded to eight diphosphonates in a monodentate fashion, rubidium is bonded to two diphosphonates in a bidentate fashion and another four in a monodentate mode. The hydrogen bonding is the same in both compounds: O(3)–H(3) forms a hydrogen bond with O(2) and the other acidic hydrogen atom, H(2), at the inversion center is between two O(2) atoms.

There are two distinct diphosphonates, which sit on inversion centers 2b and 2d, in the unit cell of $[Tl\{HO_3P(CH_2)_2PO_3H_2\}]$ (**6**). The thallium atoms are confined approximately to the *yz* planes at $x \approx 0.27$ and 0.77 and are coordinated dodecahedrally to oxygen atoms O(1)–O(6) of both diphosphonates, with the maximum value of the Tl–O bond length being as high as 3.47(3) Å. $TlO_8$ dodecahedra, similar to those in the potassium compound, share O(1)–O(1) and O(6)–O(6) edges to form "$TlO_6$" chains parallel to the *a*-axis; these chains are linked to one another through the O(4) atoms. The diphosphonate is bonded, in a monodentate fashion, to six thallium atoms. Similarly, the thallium atom is bonded to six phosphonate moieties of different diphosphonates. Both O(3)–H(3) and O(6)–H(6) form hydrogen bonds with O(5). H(2) and H(5), with half site-occupancies, represent two disordered positions of the other acidic hydrogen atom and are bonded, respectively, to the O(2) and O(5) atoms. O(2)–H(2) and O(5)–H(5) form hydrogen bonds with O(4) and O(3), respectively.

The nitrogen atoms in $[NH_4\{HO_3P(CH_2)_2PO_3H_2\}]$ (**7**) are confined approximately to the *ab* planes and are tetrahedrally hydrogen-bonded to oxygen atoms of the diphosphonates (Figure 4). The two crystallographically distinct ethylene diphosphonates sit on inversion centers 1h and 1b. All the six oxygen atoms, represented by O(4)–O(6), of one diphosphonate and only two oxygen atoms, O(1) and O(1′), of another diphosphonate are hydrogen-bonded to nitrogen. The connectivity pattern of $NO_4$ tetrahedra and "$PO_3C$" phosphonate moieties results in ladder-like chains parallel to the *a*-axis (Figure 4), with porous regions between them. Such a pattern is also observed[20] in $[NH_4(HO_3PC_6H_5)(H_2O_3PC_6H_5)]$. These chains in the adja-

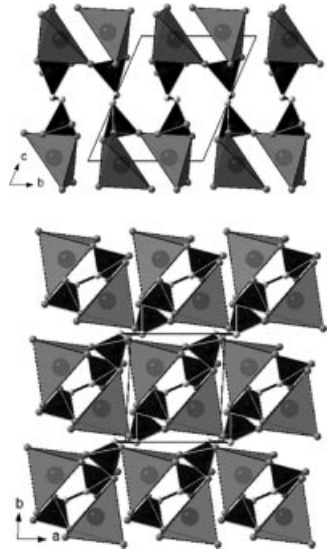

Figure 4. Polyhedral representation of the unit cell of $[NH_4\{HO_3P(CH_2)_2PO_3H_2\}]$ (**7**) viewed along the *a*-axis (top) and the *c*-axis (bottom).

 © 2006 Wiley-VCH Verlag GmbH & Co. KGaA, Weinheim 

cent layers are connected three-dimensionally through the C–C bonds of the $PO_3C$ phosphonate moieties. O(3)–H(3) and O(6)–H(6) form hydrogen bonds with O(4) and O(1), respectively, and O(2)–H(2) is strongly hydrogen bonded to O(5).

In the five compounds **1**, **3**, **4**, **5**, and **7**, the values of the P–O, P–C, and C–C bond lengths vary in the ranges 1.493(3)–1.575(2), 1.790(4)–1.795(3), and 1.522(5)–1.542(7) Å, respectively. These values compare with the 1.501(1)–1.553(2) Å range of P–O bond lengths, the 1.786(2) Å P–C bond length, and the 1.544(4) Å C–C bond length reported[22] for ethylenediphosphonic acid. The corresponding bond-length ranges of 1.48(2)–1.590(7), 1.74(3)–1.89(1), and 1.45(2)–1.55(2) Å in compounds **2** and **6** are a bit wider.

### Spectroscopic Studies

All seven compounds, as illustrated for **1** in Figure 5, have the following common infrared spectral features: (i) the C–H stretching vibrations[17c] of the ethylenediphosphonate group are observed around 2970 and 2924 $cm^{-1}$, whereas their bending vibrations are seen at 1380 $cm^{-1}$; (ii) the peaks in the region 1200–1000 $cm^{-1}$ are due to P–O stretching vibrations and the O–P–O bending vibrations[17c] are found in the region 540–410 $cm^{-1}$. The infrared spectrum of the ammonium compound shows two additional peaks at 3240 and 1401 $cm^{-1}$ corresponding to the stretching and bending vibrations of the ammonium ion.[23]

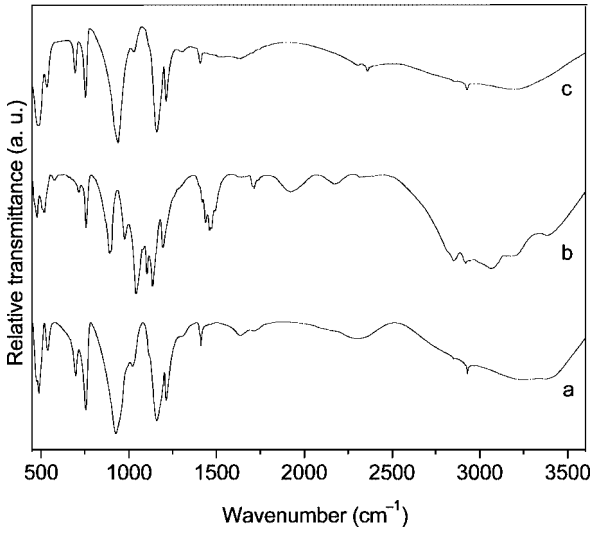


Figure 5. Infrared spectra of [Li{$HO_3P(CH_2)_2PO_3H_2$}] (**1**) (a), its intercalate **1**·$(NH_3)_{1.5}$ (b) and deintercalate (c).

### Thermal Analysis

Thermogravimetric analysis of all the seven compounds was carried out. The thermogravimetric curves of compounds **1**, **2**, and **7** are presented in Figure 6. No efforts have been made to identify the composition of the intermediate, residual solid products of decomposition and, therefore, only a factual description of these thermogravimetric curves is given. All these compounds are stable up to about 170–200 °C. Compounds **1**–**6** undergo total weight losses of 22.5–30% in the temperature range 200–800 °C, whereas the ammonium compound **7** has a maximum weight loss of 75%. These weight losses occur in two steps, with the second one at 460 °C being the major one.

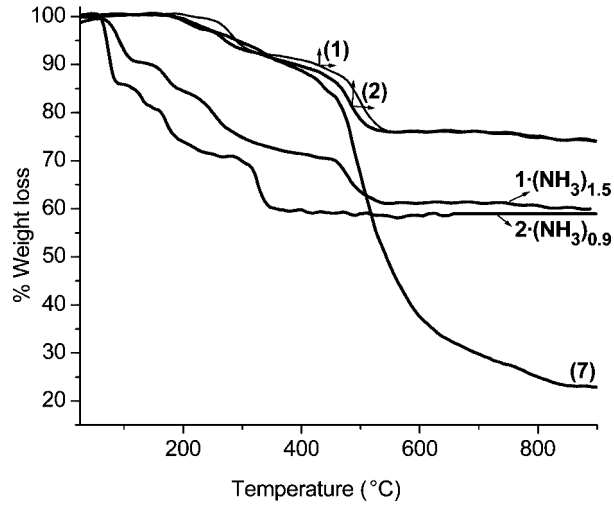


Figure 6. Thermogravimetric curves of compounds [A{$HO_3P(CH_2)_2PO_3H_2$}] [A = Li (**1**), Na (**2**), and $NH_4$ (**7**)] and ammonia intercalates **1**·$(NH_3)_{1.5}$ and **2**·$(NH_3)_{0.9}$.

### Intercalation and Deintercalation Reactions

All these ethylenediphosphonates are solid Brönsted acids. For example, the pH values of 1 M solutions of pure ligand and the sodium compound **2** are 2 and 3, respectively. Therefore, they were examined from the point of view of acid–base intercalation reactions with ammonia. These reactions, as determined from chemical analysis and spectroscopic and thermal studies, turned out to be successful. The success and extent of ammonia intercalation in the intercalates (**1**–**7**)·$(NH_3)_x$ were determined from the IR spectra and elemental analysis. The IR spectra (Figure 5) of compounds, (**1**–**6**)·$(NH_3)_x$ contain two additional peaks at 3240 and 1450 $cm^{-1}$ corresponding to the stretching and bending vibrations of the ammonium ion.[24] The $x$ values of (**1**–**7**)·$(NH_3)_x$ are 1.5, 0.9, 0.7, 0.5, 0.4, 1.0, and 1.6 respectively, and indicate partial intercalation and no systematic variation with the size and nature of A. The large value of $x$ for the lithium and ammonium compounds corroborates their large porosity and greater access to the porous regions. The differences in the powder XRD patterns of the parent diphosphonate and its ammonium intercalate are significant in the case of **1**, **3**, **6**, and **7**, which is indicative of intercalation of ammonia into the porous regions of the structure. However, the overall crystallinity decreases, as shown for **1**·$(NH_3)_{1.5}$ in Figure 7. Unlike the parent phases, the intercalates undergo a greater percentage of weight loss and begin to decompose at lower tempera-

 © 2006 Wiley-VCH Verlag GmbH & Co. KGaA, Weinheim 

tures. This is illustrated by the thermogravimetric curves of **1**·$(NH_3)_{1.5}$ and **2**·$(NH_3)_{0.9}$ in Figure 6. We also carried out ammonia deintercalation for a few selected intercalates, namely those of **1**, **2**, and **7**. They undergo deintercalation upon heating in the air-oven at about 170 °C for about 12 hours. The IR spectra (Figure 6), elemental analysis, and powder XRD patterns (Figure 7) of the deintercalated products, as illustrated in the case of **1**·$(NH_3)_{1.5}$, confirm that the deintercalation is complete and topotactic. To the best of our knowledge, this is the first time that such a reversible intercalation of ammonia in hybrid materials has been demonstrated.

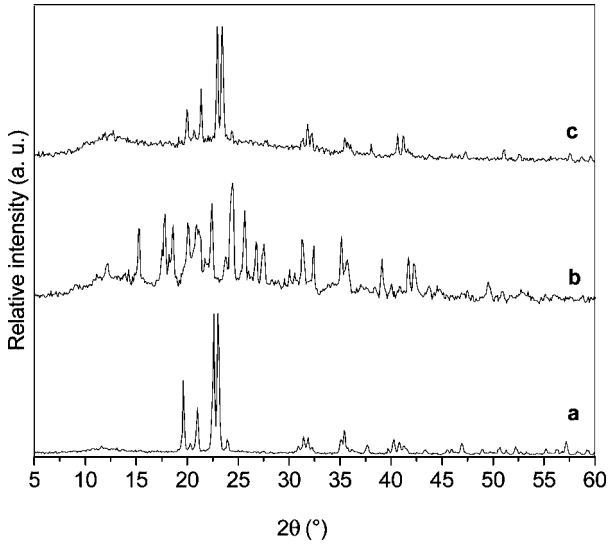


Figure 7. Powder X-ray diffraction patterns of [Li{$HO_3P(CH_2)_2PO_3H_2$}] (**1**) (a), its intercalate **1**·$(NH_3)_{1.5}$ (b) and deintercalate (c).

[$Zn(O_3PPh)$] and [$UO_2(HO_3PPh)_2(H_2O)]_2$·$8H_2O$ have been reported[9,25] to be sensors and proton conductors due to their intercalation and Brönsted-acidic properties, respectively. Compounds **1**–**7** exhibit both these properties and could be potentially useful as sensors and proton conductors.

## Concluding Remarks

A series of seven, new ethylenediphosphonates, [A{$HO_3P(CH_2)_2PO_3H_2$}] (A = alkali metal, Tl and $NH_4$), have four types of three-dimensional porous structures. They are solid Brönsted acids and undergo room-temperature intercalation reactions with ammonia. These intercalates can be deintercalated topotactically.

## Experimental Section

**Synthesis:** The high purity chemicals $A_2CO_3$ [A = Li, Na, K, $NH_4$ (SD Fine, India), Rb, Cs and Tl (Aldrich)] and 1,2-ethylenediphosphonic acid ($H_2O_3PCH_2CH_2PO_3H_2$, Lancaster) were used as purchased. The compounds [A{$HO_3P(CH_2)_2PO_3H_2$}] [A = Li (**1**), Na (**2**), K (**3**), Rb (**4**), Cs (**5**), Tl (**6**), and $NH_4$ (**7**)] were synthesized, on a 0.5–1.0-g scale, by evaporating aqueous solutions of stoichiometric reactant mixtures of ethylenediphosphonic acid and the appropriate carbonate. Slow evaporation, at room temperature, led to the formation of compounds as colorless, block-shaped or flaky crystals. However, evaporation in a steam bath yielded products in a polycrystalline form. In all the cases the yields were almost quantitative. These seven compounds were ascertained to be pure by elemental analysis with a Perkin–Elmer series 11 Model analyzer. $C_2H_7LiO_6P_2$ (195.96): calcd. C 12.25, H 3.60; found C 12.42, H 3.67. $C_2H_7NaO_6P_2$ (212.01): calcd. C 11.33, H 3.33; found C 11.80, H 3.38. $C_2H_7KO_6P_2$ (228.12): calcd. C 10.53, H 3.09; found C 10.61, H 3.00. $C_2H_7O_6P_2Rb$ (274.49): calcd. C 8.75, H 2.57; found C 8.62, H 2.67. $C_2H_7CsO_6P_2$ (321.93): calcd. C 7.46, H 2.19; found C 7.68, H, 2.23. $C_2H_7O_6P_2Tl$ (393.39): calcd. C 6.11, H 1.79; found C 6.15, H 1.79. $C_2H_{11}NO_6P_2$ (207.06): calcd. C 11.60, H 5.35, N 6.76; found C 11.62, H 5.22, N 6.50.

**Ammonia Intercalation and Deintercalation Reactions:** Intercalation of ammonia was achieved by passing ammonia gas over solid samples of ethylenediphosphonates **1**–**7** for 2 h. The amount ($x$) of intercalated ammonia was determined by analysis of the CHN content of the solid intercalates (**1**–**7**)·$(NH_3)_x$. Ammonia deintercalation was carried out by heating a sample of the intercalate in an oven at 170 °C for 12 h.

**X-ray Diffraction and Crystal Structure:** The powder X-ray diffraction (XRD) patterns of the seven ethylenediphosphontes **1**–**7** and their ammonia-intercalation products were recorded on a Shimadzu XD-D1 X-ray diffractometer using Cu-$K_\alpha$ ($\lambda$ = 1.5406 Å) radiation. Single crystals of compounds **1**–**7** suitable for X-ray diffraction were selected and mounted with glue on thin glass fibers. Crystals of compound **7** were found to be twinned. The X-ray data were gathered successfully at 25 °C, on an ENRAF-NONIUS CAD4 automated four-circle diffractometer, by standard procedures involving $\omega$–$2\theta$ techniques. These data sets were reduced by routine computational procedures. The program SHELXL-97[26] (Wingx) was employed for the structure solution and refinements and the graphic program DIAMOND[27] was used to draw the structures. The structure solutions were obtained by Patterson's method for compound **6** and by direct methods for the others. O(10) of **2** and O(1) of **6** were refined isotropically, whereas all other non-hydrogen atoms of these seven compounds were refined anisotropically. In each phosphonate moiety of compounds **1**–**7** the three oxygen atoms were labeled in increasing order of P–O bond lengths as they are different from one another. The oxygen atoms with short P–O bonds were considered to be formally double bonded to phosphorus atoms. The non-hydrogen-atom contents do not account for charge neutrality, thus indicating the presence of three acidic protons of diphosphonic acid moieties. These acidic hydrogen atoms, for all compounds except **2**, were located in the difference Fourier maps and refined with riding model restraints. Two of the three acidic hydrogen atoms of diphosphonate are bonded to the two oxygen atoms with long P–O bonds, whereas the third hydrogen atom is bonded to, or located between, those oxygen atoms with intermediate P–O bond lengths.[28] The ethylene hydrogen atoms were refined for all the seven compounds. For the ammonium compound **7**, the ammonium hydrogen atoms were located in the difference Fourier map and included in the final refinement. The structure refinement proceeded smoothly for all compounds but **2** and **6**. For compound **2**, the $R$ value was 10.5% and therefore an additional absorption correction, based on the isotropically refined model, was applied to the X-ray data using the program DIFABS.[29] The final difference Fourier map showed no residual peak with electron density of $>1$ e Å$^{-3}$ and the final $R$ value improved to around 7.8%. The C(2)–C(2)′ and C(4)–C(4)′ bond lengths in **2** were constrained to be 1.55 Å. For the thallium

 © 2006 Wiley-VCH Verlag GmbH & Co. KGaA, Weinheim 

Table 1. Pertinent crystallographic data for [AH{$HO_3P(CH_2)_2PO_3H$}] [A = Li (**1**), Na (**2**), K (**3**), Rb (**4**), Cs (**5**), Tl (**6**), and $NH_4$ (**7**)].

| Compound | **1** | **2** | **3** | **4** | **5** | **6** | **7** |
|---|---|---|---|---|---|---|---|
| Formula | $LiP_2O_6C_2H_7$ | $NaP_2O_6C_2H_7$ | $KP_2O_6C_2H_7$ | $RbP_2O_6C_2H_7$ | $CsP_2O_6C_2H_7$ | $TlP_2O_6C_2H_7$ | $NP_2O_6C_2H_{11}$ |
| Formula weight | 195.96 | 212.01 | 228.12 | 274.49 | 321.93 | 393.39 | 207.06 |
| Crystal system | monoclinic | triclinic | monoclinic | monoclinic | monoclinic | monoclinic | triclinic |
| $a$ [Å] | 16.188(2) | 5.727(8) | 9.237(1) | 10.980(3) | 11.472(7) | 8.589(3) | 6.176(1) |
| $b$ [Å] | 8.503(2) | 7.957(4) | 8.909(2) | 9.490(4) | 11.030(4) | 8.930(4) | 7.723(3) |
| $c$ [Å] | 5.381(2) | 16.52(2) | 9.484(2) | 9.222(2) | 8.443(3) | 10.094(3) | 9.183(2) |
| $\alpha$ [°] | 90 | 101.5(1) | 90 | 90 | 90 | 90 | 66.70(2) |
| $\beta$ [°] | 107.92(1) | 97.82(9) | 92.60(2) | 120.91(2) | 127.90(4) | 90.05(5) | 85.78(2) |
| $\gamma$ [°] | 90 | 98.8(1) | 90 | 90 | 90 | 90 | 85.57(3) |
| $V$ [Å$^3$] | 704.7(3) | 718.4(12) | 779.6(3) | 824.5(4) | 843.0(6) | 774.2(5) | 400.6(2) |
| Space group | $C2/c$ (no. 15) | $P\bar{1}$ (no. 2) | $P2_1/c$ (no. 14) | $C2/c$ (no. 15) | $C2/c$ (no. 15) | $P2_1/c$ (no. 14) | $P\bar{1}$ (no. 2) |
| $Z$ | 4 | 4 | 4 | 4 | 4 | 4 | 2 |
| $\rho_{calcd.}$ [g cm$^{-3}$] | 1.847 | 1.960 | 1.944 | 2.211 | 2.537 | 3.375 | 1.716 |
| $\mu$(Mo-$K_\alpha$) [mm$^{-1}$] | 0.593 | 0.645 | 1.074 | 6.376 | 4.756 | 21.256 | 0.531 |
| Total reflections | 631 | 2799 | 1455 | 765 | 783 | 2880 | 1436 |
| Independent reflections | 614 | 2523 | 1372 | 724 | 745 | 1348 | 1415 |
| $R$[a] | 0.0309 | 0.0775 | 0.0241 | 0.0237 | 0.0253 | 0.0800 | 0.0291 |
| $R_w$[b] | 0.0864 | 0.2373 | 0.0699 | 0.0663 | 0.0677 | 0.1882 | 0.0814 |

[a] $R = \Sigma||F_o| - |F_c||/\Sigma|F_o|$. [b] $R_w = [\Sigma w(|F_o|^2 - |F_c|^2)^2/\Sigma w(|F_o|^2)^2]^{1/2}$.

compound **6**, refinement with correction for twin crystal-data was carried out. The final $R$ value was about 8% and the final difference Fourier map showed twenty ghost residual peaks with electron density greater than 1 e Å$^{-3}$. No additional absorption correction was applied to the X-ray data, as it could not improve the $R$ value. The $R_w$ values for **2** and **6** are a bit high and the desired improvisation of crystal structure refinement, for lower values, was not possible. However, the qualitative picture of these structures is totally correct and the quantitative details are, to a large extent, also correct. The pertinent crystallographic data of all these seven ethylenediphosphonates are presented in Table 1.

CCDC-281082, -281083, -281084, -281085, -281086, -281087 and -281088 (for **1**–**7**) contain the supplementary crystallographic data for this paper. These data can be obtained free of charge from The Cambridge Crystallographic Data Centre via www.ccdc.cam.ac.uk/data_request/cif.

**Infrared Spectroscopic and Thermogravimetric Studies:** The infrared spectra in the range 400 to 4000 cm$^{-1}$, were measured on a Bruker IFS 66V FT-IR spectrometer. The samples were ground with dry KBr and pressed into transparent discs. Thermogravimetric analytical data were collected on a Netzsch STA 409C instrument. The samples were heated to 1000 °C at a rate of 10 °C per minute under flowing nitrogen gas.

**Supporting Information Available** (see footnote on the first page of this article): Color figures showing the polyhedral representation of the unit cells of compounds **1**–**7**.

## Acknowledgments

We gratefully acknowledge the financial support (project no. 98/37/29/BRNS) received from the Board of Research in Nuclear Sciences, Government of India. We thank the Sophisticated Analytical Instrument Facility of our institute for collecting the single-crystal X-ray data.

[1] R. C. Finn, J. Zubieta, R. C. Haushalter, *Prog. Inorg. Chem.* **2003**, *51*, 421–601.
[2] A. Clearfield, Z. Wang, *J. Chem. Soc., Dalton Trans.* **2002**, 2937–2947.
[3] A. Clearfield, *Prog. Inorg. Chem.* **1998**, *47*, 371–510.
[4] L. A. Vermeulen, *Prog. Inorg. Chem.* **1997**, *44*, 143–166.
[5] A. Clearfield, *Curr. Opin. Solid State Mater. Sci.* **1996**, *1*, 268–278.
[6] M. I. Khan, J. Zubieta, *Prog. Inorg. Chem.* **1995**, *43*, 1–149.
[7] F. Odobel, B. Bujoli, D. Massiot, *Chem. Mater.* **2001**, *13*, 163–173.
[8] a) L. Kullberg, A. Clearfield, *Solvent Extr. Ion Exch.* **1990**, *8*, 187–197; b) C. Y. Ortiz-Avila, C. Bhardwaj, A. Clearfield, *Inorg. Chem.* **1994**, *33*, 2499–2500.
[9] K. Aoki, L. C. Brousseau, T. E. Mallouk, *Sens. Actuators, B* **1993**, *13–14*, 703–704.
[10] a) M. C. C. Costa, R. A. W. Johnstone, D. Whittaker, *J. Mol. Catal. A: Chem.* **1998**, *129*, 79–89; b) K. Segawa, T. Ozawa, *J. Mol. Catal. A: Chem.* **1999**, *141*, 249–255.
[11] a) L. A. Vermeulen, M. E. Thomson, *Nature* **1992**, *358*, 656–658; b) G. Alberti, U. Costantino, M. Casciola, R. Vivani, A. Peraio, *Solid State Ionics* **1991**, *46*, 61–68; c) J. Benavente, F. Carrique, R. Pozas, S. Bruque, L. Moreno, M. Martinez, *Solid State Ionics* **1991**, *46*, 77–82.
[12] a) G. Huan, A. J. Jacobson, V. W. Day, *Angew. Chem. Int. Ed. Engl.* **1991**, *30*, 422–426; b) M. I. Khan, Y.-S. Lee, C. J. O'Connor, R. C. Haushalter, J. Zubieta, *J. Am. Chem. Soc.* **1994**, *116*, 4525–4526; c) S. Drumel, P. Janvier, D. Deniaud, B. Bujoli, *J. Chem. Soc., Chem. Commun.* **1995**, 1051–1052; d) C. B. A. Lima, C. Airoldi, *Int. J. Inorg. Mater.* **2001**, *3*, 907–914.
[13] a) V. Soghomonian, Q. Chen, R. C. Haushalter, J. Zubieta, *Angew. Chem. Int. Ed. Engl.* **1995**, *34*, 223–226; b) G. Alberti, F. Marmottini, S. Murcia-Mascaros, R. Vivani, *Angew. Chem. Int. Ed. Engl.* **1994**, *33*, 1594–1597; c) D. M. Poojary, B. Zhang, P. Bellinghausen, A. Clearfield, *Inorg. Chem.* **1996**, *35*, 4942–4949; d) M. P. Minimol, K. P. Rao, Y. R. Sai, K. Vidyasagar, *Proc. Indian Acad. Sci. (Chem. Sci.).* **2003**, *115*, 419–429; e) K. P. Rao, B. Vidyavathy, M. P. Minimol, K. Vidyasagar, *Inorg. Chem.* **2004**, *43*, 4610–4614.
[14] a) Y.-D. Chang, J. Salta, J. Zubieta, *Angew. Chem. Int. Ed. Engl.* **1994**, *33*, 325–327; b) Y.-D. Chang, J. Zubieta, *Inorg. Chim. Acta* **1996**, *245*, 177–198.
[15] a) K. Maeda, J. Akimato, Y. Kiyozumi, F. Mizukami, *Angew. Chem. Int. Ed. Engl.* **1995**, *34*, 1199–1200; b) W. T. A. Harrison, L. L. Dussack, A. J. Jacobson, *Inorg. Chem.* **1996**, *35*, 1461–1467; c) J. L. Bideau, C. Payen, P. Palvadeau, B. Bujoli, *Inorg. Chem.* **1994**, *33*, 4885–4890.
[16] a) V. Soghomonian, R. C. Haushalter, J. Zubieta, *Chem. Mater.* **1995**, *7*, 1648–1654; b) H. G. Harvey, S. J. Teat, M. P. Attfield, *J. Mater. Chem.* **2000**, *10*, 2632–2633; c) H. G. Harvey, A. C.

 © 2006 Wiley-VCH Verlag GmbH & Co. KGaA, Weinheim 

Herve, H. C. Hailes, M. P. Attfield, *Chem. Mater.* **2004**, *16*, 3756–3766; d) H. G. Harvey, J. Hu, M. P. Attfield, *Chem. Mater.* **2003**, *15*, 179–188; e) R. N. Devi, P. Wormald, P. A. Cox, P. A. Wright, *Chem. Mater.* **2004**, *16*, 2229–2237; f) M. Bujoli-doeuff, M. Evain, P. Janvier, D. Massiot, A. Clearfield, Z. Gan, B. Bujoli, *Inorg. Chem.* **2001**, *40*, 6694–6698.

[17] a) C. Bellitto, F. Federici, S. A. Ibrahim, *Chem. Mater.* **1998**, *10*, 1076–1082; b) D. M. Poojary, B. Zhang, A. Clearfield, *J. Am. Chem. Soc.* **1997**, *119*, 12550–12559; c) A. Altomare, C. Bellitto, S. A. Ibrahim, M. R. Mahmoud, R. Rizzi, *J. Chem. Soc., Dalton Trans.* **2000**, 3913–3919; d) Q. Gao, N. Guillou, M. Nogues, A. K. Cheetham, G. Férey, *Chem. Mater.* **1999**, *11*, 2937–2947; e) D. I. Arnold, X. Ouyang, A. Clearfield, *Chem. Mater.* **2002**, *#14#?#16#*, 2020–2027.

[18] a) C. Serre, G. Ferey, *Inorg. Chem.* **2001**, *40*, 5350–5353; b) F. Serpaggi, G. Ferey, *J. Mater. Chem.* **1998**, *8*, 2749–2755; c) B. A. Adair, G. D. Delgado, J. M. Delgado, A. K. Cheetham, *Solid State Sci.* **2000**, *2*, 119–126.

[19] a) R. Fu, S. Xia, S. Xiang, S. Hu, X. Wu, *J. Solid State Chem.* **2004**, *177*, 4626–4631; b) K. P. Rao, K. Vidyasagar, *Acta Crystallogr., Sect. E* **2005**, *61*, m1794–1796.

[20] K. P. Rao, K. Vidyasagar, *Eur. J. Inorg. Chem.* **2005**, 4936–4943.

[21] K. Yvon, W. Jeitschko, E. Parthe, *J. Appl. Crystallogr.* **1977**, *10*, 73–74.

[22] S. W. Peterson, E. Gebert, A. H. Reis, M. E. Druyan, G. W. Mason, D. F. Peppard, *J. Phys. Chem.* **1977**, *81*, 466–471.

[23] R. M. Silverstein, G. C. Bassler, T. C. Morrill, *Spectrometric Identification of Organic Compounds*, John Wiley & Sons, New York, **1963**, p. 128.

[24] K. J. Frink, R. C. Wang, J. L. Colon, A. Clearfield, *Inorg. Chem.* **1991**, *30*, 1438–1441.

[25] D. Grohol, M. A. Subramanian, D. M. Poojary, A. Clearfield, *Inorg. Chem.* **1996**, *35*, 5264–5271.

[26] G. M. Sheldrick, *SHELXL-97, Program for the Solution of Crystal Structures*, University of Göttingen, Germany, **1985**.

[27] DIAMOND Visual Crystal Structure Information System: W. T. Pennington, *J. Appl. Crystallogr.* **1999**, *32*, 1028–1029.

[28] R.-C. Wang, Y. Zhang, H. Hu, R. R. Frausto, A. Clearfield, *Chem. Mater.* **1992**, *4*, 864–871.

[29] N. Walker, D. Stuart, *Acta Crystallogr., Sect. A* **1983**, *39*, 158–166.

Received: August 17, 2005
Published Online: December 27, 2005

 © 2006 Wiley-VCH Verlag GmbH & Co. KGaA, Weinheim 

DOI: 10.1002/ejic.200500742

# Hydrothermal Synthesis and Structural Characterization of Two pH-Controlled Cd–Squarate Coordination Frameworks, $[Cd_2(C_4O_4)_{2.5}(H_2O)_4]\cdot(dpaH)\cdot 1.5(H_2O)$ and $[Cd(C_4O_4)(dpa)(OH_2)]$ (dpa = 2,2′-dipyridylamine)

**Chih-Chieh Wang,*[a] Cheng-Han Yang,[a] and Gene-Hsiang Lee[b]**

**Keywords:** Hydrothermal synthesis / Self-assembly / Hydrogen bonds / Squarate / Cadmium

Two extended coordination frameworks of $Cd^{II}$–squarate complexes with the formulas $[Cd_2(C_4O_4)_{2.5}(H_2O)_4](dpaH)\cdot 1.5(H_2O)$ (**1**) and $[Cd(C_4O_4)(dpa)(H_2O)]$ (**2**) (dpa = 2,2′-dipyridylamine) have been synthesized under hydrothermal conditions and characterized by single-crystal X-ray diffraction studies. Structural determination reveals that compound **1** consists of a free monoprotonated 2,2′-dipyridylamine ion ($dpaH^+$) and a two-dimensional (2D) anionic, layered framework, $\{[Cd_2(C_4O_4)_{2.5}(H_2O)_4]^-\}$, which is formed with two antiprismatic square-boxes as the fundamental building unit through the connection between $Cd^{II}$ ions and hybrid $\mu_{1,2,3}$-, $\mu_{1,2,3,4}$-squarates. Each square-box acts as a host for the inclusion of one pyridine ring of $dpaH^+$. Adjacent $dpaH^+$ cations are then self-assembled by the parallel alignment of the other pyridine ring of $dpaH^+$ to complete a 3D network with one-dimensional (1D) channels intercalated by water molecules. Compound **2** contains a distorted octahedral $Cd^{II}$ center coordinated by two squarates, two waters and one dpa ligand to form a 1D 2-legged, ladder-like framework by the connection of a $[Cd(dpa)(\mu_2\text{-}H_2O)]_2^{4+}$ dimeric unit and a $\mu_{1,2}$-squarate. Weak π–π stacking interaction and hydrogen bonds of N–H···O, O–H···O and C–H···O among the squarate, water and dpa ligands provide additional intra- and intermolecular interactions on the stabilization of these two polymeric frameworks.

(© Wiley-VCH Verlag GmbH & Co. KGaA, 69451 Weinheim, Germany, 2006)

## Introduction

Metal-organic frameworks (MOFs)[1–5] have been attracting much attention owing to their potential applications as functional solid materials in gas storage, molecular sieves, size- or shape-selective catalysis, and ion exchange,[6–9] as well as because of their versatile structural topology. The design and synthesis of new open-framework coordination polymers have been the focus in current chemical and new material research. Of particular importance is the ability of the organic molecules to influence profoundly the structures of synthesized products, and to direct their formation with specific structures and potential applications, such as magnetism, host–guest chemistry, shape specificity and catalysis. In a relevant approach, the squarate (dianion of 3,4-dihydroxycyclobut-3-ene-1,2-dione, $H_2C_4O_4$) serves as a unique ligand, which possesses a four-membered cyclic aromatic structure, characterized by extensive π-electron delocalization over all carbon and oxygen atoms. Accordingly, squarate has been known as a polyfunctional ligand providing hydrogen bonding, π–π interactions, and the construction of extended frameworks. It is also widely used as a bridging ligand bonded with metal ions in various bridging modes to create numerous amazing metal–squarate frameworks, including one-dimensional (1D) chain, two-dimensional (2D) layer, three-dimensional (3D) cube- and cage-like frameworks.[10–17] Many squarate-bridged metal complexes with $\mu_{1,2}$- or $\mu_{1,3}$-bridging modes incorporating different nitrogen-based, flexible ligands have been structurally characterized[18–24] and showed interesting magnetic behavior.[25] In this contribution, we report the hydrothermal syntheses, structures and thermal stability of two novel Cd–squarate coordination frameworks, $[Cd_2(C_4O_4)_{2.5}(H_2O)_4](dpaH)\cdot 1.5(H_2O)$ (**1**) and $[Cd(C_4O_4)(dpa)(H_2O)]$ (**2**) by using flexible dpa and rigid squarate ligands as building blocks to form 3D microporous and 1D ladder-like extended networks.

[a] Department of Chemistry, Soochow University, 111, Taipei, Taiwan
Fax: +886-2-28811053
E-mail: ccwang@mail.scu.edu.tw
[b] Instrumentation Center, National Taiwan University, Taipei, Taiwan

## Results and Discussion

### Synthesis and IR Spectroscopy of Compounds 1 and 2

The reaction was carried out under hydrothermal conditions, by adjusting various molar ratios of $[Cd(NO_3)_2]\cdot 4H_2O$, dpa and $H_2C_4O_4$ (Table 1). The results showed that compounds **1** and **2** are not controlled by stoichiometry but rather by the pH-controlled products. Compound **1** was the favored product with relatively lower pH value (pH < 4), whereas compound **2** was the dominant product with rela-

 © 2006 Wiley-VCH Verlag GmbH & Co. KGaA, Weinheim 

tively higher pH value (pH > 4). Both compounds are air-stable at ambient temperature and insoluble in common solvents, such as water, alcohol and acetonitrile. The N–H stretching vibrations of both compounds appear in the 3000–3400 $cm^{-1}$ region, and their frequencies are consistent with the existence of hydrogen bonds between N–H and several H-acceptor groups. The most relevant IR features are those associated with the chelating squarate ligands. The coordinated CO groups are characterized by medium absorptions at 1664 and 1656 $cm^{-1}$ for **1** and **2**, respectively. A very strong band centered at around 1500 $cm^{-1}$ is attributed to the vibrational modes of a combination of C–O and C–C stretching motions; the assignment of which is in agreement with the characteristic of the $(CO)_n^{2-}$ salts.[26]

Table 1. Products for different reaction conditions by adjusting molar ratios of $[Cd(NO_3)_2]\cdot 4H_2O$, dpa and $H_2C_4O_4$.

| Molar ratios in 6 mL water | | | pH value | Product |
|---|---|---|---|---|
| $[Cd(NO_3)_2]\cdot 4H_2O$ | dpa | $H_2C_4O_4$ | | |
| 0.1 mmol | 0.1 mmol | 0.1 mmol | 2.45 | **1** |
| 0.1 mmol | 0.15 mmol | 0.1 mmol | 3.17 | **1** |
| 0.1 mmol | 0.2 mmol | 0.1 mmol | 4.31 | **2** |
| 0.1 mmol | 0.125 mmol | 0.06 mmol | 4.13 | **2** |

### Crystal Structure of $[Cd_2(C_4O_4)_{2.5}(H_2O)_4](dpaH)\cdot 1.5(H_2O)$ (1)

The X-ray structure determination reveals that compound **1** consists of a 2D anionic $[Cd_2(C_4O_4)_{2.5}(H_2O)_4]^-$ layered MOF [Figure 1 (top)], a monoprotonated $dpaH^+$ [Figure 1 (bottom)], and crystallization water molecules. The 2D anionic $[Cd_2(C_4O_4)_{2.5}(H_2O)_4]^-$ layer consists of three independent slightly distorted octahedral $Cd^{II}$ ions in the asymmetric unit, in which the Cd(1) atom is bonded to six oxygen atoms from four $\mu_{1,2,3}$-squarate and two water molecules with the following bond lengths: Cd(1)–O(1) 2.336(2), Cd(1)–O(3) 2.298(2), Cd(1)–O(5) 2.307(2), Cd(1)–O(7) 2.295(2), Cd(1)–O(11) 2.255(2), and Cd(1)–O(12) 2.234(2) Å (Figure 1). The Cd(2) and Cd(3) atoms are both located at the inversion center [(1.5 2.0 0.0) for Cd(2) and (1.0 1.5 0.0) for Cd(3)] and bonded to six oxygen atoms from two $\mu_{1,2,3}$-squarate, two $\mu_{1,2,3,4}$-squarate and two water molecules with the following bond lengths: Cd(2)–O(2) 2.265(2), Cd(2)–O(9) 2.322(2), Cd(2)–O(13) 2.231(2) and Cd(3)–O(6) 2.318(2), Cd(3)–O(10) 2.279(2), and Cd(3)–O(14) 2.236(2) Å (Figure 1). The corresponding bond lengths of the Cd–$O_{sq}$ and Cd–$O_w$ bonds (Table 2) all fall in the same range analogous to those in the $[Cd(C_4O_4)(H_2O)_2]$ complex.[10] It is important to note that the squarate ligand ($C_4O_4^{2-}$), acting as a bridging ligand with two different bridging modes, plays a key role in the construction of a novel 2D anionic framework. Three crystallographically distinct squarate ligands are found: the first one (C1–C4) adopts a $\mu_{1,2,3}$-bridging mode[12] (Figure 2) to link Cd(1) with Cd(2) (5.926 and 6.065 Å) and Cd(1) with Cd(1) (8.457 Å), respectively. The second one (C5–C8) also adopts a $\mu_{1,2,3}$-bridging mode[12] to link Cd(1) with Cd(3) (5.918

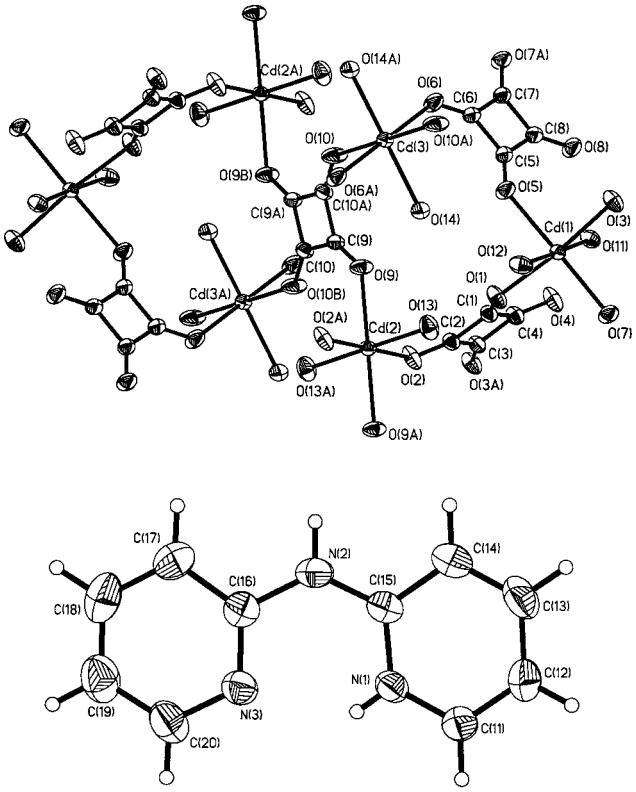


Figure 1. (top) Distorted octahedral coordination spheres of Cd(1), Cd(2) and Cd(3) ions in compound **1** with atom labelling scheme; hydrogen atoms are omitted for clarity. (bottom) Molecular structure of protonated 2,2′-dipyridylamine ($dpaH^+$) cation with atom labelling scheme; dashed lines represent N···H–N hydrogen bond interaction. (ORTEP drawing, thermal ellipsoids at 50% probability level).

Table 2. Selected bond lengths [Å] and angles [°] for compound **1**.[a]

| | | | |
|---|---|---|---|
| Cd(1)–O(1) | 2.336(2) | Cd(1)–O(3) | 2.298(2) |
| Cd(1)–O(5) | 2.307(2) | Cd(1)–O(7) | 2.295(2) |
| Cd(1)–O(11) | 2.255(2) | Cd(1)–O(12) | 2.234(2) |
| O(1)–Cd(1)–O(3) | 174.38(8) | O(1)–Cd(1)–O(5) | 84.68(9) |
| O(1)–Cd(1)–O(7) | 94.51(9) | O(1)–Cd(1)–O(11) | 93.36(8) |
| O(1)–Cd(1)–O(12) | 83.56(8) | O(3)–Cd(1)–O(5) | 89.71(9) |
| O(3)–Cd(1)–O(7) | 91.10(9) | O(3)–Cd(1)–O(11) | 86.59(8) |
| O(3)–Cd(1)–O(12) | 92.26(8) | O(5)–Cd(1)–O(7) | 178.56(8) |
| O(5)–Cd(1)–O(11) | 93.34(8) | O(5)–Cd(1)–O(12) | 84.17(8) |
| O(7)–Cd(1)–O(11) | 87.88(8) | O(7)–Cd(1)–O(12) | 94.57(9) |
| O(11)–Cd(1)–O(12) | 176.19(9) | $O(2)–Cd(2)–O(2)_i$ | 180.0 |
| Cd(2)–O(2) × 2 | 2.265(2) | Cd(2)–O(9) × 2 | 2.322(2) |
| Cd(2)–O(13) × 2 | 2.231(2) | | |
| $O(2)–Cd(2)–O(2)_i$ | 180.0 | $O(2)–Cd(2)–O(9)_i$ | 85.85(9) |
| O(2)–Cd(2)–O(9) | 94.15(9) | $O(2)–Cd(2)–O(13)_i$ | 86.16(9) |
| O(2)–Cd(2)–O(13) | 93.84(9) | O(9)–Cd(2)–O(13) | 81.87(9) |
| $O(9)–Cd(2)–O(9)_i$ | 180.0 | $O(13)–Cd(2)–O(13)_i$ | 180.0 |
| $O(9)–Cd(2)–O(13)_i$ | 98.13(9) | | |
| Cd(3)–O(6) × 2 | 2.318(2) | Cd(3)–O(10) × 2 | 2.279(2) |
| Cd(3)–O(14) × 2 | 2.236(2) | | |
| $O(6)–Cd(3)–O(6)_{ii}$ | 180.0 | O(6)–Cd(3)–O(10) | 88.3(1) |
| $O(6)–Cd(3)–O(10)_{ii}$ | 91.7(1) | O(6)–Cd(3)–O(14) | 97.58(9) |
| $O(6)–Cd(3)–O(14)_{ii}$ | 82.42(9) | $O(10)–Cd(3)–O(10)_{ii}$ | 180.0 |
| O(10)–Cd(3)–O(14) | 95.28(9) | $O(10)–Cd(3)–O(14)_{ii}$ | 84.72(9) |
| $O(14)–Cd(3)–O(14)_{ii}$ | 180.0 | | |

[a] Symmetry codes: (i) $-x + 3, -y + 4, -z$; (ii) $-x + 2, -y + 3, -z$.

 © 2006 Wiley-VCH Verlag GmbH & Co. KGaA, Weinheim 

and 6.057 Å) and Cd(1) with Cd(1) (8.434 Å), respectively. The last one (C9–C10) adopts a $\mu_{1,2,3,4}$-bridging mode[10] (Figure 2) to link Cd(2) with Cd(3) ($2\times5.854$ and $2\times6.088$ Å), Cd(2) with Cd(2) (8.434 Å) and Cd(3)···Cd(3) (8.457 Å), respectively. To the best of our knowledge, compound **1** is the first coordination framework consisting of a Cd/squarate system with hybrid $\mu_{1,2,3}$- and $\mu_{1,2,3,4}$-bridging modes of squarates. It is also noted that, independent of $\mu_{1,2,3}$- or $\mu_{1,2,3,4}$-squarates, the differences among the four C–O distances are not obvious, with the averaged C–O distances of 1.254(4) and 1.255(4) Å for $\mu_{1,2,3}$-squarate and 1.252(4) Å for $\mu_{1,2,3,4}$-squarate, respectively. The result indicates a more π-delocalization bridging mode ($D_{4h}$) close to a free squarate ring. The free, monoprotonated $dpaH^+$ cation shown in Figure 1 (bottom) adopts an *anti-anti* conformation mode. The presence of the proton H(1) bound to N(1) [0.754 Å H(1)–N(1)] and its hydrogen bond with N(3) [2.672(5) Å N(1)···N(3)] accounts for the *anti-anti* conformation of $dpaH^+$ and the quasi co-planarity of the two pyridyl rings [the dihedral angles between the mean planes of two pyridine rings is only 5.22°]. All C–C and C–N bond lengths and bond angles in the $dpaH^+$ molecule are comparable to those reported previously.[27]

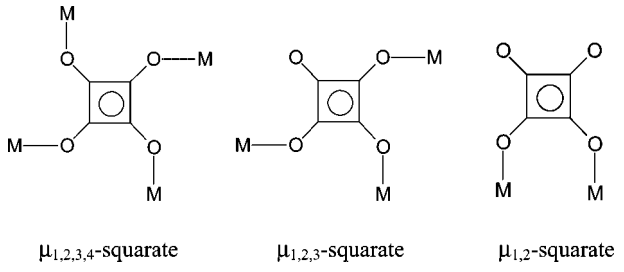


Figure 2. Binding modes of squarate in compound **1** and **2**.

The overall 3D architecture is depicted in Figure 3, and can be described as the self-assembly of 2D anionic Cd–squarate frameworks and free $dpaH^+$ cations. A face-sharing double-box shown in Figure 4 (top) is the fundamental building unit for the construction of the 2D anionic MOF. Each box consists of an antiprismatic square $Cd_8$ skeleton, bridged by four $\mu_{1,2,3}$-bridge squarates, acting as four sides of the box, and by one $\mu_{1,2,3,4}$-squarate ligand, acting as the base. Two boxes share a $\mu_{1,2,3,4}$-squarate to form a face-sharing double-box unit, whereas the neighboring double-box units share a $\mu_{1,2,3}$-squarate to complete a 2D-extended framework along the [100] and [010] directions. The dimensions of the box are approximately $5.0\times5.0\times4.9$ Å (shortest oxygen–oxygen contact distances not including the van der Waals radii), providing a vacant space for the inclusion of a pyridyl group of the $dpaH^+$ cation. It is worthy to note that the $dpaH^+$ cation plays the other important role in the construction of this 3D network. It acts not only as a counterion to balance the charge of the Cd–squarate anionic skeleton, but also as an inclusion molecule with one of the pyridyl groups in $dpaH^+$ cation inserting into each antiprismatic box. The pyridyl groups outside the boxes are then aligned parallel to one another (the separation distance of 4.2 Å between two centroid pyridyl groups) to complete the 3D-extended network, which allows a 1D microporous channel along the *c* axis (Figure 2). Two free, disordered water molecules, O15 with 0.5 occupancy and O16, O16′ with 0.67 and 0.33 occupancy, respectively, are intercalated into these channels. Hydrogen-bond formation serves as a important factor and is widely used in constructing coordination polymers.[28–32] In compound **1**, hydrogen-bonding

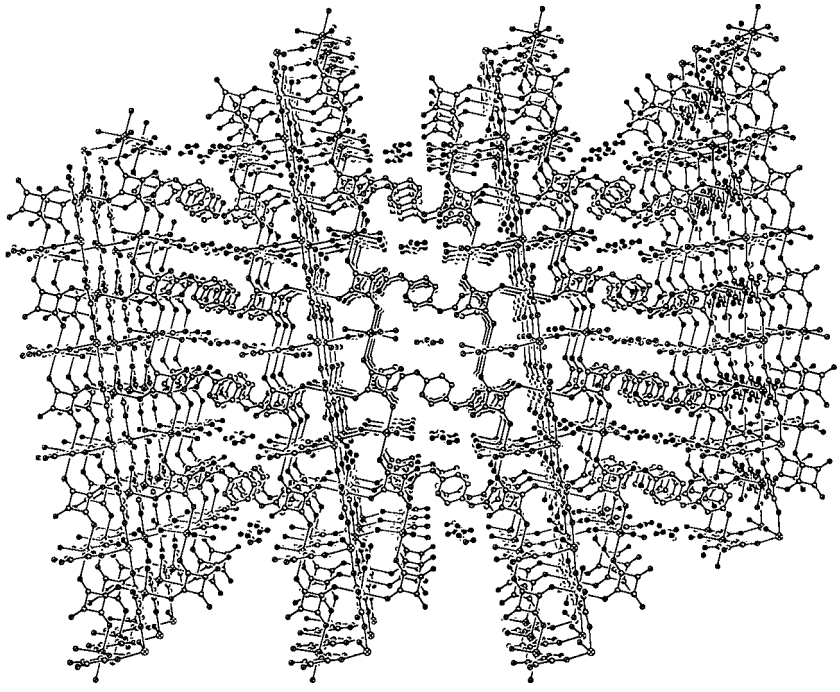

Figure 3. The three-dimensional extended network of $[Cd_2(C_4O_4)_{2.5}(H_2O)_4](dpaH)\cdot1.5H_2O$ (**1**) viewing along the *a*-axis.

 © 2006 Wiley-VCH Verlag GmbH & Co. KGaA, Weinheim 

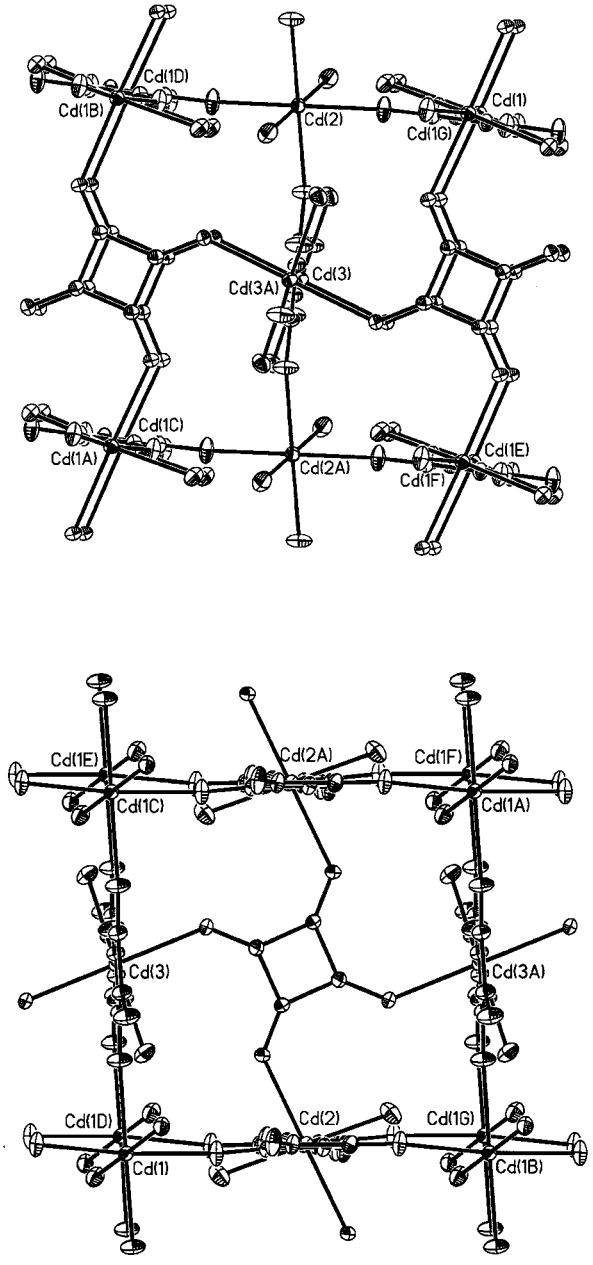


Figure 4. (top) Perspective side view (left) of double-box building unit and (bottom) top view of the *anti*-prism square box in **1**.

interactions, including the N–H···N, N–H···O and O–H···O hydrogen bonds among the $dpaH^+$, squarate ligands and water molecules, provide the additional stabilizing forces to enhance the 3D microporous network. Related bond lengths and angles of the N–H···N, N–H···O and O–H···O hydrogen bonds are summarized in Table 3.

### Crystal Structures of $[Cd(C_4O_4)(dpa)(H_2O)]$ (2)

The X-ray structural determination of compound **2** evidences a polymeric arrangement with a linear 2-legged, ladder-like MOF, which is isostructural with $[M(C_4O_4)(dpa)(H_2O)]$, M = Co, Ni, Zn.[33] The $Cd^{II}$ center is six-coordinate and adopts a slightly distorted octahedral coordination environment bonded to two nitrogen atoms from dpa ligands and two oxygen atoms from two squarate ligands and two water molecules. The related bond lengths and bond angles around the Cd center are listed in Table 4. Two Cd ions are linked together through two bridging water molecules to form a $[Cd(dpa)(H_2O)]_2^{4+}$ dimeric fragment (see Figure 5) in the equatorial plane [Figure 5 (top)] with bond lengths of Cd(1)–O(5) 2.330(2), Cd(1)–$O(5)_i$ 2.384(2), Cd(1)–N(1) 2.296(2) and Cd(3)–N(3) 2.276(2) Å. The squarate ligand adopts a $\mu_{1,2}$-binding mode[33] (Figure 2) to connect the neighboring $[Cd(dpa)(\mu_2\text{-}OH_2)]_2$ fragments at the axial sites with bond lengths of Cd(1)–O(1) 2.240(2), Cd(1)–O(2) 2.269(2) Å, constructing a 1D, linear, 2-legged, ladderlike MOF along the *a* axis [Figure 5 (bottom)]. The corresponding bond lengths of the Cd–$O_{sq}$ and Cd–$O_w$

Table 4. Selected bond lengths [Å] and angles [°] for compound **2**.[a]

| | | | |
|---|---|---|---|
| Cd(1)–O(1) | 2.240(2) | Cd(1)–O(2) | 2.269(2) |
| Cd(1)–O(5) | 2.330(2) | Cd(1)–$O(5)_i$ | 2.384(2) |
| Cd(1)–N(1) | 2.296(2) | Cd(1)–N(3) | 2.276(2) |
| O(1)–Cd(1)–O(2) | 176.56(7) | O(1)–Cd(1)–O(5) | 90.54(8) |
| O(1)–Cd(1)–$O(5)_i$ | 89.12(8) | O(1)–Cd(1)–N(1) | 91.83(8) |
| O(1)–Cd(1)–N(3) | 92.20(8) | O(2)–Cd(1)–O(5) | 88.05(8) |
| O(2)–Cd(1)–$O(5)_i$ | 87.52(8) | O(2)–Cd(1)–N(1) | 91.54(8) |
| O(2)–Cd(1)–N(3) | 88.83(8) | O(5)–Cd(1)–$O(5)_i$ | 77.78(9) |
| O(5)–Cd(1)–N(1) | 103.05(8) | O(5)–Cd(1)–N(3) | 172.63(8) |
| $O(5)_i$–Cd(1)–N(1) | 178.73(8) | $O(5)_i$–Cd(1)–N(3) | 95.42(8) |
| N(1)–Cd(1)–N(3) | 83.70(9) | | |

[a] Symmetry code: (i) –*x*, –*y*, –*z*.

Table 3. Hydrogen bond lengths [Å] and angles [°] for compound **1**.[a]

| Donor–H | | Donor···Acceptor | | H···Acceptor | | Donor–H···Acceptor | |
|---|---|---|---|---|---|---|---|
| N(1)–H(1a) | 0.754 | N(1)···N(3) | 2.672(5) | H(1a)···N(3) | 2.085 | N(1)–H(1a)···N(3) | 135.0 |
| N(2)–H(2a) | 0.860 | N(2)···O(15) | 2.951(3) | H(2a)···O(15) | 2.143 | N(2)–H(2a)···O(15) | 156.5 |
| N(2)–H(2a) | 0.860 | N(2)···$O(15)_i$ | 2.896(3) | H(2a)···$O(15)_i$ | 2.036 | N(2)–H(2a)···$O(15)_i$ | 178.00 |
| O(11)–H(11) | 0.888 | O(11)···O(4) | 2.628(3) | H(11)···O(4) | 1.741 | O(11)–H(11)···O(4) | 176.2 |
| O(11)–H(11′) | 0.895 | O(11)···$O(8)_{ii}$ | 2.687(3) | H(11′)···$O(8)_{ii}$ | 1.811 | O(11)–H(11′)···$O(8)_{ii}$ | 165.5 |
| O(12)–H(12) | 0.871 | O(12)···$O(6)_{iii}$ | 2.754(3) | H(12)···$O(6)_{iii}$ | 1.903 | O(12)–H(12)···$O(6)_{iii}$ | 165.4 |
| O(12)–H(12′) | 0.890 | O(12)···$O(2)_{ii}$ | 2.732(3) | H(12′)···$O(2)_{ii}$ | 1.849 | O(12)–H(12′)···$O(2)_{ii}$ | 171.0 |
| O(13)–H(13) | 0.873 | O(13)···O(1) | 2.744(3) | H(13)···O(1) | 1.901 | O(13)–H(13)···O(1) | 162.7 |
| O(13)–H(13′) | 0.867 | O(13)···$O(10)_{iv}$ | 2.814(3) | H(13′)···$O(10)_{iv}$ | 2.016 | O(13)–H(13′)···$O(10)_{iv}$ | 152.6 |
| O(14)–H(14) | 0.902 | O(14)···O(5) | 2.731(3) | H(14)···O(5) | 1.849 | O(14)–H(14)···O(5) | 165.1 |
| O(14)–H(14′) | 0.864 | O(14)···$O(9)_v$ | 2.802(3) | H(14′)···$O(9)_v$ | 1.973 | O(14)–H(14′)···$O(9)_v$ | 160.5 |

[a] Symmetry codes: (i) –*x*, 1 – *y*, 1 – *z*; (ii) *x*, –1 + *y*, *z*; (iii) 1 + *x*, –1 + *y*, *z*; (iv) 1 – *x*, –*y*, –*z*; (v) *x*, 1 + *y*, *z*; (vi) *x*, 2 + *y*, *z*; (vii) 1 – *x*, 1 – *y*, 1 – *z*; (viii) –1 + *x*, *y*, *z*.

 © 2006 Wiley-VCH Verlag GmbH & Co. KGaA, Weinheim 

bonds fall in the same range, analogous to those in the $[Cd(C_4O_4)(H_2O)_2]$ complex.[10] The Cd···Cd separations along the $\mu_2$-$O_{water}$ and $\mu_{1,2}$-$C_4O_4^{2-}$ bridges are 3.670(1) and 7.672(1) Å, respectively. It should be noted that adjacent ladders are displaced by half a repeating unit along the *a* and *c* axes. This arrangement effectively prevents steric hindrance between the inter-ladder dpa ligands. As a result, compound **2** favor a closer-packing building block as shown in Figure 6. The centroid pyridine rings in dpa ligands among the adjacent ladders are generally parallel and adopt a face-to-face alignment (Figure 5) with the separation distance of 3.9 Å, indicating a very weak but significant π–π stacking interaction[33–35] that may, in part, contribute to the stabilization of the extended framework. In compound **2**, two strong O–H···O hydrogen bonds [O(5)–H(5a)···O(4) and O(5)–H(5b)···O(3)] are found between uncoordinated oxygen atoms of squarate and the coordinated water molecules with the O···O distances in the range of 2.528–2.600 Å. In addition, the inter-ladder interactions are through one pair of the N–H···O [N(2)–H(2a)···O(4)] and C–H···O [C(11)–H(11a)···O(4)] hydrogen bonds from the same dpa molecule linked to the oxygen atom of squarate in the neighboring ladders to form a mixed N–H···O and C–H···O hydrogen bonds (dashed line in Figure 6). Similar hydrogen-bonding interactions have also been found in the

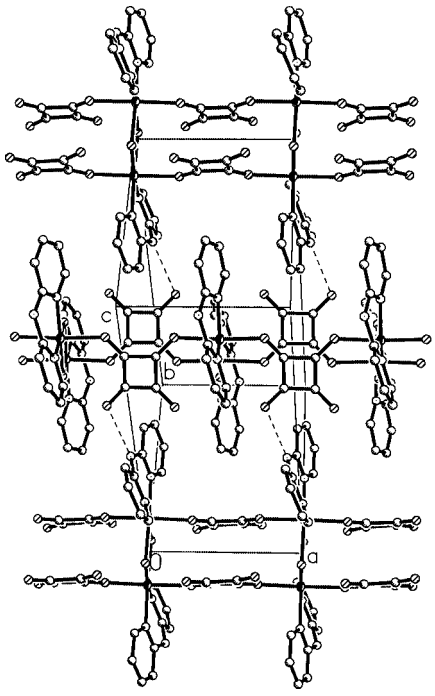

Figure 6. The molecular packing of the ladder-like framework in **2**; dashed lines represent H-bond interactions.

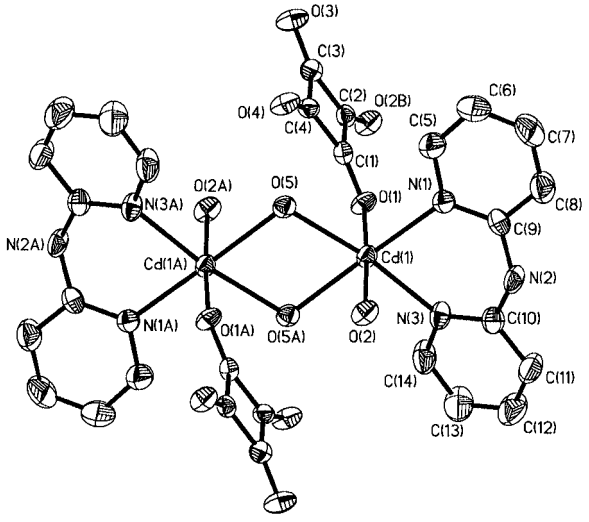


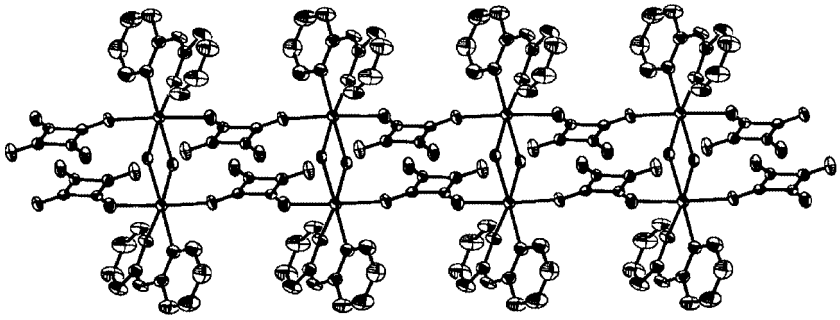

Figure 5. (top) Molecular structure of compound **2** with atom labelling scheme; hydrogen atoms are omitted for clarity. (ORTEP drawing, thermal ellipsoids at 50% probability level) (bottom) Perspective view of a 2-legged, ladder-like framework along the *a* axis in **2**.

 © 2006 Wiley-VCH Verlag GmbH & Co. KGaA, Weinheim 

Table 5. Hydrogen bond lengths [Å] and angles [°] for compound **2**.[a]

| Donor–H [Å] | | Donor···Acceptor [Å] | | H···Acceptor [Å] | | Donor–H···Acceptor [°] | |
|---|---|---|---|---|---|---|---|
| O(5)–H(5a) | 0.735 | O(5)···O(4) | 2.600(3) | H(5a)···O(4) | 1.883 | O(5)–H(5a)···O(4) | 163.1 |
| O(5)–H(5b) | 0.922 | O(5)···O(3)$_i$ | 2.590(3) | H(5b)···O(3)$_i$ | 1.672 | O(5)–H(5b)···O(3)$_i$ | 174.0 |
| N(2)–H(2a) | 0.860 | N(2)···O(4)$_{ii}$ | 2.890(3) | H(2a)···O(4)$_{ii}$ | 2.092 | N(2)–H(2a)···O(4)$_{ii}$ | 154.1 |
| C(11)–H(11a) | 0.930 | C(11)···O(4)$_{ii}$ | 3.204(4) | H(11a)···O(4)$_{ii}$ | 2.430 | C(11)–H(11a)···O(4)$_{ii}$ | 140.6 |

[a] Symmetry codes: (i) –1 + *x*, *y*, *z*; (ii) 0.5 + *x*, 0.5 – *y*, 0.5 + *z*.

[Fe(oxa)(dpa)][28] (oxa = oxalate) and [$M_2$(dpa)$_2$($C_2O_4$)-($C_4O_4$)] (M = Cu, Zn) complexes.[34] Related bond lengths and angles of the O–H···O, N–H···O and C–H···O hydrogen bonds for **2** are summarized in Table 5.

### Thermogravimetric Analysis

To investigate the thermal stability of the 3D and 1D extended framework of **1** and **2**, the thermogravimetric analyses (TGA) were performed on samples consisting of numerous single crystals under nitrogen. The TGA data of **1** suggest that the first weight lost of 11.24% (calcd. 12.75%), corresponding to the lost of 1.5 solvated and four coordinated water molecules at the cadmium center, occurred over the range of 30–174 °C. In the temperature range of 180–312 °C, **1** underwent the weight lost of 24.64% corresponding to the lost of dpaH$^+$ cations (calcd. 22.16%). The resulting solid then slowly decomposed with loss of squarate ligands to yield cadmium oxide (CdO). Compound **2** underwent a continuous single-step weight-loss process (losing coordinated water first, and then dpa and squarate groups). The on-set temperature of the weight loss is approximately at 201 °C. The decomposition process was completed at approximately 391 °C and the final product of the pyrolysis is CdO.

## Conclusion

In conclusion, under hydrothermal conditions, we have successfully synthesized two pH-controlled Cadmium(II)–squarate compounds, [$Cd_2(C_4O_4)_{2.5}(H_2O)_4$](dpaH)·1.5($H_2O$) (**1**) and [Cd($C_4O_4$)(dpa)($H_2O$)] (**2**), with metal-organic frameworks; the structures of which are well characterized by X-ray diffraction method. In compound **1**, the overall 3D network with 1D microporous channels is constructed by the following intra- and inter-molecular interactions: (1) metal–squarate covalent bonds to form a anionic 2D framework through the connectivity between Cd ions and hybrid $\mu_{1,2,3}$- and $\mu_{1,2,3,4}$-squarates, (2) molecular inclusion of dpaH$^+$ pyridyl group into the antiprism square box, (3) π–π stacking interaction of pyridyl groups between neighboring dpaH$^+$ cations and (4) hydrogen bonds between water molecules, squarate and dpaH$^+$. For compound **2**, the squarate ligands afford a $\mu_{1,2}$-bridging coordination mode as well as hydrogen-bonding capability to build a 1D 2-legged, ladder-like MOF.

## Experimental Section

**Materials and Physical Techniques:** All chemicals were of reagent grade and were used as commercially obtained without further purification. Elementary analyses (carbon, hydrogen and nitrogen) were performed using a Perkin–Elmer 2400 elemental analyzer. IR spectra were recorded with a Nicolet Fourier Transform IR, MAGNA-IR 500 spectrometer in the range of 500–4000 cm$^{-1}$ using the KBr disc technique. Thermogravimetric analyses (TGA) of compounds **1** and **2** were performed with a computer-controlled Perkin–Elmer 7 Series/UNIX TGA7 analyzer. Single-phased powder samples of **1** (4.014 mg) and **2** (1.228 mg) were loaded into alumina pans and heated with a ramp rate of 5 °C/min from room temperature to 900 °C under nitrogen.

**Synthesis of [$Cd_2(C_4O_4)_{2.5}(H_2O)_4$](dpaH)·1.5$H_2O$ (1):** The reaction of Cd($NO_3$)$_2$·4$H_2O$ (0.0325 g, 0.1 mmol), dpa (0.0175 g, 0.1 mmol), $H_2C_4O_4$ (0.0118 g, 0.1 mmol), and deionized water (6 mL, 0.3333 mol) in the molar ratio 1:1:1:3.333, in a Teflon-lined acid digestion bomb at 180 °C for three days, followed by slow cooling at 6 °C/h to room temperature, yielded colorless solutions. After evaporation for several days at room temperature, colorless crystals grew out of solution as needles and were collected after filtration and drying (yield: 0.0106 g, 34%). The final pH value was 2.45. $C_{20}H_{21}Cd_2N_3O_{15.5}$ (776.20): calcd. C 30.95, N 5.41, H 2.73; found C 30.99, N 5.39, H 2.58. IR (4000–400 cm$^{-1}$): $\tilde{\nu}$ = 3246 (m), 3083 (m), 1664 (m), 1610 (m), 1563 (m), 1506 (vs), 1457 (s), 1246 (w), 777 (m) cm$^{-1}$.

**Synthesis of [Cd($C_4O_4$)(dpa)($H_2O$)] (2):** The compounds Cd($NO_3$)$_2$·4$H_2O$ (0.0322 g, 0.1 mmol), dpa (0.0351 g, 0.2 mmol), $H_2C_4O_4$ (0.0116 g, 0.1 mmol), and deionized water (6 mL, 0.3333 mol) in the mol ratio 1:2:1:3.333 were sealed in a Teflon-lined acid digestion bomb at 180 °C for three days. They were then cooled at 6 °C/h to room temperature, yielding colorless plate crystals after filtration and drying (0.0162 g, 39%). The final pH value was 4.31. $C_{14}H_{11}CdN_3O_5$ (413.66): calcd. C 40.65, H 2.68, N 10.16; found C 40.31, H 2.81, N 10.34. IR (4000–400 cm$^{-1}$): $\tilde{\nu}$ = 3320 (w), 3206 (m), 3138 (m), 3082 (m), 3045 (m), 1656 (m), 1599 (m), 1538 (s), 1504 (vs), 1474 (vs), 1428 (s), 1373 (m), 1232 (m), 763 (m) cm$^{-1}$.

**X-ray Crystallographic Study:** Crystallographic data and experimental details of refinements for structural analyses are given in Table 6. Data collections of **1** and **2** were carried out with a Siemens SMART diffractometer with a CCD detector with Mo radiation ($\lambda$ = 0.71073 Å) at room temperature. A preliminary orientation matrix and unit cell parameters were determined from 3 runs of 15 frames each, each frame correspond to a 0.3°scan in 10 s, following by spot integration and least-squares refinement. For each structure, data were measured using $\omega$ scans of 0.3° per frame for 20 s until a complete hemisphere had been collected. Cell parameters were retrieved with SMART[36] software and refined with SAINT[37] on all observed reflections. Data reduction was performed with the SAINT[37] software and corrected for Lorentz and polarization effects. Absorption corrections were applied with the program SADABS.[38] Direct phase determination and subsequent difference Fourier map synthesis yielded the positions of all non-hydrogen atoms, which were subjected to anisotropic refinements. All hydrogen atoms were generated geometrically (C–H: 0.95) with the exception of the hydrogen atoms of the coordinated water mole-

 © 2006 Wiley-VCH Verlag GmbH & Co. KGaA, Weinheim 

cules, which were located in the difference Fourier map with the corresponding positions and isotropic displacement parameters being refined. The final full-matrix, least-squares refinement on $F^2$ was applied for all observed reflections [$I > 2\sigma(I)$]. All calculations were performed by using the SHELXTL software package.[39]

Table 6. Crystal data for compounds **1** and **2**.

| | **1** | **2** |
|---|---|---|
| Empirical formula | $C_{20}H_{21}Cd_2N_3O_{15.50}$ | $C_{14}H_{11}CdN_3O_5$ |
| Molecular weight | 776.20 | 413.66 |
| Crystal system | triclinic | monoclinic |
| Space group | $P\bar{1}$ | $P2_1/n$ |
| $a$ [Å] | 8.4341(2) | 7.6720(3) |
| $b$ [Å] | 8.4570(2) | 11.1502(4) |
| $c$ [Å] | 18.0891(4) | 16.8908(6) |
| $\alpha$ [°] | 81.0679(4) | |
| $\beta$ [°] | 88.2877(4) | 91.267(1) |
| $\gamma$ [°] | 87.7564(4) | |
| $V$ [Å$^3$] | 1273.25(5) | 1444.56(9) |
| $Z$ | 2 | 4 |
| $D_{calcd.}$ [g cm$^{-3}$] | 2.025 | 1.902 |
| $T$ [K] | 295(2) | 295(2) |
| $\mu$ [mm$^{-1}$] | 1.754 | 1.542 |
| Reflections collected | 17890 | 12538 |
| Reflections unique / $R_{int}$ | 5828 / 0.033 | 3319 / 0.040 |
| Reflections with [$I > 2\sigma(I)$] | 4627 | 2378 |
| $N_v$ | 395 | 216 |
| $R_F$[a], $R_w$[b] (all data) | 0.0371, 0.0676 | 0.0543, 0.0523 |
| $R_F$[a], $R_w$[b] [$I > 2\sigma(I)$] | 0.0243, 0.0540 | 0.0289, 0.0495 |
| Goodness-of-fit | 1.006 | 1.010 |
| $\Delta\rho_{max.}$ / $_{min.}$ [e Å$^3$] | +0.79 / –0.56 | +0.40 / –0.35 |

[a] $R_F = \Sigma||F_o| - |F_c||/\Sigma|F_o|$. [b] $R_w(|F|^2) = [\Sigma w(|F_o|^2 - |F_c^2|)^2/\Sigma w|F_o|^2]^{1/2}$.

CCDC-196616 (for **1**) and -205775 (for **2**) contain the supplementary crystallographic data for this paper. These data can be obtained free of charge from The Cambridge Crystallographic Data Centre via www.ccdc.cam.ac.uk/data_request/cif.

## Acknowledgments

The authors are grateful for financial support from the National Science Council of the Republic of China (R.O.C).

[1] B. F. Hoskins, R. Robson, *J. Am. Chem. Soc.* **1990**, *112*, 15461554.
[2] S. R. Batten, R. Robson, *Angew. Chem. Int. Ed.* **1998**, *37*, 1460–1494.
[3] A. N. Khlobystov, A. J. Blake, N. R. Champness, D. A. Lemenovskii, A. G. Majouga, N. V. Zyk, M. Schröder, *Coord. Chem. Rev.* **2001**, *222*, 155–192.
[4] M. Eddaoudi, D. B. Moler, H. L. Li, B. L. Chen, T. M. Reineke, M. O'Keeffe, O. M. Yaghi, *Acc. Chem. Res.* **2001**, *34*, 319–330.
[5] B. Moulton, M. J. Zaworotko, *Chem. Rev.* **2001**, *101*, 1629–1658.
[6] C. Janiak, *Angew. Chem. Int. Ed. Engl.* **1997**, *36*, 1431–1434.
[7] H. Li, M. Eddaoudi, M. O'Keeffe, O. M. Yaghi, *Nature* **1999**, *402*, 276.
[8] S. Noro, R. Kitaura, M. Kondo, S. Kitagawa, T. Ishii, H. Matsuzaka, M. Yamashita, *J. Am. Chem. Soc.* **2002**, *124*, 2568–2583.
[9] C. J. Kepert, M. J. Rosseinsky, *Chem. Commun.* **1998**, 31–32.
[10] C. R. Lee, C. C. Wang, Y. Wang, *Acta Crystallogr. Sect. B* **1996**, *52*, 966–975.
[11] D. S. Yufit, D. J. Price, J. A. K. Howard, S. O. H. Gutschke, A. K. Powell, P. T. Wood, *Chem. Commun.* **1999**, 1561–1562.
[12] K. J. Lin, K. H. Lii, *Angew. Chem. Int. Ed. Engl.* **1997**, *36*, 2076–2077.
[13] J. Spandl, I. Brüdgam, H. Hartl, *Angew. Chem. Int. Ed.* **2001**, *40*, 4018–4020.
[14] H.-A. Hosein, H. Jaggernauth, B. D. Alleyne, L. A. Hall, A. J. P. White, D. J. Williams, *Inorg. Chem.* **1999**, *38*, 3716–3720.
[15] T. K. Maji, G. Mostafa, S. Sain, J. S. Prasad, N. R. Chaudhuri, *Cryst. Eng. Commun.* **2001**, 37.
[16] a) M. I. Khan, Y. D. Chang, Q. Chen, J. Salta, Y. S. Lee, C. J. O'Connor, J. Zubieta, *Inorg. Chem.* **1994**, *33*, 6340–6350; b) A. Müller, R. Rohlfing, E. Krickemeyer, H. Bögge, *Angew. Chem. Int. Ed. Engl.* **1993**, *32*, 909–912.
[17] Q. Chen, S. Liu, J. Zubieta, *Angew. Chem. Int. Ed. Engl.* **1990**, *29*, 70–72.
[18] I. Castro, M. L. Calatayud, J. Sletten, F. Lloret, M. Julve, *J. Chem. Soc. Dalton Trans.* **1997**, 811–818.
[19] R. Soules, F. Dahan, J.-P. Laurent, P. Castan, *J. Chem. Soc. Dalton Trans.* **1988**, 587–590.
[20] J. A. C. van Ooijen, J. Reedijk, A. L. Spek, *Inorg. Chem.* **1979**, *18*, 1184–1189.
[21] C. E. Xanthopoulos, M. P. Sigalas, G. A. Katsoulos, C. A. Tsipis, C. C. Hadjikostas, A. Terzis, M. Mentzafos, *Inorg. Chem.* **1993**, *32*, 3743–3747.
[22] I. Castro, J. Faus, M. Julve, Y. Journaux, J. Sletten, *J. Chem. Soc. Dalton Trans.* **1991**, 2533–2538.
[23] X. Solans, M. Aguiló, A. Gieizes, J. Faus, M. Julve, *Inorg. Chem.* **1990**, *29*, 775–784.
[24] I. Castro, J. Faus, M. Julve, *Inorg. Chim. Acta* **1990**, *170*, 251.
[25] a) P. S. Mukherjee, S. Konar, E. Zangrando, C. Diaz, J. Ribas, N. R. Chaudhuri, *J. Chem. Soc. Dalton Trans.* **2002**, 3471–3476; b) Y. Akhriff, J. Server-Carrió, A. Sancho, J. García-Lozano, E. Escrivá, L. Soto, *Inorg. Chem.* **2001**, *40*, 6832–6840.
[26] M. Ito, R. Weiss, *J. Am. Chem. Soc.* **1963**, *85*, 2580–2584.
[27] R. Lescouëzec, G. Marinescu, M. C. Muñoz, D. Luneau, M. Andruh, F. Lloret, J. Faus, M. Julve, J. A. Mata, R. Llusar, J. Cano, *New J. Chem.* **2001**, *25*, 1224–1235.
[28] a) J. Y. Lu, A. M. Babb, *Inorg. Chim. Acta* **2001**, *318*, 186–190; b) J. Y. Lu, T. J. Schroeder, A. M. Babb, M. Olmstead, *Polyhedron* **2001**, *20*, 2445–2449.
[29] C. Janiak, *J. Chem. Soc. Dalton Trans.* **2000**, 3885–3896.
[30] S. B. Ferguson, E. M. Sanford, E. M. Seward, F. Diederich, *J. Am. Chem. Soc.* **1991**, *113*, 5410–5419.
[31] R. H. Groeneman, L. R. MacGillivray, J. L. Atwood, *Inorg. Chem.* **1999**, *38*, 208–209.
[32] J. Y. Lu, T. Paliwala, S. C. Lim, C. Yu, T. Niu, A. J. Jacobson, *Inorg. Chem.* **1997**, *36*, 923–929.
[33] C. C. Wang, C. H. Yang, G. H. Lee, H. L. Tsai, *Eur. J. Inorg. Chem.* **2005**, 1334–1342.
[34] C. H. Yang, C. M. Chou, G. H. Lee, C. C. Wang, *Inorg. Chem. Commun.* **2003**, *6*, 135–140.
[35] A. J. Blake, S. J. Hill, P. Hubberstey, W. Li, *J. Chem. Soc. Dalton Trans.* **1997**, 913–914.
[36] *SMART Software for CCD Detector System*, Siemens Analytical Instruments Division: Madison, WI, **1997**.
[37] *SAINT Software for CCD Detector System*, Siemens Analytical Instruments Division: Madison, WI, **1997**.
[38] G. M. Sheldrick, *Program for the Refinement of Crystal Structures*, University of Göttingen: Göttingen, Germany, **1997**.
[39] *SHELXTL*, Program Liberary for Structure Solution and Molecular Graphics, Siemens Analytical Instruments Division: Madison, WI, **1997**.

Received: August 23, 2005
Published Online: December 27, 2005

 © 2006 Wiley-VCH Verlag GmbH & Co. KGaA, Weinheim 

DOI: 10.1002/ejic.200500860

# Single-Electron-Transfer Reactions of α-Diimine dpp-BIAN and Its Magnesium Complex $(dpp\text{-}BIAN)^{2-}Mg^{2+}(THF)_3$

**Igor L. Fedushkin,*[a] Valentine M. Makarov,[b] Esther C. E. Rosenthal,[c] and Georgii K. Fukin[a]**

**Keywords:** Magnesium / N-ligands / Single-electron transfer

The reactions of (dpp-BIAN)$Mg(THF)_3$ (**1**) {dpp-BIAN = 1,2-bis[(2,6-diisopropylphenyl)imino]acenaphthene} with ethyl halides EtX (X = Cl, Br, I) in hexane proceed by single-electron transfer (SET) from the metal complex to the organic halide. Complexes $[(dpp\text{-}BIAN)(Et)]MgX(THF)_n$ [X = Cl, $n$ = 0 (**2**); X = Br, $n$ = 2 (**3**); X = I, $n$ = 1 (**4**)] are the products of ethyl transfer to an imine carbon atom of a coordinated diimine ligand. The compound [(dpp-BIAN)(Et)]MgBr (**3a**) was obtained from the reaction of free dpp-BIAN with ethylmagnesiumbromide in hexane. In this case SET from the Grignard reagent to the neutral diimine takes place. Compounds **2**–**4** and **3a** were isolated as crystals and characterized by $^1H$ NMR spectroscopy. The molecular structure of **3** was determined by single-crystal X-ray analysis.
(© Wiley-VCH Verlag GmbH & Co. KGaA, 69451 Weinheim, Germany, 2006)

## Introduction

Among the organometallic and coordination compounds of magnesium, only Grignard reagents are widely used in organic synthesis.[1] Despite the fact that magnesium amides, $R_2NMgX$ (X = halide), so-called Hauser bases, were found to be excellent deprotonating reagents for nitriles,[2] enolizable ketones,[3] and C–H acids,[4] they have not yet become regular reagents in organic synthesis. Reactions of Grignard reagents with organic substrates may proceed by two different mechanisms: concerted polar addition or single-electron transfer (SET) from RMgX to the organic compound.[5] The second mechanism implies oxidation of RMgX and reduction of the substrate by SET. During this process, an R–Mg bonding electron leaves the HOMO of RMgX. This leads to cleavage of this bond and formation of a radical R and an MgX cation, which then attack the respective centers of the substrate. Some time ago, we started our search for new electron transfer reagents based on main-group metals. Our original concept involved the preparation of metal complexes in which a complex HOMO is mainly ligand-localized and the ligand has further functionalities to bind the metal (e.g. heteroatom lone pairs). In these cases, the SET from the HOMO to the organic substrate should not cause cleavage of a metal–ligand bond. Long-known alkali metal naphthalenides or magnesium anthracenide are strong reducing agents, which are able to transfer electrons to different substrates. However, since the π-systems of these arenes are very weak bases, an electron transfer from these species causes not only oxidation of the ligand but also its release from the metal. α-Diimines have a low-lying LUMO (π*), which can be populated with electrons from the metal, and basic nitrogen atoms. The 1,2-bis[(2,6-diisopropylphenyl)imino]-acenaphthene (dpp-BIAN) ligand has an extended π system that is formed from diimine and naphthalene. Four-step reduction of this diimine with alkali metals produces its tetraanion.[6] Metallic magnesium easily reduces dpp-BIAN to a dianion and provides the monomeric solvated complex (dpp-BIAN)$Mg(THF)_3$ (**1**).[7] To some extent, this complex is related to Hauser bases because it readily deprotonates C–H acids,[8] ketones,[9] and nitriles.[10] Reaction of **1** with diphenylketone provides, by SET, the pinacolate complex $[(dpp\text{-}BIAN)^{-}\cdot Mg]_2(\mu\text{-}O_2C_2Ph_4)$.[11] Note that, during oxidation from dianion to radical-anion, the dpp-BIAN ligand still remains on magnesium. Iodine and some organic halides (e.g. $Ph_3SnCl$, $BrCH_2CH_2Br$) oxidize complex **1** to give radical-anionic species of the type $(dpp\text{-}BIAN)^{-}\cdot MgX$ (X = Cl, Br, I).[12] Recently we have reported the reverse process; the reduction of a magnesium-bound radical-anion to the corresponding dianion by reductive elimination of an alkyl radical from (dpp-BIAN)Mg(*i*Pr)($Et_2O$).[13] In this particular case, the SET occurred intramolecularly. Thus, the concept we wish to develop concerns the preparation of main-group metal complexes with ligands, which may vary their "oxidation state" while they are bound to the metal. This ap-

[a] G. A. Razuvaev Institute of Organometallic Chemistry of Russian Academy of Sciences,
Tropinina 49, 603950 Nizhny Novgorod, GSP-445, Russia
Fax: + 7-8312-127497
E-mail: igorfed@imoc.sinn.ru
[b] Nizhny Novgorod State Pedagogical University,
Ulyanova 1, 603095, Nizhny Novgorod, Russia
Fax: + 7-8312-364446
E-mail: chemical@nnspu.ru
[c] Institute of Chemistry, Technical University of Berlin, Sekr. C2,
Straße des 17. Juni 135, 10623 Berlin, Germany
Fax: +49-30-314-22168
E-mail: rosenthal@chem.tu-berlin.de

 © 2006 Wiley-VCH Verlag GmbH & Co. KGaA, Weinheim 

proach should provide redox-active complexes of redox-inactive metals (e.g. magnesium). In this paper, we report on the reactivity of **1** towards organic halides.

## Results and Discussion

Treatment of complex **1** with ethyl halides EtX (X = Cl, Br, I) in THF causes a color change from deep green to red within a few minutes at room temperature. Evaporation of the solvent affords a red oily residue, which solidifies only after repeated treatment with hexane and storage of the solution formed at ambient temperature for several days. Because **1** is insoluble in hexane, its reaction with EtX (X = Cl, Br, I) in this solvent proceeds only at reflux and takes up to 30 min in the case of EtI, one hour for EtBr, and several hours for EtCl. However, the use of hexane as solvent allows simple isolation of the products because the products crystallize from the reaction mixture during the reaction. Use of an excess of organic halide increases the reaction rates in hexane. Thus, when a fivefold excess of EtCl is used, the reaction in hexane is complete within 3 hours. Completion of the reaction may be seen by the disappearance of the green crystals of **1** and the precipitation of the red crystalline product.

According to the results of $^1$H NMR spectroscopy, the reaction of complex **1** with ethyl halides EtX (X = Cl, Br, I) yields the products of ethyl transfer to an imine carbon atom of the dpp-BIAN ligand coordinated to the magnesium atom (Scheme 1). The ethyl radical formed under SET from **1** to EtX attacks the radical-anion of dpp-BIAN, resulting in the formation of compounds **2**–**4** in good yields.

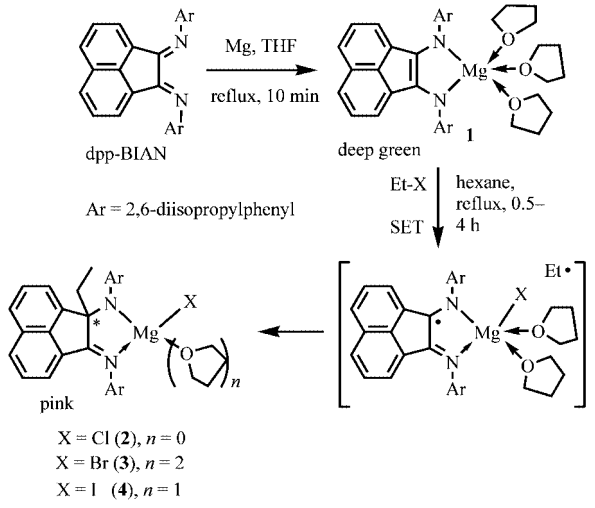


Scheme 1.

### Molecular Structure of 3

The molecular structure of **3** (Figure 1) was determined by single-crystal X-ray analysis. Free dpp-BIAN as well as the dpp-BIAN dianion in complex **1** possess two planes of symmetry, one is orthogonal to the acenaphthene plane and crosses the middle C–C bond of the naphthalene moiety, whereas the other coincides with the diimine plane. Attachment of the ethyl group to the imino carbon atom destroys this symmetry and causes the appearance of a chiral carbon atom [C(1)] in the molecule. In the unit cell *R* and *S* isomers are present. In **3** the magnesium atom is five-coordinate. The amido and imino Mg–N distances [Mg–N(1) 2.015(2) and Mg–N(2) 2.3320(19) Å, respectively] differ significantly. Asymmetric chelation of magnesium metal has already been observed in the products of addition of enolizable ketones to **1**.[9] Addition of ketones to **1** occurs with protonation of one of the nitrogen atoms of the dpp-BIAN ligand and results in an asymmetric amido/amino structure. For instance, in the addition product of 1,1-diphenylacetone, the amido and amino bond lengths are 2.051(2) and 2.410(2) Å, respectively. The N(2)–C(2) double bond in **3** [1.281(3) Å] is nearly the same as those in free dpp-BIAN (both N–C 1.28 Å).[12] The distance N(1)–C(2) [1.471(3) Å] corresponds well to a single N–C bond. The Mg–O distances [2.092(2) and 2.1286(17) Å] fall into the range of the respective distances in **1** (2.070, 2.084 and 2.224 Å).[7]

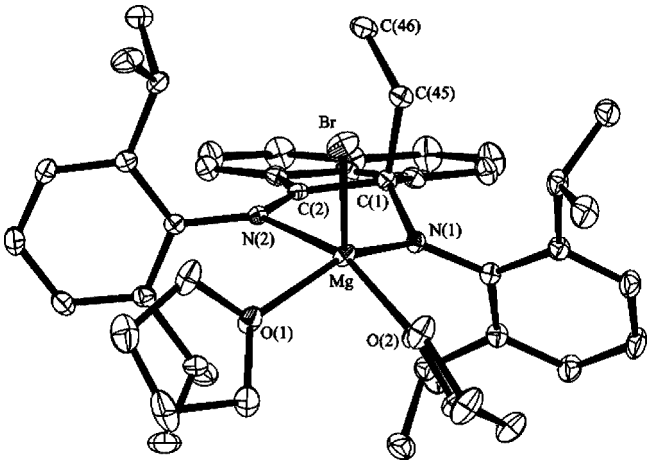


Figure 1. Molecular structure of **3** (*S* isomer). The hydrogen atoms are omitted. Thermal ellipsoids are drawn at 30% probability. Selected bond lengths [Å] and angles [°]: Mg–N(1) 2.015(2), Mg–N(2) 2.3320(19), Mg–O(1) 2.092(2), Mg–O(2) 2.1286(17), Mg–Br 2.5119(8), N(1)–C(1) 1.471(3), C(1)–C(2) 1.543(3), C(1)–C(45) 1.561(3), N(2)–C(2) 1.281(3); N(1)–Mg–O(1) 143.44(9), N(1)–Mg–O(2) 98.33(7), O(1)–Mg–O(2) 85.20(7), N(1)–Mg–N(2) 77.88(7), O(1)–Mg–N(2) 84.75(7), O(2)–Mg–N(2) 156.73(8), N(1)–Mg–Br 116.82(6), O(1)–Mg–Br 98.54(6), O(2)–Mg–Br 97.52(6), N(2)–Mg–Br 104.70(5).

### NMR Spectroscopy of 2–4

Selected $^1$H NMR spectroscopic data for **2**–**4** are given in Table 1. All three compounds reveal a similar spectral picture. The asymmetric amido/imino structure causes the twelve aromatic protons to be nonequivalent. The four methine protons of the isopropyl substituents give rise to four signals ranging from 4.85 to 2.97 ppm for **2** and **3** in [$D_8$]THF and from 5.25 to 3.06 ppm for **4** in $C_6D_6$. Because

 © 2006 Wiley-VCH Verlag GmbH & Co. KGaA, Weinheim 

of restricted rotation around the N–C(*ipso*-Ph) bond, all eight methyl groups become unique and appear as eight doublets in the range from 1.40 to –0.15 ppm. The presence of the chiral carbon atom C(1) next to the methylene protons of the ethyl group causes them to be nonequivalent (**2**: 2.75, 2.54; **3**: 2.97, 2.51; **4**: 3.23, 2.88 ppm).

Table 1. Selected $^1$H NMR spectroscopic data for **2** and **3** in [$D_8$]-THF and **4** in $C_6D_6$ (200 MHz, 293 K).

| | **2** | **3** | **4** |
|---|---|---|---|
| *H*–C($CH_3$)$_2$, septuplet[a] | 4.82<br>3.63<br>3.09<br>2.97 | 4.85<br>3.68<br>3.05<br>3.00 | 5.25<br>3.93<br>3.23<br>3.06 |
| C*H*$_2$–$CH_3$, multiplet[a] | 2.75<br>2.54 | 2.97<br>2.51 | 3.23<br>2.88 |
| H–C(C*H*$_3$)$_2$, doublet[b] | 1.39<br>1.37<br>1.28<br>1.24<br>1.13<br>0.87<br>0.46<br>–0.18 | 1.40<br>1.37<br>1.27<br>1.23<br>1.13<br>0.87<br>0.44<br>–0.15 | 1.74<br>1.72<br>1.66<br>1.23<br>1.16<br>0.98<br>0.81<br>0.14 |
| $CH_2$–C*H*$_3$, triplet[b] | –0.05 | –0.07 | 0.23 |

[a] Integral intensity corresponds to one proton. [b] Integral intensity corresponds to three protons.

Compound **3a** was prepared by the reaction of dpp-BIAN with EtMgBr (Scheme 2). Only its coordinating solvent differs from that of **3**.

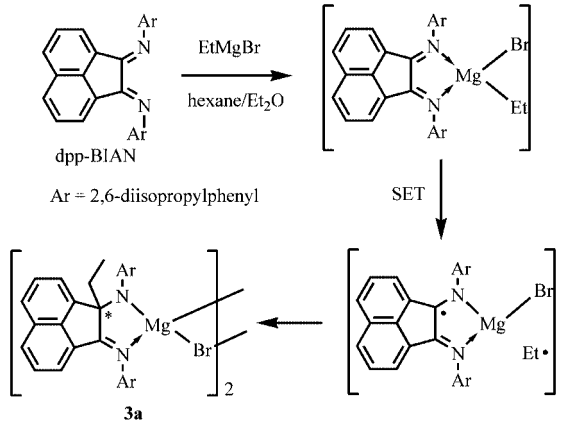


Scheme 2.

Addition of an equimolar amount of EtMgBr (1.9 M in $Et_2O$) to a stirred suspension of dpp-BIAN in hexane at room temperature causes immediate dissolution of the diimine (and provides a clear red solution). Evaporation of the solvent in vacuo leads to rapid precipitation of a microcrystalline solid, which does not dissolve in hexane again, but readily dissolves in $Et_2O$ and toluene. Although the molecular structure of this product was not confirmed by X-ray crystallography, its identity was definitely established by $^1$H NMR spectroscopy. The $^1$H NMR spectroscopic data for the product obtained, together with those acquired for **2**–**4**, indicate that in the reaction of dpp-BIAN with EtMgBr a reverse process of SET – from Grignard reagent to neutral diimine ligand – takes place. Transfer of the alkyl radical formed to the imino carbon atom of dpp-BIAN follows this SET process. The $^1$H NMR spectrum of **3a** is shown in Figure 2. According to the $^1$H NMR data, the isolated compound **3a** does not contain coordinating solvent, e.g. diethyl ether. Therefore, we suggest that compound **3a** is dimeric in the solid state. This is supported by the recently reported dimeric structure of a closely related magnesium compound formed in the reaction of **1** with $Me_3SiCl$.[12] In this case, the SET from **1** to $Me_3SiCl$ causes the formation of $Me_3Si$ radicals, which attack THF molecules to form $Me_3SiO(CH_2)_3CH_2$ radicals. Transfer of these radicals to the imino carbon atom provided a compound that is an analog of **2**–**4**.

As in the case of compound **3**, the $^1$H NMR spectrum of **3a** (Figure 2) reveals the nonequivalence of all 12 aromatic protons, whose signals range from 7.84 to 6.10 ppm. Signals of four different methine protons are positioned at 4.85, 3.70, 3.05, and 2.96 ppm. Eight different methyl groups give rise to eight doublets centered at 1.39, 1.36, 1.26, 1.22, 1.12, 0.86, 0.44, and –0.15 ppm. The ethyl group provides three signals: two multiplets at 2.97 and 2.49 (1 H each) and a triplet at –0.07 (3 H) ppm.

The reduction of α-diimines to radical-anions with main-group organometallic compounds followed either by alkyl radical transfer to a radical-anionic ligand or by an alkyl radical release has been reported. Van Koten and coworkers have studied reactions of 1,4-diazabutadienes with different dialkylzinc compounds. Tertiary, benzylic, and some secondary organozinc compounds give C-alkylation products (sometimes accompanied with 1,3-prototropic shift), whereas primary dialkylzinc compounds give N-alkylation products.[14] Recently, Bailey and coworkers reported on the reactivity of $Me_2Mg$ towards dpp-BIAN and diacetal-bis(2,6-diisopropylphenylimine) (Ar′-DAD).[15] In both cases, the reactions occur with release of a methyl radical and afford complexes of radical-anionic ligands, e.g. (L$^{-\cdot}$)-MgMe (L = dpp-BIAN or Ar′-DAD). In the case of Ar′-DAD, the methyl transfer product was isolated in low yield when the reaction was carried out at low temperature. The formation of radical-anionic products in the above-mentioned reactions of organomagnesium compounds with diimines indicates clearly that these reactions occur by SET from the magnesium compound to the diimines. In order to find confirmation for the SET process in the course of the reaction of complex **1** with ethyl bromide, we have monitored this reaction by ESR spectroscopy. Addition of EtBr to a THF solution of complex **1** at –100 °C followed by slow warming of the reaction mixture to ambient temperature resulted in the appearance of the ESR signal of the dpp-BIAN radical-anion ($g$ = 2.0045, $A_N$ = 0.44, $A_{Br}$ = 0.2 mT).[12] In the course of several minutes this signal disappeared completely, indicating the recombination of the radical-anion and the ethyl radical.

 © 2006 Wiley-VCH Verlag GmbH & Co. KGaA, Weinheim 

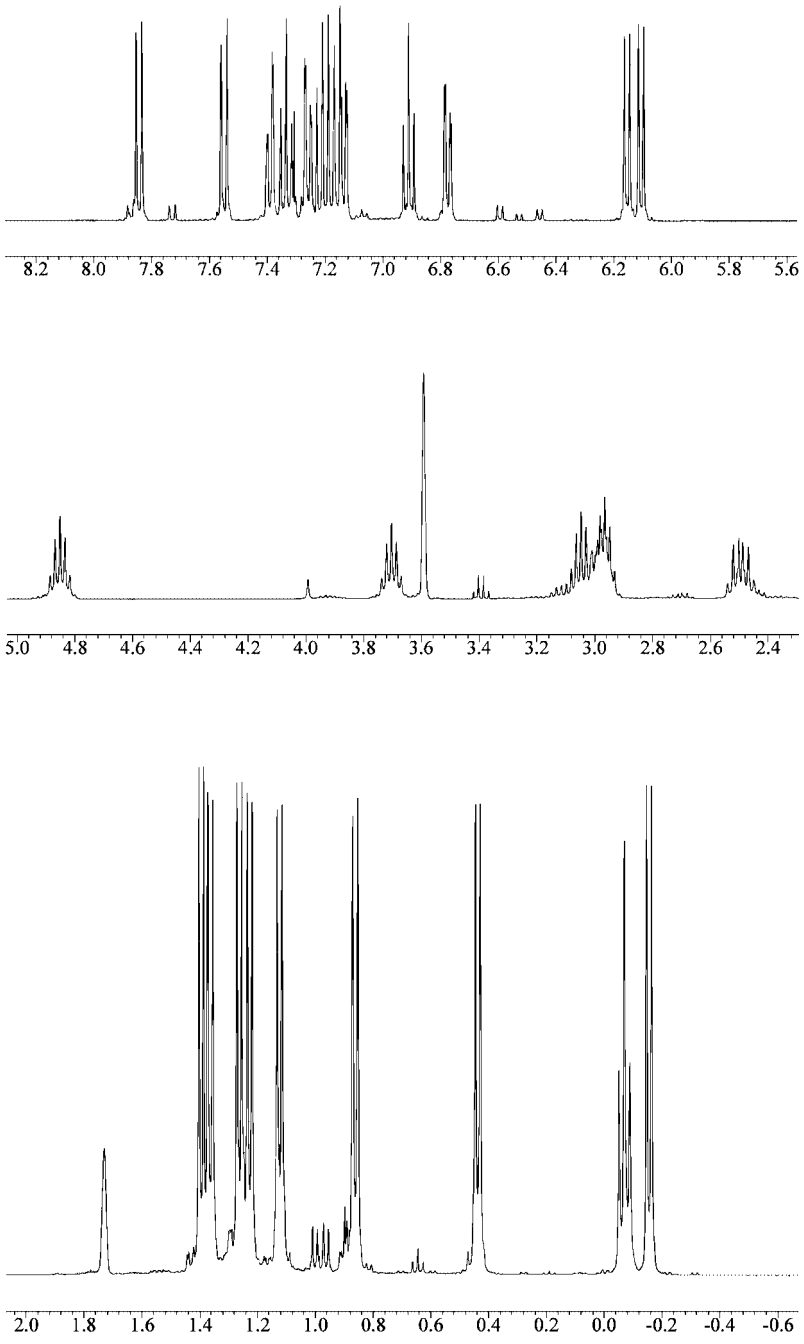


Figure 2. The $^1$H NMR spectrum of **3** divided in three sections ([$D_8$]THF, 400 MHz, 20 °C).

## Conclusions

In conclusion, we have demonstrated that diimine dpp-BIAN as well as its dianion may be involved in SET reactions. Thus, reagents having a low ionization potential, such as organometallic species, may reduce neutral dpp-BIAN. In contrast, the magnesium complex of the dpp-BIAN dianion acts as reducing agent towards organic halides. Taking into account the identity of the products isolated in both oxidation and reduction reactions one can suggest that both processes occur by the formation of the radical-anion of dpp-BIAN and an alkyl radical, which recombine to afford the final C–C coupling product.

## Experimental Section

**General Remarks:** All manipulations were carried out under vacuum using Schlenk ampoules. Tetrahydrofuran and diethyl ether were dried by distillation from sodium/benzophenone. [$D_8$]THF and $C_6D_6$ (both from Aldrich) used for NMR experiments were dried with sodium/benzophenone at ambient temperature and, just prior to use, condensed under vacuum into the NMR tubes already

 © 2006 Wiley-VCH Verlag GmbH & Co. KGaA, Weinheim 

containing the respective compound. Melting points were measured in sealed capillaries. IR spectra were recorded with an FTIR FSM-1201 spectrometer ("Monitoring Ltd."), $^1$H NMR spectra with Bruker DPX-200 and Bruker DRX-400 NMR spectrometers.

**(dpp-BIAN)Mg(THF)$_3$ (1):** Magnesium shavings (2.4 g, 100 mmol) and $I_2$ (0.5 g, 2.0 mmol) were placed in a Schlenk-like ampoule (ca. 100 mL volume) equipped with a Teflon stopcock. After evacuation of the ampoule (at $10^{-1}$ Torr for ca. 1 min), THF (40 mL) was added by condensation, and the mixture was stirred for 2 h. The $MgI_2(THF)_n$ formed was decanted together with the solvent, and the residual metal was washed three times with THF (40 mL). A suspension of dpp-BIAN (0.5 g, 1.0 mmol) in THF (20 mL) was then added to the activated magnesium metal, and the mixture was heated to reflux. Over the course of about 30 min, the reaction mixture turned deep green because of the formation of **1**. The solution was then cooled to ambient temperature and decanted from the excess magnesium. The solvent was evaporated in vacuo affording compound **1** as deep green, almost black crystals. The solid was washed three times with hexane (15 mL) and then used in the reactions with ethyl halides. The yields of the products **2**–**4** were calculated on the basis of the amount of dpp-BIAN used in the preparation of **1**.

**[(dpp-BIAN)(Et)]MgCl (2):** To a suspension of compound **1** (prepared from 0.5 g of dpp-BIAN) in hexane, was added ethyl chloride (0.32 g, 5 mmol). The reaction ampoule was sealed off under vacuum. In the course of 4 h at 80 °C, the precipitate of **1** dissolved completely. Slow cooling of the red solution to ambient temperature produced red crystals of **2** (0.39 g, 67%). M.p. 147 °C. $C_{38}H_{45}ClMgN_2$ (589.55): calcd. C 77.42, H 7.69; found C 77.11, H 7.91%. IR (Nujol): $\tilde{\nu}$ = 1626 (s), 1590 (m), 1307 (m), 1246 (m), 1188 (w), 1161 (w), 1103 (w), 1024 (m), 1015 (m), 934 (m), 857 (w), 854 (w), 800 (m), 780 (vs), 753 (s), 719 (s), 642 (w), 630 (w), 611 (w), 596 (w), 576 (w), 534 (w), 449 (s), 430 (s), 407 (vs) cm$^{-1}$. $^1$H NMR (200 MHz, [D$_8$]THF, 20 °C): $\delta$ = 7.84 (d, $J$ = 8.0 Hz, 1 H, CH arom.), 7.55 (d, $J$ = 8.3 Hz, 1 H, CH arom.), 7.39–7.15 (m, 5 H, CH arom.), 7.13 (dd, 1 H, $J$ = 7.5 and 1.7 Hz, CH arom.), 6.91 (t, $J$ = 7.5 Hz, 1 H, CH arom.), 6.77 (dd, 1 H, $J$ = 7.3 and 1.5 Hz, CH arom.), 6.17 (d, $J$ = 7.3 Hz, 1 H, CH arom.), 6.11 (d, $J$ = 7.0 Hz, 1 H, CH arom.), 4.82 [sept, 1 H, $J$ = 6.8 Hz, C$H$(CH$_3$)$_2$], 3.63 [sept, 1 H, $J$ = 6.8 Hz, C$H$(CH$_3$)$_2$], 3.09 [sept, 1 H, $J$ = 6.8 Hz, C$H$(CH$_3$)$_2$], 2.97 [sept, 1 H, $J$ = 6.8 Hz, C$H$(CH$_3$)$_2$], 2.75 (m, 1 H, C$H_2$CH$_3$), 2.54 (m,1 H, C$H_2$CH$_3$), 1.39 [d, $J$ = 6.8 Hz, 3 H, CH(C$H_3$)$_2$], 1.37 [d, $J$ = 6.8 Hz, 3 H, CH(C$H_3$)$_2$], 1.28 [d, $J$ = 6.8 Hz, 3 H, CH(C$H_3$)$_2$], 1.24 [d, $J$ = 6.8 Hz, 3 H, CH(C$H_3$)$_2$], 1.13 [d, $J$ = 6.8 Hz, 3 H, CH(C$H_3$)$_2$], 0.87 [d, $J$ = 6.8 Hz, 3 H, CH(C$H_3$)$_2$], 0.46 [d, $J$ = 6.8 Hz, 3 H, CH(C$H_3$)$_2$], –0.05 (t, $J$ = 7.3 Hz, 3 H, CH$_2$C$H_3$), –0.18 [d, $J$ = 6.8 Hz, 3 H, CH(C$H_3$)$_2$] ppm.

**[(dpp-BIAN)(Et)]MgBr(THF)$_2$ (3):** Red crystals of **3** were obtained by the procedure described for **2** using dpp-BIAN (0.5 g, 1.0 mmol) and EtBr (0.11 g, 1.0 mmol). Yield 0.5 g (63%). M.p. 76 °C. $C_{46}H_{61}BrMgN_2O_2{\cdot}0.5(C_2H_5)_2O$ (815.25): calcd. C 70.72, H 8.16; found C 70.68, H 8.09%. IR (Nujol): $\tilde{\nu}$ = 1638 (s), 1588 (w), 1315 (m), 1242 (s), 1184 (w), 1104 (w), 1073 (w), 1027 (vs), 946 (w), 919 (m), 865 (w), 854 (s), 846 (w), 834 (w), 800 (w), 784 (s), 750 (vs), 719 (m), 673 (w), 630 (w), 611 (w), 596 (w), 576 (w), 542 (w), 519 (w), 492 (w), 430 (s) cm$^{-1}$. $^1$H NMR (200 MHz, [D$_8$]THF, 20 °C): $\delta$ = 7.85 (d, $J$ = 8.2 Hz, 1 H, CH arom.), 7.55 (d, $J$ = 8.2 Hz, 1 H, CH arom.), 7.40–7.10 (m, 6 H, CH arom.), 6.91 (t, $J$ = 7.5 Hz, 1 H, CH arom.), 6.77 (dd, 1 H, $J$ = 7.5 and 1.5 Hz, CH arom.), 6.16 (d, $J$ = 7.3 Hz, 1 H, CH arom.), 6.11 (d, $J$ = 7.0 Hz, 1 H, CH arom.), 4.85 [sept, 1 H, $J$ = 6.8 Hz, C$H$(CH$_3$)$_2$], 3.68 [sept, 1 H, $J$ = 6.8 Hz, C$H$(CH$_3$)$_2$], 3.05 [sept, 1 H, $J$ = 6.8 Hz, C$H$(CH$_3$)$_2$], 3.00 [sept, 1 H, $J$ = 6.8 Hz, C$H$(CH$_3$)$_2$], 2.97 (m, 1 H, C$H_2$CH$_3$), 2.51 (m,1 H, C$H_2$CH$_3$), 1.40 [d, $J$ = 6.8 Hz, 3 H, CH(C$H_3$)$_2$], 1.37 [d, $J$ = 6.8 Hz, 3 H, CH(C$H_3$)$_2$], 1.27 [d, $J$ = 6.8 Hz, 3 H, CH(C$H_3$)$_2$], 1.23 [d, $J$ = 6.8 Hz, 3 H, CH(C$H_3$)$_2$], 1.13 [d, $J$ = 6.8 Hz, 3 H, CH(C$H_3$)$_2$], 0.87 [d, $J$ = 6.8 Hz, 3 H, CH(C$H_3$)$_2$], 0.44 [d, $J$ = 6.8 Hz, 3 H, CH(C$H_3$)$_2$], –0.07 (t, $J$ = 7.3 Hz, 3 H, CH$_2$C$H_3$), –0.15 [d, $J$ = 6.8 Hz, 3 H, CH(C$H_3$)$_2$] ppm.

**[(dpp-BIAN)(Et)]MgBr (3a):** Dropwise addition of an ether solution of EtMgBr (1.9 M, 0.6 mL) by syringe to a stirred suspension of dpp-BIAN (0.53 g, 1.06 mmol) in hexane (20 mL) at 25 °C caused instant dissolution of the orange precipitate and resulted in a red solution. Evaporation of the solvent under vacuum led to quick precipitation of the red microcrystalline solid, which was then filtered off and dried in vacuo. Yield 0.58 g (87%). M.p. 205 °C. $C_{38}H_{45}BrMgN_2$: (634.00): calcd. C 71.99, H 7.15; found C 71.05, H 6.97%. IR (Nujol): $\tilde{\nu}$ = 1623 (s), 1588 (m), 1307 (m), 1246 (m), 1188 (w), 1161 (m), 1100 (w), 1038 (w), 1011 (m), 934 (w), 854 (w), 830 (w), 800 (w), 781 (s), 750 (s), 723 (s), 642 (w), 631 (w), 611 (w), 592 (w), 577 (w), 542 (w), 527 (w), 454 (s), 427 (s), 407 (s) cm$^{-1}$. $^1$H NMR (400 MHz, [D$_8$]THF, 20 °C): $\delta$ = 7.84 (d, $J$ = 8.2 Hz, 1 H, CH arom.), 7.55 (d, $J$ = 8.2 Hz, 1 H, CH arom.), 7.39 (dd, 1 H, $J$ = 7.7 and 1.5 Hz, CH arom.), 7.33 (t, $J$ = 7.5 Hz, 1 H, CH arom.), 7.26 (dd, 1 H, $J$ = 7.7 Hz and 1.5, CH arom.), 7.21 (t, $J$ = 7.5 Hz, 1 H, CH arom.), 7.17 (dd, 1 H, $J$ = 7.5 and 7.5 Hz, CH arom.), 7.13 (dd, 1 H, $J$ = 7.7 and 1.7 Hz, CH arom.), 6.91 (t, $J$ = 7.7 Hz, 1 H, CH arom.), 6.77 (dd, 1 H, $J$ = 7.5 and 1.7 Hz, CH arom.), 6.15 (d, $J$ = 7.3 Hz, 1 H, CH arom.), 6.10 (d, $J$ = 7.1 Hz, 1 H, CH arom.), 4.85 [sept, 1 H, $J$ = 6.8 Hz, C$H$(CH$_3$)$_2$], 3.70 [sept, 1 H, $J$ = 6.8 Hz, C$H$(CH$_3$)$_2$], 3.05 [sept, 1 H, $J$ = 6.8 Hz, C$H$(CH$_3$)$_2$], 2.97 (dq, 1 H, $J$ = 14.8 and 7.3 Hz, C$H_2$CH$_3$), 2.96 [sept, 1 H, $J$ = 6.8 Hz, C$H$(CH$_3$)$_2$], 2.49 (dq, 1 H, $J$ = 14.8 and 7.3 Hz, C$H_2$CH$_3$), 1.39 [d, $J$ = 6.8 Hz, 3 H, CH(C$H_3$)$_2$], 136 [d, $J$ = 6.8 Hz, 3 H, CH(C$H_3$)$_2$], 1.26 [d, $J$ = 6.8 Hz, 3 H, CH(C$H_3$)$_2$], 1.22 [d, $J$ = 6.8 Hz, 3 H, CH(C$H_3$)$_2$], 1.12 [d, $J$ = 6.8 Hz, 3 H, CH(C$H_3$)$_2$], 0.86 [d, $J$ = 6.8 Hz, 3 H, CH(C$H_3$)$_2$], 0.44 [d, $J$ = 6.8 Hz, 3 H, CH(C$H_3$)$_2$], –0.07 (t, $J$ = 7.3 Hz, 3 H, CH$_2$C$H_3$), –0.15 [d, $J$ = 6.8 Hz, 3 H, CH(C$H_3$)$_2$] ppm.

**[(dpp-BIAN)(Et)]MgI(THF)$_2$ (4):** Red crystals of **4** were obtained by the procedure described for **2** using 0.5 g (1.0 mmol) of dpp-BIAN and 0.15 g (1.0 mmol) of ethyl iodide. The reaction completed within 30 min. Yield 0.42 g (56%). M.p. 188 °C. $C_{42}H_{53}IMgN_2O$ (753.11): calcd. C 66.98, H 7.09; found C 70.68, H 8.09%. IR (Nujol): $\tilde{\nu}$ = 1623 (s), 1584 (m), 1307 (m), 1250 (s), 1181 (m), 1100 (w), 1038 (m), 1011 (s), 949 (w), 919 (w), 869 (s), 854 (m), 834 (w), 800 (m), 784 (s), 754 (s), 723 (m), 673 (w), 630 (w), 611 (w), 596 (w), 576 (w), 542 (w), 515 (w), 496 (w), 450 (m), 427 (s) cm$^{-1}$. $^1$H NMR (200 MHz, C$_6$D$_6$, 20 °C): $\delta$ = 7.53–7.04 (m, 9 H, CH arom.), 6.89 (t, $J$ = 7.8 Hz, 1 H, CH arom.), 6.51 (d, $J$ = 7.3 Hz, 1 H, CH arom.), 6.46 (d, $J$ = 7.0 Hz, 1 H, CH arom.), 5.25 [sept, 1 H, $J$ = 6.8 Hz, C$H$(CH$_3$)$_2$], 3.93 [sept, 1 H, $J$ = 6.8 Hz, C$H$(CH$_3$)$_2$], 3.23 [sept, 1 H, $J$ = 6.8 Hz, C$H$(CH$_3$)$_2$], 3.22 (m, 1 H, C$H_2$CH$_3$), 3.06 [sept, 1 H, $J$ = 6.8 Hz, C$H$(CH$_3$)$_2$], 2.88 (m,1 H, C$H_2$CH$_3$), 1.74 [d, $J$ = 6.8 Hz, 3 H, CH(C$H_3$)$_2$], 1.72 [d, $J$ = 6.8 Hz, 3 H, CH(C$H_3$)$_2$], 1.66 [d, $J$ = 6.8 Hz, 3 H, CH(C$H_3$)$_2$], 1.23 [d, $J$ = 6.8 Hz, 3 H, CH(C$H_3$)$_2$], 1.16 [d, $J$ = 6.8 Hz, 3 H, CH(C$H_3$)$_2$], 0.98 [d, $J$ = 6.8 Hz, 3 H, CH(C$H_3$)$_2$], 0.81 [d, $J$ = 6.8 Hz, 3 H, CH(C$H_3$)$_2$], 0.23 (t, $J$ = 7.3 Hz, 3 H, CH$_2$C$H_3$), 0.14 [d, $J$ = 6.8 Hz, 3 H, CH(C$H_3$)$_2$] ppm.

**X-ray Crystallographic Study of 3:** Crystals of **3** suitable for X-ray structure determination were obtained from hexane. Crystal data: $C_{46}H_{61}BrMgN_2O_2{\cdot}0.5Et_2O$, $M$ = 815.25, triclinic, $a$ = 10.8322(6), $b$ = 12.3710(6), $c$ = 17.8518(9) Å, $U$ = 2210.7(2) Å$^3$, $T$ = 100(2) K,

 © 2006 Wiley-VCH Verlag GmbH & Co. KGaA, Weinheim 

space group $P\bar{1}$, $Z = 2$, $\mu = 0.984\ mm^{-1}$, 12387 reflections measured, 7760 unique ($R_{int} = 0.0180$) which were used in all calculations. $R_1[I > 2\sigma(I)] = 0.526$, w$R_1$(all data) = 0.0635. The structures were solved by direct methods using SHELXS-97[16] and were refined on $F^2$ using SHELXL-97.[17] All non-hydrogen atoms were refined anisotropically. The hydrogen atoms were found from Fourier synthesis except those at C(38) and C(39) in the THF molecule. The hydrogen atoms at C(38) and C(39) as well as hydrogen atoms in the lattice $Et_2O$ molecule were placed in calculated positions and refined in the riding model. SADABS[18] was used to perform area-detector scaling and absorption corrections. CCDC-282656 (**3**) contains the supplementary crystallographic data for this paper. These data can be obtained free of charge from The Cambridge Crystallographic Data Centre via www.ccdc.cam.ac.uk/data_request/cif.

## Acknowledgments

This work was supported by the Russian Foundation for Basic Research (Grant No. 03–03–32246) and the Russian Science Support Foundation.

[1] a) Ch. Elschenbroich, A. Salzer, *Organometallics* 2nd ed., Wiley-VCH, Weinheim, **1992**; b) *Handbook of Grignard Reagents* (Eds.: G. S. Silverman, P. E. Rakita), Marcel Dekker, New York, **1996**; c) *Grignard Reagents – New Developments* (Ed.: H. G. Richey, Jr.,), Wiley, Chichester, **2000**; d) P. Knochel, W. Dohle, N. Gommermann, F. F. Kneisel, F. Kopp, T. Korn, I. Sapountzis, V. A. Vu, *Angew. Chem.* **2003**, *115*, 4438; *Angew. Chem. Int. Ed.* **2003**, *42*, 4302; e) J. F. Garst, M. P. Soriaga, *Coord. Chem. Rev.* **2004**, *248*, 623.

[2] G. A. Reynolds, W. J. Humphlett, F. W. Swamer, C. R. Hauser, *J. Org. Chem.* **1951**, *16*, 165.

[3] a) J. F. Allan, W. Clegg, K. W. Henderson, L. Horsburgh, A. R. Kennedy, *J. Organomet. Chem.* **1998**, *559*, 173; b) J. F. Allan, K. W. Henderson, A. R. Kennedy, *Chem. Commun.* **1999**, 1325; c) J. F. Allan, K. W. Henderson, A. R. Kennedy, S. J. Teat, *Chem. Commun.* **2000**, 1059.

[4] K. C. Yang, C. C. Chang, J. Y. Huang, C. C. Lin, G. H. Lee, Y. Wang, M. Y. Chiang, *J. Organomet. Chem.* **2002**, *648*, 176.

[5] R. W. Hoffmann, *Chem. Soc. Rev.* **2003**, *32*, 225.

[6] a) I. L. Fedushkin, A. A. Skatova, V. A. Chudakova, G. K. Fukin, *Angew. Chem.* **2003**, *115*, 3416; *Angew. Chem. Int. Ed.* **2003**, *42*, 3294; b) I. L. Fedushkin, A. A. Skatova, V. A. Chudakova, V. K. Cherkasov, G. K. Fukin, M. A. Lopatin, *Eur. J. Inorg. Chem.* **2004**, 388.

[7] I. L. Fedushkin, A. A. Skatova, V. A. Chudakova, G. K. Fukin, S. Dechert, H. Schumann, *Eur. J. Inorg. Chem.* **2003**, 3336.

[8] I. L. Fedushkin, N. M. Khvoinova, A. A. Skatova, G. K. Fukin, *Angew. Chem.* **2003**, *115*, 5381; *Angew. Chem. Int. Ed.* **2003**, *42*, 5223.

[9] I. L. Fedushkin, A. A. Skatova, G. K. Fukin, M. Hummert, H. Schumann, *Eur. J. Inorg. Chem.* **2005**, 2332.

[10] I. L. Fedushkin, A. G. Morozov, O. V. Rassadin, G. K. Fukin, *Chem. Eur. J.* **2005**, *11*, 5749.

[11] I. L. Fedushkin, A. A. Skatova, V. K. Cherkasov, V. A. Chudakova, S. Dechert, M. Hummert, H. Schumann, *Chem. Eur. J.* **2003**, *9*, 5778.

[12] I. L. Fedushkin, A. A. Skatova, A. N. Lukoyanov, V. A. Chudakova, S. Dechert, M. Hummert, H. Schumann, *Russ. Chem. Bull.* **2004**, *113*, 2641.

[13] I. L. Fedushkin, A. A. Skatova, M. Hummert, H. Schumann, *Eur. J. Inorg. Chem.* **2005**, 1601.

[14] E. Wissing, K. van Gorp, J. Bersma, G. van Koten, *Inorg. Chim. Acta* **1994**, *220*, 55.

[15] P. J. Bailey, R. A. Coxall, C. M. Dick, S. Fabre, S. Parsons, L. J. Yellowlees, *Chem. Commun.* **2005**, 4563.

[16] G. M. Sheldrick, *SHELXS-97 Program for the Solution of Crystal Structures*; University of Göttingen, Göttingen, Germany, **1990**.

[17] G. M. Sheldrick, *SHELXL-97 Program for the Refinement of Crystal Structures*; University of Göttingen, Göttingen, Germany, **1997**.

[18] G. M. Sheldrick, *SADABS Program for Empirical Absorption Correction of Area Detector Data*; University of Göttingen, Göttingen, Germany, **1996**.

Received: September 26, 2005
Published Online: December 27, 2005

 © 2006 Wiley-VCH Verlag GmbH & Co. KGaA, Weinheim 

DOI: 10.1002/ejic.200500861

# Synthesis, Structural Characterisation and Reactions of Some Vinylgold(I) Phosphane Complexes

**Fabian Mohr,[a] Larry R. Falvello,[a] and Mariano Laguna*[a]**

**Keywords:** Gold / Vinyl ligands / Phosphane ligands

A series of vinylgold(I) complexes [Au(CR=CHR)L] (R = H, Me; L = $PPh_3$, $PPh_2Me$, $PPhMe_2$) were prepared from the reaction of the Grignard reagents [MgBr(CR=CHR)] (R = H, Me) with the gold(I) phosphane complexes [AuCl(L)] (L = $PPh_3$, $PPh_2Me$, $PPhMe_2$) at low temperature. The complexes were characterised by various spectroscopic techniques and, in the case of [Au(CMe=CHMe)($PPh_3$)], by a single-crystal X-ray structure determination. The gold–carbon bonds of these vinylgold(I) complexes are easily cleaved by acids and, in the presence of potassium permanganate, by species containing acidic protons.

(© Wiley-VCH Verlag GmbH & Co. KGaA, 69451 Weinheim, Germany, 2006)

## Introduction

Organometallic gold(I) complexes of the type [AuR(L)], where R is an alkyl, aryl or alkynyl group and L is a neutral donor ligand such as a tertiary phosphane or isocyanide, have been studied in depth over the years and numerous derivatives have been synthesised, many of which have been structurally characterised.[1–4] In marked contrast, analogous vinylgold(I) complexes [Au(CR=$CR_2$)(L)] have received very little attention to date. In the 1970s a group of Russian workers reported the synthesis and some reactions of [Au(CH=$CH_2$)($PPh_3$)] but no X-ray structure was reported and the published experimental procedure seems dubious (see below).[5,6] Around the same time, other groups were studying reactions of [AuMe(L)] complexes with the fluorinated hydrocarbons $CF_3C{\equiv}CCF_3$ and $F_2C{=}CF_2$. Stone and Mitchell first observed that UV irradiation of a benzene solution of $CF_3C{\equiv}CCF_3$ and [AuMe($PPh_3$)] afforded a colourless product, which, based on $^{19}F$ NMR spectroscopic data and elemental analysis, they formulated as the binuclear complex [$Au_2$(μ-$CF_3C{=}CCF_3$)($PPh_3$)$_2$] (**1**).[7,8] The structure was later confirmed by an X-ray diffraction study, which showed that the complex consists of a $CF_3C{=}CCF_3$ molecule bridging two $AuPPh_3$ units.[9] Similar observations were made by Puddephatt and Johnson, who studied the reactions of [AuMe($PPhMe_2$)] and [AuMe($PMe_3$)] with $CF_3C{\equiv}CCF_3$. The initial reaction products, formulated as [$AuMe_2$($CF_3C{\equiv}CCF_3$)L] (L = $PPhMe_2$, $PMe_3$), undergo ethane elimination in acetone to give the binuclear complexes [$Au_2$(μ-$CF_3C{=}CCF_3$)$L_2$] (**1**), which is analogous to those observed earlier by Stone.[10] In the case of L = $PMe_3$, the crystal structure of the complex was obtained and shown to be the mixed-valence gold(I)/gold(III) complex [$Me_3PAu^{III}(Me)_2C(CF_3){=}C(CF_3)Au^{I}PMe_3$] (**2**), which contains a bridging $CF_3C{=}CCF_3$ unit.[11]

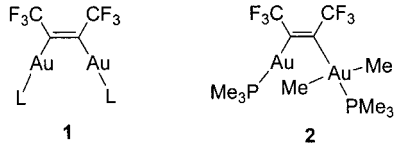


L = $PPh_3$, $PPhMe_2$, $PMe_3$

More recently, Brisdon and co-workers have prepared and structurally characterised the vinylgold(I) complexes [AuCR=$CF_2$($PPh_3$)] (R = Cl, F) by treating [AuCl($PPh_3$)] with the organolithium reagent $CF_2$=CRLi.[12] Puddephatt and Treurnicht reported the synthesis of the very thermally unstable vinylgold(I) complex [Au(CH=$CH_2$)(CNMe)], which could only be characterised by $^1H$ NMR spectroscopy at –20 °C.[13] Other approaches for adding vinyl groups to an $AuPPh_3$ unit have also been investigated. The vinyl(methyl)titanium complex [$Cp^*_2$TiMe(CH=$CH_2$)] reacts with [AuCl($PPh_3$)] to give [$Cp^*_2$TiCl(μ-C=$CH_2$)-$AuPPh_3$] (**3**), the structure of which contains a vinylidene unit bridging the titanium and gold atoms in an unsymmetrical fashion.[14] The vinylgold(I) complexes [Au{C(OR)=$CH_2$}($PPh_3$)M$(CO)_5$] (**4**) (M = Cr, Mo, W; R = Me, Et), in which the vinyl group is π-coordinated ($\eta^2$) to the M$(CO)_5$ fragment, are formed by treating the deprotonated carbene species Li[$(CO)_5$M=C(OR)$CH_2$] with [AuCl($PPh_3$)].[15] Addition of $PPh_3$ displaces the coordinated M$(CO)_5$ unit from **4** and produces the vinylgold(I) complex [Au{C(OR)=$CH_2$}($PPh_3$)].

[a] Departamento de Química Inorgánica, Instituto de Ciencia de Materiales de Aragón, Universidad de Zaragoza–C.S.I.C., 50009 Zaragoza, Spain

 © 2006 Wiley-VCH Verlag GmbH & Co. KGaA, Weinheim 

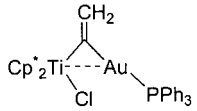


3

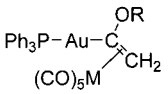


4

M = Cr, Mo, W; R = Me, Et

Our group has been studying the catalytic activity of various gold complexes in the addition of water or MeOH to terminal alkynes.[16] A vinylgold species has been suggested as a possible intermediate in this catalytic process. For this reason we were interested in preparing some vinylgold(I) complexes and studying their structures and reactivity. The results of this investigation are presented here.

## Results and Discussion

Initially, we attempted to reproduce the Russian work to prepare [Au(CH=CH$_2$)(PPh$_3$)] (**5a**). What seemed suspicious to us was the claim that the reaction between the vinyl Grignard reagent and [AuCl(PPh$_3$)] was carried out at +50 °C and that the complex was obtained in 90% yield![5] In our hands, these conditions led to complete decomposition of the reaction mixture to metallic gold. However, when vinylmagnesium bromide was added to an ethereal suspension of [AuCl(PPh$_3$)] at –78 °C the complex [Au(CH=CH$_2$)(PPh$_3$)] (**5a**) could be isolated in 73% yield after work-up. We found that when a large excess of Grignard reagent was used in the reaction and the subsequent hydrolysis was carried out with large volumes of water or aqueous NH$_4$Cl, significant decomposition to metallic gold occurred. This decomposition can be avoided by using only a small excess of Grignard reagent (ca. 10%), and simply exposing the reaction mixture to air was sufficient to hydrolyse the excess Grignard reagent. Following this procedure the vinylgold(I) complexes [Au(CR=CHR)(L)] (R = H, **5a**: L = PPh$_3$, **5b**: L = PPh$_2$Me, **5c**: L = PPhMe$_2$; R = Me, **6a**: L = PPh$_3$, **6b**: L = PPh$_2$Me, **6c**: L = PPhMe$_2$ ) were prepared in good to moderate yields (Scheme 1).

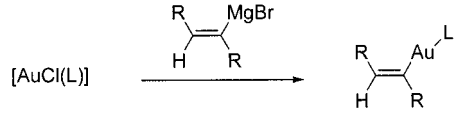


R = H
**5a**: L = PPh$_3$
**5b**: L = PPh$_2$Me
**5c**: L = PPhMe$_2$

R = Me
**6a**: L = PPh$_3$
**6b**: L = PPh$_2$Me
**6c**: L = PPhMe$_2$

Scheme 1.

All the complexes prepared are colourless, crystalline solids (except for **5c** and **6c**, which were isolated as pale-brown oils) that are air- and thermally stable in the solid state; in solution, however, decomposition occurs slowly (2–3 days) for the PPh$_3$ and PPh$_2$Me complexes, whilst the PPhMe$_2$ derivatives are stable in solution for less than 12 h. The $^1$H NMR spectra of the vinyl complexes **5a**–**5c** consists of three doublets of doublets displaying *trans,cis* and geminal coupling constants of 20, 14 and 5 Hz, respectively. The $^1$H NMR spectra of the dimethyl analogues **6a**–**6c** display a broad singlet at $\delta \approx 6.4$ ppm due to the vinylic proton. Furthermore, the two methyl groups attached to the vinyl group resonate as a broad singlet (coupling unresolved) and doublet of quartets for the α- and β-Me groups, respectively; the coupling constants confirm that the methyl groups are *trans* to each other. In the $^{13}$C NMR spectra of all six complexes we observed, in addition to the phenyl and Me signals, a singlet at $\delta \approx 129$ ppm due to the β-C of the vinyl group. The resonance of the α-C of the vinyl group attached to the gold atom could not be observed, presumably due to the large quadrupole moment of the proximal gold atom. As expected, the $^{31}$P{$^1$H} NMR spectra of all six complexes show singlet resonances whose chemical shift varies depending on the phosphane ligands. The FAB+ mass spectra of most of the complexes show weak molecular-ion peaks as well as peaks due to loss of the vinyl group and formation of higher mass ions [Au(phosphane)$_2$]$^+$; the latter are frequently observed in FAB mass spectra of gold(I) phosphane complexes.[17] The vinylgold(I) structure was confirmed by a partial X-ray diffraction study of **6a**. Due to the limited stability of the complex in solution, the crystals obtained were of poor quality and, more importantly, signs of twinning were apparent. However, the data were of sufficient quality to establish the connectivity and to derive geometric parameters of middling accuracy but wholly consistent with all other experimental data reported here and elsewhere for this and analogous compounds. A displacement ellipsoid plot of one molecule is shown in Figure 1.[18]

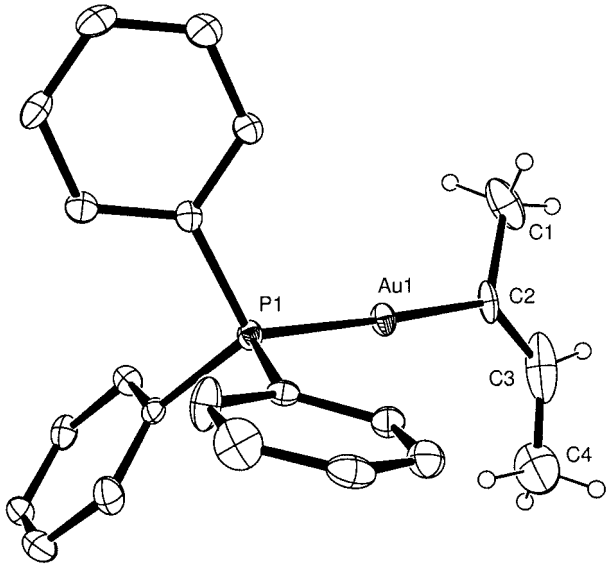


Figure 1. ORTEP view of one of the independent molecules of **6a**. Ellipsoids show 30% probability levels; phenyl hydrogen atoms have been omitted for clarity.

 © 2006 Wiley-VCH Verlag GmbH & Co. KGaA, Weinheim 

The structure was refined in the space group *C*2/*c* with two independent molecules in the asymmetric unit. Some bond lengths and angles differ slightly between the two molecules; but we do not wish to attribute chemical significance to this observation given that the differences are consistent with the inaccuracies evident in the diffraction data (vide infra) [$wR_2$ = 0.1482, $R_1$ = 0.0822, C–C bond precision 0.022 Å]. The structure of **6a** consists of a dimethylvinyl moiety (with the Me groups in a *trans* configuration) and a $PPh_3$ unit linearly [177.9(3)° and 175.4(4)°] coordinated to the gold(I) centre. The Au–P [2.3092(19) and 2.291(2) Å] and Au–C [2.004(7) and 2.053(10) Å] distances are similar to those in [Au(CF=$CF_2$)($PPh_3$)] [Au–P = 2.272(3) and Au–C = 2.028(9) Å] and [Au(CCl=$CF_2$)($PPh_3$)] [Au–P = 2.266(2) and Au–C = 2.026(10) Å].[12] The vinyl C=C distances [1.322(18) and 1.327(17) Å] are slightly longer than those in [Au(CF=$CF_2$)($PPh_3$)] [C=C = 1.297(14) Å][12] but shorter than that in [AuC(OMe)=$CH_2$($PPh_3$)Cr($CO)_5$] [C=C = 1.345(11) Å].[15]

### Reactions of Vinylgold(I) Complexes

The Russian workers studied the reactions of [Au(CH=$CH_2$)($PPh_3$)] (**5a**) with HCl, $HgCl_2$ $Br_2$, $(SCN)_2$, benzoic acid and $KMnO_4$.[6] In the first five cases the gold–carbon bond is cleaved to give [AuX($PPh_3$)] (X = Cl, Br, SCN, $O_2$CPh) as the gold-containing product. However, in the case of $KMnO_4$, neither metal–carbon bond cleavage nor oxidation of the carbon–carbon double bond occurs; instead, the acetonylgold(I) phosphane complex [Au{$CH_2C(O)CH_3$}($PPh_3$)] is formed in high yield.[6,19] The X-ray crystal structure of this complex was reported later, but neither the method of preparation nor source of the sample was mentioned.[20] In order to examine the generality of these reactions we studied the reaction of hydrochloric acid and $KMnO_4$ with the new vinylgold(I) complex **6a**. Treatment of an acetone solution of **6a** with a solution of HCl or DCl in $D_2O$ (the deuterated acid was more convenient to study by $^1$H NMR spectroscopy) results in electrophilic cleavage of the gold–carbon bond and formation of [AuCl($PPh_3$)] and *trans*-MeDC=CMeH, as was evident from the $^1$H and $^{31}$P NMR spectra; the chemical shift observed in the $^{31}$P NMR spectrum is identical to that of an authentic sample of [AuCl($PPh_3$)]. Treatment of an acetone solution of complex **6a** at 0 °C with $KMnO_4$ resulted in formation of a brown precipitate ($MnO_2$). After about 30 min reaction time a pale-yellow solid could be isolated from the mixture after filtration and removal of the solvent. On the basis of $^1$H and $^{31}$P{$^1$H} NMR spectroscopic data, this product was identified as the acetonylgold(I) complex [Au{$CH_2C(O)CH_3$}($PPh_3$)], identical to that reported by Nesmeyanov.[19] We were interested in investigating this reaction in more detail in order to gain some understanding of the mechanism and the exact role of the permanganate. To test whether species containing acidic protons, such as acetone or phenylacetylene, can react with **6a** in the absence of permanganate we treated $CDCl_3$ solutions of complex **6a** with an equivalent amount of acetone or phenylacetylene and examined the $^1$H and $^{31}$P NMR spectra over time. Even after a period of 48 h there was no evidence that any reaction had occurred − only signals from the starting complex were observed in the NMR spectra − thus confirming that permanganate is indeed required for this reaction. If a solution of $KMnO_4$ in $CD_3CN$ is then added to the NNR tubes containing complex **6a** and acetone or phenylacetylene a brown precipitate is observed after a few minutes and after about 30 min the main species in solution, determined by NMR spectroscopy, are [Au{$CH_2C(O)CH_3$}($PPh_3$)] and [Au(C≡CPh)($PPh_3$)], respectively. These results suggest that the permanganate reacts initially with the vinylgold(I) complex, probably oxidising the carbon–carbon double bond, via an intermediate gold(I)/manganese(V) cyclic ester **7** (Scheme 2). It is known that the oxidation of alkenes with permanganate proceeds via such cyclic $Mn^V$ ester intermediates, which undergo decomposition reactions to give organic products and $MnO_2$.[21] Recently, this [3+2] mechanism via cyclic $Mn^V$ esters has been confirmed by DFT calculations and kinetic isotope effect data.[22] In our case, the evidence presented above suggests that the presumed intermediate **7** causes deprotonation of acetone and phenylacetylene, thus producing the acetonyl- and alkynylgold(I) complexes as well as the diol, accompanied, perhaps even driven, by precipitation of insoluble $MnO_2$. We tried to identify the organic oxidation products by both $^1$H NMR and GC/MS spectroscopy, but no conclusive results were obtained. In an attempt to observe the intermediate species **7** we treated a $CDCl_3$ solution of **6a** with a $CD_3CN$ solution of $KMnO_4$ and observed immediate formation of a brown precipitate. The $^{31}$P NMR spectrum of the supernatant solution shows a singlet resonance at $\delta$ = 44.50 ppm, slightly shifted relative to that of the starting complex ($\delta$ = 44.77 ppm), which may be due to the intermediate. However, the presence of a multiplet at $\delta$ = 6.4 ppm in the $^1$H NMR spectrum, due to the vinylic proton, suggests that the C=C double bond in the vinyl ligand is still intact; in fact, the overall spectrum is almost identical to that of **6a**. When excess PhC≡CH is added to this solution the $^{31}$P NMR spectrum shows, in addition to the original peak at $\delta$ = 44.50 ppm, a new signal at $\delta$ = 42.15 ppm. The latter resonance is consistent with the presence of [Au(C≡CPh)($PPh_3$)], which was confirmed by comparison of chemical shifts of an authentic sample. Over a period of about 10 h the intensity of the signal due to [Au(C≡CPh)($PPh_3$)] increases, whilst that of the starting complex **6a** decreases. After about 24 h the major species in solution is [Au(C≡CPh)($PPh_3$)]. If the same experiment is carried out with acetone similar observations are made, namely the intensity of the $^{31}$P NMR signal due to the acetonylgold(I) complex [Au{$CH_2C(O)CH_3$}($PPh_3$)] increases over time, while that due to **6a** decreases. These results show that $KMnO_4$ is required for the vinylgold(I) complex to react with species containing acidic protons and, although we failed to detect any intermediate, the simple fact that addition of $KMnO_4$ to a solution of **6a** causes precipitation of

 © 2006 Wiley-VCH Verlag GmbH & Co. KGaA, Weinheim 

$MnO_2$ suggests that some reaction yielding an undetectable intermediate must be taking place. More detailed investigations are necessary to fully understand this process. Other oxidants including dichromate and $H_2O_2$ either do not react at all or, in the case of peroxide, oxidation of the phosphane occurs to give $Ph_3P{=}O$ and decomposition of the starting complex to gold metal.

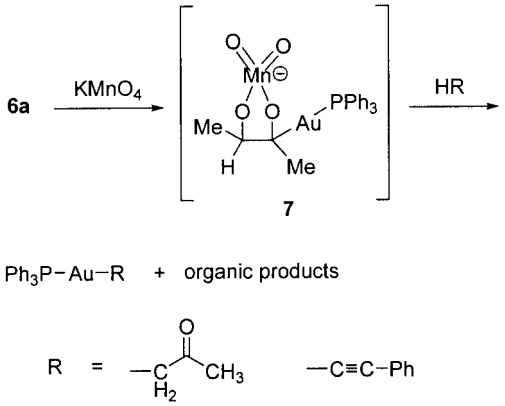


Scheme 2.

In summary, we have shown that vinylgold(I) complexes can be prepared in good yields from the reaction of a vinyl Grignard reagent with $[AuCl(PPh_3)]$ at low temperatures. The gold–vinyl–C bond is easily cleaved by acids or, in the presence of $KMnO_4$, by species containing an acidic proton such as acetone and phenylacetylene. Further work is currently in progress to further elucidate the mechanism of this reaction and to study other reactions of vinylgold(I) compounds.

## Experimental Section

**General:** All reactions were performed under an atmosphere of dry argon using Schlenk techniques. Solvents were dried by standard methods and freshly distilled under argon before use. $^1H$, $^{13}C$ and $^{31}P\{^1H\}$ NMR spectra were recorded with a 400 MHz Bruker Avance spectrometer. Chemical shifts are quoted relative to external TMS ($^1H$ and $^{13}C$) or 85% $H_3PO_4$ ($^{31}P$). FAB mass spectra were measured on a VG Autospec spectrometer in positive ion mode using NBA as matrix. Elemental analyses were obtained in-house using a Perkin–Elmer 240B microanalyser. The chlorogold(I) precursor complexes were prepared by treating equivalent amounts of [AuCl(tht)] with the tertiary phosphanes in $CH_2Cl_2$. The vinyl Grignard reagents were obtained commercially (Aldrich).

**[Au(CH=CH$_2$)(PPh$_3$)] (5a):** A suspension of $[AuCl(PPh_3)]$ (0.402 g, 0.929 mmol) in dry $Et_2O$ (10 mL) was cooled to –78 °C and treated with a solution of vinylmagnesium bromide (1.0 mL 1 M solution in THF, 1.0 mmol). The mixture was warmed to room temperature over a period of 4 h. After this time the reaction vessel was exposed to air for about 10 min. to hydrolyze any unreacted Grignard reagent. The mixture was then filtered through anhydrous $MgSO_4$ and the filtrate evaporated to dryness in vacuo to afford 0.288 g (73%) of colourless product. $^1H$ NMR (400 MHz, $CDCl_3$, 25 °C): $\delta$ = 7.42–7.61 (m, 15 H, Ph), 7.20 (dd, $J_{trans\text{-}H,H}$ = 20, $J_{cis\text{-}H,H}$ = 14 Hz, 1 H, AuC*H*), 6.04 (dd, $J_{trans\text{-}H,H}$ = 20, $J_{gem\text{-}H,H}$ = 5 Hz, 1 H, =C$H_2$), 5.53 (dd, $J_{cis\text{-}H,H}$ = 14, $J_{gem\text{-}H,H}$ = 5 Hz, 1 H, =C$H_2$) ppm. $^{13}C$ NMR (100 MHz, $CDCl_3$, 25 °C): $\delta$ = 134.3 (d, $^3J_{P,C}$ = 13 Hz, *meta*-Ph), 131.4 (s, AuC=*C*), 131.2 (s, *para*-Ph), 129.0 (d, $^2J_{P,C}$ = 10 Hz, *ortho*-Ph) ppm. $^{31}P\{^1H\}$ NMR (162 MHz, $CDCl_3$, 25 °C): $\delta$ = 44.40 ppm ppm. FAB MS: *m*/*z* (%) = = 486 (5) $[M]^+$, 459 (95) $[Au(PPh_3)]^+$, 721 (100) $[Au(PPh_3)_2]^+$. $C_{20}H_{18}AuP$ (486.3): calcd. C 49.40, H 3.73; found C 49.30, H 3.50.

Compounds **5b** and **5c** were prepared in a similar manner.

**[Au(CH=CH$_2$)(PMePh$_2$)] (5b):** Colourless solid (0.252 g, 64% yield). $^1H$ NMR (400 MHz, $CDCl_3$, 25 °C): $\delta$ = 7.60–7.70 (m, 4 H, Ph), 7.41–7.48 (m, 6 H, Ph), 7.14 (dd, $J_{trans\text{-}H,H}$ = 21, $J_{cis\text{-}H,H}$ = 14 Hz, 1 H, AuC*H*), 6.00 (dd, $J_{cis\text{-}H,H}$ = 14, $J_{gem\text{-}H,H}$ = 5 Hz, 1 H, =C$H_2$), 5.48 (dd, $J_{trans\text{-}H,H}$ = 21, $J_{gem\text{-}H,H}$ = 5 Hz, 1 H, =C$H_2$), 2.01 (d, $^2J_{P,H}$ = 8 Hz, 3 H, $PCH_3$) ppm. $^{13}C$ NMR (100 MHz, $CDCl_3$, 25 °C): $\delta$ = 132.8 (d, $^3J_{P,C}$ = 13 Hz, *meta*-Ph), 132.7 (d, $^1J_{P,C}$ = 50 Hz, *ipso*-Ph), 131.5 (s, AuC=*C*), 131.0 (s, *para*-Ph), 129.0 (d, $^2J_{P,C}$ = 10 Hz, *ortho*-Ph), 13.9 (d, $^1J_{P,C}$ = 32 Hz, P*C*H$_3$) ppm. $^{31}P\{^1H\}$ NMR (162 MHz, $CDCl_3$, 25 °C): $\delta$ = 30.10 ppm ppm. FAB MS: *m*/*z* (%) = = 379 (60) $[Au(PMePh_2)]^+$, 597 (100) $[Au(PMePh_2)_2]^+$ 821 (35) [M + $Au(PPh_2Me)]^+$. $C_{15}H_{16}AuP$ (424.2): calcd. C 42.47, H 3.80; found C 42.84, H 3.71.

**[Au(CH=CH$_2$)(PPhMe$_2$)] (5c):** Pale-brown oil (0.108 g, 55% yield). $^1H$ NMR (400 MHz, $CDCl_3$, 25 °C): $\delta$ = 7.70–7.78 (m, 2 H, Ph), 7.45–7.50 (m, 3 H, Ph), 7.10 (dd, $J_{trans\text{-}H,H}$ = 21, $J_{cis\text{-}H,H}$ = 14 Hz, 1 H, AuC*H*), 5.98 (dd, $J_{cis\text{-}H,H}$ = 12, $J_{gem\text{-}H,H}$ = 5 Hz, 1 H, =C$H_2$), 5.46 (dd, $J_{trans\text{-}H,H}$ = 21, $J_{gem\text{-}H,H}$ = 5 Hz, 1 H, =C$H_2$), 1.73 (br. s, 6 H, $PCH_3$) ppm. $^{13}C$ NMR (100 MHz, $CDCl_3$, 25 °C): $\delta$ = 133.8 (d, $^1J_{P,C}$ = 49 Hz, *ipso*-Ph), 131.77 (d, $^3J_{P,C}$ = 13 Hz, *meta*-Ph), 131.5 (s, AuC=*C*), 131.1 (s, *para*-Ph), 128.9 (d, $^2J_{P,C}$ = 10 Hz, *ortho*-Ph), 15.34 (d, $^1J_{P,C}$ = 31 Hz, P*C*H$_3$) ppm. $^{31}P\{^1H\}$ NMR (162 MHz, $CDCl_3$, 25 °C): $\delta$ = 18.65 ppm. FAB MS: *m*/*z* (%) = 335 (62) $[Au(PPhMe_2)]^+$, 473 (100) $[Au(PPhMe_2)_2]^+$.

The following complexes were prepared as described above using 1-methyl-1-propenylmagnesium bromide.

**[Au(CMe=CHMe)(PPh$_3$)] (6a):** Colourless, crystalline solid (0.206 g, 63% yield). $^1H$ NMR (400 MHz, $CDCl_3$, 25 °C): $\delta$ = 7.51–7.60 (m, 6 H, Ph), 7.40–7.51 (m, 9 H, Ph), 6.45 (m, 1 H, =C*H*Me), 2.06 (br. s, 3 H, AuC*Me*), 1.95 (dq, $^3J_{H,H}$ = 6, $^5J_{H,H}$ = 1 Hz, 3 H, =CH*Me*) ppm. $^{13}C$ NMR (100 MHz, $CDCl_3$, 25 °C): $\delta$ = 134.3 (d, $^3J_{P,C}$ = 13 Hz, *meta*-Ph), 131.4 (d, $^1J_{P,C}$ = 48 Hz, *ipso*-Ph), 130.8 (s, *para*-Ph), 129.2 (AuC=*C*), 128.9 (d, $^2J_{P,C}$ = 10 Hz, *ortho*-Ph), 30.4 (s, AuC*Me*), 20.9 (s, CH*Me*) ppm. $^{31}P\{^1H\}$ NMR (162 MHz, $CDCl_3$, 25 °C): $\delta$ = 44.77 ppm. FAB MS: *m*/*z* (%) = 514 (15) $[M]^+$, 459 (100) $[Au(PPh_3)]^+$, 721 (65) $[Au(PPh_3)_2]^+$. $C_{22}H_{22}AuP$ (514.4): calcd. C 51.37, H 4.31; found C 51.48, H 4.12. X-ray quality crystals were selected from the bulk sample.

**[Au(CMe=CHMe)(PPh$_2$Me)] (6b):** Colourless solid (0.118 g, 73% yield). $^1H$ NMR (400 MHz, $CDCl_3$, 25 °C): $\delta$ = 7.61–7.71 (m, 4 H, Ph), 7.39–7.48 (m, 6 H, Ph), 6.47 (m, 1 H, =C*H*Me), 2.06 (br. s, 3 H, AuC*Me*), 2.01 (d, $^2J_{P,H}$ = 6 Hz, 3 H, P*Me*) 1.96 (dq, $^3J_{H,H}$ = 6, $^5J_{H,H}$ = 1 Hz, 3 H, =CH*Me*) ppm. $^{13}C$ NMR (100 MHz, $CDCl_3$, 25 °C): $\delta$ = 133.2 (d, $^1J_{P,C}$ = 47 Hz, *ipso*-Ph), 132.7 (d, $^3J_{P,C}$ = 13 Hz, *meta*-Ph), 130.8 (s, *para*-Ph), 129.3 (s, AuC=*C*), 128.9 (d, $^2J_{P,C}$ = 10 Hz, *ortho*-Ph), 30.3 (s, AuC*Me*), 20.9 (s, CH*Me*), 13.7 (d, $^1J_{P,C}$ = 39 Hz, P*Me*) ppm. $^{31}P\{^1H\}$ NMR (162 MHz, $CDCl_3$, 25 °C): $\delta$ = 30.96 ppm. FAB MS: *m*/*z* (%) = 452 (10) $[M]^+$, 397 (100) $[Au(PPh_2Me)]^+$, 597 (55) $[Au(PPh_2Me)_2]^+$. $C_{17}H_{20}AuP$ (452.3): calcd. C 45.14, H 4.46; found C 45.28, H 4.32.

**[Au(CMe=CHMe)(PPhMe$_2$)] (6c):** Pale-brown oil (0.170 g, 40% yield). $^1H$ NMR (400 MHz, $CDCl_3$, 25 °C): $\delta$ = 7.68–7.80 (m, 2 H, Ph), 7.41–7.50 (m, 3 H, Ph), 6.45 (m, 1 H, =C*H*Me), 2.01 (br. s, 3 H, AuC*Me*), 1.92 (dq, $^3J_{H,H}$ = 6, $^5J_{H,H}$ = 1 Hz, 3 H, =CH*Me*),

 © 2006 Wiley-VCH Verlag GmbH & Co. KGaA, Weinheim 

1.70 (d, $^2J_{P,H}$ = 6 Hz, 6 H, P*Me*) ppm. $^{13}$C NMR (100 MHz, $CDCl_3$, 25 °C): $\delta$ = 131.8 (d, $^3J_{P,C}$ = 13 Hz, *meta*-Ph), 131.1 (s, *para*-Ph), 129.4 (s, AuC=*C*), 129.0 (d, $^2J_{P,C}$ = 11 Hz, *ortho*-Ph), 30.4 (s, AuC*Me*), 20.9 (s, CH*Me*), 15.3 (d, $^1J_{P,C}$ = 32 Hz, P*Me*) ppm. $^{31}$P{$^1$H} NMR (162 MHz, $CDCl_3$, 25 °C): $\delta$ = 19.96 ppm. FAB MS: *m/z* (%) = 390 (11) $[M]^+$, 335 (100) $[Au(PPhMe_2)]^+$, 473 (90) $[Au(PPhMe_2)_2]^+$.

**Reaction of 6a with Acid:** A few drops of an approx. 1 M solution of DCl in $D_2O$ was added to a sample of **6a** dissolved in [$D_6$] acetone in an NMR tube. $^1$H and $^{31}$P NMR spectra were recorded after about 10 min. $^1$H NMR (400 MHz, [$D_6$]acetone, 25 °C): $\delta$ = 7.53–7.66 (m, 15 H, Ph from $Ph_3PAuCl$), 5.35 (br. s, 1 H, C*H*Me), 1.54 (q, $^3J_{H,D}$ = 1 Hz, 3 H, CD*Me*), 1.53 (s, 3 H, CH*Me*) ppm. $^{31}$P{$^1$H} NMR (162 MHz, [$D_6$]acetone, 25 °C): $\delta$ = 33.97 ppm. This $^{31}$P{$^1$H} NMR chemical shift is identical to that of an authentic sample of [$AuCl(PPh_3)$].

**Reaction of 6a with $KMnO_4$:** A sample of **6a** was dissolved in acetone and treated with an acetone solution of $KMnO_4$ at about 0 °C. After around 10 min a brown precipitate ($MnO_2$) was observed. The mixture was filtered and the filtrate was evaporated to dryness. $^1$H and $^{31}$P NMR spectra of the pale-yellow solid were recorded. $^1$H NMR (400 MHz, $CDCl_3$, 25 °C): $\delta$ = 7.40–7.59 (m, 15 H, Ph), 2.71 (d, $^3J_{H,P}$ = 1 1 Hz, 2 H, AuC$H_2$), 2.22 (s, 3 H, C*Me*) ppm. $^{31}$P{$^1$H} NMR (162 MHz, $CDCl_3$, 25 °C): $\delta$ = 42.20 ppm. In addition, there are trace amounts of starting complex **6a** and a further unidentified species present ($\delta_P$ = 44.7 and 29.2 ppm, respectively).

**NMR Reactions of 6a with $KMnO_4$ and Acetone or Phenylacetylene:** A solution of $KMnO_4$ in $CD_3CN$ was added to a $CDCl_3$ solution of **6a**. A brown solid ($MnO_2$) precipitated immediately. Acetone or phenylacetylene (4 μL) was then added to the NMR tube and $^{31}$P and $^1$H NMR spectra were recorded before and after the addition.

**Reaction of 6a with $H_2O_2$:** A sample of **6a** dissolved in acetone was treated with 30% $H_2O_2$. After stirring for about 30 min a gold mirror had formed on the inside of the flask. The solvents were removed in vacuo and the residue was analysed by $^{31}$P spectroscopy. $^{31}$P{$^1$H} NMR (162 MHz, $CDCl_3$, 25 °C): $\delta$ = 29.69 ppm.

**X-ray Crystallography of Complex 6a:** Data were gathered twice, from two different crystals and using two different CCD-based diffractometers, with similar results in both cases. The results reported here were derived from data gathered using a four-circle diffractometer (Xcalibur2 with a Sapphire3 detector and sealed tube Mo Enhance source).[23] A crystal of dimensions 0.17 × 0.16 × 0.05 mm, and with a slight yellow tint as viewed under an optical microscope, was mounted with epoxy at the end of a quartz fibre and kept at 123 K for the measurements. A preliminary unit-cell determination yielded the same results that had been determined earlier using a Bruker Apex diffractometer, namely a monoclinic cell with one unusually long axis (ca. 45.8 Å). The cell dimensions were verified on the four-circle diffractometer using normal-beam axial photography. Because of the long axis, for the present data the crystal-to-detector distance was set to 90 mm and the data collection strategy was optimised accordingly. The faces of the crystal were indexed and absorption corrections were calculated numerically and applied to the integrated data. The structure was solved by direct methods and refined against $F_o^2$ using full-matrix least-squares.[24] Non-hydrogen atoms were refined anisotropically. Non-methyl hydrogen atoms were placed at calculated positions and refined as riders. Methyl hydrogen atoms were located successfully in local slant-Fourier calculations and refined as riding atoms but with a variable torsion angle about the local C–C bond. The refinement was stable and convergent, but the results showed effects that are normally considered characteristic of twinning, i.e. high residuals, some 20 difference peaks above 1 e Å$^{-3}$, and unusual analysis of variance with the worst-fit reflections largely having $F_o^2$ greater than $F_c^2$. Several twin models were tested, each of which produced some improvement in the crystallographic indicators but did not influence the chemical implications of the results. Concurrent twin models were also tested, with similar results. The results reported here are those obtained with no twin model; more information on other models can be obtained from the authors. Commonly employed structure validation tools (PLATON[25]) did not reveal the presence of missed crystallographic symmetry elements. Visual examination of the structural results suggests pseudo-translational symmetry, but at the same time reveals that the two independent molecules have very different environments and participate in quite distinct fashions in the crystal packing. One of the phenyl groups (C50–C55) shows prolate displacement ellipsoids and a short average C–C distance. While these are normally taken to be definitive symptoms of libration, we cannot rule out an association between these effects and the presence of a putative minor twin component.


[1] R. J. Puddephatt, *The Chemistry of Gold*, Elsevier Scientific Publishing Co., New York, **1978**.
[2] R. Usón, A. Laguna, *Coord. Chem. Rev.* **1986**, *70*, 1–50.
[3] H. Schmidbaur, A. Grohmann, M. E. Olmos, in *Gold Progress in Chemistry, Biochemistry and Technology* (Ed.: H. Schmidbaur), John Wiley & Sons, Chichester, **1999**.
[4] E. J. Fernández, A. Laguna, M. E. Olmos, *Adv. Organomet. Chem.* **2005**, *52*, 77–141.
[5] A. N. Nesmeyanov, E. G. Perevalova, V. V. Krivykh, A. N. Kosina, K. I. Grandberg, E. I. Smyslova, *Izv. Akad. Nauk. SSSR, Ser. Khim.* **1972**, 653–654.
[6] K. I. Grandberg, E. I. Smyslova, A. N. Kosina, *Izv. Akad. Nauk. SSSR, Ser. Khim.* **1973**, 2787–2789.
[7] C. M. Mitchell, F. G. A. Stone, *J. Chem. Soc., Chem. Commun.* **1970**, 1263–1264.
[8] C. M. Mitchell, F. G. A. Stone, *J. Chem. Soc., Dalton Trans.* **1972**, 102–107.
[9] J. C. Gilmore, P. Woodward, *J. Chem. Soc., Chem. Commun.* **1971**, 1233–1234.
[10] A. Johnson, R. J. Puddephatt, J. M. Quirk, *J. Chem. Soc., Chem. Commun.* **1972**, 938–939.
[11] J. A. J. Jarvis, A. Johnson, R. J. Puddephatt, *J. Chem. Soc., Chem. Commun.* **1973**, 373–374.
[12] N. A. Barnes, A. K. Brisdon, W. I. Cross, J. G. Fay, J. A. Greenall, R. G. Pritchard, J. Sherrington, *J. Organomet. Chem.* **2000**, *616*, 96–105.
[13] R. J. Puddephatt, I. Treurnicht, *J. Organomet. Chem.* **1987**, *319*, 129–137.
[14] R. Backhaus, J. Oster, R. Wang, U. Böhme, *Organometallics* **1998**, *17*, 2215–2221.
[15] H. G. Raubenheimer, M. W. Esterhuysen, A. Timoshkin, Y. Chen, G. Frenking, *Organometallics* **2002**, *21*, 3173–3181.
[16] R. Casado, M. Contel, M. Laguna, P. Romero, S. Sanz, *J. Am. Chem. Soc.* **2003**, *125*, 11925–11935.
[17] M. I. Bruce, M. J. Liddell, *J. Organomet. Chem.* **1992**, *427*, 263–274.
[18] $C_{22}H_{22}AuP$, monoclinic, *C2/c*, *a* = 15.4392(6), *b* = 10.8911(5), *c* = 45.7928(18) Å, $\beta$ = 98.404(4)°, *V* = 7617.4(5) Å$^3$, *Z* = 16, $\rho$ = 1.794 g cm$^{-3}$, $\mu$ = 7.809 mm$^{-1}$, 31300 data measured, 8639 unique, 98.6% completeness, $R_{int}$ = 0.0440, $R\sigma$ = 0.0653, $wR_2$ = 0.1482 (437 parameters), $R_1$ = 0.0822 [6532 data with $I > 2\sigma(I)$], quality-of-fit = 1.232. CCDC-286877 contains the supplementary crystallographic data for this paper. These data can be obtained free of charge from The Cambridge Crystallographic Data Centre via www.ccdc.cam.ac.uk/data_request/cif.
[19] A. N. Nesmeyanov, K. I. Grandberg, E. I. Smyslova, E. G. Perevalova, *Izv. Akad. Nauk. SSSR, Ser. Khim.* **1972**, 2375.


 © 2006 Wiley-VCH Verlag GmbH & Co. KGaA, Weinheim 

[20] L. G. Kuzmina, *Koord. Khim. Koordinatsionnaya Khimiya* **1994**, *20*, 540–546.
[21] D. G. Lee, J. R. Brownridge, *J. Am. Chem. Soc.* **1974**, *96*, 5517–5523.
[22] K. N. Houk, T. Strassner, *J. Org. Chem.* **1999**, *64*, 800–802.
[23] *CrysAlis CCD and CrysAlis RED: V 1.171.27p8*, Oxford Diffraction, Ltd. **1995**–**2005**.
[24] G. M. Sheldrick, *SHELXTL-NT 6.1*, University of Göttingen, **1998**.
[25] A. L. Spek, *Acta Crystallogr., Sect. A* **1990**, *46*, C34.
Received: September 20, 2005
Published Online: December 20, 2005

 © 2006 Wiley-VCH Verlag GmbH & Co. KGaA, Weinheim 

DOI: 10.1002/ejic.200500932

# Synthesis, Characterisation and Biological Activity of Chiral Platinum(II) Complexes

David Jaramillo,[a] Damian P. Buck,[b] J. Grant Collins,[b] Ronald R. Fenton,[c] Frank H. Stootman,[a] Nial J. Wheate,[a] and Janice R. Aldrich-Wright*[a]

**Keywords:** Platinum / Chiral / Intercalator / Cancer / L1210 / Induced circular dichroism

Four platinum(II) complexes of 1,10-phenanthroline (phen) and 3,4,7,8-tetramethyl-1,10-phenanthroline (3,4,7,8-$Me_4$phen), with the chiral ancillary ligands (1*R*,3*S*) and (1*S*,3*R*)-1,3-diamino-1,2,2-trimethylcyclopentane (*R*,*S*-tmcp and *S*,*R*-tmcp, respectively) have been synthesised and their biological activity quantified using an in vitro cytotoxicity assay against the L1210 murine leukaemia cell line. [Pt(*R*,*S*-tmcp)(3,4,7,8-$Me_4$phen)]$Cl_2$ and [Pt(*S*,*R*-tmcp)(3,4,7,8-$Me_4$-phen)]$Cl_2$ showed an increase in biological activity over their non-methylated complexes, [Pt(*R*,*S*-tmcp)(phen)]$Cl_2$ and [Pt(*S*,*R*-tmcp)(phen)]$Cl_2$. Some chiral discrimination was observed in the in vitro cytotoxicity experiments with the complexes having (*S*,*R*) configuration showing higher biological activity in L1210 cells. Titrations of the metal complexes into ct-DNA and observation of the changes induced in the CD spectra were used to determine the binding constants. The binding of these metal complexes to the hexamer d(GTCGAC)$_2$ was studied using two-dimensional $^1$H NMR spectroscopy. The addition of metal complexes to the hexamer produced upfield shifts of the metal complex of selected resonances, characteristic of intercalation for [Pt(tmcp)-(phen)]$Cl_2$, whereas the [Pt(tmcp)(3,4,7,8-$Me_4$phen)]$Cl_2$ complexes only partially intercalate and in a "side-on" fashion. Through the observation of NOE cross-peaks, two-dimensional NMR experiments provided some insight into the site and groove preferences of these complexes when binding to DNA. Here, we report the biological activity of platinum(II) complexes containing an intercalator and a chiral diamine, which influences the degree to which the complexes can interact with DNA.
(© Wiley-VCH Verlag GmbH & Co. KGaA, 69451 Weinheim, Germany, 2006)

## Introduction

The interaction of positively charged metallointercalators with the base-pair stack of DNA has been an area of interest for some time.[1–7] Square-planar platinum(II) complexes derived from heterocyclic ligands have produced greater in vitro cytotoxicity against human ovarian cancer cell lines, than some current therapeutic agents.[8] These intercalating complexes introduce reversible binding, a mode that is different from that of cisplatin. Compounds like [Pt(en)(phen)]$Cl_2$, which bind reversibly and non-covalently, have also been widely studied using calorimetric studies and thermodynamic calculations,[9] circular dichroism (CD) polarimetry,[10] electronic absorption studies using nucleotides[11–12] and two-dimensional $^1$H nuclear magnetic resonance (NMR) spectroscopy[13] to further understand their interaction with DNA.

We recently published[14] our investigation of a series of platinum(II) complexes, of the type [Pt(en)(phen)]$Cl_2$ containing methylated derivatives of the ligand 1,10-phenanthroline [where en = 1,2-diaminoethane, phen = 1,10-phenanthroline and phen is substituted with 4-methyl-1,10-phenanthroline (4-Mephen), 5-methyl-1,10-phenanthroline (5-Mephen), 4,7-dimethyl-1,10-phenanthroline (4,7-$Me_2$phen), 5,6-dimethyl-1,10-phenanthroline (5,6-$Me_2$phen) or 3,4,7,8-tetramethyl-1,10-phenanthroline (3,4,7,8-$Me_4$phen)] and determined that the position and number of methyl groups on the 1,10-phenanthroline structure influences biological activity. Viscometry, CD and NMR studies indicated that all the platinum(II) complexes intercalate into the DNA base pair stack.[14]

A dependence of the mutagenic and anticancer activity in covalent platinum(II) complexes upon the configuration of the ancillary ligand has been previously reported.[14,15] Cytotoxic activity of a series of chiral *cis*-diaminodichloroplatinum(II) complexes, in various cell lines, has shown an enantioselective trend.[16]

[Pt(en)(phen)]$Cl_2$ proved to be the most efficient intercalator of the platinum(II) complexes investigated, whereas [Pt(en)(3,4,7,8-$Me_4$phen)]$Cl_2$ was one of the least efficient.

[a] School of Science, Food and Horticulture, College of Science, Technology and Environment, University of Western Sydney, Penrith South, NSW, 1797, Australia
Fax: +61-246203025
E-mail: j.aldrich-wright@uws.edu.au
[b] School of Physical, Environmental and Mathematical Sciences, University College, University of New South Wales, Australian Defence Force Academy, Canberra, 2600, Australia
[c] School of Chemistry, Sydney University, Sydney, 2006, Australia
Supporting information for this article is available on the WWW under http://www.eurjic.org or from the author.

 © 2006 Wiley-VCH Verlag GmbH & Co. KGaA, Weinheim 

The wide range of biological activity seen for that series of platinum(II) complexes of 1,10-phenathrolines was encouraging and raised the question of whether other non-covalent binding platinum(II) complexes, with a wider range of substituting group-type, number and position/s on 1,10-phenanthroline and ancillary ligands have the potential to yield more active complexes.

Accordingly, we have prepared chiral platinum(II) complexes based on [Pt(en)(phen)]$Cl_2$ and [Pt(en)(3,4,7,8-$Me_4$phen)]$Cl_2$, where en is replaced by the 1*R*,3*S*- or the 1*S*,3*R*-form of 1,3-diamino-1,2,2-trimethylcyclopentane (*R*,*S*-tmcp and *S*,*R*-tmcp, respectively) (Figure 1). Each complex was examined for its growth inhibition against L1210 murine leukaemia cells, their effect on the viscometry of linear DNA, their induced circular dichroism upon addition to ct-DNA and $^1$H NMR binding with the hexanucleotide d(GTCGAC)$_2$. The results are compared with those for the parent complexes [Pt(en)(phen)]$Cl_2$ and [Pt(en)(3,4,7,8-$Me_4$phen)]$Cl_2$.

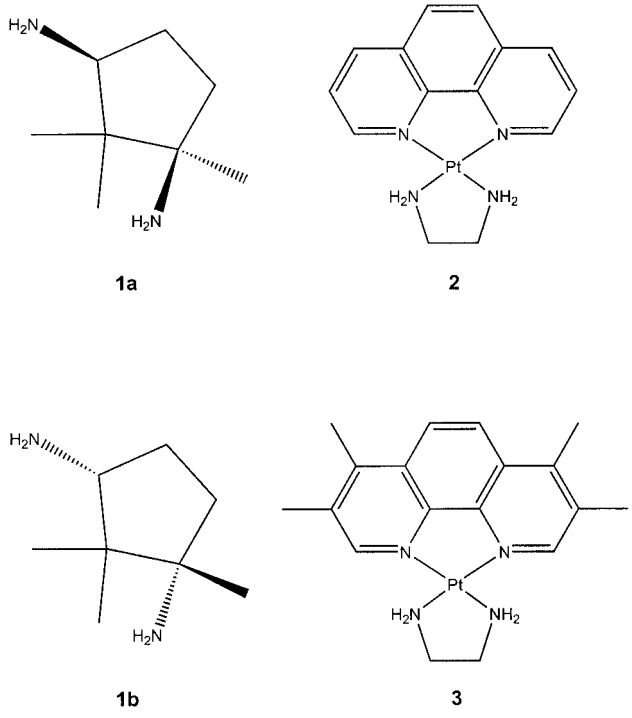


Figure 1. The structure of (1*R*,3*S*) (**1a**) and (1*S*,3*R*)-1,3-diamino-1,2,2-trimethylcyclopentane (**1b**) along with the metal complexes: [Pt(en)(phen)]$Cl_2$ (**2**) and [Pt(en)(3,4,7,8-$Me_4$phen)]$Cl_2$ (**3**).

## Results and Discussion

### Metal Complex Syntheses

The ligands **1a** and **1b** were prepared by an adapted Schmidt reaction from (*R*,*S*) and (*S*,*R*)-camphoric acid, respectively (Scheme 1). The yields and $^1$H/$^{13}$C NMR of both compounds are consistent with published data.[14] The platinum(II) complexes were prepared by refluxing aqueous solutions of [Pt(phen)$Cl_2$], or [Pt(3,4,7,8-$Me_4$phen)$Cl_2$], with the appropriate chiral ligand, until the complex had completely dissolved. Despite their structural similarities, the methylated complexes [Pt(*R*,*S*-tmcp)(3,4,7,8-$Me_4$phen)]$Cl_2$·4$H_2O$ (**3a**) and [Pt(*S*,*R*-tmcp)(3,4,7,8-$Me_4$phen)]$Cl_2$·4$H_2O$ (**3b**) took longer to react (24 hours) in comparison to [Pt(*R*,*S*-tmcp)(phen)]$Cl_2$·2$H_2O$ (**2a**) and [Pt(*S*,*R*-tmcp)(phen)]$Cl_2$·2.5$H_2O$ (**2b**) (16 hours). The variation in reaction time can be ascribed to the difference in p$K_a$, where the reactivity observed in each complex increases with a decrease in base character {[Pt(phen)$Cl_2$] p$K_a$ = 4.96; [Pt(3,4,7,8-$Me_4$phen)$Cl_2$] p$K_a$ = 6.31}.[17] All complexes were isolated as chloride salts to facilitate aqueous solubility for biological testing.

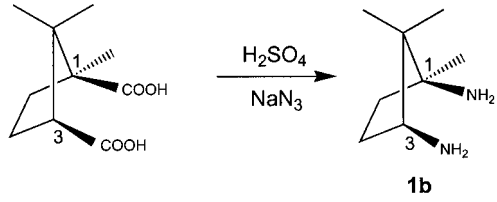


Scheme 1.

The complexes were characterised by NMR and CD spectroscopy. All $^1$H NMR spectra were recorded in [$D_6$]-DMSO in the range of 0 to 10 ppm. The C2 methyl protons of [Pt(*R*,*S*-tmcp)(phen)]$Cl_2$·2$H_2O$ (**2a**) and [Pt(*S*,*R*-tmcp)(phen)]$Cl_2$·2.5$H_2O$ (**2b**), appeared at $\delta$ = 0.80 and 1.26 ppm. The C1 methyl proton occurred downfield at $\delta$ = 1.45 ppm as a consequence of shielding due to its proximity to the nitrogen and platinum(II) atoms. The C3 methine proton occurred as a multiplet at $\delta$ = 2.91 ppm, with the C5 protons further upfield at $\delta$ = 1.78 and 1.92 ppm. Assignment of the amine protons was based on 2D DQFCOSY experiments, with the two AB spin systems occurring at $\delta$ = 6.51 ppm for C(1)$NH_2$, and 6.78 ppm for C(3)$NH_2$. The C4 protons were observed at $\delta$ = 2.15 ppm through scalar coupling to the methine proton on C3. The coordination of the diamine species rendered the aromatic ligands asymmetric, producing further splitting of the characteristic proton signals. The signals of the phenanthroline ring resonated as two doublet of doublets at $\delta$ = 8.31 and 8.29 ppm for H7/14, and a singlet at $\delta$ = 8.35 ppm for H10/11. H6/15 and H8/13 appeared as a multiplet at $\delta$ = 9.15 ppm.

The aromatic protons of [Pt(*R*,*S*-tmcp)(3,4,7,8-$Me_4$phen)]$Cl_2$·4$H_2O$ (**3a**) and [Pt(*S*,*R*-tmcp)(3,4,7,8-$Me_4$phen)]$Cl_2$·4$H_2O$ (**3b**), H6′/15′ appeared as a singlet at $\delta$ = 8.38 ppm, and for H10′/11′ two singlets in the $^1$H NMR and were observed at $\delta$ = 9.06 and 8.99 ppm. The aromatic methyl groups were upfield at $\delta$ = 2.64 and 2.80 ppm. The signals for the chiral ancillary ligand occurred at similar chemical shifts to the non-methylated complex. $^{13}$C and DEPT NMR spectra accounted for all carbon atoms present for the four complexes.

 © 2006 Wiley-VCH Verlag GmbH & Co. KGaA, Weinheim 

Table 1. Summary of the biological activity of the platinum(II) complexes.

| Compound | $IC_{50}$[a] (μM, L1210) | $K_b \times 10^5$ at 230–232 nm[c] | $n$ at 230–232 nm[c] | $K_b \times 10^5$ at 273–275 nm[c] | $n$ at 273–275 nm[c] | Relative viscosity[g] $(\eta/\eta^0)^{1/3}$ $r = 0.125$ | Relative viscosity[g] $(\eta/\eta^0)^{1/3}$ $r = 0.250$ |
|---|---|---|---|---|---|---|---|
| Cisplatin | 0.5 | | | | | 0.85 | 0.89 |
| [Pt(en)(phen)]$Cl_2$ | 9.7 ± 0.4[b] | 22.2 ± 4.6[d][e] | 2.0 ± 0.3[d,e] | | | 1.13 | 1.23 |
| [Pt(*R*,*S*-tmcp)(phen)]$Cl_2$ (**2a**) | 11.3 ± 1.8[b] | 16.1 ± 9.9[d] | 2.4 ± 0.1[d] | 11.0 ± 0.1[f] | 2.0 ± 0.1[f] | 0.90 | 0.97 |
| | | 6.6 ± 0.1[f] | 2.2 ± 0.1[f] | | | | |
| [Pt(*S*,*R*-tmcp)(phen)]$Cl_2$ (**2b**) | 11.2 ± 2.1[b] | 5.3 ± 2.2[d] | 2.4 ± 0.1[d] | 8.6 ± 0.2[f] | 2.0 ± 0.1[f] | 1.06 | 1.15 |
| | | 5.7 ± 0.1[f] | 2.0 ± 0.1[f] | | | | |
| [Pt(en)(3,4,7,8-$Me_4$phen)]$Cl_2$ | > 50[c] | 7.4 ± 3.0[d,e] | 6.0 ± 0.4[d,e] | | | 1.08 | 1.12 |
| [Pt(*R*,*S*-tmcp)(3,4,7,8-$Me_4$phen)]$Cl_2$ (**3a**) | 11.5 ± 0.7[b] | 3.1 ± 1.3[d] | 2.5 ± 0.1[d] | 2.6 ± 0.3[f] | 1.8 ± 0.1[f] | 0.86 | 0.90 |
| | | 0.7 ± 0.1[f] | 2.9 ± 0.3[f] | | | | |
| [Pt(*S*,*R*-tmcp)(3,4,7,8-$Me_4$phen)]$Cl_2$ (**3b**) | 8.5 ± 0.7[b] | 3.5 ± 1.2[d] | 3.1 ± 1.2[d] | 3.3 ± 0.1[f] | 1.9 ± 0.1[f] | 0.81 | 0.87 |
| | | 1.6 ± 0.1[f] | 2.0 ± 0.1[f] | | | | |
| DNA | | | | | | 1.00 | 1.00 |
| Ethidium | | | | | | 1.11 | 1.13 |
| Hoechst 33258 | | | | | | 1.01 | 1.03 |

[a] $IC_{50}$ values were determined for murine leukaemia L1210 cells and are reported for two experiments at 48 h continuous exposure to the metal complexes. [b] Replication = 2. [c] Replication = 4. [d] The intrinsic approach[18] was used to determine the values of α whereas the Scatchard model[18] was used to determine $K_b$ and $n$ for the CD ct-DNA titration data. [e] Data from ref.[14]. [f] Direct least-squares curve fitting, using a Levenberg–Marquardt method, to the same experimental points.[17] [g] Relative viscosity measurements were made for [metal]/[DNA] molar ratios equal to 0.125 or 0.250.

## Cytotoxicity

[Pt(*R*,*S*-tmcp)(phen)]$Cl_2$ (**2a**) and [Pt(*S*,*R*-tmcp)(phen)]-$Cl_2$ (**2b**) produced an average $IC_{50}$ values of 11.3 and 11.2 μM, respectively, a decrease in potency when compared to [Pt(en)(phen)]$Cl_2$ ($IC_{50}$ = 9.7 μM) (Table 1). [Pt(*R*,*S*-tmcp)(3,4,7,8-$Me_4$phen)]$Cl_2$ (**3a**) and [Pt(*S*,*R*-tmcp)(3,4,7,8-$Me_4$phen)]$Cl_2$, (**3b**) produced average $IC_{50}$ values of 11.5 and 8.5 μM, respectively. This is a marked increase in the potency when compared to the achiral parent complex, [Pt(en)(3,4,7,8-$Me_4$phen)]$Cl_2$, with an $IC_{50}$ value greater than 50 μM (Table 1).

## Viscosity

Platinum(II) complexes are able to bind DNA by reversible non-covalent intercalation, partial intercalation, electrostatic association or groove binding. To investigate the mode of binding the viscosity of a linearized DNA (≈ 200 bp) solution was measured in the presence of complexes (such as, ethidium bromide, cisplatin and Hoechst 33258, which each have different, known DNA binding modes) as well as the platinum(II) complexes. This provided a common reference and verified the sensitivity of the measurements towards the different binding modes.

Ethidium bromide, a classical organic DNA intercalator, increased the relative viscosity (1.13 at a binding ratio of 0.250) due to an increase in the axial length and rigidity of DNA.[19,20] Cisplatin, in contrast, produced a decrease in the relative viscosity (0.89 at a binding ratio of 0.250) as a consequence of kinking and bending that results from geometry of the Pt-DNA covalent adduct.[21] Partial intercalators also kink the DNA reducing its axial length, which is observed as a reduction in relative viscosity.[22] Hoechst 33258, a groove binder, did not alter the relative viscosity (1.00 at a binding ratio of 0.250) as it does not change the axial length of DNA.[20,23] The above results confirm the sensitivity of viscosity as a method to differentiate the modes of binding.

The viscosity of the ct-DNA solution (200 bp), decreased for [Pt(*R*,*S*-tmcp)(phen)]$Cl_2$ and [Pt(*S*,*R*-tmcp)(phen)]$Cl_2$ when compared to [Pt(en)(phen)]$Cl_2$ at binding ratios of 0.250 to 0.97, 1.15 and 1.23, respectively, as shown in Table 1. These results suggest that regardless of chirality, the bulk of the ancillary ligand impedes intercalation for both [Pt(*R*,*S*-tmcp)(phen)]$Cl_2$ and [Pt(*S*,*R*-tmcp)(phen)]$Cl_2$. The *S*,*R*-form of the diamine in [Pt(*S*,*R*-tmcp)(phen)]$Cl_2$ may reduce the extent as to how far the aromatic rings can insert into the DNA helix and because [Pt(*R*,*S*-tmcp)(phen)]$Cl_2$ accentuates this trend, this would indicate that the orientation of the *R*,*S*-isomer further obstructs the phen from full intercalation.[14,22] The viscosity results therefore indicate that [Pt(*R*,*S*-tmcp)(phen)]$^{2+}$ undergoes partial intercalation.

[Pt(en)(3,4,7,8-$Me_4$phen)]$^{2+}$ intercalates with a relative viscosity of 1.08, but its ability to increase the axial length of linearized DNA is less than [Pt(en)(phen)]$Cl_2$. It is likely that the methyl groups on the 3,4,7,8-$Me_4$phen protrude into the binding site of the DNA duplex, obstructing intercalation. This interaction is further affected with the introduction of the bulky chiral ancillary ligands. The complexes [Pt(*R*,*S*-tmcp)(3,4,7,8-$Me_4$phen)]$Cl_2$ and [Pt(*S*,*R*-tmcp)(3,4,7,8-$Me_4$phen)]$Cl_2$ showed substantial decreases in viscosity 0.90 and 0.87, respectively (Table 1). Although the viscosity is similar to that of cisplatin it can be explained by kinking of the DNA[14] as the 3,4,7,8-$Me_4$phen

 © 2006 Wiley-VCH Verlag GmbH & Co. KGaA, Weinheim 

can only partially intercalate into the DNA helix. Here the change in structure, where the DNA bends (or kinks) to accommodate the ligand, is accompanied by an increase in the biological activity of the complex.

### Circular and Induced Circular Dichroism (ICD)

CD spectra were recorded for each of the platinum(II) complexes upon titration into DNA, and the changes in ct-DNA structural conformation were observed upon binding. The titration curves for each of the complexes are presented in Figure 2 and Figure 3 as CD and ICD spectra. The initial CD is consistent with B-type DNA, with a positive peak at 275 nm, a negative peak at 245 nm, zero between the peaks at ca. 258 nm and a negative peak at 210 nm. Changes in the CD spectra for the complexes were observed, but these are more obvious when they are represented as ICD spectra (as shown in Figure 2 and Figure 3). The ICD titration spectra of each complex were used to determine the average affinity and stoichiometry of binding.

The CD spectrum of DNA from 200–300 nm, is because of the skewed orientation of the bases.[18] Changes to the secondary structure, such as unwinding of the helix, or inclination of the bases, due to interaction with a metal complex, led to an alteration in the shape of the spectrum. If the spectrum intensity changes, but the shape of the peak remains uniform, a single binding mode by the ligand can be expected.[24] If the spectrum, however, changes both in shape and intensity, a modification to the DNA-drug interaction may be taking place. Such effect may be attributed to a number of factors which include: 1) occupancy of more than one binding site as the drug concentration increases; 2) ligand–ligand interactions, 3) changes in the DNA conformation.

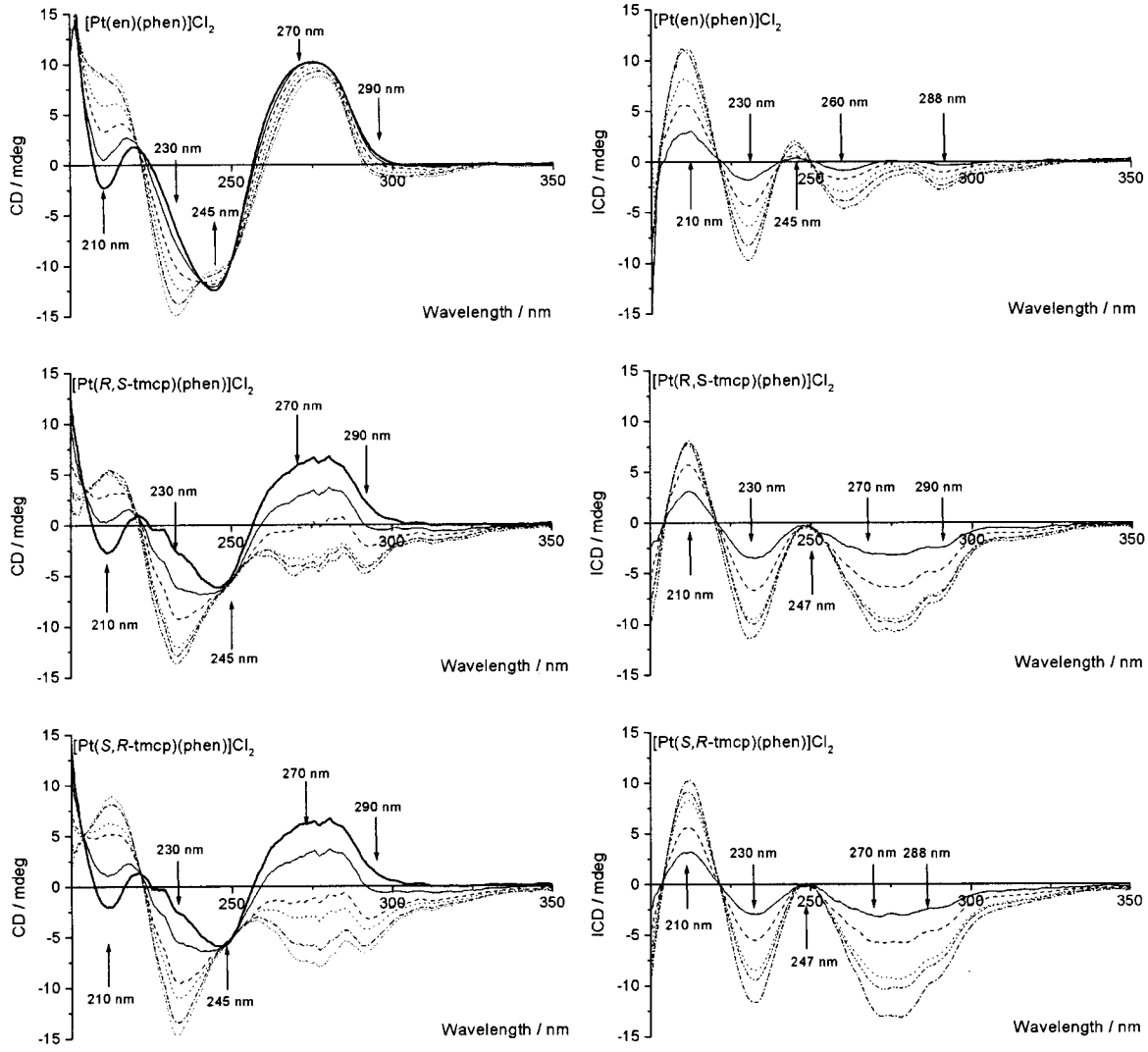


Figure 2. CD (left) and ICD (right) spectra of varying concentrations of the platinum(II) complexes, [Pt(en)(phen)]$Cl_2$ (**2**), [Pt(*R*,*S*-tmcp)(phen)]$Cl_2$ (**2a**) and [Pt(phen)(*S*,*R*-tmcp)]$Cl_2$ (**2b**) upon titration with ct-DNA solution in buffer (5 mM, Trizma, 50 mM NaCl, pH 7.5). The ratios of [Pt]/[DNA] are 0, 0.1, 0.2, 0.4. 0.5 and 1.0 and are indicated on the graph as –, –, ---, ···, ·-·, -··-, respectively.

 © 2006 Wiley-VCH Verlag GmbH & Co. KGaA, Weinheim 

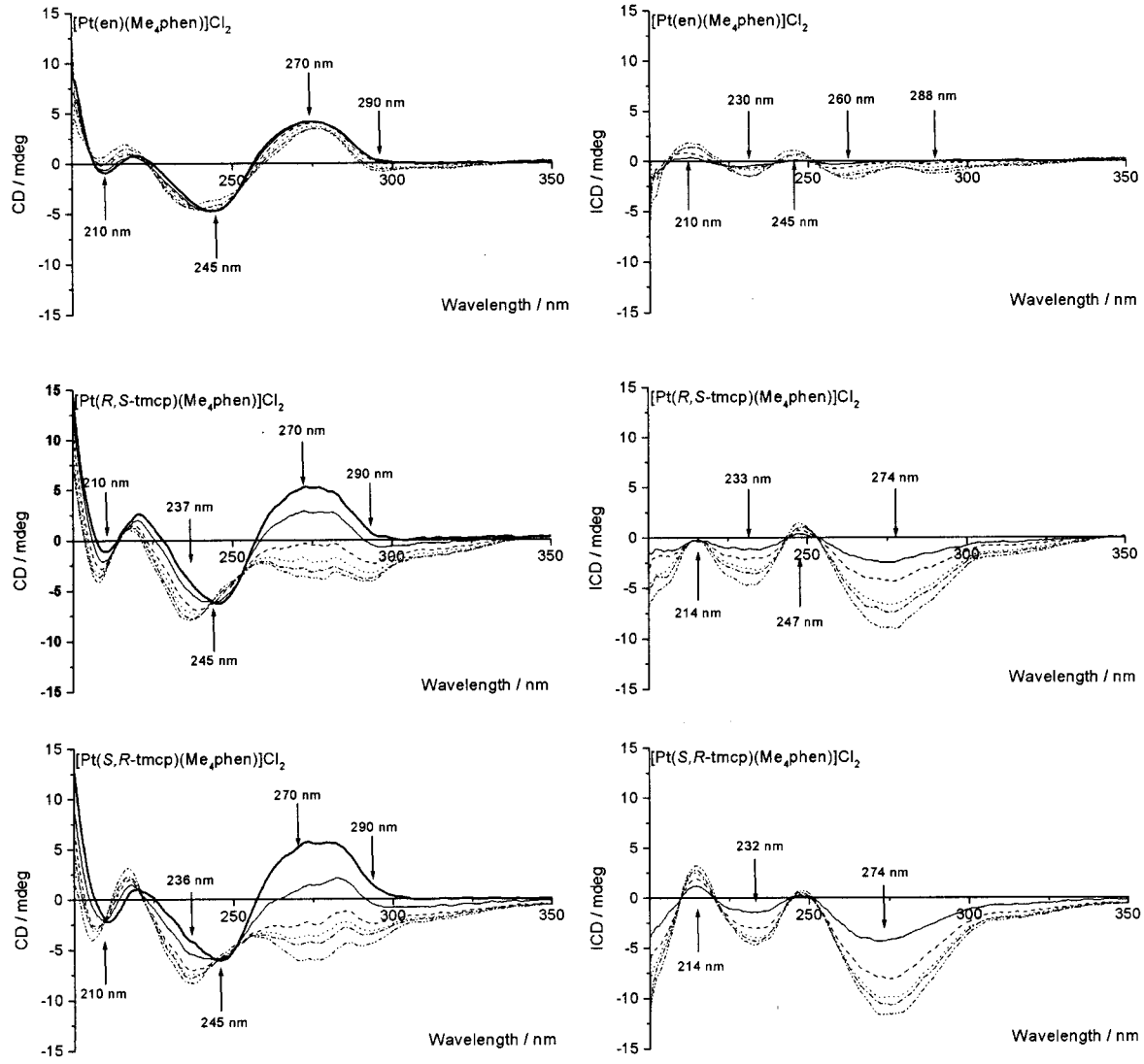


Figure 3. CD (left) and ICD (right) spectra of varying concentrations of the complexes, [Pt(en)(3,4,7,8-$Me_4$phen)]$Cl_2$ (**3**), [Pt(*R*,*S*-tmcp)(3,4,7,8-$Me_4$phen)]$Cl_2$ (**3a**) and [Pt(*S*,*R*-tmcp) (3,4,7,8-$Me_4$phen)]$Cl_2$ (**3b**) upon titration with ct-DNA solution in buffer (5 mM, Trizma, 50 mM NaCl, pH 7.5). The ratios of [Pt]/[DNA] are 0, 0.1, 0.2, 0.4. 0.5 and 1.0 and are indicated on the graph as –, – –, ---, ···, ·-·, -··-, respectively.

The ICD of [Pt(en)(phen)]$Cl_2$ (**2**), [Pt(*R*,*S*-tmcp)(phen)]-$Cl_2$ (**2a**) and [Pt(*S*,*R*-tmcp)(phen)]$Cl_2$ (**2b**) change in comparable ways below 245 nm suggesting that the interaction in DNA is of a similar nature. Above 245 nm the two discrete peaks observed for [Pt(en)(phen)]$Cl_2$, develop into one broad peak for both [Pt(*R*,*S*-tmcp)(phen)]$Cl_2$ and [Pt(*S*,*R*-tmcp)(phen)]$Cl_2$ (Figure 2). This peak is also observed for [Pt(*R*,*S*-tmcp)(3,4,7,8-$Me_4$phen)]$Cl_2$ and [Pt(*S*,*R*-tmcp)-(3,4,7,8-$Me_4$phen)]$Cl_2$ (Figure 3). The intensity of this broad peak is consistent with a deformation of the DNA helix by the complex as shown in viscosity, perhaps by partial intercalation, where $S,R > R,S$.

[Pt(en)(3,4,7,8-$Me_4$phen)]$Cl_2$ makes little impact on the structure of DNA as the ICD spectra show only very small peaks upon the addition of metal complex. Both [Pt(*R*,*S*-tmcp)(3,4,7,8-$Me_4$phen)]$Cl_2$ and [Pt(*S*,*R*-tmcp)(3,4,7,8-$Me_4$phen)]$Cl_2$ have a profound effect on the CD, which is made more obvious in the ICD. The spectra below 245 nm are significantly different from that of the phen analogues.

Binding constants were determined using the data obtained from the titrations. Previously we have used the method of Roger and Nordén[24] to determine the binding constants; however, here a different data analysis technique, which utilises direct least-squares curve fitting and a Levenberg-Marquardt method, was also employed.[18] Some inconsistencies were observed, but on the whole, the new method proved to be effective, reducing the time required to process the data from days to one hour. The inconsistencies were observed when attempts to apply a Scatchard plot to all of the data were unachievable. The calculated values for $K_b$ and $n$ using both methods are included in Table 1. This new method allowed us to review the results and investigate alternative wavelengths when calculations for $K_b$ or $n$ where not reasonable.

 © 2006 Wiley-VCH Verlag GmbH & Co. KGaA, Weinheim 

### Binding of the Pt(tmcp) Complexes to the Hexamer d(GTCGAC)$_2$

Each platinum(II) complex was titrated into a solution containing the hexamer d(GTCGAC)$_2$, with one-dimensional $^1$H NMR spectra recorded at a metal complex to hexamer ratio (R) of 0.2, 0.4, 0.6, 0.8 and 1.0 and two-dimensional spectra, DQFCOSY and NOESY, recorded at $R = 1$.

The addition of each platinum(II) complex to d(GTCGAC)$_2$ induced significant broadening of the hexamer and metal-complex resonances (for example see Figure 4), indicating that each of the [Pt(tmcp)(Me$_n$phen)]Cl$_2$ complexes bind with intermediate exchange kinetics (on the NMR timescale). The observed intermediate exchange kinetics is consistent with an intercalative binding mode and that observed in the previous study with the [Pt(en)(3,4,7,8-Me$_4$phen)]Cl$_2$ complexes.[14] For each platinum(II) complex, significant upfield shifts of all 3,4,7,8-Me$_4$phen resonances were observed upon hexamer binding (see Table 2), again consistent with intercalation. The upfield shifts of the resonances for the [Pt(*R*,*S*-tmcp)(phen)]Cl$_2$ and [Pt(*S*,*R*-tmcp)(phen)]Cl$_2$ complexes were similar, as were the shifts for the [Pt(*R*,*S*-tmcp)(3,4,7,8-Me$_4$phen)]Cl$_2$ and [Pt(*S*,*R*-tmcp)(3,4,7,8-Me$_4$phen)]Cl$_2$ complexes; however, the upfield shifts for the phen ligand resonances were considerably larger for the phen complexes than the 3,4,7,8-Me$_4$phen complexes. This may indicate that the phen complexes intercalate more fully into the hexamer base-stack than do the 3,4,7,8-Me$_4$phen complexes. The binding of the *S*,*R* complexes to d(GTCGAC)$_2$ induced larger shifts for the hexamer resonances than the corresponding *R*,*S* complexes (see Table 3), with the phen complexes generally inducing larger shifts than the 3,4,7,8-Me$_4$phen complexes (see Table 4). As most nucleotide residues exhibited significant shifts, it was not possible to deduce the metal complex binding site from the changes in chemical shift.

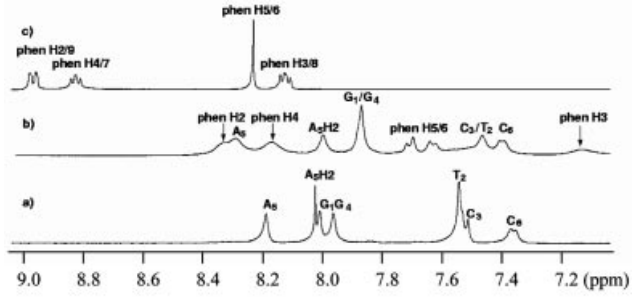


Figure 4. An expansion of the 1D NMR spectra of a) the free hexamer, b) [Pt(*S*,*R*-tmcp)(phen)]Cl$_2$ bound to d(GTCGAC)$_2$ at R = 1 and c) [Pt(*S*,*R*-tmcp)(phen)]Cl$_2$ in 10 mM phosphate buffer containing 1 mM EDTA and 20 mM NaCl at pH 7.0 and 25 °C.

NOESY spectra were recorded, at a range of temperatures and mixing times, in order to gain further information on the hexamer binding by the [Pt(tmcp)(3,4,7,8-Me$_4$phen)]-Cl$_2$ series of complexes. Figure 5 shows an expansion of the NOESY spectrum of the [Pt(*S*,*R*-tmcp)(phen)]Cl$_2$ complex bound to d(GTCGAC)$_2$ at $R = 1$. In addition to the expected intra-duplex NOEs, a range of NOE cross-peaks are also observed between the metal complex and hexamer resonances, indicating that the platinum(II) complex fully intercalates from the minor groove. A range of relatively strong NOEs are observed from the tmcp methyl protons to the hexamer minor groove protons, ie. to the A$_5$H2 and the H1′ and H4′/H5′/H5′′ protons of all nucleotide residues. In addition, NOEs are clearly observed from the phen H3 and H4 resonances to the both major and minor groove protons, whereas NOEs are only observed from the phen H5/H6 protons to the T$_2$Me protons that are located in the major groove. As all the observed intermolecular NOEs from the phen protons are to T$_2$, C$_3$, G$_4$ and A$_5$ protons, it is concluded that [Pt(*S*,*R*-tmcp)(phen)]Cl$_2$ mostly intercalates between the T$_2$·A$_5$ and C$_3$·G$_4$ base-pairs. The NOE data from the [Pt(*R*,*S*-tmcp)(phen)]Cl$_2$ complex bound to d(GTCGAC)$_2$ is similar, although the individual cross-peaks are weaker because of the greater degree of broadening of the metal complex resonances.

Due to the extreme broadening of all the resonances, it was difficult to resolve many of the intermolecular NOEs observed in NOESY spectra of the hexamer with either stereoisomer of [Pt(tmcp)(3,4,7,8-Me$_4$phen)]Cl$_2$; however, strong NOEs were observed from the tmcp-methyl protons to the hexamer A$_5$H2, H1′ and H4′/H5′/H5′′ protons. At temperatures between 40 and 50 °C a considerable number of metal complex-hexamer NOEs were clearly resolved. For

Table 2. Chemical shift [ppm] changes for the 1,10-phenanthroline ligand protons of the platinum(II) complexes [Pt(en)(phen)]Cl$_2$, [Pt(en)(3,4,7,8-Me$_4$phen)]Cl$_2$, [Pt(*R*,*S*-tmcp)(phen)]Cl$_2$, [Pt(*S*,*R*-tmcp)(phen)]Cl$_2$, [Pt(*R*,*S*-tmcp)(3,4,7,8-Me$_4$phen)]Cl$_2$ and [Pt(*S*,*R*-tmcp)(3,4,7,8-Me$_4$phen)]Cl$_2$, upon addition to the hexamer d(GTCGAC)$_2$ in 10 mM phosphate buffer containing 20 mM NaCl and 1 mM EDTA at 25 °C.

| Metal complex<br>Phen<br>Proton | en-phen[a] | en-Me$_4$phen[b] | *R*,*S*-tmcp-phen | *S*,*R*-tmcp-phen | *R*,*S*-tmcp-Me$_4$phen | *S*,*R*-tmcp-Me$_4$phen |
|---|---|---|---|---|---|---|
| 2,9 | –0.66 | –0.66 | –0.59 | –0.55 | –0.44 | –0.45 |
| 3,8 | –0.90 | | –1.07 | –1.03 | | |
| 4,7 | –0.64 | | –0.68 | –0.59 | | |
| 5 | –0.51 | –0.42 | –0.60 | –0.61 | –0.31 | –0.37 |
| 6 | –0.51 | –0.42 | –0.55 | –0.53 | –0.40 | –0.40 |
| 3/8-Me | | –0.56 | | | –0.46 | –0.52 |
| 4/7-Me | | –0.49 | | | –0.40 | –0.46 |

[a] Data taken from refs.[13,14]. [b] Data taken from ref.[14].

 © 2006 Wiley-VCH Verlag GmbH & Co. KGaA, Weinheim 

Table 3. Chemical shift [ppm] and changes in chemical shift (numbers in parentheses) of the non-exchangeable protons of $d(GTCGAC)_2$ in 10 mM phosphate buffer containing 20 mM NaCl and 1 mM EDTA at 25 °C upon binding by $[Pt(R,S\text{-tmcp})(phen)]Cl_2$ and $[Pt(S,R\text{-tmcp})(phen)]Cl_2$.

| 1:1 $d(GTCGAC)_2$/$[Pt(R,S\text{-tmcp})(phen)]^{2+}$ | | | | | | |
|---|---|---|---|---|---|---|
| Base | H8/H6 | AH2 | H1′ | H2′ | H2′′ | H3′ |
| $G_1$ | 7.93 (–0.08) | | 5.98 (–0.09) | 2.63 (–0.10) | 2.75 (–0.06) | 4.82 (0.01) |
| $T_2$ | 7.48 (–0.05) | | 6.05 (–0.16) | 2.25 (0.00) | 2.45 (–0.14) | 4.92 (–0.01) |
| $C_3$ | 7.51 (0.01) | | 5.59 (–0.13) | 2.08 (–0.07) | 2.33 (–0.09) | 4.88 (0.01) |
| $G_4$ | 7.92 (–0.04) | | 5.52 (–0.12) | 2.67 (–0.07) | 2.71 (–0.08) | 5.03 (0.00) |
| $A_5$ | 8.26 (0.07) | 8.03 (0.01) | 6.28 (–0.01) | 2.74 (0.09) | 2.90 (0.01) | 5.04 (0.02) |
| $C_6$ | 7.36 (0.01) | | 6.10 (0.03) | 2.13 (0.04) | 2.13 (0.04) | 4.48 (0.00) |
| 1:1 $d(GTCGAC)_2$/$[Pt(S,R\text{-tmcp})(phen)]^{2+}$ | | | | | | |
| Base | H8/H6 | AH2 | H1′ | H2′ | H2′′ | H3′ |
| $G_1$ | 7.86 (–0.15) | | 5.92 (–0.15) | 2.54 (–0.19) | 2.68 (–0.13) | 4.83 (–0.02) |
| $T_2$ | 7.45 (–0.08) | | 5.93 (–0.28) | 2.27 (0.02) | 2.36 (–0.23) | 4.90 (–0.03) |
| $C_3$ | 7.50 (0.00) | | 5.51 (–0.21) | 2.11 (0.06) | 2.28 (–0.14) | 4.91 (0.04) |
| $G_4$ | 7.87 (–0.09) | | 5.43 (–0.21) | 2.55 (–0.19) | 2.61 (–0.18) | 5.02 (–0.01) |
| $A_5$ | 8.30 (0.11) | 7.99 (–0.03) | 6.20 (–0.09) | 2.63 (–0.03) | 2.88 (0.01) | 5.07 (0.05) |
| $C_6$ | 7.38 (0.03) | | 6.10 (0.03) | 2.18 (0.09) | 2.18 (0.09) | 4.51 (0.03) |

Table 4. Chemical shift [ppm] and changes in chemical shift (numbers in parentheses) of the non-exchangeable protons of $d(GTCGAC)_2$ in 10 mM phosphate buffer containing 20 mM NaCl and 1 mM EDTA at 25 °C upon binding by $[Pt(R,S\text{-tmcp})(3,4,7,8\text{-}Me_4phen)]Cl_2$ and $[Pt(S,R\text{-tmcp})(3,4,7,8\text{-}Me_4phen)]Cl_2$.

| 1:1 $d(GTCGAC)_2$/$[Pt(R,S\text{-tmcp})(Me_4phen)]^{2+}$ | | | | | | |
|---|---|---|---|---|---|---|
| Base | H8/H6 | AH2 | H1′ | H2′ | H2′′ | H3′ |
| $G_1$ | 7.91 (–0.10) | | 5.98 (–0.09) | 2.60 (–0.13) | 2.73 (–0.08) | 4.82 (–0.03) |
| $T_2$ | 7.41 (–0.11) | | 6.06 (–0.15) | 2.19 (–0.06) | 2.48 (–0.11) | 4.88 (–0.05) |
| $C_3$ | 7.41 (–0.10) | | 5.60 (–0.12) | 2.03 (–0.02) | 2.35 (–0.07) | 4.88 (0.01) |
| $G_4$ | 7.90 (–0.06) | | 5.60 (–0.04) | 2.59 (–0.15) | 2.68 (–0.11) | 4.98 (0.05) |
| $A_5$ | 8.20 (0.01) | 7.91 (–0.12) | 6.24 (–0.05) | 2.66 (0.01) | 2.86 (–0.03) | 5.02 (0.00) |
| $C_6$ | 7.36 (0.01) | | 6.06 (–0.01) | 2.12 (0.03) | 2.12 (0.03) | 4.50 (0.02) |
| 1:1 $d(GTCGAC)_2$/$[Pt(S,R\text{-tmcp})(Me_4phen)]^{2+}$ | | | | | | |
| Base | H8/H6 | AH2 | H1′ | H2′ | H2′′ | H3′ |
| $G_1$ | 7.80 (–0.21) | | 5.90 (–0.17) | 2.54 (–0.19) | 2.66 (–0.15) | 4.84 (–0.01) |
| $T_2$ | 7.33 (–0.19) | | 5.95 (–0.26) | 2.12 (–0.18) | 2.40 (–0.19) | 4.84 (–0.09) |
| $C_3$ | 7.40 (–0.11) | | 5.51 (–0.21) | 2.09 (0.04) | 2.40 (–0.02) | 4.87 (0.00) |
| $G_4$ | 7.83 (–0.13) | | 5.52 (–0.12) | 2.46 (–0.28) | 2.67 (–0.12) | 4.96 (–0.07) |
| $A_5$ | 8.20 (0.01) | 7.86 (–0.17) | 6.21 (–0.08) | 2.69 (0.04) | 2.82 (–0.07) | 5.00 (–0.02) |
| $C_6$ | 7.40 (0.05) | | 6.04 (–0.03) | 2.14 (0.03) | 2.14 (0.03) | 4.52 (0.04) |

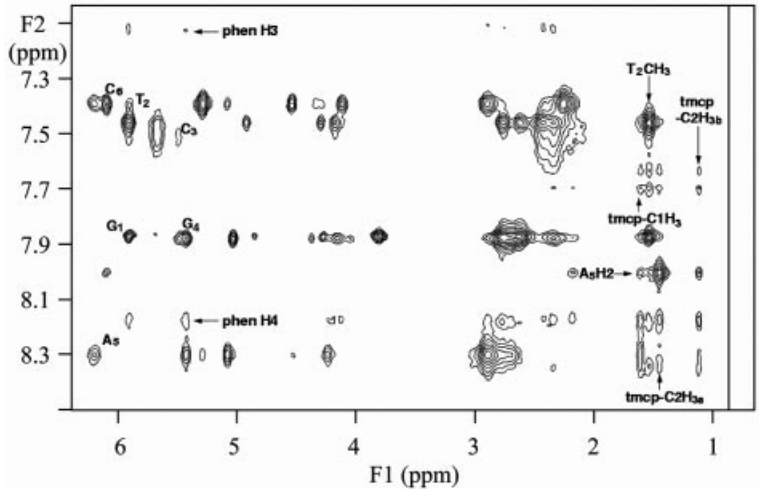


Figure 5. An expansion of the NOESY spectrum of the $[Pt(S,R\text{-tmcp})(phen)]Cl_2$ complex bound to $d(GTCGAC)_2$ at $R = 1$, in 10 mM phosphate buffer (pH, 7) containing 1 mM EDTA and 20 mM NaCl at 25 °C. The expansion shows the intermolecular connectivities between the metal complex phen and tmcp-methyl protons and the hexamer H1′ and $A_5H2$ protons, respectively.

 © 2006 Wiley-VCH Verlag GmbH & Co. KGaA, Weinheim 

the [Pt(*S*,*R*-tmcp)(3,4,7,8-$Me_4$phen)]$Cl_2$ complex, NOEs were observed from the H2/H9 protons to the $G_1$, $T_2$, $C_3$, $G_4$ and $C_6$ H1′ protons, with the strongest NOEs to the $C_3$ and $G_4$. In addition, NOEs were detected between the hexamer $A_5$H8 and the metal complex C3/C8 phenanthroline methyl protons. This data indicates that the [Pt(*S*,*R*-tmcp)(3,4,7,8-$Me_4$phen)]$Cl_2$ complex intercalates from the minor groove at all possible intercalation sites; however, based on the relative strengths of the intermolecular NOEs, with some preference for intercalation between the $T_2$·$A_5$ and $C_3$·$G_4$ base-pairs. For hexamer binding by [Pt(*R*,*S*-tmcp)(3,4,7,8-$Me_4$phen)]$Cl_2$, a similar pattern of intermolecular NOEs, but of lower intensity, to the corresponding *S*,*R* complex was observed.

As the NOESY spectra only represent exchange-averaged NOEs for the hexamer binding by the [Pt(tmcp)(3,4,7,8-$Me_4$phen)]$Cl_2$ complexes, it is not possible to draw unambiguous conclusions on the intercalation geometry; however, the NMR spectroscopic data, coupled with the viscosity data, suggest that the [Pt(tmcp)(3,4,7,8-$Me_4$phen)]$Cl_2$ complexes only partially intercalate and in a "side-on" fashion. Simple molecular modelling indicates that if the metal complex fully intercalated in a "head-on" fashion, NOEs would not be observed from the tmcp-methyl protons to the $A_5$H2 and the H1′ and H4′/H5′/H5′′ protons. Alternatively, for partial and side-on intercalation (as illustrated in Figure 6), the observed NOEs from the $A_5$H2 to the $C_2$-methyls and the strong NOEs between the tmcp-methyl protons and the H1′ and H4′/H5′/H5′′ protons would be expected, as these distances are less than 5 Å.

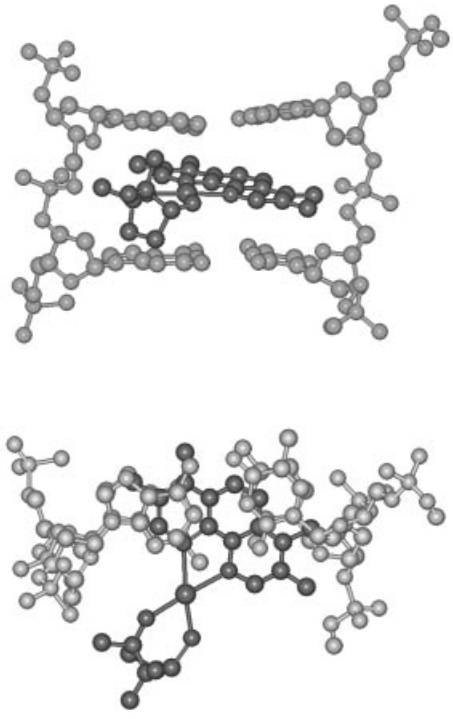

Figure 6. A HyperChem® molecular model of [Pt(*R*,*S*-tmcp)(3,4,7,8-$Me_4$phen)]$Cl_2$ (dark grey) intercalated from the minor groove of d(GTCGAC)$_2$ (light grey). For simplicity, only the $T_2$ and $C_3$ base pairs have been shown.

## Conclusions

An investigation into the biological activity of four platinum(II) complexes of 1,10-phenanthroline (phen) and 3,4,7,8-tetramethyl-1,10-phenanthroline (3,4,7,8-$Me_4$phen), with the ancillary ligands (1*R*,3*S*) and (1*S*,3*R*)-1,3-diamino-1,2,2-trimethylcyclopentane (*R*,*S*-tmcp and *S*,*R*-tmcp, respectively) has determined that the ancillary ligand can significantly influence biological activity.

In vitro cytotoxicity assays against the L1210 cell line, showed that [Pt(*R*,*S*-tmcp)(phen)]$Cl_2$ (**2a**) and [Pt(*S*,*R*-tmcp)(phen)]$Cl_2$ (**2b**) produced an average $IC_{50}$ value of 11.3 and 11.2 μM, respectively, a decrease in potency when compared to [Pt(en)(phen)]$Cl_2$ with an average $IC_{50}$ value of 9.7 μM; whereas [Pt(*R*,*S*-tmcp)(3,4,7,8-$Me_4$phen)]$Cl_2$ (**3a**) and [Pt(*S*,*R*-tmcp)(3,4,7,8-$Me_4$phen)]$Cl_2$, (**3b**) produced an average $IC_{50}$ value of 11.5 and 8.5 μM, respectively, an increase in potency when compared to [Pt(en)(3,4,7,8-$Me_4$phen)]$Cl_2$ with an average $IC_{50}$ value of $>50$ μM. This result suggests that the interaction between an intercalator, containing 3,4,7,8-$Me_4$phen, and DNA can be modulated in such a way as to increase activity.

Viscosity studies verified that the extent of intercalation had in fact been modulated, where the relative viscosities were reduced when compared to the parent complexes. Such that the viscosity of [Pt(*S*,*R*-tmcp)(phen)]$Cl_2$ and [Pt(*R*,*S*-tmcp)(phen)]$Cl_2$ were reduced to 1.15 and 0.97 respectively when compared to [Pt(en)(phen)]$Cl_2$ at 1.23 and [Pt(*R*,*S*-tmcp)(3,4,7,8-$Me_4$phen)]$Cl_2$ and [Pt(*S*,*R*-tmcp)(3,4,7,8-$Me_4$phen)]$Cl_2$ were reduced to 0.90 and 0.87 respectively when compared to [Pt(en)(3,4,7,8-$Me_4$phen)]-$Cl_2$ at 1.12. The increase in activity of the 3,4,7,8-$Me_4$phen analogues may come about because the bending of DNA is of an appropriate proportion to halt DNA replication.

Titrations of the metal complexes into ct-DNA and the observation of the changes in ICD spectra was used to determine the binding constants. The observed changes in the ICD are consistent with an intimate interaction and indicate that some small, but different, structural/conformational changes result when these complexes interact with DNA.

For each of the metal complexes studied with d(GTCGAC)$_2$, intermolecular NOE data and observed changes in chemical shift suggests that the [Pt(tcmp)(3,4,7,8-$Me_4$phen)]$Cl_2$ complexes bind the hexamer by intercalation from the minor groove, and predominantly, between the $T_2$·$A_5$ and $C_3$·$G_4$ base-pairs.

Significant differences in biological activity that are achieved by four platinum(II) complexes of 1,10-phenathrolines and 3,4,7,8-tetramethyl-1,10-phenathrolines, suggest that the use of chiral ancillary ligands can affect biological activity. Of the two stereoisomers, the *S*,*R* ligand is more active than the *R*,*S* ligand and may be related to the degree that each isomer can prevent intercalation. From both the viscosity and NMR experiments it was shown that the *R*,*S* isomer prevented intercalation in the DNA to a greater extent than the *S*,*R* isomer. As both ligands are located in the DNA minor groove when the metal complex is intercalated,

 © 2006 Wiley-VCH Verlag GmbH & Co. KGaA, Weinheim 

it is possible the *R*,*S* ligand projects one of its methyl groups more deeply into the groove, thereby creating a steric clash. The results indicate that more active complexes might be developed by changing the chiral diamine ancillary ligands. Chiral ancillary ligands that have more steric bulk may result in a reduction in cytotoxicity, or the addition of stereospecific functional groups capable of forming hydrogen bonds with the DNA backbone may result in an increase in cytotoxicity.

## Experimental Section

**Instrumentation:** The melting points were determined (uncorrected) with a Gallenkamp Melting Point apparatus. UV spectra were recorded with a Varian Cary 1E Spectrophotometer, and CD spectra were obtained with a Jasco J-810 Spectropolarimeter, both at room temperature. Viscosity measurements were carried out using a Cannon-Manning semi-micro viscometer maintained at a constant temperature of 25 °C in a water bath. ct-DNA was prepared and purified according to the method of Chaires et al.,[25] and DNA concentration was determined with a molar extinction coefficient ($\varepsilon_{260}$) of 12,824 $M^{-1}cm^{-1}$ per base pair.[25] 1D and 2D NMR spectra were recorded with a 300 or 400 MHz Varian Mercury NMR spectrometer at 25 °C, using commercially available solvents referenced to TMS or internal standards. DNA-NMR $^1$H NMR spectra were recorded with a 400-MHz Varian Unityplus-400. Two-dimensional phase-sensitive NOESY spectra were acquired by the method of States et al.,[26] using 2048 data points in $t_2$ and 256–400 $t_1$ values with a pulse-repetition delay of 1.7 s. DQFCOSY experiments were accumulated using 2048 data points in $t_2$ for 256 $t_1$ values using a pulse-repetition delay of 1.7 s. Two-dimensional NMR spectroscopic data sets were zero-filled to 1024 points in the $t_1$ dimension and apodized with either a Gaussian or a shifted sinebell function. Microchemical analyses were performed at Australian National University, Canberra.

**Materials:** (*R*,*S*)- and (*S*,*R*)-camphoric acid, 1,10-phenanthroline (phen), 3,4,7,8-tetramethyl-1,10-phenanthroline (3,4,7,8-$Me_4$phen), calf thymus DNA (ct-DNA), IRA-400 (Cl) Amberlite ion exchange resin, Trizma [tris(hydroxymethyl)aminomethane hydrochloride] and all deuterated solvents were purchased from Aldrich Chemical Company. Potassium tetrachloroplatinate(II) was bought from Precious Metals Online Pty Ltd. CM-25 Sephadex and Waters C-18 Sep-Pak columns were obtained from Pharmacia. Oligonucleotides were purchased from Geneworks Inc. All other reagents were of analytical reagent or high purity grade.

### Syntheses

**(1*R*,3*S*)-1,3-Diamino-1,2,2-trimethylcyclopentane (*R*,*S*-tmcp) (1a):** The compound was prepared by a procedure based on the method of Gillard et al.[27] To a vigorously stirred mixture of (1*R*,3*S*)-camphoric acid (20.00 g, 0.10 mol), in concentrated $H_2SO_4$ (50 mL) and ethanol-free chloroform (300 mL), at 50 °C, was added sodium azide (19.50 g, 0.30 mol) in small amounts over a period of 2 h. The mixture was then stirred for a further 18 h at 50 °C. The mixture was cooled, poured into $H_2O$ (500 mL), and the aqueous phase made strongly basic with 12 M NaOH. The amine was extracted into $CHCl_3$ (2 × 500 mL), the organic extracts dried with anhydrous $Na_2SO_4$ and the chloroform removed in vacuo to give a clear oil. The oil was dissolved in diethyl ether (100 mL), the solution filtered, and the solvent removed in vacuo to give the product as a white solid (8.09 g, 57%). M.p. 128.1 °C. CD spectrum $\lambda_{max}$ ($\Delta\varepsilon$/$mol^{-1}dm^3cm^{-1}$, water) = 217 nm (–0.12). $^1$H NMR (300 MHz, $CDCl_3$): $\delta$ = 2.98 (dd, $^3J$ = 6.9, 8.5 Hz, 1 H), 2.01 (m, 2 H), 1.62 (m, 4 H), 1.29 (m, 2 H), 1.01 (s, 3 H), 0.80 (d, $^3J$ = 3.6 Hz, 6 H) ppm. $^{13}$C NMR ($CDCl_3$): $\delta$ = 61.0 (C), 60.8 (CH), 46.2 (C), 38.3 ($CH_2$), 30.2 ($CH_2$), 25.8 ($CH_3$), 22.2 ($CH_3$), 16.3 ($CH_3$) ppm.

**(1*S*,3*R*)-1,3-Diamino-1,2,2-trimethylcyclopentane (*S*,*R*-tmcp) (1b):** The ligand was prepared as described for **1a**, using (1*S*,3*R*)-camphoric acid, to yield the product as a white solid (7.21 g, 51%). M.p. 132.4 °C. CD spectrum $\lambda_{max}$ nm ($\Delta\varepsilon$/$mol^{-1}dm^3cm^{-1}$, water) = 218 (+0.13). $^1$H NMR (300 MHz, $CDCl_3$): $\delta$ = 3.00 (dd, $^3J$ = 7.0, 8.7 Hz, 1 H), 2.02 (m, 2 H), 1.60 (m, 4 H), 1.31 (m, 2 H), 1.03 (s, 3 H), 0.81 (d, 6 H, $^3J$ = 3.5 Hz) ppm.

**(1*R*,3*S*)-1,3-Diamino-1,2,2-trimethylcyclopentane(1,10-phenanthroline)platinum(II) Dichloride Dihydrate, [Pt(*R*,*S*-tmcp)(phen)]$Cl_2$·2$H_2O$ (2a):** The complex was prepared by a similar method as described previously.[14,28] [Pt(phen)$Cl_2$] (0.09 g, 0.20 mmol) and **1a** (0.23 g, 1.60 mmol) were refluxed in $H_2O$ (20 mL) until all of the complex had dissolved to yield a pale yellow solution. This was concentrated to a small volume (5 mL) and chilled (4 °C) 1 M HCl (6 mL) was added, which caused the product to precipitate. The reaction mixture was cooled and left overnight at 4 °C before the yellow product was collected, washed with cold 1 M HCl and acetone, then dried in vacuo at room temperature (0.11 g, 88%). $C_{20}H_{26}Cl_2N_4Pt$·2$H_2O$ (624.54): calcd. C 38.46, H 4.84, N 8.97; found C 38.39, H 5.02, N 8.83. Electronic spectrum: $\lambda_{max}$ ($\varepsilon$/$mol^{-1}dm^3cm^{-1}$, water) = 227 (35769), 277 nm (30857). CD spectrum: $\lambda_{max}$ = ($\Delta\varepsilon$/$mol^{-1}dm^3cm^{-1}$, water) = 212 (–1.42), 280 nm (+1.64). $^1$H NMR (300 MHz, [$D_6$]DMSO): $\delta$ = 9.15 (m, 4 H), 8.35 (s, 2 H), 8.31 and 8.29 (2, dd, $^3J$ = 5.4, 8.3 Hz, 2 H), 6.78 (dd, $^3J$ = 11, 13.1 Hz, 2 H), 6.51 (dd, $^3J$ = 10.3, 10.6 Hz, 2 H), 2.91 (m, 1 H), 2.15 (m, 2 H), 1.92 (m, 1 H), 1.78 (m, 1 H), 1.45 (s, 3 H), 1.26 (s, 3 H), 0.80 (s, 3 H) ppm. $^{13}$C NMR ([$D_6$]DMSO): $\delta$ = 150.6 (CH), 150.3 (CH), 146.7 (2C), 141.3 (2CH), 130.7 (C), 130.6 (C), 128.1 (2 CH), 125.5 (CH), 125.4 (CH), 63.1 (C), 60.6 (CH), 47.6 (C), 34.5 ($CH_2$), 27.1 ($CH_2$), 25.1 ($CH_3$), 20.1 ($CH_3$), 16.3 ($CH_3$) ppm.

**(1*S*,3*R*)-1,3-Diamino-1,2,2-trimethylcyclopentane(1,10-phenanthroline)platinum(II) Dichloride Dihydrate, [Pt(*S*,*R*-tmcp)(phen)]$Cl_2$·2.5$H_2O$ (2b):** The complex was prepared as described for **2a**, using **1b**, to yield the product as a yellow solid (0.10 g, 80%). $C_{20}H_{26}Cl_2N_4Pt$·2.5$H_2O$ (633.55): calcd. C 37.92, H 4.93, N 8.84; found C 37.59, H 4.74, N 8.42. CD spectrum: $\lambda_{max}$ ($\Delta\varepsilon$/$mol^{-1}dm^3cm^{-1}$, water) = 213 (+1.42), 281 nm (–1.83). $^1$H NMR (300 MHz, [$D_6$]DMSO): $\delta$ = 9.11 (m, 4 H), 8.35 (s, 2 H), 8.31 and 8.28 (2, dd, $^3J$ = 5.5, 8.3 Hz, 2 H), 6.75 (dd, $^3J$ = 11.2, 13.2 Hz, 2 H), 6.50 (dd, $^3J$ = 10.4, 10.7 Hz, 2 H), 2.91 (m, 1 H), 2.12 (m, 2 H), 1.93 (m, 1 H), 1.75 (m, 1 H), 1.44 (s, 3 H), 1.26 (s, 3 H), 0.81 (s, 3 H) ppm.

**(1*R*,3*S*)-1,3-Diamino-1,2,2-trimethylcyclopentane(3,4,7,8-tetramethyl-1,10-phenanthroline)platinum(II) Dichloride Tetrahydrate, [Pt(*R*,*S*-tmcp)(3,4,7,8-Me4phen)]$Cl_2$·4$H_2O$ (3a):** This complex was prepared as described for **2a**, using [Pt(3,4,7,8-$Me_4$phen)$Cl_2$][14,20] and **1a**, to yield the product as a green solid (0.12 g, 86%). $C_{24}H_{33}N_4PtCl_2$·4$H_2O$ (715.69): calcd. C 40.27, H 5.78, N 7.83; found C 40.16, H 5.43, N 7.58. Electronic spectrum: $\lambda_{max}$ nm ($\varepsilon$/$mol^{-1}dm^3cm^{-1}$, water) = 233 (29510), 283 nm (27070). CD spectrum: $\lambda_{max}$ ($\Delta\varepsilon$/$mol^{-1}dm^3cm^{-1}$, water) = 218 (–1.53), 286 nm (+1.45). $^1$H NMR (300 MHz, [$D_6$]DMSO): $\delta$ = 9.06 (s, 1 H), 8.99 (s, 1 H), 8.38 (s, 2 H), 6.62 (dd, $^3J$ = 10.2, 11.3 Hz, 2 H), 6.55 (dd, $^3J$ = 12.2, 11.3 Hz, 2 H), 2.91 (m, 1 H), 2.80 (d, $^3J$ = 2.9 Hz, 6 H), 2.64 (d, $^3J$ = 4.4 Hz, 6 H), 2.16 (m, 2 H), 1.93 (m, 1 H), 1.78 (m, 1 H), 1.48 (s, 3 H), 1.25 (s, 3 H), 0.80 (s, 3 H) ppm. $^{13}$C NMR [$D_6$]-

 © 2006 Wiley-VCH Verlag GmbH & Co. KGaA, Weinheim 

DMSO: $\delta$ = 150.9 (CH), 150.6 (CH), 149.1 (C), 149.1 (H), 144.8 (C), 133.7 (C), 133.1 (C), 129.0 (C), 128.9 (C), 124.5 (CH), 63.2 (C), 60.5 (2 CH), 51.8 (C), 47.5 (C), 34.6 ($CH_2$), 27.3 ($CH_2$), 25.1 ($2CH_3$), 20.22 ($CH_3$), 17.6 ($CH_3$), 17.5 ($CH_3$), 16.2 ($CH_3$), 15.2 ($CH_3$) ppm.

**(1*S*,3*R*)-1,3-Diamino-1,2,2-trimethylcyclopentane(3,4,7,8-tetramethyl-1,10-phenanthroline)platinum(II) Dichloride Tetrahydrate, [Pt(*S*,*R*-tmcp)(3,4,7,8-Me$_4$phen)]Cl$_2$·4H$_2$O (3b):** This was prepared as described for **2a**, using [Pt(3,4,7,8-Me$_4$phen)Cl$_2$][14,20] and **1b**, to yield the product as a green solid (0.11 g, 83%). $C_{24}H_{38}Cl_2N_4O_2Pt$ (715.69): calcd. C 40.27, H 5.78, N 7.83; found C 40.26, H 5.50; N 7.69. CD spectrum: $\lambda_{max}$ ($\Delta\varepsilon$/mol$^{-1}$dm$^3$cm$^{-1}$, water) = 223 (+1.47), 285 nm (–1.25). $^1$H NMR (300 MHz, [D$_6$]DMSO): $\delta$ = 9.04 (s, 1 H), 8.98 (s, 1 H), 8.41 (s, 2 H), 6.60 (dd, $^3J$ = 10.3, 11.4 Hz, 2 H), 6.54 (dd, $^3J$ = 12.1, 11.2 Hz, 2 H), 2.91 (m, 1 H), 2.82 (d, $^3J$ = 2.9 Hz, 6 H), 2.62 (d, $^3J$ = 4.39 Hz, 6 H), 2.12 (m, 2 H), 1.95 (m, 1 H), 1.75 (m, 1 H), 1.45 (s, 3 H), 1.24 (s, 3 H), 0.82 (s, 3 H) ppm.

**Cytotoxicity:** In vitro cytotoxicity studies were carried out at the Peter MacCullum Cancer Institute, Melbourne by a standard method.[29] The chiral platinum(II) complexes were dissolved in warm distilled water and then diluted to the required concentrations. Results of the growth inhibition for murine leukaemia L1210 cells are reported for two experiments at 48 h continuous exposure to the metal complex. Cells were counted by Coulter Counting. The results of the growth inhibition assays of the platinum(II) complexes against the L1210 mouse leukaemia cell line are presented in Table 1. Values represent $IC_{50}$ in μM. $IC_{50}$ is the concentration of platinum(II) complex required to induce 50% inhibition of cell growth. All complexes were administered in water. Cytotoxicity of the new platinum(II) complexes are compared with cisplatin, and their individual parent compounds [Pt(en)(phen)]Cl$_2$ and [Pt(en)(3,4,7,8-Me$_4$phen)]Cl$_2$,[14] to assess the contribution of the chiral ancillary ligands.

**Viscosity Studies:** Samples were made to a volume of 300 μL and the flow time for the BPES buffer (6 mM, $Na_2HPO_4$, 2 mM $NaH_2PO_4$, 1 mM $Na_2EDTA$, pH 7.0) used was 479 (±1) s. The ct-DNA solution (100 μM per base pair, molar absorptivity of 12824 M$^{-1}$cm$^{-1}$bp$^{-1}$ at 258 nm)[25] gave a flow time of 518 (±1) and samples were prepared to give total platinum(II) complex/base pair ratios of 0.125 and 0.25. Flow times were measured after a thermal equilibration period of 20 min and ranged from 500 (±1) to 552 (±1) depending on the concentration and the complex added. Each sample flow time was measured three times and an average calculated. Relative viscosity is presented as $(\eta/\eta_o)^{1/3}$ in accordance with the theory of Cohen and Eisenberg.[30] The value $\eta$ is the viscosity of the solution in the presence of a complex, and $\eta_o$ is the viscosity of the ct-DNA solution alone. This viscosity $\eta$ is calculated from the time for the sample ($t$) to flow through the viscometer subtracted by the time measured for the buffer ($t_o$) only.

**DNA Binding and Induced Circular Dichroism:** Titrations were performed to determine the affinity constants for the chiral platinum(II) complexes with ct-DNA (Figure 2 and Figure 3) using published methods.[24] The CD was recorded over the range 200 to 350 nm, for the ct-DNA solution (3000 μL, 28 or 35 μM) in buffer (5 mM, Trizma, 50 mM NaCl, pH 7.5), and after each titration with a small volume of metal-complex solution (10 or 5 mM). The small increase in the final volume was no more than 3%. Titrations were continued until no further change was observed in the CD spectrum, indicating that saturation of the DNA had been reached.

Using the information gained from the spectra and utilising the methods of Roger and Nordén,[24] binding constants for each of the complexes were determined as described previously.[14] CD data and the methodology for calculating the binding constant are included in the supporting information (for details see the footnote on the first page of this article). The calculated values for $K_b$ and $n$ [where $K_b$ is the equilibrium binding constant and $n$ is the number of binding sites (in base pairs)] are reported in Table 1. We have also developed a different data analysis technique, which utilises direct least-squares curve fitting, using a Levenberg–Marquardt method,[18] to our experimental points. Essentially we fit the equation below to the data, where the independent variable $L_T$ is the ligand concentration, $B_T$ the total DNA concentration, and the dependent variable $\varepsilon$ the CD response. The calculated values for $K_b$ and $n$ (the number of bases per binding site) using this method are also included in Table 1.

$$\frac{\varepsilon}{\alpha} = 0.5\left[\frac{1}{K_b} + L_T + \frac{B_T}{n_s} - \sqrt{\left(\left\{\frac{1}{K_b} + L_T + \frac{B_T}{n_s}\right\}^2 - \frac{4B_TL_T}{n_s}\right)}\right]$$

**Titration of d(GTCGAC)$_2$ by the Platinum(II) Complexes:** The hexamer was converted into the sodium salt using a CM-25 Sephadex column after residual impurities were removed by elution through a C-18 Sep-Pak as described previously.[14] The hexamer was dissolved in 700 μL of phosphate buffer (10 mM, pH 7) containing 20 mM NaCl and 0.1 mM EDTA. For experiments carried out in $D_2O$ the sample was repeatedly freeze-dried from $D_2O$ and finally made up in 99.96% $D_2O$. The hexamer concentration was determined from the $A_{260}$ absorbance using an extinction coefficient of 6600 M$^{-1}$cm$^{-1}$ per nucleotide.[13,14]

**Supporting Information** (see footnote on the first page of this article): Supporting information is available in electronic format only giving a description of how the DNA binding constants were determined, including mathematical forumlae; DNA binding data; and figures of the DNA binding curves.

## Acknowledgments

The University of Western Sydney Research Grant Scheme supported this work. We thank Dr. Carleen Cullinane from the Peter MacCullum Cancer Institute for cell line testing and Grace Hey for undertaking some of the CD titrations.

[1] K. W. Jennette, S. J. Lippard, G. A. Vassiliades, W. R. Bauer, *Proc. Natl. Acad. Sci. USA* **1974**, *71*, 3839–3843.
[2] J. K. Barton, S. J. Lippard, *Nucleic Acid-Metal Ion Interactions*, (Ed.: T. G. Spiro), Wiley-Interscience, New York, **1980**, p. 31–113.
[3] A. H. Krotz, L. Y. Kuo, T. P. Shields, J. K. Barton, *J. Am. Chem. Soc.* **1993**, *115*, 3877–3882.
[4] A. M. Pyle, J. K. Barton, *Prog. Inorg. Chem., Bioinorg. Chem.* **1990**, *38*, 413–475.
[5] S. J. Lippard, *Acc. Chem. Res.* **1978**, *11*, 211–217.
[6] B. P. Hudson, C. M. Dupureur, J. K. Barton, *J. Am. Chem. Soc.* **1995**, *117*, 9379–9380.
[7] M. Cusumano, M. L. Di Pietro, A. Giannetto, *Inorg. Chem.* **1999**, *38*, 1754–1758.
[8] G. Lowe, A. S. Droz, T. Vilaivan, G. W. Weaver, J. J. Park, J. M. Pratt, L. Tweedale, L. R. Kelland, *J. Med. Chem.* **1999**, *42*, 3167–3174.
[9] A. Odani, H. Masuda, O. Yamauchi, *Inorg. Chem.* **1991**, *30*, 4484–4486.
[10] M. Cusumano, M. L. Di Pietro, A. Giannetto, F. Nicolo, E. Rotondo, *Inorg. Chem.* **1998**, *37*, 563–568.
[11] A. Odani, R. Shimata, H. Masuda, O. Yamauchi, *Inorg. Chem.* **1991**, *30*, 2133–2138.

 © 2006 Wiley-VCH Verlag GmbH & Co. KGaA, Weinheim 

[12] O. Yamanchi, A. Odani, R. Shimata, Y. Kosaka, *Inorg. Chem.* **1986**, *25*, 3337–3339.
[13] J. G. Collins, R. M. Rixon, J. R. Aldrich-Wright, *Inorg. Chem.* **2000**, *39*, 4377–4379.
[14] C. Brodie, J. G. Collins, J. R. Aldrich-Wright, *Dalton Trans.* **2004**, 1145–1152.
[15] W. R. Leopold, R. P. Batzinger, E. C. Miller, J. A. Miller, R. H. Earhart, *Cancer Res.* **1981**, *41*, 4368–4377.
[16] E. M. Rezler, R. R. Fenton, W. J. Esdale, M. J. McKeage, P. J. Russell, T. W. Hambley, *J. Med. Chem.* **1997**, *40*, 3508–3515.
[17] R. C. Conrad, J. V. Rund, *Inorg. Chem.* **1972**, *11*, 129–134.
[18] F. H. Stootman, D. M. Fisher, J. R. Aldrich-Wright, manuscript in preparation.
[19] B. H. Long, J. K. Barton, *Acc. Chem. Res.* **1990**, *23*, 271–273.
[20] D. Suh, J. B. Chaires, *Bioorg. Med. Chem.* **1995**, *3*, 723–728.
[21] S. E. Sherman, D. Gibson, A. H.-J. Wang, S. J. Lippard, *Science* **1985**, *230*, 412–417.
[22] L. Kapicak, E. J. Gabbay, *J. Am. Chem. Soc.* **1975**, *97*, 403–408.
[23] L. P. G. Wakelin, M. J. Waring, *DNA intercalating agents*, in: *Comprehensive Medicinal Chemistry* (Ed.: P. G. Sammes), Pergamon Press, Oxford, UK, **1990**, *2*, 703.
[24] A. Rodger, B. Nordén, *Circular Dichroism and Linear Dichroism*, Oxford University Press, Oxford, **1997**.
[25] J. B. Chaires, N. Dattagupta, D. M. Crothers, *Biochemistry* **1982**, *21*, 3933–3940.
[26] R. A. States, R. A. Haberkorn, D. J. Ruben, *J. Magn. Reson.* **1982**, *48*, 286–292.
[27] R. D. Gillard, P. D. Newman, R. S. Vagg, P. A. Williams, *Inorg. Chim. Acta* **1995**, *233*, 79–84.
[28] W. D. McFadyen, L. P. G. Wakelin, I. A. G. Roos, V. A. Leopold, *J. Med. Chem.* **1985**, *28*, 1113–1116.
[29] G. B. Deacon, E. T. Lawrenz, T. W. Hambley, S. Rainone, L. K. Webster, *J. Organomet. Chem.* **1995**, *493*, 205–213.
[30] G. L. Cohen, H. Eisenberg, *Biopolymers* **1969**, *8*, 45–55.

Received: October 21, 2005
Published Online: December 22, 2005

 © 2006 Wiley-VCH Verlag GmbH & Co. KGaA, Weinheim 

DOI: 10.1002/ejic.200500705

# Steric and Catalytic Effects in Tetraruthenated Manganese Porphyrins

Ildemar Mayer,[a] Genebaldo S. Nunes,[a] Henrique E. Toma,[a] and Koiti Araki*[a]

**Keywords:** Electrochemistry / Manganese / Porphyrinoids / Sensors / Supramolecular chemistry

A new tetraruthenated manganese(III) porphyrin has been obtained and characterized by spectroscopy, electrochemistry, and spectroelectrochemistry. It exhibits a saddle-shaped, nonplanar structure that conveys interesting catalytic, electrocatalytic, and spectroelectrochemical properties to the molecule. Selective steric influence induced by the peripheral ruthenium complexes has been detected in the catalytic oxidation of cyclohexane and cyclohexene with iodosylbenzene. Films formed by layer-by-layer electrostatic assembly with tetraanionic sulfonated copper phthalocyanine exhibit electrocatalytic activity for the oxidation of nitrite and sulfite, thus providing interesting applications in amperometric sensors.

(© Wiley-VCH Verlag GmbH & Co. KGaA, 69451 Weinheim, Germany, 2006)

## Introduction

Metalloporphyrins are an important class of molecules that are widely distributed in biological systems and play an enormous variety of roles, including catalysis, oxygen and signal transport, energy conversion, and electron transfer.[1–15] The development of new porphyrin compounds and derived materials is a subject of current research interest. New properties and functionalities can be generated by changing the molecular structure, stereochemistry, and interactions, in the context of molecular systems and materials. Particularly promising systems that exhibit remarkable catalytic and electrocatalytic properties[2,6,16–21] associated with high-valence oxygen donor species such as $Mn^{V}$=O[22,23] have been derived from manganese porphyrins.

Supramolecular species containing selected metal complexes attached at the periphery of the metalloporphyrin ring have been found to mimic cytochrome P-450 activity.[24] This is a consequence of the electron-withdrawing/-donating and/or electron-transfer properties of the ancillary complexes, which can also act as cofactors and create new pathways for the oxidation of organic substrates. In this sense, the understanding of their spectroscopic properties, stereochemistry, intramolecular interactions, and redox behavior is of the utmost importance.[25–29] In this work the spectroscopic and electrochemical properties of a new tetraruthenated manganese(III)porphyrin complex, [Mn(3-TRPyP)] (Figure 1), are described. Although this species can form four atropisomers, only a single configuration corresponding to a saddle geometry is inferred from molecular mechanics calculations ($MM^{+}$); this reflects the large steric hindrance of the peripheral bis(bipyridine)chlororuthenium(II) complexes attached at carbon 3 (*meta*) of the bridging pyridyl group (Figure 1).

The catalytic activity of [Mn(3-TRPyP)] in the oxidation of cyclohexane and cyclohexene has been investigated. In addition, the possibility to generate ultrathin supramolecular films of such species has been exploited in electrocatalysis for the oxidation of nitrite and sulfite ions in aqueous solution with the aim of generating new, efficient amperometric sensors.

## Results and Discussion

### Spectroscopic Properties

The insertion of $Mn^{2+}$ ions into the free-base $H_2$(3-TPyP) is very fast and its oxidation to $Mn^{3+}$ can be carried out readily in the presence of air. The resulting [Mn(3-TRPyP)] is soluble in common solvents such as methanol, ethanol, DMF, acetone, acetonitrile, and acetic acid and is sparingly soluble in water as its trifluoromethanesulfonate salt. It should be mentioned that the binding of the ruthenium complexes increases the total molecular charge to +5, thus enhancing its solubility in polar solvents. The $^{1}$H NMR spectrum is complicated by the superimposition of the 2,2′-bipyridine and $Mn^{III}$TPyP peaks, in addition to the low molecular symmetry and to the paramagnetic character of the $Mn^{III}$P center. Accordingly, the structural characterization was carried out by mass spectrometry. The fragmentation profiles of the polymetalated pyridylporphyrins were found to be analogous to those previously found for the derivatives $H_2$(3-TRPyP) and Zn(3-TRPyP).[26,27,30,31] The peak for the [Mn(3-TRPyP)] molecular ion ($[C_{120}H_{88}Cl_4MnN_{24}Ru_4]^{5+}$ = 2467.21 g mol$^{-1}$) was found at *m*/*z* 494 with Δ(*m*/*z*) = 0.20 and *m*/*z* 617 with Δ(*m*/*z*) = 0.25,

[a] Instituto de Química, Universidade de São Paulo, Caixa Postal 26077, CEP 05513-970, São Paulo (SP), Brazil
E-mail: koiaraki@iq.usp.br

 © 2006 Wiley-VCH Verlag GmbH & Co. KGaA, Weinheim 

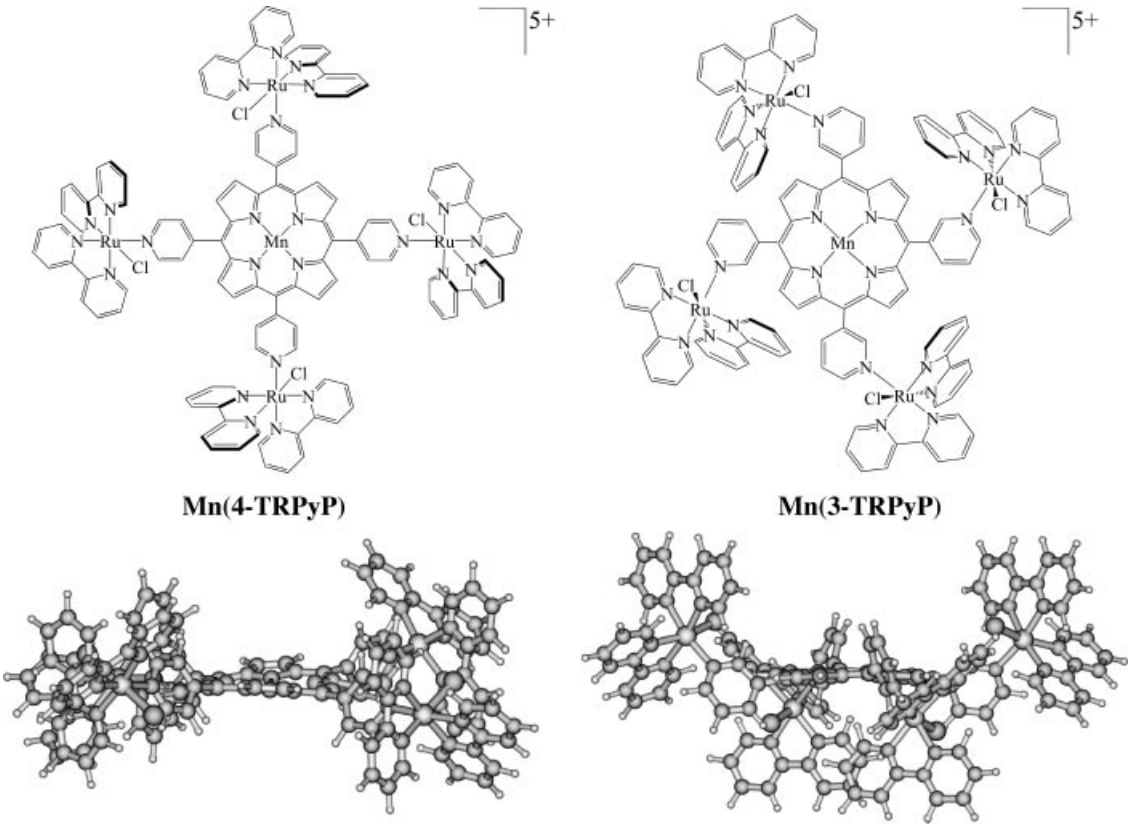


Figure 1. Structures of the tetraruthenated manganese(III) porphyrins [MnTRPyP].

suggesting the occurrence of a $Mn^{III/II}$ redox process in the spray.

[Mn(3-TRPyP)] displays a typical electronic spectrum in methanol,[32] reflecting the strong coupling between the molecular orbitals of the $Mn^{III}$ ion and porphyrin ring.[33,34] The porphyrin bands were found at 464 nm (log $\varepsilon$ = 5.2), attributed to the so-called band V, and 560 (4.3) and 595 nm (3.9), assigned to the IV or $Q_{(1-0)}$ and III or $Q_{(0-0)}$ porphyrin bands, respectively. The MLCT bands of the ruthenium complexes usually found at 360 and 480 nm are hidden by the bands VI (374 nm, log $\varepsilon$ = 4.9) and $V_a$ (399 nm, log $\varepsilon$ = 4.9). The 2,2′-bipyridine intraligand $p\pi \rightarrow p\pi^*$ transitions of the peripheral ruthenium complexes appear at 294 nm (5.3). Finally, the $Mn^{III}$ porphyrin bands II and I appear at 680 (1.6) and 770 nm (1.4) and are assigned to charge-transfer transitions (normally $a_{1u}$ and $a_{2u} \rightarrow d_{xz}$ and $d_{yz}$ transitions, respectively). They tend to become more evident when strongly coordinating ligands such as pyridine, imidazole, and pyrazine are axially coordinated.[35]

## Electrochemistry

The electrochemical behavior of the polymetalated porphyrins was investigated by cyclic voltammetry and spectroelectrochemistry. The voltammograms of a solution of [Mn(3-TRPyP)] in DMF follow the general pattern previously described for the [Mn(4-TRPyP)] isomer.[32] The reversible $Ru^{III/II}$ process is observed at $E_{1/2}$ = 0.93 V (Figure 2), with a cathodic shift of 20 mV in comparison with the *para* isomer.[32] This suggests that the $Mn^{III}$TPyP center is acting as an electron-withdrawing group stabilizing the reduced $[Ru^{II}(bpy)_2(pyP)Cl]$ species. However, no such electronic coupling between the porphyrin ring and the peripheral ruthenium complexes is expected in the case of the *meta* isomer because of the molecular geometry. The porphyrin ring $Mn^{III}P^{+/0}$ redox process was not observed, even at potentials up to 1.50 V.

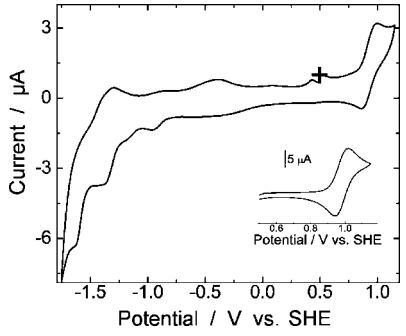


Figure 2. CV of a $2 \times 10^{-3}$ M [Mn(3-TRPyP)] solution in DMF containing 0.1 M $TEAClO_4$ (scan rate: 20 mV $s^{-1}$).

The broad cathodic wave starting around –0.3 V was assigned to the $Mn^{III/II}P$ process and confirmed by spectroelectrochemistry. The waves at $E_{pc}$ = –0.94 and –1.17 V can be tentatively assigned to the successive monoelectronic re-

 © 2006 Wiley-VCH Verlag GmbH & Co. KGaA, Weinheim 

duction of the porphyrin ring to the radical anion and dianion (Figure 2), respectively, by comparison with analogous derivatives.[11,32,36–39] However, the possibility of formation of a species with $Mn^{I}P$ character, as in the case of the respective cobalt derivative,[36–39] cannot be discarded. The single-electron reduction of one and two bipyridyl ligands of each peripheral ruthenium complex was observed at $E_{pc}$ = –1.39 and –1.63 V, respectively. All those processes should be coupled to chemical reactions involving the solvent, and the intensity of the wave associated with the reverse anodic process is lower than for the reduction process. The anodic wave at 0.35 V can be assigned to reduced species formed in the cathodic scan because only the reversible $Ru^{III/II}$ pair of waves at $E_{1/2}$ = 0.93 V was found when the scans were limited to the 0.0 to 1.2 V range.

### Spectroelectrochemistry

The spectroeletrochemical behavior of [Mn(3-TRPyP)] in DMF in the –2.2 to +1.1 V range is shown in Figure 3. The most stable form of this supramolecular complex exhibits the transition metal ions as $Mn^{III}$ and $Ru^{II}$ complexes. When the potential was increased from 0.5 to 1.1 V the peripheral ruthenium complex band (bpy, pπ→pπ*) at 297 nm and the MLCT bands at about 490 and 370 nm disappeared, while an absorption band rose at 316 nm. In contrast, the characteristic $Mn^{III}P$ absorption bands (III, IV, V, $V_a$, and VI) remained essentially unchanged. Such spectral changes (Figure 3, A) are characteristic of a reversible $Ru^{II/III}$ process, as suggested by the presence of several isosbestic points. No changes were observed in the 1.1 to 1.5 V range.

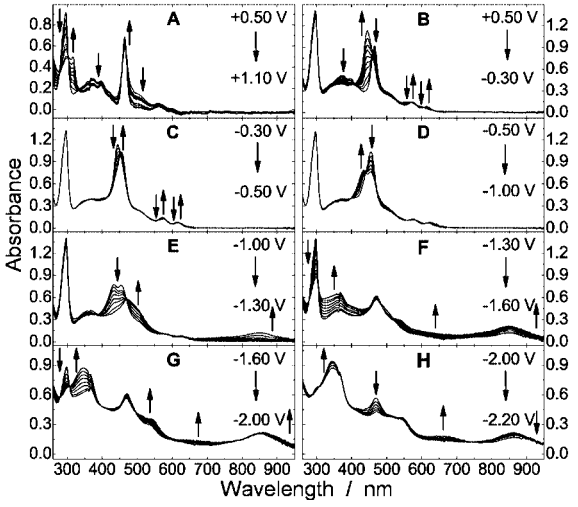


Figure 3. Spectroelectrochemistry of an approx. 80 μM solution of [Mn(3-TRPyP)] in DMF containing 0.10 M $TEAClO_4$ in the 1.1 to –2.2 V range.

The first redox process observed in the 0.5 to –0.3 V range (Figure 3, B), leads to a shift and broadening of the porphyrin Soret band from 464 to 444 nm, characteristic of the reduction of $Mn^{III}P$ to $Mn^{II}P$.[35] Interestingly, a shift of the Soret band maximum to 455 nm was observed at –0.50 V, as a function of time (Figure 3, C), giving a more symmetric and slightly less intense band. This unexpected behavior does not seem to involve a redox process and is probably associated with some axial ligand equilibrium. In this case, the participation of adventitious water molecules[5,6,32] cannot be the cause since quite negative limiting potentials (–2.2 V) could be attained.

When the potential was shifted to –1.0 V a double-peaked Soret band was formed due to the rise of a new absorption band at 433 nm and decrease of the peak at 455 nm (Figure 3, D). This behavior is not consistent with the reduction of the porphyrin ring to the respective radical anion because no characteristic band could be found around 750 nm. An equilibrium involving a face-to-face dimer is another possibility, although this doesn't involve an electron-transfer process. Accordingly, this spectroelectrochemical process was assigned to the formation of a reduced species with $Mn^{I}P$ character, as evidenced by the electrocatalytic activity of GCE modified with films of [Mn(TRPyP)]/[CuTSPc].

The reduction of the porphyrin ring was observed at –1.3 V, where a decay of the double-peaked Soret band and an increase of the absorptions at 500 and 850 nm were observed (Figure 3, E). The next two processes were observed in the ranges –1.3 to –1.6 V (Figure 3, F) and –1.6 to –2.0 V (Figure 3, G) and involve the successive decrease of the bipyridine pπ–pπ* band at 298 nm to half its value, followed by its disappearance, while a broad band rose at 350 nm. Accordingly, they were assigned to the successive single-electron reduction of the first and second bpy ligands of each peripheral ruthenium complex. Interestingly, when the potential was further shifted to –2.2 V the small peak at 470 nm associated with the porphyrin radical anion decreased as the absorbance at 660 nm increased (Figure 3, H). Those changes are typical of the formation of the porphyrin dianion. Generally, this process occurs about 200 mV after the $P^{0/-}$ process, but the reduction of the bpy ligands should shift that redox process to potentials below –2.0 V, as observed in the case of the corresponding [Co(TRPyP)] derivatives.[5,6,32,36,37]

### Electrocatalytic Properties

[Mn(TRPyP)] can form stable ultrathin films of a supramolecular nanomaterial on GCE that, however, exhibit appreciable solubility in aqueous solution. This inconvenience can be eliminated by means of a layer-by-layer electrostatic assembly[32,40] with the structurally complementary tetraanionic sulfonated copper phthalocyanine [CuTSPc]. A remarkable electrochemical activity was observed for the modified electrodes (Figure 4), showing that it is possible to transfer the molecular properties of those tetraruthenated manganese porphyrins to the electrode surface. Typical CVs of GCE modified with [Mn(TRPyP)]/[CuTSPc] films in aqueous solution, at pH 4.7, exhibit a couple of reversible sine-shaped waves at $E_{1/2}$ = 0.95 V assigned to the $Ru^{III/II}$ process. The anodic and cathodic peak current intensities

 © 2006 Wiley-VCH Verlag GmbH & Co. KGaA, Weinheim 

increase linearly as a function of the scan rate, as expected for redox species immobilized on the surface.[9,27,40]

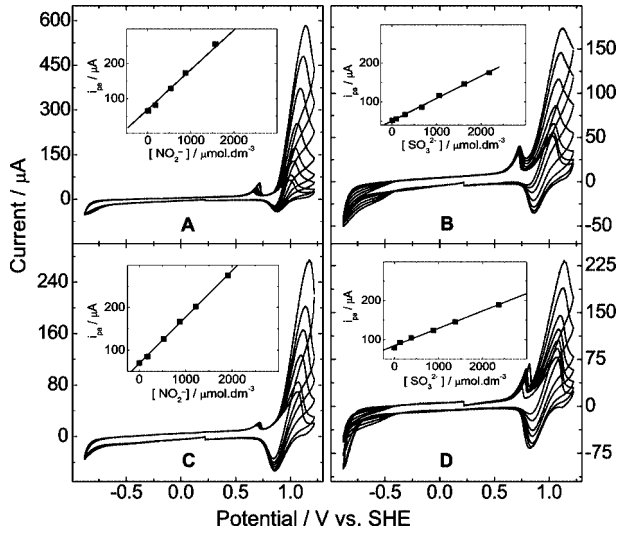


Figure 4. CVs of a GCE modified with layer-by-layer electrostatically assembled films of (A, B) [Mn(4-TRPyP)]/[CuTSPc] ($\Gamma$ = 1.6 and 1.2 nmol cm$^{-2}$) and (C, D) [Mn(3-TRPyP)]/[CuTSPc] ($\Gamma$ = 1.7 and 1.6 nmol cm$^{-2}$) in the presence of increasing concentrations of nitrite (A, C) and sulfite (B, D) in 0.025 M acetate buffer (pH 4.7) and $KNO_3$ (0.5 M). Scan rate: 0.1 V s$^{-1}$. Inset: plot of $i_{pa}$ vs. [substrate].

As aliquots of a stock solution of nitrite and sulfite were added to the electrolyte solution (Figure 4) the anodic wave at 1 V intensified linearly as a function of the concentration of those species. This indicates a relatively fast heterogeneous charge-transfer process mediated by the supramolecular films, in contrast with the bare electrodes, which exhibit broad, irreproducible responses. There is no significant difference in the electrocatalytic properties of the supramolecular nanomaterials obtained with both isomers for the oxidation of sulfite and nitrite. On the other hand, both modified electrodes are ineffective for the reduction of nitrite until –0.85 V. However, this does not seem to be the case for the reduction of sulfite, for which the activity of the *meta* isomer is clearly higher. The broad reduction wave starting at –0.5 V is assigned to the reduction of sulfite directly on the GCE surface.[41,42] This contrasts with the results obtained for [Ni(TRPyP)]/[CuTSPc] and [Co(TRPyP)]/[CuTSPc] films,[43] which exhibit high activity for the reduction of both substrates. This reductive electrocatalytic activity is due to the formation of reduced species with $M^{I}P$ character, such as $Ni^{I}P$ and $Co^{I}P$, which should be responsible for the efficient electron-transfer to nitrite and sulfite. Analogously, this result for the [Mn(TRPyP)]/[CuTSPc] films reinforces our previous assignment of the spectroelectrochemistry event observed at around –1 V to the formation of a species with $Mn^{I}P$ character.

## Catalytic Properties

The catalytic activity of [Mn(3-TRPyP)] species for cyclohexane hydroxylation and cyclohexene epoxidation with iodosylbenzene (PhIO) was evaluated relative to the activity of the [Mn(4-TRPyP)] isomer.[32] [Mn(3-TRPyP)] in acetonitrile solution exhibits bands V, IV, and III at 473, 574, and 616 nm, respectively. Upon adding a PhIO solution in $CH_2Cl_2/CH_3OH/H_2O$ (80:18:2) band V immediately shifts to 427 nm and bands IV and III disappear, giving rise to broad absorptions. These features are characteristic of high-valent $O{=}Mn^{IV}P$ species. However, within about a minute the spectrum of the $Mn^{III}P$ species is regenerated, indicating the consumption of PhIO and the reaction of $O{=}Mn^{IV}P$ with solvent species such as water and methanol. This suggests that the actual catalytically active species ($O{=}Mn^{V}P$) is a much more effective oxidant and oxygen atom donor (Figure 5).

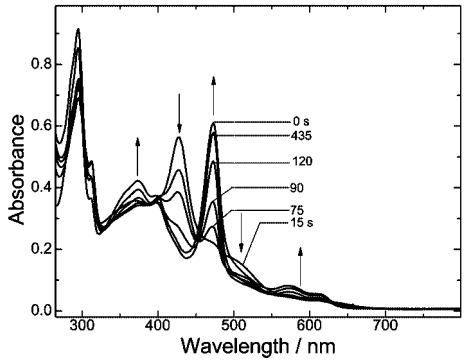


Figure 5. UV/Vis spectra showing the regeneration of $Mn^{III}P$ after reaction of a $4\times10^{-6}$ M acetonitrile solution of [Mn(3-TRPyP)] with a PhIO solution in $CH_2Cl_2/CH_3OH/H_2O$ (80:18:2). [Mn(3-TRPyP)]:[PhIO] = 1:10.

The catalytic activity of [Mn(TRPyP)] for the oxidation of cyclohexane was verified with iodosylbenzene as oxygen donor. Typically, $9.2\times10^{-4}$ mol of cyclohexane, $1.21\times10^{-7}$ mol of catalyst, and $2.7\times10^{-6}$ mol of PhIO were mixed in DCE/ACN (200/80 μL), at 298 K, in a sealed vial. The products were determined by gas chromatography after 15 min and the results are shown in Table 1. Cyclohexanol and cyclohexanone are the main products of the reaction, but small amounts of chlorocyclohexane are also observed. Interestingly, the *meta* isomer exhibits higher selectivity (alcohol/ketone ratio = 3.6 vs. 2.3) and reactivity (44% vs. 34%) than the *para* species.

More clear-cut evidence for the distinct activity of those isomers was obtained when the tetraruthenated manganese porphyrins were used as catalysts for the oxidation of cyclohexene. In general, the *meta* isomer has a significantly higher activity, converting all PhIO into oxygenated products but with a lower epoxide yield. In contrast, the *para* isomer shows a conversion of only about 60%, with a much higher selectivity for epoxide formation (Table 2).

The results described above reveal that [Mn(TRPyP)] has a catalytic activity for the oxidation of cyclohexane by PhIO similar to that of other manganese porphyrins.[44–46] For example, Iamamoto et al.[44] obtained 43% of cyclohexanol and 23% of cyclohexanone (ol/one ratio 2) with [Mn(TPP)-Cl] (chloromanganese tetraphenylporphyrin) in DCM. In general, the lower selectivity in polar solvents (for example

 © 2006 Wiley-VCH Verlag GmbH & Co. KGaA, Weinheim 

Table 1. Cyclohexane hydroxylation with PhIO catalyzed by tetraruthenated manganese(III) porphyrins.[a]

| Catalyst | C-ol [%][c] | C-one [%][c] | C-Cl [%][c] | Ratio alcohol:ketone | Total yield [%] | TON[b] |
|---|---|---|---|---|---|---|
| [Mn(3-TRPyP)] | 32 | 9 | 3 | 3.6 | 44 | 11 |
| [Mn(4-TRPyP)] | 23 | 10 | 1 | 2.3 | 34 | 9 |

[a] MnP: $1.2\times10^{-7}$ mol; PhIO: $2.7\times10^{-6}$ mol; cyclohexane: $9.2\times10^{-4}$ mol; 1,2-dichloroethane (DCE): 200 μL; acetonitrile (ACN): 80 μL; chlorobenzene as internal standard; all solvents purged with $N_2$; $T$ = 298 K. C-ol = cyclohexanol, C-one = cyclohexanone, C-Cl = chlorocyclohexane. [b] TON = mol products/mol catalyst. [c] Based on the initial amount of PhIO. Average error: ±3%.

Table 2. Cyclohexene oxidation with PhIO catalyzed by tetraruthenated maganese porphyrins.[a]

| Catalyst | Epoxide [%][b] | C-ol [%][b] | C-one [%][b] | Allyl. oxid. | Total yield [%][b] |
|---|---|---|---|---|---|
| [Mn(3-TRPyP)] | 24 | 40 | 43 | 0.3 | 107 |
| [Mn(4-TRPyP)] | 37 | 15 | 11 | 1 | 63 |

[a] MnP: $1.2\times10^{-7}$ mol; PhIO: $2.7\times10^{-6}$ mol; cyclohexene: $4.9\times10^{-4}$ mol; 1,2-dichloroethane (DCE): 250 μL; acetonitrile (ACN): 44 μL; chlorobenzene as internal standard; all solvents purged with $N_2$; $T$ = 298 K. C-ol = cyclohexen-2-ol, C-one = cyclohexen-2-one, allyl. oxid. = percentage of allylic oxidation products. [b] Based on the initial amount of PhIO. Average error ±3%.

ACN) is associated with the formation of the radical intermediate species $O{=}Mn^{IV}P^{+\cdot}$,[44,47,48] as well as the possible coordination of the solvent molecules to the Mn center. This does not seem to be the case for the [Mn(TRPyP)] complexes, however, which have a higher selectivity in DCE/ACN, in which they are more soluble because of their higher ionic character.

In the case of cyclohexane (Table 1), the higher efficiency suggests that the catalytically active high-valent oxomanganese species formed by [Mn(3-TRPyP)] is more reactive than that formed by [Mn(4-TRPyP)]. Another possibility is the involvement of two different activated species[49] as a consequence of electronic effects or interaction of the oxidant and/or the substrate with the peripheral $[Ru(bpy)_2Cl]^+$ groups. In fact, the ruthenium complexes in [Mn(3-TRPyP)] are positioned above and below the manganese porphyrin center. Accordingly, two pockets of suitable size for interaction with those organic substrates are generated, probably inducing the formation of a structurally more favorable activated complex. In contrast, the *para* isomer has a more symmetric and planar structure, ruling out such a possibility.[32]

The small amount of chlorocyclohexane (Table 1) generated in the oxidation reaction also gives some clues about the role of the peripheral ruthenium complexes in the activated complex. This by-product is likely to be formed when the cyclohexyl radical does not combine with the OH bond at the MnP center and escapes from the "cage". Consequently, its yield should be higher when the peripheral ruthenium complexes are close or interacting with the species participating in the activated complex. This proximity should facilitate the abstraction of a chloro atom from the $[Ru(bpy)_2Cl]$ groups, although the possibility of abstraction from the solvent cannot be discarded. In fact, experiments under similar conditions using another supramolecular species containing four trinuclear ruthenium acetate clusters with no coordinated chloride showed no chlorocyclohexane formation, thus ruling out the hypothesis of chlorine atom abstraction from the solvent. Considering that the redox and electronic properties of both species are similar, the significantly higher amount of chlorocyclohexane generated by the *meta* isomer is strong evidence that its higher catalytic activity can be assigned to the favorable stereochemical effects induced by the peripheral $[Ru(bipy)_2Cl]^+$ groups.

Finally, it is well known that conventional Mn–porphyrin species undergo severe degradation during the catalytic cycles,[44–48] and for this reason new, more-stable catalysts have been pursued, for example involving chlorinated or fluorinated porphyrins. In the case of the [Mn(TRPyP)] catalysts no evidence of decomposition could be detected spectroscopically after at least 10 turnover cycles, or 15 min, corresponding to the time of a typical experiment. Therefore, in spite of their secondary role in catalysis, the peripheral $[Ru(bipy)_2Cl]^+$ groups do provide an important steric protection around the highly reactive $Mn^V{=}O$ site, thereby preventing the degradation of the porphyrin center under such highly oxidizing conditions. Furthermore, they can provide interaction sites for the occurrence of steric effects, inducing changes in the geometry of the activated complex. The last two effects are probably the greatest advantage associated with these [Mn(TRPyP)] catalysts, in addition to their improved selectivity and high solubility in organic solvents.

## Conclusions

A new stereochemically hindered tetraruthenated manganese(III) porphyrin has been obtained and its structural, spectroelectrochemical, catalytic, and electrocatalytic properties investigated. The metalloporphyrin reduction and ruthenium complex oxidation potentials are shifted to more negative potentials in comparison with the planar isomer, suggesting a higher electronic density on the porphyrin ring. Stable and electrocatalytically active ultrathin films of layer-by-layer electrostatic assembled films of [Mn(TRPyP)]/[CuTSPc] can be easily prepared and used as nitrite and sulfite detectors. The activity of the [Mn(3-TRPyP)]/[CuTSPc]-modified GC electrodes for the reduction of sulfite is ascribed to the formation of a reduced species with $Mn^IP$ character at around –0.85 V, as observed by spectroelectrochemistry.

 © 2006 Wiley-VCH Verlag GmbH & Co. KGaA, Weinheim 

Very significant differences in the P-450 catalytic activity were found for the oxidation of cyclohexene and cyclohexane with iodosylbenzene. In fact, the *meta* isomer is consistently more active than the *para* isomer in both cases, although the selectivity for epoxide is higher for the latter. Such differences are due to steric effects induced by the peripheral [$Ru(bpy)_2Cl$] groups, which are positioned above and below the MnP ring and can therefore direct the activation of the substrates, thus improving the selectivity of the catalytic reactions. In comparison with conventional manganese porphyrins, the great advantage associated with the [Mn(TRPyP)] catalysts is their pronounced stability and improved selectivity in oxygen-transfer reactions.

## Experimental Section

**Materials and Methods:** UV/Vis spectra were recorded with a HP-8453A diode array spectrophotometer, in the 190–1100 nm range, either in $CH_3OH$ or $CH_3CN$. Cyclic voltammograms of [Mn(TRPyP)] in DMF solution were obtained with an AUTOLAB PGSTAT30 potentiostat/galvanostat. A conventional three-electrode cell was employed, consisting of a platinum disk as working electrode, $Ag/Ag^+$ (0.010 M, in $CH_3CN$) as reference electrode, and coiled platinum wire as auxiliary electrode. The solvents were HPLC grade; DMF was dried with anhydrous $CuSO_4$ and distilled under vacuum immediately before use. The electrolyte $[(C_2H_5)_4N]ClO_4$ was prepared by the reaction of $[(C_2H_5)_4N]OH$ with $HClO_4$, recrystallized from water, and dried under vacuum. A similar arrangement, except for the Ag|AgCl|KCl 1.00 M reference electrode, was used in the electrochemical studies using glassy carbon electrodes (GCE) modified with ultrathin electrostatic assembled films of [Mn(3-TRPyP)]/[CuTSPc] or [Mn(4-TRPyP)]/[CuTSPc]. All potentials were converted into the SHE scale by adding 0.503 or 0.222 V to the experimental values in organic or aqueous solution, respectively. Phosphate (25 mM, pH 6.80) and acetate (25 mM, pH 4.70) buffers in 0.50 M $KNO_3$ solution were used as electrolyte. The spectroelectrochemistry data were collected with a previously described homemade thin-layer cell[50] and a PAR model 173 potentiostat/galvanostat in parallel with an HP-8453A spectrophotometer. Electrospray mass spectra were recorded with a Q-Tof (Micromass) mass spectrometer with a quadrupole (Qq) and high-resolution orthogonal time of flight (o-TOF) configuration. The sample was injected with a syringe pump (Harvard Apparatus, Pump 11) at a rate of 10 $\mu L\,min^{-1}$ through an uncoated fused-silica capillary. All samples were dissolved in pure methanol. The ESI mass spectra were acquired at an ESI capillary voltage of 3 kV and a cone voltage of 10 V. Isotopic patterns were calculated using the MassLynx software. The products of the catalytic oxidation reactions were analyzed by gas chromatography using a Shimadzu model GC-17A equipment with flame ionization detector and OV-1701 0.50 micron capillary column (30 m × 0.25 mm). The carrier gas was $N_2$. Acetonitrile (HPLC grade) was dried over 3-Å molecular sieves before use. *n*-Octane was purified with concentrated sulfuric acid, washed with water, and distilled. Dichloromethane was distilled from over $P_2O_5$ and stored over molecular sieves. All other chemicals were reagent grade (1,2-dichloroethane, cyclohexane, methanol, and deuterated cyclohexane with >99% D) and used as received. Iodosylbenzene was prepared from iodobenzene diacetate as described in the literature.[51] All reactions were carried out in a thermostatted 2-mL vial with a septum, containing a magnetic stirring bar, at 25.0 ± 0.1 °C, under argon. 1,2-Dichloroethane, cyclohexane, and *n*-octane (internal reference for GC) were successively syringed into the vial, and $1.14 \times 10^{-5}$ mol of PhIO was added. A suitable volume of acetonitrile stock solution of the catalyst was then introduced in order to obtain the desired concentration.

**Syntheses:** The preparation of the *cis*-dichlorobis(2,2′-bipyridine)-ruthenium(II) complex $[Ru(bpy)_2Cl_2]$ has been described previously.[52] [Mn(3-TPyP)] was obtained by treating 500 mg (0.80 mmol) of the free-base porphyrin $H_2$(3-TPyP) with 147 mg (0.85 mmol) of manganese(II) acetate in refluxing glacial acetic acid for an hour, whilst stirring. The reaction mixture was cooled to room temperature and the solvent removed in a flash evaporator. The solid was washed with water, filtered, and dried under vacuum. Yield: 97%. $C_{40}H_{24}N_8Mn(CH_3COO)\cdot H_2O$ (748.2): calcd. C 67.38, H 3.90, N 14.97; found C 67.76, H 4.12, N 15.98. [Mn(3-TRPyP)] was obtained from the reaction of 101 mg (0.15 mmol) of [Mn(3-TPyP)] with 300 mg (0.62 mmol) of $[Ru(bpy)_2Cl_2]$ in 100 mL of refluxing glacial acetic acid for an hour, whilst stirring. The solvent was removed in a flash evaporator and the residue redissolved in methanol and refluxed for 30 min to assure the coordination of four ruthenium complexes to the peripheral pyridyl nitrogen atoms. The solvent was removed, the solid redissolved in a minimum volume of DMF, and this solution added dropwise to 10 mL of an aqueous lithium trifluoromethanesulfonate solution. The brown amorphous precipitate obtained was filtered, dried under vacuum, purified by successive recrystallization, and finally by neutral alumina column chromatography using a mixture of dichloromethane and ethanol (10:1) as eluent. Yield: 89%. $C_{120}H_{88}Cl_4MnN_{24}Ru_4(CF_3SO_3)_5\cdot 8H_2O$ (3356.7): calcd. C 44.73, H 3.12, N 10.01; found C 44.52, H 3.27, N 9.49.

## Acknowledgments

Financial support by FAPESP (Fundação de Amparo à Pesquisa do Estado de São Paulo), CNPq (Conselho Nacional de Desenvolvimento Científico e Tecnológico), CAPES/PICD, RENAMI (Rede de Nanomateriais Moleculares e de Interface), and the Millenium Institute of Complex Materials is gratefully acknowledged.

[1] Y. Murakami, J. Kikuchi, Y. Hisaeda, O. Hayashida, *Chem. Rev.* **1996**, *96*, 721.
[2] B. Meunier, *Chem. Rev.* **1992**, *92*, 1411.
[3] L. R. Milgrom, in *The Colours of Life: An Introduction to the Chemistry of Porphyrins and Related Compounds*, Oxford University Press, Oxford, **1997**.
[4] J. R. C. Rocha, L. Angnes, M. Bertotti, K. Araki, H. E. Toma, *Anal. Chim. Acta* **2002**, *452*, 23.
[5] S. Dovidauskas, K. Araki, H. E. Toma, *J. Porphyrins Phthalocyanines* **2000**, *4*, 727.
[6] S. Dovidauskas, H. E. Toma, K. Araki, H. C. Sacco, Y. Iamamoto, *Inorg. Chim. Acta* **2000**, *305*, 206.
[7] C. M. N. Azevedo, K. Araki, H. E. Toma, L. Angnes, *Anal. Chim. Acta* **1999**, *387*, 175.
[8] K. Araki, S. Dovidauskas, H. Winnischofer, A. D. P. Alexiou, H. E. Toma, *J. Electroanal. Chem.* **2001**, *498*, 152.
[9] K. Araki, L. Angnes, H. E. Toma, *Adv. Mater.* **1995**, *7*, 554.
[10] K. Araki, H. E. Toma, *J. Photochem. Photobiol., A* **1994**, *83*, 245.
[11] K. Araki, H. E. Toma, *J. Chem. Res. Synop.* **1994**, 290.
[12] L. Angnes, C. M. N. Azevedo, K. Araki, H. E. Toma, *Anal. Chim. Acta* **1996**, *329*, 91.
[13] L. Flamigni, A. M. Talarico, B. Ventura, G. Marconi, C. Sooambar, N. Solladie, *Eur. J. Inorg. Chem.* **2004**, 2557.
[14] E. Iengo, E. Zangrando, E. Alessio, *Eur. J. Inorg. Chem.* **2003**, 2371.
[15] J. Wojaczynski, M. Stepien, L. Latos-Grazynski, *Eur. J. Inorg. Chem.* **2002**, 1806.

 © 2006 Wiley-VCH Verlag GmbH & Co. KGaA, Weinheim 

[16] T. C. Zheng, D. E. Richardson, *Tetrahedron Lett.* **1995**, *36*, 833.
[17] Z. W. Tong, T. Shichi, K. Takagi, *Mater. Lett.* **2003**, *57*, 2258.
[18] Y. Naruta, M. Sasayama, *Chem. Lett.* **1994**, 2411–2414.
[19] T. J. Groves, M. K. Stern, *J. Am. Chem. Soc.* **1988**, *110*, 8628.
[20] L. Cavallo, H. Jacobsen, *Eur. J. Inorg. Chem.* **2003**, 892.
[21] E. Porhiel, A. Bondon, J. Leroy, *Eur. J. Inorg. Chem.* **2000**, 1097.
[22] N. Jin, J. T. Groves, *J. Am. Chem. Soc.* **1999**, *121*, 2923.
[23] J. T. Groves, J. Lee, S. S. Marla, *J. Am. Chem. Soc.* **1997**, *119*, 6269.
[24] B. Meunier, S. P. Visser, S. Shaik, *Chem. Rev.* **2004**, *104*, 3947.
[25] D. M. Tomazela, F. C. Gozzo, I. Mayer, F. M. Engelmann, K. Araki, H. E. Toma, M. N. Eberlin, *J. Mass Spectrom.* **2004**, *39*, 1161.
[26] I. Mayer, A. L. B. Formiga, F. M. Engelmann, H. Winnischofer, P. V. Oliveira, D. M. Tomazela, M. N. Eberlin, H. E. Toma, K. Araki, *Inorg. Chim. Acta* **2005**, *358*, 2629.
[27] I. Mayer, M. N. Eberlin, D. M. Tomazela, H. E. Toma, K. Araki, *J. Braz. Chem. Soc.* **2005**, *16*, 418.
[28] M. G. Ribeiro, G. C. Azzellini, *J. Braz. Chem. Soc.* **2003**, *14*, 914.
[29] H. E. Toma, *J. Braz. Chem. Soc.* **2003**, *14*, 845.
[30] K. Araki, H. E. Toma, *J. Coord. Chem.* **1993**, *30*, 9.
[31] H. E. Toma, K. Araki, *Coord. Chem. Rev.* **2000**, *196*, 307.
[32] K. Araki, H. Winnischofer, H. E. B. Viana, M. M. Toyama, F. M. Engelmann, I. Mayer, A. L. B. Formiga, H. E. Toma, *J. Electroanal. Chem.* **2004**, *562*, 145.
[33] S. Asher, K. Sauer, *J. Chem. Phys.* **1976**, *64*, 4115.
[34] M. Gouterman, in *The Porphyrins* (Ed.: D. Dolphin), Academic Press, New York, **1979**, vol. III, p. 347.
[35] L. J. Boucher, *Coord. Chem. Rev.* **1972**, *7*, 289.
[36] D. Sazou, C. Araullomcadams, B. C. Han, M. M. Franzen, K. M. Kadish, *J. Am. Chem. Soc.* **1990**, *112*, 7879.
[37] F. Dsouza, A. Villard, E. Vancaemelbecke, M. Franzen, T. Boschi, P. Tagliatesta, K. M. Kadish, *Inorg. Chem.* **1993**, *32*, 4042.
[38] K. Araki, L. Angnes, C. M. N. Azevedo, H. E. Toma, *J. Electroanal. Chem.* **1995**, *397*, 205.
[39] K. Araki, H. E. Toma, *Inorg. Chim. Acta* **1991**, *179*, 293.
[40] K. Araki, M. J. Wagner, M. S. Wrighton, *Langmuir* **1996**, *12*, 5393.
[41] S. M. Chen, *J. Electroanal. Chem.* **1996**, *407*, 123.
[42] S. M. Chen, S. W. Chiu, *Electrochim. Acta* **2000**, *45*, 4399.
[43] I. Mayer, H. E. Toma, K. Araki, submitted.
[44] Y. Iamamoto, M. D. Assis, K. J. Ciuffi, C. M. C. Prado, B. Z. Prellwitz, M. Moraes, O. R. Nascimento, H. C. Sacco, *J. Mol. Catal. A: Chem.* **1997**, *116*, 365.
[45] C.-C. Guo, H.-P. Li, J.-B. Xu, *J. Catal.* **1999**, *185*, 345.
[46] C.-C. Guo, J.-X. Song, X.-B. Chen, G.-F. Jiang, *J. Mol. Catal. A: Chem.* **2000**, *157*, 31.
[47] M. Gunter, P. Turner, *J. Mol. Catal.* **1991**, *66*, 121.
[48] A. Tellend, P. Bationi, D. Mansuy, *J. Chem. Soc., Chem. Commun.* **1994**, 1035.
[49] R. D. Arasasingham, G.-X. He, T. C. Bruice, *J. Am. Chem. Soc.* **1993**, *115*, 7985.
[50] H. E. Toma, K. Araki, *Curr. Org. Chem.* **2002**, *6*, 21.
[51] H. Saltzman, J. G. Sharefkin, *Org. Synth.* **1963**, *43*, 61.
[52] F. M. Engelmann, P. Losco, H. Winnischofer, K. Araki, H. E. Toma, *J. Porphyrins Phthalocyanines* **2002**, *6*, 33.

Received: August 4, 2005
Published Online: December 20, 2005

 © 2006 Wiley-VCH Verlag GmbH & Co. KGaA, Weinheim 

DOI: 10.1002/ejic.200500812

# Polar Cofacially Fixed Sandwich Complexes: Do They Demonstrate Second Harmonic Generation (SHG)?

**Maik Malessa,[a] Jürgen Heck,*[a] Jürgen Kopf,[a] and M. Helena Garcia[b]**

*Dedicated to Prof. Dr. Wittko Francke on the occasion of his 65th birthday*

**Keywords:** Heterometallic complexes / Sandwich complexes / Donor–acceptor systems / Nonlinear optics / Through-space interaction

For the purpose of possible second harmonic generation (SHG) a cationic and a neutral sandwich unit were cofacially arranged in a three-step synthesis starting from 1,8-diiodonaphthalene. First, 1-cyclopentadienyl-8-iodonaphthalene (**2**) was formed, then the neutral ferrocenyl substituent was fixed in the 8-position by a Negishi cross-coupling reaction. The deprotonation of the cyclopentadienyl substituent, and the subsequent coordination of the half-sandwich fragments ML = $[Fe(\eta^5\text{-}C_5Me_5)]^+$, $[Rh(\eta^5\text{-}C_5Me_5)]^{2+}$, $[Ir(\eta^5\text{-}C_5Me_5)]^{2+}$, $[Ru(\eta^6\text{-}C_6H_6)]^{2+}$ to the cyclopentadienyl anion revealed the desired dinuclear complexes 1-[($\eta^5$-cyclopentadienediyl)-($\eta^5$-pentamethylcyclopentadienyl)iron(II)]-8-ferrocenylnaphthalene (**5**), 1-[($\eta^5$-cyclopentadienediyl)($\eta^5$-pentamethylcyclopentadienyl)rhodium(III)]-8-ferrocenylnaphthalene hexafluorophosphate (**6**$PF_6$), 1-[($\eta^5$-cyclopentadienediyl)($\eta^5$-pentamethylcyclopentadienyl)iridium(III)]-8-ferrocenylnaphthalene hexafluorophosphate (**7**$PF_6$), and 1-[($\eta^6$-benzene)($\eta^5$-cyclopentadienediyl)ruthenium(II)]-8-ferrocenylnaphthalene hexafluorophosphate (**8**$PF_6$). The neutral complex **5** was oxidized to the paramagnetic cation 1-[($\eta^5$-cyclopentadienediyl)-($\eta^5$-pentamethylcyclopentadienyl)iron(III)]-8-ferrocenylnaphthalene hexafluorophosphate (**5**$PF_6$). Compounds **3**, **5**$PF_6$, **6**$PF_6$, and **7**$PF_6$ were characterized by X-ray structure determination; the neutral compound **3** crystallizes in the space group $P2_1/c$, whereas all of the cationic dinuclear complexes crystallize in the chiral space group $C222_1$. A cyclic voltammetry study points to a predominant "through-space" interaction between the cationic sandwich unit and the neutral ferrocene substituent. The compounds **5**$PF_6$, **6**$PF_6$, **7**$PF_6$, and **8**$PF_6$ were subjected to hyper-Rayleigh scattering (HRS) and Kurtz-powder measurements. In both studies no SHG intensity could be observed.
(© Wiley-VCH Verlag GmbH & Co. KGaA, 69451 Weinheim, Germany, 2006)

## Introduction

Cofacially stacked arrays of organic and organometallic π-systems are of increasing interest for chemists and physicists, because of novel electrical,[1,2] optical,[2] and magnetic[3] properties. Just recently, theoretical[4] and experimental[5] work has demonstrated that stacked donor–acceptor arrangements of π-systems are suitable for second harmonic generation (SHG) effected by through-space (hyper)polarization (Figure 1).

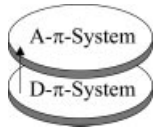


Figure 1. Cofacially stacked arrangement of donor(D)–acceptor(A) π-systems for second harmonic generation (SHG) due to polar "through-space" interaction.

Conventional types of compounds revealing nonlinear optical (NLO) properties, i.e. SHG, are composed of donor and acceptor units linked by conjugated π-bonds, which very often suffer from absorbance in the region of the SHG, and are thus not suitable for practical applications. In contrast, π-stacked donor-acceptor combinations seem to provide a better optical transparency.[6] Our approach to stacked organometallic π-complexes with donor–acceptor combinations, which may call forth SHG, is based on Rosenblum's concept of 1,8-disubstituted naphthalene derivatives containing two sandwich complexes in the *peri* position. Whereas the Rosenblum naphthalene derivatives are symmetrically constructed with the same sandwich complexes in the *peri* position,[7,8] our desired target molecules should contain different sandwich complexes,[9] one of which is a cation, generating an overall dipole moment, which is a possible prerequisite for SHG (Figure 2).

[a] Institut für Anorganische und Angewandte Chemie, Universität Hamburg,
Martin-Luther-King-Platz 6, 20146 Hamburg
[b] Faculdade de Ciências da Universidade de Lisboa, Ed. C8, Campo Grande, 1749-016 Lisboa, Portugal

 © 2006 Wiley-VCH Verlag GmbH & Co. KGaA, Weinheim InterScience 

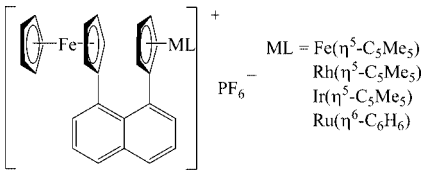


Figure 2. Unsymmetrically 1,8-disandwich-substituted naphthalene derivatives.

## Results and Discussion

### Synthesis

The assembly of different sandwich complexes in *peri* position of naphthalene requires a stepwise synthesis. Starting with a cross-coupling reaction of 1,8-diiodonaphthalene (**1**) [10] with cyclopentadienylzinc chloride[7a,9a] (Scheme 1), results in the formation of 1-cyclopentadienyl-8-iodonaphthalene (**2**). For the second step, a Pd-catalyzed Negishi cross-coupling reaction with ferrocenylzinc chloride[11,12] was performed, revealing complex **3**, which is composed of the two different isomers **3a** and **3b** (see Exp. Sect.). In order to synthesize the unsymmetrical disandwich-substituted naphthalene derivatives, complex **3** was subjected to a deprotonation by sodium bis(trimethylsilyl)amide to yield **4**, and a consecutive coordination reaction with the proper half-sandwich complexes (Scheme 1). For Rh, Ir, and Ru complexes **6**$PF_6$, **7**$PF_6$, and **8**$PF_6$, the deprotonated complex **4** was treated with thallium chloride in acetonitrile to replace the counterion $Na^+$ with $Tl^+$.[13] This cation exchange is necessary to obtain good yields of the desired dinuclear cationic complexes with Ru, Rh and Ir. In order to achieve the polar structure of the diiron derivative, compound **5** was oxidized to the paramagnetic monocation **5**$PF_6$ by addition of a stoichiometric amount of ferrocenium hexafluorophosphate (Scheme 2), and a dark red-brown crystalline material was obtained. All compounds were fully characterized by elemental analyses, spectroscopic methods and cyclic voltammetry. For compound **3a**, **5**$PF_6$, **6**$PF_6$ and **7**$PF_6$ X-ray structure analyses were determined.

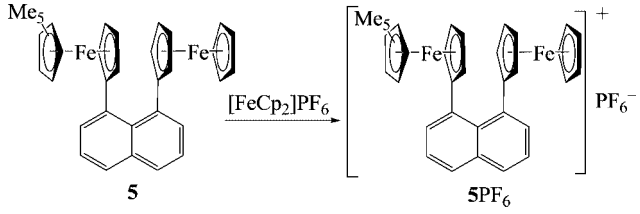


Scheme 2. Oxidation of **5** with ferrocenium hexafluorophosphate.

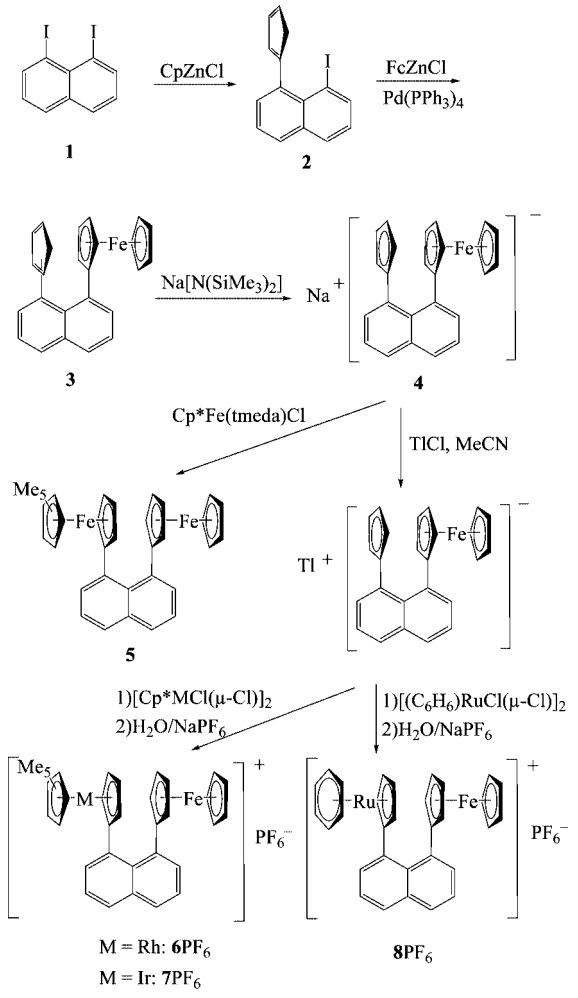


Scheme 1. Synthesis of polar cofacially fixed sandwich complexes.

### Crystal Structures

The solid-state structures of **3a**, **5**$PF_6$, **6**$PF_6$ and **7**$PF_6$ are displayed in Figures 3, 4, 5 and 6. The mononuclear complex **3a** crystallizes in the monoclinic space group $P2_1/c$, whereas the space group for the dinuclear monocationic species is found to be orthorhombic and chiral with $C222_1$. Not surprisingly, the structural data of the sandwich units are very similar to those of published data for corresponding prototype sandwich complexes (Table 1).[14–17]

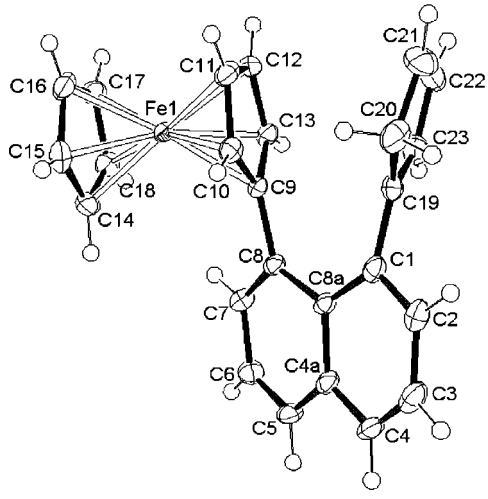


Figure 3. Molecular structure of **3a** (50% ellipsoids).

 © 2006 Wiley-VCH Verlag GmbH & Co. KGaA, Weinheim 

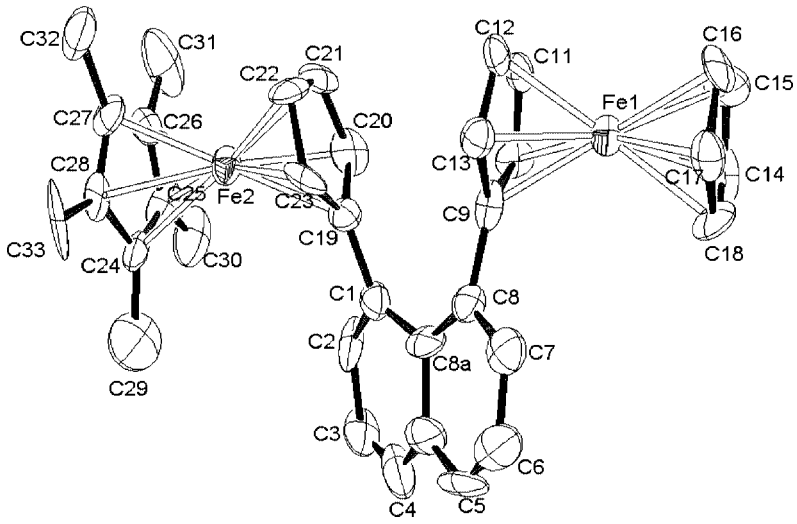


Figure 4. Molecular structure of **5**$PF_6$ (50% ellipsoids, hydrogen atoms and counterion are omitted for clarity).

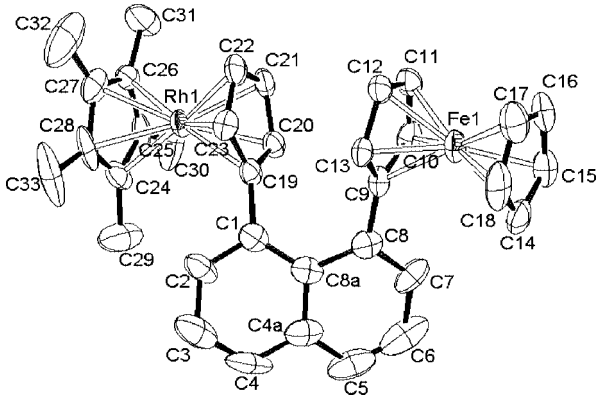


Figure 5. Molecular structure of **6**$PF_6$ (50% ellipsoids, hydrogen atoms and counterion are omitted for clarity).

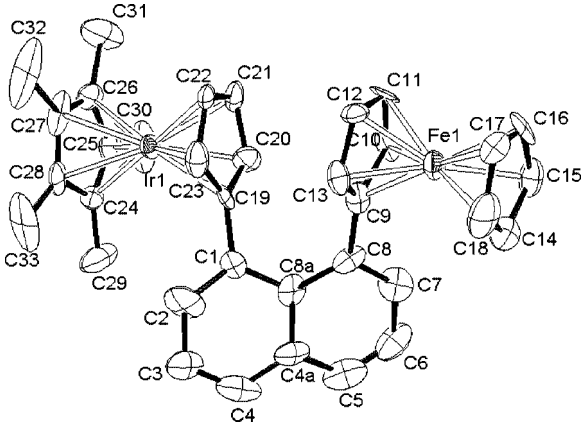


Figure 6. Molecular structure of **7**$PF_6$ (50% ellipsoids, hydrogen atoms and counterion are omitted for clarity).

Table 1. Selected bond lengths [pm] of the metallocene units in **3a**, **5**$PF_6$, **6**$PF_6$, **7**$PF_6$.

| | **3a** | **5**$PF_6$ | **6**$PF_6$ | **7**$PF_6$ |
|---|---|---|---|---|
| Fe(1)–C(9) | 207.8(3) | 206(1) | 208(1) | 208(2) |
| Fe(1)–C(10) | 204.8(3) | 205(1) | 206(1) | 204(3) |
| Fe(1)–C(11) | 203.7(4) | 203(1) | 205(1) | 201(3) |
| Fe(1)–C(12) | 204.0(4) | 204(1) | 204(1) | 201(2) |
| Fe(1)–C(13) | 204.5(3) | 206(1) | 203(1) | 204(2) |
| Fe(1)–$Cent_{[C(9)–C(13)]}$[a] | 164.47(18) | 165(1) | 166(1) | 165(1) |
| Fe(1)–C(14) | 203.8(4) | 204(2) | 206(1) | 206(3) |
| Fe(1)–C(15) | 203.9(4) | 202(2) | 204(1) | 210(2) |
| Fe(1)–C(16) | 205.3(4) | 205(2) | 204(1) | 203(3) |
| Fe(1)–C(17) | 204.8(3) | 204(1) | 205(2) | 208(2) |
| Fe(1)–C(18) | 204.7(4) | 205(1) | 204(1) | 203(3) |
| Fe(1)–$Cent_{[C(14)–C(18)]}$[a] | 165.0(2) | 166(1) | 165(1) | 168(1) |
| M–C(19) | – | 215(1) | 224(1) | 219(2) |
| M–C(20) | – | 207(2) | 221(1) | 217(3) |
| M–C(21) | – | 206(2) | 215(1) | 219(2) |
| M–C(22) | – | 205(1) | 214(1) | 217(2) |
| M–C(23) | – | 210(1) | 218(1) | 220(2) |
| M–$Cent_{[C(19)–C(23)]}$[a] | – | 171(1) | 181(1) | 183(1) |
| M–C(24) | – | 210(2) | 219(1) | 215(3) |
| M–C(25) | – | 210(2) | 217(1) | 224(3) |
| M–C(26) | – | 202(2) | 215(1) | 220(3) |
| M–C(27) | – | 207(2) | 217(1) | 218(2) |
| M–C(28) | – | 217(2) | 221(1) | 220(3) |
| M–$Cent_{[C(24)–C(28)]}$[a] | – | 170(1) | 181(1) | 182(1) |
| C(19)–C(20) | 141.9(6) | 144(2) | 144(1) | 139(3) |
| C(20)–C(21) | 148.1(7) | 139(2) | 143(2) | 146(4) |
| C(21)–C(22) | 142.0(8) | 140(2) | 140(2) | 133(3) |
| C(22)–C(23) | 141.4(7) | 142(2) | 140(2) | 145(3) |
| C(23)–C(19) | 140.7(6) | 137(2) | 144(2) | 143(3) |
| C(24)–C(25) | – | 147(3) | 143(2) | 148(4) |
| C(25)–C(26) | – | 137(2) | 143(2) | 146(5) |
| C(26)–C(27) | – | 139(2) | 141(2) | 139(4) |
| C(27)–C(28) | – | 145(2) | 144(2) | 144(4) |
| C(28)–C(24) | – | 143(2) | 143(2) | 141(5) |

[a] Cent: centroid of the corresponding cyclopentadienyl rings.

The most eye-catching feature of all structures under study is the distortion of the compound entities (Figure 7, Table 2); a common occurrence for naphthalene derivatives disubstituted in the 1,8-positions by aromatic moieties.[8,18] The tilt angle between the best plane of the naphthalene-bound Cp ligands and the best planes of the connected six-membered naphthalene rings varies from 45.6(6)° (**5**$PF_6$) to 77.9(8)° (**6**$PF_6$) (Table 2). For the less crowded example **3a**, with only one sandwich unit, intermediate tilt angles of 53.5(2)° and 53.0(2)° are found. Remarkably, the permethylation of one of the distal Cp ligands in the cationic species

 © 2006 Wiley-VCH Verlag GmbH & Co. KGaA, Weinheim 

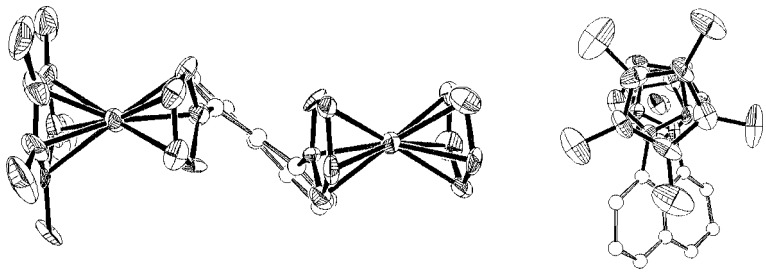

Figure 7. Cofacial arrangement of metallocene fragments in **5**$PF_6$; left: showing the interplanar distortion between the naphthalene moiety and the sandwich units; right: view along the metallocene axes; (50% ellipsoids, hydrogen atoms and counterion are omitted for clarity).

Table 2. Selected interplanar und torsion angles [°], bond lengths and interatomic distances [pm] between the naphthalene und metallocene units.

| | **3a** | **5**$PF_6$ | **6**$PF_6$ | **7**$PF_6$ | **9**$BF_4$[8b] |
|---|---|---|---|---|---|
| $Cp_{C(9)–C(13)}$–$Cp_{C(19)–C(23)}$ | 22.3(2) | 20.5(8) | 19.7(6) | 19.1(15) | 17.5 |
| $Cp_{C(9)–C(13)}$–naphthalene[a] | 53.5(2) | 45.6(6) | 77.9(8) | 45.6(12) | 58.0 |
| $Cp_{C(19)–C(23)}$–naphthalene[a] | 53.0(2) | 48.4(7) | 60.5(8) | 48.6(12) | 60.8 |
| C(19)–C(1)–C(8)–C(9) | 23.3 | 31.3 | 28.9 | 29.4 | 25.2 |
| C(1)–C(19) | 148.0(5) | 147(2) | 148(2) | 149(3) | 148.4 |
| C(8)–C(9) | 148.3(5) | 151(2) | 150(2) | 153(3) | 148.9 |
| C(1)–C(8) | 255.6(5) | 254(2) | 257(2) | 258(2) | 254.1 |
| C(9)–C(19) | 291.4(5) | 291(2) | 288(1) | 290(2) | 286.9 |
| Fe(1)–M | – | 651.9 | 658.6 | 657.9 | 651.3 |
| $Cent_{C(9)–C(13)}$–$Cent_{C(14)–C(18)}$[b] | 330.5(3) | 331.0(9) | 330.8(8) | 332(2) | 329.6 |
| $Cent_{C(19)–C(23)}$–$Cent_{C(24)–C(28)}$[b] | – | 341(1) | 362.5(8) | 365(2) | 343.5 |
| $Cent_{C(9)–C(13)}$–$Cent_{C(19)–C(23)}$[b] | 330.4(3) | 323.1(9) | 318.6(7) | 319(2) | 317.9 |

[a] Best plane of the adjacent six-membered naphthalene ring. [b] Cent: centroid of the corresponding Cp ligand.

does not cause tilt angles that deviate distinctly from those obtained for other comparable naphthalene derivatives,[8,18] which points out that the distortion is not a consequence of the steric hindrance between the positions C2 and C7, and the distal Cp ligands, but rather a result of the steric repulsion of the two-faced Cp units in the *peri* position (compare also data in Table 2). Despite the distortion of the entire *peri*-disubstituted naphthalene derivatives, a projection along the molecular axis of the sandwich complexes still shows an almost complete face-to-face arrangement of the sandwich units (Figure 7). This nicely demonstrates the clamp function of the naphthalene backbone for the purpose of stacking the sandwich units.

## Spectroscopic Properties

The NMR signals of the complexes **3**, **5**, **6**$PF_6$, **7**$PF_6$ and **8**$PF_6$ have been assigned by means of $^1H$, $^{13}C$, $^1H^1H$ COSY, HMQC, ATP and $^1H^1H$ NOESY spectra. For comparison, the symmetrical diferrocenyl-substituted naphthalene congener **9**[8] was studied. The $^1H$ NMR signals of the sandwich units are found in the typical range for the corresponding unsubstituted derivatives. The deviations are difficult to explain, because they are small and probably strongly dominated by the anisotropy effects of the neighboring sandwich complex. The $^{13}C$ NMR shifts, which are less influenced by anisotropy effects compared to the overall shift range, illustrate a slight but distinct low-field shift for the signals of the unsubstituted Cp ligand as well as of the carbon nuclei in 2,5- and 3,4-positions of the naphthalene-bound Cp ligand of the ferrocenyl substituent in the order **5** < **9** < **3** < **8**$PF_6$ < **6**$PF_6$ < **7**$PF_6$. The order may reflect a subtle decrease of the electron repulsion between the ferrocenyl substituent and the neighboring sandwich complex (Table 3).

UV/Vis spectroscopy is a well-tried tool for obtaining initial information about potential nonlinear optical (NLO) behavior in virtue of the solvatochromism of dipolar com-

Table 3. NMR spectroscopic data of the ferrocenyl substituents in **3a**, **5**, **6**$PF_6$, **7**$PF_6$, **8**$PF_6$ and **9**.

| | ML | $\delta(C_5H_5)$ | $\delta$(H-2′′,5′′) | $\delta$(H-3′′,4′′) | $\delta(C_5H_5)$ | $\delta$(C-2′′,5′′) | $\delta$(C-3′′,4′′) | $\delta$(C-1′′) |
|---|---|---|---|---|---|---|---|---|
| **3a** | – | 3.96 | 4.30 | 4.03 | 69.9 | 72.1/70.7 | 67.2/66,7 | n.d.[a] |
| **5** | [FeCp*] | 3.83 | 4.12 | 3.86 | 69.4 | 70.5 | 66.4 | 87.5 |
| **6**$PF_6$ | $[RhCp^*]^+$ | 3.98 | 4.31 | 4.10 | 70.5 | 72.2 | 68.3 | 92.5 |
| **7**$PF_6$ | $[IrCp^*]^+$ | 3.99 | 4.35 | 4.14 | 71.0 | 72.7 | 68.7 | 92.8 |
| **8**$PF_6$ | $[Ru(C_6H_6)]^+$ | 3.98 | 4.32 | 4.11 | 69.9 | 71.8 | 67.6 | n.d.[a] |
| **9** | [FeCp] | 3.86 | 4.11 | 3.84 | 69.5 | 70.9 | 66.5 | 91.3 |

[a] n.d.: not detectable.

 © 2006 Wiley-VCH Verlag GmbH & Co. KGaA, Weinheim 

Table 4. UV/Vis data of the complexes **3a**, **5**, **5**$PF_6$, **6**$PF_6$, **7**$PF_6$ and **8**$PF_6$.

| | | $\lambda_{max}$[a] ($\varepsilon$)[b] $\tilde{\nu}_{max}$[c] | | $\lambda_{max}$[a] ($\varepsilon$)[b] $\tilde{\nu}_{max}$[c] | |
|---|---|---|---|---|---|
| | ML | MeOH | $CH_2Cl_2$ | MeOH | $CH_2Cl_2$ |
| **3a** | – | 296 (6000) | | 458 (290) | 456 (540) |
| | | 33784 | [d] | 21834 | 21930 |
| **5** | [FeCp*] | 296 (13000) | | 477 (1355) | 481 (1930) |
| | | 33794 | [d] | 20964 | 20790 |
| **5**$PF_6$ | $[FeCp^*]^+$ | 304 (24780) | | 428 (3712, sh)[e] | 433 (2850, sh)[e] |
| | | 32895 | [d] | 23364 | 23095 |
| **6**$PF_6$ | $[RhCp^*]^+$ | 293 (19170) | | | |
| | | 34130 | [d] | [f] | [f] |
| **7**$PF_6$ | $[IrCp^*]^+$ | 289 (5271) | | 450 (220) | 454 (780) |
| | | 34602 | [d] | 22222 | 22026 |
| **8**$PF_6$ | $[Ru(C_6H_6)]^+$ | 286 (3758) | | 461 (190) | 463 (960) |
| | | 34965 | [d] | 21602 | 21598 |

[a] In nm. [b] In $M^{-1}\cdot cm^{-1}$. [c] In $cm^{-1}$. [d] Beyond solvent range. [e] Shoulder. [f] Shoulder, not resolved.

pounds. If the dipole moments of the ground and an excited state are different, a variation of the solvent polarity will stabilize the two states differently, resulting in a bathochromic or hypsochromic shift of the absorption maximum.[19,20] Therefore, the UV/Vis spectra of the complexes **3**, **5**, **5**$PF_6$, **6**$PF_6$, **7**$PF_6$ and **8**$PF_6$ were recorded in dichloromethane and methanol (Table 4). For both solvents, weak absorption bands can be detected in the region at $\lambda \approx 300$ and 450 nm because of d–d transitions typical for ferrocenes.[21,22] The high-energy d–d transition is superimposed by a strong π–π* transition at $\lambda < 300$ nm, and is thus only observable as a shoulder. The dependence of the absorption maxima on the polarity of the solvent is minor: only a small hypsochromic shift is observed for the low-energy d–d transition. **5**$PF_6$ and **9**$PF_6$ demonstrate additional absorption bands at $\lambda_{max} = 813$ nm ($\varepsilon = 649\ M^{-1}cm^{-1}$) and at about 840 nm ($\varepsilon = 800\ M^{-1}cm^{-1}$),[8a] respectively, which are typical for ferrocenium derivatives, as well as very broad absorption bands at $\lambda_{max} = 1284$ nm ($\tilde{\nu} = 7788\ cm^{-1}$) and $\lambda_{max} = 1500$ nm[8a] ($\tilde{\nu} = 6667\ cm^{-1}$) ($\Delta\tilde{\nu}_{1/2} > 4000\ cm^{-1}$, $\varepsilon < 100\ M^{-1}cm^{-1}$, respectively. The NIR bands are indicative of mixed-valence charge-transfer (MVCT) transitions in mixed-valence compounds of class II.[9a,9b,23a,23b]

## Redox Properties

Cyclic voltammograms were obtained for all of the naphthalene derivatives in this study. For comparison, the redox behavior of the 1,8-diferrocenyl-substituted naphthalene **9** was additionally investigated. As expected, all complexes reveal an electrochemically reversible one-electron oxidation in the range of ferrocene itself (Table 5, Figure 8), and can thus be assigned to the oxidation of the ferrocenyl substituent. The peak-to-peak separations found ($\Delta E_p = E_{pc} - E_{pa}$) are generally larger than the ideal value of 60 mV for a fully reversible one-electron process, which is probably due to the uncompensated solution resistance.

The cyclic voltammograms of the diiron complexes **5** and **9** contain an additional reversible one-electron redox wave due to the oxidation of the second ferrocenyl unit. The permethylation of one of the cyclopentadienyl ligands causes a more pronounced cathodic shift of the first oxidation step for **5** relative to **9**. The rhodium and ruthenium congeners display an irreversible reduction beyond –2000 mV vs. ferrocene/ferrocenium, which is caused by the reduction of the cationic sandwich unit;[24,25] for the iridium derivative **7**$PF_6$ a corresponding reduction was not observed within the accessible range, which seems reasonable, as the reduction potential for the cationic sandwich complex $[CpIr(C_5Me_5)]^+$ is about 500 mV more negatively shifted than for the corresponding rhodium complex.[25] A reduction of the aromatic π-system of the naphthalene unit is not expected within the scan range, because naphthalene reveals a reduction beyond –3 V vs. ferrocene/ferrocenium.[26]

When the oxidation potentials of the ferrocene units of all the monocationic species under study are compared, an increase is observed in the order **5**$PF_6$ < **3** < **7**$PF_6$ < **6**$PF_6$ < **8**$PF_6$ < **9**$PF_6$. It is still under discussion whether the

Table 5. Redox potentials[a] of the complexes **3a**, **5**$PF_6$, **6**$PF_6$, **7**$PF_6$, **8**$PF_6$ and **9**$PF_6$.

| | ML | $E_{1/2}$ (1)[b] | $\Delta E_p$ (1)[c] | $E_{1/2}$ (2)[b] | $\Delta E_p$ (2)[c] | $E_{pc}$[d] | $\Delta E$ |
|---|---|---|---|---|---|---|---|
| **3a** | – | –0.036 | 0.102 | – | – | – | – |
| **5**$PF_6$ | $[FeCp^*]^+$ | –0.042 | 0.097 | –0.532 | 0.107 | – | 0.490[e] |
| **6**$PF_6$ | $[RhCp^*]^+$ | 0.041 | 0.073 | – | – | –2.157[d] | 2.198[f] |
| **7**$PF_6$ | $[IrCp^*]^+$ | 0.036 | 0.084 | – | – | – | – |
| **8**$PF_6$ | $[Ru(C_6H_6)]^+$ | 0.053 | 0.070 | – | – | –2.345[d] | 2.398[f] |
| **9**$PF_6$ | $[FeCp]^+$ | 0.106 | 0.069 | –0.098 | 0.84 | – | 0.204[e] |

[a] In $CH_2Cl_2$ at room temperature, $[nBu_4N]PF_6$ (0.4 M) as supporting electrolyte, $Ag/AgPF_6$ as standard elektrode referenced vs. $E_{1/2}$(ferrocene/ferrocenium) = 0 V, scan rate 100 mV/s. [b] Potentials $E$ ±0.005 V. [c] $\Delta E_p = |E_{pc} - E_{pa}|$. [d] Peak potential $E_{pc}$ of the irreversible reduction. [e] $\Delta E = |E_{1/2}(1) - E_{1/2}(2)|$. [f] $\Delta E = |E_{1/2}(1) - E_{pc}|$.

 © 2006 Wiley-VCH Verlag GmbH & Co. KGaA, Weinheim 

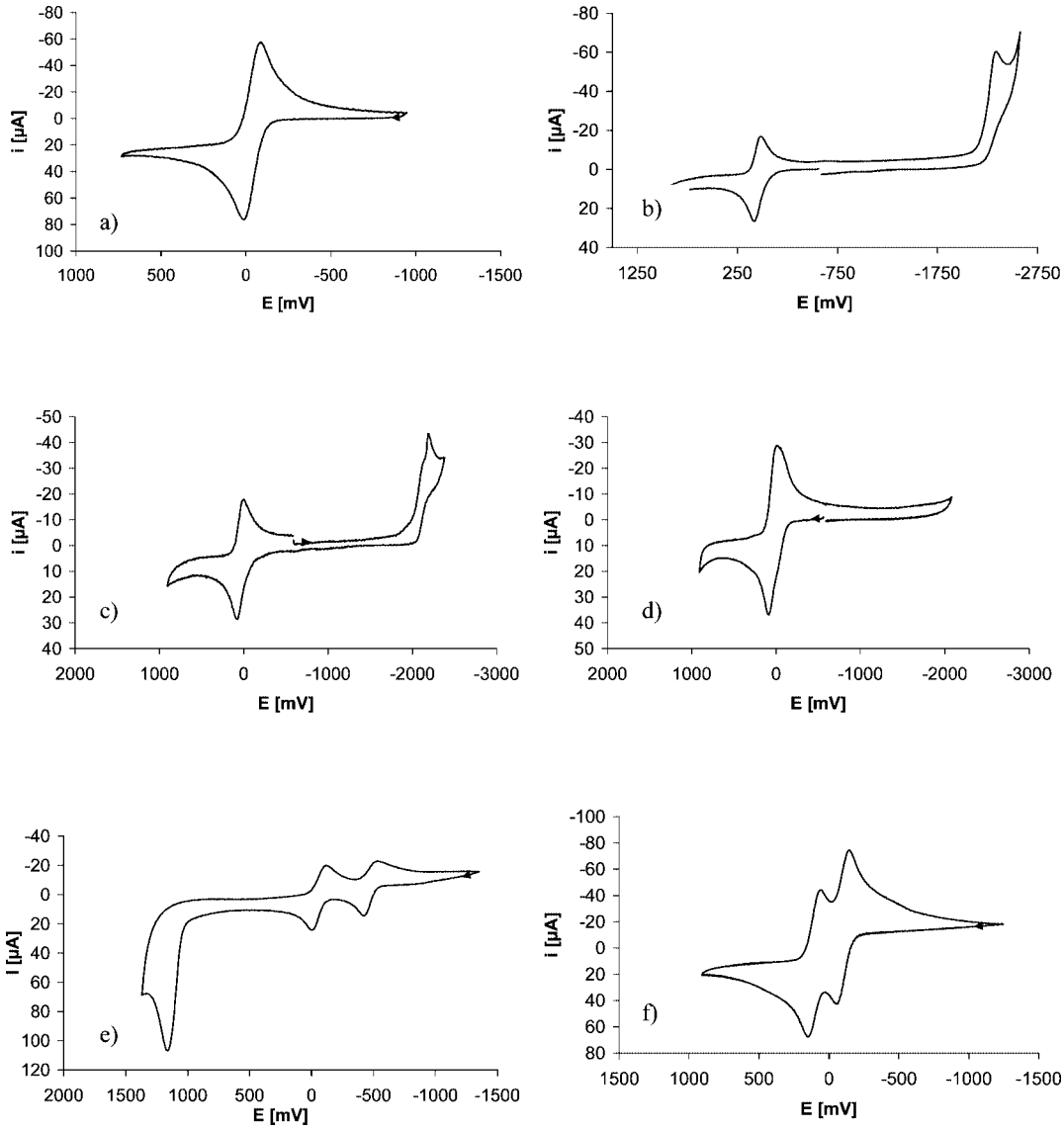


Figure 8. Cyclic voltammograms of **3** (a), **8**$PF_6$ (b), **6**$PF_6$ (c), **7**$PF_6$ (d), **5**$PF_6$ (e), **9** (f) (for more details see Table 5).

oxidation potentials are mainly influenced by a direct "through-space" interaction of the sandwich units, which are in an almost perfect face-to-face arrangement, or by a "through-bond" interaction facilitated by the π-bonding system of the naphthalene core. However, some arguments point to a predominant contribution of the "through-space" interaction: (i) the almost perpendicular conformation of the sandwich substituents with respect to the naphthalene plane hampers the interaction between the sandwich and naphthalene π-bonding systems and (ii) the 1,8-disubstitution of the aromatic naphthalene system disfavours the π-interaction between the substituents. This has been demonstrated by 1,3-diferrocenylated benzene derivatives, which may be regarded electronically similar to the 1,8-diferrocenylated naphthalene species; the benzene compounds reveal a difference in the oxidation potentials for the ferrocene units of less than 100 mV, although the ferrocene substituents rotate around the benzene–ferrocene σ-bond and can thus adopt a coplanar conformation of the ferrocene and benzene π-systems suitable for a proper π-interaction.[27,28] In contrast to this and in accordance with others,[8] a difference in the oxidation potentials of about 200 mV was found for **9**. The interpretation of an important "through-space" interaction in face-to-face stacked sandwich complexes is also in harmony with the explanation of an antiferromagnetic coupling between two paramagnetic trovacene complexes in *peri* position of naphthalene.[18]

## Measurements Concerning Second Harmonic Generation

In order to elucidate the NLO activity of the stacked sandwich compounds with respect to second harmonic generation (SHG), hyper-Rayleigh scattering (HRS) measurements were performed for liquid solution samples of **5**$PF_6$,

 © 2006 Wiley-VCH Verlag GmbH & Co. KGaA, Weinheim 

**6**$PF_6$, **7**$PF_6$, **8**$PF_6$, and **9**$PF_6$ with a pulsed Nd:YAG laser at $\lambda$ = 1064 and 1500 nm. The measurements were carried out as described in the literature.[29,30] Dichloromethane and acetonitrile were used as solvents. In addition, the Kurtz-powder method[31] was applied for crystalline samples of **5**$PF_6$, **6**$PF_6$ and **7**$PF_6$, because they crystallize in the chiral space group $C222_1$. However, no method could detect a measurable intensity of a frequency-doubled light. One explanation for the lack of SHG of the liquid solution samples is the weak polarizability and thus hyperpolarizability of the polar complexes, which can already be suggested from small solvatochromism. Even for the mixed-valence diferrocenyl species **5**$PF_6$ and **9**$PF_6$, which illustrate broad absorption bands in the NIR region (vide supra), no frequency-doubled signal could be detected, although SHG has been observed for species containing two ferrocene termini, which are separated by a cumulenium bridge.[32] The considerable absorption of **5**$PF_6$ and **9**$PF_6$ at $\lambda < 800$ nm may hamper the recognition of the second harmonic signal by absorption of light over a long range in the visible region. The lack of a SHG of the crystalline phase may be due to the orthorhombic crystal space group $C222_1$, which is a less effective space group for second harmonic generation.[33]

## Conclusions

In order to create second harmonic generation by "through-space" hyperpolarization in two face-to-face, but polar arranged sandwich complexes, four novel disandwich complexes have been synthesized, wherein a ferrocene and a cationic sandwich complex are combined and held together by a naphthalene clamp. The synthesis was performed by two consecutively conducted cross-coupling reactions of cyclopentadienylzinc chloride and ferrocenylzinc chloride, respectively, with 1,8-diiodonaphthalene as starting material. After deprotonation of the free cyclopentadienyl substituent, the coordination of different half-sandwich units revealed the desired dinuclear complexes. In addition, the neutral, but unsymmetrical diferrocenyl derivative **5**, was oxidized to the monocationic dipolar compound **5**$PF_6$. For compounds **3**, **5**$PF_6$, **6**$PF_6$, **7**$PF_6$ the molecular structures have been determined by X-ray structure analysis. Complex **3** crystallizes in the space group $P2_1/c$, whereas the dinuclear species crystallize in the chiral space group $C222_1$. The fixation of the sandwich entities in the *peri* position of the naphthalene backbone causes severe distortion of the entire complex, but warrants an almost linear face-to-face alignment of the two sandwich units. The redox properties of all of these complexes turned out a "through-space" polar interaction, which influences the oxidation potential of the ferrocene unit in **5**$PF_6$, **6**$PF_6$, **7**$PF_6$ and **8**$PF_6$. However, no SHG effect could be detected by means of HRS measurements. Having in mind the chirality of the crystalline material of **5**$PF_6$, **6**$PF_6$ and **7**$PF_6$, the Kurtz-powder method has been applied, but again, no SHG effect could be observed. The lack of SHG in the stacked sandwich entities may raise some doubts about the applicability for SHG in stacked π-systems. To obtain a deeper insight into the "through-space" interaction concerning NLO effects it would be worthwhile to extend the amount of face-to-face stacked sandwich complexes in a polar fashion to make the π-electronic system more polarizable, which is subject of current work.

## Experimental Section

**General:** Manipulations were carried out under dry nitrogen using standard Schlenk technique. Solvents were saturated with nitrogen. Diethyl ether ($Et_2O$), tetrahydrofuran (THF), *n*-hexane and toluene were freshly distilled from the appropriate alkali metal or metal alloy. Dichloromethane ($CH_2Cl_2$) and nitromethane ($MeNO_2$) were dried with calcium hydride. NMR: Varian Gemini 200 BB; Bruker AM 360; measured at 295 K rel. to TMS. UV/Vis: Perkin–Elmer Model 554. IR: KBr pellets; FT-IR Perkin–Elmer Model 325. MS: Finnigan MAT 311 A (EI-MS). Elemental analyses: CHN-O-Rapid, Fa. Heraeus, Zentrale Elementanalytik, Fachbereich Chemie, Universität Hamburg. 1,8-Diiodonaphthalene,[10] di-μ-chlorobis[chloro(η$^5$-pentamethylcyclopentadienyl)rhodium(III)] [Cp*$RhCl_2]_2$,[34] di-μ-chlorobis[chloro(η$^5$-pentamethylcyclopentadienyl)iridium(III)] [Cp*$IrCl_2]_2$,[34] di-μ-chlorobis[chloro(η$^6$-benzene)ruthenium(II)] $[(C_6H_6)RuCl_2]_2$,[35] ferrocenium hexafluorophosphate [FcH]$PF_6$,[36] chloro-(η$^5$-pentamethylcyclopentadienyl)-(tetramethylethylenediamine)iron(II) [Cp*Fe(tmeda)Cl][37] were synthesized according to literature procedures. Zinc chloride was dried by stirring in thionyl chloride unter reflux for several hours. $[Pd(PPh_3)_4]$ was purchased commercially.

**1-Cyclopentadienyl-8-iodonaphthalene (2):** The synthesis was carried out similar to the reaction described in the literature.[7c] Cyclopentadienyllithium (1.82 g, 25.25 mmol) and anhydrous zinc chloride (7.35 g, 53.95 mmol) were stirred in THF (70 mL) at 0 °C for 45 min. 1,8-Diiodonaphthalene (**1**) (4.97 g, 13.08 mmol) was added, the reaction mixture was warmed to room temperature and was stirred for 50 h. The reaction mixture was hydrolyzed with saturated $NH_4Cl$ solution (150 mL), and the products were extracted with $Et_2O$ (total amount 450 mL). The organic layer was dried with $MgSO_4$ and the solvents were evaporated to dryness. Extraction with hexane revealed 1-cyclopentadienyl-8-iodnaphthalene (**2**) as a yellow oil composed of three different isomers (3.55 g, 85.2%). M.p. ca. –10 °C. $^1$H NMR (360 MHz, $CDCl_3$, rel. to TMS, room temp.): $\delta$ = 8.21 (dd, $^3J_{6,7}$ = 7.2, $^4J_{5,7}$ = 3.6 Hz, 1 H, 7-H), 7.86 (dd, $^3J_{5,6}$ = 7.2, $^4J_{5,7}$ = 3.6 Hz, 1 H, 5-H), 7.75–7.79 (m, 1 H, 3-H), 7.44 (d, $^3J_{2,3}$ = 5 Hz, 1 H, 2-H), 7.42 (d, $^3J_{3,4}$ = 5 Hz, 1 H, 4-H), 7.07 ("t", $^3J_{6,7}$ = $^3J_{5,6}$ = 7.2 Hz, 1 H), 6.62–6.70 (m, 3 H, Cp-$H_{vinyl}$), 3.12–3.14 (m, 1 H, sp$^3$-CpH) ppm. IR (KBr): $\tilde{\nu}$ = 3049, 2960, 2927, 2908, 2846, 1927, 1802, 1719, 1595, 1571, 1536, 1498 1437, 1419, 1362, 1352, 1321, 1250, 1221, 1194, 1175, 1139, 1106, 1037, 1001, 950, 928, 890, 860, 826; 815, 764, 726, 681, 641, 606, 581, 557, 522, 505, 466, 419 cm$^{-1}$.

**Monolithioferrocene:** Monolithioferrrocene was prepared similar to the procedure described in the literature.[11] A pentane solution of *t*BuLi (1.48 M, 35 mL, 51.63 mmol) was added dropwise to a solution of ferrocene (10.0 g, 5.37 mmol) in THF (25 mL) at room temperature. After 15 min of stirring, the solution was cooled to –15 °C. The addition of *n*-hexane led to the precipitation of the lithiated products, which contain the monolithiated ferrocene as the main product (3.50 g, 34%). The orange solid material is extremely oxygen- and moisture-sensitive.

 © 2006 Wiley-VCH Verlag GmbH & Co. KGaA, Weinheim 

**1-Cyclopentadienyl-8-ferrocenylnaphthalene (3):** Anhydrous zinc chloride (2.21 g, 16.2 mmol) was added to a solution of monolithioferrocene (2.317 g, 12,07 mmol) in THF (30 mL) at 0 °C. After stirring for 1 h, the red solution was added to a solution of 1-cyclopentadienyl-8-iodonaphthalene (**2**) (2.57 g, 8.08 mmol) and tetrakis(triphenylphosphane)palladium(0) (0.55 g, 0.48 mmol, 6 mol-%) in THF (10 mL). The reaction mixture was stirred at room temperature for 4 h and poured into a solution of saturated ammonium chloride (200 mL). The mixture was vigorously stirred and extracted with $Et_2O$. The orange-red organic layer was dried with $MgSO_4$. The volume of the solution was reduced to a minimum amount, dissolved in hexane/$Et_2O$ (10:1), filtered through a column of alumina (5% water), and subjected to column chromatography on basic alumina [5% water, hexane/$Et_2O$ (1:0 to 10:1)]. Unreacted ferrocene could be separated first. The second fraction contained the desired compound **3** as an orange-red solid material, consisting of two isomers: 1-(cyclopentadien-1′-yl)-8-(ferrocen-1′′-yl)naphthalene (**3a**) and 1-(cyclopentadien-2′-yl)-8-(ferrocen-1′′-yl)naphthalene (**3b**) (1.90 g, 63%). $C_{25}H_{20}Fe$ (376.28): calcd. C 79.80, H 5.36; found C 79.74, H 5.80. M.p. 122–125 °C; ref.[7c] 134–140 °C. $^1$H NMR (200 MHz, $CDCl_3$, rel. to TMS, room temp.): $\delta$ = 8.18 (d, $^3J_{6,7}$ = 8 Hz, 1 H, 7-H), 7.79 (m, 2 H, H-2, 5-H), 7.50 (t, $^3J_{6,7}$ = $^3J_{5,6}$ = 7.5 Hz, 1 H, 6-H), 7.32–7.42 (m, 2 H, H-3, 4-H), 5.88–6.30 (m, 3 H, Cp-$H_{vinyl}$), 4.30, 4.26 (br. t, 2 H, Fc-$H_{2,5}$, isomer **3a** and **3b**), 4.03 (br. t, Fc-$H_{3,4}$, 1.2 H, isomer **3b**), 3.96 (br. s, 5.8 H, Fc-H, isomer **3a** and **3b**, Fc-$H_{3,4}$ isomer **3a**), 2.89 (br. s, 0.6 H, sp$^3$-CpH, isomer **3b**), 2.68 (br. s, 0.4 H, sp$^3$-CpH, isomer **3a**) ppm. $^{13}$C NMR (50 MHz, $CDCl_3$, rel. to TMS, room temp.): $\delta$ = 137.4, 136.3 (C-1, C-8); 133.2, 132.6, 132.1, 131.9, 129.5, 129.5, 129.20, 128.7, 128.2, 127.8, 125.5, 125.1, 72.1, 70.7 (C-2′′,5′′); 69.9 ($C_5H_5$), 67.2, 66.7 (C-3′′,4′′), 44.7, 41.7 (sp$^3$C-$C_5H_5$) ppm. IR (KBr): $\tilde{\nu}$ = 3076, 3046, 2916, 2897, 2871, 1637, 1591, 1570, 1500, 1478, 1422, 1365, 1105, 1052, 1032, 1022, 999, 952, 894, 824, 810, 773, 673, 485 cm$^{-1}$. MS (EI): *m/z* (%) = 376.3 (100) [M$^+$], 310.3 (59) [M – $C_5H_6$]$^+$, 254 (23) [$C_{10}H_6(C_5H_4)_2^+$], 189 (16) [$C_{10}H_5(C_5H_4)^+$], 121 (16) [FeCp$^+$]. UV/Vis ($CH_2Cl_2$): $\lambda_{max}$ ($\varepsilon$) = 382 (1420, sh), 456 (536 M$^{-1}$cm$^{-1}$) nm; (MeOH): $\lambda_{max}$ ($\varepsilon$) = 295 (ca. 6000), 378 (ca. 800), 458 (ca. 300 M$^{-1}$cm$^{-1}$) nm.

**1-[(η$^5$-Cyclopentadienediyl)(η$^5$-pentamethylcyclopentadienyl)iron(II)]-8-ferrocenylnaphthalene (5):** 1-Cyclopentadienyl-8-ferrocenylnaphthalene (**3**) (0.182 g, 0.48 mmol) was dissolved in THF (10 mL), treated with an Na[N($SiMe_3$)$_2$] solution in THF (1 M, 0.5 mL, 0.5 mmol) at 0 °C and stirred for 90 min. To this solution, which was cooled to –78 °C, [Cp*Fe(tmeda)Cl] (0.412 g, 1.2 mmol) was added. After stirring overnight and warming to room temperature, the reaction mixture was concentrated to dryness. The residue was dissolved in a minimum amount of toluene and filtered through alumina (neutral, 5% water) and the filtrate was purified by column chromatography on alumina (neutral, 5% water). As eluent *n*-hexane/toluene (10:1) was used. The eluate was concentrated to dryness, to yield 1-[(η$^5$-cyclopentadienediyl)(η$^5$-pentamethylcyclopentadienyl)iron(II)]-8-ferrocenylnaphthalene (**5**) (0.18 g, 65%) as an orange crystalline material (Figure 9). $C_{35}H_{34}Fe_2$ (566.35): calcd. C 74.23, H 6.05; found C 73.99, H 6.59. M.p. 150 °C. $^1$H NMR (200 MHz, $CDCl_3$ rel. to TMS, room temp.): $\delta$ = 8.06 (dd, $^3J_{6,7}$ = 7.5, $^4J_{5,7}$ = 2 Hz, 1 H, 7-H), 7.93 (d, $^3J_{2,3}$ = 6.5 Hz, 1 H, 2-H), 7.74 (dt, 2 H, H-4, 5-H), 7.48 (t, $^3J_{6,7}$ = $^3J_{5,6}$ = 7.5 Hz, 1 H, 6-H), 7.45 (t, $^3J_{3,4}$ = $^3J_{2,3}$ = 6.5 Hz, 1 H, 3-H), 4.12 (t, $^3J$ = 2 Hz, 2 H, 2′′,5′′-H), 3.86 (t, $^3J$ = 2 Hz, 2 H, 3′′,4′′-H), 3.83 (s, 5 H, $C_5H_5$), 3.64 (t, $^3J$ = 2 Hz, 2 H, 2′,5′-H), 3.38 (t, $^3J$ = 2 Hz, 2 H, 3′,4′-H), 1.60 (s, 15 H, $C_5Me_5$) ppm. $^{13}$C NMR (50 MHz, $CDCl_3$ rel. to TMS, room temp.): $\delta$ = 136.9 (C-8), 135.3 (C-1), 131.2 (C-7), 130.5 (C-2), 126.6, 126.1 (C-4,5), 124.2 (C-6), 124.0 (C-3), 91.2 (C-1′), 87.5 (C-1′′), 79.7 ($C_5Me_5$), 72.8 (C-2′,5′), 71.5 (C-3′,4′), 70.5 (C-2′′,5′′), 69.4 ($C_5H_5$), 66,40 (C-3′′,4′′), 10,81 ($C_5Me_5$) ppm. IR (KBr):$\tilde{\nu}$ = 3089, 3054, 2943, 2900, 2853, 1636, 1571, 1506, 1476, 1448, 1425, 1414, 1377, 1365, 1314, 1266, 1182, 1137, 1105, 1066, 1032, 999, 935, 912, 881, 843, 825, 811, 788, 772, 692, 661, 640, 602, 587, 533, 521, 510, 494, 483, 460, 432, 423, 414, 408 cm$^{-1}$. MS (EI): *m/z* (%) = 566 (100) [M$^+$], 501 (24) [M – Cp]$^+$, 431 (12) [M – Cp*]$^+$, 445 (6) [M – Cp]$^+$, 375 (3) [M – FeCp*]$^+$, 310 (46) [M – CpFeCp*]$^+$, 254 (6) [$C_{10}H_6(C_5H_4)_2$]$^+$, 189 (6) [$C_{10}H_5(C_5H_4)$]$^+$, 121 (5) [FeCp]$^+$. UV/Vis ($CH_2Cl_2$): $\lambda_{max}$ ($\varepsilon$) = 298 (18240), 391 (2390, sh), 481 (1932 M$^{-1}$cm$^{-1}$) nm; (MeOH): $\lambda_{max}$ ($\varepsilon$) = 296 (ca. 13000), 398 (ca. 1600, sh), 477 (ca. 1355 M$^{-1}$cm$^{-1}$) nm.

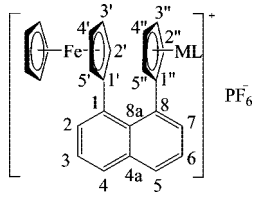


Figure 9. Numbering scheme for the assignment of the NMR signals.

**1-[(η$^5$-Cyclopentadienediyl)(η$^5$-pentamethylcyclopentadienyl)iron(III)]-8-ferrocenylnaphthalene Hexafluorophosphate (5PF$_6$):** 1-[(η$^5$-Cyclopentadienediyl)(η$^5$-pentamethylcyclopentadienyl)iron(II)]-8-ferrocenylnaphthalene (**5**) (0.314 g, 0.55 mmol) was dissolved in $CH_2Cl_2$ (30 mL). Ferrocenium hexafluorophosphate (0.166 g, 0.50 mmol) was added, whereupon the color of the reaction mixture changed form orange-red to dark brown. After stirring at room temperature for 80 min, *n*-hexane (60 mL) was layered on the $CH_2Cl_2$ solution, and the reaction flask was stored at –30 °C for 2 d. The precipitated crystals were filtered off and dried in vacuo. 1-[(η$^5$-Cyclopentadienediyl)(η$^5$-pentamethylcyclopentadienyl)iron(III)]-8-ferrocenylnaphthalene hexafluorophosphate (**5**PF$_6$) was obtained in dark red-brown crystals (0.32 g, 0.45 mmol, 82%). $C_{35}H_{34}Fe_2PF_6{\cdot}(CH_2Cl_2)_{0.66}$ (767.94): calcd. C 55.78, H 4.64; found C 55.98, H 4.70. M.p. 189 °C (dec). $^1$H NMR (360 MHz, [D$_6$]acetone, rel. to TMS, room temp.): $\delta$ = 34.2 (2′,5′-H), 24.9 (2′′,5′′-H), 22.5 (3′′,4′′H), 18.5 (3′,4′-H), 10.9 ($C_5H_5$), 1.87 (4-H, 5-H), –2.22 (6-H), –10.81 (7-H), –25.26 (3-H), –36.55 ($C_5Me_5$), –55.84 (2-H). IR (KBr): $\tilde{\nu}$ = 3121, 3051, 2963, 2916, 1631, 1587, 1502, 1474, 1448, 1423, 1412, 1389, 1314, 1268, 1185, 1133, 1105, 1070, 1032, 1000, 935, 919, 846, 837, 775, 732, 699, 692, 638, 598, 557, 533, 521, 510, 494, 483, 460, 432, 423, 414, 408 cm$^{-1}$. MS (FAB): *m/z* (%) = 566 (100) [M$^+$], 501 (8) [M – Cp]$^+$, 445 (12) [M – FeCp]$^+$, 431 (20) [M – Cp*]$^+$, 310 (44) [M – CpFeCp*]$^+$. UV/Vis ($CH_2Cl_2$): $\lambda_{max}$ ($\varepsilon$) = 433 (2850, sh), 813 (649), 1284 (122 M$^{-1}$cm$^{-1}$) nm; MeOH: $\lambda_{max}$ ($\varepsilon$) = 304 (24780), 428 (3712, sh), 801 (953 M$^{-1}$cm$^{-1}$) nm.

**1-[(η$^5$-Cyclopentadienediyl)(η$^5$-pentamethylcyclopentadienyl)-rhodium(III)]-8-ferrocenylnaphthalene Hexafluorophosphate (6PF$_6$):** 1-Cyclopentadienyl-8-ferrocenylnaphthalene (**3**) (0.29 g, 0.77 mmol) was dissolved in THF (15 mL), and treated with a solution of Na[N($SiMe_3$)$_2$] in THF (1 M, 0.75 mL, 0.75 mmol) at 0 °C. After stirring for 80 min, the solvent was stripped off in vacuo, and the residue was redissolved in acetonitrile (50 mL), whereupon thallium(I) chloride (0.185 g, 0,77 mmol) was added. The reaction mixture was stirred at room temperature for 3 h and at 40 °C for 18 h. [Cp*RhCl$_2$]$_2$ (0.236 g, 0.38 mmol) was added and the mixture stirred at 45 °C for 3 h and at room temperature for 20 h. The reaction solution was filtered through Celite, and the filtrate was concentrated to dryness. The solid red residue was dissolved in water (60 mL) and, after filtration, $NH_4PF_6$ (0.150 g, 1.03 mmol), dis-

 © 2006 Wiley-VCH Verlag GmbH & Co. KGaA, Weinheim 

solved in water (5 mL), was added to the filtrate. An orange, voluminous precipitate formed, which was collected on a filter frit, washed with water and $Et_2O$ and dried in vacuo. For recrystallization the orange-red powder of **6**$PF_6$ (0.425 g, 0.57 mmol, 74%) was redissolved in $CH_2Cl_2$ and overlayered with $Et_2O$. $C_{35}H_{34}FeRhPF_6$ (758.37): calcd. C 55.43, H 4.52; found C 56.48, H 4.87. M.p. 172 °C (dec). $^1$H NMR (200 MHz, [D$_6$]acetone, rel. to TMS, room temp.): $\delta$ = 8.33 (dd, $^3J_{2,3}$ = 7.5, $^4J_{2,4}$ = 1,5 Hz, 1 H, 2-H), 8.03 (dd, $^3J_{6,7}$ = 8, $^4J_{5,7}$ = 2 Hz, 1 H, 7-H), 7.94 (dd, $^3J_{3,4}$ = 8, $^4J_{2,4}$ = 1.5 Hz, 1 H, 4-H), 7.74–7.61 (m, 3 H, 3-H, 5-H, 6-H), 5.62 (t, 2 H, $^3J$ = 2 Hz, 2′,5′-H), 5.38 (t, $^3J$ = 2 Hz, 2 H, 3′,4′-H), 4.31 (t, $^3J$ = 2 Hz, 2 H, 2′′,5′′-H), 4.10 (t, $^3J$ = 2 Hz, 2 H, 3′,4′-H), 3.98 (s, 5 H, $C_5H_5$), 1.94 (s, 15 H, $C_5Me_5$) ppm. $^{13}$C NMR (50 MHz, [D$_6$]acetone, rel. to TMS, room temp.): $\delta$ = 136.4 (C-1), 135.9 (C-8), 133.7 (C-2), 131.9 (C-8a), 130.8 (C-7), 128.2 (C-4), 128.0 (C-4a), 126.3, 125.5 (C-5,6), 113.7 (C-1′), 101.6 [d, $^1J(^{13}C^{103}Rh)$ = 8 Hz, $C_5Me_5$], 92.5 (C-1′′), 88.4 [d, $^1J(^{13}C^{103}Rh)$ = 6 Hz C-2′, 5′], 87.7 [d, $^1J(^{13}C^{103}Rh)$ = 7.5 Hz, C-3′,4′], 72.2 (C-2′′,5′′), 70.5 ($C_5H_5$), 68.3 (C-3′′,4′′), 10.1 ($C_5Me_5$) ppm. IR (KBr): $\tilde{\nu}$ = 3093, 2919, 1626, 1500, 1476, 1455, 1425, 1389, 1314, 1266, 1185, 1133, 1106, 1068, 1028, 1001, 841, 773, 740, 692, 558, 481 cm$^{-1}$. MS (FAB): *m*/*z* (%) = 613 (100) [M$^+$], 548 (10) [M – Cp]$^+$,492 (13) [M – FeCp]$^+$,478 (18) [M – Cp*]$^+$, 375 (22) [M – RhCp*]$^+$, 357 (47) [M – Cp*-FeCp]$^+$. UV/Vis (MeOH): $\lambda_{max}$ ($\varepsilon$) = 293 (19170 M$^{-1}$ cm$^{-1}$) nm.

**1-[(η$^5$-Cyclopentadienediyl)(η$^5$-pentamethylcyclopentadienyl)-iridium(III)]-8-ferrocenylnaphthalene Hexafluorophosphate (7$PF_6$):** The synthesis of **7**$PF_6$ was carried out in the same manner as for **6**$PF_6$ with additional washing of the precipitate with toluene and hexane. Used quantities: 1-cyclopentadienyl-8-ferrocenylnaphthalene (**3**) (0.27 g, 0.72 mmol), THF (15 mL), Na[N(SiMe$_3$)$_2$] in THF (1 M, 0.72 mL, 0.72 mmol), thallium(I) chloride (0.225 g, 0.94 mmol), [Cp*IrCl$_2$]$_2$ (0.28 g, 0.35 mmol), water (60 mL), solution of $NH_4PF_6$ (0.150 g, 1.03 mmol) in water (5 mL). Yield: 0.373 g (61%) of orange-red powder of **6**$PF_6$, prior to recrystallization from $CH_2Cl_2$/$Et_2O$. $C_{35}H_{34}FeIrPF_6$·($C_6H_5CH_3$) (939.83): calcd. C 53.68, H 4.50; found C 54.11, H 4.58. M.p. 167 °C (dec). $^1$H NMR (200 MHz, [D$_6$]acetone, rel. to TMS, room temp.): $\delta$ = 8.34 (dd, $^3J_{2,3}$ = 7, $^4J_{2,4}$ = 2 Hz, 1 H, 2-H), 8.00 (dd, $^3J_{6,7}$ = 7, $^4J_{5,7}$ = 2 Hz, 1 H, 7-H), 7.93 (dd, $^3J_{3,4}$ = 7, $^4J_{2,4}$ = 2 Hz, 1 H, 4-H), 7.69 –7.60 (m, 3 H, H-3, 5-H, 6-H), 5.70 (t, 2 H, $^3J$ = 2 Hz, 2′,5′-H), 5.37 (t, 2 H, $^3J$ = 2 Hz, 3′,4′-H), 4.35 (t, $^3J$ = 2 Hz, 2 H, 2′′,5′′-H), 4.14 (t, $^3J$ = 2 Hz, 2 H, 3′′,4′′-H), 3.99 (s, 5 H, $C_5H_5$), 2.02 (s, 15 H, $C_5Me_5$) ppm. $^{13}$C NMR (50 MHz, [D$_6$]aceton/TMS, room temp.): $\delta$ = 137.0 (C-1), 136.6 (C-8), 134.5 (C-2), 133.5 (C-3), 132.6 (C-8a), 131.5 (C-7), 128.9 (C-4), 128.3 (C-4a), 126.9 (C-5), 126.2 (C-6), 107.8 (C-1′), 95.6 ($C_5Me_5$), 92.8 (C-1′′), 82.4 (C-2′,5′), 80.9 (C-3′,4′), 72.7 (C-2′′,5′′), 71.0 ($C_5H_5$), 68.7 (C-3′′,4′′), 10.0 ($C_5Me_5$) ppm. IR (KBr): $\tilde{\nu}$ = 3093, 2917, 1626, 1475, 1389, 1314, 1264, 1184, 1106, 1035, 1002, 843, 773, 692, 558, 483 cm$^{-1}$. MS (EI): *m*/*z* (%) = 703 (100) [M$^+$], 581 (14) [M – CpFe]$^+$, 568 (8) [M – Cp*]$^+$, 447 (15) [M – Cp* – FeCp]$^+$, 376 (52) [M – Cp*Ir]$^+$. UV/Vis ($CH_2Cl_2$): $\lambda_{max}$ ($\varepsilon$) = 454 (780 M$^{-1}$ cm$^{-1}$) nm; (MeOH): $\lambda_{max}$ ($\varepsilon$) = 289 (5271), 450 (220 M$^{-1}$ cm$^{-1}$) nm.

**1-[(η$^6$-Benzene)(η$^5$-cyclopentadienediyl)ruthenium(II)]-8-ferrocenylnaphthalene Hexafluorophosphate (8$PF_6$):** The synthesis of **8**$PF_6$ was carried out in the same mannere as for **6**$PF_6$ with additional washing of the precipitate with toluene and hexane. Used quantities: 1-cyclopentadienyl-8-ferrocenylnaphthalene (**3**) (0.33 g, 0.86 mmol), THF (20 mL), Na[N(SiMe$_3$)$_2$] in THF (1 M, 0.85 mL, 0.85 mmol), MeCN (50 mL), thallium(I) chloride (0.208 g, 0.87 mmol), [$C_6H_6RuCl_2$]$_2$ (0.205 g, 0.41 mmol), water (60 mL), solution of $NH_4PF_6$ (0,18 g, 1.07 mmol) in water (5 mL). Yield: 0.22 g (37%) of orange-red powder of **8**$PF_6$. $C_{31}H_{25}FeRuPF_6$·($C_6H_5CH_3$)$_{0.66}$ (760.85): calcd. C 56.30, H 4.02; found C 57.00, H 4.07. M.p. 318 °C (dec.). $^1$H NMR (200 MHz, [D$_6$]acetone, rel. to TMS, room temp.): $\delta$ = 8.33 (dd, $^3J_{2,3}$ = 7.5, $^4J_{2,4}$ = 1.5 Hz, 1 H, 2-H), 7.99–7.90 (m, 3 H, 4-H, 5-H, 7-H), 7.62 (t, $^3J_{3,4}$ = 7.5 Hz, 1 H, 3-H), 7.50 (t, $^3J_{6,7}$ = $^3J_{5,6}$ = 7.5 Hz, 1 H, 6-H), 6.13 (s, 6 H, $C_6H_6$), 5.49 (t, $^3J$ = 2 Hz, 2 H, 2′,5′-H), 5.18 (t, $^3J$ = 2 Hz, 2 H, 3′,4′-H), 4.32 (t, $^3J$ = 2 Hz, 2 H, 2′′,5′′-H), 4.11 (t, $^3J$ = 2 Hz, 2 H, 3′′,4′′-H), 3.98 (s, 5 H, $C_5H_5$) ppm. $^{13}$C NMR (50 MHz, [D$_6$]acetone, rel. to TMS, room temp.): $\delta$ = 133.6 (C-2), 133.5 (C-7), 130.3 (C-4), 129.0 (C-4a or 8a), 127.9 (C-5), 125.8 (C-3), 125.0 (C-6), 87.3 ($C_6H_6$), 82.0 (C-2′,5′), 78.4 (C-3′,4′), 71.8 (C-2′′,5′′), 69.9 ($C_5H_5$), 67.6 (C-3′′,4′′) ppm. IR (KBr): $\tilde{\nu}$ = 3090, 1629, 1509, 1480, 1441, 1395, 1365, 1187, 1146, 1106, 1067, 1028, 1002, 879, 841, 775, 739, 691, 558, 510, 484 cm$^{-1}$. MS (EI): *m*/*z* (%) = 555 (65) [M$^+$], 490 (5) [M – Cp]$^+$, 477 (15) [M – $C_6H_6$]$^+$, 376 (16) [M – $C_6H_6$Ru]$^+$, 311 (18) [M – $C_6H_6$RuCp]$^+$. UV/Vis ($CH_2Cl_2$): $\lambda_{max}$ ($\varepsilon$) = 463 (960 M$^{-1}$ cm$^{-1}$) nm; (MeOH): $\lambda_{max}$ ($\varepsilon$) = 286 (3758), 461 (190 M$^{-1}$ cm$^{-1}$) nm.

**Cyclic Voltammetry:** Measurements were performed in $CH_2Cl_2$ with 0.4 M [*n*$Bu_4N$]$PF_6$ as supporting electrolyte. An Amel 5000 system was used with a Pt wire as working electrode and a Pt plate (0.6 cm$^2$) as auxiliary electrode. The potentials were measured against Ag/$AgPF_6$ and were referenced to $E_{1/2}$(ferrocene/ferrocenium) = 0 V.

**X-ray Structure Determination:** Crystals of compound **3**, **5**$PF_6$, **6**$PF_6$ and **7**$PF_6$ suitable for an X-ray structure determination were obtained for compound **3** by careful evaporation of the solvent, and for **5**$PF_6$, **6**$PF_6$ and **7**$PF_6$ by slow diffusion of $Et_2O$ into a $CH_2Cl_2$ solution of the complexes at –30 °C. The data were collected with a four-circle diffractometer by Hilger and Watts, Mo-$K_\alpha$, $\lambda$ = 0.71073 Å (Table 6). The structures were solved by direct methods (SHELXS-86)[38a] and the refinements on $F^2$ were carried out by full-matrix least-squares techniques (SHELXL-97).[38b] All non-hydrogen atoms were refined with anisotropic thermal parameters. The hydrogen atoms were refined with a fixed isotropic thermal parameter related by a factor of 1.2 to the value of the equivalent isotropic parameter of their carrier atoms. Weights were optimized in the final refinement cycles. Residual electron density was observed for crystals of **5**$PF_6$, **6**$PF_6$, and **7**$PF_6$ pointing out diffuse incorporation of solvent molecules.[39] CCDC-279705 (**3**), -279702 (**5**$PF_6$), -279703 (**6**$PF_6$), and -279704 (**7**$PF_6$) contain the supplementary crystallographic data for this paper. These data can be obtained free of charge from The Cambridge Crystallographic Data Centre via www.ccdc.cam.ac.uk/data_request/cif.

**SHG Measurements:** The efficiency of SHG of the crystalline materials are measured with our experimental setup[40] for the Kurtz powder method.[31] The measurements were performed at 1064 nm laser pulses produced by the Nd:YAG laser at low power (50 mJ per pulse); this laser produces 40-ns pulses with a repetition rate of 10 Hz. The procedure for the measurements is as follows: for crystalline samples, the grain size was not standardized. For this reason signals between individual measurements were seen to vary in some cases by as much as ±20%. The material to be measured was ground to a fine powder and compacted in a mount and installed in the sample holder. In order to compare the new samples with the reference urea, the measurements were averaged over several laser cycles. The voltage from the photomultiplier was measured by an oscilloscope which was triggered by the signal itself. The photomultiplier voltage and the neutral density filter area were optimized to obtain a good signal-to-noise ratio and to prevent the saturation of the photomultiplier. The oscilloscope measures the

 © 2006 Wiley-VCH Verlag GmbH & Co. KGaA, Weinheim 

Table 6. Crystallographic data of **3a**, **5**$PF_6$, **6**$PF_6$ und **7**$PF_6$.

| | **3a** | **5**$PF_6$ | **6**$PF_6$ | **7**$PF_6$ |
|---|---|---|---|---|
| Empirical formula | $C_{25}H_{20}Fe$ | $C_{35}H_{34}Fe_2PF_6$ | $C_{35}H_{34}FeRhPF_6$ | $C_{35}H_{34}FeIrPF_6$ |
| $M_r$ [g/mol] | 376.25 | 711.29 | 758.35 | 847.64 |
| $T$ [K] | 153(2) | 153(2) | 153(2) | 153(2) |
| $\lambda$ [pm] | 71.073 | 71.073 | 71.073 | 71.073 |
| Crystal system | monoclinic | orthorhombic | orthorhombic | orthorhombic |
| Space group | $P2_1/c$ | $C222_1$ | $C222_1$ | $C222_1$ |
| $a$ [pm] | 1142.3(7) | 1239.8(3) | 1231.3(11) | 1234.1(8) |
| $b$ [pm] | 985.1(6) | 2377.0(5) | 2408.3(18) | 2405.1(9) |
| $c$ [pm] | 1903.2(10) | 2271.4(5) | 2277.8(18) | 2279.0(18) |
| $\beta$ [°] | 123.71(4) | | | |
| $V$ [$10^6$ pm$^3$] | 1781.5(18) | 6694(3) | 6754.1(9) | 6764(7) |
| $Z$ | 4 | 8 | 8 | 8 |
| $\rho_{calcd.}$ [Mg/m$^3$] | 1.403 | 1.412 | 1.492 | 1.665 |
| $\mu$ [mm$^{-1}$] | 0.851 | 0.971 | 1.021 | 4.463 |
| $F$(000) | 784 | 2920 | 3072 | 3328 |
| Crystal size [mm] | 0.50×0.50×0.20 | 0.30×0.40×0.50 | 0.80×0.15×0.10 | 0.50×0.20×0.50 |
| $\theta_{min,max}$ | 2.26–27.45 | 2.48–25.08 | 2.46–27.56 | 2.46–25.06 |
| Index range | $-5 \le h \le 14$ | $-1 \le h \le 14$ | $-16 \le h \le 1$ | $-7 \le h \le 14$ |
| | $-12 \le k \le 2$ | $-1 \le k \le 28$ | $-1 \le k \le 31$ | $-9 \le k \le 28$ |
| | $-24 \le l \le 22$ | $-1 \le k \le 26$ | $-1 \le l \le 29$ | $-27 \le l \le 2$ |
| Reflections total | 6429 | 4059 | 5115 | 3421 |
| Reflections independent | 4068 | 3809 | 4827 | 3314 |
| $R_{int}$ | 0.0342 | 0.0424 | 0.0349 | 0.0498 |
| Reflections [$I > 4\sigma(I)$] | 3022 | 1996 | 3880 | 2431 |
| Parameters | 253 | 436 | 437 | 402 |
| GOF[a] | 1.033 | 0.846 | 1.086 | 1.029 |
| $R_1/wR_2$[b] [$I > 2\sigma(I)$] | 0.0503/0.1158 | 0.0745/0.1548 | 0.0641/0.1733 | 0.0612/0.1371 |
| $R_1/wR_2$[b] (all data) | 0.0802/0.1307 | 0.1464/0.1842 | 0.0834/0.1891 | 0.0963/0.1534 |
| Min./max. residue [e·Å$^3$] | –0.523/0.736 | –0.398/0.905 | –0.913/1.684 | –1.681/1.564 |

[a] GOF = "Goodness-of-fit" = $\{\Sigma[w(F_o^2 - F_c^2)^2]/(n-p)\}^{1/2}$ ($n$ = number of reflections, $p$ = number of parameters). [b] $R_1 = \Sigma||F_o| - |F_c||$; $wR_2 = \{\Sigma[w(F_o^2 - F_c^2)^2]/\Sigma[w(F_o^2)]\}^{1/2}$.

time integral of the photomultiplier voltage automatically, which is proportional to the SHG efficiency. The oscilloscope also performs the average over several shots automatically. The SHG efficiency measurement for the reference sample was performed under the same experimental conditions as that of the test samples. The SHG efficiency for liquid solutions of the polar compounds was determined by means of hyper-Rayleigh scattering (HRS).[41] The HRS measurements were performed with a pulsed Nd:YAG laser at a wavelength of $\lambda$ = 1064 and 1500 nm. For the experimental setup for $HRS_{1064nm}$, see ref.[28] Solutions of the complexes in dichloromethane and acetonitrile with concentrations in the range of $10^{-4}$ to $10^{-6}$ M were used with *p*-nitroaniline as a reference [$\beta(CH_2Cl_2)_{1064} = 21.6 \cdot 10^{-30}$ esu; $\beta(MeCN)_{1064} = 29.2 \cdot 10^{-30}$ esu].[42] The measurements at 1500 nm wavelength were carried out similar to the setup described in ref.[43] Instead of the third harmonic (355 nm), generated from an Nd:YAG laser with a wavelenghth of 1064 nm, the optical parametric oscillator (OPO)[44] in use was pumped with the second harmonic (532 nm). The signal intensity at 824 nm and the fundamental at 532 nm were removed from the idler by using dichroic mirrors (HR 650–850 and HR 532), a green light and a silicon filter (transparent > 1000 nm). An additional Glan–Taylor polarizer ensured the vertical polarization of the beam into the measurement cell. Measurements were performed with ca. $10^{-4}$–$10^{-6}$ M solutions of **5**, **7** and **8** in $CH_2Cl_2$. Disperse Red 1 (DR1) was used as an external standard with a value of $\beta_{1500}$ (DR1) = $70 \cdot 10^{-30}$ esu. This value was obtained by comparing the slopes of the reference in $CH_2Cl_2$ and $CHCl_3$ to obtain the ratio of $\beta_{solute}$.[45] With the value $\beta(CHCl_3) = 80 \cdot 10^{-30}$ esu[46] the hyperpolarisibility of DR1 in $CH_2Cl_2$ is estimated to be $70 \cdot 10^{-30}$ esu. The effect of the refractive indices of the solvents was corrected using the simple Lorentz local field.[47]

## Acknowledgments

This work was supported by the Deutsche Forschungsgemeinschaft (DFG, HE 1309/3), by the DAAD (Deutsch-Portugiesicher Wissenschaftleraustausch INIDA) and by the European Community (COST D14, TMR FMRX-CT98-0166). We thank the DEGUSSA AG for a donation of $RuCl_3$, the Sartorius GmbH for a donation of microfilters, and Nelson Lopes, GoLP, Centro de Física de Plasmas, Instituto Superior Técnico, Lisboa, Portugal, for performing the Kurtz powder measurements. M. H. G. thanks for financial support by Fundação para a Ciência e Tecnologia, project POCTI/QUI/48443/2002.

[1] F. Salhi, D. M. Collard, *Adv. Mater.* **2003**, *15*, 81–85.
[2] J. Cornil, D. Beljonne, J.-P. Calbert, J.-L. Brédas, *Adv. Mater.* **2001**, *13*, 1053–1067.
[3] J. S. Miller, A. J. Epstein, W. M. Reiff, *Acc. Chem. Res.* **1988**, *21*, 114–120; H. Atzkern, P. Bergerat, H. Beruda, M. Fritz, J. Hiermeier, P. Hudeczek, O. Kahn, F. H. Köhler, M. Paul, B. Weber, *J. Am. Chem. Soc.* **1995**, *117*, 997–1011.
[4] S. Di Bella, M. A. Ratner, T. J. Marks, *J. Am. Chem. Soc.* **1992**, *114*, 5842–5849; S. Di Bella, I. L. Fragalá, M. A. Ratner, T. J. Marks, *J. Am. Chem. Soc.* **1993**, *115*, 682–686.
[5] a) J. Zyss, I. Ledoux, S. Volkov, V. Chernyak, S. Mukamel, G. P. Bartholomew, G. C. Bazan, *J. Am. Chem. Soc.* **2000**, *122*, 11956–11962; G. P. Bartholomew, S. Ledoux, S. Mukamel, G. C. Bazan, J. Zyss, *J. Am. Chem. Soc.* **2002**, *124*, 13480–13485; b) A. Bahl, W. Grahn, S. Stadler, F. Feiner, G. Bourhill, C. Bräuchle, A. Reisner, P. G. Jones, *Angew. Chem.* **1995**, *107*, 1587–1590; W. Grahn, A. Bahl, S. Link, S. Stadler, R. Dietrich, K. Meerholz, C. Bräuchle, *Proc. SPIE – Int. Soc. Opt. Eng.*

 © 2006 Wiley-VCH Verlag GmbH & Co. KGaA, Weinheim 

**1997**, *3147*, 62–73; A. Bahl, PhD Thesis, Technical University of Braunschweig, **1997**.

[6] I. Ledoux, J. Zyss, A. Jutand, C. Amatore, *Chem. Phys.* **1991**, *150*, 117–123.

[7] a) M. Rosenblum, H. M. Nugent, K. D. Jang, M. M. Labes, W. Cahalane, P. Klemarczyk, W. M. Reiff, *Macromolecules* **1995**, *28*, 6330–6342; b) D. A. R. Hudson, B. M. Foxman, M. Rosenblum, *Organometallics* **1999**, *18*, 4098–4106; c) D. A. R. Hudson, B. M. Foxman, M. Rosenblum, *Organometallics* **2000**, *19*, 469–474.

[8] a) M.-L. Lee, B. M. Foxman, M. Rosenblum, *Organometallics* **1985**, *4*, 539–547; b) R. Arnold, B. M. Foxmann, M. Rosenblum, W. B. Euler, *Organometallis* **1988**, *7*, 1253–1259.

[9] a) M. Malessa, PhD Thesis, University of Hamburg, **2001**; b) M. Malessa, J. Heck, manuscript in preparation.

[10] H. O. House, D. G. Koepsell, W. J. Campbell, *J. Org. Chem.* **1972**, *37*, 1003–1011.

[11] a) F. Rebierre, O. Samuel, H. B. Kagan, *Tetrahedron Lett.* **1990**, *31*, 3121–3124; b) U. T. Müller-Westerhoff, Z. Yang, G. Ingram, *J. Organomet. Chem.* **1993**, *463*, 163–167; c) D. Guillaneux, H. B. Kagan, *J. Org. Chem.* **1995**, *60*, 2502–2505; R. Sanders, U. T. Mueller-Westerhoff, *J. Organomet. Chem.* **1996**, *512*, 219–224.

[12] W.-Y. Wong, W.-T. Wong, *J. Chem. Soc., Dalton Trans.* **1996**, 3209–3214.

[13] G. E. Herberich, C. Engelke, W. Pahlmann, *Chem. Ber.* **1979**, *112*, 607–624.

[14] J. D. Dunitz, *Acta Crystallogr., Sect. B* **1979**, *35*, 1068–1074.

[15] J. S. Miller, J. C. Calabrese, H. Rommelmann, S. Chittipeddi, J. H. Zhang, W. M. Reiff, A. J. Epstein, *J. Am. Chem. Soc.* **1987**, *109*, 769–781.

[16] S. Rittinger, D. Buchholz, M.-H. Delville-Desbois, J. Linares, F. Varret, R. Boese, L. Zsolnai, G. Huttner, D. Astruc, *Organometallics* **1992**, *11*, 1454–1456.

[17] P. L. Holland, R. A. Andersen, R. G. Bergmann, *Organometallics* **1998**, *17*, 433–437.

[18] C. Elschenbroich, M. Wolf, O. Schiemann, K. Harms, O. Burghaus, J. Pebler, *Organometallics* **2002**, *21*, 5810–5819.

[19] C. Reichardt, *Solvents and Solvent Effects in Organic Chemistry*, 1st reprint of the 2nd ed., VCH, Weinheim, **1990**.

[20] a) J. L. Oudar, D. S. Chemla, *J. Chem. Phys.* **1977**, *66*, 2664–2668; b) J. L. Oudar, *J. Chem. Phys.* **1977**, *67*, 446–457.

[21] M. Rosenblum, *Chemistry of the iron group metallocenes*, Wiley Interscience New York, **1965**, chapter 2.

[22] Y. S. Sohn, D. N. Hendrickson, H. B. Gray, *J. Am. Chem. Soc.* **1971**, *93*, 3603–3612.

[23] a) M. B. Robin, P. Day, *Adv. Inorg. Radiochem.* **1967**, *10*, 247–422; b) C. Creutz, *Prog. Inorg. Chem.* **1983**, *30*, 1–73.

[24] O. V. Gusev, M. A. Ievlev, M. G. Peterleitner, S. M. Peregudova, L. I. Denisovich, P. V. Petrovskii, N. A. Ustynuyuk, *J. Organomet. Chem.* **1997**, *534*, 57–66.

[25] O. V. Gusev, M. G. Peterleitner, M. A. Ievlev, A. M. Kal'sin, P. V. Petrovskii, L. I. Denisovich, N. A. Ustynuyuk, *J. Organomet. Chem.* **1997**, *531*, 95–100.

[26] N. G. Conelly, W. E. Geiger, *Chem. Rev.* **1996**, *96*, 877–910.

[27] C. Patoux, C. Coudret, J.-P. Launay, C. Joachim, A. Goudron, *Inorg. Chem.* **1997**, *36*, 5037–5049.

[28] M. Iyoda, T. Kondo, T. Okabe, H. Matsuyama, S. Sasaki, Y. Kuwatani, *Chem. Lett.* **1997**, 35–36.

[29] K. Clays, A. Persoons, *Rev. Sci. Instrum.* **1992**, *63*, 3285–3289.

[30] S. Stadler, R. Dietrich, G. Bourhill, C. Bräuchle, A. Pawlik, W. Grahn, *Chem. Phys. Lett.* **1995**, *247*, 271–276.

[31] S. K. Kurtz, T. T. Perry, *J. Appl. Phys.* **1968**, *39*, 3798–3813.

[32] B. Bildstein, *Coord. Chem. Rev.* **2000**, *206–207*, 369–394.

[33] J. Zyss, J. L. Oudar, *Phys. Rev. A* **1982**, *26*, 2028–2048.

[34] J. W. Kang, K. Moseley, P. M. Maitlis, *J. Am. Chem. Soc.* **1969**, *91*, 5970–5977.

[35] a) R. A. Zelonka, M. C. Baird, *J. Organomet. Chem.* **1972**, *44*, 383–389; b) T. A. Stephenson, D. A. Tocher, *Organomet. Synth.* **1986**, *3*, 99–103.

[36] W. A. Hermann, G. Brauer, *Synthetic Methods of Organometallic and Inorganic Chemistry*, Thieme Verlag, Stuttgart, **1996**, vol. 1, p. 12.

[37] K. Jonas, P. Klusmann, R. Goddard, *Z. Naturforsch., Teil B* **1995**, *50*, 394–404.

[38] a) G. M. Sheldrick, *SHELXS-86 Program for crystal structure determination*, University of Göttingen, Germany, **1986**; b) G. M. Sheldrick, *SHELXL-97 Program for crystal structure refinement*, University of Göttingen, Germany, **1997**.

[39] P. v. Sluis, A. L. Spek, *Acta Crystallogr., Sect. A* **1990**, *46*, 194.

[40] M. H. Garcia, J. C. Rodrigues, A. Romão Dias, M. F. M. Piedade, M. T. Duarte, M. P. Robalo, N. Lopes, *J. Organomet. Chem.* **2001**, *632*, 133–144.

[41] R. W. Terhune, P. D. Maker, C. M. Savage, *Phys. Rev. Lett.* **1965**, *14*, 681.

[42] C. Dehu, F. Meyers, E. Hendrickx, K. Clays, A. Persoons, S. R. Marder, J. L. Bredas, *J. Am. Chem. Soc.* **1995**, *117*, 10127–10128.

[43] S. Stadler, R. Dietrich, G. Bourhill, C. Bräuchle, A. Pawlik, W. Grahn, *Chem. Phys. Lett.* **1995**, *247*, 271–276; T. Farrell, T. Meyer-Friedrichsen, M. Malessa, C. Wittenburg, J. Heck, A. R. Manning, *J. Organomet. Chem.* **2001**, *625*, 32–39; T. Farrell, A. R. Manning, G. Mitchell, J. Heck, T. Meyer-Friedrichsen, M. Malessa, C. Wittenburg, M. H. Prosenc, D. Cunningham, P. McArdle, *Eur. J. Inorg. Chem.* **2002**, 1677–1686.

[44] Paralite Optical Parametrical Oscillator, LAS GmbH.

[45] T. Kodaira, A. Watanabe, O. Ito, M. Matsuda, K. Clays, A. Persoons, *J. Chem. Soc., Faraday Trans.* **1997**, *93*, 3039–3044.

[46] C. Lambert, G. Nöll, E. Schmälzlin, K. Meerholz, C. Bräuchle, *Chem. Eur. J.* **1998**, *4*, 2129–2135.

[47] C. Lambert, W. Gaschler, E. Schmälzlin, K. Meerholz, C. Bräuchle, *J. Chem. Soc., Perkin Trans. 2* **1999**, 577–587.

Received: September 14, 2005
Published Online: December 22, 2005

 © 2006 Wiley-VCH Verlag GmbH & Co. KGaA, Weinheim 

EurJIC
European Journal of Inorganic Chemistry

Issue 5/2006

Pages 873–1096

*Papers available ahead of print in Early View at www.interscience.wiley.com*

*Earliest available Table of Contents:*
*Automatically, free of charge by e-mail through*
*www.interscience.wiley.com/alerts*

## COVER PICTURE

**The cover picture shows** a dendron and two types of dendritic molecules built from dendrons. The shape of these nanometric molecules resembles that of macroscopic entities; the shape of dendrons is similar to that of trees, bis-dendrons can be compared to Janus, the god with two faces, and the multidendritic species shown on the left has the shape of a tropical fish. Details of this chemistry are described in the Microreview by A.-M. Caminade, A. Maraval, and J.-P. Majoral on p. 887 ff.

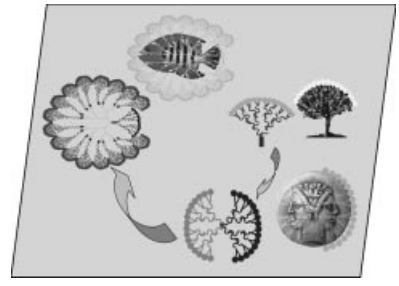

## MICROREVIEW

**Contents**

**887** **A.-M. Caminade,* A. Maraval, J.-P. Majoral***

Phosphorus-Containing Dendrons: Synthesis, Reactivity, Properties, and Use as Building Blocks for Various Dendritic Architectures

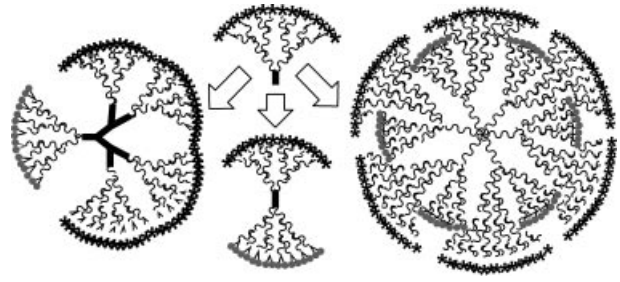

**Keywords:** Dendrimers / Phosphorus / Dendrons / Building blocks

 © 2006 Wiley-VCH Verlag GmbH & Co. KGaA, Weinheim 

# FULL PAPERS


**903** **A. Cucos, N. Avarvari, M. Andruh,* Y. Journaux,* A. Müller, M. Schmidtmann**

Reinecke Anion Derivatives and Homobinuclear Complexes as Tectons in Designing Heteropolymetallic Systems

**Keywords:** Chromium / Nickel complexes / Thiocyanato complexes / Magnetic properties / Coordination polymers

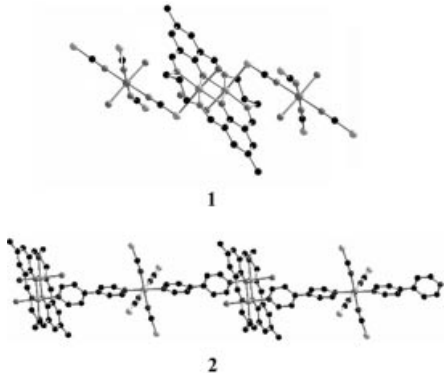


**908** **A. Dibenedetto,* M. Aresta, P. Giannoccaro, C. Pastore, I. Pápai,* G. Schubert**

On the Existence of the Elusive Mono-Methyl Ester of Carbonic Acid [$CH_3OC(O)OH$] at 300 K: $^1H$ and $^{13}C$ NMR Measurements and DFT Calculations

**Keywords:** Carbon dioxide / Density functional calculations / Methylation / NMR spectroscopy

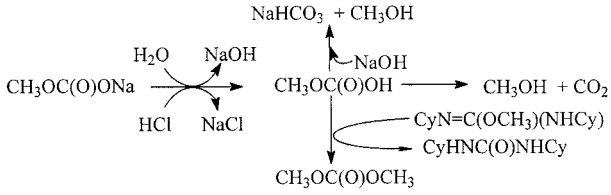


**914** **M. Bassetti,* A. Calenne, L. Mastrofrancesco, M. Salamone, G. Bocelli,* A. Cantoni, A. Musatti**

Synthesis and Characterization of a Novel Heteroditopic Macrocyclic System − Monometallic Nickel(II) and Uranyl Complexes and Their Corresponding Heterobimetallic Carbonylrhodium(I) Complexes

**Keywords:** Heterometallic complexes / Ligand design / Macrocyclic ligands / Metallacycles / Schiff bases

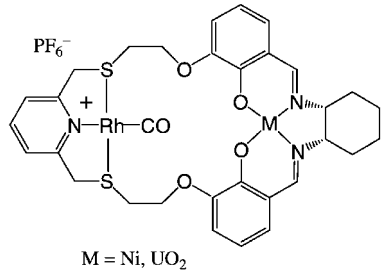


**926** **P. Štěpnička,* I. Císařová, R. Gyepes**

Synthesis and Structural Characterisation of Palladium and Group-12 Metal Complexes with a Hybrid Phosphanylphosphonate Ferrocene Ligand

**Keywords:** Group 12 metals / Phosphanes / Phosphonate esters / Palladium / Sandwich complexes / Structure eluicidation

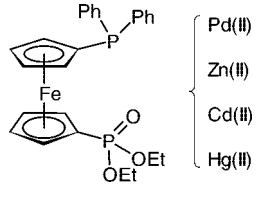



 © 2006 Wiley-VCH Verlag GmbH & Co. KGaA, Weinheim 

**939** **J.-Y. Piquemal,* L. Salles, G. Chottard, P. Herson, C. Ahcine, J.-M. Brégeault***

Another Example of the Instability of a Keggin-Type Heteropolyanion in the Presence of Aqueous Hydrogen Peroxide: From $[AsW_{12}O_{40}]^{3-}$ to Low-Nuclearity Oxoperoxotungstates − Crystal Structure of $[(n\text{Hex})_4N]_3$ $[AsO_4\{W_2O_2(\mu\text{-}O_2)_2(O_2)_2\}_2]$

**Keywords:** Oxidation / Hydrogen peroxide / Peroxo ligands / Catalysis / Tungsten

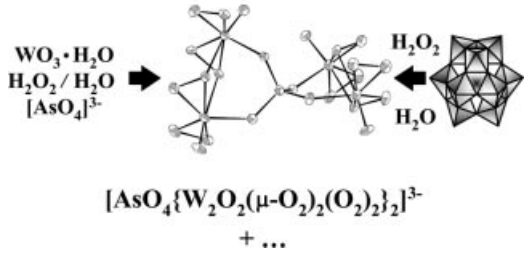


**948** **I. Ara, J. Forniés,* R. Lasheras, A. Martín, V. Sicilia***

Reactivity of the Pyrazolatopalladium(II) Complexes $[Pd(dmpz)_2(Hdmpz)_2]$ and $[Pd_2(\mu\text{-}dmpz)_2(dmpz)_2(Hdmpz)_2]$ Towards Carboxylic Acids: Hydrogen Bonds as the Driving Force That Determines the Nature of the Final Products

**Keywords:** Carboxylate ligands / Heterometallic complexes / Hydrogen bonds / N ligands / Palladium

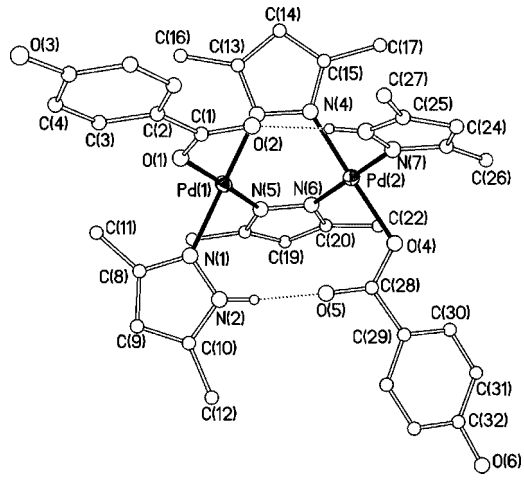


**958** **E. Schulz Lang,* G. A. Casagrande, G. Manzoni de Oliveira, G. N. Ledesma, S. S. Lemos, E. E. Castellano, U. Abram**

One-Pot Synthesis and Structure of Organochalcogen Halides with Mixed Valence States

**Keywords:** Halides / Secondary bonding / Selenium / Tellurium

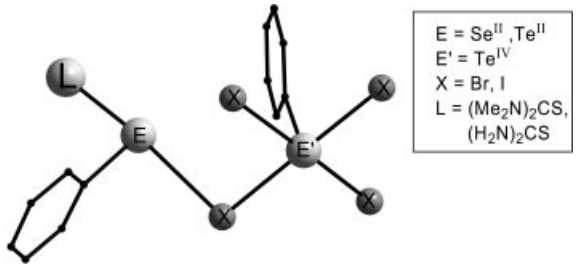


**965** **P. J. Aragón, F. Carrillo-Hermosilla, E. Villaseñor, A. Otero, A. Antiñolo, A. M. Rodríguez**

Synthesis, Structure and Reactivity in Styrene Polymerization by Heterocyclic Alkoxy- and Thiolatotitanium(IV) Complexes

**Keywords:** Heterocyclic ligands / Polymerization / Structure elucidation / Titanium

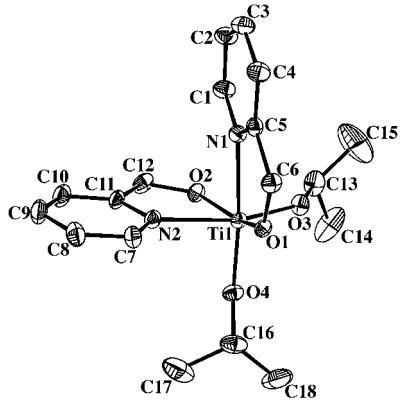


 © 2006 Wiley-VCH Verlag GmbH & Co. KGaA, Weinheim 

**972** **C. Alonso-Moreno, A. Antiñolo, F. Carrillo-Hermosilla, A. Otero,* A. M. Rodríguez, J. Sancho, V. Volkis, M. Eisen**

Synthesis, Characterization, and Catalytic Properties of *ansa*-Zirconocenes [Zr{1-$Me_2$Si-(3-$\eta^5$-$C_9H_5R)_2$}$Cl_2$] (R = Me, *n*Pr, *n*Bu, and Bz)

**Keywords:** Metallocenes / Zirconium / Homogeneous catalysis / Polymerization / Ethylene

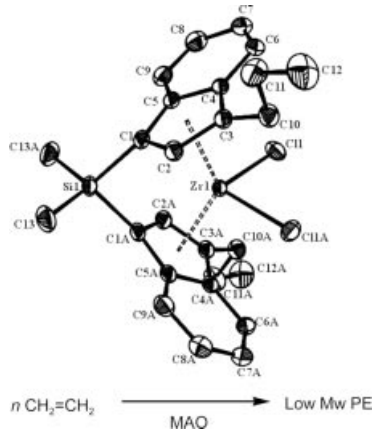


**980** **A. Carella, G. Vives, T. Cox, J. Jaud, G. Rapenne,* J.-P. Launay***

Synthesis of New Tripodal Tri-Functionalized Hydrotris(indazol-1-yl)borate Ligands and X-ray Structures of Their Cyclopentadieneruthenium Complexes

**Keywords:** Tripodal ligands / Ligand design / Ruthenium / Indazole / Stacking interactions

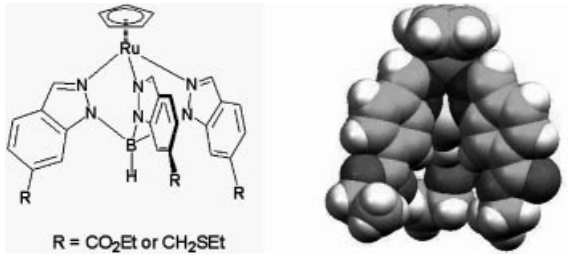


**988** **S. Chowdhury, G. Schatte, H.-B. Kraatz***

A Cyclic Fc−Histidine Conjugate: Synthesis and Properties − Interactions with Alkali Metal Ions

**Keywords:** Ferrocene / Ferrocenophane / Peptide / Bioinorganic chemistry

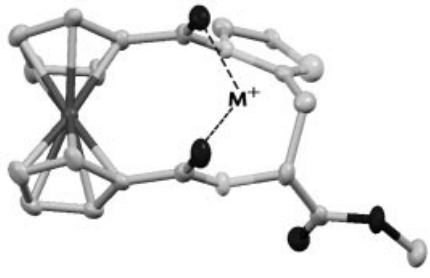


**994** **Y.-C. Lin,* T. K. Misra, T.-H. Lu, M. S. Joseph, C.-S. Chung***

Reassignment, Isolation, Spectral and X-ray Characterization of Diastereoisomers of the Macrocyclic Ligand 3,10-*meso*-3,5,7,7,10,12,14,14-Octamethyl-1,4,8,11-tetraazacyclotetradecane and their $Ni^{II}$ and $Cu^{II}$ Complexes

**Keywords:** Diastereoisomers / Macrocyclic ligands / X-ray crystallography / Coordination modes

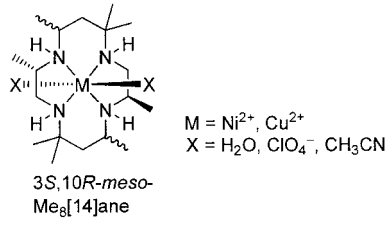


 © 2006 Wiley-VCH Verlag GmbH & Co. KGaA, Weinheim 

**1006** **S. Pavlik, F. Jantscher, G. Dazinger, K. Mereiter, K. Kirchner***

Reactions of Ruthenium−Aminophosphane Complexes with Diynes: P−N Bond Activation and Formation of Novel Phosphaallyl, Azaallyl, and Aminocarbene Complexes

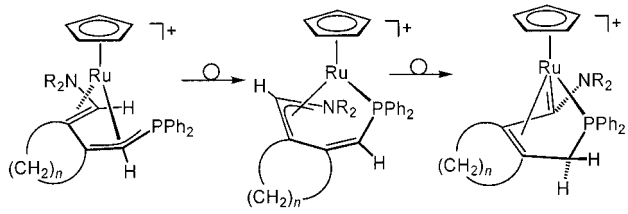

**Keywords:** Ruthenium / Phosphaallyl complexes / Azaallyl complexes / Density functional calculations

**1022** **K. Selmeczi, M. Giorgi, G. Speier, E. Farkas, M. Réglier***

Mono- versus Binuclear Copper(II) Complexes in Phosphodiester Hydrolysis

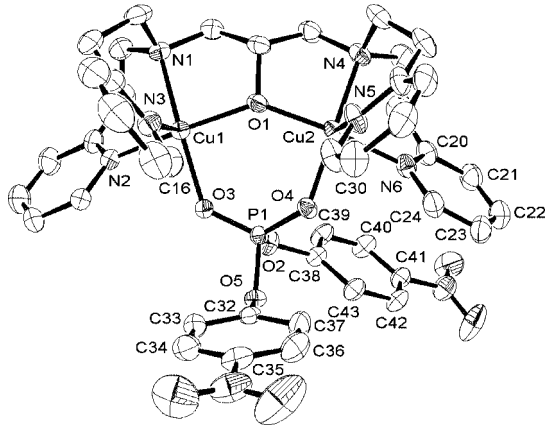

**Keywords:** Catalysis / Dinuclear copper(II) complex / Enzyme mimics / Phosphate ester hydrolysis / Tripodal ligands

**1032** **M. Forcato, F. Lake, M. Mba Blazquez, P. Renner, M. Crisma, L. H. Gade,* G. Licini,* C. Moberg***

Chiral, Enantiopure Aluminum(III) and Titanium(IV) Azatranes

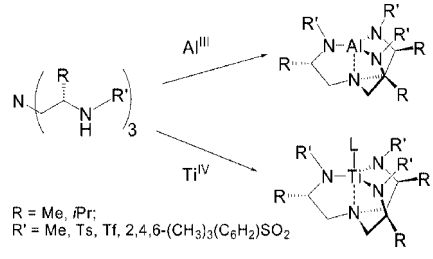

**Keywords:** Aluminum / Chirality / N ligands / Titanium / Tripodal ligands

**1041** **N. Amir,* M. Motonishi, M. Fujita, Y. Miyashita,* K. Fujisawa, K. Okamoto***

Synthesis of Novel S-Bridged Heterotrinuclear Complexes Containing Six-Membered Chelate Rings: Structural, Spectroscopic, and Electrochemical Properties of $[Co\{Rh(apt)_3\}_2]^{3+}$ (apt = 3-Aminopropanethiolate)

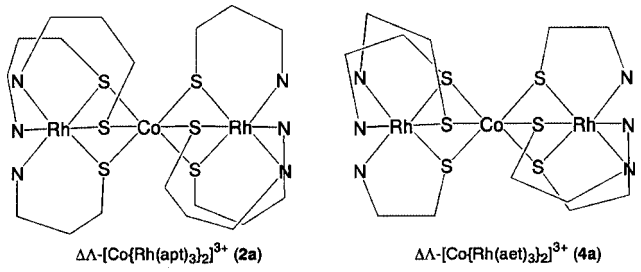

**Keywords:** 3-Aminopropanethiolate / Heterometallic complexes / Crystal structures / Six-membered chelate rings / Spectroscopy / Electrochemistry

 © 2006 Wiley-VCH Verlag GmbH & Co. KGaA, Weinheim 

**1050** **Q.-J. Pan, H.-X. Zhang,* H.-G. Fu, H.-T. Yu**

Theoretical Studies on MetalMetal Interaction and Intrinsic $^{1,3}$[σ*(d)σ(s/p)] Excited States of Dinuclear $d^{10}$ Complexes with Bridging Phosphane Ligands

**Keywords:** Metallophilicity / Excited states / Dinuclear $d^{10}$ complexes / Electronic structure / Solvent effects

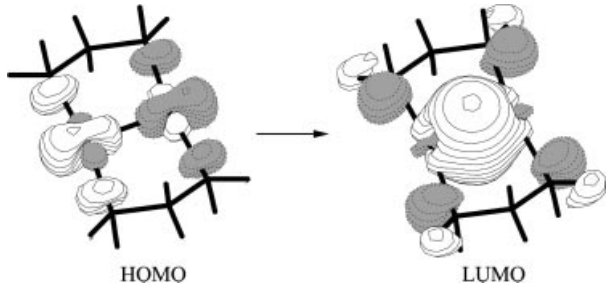


**1060** **C. Krinninger, S. Wirth, P. Klüfers, P. Mayer, I. P. Lorenz***

Absence of Dichroism in Dinuclear Rhenium Complexes with Sterically Hindered $\mu_2$-($\eta^2$-*N*,*O*)-Nitrosobenzene Ligands

**Keywords:** Dichroism / Dinuclear complexes / N ligands / Rhenium / Structure elucidation

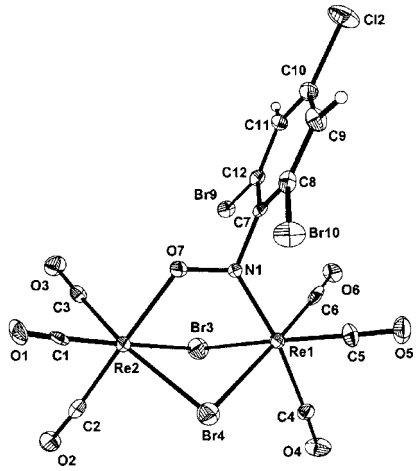


**1067** **M. Giménez-Pedrós, A. Aghmiz, N. Ruiz, A. M. Masdeu-Bultó**

New Ligands for Rh-Catalysed Hydroformylation of 1-Octene in Supercritical Carbon Dioxide − X-ray Structure of [Rh{$PPh_2$-($OC_9H_{19}$)}$_4$]$PF_6$

**Keywords:** Alkenes / Hydroformylation / P ligands / Rhodium / Supercritical fluids

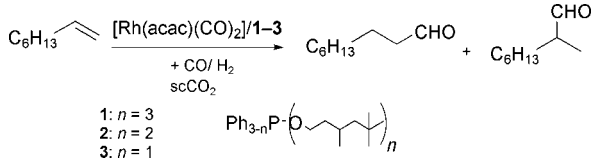


**1076** **R. Cervantes, S. Castillejos, S. J. Loeb, L. Ortiz-Frade, J. Tiburcio, H. Torrens***

Palladium(II) Compounds with Fluorinated Pincer-Type (SCS) Ligands: X-ray Structures of $C_6H_4$-1,3-($CH_2SC_6H_4F$-4)$_2$ and [PdCl(SCS−$R_f$)] [$R_f$ = $C_6H_4F$-2, $C_6H_4F$-3, $C_6H_4F$-4, $C_6H_4(CF_3)$-2, and $C_6H_4(CF_3)$-4]

**Keywords:** Fluorine / Sulfur / Pincer ligands / Thioether / Palladium compounds

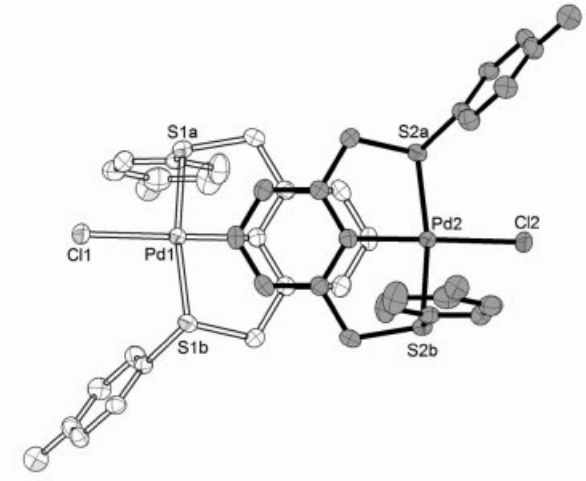


 © 2006 Wiley-VCH Verlag GmbH & Co. KGaA, Weinheim 

**1084** **P. Benkič, H. D. Brooke Jenkins, M. Ponikvar, Z. Mazej***

Synthesis and Characterisation of Alkali Metal and Thallium Polyfluoroantimonates, $ASb_nF_{5n+1}$ ($n$ = 2, 3)

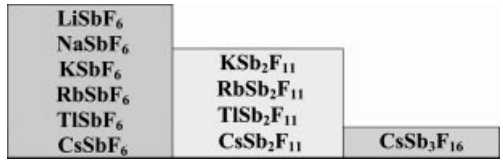


**Keywords:** Alkali metals / Antimony / Fluorides / Lewis acids / Superacidic systems

DOI: 10.1002/ejic.200500893

# Phosphorus-Containing Dendrons: Synthesis, Reactivity, Properties, and Use as Building Blocks for Various Dendritic Architectures

**Anne-Marie Caminade,*[a] Alexandrine Maraval,[a] and Jean-Pierre Majoral*[a]**

**Keywords:** Dendrimers / Phosphorus / Dendrons / Building blocks

Dendrons, also called dendritic wedges, are a special variety of dendrimers possessing one or two functional groups at the core, in addition to the numerous functional end groups. This review is focused on phosphorus-containing dendrons, which are dendrons built with one phosphorus atom at each branching point. Their synthesis, reactivity and properties are described, with emphasis on their use as building blocks for the elaboration of very complex and original dendritic architectures. Electrochemical and catalytic properties, as well as examples in the field of materials are also given.
(© Wiley-VCH Verlag GmbH & Co. KGaA, 69451 Weinheim, Germany, 2006)

## Introduction

Dendritic macromolecules constitute the fourth class of macromolecular architectures discovered about two decades ago,[1–3] after the linear, cross-linked, and branched polymers.[4] These hyperbranched architectures are expected to produce new properties and behaviours, and arouse an ever-increasing interest, with more than one thousand publications and more than one hundred patents per year over the last four years. Most of the work concerning hyperbranched architectures is focussed on the most structurally controlled compounds, i.e. dendrimers and dendrons,[5,6] which are

[a] Laboratoire de Chimie de Coordination du CNRS,
205 route de Narbonne, 31077 Toulouse Cedex 4, France
Fax: +33-5-6155-3003
E-mail: caminade@lcc-toulouse.fr
majoral@lcc-toulouse.fr

*Anne-Marie Caminade is Director of Research First Class at the CNRS. She received two Ph. D.s in Toulouse (1984 and 1988). She worked as a Post-doc at the Institut Français du Pétrole (1984) and in Pr. M. Veith's group (1988–1989, Saarbrücken, Germany). Since 1985 she has worked at the CNRS with Jean-Pierre Majoral, where she has been Director of Research since 1997. Her research interests centre on the main group elements. She developed several aspects of the chemistry of phosphorus, including low coordinated compounds, coordination of transition metals, reactivity of metallic hydrides, and synthesis of macrocycles. Her current research interest is the synthesis, reactivity and study of the properties of dendrimers and dendritic molecules. She is author of more than 210 publications and 23 patents.*

*Alexandrine Maraval is Doctor in Supramolecular Chemistry. She received her Ph. D. from the Université Paul Sabatier of Toulouse in 2000. Then she worked as a Post-doc with Prof. J. M. Basset at the high school CPE Lyon (2001–2003). Presently, she is working at the CNRS with Jean Pierre Majoral and Anne-Marie Caminade as Ingénieur Valorisation. Her research interest is mainly focused on the main group elements, especially phosphorus chemistry for the preparation of phosphorylated dendrimers. She has also worked with group 3 and 4 elements, their use in organometallic chemistry for the synthesis of new ligands and in catalysis.*

*Jean-Pierre Majoral is Director of Research Exceptional Class at the CNRS. He received his Ph. D. from the Université Paul Sabatier of Toulouse in 1972. Between 1972 and 1973 he worked as a Post-doc with Prof. A. Katritzky (University of East Anglia, Norwich, UK). He became Directeur de Recherche at the Centre National de la Recherche Scientifique in Toulouse in 1978. His research interest is mainly focused on the use of main group elements, especially phosphorus in different areas of chemistry. Presently, he is involved in the preparation and properties of macromolecules such as dendrimers and hyperbranched polymers. Emphasis is also placed on the studies of interactions between heavier main group elements and group 4 elements (titanium, zirconium, and hafnium) with applications in organic and organometallic chemistry. He is a member of the Polish Academy of Sciences and of the Academia Europaea. He is author of more than 370 publications and 31 patents.*

**MICROREVIEWS:** This feature introduces the readers to the authors' research through a concise overview of the selected topic. Reference to important work from others in the field is included.

 © 2006 Wiley-VCH Verlag GmbH & Co. KGaA, Weinheim 

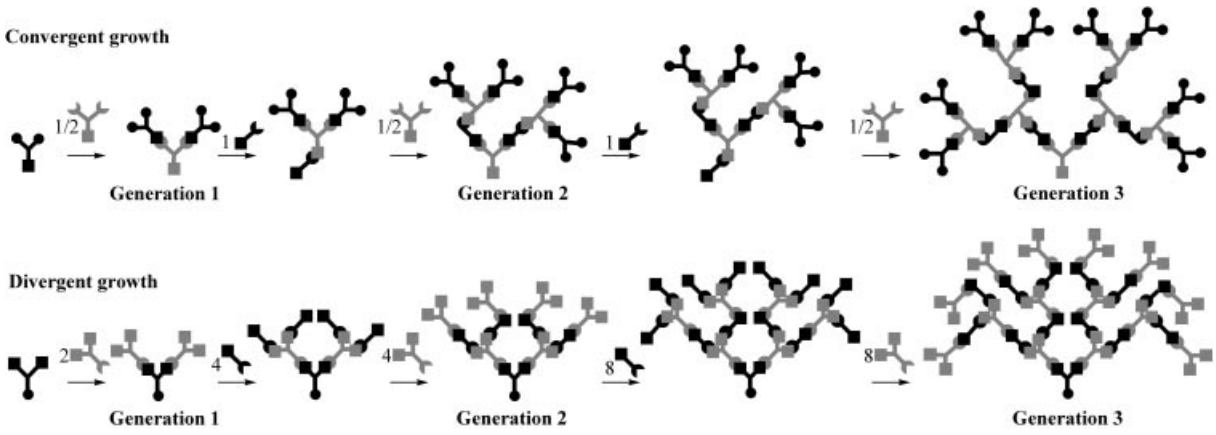


Scheme 1.

synthesised step-by-step (generation after generation) and not with polymerisation reactions. Dendrons,[7] also called dendritic wedges,[8] differ from dendrimers by the presence of one (or a few) functional group(s) located at the core, which are different from the other functional groups located at the periphery; their structure is very reminiscent of that of trees, the function at the core playing the role of the trunk. They are synthesised either by a convergent or a divergent process, generally using two types of monomers, one linear and one branched. In a convergent process, the periphery of the dendron never reacts, and only one reaction occurs at the level of the core; each generation is created by the association of two dendrons with a small molecule. In the divergent process, the periphery reacts at each step, whereas no reaction occurs at the core; each generation is created by the association of several small molecules with one dendron (Scheme 1). In both cases, the main problem is to find five types of functional groups among which one does not react with any of the other four, and four of the functional groups react specifically two-by-two.

The chemical composition of dendrimers and dendrons may be varied infinitely. We proposed about ten years ago a method of synthesis,[9,10] based on the reactivity of phosphorus derivatives, which afforded the highest well-defined generation described to date for any type of dendrimer (generation 12).[11] This method consists of condensation reactions of aldehydes with a phosphorhydrazide, and nucleophilic substitutions of Cl by hydroxybenzaldehyde under basic conditions. This method and its variants are so powerful that we have already published more than 130 papers in this field,[12] and the same method and its variants are also useful for the synthesis of dendrons. The aim of this microreview is to focus on the synthesis, reactivity, properties and use of complex architectures elaborated from dendrons possessing phosphorus at each branching point. Dendrons possessing phosphorus only at the core[13] are considered to be out of the scope of this review.

## Synthesis of Phosphorus-Containing Dendrons

The first phosphorus-containing dendrons **1-G$_n$** ($n$ = 0–2, corresponding to the generation) were synthesised in 1993 by Engel et al.,[14] but they were not recognised as dendrons but classed as dendrimers at that time. The function located at the core is a phosphane oxide, and the growing process consists of an iodination, followed by the quaternarisation of a phosphane. The phosphane oxide can be considered a masked phosphane, thus the dendrimer **1-aG$_n$** can be transformed into the dendron **1-bG$_n$** by reduction with a chlorosilane (Scheme 2). The phosphane located at the core of **1-bG$_n$** is different from all the other functional groups in the molecule, and is truly reactive, as shown by the complexation of gold.

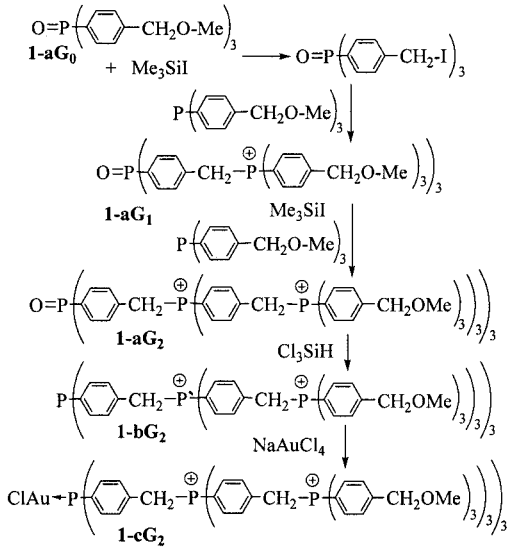


Scheme 2.

We described the second type of phosphorus-containing dendron **2-G$_n$** ($n$ = 0–7), which were also called dendrimers, but they possessed two functional groups at the core, which was different from the others (Scheme 3).[15] Indeed, the P=S groups included in P=N–P=S linkages behave differently from all the other P=S groups, and react easily with electrophiles[16] as will be illustrated later. These linkages are created by a Staudinger reaction between a phosphane such as **2-G$_0$** and a phosphorus azide such as **3**. Then the dendron is grown from the aldehydes with our classical

 © 2006 Wiley-VCH Verlag GmbH & Co. KGaA, Weinheim 

method of synthesis of dendrimers, using the phosphorhydrazide **4** in condensation reactions and hydroxybenzaldehyde sodium salt **5** for nucleophilic substitutions.[9–11] It must be emphasised that both reactions can easily be performed at a multi-gram scale. The reiteration of both steps has been carried out up to the obtaining of the seventh generation.

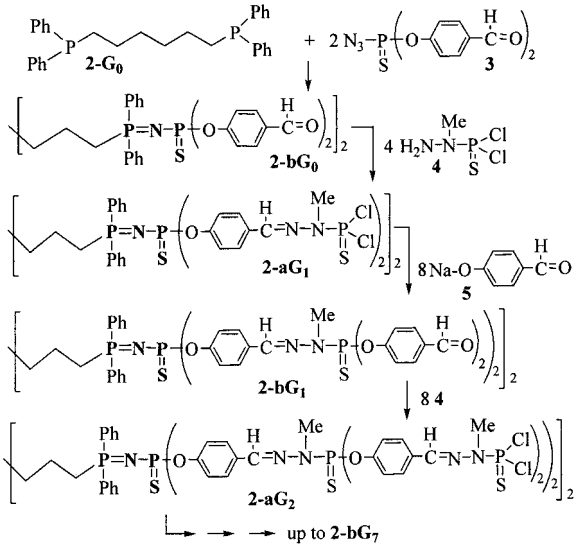


Scheme 3.

The use of Staudinger reactions allowed us to synthesise various types of dendrons possessing an R–$PPh_2$=N–P=S group at the core, starting from variously functionalised phosphanes (Scheme 4). The most often used R substituent is the vinyl group **6**,[17] but an allyl **7**,[18] a styryl **8**,[18] a methyl **9**,[19] a protected benzaldehyde **10**,[19] a triethoxysilane **11**,[20] and a diethoxyphosphonate **12**[21] have also been used as the core of these dendrons (Scheme 4 and Table 1). In addition, dendrons were built by the same process with the bis diphenylphosphanyl ferrocene **13** used as the core.[22] In most cases, the synthesis of the corresponding dendrons has been carried out up to generation 3, using the method already shown in Scheme 3, with the phosphorhydrazide **4** and hydroxybenzaldehyde **5**. Obviously, dendron growth could have been pursued up to higher generations. However, the process was voluntarily stopped at the third generation so as to be able to detect changes that occur at core level when some of these dendrons are used as building blocks for the elaboration of more complex structures. The $^{31}P$ NMR spectrum of the third generation dendron **6-aG$_3$** shows that even the phosphorus atoms located at the core are clearly distinguishable (Figure 1). The synthetic process affords directly as end groups $P(S)Cl_2$ (case a; see Scheme 4 and Table 1) and CHO (case b); various functionalised end groups have also been grafted starting from these functions. The most widely used method for the last step of the synthetic process is the substitution reaction of Cl using phenols (case e)[23] generally functionalised by nitrile (case c),[17] dimethylamine (case d),[17] diphenylphosphane (case f),[20,23] trifluoromethane (case g),[24] and free or complexed iminophosphane (cases l, m).[21] The reaction of a diamine has also been used (case i).[19] In a few cases, condensation reactions of hydrazines with the aldehyde end groups allowed the grafting of other functional groups that were either charged (case h)[25] or not (cases j, k).[19]

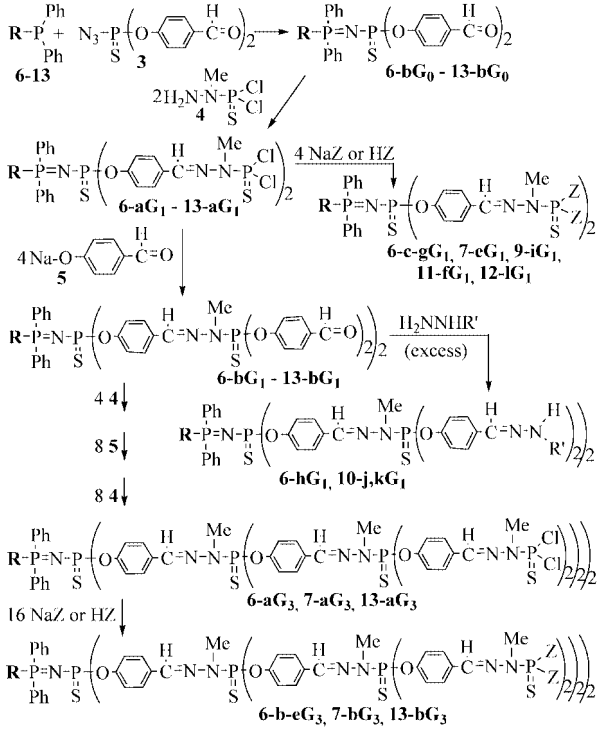


Scheme 4.

With aldehydes being one of the repetitively used units in the classical synthesis of our dendrimers and dendrons, any type of compound having at least one aldehyde and another functional group can be used as the core of dendrons, applying the same method. For instance, 4-acetoxybenzaldehyde,[26] pyridine-2,6-dicarboxaldehyde,[18] and ferrocene dicarboxaldehyde[27] have been used as cores of dendrons built by the successive reactions of the phosphorhydrazide and hydroxybenzaldehyde, affording in the final step dendrons **14-bG$_1$**, **15-bG$_2$** and **16-bG$_4$**, respectively (Scheme 5). However, this method of synthesis is not compatible with some kinds of functional groups; in particular for those sensitive to water, the condensation step must be avoided, thus we had to design alternative methods of synthesis.

For instance, the $Si(OEt)_3$ group is readily hydrolysed by traces of moisture, and the dendron **11-aG$_1$** cannot be grown by our traditional method of synthesis. Thus, the sodium salt **17** ($NaOC_6H_4PPh_2$) is used instead of $NaOC_6H_4CHO$ (**5**), then the azide **18** is reacted in a Staudinger reaction, affording directly the third generation **19-aG$_3$** with $P(S)Cl_2$ end groups. Aldehydes were grafted in the last step using the salt **5** (Scheme 6).[20] This method, based on the Staudinger reaction, was also found to be useful for the grafting of other functional groups, such as a pyrene derivative (see for instance dendron **20-G$_2$** in Scheme 6).[20]

 © 2006 Wiley-VCH Verlag GmbH & Co. KGaA, Weinheim 

Table 1. Functional groups located at the core (R) and on the periphery of the most external PS group (X) of dendrons shown in Scheme 4.

| Number | R | X | Highest generation | Ref. |
|---|---|---|---|---|
| **6-a** | $CH_2$=CH | Cl | 3 | [17] |
| **6-b** | $CH_2$=CH | O–$C_6H_4$–*p*-CHO | 3 | [17] |
| **6-c** | $CH_2$=CH | O–$C_6H_4$–*p*-CN | 3 | [17] |
| **6-d** | $CH_2$=CH | O–$C_6H_4$–*m*-$NMe_2$ | 3 | [17] |
| **6-e** | $CH_2$=CH | O–$C_6H_5$ | 3 | [23] |
| **6-f** | $CH_2$=CH | O–$C_6H_4$–*p*-$PPh_2$ | 3 | [23] |
| **6-g** | $CH_2$=CH | O–$C_6H_4$–*p*-$CF_3$ | 1 | [24] |
| **6-h** | $CH_2$=CH | O–$C_6H_4$–*p*-CH=NNHC(O)$CH_2NMe_3^+$ | 2 | [25] |
| **7-a** | $CH_2$=CH–$CH_2$ | Cl | 3 | [18] |
| **7-b** | $CH_2$=CH–$CH_2$ | O–$C_6H_4$–*p*-CHO | 3 | [18] |
| **7-e** | $CH_2$=CH–$CH_2$ | O–$C_6H_5$ | 2 | [18] |
| **8-a** | $CH_2$=CH–*p*-$C_6H_4$ | Cl | 1 | [18] |
| **8-b** | $CH_2$=CH–*p*-$C_6H_4$ | O–$C_6H_4$–*p*-CHO | 1 | [18] |
| **9-a** | Me | Cl | 1 | [19] |
| **9-i** | Me | $NHCH_2CH_2NHEt_2^+$ | 1 | [19] |
| **10-a** | [–$CH_2O$–]$_2$CH–*p*-$C_6H_4$ | Cl | 1 | [19] |
| **10-b** | [–$CH_2O$–]$_2$CH–*p*-$C_6H_4$ | O–$C_6H_4$–*p*-CHO | 1 | [19] |
| **10-j** | [–$CH_2O$–]$_2$CH–*p*-$C_6H_4$ | O–$C_6H_4$–*p*-CH=$NNH_2$ | 1 | [19] |
| **10-k** | [–$CH_2O$–]$_2$CH–*p*-$C_6H_4$ | O–$C_6H_4$–*p*-CH=N$N(CH_2PPh_2)_2$ | 1 | [19] |
| **11-a** | $(EtO)_3SiCH_2CH_2CH_2$ | Cl | 1 | [20] |
| **11-b** | $(EtO)_3SiCH_2CH_2CH_2$ | O–$C_6H_4$–*p*-CHO | 1 | [20] |
| **11-f** | $(EtO)_3SiCH_2CH_2CH_2$ | O–$C_6H_4$–*p*-$PPh_2$ | 1 | [20] |
| **12-a** | $(EtO)_2$P(O)CH=CH–*p*-$C_6H_4$ | Cl | 1 | [21] |
| **12-b** | $(EtO)_2$P(O)CH=CH–*p*-$C_6H_4$ | O–$C_6H_4$–*p*-CHO | 1 | [21] |
| **12-l** | $(EtO)_2$P(O)CH=CH–*p*-$C_6H_4$ | O–$C_6H_4$–*p*-N=CH–*o*-$C_6H_4$–$PPh_2$ | 1 | [21] |
| **12-m** | $(EtO)_2$P(O)CH=CH–*p*-$C_6H_4$ | O–$C_6H_4$–*p*-N=CH–*o*-$C_6H_4$–$PPh_2PdCl_2$ | 1 | [21] |
| **13-a** | ½[$(PPh_2Cp)_2Fe$] | Cl | 4 | [22] |
| **13-b** | ½[$(PPh_2Cp)_2Fe$] | O–$C_6H_4$–*p*-CHO | 4 | [22] |

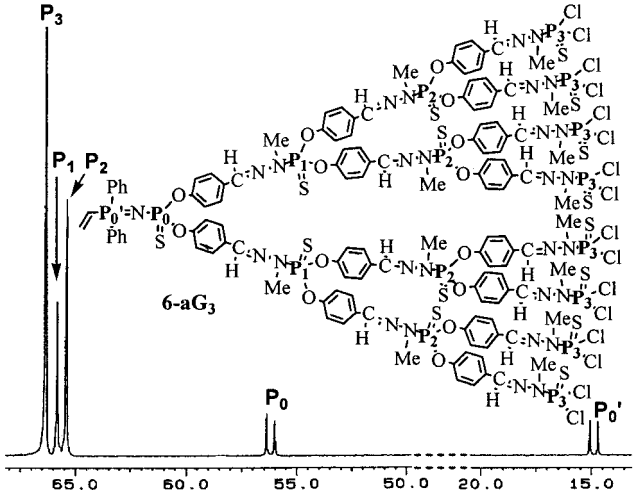


Figure 1. $^{31}$P NMR spectrum of the third generation dendron **6-aG$_3$**.

On the other hand, the presence of chlorine at the core of dendrons is incompatible both with our traditional method of synthesis, in particular with the use of the strong nucleophile **5**, and with the method shown in Scheme 6, because of the use of the salt **17**. Thus, the dendron grown from the chloromethyl phosphane oxide derivative **20-bG$_0$** is built using the repetition of three steps. The first one is the condensation reaction of methylhydrazine with aldehyde; the second is another condensation reaction, between $Ph_2PCH_2OH$ and the secondary hydrazone. The third and last step before the repetition of the three steps is the Staudinger reaction of the phosphane end groups with the azide **3**, which again affords aldehyde end groups. This dendron was grown to the fourth generation **21-bG$_4$** (Scheme 7).[18]

## Reactivity at the Core of Phosphorus-Containing Dendrons

The reactivity at the core of most of the dendrons we have synthesised is related to the presence of a P=N–P=S group. In addition to its own reactivity this group may also enhance the reactivity of other functional groups linked to it. The mesomeric form of the P=N–P=S linkage has a high electron density on sulfur ($P^+$–N=P–$S^-$) which allows the regiospecific complexation of gold, whereas the other P=S groups do not react in this way (Scheme 8).[30] The existence of this mesomeric form also allows the reaction of the P=N–P=S linkage with electrophiles such as methyl triflate. The reaction was first applied to small molecules,[28] then to dendrons.[15] Various functionalised triflates such as allyl or propargyl triflate have also been used.[29] These reactions are easily monitored by $^{31}$P NMR spectroscopy. Indeed, the P=N–P=S linkages give two very characteristic doublets at $\delta \approx 20$ ppm (P=N) and $\delta \approx 52$ ppm (P=S), which move upon *S*-alkylation to $\delta \approx 28$ ppm and $\delta \approx 33$ ppm, respectively. It should be noted that this reaction at the core occurs even for the seventh generation, illustrating the high porosity of these dendrimers, and the specificity of this reaction.[15] Indeed, the numerous other P=S groups consti-

 © 2006 Wiley-VCH Verlag GmbH & Co. KGaA, Weinheim 

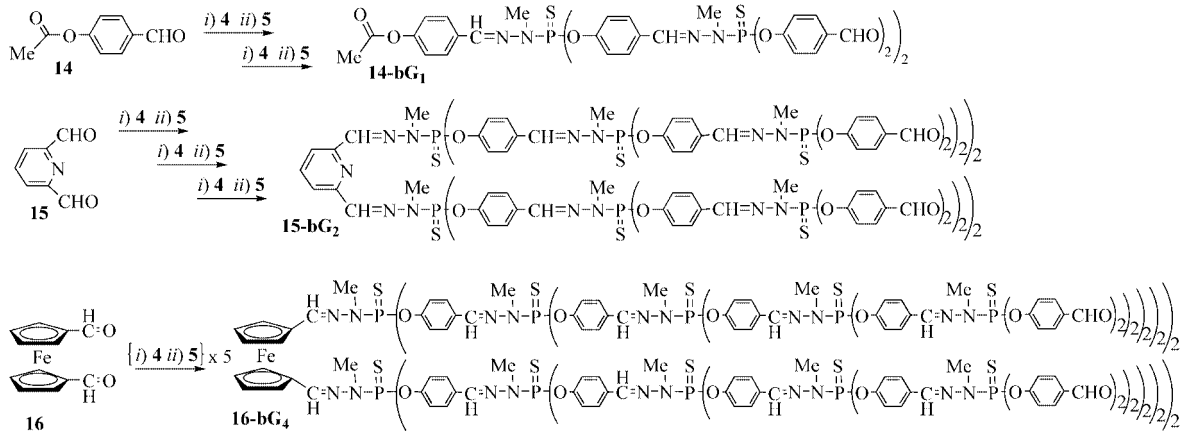

Scheme 5.

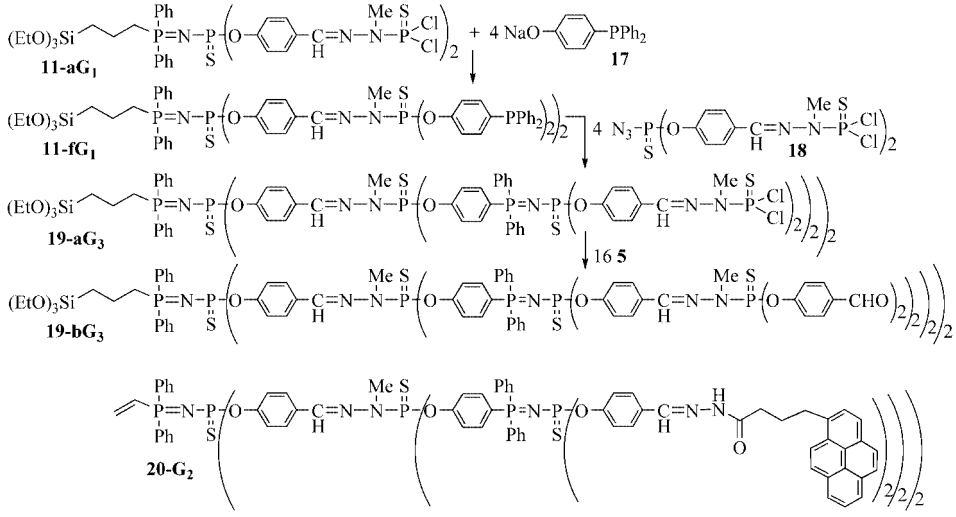

Scheme 6.

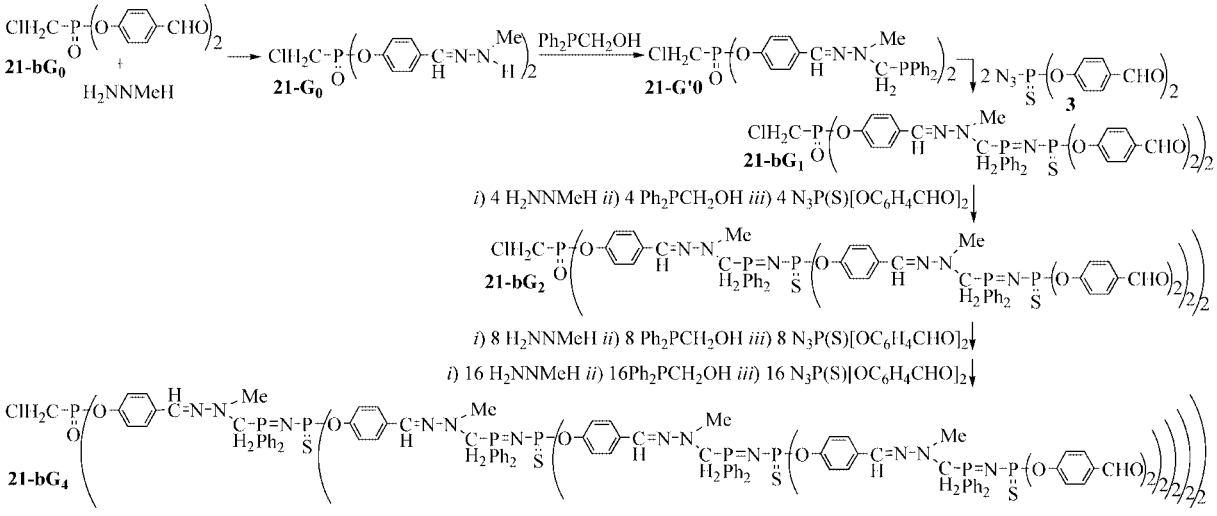

Scheme 7.

tuting the points of divergence of these dendrons are not alkylated, as shown for one example in Scheme 8, but this type of reaction has been carried out with numerous dendrons.

The alkylation of sulfur is compatible with further modifications of the periphery of the dendrons. In particular, we tried to graft water-solubilising end groups to the cationic dendron **22-aG$_1$**. In order to avoid the formation of triflic

 © 2006 Wiley-VCH Verlag GmbH & Co. KGaA, Weinheim 

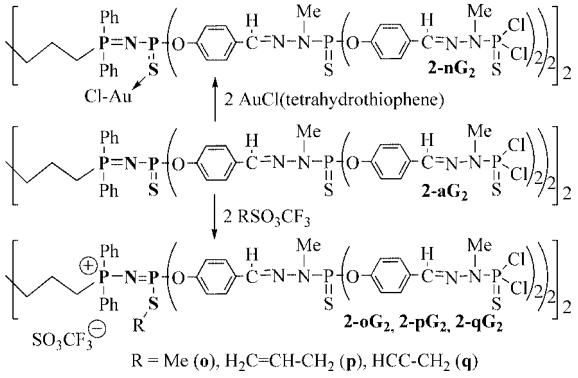


Scheme 8.

acid, which is potentially aggressive for the hydrazone linkage, the triflic counterion of **22-aG$_1$** was first replaced by tetraphenylborane. Then the reaction of 4 equiv. of *N*,*N*-diethylethylenediamine affords cleanly the pentacationic dendron **23-iG$_1$** (Scheme 9).[19]

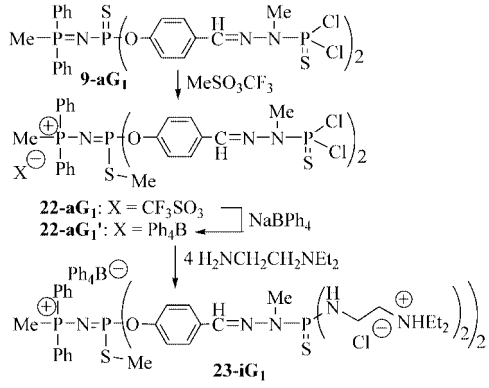


Scheme 9.

Another illustration of the specificity of the reactivity of the P=N–P=S linkages with alkyl triflates is given by the small dendron **12-bG$_0$** in which only the P=S bond is alkylated by methyl triflate, leading to **24-bG$_0$**. The conjugated P=O bond does not react with methyl triflate, but it reacts with trimethylsilyl triflate, because of the oxophilicity of silicon to afford the dicationic compound **25-bG$_0$** (Scheme 10).[21]

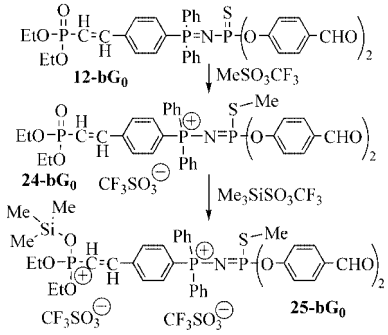


Scheme 10.

The P=N–P=S linkage also induces an electron-withdrawing effect on the functional group linked to the phosphazene, which we exploited particularly when a vinyl group is linked to this phosphorus (series of dendrons **6-G$_n$**). We demonstrated the possibility of performing Diels–Alder additions on this vinyl group,[26] but most of the reactions we carried out were Michael type additions of primary and secondary amines. They were first tested with small compounds possessing one $CH_2$=CH–$PPh_2$=N–$PR_2$=X (X = O, S) linkage,[31] then applied to dendrons. In all cases, we used functionalised amines. The reaction works nicely with primary amines (compounds **26**–**29**) and gave at the core a secondary amine together with an alkyne,[23] a triethoxysilyl group,[20,31] or even a phenol[23] (Scheme 11 and Table 2). In the latter case, the reaction of the amine is specific, no addition of the phenol is observed. Analogous reactions are obtained with secondary amines, such as diallylamine **30** and thiomorpholine **31**.[23] The reactions are carried out either at room temperature or by heating, depending on the rate of the addition, and using either a stoichiometric amount or a slight excess of reagent. The reactions are easily monitored by $^{31}$P NMR, with a deshielding effect on the signal of the P=N group from $\delta$ = 10–12 ppm for **6-G$_n$** to $\delta$ = 17–18 ppm after addition.

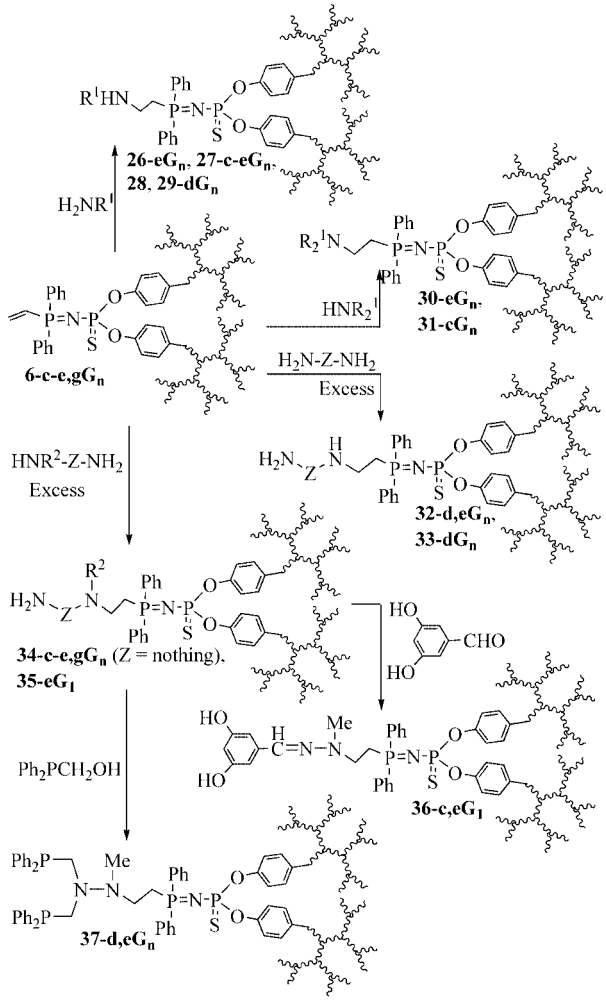


Scheme 11.

 © 2006 Wiley-VCH Verlag GmbH & Co. KGaA, Weinheim 

Table 2. Functional groups linked to the $CH_2CH_2$ group located at the core (R′) and on the periphery of the most external PS groups (X) of dendrons shown in Scheme 11.

| Number | R′ | X | Highest generation | Ref. |
|---|---|---|---|---|
| **26-e** | $NHCH_2C{\equiv}CH$ | $O–C_6H_5$ | 3 | [23] |
| **27-c** | $NH(CH_2)_3Si(OEt)_3$ | $O–C_6H_4–p$-CN | 3 | [20] |
| **27-d** | $NH(CH_2)_3Si(OEt)_3$ | $O–C_6H_4–m$-$NMe_2$ | 3 | [20] |
| **27-e** | $NH(CH_2)_3Si(OEt)_3$ | $O–C_6H_5$ | 1 | [31] |
| **28** | $NH(CH_2)_3Si(OEt)_3$ | pyrene[a] | 2 | [20] |
| **29-d** | $NH(CH_2)_2–p$-$C_6H_4$–OH | $O–C_6H_4–m$-$NMe_2$ | 3 | [23] |
| **30-e** | $N(CH_2CH{=}CH_2)_2$ | $O–C_6H_5$ | 3 | [23] |
| **31-c** | $N[–CH_2–CH_2–]_2S$ | $O–C_6H_4–p$-CN | 3 | [23] |
| **32-d** | $NH–CH_2–CH_2–NH_2$ | $O–C_6H_4–m$-$NMe_2$ | 3 | [17] |
| **32-e** | $NH–CH_2–CH_2–NH_2$ | $O–C_6H_5$ | 3 | [23] |
| **33-d** | $NH–o$-$C_6H_{10}$–$NH_2$ | $O–C_6H_4–m$-$NMe_2$ | 2 | [23] |
| **34-c** | $NMeNH_2$ | $O–C_6H_4–p$-CN | 3 | [17] |
| **34-d** | $NMeNH_2$ | $O–C_6H_4–m$-$NMe_2$ | 3 | [17] |
| **34-e** | $NMeNH_2$ | $O–C_6H_5$ | 3 | [23] |
| **34-g** | $NMeNH_2$ | $O–C_6H_4–p$-$CF_3$ | 1 | [24] |
| **35-e** | $N[(CH_2)_3NH_2]_2$ | $O–C_6H_5$ | 1 | [31] |
| **36-c** | $NMeN{=}CH–C_6H_3(OH)_2$ | $O–C_6H_4–p$-CN | 1 | [31] |
| **36-e** | $NMeN{=}CH–C_6H_3(OH)_2$ | $O–C_6H_5$ | 1 | [31] |
| **37-d** | $NMeN(CH_2PPh_2)_2$ | $O–C_6H_4–m$-$NMe_2$ | 3 | [17] |
| **37-e** | $NMeN(CH_2PPh_2)_2$ | $O–C_6H_5$ | 1 | [19] |

[a] from **20-G$_n$**.

A large excess of reagents must be used with diamines. Two cases can be distinguished: either the diamine possesses two identical primary amino groups, or it possesses one primary and one secondary amino group. In the former case, the use of several hundreds of equivalents prevents the coupling of two dendrons (cases **32** and **33** in Scheme 11 and Table 2), as shown by the loss of symmetry of the diamine, evidenced by $^1H$ and $^{13}C$ NMR spectroscopy.[17,23] The reaction is expected to be more complicated when using nonsymmetrical diamines that have two types of amino groups (primary and secondary). Indeed, besides avoiding the association of two dendrons as for symmetrical diamines, a regiospecific reaction of only one type of amine must be obtained. Such specificity was expected with methylhydrazine (considered to be a special nonsymmetrical diamine), in which the most substituted nitrogen is generally more reactive. The reaction proceeds rapidly at room temperature with an excess of methylhydrazine (30 equiv.) leading to a single product, **34-G$_n$**, corresponding to the exclusive addition of the NMeH group.[17,23,24] The same specificity for the secondary amine is observed with the diamine **35**.[31]

The series of compounds **34-G$_n$** is particularly interesting, due to the wide range of reactions available starting from a $NH_2$ group, which may enlarge the scope of functional groups located at the core of dendrons. It may afford stable hydrazones by condensation reactions with aldehydes, as shown by the synthesis of **36-c,eG$_1$**[31] (Scheme 11). We have also grafted a diphosphane group by reaction with $Ph_2PCH_2OH$ (compounds **37-G$_n$**),[17,19] a type of condensation that we have already used on the periphery of dendrimers.[32,33] A particular case of the reactions shown in Scheme 11 is afforded by dendrons possessing as end groups functions able to react with amines, because both the core and the periphery will react. An example of such a compound is provided by the dendrons **6-bG$_n$**, in which the vinyl group at the core reacts in a Michael type addition, whereas the aldehyde end groups react via condensation reactions. The use of a large excess of methylhydrazine, necessary to prevent a polymerisation reaction between the $NH_2$ of the core and the aldehydes, affords the dendrons **38-G$_n$**. Their subsequent reaction with $Ph_2PCH_2OH$ affords the dendrons **39-G$_n$** that possess a diphosphane at the core and monophosphanes as end groups (Scheme 12).[17]

However, the presence of aldehydes as end groups does not necessarily preclude a specific reaction at the core, as shown by dendrons **14-bG$_1$**. The deprotection of the acetyl

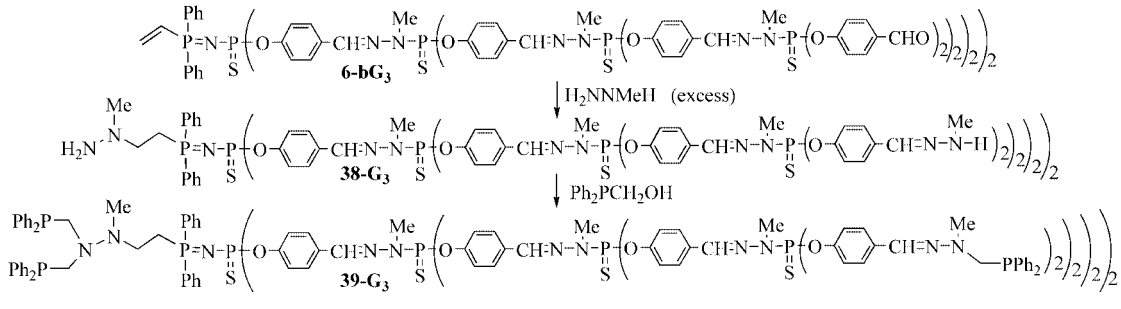


Scheme 12.

 © 2006 Wiley-VCH Verlag GmbH & Co. KGaA, Weinheim 

group by guanidine occurs cleanly and under very mild conditions to afford the phenol group of **40-bG$_1$**. This phenol is potentially useful for a number of subsequent reactions; we tested the reactivity of diisocyanatohexane, whose addition gives the dendron **41-bG$_1$**, functionalised by an isocyanate and a carbamate at the core (Scheme 13).[26]

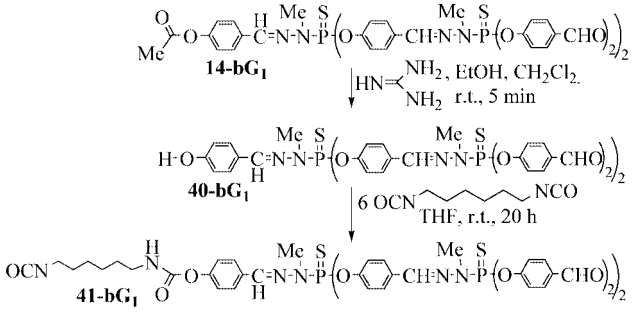

Scheme 13.

## Use of Phosphorus-Containing Dendrons for the Elaboration of Complex Dendritic Architectures

Most of the reactions at the core of dendrons described above can be applied to the elaboration of special dendritic architectures. We have been interested in this field for a long time; an example of our work being the growth of dendritic branches inside a pre-existing dendrimer.[34] In most cases, the dendrons used for building special architectures are those issued from the vinyl group at the core, but in one case the alkylated P=N–P=S core of dendron **23-iG$_1$** was used for such a purpose. Indeed, the alkylation of sulfur induces a weakening of the strength of the PS bond, which can be easily cleaved using a nucleophilic phosphane such as P(NMe$_2$)$_3$.[34,35] The dendron **42-iG$_1$** is too sensitive to oxidation to be fully isolated, but it can be directly reacted with the azide **3** to afford the small diblock dendrimer **43-iG$_1$–bG$_0$**, which possesses two types of end groups. The aldehydes can be used to afford other end groups: their reaction with methylhydrazine followed by Ph$_2$PCH$_2$OH affords **44-iG$_1$–G$_0$**, whose phosphane can be used for complexation, as illustrated by the reaction with iron, leading to the cationic complex **45-iG$_1$–G$_0$** (Scheme 14).[19]

Besides this example using the reactivity of the P=N–P=S group, all the other examples of special dendritic architectures that we have described develop from dendrons possessing an amine or phosphane at the core. The simplest type of association consists of using 2 equiv. of dendrons with 1 equiv. of a small molecule. If this molecule possesses another functional group, the resulting bis dendron is itself a dendron, as shown for instance by the condensation of 2 equiv. of the dendrons **32-c,dG$_3$** with 1 equiv. of the azidodialdehyde **3**. The azide remaining at the core of **46-c,d[G$_3$]$_2$** (Scheme 15 and Figure 2)[17] will be used later to afford more elaborate structures. The same methodology was applied to the dendron **32-gG$_1$**, which reacts with the special tetraphosphazene **47**, which possesses four types of functional groups. The reaction occurs as expected only with the aldehydes, leading to the novel type of dendrimeric species **48-g[G$_1$]$_2$**. This compound possesses several types of functional groups at the core constituted by the oligophosphazene linkage, as well as other functional groups within the branches and on the periphery (Scheme 16 and Figure 2).[24]

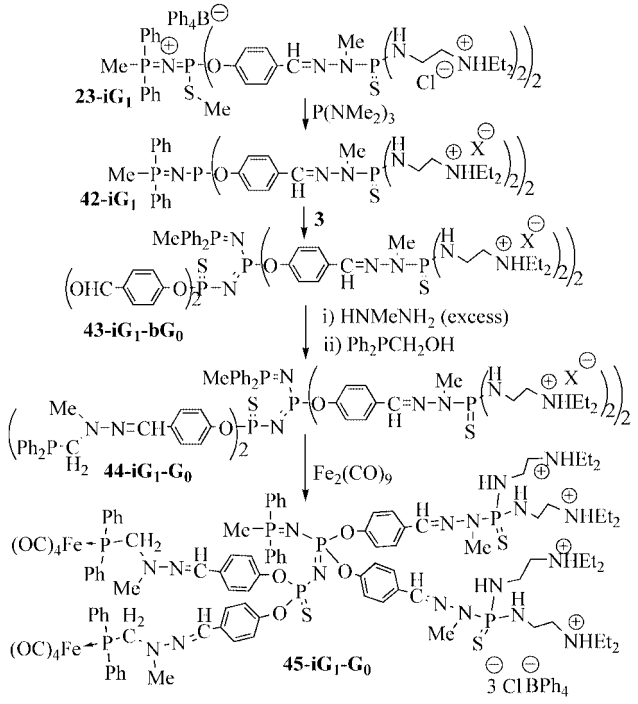

Scheme 14.

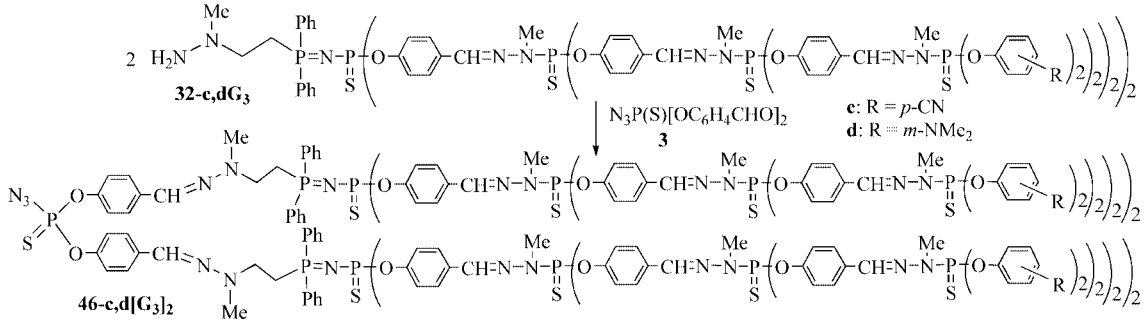

Scheme 15.

 © 2006 Wiley-VCH Verlag GmbH & Co. KGaA, Weinheim 

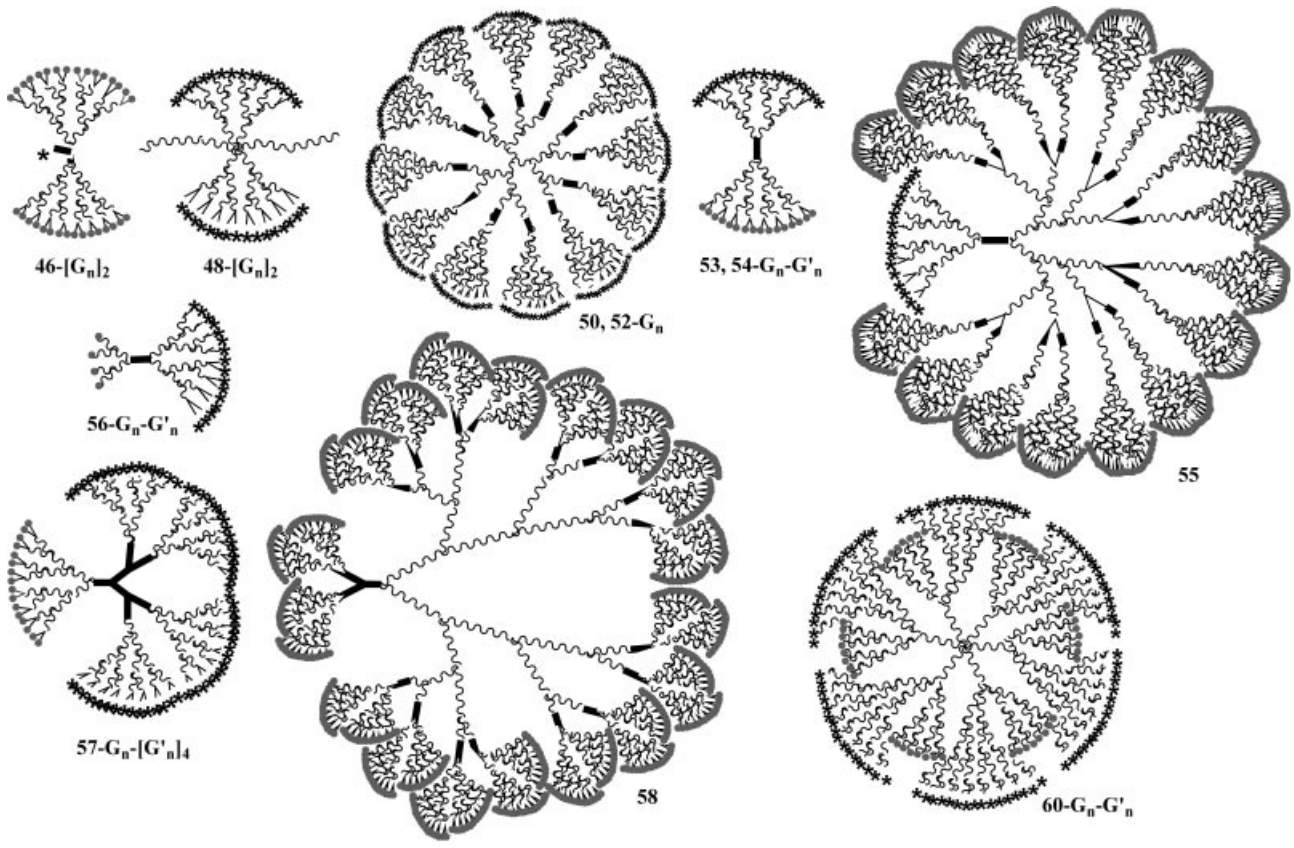


Figure 2. Various schematised special dendritic architectures elaborated from dendrons.

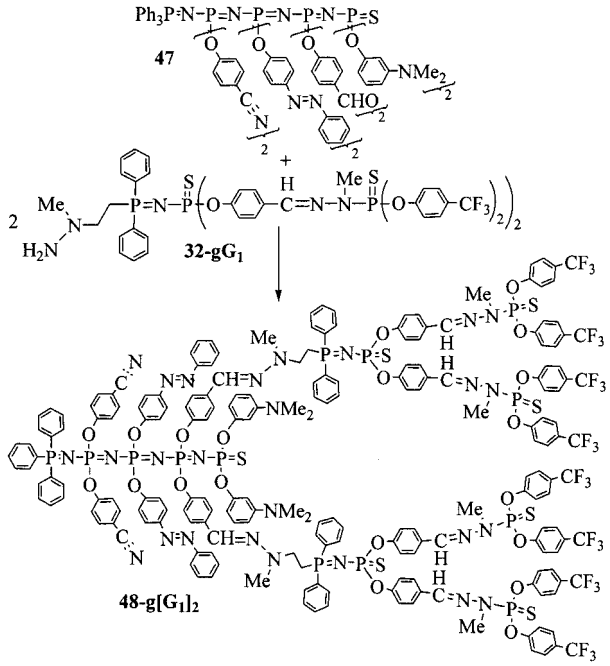


Scheme 16.

Such methodology has been extended to the synthesis in only one step of high generation layered dendrimers. Indeed, the hydrazine function located at the core of the third generation dendron **34-eG$_3$** reacts with the aldehyde end groups of the second generation dendrimer **49-bG$_2$**. The reaction is slow despite the use of an excess of dendrons, and went to completion only after 18 days, as shown with $^1$H NMR data by the disappearance of the aldehydes. Despite its length, this reaction is interesting because it affords the sixth generation of the layered dendrimer **50-eG$_6$** in only one step from the second generation (Scheme 17 and Figure 2).[23] It should be noted that an analogous reaction carried out with the third generation dendrimer **49-bG$_3$** did not continue to completion, even after 40 days. The steric hindrance precludes the insertion of approximately 1 equiv. of dendron among 24, despite the fact that the seventh generation dendrimer, and even higher generations, can be obtained step-by-step using sequentially small molecules instead of dendrons.[11]

However, the type of reaction used for connecting the dendrons to the dendrimer also has an influence on the highest generation of dendrimer usable. Indeed, the Staudinger reaction of the dendritic azide **46-b[G$_3$]$_2$** with the third generation dendrimer **51-G$_3$** affords the eighth generation of the layered dendrimers **52-cG$_8$** in one step. The P=N–P=S linkages are present only at the level of the fourth and fifth generation (Scheme 18 and Figure 2).[17]

Despite their original dendritic architectures, the compounds shown in the previous schemes possess only one type of end group. However, we have in hand all the tools necessary for synthesising large "Janus" dendrimers that are dendrimers possessing two types of end groups located in

 © 2006 Wiley-VCH Verlag GmbH & Co. KGaA, Weinheim 

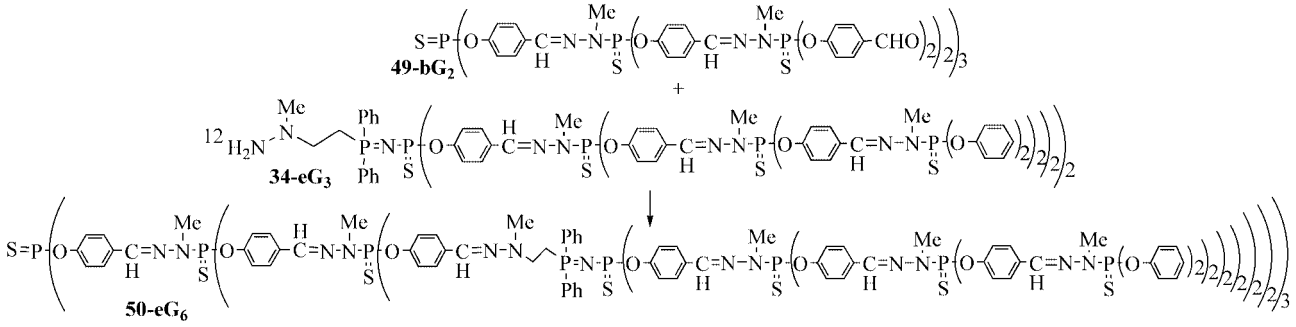


Scheme 17.

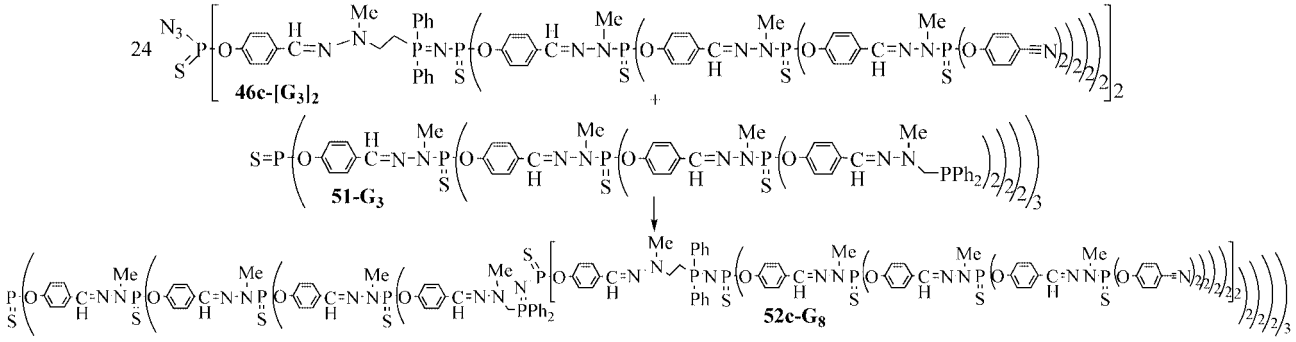


Scheme 18.

two different areas of the periphery, obtained in particular by grafting two different dendrons by their core. The first attempt involves the second generation dendrons **6-eG$_2$** and **33-dG$_2$**, which react in a Michael type addition. The resulting unsymmetrical compound **53-dG$_2$–eG$_2$** can also be viewed as a dendron, because of the presence of two NH groups at the centre of the molecule (Scheme 19 and Figure 2).[23]

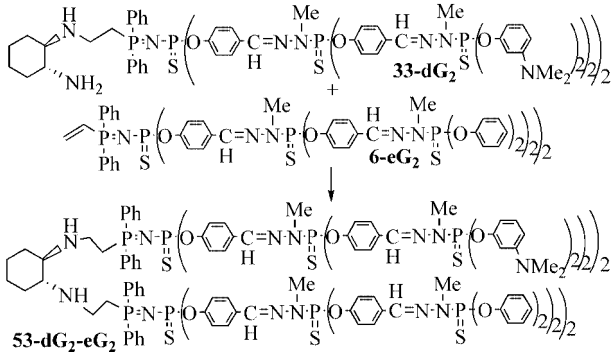


Scheme 19.

Such methodology using Michael type additions can be applied to larger generations. We decided to use compounds no higher than the third generation, in order to be able to detect the modification of the core with a sufficient intensity by NMR spectroscopy. The reaction was carried out with compounds **6-G$_3$** and **32-G$_3$**, leading to compound **54-G$_3$-G$_3$** (Scheme 20 and Figure 2).[17,23] This reaction is compatible with several types of end groups on the periphery of the dendrons, and in particular with phosphanes. This compound (**54-eG$_3$–fG$_3$**) is the precursor of the very special "fish-like" dendritic species **55**. This compound is obtained by the grafting, via a Staudinger reaction, of dendrons **46-d[G$_2$]$_2$** on only half of the periphery of **54-eG$_3$–fG$_3$**, i.e. the face that possesses phosphanes (Scheme 20 and Figure 2).[23] This unsymmetrical compound has 16 phenoxy groups as end groups on one side, two NH "central" functions, 50 P=N–P=S linkages located at four different levels in the ratio 32:16:1:1, and 512 $NMe_2$ as end groups on the other side.

As illustrated above the synthesis of complex dendritic species from dendrons can necessitate several steps, in particular to extend the number of functional groups that are usable. The reaction of the bisaldehyde azide **3** with the core of a dendron such as **37-eG$_1$** affords the possibility of growing new dendritic branches at the core of the dendron; this also allows us to multiply the possible types of functionalisation on one side of this new "Janus" dendritic molecule. Starting from the four aldehyde groups of **56-eG$_1$–bG$_1$**, we applied our classical method for the synthesis of dendrimers, using alternately the phosphorhydrazide **4** and the sodium salt of hydroxybenzaldehyde (**5**). This dendritic species has been grown up to the third generation on one side (compound **56-eG$_1$–bG$_3$**), but it could have been continued to higher generations (Scheme 21 and Figure 2).[19] This compound possesses four end groups on one side and 16 on the other.

However, the shortest method to obtain a different ratio of two types of end group obviously consists of using dendrons that have a different number of end groups. For instance, the reaction of 2 equiv. of **46-c[G$_3$]$_2$** with **37-dG$_3$** af-

 © 2006 Wiley-VCH Verlag GmbH & Co. KGaA, Weinheim 

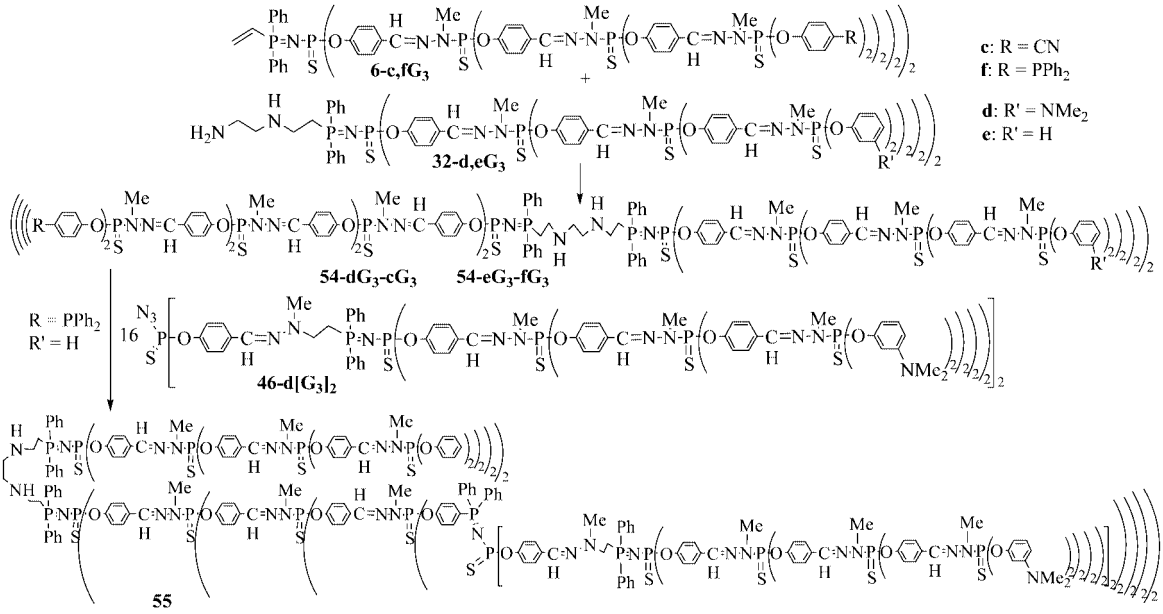


Scheme 20.

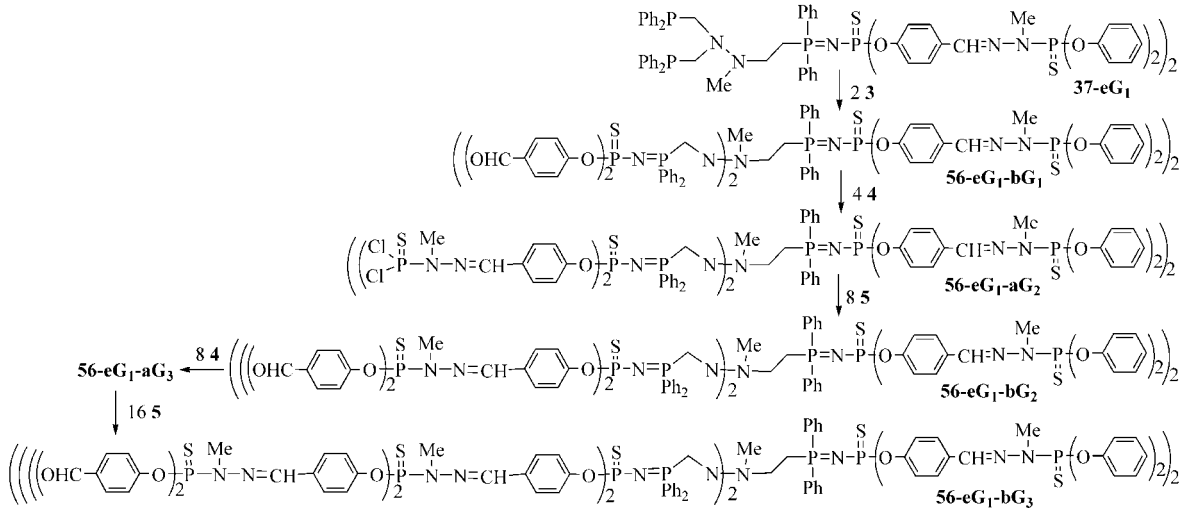


Scheme 21.

fords the straightforward compound **57-dG$_3$-c[G$_3$]$_4$**, in which the ratio of the end groups is 1:4, i.e. 16 $NMe_2$ and 64 cyano groups (Scheme 22, Figure 2).[17] The same methodology can be envisaged starting from dendron **39-G$_3$** instead of **37-dG$_3$**. The former possesses phosphanes both at the level of the core (2 $P^{III}$) and on the periphery (16 $P^{III}$), which will react in Staudinger reactions with the dendron **46-d[G$_3$]$_2$**. The result is the complex dendritic structure **58**, which is relatively reminiscent of the structure of compound **55**. However, despite its nonsymmetrical internal structure, compound **58** possesses only one type of end group (576 dimethylamino groups). Compound **58** is a kind of layered segment-block dendrimer (Scheme 23 and Figure 2).[17]

A very original distribution of two types of end groups is also obtainable from dendrons. It necessitates a dendrimer possessing reactive internal functions such as **59-eG$_3$–bG$_0$**.[34] The $NH_2$ group located at the core of dendron **34-cG$_2$** is used to react with the internal aldehydes of **59-eG$_3$–bG$_0$**. Obviously, the problem of steric hindrance evoked previously for the layered dendrimer **50-eG$_7$** might be more crucial here, where the reactions must occur inside the dendrimer and not on its periphery. The condensation is relatively slow and requires 10 days to go to completion, but it finally affords compounds **60-eG$_3$–c–G$_4$** (Scheme 24 and Figure 2),[23] confirming the high porosity of our phosphorus dendrimers, already demonstrated by NMR[15] and

 © 2006 Wiley-VCH Verlag GmbH & Co. KGaA, Weinheim 

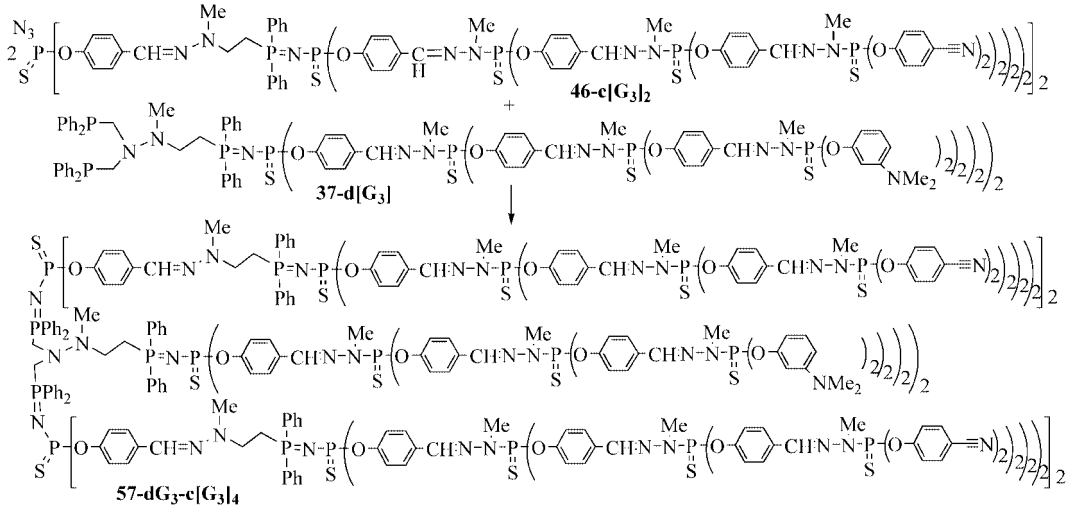


Scheme 22.

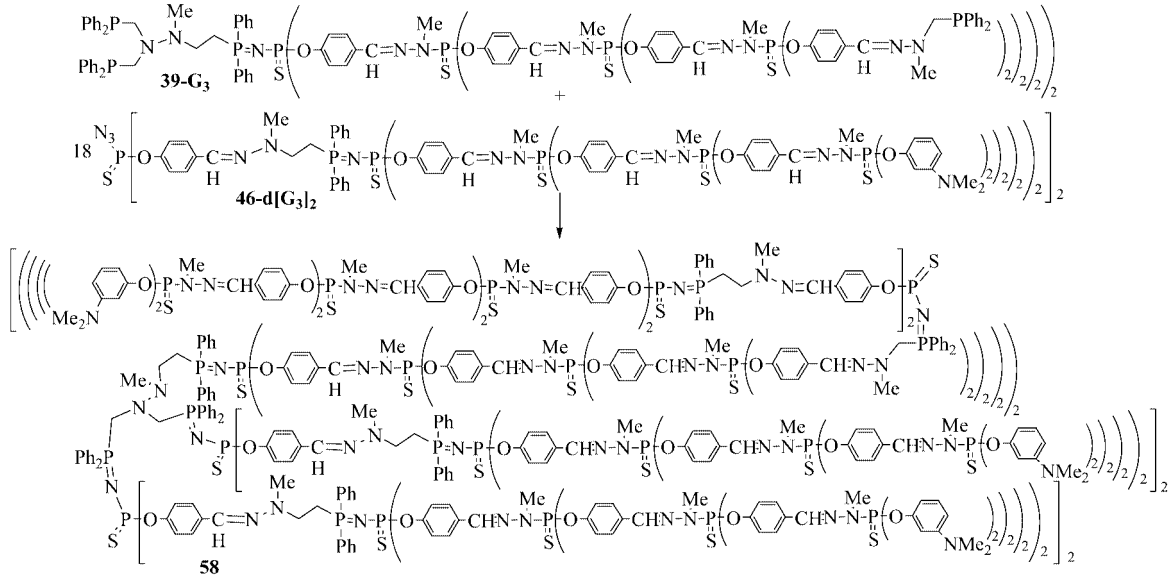


Scheme 23.

fluorescence.[36] However, **34-cG$_2$** is the largest dendron that can be accommodated inside **59-eG$_3$–bG$_0$**; indeed, the reaction of **34-cG$_3$** failed to go to completion.

## Other Properties and Uses of Phosphorus-Containing Dendrons

Besides their usefulness for the synthesis of complex dendritic architectures, dendrons offer other possible uses such as in characterising the special properties of the "dendritic state", for catalysis, or for elaborating new materials, depending on the function located at the core. Dendrons possessing a ferrocene at the core were elaborated with the aim of measuring the influence of the encapsulation of an electroactive function on the electrochemical properties. Dendrons **13-G$_n$** were relatively deceptive, because the wave detected in electrochemistry did not correspond to the oxidation of the ferrocene but of the P=N–P=S linkages. This oxidation is not reversible and induces a polymerisation of the dendron.[22] On the other hand, dendrons **16-G$_n$** do not possess any P=N–P=S linkage, and are usable, therefore, for the detection of any influence on the electrochemical properties, depending on the generation and thus the size of the dendron. Compound **16-bG$_0$** shows the characteristic quasi reversible ($I$pc/$I$pa ≅ 1) single electron oxidation process, whereas **16-bG$_1$** exhibits a slightly more irreversible process ($I$pc/$I$p$a$ = 0.88). This trend is confirmed by the pronounced irreversibility observed for **16-bG$_2$**, which gives a very weak and poorly resolved signal (Figure 3).[27] The core is undetectable presumably because it cannot approach the electrode closely enough because of the steric hindrance induced by the dendritic branches.

The presence of a diphosphanyl group at the core of dendron **37-dG$_3$** prompted us to use it as a ligand for transition metal complexes, in particular for ruthenium. Most ruthenium complexes possess catalytic properties, thus it was

 © 2006 Wiley-VCH Verlag GmbH & Co. KGaA, Weinheim 

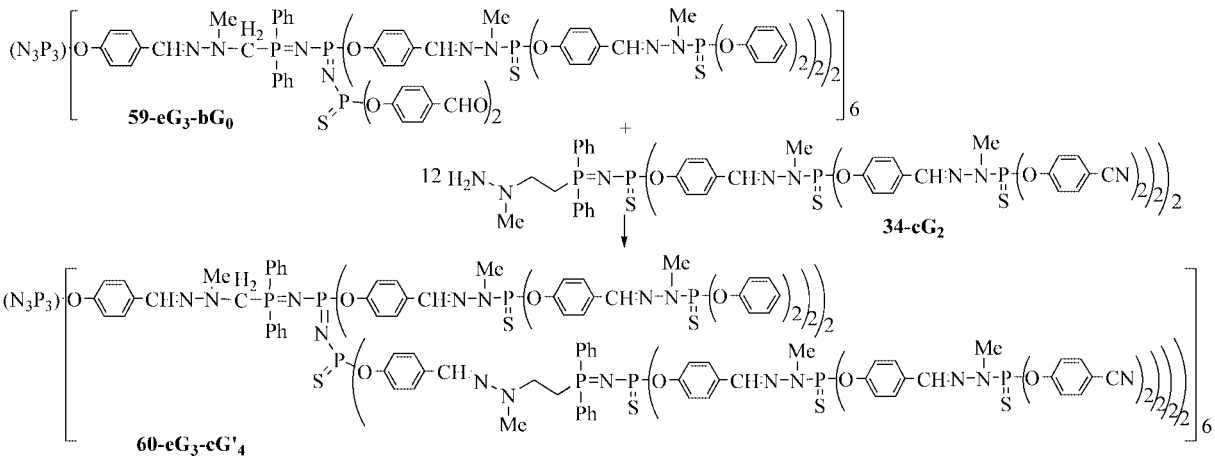


Scheme 24.

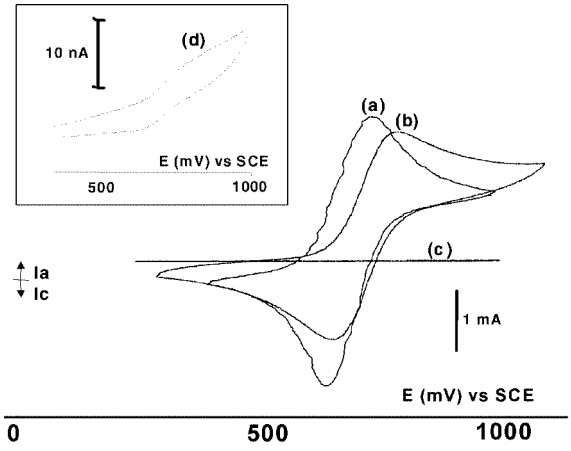


Figure 3. Cyclic voltammograms (scan rate 100 mV·s$^{-1}$) obtained for dendrimers **16-bG$_0$** (a), **16-bG$_1$** (b), **16-bG$_2$** (c), and enlargement for **16-bG$_2$** (d).

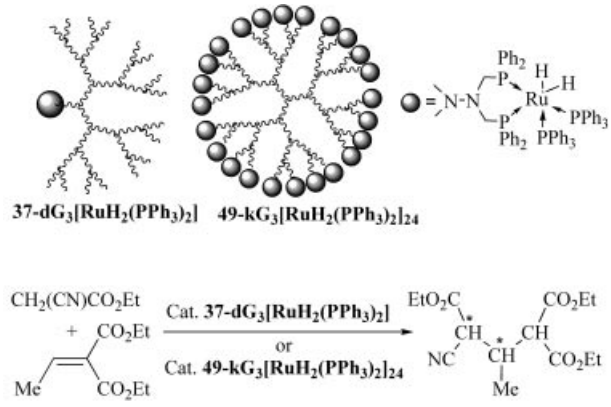


Scheme 25.

tempting to use dendron **37-dG$_3$[RuH$_2$(PPh$_3$)$_2$]** as a catalyst. Indeed, the use of dendritic complexes in catalysis is an area of intense activity, especially for those possessing phosphane complexes,[12b] mainly because of the possibility of recovering the catalyst simply by precipitation or ultra-filtration. Dendron **37-dG$_3$[RuH$_2$(PPh$_3$)$_2$]** was tested in catalysed diastereoselective Michael additions (Scheme 25). The activity of this dendron was compared to that of a third generation dendrimer possessing the same complex as end groups, **49-kG$_3$[RuH$_2$(PPh$_3$)$_2$]$_{24}$**. It was shown that both compounds have the same efficiency at the same mol-% in ruthenium (1%), and that both can be recovered by precipitation and reused twice. It was expected that the steric hindrance around the metallic centre induced by the dendrons might modify the diastereoselectivity of such a reaction, but no change was observed (Table 3).[37]

The triethoxysilyl group connected to the core of dendrons **11-G$_n$**, **27-G$_n$**, and **28-G$_n$** was used for the elaboration of new hybrid organic–inorganic materials. Indeed, the cohydrolysis of these dendrons with Si(OEt)$_4$ (TEOS) in a sol-gel process generally affords the expected functionalised silica.[20] However, the nature of the material and its porosity is highly dependant on the initial ratio of dendron/TEOS, the generation of the dendron, and the length of the linker between the Si(OEt)$_3$ group and the first branching point. It appears that the higher the dendron generation, the greater the required quantity of TEOS for the gelation. Dendron **11-bG$_0$** requires at least 10 equiv. of TEOS, whereas dendron **19-bG$_3$** requires 140 equiv. of TEOS. $^{29}$Si MAS NMR shows that the dendrons are covalently linked to the silica. The porosity of these materials was measured by nitrogen adsorption. Some materials were found to be mesoporous with a narrow or large pore size distribution, others were found to be macroporous or microporous, depending on the length of the linker, the generation of the dendron, the nature of its end groups, and the initial ratio of dendron/TEOS. Elemental and thermal analyses of the materials show that the percentage representing the organic part incorporated in the silica is always high, but inferior to the theoretical percentage.

Another way to use dendrons in materials chemistry consists of grafting them to the surface of a pre-existing material, in order to modify its properties. We have used this approach with dendrons **6-hG$_n$**, which has ammonium end groups, to modify by Michael type additions the surface of nanolatexes previously covered by cyclam (Scheme 26). A full coverage of the nanolatexes by the dendrons is observed

 © 2006 Wiley-VCH Verlag GmbH & Co. KGaA, Weinheim 

Table 3. Percentage of conversion and diastereoisomeric ratio for the reaction shown in Scheme 25, using two types of dendritic catalysts (1 mol-% in Ru in all cases). This shows the influence of the recovery and reuse of the catalyst on the efficiency.

| Catalyst | Conversion [%] | Diastereomeric ratio | Catalyst | Conversion [%] | Diastereomeric ratio |
|---|---|---|---|---|---|
| **37-dG$_3$[RuH$_2$(PPh$_3$)$_2$]** first run | 100 | 72:28 | **49-kG$_3$[RuH$_2$(PPh$_3$)$_2$]$_{24}$** first run | 100 | 73:27 |
| **37-dG$_3$[RuH$_2$(PPh$_3$)$_2$]** second run | 100 | 72:28 | **49-kG$_3$[RuH$_2$(PPh$_3$)$_2$]$_{24}$** second run | 100 | 73:27 |
| **37-dG$_3$[RuH$_2$(PPh$_3$)$_2$]** third run | 89 | 72:28 | **49-kG$_3$[RuH$_2$(PPh$_3$)$_2$]$_{24}$** third run | 90 | 73:27 |

in all cases. The number of dendron per nanolatex depends on the generation, but the total number of ammonium groups is practically the same (approximately 600 to 800 ammonium end groups per nanolatex). Interestingly, the suspensions of these modified nanolatexes are stable in water without any surfactant, in contrast to the initial nanolatex. Furthermore, the "dendrigrafted" nanoparticles can be redispersed in water after drying, which is not the case for the initial nanolatex. The dendritic shell also offers a higher thermal stability, and induces the gelation of the water solution after one week at room temperature; about 345000 water molecules were estimated to be gelled by each grafted molecule of **6-hG$_2$**.[25]

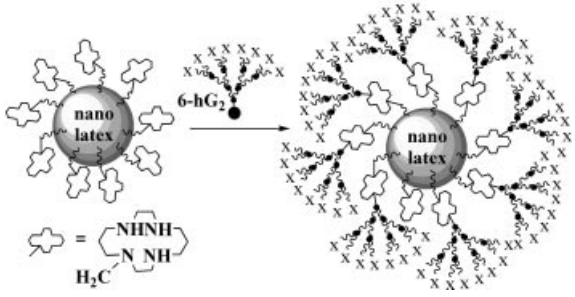


Scheme 26.

## Conclusion

This micro-review has demonstrated that phosphorus-containing dendrons are important building blocks for the elaboration of very complex and original dendritic macromolecules. Emphasis has so far been placed on fundamental research, but these dendrons and peculiar dendritic architectures have the potential for development in more applied research. Obviously, there is still considerable work to be done to determine any practical uses of phosphorus-containing dendrons, but some areas of application can be foreseen. For instance, one may consider the modification of the surface of materials, the targeted delivery of drugs, and other types of application in which the presence of two different types of function in a tailored ratio is important.

[1] E. Buhleier, W. Wehner, F. Vögtle, *Synthesis* **1978**, 155–158.
[2] D. A. Tomalia, H. Baker, J. Dewald, M. Hall, G. Kallos, S. Martin, J. Roeck, J. Ryder, P. Smith, *Polym. J.* **1985**, *17*, 117–132.
[3] G. R. Newkome, Z. Yao, G. R. Baker, V. K. Gupta, *J. Org. Chem.* **1985**, *50*, 2003–2004.
[4] D. A. Tomalia, *Materials Today* **2005**, 34–46.
[5] G. R. Newkome, F. Vögtle, C. N. Moorefield, *Dendrimers and Dendrons*, Wiley-VCH, Weinheim, Germany, **2001**.
[6] J. M. J. Fréchet, D. A. Tomalia, *Dendrimers and Other Dendritic Polymers*, John Wiley & Sons, Chichester, UK, **2001**.
[7] C. J. Hawker, J. M. J. Fréchet, *J. Am. Chem. Soc.* **1990**, *112*, 7638–7647.
[8] J. S. Moore, Z. Xu, *Macromolecules* **1991**, *24*, 5893–5894.
[9] N. Launay, A. M. Caminade, R. Lahana, J. P. Majoral, *Angew. Chem. Int. Ed. Engl.* **1994**, *33*, 1589–1592.
[10] N. Launay, A. M. Caminade, J. P. Majoral, *J. Am. Chem. Soc.* **1995**, *117*, 3282–3283.
[11] M. L. Lartigue, B. Donnadieu, C. Galliot, A. M. Caminade, J. P. Majoral, J. P. Fayet, *Macromolecules* **1997**, *30*, 7335–7337.
[12] For reviews, see in particular: a) J. P. Majoral, A. M. Caminade, *Chem. Rev.* **1999**, *99*, 845–880; b) A. M. Caminade, V. Maraval, R. Laurent, J. P. Majoral, *Curr. Org. Chem.* **2002**, *6*, 739–774; c) J. P. Majoral, A. M. Caminade, V. Maraval, *Chem. Commun.* **2002**, 2929–2942; d) J. P. Majoral, A. M. Caminade, *Topics Curr. Chem.* **2003**, *223*, 111–159; e) A. M. Caminade, J. P. Majoral, *Acc. Chem. Res.* **2004**, *37*, 341–348.
[13] See for instance: a) V. J. Catalano, N. Parodi, *Inorg. Chem.* **1997**, *36*, 537–541; b) I. Jestin, E. Levillain, J. Roncali, *Chem. Commun.* **1998**, 2655–2656; c) G. E. Oosterom, R. J. van Haaren, J. N. H. Reek, P. C. J. Kamer, P. W. N. M. van Leeuwen, *Chem. Commun.* **1999**, 1119–1120; d) Q. H. Fan, Y. M. Chen, X. M. Chen, D. Z. Jiang, F. Xi, A. S. C. Chan, *Chem. Commun.* **2000**, 789–790; e) H. J. van Manen, R. H. Fokkens, N. M. M. Nibbering, F. C. J. M. van Veggel, D. N. Reinhoudt, *J. Org. Chem.* **2001**, *66*, 4643–4650; f) A. Friggeri, H. J. van Manen, T. Auletta, X. M. Li, S. Zapotoczny, H. Schönherr, G. J. Vancso, J. Huskens, F. C. J. M. van Veggel, D. N. Reinhoudt, *J. Am. Chem. Soc.* **2001**, *123*, 6388–6395; g) B. S. Balaji, Y. Obora, D. Ohara, S. Koide, Y. Tsuji, *Organometallics* **2001**, *20*, 5342–5350; h) H. J. van Manen, R. H. Fokkens, N. M. M. Nibbering, F. C. J. M. van Veggel, D. N. Reinhoudt, *J. Org. Chem.* **2001**, *66*, 4643–4650; i) R. Kreiter, R. J. M. Klein Gebbink, G. van Koten, *Tetrahedron* **2003**, *59*, 3989–3997; j) J. Locklin, D. Patton, S. Deng, A. Baba, M. Millan, R. C. Advincula, *Chem. Mater.* **2004**, *16*, 5187–5193; B. Yi, Q. H. Fan, G. J. Deng, Y. M. Li, L. Q. Qiu, A. S. C. Chan, *Org. Lett.* **2004**, *6*, 1361–1364.
[14] R. Engel, K. Rengan, C. S. Chan, *Heteroat. Chem.* **1993**, *4*, 181–184.
[15] C. Larré, A. M. Caminade, J. P. Majoral, *Angew. Chem. Int. Ed. Engl.* **1997**, *36*, 596–599.
[16] C. Larré, B. Donnadieu, A. M. Caminade, J. P. Majoral, *Eur. J. Inorg. Chem.* **1999**, 601–611.
[17] V. Maraval, R. Laurent, B. Donnadieu, M. Mauzac, A. M. Caminade, J. P. Majoral, *J. Am. Chem. Soc.* **2000**, *122*, 2499–2511.
[18] V. Maraval, D. Prévôté-Pinet, R. Laurent, A. M. Caminade, J. P. Majoral, *New J. Chem.* **2000**, *24*, 561–566.
[19] V. Maraval, R. M. Sebastian, F. Ben, R. Laurent, A. M. Caminade, J. P. Majoral, *Eur. J. Inorg. Chem.* **2001**, 1681–1691.

 © 2006 Wiley-VCH Verlag GmbH & Co. KGaA, Weinheim 

[20] C. O. Turrin, V. Maraval, A. M. Caminade, J. P. Majoral, A. Mehdi, C. Reyé, *Chem. Mater.* **2000**, *12*, 3848–3856.
[21] R. M. Sebastian, L. Griffe, C. O. Turrin, B. Donnadieu, A. M. Caminade, J. P. Majoral, *Eur. J. Inorg. Chem.* **2004**, 2459–2466.
[22] C. O. Turrin, B. Donnadieu, A. M. Caminade, J. P. Majoral, *Z. Anorg. Allg. Chem.* **2005**, *631*, 2881–2887.
[23] V. Maraval, R. Laurent, S. Merino, A. M. Caminade, J. P. Majoral, *Eur. J. Org. Chem.* **2000**, 3555–3568.
[24] G. Magro, B. Donnadieu, A. M. Caminade, J. P. Majoral, *Chem. Eur. J.* **2003**, *9*, 2151–2159.
[25] C. Larpent, C. Geniès, A. P. De Sousa Delgado, A. M. Caminade, J. P. Majoral, J. F. Sassi, F. Leising, *Chem. Commun.* **2004**, 1816–1817.
[26] L. Brauge, V. Maraval, R. Laurent, A. M. Caminade, J. P. Majoral, *ARKIVOC (on line)* **2002**, *V*, 151–160.
[27] C. O. Turrin, J. Chiffre, D. de Montauzon, J. C. Daran, A. M. Caminade, E. Manoury, G. Balavoine, J. P. Majoral, *Macromolecules* **2000**, *33*, 7328–7336.
[28] C. Larré, B. Donnadieu, A. M. Caminade, J. P. Majoral, *Eur. J. Inorg. Chem.* **1999**, 601–611.
[29] C. Larré, B. Donnadieu, A. M. Caminade, J. P. Majoral, *J. Am. Chem. Soc.* **1998**, *120*, 4029–4030.
[30] C. Larré, B. Donnadieu, A. M. Caminade, J. P. Majoral, *Chem. Eur. J.* **1998**, *4*, 2031–2036.
[31] V. Maraval, R. Laurent, B. Donnadieu, A. M. Caminade, J. P. Majoral, *Synthesis* **2003**, 389–396.
[32] M. Slany, M. Bardají, M. J. Casanove, A. M. Caminade, J. P. Majoral, B. Chaudret, *J. Am. Chem. Soc.* **1995**, *117*, 9764–9765.
[33] M. Bardají, M. Kustos, A. M. Caminade, J. P. Majoral, B. Chaudret, *Organometallics* **1997**, *16*, 403–410.
[34] C. Galliot, C. Larré, A. M. Caminade, J. P. Majoral, *Science* **1997**, *277*, 1981–1984.
[35] J. Omelanczuk, *J. Chem. Soc., Chem. Commun.* **1992**, 1718–1719.
[36] L. Brauge, A. M. Caminade, J. P. Majoral, S. Slomkowski, M. Wolszczak, *Macromolecules* **2001**, *34*, 5599–5606.
[37] V. Maraval, R. Laurent, A. M. Caminade, J. P. Majoral, *Organometallics* **2000**, *19*, 4025–4029.

Received: October 6, 2005
Published Online: February 2, 2006

 © 2006 Wiley-VCH Verlag GmbH & Co. KGaA, Weinheim 

DOI: 10.1002/ejic.200500841

# Reinecke Anion Derivatives and Homobinuclear Complexes as Tectons in Designing Heteropolymetallic Systems

**Andrei Cucos,[a] Narcis Avarvari,[b] Marius Andruh,*[a] Yves Journaux,*[c] Achim Müller,[d] and Marc Schmidtmann[d]**

**Keywords:** Chromium / Nickel complexes / Thiocyanato complexes / Magnetic properties / Coordination polymers

Two novel $Cr^{III}$–$Ni^{II}$ heteropolynuclear complexes have been obtained through a self-assembly process involving a binuclear $Ni^{II}$ complex with a macrocyclic Robson ligand and Reinecke-type anions (*trans*-$[Cr(NCS)_4(NH_3)_2]^-$, *trans*-$[Cr(NCS)_4(4,4'\text{-bipy})_2]^-$): $[Ni_2(H_2O)_2(fsal\text{-}33)\{Cr(NCS)_4(NH_3)_2\}]\cdot 2H_2O$ (**1**) and $^1{}_\infty[Ni_2(H_2O)_2(fsal\text{-}33)\{Cr(NCS)_4(4,4'\text{-bipy})_2\}]_n\cdot n[Cr(NCS)_4(4,4'\text{-bipy})_2]$ (**2**). The compartmental ligand results from the condensation of 2,6-diformyl-4-methyl-phenol with 1,3-propanediamine. The crystal structure of **1** consists of neutral tetranuclear [CrNiNiCr] species, where each nickel ion is coordinated in one apical position by a Reinecke anion, and in the other one by an aqua ligand. The distances between the metallic centres in **1** are: Ni···Cr = 6.048 and Ni···Ni = 3.133 Å. Compound **2** contains infinite cationic chains constructed from binuclear [Ni–Ni] nodes, connected through *trans*-$[Cr(4,4'\text{-bipy})_2(NCS)_4]$ spacers, and uncoordinated *trans*-$[Cr(NCS)_4(4,4'\text{-bipy})_2]^-$ ions. The $Cr^{III}$ and $Ni^{II}$ ions are connected through 4,4′-bipyridine ligands arising from the Reinecke-type anion. The distance between the nickel and chromium ions within the chain is 11.252 Å. The magnetic properties of **1** have been investigated. Both Ni–Ni and Cr–Ni exchange interactions were found to be antiferromagnetic: $J_{NiNi} = -51.3\ cm^{-1}$; $J_{NiCr} = -22.7\ cm^{-1}$.

(© Wiley-VCH Verlag GmbH & Co. KGaA, 69451 Weinheim, Germany, 2006)

## Introduction

The search for new metal-containing building blocks is of current interest in molecular magnetism and in crystal engineering. These are relatively inert anionic complexes with potentially bridging ligands, for example cyano ($[M(CN)_6]^{3-}$,[1] $[M(bipy)(CN)_4]^-$[2]), or oxalato complexes ($[M(C_2O_4)_3]^{3-}$, $[M(bipy)(C_2O_4)_2]^-$[3]), which have been widely employed to design heterospin systems with interesting magnetic properties. It is well known that the thiocyanato anion acts as a bridge between either identical or different metal ions.[4] Nevertheless, the thiocyanato complexes have rarely been used as templates in assembling heteropolynuclear complexes.[5] A very appealing complex in this respect is the anion of the Reinecke salt, $[Cr(NCS)_4(NH_3)_2]^-$, which can interact with the second metal ion through the sulfur atom. For example, a $Cu^{II}$–$Cr^{III}$ heterobinuclear complex has been obtained by reacting the Reinecke anion with a cationic copper(II) complex.[6]

We are currently developing a research project aimed at obtaining heterometallic complexes with interesting structures and magnetic properties, by using homo- or heterobinuclear species as assembling cations. The basic idea of our strategy is to combine the magnetic behaviour of the assembling cation (exhibiting a ferro- or antiferromagnetic coupling between the two metal ions) with that of the anionic building-block. Beyond the individual magnetic behaviour, the two molecular entities may interact through the connecting ligands. This synthetic approach allowed us to obtain complexes with three different spin carriers: 2p-3d-4f,[7] 3d-3d′-4f[8] or high-dimensionality 3d-4f coordination polymers.[9] Apart from our interest in the classical Reinecke anion, we intend to enrich our chemical library with new building blocks, by replacing the $NH_3$ ligands, from the $[Cr(NCS)_4(NH_3)_2]^-$ ion, with organic molecules that can act as bridges. Such building units can be extremely versatile, having both hard and soft coordination sites (e.g. nitrogen donor atoms arising from the organic ligand and sulfur donor atoms from the isothiocyanato ligands).

## Results and Discussion

The first results concerning the synthesis of new heterobimetallics using the Reinecke anion and its derivatives as building blocks are reported herein, and consist of two

[a] Inorganic Chemistry Laboratory, Faculty of Chemistry, University of Bucharest,
Str. Dumbrava Rosie 23, 020464 Bucharest, Romania
E-mail: marius.andruh@dnt.ro
[b] Laboratoire Chimie, Ingénierie Moléculaire et Matériaux d'Angers (CIMMA) UMR 6200 CNRS- Université d'Angers,
UFR Sciences, Bât. K, 2 bd. Lavoisier, 49045 Angers, France
[c] Laboratoire de Chimie Inorganique et Matériaux Moléculaires UMR CNRS 7071, case courrier 42, Université Pierre et Marie Curie,
4 Place Jussieu, 75252 Paris cedex 05, France
[d] Fakultät für Chemie der Universität,
33501 Bielefeld, Germany

 © 2006 Wiley-VCH Verlag GmbH & Co. KGaA, Weinheim 

$Cr^{III}$–$Ni^{II}$ heteropolynuclear complexes: $[Ni_2(H_2O)_2(fsal\text{-}33)\{Cr(NCS)_4(NH_3)_2\}]\cdot 2H_2O$ (**1**) and $^1{}_\infty[Ni_2(H_2O)_2(fsal\text{-}33)\{Cr(NCS)_4(4,4'\text{-bipy})_2\}]_n\cdot n[Cr(NCS)_4(4,4'\text{-bipy})_2]$ (**2**). Compound **1** is obtained through a self-assembly process involving the Reinecke anion and a binuclear nickel(II) cationic complex, $[Ni_2(H_2O)_2(fsal\text{-}33)]^{2+}$ (fsal-33 is a dianionic macrocyclic binucleating Schiff-base ligand obtained by condensation of 2,6-diformyl-4-methyl-phenol with 1,3-propylenediamine). Compound **2** is obtained using the same nickel(II) complex and a derivative of the Reinecke salt, *trans*-$K[Cr(NCS)_4(4,4'\text{-bipy})_2]$. This Reinecke derivative is obtained by reacting $K_3[Cr(NCS)_6]$ with 4,4′-bypiridine. Its composition and structure are confirmed by chemical analysis, and by the crystal structure of compound **2** (vide infra). The infrared spectrum displays the characteristic bands of the organic ligand, as well as the band of the isothiocyanato group (2067 $cm^{-1}$). The UV/Vis spectrum shows a band with a maximum at 550 nm, which is due to the $^4A_{2g} \rightarrow {}^4T_{2g}$ transition. This transition occurs at lower energy (18180 $cm^{-1}$) than the one observed with the classical Reinecke anion, $[Cr(NCS)_4(NH_3)_2]^-$ (19610 $cm^{-1}$).

The crystal structures of compounds **1** and **2** have been solved. Compound **1** is a neutral tetranuclear $Cr^{III}$–$Ni^{II}$–$Ni^{II}$–$Cr^{III}$ complex. The chromium and nickel ions are connected through one NCS bridge (Figure 1). The two $[Cr(NCS)_4(NH_3)_2]^-$ ions are *trans* disposed with respect to the general plane of the macrocyclic ligand enclosing the nickel ions. Each nickel ion is hexacoordinate, exhibiting an elongated octahedral geometry, with an equatorial $N_2O_2$ macrocyclic donor set, and the aqua ligand and the sulfur atom from the bridge coordinated in the apical positions. The Ni–N and Ni–O distances in the equatorial plane are close and vary between 2.005(2) and 2.0278(15) Å. The apical Ni–aqua and Ni–S distances are, respectively, 2.1138(18) and 2.6057(7) Å. The distances between the metallic centres are Ni···Cr = 6.048 and Ni···Ni = 3.133 Å. The Cr–N distances within the Reinecke anion vary between 1.985(2) and 2.069(2) Å. The analysis of the packing diagram (Figure 2) reveals the formation of layers through intermolecular hydrogen bond interactions established between the aqua ligand and the crystallisation water molecule [O(2)···O(3) = 2.699(3) Å], as well as between the crystallisation water molecule and one sulfur atom from an adjacent tetranuclear unit [O(3)···S(2) = 3.282(3) Å].

The IR spectrum of **1** shows two bands due to the $NCS^-$ ligands (2066, 2104 $cm^{-1}$), in agreement with their different roles: terminal and bridging.

The second compound, $^1{}_\infty[Ni_2(H_2O)_2(fsal\text{-}33)\{Cr(NCS)_4(4,4'\text{-bipy})_2\}]_n\cdot n[Cr(NCS)_4(4,4'\text{-bipy})_2]$ (**2**), contains infinite cationic chains constructed from binuclear [Ni–Ni] nodes, connected through *trans*-$[Cr(NCS)_4(4,4'\text{-bipy})_2]$ spacers, and uncoordinated *trans*-$[Cr(NCS)_4(4,4'\text{-bipy})_2]^-$ ions taking over the charge of the cationic chain (Figure 3). Two chromium complexes acting as spacers are coordinated, through the 4,4′-bipy ligands, above and below the platform formed by the binuclear nickel complex [Ni–N(4,4′-bipy) = 2.139(16) Å] (Figure 3). The equatorial nickel–ligand distances fall in the range 2.008(16)–2.034(15) Å. The sixth coordination site at the nickel ions is occupied by an aqua ligand [Ni–O = 2.241(16) Å]. The intranode Ni···Ni distance is 3.09 Å. The shortest Ni···Cr distance within the chain is 11.25 Å. As far as the chromium building blocks are concerned, the metal ions exhibit an almost perfect octahedral stereochemistry. The Cr–N(NCS) distances (ave, 1.98 Å) are slightly shorter than the Cr–N(4,4′-bipy) ones (ave, 2.08 Å). Selected bond lengths and angles for compounds **1** and **2** are collected in Table 1.

The magnetic properties of complex **1** have been investigated. The $\chi_M T$ versus $T$ curve is represented in Figure 4. The room temperature value of the $\chi_M T$ product (5.30 $cm^3\,mol^{-1}\,K$) is slightly lower than the one corresponding to the four uncoupled metal ions (5.7 $cm^3\,mol^{-1}\,K$). By lowering the temperature, $\chi_M T$ continuously decreases, reaching 0.19 $cm^3\,mol^{-1}\,K$ at 2 K.

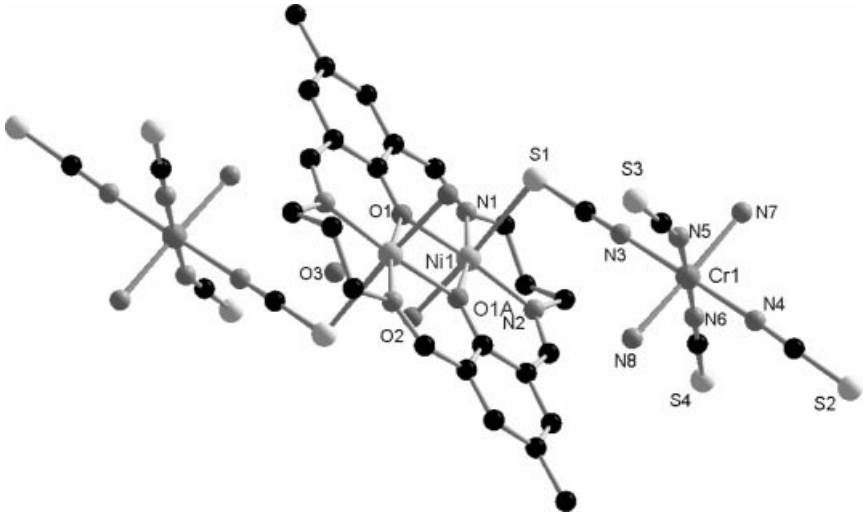


Figure 1. Perspective view of the tetranuclear complex **1**.

 © 2006 Wiley-VCH Verlag GmbH & Co. KGaA, Weinheim 

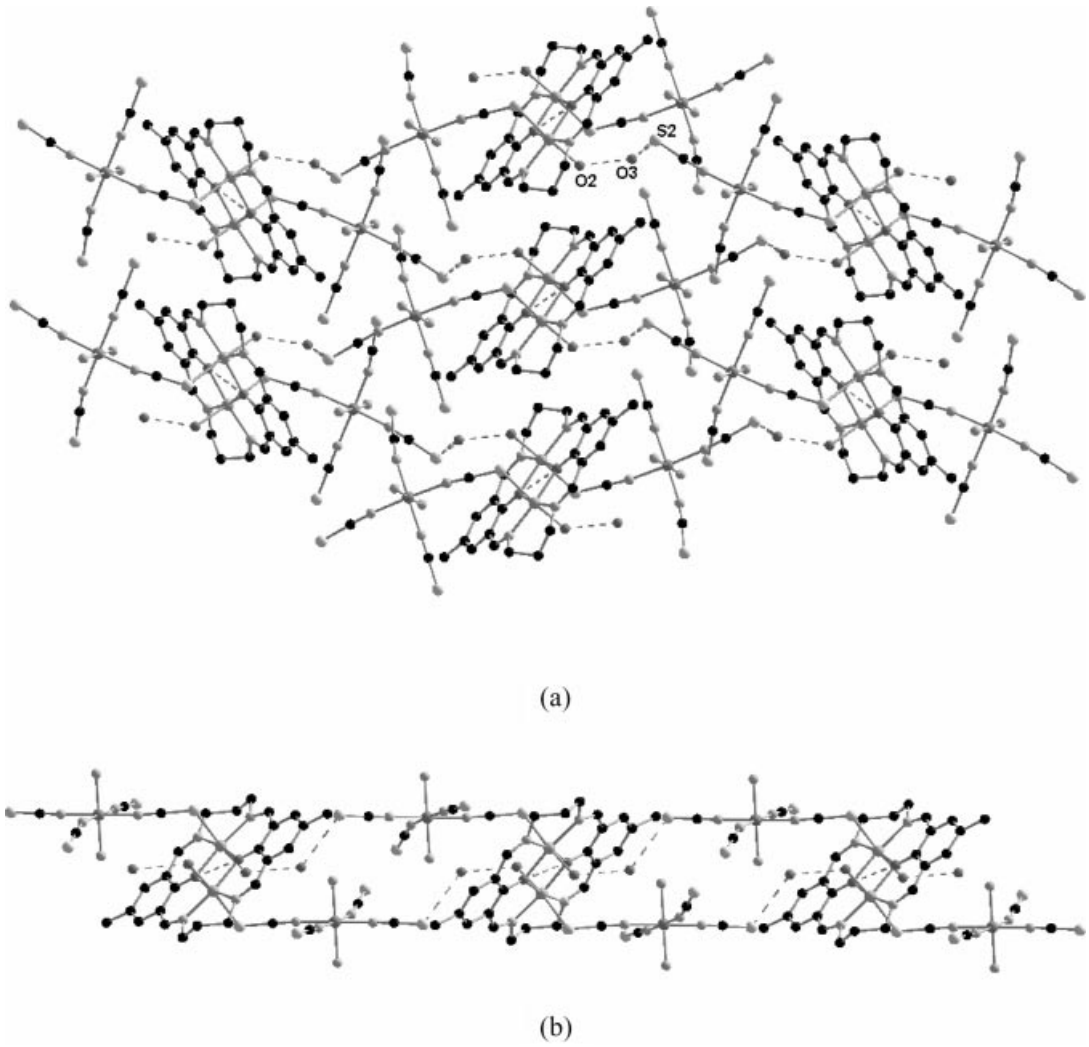


Figure 2. Packing diagram for crystal **1**, showing the formation of the supramolecular layers: a) view along the crystallographic *a* axis; b) side view.

For the centrosymmetric [CrNiNiCr] complex the energies of the low-lying spin states are obtained by using the isotropic Hamiltonian:

$\boldsymbol{H} = -J_{CrNi}(\boldsymbol{S}_{Cr1}\boldsymbol{S}_{Ni1} + \boldsymbol{S}_{Ni2}\boldsymbol{S}_{Cr2}) - J_{NiNi}\boldsymbol{S}_{Ni1}\boldsymbol{S}_{Ni2}$

The full matrix diagonalisation technique was employed to reproduce the experimental data. The best fit to the data led to:

$J_{NiCr} = -22.7\ cm^{-1}$; $J_{NiNi} = -51.3\ cm^{-1}$; $g_{Ni} = 2.2$ (fixed); $g_{Cr} = 1.98$; $R = 2.6\times10^{-4}$ {$R$ is the agreement factor defined as $\Sigma_i[(\chi_M T)_{obsd}(i) - (\chi_M T)_{calcd.}(i)]^2/\Sigma_i[(\chi_M T)_{obsd.}(i)]^2$}.

At first glance, the antiferromagnetic nature of the interaction between $Cr^{III}$ and $Ni^{II}$ is surprising, this pair of ions, both in octahedral stereochemistry, being a classical example of orthogonality of the magnetic orbitals leading to a ferromagnetic coupling. One of the most important factors influencing the sign and the magnitude of the exchange interaction is the bridging angle; more precisely, in our case, the Ni(1)–S(1)–C(13) one [106.03(8)°]. For a [$M_AXM_B$] single bridge system, the ferromagnetic interaction arising from the strict orthogonality of the magnetic orbitals is maximal for a linear $M_A$–X–$M_B$ linkage.[10,11] By decreasing the $M_A$–X–$M_B$ angle, the ferromagnetic interaction decreases also, being finally dominated by the antiferromagnetic one. For example, recent calculations for a related compound, containing the Ni–NC–Cr motif,[11] have shown that the ferromagnetic interaction between $Ni^{II}$ and $Cr^{III}$ ions through a single cyanide bridge is weakened with the bending at the cyanide bridge, becoming antiferromagnetic for values of $a \leq 148°$.

For compound **1**, the deviation from linearity is very important and consequently the relatively strong antiferromagnetic interaction between $Ni^{II}$ and $Cr^{III}$, because of the overlap of the magnetic orbitals, is not surprising. A [NiCr] thiocyanato-bridged cationic coordination polymer, –catena-μ-NCS–Ni(en)$_2$-μ-SCN–Cr(NCS)$_4$–, has recently been described.[5c] The values of the Ni–S–C angles were 93.2 and 105.1° and, accordingly, favoured an antiferromagnetic interaction ($J = -19.9\ cm^{-1}$). As far as the Ni–Ni exchange interaction is concerned, it falls in the range already observed with several other nickel complexes with the same ligand: $Ni^{II}_2L(H_2O)_2(ClO_4)_2$ ($J = -61\ cm^{-1}$),[10] $Ni^{II}_2L(py)_2(BF_4)_2$ (py = pyridine) ($J = -46\ cm^{-1}$)[12] and

 © 2006 Wiley-VCH Verlag GmbH & Co. KGaA, Weinheim 

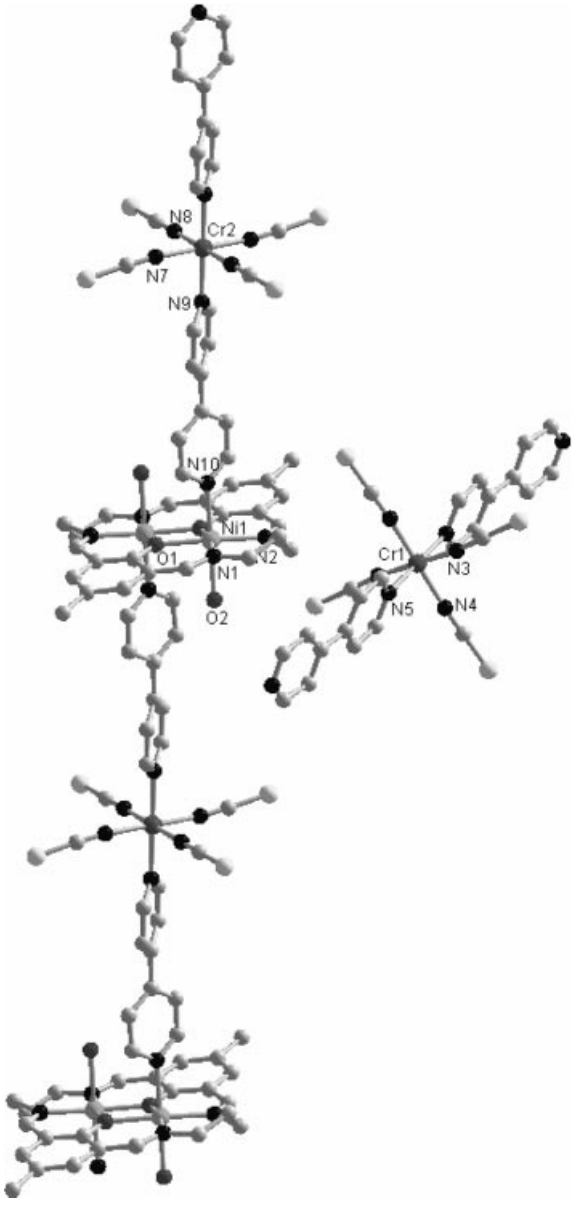


Figure 3. Perspective view of the cationic chain and of the complex anion in **2**, along with the atom-numbering scheme.

$Ni^{II}_2L(H_2O)_2Cl_2$ ($J$ = –72 cm$^{-1}$).[13] In the similar cyano-bridged [CrNiNiCr] complex, the value of the $J_{NiNi}$ parameter is –44.6 cm$^{-1}$.[11]

The functionalisation of the Reinecke anion, by replacing the $NH_3$ groups with potentially bridging ligands, as illustrated by compound **2**, opens interesting perspectives in crystal engineering. Various solid-state architectures can be thus constructed through the selective interaction of the hard (N) and soft (S) donor atoms with appropriate transition-metal ions. Two different metal ions (one hard, the other soft) can be employed simultaneously in order to obtain new solid-state architectures. Moreover, compound **2** illustrates how the building-block approach can be combined with the node-and-spacer approach, to design extended structures.

Table 1. Selected bond lengths [Å] and angles [°] for compounds **1** and **2**.

| **1** | | **2** | |
|---|---|---|---|
| Ni(1)–N(1) | 2.0230(19) | Ni(1)–N(1) | 2.029(7) |
| Ni(1)–N(2) | 2.005(2) | Ni(1)–N(2) | 2.009(7) |
| Ni(1)–O(1) | 2.0263(15) | Ni(1)–O(1) | 2.019(5) |
| Ni(1)–O(1) | 2.0278(15) | Ni(1)–O(2) | 2.241(7) |
| Ni(1)–O(2) | 2.1138(18) | Ni(1)–N(10) | 2.140(6) |
| Ni(1)–S(1) | 2.6057(7) | Cr(1)–N(3) | 2.002(8) |
| Cr(1)–N(3) | 2.017(2) | Cr(1)–N(4) | 1.969(9) |
| Cr(1)–N(4) | 1.987(2) | Cr(1)–N(5) | 2.084(7) |
| Cr(1)–N(5) | 1.993(2) | Cr(2)–N(7) | 1.989(8) |
| Cr(1)–N(6) | 1.985(2) | Cr(2)–N(8) | 1.991(6) |
| Cr(1)–N(7) | 2.069(2) | Cr(2)–N(9) | 2.079(6) |
| Cr(1)–N(8) | 2.059(2) | | |
| | | N(1)–Ni(1)–N(10) | 91.9(3) |
| N(1)–Ni(1)–O(1) | 91.16(7) | N(1)–Ni(1)–O(2) | 85.2(3) |
| N(1)–Ni(1)–O(2) | 89.86(8) | N(2)–Ni(1)–O(1) | 169.1(2) |
| N(1)–Ni(1)–S(1) | 85.35(6) | N(2)–Ni(1)–N(1) | 98.8(3) |
| N(2)–Ni(1)–N(1) | 99.21(8) | N(2)–Ni(1)–N(10) | 94.0(3) |
| N(2)–Ni(1)–O(1) | 169.63(7) | N(2)–Ni(1)–O(2) | 87.1(3) |
| N(2)–Ni(1)–O(2) | 90.02(8) | N(10)–Ni(1)–O(2) | 177.0(3) |
| N(2)–Ni(1)–S(1) | 92.73(6) | O(1)–Ni(1)–N(1) | 90.7(2) |
| O(1)–Ni(1)–O(2) | 89.99(7) | O(1)–Ni(1)–N(10) | 90.9(2) |
| O(1)–Ni(1)–S(1) | 88.10(5) | O(1)–Ni(1)–O(2) | 88.5(2) |
| O(2)–Ni(1)–S(1) | 174.80(6) | N(3)–Cr(1)–N(5) | 91.0(3) |
| N(3)–Cr(1)–N(7) | 89.49(9) | N(4)–Cr(1)–N(3) | 89.1(3) |
| N(3)–Cr(1)–N(8) | 89.48(9) | N(4)–Cr(1)–N(5) | 89.6(3) |
| N(4)–Cr(1)–N(5) | 91.06(9) | N(7)–Cr(2)–N(8) | 91.7(3) |
| N(4)–Cr(1)–N(3) | 177.17(9) | N(7)–Cr(2)–N(9) | 89.0(3) |
| N(4)–Cr(1)–N(8) | 91.13(9) | N(8)–Cr(2)–N(9) | 90.5(2) |
| N(4)–Cr(1)–N(7) | 90.01(9) | | |
| N(5)–Cr(1)–N(3) | 91.73(9) | | |
| N(5)–Cr(1)–N(8) | 87.00(10) | | |
| N(5)–Cr(1)–N(7) | 90.63(10) | | |
| N(6)–Cr(1)–N(4) | 89.63(9) | | |
| N(6)–Cr(1)–N(5) | 178.16(10) | | |
| N(6)–Cr(1)–N(3) | 87.60(9) | | |
| N(6)–Cr(1)–N(8) | 91.29(10) | | |
| N(6)–Cr(1)–N(7) | 91.07(10) | | |
| N(8)–Cr(1)–N(7) | 177.38(10) | | |

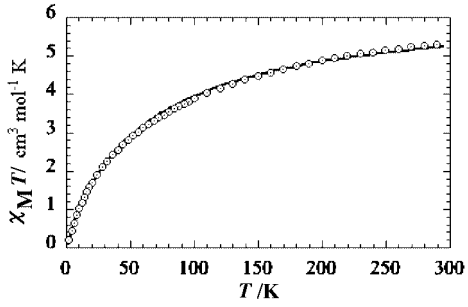


Figure 4. $\chi T$ vs $T$ diagram for complex **1**. The solid line corresponds to the best fit.

## Experimental Section

**Synthesis:** K[Cr(NCS)$_4$(4,4′-bipy)$_2$] was prepared by refluxing a *i*PrOH solution of $K_3$[Cr(NCS)$_6$] and 4,4′-bipy (in a 1:2.5 ratio) for 6 h, and isolation of the red solid appeared by cooling. IR (KBr): $\tilde{\nu}$ = 2067 (vs), 1597 (m), 1409 (m), 1218 (m), 1065 (m), 807 (m), 628 (m) cm$^{-1}$.

 © 2006 Wiley-VCH Verlag GmbH & Co. KGaA, Weinheim 

Compounds **1** and **2** were obtained by reacting the binuclear nickel(II) complex $[Ni_2(fsal\text{-}33)Cl_2]\cdot 2H_2O$[14] (in 1:1 EtOH/water solution) with, respectively, $NH_4[Cr(NCS)_4(NH_3)_2]$ (in $H_2O$) and $K[Cr(NCS)_4(4,4'\text{-bipy})_2]$ (in EtOH), in a 1:2 ratio. In both cases, light red precipitates formed and were isolated by filtration and dried. The first one was dissolved in pure methanol and allowed to evaporate slowly, generating orange needle-like crystals of **1** suitable for X-ray diffraction studies. In the second case, red single crystals of **2** were obtained by dissolving the precipitate in DMF, followed by slow diffusion of ethanol into the resulting solution. Characteristic IR bands due to the NCS ligands (KBr pellets) – **1**: 2066, 2104 $cm^{-1}$; **2**: 2062 $cm^{-1}$.

**Physical Techniques:** The IR spectra (KBr pellets) were recorded with a BIO-RAD FTS 135 spectrophotometer. The electronic spectra (diffuse reflectance technique) were recorded with a UV4 UNICAM spectrophotometer with MgO as a reference.

Magnetic measurements were carried out with a MPMS-5S (Quantum Design) SQUID magnetometer. The diamagnetic corrections for the compounds were estimated using Pascal's constants, and magnetic data were corrected for diamagnetic contributions of the sample holder.

**Crystallography:** Crystal **1** was measured at 183 K with a Bruker AXS SMART diffractometer (Mo-$K_\alpha$ radiation monochromator). Data for crystal **2** were collected at 293 K with a Stoe-IPDS imaging plate system operating with a Mo-$K_\alpha$ X-ray tube with a graphite monochromator. The structures were solved by direct methods and refined by full-matrix least-squares techniques based on $F^2$. Calculations were performed using the SHELX-97 crystallographic software package. The crystallographic data and other pertinent information are collected in Table 2.

CCDC-283332 (for **1**) and CCDC-283333 (for **2**) contain the supplementary crystallographic data for this paper. These data can be obtained free of charge from The Cambridge Crystallographic Data Centre via www.ccdc.cam.ac.uk/data_request/cif.

Table 2. Crystallographic data and structure refinement parameters for compounds **1** and **2**.

| | **1** | **2** |
|---|---|---|
| Empirical formula | $C_{32}H_{46}Cr_2N_{16}Ni_2O_6S_8$ | $C_{72}H_{58}Cr_2N_{20}Ni_2O_4S_8$ |
| $M$ | 1228.75 | 1745.28 |
| Temperature [K] | 183 | 293 |
| Wavelength [Å] | 0.71073 | 0.71073 |
| Crystal system | monoclinic | triclinic |
| Space group | $P2_1/n$ | $P\bar{1}$ |
| $a$ [Å] | 9.5752(3) | 11.3113(13) |
| $b$ [Å] | 8.7100(3) | 13.2258(13) |
| $c$ [Å] | 30.2624(10) | 15.9098(17) |
| $\alpha$ [°] | 90.00 | 80.927(12) |
| $\beta$ [°] | 91.5870(10) | 82.556(13) |
| $\gamma$ [°] | 90.00 | 89.067(13) |
| $V$ [Å$^3$] | 2522.92(14) | 2330.5(4) |
| $Z$ | 2 | 1 |
| $\rho_{(calcd)}$ [Mg m$^{-3}$] | 1.617 | 1.244 |
| $\mu$Mo [mm$^{-1}$] | 1.543 | 0.856 |
| $F(000)$ | 1260 | 894 |
| Gof (for $F^2$) | 1.035 | 0.831 |
| Final $R$, $wR$ [$I > 2\sigma(I)$] | 0.0319, 0.0776 | 0.0732, 0.1822 |
| $\Delta\rho_{max}$ and $\Delta\rho_{min}$ [e Å$^3$] | 1.009 and –0.350 | 1.101 and –0.508 |

## Acknowledgments

Financial support from the CERES Program (Project 4/130) is gratefully acknowledged.

[1] See, for example: a) K. R. Dunbar, R. A. Heintz, *Progr. Inorg. Chem.* **1997**, *45*, 283; b) M. Verdaguer, A. Bleuzen, V. Marvaud, J. Vaissermann, M. Seuleiman, C. Desplanches, A. Scuiller, C. Train, R. Garde, G. Gelly, C. Lomenech, I. Rosenman, P. Veillet, C. Cartier, F. Villain, *Coord. Chem. Rev.* **1999**, *190–192*, 1023; c) M. Ohba, H. Okawa, *Coord. Chem. Rev.* **2000**, *198*, 313; d) J. Černák, M. Orendáč, I. Potočňák, J. Chomič, A. Orendáčová, J. Skoršepa, A. Feher, *Coord. Chem. Rev.* **2002**, *224*, 51.

[2] See, for example: L. Toma, R. Lescouëzec, J. Vaissermann, F. S. Delgado, C. Ruiz-Pérez, R. Carrasco, J. Cano, F. Lloret, M. Julve, *Chem. Eur. J.* **2004**, *10*, 6130, and references therein.

[3] See, for example: a) M. Pilkington, S. Decurtins in *Magnetism: Molecules to Materials II* (Eds: J. S. Miller, M. Drillon), Wiley-VCH, Weinheim, **2001**, p. 339; b) G. Marinescu, D. Visinescu, A. Cucos, M. Andruh, Y. Journaux, V. Kravtsov, Y. A. Simonov, J. Lipkowski, *Eur. J. Inorg. Chem.* **2004**, 2914, and references therein.

[4] See, for example: J. Ribas, C. Diaz, R. Costa, J. Tercero, X. Solans, M. Font-Bardía, H. Stoeckli-Evans, *Inorg. Chem.* **1998**, *37*, 233 and references cited therein.

[5] a) G. Francese, S. Ferlay, H. W. Schmalle, S. Decurtins, *New J. Chem.* **1999**, *23*, 267; b) A. Skorupa, B. Korybut-Daszkievicz, J. Mroziński, *Inorg. Chim. Acta* **2002**, *336*, 65; c) G. Wrzeszez, L. Dobrzańska, A. Wojtczak, A. Grodzicki, *J. Chem. Soc. Dalton Trans.* **2002**, 2862; d) A. M. Madalan, V. Ch. Kravtsov, D. Pajik, K. Zadro, Yu. A. Simonov, N. Stanica, L. Ouahab, J. Lipkowski, M. Andruh, *Inorg. Chim. Acta* **2004**, *357*, 4155; e) Y.-M. Shi, W. Xu, B. Zhao, P. Cheng, D.-Z. Liao, X.-Y. Chen, *Eur. J. Inorg. Chem.* **2005**, 55.

[6] K.-L. Zhong, W. Chen, Y. Xu, Z. Wang, Z. J. Zhong, X.-Z. You, *Polyhedron* **2001**, *20*, 2033.

[7] A. M. Madalan, H. W. Roesky, M. Andruh, M. Noltemeyer, N. Stanica, *Chem. Commun.* **2002**, 1638.

[8] a) R. Gheorghe, M. Andruh, J.-P. Costes, B. Donnadieu, *Chem. Commun.* **2003**, 2778; b) M. Andruh, *Pure Appl. Chem.* **2005**, *77*, 1685.

[9] R. Gheorghe, P. Cucos, M. Andruh, J.-P. Costes, B. Donnadieu, S. Shova, *Chem. Eur. J.* **2006**, *12*, 187.

[10] O. Kahn, *Molecular Magnetism*, VCH, New York, **1993**, ch. 8.

[11] L. Toma, L. M. Toma, R. Lescouëzec, D. Armentano, G. De Munno, M. Andruh, J. Cano, F. Lloret, M. Julve, *Dalton Trans.* **2005**, 1357.

[12] C. L. Spiro, S. L. Lambert, T. J. Smith, E. N. Duesler, R. R. Gagné, D. N. Hendrickson, *Inorg. Chem.* **1981**, *20*, 1229.

[13] S. L. Lambert, D. N. Hendrickson, *Inorg. Chem.* **1979**, *18*, 2683.

[14] H. Pilkington, R. Robson, *Aust. J. Chem.* **1970**, *23*, 2225.

Received: September 21, 2005
Published Online: January 10, 2006

 © 2006 Wiley-VCH Verlag GmbH & Co. KGaA, Weinheim 

DOI: 10.1002/ejic.200500622

# On the Existence of the Elusive Monomethyl Ester of Carbonic Acid [$CH_3OC(O)OH$] at 300 K: $^1H$- and $^{13}C$ NMR Measurements and DFT Calculations

**Angela Dibenedetto,*[a] Michele Aresta,[a] Potenzo Giannoccaro,[a] Carlo Pastore,[a] Imre Pápai,*[b] and Gábor Schubert[b]**

**Keywords:** Carbon dioxide / Density functional calculations / Methylation / NMR spectroscopy

The elusive monomethyl ester of carbonic acid [$CH_3OC(O)OH$] has been prepared at 300 K by protonation of the sodium salt $NaOC(O)OCH_3$ with anhydrous HCl or water and characterized by $^1H$- and $^{13}C$ NMR spectroscopy. The stability of the acid and its reactivity towards hydroxo ions and methylating agents under ambient conditions are discussed. The energetics and the mechanism of the investigated reactions are examined on the basis of density functional calculations. For kinetic and thermodynamic reasons $CH_3OC(O)OH$ is unlikely to be formed by insertion of $CO_2$ into the O–H bond of methanol.

(© Wiley-VCH Verlag GmbH & Co. KGaA, 69451 Weinheim, Germany, 2006)

## Introduction

Carbonic acid ($H_2CO_3$, **1**) and its amino [RR′NC(O)OH, **2**] and monoalkyl derivatives [ROC(O)OH, **3**] are elusive species. Their isolation as pure compounds is not trivial as they easily decompose to afford $CO_2$ plus water [Equation (1)], amine [Equation (2)], or alcohol [Equation (3)].

$$\underset{\mathbf{1}}{H_2CO_3} \rightleftharpoons H_2O + CO_2 \quad (1)$$

$$\underset{\mathbf{2}}{RR'N\text{-}C(O)OH} \rightleftharpoons RR'NH + CO_2 \quad (2)$$

$$\underset{\mathbf{3}}{ROC(O)OH} \rightleftharpoons ROH + CO_2 \quad (3)$$

In particular, **1** has never been isolated pure (only its water solutions are known), and **2** was only very recently isolated and characterized as a dimer in the solid state. The X-ray structure shows the existence of H-bonding through the carboxylic moieties [R = $C_6H_5CH_2$, R′ = H; or R,R′ = $PhP(OCH_2CH_2)_2$].[1,2] For **3** only a report of its low-temperature IR spectrum can be found in the literature;[3] no report of its existence at room temperature or information about its stability/reactivity are available. Conversely, the salts of **1** [$MHCO_3$, $M_2CO_3$, $M'CO_3$; M = group 1 metal or ammonia; M′ = group 2 metal], **2** [RR′NC(O)OR″; R″ = ammonium or metal cation], and **3** [ROC(O)OM] or the organic esters of **2** and **3** (R, R′, R″ = alkyl or aryl group) have been known for a long time to be stable compounds at room temperature.

Despite their instability, compounds **1**–**3** are often proposed to be intermediates in reactions in which carbon dioxide is implied. Thus, **2** has been suggested to exist in solutions containing amines and carbon dioxide[4] and **3** has been proposed to be formed by direct interaction of alcohols and $CO_2$,[5] a reaction relevant to the synthesis of organic carbonates by direct carboxylation of alcohols that occurs at temperatures ranging from 330 to 450 K and at a $CO_2$ pressure of 0.1–20 MPa.[7]

In the course of our research on carbon dioxide chemistry, we have synthesized and characterized the first examples of the elusive species **2**.[1,2] We wish to report here the first evidence of the existence of $CH_3OC(O)OH$ at room temperature and describe its reactivity. Density functional calculations have also been carried out to provide a rationale for our experimental findings.

## Results and Discussion

Although it has been suggested that **3** could be formed by direct reaction[5] of ROH with $CO_2$, our $^1H$- and $^{13}C$ NMR measurements run on pressurized (5 MPa) solutions of $CO_2$ in pure, freshly distilled, and absolutely anhydrous methanol did not give any evidence of $CO_2$ insertion into

[a] Department of Chemistry, University of Bari and CIRCC, Via Celso Ulpiani 27, 70126 Bari, Italy
Fax: +39-080-544-2430
E-mail: a.dibenedetto@chimica.uniba.it
[b] Chemical Research Center, Hungarian Academy of Sciences, P.O.B. 17, 1525 Budapest, Hungary
Fax: +36-1-325-7554
E-mail: papai@chemres.hu

Supporting information for this article is available on the WWW under http://www.eurjic.org or from the author.


© 2006 Wiley-VCH Verlag GmbH & Co. KGaA, Weinheim

the O–H bond of methanol to afford $CH_3OC(O)OH$ [**4**; Equation (4)].

$$CH_3OH + CO_2 \rightleftharpoons \underset{\mathbf{4}}{CH_3OC(O)OH} \quad (4)$$

One can argue that reaction 4 may either occur through a direct bimolecular insertion [Equation (4)] or through the generation of a $CH_3O^-$ anion by autoprotolysis of methanol [Equation (5a)], which may attack the electrophilic carbon of $CO_2$ with formation of $CH_3OC(O)O^-$ [Equation (5b)]. The protonation of this latter species would afford **4** [Equation (5c)].

$$CH_3OH + CH_3OH \rightleftharpoons CH_3O^- + CH_3OH_2^+ \quad (5a)$$

$$CH_3O^- + CO_2 \longrightarrow CH_3OC(O)O^- \quad (5b)$$

$$CH_3OC(O)O^- + CH_3OH_2^+ \rightleftharpoons \underset{\mathbf{4}}{CH_3OC(O)OH} + CH_3OH \quad (5c)$$

The abundance of $CH_3O^-$ is very low in pure anhydrous methanol as it is generated by the autoprotolytic dissociation of methanol [Equation (5)], which has an equilibrium constant, $K_{dis}$, of $10^{-16}$.[6] The lack of formation of **4** under these conditions can be explained by taking into consideration the thermodynamics of reaction 4 and its kinetic aspects, as discussed below.

It is worthwhile mentioning that previous theoretical studies[8–11] on the mechanism of carbonic acid formation from $H_2O$ and $CO_2$, a reaction that is analogous to Equation (4), have excluded the possibility of a direct bimolecular insertion because the activation energy predicted for this step is about 50 kcal mol$^{-1}$,[8–10] while the energy barrier decreases substantially (to about 15 kcal mol$^{-1}$)[8] if an additional water molecule is assumed to participate in the hydration process. Our calculations carried out at the B3LYP/6-311++G** level of density functional theory for $CH_3OC(O)OH$ formation involving two $CH_3OH$ molecules (see Figure 1) predict a relatively high energy barrier for this process ($\Delta G^{\ddagger}_{gas}$ = 28.9 and $\Delta G^{\ddagger}_{solv}$ = 22.7 kcal mol$^{-1}$ if solvent effects due to the methanol environment are included), indicating that reaction 4 is likely to be kinetically hindered. Furthermore, $CH_3OC(O)OH$ is found to be thermodynamically unstable with respect to its dissociation products, since the calculations give $\Delta G_{gas}$ = +9.9 kcal mol$^{-1}$ for the gas-phase reaction shown in Figure 1, which decreases to $\Delta G_{solv}$ = +4.4 kcal mol$^{-1}$ in the solvated model [for the isolated $CH_3OC(O)OH$ molecule the calculated dissociation free-energy values are $\Delta G_{gas}$ = +15.1 and $\Delta G_{solv}$ = +11.6 kcal mol$^{-1}$].

Accordingly, **4** has been reported to be a labile species and has only been characterized so far by IR spectroscopy at low temperature.[3] Therefore, it is not likely that it will exist for a long time at temperatures above 273 K. These results suggest that the direct insertion of $CO_2$ into the O–H bond of methanol is quite unlikely to occur under reaction conditions such as those used for the synthesis of organic carbonates,[7] and $CH_3OC(O)OH$ is unlikely to be an intermediate in such a reaction.

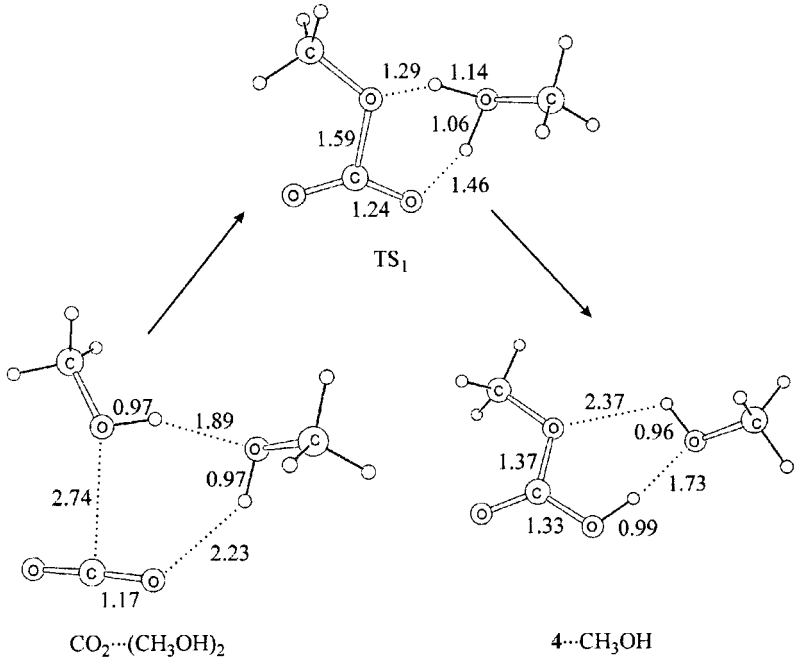


Figure 1. Formation of $CH_3OC(O)OH$ from $CO_2$ and two molecules of methanol. Selected bond lengths obtained from B3LYP/6-311++G** calculations are given in Ångstroms.

 © 2006 Wiley-VCH Verlag GmbH & Co. KGaA, Weinheim 

We generated **4** by treating the sodium salt $NaO^{13}C(O)OCH_3$ (**5**) with either anhydrous $HCl/CD_2Cl_2$ or water in a biphasic system. $NaO^{13}C(O)OCH_3$ is easily formed by reaction of sodium methoxide with $^{13}CO_2$ [Equation (6)].

$$CH_3ONa + {}^{13}CO_2 \rightleftharpoons \underset{\mathbf{5}}{NaO^{13}C(O)OCH_3} \quad (6)$$

Compound **5** is a stable, white solid that has already been described.[12] Its IR spectrum shows strong bands at 1631 and 1381 $cm^{-1}$ for the $\nu_{C=O}$ absorption of the carbonate moiety. The reaction of **5** with anhydrous $HCl/CD_2Cl_2$ or water was monitored by carrying out a detailed NMR ($^1H$ and $^{13}C$) study. $^{13}CO_2$ was used in the synthesis of **5** in order to reduce the acquisition time of the $^{13}C$ NMR spectrum, thereby minimizing the risk of decomposition of **4**.

When **5** was suspended in $CD_2Cl_2$ under 0.1 MPa of $^{13}CO_2$, the $^1H$- and $^{13}C$ NMR spectra of the solution did not show any signal that could be attributed to **5** due to its very poor solubility in the solvent. The addition of a sub-stoichiometric amount of either anhydrous $HCl/CD_2Cl_2$ or water to the suspension at 295 K caused the immediate appearance of new signals in the $^1H$- and $^{13}C$ NMR spectra.

The $^1H$ NMR spectrum shows a singlet (1 H) at $\delta$ = 4.76 and a second signal at $\delta$ = 3.38 ppm (3 H; Table 1), which are attributed to the $CD_2Cl_2$-soluble $HO^{13}C(O)OCH_3$ species formed according to reaction 7.

Table 1. Spectroscopic properties of labile $CH_3OC(O)OH$.

| Compound | νCO | νOH | $^1H$ NMR ($\delta$, ppm) | $^{13}C$ NMR ($\delta$, ppm) |
|---|---|---|---|---|
| $CH_3OC(O)OH$ | 1779 | 3484 | 4.76 (1 H, O*H*) | 50.58 (*C*$H_3$) |
| | 1730 | | 3.38 (3 H, C*H*$_3$) | 159.92 (*C*=O) |

$$\underset{\mathbf{5}}{CH_3OC(O)ONa} + HCl\,(H_2O) \rightleftharpoons \underset{\mathbf{4}}{CH_3OC(O)OH} + NaCl\,(NaOH) \quad (7)$$

The $^{13}C$ NMR spectrum confirms the formation of **4**, as demonstrated by the appearance of a signal at $\delta$ = 159.92 ppm due to the carbon atom of the hemicarbonate moiety. Continuing the addition of anhydrous HCl up to a stoichiometric amount produced an increase of the intensity of the signals mentioned above (Figure 2a). The addition of water produces broader peaks (Figure 2b), although they are located at the same positions.

If the NMR tube is left under the same conditions after the addition of the $HCl/CD_2Cl_2$ solution to $NaO(O)COCH_3$ at 295 K, the $^1H$- and $^{13}C$ NMR spectra change: the signals due to **4** slowly disappear while the signals of $CH_3OH$ [$\delta$ = 4.81 (1 H) and 3.42 ppm (3 H)] appear (Figure 2). When $CH_3O^{13}C(O)OH$ is generated using sub-stoichiometric amounts of anhydrous $HCl/CD_2Cl_2$ it has a longer lifetime than when it is generated with water. Therefore aged solutions of **4** show a different behavior according to their preparation. In fact, when anhydrous HCl is used

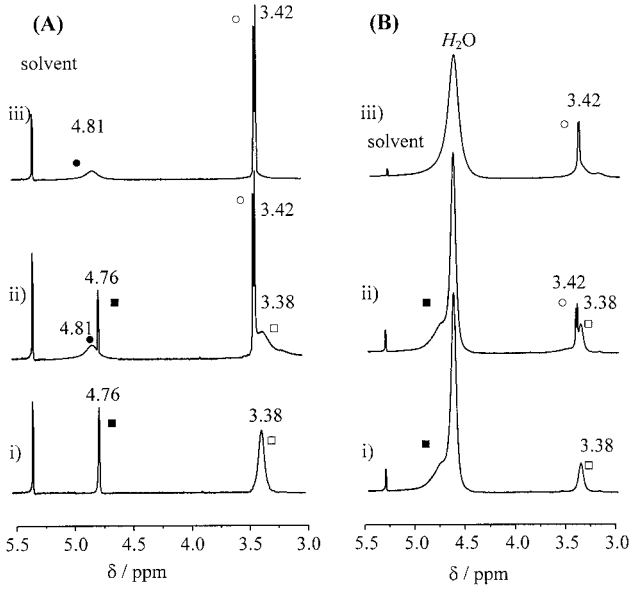


Figure 2. Evolution of the $^1H$ NMR spectrum of $CH_3OC(O)OH$ formed upon addition of (A) $HCl/CD_2Cl_2$ and (B) $H_2O$ to $CH_3OC(O)ONa$ suspended in $CD_2Cl_2$. i) soon after the addition; ii) after 10 min; iii) after 60 min. ■ $CH_3OC(O)OH$; □ $CH_3OC(O)OH$; ● $CH_3OH$; ○ $CH_3OH$.

the signal of free $CO_2$ generated by conversion of **4** is found at $\delta$ = 121.4 ppm. Conversely, when water is used a second signal appears at $\delta$ = 159.62 ppm in the $^{13}C$ NMR spectrum besides the signal at $\delta$ = 159.92 ppm that is attributed to $NaH^{13}CO_3$. In the latter case, the formation of methanol and $NaH^{13}CO_3$ can occur according to two mechanisms:
i) decomposition of $CH_3O^{13}C(O)OH$ into methanol and $^{13}CO_2$ [Equation (8a)] and subsequent reaction [Equation (8b)] of $^{13}CO_2$ with the NaOH formed in reaction 7.

$$CH_3O^{13}C(O)OH \rightarrow CH_3OH + {}^{13}CO_2 \quad (8a)$$

$$^{13}CO_2 + NaOH \rightarrow NaH^{13}CO_3 \quad (8b)$$

ii) direct interaction of the hydroxy moiety $OH^-$ with $CH_3O^{13}C(O)OH$ [Equation (9a)] by attack at the methyl group with formation of methanol and concurrent formation of $NaH^{13}CO_3$ [Equation (9b)].

$$CH_3O^{13}C(O)OH + OH^- \rightarrow CH_3OH + H^{13}CO_3^- \quad (9a)$$

$$H^{13}CO_3^- + Na^+ \rightarrow NaH^{13}CO_3 \quad (9b)$$

The energy barrier obtained for the decomposition of $CH_3OC(O)OH$ via the reverse reaction shown in Figure 1 is $\Delta G^{\ddagger}_{solv}$ = 18.3 kcal mol$^{-1}$ ($\Delta G^{\ddagger}_{gas}$ = 19.0 kcal mol$^{-1}$), whereas the calculations carried out for the methyl-transfer reaction between $CH_3OC(O)OH$ and $OH^-$ (see Figure 3) give a much smaller barrier ($\Delta G^{\ddagger}_{solv}$ = 11.3 and $\Delta G^{\ddagger}_{gas}$ = 4.4 kcal mol$^{-1}$). Moreover, the $S_N2$-type nucleophile substitution depicted in Figure 3 is predicted to be highly exergonic ($\Delta G_{solv}$ = –39.4 and $\Delta G_{gas}$ = –49.5 kcal mol$^{-1}$). These data indicate that reaction 9a is both kinetically and thermodynamically more feasible than the direct decomposition of $CH_3OC(O)OH$. This agrees with the experimental obser-

 © 2006 Wiley-VCH Verlag GmbH & Co. KGaA, Weinheim 

vation of the stability of **4** in the absence and presence of hydroxy ions.

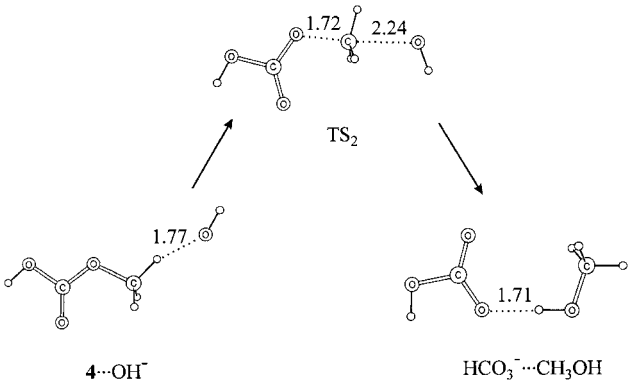


Figure 3. Stationary points located for the methyl-transfer reaction from $CH_3OC(O)OH$ to $OH^-$ forming $HCO_3^-$ and $CH_3OH$. Selected bond lengths obtained from B3LYP/6-311++G** calculations are given in Ångstroms.

The rate of conversion of **4** into methanol and $CO_2$ in the presence of $OH^-$ is affected by the solvent: an apolar solvent slows the reaction as it does not favor the formation of hydroxy ions in solution from insoluble NaOH. Conversely, when a polar organic solvent or a stoichiometric amount of water is added to $CD_2Cl_2$ containing **5**, **4** is transformed so rapidly that it cannot be detected and only the final products ($CH_3OH$ and $NaHCO_3$) are observed. These experimental data support the direct interaction of **4** with $OH^-$ more than the dissociation of **4** into $CH_3OH$ and $CO_2$ and the subsequent reaction of the latter with NaOH. However, this study gives thermodynamic and kinetic information about **4** and allows us to complete, with the $^1H$- and $^{13}C$ NMR spectra, the characterization of the labile species **4** for which only the low-temperature IR spectrum had been reported so far.

As noted in a previous theoretical study,[13] the global energy-minimum of the $CH_3OC(O)OH$ molecule corresponds to the *trans-trans* orientation of the $CH_3$ and OH groups (see Scheme 1). Our present calculations predict two other conformations that lie only 1.3 (*cis-trans*) and 3.2 kcal mol$^{-1}$ (*trans-cis*) above the most stable isomer to be local minima on the gas-phase potential energy surface. We also estimated the acidity of $CH_3OC(O)OH$ by computing the aqueous p$K_a$ value for the *trans-trans* isomer (see Computational Details) and found that $CH_3OC(O)OH$ is slightly less acidic than $H_2CO_3$. In fact, we calculated a p$K_a$ for $CH_3OC(O)OH$ of 1.7 and for $H_2CO_3$ of 1.1; the experimental p$K_a$ value for $H_2CO_3$ is 3.6. The difference between calculated and experimental p$K_a$ values for $H_2CO_3$ is within the range of typical errors obtained with similar calculations[14] and can be attributed to the simplified solvation model.

Besides the conversion of **4** into methanol and $CO_2$, we also investigated the reactivity of **4** towards a methylating

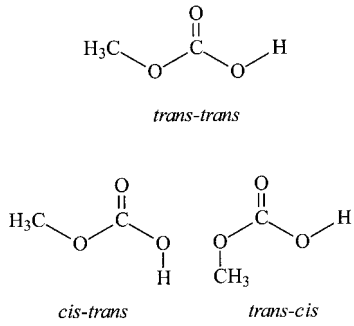


Scheme 1. Conformations of $CH_3OC(O)OH$.

agent. The interest of reaction 10 lies in the fact that the product is an organic carbonate.

$$CH_3OC(O)OH + SubOR \rightarrow CH_3OC(O)OR + SubOH \quad (10)$$

If $CH_3OC(O)OH$ could be formed from methanol and $CO_2$, reaction 10 would be an effective way to produce DMC, a chemical that has several industrial applications as an alkylating[15] or methoxycarbonylating[16] agent, a precursor of pharmaceuticals and agrochemicals,[17] a solvent,[18] and as an additive to gasoline.[19]

In particular, we investigated the reaction of **4** with the methylating agent *O*-methylisourea (**6**)[20,21] [Equation (11)], which is obtained by treating dicyclohexylcarbodiimide (DCC) with methanol [Equation (12)]. This reagent was preferred to other classical methylating systems (e.g. $BF_3$/$CH_3OH$) as the latter may carry Brønsted acids that decompose **4**.

$$CH_3OC(O)OH + CyN{=}C(OCH_3)(NHCy) \xrightarrow[\mathbf{6}]{} CH_3OC(O)OCH_3 + CyHNC(O)NHCy \quad (11)$$

$$CyN{=}C{=}NCy + CH_3OH \longrightarrow CyN{=}C(OCH_3)(NHCy) \quad (12)$$

(**6**)

When isourea **6** was added to a $CH_2Cl_2$ solution containing $HOC(O)OCH_3$ generated from $NaOC(O)OCH_3$ dimethyl carbonate was immediately formed according to reaction 11. Both products (urea and DMC) were isolated and identified from their NMR spectra ($^1H$ and $^{13}C$) and GC-MS profiles compared with those of authentic samples. When the reaction was carried out in an NMR tube it was possible to follow the disappearance of the signals of **4** and the appearance of new signals due to DMC ($\delta$ = 3.69 ppm, $CH_3$). This reaction both confirms the existence of **4** in solution and underlines the role of **6** as a methylating agent, as already reported in the literature.[20,21] If the isourea is treated with NaOC(O)OMe no methylation reaction occurs, although the addition of a small amount of water allows the reaction to proceed to form urea and DMC as $CH_3OC(O)OH$ is formed.

 © 2006 Wiley-VCH Verlag GmbH & Co. KGaA, Weinheim 

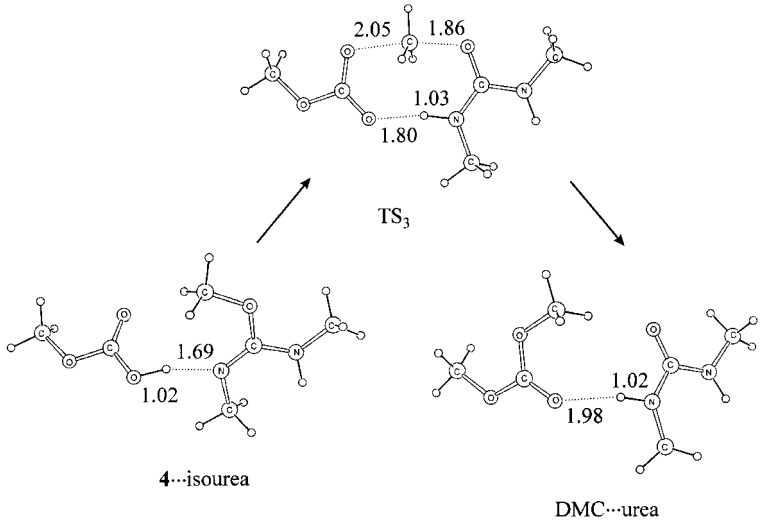


Figure 4. Stationary points located for the $CH_3OC(O)OH + CH_3N{=}C(OCH_3)(NHCH_3) \rightarrow CH_3OC(O)OCH_3 + CH_3HNC(O)NHCH_3$ model reaction. Selected bond lengths obtained from B3LYP/6-311++G** calculations are given in Ångstroms.

In order to explain the mechanism of reaction 12 we carried out DFT calculations on the reaction of **4** with a simplified model of **6** where the cyclohexyl groups have been replaced by methyl moieties (see Figure 4).

The transition state located for the model reaction describes a methyl transfer from isourea to **4**, while the O–H proton of **4** is already transferred to the iminic nitrogen of the isourea. IRC calculations indicate that the reaction takes place in a single step because the H-bonded **4**···isourea minimum is reached directly from the transition state in the reverse direction. The reaction is thermodynamically favored ($\Delta G_{solv}$ = –12.4, $\Delta G_{gas}$ = –11.8 kcal mol$^{-1}$) and the energy barrier is predicted to be $\Delta G^{\ddagger}_{solv}$ = 19.9 kcal mol$^{-1}$ ($\Delta G^{\ddagger}_{gas}$ = 25.5 kcal mol$^{-1}$), which is slightly higher than that found for reaction 13 ($\Delta G^{\ddagger}_{solv}$ = 14.5 kcal mol$^{-1}$).[20]

$$2\ ROH + CO_2 + DCC \rightarrow (RO)_2CO + CyNHC(O)NHCy \qquad (13)$$

It is worthwhile noting that the concentration of **4** in the system generated from **5** and $HCl/CD_2Cl_2$ or water decreases rapidly with an increase of temperature, and above 310 K we were not able to detect the formation of **4** at all. This agrees with the lability of **4**, which converts into methanol and $CO_2$ according to Equation (3), and makes it unlikely that $CH_3OC(O)OH$ is an intermediate in the synthesis of carbonates from alcohols and $CO_2$.

## Conclusions

Our work has demonstrated for the first time the existence of $CH_3OC(O)OH$ (**4**) at room temperature and its stability/lability under the same conditions. Although **4** is very labile, it exists in solution at room temperature for the time necessary to record its $^1$H- and $^{13}$C NMR spectra and to study its conversion with characterization of the products. It can be easily methylated to afford DMC, which is a reaction of potential practical importance. Nevertheless, **4** is not stable at temperatures above 300 K and is not formed for kinetic and thermodynamic reasons at room temperature from alcohols and $CO_2$ [nor in alcohol under 30 MPa of $CO_2$ nor in supercritical $CO_2$ (30 MPa) with added alcohol]. In order for **4** to play a role in the formation of DMC from methanol and $CO_2$, very high pressures of $CO_2$ should most probably be used (likely >>100 MPa).

## Experimental Section

All solvents and starting reagents were RP Aldrich products. Alcohols and solvents were dried, distilled,[22] and stored under dinitrogen. Carbon dioxide was purchased from Rivoira IP (99.999% purity). NMR experiments were carried out with a 300-MHz Bruker apparatus using deuterated CIL solvents. IR spectra were recorded with a FTIR Perkin–Elmer 1710 apparatus. GC-MS analyses were carried out with a Shimadzu 17 A gas chromatograph (capillary column: 30 m; MDN-5S; Ø 0.25 mm, 0.25 μm film) coupled to a Shimadzu QP5050A mass spectrometer. Quantitative determinations on the reaction solutions were recorded using a Hewlett–Packard 6850 GC-FID (capillary column: 30 m; MDN-5S; Ø 0.25 mm, 0.25 μm film).

Methylisourea was prepared as reported in the literature.[20,21]

**Synthesis of the Monomethyl Ester of Carbonic Acid [$CH_3OC(O)OH$] and NMR Studies:** NaOC(O)OMe [or $NaO^{13}C(O)OMe$] (35.0 mg, 0.36 mmol) freshly prepared from MeOH and Na under a $CO_2$ atmosphere was placed in an NMR tube in 0.7 mL of anhydrous $CD_2Cl_2$ and the tube was closed with a silicone stopper. $^1$H- and $^{13}$C NMR spectra were recorded for this sample: no signals were evident besides that of the solvent. Anhydrous HCl in $CD_2Cl_2$ was injected through the stopper in different amounts until the stoichiometric ratio was reached and the $^1$H- and $^{13}$C NMR spectra were recorded after each addition. NMR spectroscopic data are presented and discussed in the main text. Similarly, the reaction was monitored when water was added instead of anhydrous HCl.

**Reaction of 4 with Methylisourea:** $HOC(O)OCH_3$ was generated as described above from sodium methyl carbonate (78.0 mg, 0.8 mmol) and anhydrous $HCl/CD_2Cl_2$ (or water). Once the $^1$H NMR signals of **4** had reached their maximum intensity methyl-

 © 2006 Wiley-VCH Verlag GmbH & Co. KGaA, Weinheim 

isourea (200 mg, 0.8 mmol) was added to the solution. After one hour at room temperature the $^1$H NMR signal ($\delta$ = 3.69 ppm) of dimethyl carbonate became evident. The solution was dried under vacuum and the resulting solid suspended in diethyl ether. The ether solution was filtered from the solid. The latter was shown to be urea [CyHNC(O)NHCy]. DMC was isolated from the solution by evaporating the solvent.

**Computational Details:** DFT calculations were carried out at the B3LYP/6-311++G** level[23] in order to obtain information about the structures and relative energies of energy minima and transition states relevant to the reactions investigated. The nature of the stationary points obtained from the geometry optimizations was verified by subsequent vibrational frequency analysis. Intrinsic Reaction Coordinate (IRC) calculations were performed from the located transition states in order to check whether these structures indeed connect the appropriate minima on the proposed reaction pathways. Most of the investigated reactions in the present work involve charged species, therefore we estimated the solvation free-energies using a recent implementation[24] of the Polarizable Continuum Model (PCM).[25] In these calculations, the cavities of the solute molecules were constructed using the atomic radii of the universal force field (UFF)[26] model with individual hydrogen spheres to be able to describe transition states for hydrogen-transfer reactions. The dielectric constant was always chosen according to the solvent used in the experiments ($\varepsilon$ = 8.93 for $CH_2Cl_2$ and 32.63 for methanol). The Gibbs free-energies calculated for the gas phase and solvated models are denoted $\Delta G_{gas}$ and $\Delta G_{solv}$, respectively, in the text, and include the thermal corrections as well. The aqueous p$K_a$ of $CH_3OC(O)OH$ was estimated according to the procedure described by Takano and Houk[14] and using the UAHF cavity model in the PCM calculations to obtain the solvation free-energies. All these calculations were carried out using the Gaussian 03 software package.[27]

**Supporting Information** (see the footnote on the first page of this article): Cartesian coordinates and total energies of located structures.

## Acknowledgments

The Italian authors wish to thank the Ministry of Education, University and Research (COFIN grants MM03027791 and 2003039774) and the EU Project TOPCOMBI for financial support, and Dr. Paride Papadia for experimental assistance in NMR studies. The Hungarian authors acknowledge the support of the Hungarian Research Foundation (OTKA grants T037345 and T034547).

[1] M. Aresta, D. Ballivet-Tkatchenko, M. C. Bonnet, R. Faure, H. Loiseleur, *J. Am. Chem. Soc.* **1985**, *107*, 2994–2995.
[2] M. Aresta, D. Ballivet-Tkatchenko, D. Belli Dell'Amico, M. C. Bonnet, D. Boschi, F. Calderazzo, R. Faure, L. Labella, F. Marchetti, *Chem. Commun.* **2000**, 1099–1100.
[3] a) G. Gattow, W. Von Behrendt, *Angew. Chem. Int. Ed. Engl.* **1972**, *11*, 534–535; b) G. Gattow, W. Von Behrendt, *Z. Anorg. Allg. Chem.* **1973**, *398*, 198–206.
[4] M. H. Jamroz, J. C. Dobrowolski, J. E. Rode, M. A. Borowiak, *J. Mol. Struct. (Theochem)* **2002**, *618*, 101–108.
[5] K. N. West, C. Wheeler, J. P. McCarney, K. N. Griffith, D. Bush, C. L. Liotta, C. A. Eckert, *J. Phys. Chem. A* **2001**, *105*, 3947–3948.
[6] a) P. Ballinger, F. A. Long, *J. Am. Chem. Soc.* **1960**, *82*, 795–798; b) J. Hine, M. Hine, *J. Am. Chem. Soc.* **1952**, *74*, 5266–5271.
[7] M. Aresta, A. Dibenedetto, C. Pastore, *Inorg. Chem.* **2003**, *42*, 3256–3261.
[8] M. T. Nguyen, T. K. Ha, *J. Am. Chem. Soc.* **1984**, *106*, 599–602.
[9] C. A. Wight, A. I. Boldyrev, *J. Phys. Chem.* **1995**, *99*, 12125–12130.
[10] K. R. Liedl, S. Sekušak, E. Mayer, *J. Am. Chem. Soc.* **1997**, *119*, 3782–3784.
[11] P. Ballone, B. Montanari, R. O. Jones, *J. Chem. Phys.* **2000**, *112*, 6571–6575.
[12] M. Kunert, P. Wiegeleben, H. Gorls, E. Dinjus, *Inorg. Chem. Commun.* **1998**, *1*, 131–133.
[13] H. Sun, S. J. Mumby, J. R. Maple, A. T. Hagler, *J. Phys. Chem.* **1995**, *99*, 5873–5882.
[14] Y. Takano, K. N. Houk, *J. Chem. Theory Comput.* **2005**, *1*, 70–77.
[15] Y. Ono, *Appl. Catal., A* **1997**, *155*, 133–166.
[16] M. Aresta, A. Dibenedetto, E. Quaranta, *Green Chem.* **1999**, *1*, 237–242.
[17] S. C. Stinson, *Chem. Eng. News* **2001**, *79*, 15–16.
[18] A. A. G. Shaikh, S. Sivaram, *Chem. Rev.* **1996**, *96*, 951–976.
[19] M. A. Pacheco, C. L. Marshall, *Energy Fuels* **1997**, *11*, 2–29.
[20] M. Aresta, A. Dibenedetto, E. Fracchiolla, P. Giannoccaro, I. Pápai, C. Pastore, G. Schubert, *J. Org. Chem.* **2005**, *70*, 6177–6186.
[21] E. Dabritz, *Angew. Chem. Int. Ed. Engl.* **1966**, *5*, 470–477.
[22] D. D. Perrin, W. L. F. Armarego, D. R. Perrin, *Purification of Laboratory Chemicals*, Pergamon Press, Oxford, England, **1986**.
[23] a) A. D. Becke, *J. Chem. Phys.* **1993**, *98*, 5648–5652; b) C. Lee, W. Yang, R. G. Parr, *Phys. Rev. B* **1988**, *37*, 785–789; c) P. J. Stephens, F. J. Devlin, C. F. Chabalowski, M. J. Frisch, *J. Phys. Chem.* **1994**, *98*, 11623–11627.
[24] M. Cossi, G. Scalmani, N. Rega, V. Barone, *J. Chem. Phys.* **2002**, *117*, 43–54.
[25] S. Miertus, E. Scrocco, J. Tomasi, *Chem. Phys.* **1981**, *55*, 117–129.
[26] A. K. Rappi, C. J. Casewit, K. S. Colwell, W. A. Goddard III, W. M. Skid, *J. Am. Chem. Soc.* **1992**, *114*, 10024–10035.
[27] *Gaussian 03, Revision C.02*, M. J. Frisch, G. W. Trucks, H. B. Schlegel, G. E. Scuseria, M. A. Robb, J. R. Cheeseman, J. A. Montgomery Jr.,T. Vreven, K. N. Kudin, J. C. Burant, J. M. Millam, S. S. Iyengar, J. Tomasi, V. Barone, B. Mennucci, M. Cossi, G. Scalmani, N. Rega, G. A. Petersson, H. Nakatsuji, M. Hada, M. Ehara, K. Toyota, R. Fukuda, J. Hasegawa, M. Ishida, T. Nakajima, Y. Honda, O. Kitao, H. Nakai, M. Klene, X. Li, J. E. Knox, H. P. Hratchian, J. B. Cross, C. Adamo, J. Jaramillo, R. Gomperts, R. E. Stratmann, O. Yazyev, A. J. Austin, R. Cammi, C. Pomelli, J. W. Ochterski, P. Y. Ayala, K. Morokuma, G. A. Voth, P. Salvador, J. J. Dannenberg, V. G. Zakrzewski, S. Dapprich, A. D. Daniels, M. C. Strain, O. Farkas, D. K. Malick, A. D. Rabuck, K. Raghavachari, J. B. Foresman, J. V. Ortiz, Q. Cui, A G. Baboul, S. Clifford, J. Cioslowski, B. B. Stefanov, G. Liu, A. Liashenko, P. Piskorz, I. Komaromi, R. L. Martin, D. J. Fox, T. Keith, M. A. Al-Laham, C. Y. Peng, A. Nanayakkara, M. Challacombe, P. M. W. Gill, B. Johnson, W. Chen, M. W. Wong, C. Gonzalez, and J. A. Pople, Gaussian, Inc., Wallingford CT, **2004**.

Received: July 13, 2005
Published Online: January 12, 2006

 © 2006 Wiley-VCH Verlag GmbH & Co. KGaA, Weinheim 

DOI: 10.1002/ejic.200500703

# Synthesis and Characterization of a Novel Heteroditopic Macrocyclic System – Monometallic Nickel(II) and Uranyl Complexes and Their Corresponding Heterobimetallic Carbonylrhodium(I) Complexes

**Mauro Bassetti,*[a] Andrea Calenne,[a] Lucilla Mastrofrancesco,[a] Michela Salamone,[a] Gabriele Bocelli,*[b] Andrea Cantoni,[b] and Amos Musatti[b]**

**Keywords:** Heterometallic complexes / Ligand design / Macrocyclic ligands / Metallacycles / Schiff bases

A novel heteroditopic macrocyclic ligand system for selective coordination of two different transition metal ions has been obtained in the form of monometallic salen complexes of $Ni^{II}$ (LNi, **1**) and uranyl ($LUO_2$, **2**). The system is characterized by the presence of a dianionic, tetradentate salen donor system ($N_2O_2$) derived from *cis*-1,2-diaminocyclohexane and of a neutral, tridentate 2,6-bis(alkylthiomethyl)pyridine group ($NS_2$). The two binding sites are connected by two oxyethyl chains. The synthetic procedure involves the coupling of the disodium salt of 2,6-bis(mercaptomethyl)pyridine with two equivalents of 3-(2-bromoethoxy)-2-(2-propenyloxy)benzaldehyde. Removal of the protecting allyl groups from the reaction product (**I**) by palladium catalysis yields the ligand synthon 2,6-bis[2-(3-formyl-2-hydroxyphenyl)oxyethyl]thiomethylpyridine (**II**). The monometallic macrocyclic complexes **1** and **2**, obtained by metal-templated synthesis from *cis*-1,2-diaminocyclohexane, ligson **II**, and the corresponding $Ni^{II}$ or uranyl acetate salts, respectively, in the presence of barium bis(trifluoroacetate), have been fully characterized by spectroscopic techniques in solution and by X-ray diffraction analyses in the solid state. Both complexes react readily at room temperature with $[Rh(CO)_2Cl]_2$ in methanol to form the bimetallic cationic carbonyl complexes $[LNi^{II}Rh(CO)]PF_6$ (**3**) and $[LUO_2Rh(CO)]PF_6$ (**4**) upon addition of $NH_4PF_6$. Two conformers of complex **3** are observed in solution by IR and NMR spectroscopy, in a 5:1 ratio in $[D_2]$dichloromethane, which exhibit a fluxional behavior and are shown to interconvert above room temperature in $[D_3]$acetonitrile. The carbonylrhodium group in the bimetallic systems reacts further with methyl iodide in dichloromethane solution to form oxidative-addition products.

(© Wiley-VCH Verlag GmbH & Co. KGaA, 69451 Weinheim, Germany, 2006)

## Introduction

Compartmental ligands characterized by at least two different binding sites are interesting synthetic targets in the field of macrocyclic chemistry[1] as heterobimetallic macrocyclic complexes can be derived from such structures and used as appropriate models in heterogeneous or homogeneous catalysis, in which cooperative effects may arise from the vicinity of two metal centers.[2] Most dinucleating macrocycles available to date contain either one ligand type incorporated into a crown ether ring,[1a,1c,3,4] or the same donor set replicated within the macrocycle,[1a,3,5] which limits, but does not exclude, selectivity toward coordination of different transition-metal ions.[6] Although heteroditopic macrocyclic frames containing nonequivalent ring cavities are a significant advantage in this respect,[7] the introduction of different binding sites implies more elaborate synthetic approaches than those used in the preparation of systems with higher symmetry.[5c,7a,7b,7e,8] Various types of heterobimetallic macrocyclic systems have been reported.[1,5c,9]

We have planned the synthesis of a heterobifunctional macrocyclic structure bearing different donor sites. The choice of the binding units has fallen on systems widely used in catalysis and in coordination chemistry, namely the dianionic tetradentate ($N_2O_2$) salen-type ligand and the neutral tridentate ($NS_2$) 2,6-bis(alkylthiomethyl)pyridine system. The classic salen [*N*,*N*′-ethylenebis(salicylideneaminato)] metal complexes and related derivatives[5a–5c,10] are nowadays finding significant applications, most notably in host–guest chemistry,[1a,8,11] in asymmetric synthesis,[12] and in supramolecular and polymer catalysis.[13] The tridentate, neutral $NS_2$ ligands form complexes with different transition-metal ions[14] and have been used in the preparation of homo- and heterobimetallic macrocyclic structures, including those containing rhodium(I).[15] Square planar rhodium(I) complexes are of special interest in homogeneous catalysis with regard to oxidative addition and carbonylation processes.[16]

[a] CNR, Istituto di Metodologie Chimiche, Sezione Meccanismi di Reazione, and Dipartimento di Chimica, Università La Sapienza,
00185 Roma, Italy
E-mail: mauro.bassetti@uniroma1.it
[b] CNR, Istituto dei Materiali per l'Elettronica ed il Magnetismo, Parco Area delle Scienze 37a, 43010 Fontanini (Parma), Italy
E-mail: bocelli@unipr.it

Supporting information for this article is available on the WWW under http://www.eurjic.org or from the author

 © 2006 Wiley-VCH Verlag GmbH & Co. KGaA, Weinheim 

The combination of a hard and a soft metal center has driven the design and synthesis of binucleating systems.[17] In the case of metal carbonyl complexes, the proximity of the two metal atoms may activate a carbon monoxide group by interaction of the electrophilic metal center with the oxygen of CO.[18] In this context, we have selected a carbonylrhodium(I) group for coordination to the bis(mercaptomethyl)pyridine ligand and a uranyl or a nickel(II) metal center for the salen binding unit. The electrophilic character of the uranyl system has been well documented, especially its ability to coordinate organic carbonyl groups, such as that of urea, in its planar fifth coordination site,[19] or to act as an electrophilic catalyst for Michael additions[13a] and acyl-transfer reactions.[20] Detection of an intramolecular interaction of the $(NS_2)$Rh–CO group with crown-ether-complexed alkaline metal ions has been attempted.[15b]

## Results and Discussion

### Synthesis of Monometallic Macrocyclic Complexes

The synthetic strategy followed for the preparation of the target structure was directed by the fact that salen $N_2O_2$ type complexes form monometallic macrocyclic systems when a precursor molecular chain appropriately functionalized at both ends undergoes a metal-templated Schiff-base ring-closure reaction in the presence of a diamine partner and the chosen metal ion.[4b] In order to ensure the further coordination within the ring of a second metal ion, an $NS_2$ donor set was incorporated into the molecular chain. Therefore the synthesis of the ligand synthon **II**, which bears two terminal formyl-2-hydroxyaryl groups, was devised (Scheme 1). Following the preparation of monometallic macrocyclic complexes of $Ni^{II}$ and $UO_2$, derived from **II** and *cis*-1,2-diaminocyclohexane, the reaction with $[Rh(CO)_2Cl]_2$ afforded bimetallic $Ni^{II}/Rh^{I}$ and $UO_2/Rh^{I}$ species (Scheme 2). The nickel and uranyl ions were selected for the preparation of the bimetallic carbonylrhodium(I) complexes due to their different electronic and coordinative properties − uranyl is oxophilic whereas nickel(II) is not.

The synthesis of the precursor for the metal-templated ring-closure involves the coupling of the disodium salt of 2,6-bis(mercaptomethyl)pyridine[21] with 3-(2-bromoethoxy)-2-(2-propenyloxy)benzaldehyde,[22] in tetrahydrofuran, to give the allyl protected bis-formyl compound **I** (yield > 50%, Scheme 1). The allyl groups of **I** are then removed by palladium catalysis, following a method described in the literature,[20] to give ligand **II** (yield > 60%), which contains the $NS_2$ donor set, the oxyethyl spacers, and the formyl-2-hydroxyaryl sub-units. Compounds **I** and **II** were purified by column chromatography and characterized by $^1$H NMR, $^{13}$C NMR, and FT-IR spectroscopy, ESI mass spectrometry, and elemental analysis. The chemical shifts of the hydrogen atoms of the aryl rings in compound **II** were identified by a NOESY experiment, which shows correlations between the $OCH_2$ triplet at $\delta$ = 4.17 ppm and the doublet of doublets at $\delta$ = 6.93 ppm, due to the aryl 4-H *ortho* to the oxyethyl chain, as well as between the formyl H atoms at $\delta$ = 10.08 ppm and the doublet of doublets at $\delta$ = 7.20 ppm, due to the aryl 6-H.

The synthesis of the macrocyclic structures was performed by treatment of ligson **II** with *cis*-1,2-diaminocyclohexane, in the presence of $Ba(CF_3SO_3)_2$ as template, followed by transmetalation in situ with the desired metal ace-

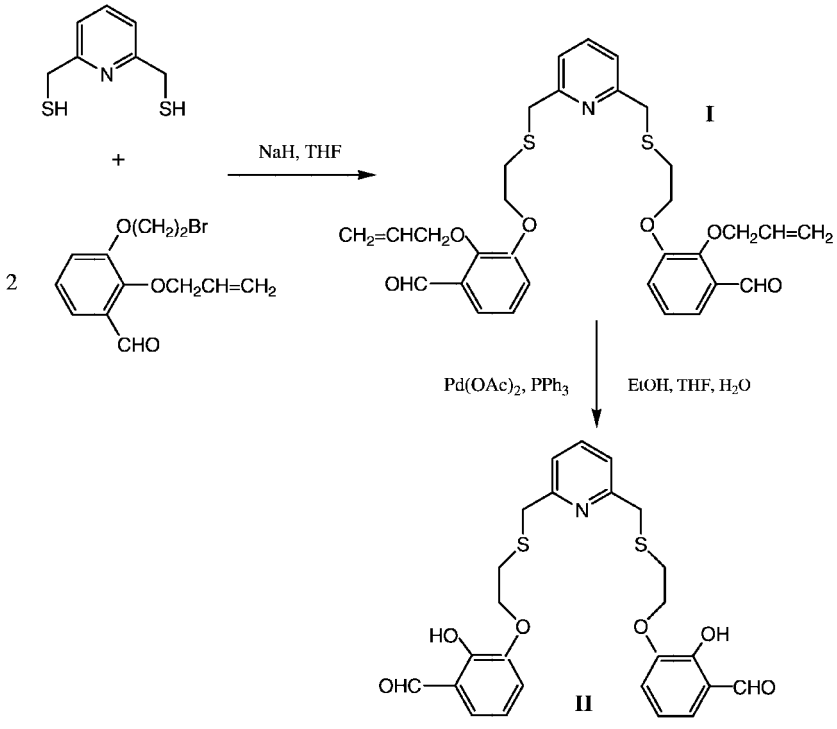


Scheme 1. Synthesis of the macrocyclic dialdehyde precursors **I** and **II**.

 © 2006 Wiley-VCH Verlag GmbH & Co. KGaA, Weinheim 

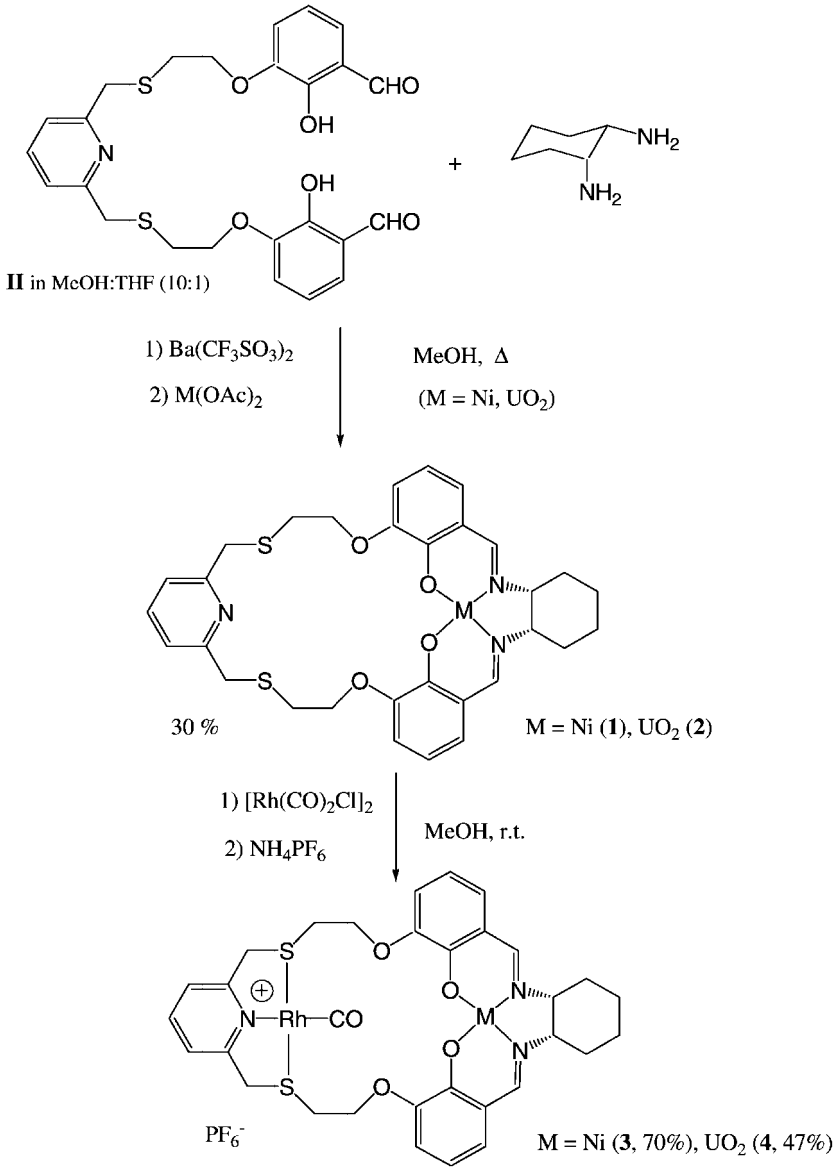


Scheme 2. Template synthesis of monometallic nickel(II) (**1**) and uranyl (**2**) macrocyclic complexes and subsequent formation of heterobimetallic nickel(II)–rhodium(I) (**3**) and uranylrhodium(I) (**4**) complexes.

tate $M(OAc)_2$ (M = Ni, $UO_2$; Scheme 2). Due to the poor solubility of **II**, which is a sticky red oil, in alcoholic solvents, the compound was added to the reaction mixture as a solution in methanol/tetrahydrofuran. The cyclization process involving the dialdehyde, the diamine, and the metal ion entails the formation of a metal–salen structure and affords the desired monometallic macrocyclic complexes **1** and **2**. Both complexes were isolated from their respective reaction mixtures as pure products by column chromatography with yields of around 30%.

The presence of $Ba^{2+}$ as a template cation has been found to be beneficial in cyclization reactions involving a diamine and a precursor containing two formyl-2-hydroxyaryl subunits linked by a polyether chain, affording the corresponding uranyl macrocyclic complexes with yields in the range 35–50% by transmetalation.[19,23] The same template has also been used successfully in the preparation of dissymmetric azamacrocyclic ligands.[7e] However, in the present case, the yields of complexes **1** and **2** were only slightly lower upon performing the reactions in the absence of the barium salt. This fact, along with the relatively low yields of the macrocyclization reactions, may be due to the lower binding ability of the hybrid thioether chain of ligand **II** toward the barium ion with respect to a polyether chain.

Complexes **1** and **2** were characterized by FT-IR, $^1H$ NMR, and $^{13}C$ NMR spectroscopy (see Experimental Section), ESI mass spectrometry, elemental analysis, and single-crystal X-ray diffraction analyses. In the $^1H$ NMR spectrum of complex **1** ([$D_2$]dichloromethane), the hydrogens of the pyridine ring (py) appear as one triplet at $\delta$ = 7.65 ppm (4-H) and one doublet at $\delta$ = 7.26 ppm (3,5-H), while the arene protons appear as two close doublets at $\delta$ = 6.79 and 6.75 ppm, due to 4,6-H, and one apparent triplet at $\delta$ = 6.45 ppm, due to 5-H, thus confirming the presence of the

 © 2006 Wiley-VCH Verlag GmbH & Co. KGaA, Weinheim 

salen and of the pyridine moieties in the expected ratio. The protons of the linking chains are also clearly identifiable. The fluxional character of the cyclohexane ring (cy) is indicated by the broad shape of the corresponding signals. One significant spectral feature is the presence of the imine CH=N protons, resulting from the coupling of the original aldehyde with the amine groups, at $\delta$ = 7.37 ppm in complex **1**. In the case of the uranyl complex **2**, the same protons appear at higher frequency, $\delta$ = 9.31 ppm, thereby indicating the stronger electron-withdrawing character of the uranyl group with respect to nickel(II). The 7-H protons of the cyclohexyl ring appear at $\delta$ = 3.45 and 4.66 ppm in complexes **1** and **2**, respectively.

In the $^{13}C$ NMR spectra, the imine carbon atoms are observed at $\delta$ = 159.2 and 167.2 ppm for **1** and **2**, respectively, while the infrared frequencies of the CH=N double bonds are virtually unaffected by the metal ion (1616 $cm^{-1}$ in dichloromethane). The electropositive uranyl center affects the rest of the molecule as well, since the $^1H$ NMR chemical shifts of the methylene hydrogens of py$CH_2$S and –S$CH_2CH_2$O– change from $\delta$ = 3.83 and 2.92 ppm in the nickel complex **1** to $\delta$ = 4.57–4.49 and 3.13 ppm, respectively, in complex **2**. The py$CH_2$S hydrogen atoms exhibit AB patterns in the $^1H$ NMR spectra, characterized by $\Delta\nu$ = 7.1 Hz (**1**, $CDCl_3$) and 24 Hz (**2**, $[D_2]$dichloromethane), due to their diastereotopic character,[15] while the same hydrogens of complex **1** appear equivalent in $[D_2]$dichloromethane. In a NOESY spectrum of complex **1** in $CDCl_3$, the absorption at $\delta$ = 6.47 ppm exhibits a cross-peak with the imine proton at $\delta$ = 7.04 ppm and is therefore assigned to the 6-H protons, while the peaks at $\delta$ = 6.71 ppm, due to 4-H, correlate with the $OCH_2$ signal at $\delta$ = 4.08 ppm.

Symmetric macrocyclic ligands containing two tetradentate salen coordination sites formed from *trans*-1,2-diaminocyclohexane, and the corresponding mono- and dinuclear nickel(II) complexes, have been reported.[24] With *trans*-1,2-diaminocyclohexane as the Schiff base counterpart, dissymmetric macrocyclic structures incorporating one nickel(II) salen unit, which acts as an intramolecular redox catalyst, and a 1,4-bis(chloromethylarene) function have been prepared by a multistep synthesis.[25] A macrocyclic compound characterized by the presence of a salen–uranyl moiety opposite a pyridine group and linked by oxyethyl chains has been reported.[23] With 1,2-phenylenediamine or *cis*-1,2-diaminocyclohexane, symmetric, dinuclear salophen or salen $UO_2$ macrocyclic complexes have been described,[26] as well as macrocyclic ligands containing 2,6-bis(alkylthiomethyl) pyridine subunits and the corresponding $[Rh(CO)][PF_6]$ dinuclear complexes.[15d] However, complexes **1** and **2** are the first macrocyclic structures in which a metal–salen unit is faced by an uncomplexed tridentate donor set that is suitable for further coordination of a second transition metal ion.

## X-ray Crystal Structure of Macrocyclic Nickel(II) (1) and Uranyl (2) Complexes

Single crystals of compounds **1** and **2** suitable for X-ray diffraction analysis were obtained by the "liquid diffusion" method from solutions of dichloromethane layered with heptane and kept at room temperature for several days. Selected bond angles and distances are reported in Tables 1 and 2 for complexes **1** and **2**, respectively.

Table 1. Selected bond lengths [Å] and angles [°] for the macrocyclic nickel(II) complex **1**.

| | | | |
|---|---|---|---|
| Ni1–O4 | 1.877(4) | C26–O29 | 1.359(8) |
| Ni1–N13 | 1.874(5) | C27–O28 | 1.319(8) |
| Ni1–N20 | 1.888(5) | O29–C30 | 1.452(7) |
| Ni1–O28 | 1.854(4) | C30–C31 | 1.483(10) |
| O4–C6 | 1.295(7) | C31–S32 | 1.825(7) |
| C12–N13 | 1.288(8) | S32–C33 | 1.787(9) |
| N13–C14 | 1.501(8) | C40–S41 | 1.867(7) |
| C19–N20 | 1.506(8) | S41–C42 | 1.802(7) |
| N20–C21 | 1.281(9) | C43–O44 | 1.456(10) |
| N20–Ni1–O28 | 94.4(2) | C12–N13–C14 | 122.63(5) |
| N13–Ni1–O28 | 177.0(2) | Ni1–N13–C14 | 111.2(4) |
| N13–Ni1–N20 | 86.5(2) | Ni1–N20–C19 | 111.0(4) |
| O4–Ni1–O28 | 85.6(2) | Ni1–N20–C21 | 124.97(5) |
| O4–Ni1–N20 | 176.8(2) | Ni1–O28–C27 | 128.2(4) |
| O4–Ni1–N13 | 93.7(2) | C31–S32–C33 | 98.6(3) |
| Ni1–O4–C6 | 126.2(4) | C40–S41–C42 | 103.3(3) |
| Ni1–N13–C12 | 126.0(5) | | |

Table 2. Selected bond lengths [Å] and angles [°] for the macrocyclic uranyl complex **2**.

| | | | |
|---|---|---|---|
| U1–O2 | 1.572(16) | C12–N13 | 1.278(21) |
| U1–O3 | 1.806(13) | N20–C21 | 1.278(17) |
| U1–O4 | 2.226(8) | C27–O28 | 1.325(15) |
| U1–O5 | 2.499(7) | C31–S32 | 1.806(19) |
| U1–N13 | 2.546(13) | S32–C33 | 1.789(16) |
| U1–N20 | 2.569(9) | C40–S41 | 1.771(23) |
| U1–O28 | 2.193(8) | S41–C42 | 1.834(22) |
| O4–C6 | 1.293(14) | | |
| O2–U1–O3 | 178.4(6) | O5–U1–N13 | 142.7(4) |
| O2–U1–O28 | 92.8(6) | O2–U1–N20 | 86.1(3) |
| O3–U1–O28 | 87.9(6) | O3–U1–N20 | 92.8(3) |
| O2–U1–O4 | 91.1(5) | O28–U1–N20 | 71.6(3) |
| O3–U1–O4 | 89.0(5) | O4–U1–N20 | 137.1(4) |
| O28–U1–O4 | 151.3(4) | O5–U1–N20 | 151.4(3) |
| O2–U1–O5 | 89.5(5) | N13–U1–N20 | 65.8(3) |
| O3–U1–O5 | 92.1(4) | C6–O4–U1 | 134.8(8) |
| O28–U1–O5 | 80.5(4) | C12–N13–U1 | 127.8(10) |
| O4–U1–O5 | 71.1(4) | C14–N13–U1 | 112.5(10) |
| O2–U1–N13 | 93.1(7) | C21–N20–U1 | 127.4(9) |
| O3–U1–N13 | 85.4(5) | C19–N20–U1 | 117.2(7) |
| O28–U1–N13 | 136.4(3) | C31–S32–C33 | 101.9(8) |
| O4–U1–N13 | 71.6(4) | C42–S41–C40 | 98.0(11) |

### *Geometry of Complex 1*

The nickel atom in the $N_2O_2$ ligand set shows a slightly deformed square-planar conformation (Figure 1) in which the bond angles around the metal range from 85.6(4)° for O(4)–Ni(1)–O(28) to 93.7(5)° for O(4)–Ni(1)–N(13); the maximum out-of-plane deformation of the five atoms of the coordination moiety is 0.06(1) Å. The average Ni–O and Ni–N(13) bond lengths [1.865 and 1.8481 Å, respectively] compare well with the values observed in other monomeric nickel macrocyclic[24] or open complexes[27] formed from *trans*-1,2-diaminocyclohexane. The complex as a whole lies approximately on a plane, with the exception of the cyclohexane and pyridine rings, which are almost orthogonal to

 © 2006 Wiley-VCH Verlag GmbH & Co. KGaA, Weinheim 

the mean plane of the macrocycle and in a relative *transoid* fashion. In fact, the dihedral angles formed by the mean C(6)–C(11), C(22)–C(27), C(34)–N(39) (py) and C(14)–C(19) (cy) ring planes with that of the coordinative moiety are 7.7(2)°, 2.9(3)°, 82.3(2)°, and 114.5(2)°, respectively. While the chain from O(29) to C(33) is planar and forms a dihedral angle of 4.4(2)° with the coordinative mean plane, the C(42) and C(43) carbon atoms lie 1.02(2) and 1.25(2) Å, respectively, out of the plane formed by the three remaining atoms of the chain. The water molecule is not coordinated to nickel [O(1W)···Ni = 3.99(5) Å] but is hydrogen bonded within the cavity through the oxygen of one ethylene chain [H(1W)···O(29) = 1.94(5) Å] and one of the methylene hydrogens of the opposite one [O(1W)···H(43) = 2.47(5) Å]. Other short contacts are an intramolecular H(1W)···O(28) contact [2.52(2) Å] and an intermolecular H(12)–O(1W)$^{i}$ ($i$ = 1 – $x$, $y$ – 1/2, 3/2 – $z$) contact [2.49(2) Å]. The C(14)–N(13) distance of the cyclohexyl equatorial bond is 1.501 Å, while the C(19)–N(20) distance of the axial bond is 1.506(7) Å. The molecules are connected in the crystal by van der Waals contacts. We have not been able to find other crystal structures of salen–nickel complexes obtained from *cis*-1,2-diaminocyclohexane in the literature. The conformation of the bis(alkylthiomethyl)pyridine ligand set in complex **1** is characterized by the presence of the sulfur atoms oriented outwards with exocyclic lone pairs, with C–S–C bond angles of 98.6(3)° and 103.3(3)°. The C–S bond lengths lie between 1.825 and 1.867 Å, in the usual range observed in macrocyclic structures including this uncomplexed ligand.[15d]

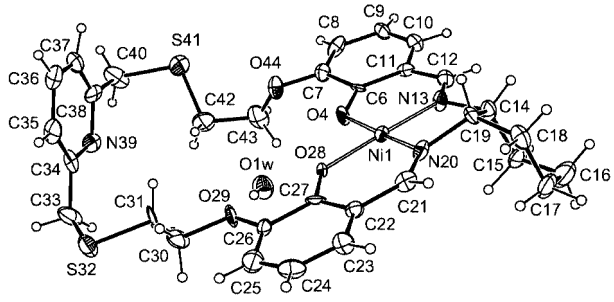


Figure 1. Molecular structure and atom-labelling scheme for the macrocyclic nickel(II) complex **1**.

### *Geometry of Complex 2*

The uranyl moiety in complex **2** exhibits a pentagonal-bipyramidal coordination (Figure 2). Two imine nitrogen atoms [N(20), N(13)], two phenoxy oxygen atoms [O(4), O(28)], and one oxygen from a molecule of water (O5) form the pentagonal base, which is almost planar, while the two uranyl oxygen atoms occupy the apex positions, with out-of-plane deviations of 1.57 and 1.81 Å, respectively. The aromatic rings are planar and the cyclohexane ring adopts the typical chair conformation. This coordinative arrangement compares well with that found for a similar complex containing a coordinated molecule of urea in place of the water molecule.[19] The pyridine ring is oriented in such a way as to form a dihedral angle of 20.7(4)° with respect to the pentagonal planar base. When compared to the S-shaped conformation of the nickel complex **1**, complex **2** can be regarded as lying approximately on a plane including the pyridine and cyclohexyl rings. Since the two phenyl rings C(6)–C(11) and C(22)–C(27) of the salen moiety form a dihedral angle of 47.5(5)° with respect to each other, this part of the complex assumes, as a whole, a butterfly orientation. These two rings are tilted by 28.2(4)° and 19.7(4)°, respectively, with respect to the mean plane formed by the five atoms coordinated by uranium. This conformation, which is due to the relatively large ionic radius of uranium pushing apart the phenyl rings, is typical of uranyl–salen complexes and is similar to that observed in other monomeric macrocyclic uranyl systems[19,28] formed from *cis*-1,2-diaminocyclohexane. The C(14)–N(13) distance of the cyclohexyl axial bond is 1.588 Å, while the C(19)–N(20) distance of the equatorial bond is 1.464 Å. In the crystals the molecules are connected by intra- [H(18a)····N(13) = 2.53(3); O(5)····N(39) = 2.76(2); O(5)····H(40) = 2.90(1) Å], and intermolecular [H(21A)···O(3)$^{i}$ (i = 1/2 – $x$, 1/2 – $y$, –$z$) = 2.33(1); H(30B)···O(5)$^{ii}$ (*ii* = –$x$, –$y$, –$z$) = 2.58(1); H(40B)···O(3)$^{iii}$ (*iii* = 1/2 – $x$, –1/2 – $y$, –$z$) = 2.49(1) Å] van der Waals contacts involving, in particular, the water molecule. The uncomplexed bis(thiomethyl)pyridine group of the uranyl complex **2** has one exocyclic and one endocyclic sulfur atom and is characterized by C–S–C bond angles of 101.9(8)° and 98.0(9)°, respectively, and C–S bond lengths in the range 1.77–1.81 Å.

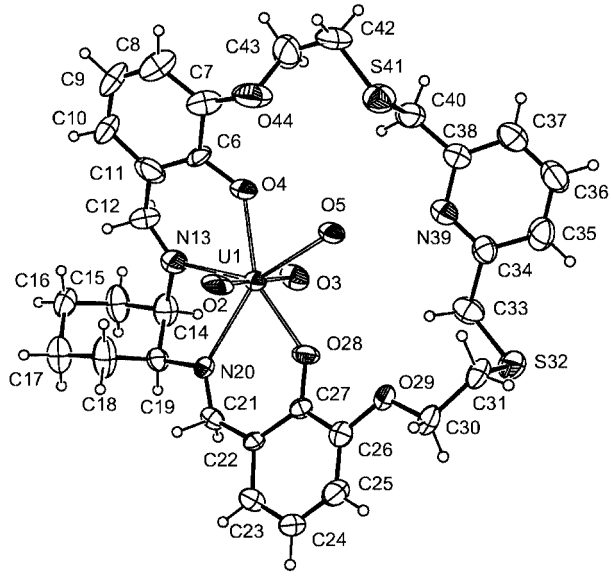


Figure 2. Molecular structure and atom-labelling scheme for the macrocyclic uranyl complex **2**.

### Synthesis of Bimetallic $Ni^{II}$–$Rh^{I}$ (3) and $UO_2$–$Rh^{I}$ (4) Macrocyclic Complexes

A suspension of the monometallic macrocyclic nickel complex **1** in methanol was treated with a methanolic solution of $[RhCl(CO)_2]_2$ (Scheme 2). The mixing of the two

 © 2006 Wiley-VCH Verlag GmbH & Co. KGaA, Weinheim 

compounds yielded a clear amber solution which, when analyzed after about 10 min, showed an intense IR band at 2009 $cm^{-1}$ and the disappearance of the absorption bands (2088 and 2014 $cm^{-1}$) of the dicarbonylchlororhodium dimer. Addition of a methanolic solution of $NH_4PF_6$ caused the formation of an orange precipitate, which corresponds to the expected macrocyclic bimetallic $Ni^{II}$–$Rh^{I}$ complex **3** (yield 70%). The monometallic uranyl complex **2** reacts with the dicarbonylchlororhodium dimer in a similar manner (yield 47%). Therefore, the macrocyclic metal–salen structure connected by a relatively short oxyethyl chain does not hinder the coordinative ability of the $NS_2$ ligand set. Both complexes **3** and **4** exhibit good solubility in organic solvents, especially in dichloromethane. This is due, presumably, to the presence of the cyclohexane ring, as a cyclohexyl group is known to increase the solubility of macrocyclic salen complexes with respect to analogous salophen derivatives.[19]

The bimetallic complexes were characterized by FT-IR, $^1H$ NMR, and $^{13}C$ NMR spectroscopy (**3**), FAB mass spectrometry, and elemental analyses. Complexation of the cationic carbonylrhodium group to the tridentate $NS_2$ ligand system is indicated by the presence of a strong split absorption at 2026–2017 $cm^{-1}$ for complex **3** and of a band at 2020 $cm^{-1}$ for complex **4**, both in dichloromethane. The $^{13}C$ NMR chemical shifts of the methylene carbons of py$CH_2$S– and –S$CH_2CH_2O$– move from $\delta$ = 37.7 and 30.0 ppm in the monometallic nickel complex **1** to $\delta$ = 47.0 and 37.3 ppm, respectively, in the bimetallic nickel–rhodium complex **3**. The $^{13}C$ NMR spectrum obtained overnight from a [$D_2$]-dichloromethane solution of the bimetallic uranylrhodium complex **4** is identical to that of the monometallic uranyl complex **2**, which suggests solvolysis of the $(RhCO)^+$ fragment. In analogy, decomposition by loss of CO was observed when monitoring a dichloromethane solution of complex **4** by IR spectroscopy over several hours.

In complex **3**, in addition to the two CO stretching bands in the IR spectrum, broad and split peaks appear in the $^1H$ NMR spectrum, indicating the existence of two isomers in an approximately 5:1 ratio in [$D_2$]dichloromethane. Split peaks are also observed in the $^{13}C$ NMR spectrum. In [$D_3$]-acetonitrile solution, the three methylene groups of py–$CH_2SCH_2CH_2O$– are well separated in the region $\delta$ = 5.2–3.0 ppm (Figure 3). At room temperature, the multiplet due to the py$CH_2$S– methylene groups is better resolved than the broad signals of the –$SCH_2CH_2O$– methylene chain, thus indicating rapid conformational equilibria along the carbon chain spacers and greater flexibility of the macrocyclic structure at these sites. The py$CH_2$S– protons display a distorted AB system ($\delta_{Ha}$ = 4.80, $\delta_{Hb}$ = 4.73 ppm; $\Delta\nu$ = 22 Hz), corresponding to the coordination of the $NS_2$ donor set to the metal ion in a stable configuration. This pattern agrees well with that observed for the open complex [Rh(L)(CO)]$PF_6$ [L = 2,6-bis(benzylthiomethyl)pyridine] in [$D_2$]dichloromethane at –65 °C,[29b] and for the macrocyclic $Rh(CO)^+$ complexes in which a 2,6-bis(thiomethyl)pyridine subunit is linked by a polyether chain.[15c] In addition, the doubled absorptions of the –$SCH_2CH_2O$– groups confirm the presence of the two isomeric species observed in [$D_2$]-dichloromethane. When the temperature is raised, interconversion of these isomers occurs with a coalescence temperature of 44 °C, at which both the chain methylene groups appear as single, broad peaks at $\delta$ = 3.50 and 4.55 ppm, respectively, while the multiplet of the py$CH_2$S– protons is only slightly affected by this temperature change. The observed isomers may arise from the relative position of the metal ions with respect to the mean ligand plane – either opposite or on the same side – and interconvert by conformational changes of the oxyethylene chains, in analogy with what is observed for the symmetric bimetallic $RhCO^+$ macrocyclic complex incorporating two 2,6-bis(alkylthiomethyl)pyridine groups.[15c] Detailed variable-temperature NMR studies involving fluxional processes related to inversion at sulfur[30] and/or conformational equilibria in the macrocyclic frame have been described for mono- and bimetallic carbonylrhodium macrocyclic complexes.[15]

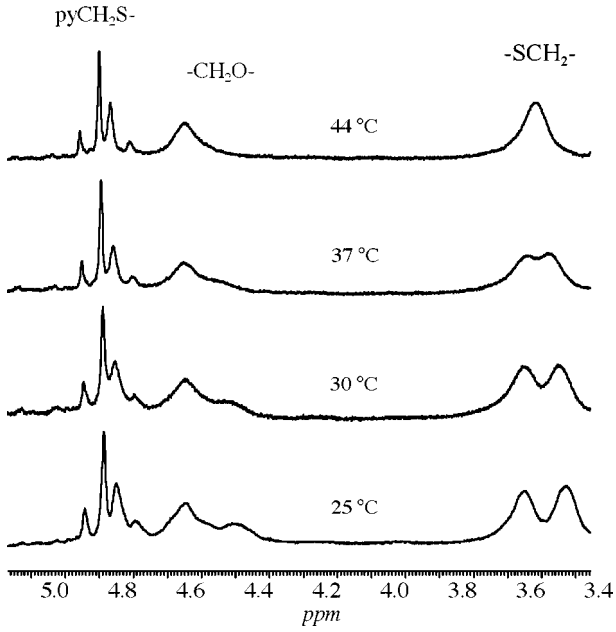


Figure 3. $^1H$ NMR spectra of the heterobimetallic $Ni^{II}$–$Rh^{I}$ complex **3** in [$D_3$]acetonitrile at different temperatures, displaying the methylene groups of the py$CH_2SCH_2CH_2O$ moiety.

The CO stretching band of the complex [Rh(L)(CO)]-$PF_6$, in which L is the "open" $NS_2$ ligand 2,6-bis(benzylthiomethyl)pyridine, is observed at 2019 $cm^{-1}$ in dichloromethane.[29] A comparison with the macrocyclic systems reported here shows that the carbonylrhodium group is not perturbed by the adjacent metal centers. It is worth mentioning that during the synthesis of the bimetallic complexes the intermediate chloride species shows a carbonyl band at 2009 $cm^{-1}$ for the nickel–rhodium complex **3** and 2015 $cm^{-1}$ for the uranylrhodium complex **4**, in methanol, indicating a small effect of the salen–metal ion on the carbonylrhodium group. The dinuclear [2+2] symmetric carbonylrhodium macrocyclic complexes incorporating two 2,6-bis(alkylthiomethyl)pyridine sub-units linked by $(CH_2)_n$ chains ($n$ = 5–10) exhibit CO stretching values in the range

 © 2006 Wiley-VCH Verlag GmbH & Co. KGaA, Weinheim 

1991–2009 $cm^{-1}$ (KBr).[15d] The values of 2013 and 2012 $cm^{-1}$ observed in the solid state (KBr) for the heterobimetallic complexes **3** and **4**, respectively, indicate a larger triple-bond character than in the homobimetallic systems. This suggests reduced electron density on rhodium, and hence reduced back-donation from rhodium to carbonyl, rather than an intramolecular CO···M contact in the heterobimetallic complex, which would have lowered the carbonyl stretching frequency.

We have recently described that the monometallic complex $[Rh(L)(CO)]PF_6$ reacts with MeI to give an intermediate methylrhodium(III) iodide species $[Rh(L)(CO)(Me)I]^+$ and an isolable acylrhodium(III) complex $[Rh(L)(COMe)I]PF_6$ as the result of consecutive oxidative addition/migratory insertion reactions.[29a] This was the first report of the organometallic reactivity of a carbonylrhodium complex of the neutral tridentate 2,6-bis(substituted thiomethyl) pyridine system. The product of oxidative addition is observed as a relatively stable intermediate that accumulates in solution and exhibits a strong infrared band at 2106 $cm^{-1}$ (acetonitrile). We therefore tested the reactivity of both complexes **3** and **4** toward methyl iodide (3.5 M) in solution in dichloromethane (Scheme 3). In the case of the nickel–rhodium complex **3**, the reaction solution, when stirred for 5 h at 40 °C, gave an abundant red precipitate, which, analyzed in $[D_3]$acetonitrile, exhibits a strong carbonyl band at 2128 $cm^{-1}$ due to the methylrhodium species, thus indicating the conversion of complex **3** into the product of oxidative addition of methyl iodide. In the case of the macrocyclic uranylrhodium complex **4**, the solution was stirred for 6 h at room temperature in order to minimize the spontaneous loss of CO. After removal of excess MeI and solvent, the spectrum showed the presence of starting material (2001 $cm^{-1}$), the oxidative-addition intermediate (2116 $cm^{-1}$), and the migratory-insertion product at 1676 $cm^{-1}$. Due to the smaller absorptivity of the acyl moiety with respect to the parent terminal $Rh^I$ and $Rh^{III}$ complexes, it can be deduced that the acyl product is more abundant than both the substrate and the methylrhodium(III) intermediate. The presence of the acyl derivative from the bimetallic $UO_2/Rh^I$ complex suggests an easier migratory-insertion reaction than in the corresponding nickel complex. It appears that the IR frequencies of the carbonyl group in the $[Rh(CO)(Me)I]^+$ moiety are affected by the different environments in the two heterobimetallic complexes and in the open system.

## Conclusions

The synthesis of a novel macrocyclic ligand system containing a neutral, tridentate $NS_2$ donor set and a tetradentate, dianionic $N_2O_2$ unity has been described, in particular the isolation and structural characterization of the corresponding monometallic salen complexes of $Ni^{II}$ and of $UO_2$ obtained from *cis*-1,2-diaminocyclohexane. These are the first examples of macrocycles in which a different uncoordinated ligand set ($NS_2$) faces the salen–metal group. Both monometallic compounds react with $[RhCl(CO)_2]_2$ to yield heterobimetallic, cationic complexes characterized by the presence of the $[(NS_2)RhCO]^+$ fragment. This synthetic method allows the sequential and selective coordination of two different metal ions onto a dissymmetric ligand frame using conventional procedures. The uranyl group enhances the lability of the CO ligand with respect to nickel(II). In fact, the $UO_2$–$Rh^I$ complex decomposes slowly by loss of CO and solvolysis of the $Rh(CO)^+$ fragment. The $Ni^{II}$–$Rh^I$ complex, which is more stable, exists in solution as two conformational isomers. The $[Rh–CO]^+$ fragment of both bimetallic complexes undergoes oxidative addition of MeI.

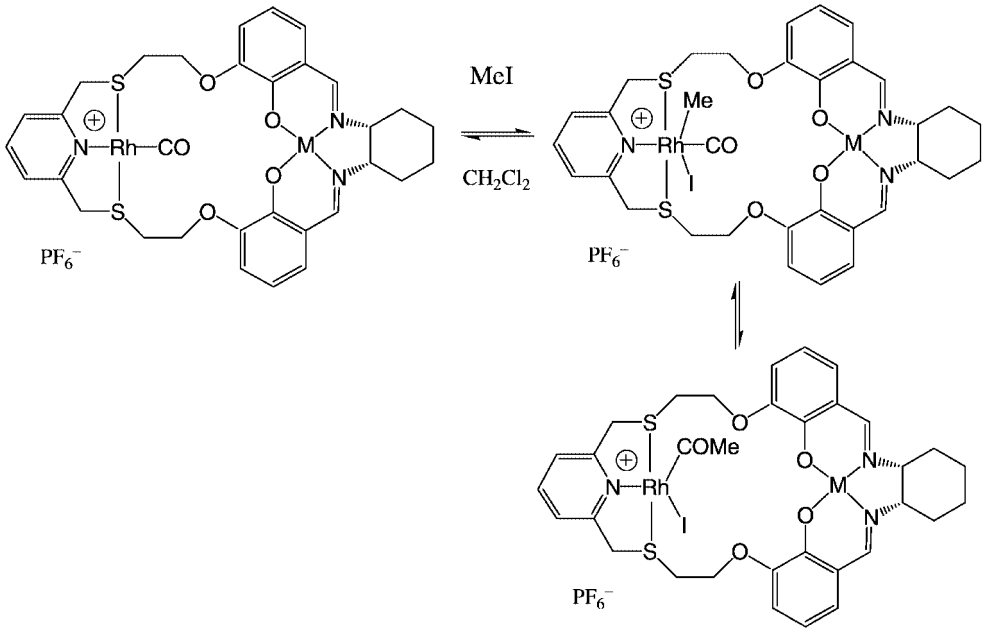


Scheme 3. Reactions of complexes **3** or **4** with methyl iodide.

 © 2006 Wiley-VCH Verlag GmbH & Co. KGaA, Weinheim 

## Experimental Section

**General Methods:** Reactions involving air- and moisture-sensitive compounds were carried out under nitrogen using standard Schlenk line techniques. Tetrahydrofuran was distilled from Na/K alloy, acetonitrile from phosphorus pentoxide, and methanol from magnesium turnings. $^1$H, $^{13}$C, and 2-D NOESY NMR spectra were obtained with a Bruker AM-300 spectrometer. Chemical shifts are reported in ppm relative to tetramethylsilane with (for $^1$H NMR) chloroform ($\delta$ = 7.24 ppm) or dichloromethane ($\delta$ = 5.32 ppm) or (for $^{13}$C NMR) $CDCl_3$ ($\delta$ = 77.0 ppm), [$D_2$]dichloromethane ($\delta$ = 53.1 ppm) or [$D_3$]acetonitrile ($\delta$ = 118.2 ppm) as internal standards. IR spectra were recorded for KBr pellets or in 0.1-mm $CaF_2$ solution cells with a FT-IR Nicolet 510 instrument using the Omnic 4 software. ESI mass spectra were recorded with a Fisons Instruments VG-Platform Benchtop LC-MS (positive ions). FAB mass spectra were obtained with *m*-nitrobenzyl alcohol as matrix on a VG-Quattro Instrument of the University of Tor Vergata, Roma. Elemental analyses were performed by the Servizio di Microanalisi of the Department of Chemistry, Università La Sapienza, Roma. The compounds 3-(2-bromoethoxy)-2-(2-propenyloxy)benzaldehyde[22] and 2,6-bis(mercaptomethyl)pyridine[21,29a] were prepared according to literature procedures. Commercial $[RhCl(CO)_2]_2$ was purified by sublimation before use. Silica gel 60 was used for preparative column chromatography, unless stated otherwise. Other chemicals were used as supplied commercially.

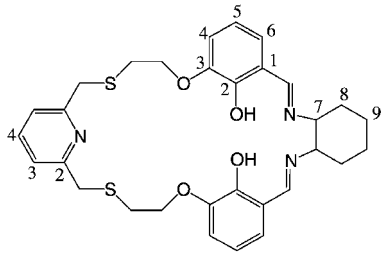

**2,6-Bis{[2-[3-formyl-2-(propenyloxy)phenyl]oxyethyl]thiomethyl}pyridine (I):** Sodium hydride (80% dispersion in mineral oil; 438 mg, 14.6 mmol) was introduced into a 250-mL, three necked flask and washed three times with dry hexane under nitrogen. Tetrahydrofuran (50 mL) and a tetrahydrofuran solution of 2,6-bis(mercaptomethyl)pyridine (1.24 g, 7.3 mmol) were introduced by cannula, and the mixture was stirred for 15 min. 3-(2-Bromoethoxy)-2-(2-propenyloxy)benzaldehyde (4.13 g, 14.5 mmol) was added dropwise to the resulting solution. After 12 h at reflux, the reaction mixture was poured into water and chloroform, and extracted with chloroform (3 × 50 mL). The combined organic layers were washed with 0.5 M NaOH (3 × 30 mL), twice with water, then dried with sodium sulfate. After filtration, evaporation of the solvent under vacuum afforded 3.9 g of crude product, which appeared in a TLC analysis (silica/chloroform) as the most intense spot with a retention factor of 0.11–012, preceded and followed by weaker spots. Purification by column chromatography with chloroform as eluent gave pure **I** as a yellow, sticky oil in 54% yield. $^1$H NMR ($CDCl_3$): $\delta$ = 10.38 (s, 2 H, CHO), 7.60 (t, $J$ = 7.7 Hz, 1 H, py 4-H), 7.38 (pseudo-t, $J$ = 4.7 Hz, 2 H, aryl 5-H), 7.23 (d, $J$ = 7.7 Hz, 2 H, py 3,5-H), 7.05 (pseudo-d, $J$ = 4.7 Hz, 4 H, aryl 4,6-H), 6.08–5.94 (m, 2 H, =CH), 5.34–5.18 (m, 4 H, =$CH_2$), 4.65–4.62 (m, 4 H, $OCH_2$), 4.11 (t, $J$ = 6.7 Hz, 4 H, $OCH_2CH_2S$), 3.85 (s, 4 H, $pyCH_2S$), 2.92 (t, $J$ = 6.5 Hz, 4 H, $OCH_2CH_2S$) ppm. $^{13}$C NMR ($CDCl_3$): $\delta$ = 190.17 (CHO), 158.06 (py C-2), 151.72, 151.20 (Ar C-2, C-3), 137.49 (py C-4), 133.03 (CH=), 130.06 (Ar C-1), 123.94, 121.24, 119.15, 118.82 (py C-3 and Ar C-4, C-5, C-6), 119.34 (=$CH_2$), 75.07 ($OCH_2CH=CH_2$), 67.98 ($OCH_2$), 38.01 ($pyCH_2S$), 30.41 ($OCH_2CH_2S$) ppm. FT-IR (dichloromethane): $\tilde{\nu}_{max}$ = 1687 cm$^{-1}$ (C=O). ESI (acetonitrile): $m/z$ = 580.7 [M + 1]$^+$, 602.4 [M + Na]$^+$, 618.8 [M + K]$^+$. $C_{31}H_{33}NO_6S_2\cdot H_2O$ (597.74): calcd. C 62.29, H 5.90, N 2.34, S 10.73; found C 62.62, H 5.64, N 2.64, S 10.82.

**2,6-Bis{[2-(3-formyl-2-hydroxyphenyl)oxyethyl]thiomethyl}pyridine (II):** Formic acid (0.28 mL, 7.5 mmol), triethylamine (freshly distilled from over sodium; 1.0 mL, 7.5 mmol), triphenylphosphane (49 mg, 0.19 mmol), palladium acetate (10 mg, 0.046 mmol), and compound **I** were dissolved in 11 mL of ethanol/water/tetrahydrofuran (5:1:5). The yellow solution was kept under reflux for 2 h, then the solvents were removed in vacuo. The residue was extracted with water (50 mL) and chloroform (3 × 50 mL). The combined extracts were washed with water (3 × 50 mL) and dried with sodium sulfate. Evaporation in vacuo gave 667 mg of crude product as a sticky, red oil. Purification of this material was carried out by column chromatography using a mixture of petroleum ether and acetone (2:1, v/v) to afford pure **II** in 60% yield. Compound **II** appears as the most intense spot in a TLC analysis from hexane/acetone (1:1) with $R_f$ = 0.56. When the reaction was performed under more dilute conditions, the deallylation process was slower and incomplete. On the other hand, longer reaction times produced decomposition of the expected product. $^1$H NMR ($CDCl_3$): $\delta$ = 11.14 (s, 2 H, OH), 10.08 (s, 2 H, CHO), 7.71 (t, $J$ = 7.7 Hz, 1 H, py 4-H), 7.41 (d, $J$ = 8.0 Hz, 2 H, py 3,5-H), 7.20 (dd, $^3J$ = 7.7, $^4J$ = 1.5 Hz, 2 H, Ar 6-H), 6.93 (dd, $^3J$ = 7.8, $^4J$ = 1.3 Hz, 2 H, Ar 4 H), 6.82 (pseudo-t, $J$ = 7.9 Hz, 2 H, Ar 5-H), 4.17 (t, $J$ = 6.2 Hz, 4 H, $OCH_2CH_2S$), 4.01 (s, 4 H, $pyCH_2S$), 2.76 (t, $J$ = 6.1 Hz, 4 H, $OCH_2CH_2S$) ppm. $^{13}$C NMR ($CDCl_3$): $\delta$ = 194.50 (CHO), 157.93 (py C-2), 151.56 (Ar C-3), 146.99 (Ar C-2), 137.99 (py C-4), 132.08 (Ar C-1), 128.53 (Ar C-5), 123.31, 122.21, 119.22 (py C-3 and Ar C-4, C-6), 69.99 ($OCH_2$), 37.39 ($SCH_2py$), 29.14 ($OCH_2CH_2S$) ppm. FT-IR (tetrahydrofuran): $\tilde{\nu}_{max}$ = 1658 cm$^{-1}$ (C=O). ESI (acetonitrile): $m/z$ = 500.4 [M + 1]$^+$, 522.3 [M + Na]$^+$. $C_{25}H_{25}NO_6S_2\cdot H_2O$ (517.62): calcd. C 58.01, H 5.26, N 2.71, S 12.39; found C 58.56, H 5.60, N 2.45, S 11.15.

**Nickel(II) Complex 1:** Separate solutions of *cis*-1,2-diaminocyclohexane (0.115 mL, 0.96 mmol) in 70 mL of methanol and dialdehyde **II** (475 mg, 0.95 mmol) in 70 mL of methanol/tetrahydrofuran were added simultaneously, within 1 h, to a refluxing solution of $Ba(CF_3SO_3)_2$ (430 mg, 0.99 mmol) in 250 mL of dry methanol. The solution of **II** was prepared by dissolving compound **II** in 10 mL of tetrahydrofuran, followed by addition of methanol up to the desired volume. After 30 min, $Ni(CH_3COO)_2\cdot 4H_2O$ (249 mg, 1.0 mmol) was added. The solution turned brown and was kept at reflux for 50 min, then cooled to room temperature. The solvent was removed under vacuum, and the residue was extracted with dichloromethane. The organic solution was washed with saturated aqueous solutions of sodium sulfate (3 × 100 mL), sodium hydrogen carbonate (1 × 100 mL), and sodium chloride (1 × 100 mL), then dried with sodium sulfate. After filtration and removal of the solvent under vacuum, the crude product was separated into two equal portions, each of which was purified by column chromatography over alumina deactivated with 3% of water. Initial elution with dichloromethane separated two yellow bands of a material which was not identified. Continued elution with dichloromethane/methanol (at first 150:1, then 100:1) moved a long, brown band, which left the product as a red-brown solid (93 mg from the first portion of crude material and 90 mg from the second; combined yield 30%). $^1$H NMR ([$D_2$]dichloromethane): $\delta$ = 7.65 (t, $J$ = 8 Hz, 1 H, py 4-H), 7.37 (s, 2 H, CH=N); 7.26 (d, $J$ = 8 Hz, 2 H, py 3,5-H), 6.79 (dd, $^3J$ = 8.2, $^4J$ = 1.5 Hz, 2 H, Ar 4-H), 6.75 (dd, $^3J$ = 7.6, $^4J$ = 1.5 Hz, 2 H, Ar 6-H), 6.45 (pseudo-t, $J$ = 7.8 Hz, 2 H, Ar

 © 2006 Wiley-VCH Verlag GmbH & Co. KGaA, Weinheim 

5-H), 4.05 (t, $J$ = 7.8 Hz, 4 H, –$CH_2$OAr), 3.83 (s, 4 H, py$CH_2$S), 3.45 (br. s, 2 H, cy 7-H), 2.92 (d, $J$ = 7.9 Hz, 4 H, –$CH_2CH_2$S), 2.29 (br. m, 2 H, cy 8-H), 1.93 (s, 2 H, $H_2O$), 1.69 (br. m, 2 H, cy 8-H), 1.41 (m, 4 H, cy 9-H) ppm. $^1$H NMR ($CDCl_3$): $\delta$ = 7.61 (t, $J$ = 7.5 Hz, 1 H, py 4-H); 7.25 (d, $J$ = 8 Hz, 2 H, py 3,5-H), 7.04 (s, 2 H, ArCHN), 6.71 (d, $J$ = 7.4 Hz, 2 H, Ar 4-H), 6.47 (d, $J$ = 7.6 Hz, 2 H, Ar 6-H), 6.30 (pseudo-t, $J$ = 7.7 Hz, 2 H, Ar 5-H), 4.08 (m, 4 H, –$CH_2$OAr), 3.84 and 3.81 (AB system: $\Delta\nu$ = 7.1 Hz, 4 H, py$CH_2$S), 3.56 (br. s, 2 H, cy 7-H), 2.89 (m, 4 H, S$CH_2CH_2$O), 2.32 (s, 2 H, $H_2O$), 2.21 (br. m, 2 H, cy 8-$H_a$), 1.60 (br. m, 2 H, cy 8-$H_b$), 1.35 (br. m, 4 H, cy 9-H) ppm. $^{13}$C NMR ($CDCl_3$): $\delta$ = 159.2 (CH=N), 158.6 (py C-2), 155.9, 149.1 (Ar C-2, C-3), 137.6 (py C-4), 125.4, 121.4, 120.8, 117.1, 113.5 (py C-3 and Ar C-1, C-4, C-5, C-6), 67.6 ($CH_2$OAr), 67.4 (br. s, cy C-7), 37.7 (py$CH_2$S), 30.0 ($CH_2$S), 27.32 (C-8), 20.9 (C-9) ppm. ESI (acetonitrile): clusters centered at $m/z$ = 635 [**1** + $H^+$], 657 [**1** + $Na^+$]. FT-IR (KBr): $\tilde{\nu}_{max}$ = 1614 cm$^{-1}$ (vs, C=N), 1572, (py) 1543, 1470, 1446 (vs, Ar), 1322, 1229 (s),1085, 1002, 864, 739 (s). Analytically pure material was obtained by precipitation upon addition of pentane to a solution in dichloromethane. $C_{31}H_{33}N_3NiO_4S_2\cdot H_2O$ (652.45): calcd. C 57.07, H 5.41, N 6.44; found C 57.38, H 4.64, N 6.15.

**Uranyl Complex 2:** Separate solutions of *cis*-1,2-diaminocyclohexane (0.068 mL, 0.576 mmol) in 50 mL of methanol and dialdehyde **II** (288 mg, 0.576 mmol) in 50 mL of methanol/tetrahydrofuran were added simultaneously, within 1 h, to a refluxing solution of $Ba(CF_3SO_3)_2$ (251 mg, 0.576 mmol) in 200 mL of dry methanol. The solution of **II** was prepared by dissolving compound **II** in 5 mL of tetrahydrofuran, followed by addition of methanol up to the desired volume. After 30 min, $UO_2(CH_3COO)_2\cdot 2H_2O$ (244 mg, 0.576 mmol) was added. The solution was kept at reflux for 30 min, then cooled to room temperature. The solvent was removed under vacuum, and the residue was extracted with dichloromethane. The organic solution was washed with saturated aqueous solutions of sodium sulfate (3 × 100 mL), sodium hydrogen carbonate (1 × 100 mL), and sodium chloride (1 × 100 mL), then dried with sodium sulfate. After filtration and removal of the solvent under vacuum, the crude product was purified by column chromatography. Elution was first performed using dichloromethane, which slowly separated a yellow band. Subsequent elution with dichloromethane/methanol (500:1) separated out a second yellow band from the top of the column. Neither of these materials was the expected product and they were not identified. A red band was eluted with dichloromethane/methanol (100:1), and collected as a red powder after removal of solvent. Pure uranyl macrocycle **2** was obtained by precipitation with hexane from a concentrated dichloromethane solution (140 mg, 29% yield). $^1$H NMR ([$D_2$]dichloromethane): $\delta$ = 9.31 (s, 2 H, CH=N), 7.79 (t, $J$ = 7.6 Hz, 1 H, py 4-H), 7.49 (d, $J$ = 7.6 Hz, 2 H, py 3,5-H), 7.24 and 7.22 (two dd, $^3J$ = 6.5, $^4J$ = 1.4 Hz, 2 H + 2 H, Ar 4-H and 6-H), 6.70 (pseudo-t, $J$ = 7.8 Hz, 2 H, Ar 5-H), 4.66 (br. m, 2 H, cy 7-H), 4.57 and 4.49 (AB system, $\Delta\nu$ = 24 Hz, 4 H, py$CH_2$S), 4.48 (t, $J$ = 5.1 Hz, 4 H, –$CH_2$OAr), 3.13 (t, $J$ = 5.1 Hz, 4 H, –$CH_2$S), 2.44 (m, 2 H, cy 8-H), 1.99 (m, 2 H, cy 8-H), 1.75 (m, 4 H, cy 9-H) ppm. $^{13}$C NMR ([$D_2$]-dichloromethane): $\delta$ = 167.2 (CH=N), 159.4 (py C-2), 157.5, 149.7 (Ar C-2, C-3), 138.48 (py C-4), 126.0, 123.3, 122.1, 116.8, 116.0 (py C-3 and Ar C-1, C-4, C-5, C-6), 71.14 (cy C-7), 69.76 (–$CH_2$OAr), 38.32 (py$CH_2$S), 31.58 ($CH_2$S), 27.36 (C-8), 21.42 (C-9) ppm. ESI (methanol): positive, cluster centered at $m/z$ = 847 [**2** + $H^+$]. FT-IR (KBr): $\tilde{\nu}_{max}$ = 1612 cm$^{-1}$ (vs, C=N), 1594 (py), 1522, 1466, 1451, 1309, 1246, 1223, 1086, 898 (s, $UO_2$), 738. FT-IR (dichloromethane): $\tilde{\nu}_{max}$ = 1616 cm$^{-1}$ (vs, C=N), 1597, 1575 (py), 1555, 1456 (vs). $C_{31}H_{33}N_3O_6S_2U\cdot 2H_2O$ (881.80): calcd. C 42.22, H 4.23, N 4.77; found C 42.77, H 4.16, N 4.62.

**$Ni^{II}$–$Rh^{I}$ Complex 3:** In a Schlenk tube, 52.1 mg (0.082 mmol) of the macrocyclic nickel complex **1** was suspended in 3 mL of dry methanol and stirred under argon at room temperature. [$RhCl(CO)_2]_2$ (16 mg, 0.041 mmol) dissolved in 2 mL of methanol was then added with a cannula from another Schlenk tube into the suspension of **3** to afford a clear, amber solution. An infrared analysis of the solution after 10 min showed the presence of an intense peak at 2009 cm$^{-1}$, and the absence of the 2088 and 2014 cm$^{-1}$ bands of the dicarbonylchlororhodium dimer. Addition of a methanolic solution (2 mL) of $NH_4PF_6$ (85 mg) caused the formation of an orange solid, and the mixture was stirred for a few minutes. The solid was then allowed to deposit and the solvent was decanted off. The precipitate was washed twice with cold methanol and vacuum-dried to leave 42 mg of an orange powder. Addition of 0.5 mL of pentane to the reaction solution caused the precipitation of an additional 10 mg of solid. Both materials were characterized by intense infrared absorptions near 2020 cm$^{-1}$ in dichloromethane solution. Overall yield 70%. The compound is moderately air-sensitive, as indicated by the slow decay of intensity of the carbonyl infrared band upon standing in air. $^1$H NMR ([$D_2$]dichloromethane): $\delta$ = 7.98 (t, $J$ = 7 Hz, 4-H py) and 7.86 (m due to the minor isomer, 1 H, py 4-H), 7.59 (d, $J$ = 8 Hz, 2 H, py 3,5-H), 7.31 and 7.38 (2 × s due to the minor isomer, 2 H, CH=N), 6.83 (d, $J$ = 7 Hz, 2 H, Ar 4-H), 6.68 (br. s, 2 H, Ar 6-H), 6.40 (br. s, 2 H, Ar 5-H), 4.72–4.50 (br. m, 8 H, py$CH_2$S and –$CH_2$OAr), 3.47 and 3.68 (2 × m, due to the minor isomer, 4 H, $CH_2$S; 5:1 ratio), 3.22 (br. s, 2 H, cy C-7), 2.24, 1.76, 1.39 (br. m, 8 H, cy 8,9-H) ppm. $^{13}$C NMR ([$D_3$]acetonitrile, peaks of the major isomer): $\delta$ = 161.8 (ArCHN), 161.4 (py C-2), 154.9, 147.8 (Ar C-2, C-3), 140.2 (py C-4), 127.5, 122.1, 121.9, 119.0, 115.3 (py C-3 and Ar C-1, C-4, C-5, C-6), 69.7 (br. s, cy C-7), 68.4 (–$CH_2$OAr), 47.0 (py$CH_2$S), 37.3 (–$CH_2$S), 27.8 (C-8), 21.4 (C-9) ppm. FT-IR (dichloromethane): $\tilde{\nu}_{max}$ 2026, 2017 cm$^{-1}$ (vs, CO), 1618 (s, C=N), 1606 (w, py), 1545, 1470, 1446. FT-IR (KBr): $\tilde{\nu}_{max}$ = 2013 cm$^{-1}$ (CO), 1618 (C=N), 1544, 1444, 1321, 1230, 840, 741, 558. FAB: clusters centered at $m/z$ =765.3 [**3** + $H^+$] and 737 [**3** + $H^+$ – CO]. $C_{32}H_{33}F_6N_3NiO_5PRhS_2\cdot 3H_2O$ (964.36): calcd. C 39.85, H 4.08, N 4.36; found C 39.54, H 3.52, N 4.40.

**$UO_2$–$Rh^{I}$ Complex 4:** The monometallic uranyl complex **2** (60.6 mg, 0.070 mmol) was suspended in 9 mL of methanol in a Schlenk tube and stirred at room temperature. A yellow solution of $[RhCl(CO)_2]_2$ (13.6 mg, 0.035 mmol) in 4 mL of methanol was then added with a cannula and the suspension changed into a clear red-orange solution. After 20 min, the infrared analysis of the solution showed an intense absorption at 2015 cm$^{-1}$ and the absence of the bands due to the starting rhodium dimer. A methanolic solution (3 mL) of $NH_4PF_6$ (155 mg) was added to the reaction flask, causing the immediate formation of a red-brown powder. After stirring for a few minutes the precipitate was allowed to settle, then the solution was decanted off. The solid was washed twice with cold methanol and vacuum-dried to give 17 mg of a brown-red powder. A second crop precipitated out of the mother solution upon standing under argon for a few hours (15 mg). Both crops were characterized by an intense infrared absorption at 2015 cm$^{-1}$ in dichloromethane. Yield: 42%. As in the case of complex **3**, this material is moderately air sensitive. FT-IR (dichloromethane): $\tilde{\nu}_{max}$ = 2020 cm$^{-1}$ (s, CO), 1616 (vs, C=N), 1556, 1453; (KBr): $\tilde{\nu}_{max}$ = 2011 cm$^{-1}$ (CO), 1614 (C=N), 1553, 1450, 1400, 1306, 1230, 1085, 997, 890 ($UO_2$), 844, 745, 558. FAB: clusters centered at $m/z$ = 976.7 [$\mathbf{4}^+$] and 949 [$\mathbf{4}^+$ – CO]. $C_{32}H_{33}F_6N_3O_7PRhS_2U$ (1121.7): calcd. C 34.27, H 2.97, N 3.75; found C 34.32, H 3.67, N 3.32.

**Crystal Structure Determination of the Macrocyclic Nickel Complex 1:** The data were collected on a Philips PW1100 diffractometer using Mo-$K_\alpha$ radiation ($\lambda$ = 0.71069 Å), controlled by a local pro-

 © 2006 Wiley-VCH Verlag GmbH & Co. KGaA, Weinheim 

gram.[31] The preliminary cell parameters were obtained from least-squares plots of the ($\theta$,$\chi$,$\varphi$) angular values of 25 reflections ($\theta$ range = 7.3–12.7°) accurately centered on the diffractometer. The intensity of one standard reflection, recorded for every 100, showed a decomposition of about 29%. The recorded data ($\theta$ range = 3–27°) were corrected for this decay, for polarization, and for Lorentz effects. The absorption correction was performed with the method of Walker and Stuart,[32] using a program written by Gluzinski.[33] The low quality of the employed crystal resulted in the low number of observed reflections. The structure was solved by direct methods with SIR97,[34] and refined full-matrix anisotropic least-squares methods with SHELX97.[35] Most of the H atoms were found in a difference Fourier map, and the remainder were put in their theoretical positions, refined by a few cycles with isotropic thermal parameters, and then blocked in the refined positions. The ORTEP drawings were produced with the ORTEP-3 program.[36]

**Crystal Structure Determination of the Macrocyclic Uranyl Complex 2:** The data were collected on a Bruker AXS Smart CCD diffractometer with Mo-$K_\alpha$ radiation ($\lambda$ = 0.71069 Å) ($\theta$ range = 3–29°). Auto-indexing was performed with an algorithm operating on difference vectors derived from the input reflections. During the data collection the specimen decomposed by about 23%. Data reduction, absorption, and decomposition corrections, structure solution and refinement were all performed with the programs contained in SHELXTL-NT V5.1.[37] The small dimensions of the employed crystal and its low quality resulted in a small number of observed reflections. All the non-hydrogen atoms were refined anisotropically. While most of the hydrogen atoms were found in a difference Fourier map, the remainder ones were put in their geometrical positions, refined by a few cycles with isotropic thermal parameters, and then blocked in the refined positions. The hydrogen atoms of the water molecule were not localized. Experimental crystallographic information for both complexes **1** and **2** are reported in Table 3.

Table 3. Selected crystallographic details for complexes **1** and **2**.

| | **1** | **2** |
|---|---|---|
| Formula | $C_{31}H_{33}N_3NiO_4S_2{\cdot}H_2O$ | $C_{31}H_{33}N_3O_6S_2U{\cdot}H_2O$ |
| Formula weight | 652.45 | 863.79 |
| Crystal color | amber | red |
| Crystal shape | prism | prism |
| Size [mm] | 0.29×0.34×0.39 | 0.09×0.15×0.20 |
| Crystal system | monoclinic | monoclinic |
| Space group | $P2_1/c$ | $C2/c$ |
| $a$ [Å] | 15.866(3) | 23.788(2) |
| $b$ [Å] | 11.983(4) | 13.353(1) |
| $c$ [Å] | 16.505(2) | 21.737(2) |
| $\beta$ [°] | 106.98(4) | 112.24(3) |
| Cell volume [Å$^3$] | 3001.17 | 6390.91 |
| $\mu_{calcd.}$ [cm$^{-1}$] | 8.25 | 49.91 |
| Temperature [K] | 293(2) | 293(2) |
| $Z$ | 4 | 8 |
| $h$, $k$, $l$ ranges | –20/19, 0/15, 0/21 | –30/14, –15/16, –28/28 |
| No. collected reflns. | 7085 | 19496 |
| No. indep. reflns. | 6261 | 6843 |
| $R_{int}$ | 0.08 | 0.14 |
| No. reflns. obsd. [$I > 2\sigma(I)$] | 1828 | 2730 |
| Final $R$ factor | 0.067 | 0.058 |
| Final $R_w$ factor | 0.147 | 0.132 |
| GOF | 0.69 | 0.78 |

CCDC-253882 (for **1**) and -253883 (for **2**) contain the supplementary crystallographic data for this paper. These data can be obtained free of charge from The Cambridge Crystallographic Data Center via www.ccdc.cam.ac.uk/data_request/cif.

**Supporting Information** (see footnote on the first page of this article): $^1$H NMR, $^{13}$C NMR, and FT-IR spectra of complexes **1**–**4**. FT-IR spectra of the products of oxidative addition of methyl iodide to complexes **3** and **4**.

## Acknowledgments

We wish to thank Prof. Frank van Veggel for discussions during the early stages of this project, Dr. Valeria van Axel Castelli for many helpful suggestions throughout the work, and Dr. Giovanna Mancini for the 2D NMR measurements. Partial funding from MIUR (projects COFIN1999 "Effetti cooperativi in sistemi organometallici polifunzionali" and COFIN2003 "Effetti cooperativi in nuovi sistemi metallo-ciclopentadienilici polifunzionali") is gratefully acknowledged.

[1] a) F. C. J. M. van Veggel, W. Verboom, D. N. Reinhoudt, *Chem. Rev.* **1994**, *94*, 279; b) D. G. McCollum, B. Bosnich, *Inorg. Chim. Acta* **1998**, *270*, 13; c) V. Arion, M. Revenco, J. Gradinaru, Y. Simonov, V. Kravtsov, N. Gerbeleu, E. Saint-Aman, F. Adams, *Rev. Inorg. Chem.* **2001**, *21*, 1; d) A. Ingham, M. Rodopoulos, K. Coulter, T. Rodopoulos, S. Subramanian, A. McAuley, *Coord. Chem. Rev.* **2002**, *233–234*, 255.

[2] a) P. Braunstein, J. Rose, *Catalysis and Related Reactions with Compounds Containing Heteronuclear Metal–Metal Bonds*, in *Comprehensive Organometallic Chemistry II* (Eds.: E. W. Abel, F. G. A. Stone, G. Wilkinson), Pergamon, Oxford, UK, **1995**, vol. 10, p. 351; b) H. Sasai, T. Arai, Y. Satow, K. N. Houk, M. Shibasaki, *J. Am. Chem. Soc.* **1995**, *117*, 6194; c) E. K. Van Den Beuken, B. L. Feringa, *Tetrahedron* **1998**, *54*, 12985; d) N. D. Jones, B. R. James, *Adv. Synth. Catal.* **2002**, *344*, 1126.

[3] N. V. Gerbeleu, V. B. Arion, J. Burgess, *Template Synthesis of Macrocyclic Compounds*, Wiley-VCH, Weinheim, **1999**, chapter 8.

[4] For example: a) C. O. Dietrich-Buchecker, J. P. Sauvage, *Tetrahedron Lett.* **1983**, *24*, 5091; b) C. J. van Staveren, J. van Eerden, F. C. J. M. van Veggel, S. Harkema, D. N. Reinhoudt, *J. Am. Chem. Soc.* **1988**, *110*, 4994–5008; c) J. E. Kickham, S. J. Loeb, *Inorg. Chem.* **1994**, *33*, 4351.

[5] Reviews: a) J. Nelson, V. Mckee, G. Morgan, *Progr. Inorg. Chem.* (Ed.: K. D. Karlin), John Wiley & Sons, **1998**, vol. 47, p. 167; b) S. Brooker, *Eur. J. Inorg. Chem.* **2002**, 2535; c) P. A. Vigato, S. Tamburini, *Coord. Chem. Rev.* **2004**, *248*, 1717; d) B. Kersting, *Z. Anorg. Allg. Chem.* **2004**, *630*, 765; e) G. Ferraudi, J. C. Canales, B. Kharizov, J. Costamagna, J. G. Zagal, G. Cardenas-Jirón, M. Paez, *J. Coord. Chem.* **2005**, *58*, 89. For specific examples, see: f) N. H. Pilkington, R. Robson, *Aust. J. Chem.* **1970**, *23*, 2225; g) P. D. Beer, J. E. Nation, M. E. Harman, M. B. Hursthouse, *J. Organomet. Chem.* **1992**, *441*, 465; h) S. Guo, D. E. Fenton, *Inorg. Chim. Acta* **1994**, *223*, 169; i) J.-M. Kern, J. P. Sauvage, J.-L. Weidmann, N. Armaroli, L. Flamigni, P. Ceroni, V. Balzani, *Inorg. Chem.* **1997**, *36*, 5329; j) S. R. Korupoju, N. Mangayarkarasi, S. Ameerunisha, E. J. Valente, P. S. Zacharias, *J. Chem. Soc., Dalton Trans.* **2000**, 2845; k) P. L. Arnold, A. J. Blake, C. Wilson, J. B. Love, *Inorg. Chem.* **2004**, *43*, 8206; l) J. B. Fontecha, S. Goetz, V. McKee, *Dalton Trans.* **2005**, 923.

[6] a) B. F. Hoskins, R. Robson, G. A. Williams, *Inorg. Chim. Acta* **1976**, *16*, 121; b) K. D. Matthews, R. A. Fairman, A. Johnson, K. V. N. Spence, I. A. Kahwa, G. L. McPherson, H. Robotham, *J. Chem. Soc., Dalton Trans.* **1993**, 1719; c) H. Okawa,

 © 2006 Wiley-VCH Verlag GmbH & Co. KGaA, Weinheim 

H. Furutachi, D. E. Fenton, *Coord. Chem. Rev.* **1998**, *174*, 51; d) J. Lisowski, *Inorg. Chim. Acta* **1999**, *285*, 233; e) T. K. Ronson, J. Nelson, G. B. Jameson, J. C. Jeffery, S. Brooker, *Eur. J. Inorg. Chem.* **2004**, 2570.

[7] a) L. Wei, A. Bell, S. Warner, I. D. Williams, S. J. Lippard, *J. Am. Chem. Soc.* **1986**, *108*, 8302; b) J.-C. Chambron, J. P. Sauvage, *Tetrahedron* **1987**, *43*, 895; c) A. R. van Doorn, D. J. Rushton, W. F. van Straaten-Nijenhuis, W. Verboom, D. N. Reinhoudt, *Recl. Trav. Chim. Pays-Bas* **1992**, *111*, 421; d) A. Bashall, M. McPartlin, B. P. Murphy, H. R. Powell, S. Waikar, *J. Chem. Soc., Dalton Trans.* **1994**, 1383; e) S. Brooker, T. J. Simpson, *J. Chem. Soc., Dalton Trans.* **1998**, 1151.

[8] J. W. Canary, B. C. Gibb, *Prog. Inorg. Chem.* (Ed.: K. D. Karlin), John Wiley & Sons, **1997**, vol. 45, p. 1.

[9] a) U. Casellato, D. Fregona, S. Sitran, S. Tamburini, P. A. Vigato, *Inorg. Chim. Acta* **1986**, *119*, 215; b) H. Ōkawa, J. Nishio, M. Ohba, M. Tadokoro, N. Matsumoto, M. Koikawa, S. Kida, D. E. Fenton, *Inorg. Chem.* **1993**, *32*, 2949; c) D. G. McCollum, G. P. A. Yap, A. L. Rheingold, B. Bosnich, *J. Am. Chem. Soc.* **1996**, *118*, 1365; d) T. A. Zevaco, H. Görls, E. Dinjus, *Polyhedron* **1998**, *17*, 613; e) M. Yonemura, K. Arimura, K. Inoue, N. Usuki, M. Ohba, H. Ōkawa, *Inorg. Chem.* **2002**, *41*, 582; f) I. Yoon, M. Goto, T. Shimizu, S. S. Lee, M. Asakawa, *Dalton Trans.* **2004**, 1513.

[10] a) M. D. Hobday, T. D. Smith, *Coord. Chem. Rev.* **1973**, *9*, 311; b) J. Costamagna, J. Vargas, R. Latorre, A. Alvarado, G. Mena, *Coord. Chem. Rev.* **1992**, *119*, 67. Although the term salen refers to the *N*,*N*′-bis(salicylidene)-1,2-ethylenediimine ligand, it is used in this manuscript to apply to bis(salicylaldimine)ligands in general.

[11] a) A. Dalla Cort, J. I. M. Murua, C. Pasquini, M. Pons, L. Schiaffino, *Chem. Eur. J.* **2004**, *10*, 3301; b) M. Cametti, M. Nissinen, A. Dalla Cort, L. Mandolini, K. Rissanen, *Chem. Commun.* **2003**, 2420; c) F. C. J. M. van Veggel, H. G. Noorlander Bunt, W. L. Jorgensen, D. N. Reinhoudt, *J. Org. Chem.* **1998**, *63*, 3554, and references cited therein; d) A. R. van Doorn, M. Bos, S. Harkema, J. van Heerden, W. Verboom, D. N. Reinhoudt, *J. Org. Chem.* **1991**, *56*, 2371–2380.

[12] a) R. A. Johnson, K. B. Sharpless, *Catalytic Asymmetric Synthesis* (Ed.: I. Ojima), VCH, Weinheim, **1993**, p. 103; b) M. S. Sigman, N. E. Jacobsen, *J. Am. Chem. Soc.* **1998**, *120*, 5315; c) Y. N. Belokon, S. Caveda-Cepas, B. Green, N. S. Ikonnikov, V. N. Khrustalev, V. S. Larichev, M. A. Moscalenko, M. North, C. Orizu, V. I. Tararov, M. Tasinazzo, G. I. Timofeeva, L. V. Yashkina, *J. Am. Chem. Soc.* **1999**, *121*, 3968; d) T. Takeda, R. Irie, Y. Shinoda, T. Katsuki, *Synlett* **1999**, 1157; e) J. M. Ready, E. N. Jacobsen, *Angew. Chem. Int. Ed.* **2002**, *41*, 1374.

[13] a) V. van Axel Castelli, A. Dalla Cort, L. Mandolini, D. N. Reinhoudt, *J. Am. Chem. Soc.* **1998**, *120*, 12688; b) N. C. Gianneschi, P. A. Bertin, S. T. Nguyen, C. A. Mirkin, L. N. Zakharov, A. L. Rheingold, *J. Am. Chem. Soc.* **2003**, *125*, 10508; c) D. J. Darensbourg, R. M. Mackiewicz, A. L. Phelps, D. R. Billodeaux, *Acc. Chem. Res.* **2004**, *37*, 836–844.

[14] a) G. Weber, *Inorg. Chim. Acta* **1982**, *58*, 27; b) E. C. Constable, J. Lewis, V. E. Marquez, P. R. Raithby, *J. Chem. Soc., Dalton Trans.* **1986**, 1747; c) F. Teixidor, L. Escriche, I. Rodriguez, J. Casabò, J. Rius, E. Molins, B. Martinez, C. Miravitlles, *J. Chem. Soc., Dalton Trans.* **1989**, 1381; d) L. Escriche, M. Sanz, J. Casabò, F. Teixidor, E. Molins, C. Miravitlles, *J. Chem. Soc., Dalton Trans.* **1989**, 1739.

[15] a) D. Parker, J.-M. Lehn, J. Rimmer, *J. Chem. Soc., Dalton Trans.* **1985**, 1517; b) A. Carroy, J.-M. Lehn, *J. Chem. Soc., Chem. Commun.* **1986**, 1232; c) I. M. Helps, K. E. Matthes, D. Parker, G. Ferguson, *J. Chem. Soc., Dalton Trans.* **1989**, 915; d) E. C. Constable, A. C. King, P. R. Raithby, *Polyhedron* **1998**, *17*, 4275.

[16] a) P. M. Maitlis, A. Haynes, G. J. Sunley, M. J. Howard, *J. Chem. Soc., Dalton Trans.* **1996**, 2187; b) A. Roodt, G. J. J. Steyn, *Rec. Dev. Inorg. Chem.* **2000**, *2*, 1; c) L. Cavallo, M. Solà, *J. Am. Chem. Soc.* **2001**, *123*, 12294; d) L. Gonsalvi, H. Adams, G. J. Sunley, E. Ditzel, A. Haynes, *J. Am. Chem. Soc.* **2002**, *124*, 13597; e) V. Chauby, J.-C. Daran, C. Serra-Le Berre, F. Malbosc, P. Kalck, O. Delgado Gonzales, C. E. Haslam, A. Haynes, *Inorg. Chem.* **2002**, *41*, 3280; f) L. Gonsalvi, J. A. Gaunt, H. Adams, A. Castro, G. J. Sunley, A. Haynes, *Organometallics* **2003**, *22*, 1047.

[17] For example: a) N. Wheatley, P. Kalck, *Chem. Rev.* **1999**, *99*, 3379; b) S. E. Watkins, D. C. Craig, S. B. Colbran, *J. Chem. Soc., Dalton Trans.* **2002**, 2423; c) M. A. A. F. Hernandez-Gruel, J. J. Perez-Torrente, M. A. Ciriano, A. B. Rivas, F. J. Lahoz, I. T. Dobrinovitch, L. A. Oro, *Organometallics* **2003**, *22*, 1237; d) M. Pizzotti, R. Ugo, C. Dragonetti, E. Annoni, F. Demartin, P. Mussini, *Organometallics* **2003**, *22*, 4001; e) R. Fandos, C. Hernandez, A. Otero, A. Rodriguez, M. J. Ruiz, P. Terreros, *Chem. Eur. J.* **2003**, *9*, 671.

[18] a) J. P. Collman, R. G. Finke, J. N. Cawse, J. I. Brauman, *J. Am. Chem. Soc.* **1978**, *100*, 4766; b) S. B. Butts, S. H. Strauss, E. M. Holt, R. E. Stimson, N. W. Alcock, D. F. Shriver, *J. Am. Chem. Soc.* **1980**, *102*, 5093; c) T. G. Richmond, F. Basolo, D. F. Shriver, *Inorg. Chem.* **1982**, *21*, 1272; d) S. J. La Croce, A. L. Cutler, *J. Am. Chem. Soc.* **1982**, *104*, 2312; e) J. Powell, M. Gregg, A. Kuksis, P. Meindl, *J. Am. Chem. Soc.* **1983**, *105*, 1064–1065; f) T. C. Forschner, A. R. Cutler, *Organometallics* **1985**, *4*, 4015; g) P. Y. Zheng, T. T. Nadasdi, D. G. Stephan, *Organometallics* **1989**, *8*, 1393; h) M. A. Casado, J. J. Pérez-Torrente, M. A. Ciriano, L. A. Oro, A. Orejón, C. Claver, *Organometallics* **1999**, *18*, 3035; i) F. Burgos, I. Chávez, J. M. Manriquez, M. Valderrama, *Organometallics* **2001**, *20*, 1287; j) J. N. L. Dennett, J. Jacke, G. Nilsson, A. Rosborough, M. J. Ferguson, M. Wang, R. McDonald, J. Takats, *Organometallics* **2004**, *23*, 4478.

[19] A. R. van Doorn, R. Schaafstra, M. Bos, S. Harkema, J. van Heerden, W. Verboom, D. N. Reinhoudt, *J. Org. Chem.* **1991**, *56*, 6083.

[20] V. van Axel Castelli, R. Cacciapaglia, G. Chiosis, F. C. J. M. van Veggel, L. Mandolini, D. N. Reinhoudt, *Inorg. Chim. Acta* **1996**, *246*, 181.

[21] H. J. J. B. Martel, S. McMahon, M. Rasmussen, *Aust. J. Chem.* **1979**, *32*, 1241.

[22] F. C. J. M. van Veggel, M. Bos, S. Harkema, H. van de Bovenkamp, W. Verboom, J. Reedijk, D. N. Reinhoudt, *J. Org. Chem.* **1991**, *56*, 225.

[23] A. R. van Doorn, W. Verboom, S. Harkema, D. N. Reinhoudt, *Synthesis* **1992**, 119.

[24] Z. Li, C. Jablonski, *Inorg. Chem.* **2000**, *39*, 2456.

[25] R. J. Janssen, J. H. P. Utley, E. Carré, E. Simon, H. Schirmer, *J. Chem. Soc., Perkin Trans. 2* **2000**, 1573.

[26] S. M. Lacy, D. M. Rudkevich, W. Verboom, D. N. Rheinhoudt, *J. Chem. Soc., Perkin Trans. 2* **1995**, 135.

[27] V. Annamalai, E. F. DiMauro, P. J. Carroll, M. C. Kozlowski, *J. Org. Chem.* **2003**, *68*, 1973.

[28] D. M. Rudkevich, W. Verboom, Z. Brzozka, M. J. Palys, W. P. R. V. Stauthamer, G. J. van Hummel, S. M. Franken, S. Harkema, J. F. J. Engbersen, D. N. Reinhoudt, *J. Am. Chem. Soc.* **1994**, *116*, 4341.

[29] a) M. Bassetti, A. Capone, L. Mastrofrancesco, M. Salamone, *Organometallics* **2003**, *22*, 2535; b) M. Bassetti, A. Capone, M. Salamone, *Organometallics* **2004**, *23*, 247.

[30] a) E. W. Abel, D. Ellis, K. G. Orrell, *J. Chem. Soc., Dalton Trans.* **1992**, 2243; b) E. W. Abel, K. G. Orrell, M. C. Poole, V. Šik, *Polyhedron* **1999**, *18*, 1345.

[31] D. Belletti, *FEBO, A New Hardware and Software System for Controlling a Philips PW1100 Single Crystal Diffractometer*, **1996**, Internal Report 1-96, Centro di Studio per la Strutturistica Diffrattometrica del CNR, Parma, Italy.

[32] N. Walker, D. Stuart, *Acta Crystallogr., Sect. A* **1983**, *39*, 158.

[33] P. Gluzinski, *Set of Programs for X-ray Structural Calculation*, **1989**; IChO, Polish Academy of Sciences, Warszawa, Poland.

 © 2006 Wiley-VCH Verlag GmbH & Co. KGaA, Weinheim 

[34] A. Altomare, M. C. Burla, M. Camalli, G. Cascarano, C. Giacovazzo, A. Guagliardi, A. G. G. Moliterni, G. Polidori, R. Spagna, *Acta Crystallogr.* **1999**, *32*, 115.
[35] G. M. Sheldrick, *SHELX97 Program for Crystal Structure Solution and Refinement*, University of Göttingen, Germany, **1997**.
[36] L. J. Farrugia, *ORTEP-3 for Windows*, **1999**, University of Glasgow, Scotland, UK.
[37] Bruker Axs Inc., 6300 Enterprise Lane, Madison, WI 53719-1173, USA, **1999**.

Received: August 4, 2005
Published Online: January 9, 2006

 © 2006 Wiley-VCH Verlag GmbH & Co. KGaA, Weinheim 

DOI: 10.1002/ejic.200500725

# Synthesis and Structural Characterisation of Palladium and Group-12 Metal Complexes with a Hybrid Phosphanylphosphonate Ferrocene Ligand

**Petr Štěpnička,*[a] Ivana Císařová,[a] and Róbert Gyepes[a]**

**Keywords:** Group 12 metals / Phosphanes / Phosphonate esters / Palladium / Sandwich complexes / Structure eluicidation

Diethyl [1′-(diphenylphosphanyl)ferrocenyl]phosphonate (**1**) was synthesised by stepwise metallation/functionalisation of 1,1′-dibromoferrocene and studied as a ligand for palladium(II) and group-12 metals. Treatment of $[PdCl_2(cod)]$ (cod = $\eta^2$:$\eta^2$-cycloocta-1,5-diene) with **1** in 1:1 or 1:2 molar ratios gave, respectively, the dinuclear, chloride-bridged complex $[\{Pd(\mu\text{-}Cl)Cl(\mathbf{1}\text{-}\kappa P^2)\}_2]$ (**2**) and the mononuclear complex *trans*-$[PdCl_2(\mathbf{1}\text{-}\kappa P^2)_2]$ (**3**), where **1** coordinates exclusively through the phosphane function. The reactions between **1** and group-12 metal bromides $MBr_2$ in a 1:1 molar ratio gave the adducts $[MBr_2(\mathbf{1})]$ [M = Zn (**4**), Cd (**5**), and Hg (**6**)], whose crystal structures change considerably with the metal ion. Thus, whereas **4** is a molecular complex with **1** coordinating as an $O^1,P^2$-chelate, its cadmium(II) analogue is a polymer built up from symmetric $\{CdBr(\mu\text{-}Br)\}_2$ units interconnected by pairs of $O^1,P^2$-bridging phosphanylphosphonate ligands. Finally, the mercury(II) complex **6** is a halide-bridged dimer, $[\{Hg(\mu\text{-}Br)Br(\mathbf{1}\text{-}\kappa P^2)\}_2]$. However, this compound is structurally fluxional in solution (NMR spectra) and, in the crystal, it attains a structure similar to **5** owing to weak interactions between mercury and phosphonate-$O^1$ atoms from adjacent molecules. An isomer to **6**, $[\{HgBr_2(\mathbf{1}\text{-}\kappa^2 O^1,P^2)\}_2]$ (**7**), was isolated from attempted alkylation of **6** and structurally characterised as a dimer, where ligands **1** bridge two $\{HgBr_2\}$ units. All compounds were studied by spectroscopic methods (IR, NMR, mass) and the solid-state structures of **1**, **2**·½$H_2O$, **3**·4 $CHCl_3$, **4**, **5**, **6**·5 $C_6H_6$, and **7** have been determined by single-crystal X-ray diffraction.
(© Wiley-VCH Verlag GmbH & Co. KGaA, 69451 Weinheim, Germany, 2006)

## Introduction

Ferrocene donors have attracted considerable attention as valuable ligands for coordination compounds and catalytic applications. Among the numerous multidentate ferrocene donors that have been synthesised during the last few decades, chiral, mixed-donor (typically PN) ligands derived from a 1,2-disubstituted ferrocene backbone have proved to be particularly successful.[1] In contrast, the related unsymmetrical, 1,1′-disubstituted ferrocene derivatives have been studied much less.[2] This applies particularly to donors whose asymmetry arises from the presence of two different phosphorus groups. To date only a few ferrocene diphosphanes $Ph_2PfcPR_2$ {fc = ferrocene-1,1′-diyl; $PR_2$ = PPh(*t*Bu),[3] P(*t*Bu)$_2$,[4] and $P(C_6H_4Y\text{-}4)_2$, Y = OMe, $CF_3$[5]}, phosphanylphosphonites $Ph_2PfcP(OR)_2$,[6] and dppf semi-chalcogenides $Ph_2PfcP(E)R_2$ (E = O,[7] S, and Se[8]) have been reported in the literature, which stands markedly against the vast chemistry of the "popular", symmetric ferrocene diphosphane 1,1′-bis(diphenylphosphanyl)-ferrocene (dppf).[9]

Recent interest in the synthesis and coordination chemistry of ferrocene phosphonate esters and acids[10] led us to design the ferrocene phosphanylphosphonate ligand $Ph_2PfcP(O)(OEt)_2$ (**1**) and study its coordination behaviour. In this contribution, we report the synthesis, characterisation and structures of this ligand and its complexes with palladium(II) and group-12 metals. It should be noted that compound **1** was reported as an intermediate in the synthesis of diphosphanes $Ph_2PfcPH_2$ and $Ph_2PfcPR_2$ [$PR_2$ = (*R*,*R*)-2,5-dimethylphospholan-1-yl] while this work was in progress.[11] However, no investigation into its donor properties was mentioned.

## Results and Discussion

Diethyl [1′-(diphenylphosphanyl)ferrocenyl]phosphonate (**1**) was prepared by lithiation of 1-bromo-1′-(diphenylphosphanyl)ferrocene followed by addition of diethyl chlorophosphate to the formed lithio intermediate, using the general methodology developed by Butler et al.[7a] Subsequent chromatography of the crude product contaminated with (diphenylphosphanyl)ferrocene and some other minor impurities on alumina furnished a good yield of pure **1** as an amber oil, which slowly crystallised upon standing at room temperature (faster at +4 °C) to give an orange, waxy solid. The compound was characterised by standard spectroscopic methods and its structure determined by X-ray diffraction analysis (see Figure 1 and the section dealing with the crystal structures below). It was then studied as a ligand in palladium(II) and group-12 metal complexes.

[a] Department of Inorganic Chemistry, Faculty of Science, Charles University,
Hlavova 2030, 12840 Prague, Czech Republic
E-mail: stepnic@natur.cuni.cz
Supporting information for this article is available on the WWW under http://www.eurjic.org or from the author.

 © 2006 Wiley-VCH Verlag GmbH & Co. KGaA, Weinheim 

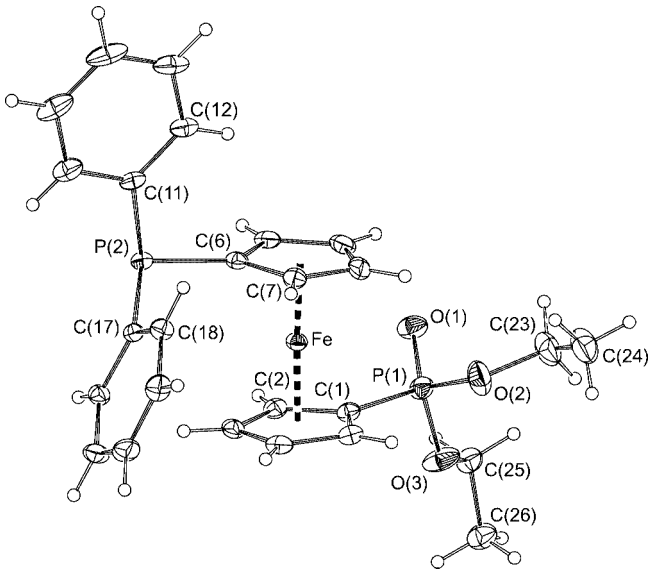


Figure 1. Molecular structure of **1** showing the atom-labelling scheme; for the consecutively numbered ring atoms, only labels of the pivotal atom and its adjacent ring carbon atoms are shown for clarity (note: the atom-numbering scheme adopted for the ligand moieties in all complexes is similar). Displacement ellipsoids are scaled to the 30% probability level. Selected distances [Å] and angles [°]: Fe–Cg(1) 1.6488(9), Fe–Cg(2) 177.00(5), P(1)–O(1) 1.467(2), P(1)–O(2) 1.587(2), P(1)–O(3) 1.572(2), P(1)–C(1) 1.761(2), P(2)–C(6) 1.813(2), P(2)–C(11) 1.838(2), P(2)–C(17) 1.831(2); Cg(1)–Fe–Cg(2) 177.00(5), range of O–P(1)–O angles 105.9(1)–115.7(1), range of C(1)–P(1)–O angles 98.59(9)–117.7(1), range of C–P(2)–C angles: 100.88(9)–102.13(8), ∠ Cp1,Cp2 4.5(1)°, $\tau$[C(1)–Cg(1)–Cg(2)–C(6)] = 155.2(1)°; Cg(1) and Cg(2) are the centroids of the cyclopentadienyl rings C(1–5) (Cp1) and C(6–10) (Cp2), respectively.

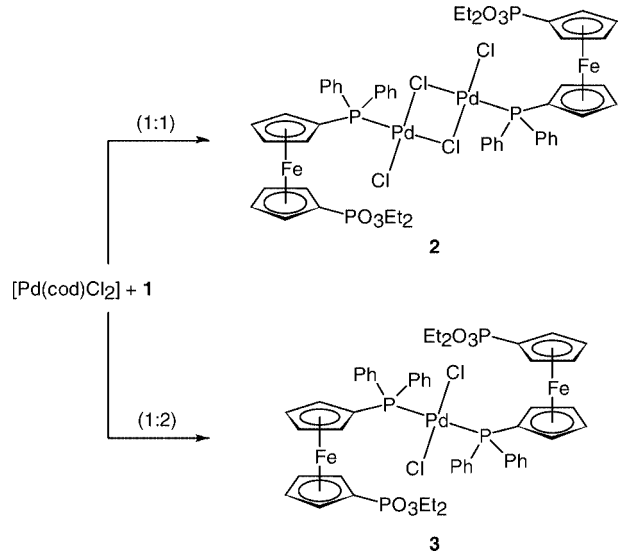


Scheme 1.

## Palladium(II) Complexes

Depending on the stoichiometry, the reaction of [Pd(cod)$Cl_2$] (cod = $\eta^2$:$\eta^2$-cycloocta-1,5-diene) with **1** gives either the chloride-bridged dipalladium(II) complex *trans*-[{Pd(μ-Cl)Cl(**1**-κ$P^2$)}$_2$] (**2**) or the bis(phosphane) complex *trans*-[$PdCl_2$(**1**-κ$P^2$)$_2$] (**3**; Scheme 1). Attempted removal of the chloride ligands from **3** by treatment with $AgClO_4$ gave an intractable, dark-red, oily residue that shows broad signals in the NMR spectra.

The reaction in a 1:1 molar ratio in methanol produced a dark-red, crystalline solid, which was structurally characterised as *trans*-[{Pd(μ-Cl)Cl(**1**-κ$P^2$)}$_2$] (**2**). The spectroscopic data for **2** give no clear signs about the coordination mode of the phosphanylphosphonate ligand and do not allow us to distinguish between two possible isomeric forms, namely **2** and [$PdCl_2$(**1**-κ$^2O^1$,$P^2$)]. For instance, the $^1$H NMR spectra exhibit markedly downfield-shifted ferrocene signals (as compared to **1** and **3**) but practically unaffected signals for the ethoxy groups [$\Delta\delta_H(CH_2) \approx +0.03$ ppm] whilst the $^{31}$P NMR spectra show two distinct signals at $\delta_P$ = 24.6 and 31.1 ppm due to the phosphonate and phosphanyl groups, respectively {coordination shifts [$\Delta\delta_P$ = $\delta_P$(complex) – $\delta_P$(ligand)] of 48.1 ($P^{III}$) and –1.1 ppm ($P^V$), recorded in $CDCl_3$}.

More information about the structure of **2** was obtained from the far-IR spectrum, which contains a strong band at 356 cm$^{-1}$ (with shoulder at 350 cm$^{-1}$), and several bands at 249–256 cm$^{-1}$ attributable to ν(PdCl) stretching vibrations involving the terminal and bridging chloride ligands, respectively. An unambiguous proof of the compound structure came from the X-ray diffraction analysis (Figure 2). Crystals amenable to the diffraction analysis were obtained directly from the reaction mixture. However, since the poor quality of the available crystals (disorder of the phosphonate group and crystal defects) resulted in a relatively low overall quality of the structural data, only the most important structural features will be addressed here.[12]

The structure determination for **2** revealed a doubly halide-bridged dimeric structure with a *sym-trans* geometry. Remarkably, the dihedral angle subtended by the {$PdCl_2P$} least-squares planes is as high as 40.91(5)°, which is rather uncommon for compounds of this type. A search in the Cambridge crystallographic database[13] revealed that the observed tilting of the coordination planes is among the highest observed.[14] As expected, the Pd–Cl bonds to terminal chlorides (2.27 Å) are significantly shorter than those to bridging ones (2.33–2.44 Å). The Pd–P bonds in **2** are about 0.12 Å shorter than those in **3** (see below), which can be ascribed to a lower *trans* influence of the chloride ligand in comparison with the phosphane donor, and possibly also to a less sterically strained structure of **2** where the two bulky phosphanylphosphonate ligands are separated by the Pd(μ-Cl)$_2$Pd core.

For complex **3**, which is formed at a 2:1 ligand-to-metal ratio, the exclusive P-coordination of **1** is clearly manifested by a considerable shift to lower fields for the phosphanyl signal and practically unaffected phosphonate resonance [$\Delta\delta_P(P^{III})$ = 32.3 ppm/$\Delta\delta_P(P^V)$ = –0.6 ppm]. The $^{31}$P coordination shifts for the palladium complexes reflect a relatively higher *trans* influence of the phosphane donor (see also

 © 2006 Wiley-VCH Verlag GmbH & Co. KGaA, Weinheim 

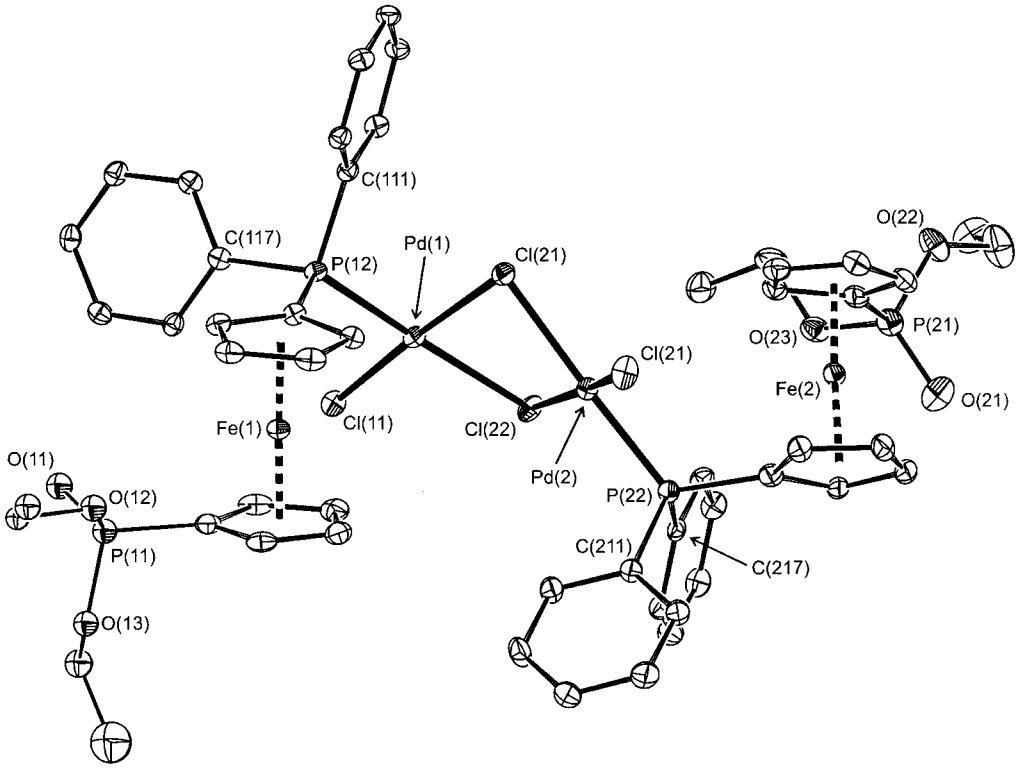


Figure 2. A view of the structure of complex **2** as determined for the solvate **2**·½$H_2O$. For clarity, the solvating water molecule and hydrogen atoms have been omitted and only one orientation of the disordered phosphonate group [the group involving the P(11) atom] is shown. Displacement ellipsoids are drawn at the 20% probability level. The atom-numbering scheme is analogous to that of **1**; the first digit is added to distinguish the symmetrically independent molecular parts. Selected distances [Å] and angles [°]: Pd(1)–Cl(11) 2.273(2), Pd(1)–Cl(12) 2.329(2), Pd(1)–Cl(22) 2.443(2), Pd(1)–P(12) 2.229(2), Pd(2)–Cl(21) 2.273(2), Pd(2)–Cl(12) 2.415(2), Pd(2)–Cl(22) 2.325(2), Pd(2)–P(22) 2.227(2); Cl(11)–Pd(1)–Cl(22) 92.48(5), Cl(11)–Pd(1)–P(12) 93.54(6), Cl(12)–Pd(1)–Cl(22) 83.88(5), Cl(12)–Pd(1)–P(12) 90.06(6), Cl(12)–Pd(2)–Cl(21) 91.70(6), Cl(12)–Pd(2)–Cl(22) 84.58(6), Cl(21)–Pd(2)–P(22) 88.19(7), Cl(22)–Pd(2)–P(22) 95.85(6), Pd(1)–Cl(12)–Pd(2) 89.50(6), Pd(1)–Cl(12)–Pd(2) 88.92(5).

above), which causes the $^{31}P$ NMR resonance to shift to higher field.[16] Simple phosphanes behave similarly; see, for instance, the pair of related complexes *trans*-[{Pd(μ-Cl)-Cl(L)}$_2$] ($\Delta\delta_P$ = 39.5 ppm) and *trans*-[$PdCl_2L_2$] ($\Delta\delta_P$ = 29.4 ppm), where L is tri-*p*-tolylphosphane.[15]

The $^1H$ NMR spectra of **3** spectra exhibit a shift to lower field for all ferrocene signals but virtually no change for the phosphonate ethoxy groups. The $^{13}C$ NMR spectrum displays resonances due to the carbon atoms at the phosphanyl-substituted cyclopentadienyl and phenyl rings as virtually coupled triplets arising from ABX spin systems [$^{12}C$-$^{31}P(A)$-(metal)-$^{31}P(B)$-$^{13}C(X)$] with relatively large $J_{A,B}$ values.[16] Very similar features have been observed for the related complex with P-monodentate 1′-(diphenylphosphanyl)ferrocenecarboxylic acid (Hdpf), *trans*-[$PdCl_2$(Hdpf-κ*P*)$_2$].[17] The solid-state structure of the solvate **3**·4$CHCl_3$ was determined by single-crystal X-ray diffraction analysis (see below).

### Group-12 Metal Complexes

Mixing the phosphanylphosphonate **1** with bromides of divalent group-12 metals in a 1:1 molar ratio in acetone and subsequent crystallisation by diffusion of diethyl ether vapour gave adducts [$MBr_2$(**1**)] [M = Zn (**4**), Cd (**5**), and Hg (**6**)] as air-stable, yellow-orange, crystalline solids.[18] However, the exact formulation for these compounds as based on spectral evidence and crystallographic data (see below) is rather complex and differs for all the members of the series. Thus, whereas compound **4** is a monomeric tetrahedral complex featuring **1** as an *O*,*P*-chelating donor, [$ZnBr_2$(**1**-κ$^2O^1$,$P^2$)], its cadmium analogue is a coordination polymer in which dinuclear {Cd(μ-Br)Br}$_2$ units are linked into infinite chains by means of symmetric pairs of the $O^1$,$P^2$-bridging phosphanylphosphonate ligands (see Scheme 2). This is reflected also by the very poor solubility of **5** compared to the well soluble **4** and **6**.

The $^{31}P$ NMR spectrum of **4** is clearly indicative of *O*,*P*-chelate coordination by showing a pair of doublets at $\delta_P$ = –19.9 and 26.1 ppm ($^3J_{P,P}$ = 5 Hz) assignable to the mutually coupled phosphane and phosphonate phosphorus atoms, respectively. The coordination shifts ($\Delta\delta_P$) of –2.9 ($P^{III}$) and +0.4 ($P^V$) ppm correspond favourably with the shifts observed for [$ZnCl_2$L] complexes with *P*,*P*′-chelating symmetric ferrocene diphosphanes [L/$\Delta\delta_P$ = dppf/–4.5 ppm,[19] and dippf/–6.6 ppm; dippf = 1,1′-bis(diisopropylphosphanyl)ferrocene],[20] and a complex containing two $O^1$-monodentate diethyl ferrocenylphosphonate ligands,

 © 2006 Wiley-VCH Verlag GmbH & Co. KGaA, Weinheim 

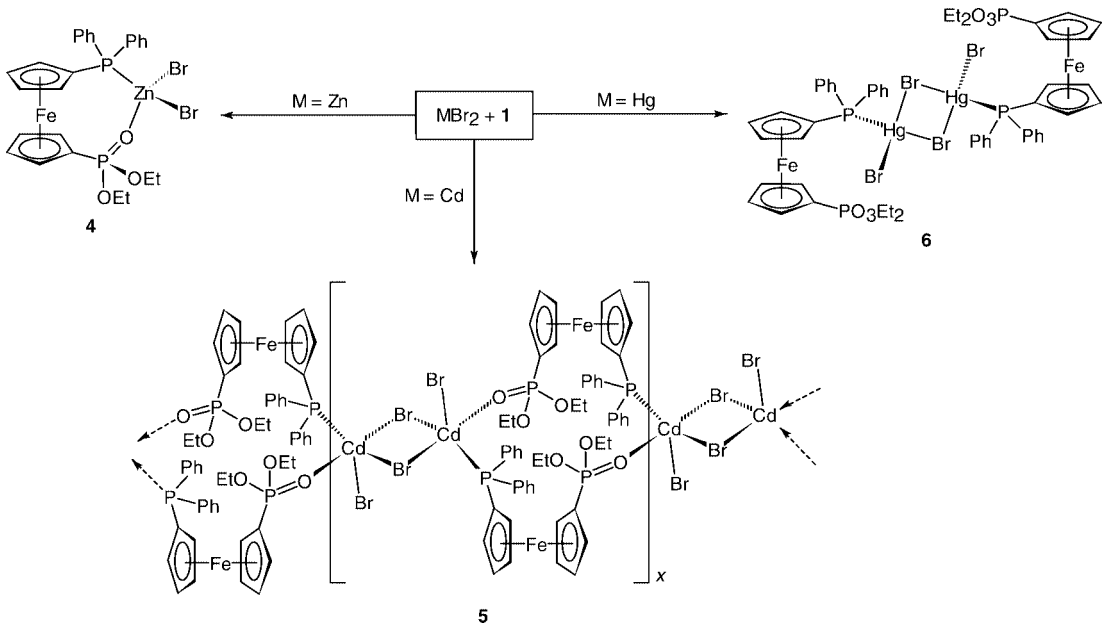


Scheme 2. Schematic drawing of structures of the products arising from group-12 metal dibromides and **1**. For compound **5**, the arrows indicate where propagation of the one-dimensional infinite polymeric chain occurs.

$[ZnCl_2\{FcPO_3Et_2\text{-}\kappa O^1\}_2]$ ($\Delta\delta_P$ = +0.7 ppm in $CD_3OD$, Fc = ferrocenyl).[10c] Furthermore, the coordination of the phosphonate group is manifested by a shift of the multiplet due to the $OCH_2$ protons by about 0.3 ppm to lower field in the $^1H$ NMR spectrum.

The IR spectra of **4** and **5** in the region down to about 300 $cm^{-1}$ exhibit mostly bands due to the ligand; useful information about the coordination geometry is provided by the far-IR region. In the case of **4**, two bands attributable to symmetric and antisymmetric ν(ZnBr) stretching vibrations are observed at 219 and 251–254 $cm^{-1}$, respectively, close to the values reported for $[ZnBr_2(PPh_3)_2]$ (236 and 205 $cm^{-1}$).[21] The far-IR spectrum of **5** exhibits a pair of bands as well (at 193 and 158 $cm^{-1}$). The positions of these bands assignable to ν(CdBr) stretching vibrations involving terminal and bridging bromide atoms correspond to those of the binuclear, halide-bridged complex $[\{Cd(\mu\text{-}Br)Br(PCy_3)\}_2]$, which, however, features only tetracoordinate cadmium centres (208 and 169–144 $cm^{-1}$).[22] Notably, the ν(ZnBr)/ν(CdBr) ratios for the band pairs (1.31 and 1.39) correspond well to the expected value obtained from the mass factor: $[A_r(Cd)/A_r(Zn)]^{1/2} \approx 1.31$.

As revealed by X-ray analysis, compound **6** is a symmetric, halide-bridged dimer with the ligand coordinating as a simple phosphane: $[\{Hg(\mu\text{-}Br)Br(\mathbf{1}\text{-}\kappa P^2)\}_2]$ (Scheme 2). The solution NMR spectroscopic data, particularly the relatively large $^1J_{Hg,P}$ coupling constant and the coordination shift $\Delta\delta_P(P^{III})$ of 41.4 ppm, indicate that this structure is most likely retained in solution (cf. the parameters for $[HgBr_2(PPh_3)_2]$ ($^1J_{Hg,P}$ = 4240 Hz/$\Delta\delta_P$ = 27.3 ppm) and $[\{Hg(\mu\text{-}Br)Br(PPh_3)\}_2]$ ($^1J_{Hg,P}$ = 6450 Hz/$\Delta\delta_P$ = 32.6 ppm) recorded in $CDCl_3/CH_2Cl_2$, 1:1[23]). However, a detailed NMR study revealed a fluxional behaviour in solution: the spectra of **6** change with temperature, solvent and also with the sample concentration (see Table 1 and Figures S1 and S2 in the Supporting Information). Upon raising the sample temperature, the signal due to the phosphane group ($P^{III}$) in the $^{31}P$ NMR spectrum shifts to lower fields while the coupling to $^{199}Hg$ increases. In contrast, the phosphonate resonance moves upfield with increasing temperature. In the $^1H$ NMR spectrum the major change occurs in the region of the ferrocene cyclopentadienyl resonances: the signals due to the phosphonate ethoxy groups exhibit practically constant chemical shifts (note that the multiplet of the methylene group is not entirely invariant as it becomes better resolved at *higher* temperatures).

Table 1. Variable temperature (VT) $^{31}P\{^1H\}$ NMR spectroscopic data for **6**.[a]

| *T* [°C] | $\delta(P^V)$ [ppm] | $\delta(P^{III})$ [ppm] | $^1J_{Hg,P^{III}}$ [Hz] |
|---|---|---|---|
| +50 | 23.73 | – | –[b] |
| +25 | 23.88 | 24.38 | 6587 |
| 0 | 24.06 | 23.69 | 6702 |
| –25 | 24.22 | 23.52 | 6809 |
| –50 | 24.35 | 23.02 | 6908 |
| +25[c] | 23.88 | 24.56 | 6560 |

[a] The spectra were recorded for a 0.036 M solution in $CDCl_3$. The VT $^1H$ and $^{31}P\{^1H\}$ NMR spectra are available as Supporting Information (see Figures S1 and S2, respectively). Reference data for **1**: $\delta_P$ = –17.0 ($P^{III}$) and 25.7 ppm ($P^V$) (in $CDCl_3$ at 25 °C). [b] Not detected due to signal broadening. [c] Data for a 0.018 M solution.

These spectral characteristics resemble in some respects the solution behaviour of the phosphane complexes $[HgX_2(PR_3)_2]$,[23] and are clearly indicative of structural fluxionality. Considering the NMR and structural data (see below), as well as the donor ability of the ligand, the dynamic processes occurring in solutions of $[HgBr_2(\mathbf{1})]$ may

 © 2006 Wiley-VCH Verlag GmbH & Co. KGaA, Weinheim 

be formulated as shown in Scheme 3. One may expect the hybrid donor **1** to coordinate to the soft mercury atom more strongly through its phosphane group than through the phosphonate oxygen. The inherent weakness of Hg–O bonds would facilitate the formation of tricoordinate species **I** which, in turn, can give rise to intermediate **II** (by closure of the *O*,*P*-chelate ring with the Hg–P bond acting as a pivot) or, by dimerisation, to the halide (**6**) or *O*,*P*-**1**-bridged (**7**) dimers. As mentioned above, the NMR spectroscopic data indicate that the solution equilibrium is shifted in favour of dimer **6**. However, since solvent, concentration and temperature influence the overall distribution, individual components may separate from solutions of [$HgBr_2$(**1**)] depending on their relative solubility in the reaction media (see the structure of **7** below).

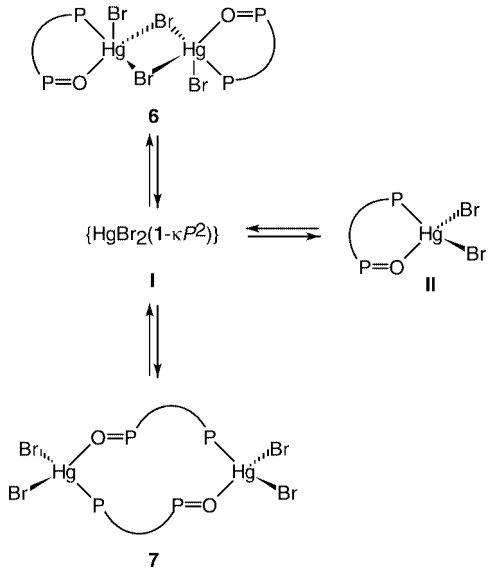


Scheme 3. Schematic depiction of the exchange equilibria of [$HgBr_2$(**1**)].

## Crystal Structures

The crystal structure of the solvate **3**·4$CHCl_3$ (Figure 3, Table 2) corroborates the expected *trans* square-planar coordination of the palladium atom. The molecule of the complex is perfectly planar and centrosymmetric due to the imposed crystallographic symmetry. Nevertheless, owing to the steric bulk of the P-bonded (diphenylphosphanyl)ferrocenyl ligands, the interligand angles deviate slightly from the ideal value of 90°. The ferrocene units in **3** are rotated with respect to the coordination plane by approximately 53°, which seems to minimise the steric interactions of the bulky phosphane ligands by bringing the "$PC_3$" moieties of the phosphanylferrocene ligands into a close-to-staggered conformation. This coordination geometry seems to be common to all structurally characterised complexes involving 1′-functionalised ferrocene phosphanes: *trans*-[$PdCl_2$($Ph_2$PfcX-κ*P*)], where X = $CO_2H$,[17] $P(O)Ph_2$,[24] SMe,[25] and (*S*)-4-isopropyl-4,5-dihydrooxazolyl-1-yl.[26]

Table 2. Selected bond lengths [Å] and angles [°] for **2**·4$CHCl_3$.[a]

| | | | |
|---|---|---|---|
| Pd–Cl | 2.2984(7) | Cl–Pd–P(2) | 86.71(2) |
| Pd–P(2) | 2.3467(6) | Cl–Pd–P(2$^i$) | 93.29(2) |
| P(1)–O(1) | 1.467(3) | O–P(1)–O[b] | 101.3(2)–115.3(2) |
| P(1)–O(2) | 1.572(3) | C(1)–P(1)–O[c] | 100.4(1)–115.6(2) |
| P(1)–O(3) | 1.593(3) | Pd–P(2)–C[d] | 110.89(9)–121.1(1) |
| P(1)–C(1) | 1.755(3) | C–P(2)–C[e] | 102.3(1)–104.8(1) |
| P(2)–C(6) | 1.802(3) | | |
| Fe–Cg(1) | 1.650(1) | ∠ Cp1,Cp2 | 2.7(2) |
| Fe–Cg(2) | 1.650(1) | $\tau$[f] | –135.8(2) |

[a] Symmetry operations used to generate equivalent positions: *i*: –*x*, –*y*, 2 – *z*. Definition of the ring planes: Cp1: C(1–5); Cp(2): C(6–1). Cg(1) and Cg(2) are the respective ring centroids. [b] The range of O(1)–P–O(2,3) and O(2)–P(1)–O(3) angles. [c] The range of C(1)–P(1)–O(1,2,3) angles. [d] The range of Pd–P(2)–C(6,11,17) angles. [e] The range of C(6)–P(2)–C(11,17) and C(11)–P(2)–C(17) angles. [f] Torsion angle C(1)–Cg(1)–Cg(2)–C(6).

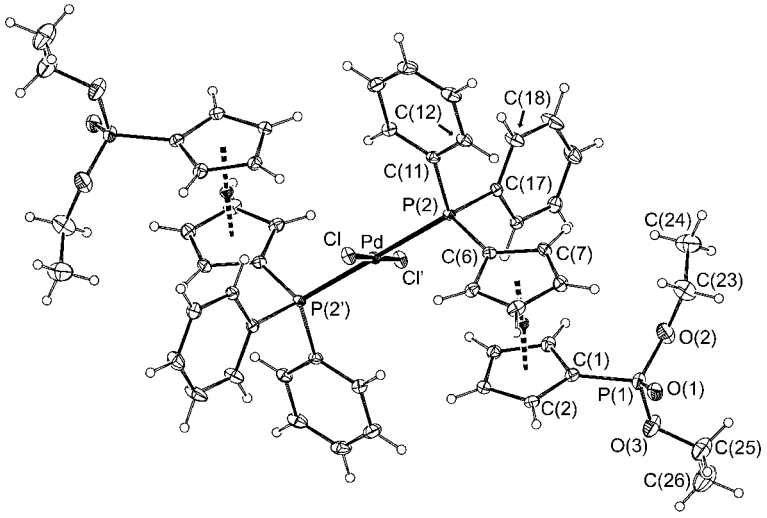


Figure 3. Molecular structure of **3**·4$CHCl_3$. Displacement ellipsoids are drawn at the 30% probability level; the solvate molecules have been omitted for clarity. Half of the molecule is generated by a (crystallographic) inversion operation, the centre of which coincides with the palladium atom.

 © 2006 Wiley-VCH Verlag GmbH & Co. KGaA, Weinheim 

The ligand phosphonate groups, which do not participate in coordination, are rotated away from the phosphanyl substituent such that the disubstituted ferrocene framework adopts a conformation near to anti-eclipsed with a $\tau$ angle of 136° (cf. the ideal value of 144°). Due to the symmetry of the crystal assembly, the phosphonate groups in individual molecules are inclined towards each other, forming polar domains that accommodate the solvate: each phosphonate moiety binds two solvent molecules by O···H–$CCl_3$ hydrogen bonds to its phosphoryl oxygen atom [C(80)–H(80)···O(1$^i$): C(80)···O(1$^i$) 3.134(5) Å, angle at H(80) 147°; C(90)–H(90)···O(1$^i$): C(90)···O(1$^i$) 3.014(5) Å, angle at H(80) 167°; $i$ ($x$, 1 + $y$, $z$). Consequently, the overall crystal packing can be described as molecular, built up from {**2**$(CHCl_3)_4$} repeating units.

As mentioned above, the solid-state structures of 1:1 complexes involving all group-12 metals [$MBr_2$(**1**)] [M = Zn (**4**), Cd (**5**) and Hg (**6**)] were established by single-crystal X-ray diffraction. Furthermore, an isomer of the latter compound (denoted as **7**, Scheme 3) was also structurally characterised. Crystals of **7** suitable for diffraction analysis were obtained from an attempted alkylation of **6** with iodomethane in methanol, followed by evaporation and crystallisation of the residue from acetone/diethyl ether. Although the IR and solution NMR spectra of the bulk material are virtually identical with the starting material **6**, their crystal structures differ markedly. Structural drawings for **4**–**7** are shown below; selected structural parameters are listed in the appropriate tables.

Clearly, the structures change with the metal and are dictated by a subtle interplay between the hardness of the central atom and the donor abilities of the functional groups available at the ferrocene ligand. With zinc, the smallest and hardest (though polarizable) metal in group 12, the ligand coordinates through both donor groups to form a molecular chelate (Figure 4, Table 3). The unit cell of **4** contains two symmetrically independent but structurally very similar molecules of the complex that differ slightly in the mutual orientation of the ferrocene ligand and the embedded $ZnBr_2$ motif, and further by conformation of the flexible ferrocene, phenyl and ethoxy groups. The coordination spheres around the zinc atoms in both molecules are quite regularly tetrahedral, albeit with rather varying zinc–donor distances: the coordination mode can be described as [3+1] with Zn–Br ≈ Zn–P > Zn–O. The individual bond lengths are comparable with the data reported for

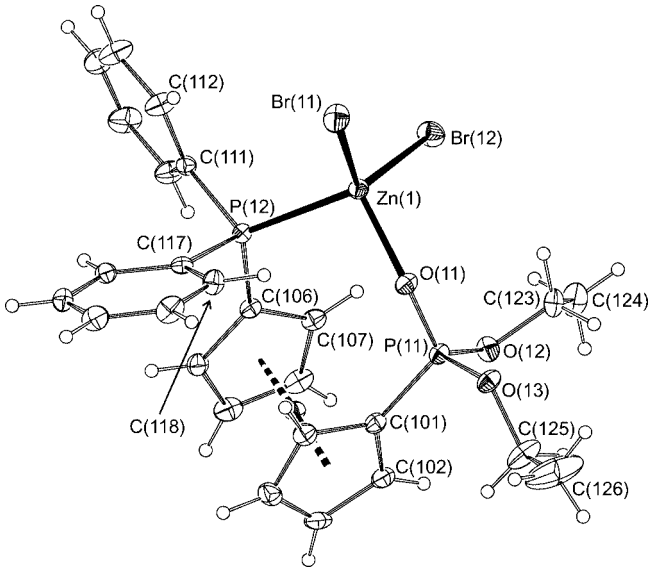


Figure 4. A view of the molecular structure of complex **4** (molecule 1). Displacement ellipsoids enclose 30% probability. Atom labels for molecule 2 (see text) are obtained by adding one to the first digit of the respective atom label in molecule 1.

Table 3. Selected bond lengths [Å] and angles [°] for **4**.[a]

| Molecule 1 | | Molecule 2 | |
|---|---|---|---|
| Zn(1)–Br(11) | 2.3602(5) | Zn(2)–Br(21) | 2.3661(5) |
| Zn(1)–Br(12) | 2.3401(5) | Zn(2)–Br(22) | 2.3636(5) |
| Zn(1)–P(12) | 2.4097(8) | Zn(2)–P(22) | 2.4249(8) |
| Zn(1)–O(11) | 2.008(2) | Zn(2)–O(21) | 2.004(2) |
| P(11)–O(11) | 1.479(2) | P(21)–O(21) | 1.481(2) |
| P(11)–O(12) | 1.559(2) | P(21)–O(22) | 1.551(2) |
| P(11)–O(13) | 1.577(2) | P(21)–O(23) | 1.571(2) |
| P(11)–C(101) | 1.757(3) | P(21)–C(201) | 1.747(3) |
| P(12)–C[b] | 1.794(3)–1.824(3) | P(12)–C[c] | 1.800(3)–1.825(3) |
| Angles at Zn(1) | 101.44(6)–116.85(2) | angles at Zn(2) | 99.17(6)–115.73(2) |
| Zn(1)–O(11)–P(11) | 144.0(1) | Zn(2)–O(21)–P(21) | 145.3(1) |
| O–P(11)–O[d] | 101.8(1)–116.4(1) | O–P(21)–O[e] | 101.5(1)–116.7(1) |
| C–P(12)–C[f] | 103.6(1)–106.8(1) | C–P(22)–C[g] | 104.5(1)–107.9(1) |
| Fe(1)–Cg(11) | 1.650(1) | Fe(2)–Cg(21) | 1.645(2) |
| Fe(1)–Cg(21) | 1.647(1) | Fe(2)–Cg(21) | 1.648(2) |
| ∠ Cp(11),Cp(12) | 2.9(2) | ∠ Cp(21),Cp(22) | 1.8(2) |
| $\tau$(1)[h] | 53.0(2) | $\tau$(2)[i] | –60.2(2) |

[a] Definitions of the ring planes: Cp(11) C(101–105), Cp(12) C(106–110), Cp(21) C(201–205), Cp(22) C(206–210). Cg(*ij*) denotes the respective ring centroid. [b] The range of P(12)–C(106,C111,C117) bond lengths. [c] The range of P(22)–C(206,C211,C217) bond lengths. [d] The range of O(11)–P(11)–O(12,13) and O(12)–P(11)–O(13) angles. [e] The range of O(21)–P(21)–O(22,23) and O(22)–P(21)–O(23) angles. [f] The range of C(106)–P(12)–C(111,117) and C(111)–P(12)–C(117) angles. [g] The range of C(206)–P(22)–C(211,217) and C(211)–P(22)–C(217) angles. [h] Torsion angle C(101)–Cg(11)–Cg(12)–C(106). [i] Torsion angle C(201)–Cg(21)–Cg(22)–C(206).

 © 2006 Wiley-VCH Verlag GmbH & Co. KGaA, Weinheim 

$[ZnCl_2\{FcP(O)(OEt)_2\text{-}\kappa O^1\}_2]$ [Zn–O 1.978(4), P=O 1.467(4), P–OEt 1.555(4) and 1.568(4), P–C 1.770(6) Å][10c] and $[ZnCl_2(dippf\text{-}\kappa^2 P,P')]$ (Zn–P av. 2.415 Å).[20b]

The solid-state structure of cadmium complex **5** (Figure 5) is relatively complicated (Scheme 2, Table 4). Formally, the "$CdBr_2$" units associate into dimers through two bromide bridges. In addition, each cadmium atom is coordinated to two phosphanylphosphonate ligands (once through P=*O* and once through *P*$Ph_2$) and thus has a coordination number of five. The dicadmium $\{Cd_2Br_4\}$ units are interconnected by means of symmetric ligand pairs to form infinite one-dimensional ribbons (Scheme 2; see also Figure 6).

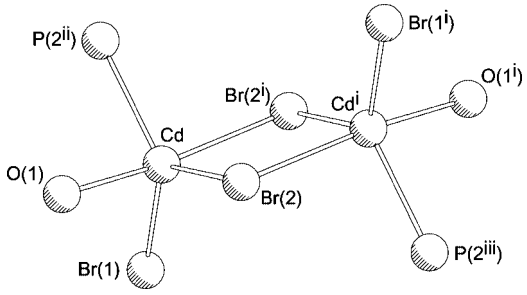


Figure 5. A view of the dicadmium core in **5**. Atomic radii correspond to the isotropic displacement parameters ($U_{iso}$); symmetry codes: *i*: 1 – *x*, 1 – *y*, –*z*; *ii*: 1 – *x*, 1 – *y*, 1 – *z*; *iii*: *x*, *y*, *z* – 1.

Table 4. Selected bond lengths [Å] and angles [°] for **5**.[a]

| | | | |
|---|---|---|---|
| Cd–Br(1) | 2.5556(4) | O(1)–Cd–Br(2$^i$) | 167.50(5) |
| Cd–Br(2) | 2.6458(4) | O(1)–Cd–Br(1) | 94.82(5) |
| Cd–Br(2$^i$) | 2.8373(3) | O(1)–Cd–Br(2) | 86.82(5) |
| Cd–P(2$^{ii}$) | 2.6306(7) | O(1)–Cd–P(2$^{ii}$) | 87.60(5) |
| Cd–O(1) | 2.394(2) | Br(2$^i$)–Cd–Br(1) | 97.05(1) |
| Cd···Cd$^i$ | 4.0737(3) | Br(2$^i$)–Cd–Br(2) | 84.10(1) |
| P(1)–O(1) | 1.481(2) | Br(2$^i$)–Cd–P(2$^{ii}$) | 89.41(2) |
| P(1)–O(2) | 1.571(2) | Br(1)–Cd–Br(2) | 118.44(1) |
| P(1)–O(3) | 1.566(2) | Br(1)–Cd–P(2$^{ii}$) | 122.06(2) |
| P(1)–C(1) | 1.771(3) | Br(2)–Cd–P(2$^{ii}$) | 119.50(2) |
| P(2)–C[b] | 1.804(2)–1.823(3) | O–P(1)–O[c] | 100.3(1)–115.0(1) |
| | | C–P(2)–C[d] | 103.2(1)–104.5(1) |
| Fe–Cg(1) | 1.648(2) | ∠ Cp(1),Cp(2) | 1.3(2) |
| Fe–Cg(2) | 1.643(2) | $\tau$(1)[e] | –155.9(2) |

[a] Definitions of the ring planes: Cp(1) C(1–5), Cp(2) C(6–10); Cg(*i*) denotes the respective ring centroid. Symmetry operations used to generate equivalent positions: *i*: 1 – *x*, 1 – *y*, –*z*; *ii*: 1 – *x*, 1 – *y*, 1 – *z*. [b] The range of P(2)–C(6,11,17) bonds lengths. [c] The range of O(1)–P(1)–O(2,3) and O(2)–P(1)–O(3) angles. [d] The range of C(6)–P(2)–C(11,17) and C(11)–P(2)–C(17) angles. [e] Torsion angle C(1)–Cg(1)–Cg(2)–C(6).

The dicadmium core in **5** (Figure 5) is centrosymmetric and its geometry is best described as two identical trigonal bipyramids sharing an edge connecting the axial and equatorial positions. Because of the steric demands of the ligands and the different cadmium–donor distances [Cd–O(1$^i$) < Cd–Br(1) < Cd–P(2$^{ii}$) ≈ Cd–Br(2) < Cd–Br(2$^i$); for symmetry codes, see Figure 5], the trigonal bipyramidal arrangements are markedly distorted. Nonetheless, the structural index parameter proposed by Addison et al.[27] allows us to classify the donor set around the cadmium atoms as trigonal bipyramid rather than a square pyramid (this parameter has a value of 0.76; the values for an idealised trigonal bipyramid and square pyramid are 1 and 0, respectively). It should be noted that pentacoordinate cadmium centres are relatively common, in line with the larger atomic radius of the metal,[28] and has even precedents among structurally characterised complexes featuring simple[29a] and functionalised phosphanes.[29b,29c]

The molecular structure of mercury complex **6** seems, a priori, to be different from **5** as it consists of dimeric $[\{HgBr_2(\mathbf{1}\text{-}\kappa P^2)\}_2]$ units (Figure 7, Table 5) as commonly observed for 1:1 phosphane–mercury(II) halide complexes. However, a closer inspection of the crystal structure reveals the structures to be very similar. The atoms within the cells of both compounds are distributed in a similar manner (see Figure 6), which brings the phosphoryl oxygen O(1) and mercury atoms from neighbouring molecules into proximity [Hg···O = 2.788(2) Å]. Thus, the O(1) atom is capping the {Br(1),Br(2),P(2)} face of a severely distorted tetrahedral donor array formed by phosphane and bromide ligands, although somewhat asymmetrically with respect to the Hg–Br(2$^i$) axis (*i*: 1 – *x*, –*y*, 1 – *z*), being displaced towards the Br(2)···P(2) edge. As a result, the primary donor set around the mercury atom exhibits severe angular deformation. The protrusion of an extra donor into the coordination sphere of mercury leads to a considerable opening of the Br(2)–Hg–P(2) and, mainly, Br(1)–Hg–P(2) angles (up to about 134° in the latter case), which is compensated by closure of the Br(2)–Hg–Br(2$^i$) and Br(2$^i$)–Hg–P(2) angles. It should be noted that in view of the asymmetric "[4+1]" donor environment around the mercury atom, the bonding situation can be described equally well as highly distorted trigonal pyramidal.

The coordination sphere around the mercury atom in **6** is also asymmetric as far as the mercury–donor atom bond lengths are concerned: the three different Hg–Br bond lengths vary by as much as 0.45 Å. As expected, the bond to the terminal bromide Hg–Br(1) is the shortest one while the Hg–Br(2$^i$) distance is the longest. This clearly points to a competition between the O(1) and Br(2$^i$) atoms for the coordination site at the mercury.

The bonding situation in solid **7**, yet another isomer of the $[HgBr_2(\mathbf{1})]$ adduct, is more straightforward. The crystal structure (Figure 8, Table 6) consists of discrete centrosymmetric dimers where two phosphanylphosphonate ligands span two $HgBr_2$ units {i.e., **7** can be formulated as $[(\mu\text{-}1\kappa P^2{:}2\kappa O^1\text{-}\mathbf{1})(\mu\text{-}1\kappa O^1{:}2\kappa P^2\text{-}\mathbf{1})(HgBr_2)_2]$}. The coordination sphere around the mercury centres departs slightly from a regular tetrahedron, most likely due to the presence of the sterically encumbered phosphanylferrocene moiety and its orientation towards the {Hg,Br(1),Br(2)} plane: the P(2)–Hg–Br(1,2) angles are less acute, which, in turn, causes a closure of the O(2$^{ii}$)–Hg–Br(1,2) and O(2$^{ii}$)–Hg–P(1) angles (*i*: –*x*, 2 – *y*, –*z*). However, the deformation is much less pronounced than in **6**. The Hg–Br distances in **7** are very similar and do not differ much from the remaining Hg–

 © 2006 Wiley-VCH Verlag GmbH & Co. KGaA, Weinheim 

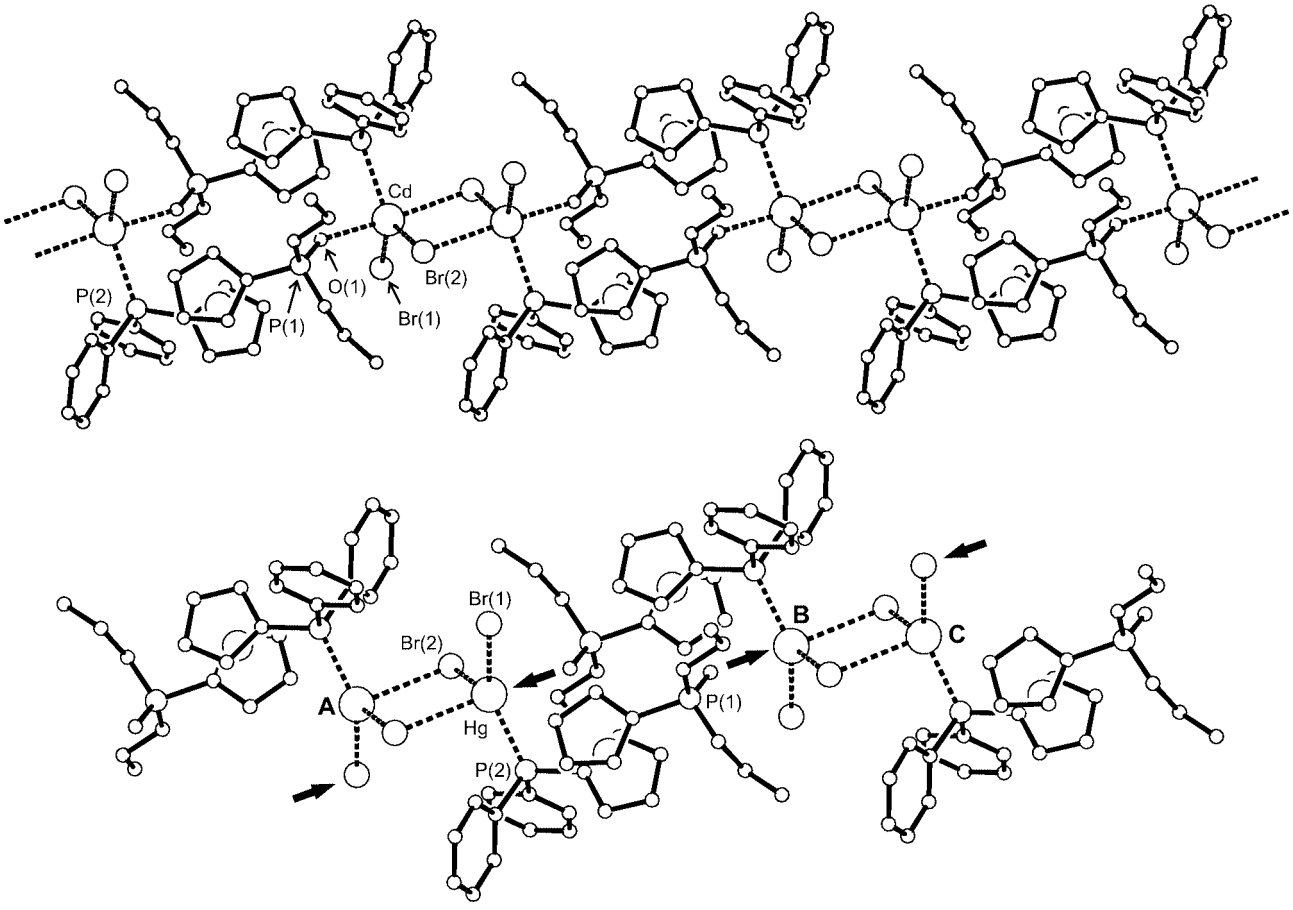


Figure 6. Views of the individual polymeric chain in the structure of **5** (top) and a part of the linear assembly of the dimeric molecules of **6** in the solid state, emphasising the similarity of both structures [intermolecular Hg···O contacts are indicated with arrows; symmetry operations: **A**: 1 – *x*, –*y*, 1 – *z*; **B**: 1 – *x*, 1 – *y*, 1 – *z*; **C**: *x*, 1 + *y*, *z*]. Hydrogen atoms and solvate molecules have been omitted to avoid complicating the figure.

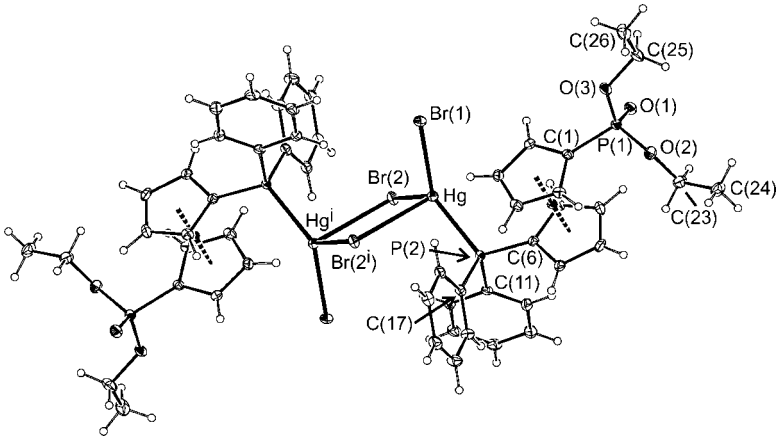


Figure 7. A view of the molecular structure of complex **6** as determined for the solvate **6**·5$C_6H_6$ (solvent molecules have been omitted for clarity). The dimeric molecule is perfectly centrosymmetric due to the imposed symmetry: the halves lie across the crystallographic inversion centre that coincides with the midpoint of the central {$Hg_2Br_2$} ring. Displacement ellipsoids are drawn with 30% probability. Symmetry operations: *i*: 1 – *x*, –*y*, 1 – *z*.

donor bond lengths (compare with **6**). Remarkably, the Hg–O(1$^{ii}$) distance in **7** is only about 5% shorter than that in **6**.[30]

A comparison of the structures determined for the free and several forms of coordinated ligand **1** reveals that coordination of the ligand moiety does not alter its structure in any significant way. The P=O bond lengths are practically identical in all compounds regardless of whether the phosphonate group is free or bonded to a metal (the relative elongation accompanying the coordination is typically less

 © 2006 Wiley-VCH Verlag GmbH & Co. KGaA, Weinheim 

Table 5. Selected bond lengths [Å] and angles [°] for **6**·5 $C_6H_6$.[a]

| | | | |
|---|---|---|---|
| Hg–Br(1) | 2.5362(5) | Br(1)–Hg–Br(2) | 105.48(1) |
| Hg–Br(2) | 2.6523(4) | Br(1)–Hg–Br(2$^i$) | 100.76(1) |
| Hg–Br(2$^i$) | 2.9858(4) | Br(1)–Hg–P(2) | 134.49(3) |
| Hg–P(2) | 2.4342(9) | Br(2)–Hg–Br(2$^i$) | 83.85(1) |
| P(1)–O(1) | 1.472(3) | Br(2)–Hg–P(2) | 118.95(3) |
| P(1)–O(2) | 1.578(3) | Br(2$^i$)–Hg–P(2) | 93.59(2) |
| P(1)–O(3) | 1.571(4) | Hg–Br(2)–Hg$^i$ | 96.15(1) |
| P(1)–C(1) | 1.776(4) | O–P(1)–O[b] | 102.3(2)–115.3(2) |
| P(2)–C[c] | 1.791(4)–1.824(3) | C–P(2)–C[d] | 104.2(2)–106.1(2) |
| Fe–Cg(1) | 1.657(2) | ∠Cp(1),Cp(2) | 1.0(2) |
| Fe–Cg(2) | 1.654(2) | $\tau$(1)[e] | –155.9(2) |

[a] Definitions of the ring planes: Cp(1) C(1–5), Cp(2) C(6–10); Cg(*i*) denotes the respective ring centroid. Symmetry operation used to generate equivalent positions: *i*: 1 – *x*, –*y*, 1 – *z*. [b] The range of O(1)–P(1)–O(2,3) and O(2)–P(1)–O(3) angles. [c] The range of P(2)–C(6,11,17) bonds lengths. [d] The range of C(6)–P(2)–(11,17) and C(11)–P(2)–C(17) angles. [e] Torsion angle C(1)–Cg(1)–Cg(2)–C(6).

Table 6. Selected bond lengths [Å] and angles [°] for **7**.[a]

| | | | |
|---|---|---|---|
| Hg–Br(1) | 2.5939(6) | Br(1)–Hg–Br(2) | 110.10(2) |
| Hg–Br(2) | 2.5692(7) | Br(1)–Hg–P(2) | 127.60(3) |
| Hg–P(2) | 2.446(2) | Br(1)–Hg–O(1$^i$) | 99.8(1) |
| Hg–O(1$^i$) | 2.638(4) | Br(2)–Hg–P(2) | 122.14(4) |
| P(1)–O(1) | 1.468(5) | Br(2)–Hg–O(1$^i$) | 89.06(9) |
| P(1)–O(2) | 1.574(5) | P(2)–Hg–O(1$^i$) | 86.4(1) |
| P(1)–O(3) | 1.571(5) | O–P(1)–O[b] | 102.2(2)–115.6(2) |
| P(1)–C(1) | 1.777(5) | C–P(2)–C[c] | 104.2(3)–106.0(3) |
| P(2)–C[d] | 1.799(5)–1.813(6) | | |
| Fe–Cg(1) | 1.654(3) | ∠ Cp(1),Cp(2) | 0.3(3) |
| Fe–Cg(2) | 1.645(3) | $\tau$(1)[e] | 155.2(5) |

[a] Definitions of the ring planes: Cp(1) C(1–5), Cp(2) C(6–10); Cg(*i*) are the respective ring centroids. Symmetry operation used to generate equivalent positions: *i*: –*x*, 2 – *y*, –*z*. [b] The range of O(1)–P(1)–O(2,3) and O(2)–P(1)–O(3) angles. [c] The range of C(6)–P(2)–(11,17) and C(11)–P(2)–C(17) angles. [d] The range of P(2)–C(6,11,17) bonds lengths. [e] Torsion angle C(1)–Cg(1)–Cg(2)–C(6).

than 1%). Likewise, the O–P–O angles at the phosphonate group do not change upon coordination; in all the structures determined, the O(1)–P(1)–O(2,3) angles are about 10–15° less acute than the remaining angle O(2)–P(1)–O(3). On the other hand, the coordination of the diphenylphosphanyl moiety leads to a slight opening of the C–P(2)–C angles, which thus approach values closer to the tetrahedral ones, albeit without influencing the P(2)–C bond lengths in any significant manner.

More importantly, coordination causes conformational changes to the ferrocene framework. In the free ligand as well and in the complexes, where it acts as an O,P bridge in a discrete dimer (**7**), a polymeric chain (**5**), and in a supramolecularly interacting assembly (**6**), the 1,1′-disubstituted ferrocene unit adopts a conformation between *syn*-eclipsed ($\tau$ = 144°) and *anti*-staggered ($\tau$ = 180°), with the torsion angles falling in the very narrow range of 155–156°.[31] On the other hand, the $P^2$-monodentate ligands in hydrated **2** and **3**·4 $CHCl_3$ have the donor groups rotated towards each other, as indicated by $\tau$ values of 103/92° (for ligand moieties 1/2) and about 136°, respectively. Chelate coordination of **1** in the zinc(II) complex **4** brings the donor groups even further into proximity, which is reflected by the $\tau$ values of around 53° and 60° for molecules 1 and 2, respectively, indicating an intermediate conformation between *syn*-staggered (36°) and *syn*-eclipsed (72°) for the ferrocene unit.

## Conclusions

In summary, organometallic phosphanylphosphonate **1**, which is accessible in good yield by sequential metallation/functionalisation of 1,1′-dibromoferrocene, is a typical example of a hybrid ligand that is novel to ferrocene chemistry. In palladium(II) complexes it binds predominantly through the phosphanyl group. However, the participation

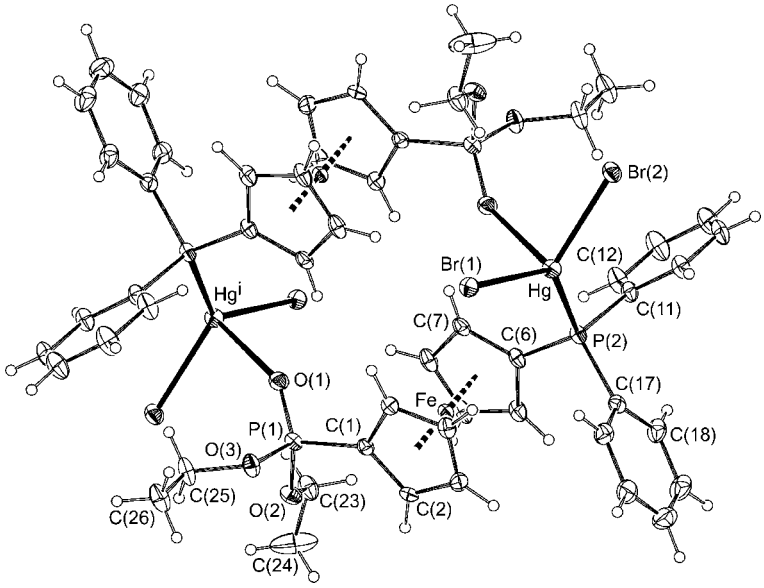


Figure 8. Molecular structure of compound **7**. Similarly to **6**, the parts of the dimeric structure are related by a crystallographic inversion operation. Displacement ellipsoids are shown with 30% probability.

 © 2006 Wiley-VCH Verlag GmbH & Co. KGaA, Weinheim 

in coordination of the hard phosphonate group can be triggered by increasing the hardness of the ligated metal. This is exemplified by the crystal structures of group-12 metal complexes **4**–**7**, where the increasing hardness of the metal cation results in an increase of the role of $O^1 \rightarrow M$ dative bonding. The hybrid nature of **1** is reflected also by the behaviour of "[$HgBr_2$(**1**)]" in solution: the presence of a weakly coordinating group (phosphonate) renders this adduct structurally fluxional and also allows for isolation of isomeric complexes (**6** and **7**).

It should be pointed out that the direct structural (crystallographic) data discussed in this paper represent the most complete series available thus far for a single phosphanylphosphonate ligand.[32] The data not only demonstrate the flexible nature of **1** as a ligand in the individual molecules of the complexes but also its potential to act as a building block in supramolecular coordination structures. Further investigations into the coordination properties of **1** aimed at new structural motifs are currently underway.

## Experimental Section

**Materials and Methods:** The synthesis of **1** was carried out under argon using tetrahydrofuran (THF) freshly distilled from potassium-benzophenone ketyl. The complexes were synthesised in argon-flushed vessels with exclusion of direct daylight. Chloroform and benzene were dried with anhydrous potassium carbonate and potassium, respectively. Acetone was dried with phosphorus pentoxide, distilled, and stored over activated molecular sieves (4 Å). 1-Bromo-1′-(diphenylphosphanyl)ferrocene was prepared from 1,1′-dibromoferrocene as reported in the literature.[7a] Other chemicals (Lachema, Fluka) and solvents used for crystallisations (methanol, diethyl ether and hexane; Lachema) were used as received.

NMR spectra were recorded with a Varian Unity Inova spectrometer ($^1$H: 399.95; $^{13}$C: 100.58; $^{31}$P: 161.90 MHz) at 25 °C (unless noted otherwise). Chemical shifts ($\delta$, ppm) are given relative to internal tetramethylsilane ($^{13}$C and $^1$H) or to external 85% aqueous $H_3PO_4$ ($^{31}$P). The phosphorus-substituted cyclopentadienyl rings represent AA′BB′X spin systems (A, B = $^1$H, X = $^{31}$P), which give rise to characteristic non-binomial multiplets in the $^1$H NMR spectra. Hence, the multiplicity of the signals of these magnetically nonequivalent protons is given as virtual triplet (vt) or virtual quartet (vq). A similar notation is used for virtual triplets occurring in the $^{13}$C{$^1$H} NMR spectrum of **3**. Note: the $J'$ values given below represent an average of the $^{(n)}J_{P,C}$ and $^{(n+2)}J_{P,C}$ coupling constants in the ABX spin system $^{12}$C-$^{31}$P(*A*)-(metal)-$^{31}$P(*B*)-$^{13}$C(*X*).[16] IR spectra were measured with an FT IR Nicolet Magna 650 (all compounds in the range 4000–400 cm$^{-1}$, the complexes also in the far-IR region: 600–100 cm$^{-1}$). Positive-ion electron impact (EI) and fast atom bombardment (FAB) mass spectra were measured with a ZAB SEQ spectrometer. Electrospray (ESI) mass spectra were recorded with a Bruker Esquire 3000 spectrometer; the samples were dissolved in methanol or firstly in a little chloroform and then diluted with a large excess of methanol.

**Diethyl [1′-(Diphenylphosphanyl)ferrocenyl]phosphonate (1):** Butyllithium (2.4 mL 2.5 M in hexanes, 6 mmol) was slowly added to a stirred solution of 1-bromo-1′-(diphenylphosphanyl)ferrocene (2.25 g, 5.0 mmol) in THF (50 mL) at –80 °C (temperature in bath). The mixture, which darkened somewhat during the addition, was stirred for another 30 min at the same temperature and then treated with diethyl chlorophosphate (0.9 mL, 6 mmol). The resulting yellow-brown solution was stirred for another 15 min at –80 °C and then for 3 h at room temperature. The mixture was evaporated under reduced pressure and the resulting orange-brown oil (containing precipitated LiCl) was purified by column chromatography on alumina with chloroform/diethyl ether (2:3) as the eluent. The first fraction containing mostly (diphenylphosphanyl)ferrocene was discarded and the second, major band was collected and carefully evaporated under vacuum to give **1** as a viscous, amber oil, which crystallised upon standing at +4 °C. Yield: 2.185 g (86%). $^1$H NMR ($CDCl_3$): $\delta$ = 1.30 (t, $^3J_{H,H}$ = 7.1 Hz, 6 H, $CH_3$), 4.03–4.14 (m, 4 H, $OCH_2$), 4.21 (vt, 2 H), 4.26 (d of vt, 2 H), 4.39 (vq, 2 H), 4.58 (vt, 2 H) (fc), 7.29–7.38 (m, 10 H, $PPh_2$) ppm. $^{13}$C{$^1$H} NMR ($CDCl_3$): $\delta$ = 16.44 (d, $^3J_{P,C}$ = 7 Hz, $CH_3$), 61.73 (d, $^2J_{P,C}$ = 6 Hz, $OCH_2$), 67.59 (d, $^1J_{P,C}$ = 215 Hz, $CP^V$ of fc), 72.29 (d, $J_{P,C}$ = 15 Hz), 72.92 (dd, $J_{P,C}$ = 14 and 1 Hz), 73.39 (d, $J_{P,C}$ = 4 Hz), 74.26 (d, $J_{P,C}$ = 14 Hz) (4 × CH of fc), 77.70 (d, $^1J_{P,C}$ = 8 Hz, $CP^{III}$ of fc), 128.19 (d, $J_{P,C}$ = 7 Hz), 128.62, 133.44 (d, $J_{P,C}$ = 20 Hz) (3 × CH of $PPh_2$), 138.60 (d, $^1J_{P,C}$ = 10 Hz, $C_{ipso}$ of $PPh_2$) ppm. $^{31}$P{$^1$H} NMR ($CDCl_3$): $\delta$ = –17.0 ($P^{III}$), +25.7 ($P^V$) ppm. IR (neat): $\tilde{\nu}$ = 3069 (m), 3052 (m), 2981 (s), 2903 (m) ν(C–H); 1478 (s), 1434 (s), 1389 (s), 1369 (m), 1249 (vs), 1188 (s), 1162 (m), 1096 (m), 1050 (vs), 1030 (vs), 961 (vs), 831 (s), 794 (m), 746 (s), 699 (s), 595 (s), 492 (s), 454 (m) cm$^{-1}$. EI MS: *m*/*z* (%) = 507 (25), 506 (100) [$M^{+\cdot}$], 449 (5) [M – $C_4H_9$]$^+$ or [M – $C_2H_5$ – $C_2H_4$]$^+$, 321 (12) (possibly [$FeC_5H_4POPh_2$]$^+$; see ref.[33]), 226 (6), 225 (18), 201 (19), 198 (6), 197 (5), 183 (35), 171 (16), 170 (10), 141 (5), 133 (8), 121 (14), 119 (13), 56 (5). HRMS calcd. for $C_{26}H_{28}{}^{56}FeO_3P_2$: 506.0863; found 506.0860.

**Preparation of *trans*-[{Pd(μ-Cl)Cl(1-κ*P*$^2$)}$_2$] (2):** Solid [$PdCl_2$(cod)] (57 mg, 0.20 mmol) and **1** (107 mg, 0.21 mmol) were mixed with methanol (3 mL). The solids quickly dissolved to give a burgundy-red solution. The mixture was stirred at room temperature for 90 min and then allowed to stand at –18 °C for several days. The separated microcrystalline solid was filtered off, washed with diethyl ether and dried under vacuum. Yield: 105 mg (76%) of dark red-brown solid (the product typically contains traces of **2** detectable in the $^{31}$P NMR spectrum). A crystal selected directly from the reaction mixture (prior to the isolation) was shown to be the solvate **2**·½$H_2O$. $^1$H NMR ($CDCl_3$): $\delta$ = 1.33 (t, $^3J_{H,H}$ = 7.1 Hz, 6 H, $CH_3$), 4.07–4.20 (m, 4 H, $OCH_2$), 4.70 (vq, 2 H), 4.76 (vq, 4 H), 4.81 (vq, 2 H), 5.27 (br. s, 2 H) (fc), 7.34–7.65 (m, 10 H, $PPh_2$) ppm. $^{13}$C{$^1$H} NMR ($CDCl_3$): $\delta$ = 16.49 (d, $^3J_{P,C}$ = 6 Hz, $CH_3$), 62.03 (d, $^2J_{P,C}$ = 6 Hz, $OCH_2$), 68.96 (very br. d, $^1J_{P,C} \approx$ 210 Hz, $CP^V$ of fc), 70.22 (d, $^1J_{P,C}$ = 67 Hz, $CP^{III}$ of fc), 73.59 (d, $J_{P,C}$ = 15 Hz), 74.35 (d, $J_{P,C}$ = 9 Hz), 75.89 (d, $J_{P,C}$ = 13 Hz), approx. 76.97 (d, $J_{P,C} \approx$ 10 Hz, CH of fc; partly obscured by the solvent signal), 128.23 (d, $J_{P,C}$ = 6 Hz, CH of $PPh_2$), 128.34 (d, $^1J_{P,C}$ = 61 Hz, $C_{ipso}$ of $PPh_2$), 134.69 (d, $J_{P,C}$ = 2 Hz), 133.70 (d, $J_{P,C}$ = 12 Hz, CH of $PPh_2$) ppm. $^{31}$P{$^1$H} NMR ($CDCl_3$): $\delta$ = +24.6 ($P^V$), +31.1 ppm ($P^{III}$) (tentative assignment). IR (Nujol): $\tilde{\nu}$ = 1246 (m), 1184 (m), 1166 (m), 1100 (m), 1027 (vs), 969 (m), 956 (m), 842 (w), 753 (m), 692 (m), 594 (m), 545 (m), 522 (m), 480 (s) cm$^{-1}$. Far-IR (polyethene): $\tilde{\nu}$ = 356 (s), 350 (sh), 258 (s), 147 (m), 229 (w), 155 (w) cm$^{-1}$. ESI MS: *m*/*z* = 933, 647 [Pd(**1**)Cl]$^+$. $C_{52}H_{56}Cl_4Fe_2O_6P_4Pd_2$ (1367.3): calcd. C 45.68, H 4.13; found C 45.24, H 4.17.

**Preparation of *trans*-[$PdCl_2$(1-κ*P*$^2$)$_2$] (3):** Neat **1** (112 mg, 0.22 mmol) was added to a suspension of [$PdCl_2$(cod)] (29 mg, 0.10 mmol) in chloroform (4 mL). The yellow complex quickly dissolved to give a red solution, which was allowed to stand for 30 min at room temperature and was then layered with hexane (ca. 10 mL) and allowed to crystallise at 0 °C for several days to afford **2** as an orange, crystalline solid. The complex forms solvates with varying chloroform content: the crystals isolated directly from the mother

 © 2006 Wiley-VCH Verlag GmbH & Co. KGaA, Weinheim 

liquor and immediately analysed by X-ray diffractions were shown to be the solvate **3**·4 $CHCl_3$. The main portion of the crystalline product, which was isolated by filtration, washed with a little hexane and dried in air, was characterised as **3**·3 $CHCl_3$ (114 mg, 74%; orange crystals). $^1H$ NMR ($CDCl_3$): $\delta$ = 1.30 (td, $^3J_{H,H}$ = 7.1, $^4J_{P,H}$ = 0.5 Hz, 6 H, $CH_3$), 4.02–4.15 (m, 4 H, $OCH_2$), 4.58 (vq, 2 H), 4.66 (s, 4 H), 4.89 (d of vt, 2 H) (fc), 7.34–7.62 (m, 10 H, $PPh_2$) ppm. $^{13}C\{^1H\}$ NMR ($CDCl_3$): $\delta$ = 16.45 (d, $^3J_{P,C}$ = 7 Hz, $CH_3$), 61.85 (d, $^2J_{P,C}$ = 6 Hz, $OCH_2$), 68.33 (d, $^1J_{P,C}$ = 214 Hz, $CP^V$ of fc), 72.83 (vt, $J'$ = 27 Hz, $CP^{III}$ of fc), 72.95 (d, $J_{P,C}$ = 15 Hz, CH of $C_5H_4P^V$), 74.35 (vt, $J'$ = 4 Hz, CH of $C_5H_4P^{III}$), 74.92 (d, $J_{P,C}$ = 13 Hz, CH of $C_5H_4P^V$), 76.70 (m, CH of $C_5H_4P^{III}$; obscured by the solvent signal), 127.84 (vt, $J'$ = 5 Hz), 130.43 (2 × CH of $PPh_2$), 130.90 (vt, $J'$ = 25 Hz, $C_{ipso}$ of $PPh_2$), 134.11 (vt, $J'$ = 6 Hz, CH of $PPh_2$) ppm. $^{31}P\{^1H\}$ NMR ($CDCl_3$): $\delta$ = +15.3 ($P^{III}$), +25.1 ($P^V$) ppm. IR (Nujol): $\tilde{\nu}$ = 1248 (s), 1179 (s), 1169 (s), 1096 (m), 1056 (s), 1030 (vs), 965 (vs), 836 (m), 797 (m), 745 (s), 692 (m), 592 (m), 504 (s) $cm^{-1}$. Far-IR (polyethene): $\tilde{\nu}$ = 354 (m), 189 (w) $cm^{-1}$. ESI MS: *m/z* = 1211/1213 $[M + Na]^+$, 1153/1155 $[M - Cl]^+$, 1119/1121 $[Pd(\mathbf{1}) + H]^+$, 861 $[Pd(\mathbf{1})_2 - FeC_5H_4PO_3Et_2]^+$. $C_{52}H_{56}Cl_2Fe_2O_6P_4Pd$·3 $CHCl_3$ (1654.5): calcd. C 42.67, H 3.84; found C 42.71, H 3.82.

**Preparation of [$ZnBr_2$(1-κ$^2O^1$,$P^2$)] (4):** Phosphonate **1** (58 mg, 0.11 mmol) and anhydrous zinc(II) bromide (23 mg, 0.10 mmol) were dissolved in acetone (2 mL). The resulting orange solution was stirred for one day and then allowed to crystallise by diffusion of diethyl ether vapour. Well-developed orange crystals of the product, which formed during several days, were filtered off, washed with hexane and dried under reduced pressure. Yield: 52 mg (71%). $^1H$ NMR ($CDCl_3$): $\delta$ = 1.41 (td, $^3J_{H,H}$ = 7.0, $^4J_{P,H}$ = 0.7 Hz, 6 H, $CH_3$), 4.26–4.37 (m, 4 H, $OCH_2$ and CH of fc), 4.45 (ddq, *J* = 7.8, 9.9 Hz, $^3J_{H,H}$ = 7.0 Hz, 2 H, $OCH_2$), 4.56 (vq, 2 H), 4.65 (d of vt, 2 H), 4.79 (vq, 2 H) (fc), 7.39–7.71 (m, 10 H, $PPh_2$) ppm. $^{13}C\{^1H\}$ NMR ($CDCl_3$): $\delta$ = 16.19 (d, $^3J_{P,C}$ = 7 Hz, $CH_3$), 64.46 (d, $^1J_{P,C}$ = 223 Hz, $CP^V$ of fc), 64.61 (d, $^2J_{P,C}$ = 6 Hz, $OCH_2$), 69.19 (d, $^1J_{P,C}$ = 42 Hz, $CP^{III}$ of fc), 72.83 (d, $J_{P,C}$ = 15 Hz), 73.37 (d, $J_{P,C}$ = 7 Hz), 73.62 (d, $J_{P,C}$ = 16 Hz), 75.52 (d, $J_{P,C}$ = 11 Hz) (CH of fc), 128.88 (d, $J_{P,C}$ = 7 Hz, CH of $PPh_2$), 129.37 (d, $^1J_{P,C}$ = 38 Hz, $C_{ipso}$ of $PPh_2$), 131.06 (d, $J_{P,C}$ = 2 Hz), 133.74 (d, $J_{P,C}$ = 13 Hz) (CH of $PPh_2$) ppm. $^{31}P\{^1H\}$ NMR ($CDCl_3$): $\delta$ = –19.9 (d, $^3J_{P,P}$ = 5 Hz, $P^{III}$), +26.1 (d, $^3J_{P,P}$ = 5 Hz, $P^V$). IR (Nujol): $\tilde{\nu}$ = 1212 (s), 1177 (s), 1100 (m), 1027 (vs), 983 (w), 966 (w), 845 (w), 828 (m), 813 (m), 754 (m), 743 (m), 694 (m), 592 (s), 489 (s), 466 (s) $cm^{-1}$. Far-IR (polyethene): $\tilde{\nu}$ = 356 (m), 317 (m), 317 (m), 2351 (s), 244 (s), 219 (s) $cm^{-1}$. ESI MS: *m/z* = 651 $[Zn(\mathbf{1})Br]^+$, 529 $[\mathbf{1} + Na]^+$. $C_{26}H_{28}Br_2FeO_3P_2Zn$ (731.50): calcd. C 42.69, H 3.86; found C 42.68, H 3.76.

**Preparation of [$CdBr_2$(1-κ$^2O$,$P^2$)] (5):** Phosphonate **1** (56 mg, 0.11 mmol) and $CdBr_2$·4 $H_2O$ (35 mg, 0.10 mmol) were suspended in a mixture of acetone (2 mL) and methanol (1 mL), and the reaction mixture was stirred for 1 d. The solids quickly dissolved to give a clear, orange solution. Crystallisation and isolation as above afforded **5** as an orange, crystalline solid (64 mg, 82%). IR (Nujol): $\tilde{\nu}$ = 1212 (vs), 1178 (vs), 1095 (m), 1067 (m), 1047 (m), 1022 (vs), 982 (m), 964 (m), 837 (w), 795 (w), 751 (s), 697 (s), 591 (s), 498 (s), 486 (m), 458 (w), 442 (w) $cm^{-1}$. Far-IR (polyethene): $\tilde{\nu}$ = 367 (m), 336 (m), 321 (m), 266 (m), 254 (m), 214 (w), 193 (s), 158 (s), 116 (m) $cm^{-1}$. ESI MS: *m/z* = 699 $[Cd(\mathbf{1})Br]^+$, 529 $[\mathbf{1} + Na]^+$. $C_{26}H_{28}CdBr_2FeO_3P_2$ (778.52): calcd. C 40.11, H 3.63; found C 40.04, H 3.62.

**Reaction of $HgBr_2$ with 1 to Form 6:** A mixture of phosphonate **1** (57 mg, 0.11 mmol), $HgBr_2$ (36 mg, 0.10 mmol) and acetone (2 mL) was stirred at room temperature. The solids dissolved quickly to give a clear, orange solution, which immediately deposited a yellow precipitate. After stirring for 30 min, the mixture was transferred to a freezer and allowed to stand at –18 °C overnight. The separated solid was filtered off, washed with diethyl ether (3 × 2 mL) and dried under vacuum. Yield of **6**: 75 mg (87%) of a yellow, powdery solid. A similar reaction in benzene as the solvent (3 mL) gave the microcrystalline solvate **6**·5 $C_6H_6$, which quickly decomposes in air by losing solvent. Crystals suitable for X-ray measurements were taken directly from the reaction and covered with paraffin oil to prevent their decomposition. The selected specimen was fixed onto a glass fibre with wax and transferred to the diffractometer (see also X-ray crystallography below). $^1H$ NMR ($CDCl_3$): $\delta$ = 1.29 (t, $^3J_{H,H}$ = 7.1 Hz, 6 H, $CH_3$), 4.00–4.14 (m, 4 H, $OCH_2$), 4.47 (vq, 2 H), 4.69 (d of vt, 2 H), 4.77 (br. vq, 2 H), 4.86 (br. vt, 2 H) (fc), 7.52–7.79 (m, 10 H, $PPh_2$) ppm. $^{13}C\{^1H\}$ NMR ($CDCl_3$): $\delta$ = 16.42 (d, $^3J_{P,C}$ = 7 Hz, $CH_3$), 62.05 (d, $^2J_{P,C}$ = 6 Hz, $OCH_2$), 68.11 (d, $^1J_{P,C}$ = 60 Hz, $CP^{III}$ of fc), 69.11 (d, $^1J_{P,C}$ = 60 Hz, $CP^V$ of fc), 73.34 (d, $J_{P,C}$ = 15 Hz), 74.30 (d, $J_{P,C}$ = 13 Hz), 75.08 (d, $J_{P,C}$ = 13 Hz), 75.94 (d, $J_{P,C}$ = 9 Hz) (CH of fc), 127.71 (d, $^1J_{P,C}$ = 54 Hz, $C_{ipso}$ of $PPh_2$), 129.55 (d, $J_{P,C}$ = 12 Hz, CH of $PPh_2$), 132.46 (d, $J_{P,C}$ = 3 Hz), 133.53 (d, $J_{P,C}$ = 13 Hz) (CH of $PPh_2$) ppm. $^{31}P\{^1H\}$ NMR ($CDCl_3$): $\delta$ = 24.3 (s with $^{199}Hg$ satellites, $^1J_{Hg,P}$ = 6610 Hz, $P^{III}$), +23.9 (d, $^3J_{P,P}$ = 5 Hz, $P^V$). Note: the spectra change with the sample concentration (see Table 1). IR (Nujol): $\tilde{\nu}$ = 1225 (s), 1185 (m), 1099 (m), 1065 (m), 1051 (m), 1019 (s), 977 (w), 963 (m), 845 (m), 750 (m), 694 (m), 596 (m), 518 (w), 498 (s), 845 (w), 468 (w) $cm^{-1}$. Far IR (polyethene): $\tilde{\nu}$ = 343 (w), 316 (w), 264 (w), 254 (m), ν(HgBr) 182 (sh), 176 (s) $cm^{-1}$. ESI MS: *m/z* = 787 $[Hg(\mathbf{1})Br]^+$, 529 $[\mathbf{1} + Na]^+$. $C_{26}H_{28}Br_2FeHgO_3P_2$ (866.70): calcd. C 36.03, H 3.26; found C 35.95, H 3.24.

**Attempted Alkylation of 6. Isolation of 7:** Neat methyl iodide (0.31 mL, 5 mmol) was added to a solution of **6** prepared in situ by stirring $HgBr_2$ (36 mg, 0.10 mmol) and **1** (57 mg, 0.11 mmol) in methanol (2 mL) for 15 min. The mixture was stirred for 1 h at room temperature, allowed to stand at 0 °C overnight, and then evaporated under vacuum. The oily residue was dissolved in acetone (ca. 2 mL) and crystallised by gas-phase diffusion of diethyl ether over several days. The crystalline solid formed was filtered off, washed with diethyl ether and dried under vacuum to give **7** as an orange microcrystalline solid. Yield: 81 mg (93%). IR and solution NMR spectra of **7** are identical to those of **6**.

**X-ray Crystallography:** Crystals suitable for single-crystal X-ray diffraction analysis were selected directly from the reaction batch [**1**: orange plate, 0.08 × 0.25 × 0.50 mm; **4**: orange prism, 0.30 × 0.33 × 0.45 mm; **5**: orange block, 0.15 × 0.20 × 0.20 mm, **6**·5 $C_6H_6$: fragment of a yellow plate, 0.08 × 0.08 × 0.28 mm (see preparation of this compound above), **7**: orange prism, 0.05 × 0.08 × 0.08 mm] or grown by recrystallisation from chloroform/hexane (**2**·4 $CHCl_3$: orange plate, 0.10 × 0.30 × 0.43 mm). Full-set diffraction data ($\theta \leq 27.5°$) were collected on a Nonius KappaCCD diffractometer equipped with a Cryostream Cooler (Oxford Cryosystems) using graphite-monochromated Mo-$K_\alpha$ radiation ($\lambda$ = 0.71073 Å) and analysed with the HKL program package.[34] The data were corrected for absorption by using the routines incorporated in the diffractometer software (**1**, **4**, **5**, and **6**·5 $C_6H_6$: Gaussian correction after indexation of the crystal faces; **2**·4 $CHCl_3$: numerical correction from the indexed crystal shape; **7**: numerical correction based on multiply measured diffractions); transmission factor ranges are given in Table 7. The structures were solved by direct methods (SIR97[35]) and refined by a weighted full-matrix least-squares procedure on $F^2$ (SHELXL97[36]). All non-hydrogen atoms were refined with anisotropic thermal motion param-

 © 2006 Wiley-VCH Verlag GmbH & Co. KGaA, Weinheim 

Table 7. Crystallographic data and data-collection and structure-refinement parameters for **2**·4 $CHCl_3$, and **4**–**7**.[a]

| Compound | **1** | **2**·4 $CHCl_3$ | **4** | **5** | **6**·5 $C_6H_6$ | **7** |
|---|---|---|---|---|---|---|
| Formula | $C_{26}H_{28}FeO_3P_2$ | $C_{56}H_{60}Cl_{14}Fe_2O_6P_4Pd$[a] | $C_{26}H_{28}Br_2FeO_3P_2Zn$ | $C_{26}H_{28}CdBr_2FeO_3P_2$ | $C_{82}H_{86}Br_4Fe_2Hg_2O_6P_4$[b] | $C_{52}H_{56}Br_4Fe_2Hg_2O_6P_4$ |
| M [g mol$^{-1}$] | 506.27 | 1667.32 | 731.46 | 778.49 | 2123.91 | 1733.37 |
| Crystal system | triclinic | triclinic | orthorhombic | triclinic | triclinic | triclinic |
| Space group | $P\bar{1}$ (no. 2) | $P\bar{1}$ (no. 2) | $Pca2_1$ (no. 29)[c] | $P\bar{1}$ (no. 2) | $P\bar{1}$ (no. 2) | $P\bar{1}$ (no. 2) |
| $a$ [Å] | 8.4620(2) | 9.2420(2) | 19.1144(2) | 11.2372(2) | 11.3805(3) | 11.4381(2) |
| $b$ [Å] | 12.4184(2) | 9.6900(1) | 17.1194(1) | 11.4026(3) | 13.1881(2) | 11.4585(2) |
| $c$ [Å] | 12.7060(2) | 20.6309(4) | 17.5230(2) | 13.0812(3) | 14.8156(4) | 12.1543(2) |
| $\alpha$ [°] | 74.290(1) | 98.613(1) | | 70.580(1) | 87.526(2) | 88.924(1) |
| $\beta$ [°] | 72.094(1) | 90.8192(9) | | 78.680(1) | 73.830(1) | 83.964(1) |
| $\gamma$ [°] | 77.3483(9) | 109.896(1) | | 61.164(1) | 68.706(1) | 61.7160(8) |
| $Z$ | 2 | 1 | 8 | 2 | 1 | 1 |
| $V$ [Å$^3$] | 1209.56(4) | 1713.49(5) | 5734.00(9) | 1383.46(5) | 1985.68(8) | 1394.14(4) |
| $D_{calcd.}$ [g mL$^{-1}$] | 1.390 | 1.616 | 1.695 | 1.869 | 1.776 | 2.065 |
| $T$ [K] | 150(2) | 150(2) | 150(2) | 150(2) | 150(2) | 150(2) |
| $\mu$(Mo-$K_\alpha$) [mm$^{-1}$] | 0.781 | 1.363 | 4.267 | 1.323 | 6.356 | 9.027 |
| $T$[d] | 0.747–0.930 | 0.670–0.859 | 0.227–0.387 | 0.367–0.613 | 0.273–0.664 | 0.379–0.539 |
| Reflns. total | 35528 | 29888 | 97688 | 24724 | 31669 | 48178 |
| $R_{int}$ [%][e] | 3.93 | 4.24 | 5.11 | 4.05 | 5.43 | 7.95 |
| Unique/obsd.[f] reflns. | 5556/4944 | 7818/6733 | 13125/11869 | 6346/5734 | 9106/7962 | 6395/5095 |
| $R$ (obsd. data) [%][g] | 3.55 | 4.08 | 2.67 | 2.55 | 3.00 | 3.59 |
| $R$, w$R$ (all data)[%][g] | 4.11, 9.89 | 5.01, 10.3 | 3.47, 5.27 | 3.03, 6.19 | 3.85, 714 | 5.56, 8.36 |
| $\Delta\rho$ [e Å$^{-3}$] | 1.05, –0.98 | 1.46, –0.54 | 1.34, –0.99 | 1.12, –0.94 | 0.98, –2.03 | 1.37, –1.74 |

[a] $(C_{52}H_{56}Cl_2Fe_2O_6P_4Pd)(CHCl_3)_4$. [b] $(C_{26}H_{28}Br_2FeHgO_3P_2)_2(C_6H_6)_5$. [c] Flack's enantiomorph parameter: –0.007(4). [d] The range of transmission coefficients. [e] $R_{int} = \Sigma|F_o^2 - F_o^2(mean)|/\Sigma F_o^2$, where $F_o^2(mean)$ is the average intensity for symmetry-equivalent reflections. [f] Diffractions with $I_o > 2\sigma(I_o)$. [g] $R = \Sigma||F_o| - |F_c||/\Sigma|F_o|$, w$R = [\Sigma\{w(F_o^2 - F_c^2)^2\}/\Sigma w(F_o^2)^2]^{1/2}$.

eters whilst the hydrogen atoms were included in the calculated positions and refined using the riding model. Relevant crystallographic data are given in Table 7. Geometric parameters and structural drawing were produced with a recent version of the Platon program.[37]

CCDC-281044 (for **1**), -281045 (for **2**·½ $H_2O$), -281046 (for **3**·4 $CHCl_3$), -281047 (for **4**), -281048 (for **5**), -281049 (for **6**·5 $C_6H_6$), and -281050 (for **7**) contain the supplementary crystallographic data for this paper. These data can be obtained free of charge from The Cambridge Crystallographic Data Centre via www.ccdc.cam.ac.uk/data_request/cif.

**Supporting Information** (see footnote on the first page of this article): The Supporting Information contains VT $^1H$ and $^{31}P\{^1H\}$ NMR spectra for **6** (Figures S1 and S2).

## Acknowledgments

This work was financially supported by the Grant Agency of the Czech Republic (grant no. 104/05/0192).

[1] a) *Ferrocenes: Homogeneous Catalysis, Organic Synthesis Materials Science* (Eds.: A. Togni, T. Hayashi); VCH, Weinheim, **1995**; b) A. Togni, in *Metallocenes: Synthesis, Reactivity, Applications* (Eds.: A. Togni, R. L. Halterman), Wiley-VCH, Weinheim, **1998**; vol. 2, chapter 11, p. 685; c) T. J. Colacot, *Chem. Rev.* **2003**, *103*, 3101.

[2] R. C. J. Atkinson, V. C. Gibson, N. J. Long, *Chem. Soc. Rev.* **2004**, *33*, 313.

[3] I. R. Butler, W. R. Cullen, T. J. Kim, S. J. Rettig, J. Trotter, *Organometallics* **1985**, *4*, 972.

[4] I. R. Butler, S. J. Coles, M. B. Hursthouse, D. J. Roberts, N. Fujimoto, *Inorg. Chem. Commun.* **2003**, *6*, 760.

[5] a) M. Yamashita, J. V. C. Vicario, J. F. Hartwig, *J. Am. Chem. Soc.* **2003**, *125*, 16347; b) T. Tu, W.-P. Deng, X.-L. Hou, L.-X. Dai, X.-C. Dong, *Chem. Eur. J.* **2003**, *9*, 3073.

[6] a) M. Laly, R. Broussier, B. Gautheron, *Tetrahedron Lett.* **2000**, *41*, 1183; b) J.-C. Hierso, F. Lacassin, R. Broussier, R. Amardeil, P. Meunier, *J. Organomet. Chem.* **2004**, *689*, 766.

[7] a) I. R. Butler, R. L. Davies, *Synthesis* **1996**, 1350; b) V. V. Grushin, *Organometallics* **2001**, *20*, 3950; c) T. S. A. Hor, H. S. O. Chan, K. L. Tan, L. T. Phang, Y. K. Yan, L. K. Liu, Y. S. Wen, *Polyhedron* **1991**, *10*, 2437; d) L. T. Phang, K. S. Gan, H. K. Lee, T. S. A. Hor, *J. Chem. Soc., Dalton Trans.* **1993**, 2697; e) G. Pilloni, B. Longato, G. Bandoli, *Inorg. Chim. Acta* **1998**, *277*, 163; f) R. J. Coyle, Yu. L. Slovokhotov, M. Yu. Antipin, V. V. Grushin, V. Vladimir, *Polyhedron* **1998**, *17*, 3059.

[8] a) G. Pilloni, B. Longato, G. Bandoli, *Inorg. Chim. Acta* **1998**, *277*, 163; b) R. Broussier, E. Bentabet, M. Laly, P. Richard, L. G. Kuzmina, P. Serp, N. Wheatley, P. Kalck, B. Gautheron, *J. Organomet. Chem.* **2000**, *613*, 77.

[9] a) T. S. A. Hor in ref.[1a], chapter 1, p. 3; b) G. Bandoli, A. Dolmela, *Coord. Chem. Rev.* **2000**, *209*, 161.

[10] a) T. L. Schull, D. A. Knight, *Coord. Chem. Rev.* **2005**, *249*, 1269; b) S. R. Alley, W. Henderson, *J. Organomet. Chem.* **2001**, *637–639*, 216 and references cited therein; c) O. Oms, F. Maurel, F. Carré, J. Le Bideau, A. Vioux, D. Leclercq, *J. Organomet. Chem.* **2004**, *689*, 2654.

[11] S. Basra, J. G. de Vries, D. J. Hyett, G. Harrison, K. M. Heslop, A. G. Orpen, P. G. Pringle, K. von der Luehe, *Dalton Trans.* **2004**, 1901.

[12] Crystallographic data for **3**: $C_{52}H_{56}Cl_4Fe_2O_6P_4Pd_2$·½ $H_2O$ (solvating water), triclinic, space group $P\bar{1}$ (no. 2), $a$ = 9.8080(3), $b$ = 16.6990(7), $c$ = 17.2320(8) Å; $\alpha$ = 93.588(2)°, $\beta$ = 105.485(3)°, $\gamma$ = 95.326(3)°; $V$ = 2696.9(2) Å$^3$, $Z$ = 2, $\mu$(Mo-$K_\alpha$) = 1.550 mm$^{-1}$ (Gaussian absorption correction applied, $T$ range: 0.744–0.940); 36531 total, 9465 unique and 6850 observed [$I_o > 2\sigma(I_o)$] reflections, final $R$ (observed data) = 5.07%; w$R$ (all data) = 13.21%. Atoms in the disordered phosphonate group were refined over two positions (with idealised distances) with isotropic thermal motion parameters. All other heavy atoms were refined anisotropically; hydrogen atoms were included in calculated positions and refined using the riding model (SHELXL97).

[13] CSD version 5.24 (November **2004**) with updates of February and May **2005**.

 © 2006 Wiley-VCH Verlag GmbH & Co. KGaA, Weinheim 

[14] A search for structural fragments $\{Pd(\mu\text{-}X)X(P)\}_2$, where X is any halide, furnished 36 hits with *R* below 10%. Most of them are planar molecules (mostly due to imposed symmetry) with the dihedral angle, $\varphi$, equal or close to 0°. Only four structures exhibit $\varphi$ higher than 15°; refcode ($\varphi$, °): NEHVUR (16.2), QAHNOC (29.2), QIVLEM (38.0 and 41.9, two independent fragments), WAVPOY (16.2); $\varphi$ is the dihedral angle subtended by the $\{PdX_2P\}$ planes.
[15] The $\Delta\delta_P$ values were calculated from shifts given in ref.[16] (the complexes) and in: S. O. Grim, A. W. Yanowsky, S. A. Bruno, W. J. Bailey, E. F. Davidoff, T. J. Marks, *J. Chem. Eng. Data* **1970**, *15*, 497 (the ligand).
[16] P. S. Pregosin, R. W. Kunz, in *$^{31}$P and $^{13}$C NMR of Transition Metal Phosphane Complexes*, *NMR Basic Principles and Progress* (Eds.: P. Diehl, E. Fluck, R. Kosfeld), Springer, Berlin, **1979**, vol. 16, ch. E, p. 65 and references cited therein.
[17] P. Štěpnička, J. Podlaha, R. Gyepes, M. Polášek, *J. Organomet. Chem.* **1998**, *552*, 293.
[18] Similar reactions with a 2:1 molar ratio gave no defined solid products, possibly due to a higher solubility of the compounds formed.
[19] $[MCl_2(dppf\text{-}\kappa P,P')]$: M ($\Delta\delta_P$) = Zn (–4.5 ppm), Cd (8.1 ppm) and Hg (+36.0 ppm). Data from: B. Corrain, B. Longato, G. Favero, D. Ajò, G. Pilloni, U. Russo, F. R. Kreissl, *Inorg. Chim. Acta* **1989**, *157*, 259.
[20] $[MCl_2(dippf\text{-}\kappa P,P')]$: M ($\Delta\delta_P$) = Zn (–6.6 ppm), Cd (+9.8 ppm) and Hg (+40.3 ppm). The shifts were calculated from the data cited in: a) A. R. Elsagir, F. Gassner, H. Görls, E. Dinjus, *J. Organomet. Chem.* **2000**, *597*, 139; b) J. H. L. Ong, C. Nataro, J. A. Golen, A. L. Rheingold, *Organometallics* **2003**, *22*, 5027.
[21] A. K. S. Chauhan, N. Singh, R. D. Srivastava, *Appl. Organomet. Chem.* **2003**, *17*, 586 and references cited therein.
[22] R. G. Goel, W. P. Henry, N. K. Jha, *Inorg. Chem.* **1982**, *21*, 2551.
[23] G. A. Bowmaker, J. J. Clase, N. W. Alcock, J. M. Kessler, J. H. Nelson, J. S. Frye, *Inorg. Chim. Acta* **1993**, *210*, 107.
[24] R. J. Coyle, Y. L. Slovokhotov, M. Y. Antipitin, V. V. Grushin, *Polyhedron* **1998**, *17*, 3059.
[25] V. C. Gibson, N. J. Long, A. J. P. White, C. K. Williams, *J. Chem. Soc., Dalton Trans.* **2002**, 3280.
[26] D. Drahoňovský, I. Císařová, P. Štěpnička, D. Dvořáková, P. Maloň, D. Dvořák, *Collect. Czech. Chem. Commun.* **2001**, *66*, 588.
[27] A. W. Addison, T. N. Rao, J. Reedijk, J. van Rijn, G. C. Verschoor, *J. Chem. Soc., Dalton Trans.* **1984**, 1349.
[28] The ionic radii for divalent metals with coordination number of six are 0.88 (Zn), 1.09 (Cd) and 1.16 Å (Hg). Besides, cadmium(II), like any other metal ion with a $d^{10}$ configuration, has no preferred coordination geometry due to ligand-field stabilisation. Consequently, the coordination geometries are determined chiefly by interplay of electrostatic forces, the nature of the ligands and steric factors. For a reference see, for example: F. A. Cotton, G. Wilkinson, C. A. Murillo, M. Bochmann, *Advanced Inorganic Chemistry*, 6th ed., Wiley, New York, **1999**, chapter 15, p. 598 ff.
[29] The following structures of phosphane–halide complexes featuring pentacoordinate cadmium(II) centres have been retrieved from the Cambridge Crystallographic Database (version 5.26 of November **2004** with updates from February and May **2005**). None of the above compounds is polymeric; a) N. A. Bell, T. D. Dee, I. W. Nowell, *Inorg. Chim. Acta* **1982**, *65*, L87 (code: BIYDIW); b) L. W. Houk, P. K. S. Gupta, M. B. Hossain, D. van der Helm, *Acta Crystallogr., Sect. B* **1982**, *38*, 91 (code: BAZMIY); c) J. T. Mague, J. L. Krinsky, *Inorg. Chem.* **2001**, *40*, 1962 (code: QIWBON).
[30] Notably, the mercury-to-oxygen distances in **6** and **7** fall between the sum of covalent (2.38 Å) and contact (4.02 Å) radii (atomic radii were taken from the Platon program[37]). The flexibility of Hg←O dative bonding can be accounted for by its relative weakness because a variation of the Hg–O distance will result in relatively low energy changes which can, in turn, be compensated by other operating effects, such as steric factors and crystal packing forces.
[31] See also the discussion of conformations adopted by the related ligand 1′-(diphenylphosphanyl)ferrocenecarboxylic acid in the solid state: P. Štěpnička, *Eur. J. Inorg. Chem.* **2005**, 3787.
[32] According to the CSD,[13] the only other structurally characterised ligand is diethyl 2-(diphenylphosphanyl)phenylphosphonate whereas the complexes featuring this and some related donors whose structures were determined are limited exclusively to those with palladium(II) and platinum(II) and just a few examples for each ligand. Representative examples for diethyl 2-(diphenylphosphanyl)phenylphosphonate: a) D. D. Ellis, G. Harrison, A. G. Orpen, H. Phetmung, P. G. Pringle, J. G. de Vries, H. Oevering, *J. Chem. Soc., Dalton Trans.* **2000**, 67 (ligand and Pt complex); for diethyl 2-(diphenylphosphanyl)-ethylphosphonate: b) S. Ganguly, J. T. Mague, D. M. Roundhill, *Inorg. Chem.* **1992**, *31*, 3500 (Pd complex); for diethyl 3-(diphenylphosphanyl)propylphosphonate: c) G. Guerrero, P. H. Mutin, F. Dahan, A. Vioux, *J. Organomet. Chem.* **2002**, *649*, 113 (Pd and Pt complexes).
[33] M. Polášek, P. Štěpnička, *J. Mass Spectrom.* **1998**, *33*, 739.
[34] Z. Otwinowski, W. Minor, *HKL Denzo and Scalepack Program Package*, Nonius BV, Delft, The Netherlands. For a reference, see: Z. Otwinowski, W. Minor, *Methods Enzymol.* **1997**, *276*, 307.
[35] A. Altomare, M. C. Burla, M. Camalli, G. L. Cascarano, C. Giacovazzo, A. Guagliardi, A. G. G. Moliterni, G. Polidori, R. Spagna, *J. Appl. Crystallogr.* **1999**, *32*, 115.
[36] G. M. Sheldrick, *SHELXL97. Program for Crystal Structure Refinement from Diffraction Data*, University of Göttingen, Germany, **1997**.
[37] A. L.Spek, *Platon, a multipurpose crystallographic tool*, Utrecht University, Utrecht, The Netherlands, **2003** and updates. Distributed via Internet; home page: http://www.cryst.chem.uu.nl/platon/.

Received: August 15, 2005
Published Online: January 16, 2006

 © 2006 Wiley-VCH Verlag GmbH & Co. KGaA, Weinheim 

DOI: 10.1002/ejic.200500758

# Another Example of the Instability of a Keggin-Type Heteropolyanion in the Presence of Aqueous Hydrogen Peroxide: From $[AsW_{12}O_{40}]^{3-}$ to Low-Nuclearity Oxoperoxotungstates – Crystal Structure of $[(n\text{Hex})_4N]_3[AsO_4\{W_2O_2(\mu\text{-}O_2)_2(O_2)_2\}_2]$

**Jean-Yves Piquemal,*[a] Laurent Salles,[b] Geneviève Chottard,[c] Patrick Herson,[c] Chehrazed Ahcine,[b] and Jean-Marie Brégeault*[b]**

**Keywords:** Oxidation / Hydrogen peroxide / Peroxo ligands / Catalysis / Tungsten

The Keggin dodecatungstoarsenato anion of $HNa_2[AsW_{12}O_{40}]$ is inherently unstable in aqueous hydrogen peroxide and is mainly degraded to $[AsO_4\{W_2O_2(\mu\text{-}O_2)_2(O_2)_2\}_2]^{3-}$, $[HAsO_4\{W_2O_2(\mu\text{-}O_2)_2(O_2)_2\}]^{2-}$ and $[\{WO(O_2)_2(H_2O)\}_2(\mu\text{-}O)]^{2-}$. These anions were isolated as salts and identified by elemental and spectroscopic analyses. The salt with the formula $[(n\text{C}_6\text{H}_{13})_4]_3[AsO_4\{W_2O_2(\mu\text{-}O_2)_2(O_2)_2\}_2]$ was obtained from the reaction of tungstic acid, "$H_2WO_4$" (or $HNa_2[AsW_{12}O_{40}]\cdot n\text{H}_2\text{O}$), with aqueous hydrogen peroxide, $HNa_2[AsO_4]\cdot 7\text{H}_2\text{O}$ and $[(n\text{C}_6\text{H}_{13})_4\text{N}]\text{Cl}$. The structure was refined with $R_1 = 0.058$ and $wR_2 = 0.067$ [monoclinic $C2$ (no. 5); $a = 20.516(6)$ Å, $b = 15.923(4)$ Å, $c = 14.902(2)$ Å, $\beta = 91.64(1)°$, $Z = 2$]. The vibrational spectra (IR and Raman) suggest that the overall structure is maintained in organic solvents. The close relation between the phosphate- and arsenate-based complexes indicates that fluxional behaviour may exist for all these di- and tetranuclear complexes. Fluxionality may play a key role in the transfer of active oxygen (from peroxo groups) to organic substrates via $\{WO(O_2)_2\}$ units. It is shown that the heteroligand $[XO_p]^{n-}$ (X = As, HAs, MeAs, P, HP, etc.) has a marked effect on the stoichiometric and regioselective epoxidation of (*R*)-(+)-limonene to 1,2-epoxide at ambient temperature, for a given pH of the aqueous phase. The oxodiperoxo complexes can be used to carry out epoxidation stoichiometrically and regioselectively with (*R*)-(+)-limonene, but can also be employed in a catalytic process in a two-phase mixture at room temperature.

(© Wiley-VCH Verlag GmbH & Co. KGaA, 69451 Weinheim, Germany, 2006)

## Introduction

Heteroligand peroxo-transition-metal complexes possess coordination spheres composed of one to three peroxo groups, and one or more monodentate or polydentate ligands. The stability of the peroxo complex can be enhanced and the reactivity of the coordinated peroxo group changed by specific heteroligand combinations.[1–7] A novel class of heteropolyoxoperoxometalate complexes has attracted attention.[1–14] Representatives of this class are the tetranuclear complexes $Q_3[PO_4\{M_2O_2(\mu\text{-}O_2)_2(O_2)_2\}_2]$ (denoted "$PM_4$"; compound **1**: M = Mo and $Q^+$ = amino-2 pyridinium[8] or $Q^+ = [(n\text{Hex})_4\text{N}]^+$;[9] compound **2**: M = W and $Q^+ = [(n\text{Hex})_4\text{N}]^+$[10–12]) and the parent dinuclear complexes $[(n\text{Bu})_4\text{N}]_2[REO_3\{W_2O_2(\mu\text{-}O_2)_2(O_2)_2\}]\cdot x\text{H}_2\text{O}$ (compound **3**: R = OH and E = P[13] with $x = 0$; compound **4**: R = OH and E = As[14] with $x = 0$; compound **5**: R = $CH_3$ and E = As[14] with $x = 1$).

The dimeric moiety $[M_2O_2(\mu\text{-}O_2)_2(O_2)_2]$ is a building block for these five anions. To the best of our knowledge, it has not been observed in peroxotungsten complexes with oxo,[15] oxalate[16] and carbonate[17] or in oxoperoxomolybdates[18,19] with molybdate as assembling ligands, $[\{MoO(O_2)_2\}_2(\mu\text{-}MoO_4)\{\mu\text{-}O\}]^{4-}$ and $[\{\{MoO(O_2)_2\}_2(\mu\text{-}O)\}_2(\mu_4\text{-}MoO_4)]^{6-}$. Complexes with[20] and without[20,21] the dimeric moiety $[M_2O_2(\mu\text{-}O_2)_2(O_2)_2]$ have been synthesised with sulfate as the assembling ligand.

On the one hand, it was shown that both the "$H_3[PW_{12}O_{40}]\cdot n\text{H}_2\text{O}/(H_2O_2/H_2O)$" and the "$H_2WO_4/H_3PO_4/(H_2O_2/H_2O)$" systems involve common species, $[PW_xO_y]^{w-}$, $x = 1$–4. The Keggin-type heteropolyoxometalate (POM) is degraded by $H_2O_2$ to form a variety of phosphatooxoperoxo complexes. These, along with other pure oxoperoxotungstates,[13,22,23] for example $[\{WO(O_2)_2(H_2O)\}_2(\mu\text{-}O)]^{2-}$, have been characterised by IR, Raman, $^{31}$P and $^{183}$W NMR spectroscopy. In contrast with $H_4[SiW_{12}O_{40}]\cdot n\text{H}_2\text{O}$, more drastic conditions (70% $H_2O_2$ in water) have to be used to degrade the Keggin-type polyanionic structure.[23] On the other hand, a new lacunary heteropolyoxotetraperoxotungstate, related to the Keggin structure

[a] ITODYS, Université Denis Diderot/CNRS, case 7090, 2 place Jussieu, 75251 Paris cedex 05, France
E-mail: piquemal@ccr.jussieu.fr
[b] Systèmes Interfaciaux à l'Echelle Nanométrique, Université Pierre et Marie Curie/CNRS, case 196, 4 place Jussieu, 75252 Paris cedex 05, France
E-mail: bregeaul@ccr.jussieu.fr
[c] Chimie Inorganique et Matériaux Moléculaires, Université Pierre et Marie Curie/CNRS, case 42, 4 place Jussieu, 75252 Paris cedex 05, France

 © 2006 Wiley-VCH Verlag GmbH & Co. KGaA, Weinheim 

$[(Co^{II}O_4)W_{11}O_{31}(O_2)_4]^{10-}$, has been characterised by single-crystal X-ray diffraction.[24] The authors underlined that the different reactivities of lacunary and saturated Keggin complexes (i.e. $[PM_{12}O_{40}]^{3-}$ where M = Mo or W) towards aqueous $H_2O_2$ may be related to the longer M=O bonds of the terminal oxygen atoms of *cis*-$W(O)_2$ groups around the vacancy that lead to *cis*-$W(O)(O_2)$. The conversion of $H_3[PM_{12}O_{40}]\cdot nH_2O$ in the presence of hydrogen peroxide should also require the intervention of lacunary precursors, but in equilibrium with $\{MO_2(OH)\}^+$ or $\{MO_2\}^{2+}$ species, which are converted to $\{MO(O_2)_2(H_2O)_2\}$ moieties.[6,13,25] Recent review articles focus on $H_2O_2$-based epoxidation catalysed by lacunary polyoxometalates,[7] e.g. $[\gamma\text{-}SiW_{10}O_{34}(H_2O)_2]^{4-}$. The nonlacunary heteropolyoxoperoxometalates $[PTiW_{11}O_{39}(O_2)]^{5-}$ and $[PTi_2W_{10}O_{38}(O_2)_2]^{7-}$ have also been reported.[26,27] In these compounds, the peroxo ligands are probably bonded to the Ti atom (statistical disorder makes it impossible to locate the Ti atoms and the peroxo ligands). These substituted polyoxometalates are moderately active for olefin epoxidation with the use of 30% $H_2O_2$ ($O_{peroxo}$/catalyst = 1200:2 mol/mol). It is inferred that there is no degradation of the Keggin-structured framework at 50 °C over 24 h,[27] although synergy may exist between the tungsten and titanium centres. The retention of the Keggin unit of this Ti–POM was reinvestigated,[28] but in some systems the isolable species are often not those that lie along the principal reaction coordinates for the catalysis.[6,25]

Although it was formerly accepted that the O–O bond lengths are fairly constant and do not depend on the nature of the metal ligands, we were interested in a systematic study of the heteroligand effect. This is of major importance for catalysis in homogeneous[6,29] or two-phase-medium[6,9,13,22,23,30,31] conditions, for grafting onto (or inserting in) polymeric supports[6,30,32–38] or for the comprehensive study of the synthesis of transition-metal-containing mesostructured materials from peroxo species.[39,40] We report here the synthesis and structural characterisation of $[(n\text{Hex})_4N]_3[AsO_4\{W_2O_2(\mu\text{-}O_2)_2(O_2)_2\}_2]$ (**6**). Salts of the anion have been prepared by several groups;[11–12,41–43] despite many attempts to show that **1**, **2** and **6** are isomorphous, it was previously difficult to isolate single crystals of **6** suitable for X-ray measurements. The profiles of the Raman and infrared spectra of **6** are compared with those of tetra-*n*-butylammonium (μ-hydrogenoarsenato)bis(μ-peroxo)bis-(oxoperoxotungstate)(2–) (**4**)[14] and with those of the methylarsenato analogue (**5**).[14] Moreover, it is shown that the interaction of excess $H_2O_2$ (30%) with an aqueous solution of $[AsW_{12}O_{40}]^{3-}$ leads to the degradation of the Keggin unit and to the formation of a less-condensed oxoperoxo species in the same way as $H_3[PW_{12}O_{40}]\cdot nH_2O$ in the presence of $H_2O_2$. These complexes are active oxygen-to-olefin transfer agents at room temperature and are active catalysts in the oxidation of model organic substrates using 30% $H_2O_2$ in water in a two-phase medium.

## Results and Discussion

### Syntheses of 6: Peroxide-Mediated Decomposition of $[AsW_{12}O_{40}]^{3-}$ or Reaction of $H_2O_2$ with Tungstic Acid in the Presence of Arsenate

The synthesis of $[(n\text{Hex})_4N]_3[AsO_4\{W_2O_2(\mu\text{-}O_2)_2(O_2)_2\}_2]$ (**6**) from "$H_2WO_4$" is based on methods that generate oxoperoxo species,[44] mainly $[WO(O_2)_2(H_2O)_2]$, $[WO(OH)(O_2)_2]^-$ and $[\{WO(O_2)_2H_2O\}_2(\mu\text{-}O)]^{2-}$ [with peroxide/tungsten(VI) > 2] which are subsequently coordinated by the assembling anion $[AsO_4]^{3-}$. Another procedure can be developed with the use of $Na_2H[AsW_{12}O_{40}]\cdot NaCl\cdot 30H_2O$, which is degraded by excess $H_2O_2$ (Scheme 1); these results compare well with previously reported data,[22,23] and spectroscopic evidence shows that the "$H_3[PW_{12}O_{40}]\cdot nH_2O/H_2O_2/H_2O$" and "$H_2WO_4/H_3PO_4/H_2O_2/H_2O$" systems give the same oxoperoxo species.[4,6,10,13,22,23] To precipitate one of the anions formed from $[AsW_{12}O_{40}]^{3-}$ and excess $H_2O_2$, we added tetra-*n*-butylammonium chloride and isolated the complex $[(n\text{Bu})_4N]_3[AsO_4\{W_2O_2(\mu\text{-}O_2)_2(O_2)_2\}_2]$, and subsequently added potassium chloride to give $K_2[\{WO(O_2)_2(H_2O)\}_2(\mu\text{-}O)]$. Therefore, the appropriate choice of counteranions allowed us to obtain the two oxoperoxo salts selectively (Scheme 1). The products have been fully characterised by an active oxygen assay, elemental analysis and vibrational studies (IR and Raman spectra, vide infra). The isolation of **6** led to structural X-ray data.

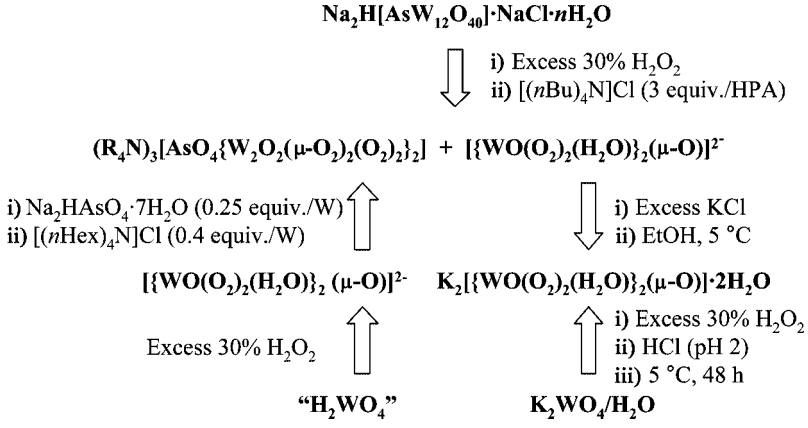


Scheme 1. Synthesis of anionic peroxo complexes involving the arsenato ligand (R = *n*Bu or *n*Hex).

 © 2006 Wiley-VCH Verlag GmbH & Co. KGaA, Weinheim 

### Structure of the Tetranuclear Complex $[(n\text{Hex})_4N]_3[AsO_4\{W_2O_2(\mu\text{-}O_2)_2(O_2)_2\}_2]$ (6)

The arsenic atom of $[AsO_4]^{3-}$ and one of the nitrogen atoms, N(2), lie on a binary axis. The neutral moiety, $\{W_2O_2(\mu\text{-}O_2)_2(O_2)_2\}$, and the other nitrogen atom, N(1), are in general positions, while the other two locations are generated by the binary axis.

Single-crystal X-ray analyses show that **1**,[9] **2**[10] and **6** (this work) are isomorphous and are structurally very similar. The anion of **6** (Figure 1) consists of a slightly distorted tetrahedral assembling anion, $[AsO_4]^{3-}$, and two neutral units, $\{W_2O_2(\mu\text{-}O_2)_2(O_2)_2\}$, in which the tungsten(VI) atoms are coordinated by seven oxygen atoms in a pentagonal-bipyramidal arrangement (PBPY-7, IUPAC Nomenclature). The four oxygen atoms of the anion are corner sharing with the four different basal planes of the pentagonal bipyramids. Atoms O(3) and O(4) of the arsenate bridge two tungsten atoms within a dinuclear unit. The geometry about the arsenic atom does not deviate significantly from that of a tetrahedral arrangement (Table 1), with a mean bond angle of 109.5°. The As–O bond lengths average 1.66 Å, in agreement with those of **4**, **5**[14] and many tungsten(VI) arsenates containing heteropolyanions, and with values found for arsenates and organoarsenates.[45,46] The tungsten atoms have two differently bound peroxo ligands: one is in the $\eta^2$-side-bound configuration, [W(1)–O(11)–O(12) and W(2)–O(21)–O(22)] (Figure 1), and the other is in the $\mu_2$-$\eta^2$:$\eta^1$ mode (or unsymmetrical bridging). Thus, in **6**, the tungsten atoms are connected in pairs not only by the $[AsO_4]^{3-}$ group, but also by the unique $\mu_2$-$\eta^2$:$\eta^1$ peroxo bridges, and the two pentagonal bipyramids associated in this way share one edge of the nonbasal plane, O(13)···O(23). It is important to note that a similar unit exists only in the anion of **1**[9] and **2**[10], and in the dinuclear complexes that have recently been isolated: **3**,[13] **4**,[14] **5**[14] and $[P(C_6H_5)_4]_2[(C_6H_5)_2SiO_2\{W_2O_2(\mu\text{-}O_2)_2(O_2)_2\}]$ (**7**).[39] The least-squares planes for the anion of **6** are such that the pentagonal bipyramids of the oxygen atoms surrounding the two tungsten atoms are almost identical. Each pentagonal girdle is generated by two peroxo groups and one oxygen atom of the arsenate group. A summary of bond lengths and angles of the anion is presented in Table 1. One of the axial positions is occupied by a terminal oxo ligand $O^{2-}$ (W=O: 1.77, 1.70 Å) and the other by an oxygen atom of a bridging unsymmetrical peroxo group with a notably long bond (W–O: 2.42, 2.37 Å), similar to those found for **4**, **5**[14] and **7**.[39] The oxygen atoms that define the equatorial plane are coplanar to within 0.004–0.143 Å. As is the case for octahedral coordination in polyoxometalates, W(1) and W(2) are located outside the mean plane defined by the five equatorial O atoms (0.37 Å and 0.40 Å, respectively). These distances are also found for the other structural units in **3**, **4**, **5** and **7**.[13,14,39] In the $\eta^2$-peroxo groups, O(11)–O(12) and O(21)–O(22) are nearly symmetrically coordinated to W(1) and W(2), respectively [W(1)–O(11) and W(1)–O(12) have bond lengths of 1.92 and 1.90 Å, respectively]. The O(11)–O(12) and O(21)–O(22) bond lengths (1.49 and 1.48 Å, respectively) are in the usual range (1.40–1.50 Å),[1–4] and the corresponding three-membered –W–O–O– rings are nearly isosceles. In contrast to these structural data, the bridging peroxo groups $\mu_2$-$\eta^2$:$\eta^1$ [O(13)–O(14) and O(23)–O(24)] are dissymetrically coordinated to W(1) and W(2), which results in a relatively long W–O bond with the bridging oxygen atoms [W(1)–O(13) and W(2)–O(23) are 2.06 and 2.00 Å, respectively] and a shorter bond with the second oxygen atom (1.93 and 1.90 Å, respectively), similar to those found for the side-bound peroxo group. The OWO angles are unchanged (about 45°), whereas the peroxo bond lengths lie between 1.48 and 1.52 Å. It is well known that the addition of suitable ancillary ligands (hexamethylphosphorotriamide, HMPA,[47] or pyridine *N*-oxide, pyO)[48] to "$H_2WO_4$" ("$WO_3{\cdot}H_2O$") or tungsten powder in 30% $H_2O_2$ in water leads to the formation of well-characterised molecular complexes: $[WO(O_2)_2L^1L^2]$ where $L^1$ = HMPA, $L^2$ = $H_2O$,[47] or $L_1$ = $L_2$ = pyO.[48] The dinuclear anion, $[\{WO(O_2)_2(H_2O)\}_2(\mu\text{-}O)]^{2-}$, can also be formed at an early stage of the reaction; it seems likely that the anions of **4**, **5** and **6** are obtained by reactions of the molecular complexes

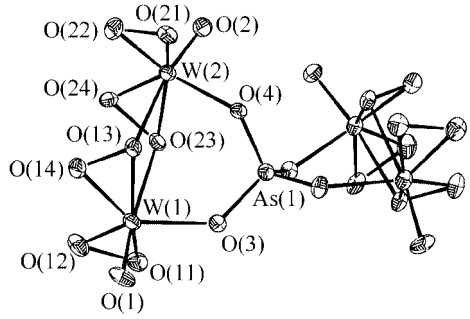


Figure 1. CAMERON view of the anion in **6**, showing the atom-labelling scheme. Atoms are represented by thermal ellipsoids at the 25% level.

Table 1. Selected bond lengths [Å] and angles [°] for $[(n\text{Hex})_4N]_3[AsO_4\{W_2O_2(\mu\text{-}O_2)_2(O_2)_2\}_2]$.

| | | | |
|---|---|---|---|
| W(1)–O(1) | 1.773(14) | O(11)–W(1)–O(12) | 45.9(6) |
| W(1)–O(3) | 2.011(11) | O(13)–W(1)–O(14) | 43.2(5) |
| W(1)–O(11) | 1.917(12) | O(1)–W(1)–O(23) | 171.4(6) |
| W(1)–O(12) | 1.903(13) | O(2)–W(2)–O(13) | 169.5(5) |
| W(1)–O(13) | 2.059(13) | O(21)–W(2)–O(22) | 45.3(6) |
| W(1)–O(14) | 1.928(13) | O(23)–W(2)–O(24) | 45.9(5) |
| W(1)–O(23) | 2.415(13) | O(3)–As(1)–O(4) | 109.7(5) |
| W(2)–O(2) | 1.700(13) | O(3)′–As(1)–O(4)′ | 109.7(5) |
| W(2)–O(4) | 2.008(11) | O(4)–As(1)–O(4)′ | 113.1(8) |
| W(2)–O(13) | 2.366(14) | O(4)–As(1)–O(3)′ | 107.3(6) |
| W(2)–O(21) | 1.931(11) | O(3)–As(1)–O(4)′ | 107.3(6) |
| W(2)–O(22) | 1.903(12) | O(3)–As(1)–O(3)′ | 109.8(9) |
| W(2)–O(23) | 1.994(11) | | |
| W(2)–O(24) | 1.899(12) | | |
| As(1)–O(3) | 1.667(12) | | |
| As(1)–O(4) | 1.650(10) | | |
| O(11)–O(12) | 1.489(19) | | |
| O(13)–O(14) | 1.472(18) | | |
| O(21)–O(22) | 1.48(2) | | |
| O(23)–O(24) | 1.521(17) | | |

 © 2006 Wiley-VCH Verlag GmbH & Co. KGaA, Weinheim 

($L^1$ = $L^2$ = $H_2O$) and/or of dinuclear species with $H_{3-\varepsilon}$-$[AsO_4]^{\varepsilon-}$ species in the same way as that for the phosphatooxoperoxotungstate species for which, according to NMR spectroscopic studies, there are several equilibria.[6,13,22,23]

### Infrared and Raman Spectra: Correlation of Vibrational Data with the Structure of Complexes 4, 5 and 6

Attempts to measure the Raman spectra of **1**, **2** and **6** in a benzene solution were unsuccessful,[42] but the solid state and acetonitrile solutions show common features in the 500–1000 $cm^{-1}$ region, which suggests that the structures of the anions of **4**, **5** and **6** are maintained in some organic solvents (here acetonitrile) at room temperature, as proposed in a preliminary structural study.[14] The IR and Raman spectra of **6** are presented in Figure 2 and the attributions of the main infrared and Raman vibrations are given in Table 2.

The infrared and Raman spectra of arsenate-containing complexes show strong bands in the 960–990 $cm^{-1}$ region assigned to $\tilde{\nu}$(W=O) of the terminal oxo group (see Table 2). For tetrahedral $XO_4$ compounds, four vibrations are expected: $\tilde{\nu}_1(A_1)$, $\tilde{\nu}_2(E)$, $\tilde{\nu}_3(F_2)$ and $\tilde{\nu}_4(F_2)$. With free $[AsO_4]^{3-}$, these maxima are at about 878 ($\tilde{\nu}_3$), 837 ($\tilde{\nu}_1$), 463 ($\tilde{\nu}_4$) and 349 ($\tilde{\nu}_2$) $cm^{-1}$.[49] Although all of them are Raman-active, only $\tilde{\nu}_3$ and $\tilde{\nu}_4$ are infrared-active for $T_d$ symmetry.[50] We propose that the two strong infrared and Raman bands in the 915–865 $cm^{-1}$ region be attributed to vibrations of the arsenato ligand, i.e. As–O stretches (see Table 2). For "$Na_3[AsW_{12}O_{40}]\cdot nH_2O$"[51] (reformulated as $Na_2H[AsW_{12}O_{40}]\cdot NaCl\cdot 30H_2O$ – see Experimental Section), an infrared band located at 911 $cm^{-1}$ is attributed to the $\tilde{\nu}_{asym}$(As–O) vibration.[51] Two infrared bands at 892 and 875 $cm^{-1}$ are also tentatively attributed to the $\tilde{\nu}(AsO_4)$ stretches of the arsenato-containing tetranuclear species.[50]

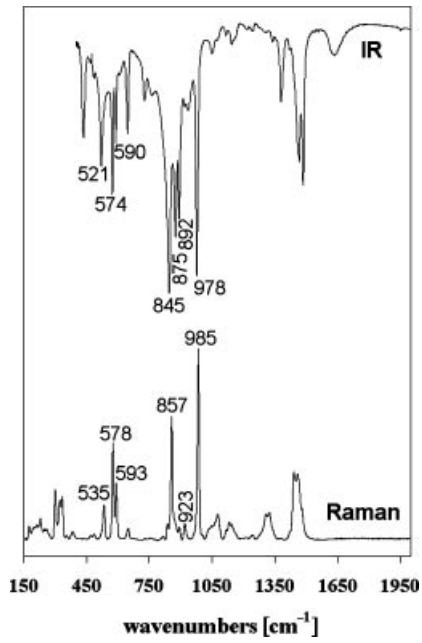


Figure 2. Infrared and Raman spectra of solid samples of $[(n\text{Hex})_4N]_3[AsO_4\{W_2O_2(\mu\text{-}O_2)_2(O_2)_2\}_2]$ (**6**).

The bands at 857–861 $cm^{-1}$ (Raman spectra) and at 843–849 $cm^{-1}$ in the IR spectra are related to the Raman- and infrared-active $\tilde{\nu}$(O–O) vibrations of the peroxo ligands. These values are in agreement with previously obtained values for tungsten oxoperoxometalates involving other assembling anions and $\{W_2O_2(\mu\text{-}O_2)_2(O_2)_2\}$ units,[9,13,14,20,22,23] and also with those from the Raman spectra of many unactivated organic peroxides. We propose to limit the wavenumber region expected for the $\tilde{\nu}$(O–O) to 830–885 $cm^{-1}$. Thus, we observed the O–O stretch at 876 $cm^{-1}$ in the spectrum of hydrogen peroxide (30% $H_2O_2$ in water). Barium peroxide ($BaO_2$), which is registered in

Table 2. Vibrational wavenumbers [$cm^{-1}$] of arsenatooxoperoxotungstate complexes **4**, **5** and **6** (main Raman and IR bands).[a]

| $\tilde{\nu}$ [$cm^{-1}$] | | Compound | | | | | |
|---|---|---|---|---|---|---|---|
| | | $(n\text{Hex}_4N)_3[AsW_4O_{24}]$ **6** | | $(n\text{Bu}_4N)_2[HAsW_2O_{14}]$ **4** | | $(n\text{Bu}_4N)_2[CH_3AsW_2O_{13}]\cdot H_2O$ **5** | |
| | | solid | $CH_3CN$ solution | solid | $CH_3CN$ solution | solid | $CH_3CN$ solution |
| $\tilde{\nu}$(W=O) | IR | 978 vs | 976 vs | 966 vs | 970 vs | 976 s<br>964 vs | 966 s |
| | Raman | 985(10) | 983(10) | 978(10) | 980(10) | 965(10) | 974(10) |
| $\tilde{\nu}(AsO_4)$ | IR | 892 vs<br>875 vs | 918 vs<br>885 vs | 932 m<br>870 vs | 918 vs<br>874 vs | 922 s<br>868 s | 918 vs<br>872 s |
| | Raman | 923(1)<br>896(1) | 911(8) | 910(3)<br>885(4) | 911(5)<br>881(3) | 910(3)<br>881(2) | 911(5) |
| $\tilde{\nu}$(O–O) | IR | 845 vs | 849 vs | 843 vs | 847 vs | 843 vs | 845 vs |
| | Raman | 857(7) | 861(8) | 855(8) | 858(7) | 837(5) | 845(4) |
| $\tilde{\nu}_{asym}[W(O)_2]$ | IR | 590 s<br>574 s | 594 m<br>577 s | 585 m<br>569 m | 587 m<br>576 s | 584 s<br>571 s | 587 s<br>573 m |
| | Raman | 593(3)<br>578(5) | 594(2)<br>579(5) | 586(4)<br>577(6) | 589(2)<br>577(4) | 584(4)<br>573(7) | 584(1)<br>573(3) |
| $\tilde{\nu}_{sym}[W(O)_2]$ | IR | 521 s | 518 s | 511 m | 514 s | 513 m | 517 s |
| | Raman | 535(2) | 532(2) | 528(2) | 530(2) | 520(2) | 524(1) |

[a] Relative intensities in parentheses for Raman data; bands resulting from the quaternary cations and water (complex **5**) are not listed.

 © 2006 Wiley-VCH Verlag GmbH & Co. KGaA, Weinheim 

the "peroxide class" of ionic compounds with isolated $[O_2]^{2-}$ ions, presents a Raman band at 842 $cm^{-1}$ that is unambiguously assigned to $\tilde{\nu}$(O–O).[52] Hence, spectroscopic data cannot differentiate all the ionic peroxide from the iono-covalent transition-metal complexes. In contrast, the peroxide function has a marked influence on the asymmetric and a less-marked influence on the symmetric stretches of the $\{W(O_2)_2\}$ moieties; their attributions, according to literature data,[50] are given in Table 2 for **4**, **5** and **6**. Two maxima are observed for $\tilde{\nu}_{asym}[W(O)_2]$ that correspond to the structural data (vide supra).

### Stoichiometric Epoxidation of (*R*)-(+)-Limonene

The reaction is highly chemoselective and regioselective, i.e. no bis-epoxides, no diols and no 8,9-epoxides were obtained (Scheme 2). Limonene oxide (0.7:1 to 1:1 mixtures of *cis* and *trans* 1,2-epoxide) was characterised and isolated.[13,30] Figure 3 shows that half of the peroxide oxygen is transferred to the olefinic substrate at room temperature, a result which differs from that of the MTO/$H_2O_2$ systems.[29,53] Comparative experiments with "$CH_3ReO_3$ + $2H_2O_2$/solvent" show complete transfer of the peroxide oxygen.

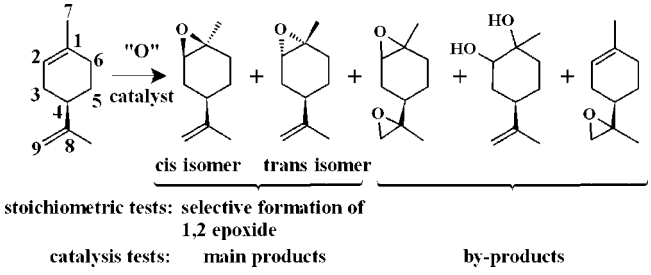


Scheme 2. Oxidation products of (*R*)-(+)-limonene.

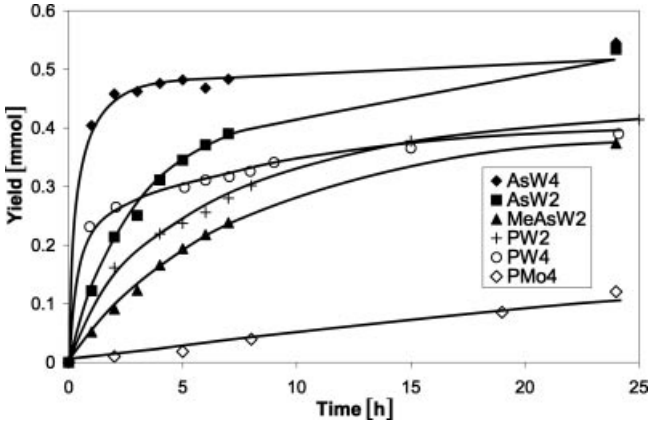


Figure 3. Stoichiometric epoxidation of (*R*)-(+)-limonene. $[(nBu)_4N]^+$ salts, 0.25 mmol for $XW_2$ and 0.125 mmol for $XW_4$ or $XMo_4$; active oxygen content due to oxoperoxo complex = 1 mmol; (*R*)-(+)-limonene: 1.5 mmol; 20 °C; solvent: dry $CH_2Cl_2$ (5 mL); $N_2$ ($P \approx 0.1$ MPa), internal standard: *n*-decane.

The kinetic curves also show that $[AsW_4O_{24}]^{3-}$ is more efficient than $[HAsW_2O_{14}]^{2-}$ and that there is a dramatic change from $[PMo_4O_{24}]^{3-}$ to $[AsW_4O_{24}]^{3-}$, which can be correlated with $\tilde{\nu}$(O–O).[13] It appears that the assembling ligand and the metal have a marked influence on the activity of these species, which all initially contain bridging $\mu$-$\eta^2$:$\eta^1$ peroxo ligands.

It was demonstrated by variable-temperature $^{31}P$ NMR spectroscopy that $[PM_4O_{24}]^{3-}$ species (M = Mo, W) and even the $[HPW_2O_{14}]^{2-}$ complex are fluxional.[25,43] In these anionic complexes, tridentate peroxo can also bind in a bidentate mode. The rearrangement involves the well-known seven-coordinate and six-coordinate tungsten moieties that were recently characterised;[40] at room temperature, the phosphate anion conserves its tetradentate character of a $\mu_4$-assembling ligand. We cannot run these same NMR spectroscopic experiments with the arsenato analogues, but the structural and spectrometric data related to **2**[10] and **6**, and also to **3**,[13] **4** and **5**,[14] lead us to consider that the phosphatooxoperoxotungstate species and the arsenato analogues behave similarly. Thus, rigid models are only a first approach for the transfer of active oxygen (from peroxo species) to olefinic substrates.[25,43] Rapid equilibria exist between anionic structures with tridentate ($\mu$-$\eta^2$:$\eta^1$-$O_2^{2-}$) and bidentate ($\eta^2$-$O_2^{2-}$) modes of coordination for the two kinds of peroxo groups of the $\{M_2O_2(\mu\text{-}O_2)_2(O_2)_2\}$ moieties, which play a key role in the activation and transfer of the oxygen of the peroxo groups, probably in the form of $\{\equiv As\text{–}OMO(O_2)_2\}$ and even free $\{MO(O_2)_2\}$ moieties.

### Catalysis Tests

Alkene epoxidation catalysed by "$AsW_4$" peroxo complexes has been investigated by several groups.[11,30,42,43,54] The Arquad 2HT® salts of complexes "$AsW_4$" and "$AsW_2$" are active precursors and catalysts in olefin oxidation, and form epoxides in the range 20–60 °C in two-phase "$H_2O_2$/$H_2O$/$CHCl_3$ or toluene" systems under phase-transfer catalysis (PTC) conditions (see Table 3, Entries 2 to 4). They transfer active oxygen to (*R*)-(+)-limonene to mostly give the monoepoxides, which are known to be acid-sensitive.[55–57] Complete optimisation must consider the effects of the organic solvent, the nature of $Q^+$, the assembling ligand X and the anionic species ($Cl^-$, $Br^-$, $HSO_4^-$, etc.), the pH of the aqueous phase, the presence of $Na^+Cl^-$ and the W/X/$Q^+$ ratios, and these factors have been analysed in detail by several groups.[30,58,59] For example, it has recently been shown that under PTC, a system such as W/$[PO_4]^{3-}$/$Q^+$ = 2:1:0.4 was more effective than the system 2:1:2 or 4:1:3 corresponding to the onium salts of "$PW_2$" and "$PW_4$", respectively.[31] The use of a large excess of $Q^+$ leads to low yields and turnover numbers, as shown previously.[30] If a tetra-*n*-hexylammonium cation is used instead of Arquad 2HT®, the conversion is very low (see Table 3, Entry 1).

Comparative studies for the recycling of different catalytic systems for epoxidation are under investigation by our group, and limitations exist for all of them except for the non-chlorinated solvents. Inexpensive buffer systems are

 © 2006 Wiley-VCH Verlag GmbH & Co. KGaA, Weinheim 

Table 3. (*R*)-(+)-Limonene epoxidation by arsenatooxoperoxotungsten complexes under phase transfer catalysis (PTC) conditions[a] at room temperature after 6 h reaction time.

| Entry | $W/[AsO_4]^{3-}/Q^+$ | $Q^+Cl^-$ | Organic solvent | Conversion[b] [%] | Selectivity[c] [%] | *Cis* isomer/ *Trans* isomer[d] |
|---|---|---|---|---|---|---|
| 1 | 4:1:3[e] | $(n\text{Hex})_4N^+Cl^-$ | Toluene | <1 | – | – |
| 2 | 4:1:2.8 | Arquad 2HT® | Toluene | 96 | 50 | 7.0 |
| 3 | 4:1:2.8 | Arquad 2HT® | $CHCl_3$ | 99 | 78 | 1.9 |
| 4 | 2:1:1.4 | Arquad 2HT® | $CHCl_3$ | 98 | 88 | 1.2 |

[a] General PTC procedure: organic solvent (5 mL, 15%); $H_2O_2$ (4 mL, 19.6 mmol); Teflon-coated bar driven externally by a magnetic stirrer (1200 rpm); limonene (6.2 mmol). [W]/[limonene] = 2%. [b] Conversion based on (*R*)-(+)-limonene was determined by GC using *n*-decane as an internal standard. [c] The selectivity is defined as S = [mol. *cis*- and *trans*-limonene oxide]/[mol. of converted limonene]. [d] See Scheme 2. [e] Catalysis test with **6**.

now easily used and recycled, as well as solid catalysts that are highly resistant to leaching. Note that the use of toluene as the organic solvent instead of $CHCl_3$ leads to a similar conversion but to a lower selectivity towards mono-epoxides (*cis* and *trans*).

Controlled addition of more appropriate weak bases ($Na_2[HAsO_4]$ is used here) to generate a buffer mixture [$pK_a$ ($H_2AsO_4^-/HAsO_4^{2-}$) = 6.95] leads to very high selectivity (>97%), but with a higher reaction time (e.g. 12 h for 99% conversion of limonene at room temperature).

It is clear that certain Keggin-type polyoxometalates can be stable under certain reaction conditions.[26–28] Parameters to consider in this context are solvent, concentrations, pH (more generally the acidity function), temperature, counterions, etc. In this paper, all the species of the catalyst pool, using the dodecatungstate anion as the catalyst precursor, have not been identified. To the best of our knowledge, it is not possible to find spectrometric evidence for all the oxoperoxo complexes. Unfortunately, we cannot perform kinetics or time-resolved studies, and the true catalytic species may be present only at low concentrations and are not amenable to characterisation. It was against this backdrop that we published refs.[25,43]. The catalyst of Noyori et al.[58] is not isolable.

## Conclusion

The addition of arsenate to oxoperoxotungstate species (peroxide/tungsten > 2), as well as the use of polyoxometalates such as the Keggin dodecatungstoarsenate anion of $Na_2H[AsW_{12}O_{40}]\cdot nH_2O$ or "$AsW_{12}$", give, with excess aqueous hydrogen peroxide, arsenatooxoperoxotungstate complexes: $Q_3[AsO_4\{W_2O_2(\mu\text{-}O_2)_2(O_2)_2\}_2]$ or "$AsW_4$", $Q_2[HAsO_4\{W_2O_2(\mu\text{-}O_2)_2(O_2)_2\}]$ or "$AsW_2$", etc. isolated with $Q^+$ = onium cation and $Q'_2[\{WO(O_2)_2(H_2O)\}_2(\mu\text{-}O)]$. All these anionic species are highly effective for epoxidation procedures (complete optimisation must consider the effects of the nature of $Q^+$ or $Q'^+$, the organic solvent, the assembling ligand X, the pH of the aqueous phase and the $W/X/Q^+$ ratios, as we showed previously).[6,9,30,31] Thus, the heteropolyanion can only be a precursor of the true catalysts (e.g. "$AsW_4$", "$AsW_2$", etc.). The "$AsW_n$" complexes, which have no coordinated water, are lipophilic and are easily transferred into an organic phase with selected $Q^+$. The facile transfer of active oxygen from these peroxo species to olefinic substrates can be related to their structure and their fluxionality. We propose that the lack of solvolytic stability of "$AsW_{12}$" and of its analogues in aqueous hydrogen peroxide can be attributed to the equilibria between Keggin and lacunary heteropolyanions and $\{WO_2(OH)\}^+$; this mononuclear group subsequently reacts with $H_2O_2$ to generate the well-known Mimoun species, $[WO(O_2)_2(H_2O)_2]$, and with X, thus forming "$AsW_4$", "$AsW_2$", etc. On the contrary, as shown recently,[7] $[\{WO(O_2)_2(H_2O)\}_2(\mu\text{-}O)]^{2-}$ is a preferred catalyst in water for the epoxidation of various allylic alcohols. The crystal structures of "$AsW_4$", "$AsW_2$" and of their methylarsenato analogue show that they contain the unique $\{W_2O_2(\mu\text{-}O_2)_2(O_2)_2\}$ moieties of the Venturello complex.

## Experimental Section

### Syntheses

**$Na_2H[AsW_{12}O_{40}]\cdot NaCl\cdot 30H_2O$:** This sodium salt was prepared according to the previously described procedure in which concentrated aqueous HCl (12 M) is used.[51] Note that we found chlorine in the final product, which corresponds to a monohydrogenodisodium salt (yield 72%). $H_{61}AsClNa_3O_{70}W_{12}$ (3566.98): calcd. As 2.10, Cl 0.99, Na 1.93, W 61.85; found As 1.99, Cl 0.84, Na 2.09, W 62.58.

**$[(n\text{Hex})_4N]_3[AsO_4\{W_2O_2(\mu\text{-}O_2)_2(O_2)_2\}_2]$ (6) and $K_2[\{WO(O_2)_2(H_2O)\}_2(\mu\text{-}O)]\cdot 2H_2O$:** This complex was first prepared from the "$H_2WO_4/H_2O_2/H_2O/Na_2H[AsO_4]\cdot 7H_2O/[(n\text{Hex})_4N]Cl$" systems. The synthesis was adapted from methods previously described for the preparation of **6**[60] and **1**, **2**.[9,11] Tungstic acid, "$H_2WO_4$", (2.5 g, 10 mmol) was added to a 30% aqueous solution of hydrogen peroxide (7 mL, 69 mmol). After 40 min of stirring at 60 °C, and then cooling to room temperature and centrifugation (15 min at 2000 rpm), the supernatant liquid (solution A) was added to an aqueous solution of $Na_2H[AsO_4]\cdot 7H_2O$ (2 mL, 0.78 g, 2.5 mmol). After 15 min of stirring, a solution of $[(n\text{Hex})_4N]Cl$ (1.56 g, 4 mmol) in toluene (25 mL) was slowly added. After 60 min of vigorous stirring, the white precipitate formed at the interface was filtered off, washed thoroughly with distilled water (10 mL), toluene (10 mL) and diethyl ether (10 mL) and dried with $P_4O_{10}$ (yield: 2.82 g, 50%). $C_{72}H_{156}AsN_3O_{24}W_4$ (2258.37): calcd. C 38.29, H 6.96, As 3.32, N 1.86, W 32.56; found C 38.07, H 7.10, As 3.15, N 1.75, W 32.16. IR and Raman spectroscopy: see Table 2. Although tetra-*n*-butylammonium and bis(triphenylphosphoranylidene) ammonium salts were prepared in powder or microcrystalline forms, only the tetra-*n*-hexylammonium salts gave single crystals of an appropriate size from acetonitrile solutions in the presence of a slight excess of hydrogen peroxide, otherwise Keggin salts are

 © 2006 Wiley-VCH Verlag GmbH & Co. KGaA, Weinheim 

formed. Compound **6** was also synthesised from "$Na_2H[AsW_{12}O_{40}]$·$NaCl$·$30H_2O/H_2O_2/H_2O/[(n\text{Hex})_4]Cl$ or $[(n\text{Bu})_4N]Cl$" systems. Aqueous hydrogen peroxide (30%, 100 mmol; 10 mL) was slowly added to a solution of the $[AsW_{12}O_{40}]^{3-}$ salt (vide supra, 0.5 mmol, 1.57 g) in water (1 mL). After 30 min of stirring at room temperature, an aqueous solution of tetra-*n*-butylammonium chloride (3 mL, 1.6 mmol, 0.45 g) was slowly added. The white precipitate was filtered off, washed with water (2 × 10 mL) and then dried with $P_4O_{10}$ (yield: 0.47 g, 41.5% based on As). Higher yields (≥90%) were obtained when an excess of $Na_2H[AsO_4]$·$7H_2O$ was added to the aqueous phase. Excess potassium chloride (7 mmol) can also be added to the recovered filtrate. A few millilitres of ethanol were added to the solution that was cooled to 5 °C until a snow-white precipitate appeared. After filtration and washing with ethanol, the precipitate, $K_2[\{WO(O_2)_2(H_2O)_2\}(\mu\text{-}O)]$·$2H_2O$, was air dried (yield 60% based on the initial precursor). See Scheme 1 for the appropriate choice of counteranions in order to obtain the two oxoperoxo salts selectively.

**$[(n\text{Bu})_4N]_2[HAsO_4\{W_2O_2(\mu\text{-}O_2)_2(O_2)_2\}]$ (4):** Solution A (vide supra) and a solution of $Na_2H[AsO_4]$·$7H_2O$ (1.59 g; 5.1 mmol) in water (2 mL) were mixed at room temperature. After 20 min of stirring, an aqueous solution of $[(n\text{Bu})_4N]Cl$ (2.78 g, 10 mmol in 10 mL) was slowly added while slow stirring was maintained. The white precipitate was filtered off on a fritted glass disc, washed thoroughly with cold water (10 mL) and diethyl ether (10 mL) and dried with $P_4O_{10}$ (yield: 4.46 g, 77%). $C_{32}H_{73}AsN_2O_{14}W_2$ (1152.56): calcd. C 33.34, H 6.38, As 6.50, N 2.43, W 31.90; found C 33.49, H 6.45, As 6.15, N 2.55, W 30.92. IR and Raman spectroscopy: see Table 2. (Compound **4** can also be prepared from $[AsW_{12}O_{40}]^{3-}$, but it is more convenient to use a direct method).

**$[(n\text{Bu})_4N]_2[CH_3AsO_3\{W_2O_2(\mu\text{-}O_2)_2(O_2)_2\}]$ (5):** This was prepared in a similar manner. $Na_2[CH_3AsO_3]$·$6H_2O$ (1.49 g, 5.1 mmol), dissolved in water (2 mL), was added to solution A. After 30 min of stirring $[(n\text{Bu})_4N]Cl$ (2.78 g in 7.5 mL water) was slowly added. Well-formed crystals suitable for X-ray measurements were obtained by slow evaporation of acetonitrile/$H_2O_2$ solutions of the microcrystalline precipitates of **4** and **5**.[14]

**Structure Determinations:** Single crystals of **6** were grown from $CH_2Cl_2/(C_2H_5)_2O/H_2O_2$ (2:1:0.1), or better from $CH_3CN/H_2O_2/H_2O$ mixtures, by slow evaporation at +5 °C. Although highly precise crystal structure analyses are not easily obtained with the tetra-*n*-hexylammonium cation[9,10] (a result of the flexibility of the long alkyl chain, solvent molecules that are incorporated in the crystals and disorder for some of the cations[61]), X-ray measurements were undertaken, because, at least, the structure of the anion could be elucidated, which would provide valuable information for the chemistry of heteropolyanions containing the $[AsO_4]^{3-}$ assembling ligand and for the relationship of some Keggin anions and Venturello–Ishii systems.

**$[(n\text{Hex})_4N][AsO_4\{W_2O_2(\mu\text{-}O_2)_2(O_2)_2\}_2]$ (6):** $C_{72}H_{156}AsN_3O_{24}W_4$, $M_r$ = 2258.37, monoclinic, space group *C*2 (no. 5); $a$ = 2051.6(6), $b$ = 1592.3(4), $c$ = 1490.2(2) pm, $\beta$ = 91.64(1)°, $V$ = 4.866(1) nm$^3$, $Z$ = 2, $\rho_{calcd.}$ = 1.54 Mg m$^{-3}$, $F(000)$ = 2260, $\lambda$ = 71.073 pm, $T$ = 293 K, $\mu$(Mo-$K_\alpha$) = 0.5112 mm$^{-1}$, crystal dimensions 0.1 × 0.3 × 0.4 mm (parallelepiped), 2° ≤ 2$\theta$ ≤ 50°, 13697 measured reflections, 7412 were unique, 206 parameters refined in full-matrix, $R_1$ = 0.058 with 5318 reflections [$I > 3\sigma(I)$], $wR_2$ = 0.067, $w \neq 1$ [weighting scheme of the form $w = w'[1 - \{(||F_o| - |F_c||)/6\sigma(F_o)\}^2]^2$ with $w' = 1/\Sigma_r A_r T_r(X)$ with coefficients 0.417, 0.302 and 0.177 for a Chebyshev series for which $X = F_c/F_{c(max)}$].[62] Min./max. residual electron density –127/153 e mm$^{-3}$. Goodness of fit: 0.93. The data were collected with a KAPPACCD-Enraf Nonius automated diffractometer at room temperature. (At low temperature the crystal collapsed.) Unit cell dimensions with estimated standard deviations were obtained from least-squares refinements of the setting angles of 35 well-centered reflections. Corrections were made for Lorentzian and polarization effects; an absorption correction (sadabs) was also applied. The structure was solved by direct methods (SHELX-86 program)[63] and subsequent Fourier difference techniques. Some of the carbon atoms of the ammonium counterions showed high thermal parameters as a result of the flexibility of the long alkyl chain and were not refined, even with reduced occupancy. Only 34 carbon atoms could be well located in the difference Fourier map. These problems probably arise from low-solvent content and from the fact that the crystal decomposes slowly. Computations were performed using CRYSTALS,[64] adapted to a PC computer. Atomic form factors for neutral C, N, As, O and W were taken from ref.[65] Refinements were carried out by minimising the functions $R = \Sigma||F_o| - |F_c||/\Sigma|F_o|$ and $Rw^* = [\Sigma w(||F_o| - |F_c||)^2/\Sigma wF_o^2]^{1/2}$, where $F_o$ and $F_c$ are the observed and calculated structure factors, respectively. A representation of the anion was drawn with CAMERON[66] (see Figure 1).

CCDC-276917 for **6** contains the supplementary crystallographic data for this paper. These data can be obtained free of charge from The Cambridge Crystallographic Data Centre via www.ccdc.cam.ac.uk/data_request/cif.

**General:** The solvents were purified by standard procedures for the stoichiometric and catalytic tests. Commercial, stabilised 30% w/v aqueous solutions of hydrogen peroxide (pH ≈ 1.5) either contained a phosphorus(V) concentration lower than 1.5 mM or were without phosphates (Aldrich) in order to avoid the formation of phosphatooxoperoxotungstate species. Tungstic acid, "$H_2WO_4$" was supplied by Eurotungstène. $Na_2H[AsO_4]$·$7H_2O$ and $Na_2[CH_3AsO_3]$·$6H_2O$ were obtained from Prolabo/VWR. The onium salts are marketed by Aldrich and Lancaster Synthesis. (*R*)-(+)-Limonene (Lancaster) was shown to be more than 97% pure by GC and NMR analyses. GC analyses were carried out with a Girdel chromatograph (FID) fitted with a SPB™ 1701 capillary column with helium as the carrier gas. Analyses were performed at temperatures ranging from 70 to 200 °C (5 °C min$^{-1}$, $P_{He}$: 0.16 MPa). GC–MS analyses were performed with a GC apparatus coupled with a mass spectrometer (Girdel 30/Delsi-Nermag and Trace GC 2000 series-Thermofinnigan) coupled to a Trace MS mass spectrometer (EI or CI/$NH_3$). $^1H$ and $^{13}C$ NMR spectra were recorded at ambient temperature with a Fourier transform apparatus (Bruker AC 200), using $CDCl_3$ as the solvent and TMS as the internal reference. IR spectra (resolution: 2–4 cm$^{-1}$) were measured with a Fourier transform apparatus (Bruker IFS 45 or Equinox 55) in Nujol suspension, either between two caesium bromide plates or KBr pellets. Solution spectra of **4**, **5** and **6** in acetonitrile (0.05 M) were recorded at room temperature with a standard sodium chloride cell (0.1 mm thickness). Acetonitrile has a window between 500–910 cm$^{-1}$, which is suitable for studying $\tilde{\nu}$(O–O), $\tilde{\nu}_{sym}[W(O_2)]$ and $\tilde{\nu}_{asym}[W(O_2)]$ bands.

Raman spectra were recorded at room temperature with a Jobin–Yvon U1000 spectrometer with a resolution of 4 cm$^{-1}$. Solid samples of the complexes were mounted on a disc rotating at about 1000 rpm in order to avoid decomposition and/or photoreduction by the laser beam (excitation line, 514.5 nm of an $Ar^+$ laser; source power, 30–50 mW; scanning time, ca. 2 h). Solutions of **6** (0.25 M), **4** (0.5 M) and **5** (0.5 M) were studied. Elemental analyses (C, H, As, N and W) were carried out at the Service Central d'Analyses CNRS, Vernaison.

**Stoichiometric Regioselective Epoxidation with Six Oxoperoxo Complexes:** These were conducted under dinitrogen using Schlenk

 © 2006 Wiley-VCH Verlag GmbH & Co. KGaA, Weinheim 

techniques and deaerated solvents. (*R*)-(+)-Limonene (1.5 mmol) was rapidly added to a thermostatted (20 °C) solution of the complex (0.25 mmol for $XW_2$ and 0.125 mmol for $XW_4$ or $XMo_4$, active oxygen content, i.e. $[O_2]^{2-}$: 1 mmol) in dry $CH_2Cl_2$ (5 mL). The solution was stirred under dinitrogen. GC analyses were performed periodically with *n*-decane as internal standard. (*R*)-(+)-Limonene oxide (mixture of *cis* and *trans*) was obtained and isolated. It was identified by MS and by $^1H$ and $^{13}C$ NMR spectroscopy.[13]

**Catalysis Tests:** Our previous procedure[13,23] was followed. "$H_2WO_4$" was treated with 15% $H_2O_2$ (4 mL, 19.6 mmol). After 15 min of stirring (necessary for the precursor to react completely at 60 °C) and cooling at room temperature, $Na_2H[AsO_4]\cdot 7H_2O$ was added (see Table 3). $Q^+Cl^-$, dissolved in the organic solvent, was then added with the substrate (6.2 mmol). The two-phase mixture was stirred vigorously (1200 rpm) for 6 h at 20 °C under dinitrogen. The organic extract was analysed by GC and/or GC–MS and in some cases by $^1H$ NMR spectroscopy.

## Acknowledgments

We thank Dr. John Lomas for constructive discussions and for correcting the manuscript, and Mme F. Sarrazin for preparing the text.

[1] C. L. Hill, C. M. Prosser-McCartha, *Coord. Chem. Rev.* **1995**, *143*, 407–455.
[2] T. Okuhara, N. Mizuno, M. Misono, *Adv. Catal.* **1996**, *41*, 113–252.
[3] R. Neumann, *Prog. Inorg. Chem.* **1998**, *47*, 317–370.
[4] I. V. Kozhevnikov, *Chem. Rev.* **1998**, *98*, 171–198.
[5] C. Jost, G. Wahl, D. Kleinhenz, J. Sundermeyer in *Peroxide Chemistry* (Ed.: W. Adam), Wiley-VCH Verlag GmbH, Weinheim, **2000**, pp. 341–364.
[6] J.-M. Brégeault, *Dalton Trans.* **2003**, 3289–3302.
[7] N. Mizuno, K. Yamaguchi, K. Kamata, *Coord. Chem. Rev.* **2005**, *249*, 1944–1956.
[8] R. G. Beiles, Z. E. Rozmanova, O. B. Andreeva, *Zh. Neorg. Khim.* **1969**, *14*, 2139–2142.
[9] L. Salles, C. Aubry, F. Robert, G. Chottard, R. Thouvenot, H. Ledon, J.-M. Brégeault, *New J. Chem.* **1993**, *17*, 367–375.
[10] C. Venturello, R. d'Aloisio, J. C. J. Bart, M. Ricci, *J. Mol. Catal.* **1985**, *32*, 107–110.
[11] C. Venturello, R. d'Aloisio, J. C. J. Bart, M. Ricci, *European Patent Appl*. 0146374, **1985**.
[12] C. Venturello, M. Gambaro, *J. Org. Chem.* **1991**, *56*, 5924–5931.
[13] L. Salles, C. Aubry, R. Thouvenot, F. Robert, C. Dorémieux-Morin, G. Chottard, H. Ledon, Y. Jeannin, J.-M. Brégeault, *Inorg. Chem.* **1994**, *33*, 871–878.
[14] J.-Y. Piquemal, L. Salles, C. Bois, F. Robert, J.-M. Brégeault, *C. R. Acad. Sci., Ser. IIb: Mec., Phys., Chim., Astron.* **1994**, *319*, 1481–1487.
[15] F. W. B. Einstein, B. R. Penfold, *Acta Crystallogr.* **1964**, *17*, 1127–1133.
[16] M. Hashimoto, T. Ozeki, H. Ichida, Y. Sasaki, K. Matsumoto, T. Kudo, *Chem. Lett.* **1987**, 1873–1876.
[17] R. Stomberg, *Acta Chem. Scand. Ser. A* **1985**, *39*, 507–514.
[18] L. Trysberg, R. Stomberg, *Acta Chem. Scand. Ser. A* **1981**, *35*, 823–825.
[19] I. Persdotter, L. Trysberg, R. Stomberg, *Acta Chem. Scand. Ser. A* **1986**, *40*, 1–7.
[20] L. Salles, F. Robert, V. Semmer, Y. Jeannin, J.-M. Brégeault, *Bull. Soc. Chim. Fr.* **1996**, *133*, 319–328.
[21] M. Hashimoto, T. Iwamoto, H. Ichida, Y. Sasaki, *Polyhedron* **1991**, *10*, 649–651.
[22] J.-M. Brégeault, C. Aubry, G. Chottard, N. Platzer, F. Chauveau, C. Huet, H. Ledon, *Stud. Surf. Sci. Catal.* **1991**, *66*, 521–529.
[23] C. Aubry, G. Chottard, N. Platzer, J.-M. Brégeault, F. Chauveau, C. Huet, H. Ledon, *Inorg. Chem.* **1991**, *30*, 4409–4416.
[24] J. Server-Carrio, J. Bas-Serra, M. E. Gonzales-Nunez, A. Garcia-Gastaldi, G. B. Jameson, L. C. W. Baker, R. Acerete, *J. Am. Chem. Soc.* **1999**, *121*, 977–984.
[25] L. Salles, R. Thouvenot, J.-M. Brégeault, *Dalton Trans.* **2004**, 904–907.
[26] T. Yamase, T. Ozeki, S. Motomura, *Bull. Chem. Soc. Jpn.* **1992**, *65*, 1453–1459.
[27] T. Yamase, E. Ishikawa, Y. Asai, S. Kanai, *J. Mol. Catal. A: Chem.* **1996**, *114*, 237–245.
[28] O. A. Kholdeeva, T. A. Trubitsina, M. N. Timofeeva, G. M. Maksimov, R. I. Maksimovskaya, V. A. Rogov, *J. Mol. Catal. A: Chem.* **2005**, *232*, 173–178.
[29] J.-M. Brégeault, C. Lepetit, F. Ziani-Derdar, O. Mohammedi, L. Salles, A. Deloffre, *Stud. Surf. Sci. Catal.* **1997**, *110*, 545–556.
[30] J.-M. Brégeault, R. Thouvenot, S. Zoughebi, L. Salles, A. Atlamsani, E. Duprey, C. Aubry, F. Robert, G. Chottard, *Stud. Surf. Sci. Catal.* **1994**, *82*, 571–581.
[31] L. Salles, J.-M. Brégeault, R. Thouvenot, *C. R. Acad. Sci., Ser. IIc: Chim.* **2000**, *3*, 183–187.
[32] E. Duprey, J. Maquet, P. P. Man, J.-M. Manoli, M. Delamar, J.-M. Brégeault, *Appl. Catal., A* **1995**, *128*, 89–96.
[33] J.-Y. Piquemal, E. Briot, M. Vennat, J.-M. Brégeault, G. Chottard, J.-M. Manoli, *Chem. Commun.* **1999**, 1195–1196.
[34] J.-Y. Piquemal, J.-M. Manoli, P. Beaunier, A. Ensuque, P. Tougne, A.-P. Legrand, J.-M. Brégeault, *Microporous Mesoporous Mater.* **1999**, *29*, 291–304.
[35] E. Briot, J.-Y. Piquemal, M. Vennat, J.-M. Brégeault, G. Chottard, J.-M. Manoli, *J. Mater. Chem.* **2000**, *10*, 953–958.
[36] J.-M. Brégeault, J.-Y. Piquemal, E. Briot, E. Duprey, F. Launay, L. Salles, M. Vennat, A.-P. Legrand, *Microporous Mesoporous Mater.* **2001**, *44–45*, 409–417.
[37] E. Briot, J.-Y. Piquemal, J.-M. Brégeault, *New J. Chem.* **2002**, *26*, 1443–1447.
[38] J.-Y. Piquemal, E. Briot, G. Chottard, P. Tougne, J.-M. Manoli, J.-M. Brégeault, *Microporous Mesoporous Mater.* **2003**, *58*, 279–289.
[39] J.-Y. Piquemal, C. Bois, J.-M. Brégeault, *Chem. Commun.* **1997**, 473–474.
[40] J.-Y. Piquemal, S. Halut, J.-M. Brégeault, *Angew. Chem. Int. Ed. Engl.* **1998**, *37*, 1146–1149.
[41] L. J. Csanyi, K. Jacky, *J. Catal.* **1991**, *127*, 42–50.
[42] A. C. Dengel, W. P. Griffith, B. C. Parkin, *J. Chem. Soc., Dalton Trans.* **1993**, 2683–2688.
[43] L. Salles, J.-Y. Piquemal, R. Thouvenot, C. Minot, J.-M. Brégeault, *J. Mol. Catal. A: Chem.* **1997**, *117*, 375–387.
[44] O. W. Howarth, *Dalton Trans.* **2004**, 476–481.
[45] M. A. G. Aranda, J. P. Attfield, S. Bruque, M. Martinez-Lara, *Inorg. Chem.* **1992**, *31*, 1045–1049.
[46] M. I. Khan, Y. Chang, Q. Chen, H. Hope, S. Parking, D. P. Goshorn, J. Zubieta, *Angew. Chem. Int. Ed. Engl.* **1992**, *31*, 1197–1200.
[47] J.-M. Le Carpentier, A. Mitschler, R. Weiss, *Acta Crystallogr. Acta Crystallogr., Sect. B* **1972**, *28*, 1278–1288.
[48] W. P. Griffith, A. M. Z. Slawin, K. M. Thompson, D. J. Williams, *J. Chem. Soc., Chem. Commun.* **1994**, 569–570.
[49] H. Siebert, *Z. Anorg. Allg. Chem.* **1954**, *275*, 225–240.
[50] K. Nakamoto, *Infrared and Raman Spectra of Inorganic and Coordination Compounds, Part A: Theory and Applications in Inorganic Chemistry*, 5th ed., John Wiley, New York, **1997**, pp. 189–201.
[51] C. Rocchiccioli-Deltcheff, M. Fournier, R. Franck, R. Thouvenot, *Inorg. Chem.* **1983**, *22*, 207–216.
[52] J.-M. Brégeault, G. Chottard, *unpublished results.*

 © 2006 Wiley-VCH Verlag GmbH & Co. KGaA, Weinheim 

[53] F. E. Kühn, C. C. Romão, W. A. Hermann in *Science Synthesis: Ho uben Weyl Methods of Molecular Transformations* (Ed.: T. Imamoto), Georg. Thieme Verlag, Stuttgart, **2003**, *2*, pp. 111–153.
[54] L. J. Csányi, K. Jáky, *J. Mol. Catal.* **1990**, *61*, 75–84.
[55] J.-M. Brégeault, C. Lepetit, F. Ziani-Derdar, O. Mohammedi, L. Salles, A. Deloffre, *Stud. Surf. Sci. Catal.* **1997**, *110*, 545–556.
[56] A. Deloffre, S. Halut, L. Salles, J.-M. Brégeault, J. Ribeiro Gregorio, B. Denise, H. Rudler, *J. Chem. Soc., Dalton Trans.* **1999**, 2897–2898.
[57] H. Rudler, J. Ribeiro Gregorio, B. Denise, J.-M. Brégeault, A. Deloffre, *J. Mol. Catal. A: Chem.* **1998**, *133*, 255–265.
[58] K. Sato, M. Aoki, M. Ogawa, T. Hashimoto, D. Panyella, R. Noyori, *Bull. Chem. Soc. Jpn.* **1997**, *70*, 905–915.
[59] M.-L. Wang, T.-H. Huang, *J. Chem. Eng. Jpn.* **2003**, *36*, 231–242.
[60] N. M. Gresley, W. P. Griffith, A. C. Laemmel, H. I. S. Nogueira, B. C. Parkin, *J. Mol. Catal. A: Chem.* **1997**, *117*, 185–198.
[61] A. Eichhöfer, O. Hampe, M. Blom, *Eur. J. Inorg. Chem.* **2003**, 1307–1314.
[62] R. J. Carruthers, D. J. Watkin, *Acta Crystallogr., Sect. A* **1979**, *35*, 698–699.
[63] G. M. Sheldrick, SHELX-86, *Program for the Solution of Crystal Structure*s, University of Göttingen, Germany, **1986**.
[64] D. J. Watkin, C. K. Prout, R. J. Carruthers, P. W. Betteridge, R. I. Cooper, *CRYSTALS, An Advanced Crystallographic Program System*, Chemical Crystallography Laboratory, University of Oxford, **2001**.
[65] D. T. Cromer, J. T. Waber, *International Tables for X-ray Crystallography*, Kynoch Press, Birmingham, **1974**, vol. IV, p. 99.
[66] D. J. Watkin, C. K.Prout, L. J. Pearce, *CAMERON, A Program for Plotting Molecular Structure*, Chemical Crystallography Laboratory, University of Oxford, **1996**.

Received: August 29, 2005
Published Online: January 12, 2006

 © 2006 Wiley-VCH Verlag GmbH & Co. KGaA, Weinheim 

DOI: 10.1002/ejic.200500791

# Reactivity of the Pyrazolatopalladium(II) Complexes $[Pd(dmpz)_2(Hdmpz)_2]$ and $[Pd_2(\mu\text{-}dmpz)_2(dmpz)_2(Hdmpz)_2]$ towards Carboxylic Acids: Hydrogen Bonds as the Driving Force That Determines the Nature of the Final Products

**Irene Ara,[a] Juan Forniés,*[a] Roberto Lasheras,[b] Antonio Martín,[a] and Violeta Sicilia*[b]**

**Keywords:** Carboxylate ligands / Heterometallic complexes / Hydrogen bonds / N ligands / Palladium

The compound $[Pd(Hdmpz)_4](O_2CCH_2NHCOCH_3)_2$ (**1**; (Hdmpz = 3,5-dimethylpyrazole) has been obtained by treatment of $[Pd(dmpz)_2(Hdmpz)_2]$ (**A**) with two equivalents of *N*-acetylglycine ($HO_2CCH_2NHCOCH_3$). The X-ray study on a crystal of **1** revealed that the *N*-acetylglycinate anion links to the cationic complex $[Pd(Hdmpz)_4]^{2+}$ through the carboxylate group by charge assisted $N–H^{(+)}\cdots O^{(-)}$ hydrogen bonds. Additionally, the remaining N–H and C=O groups allow the *N*-acetylglycinate anions to self-assemble through N–H···O hydrogen bonds to generate infinite chains. The compounds $[Pd_2(\mu\text{-}dmpz)_2(O_2CCH_2NHCOCH_3\text{-}\kappa O)_2(Hdmpz)_2]$ (**2**) and $[Pd_2(\mu\text{-}dmpz)_2(O_2CC_6H_4\text{-}R\text{-}\kappa O)_2(Hdmpz)_2]$ [R = *m*-$NO_2$ (**3a**), *p*-$N(CH_3)_2$ (**3b**), *p*-$NH_2$ (**3c**), *p*-$OCH_3$ (**3d**), *p*-OH (**3e**)] have been obtained by treatment of $[Pd_2(\mu\text{-}dmpz)_2(dmpz)_2(Hdmpz)_2]$ (**B**) with two equivalents of the monocarboxylic acids *N*-acetylglycine ($HO_2CCH_2NHCOCH_3$) and the benzoic derivatives $HO_2CC_6H_4R$ [R = *m*-$NO_2$, *p*-$N(CH_3)_2$, *p*-$NH_2$, *p*-$OCH_3$, *p*-OH] respectively. The X-ray study on complexes **3d** and **3e** shows that in these complexes the carboxylate anion bonded to one Pd atom and the terminal Hdmpz group bonded to the other one have the right arrangement to establish an N–H···O hydrogen bond. The H···O and N···O distances are in the range of those corresponding to charge-assisted $N–H^{(+)}\cdots O^{(-)}$ interactions. In complexes **3a**–**3e**, the H atoms of the terminal Hdmpz groups can be replaced by $Ag^+$ to give the mixed-metal complexes $[Pd_2Ag_2(\mu\text{-}dmpz)_4(\mu\text{-}O_2CC_6H_4\text{-}R\text{-}\kappa O)_2(Hdmpz)_2]$ [R = *m*-$NO_2$ (**4a**), *p*-$N(CH_3)_2$ (**4b**), *p*-$NH_2$ (**4c**), *p*-$OCH_3$ (**4d**), *p*-OH (**4e**)]. Compounds **4a**–**4e**, which exhibit a transoid conformation of the carboxylate groups with respect to the Pd···Pd line, isomerise to the cisoid species (**4a′**–**4e′**). The X-ray structure of the DMSO adduct of **4d′** is also reported.
(© Wiley-VCH Verlag GmbH & Co. KGaA, 69451 Weinheim, Germany, 2006)

## Introduction

The coordination chemistry of neutral pyrazole (HRpz) or anionic pyrazolate (Rpz) ligands has been intensively developed over many years[1] and has been thoroughly reviewed.[2–5] Recently, unprecedented compounds showing new bonding modes for pyrazolate ligands have been reported.[6–10] In spite of this, the number of palladium and platinum compounds is rather low. Only a few examples of mono- ($[Pt(pz)_2(Hpz)_2]$,[11,12] $[Pt(Hpz)_4]Cl_2$,[11] $[Pd(Hpz)_4]Cl_2$,[12] $[Pd(dmpz)_2(Hdmpz)_2]$[13]), di- {$[Pd_2(\mu\text{-}dmpz)_2(dmpz)_2(Hdmpz)_2]$,[14] $[Pd_2(\mu\text{-}3\text{-}t\text{Bupz})_2(3\text{-}t\text{Bupz})_2(H_3\text{-}t\text{Bupz})_2]$,[12] $[Pd_2(\mu\text{-}pz)_2(Hpz)_4](BF_4)_2$[15]} or trinuclear ($[\{Pt(\mu\text{-}pz)_2\}_3]$,[12,16] $[\{Pd(\mu\text{-}pz)_2\}_3]$,[12] $[\{Pd(\mu\text{-}4\text{-}Mepz)_2\}_3]$,[12] $[\{Pd(\mu\text{-}3\text{-}Phpz)_2\}_3]$[17]) compounds containing only pyrazoles (HRpz) and/or pyrazolates (Rpz) as ligands have been reported up to now, one of them, $[Pd_2(\mu\text{-}dmpz)_2(dmpz)_2(Hdmpz)_2]$ having been published recently by us.[14] This kind of compound often contains inter-[11–13] or intramolecular[12,14] N–H···N hydrogen bonds involving neutral pyrazole (HRpz) and anionic pyrazolate (Rpz) groups, and the protons of the coordinated pyrazoles can be replaced by metal ions as $Cu^I$, $Ag^I$ and $Au^I$ to give heterometallic polynuclear complexes.[12–14]

The mono- and dinuclear complexes $[Pd(dmpz)_2(Hdmpz)_2]$ (**A**)[13] and $[Pd_2(\mu\text{-}dmpz)_2(dmpz)_2(Hdmpz)_2]$ (**B**)[14] have terminal dmpz and Hdmpz ligands bonded to each palladium centre, that is, on each side of both complexes there is a dmpz group, which is a hydrogen-bond acceptor, and an Hdmpz ligand, which is a hydrogen-bond donor. We therefore considered it of interest to use these compounds as starting materials to obtain organic–organometallic hydrogen-bonded networks by reaction of both complexes with carboxylic acids. A carboxylic acid group (COOH) can form complementary hydrogen bonds with the dmpz and Hdmpz ligands on the same side of each complex (Figure 1a) or transfer its proton to the dmpz ligand. Should this be the case, charge-assisted $N–H^{(+)}\cdots O^{(-)}$ hydrogen bonds would be formed between complex cations and

[a] Departamento de Química Inorgánica, Instituto de Ciencia de Materiales de Aragón, Facultad de Ciencias, Universidad de Zaragoza-CSIC,
Pl. S. Francisco s/n 50009 Zaragoza, Spain
E-mail: juan.fornies@unizar.es
[b] Departamento de Química Inorgánica, Instituto de Ciencia de Materiales de Aragón, Escuela Universitaria de Ingeniería Técnica Industrial, Universidad de Zaragoza-CSIC,
Campus Universitario del Actur, Edificio Torres Quevedo, 50018, Zaragoza, Spain
E-mail: sicilia@unizar.es

 © 2006 Wiley-VCH Verlag GmbH & Co. KGaA, Weinheim 

carboxylate anions yielding a heteromeric synthon of type $R_2(10)$[18,19] (Figure 1b). Additionally, the substitution of dmpz by carboxylate groups could also take place.

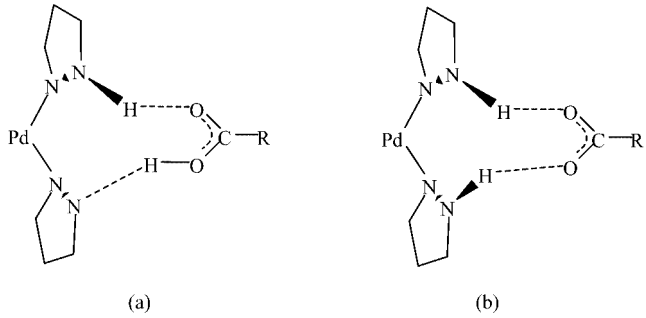

(a) (b)

Figure 1. a) Complementary hydrogen bonds between the neutral carboxylic group and the "*cis*-Pd(dmpz)(Hdmpz)" fragment. b) Charge-assisted $N–H^{(+)}\cdots O^{(-)}$ hydrogen bonds between a carboxylate anion and the cationic "*cis*-$Pd(Hdmpz)_2$" fragment.

In this paper we report the reactivity of complexes $[Pd(dmpz)_2(Hdmpz)_2]$ (**A**) and $[Pd_2(\mu\text{-}dmpz)_2(dmpz)_2(Hdmpz)_2]$ (**B**) towards monocarboxylic acids such as *N*-acetylglycine ($HO_2CCH_2NHCOCH_3$) and benzoic acid derivatives [$HO_2CC_6H_4$-R, R = *m*-$NO_2$, *p*-$N(CH_3)_2$, *p*-$NH_2$, *p*-$OCH_3$, *p*-OH]. Some of these carboxylic acids contain an additional functional group that is able to form an extra molecular hydrogen bond. As a result, a new mononuclear complex and new dinuclear heteroleptic compounds containing pyrazolate and carboxylate ligands in the same molecule have been obtained. Replacement of the protons of coordinated Hdmpz in the dinuclear complexes by $Ag^I$ gives new heteropolynuclear Pd-Ag ones.

## Results and Discussion

### Reactivity of $[Pd(dmpz)_2(Hdmpz)_2]$ (A) towards the Monoprotic Weak Acids *N*-Acetylglycine and $HO_2CC_6H_4$-R [R = *m*-$NO_2$, *p*-$N(CH_3)_2$, *p*-$NH_2$, *p*-$OCH_3$, *p*-OH]

$[Pd(dmpz)_2(Hdmpz)_2]$ (**A**) reacts with two equivalents of *N*-acetylglycine in dichloromethane/methanol solution to give $[Pd(Hdmpz)_4](O_2CCH_2NHCOCH_3)_2$ (**1**) as a pure compound in a very high yield (path a in Scheme 1) by selective protonation of the anionic monodentate dmpz ligands. The X-ray study of a crystal of **1** revealed that the *N*-acetylglycinate anion interacts with the cationic complex $[Pd(Hdmpz)_4]^{2+}$ through N–H···O hydrogen bonds.

The reactions of $[Pd(dmpz)_2(Hdmpz)_2]$ (**A**) with the benzoic derivatives $HO_2CC_6H_4$-R [R = *m*-$NO_2$, *p*-$N(CH_3)_2$, *p*-$NH_2$, *p*-$OCH_3$, *p*-OH] under similar conditions do not give rise to pure compounds: their $^1H$ NMR spectra seem to indicate that species of stoichiometry $[Pd(Hdmpz)_4](O_2CC_6H_4\text{-}R)_2$ [R = *m*-$NO_2$, *p*-$N(CH_3)_2$, *p*-$NH_2$, *p*-$OCH_3$, *p*-OH] could be present in all mixtures, but we have not been able to separate and characterise them.

Elemental analyses and the IR and $^1H$ NMR spectroscopic data of $[Pd(Hdmpz)_4](O_2CCH_2NHCOCH_3)_2$ (**1**) (see Experimental Section) are in agreement with this stoichiometry, which was confirmed later by an X-ray diffraction

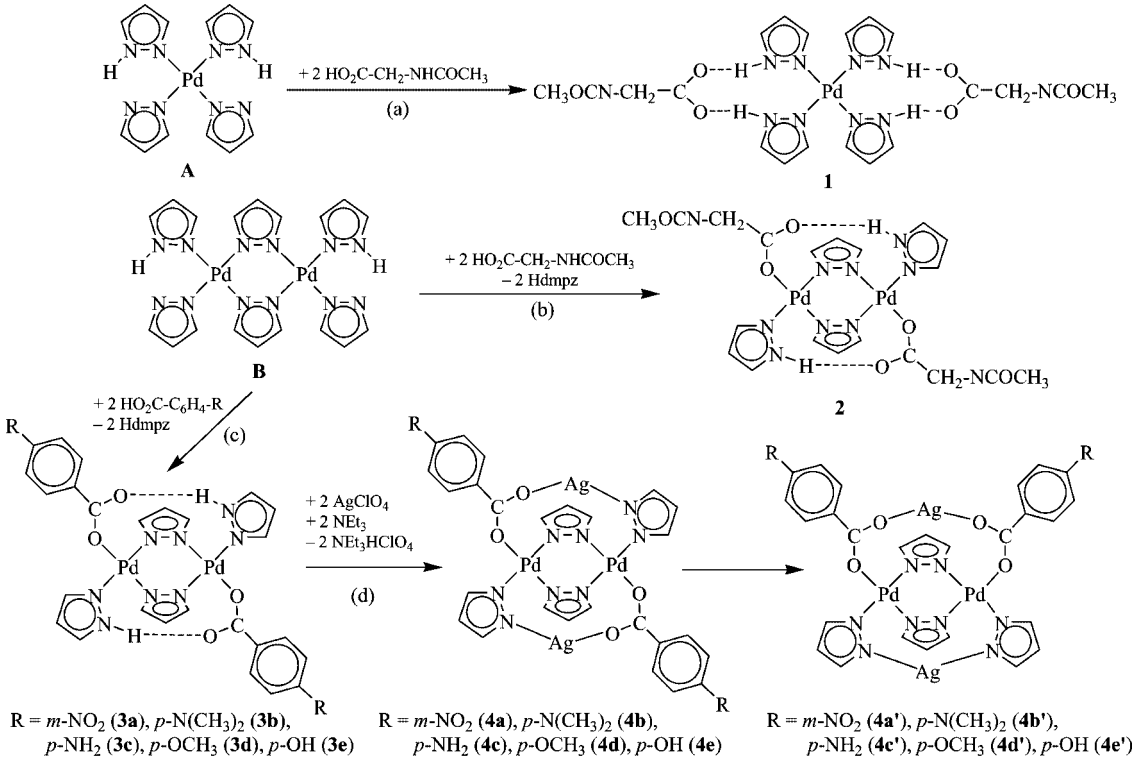


(note: Me groups of the 3,5-dmpz or 3,5-Hdmpz have been omited for clarity)

Scheme 1.

 © 2006 Wiley-VCH Verlag GmbH & Co. KGaA, Weinheim 

study. The $^1$H NMR spectrum of **1** in solution reveals the equivalence of the four Hdmpz ligands since only one set of signals is observed [$\delta$ = 15.45 (s, 4 H, N–H), 5.72 (s, 4 H, H$^4$), 2.49 (s, 12 H, $CH_3$), 2.25 (s, 12 H, $CH_3$) ppm]. The two *N*-acetylglycinate anions also give only one set of signals [$\delta$ = 6.56 (s, 2 H, N–H), 4.05 (d, $^3J_{H,H}$ = 3.74 Hz, 4 H, $CH_2$), 2.06 (s, 6 H, $CH_3$) ppm].

The molecular and supramolecular structures of compound **1** are shown in Figures 2 and 3, respectively. Table 1 lists a selection of intra- and intermolecular bond distances and angles.

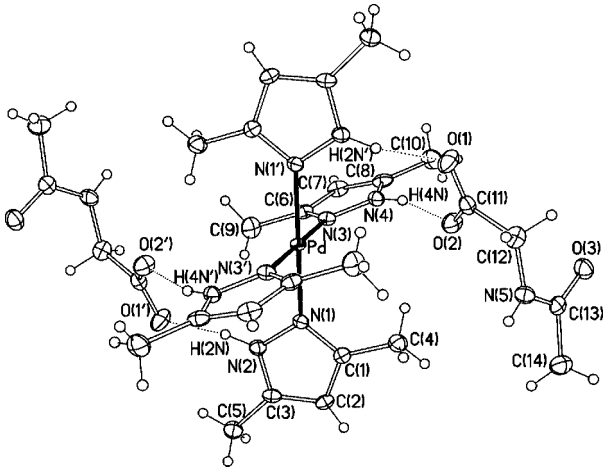


Figure 2. Molecular structure of **1** (50% probability ellipsoids).

In the $[Pd(Hdmpz)_4]^{2+}$ part of the complex the Pd centre shows an almost square-planar coordination environment with all the Pd–N bond lengths in the range of those found in palladium complexes with this kind of ligand.[6,11–13,15–17,20,21] Each pair of mutually *trans* Hdmpz groups are coplanar to each other (interplanar angle of 0° between planes 2 and 2′ and planes 3 and 3′. See Table 1 for the definition of the planes used in this discussion) and almost perpendicular to the other pair of Hdmpz groups [interplanar angle of 86.6(1)°]. All Hdmpz ligands are almost perpendicular to the best least-squares coordination plane of the metal centre (plane 1), since the interplanar angles are 80.9(1)° [planes 1 and 2 (2′)] and 76.7(1)° [planes 1 and 3 (3′)].[22] The Hdmpz groups are turned in such a way that the N–H bonds of the two Hdmpz ligands in the *cis* positions point roughly to the same side of the palladium coordination plane.

The *N*-acetylglycinate anions are bonded to the cation through hydrogen bonds. The two N–H groups pointing to the same side of the palladium coordination plane form N–H···O hydrogen bonds with the two oxygen atoms of the same carboxylate group. These N–H···O hydrogen bonds seem to be quite strong as the H···O and N···O distances are perceptibly shorter than those involved in neutral molecules[23,24] and are even at the lower end of the range observed for charge-assisted N–H$^{(+)}$···O$^{(-)}$ hydrogen bonds.[24–30] According to these structural data, the C–O distances within the $COO^-$ moieties indicate that the carboxylic acid does not retain its acidic hydrogen, which has been transferred to the monodentate dmpz groups[31] such that the complex cations and the carboxylate anions are joined by a heteromeric synthon of type $R_2(10)$[18,19] (Figure 1b). Compound **1** is a new example in which the N–H···O interaction is reinforced by an electrostatic one, the

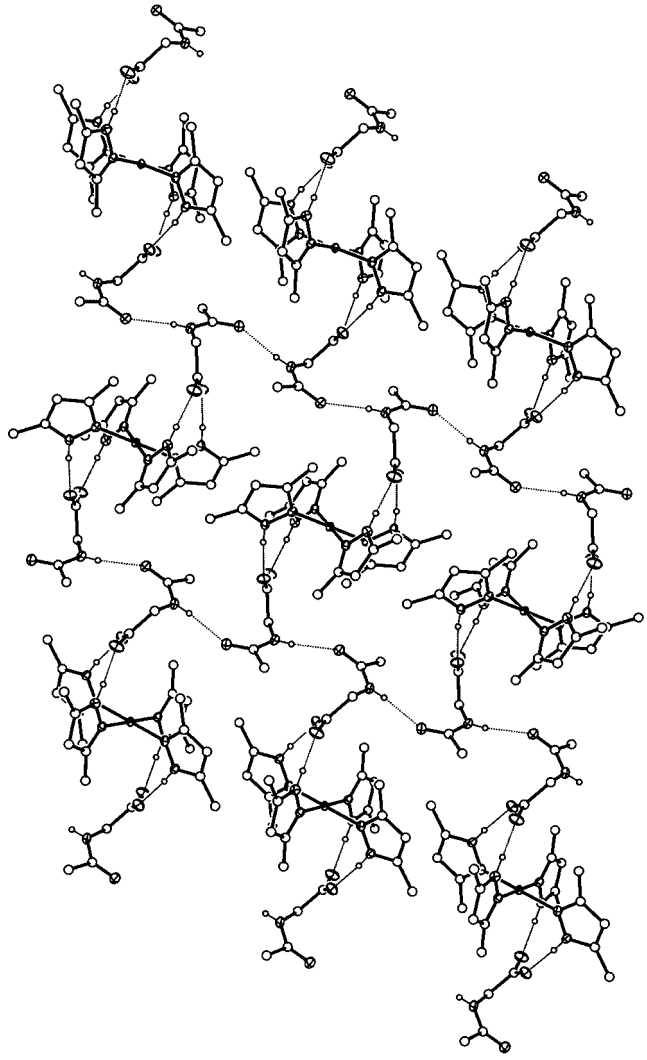

Figure 3. Supramolecular structure of **1**.

Table 1. Bond lengths [Å] and angles [°] for $[Pd(Hdmpz)_4](O_2CCH_2NHCOCH_3)_2$ (**1**).[a]

| | | | | |
|---|---|---|---|---|
| Pd–N(1) | 2.029(2) | Pd–N(3) | 2.018(2) | |
| C(11)–O(1) | 1.252(4) | C(11)–O(2) | 1.247(3) | |
| N(1)–Pd–N(3) | 91.16(9) | N(1)–Pd–N(3′) | 88.84(9) | |
| N–(H)···O | *d*(N–H) | *d*(H···O) | *d*(N···O) | <(NHO) |
| N(2)–(H2N)···O(1) | 0.89(4) | 1.76(4) | 2.647(3) | 166(3) |
| N(4)–(H4N)···O(2) | 0.95(4) | 1.73(4) | 2.645(3) | 164(4) |
| N(5)–(H5N)···O(3) | 0.79(3) | 2.16(3) | 2.937(3) | 168(3) |
| Plane1: Pd, N(1), N(3), N(1′), N(3′) | | | | |
| Plane2: N(1), N(2), C(1), C(2), C(3) | | | | |
| Plane2′: N(1′), N(2′), C(1′), C(2′), C(3′) | | | | |
| Plane3: N(3), N(4), C(6), C(7), C(8) | | | | |
| Plane3′: N(3′), N(4′), C(6′), C(7′), C(8′) | | | | |

[a] The symmetry transformation used to generate the equivalent primed atoms is $-x$, $-y + 1$, $-z + 1$.

 © 2006 Wiley-VCH Verlag GmbH & Co. KGaA, Weinheim 

H-bond acceptor being a carboxylate anion and the H-bond donor an organometallic cation containing N–H groups.

In addition, the *N*-acetylglycinate anions self-assemble through N–H···O links to generate infinite chains. The H···O and N···O distances are longer than those involving the carboxylate group, but within the range observed for this kind of interaction between neutral molecules.[23,25] The supramolecular architecture of compound **1** is a 2D network which can be described as being formed by infinite chains of *N*-acetylglycinate anions ($CH_3CONHCH_2COO^-$) linked through the carboxylate group ($COO^-$) to the $[Pd(Hdmpz)_4]^{2+}$ cations by charge-assisted $N–H^{(+)}\cdots O^{(-)}$ hydrogen bonds.

### Reactivity of $[Pd_2(\mu\text{-dmpz})_2(dmpz)_2(Hdmpz)_2]$ (B) towards the Monoprotic Weak Acids *N*-Acetylglycine and $HO_2CC_6H_4$-R [R = *m*-$NO_2$, *p*-$N(CH_3)_2$, *p*-$NH_2$, *p*-$OCH_3$, *p*-OH]

$[Pd_2(\mu\text{-dmpz})_2(dmpz)_2(Hdmpz)_2]$ (**B**) reacts with the monocarboxylic acids *N*-acetylglycine and the benzoic derivatives $HO_2CC_6H_4$-R [R = *m*-$NO_2$, *p*-$N(CH_3)_2$, *p*-$NH_2$, *p*-$OCH_3$, *p*-OH] in a 1:2 molar ratio, but in a different way to $[Pd(dmpz)_2(Hdmpz)_2]$ (**A**). In these cases selective protonation of the monodentate dmpz groups (one from each palladium atom), their elimination as Hdmpz, and their further displacement by the carboxylate anions generated takes place. These carboxylate groups interact with the palladium atoms in a monodentate way to give compounds $[Pd_2(\mu\text{-dmpz})_2(O_2CCH_2NHCOCH_3\text{-}\kappa O)_2(Hdmpz)_2]$ (**2**) and $[Pd_2(\mu\text{-dmpz})_2(O_2CC_6H_4\text{-R-}\kappa O)_2(Hdmpz)_2]$ [R = *m*-$NO_2$ (**3a**), *p*-$N(CH_3)_2$ (**3b**), *p*-$NH_2$ (**3c**), *p*-$OCH_3$ (**3d**), *p*-OH (**3e**)] (paths b and c in Scheme 1).

The IR absorptions corresponding to the carboxylate groups (see Experimental Section) are in agreement with the monodentate coordination mode of these anions,[32] as confirmed by the X-ray structures of compounds **3d** and **3e**.

According to the symmetry of these compounds ($C_2$), their $^1H$ NMR spectra show a set of signals corresponding to one half of each complex, namely "Pd(μ-dmpz)($O_2CC_6H_4$-R-κ*O*)(Hdmpz)" (see Experimental Section, Scheme 2). The methyl signals corresponding to bridging dmpz or terminal Hdmpz groups were unambiguously assigned by NOE experiments.

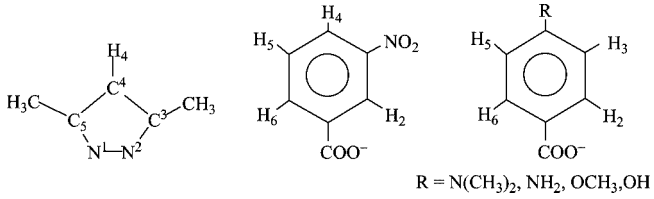


Scheme 2.

A common way to synthesise pyrazolate complexes is by treating carboxylate derivatives with the neutral pyrazole (HRpz) in the presence of $NEt_3$. These reactions proceed with elimination of the carboxylic acid and coordination of the pyrazolate anion $Rpz^-$ to the metal centre.[33,34] The substitution of $Rpz^-$ anions by carboxylate groups has seldom been used as carboxylate complexes are much easier to make than pyrazolates. As far as we know, only $[Ru_2(\mu\text{-}O_2CR)_2(Hpz)_2(CO)_4]$ has been prepared in such a way;[35] the carboxylic acid is added in a large excess to induce protonation of all Rpz groups in the starting material. However, in the synthesis of complexes **2** and **3a**–**3e** the carboxylic acids are added to compound **B** in a stoichiometric manner (1:2) and selective protonation of the terminal dmpz groups takes place. Thus, the selectivity of this process is the key to synthesising mixed-ligand complexes.

An X-ray study was performed on complexes **3d** and **3e** to try to ascertain if the OH groups of the carboxylate anions of different complexes are involved in hydrogen-bonding interactions to generate supramolecular structures. Unfortunately, no supramolecular aggregates were found and both complexes show discrete dinuclear structures. The molecular structures of complexes **3d** and **3e** are shown in Figures 4 and 5, respectively, and a selection of bond lengths and angles is given in Tables 2 and 3.

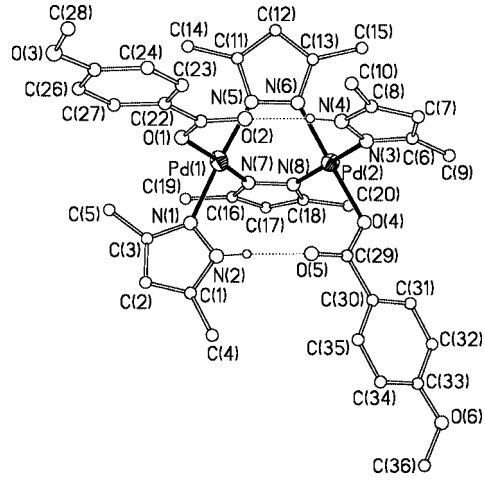


Figure 4. Molecular structure of **3d**.

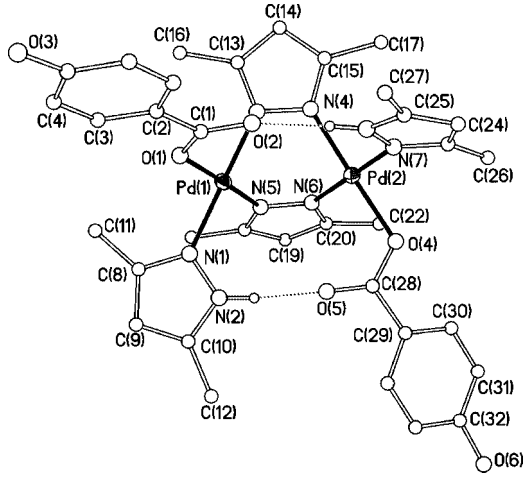


Figure 5. Molecular structure of **3e**.

Complexes **3d** and **3e** are dinuclear species of $Pd^{II}$ with two 3,5-dmpz groups bridging the two metal atoms, which

 © 2006 Wiley-VCH Verlag GmbH & Co. KGaA, Weinheim 

Table 2. Bond lengths [Å] and angles [°] for $[Pd_2(\mu\text{-dmpz})_2(O_2C\text{-}C_6H_4OCH_3\text{-}\kappa O)_2(Hdmpz)_2]$ (**3d**).

| | | | | |
|---|---|---|---|---|
| Pd(1)–O(1) | 2.001(2) | Pd(1)–N(1) | | 2.016(2) |
| Pd(1)–N(5) | 1.989(2) | Pd(1)–N(7) | | 1.994(2) |
| Pd(2)–O(4) | 2.015(2) | Pd(2)–N(3) | | 2.011(2) |
| Pd(2)–N(6) | 2.001(2) | Pd(2)–N(8) | | 1.989(2) |
| C(21)–O(1) | 1.271(3) | C(21)–O(2) | | 1.234(3) |
| C(29)–O(4) | 1.278(3) | C(29)–O(5) | | 1.232(3) |
| N(5)–Pd(1)–O(1) | 92.74(8) | O(1)–Pd(1)–N(1) | | 86.06(9) |
| N(5)–Pd(1)–N(7) | 89.04(9) | N(7)–Pd(1)–N(1) | | 92.64(9) |
| N(8)–Pd(2)–O(4) | 89.90(8) | O(4)–Pd(2)–N(3) | | 90.26(8) |
| N(8)–Pd(2)–N(6) | 89.97(9) | N(6)–Pd(2)–N(3) | | 90.00(9) |
| C(21)–O(1)–Pd(1) | 122.89 | C(29)–O(4)–Pd(2) | | 116.60 |
| N–(H)···O | *d*(N–H) | *d*(H···O) | *d*(N···O) | <(NHO) |
| N(2)-(H2)···O(5) | 0.88 | 1.85 | 2.725(3) | 173.8(2) |
| N(4)-(H4)···O(2) | 0.88 | 1.85 | 2.703(3) | 163.3(2) |

Table 3. Bond lengths [Å] and angles [°] for $[Pd_2(\mu\text{-dmpz})_2(O_2C\text{-}C_6H_4OH\text{-}\kappa O)_2(Hdmpz)_2]$ (**3e**).

| | | | | |
|---|---|---|---|---|
| Pd(1)–N(1) | 2.017(2) | Pd(1)–N(5) | | 1.998(2) |
| Pd(1)–O(1) | 2.004(2) | Pd(1)–N(3) | | 1.988(2) |
| Pd(2)–N(4) | 1.986(2) | Pd(2)–O(4) | | 2.0098(17) |
| Pd(2)–N(6) | 1.995(2) | Pd(2)–N(7) | | 2.014(2) |
| C(1)–O(1) | 1.289(3) | C(1)–O(2) | | 1.239(3) |
| C(28)–O(4) | 1.292(3) | C(28)–O(5) | | 1.234(3) |
| N(3)–Pd(1)–O(1) | 91.72(8) | O(1)–Pd(1)–N(1) | | 88.06(8) |
| N(3)–Pd(1)–N(5) | 89.76(8) | N(5)–Pd(1)–N(1) | | 90.48(8) |
| N(6)–Pd(2)–O(4) | 89.92(8) | O(4)–Pd(2)–N(7) | | 90.03(8) |
| N(4)–Pd(2)–N(6) | 89.75(8) | N(4)–Pd(2)–N(7) | | 90.39(8) |
| C(1)–O(1)–Pd(1) | 124.29(16) | C(28)–O(4)–Pd(2) | | 118.23(16) |
| N-(H)···O | *d*(N–H) | *d*(H···O) | *d*(N···O) | <(NHO) |
| N(2)–(H2)···O(5) | 0.88 | 1.827(2) | 2.704(3) | 174.26(18) |
| N(8)–(H8)···O(2) | 0.88 | 1.852(2) | 2.729(3) | 174.47(18) |

are located at 3.269 (**3d**) and 3.272 Å (**3e**). The $Pd_2N_4$ ring shows a typical boat-like conformation, the dihedral angle between both Pd–N–N–Pd fragments being 73.5(1)° (**3d**) and 72.9(1)° (**3e**).[22] In addition, each Pd atom is bonded to a nitrogen of a neutral, monodentate 3,5-dimethylpyrazole and to an oxygen of the carboxylate anion to complete a square-planar coordination environment. The angles defined by two ligands in *cis* positions and the metal centre are close to 90°. The Pd–N distances are in the range of distances found in other complexes with this kind of ligand.[6,11–17,20,21,36] No significant differences are observed in the Pd–N distances corresponding to terminal Hdmpz or bridging dmpz groups. The Pd–O bond lengths (ca. 2.00 Å) are similar to those observed in palladium complexes with monodentate carboxylate groups.[37–43] The two Pd–O–C angles are surprisingly different to each other: while one of them is smaller than 120° [C(29)–O(4)–Pd(2): 116.6° (**3d**); C(28)–O(4)–Pd(2): 118.2° (**3e**)] and similar to those found in other complexes with this type of ligand, such as $[Pd(phen)(MeCO_2)_2]$ (Pd–O–C: 114.3° and 118.5°),[37] $[Pd\{3,3'\text{-}[CH_2CH(COOEt)_2]\text{-}2,2'\text{-byp-}\kappa N,N'C^{\beta}\}(O_2CCH_3)]$ (Pd–O–C: 116.9°–119.9°),[38] the other is, unusually, greater than 120° [C(21)–O(1)–Pd(1): 122.9° (**3d**); C(1)–O(1)–Pd(1): 124.3° (**3e**)]. The C–O distances within the $COO^-$ moieties (1.232–1.292 Å) indicate that the carboxylic acid molecules do not retain their acidic hydrogen, which has been transferred to the monodentate dmpz groups to generate Hdmpz ones.[31]

The monodentate carboxylate anion bonded to a Pd atom and the terminal Hdmpz group bonded to the other Pd atom have an adequate arrangement to establish an N–H···O hydrogen bond. The H···O and N···O distances are in the range of those corresponding to charge-assisted $N\text{–}H^{(+)}\cdots O^{(-)}$ bonds. In addition, the N–H···O angles are in the range observed for these kinds of interactions.[24–30]

### Reactivity of $[Pd_2(\mu\text{-dmpz})_2(O_2CC_6H_4\text{-R-}\kappa O)_2(Hdmpz)_2]$ [R = *m*-$NO_2$ (3a), *p*-$N(CH_3)_2$ (3b), *p*-$NH_2$(3c), *p*-$OCH_3$ (3d), *p*-OH (3e)] towards $AgClO_4$

The reactions of $[Pd_2(\mu\text{-dmpz})_2(O_2CC_6H_4\text{-R-}\kappa O)_2(Hdmpz)_2]$ [R = *m*-$NO_2$ (**3a**), *p*-$N(CH_3)_2$ (**3b**), *p*-$NH_2$ (**3c**), *p*-$OCH_3$ (**3d**), *p*-OH (**3e**)] with $AgClO_4$ in a 1:2 molar ratio in the presence of $NEt_3$ produce the deprotonation of the terminal Hdmpz groups and formation of $[Pd_2Ag_2(\mu\text{-dmpz})_4(O_2CC_6H_4\text{-R-}\kappa O)_2]$ [R = *m*-$NO_2$ (**4a**), *p*-$N(CH_3)_2$ (**4b**), *p*-$NH_2$(**4c**), *p*-$OCH_3$ (**4d**), *p*-OH (**4e**)]. In these reactions the $NHEt_3ClO_4$ by-product is eliminated by washing with methanol, where compounds **4a**–**4e** are insoluble.

This method has previously been used in the synthesis of the Pd-Ag pyrazolate complexes $[Pd_2Ag_4(dmpz)_8]$[13] and $[Pd_2Ag_2(dmpz)_6]$[14] from $[Pd(dmpz)_2(Hdmpz)_2]$ and $[Pd(\mu\text{-dmpz})_2(dmpz)_2(Hdmpz)_2]$, respectively.

Elemental analysis and IR and $^1H$ NMR spectroscopic data (Experimental Section, Scheme 2) are in agreement with the stoichiometry proposed and presented in Scheme 1. With the exception of the signal corresponding to the acidic N–H protons, the number of signals observed in the $^1H$ NMR spectra of compounds **4a**–**e** is the same as that observed in the spectra of the starting complexes (**3a**–**3e**). We thus propose the molecular structure represented in Scheme 3a for compounds **4a**–**e**, in which the two acidic H atoms of complexes **3a**–**3e** have been replaced by Ag ones, keeping the carboxylate groups in a transoid conformation with respect to the Pd···Pd axis. If acetone solutions of compounds **4a**–**4e** are left at room temperature until the solvent has completely evaporated the resulting solids exhibit different $^1H$ NMR spectra (Experimental Section, Scheme 2) to those shown by the starting compounds (**4a**–**4e**), revealing a change in the molecular structure to give the isomers **4a′**–**4e′** (Scheme 3b). The $^1H$ NMR spectra of these complexes display two signals corresponding to the $H^4$ atoms

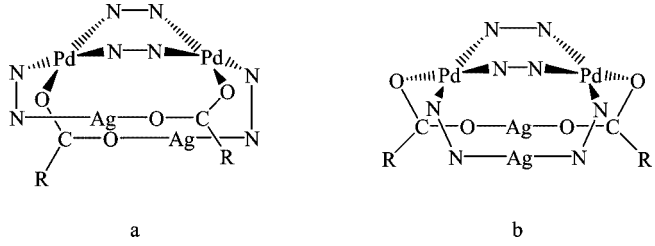


Scheme 3.

 © 2006 Wiley-VCH Verlag GmbH & Co. KGaA, Weinheim 

of the $Pd_2(\mu\text{-dmpz})_2$ groups. A cisoid arrangement of the carboxylate groups with respect to the Pd···Pd axis could account for these two signals.

Single crystals of $[Pd_2Ag_2(\mu\text{-dmpz})_4(p\text{-}O_2CC_6H_4OCH_3\text{-}\kappa O)_2(DMSO)]$ were obtained from a solution of **4d** in DMSO. Its $^1H$ NMR spectrum is similar to that of **4d′** in DMSO, indicating that the structure of the skeleton of both complexes is the same. The X-ray study of a single crystal allowed us to unambiguously establish the structure proposed for these compounds. The molecular structure of $[Pd_2Ag_2(\mu\text{-dmpz})_4(p\text{-}O_2CC_6H_4OCH_3\text{-}\kappa O)_2(DMSO)]$ is shown in Figure 6, and Table 4 contains a selection of bond lengths and angles in the complex.

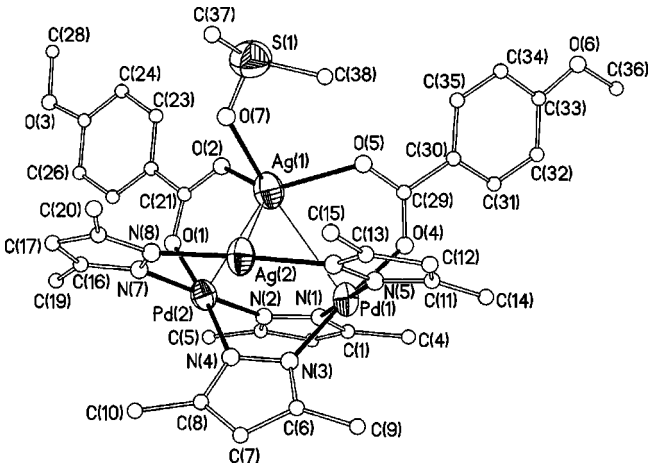


Figure 6. Molecular structure of $[Pd_2Ag_2(\mu\text{-dmpz})_4(\mu\text{-}O_2CC_6H_4OCH_3)_2(DMSO)]$.

Table 4. Bond lengths [Å] and angles [°] for $[Pd_2Ag_2(\mu\text{-dmpz})_4(O_2CC_6H_4OCH_3\text{-}\kappa O)_2(DMSO)]$ from **4d′**.

| | | | |
|---|---|---|---|
| Pd(1)–N(1) | 2.025(7) | Pd(1)–N(3) | 2.002(6) |
| Pd(1)–N(5) | 2.020(6) | Pd(1)–O(4) | 2.007(6) |
| Pd(2)–N(2) | 1.991(7) | Pd(2)–N(4) | 1.994(6) |
| Pd(2)–N(7) | 2.019(7) | Pd(2)–O(1) | 2.008(6) |
| Ag(1)–O(2) | 2.259(6) | Ag(1)–O(5) | 2.262(6) |
| Ag(1)–O(7) | 2.409(8) | Ag(2)–N(6) | 2.069(7) |
| Ag(2)–N(8) | 2.075(6) | Ag(1)···Ag(2) | 2.9208(12) |
| Ag(1)···Pd(2) | 2.9586(12) | Ag(1)···Pd(1) | 3.0652(12) |
| O(4)–Pd(1)–N(5) | 90.5(3) | N(5)–Pd(1)–N(3) | 90.8(3) |
| N(3)–Pd(1)–N(1) | 88.8(3) | N(1)–Pd(1)–O(4) | 89.9(2) |
| O(1)–Pd(2)–N(7) | 89.2(3) | O(1)–Pd(2)–N(2) | 90.2(3) |
| N(7)–Pd(2)–N(4) | 91.3(3) | N(4)–Pd(2)–N(2) | 89.4(3) |
| O(2)–Ag(1)–O(7) | 98.4(3) | O(2)–Ag(1)–O(5) | 117.2(3) |
| O(5)–Ag(1)–O(7) | 98.8(2) | O(2)–Ag(1)–Ag(2) | 136.4(2) |
| O(5)–Ag(1)–Ag(2) | 106.4(2) | O(7)–Ag(1)–Ag(2) | 73.8(2) |
| O(2)–Ag(1)–Pd(2) | 76.0(2) | O(5)–Ag(1)–Pd(2) | 136.96(16) |
| O(7)–Ag(1)–Pd(2) | 120.6(2) | Ag(2)–Ag(1)–Pd(2) | 72.27(3) |
| O(2)–Ag(1)–Pd(1) | 124.67(19) | O(5)–Ag(1)–Pd(1) | 70.22(17) |
| O(7)–Ag(1)–Pd(1) | 136.2(2) | Ag(2)–Ag(1)–Pd(1) | 69.57(3) |
| Pd(2)–Ag(1)–Pd(1) | 69.33(3) | N(6)–Ag(2)–N(8) | 176.9(3) |
| N(6)–Ag(2)–Ag(1) | 94.03(19) | N(8)–Ag(2)–Ag(1) | 85.45(18) |

$[Pd_2Ag_2(\mu\text{-dmpz})_4(p\text{-}O_2CC_6H_4OCH_3\text{-}\kappa O)_2(DMSO)]$ is a palladium/silver tetranuclear compound with both palladium atoms bridged by two 3,5-dmpz groups in such a way that the $Pd_2N_4$ ring shows a typical boat-like conformation, the dihedral angle between both Pd–N–N–Pd fragments being 70.5(2)°.[22] Both palladium atoms complete their square-planar coordination environments by bonding to one nitrogen of another 3,5-dmpz group and one oxygen of the carboxylate anion. In this complex the two 3,5-dmpz groups outside the $Pd_2N_4$ ring are in cisoid positions with respect to the Pd···Pd axis, as are both carboxylate groups, although in the starting complex $[Pd_2(\mu\text{-dmpz})_2(O_2CC_6H_4\text{-}OCH_3\text{-}\kappa O)_2(Hdmpz)_2]$ (**3d**) transoid positions are observed. The Pd–N[6,11–17,20,21,36] and Pd–O[44,45]distances are in the range of those found in palladium compounds with the same kind of ligands.

One of the silver atoms, Ag(2), is bonded to two 3,5-dmpz groups in an almost linear coordination environment [N(8)–Ag(2)–N(6) = 176.9(3)°]. The 3,5-dmpz groups bridging Ag(2) and both palladium atoms are almost coplanar [interplanar angle of 4.7(3)°] and the dihedral angles between them and the coordination planes of the corresponding palladium atoms are 52.3(3)° [Pd(1)] and 51.5(3)° [Pd(2)].[22] The Ag–N distances are similar to those found in other silver pyrazolate complexes.[13]

The other silver atom, Ag(1), is coordinated to two oxygen atoms, one from each carboxylate group, which act as a bridge between this atom] and both palladium atoms. Ag(1) completes its coordination environment with the oxygen of one molecule of DMSO used as crystallisation solvent. All Ag–O distances are in the range of those observed in silver complexes with these kinds of ligands.[44–49] Ag(1) also contacts with Ag(2), the Ag(1)···Ag(2) distance being 2.9208(12) Å, which is similar to distances found in other complexes with Ag···Ag interactions.[50–53] In addition, Ag(1) contacts with Pd(1) [Ag(1)···Pd(1) = 3.0652(12) Å] and Pd(2) [Ag(1)···Pd(2) = 2.9586(12) Å] and the Ag–Pd vectors are nearly perpendicular to the square coordination planes of the Pd(1) and Pd(2) centres [9.2(1)° and 9.7(1)° respectively]. Both facts indicate weak Pd···Ag interactions.[54,55]

The planar "C–$CO_2$" fragment from the carboxylate group bonded to Pd(1) forms angles of 69.8(3)° and 72.3(4)° with the palladium coordination plane and the 3,5-dmpz group outside the $Pd_2N_4$ ring, respectively.[22] The same parameters for Pd(2) are 86.6(3)° and 87.1(4)°. The interplanar angle between both "C–$CO_2$" fragments is 68.1(4)°.

## Conclusion

In summary, *N*-acetylglycine reacts with $[Pd(dmpz)_2(Hdmpz)_2]$ (**A**) in a 2:1 molar ratio to give $[Pd(Hdmpz)_4](O_2CCH_2NHCOCH_3)_2$ (**1**) by selective protonation of the anionic monodentate dmpz ligands. The cationic complex $[Pd(Hdmpz)_4]^{2+}$ is bonded to the *N*-acetylglycinate anion through charge-assisted $N–H^{(+)}\cdots O^{(-)}$ hydrogen bonds. *N*-acetylglycine also reacts with $[Pd_2(\mu\text{-dmpz})_2(dmpz)_2(Hdmpz)_2]$ (**B**) in a 2:1 molar ratio, but in this case, the

 © 2006 Wiley-VCH Verlag GmbH & Co. KGaA, Weinheim 

selective protonation of the monodentate dmpz groups (one from each palladium atom) is followed by their displacement by the carboxylate anions generated and their elimination as Hdmpz. In the resulting compound, $[Pd_2(\mu\text{-dmpz})_2(O_2CCH_2NHCOCH_3\text{-}\kappa O)_2(Hdmpz)_2]$ (**2**), the monodentate carboxylate groups exhibit a transoid conformation with respect to the Pd···Pd axis. The benzoic derivatives, $HO_2CC_6H_4$-R [R = *m*-$NO_2$, *p*-$N(CH_3)_2$, *p*-$NH_2$, *p*-$OCH_3$, *p*-OH] react with **B** in the same way that *N*-acetylglycine does to give compounds $[Pd_2(\mu\text{-dmpz})_2(O_2CC_6H_4\text{-R-}\kappa O)_2(Hdmpz)_2]$ [R = *m*-$NO_2$ (**3a**), *p*-$N(CH_3)_2$ (**3b**), *p*-$NH_2$ (**3c**), *p*-$OCH_3$ (**3d**), *p*-OH (**3e**)]. In the complexes **3a**–**3e**, the H atoms of the terminal Hdmpz groups can be replaced by $Ag^+$ to give $[Pd_2Ag_2(\mu\text{-dmpz})_4(\mu\text{-}O_2CC_6H_4\text{-R-}\kappa O)_2(Hdmpz)_2]$ [R = *m*-$NO_2$ (**4a**), *p*-$N(CH_3)_2$ (**4b**), *p*-$NH_2$ (**4c**), *p*-$OCH_3$ (**4d**), *p*-OH (**4e**)], keeping the carboxylate groups in a transoid conformation. Compounds **4a**–**4e** isomerise in acetone solution at room temperature to the cisoid species **4a′**–**4e′**.

## Experimental Section

**General Procedures and Materials:** $[Pd_2(\mu\text{-dmpz})_2(dmpz)_2(Hdmpz)_2]$[14] and $[Pd(dmpz)_2(Hdmpz)_2]$[13] were prepared as described elsewhere. All reagents were commercially available and used as received from Aldrich. Elemental analyses were performed with a Perkin–Elmer 240-B microanalyser. IR spectra were recorded with a Perkin–Elmer 599 spectrophotometer (Nujol mulls between polyethylene plates in the range 400–4000 $cm^{-1}$). NMR spectra were recorded with a Varian Unity-300 spectrometer using standard references.

**$[Pd(Hdmpz)_4](O_2CCH_2NHCOCH_3)_2$ (1):** *N*-acetylglycine (0.12 g, 1.0227 mmol) was added to a solution of $[Pd(dmpz)_2(Hdmpz)_2]$ (**A**; 0.250 g, 0.5113 mmol) in $CH_2Cl_2$/MeOH (25:5 mL). The mixture was stirred at room temperature for 2 h and then the solvent was evaporated to dryness. Addition of $Et_2O$ (5 mL) to the residue yielded **1** (0.3436 g, 93%). $C_{28}H_{44}N_{10}O_6Pd$ (723.12): calcd. C 46.51, H 6.13, N 19.36; found C 46.63, H 5.90, N 19.07. IR: $\tilde{\nu}_{max}$ = 3450–3000 $cm^{-1}$ (s, br), 1667 (m), 1628 (vs), 1583 (s), 1376 (s), 1287 (s), 1068 (m), 1035 (m), 783 (m, sh), 650 (m), 597 (m), 555 (m), 517 (m).

**$[Pd_2(\mu\text{-dmpz})_2(O_2CCH_2NHCOCH_3)_2(Hdmpz)_2]$ (2):** A solution of *N*-acetylglycine (0.06 g, 0.51 mmol) in methanol (10 mL) was added to a solution of $[Pd_2(\mu\text{-dmpz})_2(dmpz)_2(Hdmpz)_2]$ (**B**; 0.200 g, 0.2546 mmol) in $CH_2Cl_2$ (50 mL). The mixture was stirred at room temperature for 2 h and the solution was then filtered through celite and the solvent evaporated to dryness. Addition of $Et_2O$ (5 mL) to the residue yielded **2** (0.110 g, 51%). $C_{28}H_{42}N_{10}O_6Pd_2$ (721.11): calcd. C 40.64, H 5.12, N 16.92; found C 40.71, H 5.08, N 16.60. IR: $\tilde{\nu}_{max}$ = 3450–3000 $cm^{-1}$ (s, br), 1627 (vs), 1583 (vs), 1376 (s), 1282 (s), 1175 (m), 1035 (m), 814 (m), 775 (m), 660 (w). $^1H$ NMR (300 MHz, $CDCl_3$, 23 °C): $\delta$ = 1.80 (s, 6 H, $CH_3$, dmpz), 1.86 (s, 6 H, $CH_3$, *N*-acetylglycine), 2,18 (s, 6 H, $CH_3$, Hdmpz), 2.26 (s, 6 H, $CH_3$, dmpz), 2.64 (s, 6 H, $CH_3$, Hdmpz), 3.74 ($\nu_A$, $^2J_{H,H}$ = 4.0 Hz, 2 H, $CH_2$, acetylglycine), 3.76 ($\nu_B$, 2 H, $CH_2$, acetylglycine), 5.41 (s, 2 H, 4-H, dmpz), 5.80 (s, 2 H, 4-H, Hdmpz), 5.99 (s, 2 H, N-H, acetylglycine), 13.07 (s, 2 H, N-H, Hdmpz) ppm.

**$[Pd_2(\mu\text{-dmpz})_2(O_2CC_6H_4NO_2\text{-}\kappa O)_2(Hdmpz)_2]$ (3a):** A solution of *m*-nitrobenzoic acid (0.1067 g, 0.638 mmol) in methanol (3 mL) was added to a yellow solution of **B** (0.2496 g, 0.318 mmol) in $CH_2Cl_2$ (35 mL). The mixture was stirred at room temperature for 2 h and the solvent was then evaporated to dryness. Addition of diethyl ether (12 mL) to the residue gave **3a** as a yellow solid, which was filtered off and dried (0.055 g, 32% yield). $C_{34}H_{38}N_{10}O_8Pd_2$ (927.54): calcd. C 44.03, H 4.13, N 15.09; found C 43.93, H 4.27, N 14.83. IR: $\tilde{\nu}_{max}$ = 1631 $cm^{-1}$ (vs), 1586 (s), 1531 (s), 1378 (vs), 1348 (s), 1155 (m), 1072 (m), 820 (m), 782 (m), 760 (m). $^1H$ NMR (300 MHz, [D$_6$]acetone, 23 °C): $\delta$ = 1.94 (s, 6 H, $CH_3$, dmpz), 2.36 (s, 6 H, $CH_3$, Hdmpz), 2.40 (s, 6 H, $CH_3$, dmpz), 2.93 (s, 6 H, $CH_3$, Hdmpz), 5.47 (s, 2 H, 4-H, dmpz), 6.10 (s, 2 H, 4-H, Hdmpz), 7.70 (t, $^3J_{H,H}$ = 7.7 Hz, 2 H, 5-H), 8.33 (d, $^3J_{H6,H5}$ = 7.7 Hz, 2 H, 6-H), 8.40 (d, $^3J_{H4,H5}$ = 7.7 Hz, 2 H, 4-H), 8.80 (s, 2 H, 2-H), 13.78 (s, 2 H, N-H, Hdmpz) ppm.

**$[Pd_2(\mu\text{-dmpz})_2\{O_2CC_6H_4N(CH_3)_2\text{-}\kappa O\}_2(Hdmpz)_2]$ (3b):** Prepared similarly to **3a** from **B** (0.3000 g, 0.382 mmol) and *p*-dimethylaminobenzoic acid (0.1262 g, 0.764 mmol). Addition of methanol (7 mL) to the residue gave **3b** (0.2904 g, 82%). $C_{38}H_{50}N_{10}O_4Pd_2$ (923.68): calcd. C 49.41, H 5.46, N 15.16; found C 49.15, H 5.45, N 15.17. IR: $\tilde{\nu}_{max}$ = 1609 $cm^{-1}$ (vs), 1589 (s), 1543 (s), 1525 (s), 1356 (vs), 1307 (s), 1230 (m), 1194 (vs), 1140 (m), 1063 (m), 946 (m), 837 (m), 810 (m), 778 (vs). $^1H$ NMR (300 MHz, [D$_6$]DMSO, 23 °C): $\delta$ = 1.83 (s, 6 H, $CH_3$, dmpz), 2.25 (s, 6 H, $CH_3$, Hdmpz), 2.30 (s, 6 H, $CH_3$, dmpz), 2.78 (s, 6 H, $CH_3$, Hdmpz), 2.92 (s, 12 H, $NMe_2$), 5.45 (s, 2 H, 4-H, dmpz), 6.07 (s, 2 H, 4-H, Hdmpz), 6.65 (d, $^3J_{H2,H3}$ = $J_{H5,H6}$ = 8.8 Hz, 4 H, 3-H, 5-H), 7.71 (d, $^3J_{H2,H3}$ = $J_{H5,H6}$ = 8.8 Hz, 4 H, 2-H, 6-H), 14.00 (s, 2 H, N-H, Hdmpz) ppm.

**$[Pd_2(\mu\text{-dmpz})_2(O_2CC_6H_4NH_2\text{-}\kappa O)_2(Hdmpz)_2]$ (3c):** Prepared similarly to **3a** from **B** (0.2027 g, 0.258 mmol) and *p*-aminobenzoic acid (0.071 g, 0.516 mmol). Yield: 0.2017 g (90%). $C_{34}H_{42}N_{10}O_4Pd_2$ (867.58): calcd. C 47.07, H 4.88, N 16.14; found C 46.76, H 4.72, N 15.83. IR: $\tilde{\nu}_{max}$ = 3386 $cm^{-1}$ (m), 3329 (m), 3176 (m), 3125 (m), 1642 (m), 1600 (vs), 1548 (m), 1513 (m), 1376 (vs), 1297 (s), 1174 (s), 1066 (m), 849 (m), 813 (m), 782 (m), 649 (m), 505 (m). $^1H$ NMR (300 MHz, [D$_6$]acetone, 23 °C): $\delta$ = 1.94 (s, 6 H, $CH_3$, dmpz), 2.36 (s, 12 H, $CH_3$, dmpz, Hdmpz), 2.89 (s, 6 H, $CH_3$, Hdmpz), 4.98 (s, 4 H, $NH_2$), 5.41 (s, 2 H, 4-H, dmpz), 6.00 (s, 2 H, 4-H, Hdmpz), 6.60 (m, 4 H, 3-H, 5-H), 7.77 (m, 4 H, 2-H, 6-H), 14.34 (s, 2 H, N-H, Hdmpz) ppm.

**$[Pd_2(\mu\text{-dmpz})_2(O_2CC_6H_4OCH_3\text{-}\kappa O)_2(Hdmpz)_2]$ (3d):** Prepared similarly to **3a** from **B** (0.2995 g, 0.381 mmol) and *p*-methoxybenzoic acid (0.1161 g, 0.763 mmol). The addition of methanol (8 mL) to the residue gave **3d** as a yellow solid (0.2165 g, 63%). $C_{36}H_{44}N_8O_6Pd_2$ (897.60): calcd. C 48.17, H 4.94, N 12.48; found C 47.87, H 4.82, N 12.35. IR: $\tilde{\nu}_{max}$ = 1609 $cm^{-1}$ (vs), 1586 (s), 1570 (s), 1533 (s), 1509 (s), 1364 (vs), 1305 (s), 1253 (s), 1168 (s), 1031 (s), 851 (m), 819 (m), 778 (s). $^1H$ NMR (300 MHz, [D$_6$]acetone, 23 °C): $\delta$ = 1.94 (s, 6 H, $CH_3$, dmpz), 2.35 (s, 6 H, $CH_3$, Hdmpz), 2.36 (s, 6 H, $CH_3$, dmpz), 2.89 (s, 6 H, $CH_3$, Hdmpz), 3.81 (s, 6 H, $OCH_3$), 5.42 (s, 2 H, 4-H, dmpz), 6.02 (s, 2 H, 4-H, Hdmpz), 6.91 (d, $^3J_{H2,H3}$ = $J_{H5,H6}$ = 8.8 Hz, 4 H, 3-H, 5-H), 7.97 (d, $^3J_{H2,H3}$ = $J_{H5,H6}$ = 8.8 Hz, 4 H, 2-H, 6-H), 14.16 (s, 2 H, N-H, Hdmpz) ppm.

**$[Pd_2(\mu\text{-dmpz})_2(O_2CC_6H_4OH\text{-}\kappa O)_2(Hdmpz)_2]$ (3e):** Prepared similarly to **3a** from **B** (0.2120 g, 0.269 mmol) and *p*-hydroxybenzoic acid (0.0745 g, 0.539 mmol). Yield: 0.2211 g (94%). $C_{34}H_{40}N_8O_6Pd_2$ (869.54): calcd. C 46.96, H 4.60, N 12.89; found C 47.23, H 5.00, N 12.93. IR: $\tilde{\nu}_{max}$ = 3331 $cm^{-1}$ (m), 1610 (vs), 1597 (vs), 1537 (vs), 1503 (vs), 1377 (vs), 1288 (vs), 1234 (vs), 1167 (vs), 1054 (m), 857 (m), 788 (s), 777 (s), 651 (m). $^1H$ NMR (300 MHz, [D$_6$]acetone, 23 °C): $\delta$ = 1.94 (s, 6 H, $CH_3$, dmpz), 2.35 (s, 12 H, $CH_3$, dmpz, Hdmpz), 2.88 (s, 6 H, $CH_3$, Hdmpz), 5.42 (s,

 © 2006 Wiley-VCH Verlag GmbH & Co. KGaA, Weinheim 

2 H, 4-H, dmpz), 6.00 (s, 2 H, 4-H, Hdmpz), 6.80 (d, $^3J_{H2,H3}$ = $J_{H5,H6}$ = 8.4 Hz, 4 H, 3-H, 5-H), 7.89 (d, $^3J_{H2,H3}$ = $J_{H5,H6}$ = 8.4 Hz, 4 H, 2-H, 6-H), 14.19 (s, 2 H, N-H, Hdmpz) ppm.

**[$Pd_2Ag_2$(μ-dmpz)$_4$($O_2CC_6H_4NO_2$-κ*O*)$_2$] (4a):** $AgClO_4$ (0.0663 g, 0.3198 mmol) and $NEt_3$ (0.5 mL) were added to a solution of **3a** (0.1412 g, 0.152 mmol) in acetone (12 mL). The resulting solution was stirred for 75 min and then filtered through celite to eliminate some impurities. The solution was evaporated to dryness and MeOH (15 mL) added to the residue. The yellow solid was filtered and washed with diethyl ether (6 mL). Yield of **4a**: (0.165 g, 74%). $C_{34}H_{36}Ag_2N_{10}O_8Pd_2$ (1141.3): calcd. C 35.78, H 3.18, N 12.27; found C 35.58, H 2.95, N 12.08. IR: $\tilde{\nu}_{max}$ = 1598 $cm^{-1}$ (vs), 1564 (vs), 1399 (vs), 1349 (vs), 1160 (m), 1081 (m), 1050 (m), 780 (m), 654 (w). $^1H$ NMR (300 MHz, [$D_6$]acetone, 23 °C): $\delta$ = 2.17 [s, 6 H, $CH_3$, $Pd_2$(μ-dmpz)$_2$], 2.52 [s, 6 H, $CH_3$, $Pd_2Ag$(μ-dmpz)$_2$], 2.60 [s, 6 H, $CH_3$, $Pd_2$(μ-dmpz)$_2$], 2.85 [s, 6 H, $CH_3$, $Pd_2Ag$(μ-dmpz)$_2$], 5.64 [s, 2 H, 4-H, $Pd_2$(μ-dmpz)$_2$], 5.74 [s, 2 H, 4-H, $Pd_2Ag$(μ-dmpz)$_2$], 7.80 (m, 2 H, 5-H), 8.43 (m, 4 H, 4-H, 6-H), 8.80 (m, 2 H, 2-H) ppm. Slow evaporation of a solution of **4a** in acetone at room temperature gave **4a′**. $^1H$ NMR (300 MHz, [$D_6$]acetone, 23 °C): $\delta$ = 1.90 [s, 6 H, $CH_3$, $Pd_2$(μ-dmpz)$_2$], 2.22 [s, 6 H, $CH_3$, $Pd_2Ag$(μ-dmpz)$_2$], 2.58 [s, 6 H, $CH_3$, $Pd_2$(μ-dmpz)$_2$], 2.66 [s, 6 H, $CH_3$, $Pd_2Ag$(μ-dmpz)$_2$], 5.62 [s, 1 H, 4-H, $Pd_2$(μ-dmpz)$_2$], 5.64 [s, 1 H, 4-H, $Pd_2$(μ-dmpz)$_2$],5.86 [s, 2 H, 4-H, $Pd_2Ag$(μ-dmpz)$_2$], 7.75 (m, 2 H, 5-H), 8.37 (ddd, $^3J_{H4,H5}$ = 8.2, $^4J_{H4,H2}$ = 2.4, $^4J_{H4,H6}$ = 1.2 Hz, 2 H, 4-H), 8.41 (dt, $^3J_{H6,H5}$ = 7.8, $^4J_{H6,H4}$ = $^4J_{H6,H2}$ = 1.2 Hz, 2 H, 6-H), 8.77 (m, 2 H, 2-H) ppm.

**[$Pd_2Ag_2$(μ-dmpz)$_4${$O_2CC_6H_4N(CH_3)_2$-κ*O*}$_2$] (4b):** Prepared similarly to **4a** from **3b** (0.2001 g, 0.202 mmol), $AgClO_4$ (0.0893 g, 0.431 mmol) and $NEt_3$ (0.7 mL). Yield of **4b**: 0.1753 g (79%). $C_{38}H_{48}Ag_2N_{10}O_4Pd_2$ (1137.4): calcd. C 40.06, H 4.24, N 12.29; found C 40.41, H 4.41, N 11.99. IR: $\tilde{\nu}_{max}$ = 1603 $cm^{-1}$ (m), 1566 (m), 1512 (m), 1379 (s), 1366 (m), 1196 (m), 779 (m). $^1H$ NMR (300 MHz, $CH_2Cl_2$, 23 °C): $\delta$ = 2.04 [s, 6 H, $CH_3$, $Pd_2$(μ-dmpz)$_2$], 2.21 [s, 6 H, $CH_3$, $Pd_2Ag$(μ-dmpz)$_2$], 2.51 [s, 6 H, $CH_3$, $Pd_2$(μ-dmpz)$_2$], 2.53 [s, 6 H, $CH_3$, $Pd_2Ag$(μ-dmpz)$_2$], 3.02 (s, 12 H, $NMe_2$), 5.61 [s, 2 H, 4-H, $Pd_2$(μ-dmpz)$_2$], 5.73 [s, 2 H, 4-H, $Pd_2Ag$(μ-dmpz)$_2$], 6.63 (d, $^3J_{H2,H3}$ = $J_{H5,H6}$ = 9.1 Hz, 4 H, 3-H, 5-H), 7.87 (d, $^3J_{H2,H3}$ = $J_{H5,H6}$ = 9.1 Hz, 4 H, 2-H, 6-H) ppm. Slow evaporation of a solution of **4b** in acetone at room temperature gave **4b′**. $^1H$ NMR (300 MHz, $CD_2Cl_2$, 23 °C): $\delta$ = 1.89 [s, 6 H, $CH_3$, $Pd_2$(μ-dmpz)$_2$], 2.25 [s, 6 H, $CH_3$, $Pd_2Ag$(μ-dmpz)$_2$], 2.59 [s, 12 H, $CH_3$, $Pd_2$(μ-dmpz)$_2$, $Pd_2Ag$(μ-dmpz)$_2$], 3.02 (s, 12 H, $NMe_2$), 5.62 [s, 1 H, 4-H, $Pd_2$(μ-dmpz)$_2$], 5.71 [s, 1 H, 4-H, $Pd_2$(μ-dmpz)$_2$], 5.82 [s, 2 H, 4-H, $Pd_2Ag$(μ-dmpz)$_2$], 6.63 (d, $^3J_{H2,H3}$ = $^3J_{H5,H6}$ = 8.9 Hz, 4 H, 3-H, 5-H), 7.86 (d, $^3J_{H2,H3}$ = $^3J_{H5,H6}$ = 8.9 Hz, 4 H, 2-H, 6-H) ppm.

**[$Pd_2Ag_2$(μ-dmpz)$_4$($O_2CC_6H_4NH_2$-κ*O*)$_2$] (4c):** Prepared similarly to **4a** from **3c** (0.08 g, 0.0922 mmol), $AgClO_4$ (0.0382 g, 0.1844 mmol) and $NEt_3$ (0.5 mL). Yield of **4c**: 0.009 g (9%). $C_{34}H_{40}Ag_2N_{10}O_4Pd_2$ (1081.3): calcd. C 37.77, H 3.73, N 12.95; found C 37.68, H 3.67, N 12.65. IR: $\tilde{\nu}_{max}$ = 3363 $cm^{-1}$ (m), 1619(m), 1602 (m), 1584 (s), 1523 (m, sh), 1377 (s), 1299 (m), 1176 (m), 841 (w), 776 (m), 641 (w), 500 (w). $^1H$ NMR (300 MHz, $CDCl_3$, 23 °C): $\delta$ = 2.02 [s, 6 H, $CH_3$, $Pd_2$(μ-dmpz)$_2$], 2.16 [s, 6 H, $CH_3$, $Pd_2Ag$(μ-dmpz)$_2$], 2.47 [s, 6 H, $CH_3$, $Pd_2$(μ-dmpz)$_2$], 2.49 [s, 6 H, $CH_3$, $Pd_2Ag$(μ-dmpz)$_2$], 3.92 (s, 4 H, $NH_2$), 5.30 [s, 2 H, 4-H, $Pd_2$(μ-dmpz)$_2$], 5.55 [s, 2 H, 4-H, $Pd_2Ag$(μ-dmpz)$_2$], 6.58 (d, $^3J_{H2,H3}$ = $J_{H5,H6}$ = 8.4 Hz, 4 H, 3-H, 5-H), 7.81 (d, $^3J_{H2,H3}$ = $J_{H5,H6}$ = 8.4 Hz, 4 H, 2-H, 6-H) ppm. Slow evaporation of a solution of **4c** in acetone at room temperature gave **4c′**. $^1H$ NMR (300 MHz, [$D_6$]acetone, 23 °C): $\delta$ = 1.87 [s, 6 H, $CH_3$, $Pd_2$(μ-dmpz)$_2$], 2.21 [s, 6 H, $CH_3$, $Pd_2Ag$(μ-dmpz)$_2$], 2.57 [s, 6 H, $CH_3$, $Pd_2$(μ-dmpz)$_2$], 2.63 [s, 6 H, $CH_3$, $Pd_2Ag$(μ-dmpz)$_2$], 3.92 (s, 4 H, $NH_2$), 5.60 [s, 1 H, 4-H, $Pd_2$(μ-dmpz)$_2$], 5.63 [s, 1 H, 4-H, $Pd_2$(μ-dmpz)$_2$], 5.81 [s, 2 H, 4-H, $Pd_2Ag$(μ-dmpz)$_2$], 6.60 (d, $^3J_{H2,H3}$ = $^3J_{H5,H6}$ = 8.4 Hz, 4 H, 3-H, 5-H), 7.75 (d, $^3J_{H2,H3}$ = $^3J_{H5,H6}$ = 8.4 Hz, 4 H, 2-H, 6-H) ppm.

**[$Pd_2Ag_2$(μ-dmpz)$_4$($O_2CC_6H_4OCH_3$-κ*O*)$_2$] (4d):** Prepared similarly to **4a** from **3d** (0.1810 g, 0.202 mmol), $AgClO_4$ (0.0836 g, 0.403 mmol) and $NEt_3$ (0.7 mL). Yield of **4d**: 0.165 g (74%). $C_{36}H_{42}Ag_2N_8O_6Pd_2$ (1111.3): calcd. C 38.91, H 3.81, N 10.08; found C 38.91, H 3.78, N 10.03. IR: $\tilde{\nu}_{max}$ = 1610 $cm^{-1}$ (s), 1591 (s), 1546 (s), 1378 (s), 1260 (s), 1171 (m), 1032 (m), 848 (m), 778 (s), 765 (m), 642 (m), 628 (m). $^1H$ NMR (300 MHz, [$D_6$]DMSO, 23 °C): $\delta$ = 2.02 [s, 6 H, $CH_3$, $Pd_2$(μ-dmpz)$_2$], 2.24 [s, 6 H, $CH_3$, $Pd_2Ag$(μ-dmpz)$_2$], 2.47 [s, 6 H, $CH_3$, $Pd_2$(μ-dmpz)$_2$], 2.60 [s, 6 H, $CH_3$, $Pd_2Ag$(μ-dmpz)$_2$], 3.91 (s, 6 H, $OCH_3$), 5.70 [s, 2 H, 4-H, $Pd_2$(μ-dmpz)$_2$], 5.83 [s, 2 H, 4-H, $Pd_2Ag$(μ-dmpz)$_2$], 7.09 (d, $^3J_{H2,H3}$ = $J_{H5,H6}$ = 9.1 Hz, 4 H, 3-H, 5-H), 7.99 (d, $^3J_{H2,H3}$ = $J_{H5,H6}$ = 9.1 Hz, 4 H, 2-H, 6-H) ppm. Slow evaporation of a solution of **4d** in acetone at room temperature gave **4d′**. $^1H$ NMR (300 MHz, [$D_6$] DMSO, 23 °C): $\delta$ = 1.77 [s, 6 H, $CH_3$, $Pd_2$(μ-dmpz)$_2$], 2.18 [s, 6 H, $CH_3$, $Pd_2Ag$(μ-dmpz)$_2$], 2.46 [s, 6 H, $CH_3$, $Pd_2$(μ-dmpz)$_2$], 2.59 [s, 6 H, $CH_3$, $Pd_2Ag$(μ-dmpz)$_2$], 3.80 (s, 6 H, $OCH_3$), 5.59 [s, 1 H, 4-H, $Pd_2$(μ-dmpz)$_2$], 5.60 [s, 1 H, 4-H, $Pd_2$(μ-dmpz)$_2$], 5.83 [s, 2 H, 4-H, $Pd_2Ag$(μ-dmpz)$_2$], 6.94 (d, $^3J_{H2,H3}$ = $^3J_{H5,H6}$ = 8.7 Hz, 4 H, 3-H, 5-H), 7.89 (d, $^3J_{H2,H3}$ = $^3J_{H5,H6}$ = 8.7 Hz, 4 H, 2-H, 6-H) ppm.

**[$Pd_2Ag_2$(μ-dmpz)$_4$($O_2CC_6H_4OH$-κ*O*)$_2$] (4e):** Prepared similarly to **4a** from **3e** (0.17 g, 0.196 mmol), $AgClO_4$ (0.0812 g, 0.392 mmol) and $NEt_3$ (0.75 mL). Yield of **4e**: 0.08 g (38%). $C_{34}H_{38}Ag_2N_8O_6Pd_2$ (1083.3): calcd. C 37.70, H 3.53, N 10.34; found C 37.39, H 3.16, N 10.51. IR: $\tilde{\nu}_{max}$ = 3606 $cm^{-1}$ (m), 1610 (m), 1594 (s), 1538 (s, sh), 1377 (s), 1274 (m), 1236 (m), 1166 (m), 1095 (m), 848 (m), 780 (s), 768 (s), 643 (m). $^1H$ NMR (300 MHz, [$D_6$]acetone, 23 °C): $\delta$ = 2.04 [s, 6 H, $CH_3$, $Pd_2$(μ-dmpz)$_2$], 2.16 [s, 6 H, $CH_3$, $Pd_2Ag$(μ-dmpz)$_2$], 2.51 [s, 6 H, $CH_3$, $Pd_2$(μ-dmpz)$_2$], 2.57 [s, 6 H, $CH_3$, $Pd_2Ag$(μ-dmpz)$_2$], 5.60 [s, 2 H, 4-H, $Pd_2$(μ-dmpz)$_2$], 5.72 [s, 2 H, 4-H, $Pd_2Ag$(μ-dmpz)$_2$], 6.87 (d, $^3J_{H2,H3}$ = $J_{H5,H6}$ = 8.9 Hz, 4 H, 3-H, 5-H), 7.93 (d, $^3J_{H2,H3}$ = $J_{H5,H6}$ = 8.9 Hz, 4 H, 2-H, 6-H) ppm. Slow evaporation of a solution of **4e** in acetone at room temperature gave **4e′**. $^1H$ NMR (300 MHz, [$D_6$]acetone, 23 °C): $\delta$ = 1.88 [s, 6 H, $CH_3$, $Pd_2$(μ-dmpz)$_2$], 2.21 [s, 6 H, $CH_3$, $Pd_2Ag$(μ-dmpz)$_2$], 2.57 [s, 6 H, $CH_3$, $Pd_2$(μ-dmpz)$_2$], 2.64 [s, 6 H, $CH_3$, $Pd_2Ag$(μ-dmpz)$_2$], 5.61 [s, 1 H, 4-H, $Pd_2$(μ-dmpz)$_2$], 5.64 [s, 1 H, 4-H, $Pd_2$(μ-dmpz)$_2$], 5.83 [s, 2 H, 4-H, $Pd_2Ag$(μ-dmpz)$_2$], 6.82 (d, $^3J_{H2,H3}$ = $^3J_{H5,H6}$ = 8.9 Hz, 4 H, 3-H, 5-H), 7.89 (d, $^3J_{H2,H3}$ = $^3J_{H5,H6}$ = 8.7 Hz, 4 H, 2-H, 6-H) ppm.

**X-ray Structure Determination:** Crystal data and other details of the structure analysis are presented in Table 5. Single crystals of **1** were obtained by slow diffusion of *n*-hexane into a solution of **1** in chloroform at room temperature. Single crystals of **3d** and **3e** were obtained by slow diffusion of *n*-hexane into their respective solutions in acetone at room temperature. Single crystals of **4d′** were obtained by slow diffusion of diethyl ether into a solution of **4d** in DMSO at room temperature. For **3d·$Me_2CO$**, the acetone solvent molecule was found to be disordered over two sets of positions that were refined with partial occupancy 0.50:0.50. A common set of anisotropic parameters was used for each pair of homologous atoms. For **3e·2$Me_2CO$**, one of the acetone solvent molecules was modelled as disordered over two positions with partial occupancy 0.75:0.25, with the central C atom (C38) being common for the two sets. For **4d′·0.7$Me_2SO$**, the sulfur atom of the $Me_2SO$ molecule coordinated to Ag(1) was disordered over two positions [S(1)/S(1′)] refined with partial occupancy 0.80:0.20. For this molecule, all the

 © 2006 Wiley-VCH Verlag GmbH & Co. KGaA, Weinheim 

Table 5. Crystal data and structure refinement for complexes **1**, **3d**·$Me_2CO$, **3e**·2$Me_2CO$ and **4d′**·0.7$Me_2SO$.

| Complex | **1** | **3d**·$Me_2CO$ | **3e**·2$Me_2CO$ | **4d′**·0.7$Me_2SO$ |
|---|---|---|---|---|
| Empirical formula | $C_{28}H_{44}N_{10}O_6Pd$ | $C_{36}H_{44}N_8O_6Pd_2$·$Me_2CO$ | $C_{34}H_{40}N_8O_6Pd_2$·2$Me_2CO$ | $C_{38}H_{48}Ag_2N_8O_7Pd_2S$·0.7$Me_2SO$ |
| Formula mass | 723.13 | 955.67 | 985.7 | 1244.13 |
| $T$ [K] | 150(1) | 173(1) | 100(1) | 173(1) |
| $\lambda$ [Å] | 0.71073 | 0.71073 | 0.71073 | 0.71073 |
| Crystal system | monoclinic | monoclinic | monoclinic | triclinic |
| Space group | $P2_1/n$ | $P2_1/n$ | $Cc$ | $P\bar{1}$ |
| $a$ [Å] | 8.3462(6) | 8.5194(6) | 17.8303(7) | 12.867(5) |
| $b$ [Å] | 9.4493(5) | 22.1527(15) | 12.8679(5) | 13.823(5) |
| $c$ [Å] | 20.7037(15) | 22.9327(16) | 20.9510(9) | 14.585(5) |
| $\alpha$ [°] | 90 | 90 | 90 | 99.922(7) |
| $\beta$ [°] | 95.491(10) | 96.938(1) | 113.957(1) | 101.816(8) |
| $\gamma$ [°] | 90 | 90 | 90 | 100.341(6) |
| $V$ [Å$^3$] | 1625.32(19) | 4614.5(5) | 4392.8(3) | 2438.3(15) |
| $Z$ | 2 | 4 | 4 | 2 |
| $D_c$ [g cm$^{-3}$] | 1.478 | 1.477 | 1.490 | 1.695 |
| $\mu$ (Mo-$K_\alpha$) [mm$^{-1}$] | 0.628 | 0.892 | 0.877 | 1.643 |
| $\theta$ range [°] | 2.37–24.97 | 2.01–25.03 | 2.02–28.47 | 1.93–25.03 |
| Data collected | 3045 | 32062 | 19098 | 13477 |
| Independent data ($R_{int}$) | 2835 (0.0222) | 7570 (0.0336) | 9547 (0.0232) | 8529 (0.0330) |
| Goodness-of-fit on $F^2$[a] | 1.050 | 1.010 | 1.030 | 1.032 |
| Final $R$ indices [$I > 2\sigma(I)$][b] | $R_1 = 0.0292$; $wR_2 = 0.0722$ | $R_1 = 0.0305$; $wR_2 = 0.0687$ | $R_1 = 0.0230$; $wR_2 = 0.0583$ | $R_1 = 0.0589$; $wR_2 = 0.1344$ |
| $R$ indices (all data)[c] | $R_1 = 0.0438$; $wR_2 = 0.0782$ | $R_1 = 0.0374$; $wR_2 = 0.0710$ | $R_1 = 0.0234$; $wR_2 = 0.0585$ | $R_1 = 0.0806$; $wR_2 = 0.1476$ |

[a] Goodness-of-fit = $[\Sigma w (F_o^2 - F_c^2)^2/(N_{obs} - N_{param})]^{0.5}$. [b] $R_1 = \Sigma(|F_o| - |F_c|)/\Sigma|F_o|$. [c] $wR_2 = [\Sigma w(F_o^2 - F_c^2)^2/\Sigma w(F_o^2)^2]^{0.5}$.

S–C and S–O distances were restrained to be equal for both S atoms. No attempts were made to include the methyl hydrogen atoms of this molecule in the final model.

CCDC-271570–271573 (for **1**, **3d**, **3e** and **4d′**, respectively) contain the supplementary crystallographic data for this paper. These data can be obtained free of charge from The Cambridge Crystallographic Data Centre via www.ccdc.cam.ac.uk/data_request/cif.

## Acknowledgments

This work was supported by the Spanish MCYT (DGI)/FEDER (Project BQU 2002-03997-CO2-02) and the Gobierno de Aragón (Grupo Consolidado: Química inorgánica y de los compuestos organometálicos).

[1] S. Trofimenko, *Chem. Rev.* **1972**, *72*, 497–508.
[2] G. La Monica, G. A. Ardizzoia, *Prog. Inorg. Chem.* **1997**, *46*, 151–238.
[3] A. P. Sadimenko, S. S. Basson, *Coord. Chem. Rev.* **1996**, *147*, 247–297.
[4] A. P. Sadimenko, *Adv. Heterocycl. Chem.* **2001**, *80*, 157–240.
[5] S. Trofimenko, *Prog. Inorg. Chem.* **1986**, *34*, 115–210.
[6] L. R. Falvello, J. Forniés, A. Martín, R. Navarro, V. Sicilia, P. Villarroya, *Chem. Commun.* **1998**, 2429–2430.
[7] G. B. Deacon, E. E. Delbridge, C. M. Forsyth, B. W. Skelton, A. H. White, *J. Chem. Soc., Dalton Trans.* **2000**, 745–751.
[8] K. R. Gust, J. E. Knox, M. J. Heeg, H. B. Schlegel, C. H. Winter, *Angew. Chem.* **2002**, *114*, 1661–1664; *Angew. Chem. Int. Ed.* **2002**, *41*, 1591–1594.
[9] G. B. Deacon, C. M. Forsyth, A. Gitlits, R. Harika, P. C. Junk, B. W. Skelton, A. H. White, *Angew. Chem.* **2002**, *114*, 3383–3385; *Angew. Chem. Int. Ed.* **2002**, *41*, 3249–3251.
[10] J. R. Perera, M. J. Heeg, H. B. Schlegel, C. H. Winter, *J. Am. Chem. Soc.* **1999**, *121*, 4536–4537.
[11] W. Burger, J. Strähle, *Z. Anorg. Allg. Chem.* **1986**, *539*, 27–32.
[12] K. Umakoshi, Y. Yamauchi, K. Nakamiya, T. Kojima, M. Yamasaki, H. Kawano, M. Onishi, *Inorg. Chem.* **2003**, *42*, 3907–3916.
[13] G. A. Ardizzoia, G. La Monica, S. Cenini, M. Moret, N. Masciocchi, *J. Chem. Soc., Dalton Trans.* **1996**, 1351–1357.
[14] J. Forniés, A. Martín, V. Sicilia, L. F. Martín, *Chem. Eur. J.* **2003**, *9*, 3427–3435.
[15] A. Boixassa, J. Pons, X. Solans, M. Font-Bardia, J. Ros, *Inorg. Chem. Commun.* **2003**, *6*, 922–925.
[16] W. Burger, J. Strähle, *Z. Anorg. Allg. Chem.* **1985**, *529*, 111–117.
[17] P. Baran, C. M. Marrero, S. Pérez, R. G. Raptis, *Chem. Commun.* **2002**, 1012–1013.
[18] M. C. Etter, *Acc. Chem. Res.* **1990**, *23*, 120–126.
[19] M. C. Etter, J. C. MacDonald, J. Bernstein, *Acta Crystallogr., Sect. B* **1990**, *46*, 256–262.
[20] A. B. Goel, S. Goel, D. Vanderveer, *Inorg. Chim. Acta* **1984**, *82*, L9–L10.
[21] J. Ruiz, F. Florenciano, M. A. Sánchez, G. López, M. C. Ramírez de Arellano, J. Pérez, *Eur. J. Inorg. Chem.* **2000**, 943–949.
[22] M. Nardelli, *Comput. Chem.* **1983**, *7*, 95–98.
[23] A. Martín, *J. Chem. Educ.* **1999**, 578–583.
[24] D. Braga, L. Maini, F. Grepioni, A. De Cian, O. Félix, J. Fischer, M. W. Hosseini, *New J. Chem.* **2000**, *24*, 547–553.
[25] D. Braga, L. Maini, G. de Sanctis, K. Rubini, F. Grepioni, M. R. Chierotti, R. Gobetto, *Chem. Eur. J.* **2003**, *9*, 5538–5548.
[26] R. Atencio, M. Chacón, T. González, A. Briceño, G. Agrifoglio, A. Sierraalta, *Dalton Trans.* **2004**, 505–513.
[27] J. P. Guo, W. K. Wong, W. Y. Wong, *Polyhedron* **2005**, *24*, 927–939.
[28] D. Braga, M. Polito, F. Grepioni, *Cryst. Growth Des.* **2004**, *4*, 769–774.
[29] M. Casarin, C. Corvaja, C. Di Nicola, D. Falcomer, L. Franco, M. Monari, L. Pandolfo, C. Pettinari, F. Piccinelli, P. Togliatesta, *Inorg. Chem.* **2004**, *43*, 5865–5876.
[30] C. Foces-Foces, A. Echevarría, N. Jagerovic, I. Alkorta, J. Elguero, U. Langer, O. Klein, M. Minguet-Bonvehi, H. H. Limbach, *J. Am. Chem. Soc.* **2001**, *123*, 7898–7906.
[31] D. Braga, L. Maini, M. Mazzotti, K. Rubini, A. Masic, R. Gobetto, F. Grepioni, *Chem. Commun.* **2002**, 2296–2297.
[32] K. Nakamoto, *Infrared and Raman Spectra of Inorganic and Coordination Compounds, Part B*, 5th ed., John Wiley & Sons Inc., New York, **1997**.

 © 2006 Wiley-VCH Verlag GmbH & Co. KGaA, Weinheim 

[33] J. Forniés, A. Martín, V. Sicilia, P. Villarroya, *Organometallics* **2002**, *21*, 4604–4610.
[34] V. K. Jain, S. Kannan, E. R. T. Tiekink, *J. Chem. Soc., Dalton Trans.* **1993**, 3625–3628.
[35] F. Neumann, G. Süss-Fink, *J. Organomet. Chem.* **1989**, *367*, 175–185.
[36] V. K. Jain, S. Kannan, E. R. T. Tiekink, *J. Chem. Soc., Dalton Trans.* **1992**, 2231–2234.
[37] B. Milani, E. Alessio, G. Mestroni, A. Sammazzi, F. Garbassi, E. Zangrando, N. Bresciani-Pahor, L. Randaccio, *J. Chem. Soc., Dalton Trans.* **1994**, 1903–1911.
[38] G. R. Newkome, W. E. Puckett, G. E. Kiefer, V. K. Gupta, F. R. Froncek, D. C. Pantaleo, G. L. McClure, J. B. Simpson, W. A. Deustsch, *Inorg. Chem.* **1985**, *24*, 811–826.
[39] G. A. Grasa, R. Singh, E. D. Stevens, S. P. Nolan, *J. Organomet. Chem.* **2003**, *687*, 269–279.
[40] J. A. Mueller, M. S. Sigman, *J. Am. Chem. Soc.* **2003**, *125*, 7005–7013.
[41] A. J. Canty, M. C. Denney, B. W. Skelton, A. H. White, *Organometallics* **2004**, *23*, 1122–1131.
[42] C. González-Arellano, E. Gutiérrez-Puebla, M. Iglesias, F. Sánchez, *Eur. J. Inorg. Chem.* **2004**, 1955–1962.
[43] I. Favier, M. Gómez, J. Granell, M. Martínez, X. Solans, M. Font-Bardía, *Dalton Trans.* **2005**, 123–132.
[44] Y. C. Neo, J. J. Vittal, T. S. A. Hor, *J. Chem. Soc., Dalton Trans.* **2002**, 337–342.
[45] A. A. D. Tulloch, S. Winston, A. A. Danopoulos, G. Eastham, M. B. Hursthouse, *Dalton Trans.* **2003**, 699–708.
[46] D. Song, S. Wang, *Eur. J. Inorg. Chem.* **2003**, 3774–3782.
[47] V. J. Catalano, H. M. Kar, B. L. Bennett, *Inorg. Chem.* **2000**, *39*, 121–127.
[48] J. C. Garrison, R. S. Simons, W. G. Kofron, C. A. Tessier, W. J. Youngs, *Chem. Commun.* **2001**, 1780–1781.
[49] H. Abbas, A. L. Pickering, D.-L. Long, P. Kogerler, L. Cronin, *Chem. Eur. J.* **2005**, *11*, 1071–1078.
[50] Y. Lin, S.-W. Lai, C.-M. Che, K.-K. Cheung, Z.-Y. Zhou, *Organometallics* **2002**, *21*, 2275–2282.
[51] R. Usón, J. Forniés, B. Menjón, F. A. Cotton, L. R. Falvello, M. Tomás, *Inorg. Chem.* **1985**, *24*, 4651–4656.
[52] F. Bachedu, J. Ott, L. M. Venanzi, *J. Am. Chem. Soc.* **1985**, *107*, 1760–1761.
[53] N. Masciocchi, M. Moret, P. Cairati, A. Sironi, G. A. Ardizzoia, G. La Monica, *J. Am. Chem. Soc.* **1994**, *116*, 7668–7676.
[54] E. Alonso, J. Forniés, C. Fortuño, A. Martín, A. G. Orpen, *Organometallics* **2003**, *22*, 5011–5019 and references cited therein.
[55] *CRC Handbook of Chemistry and Physics*, 61st ed., Chemical Rubber Publishing Co., Cleveland, **1980**.

Received: September 7, 2005
Published Online: January 10, 2006

 © 2006 Wiley-VCH Verlag GmbH & Co. KGaA, Weinheim 

DOI: 10.1002/ejic.200500803

# One-Pot Synthesis and Structure of Organochalcogen Halides with Mixed Valence States

**Ernesto Schulz Lang,*[a] Gleison Antônio Casagrande,[a] Gelson Manzoni de Oliveira,[a] Gabriela Nanci Ledesma,[a] Sebastião S. Lemos,[b] Eduardo Ernesto Castellano,[c] and Ulrich Abram[d]**

**Keywords:** Halides / Secondary bonding / Selenium / Tellurium

Treatment of the diorganodichalcogenides PhEEPh (E = Se, Te) with one equivalent of elemental halogen (bromine or iodine) in methanol followed by addition of a sulfur donor and one more equivalent of the corresponding organochalcogen trihalide $PhTeX_3$ affords the mixed-oxidation-state organochalcogen halides $[PhE^{II}(L)PhE'^{IV}X_4]$ (E = Se, Te; E′ = Te; X = Br, I; L = thiourea, tetramethylthiourea) in a one-pot procedure. The X-ray structural analyses of these compounds suggest a strong dependence of the formation of supramolecular assemblies on the nature of the halogen bonded to the tellurium atom. The halogen can induce intramolecular and intermolecular secondary interactions among the heavy atoms simultaneously and, in addition to Te···X and X···X secondary bonds, intramolecular interactions of the type Te···$\eta^6$-$\pi$-aryl can be formed.

(© Wiley-VCH Verlag GmbH & Co. KGaA, 69451 Weinheim, Germany, 2006)

## Introduction

The chemistry of organochalcogen halides is also the chemistry of secondary bonds and as such is the subject of considerable current interest. The bonding in these compounds eludes simple description, and concepts like hypervalence, multicenter bonding, charge-transfer interactions, and secondary bonds have been invoked to understand their structural and chemical properties.[1–9] Intermolecular bonding of the type E···X and X···X (E = Se, Te; X = Cl, Br, I) of various strengths leads to the formation of polymeric chains, dimeric structures, or monomers with fairly strong intermolecular interactions. Many of these halogen compounds lie close to the ionic/covalent borderline, and several identified species have been found to be dependent on the substituents R, the donor atom, the identity of the halogen, and, in some cases, also on the dielectric constant of the solvent in which they have been prepared.[10–12]

Recently, as part of our research on the coordination of organotellurium compounds, we have reported the syntheses and the molecular structures of organotellurium trihalides[13,14] and organotellurium monohalides,[11,15,16] as well as several studies involving structures of phenyltellurate halides stabilized by different cations.[17–19] Most of the crystal structures reported for the $RTeX_3$ species show that the occurrence of intra- and intermolecular interactions (secondary bonding), together with the nature of the organic groups bonded to the tellurium atoms, exert influence on the geometry around the tellurium(IV) center and consequently define the structural patterns of these compounds.[14,20–26] The apparent bisphenoidal coordination sphere of the central tellurium atom is extended by the presence of intermolecular Te···X and X···X secondary interactions. It has been assumed that for $RTeX_3$ compounds there is a tendency for the chlorides to be polymeric, the bromides either polymeric or dimeric, the iodides dimeric, and, if R is particularly bulky, monomeric structures would be the norm. Here, the size of the halogen should be the other determining factor, with dimeric structures preferred as the halogen size increases.[27,28] A comparison of the structure of $[(2,4,6\text{-}Ph_3C_6H_2)TeI_3]$ with the bonding situation in other organotellurium(IV) triiodides suggests a strong dependence of the formation of supramolecular assemblies on the nature of the organic substituents.[14]

More recently, we have extended our studies to investigate the reaction conditions needed to obtain and isolate the corresponding mono-iodide of the more bulky substituted ditellurides $(MesTe)_2$ or $(2,4,6\text{-}Ph_3C_6H_2Te)_2$. The presence of the methyl or phenyl groups on the aromatic rings probably prevents the formation of stable tetrameric subunits similar to $(PhTeI)_4$.[11] Attempts to crystallize the corresponding aryltellurenyl mono-iodide (RTeI) were un-

[a] LMI – Departamento de Química, Universidade Federal de Santa Maria,
97105-900 Santa Maria, RS, Brazil
Fax: +55-55-220-8031
E-mail: eslang@quimica.ufsm.br
[b] Instituto de Química, Universidade de Brasília,
70904-970, Brasília, DF, Brazil
[c] Instituto de Física de São Carlos, Departamento de Física e Informática – Universidade de São Paulo
13560-970, São Carlos, SP, Brazil
[d] Freie Universität Berlin, Institute of Chemistry,
Fabeckstr. 34–36, 14195 Berlin, Germany

 InterScience © 2006 Wiley-VCH Verlag GmbH & Co. KGaA, Weinheim 

successful as it decomposes to other aryltellurium derivatives.[11,15,16] Thus, for example, $(MesTe)_2$ [Mes = 2,4,6-$(CH_3)C_6H_2$] reacts with iodine to produce [MesTeI], which disproportionates to [$MesTeI_3$], elemental tellurium, and [$MesTe(TeMes_2)I$].[16] When the same reaction is carried out with [(2,4,6-$Ph_3C_6H_2$)Te]$_2$, the compound [(2,4,6-$Ph_3C_6H_2$)-$TeI_3$][14] is formed as a result of a disproportion reaction under inert atmosphere or an oxo-bridged tellurium(IV) compound in the presence of air.[15] We are investigating this process further as it seems to have not only a steric influence but also an electronically directed behavior. The compound [$MesTe(TeMes_2)I$] is a representative example of a wider class of compounds of general formula [RTe(L)X] (where L is a neutral donor ligand), which were reported for the first time in the pioneering work of Foss and Huseby.[29] More recently, Godfrey,[12] Sadekov et al.,[30] and Singh et al.[31,32] have reported new examples.

Taking into account the unexpected reactivity and the interesting structural arrays previously obtained for several organochalcogen halides, we have turned our attention to the possibility of preparing organochalcogen halides with chalcogen atoms presenting mixed valence states in the same molecule.

There are only a few examples of this class of compounds in the literature. One of these is [$(DMSeU)_2Te_2Br_6$] (DMSeU = *N*,*N*-dimethylselenourea), which was obtained during the preparation of thin films of Te–Se alloys.[33] This compound contains both $Te^{IV}$ and $Te^{II}$ in the same molecule and there are no previously reported cases of such structures involving tellurium. Recently the synthesis and structural elucidation of [$Me_2TeCCTeMe$]I, the first alkynyltelluronium species, was reported.[34] A further search in the Cambridge Crystallographic Database reveals one more structure showing the coexistence of $Ph_3TeI$ and MesTeI in a ratio of 4:2 in the same compound.[3,35] The iodine atoms bridge the $Te^{IV}$ and $Te^{II}$ atoms to build blocks containing six molecules.

In the light of these previous results and to expand our studies on the molecular structures and intermolecular bonding in organotellurium derivatives, we have prepared organic models which should allow the study of the interaction processes of tellurium(II) cations with tellurolate anions. In this paper we report the synthesis and the structural characterization of the four new complexes [(TMTU)-PhTe(μ-Br)$TeBr_3Ph]_2$ (**1**), [(TU)PhTe(μ-I)$TeI_3Ph]_2$ (**2**), [PhSe(TU)][$PhTeI_4$] (**3**), and [PhSe(TU)][$PhTeBr_4$] (**4**).

## Results and Discussion

The reactions between diaryl dichalcogenides and an equivalent amount of halogen in methanol at room temperature afford the corresponding arylchalcogen halides stabilized by a sulfur donor. The arylchalcogenide trihalide was added to the mixture and stirred at slow reflux for 2 h. The final solution was filtered and crystals suitable for X-ray analysis were achieved by slow evaporation of the solvent. Compounds **1**–**4** were obtained in yields of 63–85 % [Equation (1)].

$$1/2\ (PhE)_2 \xrightarrow{1/2\ X_2} PhEX \xrightarrow{L} PhE(L)X \xrightarrow{PhE'X_3} PhE(L)PhE'X_4 \quad (1)$$

E = Se, Te; E′ = Te; X = Br, I; L = $(Me_2N)_2CS$ (TMTU), $(H_2N)_2$-CS (TU)

Several attempts to recrystallize **1**–**4** in order to obtain compounds with a high purity resulted in disproportionation to yield mainly $Ph_2TeX_2$ and $PhEX_3$ (E = Se, Te; X = Br, I).[11,16] Besides elucidating the structures of **1**–**4**, we were also interested in the structure of similar compounds containing chlorine. Attempts to obtain PhTeCl[36] by treatment of $(PhTe)_2$ with $SO_2Cl_2$ and then [PhE(L)PhE′$Cl_4$] according to Equation (1) failed; the analysis of the final material revealed merely the presence of [PhTe(TU)Cl][18] and the starting materials $PhTeCl_3$ or $PhSeCl_3$.

### X-ray Crystallography

The X-ray studies showed that the asymmetric units of compounds **1** and **2** (Figures 1 and 2, respectively) present the general formula [PhTe(L)$PhTeX_4$] [**1**: L = TMTU (tetramethylthiourea), X = Br; **2**: L = TU (thiourea), X = I] Since the Te2–Br2 and Te2–I4 distances in **1** and **2** [3.1757(13) and 3.1687(8) Å] are similar to the Te1–Br2 and Te1–I4 distances, but much smaller than the Te1–Br3′ and Te1–I4′ bond lengths of 3.8471(13) and 3.7602(12) Å. According to Alcock's concept of secondary bonds,[1] the latter bonds are examples of this type of interaction. Thus, it is plausible to state that the asymmetric units are neutral monomers connected by secondary Te···X interactions into dimers with the formula [LPhTe(μ-X)$TeX_3Ph]_2$. The crystal structures of compounds **3** and **4** (Figures 3 and 4, respectively) are built up of discrete $[PhTeX_4]^-$ anions (**3**: X = I; **4**: X = Br) and the corresponding $[PhSe(TU)]^+$ cations. Considering the E···X secondary bonds, the complex salts **3** and **4** should be classified as pseudo-dimeric (**3**) or polymeric (**4**) assemblies.

The two PhTe(TMTU)$PhTeBr_4$ units in complex **1** are related by a center of inversion in the center of the rectangle formed by the atoms Te1, Br3, Te1′, and Br3′ (Figure 1). The Br3 and Br3′ atoms form secondary bonds to the Te1′ and Te1 atoms, respectively, thereby closing the dimeric arrangement. The geometry around the $Te^{IV}$ atom (Te1) may be described as distorted octahedral with bonds to five bromine atoms (Br1, Br2, Br3, Br4, and Br3′) and to one aromatic carbon atom (C11). The geometry around the $Te^{II}$ atom (Te2) presents a T-shape and involves a bromine atom (Br2), a sulfur atom, and an aromatic carbon (C21). The Br2 atom is shared by both tellurium atoms located in the same asymmetric unit, thereby suggesting the occurrence of a charge-transfer compound. The sum of the van der Waals radii of Te and Br is 4.0 Å.[37] The Te2–S bond length of 2.455(3) Å agrees with similar examples in the literature containing a Br–Te–S arrangement.[29] An intramolecular contact is observed between $Te^{II}$ and the π-system of the phenyl ring C11–C16, resulting in a relatively short distance

 © 2006 Wiley-VCH Verlag GmbH & Co. KGaA, Weinheim 

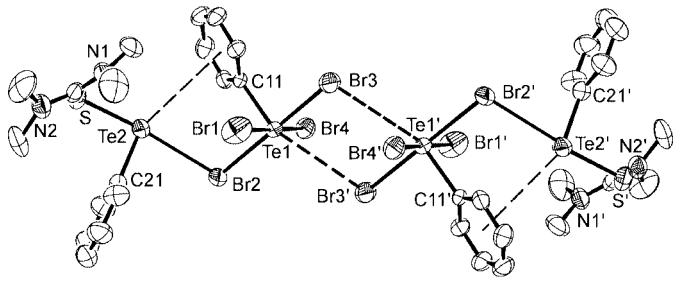


Figure 1. Crystal structure of **1** (hydrogen atoms omitted). Ellipsoids are drawn at 50 % probability. Selected bond lengths [Å] and angles [°]: Te1–Br1 2.6446(15), Te1–Br2 2.7728(14), Te1–Br3 2.6300(13), Te1–Br4 2.7090(16), Te1–Br3′ 3.8471(13), Te1–C11 2.142(7), Te2–Br2 3.1757(13), Te2–S 2.455(3), Te2–C21 2.097(9); Br1–Te1–Br2 88.53(4), Br1–Te1–Br3 90.49(5), Br1–Te1–Br4 177.58(4), Br1–Te1–Br3′ 81.18(4), C11–Te1–Br1 89.4(2), C11–Te1–Br2 89.4(2), C11–Te1–Br3 90.1(2), C11–Te1–Br4 88.9(2), Te1–Br2–Te2 102.27(4), Br2–Te2–S 173.38(7), Br2–Te2–C21 82.2(2), C21–Te2–S 91.2(2). Symmetry transformation used to generate equivalent atoms (′): $-x - 1$, $-y + 1$, $-z + 1$.

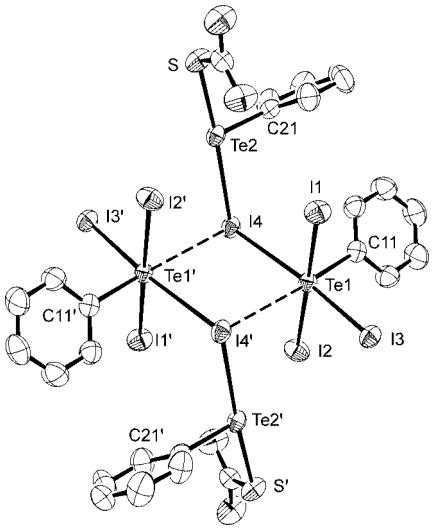


Figure 2. Crystal structure of **2** (hydrogen atoms omitted). Ellipsoids are drawn at 50 % probability. Selected bond lengths [Å] and angles [°]: Te1–I1 2.9053(8), Te1–I2 2.9519(8), Te1–I3 2.7953(7), Te1–I4 3.2651(7), Te1–I4′ 3.7602 (12), Te1–C11 2.144(6), Te2–I4 3.1687(8), Te2–S 2.4924(18), Te2–C21 2.110(6); I1–Te1–I2 178.21(2), I1–Te1–I3 88.36(2), I1–Te1–I4 90.52(17), I1–Te1–I4′ 82.31(2), C11–Te1–I1 91.88(17), C11–Te1–I2 89.85(17), C11–Te1–I3 94.40(17), Te1–I4–Te2 106.84(2), I4–Te2–S 176.11(5), I4–Te2–C21 90.19(17), C21–Te2–S 91.93(18). Symmetry transformation used to generate equivalent atoms (′): $1 - x$, $1 - y$, $1 - z$.

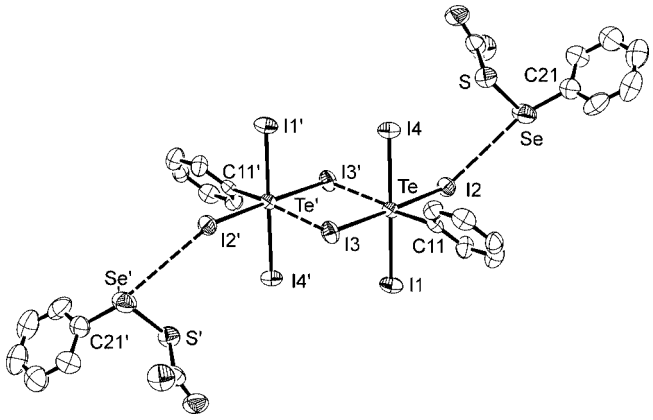


Figure 3. Crystal structure of **3** (hydrogen atoms omitted). Ellipsoids are drawn at 50 % probability. Selected bond lengths [Å] and angles [°]: Te–I1 2.9211(7), Te–I2 2.9614(8), Te–I3 2.9218(8), Te–I4 2.9521(7) Te–I3′ 3.8343(10), Te–C11 2.159(8), Se–I2 3.9485(12), Se–S 2.194(3), Se–C21 1,919(10); I1–Te–I2 89.64(2), I1–Te–I3 90.65(2), I1–Te–I4 176.89(3), I1–Te–I3′ 88.54(2), C11–Te–I1 91.93(18), C11–Te–I2 91.56(18), C11–Te–I3 90.97(18), Te–I2–Se 139.56(3), I2–Se–S 81.86(7), I2–Se–C21 154.2(3), C21–Se–S 100.0(3). Symmetry transformation used to generate equivalent atoms (′): $-x$, $-y$, $-z + 2$.

between $Te^{II}$ and C12 [3.577(23) Å] in the solid-state structure of **1**. The distance between the $Te^{II}$ atom and the centroid of the phenyl ring is 3.935(18) Å and can be interpreted as a Te–$\eta^6$-π-interaction.[38]

The PhTe(TU)PhTe$I_4$ units in complex **2** are also related by a center of inversion in the middle of the rectangle formed by the atoms Te1, I4, Te1′, and I4′. The dimer is connected through the I4 and I4′ atoms. The geometry around the Te1 atom may also be described as distorted octahedral, with bonds to five iodine atoms (I1, I2, I3, I4, and I4′) and to one aromatic carbon atom (C11). The Te1–I3 bond [2.7953(7) Å] is shorter than the *trans* Te1–I4 [3.2651(7) Å] and the Te2–I4 [3.1687(8) Å] bonds, probably due to the bridging role of the I4 atom,. The I4 atom is shared by both tellurium atoms located in the same asymmetric unit, which also suggests the occurrence of a charge-transfer process as in compound **1**.

In a recent work Aragoni et al.[6] discussed the ionic {[RSeCN]$^+$I$^-$} or "T-shaped" hypervalent {R(I)SeCN} features of an ICN adduct with a selenium donor. Density functional theory (DFT) calculations, among other studies, have accounted for the strong polarity of the Se–I bond as being due to the selenium atom having a partial hypervalent state. These results allowed the authors to conclude that the compound can be described as the product of a donor–acceptor interaction between I and the selenium atom of the organic cation [RSeCN]$^+$. This evidence can also be used to support our molecular interpretation of the monomeric fragments LPhTe(μ-X)Te$X_3$Ph of compounds **1** and **2**, although with a reasonably strong polarization of the bonds Br2–Te2 in **1** and I4–Te1 in **2**. The [PhTeS(R)]$^+$ fragment of **1** and **2** would correspond to the organic cation [RSeCN]$^+$ of Aragoni and co-workers.[6] The dimerization

 © 2006 Wiley-VCH Verlag GmbH & Co. KGaA, Weinheim 

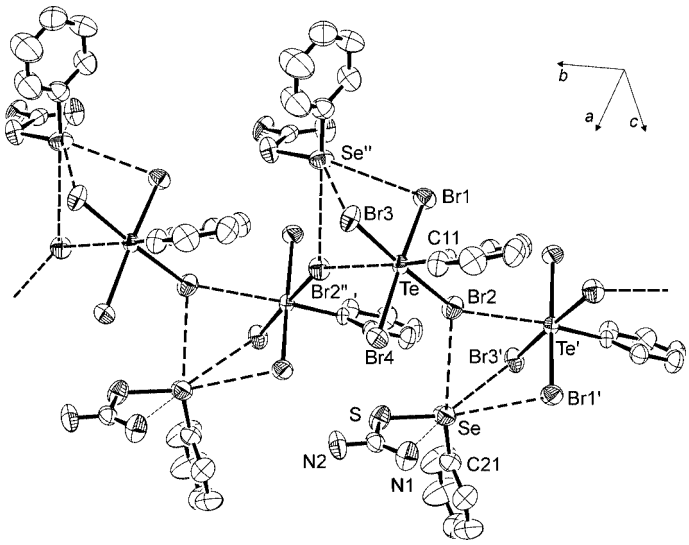


Figure 4. Crystal structure of **4** (hydrogen atoms omitted). Ellipsoids are drawn at 50 % probability. Selected bond lengths [Å] and angles [°]: Te–Br1 2.6535(12), Te–Br2 2.7688(12), Te–Br3 2.6163(12), Te–Br4 2.7309(12), Br2–Te′ 3.5775(13), Te–C11 2.148(9), Se–Br1′ 3.7113(18), Se–Br2 3.6853(16), Se–Br3′ 3.9395(17), Se–S 2.196(4), Se–C21 1.930(11), Se–N1 3.1681(97); Br1–Te–Br2 87.29(4), Br1–Te–Br3 89.69(4), Br1–Te–Br4 176.28(4), C11–Te–Br1 92.3(2), C11–Te–Br2 90.2(2), C11–Te–Br3 89.4(2), Te–Br1–Se′′ 94.02(4), Te–Br2–Se 124.00(5), Te–Br3–Se′′ 89.53(4), Br2–Se–S 93.87(10), Br2–Se–C21 156.1(3), C21–Se–S 100.3(4). Symmetry transformation used to generate equivalent atoms (′): $-x$, $y - 0.5$, $-z + 1$; (′′): $-x$, $y + 0.5$, $-z + 1$.

of the compounds through secondary Te···X bonds indicates the presence of a partial positive charge on the Te atom, as expected in hypervalent adducts with halogens. However, complexes **1** and **2** cannot be classified as charge-transfer (CT) complexes. Indeed, based on their structures and literature precedents[4,6] they should be considered CT-type compounds where the donor–acceptor interaction occurs from the μ-Br2 and μ-I4 atoms of the octahedral $[PhTeX_4]$ fragment, which acts as donor, to the empty σ* molecular orbital located on the S–Te axis of the $[PhTeS(R)]^+$ moiety.

The crystal structure of complex **3** is built up of $[PhTeI_4]_2^{2-}$ anions stabilized by two $[PhSeTU]^+$ cationic units. The I3 and I3′ atoms connect the $[PhTeI_4]^-$ anionic units and the I2 and I2′ atoms present a weak interaction with the Se and Se′ atoms of cationic $[PhSeTU]^+$ units. The geometry around the Te atom can be described as distorted octahedral as it is bonded to five halogen atoms (I1, I2, I3, I4 and I3′) and to one aromatic carbon atom (C11). The geometry around the Se atom shows a distorted T-shaped form; the Se atom is bonded to one sulfur atom, one aromatic carbon atom (C21), and weakly bonded to one iodine atom [Se–I2 = 3.9485(12) Å]. The ionic formulation of compound **3** is supported by the fact that the Se–I bond length is much longer than analogous bond lengths in previously reported structures [Se–I = 2.564(1)–2.720(1) Å].[39,40] The structure of **3** is quite different from that of compound **1** with regards to the coordination sphere of the $Te^{II}$ and $Se^{II}$ atoms. The $Te^{II}$ atom in **1** has a tendency to form an intramolecular bond of the type Te···$\eta^6$-π-aryl, while for **3** the $Se^{II}$ atom coordinates preferentially to iodide atoms. Weak $Se^{II}$···I secondary interactions link the neighboring molecules into a chain along the crystallographic *b* axis. Also of interest in the structure of **3** is the presence of four identical weak I···I secondary interactions [3.7128(8) Å] with adjacent molecules to give a polymeric, double-zigzag chain along the crystallographic *a* axis. As in **2** and in other organotellurium triiodides,[14] intramolecular I···I and Te···I secondary interactions contribute to the formation of continuous supramolecular chains in the crystal packing.

The crystal structure of complex **4** is built up of discrete cationic $[PhSeTU]^+$ and anionic $[PhTeBr_4]^-$ units, with halogen atoms bridging secondary adjacent tellurium atoms to give a single zigzag polymeric chain along the crystallographic *b* axis. The chain character is additionally reinforced by three secondary bonds from cationic selenium atoms to the bromine ligands of the surrounding anionic units (Figure 4). The geometry around the Te atom, which is bonded to five bromine atoms (Br1, Br2, Br3, Br4, and Br2′′) and to one aromatic carbon atom (C11), may be described as distorted octahedral. The Se atom shows a highly distorted octahedral geometry, with secondary bonds to three bromine atoms (Br1, Br2′′, Br3) and primary bonds with one aromatic carbon atom (C21) and the sulfur/nitrogen atoms of the thiourea ligand. The interionic Se···Br secondary bonds of **4**, with distances varying from 3.6853(16) (Se–Br2) to 3.9395(17) Å (Se–Br3′) can be considered weak interactions when compared with the Se–Br bond lengths of 2.3331(8) Å in $2\text{-}Me_2NCH_2C_6H_4SeBr$,[32,41] for example. The Se–N1 bond length of 3.1681(97) Å in **4** is also a very weak interaction when compared with Se–N bond lengths of other compounds such as $2\text{-}Me_2NCH_2C_6H_4SeX$: [X = Cl: Se–N = 2.135(4) Å; Br: 2.143(6) Å; I: 2.172(3) Å].[42]

### $^{125}$Te and $^{77}$Se NMR Spectroscopy

Attempts to study the title complexes in noncoordinating solvents by means of NMR spectroscopy were unsuccessful

 © 2006 Wiley-VCH Verlag GmbH & Co. KGaA, Weinheim 

due to their poor solubility. Since compounds **1**–**4**, as expected, do not show many significant features in their $^{1}H$ or $^{13}C$ NMR spectra, our attention turned to $^{125}Te$ and $^{77}Se$ NMR spectroscopy. A mixture of [$D_6$]acetone and [$D_6$]-DMSO (9:1 by volume) was employed for the NMR studies. The two signals detected for **1** at $\delta$ = 1203.3 and 828.8 ppm (for **2** only one broad signal is observed at $\delta$ = 946 ppm) appear very close to the two peaks observed at $\delta$ = 1202.3 and 824.8 ppm for $PhTeBr_3$, whose spectrum was recorded under the same conditions for comparison purposes. The dissolution of $PhTeBr_3$ presumably produces the ionic species shown in Equation (2).

$$2\ PhTeBr_3 \xrightarrow{DMSO} [PhTe^{IV}Br_2]^+ + [PhTe^{IV}Br_4]^- \quad (2)$$

The major signal of compound **1** at $\delta$ = 1203.3 (s) ppm should correspond to the ionic form $[PhTe^{IV}Br_4]^-$, which occurs at $\delta$ = 1199.8 ppm for the standard compound $(NEt_4)[PhTeBr_4]$. This result allows also us to conclude that the dissolution of compound **1** (and probably also of **2**) leads to the cleavage of all the bonds represented by dotted lines in Figure 1 (e.g., the secondary Te1–Br3′ and the primary Te2–Br2 bonds). This also supports the assumption that the second signal of compound **1** [$\delta$ = 828.8 (s) ppm] should correspond to the cationic species $[PhTe(L)]^+$.

The selenium derivatives **3** and **4** seem to exhibit a different behavior in solution. While compound **4** presents only a sharp $^{125}Te$ resonance at $\delta$ = 1230.2 ppm, compound **3** does not show any NMR signal even though different windows were investigated. Furthermore, in the case of **4** two sharp $^{77}Se$ resonances are found at $\delta$ = 655.9 and 446.5 ppm in an approximate proportion of 1:1. This result supports the hypothesis of a partial disruption of the polymer according to Equation (3).

$$\{[PhSe(TU)][PhTeBr_4]\}_n \rightarrow n/2\ \{PhSe(TU)[PhTeBr_4]_2\}^- + n/2\ [PhSe(TU)]^+ \quad (3)$$

The anionic species might be fluxional and variable-temperature studies would be needed to characterize such a system. Unfortunately, we could not do this because of the limited solubility of all compounds in solvents adequate for low-temperature studies.

## Conclusions

A good familiarity with the coordination chemistry and reactivity of organyl chalcogen compounds in the single oxidation states +2 and +4 is required and desirable for the adequate planning of different syntheses (one pot) to give good yields of organyl chalcogenides derivatives with mixed valence states.

The X-ray analytical data of the structures of compounds **1**–**4** show a strong tendency to dimerize for **1** and **2** and suggest that the formation of supramolecular assemblies depends on the nature of the halogen bonded to the tellurium atom. The halogen can induce simultaneous intra- and intermolecular secondary interactions among the heavy atoms and, in addition to Te···X and X···X secondary bonds, intramolecular interactions of the type Te···$\eta^6$-π-aryl can be formed. Secondary bonds are usually not strong enough to remain in solution, especially in coordinating solvents, but they can have spectacular effects in the building of a crystal by creating the secondary structure that defines the supramolecular arrangement in the solid state.[43,44] These findings also suggest further investigations of the steric influence of the organic substituents on the final architecture of the compounds.

## Experimental Section

**General Procedure:** All manipulations were conducted under dinitrogen, using standard Schlenk techniques. Methanol was dried with sodium and distilled prior to use. Diphenyl diselenide and diphenyl ditelluride were prepared according to literature methods.[45,46]

**X-ray Structural Determination:** The structures were solved by direct methods using SHELXS-97.[47] Subsequent Fourier-difference map analyses yielded the positions of the non-hydrogen atoms. Refinements were carried out with the SHELXL-97 package.[47] All refinements were made by full-matrix least-squares on $F^2$ with anisotropic displacement parameters for all non-hydrogen atoms. Hydrogen atoms were included in the refinement in calculated positions. Crystal data and more details of the data collections and refinements are contained in Table 1.
CCDC-286671–286674 (**1**–**4**) contain the supplementary crystallographic data for this paper. These data can be obtained free of charge from The Cambridge Crystallographic Data Centre via www.ccdc.cam.ac.uk/data_request/cif.

**NMR Spectroscopy:** All NMR spectra were recorded with a Varian Mercury plus spectrometer (7.05 T) operating at 94.74 MHz for $^{125}Te$ and 57.23 MHz for $^{77}Se$. $^{125}Te$ and $^{77}Se$ NMR spectra were acquired in a mixture of [$D_6$]acetone and [$D_6$]DMSO (9:1 by volume) and were externally referenced to $Me_2Te$ and $Me_2Se$ checked against $Te_2Ph_2$ in $CDCl_3$ ($\delta$ = 450.0 ppm)[48] and $Se_2Ph_2$ in $CDCl_3$ ($\delta$ = 461.0 ppm),[49] respectively. The sample temperature was maintained at 300 K during the acquisitions.

**General Procedure for the Synthesis of PhE(L)PhE′$X_4$. PhTe(TU)-$PhTeI_4$:** Iodine (1 mmol, 0.2538 g) was added to a solution of diphenyl ditelluride (1 mmol, 0.4092 g) in methanol at room temperature. The mixture was stirred for 10 min until the color changed from red to black. Thiourea (2 mmol, 0.1522 g) was then added to the mixture − the color of the solution changed from black to red − and soon afterwards $PhTeI_3$ (2 mmol, 1.1706 g) was added. The solution was kept at slow reflux for 2 h. The final solution was filtered at room temperature and crystals suitable for X-ray analysis were grown by slow evaporation.
**1:** Yield: 1.0141 g (65 %). M.p. 189–192 °C. $C_{17}H_{22}Br_4N_2STe_2$: calcd. C 23.71, H 2.57, N 3.25; found C 24.44, H 2.81, N 3.89. $^{125}Te$ NMR: $\delta$ 1203.3 (s), 828.8 (s) ppm.
**2:** Yield: 1.2907 g (63 %). M.p. 147–149 °C; $C_{13}H_{14}I_4N_2STe_2$: calcd. C 15.72, H 1.42, N 2.82; found C 16.00, H 1.47, N 2.73. $^{125}Te$ NMR: $\delta$ = 946 ppm (br).
**3:** Yield: 1.2840 g (68 %). M.p. 168–170 °C; $C_{13}H_{14}I_4N_2SSeTe$: calcd. C 16.53, H 1.49, N 2.97; found C 16.82, H 1.42, N 2.89.
**4:** Yield: 1.2853 g (85 %), Melting point: 178–180 °C; $C_{13}H_{14}Br_4N_2SSeTe$: calcd. C 20.64, H 1.87, N 3.70; found C 19.42, H 2.05, N 3.88. $^{125}Te$ NMR: $\delta$ = 1230.2 ppm (s). $^{77}Se$ NMR: $\delta$ = 655.9 (s), 446.5 (s) ppm.

 © 2006 Wiley-VCH Verlag GmbH & Co. KGaA, Weinheim 

Table 1. X-ray data collection and refinement parameters.

| | **1** | **2** | **3** | **4** |
|---|---|---|---|---|
| Empirical formula | $C_{17}H_{22}Br_4N_2STe_2$ | $C_{13}H_{14}I_4N_2STe_2$ | $C_{13}H_{14}I_4N_2SSeTe$ | $C_{13}H_{14}Br_4N_2SSeTe$ |
| Mol. wt. | 861.27 | 993.12 | 944.48 | 756.52 |
| $a$ [Å] | 9.2793(13) | 9.3392(16) | 9.3920(4) | 8.8030(3) |
| $b$ [Å] | 11.529(3) | 10.7434(16) | 9.7050(6) | 9.2070(4) |
| $c$ [Å] | 12.249(2) | 12.052(4) | 13.2290(7) | 13.0240(5) |
| $\alpha$ [°] | 100.12(3) | 91.833(14) | 74.580(3) | |
| $\beta$ [°] | 103.511(14) | 105.699(10) | 73.040(3) | 98.460(3) |
| $\gamma$ [°] | 93.40(2) | 94.491(13) | 88.710(3) | |
| $V$ [Å$^3$] | 1247.3(4) | 1158.8(4) | 1109.87(10) | 1044.10(7) |
| $Z$ | 2 | 2 | 2 | 2 |
| $D_c$ [g cm$^{-3}$] | 2.293 | 2.846 | 2.826 | 2.406 |
| Crystal system | triclinic | triclinic | triclinic | monoclinic |
| Space group | $P\bar{1}$ | $P\bar{1}$ | $P\bar{1}$ | $P2_1$ |
| Cryst. size [mm] | 0.15 × 0.1 × 0.05 | 0.14 × 0.1 × 0.08 | 0.14 × 0.1 × 0.05 | 0.13 × 0.1 × 0.07 |
| $2\theta_{max}$ [°] | 54 | 54 | 50 | 50 |
| Linear absorption coefficient [mm$^{-1}$] | 8.835 | 7.934 | 8.635 | 10.918 |
| Absorption correction | DELABS[50] | DELABS[50] | SORTAV[51] | SORTAV[51] |
| $T_{min}$ | 0.3508 | 0.7003 | 0.3777 | 0.3310 |
| $T_{max}$ | 0.6664 | 0.9413 | 0.6720 | 0.5327 |
| Measured reflections | 6413 | 5934 | 9872 | 7476 |
| Independent reflections/$R_{int}$ | 5403/0.0662 | 5010/0.0243 | 3915/0.0479 | 3428/0.0876 |
| Refined parameters | 235 | 200 | 200 | 200 |
| $R1$ ($F$)/$wR2$ ($F^2$) [$I > 2\sigma(I)$] | 0.0597/0.1707 | 0.0401/0.1043 | 0.0380/0.1025 | 0.0429/0.1101 |
| Device | CAD4 | CAD4 | BRUKER CCD | BRUKER CCD |
| Radiation | Mo-$K_\alpha$ | Mo-$K_\alpha$ | Mo-$K_\alpha$ | Mo-$K_\alpha$ |
| GOF ($F^2$) | 1.010 | 1.155 | 1.032 | 1.034 |

## Acknowledgments

We are grateful to the FAPERGS and CNPq for financial support.

[1] N. W. Alcock, *Adv. Inorg. Chem. Radiochem.* **1972**, *15*, 1–58.
[2] B. Krebs, F.-P. Ahlers, *Adv. Inorg. Chem.* **1990**, *35*, 235–317.
[3] W.-W. Du Mont, J. Jeske, P. G. Jones, *Phosphorus, Sulfur Silicon Relat. Elem.* **1998**, *136–138*, 305–308.
[4] M. C. Aragoni, M. Arca, F. Demartin, F. A. Devillanova, A. Garau, F. Lelj, V. Lippolis, G. Verani, *Chem. Eur. J.* **2001**, *7*, 3122–3133.
[5] M. C. Aragoni, M. Arca, A. J. Blake, F. A. Devillanova, W. W. du Mont, A. Garau, F. Isaia, V. Lippolis, G. Verani, C. Wilson, *Angew. Chem.* **2001**, *113*, 4359–4362; *Angew. Chem. Int. Ed.* **2001**, *40*, 4229–4232.
[6] M. C. Aragoni, M. Arca, F. Demartin, F. A. Devillanova, A. Garau, P. Grimaldi, F. Isaia, F. Lelj, V. Vippolis, G. Verani, *Eur. J. Inorg. Chem.* **2004**, 2363–2368.
[7] P. C. Srivastava, S. Bajpai, S. Bajpai, C. Ram, R. Kumar, J. P. Jasinski, R. J. Butcher, *J. Organomet. Chem.* **2004**, *689*, 194–202.
[8] A. K. S. Chauhan, Anamika, A. Kumar, R. C. Srivastava, R. J. Butcher, J. Beckmann, A. Duthie, *J. Organomet. Chem.* **2005**, *690*, 1350–1355.
[9] P. C. Srivastava, *Phosphorus, Sulfur Silicon Relat. Elem.* **2005**, *180*, 969–983.
[10] P. D. Boyle, W. I. Cross, S. M. Godfrey, C. A. McAuliffe, R. G. Pritchard, S. J. Teat, *J. Chem. Soc., Dalton Trans.* **1999**, 2845–2852.
[11] E. Schulz Lang, R. M. Fernandes Jr., E. T. Silveira, U. Abram, E. M. Vázquez-López, *Z. Anorg. Allg. Chem.* **1999**, *625*, 1401–1404.
[12] P. D. Boyle, W. I. Cross, S. M. Godfrey, C. A. McAuliffe, R. G. Pritchard, S. Sarwar, J. M. Sheffield, *Angew. Chem.* **2000**, *112*, 1866–1868; *Angew. Chem. Int. Ed.* **2000**, *39*, 1796–1798.
[13] E. Schulz Lang, G. Manzoni de Oliveira, E. T. Silveira, R. A. Burrow, E. M. Vázquez-López, *J. Organomet. Chem.* **2002**, *664*, 306–309.
[14] G. N. Ledesma, E. Schulz Lang, U. Abram, *J. Organomet. Chem.* **2004**, *689*, 2092–2095.
[15] E. Schulz Lang, U. Abram, J. Strähle, *Z. Anorg. Allg. Chem.* **1997**, *623*, 1968–1972.
[16] G. N. Ledesma, E. Schulz Lang, E. M. Vázquez-López, U. Abram, *Inorg. Chem. Commun.* **2004**, *7*, 478–480.
[17] E. Schulz Lang, R. M. Fernandes Jr., C. Peppe, R. A. Burrow, E. M. Vázquez-López, *Z. Anorg. Allg. Chem.* **2003**, *629*, 215–218.
[18] E. Schulz Lang, G. Manzoni de Oliveira, R. M. Fernandes Jr., E. M. Vázquez-López, *Inorg. Chem. Commun.* **2003**, *6*, 869–872.
[19] E. Schulz Lang, G. Manzoni de Oliveira, R. M. Fernandes Jr., E. M. Vázquez-López, *Z. Anorg. Allg. Chem.* **2004**, *630*, 717–721.
[20] C. Knobler, J. D. McCullough, *Inorg. Chem.* **1977**, *16*, 612–615.
[21] R. K. Chadha, J. E. Drake, *J. Organomet. Chem.* **1985**, *293*, 37–43.
[22] N. Al-Salim, A. A. West, W. R. McWhinnie, T. A. Hamor, *J. Chem. Soc., Dalton Trans.* **1988**, 2363–2371.
[23] H. B. Singh, N. Sudha, R. T. Butcher, *Inorg. Chem.* **1992**, *31*, 1431–1435.
[24] J. Nvosad, K. W. Törnroos, M. Necas, A. M. Z. Slawin, J. D. Woollins, S. Huseby, *Polyhedron* **1999**, *18*, 2861–2867.
[25] M. Necas, J. Novosad, S. Huseby, *J. Organomet. Chem.* **2001**, *623*, 124–130.
[26] H. Fleischer, B. Mathiasch, D. Schollmeyer, *Organometallics* **2002**, *21*, 526–533.
[27] N. W. Alcock, W. D. Harrison, *Acta Crystallogr., Sect. B* **1982**, *38*, 2677–2679.
[28] N. W. Alcock, W. D. Harrison, *J. Chem. Soc., Dalton Trans.* **1984**, 869–875.
[29] O. Foss, S. Huseby, *Acta Chem. Scand.* **1966**, *20*, 132–142.

 © 2006 Wiley-VCH Verlag GmbH & Co. KGaA, Weinheim 

[30] I. D. Sadekov, V. I. Minkin, A. V. Zakharov, A. G. Starikov, G. S. Borodkin, S. M. Aldoshin, V. V. Tkachev, G. V. Shilov, F. J. Berry, *J. Organomet. Chem.* **2005**, *689*, 103–119.
[31] S. C. Menon, H. B. Singh, J. M. Jasinski, J. P. Jasinski, R. J. Butcher, *Organometallics* **1996**, *15*, 1707–1712.
[32] G. Mugesh, H. B. Singh, R. J. Butcher, *Tetrahedron: Asymmetry* **1999**, *10*, 237–242.
[33] H. M. K. K. Pathirana, J. H. Reibenspies, E. A. Meyers, R. A. Zingaro, *Acta Crystallogr., Sect. C* **1991**, *47*, 516–519.
[34] D. B. Werz, R. Gleiter, F. Rominger, *J. Organomet. Chem.* **2004**, *689*, 627–630.
[35] P. G. Jones, J. Jeske, *Private Communication*, **2004**, CCDC 239392.
[36] K. Giselbrecht, B. Bildstein, F. Sladky, *Chem. Ber.* **1989**, *122*, 1255–1256.
[37] *Periodic Table of the Elements*, VCH, Weinheim, **1986**.
[38] J. Zukerman-Schpector, I. Haiduc, *CrystEngComm* **2002**, *4*, 178–192.
[39] O. Vikane, *Acta Chem. Scand.* **1975**, *A29*, 787–793.
[40] S. M. Godfrey, D. G. Kelly, C. A. McAuliffe, A. G. Mackie, R. G. Pritchard, S. M. Watson, *J. Chem. Soc., Chem. Commun.* **1991**, 1163–1164.
[41] F. Cristiani, F. Demartin, F. A. Devillanova, F. Isaia, V. Lippolis, G. Verani, *Inorg. Chem.* **1994**, *33*, 6315–6324.
[42] T. M. Klapötke, B. Krumm, K. Polborn, *J. Am. Chem. Soc.* **2004**, *126*, 710–711.
[43] J. D. McCullough, C. Knobler, *Inorg. Chem.* **1976**, *15*, 2728–2731.
[44] J. D. McCullough, *Inorg. Chem.* **1977**, *16*, 2318–2321.
[45] H. J. Reich, J. M. Renga, I. L. Reich, *J. Am. Chem. Soc.* **1975**, *97*, 5434–5447.
[46] a) K. J. Irgolic, *Houben-Weyl Methods of Organic Chemistry*, Vol. E 12b, Organotellurium Compounds (Ed.: D. Klamann), **1990**, 273; b) W. S. Haller, K. J. Irgolic, *J. Organomet. Chem.* **1972**, *38*, 97–103.
[47] G. M. Sheldrick, *SHELXS-97 and SHELXL-97*, Programs for Crystal Structure Solution and Refinement; University of Göttingen, Germany, **1997**.
[48] M. Asahara, M. Tanaka, T. Erabi, M. Wada, *J. Chem. Soc., Dalton Trans.* **2000**, 3493–3499.
[49] S. Kumar, S. K. Tripathi, H. B. Singh, G. Wolmershäuser, *J. Organomet. Chem.* **2004**, *689*, 3046–3055.
[50] N. Walker, D. Stuart, *Acta Crystallogr., Sect. A* **1983**, *39*, 158–166.
[51] R. H. Blessing, *Acta Crystallogr., Sect. A* **1995**, *51*, 33–38.
Received: September 12, 2005
Published Online: January 12, 2006

 © 2006 Wiley-VCH Verlag GmbH & Co. KGaA, Weinheim 

DOI: 10.1002/ejic.200500826

# Synthesis, Structure and Reactivity in Styrene Polymerization by Heterocyclic Alkoxy- and Thiolatotitanium(IV) Complexes

**Pedro J. Aragón,[a] Fernando Carrillo-Hermosilla,[a] Elena Villaseñor,[a] Antonio Otero,*[a] Antonio Antiñolo,[a] and Ana M. Rodríguez[a]**

**Keywords:** Heterocyclic ligands / Polymerization / Structure elucidation / Titanium

The reaction of $[Ti(OiPr)_4]$ or $[TiCl_4(THF)_2]$ with two equivalents of pyridyl alcohols or pyridyl or pyrimidinyl thiols has proven to be a good preparative method to obtain a variety of non-metallocene diisopropoxo- or dichlorotitanium(IV) complexes. The complexes $[Ti(X)_2\{2\text{-}(OCH_2)\text{-}6\text{-}R\text{-}(C_5H_3N)\}_2]$ were found to be dynamic at room temperature, with the heterocyclic alkoxy ligand dissociating and recoordinating in a $\kappa^2$-N,O chelate fashion, as revealed by a single-crystal X-ray analysis of $[Ti(OiPr)_2\{2\text{-}(OCH_2)(C_5H_4N)\}_2]$ (**1**). The dynamic behavior of some of the resulting thiolato complexes was also studied and the single-crystal X-ray analysis of $[Ti(OiPr)_2\{2\text{-}S\text{-}4,6\text{-}Me_2\text{-}(C_4HN_2)\}_2]$ (**5**) revealed a $\kappa^2$-N,S system for these complexes. These complexes show catalytic activity in the polymerization of styrene upon activation with methylaluminoxane.

(© Wiley-VCH Verlag GmbH & Co. KGaA, 69451 Weinheim, Germany, 2006)

## Introduction

The coordination chemistry of the transition metals has experienced significant developments during the last three decades and at present constitutes an area of great importance due to its theoretical interest and diverse applications in organic synthesis and catalytic processes. The chemistry of the group 4 elements is dominated by complexes that contain cyclopentadienyl ligands or their derivatives. This is due to the fact that in recent years this field has undergone a significant expansion aimed at exploiting applications of these complexes as catalysts in olefin polymerization, hydrogenation, and hydrosilylation reactions. Nevertheless, increasing interest is being shown in the use of alternative ligands, such as alkoxy or amido derivatives, that are capable of stabilizing metal complexes in high oxidation states. In this way, it is possible to design ligands that can stabilize active species in certain catalytic processes so that they can be used instead of Cp ligands.[1]

In this paper we describe the synthesis and characterization of new alkoxy- and thiolatotitanium(IV) complexes bearing heterocyclic rings in the ligands. In addition, the activity of these complexes as styrene polymerization catalysts has been studied.

[a] Departamento de Química Inorgánica, Orgánica y Bioquímica, Facultad de Ciencias Químicas, Universidad de Castilla-La Mancha,
Campus Universitario, 13071-Ciudad Real, Spain
Fax: +34-926-295-318
E-mail: Antonio.Otero@uclm.es

## Results and Discussion

The new complexes $[Ti(X)_2\{2\text{-}(OCH_2)\text{-}6\text{-}R\text{-}(C_5H_3N)\}_2]$ [X = O*i*Pr, R = H (**1**); X = Cl, R = H (**2**); X = Cl, R = Me (**3**)], $[Ti\{2,6\text{-}(OCH_2)_2(C_5H_3N)\}_2]$ (**4**), $[Ti(X)_2(SR)_2]$ [X = O*i*Pr, SR = 2-S-4,6-$Me_2$-$(C_4HN_2)$ (**5**); X = Cl, SR = 2-S-4,6-$Me_2$-$(C_4HN_2)$ (**6**); X = O*i*Pr, SR = 2-S-$(C_4H_3N_2)$ (**7**); X = Cl, SR = 2-S-$(C_4H_3N_2)$ (**8**); X = O*i*Pr, SR = 2-S-$(C_5H_4N)$ (**9**)], and $[TiCl_2\{2\text{-}S\text{-}(C_5H_4N)\}\{O(CH_2)_4Cl\}]$ (**10**) were prepared by reaction of the corresponding alcohol or thiol with $[Ti(OiPr)_4]$ or $[TiCl_4(THF)_2]$ (Scheme 1).

Complexes **1**–**3** were isolated as white, air-sensitive solids. Complex **1** is very soluble in THF but complexes **2** and **3** are only sparingly soluble in this solvent.

The presence of two isopropoxide or chloride groups and two alkoxypyridine ligands means that several stereochemical configurations are possible, with the possibility of $\kappa^2$-O,N coordination of the latter ligands to the metal center. A single-crystal X-ray analysis of compound **1** was carried out in order to provide precise structural details of this compound and the related complexes **2** and **3**. The structure of complex **1** is shown in Figure 1, together with the atom-numbering scheme. The bond lengths and angles for this structure are given in Table 1. Complex **1** crystallizes in the monoclinic space group $P2_1/n$. The Ti atom has a markedly distorted pseudoctahedral geometry, with the alkoxypyridine ligands occupying four sites in a chelate fashion. This arrangement is consistent with the $^{13}C$ NMR spectra of complexes **1**–**3**, in which the signals assigned to the C2 and C6 atoms of the pyridine moiety are shifted to slightly lower field in comparison with those in the free ligand. In this way, each ligand is bonded to the metal center through both

 © 2006 Wiley-VCH Verlag GmbH & Co. KGaA, Weinheim 

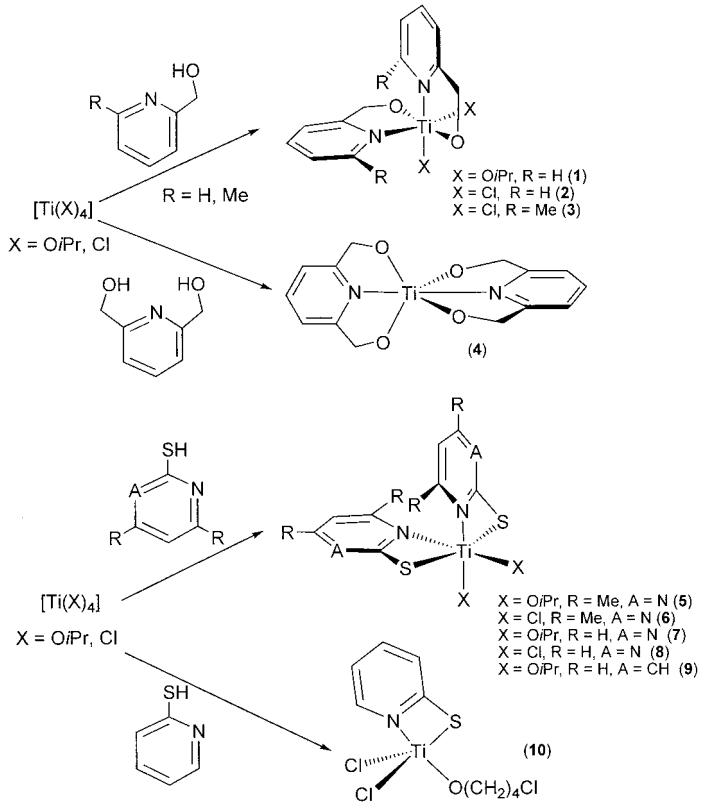


Scheme 1.

the nitrogen and the oxygen atoms. The Ti–O1 and Ti–O2 distances are slightly longer than those found in [Ti($\eta^5$-$C_5H_5$){2-(OC*i*Pr$_2$)-($C_5H_4$N)}Cl$_2$] [1.8267(9) Å],[2] which may indicate low O(pπ)–Ti(dπ) donation to the metal. In contrast, the Ti–N distances are similar in both complexes.

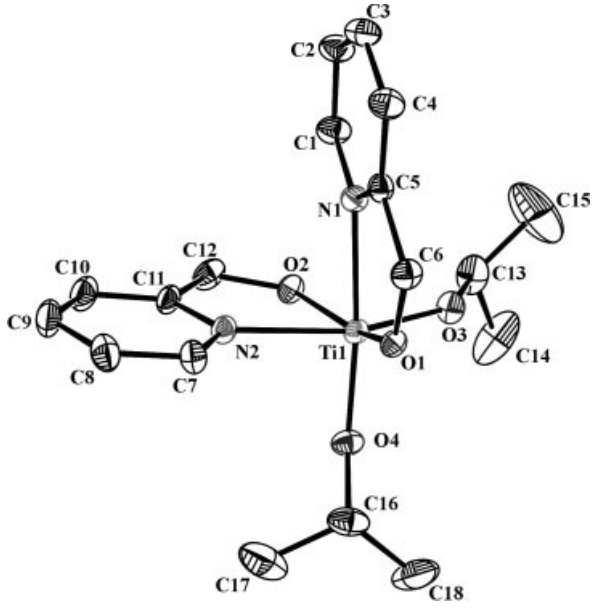


Figure 1. An ORTEP drawing of **1** with the numbering scheme.

It is worth noting that this configuration makes the two hydrogen atoms in the methylene groups inequivalent. In contrast, the $^1$H NMR spectrum of complex **1** shows one single peak for these hydrogen atoms at room temperature. This behavior can be explained in terms of a dynamic process in solution for this molecule. In this process, the alkoxypyridine ligands probably change their $\kappa^2$-N,O coordination to a $\kappa^1$-O coordination through a rupture of the metal–nitrogen bonds (Scheme 2). A similar behavior has been observed in zirconium complexes with oxypyridine and oxypyrimidine ligands.[3]

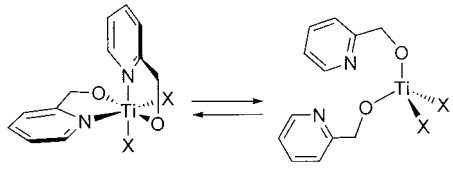

Scheme 2.

A variable-temperature $^1$H NMR study was also carried out on the complexes. When the $^1$H NMR spectrum of complex **1** was recorded at 213 K, an AB spin system ($\delta_A$ = 5.92, $\delta_B$ = 5.89 ppm; $J_{AB}$ = 18.55 Hz) was observed for the inequivalent methylene protons, indicating that, at this temperature, the alkoxypyridine ligands are coordinated in a chelate fashion [$\Delta G^{\ddagger}$ = 54.5(6) kJ mol$^{-1}$], as found in the X-ray structure. In addition, two signals for the methyl groups of the isopropoxide ligands were found, indicating that free rotation does not occur at this temperature [$\Delta G^{\ddagger}$ = 51.2(5) kJ mol$^{-1}$]. A similar behavior was observed for complex **2**. The low solubility of complex **3** prevented us from

 © 2006 Wiley-VCH Verlag GmbH & Co. KGaA, Weinheim 

Table 1. Bond lengths [Å] and angles [°] for **1** and **5**.

| | | | |
|---|---|---|---|
| | **1** | | |
| Ti(1)–O(3) | 1.818(2) | O(1)–Ti(1)–O(2) | 154.47(6) |
| Ti(1)–O(4) | 1.820(1) | O(4)–Ti(1)–N(1) | 165.27(6) |
| Ti(1)–O(1) | 1.902(1) | O(3)–Ti(1)–N(2) | 165.21(6) |
| Ti(1)–O(2) | 1.903(1) | C(6)–O(1)–Ti(1) | 125.6(1) |
| Ti(1)–N(1) | 2.242(2) | C(12)–O(2)–Ti(1) | 125.6(1) |
| Ti(1)–N(2) | 2.244(2) | C(13)–O(3)–Ti(1) | 138.5(1) |
| O(1)–C(6) | 1.381(2) | C(16)–O(4)–Ti(1) | 141.6(1) |
| O(2)–C(12) | 1.385(2) | C(5)–N(1)–Ti(1) | 114.6(1) |
| O(3)–C(13) | 1.396(2) | C(11)–N(2)–Ti(1) | 114.3(1) |
| O(4)–C(16) | 1.401(2) | O(1)–C(6)–C(5) | 111.5(1) |
| N(1)–C(5) | 1.325(2) | O(2)–C(12)–C(11) | 111.5(1) |
| N(1)–C(1) | 1.347(2) | | |
| N(2)–C(7) | 1.337(2) | | |
| N(2)–C(11) | 1.337(2) | | |
| C(5)–C(6) | 1.502(2) | | |
| C(11)–C(12) | 1.500(3) | | |
| | **5** | | |
| Ti(1)–O(1) | 1.757(3) | O(2)–Ti(1)–N(1) | 154.5(1) |
| Ti(1)–O(2) | 1.766(3) | O(1)–Ti(1)–N(3) | 155.2(1) |
| Ti(1)–N(1) | 2.231(3) | S(1)–Ti(1)–S(2) | 156.75(4) |
| Ti(1)–N(3) | 2.312(3) | C(11)–S(1)–Ti(1) | 81.5(1) |
| Ti(1)–S(1) | 2.470(1) | C(17)–S(2)–Ti(1) | 82.8(1) |
| Ti(1)–S(2) | 2.472(1) | C(1)–O(1)–Ti(1) | 156.6(2) |
| S(1)–C(11) | 1.727(4) | C(4)–O(2)–Ti(1) | 147.2(3) |
| S(2)–C(17) | 1.731(3) | C(11)–N(1)–Ti(1) | 99.6(2) |
| O(1)–C(1) | 1.423(4) | C(17)–N(3)–C(20) | 117.6(3) |
| O(2)–C(4) | 1.427(5) | C(17)–N(3)–Ti(1) | 98.0(2) |
| N(1)–C(14) | 1.351(4) | | |
| N(1)–C(11) | 1.357(5) | | |
| N(3)–C(17) | 1.349(4) | | |
| N(3)–C(20) | 1.354(4) | | |
| C(1)–C(2) | 1.496(7) | | |
| C(1)–C(3) | 1.504(6) | | |
| C(4)–C(5) | 1.465(8) | | |

obtaining conclusive results for this complex, although one would expect a similar situation to occur in all three cases.

Attempts to obtain a complex of the type $[Ti(X)_2\{2,6\text{-}(OCH_2)_2\text{-}(C_5H_3N)\}]$ were unsuccessful. In all cases, $[Ti\{2,6\text{-}(OCH_2)_2\text{-}(C_5H_3N)\}_2]$ (**4**) was obtained as a very insoluble white solid.

The $^{13}C$ NMR spectrum of complex **1** is consistent with a disposition in which the dialkoxide ligand shows tridentate coordination and is bonded to the metal atom in a "pincer" fashion.[4]

Similarly, it was not possible to obtain the analogous compound of complex **3** with isopropoxide ligands − a complex mixture of unidentified compounds was obtained in all cases. A possible explanation for this behavior involves the high level of steric hindrance associated with the ligands on the metal center in comparison with the less-crowded chloride complex **3**.

Thiolato complexes **5**–**10** were obtained as yellow (**5**–**9**) or pale-orange (**10**) very air-sensitive solids, with the chloride complexes **6**, **8**, and **10** being only sparingly soluble in THF. The $^1H$ NMR spectrum of **5** shows a broad singlet at $\delta$ = 2.42 ppm due to the thiolato methyl groups, indicating that fluxional behavior may be occurring in the molecule. This behavior is probably due to an interchange in the positions of the nitrogen atoms of the pyrimidine groups in the coordination sphere of the titanium atom by rotation around the S–C bonds (see Scheme 3).[3,5] Kempe[6] has described similar complexes with isolobal aminopyridinato ligands. These complexes undergo a dynamic process that implies an interchange between the aminopyridinato ligands. This exchange proceeds via a tetrahedral transition state similar to that we postulate for the exchange in the thiolato complexes

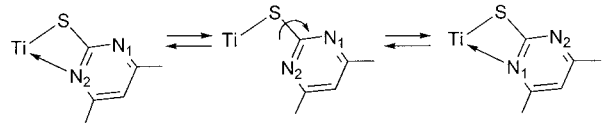


Scheme 3.

A variable-temperature $^1H$ NMR study was carried out on this complex. When the $^1H$ NMR spectrum was recorded at 223 K, two signals corresponding to the methyl groups of the pyrimidine fragments were observed, indicating that rotation around the S–C bond is hindered [$\Delta G^{\ddagger}$ = 60.5(2) kJ mol$^{-1}$] for both thiolate ligands, which act as chelate ligands. As the temperature increases, the rotation becomes easier and at temperatures above 293 K only one signal is observed, corresponding to the free rotation of the two equivalent ligands. A similar behavior was observed for complex **7**. The lack of solubility of complexes **6** and **8** prevented us from obtaining results for these compounds, although the $^{13}C$ NMR spectra indicate that some chelate interaction is present in **6** but not in **8** at room temperature.

A single-crystal X-ray analysis of complex **5** was carried out in order to obtain more precise structural information for this compound and analogous complexes **6**–**10**. The structure of complex **5** is shown in Figure 2, and bond lengths and angles for this structure are given in Table 1.

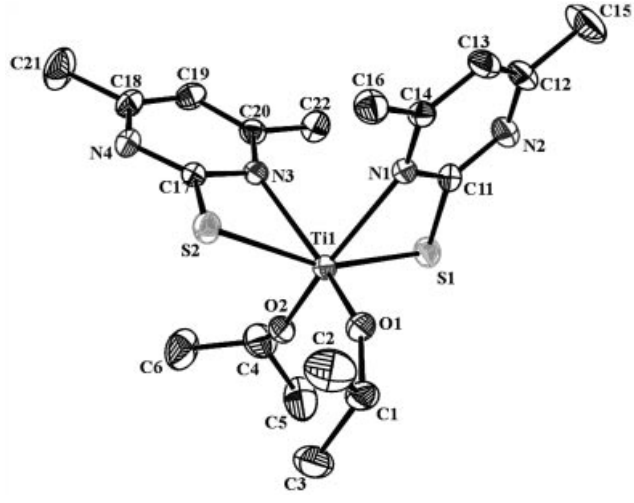


Figure 2. An ORTEP drawing of **5** with the numbering scheme.

To the best of our knowledge, only three structurally characterized titanium thiolatopyridine or -pyrimidine complexes have been described,[7a–7c] and two of these contain cyclopentadienyl ligands. Complex **5** crystallizes in the

 © 2006 Wiley-VCH Verlag GmbH & Co. KGaA, Weinheim 

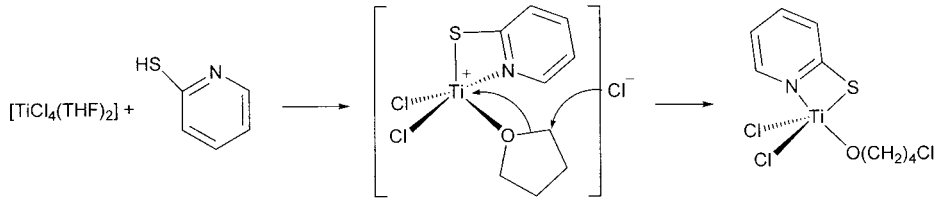


Scheme 4.

monoclinic space group $P2_1/n$. The Ti atom shows a highly distorted pseudooctahedral geometry, with two isopropoxide ligands occupying two sites and the other four sites occupied by the thiolatopyrimidine ligands in a chelate fashion. The bonding of the didentate thiolate to the metal center can be considered as being intermediate between the pyridine-2-thiolate form and the canonic amide-thione. The Ti–S distances are longer than those found in cyclopentadienyl and noncyclopentadienyl titanium complexes with thiolato ligands.[7,8] This suggests weaker Ti–S bonds in complex **5**. The Ti–N distances are even longer than those found in the aminopyridinate complexes described above,[6] in accordance with the lability of the Ti–N(pyridine) bonds.

Table 2. Summary of styrene polymerization results. Polymerization conditions: 6 μmol Ti, 2 mL styrene, Al/Ti = 2000:1, $t$ = 90 min.

| Precatalyst | $T$ [K] | Activity [Kg PS/mol Ti/h] |
|---|---|---|
| **1** | 273 | 9 |
| **1** | 298 | 101 |
| **1** | 333 | 122 |
| **1** | 363 | 117 |
| **2** | 273 | 91 |
| **2** | 298 | 133 |
| **2** | 333 | 156 |
| **2** | 363 | 167 |
| **3** | 273 | 40 |
| **3** | 298 | 21 |
| **3** | 333 | 49 |
| **3** | 363 | 39 |
| **5** | 273 | 109 |
| **5** | 298 | 48 |
| **5** | 333 | 62 |
| **5** | 363 | 106 |
| **6** | 273 | 0 |
| **6** | 298 | 50 |
| **6** | 333 | 102 |
| **6** | 363 | 113 |
| **7** | 273 | 90 |
| **7** | 298 | 60 |
| **7** | 333 | 68 |
| **7** | 363 | 84 |
| **8** | 273 | 0 |
| **8** | 298 | 0 |
| **8** | 333 | 0 |
| **8** | 363 | 0 |
| **9** | 273 | 190 |
| **9** | 298 | 76 |
| **9** | 333 | 61 |
| **9** | 363 | 118 |
| **10** | 273 | 13 |
| **10** | 298 | 42 |
| **10** | 333 | 82 |
| **10** | 363 | 37 |

Whereas the reaction of 2-HS-($C_5H_4N$) with [Ti(O*i*Pr)$_4$] gives rise to the complex [Ti(O*i*Pr)$_2${2-S-($C_5H_4N$)}$_2$] (**9**), the reaction with [$TiCl_4(THF)_2$] gives a complex in which the opening of a THF molecule was observed, i.e., [$TiCl_2${2-S-($C_5H_4N$)}{$O(CH_2)_4Cl$}] (**10**), as deduced from the $^1$H NMR spectrum. A similar reactivity has been described previously by some of us[1f,9] in heteroscorpionate complexes of titanium. The formation of this complex can be envisaged as being the result of a nucleophilic THF ring-opening reaction of the intermediate cationic species [$TiCl_2$(THF){2-S-($C_5H_4N$)}]Cl, which itself results from the coordination of a thiolate ligand and subsequent loss of a chloride ligand (Scheme 4).

Chelate coordination of the pyridinethiolate ligand can be proposed for both complexes **9** and **10** on the basis of the $^{13}$C NMR spectra.

Finally, the catalytic activities of some of the complexes obtained were investigated for styrene polymerization in the range 273–363 K in the presence of 2000 equivalents of methylaluminoxane (MAO) in toluene (Table 2). In all cases, the fraction that was insoluble in 2-butanone contained the majority of the resulting polymer (>98%). In addition, the $^{13}$C NMR spectrum in $CDCl_2CDCl_2$ at 393 K contains the characteristic peaks of syndiotactic polystyrene.[10] As can be seen from Table 2, for the alkoxypyridine complexes the activity increases with reaction temperature. In contrast, thiolato complexes show higher activities at low temperature, where they are probably more stable. In any case, the activities are similar to that found for the complex [Ti(O*i*Pr)$_4$] (140 Kg PS/mol Ti/h at 293 K).

## Conclusions

The results reported here show that a range of diisopropoxy- or dichlorotitanium(IV) complexes bearing alkoxy or thiolato heterocyclic ligands can be easily prepared by reaction of the simple precursors [Ti(O*i*Pr)$_4$] and [$TiCl_4(THF)_2$] with the corresponding alcohols or thiols. The molecular structures of **1** and **5**, as determined by X-ray diffraction, show hexacoordination around the titanium atom, with two chelate heterocyclic substituents. These compounds, as well as some of their analogs, have a dynamic bonding process in solution. Finally, these new complexes, which do not contain cyclopentadienyl units, exhibit moderate activities in styrene polymerization in conjunction with MAO.

 © 2006 Wiley-VCH Verlag GmbH & Co. KGaA, Weinheim 

## Experimental Section

**General Remarks:** All operations were performed under an inert atmosphere using standard vacuum-line (Schlenk) techniques or an MBRAUN glove-box. Solvents were purified by distillation from the appropriate drying agents before use. Titanium precursors and different alcohols and thiols were purchased from Aldrich, stored under an inert atmosphere, and deoxygenated before use. NMR spectra were obtained with a Varian Inova FT-500 instrument.

**Preparation of [Ti(O*i*Pr)$_2${2-(OCH$_2$)(C$_5$H$_4$N)}$_2$] (1):** [Ti(O*i*Pr)$_4$] (1 mL, 3.26 mmol) was added to a solution of 2-(hydroxymethyl) pyridine (0.65 mL, 6.52 mmol) in $CH_2Cl_2$ (50 mL) and the reaction mixture was stirred for 2 h at room temperature. The resulting colorless solution was evaporated to dryness to give complex **1** as a white solid, which was purified by washing with hexane (yield: 1.22 g, 98%). $^1$H NMR (500 MHz, $CDCl_3$): $\delta$ = 1.01 (d, $J$ = 6.1 Hz, 12 H, C$H_3$ isopropoxide), 4.61 (sept, $J$ = 6.1 Hz, 2 H, C*H*O isopropoxide), 5.55 (s, 4 H, C$H_2$ pyridine), 7.13 (dd, $J_{5,6}$ = 4.6 Hz, $J_{5,4}$ = 8 Hz, 2 H, 5-H pyridine), 7.15 (d, $J$ = 8 Hz, 2 H, 3-H pyridine), 7.61 (dd, $J_{4,5}$ = 8 Hz, $J_{4,3}$ = 8 Hz, 2 H, 4-H pyridine), 8.61 (d, $J$ = 4.6 Hz, 2 H, 6-H pyridine) ppm. $^{13}$C NMR (500 MHz, $CDCl_3$): $\delta$ = 25.66 (*C*H$_3$ isopropoxide), 74.30 (*C*H$_2$ pyridine), 75.30 (*C*HO isopropoxide), 118.91 (C-5 pyridine), 121.78 (C-3 pyridine), 137.45 (C-4 pyridine), 147.19 (C-6 pyridine), 166.06 (C-2 pyridine) ppm. $C_{24}H_{26}N_2O_4Ti$ (453.86): calcd. C 56.55, H 6.86, N 7.33; found C 56.31, H 6.56, N 7.95.

**Preparation of [Ti(Cl)$_2${2-(OCH$_2$)(C$_5$H$_4$N)}$_2$] (2):** 2-(Hydroxymethyl)pyridine (0.30 mL, 3.01 mmol) was added to a solution of [TiCl$_4$(THF)$_2$] (0.50 g, 1.50 mmol) in THF (25 mL) and the resulting white suspension was stirred for 16 h at room temperature. A white precipitate formed and when the sedimentation was complete the solution was filtered and the white precipitate washed with THF (50 mL) at 60 °C and filtered again. The two solutions were combined and the solvent was evaporated to give complex **2** as a pale-brown solid (yield: 0.20 g, 41%). $^1$H NMR (500 MHz, [D$_6$]-DMSO): $\delta$ = 4.86 (s, 4 H, C$H_2$ pyridine), 7.85 (dd, $J_{5,4}$ = 8 Hz, $J_{5,6}$ = 6 Hz, 2 H, 5-H pyridine), 7.96 (d, $J$ = 8.5 Hz, 2 H, 3-H pyridine), 8.47 (dd, $J_{4,5}$ = 8 Hz, $J_{4,3}$ = 8.5 Hz, 2 H, 4-H pyridine), 8.75 (d, $J$ = 6 Hz, 2 H, 6-H pyridine) ppm. $^{13}$C NMR (500 MHz, [D$_6$]-DMSO): $\delta$ = 59.96 (*C*H$_2$ pyridine), 123.93 (C-3 pyridine), 124.95 (C-5 pyridine), 141.76 (C-6 pyridine), 144.96 (C-4 pyridine), 157.27 (C-2 pyridine) ppm. $C_{12}H_{12}Cl_2N_2O_2Ti$ (334.86): calcd. C 43.02, H 3.61, N 8.36; found C 42.81, H 3.56, N 8.95.

**Preparation of [Ti(Cl)$_2${2-(OCH$_2$)-6-Me-(C$_5$H$_3$N)}$_2$] (3):** 6-Methyl-2-pyridylmethanol (0.18 mL, 1.49 mmol) was added to a solution of [TiCl$_4$(THF)$_2$] (0.25 g, 0.75 mmol) in THF (25 mL) and the resulting white suspension was stirred for 16 h at room temperature. A gray precipitate formed and when sedimentation was complete the solution was filtered to give complex **3** as a gray solid. The solid was washed with hexane (50 mL) and dried under vacuum (yield: 0.27 g, 87%). $^1$H NMR (500 MHz, [D$_6$]DMSO): $\delta$ = 2.72 (s, 6 H, C$H_3$ pyridine), 4.83 (s, 4 H, C$H_2$ pyridine), 7.72 (d, $J$ = 7.8 Hz, 2 H, 5-H pyridine), 7.79 (d, $J$ = 7.8 Hz, 2 H, 3-H pyridine), 8.37 (t, $J$ = 7.8 Hz, 2 H, 4-H pyridine) ppm. $^{13}$C NMR (500 MHz, [D$_6$]-DMSO): $\delta$ = 20.01 (*C*H$_3$ pyridine), 60.29 (*C*H$_2$ pyridine), 121.98 (C-3 pyridine), 126.14 (C-5 pyridine), 145.75 (C-4 pyridine), 157.49, 154.04 (C-2, C-6 pyridine) ppm. $C_{14}H_{16}Cl_2N_2O_2Ti$ (362.86): calcd. C 58.54, H 7.37, N 6.83; found C 58.15, H 7.52, N 6.91.

**Preparation of [Ti{2,6-(OCH$_2$)$_2$(C$_5$H$_3$N)}$_2$] (4):** [Ti(O*i*Pr)$_4$] (1 mL, 3.26 mmol) was added to a solution of 2,6-bis(hydroxymethyl)pyridine (0.93 g, 6.52 mmol) in $CH_2Cl_2$ (50 mL) and the reaction mixture was stirred for 4 h at room temperature. The resulting colorless solution was evaporated to dryness to give complex **4** as a white solid. The solid was purified by washing with hexane (yield: 1.00 g, 95%). $^1$H NMR (500 MHz, $CDCl_3$): $\delta$ = 5.85 (s, 8 H, C$H_2$ pyridine), 7.32 (d, $J$ = 7.7 Hz, 4 H, 3-H, 5-H pyridine), 7.88 (t, $J$ = 7.7 Hz, 2 H, 4-H pyridine) ppm. $^{13}$C NMR (500 MHz, $CDCl_3$): $\delta$ = 78.75 (*C*H$_2$ pyridine), 116.60 (C-3, C-5 pyridine), 140.52 (C-4 pyridine), 168.44 (C-2, C-6 pyridine) ppm. $C_{14}H_{14}N_2O_4Ti$ (321.80): calcd. C 52.20, H 4.38, N 8.70; found C 51.64, H 5.01, N 8.37.

**Preparation of [Ti(O*i*Pr)$_2${2-S-4,6-Me$_2$-(C$_4$HN$_2$)}$_2$] (5):** [Ti(O*i*Pr)$_4$] (1 mL, 3.26 mmol) was added to a solution of 2-mercapto-4,6-dimethylpyrimidine (0.92 g, 6.52 mmol) in $CH_2Cl_2$ (50 mL) and the reaction mixture was stirred for 2 h at room temperature. The resulting yellow solution was evaporated to dryness to give complex **5** as a yellow, crystalline solid, which was washed with hexane (yield: 1.17 g, 81%). $^1$H NMR (500 MHz, $CDCl_3$): $\delta$ = 1.26 (d, 12 H, C$H_3$ isopropoxide), 2.42 (broad signal, 12 H, C$H_3$ pyrimidine), 4.81 (sept, $J$ = 6.2 Hz, 2 H, C*H*O isopropoxide), 6.50 (s, 2 H, 5-H pyrimidine) ppm. $^{13}$C NMR (500 MHz, $CDCl_3$): $\delta$ = 23.80, 26.23 (*C*H$_3$ C$_4$, *C*H$_3$, C$_6$ pyrimidine), 25.36 (*C*H$_3$ isopropoxide), 81.64 (*C*HO isopropoxide), 115.17 (C-5 pyrimidine), 168.71 (C-4 pyrimidine), 164.25 (C-6 pyrimidine), 179.20 (C-2 pyrimidine) ppm. $C_{18}H_{28}N_4O_2TiS_2$ (307.52): calcd. C 48.64, H 6.35, N 12.61, S 14.14; found C 49.10, H 5.89, N 12.10, S 13.85.

**Preparation of [TiCl$_2${2-S-4,6-Me$_2$-(C$_4$HN$_2$)}$_2$] (6):** A solution of 2-mercapto-4,6-dimethylpyrimidine (0.42 mL, 3.00 mmol) in THF (10 mL) was added dropwise to a solution of [TiCl$_4$(THF)$_2$] (0.50 g, 1.50 mmol) in THF (25 mL) and the resulting brown-red suspension was stirred for 16 h at room temperature. Complex **6** was obtained as a pale-yellow solid after sedimentation, subsequent filtration, and drying under vacuum (yield: 0.46 g, 78%). $^1$H NMR (500 MHz, [D$_6$]DMSO): $\delta$ = 2.41 (s, 12 H, C$H_3$ pyrimidine), 6.95 (s, 2 H, 5-H pyrimidine) ppm. $^{13}$C NMR (500 MHz, [D$_6$]DMSO): $\delta$ = 23.85 (*C*H$_3$ pyrimidine), 118.45 (C-5 pyrimidine), 167.86 (C-4, C-6 pyrimidine), 168.53 (C-2 pyrimidine) ppm. $C_{12}H_{14}ClN_2S_4Ti$ (396.60): calcd. C 36.29, H 3.55, N 14.11, S 16.15; found C 36.46, H 3.22, N 14.45, S 16.52.

**Preparation of [Ti(O*i*Pr)$_2${2-S-(C$_4$H$_3$N$_2$)}$_2$] (7):** [Ti(O*i*Pr)$_4$] (1 mL, 3.26 mmol) was added to a solution of 2-mercaptopyrimidine (0.75 g, 6.52 mmol) in $CH_2Cl_2$ (50 mL) and the reaction mixture was stirred for 2 h at room temperature. The resulting yellow solution was evaporated to dryness and complex **7** was obtained as a yellow, crystalline solid, which was washed with hexane. (yield: 1.24 g, 98%). $^1$H NMR (500 MHz, $CDCl_3$): $\delta$ = 1.24 (d, $J$ = 6 Hz, 12 H, C$H_3$ isopropoxide), 4.70 (sept, $J$ = 6 Hz, 2 H, C*H*O isopropoxide), 6.79 (t, $J$ = 5 Hz, 2 H, 5-H pyrimidine), 8.47 (d, $J$ = 5 Hz, 4 H, 4-H, 6-H pyrimidine) ppm. $^{13}$C NMR (500 MHz, $CDCl_3$): $\delta$ = 25.60 (*C*H$_3$ isopropoxide), 81.54 (*C*HO isopropoxide), 114.73 (C-5 pyrimidine), 151.70 (C-4 pyrimidine), 159.92 (C-6 pyrimidine), 179.82 (C-2 pyrimidine) ppm. $C_{14}H_{20}N_4O_2S_2Ti$ (387.86): calcd. C 43.30, H 5.19, N 14.43, S 16.51; found C 43.85, H 5.85, N 14.01, S 16.01.

**Preparation of [TiCl$_2${2-S-(C$_4$H$_3$N$_2$)}$_2$] (8):** A solution of 2-mercaptopyrimidine (0.27 mL, 2.40 mmol) in THF (10 mL) was added dropwise to a solution of [TiCl$_4$(THF)$_2$] (0.40 g, 1.20 mmol) in THF (50 mL) and the resulting yellow suspension was stirred for 5 h at room temperature. Complex **8** was obtained as a pale-yellow solid after sedimentation, subsequent filtration, and drying under vacuum (yield: 0.37 g, 91%). $^1$H NMR (500 MHz, [D$_6$]DMSO): $\delta$ = 6.89 (t, $J$ = 5.3 Hz, 2 H, 5-H pyrimidine), 8.33 (d, $J$ = 5.3 Hz, 4 H, 4-H, 6-H pyrimidine) ppm. $^{13}$C NMR (500 MHz, [D$_6$]DMSO): $\delta$ = 119.84 (C-5 pyrimidine), 159.26 (C-4, C-6 pyrimidine), 168.51

 © 2006 Wiley-VCH Verlag GmbH & Co. KGaA, Weinheim 

Table 3. Crystal data and structure refinement for **1** and **5**.

| | **1** | **5** |
|---|---|---|
| Empirical formula | $C_{18}H_{26}N_2O_4Ti$ | $C_{18}H_{28}N_4O_2S_2Ti$ |
| Formula weight | 382.31 | 444.46 |
| Temperature [K] | 200(2) | 230(2) |
| Wavelength [Å] | 0.71073 | 0.71073 |
| Crystal system | monoclinic | monoclinic |
| Space group | $P2_1/n$ | $P2_1/n$ |
| $a$ [Å] | 11.222(4) | 13.156(5) |
| $b$ [Å] | 14.745(5) | 12.185(1) |
| $c$ [Å] | 12.124(7) | 14.893(8) |
| $\beta$ [°] | 92.77(3) | 105.26(6) |
| Volume [Å$^3$] | 2004(1) | 2303(1) |
| $Z$ | 4 | 4 |
| Density (calculated) [g cm$^{-3}$] | 1.267 | 1.282 |
| Absorption coefficient [cm$^{-1}$] | 4.50 | 5.72 |
| $F$(000) | 808 | 936 |
| Crystal size [mm] | 0.4 × 0.3 × 0.2 | 0.3 × 0.2 × 0.2 |
| Index ranges | $-14 \le h \le 14$ | $-17 \le h \le 16$ |
| | $0 \le k \le 19$ | $0 \le k \le 16$ |
| | $0 \le l \le 16$ | $0 \le l \le 19$ |
| Reflections collected | 5021 | 5731 |
| Independent reflections | 4804 [$R$(int) = 0.0145] | 5532 [$R$(int) = 0.0295] |
| Data/restraints/parameters | 4804/0/230 | 5532/0/244 |
| Goodness-of-fit on $F^2$ | 1.034 | 1.011 |
| Final $R$ indices [$I > 2\sigma(I)$] | $R_1$ = 0.0382, $wR_2$ = 0.0974 | $R_1$ = 0.0611, $wR_2$ = 0.1853 |
| $R$ indices (all data) | $R_1$ = 0.0556, $wR_2$ = 0.1052 | $R_1$ = 0.0956, $wR_2$ = 0.2105 |
| Largest diff. peak and hole [e Å$^{-3}$] | 0.250 and –0.407 | 0.730 and –0.394 |

(C-2 pyrimidine) ppm. $C_8H_6Cl_2N_4S_2Ti$ (340.70): calcd. C 28.17, H 1.77, N 16.43, S 18.80; found C 28.40, H 1.54, N 16.68, S 19.23.

**Preparation of [Ti(O*i*Pr)$_2${2-S-(C$_5$H$_4$N)}$_2$] (9):** [Ti(O*i*Pr)$_4$] (1 mL, 3.26 mmol) was added to a solution of 2-mercaptopyridine (0.73 g, 6.52 mmol) in $CH_2Cl_2$ (50 mL) and the reaction mixture was stirred for 2 h at room temperature. The resulting yellow solution was evaporated to dryness and complex **9** was obtained as a yellow solid, which was washed with hexane (yield: 1.19 g, 95%). $^1$H NMR (500 MHz, $CDCl_3$): $\delta$ = 1.20 (d, $J$ = 5.9 Hz, 12 H, C$H_3$ isopropoxide), 4.70 (sept, $J$ = 5.9 Hz, 2 H, C$H$O isopropoxide), 6.72 (dd, $J_{5,6}$ = 6 Hz, $J_{5,4}$ = 7.8 Hz, 2 H, 5-H pyridine), 7.11 (d, $J$ = 8.1 Hz, 2 H, 3-H pyridine), 7.39 (dd, $J_{4,5}$ = 7.8 Hz, $J_{4,3}$ = 8.1 Hz, 2 H, 4-H pyridine), 8.35 (d, $J$ = 8.1 Hz, 2 H, 6-H pyridine) ppm. $^{13}$C NMR (500 MHz, $CDCl_3$): $\delta$ = 25.56 (*C*H$_3$ isopropoxide), 80.34 (*C*HO isopropoxide), 116.97 (C-5 pyridine), 126.54 (C-3 pyridine), 137.94 (C-4 pyridine), 144.31 (C-6 pyridine), 170.74 (C-2 pyridine) ppm. $C_{16}H_{22}N_2O_2S_2Ti$ (385.70): calcd. C 49.74, H 5.74, N 7.25, S 16.60; found C 49.21, H 5.25, N 6.87, S 16.21.

**Preparation of [TiCl$_2${2-S-(C$_5$H$_4$N)}{O(CH$_2$)$_4$Cl}] (10):** A solution of 2-mercaptopyridine (0.33 g, 3.00 mmol) in THF (10 mL) was added dropwise to a solution of [$TiCl_4(THF)_2$] (0.50 mL, 1.50 mmol) in THF (25 mL). The resulting orange suspension was stirred for 16 h at room temperature. Complex **10** was obtained as a pale-orange solid after sedimentation, subsequent filtration, and drying under vacuum (yield: 0.38 g, 76%). $^1$H NMR (500 MHz, [D$_6$]DMSO): $\delta$ = 1.78 [m, 4 H, (C$H_2$)$_2$], 3.22 (m, 2*H* C$H_2$Cl), 4.73 (t, $J$ = 5.8 Hz, 2 H, C$H_2$O), 7.20 (m, 1 H, 5-H pyridine), 7.40 (d, $J$ = 8.4 Hz, 1 H, 3-H pyridine), 7.75 (m, 1 H, 4-H pyridine), 8.46 (d, $J$ = 6.4 Hz, 1 H, 6-H pyridine) ppm. $^{13}$C NMR (500 MHz, [D$_6$]-DMSO): $\delta$ = 30.19, 32.27 [(*C*H$_2$)$_2$], 60.78 (*C*H$_2$Cl), 85.37 (*C*H$_2$O), 120.09 (C-5 pyridine), 122.33 (C-3 pyridine), 137.96 (C-4 pyridine), 148.20 (C-6 pyridine), 157.89 (C-2 pyridine) ppm. $C_9H_{12}Cl_3NOSTi$ (332.50): calcd. C 32.12, H 3.59, N 4.16, S 9.53; found C 32.41, H 4.00, N 4.32, S 9.14.

**Styrene Polymerizations:** Polymerizations of styrene using the various catalyst precursors were carried out by adding a suspension of the titanium precursor (6 μmol) in toluene to a 100-mL flask, under an inert atmosphere, containing styrene (2 mL, previously dried with alumina) and a solution of 10% MAO (12 mmol) in toluene. The final volume of the resulting mixture was 12 mL. Polymerization reactions were run for 90 min at different temperatures and quenched by the addition of 10% HCl/methanol mixture (50 mL). The resulting polymers were filtered off, washed with methanol, and dried. The bulk polymers were extracted by refluxing in 2-butanone (35 mL) at 80 °C for four hours. The resulting polymers were dried and weighed.

**X-ray Crystal-Structure Determinations:** Single crystals of a colorless block of **1** and a yellow prism of **5** were placed in a cooled nitrogen gas stream at 200 and 230 K, respectively, on a NONIUS-MACH3 diffractometer equipped with a graphite-monochromated Mo-$K_\alpha$ radiation source ($\lambda$ = 0.71073 Å). Table 3 summarizes the crystal data, data collection, and structural solution and refinement parameters for both compounds. Intensity data were collected by using an $\omega/2\theta$ scan technique. Data were corrected for Lorentz and polarization effects and absorption correction was not necessary. The structures were solved by direct methods using the SHELXS computer program,[11] completed by subsequent difference Fourier syntheses, and refined by full-matrix least-squares procedures (SHELXL97)[12] on $F^2$. All non-hydrogen atoms were refined with anisotropic thermal parameters. The hydrogen atoms were placed using a "riding model" and included in the refinement at calculated positions.

CCDC-283896 (**1**) and -283897 (**5**) contain the supplementary crystallographic data for this paper. These data can be obtained free

 © 2006 Wiley-VCH Verlag GmbH & Co. KGaA, Weinheim 

of charge from The Cambridge Crystallographic Data Centre via www.ccdc.cam.ac.uk/data_request/cif.


[1] a) V. C. Gibson, S. K. Spitmesser, *Chem. Rev.* **2003**, *103*, 283; b) C. L. Boyd, T. Toupance, B. R. Tyrrell, B. D. Ward, C. R. Wilson, A. R. Cowley, P. Mountford, *Organometallics* **2005**, *24*, 309; c) A. Krajete, G. Steiner, H. Kopacka, K.-H. Ongania, K. Wurst, M. O. Kristen, P. Preishuber-Pflügl, B. Bildstein, *Eur. J. Inorg. Chem.* **2004**, 1740; d) U. G. Joung, T. H. Kim, D. J. Joe, B. Y. Lee, D. M. Shin, Y. K. Cheng, *Polyhedron* **2004**, *23*, 1587; e) Y. Li, A. Turnas, J. T. Ciszewski, A. L. Odom, *Inorg. Chem.* **2002**, *41*, 6298; f) A. Otero, J. Fernández-Baeza, A. Antiñolo, F. Carrillo-Hermosilla, J. Tejeda, E. Díez-Barra, A. Lara-Sánchez, L. Sánchez-Barba, I. López-Solera, *Organometallics* **2001**, *20*, 2428; g) K. K. Kang, S.-P. Hong, Y.-T. Jeong, T. Shiono, T. Ikeda, *J. Polym. Sci., Part A: Polym. Chem.* **1999**, *37*, 3756; h) F. Guérin, D. H. McConville, J. V. Vittal, G. A. P. Yap, *Organometallics* **1998**, *17*, 5172; i) F. Guérin, D. H. McConville, J. J. Vittal, *Organometallics* **1997**, *16*, 1491; j) C. H. Zambrano, A. K. McMullen, L. M. Kobriger, P. E. Fanwick, I. P. Rothwell, *J. Am. Chem. Soc.* **1990**, *112*, 6565.

[2] S. Doherty, R. J. Errington, A. P. Jarvis, S. Collins, W. Clegg, M. R. J. Elsegood, *Organometallics* **1998**, *17*, 3408.

[3] A. Antiñolo, F. Carrillo-Hermosilla, A. E. Corrochano, R. Fandos, J. Fernández-Baeza, A. M. Rodríguez, M. J. Ruiz, A. Otero, *Organometallics* **1999**, *18*, 5219.

[4] R. Fandos, I. López-Solera, A. Otero, A. Rodríguez, M. J. Ruiz, *Organometallics* **2004**, *23*, 5030.

[5] A. Antiñolo, F. Carrillo-Hermosilla, A. E. Corrochano, J. Fernández-Baeza, M. Lanfranchi, A. Otero, M. A. Pellinghelli, *J. Organomet. Chem.* **1999**, *577*, 174.

[6] R. Kempe, P. Arndt, *Inorg. Chem.* **1996**, *35*, 2644.

[7] a) Y. Nakayma, K. Miyamoto, N. Ueyama, A. Nakamura, *Chem. Lett.* **1999**, 391; b) D. R. Corbin, L. C. Francesconi, D. N. Hendrickson, G. D. Stucky, *Inorg. Chem.* **1979**, *18*, 3069; c) D. R. Corbin, L. C. Francesconi, D. N. Hendrickson, G. D. Stucky, *J. Chem. Soc., Chem. Commun.* **1979**, 248; d) R. A. Jones, S. T. Schwab, E. R. Whittlesey, *Polyhedron* **1984**, *3*, 505; e) G. A. Sigel, P. P. Power, *Inorg. Chem.* **1987**, *26*, 2819; f) M. Könemann, W. Stüer, K. Kirschbaum, D. M. Giolando, *Polyhedron* **1994**, *13*, 1415.

[8] a) T. T. Nadasdi, Y. Huang, D. W. Stephan, *Inorg. Chem.* **1993**, *32*, 347; b) A. V. Firth, D. W. Stephan, *Organometallics* **1998**, *17*, 3716; c) T. A. Wark, D. W. Stephan, *Organometallics* **1989**, *8*, 2836.

[9] A. Otero, J. Fernández-Baeza, A. Antiñolo, F. Carrillo-Hermosilla, J. Tejeda, A. Lara-Sánchez, L. Sánchez-Barba, M. Fernández-López, A. M. Rodríguez, I. López-Solera, *Inorg. Chem.* **2002**, *41*, 5193.

[10] a) Y. Inoue, A. Nishioka, R. Chujo, *Makromol. Chem.* **1972**, *156*, 207; b) K. Matsuzaki, T. Uryu, K. Osada, T. Kawamura, *Macromolecules* **1972**, *5*, 816; c) J. C. Randal, *J. Polym. Sci., Polym. Phys. Ed.* **1975**, *13*, 889; d) H. Sato, Y. Tanaka, K. Hatada, *J. Polym. Sci., Polym. Phys. Ed.* **1983**, *21*, 1667.

[11] SHELXS-97, Program for Structure Solution: G. M. Sheldrick, *Acta Crystallogr. Sect. A* **1990**, *46*, 467.

[12] G. M. Sheldrick, *SHELXL-97, Program for Crystal Structure Refinement*, University of Göttingen, **1997**.


Received: September 16, 2005
Published Online: January 19, 2006

 © 2006 Wiley-VCH Verlag GmbH & Co. KGaA, Weinheim 

DOI: 10.1002/ejic.200500845

# Synthesis, Characterization, and Catalytic Properties of *ansa*-Zirconocenes [Zr{1-$Me_2Si$(3-$\eta^5$-$C_9H_5R)_2$}$Cl_2$] (R = Me, *n*Pr, *n*Bu, and Bz)

**Carlos Alonso-Moreno,[a] Antonio Antiñolo,[a] Fernando Carrillo-Hermosilla,[a] Antonio Otero,*[a] Ana M. Rodríguez,[a] José Sancho,[b] Victoria Volkis,[c] and Moris Eisen[c]**

*Dedicated to Professor Victor Riera on the occasion of his 70th birthday[‡]*

**Keywords:** Metallocenes / Zirconium / Homogeneous catalysis / Polymerization / Ethylene

The *ansa*-indene ligands {1-$Me_2Si$(3-$C_9H_6R)_2$} [R = Me (**1**), *n*Pr (**2**), *n*Bu (**3**), and Bz (**4**)] were prepared by alkylation of the unsubstituted *ansa*-indene. These ligands were converted, by reaction with *n*BuLi, to the di-lithium compounds [$Li_2$1-$Me_2Si$(3-$C_9H_5R)_2$}] [R = Me (**5**), *n*Pr (**6**), *n*Bu (**7**), and Bz (**8**)]. *ansa*-Zirconocenes, [Zr{1-$Me_2Si$(3-$\eta^5$-$C_9H_5R)_2$}$Cl_2$] [R = Me (**9**), *n*Pr (**10**), *n*Bu (**11**), and Bz (**12**)], have been prepared by the reaction of $ZrCl_4$ with **5**–**8** in diethyl ether/toluene at –78 °C. The molecular structure of *meso*-[Zr{1-$Me_2Si$[3-$\eta^5$-$C_9H_5(CH_3)]_2$}$Cl_2$] (**9**) and *rac*-[Zr{1-$Me_2Si$[3-$\eta^5$-$C_9H_5$-$(CH_2CH_2CH_3)]_2$}$Cl_2$] (**10**) have been determined by single-crystal X-ray diffraction studies. Ethylene polymerization catalysis has been studied for complexes **9**–**12** as a mixture of *meso* and *rac* isomers in the presence of methylaluminoxane (MAO) as cocatalyst. Complexes **9**–**12** exhibit high activities and give rise to polyethylene with low molecular weights without the introduction of molecular hydrogen. In addition, active species from these complexes were found to be very stable in comparison with unsubstituted analogues.

(© Wiley-VCH Verlag GmbH & Co. KGaA, 69451 Weinheim, Germany, 2006)

## Introduction

A large number of new catalysts for olefin polymerization, classified as metallocene catalysts, have been prepared during the last decade.[1] The majority of these catalysts consist of a zirconium complex with the general formula LL′$ZrCl_2$ and these systems are activated by methylaluminoxane (MAO). The ligands L and L′ are typically equal or different dienyl ligands that may be linked together by a bridge. A major evolution has been achieved in the field of polypropylene, which can now be produced with different types and degrees of stereoregularity.[2] In fact, a new class of catalysts based on $C_2$-symmetric metallocenes, with *ansa*-bis(indenyl) ligands, produce almost isotactic polypropylenes. The best-known example is Brintzinger's *rac*-[Zr{1-$(C_2H_4)$($\eta^5$-$C_9H_6)_2$}$Cl_2$].[3] Although the introduction of an alkyl substituent in the cyclopentadienyl fragment of the indenyl group has been studied,[4] few examples of *ansa*-bis-indenyl complexes, bearing $SiMe_2$ bridges, have been described[5–9] and, to the best of our knowledge, there is not a complete structural characterization of these complexes. The target for these catalysts was to study the influence of the metallocene structure in the performance of propylene polymerization. Less attention has been paid to the study of the influence on the properties of the polyethylene obtained with these catalysts, i.e., on the molecular weight of the obtained polymer. Usually, this parameter can be controlled during the polymerization by either adjusting the temperature of the polymerization or by adding molecular hydrogen, which acts as a chain transfer agent.[10]

With this in mind, and as part of our continued interest in this field,[11] we have developed new examples of *ansa*-zirconocene catalysts of the general formula [Zr{1-$Me_2Si$(3-$\eta^5$-$C_9H_5R)_2$}$Cl_2$]. These catalysts have proved to be very active and are able to produce polyethylene with low molecular weight without introducing molecular hydrogen to control the process. It was of particular interest to compare the results with the analogous unsubstituted complex [Zr{1-$Me_2Si$($\eta^5$-$C_9H_6)_2$}$Cl_2$].[12]

Here we provide the details of the preparation and polymerization behavior of four members of this class of catalysts [Zr{1-$Me_2Si$(3-$\eta^5$-$C_9H_5R)_2$}$Cl_2$] [R = Me (**9**), *n*Pr (**10**), *n*Bu (**11**), and Bz (**12**)]. The activities of these systems in the polymerization of ethylene and the molecular weights

[a] Departamento de Química Inorgánica, Orgánica y Bioquímica, Facultad de Ciencias Químicas, Universidad de Castilla-La Mancha, Campus Universitario de Ciudad Real, 13071 Ciudad Real, Spain
E-mail: Antonio.Otero@uclm.es
Fernando.Carrillo@uclm.es
[b] Centro Tecnológico Repsol-YPF, Carretera de Extremadura, Km. 18, 28931 Móstoles, Spain
[c] Department of Chemistry and Institute of Catalysis Science and Technology Technion, Israel Institute of Technology, Haifa 32000, Israel
[‡] In recognition of his important contribution to organometallic chemistry and as a mark of friendship.

 © 2006 Wiley-VCH Verlag GmbH & Co. KGaA, Weinheim 

of the resulting polymers are discussed. In addition, the molecular structures of *rac*-**10** and *meso*-**9** have been determined by X-ray diffraction methods.

## Results and Discussion

The preparation of the substituted *ansa*-indene precursors {1-$Me_2Si$(3-$C_9H_6R)_2$} [R = Me (**1**), *n*Pr (**2**), *n*Bu (**3**) and Bz (**4**)] was achieved by alkylation of the dilithium salt of {1-$Me_2Si$(3-$C_9H_7)_2$}, generated with *n*BuLi in $Et_2O$, with a large excess of RX (X = I and R = Me for **1**, X = Br and R = *n*Pr for **2**, X = Br and R = *n*Bu for **3**, and X = Br and R = Bz for **4**) (Scheme 1). Column chromatography was used to purify the ligands **1**–**4**.

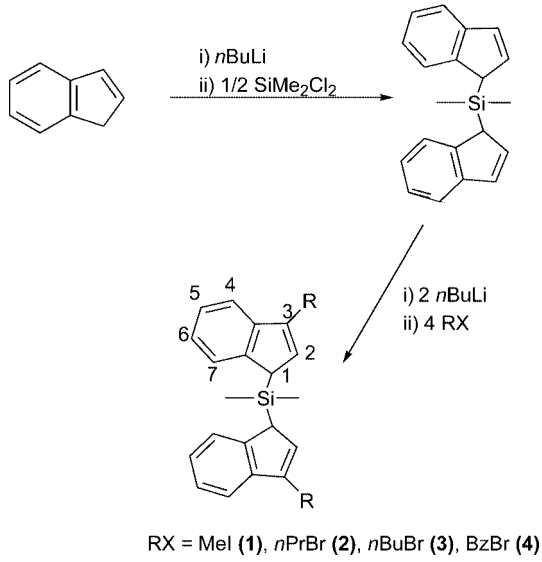


Scheme 1.

This is the preferred route because of the very simple synthesis and purification of the intermediate {1-$Me_2Si(C_9H_7)_2$} and because of its intrinsic versatility. In fact, {1-$Me_2Si(C_9H_7)_2$} is a convenient starting material for the synthesis of a series of different 3-alkyl- and 3-silyl-*ansa*-bisindenyl ligands.[13] The $^1$H NMR spectra show the *meso*-isomer as the major isomer for derivatives **1**–**4**, with two singlets for the *ansa*-bridge methyl groups, a doublet for H1, a doublet for H2, and four multiplets corresponding to the protons of the $C_6$ ring of the indenyl moiety. In addition, the corresponding signals were observed for the pendant alkyl chain (see Exp. Sect.).

As shown in Scheme 2, the deprotonation of **1**–**4** with *n*BuLi gave the lithium salts [$Li_2${1-$Me_2Si$(3-$C_9H_5R)_2$}] [R = Me (**5**), *n*Pr (**6**), *n*Bu (**7**), and Bz (**8**)]. The subsequent reaction of the lithium salts with $ZrCl_4$, in diethyl ether/toluene, gave the corresponding zirconocene complexes [Zr{1-$Me_2Si$(3-$\eta^5$-$C_9H_5R)_2$}$Cl_2$] [R = Me (**9**), *n*Pr (**10**), *n*Bu (**11**), and Bz (**12**)]. The orange solids obtained are sensitive towards air and moisture and are soluble in polar solvents.

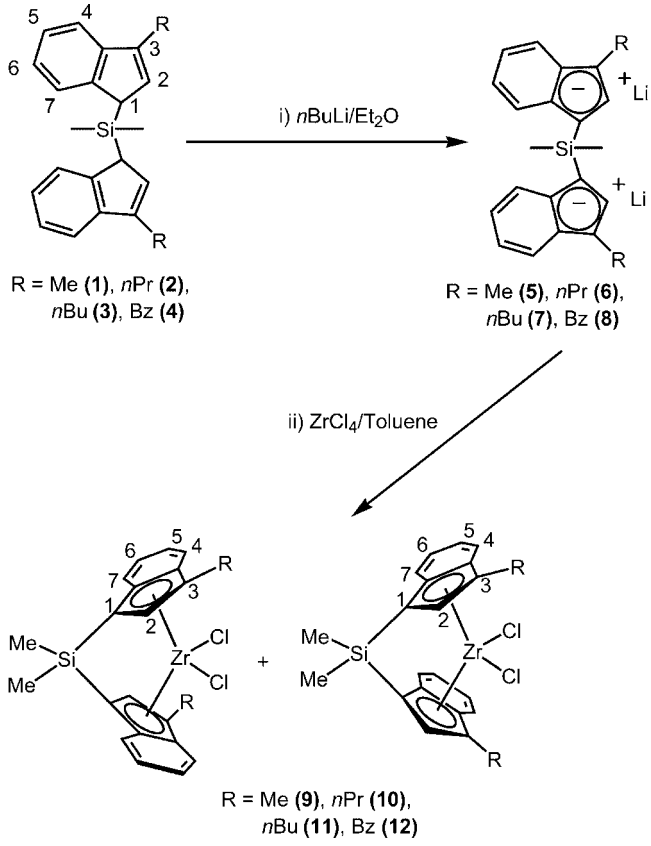


Scheme 2.

While the total yield of this last step is satisfactory, a random *rac*/*meso* ratio is obtained. In general, the *rac*/*meso* ratio ranges from 0.6:1 (**10**) to 1.86:1 (**12**). For complex **9**, samples of the pure *meso* diastereomer and a product enriched in the *rac* isomer (11.5:1) were obtained by careful recrystallization from $CH_2Cl_2/Et_2O$.

The $^1$H NMR spectra for the *meso* isomers of the complexes **9**–**12** show the following signals: two singlets for the *ansa*-bridge methyl groups, a singlet for the proton of the indenyl $C_5$ ring, and four multiplets corresponding to the protons of the $C_6$ ring of the indenyl moiety. In addition, the appropriate signals were observed for the pendant alkyl chain (see Exp. Sect.). Furthermore, the following signals were observed for the *rac* isomers of the complexes **9**–**12**: a singlet for the *ansa*-bridge methyl groups, a singlet for the proton of the indenyl $C_5$ ring, and four multiplets corresponding to the protons of the $C_6$ ring of the indenyl moiety. In addition, several signals were observed for the pendant alkyl chain (see Exp. Sect.).

$^1$H NMR nuclear Overhauser effect (NOE) difference spectroscopy allowed unambiguous identification of each isomer. Irradiation of the signal due to H2 in the *meso* isomer (which appears as a singlet in the NMR spectrum) led to measurable enhancement of the protons of the C3-alkyl substituent and the protons in one of the methyl groups of the $SiMe_2$ bridge. However, a similar irradiation in the *rac* isomer led to enhancement of the corresponding signals due to the C3-alkyl and the silicon methyl groups as well as the

 © 2006 Wiley-VCH Verlag GmbH & Co. KGaA, Weinheim 

aromatic proton H7 on the opposite indenyl ring (Figure 1). In the *meso* isomer, these $SiMe_2$ methyl groups are located in very different chemical environments (one is sandwiched between the two $C_6$ aromatic rings, and the other is only flanked by the Cp rings), while in the *rac* isomer the two methyl groups are equivalent.

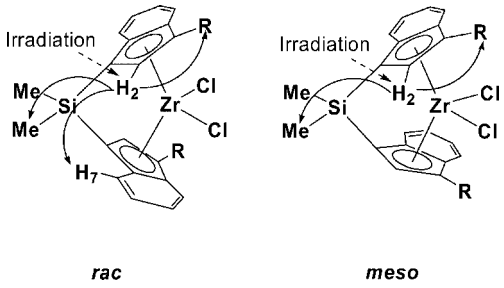


Figure 1. $^1H$ NOE difference experiments provide information on the spatial proximity between protons.

The carbon signal assignments were made following a procedure on the basis of $^1H$ and $^{13}C$ NMR correlated spectroscopy (HETCOR) (see Exp. Sect.). For the *meso* isomer of these compounds **9**–**12**, the $^{13}C$ analysis showed two signals for the *ansa*-bridge methyl groups, a signal for the carbon C2 of the indenyl $C_5$ ring, and four signals corresponding to the carbons (C4–C7) of the $C_6$ ring of the indenyl moiety. For the *rac* isomers, only one signal was found for the ansa-bridge methyl groups. In addition, a signal of the carbon C2 of the indenyl $C_5$ ring was observed, and four signals corresponding to the carbons (C4–C7) of the $C_6$ ring of the indenyl moiety. The corresponding signals were observed for the pendant alkyl chain for both isomers (see Exp. Sect.).

### X-ray Molecular Structures of Complexes *meso*-9 and *rac*-10

Single crystals of *meso*-**9** and *rac*-**10** that were suitable for X-ray diffraction were obtained from $CH_2Cl_2$/ether and toluene. Their molecular structures, as determined by the crystallographic analysis, are depicted in Figure 2.

The *meso*-**9** complex crystallizes in the triclinic space group $P\bar{1}$. The crystal structure reveals the existence of one unique isomer. The *rac*-**10** complex crystallizes in the monoclinic space group $P_2/c$ with a solvate toluene molecule. The crystal structure reveals the existence of two racemic enantiomers. The bonding parameters for *meso*-**9** and *rac*-**10** are summarized in Table 1. The mutual arrangement of the indenyl fragments corresponds to $C_2$ symmetry for *rac* and $C_s$ for *meso*.

In both cases the zirconium atom is in a pseudotetrahedral environment formed by the two chloride ligands and two $\eta^5$-coordinated indenyl ligands. The Zr–C bond lengths of five-membered rings range between 2.448(6) and 2.662(6) Å. These values are close to that found in other *ansa*-bis(indenyl) zirconocene complexes (2.5 Å).[14] The Zr–Cl distances for these complexes are within the range

Table 1. Selected bond lengths [Å] and angles [°] for *meso*-**9** and *rac*-**10**.

| | *meso*-**9** | *rac*-**10** |
|---|---|---|
| *Bond lengths* | | |
| Zr(1)–Cent(1)[a] | 2.246(1) | 2.243 |
| Zr(1)–Cent(2)[b] | 2.252(1) | |
| *av*[c] Zr(1)–C[Cent(1)][a] | 2.550(6) | 2.548(3) |
| *av*[c] Zr(1)–C[Cent(2)][b] | 2.556(6) | |
| Zr(1)–Cl(1) | 2.409(2) | 2.4130(11) |
| Zr(1)–Cl(2) | 2.4375(19) | |
| Zr(1)–C(1) | 2.448(6) | 2.451(3) |
| Zr(1)–C(2) | 2.467(6) | 2.483(3) |
| Zr(1)–C(3) | 2.631(6) | 2.619(3) |
| Zr(1)–C(4) | 2.662(6) | 2.656(3) |
| Zr(1)–C(5) | 2.540(6) | 2.529(3) |
| *Bond angles* | | |
| Cent(1)[a]–Zr–Cent(2)[b] | 128.84 | 128.81 |
| Si(1)–C(1)–Cent(1)[a] | 163.6(4) | 163.5 |
| Si(1)–C(11)–Cent(2)[b] | 163.5 | |
| Cl(1)–Zr–Cent(1)[a] | 106.71 | 106.76(3) |
| Cl(1)–Zr–Cent(2)[b] | 106.65(5) | 106.82(2) |
| Cl(2)–Zr–Cent(1)[a] | 106.40 | |
| Cl(2)–Zr–Cent(2)[b] | 106.97 | |

[a] Cent(1) is the centroid of C(1)–C(5) for both complexes. [b] Cent(2) is the centroid of C(11)–C(15) for the complex *meso*-**9**. [c] Refers to the average bond length between Zr(1) and the carbon atoms of the $C_5$ ring of the cyclopentadienyl moiety.

observed previously for other bis(indenyl)-zirconium dichlorides [2.407(1)–2.465(2) Å].[15–20]

The angles between some relevant planes are collected in Table 2 along with the geometrical parameters described in Figure 3 for compounds *meso*-**9**, *rac*-**10**, and the unsubstituted parent *rac*-[Zr{1-$Me_2Si(\eta^5$-$C_9H_6)_2$}$Cl_2$].[12] As usual for bent metallocenes, the overall coordination environment is best described by the set of parameters depicted in Figure 3, which describes the metal accessibility. In particular, the smaller the "bite angle" $\beta$ and the larger the Cp–M–Cp′ $\alpha$ angle, the more the metal is tucked into the ligand envelope.

The main geometrical difference of *meso*-**9** and *rac*-**10** from *rac*-[Zr{1-$Me_2Si(\eta^5$-$C_9H_6)_2$}$Cl_2$] is associated with the angle $\beta$ and the range of Zr–$C_{Cp}$ bond lengths. $\beta$, in *meso*-**9** (63.9°) and *rac*-**10** (62.9°), is increased compared to that of *rac*-[Zr{1-$Me_2Si(\eta^5$-$C_9H_6)_2$}$Cl_2$] (60.2°). The range of $Zr–C_{Cp}$ for both complexes (0.21 Å for *meso*-**9** and 0.20 Å for *rac*-**10**) is similar to that in *rac*-[Zr{1-$Me_2Si(\eta^5$-$C_9H_6)_2$}$Cl_2$] (0.20 Å).

These differences are, likely, caused by the bulky R substituents at C(3) of both indenyl fragments. This conclusion is supported by significant displacements of the C(3)–R bonds from the planes of the parent cyclopentadienyl rings opposite to Zr (4.1° and 4.5° for *meso*-**9**, and 4.2° for *rac*-**10**).

It can be seen from Figure 2 that, for the structures of the complexes *meso*-**9** and *rac*-**10**, both $C_5$ rings are eclipsed, including, in the case of *meso*-**9**, the methyl-substituent in position 3. In *meso*-**9**, it can be observed that one of the chloride ligands is very close to the $C_6$ aromatic rings, whereas the other one is in an intermediate location between the methyl-substituents. In the case of *rac*-**10**, each

 © 2006 Wiley-VCH Verlag GmbH & Co. KGaA, Weinheim 

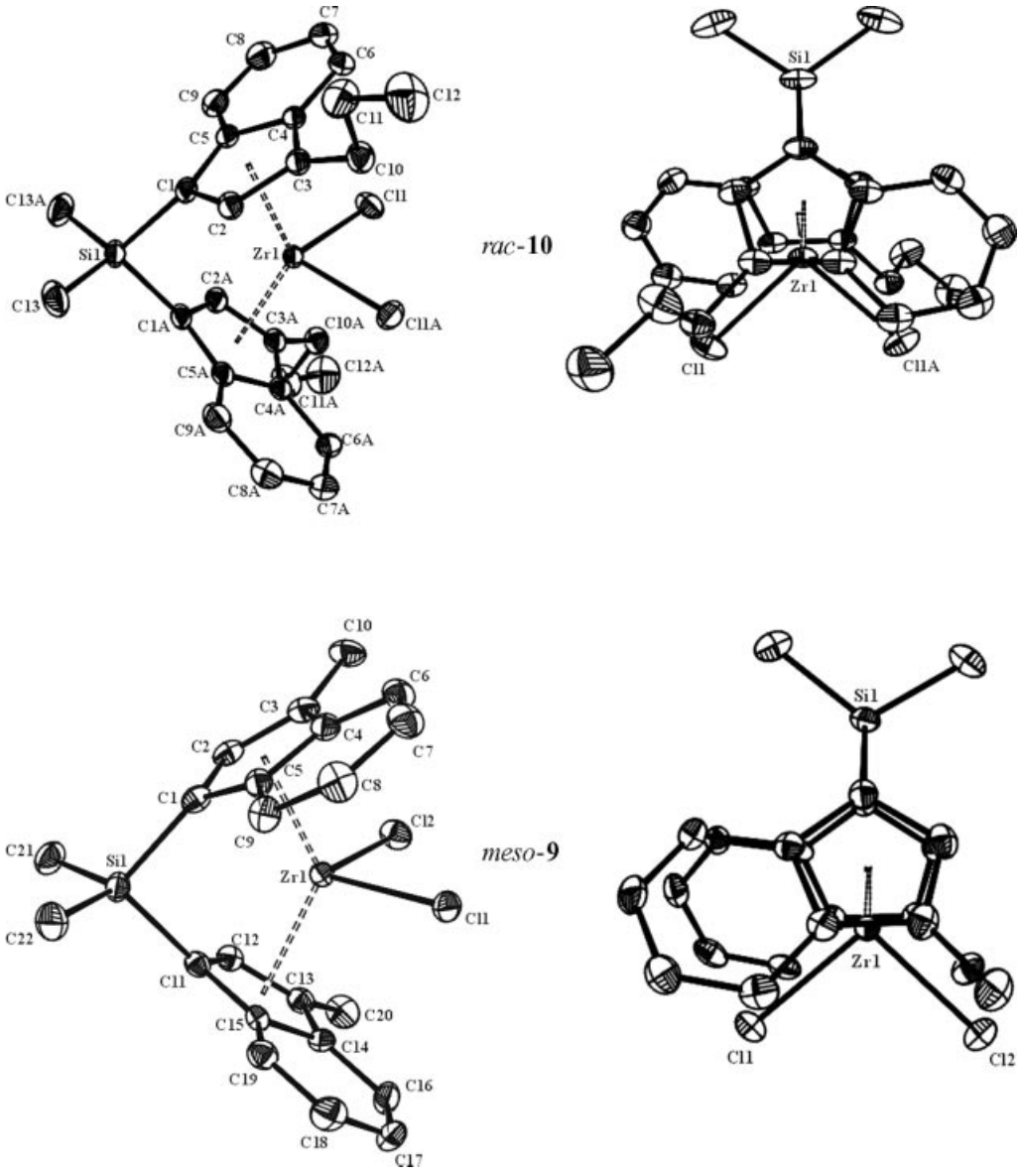


Figure 2. Solid state structure of *rac*-**10** and *meso*-**9** (hydrogen atoms are omitted for clarity).

Table 2. Relevant geometrical parameters.[a]

| | *meso*-**9** | *rac*-**10** | *rac*-[$Me_2Si(Ind)_2$]$ZrCl_2$ |
|---|---|---|---|
| $\alpha$ | 128.7 | 128.8 | 127.8 |
| $\beta$ | 63.9 | 62.9 | 60.2 |
| $\delta$ | 83.6, 83.4 | 83.9 | 85.7 |
| $\varphi$ | 95.3 | 95.3 | 94.4 |
| $\gamma$ | 15.6, 15.8 | 16.1 | 17.8; 16.4 |
| $r$(Zr–CCp), $\Delta r$ | 2.45–2.66, 0.21 | 2.45–2.65, 0.20 | 2.46–2.66, 0.20 |

[a] All quantities in degrees, apart from Δ (Å). The angles α, $\beta$, $\gamma$, $\delta$, and $\varphi$ are defined in Figure 3. Δ is the distance between the perpendicular projection of the heavy atom on the ring least-squares plane and the ring centroid.

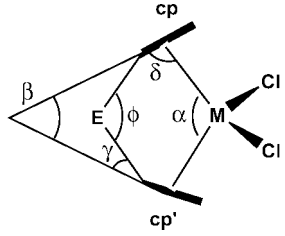


Figure 3. Schematic representation of an *ansa*-metallocene detailing the angles listed in Table 2.

chloride ligand is between a ring and an alkyl substituent. This situation could give rise to a great influence of the rings and their alkyl substituents on the positions occupied by the active sites of the catalysts. These features could be established to control the molecular weight of the polymers obtained.

### Polyethylene Polymerization using Complexes 9–12

Complexes **9**–**12**, used as *rac*/*meso* mixtures, after being activated with methylaluminoxane (MAO), are very active

 © 2006 Wiley-VCH Verlag GmbH & Co. KGaA, Weinheim 

Table 3. Homogeneous ethylene polymerization results for **9**–**12** and [Zr{1-$Me_2Si(\eta^5$-$C_9H_6)_2$}$Cl_2$] as reference. Conditions: 343 K, 1.5 bar monomer pressure, 6 μmol Zr, MAO/Zr = 2000, 100 mL toluene, $t_{pol}$ = 30 min.

| Complex | Activity[a] [$kg_{PE}/mol_{Zr} \times h$] | Activity (after 12 h)[a][b] [$kg_{PE}/mol_{Zr} \times h$] | $M_w$ [$g\,mol^{-1}$] | $M_n$ | $M_w/M_n$ | M.p. [°C] |
|---|---|---|---|---|---|---|
| [Zr{1-$Me_2Si$[3-($\eta^5$-$C_9H_5$)Me]$_2$}$Cl_2$] (**9**) | 6333 | 1757 | 82000 | 21000 | 3.82 | 132 |
| [Zr{1-$Me_2Si$[3-($\eta^5$-$C_9H_5$)*n*Pr]$_2$}$Cl_2$] (**10**) | 3473 | 2333 | 87000 | 26000 | 3.40 | 134 |
| [Zr{1-$Me_2Si$[3-($\eta^5$-$C_9H_5$)*n*Bu]$_2$}$Cl_2$] (**11**) | 2946 | 1856 | 74000 | 17000 | 4.35 | 132 |
| [Zr{1-$Me_2Si$[3-($\eta^5$-$C_9H_5$)Bz]$_2$}$Cl_2$] (**12**) | 1849 | 1843 | 70000 | 17000 | 4.06 | 134 |
| [Zr{1-$Me_2Si(Ind)_2$}$Cl_2$] | 3573 | No reaction | 166000 | 53000 | 3.16 | 136 |

[a] Average value for three different runs. [b] Precatalyst/MAO solutions were aged for 12 h, at room temperature, before monomer introduction.

catalysts for the polymerization of ethylene. In the present study, we used a 10% solution of MAO in toluene, which contains about 20–30% of $AlMe_3$. In all polymerization experiments, Al(*i*Bu)$_3$ was used to scavenge possible impurities in the monomer. The polymerization results are compared with those of one of the best zirconocene catalysts, i.e., [Zr{1-$Me_2Si(\eta^5$-$C_9H_6)_2$}$Cl_2$].[12] The polymerization results and the available polymer characterization data are shown in Table 3.

Complexes **9**–**12** show similar or higher activities than the reference complex and, moreover, these new catalysts produced lower molecular weight polyethylene than the reference catalyst. Although it is not possible to establish any relation between the size of the substituent and the polymer molecular weight, we suggest that this low molecular weight arises due to the steric influence of the substituents. The activities of complexes **9**–**12** decrease as the bulk of the substituent in position 3 increases.

In addition, the melting points of all the polymers were determined (see Table 3). The catalysts **9**–**12** produced crystalline materials with relatively high melting points (near 130 °C).

The stability of metallocene complexes is one of the most important variables for its future industrial use. The activities of activated forms of complexes **9**–**12** were tested after 12 h of contact between the complexes and MAO solution. It is worth noting that these complexes maintained a reasonable level of activity after this contact time. In contrast, the reference complex ([Zr{1-$Me_2Si(\eta^5$-$C_9H_6)_2$}$Cl_2$]) did not give any reaction with ethylene after the same time of contact with MAO. It therefore appears that an increase in the volume of the substituent in the 3-position leads to an increase in the stability of the catalyst.

## Conclusions

We have carried out the synthesis of new examples of *ansa*-bis-indenylzirconocene complexes, bearing a $SiMe_2$ bridge, with alkyl substituents in the 3 position. The presence of these groups allows stable and very active catalysts to be obtained in ethylene polymerization, producing polyethylenes of low molecular weight, in comparison with the unsubstituted analogue. In addition, complexes *meso*-[Zr{1-$Me_2Si$[3-$\eta^5$-$C_9H_5(CH_3)]_2$}$Cl_2$] and *rac*-[Zr{1-$Me_2Si$[3-$\eta^5$-$C_9H_5(CH_2CH_2CH_3)]_2$}$Cl_2$] have been characterized by X-ray diffraction methods.

## Experimental Section

**General Remarks:** All reactions were carried out using standard Schlenk-tube and glove-box techniques in dry nitrogen. Solvents were distilled from appropriate drying agents and degassed before use. $ZrCl_4$, indene, $SiMe_2Cl_2$, $ICH_3$, $BrCH_2CH_2CH_3$, $BrCH_2CH_2CH_2CH_3$, and $BrCH_2Ph$ were purchased from Aldrich and used directly. $^1H$ and $^{13}C$ spectra were recorded with Varian GEMINI FT-400 and Varian INNOVA FT-500 spectrometers and referenced to the residual deuterated solvent. Microanalyses were carried out with a Perkin–Elmer 2400 microanalyzer. Mass spectrometry was performed with a Hewlett–Packard 5988A (*m*/*z* = 50–1000) (electron impact) spectrometer.

**Preparation of {1-$Me_2Si$[3-$C_9H_6(CH_3)]_2$} (1):** *n*BuLi (1.60 M in hexane) (38.00 mL, 60.74 mmol) was added over 15 min to a cooled (–78 °C) solution of [$Me_2Si(C_9H_7)$] (7.30 g, 25.31 mmol) in $Et_2O$ (100 mL) in a 250-mL Schlenk tube. At the end of the addition the solution was allowed to reach room temperature and stirred for 4 h, cooled again to –78 °C, and MeI (14.37 g, 101.24 mmol) was added. The reaction mixture was allowed to reach room temperature and stirred for 16 h. The solvent was removed in vacuo and hexane (100 mL) was added. Water (200 mL) was added, the organic product was extracted with hexane, the aqueous layer was washed with hexane (3 × 50 mL), the organic layers combined, dried with $MgSO_4$, filtered and the solvent removed from the filtrate under reduced pressure to yield the title compound as a yellow oil. Compound **1** was purified by column chromatography ($Et_2O$/hexane, 1:9) (yield 7.05 g, 88%). $^1H$ NMR (400 MHz, $CDCl_3$) (for the predominant isomer): $\delta$ = 0.10 and 0.14 (2 s, each 3 H, $SiMe_2$), 0.82 (m, 6 H, $CH_3$), 3.56 (d, $J$ = 1.8 Hz, 2 H, 1-H), 6.82 (d, $J$ = 1.8 Hz, 2 H, 2-H), 7.11–7.37 (m, 8 H, 4-H–7-H) ppm. MS electron impact: *m*/*z* (%) = 316 (3) [M, {1-$Me_2Si$[3-$C_9H_6(CH_3)]_2$}]$^+$, 187 (100) [M – (3-Me – $C_9H_6$)]$^+$, 129 (56) [M – $Me_2Si$]$^+$.

**Preparation of {1-$Me_2Si$(3-$C_9H_6(CH_2CH_2CH_3))_2$} (2):** The synthesis of **2** was carried out in an identical manner to **1**. [$Me_2Si(C_9H_7)$] (7.30 g, 25.31 mmol), *n*BuLi (1.60 M in hexane) (38.00 mL, 60.74 mmol), and $BrCH_2CH_2CH_3$ (12.45 g, 101.24 mmol). Yield 8.48 g (89%). $^1H$ NMR (400 MHz, $CDCl_3$) (for the predominant isomer): $\delta$ = 0.19 and 0.32 (2 s, each 3 H, $SiMe_2$), 0.95 (m, 6 H, $CH_2CH_2CH_3$), 1.39–2.73 (m, 8 H, -$CH_2CH_2CH_3$), 3.50 (d, $J$ = 1.8 Hz, 2 H, 1-H), 6.98 (d, $J$ = 1.8 Hz, 2 H, 2-H), 7.10–7.50 (m, 8 H, 4-H–7-H) ppm. MS electron impact: *m*/*z* (%) = 372 (3) [M, {1-$Me_2Si$(3-$C_9H_6(CH_2CH_2CH_3))_2$}]$^+$, 216 (100) [M – (3-Pr – $C_9H_6$)]$^+$, 156 (23) [M – $Me_2Si$]$^+$.

**Preparation of {1-$Me_2Si$(3-$C_9H_6(CH_2CH_2CH_2CH_3))_2$} (3):** The synthesis of **3** was carried out in an identical manner to **1**. [$Me_2Si(C_9H_7)$] (7.30 g, 25.31 mmol), *n*BuLi (1.60 M in hexane) (38.00 mL, 60.74 mmol), and $BrCH_2CH_2CH_2CH_3$ (13.87 g, 101.24 mmol). Yield 9.13 g (90%). $^1H$ NMR (400 MHz, $CDCl_3$) (for the predominant isomer): $\delta$ = 0.22 and 0.08 (2 s, each 3 H,

 © 2006 Wiley-VCH Verlag GmbH & Co. KGaA, Weinheim 

$SiMe_2$), 0.95–2.73 (m, 18 H, -$CH_2CH_2CH_2CH_3$), 3.80 (d, $J$ = 1.8 Hz, 2 H, 1-H), 6.89 (d, $J$ = 1.8 Hz, 2 H, 2-H), 7.10–7.50 (m, 8 H, 4-H–7-H) ppm. MS electron impact: $m/z$ (%) = 400 (3) [M, {1-$Me_2Si(3\text{-}C_9H_6(CH_2CH_2CH_3))_2$}]$^+$, 228 (100) [M – (3-Bu-$C_9H_6$)]$^+$, 59 (55) [M – $Me_2Si(C_9H_6)$]$^+$.

**Preparation of {1-$Me_2Si(3\text{-}C_9H_6(CH_2C_6H_5))_2$} (4):** The synthesis of **4** was carried out in an identical manner to **1**. [$Me_2Si(C_9H_7)$] (7.30 g, 25.31 mmol), *n*BuLi (1.60 M in hexane) (38.00 mL, 60.74 mmol), and $BrCH_2C_6H_5$ (8.66 g, 50.62 mmol). Yield 5.34 g (45%). $^1$H NMR (400 MHz, $CDCl_3$) (for the predominant isomer): $\delta$ = 0.16 and 0.13 (2s, each 3 H, $SiMe_2$), 2.72–3.00 (m, 4 H, -$CH_2C_6H_5$), 3.54 (d, $J$ = 1.8 Hz, 2 H, 1-H), 6.78 (d, $J$ = 1.8 Hz, 2 H, 2-H), 7.14–7.39 (m, 18 H, 4-H–7-H, $CH_2C_6H_5$) ppm. MS electron impact: $m/z$ (%) = 468 (2) [M, {1-$Me_2Si(3\text{-}C_9H_6(CH_2C_6H_5))_2$}]$^+$, 264 (83) [M – (3-Bz-$C_9H_6$)]$^+$, 91 (100) [M – $Me_2Si(C_9H_6)$]$^+$.

**Preparation of $Li_2${1-$Me_2Si(3\text{-}C_9H_5(CH_3))_2$} (5):** *n*BuLi (1.60 M in hexane) (23.79 mL, 37.92 mmol) was added dropwise over 15 min to a cooled (–80 °C), stirred solution of {1-$Me_2Si(3\text{-}C_9H_6(CH_3))_2$} (**1**) (5.00 g, 15.80 mmol) in $Et_2O$ (80 mL) in a 250-mL Schlenk tube. The solution was warmed up to room temperature and stirred for 4 h. An increasing turbidity developed and this finally led to the formation of a yellow-orange suspension. The solvent was removed in vacuo to give a yellow solid, which was washed with hexane (2 × 50 mL) and dried under vacuum to yield **5** as a free flowing yellow solid (yield 3.94 g, 76%). $C_{22}H_{22}Li_2Si$ (328.28): calcd. C 80.47, H 6.75; found C 80.53, H 6.80.

**Preparation of $Li_2${1-$Me_2Si(3\text{-}C_9H_5(CH_2CH_2CH_3))_2$} (6):** The synthesis of **6** was carried out in an identical manner to **5**. {1-$Me_2Si(3\text{-}C_9H_6(CH_2CH_2CH_3))_2$} (**2**) (5.00 g, 13.28 mmol), *n*BuLi (1.60 M in hexane), and (19.91 ml, 31.85 mmol). Yield 4.48 g (87%). $C_{26}H_{30}Li_2Si$ (384.48): calcd. C 81.22, H 7.86; found C 81.43, H 7.93.

**Preparation of $Li_2${1-$Me_2Si(3\text{-}C_9H_5(CH_2CH_2CH_2CH_3))_2$} (7):** The synthesis of **7** was carried out in an identical manner to **5**. {1-$Me_2Si(3\text{-}C_9H_6(CH_2CH_2CH_2CH_3))_2$} (**3**) (5.00 g, 12.48 mmol) and *n*BuLi (1.60 M *in* hexane) (18.72 mL, 29.95 mmol). Yield (4.37 g, 85%). $C_{28}H_{34}Li_2Si$ (412.54): calcd. C 81.52, H 8.31; found C 81.43, H 8.40.

**Preparation of $Li_2${1-$Me_2Si(3\text{-}C_9H_5(CH_2C_6H_5))_2$} (8):** The synthesis of **8** was carried out in an identical manner to **5**. {1-$Me_2Si(3\text{-}C_9H_6(CH_2C_6H_5))_2$} (**4**) (5.00 g, 10.67 mmol) and *n*BuLi (1.60 M in hexane) (16.00 mL, 26.21 mmol). Yield 4.10 g (80%). $C_{34}H_{30}Li_2Si$ (480.57): calcd. C 84.97, H 6.29; found C 84.83, H 6.34.

**Preparation of [Zr{1-$Me_2Si(3\text{-}\eta^5\text{-}C_9H_5(CH_3))_2$}$Cl_2$] (9):** A cooled (–78 °C) slurry of $ZrCl_4$ (2.79 g, 12.00 mmol) in toluene (80 mL) was rapidly added to a cooled (–78 °C) solution of $Li_2${1-$Me_2Si(3\text{-}C_9H_5(CH_3))_2$} (**5**) (3.94 g, 12.00 mmol) in $Et_2O$ (80 mL) in a 250-mL Schlenk tube. The reaction mixture was stirred for 30 min at –20 °C and then overnight at room temperature (16 h). The orange suspension was filtered through a G4 frit with Celite. The filtrate was evaporated to dryness under reduced pressure to yield a sticky dark-orange product. The product was washed with $Et_2O$ (30 mL) and the residue was dried to give an orange solid (0.86 g, 15%). *rac*/*meso* = 55:45. For this complex, samples of the pure *meso* diastereomer and a product enriched in the *rac* isomer (11.5:1) were obtained by careful recrystallization from $CH_2Cl_2$/$Et_2O$.

***meso* Isomer:** $^1$H NMR (500 MHz, $CD_2Cl_2$): $\delta$ = 0.80 [s, 3 H, $Si(CH_3)$ *exo*], 1.27 [s, 3 H, $Si(CH_3)$ *endo*], 2.35 (s, 6 H, $CH_3$), 5.50 (s, 2 H, 2-H), 6.83 and 7.09 (2t, $J$ = 8.8 Hz, each 2 H, *5-H*, 6-H), 7.32 and 7.44 (2d, $J$ = 8.8 Hz, each 2 H, 4-H, 7-H) ppm. $^{13}$C{$^1$H} NMR (125 MHz, $CD_2Cl_2$): $\delta$ = 13.03 [$Si(CH_3)$ *exo*], 13.62 [$Si(CH_3)$ *endo*], 43.62 ($CH_3$), 76.78, 86.00 (C1, C3), 118.40 (C2), 123.21 and 125.11 (C5, C6), 126.15, 126.48 (C4, C7) ppm.

***rac* Isomer:** $^1$H NMR (500 MHz, $CD_2Cl_2$): $\delta$ = 1.09 [s, 6 H, $Si(CH_3)_2$], 2.22 (s, 6 H, $CH_3$), 5.68 (s, 2 H, 2-H), 6.97 and 7.23 (2t, $J$ = 8.8 Hz, each 2 H, 5-H, 6-H), 7.35 and 7.38 (2d, $J$ = 8.8 Hz, each 2 H, 4-H, 7-H) ppm. $^{13}$C NMR (125 MHz, $CD_2Cl_2$): $\delta$ = –1.44 ppm [$Si(CH_3)_2$], 13.34 ($CH_3$), 78.04, 86.40 (C1, C3), 119.32 (C2), 124.25 and 125.06 (C5, C6), 126.55 and 126.85 (C4, C7) ppm.

**Both Isomers:** $C_{22}H_{22}Cl_2SiZr$ (476.6): calcd. C 55.44, H 4.65; found C 55.63, H 4.68.

**Preparation of [Zr{1-$Me_2Si[3\text{-}\eta^5\text{-}C_9H_5(CH_2CH_2CH_3)]_2$}$Cl_2$] (10):** The synthesis of **10** was carried out in an identical manner to **9**. $Li_2${1-$Me_2Si[3\text{-}C_9H_5(CH_2CH_2CH_3)]_2$} (**6**) (4.48 g, 11.65 mmol) and $ZrCl_4$ (2.72 g, 11.65 mmol). Yield 1.61 g (26%). *rac*/*meso* = 38:62.

***meso* Isomer:** $^1$H NMR (500 MHz, $CDCl_3$): $\delta$ = 1.04 [s, 3 H, $Si(CH_3)$ *exo*], 1.51 [s, 3 H, $Si(CH_3)$ *endo*], 1.07 (t, 6 H, $J$ = 7.9 Hz, $CH_2CH_2CH_3$), 1.74 (m, 4 H, $CH_2CH_2CH_3$), 2.98 (m, 4 H, $CH_2CH_2CH_3$), 5.73 (s, 2 H, 2-H), 7.07 and 7.32 (2t, $J$ = 8.8 Hz, each 2 H, 5-H, 6-H), 7.57 and 7.65 (2d, $J$ = 8.8 Hz, each 2 H, 4-H, 7-H) ppm. $^{13}$C{$^1$H} NMR (125 MHz, $CDCl_3$): $\delta$ = –2.45 [$Si(CH_3)$ *exo*], –0.71 [$Si(CH_3)$ *endo*], 14.46 ($CH_2CH_2CH_3$), 23.62 ($CH_2CH_2CH_3$), 30.78 ($CH_2CH_2CH_3$), 77.30, 80.10 (C1, C3), 117.27 (C2), 124.36 and 126.04 (C5, C6), 126.30 and 126.47 (C4, C7) ppm.

***rac* Isomer:** $^1$H NMR (500 MHz, $CDCl_3$): $\delta$ = 1.25 [s, 6 H, $Si(CH_3)_2$], 1.03 (t, 6 H, $J$ = 7.9 Hz, $CH_2CH_2CH_3$), 1.65 (m, 4 H, $CH_2CH_2CH_3$), 2.84 (m, 4 H, $CH_2CH_2CH_3$), 5.91 (s, 2 H, *2-H*), 7.19 and 7.47 (2t, $J$ = 8.8 Hz, each 2 H, 5-H, 6-H), 7.57 and 7.65 (2d, $J$ = 8.8 Hz, each 2 H, 4-H, 7-H) ppm. $^{13}$C{$^1$H} NMR (125 MHz, $CDCl_3$): $\delta$ = –1.12 ppm [$Si(CH_3)_2$], 14.34 ($CH_2CH_2CH_3$), 23.54 ($CH_2CH_2CH_3$), 30.49 ($CH_2CH_2CH_3$), 77.40, 85.31 (C1, C3), 117.27 (C2), 124.55 and 124.92 (C5, C6), 126.62 and 126.72 (C4, C7) ppm.

**Both Isomers:** $C_{26}H_{30}Cl_2SiZr$ (532.73): calcd. C 58.62, H 5.68; found C 58.71, H 5.69.

**Preparation of [Zr{1-$Me_2Si[3\text{-}\eta^5\text{-}C_9H_5(CH_2CH_2CH_2CH_3)]_2$}$Cl_2$] (11):** The synthesis of **11** was carried out in an identical manner to **9**. $Li_2${1-$Me_2Si[3\text{-}C_9H_5(CH_2CH_2CH_2CH_3)]_2$} (**7**) (4.37 g, 10.59 mmol) and $ZrCl_4$ (2.47 g, 10.59 mmol). Yield 2.08 g (35%). *rac*/*meso* = 59:41.

***meso* Isomer:** $^1$H NMR (500 MHz, $CDCl_3$): $\delta$ = 0.87 [s, 3 H, $Si(CH_3)$ *exo*], 1.36 [s, 3 H, $Si(CH_3)$ *endo*], 0.89 (t, $J$ = 7.9 Hz, 6 H, $CH_2CH_2CH_2CH_3$), 1.34 (m, 4 H, $CH_2CH_2CH_2CH_3$), 1.51 (m, 4 H, $CH_2CH_2CH_2CH_3$), 2.72 (m, 4 H, $CH_2CH_2CH_2CH_3$), 5.58 (s, 2 H, 2-H), 6.91 and 7.16 (2t, $J$ = 8.8 Hz, each 2 H, 5-H, 6-H), 7.41 and 7.49 (2d, $J$ = 8.8 Hz, each 2 H, 4-H, 7-H) ppm. $^{13}$C{$^1$H} NMR (125 MHz, $CDCl_3$): $\delta$ = –2.69 [$Si(CH_3)$ *exo*], –0.96 [$Si(CH_3)$ *endo*], 13.95 ($CH_2CH_2CH_2CH_3$), 22.77 ($CH_2CH_2CH_2CH_3$), 28.24 ($CH_2CH_2CH_2CH_3$), 32.29 ($CH_2CH_2CH_2CH_3$), 77.10, 84.81 (C1, C3), 116.88 (C2), 123.98 and 125.77 (C5, C6), 126.03, 126.19 (C4, C7) ppm.

***rac* Isomer:** $^1$H NMR (500 MHz, $CDCl_3$): $\delta$ = 1.11 [s, 6 H, $Si(CH_3)_2$], 0.90 (t, 6 H, $J$ = 7.9 Hz $CH_2CH_2CH_2CH_3$), 1.34 (m, 4 H, $CH_2CH_2CH_2CH_3$), 1.51 (m, 4 H, $CH_2CH_2CH_2CH_3$), 2.82 (m, 4 H, $CH_2CH_2CH_2CH_3$), 5.77 (s, 2 H, 2-H), 7.06 and 7.32 (2t, $J$ = 8.8 Hz, each 2 H, 5-H, 6-H), 7.41 and 7.49 (2d, $J$ = 8.8 Hz, each 2 H, *4-H*, 7-H) ppm. $^{13}$C{$^1$H} NMR (125 MHz, $CDCl_3$): $\delta$ = –1.37 [$Si(CH_3)_2$], 13.95 ($CH_2CH_2CH_2CH_3$), 22.77 ($CH_2CH_2CH_2CH_3$), 28.12 ($CH_2CH_2CH_2CH_3$), 32.29 ($CH_2CH_2CH_2CH_3$), 77.69, 85.06 (C1, C3), 117.00 (C2), 124.08 and 124.67 (C5, C6), 126.34 and 126.43 (C4, C7) ppm.

 © 2006 Wiley-VCH Verlag GmbH & Co. KGaA, Weinheim 

**Both Isomers:** $C_{28}H_{34}Cl_2SiZr$ (560.79): calcd. C 59.97, H 6.11; found C 60.21, H 6.19.

**Preparation of [Zr{1-Me$_2$Si[3-η$^5$-C$_9$H$_5$(CH$_2$C$_6$H$_5$)]$_2$}Cl$_2$] (12):** The synthesis of **12** was carried out in an identical manner to **9**. $Li_2${1-$Me_2Si[3$-$C_9H_5(CH_2C_6H_5)]_2$} (**8**) (4.10 g, 8.53 mmol) and $ZrCl_4$ (2.00 g, 8.53 mmol). Yield 2.15 g (40%). *rac*/*meso* = 65:35.

***meso* Isomer:** $^1$H NMR (500 MHz, $CDCl_3$): $\delta$ = 1.01 [s, 3 H, Si($CH_3$) *exo*], 1.29 [s, 3 H, Si($CH_3$) *endo*], $\delta_A$ = 4.28, $\delta_B$ = 4.22 (AB, $J_{AB}$ = 21.6 Hz, 4 H, $CH_2C_6H_5$), 5.77 (s, 2 H, *2-H*), 7.02–7.48 (m, 8 H, 4-H–7-H), 7.02–7.48 (m, 10 H, $CH_2C_6H_5$) ppm. $^{13}$C{$^1$H} NMR (125 MHz, $CDCl_3$): $\delta$ = –1.40 [Si($CH_3$) *exo*], –0.99 [Si($CH_3$) *endo*], 34.22 ($CH_2C_6H_5$), 65.84, 85.90 (C1, C3), 118.12 (C2), 124.06 and 125.85 (C5, C6), 126.12 and 126.14 (C4, C7), 118.04–140.17 ($CH_2C_6H_5$) ppm.

***rac* Isomer:** $^1$H NMR (500 MHz, $CDCl_3$): $\delta$ = 0.79 [s, 6 H, Si($CH_3$)], $\delta_A$ = 4.17, $\delta_B$ = 4.04 (AB, $J_{AB}$ = 19.6 Hz, 4 H, $CH_2C_6H_5$), 5.59 (s, 2 H, 2-H), 7.02–7.48 (m, 8 H, 4-H–7-H), 7.02–7.48 (m, 10 H, $CH_2C_6H_5$) ppm. $^{13}$C{$^1$H} NMR (125 MHz, $CDCl_3$): $\delta$ = –2.85 [Si($CH_3$)$_2$], 34.58 ($CH_2C_6H_5$), 65.94, 86.32 (C1, C3), 118.04 (C2), 124.25 and 124.74 (C5, C6), 126.57 and 126.78 (C4, C7), 118.04–140.17 ($CH_2C_6H_5$) ppm.

**Both Isomers:** $C_{34}H_{30}Cl_2SiZr$ (628.82): calcd. C 64.94, H 4.81; found C 65.02, H 4.86.

**Polymerization Experiments:** Polymerizations (three runs for catalyst) were carried out in a 250 mL glass reactor using toluene as a solvent (100 mL). Catalysts (6 μmol) were treated with the appropriate quantity (Al/Zr = 2000) of a commercial (CROPTOM) solution of MAO in toluene (10% Al) for 15 min. Toluene (80 mL), Al($i$Bu)$_3$ scavenger (2 mL), and activated catalyst were introduced, in this order, into the reactor and the temperature was maintained at 343 K. The nitrogen atmosphere was removed and a continuous flow of ethylene (1.5 bar) was introduced over 30 min. The reaction mixture was then quenched by the addition of acidified methanol. The polymer was collected by filtration, washed with methanol, and dried under vacuum at room temperature for 24 h.

**Polymer Analysis Procedures:** $M$w, $M$n, and $M$w/$M$n were measured with an Alliance GPC-2000 high temperature GPG device from Waters Corp., Milford, MA, USA. The mobile phase was 2,4,5-trichlorobenzene (HPLC grade, J. T. Baker Ltd.) at 150 °C. Prior to use as a mobile phase, TCB was filtered through a 0.2-μ fiberglass filter (PALL Corp.). The GPC device was completed with 3 Styragel® columns (Waters Corp.) and an additional GARD column. All columns were placed in an oven and heated to 150 °C. The RI detector at 150 °C was used for MW determination by the relative method. Data processing was performed using Millennium® ver. 4.2 Software (Waters Corp.). The sample (0.020 g) was dissolved in 2,4,5-trichlorobenzene (10.0 mL) (HPLC grade, J. T. Baker Ltd.) at 150 °C over 7 h. The solution was stirred four times during this period. The hot solution (7 mL) of each sample was placed into the metal vial equipped with a mechanism for automatic filtration through 0.2-μ metal filters prior to injection. The vials were immediately placed in an autosampler heated continually at 150 °C. The sample was stirred for 15 min in the autosampler prior to injection. 12 PS narrow standards in the range of $M_W$ from 2430 Dalton to 1.800.000 Dalton (Aldrich) were used for the calibration of the GPC device. The standards were prepared analogous to the sample preparation. The concentrations of standard solutions were calculated according the recommendations of Aldrich. The calibration curve is linear in all range of $M_W$ and indicates the good working order of the device and especially the columns.

**X-ray Crystal Structure Determination of *meso*-9 and *rac*-10:** Intensity data were collected with a Nonius-MACH3 diffractometer equipped with a graphite monochromator and a Mo-$K_\alpha$ radiation source ($\lambda$ = 0.71073 Å) using a $\omega/2\theta$-scan technique. The final unit cell parameters were determined from 25 well-centered reflections and refined by least-squares methods. Data were corrected for Lorentz and polarization effects and a semi-empirical absorption correction (Psi-scans) was made.[21]

The structures were solved using direct methods,[22] completed by subsequent difference Fourier syntheses, and refined by full-matrix least-squares procedures on $F^2$.[23] All non-hydrogen atoms were refined with anisotropic thermal parameters. The hydrogen atoms were placed using a "riding model" and included in the refinement at calculated positions. Weights were optimized in the final cycles. Crystallographic data are given in Table 4.

Table 4. Crystal data and structure refinement for *meso*-**9** and *rac*-**10**.

| | *meso*-**9** | *rac*-**10** |
|---|---|---|
| Empirical formula | $C_{22}H_{22}Cl_2SiZr{\cdot}CH_2Cl_2$ | $C_{26}H_{30}Cl_2SiZr{\cdot}0.5C_7H_8$ |
| Formula weight | 561.53 | 578.78 |
| Temperature [K] | 290(2) | 250(2) |
| Wavelength [Å] | 0.71073 | 0.71073 |
| Crystal system | triclinic | monoclinic |
| Space group | $P\bar{1}$ | $P2/c$ |
| $a$ [Å] | 9.994(5) | 11.062(4) |
| $b$ [Å] | 10.430(8) | 12.206(4) |
| $c$ [Å] | 12.264(5) | 11.311(3) |
| $\alpha$ [°] | 86.23(4) | |
| $\beta$ [°] | 70.28(4) | 91.59(3) |
| $\gamma$ [°] | 78.74(6) | |
| Volume [Å$^3$] | 1180(1) | 1526.7(8) |
| $Z$ | 2 | 2 |
| Density (calculated) [g/cm$^3$] | 1.580 | 1.259 |
| Absorption coefficient [cm$^{-1}$] | 9.78 | 5.89 |
| $F$(000) | 568 | 598 |
| Crystal size [mm] | 0.3×0.2×0.1 | 0.4×0.3×0.2 |
| Index ranges | $-12 \le h \le 13$ | $-14 \le h \le 14$ |
| | $-13 \le k \le 13$ | $0 \le k \le 16$ |
| | $0 \le l \le 16$ | $0 \le l \le 14$ |
| Reflections collected | 5894 | 3858 |
| Independent reflections | 5638 [$R$(int) = 0.0497] | 3674 [$R$(int) = 0.0168] |
| Data/restraints/parameters | 5638/0/266 | 3674/0/147 |
| Goodness-of-fit on $F_2$ | 1.056 | 1.111 |
| Final $R$ indices [$I > 2\sigma(I)$] | $R_1$ = 0.0630 | $R_1$ = 0.0466 |
| | $wR_2$ = 0.1479 | $wR_2$ = 0.1460 |
| $R$ indices (all data) | $R_1$ = 0.1260 | $R_1$ = 0.0656 |
| | $wR_2$ = 0.1745 | $wR_2$ = 0.1567 |
| Largest diff. peak/hole [e·Å$^{-3}$] | 1.076/–1.384 | 1.218/–0.461 |

$R_1 = \Sigma||F_o| - |F_c||/\Sigma|F_o|$; $wR_2 = \Sigma[w(F_o^2 - F_c^2)^2]/\Sigma[w(F_o^2)^2]^{0.5}$

CCDC-283808 and -283809 contain the supplementary crystallographic data for this paper. These data can be obtained free of charge from The Cambridge Crystallographic Data Centre via www.ccdc.cam.ac.uk/data_request/cif.

## Acknowledgments

We gratefully acknowledge financial support from the Ministerio de Educación y Ciencia, Spain (Grant Nos. CTQ2005-07918-C02-01/BQU and MAT2003-05345), and the Junta de Comunidades de Castilla-La Mancha (Grant No. PBI05-029). C. A. acknowledges a fellowship from REPSOL-YPF-UCLM (contract CTR-00-084).

 © 2006 Wiley-VCH Verlag GmbH & Co. KGaA, Weinheim 

[1] See reviews by: a) P. C. Möring, N. J. Coville, *J. Organomet. Chem.* **1994**, *479*, 1; b) H.-H. Brintzinger, D. Fischer, R. Mülhaupt, B. Rieger, R. M. Waymouth, *Angew. Chem.* **1995**, *107*, 1255; *Angew. Chem. Int. Ed. Engl.* **1995**, *34*, 1143; c) T. J. Marks, J. C. Stevens, *Topics Catal.* **1999**, *7*, 1; d) J. A. Gladysz, *Chem. Rev.* **2000**, *100*, 1167; e) M. Bochmann, *J. Organomet. Chem.* **2004**, *689*, 3982; f) W. Kaminsky, *J. Polym. Sci., Part A: Polym. Chem.* **2004**, *42*, 3911.
[2] J. A. Ewen, M. J. Elder, R. L. Jones, L. Haspeslagh, J. L. Atwood, S. G. Bott, K. Robinson, *Makromol. Chem. Macromol. Symp.* **1991**, *48/49*, 253.
[3] W. Kaminsky, K. Külper, H.-H. Brintzinger, F. Wild, *Angew. Chem. Int. Ed. Engl.* **1985**, *24*, 507.
[4] a) W. Spaleck, M. Antberg, J. Rohrmann, A. Winter, B. Bachmann, P. Kiprof, J. Behm, W. Herrmann, *Angew. Chem. Int. Ed. Engl.* **1992**, *31*, 1347; b) L. Resconi, F. Piemontesi, I. Camurati, O. Sudmeijer, I. E. Ninfant'ev, P. V. Ivchenko, L. G. Kuz'mina, *J. Am. Chem. Soc.* **1998**, *120*, 2308.
[5] T. H. Warren, G. Erker, R. Fröhlich, B. Wibbleing, *Organometallics* **2000**, *19*, 127.
[6] W. Spaleck, M. Antberg, L. Böhm, L. Rohrmann, J. Lüker, *EP0399348*, **1990**.
[7] J. A. Ewen, *Macromol. Symp.* **1995**, *89*, 181.
[8] S. C. Yoon, J.-W. Park, H. S. Jung, H. Song, J. T. Park, S. I. Woo, *J. Organomet. Chem.* **1998**, *559*, 149.
[9] D. Balboni, G. Moscardi, G. Baruzzi, V. Braga, I. Camurati, F. Piemontesi, L. Resconi, I. E. Nifant'ev, V. Venditto, S. Antinucci, *Macromol. Chem. Phys.* **2001**, *202*, 2010.
[10] R. Blom, I. M. Dahl, *Macromol. Chem. Phys.* **1999**, *200*, 442.
[11] a) C. Alonso-Moreno, A. Antinolo, F. Carrillo-Hermosilla, P. Carrión, I. López-Solera, A. Otero, S. Prashar, J. Sancho, *Eur. J. Inorg. Chem.* **2005**, 2924; b) A. Antinolo, R. Fernandez-Galan, A. Otero, S. Prashar, I. Rivilla, A. M. Rodriguez, M. A. Maestro, *Organometallics* **2004**, *23*, 5108; c) A. Antinolo, I. Lopez-Solera, A. Otero, S. Prashar, A. M. Rodriguez, E. Villaseñor, *Organometallics* **2002**, *21*, 2460.
[12] W. A. Herrmann, J. Rohrmann, E. Herdtweck, W. Spaleck, A. Winter, *Angew. Chem. Int. Ed. Engl.* **1989**, *28*, 1511.
[13] L. Resconi, L. Caballo, A. Fait, F. Piemontesi, *Chem. Rev.* **2000**, *100*, 1253.
[14] a) M. Toto, L. Cavallo, P. Corradini, G. Moscardi, L. Resconi, G. Guerra, *Macromolecules* **1998**, *31*, 3431; b) L. Resconi, D. Balboni, G. Baruzzi, C. Fiori, S. Guidotti, P. Mercandelli, A. Sironi, *Organometallics* **2000**, *19*, 420.
[15] a) G. Erker, B. Temme, *J. Am. Chem. Soc.* **1992**, *114*, 4004; b) G. Erker, M. Aulbach, M. Knickmeier, D. Wingbermühle, C. Kruger, M. Nolte, S. Werner, *J. Am. Chem. Soc.* **1993**, *115*, 4590.
[16] C. Krüger, F. Lutz, M. Notle, G. Erker, M. Aulbach, *J. Organomet. Chem.* **1993**, *452*, 79.
[17] N. E. Grimmer, N. J. Coville, C. B. de Koning, J. M. Smith, L. M. Cook, *J. Organomet. Chem.* **1993**, *616*, 112.
[18] G. Jany, M. Gustafsson, T. Repo, E. Aitola, J. A. Dobado, M. Klinga, M. Leskelä, *J. Organomet. Chem.* **1998**, *558*, 11.
[19] R. L. Halterman, D. R. Fahey, E. F. Baillo, D. W. Docker, O. Stenzel, J. L. Shipman, M. A. Khan, S. Dechert, H. Suman, *Organometallics* **2000**, *19*, 5464.
[20] S. Knüppel, J.-L. Fauré, G. Erker, G. Kehr, M. Nissinen, R. Fröhlich, *Organometallics* **2000**, *19*, 1262.
[21] A. C. T. North, D. C. Phillips, F. S. Mathews, *Acta Crystallogr. Sect. A* **1968**, *24*, 351–359.
[22] *SIR92*, A program for crystal structure solution: A. Altomare, G. Cascarano, C. Giacovazzo, A. Guagliardi, *J. Appl. Crystallogr.* **1993**, *26*, 343–350.
[23] G. W. Sheldrick, *SHELXL-97*, Program for the Refinement of Crystal Structures from Diffraction Data, University of Göttingen, **1997**.

Received: September 22, 2005
Published Online: January 19, 2006

 © 2006 Wiley-VCH Verlag GmbH & Co. KGaA, Weinheim 

DOI: 10.1002/ejic.200500851

# Synthesis of New Tripodal Tri-Functionalized Hydrotris(indazol-1-yl)borate Ligands and X-ray Structures of Their Cyclopentadieneruthenium Complexes

**Alexandre Carella,[a] Guillaume Vives,[a] Tara Cox,[a] Joël Jaud,[a] Gwénaël Rapenne,*[a] and Jean-Pierre Launay*[a]**

**Keywords:** Tripodal ligands / Ligand design / Ruthenium / Indazole / Stacking interactions

Two new tripodal ligands designed to anchor complexes onto surfaces have been synthesized. They integrate ester or thioether functions at the 6-position of the indazoles. Potassium hydrotris[6-(ethoxycarbonyl)indazolyl]borate and potassium hydrotris{6-[(ethylsulfanyl)methyl]indazolyl}borate exhibit three pendant groups oriented to anchor complexes onto an oxide and a metallic surface, respectively. Their complexation with $[RuCp(CH_3CN)_3]PF_6$ yielded two piano-stool-shaped complexes that were characterized by X-ray diffraction. Comparison with the synthesized unfunctionalized analog showed that the three 6-substituted functions do not interfere with the coordination site and are particularly well oriented for surface deposition.

(© Wiley-VCH Verlag GmbH & Co. KGaA, 69451 Weinheim, Germany, 2006)

## Introduction

In the last decade, the continuous improvement of near-field microscopy techniques such as scanning tunneling microscopy (STM) and atomic force microscopy (AFM) has led to the imaging and the study of physicochemical properties of various molecules.[1] These techniques allow the visualization and manipulation of only one molecule and therefore the electrical[2] and mechanical properties[3] of a single molecule deposited on a surface can be investigated. As single-molecule experiments require the control of the shape of the molecule deposited, the design and the synthesis of rigid ligands able to be covalently attached on surfaces with a minimum number of degrees of freedom is an active field of research.[4] In particular, the movement of a molecule can be efficiently restricted by attaching the molecule to a surface with a tripod,[5] which prevents translation. Some rigid organic molecules with three points of attachment have already been used in AFM or STM studies.[6] However, the absence of coordination sites restricts their field of application. Therefore, a structurally rigid bifunctional molecule combining coordinating sites and anchoring groups is of special interest. It would allow the covalent attachment of coordination complexes on a surface, for instance giving rise to surface-mounted molecular gears or motors.[6,7]

Since their discovery by Trofimenko in the late 1960s,[8] the trispyrazolylborate ligands, also known as scorpionate ligands, have been used increasingly in bioinorganic, organometallic, and coordination chemistry.[9] This last aspect has been extensively developed with a particular interest in the modification of the functional groups connected to the pyrazolyl moiety in order to control or modify the steric and electronic environment surrounding the metal center. However its analogue, hydrotris(indazolyl)borate ($Tp^{4Bo}$), has not stimulated intense studies since its synthesis in 1995.[10] Nevertheless tris(indazolyl)borate bears two advantages over trispyrazolylborate. First it is larger, but the increase in size is not accompanied by a decrease in the rigidity of the molecule. Furthermore, by withdrawing the metal away from the surface, it allows interferences caused by metal–surface interactions to be minimized, which is particularly important for near-field microscopy experiments. The rigidity of its indazolyl fragments, conjugated with its tripodal shape, should make it a good candidate for surface deposition of metal complexes onto surfaces.

Here we report the synthesis of two new scorpionate ligands incorporating functional groups on the indazole, designed to interact with metallic or oxide surfaces. The functionalized borate ligands were designed to have three functional groups pointing in the opposite direction of the coordination site in order not to interfere sterically with it. Each of the three legs of the tripodal unit bears a functional group connected at the 6-position of indazole, which should be the optimal orientation for anchoring on a surface. The ester function has been found to strongly interact with oxide surfaces,[11] spontaneous deprotection yielding carboxylic groups that covalently bind the metallic oxide. In order to interact with a metallic surface, the thioether function was chosen to alleviate the problem encountered with oxidatively unstable thiols. Acetyl-protected thiols were also

[a] NanoSciences Group, CEMES-CNRS,
29 rue Jeanne Marvig, BP 94347,
31055 Toulouse Cedex 4, France
Fax: +33-5-62257999
E-mail: rapenne@cemes.fr

 InterScience © 2006 Wiley-VCH Verlag GmbH & Co. KGaA, Weinheim 

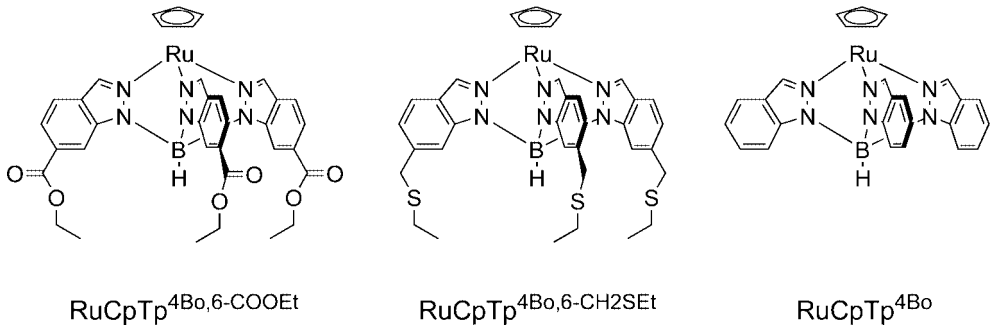


Figure 1. Structure of the triester-functionalized, trithioether-functionalized, and unfunctionalized ruthenium(II) complexes.

good candidates because of their spontaneous deprotection on a gold surface,[12] but preliminary experiments showed their incompatibility with the last step of the synthesis of the borate ligand, which requires sodium borohydride, yielding the reduction of the acetyl-protected thiol. The thioether group is stable in a wider range of conditions and is also known to interact strongly with a gold surface.[13] The synthesis of the hydrotris[6-(ethoxycarbonyl)indazol-1-yl]borate ligand incorporating three ester functions and the hydrotris{6-[(ethylsulfanyl)methyl]indazol-1-yl}borate ligand with three pendant thioether arms is described, followed by the preparation and X-ray structures of the corresponding $\eta^5$-cyclopentadienylruthenium complexes with both functionalized tripodal ligands and also with the unfunctionalized ligand. Following Trofimenko's scorpionate nomenclature,[9] the 6-functionalized ligands can be noted as $KTp^{4Bo,6\text{-}COOEt}$ for the ester-functionalized and $KTp^{4Bo,6\text{-}CH2SEt}$ for the thioether-functionalized ligand, and similarly the ruthenium complexes can be noted as $RuCpTp^{4Bo,6\text{-}COOEt}$, $RuCpTp^{4Bo,6\text{-}CH2SEt}$, and $RuCpTp^{4Bo}$ (Figure 1).

## Results and Discussion

### Ligand Syntheses

The strategy we followed consisted in the synthesis of a functionalized indazole in a first step, and its subsequent reaction with potassium borohydride to yield the potassium hydrotris(indazol-1-yl)borate ligand. Purification methods used in classical organic chemistry, such as column chromatography, are not suited to the purification of salts. Trituration with an apolar solvent can selectively dissolve the indazole precursor, and an additional sublimation step provides pure material. Potassium hydrotris[6-(ethoxycarbonyl)indazol-1-yl]borate ($KTp^{4Bo,6\text{-}COOEt}$) was synthesized in three steps starting with 3-amino-4-methylbenzoic acid (**1**) (Scheme 1). The esterification of **1** in ethanol mediated by thionyl chloride[14] afforded ethyl 3-amino-4-methylbenzoate (**2**) quantitatively. The conversion of **2** into ethyl indazole-6-carboxylate (**3**) was performed using the Jacobson procedure[15] by reaction of **2** with potassium acetate, acetic anhydride, and isopentyl nitrite in refluxing toluene to give ethyl 1-acetylindazole-6-carboxylate, which was deprotected with HCl, affording **3** in 64% yield.

The formation of the indazolyl ring was demonstrated by $^1$H NMR where the NH proton resonates with a characteristic signal at $\delta$ = 11 ppm. Reaction of **3** at 180 °C for 5 h with potassium borohydride gave the triester-functionalized $KTp^{4Bo,6\text{-}COOEt}$ in 68% yield after purification by repetitive trituration with hot toluene and sublimation of the unreacted ethyl indazole-6-carboxylate. It is noteworthy that by conducting the reaction at 150 °C instead of 180 °C, the bis(indazolyl)borate was mainly obtained. As known from the literature,[16] the signal of the BH proton is very broad and difficult to find but very informative to differentiate the

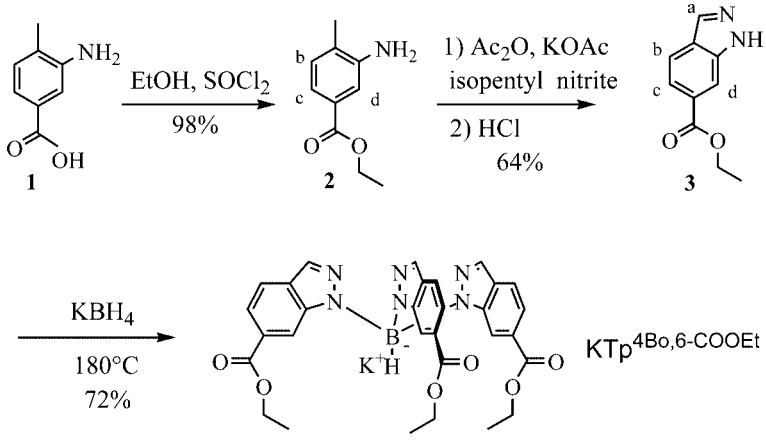


Scheme 1. Synthesis of potassium hydrotris[6-(ethoxycarbonyl)indazol-1-yl]borate.

 © 2006 Wiley-VCH Verlag GmbH & Co. KGaA, Weinheim 

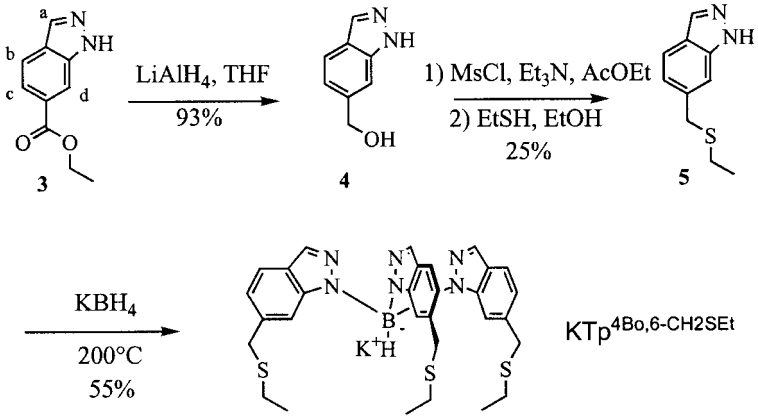


Scheme 2. Synthesis of potassium hydrotris{6-[(ethylsulfanyl)methyl]indazol-1-yl}borate.

bis (signal near 3.5 ppm) and tris ($\delta$ = 5 ppm) indazolylborates.

Concerning the regiochemistry of the reaction, Trofimenko has shown on the hydrotris(indazol-1-yl)borate ligand[10] that the interplay of steric and electronic factors tilts in favor of the latter, giving a product that is sterically hindered around the boron atom but not on the coordination side. Similarly, we obtained exclusively the product resulting from the fusion of the benzo ring at the 4–5-position (giving the $Tp^{4Bo}$ product) in which the boron atom is bound to the more hindered nitrogen atom and no trace of the 3–4 fusion product ($Tp^{3Bo}$). This regiospecificity is maintained with ester groups at the 6-position of the indazole, as confirmed by the X-ray structure of the ruthenium complex.

The synthesis of 6-[(ethylsulfanyl)methyl]indazole (**5**) was achieved in two steps from **3** (Scheme 2). Reduction of the ethyl ester function using $LiAlH_4$ gave 6-(hydroxymethyl)-indazole (**4**) with a very good yield. Mesylation of the alcohol followed by reaction with thioethanol allowed the thioether-substituted indazole **5** to be obtained in a one-pot procedure. The same procedure used to obtain $KTp^{4Bo,6\text{-}COOEt}$ was applied to **5**, yielding potassium hydrotris{6-[(ethylsulfanyl)methyl]indazol-1-yl}borate ($KTp^{4Bo,6\text{-}CH2SEt}$).

### Complex Formation and Characterization

The coordination chemistry of the two ligands was consistent with the absence of steric hindrance on the metal coordination face. Complexation of $KTp^{4Bo}$, $KTp^{4Bo,6\text{-}COOEt}$, and $KTp^{4Bo,6\text{-}CH2SEt}$ with $[RuCp(CH_3CN)_3]PF_6$ was performed by heating the scorpionate ligand with 1 equiv. of ruthenium complex in anhydrous and degassed acetonitrile. The $\eta^5$-cyclopentadienylruthenium(II) complexes of each tripodal ligand were obtained; $\eta^5$-cyclopentadienyl(hydrotris{6-[(ethylsulfanyl)methyl]indazol-1-yl}borato)ruthenium(II) ($RuCpTp^{4Bo,6\text{-}CH2SEt}$) and $\eta^5$-cyclopentadienyl(hydrotris[6-(ethoxycarbonyl)indazol-1-yl]-borato)ruthenium(II) ($RuCpTp^{4Bo,6\text{-}COOEt}$) were obtained with a lower yield compared to the complex formed with the unfunctionalized ligand. For solubility reasons, the synthesis of $RuCpTp^{4Bo,6\text{-}COOEt}$ required the use of anhydrous DMF as cosolvent. The three complexes were fully characterized.

The cyclic voltammogram of the unfunctionalized complex exhibits a reversible metal-centered oxidation at 0.49 V/SCE, that is 100 mV higher than the pyrazolyl analog in the same conditions (Table 1). This shows that ruthenium(II) is more stabilized in $RuCpTp^{4Bo}$ than in its pyrazolyl analog synthesized by Mann et al.,[17] which can be explained by the more pronounced $\pi$-acceptor character of the hydrotris(indazolyl)borate compared to its pyrazolyl analog. In the ruthenium complex $RuCpTp^{4Bo,6\text{-}COOEt}$, which incorporates the triester-functionalized ligand, oxidation occurs at a higher potential: 0.63 V/SCE, the ethoxycarbonyl electron-withdrawing groups stabilizing the ruthenium(II) state further. The ester substituents decrease the $\sigma$-donor character and increase the $\pi$-acceptor character of the scorpionate ligand. The combination of this low $\sigma$-donor character and solubility problems could explain the moderate yield of the coordination step. The coordinating nitrogen of the ester-functionalized scorpionate ligand being less donor than its unfunctionalized analog, is thus less efficient in the displacement of the acetonitrile ligands of the ruthenium precursor. In the ruthenium complex $RuCpTp^{4Bo,6\text{-}CH2SEt}$, which incorporates the thioether functions, oxidation occurs at a slightly lower potential of 0.48 V/SCE, the slightly electron-donating (ethylsulfanyl)-methyl groups destabilizing the ruthenium(II) state.

Table 1. Cyclic voltammetry data.[a]

| Compound | $E_{1/2}$(ox) $Ru^{II}$–$Ru^{III}$ (V/SCE)[b] |
|---|---|
| $RuCpTp^{4Bo,6\text{-}COOEt}$ | 0.63 |
| $RuCpTp^{4Bo}$ | 0.49 |
| $RuCpTp^{4Bo,6\text{-}CH2SEt}$ | 0.48 |
| RuCpTp | 0.39[c] |

[a] Cyclic voltammograms were carried out at a scan rate of 100 mV $s^{-1}$ in acetonitrile containing 0.1 M $Bu_4NPF_6$ as supporting electrolyte. Potentials were measured vs SCE using a Pt working electrode. [b] All couples are reversible. [c] Obtained from ref.[17]

 © 2006 Wiley-VCH Verlag GmbH & Co. KGaA, Weinheim 

Variable temperature $^1$H NMR experiments have shown that the rotation of the Cp ligand in the complexes is fast compared to the NMR timescale down to at least –90 °C in deuterated dichloromethane, indicating that the coordination site is not sterically affected by the ethoxycarbonyl or (ethylsulfanyl)methyl substituents.

### Crystal Structures of the Complexes

Crystals suitable for X-ray diffraction were grown by the slow diffusion of methanol over a dichloromethane solution of the complex. The ORTEP representations with atom numbering are shown in Figure 2, while selected bond lengths and angles are listed in Table 2.

$RuCpTp^{4Bo,6\text{-}COOEt}$ and $RuCpTp^{4Bo}$ crystallized in the *Pccn* space group while $RuCpTp^{4Bo,6\text{-}CH2SEt}$ crystallized in the $P\bar{1}$ group. The triester-functionalized complex cocrystallized with molecules of methanol (0.5 equiv. per ruthenium complex), which are located on a symmetry axis and are highly disordered. In line with the $^1$H NMR spectroscopic data, the three complexes have a piano stool shape where the scorpionate ligand binds the ruthenium center in a facial tripodal mode (i.e. $\kappa^3$-*N*,*N*′,*N*′′), as shown by Trofimenko for scorpionate complexes. The crystal structure of complexes with the triester- and (ethylsulfanyl)-methyl-functionalized ligands confirmed the regiochemistry of the scorpionate formation, which is the expected $Tp^{4Bo}$ isomer. Moreover, the functional groups at the 6-position of indazole are well oriented, pointing in the opposite direction of the coordination site, which is thus free of any steric hindrance as seen in solution by a variable temperature $^1$H NMR experiment. The lack of interference between the coordination site and the attaching groups suggests that this molecule can be expected to be truly bifunctional, acting both as ligand and anchor to fix metal complexes onto a surface.

Table 2. Selected bond lengths [Å] and angles [°] in the ruthenium complexes.[a]

| | $RuCpTp^{4Bo}$ | $RuCpTp^{4Bo,6\text{-}COOEt}$ | $RuCpTp^{4Bo,6\text{-}CH2SEt}$ |
|---|---|---|---|
| Ru–N(1) | 2.141(8) | 2.113(4) | 2.128(5) |
| Ru–N(3) | 2.108(7) | 2.129(4) | 2.126(5) |
| Ru–N(5) | 2.099(7) | 2.103(4) | 2.120(5) |
| Ru–C(22) | 2.141(10) | 2.166(5) | 2.140(6) |
| Ru–C(23) | 2.156(11) | 2.152(5) | 2.160(6) |
| Ru–C(24) | 2.166(11) | 2.148(5) | 2.159(5) |
| Ru–C(25) | 2.145(11) | 2.162(5) | 2.154(5) |
| Ru–C(26) | 2.131(11) | 2.161(5) | 2.147(6) |
| N(1)–Ru–N(3) | 84.4(3) | 83.46(14) | 83.55(18) |
| N(3)–Ru–N(5) | 84.2(3) | 84.97(14) | 85.87(17) |
| N(5)–Ru–N(1) | 85.6(3) | 86.46(14) | 84.01(17) |
| N(2)–B–N(4) | 108.3(8) | 107.3(4) | 107.5(4) |
| N(4)–B–N(6) | 110.2(7) | 108.4(4) | 108.3(4) |
| N(6)–B–N(2) | 106.8(7) | 108.9(4) | 108.5(4) |

[a] Numbers in parentheses are estimated standard deviations.

It must be noted that these complexes combine a $C_5$-symmetry cyclopentadienyl ligand and a $C_3$-symmetry tripodal ligand, and as a result, have a low symmetry. In order to facilitate the discussion and by analogy with ethane, two

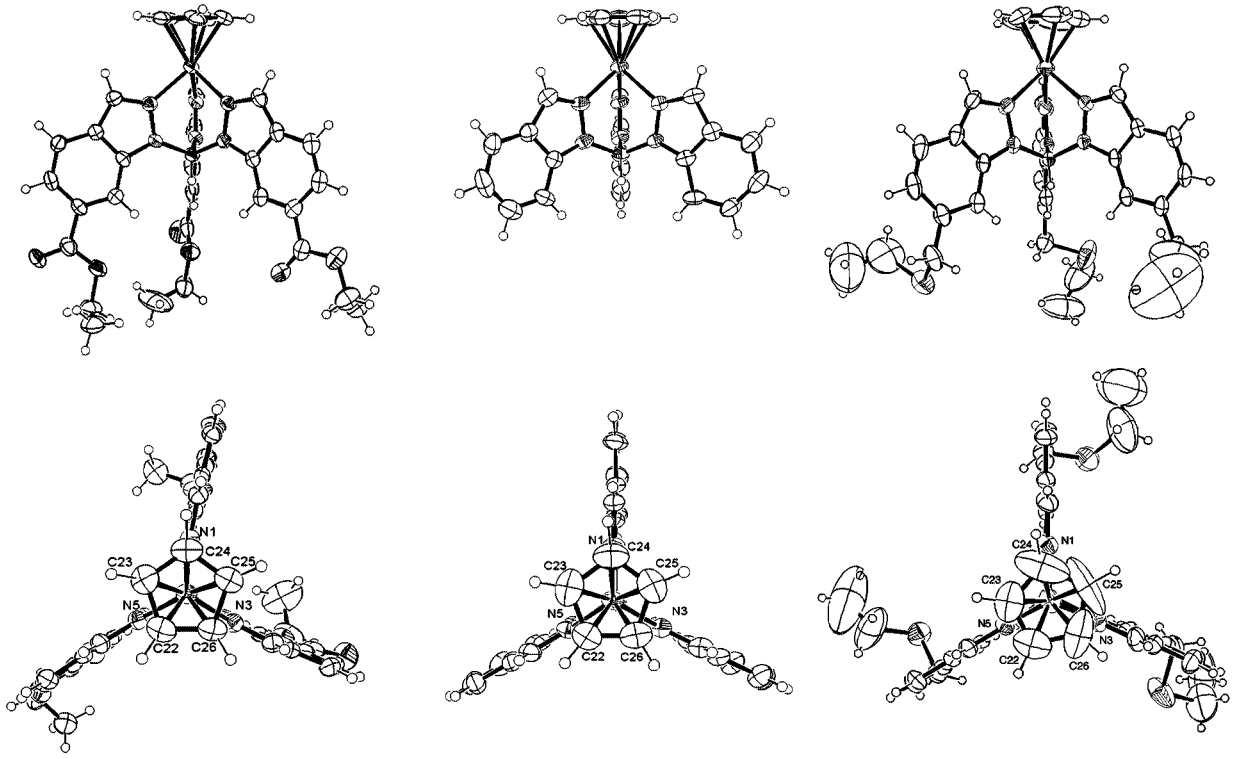


Figure 2. Thermal ellipsoid diagram of ($RuCpTp^{4Bo,6\text{-}COOEt}$) (left), ($RuCpTp^{4Bo}$) (center), and ($RuCpTp^{4Bo,6\text{-}CH2SEt}$) (right), side view (top) and top view (bottom). The ellipsoids are drawn at the 50% probability level and the molecules of cocrystallizing solvent (MeOH) have been removed for clarity.

 © 2006 Wiley-VCH Verlag GmbH & Co. KGaA, Weinheim 

significant conformations can be defined (Figure 3). The first one can be considered as an eclipsed conformation in which one of the dihedral angles between a CH bond of the cyclopentadienyl ligand and one indazole of the scorpionate ligand is 0°. In the second one, the staggered conformation, two of these dihedral angles are equal to 12°. Because of the symmetry of each ligand, a rotation of 24° is invariant. A 12° rotation of one ligand with respect to the other allows the interconversion between staggered and eclipsed conformations.

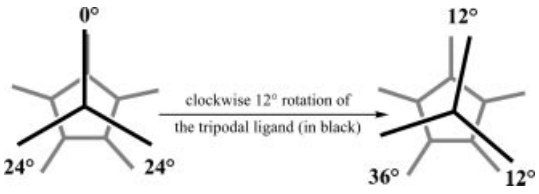


Figure 3. Eclipsed (left) and staggered (right) conformations of a complex containing both $C_3$- and $C_5$-symmetry ligands. Interconversion occurs upon a 12° rotation. For symmetry reasons, the staggered conformation appears every 24°.

On purely steric grounds, the staggered conformer is expected to be the most stable, as obtained in the case of the pyrazolyl analog RuCpTp.[15] On the contrary, RuCpTp$^{4Bo}$ adopts an almost eclipsed conformation in the solid state, with a dihedral angle between the C(24)–H(24) bond and the plane of the N(1)-containing indazole equal to 0.3° (Figure 2, bottom view). An explanation for a favored eclipsed conformation must be found in the crystal packing and in the intermolecular forces involved in the solid state. A careful examination of the crystal packing of the unfunctionalized and both functionalized complexes showed π-stacking interactions between the two indazoles of neighboring complexes. As shown for the unfunctionalized complex in Figure 4, the two indazoles face each other in a head-to-tail mode, the electron-rich part of one indazole being exactly above the electron-poor part of the other indazole, which provides further stabilization by donor–acceptor interactions. The distance between the planes of two consecutive indazoles is ideal for stacking: 3.62 Å for the triester complex, 3.59 Å for the tris (ethylsulfanyl)methyl complex, and 3.56 Å for the unfunctionalized complex.

Moreover, average Ru–C distances of 2.15 Å (for cyclopentadienyl) and Ru–N bond lengths of 2.11 Å (for trisindazolylborate) are found in the three complexes, showing that the coordination of the tripodal ligand is not influenced by the presence of the functional groups at the 6-position of the indazole rings. The moderate reactivity of the triester-functionalized ligand towards complexation with $[RuCp(CH_3CN)_3]PF_6$ is thus justified purely by electronic considerations, while steric hindrance due to the ester groups can be ruled out.

## Conclusions

In summary, we have described the preparation and coordination of two new tripodal ligands that bear functional groups suitable for surface deposition. The orientation of the three anchoring groups, as shown by the X-ray structures, seems to be ideal for surface deposition of organometallic complexes. Work is underway to anchor these complexes on surfaces and integrate the triester-functionalized ligand into molecular machines such as a molecular rotary motor[7] designed to be studied as a single molecule deposited on an oxide surface.

## Experimental Section

All commercially available chemicals were of reagent grade and were used without further purification. $[RuCp(CH_3CN)_3]PF_6$ was purchased from Strem. Potassium hydrotris(indazol-1-yl)borate ($KTp^{4Bo}$) was prepared according to a literature procedure.[10] NMR spectra were recorded with Bruker AM 250 or Avance 500 spectrometers and full assignments were made using COSY, ROESY, HMBC, and HMQC methods when necessary. The numbering scheme for the indazol derivatives is given in molecule **3** (see Scheme 1 and Scheme 2). Chemical shifts are defined with respect to TMS = 0 ppm for $^1H$ and $^{13}C$ NMR spectra and were measured relative to residual solvent peaks. UV/Vis spectra were recorded with a Shimadzu UV-3100 spectrometer. FAB and DCI mass spectrometry was performed using a Nermag R10–10. The melting points were measured on a Kofler Reichert apparatus and are not corrected.

**Ethyl 3-Amino-4-methylbenzoate (2):** 3-Amino-4-methylbenzoic acid (**1**) (2.00 g, 13.3 mmol, 1 equiv.) was dissolved in absolute eth-

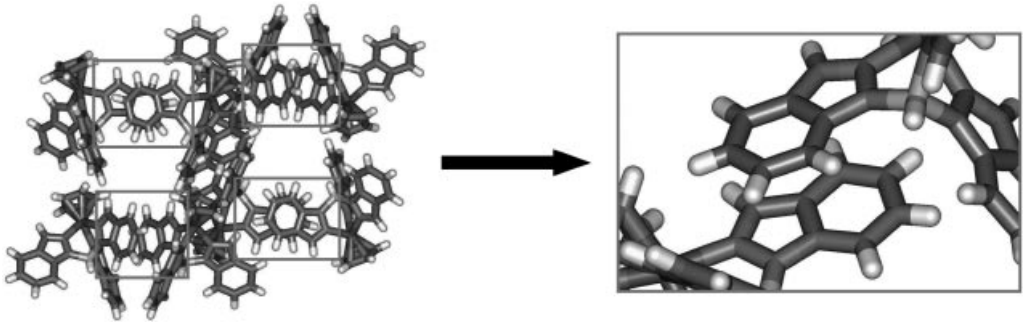

Figure 4. Stabilization in the crystal structure of RuCpTp$^{4Bo}$ by π-stacking interactions between neighboring indazolyl pairs. Zooming in shows the donor–acceptor interactions between two indazolyl groups positioned in a head-to-tail arrangement with an interplane distance of 3.56 Å.

 © 2006 Wiley-VCH Verlag GmbH & Co. KGaA, Weinheim 

anol (50 mL). Thionyl chloride (2 mL, 27.4 mmol, 2 equiv.) was added dropwise and the reaction mixture was heated at reflux overnight, during which the color of the solution turned from purple to pink. Ethanol was removed under reduced pressure, and the residual oil was dissolved in ethyl acetate (50 mL) and washed with a saturated sodium carbonate solution (3 × 20 mL). The combined aqueous phases were extracted with ethyl acetate (20 mL). Then the combined organic phases were dried with $MgSO_4$ and the solvent removed under reduced pressure to afford ethyl 3-amino-4-methylbenzoate (**2**) (2.33 g, 13.0 mmol, 98%) as a pink oil which was used without further purification. DCI-MS ($NH_3$): *m*/*z* (%) = 180 [M + H]$^+$, 197 [M + $NH_4$]$^+$. $^1$H NMR (250 MHz, $CDCl_3$): $\delta$ = 7.26–7.30 (m, 2 H, H$^{c-d}$), 6.92 (d, $^3J$ = 7.8 Hz, 1 H, H$^b$), 4.31 (q, $^3J$ = 6.9 Hz, 2 H, C$H_2$CH$_3$), 3.91 (broad s, 2 H, $NH_2$), 2.00 (s, 3 H, Me), 1.21 (t, $^3J$ = 6.9 Hz, 3 H, CH$_2$C$H_3$) ppm.

**Ethyl 1*H*-Indazole-6-carboxylate (3):** In a three-necked round-bottomed flask, ethyl 3-amino-4-methylbenzoate (**2**) (2.30 g, 12.8 mmol, 1 equiv.), potassium acetate (1.3 g, 13.2 mmol, 1.1 equiv.), and acetic anhydride (4.4 mL, 47 mmol, 3.6 equiv.) were suspended in toluene (50 mL). Isopentyl nitrite (3.6 mL, 24.6 mmol, 2.1 equiv.) was added dropwise to this suspension over a 15-min period. The gelatinous mixture was heated at reflux overnight giving an orange solution, which was evaporated to dryness. HCl (5 M, 10 mL) and concentrated HCl (5 mL) were added and the red solution was heated at 50 °C for 1 h followed by 10 min at 60 °C. After cooling down, the acid layer was extracted twice with toluene (20 mL) to remove neutral compounds. The red combined organic phases were washed three times with concentrated HCl. The acid phase was then carefully neutralized with ammonia, causing precipitation of the compound. After filtration, the product was dissolved in dichloromethane then dried with $MgSO_4$ and the solvent removed under reduced pressure to afford **3** (1.56 g, 8.2 mmol, 64%) as a brown solid. The product can be sublimed (0.1 Torr, 160 °C) or used without further purification. DCI-MS ($NH_3$): *m*/*z* (%) = 191 [M + H]$^+$. High resolution LSI calculated [M + H]$^+$: 191.0821 ($C_{10}H_{11}N_2O_2$); found: 191.0827 (100% [M + H]$^+$). M.p. 125 °C. $^1$H NMR (250 MHz, $CDCl_3$): $\delta$ = 11.15 (s, 1 H, NH), 8.27 (d, $^4J$ = 1 Hz, 1 H, H$^a$), 8.14 (s, 1 H, H$^d$), 7.88–7.77 (m, 2 H, H$^{b-c}$), 4.42 (q, 2 H, $^3J$ = 7.0 Hz, C$H_2$CH$_3$), 1.44 (t, 3 H, $^3J$ = 7.2 Hz, CH$_2$C$H_3$) ppm. $^{13}$C NMR (63 MHz, $CDCl_3$): $\delta$ = 166.8 (CO), 139.5, 135.0 (C$^a$), 129.0, 125.7, 121.6 (C$^c$), 120.7 (C$^b$), 112.1 (C$^d$), 61.3 ($CH_2$), 14.4 ($CH_3$) ppm. $C_{10}H_{10}N_2O_2$: calcd. C 63.2, H 5.30, N 14.7; found: C 62.8, H 5.11, N 14.5.

**Potassium Hydrotris[6-(ethoxycarbonyl)indazol-1-yl]borate (KTp$^{4Bo,6-COOEt}$):** Ethyl indazole-6-carboxylate (**3**) (700 mg, 3.68 mmol, 3.5 equiv.) and potassium borohydride (56 mg, 1.05 mmol, 1 equiv.) were ground up in a mortar then dried under vacuum and the vessel was filled with argon. The mixture was heated in a sand bath at 180 °C until the gas evolution had ceased (5–6 h). The reaction was then quenched by addition of toluene. The solid was filtered off and purified by trituration with hot toluene, which dissolved the unreacted **3**. After drying under vacuum, the solid was ground in a mortar and any remaining unreacted indazole was removed by sublimation, by heating the sample at 160 °C under vacuum. By repeating alternating trituration and sublimation, potassium hydrotris[6-(ethoxycarbonyl)indazol-1-yl]borate (KTp$^{4Bo,6-COOEt}$) (440 mg, 0.712 mmol, 68%) was obtained as a pale yellow solid. FAB-MS (MeOH, Gly-Thio, negative mode): *m*/*z* (%) = 579 [M – K]$^-$. High resolution LSI calculated [M – K]$^-$: 578.2085 ($C_{30}H_{27}BN_6O_6$); found: 578.2099 (100% [M – K]$^-$). $^1$H NMR (250 MHz, [D$_6$]DMSO): $\delta$ = 8.20 (s, 3 H, H$_a$), 8.15 (d, $^4J$ = 1 Hz, 3 H, H$^d$), 7.81 (d, $^3J$ = 8.5 Hz, 3 H, H$^c$), 7.59 (dd, $^3J$ = 8.5 Hz, $^4J$ = 1 Hz, 3 H, H$^b$), 4.33 (q, $^3J$ = 7 Hz, 6 H, C$H_2$CH$_3$), 1.34 (t, $^3J$ = 7 Hz, 9 H, CH$_2$C$H_3$) ppm. $^{13}$C NMR (63 MHz, [D$_6$]-DMSO): $\delta$ = 166.3 (CO), 144.3, 133.0 (C$^a$), 126.3, 123.2, 120.6 (C$^c$), 120.3 (C$^b$), 112.7 (C$_d$), 61.0 ($CH_2$), 14.3 ($CH_3$).

**$\eta^5$-Cyclopentadienyl(hydrotris[6-(ethoxycarbonyl)indazol-1-yl]borato)ruthenium(II) (RuCpTp$^{4Bo,6-COOEt}$):** Potassium hydrotris[6-(ethoxycarbonyl)indazol-1-yl]borate (KTp$^{4Bo,6-COOEt}$) (62 mg, 0.1 mmol, 1 equiv.) was dissolved in dry DMF (2 mL), dry acetonitrile was added (20 mL), and the mixture was purged with argon. [RuCp(CH$_3$CN)$_3$]PF$_6$ (43 mg, 0.1 mmol, 1 equiv.) was added to this solution, which was then refluxed overnight. Evaporation of the solvent followed by a purification by column chromatography ($SiO_2$: cyclohexane/ethanol 0–20%) afforded $\eta^5$-cyclopentadienyl-[hydrotris[6-(ethoxycarbonyl)indazol-1-yl]borato]ruthenium(II) (RuCpTp$^{4Bo,6-COOEt}$) (39 mg, 0.052 mmol, 52%) as a yellow solid. DCI-MS ($NH_3$): 747 [M + H]$^+$, 764 [M + $NH_4$]$^+$. High resolution LSI calculated [M + H]$^+$: 747.1676 ($C_{35}H_{34}BN_6O_6Ru$); found: 747.1700 (100% [M + H]$^+$). M.p. 212 °C dec. $^1$H NMR (250 MHz, $CD_2Cl_2$): $\delta$ = 8.66 (d, $^4J$ = 0.9 Hz, 3 H, H$^a$), 8.62 (d, $^4J$ = 1.2 Hz, 3 H, H$^d$), 7.69 (dd, $^3J$ = 8.5 Hz, $^4J$ = 1.2 Hz, 3 H, H$^c$), 7.62 (dd, $^3J$ = 8.5 Hz, $^4J$ = 0.9 Hz, 3 H, H$^b$), 4.63 (s, 5 H, Cp), 4.42 (q, $^3J$ = 7 Hz, 6 H, C$H_2$CH$_3$), 1.43 (t, $^3J$ = 7.2 Hz, 9 H, CH$_2$C$H_3$) ppm. $^{13}$C NMR (63 MHz, $CD_2Cl_2$): $\delta$ = 167.6 (CO), 143.1, 140.2 (C$^a$), 129.2, 126.8, 122.0 (C$^c$), 119.7 (C$^b$), 114.6 (C$^d$), 72.8 (Cp), 62.0 ($CH_2$), 15.0 ($CH_3$) ppm. $E_{Ru^{II}:Ru^{III}}$ (V/SCE): +0.63 rev (sweep rate: 100 mV s$^{-1}$). UV/Vis ($CH_2Cl_2$): $\lambda_{max}$ ($\varepsilon$ in L mol$^{-1}$ cm$^{-1}$) = 222 (60300), 256 (14000), 334 (12800), 418 nm (6900).

**$\eta^5$-Cyclopentadienyl[hydrotris(indazol-1-yl)borato]ruthenium(II) (RuCpTp$^{4Bo}$):** A solution of potassium hydrotris(indazol-1-yl)borate (KTp$^{4Bo}$) (81 mg, 0.2 mmol, 1 equiv.) in acetonitrile (20 mL) was purged with argon and [RuCp(CH$_3$CN)$_3$]PF$_6$ (87 mg, 0.2 mmol, 1 equiv.) was added. The solution was refluxed for 1.5 h. The solution, initially yellow, turned to orange-brown. Upon cooling to room temperature, an orange precipitate appeared. Recrystallization from chloroform/methanol gave pure RuCpTp$^{4Bo}$ (70 mg, 0.132 mmol, 65%) as an orange microcrystalline product. DCI-MS ($NH_3$): *m*/*z* (%) = 548 [M + $NH_4$]$^+$, 531 [M + H]$^+$. High resolution LSI calculated [M + H]$^+$: 531.1042 ($C_{26}H_{22}BN_6Ru$); found: 531.1061 (100% [M + H]$^+$). M.p. 222 °C dec. $^1$H NMR (250 MHz, $CDCl_3$): $\delta$ = 8.61 (s, 3 H, H$_a$), 7.90 (d, $^3J$ = 8.75 Hz, 3 H, H$^b$), 7.6 (d, $^3J$ = 7.25 Hz, 3 H, H$_d$), 7.32 (t, $^3J$ = 7.25 Hz, 3 H, H$^c$), 7.05 (t, $^3J$ = 7.25 Hz, 3 H, H$^6$), 4.56 (s, 5 H, Cp) ppm. $^{13}$C NMR (63 MHz, $CDCl_3$): $\delta$ = 138.9 (C$^a$), 125.9, 123.7, 120.5 (C$^c$), 119.2 (C$^b$), 111.5 (C$^d$), 70.7 (Cp) ppm. UV/Vis ($CH_2Cl_2$): $\lambda_{max}$ ($\varepsilon$ in L mol$^{-1}$ cm$^{-1}$) = 231 (21400), 298 (15000), 307 (12200), 325 (9700), 388 nm (4600). CV ($CH_3CN$, $Bu_4NPF_6$) $E_{Ru^{II}:Ru^{III}}$ (V/SCE): +0.49 rev (sweep rate: 100 mV s$^{-1}$).

**6-(Hydroxymethyl)-1*H*-indazole (4):** $LiAlH_4$ (1.6 g, 42.5 mmol, 4 equiv.) was added carefully in portions to a solution of **3** (2 g, 10.5 mmol, 1 equiv.) in freshly distilled THF (100 mL) at 0 °C. After 2 h of vigorous stirring, TLC analysis showed a complete disappearance of the starting material and the presence of a single product. The reaction mixture was carefully quenched with water (1.6 mL) followed by a 15% NaOH solution (1.6 mL) and then water (4 mL). The mixture was filtered through Celite and the filter cake was washed several times with dichloromethane. The filtrate was dried with $MgSO_4$ and the solvent was removed under reduced pressure, affording 6-(hydroxymethyl)indazole (**4**) (1.45 g, 9.8 mmol, 93%). This compound was used without further purification. ESI-MS: *m*/*z* (%) = 149 [M + H]$^+$. M.p. 159 °C. $^1$H NMR (250 MHz, [D$_6$]DMSO): $\delta$ = 12.97 (s, 1 H, NH), 8.00 (s, 1 H, H$^a$), 7.65 (d, $^3J$ = 8.4 Hz, 1 H, H$^d$), 7.46 (s, 1 H, H$^b$), 7.04 (d, $^3J$ = 8.4 Hz, 1 H, H$_c$), 5.28 (br. s, 1 H, OH), 4.61 (d, $^3J$ = 5.9 Hz, 2 H, $CH_2$).

 © 2006 Wiley-VCH Verlag GmbH & Co. KGaA, Weinheim 

**6-[(Ethylsulfanyl)methyl]-1*H*-indazole (5):** Mesyl chloride (0.65 mL, 8.4 mmol, 1 equiv.) was added dropwise to a solution of 6-(hydroxymethyl)indazole (**4**) (1.24 g, 8.4 mmol, 1 equiv.) and triethylamine (2.5 mL) in ethyl acetate (170 mL) at 0 °C. The mixture was stirred at room temperature for 12 h, the organic phase was washed three times with water (50 mL), and the combined aqueous phases were extracted once with ethyl acetate. The combined organic phases were dried with $MgSO_4$ and the solvent removed under reduced pressure, giving a pale yellow solid that was used without purification in the next step. The mesylate yellow solid was dissolved in dry THF (75 mL) and added dropwise to a solution of ethane thiol (0.62 mL, 8.4 mmol, 1 equiv.) in ethanol (75 mL) with KOH (0.7 g, 12.5 mmol, 1.5 equiv.). The solvent was removed under reduced pressure and the crude material was purified by column chromatography ($SiO_2$, cyclohexane/$Et_2O$ 40%) to give 6-[(ethylsulfanyl)methyl]indazole (**5**) (400 mg, 2.08 mmol, 25%) as a white solid. DCI-MS ($NH_3$): *m*/*z* (%) = 193 $[M + H]^+$. High resolution LSI calculated $[M + H]^+$: 193.0799 ($C_{10}H_{13}N_2S$); found: 193.0804 (100% $[M + H]^+$). M.p. 61 °C. $^1H$ NMR (250 MHz, $CD_2Cl_2$): $\delta$ = 11.35 (s, 1 H, NH), 8.01 (s, 1 H, $H^a$), 7.68 (d, $^3J$ = 8.3 Hz, 1 H, $H^d$), 7.44 (s, 1 H, $H^b$), 7.08 (d, $^3J$ = 8.3 Hz, 1 H, $H^c$), 3.86 (s, 2 H, $CH_2$), 2.39 (q, $^3J$ = 7.3 Hz, 2 H, $CH_2CH_3$), 1.15 (t, $^3J$ = 7.3 Hz, 3 H, $CH_2CH_3$) ppm. $^{13}C$ NMR (63 MHz, $CD_2Cl_2$): $\delta$ = 140.4, 138.0 ($C^a$), 134.4, 122.7 ($C^c$), 120.8 ($C^b$), 109.6 ($C^d$), 36.3 ($CH_2S$), 25.4 ($CH_2$), 14.3 ($CH_3$) ppm. $C_{10}H_{12}N_2S$: calcd. C 62.5, H 6.29, N 14.6; found C 62.2, H 6.14, N 14.5.

**Potassium Hydrotris{6-[(ethylsulfanyl)methyl]indazol-1-yl}borate ($KTp^{4Bo,6\text{-}CH2SEt}$):** 6-[(Ethylsulfanyl)methyl]indazole (**5**) (300 mg, 1.56 mmol, 3.4 equiv.) and potassium borohydride (25 mg, 46 mmol, 1 equiv.) were ground up in a mortar, dried under vacuum and the vessel was filled with argon. The mixture was heated in a sand bath at 200 °C; 5 h were needed until the gas evolution had ceased. The solid was ground in a mortar and any remaining unreacted indazole was removed by sublimation, by heating the sample at 160 °C under vacuum. By repeating alternating trituration with toluene and sublimation, potassium hydrotris{6-[(ethylsulfanyl)methyl]indazol-1-yl}borate ($KTp^{4Bo,6\text{-}CH2SEt}$) (160 mg, 0.25 mmol, 55%) was obtained as a pale yellow sticky solid. FAB-MS (MeOH, Gly-Thio, negative mode): *m*/*z* (%) = 584 $[M - K]^-$. High resolution LSI calculated $[M - K]^-$: 584.2022 ($C_{30}H_{33}BN_6S_3$); found: 584.2042 (100% $[M - K]^-$). $^1H$ NMR (250 MHz, $[D_6]$-DMSO): 7.82 (d, $^4J$ = 1 Hz, 3 H, $H^a$), 7.52 (d, $^3J$ = 8.0 Hz, 3 H, $H^c$), 6.92 (s, 3 H, $H^d$), 6.84 (dd, $^3J$ = 8.0 Hz, $^4J$ = 1 Hz, 3 H, $H^b$), 3.57 (s, 2 H, $CH_2S$), 2.05 (q, $^3J$ = 7.4 Hz, 6 H, $CH_2CH_3$), 0.97 (t, $^3J$ = 7 Hz, 9 H, $CH_2CH_3$), 5.73 (br. s, 1 H, B*H*) ppm. $^{13}C$ NMR (63 MHz, $[D_6]$DMSO): $\delta$ = 143.8, 133.3 ($C^a$), 131.9, 121.9, 120.0 ($C^c$), 119.5 ($C^b$), 112.6 ($C^d$), 35.2 ($CH_2S$), 24.0 ($CH_2$), 14.2 ($CH_3$) ppm. $^{11}B$ NMR (160 MHz, $[D_6]$DMSO): –2.57 (s, 1 H) ppm.

**$\eta^5$-Cyclopentadienyl(hydrotris{6-[(ethylsulfanyl)methyl]indazol-1-yl}borato)ruthenium(II) ($RuCpTp^{4Bo,6\text{-}CH2SEt}$):** Potassium hydrotris{6-[(ethylsulfanyl)methyl]indazol-1-yl}borate ($KTp^{4Bo,6\text{-}CH2SEt}$) (62 mg, 0.1 mmol, 1 equiv.) was dissolved in dry acetonitrile (20 mL) and the mixture was purged with argon. $[RuCp(CH_3CN)_3]PF_6$ (43 mg, 0.1 mmol, 1 equiv.) was added to this solution and it was then refluxed for 2 h. Evaporation of the solvent followed by a purification by column chromatography ($SiO_2$: cyclohexane/dichloromethane 0–50%) afforded $\eta^5$-cyclopentadienyl(hydrotris{6-[(ethylsulfanyl)methyl]indazol-1-yl}borato)ruthenium(II) ($RuCpTp^{4Bo,6\text{-}CH2SEt}$) (10 mg, 0.013 mmol, 13%) as a yellow solid. DCI-MS ($NH_3$): 753 $[M + H]^+$. High resolution LSI calculated $[M + H]^+$: 753.1613 ($C_{35}H_{40}BN_6RuS_3$); found: 753.1637 (100% $[M + H]^+$). M.p. 206 °C dec. $^1H$ NMR (500 MHz, $CD_2Cl_2$): $\delta$ = 8.57 (s, 3 H, $H^a$), 7.78 (s, 3 H, $H^d$), 7.55 (d, 3 H, $^3J$ = 8.3 Hz, $H^b$), 7.08 (d, 3 H, $^3J$ = 8.3 Hz, $H^c$), 4.55 (s, 5 H, Cp), 3.87 (s, 6 H, $CH_2$), 2.15 (q, 6 H, $^3J$ = 7.3 Hz, $CH_2CH_3$), 1.22 (t, 9 H, $^3J$ = 7.3 Hz, $CH_2CH_3$) ppm. $^{13}C$ NMR (126 MHz, $CD_2Cl_2$): $\delta$ = 143.0, 138.9 ($C^a$), 136.9, 122.7, 122.3 ($C^c$), 119.3 ($C^b$), 111.0 ($C^d$), 70.7 (Cp), 36.4 ($CH_2S$), 25.2 ($CH_2$), 14.3 ($CH_3$) ppm. $E_{Ru^{II}:Ru^{III}}$ (V/SCE): +0.49 rev (sweep rate: 100 mV s$^{-1}$). UV/Vis ($CH_2Cl_2$): $\lambda_{max}$ ($\varepsilon$ in L mol$^{-1}$ cm$^{-1}$) = 231 (30500), 309 (14700), 327 (13500), 390 nm (6200).

**X-ray Crystallographic Study:** Crystal data for $\eta^5$-cyclopentadienyl(hydrotris[6-(ethoxycarbonyl)indazol-1-yl]borato)ruthenium(II) ($RuCpTp^{4Bo,6\text{-}COOEt}$). Orange prismatic crystals suitable for X-ray analysis were obtained by slow evaporation of a solution of the complex in a pentane/methanol (1:1) mixture. $C_{35}H_{33}BN_6O_6Ru\cdot 0.5CH_3OH$: $M_r$ = 1523.17, orthorhombic, space group *Pccn*, *a* (Å) = 22.682(6), *b* (Å) = 15.0415(13), *c* (Å) = 19.813(3), *V* (Å$^3$) = 6760(2), *Z* = 4, $\rho_{calcd.}$ = 1.497 g cm$^{-3}$, $\mu$(Mo-$K_\alpha$) (mm$^{-1}$) = 0.521. Data were collected on a Nonius-Kappa CCD diffractometer using Mo-$K_\alpha$ graphite-monochromated radiation ($\lambda$ = 0.71073 Å) at 200 K; 3983 reflections having $I > 2\sigma(I)$ were used for structure determination (4.06° < $\theta$ < 27.00°). For all computations the Bruker maXus software package was used. Final results: $R(F)$ = 0.0507, $Rw(F)$ = 0.1004, Gof = 1.032.

**Crystal Data for $\eta^5$-Cyclopentadienyl[hydrotris(indazol-1-yl)borato]-ruthenium(II) ($RuCpTp^{4Bo}$):** Orange prismatic crystals suitable for X-ray analysis were obtained by dissolution of the compound in dichloromethane and slow liquid diffusion of methanol. $C_{26}H_{21}BN_6Ru$: $M_r$ = 529.377, orthorhombic, space group *Pccn*, *a* (Å) = 13.2676(12), *b* (Å) = 18.891(2), *c* (Å) = 19.4177(13), *V* (Å$^3$) = 4866.8(7), *Z* = 8, $\rho_{calcd.}$ = 1.445 g cm$^{-3}$, $\mu$(Mo-$K_\alpha$) (mm$^{-1}$) = 0.67. Data were collected on a Nonius-Kappa CCD diffractometer using Mo-$K_\alpha$ graphite-monochromated radiation ($\lambda$ = 0.71073 Å) at 298 K; 2103 reflections having $I > 3\sigma(I)$ were used for structure determination (0° < $\theta$ < 35.00°). For all computations the Bruker maXus software package was used. Final results: $R(F)$ = 0.047, $Rw(F)$ = 0.108, Gof = 1.055.

**Crystal Data for $\eta^5$-Cyclopentadienyl(hydrotris{6-[(ethylsulfanyl)-methyl]indazol-1-yl}borato)ruthenium(II) ($RuCpTp^{4Bo,6\text{-}CH2SEt}$):** Yellow prismatic crystals suitable for X-ray analysis were obtained by dissolution of the compound in dichloromethane and slow liquid diffusion of methanol. $C_{35}H_{39}BN_6RuS_3$: $M_r$ = 751.81, triclinic, space group $P\bar{1}$, *a* (Å) = 9.883(3), *b* (Å) = 14.032(3), *c* (Å) = 14.889(4), *V* (Å$^3$) = 1802.7(7), *Z* = 2, $\rho_{calcd.}$ = 1.385 g cm$^{-3}$, $\mu$(Mo-$K_\alpha$) (mm$^{-1}$) = 0.642. Data were collected on a Nonius-Kappa CCD diffractometer using Mo-$K_\alpha$ graphite-monochromated radiation ($\lambda$ = 0.71073 Å) at 298 K; 3927 reflections having $I > 2\sigma(I)$ were used for structure determination (0° < $\theta$ < 27.00°). For all computations the Bruker maXus software package was used. Final results: $R(F)$ = 0.072, $Rw(F)$ = 0.131, Gof = 1.064.

CCDC-254040 (for $RuCpTp^{4Bo}$), -254041 (for $RuCpTp^{4Bo,6\text{-}COOEt}$), and -284359 (for $RuCpTp^{4Bo,6\text{-}CH2SEt}$) contain the supplementary crystallographic data for this paper. These data can be obtained free of charge from The Cambridge Crystallographic Data Centre via www.ccdc.cam.ac.uk/data_request/cif.

**Electrochemistry:** The voltammetric experiments were measured with an AUTOLAB PGSTAT 100 potentiostat using a Pt disc (1 mm diameter) as working electrode and a Pt counter electrode. The reference electrode used was the saturated calomel electrode (SCE). Tetra-*n*-butylammonium hexafluorophosphate ($Bu_4NPF_6$, 0.1 M) acted as the electrolyte. All solutions were degassed thoroughly for at least 15 min with argon and an inert gas blanket was maintained over the solution during the measurements.

 © 2006 Wiley-VCH Verlag GmbH & Co. KGaA, Weinheim 

## Acknowledgments

A. C. thanks the French Ministry of National Education and the Institut Universitaire de France for a Ph.D. Fellowship. T. C. thanks the European Union for an ERASMUS Fellowship. G. V. thanks the French Ministry of National Education and the Ecole Normale Supérieure of Lyon for a Ph.D. Fellowship. Drs André Gourdon and Christophe Coudret are gratefully acknowledged for useful discussions. Christine Viala is also thanked for the measurement of the NMR spectra.

[1] a) F. Moresco, *Phys. Rep.* **2004**, *399*, 175–225; b) A. Gourdon, *Eur. J. Org. Chem.* **1998**, 2797–2801.
[2] a) C. Joachim, J. K. Gimzewski, A. Aviram, *Nature* **2000**, *408*, 541–548; b) C. Joachim, J. K. Gimzewski, *Chem. Phys. Lett.* **1997**, *265*, 353–357.
[3] a) C. Joachim, J. K. Gimzewski, *Struct. Bonding (Berlin)* **2001**, *99*, 1–18; b) V. L. Popov, *Phys. Rev. E* **2003**, *68*, 026608; c) F. Moresco, G. Meyer, K.-H. Rieder, H. Tang, A. Gourdon, C. Joachim, *Phys. Rev. Lett.* **2001**, *86*, 672–675; d) G. Rapenne, *Org. Biomol. Chem.* **2005**, *3*, 1165–1169.
[4] a) J. K. Whitesell, H. K. Chang, *Science* **1993**, *261*, 73–76; b) Q. Li, A. V. Rukavishnikov, P. A. Petukhov, T. O. Zaikova, C. Jin, J. F. W. Keana, *J. Org. Chem.* **2003**, *68*, 4862–4869; c) E. Galoppini, W. Guo, W. Zhang, P. G. Hoertz, P. Qu, G. J. Meyer, *J. Am. Chem. Soc.* **2002**, *124*, 7801–7811; d) E. Galoppini, *Coord. Chem. Rev.* **2004**, *248*, 1283–1297; e) Q. Li, C. Jin, P. A. Petukhov, A. V. Rukavishnikov, T. O. Zaikova, A. Phadke, D. H. LaMunyon, M. D. Lee, J. F. W. Keana, *J. Org. Chem.* **2004**, *69*, 1010–1019.
[5] a) A. V. Rukavishnikov, A. Phadke, M. D. Lee, D. H. LaMunyon, P. A. Petukhov, J. F. W. Keana, *Tetrahedron Lett.* **1999**, *40*, 6353–6356; b) Y. Yao, J. M. Tour, *J. Org. Chem.* **1999**, *64*, 1968–1971; c) W. Guo, E. Galoppini, G. Rydja, G. Pardi, *Tetrahedron Lett.* **2000**, *41*, 7419–7421; d) D. Hirayama, K. Takimiya, Y. Aso, T. Otsobu, T. Hasobe, H. Yamada, H. Imahori, S. Fukuzumi, Y. Sakata, *J. Am. Chem. Soc.* **2002**, *124*, 532–533; e) Q. Li, A. V. Rukavishnikov, P. A. Petukhov, T. O. Zaikova, J. F. W. Keana, *Org. Lett.* **2002**, *4*, 3631–3634.
[6] a) J. Vacek, J. Michl, *New J. Chem.* **1997**, *21*, 1259–1268; b) M. C. Hersam, N. P. Guisinger, J. W. Lyding, *Nanotechnology* **2000**, *11*, 70–76; c) R. Yasuda, H. Noji, K. Kinosita, M. Yoshida, *Cell* **1998**, *93*, 1117–1124; d) R. Yasuda, H. Noji, K. Kinosita, H. Itoh, *Nature* **2001**, *410*, 898–904; e) H. Jian, J. M. Tour, *J. Org. Chem.* **2003**, *68*, 5091–5103.
[7] A. Carella, G. Rapenne, J.-P. Launay, *New J. Chem.* **2005**, *29*, 288–290.
[8] a) S. Trofimenko, *J. Am. Chem. Soc.* **1966**, *88*, 1842–1844; b) S. Trofimenko, *J. Am. Chem. Soc.* **1967**, *89*, 6288–6294.
[9] a) S. Trofimenko, *Scorpionates – Polypyrazolylborate Ligands and Their Coordination Chemistry*, Imperial College Press, London, **1999**; b) S. Trofimenko, *Chem. Rev.* **1993**, *93*, 943–980; c) A. Shaver, in *Comprehensive Coordination Chemistry* (Eds.: G. Wilkinson, R. D. Gillard, J. McCleverty), Pergamon, Oxford, **1987**, vol. 13, pp. 245–259; d) C. Pettinari, C. Santini, in: *Comprehensive Coordination Chemistry II* (Ed.: A. B. P. Lever), Elsevier, Amsterdam, **2003**, vol. 1, pp. 159–210; e) D. L. Reger, *Coord. Chem. Rev.* **1996**, *147*, 571–595; f) G. Parkin, *Adv. Inorg. Chem.* **1995**, *42*, 291–393; g) M. Etienne, *Coord. Chem. Rev.* **1996**, *156*, 201–236; h) P. K. Byers, A. J. Canty, R. T. Honeyman, *Adv. Organomet. Chem.* **1992**, *34*, 1–65.
[10] a) A. L. Rheingold, G. P. A. Yap, S. Trofimenko, *Inorg. Chem.* **1995**, *34*, 759–760; b) A. L. Rheingold, B. S. Haggerty, G. P. A. Yap, S. Trofimenko, *Inorg. Chem.* **1997**, *36*, 5097–5103; c) C. Janiak, S. Temizdemir, S. Dechert, *Inorg. Chem. Commun.* **2000**, *3*, 271–275.
[11] a) K. Kalyanasundaram, M. Grätzel, *Coord. Chem. Rev.* **1998**, *177*, 347–414; b) E. Galoppini, W. Guo, P. Qu, G. J. Meyer, *J. Am. Chem. Soc.* **2001**, *123*, 4342–4343; c) P. G. Hoertz, R. A. Carlisle, G. J. Meyer, D. Wang, P. Piotrowiak, E. Galoppini, *Nano Lett.* **2003**, *3*, 325–330.
[12] a) J. M. Tour, L. Jones, D. L. Pearson, J. J. S. Lamba, T. P. Burgin, G. M. Whitesides, D. L. Allara, A. N. Parikh, S. Atre, *J. Am. Chem. Soc.* **1995**, *117*, 9529–9534; b) D. T. Gryko, C. Clausen, J. S. Lindsey, *J. Org. Chem.* **1999**, *64*, 8635–8647.
[13] a) E. B. Troughton, C. D. Bain, G. M. Whitesides, R. G. Nuzo, D. L. Allara, M. D. Porter, *Langmuir* **1988**, *4*, 365–385; b) J. Noh, T. Murase, K. Nakajima, H. Lee, M. Hara, *J. Phys. Chem. B* **2000**, *104*, 7411–7416; c) K. W. Kittredge, M. A. Minton, M. A. Fox, J. K. Whitesell, *Helv. Chim. Acta* **2002**, *85*, 788–798; d) K. Furukawa, K. Ebata, H. Nakashima, Y. Kashimura, K. Torimitsu, *Macromolecules* **2003**, *36*, 9–11.
[14] B. D. Hosangadi, R. H. Dave, *Tetrahedron Lett.* **1996**, *37*, 6375–6378.
[15] a) C. Ruechardt, V. Hassmann, *Synthesis* **1972**, 375–376; b) D. G. Batt, J. J. Petraitis, G. C. Houghton, D. P. Modi, G. A. Cain, M. H. Corjay, S. A. Mousa, P. J. Bouchard, M. S. Forsythe, P. P. Harlow, F. A. Barbera, S. M. Spitz, R. R. Wexler, P. K. Jadhav, *J. Med. Chem.* **2000**, *43*, 41–58.
[16] C. Lopez, R. M. Claramunt, D. Sanz, C. F. Foces, F. H. Cano, R. Faure, E. Cayon, J. Elguero, *Inorg. Chim. Acta* **1990**, *176*, 195–204.
[17] A. N. McNair, D. C. Boyd, K. R. Mann, *Organometallics* **1986**, *5*, 303–310.

Received: September 23, 2005
Published Online: January 16, 2006

 © 2006 Wiley-VCH Verlag GmbH & Co. KGaA, Weinheim 

DOI: 10.1002/ejic.200500887

# A Cyclic Fc–Histidine Conjugate: Synthesis and Properties – Interactions with Alkali Metal Ions

**Somenath Chowdhury,[a] Gabriele Schatte,[b] and Heinz-Bernhard Kraatz*[a]**

**Keywords:** Ferrocene / Ferrocenophane / Peptide / Bioinorganic chemistry

The synthesis of the novel $N,N^{\pi}$-(ferrocenophane-1,1′-diyldicarbonyl)-bridged histidine methyl ester **1** and of the acyclic bis(histidine methyl ester) derivative **3** are reported. The structure of **1** was studied in the solid state and in solution. The single-crystal structure of **1** shows that both proximal ferrocenyl (Fc) carbonyl groups are *syn* with respect to each other, which is a new structural motif for Fc–amino acid conjugates. This new *syn* conformation allows effective binding to alkali metal cations. Binding is evaluated by cyclic voltammetry monitoring the halfwave potential of the Fc group. Cation binding causes a shift to lower potential ($Na^+ > Li^+ > K^+$, $Cs^+$). Upon binding, compound **1** shows selectivity towards $Na^+$ ions.

(© Wiley-VCH Verlag GmbH & Co. KGaA, 69451 Weinheim, Germany, 2006)

## Introduction

With the increased interest in chemical sensor technology, redox-based sensing of molecular recognition events in host–guest systems has received considerable attention in recent years.[1] Binding of the guest to a host can affect the structure of the host and/or its electronic properties, which can be detected by a suitable redox-active probe, such as ferrocene (Fc). In this regard, specifically designed macrocycles have been studied to electrochemically recognize cationic or anionic species in polar solvents and in some cases neutral molecules.[2–4] Cyclic amides, a class of natural macrocycles are well known for their biological activities as antibiotics and ion-transport regulators in membranes.[5] These properties are attributed to their capability to capture and release metal ions.[6] However, it is recognized that to achieve good artificial cyclopeptide ionophores, a decrease of the conformational freedom is beneficial and can be achieved by introducing some constraints to the cyclic skeleton.[7] Recently, Cheng and co-workers used 1,*n*′-Fc-labelled cyclopeptides to recognize alkali ions,[8] in which the metal ions are thought to bind to the amide carbonyl groups. However, no structural details were provided, although it is proposed that the binding of the ions to the 1,*n*′-dicarbonyl groups proximal to the Fc unit are largely responsible for the changes in the half-wave potential upon metal ion binding. Various studies show that in acyclic[9–10] as well as in cyclic[11] 1,*n*′-dipeptide-substituted Fc conjugates both the carbonyl groups directly attached to the Fc unit adopt an *anti* conformation. Herein, we report the synthesis, characterization and electrochemical studies of a novel histidine-containing ferrocenophane, where both Fc-carbonyl groups adopt a *syn* conformation, which generates a recognition site for metal ions. As part of this study, we compare the binding properties of this new cyclic ferrocene conjugate with its acyclic 1,1′-bis(histidine methyl ester) derivative, which is prepared as part of this study.

## Results and Discussions

The target ferrocenophane **1** was synthesized from 1,1′-ferrocenedicarboxylic acid and histidine methyl ester at very high dilutions in order to avoid oligomerization (Scheme 1). After purification by column chromatography, a reddish, crystalline solid was obtained in 38% yield.

The product was characterized by standard spectroscopic methods. The $^1$H NMR spectrum shows the presence of an amide resonance at $\delta$ = 7.57 ppm, and seven resonances in a 1:1:1:1:1:1:2 intensity ratio in the region of $\delta$ = 4.86–4.36 ppm. The α-H is observed as a multiplet at $\delta$ = 4.88 ppm. The $^{13}$C NMR spectrum reveals three signals at $\delta$ = 172.3, 172.2, and 169.5 ppm from carbonyl groups, the first of which is assigned to the ester C=O group, while the latter two are amide carbonyl groups. The IR spectrum shows the expected ester carbonyl band at 1731 cm$^{-1}$ and a strong peak at 1652 cm$^{-1}$ due to the amide group. Like most Fc–peptide derivatives, compound **1** exhibits a weak and broad absorbance in the visible region at $\lambda_{max}$ = 449 nm. This band does not show a sizeable Cotton effect in the CD spectrum (Figure 4). Because the rotation about the Cp–Fe–Cp axis is restricted by the two substituents, the Fc unit

[a] Department of Chemistry, University of Saskatchewan,
110 Science Place, Saskatoon, S7N 5C9, Canada
Fax: + 1-306-966-4730
E-mail: kraatz@skyway.usask.ca
[b] Saskatchewan Structural Science Centre, University of Saskatchewan,
110 Science Place, Saskatoon, SK S7N 5C9, Canada

Supporting information for this article is available on the WWW under http://www.eurjic.org or from the author.

 InterScience © 2006 Wiley-VCH Verlag GmbH & Co. KGaA, Weinheim 

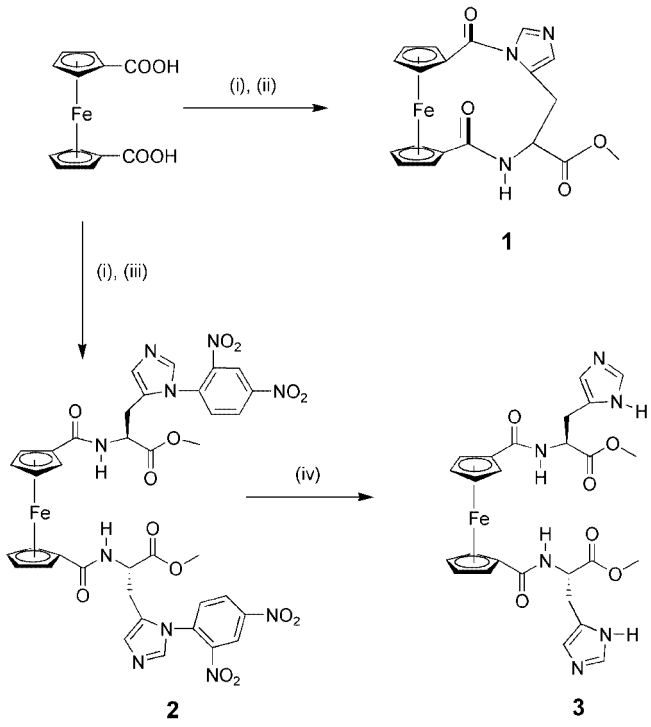


Scheme 1. Synthesis of of ferrocene–histidine conjugates **1** and **3**: (i) activation by EDC/HOBt, (ii) addition of a solution of histidine methyl ester and triethylamine at very high dilution at 0 °C after 30 min and stirring at room temperature for 12 h, (iii) addition of a solution of triethylamine and H-His(DNP)-OMe (cooling with ice bath), (iv) stirring with 10-fold molar excess of thiophenol in methanol at room temperature.

should show helical chirality.[9a,10a] As for other L-amino acids, we would have expected a strong positive band indicating a (*P*)-helical isomer. However, in the absence of a large database for CD spectra, two possibilities have to be considered: (a) compounds of this type display weak CD bands in the Fc region or (b) the absence of an intramolecular H-bond prevents the formation of a single conformation in solution and potentially both (*P*)- and (*M*)-helical isomers are formed in equimolar amounts. DFT calculations by Heinze have shown that (*P*)-helical conformations are energetically preferred for 1,1′-disubstituted Fc–L-amino acid conjugates.[12]

The acyclic compound **3** was prepared in order to compare its properties to those of the ferrocenophane **1**. Compound **3** was synthesized from ferrocenedicarboxylic acid by coupling with 2 equiv. of L-histidine(DNP) methyl ester in dichloromethane, followed by the deprotection of the imidazole group in methanol.[13] The desired compound **3** was obtained in 72% and was characterized spectroscopically. As shown in Figure 4, compound **3** displays a strong positive band in the CD spectrum in the Fc region indicating (*P*) helicity and a "Herrick-type" conformation of the system, as would be expected from an L-amino acid conjugate.[10a] This is in contrast to the very weak signal of the cyclic compound **1**.

Compound **1** was readily crystallized to yield rod-like red crystals by slow diffusion of hexanes into a dilute solution of compound **1** in chloroform. The structural presentation of compound **1** is given in Figure 1 and shows that one Fc unit is linked through the two carbonyl groups to the α-amino group as well as to the $N^{\pi}$ atom of the imidazole group.

Figure 2 shows a packing diagram of compound **1** indicating the formation of a supramolecular helical structure in the absence of intermolecular H-bonding, reminiscent of Hirao's chirality assembly.[10a] The Fe–C(Cp) distances fall into the expected range of 2.033(3)–2.061(3) Å.

The two Cp rings are parallel [angle between the two Cp planes: 2.5(2)°]. The Cp–CO bond lengths are significantly different. The Cp ring attached to the α-N atom of His exhibits a Cp–CO distance of 1.485(4) Å, whereas the Cp–CO distance of the Cp ring connected to the $N^{\pi}$ atom of the imidazole ring is shortened to 1.469(4) Å. This has also been observed in the structure of $Fc(CO–His–OMe)_2$.[14] The shortening of the Cp–CO distance is probably because of a greater electronic interaction of this Cp ring with the imidazole ring. As already observed in the structure of $Fc(CO–His–OMe)_2$ the Cp ring and the imidazole ring are not coplanar. However, the twist angle of 49.2(1)° is much larger than in $Fc(CO–His–OMe)_2$ (twist angle of 36.5°). The Cp–amide twist angle of 11.9(2)° is identical to the Cp–amide twist angle in $Fc(CO–His–OMe)_2$ (11.8°). The range of Cp–amide angles for Fc–amides and –peptides is between 5 and 20°.

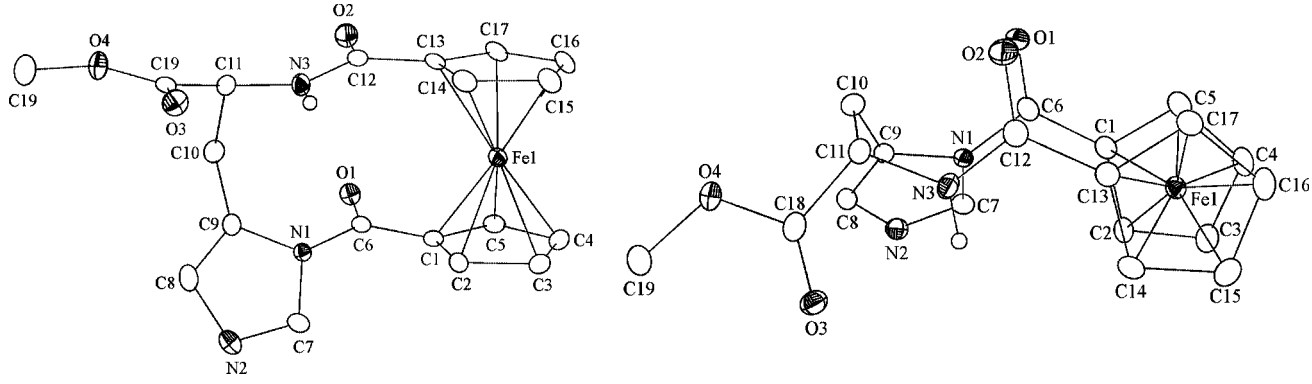


Figure 1. Two ORTEP diagrams of compound **1** showing all non-hydrogen atoms. Both C=O groups proximal to the Fc group are *syn* with respect to each other. All atoms are shown at the 30% probability level.

 © 2006 Wiley-VCH Verlag GmbH & Co. KGaA, Weinheim 

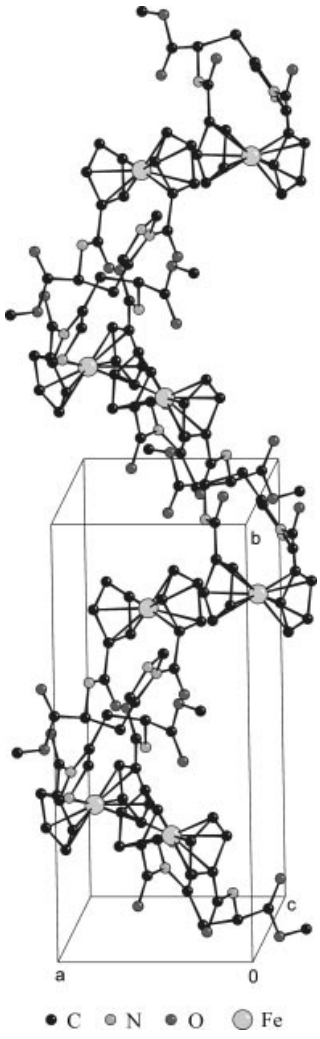


Figure 2. Helical intermolecular arrangement of compound **1**; view along the *c*-axis.

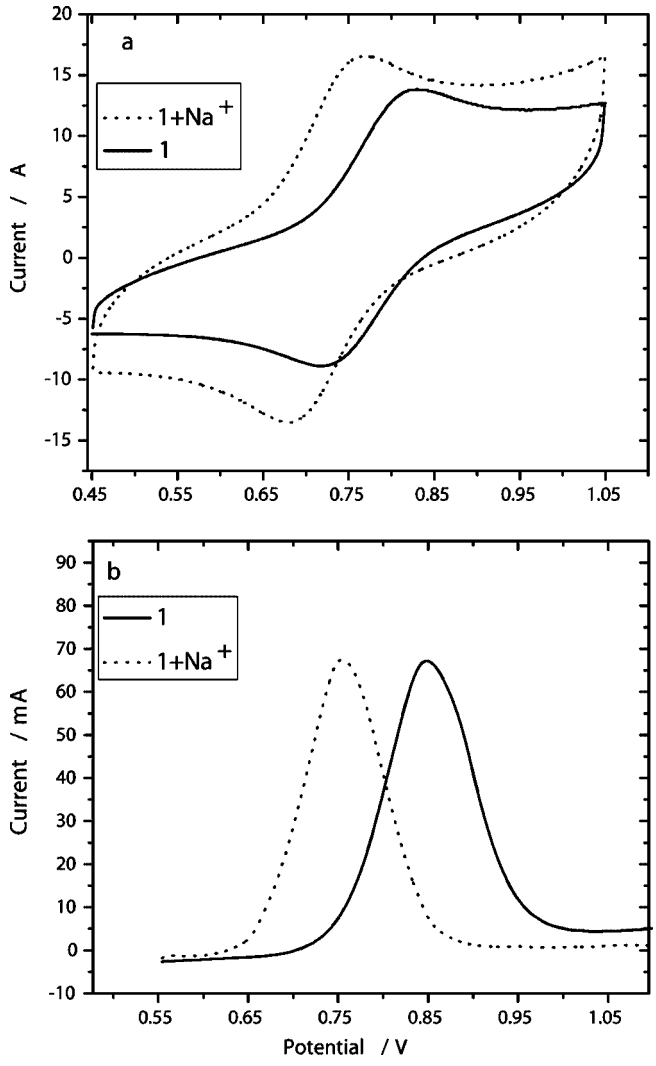


Figure 3. (a) Cyclic voltamogram at a scan rate of 0.1 V and (b) differential pulse voltamogram at a pulse width of 0.05 s of compound **1** before (——) and after (·····) the addition of $NaClO_4$ to the solution (1 mM solute in MeCN) using TBAP (0.1 M) as supporting electrolyte. Glassy carbon was used as working electrode, Ag/AgCl as reference and Pt as counter electrode.

Electrochemical studies [cyclic voltammetry (CV) and differential pulse voltammetry (DPC)] of compounds **1** and **3** were carried out in acetonitrile solutions with TBAP (0.1 M) as the supporting electrolyte. The CVs and DPVs for the compounds **1** and **3** are shown in Figure 3. Both compounds show quasi-reversible behavior ($i_a/i_c$ = 1.1, and 1.09) with a halfwave potential 794 and 751 mV, for **1** and **3**, respectively.

In comparison, the monosubstituted compound Fc(CO–His–OMe) shows a reversible one-electron oxidation at 630 mV. $Fc(CO–His–OMe)_2$, having an addition Fc group linked to the $N^{\pi}$ atom of the Im ring of His exhibits an additional wave at 762 mV.[14]

In the presence of alkali metal ions, some shifts in the $E_{1/2}$ value for compound **1** are noticeable. The halfwave potentials for the compounds **1** and **3** before and after addition of alkali metal ions are summarized in Table 1. Whereas the shift in the halfwave potential of **1** in the presence of $Li^+$ is shifted by 46 mV to lower potential, the presence of $Na^+$ causes a shift of 100 mV, making it significantly easier to oxidize the Fc group. The presence of other alkali metal ions does not cause any significant shifts in the halfwave potential.

We rationalize these potential shifts by the direct interaction of the metal ions with the two proximal *syn* carbonyl groups on the Fc unit. Association of $ClO_4^-$ anions with the Fc unit will result in a lower redox potential as bound metal ions are very close to the Fc unit and surrounded by $ClO_4^-$. The larger metal ions $K^+$ and $Cs^+$ may not fit into the cavity provided by the two carbonyl groups and thus do not affect the electrochemical properties of the Fc group.

For compound **3** on the other hand, the addition of alkali ions causes no electrochemical change but only minor effects, as in the case of $Cs^+$. Here, the two proximal C=O groups are *anti*, and binding occurs through the ester carbonyl group and/or the imidazole nitrogen atom, which both are far away from the Fc moiety. Cation binding to

 © 2006 Wiley-VCH Verlag GmbH & Co. KGaA, Weinheim 

Table 1. Half-wave potentials [mV] (±5) of ferrocene conjugates **1** and **3** with or without alkali metal ions.[a]

| Composition | **1** | **3** |
|---|---|---|
| Pure | 794 | 751 |
| Li | 748 | 751 |
| Na | 695 | 748 |
| K | 772 | 754 |
| Cs | 772 | 773 |

[a] Measured by differential pulse voltammetry using glassy carbon as working vs. Ag/AgCl as reference, and Pt as counter electrode. Compounds **1** and **3** were at 1 mM concentration in $CH_3CN$ containing 0.1 M TBAP. The $E_{1/2}$ value of the $Fc/Fc^+$ couple under the experimental conditions is 448(±5) mV (vs. Ag/AgCl). Halfwave potential recorded for pure compound and upon addition of 10 mol-equiv. of $MClO_4$ (M = Li, Na, K, Cs).

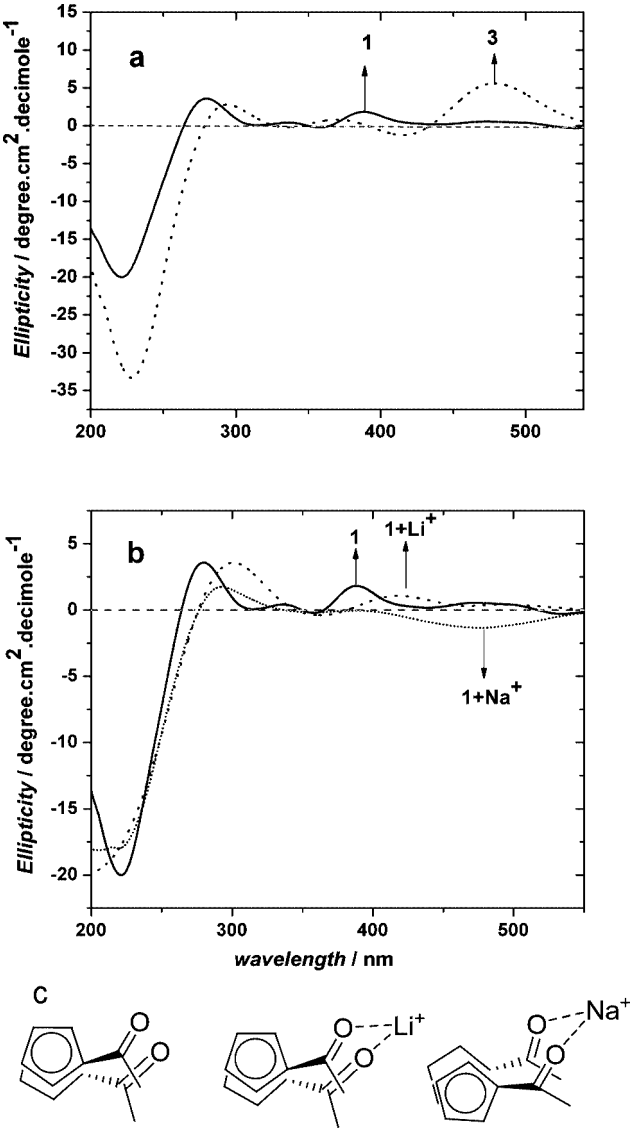


Figure 4. CD spectra in 1 mM solution in acetonitrile of (a) **1** and (b) **3** in the absence and presence of 10 equiv. of alkali metal (Li and Na) perchlorate salts and (c) schematic representation of change in conformation of the Fc entity of **1** with the addition of alkali metal salts.

the carbonyl groups causes the cathodic shift in the redox potential. Association of the $ClO_4^-$ anion with the alkali cation does not appear to influence the redox potential of the Fc group.

We postulated that binding of the ions to the two proximal *syn* C=O group may in fact cause small structural changes in the Fc core. We decided to investigate compound **1** in the presence of alkali metal ions by CD spectroscopy, which allows us to evaluate if structural changes occur involving the helicity of the ferrocene. Figure 4 shows the CD spectra of compounds **1** and **3** and changes of conformation of Fc in **1** upon addition of alkali metal salts. In comparison to **3**, the Fc-based CD band of compound **1** around 400–450 nm is very weak, which indicates weak helical chirality.

However, in the presence of alkali metals, there are noticeable changes occurring in this region. Figure 4 shows the CD spectra of compound **1** in the presence of $Li^+$ and $Na^+$. $Li^+$ causes a bathochromic shift and the band broadens. The conformation of the Fc unit is not affected. The larger $Na^+$ ion, which in the electrochemistry studies shows the largest effect, causes an apparent change in the conformation of the Fc unit. The Fc band now has an apparent negative Cotton effect. Assuming coordination of the metal ion to the two proximal *syn* carbonyl groups, the smaller $Li^+$ will fit into the "binding site" established by compound **1** with only minor adjustment, whereas the larger $Na^+$ requires that the Cp rings slightly rotate towards (*M*) helicity (Figure 4). Interestingly, for compound **3**, only $Cs^+$ causes a sizeable effect in the halfwave potential. The CD spectrum of compound **3** in the presence of $Cs^+$ clearly shows that the intensity of the Fc band indicating (*P*) helicity decreases drastically, corroborating a structural argument for the influence of alkali metal binding on these Fc conjugates (Figure S1).

## Conclusion

In conclusion, we provide details of the synthesis of a novel ferrocenophane, which displays an unusually *syn* conformation of the two proximal carbonyl groups, having the two Cp rings in an 1,1′-conformation. To the best of our knowledge this is the first example of an Fc–amino acid or –peptide conjugate that deviates from the classic Herrick conformation in such a drastic fashion. This conformation has consequences for the metal-recognition properties of this complex. The ferrocenophane **1** has the ability to recognize specific alkali elements, and displays the strongest change in the halfwave potential in the presence of $Na^+$ ions. The change in the halfwave potential is related to small structural changes that take place upon binding of the alkali metal ion to the proximal ferrocenyl C=O groups and small rotations of the two Cp rings of the metallocene.

## Experimental Section

**Synthesis and Characterization:** All syntheses were carried out in air unless otherwise indicated. $CH_2Cl_2$ (BDH; ACS grade) used for

 © 2006 Wiley-VCH Verlag GmbH & Co. KGaA, Weinheim 

synthesis was dried with $CaH_2$ and distilled prior to use. $CDCl_3$ (Aldrich) was dried with $CaH_2$, and stored over molecular sieves (8–12 mesh; effective pore size 4 Å; Fisher) before use. EDC·HCl, HOBt (Quantum), BOP (Advanced Chemtech), $MgSO_4$, and $NaHCO_3$ (VWR) were used as received. For column chromatography, a column (i.d. 2.7 cm; length 45 cm) was packed 18–22 cm high with 230–400 mesh silica gel (VWR). For TLC, aluminum plates coated with silica gel 60 $F_{254}$ (EM Science) were used. NMR spectra were recorded with a Bruker Avance 500 MHz spectrometer using a 5-mm broadband probe operating at 500.134 MHz ($^1$H) and 125.766 MHz ($^{13}$C{$^1$H}). Peak positions in both $^1$H and $^{13}$C NMR spectra are reported in ppm relative to TMS. The $^1$H NMR spectra are referenced to the residual $CHCl_3$ signal at $\delta$ = 7.27 ppm. All $^{13}$C{$^1$H} spectra are referenced to the $CDCl_3$ signal at $\delta$ = 77.23 ppm. Mass spectrometry was carried out with a VG Analytical 70/20 VSE instrument. Infrared spectra were obtained in KBr and recorded with a Perkin–Elmer model 1605 FT-IR (resolution: 4 cm$^{-1}$). 1,1′-Ferrocenedicarboxylic acid was synthesized from diacetylferrocene, which was synthesized from ferrocene by a known procedure.[15]

**Synthesis of 1:** 1,1′-Ferrocenedicarboxylic acid (0.0558 g, 0.2 mmol) was suspended in dichloromethane (100 mL). Diisopropylethylamine (DIPEA, 1 mL) was added to the solution at 0 °C. His-OMe·2HCl was added (0.048 g, 0.2 mmol) and stirring was continued. After 30 min, $CH_2Cl_2$ was added to the solution up to a total volume of 2 L. The reaction mixture was cooled to 0 °C (ice bath) for 15 min, followed by the addition of BOP (0.8 g, 2 mmol). After stirring at room temperature for 24 h, the volume of the solution was reduced to 400 mL by roto-evaporation. The organic solution was sequentially washed with saturated aqueous $NaHCO_3$, 10% aqueous citric acid, saturated $NaHCO_3$, and finally water. Traces of water were removed using anhydrous $Na_2SO_4$. After concentration, the crude product was purified by flash column chromatography using a chloroform/methanol solvent mixture (93:7, v/v; $R_f$ = 0.35). The solvents were removed under reduced pressure. Compound **1** was obtained as a red crystalline solid in 32% yield (0.032 g). HRMS (ES): calcd. for $C_{19}H_{17}FeN_3O_4$ 407.1449; found 407.1410 [M]$^+$. FT-IR (KBr): $\tilde{\nu}$ = 3530 (br., s, N–H, w), 1731 (s, C=O, ester) 1652 (s, C=O, amide I), 1538 (s, amide II) cm$^{-1}$. UV/Vis ($CH_3CN$): $\lambda$ ($\varepsilon$) = 449 (254 M$^{-1}$ cm$^{-1}$) nm. $^1$H NMR ($CDCl_3$): $\delta$ = 7.68 (s, 1 H, *o*-H of imidazole ring), 7.57 (br., s, 1 H, amide NH), 6.89 (s, 1 H, *m*-H of imidazole ring), 4.88 (m, 1 H, *α*-H of His), 4.86 (s, 1 H, *o*-H of Cp to Im ring), 4.80 (s, 1 H, *o*-H of Cp to Im ring), 4.77 (s, 1 H, *o*-H of Cp to CONH), 4.71 (s, 1 H, *o*-H of Cp to CONH), 4.48 (s, 1 H, *m*-H of Cp to Im ring), 4.46 (s, 1 H, *m*-H of Cp to Im ring), 4.36 (s, 2 H, *m*-H of other Cp attached to CONH), 3.82 (3 H, $CH_3$ of methyl ester), 3.24 (m, 2 H, β-H of His) ppm. $^{13}$C{$^1$H}NMR ($CDCl_3$): $\delta$ = 172.3, 172.2, 169.5, 135.4, 135.0, 73.6, 73.5, 72.7, 72.5, 72.3, 72.0, 71.9, 70.5, 70.0, 53.0, 52.7, 29.3 ppm.

**Synthesis of 2:** To a solution of ferrocenedicarboxylic acid (0.274 g, 1 mmol), dissolved in dry $CH_2Cl_2$ (50 mL), was added HOBt (0.38 g, 2.5 mmol), and EDC·HCl (0.48 g, 2.5 mmol). The reaction mixture was stirred for 0.5 h and then cooled to 0 °C (ice bath). H–His(DNP)–OMe (0.67 g, 2 mmol) was dissolved in dichloromethane (40 mL) and $Et_3N$ (0.5 mL, ca. 6 mmol) was added at 0 °C. The mixture was stirred at room temperature for 12 h. Workup was identical to that described for compound **1**. The crude product was purified by flash column chromatography using chloroform ($R_f$ = 0.28) and afforded a reddish yellow solid of **2** (0.70 g, 77%). $^1$H NMR ($CDCl_3$): $\delta$ = 8.84 (s, 1 H, 3-H of DNP), 8.04 (d, $J_{HH}$ = 9 Hz, 1 H, 5-H of DNP), 7.86 (d, $J_{HH}$ = 9 Hz, 1 H, 6-H of DNP), 7.85 (d, $J$ = 9 Hz, 1 H, NH of amide), 7.60 (s, 1 H, *o*-H of imidazole), 6.91 (s, 1 H, *m*-H of imidazole), 4.89 (m, 1 H, α-H of His), 4.69 (s, 1 H, *o*-H of Fc), 4.66 (s, 1 H, *o*-H of Fc), 4.41 (s, 1 H, *m*-H of Fc), 4.36 (s, 1 H, *m*-H of Fc), 3.70 (3 H, $CH_3$ of methyl ester), 3.18 (m, 2 H, β-H of His) ppm.

**Synthesis of 3:** Compound **2** (0.45 g, 0.5 mmol) was dissolved in methanol (20 mL) and thiophenol (1.2 g, 10 mmol) was added. After stirring of the reaction mixture at room temperature for 7 h, methanol was removed and the product was purified by flash chromatography ($CHCl_3$/MeOH, 80:20; $R_f$ = 0.27). The final product was obtained as an orange solid in 65% yield (0.19 g). HRMS (ES): calcd. for $C_{26}H_{28}FeN_6O_6$ 576.2214; found 576.2191 [M]$^+$. FT-IR (KBr): $\tilde{\nu}$ = 3540 (br., s, N–H), 1731 (s, C=O, ester), 1639 (s, C=O, amide I), 1533 (s, amide II) cm$^{-1}$. UV/Vis ($CH_3CN$): $\lambda$ ($\varepsilon$) = 442 (240 M$^{-1}$ cm$^{-1}$) nm. $^1$H NMR $CDCl_3$): $\delta$ = 7.84 (d, $J$ = 8 Hz, 1 H, NH of amide), 7.54 (s, 1 H, *o*-H of imidazole), 6.87 (s, 1 H, *m*-H of imidazole) 4.89 (m, 1 H, α-H of His), 4.69 (s, 1 H, *o*-H of Fc), 4.66 (s, 1 H, *o*-H of Fc), 4.41 (s, 1 H, *m*-H of Fc), 4.36 (s, 1 H, *m*-H of Fc), 3.70 (3 H, $CH_3$ of methyl ester), 3.18 (m, 2 H, β-$CH_2$ of His) ppm. $^{13}$C{$^1$H}NMR ($CDCl_3$): $\delta$ = 173.3, 171.2, 135.5, 135.4, 131.4, 98.0, 72.2, 72.1, 71.3, 70.4, 53.4, 53.3, 28.8 ppm.

**CD Measurements:** CD spectra of $CH_3CN$ solutions with a concentration of $1.0\cdot10^{-3}$ M were recorded under argon at 25 °C with a PiStar-180 spectropolarimeter (Applied Biophysics) using a quartz cell (path length 1 cm).

**X-ray Crystallography:** An orange plate-like crystal of compound **1** ($C_{19}H_{17}Fe_1N_3O_4$) (Table 2) with the approximate dimensions of 0.08 × 0.05 × 0.05 mm, coated with oil (Paratone 8277, Exxon), was mounted onto a nylon fiber of a CryoLoop™ device (diameter of the nylon fiber: 10 microns; loop diameter 0.1–0.2 mm; Hampton

Table 2. Crystallographic data for compound **1**.

| | |
|---|---|
| Empirical formula | $C_{19}H_{17}Fe_1N_3O_4$ |
| Formula mass | 407.21 |
| Crystal color, habit | orange, plate |
| Crystal dimensions [mm] | 0.08× 0.05× 0.05 |
| Crystal system | orthorhombic |
| Space group | $P2_12_12_1$ |
| Unit cell parameters: | |
| $a$ [Å] | 7.2350(2) |
| $b$ [Å] | 16.5440(4) |
| $c$ [Å] | 14.0700(5) |
| $V$ [Å$^3$] | 1684.12(9) |
| $Z$ | 4 |
| $F$(000) | 840 |
| $\rho_{calcd.}$ [Mg/m$^3$] | 1.606 |
| $\mu$ [mm] | 0.928 |
| Radiation | Mo-$K_\alpha$ ($\lambda$ = 0.71073 Å) |
| Temperature [K] | 173(2) |
| $\theta$ range for data collection [°] | 1.90–26.37 |
| Total reflections | 6450 |
| Independent reflections [$F_o^2 \geq 3\sigma(F_o^2)$] | 3445 ($R_{int}$ = 0.0426) |
| Observed reflection [$F_o^2 > 2\sigma(F_o^2)$] | 2969 |
| Index ranges | $-9 \leq h \leq 9, -19 \leq k \leq 20, -17 \leq l \leq 17$ |
| Data/restraints/parameters | 3445/0/245 |
| Absolute structure parameter | –0.020(18) (1457 Friedel pairs) |
| $S$ (Goodness-of-fit on $F^2$) | 1.066 |
| Final $R$ indices: | |
| $R_1$[a] [$I_o > 2\sigma(I_o)$] | 0.0401 |
| $wR_2$[b] (all data) | 0.0764 |
| Max. shift/error in final cycle | 0.001 |
| Largest difference peak/hole [e$^-$ Å$^3$] | 0.275/–0.318 |

[a] $R_1 = [\Sigma||F_o| - |F_c||]/[\Sigma|F_o|]$. [b] $wR_2 = \{[\Sigma w(F_o^2 - F_c^2)^2]/[\Sigma w(F_o^2)^2]\}^{1/2}$, where $w = [\sigma(F_o^2) + (0.0085\cdot P)^2 + (0.6243\cdot P)]^{-1}$ and $P = [\max(F_o^2,0) + 2F_c^2]/3$.

 © 2006 Wiley-VCH Verlag GmbH & Co. KGaA, Weinheim 

Research, USA) under a microscope. The crystal was then mounted onto the goniometer head, which was quickly transferred to the cold stream of the X-ray diffractometer. All measurements were made with a Nonius KappaCCD 4-Circle Kappa FR540C diffractometer using monochromated Mo-$K_\alpha$ radiation ($\lambda$ = 0.71073 Å) at –100 °C. An initial orientation matrix and cell was determined from 10 frames using $\varphi$ scans.[16] The X-ray data were measured using $\varphi$- and $\omega$-scans.[16] Data reduction was performed with the HKL DENZO and SCALEPACK software,[17] which corrects for beam inhomogeneity, possible crystal decay, Lorentz and polarization effects. A multi-scan absorption correction was applied (SCALEPACK).[17] The structure was solved by direct methods (SHELXS-97)[18] and refined by full-matrix least-squares methods on $F^2$ with SHELXL97-2.[19] The non-hydrogen atoms were refined anisotropically. Hydrogen atoms were included at geometrically idealized positions (C–H bond lengths 0.95/0.98/1.00 Å, N–H bond lengths 0.88 Å) and were not refined. The isotropic thermal parameters of the hydrogen atoms were fixed at 1.2 times that of the preceding carbon atom. CCDC-285760 contains the supplementary crystallographic data for this paper. These data can be obtained free of charge from The Cambridge Crystallographic Data Centre via www.ccdc.cam.ac.uk/data_request/cif.

**Electrochemical Measurements:** The electrochemical experiments were carried out at room temperature with a CV-50W voltammetric analyzer. A gold electrode (diameter 50 μm) was used as the working electrode. 1 mM $CH_3CN$ solutions of compounds **1** and **3** were prepared containing 0.1 M tetrabutylammonium perchlorate (TBAP). The measurements were carried out in a low scan rate of 100 and 10 mV/s for cyclic voltammetry (CV) and differential pulse voltammetry (DPV), respectively. A platinum wire (1 mm) was used as the counter electrode. The reference electrode was Ag/AgCl (BAS). The $E_{1/2}$ value of the $Fc/Fc^+$ couple under the experimental conditions was 448(± 5) mV (vs. Ag/AgCl).

**Supporting Information** (see footnote on the first page of this article): CD spectra and CVs of compound **3** with and without $Cs^+$.

## Acknowledgments

The authors would like to acknowledge the financial support from NSERC in the form of an operating grant and the Canada Foundation for Innovation (CFI) and the Saskatchewan Innovation Fund (SIF) for additional funding. H.-B. K. is Canada Research Chair in Biomaterials. We are grateful to Ken Thoms for recording the mass spectra, and to the SSSC for instrument time (NMR, X-ray, MS).

[1] a) P. D. Beer, *Chem. Soc. Rev.* **1989**, *18*, 409–450; b) P. L. Boulas, M. Gomez-Kaifer, L. Echegoyen, *Angew. Chem. Int. Ed.* **1998**, *37*, 216–247; c) L. Fabbrizzi, A. Poggi, *Chem. Soc. Rev.* **1995**, *24*, 197–202.

[2] a) P. D. Beer, N. Berry, O. D. Fox, M. E. Padilla-Tosta, S. Patell, M. G. B. Drew, *Chem. Commun.* **2001**, 199–200; b) P. D. Beer, *Acc. Chem. Res.* **1998**, *31*, 71–80; c) P. R. A. Webber, G. Z. Chen, M. G. B. Drew, P. D. Beer, *Angew. Chem. Int. Ed.* **2001**, *40*, 2265–2268; d) P. D. Beer, D. Hesek, K. C. Nam, M. G. B. Drew, *Organometallics* **1999**, *18*, 3933–3943.

[3] a) M. A. Herranz, B. Colonna, L. Echegoyen, *Proc. Natl. Acad. Sci. U.S.A.* **2002**, *99*, 5040–5047; b) S.-G. Liu, H. Liu, K. Bandyopadhyay, Z. Gao, L. Echegoyen, *J. Org. Chem.* **2000**, *65*, 3292–3298; c) M. J. van Eis, P. Seiler, F. Diederich, R. J. Alvarado, L. Echegoyen, *Chem. Commun.* **2000**, 1859–1860.

[4] a) M. R. Bryce, A. S. Batsanov, T. Finn, T. K. Hansen, A. J. Moore, J. A. K. Howard, M. Kamenjicki, I. K. Lednev, S. A. Asher, *Eur. J. Org. Chem.* **2001**, 933–940; b) T. Nabeshima, D. Nishida, T. Saiki, *Tetrahedron* **2003**, *59*, 639–647; c) C. D. Hall, G. J. Kirkovits, A. C. Hall, *Chem. Commun.* **1999**, 1897–1898; d) T.-Y. Dong, C.-K. Chang, C.-H. Cheng, K.-J. Lin, *Organometallics* **1999**, *18*, 1911–1922.

[5] Y. A. Ovchinnikov, V. T. Ivanov, *Tetrahedron Report*, Pergamon Press, New York, **1976**, No. 1.

[6] a) R. M. Izatt, J. S. Bradshaw, S. A. Nielson, J. D. Lamb, J. J. Christensen, D. Sen, *Chem. Rev.* **1985**, *85*, 271–339; b) T. J. Marrone, K. M. Merz, Jr., *J. Am. Chem. Soc.* **1995**, *117*, 779–791.

[7] a) D. Seebach, J. L. Matthews, *Chem. Commun.* **1997**, 2015–2022; b) T. D. Clark, L. K. Buehler, M. R. Ghadiri, *J. Am. Chem. Soc.* **1998**, *120*, 651–656; c) D. Seebach, J. L. Matthews, A. Meden, T. Wessels, C. Baerlocher, L. B. McCusker, *Helv. Chim. Acta* **1997**, *80*, 173–182; d) I. L. Karle, B. K. Handa, C. H. Hassall, *Acta Crystallogr., Sect. B* **1975**, *31*, 555–560; e) D. Ranganathan, *Acc. Chem. Res. Acc. Chem. Res.* **2001**, *34*, 919–930; f) C. Garcia-Echeverria, F. Albericio, E. Giralt, M. Pons, *J. Am. Chem. Soc.* **1993**, *115*, 11663–11670; g) I. L. Karle, R. Kishore, S. Raghothama, P. Balaram, *J. Am. Chem. Soc.* **1988**, *110*, 1958–1963; h) R. Kishore, A. Kumar, P. Balaram, *J. Am. Chem. Soc.* **1985**, *107*, 8019–8023; i) S. Kubik, *J. Am. Chem. Soc.* **1999**, *121*, 5846–5855.

[8] H. Huang, L. Mu, J. He, J.-P. Cheng, *J. Org. Chem.* **2003**, *68*, 7605–7611.

[9] a) R. van Staveren, N. Metzler-Nolte, *Chem. Rev.* **2004**, *104*, 5931–5985; b) D. R. van Staveren, T. Weyhermuller, N. Metzler-Nolte, *Dalton Trans.* **2003**, 210–220.

[10] a) T. Moriuchi, A. Nomoto, K. Yoshida, A. Ogawa, T. Hirao, *J. Am. Chem. Soc.* **2001**, *123*, 68–75; b) T. Moriuchi, K. Yoshida, T. Hirao, *Org. Lett.* **2003**, *5*, 4285–4288; c) A. Nomoto, T. Moriuchi, S. Yamazaki, A. Ogawa, T. Hirao, *Chem. Commun.* **1998**, 1963–1964; d) T. Moriuchi, K. Yoshida, T. Hirao, *J. Organomet. Chem.* **2003**, *668*, 31–34; e) T. Moriuchi, A. Nomoto, K. Yoshida, T. Hirao, *Organometallics* **2001**, *20*, 1008–1013.

[11] S. Chowdhury, G. Schatte, H. B. Kraatz, *Dalton Trans.* **2004**, 1726–1730.

[12] K. Heinze, M. Beckmann, *Eur. J. Inorg. Chem.* **2005**, 3450–3457.

[13] Catalog and Peptide Synthesis Handbook, Novabiochem, (**1997**–**1998**).

[14] H. S. Mandal, H.-B. Kraatz, *J. Organomet. Chem.* **2003**, *674*, 32–37.

[15] A. Sonoda, I. Moritani, *J. Organomet. Chem.* **1971**, *26*, 133–140.

[16] *COLLECT* data collection software, Nonius B. V., **1998**.

[17] HKL DENZO and SCALEPACK v1.96: Z. Otwinowski, W. Minor, *Processing of X-ray Diffraction Data Collected in Oscillation Mode, Methods in Enzymology*, vol. 276 ("Macromolecular Crystallography", part A) (Eds.: C. W.Carter, R. M., Sweet, Jr.,), Academic Press, San Diego, CA, **1997**, pp. 307–326.

[18] G. M. Sheldrick, *SHELXS-97, Program for the Solution of Crystal Structures*, University of Göttingen, Göttingen, Germany, **1997**.

[19] G. M. Sheldrick, *SHELXL97-2, Program for the Solution of Crystal Structures*, University of Göttingen, Göttingen, Germany, **1997**.

Received: October 5, 2005
Published Online: January 12, 2006

 © 2006 Wiley-VCH Verlag GmbH & Co. KGaA, Weinheim 

DOI: 10.1002/ejic.200500889

# Reassignment, Isolation, Spectral and X-ray Characterization of Diastereoisomers of the Macrocyclic Ligand 3,10-*meso*-3,5,7,7,10,12,14,14-Octamethyl-1,4,8,11-tetraazacyclotetradecane and their $Ni^{II}$ and $Cu^{II}$ Complexes

**Yung-Chan Lin,*[a] Tarun Kumar Misra,[b] Tian-Huey Lu,[c] Maddirala Shambabu Joseph,[d] and Chung-Sun Chung*[d]**

**Keywords:** Diastereoisomers / Macrocyclic ligands / X-ray crystallography / Coordination modes

Reduction of the macrocyclic ligand, 3,10-*meso*-3,5,7,7,10,12,14,14-octamethyl-1,4,8,11-tetraazacyclotetradecane-4,11-diene dihydroperchlorate (L), with sodium borohydride yielded three [$L_b$ (**1**), $L_c$ (**2**), and $L_d$ (**3**)] of four possible diastereoisomers. The diastereoisomeric macrocycles and their $Ni^{II}$ and $Cu^{II}$ complexes have been characterized and confirmed by IR, UV/Vis, and NMR spectroscopy as well as X-ray crystallography. The chiral carbon centers and methyl groups at the 5 and 12 positions of **1**, **2** and **3** have the 5*S*,12*R*-C-*meso*, 5*S*,12*S*-C-*racemic*, and 5*R*,12*R*-C-*racemic* configurations, respectively. In accordance with the X-ray structure determination, the geometry around the $Ni^{II}$ ion in the complexes is approximately square-planar and the $Cu^{II}$ ion has an octahedral geometry. The N–H configuration of $[NiL_c](ClO_4)_2(H_2O)_{0.5}$ (**5**) is *trans*-II, different from the most thermodynamically stable *trans*-III configuration that is found in $[NiL_b](ClO_4)_2$ (**4**), $[CuL_b(H_2O)_2](ClO_4)_2$ (**7**), and $[CuL_d(ClO_4)_2]$ (**8**). UV/Vis spectra reveal that $Ni^{II}$ complexes exhibit almost 100 % planar species in aqueous solution resulting from steric effects produced by numerous methyl groups, especially axial orientations and distorted structures. In six coordinate $Cu^{II}$ complexes, acetonitrile acts as a better axial donor than the water molecule; the weaker axial bonding is a result of steric interactions that lead to stronger in-plane coordinations.

(© Wiley-VCH Verlag GmbH & Co. KGaA, 69451 Weinheim, Germany, 2006)

## Introduction

The 14-membered tetraazacyclotetradecane macrocyclic ligands have been exploited extensively in different fields of research such as catalysis, bioinorganic, biomimetic, building blocks in supramolecular, and coordination chemistry.[1] These ligands have provided the ideal coordination sites for many metal ions and have been used as metal ion binding sites in medical techniques such as MRI and radioimmunotherapy.[2] Many of these metal complexes can be used as catalysts in redox reactions.[3] For instance, nickel complexes are used to produce CO through the photochemical and electrochemical reduction of $CO_2$.[4]

The stereochemistry of the 14-membered tetraazacyclotetradecane macrocyclic ligands and their metal complexes is very rich because of the presence of several asymmetric carbons and four N–H groups on their skeleton.[5] One such macrocyclic ligand can have numerous diastereoisomeric forms.[5] The macrocyclic molecule 3,5,7,7,10,12,14,14-octamethyl-1,4,8,11-tetraazacyclo-tetradecane-4,11-diene, $Me_8$-[14]diene, which has two chiral centers at the 3 and 10 positions, exhibits three noninterconvertible diastereoisomers, 3*S*,10*R*-*meso*- $Me_8$[14]diene (L), 3*R*,10*R*-*racemic*-$Me_8$[14]-diene, and 3*S*,10*S*-*racemic*-$Me_8$[14]diene (Scheme 1). Nickel(II) complexes of these ligands were obtained from a template reaction of tris[(±)-1,2-propanediamine]nickel(II) perchlorate, tris[(+)-1,2-propanediamine]nickel(II) perchlorate, or tris[(–)-1,2-propanediamine]nickel(II) perchlorate with acetone and were characterized by proton NMR spectroscopy.[6] In addition, the Nickel(II) complex of 3,10-*meso*-$Me_8$[14]diene was confirmed by X-ray crystallography.[6a,7] In a different approach, the reaction of (±)-1,2-propanediamine hydroperchlorate with acetone yields stereospecifically only the crystalline 3,10-*meso*-$Me_8$[14]-diene·$2HClO_4$.[6a,8] Failure to isolate any C-*rac* isomer apparently results from a higher solubility of the C-*rac* salt. Treatment of (–)-1,2-propanediamine hydroperchlorate with

[a] Material and Chemical Research Laboratories, Industrial Technology Research Institute,
Hsinchu 300, Taiwan, R. O. C.
E-mail: lin0797@itri.org.tw
[b] Department of Chemistry, National Taiwan University,
Taipei 106, Taiwan, R. O. C.
[c] Department of Physics, National Tsing Hua University,
Hsinchu 300, Taiwan, R. O. C.
[d] Department of Chemistry, National Tsing Hua University,
Hsinchu 300, Taiwan, R. O. C.
E-mail: cschung@mx.nthu.edu.tw
Supporting information for this article is available on the WWW under http://www.eurjic.org or from the author.

 © 2006 Wiley-VCH Verlag GmbH & Co. KGaA, Weinheim 

acetone yields no crystalline product under these conditions.[6a] The configuration of 3,10-*meso* is designated as 3*S**,10*R**-*meso*. Reduction of 3,10-*meso*-$Me_8$[14]diene with $NaBH_4$ generates another two chiral centers at the 5 and 12 positions and gives an isomeric mixture of the corresponding saturated macrocycles, 3,10-*meso*-$Me_8$[14]anes.[8] These molecules and their *N*-alkylated derivatives have been characterized and studied in the field of kinetics, coordination chemistry, and environmental monitoring.[9] The $Cr^{III}$ complexes of these ligands have been used as sensor materials, artificial ionophores, and in membrane electrodes.[10] Antimicrobial activity of these ligands and their complexes have been investigated.[11] Despite their huge importance and usefulness in different fields of science, proper assignment of these diastereoisomeric ligands and their complexes has been lacking.

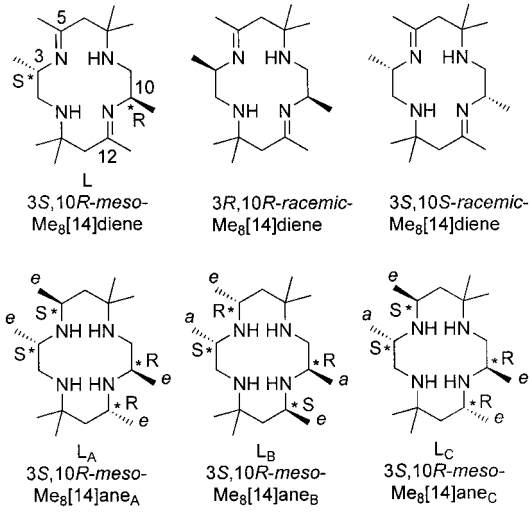


Scheme 1.

Although the assignment of diastereoisomeric forms of macrocyclic ligands and their complexes are an arduous problem, Bembi et al.[8] argued that the reduction of 3,10-*meso*-$Me_8$[14]diene would give three isomeric 3,10-*meso*-$Me_8$[14]anes. These were isolated and denoted as 3,10-*meso*-$Me_8$[14]$ane_A$ ($L_A$), 3,10-*meso*-$Me_8$[14]$ane_B$ ($L_B$) and 3,10-*meso*-$Me_8$[14]$ane_C$ ($L_C$) (Scheme 1). Bembi and coworkers characterized these ligands and their complexes by either NMR spectroscopy on its own or by both NMR spectroscopy and X-ray crystallography. In this context we have found two main flaws with their assignment and characterization of these ligands and their complexes: (i) The basis on which they have assigned the ligands $L_A$–$L_C$ is nebulous. The *RS*-configuration of the chiral methyls of $L_A$ and $L_C$ are the same. $L_C$ differs from $L_A$ in having one chiral methyl at the axial position. Thus, $L_C$ is nothing but a conformer of $L_A$. The methyl orientations (axial or equatorial) of ligand $L_A$ (or $L_C$) in its complexes with metals match those of $L_b$ rather than those of $L_A$ (or $L_C$), although they have the same *RS*-configuration, i.e., $L_A$ and $L_C$ are conformers of $L_b$. (ii) Ligand $L_B$ and its $Ni^{II}$ complex, $[NiL_{B\alpha}](ClO_4)_2$, were characterized by X-ray crystallography,[8,9h] but if one undertakes a critical investigation it can be seen that in both cases crystal structures of the ligand moiety appeared as the conformer of $L_A$ and not $L_B$. Thus, proper assignment of the diastereoisomers obtained from the reduction reaction of 3,10-*meso*-$Me_8$[14]diene is very much needed and important. In this paper we describe the reassignment, isolation, spectral and X-ray characterization of diastereoisomers of 3,10-*meso*-3,5,7,7,10,12,14,14-octamethyl-1,4,8,11-tetraazacyclotetradecane and their $Ni^{II}$ and $Cu^{II}$ complexes. The assignment of diastereoisomers has been performed on the basis of *RS*-configuration. Thus, reduction of 3,10-*meso*-$Me_8$[14]diene would give four diastereoisomeric macrocycles, $L_a$ (*SRRS*), $L_b$ (**1**, *SSRR*), $L_c$ (**2**, *SSRS*) and $L_d$ (**3**, *SRRR*) (Scheme 2). Over the course of reduction, the configurations of chiral methyls at position 3 (3*S*) and 10 (10*R*) remain intact. $L_a$ and **1** have mesomeric configuration whereas **2** and **3** are enantiomers of one another. Isomers were separated by fraction crystallization from a methanol/water mixture. The solubility of the *meso* isomers is lower and hence they separated first. Isomer $L_a$ cannot be isolated following the experimental methods described in the text, but we have still assigned it as 3*S*,10*R*-C-*meso*-5*R*,12*S*-C-*meso*-$Me_8$[14]ane. According to the results from NMR spectroscopy and X-ray crystallography studies, the structures of isomers **2** and **3** are indeed different from the literature reports. The square-planar $Ni^{II}$ and elongated octahedral $Cu^{II}$ complexes have also been characterized by UV/Vis spectroscopy in order to study the behavior of the d–d transitions and axial additions.

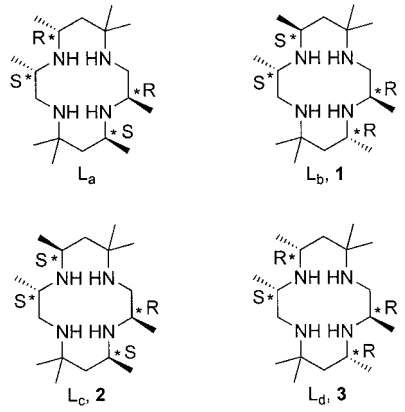


Scheme 2.

## Results and Discussion

### Synthesis

Reduction of L with $NaBH_4$ gave an isomeric mixture of the corresponding saturated macrocycles, 3*S*,10*R*-*meso*-$Me_8$[14]anes. 3*S*,10*R*-C-*meso*-$Me_8$[14]ane exists as four diastereoisomeric isomers, two 5,12-C-*meso* ($L_a$, **1**) and two 5,12-C-*racemic* (**2**, **3**) forms. By using the partial crystallization method, the *meso* and *racemic* isomers could easily be separated. Although the isomer $L_a$ could not be isolated following the experimental methods described in the text, we have assigned it as 3*S*,10*R*-C-*meso*-5*R*,12*S*-C-*meso*-

 © 2006 Wiley-VCH Verlag GmbH & Co. KGaA, Weinheim 

$Me_8$[14]ane. The two *rac* forms are enantiomers of each other and are difficult to separate completely because of their similar chemical properties. To date no effective method has been found to separate isomeric C-*rac*-macrocycles, e.g. a (7*S*,14*S*)/(7*R*,14*R*)-C-*rac*-$Me_6$[14]ane (tet b) or (5*S*,12*S*)/(5*R*,12*R*)-C-*rac*-$Me_2$[14]ane mixture. Crystals of **1** and **2** were obtained from ether solutions. The reactions of isomeric ligands with nickel acetate tetrahydrate in a refluxing methanol solution produced green nickel(II) complexes. After adding lithium perchlorate trihydrate, the yellow square-planar nickel(II) complexes were obtained. The complexes were crystallized from acetonitrile or a water/methanol mixture. Reacting copper perchlorate hexahydrate with the isomeric ligands provided the octahedral $Cu^{II}$ complexes. Crystals were obtained from the methanol/water mixture.

## $^1$H NMR Spectroscopy

Although the one-dimensional $^1$H NMR spectra of macrocycles and their $Ni^{II}$ complexes are not well resolved, they present some key features that can be used to assign their configurations. From the $^1$H NMR spectra the chiral and geminal methyl groups can easily be identified as well as the equatorial and axial methyls. The splitting pattern of the signals for the chiral methyls is a doublet whereas for the geminal methyls a singlet signal is seen. Thus geminal dimethyl groups give two singlet signals, one for the equatorial and the other for the axial methyl group. The number of chiral methyl signals varies depending on their axial and equatorial positions. The singlet at the higher field is assigned to the signal for the equatorial methyl protons and the remaining intense singlet to the axial group.[6b,8,9c,9h,12] In the case of **1** and **4**, $^1$H NMR spectra (Table 1) show four signals; two for the geminal dimethyls and the remaining two for the chiral methyls. This reveals that the molecules **1** and **4** have centrosymmetric symmetry. In the case of **2** and **5** eight signals are observed, four for the geminal dimethyls and the remaining four for the chiral methyls. This reveals that the molecules **2** and **5** are asymmetric.

Table 1. Selected $^1$H NMR spectroscopic data of ligands **1**–**2** and $Ni^{II}$ complexes **4**–**5**.[a]

| Ligands / Complexes | Geminal dimethyl | Methyl on chiral carbon atoms |
|---|---|---|
| **1** | 1.05 s (*e*, 6 H) | 0.96 d (*e*, 6 H) |
| | 1.11 s (*a*, 6 H) | 1.01 d (*a*, 6 H) |
| **2** | 0.98 s (*e*, 3 H) | 0.91 d (*e*, 3 H) |
| | 0.99 s (*e*, 3 H) | 0.97 d (*a*, 3 H) |
| | 1.03 s (*a*, 3 H) | 1.01 d (*a*, 3 H) |
| | 1.06 s (*a*, 3 H) | 1.02 d (*a*, 3 H) |
| **4** | 1.20 s (*e*, 6 H) | 1.15 d (*e*, 6 H) |
| | 1.81 s (*a*, 6 H) | 1.60 d (*a*, 6 H) |
| **5** | 1.17 s (*e*, 3 H) | 1.14 d (*e*, 3 H) |
| | 1.27 s (*e*, 3 H) | 1.19 d (*e*, 3 H) |
| | 2.29 s (*a*, 3 H) | 1.50 d (*a*, 3 H) |
| | 2.49 s (*a*, 3 H) | 1.93 d (*a*, 3 H) |

[a] s = singlet, d = doublet, *a* = axial, *e* = equatorial.

### *Ligand 1 and Complex 4*

In both cases, the methyl signals appear as two singlets and two doublets corresponding to six protons each. This requires the structure to have centrosymmetric symmetry, since the methyl groups are clearly pair-wise equivalent. In the case of **1**, two singlets at $\delta$ = 1.05 and 1.11 ppm can be assigned to the geminal dimethyl groups at the 7 and 14 positions. The upfield singlet at $\delta$ = 1.05 ppm can be assigned to equatorial methyl groups and the downfield singlet at $\delta$ = 1.11 ppm to axial methyl groups. The upfield doublet at $\delta$ = 0.96 ppm is due to two equatorially oriented methyl groups, whereas the downfield doublet at $\delta$ = 1.01 ppm is assigned to two axially oriented methyl groups. Similar observations have also been found in the case of **4**, two singlets at $\delta$ = 1.20 and 1.81 ppm can be assigned to geminal dimethyl groups at the 7 and 14 positions. The upfield singlet at $\delta$ = 1.20 ppm can be assigned to equatorial methyl groups and the downfield singlet at $\delta$ = 1.81 ppm to axial methyl groups. The 1.15 ppm ($J_{HH}$ = 5.75 Hz) doublet is assigned to two equatorially oriented methyl groups, while the 1.60 ppm ($J_{HH}$ = 6.71 Hz) doublet is assigned to two axially oriented methyl groups. A diequatorial-diaxial arrangement for the four chiral methyl groups is possible in **1** and **4**.

### *Ligand 2 and Complex 5*

Differing greatly from **1**, the spectra of **2** and **5** show that the methyl signals give four singlets and four doublets, where each signal corresponds to three protons. In the case of **2**, the singlets at 0.98, 0.99, 1.03, and 1.06 ppm can be assigned to geminal dimethyl groups at the 7 and 14 positions and the doublets at 0.91, 0.97, 1.01, and 1.02 ppm can be assigned to four chiral methyl groups at the 3, 5, 10, and 12 positions. Two upfield singlets at $\delta$ = 0.98 and 0.99 ppm appear due to two equatorially oriented methyl groups, while the downfield doublet at $\delta$ = 1.03 and 1.06 ppm is assigned to two axially oriented methyl groups. The doublet at the highest field can be assigned to an equatorially oriented methyl group and another doublet at $\delta$ = 0.97 ppm to an axially oriented methyl group. The similar chemical shifts and coupling constants of the two remaining doublets at $\delta$ = 1.01 and 1.02 ppm indicate that the two chiral methyl groups have a similar chemical environment. Therefore, the two doublets at the lower field should be assigned to axial oriented methyl groups. Thus an equatorial-triaxial arrangement for the four chiral methyl groups is possible in the structure. In the case of **5**, the methyl signals also give four singlets and four doublets, where each signal corresponds to three protons. The singlets at 1.17, 1.27, 2.29, and 2.49 ppm can be assigned to the 7,7,14,14-tetramethyl groups. Two upfield singlets at $\delta$ = 1.17 and 1.27 ppm appear due to two equatorially oriented methyl groups and the downfield doublets at $\delta$ = 2.29 and 2.49 ppm are due to two axially oriented methyl groups. The doublets at 1.14 ($J_{HH}$ = 6.46 Hz), 1.19 ($J_{HH}$ = 5.75 Hz), 1.50 ($J_{HH}$ = 7.21 Hz), and 1.93 ($J_{HH}$ = 7.43 Hz) ppm can be assigned to four chiral methyl groups, where the two doublets at higher field can be assigned to equatorially oriented methyl groups

 © 2006 Wiley-VCH Verlag GmbH & Co. KGaA, Weinheim 

and the other two doublets to the axially oriented methyl group. A diequatorial-diaxial arrangement for the four chiral methyl groups is possible in the structure. The different results of the methyl orientations in **2** and **5** are because of the nitrogen inversions.

### $^{13}C$ NMR Spectroscopy

On the basis of $^{13}C$ NMR spectra, the symmetric and asymmetric macrocyclic ligands and their nickel(II) complexes can clearly be distinguished. Each stereochemically distinct carbon atom displays a separate resonance. However, most resonances cannot be assigned to corresponding carbons by using $^{13}C$ NMR spectra alone. Even so, there is enough evidence to define whether the structures are symmetric or asymmetric from the $^{1}H$ NMR, $^{13}C$ NMR and X-ray spectral studies. The $^{13}C$ NMR spectra of **1** and **4** show nine peaks as a result of pair-wise equivalence of the carbon atoms, while eighteen peaks are seen in the case of **2** and **5** because of the eighteen nonequivalent carbon atoms. On the basis of DEPT-135 experiments, the peaks in the range from 15 to 30 ppm can be assigned to eight carbon atoms of peripheral methyl groups and the remaining peaks in the range from 40 to 60 ppm correspond to ring carbon atoms. The results are supported by similar observations for C-*meso*-$Me_8$[14]diene and $Me_4$[14]denen. Both complexes, [Ni(*Aα*-$Me_4$[14]denen)]$^{2+}$ (symmetry) and [Ni(*Bβ*-$Me_4$[14]denen)]$^{2+}$ (asymmetry), containing fourteen carbon atoms show fourteen and seventeen peaks, respectively.[13] Similar observations have also been found in the case of two isomeric *trans*-[Co([15]ane)$Cl_2$]$^{+}$ complexes.[14] In the case of symmetric C-*meso* and C-*rac*-$Me_6$[22]ane, twelve peaks are seen owing to the pair-wise equivalence of the carbon atoms.[15]

$Cu^{II}$ complexes (**7** and **8**) are NMR inactive. Hence, these were confirmed by X-ray crystallography.

### Crystal Structures

The crystal structures of ligands and complexes are shown in Figures 1, 2, 3, 4, 5, and 6, which are drawn with ORTEP at the 30% probability level. Structural configurations and methyl orientations are shown in Scheme 3. Selected bond lengths and bond angles are listed in Tables 2, 3, and 4. The geometry around the nickel(II) ion in the complexes is approximately square-planar and around the copper(II) ion it is octahedral.

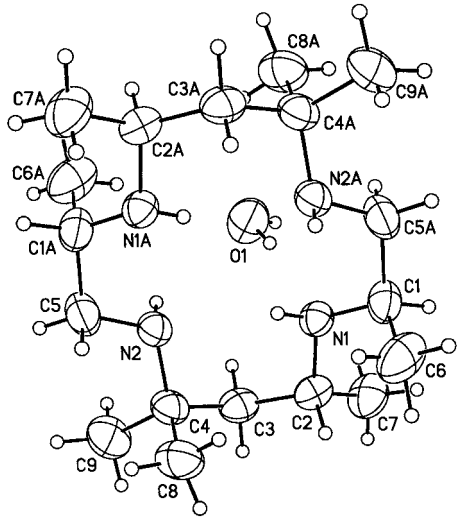


Figure 1. An ORTEP view of ligand **1**.

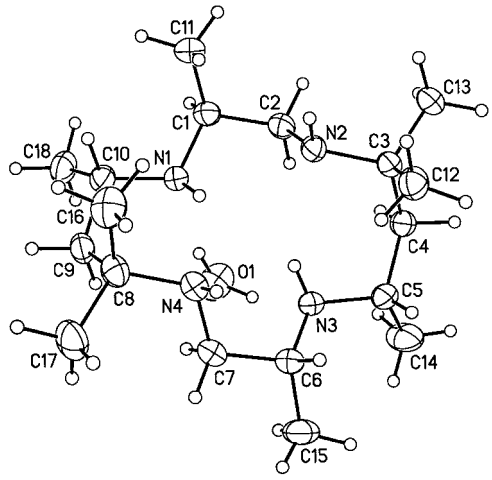


Figure 2. An ORTEP view of ligand **2**.

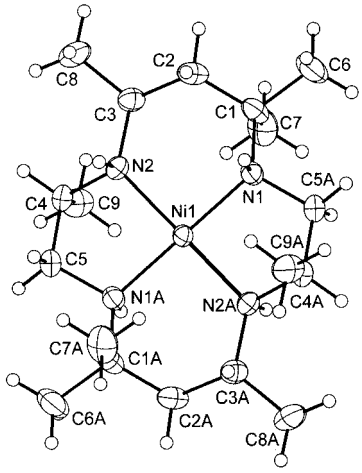


Figure 3. An ORTEP view of complex **4**.

#### *Ligand 1*

An inversion center is present in the molecule. The structure determination indicates that the ring lies in a zigzag shape with tetramine equatorial positions. The configurations of the four chiral carbon centers are 3*S*, 5*S*, 10*R*, and 12*R*. The 3,10-dimethyl groups occur on opposite sides of the ring in a *meso* configuration and have an axial orientation. Moreover, the 5,12-dimethyl groups also occur on opposite sides of the ring in a *meso* configuration but have an equatorial orientation. All distances and angles fall within the normal ranges. The H(1) atom of the water molecule forms an O–H···N hydrogen bond with a length of 2.129(1) Å with the N(1) atom of the secondary amine. The other distance, between the water H(1) atom and the amine

 © 2006 Wiley-VCH Verlag GmbH & Co. KGaA, Weinheim 

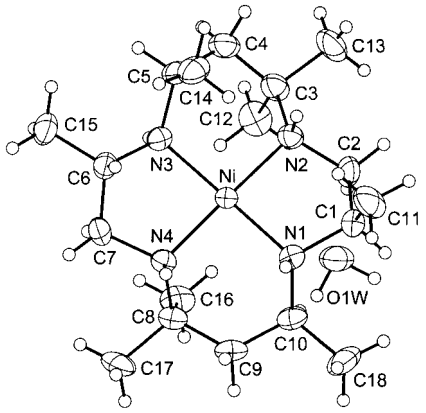


Figure 4. An ORTEP view of complex **5**.

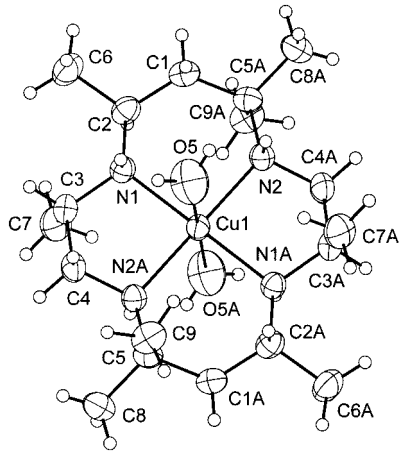


Figure 5. An ORTEP view of complex **7**.

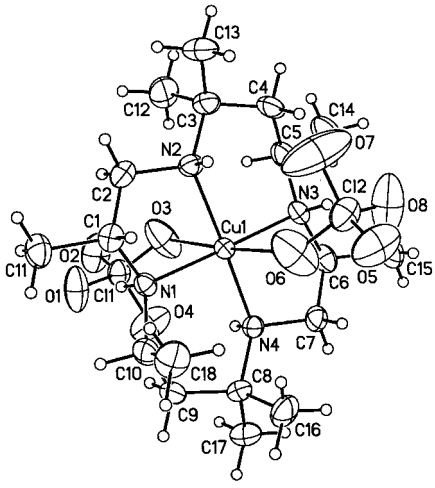


Figure 6. An ORTEP view of complex **8**.

N(2) atom, is 2.993(2) Å. The distance, 2.619(2) Å, between the O(1) atom and the H(2A) atom shows that the water O(1) atom is also slightly hydrogen bonded to the amine H(2A) atom. A diequatorial-diaxial arrangement for the four chiral methyl groups is observed in the structure, where the methyl groups at the 5 and 12 positions occupy a *meso* configuration.

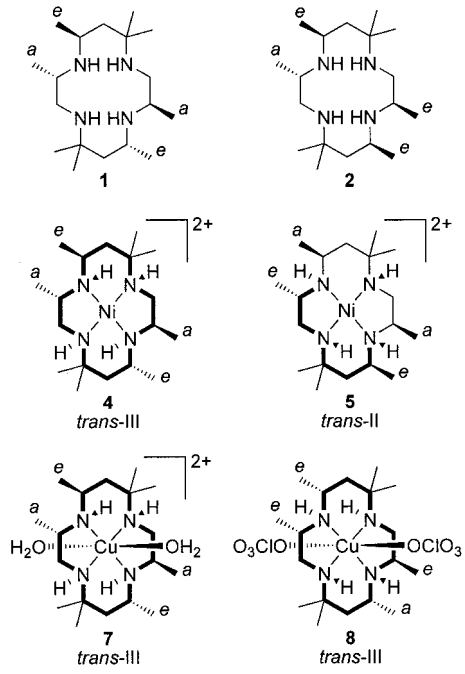


Scheme 3. *gauche* conformations of the five-membered chelate rings and chair conformations of the six-membered chelate rings are indicated by heavier lines.

### *Ligand 2*

The 14-membered ring has a noncentrosymmetric and folded structure where two diagonal nitrogen atoms point up and the other two down, and a water molecule is located on a crystallographic two-fold center. The configurations of the four chiral carbon centers are 3*S*, 5*S*, 10*R*, and 12*S*. All four NH groups and the 3-methyl group lie on the same side of the ring, while the water molecule and 5,10,12-trimethyl groups are on the other side. The 3-methyl group retains an axial orientation and the 5,10,12-trimethyl groups have an equatorial orientation with 3,10-dimethyl in a *meso* configuration and 5,12-dimethyl in a *racemic* configuration. The distances of the intermolecular O(1)–H(1A)···N(1) and O(1)–H(1B)···N(3) hydrogen bonds are 2.218(1) and 2.052(1) Å, respectively. An equatorial-triaxial arrangement for the four chiral methyl groups is possible in the structure, where the methyl groups at the 5 and 12 positions occupy a *racemic* configuration.

### *Complex 4*

The X-ray analysis reveals that the $Ni^{II}$ ion is located on a center of inversion and coordinated by four nitrogen atoms in equatorial positions to form a distorted square-planar geometry. The 14-membered ring consists of two six-membered chelate rings in chair conformations and two five-membered chelate rings in *gauche* conformations. The complex has a 1*R*,4*S*,8*S*,11*R* configuration of the four N chiral centers. The most thermodynamically stable nitrogen configuration is supposed to be the *trans*-III (–++–)[5a] configuration. The four chiral carbon centers are in the

 © 2006 Wiley-VCH Verlag GmbH & Co. KGaA, Weinheim 

Table 2. Selected bond lengths [Å] and angles [°] for ligands **1** and **2**.[a]

| | | | |
|---|---|---|---|
| **1** | | | |
| N(1)–C(1) | 1.464(2) | N(1)–C(2) | 1.469(2) |
| N(2)–C(5) | 1.460(1) | N(2)–C(4) | 1.480(1) |
| C(1)–C(5$^{i}$) | 1.523(2) | C(1)–C(6) | 1.527(2) |
| C(2)–C(7) | 1.524(2) | C(2)–C(3) | 1.527(2) |
| C(3)–C(4) | 1.541(2) | C(4)–C(8) | 1.528(2) |
| C(4)–C(9) | 1.541(2) | C(5)–C(1$^{i}$) | 1.523(2) |
| C(1)–N(1)–C(2) | 116.73(8) | C(5)–N(2)–C(4) | 117.02(9) |
| N(1)–C(1)–C(5$^{i}$) | 108.60(9) | N(1)–C(1)–C(6) | 114.57(10) |
| C(5$^{i}$)–C(1)–C(6) | 112.17(10) | N(1)–C(2)–C(7) | 110.03(9) |
| N(1)–C(2)–C(3) | 110.74(8) | C(7)–C(2)–C(3) | 109.47(9) |
| C(2)–C(3)–C(4) | 119.39(9) | N(2)–C(4)–C(8) | 109.43(9) |
| N(2)–C(4)–C(3) | 107.32(8) | C(8)–C(4)–C(3) | 110.93(10) |
| N(2)–C(4)–C(9) | 111.95(9) | C(8)–C(4)–C(9) | 109.35(11) |
| C(3)–C(4)–C(9) | 107.85(10) | N(2)–C(5)–C(1$^{i}$) | 111.46(9) |
| **2** | | | |
| N(1)–C(10) | 1.461(2) | N(1)–C(1) | 1.467(2) |
| N(2)–C(2) | 1.458(2) | N(2)–C(3) | 1.489(2) |
| N(3)–C(6) | 1.464(2) | N(3)–C(5) | 1.471(2) |
| N(4)–C(7) | 1.457(2) | N(4)–C(8) | 1.486(2) |
| C(1)–C(2) | 1.526(2) | C(1)–C(11) | 1.527(2) |
| C(3)–C(12) | 1.515(2) | C(3)–C(4) | 1.536(2) |
| C(3)–C(13) | 1.536(2) | C(4)–C(5) | 1.524(2) |
| C(5)–C(14) | 1.536(3) | C(6)–C(15) | 1.514(2) |
| C(6)–C(7) | 1.518(2) | C(8)–C(16) | 1.524(2) |
| C(8)–C(9) | 1.540(2) | C(8)–C(17) | 1.541(2) |
| C(9)–C(10) | 1.526(2) | C(10)–C(18) | 1.517(2) |
| C(10)–N(1)–C(1) | 118.06(10) | C(2)–N(2)–C(3) | 118.33(10) |
| C(6)–N(3)–C(5) | 116.28(10) | C(7)–N(4)–C(8) | 116.62(11) |
| N(1)–C(1)–C(2) | 107.35(10) | N(1)–C(1)–C(11) | 115.09(12) |
| C(2)–C(1)–C(11) | 112.31(12) | N(2)–C(2)–C(1) | 110.62(10) |
| N(2)–C(3)–C(12) | 105.55(10) | N(2)–C(3)–C(4) | 111.34(10) |
| C(12)–C(3)–C(4) | 111.00(12) | N(2)–C(3)–C(13) | 111.51(11) |
| C(12)–C(3)–C(13) | 109.20(12) | C(4)–C(3)–C(13) | 108.24(11) |
| C(5)–C(4)–C(3) | 120.48(11) | N(3)–C(5)–C(4) | 111.24(10) |
| N(3)–C(5)–C(14) | 111.20(13) | C(4)–C(5)–C(14) | 107.42(12) |
| N(3)–C(6)–C(15) | 112.86(13) | N(3)–C(6)–C(7) | 109.72(11) |
| C(15)–C(6)–C(7) | 108.83(13) | N(4)–C(7)–C(6) | 112.79(11) |
| N(4)–C(8)–C(16) | 106.28(11) | N(4)–C(8)–C(9) | 110.66(10) |
| C(16)–C(8)–C(9) | 111.03(13) | N(4)–C(8)–C(17) | 111.78(12) |
| C(16)–C(8)–C(17) | 109.23(13) | C(9)–C(8)–C(17) | 107.90(12) |
| C(10)–C(9)–C(8) | 118.78(11) | N(1)–C(10)–C(18) | 110.42(11) |

[a] Symmetry transformations used to generate equivalent atoms: (i) $-x + 1, -y + 1, -z$.

Table 3. Selected bond lengths [Å] and angles [°] for complexes **4** and **5**.[a]

| | | | |
|---|---|---|---|
| **4** | | | |
| Ni(1)–N(1) | 1.955(2) | Ni(1)–N(2) | 1.962(2) |
| N(1)–Ni(1)–N(1$^{i}$) | 180.0 | N(1)–Ni(1)–N(2) | 94.23(10) |
| N(1)–Ni(1)–N(2$^{i}$) | 85.77(10) | | |
| **5** | | | |
| Ni–N(1) | 1.949(4) | Ni–N(4) | 1.925(4) |
| Ni–N(2) | 1.932(4) | Ni–N(3) | 1.933(4) |
| N(4)–Ni–N(2) | 176.22(17) | N(4)–Ni–N(1) | 91.97(15) |
| N(4)–Ni–N(3) | 86.79(16) | N(2)–Ni–N(1) | 87.46(16) |
| N(2)–Ni–N(3) | 94.23(16) | N(3)–Ni–N(1) | 172.93(16) |

[a] Symmetry transformations used to generate equivalent atoms: (i) $-x + 1, -y + 1, -z + 2$.

3*S*,5*S*,10*R*,12*R* configuration. 3,10-Dimethyl groups on five-membered chelate rings have an axial orientation in a *meso* configuration *trans* to the H atom of the neighboring amine group. 5,12-Dimethyl groups on six-membered chelate rings also occur on opposite sides of the macrocyclic ring in a *meso* configuration but have stable equatorial orientations and lie away from the $Ni^{II}$ ion center. A diequatorial-diaxial arrangement of the four chiral methyl groups is observed in the structure.

The Ni–N distances 1.955(2) and 1.962(2) Å are almost equivalent to the reported values in [Ni(3,10-C-*meso*-5,12-C-*meso*-$Me_8$[14]ane$_{Ba}$)]$(ClO_4)_2$ ([1.953(2) and 1.962(2) Å][9g] and [Ni(3,10-C-*meso*-5,12-C-*meso*-$Me_8$[14]ane$_{Ca}$)]$(ClO_4)_2$ [1.948(3) and 1.961(2) Å],[9a] but shorter than the values found in [Ni(1,8-bis(2-cyanoethyl)-3,10-C-*meso*-5,12-C-*meso*- $Me_8$[14]ane)]$(ClO_4)_2$ [1.972(2) and 2.008(2) Å][9j] and [Ni(1,8-diallyl-3,10-C-*meso*-5,12-C-*meso*-$Me_8$[14]ane$_{Ca}$)]-$(ClO_4)_2$ [1.984(2) and 2.000(2) Å].[16] The N–Ni–N bond angle [85.77(10)°] involved in the five-membered chelate ring is smaller than that [94.23(10)°] in the six-membered chelate ring, as usual. In the perchlorate group, the anion

 © 2006 Wiley-VCH Verlag GmbH & Co. KGaA, Weinheim 

Table 4. Selected bond lengths [Å] and angles [°] for complexes **7** and **8**.[a]

| | | | |
|---|---|---|---|
| **7** | | | |
| Cu(1)–N(1) | 2.035(3) | Cu(1)–O(5) | 2.816(4) |
| Cu(1)–N(2) | 2.038(3) | | |
| N(1)–Cu(1)–N(2) | 85.38(10) | N(1)–Cu(1)–N(1$^{i}$) | 180.00 |
| N(2)–Cu(1)–N(1$^{i}$) | 94.62(10) | N(2)–Cu(1)–N(2$^{i}$) | 180.00 |
| N(1)–Cu(1)–O(5) | 77.84(10) | N(2)–Cu(1)–O(5) | 82.61(11) |
| O(5)–Cu(1)–O(5$^{i}$) | 180.00 | | |
| **8** | | | |
| Cu(1)–N(1) | 2.015(2) | Cu(1)–N(2) | 2.047(2) |
| Cu(1)–N(4) | 2.021(2) | Cu(1)–O(3) | 2.731(3) |
| Cu(1)–N(3) | 2.043(2) | Cu(1)–O(6) | 2.570(4) |
| N(1)–Cu–N(2) | 84.43(7) | N(1)–Cu–N(3) | 176.89(8) |
| N(1)–Cu–N(4) | 94.42(8) | N(2)–Cu–N(3) | 95.73(7) |
| N(2)–Cu–N(4) | 177.17(7) | N(3)–Cu–N(4) | 85.28(7) |
| N(1)–Cu(1)–O(3) | 85.01(8) | N(1)–Cu(1)–O(6) | 98.61(9) |
| N(2)–Cu(1)–O(3) | 92.94(9) | N(2)–Cu(1)–O(6) | 85.91(9) |
| N(3)–Cu(1)–O(3) | 91.88(8) | N(3)–Cu(1)–O(6) | 84.50(9) |
| N(4)–Cu(1)–O(3) | 84.38(9) | N(4)–Cu(1)–O(6) | 96.82(9) |
| O(3)–Cu(1)–O(6) | 176.07(10) | | |

[a] Symmetry transformations used to generate equivalent atoms: (i) $-x + 1, -y, -z + 2$.

is hydrogen bonded to pairs of adjacent N–H groups with normal N···O distances of 2.983 and 3.151 Å.

### *Complex 5*

The $Ni^{II}$ ion is four-coordinate in a distorted square-planar geometry with the four N-atoms of **2**. The complex cation is a noncentrosymmetric structure and has a 1*S*,4*R*,8*S*,11*S* configuration of the four chiral nitrogen centers in the *trans*-II (+–++) configuration, different from the most thermodynamically stable *trans*-III. The chiral carbon centers and 3,5,10,12-tetramethyl groups are in configurations of 3*S*,10*R*-C-*meso* and 5*S*,12*S*-C-*racemic*, where 3,12-dimethyl groups occupy an equatorial orientation and 5,10-dimethyl groups an axial orientation. The five-membered chelate ring, Ni, N(3), C(6), C(7), N(4), has a thermodynamically stable *gauche* conformation with the equatorial methyl group in the one structure and a distorted eclipsed conformation with the axial methyl group in the other. The six-membered chelate ring, Ni, N(4), C(8), C(9), C(10), N(1), has a chair conformation with the equatorial methyl group in the one structure and a twist-boat conformation with the axial methyl group in the other. The 3-methyl group and the neighboring amine group are found on the same side of the coordination plane *trans* to the other methyl and amine groups. A diequatorial-diaxial arrangement of the four chiral methyl groups is observed in the structure.

The Ni–N bond lengths in the range 1.925(4) to 1.949(4) Å are shorter than the values found in **4**, but similar to those found in [Ni(3,10-C-*rac*-5,12-C-*rac*-$Me_8$[14]ane)]$(ClO_4)_2$ [1.926(2) and 1.931(2) Å],[17] where the four N–H groups are on the same side and the 14-membered ring has a basket configuration. The N–Ni–N bond angles of the *gauche* and chair chelate rings are 86.79(16) and 91.97(15)°, respectively, smaller than those found in the eclipse [87.46(16)°] and twist-boat chelate rings [94.23(16)°]. In the second perchlorate ion [Cl(2)], three oxygen atoms are found to be disordered over two positions. The abnormal O–Cl(2)–O bond angles of the perchlorate ions, ranging from 52.2(8) to 135.9(9)°, suggest further complicated disorder. Hydrogen bonds between water molecules, perchlorate ions, and amine groups help to stabilize the crystal structure. The water molecule is placed between two perchlorate ions to form HO–H···O–$ClO_3$ hydrogen bonds in the range 2.094 to 2.628 Å. The distances of the hydrogen bonds between the perchlorate O atom and the amine H atom are in the range 2.063 to 2.508 Å.

### *Complex 7*

The copper(II) ion is coordinated by four nitrogen atoms in equatorial positions and two oxygen atoms in *trans* axial positions from water to form a distorted octahedron. The complex cation has a 1*R*,4*S*,8*S*,11*R* configuration of the four chiral nitrogen centers in the *trans*-III (–++–) configuration with both six-membered chelate rings in chair conformations and both five-membered chelate rings in *gauche* conformations. Each of the two methyl groups on the five-membered chelate rings has an axial orientation *trans* to the H atom of the neighboring amine group. Four of the six methyl groups at the 5, 7, 12, and 14 positions on the six-membered chelate rings are in a stable equatorial plane and lie away from the metal ion center. A diequatorial-diaxial arrangement for the four chiral methyl groups is observed in the structure.

The Cu–O (axial) bond is considered to be very weakly coordinated, since the Cu–O(5) distance of 2.816(4) Å is longer than the typical values for $Cu^{II}$ complexes and is significantly longer than the four Cu–N (equatorial) distances, 2.035(3) and 2.038(3) Å. In fact, the axial bonds of most six-coordinate $Cu^{II}$ complexes are often elongated as a result of the Jahn–Teller effect. These facts support the complex belonging to a six-coordinate (4 + 2) geometry.[18] The axial Cu–O bond length is compared to those in [Cu(3,10-C-*meso*-5,12-C-*meso*-$Me_8$[14]ane)$(H_2O)_2$]$(NO_3)_2$,[9d] [Cu(C-*meso*-1,5,8,12-tetramethyl-1,4,8,11-tetraazacyclotetradecane)$(H_2O)_2$]$(NO_2)_2$,[19a] and [Cu(C-*meso*-5,12-dimethyl-1,4,8,11-tetraazacyclotetradecane)$(H_2O)_2$]$Cl_2$-$(H_2O)_2$.[19b] Each of the water molecules forms intramolecular hydrogen bonds with one H atom of an amine group and one O atom of the perchlorato group, as well as an intermolecular hydrogen bond with the perchlorate O atom of a neighboring molecule. The N(1)–H(1)···O(5) distance is 2.428 Å and the N(2)–H(2)···O(5) distance 2.713 Å. The distances between the coordinated water H(5B) atom and the perchlorate O atoms are in the range 2.097 to 2.973 Å.

### *Complex 8*

The complex has a distorted octahedral coordination geometry with the macrocyclic tetradentate amine N atoms in equatorial positions and two O atoms of two perchlorato groups in *trans* axial positions with the angle O(6)–Cu–O(3) equal to 176.07(10)°. The four N atoms of the macrocyclic ligand form a square plane. The largest deviation from the

 © 2006 Wiley-VCH Verlag GmbH & Co. KGaA, Weinheim 

least-squares plane is 0.0044(10) Å. The deviation of the Cu atom from the relevant plane is 0.0507(10) Å. The tetradentate ligand adopts its most stable conformation with two six-membered chelate rings in chair conformations and two five-membered chelate rings in *gauche* conformations. The complex has a 1*S*,4*R*,8*R*,11*S* configuration of the four chiral N centers in the *trans*-III (+—+) configuration. The configurations of the four chiral carbon centers are 3*S*, 5*R*, 10*R*, and 12*R* with 3,5,10-trimethyl groups in equatorial positions and the 12-methyl group in an axial position. The axial methyl group on the six-membered chelate ring makes the chair conformation unstable while the methyl group on the other six-membered chelate ring is in the stable equatorial position. A triequatorial-axial arrangement for the four chiral methyl groups is observed in the structure.

The Cu–O(3) distance [2.731(3) Å] is longer than the other axial Cu–O(6) distance [2.570(4) Å] and the four Cu–N distances [2.015(2)–2.047(2) Å]. This result shows that $[CuL_d(ClO_4)_2]$ forms an unusual six-coordinate (4 + 1 + 1′) structure in which the complex has four strongly coordinated atoms, one weakly coordinated atom and one very weakly coordinated atom. The Cu–O bond lengths are compared to those in [Cu(1,4,7,11-tetraazacyclotetradecane)$(ClO_4)_2$][20a] and [Cu(C-*meso*-1,5,8,12-tetramethyl-1,4,8,11-tetraazacyclotetradecane)$(ClO_4)_2$].[20b] The N–Cu–N angles of five- and six-membered rings are in the expected range. Hydrogen bonds between amine hydrogen atoms and O atoms of perchlorato groups help to stabilize the crystal structure. The distances are N(1)–H(1B)···O(1) 2.146 Å, N(2)–H(2C)···O(7) 2.645 Å, N(3)–H(3A)···O(8) 2.211 Å, and N(4)–H(4C)···O(4) 2.491 Å.

### Spectra and Properties

The infrared spectra of the $Ni^{II}$ and $Cu^{II}$ complexes show a sharp NH stretching vibration of secondary amines around 3200 $cm^{-1}$ with a broad strong band at about 1100 $cm^{-1}$ resulting from the perchlorate anions.

The UV/Vis spectra of the $Ni^{II}$ complexes, **4** and **5**, show strong absorption bands of the planar chromophore at 469 and 455 nm, respectively. For low-spin nickel(II) tetramine complexes the energy of the d–d band is a measure of the energy of the equatorial Ni–N interactions. The single absorption band of **4** at 469 nm (21,322 $cm^{-1}$) is assigned to the $^1A_{1g} \rightarrow {}^1E_g$ transition of the square planar nickel(II) complex and is approximately 656 $cm^{-1}$ lower in frequency than that of **5** at 455 nm (21,978 $cm^{-1}$), establishing that **4** exerts weaker metal-donor atom interactions than its diastereoisomeric complex **5**. Similar observations have been found with $[Ni(tet\ a)]^{2+}$ (*meso*) and $[Ni(tet\ b)]^{2+}$ (*racemate*).[21] In aqueous solution, $Ni^{II}$ complexes of 14-membered tetrazamacrocyclic ligands exist as an equilibrium mixture of low-spin square planar (yellow, planar) and high-spin pseudooctahedral (blue, *cis*-diaqua and *trans*-diaqua) complex cations.[22] The *cis*-diaqua form is much more unstable than the low-spin square-planar and *trans*-diaqua high-spin pseudooctahedral complex cations. The equilibrium can be affected by various factors: addition of salts, temperature, solvent, ionic strength, pH value, and steric effect, etc.[23] In addition, the proportion of planar species also increases by an increase in the number of methyl groups on the macrocyclic ligand.[24] In nitromethane (a noncoordinating solvent), **4** and **5** have molar extinction coefficients of $\varepsilon$ = 77.9 and 90.6 $dm^3 mol^{-1} cm^{-1}$ in 100% planar species, respectively.[25] The values are almost equal to those found in aqueous solution over a range of temperatures. This result shows that the intensities of the bands are temperature-independent and axial additions are not observed. In other words, **4** and **5** exhibit almost 100% planar species in aqueous solution, which may result from the steric effect produced by numerous methyl groups, especially axial orientations and the distorted structures.

Both $Cu^{II}$ complexes, **7** and **8**, exhibit two bands, one falls in the visible region and the other falls in the ultraviolet region. Previous studies show that the most $Cu^{II}$ complexes are six-coordinate tetragonal with long axial bonds. The higher energy band (≈270 nm) in the ultraviolet region is assigned to ligand-metal charge-transfer transitions associated with the nitrogen donors.[26] The lower d–d transition in the visible region of the spectrum is believed to be a combination of the three possible transitions $d_{xy}$, $d_{xz}$, $d_{yz} \rightarrow d_{x^2-y^2}$ and is characteristic of many $Cu^{II}$ complexes.[26] The expected $d_{z^2} \rightarrow d_{x^2-y^2}$ transition appearing at the lowest energy (near-IR region), indicative of the splitting of the $e_g$ (in $O_h$) caused by the tetragonal distortion (Jahn–Teller), was not observed in the visible region. Cheng and Chung reported that the rod-like acetonitrile is coordinated more strongly than $H_2O$ in the axial position of $[Ni(tet\ b)]^{2+}$ because of steric interactions, even though the donor ability of $H_2O$ is greater than acetonitrile,[26d] indicating that acetonitrile is a better axial donor. As the axial bond weakens, the copper atom becomes more positive, and attracts the in-plane ligands more strongly. Some interesting results are provided in the visible spectra where the visible band of **7** at 511 nm (19,569 $cm^{-1}$) in acetonitrile is some 391 $cm^{-1}$ lower in frequency than that at 501 nm (19,960 $cm^{-1}$) in aqueous solution, while the bands of **8** are observed at 528 nm (18,939 $cm^{-1}$) in both acetonitrile and aqueous solution. These results indicate that the axial donor is more strongly bound in **8** than that found in **7**, as seen from the crystal structures, resulting in weaker in-plane coordinations.[26a] In this work, the axial coordination is largely affected by the steric interactions between the axial donor and the axial methyl groups. When **7** is dissolved in aqueous solution, the entire band envelope shifts to the blue region, indicating that water molecules are more weakly bound or unbound since the axial methyl groups almost sterically congest the axial sites.

## Conclusions

In summary, four diastereoisomers of 3,10-*meso*-3,5,7,7,10,12,14,14-octamethyl-1,4,8,11-tetraazacyclotetradecane were distinguished by the *RS*-configurations of the

 © 2006 Wiley-VCH Verlag GmbH & Co. KGaA, Weinheim 

chiral methyls at the 5 and 12 positions. Ligands **1**, **2**, and **3** were isolated and assigned as 5*S*,12*R*-C-*meso*, 5*S*,12*S*-C-*racemic* and 5*R*,12*R*-C-*racemic*, respectively. The isomer $L_a$ could not be isolated following the experimental methods described in the text, and we assigned it as 5*R*,12*S*-C-*meso*-$Me_8$[14]ane. Spectral studies show that **1** is centrosymmetric whereas **2** and **3** are noncentrosymmetric. Nickel(II) and copper(II) complexes of these ligands were isolated. In accordance with the X-ray structure determination, the geometry around the $Ni^{II}$ ion in the complexes is approximately square-planar and the $Cu^{II}$ ion octahedral. The configuration of **5** is *trans*-II, different from the most thermodynamically stable *trans*-III complex as shown in **4**, **7**, and **8**. In complexes **7** and **8** unusual six-coordinate (4 + 2) and (4 + 1 + 1′) geometries, respectively, were formed because of the longer Cu–O distances compared with the equatorial Cu–N distances. UV/Vis spectra show that both $Ni^{II}$ complexes exhibit almost 100% planar species in aqueous solution as a result of the steric effect produced by numerous methyl groups, especially axial orientations and the distorted structures. In six coordinate $Cu^{II}$ complexes, acetonitrile turns out to be a better axial donor than the water molecule, and the weaker axial bonding is a result of the steric interactions producing stronger in-plane coordinations.

## Experimental Section

**Physical Measurements:** A Bruker DMX-600 MHz or AC300 MHz spectrometer was used to obtain $^1H$ and $^{13}C$ NMR spectra that are referenced to the solvent. Infrared spectra were recorded with a Perkin–Elmer System 2000 FT-IR spectrophotometer as KBr pellets. UV/Vis spectra were recorded with a Hitachi Model U-3300 spectrophotometer. High-resolution mass spectra were obtained using a MAT-95XL mass spectrometer. Microanalysis (C, H, N) was performed using a Heraeus CHNOS Rapld F002 elemental analyzer.

**Synthesis of Ligands and Complexes:** All the chemicals used were of reagent grade and were not purified further. The reaction of (±)-1,2-propanediamine with acetone in perchloric acid yielded stereospecifically only the crystalline 3,10-*meso*-$Me_8$[14]diene·$2HClO_4$.[6a,8]

***Caution!*** Although no problem was encountered in this work, the transition metal perchlorate is potentially explosive. It should be prepared in small quantities and handled with care.

**$L_b$ (1):** Ligand L (73.0 g, 143 mmol) was suspended in methanol (300 mL) and stirred. An aqueous solution of sodium hydroxide (25.0 g of NaOH in 250 mL of $H_2O$) was then added until the ligand L completely dissolved. Thereafter sodium borohydride (43.0 g, 1.14 mol) was added pinchwise to the solution until no more bubbles appeared. The mixture was then refluxed for 3.0 h. After the mixture had cooled to room temperature, an aqueous solution of sodium hydroxide (16.0 g of NaOH in 400 mL of $H_2O$) was added and stirred for 30 min; a white precipitate subsequently appeared. This precipitate, a mixture of isomers 3*S*,10*R*-C-*meso*-$Me_8$[14]anes (34.5 g, 77%), was washed with cold water and dried. The isomer **1** was separated by the partial crystallization method: a mixture of isomers of 3*S*,10*R*-C-*meso*-$Me_8$[14]anes (30.0 g, 96.1 mmol) was dissolved in boiling methanol (400 mL) and filtered while hot. Deionized water (400 mL) was added to the hot filtrate and stirred until the solution had cooled to room temperature. A white precipitate of **1** was formed, which was filtered and recrystallized from hot ether. Yield 18.2 g (61%). M.p. 125 °C (from ether). $C_{18}H_{40}N_4$ (312.54): calcd. C 69.17, H 12.90, N 17.93; found C 69.02, H 12.82, N 17.85. FT-IR (KBr disk): $\tilde{\nu}$ = 3265, 2966, 2910, 2826, 1475, 1185 $cm^{-1}$. $^1H$ NMR (600 MHz, $CDCl_3$): $\delta$ = 0.96 (d, $J$ = 6.14 Hz, 6 H), 1.01 (d, $J$ = 6.44 Hz, 6 H), 1.05 (s, 6 H), 1.11 (s, 6 H), 1.22 (d, $J$ = 2.58 Hz, 1 H), 1.25 (d, $J$ = 2.57 Hz, 1 H), 1.62 (m, 2 H), 2.57 (m, 2 H), 2.64 (m, 2 H), 2.99 (m, 2 H), 3.08 (m, 2 H) ppm. $^{13}C$ NMR (125 MHz, $CDCl_3$): $\delta$ = 16.6 ($CH_3$), 20.4 ($CH_3$), 25.7 ($CH_3$), 29.1 ($CH_3$), 45.4 (CH), 47.4 (CH), 47.6 ($CH_2$), 48.7 ($CH_2$), 52.9 (C) ppm. HRMS ($EI^+$, $m/z$): calcd. for $C_{18}H_{40}N_4$ 312.3253, found 312.3253. The filtrate ($F_1$) was kept for further treatment.

**$L_c$ (2):** Deionized water (200 mL) was added to the above filtrate ($F_1$) and continuously stirred for 30 min. A small amount of white precipitate containing a mixture of the isomers was removed. The filtrate ($F_2$) was then evaporated on a rotary evaporator and gave a mixture of *rac* isomers, $L_c$ and $L_d$. Yield 10.4 g (35%). This mixture was then dissolved in ether and partial crystals of **2** were obtained in the first fraction by slow evaporation at room temperature. M.p. 91 °C (from ether). $C_{18}H_{40}N_4{\cdot}H_2O$ (330.56): calcd. C 65.40, H 12.81, N 16.95; found C 65.29, H 12.73, N 16.88. FT-IR (KBr disk): $\tilde{\nu}$ = 3246, 2966, 2930, 2837, 1500, 1174 $cm^{-1}$. $^1H$ NMR (600 MHz, $CDCl_3$): $\delta$ = 0.91 (d, $J$ = 6.11 Hz, 3 H), 0.97 (d, $J$ = 6.76 Hz, 3 H), 1.01 (d, $J$ = 2.88 Hz, 3 H), 0.98 (s, 3 H), 0.99 (s, 3 H), 1.01 (d, $J$ = 2.88 Hz, 3 H), 1.02 (d, $J$ = 2.44 Hz, 3 H), 1.03 (s, 3 H), 1.04 (d, $J$ = 2.83 Hz, 1 H), 1.06 (s, 3 H), 1.08 (d, $J$ = 2.56 Hz, 1 H), 1.67 (m, 2 H), 2.44 (m, 3 H), 2.63 (m, 1 H), 2.76 (m, 2 H), 2.97 (m, 2 H) ppm. $^{13}C$ NMR (125 MHz, $CDCl_3$): $\delta$ = 16.2 ($CH_3$), 20.5 ($CH_3$), 21.5 ($CH_3$), 25.3 ($CH_3$), 27.1 ($CH_3$), 27.6 ($CH_3$), 29.1 ($CH_3$), 29.5 ($CH_3$), 43.5 ($CH_2$), 45.9 (CH), 46.0 ($CH_2$), 47.2 (CH), 47.4 ($CH_2$), 49.4 ($CH_2$), 50.8 (CH), 52.3 (C), 53.1 (C), 54.4 (CH) ppm. HRMS ($EI^+$, $m/z$): calcd. for $C_{18}H_{40}N_4$ 312.3253, found 312.3253. After removing all the crystals, the filtrate ($F_3$) was kept for further treatment.

**$L_d$ (3):** The above filtrate ($F_3$) was air-dried and a white damp residue ($R_1$) was obtained with no crystals. We had hoped it contained a small amount of **2** but only the predominant form of 3 was present. Since these two *racemic* forms are enantiomers of each other and have identical chemical properties it was very difficult to separate them completely and characterize them separately by spectral studies. An X-ray study was the ideal tool for a unique characterization of **3** and was therefore obtained for $[CuL_d(ClO)_2]$ to provide the necessary evidence.

**$[NiL_b](ClO_4)_2$ (4):** A methanol solution (20 mL) of **1** (0.520 g, 1.66 mmol) was added to a boiling methanol solution (20 mL) of nickel acetate tetrahydrate (0.411 g, 1.65 mmol). The solution was heated over a steam bath for 2.0 h and the volume was reduced to 30 mL. After adding lithium perchlorate trihydrate (0.610 g, 3.80 mmol), the reaction mixture was again heated for 5 min and then cooled to room temperature. A bright orange-yellow precipitate was filtered off and washed with methanol followed by ether. The solid was then dissolved in a hot acetonitrile solution. Slow evaporation of the solvent at room temperature gave an orange-yellow crystalline complex **4** that was filtered off and air-dried. Yield 0.634 g (67%). $C_{18}H_{40}Cl_2N_4NiO_8$ (570.13): calcd. C 37.92, H 7.07, N 9.83; found C 37.75, H 7.03, N 9.78. UV/Vis ($CH_3NO_2$): $\lambda$ ($\varepsilon$) = 469 nm (77.9 $dm^3\,mol^{-1}\,cm^{-1}$). FT-IR (KBr disk): $\tilde{\nu}$ = 3541, 3245, 3026, 2975, 1438, 1086 $cm^{-1}$. $^{13}C$ NMR (75 MHz, $CD_3NO_2$): $\delta$ = 13.1 ($CH_3$), 16.2 ($CH_3$), 21.2 ($CH_3$), 24.7 ($CH_3$), 45.5 (CH), 46.4 ($CH_2$), 49.1 ($CH_2$), 50.4 (CH), 53.5 (C) ppm.

 © 2006 Wiley-VCH Verlag GmbH & Co. KGaA, Weinheim 

**$[NiL_c](ClO_4)_2(H_2O)_{0.5}$ (5):** A methanol solution (20 mL) of **2** (1.49 g, 4.78 mmol) was added to a boiling methanol solution (20 mL) of nickel acetate tetrahydrate (1.19 g, 4.78 mmol). The pH of this solution was adjusted between 11 and 12 with sodium hydroxide. After stirring for 3.0 h, lithium perchlorate trihydrate (1.49 g, 9.29 mmol) was added and the solution was cooled to room temperature. The pH of the solution was adjusted to neutrality with perchlorate acid. Yellow crystals were obtained by slow evaporation of the water/methanol mixture. The bright yellow complex **5** was filtered off and washed with methanol and ether. Yield 1.66 g (61%). $C_{18}H_{41}Cl_2N_4NiO_{8.50}$ (579.14): calcd. C 37.33, H 7.14, N 9.67; found C 37.15 H 7.08, N 9.60. UV/Vis ($CH_3NO_2$): $\lambda$ ($\varepsilon$) = 455 nm (90.6 $dm^3 mol^{-1} cm^{-1}$). FT-IR (KBr disk): $\tilde{\nu}$ = 3430, 3195, 2975, 2873, 1635, 1462, 1115 $cm^{-1}$. $^{13}C$ NMR (75 MHz, $CD_3NO_2$): $\delta$ = 9.84 ($CH_3$), 16.9 ($CH_3$), 17.1 ($CH_3$), 19.9 ($CH_3$), 21.5 ($CH_3$), 24.3 ($CH_3$), 26.6 ($CH_3$), 27.3 ($CH_3$), 43.7 ($CH_2$), 44.3 (CH), 47.5 ($CH_2$), 48.0 ($CH_2$), 48.4 (CH), 49.2 ($CH_2$), 51.5 (CH), 53.7 (C), 54.6 (CH), 56.1 (C) ppm.

**$[NiL_d](ClO_4)_2\ x{\cdot}H_2O$ (6):** This complex was synthesized by following the same method as used for **5**, except ligand **3** was used instead of **2**. Spectral data are not given because they are identical to those of **5**. Unfortunately we were unable to obtain single crystals of this compound.

**$[CuL_b(OH_2)_2](ClO_4)_2$ (7):** A methanol solution (20 mL) of copper perchlorate hexahydrate (2.73 g, 7.38 mmol) was added to a methanol solution (20 mL) of **1** (2.18 g, 6.98 mmol). The mixture was refluxed for 1.0 h and then cooled to room temperature. The pink solid that precipitated was separated by filtration and washed several times with methanol and ether. The solid was then dissolved in a hot methanol/water mixture. Slow evaporation of the solvent at room temperature gave the purplish red crystalline complex **7**, which was filtered off and air-dried. Yield 4.02 g (84%). $C_{18}H_{44}Cl_2CuN_4O_{10}$ (611.01): calcd. C 35.38, H 7.26, N 9.17; found C 35.18, H 7.21, N 9.11. UV/Vis ($H_2O$): $\lambda$ ($\varepsilon$) = 279 (10464), 501 nm (131 $dm^3 mol^{-1} cm^{-1}$). FT-IR (KBr disk): $\tilde{\nu}$ = 3463, 3152, 2971, 2880, 1147, 1088 $cm^{-1}$.

**$[CuL_d(ClO_4)_2]$ (8):** Copper perchlorate hexahydrate (0.593 g, 1.60 mmol) was added to a methanol solution (20 mL) of $R_1$ (0.501 g, 1.60 mmol). The mixture was refluxed for 1.0 h and cooled to room temperature. The red precipitate was filtered off and washed with methanol and ether. Red crystals of **8** were obtained by slow evaporation of the methanol/water mixture. Yield 0.791 g (86%). $C_{18}H_{40}Cl_2CuN_4O_8{\cdot}H_2O$ (574.98): C 37.60, H 7.01, N 9.74; found C 37.41, H 6.96, N 9.69. UV/Vis ($H_2O$): $\lambda$ ($\varepsilon$) = 275 (6956), 527 nm (151 $dm^3 mol^{-1} cm^{-1}$). FT-IR (KBr disk): $\tilde{\nu}$ = 3183, 2967, 2893, 1146, 1090 $cm^{-1}$.

**$[CuL_c(ClO_4)_2]$ (9):** The complex was synthesized by following the same method used for **8**, except ligand **2** was used instead of **3**. Spectral data are not given because these are identical to those of **8**. Unfortunately we were unable to obtain single crystals of this compound.

**Crystallography:** Single crystals of ligands were obtained by slow evaporation of either ether solutions, methanol/water mixtures, or acetonitrile solutions. Intensity data were collected with a Siemens Smart CCD diffractometer using graphite-monochromated Mo-$K_\alpha$ radiation ($\lambda$ = 0.71073 Å). Data reduction and empirical absorption corrections were performed with the XTAL package or NRCVAX programs.[27] Structures were solved by the heavy atom method with SHELXS 97 and refined by full-matrix least-squares analysis on $F^2$ with SHELXL.[28] All the non-hydrogen atoms were refined anisotropically and the hydrogen atoms fixed at calculated positions and refined using a riding model. A summary of the crys-

Table 5. Summery of crystallographic data for ligands **1**–**2**.

| | **1** | **2** |
|---|---|---|
| Empirical formula | $C_{18}H_{42}N_4O$ | $C_{18}H_{42}N_4O$ |
| Formula mass | 330.56 | 330.56 |
| Temperature [K] | 296(2) | 294(2) |
| Crystal system | monoclinic | monoclinic |
| Space group | *C*2/*c* | $P2_1/n$ |
| *a* [Å] | 11.4892(8) | 9.9814(6) |
| *b* [Å] | 14.7100(8) | 19.2850(10) |
| *c* [Å] | 12.6084(8) | 10.8842(6) |
| $\alpha$ [°] | 90 | 90 |
| $\beta$ [°] | 99.269(2) | 93.405(1) |
| $\gamma$ [°] | 90 | 90 |
| *V* [Å$^3$] | 2103.1(2) | 2091.4(2) |
| *Z* | 4 | 4 |
| $D_{calcd.}$ [Mg m$^{-3}$] | 1.044 | 1.050 |
| Absorption coefficient [mm$^{-1}$] | 0.065 | 0.066 |
| *F*(000) | 744 | 744 |
| Crystal size [mm] | 0.50 × 0.30 × 0.20 | 0.40 × 0.30 × 0.15 |
| $\theta$ range [°] | 2.27 to 28.29 | 2.11 to 28.30 |
| | $-15 \le h \le 15$ | $-9 \le h \le 13$ |
| | $-19 \le k \le 19$ | $-25 \le k \le 25$ |
| | $-16 \le l \le 16$ | $-14 \le l \le 14$ |
| Reflections collected | 10646 | 15466 |
| Independent reflections | 2534 [*R*(int) = 0.0305] | 5191 [*R*(int) = 0.0380] |
| Data/restraints/parameters | 2534/0/105 | 5191/0/208 |
| Final *R* indices [$I > 2\sigma(I)$] | $R_1$ = 0.0422 | $R_1$ = 0.0511 |
| | $wR_2$ = 0.1235 | $wR_2$ = 0.1308 |
| *R* indices (all data) | $R_1$ = 0.0649 | $R_1$ = 0.0834 |
| | $wR_2$ = 0.1311 | $wR_2$ = 0.1450 |
| GOF on $F_2$ | 0.989 | 0.897 |
| Largest difference peak/hole [e Å$^{-3}$] | 0.229/–0.113 | 0.208/–0.174 |

 © 2006 Wiley-VCH Verlag GmbH & Co. KGaA, Weinheim 

Table 6. Summery of crystallographic data for complexes **4**,**5** and **7**,**8**.

| | **4** | **5** | **7** | **8** |
|---|---|---|---|---|
| Empirical formula | $C_{18}H_{40}Cl_2N_4NiO_8$ | $C_{18}H_{41}Cl_2N_4NiO_{8.5}$ | $C_{18}H_{44}Cl_2CuN_4O_{10}$ | $C_{18}H_{40}Cl_2CuN_4O_8$ |
| Formula mass | 570.15 | 579.16 | 611.01 | 574.98 |
| Temperature [K] | 294(2) | 294(2) | 294(2) | 294(2) |
| Crystal system | monoclinic | orthorhombic | monoclinic | monoclinic |
| Space group | $P2_1/c$ | $P2_12_12_1$ | $P2_1/c$ | $P2_1/c$ |
| $a$ [Å] | 8.6052(6) | 9.0716(8) | 8.2077(5) | 9.4358(6) |
| $b$ [Å] | 17.3298(13) | 13.4218(12) | 16.0955(10) | 31.5816(19) |
| $c$ [Å] | 8.9614(7) | 21.526(2) | 10.4400(6) | 8.9911(6) |
| $\alpha$ [°] | 90 | 90 | 90 | 90 |
| $\beta$ [°] | 104.325(1) | 90 | 103.295(1) | 102.510(1) |
| $\gamma$ [°] | 90 | 90 | 90 | 90 |
| $V$ [Å$^3$] | 1294.83(17) | 2620.9(4) | 1342.23(14) | 2615.7(3) |
| $Z$ | 2 | 4 | 2 | 4 |
| $D_{calcd.}$ [Mg m$^{-3}$] | 1.462 | 1.468 | 1.512 | 1.460 |
| Absorption coefficient [mm$^{-1}$] | 1.003 | 0.994 | 1.069 | 1.087 |
| $F(000)$ | 604 | 1228 | 646 | 1212 |
| Crystal size [mm] | 0.50 × 0.30 × 0.30 | 0.15 × 0.10 × 0.10 | 0.50 × 0.40 × 0.40 | 0.70 × 0.10 × 0.05 |
| $\theta$ range [°] | 2.35 to 28.26 | 1.79 to 28.36 | 2.37 to 25.70 | 1.29 to 25.69 |
| | $-9 \le h \le 11$ | $-12 \le h \le 11$ | $-7 \le h \le 10$ | $-10 \le h \le 11$ |
| | $-20 \le k \le 23$ | $-17 \le k \le 17$ | $-19 \le k \le 14$ | $-29 \le k \le 38$ |
| | $-11 \le l \le 10$ | $-20 \le l \le 28$ | $-12 \le l \le 11$ | $-10 \le l \le 10$ |
| Reflections collected | 8223 | 19612 | 7360 | 15869 |
| Independent reflections | 3067 [$R$(int) = 0.0330] | 6525 [$R$(int) = 0.0710] | 2551 [$R$(int) = 0.0249] | 4958 [$R$(int) = 0.0449] |
| Data/restraints/parameters | 3067/0/151 | 6525/4/328 | 2551/0/160 | 4958/0/298 |
| Final $R$ indices [$I > 2\sigma(I)$] | $R_1$ = 0.0478 | $R_1$ = 0.0469 | $R_1$ = 0.0498 | $R_1$ = 0.0375 |
| | $wR_2$ = 0.1467 | $wR_2$ = 0.1197 | $wR_2$ = 0.1431 | $wR_2$ = 0.0949 |
| $R$ indices (all data) | $R_1$ = 0.0680 | $R_1$ = 0.1180 | $R_1$ = 0.0555 | $R_1$ = 0.0554 |
| | $wR_2$ = 0.1549 | $wR_2$ = 0.0959 | $wR_2$ = 0.1494 | $wR_2$ = 0.1033 |
| GOF on $F_2$ | 1.025 | 0.673 | 1.066 | 0.604 |
| Largest difference peak/hole [e Å$^{-3}$] | 0.603/–0.522 | 0.499/–0.242 | 1.001/–0.447 | 0.451/–0.284 |

tallographic data and structure refinement parameters is given in Tables 5 and 6.

CCDC-279963 (for **1**), -279964 (for **2**), -279803 (for **4**), -279802 (for **5**), -279961 (for **7**), and -279962 (for **8**) contain the supplementary crystallographic data for this paper. These data can be obtained free of charge from The Cambridge Crystallographic Data Centre via www.ccdc.cam.ac.uk/data_request/cif.

## Acknowledgments

This research was supported in part by the National Science Council (Grants NSC 92-2113-M-007-045 and NSC 93-2511-S-007-004) of the Republic of China.

[1] a) M. Shionoya, E. Kimura, Y. Iitaka, *J. Am. Chem. Soc.* **1990**, *112*, 9237–9245 and references cited therein; b) G. J. Bridger, R. T. Skerlj, S. Padmanabhan, D. Thornton, *J. Org. Chem.* **1996**, *61*, 1519–1522; c) X. Liang, J. A. Parkinson, M. Weishaupl, R. O. Gould, S. J. Paisey, H.-S. Park, T. M. Hunter, C. A. Blindauer, S. Parsons, P. J. Sadler, *J. Am. Chem. Soc.* **2002**, *124*, 9105–9112; d) J. Larionova, R. Clérac, B. Donnadieu, S. Willemin, C. Guérin, *Cryst. Growth Des.* **2003**, *3*, 267–272; e) E. Colacio, I. B. Maimoun, F. Lloret, J. Suārez-Varela, *Inorg. Chem.* **2005**, *44*, 3771–3773; f) O. Enoki, T. Imaoka, K. Yamamoto, *Org. Lett.* **2003**, *5*, 2547–2549; g) T. K. Misra, C.-S. Chung, J. Cheng, T.-H. Lu, *Polyhedron* **2001**, *20*, 3149–3154.

[2] a) B. Konig, M. Pelka, H. Zieg, P. G. Jones, I. Dix, *Chem. Commun.* **1996**, 471–472; b) S. Aime, M. Botta, S. G. Crich, G. B. Giovenzana, G. Jommi, R. Pagliarin, M. Sisti, *J. Chem. Soc., Chem. Commun.* **1995**, 1885–1886; c) T. J. Norman, D. Parker, F. C. Smith, D. J. King, *J. Chem. Soc., Chem. Commun.* **1995**, 1879–1880.

[3] E. K. Barefield, G. M. Freeman, D. G. Van Derveer, *Inorg. Chem.* **1986**, *25*, 552–558.

[4] a) D. J. Szalda, E. Fujita, R. Sanzenbacher, H. Paulus, H. Elias, *Inorg. Chem.* **1994**, *33*, 5855–5863 and references cited therein; b) E. Kimura, M. Haruta, T. Koike, M. Shionoya, K. Takenouchi, Y. Iitaka, *Inorg. Chem.* **1993**, *32*, 2779–2784.

[5] a) B. Bosnich, C. K. Poon, T. Tobe, *Inorg. Chem.* **1965**, *4*, 1102–1108; b) J.-W. Chen, C.-S. Chung, *Inorg. Chem.* **1986**, *25*, 2841–2846; c) R. W. Hay, R. Bembi, D. A. House, *J. Chem. Soc., Dalton Trans.* **1984**, 1921–1925.

[6] a) N. F. Curtis, D. A. Swan, T. N. Waters, I. E. Maxwell, *J. Am. Chem. Soc.* **1969**, *91*, 4588–4589; b) T. Ito, D. H. Busch, *Inorg. Chem.* **1974**, *13*, 1770–1772.

[7] D. A. Swan, T. N. Waters, N. F. Curtis, *J. Chem. Soc., Dalton Trans.* **1972**, 1115–1120.

[8] R. Bembi, S. M. Sondhi, A. K. Singh, A. K. Jhanji, T. G. Roy, J. W. Lown, R. G. Ball, *Bull. Chem. Soc. Jpn.* **1989**, *62*, 3701–3705.

[9] a) G. Ferguson, A. J. Lough, *Acta Crystallogr., Sect. C* **1990**, *46*, 213–215; b) R. Bembi, T. G. Roy, A. K. Jhanji, A. J. Maheswari, *Chem. Soc., Dalton Trans.* **1990**, 3531–3534; c) R. Bembi, M. G. B. Drew, R. Singh, T. G. Roy, *Inorg. Chem.* **1991**, *30*, 1403–1406; d) S. K. S. Hazari, T. G. Roy, B. K. Dey, S. C. Das, E. R. T. Tiekink, *Metal-Based Drugs* **1997**, *4*, 255–265; e) R. W. Hay, I. Fraser, *Polyhedron* **1998**, *17*, 1931–1936; f) K.-Y. Choi, K. M. Chun, I.-H. Suh, *Inorg. Chem. Commun.* **1999**, *2*, 210–213; g) K.-Y. Choi, I.-H. Suh, *Main Group Met. Chem.* **1999**, *22*, 123–126; h) S.-G. Kang, J. Song, J. H. Jeong, *Inorg. Chim. Acta* **2000**, *310*, 196–202; i) T. G. Roy, R. Bembi, S. K. S. Hazari, B. K. Dey, T. K. Acharjee, E. Horn, E. R. T. Tiekink, *J. Coord. Chem.* **2002**, *55*, 853–862; j) S.-G. Kang, K. Ryu, J. Kim, *Bull. Korean Chem. Soc.* **2002**, *23*, 81–85; k) T. G. Roy, *J. Bangl.*

 © 2006 Wiley-VCH Verlag GmbH & Co. KGaA, Weinheim 

*Chem. Soc.* **2002**, *15*, 23–29; l) T.-J. Lee, T.-Y. Lee, W.-B. Juang, C.-S. Chung, *Acta Crystallogr., Sect. C* **1985**, *C41*, 1596–1598; m) S. K. S. Hazari, T. G. Roy, B. K. Dey, H. A. Miah, S. Dutta, E. R. T. Tiekink, *Z. Kristallogr. New Cryst. Struct.* **2001**, *216*, 441–442.

[10] a) A. K. Singh, A. Kumar, S. Panwar, S. Baniwal, *Analyst* **1999**, *124*, 521–525; b) K. Kimura and T. Shono, *Cation Binding by Macrocycles. Complexation of Cationic Species by Crown Ethers* (Eds.: Y. Inoue, G. W. Gokel), Marcel Dekker, New York, **1990**, p. 429; c) H. Tsukube, *Talanta* **1993**, *40*, 1313–1324.

[11] T. G. Roy, S. K. Hazari, b. K. Dey, H. A. Miah, C. Bader, D. Rehder, *Eur. J. Inorg. Chem.* **2004**, 4115–4123.

[12] S. Seiji, T. C. Bruice, *J. Am. Chem. Soc.* **1973**, *95*, 7528–7530.

[13] G. H. Searle, R. W. Hay, B. Jeragh, *Aust. J. Chem.* **1980**, *33*, 1447–1461.

[14] Y. Hung, L. Y. Martin, S. C. Jackels, A. M. Tait, D. H. Busch, *J. Am. Chem. Soc.* **1977**, *99*, 4029–4039.

[15] R. W. Hay, M. P. Pujari, *Inorg. Chim. Acta* **1985**, *99*, 75–79.

[16] S.-G. Kang, J. Song, *Bull. Korean Chem. Soc.* **2000**, *21*, 1106–1110.

[17] T. Ito, H. Ito, K. Toriumi, *Acta Crystallogr., Sect. B* **1981**, *37*, 1412–1415.

[18] T.-J. Lee, T.-H. Lu, C.-S. Chung, T.-Y. Lee, *Acta Crystallogr., Sect. C* **1984**, *40*, 70–72.

[19] a) T.-H. Lu, S.-C. Lin, H. Aneetha, K. Panneerselvam, C.-S. Chung, *J. Chem. Soc., Dalton Trans.* **1999**, 3385–3391; b) K. Panneerselvam, T.-H. Lu, T.-Y. Chi, S.-F. Tung, C.-S. Chung, *Acta Crystallogr., Sect. C* **2000**, *56*, 301–302.

[20] a) K. Panneerselvam, T.-H. Lu, S.-F. Tung, T.-Y. Chi, C.-S. Chung, *Anal. Sci.* **1998**, *14*, 1029–1030; b) K. Panneerselvam, T.-H. Lu, T.-Y. Chi, F.-L. Liao, C.-S. Chung, *Anal. Sci.* **2000**, *16*, 439–440.

[21] a) J. R. Röper, H. Elias, *Inorg. Chem.* **1992**, *31*, 1210–1214; b) N. Jubran, D. Meyerstein, J. Koresh, H. Cohen, *J. Chem. Soc., Dalton Trans.* **1986**, 2509–2513.

[22] a) L. Sabatini, L. Fabbrizzi, *Inorg. Chem.* **1979**, *18*, 438–444; b) L. Fabbrizzi, M. Micheloni, P. Paoletti, *J. Chem. Soc., Dalton Trans.* **1980**, 134–136; c) Y.-C. Lin, T. K. Misra, P.-S. Wang, C.-S. Chung, *Inorg. Chim. Acta* **2005**, *358*, 1777–1784.

[23] a) L. Fabbrizzi, *Inorg. Chim. Acta* **1977**, *24*, L21–L23; b) L. Fabbrizzi, *J. Chem. Soc., Dalton Trans.* **1979**, 1857–1861.

[24] a) M. Ciampolini, L. Fabbrizzi, M. Licchelli, F. Perotti, F. Pezzini, A. Poggi, *Inorg. Chem.* **1986**, *25*, 4131–4135; b) R. W. Hay, B. Jeragh, G. Ferguson, B. Kaitner, B. L. Ruhl, *J. Chem. Soc., Dalton Trans.* **1982**, 1531–1539.

[25] R. W. Hay, B. Kinsman, C. I. Smith, *Polyhedron* **1995**, *14*, 1245–1249.

[26] a) A. B. O. Lever, *Inorganic Electronic Spectroscopy*, American Elsevier, New York, N. Y., **1984**, pp 355, 554–572; b) J. C. Kim, J. C. Fettinger, Y. I. Kim, *Inorg. Chim. Acta* **1999**, *286*, 67–73; c) T. M. Donlevy, L. R. Gahan, T. W. Hambley, G. R. Hanson, K. L. McMahon, R. Stranger, *Inorg. Chem.* **1994**, *33*, 5131–5137; d) J.-W. Chen, C.-S. Chung, *Inorg. Chem.* **1986**, *25*, 2841–2846.

[27] a) G. M. Sheldrick, *SHELXTL PLUS*, Siemens Analytical X-ray Instruments Inc., Madison, WI, **1990**; b) A. C. T. North, D. C. Phillips, F. S. Mathews, *Acta Crystallogr., Sect. A* **1968**, *24*, 351–359.

[28] a) G. M. Sheldrick, *Acta Crystallogr., Sect. A* **1990**, *46*, 467–473; b) G. M. Sheldrick, *SHELXL 97, Program for Refinement of Crystal Structures*, University of Göttingen, **1997**.

Received: October 5, 2005
Published Online: January 19, 2006

 © 2006 Wiley-VCH Verlag GmbH & Co. KGaA, Weinheim 

DOI: 10.1002/ejic.200500942

# Reactions of Ruthenium–Aminophosphane Complexes with Diynes: P–N Bond Activation and Formation of Novel Phosphaallyl, Azaallyl, and Aminocarbene Complexes

**Sonja Pavlik,[a] Florian Jantscher,[a] Georg Dazinger,[a] Kurt Mereiter,[b] and Karl Kirchner*[a]**

**Keywords:** Ruthenium / Phosphaallyl complexes / Azaallyl complexes / Density functional calculations

The aminophosphane complexes $[RuCp(PPh_2NRR'_2)(CH_3CN)_2]^+$ and $[RuCp^*(PPh_2NRR'_2)(CH_3CN)_2]^+$ (NRR′ = NH*n*Pr, $NEt_2$, $NC_5H_5$) react with 1,6-heptadiyne and 1,7-octadiyne to yield novel $\eta^3$-phosphaallyl–$\eta^2$-vinylamine complexes of the types $[RuCp\{\eta^3\text{-}(P,C,C)\text{-}PPh_2CH{=}C{-}(CH_2)_n{-}\eta^2\text{-}(C,C){-}C{=}CHNRR'_2\}]^+$ and $[RuCp^*\{\eta^3\text{-}(P,C,C)\text{-}PPh_2CH{=}C{-}(CH_2)_n{-}\eta^2\text{-}(C,C)\text{-}C{=}CHNRR'_2\}]^+$ ($n$ = 3, 4). These complexes are the kinetic products but eventually form the $\eta^1$-phosphaallyl–$\eta^3$-azaallyl complexes $[RuCp\{\eta^1\text{-}(P)\text{-}PPh_2CH{=}C{-}(CH_2)_n{-}\eta^3\text{-}(C,C,N)\text{-}CCHNRR'_2\}]^+$ and $[RuCp^*\{\eta^1\text{-}(P)\text{-}PPh_2CH{=}C{-}(CH_2)_n{-}\eta^3\text{-}(C,C,N)\text{-}CCHNRR'_2\}]^+$, respectively. With $n$ = 3 elevated temperatures are required, while with $n$ = 4 this conversion takes places already at room temperature. The only exception is $[RuCp^*(PPh_2NH{n}Pr)(CH_3CN)_2]^+$ where amido butadiene complexes $[RuCp^*\{\eta^1\text{-}(N)\text{-}N{n}PrPPh_2\text{-}\eta^4\text{-}CH{=}C(CH_2)_nCH{=}CH_2\}]PF_6$ ($n$ = 3, 4) are obtained instead. In the case of $[RuCp\{\eta^1\text{-}(P)\text{-}PPh_2CH{=}C{-}(CH_2)_3{-}\eta^3\text{-}(C,C,N)\text{-}CCHNRR'_2\}]^+$ with NRR′ = $NEt_2$ and $NC_5H_5$, a further rearrangement took place at elevated temperatures affording the aminocarbenes $[RuCp\{{=}C(NRR')\text{-}\eta^2\text{-}(C,C)\text{-}C(CH_2)_3C{-}CH_2{-}(\eta^1\text{-}(P)\text{-}PPh_2)\}]^+$. Representative X-ray structures are presented. Moreover, conceivable mechanisms for all these reaction sequences are established by means of DFT/B3LYP calculations.

(© Wiley-VCH Verlag GmbH & Co. KGaA, 69451 Weinheim, Germany, 2006)

## Introduction

Aminophosphanes that contain one or more direct $P^{III}$–N bonds have received considerable attention in recent years as ligands for transition metals.[1] They are accessible in large quantities through the use of relatively simple condensation processes from inexpensive starting materials, that is, primary or secondary amines and $PR_2Cl$ compounds which contain dialkyl or diaryl substituents as well as achiral and chiral P–O- and P–N-containing phosphane units. Accordingly, variations of electronic, steric, and stereochemical parameters may be achieved in a very facile fashion. The most common structural types of such ligands contain either one P–N unit (e.g. **I**),[2] two or more P–N units which are not directly bound (e.g. **II**),[3,4] or a P–N–P framework (e.g. **III**).[5,6] It should be noted that in some cases $P^{III}$–N bonds were found to be sensitive towards acid- or base-catalyzed hydrolysis during complexation reactions.[7] However, by choosing appropriate substituents on both phosphorus and nitrogen centers, P–N bond cleavage can be avoided.

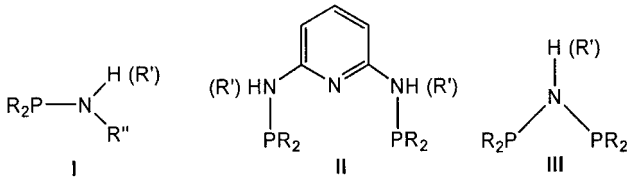


I II III

We have recently started to investigate the chemistry of RuCp, RuCp*, and RuTp complexes that contain one or two aminophosphane ligands of the most simple $PR_2NHR'$ type, **I**. In these compounds coordination takes place exclusively through the phosphorus donor leaving the N-site available for further reactions. We have shown, for instance, that in the vinylidene and allenylidene complexes $[RuCp(PPh_2NHR)_2\{{=}C{=}(C)_n{=}CHR'\}]^+$ and $[RuTp(PPh_2NHR)_2\{{=}C{=}(C)_n{=}CHR'\}]^+$ ($n$ = 0, 1; R = Ph, *n*Pr; R′ = alkyl, aryl) an intramolecular addition of the NHR′ moiety to the α-carbon of the cumulene moiety takes place, resulting in the formation of novel four-membered aza-phospha-carbenes.[8] Complexes of the types $[RuCp(PPh_2NHPh)(CH_3CN)_2]^+$ and $[RuCp^*(PR_2NHR')(CH_3CN)_2]^+$ (R = Ph, *i*Pr, R′ = Ph, $C_6F_5$) have been found to react with terminal alkynes and diynes to give amido butadiene complexes.[9,10] In all these reactions, the N–H bond but not the P–N bond is cleaved unless larger amounts of water are present. Recently, when we switched over to a complex where the aminophosphane lacks a N–H bond viz. [RuCp-

[a] Institute of Applied Synthetic Chemistry, Vienna University of Technology,
Getreidemarkt 9, 1060 Vienna, Austria
Fax: +43-1-58801-15499
E-mail: kkirch@mail.zserv.tuwien.ac.at
[b] Institute of Chemical Technologies and Analytics, Vienna University of Technology,
Getreidemarkt 9, 1060 Vienna, Austria

 InterScience © 2006 Wiley-VCH Verlag GmbH & Co. KGaA, Weinheim 

$(PPh_2NEt_2)(CH_3CN)_2]^+$, we discovered that it reacts with diynes to afford unusual and unprecedented phosphaallyl complexes which readily rearrange to give azaallyl complexes.[11] This process formally constitutes an insertion of an unsaturated carbon C4 chain into the P–N bond, that is, in the course of this reaction the P–N bond is cleaved. The present work is intended to investigate in detail the formation of phosphaallyl complexes and their conversion to azaallyl complexes and we report here the reaction of $[RuCp(PPh_2NRR')(CH_3CN)_2]PF_6$ and $[RuCp^*(PPh_2NRR')(CH_3CN)_2]PF_6$ (NRR′ = NH*n*Pr, $NEt_2$, $NC_5H_{10}$) with diynes. The mechanistic considerations will be supported by DFT/B3LYP calculations.

## Results and Discussion

### Starting Materials

The starting complexes **1a**–**c** were obtained in highly isolated yields by reacting $[RuCp(CH_3CN)_3]PF_6$ with 1 equiv. of the respective aminophosphane $PPh_2NRR'$ (NRR′ = NH*n*Pr, $NEt_2$, $NC_5H_{10}$) at room temperature. The analogous RuCp* complexes were obtained in a similar fashion by reacting $[RuCp^*(CH_3CN)_3]PF_6$ with $PPh_2NRR'$ affording complexes **2a**–**c**. All these complexes are stable to air in the solid state but decompose slowly in solutions on exposure to air. Complexes **1a**–**c** and **2a**–**c** exhibit a singlet resonance in the $^{31}P\{^1H\}$ NMR spectrum in the range of 83–102 ppm. Structural views of **1a** and **2c** are shown in Figure 1 and Figure 2 with selected bond lengths given in the captions.

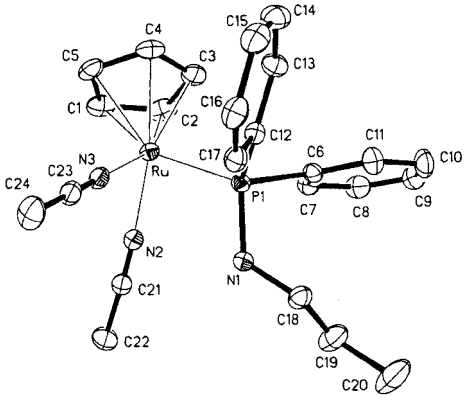


Figure 1. Structural view of $[RuCp(PPh_2NH{\it n}Pr)(CH_3CN)_2]PF_6$ (**1a**) showing 50% thermal ellipsoids ($PF_6^-$ omitted for clarity). Selected bond lengths [Å]: Ru–C(1–5)$_{av}$ 2.187(2), Ru–N(2) 2.064(2), Ru–N(3) 2.064(2), Ru–P(1) 2.2823(5), P(1)–N(1) 1.657(2).

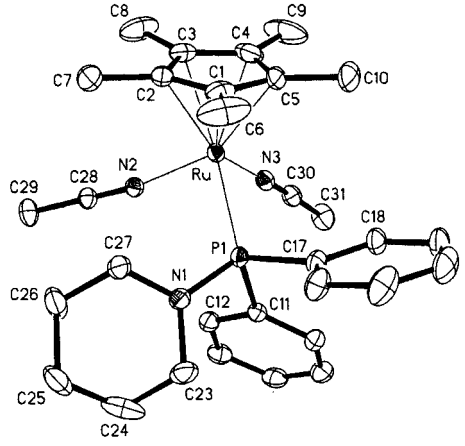


Figure 2. Structural view of $[RuCp^*(PPh_2NC_5H_{10})(CH_3CN)_2]PF_6$ (**2c**) showing 20% thermal ellipsoids ($PF_6^-$ omitted for clarity). Selected bond lengths [Å]: Ru–C(1–5)$_{av}$ 2.191(2), Ru–P(1) 2.3322(5), Ru–N(2) 2.064(2), Ru–N(3) 2.059 (2), P(1)–N(1) 1.668(2).

### Reaction of $[RuCp(PPh_2NRR')(CH_3CN)_2]^+$ (NRR′ = NH*n*Pr, $NEt_2$, $NC_5H_{10}$) with Diynes

Within a few minutes, treatment of **1a**–**c** with 1,6-heptadiyne results in the formation of the $\eta^3$-phosphaallyl–$\eta^2$-vinylamine complexes $[RuCp\{\eta^3\text{-}(P,C,C)\text{-}PPh_2CH{=}C\text{–}(CH_2)_3\text{-}\eta^2\text{-}(C,C)\text{–}C{=}CH\text{–}NH{\it n}Pr\}]^+$ (**3a**), $[RuCp\{\eta^3\text{-}(P,C,C)\text{-}PPh_2CH{=}C\text{–}(CH_2)_3\text{–}\eta^2\text{-}(C,C)\text{-}C{=}CH\text{–}NEt_2\}]^+$ (**3b**), and $[RuCp\{\eta^3\text{-}(P,C,C)\text{-}PPh_2CH{=}C\text{–}(CH_2)_3\text{–}\eta^2\text{-}(C,C)\text{-}C{=}CH\text{–}NC_5H_{10}\}]^+$ (**3c**) in high yields (Scheme 1).[12,13] It is interesting to note that despite the fact that the aminophosphane ligand of **1a** bears a NH proton, a phosphaallyl complex rather than an amido butadiene complex is formed, as has been observed recently for $[RuCp(Ph_2PNHPh)(CH_3CN)_2]^+$. This may be attributed to the lower acidity of the NH proton (in other words, a stronger N–H bond) in $PPh_2NH{\it n}Pr$ as compared to the NH bond in $PPh_2NHPh$. Accordingly, P–*N* rather than N–H bond activation is favored. The phosphaallyl composition proved not to be the most stable one. In fact, if a solution of **3a**–**c** is kept at 90 °C for several hours, further rearrangement takes place, leading eventually to the thermodynamically more stable $\eta^1$-phosphaallyl–$\eta^3$-azaallyl complexes $[RuCp\{\eta^1\text{-}(P)\text{-}PPh_2CH{=}C\text{–}(CH_2)_3\text{–}\eta^3\text{-}(C,C,N)\text{-}C{=}CH\text{–}NH{\it n}Pr\}]^+$ (**4a**), $[RuCp\{\eta^1\text{-}(P)\text{-}PPh_2CH{=}C\text{–}(CH_2)_3\text{–}\eta^3\text{-}(C,C,N)\text{-}C{=}CH\text{–}NEt_2\}]^+$ (**4b**), and $[RuCp\{\eta^1\text{-}(P)\text{-}PPh_2CH{=}C\text{–}(CH_2)_3\text{–}\eta^3\text{-}(C,C,N)\text{-}C{=}CH\text{–}NC_5H_{10}\}]^+$ (**4c**) in essentially quantitative yields (Scheme 1).[14] On the other hand, with **1a** and 1,7-octadiyne no $\eta^3$-phosphaallyl–$\eta^2$-vinylamine complex could be observed and the $\eta^1$-phosphaallyl–$\eta^3$-azaallyl **4d** was obtained directly. In the case of **1b** and **1c** the respective $\eta^3$-phosphaallyl–$\eta^2$-vinylamine complexes **3d** and **3e** could be observed spectroscopically but rearranged rapidly at room temperature to afford the corresponding $\eta^1$-phosphaallyl–$\eta^3$-azaallyl complexes **4e** and **4f**. All compounds, which are air-stable both in solution and in the solid state, were fully characterized by $^1H$, $^{13}C\{^1H\}$, and $^{31}P\{^1H\}$ NMR spectroscopy as well as elemental analysis.

The $^1H$ NMR spectroscopic data for **3a** include characteristic resonances at 4.14 (d, $J_{HP}$ = 4.4 Hz) and 3.99 ppm (d, $J_{H,P}$ = 7.6 Hz, 1 H) assignable to the protons $H^1$ and $H^4$ of the $\eta^3$-phosphaallyl and $\eta^2$-vinylamine units, respectively. In the $^{13}C\{^1H\}$ NMR spectrum the characteristic resonance of the coordinated $sp^2$ carbon atoms $C^1$, $C^2$, $C^3$, and $C^4$ of the $\eta^3$-phosphaallyl–$\eta^2$-vinylamine moiety exhi-

 © 2006 Wiley-VCH Verlag GmbH & Co. KGaA, Weinheim 

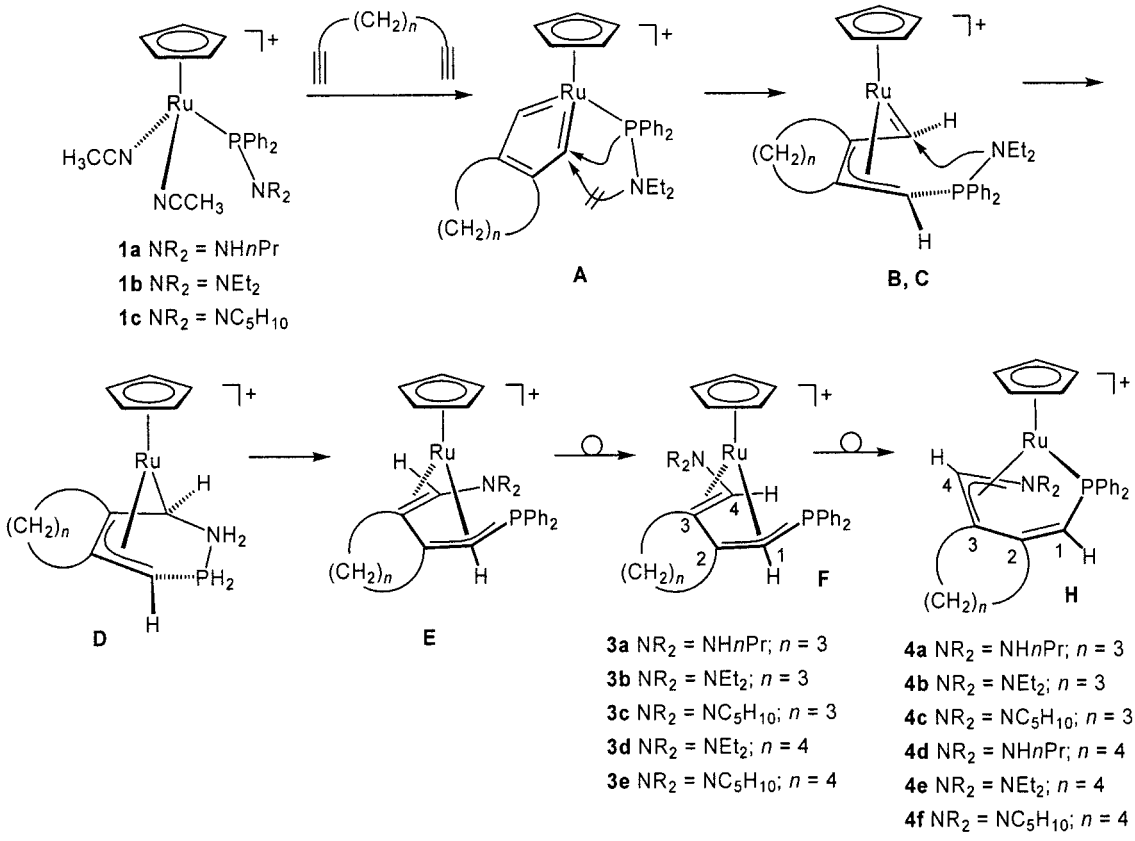


Scheme 1.

bit resonances at 41.6 (d, $J_{CP}$ = 24.5 Hz), 82.1, 116.8 (d, $J_{CP}$ = 3.8 Hz), and 106.9 ppm (d, $J_{CP}$ = 6.1 Hz), respectively. In the $^{31}P\{^1H\}$ NMR spectrum the phosphaallyl ligand exhibits a singlet at 9.3 ppm. Concurrent NMR spectra are observed for **3b**–**e**.

The NMR spectroscopic data of **4a**–**f** are quite different from those of **3a**–**e**. As the overall spectroscopic features are very similar, we describe here only those of **4a**. The $^1H$ NMR spectrum exhibits resonances at 5.98 (d, $J_{HP}$ = 10.1 Hz) and 6.02 ppm, which can be assigned to the olefinic hydrogen atom $H^1$ and the allyl proton $H^4$. The most characteristic features in the $^{13}C\{^1H\}$ NMR spectrum are a low-field doublet resonance at $\delta$ = 170.1 ppm (d, $J_{CP}$ = 29.1 Hz) and doublet resonances at 111.9 (d, $J_{CP}$ = 47.2 Hz), 85.8 (d, $J_{CP}$ = 1.9 Hz), and 74.4 ppm assignable to the terminal allyl carbon atom $C^3$, the two olefinic carbon atoms $C^1$ and $C^2$, and the central allyl carbon atom $C^4$ bearing the NH*n*Pr unit. In the $^{31}P\{^1H\}$ NMR spectrum the $\eta^1$-(P)-phosphaallyl ligand exhibits a singlet at $\delta$ = 70.3 ppm (cf. 9.3 ppm in **3a**).

The solid-state structures of **3a**, **3c**, and **4f** were determined by single-crystal X-ray diffraction. ORTEP diagrams are depicted in Figure 3, Figure 4, and Figure 5 with selected bond lengths given in Table 1. The structures of **3a** and **3c** can be described as a three-legged piano stool geometry with the $\eta^3$-phosphaallyl moiety and the C=C bond of the vinylamine unit as the legs. The $\eta^3$-phosphaallyl functionality is nearly symmetrically bonded to the metal with the Ru–P, Ru–C(18), and Ru–C(19) bond lengths being 2.2763(5), 2.241(2), and 2.220(2) Å in **3a** and 2.2505(4), 2.239(2), and 2.203(2) Å in **3c**, respectively. The olefin part of the vinylamine moiety is strongly asymmetrically bonded to the metal center with the Ru–C bonds to the carbon

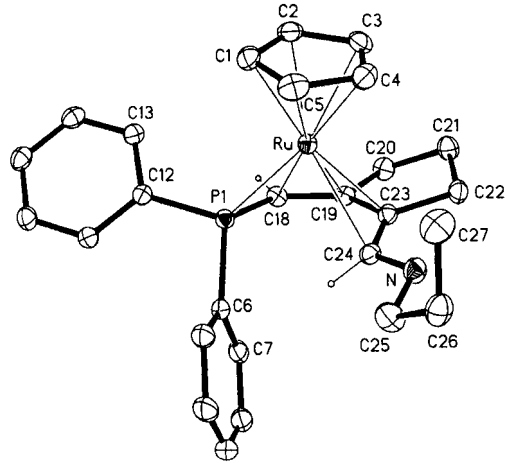


Figure 3. Structural view of [RuCp{$\eta^3$-(P,C,C)-$PPh_2CHC–(CH_2)_3$–$\eta^2$-(C,C)-CCHNH*n*Pr}]$PF_6$ (**3a**) showing 40% thermal ellipsoids ($PF_6^-$ omitted for clarity). Selected bond lengths [Å]: Ru–C(1–5)$_{av}$ 2.197(2), Ru–P(1) 2.2763(5), Ru–C(18) 2.241(2), Ru–C(19) 2.220(2), Ru–C(23) 2.236(2), Ru–C(24) 2.490(2), P(1)–C(18) 1.768(2), C(18)–C(19) 1.4129(34), C(19)–C(23) 1.437(3), C(23)–C(24) 1.396(3), C(24)–N 1.344(2).

 © 2006 Wiley-VCH Verlag GmbH & Co. KGaA, Weinheim 

atoms C(23) and C(24) being 2.236(2) and 2.490(2) Å in **3a** and 2.219(2) and 2.551(2) Å in **3c**, respectively. Strong alteration of olefin binding by π-donor substituents has also been observed in $[FeCp(CO)_2(H_2C{=}CHNMe_2)]^+$ where the vinylamine is essentially $\eta^1$-bound [the nonbonded Fe···C separation is 2.823(11) Å].[15] In turn, the C(24)–N bonds in **3a** and **3c** exhibit already double bond character being 1.344(2) and 1.359(2) Å, respectively. The bonding situation of the –C=CHNH*n*Pr and $-C{=}CHNC_5H_{10}$ units might be described as intermediate between the limiting vinylamine and imine forms or alternatively perhaps even as $\eta^1$-(C)-azaallyl. Accordingly, rotation about the C(23)–C(24) bond is expected to be facile, putting the amine moiety rapidly in a *syn*-conformation for steric reasons (conversion **D** to complexes **3** in Scheme 1).

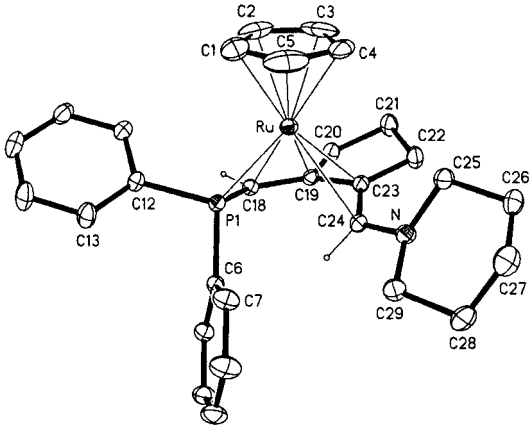


Figure 4. Structural view of $[RuCp\{\eta^1\text{-}(P)\text{-}PPh_2CH{=}C\text{–}(CH_2)_3\text{–}\eta^3\text{-}(C,C,N)\text{-}CCHNC_5H_{10}\}]PF_6$ (**3c**) showing 40% thermal ellipsoids ($PF_6^-$ omitted for clarity). Selected bond lengths [Å]: Ru–C(1–5)$_{av}$ 2.182(2), Ru–P(1) 2.2505(4), Ru–C(18) 2.239(2), Ru–C(19) 2.203(2), Ru–C(23) 2.219(2), Ru–C(24) 2.551(2), P(1)–C(18) 1.774(2), C(18)–C(19) 1.415(2), C(19)–C(23) 1.438(2), C(23)–C(24) 1.406(2), C(24)–N 1.359(2).

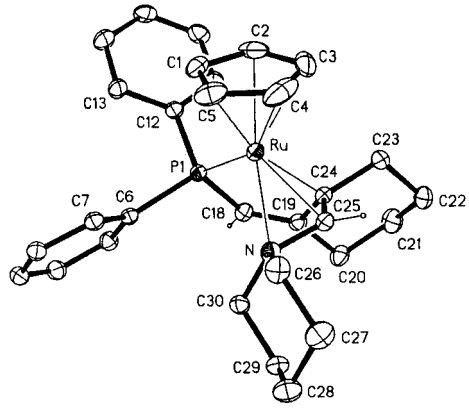


Figure 5. Structural view of $[RuCp\{\eta^1\text{-}(P)\text{-}PPh_2\text{-}CH{=}C(CH_2)_4\text{-}\eta^3\text{-}(C,C,N)\text{-}CH\text{-}NC_5H_{10}\}]PF_6$ (**4f**) showing 40% thermal ellipsoids ($PF_6^-$ omitted for clarity). Selected bond lengths [Å]: Ru–C(1–5)$_{av}$ 2.210(2), Ru–N 2.186(2), Ru–C(25) 2.089(2), Ru–C(24) 2.204(2), Ru–P(1) 2.2791(5), P(1)–C(18) 1.796(2), C(18)–C(19) 1.336(2), C(19)–C(24) 1.505(2), C(24)–C(25) 1.418(2), C(25)–N 1.415(2).

The structure of **4f** also adopts a three-legged piano stool conformation with the $\eta^3$-azaallyl moiety and the P atom as the legs. The $\eta^3$-azaallyl unit, being *exo*-oriented with respect to the phosphane moiety, is asymmetrically bonded

Table 1. Details for the crystal structure determinations of complexes **1a**, **2c**, **3a**, **3c**, **4f**, and **5a**.

| | **1a** | **2c** | **3a** | **3c** | **4f** | **5a** |
|---|---|---|---|---|---|---|
| Empirical formula | $C_{24}H_{29}F_6N_3P_2Ru$ | $C_{31}H_{41}F_6N_3P_2Ru$ | $C_{27}H_{31}F_6NP_2Ru$ | $C_{29}H_{33}F_6NP_2Ru$ | $C_{30}H_{35}F_6NP_2Ru$ | $C_{28}H_{33}F_6NP_2Ru$ |
| Formula mass | 636.51 | 732.68 | 646.54 | 672.57 | 686.60 | 660.56 |
| Crystalsize [mm] | 0.46×0.34×0.22 | 0.62×0.48×0.33 | 0.62×0.37×0.07 | 0.62×0.24×0.09 | 0.52×0.29×0.14 | 0.47×0.36×0.21 |
| Space group | $P2_1/c$ (no. 14) | $C2/c$ (no. 15) | $P2_1/n$ (no. 14) | $P2_1/n$ (no. 14) | $P2_1/c$ (no. 14) | $P2_1/n$ (no. 14) |
| $a$ [Å] | 17.4288(10) | 21.7560(17) | 9.7404(5) | 17.6384(8) | 14.9183(7) | 8.9199(4) |
| $b$ [Å] | 8.9607(5) | 18.7520(14) | 18.3098(9) | 8.8425(4) | 10.1274(5) | 15.6117(7) |
| $c$ [Å] | 17.2306(10) | 18.6960(14) | 14.7423(8) | 18.9241(9) | 19.5913(9) | 20.3315(10) |
| $\alpha$ [°] | 90 | 90 | 90 | 90 | 90 | 90 |
| $\beta$ [°] | 93.502(1) | 120.954(1) | 90.134(1) | 108.100(1) | 91.835(1) | 93.219(1) |
| $\gamma$ [°] | 90 | 90 | 90 | 90 | 90 | 90 |
| $V$ [Å$^3$] | 2686.0(3) | 6541.1(9) | 2629.2(2) | 2805.5(2) | 2958.4(2) | 2826.8(2) |
| $Z$ | 4 | 8 | 4 | 4 | 4 | 4 |
| $\rho_{calcd}$ [g/cm$^3$] | 1.574 | 1.488 | 1.633 | 1.592 | 1.542 | 1.552 |
| $T$ [K] | 173(2) | 173(2) | 173(2) | 173(2) | 173(2) | 173(2) |
| $\mu$ [mm$^{-1}$] (Mo-$K_\alpha$) | 0.763 | 0.637 | 0.779 | 0.733 | 0.697 | 0.726 |
| $F$(000) | 1288 | 3008 | 1312 | 1368 | 1400 | 1344 |
| $\theta_{max}$ [°] | 30 | 30 | 30 | 30 | 30 | 27 |
| Measured reflections | 24957 | 48057 | 37914 | 40276 | 40996 | 25939 |
| Unique reflections | 7787 | 9522 | 7615 | 8167 | 8570 | 5719 |
| No. of reflections $I > 2\sigma(I)$ | 6857 | 8133 | 6543 | 6947 | 7656 | 5024 |
| Parameters | 345 | 416 | 343 | 375 | 367 | 343 |
| $R_1$ $[I > 2\sigma(I)]$[a] | 0.0337 | 0.0343 | 0.0292 | 0.0282 | 0.0316 | 0.0899 |
| $R_1$ (all data) | 0.0396 | 0.0424 | 0.0380 | 0.0361 | 0.0360 | 0.0992 |
| $wR_2$ (all data) | 0.0838 | 0.0949 | 0.0823 | 0.0732 | 0.0881 | 0.2279 |
| $\Delta\rho_{min/max}$ [e/Å$^3$] | –0.52/1.04 | –0.50/0.77 | –0.33/1.03 | –0.43/0.80 | –0.58/0.97 | –1.08/1.96 |

[a] $R_1 = \Sigma||F_o| - |F_c||/\Sigma|F_o|$, $wR_2 = \{\Sigma[w(F_o^2–F_c^2)^2]/\Sigma[w(F_o^2)^2]\}^{1/2}$.

 © 2006 Wiley-VCH Verlag GmbH & Co. KGaA, Weinheim 

to the metal with the Ru–C bond length to the central allyl carbon atom C(25) [2.089(2) Å] distinctly shorter than the Ru–N and Ru–C(24) bonds to the terminal allyl atoms N and C(24) [2.186(2) and 2.204(2) Å, respectively].

Upon keeping a $CH_3CN$ solution of **4b** at 90 °C for 12 h, an unexpected rearrangement took place affording the aminocarbene $[RuCp\{=C(NEt_2)\text{-}\eta^2\text{-}(C,C)\text{-}C(CH_2)_3CCH_2\text{-}(\eta^1\text{-}(P)\text{-}PPh_2)\}]^+$ (**5a**) in essentially quantitative yield (71% isolated yield) as monitored by $^1H$ and $^{31}P\{^1H\}$ NMR spectroscopy (Scheme 2). The same isomerization reaction was observed for **4c** yielding $[RuCp\{=C(NC_5H_{10})\text{-}\eta^2\text{-}(C,C)\text{-}C(CH_2)_3CCH_2\text{-}(\eta^1\text{-}(P)\text{-}PPh_2)\}]^+$ (**5b**) but the reaction was not quantitative. Attempts to isolate **5b** in pure form were unsuccessful and only mixtures of **4c** and **5b** were obtained. All other azaallyl complexes turned out to be thermally stable and there was no evidence for the formation of an aminocarbene. In the course of this process, the hydrogen of the central allyl carbon atom $C^4$ is transferred onto the olefinic carbon $C^1$. It is interesting to note that this reaction takes place only in the coordinating solvent $CH_3CN$, but not in $CH_3NO_2$. It may be speculated that such a formal 1,4 hydrogen shift reaction proceeds most likely by a metal mediated C–H activation step and the intermediacy of a hydride species (Scheme 2). Addition of the coordinating solvent may cause a hapticity change of the $\eta^3$ azaallyl moiety to give a $\eta^2$ vinylamine, thereby providing a latent vacant coordination site for a subsequent C–H bond activation step. Insertion of the noncoordinated olefin moiety into the Ru–H bond may then afford the aminocarbene complex. The conversion of activated olefins to heteroatom-stabilized carbenes is well documented.[16]

Characteristic features of **5a** and **5b** comprise, in the $^{13}C\{^1H\}$ NMR spectrum, a low-field doublet resonance in the range of 225.2 (d, $J_{CP}$ = 13.0 Hz) and 222.9 (d, $J_{CP}$ = 12.3 Hz) ppm, respectively, assignable to the carbene carbon atoms. The $sp^3$ carbon atom $C^1$ gives rise to a doublet resonance at 37.9 (d, $J_{CP}$ = 35.3 Hz) and 36.7 (d, $J_{CP}$ = 35.3 Hz). The $^{31}P\{^1H\}$ NMR spectrum reveals an unusually high-field shifted resonance at –34.3 and –37.8 ppm (cf. 9.3 and 4.3 ppm in **3b** and **3c**, and 74.1 and 73.3 ppm in **4b** and **4c**) with a small coupling constant of 36 Hz. The structural identity of **5a** was unequivocally proven by X-ray crystallography. The result is depicted in Figure 6 with important bond lengths given in the caption. Overall, **5a** adopts a typical three-legged piano stool conformation with $PPh_2$, the

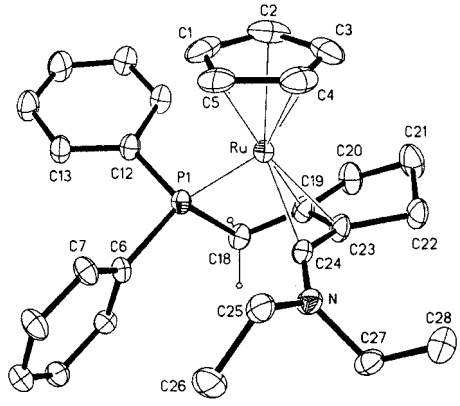


Figure 6. Structural view of $[RuCp\{=C(NEt_2)\text{-}\eta^2\text{-}(C,C)\text{-}C(CH_2)_3\text{-}C\text{–}CH_2\text{-}(\eta^1\text{-}(P)\text{-}PPh_2)\}]PF_6$ (**5a**) showing 20% thermal ellipsoids ($PF_6^-$ omitted for clarity). Selected bond lengths [Å]: $Ru\text{–}C(1\text{–}5)_{av}$ 2.204(9), Ru–C(24) 2.006(7), Ru–C(23) 2.201(7), Ru–C(19) 2.444(8), Ru–P(1) 2.263(2), P(1)–C(18) 1.818(7), C(18)–C(19) 1.493(12), C(19)–C(23) 1.421(12), C(23)–C(24) 1.508(11), C(24)–N 1.147(9).

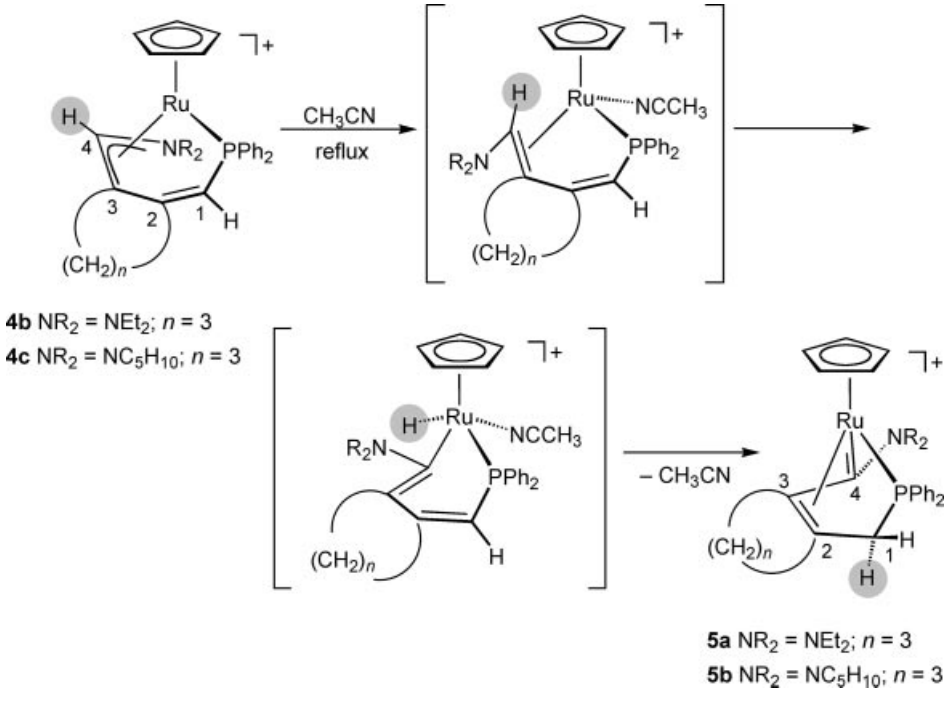


Scheme 2.

 © 2006 Wiley-VCH Verlag GmbH & Co. KGaA, Weinheim 

two C=C bonds of the vinyl moiety and the carbene carbon atom as the legs. The most notable feature is the comparatively short Ru–C(24) bond length of 2.006(7) Å reflecting metal carbon double bond character which is typical for aminocarbenes. The $\eta^2$-vinyl unit is asymmetrically bonded to the metal center with Ru–C(23) and Ru–C(19) bond lengths of 2.201(7) and 2.444(8) Å, respectively.

### Reaction of $[RuCp^*(PPh_2NRR')(CH_3CN)_2]^+$ (NRR′ = NH*n*Pr, $NEt_2$, $NC_5H_5$) with Diynes

Given the previously observed behavior differences between $[CpRu(PR_3)(CH_3CN)_2]^+$ and the homologous $[Cp^*Ru(PR_3)(CH_3CN)_2]^+$ complexes with respect to the C–H activation processes,[17] we have addressed the question of whether P–N bond activation occurs also in the case of the Cp* aminophosphane complexes **2a**–**c**. In contrast to **1a**–**c**, the reaction of **2a** both with 1,6-heptadiyne and 1,7-octadiyne results in the clean formation of the amido butadiene complexes $[RuCp^*\{\eta^1\text{-}(N)\text{-}NnPrPPh_2\text{-}\eta^4\text{-}CH{=}C(CH_2)_3CH{=}CH_2\}]PF_6$ (**6a**) and $[RuCp^*\{\eta^1\text{-}(N)\text{-}NnPrPPh_2\text{-}\eta^4\text{-}CH{=}C(CH_2)_4CH{=}CH_2\}]PF_6$ (**6b**) in high yields (Scheme 3). There was no evidence that phosphaallyl or azaallyl complexes were formed. The same reaction has been found for $[RuCp(PPh_2NHPh)(CH_3CN)_2]^+$ and $[RuCp^*(PR_2NHR')(CH_3CN)_2]^+$ (R = Ph, *i*Pr, R′ = Ph, $C_6F_5$).[10,11] Compounds **6a** and **6b** are air-stable both in solution and in the solid state and were characterized by $^1H$, $^{13}C\{^1H\}$, and $^{31}P\{^1H\}$ NMR spectroscopy as well as elemental analysis.

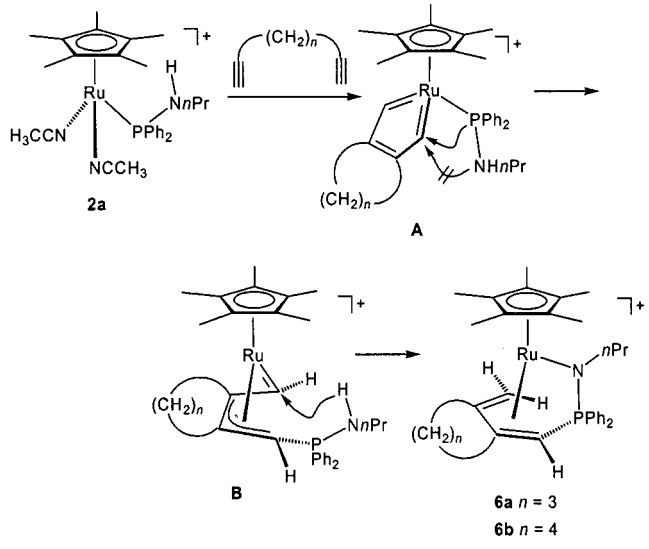


Scheme 3.

As these compounds exhibit similar spectroscopic features to the RuCp $\eta^4$-butadiene amido complexes already described recently,[10,11] they are not discussed here. The solid-state structures of **6a** and **6b** were determined by single-crystal X-ray diffraction. ORTEP diagrams are depicted in Figure 7 and Figure 8 with selected bond lengths reported in the captions.

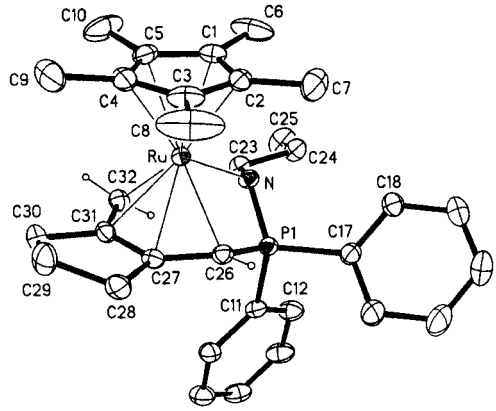


Figure 7. Structural view of $[RuCp^*\{\eta^1\text{-}(N)\text{-}NnPrPPh_2\text{-}\eta^4\text{-}CH{=}C(CH_2)_3CH{=}CH_2\}]PF_6$ (**6a**) showing 40% thermal ellipsoids ($PF_6^-$ omitted for clarity). Selected bond lengths [Å]: $Ru\text{–}C(1\text{–}5)_{av}$ 2.207(3), Ru–N = 2.183(2), Ru–C(26) 2.222(2), Ru–C(27) 2.232(2), Ru–C(31) 2.227(2), Ru–C(32) 2.204(2), P(1)–N 1.600(2), P(1)–C(26) 1.769(2), C(26)–C(27) 1.416(3), C(27)–C(31) 1.432(3), C(31)–C(32) 1.401(3).

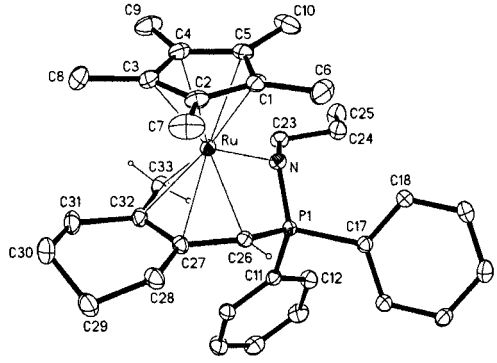


Figure 8. Structural view of $[RuCp^*\{\eta^1\text{-}(N)\text{-}NnPrPPh_2\text{-}\eta^4\text{-}CH{=}C(CH_2)_4CH{=}CH_2\}]PF_6$ (**6b**) showing 20% thermal ellipsoids ($PF_6^-$ omitted for clarity; only the first of three independent Ru complexes is shown). Selected bond lengths [Å]: $Ru\text{–}C(1\text{–}5)_{av}$ 2.220(2), Ru–N 2.184(2), Ru–C(26) 2.191 (2), Ru–C(27) 2.249(2), Ru–C(32) 2.244(2), Ru–C(33) 2.172(2), P(1)–N 1.600(2), P(1)–C(26) 1.771(2), C(26)–C(27) 1.423(3), C(27)–C(32) 1.436(3), C(32)–C(33) 1.406(4).

In similar fashion to the RuCp complexes **1a**–**c**, with 1,6-heptadiyne, 1,7-octadiyne, **2b**, and **2c**, the $\eta^1$-phosphaallyl–$\eta^3$-azaallyl complexes $[RuCp^*\{\eta^1\text{-}(P)\text{-}PPh_2\text{–}CH{=}C(CH_2)_3\text{-}\eta^3\text{-}(C,C,N)\text{-}CCHNEt_2\}]PF_6$ (**8a**), $[RuCp^*\{\eta^1\text{-}(P)\text{-}PPh_2\text{–}CH{=}C(CH_2)_3\text{-}\eta^3\text{-}(C,C,N)\text{-}CCHNC_5H_{10}\}]PF_6$ (**8b**), $[RuCp^*\{\eta^1\text{-}(P)\text{-}PPh_2\text{–}CH{=}C(CH_2)_4\text{-}\eta^3\text{-}(C,C,N)\text{-}CCHNEt_2\}]PF_6$ (**8c**), and $[RuCp^*\{\eta^1\text{-}(P)\text{-}PPh_2\text{–}CH{=}C(CH_2)_4\text{-}\eta^3\text{-}(C,C,N)\text{-}CCHNC_5H_{10}\}]PF_6$ (**8d**), respectively, are obtained in high isolated yields (Scheme 4). While in the case of 1,6-heptadiyne the intermediacy of $\eta^3$-phosphaallyl–$\eta^2$-vinylamine complexes **7a** and **7b** could be observed by NMR spectroscopy, in the case of 1,7-octadiyne no intermediates were detected. Again, all compounds were fully characterized by a combination of $^1H$, $^{13}C\{^1H\}$, and $^{31}P\{^1H\}$ NMR spectroscopy and elemental analysis. Overall, the spectroscopic features of complexes **7** and **8** are very similar to those of complexes **3** and **4** and are thus not discussed here. In ad-

 © 2006 Wiley-VCH Verlag GmbH & Co. KGaA, Weinheim 

dition, the solid-state structures of **8c** and **8d** were determined by single-crystal X-ray diffraction. ORTEP plots are depicted in Figure 9 and Figure 10 with selected bond lengths reported in the captions.

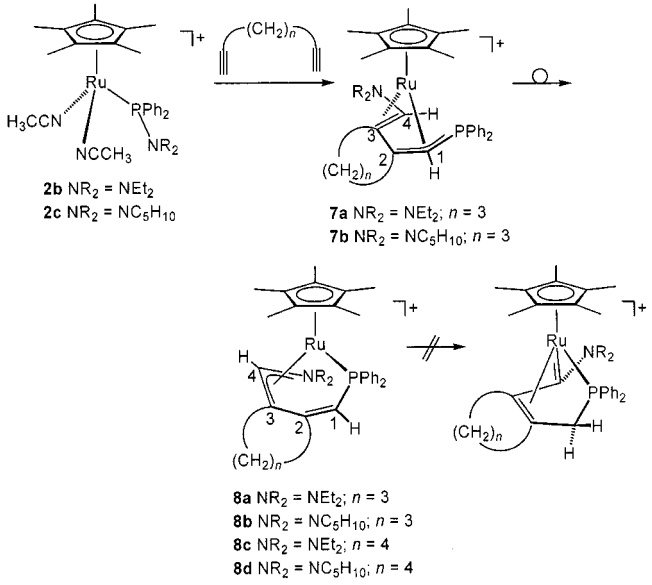


Scheme 4.

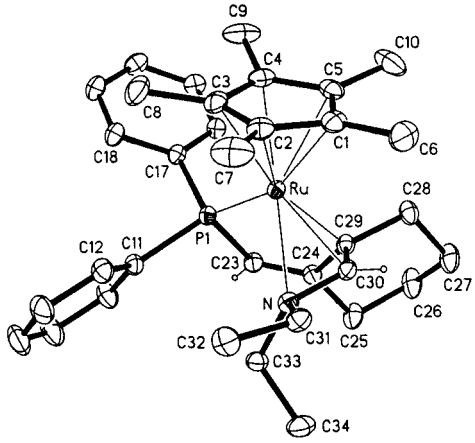

Figure 9. Structural view of [RuCp*{$\eta^1$-(P)-$PPh_2CH{=}C(CH_2)_4$-$\eta^3$-(C,C,N)-C=CH–$NEt_2$}]$PF_6{\cdot}CH_2Cl_2$ (**8c**·$CH_2Cl_2$) showing 30% thermal ellipsoids ($PF_6^-$ and solvent omitted for clarity). Selected bond lengths [Å]: Ru–$C(1–5)_{av}$ 2.239(2), Ru–P(1) 2.3020(6), Ru–C(29) 2.253(2), Ru–C(30) 2.092(2), Ru–N 2.243(2), P(1)–C(23) 1.795(2), C(23)–C(24) 1.325(3), C(24)–C(29) 1.510(3), C(29)–C(30) 1.425(3), N–C(30) 1.421(3).

Finally, as part of our ongoing effort to investigate the chemistry of complexes with ligands which possess direct $P^{III}$–N bonds towards alkynes, we set out here to prepare a complex with a diphenylphosphanylhydrazide ligand, that is, a ligand having a $P^{III}$–N–N unit. It should be noted that transition-metal complexes with $R_2PNHNR'_2$ ligands are comparatively rare. With respect to late transition metals, they have been found to coordinate either as monodentate or bidentate ligands in $\kappa^1$-P and $\kappa^2$-P,N fashion, respectively.[18] Accordingly, treatment of [RuCp$(CH_3CN)_3$]$PF_6$ with 1 equiv. of $PPh_2NHNMe_2$ in $CH_2Cl_2$ as the solvent

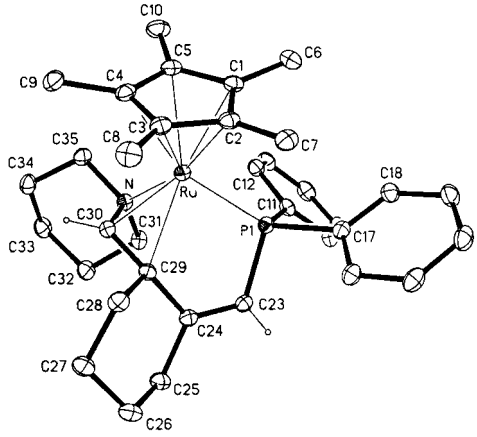

Figure 10. Structural view of [RuCp*{$\eta^1$-(P)-$PPh_2CH{=}C(CH_2)_4$-$\eta^3$-(C,C,N)-C=CH–$N(CH_2)_5$}]$PF_6$ (**8d**) showing 30% thermal ellipsoids ($PF_6^-$ omitted for clarity). Selected bond lengths [Å]: Ru–$C(1–5)_{av}$ 2.228(2), Ru–P(1) 2.2978(5), Ru–C(29) 2.252(2), Ru–C(30) 2.090(2), Ru–N 2.233(2), P(1)–C(23) 1.796(2), C(23)–C(24) 1.326(3), C(24)–C(29) 1.508(3), C(29)–C(30) 1.418(3), N–C(30) 1.418(2).

at room temperature yields, upon workup, a 5:1 mixture of [RuCp{$\kappa^1$(P)-$PPh_2NHNMe_2$}$(CH_3CN)_2$]$PF_6$ (**9**) and [RuCp{$\kappa^2$(P,N)-$PPh_2NHNMe_2$}$(CH_3CN)$]$PF_6$ (**10**) where the $PPh_2NHNMe_2$ ligand is attached to the metal center in the $\kappa^1$-P and $\kappa^2$-P,N mode, respectively (Scheme 5). Complex **9** is obtained in pure form, when the reaction is performed in the presence of 1 equiv. of $CH_3CN$. Both complexes were characterized by means of $^1H$, $^{13}C\{^1H\}$, and $^{31}P\{^1H\}$ NMR spectroscopy and elemental analysis in the case of **9**. Crystals of **10** could be grown by diffusion of diethyl ether into a $CH_2Cl_2$ solution of a reaction mixture containing both **9** and **10**. A structural view of **10** is depicted in Figure 11 with selected bond lengths and angles reported in the caption.

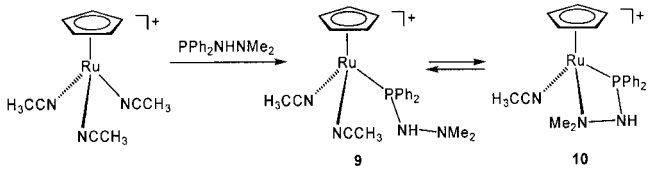


Scheme 5.

Complexes **9** and **10** exhibit singlet resonances in the $^{31}P\{^1H\}$ NMR spectrum at 90.6 to 61.4 ppm, respectively. In the case of **10** where the $PPh_2NHNMe_2$ ligand is bound in $\kappa^2$-P,N fashion the $^1H$ and $^{13}C\{^1H\}$ NMR spectra show the two methyl groups to be inequivalent, giving rise to two signals at $\delta$ = 3.35 and 2.82 ppm and 63.9 and 57.8 ppm, respectively [cf. complex **9** exhibits one singlet at $\delta$ = 2.27 ppm and a doublet centered at $\delta$ = 49.9 ppm ($J_{CP}$ = 3.4 Hz)].

Unfortunately, in contrast to the clean reactions of complexes **1** and **2** with diynes, the reaction of **9** with 1,6-heptadiyne and 1,7-octadiyne afforded only mixtures of intractable materials. Thus as yet no further reactions have been performed with **9**.

 © 2006 Wiley-VCH Verlag GmbH & Co. KGaA, Weinheim 

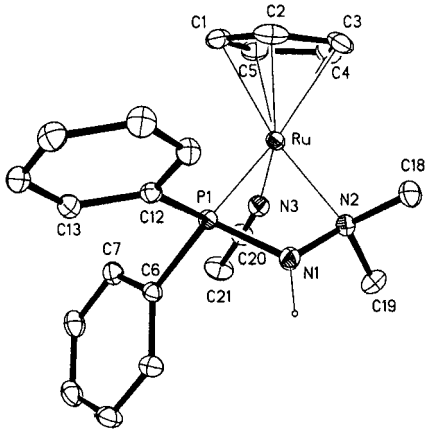


Figure 11. Structural view of $[RuCp\{\kappa^2\text{-}(P,N)\text{-}PPh_2NHNMe_2\}(CH_3CN)]PF_6$ (**10**) showing 30% thermal ellipsoids ($PF_6^-$ omitted for clarity). Selected bond lengths [Å] and angles [°]: Ru–$C(1–5)_{av}$ 2.173(2), Ru–P(1) 2.2915(2), Ru–N(2) 2.216(2), Ru–N(3) 2.050(2), P(1)–N(2) 1.688(2), N(1)–N(2) 1.456(2), P(1)–Ru–N(2) 67.03(4).

### Mechanistic Aspects

For the present conversion of **1** and **2** to the respective phosphaallyl complexes **4**, unfortunately, no intermediate products could be detected spectroscopically. From previous experimental data[19] it is reasonable to assume that the formation of the $\eta^3$-phosphaallyl–$\eta^2$-vinylamine proceeds via the intermediacy of the cationic metallacyclopentatriene **A** and the $\eta^3$-allyl carbene complex **B**. The formation of the latter involves migration of the $\kappa^1$(P) coordinated $PPh_2NRR'$ ligand to one of the two electrophilic carbene carbon atoms of **A**.[19] Accordingly, we have chosen **B** (in the form of the two model complexes $[CpRu\{=CH\text{–}(\eta^3\text{-}CHCHCH\text{–}PH_2NH_2)\}]^+$ and $[CpRu\{=CH\text{-}(\eta^3\text{-}CHCHCH\text{–}PMe_2NHMe)\}]^+$) as the starting point of our theoretical mechanistic investigation based on DFT/B3LYP calculations. The energy profile for the conversion of **B** to the $\eta^3$-phosphaallyl–$\eta^2$-vinylamine complexes **4** is shown in Figure 12. The models of **4** with $PH_2NH_2$ and $PMe_2NHMe$ will be called **F** (in Figure 12 the energy values in parentheses refer to $PMe_2NHMe$). The reliability of the computational method (details in Experimental Section) is supported by the good agreement between the calculated geometries of **F** with the X-ray structures of the related complexes (e.g. **3a** and **3c**).

The first step **B** to **C** constitutes a rotation of the aminophosphane substituent about the C–P bond, which is required to place the amine moiety in a position suitable for nucleophilic attack at the carbene carbon atom. This process is slightly endothermic by 3.2 kcal/mol and possesses a small activation barrier (6.7 kcal/mol). Subsequent nucleophilic attack of the amine moiety at the carbene carbon atom of **C** yields intermediate **D**, which features an unusual six-membered aza-phosphacycle. The transition state for this process, $\mathbf{TS_{CD}}$, is very similar to the structure of **D**, indicating that the transition state structure occurs quite late along the reaction coordinate and is merely 0.3 kcal/

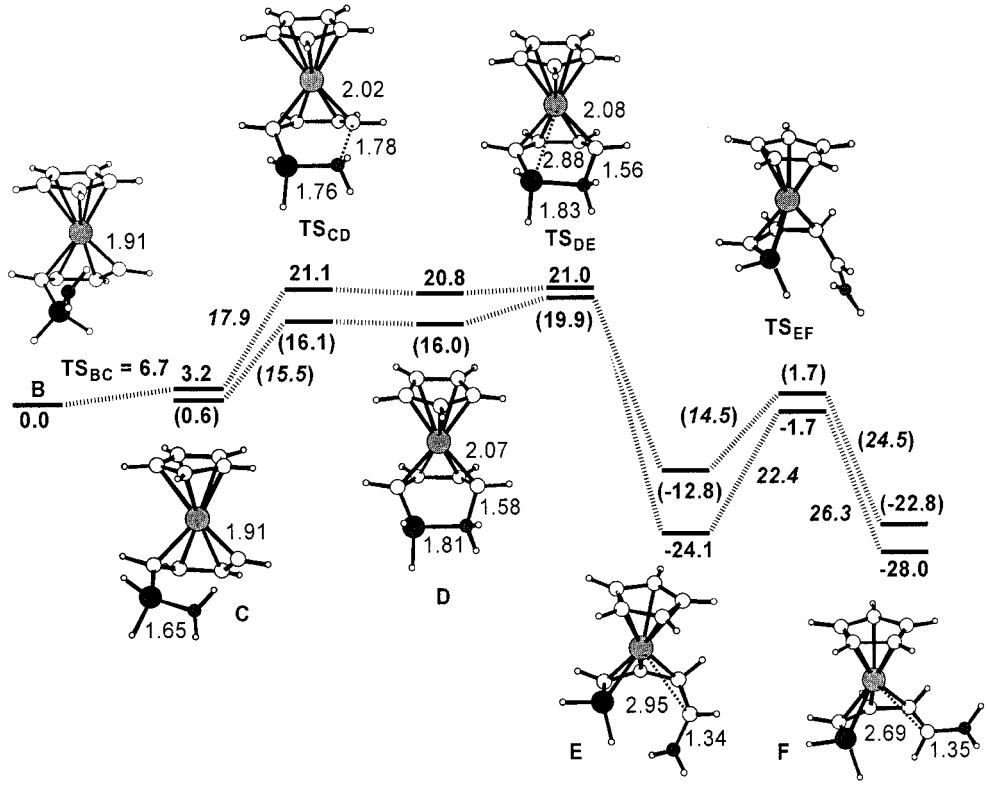


Figure 12. Energy profile (in kcal/mol, relative to **B**) for the conversion of **B** to **F** with $PH_2NH_2$ as model aminophosphane ligand. The numbers in parentheses refer to $PMe_2NHMe$ as the model ligand.

 © 2006 Wiley-VCH Verlag GmbH & Co. KGaA, Weinheim 

mol higher in energy than **D**. In the course of this reaction, a new N···C bond starts to form. It is 1.78 Å in $\mathbf{TS_{CD}}$ and finally reaches 1.58 Å in species **D**. This process requires an activation energy of 17.9 kcal/mol. The P–N bond in **D** is rather weak as judged from the long P–N bond length of 1.81 Å. Accordingly, this bond is readily cleaved, yielding the $\eta^3$-phosphaallyl–$\eta^2$-vinylamine complex **E**. This transformation is strongly exothermic, releasing 44.9 kcal/mol. The transition state connecting **D** and **E** is reached at an early stage and thus its structure is very similar to **D**. In fact, the only noticeable change from **D** to $\mathbf{TS_{DE}}$ is a weak but apparently important Ru···P interaction of 2.88 Å. In **E** the Ru–P bond is fully developed (2.30 Å), while the Ru–$C^4$ bond becomes very weak or almost nonbonding (2.95 Å). On going from **D** to **E**, the amino substituent is initially placed in an *anti* position, that is, pointing towards the phosphane moiety, which is sterically unfavorable, especially if the amine is mono- or even disubstituted (repulsive interactions) such as in **3b**, **3c**, **3d**, or **3e**. Rotation of the amine unit about the $C^3$–$C^4$ bond yields the experimentally observed and isolated *syn* isomer **F**. Surprisingly, despite the fact that the Ru–$C^4$ bond is rather long (2.95 Å), the activation barrier for this rotation is relatively high, requiring 22.4 kcal/mol. However, in the case of the more realistic model ligand $PMe_2NHMe$, the activation barrier becomes significantly smaller (14.5 kcal/mol) and unfavorable steric interactions are better taken into account (Figure 12, numbers in parentheses).

Experimentally it has been observed that $\eta^3$-phosphaallyl–$\eta^2$-vinylamine complexes (**F**) are the kinetic products but isomerize (in some cases already at room temperature) to the thermodynamically more stable $\eta^1$-phosphaallyl–$\eta^3$-azaallyl complexes **H**. The energy profiles for this conversion are presented in Figures 12 (**F** → **E**) and 13 (**E** → **H**). In agreement with experimental data, the overall process is thermodynamically favored. This rearrangement exhibits a *syn–anti* isomerization of the $NH_2$ substituent and thus proceeds most likely again via the intermediacy of **E** (Figure 12). This first step needs an activation energy of 26.3 kcal/mol for the parent $PH_2NH_2$ ligand and 24.5 kcal/mol for $PMe_2NHMe$ and is thus rate determining. Once **E** is re-formed, the subsequent processes are facile. Complex **E** proceeds through transition state $\mathbf{TS_{EG}}$ to afford the metallacycle **G**. This reaction is energetically slightly unfavorable by 6.7 kcal/mol with an activation energy of 12.1 kcal/mol. These values, however, are comparatively small taking into account that in the course of this reaction two Ru–C bonds are broken, which are counterbalanced only by one weak Ru–C interaction (2.65 Å). Moreover, as a consequence of that ongoing from **E** by $\mathbf{TS_{EG}}$ to **G**, the C4 chain experiences a severe distortion, as is apparent from the changes of the respective torsion angles C–C–C–C being 39.2, 58.1, and finally 111.5°, respectively. This may also explain why the formation of azaallyl complexes is far more facile in the case of 1,7-octadiyne where the phosphaallyl complexes contain a six-membered ring system than with 1,6-heptadiyne where these complexes feature a more rigid five-membered ring. The subsequent conversion of **G** to the $\eta^1$-phosphaallyl–$\eta^3$-azaallyl complexes **H** requires merely 0.4 kcal/mol activation energy and is energetically very favorable, releasing 18.5 kcal/mol (Figure 13).

Finally, we also looked for a plausible mechanism of the formation of amido-butadiene complexes (**I**) from allyl carbene complexes (**B**). This reaction is obviously restricted to aminophosphane ligands possessing NH protons. An energetically feasible pathway with the model complexes [CpRu{=CH-($\eta^3$-CHCHCH–$PH_2NH_2$)}]$^+$ and [CpRu{=CH-($\eta^3$-CHCHCH–$PMe_2NHMe$)}]$^+$ (**A**) is shown in Figure 14. Accordingly, the N–H proton in **B** is transferred to the carbene carbon atom by transition state $\mathbf{TS_{HI}}$ without any involvement of the metal center. This reaction has an activation barrier of 17.7 kcal/mol (18.1 kcal/mol for $PMe_2NHMe$) and is exothermic releasing 8.4 kcal/mol (11.0 kcal/mol for $PMe_2NHMe$). Therefore, in the case of complexes with

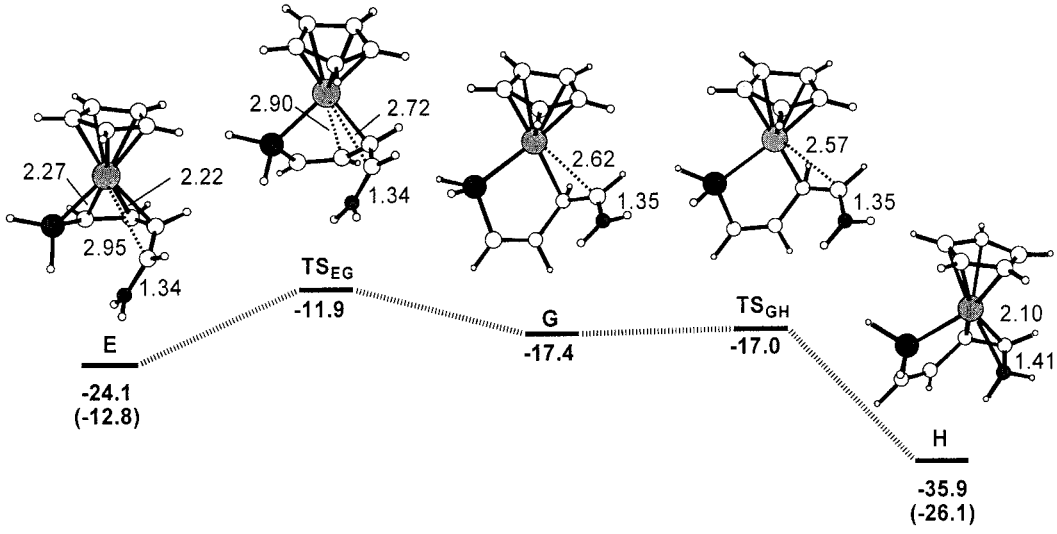


Figure 13. Energy profile (in kcal/mol, relative to **B**) for the conversion of **E** to **H** with $PH_2NH_2$ as model aminophosphane ligand. The numbers in parentheses refer to $PMe_2NHMe$ as the model ligand.

 © 2006 Wiley-VCH Verlag GmbH & Co. KGaA, Weinheim 

aminophosphanes that contain N–H bonds, this pathway becomes competitive with the formation of phosphaallyl (**F**) and azaallyl complexes (**H**). It should be noted that we were unable to find an alternative pathway to obtain amido butadiene complexes by oxidative addition of the N–H bond to the metal center.

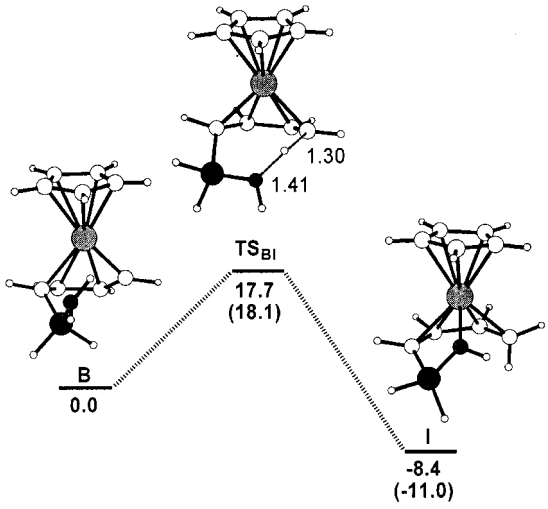


Figure 14. Energy profile (in kcal/mol, relative to **B**) for the reaction of **B** to **I** with $PH_2NH_2$ as model aminophosphane ligand. The numbers in parentheses refer to $PMe_2NHMe$ as the model ligand.

## Experimental Section

**General:** Manipulations were performed under inert purified argon by using Schlenk techniques and/or a glovebox. All chemicals were standard reagent grade and used without further purification. The solvents were purified according to standard procedures.[20] The deuterated solvents were purchased from Aldrich and dried with 4 Å molecular sieves. $[RuCp(CH_3CN)_3]PF_6$,[21] $[RuCp^*(CH_3CN)_3]PF_6$,[22] and $PPh_2NHNMe_2$[23] were prepared according to the literature. $^1H$, $^{13}C\{^1H\}$, and $^{31}P\{^1H\}$ NMR spectra were recorded with Bruker Avance-250 and -300 spectrometers and were referenced to $SiMe_4$ and $H_3PO_4$ (85%), respectively. $^1H$ and $^{13}C\{^1H\}$ NMR signal assignments were confirmed by $^1H$-COSY, 135-DEPT, and HSQC($^1H$-$^{13}C$) experiments.

**$[RuCp(PPh_2NH$*n*$Pr)(CH_3CN)_2]PF_6$ (1a):** $PPh_2NH$*n*Pr (185 mg, 0.76 mmol) was added to a solution of $[RuCp(CH_3CN)_3]PF_6$ (300 mg, 0.69 mmol) in $CH_2Cl_2$ (10 mL) and the mixture was stirred for 2 h at room temperature. After removal of the solvent, a yellow powder was obtained which was collected on a glass frit, washed with $Et_2O$ (3 × 10 mL), and dried under vacuum. Yield: 421 mg (95%). $C_{24}H_{29}F_6N_3P_2Ru$ (636.52): calcd. C 45.29, H 4.59, N 6.60; found C 45.23, H 4.79, N 6.74. $^1H$ NMR ($CD_2Cl_2$, 20 °C): $\delta$ = 7.69–7.42 (m, 10 H, Ph), 4.43 (s, 5 H, Cp), 2.85–2.66 (m, 2 H, *n*Pr), 2.50–2.32 (m, 1 H, N*H**n*Pr), 2.20 (d, $J_{HP}$ = 1.4 Hz, 6 H, $CH_3CN$), 1.51 –1.30 (m, 2 H, *n*Pr), 0.80 (t, $J_{HH}$ = 7.4 Hz, 3 H, *n*Pr) ppm. $^{13}C\{^1H\}$ NMR ($CD_2Cl_2$, 20 °C): $\delta$ = 136.1 (d, $^1J_{CP}$ = 48.7 Hz, Ph$^1$), 131.6 (d, $^2J_{CP}$ = 11.9 Hz, Ph$^{2,6}$), 130.0 (d, $^4J_{CP}$ = 1.9 Hz, Ph$^4$), 128.2 (d, $^3J_{CP}$ = 10.0 Hz, Ph$^{3,5}$), 126.7 ($CH_3CN$), 76.6 (d, $J_{CP}$ = 2.3 Hz, Cp), 45.8 (d, $J_{CP}$ = 8.0 Hz, $CH_2$), 24.9 (d, $J_{CP}$ = 5.8 Hz, $CH_2$), 11.0 ($CH_3$), 3.7 ($CH_3CN$) ppm. $^{31}P\{^1H\}$ NMR ($CD_2Cl_2$, 20 °C): $\delta$ = 86.0 ($PPh_2$), –143.0 ($^1J_{FP}$ = 708.3 Hz, $PF_6$) ppm.

**$[RuCp(PPh_2NEt_2)(CH_3CN)_2]PF_6$ (1b):** This complex has been prepared analogously to **1a** with $[RuCp(CH_3CN)_3]PF_6$ (300 mg, 0.69 mmol) and $PPh_2NEt_2$ (179 mg, 0.69 mmol) as starting materials. Yield: 416 mg (93%). $C_{25}H_{31}F_6N_3P_2Ru$ (650.55): calcd. C 46.16, H 4.80, N 6.46; found C 46.10, H 4.72, N 6.55. $^1H$ NMR ($CD_2Cl_2$, 20 °C): $\delta$ = 7.61–7.30 (m, 10 H, Ph), 4.26 (s, 5 H, Cp), 3.42–3.20 (m, 4 H, Et), 2.22 (6 H, $CH_3CN$), 0.96 (t, $J_{HH}$ = 7.1 Hz, 3 H, Et) ppm. $^{13}C\{^1H\}$ NMR ($\delta$, $CD_2Cl_2$, 20 °C): 137.4 (d, $^1J_{CP}$ = 46.0 Hz, Ph$^1$), 131.4 (d, $^2J_{CP}$ = 11.5 Hz, Ph$^{2,6}$), 129.7 (d, $^4J_{CP}$ = 1.9 Hz, Ph$^4$), 128.0 (d, $^3J_{CP}$ = 9.6 Hz, Ph$^{3,5}$), 127.3 ($CH_3CN$), 77.4 (d, $J_{CP}$ = 2.3 Hz, Cp), 42.4 (d, $J_{CP}$ = 6.5 Hz, $CH_2$), 13.6 (d, $J_{CP}$ = 2.3 Hz, $CH_3$), 3.7 ($CH_3CN$) ppm. $^{31}P\{^1H\}$ NMR ($\delta$, $CD_2Cl_2$, 20 °C): 102.1 ($PPh_2$), –143.0 ($^1J_{FP}$ = 711.8 Hz, $PF_6$) ppm.

**$[RuCp(PPh_2NC_5H_{10})(CH_3CN)_2]PF_6$ (1c):** This complex has been prepared analogously to **1a** with $[RuCp(CH_3CN)_3]PF_6$ (374 mg, 0.86 mmol) and $PPh_2NC_5H_{10}$ (232 mg, 0.86 mmol) as starting materials. Yield: 500 mg (88%). $C_{26}H_{31}F_6N_3P_2Ru$ (662.56): calcd. C 47.13, H 4.72, N, 6.34; found C 46.66, H 4.89, N 6.51. $^1H$ NMR ($CD_2Cl_2$, 20 °C): $\delta$ = 7.66–7.26 (m, 10 H, Ph), 4.23 (s, 5 H, Cp), 3.30–3.01 (m, 4 H, $NC_5H_{10}$), 2.20 (d, $J_{HP}$ = 1.0 Hz, 6 H, $CH_3CN$), 1.72–1.36 (m, 6 H, $NC_5H_{10}$) ppm. $^{13}C\{^1H\}$ NMR ($CD_2Cl_2$, 20 °C): $\delta$ = 136.6 (d, $^1J_{CP}$ = 46.0 Hz, Ph$^1$), 131.2 (d, $^2J_{CP}$ = 11.1 Hz, Ph$^{2,6}$), 129.7 (d, $^4J_{CP}$ = 1.9 Hz, Ph$^4$), 128.1 (d, $^3J_{CP}$ = 9.6 Hz, Ph$^{3,5}$), 127.3 ($CH_3CN$), 77.4 (d, $J_{CP}$ = 2.3 Hz, Cp), 50.1 (d, $J_{CP}$ = 3.4 Hz, $CH_2$), 27.0 (d, $J_{CP}$ = 5.4 Hz, $CH_2$), 24.4 ($CH_2$), 3.7 ($CH_3CN$) ppm. $^{31}P\{^1H\}$ NMR ($CD_2Cl_2$, 20 °C): $\delta$ = 98.8 ($PPh_2$), –143.0 ($^1J_{FP}$ = 710.5 Hz, $PF_6$) ppm.

**$[RuCp^*(PPh_2NH$*n*$Pr)(CH_3CN)_2]PF_6$ (2a):** $PPh_2NH$*n*Pr (145 mg 0.60 mmol) was added to a solution of $[RuCp^*(CH_3CN)_3]PF_6$ (300 mg, 0.60 mmol) in $CH_2Cl_2$ (5 mL) and the mixture was stirred for 2 h at room temperature. The volume of the solution was then reduced to about 1 mL and $Et_2O$ (5 mL) was added. A yellow precipitate was formed, which was washed with $Et_2O$ (2 × 5 mL) and dried under vacuum. Yield: 336 mg (80%) $C_{29}H_{39}F_6N_3P_2Ru$ (706.66): calcd. C 49.29, H 5.56, N 5.95; found: C 48.94,; H 6.09, N 5.59. $^1H$ NMR ($CD_2Cl_2$, 20 °C): $\delta$ = 7.65–7.40 (m, 10 H, Ph), 3.09–2.85 (m, 1 H, NH), 2.74 (m, $J_{HH}$ = 6.9 Hz, 2 H, $CH_2$), 2.23 (d, $J_{HP}$ = 1.3 Hz, 6 H, $CH_3CN$), 1.49 (d, $J_{HP}$ = 1.7 Hz, 15 H, Cp*), 1.27–1.21 (m, 2 H, $CH_2$), 0.84 (t, $J_{HH}$ = 7.5 Hz, 3 H, $CH_3$) ppm. $^{13}C\{^1H\}$ NMR ($CD_2Cl_2$, 20 °C): $\delta$ = 135.4 (d, $^1J_{CP}$ = 43.7 Hz, Ph$^1$), 132.0 (d, $^2J_{CP}$ = 11.5 Hz, Ph$^{2,6}$), 129.7 (Ph$^4$), 128.0 (d, $^3J_{CP}$ = 9.2 Hz, Ph$^{3,5}$), 124.7 ($CH_3CN$), 86.8 (Cp*), 46.0 (d, $J_{CP}$ = 9.2 Hz, $CH_2$), 25.0 (d, $J_{CP}$ = 6.1 Hz, $CH_2$), 10.5 ($CH_3$), 9.1 (Cp*), 3.8 ($CH_3CN$) ppm. $^{31}P\{^1H\}$ NMR ($CD_2Cl_2$, 20 °C): $\delta$ = 82.9 ($PPh_2$), –144.5 ($^1J_{FP}$ = 710.2 Hz, $PF_6$) ppm.

**$[RuCp^*(PPh_2NEt_2)(CH_3CN)_2]PF_6$ (2b):** This complex has been prepared analogously to **2a** with $[RuCp^*(CH_3CN)_3]PF_6$ (300 mg, 0.60 mmol) and $PPh_2NEt_2$ (153 mg 0.60 mmol) as starting materials. Yield: 350 mg (82%) $C_{30}H_{41}F_6N_3P_2Ru$ (720.68): calcd. C 50.00, H 5.73, N 5.83; found C 50.24, H 5.44, N 5.59. $^1H$ NMR ($CD_2Cl_2$, 20 °C): $\delta$ = 7.58–7.18 (m, 10 H, Ph), 3.30–3.13 (m, 4 H, $CH_2$), 2.74 (m, $^3J_{HH}$ = 6.9 Hz, 2 H, $CH_2$), 2.24 (d, $J_{HP}$ = 1.1 Hz, 6 H, $CH_3CN$), 1.32 (d, $J_{HP}$ = 1.7 Hz, 15 H, Cp*′), 1.00 (t, $^3J_{HH}$ = 7.1 Hz, 6 H, $CH_3$) ppm. $^{13}C\{^1H\}$ NMR ($CD_2Cl_2$, 20 °C): $\delta$ = 136.7 (d, $^1J_{CP}$ = 41.4 Hz, Ph$^1$), 131.8 (d, $^2J_{CP}$ = 11.5 Hz, Ph$^{2,6}$), 129.4 (Ph$^4$), 127.9 (d, $^3J_{CP}$ = 9.2 Hz, Ph$^{3,5}$), 125.5 ($CH_3CN$), 87.2 (Cp*), 41.6 (d, $J_{CP}$ = 7.7 Hz, $CH_2$), 12.9 (d, $J_{CP}$ = 3.1 Hz, $CH_3$), 8.7 (Cp*), 3.8 ($CH_3CN$) ppm. $^{31}P\{^1H\}$ NMR ($CD_2Cl_2$, 20 °C): $\delta$ = 101.3 ($PPh_2$), –144.4 ($^1J_{FP}$ = 712.0 Hz, $PF_6$) ppm.

**$[RuCp^*(PPh_2NC_5H_{10})(CH_3CN)_2]PF_6$ (2c):** This complex has been prepared analogously to **2a** with $[RuCp^*(CH_3CN)_3]PF_6$ (300 mg, 0.60 mmol) and $PPh_2NC_5H_{10}$ (160 mg 0.60 mmol) as starting mate-

 © 2006 Wiley-VCH Verlag GmbH & Co. KGaA, Weinheim 

rials. Yield: 380 mg (87%) $C_{31}H_{41}F_6N_3P_2Ru$ (732.69): calcd. C 50.82, H 5.64, N 5.74; found C 50.14, H 5.46, N 5.78. $^1$H NMR ($CD_2Cl_2$, 20 °C): $\delta$ = 7.51–7.35 (m, 10 H, Ph), 3.06–2.90 (m, 4 H, $CH_2$), 2.24 (d, $J_{HP}$ = 1.26 Hz, 6 H, $CH_3CN$), 1.62–1.48 (m, 6 H, $CH_2$), 1.32 (d, $J_{HP}$ = 1.7 Hz, 15 H, Cp*′) ppm. $^{13}$C{$^1$H} NMR ($CD_2Cl_2$, 20 °C): $\delta$ = 135.8 (d, $^1J_{CP}$ = 40.6 Hz, Ph$^1$), 131.5 (d, $^2J_{CP}$ = 10.7 Hz, Ph$^{2,6}$), 129.3 (Ph$^4$), 128.0 (d, $^3J_{CP}$ = 9.2 Hz, Ph$^{3,5}$), 125.3 ($CH_3CN$), 87.2 (Cp*), 50.4 (d, $J_{CP}$ = 3.8 Hz, $CH_2$), 26.9 (d, $J_{CP}$ = 6.9 Hz, $CH_2$), 24.3 ($CH_2$), 8.7 (Cp*), 3.8 ($CH_3CN$) ppm. $^{31}$P{$^1$H} NMR ($CD_2Cl_2$, 20 °C): $\delta$ = 96.1 ($PPh_2$), –144.4 ($^1J_{FP}$ = 710.8 Hz, $PF_6$) ppm.

**[RuCp{η³-(P,C,C)-PPh₂CHC–(CH₂)₃–η²-(C,C)-CCHNH*n*Pr}]PF₆ (3a):** 1.1 equiv. of 1,6-heptadiyne (26.7 μL, 0.23 mmol) was added to a solution of **1a** (135 mg, 0.21 mmol) in $CH_2Cl_2$ (10 mL) and the mixture was stirred for 2 h at room temperature. After removal of the solvent under reduced pressure, an orange solid was obtained, which was washed with $Et_2O$ (5 mL), and dried under vacuum. Yield: 99 mg (73%). $C_{27}H_{31}F_6NP_2Ru$ (646.56): calcd. C 50.16, H 4.83, N 2.17; found C 49.88, H 5.02, N 2.22. $^1$H NMR ($CD_2Cl_2$, 20 °C): $\delta$ = 7.79–7.25 (m, 10 H, Ph), 5.05 (s, 5 H, Cp), 4.30–4.09 (m, 1 H, N*H*nPr), 4.14 (d, $^2J_{HP}$ = 5.4 Hz, 1 H, H$^1$), 3.99 (d, $J_{HP}$ = 7.6 Hz, 1 H, H$^4$), 3.37–3.20 (m, 1 H), 2.97–2.66 (m, 3 H), 2.62–2.39 (m, 2 H), 2.36–2.17 (m, 1 H), 2.09–1.86 (m, 1 H), 1.46–1.08 (m, 2 H), 0.77 (t, $J_{HH}$ = 7.4, 3 H) ppm. $^{13}$C{$^1$H} NMR ($CD_2Cl_2$, 20 °C): $\delta$ = 133.8 (d, $^2J_{CP}$ = 11.5 Hz, Ph$^{2,6}$), 132.4 (d, $^2J_{CP}$ = 12.3 Hz, Ph$^{2',6'}$), 131.6 (d, $^4J_{CP}$ = 3.4 Hz, Ph$^4$), 131.7–131.6 (d, $^4J_{CP}$ = 3.4 Hz, Ph$^{4'}$), 129.9 (d, $^3J_{CP}$ = 12.3 Hz, Ph$^{3,5}$), 129.1 (d, $^3J_{CP}$ = 12.3 Hz, Ph$^{3',5'}$), 122.1 (d, $^1J_{CP}$ = 52.1 Hz, Ph$^1$), 116.8 (d, $J_{CP}$ = 3.8 Hz, C$^3$), 106.9 (d, $J_{CP}$ = 6.1 Hz, C$^4$), 82.1 (C$^2$), 81.7 (Cp), 50.4 ($CH_2$), 41.6 (d, $J_{CP}$ = 24.5 Hz, C$^1$), 37.1 (d, $J_{CP}$ = 7.7 Hz, $CH_2$), 31.6 ($CH_2$), 22.6 ($CH_2$), 21.9 ($CH_2$), 11.8 ($CH_3$) ppm. $^{31}$P{$^1$H} NMR ($CD_2Cl_2$, 20 °C): $\delta$ = 9.3 ($PPh_2$), –142.9 ($^1J_{FP}$ = 711.5 Hz, $PF_6$) ppm.

**[RuCp{η³-(P,C,C)-PPh₂CHC–(CH₂)₃–η²-(C,C)-CCHNEt₂}]PF₆ (3b):** This complex has been prepared analogously to **3a** with **1b** (100 mg, 0.15 mmol) and 1,6-heptadiyne (19.5 μL, 0.17 mmol) as the starting materials. Yield: 75 mg (76%). $C_{28}H_{33}F_6NP_2Ru$ (660.58): calcd. C 50.91, H 5.09, N 2.12; found C 50.83, H 5.11, N 2.19. $^1$H NMR ($CD_2Cl_2$, 20 °C): $\delta$ = 7.68–7.41 (m, 10 H, Ph), 5.09 (s, 5 H, Cp), 4.01 (d, $^2J_{HP}$ = 4.7 Hz, 1 H, H$^1$), 3.58 (d, $J_{HP}$ = 5.7 Hz, 1 H, H$^4$), 3.01–2.86 (m, 2 H), 2.82–2.51 (m, 6 H), 2.39–2.27 (m, 2 H), 0.96 (t, $J_{HH}$ = 7.1 Hz, 3 H) ppm. $^{13}$C{$^1$H} NMR ($CD_2Cl_2$, 20 °C): $\delta$ = 133.2 (d, $^2J_{CP}$ = 11.9 Hz, Ph$^{2,6}$), 132.4 (d, $^2J_{CP}$ = 12.3 Hz, Ph$^{2',6'}$), 132.1 (d, $^4J_{CP}$ = 3.5 Hz, Ph$^4$), 131.6 (d, $^4J_{CP}$ = 2.3 Hz, Ph$^{4'}$), 129.8 (d, $^3J_{CP}$ = 11.5 Hz, Ph$^{3,5}$), 129.0 (d, $^3J_{CP}$ = 11.9 Hz, Ph$^{3',5'}$), 125.9 (d, $^1J_{CP}$ = 47.9 Hz, Ph$^1$), 117.8 (d, $J_{CP}$ = 6.9 Hz, C$^4$), 117.4 (d, $J_{CP}$ = 4.6 Hz, C$^3$), 79.1 (d, $J_{CP}$ = 1.5 Hz, Cp), 75.8 (C$^2$), 46.8 ($CH_2$), 40.8 (d, $J_{CP}$ = 24.2 Hz, C$^1$), 36.0 (d, $J_{CP}$ = 7.3 Hz, $CH_2$), 33.2 ($CH_2$), 23.1 ($CH_2$), 12.1 ($CH_3$) ppm. $^{31}$P{$^1$H} NMR ($CD_2Cl_2$, 20 °C): $\delta$ = 4.2 ($PPh_2$), –143.0 ($^1J_{FP}$ = 710.8 Hz, $PF_6$) ppm.

**[RuCp{η³-(P,C,C)-PPh₂CHC–(CH₂)₃–η²-(C,C)-CCHNC₅H₁₀}]PF₆ (3c):** This complex has been prepared analogously to **3a** with **1c** (105 mg, 0.16 mmol) and 1,6-heptadiyne (19 μL, 0.17 mmol) as the starting materials. Yield: 74 mg (69%). $C_{29}H_{33}F_6NP_2Ru$ (672.59): calcd. C 51.79, H 4.95, N 2.08; found C 51.87, H 5.09, N 2.14. $^1$H NMR ($CD_2Cl_2$, 20 °C): $\delta$ = 7.72–7.31 (m, 10 H, Ph), 5.14 (s, 5 H, Cp), 4.03 (d, $^2J_{HP}$ = 4.7 Hz, 1 H, H$^1$), 3.30 (d, $J_{HP}$ = 5.7 Hz, 1 H, H$^4$), 3.24–3.09 (m, 1 H), 2.99–2.64 (m, 5 H), 2.39–2.13 (m, 4 H), 1.63–1.37 (m, 6 H) ppm. $^{13}$C{$^1$H} NMR ($CD_2Cl_2$, 20 °C): $\delta$ = 133.6 (d, $^2J_{CP}$ = 11.9 Hz, Ph$^{2,6}$), 132.2 (d, $^2J_{CP}$ = 12.3 Hz, Ph$^{2',6'}$), 132.2 (d, $^4J_{CP}$ = 3.3 Hz, Ph$^4$), 131.4–131.6 (d, $^4J_{CP}$ = 3.4 Hz, Ph$^{4'}$), 129.7 (d, $^3J_{CP}$ = 12.3 Hz, Ph$^{3,5}$), 129.7 (d, $^3J_{CP}$ = 12.3 Hz, Ph$^{3,5}$), 129.0 (d, $^3J_{CP}$ = 12.3 Hz, Ph$^{3',5'}$), 126.5 (d, $^1J_{CP}$ = 50.6 Hz, Ph$^1$), 117.8 (d, $J_{CP}$ = 3.8 Hz, C$^3$), 116.8 (d, $J_{CP}$ = 5.8 Hz, C$^4$), 79.1 (d, $J_{CP}$ = 1.5 Hz, Cp), 76.1 (C$^2$), 52.4 ($CH_2$), 41.3 (d, $J_{CP}$ = 24.2 Hz, C$^1$), 35.7 (d, $J_{CP}$ = 6.9 Hz, $CH_2$), 33.3 ($CH_2$), 24.9 ($CH_2$), 23.2 ($CH_2$), 23.1 ($CH_2$) ppm. $^{31}$P{$^1$H} NMR ($CD_2Cl_2$, 20 °C): $\delta$ = 8.1 ($PPh_2$), –142.9 ($^1J_{FP}$ = 710.8 Hz, $PF_6$) ppm.

**Reaction of 1b with 1,7-Octadiyne in $CD_2Cl_2$. Formation of [RuCp{η³-(P,C,C)–PPh₂–CH–C(CH₂)₄-η²-(C,C)-CCHNEt₂}]PF₆ (3d) and [RuCp{η¹-(P)-PPh₂–CH=C(CH₂)₄-η³-(C,C,N)-CCHNEt₂}]PF₆ (4e):** A 5-mm NMR tube was charged with **1b** (30 mg, 0.05 mmol) in $CD_2Cl_2$ (0.5 mL) and 1,7-octadiyne (6,1 μL, 0.05 mmol) was added by syringe. The reaction was then monitored by $^1$H and $^{31}$P{$^1$H} NMR spectroscopy. After 20 min both **3d** and **4e** were formed in an approximately 3:1 ratio. After 5 h this ratio changed to about 1:6. Because of spectral overlap with **4e** only the most characteristic signals of **3d** could be unequivocally assigned. $^1$H NMR ($CD_2Cl_2$, 20 °C): $\delta$ = 5.10 (s, 5 H, Cp), 3.53 (d, $^2J_{HP}$ = 4.7 Hz, 1 H, H$^1$), 2.90 (d, $J_{HP}$ = 7.6 Hz, 1 H, H$^4$), 0.83 (t, $J_{HH}$ = 7.1 Hz, 6 H, Et) ppm. $^{31}$P{$^1$H} NMR ($CD_2Cl_2$, 20 °C): $\delta$ = 3.3 ($PPh_2$), –143.0 ($^1J_{FP}$ = 710.8 Hz, $PF_6$) ppm. After heating at 40 °C for 8 h, the **3d** was completely converted to **4e**.

**Reaction of 1c with 1,7-Octadiyne in $CD_2Cl_2$. Formation of [RuCp-{η³-(P,C,C)–PPh₂–CH–C(CH₂)₄-η²-(C,C)-CCHNC₅H₁₀}]PF₆ (3e) and [RuCp{η¹-(P)-PPh₂–CH=C(CH₂)₄-η³-(C,C,N)-CCHNC₅H₁₀}]PF₆ (4f):** A 5-mm NMR tube was charged with **1c** (34 mg, 0.05 mmol) in $CD_2Cl_2$ (0.5 mL) and 1,7-octadiyne (6,1 μL, 0.05 mmol) was added by syringe. The reaction was then monitored by $^1$H and $^{31}$P{$^1$H} NMR spectroscopy. After 30 min both **3e** and **4f** were formed in an approximately 8:1 ratio. After 5 h this ratio changed to about 3:1. Because of spectral overlap with **4f** only the most characteristic signals of **3e** could be unequivocally assigned. $^1$H NMR ($CD_2Cl_2$, 20 °C): $\delta$ = 5.20 (s, 5 H, Cp), 3.51 (d, $^2J_{HP}$ = 5.1 Hz, 1 H, H$^1$), 2.62 (d, $J_{HP}$ = 7.0 Hz, 1 H, H$^4$) ppm. $^{31}$P{$^1$H} NMR ($CD_2Cl_2$, 20 °C): $\delta$ = 7.9 ($PPh_2$), –142.9 ($^1J_{FP}$ = 710.8 Hz, $PF_6$) ppm. After heating at 40 °C for 8 h, **3e** was completely converted to **4f**.

**[RuCp{η¹-(P)-PPh₂CH=C–(CH₂)₃–η³-(C,C,N)-CCHNH*n*Pr}]PF₆ (4a):** A stirred solution of **3a** (50 mg, 0,08 mmol) in $CH_3NO_2$ (5 mL) was kept at 90 °C for 3 h. After removal of the solvent under reduced pressure, an orange solid was obtained which was washed with $Et_2O$ (5 mL), and dried under vacuum. Yield: 37 mg (73%). $C_{27}H_{31}F_6NP_2Ru$ (646.56): calcd. C 50.16, H 4.83, N 2.17; found C 49.68, H 4.82, N 2.23. $^1$H NMR ($CD_3NO_2$, 20 °C): $\delta$ = 8.01–7.87 (m, 2 H, Ph), 7.68–7.45 (m, 6 H, Ph), 7.33–7.18 (m, 2 H, Ph), 6.02 (1 H, H$^4$), 5.98 (d, $J_{HP}$ = 10.1 Hz, 1 H, H$^1$), 4.85 (s, 5 H, Cp), 3.06–2.89 (m, 1 H), 2.86–2.40 (m, 5 H), 2.21–2.00 (m, 2 H), 1.47–1.11 (m, 2 H), 0.59 (t, $J_{HH}$ = 7.4 Hz, 3 H) ppm. The NH proton could not be detected. $^{13}$C{$^1$H} NMR ($CD_3NO_2$, 20 °C): $\delta$ = 170.1 (d, $J_{CP}$ = 29.1 Hz, C$^3$), 136.4 (d, $^1J_{CP}$ = 52.1 Hz, Ph$^1$), 134.2 (d, $^2J_{CP}$ = 11.5 Hz, Ph$^{2,6}$), 131.3 (d, $^4J_{CP}$ = 2.3 Hz, Ph$^4$), 131.2 (d, $^1J_{CP}$ = 41.4 Hz, Ph$^{1'}$), 130.4 (d, $^2J_{CP}$ = 11.1 Hz, Ph$^{2',6'}$), 130.0 (d, $^4J_{CP}$ = 2.7 Hz, Ph$^{4'}$), 128.8 (d, $^3J_{CP}$ = 10.4 Hz, Ph$^{3,5}$), 128.7 (d, $^3J_{CP}$ = 11.1 Hz, Ph$^{3',5'}$), 111.9 (d, $J_{CP}$ = 47.2 Hz, C$^1$), 85.8 (d, $J_{CP}$ = 1.9 Hz, C$^2$), 81.3 (d, $J_{CP}$ = 1.9 Hz, Cp), 74.4 (C$^4$), 57.5 ($CH_2$), 35.6 ($CH_2$), 28.9 (d, $J_{CP}$ = 19.2 Hz, $CH_2$), 25.2 ($CH_2$), 24.1 ($CH_2$), 9.6 ($CH_3$) ppm. $^{31}$P{$^1$H} NMR ($CD_3NO_2$, 20 °C): $\delta$ = 70.3 ($PPh_2$), –143.2 ($^1J_{FP}$ = 707.4 Hz, $PF_6$) ppm.

**[RuCp{η¹-(P)-PPh₂CH=C–(CH₂)₃–η³-(C,C,N)-CCHNEt₂}]PF₆ (4b):** A stirred solution of **3b** (50 mg, 0,08 mmol) in $CH_3NO_2$ (5 mL) was kept overnight at 80 °C. After removal of the solvent under reduced pressure, an orange solid was obtained, which was

 © 2006 Wiley-VCH Verlag GmbH & Co. KGaA, Weinheim 

washed with $Et_2O$ (5 mL), and dried under vacuum. Yield: 45 mg (85%). $C_{28}H_{33}F_6NP_2Ru$ (660.58): calcd. C 50.91, H 5.04, N 2.12; found C 50.60,; H 4.98, N 2.00. $^1H$ NMR ($CD_3NO_2$, 20 °C): $\delta$ = 8.08–7.88 (m, 2 H, Ph), 7.73–7.34 (m, 6 H, Ph), 7.33–7.16 (m, 2 H, Ph), 6.35 (d, $J_{HP}$ = 9.8 Hz, 1 H, $H^1$), 6.03 (s, 1 H, $H^4$), 4.76 (s, 5 H, Cp), 3.72–3.51 (m, 1 H), 3.03–2.44 (m, 4 H), 2.27–1.84 (m, 5 H), 1.21 (t, $J_{HH}$ = 7.1 Hz, 3 H), 0.81 (t, $J_{HH}$ = 7.1 Hz, 3 H) ppm. $^{13}C\{^1H\}$ NMR ($CD_3NO_2$, 20 °C): $\delta$ = 172.0 (d, $J_{CP}$ = 27.2 Hz, $C^3$), 137.5 (d, $^1J_{CP}$ = 54.4 Hz, $Ph^1$), 134.0 (d, $^2J_{CP}$ = 12.3 Hz, $Ph^{2,6}$), 131.6 (d, $^1J_{CP}$ = 47.2 Hz, $Ph^{1'}$), 131.3 (d, $^4J_{CP}$ = 2.3 Hz, $Ph^4$), 130.4 (d, $^2J_{CP}$ = 10.7 Hz, $Ph^{2',6'}$), 129.9 (d, $^4J_{CP}$ = 2.3 Hz, $Ph^{4'}$), 128.7 (d, $^3J_{CP}$ = 10.0 Hz, $Ph^{3,5}$), 128.6 (d, $^3J_{CP}$ = 10.7 Hz, $Ph^{3',5'}$), 117.4 (d, $J_{CP}$ = 47.9 Hz, $C^1$), 91.3 (d, $J_{CP}$ = 3.1 Hz, $C^2$), 82.2 (d, $J_{CP}$ = 1.9 Hz, Cp), 79.1 (d, $J_{CP}$ = 1.5 Hz, $C^4$), 58.3 ($CH_2$), 44.1 (d, $J_{CP}$ = 8.8 Hz, $CH_2$), 38.4 ($CH_2$), 28.8 (d, $J_{CP}$ = 19.6 Hz, $CH_2$), 25.1 ($CH_2$), 13.8 ($CH_3$), 12.1 ($CH_3$) ppm. $^{31}P\{^1H\}$ NMR ($CD_2Cl_2$, 20 °C): $\delta$ = 74.1 ($PPh_2$), –143.3 ($^1J_{FP}$ = 707.1 Hz, $PF_6$) ppm.

**[RuCp{η¹-(P)-PPh₂CH=C–(CH₂)₃–η³-(C,C,N)-CCHNC₅H₁₀}]PF₆ (4c):** A stirred solution of **3c** (50 mg, 0,07 mmol) in $CH_3NO_2$ (5 mL) was kept at 90 °C for 3 h. After removal of the solvent under reduced pressure, an orange solid was obtained, which was washed with $Et_2O$ (5 mL) and dried under vacuum. Yield: 38 mg (81%). $C_{29}H_{33}F_6NP_2Ru$ (672.59): calcd. C 51.79, H 4.95, N 2.08; found C 51.33, H 5.03, N 2.11. $^1H$ NMR ($CD_3NO_2$, 20 °C): $\delta$ = 8.06–7.89 (m, 2 H, Ph), 7.68–7.32 (m, 6 H, Ph), 7.30–7.14 (m, 2 H, Ph), 6.33 (d, $J_{HP}$ = 9.8 Hz, 1 H, $H^1$), 6.12 (1 H, $H^4$), 4.73 (s, 5 H, Cp), 3.39–3.05 (m, 2 H), 2.99–0.96 (m, 14 H) ppm. $^{13}C\{^1H\}$ NMR ($CD_3NO_2$, 20 °C): $\delta$ = 171.7 (d, $J_{CP}$ = 28.0 Hz, $C^3$), 137.8 (d, $^1J_{CP}$ = 54.1 Hz, $Ph^1$), 134.1 (d, $^2J_{CP}$ = 11.9 Hz, $Ph^{2,6}$), 131.9 (d, $^1J_{CP}$ = 44.9 Hz, $Ph^{1'}$), 131.2 (d, $^4J_{CP}$ = 2.3 Hz, $Ph^4$), 130.3 (d, $^2J_{CP}$ = 10.7 Hz, $Ph^{2',6'}$), 129.8 (d, $^4J_{CP}$ = 2.3 Hz, $Ph^{4'}$), 128.9 (d, $^3J_{CP}$ = 10.0 Hz, $Ph^{3,5}$), 128.6 (d, $^3J_{CP}$ = 10.4 Hz, $Ph^{3',5'}$), 117.3 (d, $J_{CP}$ = 47.9 Hz, $C^1$), 91.5 (d, $J_{CP}$ = 3.1 Hz, $C^2$), 82.3 (d, $J_{CP}$ = 1.9 Hz, Cp), 79.0 ($C^4$), 68.0 ($CH_2$), 52.6 (d, $J_{CP}$ = 7.7 Hz, $CH_2$), 38.1 ($CH_2$), 28.9 (d, $J_{CP}$ = 19.9 Hz, $CH_2$), 27.3 ($CH_2$), 24.8 (d, $J_{CP}$ = 1.5 Hz, $CH_2$), 22.3 ($CH_2$) ppm. $^{31}P\{^1H\}$ NMR ($CD_3NO_2$, 20 °C): $\delta$ = 73.3 ($PPh_2$), –143.2 ($^1J_{FP}$ = 707.1 Hz, $PF_6$) ppm.

**[RuCp{η¹-(P)-PPh₂–CH=C–(CH₂)₄–η³-(C,C,N)-CH–N*n*Pr}]PF₆ (4d):** 1.1 equiv. of 1,7-octadiyne (21.9 μL, 0.17 mmol) was added to a solution of **1a** (100 mg, 0.16 mmol) in $CH_2Cl_2$ (10 mL) and the mixture was heated for 8 h at 40 °C. After removal of the solvent under reduced pressure, an orange solid was obtained, which was washed with $Et_2O$ (5 mL) and dried under vacuum. Yield: 82 mg (78%). $C_{29}H_{35}F_6NP_2Ru$ (674.61): calcd. C 51.63, H 5.23, N 2.08; found C 51.60, H 5.11, N 2.04. $^1H$ NMR ($CD_2Cl_2$, 20 °C): $\delta$ = 7.92–7.76 (m, 2 H, Ph), 7.68–7.40 (m, 6 H, Ph), 7.37–7.20 (m, 2 H, Ph), 6.17 (d, $J_{HP}$ = 7.1 Hz, 1 H, $H^4$), 5.95 (d, $^2J_{HP}$ = 10.1 Hz, 1 H, $H^1$), 4.78 (s, 5 H, Cp), 3.16–2.88 (m, 2 H), 2.84–2.62 (m, 1 H), 2.47–2.07 (m, 4 H), 1.94–1.61 (m, 2 H), 1.57–1.23 (m, 3 H), 0.72 (t, $J_{HH}$ = 7.4 Hz, 3 H) ppm. $^{13}C\{^1H\}$ NMR ($CD_2Cl_2$, 20 °C): $\delta$ = 165.8 (d, $J_{CP}$ = 26.5 Hz, $C^3$), 136.5 (d, $^1J_{CP}$ = 52.5 Hz, $Ph^1$), 134.1 (d, $^2J_{CP}$ = 11.9 Hz, $Ph^{2,6}$), 131.8 (d, $^4J_{CP}$ = 2.3 Hz, $Ph^4$), 130.9 (d, $^1J_{CP}$ = 48.7 Hz, $Ph^{1'}$), 130.4 (d, $^4J_{CP}$ = 2.3 Hz, $Ph^{4'}$), 130.3 (d, $^2J_{CP}$ = 11.5 Hz, $Ph^{2',6'}$), 129.2 (d, $^3J_{CP}$ = 10.4 Hz, $Ph^{3,5}$), 129.0 (d, $^3J_{CP}$ = 10.7 Hz, $Ph^{3',5'}$), 119.9 (d, $J_{CP}$ = 46.0 Hz, $C^1$), 84.2 (d, $J_{CP}$ = 1.9 Hz, $C^2$), 81.8 (d, $J_{CP}$ = 1.9 Hz, Cp), 72.0 ($C^4$), 57.6 ($CH_2$), 41.1 ($CH_2$), 35.7 (d, $J_{CP}$ = 20.3 Hz, $CH_2$), 29.1 ($CH_2$), 27.7 ($CH_2$), 24.7 ($CH_2$), 10.4 ($CH_3$) ppm.

**[RuCp{η¹-(P)-PPh₂–CH=C–(CH₂)₄–η³-(C,C,N)-CH–NEt₂}]PF₆ (4e):** This complex was prepared analogously to **4d** with **1b** (100 mg, 0.15 mmol) and 1,7-octadiyne (20.8 μL, 0.17 mmol) as starting materials. Yield: 56 mg (55%). $C_{30}H_{37}F_6NP_2Ru$ (688.64): calcd. C 52.33 H 5.42, N 2.03; found C 52.25, H 5.46, N 2.12.$^1H$ NMR ($CD_2Cl_2$, 20 °C): $\delta$ = 7.96–7.79 (m, 2 H, Ph), 7.66–7.39 (m, 6 H, Ph), 7.34–7.18 (m, 2 H, Ph), 6.21 (d, $J_{HP}$ = 9.8 Hz, 1 H, $H^1$), 6.06 (s, 1 H, $H^4$), 4.69 (s, 5 H, Cp), 3.78–3.57 (m, 1 H), 3.28–3.12 (m, 1 H), 2.72–2.40 (m, 2 H), 2.34–1.68 (m, 8 H), 1.22 (t, $J_{HH}$ = 7.0 Hz, 3 H), 0.89 (t, $J_{HH}$ = 7.1 Hz, 3 H) ppm. $^{13}C\{^1H\}$ NMR ($CD_2Cl_2$, 20 °C): $\delta$ = 169.5 (d, $J_{CP}$ = 25.3 Hz, $C^3$), 137.8 (d, $^1J_{CP}$ = 54.1 Hz, $Ph^1$), 134.1 (d, $^2J_{CP}$ = 12.3 Hz, $Ph^{2,6}$), 131.8 (d, $^4J_{CP}$ = 2.3 Hz, $Ph^4$), 131.1 (d, $^1J_{CP}$ = 45.6 Hz, $Ph^{1'}$), 130.3 (d, $^4J_{CP}$ = 2.3 Hz, $Ph^{4'}$), 130.3 (d, $^2J_{CP}$ = 10.7 Hz, $Ph^{2',6'}$), 129.0 (d, $^3J_{CP}$ = 10.3 Hz, $Ph^{3,5}$), 122.5 (d, $J_{CP}$ = 48.0 Hz, $C^1$), 90.8 (d, $J_{CP}$ = 2.7 Hz, $C^2$), 82.7 (d, $J_{CP}$ = 1.9 Hz, Cp), 79.8 ($C^4$), 58.4 ($CH_2$), 44.9 ($CH_2$), 43.8 (d, $J_{CP}$ = 6.5 Hz, $CH_2$), 36.2 (d, $J_{CP}$ = 21.5 Hz, $CH_2$), 29.9 ($CH_2$), 28.3 ($CH_2$), 14.2 ($CH_3$), 12.9 ($CH_3$) ppm. $^{31}P\{^1H\}$ NMR ($CD_2Cl_2$, 20 °C): $\delta$ = 76.3 ($PPh_2$), –142.9 ($^1J_{FP}$ = 710.8 Hz, $PF_6$) ppm.

**[RuCp{η¹-(P)-PPh₂–CH=C–(CH₂)₄–η³-(C,C,N)-CH–NC₅H₁₀}]PF₆ (4f):** This complex was prepared analogously to **4d** with **1b** (100 mg, 0.15 mmol) and 1,7-octadiyne (20.8 μL, 0.17 mmol) as starting materials. Yield: 72 mg (70%). $C_{30}H_{35}F_6NP_2Ru$ (686.62): calcd. C 52.48, H 5.14, N 2.04; found C 52.27, H 5.18, N 2.18. $^1H$ NMR ($CD_2Cl_2$, 20 °C): $\delta$ = 8.00–7.77 (m, 2 H, Ph), 7.72–7.36 (m, 6 H, Ph), 7.33–7.14 (m, 2 H, Ph), 6.18 (d, $^2J_{HP}$ = 9.5 Hz, 1 H, $H^1$), 6.14 (1 H, $H^4$), 4.68 (s, 5 H, Cp), 3.41–3.07 (m, 3 H), 2.66–2.40 (m, 1 H), 2.38–1.51 (m, 11 H), 1.43–0.99 (m, 3 H) ppm. $^{13}C\{^1H\}$ NMR ($CD_2Cl_2$, 20 °C): $\delta$ = 169.3 (d, $J_{CP}$ = 25.7 Hz, $C^3$), 138.1 (d, $^1J_{CP}$ = 53.7 Hz, $Ph^1$), 134.2 (d, $^2J_{CP}$ = 12.3 Hz, $Ph^{2,6}$), 131.7 (d, $^4J_{CP}$ = 2.3 Hz, $Ph^4$), 131.3 (d, $^1J_{CP}$ = 45.6 Hz, $Ph^{1'}$), 130.2 (d, $^2J_{CP}$ = 11.1 Hz, $Ph^{2',6'}$), 130.1 (d, $^4J_{CP}$ = 2.3 Hz, $Ph^{4'}$), 129.2 (d, $^3J_{CP}$ = 10.0 Hz, $Ph^{3,5}$), 128.9 (d, $^3J_{CP}$ = 10.7 Hz, $Ph^{3',5'}$), 122.2 (d, $J_{CP}$ = 47.5 Hz, $C^1$), 91.0 (d, $J_{CP}$ = 2.7 Hz, $C^2$), 82.7 (d, $J_{CP}$ = 1.9 Hz, Cp), 77.2 ($C^4$), 68.7 ($CH_2$), 44.6 ($CH_2$), 36.5 (d, $J_{CP}$ = 21.5 Hz, $CH_2$), 30.0 ($CH_2$), 28.3 ($CH_2$), 27.9 ($CH_2$), 27.4 ($CH_2$), 22.7 ($CH_2$) ppm. $^{31}P\{^1H\}$ NMR ($CD_2Cl_2$, 20 °C): $\delta$ = 76.2 ($PPh_2$), –142.9 ($^1J_{FP}$ = 710.8 Hz, $PF_6$) ppm.

**[RuCp{=C(NEt₂)-η²-(C,C)-C–(CH₂)₃–CCH₂-(η¹-(P)-PPh₂)}]PF₆ (5a):** A solution of **4b** (96 mg, 0.15 mmol) in acetonitrile was heated at 90 °C for 12 h. After removal of the solvent under reduced pressure, an orange solid was obtained, which was washed with $Et_2O$ (5 mL) and dried under vacuum. Yield: 70 mg (71%). $C_{29}H_{35}F_6NP_2Ru$ (688.64): calcd. C 52.33, H 5.42, N 2.03; found C 52.57, H 5.27, N 2.11. $^1H$ NMR ($CD_3CN$, 20 °C): $\delta$ = 7.68–7.31 (m, 10 H, Ph), 4.95 (s, 5 H, Cp), 4.06–3.79 (m, 3 H, $CH_2$, $H^1$), 3.77–3.47 (m, 3 H, $CH_2$, $H^{1'}$), 2.82–2.55 (m, 2 H), 2.27–2.07 (m, 1 H), 2.03–1.74 (m, 2 H), 1.58–1.35 (m, 1 H), 1.12 (t, $J_{HH}$ = 7.3 Hz, 3 H), 0.84 (t, $J_{HH}$ = 7.3 Hz, 3 H) ppm. $^{13}C\{^1H\}$ NMR ($CD_3CN$, 20 °C): $\delta$ = 225.2 (d, $J_{CP}$ = 13.0 Hz, $C^4$), 137.5 (d, $^1J_{CP}$ = 46.8 Hz, $Ph^1$), 132.4 (d, $^2J_{CP}$ = 12.3 Hz, $Ph^{2,6}$), 131.3 (d, $^1J_{CP}$ = 36.0 Hz, $Ph^{1'}$), 131.0 (d, $^2J_{CP}$ = 11.5 Hz, $Ph^{2',6'}$), 130.9 (d, $^4J_{CP}$ = 3.1 Hz, $Ph^4$), 130.4 (d, $^4J_{CP}$ = 3.1 Hz, $Ph^{4'}$), 128.9 (d, $^3J_{CP}$ = 10.7 Hz, $Ph^{3,5}$), 128.6 (d, $^3J_{CP}$ = 10.7 Hz, $Ph^{3',5'}$), 83.3 (Cp), 73.8 (d, $J_{CP}$ = 16.1 Hz, $C^2$), 71.7 (d, $J_{CP}$ = 3.1 Hz, $C^3$), 51.7 (d, $J_{CP}$ = 26.8 Hz, $CH_2$), 37.7 (d, $J_{CP}$ = 7.7 Hz, $CH_2$), 37.0 (d, $J_{CP}$ = 35.3 Hz, $CH_2$, $C^1$), 32.7 ($CH_2$), 22.5 ($CH_2$), 13.2 ($CH_3$), 12.4 ($CH_3$) ppm. $^{31}P\{^1H\}$ NMR ($CD_3CN$, 20 °C): $\delta$ = –34.3 ($PPh_2$), –143.1 ($^1J_{FP}$ = 706.8 Hz, $PF_6$) ppm.

**Isomerization of 3c to 4c and [RuCp{=C(NC₅H₁₀)-η²-(C,C)-C–(CH₂)₃–CCH₂-(η¹-(P)-PPh₂)}]PF₆ (5b):** A 5-mm NMR tube was charged with **3c** (30 mg, 0.04 mmol) in $CD_3CN$ (0.5 mL) and heated to 90 °C. The reaction was then monitored by $^1H$ and $^{31}P\{^1H\}$ NMR spectroscopy. After 48 h both **4c** and **5b** were formed in an approximately 3:1 ratio. Because of spectral overlap

 © 2006 Wiley-VCH Verlag GmbH & Co. KGaA, Weinheim 

with **4c** only the most characteristic signals of **5b** could be unequivocally assigned. $^1$H NMR ($CD_3CN$, 20 °C): $\delta$ = 4.93 (s, 5 H, Cp), 3.66–3.49 (m, 2 H, $H^1$) ppm. $^{13}C\{^1H\}$ NMR ($CD_3CN$, 20 °C): $\delta$ = 222.9 (d, $J_{CP}$ = 12.3 Hz, $C^4$), 83.2 (Cp), 74.3 (d, $J_{CP}$ = 16.9 Hz, $C^2$), 71.2 ($C^3$), 36.7 (d, $J_{CP}$ = 35.3 Hz, $CH_2$, $C^1$) ppm. $^{31}P\{^1H\}$ NMR ($CD_3CN$, 20 °C): $\delta$ = –37.8 ($PPh_2$), –144.6 ($^1J_{FP}$ = 707.7 Hz, $PF_6$) ppm.

**[RuCp*{η$^1$-(N)-N*n*PrPPh$_2$–η$^4$-CH=C–(CH$_2$)$_3$–C=CH$_2$}]PF$_6$ (6a):** 1 equiv. of 1,6-heptadiyne (16 μL, 0.14 mmol) was added to a solution of **2a** (100 mg, 0.14 mmol) in $CH_2Cl_2$ (5 mL) and the mixture was stirred for 2 h at room temperature. After that the volume of the solution was reduced to about 1 mL and $Et_2O$ (5 mL) was added whereupon a precipitate was formed. The yellow solid was washed with $Et_2O$ (2 × 5 mL) and dried under vacuum. Yield: 68 mg (68%). $C_{32}H_{41}F_6NP_2Ru$ (716.69): calcd. C 53.63, H 5.77, N 1.95; found C 54.01, H 5.56, N 2.06. $^1$H NMR ($CD_2Cl_2$, 20 °C): $\delta$ = 7.78–7.32 (m, 10 H, Ph), 3.88 (d, $J_{HH}$ = 3.5 Hz, 1 H, $H^4$), 3.52–3.31 (m, 2 H), 3.18 (d, $^2J_{HP}$ = 16.3 Hz, 1 H, $H^1$), 2.64 (d, $J_{HH}$ = 3.3 Hz, 1 H, $H^{4'}$), 2.56–2.40 (m, 1 H), 2.39–2.28 (m, 2 H), 2.27–2.06 (m, 3 H), 1.67 (s, 15 H, Cp*), 1.34–1.20 (m, 2 H), 0.70 (t, $J_{HH}$ = 7.3 Hz, 3 H) ppm. $^{13}C\{^1H\}$ NMR ($CD_2Cl_2$, 20 °C): $\delta$ = 133.5–128.5 (Ph), 119.1 ($C^2$), 112.5 ($C^3$), 98.1 (Cp*), 50.4 ($CH_2$), 46.7 ($C^4$), 37.0 (d, $J_{CP}$ = 7.7 Hz, $CH_2$), 35.3 ($CH_2$), 29.8 ($CH_2$), 22.0 (d, $J_{CP}$ = 112.7 Hz, $C^1$), 20.5 ($CH_2$), 11.2 ($CH_3$), 9.2 (Cp*) ppm. $^{31}P\{^1H\}$ NMR ($CD_2Cl_2$, 20 °C): $\delta$ = 47.5 ($PPh_2$), –144.4 ($^1J_{FP}$ = 710.8 Hz, $PF_6$) ppm.

**[RuCp*{η$^1$-(N)-N*n*PrPPh$_2$–η$^4$-CH=C–(CH$_2$)$_4$–C=CH$_2$}]PF$_6$ (6b):** This complex was prepared analogously to **6a** with **2a** (100 mg, 0.14 mmol) and 1,7-octadiyne (19 μL, 0.14 mmol) as the starting materials. Yield: 64 mg (63%). $C_{33}H_{43}F_6NP_2Ru$ (730.72): calcd. C 54.24, H 5.93, N 1.29; found C 54.35, H 5.88, N 1.22. $^1$H NMR ($CD_2Cl_2$, 20 °C): $\delta$ = 7.78–7.26 (m, 10 H, Ph), 3.70 (d, $J_{HH}$ = 3.5 Hz, 1 H, $H^4$), 3.15–2.87 (m, 2 H), 2.76 (d, $^2J_{HP}$ = 13.6 Hz, 1 H, $H^1$), 2.61–2.28 (m, 2 H), 2.43 (d, $J_{HH}$ = 3.8 Hz, 1 H, $H^{4'}$), 1.90–1.72 (m, 4 H), 1.69 (s, 15 H, Cp*), 1.59–1.49 (m, 4 H), 0.74 (t, $J_{HH}$ = 7.3 Hz, 3 H) ppm. $^{13}C\{^1H\}$ NMR ($CD_2Cl_2$, 20 °C): $\delta$ = 135.9–126.9 (Ph), 113.3 ($C^2$), 105.4 ($C^3$), 99.1 (Cp*), 51.3 (d, $J_{CP}$ = 3.1 Hz, $CH_2$), 48.6 ($C^4$), 30.7 (d, $J_{CP}$ = 8.4 Hz, $CH_2$), 30.4 ($CH_2$), 29.7 ($CH_2$), 23.5 (d, $J_{CP}$ = 108.1 Hz, $C^1$), 21.7 (d, $J_{CP}$ = 1.2 Hz, $CH_2$), 21.4 ($CH_2$), 11.2 ($CH_2$), 9.5 (Cp*) ppm. $^{31}P\{^1H\}$ NMR ($CD_2Cl_2$, 20 °C): $\delta$ = 55.7 ($PPh_2$), –142.9 ($^1J_{FP}$ = 710.8 Hz, $PF_6$) ppm.

**Reaction of 2b with 1,6-Heptadiyne in $CD_2Cl_2$. Formation of [RuCp*{η$^3$-(P,C,C)–PPh$_2$–CH–C(CH$_2$)$_4$–η$^2$-(C,C)-CCHNEt$_2$}]PF$_6$ (7) and [RuCp*{η$^1$-(P)-PPh$_2$–CH=C–(CH$_2$)$_3$–η$^3$-(C,C,N)-CCHNEt$_2$}]PF$_6$ (8a):** A 5-mm NMR tube was charged with **2b** (56 mg, 0.08 mmol) in $CD_2Cl_2$ (0.5 mL) and 1,6-heptadiyne (8.9 μL, 0.08 mmol) was added by syringe. The reaction was then monitored by $^1$H and $^{31}P\{^1H\}$ NMR spectroscopy. After 10 min both **7** and **8a** were formed in an approximately 1:1 ratio. Because of spectral overlap with one another only the most characteristic signals of **7** and **8a** could be unequivocally assigned. **7:** $^1$H NMR ($CD_2Cl_2$, 20 °C): $\delta$ = 4.17 (d, $^2J_{HP}$ = 4.3 Hz, 1 H, $H^1$), 3.7 (d, $J_{HP}$ = 4.4 Hz, 1 H, $H^4$), 1.67 (d, $J_{HP}$ = 1.9 Hz, 15 H, Cp*) ppm. $^{13}C\{^1H\}$ NMR ($CD_2Cl_2$, 20 °C): $\delta$ = –10.0 ($PPh_2$), –144.4 ($^1J_{FP}$ = 710.2 Hz, $PF_6$). **8a**: $^1$H NMR ($CD_2Cl_2$, 20 °C): $\delta$ = 6.08 (d, $^2J_{HP}$ = 8.4 Hz, 1 H, $H^1$), 5.17 (s, 1 H, $H^4$), 1.48 (d, $J_{HP}$ = 1.6 Hz, 15 H, Cp*) ppm. $^{31}P\{^1H\}$ NMR ($CD_2Cl_2$, 20 °C): $\delta$ = 67.8 ($PPh_2$), –144.4 ($^1J_{FP}$ = 710.2 Hz, $PF_6$) ppm.

**[RuCp*{η$^1$-(P)-PPh$_2$CH=C–(CH$_2$)$_3$–η$^3$-(C,C,N)-C=CH–N-(CH$_2$)$_5$}]PF$_6$ (8b):** 1,6-Heptadiyne (16 μL, 0.14 mol) was added to a solution of **2c** (100 mg, 0.14 mmol) in $CH_2Cl_2$ (5 mL) and the mixture was stirred for 2 h at room temperature. The volume of the solution was then reduced to about 1 mL. Addition of 5 mL of $Et_2O$ resulted in the formation of a yellow precipitate, which was washed with $Et_2O$ (2 × 5 mL) and dried under vacuum. Yield: 83 mg (82%). $C_{34}H_{43}F_6NP_2Ru$ (742.73): calcd. C 54.98, H 5.84, N 1.89; found C 54.84, H 5.76, N 1.93. $^1$H NMR ($CD_2Cl_2$, 20 °C): $\delta$ = 7.76–6.99 (m, 10 H, Ph), 6.05 (d, $J_{HP}$ = 8.7 Hz, 1 H, $H^1$), 5.07 (s, 1 H, $H^4$), 3.23–2.92 (m, 2 H), 2.88–2.69 (m, 2 H), 2.66–2.43 (m, 2 H), 2.41–1.92 (m, 3 H), 1.91–1.53 (m, 3 H), 1.48 (s, 15 H, Cp*), 1.35–1.01 (m, 4 H) ppm. $^{13}C\{^1H\}$ NMR ($CD_2Cl_2$, 20 °C): $\delta$ = 169.8 (d, $J_{CP}$ = 28.4 Hz, $C^3$), 134.1 (d, $^1J_{CP}$ = 49.8 Hz, $Ph^1$), 132.3 (d, $^2J_{CP}$ = 10.7 Hz, $Ph^{2,6,2',6'}$), 131.6 ($Ph^4$), 131.5 (d, $^1J_{CP}$ = 40.6 Hz, $Ph^{1'}$), 130.3 ($C^{4'}$), 129.2 (d, $^3J_{CP}$ = 9.2 Hz, $Ph^{3,5}$), 128.7 (d, $^3J_{CP}$ = 9.2 Hz, $Ph^{3',5'}$), 119.7 (d, $^1J_{CP}$ = 46.0 Hz, $C^1$), 92.8 (Cp*), 91.4 (d, $J_{CP}$ = 3.1 Hz, $C^2$), 85.9 ($C^4$), 64.7 ($CH_2$), 51.4 (d, $J_{CP}$ = 6.9 Hz, $CH_2$), 36.5 ($CH_2$), 29.1 (d, $J_{CP}$ = 19.2 Hz, $CH_2$), 27.7 (d, $J_{CP}$ = 17.6 Hz, $CH_2$), 25.7 ($CH_2$), 22.8 ($CH_2$), 9.6 (Cp*) ppm. $^{31}P\{^1H\}$ NMR ($CD_2Cl_2$, 20 °C): $\delta$ = 68.7 ($PPh_2$), –144.4 ($^1J_{FP}$ = 710.8 Hz, $PF_6$) ppm.

**[RuCp*{η$^1$-(P)-PPh$_2$CH=C–(CH$_2$)$_4$–η$^3$-(C,C,N)-C=CH–NEt$_2$}]PF$_6$ (8c):** This complex was prepared analogously to **8b** with **2b** (100 mg, 0.14 mmol) and 1,7-octadiyne (16 μL, 0.14 mmol) as the starting materials. Yield: 75 mg (72%). $C_{34}H_{45}F_6NP_2Ru$ (744.74): calcd. C 54.83, H 6.09, N 1.88; found C 54.62, H 6.19, N 1.98. $^1$H NMR ($CD_2Cl_2$, 20 °C): $\delta$ = 7.90–7.10 (m, 10 H, Ph), 6.08 (d, $^2J_{HP}$ = 8.5 Hz, 1 H, $H^1$), 5.22 (s, 1 H, $H^4$), 3.58 (m, 1 H), 3.16 (m, 1 H′), 2.59 (m, 1 H), 2.27–1.94 (m, 5 H), 1.93–1.53 (m, 4 H), 1.46 (d, $J_{HP}$ = 1.8 Hz 15 H, Cp*), 1.16 (t, $J_{HH}$ = 7.2 Hz, 3 H, $CH_3$), 0.84 (t, $J_{HH}$ = 7.2 Hz, 3 H, $CH_3$) ppm. $^{13}C\{^1H\}$ NMR ($CD_2Cl_2$, 20 °C): $\delta$ = 167.1 (d, $J_{CP}$ = 26.8 Hz, $C^3$), 134.6 (d, $^1J_{CP}$ = 49.8 Hz, $Ph^1$), 132.5 (d, $^2J_{CP}$ = 10.7 Hz, $Ph^{2,6,2',6'}$), 131.7 (d, $^1J_{CP}$ = 41.4 Hz, $Ph^{1'}$), 131.6 (d, $J_{CP}$ = 2.3 Hz, $Ph^4$), 130.4 (d, $J_{CP}$ = 3.1 Hz, $Ph^{4'}$), 128.9 (d, $J_{CP}$ = 9.2 Hz, $Ph^{3,5}$), 128.7 (d, $J_{CP}$ = 10.0 Hz, $Ph^{3',5'}$), 126.1 (d, $J_{CP}$ = 46.8 Hz, $C^1$), 92.9 (Cp*), 88.9 (d, $J_{CP}$ = 3.1 Hz, $C^2$), 88.1 ($C^4$), 55.7 ($CH_2$), 42.0 ($CH_2$), 41.7 (d, $J_{CP}$ = 6.1 Hz, $CH_2$), 35.9 (d, $J_{CP}$ = 20.7 Hz, $CH_2$), 29.6 ($CH_2$), 27.9 ($CH_2$), 12.8 ($CH_3$), 12.6 ($CH_3$), 9.2 (Cp*) ppm. $^{31}P\{^1H\}$ NMR ($CD_2Cl_2$, 20 °C): $\delta$ = 70.5 ($PPh_2$), –144.4 ($^1J_{FP}$ = 710.5 Hz, $PF_6$) ppm.

**[RuCp*{η$^1$-(P)-PPh$_2$CH=C–(CH$_2$)$_4$–η$^3$-(C,C,N)-C=CH–N-(CH$_2$)$_5$}]PF$_6$ (8d):** This complex was prepared analogously to **8b** with **2c** (100 mg, 0.14 mmol) and 1,7-octadiyne (19 μL, 0.14 mmol) as the starting materials. Yield: 80 mg (77%). $C_{35}H_{45}F_6NP_2Ru$ (756.75): calcd. C 55.55, H 5.99, N 1.85; found C 56.00, H 5.89, N 1.69. $^1$H NMR ($CD_2Cl_2$, 20 °C): $\delta$ = 7.77–7.32 (m, 10 H, Ph), 6.02 (d, $J_{HP}$ = 8.5 Hz, 1 H, $H^1$), 5.17 (s, 1 H, $H^4$), 3.18–2.90 (m, 4 H), 2.48–2.20 (m, 2 H), 2.19–2.96 (m, 4 H), 1.90–1.50 (m, 6 H), 1.45 (d, $J_{HP}$ = 1.7 Hz, 15 H, Cp*), 1.39–1.24 (m, 2 H) ppm. $^{13}C\{^1H\}$ NMR ($CD_2Cl_2$, 20 °C): $\delta$ = 166.4 (d, $J_{CP}$ = 26.1 Hz, $C^3$), 134.7 (d, $^1J_{CP}$ = 49.8 Hz, $Ph^1$), 132.6 (d, $^2J_{CP}$ = 10.0 Hz, $Ph^{2,6}$), 132.2 (d, $^2J_{CP}$ = 9.2 Hz, $Ph^{2',6'}$), 131.6 ($Ph^4$), 131.6 (d, $^1J_{CP}$ = 48.3 Hz, $Ph^{1'}$), 130.4 ($C^{4'}$), 129.1 (d, $^3J_{CP}$ = 10.0 Hz, $Ph^{3,5}$), 128.7 (d, $^3J_{CP}$ = 10.0 Hz, $Ph^{3',5'}$), 126.2 (d, $^1J_{CP}$ = 46.0 Hz, $C^1$), 92.8 (Cp*), 89.5 ($C^2$), 84.4 ($C^4$), 65.2 ($CH_2$), 52.6 (d, $J_{CP}$ = 4.6 Hz, $CH_2$), 45.8 ($CH_2$), 41.8 ($CH_2$), 36.1 (d, $J_{CP}$ = 20.7 Hz, $CH_2$), 29.7 ($CH_2$), 28.0 (d, $J_{CP}$ = 17.6 Hz, $CH_2$), 27.9 ($CH_2$), 23.0 ($CH_2$), 9.7 (Cp*) ppm. $^{31}P\{^1H\}$ NMR ($CD_2Cl_2$, 20 °C): $\delta$ = 72.2 ($PPh_2$), –144.4 ($^1J_{FP}$ = 710.8 Hz, $PF_6$) ppm.

**Formation of [RuCp{κ$^1$(P)-PPh$_2$NHNMe$_2$}(CH$_3$CN)$_2$]PF$_6$ (9) and [RuCp{κ$^2$(P,N)-PPh$_2$NHNMe$_2$} (CH$_3$CN)]PF$_6$ (10):** $PPh_2NHNMe_2$ (188 mg, 0.77 mmol) was added to a solution of $[RuCp(CH_3CN)_3]$-$PF_6$ (335 mg, 0.77 mmol) in $CH_2Cl_2$ (5 mL) and the mixture was stirred for 2 h at room temperature. The volume of the solution was then reduced to about 1 mL and $Et_2O$ (5 mL) was added. A

 © 2006 Wiley-VCH Verlag GmbH & Co. KGaA, Weinheim 

yellow precipitate was formed, which was collected on a glass frit, washed with $Et_2O$ (3 × 10 mL), and dried under vacuum. $^1H$ NMR spectroscopy revealed that **9** and **10** were formed in an approximately 5:1 ratio. If the same reaction was performed in the presence of acetonitrile (40 μL, 0.77 mmol), complex **9** was exclusively obtained. Yield: 398 mg (84%). $C_{23}H_{28}F_6N_4P_2Ru$ (637.51): calcd. C 43.33, H 4.43, N 8.79; found C 42.98; H 4.50, N 8.61. $^1H$ NMR ($CD_2Cl_2$, 20 °C): $\delta$ = 7.74–7.54 (m, 4 H, Ph), 7.53–7.39 (m, 6 H, Ph), 4.45 (s, 5 H, Cp), 3.51 (d, $^2J_{HP}$ = 34.1 Hz, 1 H, N*H*), 2.27 (6 H, $CH_3$), 2.26 (d, $J_{HP}$ = 1.3 Hz, 6 H, $CH_3CN$) ppm. $^{13}C\{^1H\}$ NMR ($CD_2Cl_2$, 20 °C): $\delta$ = 136.2 (d, $^1J_{CP}$ = 51.7 Hz, $Ph^1$), 132.6 (d, $^2J_{CP}$ = 12.1 Hz, $Ph^{2,6}$), 130.2 (d, $^4J_{CP}$ = 2.3 Hz, $Ph^4$), 127.9 (d, $^3J_{CP}$ = 9.8 Hz, $Ph^{3,5}$), 127.0 ($CH_3CN$), 76.4 (d, $J_{CP}$ = 2.9 Hz, Cp), 49.9 (d, $J_{CP}$ = 3.4 Hz, $CH_3$) 3.8 (d, $J_{CP}$ = 1.2 Hz, $CH_3CN$) ppm. $^{31}P\{^1H\}$ NMR ($CD_2Cl_2$, 20 °C): $\delta$ = 90.6 ($PPh_2$), –142.9 ($^1J_{FP}$ = 710.8 Hz, $PF_6$) ppm. All attempts to grow crystals of **9** were unsuccessful. Crystals of **10** were grown by diffusion of diethyl ether into a $CH_2Cl_2$ solution of the reaction mixture containing **9** and **10**. **10**: $^1H$ NMR ($CD_2Cl_2$, 20 °C): $\delta$ = 7.72–7.36 (m, 10 H, Ph), 4.48 (s, 5 H, Cp), 3.35 (s, 3 H, Me), 2.82 (s, 3 H, Me), 2.14 (d, $J_{HP}$ = 1.6 Hz, $CH_3CN$) ppm. The NH proton could not be detected. $^{13}C\{^1H\}$ NMR ($CD_2Cl_2$, 20 °C): $\delta$ = 132.9–128.5 (Ph), 128.1 ($CH_3CN$), 73.0 (Cp), 63.9 ($CH_3$), 57.8 ($CH_3$), 3.85 ($CH_3CN$) ppm. $^{31}P\{^1H\}$ NMR ($CD_2Cl_2$, 20 °C): $\delta$ = 61.4 ($PPh_2$), –142.9 ($^1J_{FP}$ = 711.5 Hz, $PF_6$) ppm.

**X-ray Structure Determination:** Crystals of **1a**, **2a**, **3c**, **3f**, **4a**, **5a**, **6a**, **6b**, **8c·$CH_2Cl_2$**, **8d**, and **10** were obtained by diffusion of $Et_2O$ or pentane into $CH_2Cl_2$ solutions. Crystal data and experimental details are given in Table 1 and Table 2. X-ray data were collected with a Bruker Smart APEX CCD area detector diffractometer using graphite-monochromated Mo-$K_\alpha$ radiation ($\lambda$ = 0.71073 Å) and 0.3° $\omega$-scan frames covering mostly complete spheres of the reciprocal space. Corrections for absorption (multi-scan method), $\lambda/2$ effects, and crystal decay were applied.[24] The structures were solved by direct methods using the program SHELXS97.[25] Structure refinement on $F^2$ was carried out with the program SHELXL97.[24] All non-hydrogen atoms were refined anisotropically. Hydrogen atoms were inserted in idealized positions and were refined riding with the atoms to which they were bonded, except for N-bound hydrogen atoms, which were refined in *x*,*y*,*z* if permitted by data quality.[26] Compound **6b** crystallizes in the acentric triclinic space group *P*1 (no. 1) with three independent Ru complexes in the unit cell. Two of these three complexes adopt a pseudocentric arrangement (pseudo space group $P\bar{1}$) while the third complex does not comply with this symmetry. In Figure 8 only the first of these three complexes is shown as a representative example.

CCDC-286740 to -286750 contain the supplementary crystallographic data for this paper. These data can be obtained free of charge from The Cambridge Crystallographic Data Centre via www.ccdc.cam.ac.uk/data_request/cif.

**Computational Details:** All calculations were performed using the Gaussian98 software package on the Silicon Graphics Origin 2000 of the Vienna University of Technology.[27] The geometry and energy of the model complexes and the transition states were optimized at the B3LYP level[28] with the Stuttgart/Dresden ECP (SDD) basis set[29] to describe the electrons of the ruthenium atom. For the C, N, P, and H atoms the 6-31g** basis set was employed.[30] A vibrational analysis was performed to confirm that the structures of the model compounds have no imaginary frequency. Transition state optimizations were performed with the Synchronous Transit-Guided Quasi-Newton Method (STQN) developed by Schlegel et al.[31] Frequency calculations were performed to confirm the nature of the stationary points, yielding one imaginary frequency for the transition states and none for the minima. The vibrational eigenvectors corresponding to the reaction coordinate (with imaginary frequency) of all transition states were visually checked to confirm the connectivity of transition states with the reactants and the products. Crucial transition states have been confirmed by IRC calculations. All geometries were optimized without symmetry constraints.

Table 2. Details for the crystal structure determinations of complexes **6a**, **6b**, **8c·$CH_2Cl_2$**, **8d**, and **10**.

| | **6a** | **6b** | **8c·$CH_2Cl_2$** | **8d** | **10** |
|---|---|---|---|---|---|
| Empirical formula | $C_{32}H_{41}F_6NP_2Ru$ | $C_{33}H_{43}F_6NP_2Ru$ | $C_{35}H_{47}Cl_2F_6NP_2Ru$ | $C_{35}H_{45}F_6NP_2Ru$ | $C_{21}H_{25}F_6N_3P_2Ru$ |
| Formula mass | 716.67 | 730.69 | 829.65 | 756.73 | 596.45 |
| Crystal size [mm] | 0.48 × 0.26 × 0.22 | 0.71 × 0.32 × 0.22 | 0.56 × 0.48 × 0.42 | 0.40 × 0.27 × 0.17 | 0.62 × 0.33 × 0.26 |
| Space group | $P2_12_12_1$ (no. 19) | *P*1 (no. 1) | $Pna2_1$ (no. 33) | *Pbca* (no. 61) | $P2_12_12_1$ (no. 19) |
| *a* [Å] | 9.8943(4) | 10.9184(5) | 17.2512(7) | 18.9953(9) | 7.9113(49) |
| *b* [Å] | 16.3485(7) | 12.1773(5) | 13.7579(6) | 18.2714(8) | 15.3880(8) |
| *c* [Å] | 19.3928(8) | 20.3660(8) | 15.7043(7) | 19.2964(9) | 19.3607(10) |
| $\alpha$ [°] | 90 | 96.037(1) | 90 | 90 | 90 |
| $\beta$ [°] | 90 | 103.790(1) | 90 | 90 | 90 |
| $\gamma$ [°] | 90 | 109.460(1) | 90 | 90 | 90 |
| *V* [Å$^3$] | 3136.9(2) | 2428.6(2) | 3727.3(3) | 6697.2(5) | 2357.0(2) |
| *Z* | 4 | 3 | 4 | 8 | 4 |
| $\rho_{calcd}$ [g/cm$^3$] | 1.517 | 1.499 | 1.478 | 1.501 | 1.681 |
| *T* [K] | 173(2) | 173(2) | 173(2) | 173(2) | 173(2) |
| $\mu$ [mm$^{-1}$] (Mo-$K_\alpha$) | 0.661 | 0.642 | 0.706 | 0.623 | 0.863 |
| *F*(000) | 1472 | 1128 | 1704 | 3120 | 1200 |
| $\theta_{max}$ [°] | 30 | 30 | 30 | 30 | 30 |
| Measured reflections | 35175 | 45589 | 80284 | 96310 | 35290 |
| Unique reflections | 9048 | 28007 | 10830 | 9743 | 6675 |
| No. of reflections $I > 2\sigma(I)$ | 8633 | 27374 | 10223 | 7562 | 6858 |
| Parameters | 385 | 1202 | 435 | 417 | 302 |
| $R_1$ [$I > 2\sigma(I)$][a] | 0.0313 | 0.0271 | 0.0288 | 0.0325 | 0.0211 |
| $R_1$ (all data) | 0.0335 | 0.0279 | 0.0325 | 0.0505 | 0.0219 |
| $wR_2$ (all data) | 0.0846 | 0.0714 | 0.0807 | 0.0765 | 0.0540 |
| $\Delta\rho_{min/max}$ [e/Å$^3$] | –0.34/0.80 | –0.42/0.94 | –0.77/1.01 | –0.34/0.46 | –0.44/0.46 |

[a] $R_1 = \Sigma||F_o| - |F_c||/\Sigma|F_o|$, $wR_2 = \{\Sigma[w(F_o^2–F_c^2)^2]/\Sigma[w(F_o^2)^2]\}^{1/2}$.

 © 2006 Wiley-VCH Verlag GmbH & Co. KGaA, Weinheim 

## Acknowledgments

Financial support from the "Fonds zur Förderung der wissenschaftlichen Forschung" is gratefully acknowledged (Project No. P16600-N11).

[1] a) J. Ansell, M. Wills, *Chem. Soc. Rev.* **2002**, *31*, 259; b) Z. Fei, P. J. Dyson, *Coord. Chem. Rev.* **2005**, *249*, 2056; c) T. Appleby, J. D. Woollins, *Coord. Chem. Rev.* **2002**, *235*, 121; d) M. S. Balakrishna, V. Sreenivasa Reddy, S. S. Krishnamurthy, J. F. Nixon, J. C. T. R. Burckett St. Laurent, *Coord. Chem. Rev.* **1994**, 1291.

[2] a) S. Priya, M. S. Balakrishna, J. T. Mague, *J. Organomet. Chem.* **2003**, *679*, 116; b) S. Priya, M. S. Balakrishna, S. M. Mobin, R. McDonald, *J. Organomet. Chem.* **2003**, *688*, 227; c) K. G. Gaw, A. M. Z. Slawin, M. B. Smith, *Organometallics* **1999**, *18*, 3255; d) D. Fenske, B. Maczek, K. Maczek, *Z. Anorg. Allg. Chem.* **1997**, *623*, 1113; e) O. Kühl, P. C. Junk, E. Hey-Hawkins, *Z. Anorg. Allg. Chem.* **2000**, *626*, 1591; f) O. Kühl, S. Blaurock, J. Sieler, E. Hey-Hawkins, *Polyhedron* **2001**, *20*, 111; g) O. Kühl, T. Koch, F. B. Somoza Jr, P. C. Junk, E. Hey-Hawkins, D. Plat, M. S. Eisen, *J. Organomet. Chem.* **2000**, *604*, 116; h) G. Suss-Fink, M. A. Pellingeelli, A. Tiripicchhio, *J. Organomet. Chem.* **1987**, *320*, 101; i) E. W. Ainscough, A. M. Brodie, S. T. Wong, *J. Chem. Soc., Dalton Trans.* **1977**, 915.

[3] a) M. Jimenez-Tenorio, M. D. Palacios, M. C. Puerta, P. Valerga, *Organometallics* **2005**, *24*, 3088; b) M. S. Balakrishna, R. M. Abhyankar, J. T. Mague, *J. Chem. Soc., Dalton Trans.* **1999**, 1407.

[4] W. Schirmer, U. Flörke, H.-J. Haupt, *Z. Anorg. Allg. Chem.* **1987**, *545*, 83.

[5] N. Biricik, Z. Fei, R. Scopelliti, P. J. Dyson, *Helv. Chim. Acta* **2003**, *86*, 3281 and references cited therein.

[6] a) M. S. Balakrishna, S. Priya, W. Sommer, S. P. Nolan, *Inorg. Chim. Acta* **2005**, *358*, 2817; b) K. Raghuraman, S. S. Krishnamurthy, M. Nethaji, *J. Organomet. Chem.* **2003**, *669*, 79; c) K. Raghuraman, S. S. Krishnamurthy, M. Nethaji, *J. Chem. Soc., Dalton Trans.* **2002**, 4289; d) S. K. Mandal, G. A. N. Gowda, S. S. Krishnamurthy, C. Zheng, S. Li, N. S. Hosmane, *Eur. J. Inorg. Chem.* **2002**, 2047; e) M. S. Balakrishna, K. Ramaswamy, R. M. Abhyankar, *J. Organomet. Chem.* **1998**, *560*, 131.

[7] a) Z. Fei, N. Biricik, D. Zhao, R. Scopelliti, P. Dyson, *Inorg. Chem.* **2004**, *43*, 2228; b) S. Priya, M. S. Balakrishna, J. T. Mague, S. M. Mobin, *Inorg. Chem.* **2003**, *42*, 1272; c) M. Varrone, A. D. Burrows, M. F. Mahon, M. T. Palmer, *Inorg. Chem.* **2002**, *41*, 1695; d) M. S. Balakrishna, S. S. Krishnamurthy, *Ind. J. Chem.* **1991**, *30*, 536; e) M. G. Newton, R. B. King, M. Chang, J. Gimeno, *J. Am. Chem. Soc.* **1978**, *100*, 1632; f) J. Geicke, I. P. Lorenz, P. Murschel, K. Polborn, *Z. Naturforsch., Teil B* **1997**, *52*, 593.

[8] S. Pavlik, K. Mereiter, M. Puchberger, K. Kirchner, *Organometallics* **2005**, *24*, 3561.

[9] S. Pavlik, K. Mereiter, R. Schmid, K. Kirchner, *Organometallics* **2003**, *22*, 1771.

[10] M. Jimenez-Tenorio, M. C. Puerta, P. Valerga, *Eur. J. Inorg. Chem.* **2005**, 2631.

[11] S. Pavlik, F. Jantscher, K. Mereiter, K. Kirchner, *Organometallics* **2005**, *24*, 4899.

[12] For related ruthenium $\eta^3$-phosphaallyl complexes see: a) H. L. Ji, J. H. Nelson, A. DeCian, J. Fischer, L. Solujic, E. B. Milosavljevic, *Organometallics* **1992**, *11*, 401; b) L. P. Barthel-Rosa, K. Maitra, J. Fischer, J. H. Nelson, *Organometallics* **1997**, *16*, 1714; c) D. Duraczynska, J. H. Nelson, *Dalton Trans.* **2003**, 449; d) D. Duraczynska, J. H. Nelson, *Dalton Trans.* **2005**, 92.

[13] a) R. Appel, W. Schuhn, F. Knoch, *Angew. Chem. Int. Ed. Engl.* **1985**, *24*, 420; b) F. Mathey, *J. Organomet. Chem.* **1990**, *400*, 149; c) J. F. Nixon, *Chem. Rev.* **1988**, *88*, 1353; d) F. Mercier, J. Fischer, F. Mathey, *Angew. Chem. Int. Ed. Engl.* **1986**, *25*, 357; e) F. Mercier, C. Hugel-LeGoff, F. Mathey, *Organometallics* **1988**, *7*, 955; f) E. Niecke, B. Kramer, M. Nieger, *Organometallics* **1991**, *10*, 10; g) F. Mercier, C. Hugel-LeGoff, L. Ricard, F. Mathey, *J. Organomet. Chem.* **1990**, *398*, 389; h) C. Hugel-LeGoff, F. Mercier, L. Ricard, F. Mathey, *J. Organomet. Chem.* **1989**, *363*, 325; i) F. Mercier, F. Mathey, *Organometallics* **1990**, *9*, 863.

[14] For a recent review of azaallyl complexes see: C. F. Caro, M. F. Lappert, P. G. Merle, *Coord. Chem. Rev.* **2001**, *219–221*, 605.

[15] L. A. Watson, B. Franzman, J. C. Bollinger, K. G. Caulton, *New J. Chem.* **2003**, *27*, 1769.

[16] a) C. M. Standfest-Hauser, K. Mereiter, R. Schmid, K. Kirchner, *Eur. J. Inorg. Chem.* **2003**, 1883; b) J. N. Coalter, G. J. Spivak, G. Gerard, E. Clot, E. R. Davidson, O. Eisenstein, K. G. Caulton, *J. Am. Chem. Soc.* **1998**, *120*, 9388; c) J. N. Coalter, J. C. Bollinger, J. C. Huffman, U. W. Zwanziger, K. G. Caulton, E. R. Davidson, H. Gerard, E. Clot, O. Eisenstein, *New J. Chem.* **2000**, *24*, 9.

[17] E. Rüba, K. Mereiter, R. Schmid, K. Kirchner, E. Bustelo, M. C. Puerta, P. Valerga, *Organometallics* **2002**, *21*, 2912.

[18] A. R. Cowley, J. R. Dilworth, A. K. Nairn, A. J. Robbie, *Dalton Trans.* **2005**, 680.

[19] a) R. Schmid, K. Kirchner, *Eur. J. Inorg. Chem.* **2004**, 2609; b) E. Becker, K. Mereiter, M. Puchberger, R. Schmid, K. Kirchner, A. Doppiu, A. Salzer, *Organometallics* **2003**, *22*, 3164; c) E. Rüba, K. Mereiter, R. Schmid, V. N. Sapunov, K. Kirchner, H. Schottenberger, M. J. Calhorda, L. F. Veiros, *Chem. Eur. J.* **2002**, *8*, 3948.

[20] D. D.Perrin, W. L. F. Armarego, *Purification of Laboratory Chemicals*, 3rd ed., Pergamon, New York, **1988**.

[21] a) T. P. Gill, K. R. Mann, *Organometallics* **1982**, *1*, 485; b) E. P. Kündig, F. R. Monnier, *Adv. Synth. Catal.* **2004**, *346*, 901.

[22] B. Steinmetz, W. A. Schenk, *Organometallics* **1999**, *18*, 943.

[23] a) R. P. Nielsen, H. H. Sisler, *J. Chem. Soc.* **1962**, 3818; b) H. H. Sisler, R. P. Nielsen, *Inorg. Synth.* **1966**, *8*, 74.

[24] Bruker programs: SMART, version 5.054; SAINT, version 6.2.9; SADABS, version 2.03; XPREP, version 5.1; SHELXTL, version 5.1 (Bruker AXS Inc., Madison, WI, 2001).

[25] G. M. Sheldrick, *SHELX97: Program System for Crystal Structure Determination*, University of Göttingen, Göttingen, Germany, **1997**.

[26] A. L. Spek, *PLATON: A Multipurpose Crystallographic Tool*, University of Utrecht, Utrecht, The Netherlands, **2003**.

[27] M. J. Frisch, G. W. Trucks, H. B. Schlegel, G. E. Scuseria, M. A. Robb, J. R. Cheeseman, V. G. Zakrzewski, J. A. Montgomery Jr, R. E. Stratmann, J. C. Burant, S. Dapprich, J. M. Millam, A. D. Daniels, K. N. Kudin, M. C. Strain, O. Farkas, J. Tomasi, V. Barone, M. Cossi, R. Cammi, B. Mennucci, C. Pomelli, C. Adamo, S. Clifford, J. Ochterski, G. A. Petersson, P. Y. Ayala, Q. Cui, K. Morokuma, D. K. Malick, A. D. Rabuck, K. Raghavachari, J. B. Foresman, J. Cioslowski, J. V. Ortiz, A. G. Baboul, B. B. Stefanov, G. Liu, A. Liashenko, P. Piskorz, I. Komaromi, R. Gomperts, R. L. Martin, D. J. Fox, T. Keith, M. A. Al-Laham, C. Y. Peng, A. Nanayakkara, C. Gonzalez, M. Challacombe, P. M. W. Gill, B. Johnson, W. Chen, M. W. Wong, J. L. Andres, C. Gonzalez, M. Head-Gordon, E. S. Replogle, J. A. Pople, *Gaussian 98*, revision A.7, Gaussian, Inc., Pittsburgh, PA, **1998**.

[28] a) A. D. Becke, *J. Chem. Phys.* **1993**, *98*, 5648; b) B. Miehlich, A. Savin, H. Stoll, H. Preuss, *Chem. Phys. Lett.* **1989**, *157*, 200; c) C. Lee, W. Yang, G. Parr, *Phys. Rev. B* **1988**, *37*, 785.

[29] a) U. Haeusermann, M. Dolg, H. Stoll, H. Preuss, *Mol. Phys.* **1993**, *78*, 1211; b) W. Kuechle, M. Dolg, H. Stoll, H. Preuss, *J. Chem. Phys.* **1994**, *100*, 7535; c) T. Leininger, A. Nicklass, H. Stoll, M. Dolg, P. Schwerdtfeger, *J. Chem. Phys.* **1996**, *105*, 1052.

[30] a) A. D. McClean, G. S. Chandler, *J. Chem. Phys.* **1980**, *72*, 5639; b) R. Krishnan, J. S. Binkley, R. Seeger, J. A. Pople, *J. Chem. Phys.* **1980**, *72*, 650; c) A. H. Wachters, *J. Chem. Phys.*

 © 2006 Wiley-VCH Verlag GmbH & Co. KGaA, Weinheim 

**1970**, *52*, 1033; d) P. J. Hay, *J. Chem. Phys.* **1977**, *66*, 4377; e) K. Raghavachari, G. W. Trucks, *J. Chem. Phys.* **1989**, *91*, 1062; f) R. C. Binning, L. A. Curtiss, *J. Comput. Chem.* **1990**, *11*, 1206; g) M. P. McGrath, L. Radom, *J. Chem. Phys.* **1991**, *94*, 511.

[31] a) C. Peng, P. Y. Ayala, H. B. Schlegel, M. J. Frisch, *J. Comput. Chem.* **1996**, *17*, 49; b) C. Peng, H. B. Schlegel, *Isr. J. Chem.* **1994**, *33*, 449.

Received: October 25, 2005
Published Online: January 16, 2006

 © 2006 Wiley-VCH Verlag GmbH & Co. KGaA, Weinheim 

DOI: 10.1002/ejic.200500595

# Mono- versus Binuclear Copper(II) Complexes in Phosphodiester Hydrolysis

**Katalin Selmeczi,[a,c] Michel Giorgi,[c] Gábor Speier,[a,b] Etelka Farkas,[d] and Marius Réglier*[c]**

**Keywords:** Catalysis / Dinuclear copper(II) complex / Enzyme mimics / Phosphate ester hydrolysis / Tripodal ligands

Mono- and dinuclear copper(II) complexes [Cu(**L$^1$OH**)]-$(CF_3SO_3)_2$ (**1**) and [$Cu_2$(**L$^2$O**)]$(CF_3SO_3)_3$ (**2**) have been synthesized and characterized by X-ray crystallography. Complexes **1** and **2** were then tested as catalysts for the hydrolysis of bis(*p*-nitrophenyl)phosphate (BNPP). At pH 6, the dinuclear complex **2** was found to be 20-fold more active than complex **1** and the reaction up to 600-fold faster than the un-promoted reaction. On the basis of potentiometric studies, we were able to demonstrate that the bis(aqua)copper complex was the active species by the formation of a ternary complex in which one copper atom binds to a hydroxide and the second, to the substrate. We also propose that BNPP reacts with the bis(aqua)copper complex to give a stable, hydrolytically inactive BNPP-**2** complex (**3**).
(© Wiley-VCH Verlag GmbH & Co. KGaA, 69451 Weinheim, Germany, 2006)

## Introduction

During the last decade, there has been increasing interest in the development of metal complexes which promote the hydrolysis of phosphate ester linkages.[1,2] The main approach developed in this domain concerns the design of functional models for hydrolytic metalloenzymes. Beside their important roles in the understanding of their mechanisms, the development of hydrolytic metalloenzyme mimics are of great importance in biotechnology for the design of synthetic nucleases which could be used as artificial restriction enzymes. On the other hand, since a number of phosphate esters and related phosphorus(V) compounds are used in agriculture as pesticides or, unfortunately, as potent nerve agents in chemical weaponry (mustard gases), the development of catalytic systems able to hydrolyze and destroy such compounds is of considerable environmental and medicinal importance.

Among the metalloenzymes which catalyze the hydrolysis of the phosphate ester linkage, metallonucleases are important because they are ubiquitous and essential for living organisms.[3] Certainly, due to its high natural abundance and good Lewis acid properties, $Mg^{2+}$ is the most important metal encountered in nuclease active sites. Multinuclear transition metal centers with $Zn^{2+}$, $Mn^{2+}$ and $Fe^{2+}$ are often present too. As examples, in enzymes which hydrolyze phosphodiesters into phosphomonoesters, the active site of alkaline phosphatase contains a dinuclear $Zn^{2+}$ core,[4] while the active site present in purple acid phosphatases (PAPs) contains one $Fe^{3+}$ associated to a $Fe^{2+}$ (or $Zn^{2+}$, $Mn^{2+}$).[5] In the commonly disclosed mechanism, one of the metal ions (the one with the highest Lewis acidity) favors the formation and co-ordination of a hydroxide ion at physiological pH, while the second one activates the phosphate ester group for intramolecular nucleophilic attack by the adjacent hydroxide. On the basis of this mechanism, nuclease mimics incorporating dinuclear metal centers with Co,[6,7] Ln,[8,9] Zn[10,11] and Fe[12] were recently published as efficient bioinspired catalysts for phosphoester hydrolysis.

While the copper ion has never been identified as a cofactor in natural nucleases, $Cu^{2+}$ exhibits some interesting features rendering it attractive for artificial nucleases: (*i*) $Cu^{2+}$ is substitutionally labile and at the same time a strong Lewis acid necessary for the activation of the phosphodiester bond towards nucleophilic attack and (*ii*) $Cu^{2+}$ lowers the p$K_a$ of coordinated water, thereby providing metal-bound hydroxide at near-neutral pH. That is why binuclear[13,14] complexes of $Cu^{2+}$ have also been described as efficient bioinspired catalysts in phosphoester hydrolysis.

The importance of nuclearity (mononuclear vs. dinuclear) was clearly demonstrated for $Fe^{3+}$.[12] The situation is less clear for copper since mononuclear $Cu^{2+}$ complexes were also reported in the literature as agents with good activity.[15,16] We report in this paper the kinetics of BNPP hydrolysis by the dinuclear [$Cu_2$(**L$^2$O**)]$(CF_3SO_3)_3$ (**2**), in order to study the influence of the nuclearity of copper com-

[a] Research Group for Petrochemistry, Hungarian Academy of Sciences,
8200 Veszprém, Hungary
[b] Department of Organic Chemistry, University of Veszprém,
8201 Veszprém, Hungary
[c] Chimie, Biologie et Radicaux Libres, UMR CNRS 6517, Faculté des Sciences et Techniques, case 432, Université Paul Cézanne Aix-Marseille III,
Avenue Escadrille Normandie-Niemen, 13397 Marseille Cedex 20, France
Fax: +33-491-983-208
E-mail: marius.reglier@univ.u-3mrs.fr
[d] Department of Inorganic and Analytical Chemistry, Faculty of Science, University of Debrecen,
4010 Debrecen, Hungary

 © 2006 Wiley-VCH Verlag GmbH & Co. KGaA, Weinheim 

plexes, including a quantitative comparison with the mononuclear parent complex [Cu(**L$^1$OH**)](CF$_3$SO$_3$)$_2$ (**1**).

## Results and Discussion

**Synthesis:** Michael addition of 2-ethanolamine or 1,3-diamino-2-hydroxypropane to freshly distilled 2-vinylpyridine in methanol/acetic acid leads to ligands **L$^1$OH** and **L$^2$OH**, respectively.[17] The corresponding copper(II) complexes **1** and **2** were obtained in good yields by treatment with 1 equiv. of ligands **L$^1$OH** and **L$^2$OH** in dichloromethane with 1 and 2 equiv. of copper(II) triflate, respectively.[18] Complex **3** was prepared by mixing 1 equiv. of complex **2** in water with 1 equiv. of BNPP in methanol at room temperature (Scheme 1).

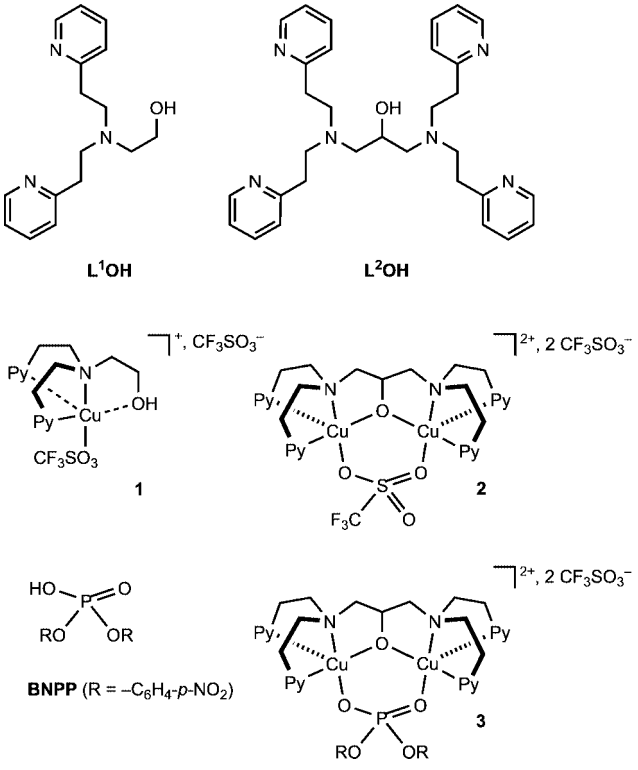


Scheme 1.

**Crystal Structures:** Crystal data for complexes **1** and **3**, together with details of the X-ray diffraction experiment, are reported in Table 5.

Single crystals of [Cu(**L$^1$OH**)](CF$_3$SO$_3$)$_2$ (**1**) suitable for X-ray diffraction analysis were obtained by slow diethyl ether vapor diffusion into a saturated acetone solution of the copper complex **1**. [Cu(**L$^1$OH**)](CF$_3$SO$_3$)$_2$ (**1**) is a mononuclear complex with a five-coordinate copper(II) cation (Figure 1). The geometry around the copper(II) ion is clearly a quite perfect square pyramid as it can be seen from the geometric parameters and the $\tau$ factor which is equal to 0.04.[19] The equatorial positions are occupied by one pyridine N atom (N3) and the nitrogen N1 and oxygen O19 of the ethanolamine moiety. The fourth equatorial ligand is the oxygen atom of a triflate counterion. The nitrogen N2 of the second pyridine occupies the axial coordination site at a distance equal to 2.171(4) Å from the copper, which is typically somewhat longer than the equatorial copper to pyridine distance [$d_{Cu–N3}$ = 1.979(4) Å]. The deviation of the copper atom from the mean basal plane defined by atoms N1, N3, O1 and O19 is equal to 0.291 Å.

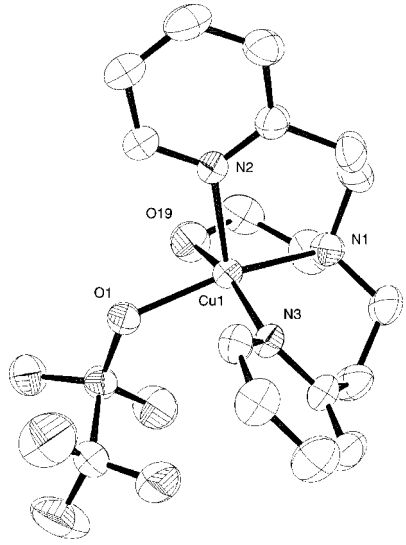


Figure 1. ORTEP perspective view of copper(II) complex [Cu(**L$^1$OH**)](CF$_3$SO$_3$)$_2$ (**1**). The H atoms and one CF$_3$SO$_3^-$ counterion are omitted for clarity. Bond lengths are in Å: Cu–N1 2.044(4), Cu–N2 2.171(4), Cu–N3 1.979(4), Cu–O1 2.042(3), Cu–O19 1.973(4). Bond angles are in °: N1–Cu–N2 96.93(16), N3–Cu–O1 88.51(15), N3–Cu–N2 100.28(19), N3–Cu–N1 95.26(17), O1–Cu–N2 98.14(15), O19–Cu–N1 84.54(18), O19–Cu–N2 98.4(2), O1–Cu–N1 163.55(16), O19–Cu–O1 86.77(17), O19–Cu–N3 161.21(18). Numbers in parentheses are the estimated standard deviation in the least significant digits.

For the complex **2**, suitable crystals for X-ray diffraction analysis were obtained by slow diethyl ether vapor diffusion into a saturated dichloromethane solution. The structure of [Cu$_2$(**L$^2$O**)](CF$_3$SO$_3$)$_3$ (**2**), already described in a previous paper,[18] consists of a binuclear complex with two tetragonally coordinated Cu$^{II}$ ions bridged in the equatorial positions by the alkoxide and triflate ligands (Figure 2). The Cu–Cu distance was found to be 3.699(3) Å. This is somewhat longer than that found e.g. in the similar [Cu$_2$(**L$^2$O**)(OMe)](PF$_6$)$_2$ [2.995(2) Å].[20] The two positions in the basal plane of the copper ions are occupied by one of the pyridine nitrogen atoms and the aliphatic nitrogen of the ligand **L$^2$OH**. The other two equatorial positions are occupied by the oxygen atoms O1 of the ligand **L$^2$OH** and O2 of the triflate anion. As in complex **1**, the geometry around both coppers is a square pyramidal ($\tau$ = 0.11) and the distance of the Cu–atoms to the mean plane defined by atoms O1, O2, N1 and N2 is equal to 0.308 Å. The axial pyridine N3 donor, which is bound to the Cu$^{II}$ atom at a distance of 2.179(4) Å, is a bit longer than the equatorial pyridine donor N2 [Cu1–N2 2.009(3) Å]. The bond lengths

 © 2006 Wiley-VCH Verlag GmbH & Co. KGaA, Weinheim 

and bond angles of **2** shows similarities to other dicopper complexes with ligands derived from 1,3-diamino-2-hydroxypropane.[20–22]

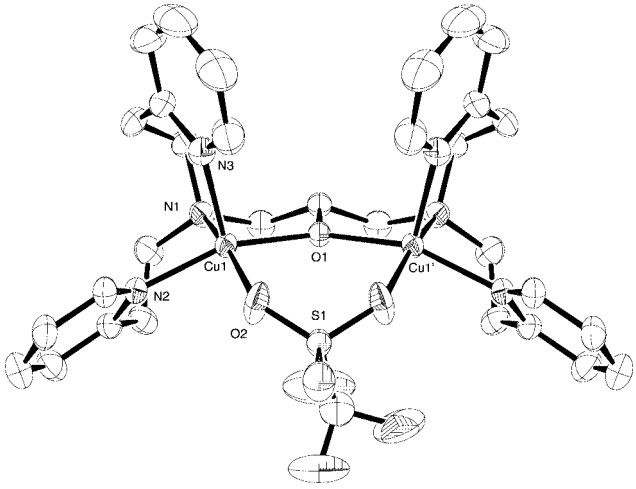


Figure 2. ORTEP perspective view of the copper(II) complex $[Cu(\mathbf{L^2O})](CF_3SO_3)_2$ (**2**). The H atoms and 2 $CF_3SO_3^-$ counterion are omitted for clarity. Bond lengths are in Å: Cu1–O1 1.9695(12), Cu1–N2 2.009(3), Cu1–N1 2.032(3), Cu1–O2 2.047(3), Cu1–N3 2.179(4). Bond angles are in °: O1–Cu1–N2 159.45(14), O1–Cu1 N1 87.04(12), N2–Cu1–N1 94.17(12), O1–Cu1–O2 90.54(12), N2–Cu1–O2 83.10(13), N1–Cu1–O2 165.31(15), O1–Cu1–N3 104.69(11), N2–Cu1–N3 95.40(10), N1–Cu1–N3 98.93(14), O2–Cu1–N3 95.71(16). Numbers in parentheses are the estimated standard deviation in the least significant digits.

Slow solvent evaporation of a solution of $[Cu_2(\mathbf{L^2O})(BNPP)](CF_3SO_3)_2$ (**3**) (Figure 3) gave deep blue crystals suitable for X-ray diffraction analysis. The structure of **3** consists of a binuclear copper(II) complex in which the Cu atoms are bridged together through the BNPP in a bidentate coordination and the alkoxide of the ligand $\mathbf{L^2OH}$. The geometries of the metals are approximately distorted square pyramidal, the $\tau$ parameter is equal to 0.14 and 0.26 for Cu1 and Cu2, respectively. As in complex **2**, the equatorial positions are occupied by the N atom from a pyridine, the nitrogen and the O atoms of the ethanolamine moiety, as well as the O atom of the BNPP ligand. The apical positions are taken by the nitrogen atoms of the remaining pyridines. The copper to nitrogen distances are slightly longer than in complex **2**: Cu1–N3 2.2432(4) Å and Cu2–N5 2.1864(4) Å. As for **2**, the bases of both pyramids, defined by atoms O1, O3, N1, N2 and O1, O4, N4, N6, respectively, are close to planarity and the out of plane distances of the copper atoms are equal to 0.25 Å and 0.27 Å for Cu1 and Cu2, respectively. The distance between the two copper ions is equal to 3.7252(2) Å which is slightly longer than that observed for complex **2**. This can be explained by the nature of the BNPP ligand which is coordinated to the complex by the two nitrophenyl rings and shows a stabilizing interaction with the $\mathbf{L^2OH}$ ligand which is not observed in complex **2**. The phenyl ring of the BNPP ligand, defined by the atoms C38–C43, is involved in a π-stacking interaction with the pyridine, defined by atoms N6, C20–C24. On the another hand, the second nitrophenyl ring of the BNPP ligand is involved in a CH-π contact with the two apical pyridines of the $\mathbf{L^2OH}$ ligand (the distances between the centroid of the ring, defined by the atoms C32–C37 and the H atoms of C16 and C30, are equal to 3.46 Å and 3.73 Å, respectively). Consequently, the distance between the centroid of the axial pyridines is longer than in complex **2** [$d$ = 5.4236(5) Å for **3** and $d$ = 4.958(4) for **2**] and the dihedral angle between both aromatic rings increases from 77° in **2** to 84.18° in **3**.

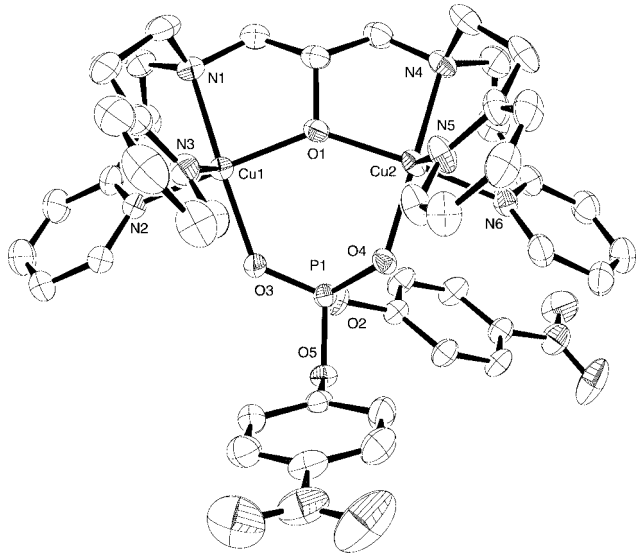


Figure 3. ORTEP perspective view of the copper(II) complex $[Cu_2(\mathbf{L^2O})(BNPP)](CF_3SO_3)_2$ (**3**). The H atoms and 2 $CF_3SO_3^-$ counterion are omitted for clarity. Bond lengths are in Å: Cu1–O1 1.9823(3), Cu1–O3 1.9854(3), Cu1–N1 2.0628(4), Cu1–N2 2.0116(4), Cu1–N3 2.2432(4), Cu2–O1 1.9874(3), Cu2–O4 1.9733(3), Cu2–N4 2.0595(4), Cu2–N5 2.1864(4), Cu2–N6 2.0230(4). Bond angles are in °: O1–Cu1–O3 92.409(13), O1–Cu1–N1 86.28(2), O1–Cu1–N2 161.41(2), O1–Cu1–N3 102.662(14), O3–Cu1–N1 169.72(2), O3–Cu1–N2 86.358(15), O3–Cu1–N3 94.77(2), N1–Cu1–N2 91.63(2), N1–Cu1–N3 95.47(2), N2–Cu1–N3 95.92(2), O1–Cu2–O4 92.451(12), O1–Cu2–N4 86.62(2), O1–Cu2–N5 106.976(14), O1–Cu2–N6 157.079(15), O4–Cu2–N4 172.71(2), O4–Cu2–N5 91.56(2), O4–Cu2–N6 86.104(15), N4–Cu2–N5 95.63(2), N4–Cu2–N6 91.93(2), N5–Cu2–N6 95.93(2). Numbers in parentheses are the estimated standard deviation in the least significant digits.

**Acid-Base Equilibrium Determination:** The distribution of different species in an aqueous solution is essential for understanding the activity of the complexes in phosphate ester hydrolysis. The protonation constants of the ligands $\mathbf{L^1OH}$ and $\mathbf{L^2OH}$ (Table 1), as well as the stability constants of their copper complexes and the p$K_a$ values of their copper-bound water molecules (Table 2), were determined by potentiometric titration in 0.2 M aqueous KCl at 40 °C.

In the case of $\mathbf{L^1OH}$, three protonation steps were found in the 2–11 pH range. The p$K_a$ values of 2.82(2) and 3.89(2) are assigned to the deprotonation of the pyridine N atoms and the third at 7.71(1) to that of the tertiary amine. Deprotonation of the OH group does not occur in the detectable pH range.

 © 2006 Wiley-VCH Verlag GmbH & Co. KGaA, Weinheim 

Table 1. Protonation constants of the ligands at 40 °C [$I$ = 0.2 M (KCl)].

| Species | p$K$ | |
|---|---|---|
| | **L$^1$OH** | **L$^2$OH** |
| $[LH_6]^{6+}$ | | <<2 |
| $[LH_5]^{5+}$ | | 2.66(2) |
| $[LH_4]^{4+}$ | | 3.41(5) |
| $[LH_3]^{3+}$ | 2.82(2) | 4.25(5) |
| $[LH_2]^{2+}$ | 3.89(2) | 5.83(7) |
| $[LH]^{+}$ | 7.71(1) | 7.92(1) |

Table 2. Overall stability constants (log$\beta$) and stepwise deprotonation constants (p$K$) of the copper complexes at 40 °C [$I$ = 0.2 M (KCl)].

| Species | **L$^1$OH** | | **L$^2$OH** | |
|---|---|---|---|---|
| | log$\beta$ | p$K$ | log$\beta$ | p$K$ |
| $\{[\mathbf{L^1OH_2}]Cu(H_2O)\}^{3+}$ (**C**) | 11.48(8) | | | |
| $\{[\mathbf{L^1OH}]Cu(H_2O)\}^{2+}$ (**A**) | 9.02(3) | 2.46 | | |
| $\{[\mathbf{L^1O}]Cu(H_2O)\}^{+}$ (**B**) | 2.91(5) | 6.11 | | |
| $\{[\mathbf{L^2OH}]Cu_2(H_2O)_2\}^{4+}$ (**D**) | | | 17.88(2) | |
| $\{[\mathbf{L^2O}]Cu_2(H_2O)_2\}^{3+}$ (**E**) | | | 14.14(6) | 3.74 |
| $\{[\mathbf{L^2O}]Cu_2(H_2O)(OH)\}^{2+}$ (**F**) | | | 8.0(6) | 6.14 |

In the case of **L$^2$OH**, three additional deprotonation steps were observed; the first is estimated to occur at a pH less than 2 which is out of the detectable range. In the following steps one proton is removed from each pyridine N atom and the p$K_a$ values at 5.83(7) and 7.92(1) correspond to the deprotonation of the two tertiary amines. Again, the proton of the OH group is not removed up to pH 11.

Titration of the ligands in the presence of various equivalents of $Cu^{2+}$ was also analyzed (Figure 4). In aqueous solution it is reasonable to assume that the bridging triflate anions in **1** and **2** are replaced by water molecules. For the [**L$^1$OH**]:[$Cu^{2+}$] 1:1 system, at a pH higher than 8 and for the [**L$^1$OH**]:[$Cu^{2+}$] 1:2 system at a pH higher than 4, precipitation of copper hydroxide was observed, and neither the mononuclear species at pH > 8 nor the dinuclear species could be determined. Equilibrium modeling from the titration results indicate that two predominant species $\{[\mathbf{L^1OH}]Cu(H_2O)\}^{2+}$ (**A**) and $\{[\mathbf{L^1O}]Cu(H_2O)\}^{+}$ (**B**) are formed in addition to a small amount of the species (**C**) (Scheme 2), where one pyridine N atom is protonated. At a p$K_a$ of 6.11 the ligand OH group in **A** is deprotonated to give the species $\{[\mathbf{L^1O}]Cu(H_2O)\}^{+}$ (**B**). The formation of this species was confirmed by spectrophotometric titration (Figure 5) where an important increase in $\varepsilon$ was observed at 374 nm in the pH range 5.5–7 this was attributed to the formation of the RO–Cu$^{II}$ LMCT band ($\varepsilon$ = 60 M$^{-1}$cm$^{-1}$ at pH 5.5 and $\varepsilon$ = 570 M$^{-1}$cm$^{-1}$ at pH 7). No formation of binuclear species in the pH range examined was observed by ESR spectroscopy.

In the case of **L$^2$OH**, no precipitation of copper hydroxide occurs, and the formation of a dinuclear species starts at a relatively low pH value. The deprotonation of the ligand OH in **D** is observed at acidic pH (p$K$ = 3.74) which is in agreement with the spectrophotometric titration in this pH range (Figure 6). A distinct peak forms at 365 nm ($\varepsilon$ =

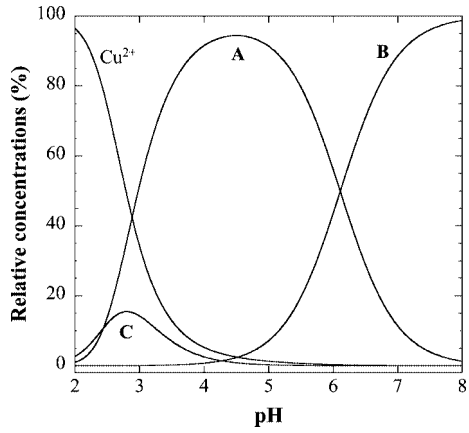


Figure 4. Species distribution of the complexes of **L$^1$OH** (5 mM) with 1 equiv. $Cu^{2+}$ in 0.2 M KCl at 40 °C.

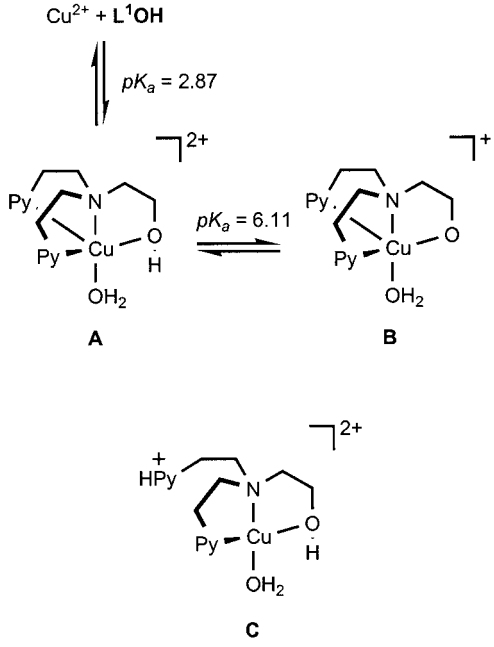


Scheme 2.

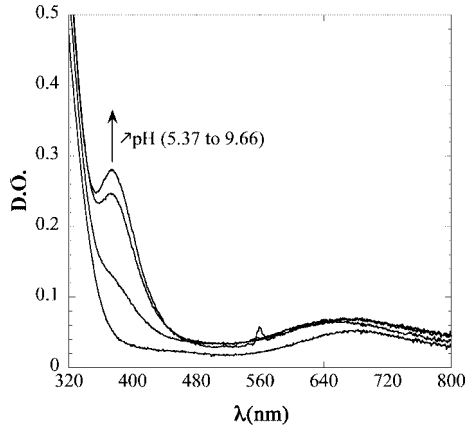


Figure 5. UV/Vis spectra of **1** at various pH values (5.37, 4.83, 7.67 and 9.66).

 © 2006 Wiley-VCH Verlag GmbH & Co. KGaA, Weinheim 

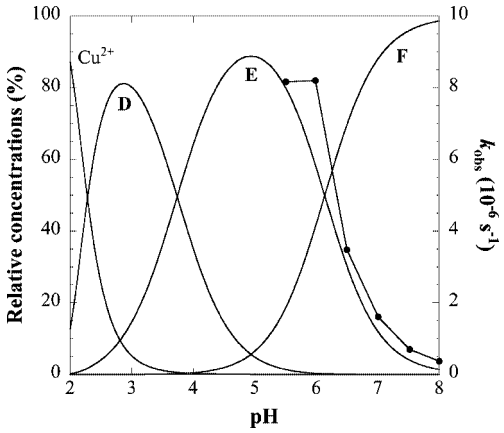


Figure 6. Species distribution of the complexes of **L²OH** (5 mM) with 2 equiv. $Cu^{2+}$ in 0.2 M KCl at 40 °C and pH/rate profile for BNPP hydrolysis promoted by **2**; [**2**] = 0.488 mM, [BNPP] = 0.192 mM at 40 °C.

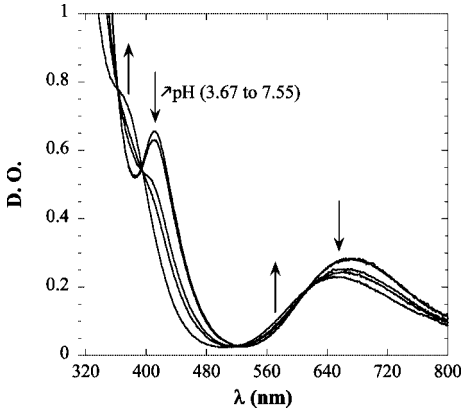


Figure 7. UV/Vis spectra of **2** at various pH values (3.67, 4.53, 5.77, 6.11 and 7.55).

2100 $M^{-1}cm^{-1}$) when the pH is raised and it can be assigned as the RO–$Cu^{II}$ LMCT band. A p$K_a$ of 6.14 for {[**L²O**]-$Cu_2OH(H_2O)$}$^{2+}$ signifies that the metal-bound water is deprotonated. At this pH, the UV/Visible absorption spectrum shows some variations, the peak at 365 nm becomes a weak shoulder with an important decrease in intensity (Figure 7; $\varepsilon$ = 1030 $M^{-1}cm^{-1}$). Similar UV/Visible features have been previously observed for several related (μ-phenoxo)dicopper(II) complexes.[23,24] This probably indicates the formation of the double bridged (μ-alkoxo)(μ-hydroxo)-dicopper(II) complex **G**. ESR silent spectra observed at a pH higher than 7, seem to confirm this proposal.

**Phosphate Hydrolysis:** The efficiency of [$Cu_2$(**L²O**)]($CF_3SO_3$)$_3$ (**2**) was studied in the 5.5–8 pH range with respect to BNPP hydrolysis and compared to the activity of the parent complex [Cu(**L¹OH**)]($CF_3SO_3$)$_2$ (**1**) (Scheme 3, Table 3). Since, the hydrolysis of BNPP by **1** or **2** proceeds cleanly to give *p*-nitrophenol (PNP) and *p*-nitrophenyl phosphate (MNPP), as revealed by thin-layer chromatography, the progress of the reaction was monitored by the visible absorbance change at 400 nm due to the release of 4-nitrophenolate anion.

Values for the observed initial rate ($V_i$) and the first-order rate ($k_{obs}$ = $V_i$/[BNPP]) constants for the appearance of the *p*-nitrophenolate anion are listed in Table 4 and Table 5 as a function of the pH (Figure 8). While an important effect of pH on the BNPP hydrolysis was observed for **2** (Table 4), the mononuclear complex **1** exhibited only a slight pH effect (Table 5). For **2**, we observed the maximal activity in the 5.5–6 pH range.

In order to find the reactive species, the pH dependence of the initial rate was measured and compared with the species distributions. The plots of $k_{obs}$ vs. pH give a sigmoidal curve and follow the distribution of the complex {[**L²O**]-$Cu_2(H_2O)_2$}$^{3+}$ (**E**) which must be the active species in the

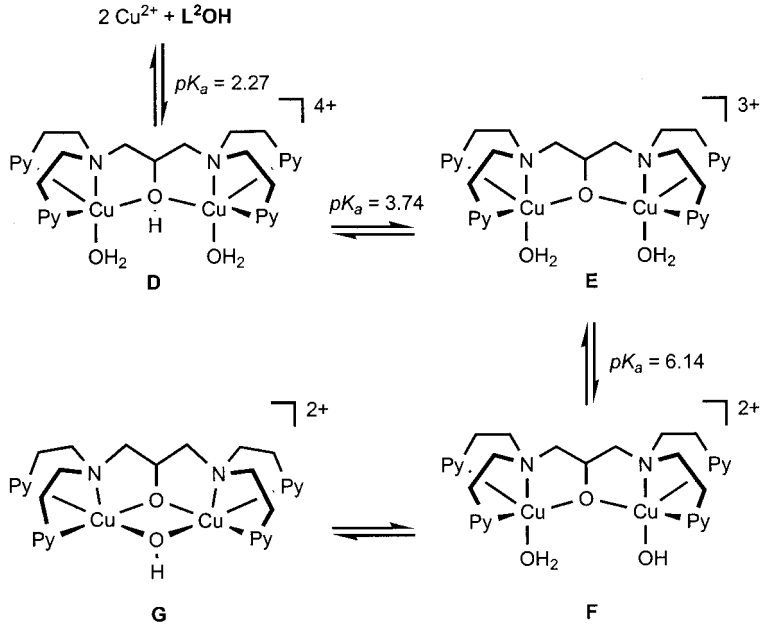


Scheme 3.

 © 2006 Wiley-VCH Verlag GmbH & Co. KGaA, Weinheim 

Table 3. Kinetic data for the hydrolysis of BNPP promoted by **2**. Reaction condition: [BNPP] = 0.194 mM, [**2**] = 0.488 mM, buffer = 50 mM (MES for pH 5.5–6.5, HEPES for pH 7–8), [KCl] = 0.1 M, 40 °C [*calculated from the hydrolysis of BNPP (1.92 mM) at 40 °C].

| pH | $V_i$ $10^{-10}$ M s$^{-1}$ | $k_{obs}$ $10^{-6}$ s$^{-1}$ | $k_2$[2] $10^{-3}$ M$^{-1}$ s$^{-1}$ | $k_{uncat}$* $10^{-8}$ s$^{-1}$ | $k_{obs}/k_{uncat}$ |
|---|---|---|---|---|---|
| 5.5 | 15.8 | 8.10 | 21 | 1.36 | 596 |
| 6.0 | 16.1 | 8.26 | 29.4 | 1.31 | 630 |
| 6.5 | 6.8 | 3.49 | 23.2 | 1.28 | 272 |
| 7.0 | 3.14 | 1.61 | 26.7 | 1.24 | 130 |
| 7.5 | 1.37 | 0.70 | 34.5 | 1.39 | 50 |
| 8.0 | 0.78 | 0.40 | 52.8 | 2.26 | 18 |

Table 4. Kinetic data for the hydrolysis of BNPP promoted by **1**. Reaction condition: [BNPP] = 0.194 mM, [**1**] = 0.486 mM, buffer = 50 mM (MES for pH 5.5–6.5, HEPES for pH 7–8), [KCl] = 0.1 M, 40 °C.

| pH | $V_i$ $10^{-10}$ M s$^{-1}$ | $k_{obs}$ $10^{-6}$ s$^{-1}$ | $k$[1] $10^{-3}$ M$^{-1}$ s$^{-1}$ | $k_{obs}$[2]/$k_{obs}$[1] |
|---|---|---|---|---|
| 5.5 | 0.47 | 0.24 | 2.62 | 34 |
| 6.0 | 0.76 | 0.39 | 1.79 | 21 |
| 6.5 | 1.32 | 0.68 | 1.97 | 5 |
| 7.0 | 1.50 | 0.77 | 1.80 | 2 |
| 7.5 | 1.05 | 0.54 | 1.16 | 1.3 |
| 8.0 | 1.0 | 0.51 | 1.05 | 0.8 |

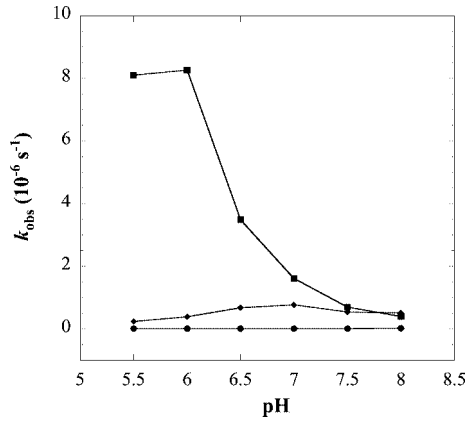


Figure 8. pH dependence on $k_{obs}$ for BNPP hydrolysis promoted by copper complexes **1** (filled diamond) and **2** (filled square) and un-promoted (filled circle).

hydrolysis (Figure 5). For this case the second order constants $k_2$ (M$^{-1}$s$^{-1}$) can be obtained taking into account the quantities of species **E** ($k_2$[2] = $k_{obs}$/[**E**]) (Table 4).

From these kinetic data, it becomes apparent that: (*i*) **2** is more efficient in promoting the hydrolysis of BNPP than the mononuclear copper complex **1** (Table 5, ratio $k_{obs}$[2]/$k_{obs}$[1] > 20) and (*ii*) the rate of the **2**-promoted reaction is up to 600 times faster than the unpromoted reaction. This

Table 5. Crystallographic data for the copper(II) complexes **1** and **3**.

| Complexes | **1** | **3** |
|---|---|---|
| ***Crystal data*** | | |
| formula | $C_{18}H_{21}CuF_6N_3O_7S_2$ | $C_{45}H_{45}Cu_2F_6N_8O_{15}PS_2$ |
| $M_r$ | 633.02 | 1482.106 |
| crystal size | 0.6×0.4×0.2 | 0.5×0.3×0.2 |
| crystal color | blue | blue |
| $a$ [Å] | 8.4863(4) | 10.3462(3) |
| $b$ [Å] | 14.9831(4) | 14.0513(6) |
| $c$ [Å] | 10.0586(4) | 20.1235(9) |
| α [°] | | 94.287(1) |
| $\beta$ [°] | 106.410(1) | 102.043(2) |
| $\gamma$ [°] | | 107.853(2) |
| $V$ [Å$^3$] | 1226.9(8) | 2692.9(2) |
| $Z$ | 2 | 2 |
| $D_{calcd.}$ [g cm$^{-3}$] | 1.714 | 1.828 |
| crystal system | monoclinic | triclinic |
| space group | $P2_1$ | $P\bar{1}$ |
| $\mu$(Mo-$K_\alpha$) [cm$^{-1}$] | 11.51 | 13.5 |
| absorption correction | none | none |
| ***Data collection*** | | |
| $T$ [K] | 293 | 293 |
| scan mode | Phi scan | Phi scan |
| scan width [°] | 2 | 2 |
| $2\theta_{max}$ [°] | 53.74 | 53.9 |
| unique reflections | 2551 | 9931 |
| ***Structure refinement*** | | |
| reflections used for refinement | 2551 | 7827 ($F_2 > 3\sigma F_2$) |
| reflections parameters | 333 | 712 |
| H atoms | calculated | calculated |
| $R$ | 0.043 | 0.043 |
| $R_w$ | 0.117[a] | 0.054[b] |
| Goodness of fit | 1.105 | 1.76 |
| $\Delta\rho_{fin}$(max./min.) [e·Å$^{-3}$] | 0.449/–0.730 | 0.56/–0.29 |

[a] $w = 1/[\sigma^2(F_o^2) + 0.1P^2]$, $P = (F_o^2 + 2F_c^2)/3$. [b] $w = 1/[\sigma^2(F_o^2) + 0.03\ F_o^2]$.

 © 2006 Wiley-VCH Verlag GmbH & Co. KGaA, Weinheim 

means that the copper complex **2** is a good catalyst for phosphate ester hydrolysis in the pH range 5.5–6.0.

In order to gain a better insight into the mechanism, the initial rate was measured as a function of **2** and BNPP concentrations. The rate of BNPP hydrolysis shows a first order dependence on the concentration of the complex **2** (Figure 9). This means that one molecule of **2** is involved in the BNPP hydrolysis. The same result was obtained for complex **1**.

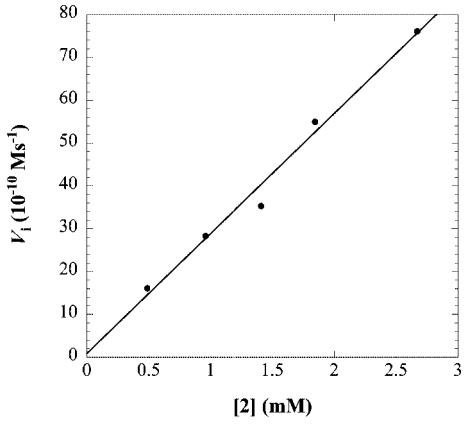


Figure 9. $V_i$ vs. [**2**] of hydrolysis of BNPP. Each reaction mixture contained 50 mM MES/0.1 M KCl, pH 6 at 40 °C and 0.192 mM BNPP. The plotted lines are the computer-generated best fit with $R = 0.9920$.

As shown in Figure 10, saturation was observed when the concentration of BNPP was 1 mM. This indicates a pre-equilibrium related to the formation of the active complex (**2**/substrate) followed by the rate-determining transformation of the substrate with the complex. The treatment of the data, using the Michaelis–Menten model, showed the following constants: $K_M = 0.17$ mM and $k_{cat} = 11.2 \cdot 10^{-6}$ s$^{-1}$. For the complex **1** (0.5 mM) at pH 7, $K_M = 0.65$ mM

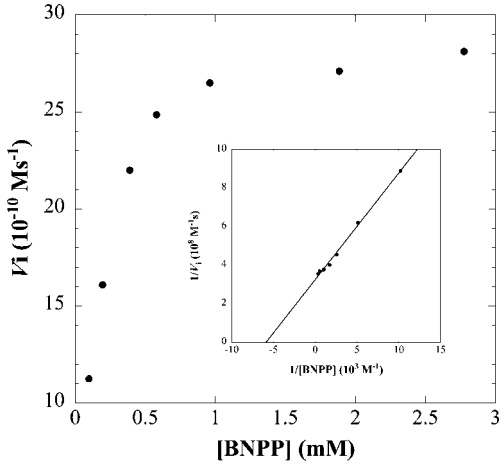


Figure 10. Saturation kinetics of copper complex **2** by BNPP. Each reaction mixture contained 50 mM MES/0.1 M KCl, pH 6 at 40 °C and 0.5 mM **2**. Inset: Lineweaver–Burk plot, the plotted line is the computer-generated best fit ($R = 0.9978$) according to $1/V_i = K_M/(V_{max}[BNPP]) + 1/V_{max}$, where $K_M = 0.17$ mM, $V_{max} = 3.07 \cdot 10^{-9}$ M s$^{-1}$ and $k_{cat} = 11.2 \cdot 10^{-6}$ s$^{-1}$, $\{[\mathbf{L^2O}]Cu_2(H_2O)_2\}^{3+} = 0.55$[**2**].

and $k_{cat} = 1.38 \cdot 10^{-6}$ s$^{-1}$ were obtained taking $[\{[\mathbf{L^1O}]Cu(H_2O)\}^{+}] = 0.89$[**1**].

On the basis of the potentiometric titration study and kinetic data we assume that the bis(aqua)copper complex $\{[\mathbf{L^2O}]Cu_2(H_2O)_2\}^{3+}$ (**E**) is responsible for the BNPP hydrolysis (Figure 5) according to a double Lewis acid activation mechanism. As shown in Scheme 4, the cleavage process may involve the following steps: (*i*) the phosphodiester BNPP coordinates to one copper ion as a monodentate ligand by replacing one water molecule (**E** → **H**); (*ii*) deprotonation of the second water ligand by a phosphate group and the subsequent nucleophilic attack of the phosphate by hydroxide leads to a pentavalent intermediate (**H** → **I**). Nucleophilic attack by free water molecule (Scheme 4, pathway b) can be excluded since the dinuclear complex **2** is more efficient in promoting hydrolysis of BNPP than the mononuclear complex **1** (Table 4, ratio $k_{obs}^{[2]}/k_{obs}^{[1]} > 20$); (*iii*) the P–O bond breaks to give *p*-nitrophenolate followed by the formation of the monoester complex (**I** → **J**); (*iv*) replacement of MNPP by water leads to the active species (**J** → **E**). This mechanism is in good agreement with the results described in the literature. It is generally believed that one of the metal ions serves to reversibly bind the phosphoester substrate whereas the second ion serves to activate a hydroxide ion at a physiological pH. The second metal ion also serves to increase the electrophilic susceptibility of the substrate and neutralizes the anionic substrate, thus moderating the electrostatic repulsion of the attacking nucleophile. The reaction then consists of an intramolecular nucleophilic attack of the adjacent hydroxide at the substrate (P–O bond cleavage).

Other pathways that should be considered are the formation of a bridged phosphate complex **3** (**K**). Due to an appropriate Cu–Cu distance, the formation of these complexes is favorable and stabilizes the phosphate ester. Indeed, complex **3** was prepared independently and under the reaction conditions (40 °C, 50 mM MES pH 6) it was not hydrolysed into *p*-nitrophenol and *p*-nitrophenyl phosphate even after 3 h. The easy formation and stability of such intermediates limits the performance of the catalyst. The copper(II) complex **2** behaves like ribonuclease which, in addition to a correct enzyme-substrate complex, also forms non-reactive enzyme-substrate complexes that do not form products but inhibit the reactions.

## Conclusion

We have demonstrated that the dinuclear complex **2** hydrolyzes the activated phosphodiester BNPP 20-fold faster than the mononuclear complex **1** and up to 600-fold faster than the un-promoted reaction at a slightly acidic pH (pH 6). The mechanism for the hydrolysis of BNPP appears to be classic according to a double Lewis acid activation. Our results are interesting for the design of more efficient copper catalysts for hydrolysis of phosphodiesters. What should be solved next is (*i*) the stabilization of the species **F** in preventing the formation of a double bridged (μ-alk-

 © 2006 Wiley-VCH Verlag GmbH & Co. KGaA, Weinheim 

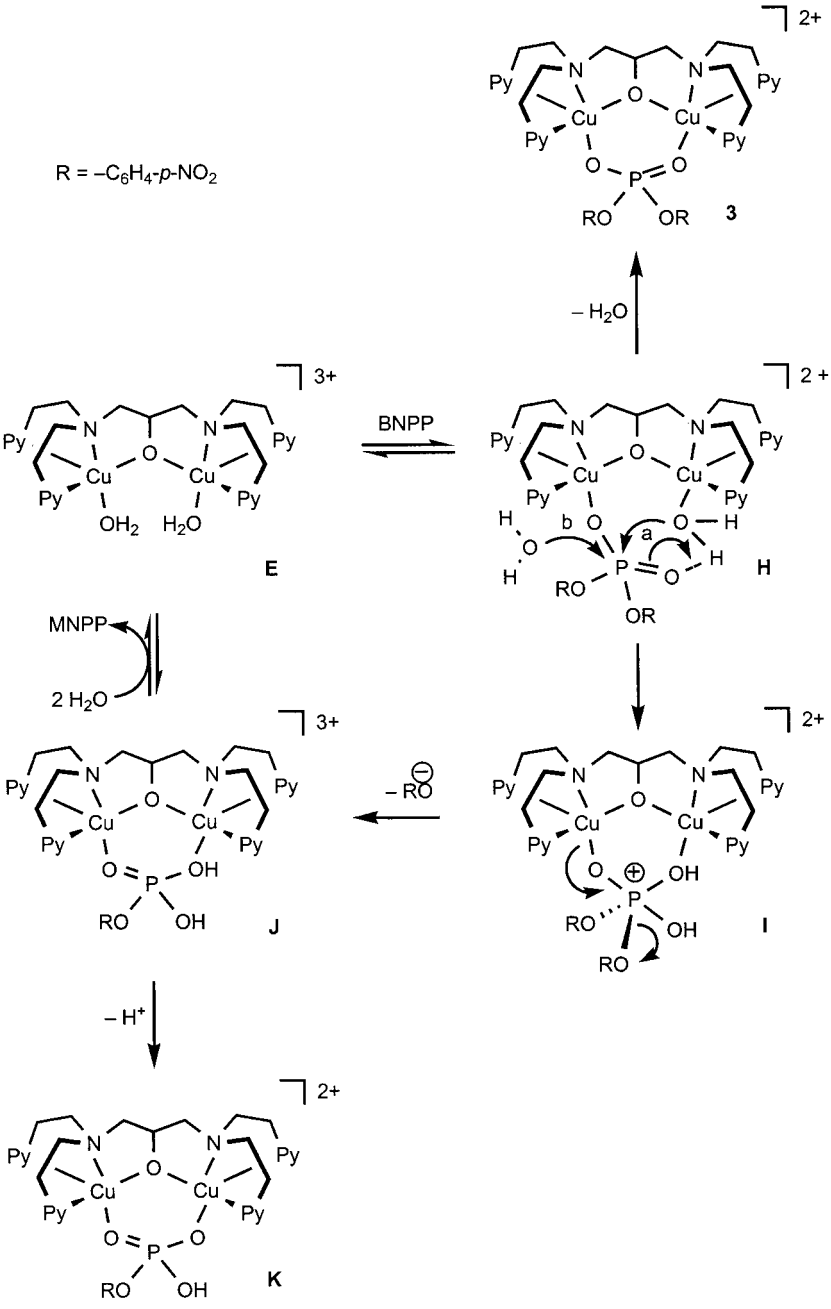


Scheme 4. Proposed mechanism for BNPP hydrolysis promoted by the copper complex **2**.

oxo)(μ-hydroxo)dicopper(II) complex **G** which seems not reactive in the hydrolysis of BNPP; (*ii*) to solve the problem of product (substrate) inhibition in preventing the formation of species such as **K** (**3**). Ligands, which could solve these problems, are currently under investigation in our laboratory.

## Experimental Section

**General Remarks:** NMR spectra were recorded at 25 °C in $CDCl_3$ using a Bruker AC-300 spectrometer. Chemical shifts are reported in ppm as $\delta$ values downfield from an internal standard of TMS. Infrared spectra were measured using neat films or KBr pellets using a Specord M80 (Carl Zeiss Jena) instrument. UV/Vis absorption spectra were recorded in $CH_2Cl_2$ using a Shimadzu UV-120A spectrometer. Elemental analyses were measured using a C, H, N, S Carlo Erba EA 1108 analyzer.

**Materials:** Solvents were freshly distilled under Ar (MeOH/Mg, $Et_2O$/Na-benzophenone ketyl, acetone/$CaH_2$ and $CH_2Cl_2/P_2O_5$). Commercial starting materials were used without purification, except for 2-vinylpyridine which was chromatographed using silica gel prior to use. Ligand **L²OH** was prepared by the Michael addition of 1,3-diamino-2-hydroxypropane to 2-vinylpyridine.[17] Complex $[Cu_2(\mathbf{L^2O})](CF_3SO_3)_3$ (**2**) was prepared by the reaction of $Cu(CF_3SO_3)_2$ with the ligand **L²OH** in $CH_2Cl_2$.[18]

***N*,*N*-Bis[2-(2-pyridyl)ethyl]ethanolamine (L¹OH):** 2-Ethanolamine (1.83 g, 1.81 mL, 30 mmol) and 2-vinylpyridine (25.2 g, 25.9 mL,

 © 2006 Wiley-VCH Verlag GmbH & Co. KGaA, Weinheim 

0.24 mol) were heated under reflux in MeOH (150 mL) with acetic acid (4.41 g, 4.2 mL, 73.5 mmol) for 5 days. Methanol was evaporated under vacuum. The resulting brown mixture was dissolved in $CH_2Cl_2$ (100 mL), washed with 15% aqueous NaOH (2 × 50 mL) and brine (2 × 50 mL). The organic layer was dried with $Na_2SO_4$. The solvent was removed by rotary evaporation to give an oil. This oil was dried under vacuum (ca. 0.01 Torr) at 40 °C to remove excess 2-vinylpyridine. The residue was chromatographed on silica gel ($CH_2Cl_2$/MeOH, 85:15) to yield the pure ligand **L¹OH**. Yield: 6.18 g, 76%. $^1$H NMR (200 MHz, $CDCl_3$): $\delta$ = 2.60 (t, $J$ = 5.1 Hz, 2 H), 2.70–2.90 (m, 8 H), 3.40 (t, $J$ = 5.1 Hz, 2 H), 6.85–7.0 (m, 4 H), 7.40 (td, $J$ = 5.8 Hz and $J$ = 1.7 Hz, 2 H), 8.40 (dd, $J$ = 3.1 Hz and $J$ = 1.0 Hz, 2 H) ppm. $^{13}$C NMR (50 MHz, $CDCl_3$): $\delta$ = 35.8 ($CH_2$), 53.9 ($CH_2$), 55.9 ($CH_2$), 59.4 ($CH_2$), 121.0 ($CH_{py}$), 123.3 ($CH_{py}$), 136.2 ($CH_{py}$), 148.9 ($CH_{py}$), 160.3 ($C_{py}$) ppm. IR (neat film): $\tilde{\nu}$ = 3300 ($\nu_{OH}$), 3010 ($\nu_{C-H}$ aromatic), 2900 ($\nu_{C-H}$ aliphatic), 1600, 1570, 1480, 1440 ($\nu_{C-C}$ pyridine ring), 1055 ($\nu_{C-O}$), 770, 756 ($\gamma_{C-H}$, $\gamma_{C-C}$ aromatic) cm$^{-1}$. UV/Vis (MeOH): $\lambda_{max}$/nm ($\varepsilon$/M$^{-1}$ cm$^{-1}$) = 230 (4200), 260 (7700).

**[Cu(L¹OH)](CF$_3$SO$_3$)$_2$ (1):** Ligand **L¹OH** (590 mg, 2 mmol) dissolved in $CH_2Cl_2$ (10 mL) was added dropwise to a suspension of $Cu(CF_3SO_3)_2$ (723.4 mg, 2 mmol) in $CH_2Cl_2$ (10 mL). After stirring at room temperature for 2 h, a deep blue oil was formed. This oil was allowed to settle and washed with $Et_2O$ until the formation of a solid. Drying under vacuum afforded the copper(II) complex **1**. Yield: 786 mg, 63%. IR (KBr): $\tilde{\nu}$ = 3450 ($\nu_{O-H}$), 3020 ($\nu_{C-H}$ aromatic), 2920 ($\nu_{as\ C-H}$ aliphatic), 1615, 1500, 1450, ($\nu_{C-C}$ pyridine), 770, 740 ($\gamma_{C-H}$ aromatic, $\gamma_{C-C}$), 1270, 1035, 640, 518 ($\nu_{triflate}$) cm$^{-1}$. UV/Vis (MeOH): $\lambda_{max}$/nm ($\varepsilon$/M$^{-1}$ cm$^{-1}$) = 215 (4130), 262 (9650), 381 (220), 690 (120). $C_{18}H_{21}N_3CuF_6O_7S_2$ (633.02): calcd. C 34.20, N 6.65, H 3.32, Cu 10.95; found C 34.85, N 6.42, H 3.24, Cu 10.25.

**[Cu$_2$(L²O)(BNPP)](CF$_3$SO$_3$)$_2$ (3):** To a solution of the complex **2** (54.2 mg, 0.05 mmol) in $H_2O$ (10 mL) was added BNPP (17 mg, 0.05 mmol) dissolved in MeOH (5 mL). After stirring at room temperature for 2 h, the solvent was allowed to evaporate in air. Deep blue crystals suitable for X-ray diffraction were grown within a few days. Yield: 44 mg, 69%. IR (KBr): $\tilde{\nu}$ = 3120, 3080 ($\nu_{C-H}$ aromatic), 2920 ($\nu_{as\ C-H}$ aliphatic), 2880 ($\nu_{s\ C-H}$ aliphatic), 1610, 1590, 1490 ($\nu_{C-C}$ pyridine), 1520 ($\nu_{as\ NO2}$), 1355 ($\nu_{s\ NO2}$), 1220 ($\nu_{as\ P-O-C}$ aromatic), 1150 ($\nu_{C-O}$), 770–750 ($\gamma_{C-H}$, $\gamma_{C-C}$ aromatic), 1265, 1034, 640, 518 ($\nu_{triflate}$) cm$^{-1}$. $C_{45}H_{45}N_8Cu_2O_{15}F_6S_2P$ (1273.08): calcd. C 42.40, N 8.80, H 3.53, Cu 9.98; found C 41.95, N 8.58, H 3.27, Cu 10.42.

**pH Potentiometric Titration:** The pH potentiometric titrations were conducted at 40.0 ± 0.1 °C at an ionic strength of 0.2 M KCl. Calibration of the electrode and pH meter was performed using a 0.05 M KH/phthalate buffer and a p$K_w$ of 13.294 at 40 °C. Solution of ligands **L¹OH** and **L²OH** (5 mM) in 0.2 M KCl, acidified with HCl (0.2008 M), were titrated in an $N_2$ atmosphere with KOH solution (0.1941 M) at 40 °C in the presence and absence of $Cu_2(CF_3SO_3)_2$. The initial concentration of $Cu_2(CF_3SO_3)_2$ was varied between 4–10 mM. The titrations of the free ligands were run between pH 2 and 11.5, with added metal solution between pH 2 and 8 for the ligand **L¹OH** and between pH 2 and 11 for the ligand **L²OH**. To calculate the deprotonation constants and $Cu^{II}$ association constants from the titration data a multiparameter curve fitting program based on SUPERQUAD[25] and PSEQUAD[26] was used.

**Kinetics:** Hydrolysis of BNPP was monitored by following the visible absorption change at 400 nm ($\varepsilon$ = 18500 M$^{-1}$ cm$^{-1}$) due to the release of *p*-nitrophenolate anion (PNPate). Conversion from absorbance to concentration was performed by using the Lambert–Beer law [Equation (1)]. In order to take into account the concentration change of the PNPate as a function of pH, the $[PNPate]_{tot}$ was calculated following equations (2) and (3), where the p$K_a$ of PNP (7.15) was determined using the above condition. The activity of the complex was determined by the initial rate method.

$$[PNPate]_{meas} = O.\,D./18500 \quad (1)$$

$$pH = 7.15 + \log([PNPate]_{meas}/[PNP]) \quad (2)$$

$$[PNPate]_{tot} = [PNPate]_{meas} + [PNP] \quad (3)$$

In a typical kinetic experiment, freshly prepared phosphate ester stock solution in water (12 μL, 50 mM) was added to a solution of copper(II) complex (**1**: 75 μL, 20 mM; **2** 60 μL, 25 mM) at 40 °C. The copper complex solutions were buffered with MES (pH 5.5–6.5), HEPES (pH 7–8) and the ionic strength was maintained with 0.1 M KCl. The final volume was 3 mL. The pseudo-first-order rate constants for un-promoted reactions ($k_{uncat}$, s$^{-1}$) were measured by following the increase in absorbance from a 1.92 mM BNPP solution.

**X-ray Crystallographic Studies:** All the measurements were performed using a Bruker–Nonius KappaCCD diffractometer.[27] The cell determinations and data integrations were performed using the software Denzo-Scalepak.[28] The structure solutions were obtained using Sir92[29] and the refinements were carried out using SHELXL-97,[30] except for complex **3**, which was refined using the software MaXus (Table 5).[31]

CCDC-283857 (for **1**), -283855 (for **2**) and -283856 (for **1**) contain the supplementary crystallographic data for this paper. These data can be obtained free of charge from The Cambridge Crystallographic Data Centre via www.ccdc.cam.ac.uk/data_request/cif.

## Acknowledgments

This research was supported by the CNRS, the Ministère de la Recherche et de la Technologie (Balaton program), the Hungarian Research Fund (OTKA # 43414), and the Ministère des Affaires Etrangères (grant for K. S.). The authors are grateful to Dr. A. Heumann for a number of enlightening discussions.

[1] E. L. Hegg, J. N. Burstyn, *Coord. Chem. Rev.* **1998**, *173*, 133–165.
[2] A. Sreedhara, J. A. Cowan, *J. Biol. Inorg. Chem.* **2001**, *6*, 337–347.
[3] D. E. Wilcox, *Chem. Rev.* **1996**, *96*, 2435–2458.
[4] E. E. Kim, H. W. Wyckoff, *J. Mol. Biol.* **1991**, *218*, 449–464.
[5] T. Klabunde, N. Strater, R. Frohlich, H. Witzel, B. Krebs, *J. Mol. Biol.* **1996**, *259*, 737–748.
[6] R. Hettich, H.-J. Schneider, *J. Am. Chem. Soc.* **1997**, *119*, 5638–5647.
[7] N. H. Williams, W. Cheung, J. Chin, *J. Am. Chem. Soc.* **1998**, *120*, 8079–8087.
[8] B. K. Takasaki, J. Chin, *J. Am. Chem. Soc.* **1994**, *116*, 1121–1122.
[9] M. E. Branum, A. K. Tipton, S. Zhu, L. Que Jr, *J. Am. Chem. Soc.* **2001**, *123*, 1898–1904.
[10] T. Koike, E. Kimura, in: *Advances in Inorganic Chemistry* (Ed.: A. G. Sykes), Academic Press, San Diego, CA, **1996**, vol. 44, pp. 229–261.
[11] T. Koike, M. Inoue, E. Kimura, M. Shiro, *J. Am. Chem. Soc.* **1996**, *118*, 3091–3099.

 © 2006 Wiley-VCH Verlag GmbH & Co. KGaA, Weinheim 

[12] F. Verge, C. Lebrun, M. Fontecave, S. Ménage, *Inorg. Chem.* **2003**, *42*, 499–507.
[13] A. Sreedhara, J. D. Freed, J. A. Cowan, *J. Am. Chem. Soc.* **2000**, *122*, 8814–8824.
[14] T. Gajda, Y. Düpre, I. Török, J. Harmer, A. Schweiger, J. Sander, D. Kuppert, K. Hegetschweiler, *Inorg. Chem.* **2001**, *40*, 4918–4927.
[15] K. M. Deck, T. A. Tseng, J. N. Burstyn, *Inorg. Chem.* **2002**, *41*, 669–677.
[16] F. H. Fry, A. J. Fischmann, M. J. Belousoff, L. Spiccia, J. Brügger, *Inorg. Chem.* **2005**, *44*, 941–950.
[17] K. D. Karlin, Z. Tyeklár, A. Farooq, M. S. Haka, P. Ghosh, R. W. Cruse, Y. Gultneh, J. C. Hayes, P. J. Toscano, J. Zubieta, *Inorg. Chem.* **1992**, *31*, 1436–1451.
[18] K. Selmeczi, M. Réglier, M. Giorgi, G. Speier, *Coord. Chem. Rev.* **2003**, *245*, 191–201.
[19] A. W. Addison, H. M. J. Hendriks, J. Reedijk, L. K. Thomson, *Inorg. Chem.* **1981**, *20*, 103–110.
[20] K. D. Karlin, I. Sanyal, A. Farooq, R. R. Jacobson, S. N. Shaikh, J. Zubieta, *Inorg. Chim. Acta* **1990**, *174*, 13–15.
[21] K. D. Karlin, J. Shi, J. C. Hayes, J. W. McKown, J. P. Hutchinson, J. Zubieta, *Inorg. Chim. Acta* **1984**, *91*, L3–L7.
[22] K. D. Karlin, A. D. Zuberbühler, in: *Bioinorganic Catalysis* (Eds.: J. Reedijk, E. Bouwman), 2nd ed., Marcel Dekker, New York, **1999**, pp. 469–534.
[23] J. J. Maloney, M. Glogowski, D. F. Rohrbach, F. L. Urbach, *Inorg. Chim. Acta* **1987**, *127*, L33–L35.
[24] S. Torelli, C. Belle, I. Gautier-Luneau, J. L. Pierre, E. Saint-Aman, J.-M. Latour, L. Le Pape, D. Luneau, *Inorg. Chem.* **2000**, *39*, 3526–3536.
[25] L. Zékány, I. Nagypál, in: *Computational Methods for the Determination of Stability Constants* (Ed.: D. L. Leggett), Plenum Press, New York, **1985**, pp. 291–353.
[26] P. Gans, A. Sabatini, A. Vacca, *J. Chem. Soc., Dalton Trans.* **1985**, 1195–1200.
[27] Bruker-Nonius, Kappa CCD Reference Manual, Nonius B. V., P. O. Box 811, 2600 Av, Delft, The Netherlands, **1998**.
[28] Z. Otwinowski, W. Minor, in: *Methods in Enzymology* (Eds.: C. W. Carter Jr, R. M. Sweet), Academic Press, vol. 276, pp. 307–326, **1997**.
[29] A. Altomare, G. Cascarano, C. Giacovazzo, A. Guagliardi, M. C. Burla, G. Polidori, M. Camalli, *J. Appl. Crystallogr.* **1994**, *27*, 435.
[30] G. M. Sheldrick, *SHELXL-97*, University of Göttingen, **1997**.
[31] S. Mackay, C. J. Gilmore, C. Edwards, M. Tremayne, N. Stewart, K. Shankland, *MaXus: a computer program for the solution and refinement of crystal structures from diffraction data*; University of Glasgow, Scotland, UK, Nonius BV, Delft, The Netherlands and MacScience Co. Ltd., Yokohama, Japan, **1998**.

Received: July 5, 2005
Published Online: January 9, 2006

 © 2006 Wiley-VCH Verlag GmbH & Co. KGaA, Weinheim 

DOI: 10.1002/ejic.200500657

# Chiral, Enantiopure Aluminum(III) and Titanium(IV) Azatranes

Massimiliano Forcato,[a] Fredrik Lake,[b] Myriam Mba Blazquez,[a] Patrick Renner,[c] Marco Crisma,[d] Lutz H. Gade,*[c] Giulia Licini,*[a] and Christina Moberg*[b]

**Keywords:** Aluminum / Chirality / N ligands / Titanium / Tripodal ligands

$Al^{III}$ and $Ti^{IV}$ complexes of $C_3$-symmetric tetradentate trisamidoamine ligands with trigonal bipyramidal coordination geometry, containing chlorine or dialkylamido groups, or with a free coordination site in the apical position, have been synthesised by salt metathesis and amine elimination. Products with threefold symmetry were generally obtained for tetravalent titanium, whereas for the aluminium complexes either asymmetric structures with two of the three podand arms taking part in coordination to the metal or symmetric arrangements possessing the full threefold symmetry were formed depending on the steric properties of the ligands.

(© Wiley-VCH Verlag GmbH & Co. KGaA, 69451 Weinheim, Germany, 2006)

## Introduction

The preparation of chiral ligands capable of efficient chirality transfer is crucial for successful asymmetric metal catalysis.[1,2] Several factors need to be considered in the design of new ligands, including steric and electronic effects, kinetic properties, hapticity and bite angles.[3,4] Another factor that occasionally plays an important role is symmetry. $C_2$-Symmetric ligands have, in many situations, proven to offer advantageous properties over those lacking symmetry, and such ligands have been extensively employed in asymmetric catalysis and various processes involving chiral recognition.[5] $C_3$-Symmetric ligands, however, have been considerably less investigated,[6] although extensive studies have been performed on achiral ligands possessing threefold rotational axes. Particularly detailed studies have been performed by the groups of Verkade[7,8] and Schrock[9] on complexes with derivatives of tris(2-aminoethyl)amine (TREN) most of them bearing bulky substituents such as trialkylsilyl or pentafluorophenyl groups on nitrogen. Metal complexes with TREN or its derivatives have also been used in several applications. Some recent examples include nitrogen activation by $Mo^{IV}$ complexes with *N*,*N*′*N*′′-aryl-substituted TREN ligands,[10] alkene epoxidation by $Mn^{III}$ and $Fe^{III}$ complexes,[11] phosphoester hydrolysis[12] and $CO_2$ fixation[13] by $Zn^{II}$ complexes, and thiosulfate oxidation by $Cu^{II}$ complexes.[14] Furthermore, a $Cu^{II}$ complex has been shown to react reversibly with oxygen,[15] and $Cu^{II}$ and $Ni^{II}$ complexes to bind nucleobases.[16]

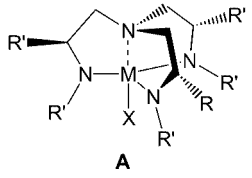


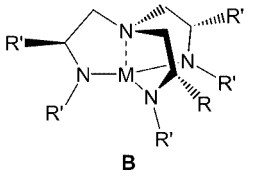


Triamidoamines usually serve as tetradentate ligands, forming rigid trigonal bipyramidal (**A**) or, in the absence of an apical ligand, trigonal monopyramidal (**B**) complexes with a variety of transition metals and main-group elements.[7,9,17] The M–$N_{ap}$ distances vary significantly, occasionally resulting in complexes lacking a transannular bond, thus leading to tridentate coordination.[7–17] Other coordination modes are possible, however, as shown by the recently determined structures of $[Ni(tren)(abpt)](NO_3)_2$ [abpt = 4-amino-3,5-bis(pyrid-2-yl)-1,2,4-triazole],[18] $[Ni(tren)Sb_2S_4]$,[19] $[Co(tren)(amino\ acidato\text{-}N,O)]X_2$,[20] and $[Co(tren)(N_3)_2]Br$,[21] which exhibit octahedral coordination.

Several methods have been employed for metal complex formation of TREN derivatives. Usually the ligand is treated with a base such as butyllithium prior to reaction with a transition metal salt,[22] although ligands with acidic protons on nitrogen may react directly with the metal com-

[a] Università degli Studi di Padova, Dipartimento di Scienze Chimiche,
Via Marzolo 1, 35131 Padova, Italy
Fax: +39-049-827-5239
E-mail: giulia.licini@unipd.it
[b] Department of Chemistry, Organic Chemistry, Royal Institute of Technology,
10044 Stockholm, Sweden
Fax: +46-8-791-2333
E-mail: kimo@kth.se
[c] Anorganisch-Chemisches Institut, Ruprecht-Karls-Universität Heidelberg,
Im Neuenheimer Feld 270, 69120 Heidelberg, Germany
Fax: +49-6221-545-609
E-mail: lutz.gade@uni-hd.de
[d] Istituto di Chimica Biomolecolare, CNR,
Via Marzolo 1, 35131 Padova, Italy
Fax: +39-049-827-5239
E-mail: marco.crisma@unipd.it
Supporting information for this article is available on the WWW under http://www.eurjic.org or from the author.

 InterScience © 2006 Wiley-VCH Verlag GmbH & Co. KGaA, Weinheim 

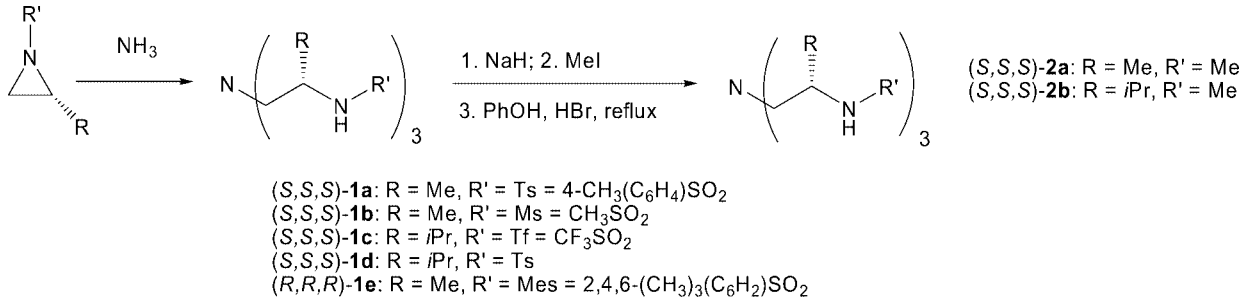


Scheme 1. Synthesis of the $C_3$-chiral TREN ligands **1a**–**1e** and **2a**,**b**.

pound.[23] Metal halides and metal amide complexes are the most commonly used metal sources.

A few chiral tetradentate TREN analogues with the chirality residing in the ligand backbone[24–27] or in substituents on the equatorial nitrogen atoms,[28] as well as tridentate ligands lacking an apical nitrogen,[29] have been prepared. Upon metal complex formation, a chiral pocket with a $C_3$-symmetric environment is created in the apical position, a favourable situation for asymmetric catalysis.[30] Some of the chiral ligands, notably those by Gade, have indeed been assessed in asymmetric reactions and were found to induce moderate to high enantioselectivity in stoichiometric[30a] and catalytic[30c] alkylations of aryl aldehydes. Proazaphosphatranes have been shown to serve as excellent catalysts in a vast number of base-mediated[31] and metal-catalysed[32] processes, but their chiral analogues[26,28,33] have not yet been applied in catalysis. Titanatranes have been employed in asymmetric ring-opening of *meso* epoxides and enantioselective oxidation of sulfides,[34] but no reports on the use of azatitanatranes, first described in 1991,[35] have appeared.

Since we have access to a versatile method for the preparation of chiral TREN derivatives,[24] we initiated a study of the formation of amido metal complexes[36,37] for potential use in asymmetric catalysis.

## Results and Discussion

### Ligand Preparation

Ligands (*S*,*S*,*S*)-**1a**–**c**[24] and -**1d**[38] were prepared as described previously, starting from the appropriate enantiopure aziridine and ammonia. Ligand (*R*,*R*,*R*)-**1e** was prepared analogously in 60% overall yield. Compounds (*S*,*S*,*S*)-**2a** and (*S*,*S*,*S*)-**2b** were obtained from (*S*,*S*,*S*)-**1a** and (*S*,*S*,*S*)-**1d**, respectively, by N-methylation followed by deprotection of the tosyl groups with HBr[24b] (Scheme 1).

Upon crystallisation by vapour-diffusion from chloroform/hexane, ligand (*R*,*R*,*R*)-**1e** afforded suitable crystals for X-ray analysis (Figure 1). Interestingly, the molecular structure of (*R*,*R*,*R*)-**1e** deviates only slightly from threefold symmetry. Two hydrogen bonds between NH functions and sulfonylic oxygen atoms (Figure 1, dashed lines) hold the ligand structure in a bent conformation which is similar to that observed upon coordination to metal ions (azametallatranes **A** and **B**). The TREN structure is approximately $C_3$-symmetric, with the angles centred around the bridgehead nitrogen atom being almost identical (Figure 1). The TREN arm labelled as **III** in Figure 1 participates in two hydrogen bonds involving carboxamide proton H3, which interacts with the sulfonyl oxygen atom in arm **I** (O12), whereas its sulfonyl unit forms a hydrogen bond with H2(N2). Both hydrogen bonds have similar metric parameters (N–H···O = 0.86 Å, N–H–O = 170°–175°).

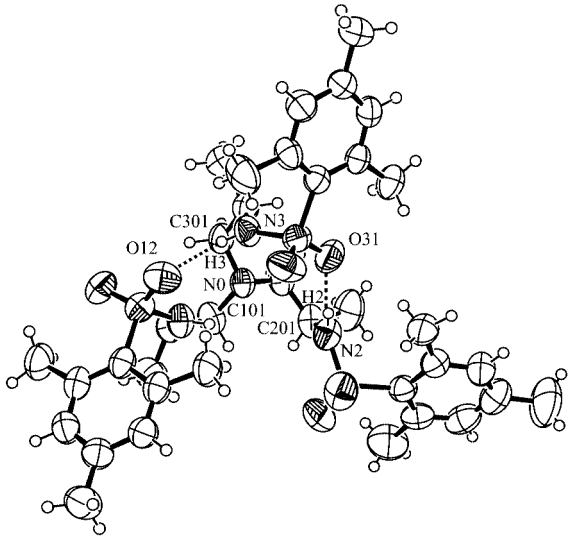


Selected bond lengths (Å) and angles (deg) for crystal structure of **1e**

| H Bonds, Å | | | N–H···O Angles (deg) | N0-Centered Angles (deg) | |
|---|---|---|---|---|---|
| | ***N-H*** | ***H···O*** | | C201-N0-C301 | 110 |
| N2-H2···O31 | 0.86 | 2.11 | 175 | C201-N0-C101 | 111 |
| N3-H3···O12 | 0.86 | 2.19 | 170 | C301-N0-C101 | 114 |

Figure 1. ORTEP view of the molecular structure of (*R*,*R*,*R*)-**1e** (30% thermal ellipsoids). Dashed lines indicate hydrogen bonds. The hydrogen atoms were included at calculated positions with fixed thermal parameters.

The ligands **1a**–**e** bearing electron-withdrawing substituents on the nitrogen atoms possess relatively acidic NH protons and were found to react directly with metal amides in a transamination reaction. On the other hand, coordination of the *N*-alkylated TREN derivatives (*S*,*S*,*S*)-**2a** and (*S*,*S*,*S*)-**2b** required initial metallation with *n*BuLi and subsequent reaction with $M^{(n)}Cl_n{\cdot}(THF)_m$ in a salt metathesis step.

 © 2006 Wiley-VCH Verlag GmbH & Co. KGaA, Weinheim 

### Metal Complex Formation: Aluminum(III) Complexes

Complex formation between ligands (*S*,*S*,*S*)-**1a**,**c** and (*R*,*R*,*R*)-**1e** and suitable $Al^{III}$ precursors was initially studied whilst monitoring the course of the reactions by $^1H$ NMR spectroscopy. Addition of one equivalent of $Al(OiPr)_3$ did not afford any new $Al^{III}$ complex, even upon prolonged heating at 100 °C. However, the addition of one equivalent of $AlMe_3$ to (*S*,*S*,*S*)-**1a** (Scheme 2) was accompanied by instantaneous gas evolution.

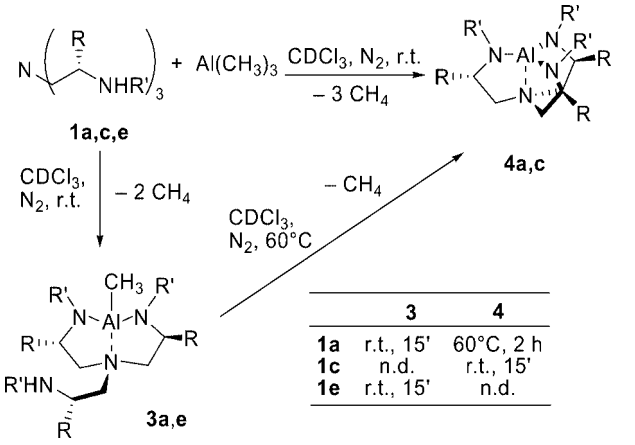


Scheme 2. Synthesis of $Al^{III}$ complexes of ligands **1a**, **1c** and **1e**.

The $^1H$ NMR spectrum recorded after 15 minutes at room temperature is consistent with the quantitative formation of a new metal complex containing three diastereotopic ligand arms and thus being devoid of threefold symmetry (Figure 2, spectrum b). The presence of one N*H* (doublet at $\delta$ = 4.70 ppm) and one Al–C$H_3$ signal (singlet at $\delta$ = –0.39 ppm) suggested the new species to be **3a** (R = Me, R′ = Ts), with a structure similar to a complex obtained from a dipodal analogue of **1** and trimethylaluminium.[39] This assumption was corroborated by the modifications observed upon heating at 60 °C. Further evolution of gas was detected, followed by the slow formation (2 h) of the symmetrical species **4a** (Scheme 2). The disappearance of the N*H* signal and the accompanying downfield shift of almost all the signals in the spectrum of **4a** with respect to those of the uncomplexed ligand (Figure 2, spectrum c) provided evidence that the coordination of (*S*,*S*,*S*)-**1a** to aluminium had occurred. A particularly evident deshielding effect ($\Delta\delta \approx 0.5$ ppm) was observed for one of the diastereotopic C$H_2$ resonances (doublet of doublets, from $\delta$ = 2.13 ppm in **1a** to $\delta$ = 2.60 ppm in **4a**).

The same experiment was repeated with (*R*,*R*,*R*)-**1e**. With this sterically more demanding ligand no symmetrical complex was obtained, and only the formation of **3e** (R = Me, R′ = Mes) was observed even after heating at 60 °C for 48 h (Scheme 1). In contrast, reaction of trimethylaluminium with the more reactive triflate derivative (*S*,*S*,*S*)-**1c** afforded **4c** (R = *i*Pr, R′ = Tf) directly without detection of any intermediate complex of type **3** (Scheme 2). The monomeric nature of **4a** and **4e** is supported by the single set of resonances in their NMR spectra ($^1H$, $^{13}C$ and $^{19}F$ in the case of complex **4e**), which reflect the $C_3$ symmetry of the complex. Verkade and co-workers provided analogous symmetry considerations derived from the NMR spectral pattern to demonstrate the monomeric nature of their *N*-trimethylsilylazaalumatrane.[40]

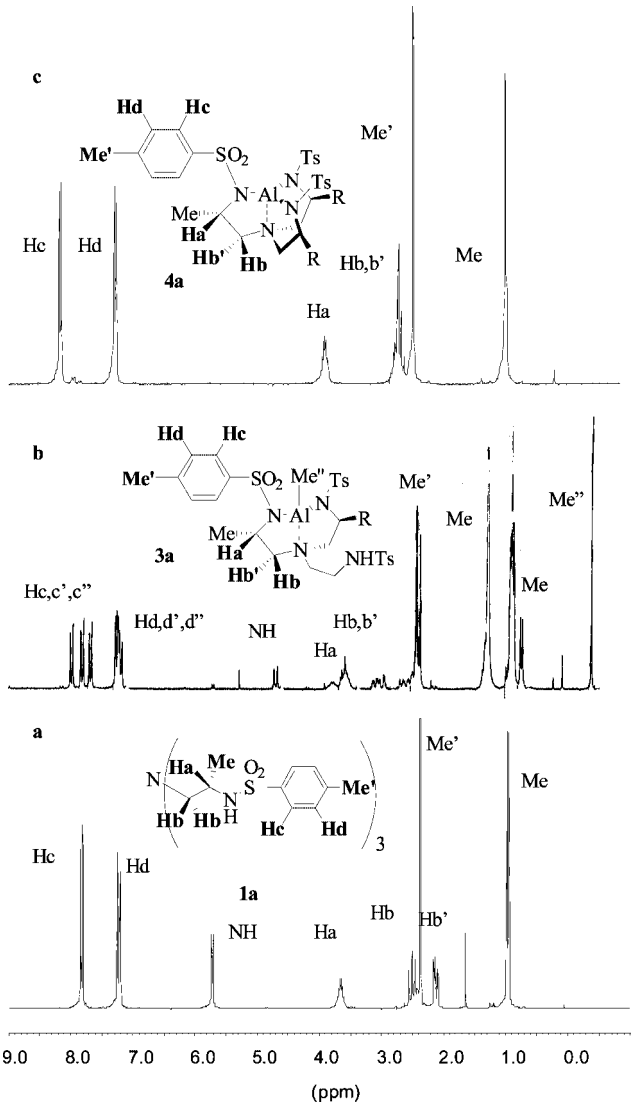


Figure 2. Reaction of $AlMe_3$ (0.020 M) with (*S*,*S*,*S*)-**1a** (0.020 M) in $CDCl_3$ under nitrogen monitored by $^1H$ NMR spectroscopy (250 MHz): a) (*S*,*S*,*S*)-**1a**; b) addition of $AlMe_3$ (1 equiv.), room temp., 15 min; c) after heating at 60 °C, 2 h: **4a**.

A synthetic procedure that allowed the preparation of **4a** on a one-gram scale was achieved by carrying out the reaction of Scheme 1 under slightly modified conditions. Complex **4a** was obtained in 99% yield by adding trimethylaluminium to a saturated solution of (*S*,*S*,*S*)-**1a** in dry THF and refluxing the reaction mixture under nitrogen until a white precipitate separated from the colourless solution. Isolation of pure **4a** was possible by washing with dry pentane and centrifugation. Despite its tendency to afford dendritic precipitates, layering of a concentrated solution of **4a** in dichloromethane with a 1:1 mixture of dichloromethane/diethyl ether and with pure diethyl ether allowed the growth

 © 2006 Wiley-VCH Verlag GmbH & Co. KGaA, Weinheim 

of colourless single crystals suitable for X-ray diffraction analysis.

The crystal structure of **4a** is depicted in Figure 3 along with the principal bond lengths and angles.

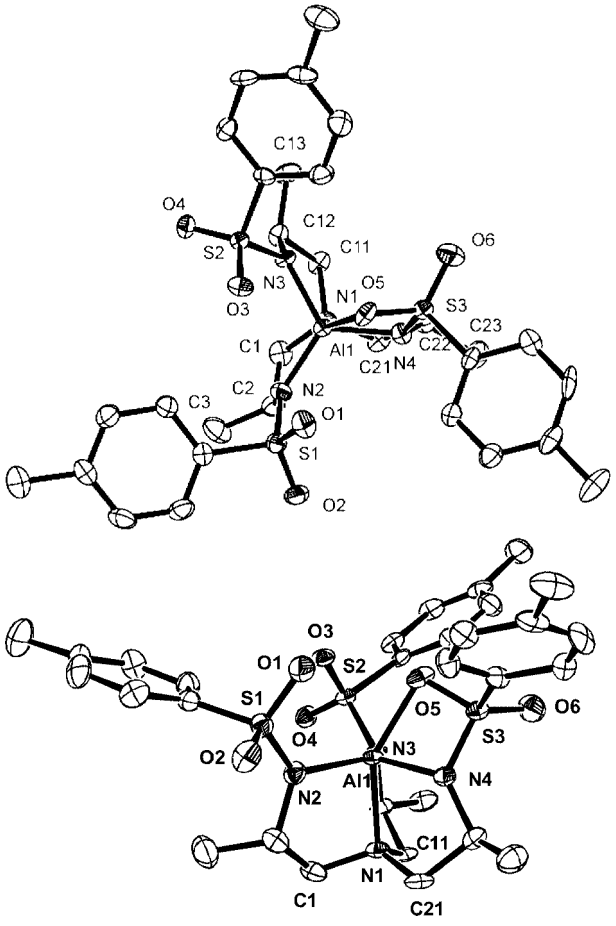


Figure 3. ORTEP views of (*S*,*S*,*S*)-**4a** (50% probability level thermal ellipsoids). Principal bond lengths [Å] and angles [°]: Al–N(1) 2.042(4), Al–N(2) 1.861(5), Al–N(3) 1.872(4), Al–N(4) 1.897(4), Al–O(5) 2.054(4), S(1)–O(1) 1.445(4), S(1)–O(2) 1.433(4), S(2)–O(4) 1.442(3), S(2)–O(3) 1.450(4), S(3)–O(5) 1.495(4), S(3)–O(6) 1.423(4); N(2)–Al–N(3) 117.5(2), N(2)–Al–N(4) 116.8(2), N(3)–Al–N(4) 122.2(2), C(1)–N(1)–C(11) 112.0(4), C(1)–N(1)–C(21) 113.3(4), C(11)–N(1)–C(21) 110.1(4), N(2)–Al–N(1) 86.4(2), N(3)–Al–N(1) 84.8(2), N(4)–Al–N(1) 80.4(2), N(1)–Al–O(5) 120.7(2), Al–O(5)–S(3) 93.9(2). All hydrogen atoms have been omitted for clarity.

Azaalumatrane **4a** crystallises in the space group $P2_12_12_1$ with a dichloromethane molecule present in the unit cell. The complex is monomeric and approximately $C_3$-symmetric, as is evident from the observed $N_{eq}$–Al–$N_{eq}$ angles (116.8–122.2°), which is in accordance with the structural features derived from the NMR spectroscopic data recorded in solution. The five-coordinate aluminium complex possesses a highly distorted trigonal-bipyramidal coordination geometry, the metal centre being slightly displaced above the equatorial plane [N(1)–Al–$N_{eq}$ = 80.4–86.4°]. The equatorial N–Al bond lengths (1.861–1.897 Å) are comparable to those reported for analogous azaalumatranes[17,41,42] and to nitrogen–aluminium distances in five-coordinate $Al^{III}$/amido complexes (1.897–1.976 Å).[43] The transannular interaction in **4a** [N(1)–Al = 2.042(4) Å] is stronger than in the *N*-methyl-substituted azaalumatrane **4f** [R = H and R′ = Me; 2.124(6) Å], which is a dimer bearing a trigonal-bipyramidal geometry around the five-coordinate aluminium.[43] On the other hand a considerably stronger transannular bond [1.983(6) Å] is found in the *N*-trimethylsilyl-substituted analogue **4g** (R = H and R′ = $SiMe_3$), in which the bulky $SiMe_3$ groups prevent dimerisation and leave a coordinatively unsaturated aluminium.[42] Interestingly, the transannular interaction observed in **4a** lies within the range found in the analogous $Al^{III}$/trialkanolamine complexes.[44] Distortion of the bipyramidal geometry is due to the coordination of one of the sulfonyl oxygen atoms belonging to a tosyl group to aluminium, the angle along the axial direction deviating considerably from 180° [N(1)–Al–O(5) = 120.7°]. This Al–O(5) interaction results in a bond length [2.054(4) Å] which is comparable to that of the transannular bond [2.042(4) Å]. As a consequence, both the sulfur–oxygen covalent bond [S(3)–O(5) = 1.495(4) Å, compared to an average S–O distance of 1.439 Å] and the $N_{eq}$–Al bond [N(4)–Al = 1.897(4) Å compared 1.861–1.872 Å for the remaining two Al–N bonds] are elongated.

As mentioned above, achiral azaalumatranes have been prepared and studied previously by Verkade.[41–43] For the monomeric complexes an interconversion between the λ and δ chelate ring conformations was observed, which was rapid on the NMR timescale down to –95 °C.[42] On the other hand, interconversion between the spiral diastereomers of **4a** was not observed at room temperature, which implies that the presence of the ring-methyl substituents of ligand **1a** increases the interconversion barrier and prevents such a conformational twist. Moreover, it is evident from the molecular structure of **4a** (Figure 3, horizontal view) that these methyl substituents play a crucial structural role and appear to determine the orientation of the N–$SO_2$–Ar moieties. This implies that the chirality of the $C_3$ cavity around the metal centre (the "chiral pocket") is determined by the orientation of the methyl groups and thus by the absolute configuration of the ligand.

The use of azaalumatranes as precursors for the synthesis of a variety of transition metal or main group element azatranes by transmetallation has been reported.[43] However, the potential of this type of complex to serve as a Lewis acid, and thus to increase the coordination number by apical coordination, is as yet essentially unexplored, although Al complexes of dipodal analogues have been employed as chiral Lewis acid catalysts.[45] We note that achiral Al complexes have in fact been used as Lewis acid catalysts in the ring-opening polymerisation of heterocycles,[39] and chiral analogues may be of interest for controlling the tacticity of the polymers.

### Metal Complex Formation: Titanium(IV) Complexes

The reaction of ligand **1a** with [Ti($NEt_2$)$_4$] in a 1:1 stoichiometry was initially performed in $CDCl_3$ in an NMR

 © 2006 Wiley-VCH Verlag GmbH & Co. KGaA, Weinheim 

tube and monitored by $^1$H NMR spectroscopy (Scheme 3). Whereas a poorly resolved spectrum was recorded after 15 min, which indicated the presence of fluxional species of low symmetry in solution, the spectral patterns simplified and sharpened up over a period of three days at ambient temperature. The highly resolved spectrum recorded at that stage is consistent with the formation of a monomeric complex with threefold symmetry (**5a**) possessing one residual diethylamido group. Complex formation was further supported by the liberation of diethylamine and the observation that the methylene proton resonances of the $Et_2N$ ligand give an AB system ($\delta$ = 4.36 and 4.51 ppm respectively). The reaction was accompanied by a change of colour from yellow to reddish-brown. An analogous complex was formed from ligand **1e** and [Ti(NEt$_2$)$_4$] within six days at room temperature or within six hours upon heating at 60 °C; **1c** exhibits higher reactivity, undergoing instantaneous complex formation (Scheme 3).

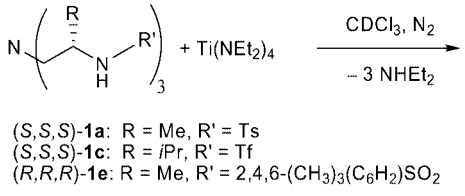


(*S*,*S*,*S*)-**1a**: R = Me, R' = Ts
(*S*,*S*,*S*)-**1c**: R = *i*Pr, R' = Tf
(*R*,*R*,*R*)-**1e**: R = Me, R' = 2,4,6-(CH$_3$)$_3$(C$_6$H$_2$)SO$_2$

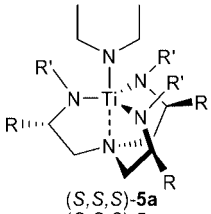

| 5 | |
|---|---|
| **1a** | r.t., 72 h |
| **1c** | r.t., 15 min |
| **1e** | 60°C, 6 h |

(*S*,*S*,*S*)-**5a**
(*S*,*S*,*S*)-**5c**
(*R*,*R*,*R*)-**5e**

Scheme 3. Synthesis of Ti$^{VI}$ complexes of ligands **1a**, **1c** and **1e**.

The $^1$H NMR spectra of azatitanatranes **5a**, **5c** and **5e** are all consistent with the formation of highly symmetric monomeric species. In all cases the resonances of the triamidoamine ligands have undergone significant shifts with respect to the uncomplexed ligand (see Table 1).

Table 1. Selected $^1$H NMR spectroscopic data [ppm] for ligands **1a**, **1c** and **1e** and complexes **5a**, **5c** and **5e**.

| | NC*H*$_2$CHR–N | | Ti–N(C*H*$_2$Me)$_2$ | |
|---|---|---|---|---|
| Ti(NEt$_2$)$_4$ | – | – | 3.46 | 3.46 |
| (*S*,*S*,*S*)-**1a** | 2.13 | 2.50 | – | – |
| (*S*,*S*,*S*)-**5a** | 2.52 | 3.05 | 4.36 | 4.50 |
| (*S*,*S*,*S*)-**1c** | 2.24 | 2.90 | – | – |
| (*S*,*S*,*S*)-**5c** | 2.62 | 3.30 | 4.24 | 4.80 |
| (*R*,*R*,*R*)-**1e** | 2.17 | 2.83 | – | – |
| (*R*,*R*,*R*)-**5e** | 3.47 | 4.63 | 3.48 | 3.92 |

A different behaviour is observed for complex **5e** and complexes **5a** and **5c**. Thus, in complex **5e** a remarkable deshielding (ca. 1 ppm) of the signals of the methylene protons of the TREN moiety is observed (from $\delta$ = 2.52 and 3.05 ppm in **5a** and $\delta$ = 2.63 and 3.30 ppm in **5c** to $\delta$ = 3.50 and 4.63 ppm in **5e**) due to a shielding of the protons of the apical diethylamido group ($\delta$ = 3.48 and 3.92 ppm vs. $\delta$ = 4.36 and 4.50 ppm for **5a** and $\delta$ = 4.24 and 4.80 ppm for **5c**). The observed difference in $\delta$ values very likely originates from a more open structure of complex **6e** compared to the other two, which is caused by the more hindered nature of the mesitylene groups. The bulkier substituents on the external part of the ligand remove the sulfonyl moieties from the inner part of the cavity, thus moving the aromatic rings closer to the methylene groups of the TREN backbone. This fact diminishes the magnetic anisotropy effect of the S=O groups on the apical ligand and increases the effect of the peripheral aromatic ring on the protons of the TREN backbone. $^1$H NOESY experiments on complexes **5a** and **5c** were in agreement with such hypothesis. In fact, a significant difference in the distances between the aromatic *meta* protons and the hydrogen atoms in the methyl group of the ligand backbone was found (3.00 and 2.25 Å for **5a** and **5e**, respectively).

A synthetic protocol allowing the preparation of Ti$^{IV}$ complex **5a** on a gram scale was worked out as well. Azatitanatrane **5a** was prepared in 95% yield and high NMR purity by carrying out the reaction in a 3:1 pentane/THF mixture at room temperature from a concentrated solution of the reactants (0.2 M); it was isolated as a yellowish solid by filtration.

Finally, the Ti complexes of **2a** and **2b** (**6a** and **6b**) were prepared as previously reported for the achiral analogue [{(MeNCH$_2$CH$_2$)$_3$N}TiCl][46] by salt metathesis of the lithium salt of the triamidoamine ligands and [TiCl$_4$(THF)$_2$] as metal source (Scheme 4). The $^1$H and $^{13}$C NMR spectra are consistent with the assumed threefold symmetry of the complexes. Unfortunately, attempts to obtain single crystals for X-ray structure determination failed.

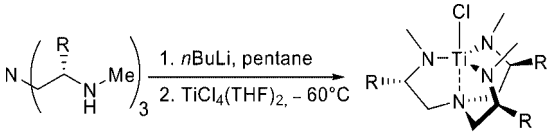


(*S*,*S*,*S*)-**2a**: R = Me
(*S*,*S*,*S*)-**2b**: R = *i*Pr

(*S*,*S*,*S*)-**6a**: R = Me
(*S*,*S*,*S*)-**6b**: R = *i*Pr

Scheme 4. Synthesis of Ti$^{VI}$ complexes of ligands **2a** and **2b**.

All attempts to displace the apical amido ligand in the N-sulfonated azatitanatranes **5a**–**c** with both O- and N-based nucleophiles only yielded mixtures or led to complex degradation, as was established upon monitoring the reactions by $^1$H NMR spectroscopy.

Several examples of reactivity studies performed with the tris-tosyl azatitanatrane **5a** are summarised in Scheme 5. Upon addition of *tert*-butyl hydroperoxide (from 1 to 10 equiv.) no formation of peroxoazatitanatrane complexes was observed (Scheme 5, path a); a complete decomposition of the starting complex occurred with concurrent slow oxidation of the free diethylamine.[47] This behaviour is in contrast to the previously established oxygenation behaviour of titanatrane complexes.[48] In the same way, treatment with racemic 2-octanol resulted, again, in complete decomposi-

 © 2006 Wiley-VCH Verlag GmbH & Co. KGaA, Weinheim 

tion of the complex with formation of ligand **1a** and titanium alkoxides (Scheme 5, path b). The oxophilic nature of titanium(IV) compounds is well documented[49] and this argument can be invoked to explain the high reactivity towards oxygen-containing species observed for **5a**. Verkade has reported that attempts to displace an apical $NMe_2$ group from an achiral azatitanatrane (R′ = Me, L = $NMe_2$) with *tert*-butyl alcohol give only a mixture of starting material, titanium alkoxide and alcoholysis products, with no detectable evidence for the displacement product.[50] Similar results were obtained in the attempted exchange of the apical diethylamido ligand for N-based nucleophiles. Addition of up to 10 equivalents of pyrrolidine to **5a** in $CDCl_3$ only returned the unreacted starting materials, and additional heating resulted in partial decomposition of the complex (Scheme 5, path c).[51]

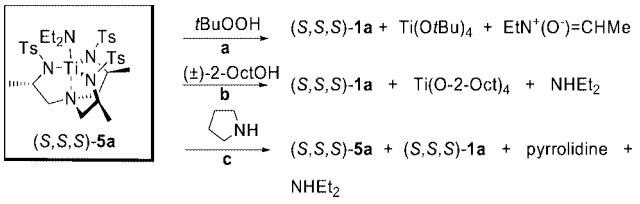


Scheme 5. Reactivity of complex **5a** with O- and N-based nucleophiles.

From these preliminary results it seems clear that the apical diethylamido ligand in complex **5a**, in analogy with the previously reported azatitanatranes,[35] is not easily displaced and this limits its use as a catalyst by the activation of apical substituents. Since apical chloro ligands can be replaced by alkylation to yield the corresponding alkyltitanium compounds[22a,52] or, alternatively, may be abstracted by treatment with silver salts to generate, for example, triflate derivatives,[49] or replaced by a siloxyl ($R_3SiO$) group by reaction with sodium siloxide,[53] such azatrane derivatives may be more suitable for use as Lewis acid catalysts. Such work is currently in progress.

## Conclusion

Enantiopure $C_3$-symmetric $Al^{III}$ and $Ti^{IV}$ complexes have been obtained from chiral trisamidoamine derivatives with threefold symmetry. Further studies are needed in order to ascertain whether the complexes have the key properties required for catalysis, such as a sufficiently large cavity for substrate binding, fast exchange of coordinated substrate, and efficient transfer of chirality from the chiral complex to the substrate undergoing reaction.

## Experimental Section

**General Remarks:** All metal-containing compounds were prepared under dry nitrogen on a high vacuum line using standard Schlenk techniques or in a glove box. All reaction flasks were heated prior to use and solvents and solutions were transferred by needle/septum techniques. Separation of solids from suspensions was performed by centrifugation with a Rotina 48 centrifuge (Hettich Zentrifugen, Tuttlingen, Germany) equipped with a specially designed Schlenk tube rotor.[54] Solvents were dried according to standard procedures and used under nitrogen: diethyl ether, THF, toluene and pentane were distilled from sodium/benzophenone and stored over a potassium mirror, except for diethyl ether, which was stored over activated 4-Å molecular sieves. Dichloromethane was distilled from calcium hydride and stored over activated 4-Å molecular sieves. The deuterated solvents used for NMR experiments were dried with activated 4-Å molecular sieves. Deuterated chloroform was additionally treated with a small amount of dry potassium carbonate. Pellets and powdered 4-Å molecular sieves were purchased from Aldrich and activated before use. The $^1H$ and $^{13}C$ NMR spectra were recorded with Bruker AC 200 SY ($^1H$: 200.13 MHz; $^{13}C$: 50.32 MHz), AC 250 ($^1H$: 250.18 MHz; $^{13}C$: 62.90 MHz), DRX 300 ($^1H$: 300.13 MHz; $^{13}C$: 75.46 MHz) and Bruker Avance 400 ($^1H$: 400.00 MHz; $^{13}C$: 100.58 MHz) instruments and referenced to the residual signals from $CDCl_3$ ($^1H$: $\delta$ = 7.26 ppm; $^{13}C$: $\delta$ = 77.2 ppm) and $C_6D_6$ ($^1H$: $\delta$ = 7.20 ppm) ppm. $^{19}F$ NMR spectra were recorded with the Bruker DRX 300 spectrometer using $CFCl_3$ as internal reference ($^{19}F$: 282.35 MHz; $CFCl_3$ $\delta$ = 0 ppm). Melting points are uncorrected and were determined withy a Reichert Austria apparatus. Optical rotations were measured with a Perkin–Elmer 241 polarimeter ($\lambda$ = 589 nm, sodium D-line) at 25 °C using a quartz cell (10 cm). Chromatographic separations were performed with Macherey–Nagel silica gel (70–230 mesh). Flash chromatography was performed as described in the literature[55] using Macherey–Nagel 60 silica gel (0.040–0.063 mm, 230–400 mesh). TLC analyses were run using Macherey–Nagel POLYGRAM®SIL G/$UV_{254}$ silica pre-coated plastic sheets (40 × 80 mm, 0.2 mm thickness). $Al(CH_3)_3$ (2.0 M solution in heptane) was purchased from Aldrich. The ligands used for the preparation of metal complexes were dried under vacuum and stored over $P_2O_5$ or under nitrogen. All other chemicals were obtained commercially and used without further purification.

**Ligand (*R*,*R*,*R*)-1e:** (*R*,*R*,*R*)-**1e** was obtained in 60% yield (0.99 g) following the procedure previously described for **3a**.[24] M.p. 177–178 °C, $[\alpha]_D^{20}$ = –82.6 (*c* = 1.2, $CHCl_3$). $^1H$ NMR (250.18 MHz, $CDCl_3$, 25 °C): $\delta$ = 0.91 (d, *J* = 6.2 Hz, 9 H), 2.17 (dd, *J* = 12.7 and 4.5 Hz, 3 H), 2.27 (s, 9 H), 2.67 (s, 18 H), 2.83 (dd, *J* = 12.6 and 11.1 Hz, 3 H), 3.68–3.91 (m, 3 H), 5.88 (d, *J* = 7.2 Hz, 3 H), 6.91 (s, 6 H) ppm. $^{13}C$ NMR (62.90 MHz, $CDCl_3$, 25 °C): $\delta$ = 19.6 [$CH_3$, 3 C, –CH(*C*$H_3$)], 20.8 ($CH_3$, 3 C, *p*-*C*$H_3$), 23.0 ($CH_3$, 6 C, *o*,*o*′-*C*$H_3$), 45.9 (CH, 3 C, $CH_2$*C*HMeN), 57.3 ($CH_2$, 3 C, N*C*$H_2$CHMe-), 131.7 (CH, 6 C, *C*H arom.), 135.8 ($C_q$, 3 C, CH*C*MeCH arom.) 138.8 ($C_q$, 6 C, -$SO_2$*C*CMeCH- arom.), 141.6 ($C_q$, 3 C, $SO_2$*C* arom.) ppm. $C_{36}H_{54}N_4O_6S_3$ (735): calcd. C 58.83, H 7.40, N 7.62; found C 58.95, H 7.42, N 7.60.

**Synthesis of $Al^{III}$ Complexes of Ligands (*S*,*S*,*S*)-1a and (*S*,*S*,*S*)-1c in situ:** Ligand **1** (0.020 mmol) was added to a 1-mL volumetric flask and dissolved in $CDCl_3$. Trimethylaluminium (2.0 M in heptane, 0.010 mL, 0.020 mmol) was then added and the solution (0.500 mL) was transferred into a screw-cap NMR tube, which was sealed under nitrogen and kept at room temperature. The reaction was followed by $^1H$ NMR spectroscopy. Once the complete formation of the complex was observed, the sample was kept at 0 °C in the refrigerator.

**Complex (*S*,*S*,*S*)-3a:** Upon addition of ligand (*S*,*S*,*S*)-**1a** (13.02 mg) to $AlMe_3$, formation of **3a** (colourless solution) was quantitative after 15 min. $^1H$ NMR (250.18 MHz, $CDCl_3$, 25 °C): $\delta$ = –0.39 (s, 3 H), 0.72 (d, *J* = 6.6 Hz, 3 H), 0.86 (d, *J* = 5.3 Hz, 3 H), 0.87 (d, *J* = 5.3 Hz, 3 H), 2.35 (s, 3 H), 2.40 (s, 3 H), 2.42 (s, 3 H), 2.47 (dd, *J* = 13.6 and 12.3 Hz, 1 H), 2.62 (dd, *J* = 16.7 and 10.1 Hz, 1

 © 2006 Wiley-VCH Verlag GmbH & Co. KGaA, Weinheim 

H), 2.98 (dd, $J$ = 15.4 and 2.2 Hz, 1 H), 3.08 (dd, $J$ = 13.6 and 4.4 Hz, 1 H), 3.69–3.42 (m, 1 H), 3.91–3.69 (m, 1 H), 4.72 (d, $J$ = 10.5 Hz, 1 H), 7.20 (d, $J$ = 8.3 Hz, 2 H), 7.27 (d, $J$ = 8.3 Hz, 4 H), 7.69 (d, $J$ = 8.3 Hz, 2 H), 7.83 (d, $J$ = 8.3 Hz, 2 H), 7.99 (d, $J$ = 8.3 Hz, 2 H) ppm.

**Complex (*R*,*R*,*R*)-3e:** This complex was prepared from $AlMe_3$ and ligand (*R*,*R*,*R*)-**1e** (14.70 mg). Quantitative formation occurred in 15 min; colourless solution. $^1$H NMR (250.18 MHz, $CDCl_3$, 25 °C): $\delta$ = –0.41 (s, 3 H), 0.56 (d, $J$ = 5.9 Hz, 3 H), 0.73 (d, $J$ = 5.6 Hz, 3 H), 0.90 (d, $J$ = 6.6 Hz, 3 H), 2.25 (s, 3 H), 2.29 (s, 3 H), 2.31 (s, 3 H), 2.36 (dd, $J$ = 14.4 and 2.9 Hz, 1 H), 2.50–2.71 (m, 2 H), 2.62 (s, 6 H), 2.67 (s, 6 H), 2.74 (s, 6 H), 3.04 (dd, $J$ = 7.9 and 4.3 Hz, 1 H), 3.20 (dd, $J$ = 14.3 and 2.9 Hz, 1 H), 3.38–3.53 (m, 1 H), 3.54–3.69 (m, 2 H), 3.70–3.91 (m, 1 H), 4.53 (d, $J$ = 10.3 Hz, 1 H), 6.87 (s, 2 H), 6.94 (s, 2 H), 6.98 (s, 2 H) ppm.

**Complex (*S*,*S*,*S*)-4a:** This complex was prepared from $AlMe_3$ and ligand (*S*,*S*,*S*)-**1a** (13.02 mg). The solution was heated at 60 °C for 15 d, resulting in 100% conversion to (*S*,*S*,*S*)-**4a**. The solution was colourless. $^1$H NMR (250.18 MHz, $CDCl_3$, 25 °C): $\delta$ = 0.87 (d, $J$ = 6.0 Hz, 9 H), 2.37 (s, 9 H), 2.43–2.76 (m, 6 H), 3.73–3.90 (m, 3 H), 7.25 (d, $J$ = 8.3 Hz, 6 H), 8.15 (d, $J$ = 8.3 Hz, 6 H) ppm. $^{13}$C NMR (62.90 MHz, $CDCl_3$, 25 °C): $\delta$ = 19.1 [$CH_3$, 3 C, –CH(*C*$H_3$)–N–], 21.5 ($CH_3$, 3 C, *C*$H_3$ arom.), 46.4 (CH, 3 C, $CH_2$C*H*MeN), 55.8 ($CH_2$, 3 C, NC*H*$_2$CHMe), 128.1 (CH, 6 C, CH arom.), 129.2 (CH, 6 C, CH arom.), 139.3 ($C_q$, 3 C, CH arom.), 142.6 ($C_q$, 3 C, CH arom.) ppm.

**Complex (*S*,*S*,*S*)-4c:** This complex was prepared from $AlMe_3$ and ligand (*S*,*S*,*S*)-**1c** (13.37 mg). Full conversion to colourless **4c** was observed after 2 h at 60 °C. $^1$H NMR (250.18 MHz, $CDCl_3$, 25 °C): $\delta$ = 0.96 (d, $J$ = 7.0 Hz, 9 H), 1.00 (d, $J$ = 7.0 Hz, 9 H), 2.02–2.90 (m, 3 H), 2.23 (dd, $J$ = 13.2 and 4.8 Hz, 3 H), 2.88 (dd, $J$ = 13.2 and 10.8 Hz, 3 H), 3.65–3.79 (m, 3 H) ppm. $^{13}$C NMR (62.90 MHz, $CDCl_3$, 25 °C): $\delta$ = 17.1 ($CH_3$, 9 C, CH*C*$H_3$), 17.9 ($CH_3$, 9 C, CH*C*$H_3$), 31.0 [CH, 3 C, –*C*H($CH_3$)$_2$], 53.1 (CH, 3 C, –$CH_2$*C*H*i*Pr), 56.9 (CH, 3 C, –*C*$H_2$CH*i*Pr), 119.2 ($C_q$, $J_{C,F}$ = 320.9 Hz, 3 C, $CF_3$) ppm. $^{19}$F NMR (282.35 MHz, $C_6D_6$, 28 °C): $\delta$ = –77.95 ppm.

**Complex (*S*,*S*,*S*)-4a:** Ligand (*S*,*S*,*S*)-**3a** (1.042 g, 1.60 mmol) was placed in a 100-mL Schlenk-tube. Dry THF (10 mL) was added followed by trimethylaluminium (2.0 M in heptane, 0.800 mL, 1.60 mmol) while stirring under nitrogen. After gently heating up to reflux, gas evolution was observed from the colourless solution. The reaction mixture was heated at 60 °C for 2 h and formation of a white precipitate was observed. Complex (*S*,*S*,*S*)-**5a** (1.069 g, 1.59 mmol, 99% yield) was isolated as a white solid after centrifugation and washing with dry THF (2 × 10 mL) and pentane (2 × 10 mL). $^1$H and $^{13}$C NMR as reported above. $C_{30}H_{39}AlN_4O_6S_3$ (675): calcd. C 53.39, H 5.82, N 8.30; found C 53.52, H 5.89, N 8.47.

**Synthesis and Characterisation of $Ti^{IV}$ Complexes of Ligands (*S*,*S*,*S*)-1a, (*S*,*S*,*S*)-1c and (*R*,*R*,*R*)-1e in situ:** Ligand **1** (0.027 mmol) was added to a 1-mL volumetric flask and dissolved in $CDCl_3$. Tetrakis(diethylamino)titanium (0.010 mL, 0.028 mmol) was then added and the solution (0.500 mL) was transferred into a screw-cap NMR tube, which was sealed and kept at room temperature. The reaction was followed by $^1$H NMR spectroscopy. Once the complex was observed, the volatile diethylamine was removed under vacuum and the sample was kept in solution at 0 °C in the refrigerator.

**Complex (*S*,*S*,*S*)-5a:** Ligand (*S*,*S*,*S*)-**5a** (17.6 mg) gave the complex quantitatively after 3 d, during which time the solution turned reddish-brown. $^1$H NMR (250.18 MHz, $CDCl_3$, 25 °C): $\delta$ = 1.03 (d, $J$ = 6.5 Hz, 9 H), 1.21 (t, $J$ = 7.4 Hz, 6 H), 2.38 (s, 9 H), 2.52 (dd, $J$ = 12.1 and 5.0 Hz, 3 H), 3.05 (dd, $J$ = 12.1 and 11.6 Hz, 3 H), 4.12–4.36 (m, 3 H), 4.36 (dq, $J$ = 11.1 and 7.4 Hz, 2 H), 4.50 (dq, $J$ = 11.1 and 7.4 Hz, 2 H), 7.23 (d, $J$ = 8.3 Hz, 6 H), 8.00 (d, $J$ = 8.3 Hz, 6 H) ppm. $^{13}$C NMR (62.90 MHz, $CDCl_3$, 25 °C): $\delta$ = 13.0 [$CH_3$, 3 C, $NCH_2$(*C*$H_3$)], 19.5 [$CH_3$, 3 C, –CH(*C*$H_3$)–N–], 21.5 ($CH_3$, 3 C, *C*$H_3$ arom.), 49.8 ($CH_2$, 6 C, N*C*$H_2$Me), 53.1 [CH, 3 C, $NCH_2$*C*H($CH_3$)–], 60.7 [$CH_2$, 3 C, N*C*$H_2$CH($CH_3$)], 127.7 (CH, 3 C, CH arom.), 129.1 (CH, 3 C, CH arom.), 141.1 ($C_q$, 3 C, CH arom.), 142.2 ($C_q$, 3 C, CH arom.) ppm.

**Complex (*S*,*S*,*S*)-5c:** Ligand (*S*,*S*,*S*)-**1c** (18.1 mg) gave the complex immediately with a 100% conversion; the solution turned dark brown. $^1$H NMR (250.18 MHz, $CDCl_3$, 25 °C): $\delta$ = 0.93 (d, $J$ = 7.2 Hz, 9 H), 1.03 (d, $J$ = 7.2 Hz, 9 H), 1.14 (t, $J$ = 7.2 Hz, 6 H), 2.22–2.42 (m, 3 H), 2.62 (dd, $J$ = 13.2 and 6.1 Hz, 3 H), 3.30 (dd, $J$ = 13.2 and 12.1 Hz, 3 H), 4.05–4.22 (m, 3 H), 4.24 (dq, $J$ = 14.8 and 7.2 Hz, 2 H), 4.80 (dq, $J$ = 14.8 and 7.2 Hz, 2 H) ppm. $^{13}$C NMR (62.90 MHz, $CDCl_3$, 25 °C): $\delta$ = 14.1 [$CH_3$, 3 C, $NCH_2$(*C*$H_3$)], 16.6 ($CH_3$, 9 C, CH*C*$H_3$), 20.2 ($CH_3$, 9 C, CH*C*$H_3$), 31.2 [CH, 3 C, –*C*H($CH_3$)$_2$], 52.8 ($CH_2$, 6 C, N*C*$H_2$Me), 55.7 (CH, 3 C, –$CH_2$*C*H*i*Pr), 64.5 (CH, 3 C, –*C*$H_2$CH*i*Pr), 120.1 ($C_q$, $J$ = 326.2 Hz, 3 C, *C*$F_3$) ppm. $^{19}$F NMR (282.35 MHz, $C_6D_6$, 28 °C): $\delta$ = –72.53 ppm.

**Complex (*R*,*R*,*R*)-5e:** Ligand (*R*,*R*,*R*)-**1e** (19.9 mg) was used. After 6 d at room temperature followed by 6 h of heating at 60 °C, a dark-yellow solution was obtained, which according to $^1$H NMR contained 90% of complex **5e**. $^1$H NMR (250.18 MHz, $CDCl_3$, 25 °C): $\delta$ = 0.97 (d, $J$ = 7.1 Hz, 9 H), 1.35 (t, $J$ = 7.1 Hz, 6 H), 2.32 (s, 9 H), 2.71 (s, 18 H), 3.47 (dd, $J$ = 12.5 and 10.9 Hz, 3 H), 3.38–3.63 (m, 2 H), 3.78–4.03 (m, 2 H), 4.38–4.55 (m, 3 H), 4.63 (dd, $J$ = 12.8 and 4.8 Hz, 2 H), 7.00 (s, 6 H) ppm. $^{13}$C NMR (62.90 MHz, $CDCl_3$, 25 °C): $\delta$ = 14.5 [$CH_3$, 3 C, N–$CH_2$(*C*$H_3$)], 18.4 [$CH_3$, 3 C, –CH(*C*$H_3$)–N–], 21.1 ($CH_3$, 3 C, *p*-*C*$H_3$), 23.9 ($CH_3$, 6 C, *o*,*o*-*C*$H_3$), 43.6 ($CH_2$, 6 C, N*C*$H_2$Me), 57.5 (CH, 3 C, $CH_2$*C*HMeN), 61.3 ($CH_2$, 3 C, N*C*$H_2$CHMe-), 132.6 (CH, 6 C, *C*H arom.), 132.9 ($C_q$, 3 C, CH*C*MeCH arom.), 140.9 ($C_q$, 6 C, -$SO_2$C*C*MeCH-arom.), 145.3 ($C_q$, 3 C, $SO_2$*C* arom.) ppm.

**Complex (*S*,*S*,*S*)-5a:** Ligand (*S*,*S*,*S*)-**1a** (1.048 g, 1.62 mmol) was placed in a 100-mL Schlenk-tube. Dry toluene (50 mL) was added and the mixture was stirred until the ligand was completely dissolved upon gently heating. Tetrakis(diethylamino)titanium (0.600 mL, 1.60 mmol) was then added while stirring under nitrogen. The reaction mixture turned from colourless to brown and it was refluxed for 4 h. The solvent was then evaporated under vacuum and the resulting brown powder was washed with dry pentane (2 × 20 mL). Pure **5a** (1.221 g, 1.59 mmol, 98% yield) was obtained as a brown powder. $^1$H and $^{13}$C NMR as reported above. $C_{34}H_{49}N_5O_6S_3Ti$ (768): calcd. C 53.18, H 6.43, N 9.12; found C 52.99, H 6.15, N 9.01.

**Complex (*S*,*S*,*S*)-6a:** Ligand (*S*,*S*,*S*)-**2a** (0.300 g; 1.29 mmol) was added with a syringe to a Schlenk flask followed by pentane (19 mL). The flask was cooled to –50 °C and *n*BuLi (2.5 M in hexanes, 1.51 mL, 3.78 mmol) was added dropwise during 15 min. The temperature was allowed to reach 0 °C during 30 min and the flask was then allowed to stand at room temperature for 2 h. The flask was cooled to –60 °C and [$TiCl_4$(THF)$_2$] (0.429 g, 1.26 mmol) was added under a stream of argon. The flask was slowly allowed to reach room temperature overnight and was then stirred for another 48 h. The flask was centrifuged and the dark-red solution was transferred with a transfer needle to a Schlenk flask. Most of the pentane was removed in vacuo and a crystalline material formed at –30 °C after a few days (0.227 g, 57% yield). $^1$H NMR

 © 2006 Wiley-VCH Verlag GmbH & Co. KGaA, Weinheim 

(200.13 MHz, $C_6D_6$, 25 °C): $\delta$ = 0.80 (d, $J$ = 6.0 Hz, 9 H), 2.16 (dd, $J$ = 11.7 and 5.1 Hz, 3 H), 2.62 (dd, $J$ = 11.6 and 11.6 Hz, 3 H), 3.20 (m, 3 H), 3.38 (s, 9 H) ppm. $^{13}$C NMR (50.32 MHz, $C_6D_6$, 25 °C): $\delta$ = 19.1 ($CH_3$, 3 C, CH*C*H$_3$), 43.6 ($CH_3$, 3 C, NC$H_3$), 60.6 (CH, 3 C, –$CH_2$*C*H–Me), 62.4 ($CH_2$, 3 C, –*C*H$_2$CHMe) ppm. $C_{12}H_{27}ClN_4Ti$ (310): calcd. C 46.39, H 8.76, N 18.03; found C 46.25, H 8.79, N 17.99.

**Complex (*S*,*S*,*S*)-6b:** The complex with ligand (*S*,*S*,*S*)-**2b** (0.395 g; 1.26 mmol) was prepared in an identical manner in 64% yield (0.318 g). $^1$H NMR (200.13 MHz, $C_6D_6$, 25 °C): $\delta$ = 0.67 (d, $J$ = 7.0 Hz, 9 H), 0.79 (d, $J$ = 8.5 Hz, 9 H), 1.73 (m, 3 H), 2.13 (dd, $J$ = 11.7 and 5.6 Hz, 3 H), 2.84 (dd, $J$ = 10.5 and 10.5 Hz, 3 H), 3.12 (m, 3 H), 3.28 (s, 9 H) ppm. $^{13}$C NMR (50.32 MHz, $C_6D_6$, 25 °C): $\delta$ = 14.2 ($CH_3$, 3 C, CH*C*H$_3$), 18.3 ($CH_3$, 3 C, CH*C*H$_3$), 26.6 [CH, 3 C, C*H*(C$H_3$)$_2$], 43.0 ($CH_3$, 3 C, NC$H_3$), 53.6 (CH, 3 C, –$CH_2$*C*H*i*Pr), 71.7 ($CH_2$, 3 C, –*C*H$_2$CH*i*Pr) ppm. $C_{18}H_{39}ClN_4Ti$ (395): calcd. C 46.39, H 8.76, N 18.03; found C 46.21, H 8.73, N 17.98.

**X-ray Diffraction**

**(*R*,*R*,*R*)-3e:** Crystallized from chloroform/hexane by vapour diffusion. Diffraction data were measured at the Istituto di Chimica Biomolecolare of CNR (Padova), with a Philips PW1100 diffractometer by using graphite-monochromated Cu-$K_\alpha$ radiation ($\lambda$ = 1.54178 Å) at 293(2) K in the $\theta$–2$\theta$ scan mode up to $\theta$ = 60°. Formula: $C_{36}H_{54}N_4O_6S_3$. Monoclinic, space group $P2_1$. Unit cell parameters: $a$ = 8.496(2), $b$ = 16.355(3), $c$ = 14.374(3) Å, $\beta$ = 98.33(4)°. $V$ = 1976.2(3) Å$^3$. $Z$ = 2. $D_{calcd.}$ = 1.235 g cm$^{-3}$. $\mu$ = 2.095 mm$^{-1}$. 3176 Collected reflections, 3053 of which were independent ($R_{int}$ = 0.029). The structure was solved by direct methods of the SHELXS 97 program[56] and refined by full-matrix block least-squares on $F^2$, using all data, with the SHELXL 97 program.[57] A planarity restraint was applied to each of the three phenyl rings. Hydrogen atoms were calculated at idealised positions and refined as riding. Data/restraints/parameters: 3053/10/455. Final $R$ indices: $R_1$ = 0.038 and $wR_2$ = 0.097 [$I > 2\sigma(I)$]; $R_1$ = 0.039 and $wR_2$ = 0.101 (all data). Goodness of fit (on $F^2$): 1.063. Max. and min. residual in the final $\Delta F$ map: +0.182 and –0.223 e Å$^{-3}$.

**(*S*,*S*,*S*)-5a:** Crystals of **5a** were grown by layering a concentrated solution of the pure compound in dichloromethane with diethyl ether, and allowing slow diffusion at room temperature. Diffraction data were collected at the Laboratoire de Chimie Organométallique et de Catalyse (Institut Le Bel, Université Louis Pasteur, Strasbourg) using a Nonius–Kappa CCD diffractometer equipped with a molybdenum source [$\lambda$(Mo-$K_\alpha$) = 0.71073 Å] at 174 K. Formula: $C_{30}H_{39}AlN_4O_6S_3{\cdot}CH_2Cl_2$. Orthorhombic, space group $P2_12_12_1$. Unit cell parameters: $a$ = 7.6495(1), $b$ = 21.4914(3), $c$ = 22.3149(4) Å. $V$ = 3668.5(1) Å$^3$. $Z$ = 4. $D_{calcd.}$ = 1.380 g cm$^{-3}$. $\mu$ = 0.418 mm$^{-1}$. 10747 Collected reflections, 6021 of which were independent ($R_{int}$ = 0.06). The Nonius OpenMoleN software package was used for all calculations.[58] The refinement was carried out by least-squares methods against $F^2$. The hydrogen atoms were included at calculated positions with fixed thermal parameters. Data/restraints/parameters: 3641/0/424. Final $R$ indices: $R_1$ = 0.051 and $wR_2$ = 0.071 [$I > 2\sigma(I)$]. Goodness of fit (on $F^2$): 1.292. Max. and min. residual in the final $\Delta F$ map: +0.679 and –0.161 e·Å$^{-3}$.

CCDC-277426 and -278811 contain the supplementary crystallographic data for (*R*,*R*,*R*)-**3e** and (*S*,*S*,*S*)-**5a**, respectively. These data can be obtained free of charge from the Cambridge Crystallographic Data Centre via www.ccdc.cam.ac.uk/data_request/cif.

**Supporting Information** (see footnote on the first page of this article): 2D NMR spectra of complex **5a** (NOESY) and **5e** (TOCSY and NOESY).

## Acknowledgments

This work was supported financially by the Göran Gustafsson Foundation for Research in Sciences and Medicine and the European Community's Human Potential Programme under contract HPRN-CT-2001-00187, [AC3S]. M.F. acknowledges financial support for an STSM provided by COST Action D24 "Sustainable Chemical Processes: Stereoselective Transition Metal-Catalysed Reactions" (WG D24/0005/02).

[1] I. Ojima, *Catalytic Asymmetric Synthesis*, 2nd ed., Wiley, New York, **2000**.
[2] J. Seyden-Penne, *Chiral Auxiliaries and Ligands in Asymmetric Synthesis*, John Wiley & Sons, Inc., New York, **1995**.
[3] a) C. A. Tolman, *Chem. Rev.* **1977**, *77*, 313–348; b) C. A. Tolman, *J. Am. Chem. Soc.* **1970**, *92*, 2953–2956; c) C. A. Tolman, *J. Am. Chem. Soc.* **1970**, *92*, 2956–2965.
[4] P. W. N. M. Van Leeuwen, P. C. J. Kamer, J. N. H. Reek, P. Dierkes, *Chem. Rev.* **2000**, *100*, 2741–2770.
[5] J. K. Whitesell, *Chem. Rev.* **1989**, *89*, 1581–1590.
[6] C. Moberg, *Angew. Chem.* **1998**, *110*, 260–281; *Angew. Chem. Int. Ed. Engl.* **1998**, *37*, 249–268.
[7] J. G. Verkade, *Acc. Chem. Res.* **1993**, *26*, 483–489.
[8] J. Pinkas, J. Tang, Y. Wan, J. G. Verkade, *Phosphorus, Sulfur Silicon Relat. Elem.* **1994**, *87*, 193–207.
[9] R. R. Schrock, *Acc. Chem. Res.* **1997**, *30*, 9–16.
[10] D. V. Yandulov, R. R. Schrock, *Inorg. Chem.* **2005**, *44*, 1103–1117 and references cited therein.
[11] J. Chen, L. K. Woo, *J. Organomet. Chem.* **2000**, *601*, 57–68.
[12] M. M. Ibrahim, N. Shimomura, K. Ichikawa, M. Shiro, *Inorg. Chim. Acta* **2001**, *313*, 125–136.
[13] M. M. Ibrahim, K. Ichikawa, M. Shiro, *Inorg. Chem. Commun.* **2003**, *6*, 1030–1034.
[14] A. J. Fischmann, A. C. Warden, J. Black, L. Spiccia, *Inorg. Chem.* **2004**, *43*, 6568–6578.
[15] M. Becker, F. W. Heinemann, S. Schindler, *Chem. Eur. J.* **1999**, *5*, 3124–3129.
[16] M. A. Salam, K. Aoki, *Inorg. Chim. Acta* **2001**, *314*, 71–82.
[17] J. G. Verkade, *Coord. Chem. Rev.* **1994**, *137*, 233–295.
[18] M. Shakir, S. Parveen, N. Begum, P. Chingsubam, *Transition Met. Chem.* **2004**, *29*, 196–199.
[19] R. Stähler, W. Bensch, *Eur. J. Inorg. Chem.* **2001**, 3073–3078.
[20] J. Cai, X. Hu, X. Feng, W. Shao, L. Ji, I. Bernal, *Eur. J. Inorg. Chem.* **2000**, 2199–2205.
[21] M. K. Saha, F. R. Fronczek, L. H. Rees, I. Bernal, *Inorg. Chem. Commun.* **2003**, *6*, 983–988.
[22] Selected examples: a) C. C. Cummins, R. R. Schrock, W. M. Davis, *Organometallics* **1992**, *11*, 1452–1454; b) C. C. Cummins, R. R. Schrock, W. M. Davis, *Inorg. Chem.* **1994**, *33*, 1448–1457.
[23] Selected examples: a) M. Kol, R. R. Schrock, R. Kempe, W. M. Davis, *J. Am. Chem. Soc.* **1994**, *116*, 4382–4390; b) G. E. Greco, A. I. Popa, R. R. Schrock, *Organometallics* **1998**, *17*, 5591–5593; c) G. E. Greco, R. R. Schrock, *Inorg. Chem.* **2001**, *40*, 3850–3860.
[24] a) M. Cernerud, H. Adolfsson, C. Moberg, *Tetrahedron: Asymmetry* **1997**, *8*, 2655–2662; b) Y. Pei, B. Brade, L. Hagberg, F. Lake, C. Moberg, *Eur. J. Org. Chem.* **2005**, 2835–2840.
[25] S. P. Hajela, A. R. Johnson, J. Xu, C. J. Sunderland, S. M. Cohen, D. L. Caulder, K. N. Raymond, *Inorg. Chem.* **2001**, *40*, 3208–3216.
[26] J. You, A. E. Wróblewski, J. G. Verkade, *Tetrahedron* **2004**, *60*, 7877–7883.
[27] K. Ishihara, Y. Karumi, S. Kondo, H. Yamamoto, *J. Org. Chem.* **1998**, *63*, 5692–5695.
[28] X. Liu, P. Ilankuraman, I. A. Guzei, J. G. Verkade, *J. Org. Chem.* **2000**, *65*, 701–706.
[29] Review: L. H. Gade, *Acc. Chem. Res.* **2002**, *35*, 575–582.

 © 2006 Wiley-VCH Verlag GmbH & Co. KGaA, Weinheim 

[30] a) L. H. Gade, P. Renner, H. Memmler, F. Fecher, C. H. Galka, M. Laubender, S. Radojevic, M. McPartlin, J. Lauher, *Chem. Eur. J.* **2001**, *7*, 2563–2580; b) P. Renner, C. H. Galka, L. H. Gade, S. Radojevic, M. McPartlin, *Eur. J. Inorg. Chem.* **2001**, 1425–1430; c) P. Renner, L. H. Gade, unpublished results.
[31] a) J. G. Verkade, P. B. Kisanga, *Tetrahedron* **2003**, *59*, 7819–7858; b) J. G. Verkade, *Top. Curr. Chem.* **2003**, *223*, 1–44.
[32] a) S. Urgaonkar, M. Nagarajan, J. G. Verkade, *Tetrahedron Lett.* **2002**, *43*, 8921–8924; b) J. You, J. G. Verkade, *Angew. Chem.* **2003**, *115*, 5205–5207; *Angew. Chem. Int. Ed.* **2003**, *42*, 5051–5053; c) J. You, J. Xu, J. G. Verkade, *Angew. Chem.* **2003**, *115*, 5208–5210; *Angew. Chem. Int. Ed.* **2003**, *42*, 5054–5056; d) J. You, J. G. Verkade, *J. Org. Chem.* **2003**, *68*, 8003–8007; e) S. Urgaonkar, J.-H. Xu, J. G. Verkade, *J. Org. Chem.* **2003**, *68*, 8416–8423; f) S. Urgaonkar, M. Nagarajan, J. G. Verkade, *Org. Lett.* **2003**, *5*, 815–818; g) W. Su, S. Urgaonkar, J. G. Verkade, *Org. Lett.* **2004**, *6*, 1421–1424.
[33] F. Lake, L. Hagberg, M. Svensson, C. Moberg, *Collect. Czech. Chem. Commun.* **2000**, *65*, 570–576.
[34] F. Di Furia, G. Licini, G. Modena, R. Motterle, W. A. Nugent, *J. Org. Chem.* **1996**, *61*, 5175–5177.
[35] A. A. Naiini, W. M. P. B. Menge, J. G. Verkade, *Inorg. Chem.* **1991**, *30*. 5009–5012.
[36] L. H. Gade, *Chem. Commun.* **2000**, 173–181.
[37] R. Kempe, *Angew. Chem.* **2000**, *112*, 478–504; *Angew. Chem. Int. Ed.* **2000**, *39*, 468–493.
[38] F. Lake, C. Moberg, *Eur. J. Org. Chem.* **2002**, 3179–3188.
[39] N. Emig, H. Nguyen, H. Krautscheid, R. Réau, J.-B. Cazaux, G. Bertrand, *Organometallics* **1998**, *17*, 3599–3608.
[40] J. Pinkas, B. Gaul, J. G. Verkade, *J. Am. Chem. Soc.* **1993**, *115*, 3925–3931.
[41] J. Pinkas, T. Wang, R. A. Jacobson, J. G. Verkade, *Inorg. Chem.* **1994**, *33*, 4202–4210.
[42] J. Pinkas, T. Wang, R. A. Jacobson, J. G. Verkade, *Inorg. Chem.* **1994**, *33*, 5244–5253.
[43] a) K. Kincaid, C. P. Gerlach, G. R. Giesbrecht, J. R. Hagadorn, G. D. Whitener, A. Shafir, J. Arnold, *Organometallics* **1999**, *18*, 5360–5366; b) G. H. Robinson, S. A. Sagokoya, *J. Am. Chem. Soc.* **1987**, *109*, 6852–6853.
[44] The transannular bond length averages 2.069 Å in the tetrameric complex $[N(CH_2CH_2O)_3Al]_4$: V. E. Shklover, Y. T. Struchkov, M. G. Voronkov, Z. A. Ovchinnikova, V. P. Baryshok, *Dokl. Akad. Nauk SSSR (Engl. Transl.)* **1984**, *277*, 723, while values in the range 2.073–2.084 Å have been observed for $[N\{CH_2CH(Ph)O\}_3Al]_2$: M. Forcato, L. H. Gade, G. Licini, F. Santin, unpublished results.
[45] a) S. G. Nelson, T. J. Peelen, Z. Wan, *J. Am. Chem. Soc.* **1999**, *121*, 9742–9743; b) S. G. Nelson, B.-K. Kim, T. J. Peelen, *J. Am. Chem. Soc.* **2000**, *122*, 9318–9319. For a Highlight, see: c) C. Schneider, *Angew. Chem.* **2002**, *114*, 771–772; *Angew. Chem. Int. Ed.* **2002**, *41*, 744–746.
[46] M. Schubart, L. O'Dwyer, L. H. Gade, W.-S. Li, M. McPartlin, *Inorg. Chem.* **1994**, *33*, 3893–3898.
[47] Homogeneous $Ti^{IV}$ complexes have been found to be effective catalysts for the selective oxidation of secondary amines to nitrones by alkyl hydroperoxides: M. Forcato, W. A. Nugent, G. Licini, *Tetrahedron Lett.* **2003**, *44*, 49–52.
[48] M. Bonchio, G. Licini, G. Modena, O. Bortolini, S. Moro, W. A. Nugent, *J. Am. Chem. Soc.* **1999**, *121*, 6258–6268.
[49] F. A. Cotton, G. Wilkinson, *Advanced Inorganic Chemistry*, 5th Edition, John Wiley and Sons, New York, **1988**, pp.652–665.
[50] A. A. Naiini, W. M. B. P. Menge, J. G. Verkade, *Inorg. Chem.* **1991**, *30*, 5009–5012.
[51] Attempts to displace the dimethylamido ligand from dimeric titanatrane by diethylamine was reported to afford low yields (<10%) of diethylamido titanatrane only upon refluxing in toluene Higher yields were obtained of the diisopropylamido titanatrane (61%) but only after refluxing in pure diisopropylamine. Under these conditions displacement of the diethylamido group afforded the diisopropyl analogue in only 24% yield. See A. A. Naiini, S. L. Ringrose, Y. Su, R. A. Jacobson, J. G. Verkade, *Inorg. Chem.* **1993**, *32*, 1290–1296.
[52] R. R. Schrock, C. C. Cummins, T. Wilhelm, S. Lin, S. M. Reid, M. Kol, W. M. Davis, *Organometallics* **1996**, *15*, 1470–1476.
[53] Z. Duan, A. A. Naiini, J.-H. Lee, J. G. Verkade, *Inorg. Chem.* **1995**, *34*, 5477–5482.
[54] K. W. Hellmann, L. H. Gade, *Verfahrenstechnik (Berlin)* **1997**, *31*, 70–71.
[55] C. W. Still, *J. Org. Chem.* **1978**, *43*, 2923–2925.
[56] G. M. Sheldrick, *SHELXS 97, Program for the Solution of Crystal Structures*, University of Göttingen, Germany, **1997**.
[57] G. M. Sheldrick, *SHELXL 97, Program for the Refinement of Crystal Structures*, University of Göttingen, Germany, **1997**.
[58] *OpenMoleN, Interactive Structure Solution*; Nonius: Delft, **1997**.

Received: July 24, 2005
Published Online: January 3, 2006

 © 2006 Wiley-VCH Verlag GmbH & Co. KGaA, Weinheim 

DOI: 10.1002/ejic.200500701

# Synthesis of Novel S-Bridged Heterotrinuclear Complexes Containing Six-Membered Chelate Rings: Structural, Spectroscopic, and Electrochemical Properties of $[Co\{Rh(apt)_3\}_2]^{3+}$ (apt = 3-Aminopropanethiolate)

**Nagina Amir,*[a] Masaru Motonishi,[a] Mitsuharu Fujita,[a] Yoshitaro Miyashita,*[a] Kiyoshi Fujisawa,[a] and Ken-ichi Okamoto*[a]**

**Keywords:** 3-Aminopropanethiolate / Heterometallic complexes / Crystal structures / Six-membered chelate rings / Spectroscopy / Electrochemistry

A bidentate ligand, 3-aminopropanethiolate (apt), was synthesized and treated with $RhCl_3 \cdot 3H_2O$ in basic water to yield a novel mononuclear complex, *fac*(*S*)-$[Rh(apt)_3]$ (**1**), which was characterized by spectroscopic methods. Furthermore, the reaction of **1** with $CoCl_2 \cdot 6H_2O$ in water formed the linear-type, S-bridged trinuclear complexes $\Delta\Lambda$-$[Co\{Rh(apt)_3\}_2]^{3+}$ (**2a**) and $\Delta\Delta/\Lambda\Lambda$-$[Co\{Rh(apt)_3\}_2]^{3+}$ (**2b**), which were characterized by stereochemical, spectrochemical, and electrochemical methods. **2a** and **2b** are stable and exhibit trivalency in water. X-ray crystallographic analysis of **2a** and **2b** showed that all of the bridging sulfur atoms are fixed in the *R* configuration for the $\Delta$ unit and in the *S* configuration for the $\Lambda$ unit, and each complex has six six-membered chelate rings, all of which are in the chair conformation. The crystal structure of the corresponding 2-aminoethanethiolate (aet) trinuclear complex $\Delta\Lambda$-$[Co\{Rh(aet)_3\}_2]^{3+}$ (**4a**) was also determined. The structures of **2a** and **2b** have some differences from that of **4a** as a result of the six-membered chelate rings. The Co···Rh distances in **2a** and **2b** [3.0490(4) and 3.063(1) Å] are significantly longer than this distance in the aet complex **4a** [2.9139(2) Å]. The UV/Vis absorption spectra of **2a** and **2b** indicate a shift to higher energies as compared with **4a** and $\Delta\Delta/\Lambda\Lambda$-$[Co\{Rh(aet)_3\}_2]^{3+}$ (**4b**). The chemical shifts for the $NCH_2$ and $SCH_2$ carbon atoms in **2a** and **2b** are shifted to higher fields than those for **4a** and **4b** in the NMR spectra. The $Co^{III/II}$ redox potential values are –0.56 V (**2a**) and –0.57 V (**2b**) compared with –0.35 V (**4a**) and –0.36 V (**4b**). This shows that the $Co^{III}$ state is more stable in **2a** and **2b** than it is in **4a** and **4b**.

(© Wiley-VCH Verlag GmbH & Co. KGaA, 69451 Weinheim, Germany, 2006)

## Introduction

The chemistry of sulfur-bridged metal complexes has attracted much interest because of the importance of coordinated thiolato groups in a variety of systems ranging from inorganic to organic and biological chemistry. It has been recognized that, because of their high Lewis basicity, coordinated thiolato groups have an affinity to form S-bridged polynuclear structures with transition-metal ions. Therefore, mononuclear complexes, *fac*(*S*)-$[M(aet)_3]$ (M = $Co^{III}$, $Rh^{III}$, $Ir^{III}$; aet = 2-aminoethanethiolate), could function as metalloligands to other transition-metal ions, using sulfur atoms.[1] The polynuclear complexes obtained so far have shown unique stereochemical, spectrochemical, and electrochemical properties, depending highly upon the nature of the central metal ions and the metal ions in the terminal building blocks (Scheme 1).[1–5]

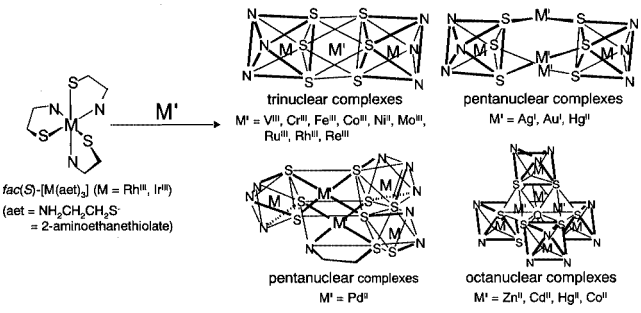


Scheme 1.

The complex $[Co(tn)_3]^{3+}$ (tn = 1,3-propanediamine) containing an additional methylene group shows some interesting differences in properties when compared with the corresponding complex $[Co(en)_3]^{3+}$ (en = ethylenediamine).[6–13] For example, six-membered chelate rings give rise to a larger bite angle (N···N distances in chelates) than five-membered rings.[6–9] It was reported that both the conformational flexibility and the structural bulkiness are larger in $[M(tn)_3]^{3+}$ than in $[M(en)_3]^{3+}$ (M = $Co^{III}$ or $Cr^{III}$

[a] Department of Chemistry, Graduate School of Pure and Applied Sciences, University of Tsukuba,
Tsukuba 305–8571, Japan
Fax: +81-29-853-4323-6503
E-mail: nagina@chem.tsukuba.ac.jp
ymiya@chem.tsukuba.ac.jp
okamoto@chem.tsukuba.ac.jp

Supporting information for this article is available on the WWW under http://www.eurjic.org or from the author.

 © 2006 Wiley-VCH Verlag GmbH & Co. KGaA, Weinheim 

ion).[10,11] It was also observed that the ring–ring interactions, which give rise to the energy differences between conformations, are more severe and more numerous in the six-membered chelate ring complexes than in five-membered systems.[10] Moreover, the absorption maxima in the first d–d transition region in the tn complexes shift to lower energies than those in the corresponding en complexes.[12,13]

Similar to the complexes $[Co(tn)_3]^{3+}$ and $[Co(en)_3]^{3+}$ with N–N donor ligands, complexes containing five- and six-membered chelate rings with N–S donor ligands also show interesting differences in properties. For example, an additional methylene group led to differences in reactivity: all the attempts to synthesize $[Co(apt)_3]$ (apt = 3-aminopropanethiolate) were unsuccessful, unlike the corresponding complex $[Co(aet)_3]$, which was obtained easily.[14] Similarly, $[Ni(apt)_2]$ was obtained under more drastic conditions than $[Ni(aet)_2]$. Moreover, differences in chemical properties were also observed: $[Ni(apt)_2]$ gave $[Ni\{Ni(apt)_2\}_2]^{2+}$ when dissolved in polar solvents, whereas $[Ni(aet)_2]$ remained practically insoluble. The aqueous solutions of $[Ni\{Ni(apt)_2\}_2]^{2+}$ were less stable than those of the homologous trinuclear complex $[Ni\{Ni(aet)_2\}_2]^{2+}$.[15] The solubility of complexes with six-membered chelate rings, e.g. $[Ni\{Ni(apt)_2\}_2]^{2+}$, was lower than that of complexes with five-membered chelate rings, e.g. $[Ni\{Ni(aet)_2\}_2]^{2+}$.[16] As far as structure was concerned, the most striking difference resulting from the presence of an additional methylene group was found to be the opening of the dihedral angle by 30°. This can be attributed to the steric requirements of the enlargement of the chelate ring. The electronic properties are also influenced by the additional methylene group, which could be explained in terms of different bond lengths and angles of the chromophores in these complexes.[15]

It has been well explained in the literature that the variations in the bridging ligands provide remarkable control over the electronic structures and photophysics of complexes. In one of the reports it was found that bpa dimers [bpa = 1,2-bis(4-pyridyl)ethane] exhibit a broad, low-energy emission from a metal-centered $^3$LF excited state, whereas the bpe and bpy dimers [bpe = *trans*-1,2-bis(4-pyridyl)ethylene, bpy = 4,4′-bipyridyl] exhibit structured emission from the lowest pyridyl-centered $3(\pi–\pi^*)$ excited state.[17] In another report, complexes of 4-pyridine thiolate with $Co^{II}$, $Ni^{II}$, $Zn^{II}$, $Cd^{II}$, $Hg^{II}$, $Pt^{II}$, $Sn^{IV}$, and $Bi^{III}$ involve bonding through sulfur rather than nitrogen,[18] while complexes of 2-(2-mercaptoethyl)pyridine with $Co^{II}$, $Ni^{II}$, $Pd^{II}$, and $Pt^{II}$ involve bonding through sulfur as well as nitrogen.[19] It can therefore be demonstrated that the modifications of the bridging ligand provide exquisite control over the electronic structures and photophysics of the compounds, including the orbital character of the lowest emissive state. It is also assumed that the complexes using apt, which has an additional methylene group as compared with aet, can lead to somewhat different structural, spectrochemical, or electrochemical properties, which might be quite interesting.

No doubt metal complexes of aet ligands have been widely studied, many of them form stable chelates, but those of apt have received little attention up to now. Only a few $Co^{III}$, $Ni^{II}$, $Zn^{II}$, $Cd^{II}$, $Hg^{II}$, and $Fe^{III}$ complexes have been reported.[14,15,20,21] The polynuclear complexes obtained were homopolynuclear complexes only, and to the best of our knowledge, there is no report of heteropolynuclear complexes. The choice of apt is based on the simplicity of the ligand and the fact that the ligand had been poorly studied. Turning to six-membered rings in the mononuclear unit, we are interested in the effects of changes in the three-dimensional structure on the metal, spectroscopic, and electrochemical properties.

In this paper, we report on the stepwise synthesis of aptH·HCl from 3-aminopropanol following literature methods with some modifications.[22–24] After synthesis, aptH·HCl was treated with the $Rh^{III}$ ion to obtain a mononuclear complex *fac*(*S*)-$[Rh(apt)_3]$ (**1**), which reacts with the $Co^{II}$ ion to form heterotrinuclear complexes $[Co\{Rh(apt)_3\}_2]^{3+}$ in *meso* (**2a**) and *racemic* (**2b**) forms. Crystal structural analysis and spectrochemical characterization have been described comparatively for the corresponding aet complexes. Electrochemical measurements were also performed.

## Results and Discussion

### Synthesis of Ligand

The ligand aptH·HCl was prepared by modified literature methods.[22–24] There was only a very simple description for the synthesis of the aminoalkanethiol series in the literature. Therefore, the synthesis of aptH·HCl was examined in detail and improved. The ligand was obtained by the three-step reaction shown in Scheme 2. Each compound was characterized by elemental analysis and NMR spectroscopy.

The first step of the reaction was vigorous and was therefore carried out in an ice bath. From this step, the compound 1-amino-3-propylsulfate (**I**) was obtained. The second step gave tetrahydro-1,3-thiazine-2-thione (**II**) with the ring-formation reaction of **I** and carbon disulfide. Compound **II** is a thione-thiol tautomer that consists of tetrahydro-1,3-thiazine-2-thione and 5,6-dihydro-1,3-thiazine-2-thiol (Figure 1). The X-ray crystal structure of **II** is shown in Figure 2, and bond lengths and angles are listed in Table 1. The six-membered ring is not a planar structure because of the $sp^3$ carbon atoms C1 and C2, and the $sp^3$ sulfur atom S1, although the C1, S1, C4, N1, C3, and S2 atoms are almost on the same plane. The S2–C4 distance [1.692(3) Å] is shorter than the length of the single bond S1–C1 [1.814(4)] and S1–C4 [1.729(3) Å]. It is reported that the length of the single bond S–C of typical thiol compounds is 1.82 Å, and that of typical thione compounds is 1.56 Å.[25–28] Similarly, the N1–C4 distance [1.321(4) Å] is shorter than the length of the single bond N1–C3 [1.471(5) Å], which suggests multibonding. Thus, the C4 atom is in an $sp^2$ hybridized state. The S1–C4 distance in **II** is similar to the corresponding S–C distance [1.722(7) Å] in *N*,*N*′-trimethylenethiourea.[29]

 © 2006 Wiley-VCH Verlag GmbH & Co. KGaA, Weinheim 

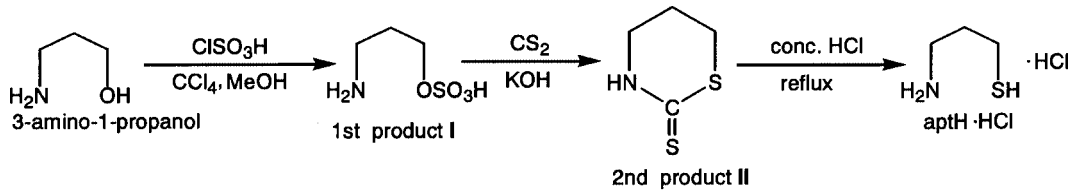


Scheme 2.

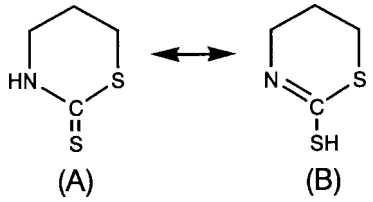


Figure 1. Two tautomers of **II**.

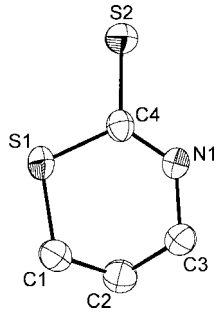


Figure 2. Crystal structure of **II**.

Table 1. Bond lengths [Å] and angles [°] of **II**.

| | | | |
|---|---|---|---|
| S1–C1 | 1.814(4) | S1–C4 | 1.729(3) |
| S2–C4 | 1.692(3) | N1–C3 | 1.471(5) |
| N1–C4 | 1.321(4) | C1–C2 | 1.502(5) |
| C2–C3 | 1.513(5) | | |
| C1–S1–C4 | 105.2(2) | C3–N1–C4 | 127.0(3) |
| S1–C1–C2 | 110.9(2) | C1–C2–C3 | 111.7(3) |
| N1–C3–C2 | 112.1(3) | S1–C4–S2 | 115.1(2) |
| S1–C4–N1 | 122.2(2) | S2–C4–N1 | 122.7(2) |

The third step in the reaction of **II** gave aptH·HCl as a result of ring opening. This ligand is hygroscopic and soluble in water, methanol, ethanol, and acetone, and less soluble in other solvents. The overall process was carried out in a manner similar to that of the synthesis of 1-Meaet (1-Meaet = 1-amino-2-propanethiolate).[30]

### Syntheses of Complexes

Preparation of the apt mononuclear complex *fac*(*S*)-[Rh(apt)$_3$] (**1**) (Scheme 3) was carried out by a modified method of the synthesis of the aet mononuclear complex, *fac*(*S*)-[Rh(aet)$_3$] (**3**).[31,32] The difference between the syntheses was the order in which the starting materials were added. For the synthesis of the aet mononuclear complex, $RhCl_3 \cdot 3H_2O$ was added to a basic aqueous solution containing the ligand, and the mixture was heated to reflux under nitrogen. However, in this work, the apt was added at the end and gave a higher yield than a similar method for synthesizing the aet mononuclear complex. The resulting yellow powder was found to be **1**. This neutral complex is not soluble in general solvents, but soluble in acidic water following the protonation of the sulfur atoms of the coordinated thiolato group. Complex **1** was obtained more easily and in a purer form than the complexes *fac*(*S*)-[Co(apt)$_3$] and *trans*(*S*)-[Ni(apt)$_2$], which were obtained under more drastic conditions.[15]

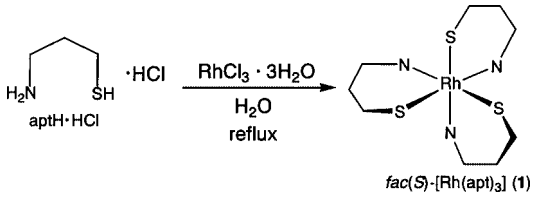


Scheme 3.

The trinuclear complexes ΔΛ-[Co{Rh(apt)$_3$}$_2$](NO$_3$)$_3$ [**2a**(NO$_3$)$_3$] and ΔΔ/ΛΛ-[Co{Rh(apt)$_3$}$_2$]Br$_3$ (**2b**Br$_3$) were synthesized by the reported procedure, but using aptH instead of aetH.[33] It was found that, in the case of **2a**(NO$_3$)$_3$ and **2b**Br$_3$, the reaction gave the trivalent Co$^{III}$ complexes under nitrogen or air. This result is different from the case of ΔΛ-[Co{Rh(aet)$_3$}$_2$](NO$_3$)$_3$ [**4a**(NO$_3$)$_3$] and ΔΔ/ΛΛ-[Co{Rh(aet)$_3$}$_2$]Br$_3$ (**4b**Br$_3$), which gave divalent Co$^{II}$ complexes under such conditions, in which case $H_2O_2$ was used for oxidation.[33] This difference in reactivity can be related to the difference in the redox potential of the Co$^{III}$ ion in trinuclear structures (vide infra). Complexes **2a** and **2b** (Scheme 4) were obtained both in *meso* and *racemic* forms similar to **4a** and **4b**. Selective crystallization using suitable counter anions was achieved. This is different from the case of the Co$^{III}$ complexes in which [Co{Co(aet)$_3$}$_2$]Cl$_3$ gave both *meso* and *racemic* forms while [Co{Co(apt)$_3$}$_2$]Cl$_3$ gave only the *meso* form.[14,21]

### Crystal Structures of Complexes 2a, 2b, and 4a

The results of the ICP analysis and elemental analysis confirmed that the ratio of Co to Rh was 1:2 in **2a** and **2b**. The values obtained for the molar conductivity in aqueous solution for the apt complexes **2a** and **2b** (329 and 363 S·cm$^2$·mol$^{-1}$, respectively) are comparable to the values of the aet complexes **4a** and **4b** (384 and 401 S·cm$^2$·mol$^{-1}$, respectively). These values are also within the range normally observed for other trivalent trinuclear complexes containing *fac*(*S*)-[Rh(aet)$_3$] units (323–404 S·cm$^2$·

 © 2006 Wiley-VCH Verlag GmbH & Co. KGaA, Weinheim 

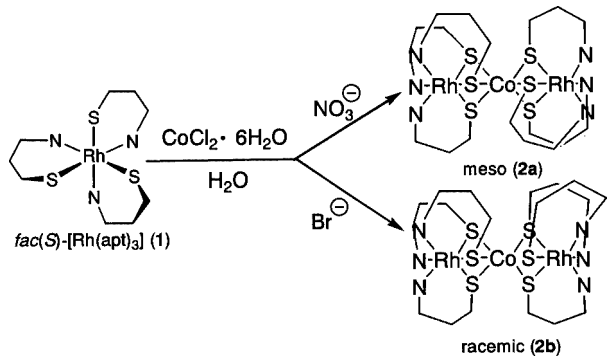


Scheme 4.

mol$^{-1}$).[2,3,34,35] The structures of **2a**, **2b**, and **4a**, determined by X-ray structural analysis, are shown in Figures 3, 4, and 5, respectively. The crystal structure of **4a** was determined for purposes of comparison. The selected bond lengths and angles are summarized in Table 2 and Table 3. Compounds **2a** and **2b** consist of two approximately octahedral *fac*(*S*)-[Rh(apt)$_3$] units and one Co atom, forming the completely linear-type, S-bridged trinuclear structures, ΔΛ-[Co{Rh(apt)$_3$}$_2$]$^{3+}$ (for **2a**) and ΔΔ/ΛΛ-[Co{Rh(apt)$_3$}$_2$]$^{3+}$ (for **2b**). Only the ΛΛ configuration of **2b** is shown in Figure 4. All of the bridging sulfur atoms in **2a** and **2b** have the *R* configuration for the Δ unit and the *S* configuration for the Λ unit, which corresponds to the results in all of the reported trinuclear structures. Each complex has six six-membered chelate rings in a molecule, and all of the rings are in the chair conformation.

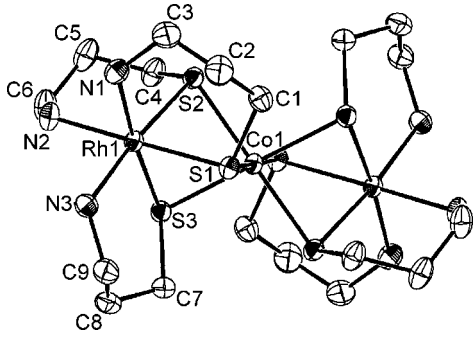


Figure 3. Crystal structure of **2a**.

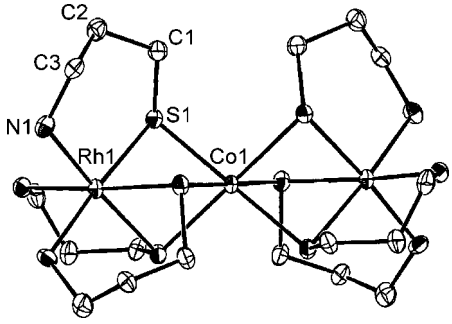


Figure 4. Crystal structure of **2b**.

The Co···Rh distances in apt complexes **2a** and **2b** [3.0490(4) and 3.063(1) Å] are significantly longer than that in the aet complex **4a** [2.9139(2) Å]. The Rh–S [av. 2.322(1) Å], Rh–N [av. 2.133(5) Å], and Co–S [av. 2.291(1) Å] distances in **2a** are slightly longer than those in **4a** [av. 2.306(8), av. 2.121(3), and av. 2.290(9) Å]. The S–Rh–S (av. 80.43(4)°), N–Rh–N [av. 88.2(2)°], and S–Co–S [av. 81.71(4)°] angles in **2a** are more acute than those in **4a** [av. 83.75(3), av. 96.2(1), and av. 84.45(3)°] while Co–S–Rh angles [av. 82.73(4)°] in **2a** are more obtuse than those in **4a** [av. 78.67(3)°]. These differences in the bond lengths and angles are attributed to the presence of six-membered chelate rings that are formed between the metal and ligands in the case of apt complexes **2a** and **2b** compared with the five-membered chelate rings found in the case of aet complex **4a**. It can be concluded that increasing the number of methylene groups in the chelate rings influences the stereochemistry of the complexes. Six-membered chelate rings give rise to a larger bite angle than five-membered rings, which is very clearly observed in the present case. The S–Rh–N bite angles in **2a** [av. 96.0(1)°] and **2b** [98.5(3)°] are significantly larger than those in **4a** [av. 87.0(1)°].

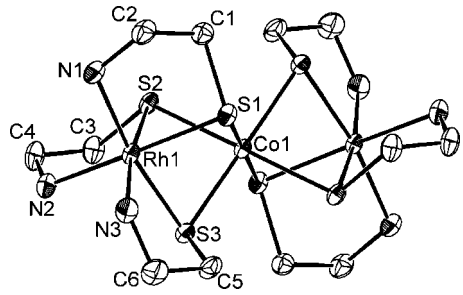


Figure 5. Crystal structure of **4a**.

## Spectroscopic Properties

### *UV/Visible Spectra*

Diffuse reflectance (DR) spectra of **1** and **3** were measured in the solid state, since the neutral mononuclear complexes are sparingly soluble in water. Both complexes exhibit the characteristic intense bands at ca. $40\times10^3$ cm$^{-1}$. These bands may be due to charge transfer (CT) transitions from the sulfur atoms to the Rh$^{III}$ ion. This suggests that **1** is the apt mononuclear complex *fac*(*S*)-[Rh(apt)$_3$] with the same geometry as **3**.

UV/Vis absorption (AB), DR, and circular dichroism (CD) spectra of **2a** and **2b** are shown in Figure 6. It was found that **2a** and **2b** exhibit characteristic AB and CD spectra of the trinuclear structure just as for complexes **4a** and **4b** with some shift towards the higher energy side.[33] The observed AB peaks arise from d–d transitions and CT transitions from the sulfur atoms to the metal ions. The peaks observed at about $40–50\times10^3$ cm$^{-1}$ are due to CT transitions from the sulfur atoms to the Rh$^{III}$ ion. DR and AB spectra show similar patterns, and therefore it is believed that the symmetry of **2a** and **2b** is not altered in solution. Furthermore, AB did not change with time. This means that **2a** and **2b** are stable for a long time in solution.

 © 2006 Wiley-VCH Verlag GmbH & Co. KGaA, Weinheim 

Table 2. Selected bond lengths [Å] and angles [°] of **2a** and **4a**.

| | **2a** | **4a** | | **2a** | **4a** |
|---|---|---|---|---|---|
| Rh1–S1 | 2.316(1) | 2.3121(9) | Rh1–S2 | 2.330(1) | 2.3077(9) |
| Rh1–S3 | 2.320(1) | 2.2993(7) | Rh1–N1 | 2.138(5) | 2.122(3) |
| Rh1–N2 | 2.127(4) | 2.123(4) | Rh1–N3 | 2.136(5) | 2.120(3) |
| Co1–S1 | 2.291(1) | 2.2853(9) | Co1–S2 | 2.294(1) | 2.3069(9) |
| Co1–S3 | 2.290(1) | 2.2796(7) | Rh1···Co1 | 3.0490(4) | 2.9139(2) |
| Rh1–S1–Co1 | 82.87(4) | 78.66(3) | Rh1–S2–Co1 | 82.51(4) | 78.31(3) |
| Rh1–S3–Co1 | 82.82(5) | 79.04(2) | S1–Rh1–S2 | 80.74(4) | 83.29(3) |
| S1–Rh1–S3 | 80.77(4) | 84.32(3) | S2–Rh1–S3 | 79.83(5) | 83.63(3) |
| N1–Rh1–N2 | 87.0(2) | 96.0(1) | N1–Rh1–N3 | 88.2(2) | 96.4(1) |
| N2–Rh1–N3 | 89.4(2) | 96.2(1) | S1–Co1–S2 | 81.99(4) | 83.90(3) |
| S1–Co1–S3 | 81.94(4) | 85.38(3) | S2–Co1–S3 | 81.20(5) | 84.08(3) |
| S1–Rh1–N1 | 96.3(1) | 87.04(9) | S2–Rh–N2 | 95.2(1) | 87.0(1) |
| S3–Rh1–N3 | 96.5(1) | 87.06(8) | | | |

Table 3. Selected bond lengths [Å] and angles [°] of **2b**.

| | | | |
|---|---|---|---|
| Rh1–S1 | 2.327(3) | Rh1–N1 | 2.13(1) |
| Co1–S1 | 2.304(3) | Rh1···Co1 | 3.063(1) |
| Rh1–S1–Co1 | 82.82(9) | S1–Rh1–S1[a] | 80.5(1) |
| N1–Rh1–N1[a] | 86.7(5) | S1–Co1–S1[a] | 81.5(1) |
| S1–Rh1–N1 | 98.5(3) | | |

[a] Symmetry code: $1 - y, x - y, z$.

When comparative studies were performed, it was found that there was no significant difference between the electronic spectra of the aqueous solutions of **2a**, **2b** and **4a**, **4b**. This trend is similar to that of $[Co\{Co(aet \text{ or } apt)_3\}_2]^{3+}$ [14,21], whereas it is different from that of $[Ni\{Ni(aet \text{ or } apt)_2\}_2]^{2+}$, in which important differences were observed.[15] The AB peaks in **2a** and **2b** were observed at higher energy levels compared with those in the corresponding $Co^{III}$ and $Ni^{II}$ complexes. It is therefore concluded that the addition of another methylene group to the chelate ring in octahedral trinuclear complexes does not cause important modifications in the chromophores, and the structures are very similar in both cases.

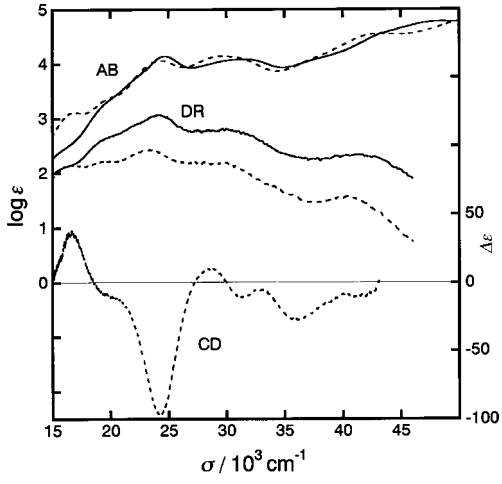


Figure 6. UV/Vis AB (log $\varepsilon$), DR (arbitrary scale), and CD ($\Delta\varepsilon$) spectra of **2a** (———) and $(-)^{CD}_{412}$-**2b** (- - - - -).

The CD spectrum of **2b**, which was optically resolved with an SP-Sephadex C-25 column, shows bands in the region $15–40 \times 10^3$ cm$^{-1}$. These CD bands correspond well to the d–d and CT bands for $[Co\{Rh(apt)_3\}_2]^{3+}$ in the AB spectra. It seems that $(-)^{CD}_{412}$-**2b** is the ΛΛ isomer and $(+)^{CD}_{412}$-**2b** is the ΔΔ isomer. The CD spectrum of **2b** is also in agreement with that of **4b**. In the CD spectra, no significant changes were observed with time over several hours. This illustrates that the trinuclear structures are fairly stable, retaining their oxidation state even under aerobic conditions.

### *IR and Far-IR Spectra*

The IR and far-IR spectra of **I**, **II**, and aptH·HCl show all the characteristic bands for the vibration and bending modes of the $NH_2$ and $CH_2$ groups (Figure S1). The overall IR spectral pattern of **1** is in good agreement with that of **3**.[35] The IR spectral patterns of **2a**$(NO_3)_3$ and **2b**$Br_3$ are similar to each other, reflecting the similarity between the isomers (Figure S2). Moreover, these spectral patterns are typical for linear-type, S-bridged trinuclear complexes in the range 4000–400 cm$^{-1}$.[2,3,35–38] The IR spectra of **1**, **2a**$(NO_3)_3$, and **2b**$Br_3$ show characteristic bands in the range 3500–2800 cm$^{-1}$, corresponding to the vibration modes of the $NH_2$ and $CH_2$ groups. The bands for the bending mode of the $NH_2$ and $CH_2$ groups are observed at 1700–1000 cm$^{-1}$. The IR spectra show similar patterns in the range 3500–2800 cm$^{-1}$, but in the range 1700–1000 cm$^{-1}$, there are small differences between the spectrum of the mononuclear complex **1** and those of the trinuclear complexes **2a**$(NO_3)_3$ and **2b**$Br_3$. The bands at ca. 1100 cm$^{-1}$ in **1** are shifted to higher energies in **2a**$(NO_3)_3$ and **2b**$Br_3$, which reflects the change from mononuclear to trinuclear geometry. The same trend is observed in the case of $Co^{II}$, $Ni^{II}$, $Zn^{II}$, $Cd^{II}$, and $Hg^{II}$ complexes with apt.[14,15,20,21] The similarity between the IR spectral patterns of **1** and those of the trinuclear **2a**$(NO_3)_3$ and **2b**$Br_3$ shows that the terminal units retain their structure during the formation of S-bridged complexes. The absence of bands in the range 2550–2600 cm$^{-1}$ (υS–H) is characteristic of coordinated sulfur. The far-IR spectra of **1**, **2a**$(NO_3)_3$, and **2b**$Br_3$ are quite complicated, but show little difference in the region 500–420 cm$^{-1}$ be-

 © 2006 Wiley-VCH Verlag GmbH & Co. KGaA, Weinheim 

Table 4. $^1$H- and $^{13}$C NMR spectral data (coupling constants/Hz).[a]

| | N*H* | NC$H_2$ | C$H_2$ | SC$H_2$ |
|---|---|---|---|---|
| **I** | –[c] | 4.17 (t, 2 H, 5.7) | 2.07 (2 H, quint, 6.4) | 3.15(t, 2 H, 7.2)[d] |
| **II**[b] | 9.02 (s, 1 H) | 3.48 (t, 2 H, 4.1) | 2.18 (2 H, quint, 5.7) | 3.00 (t, 2 H, 5.9) |
| aptH·HCl | –[c] | 3.12 (t, 2 H, 7.6) | 2.10 (2 H, quint, 7.3) | 2.82 (t, 2 H, 7.1) |
| **2a** | 4.15[c] | 2.98 (m, 2 H) | 2.15 (d, 1 H, 15.6) | 2.45 (dd, 1 H, 5.1, 4.9) |
| | 3.41[c] | | 1.83 (dd, 1 H, 11.6, 13.3) | 2.08 (t, 1 H, 13.5) |
| **2b** | 4.14[c] | 2.98 (dd, 1 H, 5.5, 5.2) | 2.18 (d, 1 H, 15.7) | 2.46 (dd, 1 H, 5.2, 5.1) |
| | 3.33[c] | 2.92 (dd, 1 H, 10.6, 12.9) | 1.74 (dd, 1 H, 6.0, 12.7) | 1.89 (t, 1 H, 12.5) |
| **4a** | –[c] | 3.15 (d, 1 H, 11.2) | | 2.49 (d, 1 H, 13.2) |
| | –[c] | 2.73 (dd, 1 H, 22.5, 13.9) | | 1.86 (td, 1 H, 13.5, 3.3) |
| **4b** | –[c] | 3.16 (d, 1 H, 12.9) | | 2.39 (d, 1 H, 11.2) |
| | –[c] | 2.73 (dd, 1 H, 23.7, 10.5) | | 1.73 (td, 1 H, 13.5, 3.6) |
| | *C*=S | NC$H_2$ | C$H_2$ | SC$H_2$ |
| **I** | | 68.92 | 29.19 | 39.61[e] |
| **II**[b] | 194.61 | 44.30 | 20.46 | 30.02 |
| aptH·HCl | | 40.72 | 28.60 | 36.39 |
| **2a** | | 44.04 | 29.82 | 30.72 |
| **2b** | | 43.82 | 30.84 | 31.18 |
| **4a** | | 49.89 | | 34.40 |
| **4b** | | 50.11 | | 34.62 |

[a] ppm from $D_2O$ containing DSS. [b] ppm from $CHCl_3$ containing TMS. [c] N$H_2$ signals were broad or missing due to H–D exchange. [d] OC$H_2$. [e] OC$H_2$.

tween the mononuclear complex **1** and the two trinuclear complexes **2a**$(NO_3)_3$ and **2b**$Br_3$ (Figure S2). Because the far-IR spectra were complicated, it was difficult to assign the bands for the shifts resulting from the vibrations of the Co–S bonds.

### *NMR Spectra*

The $^1$H- and $^{13}$C NMR spectra were measured for each product during the synthesis of ligands **2a** and **2b**. The ligand aptH·HCl as well as **I** and **II** show three sharp signals for the C$H_2$ protons and three sharp signals for the *C*$H_2$ carbons. The proton signals in the $^{13}$C-$^1$H heteronuclear multiple-bond correlation spectrum (HMBC) of aptH·HCl show coupling with the corresponding carbon signals (Figure S3). Moreover, the proton signals in the $^1$H-$^1$H correlation spectroscopy (COSY) indicate coupling between the corresponding proton signals. Both **2a** and **2b** also exhibit three sets of sharp proton signals and three carbon signals resulting from the six apt ligands (Figure S4). This means that the $S_6$ or $D_3$ symmetrical, S-bridged, trinuclear structures observed in the crystals are retained in aqueous solution. The details of the NMR spectroscopic data are shown in Table 4. In **2a** and **2b**, the chemical resonances in the $^1$H NMR spectra show shifts to lower fields for the NC$H_2$ protons and to higher fields for the SC$H_2$ protons. Moreover, the splitting pattern for the protons is also different from that observed in **4a** and **4b**.[35] It is worth noting that the chemical shifts for the N*C*$H_2$ and S*C*$H_2$ carbon atoms in **2a** and **2b** show shifts to higher fields than those for **4a** and **4b**.

### Electrochemical Properties

Cyclic voltammetry experiments were performed for **2a** and **2b**. The cyclic voltammogram obtained for **2b** is shown in Figure 7. For the already reported complexes of apt with $Co^{III}$, $Ni^{II}$, $Zn^{II}$, $Cd^{II}$, and $Hg^{II}$, there is no information about the electrochemical properties.[14,15,20,21] Therefore, to the best of our knowledge, this is the first report on the electrochemistry of S-bridged complexes containing apt. Each of the voltammograms displays a quasi-reversible redox couple in the negative potential region. In analogy to the characterized electrochemistry of the $[Co\{M(aet)_3\}_2]^{3+}$ (M = $Rh^{III}$, $Co^{III}$) system,[33,39–41] this redox process is assigned as the redox couple corresponding to $Co^{III/II}$. The redox couples of the apt complexes **2a** (–0.56 V) and **2b** (–0.57 V) are more negative than those of the aet complexes **4a** (–0.35 V) and **4b** (–0.36 V).[33,39] This means that the $Co^{III}$ state in apt complexes is more stable than that in **4a** and **4b**. A possible reason for this might be the difference in nucleophilicity of sulfur or structural differences of the $Co^{III}$ ion resulting from the additional methylene group in apt, which forms six-membered chelates rather than five-membered ones, as is the case for aet. Since the difference in reduction potential resulting from the difference in the configuration of complexes is very slight, the $E_{1/2}$ value for the *meso* isomer **2a** is only 0.01 V more positive than that for the corresponding *racemic* isomer **2b**. A profound difference was observed when the ligand was changed from *fac*(*S*)-[Rh(aet)$_3$] to *fac*(*S*)-[Rh(apt)$_3$], where **2b** is reduced (0.21 V) more easily than **4b**. The redox process of **2b** is reversible, as with **4a** and **4b**. However, in the case of **2a**, the observed peak separation was too broad to establish whether the redox process is reversible. The difference in electrochemical properties of **2a**, **2b** and **4a**, **4b** could be related to the difference of reactivity explained in the synthetic part, where it was found that, in the case of **2a** and **2b**, the reaction under nitrogen or air gave the trivalent $Co^{III}$ complexes as compared with the case of **4a** and **4b**, where $H_2O_2$ was used for oxidation.

 © 2006 Wiley-VCH Verlag GmbH & Co. KGaA, Weinheim 

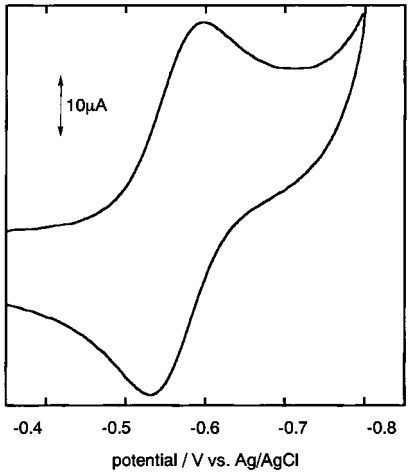


Figure 7. Cyclic voltammogram of **2b**.

## Conclusions

A novel mononuclear complex *fac*(*S*)-[Rh(apt)$_3$] (**1**) was synthesized and characterized by spectroscopic methods. The reaction of **1** with $CoCl_2 \cdot 6H_2O$ in water formed linear-type, S-bridged trinuclear complexes ΔΛ-[Co{Rh(apt)$_3$}$_2$]$^{3+}$ (**2a**) and ΔΔ/ΛΛ-[Co{Rh(apt)$_3$}$_2$]$^{3+}$ (**2b**), unlike ΔΛ-[Co{Rh(aet)$_3$}$_2$]$^{3+}$ (**4a**) and ΔΔ/ΛΛ-[Co{Rh(aet)$_3$}$_2$]$^{3+}$ (**4b**) where an oxidizing agent was required. The complexes were characterized by stereochemical, spectrochemical, and electrochemical techniques. The Co···Rh, Rh–S, and Rh–N distances in **2a** and **2b** are longer than those of **4a**. The differences in bond lengths and angles are due to the presence of six-membered chelate rings in **2a** and **2b**, rather than the five-membered chelate rings in **4a**. The absorption bands in **2a** and **2b** are shifted to higher energies than those of **4a**. The results of IR and far-IR spectra indicate that the terminal units retain their structure during the formation of S-bridged complexes. NMR spectra of **2a** and **2b** show that the chemical shift values in $^{13}C$ NMR are shifted to higher fields as compared to **4a** and **4b**. In addition, the $Co^{III}$ oxidation state in **2a** and **2b** is more stable than that in **4a** and **4b**. It can be concluded that the properties of complexes are greatly influenced by increasing the number of methylene groups in the chelate rings.

## Experimental Section

### Materials

The aet complexes *fac*(*S*)-[Rh(aet)$_3$] (**3**), ΔΛ-[Co{Rh(aet)$_3$}$_2$](NO$_3$)$_3$ [**4a**(NO$_3$)$_3$], and ΔΔ/ΛΛ-[Co{Rh(aet)$_3$}$_2$]Br$_3$ (**4b**Br$_3$) were prepared by procedures similar to those in the literature.[31–33] All reagents were purchased from Wako Pure Chemical Ind. Ltd. All chemicals were of reagent grade and were used without further purification.

### Preparation of Ligand

The ligand was prepared by literature methods with some modifications as follows.[22–24]

**1-Amino-3-propylsulfate (I):** A mixture of 3-amino-1-propanol (75.1 g, 1.0 mol) and carbon tetrachloride (200 cm$^3$) was cooled in an ice bath. Chlorosulfonic acid (116.5 g, 1.0 mol) was slowly added to the mixture. The reaction mixture was kept overnight, and carbon tetrachloride was removed in vacuo. The crude solid was crushed with methanol (400 cm$^3$), and isolated by filtration. A pure white powder of 1-amino-3-propylsulfate was obtained by recrystallization from water/methanol. Yield: 123.5 g, 79%. $C_3H_9NO_4S$ (155.17): calcd. C 23.35, H 5.66, N 9.15; found C 22.87, H 5.57, N 8.88.

**Tetrahydro-1,3-thiazine-2-thione (II):** To a suspension containing 1-amino-3-propylsulfate (252.2 g, 1.62 mol) and carbon disulfide (150.0 g, 1.94 mol) in ethanol (50%, 700 cm$^3$) was added slowly in an ice bath NaOH (141.8 g, 3.56 mol) in ethanol (50%, 300 cm$^3$). After the reaction mixture was heated to reflux for 30–40 min the ethanol was removed by evaporation. Colorless crystals of tetrahydro-1,3-thiazine-2-thione were obtained by recrystallization from hot water. Yield: 149.0 g, 70%. $C_4H_7NS_2$ (133.22): calcd. C 36.06, H 5.30, N 10.51; found C 35.40, H 5.06, N 10.34.

**3-Aminopropanethiol Hydrochloride (aptH·HCl):** A suspension of tetrahydro-1,3-thiazine-2-thione (149.0 g, 1.12 mol) in conc. HCl (800 cm$^3$) was heated to reflux for 3 weeks. After evaporating until an oil remained, a white precipitate of aptH·HCl was obtained by the addition of ethanol/ether. Yield 133.0 g, 95%. $C_3H_{10}ClNS$ (127.63): calcd. C 28.23, H 7.89, N 10.97; found C 29.05, H 6.67, N 10.30.

### Preparation of Complexes

***fac*(*S*)-[Rh(apt)$_3$] (1):** To a solution containing NaOH (0.61 g, 15 mmol) in water (10 cm$^3$) was added $RhCl_3 \cdot 3H_2O$ (0.10 g, 0.38 mmol). A solution of aptH·HCl (1.10 g, 8.6 mmol) in water (40 cm$^3$) was then added to this mixture . The mixture gave a yellow precipitate after slight heating and was then heated to reflux for a further 1–1.5 h. The yellow precipitate was collected by filtration and washed with water, methanol, and acetone. Yield of **1**·2H$_2$O: 0.075 g, 53%. $C_9H_{28}N_3O_2RhS_3$ (409.42): calcd. C 28.05, H 6.63, N 10.90; found C 28.02, H 6.11, N 10.34. Reflectance maxima ($\sigma$/$10^3$ cm$^{-1}$): 13.5, 28.5, 34.1 sh, 40.4.

**ΔΛ-[Co{Rh(apt)$_3$}$_2$](NO$_3$)$_3$ [2a(NO$_3$)$_3$] and ΔΔ/ΛΛ-[Co{Rh(apt)$_3$}$_2$]Br$_3$ (2bBr$_3$):** To a suspension containing **1** (0.20 g, 0.55 mmol) in water (10 cm$^3$) was added a solution containing $CoCl_2 \cdot 6H_2O$ (0.65 g, 2.7 mmol) in water (5 cm$^3$). The mixture was stirred at room temperature for 30 min and filtered. A saturated aqueous solution of $NaNO_3$ (5 cm$^3$) was added to the dark brown filtrate, and the resulting dark red crystals [**2a**(NO$_3$)$_3$·2H$_2$O] were collected by filtration. A saturated aqueous solution of NaBr (5 cm$^3$) was added to the filtrate, and the resulting dark red crystals (**2b**Br$_3$·3.5H$_2$O) were collected by filtration. Crystals suitable for X-ray crystallography were obtained by recrystallization of **2a**(NO$_3$)$_3$·2H$_2$O and **2b**Br$_3$·3.5H$_2$O from the aqueous solutions containing $NaNO_3$ and NaCl. Yield of **2a**(NO$_3$)$_3$·2H$_2$O: 0.065 g, 12%. $C_{18}H_{52}CoN_9O_{11}Rh_2S_6$ (1027.77): calcd. C 21.04, H 5.10, N 12.27; found C 21.19, H 4.98, N 11.89. Absorption maxima [$\sigma$/$10^3$ cm$^{-1}$ (log $\varepsilon$/mol$^{-1}$·dm$^3$·cm$^{-1}$)]: 14.5 (2.11), 20.9 (3.49), 24.7 (4.14), 31.5 (4.08 sh), 38.6 (4.13 sh), 48.7 (4.78). Reflectance maxima ($\sigma$/$10^3$ cm$^{-1}$): 15.3, 19.0, 24.2, 29.6 sh, 41.1. Yield of **2b**Br$_3$·3.5H$_2$O: 0.045 g, 7.9%. $C_{18}H_{55}Br_3CoN_6O_{3.5}Rh_2S_6$ (1100.49): calcd. C 19.50, H 5.00, N 7.58; found: C 19.73, H 5.08, N 7.96. Absorption maxima [$\sigma$/$10^3$ cm$^{-1}$ (log $\varepsilon$/mol$^{-1}$·dm$^3$·cm$^{-1}$)]: 16.7 (3.11), 18.3 (3.14), 24.3 (4.06), 29.7 (4.14 sh), 40.2 (4.35 sh), 51.0 (4.80). Reflectance maxima ($\sigma$/$10^3$ cm$^{-1}$): 16.5, 19.1, 23.4, 29.5 sh, 40.3.

### Column Chromatography

Column chromatography was also performed with an SP-Sephadex C-25 column ($Na^+$ form). When the reddish brown filtrate was

 © 2006 Wiley-VCH Verlag GmbH & Co. KGaA, Weinheim 

eluted with a NaCl solution (0.5 M), two bands were obtained: a reddish brown band followed by a greenish brown band. The UV/Vis absorption spectra of the bands showed that the reddish brown band contains **2a** and the greenish brown band contains **2b**. The purity of the isomers that had been obtained by fractional precipitation, was confirmed by column chromatography [SP-Sephadex C-25 column ($Na^+$ form)].

**Optical Resolution of 2b**

Compound **2b** was optically resolved with an SP-Sephadex C-25 column ($K^+$ form). An aqueous solution of **2b** was charged onto the column and adsorbed. The column was first eluted with an aqueous solution of $K_2[Sb_2(R,R\text{-tartrato})_2]\cdot 5H_2O$ (0.15 M), whereupon two distinct greenish brown bands were separated. The bands were finally eluted and collected by an aqueous solution of KCl (0.5 M). The CD spectra of the two bands were measured, which had a positive or negative CD sign at 412 nm. The CD spectra of two bands were just opposite to each other. The $\Delta\varepsilon$ values of each eluent containing the $(+)_{412}^{CD}$ and $(-)_{412}^{CD}$-**2b** isomers were evaluated on the basis of the absorption spectroscopic data of **2b**$Br_3\cdot 3.5H_2O$. CD extrema [$\sigma/10^3$ $cm^{-1}$ ($\Delta\varepsilon$/$mol^{-1}\cdot dm^3\cdot cm^{-1}$)]: **2b** (lower) 16.73 (–41.06), 24.26 (+99.62), 28.62 (–11.27), 31.38 (+10.65), 35.94 (+28.10), 42.05 (+10.96); **2b** (upper) 16.62 (+38.24), 24.19 (–96.92), 28.80 (+10.45), 31.46 (–11.07), 36.23 (–27.98), 41.87 (–10.12).

**Measurements**

Elemental analysis (C, H, and N) was performed by the Department of Chemistry in the University of Tsukuba. The concentrations of Co and Rh in the complexes were determined with a NIPPON Jarrell-Ash ICPA-575 spectrometer. UV/Vis absorption spectra were recorded with a JASCO V-560 spectrophotometer and solid-state diffuse reflectance spectra were recorded with a JASCO V-570 spectrophotometer equipped with an integrating sphere apparatus (JASCO ISN-470) using powder samples diluted with MgO. IR and far-IR spectra were recorded with a JASCO FT/IR-550 spectrometer using KBr disks in the range 4000–400 $cm^{-1}$ and Nujol mulls between polyethylene pellets in the range 650–50 $cm^{-1}$. $^1H$ and $^{13}C$ NMR spectra were recorded with a BRUKER AM500 and AM600 NMR spectrometer in $D_2O$ using sodium 4,4-dimethyl-4-silapentane-1-sulfonate (DSS) as an internal reference or $CDCl_3$ using tetramethylsilane (TMS) as an internal reference. The molar conductance of the complexes was measured with a HORIBA conductivity meter (DS-14). Electrochemical experiments were performed with a CV-50W voltammetry analyzer, Bioanalytical Systems, Inc. (BAS) with a platinum-working electrode (BAS, Pt). In the electrochemical experiments an aqueous Ag/AgCl/NaCl (3 $mol\cdot dm^{-3}$) (BAS, RE-1B) and platinum wire were used as the reference and auxiliary electrodes, respectively. All the measurements were carried out at room temperature in an aqueous solution, which was bubbled with $N_2$ gas, and contained $Na_2SO_4$ (0.1 $mol\cdot dm^{-3}$) as a supporting electrolyte.

**X-ray Crystal Structure Determinations**

Single-crystal X-ray data collections were performed with a Rigaku AFC-7S Mercury CCD area detector with a graphite monochromatized Mo-$K_\alpha$ (0.71070 Å) radiation using the CrystalClear (Rigaku) program package. Crystallographic data of **II** and complexes **2a**$(NO_3)_3\cdot 2H_2O$, **2b**$Cl_3$, and **4a**$(NO_3)_3\cdot 3H_2O$ are listed in Table 5. The positions of Rh, Co, and non-hydrogen atoms were determined by direct methods (SHELX 97 **2a**, **4a**)[42] or (SIR97 **II**, **2b**),[43] and some remaining atom positions were found by successive difference Fourier techniques (DIRDIFF-99).[44] The structures were refined by full-matrix least-squares techniques using anisotropic thermal parameters for non-hydrogen atoms. All hydrogen atoms except for those of **II** were included in calculated positions but not refined. The CrystalStructure (Rigaku) program package was used for the calculations.[45]

CCDC-279990–CCDC-279993 contain the supplementary crystallographic data for this paper. These data can be obtained free of charge from The Cambridge Crystallographic Data Centre via www.ccdc.cam.ac.uk/data_request/cif.

**Supporting Information** (see footnote on the first page of this article): IR and far-IR spectra of **I**, **II**, and aptH·HCl (Figure S1); IR and far-IR spectra of complexes **1**, **2a**, and **2b** (Figure S2); $^1H$-$^1H$

Table 5. Crystallographic Data for **II**, **2a**$(NO_3)_3\cdot 2H_2O$, **2b**$Cl_3$, and **4a**$(NO_3)_3\cdot 3H_2O$.

| | **II** | **2a**$(NO_3)_3\cdot 2H_2O$ | **2b**$Cl_3$ | **4a**$(NO_3)_3\cdot 3H_2O$ |
|---|---|---|---|---|
| Empirical formula | $C_4H_7NS_2$ | $C_{18}H_{52}CoN_9O_{11}Rh_2S_6$ | $C_{18}H_{48}Cl_3CoN_6Rh_2S_6$ | $C_{12}H_{42}CoN_9O_{12}Rh_2S_6$ |
| Formula weight | 133.23 | 1027.77 | 912.08 | 961.62 |
| Dimensions [mm] | 0.55×0.30×0.10 | 0.27×0.20×0.05 | 0.15×0.13×0.10 | 0.25×0.25×0.10 |
| Crystal system | monoclinic | monoclinic | hexagonal | triclinic |
| Space group | $P2_1/n$ (#14) | $C2/c$ (#15) | $P6/mcc$ (#192) | $P\bar{1}$ (#2) |
| $a$ [Å] | 4.9986(5) | 17.2186(7) | 12.8060(2) | 8.8570(1) |
| $b$ [Å] | 6.2381(7) | 9.3370(2) | | 8.9760(1) |
| $c$ [Å] | 19.717(2) | 23.2258(10) | 26.3105(5) | 12.0893(1) |
| $\alpha$ [°] | | | | 70.854(8) |
| $\beta$ [°] | 93.486(2) | 98.1420(5) | | 69.761(8) |
| $\gamma$ [°] | | | | 77.198(9) |
| Volume [Å$^3$] | 613.69(11) | 3696.4(2) | 3736.69(11) | 845.52(2) |
| $Z$ | 4 | 4 | 4 | 1 |
| $D_{calcd.}$ [$g\cdot cm^{-3}$] | 1.442 | 1.847 | 1.621 | 1.888 |
| $\mu$ [$cm^{-1}$] | 7.39 | 17.25 | 18.79 | 18.80 |
| Total reflections | 9380 | 29146 | 31160 | 13730 |
| Unique reflections | 1444 | 4413 | 1771 | 3820 |
| $R_{int}$ | 0.020 | 0.030 | 0.073 | 0.016 |
| Used [$I > 3\sigma(I)$] | 1113 | 2701 | 699 | 3482 |
| No. Variables | 64 | 239 | 65 | 250 |
| Used/ Variables | 17.39 | 11.30 | 10.75 | 13.93 |
| Final $R$ [$I > 3\sigma(I)$] | 0.062 | 0.036 | 0.074 | 0.039 |
| Final $Rw$ [$I > 3\sigma(I)$] | 0.194 | 0.092 | 0.195 | 0.126 |
| Goodness of fit | 1.000 | 1.019 | 1.002 | 1.002 |

 © 2006 Wiley-VCH Verlag GmbH & Co. KGaA, Weinheim 

COSY and $^{1}H$-$^{13}C$ HMQC NMR spectra of aptH·HCl (Figure S3); $^{1}H$-$^{1}H$ COSY of **2a** and **2b** (Figure S4).

## Acknowledgments

This work was supported by a Grant-in-Aid for Scientific Research, Center of Excellence (COE) program from the Japanese Society for the Promotion of Science, and University of Tsukuba Research Projects.

[1] T. Konno, *Bull. Chem. Soc. Jpn.* **2004**, *77*, 627–649 and the references found therein.
[2] N. Mahboob (Amir), Y. Miyashita, Y. Yamada, K. Fujisawa, K. Okamoto, *Inorg. Chim. Acta* **2004**, *357*, 75–82.
[3] N. Amir, Y. Miyashita, M. Fujita, K. Fujisawa, K. Okamoto, *Mol. Cryst. Liq. Cryst.* **2005**, *428*, 101–110.
[4] Y. Chikamoto, M. Hirotsu, T. Yamaguchi, T. Yoshimura, T. Konno, *Dalton Trans.* **2004**, 3654–3661.
[5] Y. Chikamoto, T. Kawamoto, A. Igashira-Kamiyama, T. Konno, *Inorg. Chem.* **2005**, *44*, 1601–1610.
[6] E. N. Duesler, K. N. Raymond, *Inorg. Chem.* **1971**, *10*, 1486–1492.
[7] Y. Saito, K. Nakatsu, M. Shiro, H. Kuroya, *Bull. Chem. Soc. Jpn.* **1957**, *30*, 795–799.
[8] Y. Saito, K. Nakatsu, M. Shiro, H. Kuroya, *Acta Crystallogr.* **1955**, *8*, 729–730.
[9] S. R. Niketic, F. Woldbye, *Acta Chem. Scand.* **1973**, *27*, 621–642.
[10] F. A. Jurnak, K. N. Raymond, *Inorg. Chem.* **1972**, *11*, 3149–3152.
[11] E. J. Corey, J. C. Bailer, *J. Am. Chem. Soc.* **1959**, *81*, 2620–2629.
[12] J. R. Gollogly, C. J. Hawkins, *Chem. Commun.* **1968**, 689–690.
[13] S. Sato, Y. Saito, J. Fujita, H. Ogino, *Inorg. Nucl. Chem. Lett.* **1974**, *10*, 669–673.
[14] H. Barrera, J. Suades, *Transition Met. Chem.* **1984**, *9*, 342–344.
[15] H. Barrera, J. Suades, M. C. Perucaud, J. L. Brianso, *Polyhedron* **1984**, *3*, 839–843.
[16] G. J. McDougll, R. D. Hancock, J. C. A. Boeyens, *J. Chem. Soc., Dalton Trans.* **1978**, 1438–1444.
[17] H. Jude, J. A. K. Bauer, W. B. Connick, *Inorg. Chem.* **2005**, *44*, 1211–1220.
[18] B. P. Kennedy, A. B. P. Lever, *Can. J. Chem.* **1972**, *50*, 3488–3507.
[19] M. A. Ali, S. E. Livingstone, *Coord. Chem. Rev.* **1974**, *13*, 101–132.
[20] H. Barrera, J. Pons, J. Suades, *An. Quim., Ser. B.* **1984**, *80*, 311–314.
[21] J. Suades, X. Solans, M. Font-Altaba, M. Aguilo, *Inorg. Chim. Acta* **1985**, *99*, 1–4.
[22] S. D. Turk, R. P. Louthan, R. L. Cobb, C. R. Bresson, *J. Org. Chem.* **1962**, *27*, 2846–2853.
[23] H. Wenker, *J. Am. Chem. Soc.* **1935**, *57*, 2328.
[24] T. C. Owen, *J. Chem. Soc., C* **1967**, 1373–1376.
[25] E. S. Raper, J. R. Creighton, *Acta Crystallogr., Sect. B* **1983**, *39*, 355–360.
[26] C. Chieh, S. K. Cheung, *Can. J. Chem.* **1983**, *61*, 211–213.
[27] N. Trinajstic, *Tetrahedron Lett.* **1968**, *9*, 1529–1532.
[28] P. J. Wheatley, *Acta Crystallogr.* **1953**, *6*, 369–377.
[29] H. W. Dias, M. R. Truter, *Acta Crystallogr.* **1964**, *17*, 937–943.
[30] M. Fujita, Y. Miyashita, N. Amir, Y. Kawamoto, K. Kanamori, K. Fujisawa, K. Okamoto, *Polyhedron* **2005**, *24*, 1991–2001.
[31] M. Kita, K. Yamanari, Y. Shimura, *Bull. Chem. Soc. Jpn.* **1983**, *56*, 3272–3275.
[32] T. Konno, K. Okamoto, J. Hidaka, *Inorg. Chem.* **1994**, *33*, 538–544.
[33] T. Konno, S. Aizawa, K. Okamoto, J. Hidaka, *Bull. Chem. Soc. Jpn.* **1990**, *63*, 792–798.
[34] Y. Miyashita, N. Sakagami, Y. Yamada, T. Konno, J. Hidaka, K. Okamoto, *Bull. Chem. Soc. Jpn.* **1998**, *71*, 661–670.
[35] Y. Miyashita, N. Mahboob (Amir), S. Tsuboi, Y. Yamada, K. Fujisawa, K. Okamoto, *Bull. Chem. Soc. Jpn.* **2001**, *74*, 1295–1301.
[36] Y. Miyashita, H. Hamajima, Y. Yamada, K. Fujisawa, K. Okamoto, *J. Chem. Soc., Dalton Trans.* **2001**, 2089–2094.
[37] Y. Miyashita, Y. Yamada, K. Fujisawa, T. Konno, K. Kanamori, K. Okamoto, *J. Chem. Soc., Dalton Trans.* **2000**, 981–987.
[38] N. Mahboob (Amir), Y. Miyashita, Y. Yamada, K. Fujisawa, K. Okamoto, *Polyhedron* **2002**, *21*, 1809–1816.
[39] T. Konno, K. Nakamura, K. Okamoto, J. Hidaka, *Bull. Chem. Soc. Jpn.* **1993**, *66*, 2582–2589.
[40] S. Aizawa, K. Okamoto, H. Einaga, J. Hidaka, *Bull. Chem. Soc. Jpn.* **1988**, *61*, 1601–1606.
[41] S. Miyanowaki, T. Konno, K. Okamoto, J. Hidaka, *Bull. Chem. Soc. Jpn.* **1988**, *61*, 2987–2989.
[42] G. M. Sheldrick, SHELXL97 program for Crystal Structure Refinement from Diffraction Data, University of Göttingen, Göttingen, Germany, **1997**.
[43] A. Altomare, M. Burla, M. Camalli, G. Cascarano, C. Giacovazzo, A. Guagliardi, A. Moliterni, G. Polidori, R. Spagna, *J. Appl. Crystallogr.* **1999**, *32*, 115–119.
[44] P. T. Beurskens, G. Admiraal, G. Beurskens, W. P. Bosman, R. de Gelder, R. Israel, J. M. M. Smits, *The DIRDIF-99 Program System*, Technical Report of the Crystallography Laboratory, University of Nijmegen, The Netherlands, **1999**.
[45] Crystal Structure Analysis Package, Rigaku and Rigaku/MSC, 9009 New Trails Dr. The Woodlands TX 77381 USA, **2002**–**2003**.

Received: August 4, 2005
Published Online: January 5, 2006

 © 2006 Wiley-VCH Verlag GmbH & Co. KGaA, Weinheim 

DOI: 10.1002/ejic.200500729

# Theoretical Studies on Metal–Metal Interaction and Intrinsic $^{1,3}$[σ*(d)σ(s/p)] Excited States of Dinuclear d$^{10}$ Complexes with Bridging Phosphane Ligands

Qing-Jiang Pan,[a,b] Hong-Xing Zhang,*[a] Hong-Gang Fu,[b] and Hai-Tao Yu[b]

**Keywords:** Metallophilicity / Excited states / Dinuclear d$^{10}$ complexes / Electronic structure / Solvent effects

To explore the metal–metal interaction and spectroscopic properties, the ground- and excited-state structures of $[M_2(dpm)_2]^{2+}$ [M = Ag (**2**), Cu (**3**), dpm = bis(diphosphanyl)-methane] and their solvated species $[M_2(dpm)_2]^{2+}\cdot(MeCN)_2$ were optimized by the MP2 and CIS methods, respectively. In the ground states, the calculated M–M distances and their corresponding M–M stretching frequencies for **2** and **3** indicate the presence of metallophilic attraction; there is strong N→Cu/Ag coordination in acetonitrile, which is different from the case in previous studies of $[Au_2(dpm)_2]^{2+}$ (**1**). CIS calculations show that **2** and **3** have $^{1,3}[\sigma^*(d)\sigma(s/p)]$ as their lowest-energy excited state, as is also the case for **1**, confirmed by unrestricted MP2 calculations. On the basis of the CIS-optimized structures, the TD-DFT (B3LYP) method was employed to calculate the emission spectra of such complexes. For **3**, the phosphorescent emissions were calculated at 424 and 514 nm in the solid state and acetonitrile, which is comparable to the experimental data of 475 and 480 nm, respectively. The comparison between the gas-phase and solution emissions for **1**–**3** reveals that the N→M coordination results in a large red-shift of the emission wavelength. Taking previous studies into account , we found that the M–M distances are linearly correlated with the M–M stretching frequencies for the dinuclear d$^{10}$ complexes.
(© Wiley-VCH Verlag GmbH & Co. KGaA, 69451 Weinheim, Germany, 2006)

## Introduction

Despite the fact that two closed-shell metal cations would normally be expected to repel each other, a larger number of inorganic and organometallic complexes have been described whose structures indicate strong metal–metal interactions.[1–5] Among these interactions, the Au$^{I}$–Au$^{I}$ interaction has been intensively investigated both experimentally[6–11] and theoretically,[2–4,12–17] and coined as "aurophilicity" by Schmidbaur.[18] The energy of the aurophilic attraction in the solid state and solution was estimated to be 7–15 kcal/mol,[3] comparable to that of hydrogen bonds. Pyykkö et al.[1–4] have attributed the attraction to correlation effects that are strengthened by relativistic effects.

The Au–Au aurophilic attractions often result in unusual photochemical and photophysical properties for the Au$^{I}$ complexes.[6–11] It was found that their unique spectroscopic features in the absorption and emission spectra clearly relate to the presence of the Au–Au interactions. The luminescence of Au$^{I}$ complexes was assigned as a metal-centered (MC) transition or a metal–metal-to-ligand charge-transfer (MMLCT) transition.[12–17] Recently, we calculated the aurophilic interactions and excited-state properties of model complexes $[Au_2(dpm)_2]^{2+}$ (**1**),[12,13] $[Au_2(dpm)(i\text{-}mnt)]$ (**4**),[16] and $[(AuPH_3)_2(i\text{-}mnt)]$ (**5**)[16,17] [dpm = bis(diphosphanyl)-methane and i-mnt = i-malononitriledithiolate]. The results revealed that the 507-nm phosphorescent emission of **1** in acetonitrile has the σ[s(Au$_2$)]→σ*[d(Au$_2$)] (MC) transition property,[13] while the 512 and 495-nm emissions in the $CH_2Cl_2$ solution for **4** and **5**, respectively, arise from the Au–Au to i-mnt charge-transfer (MMLCT) transition.[16] The Au$^{I}$–Au$^{I}$ interaction is strengthened in these emissive excited states, resulting from the formation of a σ single bond between the Au$^{I}$ centers upon excitation.

Though aurophilic attraction between gold(I) atoms is widely acknowledged,[1–20] the development of silver–silver (argentophilicity)[21,22] and copper–copper (cuprophilicity)[22–24] bonding interactions remains in its infancy. Che and coworkers[25–32] have structurally characterized a series of luminescent dinuclear d$^{10}$ complexes with bridging phosphane ligands. The d$^{10}$–d$^{10}$ metallophilicity in these complexes was confirmed by Raman spectroscopy. For $[M_2(dcpm)_2](X)_2$ [M = Au, Ag, and Cu; X = counteranion; dcpm = bis(dicyclohexylphosphanyl)methane], with metal–metal distances of 2.939, 2.960, and 2.731 Å, respectively, the 88, 80, and 104-cm$^{-1}$ fundamental bands were assigned to the M–M stretching vibrations.[27–29] These d$^{10}$ complexes exhibit intense luminescence either in the solid state or in solution, which is experimentally attributed to the σ[(*n* + 1)p]→σ*(*n*d) transitions.

Apart from the above fundamental interest, the existing and/or potential applications based on d$^{10}$ coinage metal

[a] State Key Laboratory of Theoretical and Computational Chemistry, Institute of Theoretical Chemistry, Jilin University, Changchun 130023, China
[b] College of Chemistry and Chemical Engineering, Heilongjiang University, Haerbin 150080, China
Supporting information for this article is available on the WWW under http://www.eurjic.org or from the author.

 © 2006 Wiley-VCH Verlag GmbH & Co. KGaA, Weinheim 

complexes such as optical materials, photocatalysts, biosensors, and molecular pharmacology have also received the attention of many researchers.[6,22–24,33–37] For example, it has been suggested that the therapeutic action of gold drugs for rheumatoid arthritis is related to the ability of the $Au^I$ complexes to quench the singlet oxygen $^1\Delta_g$ state at 7752 $cm^{-1}$.[37] Such applications of the $d^{10}$ complexes are clearly pertinent to their excited-state properties. Therefore, the theoretical investigation of the electronic structures of the ground- and excited states of the complexes is also of practical significance.

So far, computational methods are sufficiently advanced to allow calculation of ground- and excited states of relatively large molecular complexes.[38] At the same time, experiments provide wide and accurate information that can serve as a test for the computational methods. In theory these make both the systematic investigations of the M–M interactions and the luminescence of the $d^{10}$ coinage metal complexes possible. Since the presence of a bridging ligand facilitates the intramolecular interaction,[4] the series of complexes, $[M_2(P–P)_2]^{2+}$ [M = Au, Ag, and Cu; P–P = dmpm, dppm, and dcpm; dmpm = bis(dimethylphosphanyl)methane and dppm = bis(diphenylphosphanyl)methane], with eight-membered-ring conformation,[24–31,38–44] are ideal candidates for such investigations.

Here, we use the second-order Møller–Plesset perturbation (MP2)[46] and single excitation configuration interaction (CIS)[38] methods to fully optimize the ground- and excited-state structures of model complexes $[M_2(dpm)_2]^{2+}$ [M = Ag (**2**) and Cu (**3**)] and their solvated species $[M_2(dpm)_2]^{2+}\cdot(MeCN)_2$, respectively. On the basis of the MP2- and CIS-optimized structures, the absorption and emission spectra of such complexes were obtained from TD-DFT (time-dependent density functional theory)[47–49] calculations, respectively. Combined with the previous studies on **1**, the calculated M–M distances (3.03–3.16 Å) and their corresponding M–M stretching frequencies (69–89 $cm^{-1}$) for **1**–**3** indicate the presence of metallophilic attraction in the ground states. Complexes **1**–**3** give rise to the metal-centered $\sigma(s, p_z)\rightarrow\sigma^*(d_{x^2-z^2}, d_{y^2})$ emissions, both in the gas phase and in solution, revealing that the dinuclear $d^{10}$ complexes with bridging phosphane ligands have the intrinsic $^{1,3}[\sigma^*(d)\sigma(s/p)]$ excited states (the $M_2P_4$ unit lies in the *xz* plane and the *z* axis goes through the two metal atoms).

## Computational Details and Theory

It has been found that the complexes, $[M_2(P–P)_2]^{2+}$ (M = Au, Ag, and Cu; P–P = dmpm, dppm, and dcpm), form a series of discrete dinuclear M(I) dimers in the crystalline phase, i.e. no intermolecular M(I)–M(I) interactions.[25–30,40–45] There are close cation–anion contacts of 2.692 and 2.687 Å (M···O) in the crystal lattices of $[Ag_2(dcpm)_2]\cdot(CF_3SO_3)_2$[28] and $[Cu_2(dcpm)_2]\cdot(ClO_4)_2$,[29] respectively, but such interactions are not apparent in the X-ray structure of the gold(I) congener $[Au_2(dcpm)_2]\cdot(ClO_4)_2$ (closest Au···$OClO_3$, 3.362 Å).[25,26] Therefore, these types of complexes can be modeled by $[M_2(dpm)_2]^{2+}$ and $[M_2(dpm)_2]\cdot(ClO)_2$, which reflect the behaviors in the gas phase and solid state, respectively. To save the computational resources, the hydrogen was used to replace methyl, phenyl, cyclohexyl and other heavy substituents in the ab initio studies. A similar model has been applied in many studies.[12–17,50,51]

In this work, we employed the $C_i$ symmetry to settle the ground- and excited-state conformations of $[M_2(dpm)_2]^{2+}$ [M = Ag (**2**) and Cu (**3**)], which are consistent with the results from the X-ray diffraction study of $[M_2(dcpm)_2]\cdot(X)_2$ (X = counteranion).[28–30] Because the solvent affects the luminescence of the complexes,[12,13,16,17,25–32,40] we used the solvated species $[M_2(dpm)_2]^{2+}\cdot(MeCN)_2$ to establish the solvent effects of acetonitrile.

All the calculations were carried out using the GAUSSIAN03 program package.[52] The ground- and excited-state structures of **2** and **3** and their solvated species were fully optimized by the MP2[46] and CIS[38] methods, respectively. On the basis of such optimized structures, the TD-DFT (B3LYP)[47–49] method was performed to calculate the absorption and emission spectra of the complexes.

In the calculations, quasi-relativistic pseudopotentials of the Ag, Cu, and P atoms proposed by Hay and Wadt[53,54] with 19, 19, and 5 valence electrons, respectively, were employed, and the LanL2DZ basis sets associated with the pseudopotential were adopted. In order to describe the $d^{10}$–$d^{10}$ metallophilic attraction and the molecular properties precisely, one additional function was implemented for Ag ($\alpha_f$ = 0.22), Cu ($\alpha_f$ = 0.24), and P ($\alpha_d$ = 0.34).[2–4] The basis sets were taken as Ag(8s6p4d1f/3s3p2d1f), Cu(8s5p5d1f/3s3p2d1f), P(3s3p1d/2s2p1d), N(10s5p/3s2p), C(10s5p/3s2p), and H(4s/2s). Thus, 152 basis functions and 80 electrons for **2** and **3** and 218 basis functions and 124 electrons for **2**·$(MeCN)_2$ and **3**·$(MeCN)_2$ were included in the calculations.

## Results and Discussion

### Ground-State Structures

We used the MP2 method to fully optimize the ground-state structures of **2** and **3** and solvated species **2**·$(MeCN)_2$ and **3**·$(MeCN)_2$. Their structures are depicted in Figure 1. Under the $C_i$ symmetry, these complexes have $^1A_g$ ground states. The main optimized geometry parameters are listed in Table 1 and Table 2, together with the data from X-ray crystal diffraction studies for $[M_2(dcpm)_2]\cdot(X)_2$ (M = Ag, X = $CF_3SO_3^-$; M = Cu, X = $ClO_4^-$).[28,29] For **2** and **3**, the $d^{10}$ metal atoms take on a nearly linear two-coordinate geometry; the calculated P–M–P angles are 178.9° and 179.1°, comparable to the experimental values of 172.4° and 162.5°, respectively, as shown in Table 1. In the crystalline structure, the cation–anion interactions (M···O = 2.692 and 2.687 Å for the Ag and Cu complexes, respectively) result in a large difference between the calculated and experimental results.

 © 2006 Wiley-VCH Verlag GmbH & Co. KGaA, Weinheim 

Table 1. Optimized geometry parameters of $[Ag_2(dpm)_2]^{2+}$ (**2**) and $[Cu_2(dpm)_2]^{2+}$ (**3**) using the MP2 method for the $^1A_g$ ground state and the CIS method for the $^1A_u$ and $^3A_u$ excited states.

| | **2** | | | | **3** | | | |
|---|---|---|---|---|---|---|---|---|
| Parameters | $^1A_g$ | Exp.[a] | $^1A_u$ | $^3A_u$ | $^1A_g$ | Exp.[a] | $^1A_u$ | $^3A_u$ |
| Bond length [Å] | | | | | | | | |
| M–M | 3.160 | 2.960 | 2.981 | 3.056 | 3.061 | 2.731 | 2.667 | 2.704 |
| M–P | 2.498 | 2.405 | 2.827 | 2.840 | 2.230 | 2.229 | 2.566 | 2.543 |
| P···P | 3.112 | | 3.116 | 3.125 | 3.099 | | 3.125 | 3.113 |
| Bond angle [°] | | | | | | | | |
| P–M–P | 178.9 | 172.4 | 177.3 | 178.6 | 179.1 | 162.5 | 169.8 | 170.8 |
| P–M–M | 89.5 | 91.8 | 91.4 | 90.7 | 90.5 | | 95.1 | 94.6 |
| Dihedral angle [°] | | | | | | | | |
| P–M–M–P | 180.0 | | 180.0 | 180.0 | 180.0 | | 180.0 | 180.0 |

[a] Experimental values of $[Ag_2(dcpm)_2]\cdot(CF_3SO_3)_2$ and $[Cu_2(dcpm)_2]\cdot(ClO_4)_2$ are from ref.[27] and ref.[28], respectively.

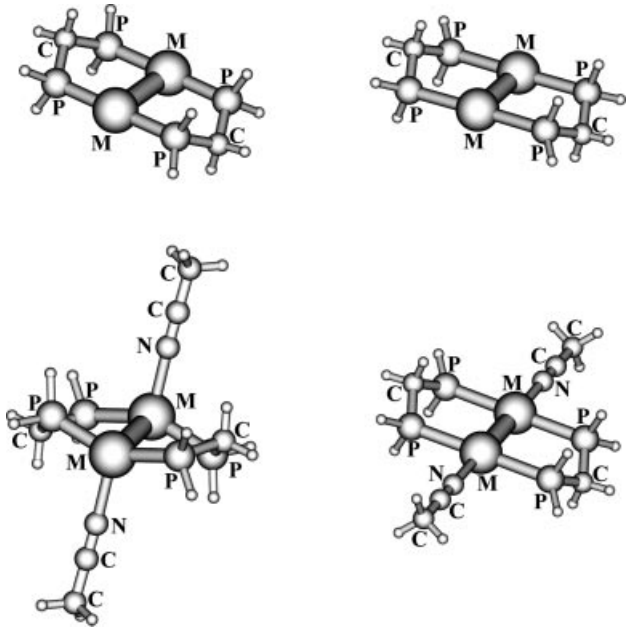

Figure 1. Ground- (left side) and excited- (right side) state structures for $[M_2(dpm)_2]^{2+}$ [M = Ag (**2**) and Cu (**3**)] and their weakly solvated species $[M_2(dpm)_2]^{2+}\cdot(MeCN)_2$.

The calculated 180.0° dihedral angles of P–M–M–P for **2** and **3** indicate that the $M_2P_4$ unit is coplanar. However, the interaction between the M(I) atom and acetonitrile in **2**·$(MeCN)_2$ and **3**·$(MeCN)_2$ results in $M_2P_4$ distortion from the original planarity, which is reflected by the calculated P–M–M–P dihedral angles of 151.3° and 138.4° (Table 2). The M–N distances are 2.380 and 1.976 Å for **2**·$(MeCN)_2$ and **3**·$(MeCN)_2$, respectively, which are very close to the experimental distances of 2.382 and 2.029 Å for $[Ag_2(dppa)_2(MeCN)_2]\cdot(PF_6)_2$ (dppa = $Ph_2PNHPPh_2$)[22] and $[Cu_2(dcpm)_2(MeCN)_2]\cdot(Y)_2$ ($Y^-$ = $ClO^-$ and $BF_4^-$)[29,30] and similar to the distances of 2.116 and 1.886 Å for $[M_2(form)_2]$ [M = Ag and Cu, form = (*p*-$CH_3C_6H_4$)NCHN(*p*-$CH_3C_6H_4$)].[55] In previous studies,[13] the calculated Au–N distance in **1**·$(MeCN)_2$ is 2.600 Å (Table S1 of the Supporting Information), which is much longer than the Au–N distance of 2.090 Å in $[Au_2(dpim)_2]\cdot(ClO_4)_2$ [dpim = 2-(diphenylphosphanyl)-1-methylimidazole].[56] Our calculated M–N distances for **1**–**3** in acetonitrile suggest that the M···N interactions are strong enough to form an M–N single bond for the Ag and Cu complexes, but very weak in the Au complex. The M–N bonding energies in (**1**–**3**)·$(MeCN)_2$ were estimated by using the Counterpoise method at the MP2 level. They are approximately 18.9, 27.0, and 36.5 kcal/mol, respectively. The present studies substantiate the previous conclusion that the $Au^I$ atom favors a linear two-coordinate arrangement, while the $Ag^I$ and $Cu^I$ atoms have the formal three coordination.[57]

Table 2. Optimized geometry parameters of $[Ag_2(dpm)_2]^{2+}\cdot(MeCN)_2$ [**2**·$(MeCN)_2$] and $[Cu_2(dpm)_2]^{2+}\cdot(MeCN)_2$ [**3**·$(MeCN)_2$] using the MP2 method for the $^1A_g$ ground state and the CIS method for the $^1A_u$ and $^3A_u$ excited states.

| | **2**·$(MeCN)_2$ | | | **3**·$(MeCN)_2$ | | |
|---|---|---|---|---|---|---|
| Parameters | $^1A_g$ | $^1A_u$ | $^3A_u$ | $^1A_g$ | $^1A_u$ | $^3A_u$ |
| Bond length [Å] | | | | | | |
| M–M | 3.069 | 2.986 | 3.046 | 2.875 | 2.920 | 3.003 |
| M–P | 2.517 | 2.917 | 2.838 | 2.299 | 2.768 | 2.646 |
| M–N | 2.380 | 2.401 | 2.441 | 1.976 | 2.102 | 2.149 |
| P···P | 3.073 | 3.063 | 3.086 | 3.034 | 3.042 | 3.061 |
| Bond angle [°] | | | | | | |
| P–M–P | 150.9 | 178.4 | 179.2 | 138.1 | 177.4 | 178.7 |
| P–M–M | 92.6 | 90.7 | 90.4 | 93.7 | 91.3 | 90.6 |
| N–M–M | 109.5 | 179.8 | 179.8 | 113.9 | 179.8 | 180.0 |
| Dihedral angle [°] | | | | | | |
| P–M–M–P | 151.3 | 179.5 | 179.7 | 138.4 | 179.7 | 179.9 |

The M(I)–M(I) separations that were calculated are 3.033, 3.160, and 3.061 Å for **1**–**3** in the ground states, which correspond to the experimental data of 2.939, 2.960, and 2.731 Å, respectively.[26,28,29] There is a large difference, especially for the Ag and Cu complexes. The following two reasons may be responsible for this. First, the choice of basis sets may cause such a difference. Hence, the SDD basis set, which is larger than the LanL2DZ basis set, was used to optimize **1**–**3** in order to judge the basis-set effect. The calculated results show that the Ag–Ag distance is shortened by about 0.1 Å but the Au–Au and Cu–Cu distances are nearly unchanged upon increasing the basis sets as shown in Table S2 of the Supporting Information. Second, in our calculations we used the model complex $[M_2(dpm)_2]^{2+}$ to replace the real complex $[M_2(P–P)_2]^{2+}$ (P–P = dmpm, dppm, and dcpm). This substituent approximation may affect the geometry parameters of the complexes. In Table S2,

 © 2006 Wiley-VCH Verlag GmbH & Co. KGaA, Weinheim 

we list the optimized geometry parameters of $[M_2(dmpm)_2]^{2+}$ (M = Au, Ag, and Cu) and the data for $[M_2(P–P)_2](X)_2$ (M = Au, Ag, and Cu; P–P = dmpm, dppm, and dcpm; X = counteranion) that were determined from experiments.[22,26,28,29,40–45] One can see that the calculated results have now improved. The M–M distances of $[M_2(dmpm)_2]^{2+}$ (M = Au, Ag, and Cu) are 2.985, 3.021 and 2.818 Å, respectively and approach the experimental values. Table S2 of the Supporting Information indicates that although the use of the larger basis sets (SDD) and heavy substituent on the phosphorous atoms (e.g. dmpm ligand) in the calculations presents results that are closer to the experimental values, the calculated results for $[M_2(dpm)_2]^{2+}$ with the LanL2DZ basis sets can also describe the essential characteristics of real complexes.

The natural bond orbital (NBO) analysis[58–60] using the MP2 density shows that the M atoms of **1**–**3** have net electronic charges of +0.31, +0.56, and +0.56, respectively, while electronic charges residing on the P atoms are +0.39, +0.28, and 0.27. This indicates that the electrons of the P atoms transfer to the original $(n + 1)$s and $(n + 1)$p empty orbitals of M(I). Consequently, the closed-shell electronic configurations, $nd^{10}(n + 1)s^0$, are no longer kept in **1**–**3** but become $5d^{9.76}6s^{0.87}6p^{0.03}4f^{0.03}$ (Au), $4d^{9.89}5s^{0.52}5p^{0.02}4f^{0.01}$ (Ag), and $3d^{9.86}4s^{0.56}4p^{0.02}4f^{0.01}$ (Cu) instead. Because the relativistic effects are stronger on Au than on Ag and Cu,[61] there is more 5d→6(s, p) population transfer for the Au atom. Such a destruction of metal closed-shell structures may be one of the predominant driving forces in causing metallophilic attraction.

### Absorption Spectra

According to the vertical electron-transition mechanism in the absorption process, the optimized ground-state structures of (**1**–**3**)·$(MeCN)_2$ were kept, while TD-DFT (B3LYP) calculations were performed in order to calculate the excited states related to the absorption. With respect to the $^1A_g$ ground state under the $C_i$ point group, the $^1A_g$→$^1A_u$ transition is spin-dipole-allowed. We obtained low-lying dipole-allowed transitions of (**1**–**3**)·$(MeCN)_2$ that represent the possible absorptions of **1**–**3** in acetonitrile. Transition energies (eV/nm) of these absorptions are presented in Table 3, together with the corresponding oscillator strengths and experimental values available.[8,25,28,29,31,32,39] In order to conveniently assign the calculated electronic absorptions, the electron density diagrams of the frontier molecular oribitals involved in the transitions are displayed in Figure 2.

For **1**·$(MeCN)_2$, we obtained three low-lying absorptions from the TD-DFT calculations. In Figure 2, one can see that the orbitals involved in the transitions are mainly Au in character. The analyses of the wave functions of **1**·$(MeCN)_2$ suggest that the $29a_u$ (HOMO–3), $30a_u$ (HOMO–2), $31a_u$ (HOMO), and $32a_g$ (LUMO) orbitals mainly have σ(Au–P), $\sigma^*(d_{y^2-z^2})$, $\sigma^*(s, d_{z^2})$, and $\sigma(sp_z)$ character, respectively (the $Au_2P_4$ unit lies in the *xz* plane and the *z* axis goes through the two Au atoms).

The lowest-energy absorption of **1** in acetonitrile was calculated at 291 nm, which results from the $31a_u$→$32a_g$ (HOMO→LUMO) configuration with the largest CI coefficient of 0.673 in the wave functions (Table 3). We attributed this absorption to a metal-centered $\sigma^*(s, d_{z^2})$→$\sigma(sp_z)$ transition. It has been found that $[Au_2(P–P)_2]^{2+}$ (P–P = dmpm, dppm, and dcpm)[8,25,31,32,39] display intense absorption bands at 269, 292, and 278 nm in acetonitrile, respectively. These absorptions correspond to the calculated 291-nm absorption and also arise from a $\sigma^*(s, d_{z^2})$→$\sigma(sp_z)$ transition. The $B^1A_u$ excited state of **1**·$(MeCN)_2$ gives the absorption at 237 nm, which corresponds to the experimental absorption at 239–267 nm (in Table 3).[8,25,31,32,39] The absorption also has the nature of a MC transition, a $\sigma^*(d_{y^2-z^2})$→$\sigma(sp_z)$ transition. There is much contribution from the phosphane ligands for the $X^1A_g$→$C^1A_u$ transition, which is intuitively reflected in Figure 2. We assigned the 224-nm absorption to a σ(Au–P)→$\sigma(sp_z)$ transition.

With respect to analogous Ag and Cu complexes, we obtained three and four low-lying electronic transitions in ace-

Table 3. Calculated absorptions of $[Au_2(dpm)_2]^{2+}$·$(MeCN)_2$, $[Ag_2(dpm)_2]^{2+}$·$(MeCN)_2$, and $[Cu_2(dpm)_2]^{2+}$·$(MeCN)_2$ at the TD-DFT (B3LYP) level.

| | States | Conf. | \|CI coeff.\| > 0.2 | Trans. ener. | | *f* | Exp. [nm][a] | | |
|---|---|---|---|---|---|---|---|---|---|
| | | | | [nm] | [eV] | | dcpm | dmpm | dppm |
| Au | $A^1A_u$ | $31a_u$→$32a_g$ | 0.67310 | 291 | 4.26 | 0.162 | 278 | 269 | 292 |
| | $B^1A_u$ | $30a_u$→$32a_g$ | 0.68089 | 237 | 5.23 | 0.050 | 243 | 239 | 267 |
| | $C^1A_u$ | $29a_u$→$32a_g$ | 0.68087 | 224 | 5.53 | 0.022 | | 213 | |
| Ag | $A^1A_u$ | $31a_u$→$32a_g$ | 0.68321 | 256 | 4.84 | 0.132 | 261 | | |
| | $B^1A_u$ | $30a_u$→$32a_g$ | 0.68629 | 238 | 5.22 | 0.070 | | | |
| | $C^1A_u$ | $31a_u$→$33a_g$ | 0.43752 | 201 | 6.18 | 0.003 | | | |
| | | $29a_u$→$32a_g$ | 0.42265 | | | | | | |
| | | $31a_g$→$32a_u$ | 0.25181 | | | | | | |
| Cu | $A^1A_u$ | $31a_u$→$32a_g$ | 0.53146 | 283 | 4.39 | 0.036 | 319 | | |
| | | $30a_u$→$32a_g$ | –0.43078 | | | | | | |
| | $B^1A_u$ | $29a_u$→$32a_g$ | 0.68166 | 246 | 5.04 | 0.071 | 269 | | |
| | $C^1A_u$ | $28a_u$→$32a_g$ | 0.67986 | 231 | 5.38 | 0.011 | | | |
| | $D^1A_u$ | $27a_u$→$32a_g$ | 0.66148 | 219 | 5.66 | 0.009 | | | |

[a] The absorptions in acetonitrile of $[M_2(dcpm)_2]^{2+}$ (M = Au, Ag, and Cu) are from ref.[24], ref.[27] and ref.[28], respectively. The results of $[Au_2(dmpm)_2]^{2+}$ are from ref.[8] and those of $[Au_2(dppm)_2]^{2+}$ from ref.[30,31,38]

 © 2006 Wiley-VCH Verlag GmbH & Co. KGaA, Weinheim 

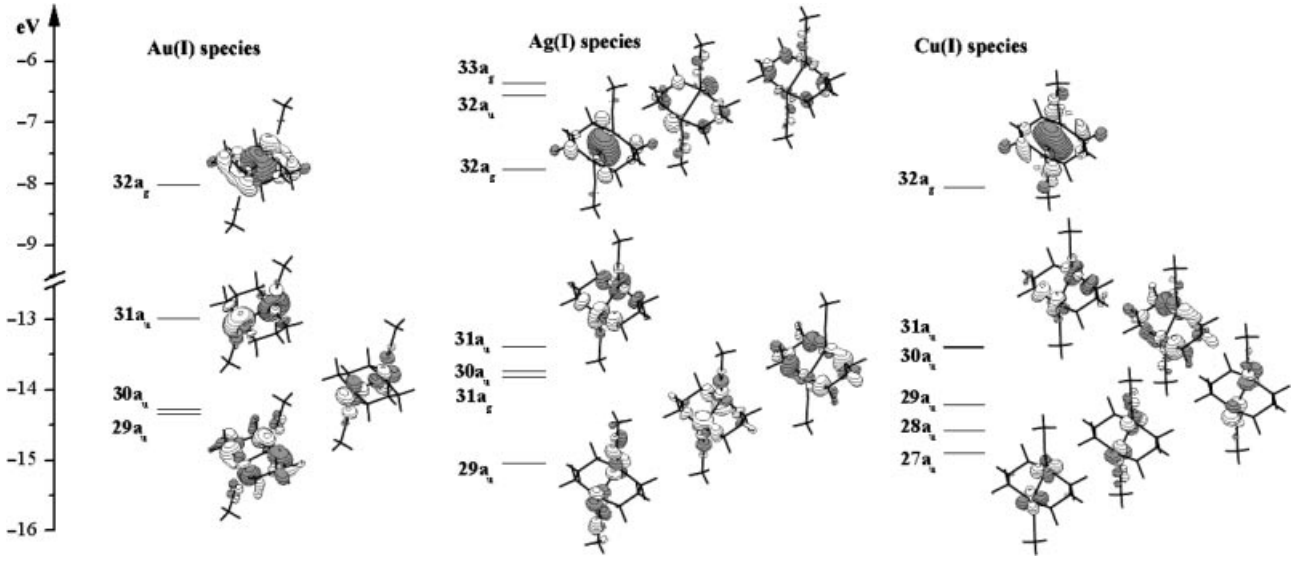


Figure 2. Frontier molecular diagrams of $[M_2(dpm)_2]^{2+}\cdot(MeCN)_2$ (M = Au, Ag, and Cu) in the TD-DFT (B3LYP) calculations.

tonitrile, respectively. By combining the information from Table 3 and Figure 2, one can see that **2** and **3** have relatively more complicated transitions than **1**. The calculated lowest-energy absorption of 256 nm for **2** in acetonitrile was assigned to a $\sigma^*(s, d_{z^2})\rightarrow\sigma(sp_z)$ transition, with a maximum oscillator strength of 0.132; we relate this to the 261-nm absorption band of $[Ag_2(dcpm)_2]^{2+}$ recorded in acetonitrile.[28] The lowest-energy absorption of 283 nm for **3** in acetonitrile is not a pure metal-centered $\sigma^*(s, d_{z^2})\rightarrow\sigma(sp_z)$ transition, which is different from those of **1** and **2**. The absorption (Table 3) results from the $31a_u\rightarrow32a_g$ (HOMO→LUMO) and $30a_u\rightarrow32a_g$ (HOMO–1→LUMO) configurations and is attributed to the mixture of $\sigma^*(s, d_{z^2})\rightarrow\sigma(sp_z)$ and $\sigma(Cu–P)\rightarrow\sigma(sp_z)$ transitions. Our calculated absorptions agree well with the experimental observations and provide more detailed information about the transition properties of the absorptions.

Such analyses show that relativistic effects play a significant role in the electronic transitions of **1**–**3** in acetonitrile, especially for the lowest-energy HOMO→LUMO transitions. As far as **1**–**3** are concerned, relativistic effects destabilize the $\sigma^*[nd_{z^2}(M_2)]$ orbital but stabilize the $\sigma[(n + 1)sp_z(M_2)]$, which result in the net effect of a decrease in the HOMO–LUMO energy gap. Because the later-row transition metals have stronger relativistic effects, **1** has a smaller HOMO–LUMO gap (Figure 2) and lower-energy HOMO→LUMO absorption than **2** and **3** (Table 3). Since the relativistic effects of Ag are larger than those of Cu, **2** should have a lower HOMO→LUMO absorption in acetonitrile. However, this is not the case in the present calculations (Table 3). We think that the M–M interactions are also one of the more important factors that affect the transition energies for **2** and **3**. Table 2 shows that the M–M distance of 2.875 Å for **3** is much shorter than that of 3.069 Å for **2**, which greatly facilitates the lower-energy transition for the Cu complex. It could be said[1] that among the coinage metals (Au, Ag, and Cu), only silver is "normal". As already mentioned, gold is anomalous because of its large relativistic effects. As the underlying nodeless d shell of copper is more compact than that of silver or gold, copper is often seen to behave differently. This suggestion has been, to some extent, reflected in such studies on the electronic absorptions of **1**–**3**. Additionally, it is worth noting that the spin-orbit interactions are an important influence on the transition moments, even if they are perhaps quenched in the molecular field.

In addition, we also calculated the absorptions of **1**–**3** in the acetonitrile solution using the CIS method. Their lowest-energy absorptions mainly feature the HOMO→LUMO transitions and the $\sigma^*(s, d_{z^2})\rightarrow\sigma(sp_z)$ characters, as do those from the TD-DFT calculations. However, the transition energies of 5.60, 6.66, and 6.68 eV for **1**–**3**, respectively, from the CIS calculations were severely overestimated relative to the experimental values. The TD-DFT calculations yield a better estimation of transition energies of absorptions than the CIS method.

### Excited-State Structures

To describe the luminescent properties of **2** and **3**, the CIS method was used to optimize the excited-state structures, both in the gas phase and in acetonitrile. Their structures are shown in Figure 1 and the main optimized geometry parameters are listed in Table 1 and Table 2.

With respect to the $^1A_u/^3A_u$ excited states of **2** and **3**, the optimized structures show significant changes compared with those of their corresponding $^1A_g$ ground states as can be seen in Table 1. The M(I)–M(I) distances are shortened from 3.160 and 3.061 Å to 2.981/3.056 and 2.667/2.704 Å for **2** and **3**, respectively. The bonding interactions between the two M(I) atoms in the $^1A_u/^3A_u$ excited states weaken the P→M dative bonds.

In solution, the acetonitrile molecules coordinate to the metal atoms of **2** and **3** with N–M–M angles of 109.5° and

 © 2006 Wiley-VCH Verlag GmbH & Co. KGaA, Weinheim 

113.9° in the $^1A_g$ ground states, respectively; in the $^1A_u/^3A_u$ excited states, the N–M–M angles are close to 180° (Table 2). The M–N interactions in **2**·$(MeCN)_2$ and **3**·$(MeCN)_2$ are slightly weaker in the $^1A_u/^3A_u$ excited states than in the ground states, thus elongating by ca. 0.02/0.06 and 0.03/0.07 Å, respectively. However, the interaction between the $Au^I$ and N atoms in acetonitrile is greatly enhanced in the excited states since the Au–N distances of the $^1A_u/^3A_u$ excited states are about 0.17/0.22 Å shorter than that of the $^1A_g$ ground state (Table S1 of Supporting Information). Our previous studies on **1** showed that the N→Au coordination in acetonitrile results in about a 200-nm red-shift of the emission wavelength in the $^3A_u$ excited state.[13] Thus, we conjecture that the influence of acetonitrile on emissions of **2** and **3** is not as significant as on **1**.

To certify the validity of the CIS-optimized geometries, we used the unrestricted MP2 method (UMP2) to optimize the lowest-energy triplet excited states of **1**–**3**. The main optimized geometry parameters of the $^3A_u$ excited states are given in Table 4. The wave functions of the excited states demonstrate that the HOMOs are the σ bonding orbitals, mainly contributed to by the metal $(n + 1)(sp_z)$ atomic orbitals, and the LUMOs possess $\sigma^*(nd_{z^2})$ character. The $^3A_u$ excited state from the UMP2 calculations has orbital character that is very similar to that of the $^3A_u$ excited state from the CIS calculations for each complex. Thus, the $^3[\sigma^*(d)\sigma(sp)]$ states from the UMP2 calculations correspond to those from the CIS calculations. In comparison with those optimized by the CIS method, the geometry parameters of the $^3A_u$ excited states from the UMP2 method are more unrelaxed (Table 1 and Table 4). This is because the latter includes more electron correlation effects.[2–4] Despite some differences between the UMP2 and CIS methods in optimized geometry parameters for **1**–**3**, the two methods can reasonably predict the excited-state properties of the complexes.

Table 4. Optimized geometry parameters of the lowest-energy $^3A_u$ triplet excited states by the UMP2 method for $[Au_2(dpm)_2]^{2+}$ (**1**), $[Ag_2(dpm)_2]^{2+}$ (**2**), and $[Cu_2(dpm)_2]^{2+}$ (**3**).

| Parameters | **1**[a] | **2** | **3** |
|---|---|---|---|
| Bond length [Å] | | | |
| M–M | 2.678 | 2.709 | 2.408 |
| M–P | 2.404 | 2.545 | 2.307 |
| P···P | 3.109 | 3.125 | 3.385 |
| Bond angle [°] | | | |
| P–M–P | 169.7 | 170.6 | 155.5 |
| P–M–M | 95.1 | 94.7 | 102.2 |
| Dihedral angle [°] | | | |
| P–M–M–P | 180.0 | 179.3 | 179.3 |

[a]. The results of the $^3A_u$ triplet excited state of $[Au_2(dpm)_2]^{2+}$ (**1**) are from ref.[13]

We have performed the frequency calculations on **1**–**3** at the MP2 level for the ground and triplet excited states. No imaginary frequencies available indicate that these ground- and excited structures are minimum points. The calculated M–M stretching frequencies (Table 5) are ca. 89, 69, and 69 $cm^{-1}$ for **1**–**3** in the ground states, which are comparable to the experimental data of 88, 80, and 104 $cm^{-1}$ for $[Au_2(dcpm)_2]\cdot(ClO_4)_2$,[27] $[Ag_2(dcpm)_2]\cdot(CF_3SO_3)_2$,[28] and $[Cu_2(dcpm)_2]\cdot(ClO_4)_2$,[29] respectively. Keeping the experimental M–M distances from the MP2 calculations, we optimized the structures of **1**–**3** and present the calculated M–M frequencies in Table 5. The M–M stretching frequencies provide evidence for weak metallophilic attraction between the two $d^{10}$ metal atoms in the ground states.

Relative to those in the ground states, the M–M stretching frequencies greatly increase in the $^3A_u$ excited states. The 144, 142, and 170 $cm^{-1}$ M–M stretching frequencies of **1**–**3** correspond to 175, 180, and 150 $cm^{-1}$ frequencies estimated by Raman Resonance spectroscopy, respectively.[27–29] Such MP2 calculations suggest that the M–M interaction is weak in the ground state (mean M–M dis-

Table 5. Calculated Au–Au stretching frequencies for the ground states and lowest-energy triplet excited states of $[Au_2(dpm)_2]^{2+}$ (**1**), $[Ag_2(dpm)_2]^{2+}$ (**2**), $[Cu_2(dpm)_2]^{2+}$ (**3**), and related dinuclear $Au^I$ complexes at the MP2 level, together with the data from the Raman Resonance spectra.[a]

| | Ground state | | | Triplet excited state | | |
|---|---|---|---|---|---|---|
| | M–M [Å] | Freq. [$cm^{-1}$] | | M–M [Å] | Freq. [$cm^{-1}$] | |
| | | Calcd. | Exp. | | Calcd. | Exp. |
| **1** | 3.033 (2.939)[b] | 89 (104)[c] | 88 | 2.678 | 144 | 175 |
| **2** | 3.160 (2.960)[b] | 69 (94)[c] | 80 | 2.709 | 142 | 180 |
| **3** | 3.061 (2.731)[b] | 69 (89)[c] | 104 | 2.408 | 170 | 150 |
| **4**[d] | 2.913 | 110 | | 2.787 | 135 | |
| **5**[d] | 2.945 | 96 | | 2.786 | 119 | |
| **6**[d] | 3.011 | 93 | | 2.778 | 126 | |
| **7**[d] | 2.989 | 96 | | 2.620 | 164 | |
| **8**[d] | 2.979 | 96 | | 2.619 | 165 | |
| **9**[d] | 2.972 | 97 | | 2.572 | 189 | |
| **10**[d] | 2.944 | 101 | | 2.583 | 179 | |

[a] The M–M frequencies of Raman Resonance spectra are from ref.[26–28]. [b] The M–M distances in parentheses were determined from X-ray crystal diffraction studies for $[Au_2(dcpm)_2]\cdot(ClO_4)_2$,[25] $[Ag_2(dcpm)_2]\cdot(CF_3SO_3)_2$,[27] and $[Cu_2(dcpm)_2]\cdot(ClO_4)_2$[28]. [c] The M–M stretching frequencies in parentheses were obtained on the basis of the optimized geometries of **1**, **2**, and **3** with the fixed experimental M–M distances. [d] Complexes **4**–**10** are $[Au_2(PH_2CH_2PH_2)(i\text{-}mnt)]$, $[Au_2(PH_3)_2(i\text{-}mnt)]$, $[Au_2(PH_2CH_2PH_2)(SCH_2S)]$, $[Au_2(PH_2CH_2PH_2)(SHCH_2SH)]^{2+}$, *trans*-$[Au_2(PH_2CH_2SH)_2]^{2+}$, *cis*-$[Au_2(PH_2CH_2SH)_2]^{2+}$, and $[Au_2(SHCH_2SH)_2]^{2+}$ (i-mnt = i-malononitriledithiolate), respectively. Their Au–Au distances and stretching frequencies are from ref.[13] and ref.[16], respectively.

 © 2006 Wiley-VCH Verlag GmbH & Co. KGaA, Weinheim 

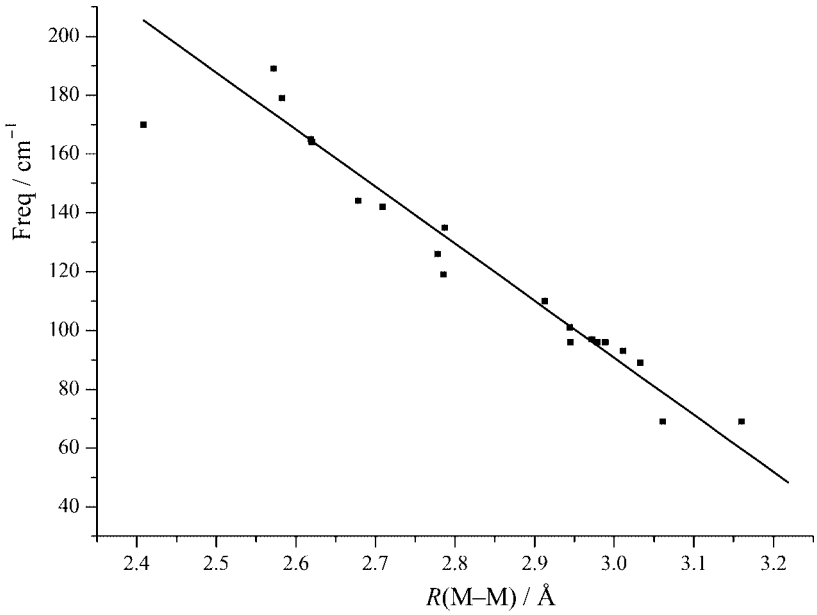


Figure 3. Plot of M–M distances versus stretching frequencies in the ground and lowest-energy triplet excited states for a series of dinuclear $d^{10}$ complexes, **1**–**10**, from the MP2 and UMP2 calculations, respectively.

tance: 3.10 Å, and M–M stretching frequency: 80 $cm^{-1}$), but is strongly enhanced in the triplet excited state (mean M–M distance: 2.60 Å, and M–M stretching frequency: 150 $cm^{-1}$).

In Table 5, we summarize the calculated M–M distances and stretching frequencies in the ground and lowest-energy triplet excited states for a series of dinuclear $d^{10}$ complexes, **1**–**10**, from MP2 and UMP2 calculations, respectively.[13,16] The plot of the M–M distances versus stretching frequencies in Figure 3 intuitively illustrates that the M–M distances are linearly correlated with the M–M stretching frequencies for the dinuclear $d^{10}$ complexes.

## Emission Spectra

It has been found that the CIS excited-state geometries are more accurate than the CIS transition energies as indicated in the literature.[62,63] The large deviations in the excitation energies are caused by an unbalanced description of the ground- and excited states. TD-DFT calculations, based on linear-response theory, have recently been reformulated to yield better transition energies than the CIS method.[63–66] Since the CIS method can present the accurate excited-state geometry and potential-energy surface, and the TD-DFT calculations can reasonably predict the

Table 6. Calculated emissions of $[Au_2(dpm)_2]^{2+}$ (**1**), $[Ag_2(dpm)_2]^{2+}$ (**2**) and $[Cu_2(dpm)_2]^{2+}$ (**3**) in the gas phase, solid state and acetonitrile solution at the CIS and TD-DFT (B3LYP) levels.

| | | | CIS | | TD-DFT | | Exp.[a] | | |
|---|---|---|---|---|---|---|---|---|---|
| | | | λ [nm/eV] | *f* | λ [nm/eV] | *f* | dcpm | dmpm | dppm |
| **1** | Gas phase | $^1A_u$ | 247/5.03 | 0.303 | 318/3.89 | 0.161 | | | |
| | | $^3A_u$ | 301/4.12 | | 381/3.25 | | | | |
| | Solid state[b] | $^3A_u$ | 304/4.08 | | 402/3.08 | | 368 | | |
| | Solution | $^1A_u$ | 339/3.66 | 0.188 | 484/2.56 | 0.116 | | | |
| | | $^3A_u$ | 507/2.44 | | 818/1.51 | | 490–530 | 555 | 565–593 |
| **2** | Gas phase | $^1A_u$ | 216/5.75 | 0.127 | 302/4.11 | 0.088 | | | |
| | | $^3A_u$ | 259/4.78 | | 356/3.49 | | | | |
| | Solid state[b] | $^3A_u$ | 263/4.71 | | 366/3.39 | | 417 | | |
| | Solution | $^1A_u$ | 238/5.19 | 0.130 | 366/3.39 | 0.093 | | | |
| | | $^3A_u$ | 277/4.48 | | 424/2.93 | | | | |
| **3** | Gas phase | $^1A_u$ | 214/5.78 | 0.187 | 328/3.78 | 0.094 | | | |
| | | $^3A_u$ | 252/4.93 | | 397/3.13 | | | | |
| | Solid state[b] | $^3A_u$ | 258/4.81 | | 424/2.92 | | 475 | | |
| | Solution | $^1A_u$ | 249/4.97 | 0.122 | 435/2.85 | 0.084 | | | |
| | | $^3A_u$ | 281/4.41 | | 514/2.41 | | 480 | | |

[a] The emissions of $[M_2(dcpm)_2]^{2+}$ (M = Au, Ag, and Cu) in acetonitrile are from ref.[24,25], ref.[27] and ref.[28,29], respectively. The results of $[Au_2(dmpm)_2]^{2+}$ are from ref.[8] and those of $[Au_2(dppm)_2]^{2+}$ from ref.[30,31,38]. [b] The results from $[M_2(dpm)_2]\cdot(ClO)_2$ (M = Au, Ag, and Cu) with fixed experimental M···O distances of 3.362, 2.692, and 2.687 Å, respectively.

 © 2006 Wiley-VCH Verlag GmbH & Co. KGaA, Weinheim 

transition energies, the combination of the benefits of the two methods is a practical approach to describe the excited-state properties of molecules.

In this paper, we have used the CIS method to optimize the lowest-energy singlet and triplet excited states for **2** and **3** and their solvated species. On the basis of these optimized structures, the TD-DFT (B3LYP) method was performed to calculate the emission spectra of **2** and **3** in the gas phase and in solution. The calculated emissions are listed in Table 6, together with the experimental values for $[M_2(dcpm)_2]\cdot(X)_2$ (M = Ag, X = $CF_3SO_3^-$; M = Cu, X = $ClO_4^-$).[28–30]

From the TD-DFT calculations, the $^1A_u/^3A_u$ excited states of **2** and **3** give rise to the 302/356 and 328/397-nm emissions in the gas phase, and 366/424 and 435/514-nm emissions in acetonitrile, respectively. According to the analyses of the wave functions of these excited states, we attribute the emissions to the metal-centered σ(s, $p_z$)→σ*($d_{x^2-z^2}$, $d_{y^2}$) transitions, as is the case for those of **1** in previous studies.[13] The detailed information on the electronic structures of the $^3A_u$ excited states for **1**–**3** are presented in Table S3 of the Supporting Information, contributing to our understanding of such MC transitions. Compared with those in the gas phase, the calculated emissions in acetonitrile are red shifted by about 64/68 and 107/117 nm for the $^1A_u/^3A_u$ excited states of **2** and **3**, respectively. The interactions between cation and solvent molecules result in a large red shift. Since the lowest-energy emissions of **1**–**3** arise from the metal-centered σ(s, $p_z$)→σ*($d_{x^2-z^2}$, $d_{y^2}$) transitions, either in the gas phase or in solution, we think that the dinuclear $d^{10}$ complexes with bridging phosphane ligands have the intrinsic $^{1,3}$[σ*(d)σ(s/p)] excited states.

In the crystalline phase of $[Ag_2(dcpm)_2]\cdot(CF_3SO_3)_2$[28] and $[Cu_2(dcpm)_2]\cdot(ClO_4)_2$,[29] very close cation-anion contacts were determined by X-ray crystal diffraction [2.692 and 2.687 Å (M···O), respectively]. The presence of anions near the $[M_2(dcpm)_2]^{2+}$ cations affects the solid-state emission. In previous studies of **1**,[12] the less bulky $ClO^-$ anion was used to replace the original $ClO_4^-$ anion in the $[Au_2(dcpm)_2]\cdot(ClO_4)_2$ crystalline phase, i.e. **1**·$(ClO)_2$ was applied to simulate the solid-state behaviors of the Au complex. Similar models, **2**·$(ClO)_2$ and **3**·$(ClO)_2$, were used in the calculations in order to represent the real complexes, $[Ag_2(dcpm)_2]\cdot(CF_3SO_3)_2$ and $[Cu_2(dcpm)_2]\cdot(ClO_4)_2$, respectively. When the *R*(M–OCl) distance changes from 5.5 to 2.5 Å, the corresponding phosphorescent emission varies in the ranges 382–535, 398–440, and 356–370 nm for the Au, Ag and Cu complexes, respectively. Figure 4 clearly reflects the correlation between the emission wavelength and *R*(M–OCl) for **1**–**3**·$(ClO)_2$. The emission of **1**·$(ClO)_2$ is very sensitive to the *R*(M–OCl) distance, especially when *R*(M–OCl) < 3.5 Å, while those of **2**·$(ClO)_2$ and **3**·$(ClO)_2$ are relatively insensitive. When *R*(M–OCl) > 4.0 Å, the anion slightly affects the emissions of the complexes. Keeping the experimental M···O distances 3.362, 2.692, and 2.687 Å in the calculations on $[M_2(dpm)_2]\cdot(ClO)_2$ (M = Au, Ag, and Cu), respectively, we obtained the emissions of **1**–**3** in the solid state. The calculated phosphorescent emissions are 402, 366, and 424 nm, which are comparable to the experimental emissions of 368, 417, and 475 nm in the solid state, respectively.[28,29]

From Table 6, one can see that the CIS method overestimates the emission energies by ca. 2 eV with respect to the experimental values for the Ag and Cu complexes, while those predicted by TD-DFT are closer to the experimental values. For **3**, the phosphorescent emissions were calculated at 4.81 eV (258 nm) and 4.41 eV (281 nm) in the solid state and acetonitrile, respectively, while the experimental values were severely overestimated [2.61 eV (475 nm) and 2.58 eV (480 nm)] for $[Cu_2(dcpm)_2]\cdot(ClO_4)_2$.[29,30] TD-DFT calculations were carried out at the CIS-optimized excited-state

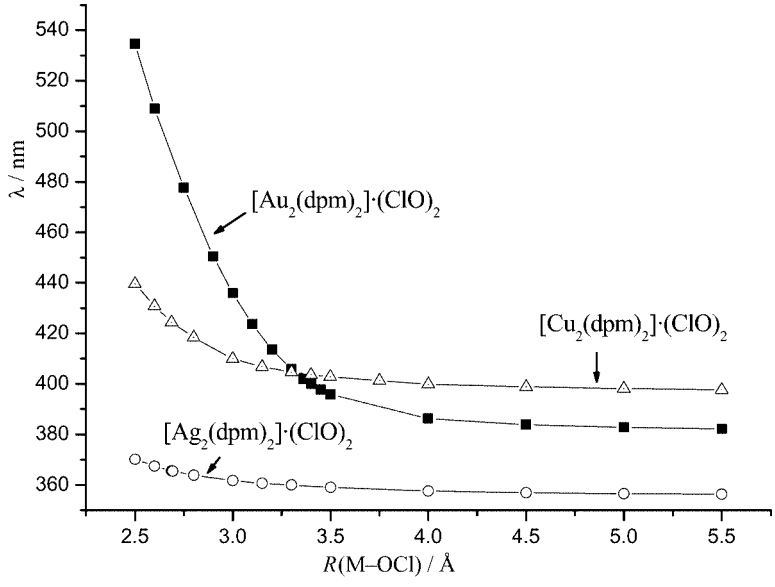


Figure 4. Plot of emission wavelength versus *R*(M–OCl) (distance between M atom and $ClO^-$ anion) for $[M_2(dpm)_2]^{2+}\cdot(ClO)_2$ (M = Au, Ag, and Cu) in the TD-DFT (B3LYP) calculations.

 © 2006 Wiley-VCH Verlag GmbH & Co. KGaA, Weinheim 

structure to obtain more accurate estimates of the emission energies. With TD-DFT, the phosphorescent emission energies were predicted to be 2.92 eV (424 nm) and 2.41 eV (514 nm) in the solid state and in acetonitrile, respectively, which are much closer to the experimental observations. However, with respect to the Au complex, the CIS and TD-DFT calculations over- and underestimated the emission energies, respectively, relative to the available experimental data.[8,25,26,31,32,39]

## Conclusions

In the paper, we used theoretical methods to study the electronic structures and spectroscopic properties of **2** and **3** and their solvated species. Taking previous studies into account on **1**,[13] we have come to the following conclusions.

For the dinuclear $d^{10}$ complexes of **1**–**3**, the calculated M–M distances (3.03–3.16 Å) and their corresponding M–M stretching frequencies (69–89 $cm^{-1}$) at the MP2 level indicate the presence of metallophilic attraction in the ground states. This is also supported by the NBO analysis on the electronic configurations of the metal atoms. In acetonitrile, the N→M coordination is strong enough to form a σ single bond in the Ag and Cu species, but is very weak in the Au analog. This agrees with the usual coordinated geometries of the Au, Ag, and Cu atoms.

In the excited states of **1**–**3**, the M–M interactions are strengthened, resulting from the promotion of electrons from the σ*(d) antibonding orbital to the σ(s/p) bonding orbital upon excitation. These complexes give rise to the metal-centered $\sigma(s, p_z)\rightarrow\sigma^*(d_{x^2-z^2}, d_{y^2})$ emissions, both in the gas phase and in solution, revealing that the dinuclear $d^{10}$ complexes with bridging phosphane ligands have the intrinsic $^{1,3}[\sigma^*(d)\sigma(s/p)]$ excited states. The comparison between the gas-phase and solution emissions for **1**–**3** shows that the N→M coordination results in a large red shift of the emission wavelength.

Taking previous studies into account, we found that the M–M distances are linearly correlated with the M–M stretching frequencies for the dinuclear $d^{10}$ complexes in the ground and lowest-energy triplet excited states.

In comparison with experimental values, the CIS calculations severely overestimate the transition energies of the Ag and Cu complexes, but the TD-DFT calculations reasonably predict their transition energies. However, with respect to the Au analog, the CIS and TD-DFT methods over- and under-estimate the transition energies, respectively.

**Supporting Information** (see footnote on the first page of this article): Table of optimized geometry parameters of $[Au_2(dpm)_2]^{2+}$ (**1**) and **1**·$(MeCN)_2$ in the ground and excited states. Table of optimized geometry parameters of $[M_2(dmpm)_2]^{2+}$ (M = Au, Ag and Cu) in the MP2 calculations. Table of compositions of HOMO and LUMO for the $^3A_u$ excited states of **1**–**3** and **1**–**3**·$(MeCN)_2$ in the TD-DFT calculations.

## Acknowledgments

This work was supported by the Natural Science Foundation of China (20301006, 20173021).

[1] P. Pyykkö, *Chem. Rev.* **1997**, *97*, 597–636.
[2] P. Pyykkö, *Angew. Chem. Int. Ed.* **2004**, *43*, 4412–4456.
[3] P. Pyykkö, N. Runeberg, F. Mendizabal, *Chem. Eur. J.* **1997**, *3*, 1451–1457.
[4] P. Pyykkö, F. Mendizabal, *Inorg. Chem.* **1998**, *37*, 3018–3025.
[5] É. Fournier, A. Dechken, P. D. Harvey, *Eur. J. Inorg. Chem.* **2004**, 4420–4429.
[6] M. A. Rawashdeh-Omary, M. A. Omary, H. H. Patterson, J. P. Fackler Jr., *J. Am. Chem. Soc.* **2001**, *123*, 11237–11247.
[7] M. Bardají, P. G. Jones, A. Laguna, M. D. Villacampa, N. Villaverde, *Dalton Trans.* **2003**, 4529–4536.
[8] V. W.-W. Yam, T.-F. Lai, C.-M. Che, *J. Chem. Soc., Dalton Trans.* **1990**, 3747–3752.
[9] A. A. Mohamed, I. Kani, A. O. Ramirez, J. P. Fackler Jr., *Inorg. Chem.* **2004**, *43*, 3833–3839.
[10] K. H. Leung, D. L. Phillips, Z. Mao, C.-M. Che, V. M. Miskowski, C.-K. Chan, *Inorg. Chem.* **2002**, *41*, 2054–2059.
[11] S. D. Hanna, J. I. Zink, *Inorg. Chem.* **1996**, *35*, 297–302.
[12] H.-X. Zhang, C.-M. Che, *Chem. Eur. J.* **2001**, *7*, 4887–4893.
[13] Q.-J. Pan, H.-X. Zhang, *J. Phys. Chem. A* **2004**, *108*, 3650–3661.
[14] Q.-J. Pan, H.-X. Zhang, *J. Chem. Phys.* **2003**, *119*, 4346–4352.
[15] Q.-J. Pan, H.-X. Zhang, *Chem. Phys. Lett.* **2004**, *394*, 155–160.
[16] Q.-J. Pan, H.-X. Zhang, *Organometallics* **2004**, *23*, 5198–5209.
[17] Q.-J. Pan, H.-X. Zhang, *Eur. J. Inorg. Chem.* **2003**, 4202–4210.
[18] H. Schmidbaur, *Chem. Soc. Rev.* **1995**, *24*, 391–400.
[19] E. J. Fernández, J. M. López-de-Luzuraga, M. Monge, M. A. Rodríguez, O. Crespo, M. C. Gimeno, A. Laguna, P. G. Jones, *Inorg. Chem.* **1998**, *37*, 6002–6006.
[20] P. Schwerdtfeger, A. E. Bruce, M. R. M. Bruce, *J. Am. Chem. Soc.* **1998**, *120*, 6587–6597.
[21] L. Magnko, M. Schweizer, G. Rauhut, M. Schütz, H. Stoll, H.-J. Werner, *Phys. Chem. Chem. Phys.* **2002**, *4*, 1006–1013.
[22] H. Liu, M. J. Calhorda, M. G. B. Drew, V. Félix, J. Novosad, L. F. Veiros, F. F. De Biani, P. Zanello, *J. Chem. Soc., Dalton Trans.* **2002**, 4365–4374.
[23] H. L. Hermann, G. Boche, P. Schwerdtfeger, *Chem. Eur. J.* **2001**, *7*, 5333–5342.
[24] P. D. Harvey, M. Drouin, T. Zhang, *Inorg. Chem.* **1997**, *36*, 4998–5005.
[25] W.-F. Fu, K.-C. Chan, V. M. Miskowski, C.-M. Che, *Angew. Chem. Int. Ed.* **1999**, *38*, 2783–2785.
[26] W.-F. Fu, K.-C. Chan, K.-K. Cheung, C.-M. Che, *Chem. Eur. J.* **2001**, *7*, 4656–4664.
[27] K. H. Leung, D. L. Phillips, M.-C. Tse, C.-M. Che, V. M. Miskowski, *J. Am. Chem. Soc.* **1999**, *121*, 4799–4803.
[28] C.-M. Che, M.-C. Tse, M. C. W. Chan, K.-K. Cheung, D. L. Phillips, K.-H. Leung, *J. Am. Chem. Soc.* **2000**, *122*, 2464–2468.
[29] C.-M. Che, Z. Mao, V. M. Miskowski, M.-C. Tse, C.-K. Chan, K.-K. Cheung, D. L. Phillips, K.-H. Leung, *Angew. Chem. Int. Ed.* **2000**, *39*, 4084–4088.
[30] W.-F. Fu, X. Gan, C.-M. Che, Q.-Y. Cao, Z.-Y. Zhou, N. N.-Y. Zhu, *Chem. Eur. J.* **2004**, *10*, 2228–2236.
[31] C.-M. Che, H.-L. Kwong, C.-K. Poon, V. W.-W. Yam, *J. Chem. Soc., Dalton Trans.* **1990**, 3215–3219.
[32] C.-M. Che, H.-L. Kwong, V. W.-W. Yam, K.-C. Cho, *J. Chem. Soc., Chem. Commun.* **1989**, 885–886.
[33] V. W.-W. Yam, K. K.-W. Lo, *Chem. Soc. Rev.* **1999**, *28*, 323–334.
[34] C. Leiggener, G. Calzaferri, *ChemPhysChem* **2004**, *5*, 1593–1596.
[35] S. M. Kanan, M. A. Omary, H. H. Patterson, M. Matsuoka, M. Anpo, *J. Phys. Chem. B* **2000**, *104*, 3507–3517.
[36] M. Anpo, M. Matsuoka, H. Yamashita, *Catal. Today* **1997**, *35*, 177–181.
[37] E. J. Corey, M. M. Mahrotra, A. U. Khan, *Science* **1987**, *236*, 68–69.

 © 2006 Wiley-VCH Verlag GmbH & Co. KGaA, Weinheim 

[38] J. B. Foresman, M. Head-Gordon, J. A. Pople, M. J. Frisch, *J. Phys. Chem.* **1992**, *96*, 135–149.
[39] C. King, J.-C. Wang, M. N. I. Khan, J. P. Fackler Jr., *Inorg. Chem.* **1989**, *28*, 2145–2149.
[40] D. Perreault, M. Drouin, A. Michel, V. M. Miskowski, W. P. Schaefer, P. D. Harvey, *Inorg. Chem.* **1992**, *31*, 695–702.
[41] N. C. Payne, R. J. Puddephatt, R. Ravindranath, I. Treurnicht, *Can. J. Chem.* **1988**, *66*, 3176–3183.
[42] J. Kozelka, H. R. Oswald, E. Dubler, *Acta Crystallogr., Sect. C* **1986**, *42*, 1007–1009.
[43] J.-C. Wang, Md. N. I. Khan, J. P. Fackler Jr., *Acta Crystallogr., Sect. C* **1989**, *45*, 1482–1485.
[44] L. C. Porter, Md. N. I. Khan, C. King, J. P. Fackler Jr., *Acta Crystallogr., Sect. C: Cryst. Struct. Commun.* **1989**, *45*, 947–949.
[45] E. R. T. Tiekink, *Acta Crystallogr., Sect. C, Cryst. Struct. Commun.* **1990**, *46*, 235–238.
[46] C. Møller, M. S. Plesset, *Phys. Rev.* **1934**, *46*, 618–622.
[47] M. E. Casida, C. Jamorski, K. C. Casida, D. R. Salahub, *J. Chem. Phys.* **1998**, *108*, 4439–4449.
[48] R. E. Statmann, G. E. Scuseria, *J. Chem. Phys.* **1998**, *109*, 8218–8224.
[49] R. Bauernschmitt, R. Ahlrichs, *Chem. Phys. Lett.* **1996**, *256*, 454–464.
[50] E. J. Fernández, M. C. Gimeno, P. G. Jones, A. Laguna, M. Laguna, J. M. López-de-Luzuriaga, M. A. Rodriguez, *Chem. Ber.* **1995**, *128*, 121–124.
[51] B. A. Bowmaker, H. Schmidbaur, S. Krüger, N. Rösch, *Inorg. Chem.* **1997**, *36*, 1754–1757.
[52] M. J. Frisch, G. W. Trucks, H. B. Schlegel, G. E. Scuseria, M. A. Robb, J. R. Cheeseman, J. A. Montgomery Jr., T. Vreven, K. N. Kudin, J. C. Burant, J. M. Millam, S. S. Iyengar, J. Tomasi, V. Barone, B. Mennucci, M. Cossi, G. Scalmani, N. Rega, G. A. Petersson, H. Nakatsuji, M. Hada, M. Ehara, K. Toyota, R. Fukuda, J. Hasegawa, M. Ishida, T. Nakajima, Y. Honda, O. Kitao, H. Nakai, M. Klene, X. Li, J. E. Knox, H. P. Hratchian, J. B. Cross, C. Adamo, J. Jaramillo, R. Gomperts, R. E. Stratmann, O. Yazyev, A. J. Austin, R. Cammi, C. Pomelli, J. W. Ochterski, P. Y. Ayala, K. Morokuma, G. A. Voth, P. Salvador, J. J. Dannenberg, V. G. Zakrzewski, S. Dapprich, A. D. Daniels, M. C. Strain, O. Farkas, D. K. Malick, A. D. Rabuck, K. Raghavachari, J. B. Foresman, J. V. Ortiz, Q. Cui, A. G. Baboul, S. Clifford, J. Cioslowski, B. B. Stefanov, G. Liu, A. Liashenko, P. Piskorz, I. Komaromi, R. L. Martin, D. J. Fox, T. Keith, M. A. Al-Laham, C. Y. Peng, A. Nanayakkara, M. Challacombe, P. M. W. Gill, B. Johnson, W. Chen, M. W. Wong, C. Gonzalez, J. A. Pople, *Gaussian 03, Revision B.03*, Gaussian, Inc., Pittsburgh PA, **2003**.
[53] W. R. Wadt, P. J. Hay, *J. Chem. Phys.* **1985**, *82*, 284–298.
[54] P. J. Hay, W. R. Wadt, *J. Chem. Phys.* **1985**, *82*, 299–310.
[55] F. A. Cotton, X. Feng, M. Matusz, R. Poli, *J. Am. Chem. Soc.* **1988**, *110*, 7077–7083.
[56] V. J. Catalano, S. J. Horner, *Inorg. Chem.* **2003**, *42*, 8430–8438.
[57] P. Schwerdtfeger, H. L. Hermann, H. Schmidbaur, *Inorg. Chem.* **2003**, *42*, 1334–1342.
[58] J. P. Foster, F. Weinhold, *J. Am. Chem. Soc.* **1980**, *102*, 7211–7218.
[59] A. E. Reed, R. B. Weinstock, F. Weinhold, *J. Chem. Phys.* **1985**, *83*, 735–746.
[60] A. E. Reed, L. A. Curtiss, F. Weinhold, *Chem. Rev.* **1988**, *88*, 899–926.
[61] P. Pyykkö, *Chem. Rev.* **1988**, *88*, 563–594.
[62] J. F. Stanton, J. Gauss, N. Ishikawa, M. Head-Gordon, *J. Chem. Phys.* **1995**, *103*, 4160–4174.
[63] I. Frank, *Excited State Molecular Dynamics* Invited Review, SIMU Newsletter, **2001**, *3*, 63–77.
[64] S. J. A. van Gisbergen, F. Kootstra, P. R. T. Schipper, O. V. Gritsenko, J. G. Snijders, E. J. Baerends, *Phys. Rev. A: At. Mol. Opt. Phys.* **1998**, *57*, 2556–2571.
[65] N. N. Matsuzawa, A. Ishitani, D. A. Dixon, T. Uda, *J. Phys. Chem. A.* **2001**, *105*, 4953–4962.
[66] P. Boulet, H. Chermette, C. Daul, F. Gilardoni, F. Rogemond, J. Weber, G. Zuber, *J. Phys. Chem. A* **2001**, *105*, 885–894.

Received: August 17, 2005
Published Online: January 16, 2006

 © 2006 Wiley-VCH Verlag GmbH & Co. KGaA, Weinheim 

DOI: 10.1002/ejic.200500772

# Absence of Dichroism in Dinuclear Rhenium Complexes with Sterically Hindered $\mu_2$-($\eta^2$-*N*,*O*)-Nitrosobenzene Ligands

**Christoph Krinninger,[a] Stefan Wirth,[a] Peter Klüfers,[a] Peter Mayer,[a] and Ingo Peter Lorenz*[a]**

**Keywords:** Dichroism / Dinuclear complexes / N ligands / Rhenium / Structure elucidation

The substitution reactions of $[Re(CO)_5X]$ (X = Cl, Br) with 2,6-dihalo-substituted nitrosobenzene derivatives $C_6H_2YZ_2NO$ (Y = H, Cl, Br; Z = Cl, Br) leads to the formation of dinuclear $\mu_2$-$\eta^2$-*N*,*O*-nitrosobenzene-bridged complexes of the type $[\{(CO)_3Re(\mu\text{-}X)\}_2ONC_6H_2YZ_2]$ (**6a**,**b**, **7a**,**b**, **8a**,**b**, **9a**). The turquoise coloured solutions of the complexes in $CH_2Cl_2$ show only one UV/Vis absorption of medium intensity in the region 670–710 nm, depending on the halogen bridges X and substituents Z. Single crystals of the complexes do not exhibit any dichroic properties. This may be due to the almost perpendicular orientation of the phenyl ring towards the Re–O–N–Re plane. The molecular structures of six compounds, as determined by single-crystal X-ray analyses, show two face-joined octahedra with Re centres that are bridged by two halogens X and one NO group. NO coordinates in a nonsymmetrical $\eta^2$-like fashion with N- or O-linkage to each Re centre. The phenyl rings do not lie within the symmetry plane containing the atoms Re, N and O, but are almost perpendicular to this (torsion angle O–N–C–C = 83.5–85.4°) because of the 2,6-dihalogen substituents Z.
(© Wiley-VCH Verlag GmbH & Co. KGaA, 69451 Weinheim, Germany, 2006)

## Introduction

The coordination chemistry of organic RNO nitroso compounds has been extensively investigated,[1] and their many different coordination modes have been summarised in schemes in previous accounts of our work, as well as by others.[2,3] The dominant bonding mode bridging two metal centres is of the type $\mu$-$\eta^1$-*N*, $\mu$-$\eta^1$:$\eta^2$-*N*,*O*, $\mu$-$\eta^1$:$\eta^1$-*N*,*O* or $\mu$-$\eta^2$:$\eta^2$-*N*,*O* (Scheme 1), although the unassisted ligand function $\mu$-$\eta^1$:$\eta^1$-*N*,*O* (type I) with a simple bridging coordination mode is less common. Co-assisted ligand functions, that is those with additional coordination by a further donor system (e.g. amido or carbonyl groups), have been verified in most examples and form additional five- (type Ia)[4] or six-membered rings (type Ib).[5] Furthermore, type I has been only observed in a unique neutral complex of platinum[6] and in a dinuclear rhodium cation with thiolato bridges.[7]

We have recently published a series of complexes[2,3] that are the first simple, neutral and dinuclear *C*-nitroso complexes to exhibit this rare, unassisted $\mu$-$\eta^1$:$\eta^1$-*N*,*O* ligand function (type I), and contain only single atoms, X, as additional bridges (X = Cl, Br, I). All of these complexes show dichroic properties and form deep-blue solutions. In the UV/Vis spectra, one very intense broad absorption is found at $\lambda$ = 600–650 nm (log $\varepsilon$ > 30000), which is due to a solvochromic ligand-to-metal CT band ([NO–Re$^I$]). Light reflected from microcrystalline powders of the substances shines with different colours (like shells). Visual inspection of suitable crystals with polarized light under a microscope clearly showed a polarisation-dependent absorption. In the case of $[\{(CO)_3Re(\mu\text{-}Br)\}_2ONC_6H_4NEt_2]$ sufficiently large single crystals showed a pronounced linear dichroism.[3] We were able to correlate this dichroism with the arrangement of the molecules in the unit cells, which show alignment of the RNO units along a crystal plane. It is worthwhile to note that the dihedral angles Re–O–N–Re and O–N–C–C (phenyl ring) are less than 5° and 3°, respectively. This means that the NO group and the phenyl ring (together with the $NR_2$ substituent)[2,3] lie almost within the symmetry plane of the dinuclear complexes. To prove this correlation, we decided to synthesise analogous complexes with nitrosobenzene ligands that are sterically hindered in both *ortho* positions. Our aim was, therefore, to twist the phenyl

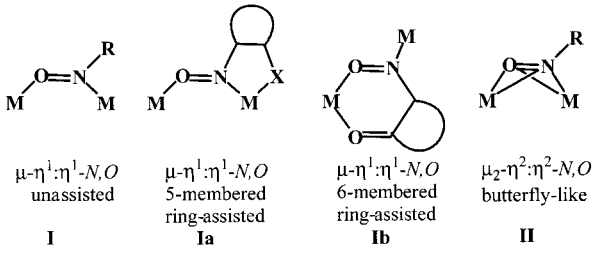


Scheme 1. Bonding modes of *C*-nitroso compounds bridging two metals ($\mu$-$\eta^2$-*N*,*O*).

[a] Ludwig Maximilian University Munich, Department of Chemistry and Biochemistry,
Butenandtstr. 5–13, 81377 Munich, Germany
Fax: +49-89-2180-77867
E-mail: ipl@cup.uni-muenchen.de

 © 2006 Wiley-VCH Verlag GmbH & Co. KGaA, Weinheim 

ring out of the plane and to observe the effect this had on the dichroism. We undertook the reaction of 2,6-dihalo-substituted nitrosobenzenes with $[Re(CO)_5X]$ (X = Cl, Br), and obtained the corresponding dinuclear complexes $[\{(CO)_3Re(\mu\text{-}X)\}_2ONC_6H_2YZ_2]$, which exhibit the same nitroso ligand function $\mu_2$-$\eta^1$:$\eta^1$-*O*, but with a perpendicular orientation of the phenyl ring towards the plane formed by the atoms Re, O, N and Re. As a consequence of this, the dichroism is lost.

## Results and Discussion

The reaction of $[Re(CO)_5X]$ (X = Cl, Br) (**1a**,**b**) with the sterically hindered *C*-nitroso compounds 4-Y-2,6-$Z_2C_6H_2NO$ [Y = H, Z = Cl (**2**), Br (**3**); Y = Cl, Z = Br (**4**); Y = Br, Z = Cl (**5**)] leads to the dinuclear complexes **6a**,**b**–**8a**,**b** and **9a** (Scheme 2). All reactions were carried out in boiling $CH_2Cl_2$. Whereas **9a** was obtained in good yield (65%), **9b** could not be isolated under the same reaction conditions. It is interesting to note that using boiling toluene as solvent resulted in the dimeric halo complexes $[(CO)_4ReX]_2$ (X = Cl, Br); no reaction occurred when $[Re(CO)_5I]$ was used as the starting material.

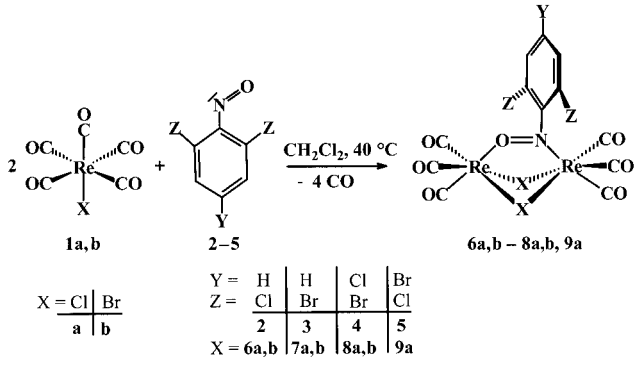


Scheme 2. Synthesis of sterically hindered $\mu_2$-($\eta^2$-*N*,O)-nitrosobenzene complexes **6**–**9**.

Compounds **6a**,**b**–**8a**,**b** and **9a** were obtained as dark-green crystals that are stable in air for some days. The complexes are soluble in THF, acetone, $CHCl_3$, $CH_2Cl_2$, and even in toluene, but nearly insoluble in pentane or hexane. The turquoise solutions formed in these solvents can be kept in air for several days without decomposition. In the UV/Vis spectra ($CH_2Cl_2$) two broad absorptions are observed, one lies consistently at about $\lambda_1$ = 375–380 nm, whereas the second, which originates from a ligand-to-metal CT (NO–$Re^I$), is observed over a larger range at $\lambda_2$ = 670–710 nm. It is shifted to lower frequency with respect to the corresponding π–π*-NO electronic transition of the free ligands. It is noteworthy that they are also observed at lower frequencies and with smaller intensities than those of the corresponding nitrosoaniline complexes published previously,[2,3] where the NO group, phenyl ring and the $NR_2$ substituent lie exactly within the symmetry plane of the dinuclear complexes. In spite of the frequency range of $\lambda_2$, there is no dependence of its spectral position on either the halogen bridges or substituents.

The X-ray structure analyses of **6a**,**b**–**8a**,**b** show that the phenyl ring with both halo substituents in the *ortho* positions is orientated perpendicular to the symmetry plane. As is therefore expected, the light reflected from crystalline powders of these complexes does not shine in different colours and neither does it show any polarisation-dependent absorption of the type mentioned above.[2,3] Therefore, they do not exhibit any significant dichroic properties.

The IR spectra of **6a**,**b**–**8a**,**b** and **9a** show five ν(CO) absorptions. As the NO group is bonded by N and O to different Re centres, the electronic situation at both Re centres is different. This normally results in two different *fac*-$Re(CO)_3$ fragments, each with local $C_{3v}$ symmetry. However, because of the bulky substituents in the *ortho* position of the nitrosobenzenes, the local symmetry of the $Re(CO)_3$ fragment at N is reduced to $C_s$. Therefore, three bands of the type 2A′ + A′′ are detected. Due to electronic reasons the *N*-bonded $Re(CO)_3$ moiety should be more electron rich and act as a better π-donor for the CO ligands than the O-bonded one. Therefore, the absorptions at higher wavenumbers with varying intensities have been assigned to the $\{(CO)_3Re\text{–}O\}$ fragment [$\tilde{\nu}$ = 2086–2091 ($A_1$), 2006–2012 $cm^{-1}$ (E)] and the three absorptions at lower wavenumbers and similar intensities to the $\{(CO)_3Re\text{–}N\}$ fragment [$\tilde{\nu}$ = 2024–2058 (A′), 1961–1970 (A′), 1913–1949 $cm^{-1}$ (A′′)]. Because several bands lie very close together it is not possible to draw any conclusions about the halogens as substituents or bridges. The ν(NO) band of the complexes is found at 1329–1350 $cm^{-1}$, which is a shift to lower frequency of about 115 $cm^{-1}$ with respect to the free *C*-nitroso ligand and of about 50 $cm^{-1}$ compared with other complexes.[2,3]

The $^1H$ NMR spectrum of **6a** shows three separate doublets at $\delta$ = 7.40, 7.42 and 7.44 ppm. In the case of **6b**, only a multiplet between $\delta$ = 7.38–7.44 ppm can be detected. In the spectra of **7a** two doublets for the ring protons in the 3,5-positions are detected at $\delta$ = 7.26 and 7.37 ppm, and one triplet for the proton in the 4-position at $\delta$ = 7.67 ppm. Complex **7b** exhibits a triplet at $\delta$ = 7.27 ppm, a doublet at $\delta$ = 7.38 ppm and a multiplet at $\delta$ = 7.61–7.64 ppm, whereas **8a** only shows one broad signal at $\delta$ = 7.66 ppm, and **8b** and **9a** exhibit singlets at $\delta$ = 7.64 and 7.60 ppm, respectively. It is noteworthy that in spite of the mirror symmetry in the $Re_2NO$ plane compounds **6a**,**b** and **7a**,**b** with the benzene ring substituted in 2,6-positions exhibit different signals for the three protons in the 3,4- and 5-positions. Compounds **8a**,**b**, and **9a**, however, show only one resonance for the 3,5-protons.

In the $^{13}C$ NMR spectra of **6a**,**b**–**8a**,**b** and **9a** the signals for the phenyl groups are detected at $\delta$ = 124.1–140.9 ppm. Here, we observe three signals for the three different types of C-atoms in the 2,6-, 3,5- and 4-positions. The *N*-bonded quaternary carbon is observed at $\delta$ = 160.2–164.5 ppm and the signals corresponding to the CO ligands at the Re centres appear at $\delta$ = 181–192 ppm.

 © 2006 Wiley-VCH Verlag GmbH & Co. KGaA, Weinheim 

The parent peaks as well as peaks corresponding to fragments resulting from the successive loss of up to six CO ligands are observed in the mass spectra (DEI-MS) of **6a**,**b**–**8a**,**b** and **9a**.

The compositions and structures of complexes **6a**,**b**–**8a**,**b** were confirmed by X-ray structure analysis (see Table 2). Single crystals of complexes **6a**,**b**–**8a**,**b** were obtained by the diffusion of pentane into solutions of the complexes in $CHCl_3$. The molecular structures and selected bond lengths and angles are given in Figures 1 (**6a**), 2 (**6b**), 3 (**7a**), 4 (**7b**), 5 (**8a**) and 6 (**8b**). They show two face-joined octahedra with two halogens and the NO group as bridging ligands. The N–O distances are approximately 1.299 Å, similar to the values for analogous complexes,[1–3] but significantly longer than the average N–O distances of free *C*-nitroso compounds (1.21 Å).[8] There is no significant dependence of the NO lengths upon varying the halo bridges. In all cases, and in contrast to the recently published analogous complexes,[2,3] the Re–O bonds (approx. 2.10 Å) are significantly longer than the Re–N bonds (approx. 1.99 Å), whereas all the bridging Re–X bonds in the complexes are similar in length. For better comparison, the most important structural parameters of all complexes are summarised in Table 1.

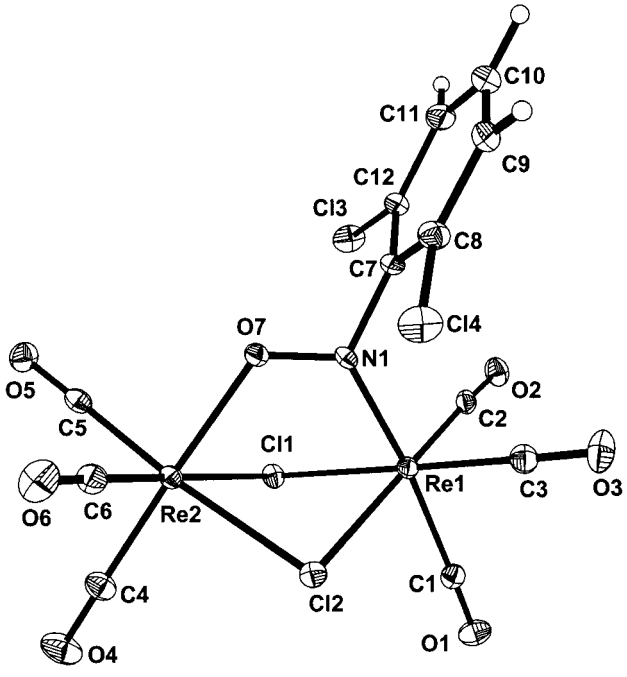


Figure 1. Molecular structure of **6a**. Selected bond lengths [Å] and angles [°]: Re(1)–N(1) 1.994(4), Re(2)–O(7) 2.124(4), Re(1)–Cl(1) 2.4914(14), Re(1)–Cl(2) 2.4726(14), Re(2)–Cl(1) 2.5024(14), Re(2)–Cl(2) 2.5056(14), O(7)–N(1) 1.282(6), N(1)–C(7) 1.457(6), Re(1)–C(1) 2.031(6), Re(1)–C(2) 1.952(6), Re(1)–C(3) 1.917(7), Re(2)–C(4) 1.928(6), Re(2)–C(5) 1.902(6), Re(2)–C(6) 1.908(6); N(1)–O(7)–Re(2) 120.2(3), O(7)–N(1)–Re(1) 123.9(3), O(7)–Re(2)–Cl(2) 82.82, O(7)–Re(2)–Cl(1) 82.82(11), N(1)–Re(1)–Cl(1) 84.52(13), N(1)–Re(1)–Cl(2) 85.96(13), Cl(2)–Re(1)–Cl(1) 80.83(5), Cl(1)–Re(2)–Cl(2) 79.98(5), O(7)–N(1)–C(7) 110.3(4), O(7)–N(1)–C(7)–C(8) 84.74.

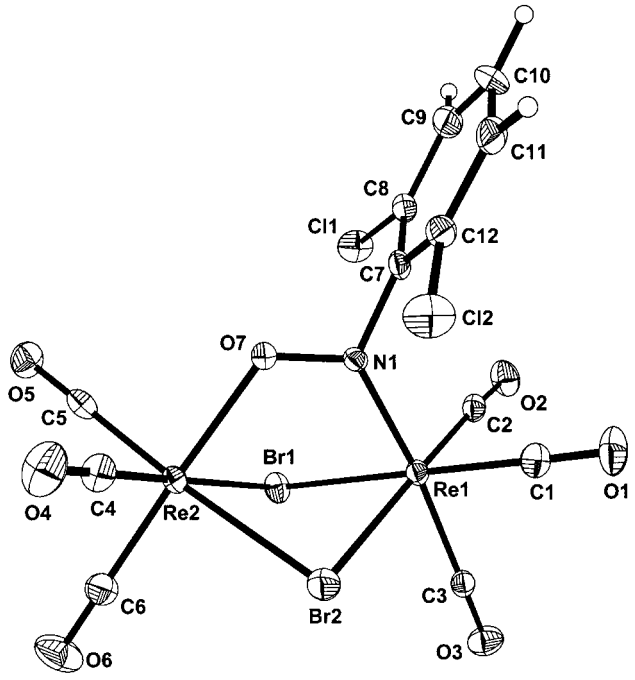


Figure 2. Molecular structure of **6b**. Selected bond lengths [Å] and angles [°]:Re(1)–N(1) 1.990(6), Re(2)–O(7) 2.116(5), Re(1)–Br(1) 2.6115(13), Re(1)–Br(2) 2.5965(11), Re(2)–Br(1) 2.6199(10), Re(2)–Br(2) 2.6305(12), O(7)–N(1) 1.299(8), N(1)–C(7) 1.451(9), Re(1)–C(1) 1.923(9), Re(1)–C(2) 1.936(9), Re(1)–C(3) 2.020(9), Re(2)–C(4) 1.902(8), Re(2)–C(5) 1.891(9), Re(2)–C(6) 1.907(9); N(1)–O(7)–Re(2) 121.8(4), O(7)–N(1)–Re(1) 126.5(5), O(7)–Re(2)–Br(2) 84.25(14), O(7)–Re(2)–Br(1) 83.58(4), N(1)–Re(1)–Br(1) 85.84(17), N(1)–Re(1)–Br(2) 86.73(17), Br(2)–Re(1)–Br(1) 82.89(4), Br(1)–Re(2)–Br(2) 82.07(4), O(7)–N(1)–C(7) 109.7(5), O(7)–N(1)–C(7)–C(12) 85.44.

The dihedral angles Re–O–N–$C_{Ph}$ of all complexes are smaller than 1.4°. The main difference between these complexes compared to those recently published[2,3] is that the dihedral angles O(7)–N(1)–C(7)–C(8/12) lie between 83.5–85.4°. This means that there is a near perpendicular orientation of the phenyl ring towards the plane formed by the atoms Re, O, N and Re. The consequence of this is the loss of dichroism. No Re–Re interaction is observed in any of the compounds, although the Re–Re distance varies with the size of the halogen bridges [Re(1)–Re(2) ≈ 3.47 (**6a**, **7a**, **8a**) and 3.54 Å (**6b**, **7b**, **8b**)].

It is worthwhile to emphasise that the orientation of the molecules described in this paper within the lattice is similar to that reported earlier[3] for the dichroic molecules. The triclinic crystal system is observed in both cases, although the packing of the dichroic molecules is closer, in particular with respect to the parallel phenyl rings of adjacent molecules, and the π-delocalisation is more widespread. Both effects lead to the significant anisotropy that is necessary for dichroism. Such close contact between the phenyl rings of the present molecules is not possible and the π-delocalisation is less. Therefore, it can be concluded that the absence of dichroism in **6a**,**b**–**8a**,**b** and **9a** is a result of the non-planar arrangement of the phenyl rings with respect to the

 © 2006 Wiley-VCH Verlag GmbH & Co. KGaA, Weinheim 

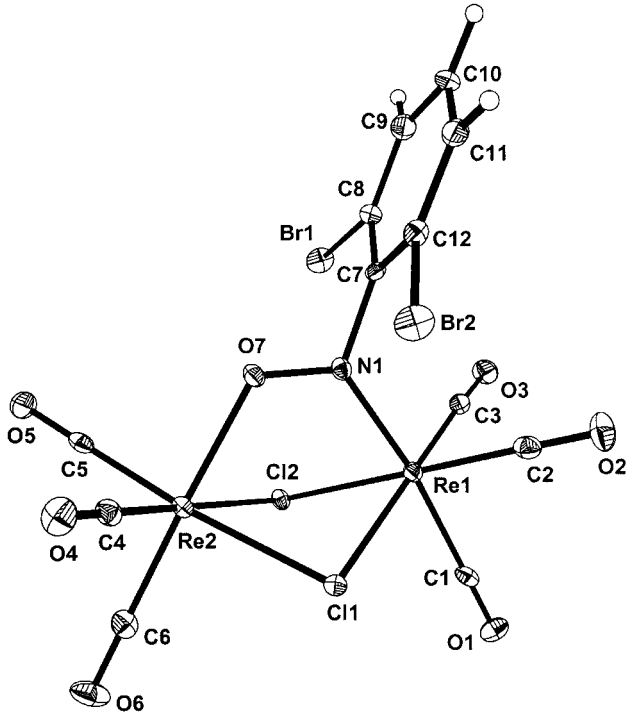


Figure 3. Molecular structure of **7a**. Selected bond lengths [Å] and angles [°]: Re(1)–N(1) 1.991(4), Re(2)–O(7) 2.126(4), Re(1)–Cl(1) 2.4801(12), Re(1)–Cl(2) 2.5000(12), Re(2)–Cl(1) 2.5117(12), Re(2)–Cl(2) 2.5144(11), O(7)–N(1) 1.282(5), N(1)–C(7) 1.460(7), Re(1)–C(1) 2.030(6), Re(1)–C(2) 1.923(6), Re(1)–C(3) 1.930(6), Re(2)–C(4) 1.903(5), Re(2)–C(5) 1.914(6), Re(2)–C(6) 1.920(6); N(1)–O(7)–Re(2) 120.3(3), O(7)–N(1)–Re(1) 126.2(3), O(7)–Re(2)–Cl(2) 82.82(9), O(7)–Re(2)–Cl(1) 83.78(11), N(1)–Re(1)–Cl(1) 86.47(12), N(1)–Re(1)–Cl(2) 84.65(12), Cl(2)–Re(1)–Cl(1) 80.87(4), Cl(1)–Re(2)–Cl(2) 79.98(5), O(7)–N(1)–C(7) 109.9(4), O(7)–N(1)–C(7)–C(12) 85.28.

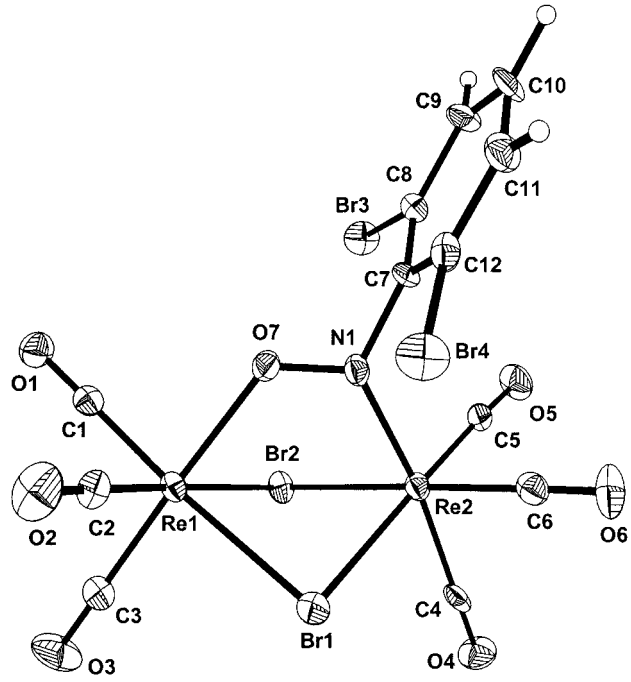


Figure 4. Molecular structure of **7b**. Selected bond lengths [Å] and angles [°]: Re(2)–N(1) 2.012(8), Re(1)–O(7) 2.123(7), Re(1)–Br(1) 2.6364(10), Re(1)–Br(2) 2.6292(10), Re(2)–Br(1) 2.6057(10), Re(2)–Br(2) 2.6182(10), O(7)–N(1) 1.279(9), N(1)–C(7) 1.453(12), Re(1)–C(1) 1.874(11), Re(1)–C(2) 1.902(10), Re(1)–C(3) 1.936(12), Re(2)–C(4) 2.043(12), Re(2)–C(5) 1.920(11), Re(2)–C(6) 1.908(11); N(1)–O(7)–Re(1) 122.7(6), O(7)–N(1)–Re(2) 123.4(6), O(7)–Re(1)–Br(2) 83.53(16), O(7)–Re(1)–Br(1) 84.39(16), N(1)–Re(2)–Br(1) 87.1(2), N(1)–Re(2)–Br(2) 85.6(2), Br(1)–Re(1)–Br(2) 82.51(3), Br(2)–Re(2)–Br(1) 81.72(3), O(7)–N(1)–C(7) 110.9(7), O(7)–N(1)–C(7)–C(12) 84.91.

$Re_2NO$ plane. In addition, it is interesting to note that this is the only structural parameter that changes in comparison with the dichroic complexes.[3]

In summary, we have synthesised a novel series of analogous[2,3] neutral and dinuclear Re complexes with *C*-nitroso ligands. They also contain an unassisted $\mu_2$-$\eta^1$:$\eta^1$-*N*,O bridge (type I, Scheme 1) and only single atoms (X = Cl, Br) as additional bridges. However, the complexes do not possess any dichroic properties. This is a result of the different orientation of the *C*-nitroso ligand, which is almost perpendicular to the Re–O–N–Re symmetry plane. This is caused by the two substituents (Z) in the two *ortho* positions of the phenyl ring. A considerably different reaction pathway has been found for the reaction of $[Re(CO)_5X]$ (X = Cl, Br, I) with more sterically demanding *C*-nitroso ligands (e.g. 1-nitroso-2-naphthol), whereby HX or $CO_2$ elimination has been observed, and quite different mononuclear products have been obtained.[9]

## Experimental Section

All operations were carried out under argon in dry solvents.[10] $[Re(CO)_5X]$ (X = Cl, Br),[11] 2,6-dibromonitrosobenzene, 2,6-dichloronitrosobenzene, 2,6-dibromo-4-chloronitrosobenzene and, 4-bromo-2,6-dichloronitrosobenzene were prepared according to a literature procedure.[12] NMR spectra were recorded with a Jeol Ex 400 ($^1$H: 399.78 MHz; $^{13}$C: 100.54 MHz) or a Jeol Eclipse 270 MHz spectrometer ($^1$H: 270.17 MHz; $^{13}$C: 67.94 MHz) in $CDCl_3$. Mass spectra were obtained with a Jeol Mstation JMS 700. IR and UV/Vis spectra were measured with a Perkin–Elmer Spectrum One FT-IR or Perkin–Elmer Lambda 16 spectrometer. Elemental analyses were performed with a Heraeus Elementar Vario EL. For X-ray data see Table 2.

**Synthesis of 6–9 from 1a,b. General Procedure:** $[Re(CO)_5X]$ (X = Cl, Br) (**1a**,**b**) and 4-Y-2,6-$Z_2C_6H_2NO$ [Y = H, Z = Cl (**2**), Z = Br (**3**); Y = Cl, Z = Br (**4**); Y = Br, Z = Cl (**5**)] were dissolved in 20 mL of dichloromethane and heated for 40 h under reflux, whereby the solution turned green. The solvent was then evaporated and the green residue was purified by column chromatography ($CH_2Cl_2$).

**$\mu_2$-($\eta^2$-*N*,*O*-2,6-Dichloronitrosobenzene)bis[$\mu$-chlorotricarbonylrhenium(I)] (6a):** Synthesised from 116 mg (0.321 mmol) of **1a** and 42.4 mg (0.240 mmol) of **3**. Yield: 51.7 mg (0.066 mmol, 41%) green crystals, m.p. 145 °C (dec.). $^1$H NMR (399.78 MHz, $CDCl_3$): $\delta$ = 7.40 (d, $^3J$ = 6.54 Hz, 1 H, $CH_{arom.}$), 7.42 (d, $^4J$ = 0.66 Hz, 1 H, $CH_{arom.}$), 7.44 (d, $^4J$ = 2.04 Hz, 1 H, $CH_{arom.}$) ppm. $^{13}$C NMR (100.53 MHz, $CDCl_3$): $\delta$ = 124.1 ($CH_{arom.}$), 129.2 ($CH_{arom.}$), 131.5 ($CH_{arom.}$), 161.3 (ON-$C_q$), 185.1 (CO), 192.2 (CO) ppm. IR (KBr): $\tilde{\nu}$ = 2965 cm$^{-1}$ (w), 2405 (w), 2338 (w) 2098 (m), 2037 (vs), 2012 (vs), 1970 (s), 1949 (s), 1931 (vs), 1618 (m), 1566 (m), 1437 (m), 1350 (m), 1319 (m), 1293 (w), 1263 (w), 1207 (w), 1192 (s), 1154

 © 2006 Wiley-VCH Verlag GmbH & Co. KGaA, Weinheim 

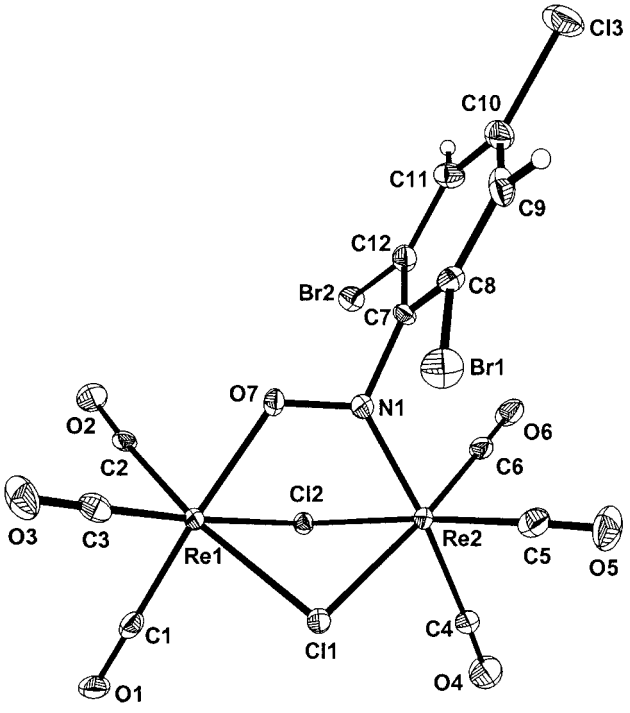


Figure 5. Molecular structure of **8a**. Selected bond lengths [Å] and angles [°]: Re(2)–N(1) 2.007(8), Re(1)–O(7) 2.099(6), Re(1)–Cl(2) 2.497(3), Re(1)–Cl(1) 2.500(2), Re(2)–Cl(2) 2.474(2), Re(2)–Cl(1) 2.482(2), O(7)–N(1) 1.297(10), N(1)–C(7) 1.440(11), Re(1)–C(1) 1.920(11), Re(1)–C(2) 1.927(10), Re(1)–C(3) 1.899(11), Re(2)–C(4) 2.018(10), Re(2)–C(5) 1.934(12), Re(2)–C(6) 1.941(11); N(1)–O(7)–Re(1) 120.8(5), O(7)–N(1)–Re(2) 123.3(6), O(7)–Re(1)–Cl(1) 83.50(18), O(7)–Re(1)–Cl(2) 83.67(18), N(1)–Re(2)–Cl(2) 85.4(2), N(1)–Re(2)–Cl(1) 85.0(2), Cl(2)–Re(1)–Cl(1) 79.27(8), Cl(2)–Re(2)–Cl(1) 80.06(8), O(7)–N(1)–C(7) 110.9(7), O(7)–N(1)–C(7)–C(12) 84.84.

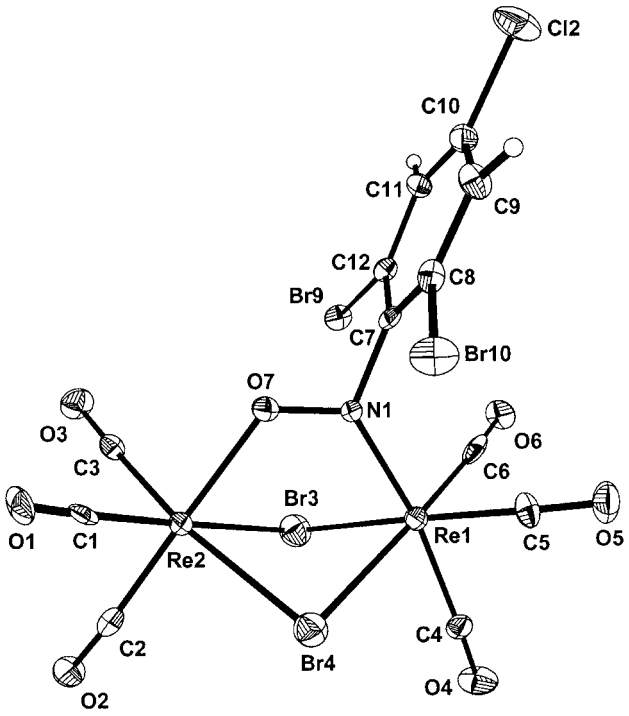


Figure 6. Molecular structure of **8b**. Selected bond lengths [Å] and angles [°]: Re(1)–N(1) 2.001(12), Re(2)–O(7) 2.127(11), Re(1)–Br(3) 2.578(2), Re(1)–Br(4) 2.611(2), Re(2)–Br(3) 2.589(2), Re(2)–Br(4) 2.637(2), O(7)–N(1) 1.257(15), N(1)–C(7) 1.458(19), Re(2)–C(1) 1.963(19), Re(2)–C(2) 1.95(2), Re(2)–C(3) 1.903(17), Re(1)–C(4) 2.08(2), Re(1)–C(5) 1.908(19), Re(1)–C(6) 1.99(2); N(1)–O(7)–Re(2) 123.7(9), O(7)–N(1)–Re(1) 123.3(10), O(7)–Re(2)–Br(3) 83.5(3), O(7)–Re(2)–Br(4) 83.5(3), N(1)–Re(1)–Br(3) 86.6(3), N(1)–Re(1)–Br(4) 86.4(4), Br(3)–Re(1)–Br(4) 81.10(7), Br(3)–Re(2)–Br(4) 80.40(7), O(7)–N(1)–C(7) 109.9(11), O(7)–N(1)–C(7)–C(12) 83.49.

(w), 1101 (w), 1067 (w), 946 (w), 929 (w), 895 (w), 929 (w), 895 (w), 854 (w), 799 (m), 786 (s), 743 (w), 726 (w), 681 (w), 643 (w), 617 (m), 529 (w). IR ($CH_2Cl_2$): $\tilde{\nu}$ = 2090 $cm^{-1}$ (m), 2033 (s), 2011 (vs), 1962 (s), 1941 (s). UV/Vis ($CH_2Cl_2$): $\lambda_{max}$ (log $\varepsilon$) = 376 nm (4685), 670 (7892). $C_{12}H_3Cl_4NO_7Re_2$ (787.30): calcd. C 18.30, H 0.38, N 1.78; found C 18.39, H 0.41, N 1.76. MS (DEI): *m*/*z* (%) = 786.3 (50) [$M^+$], 702.4 (38) [$M^+$ – 3 CO], 674.4 (36) [$M^+$ – 4 CO], 646.5 (92) [$M^+$ – 5 CO], 618.5 (100) [$M^+$ – 6 CO].

**$\mu_2$-($\eta^2$-*N*,*O*-2,6-Dichloronitrosobenzene)bis[$\mu$-bromotricarbonylrhenium(I)] (6b):** Synthesised from 152 mg (0.419 mmol) of **1b** and 43.4 mg (0.247 mmol) of **2**. Yield: 112 mg (0.128 mmol, 60%) green crystals; m.p. 147 °C (dec.). $^1$H NMR (399.78 MHz, $CDCl_3$): $\delta$ = 7.38–7.44 (m, 3 H, $CH_{arom.}$) ppm. $^{13}$C NMR (100.53 MHz, $CDCl_3$): $\delta$ = 126.3 ($CH_{arom.}$), 129.2 ($CH_{arom.}$), 130.8 ($CH_{arom.}$), 161.8 (ON-$C_q$), 184.8 (CO), 191.5 (CO) ppm. IR (KBr): $\tilde{\nu}$ = 3080 $cm^{-1}$ (m), 2997 (w), 2094 (m), 2024 (vs),2007 (vs), 1970 (s), 1930 (vs),1614 (m), 1577 (s), 1475 (s), 1438 (vs), 1333 (s), 1290 (m), 1206 (s), 1161 (w), 1132 (w), 1100 (m), 1069 (w), 970 (w), 904 (m), 896 (w), 853 (w), 804 (m), 794 (s), 782 (vs), 732 (m), 640 (w), 617 (w), 581 (w), 550 (w), 522 (w). IR ($CH_2Cl_2$): $\tilde{\nu}$ = 2086 $cm^{-1}$ (m), 2031 (s), 2011 (vs), 1962 (s), 1941 (s). UV/Vis ($CH_2Cl_2$): $\lambda_{max}$ (log $\varepsilon$) = 371 nm (4405), 702 (6409). $C_{12}H_3Br_2Cl_2NO_7Re_2$ (876.27): calcd. C 16.43, H 0.34, N 1.60; found C 16.34, H 0.39, N 1.62. MS (DEI): *m*/*z* (%) = 876.2 (18) [$M^+$], 848.2 (5) [$M^+$ – CO], 792.3 (13) [$M^+$ – 3 CO], 764.3 (10) [$M^+$ – 4 CO], 736.4 (21) [$M^+$ – 5 CO], 708.3 (24) [$M^+$ – 6 CO].

Table 1. Comparison of bond lengths [Å] and angles [°] of compounds **6a**,**b**–**8a**,**b**.

| | **6a** | **6b** | **7a** | **7b** | **8a** | **8b** |
|---|---|---|---|---|---|---|
| Re–$X_{av}$ | 2.488 | 2.608 | 2.496 | 2.633 | 2.499 | 2.595 |
| Re–O | 2.124 | 2.116 | 2.126 | 2.123 | 2.099 | 2.127 |
| Re–N | 1.994 | 1.990 | 1.991 | 2.012 | 2.007 | 2.001 |
| N–O | 1.282 | 1.299 | 1.282 | 1.279 | 1.297 | 1.257 |
| N–$C_{Ph}$ | 1.457 | 1.451 | 1.460 | 1.453 | 1.440 | 1.458 |
| Re–X–$Re_{av}$ | 80.41 | 82.48 | 80.43 | 82.12 | 79.67 | 80.75 |
| Re–N–O | 123.9 | 126.5 | 126.2 | 123.4 | 123.3 | 123.3 |
| Re–O–N | 120.2 | 121.8 | 120.3 | 122.7 | 120.8 | 123.7 |
| Re–O–N–$C_{Ph}$ | 1.03 | 0.53 | 1.34 | 0.78 | 0.27 | 0.82 |
| O–N–C–C(8/12) | 84.74 | 85.44 | 85.28 | 84.91 | 84.84 | 83.49 |

**$\mu_2$-($\eta^2$-*N*,*O*-2,6-Dibromonitrosobenzene)bis[$\mu$-chlorotricarbonylrhenium(I)] (7a):** Synthesised from 154 mg (0.427 mmol) of **1a** and 75.5 mg (0.285 mmol) of **3**. Yield: 106 mg (0.121 mmol, 57%) green crystals; m.p. 140 °C (dec.). $^1$H NMR (399.78 MHz, $CDCl_3$): $\delta$ = 7.26 (d, $^3J$ = 8.35 Hz, 1 H, $CH_{arom.}$), 7.37 (d, $^3J$ = 7.91 Hz, 1 H, $CH_{arom.}$), 7.67 (t, $^3J$ = 8.13 Hz, 1 H, $CH_{arom.}$) ppm. $^{13}$C NMR (100.53 MHz, $CDCl_3$): $\delta$ = 131.8 ($CH_{arom.}$), 132.3 ($CH_{arom.}$), 133.1 ($CH_{arom.}$), 163.7 (ON-$C_q$), 185.6 (CO), 192.1 (CO) ppm. IR (KBr): $\tilde{\nu}$ = 2953 $cm^{-1}$ (m), 2924 (s), 2854 (m), 2337 (w), 2097 (m), 2059 (s), 2029 (vs), 2007 (s), 1966 (s), 1913 (vs), 1624 (m), 1566 (w), 1466 (w), 1432 (m), 1416 (m), 1376 (w), 1341 (w) 1316 (w), 1262 (w), 1199 (w), 1149 (w), 1100 (w), 923 (w), 893 (w), 861 (w), 774 (w), 731 (w), 688 (w), 660 (w), 662 (w). IR ($CH_2Cl_2$): $\tilde{\nu}$ = 2089 $cm^{-1}$

 © 2006 Wiley-VCH Verlag GmbH & Co. KGaA, Weinheim 

Table 2. Summary of crystallographic data for complexes **6a**,**b**–**8a**,**b**.[13,14]

| | **6a** | **6b** | **7a** |
|---|---|---|---|
| Empirical formula | $C_{12}H_3Cl_4NO_7Re_2$ | $C_{12}H_3Br_2Cl_2NO_7Re_2$ | $C_{12}H_3Br_2Cl_2NO_7Re_2$ |
| Formula weight [g mol$^{-1}$] | 787.30 | 876.27 | 876.27 |
| Crystal size [mm] | 0.38 × 0.10 × 0.009 | 0.02 × 0.10 × 0.20 | 0.02 × 0.10 × 0.20 |
| Crystal colour, habit | black block | black plate | black plate |
| Crystal system | triclinic | triclinic | triclinic |
| Space group | $P\bar{1}$ | $P\bar{1}$ | $P\bar{1}$ |
| $a$ [Å] | 8.7459(2) | 8.8974(18) | 8.8423(2) |
| $b$ [Å] | 10.2474(2) | 10.310(2) | 10.2035(2) |
| $c$ [Å] | 11.6216(3) | 11.722(2) | 11.8154(3) |
| $\alpha$ [°] | 81.0843(11) | 80.82(3) | 81.5702(10) |
| $\beta$ [°] | 84.2984(11) | 84.79(3) | 83.8498(10) |
| $\gamma$ [°] | 65.4287(12) | 66.31(3) | 65.5635(8) |
| Volume [Å$^3$] | 935.09(4) | 971.7(3) | 958.76(4) |
| $Z$ | 2 | 2 | 2 |
| Density calcd. [g cm$^{-3}$] | 2.740 | 2.995 | 3.035 |
| Absorption coefficient [mm$^{-1}$] | 13.532 | 16.865 | 17.094 |
| $F$(000) | 696 | 784 | 784 |
| Index ranges | $-11 \le h \le 11$<br>$-13 \le k \le 13$<br>$-15 \le l \le 15$ | $-10 \le h \le 9$<br>$-11 \le k \le 0$<br>$-13 \le l \le 13$ | $-11 \le h \le 11$<br>$-13 \le k \le 13$<br>$-15 \le l \le 15$ |
| $\theta$ Range [°] | 3.17–27.48 | 2.18–23.97 | 3.15–27.49 |
| Reflections collected | 13095 | 3238 | 13564 |
| Independent reflections | 4208 | 3043 | 4342 |
| Observed reflections | 3753 | 2757 | 3715 |
| Parameter/restrains | 236/0 | 235/0 | 235/0 |
| $R1$/$wR2$ (all data) | 0.0404/0.886 | 0.0316/0.0736 | 0.0387/0.0658 |
| $R1$/$wR2$ (final) | 0.0341/0.0847 | 0.0268/0.0712 | 0.0295/0.0623 |
| Goodness of fit | 1.076 | 1.156 | 1.061 |
| Min./max. $\rho_e$ [e Å$^3$] | –2.597/1.573 | –1.450/0.591 | –2.113/1.154 |
| Temperature [K] | 200(2) | 293(2) | 200(2) |
| Diffractometer used | Nonius Kappa CCD | Nonius Mach 3 | Nonius Kappa CCD |
| Scan type | area detection | area detection | area detection |
| Solution | SHELXS-97 | SHELXS-97 | SHELXS-97 |
| Refinement | SHELXL-97 | SHELXS-97 | SHELXS-97 |
| | **7b** | **8a** | **8b** |
| Empirical formula | $C_{12}H_3Br_4NO_7Re_2$ | $C_{12}H_2Br_2Cl_3NO_7Re_2$ | $C_{12}H_2Br_4ClNO_7Re_2$ |
| Formula weight [g mol$^{-1}$] | 965.18 | 910.72 | 999.64 |
| Crystal size [mm] | 0.02 × 0.11 × 0.20 | 0.18 × 0.11 × 0.07 | 0.10 × 0.08 × 0.06 |
| Crystal colour, habit | black plate | black block | black plate |
| Crystal system | triclinic | triclinic | monoclinic |
| Space group | $P\bar{1}$ | $P\bar{1}$ | $C2/c$ |
| $a$ [Å] | 8.9736(2) | 8.6204(17) | 15.473(3) |
| $b$ [Å] | 10.2985(3) | 9.1558(18) | 39.231(8) |
| $c$ [Å] | 11.9402(5) | 15.059(3) | 14.732(3) |
| $\alpha$ [°] | 81.6543(19) | 75.97(3) | 90 |
| $\beta$ [°] | 84.3852(19) | 74.55(3) | 111.52(3) |
| $\gamma$ [°] | 66.3718(17) | 64.54(3) | 90 |
| Volume [Å$^3$] | 999.28(6) | 1023.1(4) | 8319(3) |
| $Z$ | 2 | 2 | 8 |
| Density calcd. [g cm$^{-3}$] | 3.208 | 2.956 | 3.192 |
| Absorption coefficient [mm$^{-1}$] | 20.132 | 16.150 | 19.476 |
| $F$(000) | 856 | 816 | 7104 |
| Index ranges | $-10 \le h \le 10$<br>$-12 \le k \le 12$<br>$-14 \le l \le 14$ | $-10 \le h \le 10$<br>$-10 \le k \le 10$<br>$-17 \le l \le 17$ | $-18 \le h \le 18$<br>$-46 \le k \le 45$<br>$-17 \le l \le 11$ |
| $\theta$ Range [°] | 3.30–25.03 | 3.24–25.05 | 3.15–25.09 |
| Reflections collected | 11093 | 10395 | 49979 |
| Independent reflections | 3513 | 3559 | 7365 |
| Observed reflections | 2767 | 3218 | 5029 |
| Parameter/restrains | 235/0 | 245/0 | 487/0 |
| $R1$/$wR2$ (all data) | 0.0562/0.0924 | 0.0654/0.1584 | 0.0936/0.1590 |
| $R1$/$wR2$ (final) | 0.0385/0.0837 | 0.0613/0.1535 | 0.0543/0.1397 |
| Goodness of fit | 1.023 | 1.048 | 1.060 |
| Min./max. $\rho_e$ [e Å$^3$] | –1.583/1.351 | –4.346/3.900 | –2.971/1.404 |
| Temperature [K] | 200(2) | 200(2) | 200(2) |
| Diffractometer used | Nonius Kappa CCD | Nonius Kappa CCD | Nonius Kappa CCD |
| Scan type | area detection | area detection | area detection |
| Solution | SHELXS-97 | SHELXS-97 | SHELXS-97 |
| Refinement | SHELXL-97 | SHELXS-97 | SHELXS-97 |

 © 2006 Wiley-VCH Verlag GmbH & Co. KGaA, Weinheim 

(m), 2033 (s), 2010 (vs), 1962 (m), 1940 (m). UV/Vis ($CH_2Cl_2$): $\lambda_{max}$ (log $\varepsilon$) = 260 nm (6266), 376 (2551), 699 (3973). $C_{12}H_3Br_2Cl_2NO_7Re_2$ (876.28): calcd. C 16.43, H 0.34, N 1.60; found C 16.26, H 0.37, N 1.54. MS (DEI): *m/z* (%) = 876.2 (62) [$M^+$], 848.2 (17) [$M^+$ – CO], 820.2 (4) [$M^+$ – 2 CO], 792.3 (45) [$M^+$ – 4 CO], 764.3 (23) [$M^+$ – 5 CO], 736.3 (23) [$M^+$ – 6 CO].

**$\mu_2$-($\eta^2$-*N*,*O*-2,6-Dibromonitrosobenzene)bis[$\mu$-bromotricarbonylrhenium(I)] (7b):** Synthesised from 425 mg (1.050 mmol) of **1b** and 139 mg (0.524 mmol) of **3**. Yield: 70.0 mg (0.073 mmol, 14%) green crystals; m.p. 144 °C (dec.). $^1$H NMR (399.78 MHz, $CDCl_3$): $\delta$ = 7.27 (t, $^3J$ = 8.13 Hz, 1 H, $CH_{arom.}$), 7.38 (d, $^3J$ = 8.13 Hz, 1 H, $CH_{arom.}$), 7.61–7.64 (m, 1 H, $CH_{arom.}$) ppm. $^{13}$C NMR (67.93 MHz, $CDCl_3$): $\delta$ = 132.9 ($CH_{arom.}$), 133.0 ($CH_{arom.}$), 133.6 ($CH_{arom.}$), 164.5 (ON-$C_q$), 185.2 (CO), 191.4 (CO) ppm. IR (KBr): $\tilde{\nu}$ = 3070 cm$^{-1}$ (w), 2963 (m), 2925 (m), 2096 (m), 2058 (m), 2006 (vs), 1966 (s), 1929 (vs), 1611 (w), 1563 (s), 1571 (m), 1458 (m), 1437 (vs), 1420 (s), 1372 (w), 1343 (w), 1283 (vs), 1263 (vs), 1200 (s), 1154 (w), 1097 (s), 1060 (s), 1023 (s), 923 (w), 862 (m), 847 (s), 803 (vs), 803 (vs), 733 (s), 633 (m), 577 (w). IR ($CH_2Cl_2$): $\tilde{\nu}$ = 2088 cm$^{-1}$ (m), 2032 (s), 2010 (vs), 1961 (m), 1943 (m). UV/Vis ($CH_2Cl_2$): $\lambda_{max}$ (log $\varepsilon$) = 260 nm (12896), 376 (5319), 699 (8244). $C_{12}H_3Br_4NO_7Re_2$ (965.18): calcd. C 14.93, H 0.31, N 1.45; found C 16.03, H 0.89, N 1.47. MS (DEI): *m/z* (%) = 964.1 (56) [$M^+$], 936.1 (28) [$M^+$ – CO], 880.1 (40) [$M^+$ – 3 CO], 852.2 (18) [$M^+$ – 4 CO], 824.2 (72) [$M^+$ – 5 CO], 796.2 (89) [$M^+$ – 6 CO].

**$\mu_2$-($\eta^2$-*N*,*O*-2,6-Dibromo-4-chloronitrosobenzene)bis[$\mu$-chlorotricarbonylrhenium(I)] (8a):** Synthesised from 132 mg (0.366 mmol) of **1a** and 73.0 mg (0.244 mmol) of **4**. Yield: 112 mg (0.123 mmol, 67%) green crystals; m.p. 129 °C (dec.). $^1$H NMR (399.78 MHz, $CDCl_3$): $\delta$ = 7.66 (s, 2 H, $CH_{arom.}$) ppm. $^{13}$C NMR (100.53 MHz, $CDCl_3$): $\delta$ = 131.2 ($CH_{arom.}$), 132.7 ($CH_{arom.}$), 133.9 ($CH_{arom.}$), 162.3 (ON-$C_q$), 187.5 (CO), 191.8 (CO) ppm. IR (KBr): $\tilde{\nu}$ = 3074 cm$^{-1}$ (w), 2963 (w), 2089 (vs), 2031 (vs), 2000 (vs), 1949 (vs), 1922 (vs), 1614 (m), 1562 (m), 1538 (w), 1506 (w), 1407 (w), 1447 (w), 1419 (m), 1371 (m), 1337 (m), 1294 (w), 1195 (m), 1127 (m), 1059 (w), 925 (w), 897 (m), 862 (m), 806 (w), 747 (w), 735 (w), 642 (w), 580 (w), 562 (w). IR ($CH_2Cl_2$): $\tilde{\nu}$ = 2090 cm$^{-1}$ (vs), 2034 (vs), 2010 (vs), 1962 (vs), 1941 (vs). UV/Vis ($CH_2Cl_2$): $\lambda_{max}$ (log $\varepsilon$) = 375 nm (4615), 707 (6304). $C_{12}H_2Br_2Cl_3NO_7Re_2$ (910.72): calcd. C 15.81, H 0.20, N 1.72; found C 16.21, H 0.21, N 1.63. MS (DEI): *m/z* (%) = 910.7 (15) [$M^+$], 826.7 (13) [$M^+$ – 3 CO], 798.7 (7) [$M^+$ – 4 CO], 770.7 (28) [$M^+$ – 5 CO], 742.8 (26) [$M^+$ – 6 CO].

**$\mu_2$-($\eta^2$-*N*,*O*-2,6-Dibromo-4-chloronitrosobenzene)-bis[$\mu$-bromotricarbonylrhenium(I)] (8b):** Synthesised from 137 mg (0.339 mmol) of **1b** and 73.0 mg (0.203 mmol) of **4**. Yield: 45.0 mg (0.045 mmol, 26%) green crystals; m.p. 135 °C (dec.). $^1$H NMR (399.78 MHz, $CDCl_3$): $\delta$ = 7.64 (s, 2 H, $CH_{arom.}$) ppm. $^{13}$C NMR (100.53 MHz, $CDCl_3$): $\delta$ = 131.2 ($CH_{arom.}$), 132.5 ($CH_{arom.}$), 133.9 ($CH_{arom.}$), 164.3 (ON-$C_q$), 186.3 (CO) ppm. IR (KBr): $\tilde{\nu}$ = 3073 cm$^{-1}$ (w), 2963 (w), 2086 (s), 2034 (vs), 1999 (vs), 1954 (vs), 1923 (vs), 1615 (w), 1563 (m), 1507 (w), 1481 (w), 1461 (w), 1420 (w), 1373 (w), 1353 (w), 1329 (w), 1297 (w), 1126 (w), 1105 (w), 1054 (w), 1030 (w), 924 (m), 862 (m), 807 (m), 807 (m), 747 (m), 687 (w), 637 (w), 609 (w), 576 (w), 539 (w). IR ($CH_2Cl_2$): $\tilde{\nu}$ = 2086 cm$^{-1}$ (vs), 2034 (vs), 2010 (vs), 1962 (vs), 1941 (vs). UV/Vis ($CH_2Cl_2$): $\lambda_{max}$ (log $\varepsilon$) = 373 nm (3476), 704 (3117). $C_{12}H_2Br_4ClNO_7Re_2$ (999.63): calcd. C 14.43, H 0.20, N 1.40; found C 15.87, H 0.39, N 1.66. MS (DEI): *m/z* (%) = 998.1 (1) [$M^+$], 914.2 (1) [$M^+$ – 3 CO], 858.1 (1) [$M^+$ – 5 CO], 830.3 (28) [$M^+$ – 6 CO].

**$\mu_2$-($\eta^2$-*N*,*O*-2,6-Dichloro-4-bromonitrosobenzene)bis[$\mu$-chlorotricarbonylrhenium(I)] (9a):** Synthesised from 139 mg (0.384 mmol) of **1a** and 65.3 mg (0.256 mmol) of **5**. Yield: 65.5 mg (0.076 mmol, 37%) green powder; m.p. 123 °C (dec.). $^1$H NMR (270.16 MHz, $CDCl_3$): $\delta$ = 7.60 (s, 2 H, $CH_{arom.}$) ppm. $^{13}$C NMR (100.53 MHz, $CDCl_3$): $\delta$ = 124.8 ($CH_{arom.}$), 130.3 ($CH_{arom.}$), 131.6 ($CH_{arom.}$), 160.2 (ON-$C_q$), 187.6 (CO), 191.9 (CO) ppm. IR (KBr): $\tilde{\nu}$ = 3116 cm$^{-1}$ (m), 3082 (m), 2088 (vs), 2022 (vs), 1950 (vs), 1925 (vs), 1726 (w), 1615 (s), 1560 (s), 1548 (s), 1469 (s), 1429 (w),1390 (w), 1378 (m), 1365 (w), 1333 (w), 1297 (m), 1280 (w), 1263 (w), 1182 (s), 1077 (m), 927 (m), 898 (w), 858 (s), 812 (m), 787 (m), 752 (w), 659 (w), 615 (m), 590 (w), 534 (w), 540 (w). IR ($CH_2Cl_2$): $\tilde{\nu}$ = 2091 cm$^{-1}$ (s), 2034 (vs), 2011 (vs), 1963 (vs), 1941 (vs). UV/Vis ($CH_2Cl_2$): $\lambda_{max}$ (log $\varepsilon$) = 385 nm (2952), 491 (1906). $C_{12}H_2BrCl_4NO_7Re_2$ (866.28): calcd. C 16.63, H 0.23, N 1.62; found C 17.28, H 1.38, N 1.55. MS (DEI): *m/z* (%) = 866.6 (52) [$M^+$], 782.6 (49) [$M^+$ – 3 CO], 754.6 (48) [$M^+$ – 4 CO], 726.7 (100) [$M^+$ – 5 CO], 698.6 (98) [$M^+$ – 6 CO].


[1] M. Cameron, B. G. Gowenlock, G. Vasapollo, *Chem. Soc. Rev.* **1990**, *19*, 355–379.

[2] R. Wilberger, C. Krinninger, H. Piotrowksi, P. Mayer, I.-P. Lorenz, *Eur. J. Inorg. Chem.* **2004**, *12*, 2488–2492.

[3] C. Krinninger, C. Högg, H. Nöth, J. C. Gálvez Ruiz, P. Mayer, O. Burkacky, A. Zumbusch, I.-P. Lorenz, *Chem. Eur. J.* **2005**, *11*, 7228–7236.

[4] a) E. Colacio, J. M. Dominguez-Vera, A. Escuer, R. Kivekas, A. Romerosa, *Inorg. Chem.* **1994**, *33*, 3914–3924; b) E. Colacio, J. M. Dominguez-Vera, E. Escuer, M. Klinga, R. Kivekas, A. Romerosa, *J. Chem. Soc., Dalton Trans.* **1995**, 343–348; c) E. Colacio, J. M. Dominguez-Vera, A. Escuer, R. Kivekas, M. Klinga, J.-M. Moreno, A. Romerosa, *J. Chem. Soc., Dalton Trans.* **1997**, 1685–1689; d) K. K.-H. Lee, W.-T. Wong, *J. Chem. Soc., Dalton Trans.* **1997**, 2987–2995.

[5] a) E. Colacio, J. M. Dominguez-Vera, A. Romerosa, R. Kivekas, M. Klinga, A. Escuer, *Inorg. Chim. Acta* **1995**, *234*, 61–65; b) E. Colacio, C. Lopez-Magana, V. McKee, A. Romerosa, *J. Chem. Soc., Dalton Trans.* **1999**, 2923–2926.

[6] D. L. Packett, W. C. Trogler, A. L. Rheingold, *Inorg. Chem.* **1987**, *26*, 4308–4309.

[7] T. Iwasa, H. Shimada, A. Takami, H. Matsuzaka, Y. Ishii, M. Hidai, *Inorg. Chem.* **1999**, *38*, 2851–2859.

[8] C. Romming, H. J. Talberg, *Acta Chem. Scand.* **1973**, *27*, 2246–2248.

[9] C. Krinninger, S. Wirth, J. C. Galvez Ruiz, P. Klüfers, H. Nöth, I.-P. Lorenz, *Eur. J. Inorg. Chem.* **2005**, *20*, 4094–4098.

[10] *Trocknen im Labor*, brochure from the series "Reagenzien", Merck, Darmstadt.

[11] G. Brauer, *Handbuch der Präparativen Anorganischen Chemie*, Ferdinand Enke Verlag, Stuttgart, vol. III, 3rd. ed., **1981**, 1951–1952.

[12] R. R. Holmes, R. P. Bayer, *J. Am. Chem. Soc.* **1960**, *82*, 3454–3456.

[13] CCDC-285191 (for **6a**), -283167 (for **6b**), -285190 (for **7a**), -285189 (for **7b**), -283168 (for **8a**) and -283169 (for **8b**) contain the supplementary crystallographic data for this paper. These data can be obtained free of charge from The Cambridge Crystallographic Data Centre via www.ccdc.cam.ac.uk/data_request/cif.

[14] G. M. Sheldrick, *SHELXL 97, Program for Crystal Structure Refinement*, University of Göttingen, Germany, **1997**.


Received: September 1, 2005
Published Online: January 9, 2006

 © 2006 Wiley-VCH Verlag GmbH & Co. KGaA, Weinheim 

DOI: 10.1002/ejic.200500790

# New Ligands for Rh-Catalysed Hydroformylation of 1-Octene in Supercritical Carbon Dioxide – X-ray Structure of $[Rh\{PPh_2(OC_9H_{19})\}_4]PF_6$

**Marta Giménez-Pedrós,[a] Ali Aghmiz,[a] Núria Ruiz,[a] and Anna M. Masdeu-Bultó*[a]**

**Keywords:** Alkenes / Hydroformylation / P ligands / Rhodium / Supercritical fluids

The new P-donor ligands $PPh_{3-n}(OC_9H_{19})_n$ ($n$ = 3, 2, 1) containing branched alkyl chains were synthesised and their coordination to $Rh^I$ and $Pd^{II}$ studied. The X-ray structure of $[Rh\{PPh_2(OC_9H_{19})\}_4]PF_6$ was determined. Reaction of the $[Rh(acac)(CO)_2]/PPh_{3-n}(OC_9H_{19})_n$ systems with $CO/H_2$ at 5 atm and 80 °C in toluene led to the formation of $[RhH(CO)\{PPh_{3-n}(OC_9H_{19})_n\}_3]$ as the main species. The Rh-catalysed hydroformylation of 1-octene with these ligands was investigated in supercritical carbon dioxide ($scCO_2$) and toluene as solvents. Although the catalytic systems are not soluble in $scCO_2$, they are active. The activities are higher in toluene than in $scCO_2$ but the selectivities for aldehydes in the case of the phosphonite derivative are higher in the supercritical medium than in toluene.
(© Wiley-VCH Verlag GmbH & Co. KGaA, 69451 Weinheim, Germany, 2006)

## Introduction

In the last few years supercritical carbon dioxide ($scCO_2$) has received growing attention as an alternative reaction medium for homogeneous catalysis[1] as it is an environmentally friendly and cheap solvent. More important, however, are its gas-like properties, especially in reactions in which the reactants are gases. $scCO_2$ is highly miscible with gases such as hydrogen and carbon monoxide (it can therefore avoid the gas–liquid mass transfer) and is highly compressible. It also has a low viscosity and therefore a high diffusivity. Moreover, its ability as an extraction solvent has proved useful for separating the products from the catalysts without the need for harsher conditions such as those used for the distillation of higher alkenes.[2]

The catalytic hydroformylation of long-chain alkenes is an interesting reaction for transforming alkenes into aldehydes using carbon monoxide and hydrogen.[3] The aldehydes obtained allow the synthesis of oxo alcohols used in the detergent industry and as plasticizers in the polymer industry. Rhodium catalysts associated with P-donor ligands are the most successful system for the hydroformylation of alkenes under mild conditions. Water can be used as a "green" solvent in this reaction, but this process is limited to short-chain alkenes (propene and 1-butene) because a certain degree of solubility of the alkene in water is required.[4] $scCO_2$ is a non-polar solvent in which alkenes are soluble, but ligand modification is often needed to increase the solubility of the catalytic systems. The most successful approach is to introduce perfluoroalkyl chains in the ligand.[5] However, the synthesis of perfluorinated ligands is difficult and expensive.

Cole-Hamilton and co-workers obtained good activities when they used alkylated phosphanes such as $[Rh_2(OAc)_4]/PEt_3$ systems, which are soluble in $scCO_2$, in the hydroformylation of 1-hexene, but the *n*/*iso* ratios were modest (2.1–2.6).[6] Ligands containing alkyl groups, preferably branched, with a chain length of eight carbon atoms have reportedly shown high solubility in supercritical carbon dioxide.[7] In the case of alkylphosphanes, such as $P(C_8H_{17})_3$, the Rh systems were not soluble under the conditions studied and the turnover frequency (TOF) was low (3–7 $h^{-1}$, 8–20% conversion in 2 h), although the *n*/*iso* ratios were high (up to 3.9).[6] When linear alkylated groups were introduced into the aromatic rings $[P(C_6H_4C_6H_{13})_3$, $P(C_6H_4C_{10}H_{21})_3$, and $P(C_6H_4C_{16}H_{33})_3]$, the corresponding rhodium systems, which are partially soluble in $scCO_2$, showed activities in the hydroformylation of 1-hexadecene with average TOFs of 150, 350 and 20 $h^{-1}$, respectively. This correlated with a maximum solubility of the $C_{10}H_{21}$ derivative.[5c] Other $scCO_2$-insoluble systems, such as $P(OPh)_3$, $P(p\text{-}OC_6H_4\text{-}C_9H_{19})_3$ and $PPh_2[CH_2CH(CO_2C_{16}H_{33})CH_2\text{-}CO_2C_{16}H_{33}]$, have been reported to show good activity in the hydroformylation of 1-hexene. The advantage of insoluble systems is that the products can be flushed away from the insoluble catalyst system by taking advantage of the excellent extraction ability of $scCO_2$.[8]

The incorporation of *tert*-butyl substituents into the alkyl chains of P-donor ligands has been reported to increase their solubility in $scCO_2$.[7,9] Introducing branched chains in surfactants derived from sodium bis(2-ethyl-1-hexyl)sulfosuccinate increases their solubility in $scCO_2$.[10]

[a] Departament de Química Física i Inorgànica, Facultat de Química, Universitat Rovira i Virgili,
C/Marcel·lí Domingo s/n, 43007 Tarragona, Spain
Fax: +34-977-559-563
E-mail: annamaria.masdeu@urv.net
Supporting information for this article is available on the WWW under http://www.eurjic.org or from the author.

 © 2006 Wiley-VCH Verlag GmbH & Co. KGaA, Weinheim 

In this paper we present the synthesis of three new P-donor ligands with nine-carbon, branched alkyl substituents (Figure 1) and their application to the rhodium-catalysed hydroformylation of 1-octene in $scCO_2$ and in toluene as solvents. Phosphite (**1**), phosphonite (**2**) and phosphinite (**3**) ligands were selected because the introduction of oxy groups has a positive effect on activity and regioselectivity.[3b,11] Bulky monophosphonite ligands have shown very high activities in the isomerisation/hydroformylation of octene.[11] We also studied the coordination of the new ligands to rhodium(I) and palladium(II).

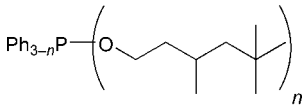


**1**: $n = 3$
**2**: $n = 2$
**3**: $n = 1$

Figure 1. P-donor ligands.

## Results and Discussion

### Synthesis of Ligands

Ligands **1**–**3** were prepared from the commercially available alcohol 3,5,5-trimethylhexanol by reaction with phosphorus trichloride or the corresponding chlorophenylphosphane in diethyl ether in the presence of pyridine (Scheme 1). The ligands were purified by flash chromatography on basic alumina eluting with hexane under an inert gas and obtained as air- and moisture-sensitive colourless oils in good yields (56–80%). The $^1H$ NNMR spectra show the methylene (-$OCH_2$-) signals at $\delta = 3.8$ ppm, the methylene and methine signals between $\delta = 1.6$ and 1.0 ppm, and the methyl doublet and singlet from the *tert*-butyl group at $\delta = 0.9$ ppm. The signals were assigned by means of COSY and HETCOR experiments. The $^{31}P\{^1H\}$ NMR singlet signals appear at $\delta = 139.9$, 156.6 and 112.5 ppm for **1**–**3**, respectively, which are typical values for this kind of phosphorus compounds.[12]

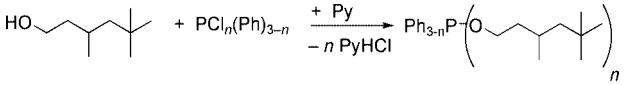


**1**: $n = 3$
**2**: $n = 2$
**3**: $n = 1$

Scheme 1. Synthesis of **1**–**3**.

### Synthesis of Complexes

To explore the coordination chemistry of the P-donor ligands **1**–**3** we decided to study their reactivity with rhodium(I) and palladium(II) complexes. We chose $[Rh(cod)_2]PF_6$ (cod = 1,5-cyclooctadiene) as a model for cationic complexes (Scheme 2). The reaction of ligands **1**–**3** with $[Rh(cod)_2]PF_6$ in anhydrous dichloromethane at room temperature should proceed by displacement of the 1,5-cyclooctadiene ligand, followed by coordination of two P-donor ligands. With tris(3,5,5-trimethylhexyl) phosphite (**1**) in a P/Rh molar ratio of 2:1, the complex $[Rh(cod)(\mathbf{1})_2]PF_6$ (**4**) was obtained as a relatively air-stable, yellow oil in high yield. Several attempts to solidify the complex were unsuccessful. Its $^{31}P\{^1H\}$ NMR spectrum shows a doublet at $\delta = 116.1$ ppm ($J_{P,Rh} = 244.0$ Hz), which corresponds to the coordinated phosphite ligand, and the characteristic septuplet of the $PF_6^-$ counteranion at $\delta = -143.2$ ppm ($J_{P,F} = 711.5$ Hz). The presence of coordinated cyclooctadiene was confirmed by the $^1H$ NMR spectrum, which shows signals at $\delta = 4.05$ ppm (HC=CH) and 2.57 and 2.36 ppm (-$CH_2$-). The $^1H$ NMR signals corresponding to the coordinated ligand are shifted slightly with respect to those of the free ligand. The mass spectrum shows a signal at $m/z = 1129.5$ corresponding to the $[Rh(cod)(\mathbf{1})_2]^+$ fragment.

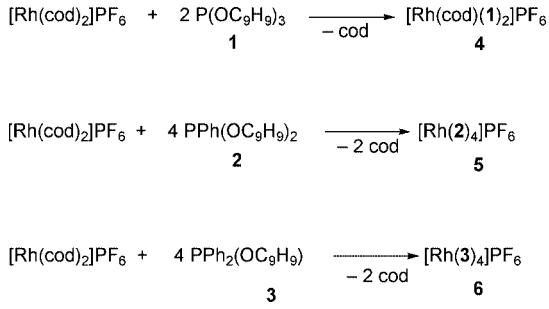


Scheme 2. Syntheses of **4**–**6**.

However, upon treatment of the same precursor complex $[Rh(cod)_2]PF_6$ with the same P/Rh molar ratio but using phosphonite **2**, the $^{31}P\{^1H\}$ NMR spectrum shows two doublets in the region of coordinated phosphorus atoms at $\delta = 146.0$ ($J_{P,Rh} = 165.9$ Hz) and 138.5 ($J_{P,Rh} = 170.8$ Hz) ppm and the $^1H$ NMR spectrum shows signals corresponding to coordinated cyclooctadiene (at $\delta = 4.0$ and 2.5–2.7 ppm). When the P/Rh molar ratio is 4:1, the $^{31}P\{^1H\}$ NMR spectrum shows only the signal at $\delta = 146.0$ ppm. There was no evidence of coordinated COD in the $^1H$ NMR spectrum, and only signals attributable to the coordinated ligand were detected. In this case, a relatively air-stable, yellow, oily solid was obtained in 76% yield. The mass spectrum of the isolated product has a signal $m/z = 1679.7$ corresponding to the cationic fragment $[Rh(\mathbf{2})_4]^+$. We propose that, at a P/Rh ratio of 2:1, a mixture of $[Rh(cod)(\mathbf{2})_2]PF_6$ and $[Rh(\mathbf{2})_4]PF_6$ (**5**) is formed and the totally substituted species **5** is formed at a P/Rh ratio of 4. Similar $[RhL_4]^+$ species have been obtained with $PPh(OCH_3)_2$,[13] with similar $^{31}P$ NMR spectroscopic data ($\delta = 148$ ppm, $J_{P,Rh} = 170$ Hz).[14]

In the reaction of $[Rh(cod)_2]PF_6$ with ligand **3** only one doublet is observed in the $^{31}P\{^1H\}$ NMR spectrum at P/Rh ratios of 2:1 and 4:1 [$\delta = 132.3$ ppm ($J_{P,Rh} = 162.2$ Hz)], which agrees with the data reported for $[Rh\{PPh_2(OR)\}_4]^+$ (R = Me: $\delta = 132.2$ ppm, $J_{P,Rh} = 159$ Hz; R = Et: $\delta = 130.5$ ppm, $J_{P,Rh} = 156$ Hz),[15] along with a septuplet signal for $PF_6^-$ at $\delta = -143.1$ ppm ($J_{F,P} = 712.6$ Hz). In the $^1H$

 © 2006 Wiley-VCH Verlag GmbH & Co. KGaA, Weinheim 

NMR spectrum there are only signals corresponding to the coordinated ligand **3**. A relatively air-stable, yellow solid was isolated in 73% yield. The X-ray crystal structure (see below) shows that this complex is $[Rh(\mathbf{3})_4]PF_6$ (**6**).

To prepare neutral palladium complexes, we chose $[PdCl_2(PhCN)_2]$ as a model precursor. The reaction of ligands **1**–**3** with $[PdCl_2(PhCN)_2]$ in anhydrous dichloromethane at room temperature proceeds by the displacement of two molecules of PhCN followed by the coordination of two P ligands to afford $[PdCl_2(\mathbf{1}–\mathbf{3})_2]$ (**7**–**9**, Scheme 3), which were obtained as relatively air-stable, yellow oils in good yields, with mass spectra in agreement with a mononuclear formulation. The $^1H$ NMR spectra of **7**–**9** show signals corresponding to the coordinated ligands. The $^{31}P\{^1H\}$ NMR spectra show only one singlet at $\delta$ = 94.2 (**7**), 122.2 (**8**) and 110.2 ppm (**9**), which indicates that only one of the two possible isomers (*cis* or *trans*) is formed. The difference between the $^{31}P$ NMR signal of the complex and that of the free ligand, known as the coordination chemical shift, $\Delta$ (= $\delta_{coord} - \delta_{free}$), for similar palladium(II) complexes is indicative of the stereochemistry of these complexes. The lowest (negative) values of $\Delta$ are found for *cis* isomers containing ligands with Tolman angles, $\Theta$, of less than 140°, and high values (positive) of $\Delta$ are found for *trans* isomers containing ligands with Tolman angles higher than 140°.[16] Based on this observation, since the values of $\Delta$ for complexes **7** and **8** are –45.7 and –34.4 ppm, respectively, we propose that the *cis* isomers are present in these complexes. In the case of complex **9** the value of $\Delta$ is –2.3 ppm. Taking into account that the estimated value of $\Theta$ from the X-ray structure is 128° (see below), we also propose the formation of the *cis* isomer for complex **9**.

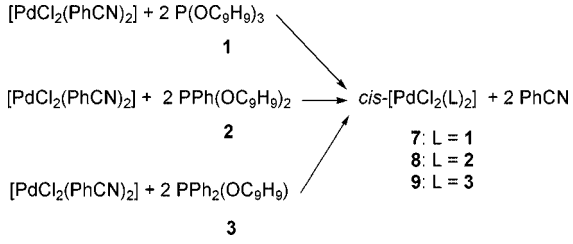


Scheme 3. Syntheses of **7**–**9**.

### X-ray Structure of 6

The crystal structure of complex **6** was solved with crystals obtained by slow diffusion of diethyl ether into a dichloromethane solution of the complex. The X-ray structure is shown in Figure 2 and selected bond lengths and angles are given in Table 1.

This cationic rhodium complex contains four coordinated phosphinite ligands **3**, as observed in solution. The Rh–P bond lengths [2.2848(6) Å] are in the range reported for other $Rh^I$ complexes with phosphinite ligands.[17] The cation has a slightly tetrahedrally distorted square-planar geometry [*trans* P–Rh–P angles of 166.64(3)°] due to intramolecular ligand repulsion. A similar distortion, but to a greater extent, has been reported for $[Rh(PMe_3)_4]^+$ (*trans* P–Rh–P angles of 148.29 and 151.46°).[18] The C–P–Rh angles [115.75(8) and 118.97(8)°] deviate from the ideal tetrahedral value, as observed in coordinated P-donor ligands. The estimated Tolman angle for **3**, calculated in accordance with the reported method,[19] is 128°. The alkoxy chains are in a staggered arrangement above and below the coordination plane in order to minimise repulsion. There is a disorder in the *t*Bu fragments. The $PF_6^-$ anions are located in the cavities formed between the four *t*Bu groups from two different cationic units.

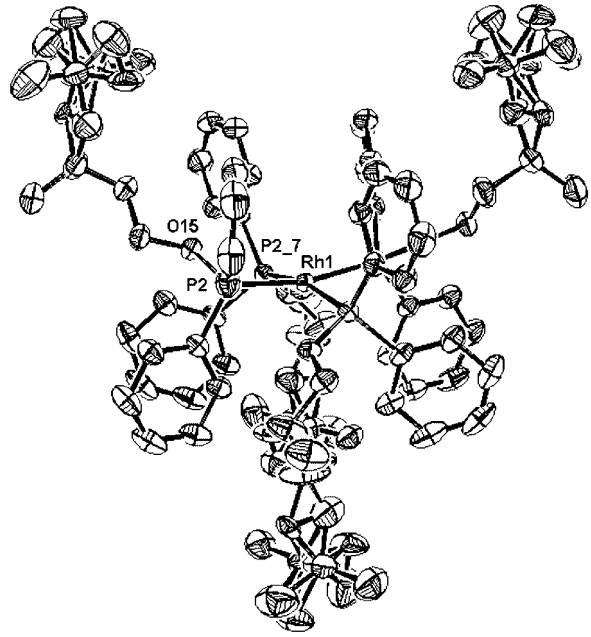


Figure 2. ORTEP drawing of complex **6**. $PF_6^-$ and hydrogen atoms have been omitted for clarity.

Table 1. Selected bond lengths [Å] and angles [°] of complex **6**.[a]

| | | | |
|---|---|---|---|
| Rh1–P2 | 2.2848(6) | $P2^i$–Rh1–$P2^{iii}$ | 90.776(3) |
| P2–C3 | 1.8222(25) | $P2^i$–Rh1–$P2^{ii}$ | 166.64(3) |
| P2–C9 | 1.815(2) | C3–P2–Rh1 | 115.75(8) |
| P2–O15 | 1.6170(17) | C9–P2–Rh1 | 118.97(8) |
| O15–C16 | 1.447(3) | O15–P2–Rh1 | 107.03(6) |
| | | C9–P2–C3 | 105.14(11) |

[a] Estimated standard deviations are given in parentheses. $P2^i$, $P2^{iii}$: phosphorus atoms located in *cis* position; $P2^i$, $P2^{ii}$: phosphorus atoms located in *trans* position.

### Reactivity of [Rh(acac)(CO)$_2$]/1–3 with CO and $H_2$

The reactivity of the systems $[Rh(acac)(CO)_2]$/**1**–**3** with CO and $H_2$ was analysed by high-pressure NMR (HPNMR) and IR (HPIR) spectroscopy. The $^{31}P\{^1H\}$ and $^1H$ NMR spectra were recorded for the complex $[Rh(acac)(CO)_2]$ in the presence of 4 equiv. of ligand **1**–**3** in $[D_6]$toluene ($[Rh] = 2\times10^{-2}$ M) with stepwise addition of $H_2$ and CO. As the IR technique is more sensitive, the IR spectra could be recorded at concentrations closer to the catalytic value ($2–5\times10^{-3}$ M) in methyltetrahydrofuran under

 © 2006 Wiley-VCH Verlag GmbH & Co. KGaA, Weinheim 

the same conditions. A list of identified species is given in Table 2.

Table 2. Identified species for [Rh(acac)(CO)$_2$]/**1**–**3** (P/Rh = 4) systems at 5 atm CO/H$_2$ (1:1) after 1 h at 80 °C.

| Complex | δ($^{31}$P) [ppm] ($J_{Rh,P}$ [Hz]) | δ($^1$H) (hydride) [ppm] ($J_{P,H}$, $J_{Rh,H}$ [Hz]) | ν(CO) [cm$^{-1}$] |
|---|---|---|---|
| [RhH(**1**)$_4$] (**10**) | 157.9 d | –11.8 dq | – |
| | (207.8) | (33.7, 9.4) | |
| [RhH(CO)(**1**)$_3$] (**11**) | 158.9 d | –10.7 quint | 2025 |
| | (212.3) | (7.8, 7.8) | |
| [RhH(CO)$_2$(**1**)$_2$] (**12**) | 154.6 d | n.d.[a] | 2049, 2005, |
| | (194.6) | | 1980, 1960 |
| [RhH(CO)(**2**)$_3$] (**13**) | 169.8 d | –10.0 quint | 2065 |
| | (189.0) | (7.7, 7.7) | |
| [RhH(CO)$_2$(**2**)$_2$] (**14**) | 168.2 d | n.d.[a] | 2073, 2042, |
| | (145.7) | | 2029, 1991 |
| [RhH(CO)(**3**)$_3$] (**15**) | 138.1 d | –9.4 dq | 2025 |
| | (163.3) | (12.3, 4.7) | |
| [RhH(CO)$_2$(**3**)$_2$] (**16**) | 136.8 d | –9.1 dt | 2044, 2006, |
| | (147.2) | (11.7, 6.3) | 1996, 1918 |

[a] n.d. = not detected.

Upon addition of 4 mol-equiv. of **1** to [Rh(acac)(CO)$_2$] in toluene, the $^{31}$P{$^1$H} spectrum shows a major, broad doublet signal at $\delta$ = 140 ppm, attributed to a mixture of the species [Rh(acac)(CO)$_n$(**1**)$_{2-n}$], along with a small multiplet at $\delta$ = 80 ppm and a singlet at $\delta$ = 0 ppm due to decomposed ligand. Addition of 2.5 atm of H$_2$ to this solution caused two new doublet signals to appear in the $^{31}$P{$^1$H} NMR spectrum at $\delta$ = 158.9 ppm ($J$ = 212.3 Hz) and $\delta$ = 157.9 ppm ($J$ = 207.8 Hz). Two new signals also appear in the hydride region of the $^1$H NMR spectrum at $\delta$ = –10.7 ppm (quint, $J$ = 7.8 Hz) and $\delta$ = –11.8 ppm (dq, $J$ = 33.7, 9.4 Hz). After further addition of 2.5 atm of CO (5 atm total pressure) and heating of the system at 80 °C for 1 h, the doublet signal in the $^{31}$P{$^1$H} NMR spectrum at $\delta$ = 157.9 ppm, the multiplet signal at $\delta$ = 80 ppm and the hydride signal at $\delta$ = –11.8 ppm in the $^1$H NMR spectrum disappear and new signals are observed at $\delta$ =154.6 (d, $J_{Rh,P}$ = 194.6 Hz), 140.8 (dd, $J$ = 273.6, 164.7 Hz), 138.1 (s, free **1**) and 70.2 (dt, $J$ = 273.4, 94.3 Hz) ppm. We assigned the signals at $\delta$ = 157.9 ppm and the hydride doublet of quintuplets at $\delta$ = –11.8 ppm to the species [RhH(**1**)$_4$] (**10**) by comparison with published data for the analogous species [RhH{P(OPh)$_3$}$_4$] [$\delta_P$ = 129.7 ($J_{Rh,P}$ = 232.8 Hz) ppm; $\delta_H$(hydride) = –10.6 ($J_{Rh,H}$ = 44, $J_{P,H}$ = 7 Hz) ppm].[20] We assigned the major doublet signal at $\delta$ = 158.9 ppm in the $^{31}$P{$^1$H} NMR spectrum together with the quintuplet at $\delta$ = –10.7 ppm in the $^1$H NMR spectrum to [RhH(CO)(**1**)$_3$] (**11**). The multiplicity of the hydride signal (quintuplet) is explained by the accidentally identical values of $^1J_{Rh,H}$ and $^2J_{P,H}$, as was also reported for [RhH(CO){P(OPh)$_3$}$_3$] [$\delta_P$ = 141.1 ($J_{Rh,P}$ = 240 Hz) ppm; $\delta_H$(hydride) = –10.9 ($J_{Rh,H}$ = $J_{P,H}$ = 3 Hz) ppm].[20] The minor signal at $\delta$ = 154.6 ($J_{Rh,P}$ = 194.6 Hz) ppm is attributed to the dicarbonyl species [RhH(CO)$_2$(**1**)$_2$] (**12**), whose hydride signal is not detected in the $^1$H NMR spectrum due to its low concentration. The signals at $\delta$ = 140.8 and 70.2 ppm could correspond to mixed complexes with phosphite/phosphonate and carbon monoxide ligands formed by the partially decomposed ligand. Coordination of phosphonates to rhodium complexes has been described in the literature[21] and the chemical shifts observed here correlate with those reported for mixed species. At the end of the experiment, the pressure was released and water was added to decompose the remaining ligand. The signals at $\delta$ = 140.8 and 70.2 ppm disappeared and new signals appeared, which could correspond to species with only phosphonate ligands.

The HPIR spectra of [Rh(acac)(CO)$_2$]/**1** at 5 atm CO/H$_2$ (1:1) in the ν(CO) region initially show signals at 2049, 2025, 2005, 1980 and 1960 cm$^{-1}$. By comparison with published data for [RhH(CO){P(OPh)$_3$}$_3$] [ν(CO) = 2060 (m) cm$^{-1}$],[22] the band at 2025 cm$^{-1}$ was assigned to **11**. The absorptions at 2049 and 1980 cm$^{-1}$ could correspond to the equatorial/equatorial isomer **ee-12** and those at 2005 and 1960 cm$^{-1}$ could correspond to the equatorial/axial isomer **ea-12**. The bands reported for ee-[RhH(CO)$_2${P(OPh)$_3$}$_2$] appear at 2053 and 2018 cm$^{-1}$ and for the isomer ea-[RhH(CO)$_2${P(OPh)$_3$}$_2$] at 2034 and 1992 cm$^{-1}$.[23] After 2 h at 80 °C, bands appeared at 1991 and 1828 cm$^{-1}$ attributed to rhodium species with bridging carbonyl ligands.

The $^{31}$P{$^1$H} and $^1$H NMR spectra of the [Rh(acac)(CO)$_2$]/**2** system (P/Rh = 4) in toluene under 5 atm of CO/H$_2$ (1:1), after heating at 80 °C for 1 h, show signals assigned to [RhH(CO)(**2**)$_3$] (**13**) and [RhH(CO)$_2$(**2**)$_2$] (**14**; Table 2); the hydride signals could not be detected in the $^1$H NMR spectrum. The signal of the remaining unreacted species [Rh(acac)(CO)$_n$(**2**)$_{2-n}$] appears at $\delta$ = 156 ppm. The slow reaction rate of similar precursors containing phosphite ligands with CO/H$_2$ has been reported.[24] The broad doublet at $\delta$ = 144.1 ($J_{Rh,P}$ = 168.7 Hz) ppm is better resolved at –60 °C and could correspond to dimeric Rh$^0$ complexes [Rh$_2$(CO)$_6$(**2**)$_2$] or [Rh$_2$(CO)$_4$(**2**)$_4$], as has been observed for other P-donor–rhodium systems.[25] The broad multiplets at $\delta$ = 120 and 82 ppm were attributed to mixed phosphonite/phosphonate species.

The HPIR spectrum, after 1 h under these reaction conditions, shows several absorptions in the 2200–1800 cm$^{-1}$ region that were difficult to assign. The band at 2065 could correspond to compound **13** and the ones at 2073 and 2029 cm$^{-1}$ and 2042 and 1991 cm$^{-1}$ could correspond to the ee and ea isomers of **14**, respectively. The absorptions around 1800 cm$^{-1}$ could correspond to the Rh$^0$ dimeric species.

The $^{31}$P{$^1$H} NMR spectrum of [Rh(acac)(CO)$_2$]/**3** (P/Rh = 4) at 5 atm CO/H$_2$ (1:1), after 1 h at 80 °C, shows a major signal at $\delta$ = 138.1 ppm, which, together with a hydride signal at $\delta$ = –9.4 ppm, was attributed to the species [RhH(CO)(**3**)$_3$] (**15**) by comparison with published data.[26] A minor, partially overlapped doublet at $\delta$ = 136.8 ppm, together with a hydride doublet of triplets at $\delta$ = –9.1 ppm,

 © 2006 Wiley-VCH Verlag GmbH & Co. KGaA, Weinheim 

was attributed to the species $[RhH(CO)_2(\mathbf{3})_2]$ (**16**). In comparison, $[RhH(CO)\{PPh_2(OPh)\}_3]$ shows signals at $\delta_P$ = 142 ($J_{P,Rh}$ = 169 Hz) ppm and $\delta_H$ = –9.4 (dq, $J_{H,P}$ = 13, $J_{H,Rh}$ = 3 Hz) ppm and $[RhH(CO)_2\{PPh_2(OPh)\}_2]$ shows signals at $\delta_P$ = 145 ($J_{P,Rh}$ = 165 Hz) ppm and $\delta_H$ = –9.5 ppm.[27] The signals at $\delta$ = 130.8 and 84.9 ppm in the $^{31}P\{^1H\}$ spectrum may correspond to mixed phosphinite/phosphonate species, as proposed for the other systems.

The IR spectrum of $[Rh(acac)(CO)_2]$/**3**, under the same conditions, initially shows only one band at 1987 $cm^{-1}$ in the 2200–1800 $cm^{-1}$ region. After 1 h of stirring at 80 °C, five absorptions are present at 2044, 2025, 2006, 1966 and 1918 $cm^{-1}$. The band at 2025 $cm^{-1}$ was assigned to **15**, the absorptions at 2044 and 1966 $cm^{-1}$ were attributed to isomer **ee-16**, since they are similar to ones reported for the equatorial/equatorial isomer of $[RhH(CO)_2\{PPh_2(OPh)\}_2]$ (2045, 1970 $cm^{-1}$),[27] the ones at 2006 and 1918 $cm^{-1}$ could correspond to the isomer **ea-16**.

In summary, the study of the reactivity of $[Rh(acac)(CO)_2]$/**1**–**3** with CO and $H_2$ at 5 atm ($CO/H_2$ = 1:1) and 80 °C has shown that the precursors $[RhH(CO)(\mathbf{1}–\mathbf{3})_3]$ are formed as the main species in all cases.

## Hydroformylation of 1-Octene

We studied the hydroformylation of 1-octene (**17**) to obtain the corresponding linear (**18**) and branched (**19**) aldehydes (Scheme 4) in toluene as a model solvent and in $scCO_2$.

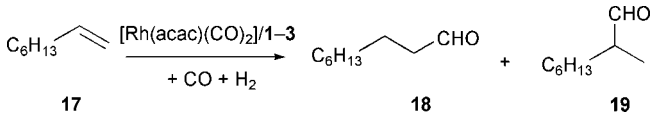


17 18 19

Scheme 4. Hydroformylation of 1-octene using different $[Rh(acac)(CO)_2]$/**1**–**3** systems.

### *Hydroformylation of 1-Octene in Toluene*

Table 3 (Entries 1–7) shows the results of 1-octene hydroformylation in toluene using $[Rh(acac)(CO)_2]$/**1**–**3** as the catalyst precursor. The products obtained were the isomeric aldehydes *n*-nonanal (**18**) and isononanal (**19**) and the isomerised products 2-octene [(*E*) and (*Z*)], (3*E*)-3-octene and (4*E*)-4-octene. No hydrogenated products were observed. The selectivity towards isomerised products is also listed.

Hydroformylation with $[Rh(acac)(CO)_2]$/**1** in toluene (Entry 1, Table 3) shows high activity (conversion = 98%) with a high selectivity for aldehydes at a P/Rh molar ratio of 4, although isomerised octenes were also formed. The *n*/*iso* ratio is relatively high (3.5), as is observed for other rhodium/phosphite systems.[3b] When the P/Rh ratio was reduced to 2, the conversion, and especially the selectivity, decreased (Entry 2, Table 3).

The catalyst precursors with ligands **2** and **3** provided very low selectivity for the aldehydes and produced octene isomers as the main products (Entries 3–7, Table 3). Since these poor donor ligands tend to form rhodium species with a high number of coordinated ligands per rhodium atom (see synthesis section above), which can inhibit hydroformylation,[28] we performed an experiment with a lower

Table 3. Hydroformylation of 1-octene using $[Rh(acac)(CO)_2]$/**1**–**3** catalyst precursors in $scCO_2$.[a]

| Entry | L | Solvent | L/Rh | *T* [°C] | $P(H_2)$ [atm] | *P*(CO) [atm] | $P_{tot}$[b] [atm] | Conv.[c] [%] | $S_a$[d] [%] | **18/19** [%] | $S_i$[e] [%] |
|---|---|---|---|---|---|---|---|---|---|---|---|
| 1 | **1** | toluene | 4 | 80 | 2.5 | 2.5 | 5 | 98 | 86 | 78:22 | 10 |
| 2 | **1** | toluene | 2 | 80 | 2.5 | 2.5 | 5 | 85 | 24 | 74:26 | 75 |
| 3 | **2** | toluene | 4 | 80 | 2.5 | 2.5 | 5 | 89 | 21 | 77:23 | 79 |
| 4[f] | **2** | toluene | 4 | 80 | 2.5 | 2.5 | 5 | 95 | 47 | 53:47 | 53 |
| 5 | **3** | toluene | 4 | 80 | 2.5 | 2.5 | 5 | 95 | 38 | 71:29 | 58 |
| 6 | **3** | toluene | 2 | 80 | 2.5 | 2.5 | 5 | 95 | 6 | 57:37[h] | 93 |
| 7[f] | **3** | toluene | 4 | 80 | 2.5 | 2.5 | 5 | 98 | 36 | 63:27 | 64 |
| 8 | **1** | – | 4 | 80 | 2.5 | 2.5 | 5 | 88 | 80 | 74:24[h] | 20 |
| 9 | **1** | $scCO_2$ | 4 | 80 | 2.5 | 2.5 | 167 | 57 | 25 | 81:19 | 74 |
| 10 | **1** | $scCO_2$ | 6 | 80 | 2.5 | 2.5 | 167 | 20 | 68 | 85:15 | 30 |
| 11 | **1** | scCO2 | 6 | 80 | 10 | 10 | 167 | 6 | 86 | 81:19 | 14 |
| 12 | **1** | scCO2 | 6 | 100 | 10 | 10 | 167 | 49 | 90 | 80:20 | 10 |
| 13 | **1** | $scCO_2$ | 6 | 100 | 10 | 10 | 250 | 82 | 89 | 78:22 | 11 |
| 14 | **2** | $scCO_2$ | 4 | 80 | 2.5 | 2.5 | 167 | 40 | 76 | 76:24 | 24 |
| 15[g] | **2** | $scCO_2$ | 4 | 80 | 2.5 | 2.5 | 167 | 15 | 12 | 45:55 | 79 |
| 16 | **2** | $scCO_2$ | 6 | 100 | 10 | 10 | 250 | 70 | 94 | 77:23 | 6 |
| 17 | **3** | $scCO_2$ | 4 | 80 | 2.5 | 2.5 | 167 | 13 | 41 | 85:15 | 59 |
| 18 | **3** | $scCO_2$ | 2 | 80 | 2.5 | 2.5 | 167 | 35 | 9 | 77:23 | 91 |
| 19 | **3** | $scCO_2$ | 6 | 100 | 10 | 10 | 250 | 24 | 79 | 75:25 | 19 |

[a] Reaction conditions: toluene: $[Rh(acac)(CO)_2]$ = 0.024 mmol, alkene = 4.8 mmol, alkene/Rh = 200, *V* = 10 mL, *t* = 3 h; $scCO_2$: $[Rh(acac)(CO)_2]$ = 0.06 mmol, alkene = 12 mmol, alkene/Rh = 200, *V* = 25 mL, *t* = 3 h. [b] Total pressure. [c] Total conversion measured by GC. [d] Selectivity for aldehydes. [e] Selectivity for isomerized products (internal octenes). [f] Preactivated system at 5 atm ($CO/H_2$ = 1), *T* = 80 °C for 1 h. [g] Preactivated system at 5 atm ($CO/H_2$ = 1), *T* = 80 °C for 1 h in diethyl ether. [h] 2-Ethylheptanal was also detected.

 © 2006 Wiley-VCH Verlag GmbH & Co. KGaA, Weinheim 

P/Rh ratio (Entry 6, Table 3); the selectivity for aldehydes decreased dramatically.

The low selectivity for aldehydes has been attributed to the nonformation of the active species $[RhH(CO)(L)_3]$. Our HPIR experiments showed that, in the case of systems with **2** and **3**, an activation time is needed before these species are detected. The system $[Rh(acac)(CO)_2]$/**2** was therefore preactivated in toluene at 5 atm ($CO/H_2$ = 1) and 80 °C for 1 h. 1-Octene was then added, the system was pressurised and again heated to 80 °C, and the reaction started. The conversion was slightly higher and the selectivity for aldehydes increased from 21 to 47% (Entry 4, Table 3). Similar results were obtained when the preactivated catalyst precursor with ligand **3** was used (Entry 7, Table 3).

Rhodium catalysts with phosphonite ligands have been shown to have very high activity in the isomerisation/hydroformylation of internal alkenes.[11] When we used $[Rh(acac)(CO)_2]$/**2** under the same conditions as for the hydroformylation of (2*E*)-2-hexene, 17% total conversion was obtained with a selectivity of 45% for aldehydes and a 1-heptanal/2-methylhexanal/3-ethylpentanal ratio of 24:54:22, which indicates that the isomerisation rate is slower than the hydroformylation rate for these systems.

### *Hydroformylation of 1-Octene in Supercritical $CO_2$*

The solubility of the catalyst precursors in $scCO_2$ was studied using a Thar autoclave equipped with sapphire windows. The purged autoclave was charged with $[Rh(acac)(CO)_2]$/**1**–**3** (P/Rh = 4), filled with $CO/H_2$ at 5 atm ($CO/H_2$ = 1:1) and pressurised with $CO_2$ up to 240 atm at 80 °C. Visual inspection through the windows showed that the supercritical phase is colourless, which indicates that there is no apparent solubility of these systems.

The catalytic experiments using $scCO_2$ with systems $[Rh(acac)(CO)_2]$/**1**–**3** are summarised in Table 3 (Entries 9–19). A reference experiment with the system $[Rh(acac)(CO)_2]$/**1** without solvent provided lower conversion and selectivity than when toluene was used as a solvent (Entry 8, Table 3).

As expected due to the low solubility of the catalyst precursors, the conversions with $scCO_2$ were lower than for the toluene systems under similar conditions. However, conversion was good with the catalyst system $[Rh(acac)(CO)_2]$/**1** (Entry 9, Table 3), although the selectivity for aldehydes fell to 25%. This led the linear/branched ratio to increase to 4.2. We optimised the conditions with this system by modifying the P/Rh ratio (Entry 10, Table 3), partial $CO/H_2$ pressure (Entry 11, Table 3), temperature (Entry 12, Table 3) and total pressure (Entry 13, Table 3). Under the best conditions (P/Rh = 6, $CO/H_2$ = 20 atm, $T$ = 100 °C, total pressure 250 atm), we achieved high conversion (82%) and high selectivity for aldehydes (89%; Entry 13, Table 3) probably because of the greater solubility of this system in $scCO_2$. Under these conditions, the linear/branched ratio was similar to that of the toluene system.

When the system $[Rh(acac)(CO)_2]$/**2** was used in $scCO_2$, the selectivity for aldehydes increased from 47% to 76%, although the conversion was lower (Entry 14 vs. Entry 4, Table 3). To favour the formation of the active species in one of the experiments (Entry 15, Table 3), the system was preactivated in diethyl ether at 5 atm ($CO/H_2$ = 1) at 80 °C for 1 h. The solvent was then evaporated and 1-octene was added. The system was pressurised and heated again to 80 °C and the reaction started. In this case the conversion and selectivity decreased considerably and decomposition of the catalyst was observed at the end of the reaction. Under the optimised conditions, we obtained high selectivity for aldehydes (94%) and a conversion of 70%.

When the system $[Rh(acac)(CO)_2]$/**3** (Entries 17–19, Table 3) was used, the best results were also obtained under the optimised conditions (selectivity for aldehydes 79% and conversion of 24%).

In summary, the catalyst precursors formed with $[Rh(acac)(CO)_2]$/**1**–**3** are active in the hydroformylation of 1-octene in $scCO_2$. In the catalyst system with the phosphite **1**, similar conversion and selectivities to those of the toluene reaction can be achieved by optimising the reaction conditions. The selectivity for aldehyde of the rhodium catalyst precursors with ligands **2** and **3** increases, especially with ligand **2**, when $scCO_2$ is used as the reaction medium instead of toluene.

## Conclusions

We have synthesised new P-donor ligands **1**–**3** with branched substituents and studied their coordination to $Rh^I$ and $Pd^{II}$. We have characterised complexes $[Rh(cod)(\mathbf{1})_2]PF_6$, $[Rh(\mathbf{2},\mathbf{3})_4]PF_6$ and $[PdCl_2(\mathbf{1}–\mathbf{3})_2]$. We have determined the X-ray structure of $[Rh(\mathbf{3})_4]PF_6$ and confirmed the formation of the tetrakis(phosphite) complex. The reactivity of $[Rh(acac)(CO)_2]$/**1**–**3** with $CO/H_2$ at 5 atm ($CO/H_2$ = 1) and 80 °C indicates that $[RhH(CO)(\mathbf{1}–\mathbf{3})_3]$ is the main species formed in solution. The solubility of the catalyst precursors $[Rh(acac)(CO)_2]$/**1**–**3** in $scCO_2$ is low but they are active in the hydroformylation of 1-octene in $scCO_2$. In this solvent, the catalyst precursor with ligand **1** gives similar activities and selectivities to those in toluene. Catalyst precursors with ligands **2** and **3** give lower conversions than in toluene but the aldehyde selectivity is higher.

## Experimental Section

**General:** All reactions were carried out under nitrogen using standard Schlenk techniques. Solvents were distilled and degassed prior to use. $^1H$, $^{13}C\{^1H\}$, $^{19}F$ and $^{31}P\{^1H\}$ NMR spectra were recorded with Varian Gemini spectrometers operating at 300 or 400 MHz ($^1H$), 75.43 or 100.57 MHz ($^{13}C$), 376.3 MHz ($^{19}F$) or 121.44 or 161.92 MHz ($^{31}P$). Chemical shifts are reported relative to tetramethylsilane for $^1H$ and $^{13}C\{^1H\}$ as internal reference, 85% $H_3PO_4$ for $^{31}P\{^1H\}$ and $CFCl_3$ for $^{19}F$. Mass spectrometry was performed with either an AUTOSPEC (EI-HR) or an AUTOFLEX spectrometer (MALDI-TOF). High-pressure NMR experiments (HPNMR) were carried out in a 10-mm-diameter sapphire tube with a titanium cap equipped with a Teflon/polycarbonate protection.[29] High-pressure IR experiments were performed in situ with an infrared autoclave.[30] Gas chromatography analyses were per-

 © 2006 Wiley-VCH Verlag GmbH & Co. KGaA, Weinheim 

formed with a Hewlett–Packard 5890A apparatus in an HP-5 (5% diphenylsilicone/95% dimethylsilicone) column (25 m × 0.2 mm) for the separation of the products.

**Catalysis:** Hydroformylation experiments were carried out in a Parr autoclave (25 mL) with magnetic stirring. The autoclave was equipped with a liquid inlet, a gas inlet, a $CO_2$ inlet and a thermocouple. An electric heating mantle kept the temperature constant.

**Standard Hydroformylation Experiment in Toluene:** The reactions in toluene were carried out in the same Parr autoclave. The complex [Rh(acac)(CO)$_2$] (0.024 mmol) and the ligand (0.096 mmol) in toluene (10 mL) were stirred at room temperature for 1 h. The substrate (4.8 mmol) was then added and the resulting solution was introduced into the evacuated autoclave. The system was pressurised and heated. When thermal equilibrium was reached, more gas mixture was introduced until the desired pressure was attained. After the required reaction time, the autoclave was cooled to room temperature and depressurised. The products were identified by GC/MS.

**Standard Hydroformylation Experiment in scCO$_2$:** The complex [Rh(acac)(CO)$_2$] (0.06 mmol) and the ligand (0.24 mmol) in diethyl ether (2 mL) were stirred at room temperature for 30 min. The resulting solution was introduced into the evacuated autoclave, and the solvent was removed in vacuo. 1-Octene (12 mmol) was then added. The system was pressurised with 5 atm of CO/H$_2$ (1:1), and liquid $CO_2$ was introduced until a total pressure of 60 bar was reached. The autoclave was heated to the desired temperature. When thermal equilibrium was reached, the total pressure was adjusted with a Thar syringe pump. After the reaction time, the autoclave was cooled down to –10 °C and depressurised. The final mixture was analysed by GC. The products were identified by GC/MS.

**Solubility Studies:** The solubility studies were carried out in a Thar reactor (100 mL) equipped with sapphire windows and magnetic stirring. The autoclave was charged with a solution of the ligand (0.220 mmol) and [Rh(acac)(CO)$_2$] (0.055 mmol) in diethyl ether. The solvent was removed in vacuo, the reactor was pressurised with syn-gas and $CO_2$, the system was heated to 80 °C, and the total pressure was adjusted to 240 atm. Solubility was monitored by visual inspection through the sapphire windows with a mirror due to safety requirements.

**HPNMR:** In a typical experiment, the NMR tube was filled under $N_2$ with a solution of [Rh(acac)(CO)$_2$] (0.04 mmol), the ligand **1**–**3** (0.16 mmol) and [D$_8$]toluene (2 mL). The tube was pressurised to 5 atm of CO/H$_2$ (1:1) and left at 80 °C for 1 h. The NMR spectra were then recorded.

**HPIR:** In a typical experiment, the HPIR cell was filled under $N_2$ with a solution of [Rh(acac)(CO)$_2$] (0.036 mmol), the ligand **1**–**3** (0.144 mmol) and methyltetrahydrofuran (15 mL). The cell was pressurised to 5 atm of CO/H$_2$ (1:1) and left at 80 °C for 1 h. The IR spectra were then recorded.

**Preparation of Tris(3,5,5-trimethylhexyl) Phosphite (1):** A solution of phosphorus trichloride (0.87 g, 6.3 mmol) in 6.5 mL of diethyl ether was added dropwise to a solution of 3,5,5-trimethylhexanol (2.74 g, 0.019 mol) and pyridine (1.50 g, 0.019 mol) in 12 mL of diethyl ether at –10 °C. The solution was stirred at room temperature for 2 h. The solution was filtered and the solvent was removed. The resulting colourless oil was purified by flash chromatography on basic alumina eluting with hexane. Yield: 2.33 g (80%) (colourless oil). $^1$H NMR (400 MHz, $CDCl_3$, 20 °C): $\delta$ = 3.74 (q, $J_{H,P}$ = $J_{H,H}$ = 7.1 Hz, 6 H, POC$H_2$), 1.57 (m, 6 H, POCH$_2$C*H*H + C*H*CH$_3$) 1.36 (m, 3 H, POCH$_2$CH*H*), 1.15 [dd, $^2J_{H,H}$ = 14.0 Hz, $^3J_{H,H}$ = 3.4 Hz, 3 H, CH(CH$_3$)C*H*H], 1.00 [dd, $^2J_{H,H}$ = 14.0 Hz, $^3J_{H,H}$ = 6.0 Hz, 3 H, CH(CH$_3$)CH*H*], 0.86 [d, $^3J_{H,H}$ = 6.4 Hz, 9 H, CH(C*H*$_3$)], 0.82 [s, 27 H, C(C*H*$_3$)$_3$] ppm. $^{13}$C NMR (100.5 MHz, $CDCl_3$, 20 °C): $\delta$ = 60.49 (d, $^2J_{P,C}$ = 10.6 Hz, PO*C*H$_2$), 51.21 [s, CH(CH$_3$)*C*H$_2$], 40.52 (d, $^3J_{P,C}$ = 4.6 Hz, POCH$_2$*C*H$_2$), 31.11 [s, *C*(CH$_3$)$_3$], 29.99 [s, C(*C*H$_3$)$_3$], 25.91 [s, *C*H(CH$_3$)], 22.53 [s, CH(*C*H$_3$)] ppm. $^{31}$P{$^1$H} NMR (161.9 MHz, $CDCl_3$, 20 °C): $\delta$ = 139.9 ppm. EIMS: *m*/*z* = 461 [M + H]$^+$. High-resolution EIMS: 461.4120 ($C_{27}H_{58}O_3P$).

**Preparation of Bis(3,5,5-trimethylhexyl) Phenylphosphonite (2):** A solution of dichloro(phenyl)phosphane (1.79 g, 0.010 mol) in 6.5 mL of diethyl ether was added dropwise to a solution of 3,5,5-trimethylhexanol (2.88 g, 0.02 mol) and pyridine (1.58 g, 0.02 mol) in 12 mL of diethyl ether at –10 °C. The solution was stirred at room temperature for 7 h and then filtered. After all the solvent had been removed under reduced pressure, the resulting colourless oil was purified by flash chromatography on basic alumina eluting with hexane. Yield: 2.21 g (56%) (colourless oil). $^1$H NMR (400 MHz, $CDCl_3$, 20 °C): $\delta$ = 7.59 (m, 2 H, Ph), 7.38 (m, 3 H, Ph), 3.87 (m, 2 H, POC*H*H), 3.75 (m, 2 H, POCH*H*), 1.64 (m, 4 H, POCH$_2$C*H*H + C*H*CH$_3$), 1.43 (m, 2 H, POCH$_2$CH*H*), 1.19 [m, 2 H, CH(CH$_3$)C*H*H], 1.05 [m, 2 H, CH(CH$_3$)CH*H*], 0.91 [d, $^3J_{H,H}$ = 8.4 Hz, 6 H, CH(C*H*$_3$)], 0.87 [s, 18 H, C(C*H*$_3$)$_3$] ppm. $^{13}$C NMR (100.5 MHz, $CDCl_3$, 20 °C): $\delta$ = 141.25 (d, $^1J_{P,C}$ = 19.2 Hz, C$_i$ Ph), 129.84 (s, C$_p$ Ph), 129.65 (d, $^3J_{P,C}$ = 2.3 Hz, C$_m$ Ph), 128.08 (d, $^2J_{C,P}$ = 4.5 Hz, C$_o$ Ph), 65.04 (d, $^2J_{P,C}$ = 9.2 Hz, PO*C*H$_2$), 64.99 (d, $^2J_{P,C}$ = 8.4 Hz, PO*C*H$_2$), 51.26 [s, CH(CH$_3$)*C*H$_2$], 51.22 [s, CH(CH$_3$)*C*H$_2$], 40.77 (d, $^3J_{C,P}$ = 4.6 Hz, POCH$_2$*C*H$_2$), 40.72 (d, $^3J_{C,P}$ = 4.3 Hz, POCH$_2$*C*H$_2$), 31.1 [s, *C*(CH$_3$)$_3$], 29.97 [s, C(*C*H$_3$)$_3$], 25.92 [s, *C*H(CH$_3$)], 22.54 [s, CH(*C*H$_3$)], 22.48 [s, CH(*C*H$_3$)] ppm. $^{31}$P{$^1$H} NMR (161.9 MHz, $CDCl_3$, 20 °C): $\delta$ = 156.6 ppm. EIMS: *m*/*z* = 394.3 [M]$^+$. High-resolution EIMS: 394.2991 ($C_{24}H_{43}O_2P$).

**Synthesis of 3,5,5-Trimethylhexyl Diphenylphosphinite (3):** A solution of chlorodiphenylphosphane (1.00 g, 4.6 mmol) in 6.5 mL of diethyl ether was added dropwise to a solution of 3,5,5-trimethylhexanol (0.66 g, 4.6 mmol) and pyridine (0.36 g, 4.6 mmol) in 12 mL of diethyl ether at –10 °C. The solution was stirred at room temperature for 2 h and then filtered. After all the solvent had been removed under reduced pressure, the resulting colourless oil was purified by chromatography on basic alumina eluting with hexane. Yield: 1.01 g (67%) (colourless oil). $^1$H NMR (400 MHz, $CDCl_3$, 20 °C): $\delta$ = 7.40 (m, 4 H, Ph), 7.22 (m, 6 H, Ph), 3.78, (m, 2 H, POC$H_2$), 1.64 (m, 1 H, POCH$_2$C*H*H), 1.55 [m, 1 H, C*H*(CH$_3$)], 1.40 (m, 1 H, POCH$_2$CH*H*), 1.13 [dd, $^2J_{H,H}$ = 13.8 Hz, $^3J_{H,H}$ = 3.8 Hz, 1 H, CH(CH$_3$)CH*H*], 0.96 [dd, $^2J_{H,H}$ = 14.2 Hz, $^3J_{H,H}$ = 6.8 Hz, 1 H, CH(CH$_3$)C*H*H], 0.82 [d, $^3J_{H,H}$ = 6.2 Hz, 3 H, CH(C*H*$_3$)], 0.77 [s, 9 H, C(C*H*$_3$)$_3$] ppm. $^{13}$C NMR (100.5 MHz, $CDCl_3$, 20 °C): $\delta$ = 142.28 (d, $^2J_{P,C}$ = 18.8 Hz, C$_i$ Ph), 130.54 (d, $^2J_{P,C}$ = 7.6 Hz, C$_o$ Ph), 130.33 (d, $^2J_{P,C}$ = 7.6 Hz, C$_o$ Ph), 129.12 (d, $^3J_{P,C}$ = 5.3 Hz, C$_m$ Ph), 128.26 (s, C$_p$ Ph), 128.19 (s, C$_p$ Ph), 68.50 (d, $^2J_{P,C}$ = 19,1 Hz, PO*C*H$_2$), 51.21 [s, CH(CH$_3$)*C*H$_2$], 40.83 (d, $^3J_{P,C}$ = 7.6 Hz, POCH$_2$*C*H$_2$) 31.08 [s, *C*(CH$_3$)$_3$], 29.99 [s, C(*C*H$_3$)$_3$] 29.95 [s, C(*C*H$_3$)$_3$], 25.92 [s, *C*H(CH$_3$)], 22.50 [s, CH(*C*H$_3$)] ppm. $^{31}$P{$^1$H} NMR (161.9 MHz, $CDCl_3$, 20 °C): $\delta$ = 112.5 ppm. EIMS: *m*/*z* = 328.2 [M]$^+$. High-resolution EIMS: 328.1961 ($C_{21}H_{29}OP$).

**Preparation of [Rh(C$_8$H$_{12}$)(1)$_2$]PF$_6$ (4):** Ligand **1** (221 mg, 0.48 mmol) was added to a solution of [Rh(cod)$_2$]PF$_6$ (93 mg, 0.20 mmol) in 2 mL of anhydrous dichloromethane. The solution turned yellow immediately and was stirred for 1 h. The solvent was then evaporated in vacuo and the product washed with cold methanol. The product was obtained as a yellow oil. Yield: 219 mg (86%). $^1$H NMR (400 MHz, $CDCl_3$, 20 °C): $\delta$ = 4.05 (m, 16 H,

 © 2006 Wiley-VCH Verlag GmbH & Co. KGaA, Weinheim 

$POCH_2$ + CH= cod), 2.57 (m, 4 H, $CH_2$ cod), 2.36 (m, 4 H, $CH_2$ cod), 1.60 (m, 18 H, $POCH_2CH_2$ + $CHCH_3$), 1.22 [dd, $^2J_{H,H}$ = 14.0 Hz, $^3J_{H,H}$ = 3.6 Hz, 6 H, $CH(CH_3)CHH$], 1.14 [dd, $^2J_{H,H}$ = 14.0 Hz, $^3J_{H,H}$ = 6.0 Hz, 6 H, $CH(CH_3)CHH$], 0.97 [d, $^3J_{H,H}$ = 6.4 Hz, 18 H, $CH(CH_3)$], 0.90 [s, 54 H, $C(CH_3)_3$] ppm. $^{13}$C NMR (100.5 MHz, $CDCl_3$, 20 °C): $\delta$ = 106.2 (m, CH= cod), 65.2 (d, $J_{C,P}$ = 6.1 Hz, $POCH_2$), 51.3 [s, $CH(CH_3)CH_2$], 39.8 (d, $POCH_2CH_2$), 31.1 [s, $C(CH_3)_3$], 29.9 [s, $C(CH_3)_3$] 26.1 [s, $CH(CH_3)$], 22.5 [s, $CH(CH_3)$] ppm. $^{19}$F NMR (376.3 MHz, $CDCl_3$, 20 °C): $\delta$ = –73.11 (d, $J_{P,F}$ = 715.4 Hz) ppm. $^{31}P\{^1H\}$ NMR (161.9 MHz, $CDCl_3$, 20 °C): $\delta$ = 116.1 (d, $J_{Rh,P}$ = 244.0 Hz), –143.2 [sept, $J_{F,P}$ = 711.5 Hz] ppm. MS (MALDI-TOF): *m*/*z* = 1129.54 [M – $PF_6$ – 3 H]$^+$, 1003.45 [M – $PF_6$ – $C_9H_{20}$ – H]$^+$.

**Preparation of [Rh(2)$_4$]PF$_6$ (5):** Ligand **2** (316 mg, 0.80 mmol) was added to a solution of $[Rh(cod)_2]PF_6$ (46.5 mg, 0.20 mmol) in 2 mL of anhydrous dichloromethane. The solution turned yellow immediately and was stirred for 1 h. The solvent was evaporated and the residue washed with cold methanol and dried in vacuo overnight to give the product as a yellow oily solid. Yield: 277 mg (76%). $^1$H NMR (400 MHz, $CDCl_3$, 20 °C): $\delta$ = 7.5 (m, 20 H, Ph), 3.47 (br. m, 8 H, POC*H*H), 3.16 (br., 8 H, POCH*H*), 1.38 (br. m, 24 H, $POCH_2CH_2$ + $CHCH_3$), 1.02 [br. m, 16 H, $CH(CH_3)CH_2$], 0.85 [d, $^3J_{H,H}$ = 5.6 Hz, 24 H, $CH(CH_3)$], 0.87 [s, 72 H, $C(CH_3)_3$] ppm. $^{13}$C NMR (100.5 MHz, $CDCl_3$, 20 °C): $\delta$ = 137.74 (br., $C_i$ Ph), 131.47 (s, $C_o$ Ph), 130.33 (s, $C_m$ Ph) 128.34 (s, $C_p$ Ph), 66.00 (br., $POCH_2$) 51.19 [s, $CH(CH_3)CH_2$], 39.91 (s, $POCH_2CH_2$), 31.01 [s, $C(CH_3)_3$], 29.90 [s, $C(CH_3)_3$], 26.21 [s, $CH(CH_3)$], 22.65 [s, $CH(CH_3)$] ppm. $^{19}$F NMR (376.3 MHz, $CDCl_3$, 20 °C): $\delta$ = –74.32 (d, $J_{F,P}$ = 710.8 Hz) ppm. $^{31}P\{^1H\}$ NMR (161.9 MHz, $CDCl_3$, 20 °C): $\delta$ = 146.0 (d, $J_{P,Rh}$ = 169.7 Hz), –143.2 (sept, $J_{P,F}$ = 711.5 Hz) ppm. MS (MALDI-TOF): *m*/*z* = 1679.7 [M – $PF_6$ – 2 H]$^+$ 1285.56 [M – $PF_6$ – 4 H]$^+$.

**Preparation of [Rh(3)$_4$]PF$_6$ (6):** Ligand **3** (158 mg, 0.47 mmol) was added to a solution of $[Rh(cod)_2]PF_6$ (80 mg, 0.20 mmol) in 2 mL of anhydrous dichloromethane. The solution turned yellow immediately and was stirred for 1 h. Diethyl ether was then added to the solution to afford a yellow solid. Yield: 228 mg (73%). $^1$H NMR (400 MHz, $CDCl_3$, 20 °C): $\delta$ = 7.2–7.3 (m, 40 H, Ph), 2.78 (br. m, 8 H, $POCH_2$), 0.80 [m, 12 H, $POCH_2CH_2CH(CH_3)$], 0.67 [dd, $^2J_{H,H}$ = 13.8 Hz, $^3J_{H,H}$ = 5.6 Hz, 4 H, $CH(CH_3)CHH$], 0.60 [s, 36 H, $C(CH_3)_3$], 0.54 [dd, $^2J_{H,H}$ = 14.0 Hz, $^3J_{H,H}$ = 3 Hz, 4 H, $CH(CH_3)CHH$], 0.42 [d, $^3J_{H,H}$ = 6.4 Hz, 12 H, $CH(CH_3)$] ppm. $^{13}$C NMR (100.5 MHz, $CDCl_3$, 20 °C): $\delta$ = 133.25 (br., $C_i$ Ph), 133.01 (s, $C_o$ Ph), 131.06 (s, $C_m$ Ph), 128.27 (s, $C_p$ Ph), 66.53 (s, $POCH_2$), 51.08 [s, $CH(CH_3)CH_2$], 37.85 (s, $POCH_2CH_2$), 31.06 [s, $C(CH_3)_3$], 29.83 [s, $C(CH_3)_3$], 26.02 [s, $CH(CH_3)$], 22.86 [s, $CH(CH_3)$] ppm. $^{31}P\{^1H\}$ NMR (161.9 MHz, $CDCl_3$, 20 °C): $\delta$ = 132.3 (d, $J_{P,Rh}$ = 162.2 Hz), –143.1 (sept. $J_{P,F}$ = 712.6 Hz) ppm.

**Preparation of [PdCl$_2$(1)$_2$] (7):** Ligand **1** (120 mg, 0.26 mmol) was added to a solution of $[PdCl_2(PhCN)_2]$ (50 mg, 0.13 mmol) in 2 mL of anhydrous dichloromethane. The solution was stirred for 1 h, then the solvent was evaporated in vacuo and the product was washed with cold methanol and dried under vacuum overnight. The product was obtained as a light-yellow oil. Yield: 124 mg (87%). $^1$H NMR (400 MHz, $CDCl_3$, 20 °C): $\delta$ = 4.15 (m, 12 H, $POCH_2$) 1.64 (m, 6 H, $POCH_2CHH$), 1.55 (m, 6 H, $CHCH_3$), 1.46 (m, 6 H, $POCH_2CHH$), 1.44 [dd, $^2J_{H,H}$ = 14.0 Hz, $^3J_{H,H}$ = 3.6 Hz, 6 H, $CH(CH_3)CHH$], 1.03 [dd, $^2J_{H,H}$ = 14.0 Hz, $^3J_{H,H}$ = 6.4 Hz, 6 H, $CH(CH_3)CHH$], 0.88 [d, $^3J_{H,H}$ = 3.2 Hz, 18 H, $CH(CH_3)$], 0.83 [s, 54 H, $C(CH_3)_3$] ppm. $^{13}$C NMR (100.5 MHz, $CDCl_3$, 20 °C): $\delta$ = 66.60 (s, $POCH_2$), 51.35 [s, $CH(CH_3)CH_2$], 39.77 (s, $POCH_2CH_2$), 31.29 [s, $C(CH_3)_3$], 30.18 [s, $C(CH_3)_3$], 26.15 [s, $CH(CH_3)$] 22.67 [s, $CH(CH_3)$] ppm. $^{31}P\{^1H\}$ NMR (161.9 MHz, $CDCl_3$, 20 °C): $\delta$ = 94.2 (s) ppm. MS (MALDI-TOF): *m*/*z* = 1063.7 [M – Cl]$^+$, 1026.7 [M – 2 Cl]$^+$.

**Preparation of [PdCl$_2$(2)$_2$] (8):** Ligand **2** (51 mg, 0.12 mmol) was added to a solution of $[PdCl_2(PhCN)_2]$ (25 mg, 0.06 mmol) in 2 mL of anhydrous dichloromethane. The solution was stirred for 1 h, then the solvent was evaporated in vacuo and the product was washed with cold methanol and dried under vacuum overnight. The product was obtained as a yellow oil. Yield: 47 mg (81%). $^1$H NMR (400 MHz, $CDCl_3$, 20 °C): $\delta$ = 7.75 (m, 4 H, Ph), 7.45 (m, 6 H, Ph), 4.20 (br. m, 4 H, POC*H*H), 3.95 (br. m, 4 H, POCH*H*), 1.71 (br. m, 4 H, $POCH_2CHH$), 1.54 (br. m, 8 H, $POCH_2CH$H + $CHCH_3$), 1.13 [br. m, 8 H, $CH(CH_3)CH_2$], 0.90 [d, $^3J_{H,H}$ = 6.4 Hz, 12 H, $CH(CH_3)$] 0.87 [s, 36 H, $C(CH_3)_3$] ppm. $^{13}$C NMR (100.5 MHz, $CDCl_3$, 20 °C): $\delta$ = 140.70 (br., $C_i$ Ph), 132.55 (s, $C_o$ Ph), 131.74 (s, $C_m$ Ph), 129.07, (s, $C_p$ Ph), 67.83 (s, $POCH_2$), 50.93 [s, $CH(CH_3)CH_2$], 39.22 (s, $POCH_2CH_2$), 30.88 [s, $C(CH_3)_3$], 29.77 [s, $C(CH_3)_3$], 25.82 [s, $CH(CH_3)$], 22.26 [s, $CH(CH_3)$] ppm. $^{31}P\{^1H\}$ NMR (161.9 MHz, $CDCl_3$, 20 °C): $\delta$ = 122.2 (s) ppm. MS (MALDI-TOF): *m*/*z* = 929.4 [M – Cl]$^+$, 894.4 [M – 2 Cl]$^+$.

**Preparation of [PdCl$_2$(3)$_2$] (9):** Ligand **3** (85.63 mg, 0.26 mmol) was added to a solution of $[PdCl_2(PhCN)_2]$ (50 mg, 0.13 mmol) in 2 mL of anhydrous dichloromethane. The solution was stirred for 1 h, the solvent was evaporated in vacuo and the residue was washed with methanol. The product was obtained as a yellow oil. Yield: 98 mg (91%). $^1$H NMR (400 MHz, $CDCl_3$, 20 °C): $\delta$ = 7.81 (m, 8 H, Ph), 7.46 (m, 12 H, Ph), 3.63 (m, 4 H, $POCH_2$), 1.31–1.19 [m, 6 H, $POCH_2CH_2$ + $CH(CH_3)$ + $CH(CH_3)CH_2$], 0.92 [d, $^3J_{H,H}$ = 4.4 Hz, 6 H, $CH(CH_3)$], 0.78 [s, $C(CH_3)_3$] ppm. $^{13}$C NMR (100.5 MHz, $CDCl_3$, 20 °C): $\delta$ = 140.4 (br. $C_i$ Ph), 132.58 (d, $^2J_{P,C}$ = 6.1 Hz, $C_o$ Ph), 132.52 (d, $^2J_{P,C}$ = 6.1 Hz, $C_o$ Ph), 131.75 (br., $C_m$ Ph), 128.20 (br., $C_p$ Ph), 67.86 (s, $POCH_2$), 50.93 [s, $CH(CH_3)CH_2$], 39.22 ($POCH_2CH_2$), 30.87 [s, $C(CH_3)_3$], 29.76 [s, $C(CH_3)_3$], 25.81 [s, $CH(CH_3)$], 22.26 [s, $CH(CH_3)$] ppm. $^{31}$P NMR (161.9 MHz, $CDCl_3$, 20 °C): $\delta$ = 110.21 (s) ppm. MS (MALDI-TOF): *m*/*z* = 796.9 [M – Cl]$^+$, 762.0 [M – 2 Cl]$^+$.

**Crystal Data for Complex 6:** Suitable crystals of complex **6** were grown by slow diffusion of diethyl ether into a solution of the complex in dichloromethane and mounted on a glass fibre. The measurements were taken at 120 K with a Bruker SMART CCD1000 diffractometer equipped with a graphite-monochromated Mo-$K_\alpha$ radiation source ($\lambda$ = 0.71073 Å). Data collection and processing were carried out with Smart and Saint from Bruker. Complex **6** ($C_{84}H_{112}O_4P_4Rh{\cdot}PF_6$) crystallised in a tetragonal *P*4/*n* space group with *a* = 18.021 (2), *c* = 13.431 (3) Å, *V* = 4361.8 (12) Å$^3$, *M* = 1557.50, *Z* = 2, $\rho_{calcd.}$ = 1.186 mg m$^{-3}$, $\mu$ = 0.345 mm$^{-1}$. The yellow crystal was prismatic and of dimensions 0.6 × 0.52 × 0.48 mm. The $\theta$ range for measurement was 1.52–26.37° and 4471 unique reflections were measured at 120 K ($R_{int}$ = 0.0381). The structure was solved by direct methods (SHELXS-97)[31] and refined on $F^2$ by full-matrix least squares (SHELXL-97)[32] of 278 parameters. All non-hydrogen atoms were refined anisotropically. The data were corrected for absorption effects with SADABS.[33] The final parameters were $R = \sum||F_o| - |F_c||/\sum|F_o|$ = 0.0393 for 3571 reflections with $F_o^2 > 2\sigma(F_o^2)$ and $wR_2 = [\sum w(F_o^2 - F_c^2)/\sum w(F_o^2)^2]^{1/2}$ = 0.1178. Goodness-of-fit = 1.1. The ORTEP diagram was generated with ORTEP-3.[34] CCDC-270199 contains the supplementary crystallographic data for this paper. These data can be obtained free of charge from The Cambridge Crystallographic Data Centre via www.ccdc.cam.ac.uk/data_request/cif.

**Supporting Information** (see footnote on the first page of this article): HPNMR and HPIR spectra of systems [Rh(acac)(CO)$_2$]/**1**–**3**.

 © 2006 Wiley-VCH Verlag GmbH & Co. KGaA, Weinheim 

## Acknowledgments

We thank the Ministerio de Educación, Cultura y Deporte (PPQ01-0452) for financial support and Prof. P. W. N. M. van Leeuwen for interesting suggestions.

[1] a) D. A. Montgenstern, R. M. LeLacheur, D. K. Morita, S. L. Borkowsky, S. Feng, G. H. Brown, L. Luan, M. F. Gross, M. J. Burk, W. Thumas, in *Green Chemistry: Designing Chemistry for the Environment* (Eds.: P. T. Anastas, T. C. Williamson), *ACS Symp. Ser.* **1996**, *626*, 132–151; b) P. G. Jessop, T. Ikaraya, R. Noyori, *Chem. Rev.* **1999**, *99*, 475–493; c) W. Leitner, *Acc. Chem. Res.* **2000**, *35*, 746–756.
[2] D. J. Cole-Hamilton, *Science* **2003**, *299*, 1702–1706.
[3] a) C. D. Frohning, C. W. Kohlpaintner, in *Applied Homogeneous Catalysis with Organometallic Compounds* (Eds.: B. Cornils, W. A. Herrmann), VCH, Weinheim, **1996**, chapter 2.1, p. 29; b) *Rhodium Catalyzed Hydroformylation* (Eds.: P. W. N. M. van Leeuwen, C. Claver), Kluwer Academic Publishers, Dordrecht, **2000**.
[4] E. Wiebus, B. Cornils, *Chem. Eng. Technol.* **1994**, *66*, 916–923.
[5] a) D. Koch, W. Leitner, *J. Am. Chem. Soc.* **1998**, *120*, 13398–13404; b) G. Franciò, W. Leitner, *Chem. Commun.* **1999**, 1663–1664; c) A. M. Banet-Osuna, W. Chen, E. G. Hope, R. D. W. Kemmit, D. R. Paige, A. M. Stuart, J. Xiao, L. Xu, *J. Chem. Soc., Dalton Trans.* **2000**, 4052–4055.
[6] a) I. Bach, D. J. Cole-Hamilton, *Chem. Commun.* **1998**, 1463–1464; b) M. F. Sellin, I. Bach, J. M. Webster, F. Montilla, V. Rosa, T. Avilés, M. Poliakoff, D. J. Cole-Hamilton, *J. Chem. Soc., Dalton Trans.* **2002**, 4569–4576.
[7] N. G. Smart, T. E. Carleson, S. Elshani, S. Wang, C. M. Wai, *Ind. Eng. Chem. Res.* **1997**, *36*, 1819–1826.
[8] M. F. Sellin, D. J. Cole-Hamilton, *J. Chem. Soc., Dalton Trans.* **2000**, 1681–1683.
[9] A. L. Lagalante, B. N. Hansen, T. J. Bruno, R. E. Sievers, *Inorg. Chem.* **1995**, *34*, 5781–5785.
[10] J. Eastoe, A. Paul, S. Nave, D. C. Steytler, B. H. Robinson, E. Rumsey, M. Thorpe, R. Heenan, *J. Am. Chem. Soc.* **2001**, *123*, 988–989.
[11] D. Selent, K.-D. Wiese, D. Röttger, A. Börner, *Angew. Chem. Int. Ed.* **2000**, *39*, 1639–1641.
[12] *Handbook of Phosphorus-31 Nuclear Magnetic Resonance Data* (Ed.: J. C. Tebby), CRC Press Inc., Boca Raton, **1991**, p. 65.
[13] L. M. Haines, *Inorg. Chem.* **1971**, *10*, 1685–1692.
[14] R. R. Schrock, J. A. Osborn, *J. Am. Chem. Soc.* **1971**, *93*, 2397–2407.
[15] J. A. S. Duncan, T. A. Stephenson, M. D. Walkinshaw, D. Hedden, D. M. Roundhill, *J. Chem. Soc., Dalton Trans.* **1984**, 801–807.
[16] A. M. Trzeciak, H. Bartosz-Bechowski, Z. Ciunik, K. Niesyty, J. J. Ziółkowski, *Can. J. Chem.* **2001**, *79*, 752–759.
[17] a) R. Kempe, M. Schwarze, K. Selke, *Z. Kristallogr.* **1995**, *210*, 555–556; b) T. V. RajanBabu, T. A. Ayers, G. A. Halliday, K. K. You, J. C. Calabrese, *J. Org. Chem.* **1997**, *62*, 6012–6028; c) C. M. Haar, J. Huang, S. P. Nolan, *Organometallics* **1998**, *17*, 5018–5024; d) M. Aghmiz, A. Aghmiz, Y. Díaz, A. M. Masdeu-Bultó, C. Claver, S. Castillón, *J. Org. Chem.* **2004**, *69*, 7502–7510.
[18] R. A. Jones, F. M. Real, G. Wilkinson, A. M. R. Galas, M. B. Hursthouse, K. M. A. Malik, *J. Chem. Soc., Dalton Trans.* **1980**, 511–518.
[19] $\Theta = (2/3) \sum_{i=1}^{3} \theta i/2$; taking $\theta i/2 = 65°$ for Ph rings: C. A. Tolman, *Chem. Rev.* **1977**, *77*, 313–348.
[20] A. M. Trzeciak, J. J. Ziółkowski, S. Aygen, R. Van Eldik, *J. Mol. Catal.* **1986**, *34*, 337–343.
[21] a) S. Aygen, R. Van Eldik, *Organometallics* **1987**, *6*, 1080–1084; b) C. G. Arena, F. Nicolò, D. Dormí, G. Bruno, F. Faraone, *J. Chem. Soc., Dalton Trans.* **1996**, 4357–4363.
[22] A. M. Trzeciak, *J. Organomet. Chem.* **1990**, *390*, 105–111.
[23] a) M. Diéguez, C. Claver, A. M. Masdeu-Bultó, A. Ruiz, P. W. N. M. Van Leeuwen, G. C. Schoemaker, *Organometallics* **1999**, *18*, 2107–2115; b) A. M. Trzeciak, J. J. Ziółkowski, *J. Mol. Catal.* **1983**, *19*, 41–55.
[24] R. Crous, M. Datt, D. Foster, L. Bennie, C. Steenkamp, J. Huyser, L. Kirsten, G. Steyl, A. Roodt, *Dalton Trans.* **2005**, 1108–1116.
[25] B. R. James, D. Mahajan, S. J. Rettig, G. M. Williams, *Organometallics* **1983**, *2*, 1452–1458.
[26] A. M. Trzeciak, J. J. Ziólkowski, *Transition Met. Chem.* **1989**, *14*, 135–138.
[27] S. C. Van der Slot, J. Duran, J. Luten, P. C. J. Kamer, P. W. N. M. Van Leeuwen, *Organometallics* **2002**, *21*, 3873–3883.
[28] A. M. Trzeciak, J. J. Ziólkowski, *J. Mol. Catal.* **1986**, *34*, 213–219.
[29] A. Cusanelli, U. Frey, D. T. Richens, A. Merbach, *J. Am. Chem. Soc.* **1996**, *118*, 5265–5271.
[30] P. C. J. Kamer, A. Van Rooy, G. C. Schoemaker, P. W. N. M. Van Leeuwen, *Coord. Chem. Rev.* **2004**, *248*, 2409–2424.
[31] G. M. Sheldrick, *Acta Crystallogr., Sect. A* **1990**, *46*, 467–473.
[32] G. M. Sheldrick, *SHELXL-97: Program for Crystal Structure Refinement*, University of Göttingen, Germany, **1997**.
[33] G. M. Sheldrick, *SADABS software for empirical absorption correction*, University of Göttingen, Germany, **2000**.
[34] *ORTEP-3 for Windows*: L. J. Farrugia, *J. Appl. Crystallogr.* **1997**, *30*, 565–565.

Received: September 7, 2005
Published Online: January 3, 2006

 © 2006 Wiley-VCH Verlag GmbH & Co. KGaA, Weinheim 

DOI: 10.1002/ejic.200500818

# Palladium(II) Compounds with Fluorinated Pincer-Type (SCS) Ligands: X-ray Structures of $C_6H_4$-1,3-$(CH_2SC_6H_4F$-4$)_2$ and [PdCl(SCS–$R_f$)] [$R_f$ = $C_6H_4F$-2, $C_6H_4F$-3, $C_6H_4F$-4, $C_6H_4(CF_3)$-2, and $C_6H_4(CF_3)$-4]

**Ruy Cervantes,[a] Sandra Castillejos,[a] Stephen J. Loeb,[b] Luis Ortiz-Frade,[a] Jorge Tiburcio,[b] and Hugo Torrens*[a]**

**Keywords:** Fluorine / Sulfur / Pincer ligands / Thioether / Palladium compounds

Metathesis reactions employing lead fluorothiolates and $C_6H_4$-1,3-$(CH_2Br)_2$ afford the corresponding pincer-type dithioether ligands $C_6H_4$-1,3-$(CH_2SR_f)_2$ [$R_f$ = $C_6H_4F$-2 (**L1**), $C_6H_4F$-3 (**L2**), $C_6H_4F$-4 (**L3**), $C_6H_4CF_3$-2 (**L4**), $C_6H_4CF_3$-3 (**L5**), and $C_6H_4CF_3$-4 (**L6**)]. A series of $Pd^{II}$ pincer-type complexes [PdCl($\kappa^3$-**Ln**)], **1** to **6**, were prepared and fully characterized. The X-ray diffraction molecular structures of $C_6H_4$-1,3-$[CH_2S(C_6H_4F$-4$)]_2$ (**L3**), [PdCl(SCS–$C_6H_4F$-2)] (**1**), [PdCl(SCS–$C_6H_4F$-3)] (**2**), [PdCl(SCS–$C_6H_4F$-4)] (**3**), [PdCl{SCS–$C_6H_4(CF_3)$-2}] (**4**), and [PdCl{SCS–$C_6H_4(CF_3)$-4}] (**6**) are also reported.

(© Wiley-VCH Verlag GmbH & Co. KGaA, 69451 Weinheim, Germany, 2006)

## Introduction

Pincer-type palladacycles are one of the most popular and well-investigated classes of cyclometalated compounds.[1,2] They have found application in diverse areas from efficient catalyst precursors[3] to molecular materials for crystalline switches and sensors.[4] In particular, SCS pincer-type palladium compounds have been widely studied as catalyst precursors, either as low-molecular-weight or PEG-supported polymers,[2a,5] for $Pd^{II}$-catalyzed Heck[6] and Suzuki[2d,7] cross-coupling reactions.[8–10] SCS pincer-type palladium compounds have also been the focus of interesting structural and conformational studies such as isomeric exchange[11] and dimer formation.[12] Macromolecular and self-assembled supramolecular chemistry have also profited from the useful properties of SCS pincer-type compounds for the construction of polymetallic complexes,[13] macrocycles,[14] large metallodendrimers,[15] functionalized polymers,[16] mixed Pd–Au nanoparticles,[17] polypincer-porphyrin compounds,[18] and supramolecular arrays of palladium.[19]

The possibility of fine tuning the steric and electronic properties of the metal center by simply changing the donor groups or their substituents is one of the features that makes this anionic, terdentate, six-electron donor ligand so flexible and amenable to a plethora of applications.[20] In particular, fluorine-containing pincer-type complexes are relatively rare.[21] The fluorous SCS pincer-type palladium complex with a SCS–$C_6H_4$-*p*-$C_6F_{13}$ ligand has recently been synthesized and shown to be catalytically active under both microwave and thermal heating.[22] The fluorinated PCP pincer-type complexes [RuCl{$C_6H_3$-2,6-$[CH_2P(C_6F_5)_2]_2$}-($PPh_3$)],[23a] [PdCl{$C_6H_3$-2,6-$[CH_2P(C_6F_5)_2]_2$}], and [Pd-($NCCH_3$){$C_6H_3$-2,6-$[CH_2P(C_6F_5)_2]_2$}]$BF_4$ have also recently been described.[23b]

As part of our interest in fluorinated sulfur-containing ligands,[24] we have synthesized a series of SCS pincer-type ligands with several fluorinated substituents at the sulfur atoms.[25] In this paper, we report on the synthesis and characterization of the pincer-type dithioether ligands $C_6H_4$-1,3-$(CH_2SR_f)_2$ [$R_f$ = $C_6H_4F$-2 (**L1**), $C_6H_4F$-3 (**L2**), $C_6H_4F$-4 (**L3**), $C_6H_4(CF_3)$-2 (**L4**) $C_6H_4(CF_3)$-3 (**L5**), and $C_6H_4(CF_3)$-4 (**L6**)] and the corresponding $Pd^{II}$ complexes [PdCl(**Ln**)], **1** to **6**, and include the X-ray diffraction structures of $C_6H_4$-1,3-$(CH_2SC_6H_4F$-4$)_2$ (**L3**), [PdCl(SCS–$C_6H_4F$-2)] (**1**), [PdCl(SCS–$C_6H_4F$-3)] (**2**), [PdCl(SCS–$C_6H_4F$-4)] (**3**), [PdCl{SCS–$C_6H_4(CF_3)$-2}] (**4**), and [PdCl{SCS–$C_6H_4(CF_3)$-4}] (**6**).

## Results and Discussion

### SCS Pincer-Type Ligands

Lead fluorothiolates, $Pb(SR_f)_2$, react with $C_6H_4$-1,3-$(CH_2Br)_2$ to give the corresponding dithioether compounds $C_6H_4$-1,3-$(CH_2SR_f)_2$ [$R_f$ = $C_6H_4F$-2 (**L1**), $C_6H_4F$-3 (**L2**), $C_6H_4F$-4 (**L3**), $C_6H_4(CF_3)$-2 (**L4**), $C_6H_4(CF_3)$-3 (**L5**), and $C_6H_4(CF_3)$-4 (**L6**)] as clear dense oils (**L1**, **L2**, **L4**, and **L5**)

[a] División de Estudios de Postgrado, Facultad de Química, UNAM, Cd. Universitaria,
04510 México D. F., México
Fax: +52-56223724
E-mail: Torrens@servidor.unam.mx
[b] Department of Chemistry & Biochemistry, University of Windsor,
Windsor, Ontario N9B 3P4, Canada

 © 2006 Wiley-VCH Verlag GmbH & Co. KGaA, Weinheim 

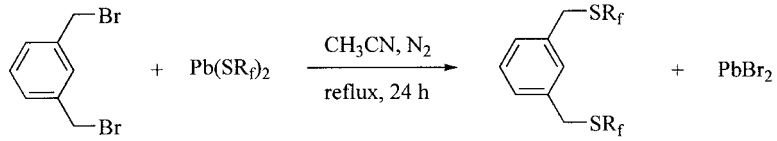


**L1** $R_f = C_6H_4F$-2
**L2** $R_f = C_6H_4F$-3
**L3** $R_f = C_6H_4F$-4
**L4** $R_f = C_6H_4(CF_3)$-2
**L5** $R_f = C_6H_4(CF_3)$-3
**L6** $R_f = C_6H_4(CF_3)$-4

Scheme 1. Synthesis of dithioether compounds **L1**–**L6**.

or crystalline white solids (**L3** and **L6**), in very good yields (see Scheme 1).

The mass spectra of all compounds show the signals corresponding to the molecular ion $[M]^+$ with significant intensities (75–90%). The $^1H$ NMR spectra of compounds **L1**–**L6** exhibit a singlet for the benzylic $CH_2$ protons. All other signals appear in the aromatic region as multiplets. The $^{13}C$ NMR spectra show quartets for the carbon atoms of the $CF_3$ groups, whereas the signals for all aromatic carbon atoms with fluorine atoms appear as doublets as a result of their magnetic coupling with the fluorine nuclei. The remaining signals have been assigned with the aid of two-dimensional HETCOR experiments. As expected, the $^{19}F$ NMR spectra for all compounds show only one signal. IR, $^1H$ and $^{19}F$ NMR spectroscopy as well as EI-MS data (reported in the Experimental Section) confirm the identity of each ligand.

The X-ray structure of $C_6H_4$-1,3-$(CH_2SC_6H_4F$-4$)_2$ (**L3**) is shown in Figure 1 and Figure 2, and the principal bond lengths and angles are reported in Table 1. The solid-state structure analysis of compound **L3** corresponds to the results obtained from $^1H$, $^{13}C$, and $^{19}F$ NMR spectroscopy, observed in solution.

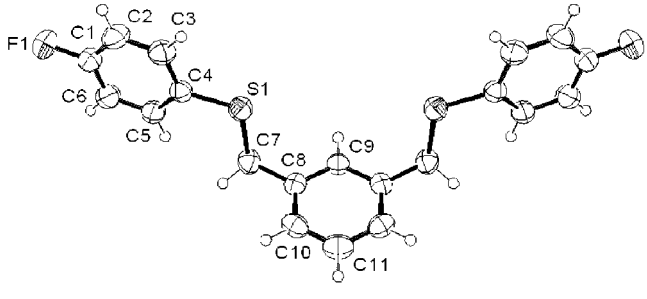


Figure 1. ORTEP drawing of compound $C_6H_4$-1,3-$(CH_2SC_6H_4F$-4$)_2$ (**L3**).

In contrast with the structure of $C_6H_4$-1,3-$(CH_2SC_6F_5)_2$,[25] in which the $SR_f$ groups are positioned on opposite sides of, and almost parallel to, the central aromatic ring, the molecular structure of **L3** has a *syn* configuration where the sulfur substituents point in the same direction as and are almost perpendicular to the central aromatic ring.

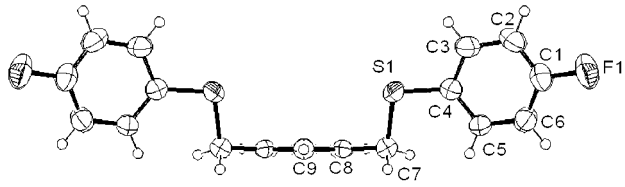


Figure 2. ORTEP drawing of compound **L3**, view along the C9–C11 axis.

Table 1. Selected bond lengths [Å] and angles [°] for compound $C_6H_4$-1,3-$(CH_2SC_6H_4F$-4$)_2$ (**L3**).

| Bond | Length | Atoms | Angle |
|---|---|---|---|
| S(1)–C(4) | 1.770(3) | C(4)–S(1)–C(7) | 104.26(12) |
| S(1)–C(7) | 1.809(3) | C(3)–C(4)–S(1) | 116.3(2) |
| C(9)–C(8) | 1.389(3) | C(5)–C(4)–S(1) | 125.2(2) |
| C(8)–C(10) | 1.383(3) | C(8)–C(7)–S(1) | 106.84(17) |
| C(10)–C(11) | 1.376(3) | C(9)–C(8)–C(7) | 121.1(2) |
| C(4)–C(3) | 1.389(4) | C(10)–C(8)–C(7) | 120.2(2) |
| C(4)–C(5) | 1.379(3) | C(5)–C(4)–C(3) | 118.5(3) |
| C(5)–C(6) | 1.380(4) | C(1)–C(6)–C(5) | 119.1(3) |
| C(6)–C(1) | 1.355(4) | C(1)–C(2)–C(3) | 118.5(3) |
| C(1)–C(2) | 1.366(4) | C(6)–C(1)–C(2) | 122.2(3) |
| C(3)–C(2) | 1.372(4) | F(1)–C(1)–C(2) | 118.8(3) |
| F(1)–C(1) | 1.355(3) | F(1)–C(1)–C(6) | 119.0(3) |
| | | C(10)–C(8)–C(9) | 118.8(2) |

## Pincer-Type Palladacycles

In our experiments, the reaction of the highly fluorinated pincer-type ligands $C_6H_4$-1,3-$(CH_2SC_6F_5)_2$ or $C_6H_4$-1,3-$(CH_2SC_6HF_4$-4$)_2$[25] with either $[PdCl_2(NCCH_3)_2]$ or $[Pd(NCCH_3)_4](BF_4)_2$ failed to produce the expected palladacycle derivatives. $SC_6F_5$ or $SC_6HF_4$-4 are much poorer donors than the corresponding protioaryl systems and, in contrast to phosphanes, they are not considered to be particularly good π acceptors.[26] Both of these effects contribute to a weaker S–Pd bond than the competing Pd–$NCCH_3$ interactions and prevent the formation of the Pd pincer-type compounds. This lack of reactivity emphasizes the importance of sulfur coordination as a preliminary step to C–Pd bond formation.

In contrast, the reaction of ligands **L1**–**L6** with $[PdCl_2(NCCH_3)_2]$ yielded the corresponding SCS pallada-

 © 2006 Wiley-VCH Verlag GmbH & Co. KGaA, Weinheim 

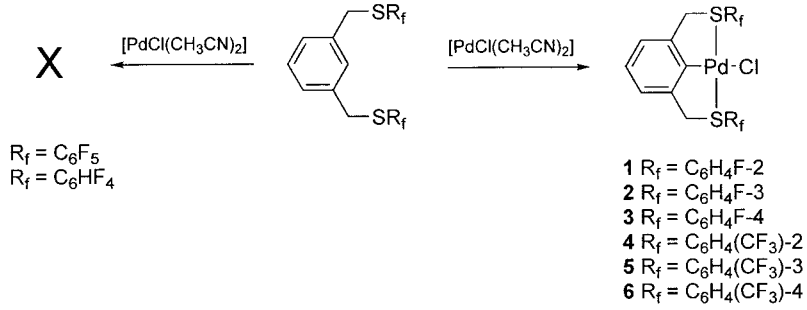


Scheme 2. Synthesis of palladium compounds **1**–**6**.

cycle compounds shown below as air-stable, yellow, crystalline solids. The yields are noticeably different for compounds bearing monofluorinated rings (**1**: 96, **2**: 81, **3**: 68%) from those with the bulkier $C_6H_4CF_3$ moiety (**4**: 79, **5**: 36, **6**: 44%), probably because they are influenced by steric factors (Scheme 2).

The $^1H$ NMR spectra of compounds **1**–**6** in $CD_3CN$ show a broad singlet for the $CH_2SR_f$ protons in the $\delta \approx$ 4.2–4.7 ppm range, probably because of a combination of *syn–anti* isomer exchange and the conformational interconversion of the $Pd^{II}$-containing five-membered rings.[27] The signal for the proton at ca. 7 ppm (C1–H) is absent, indicating complete cyclopalladation. With the exception of compound **4**, for which the low solubility precluded its measurement, the C1 shielding, as a result of cyclopalladation for the rest of the complexes, is also diagnostic of palladation at C1. The ($\delta^{13}$C1–H – $\delta^{13}$C1–Pd) values are as follows: **1** 28.29; **2** 30.74; **3** 33.57; **5** 30.37; and **6** 30.91 ppm. Likewise, the parameters defined as $\Delta_{Ln} = \delta^{13}C1 - \delta^{13}C4$ for the ligands and $\Delta_n = \delta^{13}C1 - \delta^{13}C4$ for the palladium complexes have the following values: $\Delta_{L1} = 0.74$, $\Delta_1 = 34.08$; $\Delta_{L2} = 0.57$, $\Delta_2 = 35.86$; $\Delta_{L3} = 0.87$, $\Delta_3 = 37.09$; $\Delta_{L5} = 0.63$, $\Delta_5 = 35.3$; and $\Delta_{L6} = 0.44$, $\Delta_6 = 35.87$ ppm.

$^{19}F\{^1H\}$ NMR spectra of compounds **1**–**3** and **4**–**6** exhibit a single, sharp resonance in the fluoro-aromatic region (–108.89, –113.69, –114.6 ppm) or in the $CF_3$-aromatic region (–56.56, –62.99, –62.60 ppm), respectively. Thus, isomers arising from substituent orientation relative to the square plane are not detected, which suggests that, in these complexes, sulfur inversion is either absent or faster than the NMR time scale. Palladium complexes of related thioethers exhibit relatively low energies for the process involving the inversion of configuration at the sulfur atoms ($\Delta E \approx 50$–$70$ kJ mol$^{-1}$), which is probably also true in these cases.[28]

## Molecular Structures

An X-ray structural study of compounds **1**–**3** provided solid-state evidence verifying the solution results and confirming, for all cases, the terdentate-binding mode of the SCS ligands. ORTEP drawings of [PdCl(SCS–$C_6H_4$F-2)] (**1**), [PdCl(SCS–$C_6H_4$F-3)] (**2**), and [PdCl(SCS–$C_6H_4$F-4)] (**3**) are shown in Figure 3, Figure 4 and Figure 5, respectively, and selected bond lengths and angles are reported in Table 2.

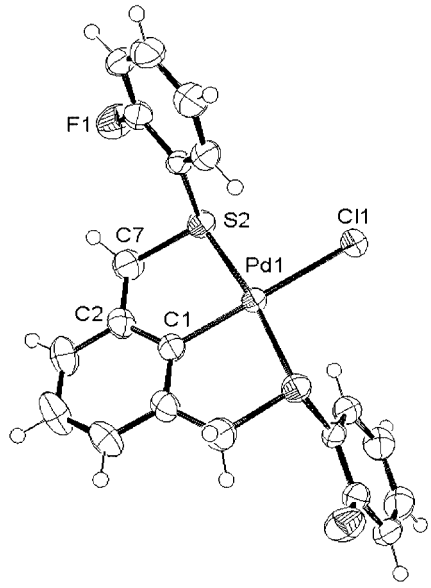


Figure 3. ORTEP drawing of compound [PdCl(SCS–$C_6H_4$F-2)] (**1**).

The Pd atoms are in slightly distorted square-planar environments: S(1)–Pd(1)–S(2), **1** 171.94(6); **2** 170.84(3); **3** 170.28(2)° and Cl(1)–Pd(1)–C(1), **1** 180.00(1); **2** 177.83(10); **3** 179.03(7)°. The bonding parameters of Pd are very similar to those observed for the complexes [PdCl{2,6-$C_6H_3$-($CH_2S$*t*Bu)$_2$}],[29] Pd–S 2.308(2); Pd(1)–Cl(1) 2.406(3); and Pd–C(1) 1.998(11) Å; [PdCl{2,3,5,6-$C_6H$-($CH_2S$*t*Bu)$_4$}],[19f] Pd–S(1) 2.297(3); Pd(1)–S(2) 2.302(3); Pd(1)–Cl(1) 2.408(3); Pd–C(1) 1.994(9) Å; and [Pd{4-(*n*BuO)-2,6-$C_6H_2$-($CH_2$SPh)$_2$}($NCCH_3$)]$^+$,[30] Pd–S(1) 2.2992(8); Pd–S(2) 2.2961(9); Pd–C(1) 1.975(2) Å.

The $C_6H_4$F-2 and $C_6H_4$F-3 groups attached to the metal-bound sulfur atoms in **1** and **2** are oriented in an *anti* fashion with respect to the square plane; a common conformation observed in these type of compounds,[19f,29–31] which allows for minimization of any steric repulsions between the aromatic rings. In contrast, the $C_6H_4$F-4 groups attached to the metal-bound sulfur atoms in **3** are oriented in a *syn* fashion with respect to the square plane; this allows for maximization of intermolecular aromatic π-stacking inter-

 © 2006 Wiley-VCH Verlag GmbH & Co. KGaA, Weinheim 

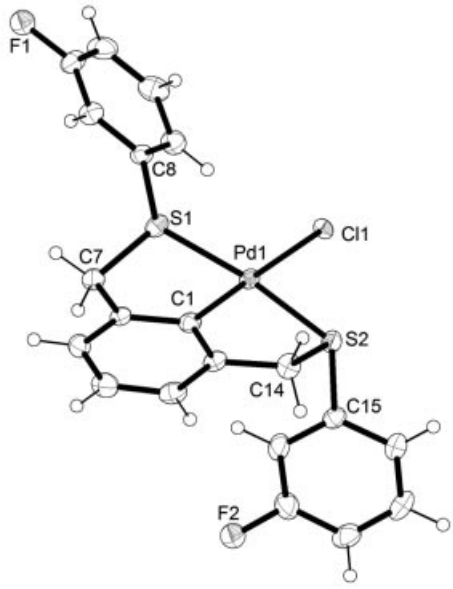


Figure 4. ORTEP drawing of compound [PdCl(SCS–$C_6H_4$F-3)] (**2**).

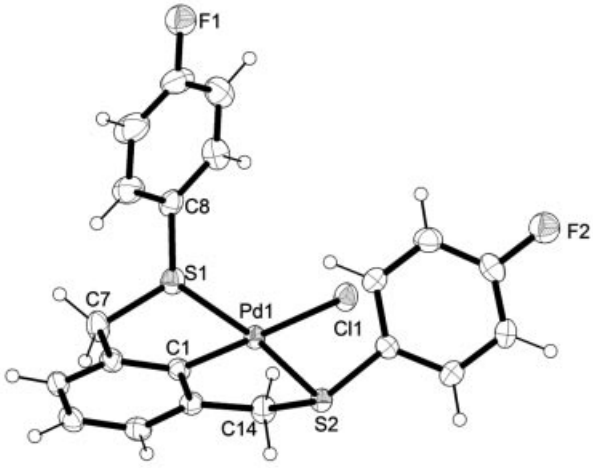


Figure 5. ORTEP drawing of compound [PdCl(SCS–$C_6H_4$F-4)] (**3**).

Table 2. Selected bond lengths [Å] and angles [°] with estimated standard deviations for complexes **1**, **2**, and **3**.

| Bond | **1** | **2** | **3** |
|---|---|---|---|
| Pd1–C1 | 1.994(7) | 1.968(4) | 1.979(2) |
| Pd1–S1 | 2.3021(10) | 2.2913(9) | 2.2970(6) |
| Pd1–S2 | 2.3021(10) | 2.3040(9) | 2.2842(6) |
| Pd1–Cl1 | 2.404(2) | 2.4284(8) | 2.3943(6) |
| S1–C7 | 1.836(5) | 1.828(4) | 1.820(2) |
| S1–C8 | 1.775(3) | 1.786(4) | 1.788(2) |
| S2–C14 | 1.836(5) | 1.826(4) | 1.837(2) |
| S2–C15 | 1.775(3) | 1.787(4) | 1.785(2) |
| Angle | | | |
| C1–Pd1–Cl1 | 180.00(1) | 177.83(10) | 179.01(7) |
| C1–Pd1–S1 | 85.97(3) | 85.28(11) | 85.37(7) |
| C1–Pd1–S2 | 85.97(3) | 85.62(11) | 84.91(7) |
| S1–Pd1–S2 | 171.94(6) | 170.84(3) | 170.28(2) |
| C7–S1–C8 | 103.7(2) | 98.04(17) | 104.38(11) |
| C14–S2–C15 | 103.7(2) | 101.30(17) | 103.41(11) |

actions between the metalated rings in adjacent molecules at ca. 3.5 Å (see Figure 6). This positive interaction probably compensates any losses derived from steric repulsions that arise as a result of the changing from an *anti* to a *syn* conformation.

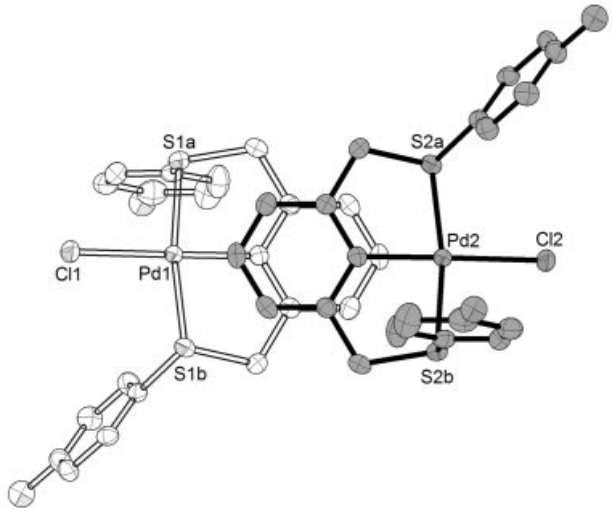


Figure 6. ORTEP drawing of compound **3** showing the aromatic π-stacking interactions between adjacent molecules (hydrogen atoms are omitted for clarity).

The X-ray diffraction molecular structure of compounds [PdCl{SCS–$C_6H_4(CF_3)$-2}] (**4**) and [PdCl{SCS–$C_6H_4(CF_3)$-4}] (**6**) are shown in Figure 7 and Figure 8, respectively and selected bond lengths and angles are reported in Table 3.

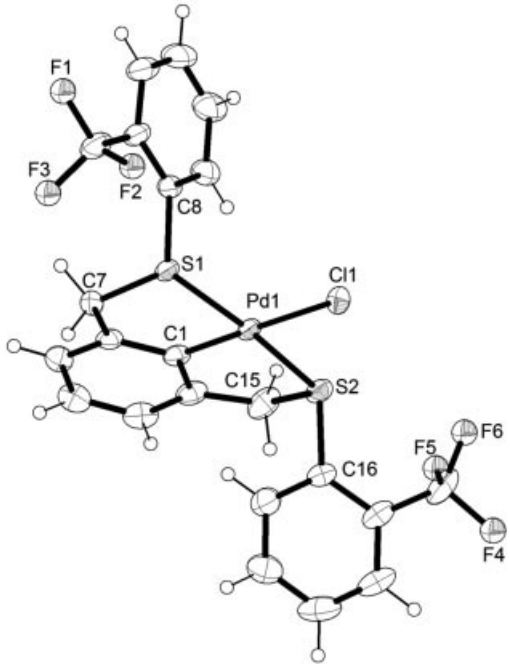


Figure 7. ORTEP drawing of compound [PdCl{SCS–$C_6H_4(CF_3)$-2}] (**4**).

In compounds **4** and **6**, the Pd atoms are also in a slightly distorted square-planar environment: S(1)–Pd(1)–S(2), **4**

 © 2006 Wiley-VCH Verlag GmbH & Co. KGaA, Weinheim 

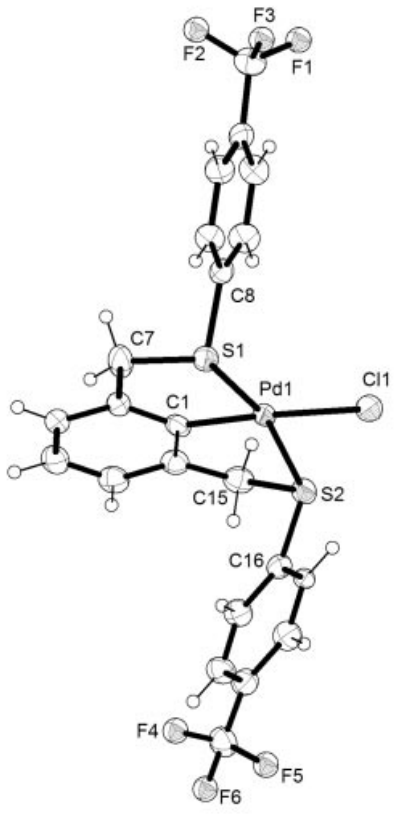


Figure 8. ORTEP drawing of compound [PdCl{SCS–$C_6H_4(CF_3)$-4}] (**6**).

Table 3. Selected bond lengths [Å] and angles [°] with estimated standard deviations for complexes **4** and **6**.

| Bond | **4** | **6** |
|---|---|---|
| Pd1–C1 | 1.983(3) | 1.982(4) |
| Pd1–S1 | 2.3044(13) | 2.2767(13) |
| Pd1–S2 | 2.2915(12) | 2.3195(13) |
| Pd1–Cl1 | 2.3893(14) | 2.3929(13) |
| S1–C7 | 1.830(3) | 1.841(5) |
| S1–C8 | 1.786(3) | 1.787(4) |
| S2–C15 | 1.830(3) | 1.815(5) |
| S2–C16 | 1.792(3) | 1.795(5) |
| Angle | | |
| C1–Pd1–Cl1 | 178.46(7) | 176.82(13) |
| C1–Pd1–S1 | 85.47(8) | 85.43(14) |
| C1–Pd1–S2 | 86.11(8) | 85.38(14) |
| S1–Pd1–S2 | 171.54(2) | 165.99(4) |
| C7–S1–C8 | 101.41(12) | 101.4(2) |
| C15–S2–C16 | 100.07(13) | 102.8(2) |

171.54(2); **6** 165.99(4)° and Cl(1)–Pd(1)–C(1), **4** 178.46(7); **6** 176.82(13)°. The bonding parameters for Pd are comparable with those observed for complexes **1**–**3** and analogous compounds.[19f,29–31] The $C_6H_4(CF_3)$-*n* (*n* = 2 or 4) groups attached to the metal-bound sulfur atoms are oriented in an *anti* fashion with respect to the square plane, as is the case for **1** and **2**.

## Summary and Conclusions

Pincer-type ligands of the SCS class can be prepared with partially fluorinated aromatic substituents. However, only those with a single F or $CF_3$ group will undergo facile palladation reactions to give the corresponding palladacycle. When the number of F atoms is increased, the resulting electronic effect on the S donor is such that coordination to palladium is too weak to allow for metallation to occur.

The solid-state structures show no unusual steric effects that would prevent these complexes from being used in a variety of catalytic reactions. We are currently testing these complexes as catalysts for the Suzuki coupling of aromatic groups. The results showing the effect of these electron-withdrawing substituted SCS pincers will be reported in due course.

## Experimental Section

**General:** All reactions were carried out under inert conditions using conventional Schlenk glassware. The solvents were dried by using established procedures and distilled under nitrogen immediately prior to use. TLC (Merck, $2 \times 5$ cm$^2$ Kieselgel 60 F254) was used to monitor the progress of the reaction under study with hexane/ethyl acetate (9:1) as the eluent. The IR spectra were measured with a Nicolet Avatar FT-IR spectrometer. $^1$H-, $^{13}$C-, and $^{19}$F NMR spectra were recorded with a Varian Unity Inova 300 spectrometer operating at 300 MHz. Chemical shifts are relative to TMS $\delta = 0$ ($^1$H, $^{13}$C) and $CFCl_3$ $\delta = 0$ ($^{19}$F) using $CD_3CN$ as the solvent. Electron impact mass spectra were recorded with a Jeol JMSSX102A mass spectrometer. Elemental analyses were determined using a Fisons EA1108 instrument. The starting material 1,3-bis(bromomethyl)benzene was obtained from Aldrich Chemical Co. and used without further purification. $C_6H_3$-1,3-$(CH_2SC_6F_5)_2$, $C_6H_3$-1,3-$(CH_2SC_6HF_4$-4$)_2$,[25] and $Pb(SR_f)_2$[32] ($R_f$ = $C_6H_4$F-2, $C_6H_4$F-3, and $C_6H_4$F-4) were prepared according to published procedures.

**Preparation of Compounds L1–L6:** $C_6H_4$-1,3-$(CH_2SC_6H_4F$-*n*$)_2$ (**L1**–**L3**) and $C_6H_4$-1,3-$[CH_2SC_6H_4(CF_3)$-*n*$]_2$ (**L4**–**L6**).

In all reactions, stoichiometric quantities of reactants were used, and since all preparations were similar, only a typical procedure is described.

$Pb(SC_6H_4F$-*n*$)_2$ or $Pb[SC_6H_4(CF_3)$-*n*$]_2$ (0.41 mmol) was added to a mixture of 1,3-bis(bromomethyl)benzene (0.113 g, 0.41 mmol) in acetonitrile (30 mL). The stirred mixture was maintained under reflux for 24 h. After this time, $PbBr_2$ was filtered off, the solvent was removed under vacuum, and the residue purified by column chromatography (silica gel; hexane/ethyl acetate 9:1).

Spectroscopic parameters follow the numbering scheme shown in the following diagram.

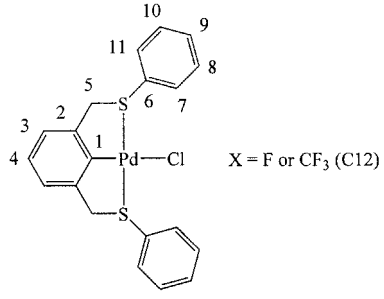


 © 2006 Wiley-VCH Verlag GmbH & Co. KGaA, Weinheim 

**$C_6H_4$-1,3-$(CH_2SC_6H_4F$-2)$_2$ (L1):** Colorless oil; yield; 0.141 g, 92%. IR (KBr): $\tilde{\nu}$ = 3030, 2922, 1593, 1472, 1220, 1260 cm$^{-1}$. EI-MS: *m*/*z* (%) = 358 [M$^+$] (90), 231 (100), 104 (45). $^1$H NMR (299.69 MHz, $CD_3CN$): $\delta$ = 4.09 (s, 4 H, 5-H), 7.08 (m, 7 H, 3-H, 4-H, 8-H, 11-H), 7.22 (m, 5 H, 1-H, 9-H, 10-H) ppm. $^{13}C\{^1H\}$ NMR (75.36 MHz, $CD_3CN$): $\delta$ = 37.5 (C-5), 116.5 (d, $^2J_{C,F}$ = 22.7 Hz, C-8), 123.7 (d, $^2J_{C,F}$ = 17.7 Hz, C-6), 125.8 (d, $^3J_{C,F}$ = 3.5 Hz, C-11), 128.8 (C-3), 129.6 (C-4), 129.8 (d, $^3J_{C,F}$ = 8.0 Hz, C-9), 130.3 (C-1), 133.2 (d, $^4J_{C,F}$ = 2.9 Hz, C-10), 138.8 (C-2), 162.1 (d, $J_{C,F}$ = 242.6 Hz, C-7) ppm. $^{19}$F NMR (281.96 MHz, $CD_3CN$): $\delta$ = –108.89 (m, $^3J_{F,H}$ = 9.59, $^4J_{F,H}$ = 6.99, $^5J_{F,H}$ = 4.82, $^4J_{F,H}$ = 0.13 Hz) ppm.

**$C_6H_4$-1,3-$(CH_2SC_6H_4F$-3)$_2$ (L2):** Colorless oil; yield: 0.138 g, 90%. IR (KBr): $\tilde{\nu}$ = 3060, 2923, 1598, 1473, 1263, 1215 cm$^{-1}$. EI-MS: *m*/*z* (%) = 358 [M$^+$] (75), 231 (100), 104 (65). $^1$H NMR (299.69 MHz, $CD_3CN$): $\delta$ = 4.15 (s, 4 H, 5-H), 6.90 (m, 2 H, 9-H), 7.05 (m, 4 H, 7-H, 11-H), 7.35 (m, 6 H, 1-H, 3-H, 4-H, 10-H) ppm. $^{13}C\{^1H\}$ NMR (75.4 MHz, $CD_3CN$): $\delta$ = 38.1 (C-5), 113.8 (d, $^2J_{C,F}$ = 21.5 Hz, C-9), 116.2 (d, $^2J_{C,F}$ = 23.1 Hz, C-7), 125.5 (d, $^4J_{C,F}$ = 3.0 Hz, C-11), 128.9 (C-3), 129.7 (C-4), 130.3 (C-1), 131.6 (d, $^3J_{C,F}$ = 8.5 Hz, C-10), 138.7 (C-2), 140.0 (d, $^3J_{C,F}$ = 8.0 Hz, C-6), 163.8 (d, $J_{C,F}$ = 244.6 Hz, C-8) ppm. $^{19}$F NMR (281.96 MHz, $CD_3CN$): $\delta$ = –113.69 (m, $^3J_{F,H}$ = 9.54, $^3J_{F,H}$ = 6.16, $^4J_{F,H}$ = 9.00, $^5J_{F,H}$ = 0.96 Hz) ppm.

**$C_6H_4$-1,3-$(CH_2SC_6H_4F$-4)$_2$ (L3):** White microcrystalline powder; yield: 0.145 g, 95%. M.p. 51–52 °C. IR (KBr): $\tilde{\nu}$ = 2918, 1595, 1490, 1239, 822 cm$^{-1}$. EI-MS: *m*/*z* (%) = 358 [M$^+$] (85), 231 (100), 104 (45). $^1$H NMR (299.69 MHz, $CD_3CN$): $\delta$ = 4.04 (s, 4 H, 5-H), 7.00 (m, 4 H, 8-H, 10-H), 7.13 (m, 4 H, 1-H, 3-H, 4-H), 7.28 (m, 4 H, 7-H, 11-H) ppm. $^{13}C\{^1H\}$ NMR (75.36 MHz, $CD_3CN$): $\delta$ = 39.8 (C-5), 116.9 (d, $^2J_{C,F}$ = 21.7 Hz, C-8, C-10), 128.7 (C-3), 129.5 (C-1), 130.4 (C-4), 132.1 (d, $^4J_{C,F}$ = 2.8 Hz, C-6), 133.7 (d, $^3J_{C,F}$ = 8.0 Hz, C-7, C-11), 139.1 (C-2), 162.8 (d, $J_{C,F}$ = 244.7 Hz, C-9) ppm. $^{19}$F NMR (281.96 MHz, $CD_3CN$): $\delta$ = –114.6 (m, $^4J_{F,H}$ = 5.21, $^3J_{F,H}$ = 9.02 Hz) ppm. $C_{20}H_{16}F_2S_2$ (358.5): calcd. C 67.02, H, 4.50, S 17.86; found C 66.94, H 4.45, S 17.23.

**$C_6H_4$-1,3-$[CH_2SC_6H_4(CF_3)$-2$]_2$ (L4):** Yellowish oil; yield: 0.158 g, 80.4%. IR (KBr): $\tilde{\nu}$ = 1312, 1112, 1172, 1034, 760, 1258, 1440, 1592 cm$^{-1}$. EI-MS: *m*/*z* (%) = 458 [M$^+$] (40), 281 (100), 104 (30). $^1$H NMR (299.69 MHz, $CD_3CN$): $\delta$ = 4.20 (s, 4 H, 5-H), 7.22 (m, 3 H, 3-H, 4-H), 7.32 (m, 3 H, 1-H, 9-H), 7.48 (m, 4 H, 10-H, 11-H), 7.66 (m, 2 H, 8-H) ppm. $^{13}C\{^1H\}$ NMR (75.36 MHz, $CD_3CN$): $\delta$ = 38.8 (C-5), 127.3 (C-9), 127.8 (q, $^3J_{C,F}$ = 5.8 Hz, C-8), 129.1 (C-3), 129.8 (C-4), 130.6 (C-1), 132.2 (C-11), 133.5 (C-10), 136.6 (C-6), 138.2 (C-2), 129.6 (q, $^2J_{C,F}$ = 30.2 Hz, C-7), 125.2 (q, $J_{C,F}$ = 273.4 Hz, C-12) ppm. $^{19}$F NMR (281.96 MHz, $CD_3CN$): $\delta$ = –56.56 ppm.

**$C_6H_4$-1,3-$[CH_2SC_6H_4(CF_3)$-3$]_2$ (L5):** Yellowish oil; yield: 0.155 g,79.3%. IR (KBr): $\tilde{\nu}$ = 1322, 1124, 1165, 1072, 695, 793, 711, 1425 cm$^{-1}$. EI-MS: *m*/*z* (%) = 458 [M$^+$] (20), 281 (75), 104 (70). $^1$H NMR (299.69 MHz, $CD_3CN$): $\delta$ = 4.18 (s, 4 H, 5-H), 7.28 (m, 3 H, 3-H, 4-H), 7.33 (m, 1 H, 1-H), 7.48 (m, 8 H, 7-H, 9-H, 10-H, 11-H) ppm. $^{13}C\{^1H\}$ NMR (75.36 MHz, $CD_3CN$): $\delta$ = 38.1 (C-5), 123.7 (q, $^3J_{C,F}$ = 4.0 Hz, C-9), 126.1 (q, $^3J_{C,F}$ = 3.7 Hz, C-7), 128.9 (C-3), 129.7 (C-4), 130.8 (C-1), 133.7 (C-10), 133.4 (C-11), 138.6 (C-2), 139.1 (C-6), 131.5 (q, $^2J_{C,F}$ = 32.3 Hz, C-8), 125.1 (q, $J_{C,F}$ = 272.4 Hz, C-12) ppm. $^{19}$F NMR (281.96 MHz, $CD_3CN$): $\delta$ = –62.99 ppm.

**$C_6H_4$-1,3-$[CH_2SC_6H_4(CF_3)$-4$]_2$ (L6):** White microcrystalline powder; yield: 0.166 g, 85%. M.p. 61–63 °C. IR (KBr): $\tilde{\nu}$ = 1327, 1121, 1095, 1063, 1164, 1605, 823, 1013 cm$^{-1}$. EI-MS: *m*/*z* (%) = 458 [M$^+$] (30), 281 (100), 104 (25). $^1$H NMR (299.69 MHz, $CD_3CN$): $\delta$ = 4.21 (s, 4 H, 5-H), 7.26 (m, 3 H, 3-H, 4-H), 7.40 (m, 5 H, 1-H, 8-H, 10-H), 7.52 (m, 4 H, 7-H, 11-H) ppm. $^{13}C\{^1H\}$ NMR (75.36 MHz, $CD_3CN$): $\delta$ = 37.3 (C-5), 129.0 (C-3), 129.9 (C-4), 130.4 (C-1), 138.4 (C-2), 143.5 (C-6), 126.6 (q, $^3J_{C,F}$ = 7.9 Hz, C-8, C-10), 128.7 (C-7, C-11), 125.5 (q, $J_{C,F}$ = 271.3 Hz, C-12), 127.9 (q, $^2J_{C,F}$ = 32.3 Hz, C-9) ppm. $^{19}$F NMR (281.96 MHz, $CD_3CN$): $\delta$ = –62.60 ppm.

**General Procedure for the Preparation of Palladium(II) Complexes 1–6:** Dichloropalladium(II) (0.216 g, 1.22 mmol) in acetonitrile (25 mL) was heated under reflux for 1 h. Silver tetrafluoroborate (0.495 g, 2.54 mmol) was added to this solution. Silver chloride was separated from the suspension by filtration through Celite. The ligand (**L1**–**L6**) (0.435 g, 1.22 mmol) was dissolved in warm acetonitrile (10 mL) and added to the filtrate. The solution immediately turned orange and was heated under reflux for 4 h. The reaction mixture turned yellow, and excess NaCl (0.189 g, 3.23 mmol) was added. The suspension was stirred overnight. The yellow precipitate was filtered off and washed three times with water and two times with ethanol. The products were obtained as yellow powders.

**[PdCl{$C_6H_3$-1,3-$(CH_2SC_6H_4F$-2)$_2$}] (1):** Yellow crystals; yield: 0.583 g, 96%. M.p. 187 °C. IR (KBr): $\tilde{\nu}$ = 750, 1470, 1449, 1221, 1262, 724, 818, 1061, 1029, 2900, 2976, 3046 cm$^{-1}$. EI-MS: *m*/*z* (%) = 500 [M + 1]$^+$ (5), 463 (60), 391 (40). $^1$H NMR (299.69 MHz, $CDCl_3$): $\delta$ = 4.65 (s, 4 H, 5-H), 7.18 (m, 4 H, 8-H, 11-H), 6.97 (m, 3 H, 3-H, 4-H), 7.45 (m, 2 H, 9-H), 8.28 (m, 2 H, 10-H) ppm. $^{13}C\{^1H\}$ NMR (75.36 MHz, $CDCl_3$): $\delta$ = 52.1 (C-5), 116.5 (d, $^2J_{C,F}$ = 21.7 Hz, C-8), 119.0 (d, $^2J_{C,F}$ = 16.1 Hz, C-6), 122.2 (C-3), 123.0 (d, $^3J_{C,F}$ = 8.2 Hz, C-9), 125.1 (d, $^3J_{C,F}$ = 3.8 Hz, C-11), 125.2 (C-4), 136.5 (C-10), 148.4 (C-2), 159.2 (C-1), 160.8 (d, $J_{C,F}$ = 251.1 Hz, C-7) ppm. $^{19}$F NMR (281.96 MHz, $CDCl_3$): $\delta$ = –106.31 ppm. $C_{20}H_{15}S_2F_2PdCl$ (499.3): calcd. C 48.11, H 3.03, S 12.84; found: C 48.30, H 3.36, S 13.01.

**[PdCl{$C_6H_3$-1,3-$(CH_2SC_6H_4F$-3)$_2$}] (2):** Yellow crystals; yield: 0.492 g, 81%. M.p. 165 °C. IR (KBr): $\tilde{\nu}$ = 727, 1472, 1214, 873, 1579, 749, 777, 1420, 674, 1264, 2922, 3053 cm$^{-1}$. EI-MS: *m*/*z* (%) = 500 [M + 1]$^+$ (5), 463 (70). $^1$H NMR (299.69 MHz, $CDCl_3$): $\delta$ = 4.62 (s, 4 H, 5-H), 7.04 (m, 5 H, 9-H, 3-H, 4-H), 7.34 (m, 2 H, 10-H), 7.51 (m, 2 H, 7-H), 7.61 (m, 2 H, 11-H) ppm. $^{13}C\{^1H\}$ NMR (75.36 MHz, $CDCl_3$): $\delta$ = 51.2 (C-5), 117.0 (d, $^2J_{C,F}$ = 21.2 Hz, C-9), 118.0 (d, $^2J_{C,F}$ = 24.2 Hz, C-7), 122.5 (C-3), 125.19 (C-4), 126.9 (d, $^4J_{C,F}$ = 3.0 Hz, C-11), 131.1 (d, $^3J_{C,F}$ = 8.1 Hz, C-10), 133.7 (d, $^3J_{C,F}$ = 8.0 Hz, C-6), 149.0 (C-2), 161.0 (C-1), 162. 5 (d, $J_{C,F}$ = 251.6 Hz, C-8) ppm. $^{19}$F NMR (281.96 MHz, $CDCl_3$): $\delta$ = –109.8 ppm. $C_{20}H_{15}S_2F_2PdCl$ (499.3): calcd. C 48.11, H 3.03, S 12.84; found C 48.05, H 3.17, S 13.01.

**[PdCl{$C_6H_3$-1,3-$(CH_2SC_6H_4F$-4)$_2$}] (3):** Yellow crystals; yield: 0.413 g, 68%. M.p. 198 °C. IR (KBr): $\tilde{\nu}$ = 1489, 1218, 1153, 826, 816, 843, 1415, 772, 3058, 298, 3085 cm$^{-1}$. EI-MS: *m*/*z* (%) = 500 [M + 1]$^+$ (10), 463 (100). $^1$H NMR (299.69 MHz, $CDCl_3$): $\delta$ = 4.67 (s, 4 H, 5-H), 7.00 (m, 3 H, 3-H, 4-H), 7.186 (m, 4 H, 8-H, 10-H), 7.94 (m, 4 H, 7-H, 11-H) ppm. $^{13}C\{^1H\}$ NMR (75.36 MHz, $CDCl_3$): $\delta$ = 53.0 (C-5), 117.6 (d, $^2J_{C,F}$ = 22.8 Hz, C-8, C-10), 123.5 (C-3), 126.0 (C-4), 129.0 (d, $^4J_{C,F}$ = 3.0 Hz, C-6), 135.3 (d, $^3J_{C,F}$ = 9.1 Hz, C-7, C-11), 150.6 (C-2), 163.1 (C-1), 164.5 (d, $J_{C,F}$ = 248.1 Hz, C-9) ppm. $^{19}$F NMR (281.96 MHz, $CDCl_3$): $\delta$ = –107.1 ppm. $C_{20}H_{15}S_2F_2PdCl$ (499.3): calcd. C 48.11, H 3.03, S 12.84; found C 44.90, H 3.03, S 12.27.

**[PdCl{SCS–$C_6H_4(CF_3)$-2}] (4):** Yellow crystals; yield: 0.450 g, 79%. M.p. 130 °C (dec). IR (KBr): $\tilde{\nu}$ = 1310, 1181, 1117, 1029, 770, 1092, 1265 cm$^{-1}$. $^1$H NMR (299.69 MHz, $CDCl_3$): $\delta$ = 4.54 (s, 4 H, 5-H), 7.03 (m, 3 H, 3-H, 4-H), 7.69 (m, 6 H, 8-H, 9-H, 11-H), 8.75 (m, 2 H, 10-H) ppm. $^{13}C\{^1H\}$ NMR (75.36 MHz, $CDCl_3$): $\delta$ = 55.7 (C-

 © 2006 Wiley-VCH Verlag GmbH & Co. KGaA, Weinheim 

Table 4. Crystallographic data, solution and refinement parameters for single crystal structure determinations of compounds **L3**, **1**, **2**, **3**, **4**, and **6**.

| | **L3** | **1** | **2** | **3** | **4** | **6** |
|---|---|---|---|---|---|---|
| Formula | $C_{20}H_{16}F_2S_2$ | $C_{20}H_{15}ClF_2PdS_2$ | $C_{20}H_{15}ClF_2PdS_2$ | $C_{20}H_{15}ClF_2PdS_2$ | $C_{22}H_{15}ClF_6PdS_2$ | $C_{22}H_{15}ClF_6PdS_2$ |
| Formula mass | 358.47 | 499.29 | 499.29 | 499.29 | 599.31 | 599.31 |
| Crystal system | orthorhombic | orthorhombic | triclinic | monoclinic | monoclinic | monoclinic |
| Space group | *P*nma | *F*dd2 | $P\bar{1}$ | $P2_1/n$ | $P2_1/c$ | $P2_1/c$ |
| $T$ [K] | 298(2) | 298(2) | 173(2) | 173(2) | 173(2) | 173(2) |
| $a$ [Å] | 6.868(5) | 35.219(5) | 8.5669(5) | 9.2552(11) | 17.173(12) | 8.371(3) |
| $b$ [Å] | 33.026(5) | 9.817(5) | 9.5228(6) | 18.417(2) | 8.809(6) | 27.069(8) |
| $c$ [Å] | 7.623(5) | 10.920(5) | 11.8512(7) | 11.2976(13) | 14.689(10) | 9.899(3) |
| $\alpha$ [°] | | | 96.153(1) | | | |
| $\beta$ [°] | | | 100.303(1) | 103.993(1) | 98.143(7) | 107.945(3) |
| $\gamma$ [°] | | | 103.385(1) | | | |
| $V$ [Å$^3$] | 1729.1(2) | 3776(3) | 914.2(1) | 1868.6(4) | 2200(3) | 2134.0(1) |
| $Z$ | 8 | 8 | 2 | 4 | 4 | 4 |
| $D_{calcd.}$ [g cm$^{-3}$] | 1.377 | 1.757 | 1.814 | 1.775 | 1.810 | 1.865 |
| $\mu$ [mm$^{-1}$] | 0.325 | 1.365 | 1.410 | 1.380 | 1.214 | 1.251 |
| reflections collected | 3154 | 1813 | 7260 | 17746 | 19198 | 20216 |
| unique reflections | 2331 | 1580 | 3201 | 3291 | 3880 | 3752 |
| $R_1/R_2w$ $[I > 2\sigma(I)]$[a] | 0.0532/0.0978 | 0.0270/0.0604 | 0.0329/0.0971 | 0.0207/0.0595 | 0.0246/0.0712 | 0.0442/0.1057 |
| $R_1/R_2w$ (all data)[b] | 0.1391/0.1229 | 0.0322/0.0622 | 0.0335/0.0976 | 0.245/0.0619 | 0.0275/0.0770 | 0.0474/0.1078 |
| GoF on $F^2$ | 0.954 | 1.066 | 1.089 | 1.026 | 1.085 | 1.088 |
| Parameters/restrains | 112/0 | 120/1 | 235/0 | 235/0 | 289/0 | 289/0 |
| Min./max. residual density [e Å$^{-3}$] | 0.275/0.259 | –0.390/0.376 | –1.13/1.41 | –0.22/0.40 | –0.52/0.55 | –1.31/1.66 |

[a] $R_1 = \Sigma||F_o| - |F_c|| / \Sigma|F_o|$;. [b] $R_2w = \{\Sigma[w(F_o^2 - F_c^2)^2] / \Sigma[w(F_o^2)^2]\}^{1/2}$, where $w = q[\sigma^2(F_o^2) + (aP)^2 + bP]^{-1}$.

5), 122.4 (C-3), 125.0 (C-4), 125.6 (C-9), 126.9 (C-8), 131.3 (C-11), 133.5 (C-10), 147.8 (C-2) ppm. $^{19}$F NMR (281.96 MHz, $CDCl_3$): $\delta$ = –59.09 ppm.

**[PdCl{SCS–C$_6$H$_4$(CF$_3$)-3}] (5):** Yellow crystals; yield: 0.205 g, 36%. M.p. 194 °C. IR (KBr): $\tilde{\nu}$ = 1320, 1122, 1176, 1103, 1072, 692, 797, 769 cm$^{-1}$. FAB(+)-MS: *m*/*z* (%) = 598 [M$^+$] (2), 563 (100), 417 (10), 385 (8), 279 (20), 135 (10). $^1$H NMR (299.69 MHz, $CDCl_3$): $\delta$ = 4.67 (s, 4 H, 5-H), 7.05 (m, 3 H, 3-H, 4-H), 7.53 (t, $^3J_{H,H}$ = 7.8 Hz, 2 H, 10-H), 7.65 (d, $^3J_{H,H}$ = 7.8 Hz, 2 H, 9-H), 8.00 (s, 2 H, 7-H), 8.13 (d, $^3J_{H,H}$ = 8.1 Hz, 2 H, 11-H) ppm. $^{13}$C{$^1$H} NMR (75.36 MHz, $CDCl_3$): $\delta$ = 51.6 (C-5), 122.6 (C-3), 123.2 (q, $J_{C,F}$ = 273.2 Hz, C-12), 125.4 (C-4), 126.8 (q, $^3J_{C,F}$ = 3.7 Hz, C-9), 127.5 (q, $^3J_{C,F}$ = 3.7 Hz, C-7), 130.3 (C-10), 132.0 (q, $^2J_{C,F}$ = 33.2 Hz, C-8), 133.3 (C-6), 135.2 (C-11), 148.6 (C-2), 160.7 (C-1) ppm. $^{19}$F NMR (281.96 MHz, $CDCl_3$): $\delta$ = –63.16 ppm. $C_{22}H_{15}F_6S_2PdCl$ (599.3): calcd. C 44.09, H 2.52, S 10.7; found C 43.80, H 2.72, S 11.28.

**[PdCl{SCS–C$_6$H$_4$(CF$_3$)-4}] (6):** Yellow crystals; yield: 0.251 g, 44%. M.p. 230 °C. IR (KBr): $\tilde{\nu}$ = 1320, 1123, 1061, 1169, 1085, 1011, 838, 1604 cm$^{-1}$. FAB(+)-MS: *m*/*z* (%) = 598 [M$^+$] (2), 563 (100), 417 (10), 385 (8), 279 (25), 135 (10). $^1$H NMR (299.69 MHz, $CDCl_3$): $\delta$ = 4.66 (s, 4 H, 5-H), 7.07 (m, 3 H, 3-H, 3-H), 7.62 (d, $^3J_{H,H}$ = 8.4 Hz, 4 H, 8-H, 10-H), 7.91 (d, $^3J_{H,H}$ = 8.1 Hz, 4 H, 7-H7, 11-H) ppm. $^{13}$C{$^1$H} NMR (75.36 MHz, $CDCl_3$): $\delta$ = 50.3 (C-5), 122.7 (C-3), 123.4 (q, $J_{C,F}$ = 270.8 Hz, C-12), 125.4 (C-4), 126.6 (q, $^3J_{C,F}$ = 3.6 Hz, C-10, C-8), 128.8 (C-6), 130.8 (C-7, C-11), 131.6 (q, $^2J_{C,F}$ = 33.2 Hz, C-9), 148.8 (C-2), 161.3 (C-1) ppm. $^{19}$F NMR (281.96 MHz, $CDCl_3$): $\delta$ = –63.40 ppm.

**Crystal Data:** Crystallographic data, solution and refinement parameters for the single crystal structure determinations of compounds **L3**, **1**, **2**, **3**, **4**, and **6** are reported in Table 4. Single crystals of all compounds were obtained from slow evaporation of saturated acetonitrile solutions. X-ray diffraction data for compounds **L3** and **1** were collected at 298 K with a Siemens P4 automatic diffractometer and analyzed using graphite-monochromated Mo-$K_\alpha$ X-ray radiation ($\lambda$ = 0.71073 Å). X-ray diffraction data for compounds **2**, **3**, **4**, and **6** were collected at 173 K with a Bruker APEX CCD single crystal diffractometer with Mo-$K_\alpha$ X-ray radiation ($\lambda$ = 0.71073 Å). The structures were solved by direct methods using SHELXS 97–2.[33] Least-squares refinement based on $F^2$ was carried out by a full-matrix method with SHELXL 97–2.[33] All non-hydrogen atoms were refined with anisotropic thermal parameters. The location of hydrogen atoms was generated geometrically and included in the refinement with an isotropic fixed thermal parameter using a "riding" model. Neutral atom scattering factors and anomalous dispersion corrections were taken from International Tables for Crystallography.[34] Molecular structure drawings were generated using ORTEP3 for Windows.[35]

CCDC-251029 (**L3**), -251028 (**1**), -254754 (**2**), -281816 (**3**), -281832 (**4**), and -281831 (**6**) contain the supplementary crystallographic data for this paper. These data can be obtained free of charge from The Cambridge Crystallographic Data Centre via www.ccdc.cam.ac.uk/data_request/cif.

## Acknowledgments

This work was supported by the CONACYT (Project 44494-Q) and DGAPA-UNAM (Project IN119305).

[1] a) T. Nabeshima, D. Nishida, S. Akine, T. Saiki, *Eur. J. Inorg. Chem.* **2004**, 3779–3782; b) P. Steenwinkel, R. A. Gossage, G. van Koten, *Chem. Eur. J.* **1998**, *4*, 759–762; c) J. Dupont, M. Pfeffer, J. Spencer, *Eur. J. Inorg. Chem.* **2001**, 1917–1927; d) M. E. van der Boom, D. Milstein, *Chem. Rev.* **2003**, *103*, 1759–1792.

[2] a) D. E. Bergbreiter, P. L. Osburn, Y. S. Liu, *J. Am. Chem. Soc.* **1999**, *121*, 9531–9538; b) I. P. Beletskaya, A. V. Chuchurjukin, H. P. Dijkstra, G. P. M. van Klink, G. van Koten, *Tetrahedron Lett.* **2000**, *41*, 1075–1079; c) R. B. Bedford, S. M. Draper, P. N. Scully, S. L. Welch, *New J. Chem.* **2000**, *24*, 745–747; d) H. P.

 © 2006 Wiley-VCH Verlag GmbH & Co. KGaA, Weinheim 

Dijkstra, N. Ronde, G. P. M. van Klink, D. Vogt, G. van Koten, *Adv. Synth. Catal.* **2003**, *345*, 364–369.
[3] T. J. Singleton, *Tetrahedron* **2003**, *59*, 1837–1857.
[4] M. Albrecht, G. van Koten, *Angew. Chem. Int. Ed.* **2001**, *40*, 3750–3781.
[5] D. E. Bergbreiter, P. L. Osburn, A. Wilson, E. M. Sink, *J. Am. Chem. Soc.* **2000**, *122*, 9058–9064.
[6] A. S. Gruber, D. Zim, G. Ebeling, A. L. Monteiro, J. Dupont, *Org. Lett.* **2000**, *2*, 1287–1290.
[7] D. Zim, A. S. Gruber, G. Ebeling, J. Dupont, A. L. Monteiro, *Org. Lett.* **2000**, *2*, 2881–2884.
[8] N. Hidetaka, O. Seiji, W. Yoshihito, *Organometallics* **2002**,*21*, 1674–1678.
[9] R. Gimenez, T. J. Swager, *Mol. Catal. A: Chem.* **2001**, *166*, 265–273.
[10] J. Kjellgren, H. Sundén, K. J. Szabó, *J. Am. Chem. Soc.* **2005**, *127*, 1787–1796.
[11] a) D. R. Evans, M. Huang, W. M. Seganish, J. C. Fettinger, T. L. Williams, *Organometallics* **2002**, *21*, 893–900; b) J. Dupont, N. Beydoun, M. Pfeffer, *J. Chem. Soc., Dalton Trans.* **1989**, 1715–1720.
[12] D. R. Evans, M. Huang, W. M. Seganish, E. W. Chege, Y. F. Lam, J. C. Fettinger, T. L. Williams, *Inorg. Chem.* **2002**, *41*, 2633–2641.
[13] C. H. M. Amijs, G. P. M. van Klink, M. Lutz, A. L. Spek, G. van Koten, *Organometallics* **2005**, *24*, 2944–2958.
[14] M. A. Hossain, S. Lucarini, D. Powell, K. Bowman-James, *Inorg. Chem.* **2004**, *43*, 7275–7277.
[15] H. J. van Manen, R. H. Fokkens, N. M. M. Nibbering, F. C. J. M. van Veggel, D. N. Reinhoudt, *J. Org. Chem.* **2001**, *66*, 4643–4650.
[16] J. M. Pollino, M. Weck, *Org. Lett.* **2002**, *4*, 753–756.
[17] A. Friggeri, H. J. van Manen, T. Auletta, X. M. Li, S. Zapotoczny, H. Schonherr, G. J. Vancso, J. Huskens, F. C. J. M. van Veggel, D. N. Reinhoudt, *J. Am. Chem. Soc.* **2001**, *123*, 6388–6395.
[18] B. M. J. M. Suijkerbuijk, M. Lutz, A. L. Spek, G. van Koten, R. J. M. K. Gebbink, *Org. Lett.* **2004**, *6*, 3023–3026.
[19] a) J. E. Kickham, S. J. Loeb, S. L. Murphy, *J. Am. Chem. Soc.* **1993**, *115*, 7031–7032; b) J. E. Kickham, S. J. Loeb, *Inorg. Chem.* **1994**, *33*, 4351–4359; c) J. E. Kickham, S. J. Loeb, *Inorg. Chem.* **1995**, *34*, 5656–5665; d) J. E. Kickham, S. J. Loeb, *Organometallics* **1995**, *14*, 3584–3587; e) J. R. Hall, S. J. Loeb, G. K. H. Shimizu, G. P. A. Yap, *Angew. Chem. Int. Ed.* **1998**, *37*, 121–123; f) S. J. Loeb, G. K. H. Shimizu, J. A. Wisner, *Organometallics* **1998**, *17*, 2324–2327; g) S. J. Loeb, S. L. Murphy, J. A. Wisner, *Crystal Eng.* **1999**, *2*, 27–36.
[20] M. H. P. Rietveld, D. M. Grove, G. van Koten, *New J. Chem.* **1997**, *21*, 751–771.
[21] a) H. Kleijn, J. T. B. H. Jastrzebski, R. A. Gossage, H. Kooijman, A. L. Spek, G. van Koten, *Tetrahedron* **1998**, *54*, 1145–1152; b) E. de Wolf, G. van Koten, B. J. Deelman, *Chem. Soc. Rev.* **1999**, *28*, 37–41; c) P. Dani, B. Richter, G. P. M. van Klink, G. van Koten, *Eur. J. Inorg. Chem.* **2001**, 125–131.
[22] D. P. Curran, K. Fischer, G. Moura-Letts, *Synlett* **2004**, *8*, 1379–1382.
[23] a) M. Gagliardo, P. A. Chase, M. Lutz, A. L. Spek, F. Hartl, R. W. A. Havenith, G. P. M. van Klink, G. van Koten, *Organometallics* **2005**, *24*, 4553–4557; b) P. A. Chase, M. Gagliardo, M. Lutz, A. L. Spek, G. P. M. van Klink, G. van Koten, *Organometallics* **2005**, *24*, 2016–2019.
[24] a) M. Arroyo, S. Bernès, J. Cerón, J. Rius, H. Torrens, *Inorg. Chem.* **2004**, *43*, 986–992; b) L. Villanueva, S. Bernès, H. Torrens, *Chem. Commun.* **2004**, 1942–1943.
[25] M. Arroyo, R. Cervantes, V. Gómez-Benítez, P. López, D. Morales-Morales, H. Torrens, *Synthesis* **2003**, *10*, 1565 –1568.
[26] S. I. Gorelsky, L. Basumallick, J. Vura-Weis, R. Sarangi, K. O. Hodgson, B. Hedman, K. Fujisawa, E. I. Solomon, *Inorg. Chem.* **2005**, *44*, 4947–4960.
[27] A. J. Canty, N. J. Minchin, *J. Chem. Soc., Dalton Trans.* **1987**, 1477–1483.
[28] E. W. Abel, S. K. Bhargava, K. G. Orrell, *Prog. Inorg. Chem.* **1984**, *32*, 1–118.
[29] J. Errington, W. S. McDonald, B. L. Shaw, *J. Chem. Soc., Dalton Trans.* **1980**, 2312–3214.
[30] H.-J. van Manen, K. Nakashima, S. Shinkai, H. Kooijman, A. L. Spek, F. C. J. M. Van Veggel, D. N. Reinnhoudt, *Eur. J. Inorg. Chem.* **2000**, 2533–2540.
[31] N. Lucena, J. Casabó, L. Escriche, G. Sánchez-Castelló, F. Teixidor, R. Kivekäs, R. Sillanpää, *Polyhedron* **1996**, *15*, 3009–3018.
[32] A. Bertrán, J. García, E. Martin, P. Sosa, H. Torrens, *Rev. Soc., Quim. Mex.* **1993**, *37*, 185–189.
[33] G. M. Sheldrick, *SHELXS-97–2, Program for Crystal Structure Refinement*, University of Göttingen, Göttingen, Germany, **1997**.
[34] A. J. C. Wilson (Ed.), *International Tables for Crystallography*, Volume C, Kluwer Academic Publishers, Dordrecht, The Netherlands, **1995**.
[35] L. Farrugia, *J. Appl. Crystallogr.* **1997**, *30*, 565.

Received: September 15, 2005
Published Online: January 19, 2006

 © 2006 Wiley-VCH Verlag GmbH & Co. KGaA, Weinheim 

DOI: 10.1002/ejic.200500856

# Synthesis and Characterisation of Alkali Metal and Thallium Polyfluoroantimonates, $ASb_nF_{5n+1}$ ($n$ = 2, 3)

**Primož Benkič,[a] H. Donald Brooke Jenkins,[b] Maja Ponikvar,[a] and Zoran Mazej*[a]**

**Keywords:** Alkali metals / Antimony / Fluorides / Lewis acids / Superacidic systems

Reactions of AF (A = K, Rb, Tl) with excess liquid $SbF_5$ in anhydrous HF (or $SO_2$) at room temperature give products having the composition $ASb_2F_{11}$. The reaction between CsF and a small excess of $SbF_5$ in anhydrous HF (0.76 mmol of CsF + 4.19 mmol of $SbF_5$ in 4 mL of aHF) yields $CsSb_2F_{11}$, whereas the reaction with a large excess of $SbF_5$ (0.79 mmol of CsF + 23 mmol of $SbF_5$ in 10 mLof aHF) yields the salt $CsSb_3F_{16}$. Efforts to prepare similar compounds using the monofluorides of Li and Na led only to the already known $ASbF_6$ compounds. Reactions of AF (A = Na, K, Rb, Cs) with liquid $SbF_5$ at 85 °C in the absence of solvents yield the products $NaSbF_6$, $ASb_2F_{11}$ (A = K, Rb) and $CsSb_3F_{16}$, respectively. A single-crystal X-ray diffraction study on the salt $KSb_2F_{11}$ [orthorhombic, at 250 K, *Pbca*, with $a$ = 1141.65(8), $b$ = 1279.96(9), $c$ = 3948.5(3) pm, $V$ = 5.7699(7) nm$^3$ and $Z$ = 24] has shown it to be isostructural with $AgSb_2F_{11}$. $CsSb_2F_{11}$, on the other hand, is monoclinic at 250 K [$P2_1/n$, with $a$ = 774.10(14), $b$ = 1425.41(17)m, $c$ = 951.30(15) pm, $\beta$ = 113.226(6)°, $V$ = 0.9646(3) nm$^3$ and $Z$ = 4]. $RbSb_2F_{11}$ and $TlSb_2F_{11}$ belong to yet a third structural type. Crystals of $CsSb_3F_{16}$ are orthorhombic at 200 K [$Pca2_1$, with $a$ = 2207(3), $b$ = 772.6(11), $c$ = 1605(3) pm, $V$ = 2.737(8) nm$^3$ and $Z$ = 8]. The vibrational spectra of $Sb_2F_{11}^-$ salts are consistent with the above crystallographic assignments, showing that $Sb_2F_{11}^-$ anions deviate strongly from $D_{4h}$ symmetry in having no symmetry at all (point group $C_1$). The vibrational spectra of $CsSb_3F_{16}$ confirm the presence of $Sb_3F_{16}^-$ anions, which adopt a *cis*-fluorine-bridged geometry consistent with the crystal structure.

(© Wiley-VCH Verlag GmbH & Co. KGaA, 69451 Weinheim, Germany, 2006)

## Introduction

Compounds of the type $ASbF_6$ (A = monovalent cation) are well known and established.[1] In contrast to $ASbF_6$ salts, reports concerning the formation of $ASb_2F_{11}$ and $ASb_3F_{16}$ compounds are scarce. $CsSb_2F_{11}$ has been prepared from CsF and $SbF_5$ in $SO_2$ solution and investigated by $^{19}F$ NMR spectroscopy.[2] Its (incomplete) vibrational spectrum was also reported.[3,4] The salt $AgSb_2F_{11}$ has been studied and its synthesis, crystal-structure determination and vibrational spectra have been published recently.[5] In the case of the $Sb_3F_{16}^-$ salts of alkali metal fluorides only the caesium compound has been reported to exist.[6]

The tendency of alkali metal fluorides to form stable, complex fluoro or oxofluoro anion salts with covalent metal fluorides or oxofluorides decreases from $Cs^+$ to $Li^+$.[7] However, the cut-off limit for salt formation in the view of the size (volume) of the $A^+$ cation appears to vary somewhat from one system to another.[7] The aim of this work was a systematic investigation of reactions between monofluorides of alkali metals (including thallium) and antimony pentafluoride [with and without the presence of solvents such as $SO_2$ and anhydrous HF (aHF)] to find out how the size of the cations influences the composition of the final products. In other words, which compounds with general formula $ASb_nF_{5n+1}$ ($n$ = 1, 2, 3) should exist for a specific cation.

[a] Jožef Stefan Institute, Department of Inorganic Chemistry and Technology,
Jamova 39, SI-1000 Ljubljana, Slovenia
Fax: +386-1-477-3155
E-mail: zoran.mazej@ijs.si
[b] Department of Chemistry, University of Warwick,
Coventry, CV4 7AL, West Midlands, United Kingdom
Fax: +44-2476-466747
E-mail: Don.Jenkins@warwick.ac.uk

## Results and Discussion

### Syntheses

Reactions of AF (A = K, Rb, Tl) with an excess of $SbF_5$ in anhydrous HF or $SO_2$ at room temperature yield products having the composition $ASb_2F_{11}$ [Equation (1)].

$$AF + 2SbF_5 \xrightarrow[298\ K]{aHF/SO_2,\ SbF_5} ASb_2F_{11}\ (A = K, Rb, Tl) \quad (1)$$

The reaction between CsF and a small excess of $SbF_5$ in anhydrous HF (0.76 mmol of CsF + 4.19 mmol of $SbF_5$ in 4 mL of aHF) yields $CsSb_2F_{11}$ whilst, in contrast, the reaction with a large excess of $SbF_5$ (0.79 mmol of CsF + 23 mmol of $SbF_5$ in 10 mL of aHF) yields $CsSb_3F_{16}$.

 © 2006 Wiley-VCH Verlag GmbH & Co. KGaA, Weinheim 

The course of the reaction between KF and $SbF_5$ (the starting molar ratio KF/$SbF_5$ being 1:2) in $SO_2$ is in agreement with previous findings for Cs salts.[2] $KSb_2F_{11}$ is similar to $CsSb_2F_{11}$ in being relatively soluble in $SO_2$.

Efforts to prepare similar compounds starting from the monofluorides of Li and Na led only to already known $ASbF_6$[1] compounds [Equation (2)].

$$AF + SbF_5 \xrightarrow[298\ K]{aHF/SO_2,\ SbF_5} ASbF_6 \quad (A = Li, Na) \tag{2}$$

The reaction between NaF and $SbF_5$ in $SO_2$ yields only $NaSbF_6$ which, like the corresponding $CsSbF_6$, is rather insoluble[2] in $SO_2$ (see Experimental Section).

The previously reported vibrational spectra of products obtained by heating equimolar mixtures of $SbF_5$ and the corresponding alkali metal fluoride under $F_2$ at 280 °C exhibited no evidence at all for the presence of polyfluoroantimonates.[8] Our results, however, show that when the reaction mixture of a sample of alkali fluoride (AF, A = Na, K, Rb, Cs) and an excess of liquid $SbF_5$ is heated at 85 °C $NaSbF_6$, $ASb_2F_{11}$ (A = K, Rb) and $CsSb_3F_{16}$ are isolated as the final products.

## Crystal Structures

Single crystals of $ASb_2F_{11}$ (A = K, Cs) were prepared by slow evaporation (over two months) of the volatiles from saturated solutions of the corresponding $ASb_2F_{11}$ salts in aHF acidified with a large excess of $SbF_5$. A similar procedure using NaF yields only single crystals of $NaSbF_6$. These results suggest that the products of the reaction between AF (A = Li, Na) and an excess of $SbF_5$ [Equation (2)] are not the result of kinetic control.

The crystal structures of $ASb_2F_{11}$ compounds can be divided into three groups. The first group corresponds to $ASb_2F_{11}$ compounds having similarly sized cations (A = $K^+$, $H_3O^+$, $Ag^+$). Crystals of $KSb_2F_{11}$ are orthorhombic at 250 K (see Experimental Section) and are isostructural to $AgSb_2F_{11}$[5] and also structurally related to $H_3OSb_2F_{11}$.[9] The complex structure of $KSb_2F_{11}$ reveals three crystallographically nonequivalent $Sb_2F_{11}^-$ anions that are highly distorted from ideal $D_{4h}$ symmetry (Figure 1). Distortions of $Sb_2F_{11}$ units are usually expressed in terms of the bridge angle $\alpha$ (bending of $F_5Sb$–F–$SbF_5$ about bridging fluorine) and the torsion angle $\psi$ (torsion of two planar $SbF_{4,eq}$ groups from eclipsed to staggered conformation). In $KSb_2F_{11}$ three different bridge (149.2°, 150.4° and 146.1°) and three corresponding dihedral (20.2°, 21.2° and 32.6°) angles for three crystallographically nonequivalent $Sb_2F_{11}$ units were identified. The bridging and dihedral angles found in $KSb_2F_{11}$ are close to the values found for the anion in the isostructural $AgSb_2F_{11}$ ($\alpha$ = 148.3°, 151.8° and 143.5°; $\psi$ = 22.5°, 18.0° and 37.1°).[5] The Sb–$F_t$ bonds are, as expected, shorter (181.2–186.4 pm) and show a wider spread than the Sb–$F_b$ bonds (202.4–204.1 pm; Table 1). The $F_{eq}$–Sb–$F_{ax}$ Bond angles are slightly greater than 90°, while the $F_{eq}$–Sb–$F_b$ are more acute by 3–7° (Table 2).

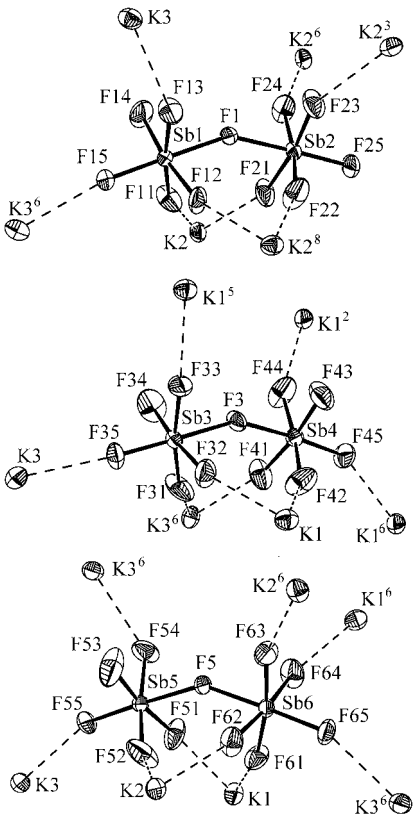


Figure 1. Three crystallographically nonequivalent $Sb_2F_{11}$ units and their interactions with $K^+$ cations in the crystal structure of $KSb_2F_{11}$ (thermal ellipsoids are drawn at 40% probability level). Superscripted numbers: symmetry operations used for generation of equivalent atoms: [1] $x, y, z$; [2] $x + ½, -y + ½, -z$; [3] $-x, y + ½, -z + ½$; [4] $-x + ½, -y, z + ½$; [5] $-x, -y, -z$; [6] $-x + ½, y + ½, z$; [7] $x, -y + ½, z + ½$; [8] $x + ½, y, -z + ½$.

There are also three crystallographically nonequivalent $K^+$ cations in the crystal structure of $KSb_2F_{11}$. The K–F bond lengths span a wide range of values (260.1–289.8 pm). By comparison, in $KSbF_6$ eight fluorine atoms, which form a slightly distorted dodecahedron, surround the K atoms at distances of between 261.8 and 320.4 pm.[10] The coordination number of the potassium atoms in $KSb_2F_{11}$ can be written as 8 for K1 and K3 and 9 for K2.

$CsSb_2F_{11}$ crystallises in the monoclinic space group $P2_1/n$ (no. 14) with the unit-cell parameters and the crystal and structure refinement data given in the Experimental Section. Selected bond lengths and angles are summarised in Tables 3 and 4, respectively. The packing diagram is depicted in Figure 2.

The structure of the $Sb_2F_{11}^-$ anion and its interactions with $Cs^+$ cations, along with the numbering scheme adopted, are given in Figure 3. The structure of $CsSb_2F_{11}$ is ionic and consists of discreet $Sb_2F_{11}^-$ anions and

 © 2006 Wiley-VCH Verlag GmbH & Co. KGaA, Weinheim 

Table 1. Selected bond lengths [pm] in $KSb_2F_{11}$.

| | | | | | | | |
|---|---|---|---|---|---|---|---|
| Sb1–F1 | 204.1(5) | Sb2–F1 | 202.4(5) | Sb3–F3 | 203.4(5) | Sb4–F3 | 202.8(5) |
| Sb1–F11 | 183.4(5) | Sb2–F21 | 184.4(6) | Sb3–F31 | 183.7(6) | Sb4–F41 | 182.9(7) |
| Sb1–F12 | 183.1(5) | Sb2–F22 | 184.1(6) | Sb3–F32 | 183.2(6) | Sb4–F42 | 184.0(6) |
| Sb1–F13 | 184.8(6) | Sb2–F23 | 185.3(6) | Sb3–F33 | 183.1(6) | Sb4–F43 | 182.7(7) |
| Sb1–F14 | 183.2(7) | Sb2–F24 | 184.7(6) | Sb3–F34 | 182.7(7) | Sb4–F44 | 184.0(6) |
| Sb1–F15 | 185.3(5) | Sb2–F25 | 183.8(5) | Sb3–F35 | 183.8(5) | Sb4–F45 | 185.1(6) |
| Sb5–F5 | 203.8(5) | Sb5–F53 | 181.6(7) | Sb6–F5 | 202.4(5) | Sb6–F63 | 184.4(6) |
| Sb5–F51 | 181.2(6) | Sb5–F54 | 182.4(6) | Sb6–F61 | 184.3(6) | Sb6–F64 | 182.9(6) |
| Sb5–F52 | 182.4(7) | Sb5–F55 | 184.9(5) | Sb6–F62 | 184.9(6) | Sb6–F65 | 186.4(5) |
| K1–F32 | 273.0(6) | K2–F11 | 269.2(6) | K3–F13 | 275.4(7) | | |
| K1–F33 | 271.6(7) | K2–F12 | 266.7(6) | K3–F15 | 280.8(5) | | |
| K1–F42 | 271.0(7) | K2–F21 | 274.7(6) | K3–F31 | 275.2(7) | | |
| K1–F44 | 276.8(8) | K2–F22 | 267.9(7) | K3–F35 | 289.6(6) | | |
| K1–F45 | 277.3(7) | K2–F23 | 291.9(6) | K3–F41 | 277.4(7) | | |
| K1–F51 | 269.4(6) | K2–F24 | 278.3(6) | K3–F54 | 284.0(8) | | |
| K1–F61 | 282.0(7) | K2–F52 | 288.4(8) | K3–F55 | 279.1(5) | | |
| K1–F64 | 283.3(6) | K2–F62 | 260.1(6) | K3–F65 | 279.7(6) | | |
| | | K2–F63 | 289.8(6) | | | | |

Table 2. Selected bond angles [°] in $KSb_2F_{11}$.

| | | | | | |
|---|---|---|---|---|---|
| F11–Sb1–F1 | 85.5(2) | F21–Sb2–F1 | 84.6(3) | F31–Sb3–F3 | 85.6(3) |
| F12–Sb1–F1 | 85.7(2) | F22–Sb2–F1 | 85.7(3) | F32–Sb3–F3 | 86.0(3) |
| F13–Sb1–F1 | 85.0(3) | F23–Sb2–F1 | 85.6(3) | F33–Sb3–F3 | 82.7(3) |
| F14–Sb1–F1 | 86.5(3) | F24–Sb2–F1 | 86.1(2) | F34–Sb3–F3 | 86.4(3) |
| F11–Sb1–F15 | 94.3(3) | F21–Sb2–F25 | 94.6(3) | F31–Sb3–F35 | 95.0(3) |
| F12–Sb1–F15 | 93.3(2) | F22–Sb2–F25 | 93.0(3) | F32–Sb3–F35 | 94.4(3) |
| F13–Sb1–F15 | 95.3(3) | F23–Sb2–F25 | 95.2(3) | F33–Sb3–F35 | 96.7(3) |
| F14–Sb1–F15 | 94.5(3) | F24–Sb2–F25 | 95.1(3) | F34–Sb3–F35 | 93.2(3) |
| | | Sb1–F1–Sb2 | 149.2(3) | | |
| F41–Sb4–F3 | 85.4(3) | F51–Sb5–F5 | 85.7(3) | F61–Sb6–F5 | 84.9(2) |
| F42–Sb4–F3 | 85.2(3) | F52–Sb5–F5 | 84.4(3) | F62–Sb6–F5 | 86.3(2) |
| F43–Sb4–F3 | 85.1(3) | F53–Sb5–F5 | 86.7(3) | F63–Sb6–F5 | 86.1(2) |
| F44–Sb4–F3 | 86.6(3) | F54–Sb5–F5 | 86.2(3) | F64–Sb6–F5 | 87.1(3) |
| F41–Sb4–F45 | 91.2(3) | F51–Sb5–F55 | 92.3(3) | F61–Sb6–F65 | 93.4(3) |
| F42–Sb4–F45 | 92.6(3) | F52–Sb5–F55 | 94.3(3) | F62–Sb6–F65 | 92.9(3) |
| F43–Sb4–F45 | 98.3(3) | F53–Sb5–F55 | 95.3(3) | F63–Sb6–F65 | 95.6(3) |
| F44–Sb4–F45 | 95.7(3) | F54–Sb5–F55 | 95.2(3) | F64–Sb6–F65 | 93.7(3) |
| Sb3–F3–Sb4 | 150.4(3) | | | Sb5–F5–Sb6 | 146.1(3) |

Table 3. Selected bond lengths [pm] in $CsSb_2F_{11}$.

| | | | | | | | |
|---|---|---|---|---|---|---|---|
| Sb1–F1 | 203.9(3) | Sb2–F1 | 203.9(3) | Cs1–F11 | 307.0(4) | Cs1–F21 | 315.8(4) |
| Sb1–F11 | 183.8(4) | Sb2–F21 | 185.8(4) | Cs1–F12 | 349.8(4) | Cs1–F21 | 355.2(4) |
| Sb1–F12 | 185.6(3) | Sb2–F22 | 184.9(4) | Cs1–F12 | 352.9(4) | Cs1–F22 | 339.6(4) |
| Sb1–F13 | 185.3(3) | Sb2–F23 | 184.6(4) | Cs1–F13 | 309.9(4) | Cs1–F23 | 345.1(4) |
| Sb1–F14 | 185.4(4) | Sb2–F24 | 185.4(4) | Cs1–F14 | 305.9(4) | Cs2–F24 | 323.0(4) |
| Sb1–F15 | 183.7(4) | Sb2–F25 | 184.9(3) | Cs1–F15 | 316.5(4) | Cs2–F25 | 310.1(3) |

Table 4. Selected bond angles [°] in $CsSb_2F_{11}$.

| | | | |
|---|---|---|---|
| F11–Sb1–F1 | 86.0(2) | F21–Sb2–F1 | 85.7(1) |
| F12–Sb1–F1 | 83.5(2) | F22–Sb2–F1 | 85.2(1) |
| F13–Sb1–F1 | 85.3(2) | F23–Sb2–F1 | 85.4(2) |
| F14–Sb1–F1 | 84.8(2) | F24–Sb2–F1 | 85.2(2) |
| F11–Sb1–F15 | 94.9(2) | F21–Sb2–F25 | 95.5(2) |
| F12–Sb1–F15 | 96.5(2) | F22–Sb2–F25 | 93.8(2) |
| F13–Sb1–F15 | 93.8(2) | F23–Sb2–F25 | 93.4(2) |
| F14–Sb1–F15 | 95.2(2) | F24–Sb2–F25 | 95.9(2) |
| | | Sb1–F1–Sb2 | 146.0(2) |

$Cs^+$ cations in a simple packing arrangement. As in the case of $KSb_2F_{11}$, the $Sb_2F_{11}^-$ anion in $CsSb_2F_{11}$ is highly distorted from ideal $D_{4h}$ symmetry ($\alpha$ = 146.0°, $\psi$ = 33.9°; Figure 3). The Sb–F bond lengths (Table 3) and F–Sb–F bond angles (Table 4) in $CsSb_2F_{11}$ are comparable to those found for $KSb_2F_{11}$ (Tables 1 and 2).

Taking the coordination number as the number of nearest neighbour atoms[9] then Cs is surrounded by 12 fluorine atoms at distances of between 307.0(4) and 355.2(4) pm. In

 © 2006 Wiley-VCH Verlag GmbH & Co. KGaA, Weinheim 

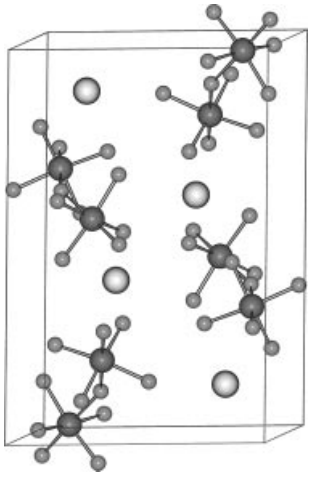

Figure 2. Packing diagram of $CsSb_2F_{11}$.

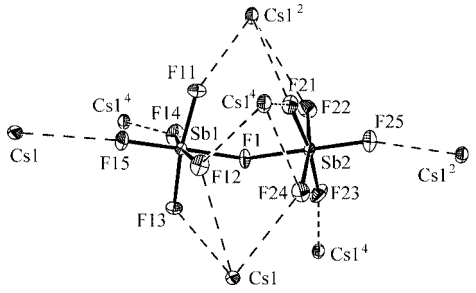


Figure 3. $Sb_2F_{11}$ unit and interacting $Cs^+$ cations in $CsSb_2F_{11}$ (thermal ellipsoids are drawn at 40% probability level). Superscripted numbers: symmetry operations used for generation of equivalent atoms: [1] $x, y, z$; [2] $-x + ½, y + ½, -z + ½$; [3] $-x, -y, -z$; [4] $x + ½, -y + ½, z + ½$.

$CsSbF_6$ twelve fluorine atoms again surround the Cs atom with six close contacts (311.6 pm) and six long contacts (338.3) pm.[11]

The X-ray powder-diffraction photographs indicate that $RbSb_2F_{11}$ and $TlSb_2F_{11}$ are isostructural and different from $KSb_2F_{11}$ or $CsSb_2F_{11}$. Their isostructurality is consistent with the close similarity shown by the ionic radii of Rb and Tl (Shannon: Rb = 175 pm, Tl = 173 pm for C.N. = 8;[12] Goldschmidt: Rb = Tl = 149 nm[13]) or their volumes [$V(Rb^+) = V(Tl^+) = 0.014$ nm$^3$].[14]

Examples of crystal structures of $Sb_3F_{16}^-$ salts are rare. The $Sb_3F_{16}^-$ anion adopts a *cis*-fluorine-bridged geometry in the crystal structures of $[OsO_3F][Sb_3F_{16}]$,[15] $[OCNCO][Sb_3F_{16}]$,[16] $[XeN(SO_2F)_2][Sb_3F_{16}]$[17] and $[Cl_3][Sb_3F_{16}]$,[18] whereas a *trans*-fluorine-bridged $Sb_3F_{16}^-$ anion has been reported in the crystal structure of $[Br_2][Sb_3F_{16}]$.[19] $CsSb_3F_{16}$ crystallises in the orthorhombic space group $Pca2_1$ (no. 29). The unit-cell parameters and the crystal and structure refinement data are given in the Experimental Section. Selected bond lengths and angles are summarised in Tables 5 and 6, respectively. The packing diagram is depicted in Figure 4.

Table 6. Selected bond angles [°] in $CsSb_3F_{16}$.

| | | | |
|---|---|---|---|
| F11–Sb1–F16 | 85(6) | F22–Sb2–F36 | 171.2(6) |
| F12–Sb1–F16 | 84(2) | F23–Sb2–F36 | 86(4) |
| F13–Sb1–F16 | 83(6) | F24–Sb2–F36 | 91(2) |
| F14–Sb1–F16 | 85(3) | F36–Sb3–F35 | 179.4(6) |
| F15–Sb1–F16 | 177.1(5) | F36–Sb3–F31 | 88(7) |
| F16–Sb2–F24 | 173.4(6) | F36–Sb3–F32 | 84(2) |
| F16–Sb2–F21 | 85(5) | F36–Sb3–F33 | 83(7) |
| F16–Sb2–F22 | 89.1(22) | F36–Sb3–F34 | 84(2) |
| F16–Sb2–F23 | 84(6) | | |
| F16–Sb2–F36 | 82(2) | Sb1–F16–Sb2 | 151.9(7) |
| F21–Sb2–F36 | 86(3) | Sb2–F36–Sb3 | 152.6(11) |
| F41–Sb4–F46 | 86(6) | F52–Sb5–F66 | 172.8(4) |
| F42–Sb4–F46 | 84(4) | F53–Sb5–F66 | 86(4) |
| F43–Sb4–F46 | 83(5) | F54–Sb5–F66 | 89.0(14) |
| F44–Sb4–F46 | 87(3) | F66–Sb6–F65 | 177.8(6) |
| F45–Sb4–F46 | 178.8(6) | F66–Sb6–F61 | 82.4(13) |
| F46–Sb4–F54 | 172.3(6) | F66–Sb6–F62 | 85(7) |
| F46–Sb5–F51 | 85(6) | F66–Sb6–F63 | 86.6(9) |
| F46–Sb5–F52 | 89.8(12) | F66–Sb6–F64 | 84(7) |
| F46–Sb5–F53 | 84(7) | | |
| F46–Sb5–F66 | 83.3(11) | Sb4–F46–Sb5 | 156.3(8) |
| F51–Sb5–F66 | 83(4) | Sb5–F66–Sb6 | 155.5(5) |

The crystal structure of $CsSb_3F_{16}$ reveals two crystallographically nonequivalent $Sb_3F_{16}^-$ anions adopting a *cis*-fluorine-bridged geometry. The structure of the $Sb_3F_{16}^-$ anions and their interactions with $Cs^+$ cations, along with the numbering scheme adopted, are given in Figure 5. The Sb–$F_t$ bond lengths (Table 5) in $CsSb_3F_{16}$ are comparable to those found for $KSb_2F_{11}$ and $CsSb_2F_{11}$ (Tables 1 and 3).

The corresponding pairs of Sb–$F_b$ bond lengths in the $F_5Sb–F_b–SbF_5$ units of $KSb_2F_{11}$ [Sb1–F1 = 204.1(5), F1–

Table 5. Selected bond lengths [pm] in $CsSb_3F_{16}$.

| | | | | | | | |
|---|---|---|---|---|---|---|---|
| Sb1–F11 | 186(6) | Sb3–F34 | 185(4) | Sb6–F61 | 186(2) | Cs1–F45 | 309(11) |
| Sb1–F12 | 186(7) | Sb3–F35 | 185(2) | Sb6–F62 | 187(4) | Cs1–F52 | 320.3(12) |
| Sb1–F13 | 187(9) | Sb3–F36 | 207(2) | Sb6–F63 | 182(2) | Cs1–F63 | 337(2) |
| Sb1–F14 | 185(6) | Sb4–F41 | 183(8) | Sb6–F64 | 183(2) | Cs2–F12 | 312(2) |
| Sb1–F15 | 183.7(18) | Sb4–F42 | 184(6) | Sb6–F65 | 185.0(12) | Cs2–F15 | 304(12) |
| Sb1–F16 | 208.9(15) | Sb4–F43 | 183(11) | Sb6–F66 | 209.5(9) | Cs2–F22 | 326.8(11) |
| Sb2–F16 | 199(11) | Sb4–F44 | 184(8) | | | Cs2–F34 | 344(3) |
| Sb2–F21 | 186(12) | Sb4–F45 | 186(2) | Cs1–F11 | 344(5) | Cs2–F35 | 307(3) |
| Sb2–F22 | 183.8(10) | Sb4–F46 | 208(2) | Cs1–F13 | 351(5) | Cs2–F41 | 341(8) |
| Sb2–F23 | 184(8) | Sb5–F46 | 196(8) | Cs1–F14 | 330(13) | Cs2–F42 | 350(20) |
| Sb2–F24 | 180(9) | Sb5–F51 | 182(10) | Cs1–F21 | 310(20) | Cs2–F43 | 366(3) |
| Sb2–F36 | 199.6(17) | Sb5–F52 | 184.6(11) | Cs1–F31 | 337(8) | Cs2–F51 | 320(20) |
| Sb3–F31 | 185(6) | Sb5–F53 | 181(4) | Cs1–F32 | 329(5) | Cs2–F61 | 353(5) |
| Sb3–F32 | 184(3) | Sb5–F46 | 196(8) | Cs1–F33 | 322(4) | Cs2–F62 | 329(7) |
| Sb3–F33 | 185(3) | Sb5–F66 | 196.4(9) | Cs1–F44 | 311(3) | Cs2–F64 | 328.6(18) |

 © 2006 Wiley-VCH Verlag GmbH & Co. KGaA, Weinheim 

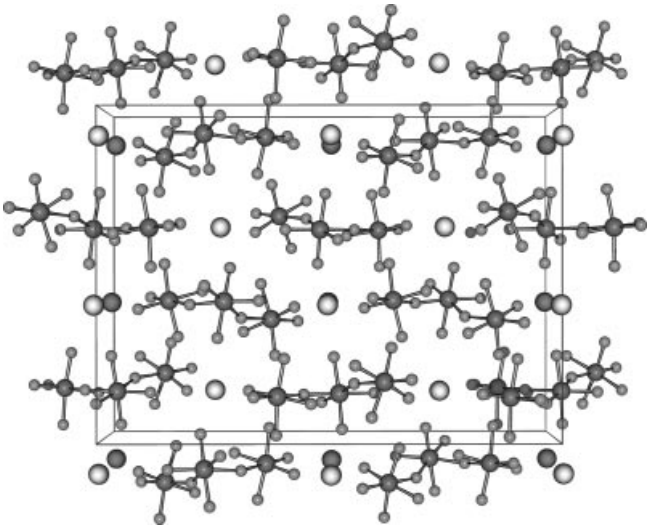

Figure 4. Packing diagram for $CsSb_3F_{16}$.

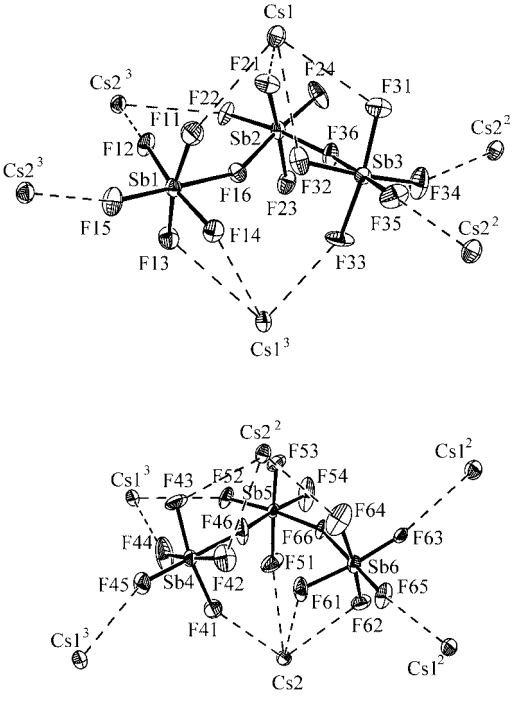


Figure 5. Two crystallographically nonequivalent $Sb_3F_{16}$ units and their interactions with $Cs^+$ cations in the crystal structure of $CsSb_3F_{16}$ (thermal ellipsoids are drawn at 40% probability level). Superscripted numbers: symmetry operations used for generation of equivalent atoms: [1] *x*, *y*, *z*; [2] –*x*, –*y*, *z* + ½; [3] –*x* + ½, *y*, *z* + ½; [4] *x* + ½, –*y*, *z*.

Sb1 = 202.4(5); Sb3–F3 = 203.4(5); F3–Sb4 = 202.8(5); Sb5–F5 = 203.8(5), F5–Sb6 = 202.4(5) pm] and $CsSb_2F_{11}$ [Sb1–F1 = 203.9(3), F1–Sb2 = 203.9(3) pm] are much closer than the corresponding pairs of Sb–$F_b$ bond lengths in the $F_5Sb–F_b–SbF_4–F_b–SbF_5$ units of $CsSb_3F_{16}$. The Sb–$F_b$ bond lengths (Sb2–F16, Sb2–F36 and Sb5–F46, Sb5–F66) between $F_b$ and the central Sb atom are much shorter [196(8)–199.6(17) pm] than the corresponding bond lengths between $F_b$ and the terminal Sb atoms (F16–Sb1, F36–Sb3 and F46–Sb4, F66–Sb6), which are in the range 207(2)–209.5(9) pm.

There are also two crystallographically nonequivalent $Cs^+$ cations in the crystal structure of $CsSb_3F_{16}$. On a similar basis to the assignment of the coordination number made in the case of $CsSb_2F_{11}$, these cations are surrounded by 12 fluorine atoms at distances of between 304(12) and 366(5) pm.

### Vibrational Spectra

The Raman and IR spectra of $ASb_2F_{11}$ (A = K, Rb, Cs, Tl) and $CsSb_3F_{16}$ are shown in Figures 6 and 7, respectively, with additional details given in Tables 7 and 8.

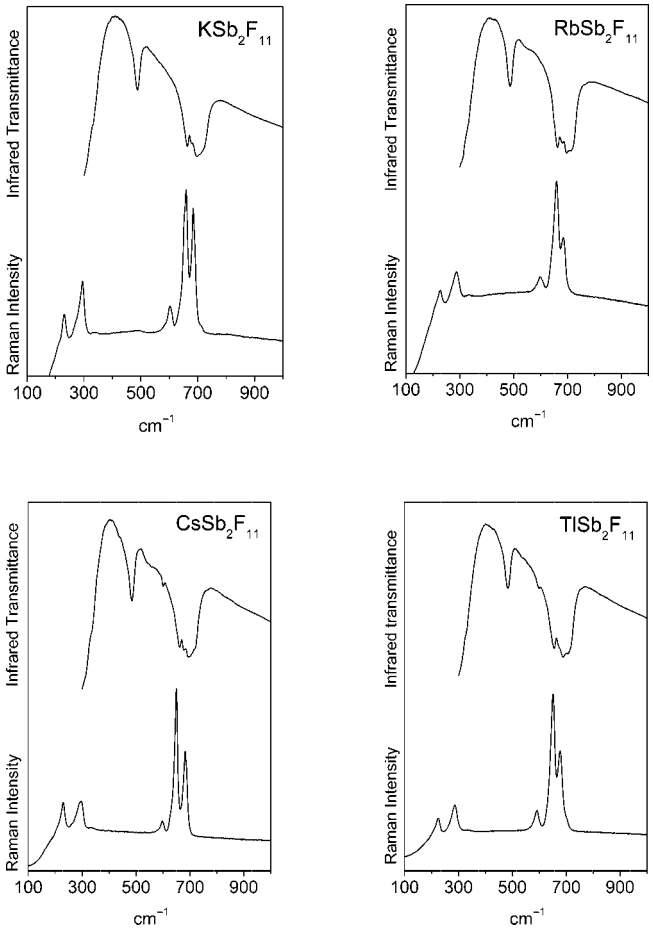


Figure 6. Infrared and Raman spectra of $ASb_2F_{11}$ (A = K, Rb, Cs, Tl).

The IR spectra (Figure 6, Table 7) were taken for powdered samples obtained from the synthesis [Equation (1)] and also for powdered samples obtained by grinding selected single crystals of $ASb_2F_{11}$ (A = K, Cs). They were found to be identical. Raman spectra taken for powdered samples obtained from the synthesis [Equation (1)] and Raman spectra taken for single crystals of $ASb_2F_{11}$ (A = K, Cs) were also identical. Small differences in the observed wavenumbers and relative intensities of some of the Raman and infrared bands of these salts arise as a consequence of

 © 2006 Wiley-VCH Verlag GmbH & Co. KGaA, Weinheim 

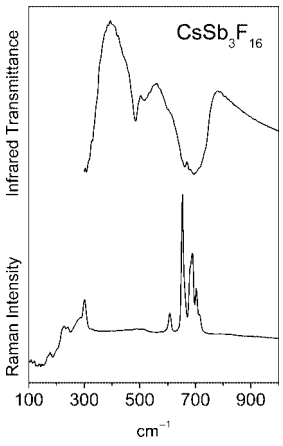


Figure 7. Infrared and Raman spectra of $CsSb_3F_{16}$.

the fact that some bands are broad, which makes the precise estimation of particular band positions difficult. A further factor contributing to these small differences are the crystal effects.

$Sb_2F_{11}^-$ anions deviate strongly from ideal $D_{4h}$ symmetry and, in fact, possess no symmetry at all (point group $C_1$). A partial assignment of the spectra of the $Sb_2F_{11}^-$ anions was made on the basis of comparison with $[M(CO)_4(Sb_2F_{11})_2]$ (M = Pd, Pt),[20] which contain two crystallographically nonequivalent and highly distorted $Sb_2F_{11}^-$ anions (Table 7, Figure 6). The bands in the regions 592–698 $cm^{-1}$ and 702–719 $cm^{-1}$ are assigned to Sb–$F_{eq}$ and Sb–$F_{ax}$ stretches, respectively, meanwhile bands around 500 $cm^{-1}$ are typical for Sb–F–Sb bridging. Bands below 300 $cm^{-1}$ were assigned to bending deformations.

Table 8. Vibrational spectra of $CsSb_3F_{16}$.

| IR[a] | Ra | Assignments[b] |
|---|---|---|
| 738(sh) | | ν($SbF_t$) |
| 719(sh) | 715(sh) | ν($SbF_t$) |
| 706(s) | 704(35) | ν($SbF_t$) |
| 694(vs) | 689(60) | ν($SbF_t$) |
| 678(s) | 680(sh) | ν($SbF_t$) |
| 662(vs) | 661(sh) | ν($SbF_t$) |
| 650(sh) | 653(100) | ν($SbF_t$) |
| 601(mw) | 607(20) | ν($SbF_t$) |
| 568(w) | | |
| 539(mw) | | |
| 517(m) | 517(1) | ν(SbFSb) |
| 486(ms) | 489(1) | ν(SbFSb) |
| 456(sh) | | ν(SbFSb) |
| 419(mw) | | |
| | 329(1) | δ(FSbF) |
| | 300(20) | δ(FSbF) |
| | 285(sh) | δ(FSbF) |
| | 240(5) | δ(FSbF) |
| | 228(7) | δ(FSbF) |
| | 177(5) | lattice vibrations |

[a] Intensities are given in parentheses; w = weak, mw = medium weak, m = medium, ms = medium strong, s = strong, vs. = very strong, sh = shoulder. [b] ν = Stretching mode, δ = deformation mode.

The vibrational spectrum of $CsSb_3F_{16}$ is similar but not identical to that for $CsSb_2F_{11}$. The $Sb_3F_{16}^-$ anion in $CsSb_3F_{16}$ exhibits very complex Raman and infrared spectra (Figure 7, Table 8). Reported vibrational data for the $Sb_3F_{16}^-$ anion are scarce. $[OsO_3F][Sb_3F_{16}]$,[15] $[ClCO][Sb_3F_{16}]$,[22] $[OCNCO][Sb_3F_{16}]$,[16] $[XeN(SO_2F)_2][Sb_3F_{16}]$,[17] $[ReF_6][Sb_3F_{16}]$[23] and $[PF_4][Sb_3F_{16}]$[24] have

Table 7. Vibrational spectra of undecafluorodiantimonates of monovalent cations.

| $KSb_2F_{11}$ | | $RbSb_2F_{11}$ | | $CsSb_2F_{11}$ | | $TlSb_2F_{11}$ | | $Pd(CO)_4(Sb2F11)_2$[a] | | Assignments[b] |
|---|---|---|---|---|---|---|---|---|---|---|
| IR[c] | Raman | IR | Raman | IR[d] | Raman[e] | IR | Raman | IR | Raman | |
| | | | | 719(sh) | | | | 718(sh) | 714(w) | ν ($SbF_{ax:}$ ) |
| 711(sh) | 713(sh) | 713(s) | | 702(s) | | 707(s) | 703(sh) | 708(vs) | 709(sh) | ν($SbF_{ax}$) |
| 698(vs) | | 696(vs) | | 693(vs) | 688(sh) | 689(vs) | | 690 (vs) | | ν($SbF_{4eq}$) |
| | 684(85) | | 684(50) | | 683(60) | | 678(60) | | 686(m) | ν($SbF_{4eq}$) |
| 678(s) | | 681(s) | | 677(s) | | 674(sh) | | 675(s) | 668(s) | ν($SbF_{4eq}$) |
| 664(vs) | 660(100) | 662(vs) | 659(100) | 662(vs) | 650(100) | 655(s) | 651(100) | 662(s) | 656(s) | ν($SbF_{4eq}$) |
| | 654(sh) | | | | | | | 648(sh) | 649(s) | ν($SbF_{4eq}$) |
| | 603(20) | | 599(15) | 601(m) | 598(5) | 599(w) | 592(16) | 604(vw) | 598(w) | ν($SbF_{4eq}$) |
| | | | | | | | | 596(w) | 585(w) | ν($SbF_{4eq}$) |
| | | 558(sh) | | 556(vw) | | 536(vw) | | | | |
| 488(ms) | | 487 (ms) | | 485(ms) | | 484(ms) | | 503(m) | | ν(SbFSb) |
| | | | | 436(sh) | | | | | | ν(SbFSb) |
| | 339(5) | | 336(3) | | 336(3) | | 346(1) | | 349(2) | |
| | | | | | | | | 315(s) | 305(m) | δ($SbF_{4eq}$) |
| | 295(40) | | 288(25) | | 298(25) | | 288(20) | 305(s) | | δ($SbF_{4eq}$) |
| | | | | | 293(25) | | | | | |
| | 271(sh) | | | | | | | | 275(w) | δ($SbF_{4eq}$) |
| | | | | | | | | 267(vs) | | δ($SbF_{4eq}$) |
| | | | | | | | | 250(sh) | | δ($SbF_{4eq}$) |
| | 231(15) | | 227(15) | | 230(10) | | 225(10) | 228(sh) | 230(m) | δ($SbF_{4eq}$) |
| | | | | | | | | 196(vw) | 201(vw) | δ($SbF_{4eq}$) |

[a] Ref.[20] [b] ν = stretching mode, δ = deformation mode. [c] Intensities are given in parentheses; vw = very weak, w = weak, m = medium, ms = medium strong, s = strong, vs. = very strong, sh = shoulder. [d] Literature data: broad band at 700 $cm^{-1}$, shoulder at 600 $cm^{-1}$, sharp and intense band at 480 $cm^{-1}$ (ref.[4]). [e] Literature data: 692/685(93), 654(100), 603/597(15), 521(1), 332(4), 300/291(39), 232(?) (ref.[21]).

 © 2006 Wiley-VCH Verlag GmbH & Co. KGaA, Weinheim 

been characterised by Raman spectroscopy and $[ClO_2][Sb_3F_{16}]$[25] by IR spectroscopy. These data vary significantly as the nature of the cation changes. The bands attributed to the $Sb_3F_{16}^-$ anion in $CsSb_3F_{16}$ show most correspondence with those found in $[ClCO][Sb_3F_{16}]$,[22] where $Sb_3F_{16}^-$ was found to exhibit a common *cis*-fluorine-bridged $Sb_3F_{16}^-$ anion consistent with the crystal structure analysis made for $CsSb_3F_{16}$.

## Conclusions

Smaller cations such as $Li^+$ [$V(Li^+)$ = 0.002 nm$^3$][14] and $Na^+$ [$V(Na^+)$ = 0.004 nm$^3$][14] yield $ASbF_6$ compounds, whereas larger $A^+$ cations (A = $Ag^+$, $H_3O^+$, $K^+$) prefer to form $ASb_2F_{11}$ salts. These latter ions, with volumes $V(Ag^+)$ = 0.006 nm$^3$,[5] $V(H_3O^+)$ = 0.008 nm$^3$[5] and $V(K^+)$ = 0.010 nm$^3$,[14] lead to salts which crystallise in an identical structural type. The coordination of the three crystallographically nonequivalent $A^+$ cations can be approximately regarded as being 5+3, (C.N. = 8), 6+3 (C.N. = 9) and 6+2 (C.N. = 8), respectively. X-ray powder diffraction patterns indicate that $RbSb_2F_{11}$ and $TlSb_2F_{11}$ are isostructural, which, as was alluded to above, is not surprising in light of their similar volumes. The larger $Cs^+$ cation [$V(Cs^+)$ = 0.019 nm$^3$][14] yields $CsSb_2F_{11}$, which represents the third structural type with the highest coordination number (C.N. = 12) found for the cation $A^+$.

In all crystal structures determined for $ASb_2F_{11}$ compounds the $Sb_2F_{11}$ units are observed to have a high degree of distortion. The bridge angle $\alpha$ and torsion angle $\psi$ in the $Sb_2F_{11}$ units may have some cation-dependence, although these values are mostly influenced by long interionic contacts in the solid state.

Only the largest of the alkali metal cations ($Cs^+$) is capable of stabilizing the weakly fluoro-basic $Sb_3F_{16}^-$ anion.

A summary of known compounds with general formula $ASb_nF_{5n+1}$ (A = monovalent metal cation; $n$ = 1, 2, 3) is shown in Table 9.

Table 9. Compounds with general formula $ASb_nF_{5n+1}$ (A = monovalent metal cation; $n$ = 1, 2, 3).

| | $SbF_6^-$ | $Sb_2F_{11}^-$ | $Sb_3F_{16}^-$ |
|---|---|---|---|
| $Li^+$ | [a] | | |
| $Cu^+$ | [b] | | |
| $Na^+$ | [a] | | |
| $K^+$ | [a] | [g] | |
| $Ag^+$ | [c] | [h] | |
| $Rb^+$ | [d] | [g] | |
| $In^+$ | [e] | | |
| $Tl^+$ | [f] | [g] | |
| $Cs^+$ | [a] | [g] | [g] |

[a] Ref.[1] [b] Ref.[26] [c] Ref.[27] [d] Ref.[28] [e] Ref.[29] [f] Ref.[30] [g] This work. [h] Ref.[5]

## Experimental Section

### Techniques

The infrared spectra, with a resolution of 4 cm$^{-1}$, of powdered samples sandwiched between AgCl windows in a leak-tight brass cell were recorded (5 scans) with a Perkin–Elmer FTIR 1710 spectrometer. Raman spectra, with a resolution of 1 cm$^{-1}$, were recorded (10–20 scans) with a Renishaw Raman Imaging Microscope System 1000, with the 632.8-nm exciting line of a He-Ne laser.

X-ray powder diffraction patterns were obtained using the Debye–Scherrer technique with Ni-filtered Cu-$K_\alpha$ radiation. Samples were loaded into quartz capillaries (0.3 mm) in a dry-box. Intensities were estimated visually.

### Reagents and Apparatus

Volatile materials were manipulated using an all-PTFE vacuum line equipped with PTFE valves. The manipulation of the non-volatile solids was accomplished under a dry argon atmosphere in a dry-box (M. Braun, Germany). The residual water in the atmosphere within the dry-box never exceeded 1 ppm. All reactions were carried out in FEP (Polytetra, Germany) reaction vessels (height: 300 mm; inner diameter: 15.5 mm; outer diameter: 18.75 mm) equipped with PTFE valves[31] and PTFE-coated stirring bars. All reaction vessels were pretreated with $F_2$ prior to use.

LiF (Merck, 99.9%), NaF (Merck, 99%), KF (Ventron, 99.9%), RbF (Aldrich, 99%), CsF (Ventron, 99.9%), $SO_2$ (Messer Griesheim, 99.9%) and fluorine (Solvay) were used as supplied. TlF was prepared by reaction between $Tl_2CO_3$ (Merck, P.A.) and aqueous HF. $SbF_3$ (Alfa Aesar, 99%) was treated with aHF in order to remove possible traces of $Sb_2O_3$. $SbF_5$ was prepared by fluorination of $SbF_3$ in a flow reaction. Its purity was checked by Raman spectroscopy. Anhydrous HF (Fluka, Purum) was treated with $K_2NiF_6$ for several hours prior to use.

### Reactions between AF and an Excess of $SbF_5$

In a dry-box a sample of the fluoride AF (A = Li – Cs, Tl) was loaded into the FEP reaction vessel. An excess of $SbF_5$ and the solvent (aHF or $SO_2$) were condensed onto the solid fluoride salt at 77 K. The reaction mixtures were left stirring for several days at room temperature. The details of the reaction conditions are given in Table 10. Clear colourless solutions were obtained in the case of reactions between NaF or KF and $SbF_5$ in aHF. However, in the case of the reaction between AF (A = Li, Rb, Cs and Tl) and $SbF_5$ in aHF, a clear, colourless liquid phase was visible above an insoluble white solid, which always formed. The reaction between KF and $SbF_5$ (molar ratio = 1:2) in $SO_2$ as solvent, yielded a clear, colourless solution. In the case of the reaction between NaF and $SbF_5$ (molar ratio = 1:2) in $SO_2$ *two* liquid phases were observed. In this latter case a clear, colourless solution was visible above a milky suspension.

Volatiles were slowly pumped off at room temperature over a few hours to leave behind white solids. The chemical analyses of the resulting isolated $ASb_2F_{11}$ salts (A = K, Rb, Cs) are given in Table 11. The Raman spectra of the products of reactions between AF (A = Li, Na) and $SbF_5$ in aHF or $SO_2$ showed only the bands [Li: 669(100), 569(10), 295(80); Na: 672(100), 581(10), 279(50)] that can be assigned to $ASbF_6$ salts.[32]

In further experiments a sample of alkali metal fluoride (AF, A = Na, K, Rb, Cs) was loaded into the FEP reaction vessel and an excess of liquid $SbF_5$ was condensed onto the solid fluoride salt at 77 K. The reaction mixture was warmed up to 85 °C. The details

 © 2006 Wiley-VCH Verlag GmbH & Co. KGaA, Weinheim 

Table 10. Reaction conditions for the reactions of AF (A = Li–Cs, Tl) with an excess of $SbF_5$ in aHF (or $SO_2$) at room temperature.

| Starting materials | | | | | Solvent | $V_{solvent}$ | Reaction time | Final product |
|---|---|---|---|---|---|---|---|---|
| AF[a] | | | $SbF_5$ | | | | | |
| AF | [g] | [mmol] | [g] | [mmol] | | [mL] | [d] | |
| LiF | 0.024 | 0.92 | 1.767 | 8.15 | aHF | 5 | 11 | $LiSbF_6$ |
| NaF | 0.036 | 0.87 | 0.815 | 3.76 | aHF | 6 | 11 | $NaSbF_6$ |
| KF | 0.054 | 0.92 | 1.560 | 7.20 | aHF | 5 | 7 | $KSb_2F_{11}$ |
| RbF | 0.103 | 0.99 | 1.800 | 8.30 | aHF | 5 | 13 | $RbSb_2F_{11}$ |
| CsF | 0.115 | 0.76 | 0.908 | 4.19 | aHF | 4 | 11 | $CsSb_2F_{11}$ |
| CsF | 0.120 | 0.79 | 5.00 | 23.00 | aHF | 10 | 3 | $CsSb_3F_{16}$ |
| TlF | 0.216 | 0.96 | 0.900 | 4.15 | aHF | 3 | 2 | $TlSb_2F_{11}$ |
| NaF | 0.035 | 0.83 | 0.361 | 1.66 | $SO_2$ | 6 | 1 | $NaSbF_6$ |
| KF | 0.055 | 0.95 | 0.411 | 1.90 | $SO_2$ | 6 | 1 | $KSb_2F_{11}$ |

[a] A = Alkali metal.

Table 11. Chemical analyses of K, Rb, and Cs polyfluoroantimonates.

| Product | Chemical analyses[a] | | | | | |
|---|---|---|---|---|---|---|
| | calcd. [%] | | | found [%] | | |
| | A[b] | Sb | F | A | Sb | F |
| $KSb_2F_{11}$[c] | 7.95 | 49.53 | 42.51 | 8.5 | 49.5 | 41.8 |
| $RbSb_2F_{11}$[c] | 15.89 | 45.26 | 38.85 | 16.4 | 45.5 | 38.5 |
| $CsSb_2F_{11}$[d] | – | 41.6 | 35.7 | – | 41.4 | 35.4 |
| $CsSb_3F_{16}$[e] | – | – | 37.90 | – | – | 37.3 |
| $CsSb_3F_{16}$[f] | – | 45.53 | 37.90 | – | 45.0 | 37.7 |

[a] The chemical analyses are given in mass percent. [b] A = alkali metal. [c] Prepared in aHF. [d] Prepared in aHF with a small excess of $SbF_5$. [e] Prepared in aHF with a large excess of $SbF_5$. [f] Prepared at 85 °C without aHF.

of the reaction conditions are given in Table 12. On the basis of the final masses of the solidified isolated solids and comparison of their vibrational spectra with the vibrational spectra obtained for the products in AF/$SbF_5$/aHF system it was concluded that the final products were $ASbF_6$ (A = Na), $ASb_2F_{11}$ (A = K, Rb) and $ASb_3F_{16}$ (A = Cs). The chemical analysis of the latter salt is given in Table 11.

Table 12. Reaction conditions for the reactions of AF (A = Na, K, Rb, Cs) with an excess of $SbF_5$ at 85 °C.

| Starting materials | | | | | Reaction time | Mass balance | | Final product |
|---|---|---|---|---|---|---|---|---|
| AF[a] | | $SbF_5$ | | | | calcd. | found | |
| AF | [g] | [mmol] | [g] | [mmol] | [d] | [g] | [g] | |
| NaF | 0.012 | 0.29 | 0.400 | 1.85 | 5 | 0.075[b] | 0.070 | $NaSbF_6$ |
| KF | 0.060 | 1.03 | 5.000 | 23.07 | 9 | 0.507[c] | 0.480 | $KSb_2F_{11}$ |
| RbF | 0.091 | 0.87 | 1.600 | 7.38 | 5 | 0.466[c] | 0.461 | $RbSb_2F_{11}$ |
| CsF | 0.158 | 1.04 | 1.250 | 5.77 | 5 | 0.834[d] | 0.823 | $CsSb_3F_{16}$ |

[a] A = alkali metal. [b] Calculated for $ASbF_6$. [c] Calculated for $ASb_2F_{11}$. [d] Calculated for $ASb_3F_{16}$.

### Preparation of Single Crystals of $ASb_2F_{11}$ (A = K, Cs) and $CsSb_3F_{16}$

Preparations were carried out in a double T-shaped apparatus consisting of two FEP tubes (19 mm o.d., and 6 mm o.d.). CsF or $KSb_2F_{11}$ (ca. 0.2 mmol of each) were loaded into the wider of the two tubes in a dry-box. $SbF_5$ (ca. 7 mmol) and aHF (ca. 4 mL) were then condensed onto the starting material at 77 K. The reaction mixtures were then brought up to room temperature. After one day the clear solutions that had developed were transferred into the narrower tube. The evaporation of the solvent from these solutions was carried out by maintaining a temperature gradient corresponding to about 10 K between both tubes for one month, and later increasing this further to about 50 K for an additional month. The effect of this treatment was to enable aHF and the excess of $SbF_5$ to be slowly evaporated from the narrower into the wider tube, leaving colourless crystals of $ASb_2F_{11}$ (A = K, Cs). A similar procedure was adopted with NaF but this yielded only single crystals of $NaSbF_6$. Crystals were selected from the compounds in a dry-box and these were then placed inside 0.3-mm quartz capillaries, which were heat-sealed and mounted on the goniometer head of the diffractometer.

When the final product of the reaction between CsF and liquid $SbF_5$ at 85 °C was checked under a microscope it was found to consist of small regular blocks. Single crystals were immersed in perfluorinated oil (ABCR, FO5960) in the dry-box, selected under the microscope and then transferred into the cold nitrogen stream of the diffractometer.

Table 13. Crystal data and structure refinement for $KSb_2F_{11}$, $CsSb_2F_{11}$ and $CsSb_3F_{16}$.

| Empirical formula | $KSb_2F_{11}$ | $CsSb_2F_{11}$ | $CsSb_3F_{16}$ |
|---|---|---|---|
| Formula mass | 507.60 | 585.41 | 802.16 |
| Temp [K] | 250 | 250 | 200 |
| *a* [pm] | 1141.65(8) | 774.10(14) | 2207(3) |
| *b* [pm] | 1279.96(9) | 1425.41(17) | 772.6(11) |
| *c* [pm] | 3948.5(3) | 951.30(15) | 1605(3) |
| *α* [°] | 90 | 90 | 90 |
| *β* [°] | 90 | 113.226(6) | 90 |
| *γ* [°] | 90 | 90 | 90 |
| *V* [nm$^3$] | 5.7699(7) | 0.9646(3) | 2.737(8) |
| *Z* | 24 | 4 | 8 |
| $D_{calcd.}$ [Mg m$^{-3}$] | 3.506 | 4.031 | 1.947 |
| *λ* [pm] | 71.069 | 71.069 | 71.069 |
| *μ* [mm$^{-1}$] | 6.19 | 9.449 | 4.335 |
| Space group | *Pbca* (no. 61) | $P2_1/n$ (no. 14) | $Pca2_1$ (no. 29) |
| *GOF* indicator | 1.101 | 1.064 | 1.422 |
| $R_1$; $wR_2$ [$I > 2.00\sigma(I)$][a] | 0.0511; 0.1213 | 0.0309; 0.0735 | 0.0609; 0.1165 |

[a] $R_1 = \Sigma||F_o| - |F_c||/\Sigma|F_o|$, $wR_2 = \Sigma[w(F_o^2 - F_c^2)^2]/\Sigma[w(F_o^2)^2]^{1/2}$, $GOF = [\Sigma[w(F_o^2 - F_c^2)^2/(N_o - N_p)]^{1/2}$, where $N_o$ = no. of reflns. and $N_p$ = no. of refined parameters.

 © 2006 Wiley-VCH Verlag GmbH & Co. KGaA, Weinheim 

### Chemical Analyses

The alkali metal content (A) was determined by flame atomic emission spectrometry.[33] The total fluoride content (F) was determined following complete decomposition of the sample with Devarda alloy in alkaline media by direct potentiometry using a fluoride ion selective electrode.[34] The antimony content was, in turn, determined potentiometrically by redox titration with $KBrO_3$ after prior reduction of the antimony with alumina powder in acidic media.[35] The results of analysis of the isolated K, Rb, and Cs polyfluoroantimonate products are given in Table 11.

### X-ray Structure Determination of $ASb_2F_{11}$ (A = K, Cs) and $CsSb_3F_{16}$ Salts

Single-crystal data of $ASb_2F_{11}$ (A = K, Cs) and $CsSb_3F_{16}$ were collected using a Mercury CCD area detector coupled with a Rigaku AFC7S diffractometer with a graphite-monochromated Mo-$K_\alpha$ radiation source. Data were corrected for Lorentz, polarisation and absorption effects and processed using the Rigaku Crystalclear software suite.[36] The structures were solved by direct methods[37] and then expanded using Fourier techniques. The salt $CsSb_3F_{16}$ crystallizes in an acentric space group ($Pca2_1$), so the Flack parameter[38] was refined. The latter converged to a twin ratio of 0.75(7). Some details of the single-crystal data collection and data processing and refinement for $ASb_2F_{11}$ (A = K, Cs) and $CsSb_3F_{16}$ are given in Table 13.

Further details of the crystal-structure investigation may be obtained from the Fachinformationzentrum Karlsruhe, 76344 Eggenstein-Leopoldshafen, Germany, on quoting the depository numbers CSD-415752 ($KSb_2F_{11}$), -415751 ($CsSb_2F_{11}$) and -415750 ($CsSb_3F_{16}$).

## Acknowledgments

The authors (Z. M., P. B. and M. P.) gratefully acknowledge the Slovenian Research Agency (ARRS) for the financial support of the present study within the research program P1-0045 Inorganic Chemistry and Technology. We are also grateful to Prof. Jack Passmore for a careful reading of the manuscript and helpful comments.

[1] C. Röhr, R. Kniep, *Z. Naturforsch., Teil B* **1994**, *49*, 650–654.
[2] J. Bacon, P. A. W. Dean, R. J. Gillespie, *Can. J. Chem.* **1969**, *47*, 1655–1659.
[3] R. J. Gillespie, B. Landa, *Inorg. Chem.* **1973**, *12*, 1383–1388.
[4] B. Bonnet, G. Mascherpa, *Inorg. Chem.* **1980**, *19*, 785–788.
[5] Z. Mazej, P. Benkič, *Inorg. Chem.* **2003**, *42*, 8337–8343.
[6] J. Burgess, R. D. Peacock, R. Sherry, *J. Fluorine Chem.* **1982**, *20*, 541–554.
[7] G. W. Drake, D. A. Dixon, J. A. Sheehy, J. A. Boatz, K. O. Chiste, *J. Am. Chem. Soc.* **1998**, *120*, 8392–8400.
[8] K. O. Christe, W. W. Wilson, C. J. Schack, *J. Fluorine Chem.* **1978**, *11*, 71–85.
[9] D. Zhang, S. J. Rettig, J. Trotter, F. Aubke, *Inorg. Chem.* **1996**, *35*, 6113–6130.
[10] G. J. Kruger, C. W. F. T. Pistorius, *Acta Crystallogr., Sect. B* **1976**, *32*, 2916–2918.
[11] M. M. de V. Steyn, A. M. Heyns, R. B. English, *J. Cryst. Spec. Res.* **1984**, *14*, 505–512.
[12] R. D. Shannon, *Acta Crystallogr., Sect. A* **1976**, *32*, 751–767.
[13] W. E. Dasent, *Inorganic Energetics*, 1st ed., Penguin Books Ltd., Harmondsworth, UK, **1970**.
[14] H. D. B. Jenkins, H. K. Roobottom, J. Passmore, L. Glasser, *Inorg. Chem.* **1999**, *38*, 3609–3620.
[15] M. Gerken, D. A. Dixon, G. J. Schrobilgen, *Inorg. Chem.* **2002**, *41*, 259–277.
[16] I. Bernhardi, T. Drews, K. Sepplet, *Angew. Chem. Int. Ed.* **1999**, *38*, 2232–2233.
[17] R. Faggiani, D. K. Kennepohl, C. J. L. Lock, G. Schrobilgen, *Inorg. Chem.* **1986**, *25*, 563–571.
[18] T. Drews, W. Koch, K. Seppelt, *J. Am. Chem. Soc.* **1999**, *121*, 4379–4384.
[19] A. J. Edwards, G. R. Jones, *J. Chem. Soc. A* **1971**, 2318–2320.
[20] H. Willner, M. Bodenbinder, R. Bröchler, G. Hwang, S. J. Rettig, J. Trotter, B. von Ahsen, U. Westphal, V. Jonas, W. Thiel, F. Aubke, *J. Am. Chem. Soc.* **2001**, *123*, 588–602.
[21] R. J. Gillespie, B. Landa, *Inorg. Chem.* **1973**, *12*, 1383–1388.
[22] K. O. Christe, B. Hoge, J. A. Boatz, G. K. S. Prakash, G. A. Olah, J. A. Sheehy, *Inorg. Chem.* **1999**, *38*, 3132–3142.
[23] G. Schrobilgen, J. H. Holloway, D. R. Russell, *J. Chem. Soc., Dalton Trans.* **1984**, 1411–1415.
[24] G. S. H. Chen, J. Passmore, *J. Chem. Soc., Dalton Trans.* **1979**, 1251–1256.
[25] A. I. Karelin, Z. K. Nikitina, Y. Y. Khariton, V. Y. Rosolovsky, *Zh. Neorg. Khim.* **1970**, *15*, 941–948; *Chem. Abstr.* **1970**, *73*, 19946.
[26] Z. Mazej, P. Benkič, *J. Fluorine Chem.* **2005**, *126*, 803–808.
[27] K. Matsumoto, R. Hagiwara, Y. Ito, O. Tamada, *J. Fluorine Chem.* **2001**, *110*, 117–122.
[28] S. Loss, C. Röhr, *Z. Naturforsch. Teil B* **1998**, *53*, 75–80.
[29] Z. Mazej, *Eur. J. Inorg. Chem.* **2005**, 3983–3987.
[30] N. Schrewelius, *Arkiv Foer Kemi, Mineralogi Och Geologi* **1943**, *16b*, 1–5; *Chem. Abstr.* **1945**, *39*, 14452.
[31] PTFE valves were constructed and made at the Jožef Stefan Institute in a similar way as shown in: O'Donnelll, *The Chemistry of Fluorine*; in *Comprehensive Inorganic Chemistry*, Pergamon Press, Oxford, **1973**, p. 1918.
[32] J. E. Griffiths, G. E. Walrafen, *Inorg. Chem.* **1972**, *11*, 427–429.
[33] J. D. Ingle, S. R. Crouch, *Spectrochemical Analysis*, Prentice Hall, Englewood Cliffs, **1988**, pp. 225– 256.
[34] M. Ponikvar, B. Sedej, B. Pihlar, B. Žemva, *Anal. Chim. Acta* **2000**, *418*, 113–118.
[35] M. Ponikvar, B. Pihlar, B. Žemva, *Talanta* **2002**, *58*, 803–810.
[36] CrystalClear: Rigaku Corporation, Woodlands, Texas, USA, **1999**.
[37] G. M. Sheldrick, SHELX97-2, University of Göttingen, Germany, **1997**.
[38] H. D. Flack, *Acta Crystallogr., Sect. A* **1983**, *39*, 876–881.

Received: September 20, 2005
Published Online: January 16, 2006

 © 2006 Wiley-VCH Verlag GmbH & Co. KGaA, Weinheim 

EurJIC
European Journal of Inorganic Chemistry

Issue 6/2006

Pages 1097–1304

*Papers available ahead of print in Early View at www.interscience.wiley.com*

*Earliest available Table of Contents: Automatically, free of charge by e-mail through www.interscience.wiley.com/alerts*

## COVER PICTURE

**The cover picture shows** the crystal structure of the cationic organometallic π-conjugated push–pull chromophore combining the mixed sandwich acceptor group $[CpFe(\eta^6\text{-}p\text{-}MeC_6H_4)]^+$, associated with the 2-*tert*-butyl-4*H*-chromen-4-ylidene donor through the asymmetric hydrazone spacer −NH−N=CH−. This dipolar chromophore exhibits solvatochromic properties, low-lying intramolecular charge-transfer transition and enhanced second-order NLO properties ($\mu\beta$), as measured with the EFISH technique at 1.907 μm. The scientific cooperation between researchers from the Southern Hemisphere (Chile) and the Northern Hemisphere (France) is symbolised not only by the Southern Cross but also by the NaCl crystals of the salt desert El Salar de Atacama. Details are discussed in the article by C. Manzur, D. Carrillo, B. Caro, J.-R. Hamon et al. on p. 1131 ff.

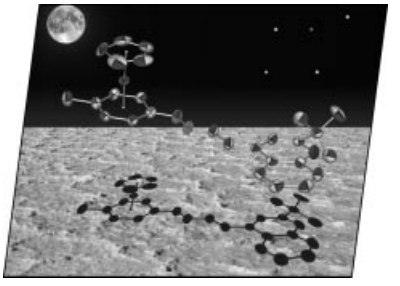

## MICROREVIEW

**Contents**

**1111** **B. Smarsly, M. Antonietti***

Block Copolymer Assemblies as Templates for the Generation of Mesoporous Inorganic Materials and Crystalline Films

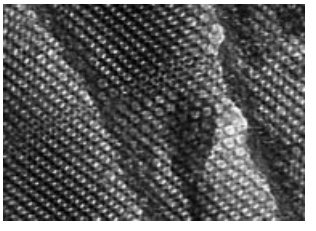

**Keywords:** Block copolymers / Mesoporous materials / Self-assembly / Sol–gel processes

 © 2006 Wiley-VCH Verlag GmbH & Co. KGaA, Weinheim 

# SHORT COMMUNICATIONS


**1121** **S. Gautron, N. Lassauque, C. Le Berre, P. Serp, L. Azam, R. Giordano, G. Laurenczy, D. Thiébaut, P. Kalck***

Analysis of the Synergistic Effect of Carbonylplatinum Complexes on the Iridium-Catalysed Carbonylation of Methanol to Acetic Acid

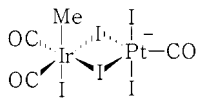


**Keywords:** Homogeneous catalysis / Carbonylation / Iridium / Platinum / Reaction mechanism

**1127** **R. Ahlrichs, D. Fenske,* A. Rothenberger,* C. Schrodt, S. Wieber**

Atom Assignment in Solid-State Structures on the Basis of X-ray Crystallography and DFT Calculations − A Case Study on a Molecular Cu−Sb Alloy

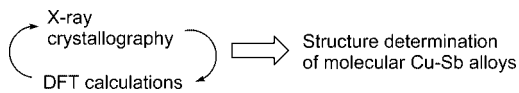


**Keywords:** DFT calculations / Molecular alloys / Sb ligands


# FULL PAPERS


**1131** **L. Millán, M. Fuentealba, C. Manzur,* D. Carrillo,* N. Faux, B. Caro,* F. Robin-Le Guen, S. Sinbandhit, I. Ledoux-Rak, J.-R. Hamon***

Dipolar Organoiron Pyranylideneacetaldehyde Hydrazone Complexes: Synthesis, Characterization, Crystal Structure, Linear and Nonlinear Optical Properties

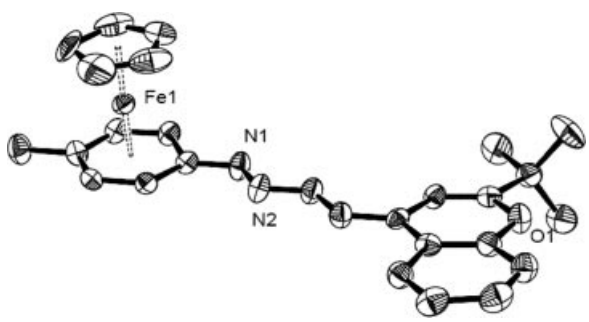


**Keywords:** Donor−acceptor systems / Iron / Pyranylideneacetaldehyde / Nonlinear optics / Sandwich complexes

**1139** **J. Gracia, J. M. Poblet,* J. Autschbach, L. P. Kazansky***

Density-Functional Calculation of the $^{183}W$ and $^{17}O$ NMR Chemical Shifts for Large Polyoxotungstates

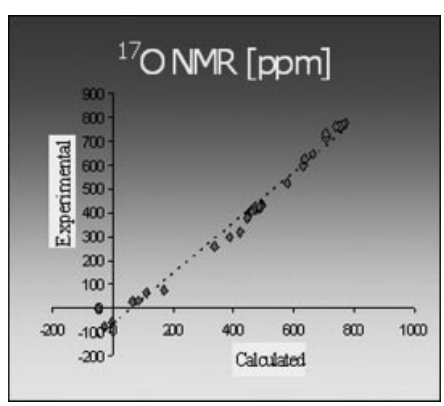


**Keywords:** Density-functional calculations / NMR spectroscopy / Oxygen / Polyoxometalates / Tungsten

**1149** **J. Gracia, J. M. Poblet,* J. Autschbach, L. P. Kazansky***

DFT Calculations of the $^{183}W$ NMR Chemical Shifts in Reduced Polyoxotungstates

**Keywords:** Density functional calculations / NMR spectroscopy / Oxygen / Polyoxometalates / Tungsten

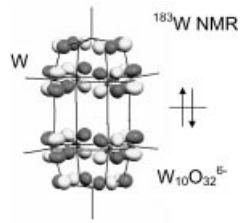


**1155** **M. García-Castro, A. Martín, M. Mena,* J.-M. Poblet, C. Yélamos**

Iodine Attack on the Metalloligand [{Ti($\eta^5$-$C_5Me_5$)($\mu$-NH)}$_3$($\mu_3$-N)]: Surprising Formation of the $[Ti_3(\eta^5\text{-}C_5Me_5)_3I_2(\mu\text{-}NH)_3(NH_3)]^+$ Cation

**Keywords:** Indium / Iodine / N ligands / Nitrido complexes / Titanium

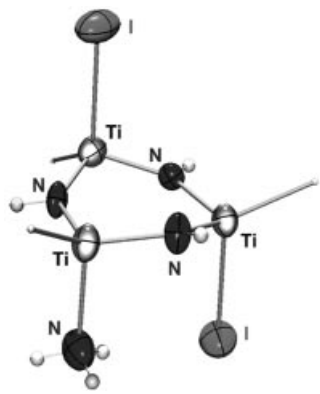


**1161** **H.-F. Hsu,* C.-L. Su, N. O. Gopal, C.-C. Wu, W.-C. Chu, Y.-F. Tsai, Y.-H. Chang, Y.-H. Liu, T.-S. Kuo, S.-C. Ke***

Redox Chemistry in the Reaction of Oxovanadium(V) with Thiolate-Containing Ligands: the Isolation and Characterization of Non-Oxo Vanadium(IV) Complexes Containing Disulfide and Thioether Groups

**Keywords:** Vanadium / S ligands / Bioinorganic chemistry / EPR spectroscopy

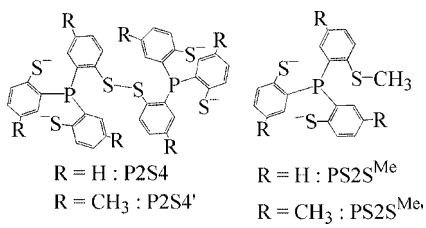


**1168** **F. Liu, W. Chen***

Oxidative Addition of $Cl_2$, HClO to Square-Planar $Pt^{II}$ Complexes: Synthesis and Structural Characterization of Platinum(II) and Platinum(IV) Bis(amidate) Complexes

**Keywords:** Platinum / Amidates / Amines

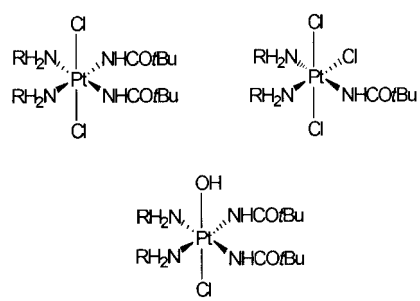


 © 2006 Wiley-VCH Verlag GmbH & Co. KGaA, Weinheim 

**1174** **B. Demerseman,* M. D. Mbaye, D. Sémeril, L. Toupet, C. Bruneau, P. H. Dixneuf**

Direct Preparation of [Ru($\eta^2$-$O_2CO$)($\eta^6$-arene)-(L)] Carbonate Complexes (L = Phosphane, Carbene) and Their Use as Precursors of [$RuH_2$(*p*-cymene)($PCy_3$)] and [Ru($\eta^6$-arene)(L)-$(MeCN)_2$][$BF_4$]$_2$: X-ray Crystal Structure Determination of [Ru($\eta^2$-$O_2CO$)(*p*-cymene)($PCy_3$)]·1/2$CH_2Cl_2$ and [Ru($\eta^2$-$O_2CO$)($\eta^6$-$C_6Me_6$)-($PMe_3$)]·$H_2O$

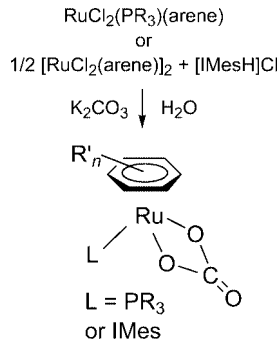


**Keywords:** Arene ligands / Hydrides / O ligands / Reactive intermediates / Ruthenium

**1182** **B. J. Frost,* C. A. Mebi, P. W. Gingrich**

Boron−Nitrogen Adducts of 1,3,5-Triaza-7-phosphaadamantane (PTA): Synthesis, Reactivity, and Molecular Structure

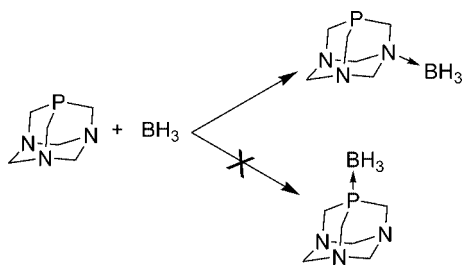


**Keywords:** Borane adducts / Boroxine / N,P ligands / Coordination modes / Structure elucidation

**1190** **D. G. Lonnon, S. B. Colbran,* D. C. Craig**

Programmed Helicity in Self-Assembled Hydrogen-Bonded Chains of Chiral Copper(II) Complexes

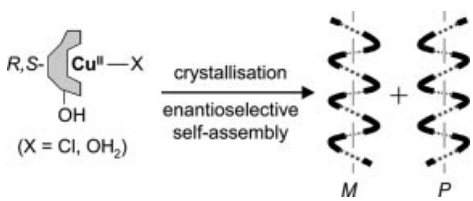


**Keywords:** Hydrogen bonds / Supramolecular / Self-assembly / Copper / Helical structures

**1198** **M. Itoi,* Y. Ono, N. Kojima,* K. Kato, K. Osaka, M. Takata**

Charge-Transfer Phase Transition and Ferromagnetism of Iron Mixed-Valence Complexes ($n$-$C_nH_{2n+1}$)$_4$N[$Fe^{II}Fe^{III}$(dto)$_3$] ($n$ = 3−6; dto = $C_2O_2S_2$)

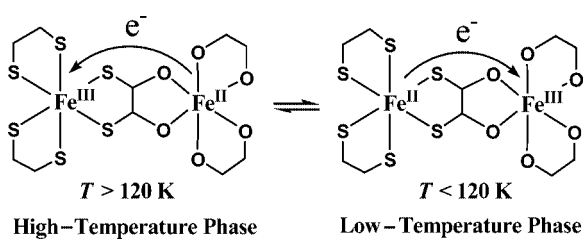


**Keywords:** Mixed-valence compounds / Iron / Magnetic properties / Charge transfer


 © 2006 Wiley-VCH Verlag GmbH & Co. KGaA, Weinheim 

**1208** **J. Yang, J.-F. Ma,* Y.-Y. Liu, J.-C. Ma, H.-Q. Jia, N.-H. Hu**

Two New $Cu^{II}$ Coordination Polymers: Studies of Topological Networks and Water Clusters

**Keywords:** Coordination polymers / Copper / Materials science / Topology / Water clusters

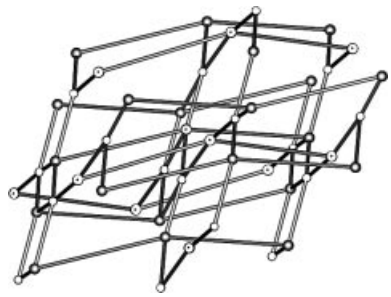

**1216** **X. Liu, H. Xia, W. Gao, L. Ye, Y. Mu,* Q. Su, Y. Ren**

Synthesis, Structures, and Luminescent Properties of Aluminum Complexes with Chelating Anilido-Imine Ligands

**Keywords:** Aluminum / N ligands / Luminescence

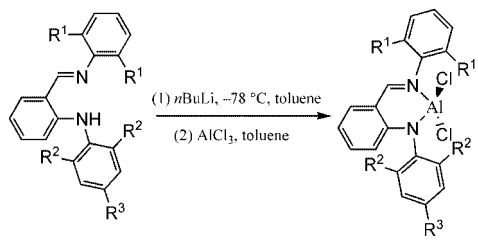


**1223** **F. Cheviré, F. Tessier,* R. Marchand**

Optical Properties of the Perovskite Solid Solution $LaTiO_2N-ATiO_3$(A = Sr, Ba)

**Keywords:** Oxynitrides / Perovskites / Solid solution / Optical properties

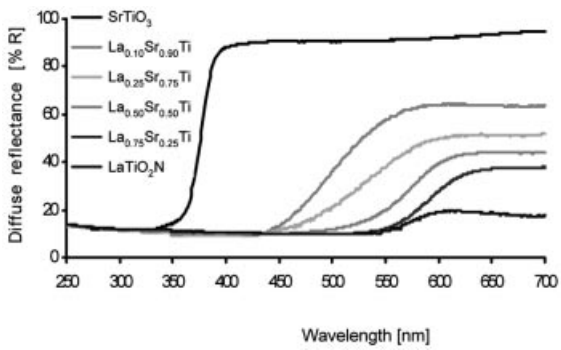


**1231** **M. del Carmen Aguirre, J. Borrás, A. Castiñeiras,* J. M. García-Monteagudo, I. García-Santos, J. Niclós, D. X. West**

Synthesis, Characterization, and Properties of Some Copper(II) Complexes of 2-Pyridineformamide Thiosemicarbazone (HAm4DH)

**Keywords:** Thiosemicarbazones / Copper complexes / One-dimensional chains / Cyclic voltammetry / DNA cleavage

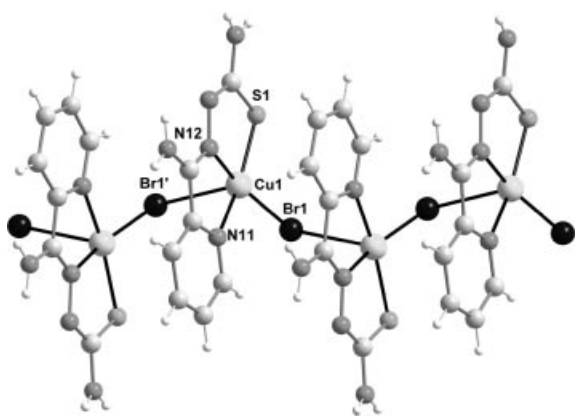


 © 2006 Wiley-VCH Verlag GmbH & Co. KGaA, Weinheim 

**1245** **M. Du,* X.-J. Jiang, X.-J. Zhao, H. Cai, J. Ribas**

Novel Metallosupramolecular Networks Constructed from $Cu^{II}$, $Ni^{II}$, and $Cd^{II}$ with Mixed Ligands: Crystal Structures, Fluorescence, and Magnetism

**Keywords:** Coordination polymers / Inclusion complexes / Supramolecular chemistry / Noncovalent interactions

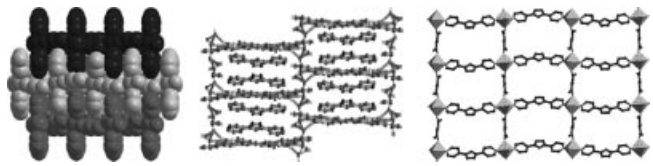

**1255** **N. D. Boscher, C. J. Carmalt, I. P. Parkin***

Atmospheric Pressure Chemical Vapour Deposition of $NbSe_2$ Thin Films on Glass

**Keywords:** Chemical vapour deposition / Metal selenide / Thin film

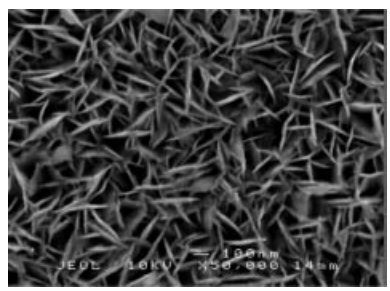

**1260** **R.-L. Sang, L. Xu***

Counteranion-Induced Formation of *cis* and *trans* Singly and Doubly $H_2$biim-Bridged Di-, Hexa-, and Polymeric Ag−$H_2$biim Complexes

**Keywords:** Crystal engineering / Luminescence / Metal−metal interactions / N ligands / Silver

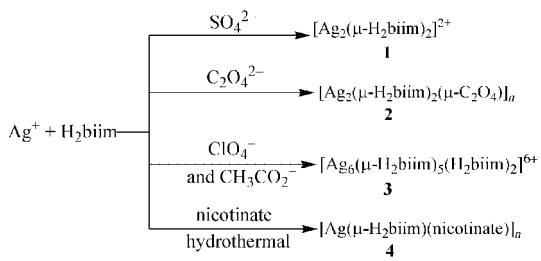


**1268** **S. Ahrens, E. Herdtweck, S. Goutal, T. Strassner***

Synthesis, Structure and Stability of New $Pt^{II}$–Bis(N-Heterocyclic Carbene) Complexes

**Keywords:** Carbene ligands / NMR spectroscopy / Platinum / Synthesis design

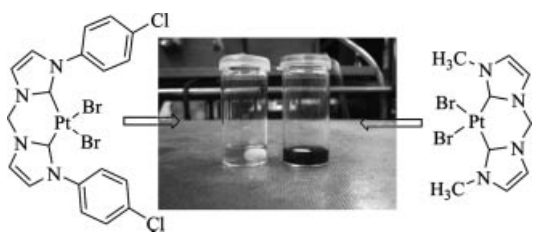


**1275** **A. R. Silva, K. Wilson, A. C. Whitwood, J. H. Clark, C. Freire***

Amine-Functionalised Hexagonal Mesoporous Silica as Support for Copper(II) Acetylacetonate Catalyst

**Keywords:** Copper / Anchoring / Mesoporous silica / EPR spectroscopy / Aziridination

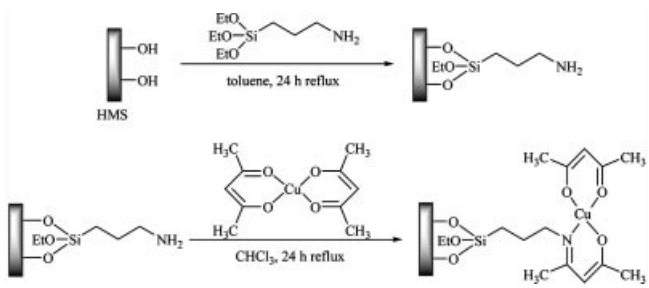


 © 2006 Wiley-VCH Verlag GmbH & Co. KGaA, Weinheim 

**1284** **V. B. Di Marco,* A. Dean, M. G. Ferlin, R. A. Yokel, H. Li, A. Venzo, G. G. Bombi**

Methyl-Hydroxypyridinecarboxylic Acids as Possible Bidentate Chelating Agents for Aluminium(III): Synthesis and Metal−Ligand Solution Chemistry

**Keywords:** Aluminium / Carboxylate ligands / Potentiometry / Chelation therapy

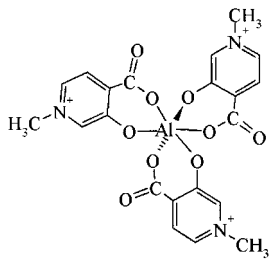

**1294** **C. G. Hrib, P. G. Jones, W.-W. du Mont,* V. Lippolis, F. A. Devillanova**

Complexes of Bidentate Phosphane Selenide Ligands with Mesitylenetellurenyl Iodide and with Tellurium Diiodide

**Keywords:** Phosphane selenides / Tellurium iodides / Heteronuclear NMR / Raman spectroscopy / Soft−soft interactions

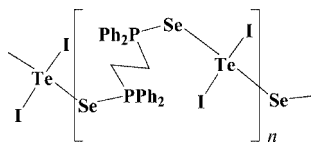

DOI: 10.1002/ejic.200501003

# Block Copolymer Assemblies as Templates for the Generation of Mesoporous Inorganic Materials and Crystalline Films

**Bernd Smarsly[a] and Markus Antonietti*[a]**

**Keywords:** Block copolymers / Mesoporous materials / Self-assembly / Sol–gel processes

This Microreview presents the synthesis of mesoporous, crystalline inorganic materials using self-assembled block copolymer mesostructures as templates. The advances in this field are discussed in light of the progress in the development of suitable polymer templates. Particular emphasis is placed on the special conditions and demands to transform the primary sol–gel films into mesoporous, aligned crystalline films for functional applications.
(© Wiley-VCH Verlag GmbH & Co. KGaA, 69451 Weinheim, Germany, 2006)

## Introduction

In the past ten years scientists have learned to develop and use appropriate amphiphilic block copolymers (soft matter) as templates to generate inorganic films and multicrystals with controlled porosity on the nanometer scale (hard matter). Such inorganic materials with a nanoscale structural set-up and large specific surfaces had not been accessible before and may play important roles in sorption, catalysis, photoconversion, or piezo- and ferroelectric devices.

[a] Max-Planck Institute of Colloids and Interfaces, Am Mühlenberg, 14476 Potsdam-Golm, Germany

This Microreview will introduce the concept of "true liquid-crystal templating",[1,2] i.e. the idea of converting a self-assembled block copolymer mesophase into its inorganic counterpart with liquid precursors (e.g. providing mesoporous silica, metal oxides, and metals), which is also termed "nanocasting".[3] We will delineate the special effects for a number of oxide crystalline systems with special functions in detail.

The field of mesoporous oxides made by templates is, of course, much bigger, and for a general overview of ordered mesoporous oxides we refer the reader to the review article by Schüth.[4] This review will be centered around the generation of mesoporous inorganic structures using block copolymers as templates, putting special emphasis on the con-

*Bernd Smarsly studied chemistry and physics at the University of Marburg, Germany, and Innsbruck, Austria, and received a Masters degree of Natural Science in 1998. He completed his PhD studies in 2001 at the Max Planck Institute of Colloids and Interfaces. Afterwards, from 2002–2003 he worked as a postdoctoral researcher at the Advanced Materials Laboratory of the University of New Mexico at Albuquerque, USA. Since 2003 he has been working as group leader at the MPI of Colloids and Interfaces. His main research interests now focus on the preparation of functional, mesostructured metal oxides, their physico-chemical properties, and the development of novel characterization techniques, especially using X-ray scattering.*

*Markus Antonietti studied chemistry in Mainz and did his doctorate with Hans Sillescu. His habilitation about nanostructured polymer gels in 1990 filled him with enthusiasm for complex materials. After his Professorship of Chemistry at the University of Marburg, he was appointed Director of the Department of Colloid Chemistry at the Max Planck Institute of Colloids and Interfaces in 1993. Markus Antonietti's contributions to the chemical community are manifold, but first of all he is interested in the creativity in research. He loves to share and impart this passion. He also likes cooking with his family and loud music.*

**MICROREVIEWS:** This feature introduces the readers to the authors' research through a concise overview of the selected topic. Reference to important work from others in the field is included.

 © 2006 Wiley-VCH Verlag GmbH & Co. KGaA, Weinheim 

ditions of crystalline metal-oxide formation and the observed textural properties. While most of the research is focused on oxide materials, a separate paragraph is reserved for the interesting emerging field of mesoporous metals.

## 1. General Mechanism

The general idea of using block copolymers as templates is based on the fact that amphiphilic block copolymers self-assemble in certain solvents to give robust, very regular superstructures that feature structural motifs on the nanometer scale (lyotropic liquid-crystalline phases). Typically, the constituting entities are spherical or cylindrical micelles or lamellar sheets with a characteristic cross-section of 5–100 nm.

The block copolymer self-assembly technique is probably the best examined mode of self-organization[5] and is governed by the microphase separation dictated by the mutual incompatibility of the different blocks, one being soluble and the other being insoluble in the solvent to be used ("amphiphilic" polymers). In most cases, aside from classical nonionic surfactants, which can be regarded as small block oligomers composed of an oligoethylene and oligo(ethylene oxide), diblock or triblock copolymers are used that feature polystyrene,[2a] polybutadiene,[6] and poly(propylene oxide) as the hydrophobic block,[7] and poly(ethylene oxide) or poly(vinylpyridines)[8] as hydrophilic blocks. Recently, a semi-commercial family of "KLE" block copolymers [KLE = *K*raton-*L*iquid-*b*-poly(*e*thylene oxide)] was introduced, which combines good chemical accessibility and high mesophase robustness with a superb application profile.[9] Kraton liquid is a hydrogenated poly(ethylene-*co*-butylene) hydrophobic block with a low glass transition. In principle, block copolymers self-assemble or microphase-separate in a variety of solvents, in particular water, but also alcohols or THF, which enables a certain width of chemistry for inorganic framework generation. This is contrary to low molecular weight surfactants, which usually rely on water and the hydrophobic effect for self-assembly.

In a typical block copolymer templating procedure (see Figure 1), such regularly ordered mesostructures of amphiphiles in water are converted into their 1:1 replica (their "negative") by solidifying the hydrophilic or solvatophilic domains between the micelles. This is done by replacing the majority of the solvent by a metal or metal oxide precursor with similar polarity and condensing this precursor around the aggregates. An especially suitable precursor for this procedure is, for instance, hydrated silicic acid, which shows a very similar polarity and proton-bridging behavior as water, such that the final assembly patterns are very similar to the ones found in water. Depending on the final material of choice, this precursor can be a hydrolysable metal species such as metal–orthoesters, but can also be a metal salt (metal chlorides, etc.), and the final structure can be made out of metal oxides, metal chalcogenides, or even the elemental metals. The organic template can also be regarded as a place holder that prevents the inorganic reaction from occurring and becomes void space upon removal either by extraction or thermal decomposition.

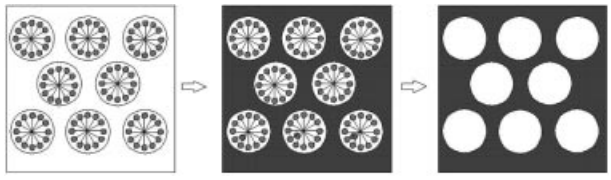

Figure 1. Illustration of the typical block copolymer templating procedure ("nanocasting"). A soft matter complex fluid is surrounded with a high concentration of inorganic precursor (left), and the continuous phase is solidified (middle). After solidification of the inorganic phase, the template is removed to give a solid negative replica ("hardcopy") of the original phase.

Figures 2 and 3 show examples of mesostructures that can be obtained by varying the polymers.[6b]

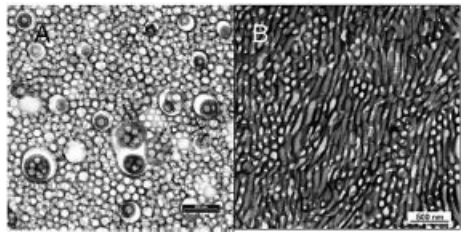


Figure 3. TEM of two mesoporous silicas obtained from PB-*b*-PEO templates,[6] illustrating the wide range of accessible structures. **A** presents a micellar phase at the borderline to a lamellar phase, which contains some vesicles as precursor structures (scale bar: 200 nm), while **B** shows the bicontinuous sponge-like $L_3$-phase (scale bar: 500 nm).

One main advantage of block copolymers over low molecular weight surfactants is their significantly higher molecular weight and their variability in size and composition, which enable a rich diversity of structures (hexagonal, cu-

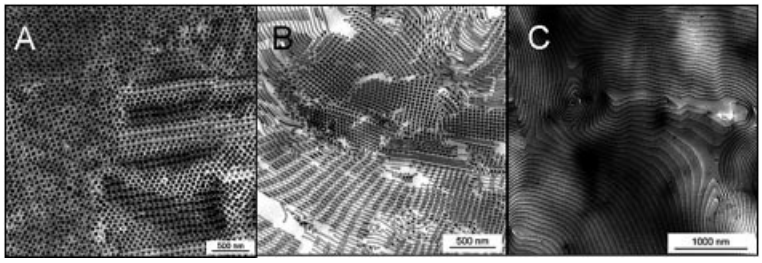


Figure 2. Microtomed films of lyotropic phases of block copolymers, as used for nanocasting. **A**: BCC phase; **B**: hexagonal phase; **C**: lamellar phase (taken from refs.[6b,6c]).

 © 2006 Wiley-VCH Verlag GmbH & Co. KGaA, Weinheim 

bic, etc.) and a wider range of accessible pore sizes, currently up to about 80 nm.[6] Initial work was pioneered by Göltner et al. using PS-*b*-PEO[2] or PS-*b*-PVP block copolymers.[8] Later, presumably independently, this work was extended by Stucky towards Pluronics block copolymers[7] and by Wiesner et al.[10] towards organically modified aluminosilica hybrids.

The assumption that the final silica mesostructure represents a 1:1 copy of the lyotropic phase was later proven by comparing the replicas with species obtained by cross-linking of lyotropic phases with γ-radiation.[11] An unusual case is shown in Figure 4, where a branched lamellar phase is replicated and compared with the original phase. The two TEM images show the original lyotropic phase (Figure 4, A) and the templated, porous silica (Figure 4, B), and it is nicely seen that one is the "negative" of the other.

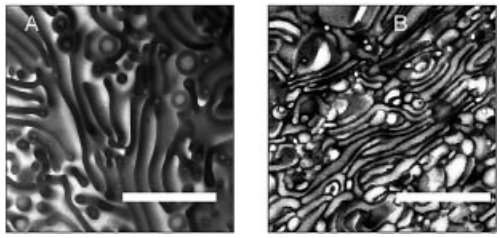


Figure 4. Original or copy? **A** represents the lyotropic phase (TEM obtained from thin cuts) leading to the corresponding silica (**B**) shown in Figure 3. This example illustrates the similarity between the original block copolymer mesophase and the silica replica. Terminal ends of lamellae, branching points, vesicles, membrane, and pores are replicated with about the same abundance and fine structural features. The scale bars represent 1000 nm.

The quality of replication plus the homogeneity has also been proved by small angle X-ray scattering. Already in the original paper by Göltner et al.[2c] the authors showed that after solidification and removal of the template the diffractogram is only shifted to slightly higher angles, while the pattern stays unaltered. This means that the material shrinks slightly but does not change its local structure. A case for quantitative fitting of the scattering curve is shown in Figure 5.

In this case (using KLE polymers as a template), TEM shows that the mesoporous silica contains a regular packing of spherical mesopores about 13 nm in diameter, which are located on the sites of a face-centered cubic arrangement. Evidently, not only are the single mesopores extremely uniform in shape and size, but the 3D arrangement is also nearly undisturbed over large areas of up to several square micrometers. This example illustrates the amazing order and control of the materials' structure that can be achieved by the nanocasting procedure, in spite of the mechanical stresses during the condensation of the matrix. Small-angle X-ray scattering (SAXS) is usually applied to provide an overall, averaged characterization of mesoporous materials. In this case (Figure 5, b), the presence of distinct SAXS patterns with pronounced maxima and minima confirms the high regularity of the mesostructure and the mesopore size and lattice type.

In the case of metal oxides the ultimate composition is readily obtained by heat-treatment in air or oxygen to give the amorphous or crystalline oxide form, and mesoporous metals are obtained by an in situ or final reduction step, either electrochemically or chemically.

## 2. Evaporation-Induced Self-Assembly for the Generation of Organized Thin Films

The general concept of nanocasting was originally developed for thick specimens (monoliths or powders), although it also holds true for the generation of bulk materials and thin films. The latter was remarkably improved and simplified by introduction of the technique of "evaporation-induced self-assembly" (EISA).[12] EISA proceeds along a different methodology, but the underlying templating mechanism is identical to nanocasting. The practical difference lies in the fact that one starts from a homogeneous solution with a significantly larger amount of volatile solvents with low viscosity.

Taking this low viscosity, which means less organized precursor solutions, coatings of excellent macroscopic

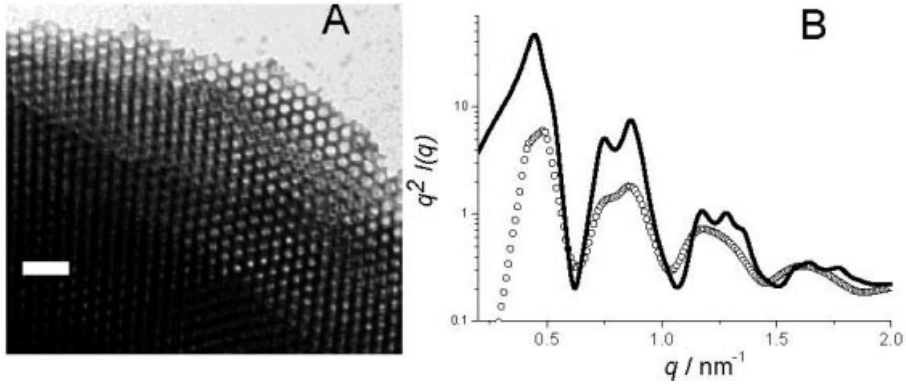


Figure 5. Mesoporous silica featuring spherical mesopores (size of about 13 nm) obtained from the KLE block copolymer [poly(ethylene-*co*-butylene)-*b*-poly(ethylene oxide)].[9a] The TEM image (**A**) reveals a highly ordered structure of spherical mesopores arranged on a fcc lattice. The scale bar is 80 nm. **B**: Small-angle X-ray scattering curve of the mesoporous silica (circles) and a fitting (solid line) based on a model of spherical mesopores with a certain polydispersity and lattice distortions[9a] In the present case, the relative polydispersity of the pore radius is only 5% (including the deviations from spherical shape).

 © 2006 Wiley-VCH Verlag GmbH & Co. KGaA, Weinheim 

homogeneity can be generated by standard coating techniques, i.e. dip-coating, spin-coating, doctor-blading, or spraying. After evaporation of the volatile solvent, a high-concentration template phase is regained. This is the return to the situation of nanocasting, although already shaped in a defined coating geometry. It must be mentioned, however, that throughout drying, large scale orientation of the otherwise unorganized lyotropic phase can be promoted to a very high extent. For EISA in thin films, the strong interaction with the substrate in the interplay with a directional drying pressure (e.g. in dip coating) usually leads to a high degree of preferred orientation, much higher than in the bulk materials.[13] An orientation is usually established that provides a maximum degree of interaction with the substrate via the densest lattice plane.[14]

For the generation of inorganic materials discussed below, low molecular weight inorganic precursors or salts are usually taken. Recent papers, however, have shown that similar constructions can also be achieved by EISA using preformed inorganic nanoparticles of sizes of only a few nanometers for structure build-up, e.g. $TiO_2$[15] or $CeO_2$,[16] as illustrated in Figure 6.

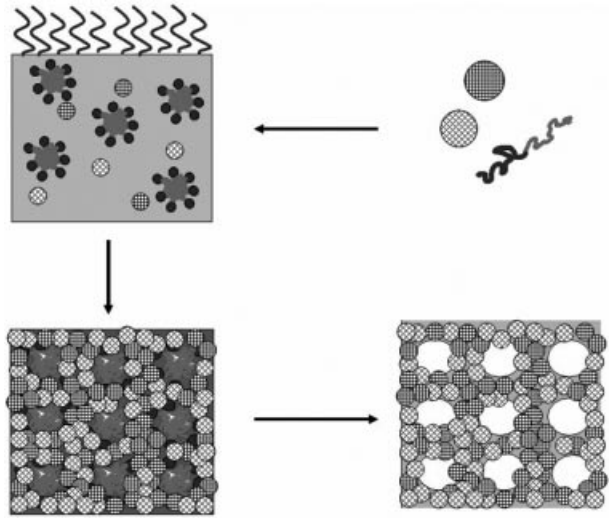

Figure 6. Block copolymer templating to generate a mesoporous scaffold starting from inorganic nanoparticles, using the EISA process. The scheme illustrates the more complicated case where two different nanoparticles ("bricks"), cross-hatched with vertical/horizontal and diagonal lines, respectively, are used for structure set-up to generate binary contacts.

It is evident that this approach faces different obstacles, for instance the colloidal stability of the initial sol, and only recently has a novel procedure for the synthesis of nanoparticles provided particles which could be sufficiently dispersed at high concentrations.[17] On the other hand, there are also benefits due to the building block approach, as the material is already crystallized and does not shrink.[16] Binary systems (i.e. two different nanoparticles) can also be easily made, thus leading to interesting binary contacts.

While the overall principle of block copolymer templating for inorganic chemistry seems to be surprisingly straightforward, it is worthwhile to highlight some key features of this process:

· Such high area interfaces between two materials can only be generated if all of the involved interfacial energies throughout the process are lowered. This compatibilization is provided by the special chemical character of the appropriate block copolymer. If a new inorganic substance is to be made porous, a block copolymer with the right binding moieties along the backbone of one block has to be chosen.

· As the formation of microphase-separated block copolymer phases is a thermodynamic phenomenon, templating is substantially governed by numerous physical parameters. Together with solvent effects, it is difficult to predict pore structures a priori, hence optimal templating conditions were found by trial-and-error experiments in many cases. In addition to these thermodynamic parameters, templating is further aggravated by strong kinetic effects, as some intermediary structures might turn out to be metastable. For instance, Gibaud et al. have shown that the rate of evaporation of the volatile solvent, even when all the other parameters are kept the same, can dramatically change the final mesophase structure.[14]

· A general problem of true liquid-crystalline sol–gel templating is the simultaneous occurrence of condensation of the inorganic species and the self-assembly process. Experimental procedures are usually needed that delay the condensation significantly until completion of micelle formation. Robust self-assembly of amphiphilic copolymers into micelles, which is the best choice for systems with higher segregation strength (or incompatibility between the two blocks), is certainly favorable for this purpose. The use of block copolymers towards larger sizes is limited for the same reason by their increasingly reduced mobility. Hence, the upper limit for block copolymer templating is, under practical conditions, currently at about 80 nm in structural size.[6]

· The solvating block is sometimes tightly bound and molecularly mixed into the inorganic phase, bringing some organic character to it, as found for PEO and silica.[18] This can result, after template removal, in extensive extra microporosity (pore size below 2 nm), as reported by various studies.[18–24] While physisorption techniques gave no unambiguous conclusion, detailed small-angle X-ray and neutron scattering (SAXS, SANS) analyses of PS-*b*-PEO-templated silicas provided a quantification of the microporosity[21–23] and showed that the micropores are actually located between the mesopores.

## 3. Synthesis of Mesoporous, Crystalline Metal Oxides

While work in the first years of block copolymer templating has been mainly focused on amorphous silica as a model case, one of the current scientific challenges is the creation of mesoporous metal oxides whose pore walls are entirely nanocrystalline. The reason for this is essentially driven by their potential applications: crystalline oxides are chemically, thermally, and mechanically more robust. In addition, oxide materials possess inherently interesting func-

 © 2006 Wiley-VCH Verlag GmbH & Co. KGaA, Weinheim 

tionality, which is improved or is accessible by the introduction of mesopores. For instance, mesoporous, crystalline $TiO_2$ could be beneficial for various applications like solid-state solar cells ("the Grätzel cell")[25] or photocatalysis.[26] In these applications, organized porosity would be helpful to improve the contact between the oxide and other species (e.g. the anode in case of solar cells). Another target is heterogeneous catalysis, where it would be desirable to generate mesoporous metal oxides such as $CeO_2$, $ZrO_2$, or $V_2O_5$.

The necessity of a high crystallinity imposes a severe problem. It is evident that the soft, self-assembled structures of amphiphilic block copolymers (ABC) are not very stable at the high temperatures needed for many crystallization processes of oxides. The use of preformed, soluble metal oxide nanoparticles for casting evidently has certain elegance because of the absence of a separate nucleation step for the oxide, but is still restricted to some readily dispersable oxides.[16] This is why the most frequently employed strategy starts from molecular metal precursors such as metal chlorides or alkoxides (e.g. $TiCl_4$, $CeCl_3{\cdot}7H_2O$, etc.). Many metal oxide precursors are indeed available that are amenable to sol–gel templating and are soluble in common solvents.

These precursors are then condensed, and nucleation and crystallization as well as the removal of the template occur concurrently and have to be dynamically balanced. This is not simple, as crystal growth can severely disrupt the fragile, soft ABC mesostructure, which would lead to pore collapse and loss of mesostructural order. Therefore, usually quite delicate and tedious heat-treatment procedures have to be used to avoid mesostructural breakdown and to balance condensation, crystallization, and calcination of the template.

Previous experiments with classical templates gave highly crystalline mesoporous oxides in only a few cases, in particular for $TiO_2$.[27–30] In the majority of these studies the materials showed either moderate crystallinity or significant damage to the mesostructural regularity (pore shape and porosity). A clever optimization of all these processes was presented by Grosso et al., who developed an in situ experiment to study the morphological changes by simultaneous small- and wide-angle X-ray scattering (SAXS/WAXS), leading to an improved understanding of the crystallization and its interference with the imprinted mesostructure.[30c] Using that technique, crystalline mesoporous anatase became accessible with traditional templates.

Novel amphiphilic block copolymer templates helped to improve the preparation of mesoporous $TiO_2$ films[31] and to extend these results also to other oxides of high chemical relevance. This is on the one hand due to the ability of these systems to self-assemble in a broader range of solvent systems: poly(ethylene-*co*-butylene)-*b*-poly(ethylene oxide) ("KLE polymers") is more robust and has more hydrophobic "contrast" than the commonly applied polymers of the Pluronics family.[31b] Poly(isobutylene)-*b*-poly(ethylene oxide) (PIB-*b*-PEO)[31a] is a similar template system with improved templating properties and good accessibility.

Secondly, due to their larger and chemically variable molecular weight, the pore structure can be adopted to match organic process parameters and properties, such as the nanocrystal size. If an inorganic system shows a small nucleation and fast growth-rate, the nanocrystals get rather big under standard conditions and the targeted pore size has to match the size of the accessible tectonic elements to form the structure. In other cases, the desired physical properties rely on a certain structural size, such as the exciton or plasmon size. Anatase just keeps its favorable indirect semiconductor properties at a size larger than 10 nm, and making the structure finer does not contribute to performance. For all those systems, the targeting of slightly larger pore sizes (ca. 20 nm) is advised.

Thirdly, the chemical functionality of the inorganic-binding block can also, in principle, be adjusted, for example by introduction of acetylacetoxy groups[32] or a variety of other metal-complexing moieties, following the hard-soft-acid-base (HSAB) principle.[33] Up to know, however, it has been possible to address all practical questions with the simple PEO binding block.

The final crystalline films are very homogeneous, crack-free, and flat on the scale of some nanometers over macroscopic dimensions. This is nicely illustrated by high resolution SEM of the surface of such an optimized anatase film (Figure 7). The depicted pores have a size of about 13 nm, are open to the surface, and at some positions even the three openings towards the lower cubic pore layer are visible. The overall flatness of this film (excluding pores) is lower than 2 nm, as determined by atomic force microscopy (AFM). It should be emphasized that these films show a rather homogeneous spherical pore shape. The structure resembles highly ordered inverse opal structures with respect to the perfection of the mutual arrangement, thus proving that crystal-like packing can also be achieved with block copolymers.

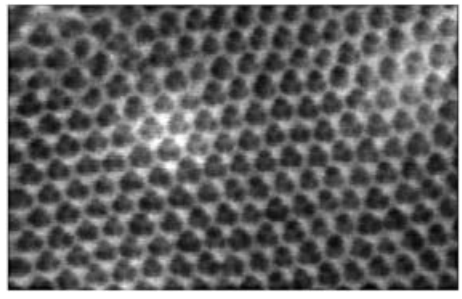

Figure 7. HRSEM of a mesoporous crystalline anatase film indicating the typical lyotropic liquid-crystalline arrangement of pores. The pores have a cross-section of about 13 nm. Note that in some pores the three entries to the lower layer of the cubically packed pores are visible.

With these improved templates, various metal oxides could be applied as highly crystalline coatings with high structural regularity of the mesopores (spherical, size larger than 12 nm).[34–36]

Beside the technically highly relevant anatase, $ZrO_2$, $CeO_2$, and a variety of mixed intermediary ternary oxide

 © 2006 Wiley-VCH Verlag GmbH & Co. KGaA, Weinheim 

mixtures of the two metals have also been synthesized (see Figure 8).[34]

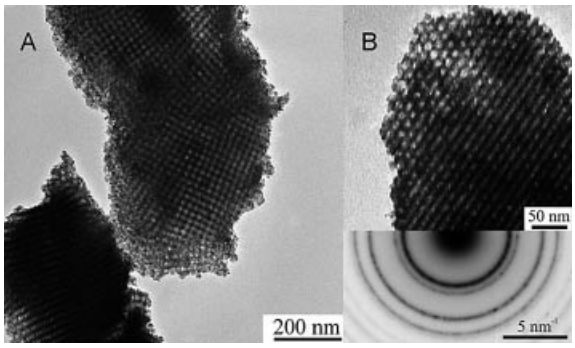


Figure 8. Crystalline, mesoporous $CeO_2$ films prepared from molecular precursors (**A**),[34b] and mesoporous powder obtained from preformed $CeO_2$ nanoparticles (**B**).[16a] The selected-area electron diffraction pattern (bottom part of **B**) proves the crystallinity of the mesopore walls.

Those ceria/zirconia systems are interesting for various applications. Compared to other metal oxides, ceria and zirconia are chemically and thermally extraordinarily stable and are therefore used as catalyst supports and in ceramic membranes for sensing and catalysis. Ceria has just one polymorph (fluorite structure), and can switch easily between $Ce^{4+}$ and $Ce^{3+}$, balancing the charge difference with oxygen vacancies. This distinct property makes cerium oxide in the form of mesoporous layers an interesting candidate for solid-oxide fuel cells.

Porous crystalline films with very high thermal stability and related crystallization temperatures, such as $Al_2O_3$[35a] and $HfO_2$,[35b] have also been made. The case studies on $HfO_2$ had the advantage that removal of the template and crystallization are thermally clearly separate processes. Here, it could be demonstrated that the transformation of the initial self-assembled composite, consisting of the block copolymer and weakly condensed metal oxyhydrates, into the final mesoporous, crystalline metal oxide proceeds through the steps of inorganic condensation, template removal, and final crystallization. WAXS/SAXS experiments performed in situ during the heat treatment revealed that the crystallization has to be adjusted to be a solid–solid transformation from an almost completely dry, water-free, amorphous metal oxide into its crystalline counterpart. It is essential that the BC template is stable enough to support the mesostructure up to a temperature (350–400 °C under nitrogen) where the anhydrous and amorphous condensed metal oxide species is formed.

As shown for $Al_2O_3$, a slightly higher structural size is also favorable for the mechanical stability of the intermediary amorphous thin pore walls and the final thermal stability. Well organized $\gamma$-$Al_2O_3$ films were only accessible when the pore size was increased to about 20 nm[35a] (Figure 9).

Furthermore, even such complex materials as perovskites (e.g. $BaTiO_3$, $SrTiO_3$, and their substitution products) can now be obtained as mesoporous films,[36] which is particularly interesting for a number of reasons (Figure 10). First, such materials are more difficult to accomplish in the desired stoichiometric composition by ordinary sol–gel methods. Secondly, the class of perovskites is linked to properties such as ferroelectricity, piezoelectricity, adjustable bandgaps, or even high-temperature superconductivity.[37]

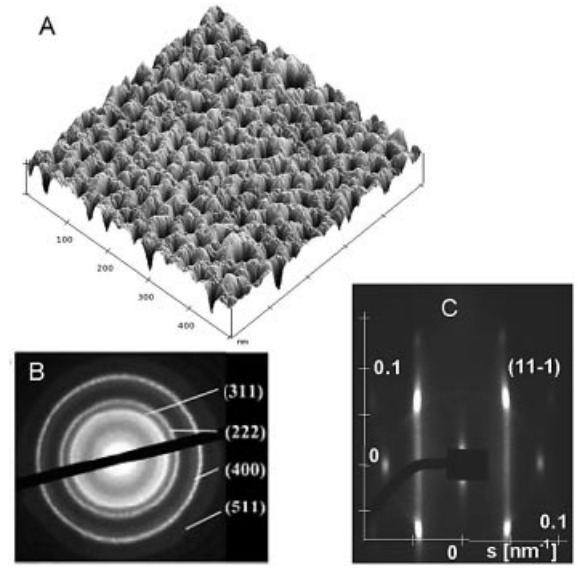


Figure 9. Crystalline, mesoporous films of $\gamma$-$Al_2O_3$, heat-treated at 900 °C.[35a] **A**: Atomic force microscopy image. **B**: Selected-area electron diffraction, underlining the polycrystalline character. **C**: 2D SAXS pattern obtained at a low angle of incidence with respect to the substrate, proving the close to perfect orientation of the mesostructure in the *z*-direction.

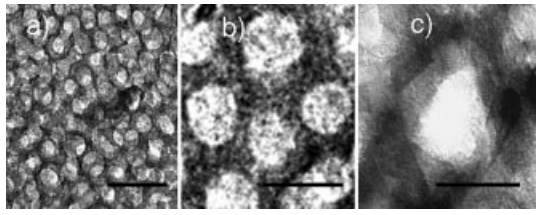


Figure 10. Structural changes in mesoporous $SrTiO_3$ perovskite films upon transformation from the amorphous (a and b) to the crystalline phase. The walls, in spite of the complex composition, are nevertheless homogeneous and single crystalline. Scale bars from left to right: 50 nm, 20 nm, and 10 nm.

For other oxide systems, such as $Nb_2O_5$, a newly emerging dynamic effect sets in. On a mesoscpic scale, these films look quite similar to all the other previously described ones (Figure 11). Both WAXS and electron diffraction, however, show that the structure is built up by aligned single nanoparticles, that is, the nanoparticles "sense" their mutual organization and orient together in one energetically favorable direction.[38] This effect also occurs for dense sol–gel films made by similar protocols and has been called "soft epitaxy". It might become the basis for the generation of oriented films by simple chemical coating means.

 © 2006 Wiley-VCH Verlag GmbH & Co. KGaA, Weinheim 

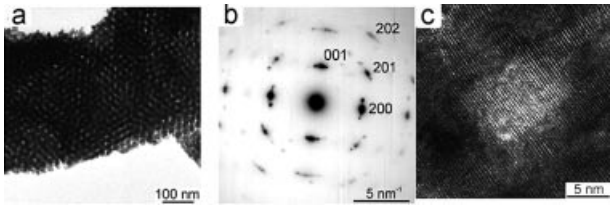


Figure 11. Soft epitaxy of mesoporous niobium oxide made by nanocasting: a) TEM of a porous film; b) electron diffraction of the same area, indicating an epitaxial alignment of the formed nanoparticles to the surface and each other; c) HRTEM of one single pore supporting the rather high degree of mutual organization.

The special functionality of crystalline oxide films has been explored both for $SnO_2$[39] and $WO_3$.[40] In the case of $SnO_2$, it was shown that the resulting porous thin-films are conducting, which is a prerequisite for their use as sensors and as electrodes. For $WO_3$, reversible electrochromism, which is the reversible change of the transparency of those films with applied electric fields, has also been observed (Figure 12). The switching time in these films is much shorter than classical thin-films analogous to this structure (already applied in switchable rear mirrors) as electrons only have to be moved from the walls to the pore interior (Figure 12).

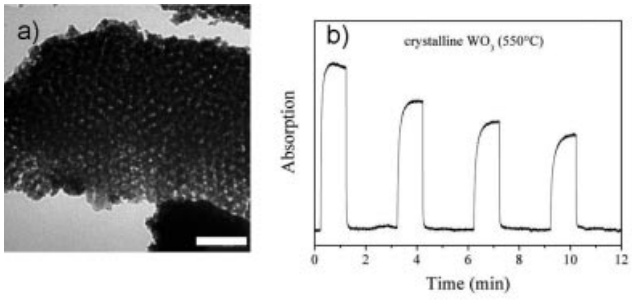


Figure 12. Mesoporous $WO_3$ (TEM, a) prepared with KLE block copolymers shows improved electrochromic switching. b) The absorption at 450 nm as a function of applied voltage. The mesoporous, crystalline mesostructure with its much higher surface area and short transport paths leads to a much faster coloration and decoloration than previous materials.

Very recently, some new approaches have been developed that extend nanocasting in a even more general frame and bypass some of the aforementioned problems. For instance, in the method of Holmes and Watkins the films are exposed to solutions of metal oxide precursors in supercritical $CO_2$.[41] This procedure has the advantage that capillary forces are absent and that the films have higher temperature stability because of the supercritical conditions. In separate work, Chmelka et al. first cross-linked the mesophases of block copolymers featuring additional double bonds,[42] and then the inorganic precursor was infiltrated. This approach reduces the disruption of the BC mesophase upon condensation of the metal salts.

Wiesner and Gruner et al.[43] have used extended amphiphilic dendrimers as templates, the self assembly of which is also expected to be rather robust against variations of the environment. Another interesting approach was introduced by Domen:[44] first, an amorphous mesoporous oxide is prepared, which is then followed by carbon deposition inside the pores, which acts as a temperature-stable scaffold. The material is then crystallized at elevated temperature, where the carbon prevents mesostructural collapse. Finally, the carbon is oxidized by calcination in oxygen to generate the pure inorganic scaffold.

## 4. Mesoporous Metals and Other Semiconductors

Aside from mesoporous metal oxides, mesoporous elemental metals, e.g. Pt, Pd, and Ni, have also been obtained by block copolymer templating. In principle, mesoporous metals are also accessible through the schematic principle depicted in Figure 1. Similar to mesoporous oxides, in the first step, reducible metal salts ($PdCl_2$, $H_2PtCl_6$, etc.) are distributed around the block copolymer domains. The preparation of the corresponding metals is more delicate because of the additional reduction step, which can be performed by electrodeposition (for instance on gold electrodes) or chemically, for example with metallic Zn. A second problem of these strategies is the high densification of matter throughout metal formation.

The Attard group has reported the electrochemical preparation of mesoporous metal electrodes (Figure 13, A),[45] which could be interesting for various applications such as fuel cells (Ni) or electrochemical hydrogenation of organic species (Pd, Pt). Yamauchi et al.[46] have described the generation of mesostructured particles of Ni (Figure 13) and Ni–Co alloys, partly by electroless methods, especially by using organic reducing agents such as dimethylaminoborane or sodium borohydride. Furthermore, Kucernak has demonstrated that it is possible to obtain mesostructures of otherwise inaccessible mesoporous "alloys" such as Pt/Ru.[47] Such two-phase, mesostructured metal blends show high promise for catalytic applications, such as in fuel cells.

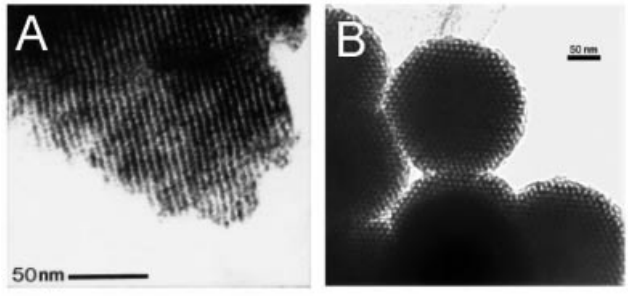


Figure 13. Mesoporous Pt[45a] (**A**) and mesoporous Ni[46a] particles (**B**).

Using oligomeric nonionic surfactants, even non-oxidic semiconductors have been made. Stupp et al.[48] have been able to mesostructure thin films of CdS, CdSe, and ZnS, while for $Ag_2S$, CuS, HgS, and PbS the same methodology only resulted in compound films without mesoscopic features. Nandhakumar et al.[49] have extended this approach

 © 2006 Wiley-VCH Verlag GmbH & Co. KGaA, Weinheim 

to synthesize mesostructuted CdTe films with excellent optical properties. As these experiments were already possible with rather short oligomeric structures, it is expected that the advantages of block copolymer templates can also be transferred to these classes of inorganic materials.

## Conclusion and Outlook

Nanocasting with block copolymer templates has turned into a powerful instrument for generating inorganic materials with mesostructure, porosity, and a high surface area, as documented by the broad variety of new materials described above. In nanocasting, the self-assembly of "soft", fragile matter is literally hard-copied into inorganic hard matter, with all the advantageous properties resulting from the inorganic world. Through the hard-copy approach, the inorganic films are fitted out with the properties that make them valuable for different areas of materials science, e.g. chemical sensing, piezoelectricity, catalysis, electrochromism, solar cells, light-emitting diodes, etc. All these applications benefit from an optimized mesostructure, conduction pathways, or addressed binary interface contacts.

It is our personal view that these new materials are the first case where self-assembly will have a significant impact on nanosciences, especially for diverse electrochemical applications where complex metal oxides are needed with high surface areas. It is also very likely that various fields such as electrochromism, batteries, and electrode materials will benefit dramatically from progress in the preparation of mesoporous inorganic materials and metals. However, there are still some important challenges that hinder a broader application of block copolymer templated mesostructures in technical devices. For instance, for catalysis and electrodes it would be desirable to prepare crystalline, mesoporous metal oxides in the form of macroscopic monoliths, which can also be obtained in arbitrary shapes. Moreover, although various mesostructures have been obtained as high quality thin films with thicknesses of up to several micrometers, the preparation of much thicker layers is still a problem. Such geometries are, however, needed for various applications, for example for catalytically active coatings.

Another point of exploration and interest are hierarchical mesostructures with their expectedly superior transport properties, because larger pores could serve as transport pores, reduce back-pressure, and enhance diffusion. Such hierarchical structures could, in principle, be obtained by mixing the corresponding block copolymer micelles of different sizes. However, this build-up of hierarchically arranged micelles is not a trivial task because block copolymers tend to form either mixed micelles or phase-separate macroscopically.[50,51]

Furthermore, new types of block copolymer could open up a new chapter in templating. So far, self-assembly has mainly been carried out in close-to-aqueous systems. If templates were available that form self-organized lyotropic structures in a variety of solvents, this would dramatically facilitate processing and allow broader synthetic access to other porous materials, in particular for substances which are sensitive to water.

Evidently, in spite of the huge progress in the field of block copolymer self-assembly, there are still fascinating new opportunities for inorganic and materials chemistry, which will, in our opinion, keep this area very active for the next few years.


[1] a) G. S. Attard, J. G. Glyde, C. G. Goltner, *Nature* **1995**, *378*, 366–368; b) G. S. Attard, C. G. Goltner, J. M. Corker, S. Henke, R. H. Templer, *Angew. Chem.* **1997**, *109*, 1372–1374; *Angew. Chem. Int. Ed. Engl.* **1997**, *36*, 1315.

[2] a) C. G. Goltner, S. Henke, M. C. Weißenberger, M. Antonietti, *Angew. Chem.* **1998**, *110*, 633–636; *Angew. Chem. Int. Ed.* **1998**, *37*, 613; b) C. G. Goltner, M. Antonietti, *Adv. Mater.* **1997**, *9*, 431; c) M. C. Weissenberger, C. G. Goltner, M. Antonietti, *Ber. Bunsen-Ges. Phys. Chem.* **1997**, *101*, 1679–1682.

[3] S. Polarz, M. Antonietti, *Chem. Commun.* **2002**, 2593–2604.

[4] U. Ciesla, F. Schuth, *Microporous Mesoporous Mater.* **1999**, *27*, 131–149.

[5] a) F. S. Bates, G. H. Fredrickson, *Annu. Rev. Phys. Chem.* **1990**, *41*, 525–557; b) I. W. Hamley, *Philos. Trans. R. Soc. London, A* **2001**, *359*, 1017–1044.

[6] a) C. G. Goltner, B. Berton, E. Kramer, M. Antonietti, *Adv. Mater.* **1999**, *11*, 395–398; b) S. Forster, B. Berton, H. P. Hentze, E. Kramer, M. Antonietti, P. Lindner, *Macromolecules* **2001**, *34*, 4610–4623; c) H. P. Hentze, E. Kramer, B. Berton, S. Forster, M. Antonietti, M. Dreja, *Macromolecules* **1999**, *32*, 5803–5809.

[7] a) D. Zhao, Q. Huo, J. Feng, B. F. Chmelka, G. D. Stucky, *J. Am. Chem. Soc.* **1998**, *120*, 6024–6036; b) D. Zhao, J. Feng, Q. Huo, N. Melosh, G. H. Fredrickson, B. F. Chmelka, G. D. Stucky, *Science* **1998**, *279*, 548–552.

[8] E. Kramer, S. Forster, C. Goltner, M. Antonietti, *Langmuir* **1998**, *14*, 2027–2031.

[9] a) A. Thomas, H. Schlaad, B. Smarsly, M. Antonietti, *Langmuir* **2003**, *19*, 4455–4459; b) M. Groenewolt, M. Antonietti, S. Polarz, *Langmuir* **2004**, *20*, 7811–7819; c) C. G. Goltner, B. Berton, E. Krämer, M. Antonietti, *Chem. Commun.* **1998**, 2287–2288.

[10] M. Templin, A. Franck, A. DuChesne, H. Leist, Y. M. Zhang, R. Ulrich, V. Schadler, U. Wiesner, *Science* **1997**, *278*, 1795–1798.

[11] H. P. Hentze, E. Krämer, B. Berton, S. Forster, M. Antonietti, *Macromolecules* **1999**, *32*, 5803–5809.

[12] C. J. Brinker, Y. F. Lu, A. Sellinger, H. Y. Fan, *Adv. Mater.* **1999**, *11*, 579–585.

[13] a) W. Ruland, B. Smarsly, *J. Appl. Crystallogr.* **2004**, *37*, 575–684; b) W. Ruland, B. Smarsly, *J. Appl. Crystallogr.* **2005**, *38*, 78–86.

[14] A. Gibaud, D. Grosso, B. Smarsly, A. Baptiste, J. F. Bardeau, F. Babonneau, D. A. Doshi, Z. Chen, C. J. Brinker, C. Sanchez, *J. Phys. Chem. B* **2003**, *107*, 6114–6118.

[15] F. Bosc, A. Ayral, P. A. Albouy, C. Guizard, *Chem. Mater.* **2003**, *15*, 2463–2468.

[16] a) A. S. Desphande, N. Pinna, B. Smarsly, M. Antonietti, M. Niederberger, *Small* **2005**, *1*, 313–316; b) J. Ba, J. Polleux, M. Antonietti, M. Niederberger, *Adv. Mater.* **2005**, DOI 10.100/adma.200501018.

[17] a) N. Pinna, G. Garnweitner, M. Antonietti, M. Niederberger, *J. Am. Chem. Soc.* **2005**, *127*, 5608–5612; b) N. Pinna, G. Garnweitner, M. Antonietti, M. Niederberger, *Adv. Mater.* **2004**, *16*, 2196–2200; c) M. Niederberger, M. H. Bard, G. D. Stucky, *J. Am. Chem. Soc.* **2002**, *124*, 13642–13643.

[18] B. Smarsly, S. Polarz, M. Antonietti, *J. Phys. Chem. B* **2001**, *105*, 10473–10483.

[19] C. G. Goltner, B. Smarsly, B. Berton, M. Antonietti, *Chem. Mater.* **2001**, *13*, 1617–1624.


 © 2006 Wiley-VCH Verlag GmbH & Co. KGaA, Weinheim 

[20] a) M. Jaroniec, M. Kruk, C. H. Ko, R. Ryoo, *Chem. Mater.* **2000**, *12*, 1961–1968; b) R. Ryoo, C. H. Ko, M. Kruk, V. Antochshuk, M. Jaroniec, *J. Phys. Chem. B* **2000**, *104*, 11465.
[21] B. Smarsly, M. Thommes, P. I. Ravikovitch, A. V. Neimark, *Adsorption* **2005**, *11*, 653–655.
[22] M. Impéror-Clerc, P. Davidson, A. Davidson, *J. Am. Chem. Soc.* **2000**, *122*, 11925–11933.
[23] B. Smarsly, C. G. Goltner, M. Antonietti, W. Ruland, E. Hoinkis, *J. Phys. Chem. B* **2001**, *105*, 831–840.
[24] a) A. Galarneau, N. Cambon, F. Di Renzo, R. Ryoo, M. Choi, F. Fajula, *New J. Chem.* **2003**, *27*, 73–79; b) B. L. Newalkar, S. Komarneni, *Chem. Mater.* **2001**, *13*, 4573–4579; c) K. Miyazawa, S. Inagaki, *Chem. Commun.* **2000**, 2121–2122.
[25] M. Grätzel, *Nature* **2001**, *414*, 338–344.
[26] I. Mora-Seró, *J. Phys. Chem. B* **2005**, *109*, 3371–3380.
[27] D. M. Antonelli, J. Y. Ying, *Curr. Opin. Colloid Interf. Sci.* **1996**, *1*, 523–529.
[28] P. D. Yang, T. Deng, D. Y. Zhao, P. Y. Feng, D. Pine, B. F. Chmelka, G. M. Whitesides, G. D. Stucky, *Science* **1998**, *282*, 2244.
[29] a) O. Dag, I. Soten, O. Celik, S. Polarz, N. Coombs, G. A. Ozin, *Adv. Funct. Mater.* **2003**, *13*, 30–36; b) S. Y. Choi, M. Mamak, N. Coombs, N. Chopra, G. A. Ozin, *Adv. Funct. Mater.* **2004**, *14*, 335–344; c) S. Y. Choi, M. Mamak, S. Speakman, N. Chopra, G. A. Ozin, *Small* **2005**, *1*, 226–232.
[30] a) D. Grosso, G. Soler-Illia, F. Babonneau, C. Sanchez, P. A. Albouy, A. Brunet-Bruneau, A. R. Balkenende, *Adv. Mater.* **2001**, *13*, 1085; b) E. L. Crepaldi, G. Soler-Illia, D. Grosso, C. Sanchez, *New J. Chem.* **2003**, *27*, 9–13; c) D. Grosso, G. J. D. A. Soler-Illia, E. L. Crepaldi, F. Cagnol, C. Sinturel, A. Bourgeois, A. Brunet-Bruneau, H. Amenitsch, P. A. Albouy, C. Sanchez, *Chem. Mater.* **2003**, *15*, 4562–4570; d) E. L. Crepaldi, G. J. de A. A. Soler-Illia, D. Grosso, F. Cagnol, F. Ribot, C. Sanchez, *J. Am. Chem. Soc.* **2003**, *125*, 9770–9786; e) D. O. de Zárate, C. Boissière, D. Grosso, P. A. Albouy, H. Amenitsch, P. Amoros, C. Sanchez, *New J. Chem.* **2005**, *29*, 141–144; f) P. C. Angelomé, S. Aldabe-Bilmes, M. E. Calvo, E. L. Crepaldi, D. Grosso, C. Sanchez, G. J. A. A. Soler-Illia, *New J. Chem.* **2005**, *29*, 59–63.
[31] a) M. Groenewolt, T. Brezesinski, H. Schlaad, M. Antonietti, P. W. Groh, B. Ivan, *Adv. Mater.* **2005**, *17*, 1158; b) B. Smarsly, D. Grosso, T. Brezesinski, N. Pinna, C. Boissière, M. Antonietti, C. Sanchez, *Chem. Mater.* **2004**, *16*, 2948–2952.
[32] H. Schlaad, T. Krasia, M. Antonietti, *J. Am. Chem. Soc.* **2004**, *126*, 11307–11310.
[33] a) M. Antonietti, S. Forster, J. Hartmann, S. Oestreich, *Macromolecules* **1996**, *29*, 3800–3806; b) M. Antoniett, S. Forster, S. Oestreich, *Macromol. Symp.* **1997**, *121*, 75–88; c) S. Klingelhofer, W. Heitz, A. Greiner, S. Oestreich, S. Forster, M. Antonietti, *J. Am. Chem. Soc.* **1997**, *119*, 10116–10120.
[34] a) T. Brezesinski, M. Groenewolt, N. Pinna, M. Antonietti, B. Smarsly, *New J. Chem.* **2005**, *29*, 237–242; b) T. Brezesinski, C. Erpen, K. I. Iimura, B. Smarsly, *Chem. Mater.* **2005**, *17*, 1683–1690.
[35] a) M. Kuemmel, D. Grosso, C. Boissière, B. Smarsly, T. Brezesinski, P. A. Albouy, H. Amenitsch, C. Sanchez, *Angew. Chem. Int. Ed.* **2005**, *44*, 4589–4592; b) T. Brezesinski, B. Smarsly, K. I. Iimura, D. Grosso, C. Boissière, H. Amenitsch, M. Antonietti, C. Sanchez, *Small* **2005**, *1*, 889–898.
[36] D. Grosso, C. Boissière, B. Smarsly, T. Brezesinski, N. Pinna, P. A. Albouy, H. Amenitsch, M. Antonietti, C. Sanchez, *Nat. Mater.* **2004**, *3*, 787–792.
[37] a) A. S. Balla, R. Guo, R. Roy, *Mat. Res. Innovat.* **2000**, *4*, 3–26; b) C. D. Chandler, C. Roger, M. J. Hampden-Smith, *Chem. Rev.* **1993**, *93*, 1205–1241.
[38] B. Smarsly, T. Brezesinski, M. Groenewolt, N. Pinna, H. Amenitsch, M. Antonietti, *Nat. Mater.*, manuscript submitted.
[39] T. Brezesinski, B. Smarsly, A. Fischer, M. Groenewolt, D. Grosso, C. Sanchez, M. Antonietti, *Adv. Funct. Mater.*, manuscript submitted.
[40] T. Brezesinski, D. Fattakhova Rohlfing, S. Sallard, M. Antonietti, B. M. Smarsly, *J. Am. Chem. Soc.*, manuscript submitted.
[41] a) K. X. Wang, B. D. Yao, M. A. Morris, J. D. Holmes, *Chem. Mater.* **2005**, *17*, 4825–4831; b) R. A. Pai, R. Humayun, M. T. Schulberg, A. Sengupta, J. N. Sun, J. J. Watkins, *Science* **2004**, *303*, 507–510.
[42] R. C. Hayward, B. F. Chmelka, E. J. Kramer, *Macromolecules* **2005**, *38*, 7768–7783.
[43] B. K. Cho, A. Jain, S. Mahajan, H. Ow, S. M. Gruner, U. Wiesner, *J. Am. Chem. Soc.* **2004**, *126*, 4070–4071.
[44] J. N. Kondo, T. Katou, D. Lu, M. Hara, K. Domen, *Stud. Surf. Sci. Cat.* **2004**, *154*, 951–957.
[45] a) G. S. Attard, P. N. Bartlett, N. R. B. Coleman, J. M. Elliott, J. R. Owen, J. H. Wang, *Science* **1997**, *278*, 838–840; b) P. A. Nelson, J. M. Elliott, G. S. Attard, J. R. Owen, *Chem. Mater.* **2002**, *14*, 524–529; c) J. M. Elliott, G. S. Attard, P. N. Bartlett, N. R. B. Coleman, D. A. S. Merckel, J. R. Owen, *Chem. Mater.* **1999**, *11*, 3602–3609.
[46] a) Y. Yamauchi, T. Momma,T. Yokoshima, K. Kuroda, T. Osaka, *J. Mater. Chem.* **2005**, *15*, 1987–1994; b) Y. Yamauchi,T. Yokoshima, T. Momma, T. Osaka, K. Kuroda, *J. Mater. Chem.* **2004**, *14*, 2935–2940; c) Y. Yamauchi, T. Yokoshima, T. Momma, T. Osaka, K. Kuroda, *Chem. Lett.* **2004**, *33*, 1576–1579; d) Y. Yamauchi, T. Yokoshima, H. Mukaibo, M. Tezuka, T. Shigeno, T. Momma, T. Osaka, K. Kuroda, *Chem. Lett.* **2004**, *33*, 543.
[47] a) J. Jiang, A. Kucernak, *Chem. Mater.* **2004**, *16*, 1362–1367; b) J. Jiang, A. Kucernak, *J. Electroanalyt. Chem.* **2003**, *543*, 187–199.
[48] P. V. Braun, P. Osenar, V. Tohver, S. B. Kennedy, S. I. Stupp, *J. Am. Chem. Soc.* **1999**, *121*, 7302–7309.
[49] I. S. Nandhakumar, T. Gabriel, X. Li, G. S. Attard, M. Markham, D. C. Smith, J. J. Baumberg, *Chem. Commun.* **2004**, *12*, 1374–1375.
[50] T. Sen, G. J. T. Tiddy, J. L. Casci, M. W. Anderson, *Angew. Chem. Int. Ed.* **2003**, *42*, 4649–4653.
[51] D. B. Kuang, T. Brezesinski, B. Smarsly, *J. Am. Chem. Soc.* **2004**, *126*, 10534–10535.

Received: November 10, 2005
Published Online: February 21, 2006

 © 2006 Wiley-VCH Verlag GmbH & Co. KGaA, Weinheim 

DOI: 10.1002/ejic.200500931

# Analysis of the Synergistic Effect of Carbonylplatinum Complexes on the Iridium-Catalysed Carbonylation of Methanol to Acetic Acid

**Samuel Gautron,[a,b] Nicolas Lassauque,[a] Carole Le Berre,[a] Philippe Serp,[a] Laurent Azam,[a] Roberto Giordano,[a] Gábor Laurenczy,[c] Daniel Thiébaut,[b] and Philippe Kalck*[a]**

**Keywords:** Homogeneous catalysis / Carbonylation / Iridium / Platinum / Reaction mechanism

High-pressure NMR mechanistic investigations into the promoting role of dicarbonyldiiodoplatinum complex in the iridium-catalysed carbonylation of methanol to acetic acid are consistent with iodide abstraction from the $[IrI_3(CH_3)(CO)_2]^-$ resting state species by $[PtI_2(CO)_2]$, unbolting the rate-limiting migratory CO insertion step. A new [Ir–Pt] heterodimetallic complex, which presumably represents the key species involved in the abstraction of $I^-$, has been characterised by NMR in tandem with FAB-MS.

(© Wiley-VCH Verlag GmbH & Co. KGaA, 69451 Weinheim, Germany, 2006)

## Introduction

Carbonylation of methanol is the major route to the production of acetic acid, and the worldwide industrial manufacture associated with this homogeneous catalytic process reaches $6 \cdot 10^6$ tons/year [Equation (1)]. This reaction involves a complex mixture of reactants consisting of water, acetic acid, methyl iodide, methyl acetate, hydroiodic acid, and traces of propionic acid, from which methanol is absent as it is immediately converted by HI into $CH_3I$. Many efforts have been aimed at the substitution of iridium for rhodium since the former tolerates low levels of water during the reaction, saving operating costs in the separation step of water from acetic acid.

$$CH_3OH + CO \xrightarrow[3\ MPa,\ 180°C]{Cat} CH_3COOH \quad (1)$$

Moreover, in the active species $H[IrI_2(CO)_2]$ (**1**) the metal centre is more nucleophilic than that in the homologous rhodium precursor used in the Monsanto process,[1] so that the rate of the first step of the catalytic cycle, the oxidative addition of $CH_3I$ affording $[IrI_3(CH_3)(CO)_2]^-$ (**2**), is largely enhanced.[2] The subsequent step, the migratory CO insertion leading to an Ir–acetyl species is so slow[3] that a process based on iridium cannot be suitable for industrial applications. In 1994, Watson et al. discovered that addition of ruthenium promoters to the iridium catalyst resulted in a dramatic increase in catalytic activity,[4] and very recent reports[5,6] have shown that this is due to the abstraction of an iodo ligand from **2**, allowing the rapid migratory insertion of CO into the Ir–$CH_3$ bond. The authors have proposed an intermediate [Ir–Ru] heterodimetallic complex, which has not been detected. In 1998, we patented the promoting effect of platinum,[7] which gives performances comparable to the iridium/ruthenium system in terms of turnover frequencies (2500 $h^{-1}$ for Ir–Pt and 2800 $h^{-1}$ for Ir–Ru, respectively, expressed with regard to Ir). For the two dimetallic systems, maximum activities are found for water concentrations close to 5 wt.-%, whereas the corresponding value approaches 14 wt.-% for the Monsanto process.

We envisaged that in both cases the catalytic cycles could present some common features. Thus, we undertook investigations on the [Ir–Pt] system in order to obtain a deeper insight into the nature of the intermediates that are formed and are responsible for the iodide abstraction from **2**. At first, we decided to study the catalytic complex mixtures by high-pressure NMR spectroscopy under conditions that closely resemble those used in the industrial process. Relevant pieces of information arise from the use of $^{13}C$-enriched reactants, such as $^{13}CO$, $^{13}CH_3{}^{13}COO{}^{13}CH_3$, and $^{13}CH_3I$ in $^{13}C$ and $^{195}Pt$ NMR spectroscopy. Thus, we were able to focus on every part of the catalytic cycle, using a procedure that leads to the detection of the transition metal complexes bearing carbonyl and methyl or acyl ligands. We

[a] Laboratoire de Catalyse, Chimie Fine et Polymères, Ecole Nationale Supérieure des Ingénieurs en Arts Chimiques et Technologiques (ENSIACET),
118 Route de Narbonne, 31077 Toulouse Cedex4, France
E-mail: Philippe.Kalck@ensiacet.fr
[b] ACETEX, AATF1, Usine de Pardies,
B. P. 17 Pardies, 64150 Mourenx, France
[c] Ecole Polytechnique Fédérale de Lausanne, Institut des Sciences et Ingénierie Chimiques, BCH-LCOM,
1015 Lausanne, Switzerland

Supporting information for this article is available on the WWW under http://www.eurjic.org or from the author.

 © 2006 Wiley-VCH Verlag GmbH & Co. KGaA, Weinheim 

present here our first mechanistic results based on high-pressure NMR ($^{13}C$, $^{1}H$, $^{195}Pt$) experiments. Moreover, in order to characterise the short-lived complexes involved in this process, we used the bis(triphenylphosphoranylidene) $[PPN]^+$ stabilising counterion and made observations at room temperature by NMR in tandem with FAB-MS. The new heterodimetallic species $[IrI(CH_3)(CO)_2(\mu\text{-}I)_2PtI_2(CO)]^-$ has been identified and its evolution monitored in solution.

The iridium complex **1** alone, initially studied by Forster[2] and Pannetier et al.,[8] is known to slowly catalyse the carbonylation of methanol to acetic acid. In mixtures similar to those employed industrially,[9] under 3 MPa and at 95 °C, we observed by high-pressure $^{13}C$ NMR spectroscopy (100.6 MHz) the spontaneous formation of the methyliridium complex $H[Ir(^{13}CH_3)I_3(^{13}CO)_2]$ (**2**) together with small amounts of the acyl species $H[Ir(^{13}CO^{13}CH_3)I_3(^{13}CO)_2]$ (**4**) (see Table 1). As previously proposed by Forster from IR observations,[2] we confirm that under these conditions the resting state is the methyl complex **2**, which is characterised by signals at $\delta$ = 157.1 (s, CO), –15.2 [q, $^1J$(C,H) = 141 Hz, $CH_3$] ppm. These NMR values are very close to those for $[PPN][Ir(CH_3)I_3(CO)_2]$, which was characterised by X-ray crystallography.[10] Small amounts of $CO_2$ were also detected, resulting from the water gas shift side reaction (WGSR). In addition, some $CH_4$ was detected. Evidence of occurrence of the WGSR was provided by the presence of $H[IrHI_3(CO)_2]$ and $H[IrI_4(CO)_2]$, as shown by the relevant NMR spectroscopic data. The low activity of **2** was also shown by the low consumption of $^{13}CO$ and

Table 1. NMR spectroscopic data for the species involved in the methanol carbonylation reaction.

| Complex | $^{13}C$ NMR ($\delta$/ppm) | Products | $^{13}C$ NMR ($\delta$/ppm) |
|---|---|---|---|
| $PPN[IrI_2(CO)_2]$ (**1**) | 169.9 (s, CO) | AcOH | 177.3 (s), 21.1 (q) |
| $H[IrHI_3(CO)_2]$ | 156.0 (s, CO) | AcOMe | 172 (s), 52 (q), 21 (q) |
| $H[IrI_4(CO)_2]$ | 151.3 (s, CO) | MeI | –25.0 (q) |
| $H[IrI_3Me(CO)_2]$ (**2**) | 157.1 (s, CO), –15.2 (q, $J_{C,H}$ = 141 Hz, $CH_3$) | MeOH | 49.3 (q) |
| $[IrI_2Me(CO)_3]$ (**3**) | 146.9 (s, CO), –22.3 (q, $J_{C,H}$ = 140 Hz, $CH_3$) | $CO_2$ | 125 (s) |
| $H[IrI_3(COMe)(CO)_2]$ (**4**) | 203.4 (s, *C*OMe), 160.7 (s, CO), 50.6 (q, $J_{C,H}$ = 140 Hz, $CH_3$) | CO | 185.4 (s) |
| $H[PtI_3(CO)]$ (**6**) | 156.8 (s, d, $J_{Pt-C}$ = 1649 Hz, CO) | $CH_4$ | –4.2 (quint) |
| $[PtI_2(CO)_2]$ (**5**) | 154.5 (s, d, $J_{Pt-C}$ = 1843 Hz, CO) | | |

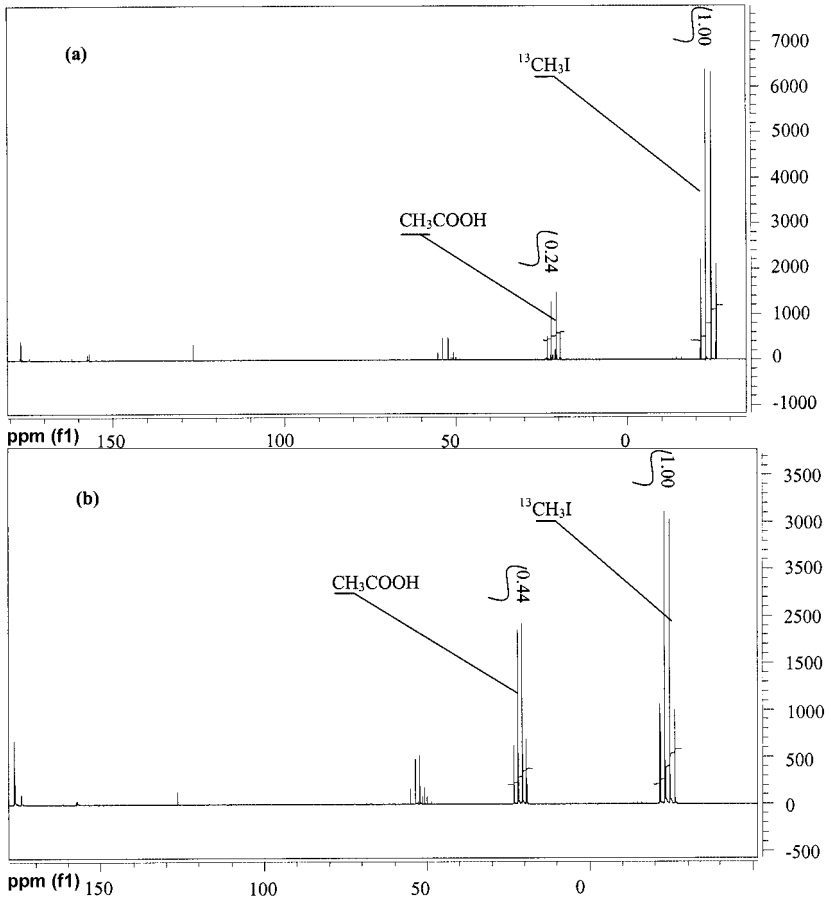


Figure 1. High-pressure $^{13}C$ NMR of the [Ir] system (a) and the [Pt–Ir] system (b).

 © 2006 Wiley-VCH Verlag GmbH & Co. KGaA, Weinheim 

$^{13}CH_3I$.[11] Thus, in the absence of any stabilising counterion, we have established the nature of the catalytic species that present the longest life-times.

Subsequently, our studies focused on the accelerating effect of platinum promoters on the iridium system. Under 3 MPa ($^{13}CO/^{12}CO$ = 1:3) and at 95 °C in a high-pressure NMR sapphire tube, addition to the catalytic iridium mixture of $[PtI_2(CO)_2]$ (**5**), which is the stable species formed from $[Pt_2I_2(\mu\text{-}I)_2(CO)_2]$ under CO, led to a significant increase in the carbonylation rate. In batch experiments using a Hastelloy® reactor, we obtained a carbonylation rate (based on the transformation of AcOMe into acetic acid) of 16 mol $L^{-1}$ $h^{-1}$ with iridium alone, compared to 35 mol $L^{-1}$ $h^{-1}$ after addition of $[PtI_2(CO)]_2$ (Pt/Ir = 3:7). $^{13}C$ NMR spectra led to observe the change in the concentration of the organic compounds during the catalytic runs

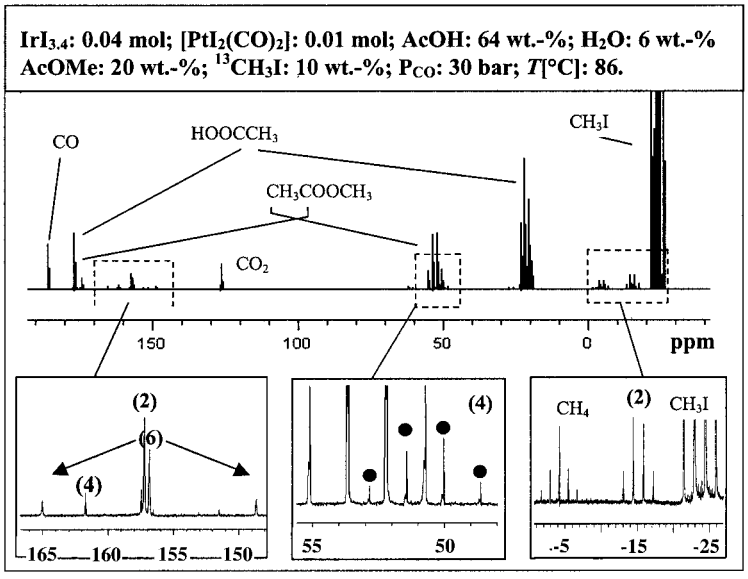


Figure 2. $^{13}C$ NMR spectroscopic data for the [Ir–Pt]/methanol carbonylation system.

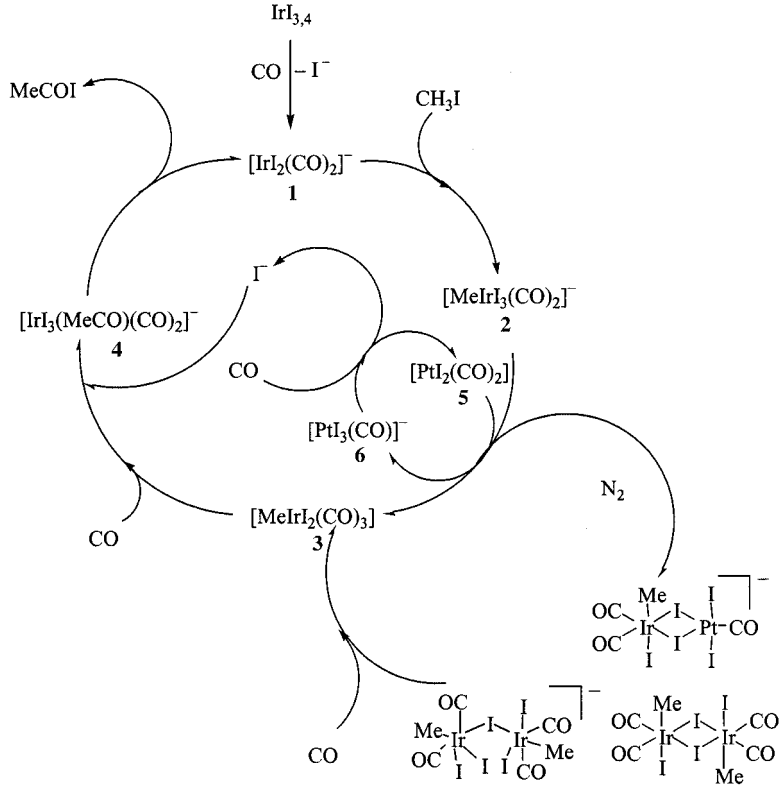


Figure 3. Proposed catalytic cycle for the [Ir–Pt] system.

 © 2006 Wiley-VCH Verlag GmbH & Co. KGaA, Weinheim 

and particularly the intensity ratio between the signals of acetic acid and methyl iodide. We have charged two high-pressure NMR tubes with $IrI_{3.4}$, $^{13}CH_3I$ (10 wt.-%), AcOMe (20 wt.-%), $H_2O$ (6 wt.-%) and AcOH (64 wt.-%) under 30 bar of a mixture of $^{13}CO/^{12}CO$, one tube containing only $IrI_{3.4}$ salt (a) and the other containing the mixture of $IrI_{3.4}$ and $[PtI_2(CO)]_2$ (b). After 3 h at 86 °C, we can compare (Figure 1) the relative intensity ratios of the two signals of $^{13}CH_3I$/AcOH and conclude that a larger amount (around two times) of $^{13}CH_3I$ was consumed[11] with the [Ir–Pt] system than with the iridium catalyst only. Under these conditions, we observed the presence of $H[PtI_3(CO)]$ (**6**) and the signals corresponding to the iridium complexes **2** and **4** in significant amounts[12] (Figure 2).

The role of platinum is mainly to assist the formation of the species $[IrI_2(CH_3)(CO)_3]$ (**3**), in which the electron density on the iridium atom is reduced; migratory CO insertion can then occur more rapidly to produce **4**. In separate experiments we checked that platinum indeed acts as a real co-catalyst, since application of 3 MPa of CO exerted on **6** provides **5** again, whereas such a platinum species alone does not catalyse the carbonylation reaction. Finally, reductive elimination of acyl iodide from **4** regenerates **1** (Figure 3).

In order to obtain a clear view of this dimetallic process, we decided to decrease the reaction rate by performing the experiments under ambient conditions and by using the $[PPN]^+$ stabilising counterion under nitrogen. A number of $^1H$ NMR (250 MHz, $CD_2Cl_2$, 25 °C) spectra were recorded while varying the Ir/Pt molar ratio. Addition of $[Pt_2I_2(\mu\text{-}I)_2(CO)_2]$ to a dichloromethane solution of **2-PPN** provided several signals at $\delta$ = 2.36, 2.28, 2.14, 2.09, 1.90 and 1.85 ppm (Figure 4). At low platinum concentrations (Ir/Pt = 9.5:1), the signal at $\delta$ = 2.14 ppm is assigned to unreacted **2-PPN**. We may tentatively assign the peak at $\delta$ = 2.09 ppm to the solvated neutral species $[IrI_2(CH_3)(CO)_2(solv)]$, in which the coordinated solvent could be $CD_2Cl_2$. Indeed, iridium(III) complexes containing coordinated $CH_2Cl_2$ have been reported previously.[13] At higher platinum concentrations (Ir/Pt = 5.3:1), significant amounts of the two isomers of $[Ir_2I_2(\mu\text{-}I)_2(CH_3)_2(CO)_4]$ were detected at $\delta$ = 1.90 and 1.85 ppm.[10]

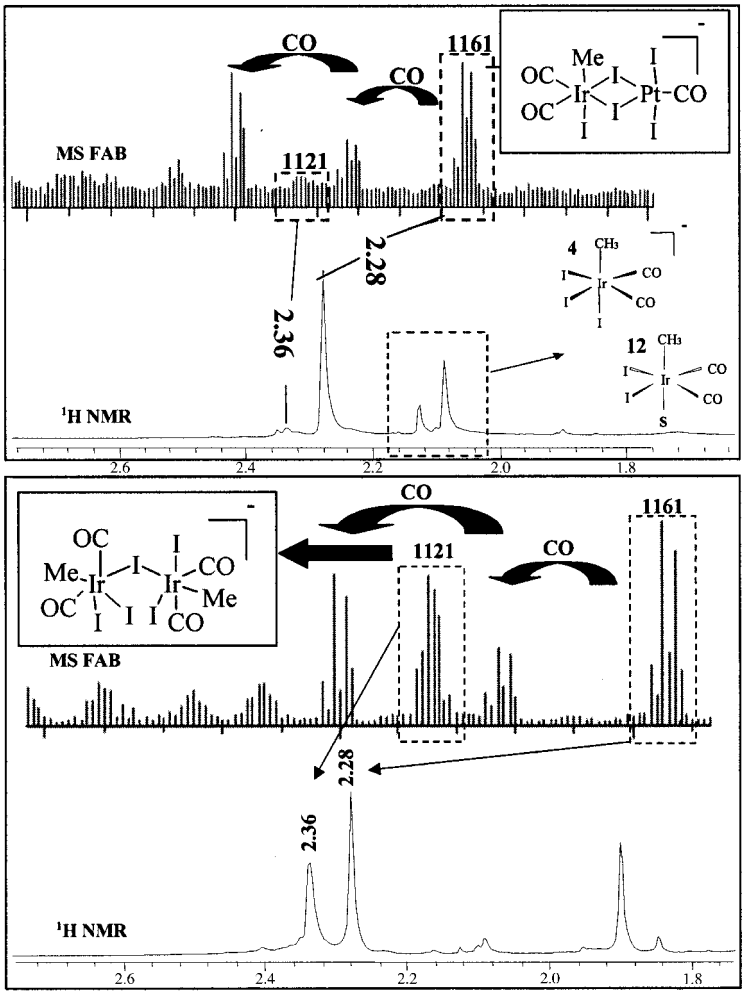


Figure 4. Detection of $[IrI(CH_3)(CO)_2(\mu\text{-}I)_2PtI_2(CO)]^-$ and $[Ir_2I_4(\mu\text{-}I)(CH_3)_2(CO)_4]^-$ by tandem NMR and FAB/MS experiments: top (Ir/Pt = 9.5:1), bottom (Ir/Pt = 5.3:1).

 © 2006 Wiley-VCH Verlag GmbH & Co. KGaA, Weinheim 

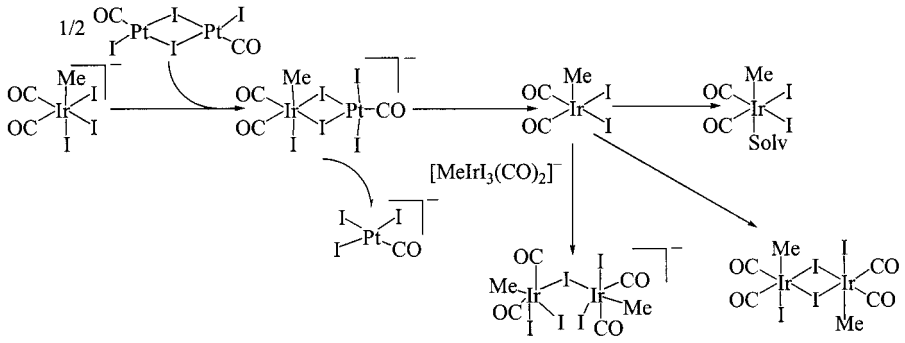


Scheme 1. Reaction route leading to $Ir_2$-bridged species through the intermediate formation of an [Ir–Pt] dimetallic moiety (from **2** and $[Pt_2I_2(\mu\text{-}I)_2(CO)_2]$).

As already stated, two additional $^1H$ NMR signals appeared at $\delta$ = 2.36 and 2.28 ppm, whose relative intensities vary with the Ir/Pt molar ratio. In order to assign these two signals, for the given Ir/Pt ratios, we recorded $^1H$ NMR spectra in tandem (analysed from the same sample) with FAB/MS experiments. Representative examples are shown in Figure 4. For an Ir/Pt = 5.3:1 molar ratio, two anionic complexes were detected at *m*/*z* = 1121 and 1161. The former molecular peak corresponds to the anionic heterodimetallic complex $[IrI(CH_3)(CO)_2(\mu\text{-}I)_2PtI_2(CO)]^-$. The latter is consistent with the formulation $[Ir_2I_4(\mu\text{-}I)(CH_3)_2(CO)_4]^-$, which was previously suggested as an intermediate in the [Ir–Ru] system.[5] In a second representative run, for an Ir/Pt = 9.5:1 molar ratio, the peak at *m*/*z* = 1121 in the FAB/MS spectra, as well as the signal at $\delta$ = 2.36 ppm in the $^1H$ NMR spectra disappeared nearly completely. Thus, the signal at $\delta$ = 2.28 ppm can be unambiguously assigned to the complex $[Ir_2I_4(\mu\text{-}I)(CH_3)_2(CO)_4]^-$. Additionally, $^{13}C$ NMR spectra reveal the signals of $[Ir_2I_4(\mu\text{-}I)(CH_3)_2(CO)_4]^-$ at $\delta$ = 154.68 ppm (s, CO), –14.83 ppm (q, $J_{C,H}$ = 141 Hz, $CH_3$) and two new carbonyl signals that correspond to $[IrI(CH_3)(CO)_2(\mu\text{-}I)_2PtI_2(CO)]^-$. The CO ligand coordinated to Pt gives a signal at $\delta$ = 154.9 ppm (s, CO) with its satellites characterised by a doublet ($^1J_{Pt,C}$ = 1650 Hz, CO). The other carbonyl signal at $\delta$ = 155.4 ppm (no coupling constant) is assigned to the two CO ligands coordinated to the iridium atom. The quadruplet at $\delta$ = –14.2 (q, $^1J_{C,H}$ = 141 Hz, $CH_3$) ppm shows no coupling between $^{13}C$ and $^{195}Pt$ and is presumably due to the $CH_3$ ligand coordinated to the iridium atom. The $^{195}Pt$ NMR spectra show a new signal at $\delta$ = –5462 (s, + satellites d, $^1J_{Pt,C}$ = 1650 Hz, CO) ppm, together with a signal of $[PtI_3(CO)]^-$ at $\delta$ = –5460 (s, + satellites d, $^1J_{Pt,C}$ = 1759 Hz, CO) ppm. Scheme 1 summarises the reaction pathway for the formation and the evolution of the mixed [Ir–Pt] complex. Under CO, the [Ir–Pt] system leads very quickly to the two complexes **3** and **6**.

This work presents circumstantial evidence that the main role of the platinum promoter during the iridium-catalysed carbonylation of methanol is to abstract an iodo ligand from $[IrI_3(CH_3)(CO)_2]^-$ (**2**) through the formation of the heterodimetallic $[IrI(CH_3)(CO)_2(\mu\text{-}I)_2PtI_2(CO)]^-$ intermediate species.

## Experimental Section

**Synthesis of the Iridium Complexes:** The synthesis of the iridium complexes has been previously reported.[10]

**Synthesis of the Platinum Complexes**

**$[PtI_2(CO)_2]$ (5) and $[PtI_2(CO)]_2$ (5′):** $[Pt(CO)_2I_2]$ was prepared by addition of $PtI_2$ (2 g, 4.45 mmol) in an autoclave containing hexane (125 mL). The mixture was pressurised with CO (12 bar) and stirred at 75 °C for 1 h. The solution was cooled in the reactor under CO (1 bar). 1.69 g (80% yield) of a red solid was obtained and dried under reduced pressure, which corresponds to $[PtI_2(CO)]_2$. Under CO, this compound leads to $[PtI_2(CO)_2]$ in 100% yield. $[PtI_2(CO)]_2$: IR ($CH_2Cl_2$): $\tilde{\nu}$ = 2111 (CO) $cm^{-1}$. $^{13}C$ NMR ($CD_2Cl_2$): $\delta$ = 154.5 (s, $^1J_{Pt-C}$ = 1843 Hz, CO) ppm. $^{195}Pt$ NMR ($CD_2Cl_2$): $\delta$ = –5328 ($^1J_{Pt-C}$ = 1843 Hz) ppm. $[PtI_2(CO)_2]$: IR ($CH_2Cl_2$): $\tilde{\nu}$ = 2127 (CO) $cm^{-1}$. $^{13}C$ NMR ($CD_2Cl_2$): $\delta$ = 166 (s, $^1J_{Pt-C}$ = 1466 Hz, CO) ppm. $^{195}Pt$ NMR ($CD_2Cl_2$): $\delta$ = –5790 ($^1J_{Pt-C}$ = 1466 Hz) ppm.

**[PPN][$PtI_3(CO)$] (6-PPN):** $[PtI_2(CO)]_2$ (1 g, 1.05 mmol) was dissolved in dichloromethane (50 mL), and HI (0.26 g, 2.10 mmol) was added to give rapidly, at room temperature, the complex $H[PtI_3(CO)]$. Then, [PPN]Cl (1.20 g, 2.10 mmol) was added to the solution. The solvent was removed under vacuum to give a yellow product. Crystallisation of this compound in $CH_2Cl_2$/hexane (1:1) gave yellow crystals of $[PPN][PtI_3(CO)]$ (1.08 g, 45%). IR ($CH_2Cl_2$): $\tilde{\nu}$ = 2075 (CO) $cm^{-1}$. $^{13}C$ NMR ($CD_2Cl_2$): $\delta$ = 152.8 (s, $^1J_{Pt-C}$ = 1759 Hz, CO) ppm. $^{195}Pt$ NMR ($CD_2Cl_2$): $\delta$ = –5460 ($^1J_{Pt-C}$ = 1759 Hz). MS ($FAB^-$): *m*/*z* = 603.

## Acknowledgments

The "Ministère de la Recherche et de la Technologie" is gratefully acknowledged for supporting an "Equipe de Recherche Technologique" (ERT 007), in our laboratory at ENSIACET. Financial support from NSF Switzerland 200020-105335/1 (to G. L.) is also gratefully acknowledged.

[1] The Monsanto process implies rhodium in a mixture containing water (14 wt.-%) at 180 °C and under 3 MPa.
[2] T. W. Dekleva, D. Forster, *Adv. Catal.* **1986**, *34*, 81.
[3] J. M. Pearson, A. Haynes, G. E. Morris, G. J. Sunley, P. M. Maitlis, *J. Chem. Soc., Chem. Commun.* **1995**, 1045.
[4] G. J. Sunley, D. J. Watson, *Catal. Today* **2000**, *58*, 293; C. J. E. Vercauteren, K. E. Clode, D. J. Watson, European patent, 616997, **1994**.

 © 2006 Wiley-VCH Verlag GmbH & Co. KGaA, Weinheim 

[5] A. Haynes, P. M. Maitlis, J. E. Morris, G. J. Sunley, H. Adams, P. W. Badger, C. M. Bowers, D. B. Cook, P. I. P. E. Elliott, T. Ghaffar, H. Green, T. R. Griffin, M. Payne, J. M. Pearson, M. J. Taylor, P. W. Vickers, R. J. Watt, *J. Am. Chem. Soc.* **2004**, *126*, 2847.
[6] R. Whyman, A. P. Wright, J. A. Iggo, B. T. Heaton, *J. Chem. Soc., Dalton Trans.* **2002**, *5*, 771.
[7] C. Le Berre, P. Serp, P. Kalck, L. Layellon, D. Thiebaut, French patent 9813954, **1998**.
[8] D. Brodzki, B. Denise, G. Pannetier, *J. Mol. Catal.* **1977**, *2*, 149.
[9] $IrI_3$, $IrI_4$ (0.05 mol), AcOH (64 wt.-%), $H_2O$ (6 wt.-%), AcOMe (20 wt.-%), $^{13}CH_3I$ (10 wt.-%).
[10] S. Gautron, R. Giordano, C. Le Berre, J. Jaud, J.-C. Daran, P. Serp, P. Kalck, *Inorg. Chem.* **2003**, *42*, 5523.
[11] As $CH_3I$ is formed by reaction of HI with methyl acetate, we monitored the decrease of $^{13}CH_3I$, whereas $^{12}CH_3I$ is produced when using unlabelled methyl acetate.
[12] Complex **4** is observed here when adding the platinum promoter, since the rate-determining step is accelerated by the $I^-$ abstraction process.
[13] R. H. Crabtree, *The Organometallic Chemistry of the Transition Metals*, 3rd ed., Wiley-Interscience, New York, **2001**, p. 109.

Received: October 20, 2005
Published Online: February 2, 2006

 © 2006 Wiley-VCH Verlag GmbH & Co. KGaA, Weinheim 

DOI: 10.1002/ejic.200501032

# Atom Assignment in Solid-State Structures on the Basis of X-ray Crystallography and DFT Calculations – A Case Study on a Molecular Cu–Sb Alloy

**Reinhart Ahlrichs,[a] Dieter Fenske,*[b,c] Alexander Rothenberger,*[b,c] Claudia Schrodt,[c] and Stephan Wieber[c]**

*Dedicated to Professor Hansgeorg Schnöckel on the occasion of his 65th birthday*

**Keywords:** DFT calculations / Molecular alloys / Sb ligands

The structure determination of the molecular Cu-Sb alloy $[Cu_{28}Sb_{12}(PEt_3)_{12}\{Sb(SiMe_3)_2\}_2]$ was performed by DFT-assisted X-ray crystallography, a powerful combination of methods, widely applicable.

(© Wiley-VCH Verlag GmbH & Co. KGaA, 69451 Weinheim, Germany, 2006)

## Introduction

Recently, some of our interests have been focused on the synthesis of Cu–Sb clusters and their structural analysis.[1,2] For the synthesis of conventional $Cu^I$–Sb complexes, $Cu^I$ salts are treated with tertiary stibane ligands to produce coordination compounds analogous to thoroughly investigated $[Cu^IX{\cdot}PR_3]$ (R = organic group, X = anion) complexes.[3] A remarkable achievement in the area of Cu–Sb compounds represents the synthesis of the thermally unstable first copper(I) antimonide complex $[Mes_2SbCu(PMe_3)_2]_2$ (Mes = 2,4,6-trimethylphenyl) by the metathesis reaction of $Mes_2SbLi$ with CuCl.[4] A different approach to the syntheses of copper(I) antimonides involves the reaction of $Sb(SiMe_3)_3$ with $Cu^I$ salts in the presence of tertiary phosphanes. As results from these studies, a series of Cu–Sb cluster complexes {e.g., $[Cu_{10}(Sb_3)_2(SbSiMe_3)_2(dppm)_6]$, $[Cu_{17}Sb_8(dppm)_7]$, and $[Cu_{20}Sb_{10}(PCy_3)_8]$ [dppm = 1,2-bis(diphenylphosphanyl)methane, Cy = cyclohexyl]} was obtained and structurally characterised.[1,2] A common feature of the majority of clusters produced in these reactions are the unexpected ratios of Cu/Sb. This is illustrated by $[Cu_{20}Sb_{10}(PCy_3)_8]$, where physical measurements showed that the concept of oxidation numbers can no longer be applied and that they are instead best described as molecular sections of Cu–Sb alloys.[1] Investigations in this field so far showed a preference for copper–antimony compounds with Cu/Sb = 2:1, a ratio which is observed in the η-phase of the rather complex Cu–Sb phase diagram.[5,6] The structural analysis of these complexes has proven to be impossible by X-ray crystallography alone, but the solid-state structure of $[Cu_{45}Sb_{16}(PEt_2Me)_{16}]$, the largest representative of molecular Cu–Sb alloys, was possible by a combined approach of DFT calculations and X-ray crystallography.[2]

## Results and Discussion

Here we describe the so far best example of DFT-assisted X-ray crystallography in the Cu–Sb alloy system, which is, due to the structural diversity, predestined for future discoveries in this field. The reaction of CuOAc and $Sb(SiMe_3)_3$ (ratio 1:1) in the presence of $PEt_3$ produces the Cu–Sb cluster $[Cu_{28}Sb_{12}(PEt_3)_{12}\{Sb(SiMe_3)_2\}_2]$ (**1**) (Scheme 1).

$$CuOAc + Sb(SiMe_3)_3 \xrightarrow[Et_2O]{PEt_3} [Cu_{28}Sb_{12}(PEt_3)_{12}\{Sb(SiMe_3)_2\}_2]\cdot 2Et_2O\ (\mathbf{1})$$

Scheme 1. Synthesis of **1**.

The initial X-ray structural analysis of black crystals of **1** led to problems with the atom assignment of Cu(5,10,17) and Sb(6,8,10) and their symmetry equivalents, indicated by unusual thermal parameters. All other atoms could be unequivocally identified. Figure 1 represents the refined structural model of **1** based on results obtained from DFT calculations.

[a] Institut für Physikalische Chemie, Universität Karlsruhe, Fritz-Haber-Weg 4, 76131 Karlsruhe
[b] Institut für Anorganische Chemie, Universität Karlsruhe, Geb. 30.45, Engesserstr. 15a, 76131 Karlsruhe
[c] Institut für Nanotechnologie, Forschungszentrum Karlsruhe GmbH, Postfach 3640, 76021 Karlsruhe, Germany
E-mail: ar252@chemie.uni-karlsruhe.de

 © 2006 Wiley-VCH Verlag GmbH & Co. KGaA, Weinheim 

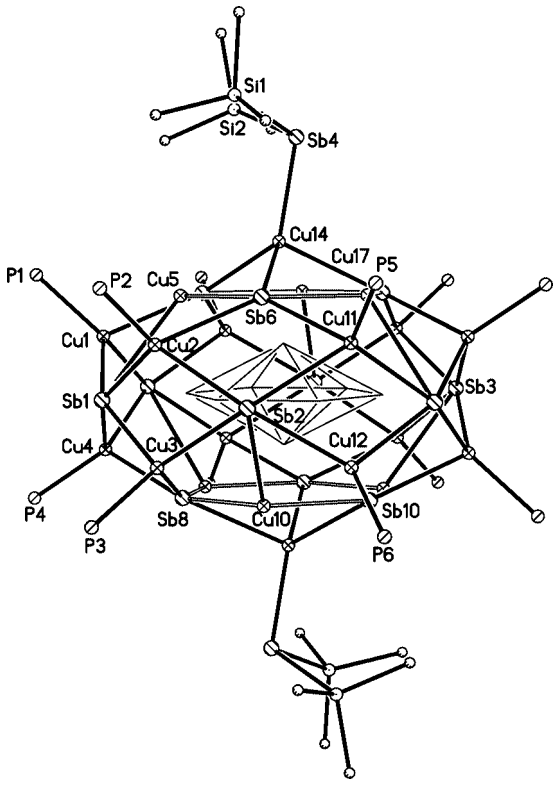


Figure 1. Molecular structure of **1**. Et groups and bonds to the inner $[Cu_8]$ unit and solvent have been omitted for clarity. Selected ranges of bond lengths [Å]: Cu–Sb 2.5322(11)–3.109(11), Cu–P 2.213(2)–2.228(2), Sb(4)–Si(1) 2.542(3), Sb(4)–Si(2) 2.547(3), short Cu–Cu distances observed in the inner $[Cu_8]$ unit 2.410(1), 2.476(1).

The DFT study was carried out to allow reliable assignment of atom types to the positions in question [Cu(5,10,17), Sb(6,8,10) and symmetry equivalents]. All calculations were performed with the TURBOMOLE program package[7] by employing the BP86 functional with the very efficient MARI-J approximation,[8] and recently developed TZVP basis sets.[9] For P–Me and –Et smaller basis sets were used. The number of contracted basis functions is as follows: Sb [6s5p3d2f], Cu [6s4p4d1f], Si [5s5p2d1f], P [5s5p2d1f], C [5s3p1d], and H [2s]. The core electrons 1s to 3d of Sb (28 electrons) were modeled by a small-core ECP (Effective Core Potential), taking into account scalar relativistic effects.[10] The results of these calculations give a clear preference to six-membered $[CuSb]_3$ rings (indicated by open bonds in Figure 1) over $Cu_6$, $Sb_6$, $Cu_4Sb_2$, $Cu_2Sb_4$, and permutations thereof. $[CuSb]_3$ rings, however, can be in different orientations relative to each other (Scheme 2).

The calculated structures of **1** and a conformer (generated by the exchange of all Cu and Sb positions within slightly puckered six-membered rings) are equally stable ($\Delta$ = 4 kJ/mol) and fit with a structure solution of X-ray crystallographic data, based on these DFT suggestions. The calculated structure of the acentric isomer of **1** (Scheme 2, right) is 28 kJ/mol more stable than calculated **1** but shows larger deviations of Cu–Sb bond lengths and would require lower crystallographic symmetry. Although an acentric structure of **1** was initially ruled out when refinement of a

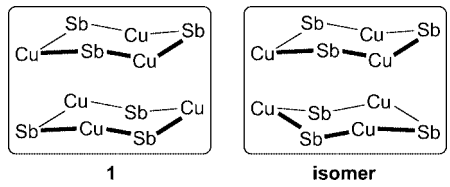


Scheme 2. Relative arrangement of $[CuSb]_3$ rings in **1** and its isomer.

structural model in the space group $P2_1$ did not indicate a preference for Cu or Sb on any site in the highlighted six-membered $[CuSb]_3$ rings (Figure 1; Scheme 2, right), the findings of DFT calculations and X-ray crystallographic results are not contradictory and point towards individual acentric cluster molecules with a 50:50 distribution. This results in a pseudo-centrosymmetric solid-state structure of **1** representing the average composition rather than an individual molecule. Based on these considerations, the structure of **1** and its conformer was solved and refined in the space group $P2_1/n$. Atomic positions within the six-membered rings were refined with 50% occupancy of both Cu and Sb. The solid-state structure of **1** (Figure 1) consists of a central hexagonal-bipyramidal arrangement of Cu atoms surrounded by a distorted icosahedral arrangement of Sb atoms and an additional layer of a capped hexagonal prism of 14 Cu atoms (Figure 2).

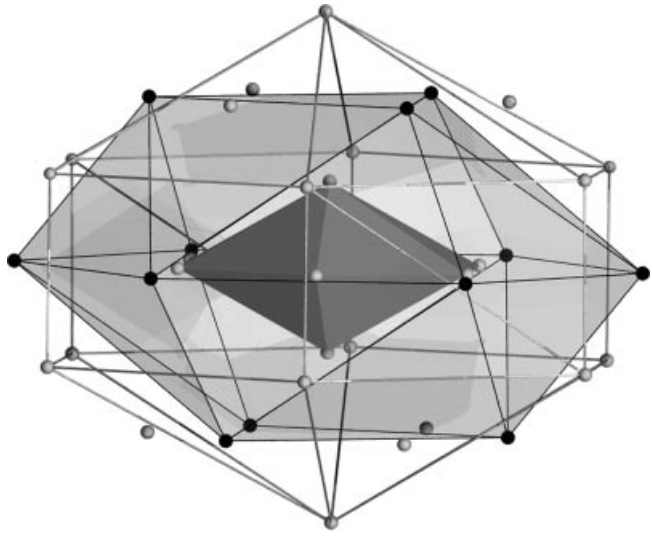

Figure 2. Polyhedral model of the cluster core found in **1** (Sb black, Cu grey).

Over six of the twelve trigonal faces of the hexagonal-prismatic arrangement Cu atoms are located, which form the crucial six-membered $[CuSb]_3$ rings together with two $Sb_3$ faces of the icosahedral arrangement of the Sb atoms (Figures 1 and 2). Cu atoms in the hexagonal prism are coordinated by P atoms of $PEt_3$ ligands [Cu–P 2.213(2)–2.228(2) Å], whilst two $[Sb(SiMe_3)_2]$ ligands coordinate the two capping Cu atoms [Cu(14) and its symmetry-equivalent atom].

 © 2006 Wiley-VCH Verlag GmbH & Co. KGaA, Weinheim 

## Conclusion

The exchange of lattice positions in other copper–transition metal compounds is well known.[11] Indications for statistical occupation of atomic positions in a molecular Cu–Sb alloy (resulting here in the cocrystallisation of two conformers), however, are in this case to the best of our knowledge observed for the first time. An increasing number of copper and antimony atoms in metal clusters could lead to even more challenging structural analyses of these species and will propagate the use of DFT methods where conventional X-ray crystallography on its own fails to give convincing results.

## Experimental Section

**General Remarks:** All operations were carried out under purified nitrogen. Hexane and diethyl ether were dried with $LiAlH_4$ and freshly distilled. $PEt_3$, $Sb(SiMe_3)_3$, and CuOAc were prepared according to published procedures.[12]

**Synthesis of 1:** CuOAc (0.24 g, 2.00 mmol) was dissolved in $Et_2O$ (8 mL) and $PEt_3$ (0.56 mL, 4.00 mmol). The yellow solution was cooled to –78 °C and $Sb(SiMe_3)_3$ (2.91 mL, 2.00 mmol, 0.31 M in hexane) was added. The brown reaction mixture was stored at –78 °C for 12 h and was then warmed up to –8 °C and stored for four weeks. Black crystals of **1** were isolated (0.08 g, 21%), but decomposed at room temperature, precluding elemental analysis. **1** is insoluble in ethereal solvents and hydrocarbons.

**X-ray Crystallographic Study of 1:** Crystallography data for the compound were collected with a Stoe IPDS II diffractometer by using graphite-monochromated Mo-$K_\alpha$ radiation ($\lambda$ = 0.71073 Å). The structure was solved by direct methods and refined by full-matrix least squares on $F^2$ (all data) using the SHELXTL software package.[13] Hydrogen atoms were placed in calculated positions, non-hydrogen atoms were assigned anisotropic thermal parameters. $C_{92}H_{238}Cu_{28}O_2P_{12}Sb_{14}Si_4$; $M$ = 5342.42; monoclinic, space group $P2_1/n$; $Z$ = 4; $a$ = 19.0392(5) Å, $b$ = 22.0502(6) Å, $c$ = 19.4760(5) Å, $\beta$ = 97.145(2)°; $V$ = 8112.9(4) Å$^3$; $T$ = 120(2) K; $F(000)$ = 5132; $D_{calcd.}$ = 2.187 g cm$^{-3}$; 52524 reflections measured, of which 17705 were unique ($R_{int}$ = 0.0689); 455 parameters; final $wR_2$ = 0.1572 (all data); $R_1$ = 0.0588 [$I > 2\sigma(I)$]; largest difference peak/hole = 3.554/–3.273°e·Å$^{-3}$; disordered components were refined with isotropic thermal parameters. A numerical absorption correction was performed. CCDC-281468 contains the supplementary crystallographic data for this paper. These data can be obtained free of charge from The Cambridge Crystallographic Data Centre via www.ccdc.cam.ac.uk/data_request/cif.

## Acknowledgments

We gratefully acknowledge the DFG (Center for Functional Nanostructures), the INT at the Forschungszentrum Karlsruhe (A. R., S. W., C. S.) and the Fonds der Chemischen Industrie for financial support.

[1] a) R. Ahlrichs, C. E. Anson, R. Clerac, D. Fenske, A. Rothenberger, M. Sierka, S. Wieber, *Eur. J. Inorg. Chem.* **2004**, *14*, 2933–2936; b) J. Besinger, J. Treptow, D. Fenske, *Z. Anorg. Allg. Chem.* **2002**, *628*, 512–515.
[2] R. Ahlrichs, D. Fenske, M. McPartlin, A. Rothenberger, C. Schrodt, S. Wieber, *Angew. Chem.* **2005**, *117*, 4002–4005; *Angew. Chem. Int. Ed.* **2005**, *44*, 3932–3936.
[3] a) W. Levason, M. L. Matthews, G. Reid, M. Webster, *Dalton Trans.* **2004**, 554–561; b) G. B. Bowmaker, R. D. Hart, A. H. White, *Aust. J. Chem.* **1997**, *50*, 621–626.
[4] A. H. Cowley, R. A. Jones, C. M. Nunn, D. L. Westmoreland, *Angew. Chem.* **1989**, *101*, 1089–1090; *Angew. Chem. Int. Ed. Engl.* **1989**, *28*, 1018–1019.
[5] *ASM Speciality Handbook, Copper and Copper Alloys* (Ed.: J. R. Davis), Danis & Associates, ASM International, **2001**.
[6] Distances in $Cu_2Sb$: Cu–Sb 2.701(1)–2.834(1), Cu···Cu 2.602(1) Å; a) W. B. Pearson, *A Handbook of Lattice Spacings and Structures of Metals and Alloys*, Pergamon Press, New York, **1967**, vol. 2; b) J. Nuss, M. Jansen, *Z. Anorg. Allg. Chem.* **2002**, *628*, 1152–1157 and references cited therein.
[7] a) R. Ahlrichs, M. Bär, M. Häser, H. Horn, C. Kölmel, *Chem. Phys. Lett.* **1989**, *162*, 165–169; b) O. Treutler, R. Ahlrichs, *J. Chem. Phys.* **1995**, *102*, 346–354.
[8] a) A. D. Becke, *Phys. Rev. A* **1988**, *38*, 3098–3100; b) S. J. Vosko, L. Wilk, M. Nusair, *Can. J. Phys.* **1980**, *58*, 1200–1211; c) J. P. Perdew, *Phys. Rev. B* **1986**, *33*, 8822–8824; d) Erratum: J. P. Perdew, *Phys. Rev. B* **1986**, *34*, 7406; e) K. Eichkorn, O. Treutler, H. Öhm, M. Häser, R. Ahlrichs, *Chem. Phys. Lett.* **1995**, *242*, 652–660; f) M. Sierka, A. Hogekamp, R. Ahlrichs, *J. Chem. Phys.* **2003**, *118*, 9136–9148.
[9] a) Available via ftp://ftp.chemie.uni-karlsruhe.de/pub/; b) F. Weigend, R. Ahlrichs, *Phys. Chem. Chem. Phys.*, in press.
[10] B. Metz, M. Schweizer, H. Stoll, M. Dolg, W. Liu, *J. Chem. Phys.* **2000**, *113*, 2563–2569.
[11] H. Jacobi, H. J. Engell, *Acta Metall.* **1971**, *19*, 701–711.
[12] a) F. Hewitt, A. K. Holliday, *J. Chem. Soc.* **1953**, 530–534; b) G. Becker, A. Münch, C. Witthauer, *Z. Anorg. Allg. Chem.* **1982**, *492*, 15–27; c) D. A. Edwards, R. J. Richards, *J. Chem. Soc., Dalton Trans.* **1973**, 2463–2468.
[13] G. M. Sheldrick, *SHELXTL-97*, University of Göttingen, **1997**.

Received: November 17, 2005
Published Online: February 2, 2006

 © 2006 Wiley-VCH Verlag GmbH & Co. KGaA, Weinheim 

DOI: 10.1002/ejic.200500955

# Dipolar Organoiron Pyranylideneacetaldehyde Hydrazone Complexes: Synthesis, Characterization, Crystal Structure, Linear and Nonlinear Optical Properties

**Lorena Millán,[a] Mauricio Fuentealba,[a] Carolina Manzur,*[a] David Carrillo,*[a] Nadège Faux,[b] Bertrand Caro,*[b] Françoise Robin-Le Guen,[b] Sourisak Sinbandhit,[c] Isabelle Ledoux-Rak,[d] and Jean-René Hamon*[e]**

**Keywords:** Donor–acceptor systems / Iron / Pyranylideneacetaldehyde / Nonlinear optics / Sandwich complexes

New cationic organoiron(II) pyranylideneacetaldehyde hydrazone complexes were prepared in high yields through condensation reactions of the organometallic hydrazine precursor $[CpFe(\eta^6\text{-}p\text{-}MeC_6H_4NHNH_2)]^+PF_6^-$ with differently substituted α- and γ-pyranylideneacetaldehydes. The mononuclear hydrazones were stereoselectively obtained as their (*E*) isomers about the N=C double bond. All the new compounds were thoroughly characterized by a combination of elemental analysis and spectroscopic techniques ($^1H$ and $^{13}C$ NMR, IR, and UV/Vis), and by a single-crystal X-ray diffraction analysis of the 2-*t*Bu-chromene derivative **5**. The spectroscopic data suggest that these complexes have a partial pyrylium character due to the electron-accepting ability of the cationic organometallic fragment and to the electron-releasing properties of the methylenepyran-based donor. The crystal structure of **5** shows that the $\eta^6$-coordinated tolyl ring and the pyran ring are coplanar (dihedral angle 3.2°), a favorable situation that allows conjugation between the intracyclic oxygen atom and the cationic iron center through the entire hydrazone backbone. Compounds **4**–**6** are strongly polarized D–π–A systems that exhibit solvatochromic properties, low-lying intramolecular charge-transfer bands in their electronic absorption spectra, and enhanced second-order NLO properties ($\mu\beta$), as measured by the EFISH technique at 1.907 μm.
(© Wiley-VCH Verlag GmbH & Co. KGaA, 69451 Weinheim, Germany, 2006)

## Introduction

The electron-donating and -accepting capabilities of organoligand–metal fragments have been successfully applied in the design and development of highly efficient dipolar chromophores in order to achieve high second-order nonlinear optical (NLO) responses.[1] This has led to a growing development of organometallic push–pull rod-shaped oligomers, mainly ferrocene-based donor–acceptor materials,[2] and, in particular, those incorporating a cationic acceptor subunit have demonstrated good second-harmonic generation (SHG) efficiency.[3,4] The potentially attractive NLO properties of ferrocene-based complexes are coupled with good thermal and photochemical stability,[5] excellent donor capability,[6] and redox-switching abilities.[7] On the other hand, the cationic isolobal electron-acceptor counterparts of ferrocene, namely the robust mixed-sandwich derivatives $[CpFe(\eta^6\text{-arene})]^+$,[8] have also been the subject of intense investigations within the domains of arene functionalization,[9] electron transfer and redox processes,[10] photochemistry,[11] and, in one case, as an organometallic chromophore to achieve second-order NLO responses.[12] Along this line, some of us have thoroughly investigated organometallic dipolar chromophores in which the electron-withdrawing cationic organometallic fragment $[CpFe(\eta^6\text{-arene})]^+$ (A) is connected to a potent donating organic[13] or ferrocenyl[14] subunit (D) by an asymmetric –NR–N=CR– (R = H, Me) hydrazone conjugated bridge (π), and have shown that in such D–π–A-type systems an effective electron delocalization or electronic interaction between the electron-donating and -accepting termini takes place through the entire hydrazone skeleton. Others of us have recently reported on donor–acceptor pentacarbonylmetal methylenepyran Fischer-type methoxycarbene complexes (metal = Cr, W).[15]

[a] Laboratorio de Química Inorgánica, Instituto de Química, Pontificia Universidad Católica de Valparaíso,
Avenida Brasil 2950, Valparaíso, Chile
Fax: +56-32-273-420
E-mail: cmanzur@ucv.cl david.carrillo@ucv.cl
[b] UMR 6226 Sciences chimiques de Rennes, CNRS – Université de Rennes 1, IUT de Lannion,
Rue E. Branly, B. P. 30219, 22300 Lannion, France
Fax: +33-296-48-57-97
E-mail: bertrand.caro@univ-rennes1.fr
[c] Centre Régional de Mesures Physiques de l'Ouest, Université de Rennes 1, Campus de Beaulieu,
35042 Rennes Cedex, France
[d] Laboratoire de Photonique Quantique et Moléculaire, UMR 8537 CNRS-ENS Cachan,
61 Avenue du Président Wilson, 94235 Cachan Cedex, France
[e] UMR 6226 Sciences chimiques de Rennes, CNRS – Université de Rennes 1, Campus de Beaulieu,
35042 Rennes-Cedex, France
Fax: +33-223-23-56-37
E-mail: jean-rene.hamon@univ-rennes1.fr
Supporting information for this article is available on the WWW under http://www.eurjic.org or from the author.

 © 2006 Wiley-VCH Verlag GmbH & Co. KGaA, Weinheim 

These complexes, which have a pyrylium character owing to the π-electron-accepting ability of the carbene fragment and to the electron-releasing properties of the methylenepyran core, exhibit a large first hyperpolarisability $\mu\beta$, as measured by the electric-field-induced-second-harmonic (EFISH) generation technique.[16] These facts, and the results of a recent theoretical study, which focused attention on the importance of pyrylium–methylenepyran duality for NLO purposes,[17] prompted us to investigate new push–pull structures that combine an ionic iron acceptor with a methylenepyran group, which should act as electron donors because of the aromaticity gain upon electron delocalization of the heterocyclic oxygen lone-pair (Scheme 1).

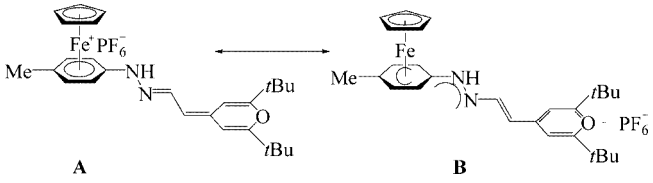


Scheme 1. Resonance forms for the methylenepyran–pyrylium mesomers.

For this purpose, we have chosen three archetypal pyranylideneacetaldehyde-type structures where the pyranyl ring is substituted at positions 2,6 (**1**) and 4,6 (**3**), or fused with a six-membered ring (**2**), as depicted in Figure 1. The present contribution reports on the preparation and full spectroscopic characterization (IR, UV/Vis, $^1$H, and $^{13}$C NMR) of

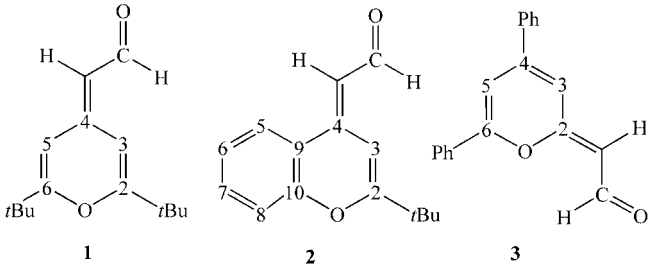


Figure 1. Substituted α- and γ-pyranylideneacetaldehydes used in this work and their labelling scheme.

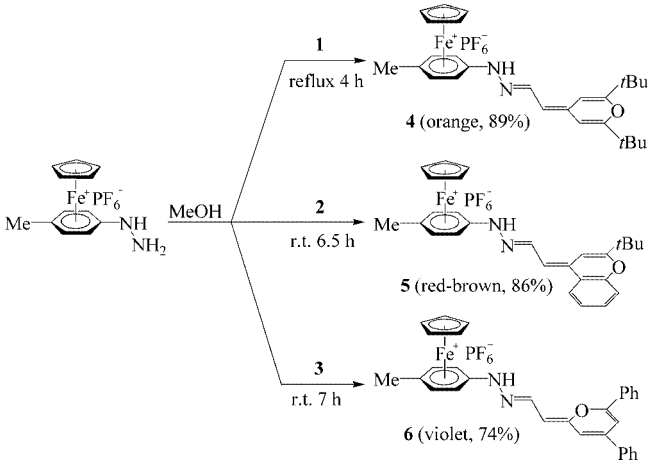


Scheme 2. Preparation of complexes **4**–**6**.

the resulting new mononuclear complexes **4**–**6**, in which a substituted α- or γ-methylenepyran fragment is attached to a [CpFe(η$^6$-*p*-tolylhydrazone)]$^+$ moiety (the structural formulae of complexes **4**–**6** are given in Scheme 2), the crystal and molecular structures of the benzopyran derivative **5** to gain insight into influence of the electron-withdrawing organometallic group on the geometry of D–π–A systems, and finally the second-order NLO properties of these three compounds by measuring the second-harmonic generation efficiency, $\mu\beta$, by the EFISH generation technique.

## Results and Discussion

### Syntheses and Spectroscopic Characterization

The new mononuclear chromophores **4**–**6** were successfully prepared by a condensation reaction of the ionic organometallic hydrazine precursor [CpFe(η$^6$-*p*-MeC$_6$H$_4$-NHNH$_2$)]$^+$PF$_6^-$ with the γ-pyranylideneacetaldehydes **1** and **2**, and the α-pyranylideneacetaldehyde **3** (see Figure 1), respectively, in ethanol solution (Scheme 2). The three complexes were isolated as orange (**4**), reddish-brown (**5**), and dark-violet (**6**) microcrystalline solids, in excellent yields of between 74 and 89% after recrystallization from a dichloromethane/diethyl ether mixture. All three mononuclear species display good thermal stability in air. Compound **6** has the same intense dark color as the methylenepyran Fischer-type carbene derivatives.[15a] Complexes **4**–**6** exhibit a good solubility in common polar organic solvents, but are insoluble in diethyl ether, hydrocarbons, and water. Their structures were inferred from satisfactory elemental analysis, $^1$H and $^{13}$C NMR, IR, and UV/Vis spectroscopy, and additionally, in the case of complex **5**, by an X-ray diffraction analysis (vide infra).

The solid-state IR spectra of compounds **4**–**6** exhibit the three typical features we have previously observed for related mononuclear organometallic hydrazones.[13] These are: (i) a weak to medium ν(N–H) stretching vibration at about 3320 cm$^{-1}$, (ii) a sharp intense band at about 1565 cm$^{-1}$ attributed to the asymmetric ν(C=N) stretching vibration, and (iii) a splitting of the very strong ν(PF$_6$) band at about 845 and 828 cm$^{-1}$ and a sharp and strong $\delta$(P–F) band at around 557 cm$^{-1}$. In addition, the IR spectra show weak bands in the 1640–1590 cm$^{-1}$ region assigned to the ν(C=C) stretching mode of the methylenepyran fragment.[18]

Interestingly, the organoiron hydrazones **4**–**6** are formed stereoselectively as the sterically less hindered (*E*) isomer (about the N=C double bond), as indicated by the unique set of signals in their $^1$H and $^{13}$C NMR spectra (see Exp. Sect.), and definitively assigned from the structural analysis of complex **5** (see below). In the $^1$H NMR spectra of all the compounds, the sandwich moiety [CpFe(η$^6$-*p*-MeC$_6$H$_4$–)]$^+$ is clearly identified by the characteristic sharp singlets of the Cp and *p*-methyl tolyl proton resonances observed at $\delta \approx 5.00$ and 2.48 ppm, respectively. In addition, the upfield-shifted signals of the aromatic protons of the coordinated C$_6$ ring ($\delta \approx 6.20$ ppm), the doublet ($\delta$ = 8.15–8.37, $^3J_{H,H}$

 © 2006 Wiley-VCH Verlag GmbH & Co. KGaA, Weinheim 

≈ 10 Hz) assigned to the deshielded imine proton, and the low-field position ($\delta$ = 9.21–9.48 ppm) of the acidic benzylic N–H signal appear in their expected regions.[13,14] On the other hand, the vinylic 3-H resonance of the methylenepyran core (see Figure 1 for labelling scheme), which is common to the three compounds under investigation, appears as a doublet ($^4J_{H,H}$ = 2.0 Hz) for **4** and as a singlet for **5** and **6**, at $\delta$ = 6.24, 6.38, and 6.85, respectively. Like the 3-H signal, 5-H also appears as a singlet, which strongly indicates that compound **6** is isolated as a single isomer about the C-2=C(exocyclic) double bond, even though the starting pyranic aldehyde **3** is a mixture of (*Z*) and (*E*) isomers.[19] However, the formation of a minor isomer, the population of which is too low to be detected by 300 MHz NMR spectroscopy, cannot be ruled out. It should be noted that the $^1$H NMR spectrum was recorded after recrystallization of the compound and that both isomers have indeed been spectroscopically characterized for a related Fischer-type carbene complex derived from the same mixture of aldehydes.[20]

Consistent with the proposed structure, the $^{13}$C NMR spectra of complexes **4**–**6** exhibit the expected characteristic sharp resonances for the $C_5$ ring and the *p*-Me substituent of the sandwich fragments at $\delta \approx$ 76 and 19 ppm, respectively. The two carbon atoms linked to a nitrogen atom appear as broad signals at lower field, with the imine carbon signal at $\delta \approx$ 143 ppm and the coordinated $C_{ipso}$ signal at $\delta \approx$ 120 ppm. This latter value suggests a partial C–N multiple-bond character, in agreement with the findings of the crystallographic study (see below). The carbon signals of the coordinated $C_6$ ring are shifted upfield relative to those of the free benzo and phenyl rings of compounds **5** and **6**, respectively. In addition, the three types of methylenepyran frameworks exhibit five resonances assigned to five types of skeletal carbon atoms. Molecule **4**, for example, shows the quaternary C-2, C-4, and C-6 carbon atoms as peaks at $\delta$ = 164.67, 134.86, and 163.91 ppm, respectively, with the vinylic C-3 and C-5 signals at $\delta$ = 98.04 and 104.35 ppm, respectively, and the exocyclic carbon signal at $\delta$ = 106.45 ppm. Moreover, the *tert*-butyl carbon atoms show up as two sets of two closely spaced singlets at $\delta$ = 27.09 and 27.13 and 35.16 and 35.47 ppm for the methyl and the quaternary carbon atoms, respectively.

The $^1$H NMR chemical shift of the 3-H proton has previously been taken as a criterion for the degree of pyrylium character.[21] In general, as the contribution of the pyrylium resonance form contributes more to the ground-state structure of a compound, the chemical shift of the signal of the hydrogen atom in the 3-position tends to shift downfield. Thus, from comparison of the observed 3-H chemical-shift values of compounds **4**–**6** with those, more deshielded (see Exp. Sect. and Tables S1 and S2), of unsaturated Fischer-type carbene complexes bearing an α- and γ-methylenepyran or γ-methylenebenzopyran group, namely [$(OC)_5$-W=C(OMe)$(CH=CH)_n$CH=(pyran)] ($n$ = 0–2),[15,20] it seems that the sandwich molecules **4**–**6** have a lower pyrylium or benzopyrylium character. This trend is also confirmed by the $^{13}$C NMR spectroscopic data (Tables S1 and S2). This would suggest that the [CpFe(η$^6$-*p*-tolyl)]$^+$ moieties have a lower electron-withdrawing ability than the [$(OC)_5$W=C(OMe)] carbene fragment. However, a decrease of the electronic transmission between the ends of the molecule through the NH–N=CH spacer should also be considered.

### X-ray Crystal Structure

The molecular structure of the cationic organometallic moiety **5**$^+$, along with the atom-labelling scheme, is presented in Figure 2. Selected bond lengths and angles are listed in Table 1, and details of data collection and refinement are provided in the Exp. Sect. Compound **5** crystallizes in the monoclinic space group $P2_1/n$ with four molecules in the unit cell. In the mixed-sandwich fragment, the iron atom is coordinated to the cyclopentadienyl ring at a ring centroid–iron distance of 1.654 Å, and to the tolyl ring at a ring centroid–iron distance of 1.554 Å. The carbocyclic rings coordinated to the iron center are essentially parallel to one another (deviation of 4.10°), which gives rise to a ring centroid–iron–ring centroid angle of 177.2°. These metrical parameters, together with those listed in Table 1, are similar to those we have already reported for related mononuclear hydrazone complexes,[13] and are typical of an η$^5$-Fe$^{II}$-η$^6$ metallocene-type coordination.[22] More interestingly, the coordinated tolyl ring and the pyran ring, as well as the two six-membered rings of the benzopyran subunit, are coplanar (dihedral angles 3.2° and 1.4°, respectively), a situation which allows conjugation between the intracyclic oxygen atom and the cationic iron center through the entire hydrazone backbone.

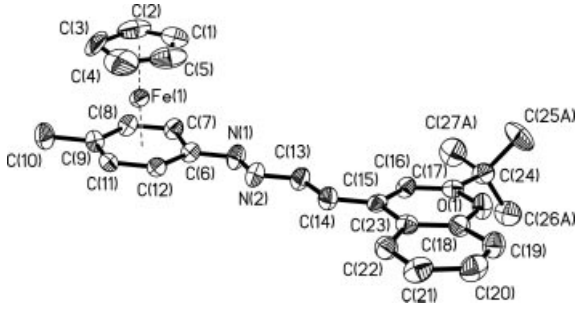


Figure 2. Molecular structure and atom-numbering scheme for **5**·$CH_2Cl_2$. Hydrogen atoms, the $PF_6^-$ counteranion, one of the disordered positions of the *tert*-butyl substituent, and the solvent molecule have been omitted for clarity. Displacement ellipsoids are at the 30% probability level.

A close inspection of Table 1 reveals characteristic structural features provoked by the electron-withdrawing CpFe$^+$ moiety on the η$^6$-coordinated arylhydrazone ligand. Thus, the Fe(1)–C(6) bond [2.198(6) Å] is longer than the mean value of the other five Fe(1)–C($C_6$ ring) bonds (2.048 Å). This elongation (0.15 Å) is a consequence of a partial delocalization of the benzylic nitrogen electron lone-pair toward the cationic mixed-sandwich moiety, and is reflected by (i) a depyramidalization of the N(1) atom, with idealized bond angles at this sp$^2$-hybridized nitrogen atom [C(6)–N(1)–

 © 2006 Wiley-VCH Verlag GmbH & Co. KGaA, Weinheim 

Table 1. Selected bond lengths [Å] and angles [°] for **5**·$CH_2Cl_2$.

| | | | |
|---|---|---|---|
| Fe(1)–C(6) | 2.198(6) | C(6)–N(1) | 1.342(7) |
| Fe(1)–C(7) | 2.087(6) | N(1)–N(2) | 1.357(7) |
| Fe(1)–C(8) | 2.044(6) | N(2)–C(13) | 1.280(7) |
| Fe(1)–C(9) | 2.065(6) | C(13)–C(14) | 1.425(8) |
| Fe(1)–C(11) | 2.040(6) | C(14)–C(15) | 1.354(8) |
| Fe(1)–C(12) | 2.083(6) | C(15)–C(16) | 1.446(8) |
| Fe(1)–C(1–5)av. | 2.061 | C(15)–C(23) | 1.455(8) |
| O(1)–C(17) | 1.372(7) | C(16)–C(17) | 1.309(8) |
| O(1)–C(18) | 1.383(7) | C(18)–C(23) | 1.381(8) |
| C(6)–C(7) | 1.410(8) | C(6)–C(12) | 1.410(8) |
| C(7)–C(8) | 1.398(8) | C(8)-C(9) | 1.366(8) |
| C(9)–C(11) | 1.395(8) | C(11)–C(12) | 1.389(8) |
| C(6)–N(1)–N(2) | 120.7(5) | N(1)–N(2)–C(13) | 115.7(6) |
| N(2)–C(13)–C(14) | 121.9(6) | C(13)–C(14)–C(15) | 126.2(6) |
| C(14)–C(15)–C(16) | 122.7(6) | C(14)–C(15)–C(23) | 123.3(6) |
| O(1)–C(17)–C(16) | 122.4(6) | O(1)–C(18)–C(23) | 122.0(5) |
| C(17)–O(1)–C(18) | 118.3(5) | | |

N(2) = 120.7(5)°], (ii) a C(6)–N(1) bond length of 1.342(7) Å, which is intermediate between a single and a double carbon–nitrogen bond,[22] and (iii) a very weak cyclohexadienyl character of the coordinated phenyl ring, with a folding dihedral angle of 3.3° about the C(7)–C(12) axis. Moreover, this cyclohexadienyl character is exemplified by two long C(6)–C(7) and C(6)–C(12) distances of 1.410(8) Å, while the remaining four other C–C bonds are significantly shorter and fall in the interval 1.366(8)–1.398(8) Å (Table 1), thus emphasizing the weight of the iminocyclohexadienyl mesomeric form (Scheme 1).[8a,13a] On the benzomethylenepyran side, we observe that the exocyclic bond C(14)–C(15) is 1.354(8) Å long, which suggests a weak benzopyrylium character. In fact, for comparison, the exocyclic bond lengths 1.393(8),[15c] 1.389(10),[23] and 1.40(1) Å[15a] measured for γ-methylenepyran Fischer-type carbene complexes have more single-bond character, in accordance with a large conjugation between the intracyclic oxygen lone-pair and the strongly electron-withdrawing carbene fragment. It is worth remarking that these findings fully corroborate the observed NMR spectroscopic data (see above). In addition, it should be noted that NMR studies have shown that the presence of a fused benzene ring decreases the electron-donating ability of the pyran heterocycle.[16]

### Linear and Nonlinear Optical Properties

The UV/Vis spectra of the three complexes under study are similar in that the spectra consist of two intense and broad absorption bands in the visible region. As expected from its dark-violet color, the low-energy absorption band of compound **6** is red-shifted relative to those of **4** and **5**. The origin of the high-energy absorption band in the range 300–380 nm is assumed to be an intra-ligand charge-transfer (ILCT) transition, and the low-energy absorption band in the region 380–550 nm is assigned to a metal-to-ligand charge-transfer (MLCT) transition.[12,13b,24] Deconvolution of the spectra with Gaussian curves gives rise to three or four absorption bands for these two CT transitions (Figure 3 and Table 2). The data of Table 2 indicate that the linear-optical properties (i.e. the energies and intensities of the absorption bands corresponding to the above-mentioned CT transitions) of **4**–**6** are in agreement with those reported for other D–π–A systems having the same $[CpFe(\eta^6\text{-arene})]^+$ fragment as electron acceptor linked to an organic electron-donating group.[12,13b] The broadening of the low-energy band is probably the result of the overlap of broad d–d visible bands of the $[CpFe(\eta^6\text{-arene})]^+$ fragment.[10a,11,25] For compounds **4** and **6**, the two characteristic CT bands exhibit bathochromic shifts when the solvent polarity is increased, thus indicating increased polarity in the excited state. The solvatochromism is much larger for **4** than for **6**, whereas the solvent influence is negligible for compound **5**. Nevertheless, solvatochromic effects can hint at the magnitude of the expected nonlinear optical properties, since they reflect the polarizability of a chromophore.[26]

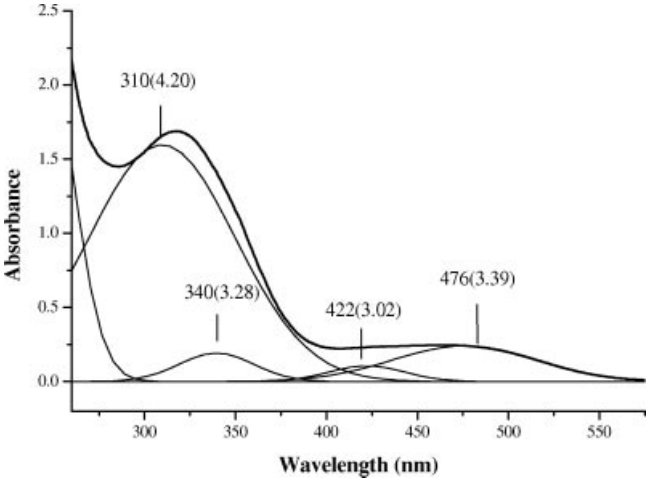


Figure 3. Deconvoluted UV/Vis spectrum of compound **5** recorded in $CH_2Cl_2$. The first number is the wavelength ($\lambda$) and the value in parentheses is log$\varepsilon$ (see Table 2).

Table 2. Electronic absorption and EFISH data.

| Compound | $\lambda$ [nm] (log$\varepsilon$) $CH_2Cl_2$ | $\lambda$ [nm] (log$\varepsilon$) DMSO | $\Delta\lambda$ [nm] | $\mu\beta$ ($\times 10^{-48}$) [esu] $CH_2Cl_2$ |
|---|---|---|---|---|
| **4** | 369 (4.48) | 382 (4.55) | +23 | 154 ± 20 |
| | 396 (3.80) | 452(3.27) | +56 | |
| | 451 (4.07) | 486 (3.69) | +35 | |
| **5** | 310 (4.20) | 309 (4.11) | –1 | 149 ± 10 |
| | 340 (3.28) | 348 (3.66) | +8 | |
| | 422 (3.02) | 415 (2.92) | –7 | |
| | 476 (3.39) | 469 (3.34) | –7 | |
| **6** | 369 (4.17) | 374 (4.05) | +5 | 83 ± 40 |
| | 453 (3.86) | 483 (3.65) | +30 | |
| | 486 (3.62) | 498 (2.94) | +12 | |
| | 523 (4.05) | 531 (3.75) | +8 | |

The second-order NLO properties of compounds **4**–**6** were investigated using the electric-field-induced second-harmonic (EFISH) generation technique, which provides information about the scalar product, $\mu\beta$, of the vectorial part of the first hyperpolarisability tensor, $\beta$, and the dipole

 © 2006 Wiley-VCH Verlag GmbH & Co. KGaA, Weinheim 

moment vector, $\mu$.[27] Compounds **4**–**6** exhibit reasonable $\mu\beta$ values (Table 2), although they remain significantly weaker than those reported for organic hydrazone molecules ($\mu\beta$ = $100–640 \times 10^{-48}$ esu).[28] However, these compounds contain a longer conjugated moiety containing two phenyl rings and are substituted with a very strong acceptor group ($NO_2$) and a good alkoxy donor substituent. The $\mu\beta$ values reported in the present work are comparable to the values of $74 \times 10^{-48}$ and $310 \times 10^{-48}$ esu determined for two Fischer-type methoxycarbene complexes bearing an identical methylenepyran donor fragment to that in **4** and **5** (Table S3).[20] This clearly indicates that the hydrazone and the methylenepyran fragments act as a good π-conjugated spacer and electron donor, respectively, and that the $[CpFe(\eta^6\text{-arene})]^+$ group, which can be functionalized by easy, $CpFe^+$-induced transformations at the coordinated arene ring,[9] could be used as a strong electron-acceptor substituent in molecular engineering for quadratic NLO.[29] Finally, it is interesting to note that the $\mu\beta$ values of **4** and **5** are practically identical, whereas that of **6** is only half as large. This behavior can be attributed to the fact that the spacer is located at the α-position of the electron-donating pyran ring in compound **6**, whereas in **4** and **5** it is located at the γ-position. As a consequence, the internal charge transfer responsible for the $\beta$ value should be smaller and the $\mu\beta$ scalar product is also reduced by the fact that $\mu$ and $\beta$ are probably not parallel to one another.

## Concluding Remarks

In summary, three new organometallic π-conjugated push-pull chromophores have been prepared in high yields by condensation reactions of cyclopentadienyliron(II)-complexed *p*-tolylhydrazines with differently substituted archetypal pyranylideneacetaldehydes. Their original design combines an organometallic acceptor group, namely the cationic mixed-sandwich fragment $[CpFe(\eta^6\text{-}p\text{-}MeC_6H_4)]^+$, associated with an α- and γ-methylenepyran donor through the asymmetric hydrazone spacer NH–N=CH. Single-crystal X-ray diffraction analysis of compound **5** has shown a favorable electronic structure resulting from the coplanarity of the coordinated tolyl ring and the pyran ring, as well as the two six-membered rings of the benzopyran subunit, thus allowing conjugation between the intracyclic oxygen atom and the cationic iron center through the entire hydrazone backbone. As such, the organometallic hydrazones described in this work can be defined as type-I non-rod-shaped dipolar chromophores,[30] and have been proven to favor electronic delocalization along the conjugated chain. Finally, compounds **4**–**6** are strongly polarized D–π–A systems that exhibit solvatochromic properties and have low-lying intramolecular charge-transfer bands in their electronic absorption spectra and enhanced second-order NLO properties ($\mu\beta$). Theoretical computations are obviously required before discussing the electronic structures of the complexes and the electronic transitions giving rise to the NLO properties in more detail; these are currently underway and will be published in due course.

## Experimental Section

**General Procedures:** Unless otherwise noted, all reactions and manipulations were performed at room temperature under dinitrogen using standard Schlenk-line techniques. Solid IR spectra were obtained from KBr disks with a Perkin–Elmer Model Spectrum One FT IR spectrophotometer. Electronic spectra were collected with a Spectronic Genesys 2 spectrophotometer. $^1H$ and $^{13}C$ NMR spectra were recorded with a Bruker Advance DPX 300, 400 Digital or a DPX 500 spectrometer, as noted within the text. All NMR spectra are reported in ppm ($\delta$) relative to tetramethylsilane, with the residual solvent proton resonance and carbon resonances used as internal standards. Coupling constants are reported in Hz. $^1H$ and $^{13}C$ NMR chemical shift assignments are supported by data obtained from $^1H$-$^1H$ COSY, $^1H$-$^{13}C$ HMQC, and $^1H$-$^{13}C$ HMBC NMR experiments, and are given according to the numbering scheme of Figure 1. Melting points were determined in evacuated capillaries and are not corrected. Microanalytical data were obtained by the Institut de Chimie de Rennes Microanalysis Service with a Thermo-FINNIGAN Flash EA 1112 CHNS/O analyzer.

**Materials:** Solvents were dried and distilled under dinitrogen by standard methods prior to use. Reagents were purchased from commercial suppliers and used without further purification. The organometallic hydrazine precursor $[CpFe(\eta^6\text{-}p\text{-}CH_3C_6H_4NHNH_2)]^+\text{-}PF_6^-$ was synthesized as described previously,[13e] and the γ-pyranylideneacetaldehydes **1**–**3** (see Figure 1) were also prepared according to published procedures.[19,31]

**($\eta^5$-Cyclopentadienyl)[(2,6-di-*tert*-butyl-4*H*-pyran-4-ylidene)acetaldehyde ($\eta^6$-*p*-tolyl)hydrazone]iron Hexafluorophosphate (4):** A Schlenk tube was charged with a magnetic stirring bar, $[CpFe(\eta^6\text{-}p\text{-}CH_3C_6H_4NHNH_2)]^+PF_6^-$ (105 mg, 0.271 mmol), (2,6-di-*tert*-butyl-4*H*-pyran-4-ylidene)acetaldehyde (**1**; 63.0 mg, 0.269 mmol), and ethanol (15 mL). The reaction mixture was refluxed for 4 h, then cooled to room temperature and stored at –30 °C overnight. The orange precipitate was filtered off, washed with diethyl ether ($2 \times 5$ mL), and dried under vacuum. It was then dissolved in a minimum amount of $CH_2Cl_2$ and the solution was layered with an equivalent volume of diethyl ether. Compound **4** was isolated as an orange, microcrystalline solid. Yield: 145 mg (89%). M.p. 212 °C (dec.). $C_{27}H_{35}F_6FeN_2OP$ (604.39): calcd. C 53.66, H 5.84, N 4.64; found C 53.53, H 6.02, N 4.85. IR (KBr pellet): $\tilde{\nu}$ = 3319 (m) ν(N–H); 3109 (vw), 3080 (vw), 2964 (m), 2928 (w), 2904 (w), 2870 (w) ν(C–H); 1668 (s), 1609 (m), 1588 (s) ν(C=C); 1570 (s) ν(C=N); 1501 (m) ν(C–O); 840 (vs), 826 (vs) ν($PF_6$); 555 (s) $\delta$(P–F) $cm^{-1}$. $^1H$ NMR (400 MHz, $CD_3COCD_3$, 25 °C): $\delta$ = 1.24, 1.26 [2 × s, 2 × 9 H, $C(CH_3)_3$], 2.47 (s, 3 H, $CH_3C_6H_4$), 4.97 (s, 5 H, Cp), 5.54 (d, $^3J_{H,H}$ = 10.4 Hz, 1 H, N=CH–C*H*=), 5.90 (d, $^4J_{H,H}$ = 2.0 Hz, 1 H, 5-H), 6.14 (d, $^3J_{H,H}$ = 6.8 Hz, 2 H, $C_6H_4$), 6.18 (d, $^3J_{H,H}$ = 6.8 Hz, 2 H, $C_6H_4$), 6.24 (d, $^4J_{H,H}$ = 2.0 Hz, 1 H, 3-H), 8.15 (d, $^3J_{H,H}$ = 10.4 Hz, 1 H, N=C*H*–CH=), 9.21 (s, 1 H, NH) ppm. $^{13}C$ NMR (125 MHz, $CD_3COCD_3$, 25 °C): $\delta$ = 19.06 ($CH_3C_6H_4$); 27.09, 27.13 [$C(CH_3)_3$]; 35.16, 35.47 [$C(CH_3)_3$]; 67.73 (*o*-$C_6H_4$); 76.09 (Cp); 86.14 (*m*-$C_6H_4$); 96.73 (*p*-$C_6H_4$); 98.04 (C-3); 104.35 (C-5); 106.45 (N=CH–*C*H=); 120.07, 120.19 ($C_{ipso}$ $C_6H_4$); 134.86 (C-4); 144.28 (N=*C*H–CH=); 163.91 (C-6); 164.67 (C-2) ppm.

**[(2-*tert*-Butyl-4*H*-chromen-4-ylidene)acetaldehyde ($\eta^6$-*p*-tolyl)hydrazone]($\eta^5$-cyclopentadienyl)iron Hexafluorophosphate (5):** A Schlenk tube was charged with a magnetic stirring bar, $[CpFe(\eta^6\text{-}p\text{-}CH_3C_6H_4NHNH_2)]^+PF_6^-$ (150 mg, 0.387 mmol), [(4*E*)-2-*tert*-butyl-4*H*-chromen-4-ylidene]acetaldehyde (**2**; 88.0 mg, 0.387 mmol), and ethanol (10 mL). The reaction mixture was stirred at room temperature for 6.5 h and was then stored at –30 °C overnight. Workup as described above yielded 200 mg (86%) of **5** as reddish-

 © 2006 Wiley-VCH Verlag GmbH & Co. KGaA, Weinheim 

brown crystals. A crystal from this crop was used for an X-ray structure determination. M.p. 239 °C (dec.). $C_{27}H_{29}F_6FeN_2OP$ (598.35): calcd. C 54.20, H 4.89, N 4.68; found C 54.35, H 4.92, N 4.76. IR (KBr pellet): $\tilde{\nu}$ = 3319 (w) ν(N–H); 3116 (vw), 2969 (w), 2920 (w), 2848 (vw) ν(C–H); 1648 (m), 1592 (m) ν(C=C); 1568 (m) ν(C=N); 1501 (m) ν(C–O); 847 (vs), 829 (vs) ν($PF_6$); 558 (m) δ(P–F) $cm^{-1}$. $^1H$ NMR (400 MHz, $CD_3COCD_3$, 25 °C): δ = 1.31 [s, 9 H, $C(CH_3)_3$], 2.49 (s, 3 H, $CH_3C_6H_4$), 5.01 (s, 5 H, Cp), 6.25 (s, 4 H, $C_6H_4$), 6.38 (s, 1 H, 3-H), 6.47 (d, $^3J_{H,H}$ = 10.0 Hz, 1 H, N=CH–CH=), 7.23–7.33 (m, 2 H, 6-H, 8-H), 7.47 (t, $^3J_{H,H}$ = 7.5 Hz, 1 H, 5-H), 7.87 (d, $^3J_{H,H}$ = 7.7 Hz, 1 H, 7-H), 8.37 (d, $^3J_{H,H}$ = 10.0 Hz, 1 H, N=CH–CH=), 9.48 (s, 1 H, NH) ppm. $^{13}C$ NMR (125 MHz, $CD_3COCD_3$, 25 °C): δ = 19.10 ($CH_3C_6H_4$), 27.15 [$C(CH_3)_3$], 35.38 [$C(CH_3)_3$], 68.28 (*o*-$C_6H_4$), 76.29 (Cp), 86.26 (*m*-$C_6H_4$), 96.69 (C-3) 97.14 (*p*-$C_6H_4$), 107.38 (N=CH–CH=), 117.62 (C-8), 119.56 ($C_{ipso}$ $C_6H_4$), 120.88 (C-4), 122.82 (C-5), 124.63 (C-6), 130.36 (C-7), 132.38 (C-10), 143.50 (N=CH–CH=), 151.97 (C-9), 162.61 (C-2) ppm.

**(η⁵-Cyclopentadienyl)[(4,6-diphenyl-2*H*-pyran-2-ylidene)acetaldehyde (η⁶-*p*-tolyl)hydrazone]iron Hexafluorophosphate (6):** A Schlenk tube was charged with a magnetic stirring bar, $[CpFe(\eta^6\text{-}p\text{-}CH_3C_6H_4NHNH_2)]^+PF_6^-$ (131 mg, 0.338 mmol), (2*Z*)-(4,6-diphenyl-2*H*-pyran-2-ylidene)acetaldehyde (**3**; 92.0 mg, 0.335 mmol), and ethanol (10 mL). The reaction mixture was stirred at room temperature for 7 h, and then stored at –30 °C overnight. Workup as above yielded 160 mg (74%) of **6** as a dark-violet powder. M.p. 254 °C (dec.). $C_{31}H_{27}F_6FeN_2OP$ (644.38): calcd. C 57.78, H 4.22, N 4.35; found C 57.63, H 4.41, N 4.08. IR (KBr pellet): $\tilde{\nu}$ = 3322 (w) ν(NH); 3058 (vw), 2964 (vw), 2920 (vw), 2848 (vw) ν(CH); 1639 (w), 1593 (w) ν(C=C); 1557 (m) ν(C=N); 1494 (m) ν(C–O); 842 (vs), 830 (vs) ν($PF_6$); 558 (m) δ(P–F) $cm^{-1}$. $^1H$ NMR (300.08 MHz, $CD_3COCD_3$, 25 °C): δ = 2.46 (s, 3 H, $CH_3C_6H_4$), 4.98 (s, 5 H, Cp), 5.63 (d, $^3J_{H,H}$ = 10.0 Hz, 1 H, N=CH–CH=), 6.18 (s, 4 H, $C_6H_4$), 6.85 (s, 1 H, 3-H), 6.90 (s, 1 H, 5-H), 7.50 (m, 6 H, *m*- and *p*-H Ph at C-4 and C-6), 7.79 (d, $^3J_{H,H}$ = 7.0 Hz, 2 H, *o*-H Ph at C-4), 7.97 (d, $^3J_{H,H}$ = 7.9 Hz, 2 H, *o*-H Ph at C-6), 8.35 (d, $^3J_{H,H}$ = 10.0 Hz, 1 H, N=CH–CH=), 9.37 (s, 1 H, NH) ppm. $^{13}C$ NMR (75.46 MHz, $CD_3COCD_3$, 25 °C): δ = 19.07 ($CH_3C_6H_4$); 67.91 (*o*-$C_6H_4$); 76.20 (Cp); 86.18 (*m*-$C_6H_4$); 96.86 (*p*-$C_6H_4$); 99.35 (N=CH–CH=); 100.42 (C-5); 116.56 (C-3); 119.94 ($C_{ipso}$ $C_6H_4$); 124.96 (*o*-C Ph at C-6); 125.65 (*o*-C Ph at C-4); 128.84, 128.95 (*m*-C Ph at C-4 and C-6); 129.18, 130.00 (*p*-C Ph at C-4 and C-6); 132.35 ($C_{ipso}$ Ph at C-6); 136.20 ($C_{ipso}$ Ph at C-4); 137.94 (C-4); 141.93 (N=CH–CH=); 155.34 (C-6); 156.36 (C-2) ppm.

**X-ray Crystal-Structure Determination for 5·$CH_2Cl_2$:** A red-orange plate of complex **5** with dimensions 0.18 × 0.11 × 0.10 mm was mounted on a glass fiber in a random orientation. Data collection was performed at room temperature with a Bruker Smart Apex diffractometer equipped with a two-dimensional CCD detector and a graphite-monochromated Mo-$K_\alpha$ radiation (λ = 0.71073 Å) source, with a nominal crystal-to-detector distance of 6.3 cm. A hemisphere of data was collected on the basis of four ω-scans runs (starting ω = 28°) at φ values of 0°, 120°, 240°, and 0°, with the detector at 2θ = 28°. In each of these runs, frames (600, 600, 600, and 50, respectively) were collected at 0.3° intervals and for 10 s per frame. The diffraction frames were integrated using the SAINT package,[32] and corrected for absorption with SADABS.[33] The positions of the heavy atoms were determined by direct methods, and successive difference electron density maps were produced with the SHEXTL 6.14 software package[34] to locate the remaining atoms. Refinement was performed by the full-matrix least-squares method based on $F^2$. The *tert*-butyl group was disordered over two positions, with an occupation multiplicity, μ, of 0.71/0.29. All non-hydrogen atoms were refined anisotropically. Hydrogen atoms were placed in their calculated positions, assigned fixed isotropic thermal parameters, and allowed to ride on their respective parent atoms. $C_{27}H_{29}F_6FeN_2OP{\cdot}CH_2Cl_2$, $M_r$ = 683.27, *a* = 10.1473(10), *b* = 18.7529(19), *c* = 16.2043(16) Å, β = 95.395(2)°, *V* = 3069.9(5) $Å^3$, monoclinic, $P2_1/n$, *Z* = 4, $D_{calcd.}$ = 1.478 $g cm^{-3}$, μ = 0.779 $mm^{-1}$, SADABS absorption correction applied, *F*(000) = 1400, *T* = 299(2) K, $2\theta_{max}$ = 28.08°, reflections collected/unique 25343/6916 [$I > 2\sigma(I)$], data/restraints/parameters 6916/126/459, $R/R_{w2}$ [$I > 2\sigma(I)$] = 0.0923/0.1923, $R/R_{w2}$ (all data) = 0.2394/0.2485, GOF = 0.962, $[\Delta\rho]_{min}/[\Delta\rho]_{max}$ = –0.346/0.476. CCDC-272776 contains the supplementary crystallographic data for this paper. These data can be obtained free of charge from The Cambridge Crystallographic Data Center via www.ccdc.cam.ac.uk/data_request/cif.

**EFISH Measurements:** The principle of the EFISH technique has been described elsewhere.[35,36] In order to avoid reabsorption of the generated second harmonics, the data were recorded using 1.907-μm, 10-ns incident laser pulses produced by a hydrogen Raman shifter pumped by an Nd:YAG laser at 1.06 μm at a repetition rate of 10 Hz. The centrosymmetry of the solution was broken by dipolar orientation of the chromophores with a high-voltage pulse (8 kV applied on 3 mm during 1 μs) synchronized with the laser pulse. The compounds were dissolved in dichloromethane at various concentrations ($10^{-3}$ to $10^{-2}$ M) and the solutions were introduced into the measurement cell where the high-voltage was applied during SHG measurements. NLO measurements were calibrated with pure dichloromethane as a reference. Acquisition and data processing were performed using a computerized home-made system.

**Supporting Information** (see footnote on the first page of this article): Tables S1 and S2 compare selected $^1H$ and $^{13}C$ NMR chemical shifts of compounds **4** and **5** with those of pentacarbonyltungsten methylenepyran Fischer-type methoxycarbene complexes, and Table S3 lists the EFISH data of these same pentacarbonyltungsten methylenepyran Fischer-type methoxycarbene complexes.

## Acknowledgments

Financial support from the Fondo Nacional de Desarrollo Científico y Tecnológico [FONDECYT, Chile; grant no. 1010318 (D. C. and C. M.)], the CNRS-CONICYT agreement no. 16771 (C. M., D. C., and J.-R. H.), the Pontificia Universidad Católica de Valparaíso, the Université de Rennes 1, and the Ministère de l'Education Nationale de la Recherche et de la Technologie (MENRT, grant to N. F.) is gratefully acknowledged.

[1] a) E. Goovaerts, W. E. Wenseleers, M. H. Garcia, G. H. Cross, in *Handbook of Advanced Electronic and Photonic Materials and Devices* (Ed.: H. S. Nalwa), *Nonlinear Optical Materials*, Academic Press, New York, **2001**, vol. 9, p. 127; b) J. Zyss, *Molecular Nonlinear Optics: Materials, Physics and Devices*, Academic Press, Boston, **1994**; c) P. N. Prasad, D. J. Williams, *Nonlinear Optical Effects in Molecules and Polymers*, John Wiley & Sons, New York, **1991**; d) *Nonlinear Optics of Organic Molecules and Polymers* (Eds.: H. S. Nalwa, S. Miyata), CRC Press, New York, **1997**; e) P. G. Lacroix, *Eur. J. Inorg. Chem.* **2001**, 339–348; f) J. A. Delaire, K. Nakatani, *Chem. Rev.* **2000**, *100*, 1817–1845; g) D. M. Burland, *Chem. Rev.* **1994**, *94*, 1–278 (special issue).

[2] For an overview see: a) B. J. Coe, N. R. M. Curati, *Comments Inorg. Chem.* **2004**, *25*, 147–184; b) E. Peris, *Coord. Chem. Rev.* **2004**, *248*, 279–297 and references cited therein; c) S. Di Bella, *Chem. Soc. Rev.* **2001**, *30*, 355–366; d) S. Barlow, S. R. Marder,

 © 2006 Wiley-VCH Verlag GmbH & Co. KGaA, Weinheim 

*Chem. Commun.* **2000**, 1555–1562; e) N. J. Long, *Angew. Chem. Int. Ed. Engl.* **1995**, *34*, 21–38.
[3] S. R. Marder, J. W. Perry, B. G. Tiemann, W. P. Schaefer, *Organometallics* **1991**, *10*, 1896–1901.
[4] a) J. Heck, S. Dabek, T. Meyer-Friedrichsen, H. Wong, *Coord. Chem. Rev.* **1999**, *190–192*, 1217–1254; b) H. Wong, T. Meyer-Friedrichsen, T. Farrell, C. Mecker, J. Heck, *Eur. J. Inorg. Chem.* **2000**, 631–646; c) T. Farrell, T. Meyer-Friedrichsen, M. Malessa, D. Haase, W. Saak, I. Asselberghs, K. Wostyn, K. Clays, A. Persoons, J. Heck, A. R. Manning, *J. Chem. Soc., Dalton Trans.* **2001**, 29–36; d) T. Meyer-Friedrichsen, C. Mecker, M. H. Prosenc, J. Heck, *Eur. J. Inorg. Chem.* **2002**, 239–248; e) T. Meyer-Friedrichsen, H. Wong, M. H. Prosenc, J. Heck, *Eur. J. Inorg. Chem.* **2003**, 936–946; f) U. Behrens, T. Meyer-Friedrichsen, J. Heck, *Z. Anorg. Allg. Chem.* **2003**, *629*, 1421–1430.
[5] a) M. Rosenblum, *Chemistry of the Iron-Group Metallocenes*, Wiley, New York, **1965**; b) E. W. Neuse, J. R. Woodhouse, G. Montaudo, C. Puglis, *Appl. Organomet. Chem.* **1988**, *2*, 53; c) *Ferrocenes: Homogenous Catalysis, Organic Synthesis Materials Science* (Eds.: A. Togni, T. Hayashi), Wiley-VCH, Weinheim, **1995**.
[6] For example: a) Y. Liao, B. E. Eichinger, K. A. Firestone, M. Haller, J. D. Luo, W. Kaminsky, J. B. Benedict, P. J. Reid, A. K. Y. Jen, L. R. Dalton, B. H. Robinson, *J. Am. Chem. Soc.* **2005**, *127*, 2758–2766; b) I. Janowska, J. Zakrzewski, K. Nakatani, J. Delaire, M. Palusiak, M. Walak, H. Scholl, *J. Organomet. Chem.* **2003**, *675*, 35–41; c) V. Alain, M. Blanchard-Desce, C. T. Chen, S. R. Marder, A. Fort, M. Barzoukas, *Synth. Met.* **1996**, *81*, 133–136.
[7] a) M. Malaun, Z. R. Reeves, R. L. Paul, J. C. Jeffery, J. A. McCleverty, M. D. Ward, I. Asselberghs, K. Clays, A. Persoons, *Chem. Commun.* **2001**, 49–50; b) I. Asselberghs, K. Clays, A. Persoons, A. M. McDonagh, M. D. Ward, J. A. McCleverty, *Chem. Phys. Lett.* **2003**, *368*, 408–411.
[8] a) J. Ruiz, F. Ogliaro, J.-Y. Saillard, J.-F. Halet, F. Varret, D. Astruc, *J. Am. Chem. Soc.* **1998**, *120*, 11693–11705; b) H. A. Trujillo, C. M. Casado, D. Astruc, *J. Am. Chem. Soc.* **1999**, *121*, 5674–5686.
[9] a) D. Astruc, *J. Organomet. Chem.* **2004**, *689*, 4332–4344 and references cited therein; b) D. Astruc, S. Nlate, J. Ruiz, *Modern Arene Chemistry: Concepts, Synthesis and Applications* (Ed.: D. Astruc), Wiley-VCH, Weinheim, **2002**, ch. 12, p. 400; c) A. S. Abd-El-Aziz, S. Bernardin, *Coord. Chem. Rev.* **2000**, *203*, 219–267; d) A. J. Pearson, *Iron Compounds in Organic Synthesis*, Academic Press, London, **1994**; e) D. Astruc, *Top. Curr. Chem.* **1991**, *160*, 47–95; f) D. Astruc, *Tetrahedron* **1983**, *39*, 4027–4095.
[10] a) J.-R. Hamon, D. Astruc, P. Michaud, *J. Am. Chem. Soc.* **1981**, *103*, 758–766; b) D. Astruc, *Chem. Rev.* **1988**, *88*, 1189–1216; c) S. Rigaut, M.-H. Delville, J. Losada, D. Astruc, *Inorg. Chim. Acta* **2002**, *334*, 225–242.
[11] a) W. A. Hendrickson, M. C. Palazzotto, in *Photosensitive Metal-Organic systems* (Eds.: C. Kutal, N. Serpone), Advanced Chemistry Series 238, ACS, Washington, DC, **1993**, p. 411; b) D. R. Chrisope, K. M. Park, G. B. Schuster, *J. Am. Chem. Soc.* **1989**, *111*, 6195–6201; c) D. R. Chrisope, G. B. Schuster, *Organometallics* **1989**, *8*, 2737–2739.
[12] C. Lambert, W. Gaschler, M. Zabel, R. Matschiner, R. Wortmann, *J. Organomet. Chem.* **1999**, *592*, 109–114.
[13] a) W. Figueroa, M. Fuentealba, C. Manzur, D. Carrillo, A. I. Vega, J.-Y. Saillard, J.-R. Hamon, *Organometallics* **2004**, *23*, 2515–2518; b) C. Manzur, L. Millán, W. Figueroa, D. Boys, J.-R. Hamon, D. Carrillo, *Organometallics* **2003**, *22*, 153–161; c) W. Figueroa, M. Fuentealba, C. Manzur, D. Carrillo, J. A. Mata, J.-R. Hamon, *J. Chil. Chem. Soc.* **2003**, *48*, 75–78; d) C. Manzur, L. Millán, W. Figueroa, J.-R. Hamon, J. A. Mata, D. Carrillo, *Bol. Soc. Chil. Quim.* **2002**, *47*, 431–440; e) C. Manzur, E. Baeza, L. Millán, M. Fuentealba, P. Hamon, J.-R. Hamon, D. Boys, D. Carrillo, *J. Organomet. Chem.* **2000**, *608*, 126–132.
[14] a) C. Manzur, L. Millán, M. Fuentealba, J. A. Mata, D. Carrillo, J.-R. Hamon, *J. Organomet. Chem.* **2005**, *690*, 1265–1272; b) W. Figueroa, M. Fuentealba, C. Manzur, A. I. Vega, D. Carrillo, J.-R. Hamon, *C. R. Chim.* **2005**, *8*, 1268–1275; c) C. Manzur, C. Zúñiga, L. Millán, M. Fuentealba, J. A. Mata, J.-R. Hamon, D. Carrillo, *New J. Chem.* **2004**, *28*, 134–144; d) A. Trujillo, M. Fuentealba, C. Manzur, D. Carrillo, J.-R. Hamon, *J. Organomet. Chem.* **2003**, *681*, 150–157; e) C. Manzur, M. Fuentealba, L. Millán, F. Gajardo, D. Carrillo, J. A. Mata, S. Sinbandhit, P. Hamon, J.-R. Hamon, S. Kahlal, J.-Y. Saillard, *New J. Chem.* **2002**, *26*, 213–221; f) C. Manzur, M. Fuentealba, L. Millán, F. Gajardo, M. T. Garland, R. Baggio, J. A. Mata, J.-R. Hamon, D. Carrillo, *J. Organomet. Chem.* **2002**, *660*, 71–77; g) C. Manzur, M. Fuentealba, D. Carrillo, D. Boys, J.-R. Hamon, *Bol. Soc. Chil. Quim.* **2001**, *46*, 409–413.
[15] a) B. Caro, B. Le Poul, F. Robin-Le Guen, J.-Y. Saillard, S. Kahlal, C. Moinet, N. Le Poul, J. Vaissermann, *Tetrahedron* **2002**, *58*, 7519–7530; b) F. Le Guen, P. Le Poul, B. Caro, R. Pichon, N. Kervarec, *J. Organomet. Chem.* **2001**, *626*, 37–42; c) B. Caro, P. Le Poul, F. Robin-Le Guen, M.-C. Sénéchal-Tocquer, J.-Y. Saillard, S. Kahlal, L. Ouahab, S. Gohlen, *Eur. J. Org. Chem.* **2000**, 577–581; d) B. Caro, P. Le Poul, F. Robin-Le Guen, M.-C. Sénéchal-Tocquer, *Tetrahedron Lett.* **1998**, *39*, 557–560.
[16] N. Faux, B. Caro, F. Robin-Le Guen, P. Le Poul, K. Nakatani, E. Ishow, *J. Organomet. Chem.* **2005**, *690*, 4982–4988.
[17] I. D. L. Albert, T. J. Marks, M. A. Ratner, *J. Am. Chem. Soc.* **1998**, *120*, 11174–11181.
[18] J. D. Hepworth, C. D. Gabbutt, B. M. Heron, in *Comprehensive Heterocyclic Chemistry*, 2nd ed. (Ed.: A. McKillop), Elsevier, Oxford, **1996**, vol. 5, p. 301.
[19] G. A. Reynolds, J. A. VanAllan, *J. Org. Chem.* **1969**, *34*, 2736–2741.
[20] N. Faux, Thesis dissertation, Université de Rennes 1, **2004**.
[21] C.-T. Chen, S. R. Marder, *Adv. Mater.* **1995**, *7*, 1030–1033.
[22] For a reference gathering a large number of interatomic and metal–ligand distances obtained from the Cambridge Crystallographic Data Base Center, see: A. G. Orpen, L. Brammer, F. H. Allen, D. Kennard, D. G. Watson, R. Taylor, *J. Chem. Soc., Dalton Trans.* **1989**, S1–S83.
[23] F. Robin-Le Guen, B. Caro, S. Golhen, unpublished work.
[24] A. Le Beuze, R. Lissilour, J. Weber, *Organometallics* **1993**, *12*, 47–55.
[25] W. H. Morrison, E. Y. Ho, D. N. Hendrickson, *Inorg. Chem.* **1975**, *14*, 500–506.
[26] a) M. S. Paley, J. M. Harris, H. Looser, J. C. Baumert, G. D. Bjorklund, D. Jundt, R. J. Twieg, *J. Org. Chem.* **1989**, *54*, 3774–3778; b) E. G. McRae, *J. Phys. Chem.* **1957**, *61*, 562–572.
[27] a) J. L. Oudar, D. S. Chemla, *J. Chem. Phys.* **1977**, *66*, 2664–2668; b) J. L. Oudar, *J. Chem. Phys.* **1977**, *67*, 446–457; c) J. L. Oudar, H. Le Person, *Opt. Commun.* **1975**, *15*, 258–262.
[28] J. Zyss, I. Ledoux, J.-F. Nicoud, in "Advances in Molecular Engineering for Quadratic Nonlinear Optics" (Eds.: D. S. Chemla, J. Zyss), *Molecular Nonlinear Optics*, Academic Press, San Diego, **1994**, p. 129.
[29] Owing to the different experimental conditions used in ref.[12] (HRS method, acetonitrile, 1.064-μm fundamental energy), comparison of our NLO data with those measured for the closely related dipolar chromophore $[CpFe(\eta^6\text{-}C_6Me_5)\text{–}C{\equiv}C\text{–}p\text{-}C_6H_4NMe_2]PF_6$ is not appropriate.
[30] a) C. Serbutoviez, C. Bosshard, G. Knöpfle, P. Weiss, P. Prêtre, P. Günter, K. Schenk, E. Solari, G. Chapuis, *Chem. Mater.* **1995**, *7*, 1198–1206; b) M. S. Wong, U. Meier, F. Pan, V. Gramlich, C. Bosshard, P. Günter, *Adv. Mater.* **1996**, *8*, 416–420.
[31] D. H. Wadsworth, M. R. Detty, B. J. Murray, C. H. Weidner, N. F. Haley, *J. Org. Chem.* **1984**, *49*, 2676–2681.
[32] *SAINT-PLUS*, Version 6.02, Bruker Analytical X-ray Systems Inc., Madison, WI, USA, **1999**.
[33] G. M. Sheldrick, *SADABS: Empirical Absorption Program*, Version 2.05, University of Götingen, Götingen, Germany.

 © 2006 Wiley-VCH Verlag GmbH & Co. KGaA, Weinheim 

[34] *SHELXTL Reference Manual*, Version 6.14, Bruker Analytical X-ray Systems Inc., Madison, WI, USA, **1998**.
[35] D. M. Burland, C. A. Walsh, F. Kajzar, C. Sentein, *J. Opt. Soc. Am. B* **1991**, 2269.
[36] I. Maltey, J. Delaire, K. Nakatani, P. Wang, X. Shi, S. Wu, *Adv. Mater. Opt. Electron.* **1996**, *6*, 233–238.
Received: October 28, 2005
Published Online: February 21, 2006

 © 2006 Wiley-VCH Verlag GmbH & Co. KGaA, Weinheim 

DOI: 10.1002/ejic.200500832

# Density-Functional Calculation of the $^{183}W$ and $^{17}O$ NMR Chemical Shifts for Large Polyoxotungstates

**Jose Gracia,[a] Josep M. Poblet,*[a] Jochen Autschbach,[c] and Leonid P. Kazansky*[b]**

**Keywords:** Density-functional calculations / NMR spectroscopy / Tungsten / Oxygen / Polyoxometalates

A phosphane sulfate relativistic DFT method (ZORA) has been used to calculate the $^{183}W$ and $^{17}O$ NMR chemical shifts for large polyoxotungstates, including $W_6O_{19}^{2-}$, $CH_3OTiW_5O_{18}^{3-}$, $W_5O_{18}W^{II}NO^{3-}$, $W_{10}O_{32}^{4-}$, α-δ-γ-$XW_{12}O_{40}^{n-}$, β-$PW_9O_{28}Br_6^{3-}$, $P_2W_{18}O_{62}^{6-}$, $PW_2O_{14}^{3-}$, and $W_7O_{24}^{6-}$, based on their optimized molecular structures. Despite sizeable deviations between the calculated and experimental values, the calculations correctly reproduce the trends in the change of the chemical shift for both nuclei. As expected, the diamagnetic term is almost constant throughout the whole series. The change in the chemical shifts is shown to be determined by the paramagnetic term, which depends on the electronic structure of the whole anion under study and, in particular, on the local geometry around a given tungsten atom. On the other hand, there is no correlation between the chemical shift and HOMO–LUMO gap, showing that deeper occupied levels and several unoccupied orbitals play an important role in the paramagnetic term. However, analysis of the components of the paramagnetic shielding has shown that the most significant transitions determining the change of both $^{183}W$ and $^{17}O$ NMR chemical shifts for anions consisting of tungsten and oxygen atoms are the occupied–occupied and not the occupied–virtual ones.

(© Wiley-VCH Verlag GmbH & Co. KGaA, 69451 Weinheim, Germany, 2006)

## Introduction

NMR spectroscopy is one of the powerful techniques for studying the problems of the chemistry of polyoxometalates (POM) formed by V, Mo, W, and other metals in high oxidation states[1] as it can be used to characterize them both in solution and in the solid state. POMs are usually built of metal–oxygen octahedra that form $M_nO_m^{z-}$ isopolyanions or $XM_nO_m^{z-}$ heteropolyanions. In many cases all nuclei can be observed in the NMR spectra, which helps to elucidate the chemical environment of the nucleus under study.

Several resonance lines may be observed in the NMR spectra depending on the complexity of an anion and its symmetry, and assigning each line to a particular atom sometimes presents a problem. The nature of the chemical shifts is therefore still to be revealed.

As a matter of fact there have been several attempts to understand the nature of the chemical shifts for POMs, and particularly for polyoxotungstates (POTs). The first such study attempted to explain the trend in the change of the $^{183}W$ NMR chemical shifts in lacunary POTs by the charge delocalization resulting from the removal of one W=O group from the Keggin anion $X^{x+}W_{12}O_{40}^{x-8}$.[2] Further, there have also been attempts to correlate the $^{17}O$ and $^{183}W$ chemical shifts with the wavelength of the lowest charge-transfer (LCT) band (the electronic transition from the MO localized mainly on the oxygen atoms to a virtual MO localized mainly on the metals),[3,4] with bond lengths,[5,6] with the inverse sum of the energy separations,[7,8] and with the calculated charges on atoms[9] obtained from EHMO calculations. However, the calculation of the actual chemical shielding for different nuclei is still to be attained.

The first attempts to calculate $^{183}W$ NMR chemical shifts were limited to small and simple molecules like $WO_{4-x}S_x^{2-}$, $W(CO)_6$, $WF_6$, and $WCl_6$, and a practically linear correlation between calculated and experimental shifts was found.[10,11] Calculation of the $^{17}O$ NMR chemical shifts in metal oxide anions $MO_4^{n-}$ has been carried out by different methods with different degrees of accuracy.[12,13]

The first calculation of the $^{183}W$ chemical shift in a large Keggin anion using DFT was not so successful, and large discrepancies have been found by Bagno and co-workers even for small molecules.[14] Later, more reasonable calculated values of the $^{183}W$ NMR chemical shifts were obtained by the same authors.[15] A number of reviews of theoretical calculations of NMR chemical shifts in transition metal compounds have been published, including the results of $^{183}W$ chemical shift calculations by first-principles meth-

[a] Departament de Quimica Fisica i Inorgánica, Universitat Rovira i Virgili,
Pc. Imperial Tarraco 1, 43005 Tarragona, Spain
E-mail: josepmaria.poblet@urv.net
[b] Institute of Physical Chemistry, Russian Academy of Sciences, 31, Leninski pr, Moscow 119991, Russia
E-mail: leoka@ipc.rssi.ru
[c] Department of Chemistry, State University of New York at Buffalo,
312 Natural Sciences Complex, Buffalo, NY 14260-3000, USA
Supporting information for this article is available on the WWW under http://www.eurjic.org or from the author.

 © 2006 Wiley-VCH Verlag GmbH & Co. KGaA, Weinheim 

ods (relativistic Hartree–Fock and DFT).[16] However, those previous calculations were limited to comparatively small systems and no exhaustive theoretical study of chemical shifts in large heavy-metal POMs has yet been reported.

In the present work we have calculated the $^{183}W$ and $^{17}O$ nuclear magnetic shielding for several POTs using DFT methods with the goal of elucidating the relationship between the shielding and the geometric characteristics as well

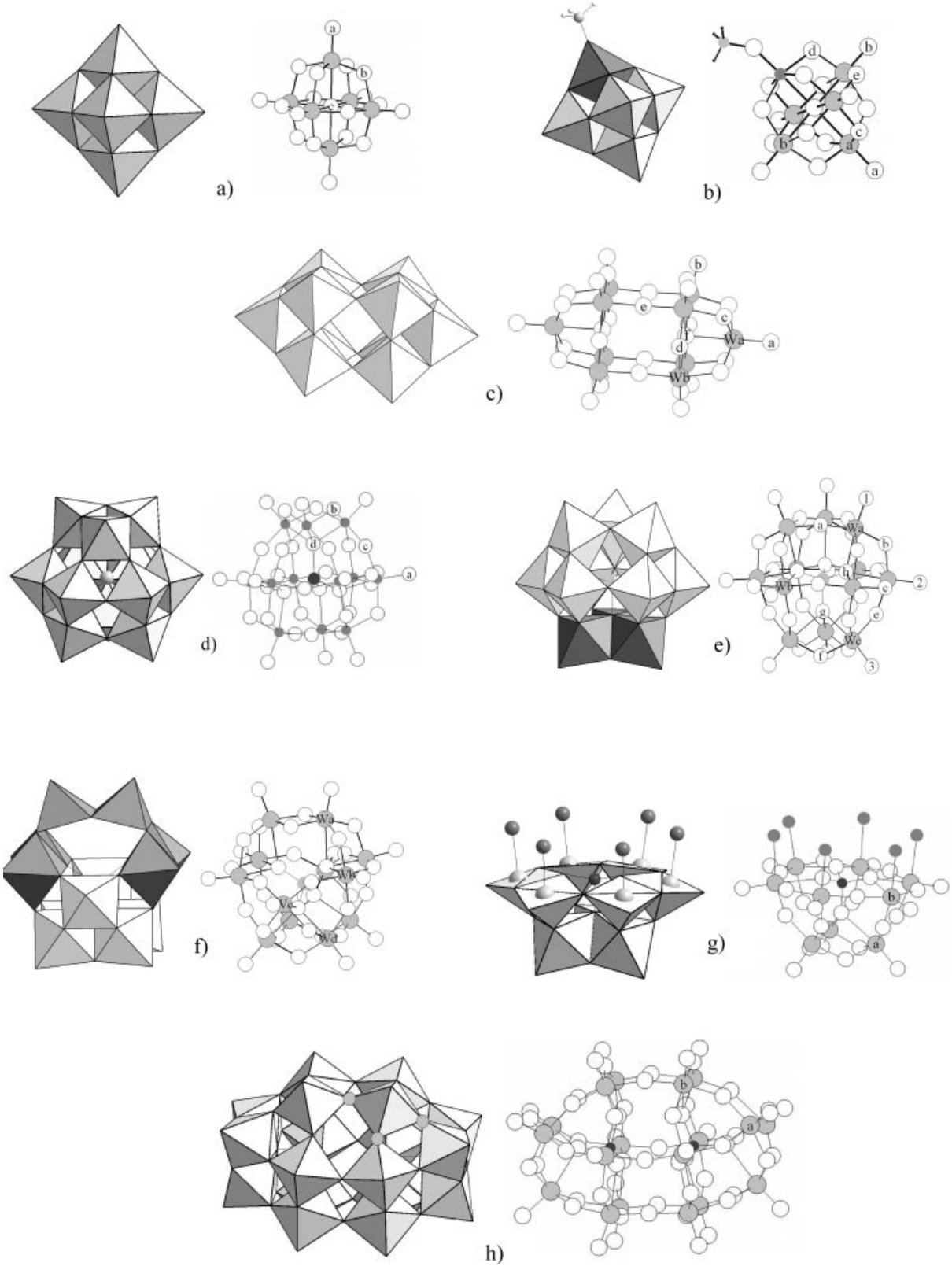


Figure 1. Polyhedral and ball-and-stick models for $W_6O_{19}^{2-}$ (a), $CH_3OTiW_5O_{18}^{3-}$ (b), $W_{10}O_{32}^{4-}$ (c), α-$XW_{12}O_{40}^{n-}$ (d), β-$SiW_{12}O_{40}^{4-}$ (e), γ-$SiW_{12}O_{40}^{4-}$ (f), β-$PW_9O_{28}Br_6^{3-}$ (g), and $P_2W_{18}O_{62}^{6-}$ (h).

 © 2006 Wiley-VCH Verlag GmbH & Co. KGaA, Weinheim 

as the influence of the latter on the chemical shifts. DFT methods have been shown to be adequate to rationalize many different aspects of the electronic structure,[17,18] magnetism,[19] and bonding[20] in POMs, and a summary of the most illustrative results can be found in a recent review.[21]

The first part of this study discusses several types of POTs (represented in Figures 1 and 2), namely the Lindqvist anion $W_6O_{19}^{2-}$ and its derivatives $CH_3OTiW_5O_{18}^{3-}$, $W_5O_{18}W^{II}NO^{3-}$, and $W_{10}O_{32}^{4-}$ (structural type I, characterized by edge sharing of $WO_6$ octahedra having a symmetry close to $C_{4v}$), the Keggin anions of general formula $XW_{12}O_{40}^{n-}$, their β and γ forms, and a bromide derivative (structural type II, with octahedra having two edge- and two corner-shared oxygen atoms), and the Dawson anion $P_2W_{18}O_{62}^{6-}$ (structural type III, where $W_bO_6$ octahedra have three corner-shared oxygen atoms). The octahedra in all these anions may be assigned as having local axial symmetry close to $C_{4v}$, with one terminal W=O bond. Finally,

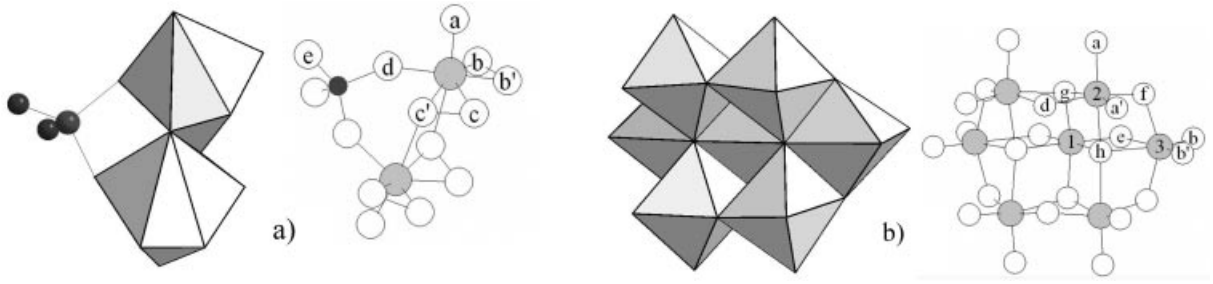


Figure 2. Polyhedral and ball-and-stick models for $PW_2O_{14}^{3-}$ (a) and $W_7O_{24}^{6-}$ (b).

Table 1. Experimental and calculated $^{183}W$ NMR shifts for several polyoxotungstates (POTs).

| Anion type | Anion | W type | $\sigma_p$ [ppm] | $\sigma_d$ [ppm] | $\sigma_t$ [ppm] | $\delta_{cal}$ [ppm] | $\delta_{exp}$ [ppm] | Ref. NMR | Ref. Struct. |
|---|---|---|---|---|---|---|---|---|---|
| 0 | $WO_4^{2-}$ | | –7002 | 9664 | 2663 | 0 | 0 | | |
| I | $W_6O_{19}^{2-}$ | | –7091 | 9658 | 2567 | 96 | 59 | [2] | [28] |
| | $CH_3OTiW_5O_{18}^{3-}$ | $W_a$ | –7115 | 9658 | 2543 | 120 | 70 | [29a] | [29a] |
| | | $W_b$[a] | –7051 | 9659 | 2608 | 55 | 37 | | |
| | $W_5O_{18}W^{II}NO^{3-}$[b] | $W_a^{VI}$ | –7183 | 9659 | 2476 | 187 | 117 | [29b] | [29b] |
| | | $W_b^{VI}$ | –7221 | 9659 | 2438 | 225 | 168 | | |
| | $W_{10}O_{32}^{4-}$ | $W_a$ | –6841 | 9659 | 2818 | –155 | –166 | [30] | [31] |
| | | $W_b$ | –6954 | 9658 | 2704 | –41 | –23 | | |
| II | $AsW_{12}O_{40}^{3-}$ | | –6897 | 9658 | 2761 | –98 | –65 | [32] | [2,4] |
| | $GaW_{12}O_{40}^{5-}$ | | –6931 | 9657 | 2726 | –63 | –89 | | |
| | $GeW_{12}O_{40}^{4-}$ | | –6888 | 9657 | 2769 | –106 | –82 | | |
| | $PW_{12}O_{40}^{3-}$ | | –6842 | 9657 | 2815 | –152 | –99 | | |
| | $SiW_{12}O_{40}^{4-}$ | | –6864 | 9657 | 2793 | –130 | –104 | | |
| | $AlW_{12}O_{40}^{3-}$ | | –6897 | 9657 | 2760 | –97 | –113 | | |
| | $BW_{12}O_{40}^{5-}$ | | –6854 | 9657 | 2803 | –140 | –131 | | |
| | β-$SiW_{12}O_{40}^{4-}$ | $W_a$ | –6828 | 9657 | 2829 | –166 | –130 | [33] | [2,34] |
| | | $W_b$ | –6833 | 9657 | 2824 | –161 | –115 | | |
| | | $W_c$ | –6871 | 9657 | 2786 | –123 | –110 | | |
| | γ-$SiW_{12}O_{40}^{4-}$ | $W_a$ | –6825 | 9658 | 2833 | –170 | –160 | [35] | [36] |
| | | $W_b$ | –6864 | 9657 | 2793 | –130 | –105 | | |
| | | $W_c$ | –6810 | 9657 | 2847 | –184 | –117 | | |
| | | $W_d$ | –6836 | 9657 | 2821 | –158 | –127 | | |
| | β-$PW_9O_{32}B_6^{3-}$ | $W_a$ | –6846 | 9658 | 2812 | –149 | –123 | [37] | [37] |
| | | $W_b$ | –7107 | 9658 | 2552 | 111 | 192 | | |
| III | $P_2W_{18}O_{62}^{6-}$ | $W_a$ | –6848 | 9657 | 2809 | –146 | –123 | [38] | [39] |
| | | $W_b$ | –6779 | 9657 | 2878 | –215 | –174 | | |
| IV | $PW_2O_{14}^{3-}$ | | –6176 | 9659 | 3483 | –820 | –676 | [40] | [40] |
| V | $W_7O_{24}^{6-}$ | $W_1$ | –7276 | 9658 | 2382 | 281 | 268 | [41] | [42] |
| | | $W_2$ | –7024 | 9660 | 2636 | 27 | –106 | | |
| | | $W_3$ | –6932 | 9662 | 2730 | –67 | –189 | | |

[a] Average value for four slightly different $W_b$ atoms due to bent $TiOCH_3$ group. [b] one $W^{VI}$=O group in $W_6O_{19}^{2-}$ is replaced by $W^{II}$-NO and the calculated shifts are given only for $W^{VI}$ (apical and belt) as for $CH_3OTiW_5O_{18}^{3-}$.

 © 2006 Wiley-VCH Verlag GmbH & Co. KGaA, Weinheim 

the peroxo complex $PW_2O_{14}^{3-}$ (structural type IV) represents a POT where the tungsten has a formal coordination number of 7, with the lowest chemical shift, and the heptatungstate $W_7O_{24}^{6-}$ (structural type V) has three types of W, each of which has two terminal oxygen atoms.

The second part of the study will describe the results of the DFT calculations of the $^{183}W$ and $^{17}O$ chemical shifts for the corresponding reduced polyoxotungstates with delocalized, unevenly delocalized, and localized electrons.

### Calculation of the Chemical Shielding

We used the ADF 2003.01 package[22] to compute the geometries of the molecules. The DFT calculations are characterized by the local density approximation featuring the *Xα* model for exchange with Becke's gradient-corrected functional,[23] and the VWN parameterization for correlation[24] corrected with Perdew's functional.[25] The basis functions for describing the valence electrons of all the atoms are Slater-type orbitals of triple-ζ+ polarization quality. The internal or core electrons are described by a relativistic core potential generated with the auxiliary program DIRAC.[22] The valence orbitals in this approach are kept orthogonal to the core orbitals by means of a single-ζ Slater-type core-orthogonalization basis set. We applied quasi-relativistic corrections to the valence shell by means of the zeroth-order relativistic approximation (ZORA). The NMR shielding tensors were computed from a parallel version of the NMR module.[26a] Although some previous studies have shown that all-electron basis sets reproduce the chemical shifts in some transition metal oxides better,[26b] we found no improvement in our results when this type of basis set was used for large POTs.

Generally, the W–O bonds in the optimized configurations are slightly longer than those observed in the X-ray structure determinations of the corresponding POTs. However, if we take the same anion but in different X-ray structures we sometimes see large discrepancies in the bond lengths. Even in a single crystal there may be two slightly different configurations with the same overall symmetry. Optimizing a structure results in a unique configuration for the given POT because, despite possible different initial coordinates, the program will end up delivering unique atomic coordinates, and although this may lead to an overestimation or underestimation of the calculated chemical shifts, such an approach is justified for comparison of the chemical shifts for different POTs, especially when accurate X-ray-determined coordinates are not available.

As usual, the calculated chemical shift, $\delta_{cal}$, is determined as the difference between the total shielding of the reference molecule, $\sigma_r$, and the shielding of the molecule under study, $\sigma_x$. For each nucleus the total shielding tensor, $\sigma_t$, is calculated as the sum of the paramagnetic ($\sigma_p$) and diamagnetic ($\sigma_d$ ) contributions and therefore:

$$\delta_{cal} = \sigma_r - \sigma_x$$

where $\sigma_x$ is the isotropic average of the shielding tensor for the nucleus in an anion and $\sigma_r$ is the shielding of the reference compound.

The simplest oxoanion, $WO_4^{2-}$, is usually used as a reference for $^{183}W$ NMR chemical shifts and the resonance line of water is used as a reference for $^{17}O$ NMR chemical shifts. For convenience, the absolute shielding of liquid water, $\sigma_t$, is accepted to be equal to +291 ppm.[27]

The experimental values of $^{183}W$ chemical shifts may vary slightly depending on the spectrometer (sometimes by up to 10 ppm, and the chemical shifts of POTs are usually more positive in organic media. On the contrary, protonation of POT generally results in a negative shift of the resonance. Moreover, it should be noted that solvation effects are not included in these theoretical studies even though they can considerably influence the calculated chemical shift, which is assumed to refer to the gaseous state of a single molecule. Hence, we can only estimate a general trend in the chemical shifts from these calculations and, at best, to make an assignment of the resonances for a complex anion with nonequivalent nuclei.

## Results

### The $^{183}W$ NMR Chemical Shift

Table 1 gives the calculated paramagnetic, diamagnetic, and total shielding along with calculated and experimental $^{183}W$ NMR shifts for the POTs shown in Figures 1 and 2. (Table S1 in the Supporting Information shows the difference in the calculated parameters for the experimental and optimized structures of $W_6O_{19}^{2-}$ as an example).

It can be seen that the chemical shift decreases as the number of corner-sharing oxygen atoms increases (structures I→II→III) and that the most positive shift for $W^1$ in $W_7O_{24}^{4-}$, which formally has no terminal oxygen atoms, and the most negative shift for $PW_2O_{14}^{3-}$ are correctly predicted by the calculations. For the bromide derivative, the resonance assigned to the six $W_b$ tungstens linked to bromide, observed at $\delta$ = +192 ppm, and the other line corresponding to $W_a$, observed at $\delta$ = –123 ppm, are also correctly predicted by the calculations. As expected, a soft ligand induces a large positive shift for the corresponding tungsten.

The order of the computed resonances corresponds to the observed one for both β-$SiW_{12}O_{40}^{4-}$ and for γ-$SiW_{12}O_{40}^{4-}$, and only the shift of $W_c$ is rather exaggerated, probably due to an inadequate geometry.

In general, for anions consisting of $WO_6$ octahedra with an axial symmetry and a single W=O bond, including the peroxo anion, we observe a nice linear correlation between the calculated and experimental shifts for the POTs studied (Figure 3). The most notable deviations from this linear trend are observed for anions with the Keggin structure, which was shown by a more detailed analysis to be due to the structure-optimization process (as will be presented elsewhere). Briefly, the results of the latter depend strongly on the overall anionic charge, although for anions with the same negative charge, for example $XW_{12}O_{40}^{5-}$ (X = $B^{III}$, $Al^{III}$, and $Ga^{III}$), the observed and calculated shifts increase regularly with an increase of the inner tetrahedron.

 © 2006 Wiley-VCH Verlag GmbH & Co. KGaA, Weinheim 

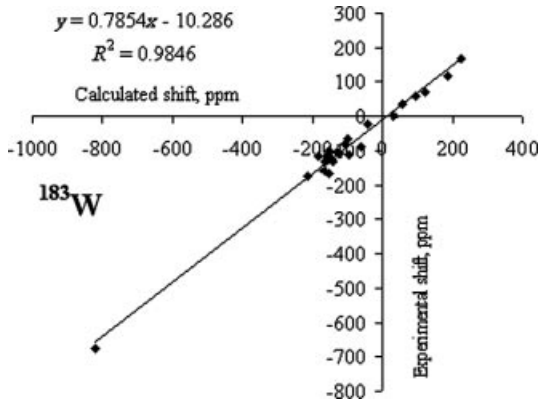


Figure 3. Correlation of the experimental and calculated $^{183}W$ NMR chemical shifts.

### The $^{17}O$ NMR Chemical Shift

The $^{17}O$ NMR shifts depend strongly on the type of bonding (terminal or bridging) and the calculated values follow the experimental trend well (Table 2). A comparison of the calculated and experimental chemical shifts shows that the magnitude of the calculated shifts is overestimated for the bridging oxygen atoms and slightly underestimated for the terminal ones (Figure 4).

In the cases where the POT contains equal numbers of slightly different bridging oxygen atoms it is impossible to assign closely spaced resonances unequivocally in the experimental spectra. However, according to the calculations, the larger chemical shift for $CH_3OTiW_5O_{18}^{3-}$ ($\delta$ = 390 ppm) can be assigned to the bridging oxygen, $O_c$, linking two different tungsten atoms, and that at $\delta$ = 380 ppm to $O_e$ (Table 2).

In the case of $W_{10}O_{32}^{4-}$, according to the calculations the two resonances at $\delta$ = 434 and 421 ppm observed in the experimental NMR spectrum should be attributed to the bridging oxygen, $O_c$, which links $W_a$ and $W_b$ and $O_d$, which is bound to two identical $W_b$ lying in a square plane. For the oxygen atoms ($O_e$) in the linear bridges the calculated shift is the lowest, although it is observed between $O_c$ and $O_d$ in the experimental spectrum.

The bridging oxygen atoms in the Keggin anions $XW_{12}O_{40}^{n-}$ give two closely spaced resonances with equal intensity in the range $\delta$ = 440–390 ppm. Using a special method, which involves replacing three tungstens by molybdenum atoms, Shum and Klemperer[43b] have shown that the line with the larger chemical shift is due to the edge-sharing oxygens ($O_b$). According to the DFT calculations, the resonance with the larger chemical shift should be assigned to the edge bridging oxygen atoms $O_b$, which fully confirms the conclusions drawn from the experiment.

The rotation of a triplet in β-$SiW_{12}O_{40}^{4-}$ should formally result in the inequivalence of the oxygen atoms, with a corresponding weight ratio (according to the atom labels) of 3:6:3 for the terminal oxygen atoms and 3:6:3:3:6:3 for the bridging ones. However, only four lines are observed in the $^{17}O$ NMR spectrum, which were assigned[43b] as follows: the highest chemical shift was assigned to the terminal oxygen atoms, the line with intensity 3 to the edge-bridging $O_c$ in the six-membered ring, the line with intensity 9 to the edge-bridging $O_b$ and $O_f$, the line with intensity 12 to the corner bridging $O_a$, $O_d$, and $O_e$, and, finally, the less-intense line was assigned to the internal oxygens $O_g$ and $O_h$. Our

Table 2. Calculated shielding and shifts and experimental $^{17}O$ shifts for several POTs.

| Type | $R_{W-O}$ [Å] | $\sigma_p$ [ppm] | $\sigma_d$ [ppm] | $\sigma_t$ [ppm] | $\delta_{cal}$ [ppm] | $\delta_{exp}$ [ppm] | Ref. |
|---|---|---|---|---|---|---|---|
| $W_6O_{19}^{2-}$ | | | | | | | |
| $O_a$ | 1.73 | 1.730 | –880 | 401 | 770 | 775 | [43] |
| $O_b$ | 1.953 | 1.953 | –596 | 413 | 474 | 416 | |
| $O_c$ | 2.357 | 2.357 | –91 | 410 | –28 | –80 | |
| $CH_3OTiW_5O_{18}^{3-}$ | | | | | | | |
| $O_b$ | 1.75 | –823 | 404 | –419 | 710 | 721 | [29] |
| $O_a$ | 1.75 | –819 | 403 | –416 | 707 | 713 | |
| $O_d$ | 1.885 | –703 | 416 | –287 | 578 | 525 | |
| $O_c$ | 1.938 | –577 | 415 | –162 | 453 | 390 | |
| $O_e$ | 1.956 | –570 | 414 | –155 | 446 | 380 | |
| $O_f$ | 2.361 | –114 | 408 | 294 | –3 | –58 | |
| $W_{10}O_{32}^{4-}$ | | | | | | | |
| $O_b$ | 1.739 | –863 | 403 | –460 | 751 | 765 | [31] |
| $O_a$ | 1.756 | –820 | 404 | –416 | 707 | 732 | |
| $O_c$ | 1.953[a] | –621 | 418 | –203 | 494 | 434 | |
| $O_e$ | 1.923 | –601 | 421 | –180 | 471 | 423 | |
| $O_d$ | 1.942 | –609 | 415 | –194 | 485 | 421 | |
| $O_f$ | 2.341[a] | –162 | 404 | 242 | –49 | –2 | |
| $PW_{12}O_{40}^{3-}$ | | | | | | | |
| $O_a$ | 1.726 | –873 | 401 | –472 | 763 | 769 | [43] |
| $O_b$ | 1.938 | –619 | 419 | –200 | 491 | 431 | |
| $O_c$ | 1.93 | –581 | 417 | –164 | 455 | 404 | |
| $O_d$ | 2.469 | –218 | 398 | 180 | 111 | 70–60 | |
| $SiW_{12}O_{40}^{4-}$ | | | | | | | |
| $O_a$ | 1.737 | –866 | 403 | –463 | 754 | 761 | [43] |
| $O_b$ | 1.943 | –620 | 419 | –201 | 492 | 427 | |
| $O_c$ | 1.935 | –584 | 418 | –166 | 457 | 405 | |
| $O_d$ | 2.38 | –176 | 400 | 224 | 67 | 27 | |
| β-$SiW_{12}O_{40}^{4-}$ | | | | | | | |
| $O_1$ | 1.735 | –864 | 403 | –461 | 742[a] | 762 | [43b] |
| $O_2$ | 1.737 | –861 | 403 | –458 | | | |
| $O_3$ | 1.735 | –858 | 403 | –455 | | | |
| $O_c$ | 1.937 | –650 | 420 | –230 | 521 | 454 | |
| $O_b$ | 1.946[a] | –614 | 419 | –195 | 485[a] | 425 | |
| $O_f$ | 1.949 | –612 | 419 | 193 | | | |
| $O_a$ | 1.934 | –588 | 419 | –169 | 460[a] | 404 | |
| $O_d$ | 1.927 | –584 | 419 | –166 | | | |
| $O_e$ | 1.941[a] | –589 | 418 | –171 | | | |
| $O_g$ | 2.390 | –183 | 400 | 217 | 84[a] | 32 | |
| $O_h$ | 2.392 | –179 | 397 | 218 | | | |
| $W_7O_{24}^{6-}$ | | | | | | | |
| $O_a$ | 1.781 | –765 | 407 | –358 | 663[a] | 648 | [41] |
| $O_{a'}$ | 1.772 | –792 | 405 | –387 | | | |
| $O_b$ | 1.795 | –686 | 407 | –279 | 570 | 590 | |
| $O_{b'}$ | 1.777 | –747 | 406 | –341 | 632 | 597 | |
| $O_e$ | 1.796 | –752 | 407 | –345 | 636 | 626 | |
| $O_d$ | 1.968 | –545 | 413 | –132 | 423 | 319 | |
| $O_f$ | 1.973[a] | –507 | 411 | –96 | 387 | 298 | |
| $O_g$ | 2.049[a] | –455 | 410 | –45 | 336 | 259 | |
| $O_h$ | 2.260[a] | –286 | 407 | 121 | 170 | 74 | |

[a] Average value.

 © 2006 Wiley-VCH Verlag GmbH & Co. KGaA, Weinheim 

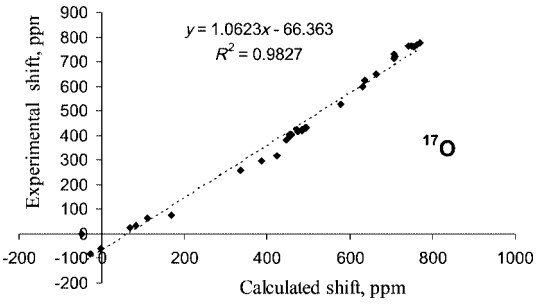


Figure 4. Correlation of the experimental and calculated $^{17}O$ NMR chemical shifts.

calculations fully confirmed the observed pattern, with the largest chemical shift for the bridging oxygen atoms $O_c$ in the ring.

For $W_7O_{24}^{4-}$ the range of the $^{17}O$ NMR chemical shifts is fairly well reproduced by the calculations; a possible assignment of the lines is given in Table 2.

In general, a rather good linear correlation between the calculated and experimental $^{17}O$ NMR chemical shifts for POTs may be seen in Figure 4.

### General Results

Taking into account all the calculated values for both $^{183}W$ and $^{17}O$ NMR chemical shifts, we have obtained good correlations between calculated and experimental values even though the NMR spectra were measured in different solvents in some cases. This shows that calculations adequately reflect the changes in chemical shifts depending on the structure. The discrepancies observed in some cases may result from the inadequacy of the optimized geometry, and the deviation of the slope from unity may be due to the basis sets used in the calculations.

## Discussion

According to the present calculations the diamagnetic shielding (Tables 1 and 2) for both $^{183}W$ and $^{17}O$ is essentially unaffected by the geometry (the chemical environment). This can be understood from the fact that the diamagnetic shielding contains the unperturbed, zero-order density. The largest contributions are due to the core shells at $^{183}W$ and $^{17}O$ nuclei. Such core shells should not change on going from one chemical environment to another and therefore yield constant diamagnetic shielding contributions that cancel out in relative chemical shifts. Thus, we will consider only the paramagnetic contribution. In the following sections we discuss the analysis of the paramagnetic shielding tensors in a gauge-including atomic orbitals (GIAO) basis where a gauge-origin independent division into a paramagnetic and a diamagnetic contribution can be achieved.[26c]

### The $^{183}W$ Paramagnetic Shielding

The paramagnetic contribution is determined by the magnetically perturbed MOs,[10] while the most important one is considered to be due to the coupling of the occupied ($\Psi_a$) and virtual ($\Psi_i$) MOs under the applied magnetic field. The magnitude of the coupling coefficients, $u_{ai}$, are given as[10]

$$u_{ai} \approx -\frac{1}{2(\varepsilon_i^0 - \varepsilon_a^0)}\langle \Psi_i | M | \Psi_a \rangle$$

where $\varepsilon_i^0$ and $\varepsilon_a^0$ are the orbital energies of the virtual and occupied MOs. We will refer to the "u-tensor" in conjunction with nuclear shielding contributions arising from these coefficients and note that inverse occupied–virtual MO energy differences enter these terms. Thus, common knowledge often relates the magnitude of the paramagnetic shielding to the size of the HOMO–LUMO gap, for example.

The paramagnetic shielding is determined by the sum of all magnetically active transitions and by atomic orbital coefficients forming the corresponding MOs. For the large anions, which consist of tungsten and oxygen atoms, so many MOs are formed that it is rather difficult to show which transitions are the most important in the paramagnetic shielding. However, a preliminary analysis of the paramagnetic shielding for $W_6O_{19}^{2-}$ shows that the largest contributions (about 15%) come from two transitions from rather deep bonding MOs ($5t_{1g}$), involving p and d orbitals of the bridging oxygen and tungsten atoms, respectively, not to the LUMO but to upper virtual orbitals ($a_{1g}$ and $e_g$), consisting of W-$d_{z^2}$ and p- and s-oxygen orbitals. Moreover, terms involving pairs of occupied orbitals should be also taken into account. In the paramagnetic shielding, this is a term, from now on dubbed "*s*-tensor", that is specific to the computation of the nuclear shielding in a GIAO basis, where the external magnetic field will change the overlap between the basis functions (atomic orbitals or AOs). In the case of $^{183}W$ shielding it can attain 15% of the total paramagnetic term, which is mostly due to the occupied–virtual transitions ("*u*-tensor"). For the paramagnetic contribution of the terminal oxygen atom in the case of the Lindqvist anion, for example, 163 occupied–occupied ("*s*-tensor") and 238 occupied–virtual (*u*-tensor) couplings should be taken into account, and for the latter less than 50 transitions exceed 10 ppm. For the bridging oxygen the number of transitions increases to 488 and 744, respectively, and some transitions contribute with opposite signs.

Two points should be mentioned. First of all, the lowest charge transfer, determined as the HOMO–LUMO gap, $E_{LCT}$, is by no means the principal contributor otherwise we should observe a correspondence between $1/E_{LCT}$ and the $^{183}W$ chemical shifts (see Table S2 in the Supporting Information). Usually, the HOMO is a nonbonding orbital consisting of the p-orbitals of the bridging oxygen atoms, especially of the inner oxygen atoms, and even for simpler complexes the transitions from deeper MOs, involving several metallic orbitals, make the largest contributions.

As already mentioned, the paramagnetic shielding includes not only the *u*-term, which involves the occupied and virtual MO coupling and plays a dominant role in the

 © 2006 Wiley-VCH Verlag GmbH & Co. KGaA, Weinheim 

change of the chemical shift, but also the occupied–occupied MO coupling (*s*-tensor) and additional "paramagnetic gauge terms". The latter are also related to the GIAO formalism (they are negligibly small in the present study, see discussion on the components of the paramagnetic shielding[44] and Table 3). In frozen-core calculations there is, in addition, a frozen-core term (dubbed "*b*-tensor" here) that stems from the change of the valence-core orthogonalization under the external magnetic-field perturbations. As for POTs, the magnitudes of the changes in the *s*- and *b*-tensors may be comparable with the *u*-term and therefore they demand more consideration in detail:

Table 3. Parameters of the paramagnetic shielding ($\sigma_p$) of $^{183}W$ NMR for some POTs.[a]

| Anion | Metal/X | *b*-term [ppm] | *s*-term [ppm] | *u*-term [ppm] | PGT [ppm] | $R_{W-O}$ [Å] | $\delta_{cal}$ [ppm] |
|---|---|---|---|---|---|---|---|
| $W_{10}O_{32}^{4-}$ | $W_a$ | 262 | –730 | –6384 | 11 | 1.966 | –155 |
| | $W_b$ | 358 | –882 | –6437 | 7 | 1.978 | –41 |
| $W_6O_{19}^{2-}$ | | 358 | –1002 | –6454 | 7 | 1.983 | 96 |
| $CH_3OTiW_5O_{18}^{3-}$ | $W_b$ | 397 | –1068 | –6385 | 7 | 1.982 | 55 |
| | $W_a$ | 366 | –1014 | –6474 | 7 | 1.983 | 120 |
| $W_5O_{18}W(II)NO^{3-}$ | $W_a$ | 321 | –917 | –6594 | 7 | 1.986 | 187 |
| | $W_b$ | 359 | –1015 | –6571 | 6 | 1.991 | 225 |
| $XW_{12}O_{40}^{n-8}$ | As | 140 | –295 | –6752 | 10 | 1.981 | –98 |
| | Ga | 119 | –212 | –6759 | 9 | 1.989 | –152 |
| | Ge | 242 | –545 | –6595 | 10 | 1.975 | –106 |
| | P | 222 | –470 | –6625 | 9 | 1.979 | –130 |
| | Si | 332 | –791 | –6482 | 10 | 1.966 | –63 |
| | Al | 323 | –746 | –6483 | 9 | 1.972 | –97 |
| | B | 228 | –475 | –6615 | 8 | 1.981 | –140 |
| $\beta$-$SiW_{12}O_{40}^{4-}$ | $W_a$ | 192 | –404 | –6624 | 8 | 1.981 | –166 |
| | $W_b$ | 232 | –499 | –6575 | 9 | 1.976 | –162 |
| | $W_c$ | 204 | –431 | –6653 | 9 | 1.984 | –123 |
| $\gamma$-$SiW_{12}O_{40}^{4-}$ | $W_a$ | 43 | –2 | –6873 | 7 | 2.017 | –171 |
| | $W_b$ | 237 | –513 | –6596 | 8 | 1.978 | –130 |
| | $W_c$ | 236 | –521 | –6535 | 10 | 1.973 | –184 |
| | $W_d$ | 201 | –433 | –6613 | 9 | 1.978 | –158 |
| $\beta$-$PW_9Br_6O_{28}^{3-}$ | $W_a$ | 74 | –90 | –6836 | 6 | 1.987 | –149 |
| | $W_b$ | 125 | –164 | –7071 | 3 | 2.078 | 111 |
| $X_2W_{18}O_{62}^{6-}$ | $W_b$ | 127 | –134 | –6785 | 13 | 1.981 | –215 |
| | $W_a$ | 8 | 134 | –6999 | 9 | 1.983 | –146 |
| $PW_2O_{14}^{3-}$ | | 482 | –533 | –6119 | –5 | 1.960 | –820 |
| $W_7O_{24}^{6-}$ | $W_1$ | 585 | –1525 | –6344 | 8 | 2.024 | 283 |
| | $W_2$ | 170 | –399 | –6797 | 2 | 1.964 | 47 |
| | $W_3$ | 158 | –372 | –6720 | 2 | 1.972 | –77 |

[a] B-tensor: direct frozen core terms (B1 tensor); S-tensor: OCC-OCC terms (paramagnetic SMAT1 tensor); U-tensor: OCC-VIR terms (paramagnetic UMAT1 tensor); PGT: DIAG. OCC-OCC terms (for gauge invariance, paramagnetic gauge tensor).

1. For anions with octahedra having only *edge-shared* oxygen atoms (the first four, Figures 1a–c) and the internal oxygen linking six and five tungsten atoms, for a span of the experimental shifts of 334 ppm (span of the calculated shifts: 380 ppm), increasing the mean $R_{WO}$ results in a negative shift (–135 ppm) due to the *b*-term but in positive shifts due to the *s*-term (338 ppm) and the *u*-term (only 210 ppm). The total shift therefore increases with $R_{WO}$.
2. As opposed to the Lindqvist-type anions, α-Keggin anions (Figure 1d), with their narrow range (89 ppm) of calculated shifts (66 ppm for experimental ones), and with two corner and two edge-shared oxygen atoms and the inner oxygen linking three W atoms and the central atom, an increase of the mean $R_{WO}$ in the optimized structures corresponds to a general decrease of the chemical shift due to a decrease in the *b*-term (213 ppm) and the *u*-term (277 ppm; both of which correspond to an increase in the chemical shift), which is outweighed by the negative shift due to the *s*-term (–579 ppm); a fine interplay of these components therefore determines the total chemical shift.

For the β-γ Keggin isomers and $P_2W_{18}O_{62}^{6-}$ a decrease of the *b*-term from 237 to 8 ppm ($\Delta$ = –229 ppm) and the *u*-term from –6534 to –6999 ppm ($\Delta$ = –465 ppm, for a total of –694 ppm) is close to the increase of the *s*-term from –521 to 134 ppm ($\Delta$ = 655 ppm).

The second point is that the absolute values of the *s*-term for the Lindqvist-type anions are almost twice as large as for the Keggin anions. On the other hand, the pentacoordination of $W_a$ in γ-$SiW_{12}O_{40}^{4-}$ (Table 3, Figure 1e) results in a rather small magnitude of the *s*-term; this is probably characteristic for pentacoordination.

It is noteworthy that the *u*-term for $W_a$ in $P_2W_{18}O_{62}^{6-}$ is the lowest of all $WO_6$ octahedra, which is difficult to explain as the local symmetry around $W_a$ is almost the same as in the Keggin system. However, despite substantial differences in the components of the paramagnetic shielding, the calculated $^{183}W$ chemical shifts for the Keggin anion and for $W_a$ of the Dawson anion proved to be almost the same, reflecting the similarity of the local geometry.

Some unusual values of the *b*- and *u*-terms for the Dawson anion may be explained by the correlations of the *b*- and *s*- against the *u*-term as the largest component (anions α-$XW_{12}O_{40}^{n-8}$, β-$SiW_{12}O_{40}^{4-}$, γ-$SiW_{12}O_{40}^{4-}$, $X_2W_{18}O_{62}^{6-}$) shown in Figure 5. It is clearly seen that three components are interrelated, but only for similar types of anions.

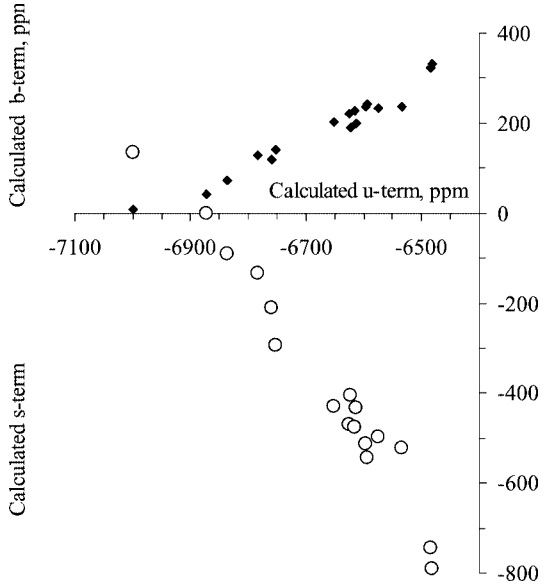


Figure 5. Interrelation between paramagnetic *u*- and *b*- (♦) and *s*- (○) terms for POTs (α-$XW_{12}O_{40}^{n-8}$, β-$SiW_{12}O_{40}^{4-}$, γ-$SiW_{12}O_{40}^{4-}$, $X_2W_{18}O_{62}^{6-}$).

In general, we can observe that increasing $R_{WO}$ results in a corresponding absolute increase in the *u*-term (the more negative the shielding the more positive the chemical shift)

 © 2006 Wiley-VCH Verlag GmbH & Co. KGaA, Weinheim 

determined by the occupied–virtual MO transitions (see Figure S1 in the Supporting Information) That, in turn, depends on the bonding system (edge, corner, inner oxygen atoms, and angles between bonds) and determines the change of the *b* and *s* shielding components. In any case, the *s*-term changes in a broader range than the *u*-term, which is usually considered as the most important. For POTs, where tungsten is surrounded only by oxygen atoms as ligands, we can suggest that the change of the chemical shift is determined by the total paramagnetic contribution, in which the occupied–occupied transitions have proved to be the most important, and a fine interplay of the components (*s*- and *u*-terms) of the paramagnetic shielding variable in quite a large range will determine the total chemical shift. Nevertheless, the calculation adequately represents the general trend in the chemical shifts.

It should be noted that the *u*- and *s*-terms decrease with $R_{WO}$ for the anions built with octahedra linked by edge-shared oxygens and therefore a close correlation between the experimental shifts and the sum of the inversed energies of the electronic transitions between d and d* orbitals calculated by the EHMO method is observed.[8]

### The $^{17}O$ Paramagnetic Shielding

For the terminal oxygen atoms the *s*-term makes no more than 5% contribution to the paramagnetic *u*-term and the core *b*-term is much lower (Table 4). For the inner oxygen the *s*-term may reach 30% and moreover is of opposite sign, therefore it makes a sizeable contribution. Only for $W_6O_{19}^{2-}$ is the *s*-term for $O_c$ negative as it binds six tungsten atoms. For $W_{10}O_{32}^{4-}$, where the inner oxygen atoms $O_f$ bind five W atoms, and for $O_d$ in the Keggin anion, which binds four atoms, the *s*-term becomes positive.

Table 4. Components of the $^{17}O$ paramagnetic shielding for some POTs.

| Anion | Atom | *b*-term [ppm] | *s*-term [ppm] | *u*-term [ppm] | PGT [ppm] | $R_{W-O}$ av. [Å] |
|---|---|---|---|---|---|---|
| $W_{10}O_{32}^{4-}$ | $O_a$ | 1 | –36 | –787 | 1 | 1.756[a] |
| | $O_c$ | –2 | –9 | –596 | –15 | 1.938, 1.969[a] |
| | $O_f$ | –7 | 114 | –276 | 8 | 2.288, 2.354[a] |
| | $O_b$ | 0 | 7 | –868 | –2 | 1.739[b] |
| | $O_d$ | –3 | –7 | –594 | –5 | 1.942[b] |
| | $O_e$ | –4 | –82 | –521 | 7 | 1.923[b] |
| $W_6O_{19}^{2-}$ | $O_a$ | 1 | –1 | –880 | 0 | 1.730 |
| | $O_b$ | –2 | –15 | –573 | –7 | 1.953 |
| | $O_c$ | –5 | –26 | –74 | 14 | 2.357 |
| $PW_{12}O_{40}^{3-}$ | $O_a$ | 1 | 34 | –905 | –3 | 1.726 |
| | $O_b$ | –2 | –14 | –593 | –9 | 1.938 |
| | $O_c$ | –4 | –23 | –556 | 2 | 1.930 |
| | $O_d$ | –8 | 121 | –355 | 23 | 2.469 |

[a] Distance to $W_a$. [b] Distance to $W_b$.

Depending on the type of oxygen atom (corner- or edge-shared), the absolute value of the *s* component is larger for the corner one. However, because the bond length in corner sharing is usually shorter than that for an edge-sharing oxygen, the absolute *u*-term is less, making more negative shift for the corner oxygen that links two equivalent tungsten atoms having the same chemical shift. If it binds two tungsten atoms with different chemical shifts (as $O_c$ in $W_{10}O_{32}^{4-}$), the magnitude becomes unpredictable.

However, from Figure 6 (taking into account data for anions $W_6O_{19}^{2-}$, $W_{10}O_{32}^{4-}$, $CH_3OTiW_5O_{18}^{3-}$, α-$PW_{12}O_{40}^{3-}$, α-$SiW_{12}O_{40}^{4-}$, and β-$SiW_{12}O_{40}^{4-}$) the interrelation between the *u*-term and the *s*-term for three types of oxygen atoms − terminal, bridging, and inner − is clearly seen. A certain similarity between this plot and the one given in Figure 5 may be noted.

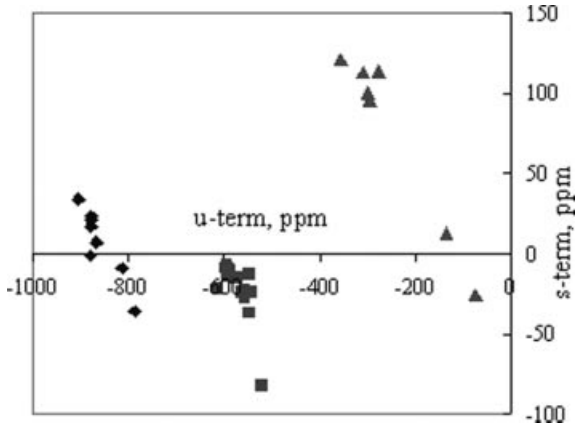


Figure 6. Interrelation of the *u*- and *s*-terms in the $^{17}O$ paramagnetic shielding for POT. ♦: terminal oxygen atoms; ■: bridging oxygen atoms; ▲: inner oxygen atoms.

For all POTs the most deshielded ones proved to be the terminal oxygen atoms. Although the shorter bond length leads to increased $\Delta E$, it is possible that an increase of the numerator exceeds the effect of decreasing $1/\Delta E$ (see formula above).

## Conclusions

Having considered the results of calculations of the $^{183}W$ and $^{17}O$ NMR chemical shifts we can come to the following conclusions: 1) Generally, the calculations reproduce the patterns of the chemical shifts for both nuclei for several types of tungsten and oxygen atoms. However, when the range of the chemical shifts is rather narrow, prediction of the chemical shifts will depend on the chosen geometric parameters, and a fine interplay of the different components of the paramagnetic shielding may result in discrepancies between the calculated and experimental chemical shifts, as, for example, for γ-$SiW_{12}O_{40}^{4-}$. 2) The accuracy of the calculated chemical shifts is far from what would be desirable and, in principle, a complete compatibility between calculated and observed chemical shifts is still not possible for such polyoxotungstate complexes because of inaccuracies in the geometric characteristics obtained by X-ray diffraction studies. Sometimes, even for rather simple peroxotungstates with overall $C_2$ symmetry, two tungstens are crystallographically not identical and their different local geometry may

 © 2006 Wiley-VCH Verlag GmbH & Co. KGaA, Weinheim 

easily give rise to differences of 200 ppm or more in the calculated chemical shifts. Therefore, for sake of consistency, the optimized structures, despite some inadequacy, may be an adequate approach for the calculation of the NMR shielding. 3) For POTs consisting of tungsten and oxygen atoms the change in the chemical shifts is determined by an interplay of the components of the paramagnetic shielding, in which the main contributor has been shown to be the *s*-term (the occupied–occupied MO coupling) along with the change in the *u*-term (the occupied–virtual MO transitions). Apparently, such a behavior of the paramagnetic shielding is characteristic, as shown by our preliminary results, for other polyoxometalates involving vanadium or molybdenum. 4) From the accumulated data the reverse task may, in principle, become possible, namely deducing the geometry from the observed chemical shifts, if the nature of the nuclear shielding is completely understood. 5) At present, the reliable assignment of the several resonance lines observed in the NMR spectra to specific atoms may be made only in the case of widely separated NMR shifts. The fine details of the anion geometry must therefore be taken into account to be able to assign the resonances correctly. 6) It is rather well known[10,11,45] that taking into account the spin-orbit coupling during calculation of the chemical shift of heavy elements notably increases the correspondence between the calculated and experimental shifts. This is especially true when the ligands around the coordinating cation are quite different and heavy. However, although our preliminary calculations for POTs where the ligand atoms are only oxygen atoms, obtained by including the SO coupling term, give slightly more reasonable values in terms of magnitude, they do not give the correct order of the resonances for the Keggin anions and even violate the sequence of the lines for β- and γ-$SiW_{12}O_{40}^{4-}$.

Thus, to improve the accuracy of computed NMR chemical shifts in polyoxometalates is not simple and will require effort in several areas, most notably to incorporate exact exchange functionals in the DFT calculations, to consider the spin-orbit coupling, and to use larger basis sets. The reader must bear in mind that the calculation of the shielding tensors for *one* atom of the Dawson anion $P_2W_{18}O_{62}^{6-}$ needs more than ten days of computer time.[46] Therefore, it will be necessary to further improve the codes of NMR calculations for large systems, and probably for clusters with relatively large *q*/*m*, where *q* is charge and *m* the number of metals, to introduce the effect of the solvent.[47]

**Supporting Information** (see also footnote on the first page of this article): Influence of the geometric parameters on calculated shieldings for $W_6O_{19}^{2-}$ and HOMO–LUMO separation for several POTs are given in Tables S1 and S2. The correlation between calculated paramagnetic shielding and mean bond length, $R_{W-O}$, in Keggin anions is given in Figure S1.

## Acknowledgments

This work was supported by the Spanish MECD (BQU2002-04110-C02-01) and the CIRIT of the Autonomous Government of Catalonia (SGR01-00315). J.A. is grateful for financial support from the CAREER program of the National Science Foundation (grant no. CHE-0447321). The authors thank the referees for comments and suggestions.

[1] a) *Chem. Rev.* **1988**, *98*, special issue, Ed.: C. Hill; b) *Polyoxometalate-Molecular Science* (Eds.: J. J. Borrás-Almenar, E. Coronado, A. Müller, M. T. Pope). NATO Science Series, II. Mathematics, Physics and Chemistry, vol. 98, Kluwer Academic Publishers, Dordrecht, The Netherlands, **2003**.
[2] O. A. Gansow, R. K. C. Ho, W. G. Klemperer, *J. Organomet. Chem.* **1980**, *187*, 27.
[3] L. P. Kazansky, *Koord. Khim.* **1977**, *3*, 327.
[4] R. Acerete, C. F. Hammer, L. C. W. Baker, *J. Am. Chem. Soc.* **1982**, *104*, 5384.
[5] L. P. Kazansky, M. A. Fedotov, V. I. Spitsyn, *Doklady Akad. Nauk SSSR* **1983**, *272*, 1179.
[6] L. P. Kazansky, *Chem. Phys. Lett.* **1994**, *223*, 289.
[7] L. P. Kazansky, P. Chaquin, M. Fournier, G. Herve, *Polyhedron* **1998**, *17*, 4353.
[8] M. Inoue, T. Yamase, L. P. Kazansky, *Polyhedron* **2003**, *22*, 1183.
[9] L. P. Kazansky, T. Yamase, *J. Phys. Chem. A* **2004**, *108*, 6437.
[10] A. Rodrigues-Fortea, P. Alemany, T. Ziegler, *J. Phys. Chem. A* **1999**, *103*, 8288.
[11] M. Hada, H. Kaneko, H. Nakatsuji, *Chem. Phys. Lett.* **1996**, *261*, 7.
[12] M. Kaupp, O. L. Malkina, V. G. Malkin, *J. Chem. Phys.* **1997**, *106*, 9201.
[13] G. Schreckenbach, T. Ziegler, *Int. J. Quantum Chem.* **1997**, *61*, 899.
[14] A. Bagno, M. Bonchio, *Chem. Phys. Lett.* **2000**, *317*, 12.
[15] A. Bagno, M. Bonchio, A. Sartorel, G. Scorrano, *ChemPhysChem.* **2003**, *4*, 4353.
[16] a) J. Autschbach, *The Calculation of NMR Parameters in Transition Metal Complexes*, in *Density Functional Theory in Inorganic Chemistry*, Vol. 112 (Eds.: N. Kaltsoyannis, J. E. McGrady), Springer, Heidelberg, **2004**; b) J. Autschbach, *Calculation of Heavy-Nucleus Chemical Shifts: Relativistic All-Electron Methods*, in *Calculation of NMR and EPR Parameters. Theory and Applications* (Eds.: M. Kaupp, M. Bühl, V. G. Malkin), Wiley-VCH, Weinheim, **2004**. See also c) M. Kaupp, V. G. Malkin, O. L. Malkina, *NMR of Transition Metal Compounds*, in *Encyclopedia of Computational Chemistry* (Ed.: P. v. R. Schleyer), John Wiley & Sons, Chichester, **1998**, pp 1857–1866; d) M. Bühl, M. Kaupp, M. O. L. Malkina, V. G. Malkin, *J. Comput. Chem.* **1999**, *20*, 91–105.
[17] M.-M. Rohmer, M. Bénard, E. Cadot, F. Sécheresse, *Polyoxometalate Chemistry: From Topology via Self-Assembly to Applications* (Eds.: M. T. Pope, A. Müller), Kluwer Academic, Dordrecht, The Netherlands, **2001**, p. 117; M.-M. Rohmer, M. Bénard, *Chem. Soc. Rev.* **2001**, *30*, 340.
[18] J. M. Maestre, X. López, C. Bo, J. M. Poblet, N. Casañ-Pastor, *J. Am. Chem. Soc.* **2001**, *123*, 3749; X. López, J. M. Maestre, C. Bo, J. M. Poblet, *J. Am. Chem. Soc.* **2001**, *123*, 9571; C. X. López, J. M. Poblet, *J. Am. Chem. Soc.* **2002**, *124*, 12574.
[19] S. A. Borshch, *Inorg. Chem.* **1998**, *37*, 3116; H. H. Duclusaud, S. A. Borshch, *J. Am. Chem. Soc.* **2001**, *123*, 2825; S. A. Borshch, H. Duclusaud, J. M. Millet, *Appl. Cat. A: General* **2000**, *200*, 103.
[20] A. Bridgeman, *Chem. Phys.* **2003**, *287*, 55; A. Bridgeman, G. Cavigliasso, *Chem. Phys.* **2002**, *279*, 143; A. Bridgeman, G. Cavigliasso, *J. Phys. Chem. A* **2003**, *107*, 6613.
[21] J. M. Poblet, X. López, C. Bo, *Chem. Soc. Rev.* **2003**, *32*, 297.
[22] ADF 2003.1; Department of Theoretical Chemistry, Vrije Universiteit, Amsterdam, J. Baerends; D. E. Ellis, P. Ros, *Chem. Phys.* **1973**, *2*, 41; L. Versluis, T. Ziegler, *J. Chem. Phys.* **1988**, *88*, 322; G. Te Velde, E. J. Baerends, *J. Comput. Phys.* **1992**, *99*, 84; C. Fonseca Guerra, J. G. Snijders, G. Te Velde, E. J. Baerends, *Theor. Chem. Acc.* **1998**, *99*, 391.

 © 2006 Wiley-VCH Verlag GmbH & Co. KGaA, Weinheim 

[23] A. D. Becke, *J. Chem. Phys.* **1986**, *84*, 4524; A. D. Becke, *Phys. Rev.* **1988**, *A38*, 3098.
[24] S. H. Vosko, L. Wilk, M. Nusair, *Can. J. Phys.* **1980**, *58*, 1200.
[25] J. P. Perdew, *Phys. Rev. B* **1986**, *33*, 8822; J. P. Perdew, *Phys. Rev. B* **1986**, *34*, 7406.
[26] The parallelized spin-orbit version of the NMR code has been improved by J. A. in order to achieve more favorable scaling with increasing system size as compared to the original implementation: a) J. Autschbach, E. Zurek, *J. Phys. Chem. A* **2003**, *107*, 4967–4972; b) R. Bouten, E. J. Baerends, E. van Lenthe, L. Visscher, G. Schreckenbach, T. Ziegler, *J. Phys. Chem. A* **2000**, *104*, 5600; c) S. K. Wolff, T. Ziegler, E. van Lenthe, E. J. Baerends, *J. Chem. Phys.* **1999**, *110*, 7689; d) G. Schreckenbach, *Theor. Chem. Acc.* **2002**, *108*, 246.
[27] D. Sundholm, J. Gauss, A. Schäfer, *J. Chem. Phys.* **1996**, *105*, 11051.
[28] a) N. I. Krylov, I. S. Kolomnikov, *Koord. Khim.* **1977**, *3*, 1895; b) J. Fuchs, W. Freiwald, H. Hartl, *Acta Crystallogr., Sect. B* **1978**, *34*, 1764.
[29] a) W. Clegg, M. R. J. Elsegood, R. J. Errington, J. J. Havelock, *J. Chem. Soc., Dalton Trans.* **1996**, 681; b) A. Proust, R. Thouvenot, S. G. Roh, J. K. Yoo, P. Gouzerh, *Inorg. Chem.* **1995**, *34*, 4106–4112.
[30] a) J. Fuchs, H. Hartl, W. Schiller, U. Gerlach, *Acta Crystallogr., Sect. B* **1976**, *32*, 740; b) Y. Sasaki, T. Yamase, Y. Ohashi, Y. Sasada, *Bull. Chem. Soc. Jpn.* **1987**, *60*, 4285.
[31] a) L. P. Kazansky, M. A. Fedotov, V. I. Spitsyn, *Dokl. Acad. Nauk SSSR* **1983**, *272*, 1179; b) D. C. Duncan, C. L. Hill, *Inorg. Chem.* **1996**, *35*, 5828.
[32] G. M. Brown, M.-R. Noe-Spirlet, W. R. Busing, H. A. Levy, *Acta Crystallogr., Sect. B* **1977**, *33*, 1038.
[33] a) K. Y. Matsumoto, A. Kobayashi, Y. Sasaki, *Bull. Chem. Soc. Jpn.* **1975**, *48*, 3146; b) J. Fuchs, A. Thiele, Z. R. Palm, *Z. Naturforsch., Teil B* **1981**, *36*, 161–171; c) F. Robert, A. Tezé, G. Hervé, Y. Jeannin, *Acta Crystallogr., Sect. B* **1980**, *36*, 11.
[34] J. Lefebvre, F. Chauveau, P. Doppelt, C. Brevard, *J. Am. Chem. Soc.* **1981**, *103*, 4589.
[35] A. Tezé, E. Cadot, V. Béreau, G. Hervé, *Inorg. Chem.* **2001**, *40*, 2000.
[36] A. Tezé, J. Canny, L. Gurban, R. Thouvenot, G. Hervé, *Inorg. Chem.* **1996**, *35*, 1001.
[37] R. J. Errington, R. L. Wingad, W. Clegg, M. R. J. Elsegood, *Angew. Chem. Int. Ed.* **2000**, *39*, 3884.
[38] a) R. Acerete, C. F. Hammer, L. C. W. Baker, *Inorg. Chem.* **1984**, *23*, 1478; b) R. Acerete, C. F. Hammer, L. C. W. Baker, *Inorg. Chem.* **1984**, *23*, 1478.
[39] a) H. D'Amour, *Acta Crystallogr., Sect. B* **1976**, *32*, 729; b) V. S. Sergienko, M. A. Porai-Loshits, S. V. Kiselev, L. A. Butman, V. F. Chuvaev, *Z. Neorgan. Khim.* **1983**, *28*, 1199.
[40] L. Salles, C. Aubry, R. Thouvenot, F. Robert, C. Doremieux-Morin, G. Chottard, H. Ledon, Y. Jeannin, J.-M. Brégeault, *Inorg. Chem.* **1994**, *33*, 871.
[41] a) K. G. Burtseva, T. S. Chernaya, M. I. Sirota, *Doklady AN SSSR* **1978**, *243*, 104; b) J. Fuchs, E. P. Flint, *Z. Naturforsch., Teil B* **1979**, *34*, 412.
[42] a) R. I. Maksimovskaya, K. G. Burtseva, *Polyhedron* **1985**, *4*, 1559; b) J. J. Hastings, O. W. Howarth, *J. Chem. Soc., Dalton Trans.* **1992**, 209.
[43] a) C. J. Besecker, W. K. Klemperer, F. J. Maltbie, *Inorg. Chem.* **1985**, *24*, 1027; b) W. Shum, thesis; W. G. Klemperer, personal communication.
[44] G. Schreckenbach, T. Ziegler, *Int. J. Quantum Chem.* **1996**, *60*, 753.
[45] a) J. Autschbach, T. Ziegler, *Relativistic Computation of NMR Shieldings and Spin-Spin Coupling Constants*, in *Encyclopedia of Nuclear Magnetic Resonance*, Vol. 9 (Eds.: D. M. Grant, R. K. Harris), John Wiley & Sons, Chichester, **2002** (see also ref.[16]); b) M. Kaupp, O. L. Malkina, V. G. Malkin, P. Pyykkö, *Chem. Eur. J.* **1998**, *4*, 118–126; c) S. K. Wolff, T. Ziegler, *J. Chem. Phys.* **1998**, *109*, 895–905.
[46] Calculation running in parallel in a five Pentium 4 (2.5 GHz) cluster.
[47] X. López, J. A. Fernández, S. Romo, J. F. Paul, L. Kazansky, J. M. Poblet, *J. Comput. Chem.* **2004**, *25*, 1542.

Received: December 1, 2005
Published Online: February 6, 2006

 © 2006 Wiley-VCH Verlag GmbH & Co. KGaA, Weinheim 

DOI: 10.1002/ejic.200500833

# DFT Calculations of the $^{183}W$ NMR Chemical Shifts in Reduced Polyoxotungstates

**Jose Gracia,[a] Josep M. Poblet,*[a] Jorge A. Fernández,[a] Jochen Autschbach,[c] and Leonid P. Kazansky*[b]**

**Keywords:** Density-functional calculations / NMR spectroscopy / Tungsten / Oxygen / Polyoxometalates

A relativistic DFT method (ZORA) is used to calculate the $^{183}W$ and $^{17}O$ NMR chemical shifts for the reduced polyoxotungstates $W_5O_{18}W^{II}NO^{3-}$, $\gamma$-$SiW_{12}O_{40}^{6-}$, $P_2W_{18}O_{62}^{8-}$, and $W_{10}O_{32}^{6-}$ with different degrees of (de)localization of the electrons introduced. Despite some discrepancies in the calculated and experimental data, the calculations adequately describe the changes in the chemical shifts upon reduction. The reduction of a fully oxidized anion is accompanied by an expansion of the geometry. The effect of the charge localization and change in geometry on the chemical shift is evaluated. The shift of the resonance of the tungsten atoms largely depends on the reduced charge acquired upon reduction. On the other hand, those tungsten atoms that do not increase the electron density upon reduction have a negative shift. The calculations also reproduce the negative shifts of all the $^{17}O$ NMR resonances upon reduction of the polyoxotungstates.
(© Wiley-VCH Verlag GmbH & Co. KGaA, 69451 Weinheim, Germany, 2006)

## Introduction

Because of the well-known ability of polyoxometalates (POM) consisting of $V^V$, $Mo^{VI}$, and $W^{IV}$ to be reversibly reduced by one, two, or more electrons, they have attracted much attention in catalysis and other fields where redox reactions are quite important.[1–4] Depending on the molecular structure, electrons delocalize over the whole of the coordination sphere or just a part of it. EPR[1,5,6] and, subsequently, $^{17}O$ NMR spectroscopy[7] have proved that a single electron can be delocalized and that this delocalization can be "frozen out" at quite low temperatures (several degrees kelvin).

The second electron introduced by a certain mechanism generally pairs with the first one. $^{17}O$ NMR[7,8] and then $^{183}W$ NMR[9–11] spectroscopy have shown that the electron pair formed is completely delocalized in the Keggin anion $SiW_{12}O_{40}^{6-}$, partly in the Dawson anion $P_2W_{18}O_{62}^{8-}$, in $W_{10}O_{32}^{6-}$ or $\gamma$-$SiW_{12}O_{40}^{6-}$, and resides completely on specific atoms in $\gamma$-$SiW_{10}W^V_2S_2O_{38}^{6-}$,[12] $\gamma$-$SiMo^V_2W_{10}O_{40}^{6-}$,[10] and $P_2W_{15}Mo_3O_{62}^{8-}$ (delocalization of the electron pair over three Mo atoms),[13] or, in the case of six electrons, in $XW_9W_3^{IV}O_{40}H_6^{x-}$ (localization of six electrons in triplet forming metal–metal bonding).[14,15] In some specific cases, the introduction of two electrons entails the localization of one electron on one atom while the second electron partially delocalizes over the tungsten atoms adjacent to the first reduced atom (for example $P_2W_{17}Mo^VO_{62}^{8-}$).[13]

Several cases, however, should be considered separately. In the nitrosyl complexes $W_5O_{18}W^{II}NO^{3-}$ with the Lindqvist-type structure,[16] $PW_{11}W^{II}NO_{40}^{8-}$, and the corresponding Ru complexes with the Keggin structure,[17–19] the electron density of the cation introduced delocalizes onto the neighboring tungsten atoms.

In all the examples mentioned above, the degree of delocalization was monitored by NMR spectroscopy and estimated by the characteristic positive shift of the resonance lines attributed to the tungstens accepting the electron density. At the same time, some resonances undergo negative shift which, depending on the structure and position of the most important atom in it, may be rather significant.

In this paper we report DFT calculations of the $^{183}W$ and $^{17}O$ chemical shifts for several reduced POMs.

## Computational Details

We used the ADF 2003.01 package[20] to compute the geometries of the molecules reported here. The density-functional theory (DFT) calculations are characterized by the local density approximation featuring the *Xa* model for exchange with Becke's gradient-corrected functional,[21] and the VWN parameterization for correlation[22] corrected

[a] Departament de Quimica Fisica i Inorgánica, Universitat Rovira i Virgili,
Marcel.lí Domingo s/n, Campus Sescelades, 43007 Tarragona, Spain
E-mail: josepmaria.poblet@urv.net
[b] Institute of Physical chemistry, Russian Academy of Sciences, 31, Leninski pr, Moscow 119991, Russia
E-mail: leoka@ipc.rssi.ru
[c] Department of Chemistry, State University of New York at Buffalo,
312 Natural Sciences Complex, Buffalo, NY 14260-3000, USA
Supporting information for this article is available on the WWW under http://www.eurjic.org or from the author.

 © 2006 Wiley-VCH Verlag GmbH & Co. KGaA, Weinheim 

with Perdew's functional.[23] The basis functions for describing the valence electrons of all the atoms are Slater-type orbitals of triple-ζ+ polarization quality. The internal or *core* electrons are described by means of single Slater functions and were generated with the auxiliary program DIRAC.[20] Quasi-relativistic corrections − *zeroth-order relativistic approximation* (ZORA) − were performed with corrected core potentials. The NMR shielding tensors were computed from a parallel version of the NMR module.[24]

The calculated chemical shift, $\delta_{cal}$, is determined as the difference between total shielding of the reference molecule, $\sigma_r$, and the shielding, $\sigma_x$, of the molecule being studied:

$\delta_{cal} = \sigma_r - \sigma_x$

For each nucleus, the total shielding tensor, $\sigma_t$, is calculated as the sum of the paramagnetic ($\sigma_p$) and diamagnetic ($\sigma_d$) contributions. The simplest oxoanion, $WO_4^{2-}$, is usually used as a reference for $^{183}W$ NMR spectroscopy (calculated $\sigma_t$ is 2663 ppm).[25] The $^{17}O$ NMR chemical shift is measured relative to pure water ($\delta$ = 0 ppm) for which the absolute shielding, $\sigma_t$, is 291 ppm.[26]

It is well known that when electrons are added to the structure the framework swells somewhat (i.e. some bonds are elongated).[15,27–30] Thus, in all cases, for both the parent oxidized POM and its reduced counterparts, the structures used were the optimized ones before and after the two electrons had been introduced.

## Results and Discussion

### $W_5O_{18}WNO^{3-}$

This anion is a derivative of the Lindqvist anion that contains one tungsten atom in the formal oxidation state 2+ with an NO group in place of the terminal oxygen atom. Formally, NO has a charge of 1+.[16] The oxidized anion has no counterpart and for purposes of comparison the Lindqvist anion is used. Although the X-ray geometry of this anion was not determined because the lattice cells are very similar, the atomic coordinates were inferred from the general description of the related anion $Mo_5O_{18}MoNO^{3-}$ and by comparison with the Lindqvist molybdate and tungstate anions. The symmetry of the anion is $C_{4v}$, which leads to three types of tungsten atoms (Figure 1). Three resonances are observed in the $^{183}W$ NMR spectrum with an intensity ratio of 1:4:1, the first of which is substantially shifted to low field (Table 1) and assigned to the reduced tungsten linked to NO. It should be noted that the experimental shift for $W_c$ is markedly lower than the expected one for a $W(d^4)$ configuration. Due to the back-donation from tungsten to the nitrosyl group less electron density is left on tungsten, which results in a smaller chemical shift. The $^{183}W$ and $^{17}O$ NMR chemical shifts calculated for the optimized structure are given in Table 1.

The calculations correctly describe the pattern of the $^{183}W$ chemical shifts, although the value for $W_c$ is considerably underestimated. The HOMO with *e* symmetry shows a π interaction between the W metal and the NO group (see Figure 1).

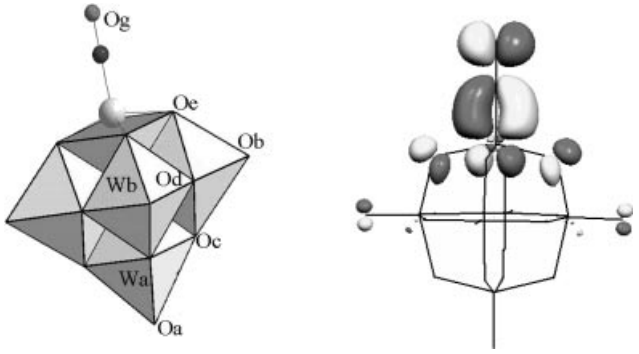


Figure 1. Structure and HOMO of $W_5O_{18}WNO^{3-}$.

Table 1. Calculated parameters and experimental $^{183}W$ and $^{17}O$ NMR shifts for $W_5O_{18}WNO^{3-}$.

| | $W_c$ | $W_b$ | $W_a$ | $O_a$ | $O_b$ | $O_c$ | $O_d$ | $O_e$ | $O_f$ |
|---|---|---|---|---|---|---|---|---|---|
| $\delta_{cal}$ [ppm] | 488 | 225 | 197 | 699 | 717 | 456 | 438 | 517 | –27 |
| $\delta_{exp}$ [ppm] | 653 | 168 | 117 | 728 | 734 | 402 | 399 | 448 | |

The $^{17}O$ NMR chemical shifts calculated for several oxygen atoms enable the lines observed for both the terminal and bridging ($O_c$ and $O_d$, respectively) atoms to be assigned. It should be pointed out that the chemical shift for the bridging $O_e$ is larger than for the other bridging atoms. This may be due to an interaction with the cation with the lowest oxidation state ($W_c$)[16] or the influence of the passing electron density. However, the oxygen atoms of this type have a higher shift[25] in $CH_3OTiW_5O_{18}^{3-}$, where no delocalization occurs. It should be noted that, as before, the chemical shifts calculated for the bridging oxygen atoms are overestimated and for the terminal ones they are underestimated.[25] Nevertheless, if compared with $W_6O_{19}^{2-}$, the computed $^{17}O$ chemical shifts correctly represent the marked decrease in the experimental shifts for all the oxygen atoms in $W_5O_{18}W_cNO^{3-}$.

### γ-$SiW_{12}O_{40}^{n-}$

The structure of this anion, determined by Tézé et al.,[10] is the result of two triplet groups ($W_a$–$W_b$–$W_b$) rotated by 60° along two $C_3$ axes of the Keggin anion (Figure 2). This structure gives rise to four resonances with a 2:1:2:1 intensity pattern. The most shielded atoms in the $^{183}W$ NMR spectrum proved to be the $W_a$ tungstens in rather a peculiar position (Table 2).[10]

According to the $^{183}W$ NMR spectrum, the two-electron-reduced form reveals an uneven distribution of the electron density over the coordination sphere. The most deshielded atoms proved to be $W_d$, which acquire the largest portion of the electron density, and the least shielded are $W_c$. Experimentally, the assignment of the resonance lines for the reduced species is ambiguous because the quality of the spectrum did not allow the spin–spin coupling to be determined. However, the present calculations unambiguously show that $W_d$ is reduced first because the LUMO that acquires two electrons mainly consists of $W_d$ $d_{xy}$ orbitals and,

 © 2006 Wiley-VCH Verlag GmbH & Co. KGaA, Weinheim 

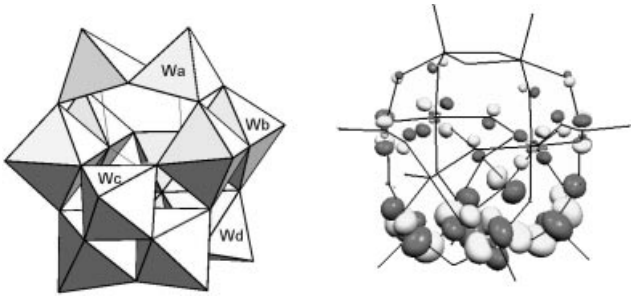


Figure 2. Structure and HOMO of the two-electron-reduced $\gamma$-$SiW_{12}O_{40}^{6-}$.

Table 2. Calculated and experimental $^{183}W$ NMR chemical shifts [ppm] for the oxidized $\gamma$-$SiW_{12}O_{40}^{4-}$ and 2e-reduced $\gamma$-$SiW_{12}O_{40}^{6-}$ anions.

| | $W_a$ | $W_b$ | $W_c$ | $W_d$ |
|---|---|---|---|---|
| $\delta^{ox}{}_{exp}$[a] | –160 | –105 | –117 | –127 |
| $\delta^{ox}{}_{cal}$[b] | –170 | –130 | –184 | –158 |
| $\delta^{red}{}_{exp}$[a] | –131 | –63 | –124 | 489 |
| $\delta^{red}{}_{cal}$[b] | –47 | –2 | –65 | 471 |
| $\delta^{*}{}_{cal}$[c] | –63 | –63 | –98 | –32 |
| $\Delta\delta_{geom}$[d] | +107 | +67 | +86 | +126 |
| $\Delta\delta_{elect}$[d] | +16 | +61 | +33 | +503 |

[a] Observed NMR chemical shifts for the fully oxidized ($\delta^{ox}{}_{exp}$) and 2e-reduced ($\delta^{red}{}_{exp}$) anions. [b] Computed NMR chemical shifts for the fully oxidized ($\delta^{ox}{}_{cal}$) and 2e-reduced ($\delta^{red}{}_{cal}$) anions in their optimal structures. [c] $\delta^{*}{}_{cal}$ is the shift computed for the oxidized anion but with the structure of the reduced anion. [d] $\Delta\delta_{geom} = \delta^{*}{}_{cal} - \delta^{ox}{}_{calc}$ represents the shift induced by the geometrical change and $\Delta\delta_{elect} = \delta^{red}{}_{cal} - \delta^{*}{}_{calc}$ the shift resulting from the incorporation of the electron density in the already deformed anion (see text for more details).

to a lesser extent, $W_b$ tungsten atoms; $W_a$ and $W_c$ are reduced afterwards. Nevertheless, in the observed spectrum of the reduced anion one of the resonance lines ($\delta$ = –131 ppm) is negatively shifted with respect to the lines of the oxidized anion. The notable positive calculated shifts (>100 ppm) of the lines assigned to $W_a$ and $W_c$ for the reduced anion will be discussed below.

It should also be noted that, despite an increase in the electron population on the reduced tungsten, the diamagnetic shielding does not differ much ($\delta$ = 5 ppm) from the diamagnetic shielding for nonreduced tungstens.

## $P_2W_{18}O_{62}^{6-}$

This is the largest anion considered in this paper (Figure 3). Its $^{183}W$ NMR spectrum completely corresponds to the two expected resonance lines with an intensity ratio of 1:2, the first of which is assigned to the cap tungsten atoms ($W_a$) (Table 3).[9] It should be noted that $W_b$ is linked to other tungsten atoms with three corner- and one edge-shared oxygen atoms, unlike $W_a$, which is linked by two corner- and two edge-shared oxygen atoms as in the Keggin anion.

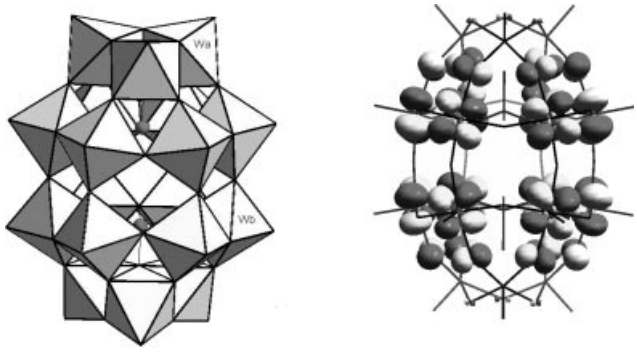


Figure 3. Structure and HOMO of the two-electron-reduced $P_2W_{18}O_{62}^{8-}$.

Table 3. Calculated and observed $^{183}W$ NMR chemical shifts [ppm] for the oxidized $P_2W_{18}O_{62}^{6-}$ and 2e-reduced $P_2W_{18}O_{62}^{8-}$ anions.[a]

| | $W_a$ | $W_b$ |
|---|---|---|
| $\delta^{ox}{}_{exp}$ | –127 | –173 |
| $\delta^{ox}{}_{cal}$ | –146 | –215 |
| $\delta^{red}{}_{exp}$ | –299 | –51 |
| $\delta^{red}{}_{cal}$ | –193 | –143 |
| $\delta^{*}{}_{cal}$ | –105 | –134 |
| $\Delta\delta_{geom}$ | 41 | 81 |
| $\Delta\delta_{elect}$ | –88 | –9 |

[a] See Table 2 for definitions of the chemical shifts.

Reducing the anion with two electrons completely delocalizes the electron pair over 12 $W_b$ atoms. As shown by different calculation approaches, the HOMO (Figure 3), which contains two electrons, is composed of symmetry-adapted $W^5$ $d_{xy}$ orbitals of the belt tungsten atoms $W_b$. This is clear from the marked positive shift of the more intense resonance line. At the same time, the resonance assigned to the cap tungsten atoms $W_a$ undergoes a substantial negative shift.

Despite the notable discrepancy between the calculated and experimental chemical shifts, and although the calculated absolute shifts upon reduction are markedly less than the observed ones (Table 3), the DFT calculation adequately reflects how the chemical shifts tend to change upon reduction.

## $W_{10}O_{32}^{4-}$

Like the Dawson anion $P_2W_{18}O_{62}^{6-}$ considered above, this decatungstate may be viewed as a combination of two fragments of the initial anion, in this case the Lindqvist anion (Figure 4). $W_{10}O_{32}^{4-}$ also gives two resonance lines in the $^{183}W$ NMR spectrum at $\delta$ = –23 and –165 ppm, with an intensity ratio of 4:1, both of which are shifted to high field with respect to the parent anion ($\delta$ = +59 ppm).[11] In contrast to the Dawson anion, two-electron reduction of $W_{10}O_{32}^{4-}$ induces positive shifts in both resonances. However, the second line shifts by only 16 ppm, while the first one shifts by 330 ppm, strongly indicating that the electron pair is delocalized over eight tungsten atoms of the $W_b$ type.

 © 2006 Wiley-VCH Verlag GmbH & Co. KGaA, Weinheim 

This is also confirmed by the nature of the HOMO, which consists of symmetry-adapted $d_{xy}$ orbitals of $W_b$ (Figure 4).

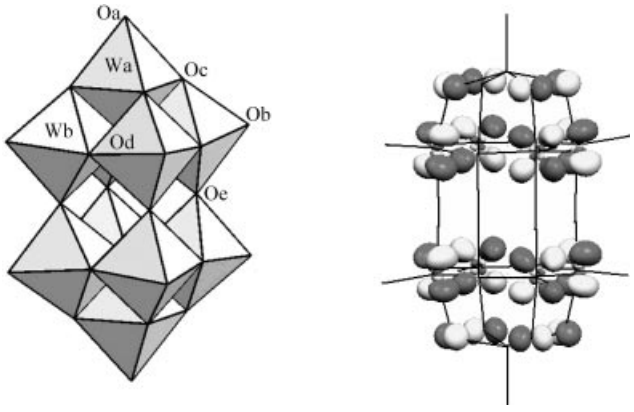


Figure 4. Structure and HOMO of the two-electron-reduced $W_{10}O_{32}^{6-}$.

A slight positive shift in the line assigned to $W_a$ might indicate the delocalization of electron density on these atoms, as was observed in $\gamma$-$SiW_{12}O_{40}^{6-}$. However, this may be misleading. We should bear in mind that when an anion is reduced, it "swells" because the bond lengths increase. According to the X-ray structure determination of the oxidized and reduced species[30] of the decatungstate, both types of $WO_6$ octahedron increase in size slightly, which is confirmed by the structures computed for oxidized and reduced anions. The geometry changes most in the belt octahedra (see the bond lengths in Table 4).

Table 4. Observed and calculated NMR shieldings for $W_{10}O_{32}^{n-}$.[a]

| | $W_a$ | $W_b$ | $O_a$ | $O_b$ | $O_c$ | $O_d$ | $O_e$ | $O_f$ |
|---|---|---|---|---|---|---|---|---|
| $W_{10}O_{32}^{4-}$ | | | | | | | | |
| $R_{WO}$ [Å] | 1.966 | 1.983 | 1.756 | 1.739 | 1.938/ 1.969 | 1.942 | 1.923 | 2.288/ 2.354 |
| $\delta^{ox}_{exp}$ [ppm] | –165 | –23 | 732 | 765 | 434 | 421 | 423 | –1.6 |
| $\delta^{ox}_{cal}$ [ppm] | –155 | –41 | 707 | 751 | 494 | 485 | 471 | –49 |
| $\delta^{*}_{cal}$ [ppm] | –39 | 109 | 733 | 784 | 524 | 505 | 480 | –58 |
| $\Delta\delta_{geo}$ [ppm] | +116 | +150 | +26 | +33 | +30 | +20 | +9 | –9 |
| $W_{10}O_{32}^{6-}$ | | | | | | | | |
| $R_{WO}$ [Å] | 1.978 | 1.994 | 1.789 | 1.762 | 1.939/ 2.024 | 1.942 | 1.928 | 2.325/ 2.365 |
| $\delta^{red}_{exp}$ [ppm] | –149 | 307 | 662 | 709 | 349 | 405 | 419 | –2.4 |
| $\delta^{red}_{cal}$ [ppm] | –58 | 249 | 632 | 693 | 412 | 465 | 479 | –50 |
| $\Delta\delta_{elect}$ [ppm] | –19 | +140 | –101 | –91 | –112 | –40 | –1 | +8 |

[a] See Table 2 for definitions of the chemical shifts.

The calculated charge on the $W_b$ atoms decreases upon reduction, and there is practically no change in $W_a$.[31] In other words, the positive shift for $W_a$ is caused by a geometrical change in the cap octahedron due to the reduction of the vicinal tungstens.

Unlike in the $^{183}W$ NMR spectrum, all the $^{17}O$ NMR resonances shift to high field upon reduction. These negative shifts may be the result of the delocalization of the electron density, the shielding of the nuclei, or the exclusion of the HOMO (LUMO before reduction) from the transitions that determine the paramagnetic term. From the calculated charges, only the $O_c$ atoms seem to reveal some increase in their negative charge upon reduction. Thus, the substantial negative shifts may be assumed to be due to an increase in the paramagnetic shielding. It should be noted that the $^{17}O$ resonance line assigned to the $O_e$ linking two fragments undergoes the least negative shift, despite delocalization of the electron pair over $W_b$. Once again, if the shifts calculated for $W_{10}O_{32}^{4-}$ and $W_{10}O_{32}^{6-}$ are compared using the geometry for the reduced anion, we see that the decrease in the shifts is larger.

It should be noted that despite localization of the electron density over the eight $W_b$ atoms, the terminal oxygen atom $W_a$ feels the presence of the electron pair in the HOMO, which is probably excluded from the principle transitions that determine the paramagnetic shielding. On the other hand, $O_e$ does not react to the presence of the electron density on the nearest $W_b$ tungsten atoms. Presumably because of selection rules, the HOMO does not participate in the transitions that determine the paramagnetic contribution of these oxygen atoms.

Electronic and geometric factors also influence the calculated chemical shifts. For example, the reduction of a tungsten ion *always* induces a positive shift in the $^{183}W$ NMR resonance in polytungstates. The present DFT calculations reproduce this phenomenon fairly well and show that the greater the electron density on a given nucleus the greater the chemical shift. It increases from the Dawson anion (2 e per 12 $W_b$), to decatungstate (2 e per 8 $W_b$), and then to the $\gamma$-Keggin anion (2 e per 4 $W_d$ and partially on another 4 $W_b$).

The incorporation of one electron into a nonbonding metal orbital is associated with a small enlargement in the reduced octahedron. By analyzing the chemical shift in several geometries we managed to separate the electronic factors from the geometric factors causing this positive shift. For some of the anions discussed above we calculated the chemical shifts for the oxidized parent anions but using the optimized geometry for the reduced form. In all cases, substantial positive shifts of the calculated values $\delta^{*}_{cal}$ were found, therefore $\Delta\delta_{geom}$ ($\delta^{*}_{cal} - \delta^{ox}_{cal}$) will be considered as the geometry factor due to the enlargement of the anion as a result of reduction. On the other hand, the shift due to incorporation of the electron density, $\Delta\delta_{elec}$, is given by $\delta^{red}_{cal} - \delta^{*}_{cal}$, where calculated values refer to the optimized structure of the reduced form. The importance of the electronic effect increases as the charge density on the reduced center increases. Hence, in the $\gamma$-$SiW_{12}O_{40}^{6-}$ anion the electronic term for $W_d$ was estimated to be four times larger than the geometric term. For $W_b$ in $W_{10}O_{32}^{6-}$ the two terms are of similar weight. The electronic effect must be much less important in the case of the Dawson anion, where the two extra electrons are shared by 12 centers, therefore the positive shift is due to enlargement of the anion (see Table 3).

We will now discuss the case of $W_{10}O_{32}^{4-}$ in some detail. The 2e-reduction shifts the signal associated to the reduced belt tungstens ($W_b$) by +330 ppm. The corresponding computed value is +290 ppm. By calculating the chemical shift of the oxidized anion with the geometry of the reduced

 © 2006 Wiley-VCH Verlag GmbH & Co. KGaA, Weinheim 

partner, we estimate that the geometrical effect is +150 ppm ($\Delta\delta_{geo}$). Thus, the addition of two electrons to the already adapted (enlarged) framework shifts the signal by a further +140 ppm ($\Delta\delta_{elec}$). For the nonreduced $W_a$, the calculated shift is +97 ppm, a very high value in comparison with the experimental value of +16 ppm. The DFT calculations probably overestimate the deformation of the cap octahedra ($\Delta\delta_{geo}$ = +116 ppm) due to the reduction of a belt site.

As mentioned above, the two added electrons in $\gamma$-$SiW_{12}O_{40}^{6-}$ are shared mainly by four tungstens. Consequently, the electronic term is much more important. $\Delta\delta_{elec}$ for $W_d$ was computed to be +503 ppm, whereas the corresponding $\Delta\delta_{geo}$ contribution is only +126 ppm. As for $W_{10}O_{32}^{4-}$, the relatively large $\Delta\delta_{geo}$ values for the nonreduced centers seem to be the cause of their large positive shift.

Figure 5 compares the calculated and experimental $^{183}W$ chemical shifts for the reduced and parent anions, and gives important data for $W_5O_{18}W_cNO^{3-}$. From the position of the points, it can be assumed that the values calculated for the reduced anions are slightly overestimated, because the linear trend seems to be positively shifted. This shows that the increase in the chemical shifts is not only due to the reduction but also because the additional electrons lead to an enlargement of the structure. The positive shift of 65 ppm of the trend may assume that the optimization of the structure in the reduced state slightly overestimates the bond lengths.

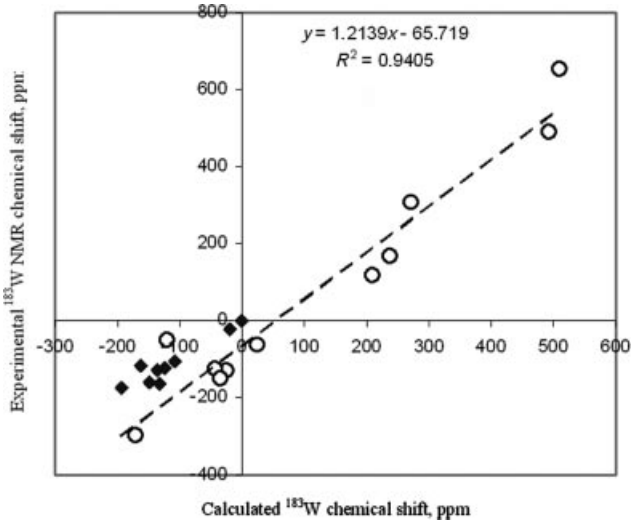


Figure 5. Correlation of the experimental and calculated $^{183}W$ chemical shifts for reduced and parent anions: ♦ oxidized anions, o reduced anions.

Analysis of the transitions responsible for the paramagnetic shielding of different tungsten atoms may clarify the situation for those atoms for which the resonances with less-positive shifts are assigned.

## Conclusions

DFT calculations have been carried out to analyze the effect of reduction on the $^{183}W$ and $^{17}O$ chemical shifts in several prototypic polyoxotungstates. In general, the experimental trends are well reproduced, although significant discrepancies were found between some computed and observed values. This deviation is especially important for the $W^{II}$ ion in the Lindqvist derivative $W_5O_{18}W^{II}NO^{3-}$, probably due to the inability of DFT methods to properly describe the interaction between the $W^{II}$ ion and the NO ligand.

The incorporation of one electron in a nonbonding metal orbital produces an enlargement of the reduced octahedron. By analyzing the chemical shift in several geometries we have been able to separate the electronic factors from the geometric factors that cause the positive shift. The importance of the electronic effect increases with the charge density on the reduced center, hence in the $\gamma$-$SiW_{12}O_{40}^{6-}$ anion the electronic term has been estimated to be three times larger than the geometric term, whereas for $W_{10}O_{32}^{6-}$ the two terms have similar weight. The electronic effect must be much less relevant in the Dawson anion, where the two extra electrons are shared by 12 centers. This means that the small positive shift should be mainly attributed to a change in the geometry as a consequence of the reduction. The present calculations have not allowed us to rationalize the extremely negative shift of the resonance line assigned to the cap $W_a$ in reduced $P_2W_{18}O_{62}^{8-}$.

The $^{17}O$ NMR lines are negatively shifted upon reduction, in contrast to the positive shifts resulting from placing the electron density on the tungsten atoms. The large negative shift of the resonance of $O_a$ in $W_{10}O_{32}^{6-}$, which is rather far away from the delocalized electron pair, is especially surprising. Further analysis of the calculated $^{17}O$ NMR chemical shifts may clarify this situation.

**Supporting Information** (see footnote on the first page of this article): Decomposition of shielding tensors into their paramagnetic and diamagnetic contributions is given as Supporting Information (Tables S1–S4).

## Acknowledgments

This work was supported by the Spanish MECD (BQU2002-04110-C02-01) and the CIRIT of the Autonomous Government of Catalonia (SGR01-00315). J.A. is grateful for financial support from the CAREER program of the National Science Foundation (grant no. CHE-0447321). The authors thank the referees for comments and suggestions.

[1] M. T. Pope, *Heteropoly and Isopoly Oxometalates*, Springer, Berlin, **1983**.
[2] a) *Polyoxometalates: From Platonic Solids to Anti-Retroviral Activity* (Eds.: M. T. Pope, A. Müller), Kluwer, Dordrecht, **1994**; b) M. T. Pope, A. Müller, *Angew. Chem. Int. Ed. Engl.* **1991**, *30*, 34–48.
[3] *Chem. Rev.* **1998**, *98*, 3 special issue, Ed.: C. Hill.
[4] *Polyoxometalates* (Eds.: J. J. Borrás-Almenar, E.Coronado, M. T. Müller, A. Pope), Molecular Science NATO Science Series. II, Mathematics, Physics and Chemistry, **2003**, vol. 98, Kluwer Academic Publishers, Dordrecht.
[5] C. Sanchez, J. Livage, J. P. Launay, M. Fournier, Y. Jeannin, *J. Am. Chem. Soc.* **1982**, *104*, 3194.
[6] C. Sanchez, J. Livage, J. P. Launay, M. Fournier, *J. Am. Chem. Soc.* **1983**, *105*, 6817.

 © 2006 Wiley-VCH Verlag GmbH & Co. KGaA, Weinheim 

[7] K. Piepgrass, J. N. Barrows, M. T. Pope, *J. Chem. Soc., Chem. Commun.* **1989**, 10.
[8] P. Kazansky, M. A. Fedotov, I. V. Potapova, V. I. Spitsyn, *Dokl. Akad. Nauk.* **1979**, *244*, 372.
[9] K. Kozik, C. F. Hammer, L. C. W. Baker, *J. Am. Chem. Soc.* **1986**, *108*, 2748.
[10] a) A. Tézé, J. Canny, L. Gurban, R. Thouvenot, G. Hervé, *Inorg. Chem.* **1996**, *35*, 1001; b) A. Tezé, E. Cadot, V. Béreau, G. Hervé, *Inorg. Chem.* **2001**, *40*, 2000.
[11] D. C. Duncan, C. L. Hill, *Inorg. Chem.* **1996**, *35*, 5828.
[12] E. Cadot, V. Bereau, B. Marg, S. Halut, F. Secheresse, *Inorg. Chem.* **1996**, *35*, 3099.
[13] K. Kozik, L. C. W. Baker, in *Polyoxometalates* (Eds.: M. T. Pope, A. Muller), Kluwer Academic Publishers, **1994**, p. 191.
[14] K. Piepgrass, M. T. Pope, *J. Am. Chem. Soc.* **1987**, *109*, 1586.
[15] T. Yamase, E. Ishikawa, *J. Chem. Soc., Dalton Trans.* **1996**, 1619.
[16] A. Proust, R. Thouvenot, S. G. Roh, J. K. Yoo, P. Gouzerh, *Inorg. Chem.* **1995**, *34*, 4106.
[17] A. Proust, M. Fournier, R. Thouvenot, P. Gouzerh, *Inorg. Chim. Acta* **1994**, *215*, 61.
[18] C. Rong, M. T. Pope, *J. Am. Chem. Soc.* **1992**, *114*, 293–298.
[19] A. Bagno, M. Bonchio, A. Sartorel, G. Scorano, *Eur. J. Inorg. Chem.* **2000**, 17.
[20] a) ADF 2003.01, Department of Theoretical Chemistry, Vrije Universiteit, Amsterdam; b) E. J. Baerends, D. E. Ellis, P. Ros, *Chem. Phys.* **1973**, *2*, 41; c) L. Versluis, T. Ziegler, *J. Chem. Phys.* **1988**, *88*, 322; d) G. Te Velde, E. J. Baerends, *J. Comput. Phys.* **1992**, *99*, 84; e) C. Fonseca Guerra, J. G. Snijders, G. Te Velde, E. J. Baerends, *Theor. Chem. Acc.* **1998**, *99*, 391.
[21] A. D. Becke, *J. Chem. Phys.* **1986**, *84*, 4524; A. D. Becke, *Phys. Rev. A* **1988**, *38*, 3098.
[22] S. H. Vosko, L. Wilk, M. Nusair, *Can. J. Phys.* **1980**, *58*, 1200.
[23] J. P. Perdew, *Phys. Rev. B* **1986**, *33*, 8822; J. P. Perdew, *Phys. Rev. B* **1986**, *34*, 7406.
[24] J. Autschbach, E. Zurek, *J. Phys. Chem. A* **2003**, *107*, 4967–4972.
[25] J. Gracia, J. M. Poblet, J. Autschbach, L. P. Kazansky, *Eur. J. Inorg. Chem.* **2006**, 1139–1148; preceding article.
[26] D. Sundholm, J. Gauss, A. Schäfer, *J. Chem. Phys.* **1996**, *105*, 11051.
[27] J. N. Barrows, G. B. Jameson, M. T. Pope, *J. Am. Chem. Soc.* **1985**, *107*, 1771.
[28] R. Neir, C. Trojanovski, R. Mattes, *J. Chem. Soc., Dalton Trans.* **1995**, 2521.
[29] E. Ishikawa, T. Yamase, *Bull. Chem. Soc. Jpn.* **2000**, *73*, 641.
[30] Y. Sasaki, T. Yamase, Y. Ohashi, Y. Sasada, *Bull. Chem. Soc. Jpn.* **1987**, *60*, 4285.
[31] L. P. Kazansky, T. Yamase, *J. Phys. Chem. A* **2004**, *108*, 6437.

Received: September 19, 2005
Published Online: February 6, 2006

 © 2006 Wiley-VCH Verlag GmbH & Co. KGaA, Weinheim 

DOI: 10.1002/ejic.200500840

# Iodine Attack on the Metalloligand [{Ti($\eta^5$-$C_5Me_5$)($\mu$-NH)}$_3$($\mu_3$-N)]: Surprising Formation of the [$Ti_3(\eta^5$-$C_5Me_5)_3I_2(\mu$-$NH)_3(NH_3)]^+$ Cation

María García-Castro,[a] Avelino Martín,[a] Miguel Mena,*[a] Josep-M. Poblet,[b] and Carlos Yélamos[a]

**Keywords:** Indium / Iodine / N ligands / Nitrido complexes / Titanium

The reactivity of the trinuclear imido-nitrido complex [{Ti($\eta^5$-$C_5Me_5$)($\mu$-NH)}$_3$($\mu_3$-N)] (**1**) and derivatives thereof with iodine has been investigated. Treatment of the indium(I) adduct [IIn{($\mu_3$-NH)$_3$Ti$_3$($\eta^5$-$C_5Me_5$)$_3$($\mu_3$-N)}] (**2**) with $I_2$ (1 equiv.) in benzene afforded the indium(III) complex [$I_3$In{($\mu_3$-NH)$_3$Ti$_3$($\eta^5$-$C_5Me_5$)$_3$($\mu_3$-N)}] (**3**), but with excess of iodine the precipitation of orange crystals of the ionic complex [$Ti_3(\eta^5$-$C_5Me_5)_3I_2(\mu$-$NH)_3(NH_3)][InI_4]$ (**4**) takes place. Analogous treatment of the metalloligand **1** with $I_2$ in toluene gave initially the iodine(I) derivative [I{($\mu_3$-NH)$_3$Ti$_3$($\eta^5$-$C_5Me_5$)$_3$($\mu_3$-N)}][$I_3$] (**5**). Surprisingly, toluene solutions of **5** at room temperature produced crystals of the ionic complex $[Ti_3(\eta^5$-$C_5Me_5)_3I_2(\mu$-$NH)_3(NH_3)][I_3]\cdot C_7H_8$ (**6**·$C_7H_8$). The trinuclear titanium cation $[Ti_3(\eta^5$-$C_5Me_5)_3I_2(\mu$-$NH)_3(NH_3)]^+$ of complexes **4** and **6** has been structurally characterized by a combination of X-ray and DFT studies.
(© Wiley-VCH Verlag GmbH & Co. KGaA, 69451 Weinheim, Germany, 2006)

## Introduction

Transition metal nitrido complexes have received considerable attention over the last decades.[1,2] Compounds of group 6–8 metals usually bear the nitrido ligand as a terminal functionality [M]≡N and the study of its reactivity is an area of increasing activity.[1,3] The analogous early transition metal derivatives have not received the same treatment due to their difficult characterization and, perhaps more importantly, the lack of a systematic method of synthesis. This could be related with the tendency of the nitrido ligand to bridge two or more early-transition metal centers, which produces singular and very often unpredictable polynuclear structures.[2,4]

The imido-nitrido complex [{Ti($\eta^5$-$C_5Me_5$)($\mu$-NH)}$_3$($\mu_3$-N)] (**1**)[5,6] shows a cyclic [$Ti_3(\mu$-$NH)_3$] system, which resembles that of other triazamacrocycles such as 1,4,7-triazacyclononanes,[7] and especially 1,3,5-triazacyclohexanes,[8] whose extensive coordination chemistry is known. In fact, we have recently shown the capacity of **1** to act as a preorganized tridentate ligand with transition,[4,9,10] and main group metals.[11] The great versatility of **1** is also confirmed by the possibility of preparing complexes with metals in low [e.g. $Mo^0$, $Ir^I$] or high oxidation states [e.g. $Ti^{IV}$, $Ta^V$]. Although the main driving force in the coordination of **1** is the electron donation of the nitrogen atom lone pair to the incorporated metals, theoretical calculations performed on adducts of **1** with transition metals in low oxidation states have shown that the presence of $Ti^{IV}$ centers in the metalloligand produces an additional stabilization through metal–metal coupling.[9]

We have recently shown the formation of indium(I) and indium(III) iodide adducts [$I_x$In{($\mu_3$-NH)$_3$Ti$_3$($\eta^5$-$C_5Me_5$)$_3$($\mu_3$-N)}] [$x$ = 1 (**2**), $x$ = 3 (**3**)] through the reaction of **1** with the corresponding metal halides,[12] and were interested in performing the oxidation reactions directly on the metallocubane system, for example preparing **3** from the indium(I) complex **2**. Here we present the results obtained in this reaction, including the opening of the metalloligand **1** in the presence of excess iodine to give ionic complexes containing the singular unprecedented cation [$Ti_3(\eta^5$-$C_5Me_5)_3I_2(\mu$-$NH)_3(NH_3)]^+$, which has been structurally characterized by X-ray and DFT studies.

## Results and Discussion

The objective of this work was to evaluate the possibility of performing oxidation processes on inorganic fragments incorporated into the preorganized metallocubane ligand [{Ti($\eta^5$-$C_5Me_5$)($\mu$-NH)}$_3$($\mu_3$-N)] (**1**). In this way, we tried to obtain the indium(III) iodide adduct [$I_3$In{($\mu_3$-NH)$_3$-Ti$_3$($\eta^5$-$C_5Me_5$)$_3$($\mu_3$-N)}] (**3**) from the indium(I) analogue [IIn{($\mu_3$-NH)$_3$Ti$_3$($\eta^5$-$C_5Me_5$)$_3$($\mu_3$-N)}] (**2**) via oxidation with iodine. In a NMR experiment, complex **3** was quanti-

[a] Departamento de Química Inorgánica, Universidad de Alcalá, 28871 Alcalá de Henares-Madrid, Spain
Fax: +34-91-8854683
E-mail: miguel.mena@uah.es
[b] Department de Química Física i Inorgánica, Universitat Rovira i Virgili,
Marcel-lí Domingo s/n, 43007 Tarragona, Spain
Fax: +34-77-559563
E-mail: josepmaria.poblet@urv.net
Supporting information for this article is available on the WWW under http://www.eurjic.org or from the author.

 © 2006 Wiley-VCH Verlag GmbH & Co. KGaA, Weinheim 

tatively formed within minutes by oxidation of **2** using a solution of $I_2$ in [$D_6$]benzene (Scheme 1). However, an excess of iodine in the reaction produced the consumption of **3**.

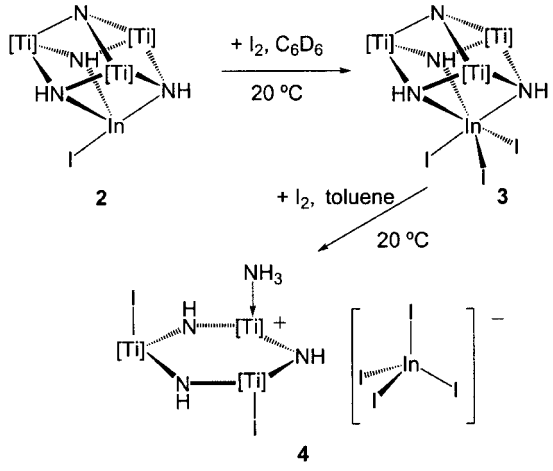


Scheme 1. Reaction of **2** with iodine. [Ti] = Ti($\eta^5$-$C_5Me_5$).

In a preparative scale reaction, a toluene solution of **3** was layered with a solution containing an excess of iodine (3 equiv.) in toluene to afford orange crystals of the ionic complex [$Ti_3(\eta^5$-$C_5Me_5)_3I_2(\mu$-$NH)_3(NH_3)$][$InI_4$] (**4**) in 49% yield. The X-ray analysis of **4** confirms the structure proposed in Scheme 1, containing a tetraiodoindiate(III) anion and a trinuclear titanium cation (see Figure 1). The $InI_4^-$ moiety found in **4** shows an average bond length for In–I of 2.703(2) Å and bond angles I–In–I of 109.5(6)°, typical for this tetrahedral fragment[13] (vide infra discussion about the cation structure). Complex **4** is not soluble in benzene or toluene and decomposes immediately in [$D_8$]tetrahydrofuran, [$D_5$]pyridine, [$D_1$]chloroform, or [$D_2$]dichloromethane, precluding its characterization by NMR spectroscopy. The IR (KBr) spectrum shows several bands in the range 3304–2942 $cm^{-1}$ and one at 1587 $cm^{-1}$ that are similar to those found for the Ti–$NH_3$-containing complex [{$Ti_2(\eta^5$-$C_5Me_5)_2Cl_3(NH_3)$}($\mu$-N)].[6] The latter absorption is assigned to the $NH_3$ bending mode.[14]

Since the metalloligand **1** coordinated to indium was affected in the reaction with $I_2$, we have also investigated the reaction of "free" **1** with iodine in toluene (Scheme 2). Treatment of **1** with excess of iodine leads to precipitation of a dark brown solid in 64% yield. Spectroscopic and analytical data are consistent with the iodine(I) derivative [I{($\mu_3$-$NH)_3Ti_3(\eta^5$-$C_5Me_5)_3(\mu_3$-N)}][$I_3$] (**5**). This complex is slightly soluble in [$D_6$]benzene and soluble in [$D_2$]dichloromethane. The $^1H$ and $^{13}C\{^1H\}$ NMR spectra show resonances for equivalent $\eta^5$-$C_5Me_5$ ligands. The *ipso* carbon resonances of the $C_5Me_5$ ligands are shifted to a lower field with respect to those of **1**, in a similar tendency to that found for our previously reported adducts [$X_nM$·**1**].[12] Resonances due to the $\mu$-NH ligands were not detected in the $^1H$ NMR spectrum, but the presence of those groups was confirmed in the IR (KBr) spectrum with two $\nu_{NH}$ absorptions at 3340 and 3218 $cm^{-1}$.

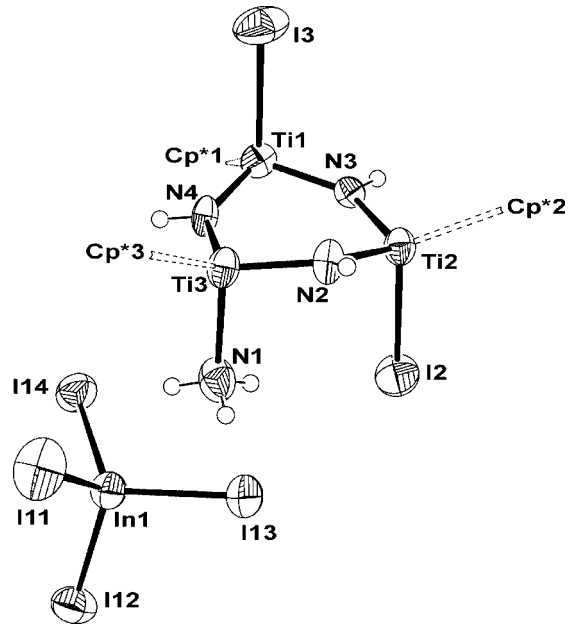


Figure 1. Simplified view of the complex [$Ti_3(\eta^5$-$C_5Me_5)_3I_2(\mu$-$NH)_3$-($NH_3$)][$InI_4$] (**4**) with thermal ellipsoids at the 50% probability level. The pentamethylcyclopentadienyl ligands are not shown for clarity.

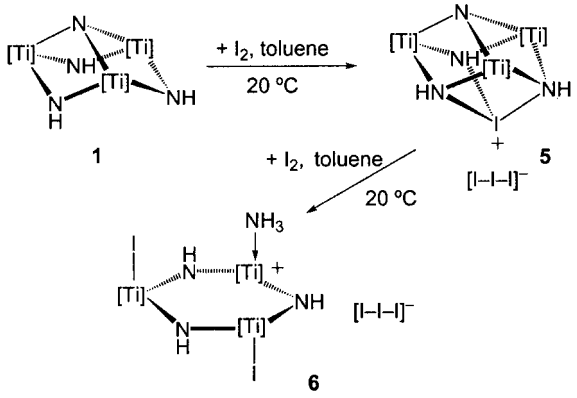


Scheme 2. Reaction of **1** with iodine. [Ti] = Ti($\eta^5$-$C_5Me_5$).

Analogous disproportionation reactions of $I_2$ in the presence of tetraazamacrocyclic or cryptand ligands to give coordination compounds of iodine(I) have been previously reported.[15] Attempts to grow suitable crystals of **5** for a X-ray crystal structure determination failed, but saturated toluene solutions of **5** at room temperature afforded orange crystals of [$Ti_3(\eta^5$-$C_5Me_5)_3I_2(\mu$-$NH)_3(NH_3)$][$I_3$]·$C_7H_8$ (**6**·$C_7H_8$) in poor yields.[16] Complex **6** is not soluble in unreactive solvents and its IR (KBr) spectrum is essentially identical to that of **4**.

The X-ray crystal structure determination of **6** shows a triiodide anion and the same trinuclear titanium cation [$Ti_3(\eta^5$-$C_5Me_5)_3I_2(\mu$-$NH)_3(NH_3)$]$^+$ found for **4** (see Figure 2). While **4** crystallizes as a solvent-free compound, crystals of **6** bear one toluene solvent molecule per complex. The $I_3^-$ ion in **6** is asymmetric [I–I distances are

 © 2006 Wiley-VCH Verlag GmbH & Co. KGaA, Weinheim 

Table 1. Selected lengths [Å] and angles [°] for the cation of complexes **4** and **6**.

| $[Ti_3(\eta^5\text{-}C_5Me_5)_3I_2(\mu\text{-}NH)_3(NH_3)]^+$ | | | | | | | |
|---|---|---|---|---|---|---|---|
| | **4** | **6** | DFT | | **4** | **6** | DFT |
| N(1)–Ti(3) | 2.167(11) | 2.149(4) | 2.191 | Ti(3)–N(2)–Ti(2) | 127.7(5) | 125.8(2) | 127.7 |
| N(2)–Ti(3) | 1.854(9) | 1.891(3) | 1.915 | Ti(2)–N(3)–Ti(1) | 137.4(5) | 138.3(2) | 133.6 |
| N(2)–Ti(2) | 1.904(9) | 1.918(3) | 1.958 | Ti(3)–N(4)–Ti(1) | 135.6(5) | 131.4(2) | 129.8 |
| N(3)–Ti(2) | 1.808(9) | 1.823(3) | 1.919 | N(3)–Ti(1)–N(4) | 101.6(4) | 102.6(1) | 105.4 |
| N(3)–Ti(1) | 1.810(9) | 1.825(3) | 1.917 | N(3)–Ti(1)–I(3) | 102.1(3) | 101.4(1) | 102.6 |
| N(4)–Ti(3) | 1.790(9) | 1.850(3) | 1.893 | N(4)–Ti(1)–I(3) | 104.0(3) | 103.6(1) | 101.7 |
| N(4)–Ti(1) | 1.845(10) | 1.880(3) | 1.962 | N(3)–Ti(2)–I(2) | 100.6(3) | 99.7(1) | 101.1 |
| Ti(1)–I(3) | 2.664(3) | 2.673(1) | 2.723 | N(2)–Ti(2)–I(2) | 102.1(3) | 102.1(1) | 101.7 |
| Ti(2)–I(2) | 2.678(3) | 2.695(1) | 2.753 | N(3)–Ti(2)–N(2) | 103.4(4) | 103.9(1) | 104.3 |
| Ti(1)···Ti(2) | 3.370(3) | 3.408(1) | 3.526 | N(4)–Ti(3)–N(2) | 105.4(4) | 108.1(1) | 108.4 |
| Ti(1)···Ti(3) | 3.366(3) | 3.399(1) | 3.490 | N(4)–Ti(3)–N(1) | 99.2(5) | 100.0(1) | 99.5 |
| Ti(2)···Ti(3) | 3.374(3) | 3.391(1) | 3.476 | N(2)–Ti(3)–N(1) | 98.8(4) | 98.5(1) | 97.9 |

2.867(1) and 3.000(1) Å, I–I–I 179.0(1)°] as determined in many other crystalline structures with such an anion.[17] Selected distances and angles of the cation structures are shown in Table 1.

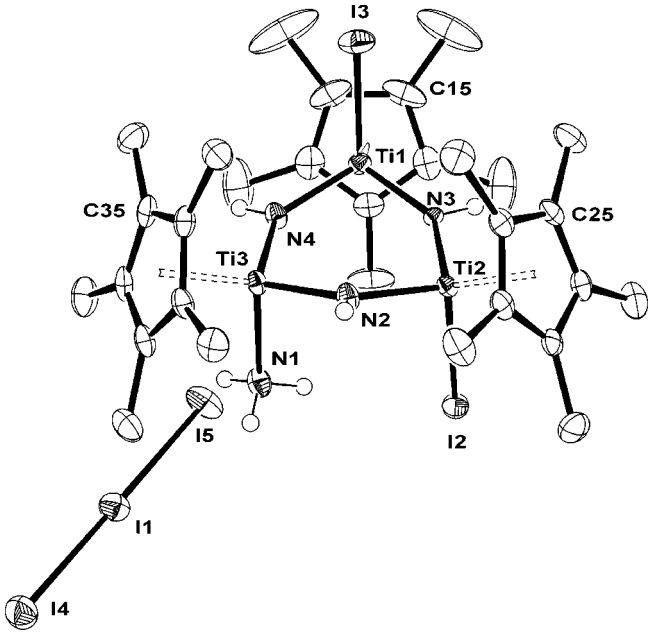


Figure 2. Perspective view of the $[Ti_3(\eta^5\text{-}C_5Me_5)_3I_2(\mu\text{-}NH)_3(NH_3)][I_3]$ (**6**) with thermal ellipsoids at the 50% probability level. Solvent molecule is not shown for clarity.

The cation of both **4** and **6** is a cyclic trinuclear complex, with three $Ti(\eta^5\text{-}C_5Me_5)L$ moieties held together by bridging (μ-NH) imido ligands. Each titanium atom has a classical three-legged piano-stool arrangement, where the legs are occupied by one iodine and two imido groups for Ti(1) and Ti(2), and one ammonia and two imido ligands for Ti(3). With respect to the plane formed by the three titanium atoms, I(3) is located above while I(2) and the ammonia molecule are below the plane. This structural disposition (two below, one above) of the ligands resembles that of the oxotitanium complexes $[\{Ti(\eta^5\text{-}C_5Me_5)L\}_3(\mu\text{-}O)_3]$ (L = Me,[18] Cl,[19] Br,[20] $CH_2CH{=}CH_2$[21]). The titanium–iodine distances of 2.677(av.) Å are in the normal range[22] and the titanium–nitrogen (ammonia) bond lengths [2.167(11) for **4** and 2.149(4) Å for **6**] are very similar to the unique crystallographic documented titanium organometallic complex with ammonia $[\{Ti_2(\eta^5\text{-}C_5Me_5)_2Cl_3(NH_3)\}(\mu\text{-}N)]$ (2.158 Å).[6] This distance is longer than that found for the Ti–$OH_2$ bonds in aquotitanium(IV) derivatives.[23] Surprisingly, only seven other examples of metal–ammonia interactions are found for groups 3, 4, and 5 when a search is performed in the CSD.[24] The bridging imido ligands are characterized by titanium–nitrogen bond lengths in the range 1.790(3)–1.918(3) Å [av. 1.85 Å], which are slightly shorter than those found in **1** [av. 1.92 Å], and angles Ti–N–Ti clearly wider 125.8(2)–138.3(2)° than those of complex **1** (93.2° av.) where the $\mu_3$-nitrogen apical atom constrains the geometry. On the other hand, distances from N(1) to I(2) of 3.661(1) in **4** and 3.623(3) Å in **6** could be indicative of the existence of an intramolecular hydrogen bonding interaction between them (sum of the van der Waals' radii 3.650 Å).[25]

DFT calculations were conducted to characterize the trinuclear fragment $[Ti_3(\eta^5\text{-}C_5Me_5)_3I_2(\mu\text{-}NH)_3(NH_3)]^+$. The optimized geometry coincides quite well with the X-ray ones, as can be seen in Table 1. Calculated distances are slightly longer than the experimental and some of the angles differ by a small number of degrees. Especially significant is the distance Ti(3)–N(1) 2.191 Å, which is only ≈0.02 and ≈0.04 Å longer than those found in complexes **3** and **6**, respectively. The cation $[Ti_3(\eta^5\text{-}C_5Me_5)_3I_2(\mu\text{-}NH)_3(NH_3)]^+$ displays a relatively large HOMO–LUMO gap of 1.88 eV, a fact that is a signal of its relative stability.

Although all the three metal atoms in the titanium complex are formally in their highest oxidation state, the Mulliken population analysis suggests that the Ti atom bonded to $NH_3$ carries a larger positive charge (+1.42 e) than the other two titaniums [computed charge for Ti(1) + Ti(2) = +0.92 e]. The LUMO is a nonbonding orbital with a larger participation of Ti(3) (Figure 3). As a matter-of-fact, the monoreduction of $[Ti_3(\eta^5\text{-}C_5Me_5)_3I_2(\mu\text{-}NH)_3(NH_3)]^+$ hardly induces changes in the geometry of the cluster, the additional metal electron being mainly localized on the Ti bonded to ammonia [spin density on Ti(3) of ≈0.5 e,

 © 2006 Wiley-VCH Verlag GmbH & Co. KGaA, Weinheim 

whereas the other two Ti share ≈0.6 e]. All these results are in concordance with the drawings proposed for the trinuclear titanium cation in Schemes 1 and 2.

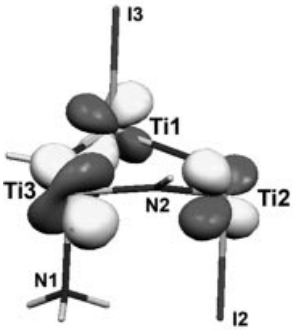


Figure 3. 3D representation of the LUMO for $[Ti_3(\eta^5\text{-}C_5Me_5)_3I_2(\mu\text{-}NH)_3(NH_3)]^+$.

In summary, the heterometallocubane $[IIn\{(\mu_3\text{-}NH)_3Ti_3(\eta^5\text{-}C_5Me_5)_3(\mu_3\text{-}N)\}]$ (**2**) allows the oxidation with iodine of the supported InI, under mild conditions, to cleanly give the expected indium(III) derivative $[I_3In\{(\mu_3\text{-}NH)_3Ti_3(\eta^5\text{-}C_5Me_5)_3(\mu_3\text{-}N)\}]$ (**3**). However, an excess of iodine in the solution produces the rupture of the preorganized structure of $[\{Ti(\eta^5\text{-}C_5Me_5)(\mu\text{-}NH)\}_3(\mu_3\text{-}N)]$ (**1**) to give the singular cation $[Ti_3(\eta^5\text{-}C_5Me_5)_3I_2(\mu\text{-}NH)_3(NH_3)]^+$. This complex is also accessible through the reaction of **1** with an excess of iodine. DFT studies support the cationic nature of the unprecedented ammonia adduct.

## Experimental Section

**General Considerations and Starting Materials:** All manipulations were carried out under argon using Schlenk line or glovebox techniques. Hexane was distilled from Na/K alloy just prior to use. Toluene was freshly distilled from sodium. NMR solvents were dried with Na/K alloy ($C_6D_6$) or calcium hydride ($CD_2Cl_2$) and vacuum-distilled. Oven-dried glassware was repeatedly evacuated with a pumping system (ca. $1\cdot10^{-3}$ Torr) and subsequently filled with inert gas. Iodine was purchased from Aldrich and sublimed under vacuum prior to use. $[\{Ti(\eta^5\text{-}C_5Me_5)(\mu\text{-}NH)\}_3(\mu_3\text{-}N)]$ (**1**),[6] $[IIn\{(\mu_3\text{-}NH)_3Ti_3(\eta^5\text{-}C_5Me_5)_3(\mu_3\text{-}N)\}]$ (**2**),[12] and $[I_3In\{(\mu_3\text{-}NH)_3Ti_3(\eta^5\text{-}C_5Me_5)_3(\mu_3\text{-}N)\}]$ (**3**)[12] were prepared according to published procedures.

Samples for infrared spectroscopy were prepared as KBr pellets. $^1H$ and $^{13}C\{^1H\}$ NMR spectra were recorded with a Varian Unity-300 spectrometer. Chemical shifts ($\delta$) are given relative to residual protons or to carbon of the solvent. Microanalyses (C,H,N) were performed with a Heraeus CHN-O-Rapid microanalyzer.

**Oxidation Reaction of 2 with Iodine:** A 5-mm valved NMR tube was charged with **2** (10 mg, 0.012 mmol), $I_2$ (3.0 mg, 0.012 mmol) and [$D_6$]benzene or [$D_8$]toluene (1.00 mL). The course of the reaction was monitored by $^1H$ NMR spectroscopy. After 5 min at room temperature the spectrum shows the complete consumption of **2** along with resonances due to complex **3**.[12]

**$[IIn\{(\mu_3\text{-}NH)_3Ti_3(\eta^5\text{-}C_5Me_5)_3(\mu_3\text{-}N)\}]$ (2):** $^1H$ NMR (300 MHz, $C_6D_6$, 20 °C): $\delta$ = 12.87 (br. s, 3 H, NH), 2.01 (s, 45 H, $C_5Me_5$) ppm.

**$[I_3In\{(\mu_3\text{-}NH)_3Ti_3(\eta^5\text{-}C_5Me_5)_3(\mu_3\text{-}N)\}]$ (3):** $^1H$ NMR (300 MHz, $C_6D_6$, 20 °C): $\delta$ = 11.58 (br. s, 3 H, NH), 1.95 (s, 45 H, $C_5Me_5$) ppm.

**Synthesis of $[Ti_3(\eta^5\text{-}C_5Me_5)_3I_2(\mu\text{-}NH)_3(NH_3)][InI_4]$ (4):** A solution of $I_2$ (0.062 g, 0.24 mmol) in toluene (10 mL) was carefully added to $[I_3In\{(\mu_3\text{-}NH)_3Ti_3(\eta^5\text{-}C_5Me_5)_3(\mu_3\text{-}N)\}]$ (**3**) (0.090 g, 0.08 mmol) in toluene (30 mL). The system was allowed to react without any stirring for 5 days to yield **4** as orange crystals suitable for X-ray analysis. The resultant red solution was concentrated in volume under vacuum until ca. 15 mL and allowed to stand at room temperature to give a second crop of crystals. The combined yield of **4** was 0.059 g (49%). IR (KBr) $\tilde{\nu}$ = 3304 (m), 3261 (m), 3192 (w),

Table 2. Experimental data for the X-ray diffraction studies on compounds **4** and **6**.

| Formula | $C_{30}H_{51}I_6InN_4Ti_3$ (**4**) | $C_{37}H_{59}I_5N_4Ti_3$ (**6**·$C_7H_8$) |
|---|---|---|
| $M_r$ | 1487.67 | 1338.08 |
| $T$ [K] | 293(2) | 150(2) |
| $\lambda$ [Å] | 0.71073 | 0.71073 |
| Crystal system | triclinic | triclinic |
| Space group | $P\bar{1}$ | $P\bar{1}$ |
| $a$ [Å]; $\alpha$ [°] | 12.063(2); 91.85(2) | 11.823(1); 79.10(1) |
| $b$ [Å]; $\beta$ [°] | 13.031(5); 99.36(4) | 13.086(1); 87.60(1) |
| $c$ [Å]; $\gamma$ [°] | 14.769(4); 90.39(2) | 15.886(1); 78.14(1) |
| $V$ [Å$^3$] | 2289.3(11) | 2362.0(3) |
| $Z$ | 2 | 2 |
| $\rho_{calcd.}$ [g cm$^{-3}$] | 2.158 | 1.881 |
| $\mu_{Mo\text{-}K\alpha}$ [mm$^{-1}$] | 5.071 | 3.791 |
| $F(000)$ | 1384 | 1280 |
| Crystal size [mm] | 0.25 × 0.20 × 0.18 | 0.34 × 0.33 × 0.22 |
| $\theta$ range | 1.40 to 24.97° | 3.06 to 27.50° |
| Index ranges | –14 to 14, –15 to 15, –17 to 0 | –15 to 15, –17 to 17, –20 to 20 |
| Reflections collected | 8382 | 20854 |
| Unique data | 8038 [$R_{int}$ = 0.052] | 10824 [$R_{int}$ = 0.033] |
| Observed data [$I > 2\sigma(I)$] | 5147 | 8331 |
| Goodness-of-fit on $F^2$ | 1.041 | 1.033 |
| Final $R$ indices [$I > 2\sigma(I)$][a] | $R_1$ = 0.062, $wR_2$ = 0.164 | $R_1$ = 0.031, $wR_2$ = 0.069 |
| $R$ indices (all data) | $R_1$ = 0.122, $wR_2$ = 0.189 | $R_1$ = 0.051, $wR_2$ = 0.074 |
| Largest diff. peak/hole [e·Å$^{-3}$] | 1.465/–0.976 | 1.529/–1.010 |

[a] $R_1 = \Sigma||F_o| - |F_c||/[\Sigma|F_o|]$ $wR_2 = \{[\Sigma w(F_0^2 - F_c^2)^2] / [\Sigma w(F_0^2)^2]\}^{1/2}$.

 © 2006 Wiley-VCH Verlag GmbH & Co. KGaA, Weinheim 

3124 (w), 2942 (w), 2910 (m), 2850 (w), 1587 (m), 1485 (m), 1450 (m), 1427 (s), 1377 (s), 1268 (s), 1067 (m), 1019 (m), 790 (vs), 753 (vs), 711 (vs), 622 (m), 548 (w), 536 (w), 494 (w), 435 (m) $cm^{-1}$. $C_{30}H_{51}I_6InN_4Ti_3$ (1487.67): calcd. C 24.22, H 3.45, N 3.77; found C 24.85, H 3.39, N 2.69.

**Synthesis of [I{(μ3-NH)3Ti3(η5-C5Me5)3(μ3-N)}][I3] (5):** A solution of $I_2$ (0.75 g, 2.96 mmol) in toluene (30 mL) was carefully added to **1** (0.40 g, 0.66 mmol) in toluene (30 mL). The system was allowed to react without any stirring for 3 days. After decantation, the resultant dark brown crystals were vacuum-dried to afford **5** (0.47 g, 64%). IR (KBr) $\tilde{\nu}$ = 3340 (m), 3218 (m), 2911 (s), 1486 (m), 1426 (s), 1376 (s), 1021 (w), 762 (s), 717 (s), 660 (vs), 638 (vs), 594 (s), 467 (m) $cm^{-1}$. $^1H$ NMR (300 MHz, $C_6D_6$, 20 °C): $\delta$ = 1.88 (s, 45 H, $C_5Me_5$) ppm. $^1H$ NMR (300 MHz, $CD_2Cl_2$, 20 °C): $\delta$ = 2.10 (s, 45 H, $C_5Me_5$) ppm, NH resonance was not detected. $^{13}C\{^1H\}$ NMR (75 MHz, $CD_2Cl_2$, 20 °C): $\delta$ = 123.8 ($C_5Me_5$), 12.3 ($C_5Me_5$) ppm. $C_{30}H_{48}I_4N_4Ti_3$ (1115.94): calcd. C 32.29, H 4.33, N 5.02; found C 31.18, H 4.23, N 4.52.

**Synthesis of [Ti3(η5-C5Me5)3I2(μ-NH)3(NH3)][I3] (6):** A saturated solution of **5** in toluene at room temperature for 5 days gave orange crystals (0.050 g) of **6**·$C_7H_8$ suitable for X-ray crystallographic studies. IR (KBr) $\tilde{\nu}$ = 3301 (m), 3234 (m), 3116 (m), 2909 (s), 2852 (w), 1587 (m), 1493 (m), 1428 (m), 1377 (s), 1271 (s), 1021 (m), 798 (vs), 753 (s), 729 (s), 710 (vs), 622 (m), 494 (w), 465 (w), 432 (m) $cm^{-1}$. $C_{37}H_{59}I_5N_4Ti_3$ (1338.08): calcd. C 33.21, H 4.44, N 4.19; found C 32.67, H 4.37, N 3.67.

**X-ray Crystal Structure Determination of Complexes 4 and 6:** Orange crystals of compounds **4** and **6** were obtained from toluene solutions at room temperature. Crystals of **4** were mounted in a glass capillary in a random orientation and transferred to an Enraf–Nonius CAD4 diffractometer for characterization and data collection at room temperature. Complex **6** crystallized with one molecule of toluene, so the crystals were removed from the Schlenk and covered with a layer of viscous perfluoropolyether (Fomblin®Y). A suitable crystal was selected with the aid of a microscope, attached to a glass fiber, and immediately placed in the low temperature nitrogen stream of the diffractometer. The intensity data sets were collected at 150 K with a Bruker–Nonius KappaCCD diffractometer equipped with an Oxford Cryostream 700 unit. Crystallographic data for all the complexes are presented in Table 2. The structures were solved, using the WINGX package,[26] by direct methods (SHELXS-97) and refined by least-squares against $F^2$ (SHELXL-97).[27] All non-hydrogen atoms of **4** and **6** were anisotropically refined. All the hydrogen atoms were positioned geometrically and refined by using a riding model except those attached to N(1) and N(2) in complex **6** which were directly located in the difference Fourier map and refined isotropically. The largest residual density peaks are located at 0.88 Å of I(14) in compound **4** and at 0.83 Å of I(4) in compound **6**. The refinement of the crystal structure of complex **6** was also performed substituting the ammonia molecule by water and the result was a decrease of the quality of the study, increased *R* values, poorer temperature factors for the oxygen atom and always the appearance of the third hydrogen atom in the difference Fourier map, excluding the existence of a water molecule.

CCDC-283509 and -283510 contain the supplementary crystallographic data for this paper. These data can be obtained free of charge from The Cambridge Crystallographic Data Centre via www.ccdc.cam.ac.uk/data_request/cif.

**Computational Details:** All DFT calculations were carried out with the ADF program[28] by using triple-ζ and polarization Slater basis sets to describe the valence electrons of C and N. For titanium, a frozen core composed of the 1s, 2s, and 2p orbitals was described by double-ζ Slater functions, the 3d and 4s orbitals by triple-ζ functions, and the 4p orbital by a single orbital. Hydrogen atoms were described by triple-ζ and polarization functions. The geometries and binding energies were calculated with gradient corrections. We used the local spin density approximation, characterized by the electron gas exchange (Xα with $a$ = 2/3) together with Vosko–Wilk–Nusair parametrization[29] for correlation. Becke's nonlocal corrections[30] to the exchange energy and Perdew's nonlocal corrections[31] to the correlation energy were added. Quasirelativistic corrections were employed by using the ZORA formalism with corrected core potentials. The quasirelativistic frozen core shells were generated with the auxiliary program DIRAC.[28]

**Supporting Information** (see footnote on the first page of this article): The $^1H$ and $^{13}C\{^1H\}$ NMR spectra of complex **5** are provided as Supporting Information.

## Acknowledgments

We are grateful to the Spanish MCYT (BQU2001-1499 and BQU2002-04110-C02-01), Comunidad de Madrid (GR/MAT/0621/2004) and the CIRIT of the Generalitat de Catalunya (SGR01-00315) for support of this research.

[1] W. A. Nugent, J. M. Mayer, *Metal-Ligand Multiple Bonds*, Wiley, New York, **1988**.
[2] a) K. Dehnicke, J. Strähle, *Angew. Chem. Int. Ed. Engl.* **1981**, *20*, 413–426; b) K. Dehnicke, J. Strähle, *Angew. Chem. Int. Ed. Engl.* **1992**, *31*, 955–978; c) K. Dehnicke, F. Weller, J. Strähle, *Chem. Soc. Rev.* **2001**, *30*, 125–135.
[3] R. A. Eikey, M. M. Abu-Omar, *Coord. Chem. Rev.* **2003**, *243*, 83–124.
[4] A. Abarca, M. Galakhov, J. Gracia, A. Martín, M. Mena, J.-M. Poblet, J. P. Sarasa, C. Yélamos, *Chem. Eur. J.* **2003**, *9*, 2337–2346, and references therein.
[5] H. W. Roesky, Y. Bai, M. Noltemeyer, *Angew. Chem. Int. Ed. Engl.* **1989**, *28*, 754–755.
[6] A. Abarca, P. Gómez-Sal, A. Martín, M. Mena, J.-M. Poblet, C. Yélamos, *Inorg. Chem.* **2000**, *39*, 642–651.
[7] For reviews, see: a) P. Chaudhuri, K. Wieghardt, *Prog. Inorg. Chem.* **1987**, *35*, 329–436; b) J. A. R. Schmidt, G. R. Giesbrecht, C. Cui, J. Arnold, *Chem. Commun.* **2003**, 1025–1033.
[8] For recent publications, see: a) R. D. Köhn, M. Haufe, G. Kociok-Köhn, S. Grimm, P. Wasserscheid, W. Keim, *Angew. Chem. Int. Ed.* **2000**, *39*, 4337–4339; b) R. D. Köhn, G. Seifert, Z. Pan, M. F. Mahon, G. Kociok-Köhn, *Angew. Chem. Int. Ed.* **2003**, *42*, 793–796; c) R. D. Köhn, Z. Pan, M. Haufe, G. Kociok-Köhn, *Dalton Trans.* **2005**, 2793–2797; d) R. D. Köhn, P. Kampe, G. Kociok-Köhn, *Eur. J. Inorg. Chem.* **2005**, 3217–3223 and references cited therein.
[9] a) A. Abarca, M. Galakhov, P. Gómez-Sal, A. Martín, M. Mena, J.-M. Poblet, C. Santamaría, J. P. Sarasa, *Angew. Chem. Int. Ed.* **2000**, *39*, 534–537; b) K. Freitag, J. Gracia, A. Martín, M. Mena, J.-M. Poblet, J. P. Sarasa, C. Yélamos, *Chem. Eur. J.* **2001**, *7*, 3644–3651.
[10] A. Abarca, A. Martín, M. Mena, C. Yélamos, *Angew. Chem. Int. Ed.* **2000**, *39*, 3460–3463.
[11] a) M. García-Castro, A. Martín, M. Mena, A. Pérez-Redondo, C. Yélamos, *Chem. Eur. J.* **2001**, *7*, 647–651; b) A. Martín, M. Mena, A. Pérez-Redondo, C. Yélamos, *Organometallics* **2002**, *21*, 3308–3310; c) M. García-Castro, A. Martín, M. Mena, C. Yélamos, *Organometallics* **2004**, *23*, 1496–1500; d) A. Martín, M. Mena, A. Pérez-Redondo, C. Yélamos, *Inorg. Chem.* **2004**, *43*, 2491–2498; e) A. Martín, M. Mena, A. Pérez-Redondo, C. Yélamos, *Dalton Trans.* **2005**, 2116–2119.

 © 2006 Wiley-VCH Verlag GmbH & Co. KGaA, Weinheim 

[12] M. García-Castro, J. Gracia, A. Martín, M. Mena, J.-M. Poblet, J. P. Sarasa, C. Yélamos, *Chem. Eur. J.* **2005**, *11*, 1030–1041.
[13] a) A. Frazer, B. Piggott, M. Harman, M. Mazid, M. B. Hursthouse, *Polyhedron* **1992**, *11*, 3013–3017; b) L. A. Kloo, M. J. Taylor, *J. Chem. Soc., Dalton Trans.* **1997**, 2693–2696; c) M. Sigl, A. Schier, H. Schmidbaur, *Eur. J. Inorg. Chem.* **1998**, 203–210.
[14] K. Nakamoto, *Infrared and Raman Spectra of Inorganic and Coordination Compounds*, 5th ed., Wiley, New York, **1997**.
[15] a) W. S. Hua, A. I. Ajiboye, G. Haining, L. McGhee, R. D. Peacock, G. Peattie, R. M. Siddique, J. M. Winfield, *J. Chem. Soc., Dalton Trans.* **1995**, 3837–3841; b) R. Le Goaller, H. Handel, P. Labbe, J.-L. Pierre, *J. Am. Chem. Soc.* **1984**, *106*, 1694–1698.
[16] Suitable crystals of **6**·$C_7H_8$ for X-ray crystallographic studies were obtained in three independent preparations although the preparative scale of **6** could not be optimized.
[17] P. H. Svensson, L. Kloo, *Chem. Rev.* **2003**, *103*, 1649–1684.
[18] S. G. Blanco, M. P. Gómez-Sal, S. M. Carrera, M. Mena, P. Royo, R. Serrano, *J. Chem. Soc., Chem. Commun.* **1986**, 1572–1573.
[19] T. Carofiglio, C. Floriani, A. Sgamellotti, M. Rosi, A. Chiesi-Villa, C. Rizzoli, *J. Chem. Soc., Dalton Trans.* **1992**, 1081–1088.
[20] S. I. Troyanov, V. Varga, K. Mach, *J. Organomet. Chem.* **1991**, *402*, 201–207.
[21] R. Andrés, M. Galakhov, M. P. Gómez-Sal, A. Martín, M. Mena, C. Santamaría, *J. Organomet. Chem.* **1996**, *526*, 135–143.
[22] a) J. Okuda, S. Fokken, T. Kleinhenn, T. P. Spaniol, *Eur. J. Inorg. Chem.* **2000**, 1321–1326; b) S. A. Harris, J. T. Ciszewski, A. L. Odom, *Inorg. Chem.* **2001**, *40*, 1987–1988.
[23] 2.08 Å is the averaged value for terminal Ti–$OH_2$ bonds: a) J. P. Fackler Jr, F. J. Kristine, A. M. Mazany, T. J. Moyer, R. E. Shepherd, *Inorg. Chem.* **1985**, *24*, 1857–1860; b) M. Bochmann, A. J. Jaggar, L. M. Wilson, M. B. Hursthouse, M. Motevalli, *Polyhedron* **1989**, *8*, 1838–1843; c) T. S. Cameron, A. Decken, E. G. Ilyin, G. B. Nikiforov, J. Passmore, *Eur. J. Inorg. Chem.* **2004**, 3865–3872.
[24] Cambridge Structural Database: F. H. Allen, *Acta Crystallogr., Sect. B* **2002**, *58*, 380–388. Updated to Aug05.
[25] N. H. Greenwood, A. Earnshaw, *Chemistry of the Elements*, 2nd ed., Butterworth Heinemann, Oxford, **1998**, p. 60.
[26] L. J. Farrugia, *J. Appl. Crystallogr.* **1999**, *32*, 837–838.
[27] G. M. Sheldrick, *SHELX-97*, Program for Crystal Structure Analysis (Release 97–2). University of Göttingen, Germany, **1998**.
[28] a) ADF 2004.01. Department of Theoretical Chemistry, Vrije Universiteit, Amsterdam; b) E. J. Baerens, D. E. Ellis, P. Ros, *Chem. Phys.* **1973**, *2*, 41–51; c) L. Versluis, T. Ziegler, *J. Chem. Phys.* **1988**, *88*, 322–328; d) G. Te Velde, E. J. Baerens, *J. Comput. Phys.* **1992**, *99*, 84–98; e) C. Fonseca Guerra, J. G. Snijders, G. Te Velde, E. J. Baerens, *Theor. Chem. Acc.* **1998**, *99*, 391–403.
[29] S. H. Vosko, L. Wilk, M. Nusair, *Can. J. Phys.* **1980**, *58*, 1200–1211.
[30] a) A. D. Becke, *J. Chem. Phys.* **1986**, *84*, 4524–4529; b) A. D. Becke, *Phys. Rev. A* **1988**, *38*, 3098–3100.
[31] a) J. P. Perdew, *Phys. Rev. B* **1986**, *33*, 8822–8824; b) J. P. Perdew, *Phys. Rev. B* **1986**, *34*, 7406–7406.

Received: September 21, 2005
Published Online: January 27, 2006

 © 2006 Wiley-VCH Verlag GmbH & Co. KGaA, Weinheim 

DOI: 10.1002/ejic.200500874

# Redox Chemistry in the Reaction of Oxovanadium(V) with Thiolate-Containing Ligands: the Isolation and Characterization of Non-Oxo Vanadium(IV) Complexes Containing Disulfide and Thioether Groups

**Hua-Fen Hsu,*[a] Chia-Ling Su,[a] Neeruganti O. Gopal,[b] Chi-Chin Wu,[a] Wei-Cheng Chu,[a] Yi-Fang Tsai,[a] Ya-Ho Chang,[a] Yi-Hung Liu,[c] Ting-Shen Kuo,[d] and Shyue-Chu Ke*[b]**

**Keywords:** Vanadium / S ligands / Bioinorganic chemistry / EPR spectroscopy

The reactions of $V^{V}O(O\text{-}iPr)_3$ with $[PS3']H_3$ and $[PS3]H_3$ {$[PS3']H_3$ = $P(C_6H_3\text{-}5\text{-}Me\text{-}2\text{-}SH)_3$, $[PS3]H_3$ = $P(C_6H_4\text{-}2\text{-}SH)_3$} led to the formation of $[V^{IV}(L)]$ [L = P2S4′ (**1a**), P2S4 (**1b**)], where L was formed by the oxidative coupling of two PS3′ or PS3 ligands by a disulfide bond. When the reaction of $V^{V}O(O\text{-}iPr)_3$ with $[PS3']H_3$ was conducted in the presence of methoxide followed by the addition of a cation, $[V^{IV}(PS3')(PS2S^{Me'})]X$ [X = $N(C_2H_5)_4$ (**2a**), $N(C_2H_5)_3(CH_2Ph)$ (**2b**)] was isolated, where $PS2S^{Me'}$ is a bis(benzenethiolato)phenylmethylthioetherphosphane ligand generated from the methylation of one thiolate group in PS3′. The structures of complexes **1a**,**b** and **2a**,**b**, determined by X-ray crystallography, contain six- and seven-coordinate non-oxo vanadium(IV) centers, respectively, with an octahedral geometry for **1a**,**b** and a pentagonal-bipyramidal geometry for **2a**,**b**. The electronic, magnetic, and electrochemical properties of these complexes were determined by UV/Vis and EPR spectroscopy, SQUID measurements, and cyclic voltammetry.
(© Wiley-VCH Verlag GmbH & Co. KGaA, 69451 Weinheim, Germany, 2006)

## Introduction

Vanadium has been shown to have an important role in biological systems and therefore its complexes are worth investigation.[1] In particular, the interactions of high-valent vanadium species with sulfur-containing bioligands, such as cysteine and glutathione, are essential subjects in various biological and medical topics.[1a,2] Vanadate interacts with the Cys residue in the catalytic site of the protein-tyrosine phosphatase (PTP), inhibiting the activity of the enzyme that might be associated with the insulin-mimetic behavior of vanadium compounds.[3] Some ascidians sequester $V^{V}$ species from seawater and reduce it to $V^{III}$ which is accumulated in high concentration in vacuoles of the blood cells.[4] The mechanism for this redox conversion is still unknown. In addition to tunichrome and NADPH, glutathione and cysteine might be candidates to act as reductants in the cell.[5] A natural vanadium(IV) complex, amavadin, was isolated from *Amanita* mushrooms.[6] Even though the structure of this complex is known, its function is still not well understood.[7] It has been suspected that amavadin might be involved in the defensive system of the mushrooms through the specific oxidation of some thiols to disulfide.[8] The toxicity of vanadium in biological systems is not well understood, however, it has been shown that the injection of vanadate in mice decreased the cellular level of glutathione, an essential antioxidant in the cell.[9] Vanadium complexes with S-donor ligands have been shown to have insulin-mimetic antidiabetic activity.[10]

From this information, efforts have been made to understand the fundamental chemistry of high-valent vanadium complexes with thiolate ligands that have similar functional groups to those in cysteine and glutathione.[11] Among those studies, the interaction of $VO^{3+}$ species with thiolate-containing ligands has not been intensively investigated.[11b,11d] Therefore, in this paper we focus on the chemistry of $VO^{3+}$ reacting with the tris(benzenethiolato)phosphane ligands, $[PS3]H_3$ and $[PS3']H_3$. The reactions led to the reduction of vanadium(V) to vanadium(IV) with the formation of the two new types of ligands, L (L = P2S4 and P2S4′) and $PS2S^{Me'}$ (see Scheme 1). The former was created by the oxidative coupling of two PS3 ligands by way of a disulfide linkage, and the latter resulted from the methylation of one thiolate group in the PS3′ ligand. We verified this chemistry by isolating the reaction products, $[V^{IV}(L)]$ [L = P2S4′ (**1a**), P2S4 (**1b**)] and $[V^{IV}(PS3')(PS2S^{Me'})]X$ [X

[a] Department of Chemistry, National Cheng Kung University, Tainan 701, Taiwan
Fax: +886-6-2740552
E-mail: konopka@mail.ncku.edu.tw
[b] Department of Physics, National Dong Hua University, Hualien, Taiwan
[c] Department of Chemistry, National Taiwan University, Taipei 117, Taiwan
[d] Department of Chemistry, National Taiwan Normal University, Taipei 116, Taiwan
Supporting information for this article is available on the WWW under http://www.eurjic.org or from the author.

 © 2006 Wiley-VCH Verlag GmbH & Co. KGaA, Weinheim 

= $N(C_2H_5)_4$ (**2a**), $N(C_2H_5)_3(CH_2Ph)$ (**2b**)] (Scheme 2). Notably, **1a**,**b** and **2a**,**b** belong to a limited set of non-oxo (or "bare") vanadium complexes.[12] The interest in non-oxo vanadium species stems from amavadin and vanadium nitrogenase that contain an eight-coordinate non-oxo vanadium center and a [V(μ-S)$_3$(His)(homocitrate)] site, respectively. Herein, we describe the syntheses, structures, spectroscopy, and magnetic properties of **1a**,**b** and **2a**,**b**, as well as the significance of the chemistry provided in this work.

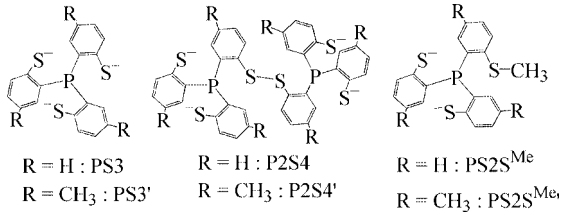


Scheme 1.

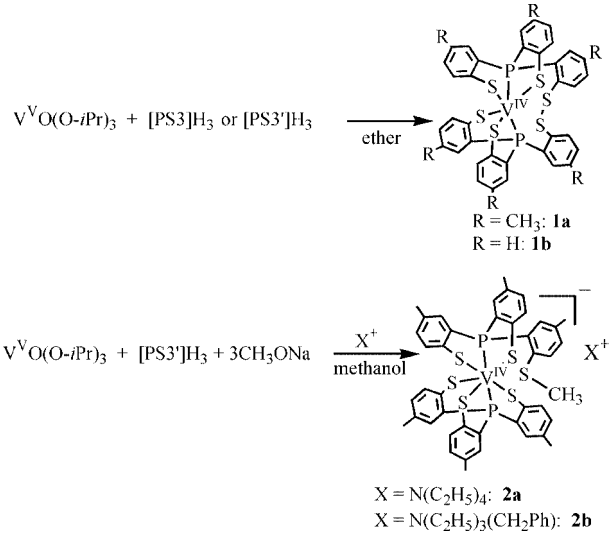


Scheme 2.

## Results and Discussion

### Syntheses and X-ray Structures

The reaction of 1 equiv. [PS3′]$H_3$ in ether with 1 equiv. $V^VO(O\text{-}iPr)_3$ in *i*PrOH generated a purple solid that was recrystallized from dichloromethane/hexane to give the crystalline form of [$V^{IV}$(P2S4′)] (**1a**). The synthetic procedure of [$V^{IV}$(P2S4)] (**1b**) was similar to that of **1a** except [PS3]$H_3$ was used and the compound was recrystallized from benzene/ether. When $V^VO(O\text{-}iPr)_3$ in *i*PrOH was added to equimolar amounts of [PS3′]$H_3$ in methanol with the presence of sodium methoxide, a transient brown solution was produced which gradually changed to a purple color in one hour. After addition of the counterion, X, the purple crystalline solid of [$V^{IV}$(PS3′)(PS2S$^{Me\prime}$)]X [X = $N(C_2H_5)_4$ (**2a**), $N(C_2H_5)_3(CH_2Ph)$ (**2b**)] precipitated from the solution by the next day. When the reactions were performed with $V^VO(O\text{-}iPr)_3$ and the ligands in a molar ratio of 1:2, there were no appreciable gains in the yields of compounds **1a**,**b** and **2a**,**b**. The solid forms of these complexes were stable in the air, however, the solution forms decomposed within minutes of exposure to the air.

The structure of **1a** was obtained by X-ray crystallography, but it was poorly refined as a result of the weak intensity of the data. Compound **1b** afforded X-ray crystallographic data of better quality and its ORTEP diagram is shown in Figure 1. It consists of a $V^{IV}$ ion coordinated to a hexadentate ligand, P2S4, with a nine-membered chelate ring containing a S–S bond. The vanadium(IV) center adopts a distorted octahedral geometry by binding to two phosphane atoms and four thiolate groups of P2S4, with the two P donor atoms in *cis* positions. The generation of P2S4 by the reaction was a consequence of the oxidative coupling of two PS3 ligands by formation of a disulfide linkage. Similar chemistry was also found in the reaction of $Os^{II}$ with the PS3 ligand, however, two disulfide linkages were formed.[13] Redox chemistry of $V^V/V^{IV}$ coupled with $RS^-$/RSSR, as demonstrated by the isolation of **1a**,**b**, is unprecedented, although the chemistry of $V^{IV}/V^{III}$ coupled with $RS^-$/RSSR has been reported.[11e,11g] To the best of our knowledge, hexadentate P2S4 and P2S4′ ligands containing two phosphane and four thiolate donor atoms have not been presented in the literature. Selected bond lengths and angles of **1b** are listed in Table 1. The V–S distances of 2.307–2.335 Å in **1b** are in the range of those for reported $V^{IV}$-thiolate complexes.[11a,11d–11h] The S atoms of the disulfide linkage remain uncoordinated, and the S–S distance of 2.055 Å is similar to those in characterized disulfide-containing compounds.[11d,11f]

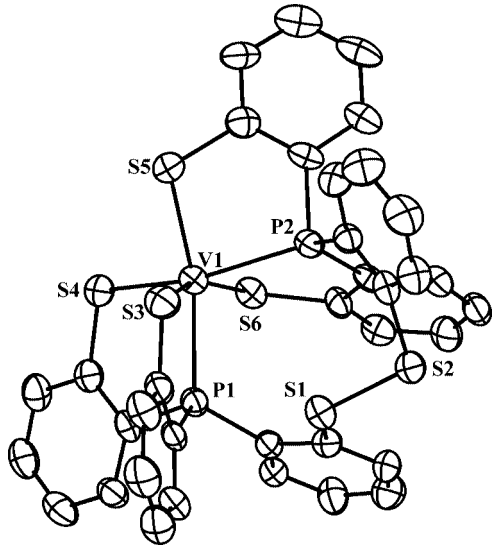


Figure 1. ORTEP diagram of **1b** shown with 35% thermal ellipsoids. All hydrogen atoms are omitted for clarity.

The structures of **2a** and **2b** were determined by X-ray crystallography and their anions are very similar (see Figure S1 and Figure 2, respectively). However, **2b** provides a better quality of X-ray crystallographic data and is discussed here. The anion of **2b** consists of a seven-coordinate $V^{IV}$

 © 2006 Wiley-VCH Verlag GmbH & Co. KGaA, Weinheim 

Table 1. Selected bond lengths [Å] and angles [°] for **1b**·$2C_6H_6$.

| | | | |
|---|---|---|---|
| V(1)–S(3) | 2.335(3) | V(1)–S(4) | 2.307(2) |
| V(1)–S(5) | 2.329(3) | V(1)–S(6) | 2.325(2) |
| S(1)–S(2) | 2.055(3) | V(1)–P(1) | 2.442(2) |
| V(1)–P(2) | 2.500(2) | | |
| S(4)–V(1)–S(3) | 107.45(9) | S(3)–V(1)–P(1) | 80.43(8) |
| S(4)–V(1)–S(6) | 84.73(9) | S(3)–V(1)–P(2) | 94.58(9) |
| S(4)–V(1)–S(5) | 90.18(9) | S(6)–V(1)–S(3) | 157.69(10) |
| S(4)–V(1)–P(1) | 84.31(8) | S(6)–V(1)–S(5) | 110.40(9) |
| S(4)–V(1)–P(2) | 156.88(9) | S(6)–V(1)–P(1) | 82.35(8) |
| S(5)–V(1)–S(3) | 88.65(10) | S(6)–V(1)–P(2) | 76.94(8) |
| S(5)–V(1)–P(1) | 165.64(9) | P(1)–V(1)–P(2) | 106.74(8) |
| S(5)–V(1)–P(2) | 83.25(8) | | |

center by binding to PS3′ and $PS2S^{Me\prime}$, where $PS2S^{Me\prime}$ is a bis(thiolato)thioetherphosphane ligand. Interestingly, during the reaction a thiolate group in the PS3′ ligand was methylated to yield the $PS2S^{Me\prime}$ ligand. The S(2)–C(10) distance of 1.763(5) Å is close to those found in methylphenyl thioether-containing compounds,[14] but is different from the reported S–O and S–OH distances found in sulfoxide and sulfenic acid, respectively.[15] The S atom of the thioether group in $PS2S^{Me\prime}$ remains uncoordinated. The structure adopts a distorted pentagonal-bipyramidal geometry with two P atoms in the equatorial plane. Seven-coordinate $V^{IV}$ complexes are unusual and the only reported example is $[V(S_2)_2(terpy)]$.[16] Selected bond lengths and angles of **2a** and **2b** are listed in Table S1 and Table 2, respectively. The distances of V–S bonds occur in a large range (2.374 to 2.551 Å). The axial V–S distances (2.374 and 2.386 Å) are comparable to those in **1b** and other reported $V^{IV}$-thiolate complexes.[11a,11d–11h] However, the equatorial V–S bond lengths (2.444, 2.434, and 2.551 Å) are much longer than those in reported $V^{IV}$-thiolate compounds, but are close to those in seven-coordinate vanadium(III)-thiolate complexes.[17]

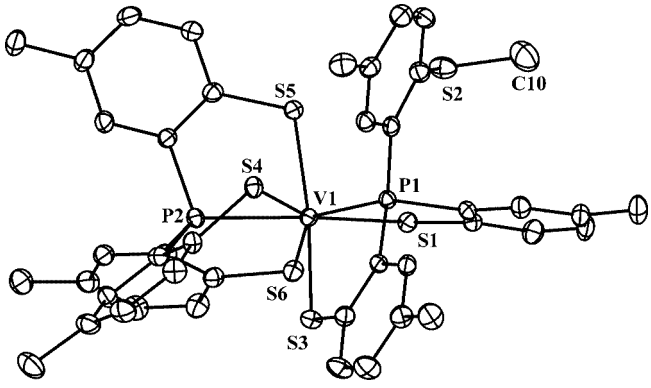


Figure 2. ORTEP diagram of **2b** shown with 35% thermal ellipsoids. The cation and all hydrogen atoms are omitted for clarity.

### Spectroscopic, Electrochemical, and Magnetic Studies

The patterns of the bands in the UV/Vis spectra of **1a**,**b** are similar to each other, but are dissimilar to that of **2a**, clearly delineating the different coordination sites of **1a**,**b** and **2a** in solution state (Figure 3). The absorptions of **1a** are slightly red-shifted relative to those of **1b** as a result of the methyl substituents of the ligand in **1a**. The intense bands appearing in these spectra are very likely caused by the ligand-to-metal charge transfers that mask d-d transitions. Cyclic voltammograms (CVs) of complexes **1a**,**b** and **2a** were measured under nitrogen with ferrocene (Fc) as an external standard. The potentials are referenced versus the $Fc^+$/Fc couple as summarized in Table 3. The CVs of **1a** and **2a** display two well-separated reversible waves of equal size as one-electron-reduction and one-electron-oxidation processes (Figure 4). The reduction processes should be interpreted as metal-centered reductions to $V^{III}$ species since the thiolate ligands are unlikely to be reduced in this potential range. Although the possibility of ligand-based oxidations should not be excluded, we are inclined to speculate that the oxidation processes are related to metal-centered oxidations since the oxidation of thiolate to thiyl radical is usually irreversible and at higher potential.[12e,12i] The potentials ($E_{1/2}$) of **1a** are much higher than the corresponding potentials of **2a**. Presumably, this is related to the six-coordinate metal center in **1a** compared with the seven-coordinate metal center in **2a**; this is in agreement with lower-coordinate complexes stabilized at lower oxidation states. The differences in potentials of these two complexes are 689 mV for the $V^{III}/V^{IV}$ couple and 498 mV for the $V^{IV}/V^{V}$ couple, indicating that the effect of the coordination number on the stabilization of the oxidation state is more pronounced for the former than the latter couple. Indeed, the potentials of redox couples of **1a** are closer to those of the corresponding couples in a six-coordinate non-oxo vanadium(IV) complex, $V^{IV}L^{P}_2$, in which $L^P$ is a tridentate bis(phenolato)phosphane ligand (Table 3).[12p] The potentials of **1a** are slightly higher than those in $V^{IV}L^{P}_2$ since the reduced form is more stable in a P2S4 environment compared with a P2O4 environment. The cyclic voltammogram of **1b** displays an irreversible reduction wave at –0.818 V and an irreversible oxidation wave at 0.149 V, presumably related to the redox processes to $V^{III}$ and $V^{V}$, respectively. The potentials of **1b** are higher than those of **1a**, consistent with the electron-donating nature of the methyl substituent in the ligand of **1a**. Some irreversible oxidized waves are observed in the potential range of 0.2 to 0.8 V for **1a**,**b** and

Table 2. Selected bond lengths [Å] and angles [°] for **2b**·$CH_3OH$.

| | | | |
|---|---|---|---|
| V(1)–S(1) | 2.4435(10) | V(1)–S(3) | 2.3743(11) |
| V(1)–S(4) | 2.5513(10) | V(1)–S(5) | 2.3861(10) |
| V(1)–S(6) | 2.4336(10) | V(1)–P(1) | 2.4891(10) |
| V(1)–P(2) | 2.4305(10) | S(2)–C(10) | 1.763(5) |
| S(1)–V(1)–S(3) | 98.05(4) | S(4)–V(1)–P(1) | 70.09(3) |
| S(1)–V(1)–S(5) | 92.00(4) | S(4)–V(1)–P(2) | 68.22(3) |
| S(1)–V(1)–S(6) | 70.05(3) | S(5)–V(1)–P(1) | 97.15(4) |
| S(1)–V(1)–P(1) | 77.52(3) | S(5)–V(1)–S(3) | 168.96(4) |
| S(1)–V(1)–P(2) | 144.00(4) | S(5)–V(1)–S(6) | 102.52(4) |
| S(3)–V(1)–S(6) | 85.30(4) | P(1)–V(1)–S(6) | 142.33(4) |
| S(3)–V(1)–P(1) | 80.68(3) | P(2)–V(1)–S(3) | 93.20(4) |
| S(4)–V(1)–S(1) | 146.71(4) | P(2)–V(1)–S(5) | 81.18(4) |
| S(4)–V(1)–S(3) | 84.40(4) | P(2)–V(1)–S(6) | 76.98(3) |
| S(4)–V(1)–S(5) | 84.69(3) | P(2)–V(1)–P(1) | 138.26(4) |
| S(4)–V(1)–S(6) | 142.97(4) | | |

 © 2006 Wiley-VCH Verlag GmbH & Co. KGaA, Weinheim 

**2a**, and are probably related to the oxidation of thiolate ligand to thiyl radical.

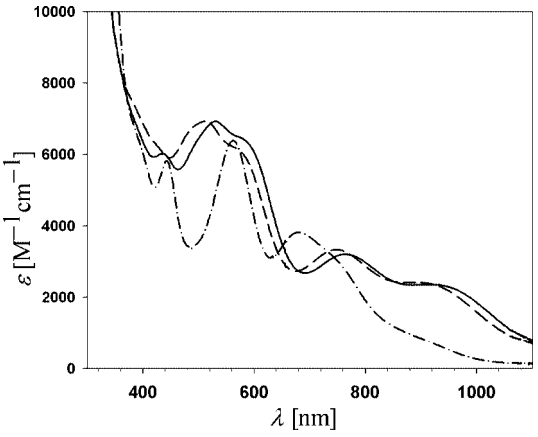


Figure 3. UV/Vis spectra of **1a**,**b** and **2a** in $CH_2Cl_2$. Solid line (**1a**), dashed line (**1b**), dashed-dotted line (**2a**).

Table 3. Electrochemical data from cyclic voltammetry.[a]

| Complex | $E_{1/2}^{red}$ [V][b] | $\Delta E_p^{red}$ [mV] | $E_{1/2}^{ox}$ [V][b] | $\Delta E_p^{ox}$ [mV] |
|---|---|---|---|---|
| **1a** | –0.872 | 98 | –0.107 | 104 |
| **1b** | –0.818[c] | – | 0.149[c] | – |
| **2a** | –1.561 | 92 | –0.605 | 86 |
| $V^{IV}L^{P}{}_2$[d] | –1.060 | – | –0.175 | – |

[a] Measured 0.5 mM solutions of **1a**,**b** and **2a** in $CH_2Cl_2$ with $n$Bu$_4$NBF$_4$ (0.05 M), Pt electrode, Ag/Ag(NO$_3$) (0.01 M in $CH_3CN$) reference, ambient temperature, scan rate 100 mV s$^{-1}$. [b] Vs. Fc/Fc$^+$. [c] Irreversible wave, the peak potentials $E_p^{ox}$ or $E_p^{red}$ are given. [d] L = bis(phenolato)phosphane (ref.[12p]).

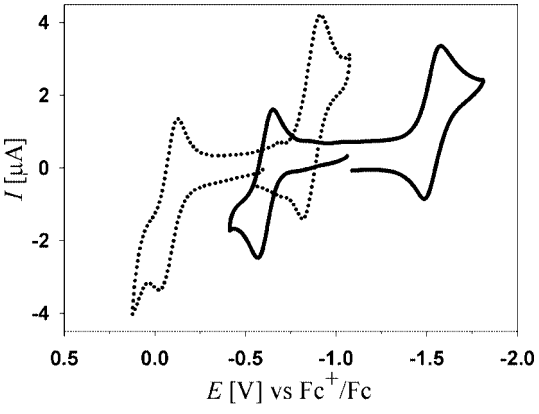


Figure 4. Cyclic voltammograms of complexes **1a** (dotted line) and **2a** (solid line) in $CH_2Cl_2$ solutions (scan rate: 100 mV s$^{-1}$).

The magnetic properties of the complexes were studied by SQUID measurements over the temperature range 5–300 K. The temperature-independent magnetic moments of **1a** and **2a** are 1.78±0.10 and 1.68±0.04 $\mu_B$, respectively, close to the spin-only value of one unpaired electron ($\mu_{eff}$ = 1.73 $\mu_B$). These results are consistent with a $V^{IV}$ ion that has a $S$ = 1/2 ground state. The $^1$H NMR spectra of **1a** and **2a** in $CD_2Cl_2$ exhibit broadened resonance signals in the range of –10 to 20 ppm, in agreement with paramagnetic species in the solution state. The EPR spectra of **1a**,**b** and **2a** in frozen $CH_2Cl_2$ solutions are presented in Figure 5. The spectra of **1a**,**b** are not highly resolved, which is probably a result of the bad quality of glass samples. Attempts to obtain better resolved spectra by preparing the samples under various conditions did not succeed. These spectra exhibit an eight-line pattern with hyperfine splitting of $108.01 \cdot 10^{-4}$ and $103.55 \cdot 10^{-4}$ cm$^{-1}$ for **1a**,**b** and **2a**, respectively, centered at $g_z \cong 1.97$ that is caused by coupling of the unpaired electron with the $^{51}$V nuclear spin ($I$ = 7/2). Spin quantification of the EPR signals account for almost 100% of all three complexes. These results confirm $S$ = 1/2 $d^1$ electronic configuration assignments of the vanadium ions. As shown in Figure 5, each member of the octet is further split into a 1:2:1 triplet of lines, indicating that the electron is coupled to two equivalent $^{31}$P nuclei ($I$ = 1/2) with a superhyperfine splitting of 2.8 and 3.2 mT for **1a**,**b** and **2a**, respectively. The magnetic parameters of the $x$ and $y$ components could not be determined directly from these spectra because of considerable overlapping of lines. We have attempted to simulate these spectra based on $S$ = 1/2 rhombic models with two equivalent coordinating phosphorus nuclei. Notably, we have assumed that the principal axis systems for the $g$, $A^V$, and $A^P$ tensors are collinear for simplicity, which may not be justified for non-oxo vanadium(IV) complexes as described by Chaudhuri and coworkers.[12p] Satisfactory fits are presented in Figure 5 and the derived EPR parameters are presented in Table 4. The EPR parameters of six-coordinate **1a**,**b** exhibit $g_z < g_{x,y} < 2$ and $A_z >> A_x$, $A_y$ characteristic of a $(d_{xy})^1$ ground state configuration.[12e,12p,18] The study of complex **2a** is the first reported EPR study of a seven-coordinate non-oxo vanadium(IV) complex with approximately $D_{5h}$ symmetry. For an ideal pentagonal-bipyramidal ($D_{5h}$) symmetry, simple crystal-field considerations place the $e_1''$ ($d_{xz}$ and $d_{yz}$) the lowest. The $a_1'$ ($d_{z^2}$) and $e_2'$ ($d_{xy}$, $d_{x^2-y^2}$) lie relatively high above $e_1''$, and the ordering of $e_2'$ and $a_1'$ depends on the relative field strength of the equatorial and the axial ligands. The system is subject to Jahn–Teller distortion. Complex **2a** adopts a pseudo $D_{5h}$ pentagonal-bipyramidal geometry with S1, P1, S4, P2, and S6 atoms forming the pentagon. The spin-Hamiltonian parameters (Table 4) are such that $g_z < g_{x,y} < 2$ and $A_z >> A_x$, $A_y$. These results are consistent with the unpaired electron being in a nondegenerate $d_{xz}$ ground state expected for a pentagonal-bipyramidal complex with a $d^1$ electron configuration. The fact that the observed $g$ anisotropy is relatively small suggests a considerable energy difference between the $d_{xz}$ and $d_{yz}$ orbitals, even though these orbitals are strongly coupled by spin-orbit interactions.

From the observed spin-Hamiltonian parameters, the Fermi contact term ($k$) at the $^{51}$V nucleus has been calculated.[19] A large value of $k$ indicates a large contribution to the hyperfine coupling constant by the unpaired electron. The values of the Fermi contact term obtained in the present work ($k$ = 0.53, 0.53, and 0.51 for **1a**, **1b**, and **2a**, respectively) indicate the moderate hyperfine coupling from the $^{51}$V nucleus. The observed spectral features, the obtained

 © 2006 Wiley-VCH Verlag GmbH & Co. KGaA, Weinheim 

Table 4. EPR parameters of **1a**,**b** and **2a**.

| Compound | $g_x$ | $g_y$ | $g_z$ | $A_x$ [$10^{-4}$ cm$^{-1}$] | $A_y$ [$10^{-4}$ cm$^{-1}$] | $A_z$ [$10^{-4}$ cm$^{-1}$] |
|---|---|---|---|---|---|---|
| **1a** | 1.999(9) | 1.989(9) | 1.976(9) | 18.68 | 29.73 | 108.01[a] |
| **1b** | 1.999(2) | 1.989(6) | 1.976(9) | 18.67 | 29.72 | 108.01[a] |
| **2a** | 1.997(9) | 1.989(2) | 1.979(9) | 17.26 | 26.00 | 103.55 |

[a] The parameter for compounds **1a** and **1b** is only accurate to $\pm 0.9 \cdot 10^{-4}$ cm$^{-1}$, because the spectra of **1a** and **1b** are not as well-resolved as **2a** in the high-field region.

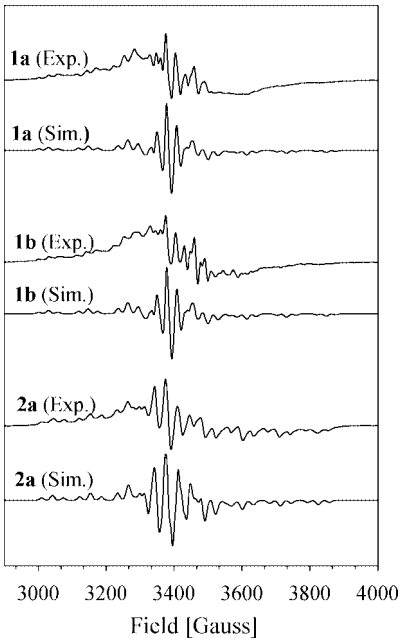


Figure 5. Experimental and simulated EPR spectra of **1a**,**b** and **2a**. Instrument settings: microwave frequency, 9.5192 GHz for **1a**, 9.5158 GHz for **1b**, 9.5152 GHz for **2a**; modulation amplitude, 8 G at 100 kHz; temperature, 5 K; microwave power, 5 mW.

spin-Hamiltonian parameters with low $k$ values, and the isotropic superhyperfine coupling from the two equivalent phosphorus nuclei signify the delocalization of the unpaired electron density away from the $V^{IV}$ metal center.

### The Disulfide Formation and the Alkylation of Coordinated Thiolate

Ligand-based reactions of metal-thiolate complexes are well-known.[11b,15a,20] The reactions include alkylation, metalation, and oxygenation of bound sulfur centers. The formation of disulfide along with the reduction of metal ions has also been seen in metal-thiolate chemistry.[11e,11g,13,21] However, it has never been reported that $V^V$ species mediate the disulfide formation and the alkylation of thiolate, as presented in this work. The mechanism of forming the thioether group contained in **2a**,**b** is less clear. The alkylation of coordinated thiolate groups is mostly limited to late-transition-metal complexes such as $Ni^{II}$, $Ru^{II}$, $Fe^{II}$, and $Zn^{II}$ thiolates, where bound sulfur atoms tend to react with electrophiles like carbonium sources.[20a,20d,20g,22] The nucleophilicity of bound sulfur atoms has been attributed to a four-electron repulsion between a sulfur lone pair and electrons in filled metal d-orbitals. However, in the case of high-valent vanadium thiolates, the electron repulsion stemming from the metal–sulfur dπ-pπ interactions is undermined by the electron deficiency of the metal center. Thus, an electrophilic attack of bound sulfur to carbon in methoxide leading to the formation of **2a**,**b** is less likely, but cannot be excluded. More likely, the methylation of thiolate might involve the homolytic cleavage of the C–O bond in methoxide by a bound thiyl radical generated by the reaction of $V^V$ with thiolate.[23] In this case, the initial step possibly involved the reduction of $V^V$ to $V^{IV}$ and the oxidation of thiolate to thiyl radical.[24] Thus, a $V^{IV}(RS\cdot)(OCH_3)$ species might be proposed as an intermediate.

## Conclusions

This work describes the redox chemistry that occurs in the reactions of vanadium(V) with thiolate groups, leading to the formation of two types of non-oxo vanadium(IV) complexes: one with disulfide- and the other with thioether-containing ligands, as shown by **1a**,**b** and **2a**,**b**, respectively. The chemistry here contrasts with the reported reactions of $VO^{3+}$ with thiolate-containing ligands, NS3 and $btap^{3-}$ {NS3 = $[N(CH_2CH_2S)_3]^{3-}$, $btap^{3-}$ = 2-[bis(ethylthiolato)-amino]-4-methylphenolate}, in which redox chemistry was not involved and oxovanadium(V) complexes binding with the title ligands were obtained.[11b,11d] Compared with NS3 and $btap^{3-}$ ligands, the PS3 system might be attributed to a better driving force of the redox process between $V^V/V^{IV}$ and $RS^-/RS\cdot$ couples, consequently generating a $V^{IV}$–RS· intermediate that might be a key species for forming **1a**,**b** and **2a**,**b**.

## Experimental Section

**General Considerations:** Manipulations were performed under nitrogen by standard Schlenk techniques or in a nitrogen-filled glove box. $[P(C_6H_4\text{-}2\text{-}SH)_3]$, $[P(C_6H_3\text{-}5\text{-}Me\text{-}2\text{-}SH)_3]$,[25] and $VO(i\text{PrO})_3$[26] were synthesized according to literature procedures. Solvents were dried, distilled, and degassed using standard techniques. All other starting materials were obtained commercially and used without further purification.

**Physical Methods:** Electronic spectra were recorded in the range of 300–1100 nm on a Hewlett Packard 8453 spectrophotometer. Electrochemical studies were performed at ambient temp. under nitrogen with a CHI 600A electrochemical analyzer. Cyclic voltammograms were obtained by using a three-component system consisting of a platinum-disk working electrode, a platinum-wire auxiliary electrode, and a $Ag/Ag(NO_3)$ (0.01 M in $CH_3CN$) reference electrode. The experiments were performed in $CH_2Cl_2$ by using tetrabutylammonium tetrafluoroborate (0.05 M) as the supporting

 © 2006 Wiley-VCH Verlag GmbH & Co. KGaA, Weinheim 

electrolyte. The ferrocenium/ferrocene ($Fc^+/Fc$) couple was measured as an external standard. Under our experimental conditions, the $Fc^+/Fc$ couple was at $E_{1/2}$ ($\Delta E_p$) = 0.161 ± 0.01 V (130 mV) vs. $Ag/Ag(NO_3)$ (0.01 M in $CH_3CN$). The $^1H$ NMR spectra were recorded with a BRUKER AMX-400 at ambient temp. EPR spectra were obtained at X-band using a Bruker EMX spectrometer equipped with a Bruker TE102 cavity and an Advanced Research System continuous-flow cryostat (3.2–200 K). The microwave frequency was measured with a Hewlett–Packard 5246L electronic counter. The instrument settings are shown in the Figure caption. SQUID magnetic measurements were performed with a QUANTUM DESIGN MPMS-7 with a field of 5000 G. The measurements were taken over the following temp. ranges with the indicated increments: 5–10 K (one data point every 1 K), 12–20 K (one data point every 2 K), 23–50 K (one data point every 3 K), 55–100 K (one data point every 5 K), 110–300 K (one data point every 10 K). Diamagnetic contributions were estimated for each compound by using Pascal's constants.

**Synthesis of [$V^{IV}$(P2S4′)] (1a):** An *i*PrOH solution of $VO(iPrO)_3$ (0.061 g, 0.25 mmol) was added to an ether solution of $[PS3']H_3$ (0.100 g, 0.25 mmol) to generate a bluish-purple solution. After stirring for 1 h, a bluish-purple solid precipitated. The solid was filtered in the air and was followed by recrystallization from $CH_2Cl_2$ and hexane in anaerobic conditions to yield the crystalline form of **1a** [0.040 g, 0.047 mmol, ca. 19% based on $VO(iPrO)_3$]. $C_{42}H_{36}P_2S_6V$ (846.01): calcd. C 59.63, H 4.29, S 22.74; found C 59.42, H 4.28, S 22.53. UV/Vis in $CH_2Cl_2$ ($\lambda$, nm; $\varepsilon$, $M^{-1}cm^{-1}$): 438 ($6.02\cdot10^3$), 531 ($6.92\cdot10^3$), 764 ($3.21\cdot10^3$), 918 ($2.40\cdot10^3$).

**Synthesis of [$V^{IV}$(P2S4′)] (1b):** An *i*PrOH solution of $VO(iPrO)_3$ (0.068 g, 0.28 mmol) was added to an ether solution of $[PS3]H_3$ (0.100 g, 0.28 mmol) to generate a bluish-purple solution. After stirring for 1 h, a bluish-purple solid precipitated. The solid was filtered in the air and was followed by recrystallization from benzene and ether in anaerobic conditions to yield the crystalline form of **1b** [0.017 g, 0.023 mmol, ca. 8.2% based on $VO(iPrO)_3$]. $C_{36}H_{24}P_2S_6V$ (761.85): calcd. C 56.75, H 3.18, S 25.25; found C 56.21, H 3.17, S 24.40. UV/Vis in $CH_2Cl_2$ ($\lambda$, nm; $\varepsilon$, $M^{-1}cm^{-1}$): 513 ($6.93\cdot10^3$), 747 ($3.33\cdot10^3$), 890 ($2.41\cdot10^3$).

**Synthesis of [$V^{IV}$(PS3′)(PS2$S^{Me'}$)][$N(C_2H_5)_4$] (2a) and [$V^{IV}$(PS3′)-(PS2$S^{Me'}$)][$N(C_2H_5)_3(CH_2Ph)$] (2b):** An *i*PrOH solution of $VO(iPrO)_3$ (0.060 g, 0.25 mmol) was added to a methanol solution of $[PS3']H_3$ (0.100 g, 0.25 mmol) and $CH_3ONa$ (0.040 g, 0.75 mmol) to generate a brown solution. The reaction mixture changed to a purple color after stirring for 30 min. After filtering through Celite, the solution was concentrated and layered with $(C_2H_5)_4NBr$ (0.050 g, 0.24 mmol) in methanol to give a purple crystalline solid of **2a** [0.020 g, 0.02 mmol, ca. 8% based on $VO(iPrO)_3$]. $C_{51}H_{59}NP_2S_6V$ (991.23): calcd. C 61.79, H 6.00, N 1.41, S 19.41; found C 60.99, H 6.19, N 1.33, S 18.73. UV/Vis in $CH_2Cl_2$ ($\lambda$, nm; $\varepsilon$, $M^{-1}cm^{-1}$): 443 ($4.53\cdot10^3$), 562 ($4.92\cdot10^3$), 677 ($2.98\cdot10^3$). The procedure for the synthesis of **2b** is the same except $(C_2H_5)_3(CH_2Ph)NBr$ was used for the cation. **2b**, $C_{56}H_{61}NP_2S_6V$ (1053.38): calcd. C 63.85, H 5.85, N 1.33, S 18.27; found C 62.99, H 6.05, N 1.32, S 17.82.

### Crystallographic Structure Determination

Each crystal was mounted on a glass fiber and quickly coated in epoxy resin. Diffraction measurements were carried out at 295(2) K for **1b** and 150(2) K for **2b** with a Bruker SMART 1000 CCD diffractometer with graphite-monochromated Mo-$K\alpha$ radiation ($\lambda$ = 0.7107 Å). Least-squares refinement of the positional and anisotropic thermal parameters for the contribution of all non-hydrogen atoms and fixed hydrogen atoms was based on $F^2$. A SADABS absorption correction was made.[27] The SHELXTL structural refinement program was employed.[28] All non-hydrogen atoms were refined with anisotropic displacement factors. All hydrogen atoms were calculated using the riding model. Detailed data and refinement parameters are summarized in Table 5 (**1b** and **2b**) and Table S2 (**2a**).

Table 5. Crystallographic data for compounds **1b** and **2b**.

| | **1b**·$2C_6H_6$ | **2b**·$CH_3OH$ |
|---|---|---|
| Formula | $C_{48}H_{36}P_2S_6V$ | $C_{57}H_{65}NOP_2S_6V$ |
| $M$ [g mol$^{-1}$] | 918.01 | 1085.34 |
| $T$ [K] | 295(2) | 150(2) |
| Crystal system | Monoclinic | Monoclinic |
| Space group | $P2_1/a$ | $P2_1/n$ |
| $a$ [Å] | 18.0270(10) | 12.58000(10) |
| $b$ [Å] | 13.8510(9) | 33.6470(3) |
| $c$ [Å] | 19.1040(11) | 14.25500(10) |
| $\alpha$ [°] | 90 | 90 |
| $\beta$ [°] | 114.260(3) | 113.58 |
| $\gamma$ [°] | 90 | 90 |
| $V$ [Å$^3$] | 4348.9(4) | 5529.99(8) |
| $Z$ | 4 | 4 |
| $D_{calcd.}$ [g cm$^{-1}$] | 1.402 | 1.304 |
| $\mu$(Mo-$K_\alpha$) [mm$^{-1}$] | 0.624 | 0.503 |
| $F$(000) | 1892 | 2284 |
| Collected data | 23029 | 33541 |
| Unique data ($R_{int}$) | 7636 (0.2093) | 9649 (0.0535) |
| Refined parameters | 515 | 613 |
| $R_1$[a] [$I > 2\sigma(I)$] | 0.0753 | 0.0525 |
| $wR_2$[b] [$I > 2\sigma(I)$] | 0.1270 | 0.1433 |
| GOF[c] | 1.226 | 1.019 |

[a] $R_1 = \Sigma||F_o| - |F_c||/\Sigma|F_o|$. [b] $wR_2 = \{\Sigma[w(F_o^2 - F_c^2)^2]/\Sigma[w(F_o^2)^2]\}^{1/2}$. [c] Goodness-of-fit on $F^2$.

CCDC-272405 (for **1b**), CCDC-287713 (for **2a**), and CCDC-272406 (for **2b**) contain the supplementary crystallographic data for this paper. These data can be obtained free of charge from The Cambridge Crystallographic Data Centre via www.ccdc.cam.ac.uk/data_request/cif.

**Supporting Information** (see footnote on the first page of this article): ORTEP diagram of **2a** (Figure S1), selected bond lengths and angles for **2a** (Table S1), and crystallographic data of **2a** (Table S2).

## Acknowledgments

We thank the National Science Council in Taiwan (NSC, 93-2113-M-006–012-) for generous support of this work. Helpful discussions with Professor I-Wen Sun at National Cheng Kung University are gratefully acknowledged.

[1] a) D. C. Crans, J. J. Smee, E. Gaidamauskas, L. Yang, *Chem. Rev.* **2004**, *104*, 849–902; b) E. J. Baran, *J. Braz. Chem. Soc.* **2003**, *14*, 878–888; c) E. J. Baran, *Coord. Chem. Rev.* **2003**, *237*, 1–286. (A special issue: "New Directions in Chemistry and Biological Chemistry of Vanadium"); d) E. J. Baran, *J. Inorg. Biochem.* **2000**, *80*, 1–194. (A special issue dedicated to biological aspects of vanadium).
[2] E. J. Baran, *J. Inorg. Biochem.* **2000**, *80*, 1–10.
[3] a) G. Huyer, S. Liu, J. Kelly, J. Moffat, P. Payette, B. Kennedy, G. Tsaprailis, M. J. Gresser, C. Ramachandran, *J. Biol. Chem.* **1997**, *272*, 843–851; b) J. E. Benabe, L. A. Echegoyen, B. Pastrana, M. Martínez-Maldonado, *J. Biol. Chem.* **1987**, *262*, 9555–9560; c) D. Rehder, *Inorg. Chem. Commun.* **2003**, *6*, 604–617.

 © 2006 Wiley-VCH Verlag GmbH & Co. KGaA, Weinheim 

[4] S. W. Taylor, B. Kammerer, E. Bayer, *Chem. Rev.* **1997**, *97*, 333–346.
[5] H. Michibata, N. Yamaguchi, T. Uyama, T. Ueki, *Coord. Chem. Rev.* **2003**, *237*, 41–51.
[6] C. D. Garner, E. M. Armstrong, R. E. Berry, R. L. Beddoes, D. Collison, J. J. A. Cooney, S. N. Ertok, M. Helliwell, *J. Inorg. Biochem.* **2000**, *80*, 17–20.
[7] R. E. Berry, E. M. Armstrong, R. L. Beddoes, D. Collison, S. N. Ertok, M. Helliwell, C. D. Garner, *Angew. Chem. Int. Ed.* **1999**, *38*, 795–797.
[8] M. F. C. Guedes da Silva, J. A. L. Silva, J. J. R. Fraústo da Silva, A. J. L. Pombeiro, C. Amatore, J.-N. Verpeaux, *J. Am. Chem. Soc.* **1996**, *118*, 7568–7573.
[9] M. Bruech, M. E. Quintanilla, W. Legrum, J. Koch, K. J. Netter, G. F. Fuhrmann, *Toxicology* **1984**, *31*, 283–295.
[10] a) H. Sakurai, H. Sano, T. Takino, H. Yasui, *J. Inorg. Biochem.* **2000**, *80*, 99–105; b) H. Sakurai, H. Watanabe, H. Tamura, H. Yasui, R. Matsushita, J. Takada, *Inorg. Chim. Acta* **1998**, *283*, 175–183; c) D. Rehder, J. C. Pessoa, C. F. Geraldes, M. M. Castro, T. Kabanos, T. Kiss, B. Meier, G. Micera, L. Pettersson, M. Rangel, A. Salifoglou, I. Turel, D. Wang, *J. Biol. Inorg. Chem.* **2002**, *7*, 384–396.
[11] a) J. J. A. Cooney, M. D. Carducci, A. E. McElhaney, H. D. Selby, J. H. Enemark, *Inorg. Chem.* **2002**, *41*, 7086; b) C. R. Cornman, T. C. Stauffer, P. D. Boyle, *J. Am. Chem. Soc.* **1997**, *119*, 5986–5987; c) J. K. Money, J. R. Nicholson, J. C. Huffman, G. Christou, *Inorg. Chem.* **1986**, *25*, 4072–4074; d) K. K. Nanda, E. Sinn, A. W. Addison, *Inorg. Chem.* **1996**, *35*, 1–2; e) W. Tsagkalidis, D. Rodewald, D. Rehder, *Inorg. Chem.* **1995**, *34*, 1943–1945; f) D. Wang, M. Ebel, C. Schulzke, C. Grüning, S. K. S. Hazari, D. Rehder, *Eur. J. Inorg. Chem.* **2001**, 935–942; g) D. Wang, A. Behrens, M. Farahbakhsh, J. Gätjens, D. Rehder, *Chem. Eur. J.* **2003**, *9*, 1805–1813; h) W. Tsagkalidis, D. Rehder, *J. Biol. Inorg. Chem.* **1996**, *1*, 507–514; i) H. Nekola, D. Wang, C. Grüning, J. Gätjens, A. Behrens, D. Rehder, *Inorg. Chem.* **2002**, *41*, 2379–2384.
[12] a) M. Farahbakhsh, H. Schmidt, D. Rehder, *Chem. Commun.* **1998**, 2009–2010; b) V. Vergopoulos, S. Jantzen, D. Rodewald, D. Rehder, *J. Chem. Soc., Chem. Commun.* **1995**, 377–378; c) T. A. Kabanos, A. J. P. White, D. J. Williams, J. D. Woollins, *J. Chem. Soc., Chem. Commun.* **1992**, 17–18; d) S. Bruni, A. Caneschi, F. Cariati, C. Delfs, A. Dei, D. Gatteschi, *J. Am. Chem. Soc.* **1994**, *116*, 1388–1394; e) P. R. Klich, A. T. Daniher, P. R. Challen, *Inorg. Chem.* **1996**, *35*, 347–356; f) S. R. Cooper, Y. B. Koh, K. N. Raymond, *J. Am. Chem. Soc.* **1982**, *104*, 5092–5102; g) M. A. A. F. de C. T. Carrondo, M. T. L. S. Duarte, J. C. Pessoa, J. A. L. Silva, J. J. R. Fraústo da Silva, M. C. T. A. Vaz, L. F. Vilas-Boas, *J. Chem. Soc., Chem. Commun.* **1988**, 1158–1159; h) U. Auerbach, B. S. P. C. D. Vedova, K. Wieghardt, B. Nuber, J. Weiss, *J. Chem. Soc., Chem. Commun.* **1990**, 1004–1005; i) T. Beissel, T. Glaser, F. Kesting, K. Wieghardt, B. Nuber, *Inorg. Chem.* **1996**, *35*, 3936–3947; j) P. Comba, L. M. Engelhardt, J. M. Harrowfield, G. A. Lawrance, L. L. Martin, A. M. Sargeson, A. H. White, *J. Chem. Soc., Chem. Commun.* **1985**, 174–176; k) A. Neves, A. S. Ceccato, I. Vencato, Y. P. Mascarenhas, C. Erasmus-Buhr, *J. Chem. Soc., Chem. Commun.* **1992**, 652–654; l) T. A. Kabanos, A. M. Z. Slawin, D. J. Williams, J. D. Woolins, *J. Chem. Soc., Dalton Trans.* **1992**, 1423–1427; m) A. A. Diamantis, M. R. Snow, J. A. Vanzo, *J. Chem. Soc., Chem. Commun.* **1976**, 264–265; n) B. Kang, L. Weng, H. Liu, D. Wu, L. Huang, C. Lu, J. Cai, X. Chen, J. Lu, *Inorg. Chem.* **1990**, *29*, 4873–4877; o) T. A. Kabanos, A. M. Z. Slawin, D. J. Williams, J. D. Woollins, *J. Chem. Soc., Chem. Commun.* **1990**, 193–194; p) T. K. Paine, T. Weyhermüller, L. D. Slep, F. Neese, E. Bill, E. Bothe, K. Wieghardt, P. Chaudhuri, *Inorg. Chem.* **2004**, *43*, 7324–7338; q) P. D. Smith, R. E. Berry, S. M. Harben, R. L. Beddoes, M. Helliwell, D. Collison, C. D. Garner, *J. Chem. Soc., Dalton Trans.* **1997**, 4509–4516.
[13] J. R. Dilworth, Y. Zheng, J. R. Miller, *J. Chem. Soc., Dalton Trans.* **1992**, 1757–1758.
[14] R. H. Laitinen, H. Riihimäki, M. Haukka, S. Jääskeläinen, T. A. Pakkanen, J. Pursiainen, *Eur. J. Inorg. Chem.* **1999**, 1253–1258.
[15] a) For instance: S=O distances in sulfoxide-containing complexes are 1.5–1.6 Å. C. A. Grapperhaus, M. Y. Darensbourg, *Acc. Chem. Res.* **1998**, *31*, 451–459; b) For instance: S–OH distance in a sulfenic acid is 1.679 Å. K. Goto, M. Holler, R. Okazaki, *J. Am. Chem. Soc.* **1997**, *119*, 1460–1461.
[16] F. T. Al-Ani, D. L. Hughes, C. J. Pickett, *J. Chem. Soc., Dalton Trans.* **1988**, 1705–1707.
[17] H.-F. Hsu, W.-C. Chu, C.-H. Hung, J.-H. Liao, *Inorg. Chem.* **2003**, *42*, 7369–7371.
[18] A. Jezierski, J. B. Raynor, *J. Chem. Soc., Dalton Trans.* **1981**, 1–7.
[19] D. Kivelson, S.-K. Lee, *J. Chem. Phys.* **1964**, *41*, 1896–1902.
[20] a) C. A. Grapperhaus, S. Poturovic, M. Mashuta, *Inorg. Chem.* **2002**, *41*, 4309–4311; b) M. Kumar, R. O. Day, G. J. Colpas, M. J. Maroney, *J. Am. Chem. Soc.* **1989**, *111*, 5974–5976; c) E. L. Blinn, D. H. Busch, *J. Am. Chem. Soc.* **1968**, *90*, 4280–4285; d) J. J. Wilker, S. J. Lippard, *Inorg. Chem.* **1997**, *36*, 969–978; e) L. F. Lindoy, D. H. Busch, *Inorg. Chem.* **1974**, *13*, 2494–2498; f) R. M. Buonomo, I. Font, M. J. Maguire, J. H. Reibenspies, T. Tuntulani, M. Y. Darensbourg, *J. Am. Chem. Soc.* **1995**, *117*, 963; g) G. Musie, J. H. Reibenspies, M. Y. Darensbourg, *Inorg. Chem.* **1998**, *37*, 302–310; h) Y.-M. Hsiao, S. S. Chojnacki, P. Hinton, J. H. Reibenspies, M. Y. Darensbourg, *Organometallics* **1993**, *12*, 870–875.
[21] B. Albela, E. Bothe, O. Brosch, K. Mochizuki, T. Weyhermüller, K. Wieghardt, *Inorg. Chem.* **1999**, *38*, 5131–5138.
[22] M. T. Ashby, J. H. Enemark, D. L. Lichtenberger, *Inorg. Chem.* **1988**, *27*, 191–197.
[23] Attempts to isolate the reaction intermediates or other products were unsuccessful.
[24] X. Shi, X. Sun, N. S. Dalal, *FEBS LETT.* **1990**, *271*, 185–188.
[25] E. Block, G. Ofori-Okai, J. Zubieta, *J. Am. Chem. Soc.* **1989**, *111*, 2327–2329.
[26] H. Hillerns, D. Rehder, *Chem. Ber.* **1991**, *124*, 2249–2254.
[27] G. M. Sheldrick, *SADABS*, *Siemens Area Detector Absorption Correction Program*, University of Göttingen, Göttingen, Germany, **1996**.
[28] G. M. Sheldrick, *SHELXTL*, *Program for Crystal Structure Determination*, Siemens Analytical X-ray Instruments Inc., Madison, WI, **1994**.

Received: September 29, 2005
Published Online: January 26, 2006

 © 2006 Wiley-VCH Verlag GmbH & Co. KGaA, Weinheim 

DOI: 10.1002/ejic.200500878

# Oxidative Addition of $Cl_2$, HClO to Square-Planar $Pt^{II}$ Complexes: Synthesis and Structural Characterization of Platinum(II) and Platinum(IV) Bis(amidate) Complexes

**Fenghui Liu[a] and Wanzhi Chen*[a]**

**Keywords:** Platinum / Amidates / Amines

New bis(amidate)platinum(II) complexes with the general formula *cis*-[Pt(RNH$_2$)$_2$(NHCO*t*Bu)$_2$] were prepared by the hydrolysis of the corresponding *cis*-[Pt(RNH$_2$)$_2$(*t*BuCN)$_2$]$^{2+}$ complex. The bis(amidate)platinum(IV) complexes with the formula *trans*,*cis*,*cis*-[PtCl$_2$(RNH$_2$)$_2$(NHCO*t*Bu)$_2$] (**5**: R = H, **6**: R = Et), *trans*,*cis*,*cis*-[PtCl(OH)(RNH$_2$)$_2$(NHCO*t*Bu)$_2$] (**8**: R = H, **9**: R = Et, and **10**: 2R = 1,2-*c*Hex), and mono(amidate) complex *mer*-[PtCl$_3$(DACH)(NHCO*t*Bu)$_2$] (**7**, DACH = *trans*-1,2-diaminocyclohexane) have been generated selectively by the oxidative addition of $Cl_2$ and HClO to the corresponding platinum(II) complexes, [Pt(RNH$_2$)$_2$(NHCO*t*Bu)$_2$], in water. All the prepared compounds were characterized by elemental analyses and $^1$H and $^{195}$Pt NMR spectroscopy. The structures of *trans*,*cis*,*cis*-[PtCl$_2$(NH$_3$)$_2$(NHCO*t*Bu)$_2$] (**5**), *trans*,*cis*,*cis*-[PtCl$_2$(EtNH$_2$)$_2$(NHCO*t*Bu)$_2$] (**6**), *mer*-[PtCl$_3$-(DACH)(NHCO*t*Bu)] (**7**), and *trans*,*cis*,*cis*-[PtCl(OH)(DACH)-(NHCO*t*Bu)$_2$] (**10**) have been confirmed by X-ray diffraction analyses. The structures of these platinum(IV) complexes adopt an octahedral geometry. The Pt–N, Pt–O, and Pt–Cl distances are in the expected ranges. These complexes are rare examples of bis(amidate)- and mono(amidate)platinum(IV) complexes.
(© Wiley-VCH Verlag GmbH & Co. KGaA, 69451 Weinheim, Germany, 2006)

## Introduction

Since the discovery of the antitumor activity of *cis*-Pt(NH$_3$)$_2$Cl$_2$ by Rosenberg and co-workers[1] a large number of platinum(II) and platinum(IV) complexes containing *cis*-(NH$_3$)$_2$Pt or *cis*-(RNH$_2$)$_2$Pt units have been prepared and characterized.[2,3] Numerous efforts have been made to develop new antitumor compounds that do not show cross-resistance with *cis*-platin. *cis*-[Pt(RNH$_2$)$_2$(amidate)$_2$] complexes, derived from *cis*-Pt(RNH$_2$)Cl$_2$ have proved to be useful building blocks to assemble homo- and heteronuclear dimeric,[3] oligomeric,[4] and polymeric complexes.[5] The two mutually *cis* amidate ligands play a critical role in favoring the association of the platinum units and other metal ions such as in the biologically active "platinum blues".[6] The amidate-bridged dimeric platinum complex [Pt$_2$(NH$_3$)$_4$(NHCO*t*Bu)L$_2$]$^{2+}$, where L is $NO_3^-$ or solvent molecules, has been found to activate C–H bonds of ketones[7] and to catalyze the ketonation of alkynes, epoxidation, and dihydroxylation of terminal olefins.[8]

It is well known that the $Pt^{IV}$ species are involved in the activation of C–H bonds such as the Shilov system, which consists of aqueous solutions of $Pt^{II}$ and $Pt^{IV}$ salts that convert alkanes to the corresponding chlorides and alcohols under mild conditions.[9] Taking into account the fascinating chemistry of bis(amidate)platinum(III) complexes, the amidatoplatinum(IV) complexes may also be useful for such types of organic transformation processes. Furthermore, although most of the platinum centered antitumor drugs are platinum(II) compounds, in recent years a number of platinum(IV) complexes have also been found to be active for antitumor treatment with improved pharmacological properties.[10] However, so far no bis(amidate)- and mono(amidate)platinum complexes having a $Pt^{IV}$ center have been reported. Here we report for the first time the preparation, $^1$H and $^{195}$Pt NMR spectra, and structural characterization of the platinum(IV) complexes *mer*-[PtCl$_3$(DACH)-(NHCO*t*Bu)] (DACH = *trans*-1,2-diaminocyclohexane), *trans*,*cis*,*cis*-[PtCl$_2$(RNH$_2$)$_2$(NHCO*t*Bu)$_2$], and *trans*,*cis*,*cis*-[PtCl(OH)(RNH$_2$)$_2$(NHCO*t*Bu)$_2$] (R = H, Et; and 2R = 1,2-cHex). These platinum(IV) complexes were prepared by oxidative addition of $Cl_2$ and HClO to their corresponding platinum(II) complexes, *cis*-[Pt(RNH$_2$)$_2$(NHCO*t*Bu)$_2$], in high yields.

## Results and Discussion

### Synthesis and NMR Characterization

The [Pt(RNH$_2$)$_2$(NHCO*t*Bu)$_2$] complexes are easily prepared in high yield by basic hydrolysis of their corresponding platinum(II)-nitrile complexes, [Pt(RNH$_2$)$_2$(*t*BuCN)$_2$]$^{2+}$. This procedure has been employed to prepare [Pt(NH$_3$)$_2$-

[a] Department of Chemistry, Zhejiang University, Xixi campus, Hangzhou 310028, China
Fax: +86-571-8827-3314
E-mail: chenwzz@zju.edu.cn
Supporting information for this article is available on the WWW under http://www.eurjic.org or from the author.

 © 2006 Wiley-VCH Verlag GmbH & Co. KGaA, Weinheim 

$(NHCOtBu)_2]$ and *cis*-$[Pt(DACH)(NHCOtBu)_2]$. *cis*-$[Pt(EtNH_2)_2(NHCOtBu)_2]$ and *cis*-$[Pt(DACH)(NHCOtBu)_2]$ were similarly obtained. The synthetic strategy for making the platinum(II) as well as platinum(IV) complexes described below is shown in Scheme 1. These platinum(II) complexes are isolated as stable colorless crystalline solids, and they are soluble in acetone, ethanol, and chloroform. The neutral square-planar complexes, *cis*-$[Pt(NH_3)_2(NHCOtBu)_2]$ and *cis*-$[Pt(EtNH_2)_2(NHCOtBu)_2]$, react with an equimolar amount of $Cl_2$ (0.3% in water) at room temperature to give the bis(amidate)platinum(IV) complexes, *trans*,*cis*,*cis*-$[PtCl_2(NH_3)_2(NHCOtBu)_2]$ (**5**) and *trans*,*cis*,*cis*-$[PtCl_2(EtNH_2)_2(NHCOtBu)_2]$ (**6**), as yellow crystals, respectively. However, *mer*-$[PtCl_3(DACH)(NHCOtBu)]$ (**7**) was generated as the sole isolated product when *cis*-$[Pt(DACH)(NHCOtBu)_2]$ was dissolved in $Cl_2/H_2O$ under the same conditions. The reactions proceeded in good yields. The initially formed $[PtCl_2(DACH)(NHCOtBu)_2]$ probably further reacted with HCl to lose one molecule of $tBuCONH_2$ and yield the final product, **7**. The isolated crystals of **5**–**7** are poorly soluble in common organic solvents, but are moderately soluble in dimethyl sulfoxide. Their $^{195}Pt$ NMR spectra exhibit a singlet at –35, –30.6, and –289 ppm, respectively, indicative of typical platinum(IV) compounds.

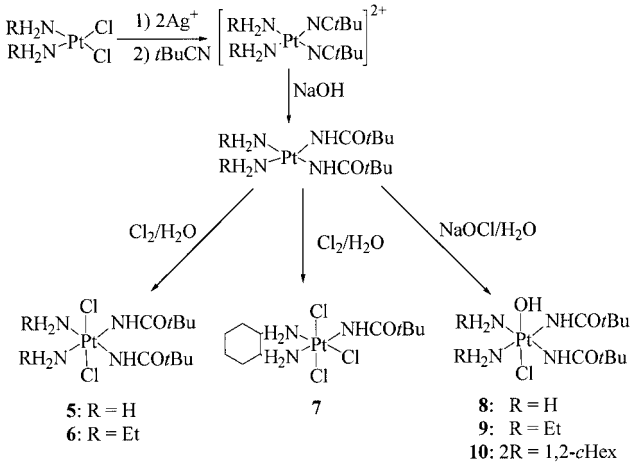


Scheme 1.

Sodium hypochlorite has proved to be a convenient oxygen source for olefin epoxidation catalyzed by transition-metal complexes.[11] We found that it also acts as a $Cl^-$ and $HO^-$ source for the preparation of (chloro)(hydroxo)platinum(IV) complexes. The platinum(II) complexes *cis*-$[Pt(NH_3)_2(NHCOtBu)_2]$, *cis*-$[Pt(EtNH_2)_2(NHCOtBu)_2]$, and *cis*-$[Pt(DACH)(NHCOtBu)_2]$ easily dissolved in an aqueous solution of NaOCl (available $Cl_2$ 5%) at room temperature and yielded *trans*,*cis*,*cis*-$[PtCl(OH)(RNH_2)_2(NHCOtBu)_2]$ {R = H, **8**; R = Et, **9**; $(RNH_2)_2$ = DACH, **10**} in moderate yields. All these chloro(hydroxo)platinum(IV) complexes were isolated as yellow solids. The $^{195}Pt$ NMR spectra of **8**–**10** in $[D_6]$acetone exhibit singlets at –134, –146, and 189 ppm, respectively, which are typical of $Pt^{IV}$ species. The $^{195}Pt$ NMR spectrum of **10** measured immediately upon dissolving in $[D_6]$DMSO shows two singlets at 189 and –193 ppm. The downfield signal disappeared and the upfield signal was intensified after the solution stood in an NMR tube for 24 h. After this time the $^1H$ NMR spectrum also became simpler. Thus the upfield signal at $\delta$ = –193 ppm is assigned to the solvated species $[Pt(OH)(DMSO)(DACH)(NHCOtBu)_2]Cl$.

The general synthetic route to platinum(IV) complexes is the oxidation of platinum(II) complexes by hydrogen peroxide or halogens.[12] The oxidative addition of HOCl with NaOCl provides a convenient route for the preparation of chloro(hydroxo)platinum(IV) complexes.

## Structural Description

The structures of compounds **4**–**7** and **10** have been determined by X-ray diffraction. A summary of the crystallographic data can be found in Table 1. Colorless crystals of **4** were obtained by slow evaporation of its acetone/water solution. Compound **4** crystallizes in a chiral orthorhombic space group $P2_12_12$, and the chiral configuration is predetermined by the diamine, 1*R*,2*R*-*trans*-diaminocyclohexane. The structure of **4** established by X-ray diffraction analysis is shown in Figure 1. As expected, the central platinum is tetra-coordinated to four nitrogen atoms in a square-planar geometry. The shortness of the C–O and C–N bond lengths illustrates the $sp^2$ character of the related atoms. The structure of **4** is the first crystal structure of a platinum(IV) complex of the type $[Pt(RNH_2)_2(trans\text{-}Cl_2)(amidate)_2]$ in which the chlorine atoms occupy the axial positions of an octahedral geometry.

Although compounds **5** and **6** crystallize in different noncentrosymmetric space groups *C*2 and *Pc*, respectively, they display the same structure. The structure of **5** is depicted in Figure 2 and the structure of compound **6** is given as Supporting Information. There are two independent molecules in the asymmetric crystallographic unit of compound **6**, which have essentially the same structure. Therefore, only one of the two molecules is shown in the Supporting Information. The coordination polyhedrons of the complexes are distorted octahedrons for both **5** and **6**. The two amine and two amidate ligands are in mutual *cis* positions, and the two chloride ions are in mutual *trans* positions. The sum of the angles of the neighboring nitrogen atoms around Pt is 359.8° for **5** and 360.5° for **6**, indicating their coplanarity. The Pt–Cl bond lengths [2.324(8) and 2.328(7) Å for **5**, 2.311(2) and 2.319(2) Å for **6**] are in good agreement with other structurally characterized platinum chloride compounds.[13] The $NH_3$ and $NH_2$ groups in **5** and **6** are involved in intra- and intermolecular hydrogen bonding. The Cl–Pt–Cl angles [179.24(8)° for **5** and 177.01(6)° for **6**] are close to 180°.

The trichloroplatinum(IV) complex **7** crystallizes in an orthorhombic space group *Pbca*. Its unit cell contains eight molecules of $[PtCl_3(DACH)(NHCOtBu)_2]$ and eight molecules of acetone. The structure of **7** consists of an octahe-

 © 2006 Wiley-VCH Verlag GmbH & Co. KGaA, Weinheim 

Table 1. Crystal data and structure refinement details for *trans,cis,cis*-$[PtCl_2(NH_3)_2(NHCOtBu)_2]$ (**5**), *trans,cis,cis*-$[PtCl_2(EtNH_2)_2(NHCOtBu)_2]$ (**6**), *mer*-$[PtCl_3(DACH)(NHCOtBu)_2]\cdot(CH_3)_2CO$ (**7**), and *trans,cis,cis*-$[PtCl(OH)(DACH)(NHCOtBu)_2]$ (**10**).

| | **4** | **5** | **6** | **7** | **10** |
|---|---|---|---|---|---|
| Formula | $C_{16}H_{40}N_4O_5Pt$ | $C_{10}H_{26}Cl_2N_4O_2Pt$ | $C_{14}H_{34}Cl_2N_4O_2Pt$ | $C_{14}H_{30}Cl_3N_3O_3Pt$ | $C_{16}H_{39}ClN_4O_5Pt$ |
| Formula mass | 563.61 | 500.34 | 556.44 | 573.84 | 598.05 |
| Crystal size [mm] | 0.08×0.15×0.36 | 0.10×0.12×0.26 | 0.24×0.30×0.31 | 0.10×0.12×0.23 | 0.08×0.08×0.28 |
| Crystal system | orthorhombic | monoclinic | monoclinic | orthorhombic | monoclinic |
| Space group | $P2_12_12$ | $C2$ | $Pc$ | $Pbca$ | $P2_1$ |
| $a$ [Å] | 21.556(5) | 24.181(11) | 11.752(14) | 18.161(4) | 12.738(4) |
| $b$ [Å] | 25.509(6) | 5.921(3) | 9.939(12) | 12.768(2) | 20.352(6) |
| $c$ [Å] | 8.3333(18) | 12.625(6) | 18.72(2) | 18.752(4) | 18.372(5) |
| $\beta$ [°] | 90 | 106.327(8) | 96.89(2) | 90 | 90.282(6) |
| $V$ [Å$^3$] | 4582.2(17) | 1734.6(14) | 2171(4) | 4348.3(14) | 4763(2) |
| $Z$ | 8 | 4 | 4 | 8 | 8 |
| $\rho_{calcd}$ [mg/m$^3$] | 1.634 | 1.916 | 1.702 | 1.937 | 1.668 |
| $\theta$ range [°] | 1.24–27.52 | 1.68–27.56 | 1.75–27.63 | 2.23–27.54 | 1.11–27.54 |
| Reflections collected | 26253 | 5387 | 11931 | 21860 | 28487 |
| Reflections unique ($R_{int}$) | 10132 (0.0363) | 3623 (0.0458) | 8102 (0.0335) | 4854 (0.0978) | 18554 (0.1010) |
| Goodness-of-fit | 1.370 | 1.024 | 1.044 | 1.035 | 0.869 |
| $R_1$, $wR_2$ [$I > 2\sigma(I)$] | 0.0718, 0.1764 | 0.0314, 0.0771 | 0.0332, 0.0873 | 0.0392, 0.0981 | 0.0678, 0.1321 |
| $R_1$, $wR_2$ (all data) | 0.0732, 0.1770 | 0.0344, 0.0789 | 0.0394, 0.0919 | 0.0609, 0.1085 | 0.1712, 0.1597 |
| Absolute structure parameter | 0.00 | –0.003(11) | 0.00 | | 0.00 |

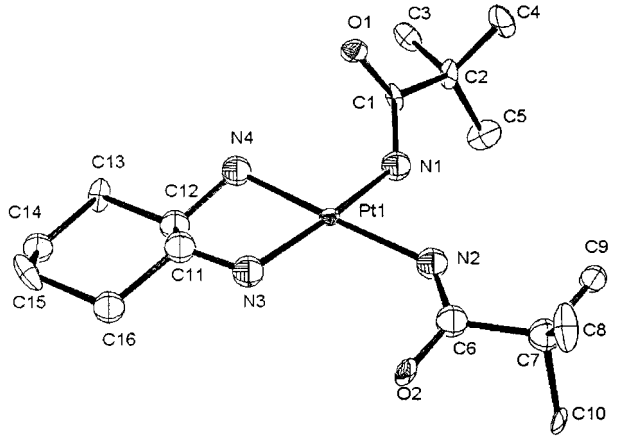


Figure 1. Molecular structure of $[Pt(DACH)(NHCOtBu)_2]$ (**4**). Selected bond lengths and angles: Pt(1)–N(1) 2.055(11), Pt(1)–N(2) 2.098(15), Pt(1)–N(3) 2.062(12), Pt(1)–N(4) 2.051(15), N(4)–Pt(1)–N(1) 93.5(5), N(4)–Pt(1)–N(3) 80.6(6), N(1)–Pt(1)–N(3) 173.2(7), N(4)–Pt(1)–N(2) 178.3(6, N(1)–Pt(1)–N(2) 85.1(5 N(3)–Pt(1)–N(2) 100.9(6).

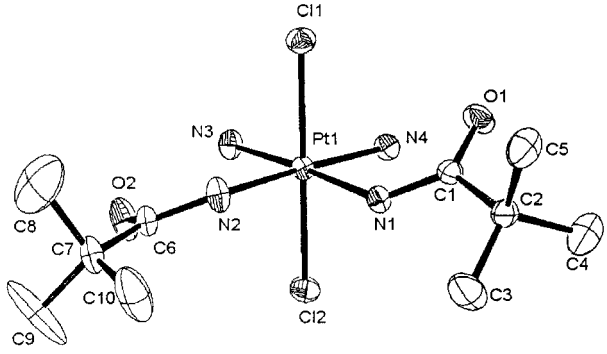


Figure 2. Molecular structure of *trans,cis,cis*-$[PtCl_2(NH_3)_2(NHCOtBu)_2]$ (**5**). Selected bond lengths [Å] and angles [°]: Pt(1)–Cl(1) 2.316(2), Pt(1)–Cl(2) 2.300(2), Pt(1)–N(1) 2.016(6), Pt(1)–N(2) 1.991(7), Pt(1)–N(3) 2.070(7), Pt(1)–N(4) 2.059(6), N(2)–Pt(1)–N(1) 86.6(3), N(2)–Pt(1)–N(4) 176.8(3), N(1)–Pt(1)–N(4) 90.7(3), N(2)–Pt(1)–N(3) 92.4(3), N(1)–Pt(1)–N(3) 177.0(3), N(4)–Pt(1)–N(3) 90.1(3), N(2)–Pt(1)–Cl(2) 89.3(2), N(1)–Pt(1)–Cl(2) 87.54(19), N(4)–Pt(1)–Cl(2) 88.8(2), N(3)–Pt(1)–Cl(2) 89.6(2), N(2)–Pt(1)–Cl(1) 91.3(2), N(1)–Pt(1)–Cl(1) 93.0(2), N(4)–Pt(1)–Cl(1) 90.6(2), N(3)–Pt(1)–Cl(1) 89.9(2), Cl(2)–Pt(1)–Cl(1) 179.24(8).

drally coordinated platinum(IV) center in which the platinum atom is surrounded by three nitrogen and three chlorine atoms in a meridional fashion. The structure is depicted in Figure 3. The cyclohexyl ring exhibits pseudoplanarity as a consequence of the racemic mixture and disorder. The Pt–Cl bond lengths are not unusual, but the chlorine atom *trans* to the nitrogen atom has a rather longer Pt–Cl distance [2.329(2) Å] than the other two in mutually *trans* positions [2.311(2) and 2.319(2) Å]. However, it should be pointed out that an opposite trend has been observed in *cis*-$[PtCl_4\{NH{=}C(Et)OMe\}_2]$.[14] All other bond lengths and angles are as expected and agree perfectly with the values already reported for bis(amidate) platinum complexes.[15]

Compound **10** crystallizes in the noncentrosymmetric space group $P2_1$, and the chirality is predetermined by the ligand 1*R*,2*R*-*trans*-1,2-diaminocyclohexane. Figure 4 depicts the molecular structure of **10** with an atomic labeling scheme. The $PtN_4$ moiety maintains its *cis*-arrangement. The chloride and hydroxide groups are located in axial positions with normal Pt–O and Pt–Cl distances. The Pt–O distance [2.043(16) Å] is consistent with those found in other platinum hydroxide complexes,[16] and the O–Pt–Cl angle is 179.1(5)°. One of the two C=O groups is oriented toward the $NH_2$ group as shown in Figure 4. The N(3)···O(3) distance is 2.71 Å, indicating intramolecular hydrogen bonding.

 © 2006 Wiley-VCH Verlag GmbH & Co. KGaA, Weinheim 

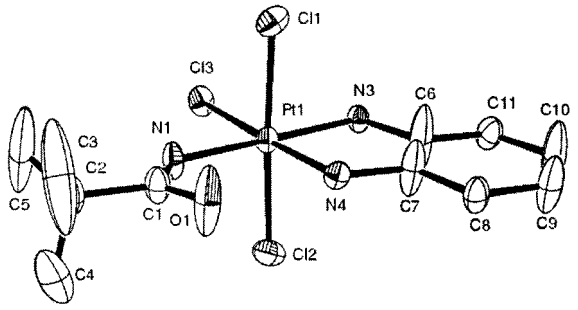


Figure 3. Molecular structure of *mer*-[$PtCl_3$(DACH)(NHCO*t*Bu)] (**7**). Selected bond lengths [Å] and angles [°]: Pt(1)–Cl(1) 2.311(2), Pt(1)–Cl(2) 2.319(2), Pt(1)–Cl(3) 2.329(2), Pt(1)–N(1) 2.009(6), Pt(1)–N(3) 2.056(5), Pt(1)–N(4) 2.051(5), N(1)–Pt(1)–N(4) 96.7(2), N(1)–Pt(1)–N(3) 179.3(3), N(4)–Pt(1)–N(3) 83.0(2), N(1)–Pt(1)–Cl(1) 91.2(2), N(4)–Pt(1)–Cl(1) 88.95(18), N(3)–Pt(1)–Cl(1) 88.21(17), N(1)–Pt(1)–Cl(2) 90.8(2), N(4)–Pt(1)–Cl(2) 87.91(18), N(3)–Pt(1)–Cl(2) 89.78(17), Cl(1)–Pt(1)–Cl(2) 176.46(7), N(1)–Pt(1)–Cl(3) 86.92(17), N(4)–Pt(1)–Cl(3) 176.38(16), N(3)–Pt(1)–Cl(3) 93.38(15), Cl(1)–Pt(1)–Cl(3) 90.57(7), Cl(2)–Pt(1)–Cl(3) 92.45(7).

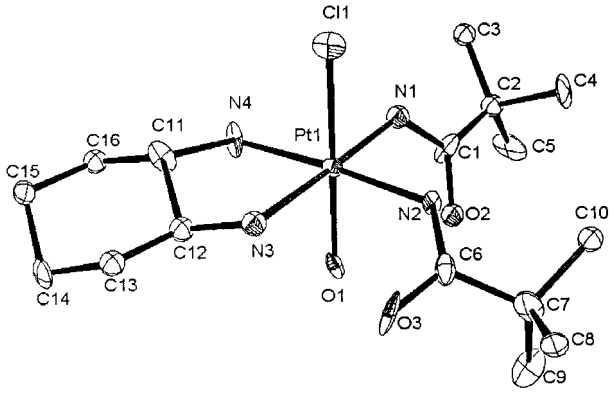


Figure 4. Molecular structure of *trans*,*cis*,*cis*-[PtCl(OH)(DACH)(NHCO*t*Bu)$_2$] (**10**). Selected bond lengths [Å] and angles [°]: Pt(1)–N(1) 2.021(17), Pt(1)–N(2) 2.014(18), Pt(1)–N(3) 2.094(18), Pt(1)–N(4) 2.07(2), Pt(1)–Cl(1) 2.338(7), Pt(1)–O(1) 2.043(16), N(2)–Pt(1)–N(1) 87.2(8), N(1)–Pt(1)–N(4) 95.0(8), N(2)–Pt(1)–N(3) 96.0(9), N(2)–Pt(1)–N(4) 176.0(9), N(1)–Pt(1)–N(3) 176.5(8), N(4)–Pt(1)–N(3) 81.8(8), N(2)–Pt(1)–O(1) 87.1(7), N(1)–Pt(1)–O(1) 92.3(6), O(1)–Pt(1)–N(4) 89.4(7), O(1)–Pt(1)–N(3) 86.4(7), N(2)–Pt(1)–Cl(1) 93.7(6), N(1)–Pt(1)–Cl(1) 87.4(5), N(3)–Pt(1)–Cl(1) 93.8(6), N(4)–Pt(1)–Cl(1) 89.8(6), O(1)–Pt(1)–Cl(1) 179.1(5).

In summary, oxidative addition of chlorine or HOCl to the neutral [$Pt(RNH_2)_2$(NHCO*t*Bu)$_2$] complexes in water yielded a number of bis(amidate) and mono(amidate) platinum(IV) complexes. Complexes **5**–**10** represent the first fully characterized examples of platinum(IV) mono(amidate) and bis(amidate) complexes derived from oxidative addition. The present study also provides a convenient synthetic route for chloro(hydroxo)platinum(IV) complexes using NaClO as the source of the chloride and hydroxide ions. Furthermore, these complexes may potentially be precursors for the preparation of some $Pt^{IV}$ compounds since the Cl atoms can easily be replaced by other anions.

## Experimental Section

**General Remarks:** *cis*-$Pt(EtNH_2)_2Cl_2$,[17] $Pt(DACH)Cl_2$ (DACH = *trans*-1,2-diaminocyclohexane),[18] *cis*-[$Pt(NH_3)_2$(NHCO*t*Bu)$_2$]·$2H_2O$,[19] and *cis*-[Pt(DACH)(NHCO*t*Bu)$_2$]·$4H_2O$[19] were prepared according to previously published procedures. $Cl_2/H_2O$ (available chlorine 0.3%), NaClO/$H_2O$ (available $Cl_2$ 5.0%), and other chemicals were purchased from commercial sources and used as received. The elemental analyses were performed with a Perkin–Elmer PE 2400II analyzer. The $^1H$ and $^{195}Pt$ NMR spectra were recorded with a Bruker 500 MHz spectrometer. The NMR chemical shifts are given in ppm relative to TMS ($^1H$) and $K_2PtCl_4$ ($^{195}Pt$), and referenced either to residual solvent signals ($^1H$) or externally ($^{195}Pt$).

CAUTION! Perchlorate salts of metal complexes are potentially explosive and should be handled with great care.

***cis*-[Pt(EtNH$_2$)$_2$(NC*t*Bu)$_2$](ClO$_4$)$_2$ (1):** A suspension of *cis*-$Pt(EtNH_2)_2Cl_2$ (0.36 g, 1.0 mmol) in water (10 mL) was treated with $AgClO_4$ (0.41 g, 2.0 mmol), and the mixture was stirred overnight in the dark. After the removal of AgCl, *t*BuCN (1.0 g, 12.0 mmol) was added to the filtrate. The resulting white precipitate was separated and washed with $H_2O$, EtOH, and $Et_2O$, and dried in vacuo. Yield: 0.53 g (82%). $C_{14}H_{32}Cl_2N_4O_8Pt$ (650.41): calcd. C 25.85, H 4.96, N 8.61; found C 25.81, H 4.87, N 8.50. $^1H$ NMR (500 MHz, [$D_6$]acetone): 2.62 (q, $J_{HH}$ = 7.0 Hz, $CH_2CH_3$, 4 H), 1.52 (s, $C(CH_3)_3$, 18 H), 1.10 (t, $CH_2CH_3$, 6 H) ppm. $^{195}Pt$ NMR (107.30 MHz, [$D_6$]acetone): $\delta$ = –2857 ppm.

***cis*-[Pt(EtNH$_2$)$_2$(NHCO*t*Bu)$_2$]·H$_2$O (2):** A suspension of **1** (1.30 g, 2.0 mmol) in water (10 mL) was treated with NaOH (0.20 g, 5.0 mmol). The mixture was stirred overnight at room temperature. The resulting white solid was collected by filtration, washed with cold water and dried in vacuo. Condensing the filtrate and cooling at 5 °C afforded the second crop of the product. Yield: 0.88 g (87%). $C_{14}H_{34}N_4O_2Pt·H_2O$ (503.54): calcd. C 33.39, H 7.21, N 11.13; found C 33.29, H 7.31, N 11.12. $^1H$ NMR (500 MHz, [$D_6$]-acetone): $\delta$ = 6.24 (br. s. $NH_2$, 4 H), 4.89 (s, NH, 2 H), 2.75 (q, $J_{HH}$ = 6.8 Hz, $CH_2$, 4 H), 1.17 (t, $CH_2CH_3$, 6 H), 1.10 (s, $C(CH_3)_3$, 18 H) ppm. $^{195}Pt$ NMR (107.00 MHz, [$D_6$]acetone): $\delta$ = –2564 ppm.

***cis*-[Pt(1*R*,2*R*-DACH)(NC*t*Bu)$_2$](ClO$_4$)$_2$ (3):** The compound was prepared according to the procedure above for **1** using Pt(1R,2R-DACH)$Cl_2$ (0.38 g, 1.0 mmol) instead of *cis*-$Pt(EtNH_2)Cl_2$. Yield: 0.62 g (92%). $C_{16}H_{32}N_4Cl_2O_8Pt$ (674.43): calcd. C 28.49, H 4.78, N 8.31; found C 28.40, H 4.92, N 8.25. $^1H$ NMR (500 MHz, [$D_6$]-acetone): 1.54 (s, $CH_3$, 18 H), 2.75, 2.20, 1.56, 1.38, 1.20 (m, $C_6H_{10}$, 10 H) ppm. $^{195}Pt$ NMR (107.30, [$D_6$]acetone): –2857 ppm.

***cis*-[Pt(1*R*,2*R*-DACH)(NHCO*t*Bu)$_2$]·3H$_2$O (4):** The compound was prepared according to the procedure above for **2** using [Pt(1R,2R-DACH)(NC*t*Bu)$_2$](ClO$_4$)$_2$ (0.62 g, 0.09 mmol) instead of [$Pt(EtNH_2)$(NC*t*Bu)$_2$](ClO$_4$)$_2$. Yield: 0.48 g (94%). $C_{16}H_{34}N_4O_2Pt·3H_2O$ (563.59): calcd. C 34.10, H 7.15, N 9.94; found C 34.44, H 6.74, N 9.94. $^1H$ NMR (500 MHz, [$D_6$]acetone): $\delta$ = 6.51, 4.65 (m, $NH_2$, each 2 H), 5.59 (s, NH, 2 H), 2.31, 1.94, 1.53, 1.35 (m, $C_6H_{10}$, 10 H), 1.08 (s, $C(CH_3)_3$, 18 H) ppm. $^{195}Pt$ NMR (107.30 MHz, [$D_6$]acetone): $\delta$ = –2626 ppm.

***trans*,*cis*,*cis*-[PtCl$_2$(NH$_3$)$_2$(NHCO*t*Bu)$_2$] (5):** [$Pt(NH_3)_2$(NHCO*t*Bu)$_2$]·$2H_2O$ (47 mg, 0.10 mmol) was suspended in $Cl_2/H_2O$ (2.36 mL, 0.3%). The mixture was stirred for 10 min to yield a yellow solution. After the solvent was removed with a rotary evaporator, the yellow solid was washed with cold water and dried in vacuo. Crystals of **5** suitable for X-ray diffraction analysis were grown by slow

 © 2006 Wiley-VCH Verlag GmbH & Co. KGaA, Weinheim 

evaporation of its aqueous solution. Yield: 42 mg (84%). $C_{10}H_{26}Cl_2N_4O_2Pt$ (500.32): calcd. C 24.01, H 5.24, N 11.20; found C 23.85, H 4.98, N 11.46. $^1$H NMR (500 MHz, [D]DMSO): $\delta$ = 6.12 (s, NH, 2 H), 5.89 (s, $NH_3$, 6 H), 1.14 (s, $C(CH_3)_3$, 18 H) ppm. $^{195}$Pt (107.00 MHz, [D]DMSO): $\delta$ = –35 ppm.

***trans*,*cis*,*cis*-[PtCl$_2$(EtNH$_2$)$_2$(NHCO*t*Bu)$_2$]·H$_2$O (6):** The compound was prepared according to the procedure above for **5** using [Pt(EtNH$_2$)$_2$(NHCO*t*Bu)$_2$]·H$_2$O (50.3 mg, 0.1 mmol) in place of [Pt(NH$_3$)$_2$(NHCO*t*Bu)$_2$]·2H$_2$O. Yield: 41.7 mg (75%). $C_{14}H_{34}Cl_2N_4O_2Pt$ (556.43): calcd. C 30.22, H 6.16, N 10.07; found C 30.10, H 6.25, N 9.96. $^1$H NMR (500 MHz, [D$_6$]DMSO): $\delta$ = 7.09 (s, $NH_2$, 4 H), 5.63 (s, NH, 2 H), 2.64 (m, $CH_2$, 4 H), 1.15, 1.06 (both t, $J_{HH}$ = 7.2 Hz, $CH_2CH_3$, each 3 H), 1.09 (s, $C(CH_3)_3$, 18 H) ppm. $^{195}$Pt (107.30 MHz, [D$_6$]DMSO): $\delta$ = –31 ppm.

***mer*-[PtCl$_3$(DACH)(NHCO*t*Bu)]·(CH$_3$)$_2$CO (7):** The compound was prepared according to the procedure above for **5** using [Pt(DACH)(NHCO*t*Bu)$_2$]·3H$_2$O (67.4 mg, 0.1 mmol) instead of [Pt(NH$_3$)$_2$(NHCO*t*Bu)$_2$]·2H$_2$O. Yield: 31.7 mg, (67%). $C_{11}H_{24}Cl_3PtO$ (473.74): calcd. C 29.30, H 5.27, N 7.32; found C 29.45, H 5.29, N 7.07. $^1$H NMR (500 MHz, [D$_6$]DMSO): $\delta$ = 7.81–6.26 (m, NH + $NH_2$, 5 H), 1.09, 1.53, 2.06, 2.71 (m, $C_6H_{10}$, 10 H), 1.12 (s, $C(CH_3)_3$, 18 H) ppm. $^{195}$Pt NMR (107.30 MHz, [D$_6$]-DMSO): $\delta$ = –289 ppm.

***trans*,*cis*,*cis*-[PtCl(OH)(NH$_3$)$_2$(NHCO*t*Bu)$_2$] (8):** *cis*-[Pt(NH$_3$)$_2$-(NHCO*t*Bu)$_2$]·2H$_2$O (47 mg, 0.10 mmol) was suspended in NaClO/H$_2$O (2 mL, available $Cl_2$ 5.0%). The mixture was stirred for 10 min to yield a yellow solution. After the solvent was removed with a rotary evaporator, the yellow solid was washed with cold water and dried in vacuo. Yield: 20.2 (42%). $C_{10}H_{27}ClN_4O_3Pt$ (481.88): calcd. C 24.92, H 5.65, N 11.63; found C 24.83, H 5.80, N 11.49. $^1$H NMR (500 MHz, [D$_6$]DMSO): $\delta$ = 6.15 (s, NH, 2 H), 5.31, 4.82 (s, $NH_3$, 6 H), 1.14 (s, $C(CH_3)_3$, 18 H) ppm. $^{195}$Pt NMR (107.30 MHz, [D$_6$]DMSO): $\delta$ = –134 ppm.

***trans*,*cis*,*cis*-[PtCl(OH)(EtNH$_2$)$_2$(NHCO*t*Bu)$_2$]·H$_2$O (9):** The compound was prepared according to the procedure above for **8** using [Pt(EtNH$_2$)$_2$(NHCO*t*Bu)$_2$]·H$_2$O (50.3 mg, 0.1 mmol) instead of [Pt(NH$_3$)$_2$(NHCO*t*Bu)$_2$]·2H$_2$O. Yield: 35 mg (63%). $C_{14}H_{35}ClN_4O_3Pt·H_2O$ (556.00): calcd. C 30.24, H 6.71, N 10.08; found C 30.24, H 6.53, N 9.89. $^1$H NMR (500 MHz, [D$_6$]DMSO): $\delta$ = 6.46 (s, NH, 2 H), 7.05, 4.92 (s, $NH_2$, 4 H), 2.70 (q, $J_{HH}$ = 7.0 Hz, $CH_2$, 4 H), 1.15 (t, $CH_2CH_3$, 6 H), 1.07 (s, $C(CH_3)_3$, 18 H) ppm. $^{195}$Pt NMR (107.30 MHz, [D$_6$]DMSO): $\delta$ = –146 ppm.

***trans*,*cis*,*cis*-[PtCl(OH)(DACH)(NHCO*t*Bu)$_2$] (10):** A suspension of [Pt(DACH)(NHCO*t*Bu)$_2$] (52 mg, 0.1 mmol) in water was treated with an aqueous solution of NaClO (2 mL, available $Cl_2$ 5%). A yellow solution was yielded after stirring for 30 min. Yellow crystals were grown upon slow evaporation of the resulting yellow solution. Yield: 43.8 mg (78%). $C_{16}H_{35}ClN_4O_3Pt$ (562.00): cacld. C 34.19, H 6.28, N 9.97; found C 34.01, H 6.59, N 9.52. $^1$H NMR (500 MHz, [D$_6$]DMSO): $\delta$ = 7.51, 7.31 (s, NH, 2 H), 5.94, 5.96 (both s, $NH_2$, 4 H), 2.65, 2.06, 1.52, 1.48 (all m, $C_6H_{10}$, 10 H), 1.15 (s, $C(CH_3)_3$, 18 H) ppm. $^{195}$Pt NMR (107.30 MHz, [D$_6$]DMSO): $\delta$ = 189 ppm.

***trans*,*cis*,*cis*-[Pt(OH)(DACH)(DMSO)(NHCO*t*Bu)$_2$]Cl:** $^1$H NMR (500 MHz, [D$_6$]DMSO): $\delta$ = 7.82 (s, NH, 2 H), 6.00 (s, $NH_2$, 4 H), 2.51, 2.08, 1.52, 1.49 (m, $C_6H_{10}$, 10 H), 1.08 (s, $C(CH_3)_3$, 18 H) ppm. $^{195}$Pt NMR (107.30, [D$_6$]DMSO): $\delta$ = –195 ppm.

**X-ray Crystallographic Study:** Single crystals of the complexes **4**–**7**, and **10** were grown by slow evaporation of solutions from the above-described preparations. In each case, suitable crystals were mounted on a glass fibre; the hemispheres of X-ray intensity data were collected with a Bruker Smart-*CCD* diffractometer equipped with Mo-$K_\alpha$ radiation ($\lambda$ = 0.71073 Å). The first 50 frames were recollected at the end of the process to monitor crystal decay. The raw frame data were integrated into the SHELX-format reflection files and corrected for Lorentz and polarization effects using SAINT.[20] All structures were solved by direct methods and refined against $F^2$ by full-matrix least-squares techniques.[21] All non-hydrogen atoms were refined anisotropically. Hydrogen atoms were introduced into their calculated positions. Compounds **6**–**8** crystallize in noncentrosymmetric space groups. The absolute configurations were determined by refinement of the Flack *x* parameters. Details of the X-ray experiments and crystal data are summarized in Table 1.

CCDC-285359 (for **4**), -195437 (for **5**), -195438 (for **6**), -195439 (for **7**), and -195440 (for **10**) contain the supplementary crystallographic data for this paper. These data can be obtained free of charge from The Cambridge Crystallographic Data Centre via www.ccdc.cam.ac.uk/data_request/cif.

## Acknowledgments

We wish to thank the National Science Foundation of China (20572096) and Zhejiang Province (R405066) for financial support of this work.

[1] a) B. Rosenberg, L. Van Camp, T. Krigas, *Nature* **1965**, *205*, 698; b) B. Rosenberg, L. Van Camp, J. E. Trosko, V. H. Mansour, *Nature* **1969**, *222*, 385.

[2] a) E. R. Jamieson, S. J. Lippard, *Chem. Rev.* **1999**, *99*, 2467–2498; b) Y. Qu, N. Farrell, *J. Am. Chem. Soc.* **1991**, *113*, 4851–4857; c) S. Komeda, M. Lutz, A. L. Spek, M. Chikuma, J. Reedijik, *Inorg. Chem.* **2000**, *39*, 4230–4236; d) V. Brabec, J. Kasparkova, O. Vrana, O. Novakova, J. W. Cox, Y. Qu, N. Farrell, *Biochemistry* **1999**, *38*, 6781–6790; e) R. K. O. Sigel, E. Freisinger, S. Metzger, B. Lippert, *J. Am. Chem. Soc.* **1998**, *120*, 12000–12007.

[3] a) M. Peilert, S. Weißbach, E. Freisinger, V. I. Korsunsky, B. Lippert, *Inorg. Chim. Acta* **1997**, *265*, 187–195; b) H. Urata, H. Moriyama, K. Matsumoto, *Inorg. Chem.* **1991**, *30*, 3914–3919; c) S. Ongeri, D. J. Aitken, H.-P. Husson, J. Kozelka, B. Viossat, *Inorg. Chem.* **2000**, *39*, 6131–6133.

[4] a) D. Holthenrich, M. Krumm, E. Zangrando, F. Pichierri, L. Randaccio, B. Lippert, *J. Chem. Soc., Dalton Trans.* **1995**, 3275–3279; b) J. A. R. Navarro, M. B. L. Janik, E. Freisinger, B. Lippert, *Inorg. Chem.* **1999**, *38*, 426–432; c) J. A. R. Navarro, E. Freisinger, B. Lippert, *Inorg. Chem.* **2000**, *39*, 2301–2305; d) R.-D. Schnebeck, E. Freisinger, F. Glahé, B. Lippert, *J. Am. Chem. Soc.* **2000**, *122*, 1381–1390; e) A. Schneider, E. Freisinger, B. Beck, B. Lippert, *J. Chem. Soc., Dalton Trans.* **2000**, 837–838.

[5] A. Erxleben, B. Lippert, *J. Chem. Soc., Dalton Trans.* **1996**, 2329–2333.

[6] K. Matsumoto, K. Sakai, *Adv. Inorg. Chem.* **1999**, *49*, 375.

[7] a) Y. Lin, H. Misawa, J. Yamada, K. Matsumoto, *J. Am. Chem. Soc.* **2001**, *123*, 569–575; b) K. Matsumoto, J. Matsunami, K. Mizuno, H. Uemura, *J. Am. Chem. Soc.* **1996**, *118*, 8959–8960.

[8] K. Matsumoto, Y. Nagai, J. Matsunami, K. Mizuno, T. Abe, R. Somazawa, J. Kinoshita, H. Shimura, *J. Am. Chem. Soc.* **1998**, *120*, 2900–2907.

[9] a) A. Shilov, G. B. Shulpin, *Chem. Rev.* **1997**, *97*, 2879–2932; b) K. Mylvaganam, G. B. Bacskay, N. S. Hush, *J. Am. Chem. Soc.* **2000**, *122*, 2041–2052; c) P. E. M. Siegbahn, R. H. Crabtree, *J. Am. Chem. Soc.* **1996**, *118*, 4442–4450.

[10] a) M. A. Fuertes, J. Castilla, C. Alonso, J. M. Perez, *Curr. Med. Chem.: Anti-Cancer Agents* **2002**, *2*, 539–551; b) A. Alvarez-Valdés, J. M. Pérez, I. López-Solera, R. Lannegrand, J. M. Continente, P. Amo-Ochoa, M. J. Camazón, X. Solans, M.

 © 2006 Wiley-VCH Verlag GmbH & Co. KGaA, Weinheim 

Font-Bardía, C. Navarro-Ranninger, *J. Med. Chem.* **2002**, *45*, 1835–1844; c) M. D. Hall, G. J. Foran, M. Zhang, P. J. Beale, T. W. Hambley, *J. Am. Chem. Soc.* **2003**, *125*, 7524–7525.
[11] a) D. Monti, A. Pastorini, G. Mancini, S. Borocci, P. Tagliatesta, *J. Mol. Catal. A: Chem.* **2002**, *179*, 125–131; b) B. Meunier, E. Guilmet, M.-E. De Carvalho, R. Poilblanc, *J. Am. Chem. Soc.* **1984**, *106*, 6668–6676.
[12] a) K. M. Kim, Y. S. Sohn, *Inorg. Chem.* **1998**, *37*, 6109–6112; b) C. F. Barnard, J. F. Vollano, P. A. Chaloner, S. Dewa, *Z. Inorg. Chem.* **1996**, *35*, 3280–3284; c) M. Galanski, B. K. Keppler, *Inorg. Chem.* **1996**, *35*, 1709–1711; d) F. Basolo, J. C. Bailar Jr, *J. Am. Chem. Soc.* **1950**, *72*, 2433–2438.
[13] a) V. Y. Kukushikin, T. B. Pakhomova, N. A. Bokach, G. Wagner, M. L. Kuznetsov, M. Galanski, A. J. L. Pombeiro, *Inorg. Chem.* **2000**, *39*, 216–225; b) W. Chen, K. Matsumoto, *Bull. Chem. Soc. Jpn.* **2002**, *75*, 1561–1562.
[14] N. A. Bokach, V. Y. Kukushkin, M. L. Kuznetsov, D. A. Garnovskii, G. Natile, A. J. L. Pombeiro, *Inorg. Chem.* **2002**, *41*, 2041–2053.
[15] W. Chen, K. Matsumoto, *Eur. J. Inorg. Chem.* **2002**, 2664–2670.
[16] a) A. Klein, K. W. Klinkhammer, T. Scheiring, *J. Organomet. Chem.* **1999**, *592*, 128–135; b) J. Müller, F. Glahè, E. Freisinger, B. Lippert, *Inorg. Chem.* **1999**, *38*, 3160–3166.
[17] F. D. Rochon, L. M. Gruia, *Inorg. Chim. Acta* **2000**, *306*, 193–204.
[18] S. G. Gill, B. Resenberg, *J. Am. Chem. Soc.* **1982**, *104*, 4598–4604.
[19] W. Chen, K. Matsumoto, *Inorg. Chim. Acta* **2003**, *342*, 88–96.
[20] G. M. Sheldrick, *SHELXS-97, Program for X-ray Crystal Structure Solution*, University of Göttingen: Göttingen, Germany, **1997**.
[21] G. M. Sheldrick, *SHELXL-97, Program for X-ray Crystal Structure Refinement*, University of Göttingen: Göttingen, Germany, **1997**.

Received: September 30, 2005
Published Online: February 2, 2006

 © 2006 Wiley-VCH Verlag GmbH & Co. KGaA, Weinheim 

DOI: 10.1002/ejic.200500973

# Direct Preparation of [Ru($\eta^2$-$O_2CO$)($\eta^6$-arene)(L)] Carbonate Complexes (L = Phosphane, Carbene) and Their Use as Precursors of [$RuH_2$(*p*-cymene)($PCy_3$)] and [Ru($\eta^6$-arene)(L)($MeCN)_2$][$BF_4]_2$: X-ray Crystal Structure Determination of [Ru($\eta^2$-$O_2CO$)(*p*-cymene)($PCy_3$)]·1/2$CH_2Cl_2$ and [Ru($\eta^2$-$O_2CO$)($\eta^6$-$C_6Me_6$)-($PMe_3$)]·$H_2O$

**Bernard Demerseman,*[a] Mbaye Diagne Mbaye,[a] David Sémeril,[a] Loïc Toupet,[a] Christian Bruneau,[a] and Pierre H. Dixneuf[a]**

**Keywords:** Arene ligands / Hydrides / O ligands / Reactive intermediates / Ruthenium

[$RuCl_2$($\eta^6$-arene)($PR_3$)] complexes react with $K_2CO_3$ in the presence of water to afford the carbonatoruthenium(II) derivatives [Ru($\eta^2$-$O_2CO$)($\eta^6$-arene)($PR_3$)] (**2**; arene = *p*-cymene, R = Cy, Ph, or Me; arene = hexamethylbenzene, R = Me) involving a planar Ru($\eta^2$-$O_2CO$) moiety as shown by X-ray crystal structure determination of **2a** (*p*-cymene, $PCy_3$) and **2d** (hexamethylbenzene, $PMe_3$). The complex [Ru($\eta^2$-$O_2CO$)(*p*-cymene)($PCy_3$)] is cleanly converted in hot methanol into the dihydride [$RuH_2$(*p*-cymene)($PCy_3$)]. The related complexes [Ru($\eta^2$-$O_2CO$)($\eta^6$-arene)(IMes)] [arene = *p*-cymene or hexamethylbenzene, IMes = 1,3-bis(2,4,6-trimethylphenyl)imidazol-2-ylidene] are straightforwardly prepared by treating [$RuCl_2$($\eta^6$-arene)$]_2$ precursors with 1,3-bis(2,4,6-trimethylphenyl)imidazolium chloride and $K_2CO_3$ in THF at reflux. The removal of the carbonato ligand from complexes **2** with $HBF_4$ in the presence of acetonitrile leads to the dicationic derivatives [Ru($\eta^6$-arene)(L)($MeCN)_2$][$BF_4]_2$ (L = $PR_3$ or IMes).
(© Wiley-VCH Verlag GmbH & Co. KGaA, 69451 Weinheim, Germany, 2006)

## Introduction

The formation of metal catalysts in situ from a metal complex and an alkali metal carbonate salt, introduced as a base, is receiving growing attention. This is the case with a variety of cross-coupling and Heck reactions catalysed by palladium complexes.[1,2] Recently, the generation of ruthenium catalysts for ring-closing enyne metathesis[3,4] or sequential alkene isomerisation/Claisen reactions,[5] by treatment of [$RuCl_2$($\eta^6$-arene)$]_2$ with an imidazolium salt and $Cs_2CO_3$ in situ, has provided other useful examples. In this case, $Cs_2CO_3$ was expected to generate an imidazolylidene carbene by deprotonation of the imidazolium salt, as was fully demonstrated by Arduengo[6] and Çetinkaya.[7] However, the question was raised whether the carbonate anion acts solely as a proton acceptor or might additionally enter into the coordination sphere of the ruthenium centre. Indeed, there are already examples of carbonatoruthenium(II) complexes, although such complexes were most often depicted as unexpected or undesired side-products. Their formation has been observed during the course of various processes, including metathetical exchange between an alkali metal carbonate and a ruthenium halide or cationic ruthenium precursor,[8–11] reaction of carbon dioxide with an oxaruthenacyclobutane,[8] hydrolysis of carbamato ligands,[12] oxidation of coordinated carbon monoxide,[13–18] and reactions involving a formal reduction of carbon dioxide ($2\ CO_2 + 2e^- \rightarrow CO + CO_3^{2-}$).[19,20] From a structural point of view, mononuclear carbonatoruthenium(II) complexes contain an Ru($\eta^2$-$O_2CO$) fragment, whereas the carbonate dianion is a bridging ligand in the dinuclear [$Ru_2$(μ-$O_2CO)_4]^{3-}$ anion[21–23] and in polynuclear, heteroleptic ruthenium complexes.[9,24,25]

The involvement of carbonatoruthenium complexes in organometallic synthesis is still uncommon but, remarkably, the carbonato complex [Ru($\eta^2$-$O_2CO$)(bipy)$_2$] has been shown to react with terminal alkynes under aqueous acidic conditions to conveniently produce [Ru(alkyl)(CO)(bipy)$_2]^+$ and [Ru(acyl)(CO)(bipy)$_2]^+$ derivatives.[26–28] We wish to report here the direct synthesis of [Ru($\eta^2$-$O_2CO$)($\eta^6$-arene)($PR_3$)] carbonatoruthenium(II) derivatives starting from [$RuCl_2$($\eta^6$-arene)($PR_3$)] precursors and $K_2CO_3$, and of related [Ru($\eta^2$-$O_2CO$)($\eta^6$-arene)(IMes)] complexes, where IMes is an imidazolylidene ligand, from [$RuCl_2$($\eta^6$-arene)$]_2$ precursors and an imidazolium salt in the presence of $K_2CO_3$. The present account illustrates the usefulness of the carbonato ligand as a protecting group for ruthenium centres that favours the access to valuable ruthenium hydride derivatives, such as the dihydride complex [$RuH_2$-

[a] Institut de Chimie de Rennes, UMR-CNRS 6509, Organométalliques et Catalyse, Université de Rennes 1,
35042 Rennes Cedex, France
Fax: +33-22-323-6939
E-mail: bernard.demerseman@univ-rennes1.fr

 WILEY InterScience DISCOVER SOMETHING GREAT © 2006 Wiley-VCH Verlag GmbH & Co. KGaA, Weinheim 

(*p*-cymene)($PCy_3$)], and to dicationic [Ru(η⁶-arene)(L)-$(MeCN)_2$][$BF_4$]$_2$ derivatives.

## Results and Discussion

### Synthesis of [Ru(η²-$O_2CO$)(η⁶-arene)(L)] Complexes

Upon stirring at room temperature, a red slurry consisting of [$RuCl_2$(*p*-cymene)($PCy_3$)] (**1a**) and $K_2CO_3$ in acetone as solvent gradually (2 d) turned yellow. Subsequent workup afforded orange-yellow crystals of the new carbonato complex [Ru(η²-$O_2CO$)(*p*-cymene)($PCy_3$)] (**2a**) in 78% yield (Scheme 1).

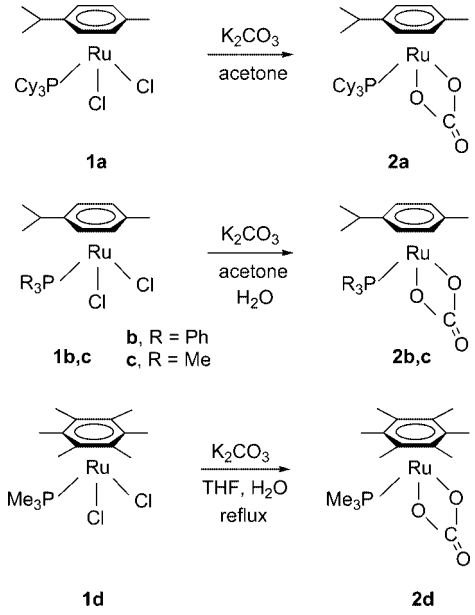


Scheme 1. Synthesis of the new carbonatoruthenium complexes **2a**–**d**.

No reaction was detected under similar conditions starting from [$RuCl_2$(*p*-cymene)($PR_3$)] precursors **1b**,**c** (**b**: R = Ph; **c**: R = Me) without the addition of a small amount of water to the reaction mixture (ca. 2 wt.-% relative to acetone) to promote the expected reaction and the formation of complexes **2b**,**c** (Scheme 1). Complexes **2b**,**c** were isolated as orange solids in 97 and 95% yield, respectively. Since very long reaction times (10 d starting from **1c**) were required, the use of methanol (instead of acetone) as a polar solvent to facilitate the cleavage of ruthenium–chloride bonds was attempted. Starting from **1b**,**c**, an obvious decomposition was observed at room temperature, whereas **1a** still led to **2a** but also gave minor amounts of the dihydride [$RuH_2$(*p*-cymene)($PCy_3$)] (**3a**) and the chloro hydride [RuCl(H)(*p*-cymene)($PCy_3$)] (**4a**), as determined by $^{31}P\{^1H\}$ NMR spectroscopy. When the yellow reaction mixture in methanol was additionally heated at reflux for 1 h, the dihydride **3a** was obtained selectively (Scheme 2). The dihydride complex **3a** was isolated as a colourless solid in yields of up to 81%. As expected, **3a** was also obtained when a solution of pure **2a** in methanol was heated at reflux (Scheme 2).

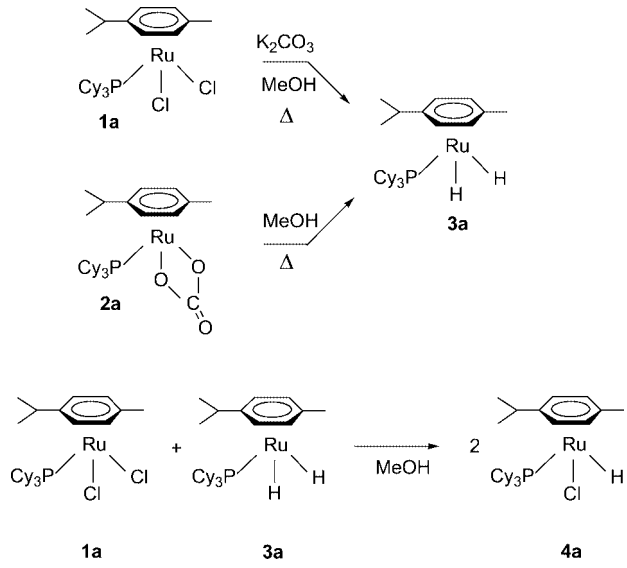


Scheme 2. Synthesis of the ruthenium hydride complexes **3a** and **4a**.

The formation of a metal alkoxide intermediate that spontaneously undergoes a β-elimination process is among the most usual routes allowing the transformation of metal–halide into metal–hydride bonds. Evidence for such a mechanism was first obtained from the study of the reaction of [RuCl(Cp)($PPh_3$)$_2$] with NaOMe,[29] and the synthesis of [RuH(Cp)($PPh_3$)$_2$] has since been more conveniently achieved using $K_2CO_3$ in methanol.[30] The formation of the hydride derivatives **3a** and **4a** that occurs in methanol can be rationalised in the same way. The use of acetone as solvent precludes the formation of any ruthenium methoxide intermediate and thus allows selective formation of **2a**. The conversion of **2a** into the dihydride complex **3a** that occurs in methanol at reflux might result from the reaction of the carbonato ligand with two molecules of methanol to generate methoxide groups along with carbon dioxide and water. Finally, the second minor compound, identified as the chloro hydride [RuCl(H)(*p*-cymene)($PCy_3$)] (**4a**), was alternatively synthesised by mixing equimolar amounts of **1a** and **3a** in methanol as solvent (Scheme 2). The synthesis of the parent complex [RuCl(H)(η⁶-benzene)($PCy_3$)] has recently been achieved by treating [$RuCl_2$(η⁶-benzene)($PCy_3$)] with sodium formate.[31]

As with the reaction with **1c**, the conversion of the more robust precursor [$RuCl_2$(hexamethylbenzene)($PMe_3$)] (**1d**) into the corresponding carbonato complex [Ru(η²-$O_2CO$)(η⁶-$C_6Me_6$)($PMe_3$)] (**2d**) needed a reaction time longer than 10 d at room temperature. The synthesis of **2d** was more rapidly (24 h) achieved by treating **1d** with $K_2CO_3$ in THF at reflux, although addition of a small amount of water was also required to reach completion of the reaction (Scheme 1).

The new complexes **2a**–**d**, **3a** and **4a** were characterised by $^1H$, $^{13}C$, $^{13}C\{^1H\}$ and $^{31}P\{^1H\}$ NMR spectroscopy and elemental analysis. The $^1H$ and $^{31}P\{^1H\}$ NMR spectra accounted for the coordination of the phosphane besides the

 © 2006 Wiley-VCH Verlag GmbH & Co. KGaA, Weinheim 

arene ligand. More specific and characteristic were the high-field $^1$H NMR resonances corresponding to the RuH protons in **3a** and **4a**. The presence of the carbonato ligand in **2a**–**d** was confirmed by $^{13}$C and $^{13}$C{$^1$H} NMR spectroscopy as a resonance between $\delta$ = 165.6 and 166.8 ppm with a small coupling constant ($^3J_{P,C} < 2.9$ Hz). The two complexes **2a**·1/2$CH_2Cl_2$ and **2d**·$H_2O$ were further characterised by an X-ray crystal structure analysis. Crystallographic data are summarised in the Exp. Sect., and ORTEP drawings of **2a** and **2d** are shown in Figures 1 and 2, respectively; selected bond lengths and angles are given in the captions.

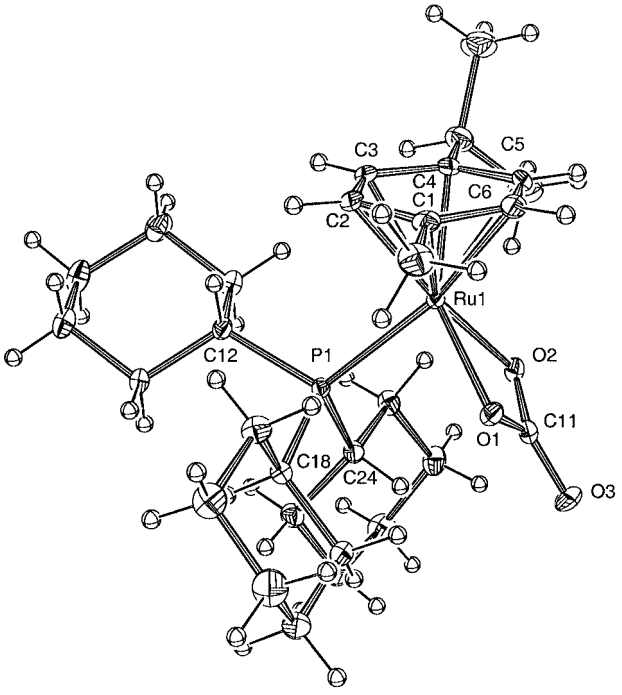


Figure 1. ORTEP drawing of **2a**·1/2$CH_2Cl_2$ showing 50% probability thermal ellipsoids. The $CH_2Cl_2$ molecule has been omitted for clarity. Selected bond lengths [Å] and angles [°]: Ru1–O1 2.079(2), Ru1–O2 2.087(2), O1–C11 1.323(3), O2–C11 1.315(3), O3–C11 1.232(3), Ru1–P1 2.3779(6); O1–Ru1–O2 62.90(7), C11–O1–Ru1 93.02(1), C11–O2–Ru1 92.90(1), O1–C11–O2 111.0(2), O1–C11–O3 124.5(2), O2–C11–O3 124.5(2), O1–Ru1–P1 86.92(5), O2–Ru1–P1 88.09(5).

Figures 1 and 2 show mononuclear species containing a carbonate dianion $\eta^2$-*O*,*O*-coordinated to the ruthenium centre. The two Ru–O bond lengths are almost identical, although they are slightly longer in **2d** [2.104(2) and 2.091(2) Å in **2d** vs. 2.087(2) and 2.079(2) Å in **2a**]. The two Ru–O bonds form a small angle [62.90(7)° in **2a**; 62.81(8)° in **2d**]. The exocyclic C=O bond in **2a** or **2d** [1.232(3) and 1.239(4) Å, respectively] is significantly shorter than the two endocyclic C–O bonds [1.323(3) and 1.315(3) Å in **2a**; 1.325(4) and 1.315(4) Å in **2d**]. It is worth noting the planar arrangement of the Ru($\eta^2$-$O_2$CO) fragment, as indicated by the sum of the angles of the four-membered ring, and around the carbon atom, both of which are very close to 360° (359.8° and 360.0° for **2a** and 359.9° and 360.0° for **2d**, respectively). This plane is approximately perpendicular

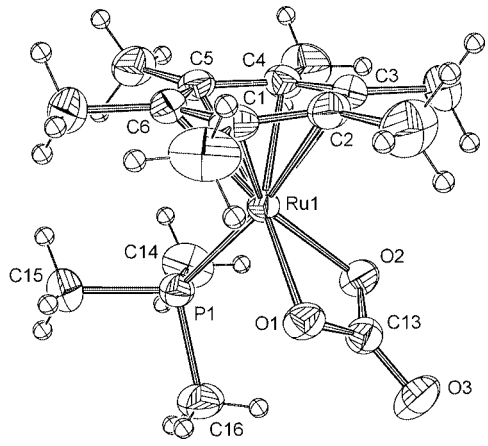


Figure 2. ORTEP drawing of **2d**·$H_2O$ showing 50% probability thermal ellipsoids. The $H_2O$ molecule has been omitted for clarity. Selected bond lengths [Å] and angles [°]: Ru1–O1 2.104(2), Ru1–O2 2.091(2), O1–C13 1.325(4), O2–C13 1.315(4), O3–C13 1.239(4), Ru1–P1 2.343(1); O1–Ru1–O2 62.81(8), C13–O1–Ru1 92.2(2), C13–O2–Ru1 93.1(2), O1–C13–O2 111.8(2), O1–C13–O3 123.7(3), O2–C13–O3 124.5(3), O1–Ru1–P1 88.61(7), O2–Ru1–P1 84.25(7).

to the Ru–P bond [**2a**: O1–Ru1–P1 = 86.92(5)°, O2–Ru1–P1 = 88.09(5)°; **2d**: O1–Ru1–P1 = 88.61(7)°, O2–Ru1–P1 = 84.25(7)°]. The Ru–P bond lengths in **2a** and **2d** are also similar [2.3779(6) and 2.343(1) Å, respectively]. Finally, these main structural features for the Ru($\eta^2$-$O_2$CO) fragment in **2a** and **2d** are in good agreement with those arising from the study of the distinct complex [Ru($CO_3$)($PPh_3$)$_2$($CO$)$_2$], obtained by hydrolysis of the carbamato ligands in [Ru($O_2CN$*i*Pr$_2$)$_2$($PPh_3$)$_2$($CO$)$_2$].[12]

The observed need for water to generate the carbonato complexes **2** suggests a lack of reactivity of the $CO_3^{2-}$ dianion. Furthermore, attempts to synthesise **2d** using $KHCO_3$ instead of $K_2CO_3$ also showed the same need for addition of water to trigger the reaction. Note that the related complex [Ru($CO_3$)($\eta^6$-$C_6Me_6$)(*i*Pr$_2$PCH$_2$CH$_2$OMe)] has been fortuitously synthesised from [RuCl($\eta^6$-$C_6Me_6$)($\eta^2$-*P*,*O*-*i*Pr$_2$PCH$_2$CH$_2$OMe)][$PF_6$] upon treatment with aqueous $Na_2CO_3$.[10] The addition of water might be expected to result in the additional presence of the more reactive hydroxide anion, and this suggested the formation of a Ru–OH bond in a chloride ligand substitution reaction as the first step in this reaction. As depicted in Scheme 3, subsequent reaction between the basic hydroxide intermediate and the acidic $HCO_3^-$ anion completes the formation of the carbonato complexes.

An insertion of carbon dioxide into the Ru–OH bond might also be considered. Indeed, the stable bicarbonato derivative [Ru($\eta^1$-$OCO_2H$)(Me)($\eta^6$-$C_6Me_6$)($PMe_3$)] has been previously been obtained by treating the hydroxide complex [Ru(OH)(Me)($\eta^6$-$C_6Me_6$)($PMe_3$)] with carbon dioxide.[32]

The reaction between $K_2CO_3$ and an imidazolium salt such as 1,3-bis(2,4,6-trimethylphenyl)imidazolium chloride has been shown to generate reactive imidazol-2-ylidene species that can be trapped with sulfur.[6] This process appeared attractive to synthesise organometallic (vs. sulfide)

 © 2006 Wiley-VCH Verlag GmbH & Co. KGaA, Weinheim 

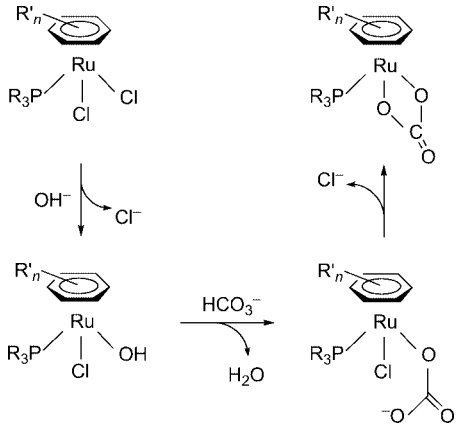

Scheme 3. Rationale accounting for the formation of complexes **2** catalysed by water.

derivatives under similar conditions. Thus, treatment of a 2:1 [H(IMes)]Cl/[$RuCl_2$(η⁶-arene)]$_2$ mixture with an excess of $K_2CO_3$ in THF at reflux led to the new carbonato complexes **2e** and **2f**, which were isolated as dark-orange solids in 79 and 46% yield, respectively (Scheme 4).

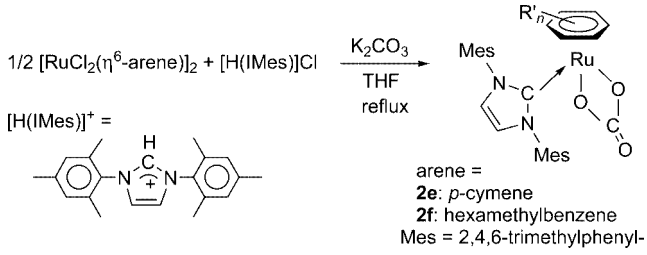

Scheme 4. Synthesis of the carbonatoruthenium complexes [Ru(η²-$O_2CO$)(η⁶-arene)(IMes)] (**2e** and **2f**).

Complexes **2e** and **2f**, which only differ from the carbonato complexes **2a**–**d** by the presence of the 1,3-bis(2,4,6-trimethylphenyl)imidazol-2-ylidene ligand instead of a phosphane, were characterised by $^1$H, $^{13}$C and $^{13}$C{$^1$H} NMR spectroscopy and elemental analysis. The $^{13}$C NMR resonance corresponding to the carbene carbon nucleus in **2e** and **2f** is located at $\delta$ = 180.5 and 183.6 ppm, respectively. The assignment of the $^{13}$C NMR resonance corresponding to the carbonato ligand in **2e** and **2f** ($\delta$ = 166.4 and 166.2 ppm, respectively) was inferred by comparison with **2a**–**d**.

The formation of the carbonato complexes [Ru(η²-$O_2CO$)(η⁶-arene)(IMes)] sheds new light on the preparation of catalysts for enyne metathesis and *O*-allyl isomerisation reactions, which were generated in situ by heating a mixture of [$RuCl_2$(*p*-cymene)]$_2$, imidazolium salt and an excess of $Cs_2CO_3$ in toluene.[3–5] The transient formation of [$RuCl_2$(*p*-cymene)(IMes)], which releases a reactive [$RuCl_2$(IMes)] moiety, was postulated. The fact that the catalytic species may arise from an [Ru($CO_3$)(*p*-cymene)(IMes)] species rather than the [$RuCl_2$(*p*-cymene)(IMes)] intermediate must now be considered.

### Synthesis of Dicationic [Ru(η⁶-arene)(L)(MeCN)$_2$][$BF_4$]$_2$ Derivatives

As previously reported for the reactivity study of the carbonato complex [Ru(η²-$O_2CO$)(bipy)$_2$],[26] double protonation of the carbonato ligand in complexes **2a**–**f** easily occurs under acidic conditions to generate carbon dioxide, water, and to formally release a 14-electron [Ru(η⁶-arene)(L)]$^{2+}$ fragment. The derivatives [Ru(η⁶-arene)(L)(MeCN)$_2$][$BF_4$]$_2$ (**5a**–**f**) were isolated in high yield (84–99%) after treating **2a**–**f** with 2 equiv. of $HBF_4$ (as its dimethyl ether adduct) in acetonitrile as solvent (Scheme 5).

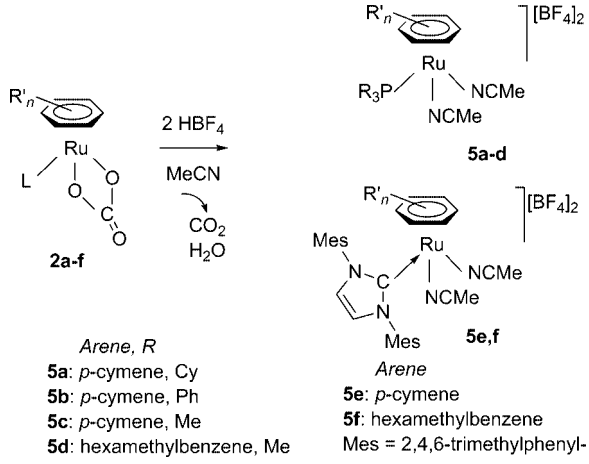

Scheme 5. Synthesis of the dicationic derivatives [Ru(η⁶-arene)(L)(MeCN)$_2$][$BF_4$]$_2$ (**5a**–**f**).

Complexes **5a**–**f** are robust yellow compounds that are highly soluble in acetonitrile. They were characterised by $^1$H, $^{13}$C, $^{13}$C{$^1$H} and $^{31}$P{$^1$H} NMR spectroscopy and elemental analysis. Remarkably, the $^{13}$C NMR resonance corresponding to the carbene carbon nucleus in **5e** and **5f** ($\delta$ = 163.7 and 164.1 ppm, respectively) is shifted upfield relative to **2e** and **2f** ($\delta$ = 180.5 and 183.6 ppm, respectively). This observation likely indicates a reduced back-donation from the metal atom in **5e** and **5f** as compared to **2e** and **2f**, which results in an enhanced imidazolium (vs. imidazolylidene) character.[33] A study of analogous [Ru(η⁶-benzene)(L)(MeCN)$_2$]$^{2+}$ complexes obtained by treatment of [Ru(η⁶-benzene)(MeCN)$_3$][OTf]$_2$ with a phosphane has recently been reported and emphasises the potential of such complexes.[34]

## Conclusions

The easy formation of carbonatoruthenium complexes on reaction of $K_2CO_3$ with $L_nRuCl_2$ precursors in the presence of water constitutes a convenient method to remove the chloride ligands and to use the carbonato ligand as a protecting group for transition metal centres. Under acidic conditions, a clean elimination of the carbonato ligand takes place to formally generate a coordinatively unsaturated dicationic moiety. Thus, the transformation of [$RuCl_2$(η⁶-arene)(L)] precursors into dicationic [Ru(η⁶-arene)(L)(MeCN)$_2$][$BF_4$]$_2$ derivatives is achieved without any

 © 2006 Wiley-VCH Verlag GmbH & Co. KGaA, Weinheim 

involvement of strong chloride scavengers such as silver or thallium salts. The carbonato ligand also allows a convenient route to useful dihydride complexes upon reaction with methanol. Finally, the formation of carbonatoruthenium intermediates may interfere in processes where a ruthenium catalyst is generated in situ from a ruthenium dichloride complex and an alkali metal carbonate as base.

## Experimental Section

**General:** The reactions were performed according to Schlenk-type techniques. Commercial solvents (99+% grade) were used without further purification except diethyl ether and dichloromethane, which were distilled under an inert gas after drying according to conventional methods. NMR spectra were recorded at 297 K with AC 200 FT and AC 300 Bruker instruments and referenced internally to the solvent peak. Elemental analyses were performed by the "Service de Microanalyse du CNRS", Vernaison, France. Complexes **1a**–**d** were obtained by treating the appropriate phosphane with dimeric $[RuCl_2(\eta^6\text{-arene})]_2$ ruthenium complexes in dichloromethane as solvent, as described in the literature.[35] For the convenience of this work, **1a** was prepared as its acetone adduct. The preparation of 1,3-bis(2,4,6-trimethylphenyl)imidazolium chloride has been described elsewhere.[36]

**$[RuCl_2(p\text{-cymene})(PCy_3)]\cdot$acetone (1a):** Stoichiometric amounts of $[RuCl_2(p\text{-cymene})]_2$ (8.07 g, 13.2 mmol) and $PCy_3$ (7.39 g, 26.4 mmol) were mixed in dichloromethane (60 mL) as reported previously.[37] After stirring for 2 h, the mixture was concentrated to dryness and acetone (60 mL) was added to the residue. The mixture was stirred to obtain a red precipitate that was collected by filtration. Yield: 16.1 g (95%). The product retains 1 equiv. of acetone per Ru, as indicated by $^1$H NMR spectroscopy.

**$[Ru(\eta^2\text{-}O_2CO)(p\text{-cymene})(PCy_3)]\cdot 1/2CH_2Cl_2$ (2a):** A mixture consisting of a sample of **1a** (6.00 g, 9.30 mmol), $K_2CO_3$ (2.00 g, 14.5 mmol) and acetone (50 mL) was stirred for 2 d. The volatiles were then removed under vacuum to leave a yellow solid, whicht was extracted with dichloromethane (50 mL). The solution was filtered and the filtrate was covered with acetone (20 mL) and then with diethyl ether (160 mL) to afford orange-yellow crystals. Yield: 4.51 g (78%). $^1$H NMR (300.13 MHz, $CD_2Cl_2$): $\delta$ = 1.25 (d, $^3J_{H,H}$ = 6.9 Hz, 6 H, CH$Me_2$), 1.16–1.89 (m, 33 H, Cy), 2.12 (s, 3 H, Me), 2.52 (m, 1 H, C$H$Me$_2$), 5.26 (d, $^3J_{H,H}$ = 6.2 Hz, 2 H, $C_6H_4$), 5.34 (d, $^3J_{H,H}$ = 6.2 Hz, 2 H, $C_6H_4$) ppm. $^{13}$C{$^1$H} NMR (75.47 MHz, $CD_2Cl_2$): $\delta$ = 18.7 (s, $Me$C$_6$H$_4$), 23.3 (s, CH$Me_2$), 27.0 (s, Cy, 1 C), 28.3 (d, $J_{P,C}$ = 10.2 Hz, Cy, 2 C), 29.9 (s, Cy, 2 C), 32.6 (s, $C$HMe$_2$), 35.4 (d, $^1J_{P,C}$ = 18.9 Hz, Cy, 1 C), 85.4 (d, $^2J_{P,C}$ = 3.8 Hz, $C_6H_4$, 2 CH), 86.6 (d, $^2J_{P,C}$ = 4.2 Hz, $C_6H_4$, 2 CH), 94.5 (s, $C$Me, *p*-cymene), 103.7 (s, $Ci$Pr, *p*-cymene), 165.6 (d, $^3J_{P,C}$ = 2.6 Hz, $CO_3$) ppm. $^{31}$P{$^1$H} NMR (121.50 MHz, $CD_2Cl_2$): $\delta$ = 37.8 ppm (s). $C_{29}H_{47}O_3PRu\cdot 1/2CH_2Cl_2$ (618.21): calcd. C 57.32, H 7.66, Cl 5.73, P 5.01; found C 57.24, H 7.82, Cl 5.52, P 5.18.

**$[Ru(\eta^2\text{-}O_2CO)(p\text{-cymene})(PPh_3)]$ (2b):** A mixture consisting of a sample of **1b** (2.71 g, 4.77 mmol), $K_2CO_3$ (1.50 g, 10.9 mmol), acetone (40 mL) and water (0.50 mL) was stirred for 3 d. The resulting yellow slurry was concentrated to dryness and the remaining solid was extracted with dichloromethane (40 mL). Acetone (10 mL) was added to the orange filtrate and this mixture was slowly concentrated to leave a crystalline orange-yellow solid, which was found to be pure by $^1$H and $^{31}$P{$^1$H} NMR spectroscopy. Yield: 2.57 g (97%). Orange crystals were obtained by recrystallisation from hot acetonitrile. $^1$H NMR (300.13 MHz, $CD_2Cl_2$): $\delta$ = 1.18 (d, $^3J_{H,H}$ = 6.7 Hz, 6 H, CH$Me_2$), 2.00 (s, 3 H, $Me$C$_6$H$_4$), 2.49 (m, 1 H, C$H$Me$_2$), 5.12 (d, $^3J_{H,H}$ = 6.1 Hz, 2 H, $C_6H_4$), 5.20 (d, $^3J_{H,H}$ = 6.2 Hz, 2 H, $C_6H_4$), 7.37–7.54 (m, 15 H, Ph) ppm. $^{13}$C{$^1$H} NMR (75.47 MHz, $CD_2Cl_2$): $\delta$ = 18.6 (s, $Me$C$_6$H$_4$), 22.9 (s, CH$Me_2$), 31.8 (s, $C$HMe$_2$), 87.1 (d, $^2J_{P,C}$ = 5.4 Hz, $C_6H_4$, 2 CH), 87.8 (d, $^2J_{P,C}$ = 4.4 Hz, $C_6H_4$, 2 CH), 96.3 (s, $C$Me, *p*-cymene), 106.8 (s, $Ci$Pr, *p*-cymene), 128.8 (d, $^2J_{P,C}$ = 9.9 Hz, Ph, *ortho*), 131.1 (s, Ph, *para*), 131.5 (d, $^1J_{P,C}$ = 44.8 Hz, Ph, *ipso*), 134.5 (d, $^3J_{P,C}$ = 9.7 Hz, Ph, *meta*), 165.1 (s, $CO_3$) ppm. $^{31}$P{$^1$H} NMR (121.50 MHz, $CD_2Cl_2$): $\delta$ = 33.0 ppm (s). $C_{29}H_{29}O_3PRu$ (557.60): calcd. C 62.47, H 5.24, P 5.55; found C 62.33, H 5.30, P 5.30.

**$[Ru(\eta^2\text{-}O_2CO)(p\text{-cymene})(PMe_3)]$ (2c):** A mixture consisting of a sample of **1c** (1.50 g, 3.92 mmol), $K_2CO_3$ (1.00 g, 7.24 mmol), acetone (40 mL) and water (0.50 mL) was stirred for 10 d. The resulting yellow slurry was concentrated to dryness and the remaining solid was extracted with dichloromethane (40 mL). The solution was filtered and the orange filtrate was slowly concentrated to leave an orange, crystalline solid, which was found to be pure by $^1$H and $^{31}$P{$^1$H} NMR spectroscopy. Yield: 1.38 g (95%). Recrystallisation from an acetone/acetonitrile mixture afforded dark-orange crystals. $^1$H NMR (300.13 MHz, $CD_2Cl_2$): $\delta$ = 1.17 (d, $^3J_{H,H}$ = 6.9 Hz, 6 H, CH$Me_2$), 1.34 (d, $^2J_{P,H}$ = 10.3 Hz, 9 H, $PMe_3$), 2.05 (s, 3 H, $Me$C$_6$H$_4$), 2.51 (m, 1 H, C$H$Me$_2$), 5.38 (d, $^3J_{H,H}$ = 5.9 Hz, 2 H, $C_6H_4$), 5.46 (d, $^3J_{H,H}$ = 5.9 Hz, 2 H, $C_6H_4$) ppm. $^{13}$C{$^1$H} NMR (75.47 MHz, $CD_2Cl_2$): $\delta$ = 14.9 (d, $^1J_{P,C}$ = 28.4 Hz, $PMe_3$), 18.9 (s, $Me$C$_6$H$_4$), 23.2 (s, CH$Me_2$), 32.2 (s, $C$HMe$_2$), 86.1 (s, $C_6H_4$, 2 CH), 86.6 (s, $C_6H_4$, 2 CH), 94.9 (s, $C$Me, *p*-cymene), 103.9 (s, $Ci$Pr, *p*-cymene), 166.7 (d, $^3J_{P,C}$ = 2.9 Hz, $CO_3$) ppm. $^{31}$P{$^1$H} NMR (121.50 MHz, $CD_2Cl_2$): $\delta$ = 8.3 ppm (s). $C_{14}H_{23}O_3PRu$ (371.38): calcd. C 45.28, H 6.24, P 8.34; found C 45.18, H 6.29, P 8.30.

**$[Ru(\eta^2\text{-}O_2CO)(\text{hexamethylbenzene})(PMe_3)]\cdot H_2O$ (2d):** A mixture consisting of a sample of **1d** (2.00 g, 4.87 mmol), $K_2CO_3$ (1.50 g, 10.9 mmol), acetone (40 mL) and water (0.60 mL) was stirred for 10 d. The resulting yellow slurry was concentrated to dryness and the remaining solid was extracted with dichloromethane (40 mL). Acetone (10 mL) was added to the orange filtrate and this mixture was slowly concentrated to leave an orange, crystalline solid, which was found to be pure by $^1$H and $^{31}$P{$^1$H} NMR spectroscopy. Yield: 1.87 g (92%). Alternatively, a mixture consisting of a sample of **1d** (1.00 g, 2.44 mmol), $K_2CO_3$ (1.00 g, 7.2 mmol), THF (40 mL) and water (0.50 mL) was heated at reflux for 24 h, then treated as above. Yield: 0.55 g (54%). Recrystallisation by diffusion of THF into a concentrated solution of the compound in dichloromethane afforded orange-red crystals. $^1$H NMR (300.13 MHz, $CD_2Cl_2$): $\delta$ = 1.22 (d, $^2J_{P,H}$ = 10.2 Hz, 9 H, $PMe_3$), 2.04 (s, 18 H, $C_6Me_6$) ppm. $^{13}$C{$^1$H} NMR (75.47 MHz, $CD_2Cl_2$): $\delta$ = 13.7 (d, $^1J_{P,C}$ = 28.0 Hz, $PMe_3$), 16.2 (s, $C_6Me_6$), 95.1 (d, $^2J_{P,C}$ = 3.4 Hz, $C_6$Me$_6$), 166.8 (d, $^3J_{P,C}$ = 2.6 Hz, $CO_3$) ppm. $^{31}$P{$^1$H} NMR (121.50 MHz, $CD_2Cl_2$): $\delta$ = 4.7 ppm (s). $C_{16}H_{27}O_3PRu\cdot H_2O$ (417.45): calcd. C 46.04, H 7.00, P 7.42; found C 45.86, H 6.92, P 7.45.

**$[Ru(\eta^2\text{-}O_2CO)(p\text{-cymene})(IMes)]$ (2e):** A mixture consisting of a sample of $[RuCl_2(p\text{-cymene})]_2$ (2.00 g, 3.27 mmol), 1,3-bis(2,4,6-trimethylphenyl)imidazolium chloride (2.27 g, 6.66 mmol), $K_2CO_3$ (3.00 g, 21.7 mmol), THF (40 mL) and dichloromethane (10 mL) was stirred overnight then heated at reflux for 20 h. The resulting slurry was concentrated to dryness and the remaining solid was extracted with dichloromethane (30 mL). The solution was filtered and the filtrate was concentrated under vacuum to leave a brown solid, which was found to be pure by $^1$H NMR spectroscopy. Yield: 3.60 g (79%). Recrystallisation from hot toluene afforded dark-orange crystals of **2e**·1/4$C_7H_8$ in 77% yield relative to crude **2e**. $^1$H

 © 2006 Wiley-VCH Verlag GmbH & Co. KGaA, Weinheim 

NMR (300.13 MHz, $CD_2Cl_2$): $\delta$ = 0.76 (d, $^3J_{H,H}$ = 6.9 Hz, 6 H, CH$Me_2$), 1.28 (s, 3 H, $Me$C$_6$H$_4$), 1.56 (m, 1 H, C$H$Me$_2$), 2.08 (s, 12 H, Mes, 4 Me), 2.25 (s, toluene), 2.27 (s, 6 H, Mes, 2 Me), 4.74 (d, $^3J_{H,H}$ = 6.1 Hz, 2 H, C$_6$H$_4$), 5.04 (d, $^3J_{H,H}$ = 6.2 Hz, 2 H, C$_6$H$_4$), 6.93 (s, 2 H, CH=), 6.93 (s, 2 H, Mes, 2 CH), 6.94 (s, 2 H, Mes, 2 CH), 7.04–7.15 (m, toluene) ppm. $^{13}$C{$^1$H} NMR (75.47 MHz, $CD_2Cl_2$): $\delta$ = 17.1 (s, $Me$C$_6$H$_4$), 18.7 (s, Mes, 4 Me), 21.2 (s, CH$Me_2$), 23.4 (s, Mes, 2 Me), 32.2 (s, $C$HMe$_2$), 84.5 (s, C$_6$H$_4$, 2 CH), 85.2 (s, C$_6$H$_4$, 2 CH), 94.7 (s, $C$Me, $p$-cymene), 100.3 (s, $Ci$Pr, $p$-cymene), 125.2 (s, NCH=), 129.2 (s, Mes, 4 CH), 136.9 (s, Mes, 4 $C$Me), 137.1 (s, Mes, 2 CN), 139.3 (s, Mes, 2 $C$Me), 166.4 (s, $CO_3$), 180.5 (s, Ru=C) ppm; the resonances of toluene have been omitted. $C_{32}H_{41}N_2O_3Ru\cdot1/4C_7H_8$ (625.80): calcd. C 64.78, H 6.60, N 4.48; found C 64.73, H 6.54, N 4.16.

**[Ru(η²-$O_2CO$)(hexamethylbenzene)(IMes)] (2f):** A mixture consisting of a sample of [RuCl$_2$(hexamethylbenzene)]$_2$ (1.50 g, 2.24 mmol), 1,3-bis(2,4,6-trimethylphenyl)imidazolium chloride (1.52 g, 4.46 mmol), $K_2CO_3$ (1.00 g, 7.24 mmol) and THF (40 mL) was stirred overnight, then heated at reflux for 24 h. The resulting slurry was concentrated to dryness and the remaining solid was extracted with dichloromethane (30 mL). The solution was filtered and the filtrate was concentrated under vacuum to leave a brown solid. Yield: 1.30 g (46%). Dark-orange crystals were obtained from hot toluene. $^1$H NMR (300.13 MHz, $CD_2Cl_2$): $\delta$ = 1.55 (s, 18 H, C$_6$Me$_6$), 2.09 (s, 6 H, Mes, 2 Me), 2.10 (s, 6 H, Mes, 2 Me), 2.27 (s, 6 H, Mes, 2 Me), 6.83 (s, 2 H, CH=), 6.90 (s, 2 H, Mes, 2 CH), 6.92 (s, 2 H, Mes, 2 CH) ppm. $^{13}$C{$^1$H} NMR (75.47 MHz, $CD_2Cl_2$): $\delta$ = 15.6 (s, C$_6$$Me_6$), 19.1 (s, Mes, 2 Me *ortho*), 19.5 (s, Mes, 2 Me *ortho*), 21.2 (s, Mes, 2 Me *para*), 92.9 (s, $C_6$Me$_6$), 125.1 (s, NCH=), 128.2 (s, Mes, 2 CH), 129.5 (s, Mes, 2 CH), 135.0 (s, Mes, 2 $C$Me *ortho*), 137.6 (s, Mes, 2 CN), 138.7 (s, Mes, 2 $C$Me *para*), 139.0 (s, Mes, 2 $C$Me *ortho*), 166.2 (s, $CO_3$), 183.6 (s, Ru=C) ppm. $^{13}$C NMR (75.47 MHz, $CD_2Cl_2$, selected values): $\delta$ = 125.1 ppm (dd, $^1J_{H,C}$ = 196, $^3J_{H,C}$ = 11.9 Hz, NCH=). $C_{34}H_{42}N_2O_3Ru$ (627.79): calcd. C 65.05, H 6.74, N 4.46; found C 64.72, H 6.57, N 4.56.

**[RuH$_2$($p$-cymene)(PCy$_3$)] (3a):** A mixture consisting of a sample of **1a** (3.29 g, 5.11 mmol), $K_2CO_3$ (1.50 g, 10.9 mmol) and methanol (40 mL) was stirred at room temperature for 0.5 h and the resulting yellow slurry was heated at reflux for 1 h. The hot solution was immediately filtered and the brown filtrate was concentrated under vacuum to leave a solid, which was washed twice with cold methanol to give a colourless, crystalline powder. Yield: 2.13 g (81%). Similarly, a solution of **2a** in methanol was heated at reflux for 1 h and then treated as above to give **3a** in 70% yield. $^1$H NMR (300.13 MHz, $C_6D_6$): $\delta$ = –11.0 (d, $^2J_{P,H}$ = 43.3 Hz, 2 H, RuH), 1.29 (d, $^3J_{H,H}$ = 6.7 Hz, 6 H, CH$Me_2$), 1.17–2.06 (m, 33 H, Cy), 2.08 (s, 3 H, Me), 2.46 (m, 1 H, C$H$Me$_2$), 5.07 (d, $^3J_{H,H}$ = 5.6 Hz, 2 H, C$_6$H$_4$), 5.16 (d, $^3J_{H,H}$ = 5.6 Hz, 2 H, C$_6$H$_4$) ppm. $^{13}$C{$^1$H} NMR (75.47 MHz, $C_6D_6$): $\delta$ = 21.7 (s, $Me$C$_6$H$_4$), 25.3 (s, CH$Me_2$), 27.7 (s, Cy, 1 C), 28.7 (d, $J_{P,C}$ = 9.8 Hz, Cy, 2 C), 31.2 (s, Cy, 2 C), 33.5 (s, $C$HMe$_2$), 40.0 (d, $^1J_{P,C}$ = 21.8 Hz, Cy, 1 C), 80.0 (d, $^2J_{P,C}$ = 3.8 Hz, C$_6$H$_4$, 2 CH), 85.7 (d, $^2J_{P,C}$ = 1.7 Hz, C$_6$H$_4$, 2 CH), 96.9 (s, $C$Me, $p$-cymene), 110.4 (s, $Ci$Pr, $p$-cymene) ppm. $^{31}$P{$^1$H} NMR (121.50 MHz, $C_6D_6$) $\delta$ = 78.1 ppm (s). $C_{28}H_{49}$PRu (517.74): calcd. C 64.96, H 9.54, P 5.98; found C 64.79, H 9.50, P 5.87.

**[RuCl(H)($p$-cymene)(PCy$_3$)] (4a):** Equimolar amounts of **3a** (1.14 g, 2.20 mmol) and **1a** (1.42 g, 2.20 mmol) were added to methanol (30 mL) and this mixture was stirred at room temperature overnight (or heated at reflux for 1 h) to afford a yellow slurry. Concentration of the mixture and subsequent analysis of the residue by $^1$H and $^{31}$P{$^1$H} NMR spectroscopy indicated a quantitative formation of **4a**. Recrystallisation by dissolution in dichloromethane (25 mL) and then diffusion of methanol (100 mL) afforded dark-orange crystals but in a moderate yield (0.94 g, 39%) owing to residual solubility. $^1$H NMR (300.13 MHz, $CD_2Cl_2$): $\delta$ = –8.0 (d, $^2J_{P,H}$ = 49.5 Hz, 1 H, RuH), 1.12 (d, $^3J_{H,H}$ = 7.0 Hz, 3 H, CH$Me_2$), 1.26 (d, $^3J_{H,H}$ = 6.8 Hz, 3 H, CH$Me_2$), 1.06–1.90 (m, 33 H, Cy), 1.95 (s, 3 H, Me), 2.14 (m, 1 H, C$H$Me$_2$), 4.28 (d, $^3J_{H,H}$ = 5.4 Hz, 1 H, C$_6$H$_4$), 4.48 (d, $^3J_{H,H}$ = 6.1 Hz, 1 H, C$_6$H$_4$), 6.05 (m, 2 H, C$_6$H$_4$) ppm. $^{13}$C{$^1$H} NMR (75.47 MHz, $CD_2Cl_2$): $\delta$ = 19.5 (s, $Me$C$_6$H$_4$), 21.2 (s, CH$Me_2$), 25.4 (s, CH$Me_2$), 27.3 (s, Cy, 1 C), 28.3 (d, $J_{P,C}$ = 9.9 Hz, Cy, 1 C), 28.4 (d, $J_{P,C}$ = 10.9 Hz, Cy, 1 C), 30.0 (s, Cy, 1 C), 30.1 (d, $J_{P,C}$ = 1.8 Hz, Cy, 1 C), 31.7 (s, $C$HMe$_2$), 36.8 (d, $^1J_{P,C}$ = 21.8 Hz, Cy, 1 C), 79.6 (d, $^2J_{P,C}$ = 2.7 Hz, C$_6$H$_4$, 1 CH), 86.7 (d, $^2J_{P,C}$ = 4.5 Hz, C$_6$H$_4$, 1 CH), 86.9 (d, $^2J_{P,C}$ = 5.4 Hz, C$_6$H$_4$, 1 CH), 91.2 (d, $^2J_{P,C}$ = 3.6 Hz, C$_6$H$_4$, 1 CH), 97.8 (s, $C$Me, $p$-cymene), 106.5 (s, $Ci$Pr, $p$-cymene) ppm. $^{31}$P{$^1$H} NMR ($CD_2Cl_2$): $\delta$ = 59.7 ppm (s). $C_{28}H_{48}$ClPRu (552.19): calcd. C 60.90, H 8.76, Cl 6.42, P 5.61; found C 60.89, H 9.06, Cl 6.68, P 5.74.

**[Ru($p$-cymene)(PCy$_3$)(MeCN)$_2$][BF$_4$]$_2$ (5a):** Complexes **5a**–**f** were quantitatively formed by treating the corresponding carbonato complex in solution in cold acetonitrile with a stoichiometric amount of $HBF_4\cdot OMe_2$. In a typical procedure, a 1.2 M solution of $HBF_4\cdot OMe_2$ in methanol (7.5 mL, 9.0 mmol) was added to a stirred solution of **2a** (2.75 g, 4.45 mmol) in cold acetonitrile (30 mL, –40 °C). The mixture was allowed to reach room temperature (1 h) and then concentrated under vacuum. The resulting solution was covered with dichloromethane (20 mL) and then diethyl ether (120 mL) to afford yellow crystals. Yield: 3.26 g (95%). $^1$H NMR (300.13 MHz, $CD_3CN$): $\delta$ = 1.41 (d, $^3J_{H,H}$ = 6.9 Hz, 6 H, CH$Me_2$), 1.48–1.94 (m, broad, 33 H, Cy), 2.10 (s, 6 H, MeCN), 2.27 (s, 3 H, $Me$C$_6$H$_4$), 2.80 (m, 1 H, C$H$Me$_2$), 6.34 (d, $^3J_{H,H}$ = 6.6 Hz, 2 H, C$_6$H$_4$), 6.42 (d, $^3J_{H,H}$ = 6.6 Hz, 2 H, C$_6$H$_4$) ppm. $^{13}$C{$^1$H} NMR (75.47 MHz, $CD_2Cl_2$): $\delta$ = 4.76 (s, $Me$CN), 18.9 (s, $Me$C$_6$H$_4$), 22.6 (s, CH$Me_2$), 26.5 (s, Cy, 1C), 27.7 (d, $J_{P,C}$ = 10.3 Hz, Cy, 2 C), 30.4 (d, $J_{P,C}$ = 1.7 Hz, Cy, 2 C), 32.2 (s, $C$HMe$_2$), 37.9 (d, $J_{P,C}$ = 19.8 Hz, Cy, 1 C), 90.8 (d, $^2J_{P,C}$ = 2.9 Hz, C$_6$H$_4$, 2 CH), 93.0 (d, $^2J_{P,C}$ = 1.7 Hz, C$_6$H$_4$, 2 CH), 103.9 (s, $C$Me, $p$-cymene), 114.3 (s, $Ci$Pr, $p$-cymene), 132.2 (s, Me$C$N) ppm. $^{31}$P{$^1$H} NMR (121.50 MHz, $CD_2Cl_2$): $\delta$ = 44.7 ppm (s). $C_{32}H_{53}B_2F_8N_2$PRu (771.44): calcd. C 49.82, H 6.93, N 3.63, P 4.02; found C 49.59, H 7.03, N 3.64, P 4.38.

**[Ru($p$-cymene)(PPh$_3$)(MeCN)$_2$][BF$_4$]$_2$ (5b):** Yield: 96%, yellow crystals. $^1$H NMR (300.13 MHz, $CD_3CN$): $\delta$ = 1.36 (d, $^3J_{H,H}$ = 6.3 Hz, 6 H, CH$Me_2$), 1.94 (s, 3 H, $Me$C$_6$H$_4$), 2.33 (s, 6 H, MeCN), 2.94 (m, 1 H, C$H$Me$_2$), 5.63 (dd, $^3J_{H,H}$ = 6.7, $^3J_{P,H}$ = 1.3 Hz, 2 H, C$_6$H$_4$), 6.27 (d, $^3J_{H,H}$ = 6.6 Hz, 2 H, C$_6$H$_4$), 7.66–7.77 (m, 15 H, Ph) ppm. $^{13}$C{$^1$H} NMR (75.47 MHz, $CD_3CN$): $\delta$ = 4.66 (s, $Me$CN), 18.7 (s, $Me$C$_6$H$_4$), 22.3 (s, CH$Me_2$), 32.3 (s, $C$HMe$_2$), 92.5 (s, C$_6$H$_4$, 2 CH), 93.9 (d, $^2J_{P,C}$ = 2.9 Hz, C$_6$H$_4$, 2 CH), 107.6 (s, $C$Me, $p$-cymene), 119.3 (s, $Ci$Pr, $p$-cymene), 129.6 (d, $^1J_{P,C}$ = 51.9 Hz, Ph, *ipso*), 130.5 (d, $^2J_{P,C}$ = 10.2 Hz, Ph, *ortho*), 132.2 (s, Me$C$N), 133.3 (d, $^4J_{P,C}$ = 2.9 Hz, Ph, *para*), 134.9 (d, $^3J_{P,C}$ = 10.2 Hz, Ph, *meta*) ppm. $^{31}$P{$^1$H} NMR (121.50 MHz, $CD_3CN$): $\delta$ = 39.4 ppm (s). $C_{32}H_{35}B_2F_8N_2$PRu (753.30): calcd. C 51.02, H 4.68, N 3.72, P 4.11; found C 50.78, H 4.68, N 3.72, P 4.10.

**[Ru($p$-cymene)(PMe$_3$)(MeCN)$_2$][BF$_4$]$_2$ (5c):** Yield: 88%, lemon-yellow crystals. $^1$H NMR (300.13 MHz, $CD_3CN$): $\delta$ = 1.32 (d, $^3J_{H,H}$ = 6.9 Hz, 6 H, CH$Me_2$), 1.84 (d, $^2J_{P,H}$ = 12.0 Hz, 9 H, PMe$_3$), 2.20 (s, 3 H, $Me$C$_6$H$_4$), 2.63 (d, $^5J_{P,H}$ = 1.3 Hz, 6 H, MeCN), 2.80 (m, 1 H, C$H$Me$_2$), 6.27 (m, 4 H, C$_6$H$_4$) ppm. $^{13}$C{$^1$H} NMR (75.47 MHz, $CD_3CN$): $\delta$ = 4.82 (s, $Me$CN), 16.7 (d, $^1J_{P,C}$ = 34.7 Hz, PMe$_3$), 18.6 (s, $Me$C$_6$H$_4$), 22.2 (s, CH$Me_2$), 32.0 (s,

 © 2006 Wiley-VCH Verlag GmbH & Co. KGaA, Weinheim 

*C*HMe$_2$), 91.7 (d, $^2J_{P,C}$ = 4.0 Hz, $C_6H_4$, 2 CH), 94.5 (d, $^2J_{P,C}$ = 3.3 Hz, $C_6H_4$, 2 CH), 102.9 (s, *C*Me, *p*-cymene), 113.0 (s, *Ci*Pr, *p*-cymene), 130.5 (s, Me*C*N) ppm. $^{31}P\{^1H\}$ NMR (121.50 MHz, $CD_3CN$): $\delta$ = 12.5 ppm (s). $C_{17}H_{29}B_2F_8N_2PRu$ (567.08): calcd. C 36.01, H 5.15, N 4.94, P 5.46; found C 35.74, H 5.19, N 4.95, P 5.83.

**[Ru(hexamethylbenzene)(PMe$_3$)(MeCN)$_2$][BF$_4$]$_2$ (5d):** Yield: 92%, lemon-yellow crystals. $^1H$ NMR (300.13 MHz, $CD_3CN$): $\delta$ = 1.55 (d, $^2J_{P,H}$ = 11.5 Hz, 9 H, $PMe_3$), 2.17 (s, 18 H, $C_6Me_6$), 2.52 (d, $^5J_{P,H}$ = 1.3 Hz, 6 H, MeCN) ppm. $^{13}C\{^1H\}$ NMR (75.47 MHz, $CD_3CN$): $\delta$ = 4.79 (s, *Me*CN), 14.8 (d, $^1J_{P,C}$ = 33.5 Hz, $PMe_3$), 16.6 (s, $C_6Me_6$), 103.6 (d, $^2J_{P,C}$ = 1.9 Hz, $C_6Me_6$), 129.8 (s, Me*C*N) ppm. $^{31}P\{^1H\}$ NMR (121.50 MHz, $CD_3CN$): $\delta$ = 8.9 ppm (s). $C_{19}H_{33}B_2F_8N_2PRu$ (595.14): calcd. C 38.35, H 5.59, N 4.71, P 5.20; found C 38.32, H 5.66, N 4.69, P 5.40.

**[Ru(*p*-cymene)(IMes)(MeCN)$_2$][BF$_4$]$_2$ (5e):** Yield: 99%, orange crystals. $^1H$ NMR (300.13 MHz, $CD_2Cl_2$): $\delta$ = 1.03 (d, $^3J_{H,H}$ = 6.9 Hz, 6 H, CH*Me$_2$*), 1.73 (s, 3 H, *Me*$C_6H_4$), 1.97 (m, 1 H, C*H*Me$_2$), 2.07 (s, 12 H, Mes, 4 Me), 2.34 (s, 6 H, Mes, 2 Me), 2.36 (s, 6 H, MeCN), 5.41 (d, $^3J_{H,H}$ = 6.3 Hz, 2 H, $C_6H_4$), 5.71 (d, $^3J_{H,H}$ = 6.5 Hz, 2 H, $C_6H_4$), 7.10 (s, 4 H, Mes, CH), 7.27 (s, 2 H, CH=) ppm. $^{13}C\{^1H\}$ NMR (75.47 MHz, $CD_2Cl_2$): $\delta$ = 4.74 (s, *Me*CN), 18.3 (s, Mes, 4 Me), 18.6 (s, *Me*$C_6H_4$), 21.2 (s, Mes, 2 Me), 22.7 (s, CH*Me$_2$*), 32.1 (s, *C*HMe$_2$), 90.6 (s, $C_6H_4$, 2 CH), 91.3 (s, $C_6H_4$, 2 CH), 104.5 (s, *C*Me, *p*-cymene), 109.0 (s, *Ci*Pr, *p*-cymene), 127.8 (s, NCH=), 129.5 (s, Me*C*N), 130.1 (s, Mes, 4 CH), 136.1 (s, Mes, 4 *C*Me), 136.4 (s, Mes, 2 CN), 141.6 (s, Mes, 2 *C*Me, Mes), 163.7 (s, Ru=C) ppm. $^{13}C$ NMR (75.47 MHz, $CD_2Cl_2$, selected values): $\delta$ = 127.8 ppm (dd, $^1J_{H,C}$ = 201, $^3J_{H,C}$ = 12 Hz, NCH=). $C_{35}H_{44}B_2F_8N_4Ru$ (795.44): calcd. C 52.85, H 5.58, N 7.04; found C 52.68, H 5.62, N 6.99.

**[Ru(hexamethylbenzene)(IMes)(MeCN)$_2$][BF$_4$]$_2$ (5f):** Yield: 84%, orange crystals. $^1H$ NMR (200.13 MHz, $CD_3CN$): $\delta$ = 1.78 (s, 18 H, $C_6Me_6$), 1.95 (s, 6 H, MeCN), 2.06 (s, 12 H, Mes, 4 Me), 2.35 (s, 6 H, Mes, 2 Me), 7.11 (s, Mes, 4 H), 7.25 (s, 2 H, CH=) ppm. $^{13}C\{^1H\}$ NMR (75.47 MHz, $CD_2Cl_2$): $\delta$ = 5.30 (s, *Me*CN), 16.5 (s, $C_6Me_6$), 18.7 (s, Mes, 4 Me), 21.2 (s, Mes, 2 Me), 101.7 (s, $C_6Me_6$), 128.5 (s, NCH=), 129.3 (s, Me*C*N), 130.3 (s, Mes, 4 CH), 136.1 (s, Mes, 4 *C*Me), 137.1 (s, Mes, 2 CN), 141.1 (s, Mes, 2 *C*Me), 164.1 (s, Ru=C) ppm. $^{13}C$ NMR (75.47 MHz, $CD_2Cl_2$, selected values): $\delta$ = 128.5 ppm (dd, $^1J_{H,C}$ = 201, $^3J_{H,C}$ = 11 Hz, NCH=). $C_{37}H_{48}B_2F_8N_4Ru$ (823.49): calcd. C 53.97, H 5.88, N 6.80; found C 53.95, H 6.09, N 6.90.

**X-ray Crystallography:** A selected crystal of **2a**·1/2$CH_2Cl_2$ was studied with a NONIUS Kappa CCD diffractometer equipped with a graphite monochromator. The cell parameters were obtained with Denzo and Scalepack,[38] and data collection with NONIUS KappaCCD software.[39] Data reduction was carried out with Denzo and Scalepack.[38] A selected crystal of **2d**·$H_2O$ was studied with a NONIUS CAD 4 automatic diffractometer equipped with a graphite monochromator.[40] After Lorenz and polarisation corrections (**2d**),[41] the structures were solved with SIR-97, which revealed the non-hydrogen atoms.[42,43] After anisotropic refinement, many hydrogen atoms might be found with Fourier difference calculations. The whole structures were refined with SHELXL-97 by full-matrix least-squares methods on $F^2$ ($x$, $y$, $z$, $\beta_{ij}$ for Ru, P, Cl,

Table 1. Crystallographic data for complexes **2a**·1/2$CH_2Cl_2$ and **2d**·$H_2O$.[a]

| Complex | **2a**·1/2$CH_2Cl_2$ | **2d**·$H_2O$ |
|---|---|---|
| Empirical formula | $C_{59}H_{96}Cl_2O_6P_2Ru_2$ | $C_{16}H_{29}O_4PRu$ |
| Molecular mass [g mol$^{-1}$] | 1236.34 | 417.43 |
| Crystal size [mm] | 0.32 × 0.22 × 0.20 | 0.32 × 0.26 × 0.22 |
| Crystal system | triclinic | monoclinic |
| Space group | $P\bar{1}$ | $P2_1/n$ |
| $a$ [Å] | 14.6292(3) | 12.900(4) |
| $b$ [Å] | 15.8474(3) | 14.846(7) |
| $c$ [Å] | 16.0019(3) | 9.764(3) |
| $\alpha$ [°] | 115.050(1) | 90 |
| $\beta$ [°] | 114.131(1) | 103.32(3) |
| $\gamma$ [°] | 94.460(1) | 90 |
| Volume [Å$^3$] | 2922.55(10) | 1819.6(12) |
| $Z$ | 2 | 4 |
| Density [g cm$^{-3}$] | 1.405 | 1.524 |
| Temperature [K] | 150(2) | 293(2) |
| $F$(000) | 1300 | 864 |
| Mo-$K_\alpha$ radiation, $\lambda$ [Å] | 0.71073 | 0.71073 |
| Absorption coefficient [mm$^{-1}$] | 0.711 | 0.963 |
| $\theta$ range [°] | 1.49 to 27.51 | 2.12 to 27.02 |
| Index ranges | $0 < h < 19$ | $-16 < h < 16$ |
| | $-20 < k < 20$ | $0 < k < 18$ |
| | $-20 < l < 18$ | $0 < l < 12$ |
| Reflections collected | 32238 | 4176 |
| Independent reflections | 12228 ($R_{int}$ = 0.0000) | 3951 ($R_{int}$ = 0.0253) |
| Reflections [$I > 2\sigma(I)$] | 10808 | 3474 |
| Data/restraints/parameters | 12923/0/641 | 3951/0/200 |
| Goodness-of-fit on $F^2$ | 1.088 | 1.018 |
| Final $R$ indices [$I > 2\sigma(I)$] | $R_1$ = 0.0328 | $R_1$ = 0.0320 |
| | $wR_2$ = 0.0759 | $wR_2$ = 0.0858 |
| $R$ indices (all data) | $R_1$ = 0.0440 | $R_1$ = 0.0397 |
| | $wR_2$ = 0.0832 | $wR_2$ = 0.0895 |
| Largest diff. peak/hole [e·Å$^{-3}$] | 0.837/–0.929 | 0.869/–0.840 |

[a] $w = 1/[\sigma^2(F_o^2) + (0.0252P)^2 + 3.4483P]$ (**2a**), $1/[\sigma^2(F_o^2) + (0.0532P)^2 + 2.1077P]$ (**2d**), where $P = (F_o^2 + 2F_c^2)/3$.

 © 2006 Wiley-VCH Verlag GmbH & Co. KGaA, Weinheim 

O and C atoms; *x*, *y*, *z* in riding mode for H atoms).[44] ORTEP views were prepared with PLATON98,[45] and ORTEP-3 for Windows.[46] In the case of **2a**, the asymmetric unit cell consists of two molecules of complex and a dichloromethane one. The two molecules are identical, although slight differences in torsion angles were detected. Further crystallographic data are given in Table 1. CCDC-287581 (**2a**), and -287580 (**2d**) contain the supplementary crystallographic data for this paper. These data can be obtained free of charge from The Cambridge Crystallographic Data Centre via www.ccdc.cam.ac.uk/data_request/cif.


[1] R. B. Bedford, C. S. J. Cazin, D. Holder, *Coord. Chem. Rev.* **2004**, *248*, 2283–2321.
[2] A. F. Littke, G. C. Fu, *Angew. Chem. Int. Ed.* **2002**, *41*, 4176–4211.
[3] D. Sémeril, C. Bruneau, P. H. Dixneuf, *Adv. Synth. Catal.* **2002**, *344*, 585–595.
[4] D. Sémeril, M. Cléran, C. Bruneau, P. H. Dixneuf, *Adv. Synth. Catal.* **2001**, *343*, 184–187.
[5] J. Le Nôtre, R. Touzani, O. Lavastre, C. Bruneau, P. H. Dixneuf, *Adv. Synth. Catal.* **2005**, *347*, 783–791.
[6] A. J. Arduengo, III, *Acc. Chem. Res.* **1999**, *32*, 913–921.
[7] B. Çetinkaya, S. Demir, I. Özdemir, L. Toupet, D. Sémeril, C. Bruneau, P. H. Dixneuf, *Chem. Eur. J.* **2003**, *9*, 2323–2330.
[8] J. F. Hartwig, R. G. Bergman, R. A. Andersen, *Organometallics* **1991**, *10*, 3344–3362.
[9] L. Maurette, B. Donnadieu, G. Lavigne, *Angew. Chem. Int. Ed.* **1999**, *38*, 3707–3710.
[10] G. Henig, M. Schulz, B. Windmüller, H. Werner, *Dalton Trans.* **2003**, 441–448.
[11] T. J. Geldbach, P. S. Pregosin, *Eur. J. Inorg. Chem.* **2002**, 1907–1918.
[12] D. Belli Dell'Amico, F. Calderazzo, L. Labella, F. Marchetti, *J. Organomet. Chem.* **2000**, *596*, 144–151.
[13] J. Valentine, D. Valentine Jr, J. P. Collman, *Inorg. Chem.* **1971**, *10*, 219–225.
[14] D. F. Christian, W. R. Roper, *J. Chem. Soc., Chem. Commun.* **1971**, 1271–1272.
[15] W. O. Siegl, S. J. Lapporte, J. P. Collman, *Inorg. Chem.* **1973**, *12*, 674–677.
[16] J. B. Letts, T. J. Mazanec, D. W. Meek, *Organometallics* **1983**, *2*, 695–704.
[17] M. Ogasawara, F. Maseras, N. Gallego-Planas, K. Kawamura, K. Ito, K. Toyota, W. E. Streib, S. Komiya, O. Eisenstein, K. G. Caulton, *Organometallics* **1997**, *16*, 1979–1993.
[18] H. Nakajima, K. Tsuge, K. Toyohara, K. Tanaka, *J. Organomet. Chem.* **1998**, *569*, 61–69.
[19] C. Becker, L. Dahlenburg, S. Kerstan, *Z. Naturforsch., Teil B* **1993**, *48*, 577–582.
[20] S. Yamazaki, Z. Taira, *J. Organomet. Chem.* **1999**, *578*, 61–67.
[21] A. J. Lindsay, M. Motevalli, M. B. Hursthouse, G. Wilkinson, *J. Chem. Soc., Chem. Commun.* **1986**, 433–434.
[22] A. J. Lindsay, G. Wilkinson, M. Motevalli, M. B. Hursthouse, *J. Chem. Soc., Dalton Trans.* **1987**, 2723–2736.
[23] F. A. Cotton, L. Labella, M. Shang, *Inorg. Chem.* **1992**, *31*, 2385–2389.
[24] A. Llobet, M. E. Curry, H. T. Evans, T. J. Meyer, *Inorg. Chem.* **1989**, *28*, 3131–3137.
[25] A. Geilenkirchen, P. Neubold, R. Schneider, K. Wieghardt, U. Flörke, H.-J. Haupt, B. Nuber, *J. Chem. Soc., Dalton Trans.* **1994**, 457–464.
[26] B. P. Sullivan, R. S. Smythe, E. M. Kober, T. J. Meyer, *J. Am. Chem. Soc.* **1982**, *104*, 4701–4703.
[27] C. Mountassir, T. Ben Hadda, H. Le Bozec, *J. Organomet. Chem.* **1990**, *388*, C13–C16.
[28] D. Ooyama, T. Tomon, K. Tsuge, K. Tanaka, *J. Organomet. Chem.* **2001**, *619*, 299–304.
[29] T. Wilczewski, M. Bocheńska, J. F. Biernat, *J. Organomet. Chem.* **1981**, *215*, 87–96.
[30] P. Crochet, B. Demerseman, C. Rocaboy, D. Schleyer, *Organometallics* **1996**, *15*, 3048–3061.
[31] Y. Miyaki, T. Onishi, S. Ogoshi, H. Kurosawa, *J. Organomet. Chem* **2000**, *616*, 135–139.
[32] J. M. Boncella, T. M. Eve, B. Rickman, K. A. Abboud, *Polyhedron* **1998**, *17*, 725–736.
[33] A. J. Arduengo III, H. V. Rasika Dias, J. C. Calabrese, F. Davidson, *J. Am. Chem. Soc.* **1992**, *114*, 9724–9725.
[34] W. Lackner, C. M. Standfest-Hauser, K. Mereiter, R. Schmid, K. Kirchner, *Inorg. Chim. Acta* **2004**, *357*, 2721–2727.
[35] H. Le Bozec, D. Touchard, P. H. Dixneuf, *Adv. Organomet. Chem.* **1989**, *29*, 163–247.
[36] A. J. Arduengo III, *Preparation of 1,3-Disubstituted Imidazolium Salts*, US Patent No. 5182405, **1993**.
[37] A. Demonceau, A. W. Stumpf, E. Saive, A. F. Noels, *Macromolecules* **1997**, *30*, 3127–3136.
[38] *Processing of X-ray Diffraction Data Collected in Oscillation Mode*: Z. Otwinowski, W. Minor, *Macromol. Crystallogr. A* **1997**, *276*, 307–326.
[39] *NONIUS KappaCCD Software*, Nonius BV, Delft, The Netherlands, **1999**.
[40] C. K. Fair, *MolEN – An Interactive Intelligent System for Crystal Structure Analysis*, Enraf–Nonius, Delft, The Netherlands, **1990**.
[41] A. L. Spek, *HELENA – A Program for the Handling of CAD4/Diffractometer Output SHELX(S/L)*, University of Utrecht, The Netherlands, **1997**.
[42] *SIR-97 – A New Tool for Crystal Structure Determination and Refinement*: A. Altomare, M. C. Burla, M. Camalli, G. Cascarano, C. Giacovazzo, A. Guagliardi, A. G. G. Moliterni, G. Polidori, R. Spagna, *J. Appl. Crystallogr.* **1998**, *31*, 74–77.
[43] *SIR-97 – A New Tool for Crystal Structure Determination and Refinement*: A. Altomare, M. C. Burla, M. Camalli, G. Cascarano, C. Giacovazzo, A. Guagliardi, A. G. G. Moliterni, G. Polidori, R. Spagna, *J. Appl. Crystallogr.* **1999**, *32*, 115–119.
[44] G. M. Sheldrick, *SHELXL97 – A Program for the Refinement of Crystal Structures*, University of Göttingen, Germany, **1997**.
[45] A. L. Spek, *PLATON – A Multipurpose Crystallographic Tool*, University of Utrecht, The Netherlands, **1998**.
[46] L. J. Farrugia, *J. Appl. Crystallogr.* **1997**, *30*, 565.


Received: November 2, 2005
Published Online: January 31, 2006

 © 2006 Wiley-VCH Verlag GmbH & Co. KGaA, Weinheim 

DOI: 10.1002/ejic.200501019

# Boron–Nitrogen Adducts of 1,3,5-Triaza-7-phosphaadamantane (PTA): Synthesis, Reactivity, and Molecular Structure

**Brian J. Frost,*[a] Charles A. Mebi,[a] and Phillip W. Gingrich[a]**

**Keywords:** Borane adducts / Boroxine / N,P ligands / Coordination modes / Structure elucidation

Addition of $BH_3$ to 1,3,5-triaza-7-phosphaadamantane (PTA) leads to the formation of the first coordination complex of PTA in which a nitrogen and not the phosphorus of PTA is involved in the bonding. Multinuclear NMR spectroscopy, X-ray crystallography, and computational chemistry are utilized in the characterization of the products. Crystal structures of PTA–$BH_3$ (**1**) and O=PTA–$BH_3$ (**2**) adducts are described. In addition a coordination polymer, $[CpRu(PTA)_2Cl(Ph_3B_3O_3)]_n$ (**3**), resulting from Lewis acid–base adduct formation between the PTA ligands of $CpRu(PTA)_2Cl$ and the product of the cyclocondensation of phenylboronic acid is described. The polymeric compound **3** was also characterized by X-ray crystallography.

(© Wiley-VCH Verlag GmbH & Co. KGaA, 69451 Weinheim, Germany, 2006)

## Introduction

The coordination chemistry and catalytic activity of metal complexes containing aminophosphane ligands has been explored extensively in recent years.[1] Much of the interest in this class of ligand arises from the variety of coordination modes possible (i.e. *N*-bound, *P*-bound, or N–P chelate). Particularly important for catalytic applications is the hemilabile nature of the hard nitrogen donor.[2] Our group,[3–5] and others,[6] have been interested in the chemistry of the heterocyclic phosphane 1,3,5-triaza-7-phosphaadamantane (PTA), which was first synthesized by Daigle in the 1970s (Figure 1).[7,8] The attractive properties of PTA are its resistance to oxidation, small size, strong binding ability, and water solubility. Although PTA is an aminophosphane, the adamantane-like structure excludes the possibility of P–N chelate formation. PTA coordinates to metal atoms through the phosphorus atom, with only one known example of a PTA complex containing a nitrogen–metal dative bond; a polymeric structure formed through the coordination of a nitrogen of a ruthenium-bound PTA ligand to silver.[9] Because metals preferentially bind to the phosphorus of PTA, the amine functionalities of PTA are the preferred site of alkylation and protonation.[7,10] We have been interested in the coordination chemistry of PTA and, specifically, why transition metals bind to the phosphorus site and other Lewis acids, such as $H^+$ and $R^+$, bind preferentially, although not exclusively, to the nitrogen sites. Methylation of PTA with MeI leads to *N*-methylated PTA (PTA-Me) with a small amount, $< 5\%$, of the *P*-methylated PTA (Me-PTA).[10,11] The synthesis of *P*-alkylated PTA derivatives may be accomplished by starting with phosphane sources such as R-$PH_2$ or $P(CH_2OH)_3$, Scheme 1.[12,13]

Figure 1. PTA.

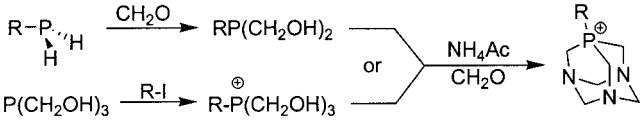


Scheme 1.

Herein we present experimental and theoretical data on the addition of $BH_3$ to PTA and O=PTA, affording the first coordination complex of PTA involving only nitrogen coordination. Also described is an extended polymeric structure, $[CpRu(PTA)_2Cl(Ph_3B_3O_3)]_n$, held together by B–N coordination of a PTA nitrogen to triphenylboroxine.

## Results and Discussion

$BH_3$ complexes of PTA and O=PTA, **1** and **2** respectively, have been synthesized in good yield by addition of $BH_3$–THF to PTA or O=PTA. In both cases, addition of $BH_3$ leads to the formation of a N–B coordination complex, Scheme 2. As it is not surprising that such complexes are formed, compound **1** is, to the best of our knowledge, the first example of a coordination complex of PTA in which only nitrogen of PTA is involved in bonding. Peruzzini et al. recently reported the first example of a coordination

[a] Department of Chemistry, University of Nevada, Reno, NV 89557, USA
Fax: +1-775-784-6804
E-mail: Frost@chem.unr.edu

 © 2006 Wiley-VCH Verlag GmbH & Co. KGaA, Weinheim 

complex involving binding of a nitrogen of PTA to another metal;[9] in this case the phosphorus of PTA is already coordinated to ruthenium. There are still no examples in the literature of a nitrogen-bound PTA–metal complex in which the phosphorus is not also coordinated to a metal.

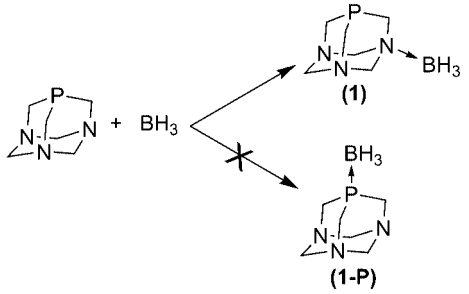


Scheme 2.

The site of $BH_3$ binding has been determined by: X-ray crystallography, computational chemistry, IR spectroscopy, $^1H$, $^{31}P$, and $^{11}B$ NMR spectroscopy, all of which indicate that addition of $BH_3$ results in preferential B–N and *not* B–P bond formation. No evidence of P–B bond formation was observed by any spectroscopic method including $^{11}B$ or $^{31}P$ NMR spectroscopy.[14,15]

Addition of $BH_3$ to PTA or O=PTA results in a slight shift of the $^{31}P$ NMR resonances with respect to PTA and O=PTA. The complexes **1** and **2** exhibit $^{31}P$ NMR resonances at –88.4 and –9.8 ppm, respectively, compared to –98.3 and –2.5 ppm for PTA and O=PTA.[7,8] These shift values are similar to those observed for the methylation of PTA; $PTA(Me)^+$ exhibits a $^{31}P$ NMR resonance at –86.1 ppm.[6] The $^{11}B$ NMR spectra of **1** and **2** were obtained with resonances at –10.8 ppm for **1** (quartet, $^1J_{BH}$ = 98 Hz) and –12.2 ppm for **2** (quartet, $^1J_{BH}$ = 95 Hz). These values compare well with other $^{11}B$ chemical shifts of other $H_3B–NR_3$ compounds. For example, the $^{11}B$ NMR chemical shift of the borane adducts of 1,3,5-trimethyl-1,3,5-triazacyclohexane[16] and 3,5-dimethyl-1,3,5-thiadiazacyclohexane[17] were found to be –12.6 ppm (q, $^1J_{BH}$ = 96 Hz) and –11.1 ppm (q, $^1J_{BH}$ = 97 Hz), respectively.

The solid-state structures of **1** and **2** were determined by X-ray crystallography. Crystals suitable for X-ray analysis were obtained by slow diffusion of hexanes into a THF solution of the complex at room temperature over 3 days.

### Structure of $PTA–BH_3$ (1)

A thermal ellipsoid representation of complex **1** is depicted in Figure 2, along with the atomic numbering scheme. Selected bond lengths and angles may be found in Table 1. The overall structure including bond lengths and angles is practically identical to that of PTA. Noteworthy is that the B–N bond length [1.58(2) Å] in **1** is similar to that found in the DABCO adduct, $N(CH_2CH_2)_3N–BH_3$ (B–N = 1.598 Å),[18] and is slightly shorter than the B–N bond in the hexamethylenetetramine–borane adduct [B–N = 1.661(7) Å].[19] Also of note is that the (B)N–C(N) bond length, 1.505(9) Å, is longer than the other N–C(N) bond lengths, 1.458(9) Å, consistent with other PTA complexes

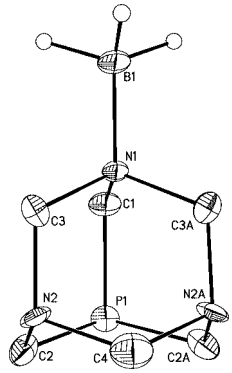


Figure 2. Thermal ellipsoid plot of $PTA–BH_3$ showing the atomic numbering scheme; hydrogen atoms have been omitted for clarity; thermal ellipsoids are plotted at 50% probability.

Table 1. Bond lengths [Å] and angles [°] for $PTA–BH_3$ (**1**).

| | |
|---|---|
| P(1)–C(2) | 1.815(9) |
| P(1)–C(1) | 1.830(12) |
| (B)N(1)–C | 1.505(11)[a] |
| N(1)–B(1) | 1.58(2) |
| N(2)–C | 1.458(9)[b] |
| C(2)–P(1)–C(1) | 95.0(4) |
| C(1)–N(1)–C(3) | 109.3(6) |
| C–N(1)–B(1) | 111.2(12), 110.0(7) |
| C–N(2)–C | 108.0(8)–110.6(8) |
| N(1)–C(1)–P(1) | 116.1(8) |
| N(2)–C(2)–P(1) | 117.2(6) |

[a] Average of two similar distances. [b] Average of three similar distances.

Table 2. Comparison of the bond lengths [Å] and angles [°] obtained from X-ray crystallography for **1**, **2**, PTA, and O=PTA.

| | PTA[21,22] | $PTA–BH_3$ (**1**) | O=PTA[21,22] | O=PTA–$BH_3$ (**2**) |
|---|---|---|---|---|
| P–C | 1.856 | 1.815(9), 1.830(12) | 1.817 | 1.810 0(17)–1.8192(16) |
| N–C(N) | 1.464 | 1.458(9), 1.464(9) | 1.465 | 1.447(2), 1.468(2) |
| (B)N–C(N) | – | 1.505(11) | – | 1.5162(19), 1.5145(19) |
| N–C(P) | 1.461 | 1.454(9), 1.504(13) | 1.472 | 1.485(2),[a] 1.5011(18) |
| N–B | – | 1.58(2) | – | 1.616(2) |
| P=O | – | – | 1.476 | 1.4903(11) |
| B–N–C | – | 110.0(7), 111.2(12) | – | 109.51(12),[a] 111.22(12) |
| C–P–C | 96.07 | 95.0(4), 95.9(6) | 100.18 | 100.42(7),[a] 101.95(8) |
| C–N–C | 108.30 | 106.8(9)–110.6(8) | 108.61 | 107.39(12)–113.15(12) |
| N–C–P | 114.06 | 117.2(6), 116.1(8) | 110.21 | 108.73(10),[a] 111.8(1) |
| C–P–O | – | – | 117.66 | 114.08(7)–119.33(7) |

[a] Average of two similar values.

 © 2006 Wiley-VCH Verlag GmbH & Co. KGaA, Weinheim 

in which one nitrogen atom of PTA has been protonated or alkylated.[20] Table 2 compares the bond lengths and angles of **1** with PTA and other PTA complexes.

### Structure of O=PTA–$BH_3$ (2)

A thermal ellipsoid representation of complex **2** is depicted in Figure 3, along with the atomic numbering scheme. Selected bond lengths and angles may be found in Table 3. The P–O bond length in **2** [1.4903(11) Å] is slightly longer than found in O=PTA (P–O = 1.476 Å).[21,22] Noteworthy is that the B–N bond length in **2** [1.616(2) Å] is slightly longer than the B–N distance in **1** [1.58(2) Å], presumably due to the more positive nature of the formally $P^V$ oxidation state of the phosphorus. Comparison of bond lengths and angles in **2** with O=PTA may be found in Table 2.

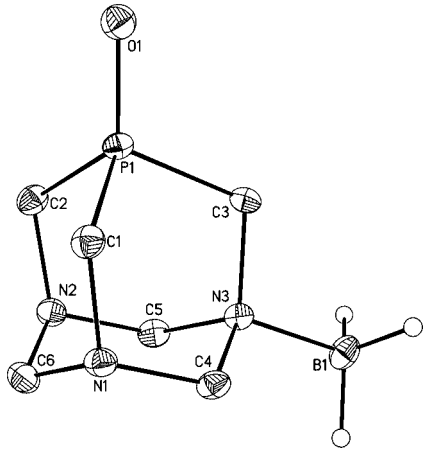


Figure 3. Thermal ellipsoid plot of O=PTA–$BH_3$ showing the atomic numbering scheme; hydrogen atoms have been omitted for clarity; thermal ellipsoids are plotted at 50% probability.

Table 3. Selected bond lengths [Å] and angles [°] for O=PTA–$BH_3$ (**2**).

| | |
|---|---|
| P(1)–O(1) | 1.4903(11) |
| P(1)–C | 1.8100(17)–1.8192(16) |
| (B)N(3)–C | 1.5011(18)–1.5162(19) |
| N(3)–B(1) | 1.616(2) |
| N–C | 1.447(2)–1.4879(19) |
| O–P(1)–C | 114.07(7)–119.33(7) |
| C–P(1)–C | 100.21(7)–101.95(8) |
| C–N(1)–C | 109.35(12)–113.15(12) |
| C–N(2)–C | 109.46(12)–112.87(12) |
| C–N(3)–C | 107.39(12)–109.58(11) |
| C–N(3)–B(1) | 109.46(12)–111.22(12) |
| N(3)–C(3)–P(1) | 111.80(10) |
| N(1)–C(1)–P, N(2)–C(2)–P | 108.88(10), 108.57(11) |
| N–C–N | 113.52(12)–113.69(12) |

### Theoretical Calculations

In an attempt to gain insight into the reactivity differences between the nitrogen and phosphorus sites of PTA, calculations were performed modeling the alkylation and $BH_3$ addition to PTA. Density Functional Theory (DFT) calculations (B3LYP/LANL2DZ) were performed on **1**, **1-P**, PTA, PTA-Me, and Me-PTA as described in the experimental section. From these calculations we predict an energy difference of 53.6 kJ/mol between **1** and **1-P**, with **1** being the more stable isomer. This is consistent with calculations comparing the alkylation of PTA at the nitrogen atom (PTA-Me) or phosphorus (Me-PTA), which predict that nitrogen is the preferred site of alkylation by ca. 39.1 kJ/mol. These results are in agreement with those obtained by Darensbourg et al.[10] Table 4 contains comparisons of calculated geometries for **1**, **1-P**, **2**, PTA, and O=PTA. The bond lengths and angles in Table 4 correspond well that those found in the crystal structures of **1**, **2**, PTA, and O=PTA.

### Reactivity of 1 and 2

Complexes of **1** and **2** are susceptible to hydrolytic cleavage of the boron–nitrogen bond in both the solid state and in solution. $BH_3$ may also be cleanly and easily removed from **1** or **2** by addition of excess diazobicyclooctane (DABCO) to an acetone solution of **1** or **2** at 50° C. One of the unusual features of **1** is that the phosphorus is now much more vulnerable to oxidation than PTA, $PTA(H)^+$, or $PTA(Me)^+$. Solids of PTA–$BH_3$ were stable in air for weeks, whereas solutions of PTA–$BH_3$ show signs of oxidation to O=PTA–$BH_3$ over the course of days, Scheme 3. In contrast, PTA, $PTAH^+$, and $PTAMe^+$ are indefinitely stable towards air oxidation in the solid state or solution. Both **1** and **2** must be stored under dry conditions, and **1** must be stored under nitrogen to prevent oxidation.

Table 4. DFT[a] calculated bond lengths and angles for **1**, **2**, PTA and O=PTA.

| | PTA–$BH_3$[N] (**1**) | $H_3B$–PTA (**1-P**)[b] | O=PTA–$BH_3$ (**2**) | PTA | O=PTA |
|---|---|---|---|---|---|
| P–B | – | 2.013 | – | – | – |
| P–C | 1.946, 1.929 | 1.927 | 1.914, 1.903 | 1.955 | 1.919 |
| N–C(N) | 1.465, 1.488, 1.540 | 1.493 | 1.466, 1.490, 1.542 | 1.492 | 1.494 |
| N–C(P) | 1.483, 1.519 | 1.483 | 1.486, 1.518 | 1.484 | 1.488 |
| N–B | 1.652 | – | 1.660 | – | – |
| B–P–C | – | 120.2 | – | – | – |
| B–N–C | 109.5, 109.6 | – | 109.5 | – | – |
| C–P–C | 94.1, 94.6 | 96.8 | 98.4, 98.5 | 93.8 | 98.0 |
| P=O | – | – | 1.610 | – | 1.614 |

[a] B3LYP/Lanl2dz. [b] $BH_3$ is phosphorus bound.

 © 2006 Wiley-VCH Verlag GmbH & Co. KGaA, Weinheim 

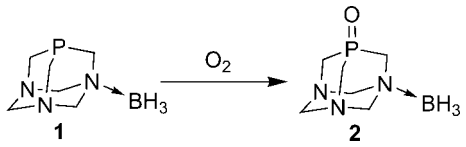


Scheme 3.

Addition of $BH_3$ appears to activate the phosphorus to alkylation as well as oxidation; addition of methyl iodide to PTA–$BH_3$ results in the formation of ca. 20% of the phosphorus-methylated product (Me-PTA) and ca. 80% of the nitrogen-methylated product (PTA-Me). Compared to the alkylation of PTA with MeI, which results in >95% PTA-Me and <5% Me-PTA the phosphorus in **1** is activated with respect to alkylation. This may open up new synthetic pathways towards high-yield synthesis of phosphorus-alkylated PTA compounds important in the further development of the chemistry of PTA and PTA derivatives. Currently phosphorus-alkylated PTA is synthesized by first alkylating $P(CH_2OH)_3$ followed by reaction with $NH_4OAc$ and formaldehyde (Scheme 1).[12,13]

### Synthesis of $[CpRu(PTA)_2Cl(Ph_3B_3O_3)]_n \cdot 1/2CH_2Cl_2$

We have previously reported the solid-state structure of $CpRu(PTA)_2Cl$.[4] In an attempt to access the cationic $CpRu(PTA)_2S^+$ complexes (where S = solvent; $CH_3CN$, $H_2O$), recently described,[23] we reacted $NaBPh_4$ with $CpRu(PTA)_2Cl$ in the presence of 1-propanol. Instead of the desired product, $[CpRu(PTA)_2S][BPh_4]$, we obtained crystals of the polymeric complex $[CpRu(PTA)_2Cl(Ph_3B_3O_3)]_n \cdot 3CH_2Cl_2$ in low yield (< 10%). The yield from this reaction is very low; the product is likely obtained due to small amounts of $Ph_3B_3O_3$ impurities in the $NaBPh_4$, or from adventitious water reacting with the tetraphenylborate anion generating triphenylboroxine. This complex was obtained in moderate yields (48%) by reaction of $CpRu(PTA)_2Cl$ with three equivalents of phenylboronic acid in dichloromethane, which affords large orange crystals of $[CpRu(PTA)_2Cl(Ph_3B_3O_3)]_n \cdot 1/2CH_2Cl_2$ (**3**). The polymer forms as a result of the cyclocondensation of phenylboronic acid, to triphenylboroxine, followed by formation of a Lewis acid–base adduct with the PTA ligands of $CpRu(PTA)_2Cl$ (Scheme 4); similar to the PTA–$BH_3$ complexes described above. Adducts of boroxines with amines have been reported;[24–30] however, compound **3** is the first involving PTA. Perzzuni et al. have described elsewhere the first heterobimetallic complex in which PTA exhibits both P and N coordination. In this case, $CpRu(PTA)_2Cl$ was treated with AgOTf leading to a polymeric structure in which PTA is bound to both ruthenium (by phosphorus) and silver (by nitrogen).[9] Complex **3** and the complexes described by Peruzzini are the only verifiable examples of PTA complexes in which the nitrogen sites of PTA are involved in dative bonding to another atom. It is now apparent that the nitrogen sites of PTA may be far from benign in the chemistry of PTA complexes. Unlike the water-soluble organometallic polymers of Peruzzini et al.,[9] compound **3** does not appear to remain polymeric in aqueous solution, presumably due to ring-cleavage hydrolysis of the coordinated $Ph_3B_3O_3$.

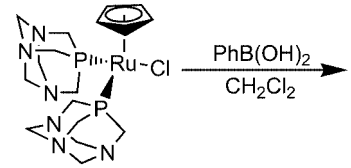


$[CpRu(PTA)_2Cl(Ph_3B_3O_3)]_n + 3n\ H_2O$

**3**

Scheme 4.

The $^{31}P$ NMR of the polymeric **3** in dichloromethane exhibits a broad singlet at –21.9 ppm, relative to the $^{31}P$ NMR chemical shift of –25.6 ppm for the parent $CpRu(PTA)_2Cl$. The $^1H$ NMR spectrum of **3**, in $CD_2Cl_2$, contains a sharp resonance attributed to the Cp protons at $\delta$ = 4.59 ppm an upfield shift of 0.16 ppm, relative to $CpRu(PTA)_2Cl$, indicating shielding of the protons by the phenyl groups of the boroxine as confirmed by the crystal structure. The N$CH_2$N protons of the PTA ligands in **3** exhibit an AB pattern centered at $\delta$ = 4.53 ppm ($^2J_{(HAHB)}$ = 13 Hz). The P$CH_2$N protons of the PTA ligands also exhibit an AB pattern centered at $\delta$ = 3.98 ppm ($^2J_{(HAHB)}$ = 15 Hz). The PTA protons are shifted downfield due to the deshielding effect of the N–B bonding. Two distinct resonances for the phenyl rings of the boroxine are observed, 8.07 ppm (5 H) and 7.5 ppm (10 H), indicating two different environments for the phenyl rings. $^{11}B$ NMR spectroscopy of **3** in acetone reveals two different boron environments with $^{11}B$ chemical shifts of 29.3 and 21.3 ppm indicative of unbound and bound boron nuclei, respectively.[31] This suggests that **3** remains polymeric in acetone with two of the boron atoms of triphenylboroxine coordinated to a PTA and remaining boron uncoordinated.

### Structure of $[CpRu(PTA)_2Cl(Ph_3B_3O_3)]_n \cdot 1/2CH_2Cl_2$

The solid-state structure of **3** was determined by X-ray crystallography. Large orange crystals suitable for X-ray diffraction were obtained by slow diffusion of hexanes into a concentrated solution of **3** in $CH_2Cl_2$. A thermal ellipsoid representation of complex **3** is depicted in Figure 4, along with the atomic numbering scheme. Selected bond lengths and angles may be found in Table 5. The structure consists of $CpRu(PTA)_2Cl$ molecules linked together in linear chains by $Ph_3B_3O_3$, cocrystallized with half a molecule of $CH_2Cl_2$. The polymeric structure is obtained through formation of a Lewis acid–base adduct from one nitrogen atom on each PTA to a boron atom of triphenylboroxin. Two of the three boron atoms in triphenylboroxin form N–B bonds, which affords a linear polymer, with the geometry about the coordinated boron sites significantly distorted

 © 2006 Wiley-VCH Verlag GmbH & Co. KGaA, Weinheim 

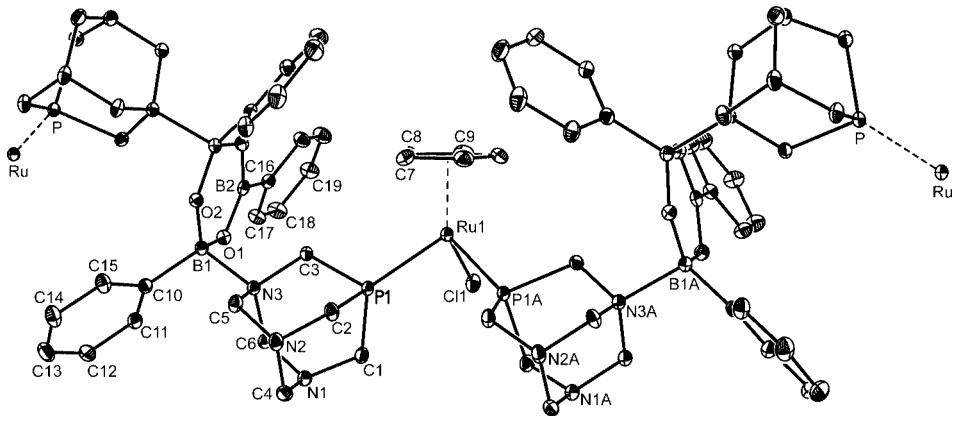


Figure 4. Thermal ellipsoid plot of **3** showing the atomic numbering scheme; hydrogen atoms have been omitted for clarity; thermal ellipsoids are plotted at 50% probability.

from planar towards tetrahedral with O–B–O angles of 115.8(2)° and N–B–C angles of 107.46(18)°. The boron atom, which is not coordinated to nitrogen is nearly planar with a O–B–O angle of 122.3(3)°. The B–N bond lengths are 1.737(3) Å, significantly longer than the N–B distances in compounds **1** and **2**, but comparable to other nitrogen-coordinated boroxin complexes which have B–N distances of 1.73–1.84 Å.[28–30] Comparison of the structure of **3** with the parent complex $CpRu(PTA)_2Cl$ and the diprotonated form $[CpRu(PTAH)_2Cl]^{2+}$, previously reported by us,[3,4] reveals that the core organometallic portion of **3** is largely unchanged, Table 6. The P–Ru–P angle is slightly less obtuse and the Ru–P bond lengths are elongated slightly (≈ 0.01 Å) in **3** vs. the other two complexes. The biggest change is in the (N)C–N distances within the PTA ligand, which have been utilized to determine when a PTA ligand has been protonated [on average the (N)C–N distance increases from ca. 1.46 to ca. 1.53 Å upon protonation].[20]

Table 5. Selected bond lengths [Å] and angles [°] for **3**.

| | |
|---|---|
| Ru(1)–P(1) | 2.2645(6) |
| Ru(1)–Cl(1) | 2.4443(8) |
| N(1)–C | 1.449(3)–1.470(4) |
| N(2)–C | 1.445(3)–1.473(3) |
| N(3)–C | 1.498(3)–1.513(3) |
| N(3)–B(1) | 1.737(3) |
| O(1)–B(2) | 1.368(3) |
| O–B(1) | 1.439(3)[a] |
| B(1)–C(10) | 1.625(4) |
| B(2)–C(16) | 1.576(5) |
| P(1)–Ru(1)–P(1)#1 | 95.46(3) |
| P(1)–Ru(1)–Cl(1) | 90.56(2) |
| C–N(3)–C | 107.80(18)–109.66(18) |
| C–N(3)–B(1) | 108.67(17)[a] |
| C(6)–N(3)–B(1) | 113.27(16) |
| B(2)–O(1)–B(1) | 121.1(2) |
| B(1)–O(2)–B(1)#2 | 123.4(3) |
| O(2)–B(1)–O(1) | 115.8(2) |
| O–B(1)–C(10) | 112.78(19)[a] |
| O–B(1)–N(3) | 103.21(16), 103.57(19) |
| C(10)–B(1)–N(3) | 107.46(18) |
| O(1)#2–B(2)–O(1) | 122.3(3) |
| O(1)–B(2)–C(16) | 118.83(16) |

[a] Average of two similar values.

Table 6. Comparison of selected bond lengths [Å] and angles [°] for **3** with those reported for $CpRu(PTA)_2Cl$[4] and $[CpRu(PTAH)_2Cl](PF_6)_2$.[3]

| | $CpRu(PTA)_2Cl$ | $[CpRu(PTAH)_2Cl](PF_6)_2$ | **3** |
|---|---|---|---|
| Ru–Cl | 2.445(2) | 2.455(2) | 2.4443(8) |
| Ru–P(1) | 2.258(3) | 2.254(3) | 2.2645(6) |
| Ru–P(2) | 2.247(3) | 2.257(3) | 2.2645(6)[c] |
| $Ru–Cp_{cent}$ | 1.852 | 1.855 | 1.850 |
| (N)C–N | 1.460(2)[a] | 1.448(11)[b] | 1.472(3)[c] |
| (N)C–N(B/H) | – | 1.516(12)[c] | 1.512(3)[d] |
| P(1)–Ru–P(2) | 96.85(5) | 99.05(10) | 95.46(3) |
| P(1)–Ru–Cl | 91.61(7) | 85.86(9) | 90.56(2) |
| P(2)–Ru–Cl | 86.46(7) | 86.80(9) | 90.56(2)[c] |

[a] Average of 12 values. [b] Average of 8 values. [c] Average of 4 values. [d] Average of 2 values.

## Conclusions

We have presented here the synthesis and characterization of three boron-coordinated PTA complexes. Peruzzini et al. published the first report of a PTA complex in which a metal is bound to a nitrogen of the PTA ligand.[9] Here we reported the second such complex, in which a nitrogen of a ruthenium-bound PTA serves as a Lewis base coordinating to the Lewis basic boron of triphenylboroxin. It should be noted that in both of these complexes the phosphorus atom of PTA is *already bound to a metal*. To the best of our knowledge, there are still no substantiated cases in the literature in which PTA serves only as a nitrogen donor ligand to a metal center. We reported here the closest example of such a structure; complex **1** represents the first coordination complex of PTA in which *only* the nitrogen of the PTA ligand is coordinated to another atom through a dative bond. Finally, it should be noted that the nitrogen sites of PTA may become involved in coordination chemistry and are not necessarily innocent bystanders. Complex **3** and the complexes previously reported by Peruzzini[9] may serve as a beginning for the use of PTA as a ligand in the building of extended structures, utilizing the ability of both the phosphorus and nitrogen sites of PTA to serve as Lewis bases.

 © 2006 Wiley-VCH Verlag GmbH & Co. KGaA, Weinheim 

## Experimental Section

**Materials and Methods:** Unless otherwise noted all manipulations where performed on a double-manifold Schlenk vacuum line under nitrogen or in a nitrogen-filled glovebox. Nitrogen was purified by passing the gas through a column of molecular sieves (Lind 13X), calcium chloride, potassium hydroxide, and dryrite. Tetrakis-(hydroxymethyl)phosphonium chloride was obtained from Cytec and used as received. Ruthenium trichloride hydrate, $D_2O$, KOH, $PPh_3$, phenyl boronic acid, dicyclopentadiene, cyclooctadiene (COD), and $BH_3$–etherate were purchased from commercial sources and used as received. 1,3,5-Triaza-7-phosphaadamantane (PTA),[7,8] 1,3,5-triaza-7-phosphaadamatane oxide (O=PTA),[7] and $CpRu(PTA)_2Cl$[4,32] were prepared according to the literature procedures. Solvents were freshly distilled from standard drying reagents or dried with activated molecular sieves. Water was distilled and deoxygenated prior to use. NMR spectra were recorded with either a Varian Unity Plus 500 FT-MNR spectrometer, a GN 300 FT-NMR/Scorpio spectrometer, or a QE 300 FT-NMR/Aquarius spectrometer. Proton spectra were referenced to residual solvent relative to TMS with the exception of aqueous spectra, which were referenced to an external standard of sodium 2,2-dimethyl-2-silapentane-5-sulfonate (DSS). Phosphorus chemical shifts are relative to an external reference of 85% $H_3PO_4$ in $D_2O$ with positive values downfield of the reference. $^{11}B$ chemical shifts are relative to an external reference of $BF_3$ in diethyl ether, with positive values downfield from the reference.

**Synthesis of PTA–$BH_3$ (1):** PTA (1.0 g, 6.4 mmol) was dissolved in a minimum amount of dichloromethane. The solution was then cooled in an ice bath and 1.1 equiv. of 1.0 M borane tetrahydrofuran complex was added via syringe (7 mL). The solution was stirred for 2 h, after which time the solvent was removed under vacuum leaving 1.01 g of a fine white solid (93% yield). $^1H$ NMR (300 MHz, [$D_6$]acetone, 25 °C): $\delta$ = 4.50–4.25 (m, 6 H, NC$H_2$N), 3.88–3.66 (m, 6 H, PC$H_2$N), 1.17 (q, $^1J_{BH}$ = 98 Hz, 3 H, $BH_3$) ppm. $^{11}B$ NMR (160 MHz, [$D_6$]acetone, 25 °C): $\delta$ = –10.8 (q, $^1J_{BH}$ = 98 Hz) ppm. $^{31}P\{^1H\}$ NMR (121 MHz, [$D_6$]acetone, 25 °C): $\delta$ = –88.4 (s) ppm. IR (KBr): $\tilde{\nu} = \upsilon_{(BH)}$: 2365 (s), 2312 (m), 2263 (m) $cm^{-1}$; $\upsilon_{(BN)}$: 1174 (s) $cm^{-1}$. IR ($CH_2Cl_2$): $\tilde{\nu} = \upsilon_{(BH)}$: 2370 (s), 2305 (m), 2271 (m) $cm^{-1}$; $\upsilon_{(BN)}$: 1172 (s) $cm^{-1}$. $C_6H_{15}BN_3P$: calcd. C 42.15, H 8.84, N 24.57; found C 42.20, H 8.90, N 25.02. X-ray quality crystals were grown by slow diffusion of hexanes into a concentrated THF solution of **1**, yielding colorless needles over the course of a week. A crystal suitable for X-ray diffraction was selected and mounted under oil on a glass fiber. Crystallographic data and data collecting parameters are listed in Table 7.

**Synthesis of O=PTA–$BH_3$ (2):** The borane complex of PTA oxide (O=PTA) was synthesized in a manner analogous to the PTA–borane complex described above. PTA=O (50 mg, 0.29 mmol) was dissolved in $CH_2Cl_2$ (20 mL) and $BH_3$–THF (1.0 mL, 1.0 M) was added at room temperature with stirring. The resultant solution turned cloudy and was stirred for an additional 1 h, after which time the product was collected by filtration. O=PTA–$BH_3$ was obtained as a fine white powder in 37% yield (20 mg). $^1H$ NMR (300 MHz, [$D_6$]acetone, 25 °C): $\delta$ = 4.5–3.8 (m, PTA), 1.47 (q, $^1J_{BH}$ = 95 Hz, $BH_3$) ppm. $^{11}B$ NMR (160 MHz, [$D_6$]acetone, 25 °C): $\delta$ = –12.2 (q, $^1J_{BH}$ = 95 Hz) ppm. $^{31}P\{^1H\}$ NMR (121 MHz, [$D_6$]-acetone, 25 °C): $\delta$ = –9.8 ppm. IR (KBr): $\tilde{\nu} = \upsilon_{(BH)}$: 2389 (s), 2325 (m), 2283 (m) $cm^{-1}$. $C_6H_{15}BN_3OP$: calcd. C 38.54, H 8.09, N 22.47; found C 38.92, H 8.51, N 22.56. Colorless X-ray quality crystals were obtained after approximately one week by layering a dilute solution of **2** in THF with hexane. A crystal suitable for X-ray diffraction was selected and mounted under oil on a glass fiber. Crystallographic data and data collecting parameters are listed in Table 7.

**Synthesis of $[CpRu(PTA)_2Cl(Ph_3B_3O_3)]_n \cdot 1/2CH_2Cl_2$ (3):** A Schlenk flask was charged with $CpRu(PTA)_2Cl$ (50 mg, 0.097 mmol) and

Table 7. Crystal data and structure refinement for **1**, **2**, and **3**.

| | PTA–$BH_3$ (**1**) | O=PTA–$BH_3$ (**2**) | $[CpRu(PTA)_2Cl(Ph_3B_3O_3)]_n$ (**3**) |
|---|---|---|---|
| Empirical formula | $C_6H_{15}BN_3P$ | $C_6H_{15}BN_3OP$ | $[(C_5H_5)Ru(C_6H_{12}N_3)_2Cl(Ph_3B_3O_3)]\cdot 1/2CH_2Cl_2$ |
| Formula mass | 170.99 | 186.99 | 875.11 |
| $T$ (K) | 100(2) K | 100(2) K | 100(2) K |
| Wavelength [Å] | 0.71073 Å | 0.71073 Å | 0.71073 Å |
| Crystal system | monoclinic | monoclinic | orthorhombic |
| Space group | *Cm* | *P*21/*n* | *Ima*2 |
| $a$ [Å] | 7.571(4) | 6.1903(5) | 22.9789(12) |
| $b$ [Å] | 9.244(4) | 11.3929(9) | 15.2606(8) |
| $c$ [Å] | 6.758(3) | 12.7715(9) | 11.4219(6) |
| $\alpha$ (°) | 90 | 90 | 90 |
| $\beta$ [°] | 114.900(10) | 93.339(2) | 90 |
| $\gamma$ [°] | 90 | 90 | 90 |
| Volume [$Å^3$] | 429.0(3) | 899.19(12) | 4005.3(4) |
| $Z$ | 2 | 4 | 4 |
| $D_{calcd.}$ [$mg/m^3$] | 1.324 | 1.381 | 1.451 |
| Abs. coefficient [$mm^{-1}$] | 0.258 | 0.261 | 0.648 |
| Crystal size [mm] | 0.28 × 0.03 × 0.03 | 0.22 × 0.01 × 0.01 | 0.775×0.18×0.16 |
| $\theta$ range for data collection | 3.32 to 22.48° | 2.40 to 27.50° | 1.60 to 32.26° |
| Index ranges | $-8 \le h \le 8$, $-9 \le k \le 9$, $-7 \le l \le 7$ | $-8 \le h \le 8$, $-14 \le k \le 14$, $-16 \le l \le 16$ | $-34 \le h \le 34$, $-22 \le k \le 22$, $-17 \le l \le 17$ |
| Reflections collected | 1360 | 10013 | 26436 |
| Independent reflections | 598 [$R$(int) = 0.1467] | 2048 [$R$(int) = 0.0396] | 7202 [$R$(int) = 0.0228] |
| Absorption correction | SADABS | SADABS | SADABS |
| Data/restraints/parameters | 598/2/65 | 2048/0/169 | 7202/1/261 |
| Goodness-of-fit on $F_2$ | 0.812 | 1.026 | 1.167 |
| Final $R$ indices [$I > 2\sigma(I)$] | $R_1$ = 0.0689, $wR_2$ = 0.1007 | $R_1$ = 0.0380, $wR_2$ = 0.0978 | $R_1$ = 0.0341, $wR_2$ = 0.1106 |
| $R$ indices (all data) | $R_1$ = 0.1247, $wR_2$ = 0.1138 | $R_1$ = 0.0470, $wR_2$ = 0.1028 | $R_1$ = 0.0344, $wR_2$ = 0.1109 |

 © 2006 Wiley-VCH Verlag GmbH & Co. KGaA, Weinheim 

$PhB(OH)_2$ (36 mg, 0.295 mmol); the solids were dissolved in a minimum volume (≈ 5 mL) of dichloromethane and stirred under nitrogen for 10 h. Addition of hexanes afforded 38 mg (48%) $[CpRu(PTA)_2Cl(Ph_3B_3O_3)]_n$·1/2 $CH_2Cl_2$ (**3**) as orange crystals. $^1H$ NMR (300 MHz, $CD_2Cl_2$, 25 °C): $\delta$ = 8.0–8.1 (m, 5 H, ArH), 7.35–7.45 (m, 10 H, ArH), 4.4–4.6 (AB spin system, $^2J_{(HAHB)}$ = 13 Hz, 17 H, Cp, $NCH_2N$), 3.9–4.1 (AB spin system, $^2J_{(HAHB)}$ = 15 Hz, 12 H, $PCH_2N$) ppm. $^{11}B$ NMR (160 MHz, [D$_6$]acetone, 25 °C): $\delta$ = 29.3 (s, $B_{uncoordinated}$), 21.3 (br. s, *B*–N) ppm. $^{31}P\{^1H\}$ NMR (121 MHz, $CD_2Cl_2$, 25 °C): $\delta$ = –21.9 (br. s, Ru–PTA) ppm. IR (KBr): $\tilde{\nu} = \upsilon_{(BO)}$: 1387, 1344, 1310 $cm^{-1}$. $C_{36}H_{45}B_3Cl_2N_6O_3P_2Ru$: calcd. C 49.35, H 5.18, N 9.59; found C 50.51, H 5.14, N 9.42. Dark orange X-ray quality crystals were grown by slow diffusion of hexanes into a $CH_2Cl_2$ solution of **3** over the course of 4 days. A crystal suitable for X-ray diffraction was selected and mounted under oil on a glass fiber. Crystallographic data and data collecting parameters are listed in Table 7.

**Computational Details:** Theoretical calculations were performed in an attempt to obtain insight into the differential reactivity of the phosphorus and nitrogen nuclei of PTA. All calculations were run on a Beowulf cluster of 16 dual processor computers operating under Linux. Theoretical calculations were performed using the Gaussian 03 program package employing the LANL2DZ basis set of Wadt and Hay[33,34] as implemented in Gaussian 03.[35] Density functional (DFT) calculations were carried out on all complexes using Becke's three-parameter hybrid method[36] coupled to the correlation functional of Lee, Yang, and Parr (B3LYP).[37] Frequency calculations were performed on all optimized structures in order to establish the nature of the extrema and to calculate values for $\Delta H$ and $\Delta G$. Full geometry optimizations were performed on **1**, **1-P**, PTA, PTA-Me, and Me-PTA starting from the crystal structures of each compound.

CCDC-288665 to -288667 contain the supplementary crystallographic data for this paper. These data can be obtained free of charge from The Cambridge Crystallographic Data Centre via www.ccdc.cam.ac.uk/data_request/cif.

## Acknowledgments

The authors would like to thank Brady Janes and Lauren Volz for their help on this project. PWG would like to thank the NSF-EPSCoR program (EPS-0132556) for a summer fellowship and UNR for an undergraduate research award supporting this project. We thank Cytec for the generous gift of $P(CH_2OH)_4Cl$. Financial support from the National Science Foundation is acknowledged for funding for the X-ray diffractometer (CHE-0226402).

[1] See for example: J. Andrieu, J.-M. Camus, P. Richard, R. Poli, L. Gonsalvi, F. Vizza, M. Peruzzini, *Eur. J. Inorg. Chem.* **2006**, 51–61; J. Andrieu, J.-M. Camus, P. Richard, R. Poli, L. Gonsalvi, F. Vizza, M. Peruzzini, *Eur. J. Inorg. Chem.* **2006**, 51–61; J. Andrieu, J.-M. Camus, C. Balan, R. Poli, *Eur. J. Inorg. Chem.* **2006**, 62–68; J. Andrieu, P. Richard, J.-M. Camus, R. Poli, *Inorg. Chem.* **2002**, *41*, 3876–3885; J. Andrieu, J.-M. Camus, J. Dietz, P. Richard, R. Poli, *Inorg. Chem.* **2001**, *40*, 1597–1605; C. Müller, C. N. Iverson, R. J. Lachicotte, W. D. Jones, *J. Am. Chem. Soc.* **2001**, *123*, 9718–9719; P. Espinet, K. Soulantica, *Coord. Chem. Rev.* **1999**, *193–195*, 499–556; F. Stöhr, D. Sturmayr, G. Kickelbick, U. Schubert, *Eur. J. Inorg. Chem.* **2002**, 2305–2311; P. Molina, A. Arques, A. García, M. C. Ramírez de Arellano, *Eur. J. Inorg. Chem.* **1998**, 1359–1368; G. R. Newkome, *Chem. Rev.* **1993**, *93*, 2067–2089; D. B. Grotjahn, D. A. Lev, *J. Am. Chem. Soc.* **2004**, *126*, 12232–12233.

[2] See for example: W. J. Knebel, R. J. Angelici, O. A. Gansow, D. J. Darensbourg, *J. Organomet. Chem.* **1974**, *66*, C11–C13; W. J. Knebel, R. J. Angelici, *Inorg. Chem.* **1974**, *13*, 632–637; W. J. Knebel, R. J. Angelici, *Inorg. Chem.* **1974**, *13*, 627–631; T. B. Rauchfuss, D. M. Roundhill, *J. Am. Chem. Soc.* **1974**, *96*, 3098–3105; G. P. C. M. Dekker, A. Buijs, C. J. Elsevier, K. Vrieze, P. W. N. M. van Leeuwen, W. J. J. Smeets, A. L. Spek, Y. F. Yang, C. H. Stam, *Organometallics* **1992**, *11*, 1937–1948.

[3] C. A. Mebi, B. J. Frost, *Organometallics* **2005**, *24*, 2339–2346.

[4] B. J. Frost, C. A. Mebi, *Organometallics* **2004**, *23*, 5317–5323.

[5] B. J. Frost, S. B. Miller, K. O. Rove, D. M. Pearson, J. D. Korinek, J. L. Harkreader, C. A. Mebi, J. Shearer, *Inorg. Chem. Acta* **2006**, *359*, 283–288.

[6] A. D. Phillips, L. Gonsalvi, A. Romerosa, F. Vizza, M. Peruzzini, *Coord. Chem. Rev.* **2004**, *248*, 955–993 and references within.

[7] D. J. Daigle, *Inorg. Synth.* **1998**, *32*, 40–45.

[8] D. J. Daigle, A. B. Pepperman Jr, S. L. Vail, *J. Heterocycl. Chem.* **1974**, *11*, 407–408.

[9] C. Lidrissi, A. Romerosa, M. Saoud, M. Serrano-Ruiz, L. Gonsalvi, M. Peruzzini, *Angew. Chem. Int. Ed.* **2005**, *44*, 2568–2572.

[10] D. J. Darensbourg, J. C. Yarbrough, S. J. Lewis, *Organometallics* **2003**, *22*, 2050–2056.

[11] D. J. Daigle, A. B. Pepperman Jr, *J. Heterocycl. Chem.* **1975**, *12*, 579–580.

[12] E. Fluck, H. J. Weissgraeber, *Chem.-Ztg.* **1977**, *101*, 304–304.

[13] B. Assmann, K. Angermaier, M. Paul, J. Riede, H. Schmidbaur, *Chem. Ber.* **1995**, *128*, 891–900.

[14] R. W. Rudolph, C. W. Schultz, *J. Am. Chem. Soc.* **1971**, *93*, 6821–6822.

[15] A. H. Cowley, M. C. Damasco, *J. Am. Chem. Soc.* **1971**, *93*, 6815–6820.

[16] L. M. R. Martinez-Aguilera, G. Cadenas-Pliego, R. Contreras, A. Flores-Parra, *Tetrahedron: Asymmetry* **1995**, *6*, 1585–1592.

[17] A. Flores-Parra, S. A. Sánchez-Ruíz, C. Guadarrama-Pérez, *Eur. J. Inorg. Chem.* **1999**, 2063–2068.

[18] A. J. Arduengo, US Patent WO9003990, 1990.

[19] F. Hanic, V. Subrtova, *Acta Crystallogr., Sect. B* **1969**, *25*, 405–409.

[20] D. J. Darensbourg, T. J. Decuir, J. H. Reibenspies, in *Aqueous Organometallic Chemistry and Catalysis* (Eds.: I. T. Horvath, F. Joo); High Technology; Kluwer: Dordrecht, The Netherlands, **1995**; pp. 61–80.

[21] K. H. Jogun, J. J. Stezowski, E. Fluck, J. Weidlein, *Phosphorus Sulfur* **1978**, *4*, 199–204.

[22] R. E. Marsh, M. Kapon, S. Hu, F. H. Herbstein, *Acta Crystallogr., Sect. B* **2002**, *58*, 62–77.

[23] S. Bolano, L. Gonsalvi, F. Zanobini, F. Vizza, V. Bertolasi, A. Romerosa, M. Peruzzini, *J. Mol. Cat. A* **2004**, *224*, 61–70.

[24] M. A. Beckett, D. S. Brassington, P. Owen, M. B. Hursthouse, M. E. Light, K. M. A. Malik, K. S. Varma, *J. Organomet. Chem.* **1999**, *585*, 7–11.

[25] M. A. Beckett, D. E. Hibbs, M. B. Hursthouse, P. Owen, K. M. A. Malik, K. S. Varma, *Main Group Chem.* **1998**, *2*, 251–258.

[26] M. A. Beckett, G. C. Strickland, K. S. Varma, D. E. Hibbs, M. B. Hursthouse, K. M. A. Malik, *J. Organomet. Chem.* **1997**, *535*, 33–41.

[27] M. A. Beckett, G. C. Strickland, K. S. Varma, D. E. Hibbs, M. B. Hursthouse, K. M. A. Malik, *Polyhedron* **1995**, *14*, 2623–2630.

[28] M. Yalpani, R. Boese, *Chem. Ber.* **1983**, *116*, 3347–3358.

[29] J. C. Norrild, I. Sotofte, *J. Chem. Soc., Perkin Trans. 2* **2002**, 303–311.

[30] L. I. Bosch, M. F. Mahon, T. D. James, *Tetrahedron Lett.* **2004**, *45*, 2859–2862.

[31] W. Kliegel, K. Drückler, B. O. Patrick, S. J. Rettig, J. Trotter, *Acta Crystallogr., Sect. E* **2002**, *58*, o831–o833.

 © 2006 Wiley-VCH Verlag GmbH & Co. KGaA, Weinheim 

[32] D. N. Akbayeva, L. Gonsalvi, W. Oberhauser, M. Peruzzini, F. Vizza, P. Brueggeller, A. Romerosa, G. Sava, A. Bergamo, *Chem. Commun.* **2003**, 264–265.
[33] W. R. Wadt, P. J. Hay, *J. Chem. Phys.* **1985**, *82*, 284–298.
[34] P. J. Hay, W. R. Wadt, *J. Chem. Phys.* **1985**, *82*, 270–283.
[35] M. J. Frisch, G. W. Trucks, H. B. Schlegel, G. E. Scuseria, M. A. Robb, J. R. Cheeseman, J. A. Montgomery Jr, T. Vreven,K. N. Kudin, J. C. Burant, J. M. Millam, S. S. Iyengar, J. Tomasi, V. Barone, B. Mennucci, M. Cossi, G. Scalmani, N. Rega, G. A. Petersson, H. Nakatsuji, M. Hada, M. Ehara, K. Toyota, R. Fukuda, J. Hasegawa, M. Ishida, T. Nakajima, Y. Honda, O. Kitao, H. Nakai, M. Klene, X. Li, J. E. Knox, H. P. Hratchian, J. B. Cross, C. Adamo, J. Jaramillo, R. Gomperts, R. E. Stratmann, O. Yazyev, A. J. Austin, R. Cammi, C. Pomelli, J. W. Ochterski, P. Y. Ayala, K. Morokuma, G. A. Voth, P. Salvador, J. J. Dannenberg, V. G. Zakrzewski, S. Dapprich, A. D. Daniels, M. C. Strain, O. Farkas, D. K. Malick, A. D. Rabuck, K. Raghavachari, J. B. Foresman, J. V. Ortiz, Q. Cui, A. G. Baboul, S. Clifford, J. Cioslowski, B. B. Stefanov, G. Liu, A. Liashenko, P. Piskorz, I. Komaromi, R. L. Martin, D. J. Fox, T. Keith, M. A. Al-Laham, C. Y. Peng, A. Nanayakkara, M. Challacombe, P. M. W. Gill, B. Johnson,W. Chen, M. W. Wong, C. Gonzalez, J. A. Pople, *Gaussian 03, Revision B.02*, Gaussian, Inc.: Pittsburgh, PA, **2003**.
[36] A. D. Becke, *Phys. Rev. A* **1988**, *38*, 3098–3100.
[37] C. Lee, W. Yang, R. G. Parr, *Phys. Rev. B* **1988**, *37*, 785–789.
Received: November 15, 2005
Published Online: February 2, 2006

 © 2006 Wiley-VCH Verlag GmbH & Co. KGaA, Weinheim 

DOI: 10.1002/ejic.200501063

# Programmed Helicity in Self-Assembled Hydrogen-Bonded Chains of Chiral Copper(II) Complexes

David G. Lonnon,[a] Stephen B. Colbran,*[a] and Donald C. Craig[a]

**Keywords:** Hydrogen bonds / Supramolecular / Self-assembly / Copper / Helical structures

The copper(II) complexes $[Cu(H_2L^1)Cl_2]_2[CuCl_4]\cdot CH_3CN\cdot H_2O$ ($HL^1$ = *N*-6-(4-hydroxyphenyl)-2-pyridylmethyl-*N*,*N*′,*N*′-trimethylethylenediamine), $[Cu(HL^2)Cl_2]$ ($HL^2$ = *N*-4-hydroxybenzylmethyl-*N*,*N*′,*N*′-trimethylethylenediamine) and $[Cu_2(\mu\text{-}L^3)_2(H_2O)(ClO_4)]ClO_4\cdot H_2O$ ($HL^3$ = *N*-2-hydroxybenzylmethyl-*N*,*N*′,*N*′-trimethylethylenediamine) were prepared and characterised in acetonitrile solution (by ESI-MS, EPR and UV/Vis-NIR spectroscopy) and in the solid state (by X-ray crystallography). Each copper(II) complex is chiral and has a potential inter-complex hydrogen-bond donor group. Upon crystallisation, all three copper(II) complexes undergo spontaneous enantioselective self-assembly into hydrogen-bond-linked helices.

(© Wiley-VCH Verlag GmbH & Co. KGaA, 69451 Weinheim, Germany, 2006)

## Introduction

Self-assembly into spiral structures is inherent in nature, from the grandest scale – e.g. spiral galaxies[1] – through everyday structures – e.g. the aesthetically pleasing spiral seashell – to the molecular scale – e. g. the structures of biological macromolecules such as proteins[2] and nucleic acids.[3] The self-organisation of the latter molecules into specific structures is, of course, vital to their function and so to all life, and has inspired the recent interest into molecules that aggregate into regular spiral topologies.[4–8] Metal coordination complexes proffer a vast array of useful catalytic, magnetic and optical properties and so, not surprisingly, helical coordination polymers are synthetic targets for emergent applications in asymmetric catalyses, in enantioselective separations and as magnetic/optical materials.[7,8] The design and construction of coordination polymers with helical topologies thus presents a contemporary challenge that spans coordination, supramolecular and materials chemistry.

In the majority of those helical coordination polymers reported in the literature, ditopic ligands are employed to bridge and link two adjacent metal centres.[7,8] Herein, we demonstrate that molecular helicity can be predictably programmed into the solid-state structures of simple copper(II) coordination complexes by judicious introduction of molecular chirality through ligand design in combination with a noncovalent recognition element that induces aggregation and hence self-organisation into a spiral arrangement upon crystallisation. The natures of the new complex species in solution were also investigated by the use of a combination of electrospray ionisation mass, UV/Visible-NIR and X-band EPR spectroscopy.

## Results and Discussion

Three ligands $HL^1$–$HL^3$ were targeted. All three are chiral and, although isolated as the racemate, upon coordination to a metal ion the chirality of the individual ligand molecule must transfer to the complex species thus formed. In $HL^1$ and $HL^2$ the positioning of the phenolic 4-OH groups prevents intramolecular hydrogen bonding interactions, but is ideal for inter-complex hydrogen bonding; therefore, these OH groups should act as a recognition element for inter-complex aggregation through hydrogen bonding. Thus, overall, simple metal complexes of $HL^1$ and $HL^2$ should be chiral and aggregate into strands through inter-complex hydrogen bonding. In contrast, the *ortho*-OH groups in $HL^3$ are ideally positioned for binding to a metal ion, because this was assumed that it would curtail the involvement of these groups in inter-complex aggregation. To test these predictions the three ligands were made, and their reactions with cupric chloride and cupric perchlorate studied.

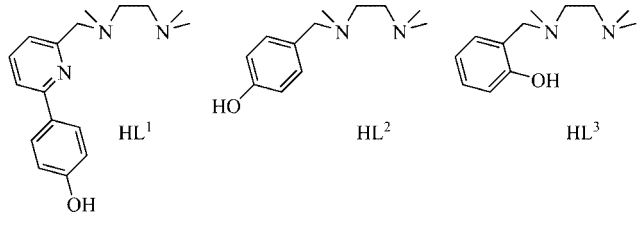


[a] School of Chemistry, The University of New South Wales, Sydney, NSW 2052, Australia
E-mail: S.Colbran@unsw.edu.au

Supporting information for this article is available on the WWW under http://www.eurjic.org or from the author.


InterScience
© 2006 Wiley-VCH Verlag GmbH & Co. KGaA, Weinheim

### Syntheses

The ligands $HL^1$–$HL^3$ were prepared by direct reductive amination reactions of *N*,*N*,*N*′-trimethylethylenediamine with the appropriate aldehyde. For $HL^1$, tetrahydropyran (THP) protected 4-phenol-6-pyridylaldehyde was used and the THP protecting group was removed with pyridinium tosylate in 95% ethanol. Three crystalline materials were obtained from the reactions of the ligands with the cupric salts: A green powder was obtained from $HL^1$ and $CuCl_2$ in methanol/ether that afforded clear, gold-brown platelets of $[Cu(HL)Cl_2]_2[CuCl_4]\cdot MeCN\cdot 2H_2O$ upon recrystallisation from acetonitrile/methanol, green crystalline $[Cu(HL^2)Cl_2]$ deposited from solution of $HL^2$ and $CuCl_2$ in methanol/ether, and dark green-black $[Cu_2(L^3)_2(H_2O)(ClO_4)]ClO_4\cdot H_2O$ crystallised from an alkaline (pH 9) aqueous solution of cupric perchlorate and $HL^3$.

### Solution Physicochemical Properties

Positive-mode ESI-MS, X-band EPR (at 77 K) and UV/Vis-NIR spectra were acquired to give information about the species in acetonitrile solutions; the data are listed in the Experimental Section and spectra are shown in the supporting information, Figure S1 and Figure S2 (for supporting information see also the footnote on the first page of this article). The ESI-MS spectrum of $[Cu(H_2L^1)Cl_2]_2[CuCl_4]$ shows only peaks for the $[Cu(H_2L^1)Cl_2]^+$ ion (at *m*/*z* 419; calcd. *m*/*z* 419.06) suggesting that this is the only cationic species in solution. The EPR spectrum of the frozen acetonitrile solution at 77 K reveals overlaid axial subspectra for two nonequivalent copper(II) centres, a four/five-coordinate tetragonally distorted ion [$g_\parallel \approx 2.26$ ($A_\parallel \approx 156$ G) >> $g_\perp \approx 2.07$] and a distorted tetrahedral species [$g_\parallel \approx 2.39$ ($A_\parallel \approx 120$ G) >> $g_\perp \approx 2.09$], which is attributed to $[CuCl_3(MeCN)_x]^-$ (in acetonitrile solution, $[CuCl_4]^{2-}$ is only observed at high chloride concentrations[11]). The UV/Vis-NIR spectrum shows a broad asymmetric band at 676 nm with a long low-energy tail, distinctive for a tetragonally distorted ion; the lowest energy transition for $[CuCl_3(MeCN)_x]^-$ is reported at 405 nm and is hidden in the intense UV tail.[11]

The ESI-MS spectrum of $[Cu(HL^2)Cl_2]$ was very weak until 1% acetic acid was added to the carrier solvent; in the presence of the acetic acid, $[Cu(HL^2)Cl]^+$ (at *m*/*z* 306; calcd. *m*/*z* 306.06) was observed along with peaks for the protonated ligand, $(H_2L^2)^+$, and ions that result from chloride–acetate exchange. The results are consistent with $[Cu(HL^2)Cl_2]$ persisting into acetonitrile solution. The EPR spectrum of the complex in acetonitrile solution at 77 K is axial and thus indicative for a tetragonally-distorted species with a $d_{x^2-y^2}$ ground-state and the UV/Vis-NIR spectrum shows a broad asymmetric visible band at 676 nm with distinct tail to low energy (identically with $[Cu(H_2L^1)Cl_2]^+$); these spectra are consistent with $[Cu(HL^2)Cl_2]$ dissolving unchanged in acetonitrile.

The main peak in the ESI-MS spectrum of $[Cu_2(L^3)_2(H_2O)](ClO_4)_2$ at *m*/*z* 270 corresponds to the monomeric species $[Cu(L^3)]^+$ (calcd. *m*/*z* 270.08). The solid complex is EPR silent indicative for antiferromagnetic coupling between the two copper(II) centres relayed by the phenolate bridges in the dimeric $[Cu_2(L^3)_2(H_2O)]^{2+}$ cation. The EPR spectrum of a frozen acetonitrile solution of the complex at 77 K shows a strong axial signal [$g_\parallel = 2.25$ ($A_\parallel = 165$ G) >> $g_\perp = 2.06$] for a tetragonal monomer suggesting that the dimer dissociates in solution according to:

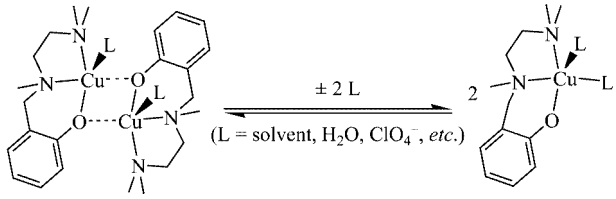


The UV/Vis-NIR spectrum differs from those of the other two complexes: It shows a relatively sharp and intense σ-phenolate → Cu$^{II}$ charge-transfer band at 430 nm[12,13] plus a weaker visible (*d*-*d*) band at 625 nm; these two bands are blue shifted by ca. 30 and 85 nm, respectively, as a 1:1 EtOH/water solution is made alkaline (pH raised from 7 to 10). The EPR and UV/Vis-NIR spectra are very similar to those of other copper(II) dimers of chelating ligands with a phenolate sidearm that break up in donor solvents to monomeric species.[12,13]

### Crystal Structures

**$[Cu(HL)Cl_2]_2[CuCl_4]\cdot CH_3CN\cdot 2H_2O$:** The crystal structure confirms the identity of the complex salt as $[Cu(H_2L^1)Cl_2]_2[CuCl_4]$. The structure of the $[Cu(H_2L^1)Cl_2]^+$ ion is illustrated in Figure 1. Immediately obvious is that the terminal tertiary amine of $HL^1$ is protonated and "dangling" in the $[Cu(H_2L^1)Cl_2]^+$ ion. This is expected: the tertiary amine is a relatively weak donor to a metal ion due to steric effects but is strongly basic and, therefore, protonation is favoured over coordination to a metal ion under the weakly acidic conditions in solutions of simple metal salts. As it must be, the $[Cu(H_2L^1)Cl_2]^+$ complex cation is chiral, with $HL^1$ wrapped about the copper centre, which is bound by the pyridyl and the adjacent chiral, tertiary amine donors (nitrogen atoms N1 and N2, respectively). Within the crystal, both enantiomers of $[Cu(H_2L^1)Cl_2]^+$ appear and are related by crystallographic inversion; see below. The Cu–N and Cu–Cl distances in the $[Cu(H_2L^1)Cl_2]^+$ ion are listed in the caption to Figure 1 and are indicative for a copper(II) centre.[13–17] The two largest angles about the copper ion, the *transoid* angles Cl1–Cu1–N2 [132.5(2)°] and Cl2–Cu1–Nl [152.2(2)°], give $\beta = 71.2°$ and $\omega = 51.4°$ [where $\beta = 90°$ and $\omega = 0°$ for square-planar geometry ($D_{4h}$) and $\beta = 54.7°$ and $\omega = 90°$ for tetrahedral geometry ($T_d$)], thus revealing the geometry of Cu1 is near to midway between ideal square-planar and ideal tetrahedral. The $[CuCl_4]^{2-}$ counteranions exhibit a much less flattened tetrahedral geometry, which is commonplace for this ion:[14] the *transoid* equatorial angles Cl3–Cu2–Cl3* [124.3(1)°] and Cl4–Cu2–Cl4* [138.7(3)°] yield $\beta = 60.3°$ and $\omega = 77.9°$.

 © 2006 Wiley-VCH Verlag GmbH & Co. KGaA, Weinheim 

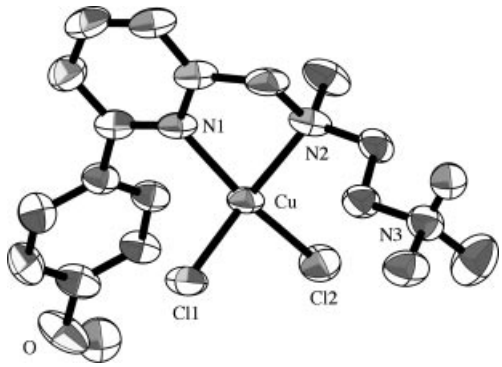


Figure 1. View of the $[Cu(S\text{-}H_2L^1)Cl_2]^+$ complex ion (50% thermal ellipsoids at 295 K are shown; hydrogen atoms on carbon are omitted for clarity). Key metric data – bond lengths [Å]: Cu1–Cl1 2.256(2), Cu2–Cl3 2.257(2), Cu1–Cl2 2.192(2), Cu2–Cl4 2.208(3), Cu1–N1 1.965(5), Cu1–N2 2.054(5); bond angles [°]: Cl1–Cu1–Cl2 101.82(7), Cl3–Cu2–Cl3* 124.3(1), Cl1–Cu1–N1 97.9(2), Cl3–Cu2–Cl4 102.2(1), Cl1–Cu1–N2 132.5(2), Cl3–Cu2–Cl4* 96.83(9), Cl2–Cu1–N1 152.2(2), Cl4–Cu2–Cl4* 138.7(3), Cl2–Cu1–N2 98.9(2), N1–Cu1–N2 81.5(2).

As predicted, homochiral $[Cu(H_2L^1)Cl_2]^+$ ions self-assemble along the *y* axis into helical chains that are held together by hydrogen bonding between the phenol OH group (O1) and the chloride co-ligand Cl1 ($H_{O1}\cdots Cl1$ 2.163 Å), Figure 2. The helices, in which the adjacent cations are inter-related by a $2_1$ crystallographic screw, are quite open with large grooves, Figure 2 (b). The helices interweave to afford layers parallel to the *yz* plane, Figure 2 (c). Within a layer all cations have the same chirality and, therefore, all helices identical (*M or P*) handedness, but adjacent helices within the layers run in the opposite direction; the *S*-enantiomer, i.e. $[Cu\{(S)\text{-}H_2L^1\}Cl_2]^+$, affords the left-handed (*M*) helices. The helices alternate in chirality parallel to the *x*-axis so adjacent layers contain cations and helices of opposite chirality. The $[CuCl_4]^{2-}$ anions are interspersed between the cation layers and each forms a $Cl\cdots H\text{–}^+NHR$ hydrogen bond (Cl3···N3 3.290 Å) to the nearest cation in the two adjacent layers. The lattice acetonitrile and water molecules fill voids in $[CuCl_4]^{2-}$ anion layers; notably each water (W) is well-positioned to form hydrogen bonds with the nearest $[Cu(H_2L^1)Cl_2]^+$ ion ($O_W\cdots$Cl2 3.259 Å) and the adjacent $[CuCl_4]^{2-}$ anion ($O_W\cdots$Cl4 3.391 Å).

**$[Cu(HL^2)Cl_2]$:** Figure 3 presents a view of the complex molecule. The copper(II) centre is four coordinate, bound by the two amine nitrogen atoms of $HL^2$ and two chloride co-ligands with Cu–N and Cu–Cl distances that are typical of those of other copper(II) chloride complexes of ethylenediamine derivatives (e.g. $[Cu(ethylenediamine)Cl_2]$[15]

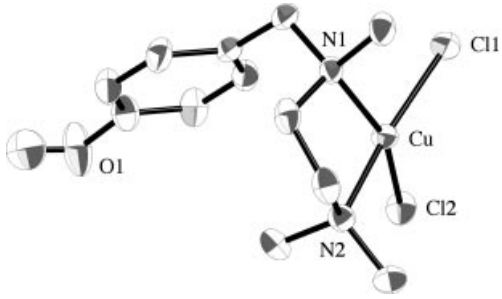


Figure 3. View of the $[Cu(R\text{-}HL^2)Cl_2]$ complex molecule (50% thermal ellipsoids at 295 K are shown; hydrogen atoms on carbon are omitted for clarity). Key metric data – bond lengths [Å]: Cu–Cl1 2.263(1), Cu–Cl2 2.269(1), Cu–N1 2.086(3), Cu–N2 2.045(3); bond angles [°]: Cl1–Cu–Cl2 93.0(1), Cl1–Cu–N1 92.9(1), Cl1–Cu–N2 171.1(1), Cl2–Cu–N1 157.7(1), Cl2–Cu–N2, 91.7(1), N1–Cu–N2 85.5(1).

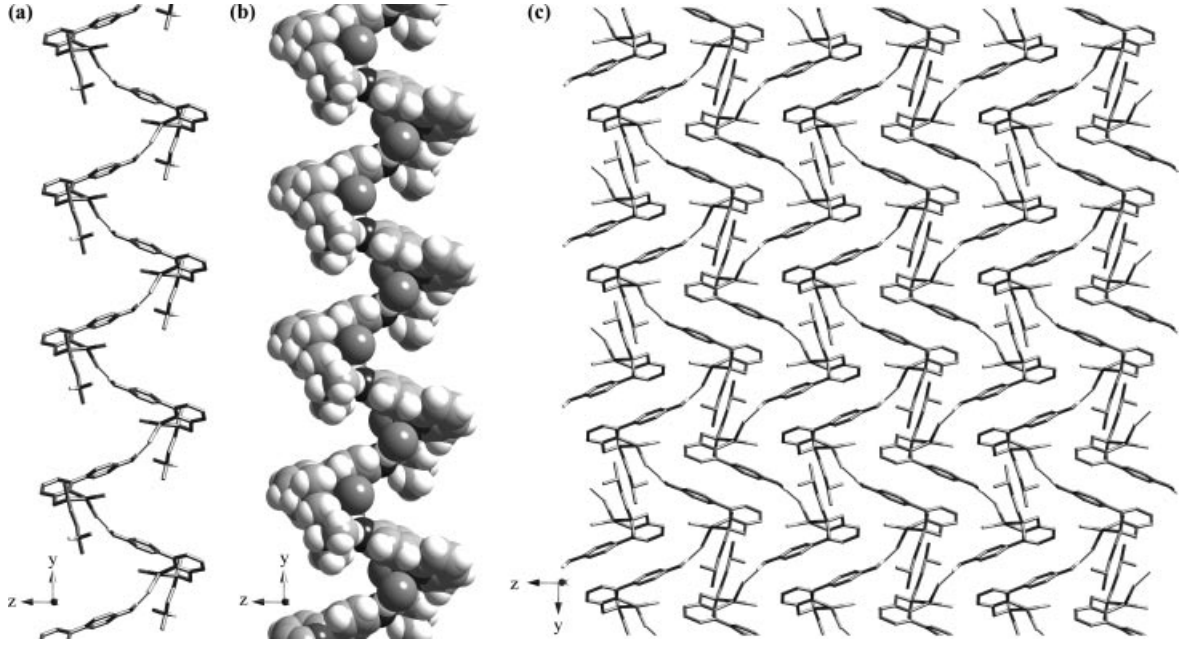


Figure 2. $[Cu(H_2L^1)Cl_2^{2+}]_\infty$ helices: (a) stick view of a *M*-helix, (b) spacefilling view (CPK van der Waal's radii) of a *M*-helix from the same perspective as (a); (c) view of a layer illustrating the antiparallel packing of the helices, all of which have the same (*M*) handedness. For clarity, those hydrogen atoms not involved in hydrogen bonding are omitted from views (a) and (c).

 © 2006 Wiley-VCH Verlag GmbH & Co. KGaA, Weinheim 

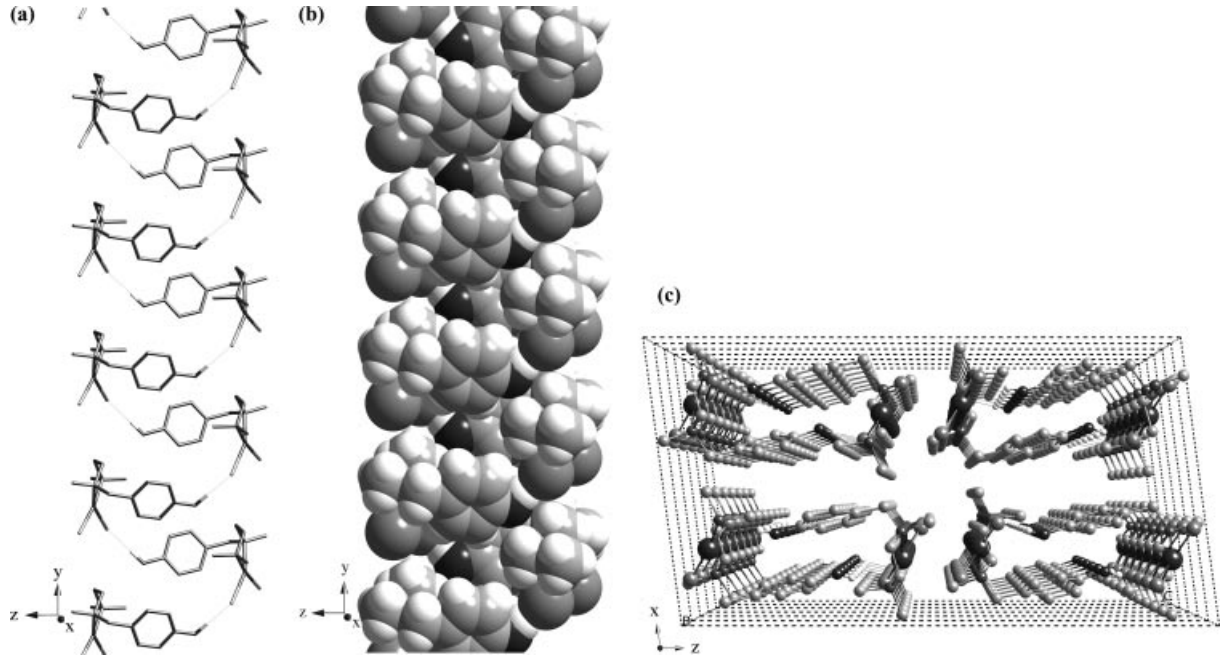


Figure 4. $[Cu(HL^2)Cl_2]_\infty$ helices: (a) view of a single *P*-helix (with carbon-bound hydrogen atoms omitted for clarity); (b) spacefilling view (CPK van der Waal's radii) showing the tight packing of complex molecules in a *P*-helix drawn from the same perspective as (a); (c) ball-and-stick perspective view of the crystal structure showing the packing of the helices of opposite chirality along the *y* axis (the top left and bottom right helices are left-handed, the others right-handed).

Cu–N 2.010 and 2.017 Å, Cu–Cl 2.286 and 2.301 Å; [Cu(*trans*-*N*,*N*,*N*′*N*′-tetramethylcyclohexane-1,2-diamine)$Cl_2$][16] Cu–N 2.052 Å, Cu–Cl 2.247 Å). The *transoid* angles about copper, N2–Cu–Cl1 171.1(1)° and N1–Cu–Cl2 157.7(1)°, give $\beta$ = 82.2° and $\omega$ = 21.9° indicative for moderate tetrahedral distortion away from square-planar geometry.

The hydroxy group of $HL^2$ is, as predicted, involved in intermolecular hydrogen bonding. The enantiomers of $[Cu(HL^2)Cl_2]$ separate and self-assemble into helices parallel to the *y* axis, Figure 4. Within each helix, the $[Cu(HL^2)Cl_2]$ molecules all have the same handedness and adjacent complexes are linked by hydrogen bonding between the chloride co-ligand (Cl2) on one and the hydroxy group of $HL^2$ on the other (Cl···H 2.103 Å), Figure 4(a). The crystal is the racemate in which the *P*-helices are comprised of the $[Cu(R\text{-}HL^2)Cl_2]$ enantiomer (i.e. from the *R*-enantiomer of the ligand). Comparison of the space-filling representations of the $[Cu(H_2L^1)Cl_2^+]_\infty$ helix, Figure 2 (b), and the $[Cu(HL^2)Cl_2]_\infty$ helix, Figure 4 (b), shows the grooves in the latter helices to be considerably more tightly packed and shallow. Thus, whereas the $[Cu(H_2L^1)Cl_2^+]_\infty$ helices interweave in the crystal (see Figure 2, c), each $[Cu(HL^2)Cl_2]_\infty$ helix packs largely independently of the others, Figure 4 (c); there are no significant interactions with the four nearest-neighbour helices, which have opposite chirality (because the chirality of the helices alternates along both the *x* and *z* axes).

**$[Cu_2(\mu\text{-}L^3)_2(H_2O)(ClO_4)]ClO_4\cdot H_2O$:** The $[Cu_2(L^3)_2(H_2O)(ClO_4)]^+$ cation, Figure 5, consists of two independent five-coordinate copper(II) centres, Cu1 and Cu2. Both copper ions are bound by the same enantiomer of $L^3$ (so the dimers are the chiral *R*,*R*- and *S*,*S*-enantiomers) and exhibit

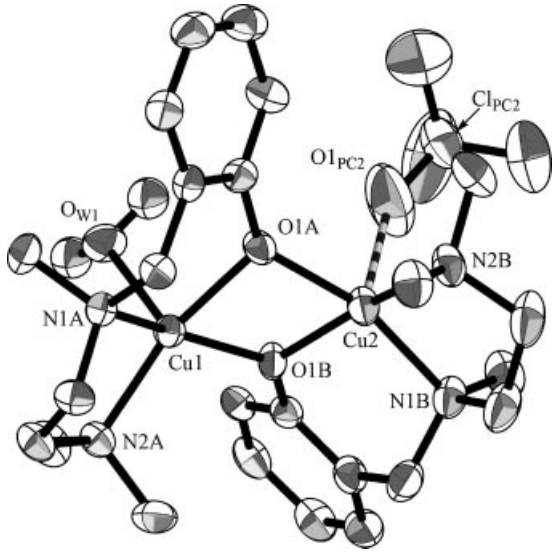


Figure 5. View of the $[Cu_2(S\text{-}L^3)_2(H_2O)(ClO_4)]^+$ complex ion (50% thermal ellipsoids at 295 K are shown;W = water, PC = perchlorate). Key metric data – bond lengths [Å]: Cu1–O1A 1.987(3), Cu2–O1A 1.955(3), Cu1–N1A 2.032(4), Cu2–O1B 1.940(3), Cu1–N2A, 2.046(4), Cu2–N1B 2.023(4), Cu1–O1B 1.995(3), Cu2–N2B, 2.034(4), Cu1–OW1, 2.223(3), Cu2···O1Pc2 2.580(3); bond angles [°]: O1A–Cu1–N1A 92.3(1), O1B–Cu2–N1B 92.6(1), O1A–Cu1–N2A 163.8(2), O1A–Cu2–N1B 163.1(2), O1A–Cu1–O1B 74.4(1), O1A–Cu2–O1B 76.3(1), O1A–Cu1–OW1 95.0(1), O1A–Cu2–O1Pc2 93.8(1), N1A–Cu1–N2A 86.5(2), N1B–Cu2–N2B 87.3(2), N1A–Cu1–O1B 156.4(1), O1B–Cu2–N2B 167.0(2), N1A–Cu1–OW1 101.1(2), N1B–Cu2–O1Pc2 99.1(2), N2A–Cu1–O1B 100.8(2), N2B–Cu2–O1Pc2 102.4(2), N2A–Cu1–OW1 101.1(1), O1A–Cu2–N2B 100.6(2), O1B–Cu1–OW1 99.4(1), O1B–Cu2–O1Pc2 90.5(1), Cu1–O1A–Cu2 101.2(1).

 © 2006 Wiley-VCH Verlag GmbH & Co. KGaA, Weinheim 

square-pyramidal geometries (trigonality indices:[17] Cu1, $\tau$ = 0.12; Cu2, $\tau$ = 0.07). The two amine nitrogen atoms and the phenolate oxygen atom of $L^3$ are equatorially bound, and each phenolate group also bonds to the fourth equatorial position of the other copper, thereby producing a phenolate-bridged dimer with Cu1···Cu2 3.047 Å. The equatorial Cu–O/N distances at 2.00 ± 0.5 Å are indicative for copper(II).[13–17] An axial water (W1) completes the coordination sphere of Cu1 [Cu1–$O_{W1}$ = 2.223(3) Å] and a weakly bound, axial perchlorate [PC2: Cu2–$O1_{Pc2}$ = 2.580(3) Å] that of Cu2; the axial water and the perchlorate ligands lie to the same side of the equatorial $Cu_2O_2$ plane and are hydrogen-bonded to a lattice water (W2).

Given that the phenol group of $L^3$ becomes involved in binding to the copper(II) ions as anticipated (see above), it was a surprise to find that the homochiral $[Cu_2(L^3)_2(H_2O)(ClO_4)]^+$ ions also self-assemble along with the (second) perchlorate counterion and a lattice water into $2_1$ helices parallel to the *y* axis, Figure 6. Spiral hydrogen-bond-linked chains comprised of the axial water ligand (W1), a perchlorate (PC1), and a lattice water (W2) form the helix cores; see Figure 6 (c). The hydrogen bond lengths in the spiral $[(H_2O)_2(ClO_4)^-]_\infty$ core are given in the Supporting Information (Figure S3). The dicopper(II) ions do not directly hydrogen bond with each other, but rather water W1, the axial ligand to Cu1, forms the link between each copper(II) dimer and the spiral core. The crystal is the racemate containing *M* and *P* helices; the chirality of the helices derives from the copper dimers with the *S,S*-enantiomer producing the *P*-helix (that shown in Figure 6, a–c). Figure 6 (d) illustrates the packing of the helices in the crystal. Helices of the same handedness align parallel to the *x*-axis and helices

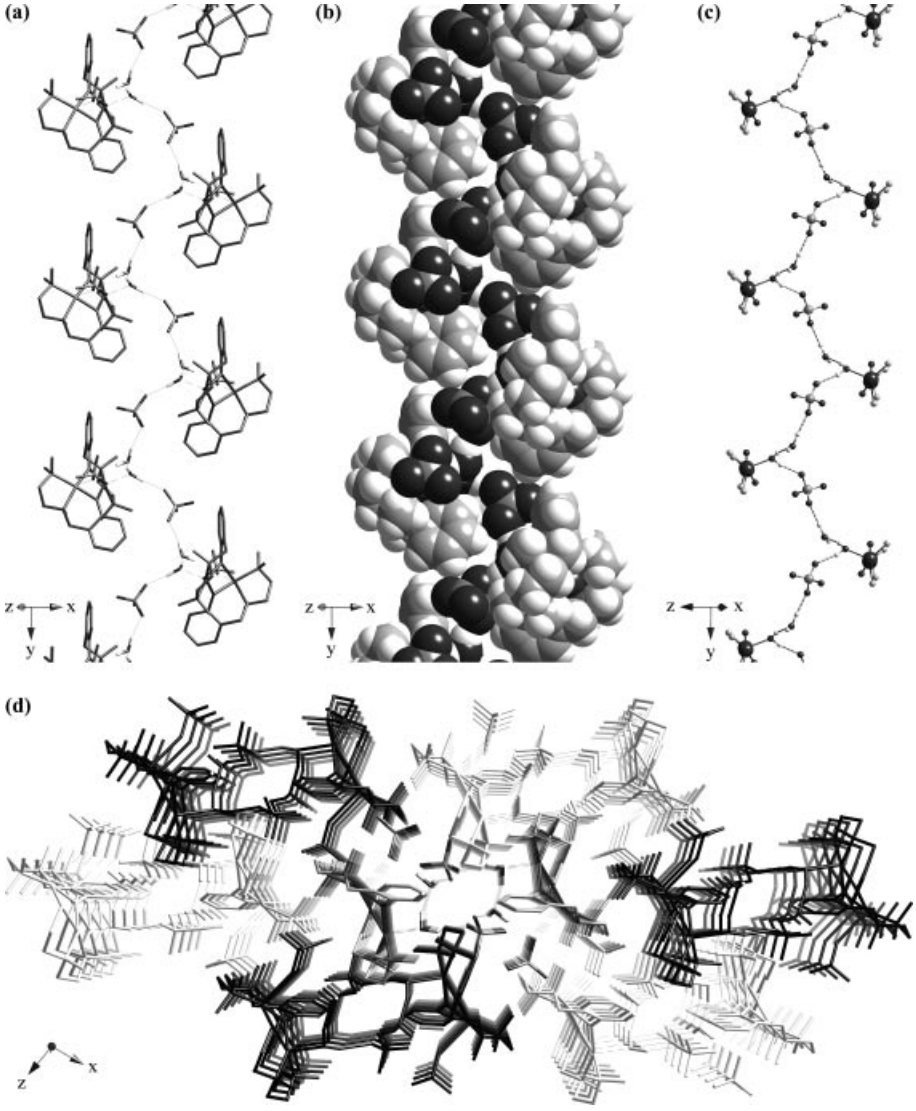


Figure 6. $[Cu_2(\mu\text{-}L^3)_2(H_2O)(ClO_4)](ClO_4)\cdot(H_2O)]_\infty$ helices: (a) view of a *P*-helix, (b) spacefilling view (CPK van der Waal's radii) of a *P*-helix from the same perspective as (a); (c) view of a *P*-helix core illustrating the spiral $[(H_2O)_2(ClO_4)^-]_\infty$ chain (with carbon atoms, the hydrogen atoms attached to these and the perchlorate ligand (PC2) all omitted for clarity); (d) perspective view down a *P*-helix showing the packing of the six surrounding helices. For clarity, the neighbour helices are alternatively shaded light and dark in view (d) and those hydrogen atoms not involved in hydrogen bonding are omitted from views (a) and (d).

 © 2006 Wiley-VCH Verlag GmbH & Co. KGaA, Weinheim 

alternate in handedness parallel to the *z*-axis, so that each helix is surrounded by six neighbours, two of the same handedness and four of the opposite handedness.

## Conclusion

Three new helical copper(II) coordination polymers have been prepared and characterised. These examples serve to demonstrate that a weak inter-ion, noncovalent recognition element, hydrogen bonds involving a phenol or water OH group within the complex species, in concert with the chiral twist of the complex cation is perfectly sufficient to cause aggregation into spirals. Zigzag chains[7,8] of hydrogen-bonded complexes alternating in chirality were not observed in this work. In the three crystal structures, the spontaneous enantioselective self-assembly of the complexes within each helix suggests a self-recognition process must play a role in each crystallisation just as hydrogen bonding between complimentary bases dictates DNA double strand formation. Notably, the adjacent copper(II) complexes are crystallographically inter-related by a $2_1$ screw. Given the weak directionality of the phenol OH···Cl–Cu or Cu–$OH_2$···O ($H_2O$ or $ClO_4^-$) hydrogen bonds, this is not surprising – it is the simplest possible symmetry relationship between the adjacent hydrogen-bonded complexes in a helix. Likewise, a majority of the recently reported coordination polymer helices[7,8] align along a twofold screw axis. The obvious implication, of course, is that a recognition element(s) of greater complexity with inbuilt directionality in the non-covalent interaction – i.e. more information content – is necessary for predictable self-assembly of helices of higher symmetry.

## Experimental Section

**General:** $^1H$ and $^{13}C\{^1H\}$ NMR spectra were recorded at 300 K with a Bruker AC 300F spectrometer (300 MHz) operating at 300.13 MHz. Electrospray Ionisation (ESI) mass spectra were acquired with a VG Quattro mass spectrometer operating with a capillary voltage of 4 kV and a cone voltage of 30 V at 60 °C with a feed solvent of $CH_3CN$/water (1:1, v/v). Electronic spectra of the complexes were recorded between 220 and 2000 nm with a CARY 5 spectrometer in the dual beam mode; solution spectra were recorded in sealed 1-cm quartz cuvettes and solid-state spectra were recorded in reflectance mode on powdered samples. X-band EPR spectra of both solids and frozen solutions and were recorded at 77 K (using a liquid nitrogen dewar) with a Bruker EMX 10 EPR spectrometer. Elemental analyses for C, H and N were carried out at the Australian National University Microanalytical Laboratory. Prior to being sent for analysis, samples were dried at 40 °C for 48 h under vacuum (0.2 Torr) over phosphorus pentoxide.

***Caution:*** Although no problems were encountered in the course of this work, perchlorate salts are potentially explosive materials and appropriate precautions should be taken when handling them.

***N*-[6-(4-Hydroxyphenyl)-2-pyridylmethyl]-*N*,*N*′,*N*′-trimethylethylenediamine ($HL^1$):** A solution of *N*,*N*,*N*′-trimethylethylenediamine (363 mg, 3.55 mmol) in 1,2-dichloroethane (15 $cm^3$) was added to a 1,2-dichloroethane (10 $cm^3$) solution of 6-(2-tetrahydropyranyl-4-phenoxyl)-2-pyridinecarbaldehyde (1.000 g, 3.54 mmol) followed by the addition of solid sodium triacetoxyborohydride (0.902 g, 4.25 mmol). The resulting white suspension was stirred for 12 h under nitrogen to give a yellow suspension, which was washed twice with a saturated $NaHCO_3$ solution (≈ 10 $cm^3$), dried with magnesium sulfate and the solvent remove under vacuum to give the tetrahydropyranyl (THP)-protected precursor, THP-$L^1$, as a viscous yellow-brown oil (1.130 g). $^1H$ NMR ($CDCl_3$): $\delta$ = 7.93 (d, 2 H, Ar), 7.67 (d, 1 H, py), 7.54 (t, 1 H, py), 7.33 (d, 1 H, py), 7.12 (d, 2 H, Ar), 5.49 (m, 1 H, $CH_2$), 3.92 (m, 2 H, $CH_2$), 3.77 (s, 2 H, $CH_2$), 3.62 (m, 2 H, $CH_2$), 2.60 (m, 2 H, $CH_2CH_2$), 2.49 (m, 2 H, $CH_2CH_2$), 2.35 (s, 3 H, $CH_3$), 2.23 (s, 6 H, 2 $CH_3$), 2.08 (m, 2 H, $CH_2$), 1.90 (m, 2 H, $CH_2$) ppm. ESI-MS: *m*/*z* (%) = 370 (100) [(THP)-$L^1$ + H]$^+$, 286 (10) $[H_2L]^+$. Removal of the THP protecting group was effected by heating pyridinium *p*-toluenesulfonate (75.3 mg, 0.30 mmol) and THP-$L^1$ (1.105 g, 3.00 mmol) in ethanol (50 $cm^3$) at 60 °C for 6 h. The solvent was removed and the resulting solid purified by column chromatography on silica gel with dichloromethane as the eluent; the main yellow band afforded the product, a clear light golden oil (0.810 g, 95%; > 98% purity by $^1H$ NMR spectroscopy). $^1H$ NMR ($CDCl_3$): $\delta$ = 7.90 (d, 2 H, Ar), 7.68 (d, 1 H, py), 7.55 (t, 1 H, py), 7.33 (d, 1 H, py), 7.15 (d, 2 H, Ar), 3.88 (m, 2 H, $CH_2$), 2.70 (m, 4 H, $CH_2CH_2$), 2.38 (s, 9 H, $CH_3$) ppm. ESI-MS: *m*/*z* (%) = 286 (100) $[H_2L^3]^+$. UV ($CH_3CN$): $\lambda_{max}$ ($\varepsilon$/$dm^3mol^{-1}$ $cm^{-1}$) = 263 (12400), 284 nm (13400).

***N*-4-(Hydroxybenzyl)methyl-*N*,*N*′,*N*′-trimethylethylenediamine ($HL^2$):** The literature method[9] was adapted as follows. A mixture of *N*,*N*,*N*′-trimethylethylenediamine (1.502 g, 14.73 mmol), 4-hydroxybenzaldehyde (1.800 g, 14.73 mmol), and sodium triacetoxyborohydride (3.751 g, 17.70 mmol), in 1,2-dichloroethane (70 $cm^3$) was stirred overnight for 16 h under nitrogen. The solvent was removed to give an orange oil that partially dissolved in acetonitrile (≈ 2 × 20 $cm^3$) leaving an off-white solid that was removed by filtering the solution through a short silica plug. Removal of the solvent in vacuo gave the product as an orange-yellow oil (2.822 g, 92%; ≈ 95% purity by $^1H$ NMR spectroscopy). $^1H$ NMR ($CDCl_3$): $\delta$ = 7.10 (d, 2 H, Ar), 6.80 (d, 2 H, Ar), 3.59 (s, 2 H, $CH_2$), 2.92 (t, 2 H, $CH_2CH_2$), 2.79 (t, 2 H, $CH_2CH_2$), 2.52 (s, 6 H, $CH_3$), 2.32 (s, 3 H, $CH_3$); $\delta_C$ ($CDCl_3$) 157.9 (Ar), 131.8 (Ar), 126.7 (Ar), 116.3 (Ar), 62.1 ($CH_2$), 54.7 ($CH_2CH_2$), 52.0 ($CH_2CH_2$), 44.3 ($CH_3$), 41.9 ($CH_3$) ppm. ESI-MS: *m*/*z* (%) = 209 (100) $[H_2L^2]^+$. UV ($CH_3CN$): $\lambda_{max}$ ($\varepsilon$/$dm^3mol^{-1}$ $cm^{-1}$) = 278 (6200), 283 (5900), 314 nm (2900).

***N*-2-Hydroxybenzylmethyl-*N*,*N*′,*N*′-trimethylethylenediamine ($HL^3$):**[10] A mixture of *N*,*N*,*N*′-trimethylethylenediamine (1.530 g, 15.00 mmol), 2-hydroxybenzaldehyde (1.832 g, 14.99 mmol), and sodium triacetoxyborohydride (3.820 g, 18.03 mmol), in 1,2-dichloroethane (40 $cm^3$) was stirred for 16 h under nitrogen. Workup as for $L^1$ afforded $HL^2$; a straw-coloured oil (2.780 g, 89%; > 98% purity by $^1H$ NMR spectroscopy). $^1H$ NMR ($CDCl_3$): $\delta$ = 7.16 (t, 1 H, Ar), 7.00 (d, 1 H, Ar), 6.83 (d, 1 H, Ar), 6.77 (t, 1 H, Ar), 3.68 (s, 2 H, $CH_2$), 2.74 (m, 4 H, $CH_2CH_2$), 2.42 (s, 6 H, $CH_3$), 2.32 (s, 3 H, $CH_3$) ppm $^{13}C$ NMR ($CDCl_3$): $\delta$ = 158.2 (Ar), 129.7 (Ar), 122.5 (Ar), 119.8 (Ar), 117.0 (Ar), 61.2 ($CH_2$), 56.1 ($CH_2CH_2$), 53.3 ($CH_2CH_2$), 44.7 ($CH_3$), 42.6 ($CH_3$) ppm. ESI-MS: *m*/*z* (%) = 209 (100) $[H_2L^3]^+$. UV ($CH_3CN$): $\lambda_{max}$ ($\varepsilon$/$dm^3mol^{-1}$ $cm^{-1}$) = 277 (6400), 330 nm (600).

**$[Cu(HL^1)Cl_2]_2[CuCl_4]$:** Methanol solutions, 5 $cm^3$ each, of $HL^1$ (140 mg, 0.49 mmol) and $CuCl_2$ (66 mg, 0.49 mmol) were stirred overnight. The resulting dark green solution when placed under diethyl ether produced a green precipitate, which was twice recrystallised, firstly from dichloromethane/acetonitrile (3:1) under diethyl ether and then from methanol/acetonitrile (1:1). This pro-

 © 2006 Wiley-VCH Verlag GmbH & Co. KGaA, Weinheim 

Table 1. Numerical crystal and refinement data for the X-ray crystal structures.

| Compound | $[Cu(H_2L^1)Cl_2]_2[CuCl_4]\cdot CH_3CN\cdot 2H_2O$ | $[Cu(HL^2)Cl_2]$ | $[Cu_2(L^3)_2(H_2O)(ClO_4)]ClO_4\cdot H_2O$ |
|---|---|---|---|
| Formula | $C_{36}H_{55}Cl_8Cu_3N_7O_4$ | $C_{12}H_{20}Cl_2Cu_1N_2O$ | $C_{24}H_{42}Cl_2Cu_2N_4O_{12}$ |
| Formula mass | 1124.1 | 342.8 | 776.6 |
| Crystal system | monoclinic | monoclinic | monoclinic |
| Space group | *C*2/*c* | *C*2/*c* | $P2_1/c$ |
| *a* [Å] | 24.295(6) | 14.287(6) | 13.597(5) |
| *b* [Å] | 12.770(2) | 8.150(2) | 13.937(2) |
| *c* [Å] | 15.726(4) | 26.416(8) | 17.152(6) |
| $\alpha$ [°] | 90 | 90 | 90 |
| $\beta$ [°] | 91.73(1) | 97.65(2) | 100.01(2) |
| $\gamma$ [°] | 90 | 90 | 90 |
| *V* [Å$^{-3}$] | 4877(2) | 3048(2) | 3201(2) |
| *Z* | 4 | 8 | 4 |
| $\mu$ [mm$^{-1}$] (radiation) | 5.998 (Cu-$K_\alpha$) | 1.780 (Mo-$K_\alpha$) | 1.562 (Mo-$K_\alpha$) |
| $\rho$ [g cm$^{-3}$] | 1.53 | 1.49 | 1.61 |
| *F*(000) | 2300.0 | 1416.0 | 1608.0 |
| Observed reflections | 2339 [$I > 2\sigma(I)$] | 1844 [$I > 3\sigma(I)$] | 3470 [$I > 3\sigma(I)$] |
| No. of parameters | 264 | 163 | 350 |
| Observed reflections | 8.9 | 11.3 | 9.9 |
| Goodness-of-fit | 1.64 | 1.28 | 1.54 |
| $R_1$, $wR_2$ | 0.054, 0.073 | 0.030, 0.039 | 0.041, 0.051 |
| Max., min. peaks in final difference map [e·Å$^{-3}$] | 0.61, –0.93 | 0.52, –0.60 | 1.07, –1.12 |

duced X-ray quality, brown, plate-like crystals of $[Cu(HL^1)Cl_2]_2[CuCl_4]$ (82 mg, 16%). $C_{34}H_{48}Cl_8Cu_3N_6O_2\cdot CH_3CN\cdot 2H_2O$: calcd. C 38.46, H 4.93, N 8.72; found C 38.16, H 4.75, N 8.82. ESI-MS (MeCN): *m*/*z* (%) = 384 (100) $[Cu(HL^1)Cl]^+$, 286 (30) $[H_2L^1]^+$. UV ($CH_3CN$): $\lambda_{max}$ ($\varepsilon$/dm$^3$mol$^{-1}$ cm$^{-1}$) = 268 (12400), 288 (13400), 460 (1100), 677 (275), 775 sh (240) nm. UV (solid): $\lambda_{max}$ ($\varepsilon$/dm$^3$mol$^{-1}$ cm$^{-1}$) = 690 nm. EPR ($CH_3CN$ glass, 77 K): $g_\parallel$ = 2.29, $g_\perp$ = 2.09, $A_\parallel$ = 156 G, $g_\parallel$ = 2.26, $g_\perp$ = 2.08, $A_\parallel$ = 120 G; EPR (powder, 77 K) $g_{iso}$ = 2.10.

**$[Cu(HL^2)Cl_2]$:** To $HL^2$ (100 mg, 0.48 mmol) in methanol (10 cm$^3$) was added $CuCl_2$ (65 mg, 0.48 mmol) to give a dark blue solution that was stirred for 2 h. The solution was then reduced to half volume and placed under diethyl ether. After two days standing a green precipitate formed which was collected by filtration and dried under vacuum to give $[Cu(HL^2)Cl_2]$ (128 mg, 78%); a portion of this solid was recrystallised from methanol under diethyl ether to give green crystals of sufficient quality for X-ray crystallographic analysis. All data obtained from the powder and crystals were identical. $C_{12}H_{20}Cl_2CuN_2O$: calcd. C 42.05, H 5.88, N 8.17; found C 41.76, H 5.78, N 8.20. ESI-MS (1% HOAc in $CH_3CN$): *m*/*z* (%) = 674 (10) $[Cu_2(HL^2)_2Cl_2(OAc)]^+$, 331 (40) $[Cu(HL^2)(OAc)]^+$, 306 (10) $[Cu(HL^2)Cl]^+$, 209 (100) $[H_2L^2]^+$. UV ($CH_3CN$): $\lambda_{max}$ ($\varepsilon$/dm$^3$mol$^{-1}$ cm$^{-1}$) = 282 (6200), 379 (1000), 678 (205), 770 sh (190) nm. UV (powder): $\lambda_{max}$ = 685. EPR ($CH_3CN$ glass, 77 K): $g_\parallel$ = 2.25, $g_\perp$ = 2.09, $A_\parallel$ = 153 G; EPR (powder) $g_{iso}$ = 2.12.

**$[Cu_2(L^3)_2(H_2O)](ClO_4)_2$:** Aqueous solutions of $L^3$ (135 mg, 0.65 mmol, in 5 mL) and $Cu(ClO_4)_2\cdot 6H_2O$ (240 mg, 0.65 mmol, in 5 mL) were combined to give a black green solution (pH = 5). NaOH (ca. 0.6 mL, 5 M) was added dropwise until a precipitate began to form (pH = 9). The mixture was stirred for 20 h, and then the solid collected by filtration and washed with ethanol, then diethyl ether and dried under vacuum to give the product as a dark green powder (124 mg, 26%). Further product was obtained from the filtrate, which was reduced to half volume then left to slowly evaporate in air. Black, block-shaped crystals (26 mg, 5%) of X-ray analysis quality were obtained. The crystals and the powder exhibited identical spectroscopic data. $C_{24}H_{38}Cl_2Cu_2N_4O_{10}\cdot 2H_2O$: calcd. C 37.12, H 5.45, N 7.21; found C 37.18, H 5.31, N 7.47. ESI-MS (MeCN): *m*/*z* (%) = 560 (15) $[Cu_2(L^3)_2(H_2O)]^{2+}$, 271 (100) $[Cu(L^3)]^+$, 209 (30) $[H_2L^3]^+$. UV ($CH_3CN$): $\lambda_{max}$ ($\varepsilon$/dm$^3$mol$^{-1}$ cm$^{-1}$) = 233 (6800), 278 (6300), 428 (2000), 639 (315). UV (water/ethanol, 1:1, pH = 7): $\lambda_{max}$ ($\varepsilon$/dm$^3$mol$^{-1}$ cm$^{-1}$) = 418 (1900), 673 (430) nm. UV (water/ethanol, 1:1, pH = 10): $\lambda_{max}$ ($\varepsilon$/dm$^3$mol$^{-1}$ cm$^{-1}$) = 389 (1800), 588 (532) nm; $\lambda_{max}$ (powder) = 627 nm. EPR ($CH_3CN$ glass, 77 K): $g_\parallel$ = 2.25, $g_\perp$ = 2.06, $A_\parallel$ = 165 G; EPR (powder, 77 K): silent.

**X-ray Crystallography:** Relevant crystal, data collection and refinement data for the X-ray crystal structures of $[Cu(H_2L^1)Cl_2]_2[CuCl_4]\cdot CH_3CN\cdot 2H_2O$, $[Cu(HL^2)Cl_2]$ and $[Cu_2(\mu\text{-}L^3)_2(H_2O)(ClO_4)]ClO_4\cdot H_2O$ are summarised in Table 1.

CCDC-290947–290949 contain the supplementary crystallographic data for this paper. These data can be obtained free of charge from The Cambridge Crystallographic Data Centre via www.ccdc.cam.ac.uk/data_request/cif.

**Supporting Information** (see footnote on the first page of this article). Plots of EPR (at 77 K) and UV/Vis-NIR spectra for all complexes in the solid state and in acetonitrile solution; a figure of a $[Cu_2(L^3)_2(H_2O)(ClO_4)](ClO_4)\cdot(H_2O)]_\infty$ helix showing hydrogen bond lengths.

[1] E. Hubble, *The Realm of the Nebulae*, Yale Univ. Press, New Haven, **1936**.
[2] L. Pauling, R. B. Corey, H. R. Branson, *Proc. Natl. Acad. Sci. USA* **1951**, *37*, 205.
[3] J. D. Watson, F. H. C. Crick, *Nature* **1953**, *171*, 737.
[4] J. M. Lehn, *Supramolecular Chemistry - Concepts and Perspectives*, VCH, Weinheim **1995**.
[5] T. J. Katz, *Angew. Chem. Int. Ed.* **2000**, *39*, 1921; A. E. Rowan, R. J. M. Nolte, *Angew. Chem. Int. Ed.* **1998**, *37*, 63; J. M. Lehn, *Angew. Chem. Int. Ed. Engl.* **1990**, *29*, 1304.
[6] F. Zhang, S. Bai, G. P. A. Yap, V. Tarwade, J. M. Fox, *J. Am. Chem. Soc.* **2005**, *127*, 10590; T. J. Wigglesworth, D. Sud, T. B. Norsten, V. S. Lekhi, N. R. Branda, *J. Am. Chem. Soc.* **2005**, *127*, 7272; A. Tanatani, A. Yokoyama, I. Azumaya, Y. Takakura, C. Mitsui, M. Shiro, M. Uchiyama, A. Muranaka, N. Kobayashi, T. Yokozawa, *J. Am. Chem. Soc.* **2005**, *127*, 8553; M. Miyasaka, A. Rajca, M. Pink, S. Rajca, *Chem. Eur. J.* **2004**, *10*, 6531; V. Mamane, P. Hannen, A. Furstner, *Chem. Eur. J.* **2004**, *10*, 4556; S. Kim, R. Bishop, D. C. Craig, I. G. Dance, M. L. Scudder, *J. Org. Chem.* **2002**, *67*, 3221; R. Custelcean,

 © 2006 Wiley-VCH Verlag GmbH & Co. KGaA, Weinheim 

M. D. Ward, *Angew. Chem. Int. Ed.* **2002**, *41*, 1724; V. Berl, I. Huc, R. G. Khoury, M. J. Krische, J. M. Lehn, *Nature* **2000**, *407*, 720; L. J. Prins, J. Huskens, F. de Jong, P. Timmerman, D. N. Reinhoudt, *Nature* **1999**, *398*, 498.

[7] L. Han, M. Hong, *Inorg. Chem. Commun.* **2005**, *8*, 406; L. J. Childs, M. J. Hannon, *Supramol. Chem.* **2004**, *16*, 7; M. Albrecht, *Chem. Rev.* **2001**, *101*, 3457; C. Piguet, G. Bernardinelli, G. Hopfgartner, *Chem. Rev.* **1997**, *97*, 2005.

[8] X. D. Chen, T. C. W. Mak, *Dalton Trans.* **2005**, 3646; R. B. Fu, S. C. Xiang, S. M. Hu, L. S. Wang, Y. M. Li, X. H. Huang, X. T. Wu, *Chem. Commun.* **2005**, 5292; X. C. Huang, J. P. Zhang, Y. Y. Lin, X. M. Chen, *Chem. Commun.* **2005**, 2232; X. J. Luan, Y. Y. Wang, D. S. Li, P. Liu, H. M. Hu, Q. Z. Shi, S. M. Peng, *Angew. Chem. Int. Ed.* **2005**, *44*, 3864; O. Mamula, M. Lama, S. G. Telfer, A. Nakamura, R. Kuroda, H. Stoeckli-Evans, R. Scopelitti, *Angew. Chem. Int. Ed.* **2005**, *44*, 2527; R. Rai, A. Saxena, A. Ohira, M. Fujiki, *Langmuir* **2005**, *21*, 3957; X. L. Wang, C. Qin, E. B. Wang, Y. G. Li, Z. M. Su, *Chem. Commun.* **2005**, 5450; C. D. Wu, W. B. Lin, *Angew. Chem. Int. Ed.* **2005**, *44*, 1958; L. Yi, X. Yang, T. B. Lu, P. Cheng, *Crystal Growth Des.* **2005**, *5*, 1215; L. J. Childs, M. Pascu, A. J. Clarke, N. W. Alcock, M. L. Hannon, *Chem. Eur. J.* **2004**, *10*, 4291; S. K. Ghosh, P. K. Bharadwaj, *Inorg. Chem.* **2004**, *43*, 2293; A. Lavalette, F. Tuna, G. Clarkson, N. W. Alcock, M. J. Hannon, *Chem. Commun.* **2003**, 2666; K. Aikawa, K. Mikami, *Angew. Chem. Int. Ed.* **2003**, *42*, 5458; L. Y. Zhang, G. F. Liu, S. L. Zheng, B. H. Ye, X. M. Zhang, X. M. Chen, *Eur. J. Inorg. Chem.* **2003**, 2965; A. J. Blake, N. R. Champness, P. A. Cooke, J. E. B. Nicolson, C. Wilson, *J. Chem. Soc., Dalton Trans.* **2000**, 3811; L. Carlucci, G. Ciani, D. M. Proserpio, S. Rizzato, *Chem. Commun.* **2000**, 1319; R. Andres, M. Gruselle, B. Malezieux, M. Verdaguer, J. Vaissermann, *Inorg. Chem.* **1999**, *38*, 4637; T. Ezuhara, K. Endo, Y. Aoyama, *J. Am. Chem. Soc.* **1999**, *121*, 3279; H. P. Wu, C. Janiak, G. Rheinwald, H. Land, *J. Chem. Soc., Dalton Trans.* **1999**, 183; M. L. Tong, X. M. Chen, B. H. Ye, S. W. Ng, *Inorg. Chem.* **1998**, *37*, 5278; E. Psillakis, J. C. Jeffery, J. A. McCleverty, M. D. Ward, *J. Chem. Soc., Dalton Trans.* **1997**, 1645.

[9] T. Yajima, Y. Shimazaki, N. Ishigami, A. Odani, O. Yamauchi, *Inorg. Chim. Acta* **2002**, *337*, 193.

[10] J. Saa, A. Llobera, A. Garcia-Raso, A. Costa, P. Deya, *J. Org. Chem.* **1988**, *53*, 4263.

[11] Q. E. Manaham, R. T. Iwamoto, *Inorg. Chem.* **1965**, *4*, 1409; J. K. Senne, B. Kratochvil, *Anal. Chem.* **1971**, *43*, 79.

[12] B. A. Jazdzewski, W. B. Tolman, *Coord. Chem. Rev.* **2000**, *200*, 633.

[13] A. Philibert, F. Thomas, C. Philouze, S. Hamman, E. Saint-Aman, J. L. Pierre, *Chem. Eur. J.* **2003**, *9*, 3803; M. Vaidyanathan, M. Palaniandavar, R. S. Gopalan, *Inorg. Chim. Acta* **2001**, *324*, 241; E. Saint-Aman, S. Menage, J. L. Pierre, E. Defrancq, G. Gellon, *New J. Chem.* **1998**, *22*, 393; S. Itoh, S. Takayama, R. Arakawa, A. Furuta, M. Komatsu, A. Ishida, S. Takamuku, S. Fukuzumi, *Inorg. Chem.* **1997**, *36*, 1407; D. Zurita, I. GautierLuneau, S. Menage, J. L. Pierre, E. Saint-Aman, *J. Biol. Inorg. Chem.* **1997**, *2*, 46; H. Adams, N. A. Bailey, I. K. Campbell, D. E. Fenton, Q. Y. He, *J. Chem. Soc., Dalton Trans.* **1996**, 2233.

[14] T. Kawata, T. Aoyama, S. Ohba, *Acta Crystallogr., Sect. C* **1993**, *49*, 137; R. Corzo-Suarez, I. Diaz, S. Garcia-Granda, V. Fernandez, *Acta Crystallogr., Sect. C* **2000**, *56*, 385; C. J. Matthews, V. Broughton, G. Bernardinelli, X. Melich, G. Brand, A. C. Willis, A. F. Williams, *New J. Chem.* **2003**, *27*, 354.

[15] D. A. Harvey, C. J. L. Lock, *Acta Crystallogr., Sect. C* **1986**, *42*, 799.

[16] S. V. Pavlova, Y. S. Wen, S. I. Chan, *Acta Crystallogr., Sect. E* **2003**, *59*, 792.

[17] A. W. Addison, A. N. Rao, J. Reedjik, J. Rijn, G. C. Verschoor, *J. Chem. Soc., Dalton Trans.* **1984**, 1349.

Received: November 29, 2005
Published Online: January 26, 2005

 © 2006 Wiley-VCH Verlag GmbH & Co. KGaA, Weinheim 

DOI: 10.1002/ejic.200500560

# Charge-Transfer Phase Transition and Ferromagnetism of Iron Mixed-Valence Complexes ($n$-$C_nH_{2n+1})_4N[Fe^{II}Fe^{III}(dto)_3]$ ($n$ = 3–6; dto = $C_2O_2S_2$)

**Miho Itoi,*[a] Yuuki Ono,[b] Norimichi Kojima,*[b] Kenichi Kato,[c,d] Keiichi Osaka,[c,d] and Masaki Takata[c,d]**

**Keywords:** Mixed-valence compounds / Iron / Magnetic properties / Charge transfer

The iron mixed-valence complex, ($n$-$C_3H_7)_4N[Fe^{II}Fe^{III}(dto)_3]$ (dto = dithiooxalato) shows a charge-transfer (CT) phase transition at $T_{CT}$ = 122.4 K. In the vicinity of $T_{CT}$, the spin state changes from $Fe^{II}$ ($S$ = 2) – $Fe^{III}$ ($S$ = 1/2) (high-temperature phase: HTP) to $Fe^{II}$ ($S$ = 0) – $Fe^{III}$ ($S$ = 5/2) (low-temperature phase: LTP) accompanied by a charge transfer between $Fe^{II}$ and $Fe^{III}$. This complex also undergoes a ferromagnetic transition at 7 K in the LTP. In order to investigate the mechanism of the CT phase transition and the ferromagnetism, we have systematically synthesized ($n$-$C_nH_{2n+1})_4N[Fe^{II}Fe^{III}(dto)_3]$ ($n$ = 3–6), and have investigated their physical properties by magnetic susceptibility, powder X-ray diffraction measurements, and ESR spectroscopy. The compounds ($n$-$C_nH_{2n+1})_4N[Fe^{II}Fe^{III}(dto)_3]$ ($n$ = 3–6) display ferromagnetic phase transitions at 7 K, 7 K (& 13 K), 19.5 K, and 22 K, respectively. For $n$ = 3 and 4, the CT phase transitions take place at $T_{CT} \approx$ 120 K and $T_{CT} \approx$ 140 K, respectively. For $n$ = 5 and 6, on the other hand, the CT phase transition does not occur, and the spin configuration of $Fe^{II}$ ($S$ = 2) and $Fe^{III}$ ($S$ = 1/2) corresponding to the HTP for $n$ = 3 and 4 is stable between 2 K and 300 K. The cation size of ($n$-$C_nH_{2n+1})_4N^+$ ($n$ = 3–6) acts as an effective internal pressure which induces the CT phase transition and the ferromagnetic ordering in the $[Fe^{II}Fe^{III}(dto)_3]^-_\infty$ layer. We also discuss the mechanism of the CT phase transition and the ferromagnetism induced by the charge-transfer interaction between $Fe^{II}$ and $Fe^{III}$.
(© Wiley-VCH Verlag GmbH & Co. KGaA, 69451 Weinheim, Germany, 2006)

## Introduction

Transition-metal complexes with $d^4$-$d^7$ configuration have a possibility of a spin transition between a low-spin (LS) state and a high-spin (HS) state. The spin-crossover phenomenon has gained a renewed importance through the discovery of Light Induced Excited Spin State Trapping (LIESST) for $[Fe(ptz)_6](BF_4)_2$ (ptz = 1-propyltetrazole)[1] and the thermally induced spin-crossover transition with a large thermal hysteresis around room temperature in a triazole-bridged iron(II) complex.[2,3]

One expects mixed-valence complexes with spin states situated in the spin-crossover region to display several new types of conjugated phenomena, coupled with spin and charge, between neighboring metal ions, that minimize the free energy in the whole system. To explore this possibility, we have synthesized iron mixed-valence complexes whose spin states are situated in that region. It is well-known that tris(dithiocarbamato) iron(III) complexes show the spin-crossover transition.[4] In these complexes, the $Fe^{III}$ atom is coordinated by six S atoms. Taking account of these particulars, we have synthesized dithiooxalato-bridged iron mixed-valence complexes. (Hereafter, dithiooxalato is denoted as dto.)

Heterometal dto complexes were first synthesized by Ōkawa et al., who described the ferromagnetism of ($n$-$C_3H_7)_4N[M^{II}Cr^{III}(dto)_3]$ ($M^{II}$ = Fe, Co, Ni)[5] and compared their ferromagnetic properties with those of ($n$-$C_4H_9)_4N[M^{II}Cr^{III}(ox)_3]$ ($M^{II}$ = Mn, Fe, Co, Ni, Cu, ox = oxalato).[6] The structures and magnetic properties of $A[M^{II}Cr^{III}(dto)_3]$ [$A^+$ = $Ph_4P^+$, ($C_nH_{2n+1})_4N^+$, $n$ = 3–5; $M^{II}$ = Mn, Fe, Co] complexes were investigated by J. M. Bradly et al.,[7] who confirmed that all the complexes were ferromagnets with Curie temperatures between 5 and 16 K except for the $[Mn^{II}Cr^{III}(dto)_3]$ complex, which did not show a long-range ordering above 2 K.

Recently, we have discovered a new type of first-order phase transition at $T_{CT} \approx$ 120 K for ($n$-$C_3H_7)_4N[Fe^{II}Fe^{III}(dto)_3]$, where the thermally induced charge-transfer between the $Fe^{II}$ and $Fe^{III}$ is reversible.[8,9] This phase transition is schematically shown in Figure 1. In the high-temperature phase (HTP), the $Fe^{III}$ ($S$ = 1/2) and $Fe^{II}$ ($S$ = 2) sites are coordinated by six S atoms and six O atoms, respectively. On the other hand, in the low-temperature

[a] Institute for Solid State Physics, The University of Tokyo, Kashiwanoha 5-1-1, Kashiwa 277-8581, Chiba, Japan
Fax: +81-4-7136-3333
E-mail: itoimiho@issp.u-tokyo.ac.jp
[b] Graduate School of Arts & Sciences, The University of Tokyo, Komaba 3-8-1, Meguro-Ku, Tokyo 153-8902, Japan
Fax: +81-3-5454-6741
E-mail: cnori@mail.ecc.u-tokyo.ac.jp
[c] SPring-8/JASRI, 1-1-1 Kouto, Mikazuki-cho, Sayo-gun, Hyogo 679-5198, Japan
[d] CREST, JST 4-1-8, Honcho, Kawaguchi-shi, Saitama 332-0012 Japan

 © 2006 Wiley-VCH Verlag GmbH & Co. KGaA, Weinheim 

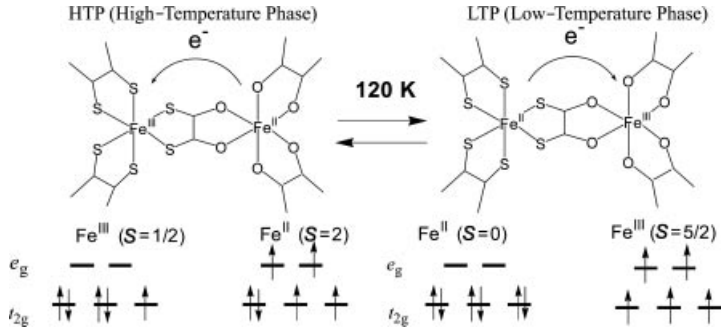


Figure 1. Schematic representation of a charge-transfer phase transition in $(n\text{-}C_3H_7)_4N[Fe^{II}Fe^{III}(dto)_3]$.

phase (LTP), the $Fe^{III}$ ($S$ = 5/2) site is coordinated by six O atoms, and the $Fe^{II}$ ($S$ = 0) site by six S atoms. Moreover, we have found a ferromagnetic transition at 7 K. The ferromagnetic interaction takes place over a long distance involving $Fe^{III}$ ($S$ = 5/2) – $S_2C_2O_2$ – $Fe^{II}$ ($S$ = 0) – $O_2C_2S_2$ – $Fe^{III}$ ($S$ = 5/2). The ferromagnetic ordering is presumably induced by the charge-transfer interaction between $Fe^{II}$ and $Fe^{III}$.

In order to investigate the mechanism of the CT phase transition and the ferromagnetism induced by the charge-transfer interaction between $Fe^{II}$ and $Fe^{III}$ for $(n\text{-}C_3H_7)_4N[Fe^{II}Fe^{III}(dto)_3]$, we have synthesized iron mixed-valence complexes, $(n\text{-}C_nH_{2n+1})_4N[Fe^{II}Fe^{III}(dto)_3]$ ($n$ = 3–6), and investigated their crystal structures and physical properties by powder X-ray diffraction, magnetic susceptibility measurements, and ESR spectroscopy. In this paper, we report our results concerning the CT phase transition and the ferromagnetic phase transition for $(n\text{-}C_nH_{2n+1})_4N[Fe^{II}Fe^{III}(dto)_3]$ ($n$ = 3–6; the complex is hereafter denoted as $n$ = 3–6). In addition, we discuss the mechanism of the CT phase transition and the ferromagnetism induced by the charge-transfer interaction between $Fe^{II}$ and $Fe^{III}$.

## Results

### Structural Characterization

The crystal structure of $(n\text{-}C_3H_7)_4N[Fe^{II}Fe^{III}(dto)_3]$ has already been determined by single-crystal X-ray diffraction analysis.[10] In this compound, $Fe^{II}$ and $Fe^{III}$ are alternately bridged by dithiooxalato molecules, which forms the 2-D honeycomb network structure of $[Fe^{II}Fe^{III}(dto)_3]^-_\infty$. The $(n\text{-}C_3H_7)_4N^+$ cation layer is intercalated between two $[Fe^{II}Fe^{III}(dto)_3]^-_\infty$ layers. This structure is common in heterometal oxalato and dithiooxalato complexes.[11,12] The space group of $(n\text{-}C_3H_7)_4N[Fe^{II}Fe^{III}(dto)_3]$ is $P6_3$.

Single crystals of $(n\text{-}C_nH_{2n+1})_4N[Fe^{II}Fe^{III}(dto)_3]$ ($n$ = 4–6) have not yet been obtained. However, crystals of $(n\text{-}C_nH_{2n+1})_4N[Fe^{II}Fe^{III}(dto)_3]$ ($n$ = 4–6) appear to have honeycomb structures that are restricted to the *ab* plane. For these crystals, the lattice parameter $c$ increases with the number of carbon atoms in $(n\text{-}C_nH_{2n+1})_4N^+$, a relationship based on results from the analogous complexes $(n\text{-}C_nH_{2n+1})_4N[M^{II}Cr^{III}(dto)_3]$ (M = Mn, Fe, Co, Ni; $n$ = 3–5) and $A[Mn^{II}Fe^{III}(dto)_3]$ [A = $N(C_nH_{2n+1})_4$ ($n$ = 3–5) and $P(C_6H_5)_4$].[7,13] In support of this suggestion, note that the infrared spectra of all the complexes show dto-ligand vibration bands; the ν(CO) stretching mode of the dithiooxalato molecule appears around 1500 $cm^{-1}$, (1490.91 $cm^{-1}$, 1496.0 $cm^{-1}$, 1490.5 $cm^{-1}$, and 1490.5 $cm^{-1}$ for $n$ = 3–6, respectively). In the case of the parent compounds $K_2(C_2O_2S_2)$ and $KBa[Fe^{III}(dto)_3]\cdot 3H_2O$, the ν(CO) vibration modes appear at higher energies (1516 $cm^{-1}$ and 1528 $cm^{-1}$). The low values of ν(CO) of the $n$ = 3–6 complexes indicate that the dto molecule acts as a bridging ligand to form the 2-D network.

The structural characteristics of $(n\text{-}C_nH_{2n+1})[Fe^{II}Fe^{III}(dto)_3]$ ($n$ = 3–6) were investigated by powder X-ray diffraction (PXD) using synchrotron radiation. Figure 2 shows the X-ray diffraction patterns for $n$ = 3–6 taken over 1 h at room temperature. The profiles are broad, and several peaks are only observed below $2\theta > 20°$. For the title complexes, the thermal vibration of $(n\text{-}C_nH_{2n+1})_4N^+$ appears to be quite large. A PXD measurement at low temperatures was carried out so that thermal vibration of the cation might be prevented; however, the diffraction profiles were still broad.

The sharpest peak can be attributed to the (002) reflection, which generally moves to a higher angle with decreasing temperature. The (002) reflections for $(n\text{-}C_nH_{2n+1})_4N[Fe^{II}Fe^{III}(dto)_3]$ systematically shift to lower angle as shown in Figure 2(a). These results suggest that the interlayer spacing becomes larger as the number of carbon atoms in the alkyl chains increases.

The unit cell parameters of $n$ = 3 and 4 were estimated by the Rietveld method as shown in Figure 2(b) and (c). For the refinement of $n$ = 4, we used the coordination of $(n\text{-}C_4H_9)_4N[Mn^{II}Fe^{III}(ox)_3]$ with the space group $P6_3$.[12] The cell parameters $a$ are 10.06 Å ($n$ = 3) and 10.09 Å ($n$ = 4). The lattice parameters $c$ are 16.18 Å ($n$ = 3) and 18.14 Å ($n$ = 4). The $c$ parameter determined by PXD differs from the result of a single-crystal X-ray diffraction (SXD) study, since the $h$ $k$ $l$ reflections obtained by the Rietveld analysis cover the range $h$ = 0–3, $k$ = 0–2, $l$ = 0–4, a data range that is much smaller than that of the single-crystal analysis ($h$ = 0–12, $k$ = –12 to 10, $l$ = –16 to 15). The error in the cell parameters in the PXD thus becomes larger than that in the SXD.

 © 2006 Wiley-VCH Verlag GmbH & Co. KGaA, Weinheim 

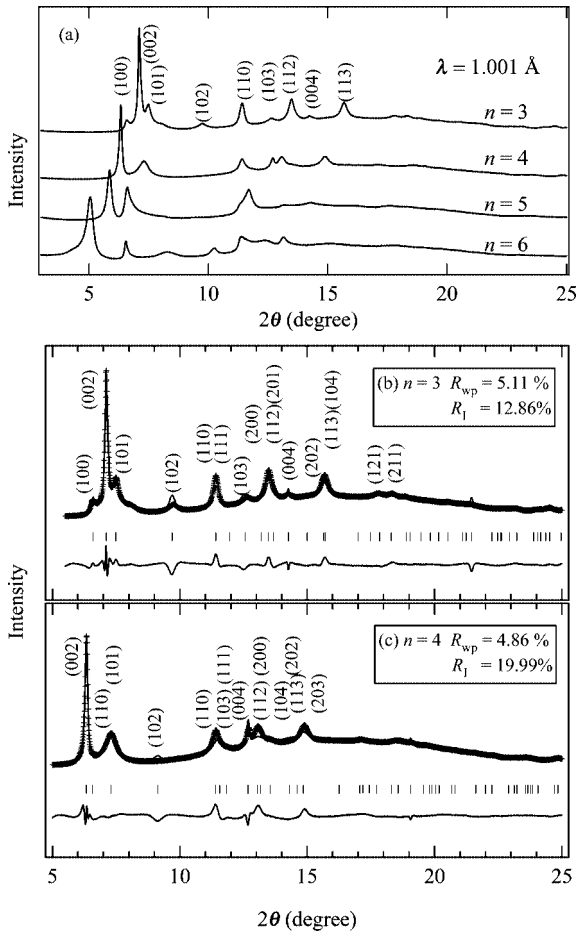


Figure 2. (a) Powder X-ray diffraction patterns for $(n\text{-}C_nH_{2n+1})_4N[Fe^{II}Fe^{III}(dto)_3]$ ($n$ = 3–6) at room temperature. (b) Result of the Rietveld refinement for $n$ = 3, and (c) for $n$ = 4. $R_{wp}$ and $R_I$ are expressed as $\{[\Sigma_i w_i(y_i - y_{i,calc})^2/\Sigma_i w_i y_i^2]^{1/2}\}$ and $\{[\Sigma_K|I_{K,calc} - I_K|/\Sigma_K I_{K,calc}]\}$, respectively.

In the cases of $n$ = 5 and 6, the cell parameter could not be determined by the Rietveld method. The estimated parameters of $c$ are 19.67 Å and 22.71 Å, respectively. The lattice parameters for $(n\text{-}C_nH_{2n+1})_4N[Fe^{II}Fe^{III}(dto)_3]$ are listed in Table 1.

Table 1. Lattice parameters for $(n\text{-}C_nH_{2n+1})_4N[Fe^{II}Fe^{III}(dto)_3]$.

| $(n\text{-}C_nH_{2n+1})_4N[Fe^{II}Fe^{III}(dto)_3]$ | $a$ [Å] | $c$ [Å] | $R^*$, $R_{WP}$** |
|---|---|---|---|
| $n$ = 3 | 10.06[a] | 16.04[a] | 0.091[a]* |
| | 10.06[b] | 16.18[b] | 0.051[b]** |
| $n$ = 4 | 10.09[b] | 18.14[b] | 0.049[b]** |
| $n$ = 5 | | 19.67[c] | |
| $n$ = 6 | | 22.71[c] | |

[a] Value obtained from single-crystal structure analysis. [b] Refined value obtained by using the Rietveld method. [c] Calculated from the position of the (002) peak. $R_{wp}$ is expressed as $\{[\Sigma_i w_i(y_i - y_{i,calc})^2/\Sigma_i w_i y_i^2]^{1/2}\}$.

## Magnetic Properties

The static magnetic susceptibilities of $n$ = 3–6 were measured in an external magnetic field of 5000 G. Figure 3 shows the $\chi T$ and the inverse magnetic susceptibility ($\chi^{-1}$) as a function of temperature for $n$ = 3–6. The magnetic susceptibilities for $n$ = 5 and 6 obey the Curie–Weiss law [$\chi^{-1} = (T - \theta)/C$] in the range 50–300 K. However, for $n$ = 3 and 4, the magnetic susceptibilities do not obey the Curie–Weiss law over this range. The change of slope is at around 100 K on the $\chi^{-1}$ curves showing a thermal dependence. The Weiss constants are +12 K ($T_{CT} < T$: 120–300 K) and +20 K ($T_{CT} > T$: 30–98.4 K) for $n$ = 3, +18 K ($T_{CT} < T$: 140–300 K), and +27 K ($T_{CT} > T$; 39.7–100 K) for $n$ = 4. Those of $n$ = 5 and 6 are +23 K and +21 K, respectively.

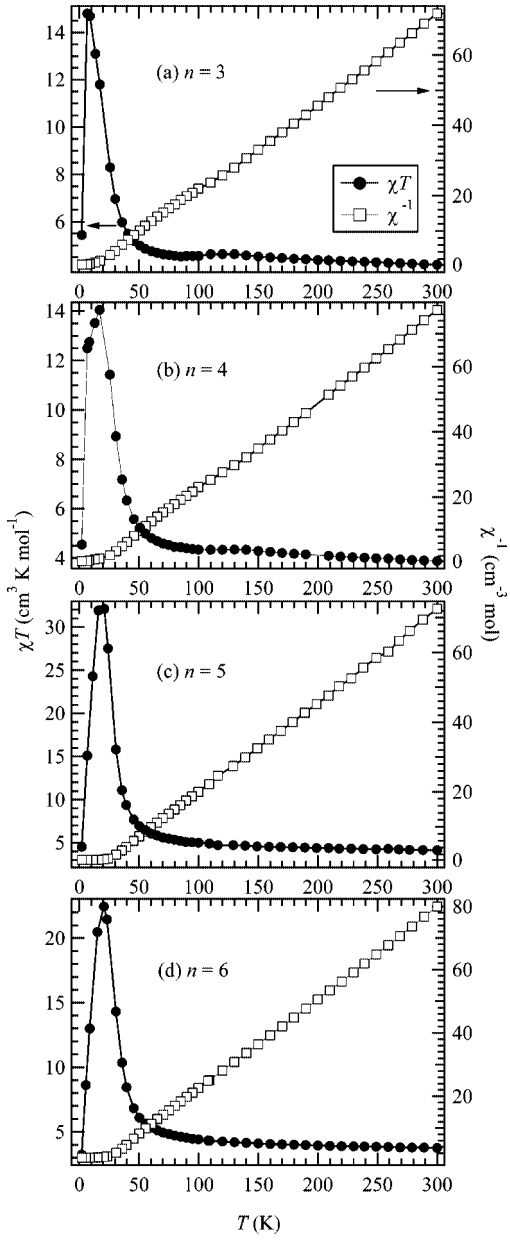


Figure 3. Temperature dependence of the magnetic susceptibility multiplied by temperature ($\chi T$) and the inverse susceptibility ($\chi^{-1}$) of $(n\text{-}C_nH_{2n+1})_4N[Fe^{II}Fe^{III}(dto)_3]$ ($n$ = 3–6).

 © 2006 Wiley-VCH Verlag GmbH & Co. KGaA, Weinheim 

All these positive Weiss constants imply the existence of a ferromagnetic interaction between $Fe^{II}$ and $Fe^{III}$. At room temperature, the effective moments, $\mu_{eff}$, are 5.87 $\mu_B$ ($n$ = 3), 5.58 $\mu_B$ ($n$ = 4), 5.94 $\mu_B$ ($n$ = 5), and 5.48 $\mu_B$ ($n$ = 6). When $kT>>|J|$, the effective moment of HTP with $Fe^{II}$ ($S$ = 2) and $Fe^{III}$ ($S$ = 1/2) is calculated as 5.91 $\mu_B$ ($g$ = 2.00).

In order to confirm the ferromagnetic phase transition, we investigated the field-cooled magnetization (FCM), the remanent magnetization (RM) and the zero-field cooled magnetization (ZFCM) for $n$ = 3–6, the results of which are shown in Figure 4. The FCM curve was obtained on cooling with an external magnetic field of 30 G. After the FCM measurement, the magnetic field was switched off at 2 K; then, the RM was measured from 2 K to 35 K. After cooling from 300 K to 2 K in zero external field, an external field of 30 G was switched on at 2 K. Then, the ZFCM was measured from 2 K to 35 K.

Figure 4(a) displays the FCM, RM, and ZFCM as a function of temperature for $n$ = 3. The FCM curve shows a rapid increase below 8 K, as well as a tendency to saturate below 6 K. The RM vanishes at about 7 K. Below 7 K, the ZFCM is smaller than the FCM, a result which is due to the fact that the applied magnetic field of 30 G is too weak to move the magnetic domain walls below the ferromagnetic temperature. The ZFCM and FCM curves overlap at 7 K, where the magnetic hysteresis disappears. From these results, we estimate the Curie temperature to be 7 K. The FCM and ZFCM curves for $n$ = 4, provided in Figure 4(b), are different from those for $n$ = 3. The FCM has a shoulder at 13 K and the ZFCM has two peaks at 7 K and 13 K. The RM vanishes at 13 K, where the ZFCM and FCM meet each other. The ZFCM of $n$ = 4 implies that two ferromagnetic phases with $Tc$ = 7 K and 13 K coexist, which we can regard as a mixture of HTP and LTP at a low temperature. The coexistence of HTP and LTP is consistent with the ESR data. Figure 4(c) and (d) show the temperature dependences of the magnetizations for $n$ = 5 and 6. The FCM steeply increases at 23 K and 26 K for $n$ = 5 and 6, respectively, and the RM disappears at 19 K and 25 K for $n$ = 5 and $n$ = 6, respectively, where the ZFCM and FCM curves meet each other. The Curie temperatures for $n$ = 3–6 were evaluated at 7 K, 7 K (&13 K), 19.5 K and 22 K, respectively, from heat capacity measurements (for $n$ = 3 and 4),[14,15] and by an *Arrott plot*,[16] i.e. $M^2 - H/M$ ($1/\chi$) plot (for $n$ = 5 and 6). The Curie temperatures for $n$ = 3–6 are listed in Table 2.

Reflecting the CT phase transition, a small bump appears in the $\chi T$ curve and the slope of $\chi^{-1}$ changes around 120 K ($n$ = 3) and 140 K ($n$ = 4). We carefully measured the magnetic susceptibility for $n$ = 3 and 4 with a sweep rate of 0.1 K min$^{-1}$ on heating and cooling, the results of which are shown in Figure 5. A thermal hysteresis loop appears between 60 K and 130 K for $n$ = 3, and between 50 K and 150 K for $n$ = 4. The $\chi T$ curve for $n$ = 4 changes by about 4% between 50 K and 150 K. This value is smaller than that for $n$ = 3, which drops by about 7% between 60 K and 130 K.

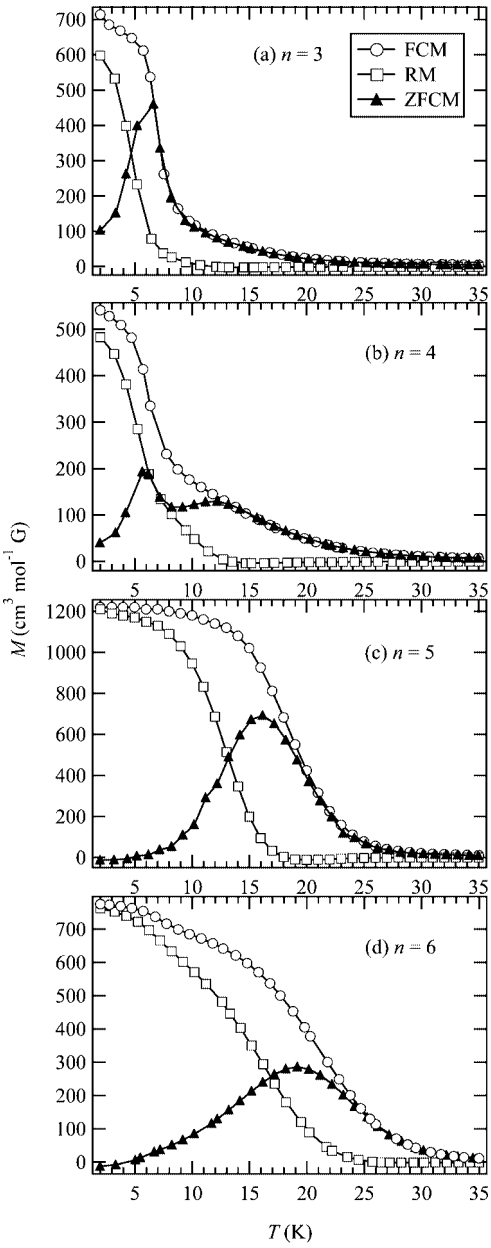


Figure 4. Temperature dependence of the field cooled magnetization (FCM:○), the remnant magnetization (RM:□), and the zero-field cooled magnetization (ZFCM:▲) for $(n\text{-}C_nH_{2n+1})_4N[Fe^{II}Fe^{III}(dto)_3]$ ($n$ = 3–6). Applied magnetic field $H$ = 30 G.

## ESR Spectroscopy

In order to investigate the CT phase transition and the spin state of the Fe atom, we obtained the ESR spectra for $n$ = 3–6 between 4 K and 300 K. The experimental conditions are as described in ref.[17]

Figure 6 shows the temperature dependence of the ESR signal of the $n$ = 3 complex. When the temperature was lowered from room temperature, an ESR signal corresponding to the $Fe^{III}$ site with $S$ = 5/2 appeared below 105 K, and its intensity strengthened with decreasing temperature. On heating, the ESR signal vanished above 130 K. The $g$ value of the ESR signal at the center of the 3200-G

 © 2006 Wiley-VCH Verlag GmbH & Co. KGaA, Weinheim 

Table 2. The parameters related to the change-transfer phase transition and ferromagnetism for $(n\text{-}C_nH_{2n+1})_4N[Fe^{II}Fe^{III}(dto)_3]$ ($n$ = 3–6).

| | $(n\text{-}C_nH_{2n+1})_4N[Fe^{II}Fe^{III}(dto)_3]$ ($n$ = 3-6) | | | |
|---|---|---|---|---|
| | $n$ = 3 | $n$ = 4 | $n$ = 5 | $n$ = 6 |
| Charge-Transfer Phase Transition | $T_{CT\downarrow}$* = 60 K | $T_{CT\downarrow}$ = 50 K | - | - |
| | $T_{CT\uparrow}$* = 130 K | $T_{CT\uparrow}$ = 145 K | - | - |
| Spin State of Fe | | | | |
| $Fe^{II}$ | $S = 2$ ($T > T_{CT}$) | $S = 2$ ($T > T_{CT}$) | $S = 2$ | $S = 2$ |
| | $S = 0$ ($T < T_{CT}$) | $S = 0$ ($T < T_{CT}$) | | |
| $Fe^{III}$ | $S = 1/2$ ($T > T_{CT}$) | $S = 1/2$ ($T > T_{CT}$) | $S = 1/2$ | $S = 1/2$ |
| | $S = 5/2$ ($T < T_{CT}$) | $S = 5/2$ ($T < T_{CT}$) | | |
| Curie Constant ($cm^3$ K $mol^{-1}$) | 3.90** | 3.56** | 3.88 | 3.52 |
| $T_C$ (K)*** | 7 | 7 (13 K) | 19,5 | 22 |
| Weiss Constant (K) | +12 (HTP), +20 (LTP) | +18 (HTP), +27 (LTP) | +23 | +21 |
| Coercive Field at 2 K (G) | 310 | 3160 | 6600 | 6800 |

* $T_{CT\uparrow}$ and $T_{CT\downarrow}$ denote, respectively, the upper-limit and the lower-limit of the thermal hysteresis loop for the charge-transfer phase transtion.
** Curie constants were estimated in the high-temperature phase (HTP).
*** Curie temperatures of $(n\text{-}C_nH_{2n+1})_4N[Fe^{II}Fe^{III}(dto)_3]$ were determined by heat capacity measurements (for $n$ = 3, 4) and by Arrott plots (for $n$ = 5, 6).

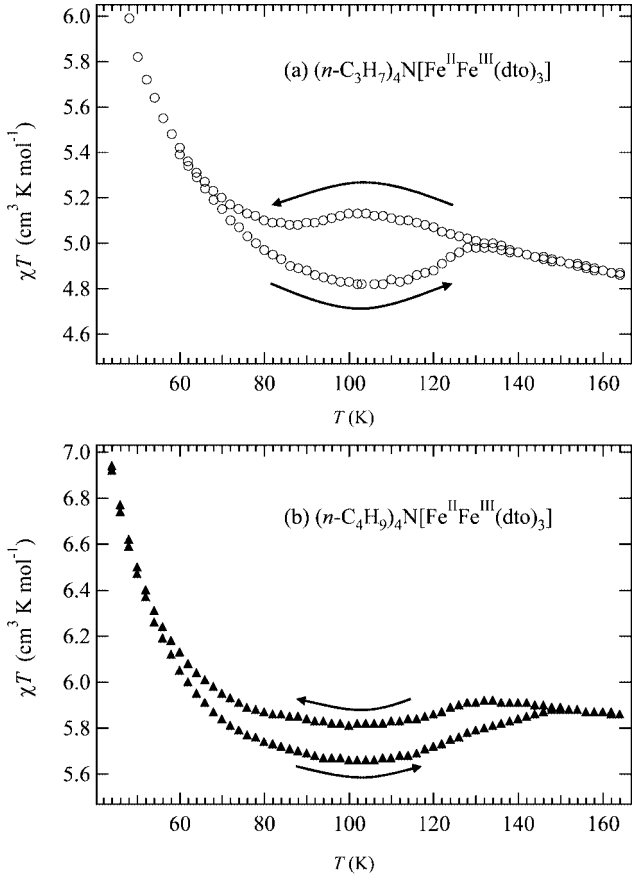


Figure 5. Temperature dependence of the magnetic susceptibility for $(n\text{-}C_3H_7)_4N[Fe^{II}Fe^{III}(dto)_3]$ and $(n\text{-}C_4H_9)_4N[Fe^{II}Fe^{III}(dto)_3]$. Temperature sweep rate is 0.1 K $min^{-1}$; (→) and (←) denote heating and cooling, respectively.

field is 2.10, which is consistent with that of the HS state ($^6A_{1g}$) of $Fe^{III}$, whose spin-orbit interaction is negligibly small. The half width ($\Delta H_{pp}$) has an almost constant value of $\Delta H_{pp}$ = 1470 G between 60 K and 120 K. In the case of $n$ = 4, as shown in Figure 7, a similar ESR signal corresponding to the HS state ($^6A_{1g}$) of $Fe^{III}$ appeared below 105 K in the cooling mode. On heating, the ESR signal almost disappeared above 145 K. The $\Delta H_{pp}$ for $n$ = 4 has an almost constant value of 1600 G between 50 and 140 K. In addition to the ESR signal due to the HS state ($^6A_{1g}$) of $Fe^{III}$, a weak signal is observed at 1600 G, whose $g$ value is 4.1. This weak signal should be attributed to the HTP fraction, i.e. the HS state ($S$ = 2; $^5T_{2g}$) of the $Fe^{II}$ and/or the LS state ($S$ = 1/2; $^2T_{2g}$) of the $Fe^{III}$. For $n$ = 5 and 6, a similar ESR signal appears at about 1600 G. Therefore, the HTP coexists with the LTP at 20 K for $n$ = 4, a finding which could account for the existence of the two peaks in the ZFCM.

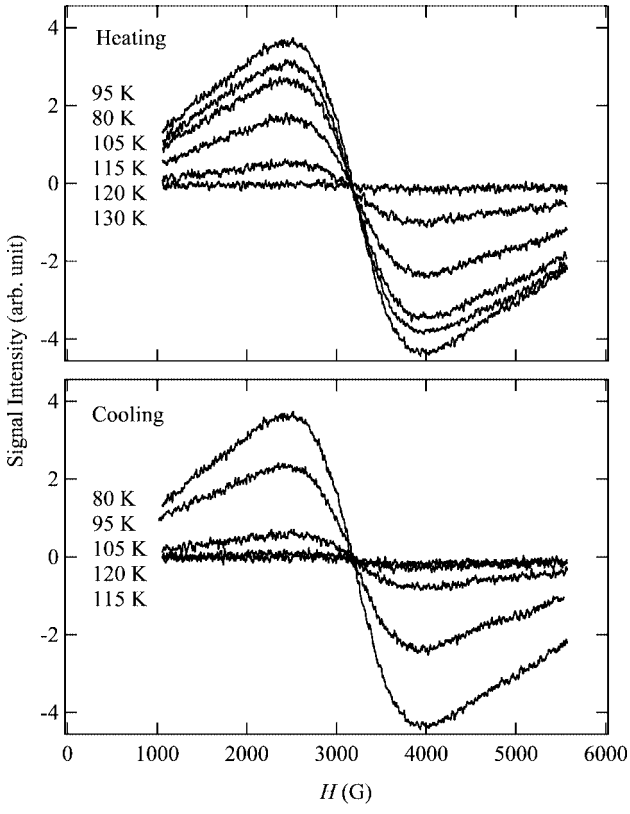


Figure 6. Temperature dependence of the ESR spectra on heating and cooling for $(n\text{-}C_3H_7)_4N[Fe^{II}Fe^{III}(dto)_3]$.

 © 2006 Wiley-VCH Verlag GmbH & Co. KGaA, Weinheim 

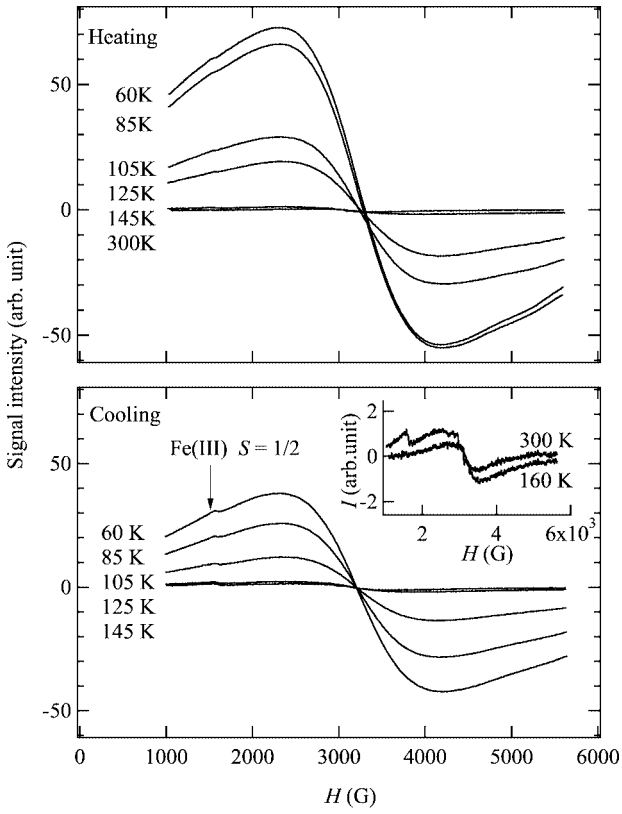


Figure 7. Temperature dependence of the ESR spectra on heating and cooling for $(n\text{-}C_4H_9)_4N[Fe^{II}Fe^{III}(dto)_3]$. Inset denotes the ESR signal corresponding to the $Fe^{III}$ ($^2T_{2g}$, $S$ = 1/2) of the HTP at 160 K and room temperature.

We estimated the spin susceptibilities corresponding to the HS state ($^6A_{1g}$) of the $Fe^{III}$ atom for $n$ = 3 and 4. The spin susceptibility is expressed as $\chi_{spin} = A(I(H) \times \{\Delta H_{PP}\}^2)$, where A is a constant value, $I(H)$ is the signal intensity, and $\Delta H_{PP}$ is the half width.[18] The spin susceptibilities for $n$ = 3 and $n$ = 4 are shown in Figure 8. The large thermal hysteresis loop in $\chi_{spin}$ for $n$ = 4 is in good agreement with that of the dc magnetic susceptibility; however, the thermal hysteresis loop in $\chi_{spin}$ for $n$ = 3 is narrower than that of the dc magnetic susceptibility.

In the cases of $KBa[Fe^{III}(dto)_3]\cdot 3H_2O$ and $(n\text{-}C_nH_{2n+1})_4N[Fe^{II}Fe^{III}(dto)_3]$ ($n$ = 5 and 6), the ESR spectra are completely different from those of $n$ = 3 and 4. For $n$ = 5 and 6, we could not observe a drastic signal change caused by the CT phase transition such as we noted for $n$ = 3 and 4. The ESR signals of $n$ = 5 and 6 are shown in Figure 9. The ESR spectra of the parent complex, $KBa[Fe^{III}(dto)_3]\cdot 3H_2O$, is shown in Figure 9(a). The paramagnetic spin of $KBa[Fe^{III}(dto)_3]\cdot 3H_2O$ has been already reported as the $Fe^{III}$ LS state ($S$ = 1/2) on the basis of magnetic susceptibility and Mössbauer spectroscopy results.[11,19,20]

The $KBa[Fe^{III}(dto)_3]\cdot 3H_2O$ complex has two ESR signals: a strong signal at 1600 G, and a weak signal at 3200 G. The $g$ values of the ESR signals at 1600 G and 3200 G are estimated at 4.10 and 2.01 and are attributed to the $g_\perp$ and $g_\parallel$ of $Fe^{III}$ ($S$ = 1/2), respectively. However, the ESR signal with $g$ = 2.01 persisted at room temperature, even though

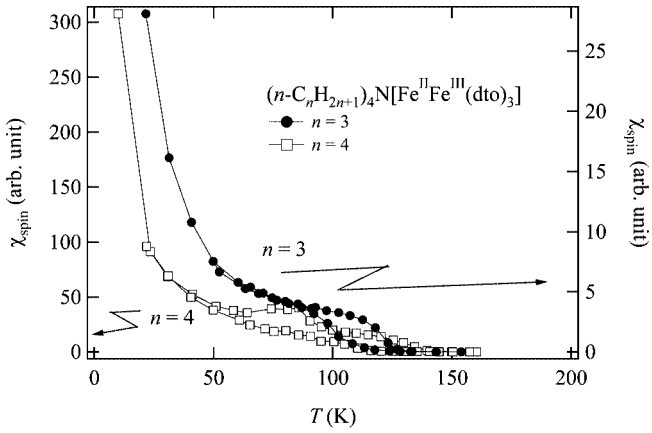


Figure 8. Temperature dependence of the spin susceptibility for $(n\text{-}C_nH_{2n+1})N[Fe^{II}Fe^{III}(dto)_3]$ ($n$ = 3 and 4).

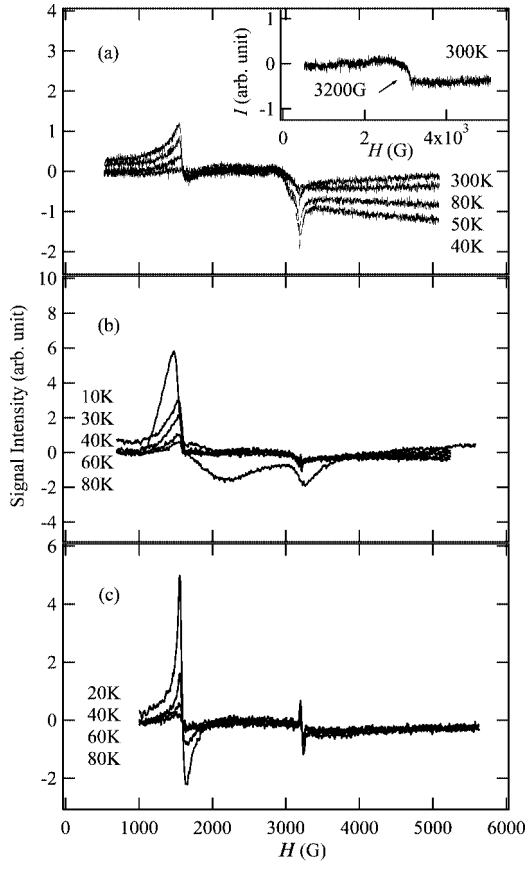


Figure 9. The ESR spectra at several temperatures for (a) $KBa[Fe^{III}(dto)_3]\cdot 3H_2O$; (b) $(n\text{-}C_5H_{11})_4N[Fe^{II}Fe^{III}(dto)_3]$; and (c) $(n\text{-}C_6H_{13})_4N[Fe^{II}Fe^{III}(dto)_3]$.

the strong signal with $g$ = 4.10 disappeared above 90 K. Therefore, we suggest that the HS state ($S$ = 5/2) of the $Fe^{III}$ atom caused by linkage isomerization ($Fe^{III}O_4S_2$ and / or $Fe^{III}O_6$) is responsible for this appearance of the ESR signal around 3200 G at room temperature. The $^{57}Fe$ Mössbauer spectrum for $KBa[Fe^{III}(dto)_3]\cdot 3H_2O$ did not enable us to distinguish the minor fraction of the $Fe^{III}$ HS state ($S$ = 5/2) caused by linkage isomerization from the LS state ($S$ = 1/2), because these Mössbauer spectra appear at almost

 © 2006 Wiley-VCH Verlag GmbH & Co. KGaA, Weinheim 

the same velocities. Therefore, the ESR signal due to the $Fe^{III}$ HS state ($S$ = 5/2) is presumably superposed on the ESR signal with $g_{\parallel}$ = 2.01 corresponding to the $Fe^{III}$ LS state ($S$ = 1/2).

For $n$ = 5 and 6, the ESR spectra were quite similar to those of $KBa[Fe^{III}(dto)_3]\cdot 3H_2O$. A strong signal at 1580 G and a weak signal at 3260 G were observed. The $g$ values of the ESR signals at 1580 G and 3260 G are estimated at 4.10 and 2.01, respectively, which are attributed to the $g_{\perp}$ and $g_{\parallel}$ of the LS state ($S$ = 1/2) of $Fe^{III}$. The signal with $g$ = 2.01 persisted at room temperature, so that an ESR signal due to the HS state ($S$ = 5/2) of the $Fe^{III}$ atom caused by linkage isomerization ($Fe^{III}O_4S_2$ and /or $Fe^{III}O_6$) appeared around 3260 G. Note that the ratio of the linkage isomer $Fe^{II}O_4S_2$ ($S$ = 2) can be estimated easily by Mössbauer spectroscopy. The percentages of the linkage isomer of $Fe^{II}O_4S_2$ are about 8% at 60 K for $n$ = 3, 14% at 25 K for $n$ = 4, 4% at 25 K for $n$ = 5, and 11% at 30 K for $n$ = 6. The $Fe^{II}O_4S_2$ persists at low temperatures without creating charge-transfer.[21]

In the cases of $n$ = 5 and 6, the ESR signals of the LS state ($S$ = 1/2) of the $Fe^{III}$ atom decrease with increasing temperature and then almost disappear above 90 K; the latter change takes place because of rapid spin-lattice relaxation. The ESR signal of the HS state ($^5T_{2g}$) of $Fe^{II}$ and the LS state ($^2T_{2g}$) of $Fe^{III}$ could not be observed in the high-temperature region. From the analysis of the ESR spectra, we conclude that the CT phase transition does not take place for $n$ = 5 and 6, in which the spin configurations of $Fe^{II}$ ($S$ = 2) and $Fe^{III}$ ($S$ = 1/2) are stable between 4 K and 300 K.

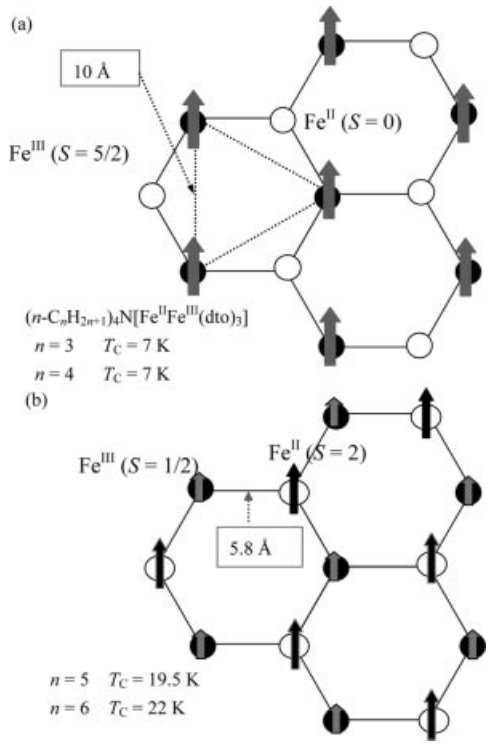


Figure 10. Schematic representation of ferromagnetic ordering for $(n\text{-}C_nH_{2n+1})_4N[Fe^{II}Fe^{III}(dto)_3]$ ($n$ = 3–6). (a) The ferromagnetic ordering for $n$ = 3 and $n$ = 4 takes place in the LTP with the spin configuration $Fe^{II}$ ($S$ = 0) and $Fe^{III}$ ($S$ = 5/2). (b) The ferromagnetic ordering for $n$ = 5 and $n$ = 6 takes place in the HTP with the spin configuration $Fe^{II}$ ($S$ = 2) and $Fe^{III}$ ($S$ = 1/2).

## Discussion

The spin state in the paramagnetic-ferromagnetic region and the existence of the charge-transfer phase transition of $(n\text{-}C_nH_{2n+1})_4N[Fe^{II}Fe^{III}(dto)_3]$ ($n$ = 3–6) are revealed by magnetic susceptibility measurements and ESR spectroscopy. The appearance of the CT phase transition and the mechanism of the ferromagnetism in an iron mixed-valence tris-dithiooxalato complex critically depend on the cation size $(n\text{-}C_nH_{2n+1})_4N^+$ ($n$ = 3–6). The CT phase transitions are observed for $n$ = 3 (120 K) and 4 (140 K), and then the $Fe^{II}$ ($S$ = 0) – $Fe^{III}$ ($S$ = 5/2) spin combination causes the ferromagnetic transition at 7 K. On the other hand, the CT phase transition is not apparent for $n$ = 5 and $n$ = 6; $Fe^{II}$ ($S$ = 2) – $Fe^{III}$ ($S$ = 1/2) spins are stable between 2 K and 300 K. The spin configuration corresponding to the HTP of $n$ = 3 and 4 is responsible for the ferromagnetic transitions at 19.5 K ($n$ = 5) and 22 K ($n$ = 6), respectively. The ferromagnetically ordered states and several parameters for $n$ = 3–6 are schematically shown in Figure 10 and Table 2.

Due to the effect of the cation size, the $[Fe^{II}Fe^{III}(dto)_3]$ layers are separated by an increment corresponding to the length of the alkyl chain from $n$ = 3 to $n$ = 6. The bulkier $(n\text{-}C_nH_{2n+1})_4N^+$ cations probably expand or distort slightly the $[Fe^{II}Fe^{III}(dto)_3]$ honeycomb ring. The cell parameter $a$ of the analogous complexes, $(n\text{-}C_nH_{2n+1})_4N[Fe^{II}Fe^{III}(ox)_3]$ ($n$ = 3–5)[22] tends to expand slightly as $n$ increases. For $n$ = 4, the slight expansion or distortion of the 2-D honeycomb ring ($\Delta a$ = 0.03 Å) might be expected to lead to an inhibition of CT between the Fe atoms; thus, the HTP spin partially remains at low temperature. We should note that $n$ = 5 shows a CT phase transition under 0.5 GPa, and the ferromagnetic transition temperature changes from 19.5 K to 7 K. In other words, the spin configuration changes from $Fe^{II}$ ($S$ = 2) – $Fe^{III}$ ($S$ = 1/2) (HTP) to $Fe^{II}$ ($S$ = 0) – $Fe^{III}$ ($S$ = 5/2) (LTP).[23] There is a limiting size of the honeycomb ring between $n$ = 4 and $n$ = 5 where the CT does not occur. Unfortunately, we could not obtain information on the crystal structure of the $(n\text{-}C_nH_{2n+1})_4N[Fe^{II}Fe^{III}(dto)_3]$ ($n$ = 5, 6) complexes by PXD. A single crystal X-ray analysis of the $n$ = 4–6 and an X-ray diffraction measurement taken under pressure are necessary to quantitatively clarify the cation size effects on the $[Fe^{II}Fe^{III}(dto)_3]^-$ layer.

The mechanism of the magnetic interaction in the iron tris-dithiooxalato complexes is dramatically changed according to whether a CT phase transition exists. Here, we will discuss the origin of the magnetic interaction in the title complexes. The ferromagnetic ordering for $n$ = 3 and 4 is considered to be established by the charge-transfer interaction between $Fe^{II}$ and $Fe^{III}$, the same mechanism as in $Fe^{III}_4[Fe^{II}(CN)_6]_3\cdot 15H_2O$ ($T_C$ = 5.5 K),[24,25] as shown in Fig-

 © 2006 Wiley-VCH Verlag GmbH & Co. KGaA, Weinheim 

ure 11(a). In contrast, for $n$ = 5 and 6, the spin configuration of $Fe^{II}$ ($S$ = 2) and $Fe^{III}$ ($S$ = 1/2) is the ground state between 2 K and 300 K. The ferromagnetic ordering for $n$ = 5 and 6 is schematically shown in Figure 11(b); each $Fe^{III}$ site in the LS state ($S$ = 1/2) accepts a $t_2$ electron with a down-spin from the neighboring $Fe^{II}$ site in the HS state ($S$ = 2). Therefore, the coupling between the ground configuration $\varphi_i[Fe^{III}(t_2^5)]\varphi_j[Fe^{II}(t_2^4e^2)]$ and the charge-transfer configuration $\varphi_i[Fe^{II}(t_2^6)]\varphi_j[Fe^{III}(t_2^3e^2)]$ stabilizes the ground state, a situation favoring ferromagnetic ordering. In the ground configuration of $\varphi_i[Fe^{III}(t_2^5)]\varphi_j[Fe^{II}(t_2^4e^2)]$, in addition to the charge-transfer interaction, the potential exchange interaction due to the orbital orthogonality between the $t_2$ electron with an up-spin $Fe^{III}$ and the $Fe^{II}$ electrons with up-spins (in $e$ orbitals and one $t_2$ orbital) induces ferromagnetic ordering, which is presumably responsible for the ferromagnetic transition with a high $T_C$ in $n$ = 5 and 6.

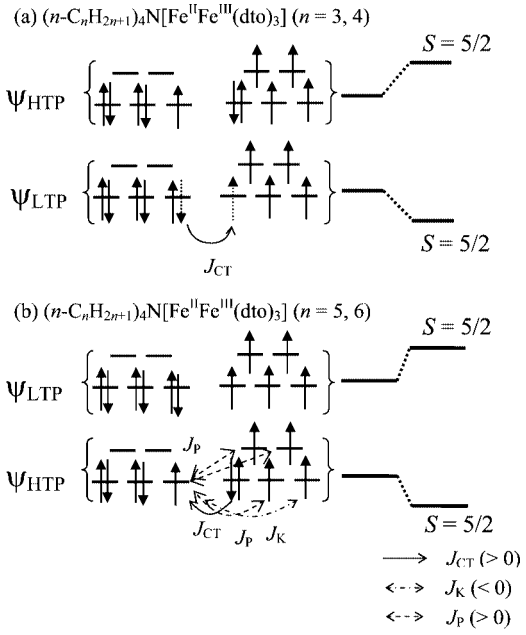


Figure 11. (a) Ferromagnetism induced by the charge-transfer interaction between $Fe^{II}$ ($S$ = 0) and $Fe^{III}$ ($S$ = 5/2) for ($n$-$C_nH_{2n+1}$)$_4$N[$Fe^{II}Fe^{III}$(dto)$_3$] ($n$ = 3, 4). (b) Ferromagnetism induced by the charge-transfer interaction as well as the potential exchange interaction between $Fe^{II}$ ($S$ = 2) and $Fe^{III}$ ($S$ = 1/2) for ($n$-$C_nH_{2n+1}$)$_4$N[$Fe^{II}Fe^{III}$(dto)$_3$] ($n$ = 5, 6). Solid line arrow: charge transfer interaction ($J_{CT} > 0$); dash-dotted line arrow: kinetic exchange interaction ($J_K < 0$); short-dashed line arrow: potential exchange interaction ($J_P > 0$).

Next, to quantify the ferromagnetic interaction between the iron atoms of ($n$-$C_nH_{2n+1}$)$_4$N[$Fe^{II}Fe^{III}$(dto)$_3$] ($n$ = 3–6), we will estimate the exchange interaction $J$ in a 2-D layer by means of the simplest Hamiltonian,

$$H = -J\sum_{<i,j>}\vec{S}_i\cdot\vec{S}_j - gh\sum_i S_i^Z .$$

Here, $h$ is the external magnetic field. For $n$ = 3 and 4, the LTP spin state with $Fe^{III}$($S$ = 5/2) – $Fe^{II}$($S$ = 0) appears via a CT phase transition, and the states produce large triangular interactions in the 2-D plane [Figure 10(a)]. In the case of the triangular lattice, the number of nearest neighbors of the $Fe^{III}$ ($S$ = 5/2) site is 6. The molar susceptibility of the triangular lattice, calculated by a high-temperature expansion up to the second order, is given by [Equation (1)]:[26]

$$\chi = \frac{NS(S+1)}{3}\beta(g\mu_B)^2 + \frac{2N\beta^2\mu_B^2g^2}{3}JS^2(S+1)^2 \qquad (1)$$

Here $\beta$ is $1/kT$, $N$ is Avogadro's number, and $\mu_B$ is the Bohr magneton. After substituting $S$ = 5/2 and $g$ = 2.00 into (1), we estimate the exchange coupling by the least-squares method. The fitting curves are shown in Figure 12(a). The range analyzed in the LTP is from 20 to 122 K for $n$ = 3, and from 20 to 140 K for $n$ = 4. The values obtained are $J$ = 3.12 K for $n$ = 3, and 2.39 K for $n$ = 4.

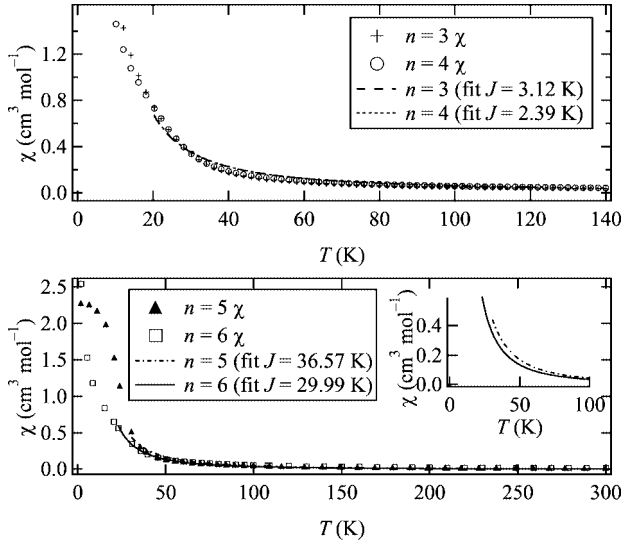


Figure 12. Temperature dependences of $\chi$ for $n$ = 3–6 with high-temperature expansion fitting. (a) dashed line: fitting for $n$ = 3; short-dashed line: fitting for $n$ = 4 in LTP spin configuration ($Fe^{III}$ $S$ = 5/2 – $Fe^{II}$ $S$ = 0) on triangular lattice. Molar susceptibility for $n$ = 3 and 4 is indicated by plus (+) and circle (○) symbols, respectively. (b) dash-dotted line: fitting for $n$ = 5; solid line: fitting for $n$ = 6 in HTP spin configuration ($Fe^{III}$ $S$ = 1/2 – $Fe^{II}$ $S$ = 2) on hexagonal lattice. Molar susceptibility for $n$ = 5 and 6 is indicated by the solid triangle (▲) and square (□) symbols, respectively.

On the other hand, for $n$ = 5 and 6, there is no CT phase transition, and the $Fe^{III}$ ($S$ = 1/2) – $Fe^{II}$ ($S$ = 2) interaction takes place on hexagonal rings [Figure 10(b)]. In the case of a hexagonal lattice, the number of nearest neighbors is 3. For $n$ = 5 and 6, the $Fe^{II}$ ($S$ = 2) atom is connected with three $Fe^{III}$ ($S$ = 1/2) atoms. The high-temperature expansion of the susceptibility for a hexagonal lattice is calculated by the same procedure as (1), and we get the molar susceptibility as follows [Equation (2)]:

$$\chi = \frac{N\beta\mu_B^2}{6}(g_AS_A(S_A+1)+g_BS_B(S_B+1)) + \frac{N\beta^2\mu_B^2}{3}g_Ag_BJS_A(S_A+1)S_B(S_B+1) \qquad (2)$$

 © 2006 Wiley-VCH Verlag GmbH & Co. KGaA, Weinheim 

After substituting $S_A$ = 1/2 and $S_B$ = 2 into (2), we estimated the exchange coupling and g values by the least-squares method. The range analyzed is from 31 to 300 K for $n$ = 5, and from 21 to 300 K for $n$ = 6. Then, we obtained $J$ = 36.57 K for $n$ = 5 and $J$ = 29.99 K for $n$ = 6, with $g_{1/2}$ = $g_2$ = 4.00 values, which were in agreement with the $T_C$ and g values obtained by the ESR spectra. The fitting curves are shown in Figure 12(b). The ferromagnetic interactions $J$ for $n$ = 3 and 4 are considerably lower than those for $n$ = 5 and 6.

## Conclusion

We have synthesized ($n$-$C_nH_{2n+1}$)$_4$N[$Fe^{II}Fe^{III}$(dto)$_3$] ($n$ = 3–6), and have investigated the cation-size effect on the CT phase transition and the ferromagnetic transition in these compounds. The result of our PXD measurement confirmed that the 2-D honeycomb network layer [$Fe^{II}Fe^{III}$(dto)$_3$]$^-$ is increasingly well separated with increases in the number $n$ of the ($n$-$C_nH_{2n+1}$)$_4$N cations. We have also determined, by magnetic susceptibility and ESR spectroscopy measurements, the spin states of the $Fe^{II}$ and $Fe^{III}$ sites for $n$ = 3–6 between 2 and 300 K. The ($n$-$C_nH_{2n+1}$)$_4$N$^+$ cation size affects the existence or nonexistence of the CT phase transition and the ferromagnetic interaction $J$ between the $Fe^{II}$ and $Fe^{III}$ sites. For $n$ = 3 and 4, we observed the thermally induced charge transfer between $Fe^{II}$ and $Fe^{III}$ around 120 K ($n$ = 3) and 140 K ($n$ = 4). The spin configuration changes from $Fe^{II}$ ($S$ = 2) – $Fe^{III}$ ($S$ = 1/2) (HTP) to $Fe^{II}$ ($S$ = 0) – $Fe^{III}$ ($S$ = 5/2) (LTP) in the vicinity of the CT phase transition temperature ($T_{CT}$). Furthermore, the $Fe^{III}$ ($S$ = 5/2) spin, which is located on a large triangular lattice, is ferromagnetically ordered at 7 K. On the other hand, for $n$ = 5 and 6, the CT phase transition did not occur, and the spin configuration of the HTP for $n$ = 3 and 4 dominated over the whole temperature range. The $Fe^{II}$ ($S$ = 2) – $Fe^{III}$ ($S$ = 1/2) spin configurations located on a hexagonal lattice produce the ferromagnetic transitions at 19.5 K ($n$ = 5) and 22 K ($n$ = 6), respectively.

## Experimental Section

### Syntheses

**$K_2C_2O_2S_2$:** Potassium dithiooxalate, $K_2C_2O_2S_2$, was prepared by the reaction of potassium hydrogensulfide KHS (14.57 g, 0.20 mol) and di-*n*-pentyl dithiooxalate ($n$-$C_5H_{11}$)$_2$($C_2O_2S_2$) (0.10 mol) in methanol. The di-*n*-pentyl dithiooxalate was obtained by the reaction of oxalyl dichloride $(COCl)_2$ (8.61 mL, 0.10 mol) and 1-pentanethiol $CH_3(CH_2)_4SH$ (25 mL, 0.20 mol). After filtration, the $K_2C_2O_2S_2$ was washed well with methanol to remove the KHS and, because $K_2C_2O_2S_2$ is highly hygroscopic,[27,28] it was dried in vacuo. $C_2K_2O_2S_2$ (198.35): calcd. C 12.11, S 32.33; found C 12.28, S 32.54.

**KBa[$Fe^{III}$(dto)$_3$]·3$H_2O$:** $Fe(NO_3)_3$·10$H_2O$ (2.10 g, 5.61·10$^{-3}$ mol) was treated with $K_2C_2O_2S_2$ (3.00 g, 15.1 mmol) in cold water (25 mL), and the solution was filtered to remove iron sulfide. Then $BaBr_2$·2$H_2O$ (2.50 g, 0.17 mol) was added to the dark purple solution, and KBa[$Fe^{III}$(dto)$_3$]·3$H_2O$ precipitated. The salt was recrystallized from water and dried for one day.[20,29,30] $C_6H_6BaFeKO_9S_6$ (646.8): calcd. C 11.14, H 0.94, S 29.75; found C 11.39, H 1.20, S 29.66.

**($n$-$C_nH_{2n+1}$)$_4$N[$Fe^{II}Fe^{III}$(dto)$_3$] ($n$ = 3–6):** The title complexes were synthesized in a way similar to the preparation of ($n$-$C_3H_7$)$_4$N-[$M^{II}Cr^{III}$(dto)$_3$] (M = Fe, Co, Ni, Zn).[5]

A solution of KBa[Fe(dto)$_3$]·3$H_2O$ (0.5 g, 0.77 mmol) in a 3:2 methanol/water mixture (20 mL) was stirred. To this was added slowly a solution of $FeCl_2$·4$H_2O$ (0.24 g, 0.77 mmol) and ($n$-$C_nH_{2n+1}$)$_4$NBr ($n$ = 3–6) (1.15 mmol) in a 3:2 methanol/water mixture (20 ml), whereupon a black powdered crystal precipitated. The compounds ($n$-$C_nH_{2n+1}$)$_4$N[$Fe^{II}Fe^{III}$(dto)$_3$] ($n$ = 3–6) were separated as powdered crystals by suction filtration and washed first with a 1:1 methanol/water mixture and then with methanol and diethyl ether. The compounds ($n$-$C_nH_{2n+1}$)$_4$N[$Fe^{II}Fe^{III}$(dto)$_3$] ($n$ = 7, 8) could not be obtained as crystalline powders. The elemental analysis for the precipitated crystal that had been stirred at 30–40 °C for 12 h was in good agreement with the calculated one; the results are listed in Table 3.

Table 3. Elemental analysis of C, H, N, and S in ($n$-$C_nH_{2n+1}$)$_4$N-[$Fe^{II}Fe^{III}$(dto)$_3$] ($n$ = 3–6).

| ($n$-$C_nH_{2n+1}$)$_4$N[$Fe^{II}Fe^{III}$(dto)$_3$] | C | H | N | S |
|---|---|---|---|---|
| $n$ = 3 found (calc) | 32.88 (32.83) | 4.46 (4.29) | 2.34 (2.13) | 29.40 (29.22) |
| $n$ = 4 | 36.73 (36.98) | 5.14 (5.08) | 1.76 (1.96) | 27.33 (26.92) |
| $n$ = 5 | 40.71 (40.52) | 5.93 (5.75) | 1.64 (1.82) | 24.72 (24.96) |
| $n$ = 6 | 43.78 (43.58) | 6.58 (6.34) | 1.64 (1.69) | 23.23 (23.27) |

**Measurements:** The powder X-ray diffraction data was taken at the BL02B2 beam line of SPring-8.[31] The as-grown powdered sample was sealed in a Lindemann capillary having a diameter of 0.3 mm, which gave a homogeneous intensity distribution in the Debye–Scherrer ring. The wavelength of the X-ray was 1.001 Å, and the exposure time at 300 K was 1 h. The static magnetic susceptibility was measured with a Quantum Design MPMS5 SQUIID magnetometer. Powdered crystals (10 mg) were wrapped in a polyethylene film and held in a plastic straw. The magnetic susceptibility obtained was corrected for the background and the core diamagnetism. The diamagnetic correction for constituting atoms was carried out using Pascal's constants.[32] The diamagnetic Pascal's corrections are as follows: –4.18·10$^{-4}$ cm$^3$ mol$^{-1}$ ($n$ = 3), –4.66·10$^{-4}$ cm$^3$ mol$^{-1}$ ($n$ = 4), –5.13·10$^{-4}$ cm$^3$ mol$^{-1}$ ($n$ = 5), and –5.60·10$^{-4}$ cm$^3$ mol$^{-1}$ ($n$ = 6). The ESR spectra for the powdered crystals were obtained with a JEOL JES-TE300 X-band ESR spectrometer. The magnetic field was monitored with an Echo Electronics ES-FC5 field meter.

## Acknowledgments

The authors wish to thank Prof. K. Asai, Prof. Y. Uwatoko, Prof. F. Varret, Prof. K. Boukheddaden, Prof. C. Itoi, Dr. Y. Kobayashi, and Dr. M. Enomoto for many helpful discussions. This work was supported by a Grant-in-Aid for Scientific Research and a Grant-in-Aid from the 21st Century COE (Center of Excellence) Program (Research Center for Integrated Science) of the Japanese Ministry of Education, Science, Sports, and Culture. The synchrotron-radiation X-ray powder experiments were performed at the SPring-8 BL02B2 with approval of the Japanese Synchrotron Radiation Research Institute (JASRI). One of the authors (M. Itoi) was sup-

 © 2006 Wiley-VCH Verlag GmbH & Co. KGaA, Weinheim 

ported by Research Fellowships of the Japanese Society for the Promotion of Science for Young Scientists.

[1] S. Decurtins, P. Gütlich, C. P. Köhler, H. Spiering, A. Hauser, *Chem. Phys. Lett.* **1984**, *105*, 1–4.
[2] J. Kröber, E. Codjovi, O. Kahn, F. Grolière, C. Jay, *J. Am. Chem. Soc.* **1993**, *115*, 9810–9811.
[3] O. Kahn, C. J. Martinez, *Science* **1998**, *279*, 44.
[4] L. Cambi, A. Cagnasso, *Atti Accad. Naz. Lincei* **1931**, *13*, 809–813.
[5] H. Ōkawa, M. Mitsumi, M. Ohba, M. Kodera, N. Matsumoto, *Bull. Chem. Soc. Jpn.* **1994**, *67*, 2139–2144.
[6] H. Tamaki, Z. J. Zhong, N. Matsumoto, S. Kida, M. Koikawa, N. Achiwa, Y. Hashimoto, H. Ōkawa, *J. Am. Chem. Soc.* **1992**, *114*, 6974–6979.
[7] J. M. Bradly, S. G. Carling, D. Visser, P. Day, D. Hautot, G. J. Long, *Inorg. Chem.* **2003**, *42*, 986–996.
[8] N. Kojima, W. Aoki, M. Seto, Y. Kobayashi, Yu. Maeda, *Synth. Met.* **2001**, *121*, 1796–1797.
[9] N. Kojima, W. Aoki, M. Itoi, Y. Ono, M. Seto, Y. Kobayashi, Yu. Maeda, *Solid State Commun.* **2001**, *120*, 165–170.
[10] M. Itoi, A. Taira, M. Enomoto, N. Matsushita, N. Kojima, Y. Kobayashi, K. Asai, K. Koyama, T. Nakano, Y. Uwatoko, *Solid State Commun.* **2004**, *130*, 415–420.
[11] Y. Ono, M. Okubo, N. Kojima, *Solid State Commun.* **2003**, *126*, 291–296.
[12] R. Pellaux, H. W. Schmalle, R. Huber, P. Fischer, T. Hauss, B. Ouladdiaf, S. Decurtins, *Inorg. Chem.* **1997**, *36*, 2301–2308.
[13] S. G. Carling, J. M. Bradley, D. Visser, P. Day, *Polyhedron* **2003**, *22*, 2317–2324.
[14] T. Nakamoto, Y. Miyazaki, M. Itoi, Y. Ono, N. Kojima, M. Sorai, *Angew. Chem. Int. Ed.* **2001**, *40*, 4716–4719.
[15] T. Nakamoto, Y. Miyazaki, M. Itoi, Y. Ono, N. Kojima, M. Sorai, to be submitted.
[16] A. Arrott, *Phys. Rev.* **1957**, *108*, 1394–1396.
[17] (1) $n = 3$: Frequency 9.15307 GHz, Microwave power 1.06 mW, modulation width 1 mT, Amplitude 63–2000 (from 10 K to 150 K) (2) $n = 4$: 9.15811 GHz, 1.00 mW, 0.1 mT, 2–1000 (from 10 K to 160 K) (3) $n = 5$: 9.16210 GHz, 1.00 mW, 0.5 mT, 160–630 (from 14 K to 206 K) (4) $n = 6$: 9.16754 GHz, 1.01 mW, 0.02 mT, 250–1000 (from 10 K to 91 K).
[18] C. P. Slichter, *Principles of Magnetic Resonance*, Springer-Verlag, Berlin, Heidelberg, **2000**.
[19] T. Bichall, K. M. Tnn, *Inorg. Chem.* **1976**, *15*, 376–380.
[20] F. P. Dwyer, A. M. Sargeson, *J. Am. Chem. Soc.* **1959**, *81*, 2335–2336.
[21] Y. Ono, *Doctoral Thesis*, The University of Tokyo, **2004**.
[22] C. Mathonière, C. J. Nuttall, S. G. Carling, P. Day, *Inorg. Chem.* **1996**, *35*, 1201–1206.
[23] Y. Kobayashi, M. Itoi, N. Kojima, K. Asai, *J. Magn. Magn. Mater.* **2004**, *272–276*, 1091–1092.
[24] B. Mayoh, P. Day, *J. Chem. Soc., Dalton Trans.* **1974**, 846–852.
[25] B. Mayoh, P. Day, *J. Chem. Soc., Dalton Trans.* **1976**, 1483–1486.
[26] T. Oguchi, *Statistical Theory of Magnetism*, SYŌKABŌ, 1st ed., **1970**, ch. 4.
[27] H. O. Jones, H. S. Tasker, *J. Chem. Soc., Trans.* **1910**, *95*, 1904–1909.
[28] C. S. Robinson, H. O. Jones, *J. Chem. Soc., Trans.* **1912**, *101*, 62–76.
[29] The number ($n = 3$) of the water of crystallization in $KBa[Fe^{III}(C_2O_2S_2)_3]\cdot nH_2O$ was determined by TG analysis.
[30] D. Coucouvanis, D. Piltingsrud, *J. Am. Chem. Soc.* **1973**, *95*, 5556–5563.
[31] E. Nishibori, M. Takata, K. Kato, M. Sakata, Y. Kubota, S. Aoyagi, Y. Kuroiwa, M. Yamamoto, N. Ikeda, The Large Debye–Scherrer Camera Installed at SPring-8 BL02B2 for Charge Density Studies, *Nuclear Instruments and Method in Physics Research A* **2001**, pp. 467–468, 1045–1048.
[32] O. Kahn, *Molecular Magnetism*, Wiley-VCH, **1993**, ch.1.

Received: June 25, 2005
Published Online: February 2, 2006

 © 2006 Wiley-VCH Verlag GmbH & Co. KGaA, Weinheim 

DOI: 10.1002/ejic.200500731

# Two New $Cu^{II}$ Coordination Polymers: Studies of Topological Networks and Water Clusters

**Jin Yang,[a] Jian-Fang Ma,*[a] Ying-Ying Liu,[a] Ji-Cheng Ma,[a] Heng-Qing Jia,[b] and Ning-Hai Hu[b]**

**Keywords:** Coordination polymers / Copper / Materials science / Topology / Water clusters

Two new $Cu^{II}$ coordination polymers, namely $[Cu_2(BDC)_2(L)_4(H_2O)_2]\cdot 14H_2O$ (**1**) and $[Cu_{1.5}(BTC)(L)_{1.5}(H_2O)_{0.5}]\cdot 2H_2O$ (**2**), where L = 1,1′-(1,4-butanediyl)bis(imidazole), BDC = 1,4-benzenedicarboxylate, and BTC = 1,3,5-benzenetricarboxylate, have been synthesized at room temperature. Complex **1** exhibits an unusual, square-planar, four-connected 2D $^{2}_{6}4$ net, which has been predicated by Wells. Interestingly, three types of water clusters, namely $(H_2O)_6$, $(H_2O)_8$, and $(H_2O)_{10}$, are observed in the hydrogen-bonded layers constructed by the BDC ligands and water molecules. The BTC anion in compound **2** is coordinated to the $Cu^{II}$ cation as tetradentate ligand to form a $(6^6)_2(4^26^48^4)_2(6^4810)$ net containing three kinds of nonequivalent points. Thermogravimetric analyses (TGA) and IR spectra for **1** and **2** are also discussed in detail. (© Wiley-VCH Verlag GmbH & Co. KGaA, 69451 Weinheim, Germany, 2006)

## Introduction

During the past few years much attention has been paid to theoretical and experimental studies of small water clusters due to their unusual properties and importance in many physical, chemical, and biological processes.[1] A detailed understanding of the numerous possible structures and stabilities of isolated water clusters in diverse surroundings can help us study the nature of water–water interactions in bulk water or ice.[2] For example, the water hexamer is the building block of ice $I_h$ and appears to be relevant to liquid water as well.[3] Several different isomers for the water hexamer, such as book, bag, ring, cage, and prism topologies, have been found from theoretical calculations.[4] Thus, the search for experimental models of these small water clusters is very important to improve our study of the structures and characteristics of liquid water and ice.

On the other hand, understanding the structure of coordination polymers is an important aspect to achieve a true advance in the synthesis and design of new materials for practical applications.[5] The analysis of network topology is a particularly useful tool for reducing multidimensional structures to simple node-and-connection reference nets. Wells has listed a large number of topologies in his classic monographs on networks,[6] and numerous fascinating archetypal structures, including diamond ($6^6$), $SiO_2$ ($6^48^2$-b), $SrSi_2$ ($10^3$-a), α-$ThSi_2$ ($10^3$-b), and PtS ($4^28^4$) have been reported[7] that are of fundamental importance in structural design and in the understanding of structure–property correlations. In this work we report two new $Cu^{II}$ coordination polymers, namely $[Cu_2(BDC)_2(L)_4(H_2O)_2]\cdot 14H_2O$ (**1**), which contains an unusual, square-planar, four-connected $^{2}_{6}4$ net and three types of water clusters, and $[Cu_{1.5}(BTC)(L)_{1.5}(H_2O)_{0.5}]\cdot 2H_2O$ (**2**), which possesses a $(6^6)_2(4^26^48^4)_2(6^4810)$ net [L = 1,1′-(1,4-butanediyl)bis(imidazole),[8] BDC = 1,4-benzenedicarboxylate, BTC = 1,3,5-benzenetricarboxylate; Scheme 1].

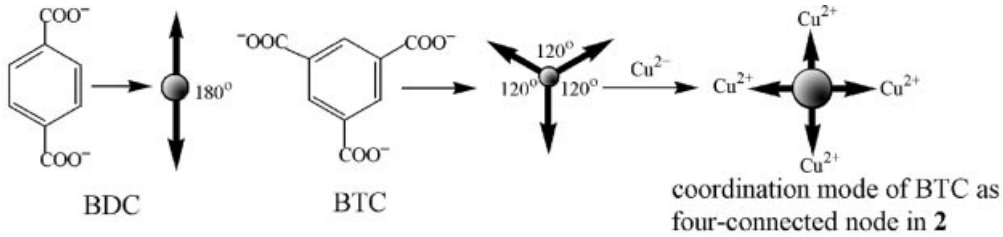


Scheme 1.

[a] Department of Chemistry, Northeast Normal University, Changchun 130024, People's Republic of China
E-mail: jianfangma@yahoo.com.cn
Fax: +86-431-568-4009
[b] Changchun Institute of Applied Chemistry, Chinese Academy of Sciences, Changchun 130022, People's Republic of China
Supporting information for this article is available on the WWW under http://www.eurjic.org or from the author.

 © 2006 Wiley-VCH Verlag GmbH & Co. KGaA, Weinheim 

## Results and Discussion

### Crystal Structures

The synthesis of complexes **1** and **2** is described in the Experimental Section. Selected bond lengths and angles for compounds **1** and **2** are listed in Table 1. Part of the structure of $[Cu_2(L)_4(H_2O)_2]\cdot(BDC)_2\cdot 14H_2O$ (**1**) is shown in Figure 1 (a). There are two crystallographically unique $Cu^{II}$ cations in the asymmetric unit. Each $Cu^{II}$ cation adopts a distorted square-pyramidal geometry by coordinating to four nitrogen atoms from four L molecules and one water molecule. Four nitrogen atoms (N1, N5, N9, and N8A for Cu1; N4, N11, N13, and N16A for Cu2) form the base of the pyramid and one water molecule (Ow1 for Cu1; Ow2 for Cu2) occupies the apical position, with respective Cu–O distances of 2.380 and 2.464 Å. The BDC anion acts as a counter-anion and structure-directing reagent, indicating that the coordination of L to the $Cu^{II}$ cation is stronger than that of the BDC anion in this case.

The structure of **1** consists of an unusual, 2D, square-planar, four-connected $^2_6$4 net, which has been predicated by Wells.[6] In this net the $Cu^{II}$ cation acts as a four-connected node and L acts as the edge of every circuit (Figure 1, b). This $^2_6$4 net is entirely different from the square-planar four-connected ($8^6$) net first reported by Tong et al. and us, which was not mentioned by Wells.[5g,8c] It is well known that when square-planar, four-connected building blocks self-assemble into extended structures, 2D (4,4) square grids are favored.[9] This observation shows that formation of a $^2_6$4 net may be attributed to the effects of the flexible L and the BDC anion. Moreover, if two of the L molecules act as each of two opposite edges, a single L molecule acts as each of the other four edges, and every $Cu^{II}$ cation can be seen as a three-connected node, the structure of **1** can be regarded as a 2D (6,3) network.

Table 1. Selected bond lengths [Å] and angles [°] for compounds **1** and **2**.

| $[Cu_2(L)_4(H_2O)_2]\cdot(BDC)_2\cdot 14H_2O$ (**1**)[a] | | | |
|---|---|---|---|
| N(1)–Cu(1) | 2.030(3) | N(4)–Cu(2) | 2.026(3) |
| N(5)–Cu(1) | 2.008(3) | N(8)–Cu(1)$^{\#1}$ | 1.991(3) |
| N(9)–Cu(1) | 2.005(3) | N(11)–Cu(2) | 1.990(3) |
| N(13)–Cu(2) | 2.004(3) | N(16)–Cu(2)$^{\#2}$ | 1.985(3) |
| OW1–Cu(1) | 2.380(3) | | |
| N(8)$^{\#1}$–Cu(1)–N(9) | 175.20(10) | N(8)$^{\#1}$–Cu(1)–N(5) | 91.32(11) |
| N(9)–Cu(1)–N(5) | 90.28(10) | N(8)$^{\#1}$–Cu(1)–N(1) | 90.19(11) |
| N(9)–Cu(1)–N(1) | 88.05(10) | N(5)–Cu(1)–N(1) | 177.40(10) |
| N(8)$^{\#1}$–Cu(1)–OW1 | 88.63(10) | N(9)–Cu(1)–OW1 | 95.89(10) |
| N(5)–Cu(1)–OW1 | 90.21(11) | N(1)–Cu(1)–OW1 | 91.95(11) |
| N(16)$^{\#2}$–Cu(2)–N(11) | 177.28(11) | N(16)$^{\#2}$–Cu(2)–N(13) | 92.13(11) |
| N(11)–Cu(2)–N(13) | 89.64(11) | N(16)$^{\#2}$–Cu(2)–N(4) | 90.95(11) |
| N(11)–Cu(2)–N(4) | 87.46(11) | N(13)–Cu(2)–N(4) | 174.22(11) |
| $[Cu_{1.5}(BTC)(L)_{1.5}(H_2O)_{0.5}]\cdot 2H_2O$ (**2**)[b] | | | |
| N(1)–Cu(2) | 1.978(4) | N(3)–Cu(1) | 1.994(4) |
| O(1)–Cu(1) | 1.952(3) | O(2)–Cu(1)$^{\#1}$ | 2.319(3) |
| O(3)–Cu(1)$^{\#2}$ | 2.014(3) | O(5)–Cu(2) | 1.937(3) |
| OW1–Cu(2) | 2.319(7) | Cu(1)–N(6)$^{\#3}$ | 1.966(4) |
| Cu(1)–O(3)$^{\#4}$ | 2.014(3) | Cu(1)–O(2)$^{\#1}$ | 2.319(3) |
| O(1)–Cu(1)–N(6)$^{\#3}$ | 94.02(17) | O(1)–Cu(1)–N(3) | 86.14(16) |
| N(6)$^{\#3}$–Cu(1)–N(3) | 173.90(18) | O(1)–Cu(1)–O(3)$^{\#4}$ | 159.37(14) |
| N(6)$^{\#3}$–Cu(1)–O(3)$^{\#4}$ | 90.98(16) | N(3)–Cu(1)–O(3)$^{\#4}$ | 86.81(15) |
| O(1)–Cu(1)–O(2)$^{\#1}$ | 107.78(14) | N(6)$^{\#3}$–Cu(1)–O(2)$^{\#1}$ | 94.97(16) |
| N(3)–Cu(1)–O(2)$^{\#1}$ | 90.78(15) | O(3)$^{\#4}$–Cu(1)–O(2)$^{\#1}$ | 91.67(13) |
| O(5)–Cu(2)–O(5)$^{\#5}$ | 178(2) | O(5)–Cu(2)–N(1) | 88.33(16) |
| O(5)$^{\#5}$–Cu(2)–N(1) | 91.87(16) | N(1)–Cu(2)–N(1)$^{\#5}$ | 168.7(3) |
| O(5)–Cu(2)–OW1 | 88.900(11) | N(1)–Cu(2)–OW1 | 95.67(14) |

[a] Symmetry codes for **1**: $^{\#1}$ $-x+1, -y, -z-1$; $^{\#2}$ $-x, -y+1, -z$. [b] Symmetry codes for **2**: $^{\#1}$ $-x+1.5, -y+1.5, -z+1$; $^{\#2}$ $x, y+1, z$; $^{\#3}$ $x, -y+1, z-0.5$; $^{\#4}$ $x, y-1, z$; $^{\#5}$ $-x+1, y, -z+1.5$.

In addition, a notable feature within complex **1** is the presence of three types of water clusters, namely $(H_2O)_6$, $(H_2O)_8$, and $(H_2O)_{10}$, in the hydrogen-bonded layer of BDC anions and water molecules (Figure 2, a). The hydrogen-bonding parameters are outlined in Table 2. Within the $(H_2O)_6$ cluster, two water molecules (OW2 and OW2A) act as two hydrogen-bond donors with OW4 and OW4A as hydrogen-bond acceptors to form a cyclic water tetramer (Figure 2, b).[10,11] Interestingly, the cyclic water tetramer is hydrogen-bonded to two neighboring free water molecules, OW6 and OW6A, yielding a water hexamer. Furthermore, the oxygen atoms O2, O2A, O5, O5A, O7, and O7A from the BDC ligands are involved in hydrogen bonds with water molecules OW4, OW4A, OW6, and OW6A to stabilize the $(H_2O)_6$ cluster. Within the $(H_2O)_{10}$ cluster, four water molecules (OW7, OW7A, OW16, and OW16A) act as both hydrogen-bond donors and acceptors (Figure 2, c). Four water molecules (OW13, OW13A, OW15, and OW15A) play the role of hydrogen-bond donors, while another two water molecules (OW14 and OW14A) only act as hydrogen-bond acceptors. Four water molecules (OW15, OW15A, OW16, and OW16A) form a cyclic water tetramer through hydrogen bonds, which is further hydrogen-bonded by water molecules OW7, OW13, OW14, OW7A, OW13A, and OW14A, leading to an $(H_2O)_{10}$ cluster. Moreover, the $(H_2O)_{10}$ cluster is stabilized by oxygen atoms O1, O1A, O3, O3A, O6A, and O6B from BDC ligands. It is of interest that the four water molecules of the cyclic water tetramer in the $(H_2O)_6$ or $(H_2O)_{10}$ clusters are completely coplanar without regard to the connectivity of the hydrogen atoms. The hydrogen-bond lengths are 2.818(4) [OW15–H(15C)···OW16], 2.879(4) [OW15–H(15D)···OW16$^{\#8}$], 2.812(4) [OW2–H(2D)···OW4], and 2.809(4) Å [OW2–H(2C)···OW4$^{\#4}$], and are slightly longer than the average hydrogen-bond length of liquid water tetramer (2.718 Å).[4a,12] In the $(H_2O)_8$ cluster, the lattice water molecules (OW8A, OW8B, OW5, and OW5A) and the coordinated water molecules (OW1 and OW1A) of the $[Cu_2(L)_4(H_2O)_2]^{4+}$ cation are associated by hydrogen bonds to form a cyclic centrosymmetric water hexamer (Figure 2, d). The average OW···OW distance is about 2.80 Å, which is slightly longer than the corresponding value in ice $I_h$ (2.759 Å) and the calculated value of 2.718 Å for cyclic water hexamer.[3] However, they are shorter than those observed in liquid water (2.854 Å).[3] The cyclic water hexamer is hydrogen-bonded to two neighboring water molecules (OW10A and OW10B), yielding a $(H_2O)_8$ cluster. It is worthwhile to note that two water molecules of the $(H_2O)_8$ cluster bind to the $Cu^{II}$ cations. Meanwhile, four water molecules are involved in hydrogen bonds with the oxygen atoms from the carboxylate groups of the

 © 2006 Wiley-VCH Verlag GmbH & Co. KGaA, Weinheim 

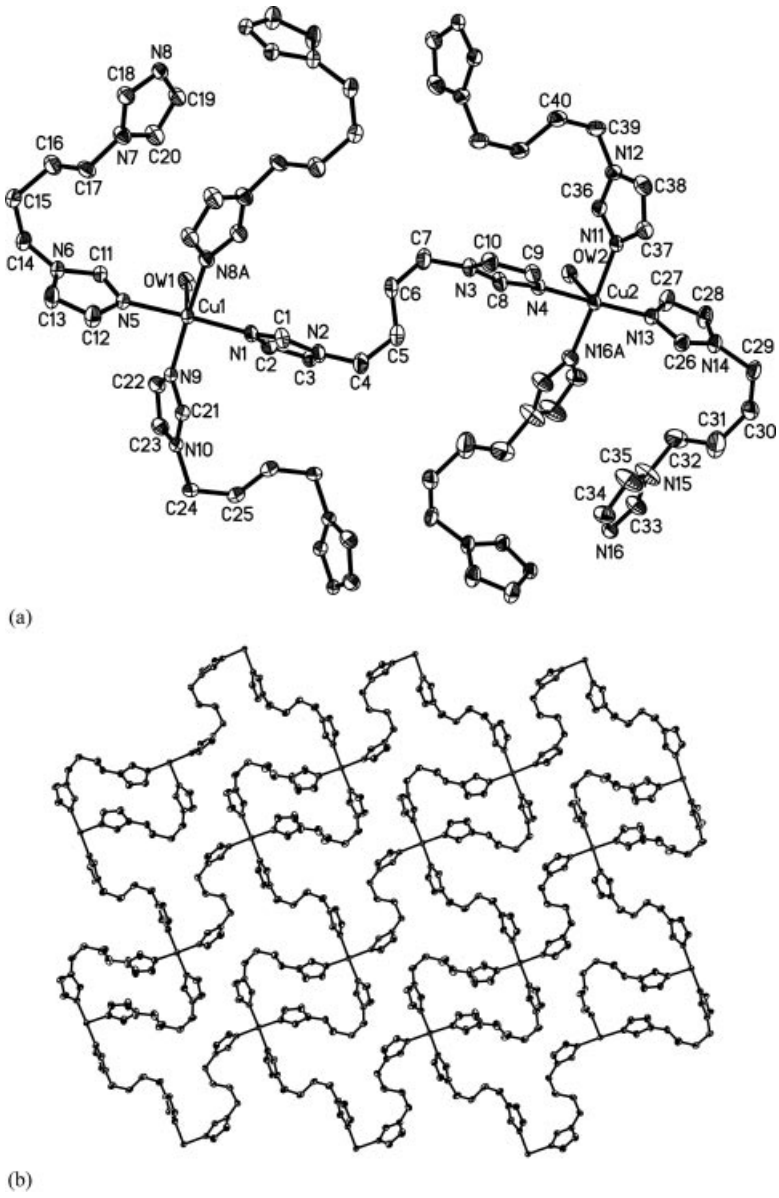


Figure 1. (a) An ORTEP view of complex **1** showing 30% thermal probability ellipsoids. (b) The square-planar, four-connected 2D $^{2}_{6}4$ network.

BDC ligands. This indicates that the $(H_2O)_8$ cluster is stabilized not only by hydrogen bonds but also by coordination interactions. The water molecule, the organic BDC anion, and the $Cu^{II}$ cation play a crucial role in the formation of the water clusters. Furthermore, the square-planar, four-connected $^{2}_{6}4$ net and the hydrogen-bonded layer are further connected through the coordinating water molecules to form 3D supramolecular structures. Figure 3 (a) displays the packing structure of compound **1**. The H-bonding layers act as a "glue" to reinforce the coordination polymeric $^{2}_{6}4$ sheet, forming an overall 3D structure. Each H-bonding layer links two polymeric sheets, and each polymeric sheet is also attached to two H-bonding layers through OW1 and OW2 molecules (Figure 3, b). Here, both water–sheet and water–water interactions are important for the stability of the overall structure.

It should be pointed out that the angles between two neighboring carboxylate groups of BDC and BTC anions are 180° and 120°, respectively, which suggests that the BTC anion may be superior to the BDC anion when it comes to meeting the configurations of $[Cu(L)_n]^{2+}$ ($n$ = 1 or 2) cations, and to coordinate to the $Cu^{II}$ cation (Scheme 1). Thus, during the construction of **2** the multi-carboxylate ligand BTC was chosen as organic anion.

The structure of **2** contains two crystallographically unique $Cu^{II}$ cations, two unique L molecules, and one unique BTC anion. As shown in Figure 4 (a), the Cu1 cation is five-coordinate in a distorted square-pyramidal ge-

 © 2006 Wiley-VCH Verlag GmbH & Co. KGaA, Weinheim 

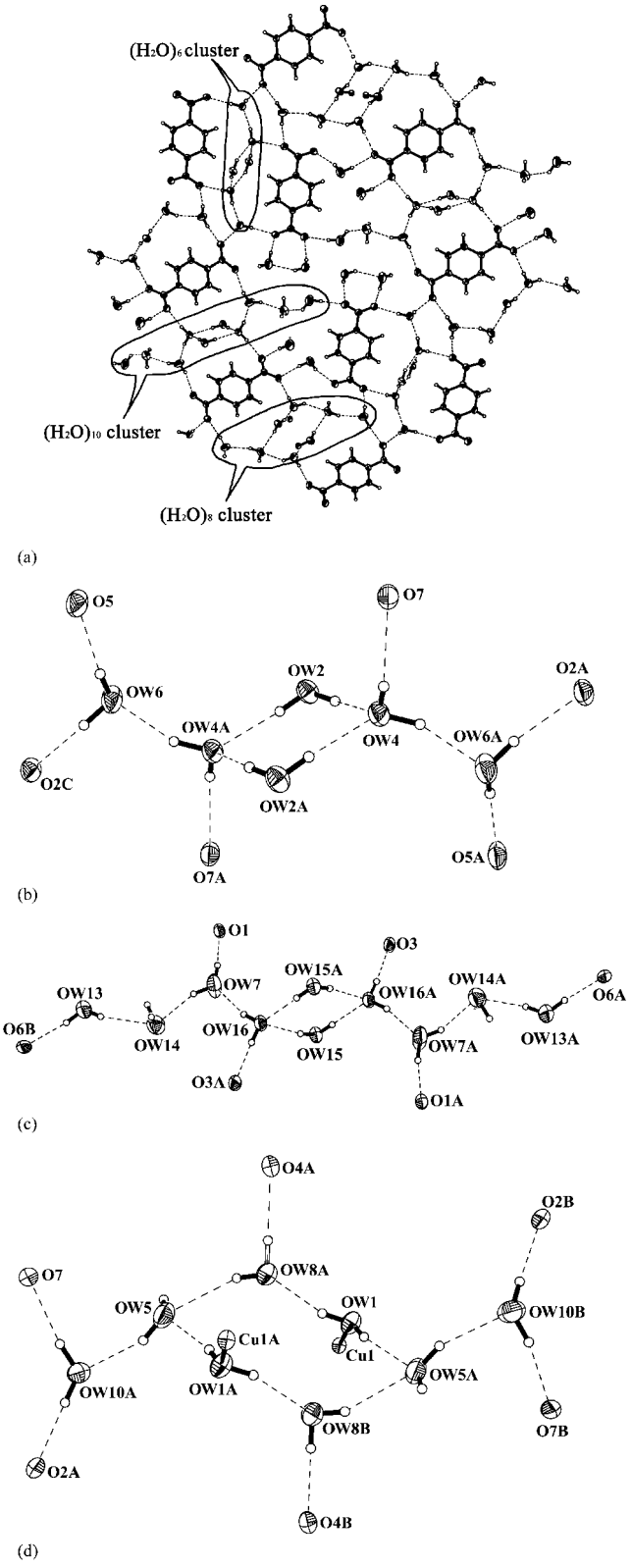


Figure 2. (a) The hydrogen-bonded layer of BDC and water molecules. (b) An ORTEP view showing the $(H_2O)_6$ cluster and its coordination environment. (c) An ORTEP view showing the $(H_2O)_{10}$ cluster and its coordination environment. (d) An ORTEP view showing the $(H_2O)_8$ cluster and its coordination environment.

ometry by coordinating to two nitrogen atoms (N3 and N6A) from two L molecules and three oxygen atoms (O1, O2A, and O3A) from three BTC molecules. The Cu2 center also has a distorted square-pyramidal coordination sphere defined by two carboxylate oxygen atoms (O5 and O5A), one water molecule (OW1), and two nitrogen atoms (N1 and N1A) from two L molecules. The BTC anions bridge the $Cu^{II}$ cations to form 2D networks, which are further connected through the L ligands to form a 3D framework structure, see Figure 4 (b) and Figure 4 (c). In addition, there are some hydrogen-bonded water molecules in the framework of **2**. These water molecules are stabilized by both hydrogen bonds and coordination interactions (OW1 coordinates to Cu2). The hydrogen-bonded water molecules not only fill the voids in the supramolecular framework but also contribute to the total lattice energy. The framework host sufficiently affects the hydrogen bonds of the water molecules and the water molecules maybe also influence the arrangement of the framework host.

If, for reasons of classifying the net, we define the BTC anion as a single point, then it can be considered as a four-connected node (Scheme 1). Thus, there are three kinds of nodes in the structure of **2**: a five-connected node for Cu1, a four-connected node for Cu2, and a four-connected node for the BTC anion. There are some unique four-, six-, eight-, and ten-membered circuits through the nodes in **2** (see Figures S1–S13 in the Supporting Information). For the four-connected BTC anion, each of six sets of links is contained in six-membered circuits (see Figures S1 and S2). Thus, the four-connected BTC anion has the Schäfli symbol $6^6$ (Figure 5, a). For the five-connected Cu1 node, ten sets of links are contained in four six-membered circuits (Figures S3–S5), two four-membered circuits (Figure S6), and four eight-membered circuits (Figures S7–10), therefore this node has the Schäfli symbol $(4^26^48^4)$ (Figure 5, b). For the four-connected Cu2 node, four sets of links are contained in a six-membered circuit (Figure S11), while the other two sets of links are contained in an eight-membered circuit (Figure S12) and a ten-membered circuit (Figure S13), respectively, therefore the four-connected Cu2 node has the Schäfli symbol $(6^4810)$ (Figure 5, c). The molar ratio of these three kinds of nodes is 2:2:1 (BTC/Cu1/Cu2), thus the structure of **2** can be symbolized as a $(6^6)_2(4^26^48^4)_2(6^4810)$ net with three kinds of nonequivalent points (Figure 5, d).[6] The topological analysis of this net was performed with OLEX.[13] The present case indicates that topological analysis is a useful tool for the description and comparison of natural and artificial networks in crystal engineering.[14]

From the above descriptions, the choice of anion is clearly critical in determining the molecular structures of the final compounds. In this work, both planar two-carboxylate anion and three-carboxylate anion were chosen to study the variation of the structures for **1** and **2**. The topological difference between **1** and **2** should therefore result from the structural features of the BDC and BTC anions. The BDC anion in **1** is not coordinated to the $Cu^{II}$ cation but acts as a counter-anion and template reagent, whereas the BTC anion in **2** meets the configuration of $[Cu(L)_n]^{2+}$

 © 2006 Wiley-VCH Verlag GmbH & Co. KGaA, Weinheim 

Table 2. Hydrogen-bonding parameters for **1**.[a]

| D–H···A [Å] | *d*(D–H) [Å] | *d*(H···A) [Å] | *d*(D···A) [Å] | <(D···H···A) [°] |
|---|---|---|---|---|
| OW1–H(1D)···OW5$^{\#3}$ | 0.88(2) | 1.93(3) | 2.778(4) | 161(5) |
| OW1–H(1C)···OW8$^{\#2}$ | 0.80(4) | 1.98(4) | 2.763(4) | 166(4) |
| OW2–H(2D)···OW4 | 0.879(18) | 1.97(2) | 2.812(4) | 159(4) |
| OW2–H(2C)···OW4$^{\#4}$ | 0.87(2) | 1.94(2) | 2.809(4) | 173(5) |
| OW3–H(3C)···O(4)$^{\#2}$ | 0.928(17) | 1.889(19) | 2.805(4) | 169(3) |
| OW3–H(3D)···O(8) | 0.868(19) | 1.99(2) | 2.850(4) | 168(4) |
| OW4–H(4D)···O(7) | 0.88(2) | 1.89(2) | 2.740(4) | 163(4) |
| OW4–H(4C)···OW6$^{\#4}$ | 0.84(4) | 1.90(4) | 2.719(4) | 165(4) |
| OW5–H(5D)···OW10$^{\#5}$ | 0.896(18) | 2.01(3) | 2.827(4) | 151(3) |
| OW6–H(6D)···O(2)$^{\#1}$ | 0.901(18) | 1.91(2) | 2.750(4) | 154(3) |
| OW6–H(6C)···O(5) | 0.871(18) | 1.91(2) | 2.780(4) | 172(3) |
| OW7–H(7C)···O(1) | 0.888(18) | 1.95(2) | 2.816(4) | 165(4) |
| OW7–H(7D)···OW14 | 0.842(18) | 2.208(16) | 2.763(5) | 123(2) |
| OW8–H(8C)···O(4) | 0.875(19) | 1.90(2) | 2.767(4) | 174(5) |
| OW8–H(8D)···OW5$^{\#2}$ | 0.90(4) | 2.03(2) | 2.849(4) | 151(4) |
| OW9–H(9C)···O(3) | 0.825(18) | 1.99(3) | 2.702(4) | 144(3) |
| OW10–H(10D)···O(2) | 0.90(4) | 1.88(4) | 2.779(4) | 170(3) |
| OW10–H(10C)···O(7)$^{\#7}$ | 0.896(18) | 1.98(2) | 2.851(4) | 164(3) |
| OW11–H(11D)···O(5)$^{\#1}$ | 0.92(4) | 1.78(2) | 2.693(4) | 176(5) |
| OW12–H(12C)···O(6)$^{\#1}$ | 0.83(5) | 2.01(5) | 2.812(4) | 163(5) |
| OW12–H(12D)···OW11 | 0.90(2) | 2.17(5) | 2.837(4) | 131(5) |
| OW13–H(13D)···O(6)$^{\#8}$ | 0.866(19) | 1.88(3) | 2.713(4) | 161(6) |
| OW13–H(13C)···OW14 | 0.999(18) | 2.134(15) | 2.791(5) | 122(4) |
| OW15–H(15C)···OW16 | 0.874(19) | 1.95(2) | 2.818(4) | 174(4) |
| OW15–H(15D)···OW16$^{\#6}$ | 0.858(18) | 2.04(2) | 2.879(4) | 167(3) |
| OW16–H(16D)···O(3) | 0.89(4) | 1.89(2) | 2.773(4) | 175(4) |
| OW16–H(16C)···OW7$^{\#6}$ | 0.89(4) | 1.82(2) | 2.672(4) | 163(4) |

[a] Symmetry transformations used to generate equivalent atoms: $^{\#1}$ $-x+1, -y, -z$; $^{\#2}$ $-x+1, -y, -z-1$; $^{\#3}$ $-x, -y, -z-1$; $^{\#4}$ $-x, -y, -z$; $^{\#5}$ $x-1, y, z$; $^{\#6}$ $-x+1, -y+1, -z-1$; $^{\#7}$ $x+1, y, z$; $^{\#8}$ $x, y+1, z$.

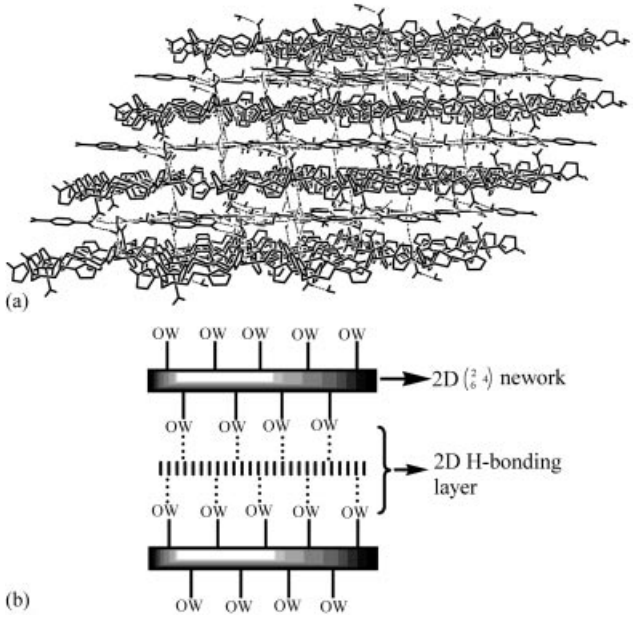


Figure 3. (a) The 3D H-bonding structure of **1**. (b) A schematic representation of the 3D H-bonding structure.

($n$ = 1 or 2) cations and coordinates to the $Cu^{II}$ cation as a four-coordinate ligand. Although different Cu/L ratios (1:1, 1:2, 1:3, and 1:4) were used in the preparations, only **1** and **2** were isolated as the products. Thus, the formation of these different frameworks is due to the effects of different organic anions.

## IR Spectra and TGA

The solid-state IR spectra of **1** and **2** in the region 4000–400 $cm^{-1}$ exhibit characteristic bands for BDC, BTC, and L ligands (see Figure S14 in the Supporting Information). The IR spectrum of **1** shows a broad band centered around 3427 $cm^{-1}$ attributable to the O–H stretching frequency of the water cluster. The IR spectrum of ice shows the O–H stretch at 3220 $cm^{-1}$, while this stretching vibration in liquid water appears at 3490 and 3280 $cm^{-1}$.[15] This indicates that the water cluster in **1** has an O–H stretching vibration similar to that of liquid water, and the slight difference is attributable to the environment that the clusters are in.[16] The peaks around 1600, 1560, 1400, and 1350 $cm^{-1}$ for **1** and **2** can be attributed to the asymmetric and symmetric vibrations of the carboxylate groups.[17]

In order to characterize the compounds **1** and **2** more fully in terms of thermal stability, we studied them by TGA. Compounds **1** and **2** were heated from 35 to 780 °C under $N_2$. As expected, the TGA curves of compounds **1** and **2** exhibit three similar weight-loss stages. The first weight loss, corresponding to the water molecules, is observed over the wide temperature range 35–90 °C (observed 18.6%, calculated 19.1%) for **1** and 35–93 °C (observed 6.7%, calculated 7.1%) for **2**. The second weight loss is 52.4% (calculated 50.6%) for **1** in the range 238–350 °C and 46.4% (calculated 45.1%) for **2** in the range 239–344 °C, and is assigned to the release of L molecules. Drastic weight losses corre-

 © 2006 Wiley-VCH Verlag GmbH & Co. KGaA, Weinheim 

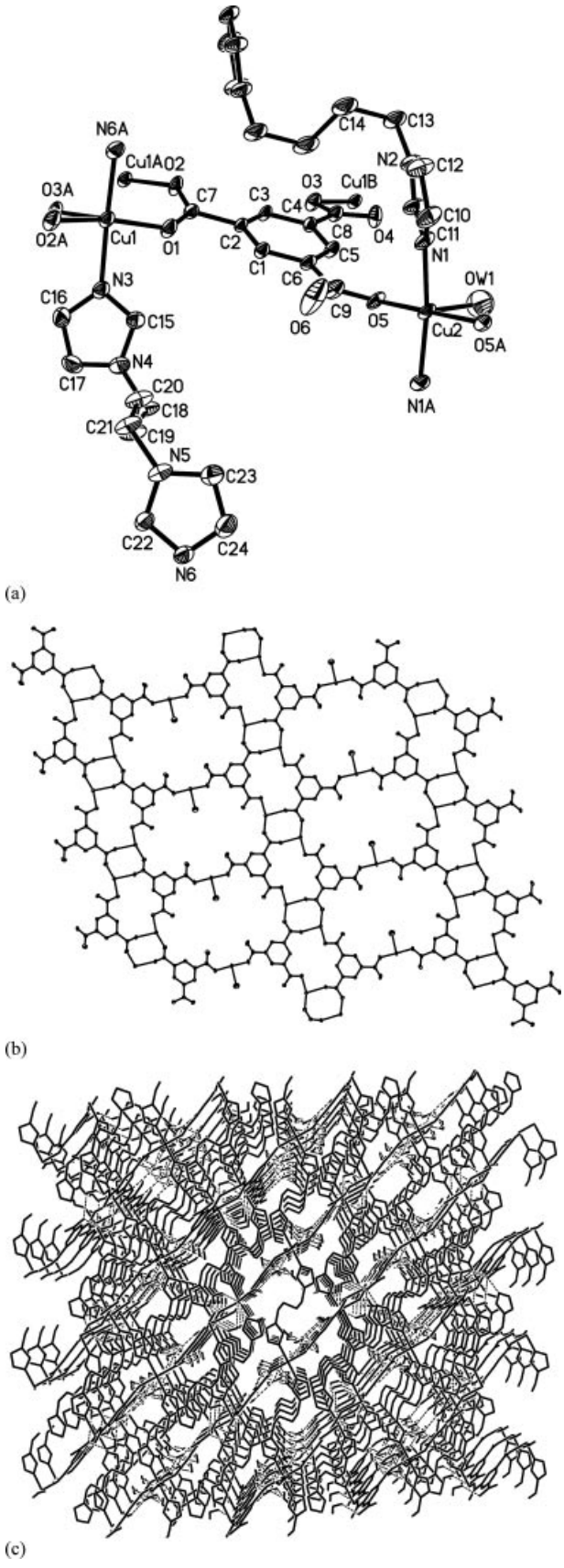


Figure 4. (a) ORTEP view of **2** showing 30% thermal probability ellipsoids. (b) The 2D layered structure constructed by BTC and $Cu^{II}$ cations. (c) The packing diagram of **2**.

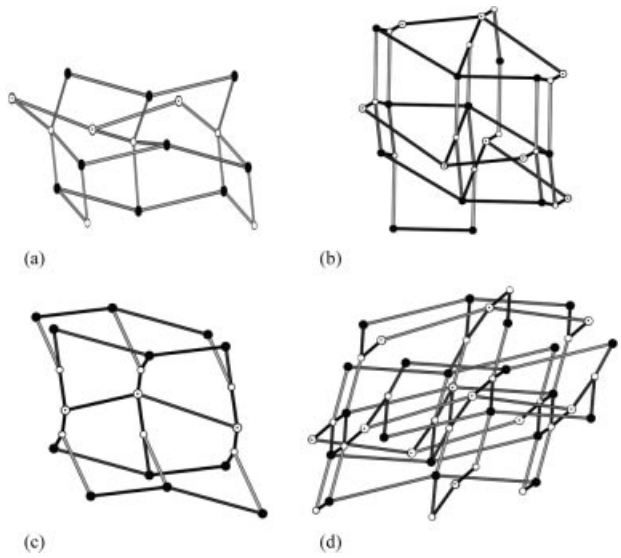


Figure 5. (a) Schematic representation of the circuits through the four-connected BTC node. (b) Schematic representation of the circuits through the five-connected Cu1 node. (c) Schematic representation of the circuits through the four-connected Cu2 node. (d) The $(6^6)_2(4^26^48^4)_2(6^4810)$ net with three kinds of nonequivalent points. (Cu2 = ⊙, BTC = ○, Cu1 = ●).

sponding to the removal of BDC and BTC were observed from 420 to 528 °C for **1** and from 423 to 524 °C for **2**, respectively.

## Conclusions

Two new $Cu^{II}$ coordination polymers with different topologies have been obtained due to the effects of different organic anions on the final frameworks' formation. When the BDC anion was chosen as the dicarboxylate anion, a coordination polymer **1** with an unusual, square-planar, four-connected $^2_6$4 net and three types of water clusters was obtained. In **2**, the BTC anion coordinates to the $Cu^{II}$ cation as a tetradentate ligand to form a $(6^6)_2(4^26^48^4)_2(6^4810)$ net with three kinds of nonequivalent points.

## Experimental Section

**Materials and Methods:** All reagents and solvents for syntheses were purchased from commercial sources and used as received. A Perkin–Elmer 240 elemental analyzer was used to collect microanalytical data, and the FT-IR spectrum was recorded from KBr pellets in the range 4000–400 $cm^{-1}$ on a Mattson Alpha-Centauri spectrometer. TGA was performed with a Perkin–Elmer TG-7 analyzer under nitrogen.

**Synthesis of 1,1′-(1,4-Butanediyl)bis(imidazole) (L):** A mixture of imidazole (3.4 g, 50 mmol) and NaOH (2.0 g, 50 mmol) in DMSO (10 mL) was stirred at 60 °C for 1 h, and then 1,4-dichlorobutane (3.2 g, 25 mmol) was added. The mixture was cooled to room temperature after stirring at 60 °C for 2 h and then poured into 200 mL of water. A white solid formed immediately, which was isolated by filtration in 86% yield (4.1 g) after drying in air. $C_{10}H_{14}N_4$ (190.25): calcd. C 63.16, H 7.37, N 29.47; found C 63.11, H 7.42, N 29.31.

 © 2006 Wiley-VCH Verlag GmbH & Co. KGaA, Weinheim 

**Synthesis of $[Cu_2(L)_4(H_2O)_2]\cdot(BDC)_2\cdot 14H_2O$ (1):** A mixture of $CuCl_2\cdot 2H_2O$ (0.171 g, 1 mmol), NaOH (0.080 g, 2 mmol), and $H_2BDC$ (0.166 g, 1 mmol) in water was stirred for 10 min at 60 °C, then 1,1′-(1,4-butanediyl)bis(imidazole) (L; 0.190 g, 1 mmol) was added to the mixture. After stirring for 30 min, the blue precipitate was collected and dissolved in a minimum amount of ammonia (14 M). Suitable blue single crystals of **1** were obtained by slow evaporation of this solution at ambient temperature in 73% yield (109.8 mg). $C_{56}H_{96}Cu_2N_{16}O_{24}$ (1504.6): calcd. C 44.66, H 6.38, N 14.89; found C 44.89, H 6.60, N 14.49.

**Synthesis of $[Cu_{1.5}(BTC)(L)_{1.5}(H_2O)_{0.5}]\cdot 2H_2O$ (2):** Compound **2** was prepared in the same way as for **1**, but with 1,3,5-benzenetricarboxylic acid ($H_3BTC$), in 53% yield (33.5 mg). $C_{24}H_{29}Cu_{1.5}N_6O_{8.5}$ (632.84): calcd. C 45.51, H 4.58, N 13.27; found C 45.22, H 4.51, N 13.79.

**X-ray Crystallography:** Single-crystal X-ray diffraction data for complexes **1** and **2** were recorded with a Rigaku RAXIS-RAPID image plate diffractometer and a Bruker-AXS Smart CCD diffractometer, respectively, using the ω-scan technique with Mo-$K_\alpha$ radiation ($\lambda$ = 0.71073 Å). All the structures were solved by direct methods with SHELXS-97[18] and refined by full-matrix least-squares techniques using the SHELXL-97 program.[19] Non-hydrogen atoms were refined with anisotropic temperature parameters the and the hydrogen atoms of the ligands were refined as rigid groups. The hydrogen atoms of the water molecules for **1** and **2** were located from the difference Fourier maps. Further details of the structural analysis are summarized in Table 3.

Table 3. Summary of X-ray crystallographic data for compounds **1** and **2**.

| Compound | **1** | **2** |
|---|---|---|
| Formula | $C_{56}H_{96}Cu_2N_{16}O_{24}$ | $C_{24}H_{29}Cu_{1.5}N_6O_{8.5}$ |
| Mol. mass | 1504.57 | 632.84 |
| Space group | $P\bar{1}$ | $C2/c$ |
| $a$ [Å] | 13.049(3) | 25.860(6) |
| $b$ [Å] | 13.334(3) | 10.185(2) |
| $c$ [Å] | 21.562(4) | 22.790(5) |
| $\alpha$ [°] | 91.46(3) | 90 |
| $\beta$ [°] | 101.60(3) | 97.671(7) |
| $\gamma$ [°] | 99.41(3) | 90 |
| $V$ [Å$^3$] | 3619.2(13) | 5949(2) |
| $Z$, $d_{calcd.}$ [g cm$^{-3}$] | 2, 1.381 | 8, 1.413 |
| $\mu$ (Mo-$K_\alpha$ [mm$^{-1}$]) | 0.672 | 1.137 |
| $F$(000) | 1588 | 2612 |
| Reflns. collected / unique | 29446 / 14091 | 18017 / 7010 |
| Reflns. obsd. [$I > 2\sigma(I)$] | 8141 | 3181 |
| GOF on $F^2$ | 0.940 | 0.885 |
| $R1$,[a] $wR2$[b] (obsd.) | 0.0462, 0.1260 | 0.0633, 0.1237 |
| ($\Delta/\sigma$) max., mean | 0.001, 0.000 | 0.001, 0.000 |
| Max., min. peaks [e Å$^{-3}$] | 0.541, –0.607 | 0.858, –0.324 |

[a] $R1 = \Sigma||F_o| - |F_c||/\Sigma|F_o|$. [b] $wR2 = [\Sigma w(|F_o|2 - |F_c|2)|/\Sigma|w(F_o)^2|^{1/2}$, where $w = 1/[\sigma^2(F_o^2) + (aP)^2 + bP]$ and $P = (F_o^2 + 2F_c^2)/3$.

CCDC-216567 (for **1**) and -281108 (for **2**) and contain the supplementary crystallographic data for this paper. These data can be obtained free of charge from The Cambridge Crystallographic Data Centre via www.ccdc.cam.ac.uk/data_request/cif.

**Supporting Information** (see footnote on the first page of this article): Figures of circuits around the nodes for **2** (Figures S1–S13). The IR spectra of compounds **1** and **2** (Figure S14).

## Acknowledgments

We thank the National Natural Science Foundation of China (no. 20471014), the Fok Ying Tung Education Foundation, and the Natural Science Foundation of Jilin province (China) for financial support.

[1] a) G. A. Jeffrey, *An Introduction to Hydrogen Bonding*, Oxford University Press, Oxford, U.K., **1997**, pp. 160–180; b) A. L. Gillon, N. Feeder, R. J. Davey, R. Storey, *Cryst. Growth Des.* **2003**, *3*, 663–673; c) R. Ludwig, *Angew. Chem. Int. Ed.* **2001**, *40*, 1808–1827.

[2] a) B.-Q. Ma, H.-L. Sun, S. Gao, *Angew. Chem. Int. Ed.* **2004**, *43*, 1374–1376; b) S. W. Benson, E. D. Siebert, *J. Am. Chem. Soc.* **1992**, *114*, 4269–4276; c) K. A. Udachin, J. A. Ripmeester, *Nature* **1999**, *397*, 420–423; d) B.-H. Ye, B.-B. Ding, Y.-Q. Weng, X.-M. Chen, *Inorg. Chem.* **2004**, *43*, 6866–6868; e) N. S. Oxtoby, A. J. Blake, N. R. Champness, C. Wilson, *Chem. Eur. J.* **2005**, *11*, 1–13.

[3] D. Eisenberg, W. Kauzmann, *The Structure and Properties of Water*, Oxford University Press, Oxford, U.K., **1969**.

[4] a) J. D. Cruzan, L. B. Braly, K. Liu, M. G. Brown, J. G. Loeser, R. J. Saykally, *Science* **1996**, *271*, 59–62; b) B. Zhao, P. Cheng, X. Chen, C. Cheng, W. Shi, D. Liao, S. Yan, Z. Jiang, *J. Am. Chem. Soc.* **2004**, *126*, 3012–3013; c) S. K. Ghosh, P. K. Bharadwaj, *Inorg. Chem.* **2003**, *42*, 8250; d) S. K. Ghosh, P. K. Bharadwaj, *Angew. Chem. Int. Ed.* **2004**, *43*, 3577–3580.

[5] a) S. Leininger, B. Olenyuk, P. J. Stang, *Chem. Rev.* **2000**, *100*, 853–908; b) S. R. Batten, R. Robson, *Angew. Chem. Int. Ed.* **1998**, *37*, 1460–1494; c) B. Moulton, M. J. Zaworotko, *Chem. Rev.* **2001**, *101*, 1629–1658; d) S.-I. Noro, R. Kitaura, M. Kondo, S. Kitagawa, T. Ishii, H. Matsuzaka, M. Yamashita, *J. Am. Chem. Soc.* **2002**, *124*, 2568–2583; e) L. Carlucci, G. Ciani, D. M. Proserpio, *Coord. Chem. Rev.* **2003**, *246*, 247–289; f) D.-L. Long, R. J. Hill, A. J. Blake, N. R. Champness, P. Hubberstey, D. M. Proserpio, C. Wilson, M. Schröder, *Angew. Chem. Int. Ed.* **2004**, *43*, 1851–1854; g) M.-L. Tong, X.-M. Chen, S. R. Batten, *J. Am. Chem. Soc.* **2003**, *125*, 16170–16171; h) L. Carlucci, G. Ciani, D. M. Proserpio, *Chem. Commun.* **2004**, 380–381.

[6] a) A. F. Wells, *Three-Dimensional Nets and Polyhedra*, Wiley-Interscience, New York, **1977**; b) A. F. Wells, *Further Studies of Three-Dimensional Nets*; ACA Monograph 8, American Crystallographic Association, **1979**.

[7] a) P. J. Hagrman, D. Hagrman, J. Zubieta, *Angew. Chem. Int. Ed.* **1999**, *38*, 2638–2684; b) Z.-R. Qu, H. Zhao, Y.-P. Wang, X.-S. Wang, Q. Ye, Y.-H. Li, R.-G. Xiong, B. F. Abrahams, Z.-G. Liu, Z.-L. Xue, X.-Z. You, *Chem. Eur. J.* **2004**, *10*, 53–60; c) T. M. Reineke, M. Eddaoudi, M. O'Keeffe, O. M. Yaghi, *Angew. Chem. Int. Ed.* **1999**, *38*, 2590–2594.

[8] a) J.-F. Ma, J.-F. Liu, Y. Xing, H.-Q. Jia, Y.-H. Lin, *J. Chem. Soc., Dalton Trans.* **2000**, 2403–2407; b) J.-F. Ma, J.-F. Liu, Y.-C. Liu, Y. Xing, H.-Q. Jia, Y.-H. Lin, *New J. Chem.* **2000**, *24*, 759–763; c) J.-F. Ma, J. Yang, G.-L. Zheng, L. Li, J.-F. Liu, *Inorg. Chem.* **2003**, *42*, 7531–7534; d) J. Yang, J.-F. Ma, Y.-Y. Liu, S.-L. Li, G.-L. Zheng, *Eur. J. Inorg. Chem.* **2005**, 2174–2180.

[9] a) X.-H. Bu, M.-L. Tong, H. C. Chang, S. Kitagawa, S. R. Batten, *Angew. Chem. Int. Ed.* **2004**, *43*, 192–195; b) J.-P. Zhang, S.-L. Zheng, X.-C. Huang, X.-M. Chen, *Angew. Chem. Int. Ed.* **2004**, *43*, 206–209.

[10] S. Supriya, S. K. Das, *New J. Chem.* **2003**, *27*, 1568–1574.

[11] J. Tao, Z.-J. Ma, R.-B. Huang, L.-S. Zheng, *Inorg. Chem.* **2004**, *43*, 6133–6135.

[12] A. Geiger, P. Mausbach, J. Schnitker, *Water and Aqueous Solutions*, Hilger, Bristol, **1986**, p. 15.

[13] O. V. Dolomanov, A. J. Blake, N. R. Champness, M. Schröder, *J. Appl. Crystallogr.* **2003**, *36*, 1283–1284.

 © 2006 Wiley-VCH Verlag GmbH & Co. KGaA, Weinheim 

[14] C.-Y. Su, M. D. Smith, A. M. Goforth, H.-C. zur Loye, *Inorg. Chem.* **2004**, *43*, 6881–6883.
[15] R. Custelcean, C. Afloroaei, M. Vlassa, M. Polverejan, *Angew. Chem. Int. Ed.* **2000**, *39*, 3094–3096.
[16] a) S. Neogi, P. K. Bharadwaj, *Inorg. Chem.* **2005**, *44*, 816–818; b) S. K. Ghosh, P. K. Bharadwaj, *Inorg. Chem.* **2004**, *43*, 6887–6889.
[17] J.-F. Ma, J. Yang, S.-L. Li, S.-Y. Song, H.-J. Zhang, H.-S. Wang, K.-Y. Yang, *Cryst. Growth Des.* **2005**, *5*, 807–812.
[18] G. M. Sheldrick, *SHELXS-97, Programs for X-ray Crystal Structure Solution*; University of Göttingen, Germany, **1997**.
[19] G. M. Sheldrick, *SHELXL-97, Programs for X-ray Crystal Structure Refinement*; University of Göttingen, Germany, **1997**.
Received: August 18, 2005
Published Online: January 27, 2006

 © 2006 Wiley-VCH Verlag GmbH & Co. KGaA, Weinheim 

DOI: 10.1002/ejic.200500740

# Synthesis, Structures, and Luminescent Properties of Aluminum Complexes with Chelating Anilido-Imine Ligands

Xiaoming Liu,[a] Hong Xia,[a] Wei Gao,[a] Ling Ye,[a] Ying Mu,*[a] Qing Su,[a] and Yi Ren[a]

**Keywords:** Aluminum / N ligands / Luminescence

The syntheses of a number of four-coordinate aluminum complexes, *ortho*-$C_6H_4(NAr')(CH{=}NAr'')AlCl_2$ [Ar′ = Ar′′ = 2,6-*i*$Pr_2C_6H_3$ (**2a**); Ar′ = 2,6-*i*$Pr_2C_6H_3$, Ar′′ = 2,6-$Me_2C_6H_3$ (**2b**); Ar′ = Ar′′ = 2,6-$Me_2C_6H_3$ (**2c**); Ar′ = *p*-$MeC_6H_4$, Ar′′ = 2,6-*i*$Pr_2C_6H_3$ (**2d**)], are described. Complexes **2a**–**2d** were synthesized from the reaction of $AlCl_3$ with lithium salt of the corresponding ligand at room temperature. All complexes were characterized by $^1H$ and $^{13}C$ NMR spectroscopy and molecular structures of complexes **2a**, **2b**, and **2d** were determined by X-ray crystallography. Luminescent properties of complexes **2a**–**2d** in both solution and the solid state were studied.
(© Wiley-VCH Verlag GmbH & Co. KGaA, 69451 Weinheim, Germany, 2006)

## Introduction

Luminescent metal complexes have attracted increasing attention because of their potential application in areas of chemistry, medicine, and material science.[1] Many luminescent complexes of main group and transition metals, such as $Al^{III}$,[2] $Zn^{II}$,[3] $Pt^{II}$,[4] $Ir^{III}$,[5] and $Re^{I}$,[6] have been designed and synthesized in recent years. Particularly, chelated aluminum complexes have attracted much attention because of their low cost, and good luminescent and electron-transporting properties. As the well-known tris(8-hydroxyquinolinyl)aluminum ($Alq_3$) was found to be a good emitter, and a highly efficient electron-transporting material and host material in organic electroluminescence devices,[7–9] a large number of its derivatives with modified 8-hydroxyquinoline ligands have been investigated.[1b,2,10] Aluminum complexes with nitrogen-containing ligands have also been reported,[11] while the luminescent properties of coordinative unsaturated aluminum complexes have not been extensively explored, probably because of their instability to air and moisture.[12,13] We have recently focused our attention on the synthesis of aluminum complexes of this type. As a continuation of our studies on the luminescent alkylaluminum complexes with chelating anilido-imine ligands (Scheme 1 A),[14d] herein we report the syntheses, characterization, and fluorescent properties of a number of aluminum dichloride complexes with anilido-imine ligands, *ortho*-$C_6H_4(NAr')(CH{=}NAr'')AlCl_2$ [Ar′ = Ar′′ = 2,6-*i*$Pr_2C_6H_3$ (**2a**); Ar′ = 2,6-*i*$Pr_2C_6H_3$, Ar′′ = 2,6-$Me_2C_6H_3$ (**2b**); Ar′ = Ar′′ = 2,6-$Me_2C_6H_3$ (**2c**); Ar′ = *p*-$MeC_6H_4$, Ar′′ = 2,6-*i*$Pr_2C_6H_3$ (**2d**)].

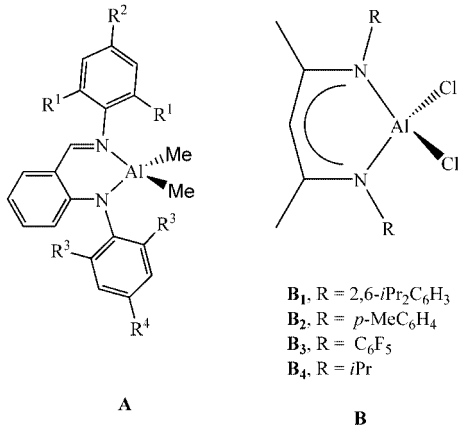


Scheme 1.

## Results and Discussion

### Ligand Synthesis

Free ligands, *ortho*-$C_6H_4(NHAr')(CH{=}NAr'')$ [Ar′ = Ar′′ = 2,6-*i*$Pr_2C_6H_3$ (**1a**); Ar′ = 2,6-*i*$Pr_2C_6H_3$, Ar′′ = 2,6-$Me_2C_6H_3$ (**1b**); Ar′ = Ar′′ = 2,6-$Me_2C_6H_3$ (**1c**); Ar′ = *p*-$MeC_6H_4$, Ar′′ = 2,6-*i*$Pr_2C_6H_3$ (**1d**)], were synthesized by a literature procedure.[15] Of these free ligands, compounds **1a**, **1c**, and **1d** are known, while **1b** is a new compound. The new ligand **1b** was prepared by the reaction of *ortho*-$C_6H_4F(CH{=}NC_6H_3Me_2\text{-}2,6)$ with LiN(H)Ar (Ar = 2,6-*i*$Pr_2C_6H_3$) (Scheme 2) in good yield (72% isolated yields). The reaction was carried out in THF and the crude product

[a] Key Laboratory for Supramolecular Structure and Materials of Ministry of Education, School of Chemistry, Jilin University, 10 Qianwei Road, Changchun 130012, People's Republic of China
Fax: +86-431-5193421
E-mail: ymu@mail.jlu.edu.cn
Supporting information for this article is available on the WWW under http://www.eurjic.org or from the author.

 © 2006 Wiley-VCH Verlag GmbH & Co. KGaA, Weinheim 

was purified by crystallization from methanol. Compound **1b** was characterized by $^1$H and $^{13}$C NMR spectroscopy along with elemental analysis. The $^1$H NMR spectrum of **1b** exhibits resonance at $\delta$ = 8.39 ppm for the imino CH proton, with the corresponding $^{13}$C NMR resonance at $\delta$ = 166.25 ppm. The NH resonance appears at characteristically low field ($\delta$ = 10.5 ppm). The infrared absorption band of the imine C=N stretch occurs in the region 1617 cm$^{-1}$. Those data are similar to the corresponding values of **1a**, **1c**, and **1d**.[14d]

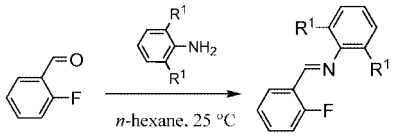


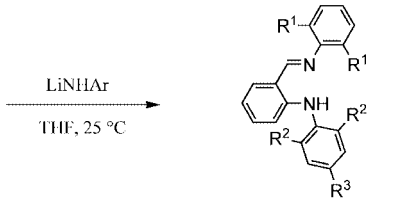


**1a** $R^1 = R^2 = i$Pr, $R^3$ = H
**1b** $R^1$ = Me, $R^2 = i$Pr, $R^3$ = H
**1c** $R^1 = R^2$ = Me, $R^3$ = H
**1d** $R^1 = i$Pr, $R^2$ = H, $R^3$ = Me

Scheme 2. Synthetic procedure of ligands **1a**–**1d**.

## Complex Synthesis

The aluminum dichloride complexes **2a**–**2d** were synthesized in reasonable yields (68–75%) by reaction of $AlCl_3$ with the lithium salt of the corresponding ligand that was generated in situ by treating the free ligand with *n*BuLi in hexanes at –78 °C (Scheme 3). All complexes are well soluble in toluene, dichloromethane, diethyl ether, and THF, but sparingly soluble in saturated hydrocarbon solvents. Complexes **2a**–**2d** were all characterized by elemental analyses, $^1$H and $^{13}$C NMR spectroscopy, and satisfactory analytic results were obtained for all compounds. In the $^1$H NMR spectra of these complexes, the resonances for the imino CH protons ($\delta$ = 7.32–7.90 ppm) shift about 1 ppm towards high field compared to the corresponding signals of the free ligands. However, the resonances ($\delta$ = 173.5–174.5 ppm) for the imino CH carbons in the $^{13}$C NMR spectra shift to low field in comparison with the corresponding ones of the free ligands and the dialkylaluminum complexes.[14d] The N–H signals of the free ligands disappear in the $^1$H NMR spectra of complexes **2a**–**2d**, which is indicative of formation of an Al–N bond in these compounds. The two methyl groups of the isopropyl units in complexes **2a**, **2b**, and **2d** are inequivalent, as the coordination of the anilido-imine ligands to the aluminum center causes rotation about the N–aryl bond to become slow on the NMR timescale.[16] In addition, $^1$H and $^{13}$C NMR spectra reveal that these complexes all have $C_s$-symmetric structures in solution. All complexes are more stable than the corresponding alkylaluminum complexes in solution; they have pretty good thermal stability and can be heated in boiling toluene for several hours without obvious decomposition.

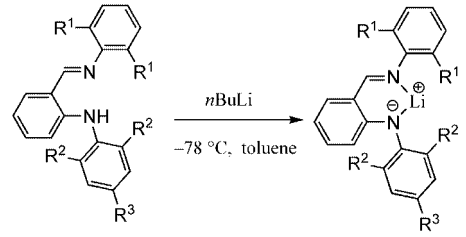


**1a** $R^1 = R^2 = i$Pr, $R^3$ = H
**1b** $R^1$ = Me, $R^2 = i$Pr, $R^3$ = H
**1c** $R^1 = R^2$ = Me, $R^3$ = H
**1d** $R^1 = i$Pr, $R^2$ = H, $R^3$ = Me

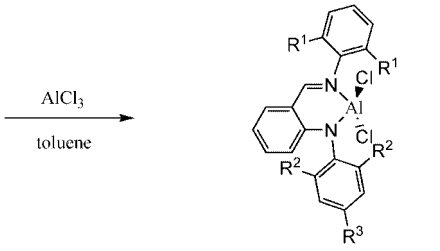


**2a** $R^1 = R^2 = i$Pr, $R^3$ = H
**2b** $R^1$ = Me, $R^2 = i$Pr, $R^3$ = H
**2c** $R^1 = R^2$ = Me, $R^3$ = H
**2d** $R^1 = i$Pr, $R^2$ = H, $R^3$ = Me

Scheme 3. Synthetic procedure of complexes **2a**–**2d**.

## Crystal Structure

The molecular structures of the complexes **2a**, **2b**, and **2d** were determined by X-ray crystallographic analysis. Crystals of all three complexes suitable for X-ray crystal structure determination were grown from *n*-hexane at room temperature. The ORTEP drawings of molecular structures of **2a**, **2b**, and **2d** are shown in Figure 1 (top), Figure 2, and Figure 3, respectively. Selected bond lengths and angles for these complexes are given in Table 1. The X-ray analysis reveals that all three complexes adopt a distorted tetrahedral geometry with the metal center chelated by the bidentate ligand through the imine and amido nitrogen atoms. The N–Al–N bite angle in **2b** [99.27 (6)°] is larger than those in **2a** [97.59 (8)°] and **2d** [97.82 (8)°], but similar to the one in the related β-diketiminato aluminum complex [Scheme 1; $\mathbf{B_1}$ 99.36 (4)°, $\mathbf{B_2}$ 99.41(12)°],[17a,17b] which contains a similar six-membered $C_3N_2Al$ metallacycle. In these three complexes, the six-membered chelating rings are nearly planar with the aluminum atom lying 0.5017, 0.0963, and 0.3065 Å out of the plane, respectively. The imino C=N bonds in these complexes retain their double bond character, being 1.303(2), 1.303(2), and 1.310(3) Å for **2a**, **2b**, and **2d**, respectively. The Al–N (amido) distances [1.8327(19) Å

 © 2006 Wiley-VCH Verlag GmbH & Co. KGaA, Weinheim 

for **2a**, 1.8397(14) Å for **2b**, 1.826(2) Å for **2d**] are much shorter than the Al–N (imine) distances [1.894(2) Å for **2a**, 1.8927(15) for **2b**, 1.8937(19) Å for **2d**] because the anionic amido nitrogen can also π-donate to the aluminum, whereas the neutral imine nitrogen does not have an available lone pair for π-donation. The Al–N (imine) distances (1.893 Å average) are shorter than the values (1.953 Å average) previously reported for *ortho*-$C_6H_4(NAr')(CH{=}NAr')AlMe_2$[14d] because of the more electrophilic aluminum center in the dichloro aluminum compounds, but larger than the one [1.850(2) Å] in $(TTP)AlCl_2$.[17b] The Cl–Al–Cl angles (109.40° average) in **2a** and **2d** are close to the ideal tetrahedral angle of 109.47°, and they are similar to that of the reported diketiminatolaluminum complex (Scheme 1; B).[17] In addition, X-ray diffraction analysis reveals that intermolecular π–π interaction appears in the solid state of complex **2a** (Figure 1, bottom). One phenyl ring in the ligand of **2a** stacks together with the corresponding one in an adjacent molecule by the π–π interaction with a distance of 3.6 Å.[18]

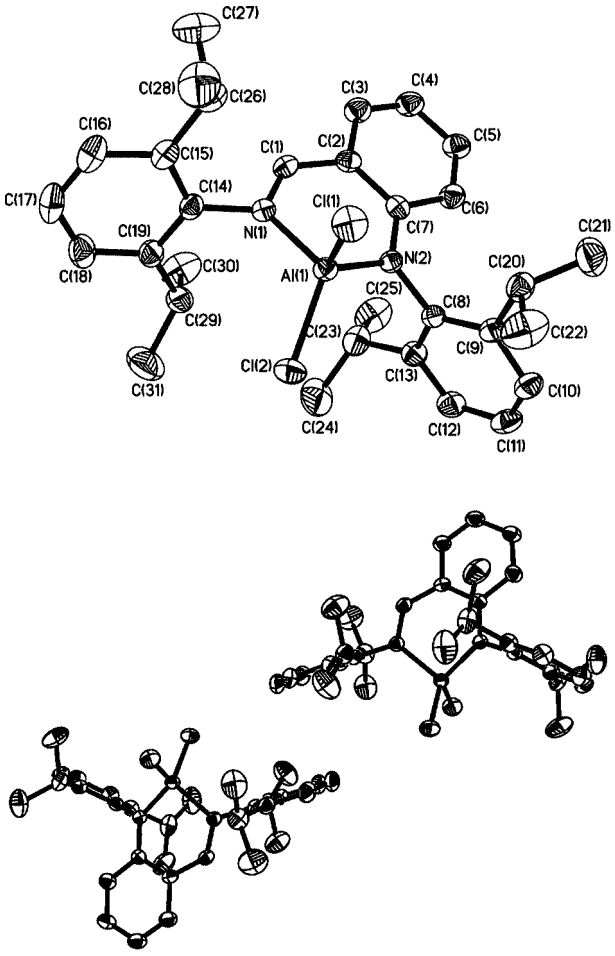


Figure 1. Top: Molecular structure of complex **2a**; bottom: Crystal packing diagram between two adjacent molecules of **2a** showing the existence of a π–π stacking interaction in the solid state. (Thermal ellipsoids are drawn at the 30% probability level.).

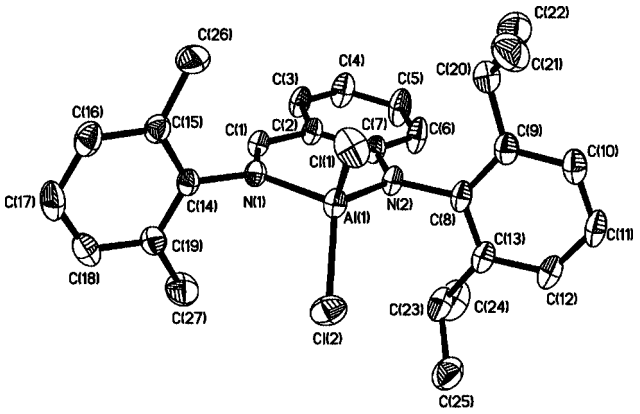


Figure 2. Molecular structure of complex **2b** (thermal ellipsoids are drawn at the 30% probability level).

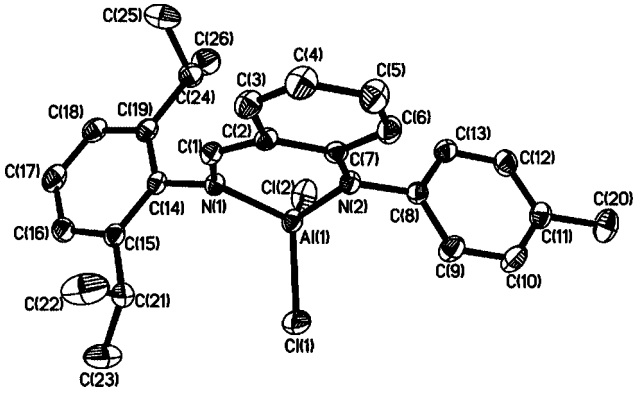


Figure 3. Molecular structure of complex **2d** (thermal ellipsoids are drawn at the 30% probability level).

## Fluorescent Properties

Table 2 summarizes the UV/Vis and fluorescent properties of compounds **1a**–**1d** and **2a**–**2d** determined in both solution and the solid state. In solution, the free ligands **1a**–**1d** have a weak emission band at $\lambda_{max}$ = 419, 420, 423, and 430 nm, respectively. When these ligands were bound to an aluminum center, strong green luminescence was observed. The observed luminescence of the complexes could be attributed to a π*–π transition of their chelated anilido-imine conjugated ligands. As shown in Figure 4, in contrast to the free ligands, each of complexes **2a**–**2d** in solution gives a broad emission band (bandwidth at half-height = 70–90 nm) with $\lambda_{max}$ = 512, 510, 505, and 554 nm, respectively. The emission energies of these complexes are significantly red-shifted in comparison with the free ligands. The role of the aluminum atom in the luminescence of **2a**–**2d** should be twofold, as pointed out in the literature for coordination complexes.[19] First, the formation of covalent bonds between the Al and N atoms by the donation of lone pairs of the N atom to the Al atom changes the emission energy, owing to the lowering of the energy gap between π* and π. Second, after coordination with the Al atom, the ligand becomes more rigid, which can reduce the loss of energy by vibrational motions and increase the emission efficiency. The emission maxima of complexes **2a**–**2c** in solution are

 © 2006 Wiley-VCH Verlag GmbH & Co. KGaA, Weinheim 

Table 1. Selected bond lengths [Å] and angles [°].

| | | | |
|---|---|---|---|
| Complex **2a** | | | |
| Al(1)–N(1) | 1.894(2) | N(1)–Al(1)–Cl(2) | 114.54(7) |
| Al(1)–N(2) | 1.8327(19) | N(2)–Al(1)–Cl(1) | 115.53(7) |
| Al(1)–Cl(2) | 2.0978(10) | N(1)–Al(1)–Cl(1) | 106.18(7) |
| Al(1)–Cl(1) | 2.1190(11) | Cl(2)–Al(1)–Cl(1) | 109.46(4) |
| N(1)–C(1) | 1.303(3) | C(1)–N(1)–Al(1) | 119.83(16) |
| N(2)–C(7) | 1.370(3) | C(14)–N(1)–Al(1) | 123.33(15) |
| N(1)–Al(1)–N(2) | 97.59(8) | C(7)–N(2)–Al(1) | 122.40(15) |
| N(2)–Al(1)–Cl(2) | 113.02(7) | C(8)–N(2)–Al(1) | 120.78(14) |
| Complex **2b** | | | |
| Al(1)–N(1) | 1.8927(15) | N(1)–Al(1)–Cl(1) | 109.36(5) |
| Al(1)–N(2) | 1.8397(14) | N(2)–Al(1)–Cl(2) | 116.17(6) |
| Al(1)–Cl(1) | 2.1154(8) | N(1)–Al(1)–Cl(2) | 110.40(5) |
| Al(1)–Cl(2) | 2.1182(9) | Cl(1)–Al(1)–Cl(2) | 107.00(4) |
| N(1)–C(1) | 1.303(2) | C(1)–N(1)–Al(1) | 121.47(11) |
| N(2)–C(7) | 1.372(2) | C(14)–N(1)–Al(1) | 122.05(10) |
| N(2)–Al(1)–N(1) | 99.27(6) | C(7)–N(2)–Al(1) | 125.07(11) |
| N(2)–Al(1)–Cl(1) | 114.36(6) | C(8)–N(2)–Al(1) | 117.04(11) |
| Complex **2d** | | | |
| Al(1)–N(1) | 1.8937(19) | N(1)–Al(1)–Cl(2) | 110.46(7) |
| Al(1)–N(2) | 1.826(2) | N(2)–Al(1)–Cl(1) | 110.55(7) |
| Al(1)–Cl(2) | 2.1064(12) | N(1)–Al(1)–Cl(1) | 113.73(7) |
| Al(1)–Cl(1) | 2.1146(10) | Cl(2)–Al(1)–Cl(1) | 109.34(5) |
| N(1)–C(1) | 1.310(3) | C(1)–N(1)–Al(1) | 120.93(15) |
| N(2)–C(7) | 1.367(3) | C(14)–N(1)–Al(1) | 123.09(13) |
| N(2)–Al(1)–N(1) | 97.82(8) | C(7)–N(2)–Al(1) | 126.00(15) |
| N(2)–Al(1)–Cl(2) | 114.65(8) | C(8)–N(2)–Al(1) | 114.41(13) |

close to each other, while the emission maximum of **2d** is red-shifted about 40 nm compared to other complexes. This result could be attributed to the differences in the number and size of the *ortho*-substituents on the rotatable aryl rings of their ligands, which might affect the conjugated extent of these complexes.[14a–14d] In addition, the lower basicity and lower electron density of the anilide may also be responsible for the emission red shift in **2d**.[14e] The quantum yields of these compounds are low in solution. Complexes **2a**–**2d** all emit bright fluorescence in the solid state when irradiated by exciting light. The emission spectra of complexes **2a**–**2d** in the solid state are shown in Figure 5. Complexes **2b**, **2c**, and **2d** each have a relatively narrow band (bandwidth at half-height: 60–70 nm) in the solid state with $\lambda_{max}$ = 497, 498, and 544 nm, respectively. The emission

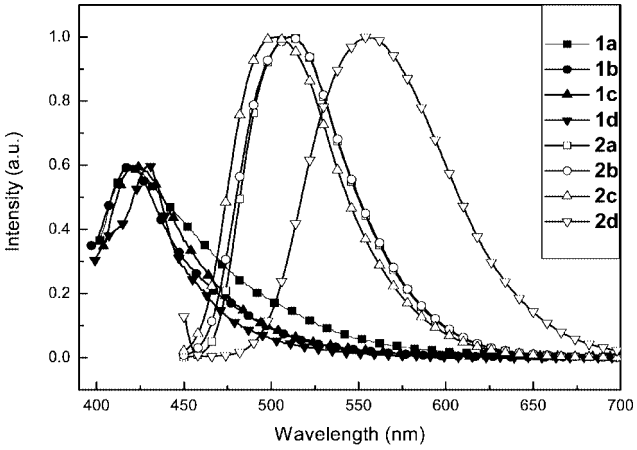


Figure 4. Emission spectra of ligands **1a**–**1d** and complexes **2a**–**2d** in *n*-hexane.

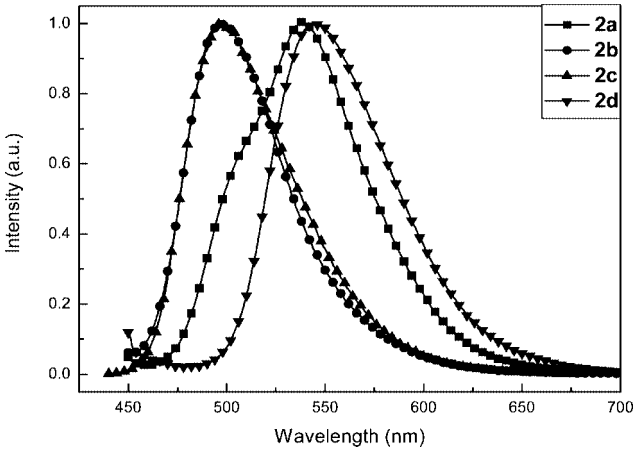


Figure 5. Emission spectra of complexes **2a**–**2d** in the solid state.

Table 2. Photoluminescent data for ligands **1a**–**1d** and complexes **2a**–**2d**.

| Compound | $\varepsilon$ [$M^{-1}\cdot cm^{-1}$] | $\lambda_{abs}$ [nm] | $\lambda_{em}$ [nm] | Quantum yields [$\Phi$][a] | Conditions |
|---|---|---|---|---|---|
| **1a** | 9011 | 370 | 419 | 0.036 | hexane, 298 K |
| | | | 431 | | solid, 298 K |
| **1b** | 11265 | 371 | 420 | 0.029 | hexane, 298 K |
| | | | 432 | | solid, 298 K |
| **1c** | 13214 | 373 | 423 | 0.023 | hexane, 298 K |
| | | | 432 | | solid, 298 K |
| **1d** | 10745 | 382 | 430 | 0.009 | hexane, 298 K |
| | | | 462 | | solid, 298 K |
| **2a** | 12645 | 437 | 512 | 0.093 | hexane, 298 K |
| | | | 540 | | solid, 298 K |
| **2b** | 12495 | 436 | 510 | 0.098 | hexane, 298 K |
| | | | 497 | | solid, 298 K |
| **2c** | 11932 | 436 | 505 | 0.085 | hexane, 298 K |
| | | | 498 | | solid, 298 K |
| **2d** | 10876 | 447 | 554 | 0.066 | hexane, 298 K |
| | | | 544 | | solid, 298 K |

[a] Determined using quinine sulfate in 0.1 M sulfuric acid as a standard.

 © 2006 Wiley-VCH Verlag GmbH & Co. KGaA, Weinheim 

maxima of these complexes in the solid state are blue shifted compared to their corresponding emission maxima in solution, which probably resulted from the reduced conjugated extent of the three complexes, as the free rotation of the aryl rings in these complexes is blocked in the solid state. The emission maximum of complex **2a** ($\lambda_{max}$ = 540 nm) in the solid state is red shifted compared to its corresponding emission maximum in solution, which is normal considering that red shifting of the emission maximum can be observed for most fluorescent compounds in the solid state, probably because of π–π stacking of aromatic rings in the molecules (see Figure 1, bottom). This result also implies that the rotation of 2,6-*i*$Pr_2$Ph groups about the N–aryl bond in complex **2a** is slow in solution, which is consistent with the $^1$H NMR experimental result.

## Conclusion

Our research results indicate that the chelating bidentate anilido-imine conjugated ligands are well suited for synthesizing the four-coordinate aluminum complexes by a salt metathesis reaction of $AlCl_3$ with the lithium salt of corresponding ligands at room temperature. $^1$H and $^{13}$C NMR spectra reveal that these aluminum complexes have $C_s$-symmetric structures in solution and X-ray diffraction analysis indicates that the six-membered chelating ring in these complexes is nearly planar with the aluminum lying slightly out of the plane. These complexes produce bright fluorescence in both solution and the solid state, and the emission color in solution can be tuned by the *ortho* substituents on the rotatable aryl rings of the ligands. The four-coordinate aluminum complexes are a new class of luminescent material with potential applications in optoelectronic devices.

## Experimental Section

All reactions were performed using standard Schlenk techniques in high-purity nitrogen or glovebox techniques. Toluene, *n*-hexane, THF, and diethyl ether were dried by refluxing over sodium and benzophenone and distilled under nitrogen prior to use. $C_6D_6$ was dried with activated 4 Å molecular sieves and vacuum-transferred to a sodium-mirrored air-free flask. $CDCl_3$ was dried with $CaH_2$ for 48 h and vacuum-transferred to an air-free flask. $AlCl_3$ and *n*BuLi were purchased from Aldrich and used as received. NMR spectra were measured using a Varian Mercury-300 NMR spectrometer. The elemental analysis was performed with a Perkin–Elmer 2400 analyzer. UV/Vis absorption spectra were recorded with a UV-3100 spectrophotometer. Fluorescence measurements were carried out on an RF-5301PC.

***ortho*-$C_6H_4$[NH($C_6H_3$*i*$Pr_2$-2,6)](CH=N$C_6H_3Me_2$-2,6) (1b):** A solution of *n*BuLi (30.32 mL, 48.5 mmol) in hexanes was added to a solution of 2,6-diisopropylaniline (8.1 mL, 48.5 mmol) in THF (30 mL) at –78 °C. The mixture was allowed to warm to room temperature and stirred overnight. The resulting solution of LiNHAr was transferred into a solution of *ortho*-$C_6H_4F$(CH=N$C_6H_3Me_2$-2,6) (11.0 g, 48.5 mmol) in THF (40 mL) at 25 °C. After stirring for 2 h, the reaction was quenched with $H_2O$ (25 mL), extracted with *n*-hexane, and the organic phase was evaporated to dryness in vacuo to give the crude product as a yellow solid. Pure product (13.4 g, 72%) was obtained as yellowish-green crystals by recrystallization from ethanol at –20 °C. $C_{27}H_{32}N_2$ (384.56): calcd. C 84.33, H 8.39, N 7.28; found C 84.28, H 8.48, N 7.24. $^1$H NMR (300 MHz, $CDCl_3$, 293 K): $\delta$ = 1.15, 1.17 [d, $J$ = 6.6 Hz, 2×6 H, CH(C$H_3$)$_2$], 2.21 (s, 6 H, C$H_3$), 3.22 [sept, $J$ = 6.6 Hz, 2 H, C$H$(CH$_3$)$_2$], 6.30 (d, $J$ = 8.1 Hz, 1 H, Ph-*H*), 6.71 (t, $J$ = 6.6 Hz, 1 H, Ph-*H*), 6.98 (t, $J$ = 7.2 Hz, 1 H, Ph-*H*), 7.09–7.38 (m, 7 H, Ph-*H*), 8.39 (s, 1 H, C*H*=NAr), 10.53 (s, 1 H, N*H*) ppm. $^{13}$C{$^1$H} NMR (300 MHz, $CDCl_3$, 293 K): $\delta$ = 18.7 (*C*H$_3$), 23.2 [CH(*C*H$_3$)$_2$], 25.0 [CH(*C*H$_3$)$_2$], 28.8 [*C*H(CH$_3$)$_2$], 112.2, 115.3, 116.5, 124.0, 127.7, 127.9, 128.3, 132.5, 134.7, 134.8, 147.7, 150.2, 151.1 (Ph), 166.2 (*C*H=NAr) ppm.

***ortho*-$C_6H_4N(C_6H_3$*i*$Pr_2$-2,6)(CH=N$C_6H_3$*i*$Pr_2$-2,6)$AlCl_2$ (2a):** A solution of *n*BuLi in hexanes (0.28 mL, 0.45 mmol) was added dropwise to a stirred toluene solution of *ortho*-$C_6H_4$NH($C_6H_3$*i*$Pr_2$-2,6)(CH=N$C_6H_3$*i*$Pr_2$-2,6) (0.20 g, 0.45 mmol) at –78 °C. After the addition, the reaction mixture was warmed to room temperature and stirred overnight. The resulting mixture was added dropwise to a toluene suspension solution of $AlCl_3$ (0.06 g, 0.45 mmol) at –78 °C with stirring. The mixture was warmed to room temperature and stirred for 12 h, and the solution was evaporated to dryness in vacuo. The solid residue was extracted with *n*-hexane (30 mL). Insoluble materials were removed by filtration through Celite. The yellow filtrate was concentrated to about 20 mL and kept at –20 °C overnight to let the product crystallize. The product was obtained as yellow-green crystals (0.18 g, 75%). $C_{31}H_{39}Al_2Cl_2N$ (537.54): calcd. C 69.27, H 7.31, N 5.21; found C 69.20, H 7.40, N 5.25. $^1$H NMR (300 MHz, $C_6D_6$, 293 K): $\delta$ = 0.93, 1.00 [d, $J$ = 6.9 Hz, 2×6 H, CH(C$H_3$)$_2$], 1.38, 1.46 [d, $J$ = 6.9 Hz, 2×6 H, CH(C$H_3$)$_2$], 3.53 [sept, $J$ = 6.9 Hz, 2×2 H, C$H$(CH$_3$)$_2$], 6.25 (t, $J$ = 6.1 Hz, 1 H, Ph-*H*), 6.41 (d, $J$ = 8.8 Hz, 1 H, Ph-*H*), 6.70 (t, $J$ = 6.6 Hz, 2 H, Ph-*H*), 7.07–7.12 (m, 6 H, Ph-*H*), 7.92 (s, 1 H, *H*C=N) ppm. $^{13}$C{$^1$H} NMR (300 MHz, $C_6D_6$, 293 K): $\delta$ = 22.9, 24.7, 25.4, 25.7 [4×CH(*C*H$_3$)$_2$], 28.7, 29.0 [2×*C*H(CH$_3$)$_2$], 115.1, 117.1, 119.3, 124.7, 125.2, 129.0, 136.9, 137.2, 137.6, 141.1, 143.5, 146.7, 158.0 (Ph), 173.5 (*C*H=NAr) ppm.

***ortho*-$C_6H_4N(C_6H_3$*i*$Pr_2$-2,6)(CH=N$C_6H_3Me_2$-2,6)$AlCl_2$ (2b):** A solution of *n*BuLi in hexanes (0.33 mL, 0.52 mmol) was added dropwise to a stirred toluene solution of *ortho*-$C_6H_4$NH($C_6H_3$*i*$Pr_2$-2,6)(CH=N$C_6H_3Me_2$-2,6) (0.20 g, 0.52 mmol) at –78 °C. After the addition, the reaction mixture was warmed to room temperature and stirred overnight. The resulting mixture was added dropwise to a toluene suspension solution of $AlCl_3$ (0.07 g, 0.52 mmol) at –78 °C with stirring. The mixture was warmed to room temperature and stirred for 12 h, and the solution was evaporated to dryness in vacuo. The solid residue was extracted with *n*-hexane (30 mL). Insoluble materials were removed by filtration through Celite. The yellow filtrate was concentrated to about 20 mL and kept at –20 °C overnight to let the product crystallize. The product was obtained as yellow-green crystals (0.18 g, 70%). $C_{27}H_{31}AlCl_2N_2$ (481.44): calcd. C 67.36, H 6.49, N 5.82; found C 67.30, H 6.44, N 5.91. $^1$H NMR (300 MHz, $C_6D_6$, 293 K): $\delta$ = 0.99 [d, $J$ = 6.6 Hz, 6 H, CH(C$H_3$)$_2$], 1.42 [d, $J$ = 6.6 Hz, 6 H, CH(C$H_3$)$_2$], 2.67 (s, 6 H, C$H_3$), 3.48 [sept, $J$ = 6.6 Hz, 2 H, C$H$(CH$_3$)$_2$], 6.27 (t, $J$ = 6.0 Hz, 1 H, Ph-*H*), 6.38 (d, $J$ = 8.7 Hz, 1 H, Ph-*H*), 6.60 (d, $J$ = 8.1 Hz, 1 H, Ph-*H*), 6.72 (t, $J$ = 6.6 Hz,1 H, Ph-*H*), 6.81–7.19 (m, 6 H, Ph-*H*), 7.35 (s, 1 H, C*H*=NAr) ppm. $^{13}$C{$^1$H} NMR (300 MHz, $C_6D_6$, 293 K): $\delta$ = 18.8 (*C*H$_3$), 24.6 [CH(*C*H$_3$)$_2$], 25.5 [CH(*C*H$_3$)$_2$], 28.6 [*C*H(CH$_3$)$_2$], 115.3, 116.7, 119.3, 125.2, 129.3, 132.7, 137.2, 137.3, 143.9, 146.7 (Ph), 173.8 (*C*H=NAr) ppm.

 © 2006 Wiley-VCH Verlag GmbH & Co. KGaA, Weinheim 

***ortho*-$C_6H_4N(C_6H_3Me_2$-2,6)(CH=$NC_6H_3Me_2$-2,6)$AlCl_2$ (2c):** A solution of *n*BuLi in hexanes (0.38 mL, 0.61 mmol) was added dropwise to a stirred toluene solution of *ortho*-$C_6H_4NH(C_6H_3Me_2$-2,6)(CH=$NC_6H_3Me_2$-2,6) (0.20 g, 0.61 mmol) at –78 °C. After the addition, the reaction mixture was warmed to room temperature and stirred overnight. The resulting mixture was added dropwise to a toluene suspension solution of $AlCl_3$ (0.08 g, 0.61 mmol) at –78 °C with stirring. The mixture was warmed to room temperature and stirred for 12 h, and the solution was evaporated to dryness in vacuo. The solid residue was extracted with *n*-hexane (30 mL). Insoluble materials were removed by filtration through Celite. The yellow filtrate was concentrated to about 20 mL and kept at –20 °C overnight to let the product crystallize. The product was obtained as yellow crystals (0.18 g, 68%). $C_{23}H_{23}AlCl_2N_2$ (425.33): calcd. C 64.95, H 5.45, N 6.59; found C 64.82, H 5.56, N 6.64. $^1$H NMR (300 MHz, $C_6D_6$, 293 K): $\delta$ = 2.27 (s, 6 H, C$H_3$), 2.37 (s, 6 H, C$H_3$), 6.33 (t, $J$ = 6.3 Hz, 1 H, Ph-*H*), 6.68 (d, $J$ = 8.5 Hz, 1 H, Ph-*H*), 6.76–7.04 (m, 8 H, Ph-*H*), 7.35 (s, 1 H, C*H*=NAr) ppm. $^{13}$C{$^1$H} NMR (300 MHz, $C_6D_6$, 293 K): $\delta$ = 18.9 (*C*$H_3$), 115.3, 116.5, 116.7, 127.2, 128.1, 129.2, 129.6, 132.9, 136.4, 137.5, 138.3, 139.8, 143.5, 156.5, 174.3 (*C*H=NAr) ppm.

***ortho*-$C_6H_4N(C_6H_4Me$-*p*)(CH=$NC_6H_3i Pr_2$-2,6)$AlCl_2$ (2d):** A solution of *n*BuLi in hexanes (0.34 mL, 0.54 mmol) was added dropwise to a stirred toluene solution of *ortho*-$C_6H_4NH(C_6H_4Me$-*p*)-(CH=$NC_6H_3i Pr_2$-2,6) (0.20 g, 0.54 mmol) at –78 °C. After the addition, the reaction mixture was warmed to room temperature and stirred overnight. The resulting mixture was added dropwise to a toluene suspension solution of $AlCl_3$ (0.08 g, 0.54 mmol) at –78 °C with stirring. The mixture was warmed to room temperature and stirred for 12 h, and the solution was evaporated to dryness in vacuo. The solid residue was extracted with hexane (30 mL). Insoluble materials were removed by filtration through Celite. The yellow filtrate was concentrated to about 20 mL and kept at –20 °C overnight to let the product crystallize. The product was obtained as yellow crystals (0.16 g, 71%). $C_{26}H_{29}AlCl_2N_2$ (467.41): calcd. C 66.81, H 6.25, N 5.99; found: C 66.92, H 6.11, N 5.90. $^1$H NMR (300 MHz, $C_6D_6$, 293 K): $\delta$ = 0.89 [d, $J$ = 6.6 Hz, 6 H, CH(C$H_3$)$_2$], 1.38 [d, $J$ = 6.6 Hz, 6 H, CH(C$H_3$)$_2$], 2.03 (s, 3 H, C$H_3$), 3.48 [sept, $J$ = 6.6 Hz, 2 H, C$H$(CH$_3$)$_2$], 6.31 (t, $J$ = 6.9 Hz, 1 H, Ph-*H*), 6.62 (d, $J$ = 8.8 Hz, 1 H, Ph-*H*), 6.72 (d, $J$ = 8.1 Hz, 1 H, Ph-*H*), 6.81 (t, $J$ = 6.6 Hz, 1 H, Ph-*H*), 6.94 (d, $J$ = 8.4 Hz, 2 H, Ph-*H*), 7.07–7.13 (m, 2 H, Ph-*H*), 7.33 (d, $J$ = 6.5 Hz, 2 H, Ph-*H*), 7.94 (s, 1 H, C*H*=NAr) ppm. $^{13}$C{$^1$H} NMR (300 MHz, $C_6D_6$, 293 K): $\delta$ = 20.8 (*C*H$_3$), 22.8 [CH(*C*H$_3$)$_2$], 26.0 [CH(*C*H$_3$)$_2$], 28.9 [*C*H(CH$_3$)$_2$], 114.7, 116.7, 117.6, 124.7, 128.5, 129.2, 131.0, 136.4, 137.0, 138.1, 140.1, 140.7, 143.8, 158.0 (Ph), 173.6 (*C*H=NAr) ppm.

**X-ray Structure Determinations of 2a, 2b, and 2d:** Single crystals of **2a**, **2b**, and **2d** suitable for X-ray structural analysis were obtained from *n*-hexane. Diffraction data were collected at 293 K with a Rigaku R-AXIS RAPID IP diffractometer equipped with graphite-monochromated Mo-$K_\alpha$ radiation ($\lambda$ = 0.71073 Å) for **2a**, **2b**, and **2d**. Details of the crystal data, data collections, and structure refinements are summarized in Table 3. The structures were solved by direct methods[20] and refined by full-matrix least-squares on $F^2$. All non-hydrogen atoms were refined anisotropically and the hydrogen atoms were included in idealized positions. All calculations were performed using the SHELXTL[21] crystallographic software packages.

CCDC-279167 (for **2a**), -279168 (for **2b**), and -279169 (for **2d**) contain the supplementary crystallographic data for this paper. These data can be obtained free of charge from The Cambridge Crystallographic Data Centre via www.ccdc.cam.ac.uk/data_request/cif.

Table 3. Crystal data and structural refinement details for **2a**, **2b**, and **2d**.

| | **2a** | **2b** | **2d** |
|---|---|---|---|
| Empirical formula | $C_{31}H_{39}AlCl_2N_2$ | $C_{27}H_{31}AlCl_2N_2$ | $C_{26}H_{29}AlCl_2N_2$ |
| Formula mass | 537.5 | 481.42 | 467.39 |
| Temp. [K] | 293(2) | 293(2) | 293(2) |
| Wavelength [Å] | 0.71073 | 0.71073 | 0.71073 |
| Crystal system | monoclinic | monoclinic | triclinic |
| Space group | *P*2(1)/*c* | *P*2(1)/*n* | $P\bar{1}$ |
| *a* [Å] | 17.474(4) | 8.9391(18) | 9.5066(19) |
| *b* [Å] | 10.448(2) | 26.151(5) | 9.866(2) |
| *c* [Å] | 17.528(4) | 11.242(2) | 14.837(3) |
| *α* [°] | 90 | 90 | 107.24(3) |
| *β* [°] | 108.65(3) | 96.02(3) | 103.70(3) |
| *γ* [°] | 90 | 90 | 99.30(3) |
| *V* [Å$^3$] | 3032.1(11) | 2613.6(9) | 1250.3(4) |
| *Z* | 4 | 4 | 2 |
| $D_{calcd}$ [Mg·m$^{-3}$] | 1.177 | 1.223 | 1.241 |
| *F*(000) | 1144 | 1016 | 492 |
| Crystal size [mm] | 0.40 × 0.28 × 0.24 | 0.51 × 0.32 × 0.21 | 0.41 × 0.28 × 0.21 |
| *θ* Range for data collection (°) | 1.23–27.50 | 3.07–27.44 | 1.51–27.48 |
| Limiting indices | $-18 \le h \le 22$ | $-11 \le h \le 11$ | $0 \le h \le 12$ |
| | $-13 \le k \le 13$ | $-31 \le k \le 33$ | $-12 \le k \le 12$ |
| | $-17 \le l \le 22$ | $-14 \le l \le 14$ | $-19 \le l \le 18$ |
| Data/restraints/parameters | 6955/0/333 | 5941/0/413 | 5697/0/396 |
| Goodness-of-fit on $F^2$ | 0.865 | 1.020 | 0.850 |
| Final *R* indices [$I > 2\sigma(I)$] | $R_1$[a] = 0.0480 | $R_1$[a] = 0.0404 | $R_1$[a] = 0.0424 |
| | $wR_2$[b] = 0.1098 | $wR_2$[b] = 0.1032 | $R_2$[b] = 0.1062 |
| *R* indices (all data) | $R_1$[a] = 0.1159 | $R_1$[a] = 0.0642 | $R_1$[a] = 0.0776 |
| | $wR_2$[b] = 0.1258 | $wR_2$[b] = 0.1157 | $wR_2$[b] = 0.1207 |
| Largest diff. peak/hole [e·Å$^{-3}$] | 0.344, –0.246 | 0.251, –0.285 | 0.850, –0.301 |

[a] $R_1 = \Sigma||F_o| - |F_c|| / \Sigma|F_o|$. [b] $wR_2 = \{\Sigma[w(F_o^2 - F_c^2)^2] / \Sigma[w(F_o^2)^2]\}^{1/2}$.

 © 2006 Wiley-VCH Verlag GmbH & Co. KGaA, Weinheim 

## Acknowledgments

This work was supported by the National Natural Science Foundation of China (No. 20374023) and the Ministry of Science and Technology of China (No. 2002CB6134003).

[1] a) S. N. Wang, *Coord. Chem. Rev.* **2001**, *215*, 79–98; b) C. H. Chen, J. Shi, *Coord. Chem. Rev.* **1998**, *171*, 161–174; c) Q. Wu, M. Esteghamatian, N. H. Hu, Z. Popovic, G. Enright, Y. Tao, M. D'Iorio, S. Wang, *Chem. Mater.* **2000**, *12*, 79–83; d) J. E. McGarrah, Y. J. Kim, M. Hisser, R. Eisenberg, *Inorg. Chem.* **2001**, *40*, 4510–4511; e) N. L. Coker, J. A. K. Brauer, R. C. Elder, *J. Am. Chem. Soc.* **2004**, *126*, 12–13; f) Y. Kunugi, K. R. Mann, L. Miller, C. L. Exstrom, *J. Am. Chem. Soc.* **1998**, *120*, 589–590; g) M. A. Mansour, W. B. Connick, R. J. Lachicotte, H. J. Gysling, R. J. Eisenberg, *J. Am. Chem. Soc.* **1998**, *120*, 1329–1330.

[2] a) V. A. Montes, G. Li, R. Pohl, J. Shinar, P. Anzenbacher Jr, *Adv. Mater.* **2004**, *16*, 2001–2003; b) R. Pohl, V. A. Montes, J. Shinar, P. Anzenbacher Jr, *J. Org. Chem.* **2004**, *69*, 1723–1725; c) R. Pohl, P. Anzenbacher Jr, *Org. Lett.* **2003**, *5*, 2769–2772.

[3] a) K. H. Chang, C. C. Huang, Y. H. Liu, Y. H. Hu, P. T. Chou, Y. C. Lin, *Dalton Trans.* **2004**, 1731–1738; b) Y. J. Kang, C. Seward, D. T. Song, S. N. Wang, *Inorg. Chem.* **2003**, *42*, 2789–2797; c) W. L. Jia, D. T. Song, S. N. Wang, *J. Org. Chem.* **2003**, *68*, 701–705; d) K. Y. Ho, W. Y. Yu, K. K. Cheung, C. M. Che, *J. Chem. Soc., Dalton Trans.* **1999**, 1581–1586.

[4] a) W. Lu, B. X. Mi, M. C. W. Chan, Z. Hui, C. M. Che, N. Y. Zhu, S. T. Lee, *J. Am. Chem. Soc.* **2004**, *126*, 4958–4971; b) J. Brooks, Y. Babayan, S. Lamansky, P. I. Djurovich, I. Tsyba, R. Bau, M. K. Thompson, *Inorg. Chem.* **2002**, *41*, 3055–3066; c) Q. D. Liu, W. L. Jia, G. Wu, S. N. Wang, *Organometallics* **2003**, *22*, 3781–3791.

[5] a) W. S. Huang, J. T. Lin, C. H. Chien, Y. T. Tao, S. S. Sun, Y. S. Wen, *Chem. Mater.* **2004**, *16*, 2480–2488; b) I. R. Laskar, T. M. Chen, *Chem. Mater.* **2004**, *16*, 111–117; c) S. Lamansky, P. Djurovoch, D. Murphy, F. Abdel-Razzaq, H. E. Lee, C. Adachi, P. E. Burrows, S. R. Forrest, M. E. Thompson, *J. Am. Chem. Soc.* **2001**, *123*, 4304–4312.

[6] a) V. W. W. Yaw, W. Y. Lo, C. H. Lam, W. K. M. Fung, K. M. C. Wong, V. C. Y. Lau, N. Y. Zhu, *Coord. Chem. Rev.* **2003**, *245*, 39–47; b) V. W. W. Yaw, Y. Yang, J. X. Zhang, B. W. K. Chu, N. Y. Zhu, *Organometallics* **2001**, *20*, 4911–4918; c) V. W. W. Yaw, C. C. Ko, L. X. Wu, K. M. C. Wong, K. C. Cheung, *Organometallics* **2000**, *19*, 1820–1822.

[7] a) C. W. Tang, S. A. Vanslyke, *Appl. Phys. Lett.* **1987**, *51*, 913–915; b) C. W. Tang, S. A. Vanslyke, C. H. Chen, *J. Appl. Phys.* **1989**, *65*, 3611–3613; c) Y. Shirota, Y. Kuwabara, H. Inada, T. Wakimoto, H. Nakada, Y. Yonemoto, S. Kawami, K. Imai, *Appl. Phys. Lett.* **1994**, *65*, 807–809.

[8] a) C. Asachi, S. Tokito, T. Tsutsui, S. Saito, *Appl. Phys. Lett.* **1990**, *56*, 799–801; b) Z. Shen, V. Bulovic, P. E. Burrows, S. R. Forrest, M. E. Thompson, *Science* **1999**, *283*, 1900–1902.

[9] a) C. T. Chen, *Chem. Mater.* **2004**, *16*, 4389–4400; b) X. H. Zhang, B. J. Chen, X. Q. Lin, O. Y. Wong, C. S. Lee, H. L. Kwong, S. T. Lee, S. K. Wu, *Chem. Mater.* **2001**, *13*, 1565–1569; c) Y. Hamada, H. Kanno, T. Tsujioka, H. Takahashi, T. Usuki, *Appl. Phys. Lett.* **1999**, *75*, 1682–1684; d) Z. Y. Xie, L. S. Hung, S. T. Lee, *Appl. Phys. Lett.* **2001**, *79*, 1048–1050.

[10] a) L. S. Sapochak, A. Padmaperuma, N. Washton, F. Endrino, G. T. Schmett, J. Marshall, D. Fogarty, P. E. Burrows, S. T. Forrest, *J. Am. Chem. Soc.* **2001**, *123*, 6300–6307; b) H. Jang, L.-M. Do, Y. Kim, J. G. Kim, T. Zyung, Y. Do, *Synth. Met.* **2001**, *121*, 1669–1670.

[11] a) J. Ashenhurst, L. Brancaleon, A. Hassan, W. Liu, H. Schmider, S. Wang, G. Wu, *Organometallics* **1998**, *17*, 3186–3195; b) J. Ashenhurst, L. Brancaleon, S. Gao, W. Liu, H. Schmider, S. Wang, G. Wu, Q. G. Wu, *Organometallics* **1998**, *17*, 5334–5338; c) S. Gao, Q. Wu, G. Wu, S. Wang, *Organometallics* **1998**, *17*, 4666–4674; d) J. Ashenhurst, S. Wang, G. Wu, *J. Am. Chem. Soc.* **2000**, *122*, 3528–3529; e) J. Ashenhurst, G. Wu, S. Wang, *J. Am. Chem. Soc.* **2000**, *122*, 2541–2547; f) S. F. Liu, C. Seward, H. Aziz, N. X. Hu, Z. Popovic, S. Wang, *Organometallics* **2000**, *19*, 5709–5714; g) J. F. Wang, G. E. Jabbour, E. A. Mash, J. Anderson, Y. Zhang, P. A. Lee, N. R. Armstrong, N. Peryhambarian, B. Kippelen, *Adv. Mater.* **1999**, *11*, 1266–1269.

[12] a) L. M. Leung, W. Y. Lo, S. K. So, K. M. Lee, W. K. Choi, *J. Am. Chem. Soc.* **2000**, *122*, 5640–5641; b) S. A. VanSlyke, US Patent 5,151,629, **1992**; c) P. S. Bryan, F. V. Lovecchio, S. A. VanSlyke, US Patent 5,141,671, **1992**.

[13] a) Y. Peng, H. Fan, H. Zhu, H. W. Roesky, J. Magull, C. E. Hughes, *Angew. Chem. Int. Ed.* **2004**, *43*, 3443–3445; b) V. Jancik, M. M. M. Cabrera, H. W. Roesky, R. Herbst-Irmer, D. Neculai, A. M. Neculai, M. Noltemeyer, H. G. Schmid, *Eur. J. Inorg. Chem.* **2004**, 3508–3512; c) V. Jancik, Y. Peng, H. W. Roesky, J. Li, D. Neculai, A. M. Neculai, R. Herbst-Irmer, *J. Am. Chem. Soc.* **2003**, *125*, 1452–1253; d) V. Jancik, L. W. Pineda, J. Pinas, H. W. Roesky, D. Neculai, A. M. Neculai, R. Herbst-Irmer, *Angew. Chem. Int. Ed.* **2004**, *43*, 2142–2145; e) D. Chakrabory, A. Rodriguez, E. Y.-X. Chen, *Macromolecules* **2003**, *36*, 5470–5481; f) H. W. Roesky, *Inorg. Chem.* **2004**, *43*, 7284–2793; g) G. Bai, Y. Peng, H. W. Roesky, J. Li, H.-G. Schmidt, M. Noltemeyer, *Angew. Chem. Int. Ed.* **2003**, *42*, 1132–1135.

[14] a) Y. Cui, Q. D. Liu, W. L. Jia, Y. Tao, S. N. Wang, *Inorg. Chem.* **2005**, *44*, 601–609; b) S. F. Lim, R. H. Friend, I. D. Rees, J. Li, Y. G. Ma, K. Robinson, A. B. Holmes, E. Hennebicq, D. Beljonne, F. Cacialli, *Adv. Funct. Mater.* **2005**, *15*, 981–988; c) F. Cacialli, B. S. Chuah, R. H. Friend, S. C. Moratti, A. B. Holmes, *Synth. Met.* **2000**, *111*, 155–158; d) X. M. Liu, W. Gao, Y. Mu, G. H. Li, L. Ye, H. Xia, Y. Ren, S. H. Feng, *Organometallics* **2005**, *24*, 1614–1619; e) M. Klessinger, J. Michl, *Excited State and Photochemistry of Organic Molecules*, VCH Publishers, Inc., New York, **1995**.

[15] P. G. Hayes, G. C. Welch, D. J. H. Emslie, C. L. Noack, W. E. Piers, M. Parvez, *Organometallics* **2003**, *22*, 1577–1579.

[16] a) J. C. Jenkins, M. Brookhart, *Organometallics* **2003**, *22*, 250–256; b) B. Y. Lee, X. H. Bu, G. C. Bazan, *Organometallics* **2001**, *20*, 5425–5431; c) V. C. Gibson, J. A. Segal, A. J. P. White, D. J. Williams, *J. Am. Chem. Soc.* **2000**, *122*, 7120–7121; d) C. E. Radzewich, I. A. Guzei, R. F. Jordan, *J. Am. Chem. Soc.* **1999**, *121*, 8673–8674.

[17] a) M. Stender, B. E. Eichler, N. J. Harman, P. P. Power, *Inorg. Chem.* **2001**, *40*, 2794–2799; b) B. Qian, M. L. Ward, M. R. Smith III, *Organometallics* **1998**, *17*, 3070–3076; c) D. Vidovic, J. A. Moore, J. N. Jones, A. H. Cowley, *J. Am. Chem. Soc.* **2005**, *127*, 4566–4567; d) N. Kuhn, J. Fahl, S. Fuchs, M. Steimann, G. Henkel, A. H. Maulitz, *Z. Anorg. Allg. Chem.* **1999**, *625*, 2108–2119.

[18] C. Janiak, *J. Chem. Soc., Dalton Trans.* **2000**, 3885–3896.

[19] a) D. Rendell (Ed.), *Fluorescence and Phosphorescence*, Wiley, New York, **1987**; b) H. Yersin, A. Vogler (Eds.), *Photochemistry and Photophysics of Coordination Compounds*, Springer-Verlag, Berlin, **1987**; c) A. W. Adamson, P. D. Fleischauer (Eds.), *Concepts of Inorganic Photochemistry*, Wiley, New York, **1975**.

[20] *SHELXTL*, PC Siemens Analytical X-ray Instruments, Madison, WI, **1993**.

[21] G. M. Sheldrick, *SHELXTL Structure Determination Programs*, Version 5.0, PC Siemens Analytical Systems, Madison, WI, **1994**.

Received: August 21, 2005
Published Online: February 2, 2006

 © 2006 Wiley-VCH Verlag GmbH & Co. KGaA, Weinheim 

DOI: 10.1002/ejic.200500743

# Optical Properties of the Perovskite Solid Solution $LaTiO_2N$–$ATiO_3$ (A = Sr, Ba)

François Cheviré,[a] Franck Tessier,*[a] and Roger Marchand[a]

**Keywords:** Oxynitrides / Perovskites / Solid solution / Optical properties

Starting from the colored oxynitride $LaTiO_2N$, new perovskite-type solid solutions have been evidenced in the systems $La_{1-x}A_xTiO_{2+x}N_{1-x}$ (A = Sr, Ba) by ammonolysis at 950 °C of the corresponding oxide precursors prepared by the molten salt route. The color of the resulting powders varies progressively from the brown of $LaTiO_2N$ to the white of the oxide with a decrease in both the nitrogen and lanthanum contents. The optical absorption was characterized by diffuse reflectance. The nonlinear variation of the optical bandgap may result from the competition between the variation of the inductive effect between lanthanum and strontium, structural changes, and the difference in electronegativity between nitrogen and oxygen. For the compounds with a low nitrogen content the observed green shade is attributed to the presence of a nitrogen-rich secondary phase: $TiO_xN_y$ in which titanium presents a mixed-valence state. Taking advantage of a chimie douce process, the amorphous citrate route, the highest oxidation state of titanium was stabilized until $x = 0.9$ in the $La_{0.1}Sr_{0.9}Ti(O,N)_3$ phase giving the powder a bright yellow color ($Eg$ = 2.49 eV).
(© Wiley-VCH Verlag GmbH & Co. KGaA, 69451 Weinheim, Germany, 2006)

## Introduction

The progressive insertion of nitrogen, a less electronegative element compared with oxygen, within an oxide network involves an increase in the covalency of the bonding. A lower optical gap value, $Eg$, and consequently a modification of the absorption properties of the compound results from this substitution. Whereas many oxides are white, the corresponding oxynitrides are often colored. For example, considering the following cross-substitution: $M^{n+} + O^{2-} = M^{(n+1)+} + N^{3-}$, $ZrO_2$ (baddeleyite) and $BaTiO_3$ (perovskite) give rise to the isostructural colored oxynitrides TaON (yellow, $Eg$ = 2.5 eV) and $BaTaO_2N$ (red brown, $Eg$ = 2.0 eV), respectively. Over the last few years, nitride-type materials have largely been studied for their optical potential as nontoxic colored pigments (see below), as novel inorganic UV absorbers,[1] or as visible light-driven photocatalysts.[2–5]

The first colored oxynitride perovskites were obtained by substituting titanium in $BaTiO_3$ by a +5 oxidation-state element, such as tantalum or niobium. Numerous novel oxynitride phases were and are still obtained by applying this substitution principle at both the 12- and 6-fold-coordinated cationic sites. This is a key principle at the origin of a rich chemistry. $ATaO_2N$ (A = Ca, Sr, Ba) and $ANbO_2N$ (A = Sr, Ba) manifest dielectric properties.[6,7] $BaTaO_2N$ and $BaNbO_2N$ crystallize in a cubic unit cell and $SrTaO_2N$ in a tetragonal one.[8–10] The substitution of barium by a lanthanide element results in the oxynitrides $RTiO_2N$ (R = La, Nd),[11] where the +4 oxidation state of titanium is stabilized by the inductive effect of the rare earth element on the Ti-(O,N) bond.[12,13] This well-known effect is based on the capacity of an electropositive element (alkaline earth or rare earth) to share some electrons with the closest transition metal–nitrogen (oxygen) bond to enhance its covalent character, and thus to stabilize it. $NdTiO_2N$ is an orthorhombic $GdFeO_3$-type perovskite, while $LaTiO_2N$ crystallizes in a unit cell with triclinic symmetry.[14] The simultaneous substitution of both barium and titanium enables access to the white phase $LaZrO_2N$, which also presents a deformed $GdFeO_3$-type perovskite structure,[14] or to the oxynitride family $RTaON_2$ (R = La → Dy) and $LaNbON_2$.[11]

On the basis of one of the specific features of nitrogen, i.e. $\chi_N < \chi_O$, we were very interested in working with oxynitride solid-solution domains as a suitable means to tune the optical properties by the progressive modification of the composition. Jansen et al. have shown the possibility of adjusting the color of oxynitride pigments in the perovskite-type system $Ca_{1-x}La_xTaO_{2-x}N_{1+x}$.[15,16] The hue varies from yellow ($CaTaO_2N$) to brown ($LaTaON_2$) through orange and red intermediate colors as a result of the nitrogen content. Grins et al. obtained similar results in the system $AZr_{1-x}Ta_xO_{3-x}N_x$ with powders evolving from the white of $AZrO_3$ to the yellow, red, or brown of $ATaO_2N$, where A corresponds to Ca, Sr, and Ba, respectively.[17] Recently, Diot has evidenced solid-solution domains in the perovskite systems $A(A,Ta)(O,N,\square)_3$ (A = Ca, Sr, Ba) and

[a] UMR CNRS 6512 "Verres et Céramiques", Institut de Chimie de Rennes, Université de Rennes 1,
35042 Rennes cedex, France
Fax: +33-2-23235683
Franck.Tessier@univ-rennes1.fr

 © 2006 Wiley-VCH Verlag GmbH & Co. KGaA, Weinheim 

$Sr(Sr,Nb)(O,N,\square)_3$ giving rise to a range of colored pigments from pale yellow to orange brown.[18] Her research has also shown the interest in using defect fluorite rare earth tungstates $R_6WO_{12}\square_2$ and $R_{14}W_4O_{33}\square_3$ (R = rare earth) to isolate oxynitride powders $R_6W(O,N,\square)_{14}$ and $R_{14}W_4(O,N,\square)_{36}$, the color of which changes progressively from the white of the oxides to bright yellow with increasing nitrogen substitution. While with large rare earth elements the ammonolysis reaction of $RTaO_4$ tantalates provides either perovskite phases $RTaON_2$[11] or pyrochlore phases $R_2Ta_2O_5N_2$,[19] Maillard et al. identified defect fluorite solid solutions $RTa(O,N,\square)_4$ with small rare earths ($r_{R3+} \leq r_{Gd3+}$).[20] Colored oxynitride solid-solution domains have also been obtained in other structure types; for example, orange $Ta_{3-x}Zr_xN_{5-x}O_x$ ($0 \leq x \leq 0.60$) isostructural with $Ta_3N_5$ and pale yellow $Ta_{1-x}Zr_xN_{1-x}O_{1+x}$ ($0 \leq x \leq 0.28$) isostructural with TaON.[21]

This study was motivated, in part, by the preparation of light-colored oxynitride powders, for which an absorption edge located at exactly 400 nm will allow the absorption of all UV radiations. Our objective was to evidence a solid-solution domain $La_{1-x}A_xTiO_{2+x}N_{1-x}$ between the colored oxynitride $LaTiO_2N$ (brown, gap = 2.0 eV[22]) and the titanate $ATiO_3$ (A = Sr, Ba; gap > 3.1 eV) absorbing in the UV range.[1] $LaTiO_2N$ crystallizes in a distorted perovskite-type structure (Figure 1), as determined by neutron diffraction refinement, with a triclinic unit cell ($I\bar{1}$, $a$ = 5.6097 Å, $b$ = 7.8719 Å, $c$ = 5.5772 Å, $\alpha$ = 90.199°, $\beta$ = 90.154°, $\gamma$ = 89.988°).[14] The structure reveals two distinct $Ti(O,N)_6$ octahedra and no nitrogen/oxygen ordering in the anionic network.

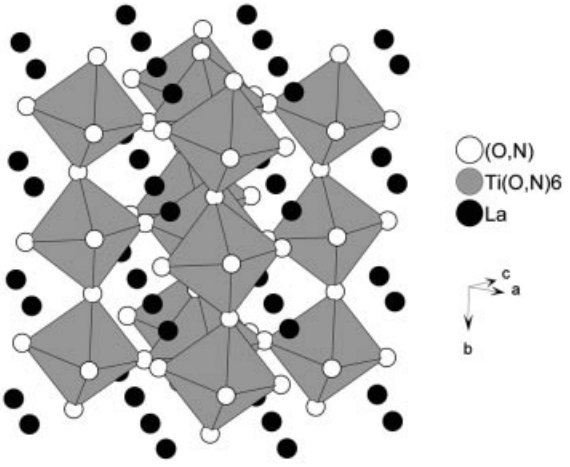


Figure 1. Crystal structure of the oxynitride perovskite $LaTiO_2N$.

## Results and Discussion

Firstly, we have considered the preparation of oxide precursors by molten salt synthesis. When $x$ = 0, $La_2Ti_2O_7$ (layered-perovskite structure) is clearly identified by X-ray diffraction. In the case of substituted compositions $La_{1-x}A_xTiO_y$, oxide precursors correspond generally to a mixture of ternary phases $La_aA_bTi_cO_d$ with variable composition. However, for $x$ values close to 1, single-phase powders present a perovskite structure close to that of the corresponding $ATiO_3$ titanate. Interestingly, the reaction of these precursors under ammonia leads systematically to the formation of single-phase perovskite-type oxynitrides, even in the case of a mixture of multinary oxides ($x < 1$). Figure 2 clearly illustrates this observation with the example of the composition $x$ = 0.5.

Table 1 details the experimental parameters of the ammonolysis experiments that were performed. All the compositions have a perovskite-structure type for which the position of the diffraction peaks continuously shifts from $LaTiO_2N$ to (Ba/Sr)$TiO_3$, as observed, for example, in the case of strontium (Figure 3). Although the structure of $LaTiO_2N$ was refined in a triclinic unit cell using neutron diffraction, the diffraction lines of the corresponding X-ray diffraction pattern can be indexed in a cubic perovskite unit cell [$a$ = 3.939(2) Å]. The asymmetry of some peaks, previously reported,[11] indicates that the real unit cell is not cubic. However, the distortion is quite weak relative to that observed for $NdTiO_2N$ and is not strong enough to determine the unit cell unambiguously by this technique. Here, it was not our purpose to refine all compositions of the solid solution by neutron diffraction. Using the cubic unit cell is an easy way to verify the linear evolution of the cell parameter and to prove the formation of the solid solution. Corresponding cubic unit-cell parameters have been plotted vs. $x$ in Figure 4. The trend follows a linear relation, in both cases, in agreement with Vegard's law. The opposite variation of the parameters, towards higher and lower values for Ba- and Sr-substitution, respectively, is explained if we compare the size of the cations in the 12-fold coordination (from Shannon:[23] La, 1.36 Å; Ba, 1.61 Å; Sr, 1.44 Å). There is a larger difference between La and Ba than there is for La and Sr, which should be balanced by the substitution of nitrogen by oxygen with increasing $x$ values. The resulting effect of such a competition within the lattices leads to the observed trend.

The brown color of the Ba-containing oxynitrides slightly lightens when increasing the alkaline earth metal amount from $x$ = 0.3 to 0.5. But the composition with $x$ = 0.75 presents a dark green shade that we attribute to a partial reduction of titanium. A decrease in the reaction temperature to 900 °C does not modify the green aspect of the color. In the case of Sr-containing oxynitrides, we observe a different color range strongly related to the substitution of a smaller cation (Table 1). A study performed by Eng et al.[24] in the perovskite system $ATiO_3$ (A = Sr, Ca) attributes the formation of a narrow conduction band leading to a higher value of the bandgap (+0.2 eV) mainly to the distortion of the linear M–O–M bonds from Sr (180°) to Ca (156°). This effect becomes more detectable with Ta than with Ti compounds because of the formation of larger conduction bands. This study just focuses on the effect of the tilting of the octahedra and does not take into account

 © 2006 Wiley-VCH Verlag GmbH & Co. KGaA, Weinheim 

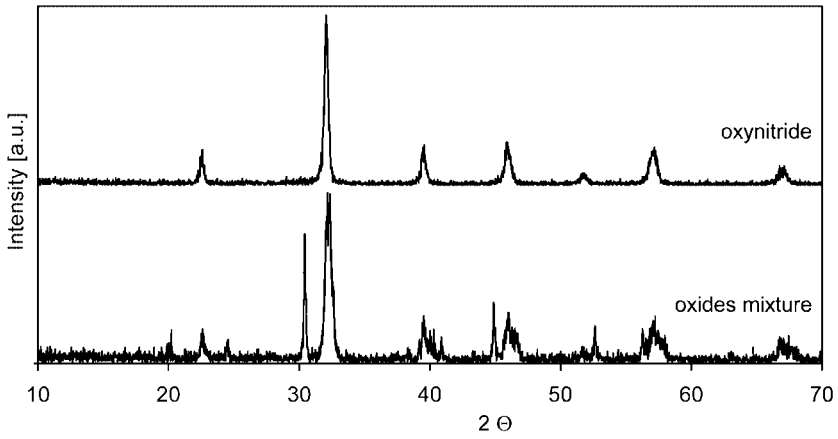


Figure 2. XRD powder pattern of the $La_{0.5}Ba_{0.5}TiO_{2.48}N_{0.52}$ oxynitride after ammonolysis of the corresponding oxide precursor.

Table 1. Experimental parameters for $La_{1-x}A_xTi(O,N)_3$ (A = Sr, Ba) oxynitrides.

| Cationic composition | Nitridation parameters | Cubic unit-cell parameter[a] [Å] | Powder color |
|---|---|---|---|
| LaTi | 950 °C/$NH_3$/15 h | 3.939(2) | brown |
| $La_{0.90}Ba_{0.10}Ti$ | 950 °C/$NH_3$/15 h | 3.945(2) | brown |
| $La_{0.70}Ba_{0.30}Ti$ | 950 °C/$NH_3$/15 h | 3.970(3) | brown |
| $La_{0.50}Ba_{0.50}Ti$ | 950 °C/$NH_3$/15 h | 3.971(2) | pale brown |
| $La_{0.25}Ba_{0.75}Ti$ | 900 °C/$NH_3$/15 h | – | khaki |
| $La_{0.25}Ba_{0.75}Ti$ | 950 °C/$NH_3$/15 h | 3.982(1) | dark green |
| $La_{0.75}Sr_{0.25}Ti$ | 950 °C/$NH_3$/15 h | 3.928(2) | red |
| $La_{0.50}Sr_{0.50}Ti$ | 950 °C/$NH_3$/15 h | 3.9187(4) | orange |
| $La_{0.25}Sr_{0.75}Ti$ | 950 °C/$NH_3$/15 h | 3.917(1) | ocher |
| $La_{0.10}Sr_{0.90}Ti$ | 850 °C/$NH_3$/15 h | – | green |
| $La_{0.10}Sr_{0.90}Ti$ | 950 °C/$NH_3$/15 h | 3.9130(3) | apple green |

[a] Refined values (using Dicvol04[36]).

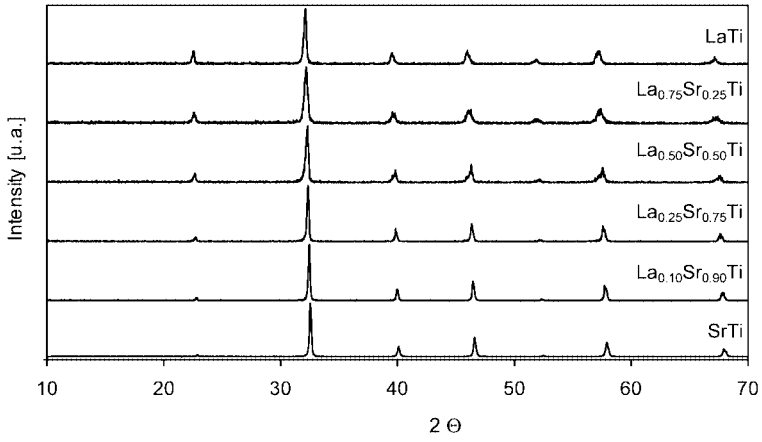


Figure 3. XRD patterns of the $La_{1-x}Sr_xTi(O,N)_3$ compositions (prepared at 950 °C) between the end terms of the solid solution.

either inductive effects or octahedral distortions. While changing the alkaline earth metal, similar color and also bandgap modifications have been observed in many phases, for example, in the perovskite-type oxynitrides, $CaTaO_2N$ (yellow), $SrTaO_2N$ (orange red), and $BaTaO_2N$ (red brown).[7,8,10,25–27] In this series, the atomic ratio O/N is constant and the modifications in the optical properties can only be explained by any changes in the structure and/or in the inductive effect relative to the choice of the alkaline earth metal. The characteristics of these phases are the following: $BaTaO_2N$ [cubic, bandgap = 1.8 eV; Ta–(O,N)–Ta = 180°], $SrTaO_2N$ [tetragonal, bandgap = 2.1 eV; Ta–(O,N)–Ta = 180° and 173.8°], $CaTaO_2N$ [orthorhombic, bandgap = 2.4 eV; Ta–(O,N)–Ta = 153.9°]. The linear evolution of the bandgap from $BaTaO_2N$ to $CaTaO_2N$ does not parallel a linear change in the Ta–(O/N)–Ta angles. As $BaTaO_2N$ and $SrTaO_2N$ display similar bond angles we expect similar bandgaps for both of them, which is not the

 © 2006 Wiley-VCH Verlag GmbH & Co. KGaA, Weinheim 

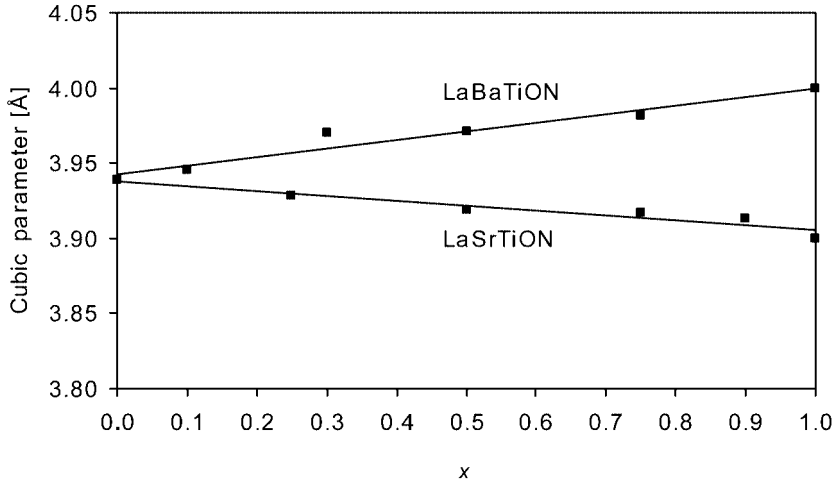


Figure 4. Variation of the unit-cell parameter in the $La_{1-x}Ba(Sr)_xTi(O,N)_3$ solid solutions.

case. Thus, the evolution of the bandgap value, and also the color, cannot only be the consequence of the deviation from linearity of the M–O–M bonds. The color change is due to several parameters including structure changes and the influence of the weaker inductive effect of strontium compared to that of barium, leading to a less covalent compound.

According to ref.,[24] the bandgap variation between $SrTiO_3$ (180°) and $CaTiO_3$ (156°) reaches 0.2 eV. However, the bond angles of $LaTiO_2N$ (160–167°) are closer to 180° than those of $CaTiO_3$, so we can expect a lower influence on the bandgap and a more diluted one for each of the intermediate compositions in the solid solution La–Sr–Ti–O–N. Between the two end members, $LaTiO_2N$ and $SrTiO_3$, the only visible effect in the bandgap position comes from the N/O substitution. The main consequence is an important red shift of the absorption edge. Thus, compared to the Ba-based system, for the same value of $x$, the absorption of the Sr-containing compositions is shifted towards lower wavelengths resulting in red and orange powders for $x$ = 0.25 and $x$ = 0.50, respectively, instead of the brown powders observed for the Ba-containing compositions. In the present system, the color of the powders varies progressively from the brown of $LaTiO_2N$ to the white of the oxide $SrTiO_3$ with the decrease in the nitrogen content. However, the $x$ = 0.9 composition is also characterized by a bright green shade close to apple-green. This greenish color of the powder may be a consequence of the combination of a yellow hue and a black component. It is effectively known that a black-unsaturated yellow appears green, then khaki, and finally black.

We ascribe the black shade to the presence of a mixed-valent-state for titanium ($Ti^{III}/Ti^{IV}$). The origin of this phenomenon may be clarified according to two hypotheses. First, the reduction of titanium may occur directly in the oxynitride product. It is then necessary to take account of a decrease in the formal cationic charge and consequently of a smaller nitrogen content in the structure, as illustrated by the following formulations with $x$ = 0.9:

$(La_{1-x}Sr_x)Ti^{IV}O_{2+x}N_{1-x} \rightarrow (La_{1-x}Sr_x)(Ti^{IV}_{1-y}Ti^{III}_y)O_{2+(x+y)}N_{1-(x+y)}$

$(La_{0.1}Sr_{0.9})Ti^{IV}O_{2.9}N_{0.1} \rightarrow (La_{0.1}Sr_{0.9})(Ti^{IV}_{1-y}Ti^{III}_y)O_{2.9+y}N_{0.1-y}$

Secondly, some reduced titanium may be present in a secondary black phase, $TiO_xN_y$. The powder then contains a mixture of a nitrogen-rich titanium oxynitride phase and a yellow $La_{0.1}Sr_{0.9}Ti(O,N)_3$ oxynitride. However, no secondary phase was detected by XRD analyses (Figure 3). From experience, it is well known that a very small amount of impurity, even indiscernible by XRD, may be sufficient to alter completely the color of the product and to overestimate nitrogen titration results. In order to avoid any reduction of titanium, ammonolysis experiments were carried out at lower temperatures (until 850 °C), but this did not allow for the stabilization of the higher oxidation state of titanium since a green shade was still observed. Grins et al. have reported similar color changes within the oxynitride solid solutions $AZr_xTa_{1-x}O_{2+x}N_{1-x}$ (A = Ca–Ba) without describing the hue progression.[16]

Nitrogen determination of the samples leads to the formulations listed in Table 2. Experimental contents are slightly higher than the calculated values (≈2%). In the case of the most greenish composition (A = Ba and $x$ = 0.75), the observed deviation (≈4%) is more important and seems to validate the hypothesis of a nitrogen-rich secondary phase. In the strontium-based oxynitride series, the black component in the apple-green shade is not very marked and suggests an extremely low amount of titanium oxynitride $TiO_xN_y$, which does not considerably affect the measured nitrogen amount.

The optical characterization of $La_{1-x}Sr_xTi(O,N)_3$ oxynitrides by diffuse reflectance highlights several significant points (Figure 5). The plot of the corresponding spectra between the two end members of the solid solution confirms the shift of the absorption edge towards higher wavelengths with increasing nitrogen content. However, this shift is not progressive. Between the oxide $SrTiO_3$ and the oxynitride $La_{0.1}Sr_{0.9}Ti(O,N)_3$ the absorption edge moves from 375 to 500 nm – a shift of 125 nm – whereas it stays between 525 and 590 nm for the lanthanum-rich compositions. In an at-

 © 2006 Wiley-VCH Verlag GmbH & Co. KGaA, Weinheim 

Table 2. Nitrogen contents and corresponding oxynitride formulations.

| Cationic composition | N wt.-%$_{calcd.}$ | N wt.-%$_{exp.}$ | Experimental formulation |
|---|---|---|---|
| LaTi | 6.02 | $6.1_7$ | $LaTiO_{1.96}N_{1.02}$ |
| $La_{0.90}Ba_{0.10}Ti$ | 5.41 | $5.5_5$ | $La_{0.90}Ba_{0.10}TiO_{2.07}N_{0.92}$ |
| $La_{0.70}Ba_{0.30}Ti$ | 4.21 | $4.4_3$ | $La_{0.70}Ba_{0.30}TiO_{2.27}N_{0.73}$ |
| $La_{0.50}Ba_{0.50}Ti$ | 3.01 | $3.1_4$ | $La_{0.50}Ba_{0.50}TiO_{2.48}N_{0.52}$ |
| $La_{0.25}Ba_{0.75}Ti$ | 1.50 | $2.0_5$ | $La_{0.25}Ba_{0.75}TiO_{2.62}N_{0.34}$ |
| $La_{0.75}Sr_{0.25}Ti$ | 4.77 | $4.9_1$ | $La_{0.75}Sr_{0.25}TiO_{2.22}N_{0.77}$ |
| $La_{0.50}Sr_{0.50}Ti$ | 3.36 | $3.5_2$ | $La_{0.50}Sr_{0.50}TiO_{2.47}N_{0.52}$ |
| $La_{0.25}Sr_{0.75}Ti$ | 1.79 | $2.0_6$ | $La_{0.25}Sr_{0.75}TiO_{2.69}N_{0.29}$ |
| $La_{0.10}Sr_{0.90}Ti$ | 0.74 | $0.9_1$ | $La_{0.10}Sr_{0.90}TiO_{2.88}N_{0.12}$ |

tempt to explain this nonlinearity, and despite the difficulty in calculating the band structure due to nitrogen/oxygen disorder, it is realistic to involve the following effects. Basically, the element located in the 12-fold coordination site does not directly influence the bandgap between the 2p(O) and 3d(Ti) bands, but rather it engenders an inductive effect on the Ti-(O,N) bond. Besides the effect of the large cation, nitrogen/oxygen substitutions modify the position of the valence band in a precise manner, so that the position of the absorption edge moves towards higher wavelengths. As nitrogen is less electronegative than oxygen, the energy level difference between the oxygen and nitrogen 2p orbitals [$E_{2p}$(O) = –14.8 eV, $E_{2p}$(N) = –13.4 eV (top of the valence band[28])] can simply explain the decrease in the bandgap between the valence and conduction bands. Also, as discussed above, by substituting La for Sr the decrease in the bond angles from 180° causes a small increase in the bandgap value that can act as a minor counter effect to the red shift (coupled with inductive effect variation) to explain parts of the nonlinearity of the bandgap values along the solid solution. By comparison with the oxide $SrTiO_3$, the absorption edge profile appears less steep and the spectral selectivity lower (Table 3), which is mainly a consequence of a lower crystallization state. We have already observed that the crystallization state of the powder influences the steepness of the diffuse reflectance spectrum in oxide systems. Thus, the absorption edge becomes steeper with an increasing crystallization state. This is probably linked to the better homogeneity of the environments of titanium. The average octahedron is $TiO_{4+2x}N_{2-2x}$, but because of the O/N disorder we consent that a large variety of O/N environments, with slightly different absorption properties, should exist around the titanium atoms, leading to the spreading of the absorption edge. Moreover, the level of the reflection plateau dramatically decreases with increasing nitrogen content. We have already observed, and not yet explained, such a phenomenon in several systems.[29,30] In the case of the composition $x$ = 0.9 the absorption edge – located at 500 nm – should correspond to a yellow color although the powder appears "apple green". This result provides further confirmation of the presence of a black component. Thus, the alteration of the expected color is effectively due to the existence of partially reduced titanium, which is no longer totally stabilized under the reducing ammonia synthesis conditions used.

A more reactive oxide precursor was synthesized by the amorphous citrate route in order to stabilize the +4 oxidation state of titanium in the $La_{0.1}Sr_{0.9}Ti(O,N)_3$ oxynitride phase. This chimie douce process allows very fine and chemically homogeneous powders to be obtained rapidly. These powders are potentially able to manifest an enhanced reactivity with ammonia at lower temperatures.[31,32] Experimental data are listed in Table 4 for both the $x$ = 0.9 and 1.0 compositions. A bright yellow powder is obtained after ammonolysis of the $x$ = 0.9 precursor at 950 °C. Reduction phenomena did not occur with longer reaction times. The corresponding diffuse reflectance spectra, shown in Figure 6, reveal an absorption domain at the same wavelengths as that for the absorption of the greenish product obtained from the molten salt precursor. Moreover, a slight gain is noticed in the maximum value of the diffuse reflectance, in possible relation with the disappearance of the black component discussed previously. In addition, the experimental nitrogen content of this phase reaches 0.81 wt.-%, in excellent agreement with the calculated content (0.74 wt.-%), and corresponds to the following formulation $La_{0.10}Sr_{0.90}TiO_{2.89}N_{0.11}$. All these results confirm the hypothesis of the presence of a small amount of titanium oxynitride as an impurity in the former results, since the use of a more chemically homogeneous precursor solves the problem. Nevertheless, the green shade appears again for the composition $x$ = 0.05, and the powder becomes yellowish green. In this case, a very small amount of dopant is present and hence it is difficult to come to a conclusion on the origin of the reduced titanium giving the green shade and also on the nature of the "impurity" phase. Many possibilities are of interest, such as the presence of a $TiO_xN_y$ or $SrTi(O,N,\square)_3$ secondary phase. When the reaction is carried out under ammonia at 750 °C a pale green powder, without any marked yellow hue, is produced. It seems that under usual ammonolysis conditions the reduction of titanium occurs before the maximum nitrogen content is obtained.

To conclude, we have synthesized new oxynitride solid solutions for the systems $La_{1-x}A_xTiO_{2+x}N_{1-x}$ (A = Sr, Ba), where it is possible to tune progressively the color of the powders from brown ($LaTiO_2N$), to red, orange, yellow, and finally white ($SrTiO_3$) with the variation of both nitrogen and lanthanum contents. The green shade observed in the presence of low nitrogen contents is attributed to mixed-

 © 2006 Wiley-VCH Verlag GmbH & Co. KGaA, Weinheim 

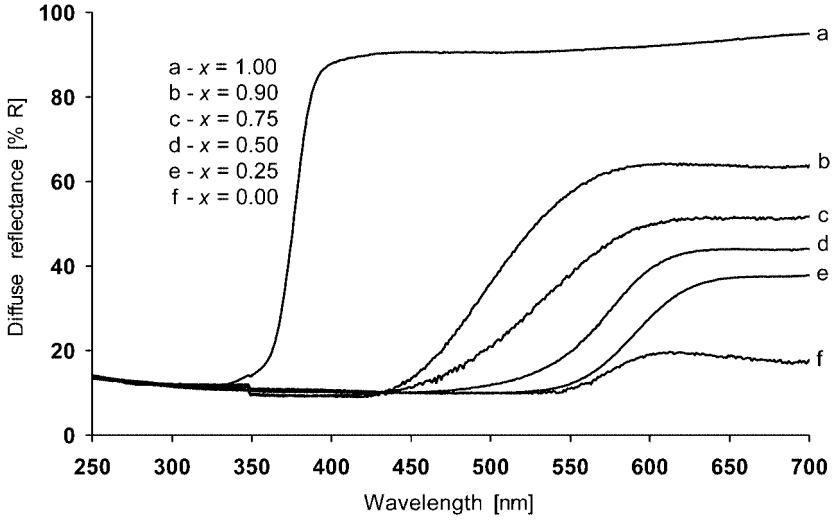


Figure 5. Diffuse reflectance spectra of $La_{1-x}Sr_xTi(O,N)_3$ compositions.

Table 3. Diffuse reflectance data of the oxynitride $La_{1-x}Sr_xTi(O,N)_3$ series obtained from precursors prepared by molten salt synthesis.

| Composition | $\lambda \pm \Delta\lambda$ [nm] | *E*g [eV] |
|---|---|---|
| $SrTiO_3$ | 376 ± 14 | 3.31 |
| $La_{0.10}Sr_{0.90}Ti(O,N)_3$ | 497 ± 63 | 2.49 |
| $La_{0.25}Sr_{0.75}Ti(O,N)_3$ | 533 ± 60 | 2.27 |
| $La_{0.50}Sr_{0.50}Ti(O,N)_3$ | 574 ± 38 | 2.07 |
| $La_{0.75}Sr_{0.25}Ti(O,N)_3$ | 590 ± 33 | 2.02 |
| $LaTiO_2N$ | 574 ± 30 | 1.96 |

valent titanium present in a black nitrogen-rich phase, $TiO_xN_y$. An attenuation of this reduction phenomenon is detected when using more chemically homogeneous and reactive precursors prepared by the amorphous citrate route. Such processes create suitable solutions to optimize the properties of (oxy)nitride materials for optical applications (colored pigments, visible-light photocatalysts). Avoiding such parasitic colors is a major synthetic problem in the preparation of light-colored materials for promising appli-

Table 4. Experimental data of the synthesis of $La_{0.1}Sr_{0.9}Ti(O,N)_3$ oxynitrides using the citrate route.

| Cationic composition | Experimental parameters | Color | $\lambda \pm \Delta\lambda$ [nm] |
|---|---|---|---|
| SrTi | 950 °C/air/15 h | white | 376 ± 20 |
| $La_{0.10}Sr_{0.90}Ti$ | 950 °C/$NH_3$/15 h | bright yellow | – |
| $La_{0.10}Sr_{0.90}Ti$ | 950 °C/$NH_3$/2 × 15 h | bright yellow | 496 ± 57 |
| $La_{0.05}Sr_{0.95}Ti$ | 750 °C/$NH_3$/15 h | pale green | – |
| $La_{0.05}Sr_{0.95}Ti$ | 900 °C/$NH_3$/2 × 15 h | pale yellow/green | 483 ± 55 |
| $La_{0.05}Sr_{0.95}Ti$ | 950 °C/$NH_3$/15 h | green | – |

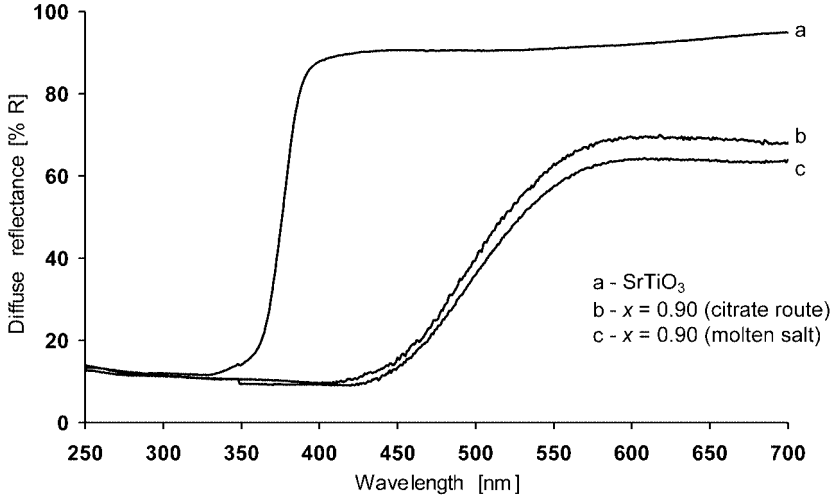


Figure 6. Comparison of the diffuse reflectance spectra of $La_{0.10}Sr_{0.90}TiO_{2.89}N_{0.11}$ prepared by ammonolysis of the molten salt and citrate precursors.

 © 2006 Wiley-VCH Verlag GmbH & Co. KGaA, Weinheim 

cations such as novel UV absorbers. Nevertheless, the interest in oxynitride solid-solution domains relies on the ability to tune the absorption edge position towards 400 nm, which is the limit between the UV and the visible ranges.

## Experimental Section

**Synthesis of Oxide Precursors:** Lanthanum-modified titanates were obtained using both a modified ceramic route and by taking advantage of the amorphous citrate route, a chimie douce method, which gives the oxide precursors an enhanced homogeneity and reactivity towards ammonia.

**Solid-State Route:** $La_{1-x}A_xTiO_{3.5-x/2}$ precursors ($x$ = 0, 0.25, 0.5, 0.75, 0.9) were prepared by heating a stoichiometric mixture of $La_2O_3$ (99.99%, Alfa Aesar), $BaCO_3$ (99%, Acros), $SrCO_3$ (99%, Alfa Aesar), and $TiO_2$ (Degussa, P25) in a molten salt medium. The melt content, corresponding to the eutectic mixture 50 mol-% NaCl and 50 mol-% KCl, was determined to form 50 wt.-% of the total reactants weight.[33] The corresponding mixture was heated at 1000 °C for 15 h in a muffle furnace. The resulting products were washed using distilled water and absolute ethyl alcohol, and then dried at 150 °C.

**Amorphous Citrate Route:** Among numerous chimie douce type processes that have been developed to prepare oxide powders in order to improve their quality (purity, chemical homogeneity, etc.) and their reactivity the process involving citric acid as a complexing agent has been preferentially used. It is not, strictly speaking, a classic sol-gel process in the usual sense in that the gel is not formed by a metal–oxygen–metal network, but rather from calcination of metal–organic complexes, thus producing ultra fine reactive powders with an excellent chemical homogeneity.[34] In order to characterize any influence of the synthesis route, the $x$ = 0.9 precursor for A = Sr was also prepared using this route. Lanthanum oxide ($La_2O_3$, 99.99%, Alfa Aesar), strontium carbonate ($SrCO_3$, 99%, Alfa Aesar), and titanium tetrabutoxide ($C_{16}H_{36}O_4Ti$, 99%, Acros) were used as starting materials and dissolved in a diluted nitric acid solution. Citric acid ($C_6H_8O_7$, Merck, > 99%) dissolved in a minimum amount of water was added to the solution in the proportion of one mole per cation valence, the addition being followed by a 30 min stirring step at 120 °C. Since the complexation of cations by citric acid is improved at pH ≥ 7, the acidic solution was neutralized by an ammonia solution (25%, Merck),[35] then stirred at 150 °C for 15 min to promote chelate formation. The liquid was progressively heated to 250 °C, leading after 15 h to an expanded black solid residue. This solid was finally ground and calcined at 600 °C in an alumina crucible until total elimination of carbon had occurred.

**Thermal Ammonolysis:** Nitridation reactions were carried out in alumina boats placed inside an electric furnace through which ammonia gas flowed at 40–50 $L\,h^{-1}$. The temperature was raised to 950–1000 °C with a heating rate of 10 °C $min^{-1}$. After a reaction time of 15 h the furnace was switched off and the nitrided powders were cooled to room temperature under a pure nitrogen atmosphere.

**X-ray Diffraction:** XRD powder patterns were recorded using a Philips PW3710 diffractometer operating with Cu-$K_\alpha$ radiation ($\lambda$ = 1.5418 Å). X′PERT software – Data Collector, Graphics, and Identify – were used for recording, analysis, and phase matching of the patterns, respectively. The lattice parameters were refined using Dicvol04.[36]

**Elemental Analysis:** Nitrogen and oxygen contents were determined with a LECO TC-436 analyzer using the inert gas fusion method. Nitrogen was detected as $N_2$ by thermal conductivity and oxygen as $CO_2$ by infrared detection. The apparatus was calibrated using $N_2$ and $CO_2$ gas (purity ≥ 99.95%) as well as ε-TaN as a nitrogen standard.[37]

**UV/Vis Spectrophotometry:** Diffuse reflectance spectra were collected using a Varian Cary 100 Scan spectrometer equipped with the Varian WinUV software and the integrating sphere Labsphere (DRC-CA-30I). Prior to measurements, the absolute reflectance of the samples was calibrated with a certified "spectralon" standard (Labsphere Cie). Experimental data were collected within the 250–800 nm range with a 1 nm step and 0.5 s integration time. The position of the absorption edge was determined graphically at the inflection point of the curve and the value of the optical gap using the theory of Kubelka–Munk.[38]


[1] F. Cheviré, Thesis no. 3061, Université de Rennes 1, France, **2004**.
[2] D. Li, H. Haneda, S. Hishita, N. Ohashi, *Mater. Sci. Eng. B* **2005**, *117*, 67–75.
[3] D. Yamasita, T. Takata, M. Hara, J. N. Kondo, K. Domen, *Solid State Ionics* **2004**, *172*, 591–595.
[4] M. Hara, T. Takata, J. N. Kondo, K. Domen, *Catal. Today* **2004**, *90*, 313–317.
[5] A. Kasahara, K. Nukumizu, T. Takata, J. N. Kondo, M. Hara, H. Kobayashi, K. Domen, *J. Phys. Chem. B* **2003**, *107*, 791–797.
[6] R. Marchand, F. Pors, Y. Laurent, *Rev. Int. Tempér. Réfract. Fr.* **1986**, *23*, 11–15.
[7] F. Pors, R. Marchand, Y. Laurent, P. Bacher, G. Roult, *Mater. Res. Bull.* **1988**, *23*, 11–15.
[8] F. Pors, P. Bacher, R. Marchand, Y. Laurent, G. Roult, *Mater. Res. Bull.* **1988**, *23*, 1447–1450.
[9] F. Pors, P. Bacher, R. Marchand, Y. Laurent, G. Roult, *Rev. Int. Tempér. Réfract. Fr.* **1988**, *24*, 239–246.
[10] Y.-I. Kim, P. M. Woodward, K. Z. Baba-Kishi, C. W. Tai, *Chem. Mater.* **2004**, *16*, 1267–1276.
[11] R. Marchand, F. Pors, Y. Laurent, *Ann. Chim. Fr.* **1991**, *16*, 553–560.
[12] J. Etourneau, J. Portier, F. Ménil, *J. Alloys Compd.* **1992**, *188*, 1–7.
[13] H.-C. Zur Loye, J. D. Houmes, D. S. Bem, *The Chemistry of Transition Metal Carbides and Nitrides* (Ed.: Ted Oyama), Blackie Academic & Professional, **1996**, *8*, 155.
[14] S. J. Clarke, B. P. Guinot, C. W. Michie, M. J. C. Calmont, M. J. Rosseinsky, *Chem. Mater.* **2002**, *14*, 288–294.
[15] M. Jansen, H. P. Letschert, *Nature* **2000**, *404*, 980–982.
[16] M. Jansen, H. P. Letschert, *European Patent no. 0627373,* **1995**.
[17] J. Grins, G. Svensson, *Mater. Res. Bull.* **1994**, *29*, 801–809.
[18] N. Diot, *Thesis no. 2222*, Université de Rennes 1, France, **1999**.
[19] F. Pors, R. Marchand, Y. Laurent, *J. Solid State Chem.* **1993**, *107*, 39–42.
[20] P. Maillard, F. Tessier, E. Orhan, F. Cheviré, R. Marchand, *Chem. Mater.* **2005**, *17*, 152–156.
[21] E. Günther, M. Jansen, *Mater. Res. Bull.* **2001**, *36*, 1399–1405.
[22] G. Hitoki, T. Takata, J. N. Kondo, M. Hara, H. Kobayashi, K. Domen, *Electrochem.* **2002**, *70*, 463–465.
[23] R. D. Shannon, *Acta Crystallogr. Sect. A* **1976**, *A32*, 751–767.
[24] H. W. Eng, P. W. Barnes, B. M. Auer, P. M. Woodward, *J. Solid State Chem.* **2003**, *175*, 94–109.
[25] F. Pors, P. Bacher, R. Marchand, Y. Laurent, G. Roult, *Rev. Int. Hautes Tempér. Réfract.* **1987**, *24*, 239–246.
[26] E. Günther, R. Hagenmayer, M. Jansen, *Z. Anorg. Allg. Chem.* **2000**, *626*, 1519–1525.
[27] S. J. Clarke, K. A. Hardstone, C. W. Michie, M. J. Rosseinsky, *Chem. Mater.* **2002**, *14*, 2664–2669.
[28] R. Hoffmann, *J. Chem. Phys.* **1963**, *39*, 1397–1412.


 © 2006 Wiley-VCH Verlag GmbH & Co. KGaA, Weinheim 

[29] F. Cheviré, F. Tessier, R. Marchand, *Sil. Ind.* **2004**, *69*, 159–163.
[30] N. Diot, O. Larcher, R. Marchand, J. Y. Kempf, P. Macaudière, *J. Alloys Compd.* **2001**, *323–324*, 45–48.
[31] F. Cheviré, F. Tessier, R. Marchand, *Mater. Res. Bull.* **2004**, *39*, 1091–1101.
[32] P. Maillard, F. Tessier, E. Orhan, F. Cheviré, R. Marchand, *Chem. Mater.* **2005**, *17*, 152–156.
[33] P. A. Fuierer, R. E. Newnham, *J. Am. Ceram. Soc.* **1991**, *74*, 2876–2881.
[34] F. Tessier, R. Marchand, *J. Solid State Chem.* **2003**, *171*, 143–151.
[35] A. Douy, P. Odier, *Mater. Res. Bull.* **1989**, *24*, 1119–1126.
[36] A. Boultif, D. Louer, *J. Appl. Crystallogr.* **2004**, *37*, 724–731.
[37] M. Dopita, B. Wollein, D. Rafaja, W. Gruner, W. Lengauer, *Defect and Diffusion Forum, Diffusion in Materials*, DIMAT-2000, **2001**, *194–199*, 1607–1612.
[38] D. Kubelka, L. Munk, *Z. Techn. Physik* **1931**, *12*, 593–601.

Received: August 23, 2005
Published Online: February 2, 2006

 © 2006 Wiley-VCH Verlag GmbH & Co. KGaA, Weinheim 

DOI: 10.1002/ejic.200500792

# Synthesis, Characterization, and Properties of Some Copper(II) Complexes of 2-Pyridineformamide Thiosemicarbazone (HAm4DH)

**María del Carmen Aguirre,[a] Joaquín Borrás,[b] Alfonso Castiñeiras,*[a] José M. García-Monteagudo[c] Isabel García-Santos,[a] Juan Niclós,[d] and Douglas X. West[e]**

**Keywords:** Thiosemicarbazones / Copper complexes / One-dimensional chains / Cyclic voltammetry / DNA cleavage

Reactions between different copper(II) salts and 2-pyridineformamide thiosemicarbazone (HAm4DH) in neutral ethanolic media led to the formation of complexes with the formulae $[Cu(HAm4DH)X_2]$ (X = Cl or Br) (**1**, **2**) and $[Cu(HAm4DH)_2]X_2$ (X = $NO_3$ or $ClO_4$) (**3**, **4**). The same reactions carried out in the presence of triethylamine gave rise to new complexes with the general formulae [Cu(Am4DH)X] (X = Cl, Br, AcO, or $NO_3$) (**5**–**8**), $[Cu(H_2O)(Am4DH)](ClO_4)$ (**9**), and $[Cu(Am4DH)_2]$ (**10**), many of which were isolated with different molecules of crystallization and contain a deprotonated thiosemicarbazone (Am4DH). These complexes were characterized by elemental analysis, and different spectroscopic and magnetic techniques. The thermal and redox behavior of the complexes was also evaluated. Complexes **1**, **2**, **5**, and **6** show better nuclease activity than $[Cu(phen)_2]^{2+}$. In addition, crystals were isolated in the cases of $[Cu(HAm4DH)Cl_2]_2$ (**5a**), $^1_\infty$[Cu(Am4DH)Cl] (**5b**), $^1_\infty$[Cu(Am4DH)Br] (**6a**), and $[Cu(HAm4DH)(H_2O)(ClO_4)_2]\cdot MeOH\cdot H_2O$ (**9a**) and these structures were analyzed by X-ray diffraction. Compound **5a** has a dimeric structure with chlorine bridges and shows weak antiferromagnetism ($J$ = –12.2 $cm^{-1}$). Complexes **5b** and **6a** are one-dimensional polymers formed through halogen bridges and the deprotonated thiosemicarbazone in the thiolate form. In compound **9a** the copper(II) is in a distorted octahedral environment with two $ClO_4$ units coordinated to the metal center.

(© Wiley-VCH Verlag GmbH & Co. KGaA, 69451 Weinheim, Germany, 2006)

## Introduction

In general, thiosemicarbazones are obtained by condensation of the corresponding thiosemicarbazide with aldehydes or ketones.[1] However, an alternative method of synthesis involves the use of nitriles as starting materials.[2] In this case, the resulting thiosemicarbazones contain an additional amino group (Scheme 1), which gives improved water solubility. This in turn can improve the biological activity of these compounds and their metal complexes. Furthermore, this amino group is undoubtedly able to participate in hydrogen bond formation, which can favor the formation of supramolecular species.

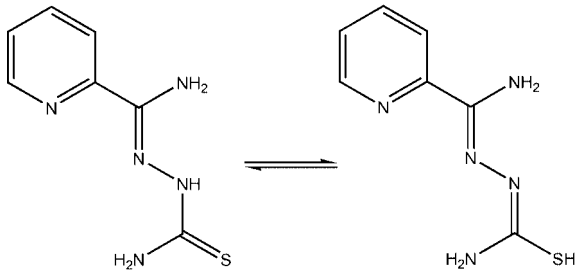


**Ia** **Ib**

Scheme 1.

Thiosemicarbazones in the solid state are in an approximately planar arrangement with a *Z* configuration around the C=N bond and the terminal thioamide sulfur atom in a *trans* disposition with respect to the azomethine nitrogen (**Ia** in Scheme 1). The fact that this system undergoes *thione–thiol* tautomerism makes the thiosemicarbazones versatile ligands for a wide range of metal ions both in the neutral and anionic forms (Scheme 1).

Thiosemicarbazones generally coordinate to metal centers through the sulfur and azomethine nitrogen atoms to give a five-membered chelate ring with the metal. The resulting complexes are usually mononuclear,[3] dinuclear,[4,5]

[a] Departamento de Química Inorgánica, Facultad de Farmacia, Universidad de Santiago de Compostela,
15782 Santiago de Compostela, Spain
Fax: +34-981547-163
E-mail: qiac01@usc.es
[b] Departamento de Química Inorgánica, Facultad de Farmacia, Universidad de Valencia,
46100 Valencia, Spain
[c] Departamento de Química Física, Facultad de Farmacia, Universidad de Santiago de Compostela,
15782 Santiago de Compostela, Spain
[d] Departamento de Química Inorgánica, Facultad de Farmacia, Universidad de Granada,
18071 Granada, Spain
[e] Department of Chemistry, University of Washington,
Box 351700, Seattle, WA 98195-1700, USA

 © 2006 Wiley-VCH Verlag GmbH & Co. KGaA, Weinheim 

or polynuclear in conjunction with an additional ligand such as a halogen.

The ability of these ligands to be deprotonated in a suitable basic medium frequently leads to the formation not only of neutral mononuclear species but also polynuclear entities in which the thiosemicarbazone acts as a bridging ligand − generally through the thiolate sulfur atom.[6–8]

Although complexes of a number of metals with 2-pyridineformamide thiosemicarbazone (HAm4DH)[9–12] or its $^4N$-substituted derivatives[13–21] have been studied, the coordination of these ligands with copper(II) has scarcely been investigated hitherto.[16,22,23] To explore their versatility further, in the work described here we prepared a number of copper(II) complexes of HAm4DH and determined their thermal, magnetic, and redox properties, the X-ray crystal structures of the complexes $[Cu(HAm4DH)Cl_2]_2$ (**5a**), $^1_\infty$[Cu(Am4DH)Cl] (**5b**), $^1_\infty$[Cu(Am4DH)Br] (**6a**), and $[Cu(HAm4DH)(H_2O)(ClO_4)_2]\cdot MeOH\cdot H_2O$ (**9a**), and the in vitro nuclease activities of a selection of these compounds.

## Results and Discussion

The reactions between different copper(II) salts and HAm4DH, in neutral or slightly basic ethanolic media, gave a series of complexes with the general formulae $[Cu(HAm4DH)X_2]$ (X = Cl or Br) (**1**, **2**), $[Cu(HAm4DH)_2]X_2$ (X = $NO_3$ or $ClO_4$) (**3**, **4**), [Cu(Am4DH)X] (X = Cl, Br, AcO, or $NO_3$) (**5**–**8**), $[Cu(H_2O)(Am4DH)](ClO_4)$ (**9**), and $[Cu(Am4DH)_2]$ (**10**). These compounds generally have melting points above 200 °C and are soluble in DMF and DMSO, partially soluble in methanol, but insoluble in other commonly used organic solvents. The mass spectra of the complexes (FAB) in some cases show the molecular ion peak, although the most significant peaks correspond to the fragments $[Cu(HAm4DH)_2]^+$, $[Cu(HAm4DH)X]^+$, and $[Cu(HAm4DH)]^+$, where X is the corresponding anion. These fragmentation patterns involve the addition or loss of a hydrogen atom from the fragments.

The molar conductivities of freshly prepared solutions of the complexes in DMF are in the range $\Lambda_m$ = 23–63 $S\cdot cm^2\cdot mol^{-1}$, which indicates that the compounds are neutral. However, $[Cu(Am4DH)(H_2O)](ClO_4)$ is a 1:1 electrolyte ($\Lambda_m$ = 96 $S\cdot cm^2\cdot mol^{-1}$). The molar conductivity values for $[Cu(HAm4DH)_2](NO_3)_2\cdot EtOH$ and $[Cu(HAm4DH)_2](ClO_4)_2$ are 152 and 168 $S\cdot cm^2\cdot mol^{-1}$, respectively, and these values correspond to 1:2 electrolytes.[24]

Single crystals of the complexes $[Cu(HAm4DH)Cl_2]_2$ (**5a**), $^1_\infty$[Cu(Am4DH)Cl] (**5b**), $^1_\infty$[Cu(Am4DH)Br] (**6a**), and $[Cu(HAm4DH)(H_2O)(ClO_4)_2]\cdot MeOH\cdot H_2O$ (**9a**) suitable for X-ray diffraction were obtained by the slow evaporation of $[Cu(Am4DH)Cl]\cdot 0.5\,EtOH$ (**5**), $[Cu(Am4DH)Br]\cdot 0.5\,EtOH$ (**6**), or $[Cu(Am4DH)(H_2O)](ClO_4)$ (**9**) solutions in 1:1 mixtures of MeOH/$CCl_4$, MeOH/$CH_3CN$, or MeOH/$CCl_4$, respectively, in air at room temperature.

### Crystal Structure of $[Cu(HAm4DH)Cl_2]_2$ (5a)

It can be seen from Figure 1 that **5a** is a centrosymmetric binuclear species. Each copper(II) center is bonded to a neutral HAm4DH molecule through the thione sulfur, azomethine nitrogen, and pyridinic nitrogen atoms. Three chlorine atoms are also bound to the metal − one terminal chlorine and the other two as bridges between the metal centers. This arrangement gives rise to an octahedral environment in such a way that the dimer is formed by two octahedra that share an edge consisting of the dimeric skeleton Cu(μ-Cl)$_2$Cu. The most significant bond lengths and angles are shown in Table 1.

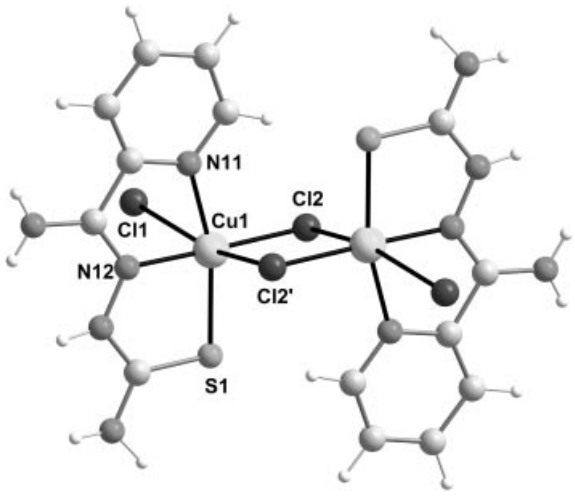


Figure 1. Perspective view of **5a** (symmetry code i: $-x + 2$, $-y$, $-z + 1$).

The formation of dimers is not unusual in copper(II) complexes of thiosemicarbazones.[4,25] However, the majority of such compounds have the formula $[Cu(L)Cl]_2$, where the bridging atom is either the sulfur or the chlorine atom, which gives rise to a coordination number of five around the metal center. In the case where L is 2-pyridinecarboxaldehyde thiosemicarbazone it was possible to obtain both structures,[4] each with a pyramidal geometry; that is, the copper(II) centers are joined either by two thiolate bridges from the thiosemicarbazone or by two chloro bridges. In contrast, compound **5a** has a coordination mode and geometry that is completely different, where the Cu(μ-Cl)$_2$-Cu skeleton has the two copper centers joined through two chloro bridges that have markedly different bond lengths: 2.219(1) Å (Cu1–Cl2$^i$, i: $-x + 2$, $-y$, $-z + 1$) and 3.139(1) Å (Cu1–Cl2). This gives rise to a rhomboidal geometry, with Cu–Cu and Cl–Cl distances of 3.837(1) and 3.850(2) Å, respectively, and Cl–Cu–Cl and Cu–Cl–Cu angles of 90.20(3) and 89.90(3)°, respectively. The existence of one weak and one strong Cu–Cl interaction is a characteristic feature in dimeric species with halogen bridges.[26,27] However, the second Cu–Cl distance in **5a** is at the higher limit of the sum of the van der Waals radii (3.15 Å), but is equal to or less than the order of magnitude for these bonds found in other copper(II) dimers with chloro bridges.[28] The three coordination positions around the copper center are occupied by the sulfur and two nitrogens of HAm4DH, with values of 2.027(2) and 1.941(2) Å for the Cu–Npyri-

 © 2006 Wiley-VCH Verlag GmbH & Co. KGaA, Weinheim 

Table 1. Selected bond lengths [Å] and angles [°] for compounds **5a**, **5b**, **6a**, and **9a**.

| Compound | **5a**[a] | **5b**[b] | **6a**[c] | **9a**[d] | |
|---|---|---|---|---|---|
| Cu1–N11 | 2.027(2) | 2.034(6) | 2.034(3) | 2.020(3) | 2.018(3) |
| Cu1–N12 | 1.941(2) | 1.934(7) | 1.938(3) | 1.921(3) | 1.919(3) |
| Cu1–S1 | 2.296(8) | 2.265(2) | 2.257(1) | 2.278(1) | 2.277(1) |
| Cu1–X1 | 3.132(1) | 2.247(2) | 2.375(1) | 2.498(3) | 2.483(3) |
| Cu1–X2 | 3.139(1) | – | – | 2.744(3) | 2.852(3) |
| Cu1–X3 | 2.219(1) | 2.945(2) | 2.957(1) | 1.964(2) | 1.966(2) |
| Cu1–Cu1$^{i}$ | 3.837(1) | 4.158(1) | 4.249(1) | 9.687(2) | – |
| N11–Cu1–N12 | 79.44(8) | 80.0(3) | 80.25(12) | 80.25(11) | 80.21(12) |
| N11–Cu1–S1 | 164.14(6) | 164.0(2) | 164.13(9) | 166.21(8) | 166.04(9) |
| N12–Cu1–S1 | 84.75(7) | 84.3(2) | 84.08(8) | 85.97(9) | 85.84(9) |
| N11–Cu1–X1 | 84.20(6) | 97.0(2) | 97.95(9) | 86.6510 | 86.71/11) |
| N11–Cu1–X2 | 90.49(6) | – | – | 81.96(11) | 77.70(11) |
| N11–Cu1–X3 | 99.43(6) | 86.9(2) | 87.50(9) | 95.41(11) | 95.64(11) |
| N12–Cu1–X1 | 83.66(6) | 166.3(2) | 166.01(9) | 92.65(11) | 94.22(11) |
| N12–Cu1–X2 | 90.49(6) | – | – | 86.17(12) | 91.60(11) |
| N12–Cu1–X3 | 178.58(7) | 98.7(2) | 99.03(9) | 173.76(11) | 173.85(11) |
| S1–Cu1–X1 | 95.48(3) | 97.6(1) | 96.65(3) | 94.15(7) | 95.08(7) |
| S1–Cu1–X2 | 97.47(3) | – | – | 97.09(9) | 102.14(8) |
| S1–Cu1–X3 | 96.39(3) | 98.7(1) | 97.48(4) | 98.33(8) | 98.20(8) |
| X1–Cu1–X2 | 165.23(2) | – | – | 168.58(10) | 162.18(10) |
| X1–Cu1–X3 | 95.38(3) | 94.5(1) | 94.73(2) | 91.56(10) | 90.04(10) |
| X2–Cu1–X3 | 90.20(3) | – | – | 88.79(12) | 83.04(10) |

[a] Symmetry transformation used to generate equivalent atoms i: $-x + 2, -y, -z + 1$; X3 = Cl2$^{i}$. [b] i: $-x - 1/2, y - 1/2, z$; X3 = Cl1$^{i}$. [c] i: $-x + 1/2, y - 1/2, z$; X3 = Br1$^{i}$. [d] X1, X2, and X3 are O11, O21, and O1 for molecule 1, and O31, O41, and O2 for molecule 2, respectively.

dine and Cu–Nazomethine, respectively, and 2.296(1) Å for the Cu–S distance. On the other hand, the Cu–Cl1 terminal distance is 3.132(1) Å, which is longer than those found in similar compounds[29,30] and is also at the higher limit of the sum of van der Waals radii (as is Cu–Cl2), a situation that confers significant ionic character to this chlorine atom.

On the basis of the information discussed above and on the assumption that each Cu is hexacoordinate, the *trans* angles N11–Cu1–S1, N12–Cu1–Cl2$^{i}$, and Cl1–Cu1–Cl2 [164.1(1), 178.6(1), and 165.2(1)°, respectively] and the distances discussed above suggest that each metal center has an octahedral coordination geometry with a growing tetragonal distortion of the 4+2 type, and a $CuCl_3N_2S$ chromophore in which the equatorial plane defined by the atoms S1, N12, N11, and Cl2$^{i}$ contains the copper(II) centers (Table 2). This plane forms a dihedral angle of 1.8(1)° with the average plane corresponding to the thiosemicarbazone chain, which in turn forms an angle of 6.0° with the pyridine ring. This situation confirms that the HAm4DH ligand is almost planar in the coordination arrangement.

The bonding parameters for the thiosemicarbazone in the complex are close to those in the free ligand − apart from the N13–N12–C16 angle, which increases from 116.7(2)° to 120.1(2)° as a consequence of the involvement of N12 in coordination with the copper center.

In the crystal packing the dimeric units interact with one another through Cl1, which participates in hydrogen bonding to form chains along the [100] direction, as shown in Figure 2. Each dimeric unit is bonded to its neighbor

Table 2. Best least-squares planes for **5a**, **5b**, **6a**, and **9a**.[a]

| Compound | Plane | Rms deviation [Å] | Largest deviation [Å] | Angle with previous plane [°] |
|---|---|---|---|---|
| **5a** | N11/N12/S1/Cl2$^{i}$ | 0.0192 | N12, 0.023(1) | |
| | C16/N12/N13/C17/S1/N14 | 0.0183 | N12, 0.036(2) | 1.8(1) |
| | N11/C11/C12/C13/C14/C15 | 0.0050 | C15, 0.007(2) | 6.0(2) |
| **5b** | N11/N12/S1/Cl1 | 0.0738 | N12, 0.088(3) | |
| | C16/N12/N13/C17/S1/N14 | 0.0252 | N13, 0.039(6) | 10.1(2) |
| | N11/C11/C12/C13/C14/C15 | 0.0075 | C11, 0.013(6) | 4.5(3) |
| **6a** | N11/N12/S1/Br1 | 0.0855 | N12, 0.104(2) | |
| | C16/N12/N13/C17/S1/N14 | 0.0125 | C17, 0.016(2) | 9.4(1) |
| | N11/C11/C12/C13/C14/C15 | 0.0041 | C13, 0.007(4) | 3.3(2) |
| **9a** | N11/C11/C12/C13/C14/C15 | 0.0045 | C15, 0.007(2) | |
| | C16/N12/N13/C17/S1/N14 | 0.0227 | N12, 0.041(2) | 4.5(2) |
| | N11/N12/S1/O1 | 0.0318 | N12, 0.036(1) | 2.4(1) |
| | N21/N22/S2/O2 | 0.0267 | N22, 0.001(1) | 1.1(1) |
| | C26/N22/N23/C27/S2/N24 | 0.0254 | N23, 0.026(3) | 2.6(11) |
| | N21/C21/C22/C23/C24/C25 | 0.0034 | C22, 0.005(3) | 5.7(2) |

[a] Symmetry transformation used to generate equivalent atoms, i: $-x + 2, -y, -z + 1$.

 © 2006 Wiley-VCH Verlag GmbH & Co. KGaA, Weinheim 

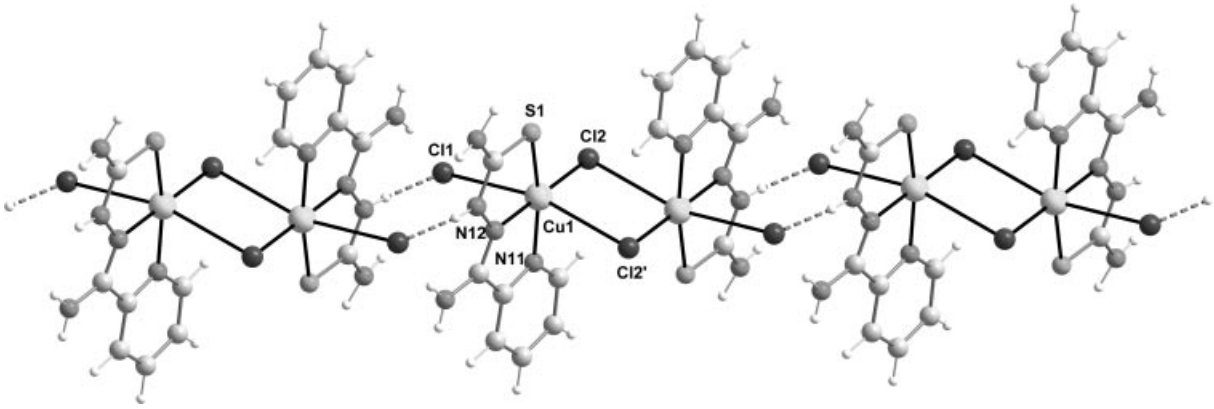


Figure 2. View of the chain structure in the crystal lattice of complex **5a**. The Cl1 atoms are responsible for linking each dimer unit to another through hydrogen bonding along the [100] direction.

through a N13–H13···Cl1$^{i}$ bond (Table 3). The same atom acts as a hydrogen-bond acceptor with the $NH_2$ groups of the thiosemicarbazones from contiguous chains acting as donors. These interactions give rise to parallel layers along the *bc* plane that stack in the [100] direction.

### Crystal Structure of $^{1}_{\infty}$[Cu(Am4DH)Cl] (5b) and $^{1}_{\infty}$[Cu(Am4DH)Br] (6a)

Compounds **5b** and **6a** are isotypic and their structures are formed by chains along the *a* axis. Each copper(II) cen-

Table 3. Hydrogen bonding interactions for **5a**, **5b**, **6a**, and **9a**.

| Compound | D–H···A | *d*(D–H) | *d*(H···A) | *d*(D···A) | ∠(DHA) |
|---|---|---|---|---|---|
| **5a**[a] | N13–H13···Cl1$^{1}$ | 0.89 | 2.19 | 3.078(2) | 174.7 |
| | N14–H14A···Cl1$^{1}$ | 0.89 | 2.88 | 3.603(3) | 139.6 |
| | N14–H14B···Cl1$^{2}$ | 0.95 | 2.86 | 3.328(2) | 111.9 |
| | N14–H14B···Cl2$^{3}$ | 0.95 | 2.95 | 3.670(3) | 133.3 |
| | N15–H15A···Cl1$^{1}$ | 0.87 | 2.52 | 3.377(2) | 173.3 |
| | N15–H15B···Cl1$^{4}$ | 0.83 | 2.48 | 3.274(2) | 161.6 |
| **5b**[b] | N14–H14A···N13$^{1}$ | 0.96 | 2.15 | 3.090(10) | 165.9 |
| | N14–H14B···S1$^{2}$ | 0.97 | 2.55 | 3.510(7) | 167.6 |
| | N15–H15B···Cl1$^{3}$ | 0.86 | 2.63 | 3.44(7) | 159.2 |
| **6a**[c] | N14–H14A···S1$^{1}$ | 0.81 | 2.69 | 3.503(4) | 173.7 |
| | N14–H14B···N13$^{2}$ | 0.85 | 2.22 | 3.074(5) | 174.8 |
| | N15–H15B···Br1$^{3}$ | 0.84 | 2.68 | 3.468(3) | 157.0 |
| **9a**[d] | O1–H1B···O33$^{1}$ | 0.77 | 2.11 | 2.862(4) | 168.3 |
| | O1–H1B···O13 | 0.77 | 2.62 | 3.077(4) | 119.4 |
| | N13–H13A···O5 | 0.97 | 1.76 | 2.723(5) | 168.2 |
| | N14–H14A···O32$^{2}$ | 0.88 | 2.09 | 2.942(4) | 162.7 |
| | N14–H14B···O34$^{3}$ | 0.90 | 2.20 | 3.011(4) | 151.0 |
| | N15–H15A···O5 | 0.84 | 2.27 | 3.078(4) | 163.4 |
| | N15–H15B···O3 | 0.90 | 2.04 | 2.894(4) | 157.9 |
| | O2–H2A···O3 | 0.87 | 1.85 | 2.710(4) | 173.4 |
| | O2–H2B···O13$^{1}$ | 0.78 | 2.12 | 2.864(4) | 161.0 |
| | O2–H2B···O33 | 0.78 | 2.53 | 3.065(4) | 126.8 |
| | N23–H23A···O6$^{4}$ | 0.92 | 1.83 | 2.744(4) | 175.4 |
| | N24–H24A···O12$^{4}$ | 0.83 | 2.15 | 2.950(4) | 164.2 |
| | N24–H24B···O14$^{3}$ | 0.91 | 2.18 | 3.028(4) | 154.9 |
| | N25–H25A···O6$^{4}$ | 0.81 | 2.31 | 3.064(4) | 155.0 |
| | N25–H25B···O4$^{5}$ | 0.87 | 2.08 | 2.907(4) | 157.9 |
| | O5–H5A···O43$^{6}$ | 0.88 | 2.15 | 2.964(5) | 154.1 |
| | O6–H6A···O14$^{1}$ | 0.95 | 2.19 | 3.038(4) | 149.4 |
| | O3–H3A···O41 | 0.87 | 2.23 | 2.830(4) | 126.2 |
| | O3–H3A···O42$^{6}$ | 0.87 | 2.39 | 3.072(4) | 135.4 |
| | O3–H3B···O22$^{7}$ | 0.76 | 2.11 | 2.810(5) | 153.9 |
| | O4–H4A···O21$^{1}$ | 0.90 | 2.30 | 2.958(5) | 129.7 |
| | O4–H4A···O24$^{8}$ | 0.90 | 2.38 | 3.025(4) | 128.0 |
| | O4–H4B···O43$^{9}$ | 0.80 | 2.11 | 2.786(4) | 141.8 |

[a] Symmetry transformations used to generate equivalent atoms: **1**: $-x + 1, -y, -z + 1$; **2**: $x, -y - 1/2, z + 1/2$; **3**: $-x + 2, y - 1/2, -z + 3/2$; **4**: $x, -y + 1/2, z + 1/2$. [b] **1**: $-x, y, -z + 1/2$; **2**: $-x, -y, -z + 1$; **3**: $-x - 1/2, -y - 1/2, z - 1/2$. [c] **1**: $-x, -y + 1, -z + 1$; **2**: $-x, y, -z + 1/2$; **3**: $-x + 1/2, -y - 1/2, z - 1/2$. [d] **1**: $-x + 1, -y + 1, -z + 1$; **2**: $x, y, z + 1$; **3**: $-x, -y + 1, -z + 1$; **4**: $x - 1, y, z$, **5**: $-x, -y + 1, -z$; **6**: $-x, -y, -z + 1$; **7**: $-x + 1, -y, -z + 1$; **8**: $x, y + 1, z + 1$; **9**: $x, y + 1, z$.

 © 2006 Wiley-VCH Verlag GmbH & Co. KGaA, Weinheim 

ter is coordinated to a deprotonated thiosemicarbazone through the thiolate sulfur atom and the azomethine and pyridine nitrogen atoms, a situation that is common with this type of ligand. The structure of the 1D coordination polymers is formed by the asymmetric halogen bridges between the metal centers, which gives rise to pentacoordination around each copper(II) center (Figure 3). In both complexes the Cu–S, Cu–Nazomethine, and Cu–Npyridine distances (Table 1) are very similar and the most marked difference (0.008 Å) is in the Cu–S bond of **5b**. This in turn is associated with the largest deviation (0.039 Å), which is not particularly significant in comparison with that in **5a**.

The Cu–Cl distances in **5b** are 2.247(2) and 2.945(2) Å and, although these are significantly different, they are more similar to one another than those found in the dimer **5a** (differences of 0.920 Å vs 0.694 Å). The shortest distance is slightly longer than those found in other copper(II) complexes with thiosemicarbazone ligands and chloro bridges[25] and the longest distance is in the range found in other systems with chloro bridges between copper centers (2.70–3.19 Å).[31,32]

In **6a** both Cu–Br bond lengths are also significantly different. However, in this case the difference is 0.582 Å, which represents the smallest difference of the three complexes under discussion. However, the bond lengths are shorter and longer, respectively, than those found in $[Cu(dmamhp)Br_2]_2$ (dmamhp = 2-dimethylaminomethyl-3-hydroxypyridine), a dimer that contains asymmetric bromo bridges with Cu–Br distances of 2.439(2) and 2.805(2) Å.[33]

The $\tau$ values found in the two complexes[34] are 0.039 for **5b** and 0.031 for **6a**, and these are consistent with the copper(II) atoms having a tetragonal pyramidal coordination environment ($\tau = 0$) with a distortion towards trigonal bipyramidal ($\tau = 1$). In this arrangement the basal plane is defined by N11, N12, S1, and X1, all of which are coplanar [maximum deviations of 0.088(3) and 0.104(2) Å in N12 for **5b** and **6a**, respectively], and the copper center is located 0.170(3) Å above this plane in **5b** and 0.173(1) Å above it in **6a** (Table 2). This basal plane forms angles of 10.1(2) and 9.4(1)° with the plane of the thiosemicarbazone chain, which in turn forms angles of 4.5(3) and 3.3(2)°, respectively, with the best least-squares plane of the pyridine ring.

The axial position is occupied by the neighboring halogen atom that forms the bridge (symmetry code: $-x - 1/2$, $y - 1/2$, $z$) and this gives rise to angles in the range 86.9(2)–98.7(1) Å in **5b** and 87.5(1)–99.0(1) Å in **6a** (Table 1). The chains develop along the [010] direction and in these chains the Cu···Cu separations are 4.158(1) and 4.249(1) Å for **5b** and **6a**, respectively. This level of separation is sufficiently large that magnetic interactions can take place between the metal centers.

In contrast to the situation in **5a**, a number of significant changes are apparent in **5b** and **6a** in terms of the bonding parameters of HAm4DH when compared to the data for the free ligand. These changes are due to deprotonation of the ligand and mainly affect the bond lengths and angles around C17. This situation gives rise to elongation of the S1–C17 and N14–C17 bonds from average values of 1.698(2) and 1.316(3) Å to 1.741(6) and 1.363(6) Å, respectively. On the other hand, the N13–C17 bond decreases in length from 1.340(2) to 1.305(8) Å. Some bond angles also experience significant changes on complexation and this is due to the presence of the thiolate form of the ligand; S1–C17–N14 and C17–N13–N12 are modified from average values of 123.0(2) and 118.3(2)° in HAm4DH to 116.8(5) and 111.3(5)°, respectively, while S1–C17–N13 changes form 120.3(2) to 125.4(5)°. These changes are clearly a result of changes in the electronic delocalization in the thiosemicarbazone chain on conversion to the thiol form of the ligand and subsequent deprotonation in the basic medium.

A number of hydrogen bonds are formed in the crystal packing arrangement. The most significant of these occur between the amino donor groups and the imine nitrogen atoms of neighboring chains, which act as acceptors (Table 3). These interactions give rise to a three-dimensional supramolecular network.

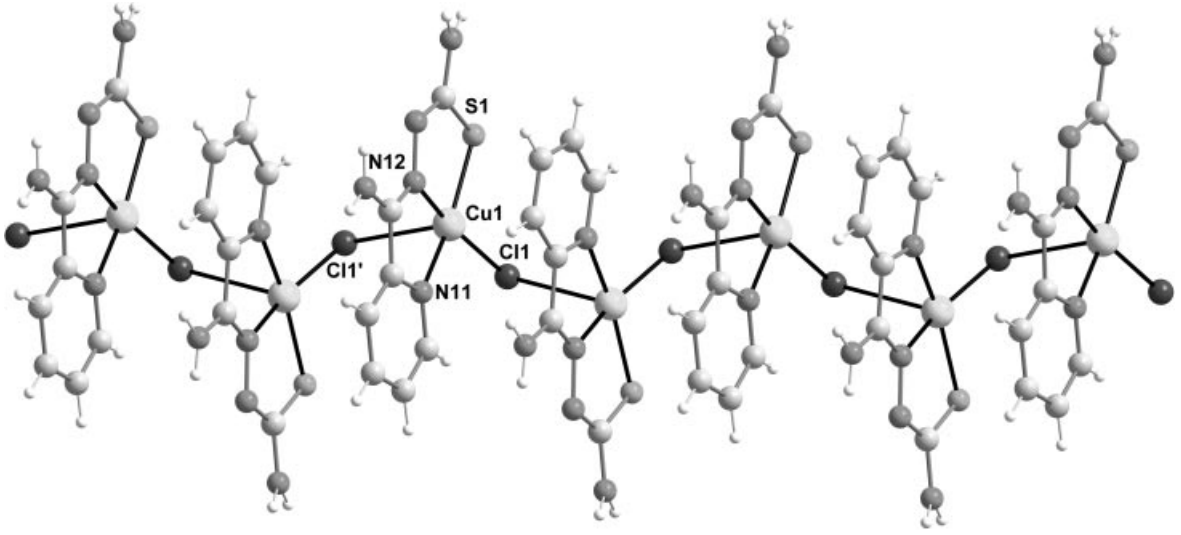


Figure 3. Perspective view of the 1D-chain structure of **5b** along the *b* axis.

 © 2006 Wiley-VCH Verlag GmbH & Co. KGaA, Weinheim 

### Crystal Structure of $[Cu(HAm4DH)(H_2O)(ClO_4)_2]\cdot MeOH\cdot H_2O$ (9a)

The asymmetric unit consists of two complex molecules that are crystallographically independent (I and II), and are separated by a Cu···Cu distance of 9.687(2) Å. In each molecule the copper(II) center is hexacoordinate by a neutral thiosemicarbazone molecule through the sulfur atoms and the usual nitrogen atoms, an oxygen atom from a water molecule, which occupies the equatorial positions, and two oxygen atoms from the perchlorate ligands, which occupy the axial positions. Figure 4 is a diagram of molecule I.

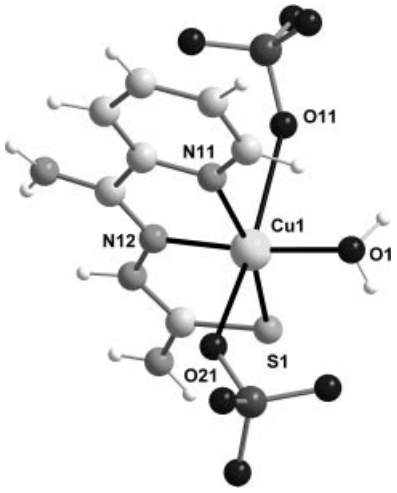


Figure 4. Representation of molecule I of **9a**.

In the equatorial plane the metal–ligand distances in the two molecules range from 1.919(3) Å for the Cu–Nazomethine distance in the second molecule to 2.278(1) Å for the Cu–S distance in the first molecule (Table 1). The axial Cu–O distances are different and this gives rise to a 4+1+1 distortion in the coordination polyhedron. One of the Cu–O distances is around 2.5 Å and the other around 2.8 Å. These distances are considerably longer than the equatorial Cu–Owater distance, which has an average value of 1.965(2) Å, but are of the same order of magnitude as those found in other copper(II) complexes with coordinated perchlorate groups.[5,26,35–37]

Another indication of the magnitude of the distortion is given by the *trans* angles in the equatorial plane, which have average values of 166.1(1)° for N11–Cu1–S1 and 173.8(1) for N12–Cu1–O1. However, the clearest evidence of distortion is provided by the *trans* angle between the axial positions, with values of 168.6(1)° in the first molecule and 162.2(1)° in the second. These bond angle values are comparable to those found in other copper(II) complexes with coordinated perchlorate ligands but are larger than the value of 155.9(2)° found in $[Cu(HL)(H_2O)(ClO_4)_2]$, where HL is 2-formylpyridine thiosemicarbazone.[5] In both molecules the equatorial plane containing each Cu atom is approximately coplanar with the corresponding thiosemicarbazone plane [dihedral angles are 2.4(1) and 2.6(1)°] (Table 2), which in turn form angles of 4.5(2) and 5.7(2)° with the best least-squares plane of the pyridine ring.

Once again in this complex − as in the case of **5a** − only the N13–N12–C16 angle changes and this angle has values of 120.7(3) and 120.2(3)° in the two molecules in the complex.

Numerous hydrogen-bonding interactions occur in the crystal packing arrangement (Table 3) and it is not only the amine and imine groups of HAm4DH that take part but also the water and ethanol molecules and the noncoordinated oxygen atoms of the perchlorate ligands.

### Spectral Studies

The IR spectra of the $Cu^{II}$ complexes contain bands in the range 3473–3158 $cm^{-1}$ and these correspond to $\nu$(NH) and, in cases where the complex contains solvent molecules, $\nu$(OH). Bands are also observed between 1610 and 1568 $cm^{-1}$ and these are due to $\nu$(CN+CC).

The C=S vibration modes are seen for the ligand HAm4DH at 853 $cm^{-1}$ and this band is observed at lower frequencies in the complexes, which shows that coordination of the thio donor to the copper center has taken place. In the free ligand the band corresponding to $\nu$(NN) is observed at 999 $cm^{-1}$, while in all of the complexes this band appears at higher frequencies because of coordination of the metal center through the sulfur and azomethine nitrogen atom.

The diffuse reflectance spectra of all of the complexes show three broad bands in the visible region. The intense band, which has the high energy, appears at 26350–26724 $cm^{-1}$ and has a shoulder on the highest energy side. This band is due to ligand transitions: $n \rightarrow \pi^*$ (main band) and $\pi \rightarrow \pi^*$ (shoulder). A second band is observed between 22624 and 24232 $cm^{-1}$ and this has various components that must correspond to metal–ligand charge-transfer processes (MLCT), probably $\sigma(S) \rightarrow d_{x^2-y^2}$ ($Cu^{II}$) or $\pi \rightarrow d_{x^2-y^2}$ ($Cu^{II}$). In contrast to other copper(II) complexes, in this case there does not seem to be a clear correlation between the position of the maximum of this band and the coordination geometry or the nature of the ligand coordinated to the metal. The band that is observed in the lower energy region of the spectrum has two components at 15244–16353 and 14245–15785 $cm^{-1}$ and these correspond to a d–d transition.[38]

The EPR spectra of polycrystalline samples, measured at room temperature, are axial and isotropic. The spectra of complexes **1** and **8** are practically identical and show an axial nature (Figure 5, a) and very similar EPR parameters for the two complexes, a situation that suggests the same coordination polyhedron around copper(II). Given that $g_{\|} > g_{\perp}$, the unpaired electron is located in a $d_{x^2-y^2}$ orbital and this is characteristic of a distorted tetragonal structure. Complex **7** gives rise to an axial spectrum that is slightly rhombic, as can be seen in Figure 5 (b). The EPR parameters of this complex are practically identical to those of the two complexes discussed above. The complexes are also quasi-isotropic.

 © 2006 Wiley-VCH Verlag GmbH & Co. KGaA, Weinheim 

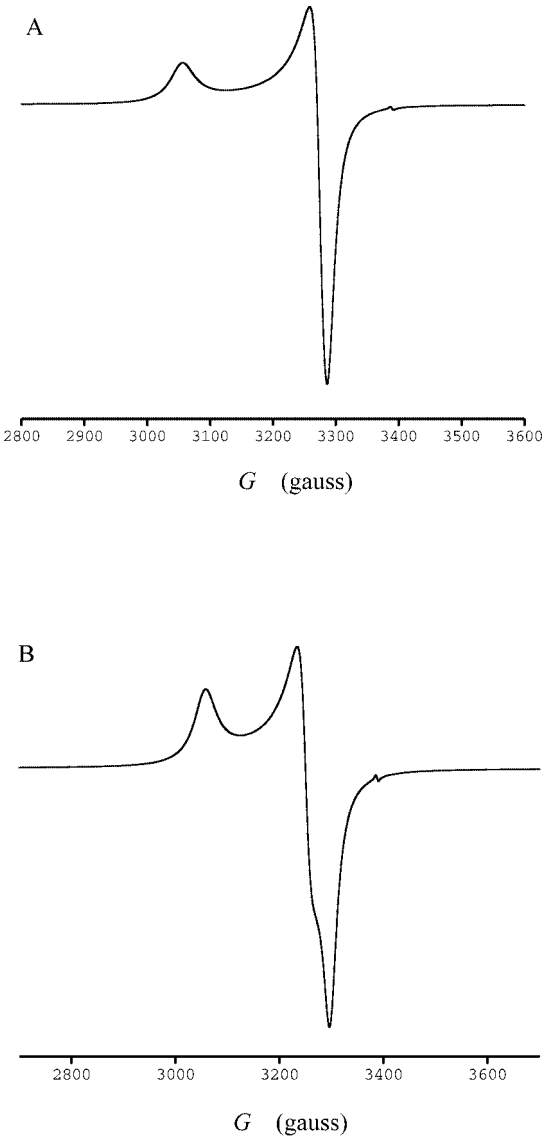


Figure 5. ESR spectra of **1** (A) and **7** (B) at room temperature.

## Magnetic Behavior

The magnetic moments of the complexes were measured at room temperature (298 K) and the majority are in the range 1.75–2.20 BM, which is characteristic of mononuclear copper(II) complexes. However, in compound **5a**, $[Cu(HAm4DH)Cl_2]_2$, the value is 1.24 BM and this is lower than the expected spin-only value, which clearly indicates antiferromagnetic coupling between the copper(II) ions. This behavior is very similar to that found in binuclear copper(II) complexes containing chloro bridges. In order to determine the extent of the magnetic interaction between the two metal ions and to elucidate the difference in the singlet–triplet energy values, the magnetic susceptibility was measured in the temperature range 2–150 K. The variation in the magnetic susceptibility with temperature is shown in Figure 6. It can be seen that the magnetic susceptibility increases to a maximum at 15 K on cooling and then falls rapidly on decreasing the temperature further. The experimental magnetic susceptibility values (corrected for diamagnetism) were adjusted using the Bleaney–Bowers equation[39] for a coupled dinuclear copper(II) species:

$$\chi_M = \{(Ng^2\beta^2)/kT[3 + \exp(-J/kT)]\}^{-1}(1 - \rho) + \rho Ng^2\beta^2/4kT + \chi_{TIP}$$

which results from considering the same values of $H = -2JS_1S_2$ and where the symbols have the accepted meanings. A nonlinear least-squares adjustment program was used to calculate $-J$ and $g$ and excellent agreement was obtained when $J = -12.2$ cm$^{-1}$, $g = 2.17$, $\chi_{TIP} = 124\times10^{-6}$, $\rho = 0.035$, and $R = 1.2\times10^{-3}$. The coupling constant calculated for the singlet–triplet exchange clearly shows that antiferromagnetic interactions exist between the copper(II) ions in **5a** in the solid phase.

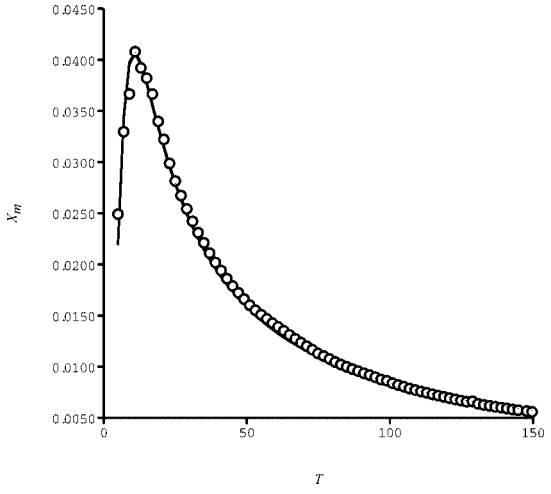


Figure 6. Temperature [K] dependence of the magnetic susceptibility $\chi_M$ (cm$^3$·mol$^{-1}$) of **5a**. The solid line represents the least-squares fit equation and the parameters described in the text.

In contrast to copper(II) complexes containing hydroxy bridges, which have equivalent Cu–O (bridge) distances, dimers with chloro bridges frequently have different Cu–Cl (bridge) distances and the singlet–triplet splitting depends on the length of the bridging bonds and the Cu–Cl–Cu angle of the bridge.[40]

Correlation studies were carried out on the magnetic and structural properties of a diverse range of dinuclear copper(II) species − particularly compounds with two chloro bridges between the metal centers and trigonal pyramidal or square-pyramidal coordination geometries. Reasonable consistency was found in that the singlet–triplet splitting and, consequently, the isotropic interaction parameter ($2J$) correlate reasonably well with the $\varphi/r$ ratio between the bridging angle Cu–Cl–Cu′ ($\varphi$) and the longest Cu–Cl distance from the basal plane ($r$). The $\varphi/r$ values between 32.5 and 34.75 °/Å correspond to ferromagnetic interaction while values outside this range correspond to antiferromagnetic behavior.[41] The $\varphi/r$ value found for compound **5a** is 28.6 °/Å and this is consistent with the correlation.

However, this situation contrasts with that found for $[(dpt)Cu(\mu\text{-}Cl)_2Cu(dpt)]Cl_2$ (dpt = dipropylenetriamine, $\varphi/r$

 © 2006 Wiley-VCH Verlag GmbH & Co. KGaA, Weinheim 

= 35.9 °/Å), where each copper(II) ion is in a trigonal bipyramidal environment and the compound shows ferromagnetic coupling between the copper(II) ions ($J$ = 42.9 $cm^{-1}$) and an interdimeric antiferromagnetic coupling ($J'$ = –3.92 $cm^{-1}$).[42] Another similar example is [(depc)(Cl)Cu(μ-$Cl)_2$Cu(Cl)(depc)] (depc = diethyl pyridine-2,6-dicarboxylate, $\varphi/r$ = 40.9 °/Å), in which each copper(II) ion is in a distorted octahedral environment and coupling constants of $J$ = 39.9 $cm^{-1}$ and $J'$ = –0.59 $cm^{-1}$ are found.[43]

## Thermochemistry

The pyrolysis of the compounds subjected to thermogravimetric analysis (**1**–**3**, **5**–**8**, **10**) occurred in four or five stages, with overall evolution of $H_2O$, $CO_2$, CO, $NH_3$, NO, $NO_2$, and $SO_2$ in all cases except that of compound **7**, for which only three stages and the evolution of only $H_2O$, $CO_2$, NO, $NO_2$, and $SO_2$ were detected (Table 4). In keeping with their observed crystal structures, compounds **1** and **7** gave off no solvent molecules, and these compounds were stable up to 226 °C and 174 °C, respectively. The remaining compounds, which are all solvated, lost solvent molecules even at room temperature, because of which the number of solvent molecules included in the working empirical formula of the starting material was calculated as that which gave the best agreement with the experimental weight loss during the first decomposition stage, assuming this stage to involve only solvent loss; for example, for compounds **3** and **10** this procedure afforded the working empirical formulae $[Cu(HAm4DH)_2](NO_3)_2 \cdot 0.52\,EtOH$ and $[Cu(Am4DH)_2] \cdot 1.27\,H_2O$, respectively. Note that the final residue of compound **7**, the only compound not to give off ammonia as well as $SO_2$ and nitrogen oxides, was $Cu(NO_3)_2$, and that for all compounds except compound **7** the final residue accounted for a greater percentage of the initial mass than would correspond to its consisting entirely of CuO, the difference being quite substantial in some cases; this suggests that in these cases, too, the residue may have contained $Cu(NO_3)_2$, or perhaps a copper(II) oxy-nitrate, even though only CuO was detected.

## Cyclic Voltammetry Studies

The reduction peak potentials for $Cu^{II}$ are shown in Table 5 along with the corresponding reoxidation peaks for $Cu^{I}$. It can be seen that the more negative the cathodic peak, the more stable the complex (for a variation in potential of 0.02 $V \cdot s^{-1}$).

Table 5. Reduction peak potentials for $Cu^{II}$ and the corresponding peaks for the reoxidation of $Cu^{I}$.

| | $V$ = 0.02 $V \cdot s^{-1}$ | | | $V$ = 0.2 $V \cdot s^{-1}$ | | |
|---|---|---|---|---|---|---|
| | $E_c$[a] | $E_a$[a] | $E_c - E_a$[a] | $E_c$[a] | $E_a$[a] | $E_c - E_a$[a] |
| **1** | –0.532 | –0.379 | –0.135 | –0.597 | –0.413 | –0.184 |
| **2** | –0.572 | – | – | –0.662 | –0.121 | –0.541 |
| **3** | –0.562 | – | – | –0.655 | –0.192 | –0.463 |
| **4** | –0.406 | – | – | –0.452 | – | – |
| **5** | –0.564 | –0.425 | –0.139 | –0.610 | –0.345 | –0.265 |
| **6** | –0.501 | –0.384 | –0.117 | –0.523 | –0.307 | –0.216 |
| **7** | –0.493 | –0.326 | –0.167 | –0.544 | –0.292 | –0.252 |
| **8** | –0.432 | – | – | –0.465 | – | – |
| **9** | –0.610 | –0.054 | –0.556 | –0.685 | 0.052 | –0.737 |
| **10** | –0.663 | –0.375 | –0.288 | –0.618 | –0.224 | –0.394 |

[a] $V$ vs. SCE.

In all cases a well-defined cathodic peak was observed and, based on the position of the peak on the potential scale (–0.4 to –0.8 V vs SCE) and its absence in the reverse measurements on the ligands, this can be attributed to the reduction of copper(II) according to the equation:

$$Cu^{2+} + e^- \leftrightarrows Cu^+$$

In the majority of the complexes the corresponding anodic peak is also observed ($E_a$) (Figure 7), although in some cases the appearance of the peak depends on the experimental conditions (e.g. potential range and length of time after preparation of the solution). The peak shapes and the separation between the cathodic and anodic peaks (when they are observed) demonstrate the irreversible nature of the electrode process.

Voltammograms were also obtained over a larger potential range and these showed a cathodic peak at around –2 V versus SCE, which is also present in the voltammograms obtained for the ligand (Figure 8). This peak can be assigned to reduction of the ligand from the thione to the thiol, as proposed by other authors for similar conditions.[44] An anodic peak was also observed in the potential range 0.5–0.6 V versus SCE (Figure 9) and the origin of this peak is not clear because of its changeable behavior.

In complexes **3**, **8**, **9**, and **10** the peak due to the reduction of copper(II) is split into two very close peaks that

Table 4. Data for the thermogravimetric analysis of $Cu^{II}$.

| | Stages | % Total | $\Delta T$ [°C] | Gases evolved in stage 1 | Gases evolved in other stages | Final residue (% exp. – % calcd.) |
|---|---|---|---|---|---|---|
| **1** | 4 | 70.85 | 226–524 | $H_2O$, $CO_2$, CO, $NH_3$, $NO_2$ | $H_2O$, $CO_2$, CO, $NH_3$, $N_2O$, NO, $NO_2$, $SO_2$ | CuO (29.15–24.13) |
| **2** | 5 | 76.04 | r.t.–737 | $H_2O$, $CO_2$ | $H_2O$, $CO_2$, CO, $NH_3$, $N_2O$, NO, $NO_2$, $SO_2$ | CuO (23.96–17.65) |
| **3** | 5 | 74.86 | r.t.–511 | $H_2O$, $CO_2$ | $H_2O$, $CO_2$, CO, $NH_3$, $N_2O$, NO, $NO_2$, $SO_2$ | CuO (33.65–25.11) |
| **5** | 4 | 71.42 | r.t.–512 | $H_2O$, $CO_2$, $NO_2$ | $H_2O$, $CO_2$, CO, $NH_3$, $N_2O$, NO, $NO_2$, $SO_2$ | CuO (28.58–25.15) |
| **6** | 5 | 76.87 | r.t.–773 | $H_2O$, $CO_2$, $NO_2$ | $H_2O$, $CO_2$, CO, $NH_3$, $N_2O$, NO, $NO_2$, $SO_2$ | CuO (23.13–22.05) |
| **7** | 3 | 66.35 | 174–474 | $H_2O$, $CO_2$, NO | $H_2O$, $CO_2$, $NO_2$, $SO_2$ | $Cu(NO_3)_2$ (27.57–29.21) |
| **8** | 4 | 65.76 | r.t.–526 | $H_2O$, $CO_2$, CO, $NH_3$, $NO_2$ | $H_2O$, $CO_2$, CO, $NH_3$, $N_2O$, NO, $NO_2$, $SO_2$ | CuO (34.24–18.54) |
| **10** | 5 | 73.86 | r.t.–524 | $H_2O$, $CO_2$, CO, $NH_3$ | $H_2O$, $CO_2$, CO, $NH_3$, $N_2O$, NO, $NO_2$, $SO_2$ | CuO (26.14–15.18) |

 © 2006 Wiley-VCH Verlag GmbH & Co. KGaA, Weinheim 

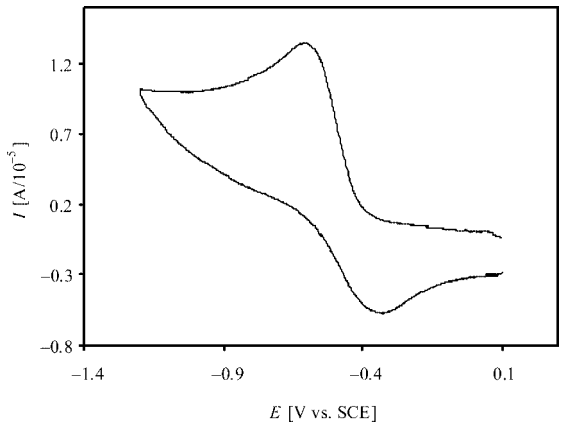


Figure 7. Cyclic voltammogram of complex **5** in $10^{-3}$ M DMF (scan rate 0.2 V·s$^{-1}$).

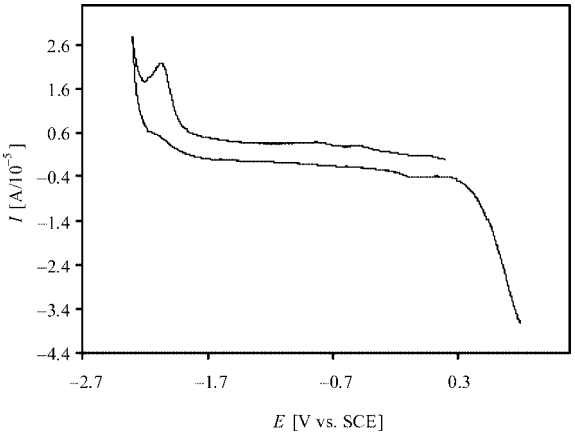


Figure 8. Cyclic voltammogram (scan rate 0.2 V·s$^{-1}$) of a 1 mM solution in DMF of HAm4DH.

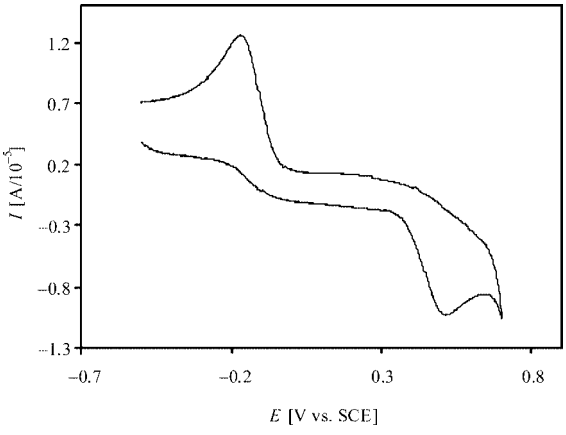


Figure 9. Cyclic voltammogram (scan rate 0.2 V·s$^{-1}$) of a 1 mM solution in DMF of **1**.

practically overlap (Figure 10) − these peaks are due to the presence of two chemically very similar species in solution. In the case of complex **9** this splitting becomes more marked as the length of time after preparation of the solution increases. This change indicates a progressive change in the structure of the ligand. Complexes **1** and **7** also show splitting of the cathodic peak because of the reduction of copper(II) (Figure 11) but, given the characteristic shape of one of the peaks, this splitting can be attributed to the fact that a proportion of the electrochemical reaction takes place at the surface.

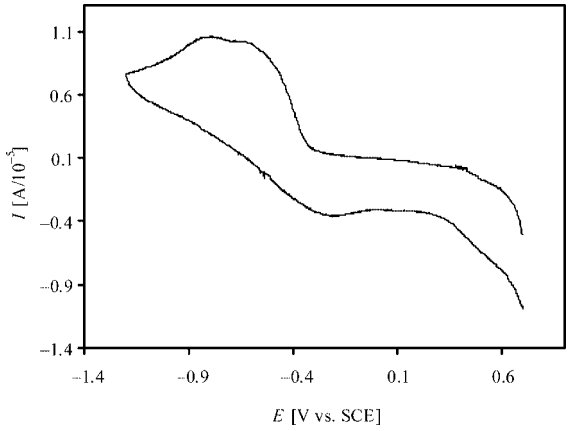


Figure 10. Cyclic voltammogram of complex **10** in $10^{-3}$ M DMF (scan rate 0.2 V·s$^{-1}$).

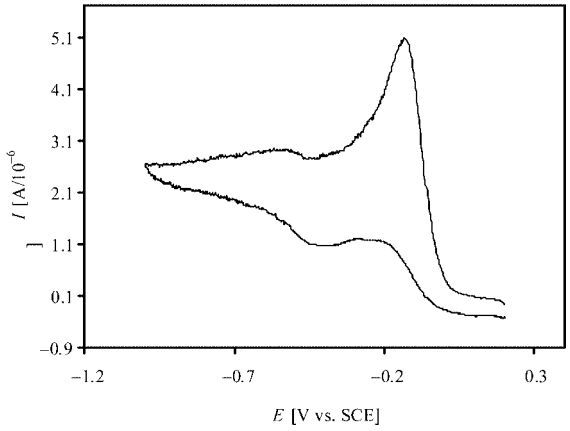


Figure 11. Cyclic voltammogram of complex **1** in $10^{-3}$ M DMF (scan rate 0.2 V·s$^{-1}$).

Similar splitting − albeit less marked − was observed in the anodic peak associated with the reoxidation of copper(I).

### The Activity of Thiosemicarbazone/Copper Complexes as DNA Nucleases

The electrophoresis studies carried out on complexes **1**, **2**, **5**, and **6** (Figure 12) show that these materials have nuclease activity because a significant proportion of the DNA, which is initially supercoiled (lane 2), appears in a circular form when incubated in the presence of 12 μM of complex (lanes 5, 7, 9, and 11, respectively). It can also be seen that the nuclease capacity of the four complexes under investigation is dependent on the concentration, as the digestion observed on incubating the DNA with 24 μM of the complex is higher than that produced with 12 μM for all four complexes.

 © 2006 Wiley-VCH Verlag GmbH & Co. KGaA, Weinheim 

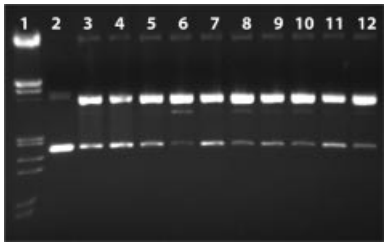


Figure 12. Agarose gel electrophoresis of pUC18 plasmid DNA treated with complexes **1**, **2**, **5** and **6** or $CuSO_4$ in the presence of 50 equiv. $H_2O_2$/ascorbate tandem. Incubation time 1 h (37 °C). Lane 1, λDNA/EcoR1 + HindIII Marker; lane 2, supercoiled DNA (control); lane 3, $Cu(SO_4)$ 40 μM; lane 4, $Cu(SO_4)$ 80 μM; lane 5, complex **2** 12 μM; lane 6, complex **2** 24 μM; lane 7, complex **6** 12 μM; lane 8, complex **6** 24 μM; lane 9, complex **1** 12 μM; lane 10, complex **1** 24 μM; lane 11, complex **5** 12 μM; lane 12, complex **5** 24 μM. Incubation time 1 h (37 °C).

It is known that copper has nuclease activity in its own right and, for this reason, the digestion produced by $CuSO_4$ under the same conditions was also determined. It can be seen from Figure 12 that the presence of $CuSO_4$ causes a proportion of the DNA to change to the circular form upon digestion (lanes 3 and 4). Complexes **1**, **5**, and **6** show practically identical nuclease activity to that shown by copper under the same conditions (cf. lanes 3–4 with 7–8, 9–10 and 11–12). The activity of these complexes must therefore be due to the presence of copper. In contrast, at a concentration of 24 μM complex **2** causes complete digestion of the supercoiled plasmid to give the circular form and a small quantity of the linear form. This complex clearly shows higher activity than $CuSO_4$ under the same experimental conditions (lanes 4 and 6).

In an effort to determine the mode of action of the nuclease process associated with complex **2**, we assessed the influence of different agents that could potentially inhibit reactive oxygen species (ROS). These compounds included hydroxy radical scavengers (DMSO and *tert*-butyl alcohol), singlet oxygen scavengers (sodium azide and 2,2,6,6-tetramethyl-4-piperidone), and superoxide radical scavengers (SOD). Finally, distamycin was tested as a species that bonds to DNA in the minor groove. Comparison of lanes 4 and 5 (Figure 13), which represent assays with DMSO and *tert*-butyl alcohol, respectively, with lane 3 (absence of inhibitor) shows that these additives do inhibit the process. This observation indicates the participation of the hydroxy radical in the DNA digestion process. Sodium azide (lane 6) and 2,2,6,6-tetramethyl-4-piperidone (lane 7) also inhibit the nuclease activity of the complex. This finding shows that singlet oxygen − or a species that behaves in a similar way − is also involved in the nuclease process. It is worth highlighting that azide can form complexes with copper and in this case the inhibition is markedly higher than that observed with 2,2,6,6-tertramethyl-4-piperidone. The presence of distamycin in the reaction mixture did not lead to changes in the activation of the complex, as can be seen in lane 8. This observation shows that the complex does not interact with DNA through the minor groove. The SOD enzyme, on the other hand, increased the nuclease activity and lane 9 shows total degradation of the plasmid. The dismutation process of the superoxide ion probably gives rise to a greater proportion of hydroxy radicals, which are produced by decomposition of hydrogen peroxide produced in the dismutation process.

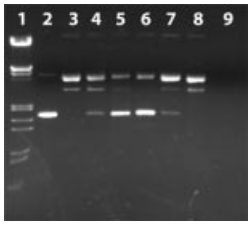


Figure 13. Agarose gel electrophoresis of pUC18 plasmid DNA treated with 24 μM of complex **2** and different inhibitors in the presence of $H_2O_2$/ascorbate (50 times more concentrated than the complex). Incubation time 1 h (37 °C). Lane 1, λDNA/EcoR1 + HindIII Marker; lane 2, supercoiled DNA (control); lane 3, complex without inhibitor; lane 4, complex + 1 M DMSO; lane 5, complex + 1 M *tert*-butyl alcohol; lane 6, complex + $NaN_3$ (100 mM); lane 7, complex + 2,2,6,6-tetramethyl-4-piperidone (100 mM); lane 8, complex + distamycin (8 μM); lane 9, complex + SOD (15 units).

These results imply that the $OH^{\cdot}$ radicals take part in the nucleic acid digestion process in the same way as singlet oxygen (or a species with similar behavior). The following mechanism can be proposed for the process:

1. reduction of $Cu^{II}$ to $Cu^{I}$;
2. interaction of the $Cu^{I}$ complex with DNA, possibly through the major groove;
3. reaction between hydrogen peroxide or oxygen with the $Cu^{I}$ to form the reactive oxygen species;
4. reaction of the hydroxy radical and singlet oxygen with DNA and destruction of the strands.

If the reactive species are not generated in the immediate vicinity of the DNA they can diffuse and be neutralized. For this reason the structures of the complexes and the nature of the ligand govern the DNA recognition process and determine the level of chemical damage.

The fact that the complex does not intercalate with the minor groove of the double helix possibly means that the reduction of $Cu^{II}$ to $Cu^{I}$ and the production of reactive oxygen species capable of attacking the DNA do not take place in the vicinity of the DNA. For this reason the digestion process is not as effective as that in cases where the complexes act by intercalation, for example, $[Cu(phen)_2]^{2+}$. This could be the reason why complex **2** shows a higher nuclease activity than the other compounds synthesized in this study.

## Experimental Section

**General:** Elemental analyses were carried out with a Carlo–Erba Model 1108 and Perkin–Elmer 240B microanalyzer. IR spectra were recorded with a Bruker IFS-66 V spectrophotometer as KBr disks (4000–400 $cm^{-1}$) or polyethylene-sandwiched Nujol mulls (500–100 $cm^{-1}$). Mass spectra were obtained with a Hewlett Packard HP598A spectrometer. Electronic spectra were obtained with a Shimadzu UV-3101PC spectrophotometer equipped with a reflectance accessory. X-band EPR spectra of the complexes were obtained in 3 mm Pyrex tubes with a Bruker EMX spectrometer using

 © 2006 Wiley-VCH Verlag GmbH & Co. KGaA, Weinheim 

a conventional Dewar insert at liquid nitrogen temperature and $Cr^{II}$ as the reference. Room temperature magnetic moments were determined on a DSM-8 magnetic susceptibility balance, and the instrument was calibrated using nickel metal. Variable-temperature (5–293 K) magnetic susceptibility measurements on a polycrystalline sample of **5a** were carried out with a Quantum Design SQUID susceptometer using an applied magnetic field of 2000 G over the whole temperature range. All data were corrected for diamagnetism of the ligands as estimated from Pascal's constants. The conductivity measurements were carried out with a CRISON digital conductivity bridge model MicroCM 2202 using freshly prepared $10^{-3}$ M solutions of the complexes in DMF. Thermogravimetric analysis from 20 to 950 °C was performed in a Shimadzu TGA-DGT 50H thermobalance using a constant 100 mL/min air flow. Evolved gases were identified from between 21 and 24 IR spectra of the gaseous products that were recorded at appropriate times during the analysis using a coupled Nicolet Magma 550 FTIR spectrophotometer; in each spectrum, the characteristic bands of the various gases were unequivocally identified by comparison with spectra in the Sigma–Aldrich FTIR library. Cyclic voltammograms were obtained on a 273 EG&G Princeton Applied Research electrochemical analyzer. The measurements were carried out at 50 mV·s$^{-1}$ under oxygen-free conditions using a three-electrode cell with a glassy carbon electrode. Tetra(*n*-butyl)ammonium perchlorate (TBAP) was used as the supporting electrolyte.

All chemicals and solvents were of analytical grade and were used as received. The TBAP used as the supporting electrolyte in electrochemical measurements was purchased from Fluka and recrystallized from hot methanol.

***Caution! Perchlorates are potentially explosive and care should be taken in handling these compounds.***

**Preparation of HAm4DH:** The ligand, HAm4DH, 2-pyridineformamide thiosemicarbazone was prepared according to a literature procedure.[2]

**Synthesis of [Cu(HAm4DH)Cl$_2$] (1):** An ethanolic solution (20 mL) of HAm4DH (0.25 g, 1.28 mmol) was added to a stirred solution of $CuCl_2 \cdot 2H_2O$ (0.22 g, 1.28 mmol) in ethanol (20 mL). The mixture was stirred for 7 days; the resulting suspension was filtered off and the bluish-green solid was washed with ethanol and dried with calcium chloride. Yield: 0.38 g (90%). $C_7H_9Cl_2CuN_5S$ (329.70): calcd. C 25.5, H 2.8, N 21.2, S 9.7; found C 25.6, H 2.8, N 21.0, S 9.5. Selected IR data: $\tilde{\nu}_{max}$ = 3437–3165 (NH), 1639–1578 (C=N + C=C), 1020 (NN), 793 (C=S), 463 (Cu–N), 349 (Cu–S), 319, 264 (Cu–Cl) cm$^{-1}$. FAB$^+$ MS [*m*/*z*, assignment]: 258 [Cu(HAm4DH)]. UV/Vis ($\lambda_{max}$, nm): 26738, 24154, 15244, 14245. EPR (X-band, solid sample): $g_{\parallel}$ = 2.19, $g_{\perp}$ = 2.04, $g_{av}$ = 2.05, $G$ = 4.75. $\mu_{eff}$ = 2.05 MB. Conductance ($\Lambda_m$/S·cm$^2$·mol$^{-1}$) in DMF: 28.

**Synthesis of [Cu(HAm4DH)Br$_2$]·0.5 EtOH·0.5 H$_2$O (2):** A solution of HAm4DH (0.20 g, 1.02 mmol) in ethanol (20 mL) was added to a solution of $CuBr_2$ (0.46 g, 2.05 mmol) in ethanol (20 mL). The mixture was stirred for one week and the resulting dark brown solid was filtered off, washed with ethanol, and dried under vacuum. Yield: 0.92 g (99%). $C_8H_{13}Br_2CuN_5OS$ (545.64): calcd. C 21.3, H 2.9, N 15.5, S 7.1; found C 22.2, H 2.3, N 15.0, S 6.5. Selected IR data: $\tilde{\nu}_{max}$ = 3408, 3324 (NH), 1562, 1515 (C=N, C=C), 1015 (NN), 789 (C=S), 464 (Cu–N2), 324 (Cu–S), 254 (Cu–Br) cm$^{-1}$. FAB$^+$ MS [*m*/*z*, assignment]: 338, [Cu(Am4DH)Br]; 257, [Cu(Am4DH)]. UV/Vis ($\lambda_{max}$, nm): 26693, 24232, 15253, 14271 cm$^{-1}$. EPR (X-band, solid sample): $g_{iso}$ = 2.04. $\mu_{eff}$ = 2.16 MB. Conductance ($\Lambda_m$/S·cm$^2$·mol$^{-1}$) in DMF: 34.6.

**Synthesis of [Cu(HAm4DH)$_2$](NO$_3$)$_2$·EtOH (3):** A solution of $Cu(NO_3)_2 \cdot 3H_2O$ (0.25 g, 1.02 mmol) and HAm4DH (0.40 g, 2.05 mmol) in ethanol (20 mL) was stirred for one week. A dark green precipitate formed and this was filtered off, washed with ethanol, and dried under vacuum. Yield: 0.25 g (40%). $C_{16}H_{24}CuN_{12}O_7S_2$ (624.11): calcd. C 30.8, H 3.9, N 26.9, S 10.3; found C 31.5, H 3.5, N 26.2, S 11.8. Selected IR data : $\tilde{\nu}_{max}$ = 3422–3171 (NH), 1599–1519 (C=N, C=C), 1384 ($NO_3$), 1016 (NN), 840 (C=S), 467 (Cu–N2), 338 (Cu–S) cm$^{-1}$. FAB$^+$ MS [*m*/*z*, assignment]: 453, [Cu(HAm4DH)$_2$]; 322, [Cu(H$_3$Am4DH)(NO$_3$)]; 259, [Cu(H$_2$Am4DH)]. UV/Vis ($\lambda_{max}$, nm): 26378, 22676, 21459, 16326, 15588. EPR (X-band, solid sample): $g_{iso}$ = 2.08. $\mu_{eff}$ = 2.16 MB. Conductance ($\Lambda_m$/S·cm$^2$·mol$^{-1}$) in DMF: 125.6.

**Synthesis of [Cu(HAm4DH)$_2$](ClO$_4$)$_2$ (4):** A solution of HAm4DH (0.25 g, 1.28 mmol) in ethanol (20 mL) was added to a solution of $Cu(ClO_4)_2 \cdot 6H_2O$ (0.47 g, 1.28 mmol) in ethanol (20 mL). The mixture was stirred for 7 days and the resulting black solid was filtered off, washed with ethanol and dried with calcium chloride. Yield: 0.64 g (76%). $C_{14}H_{18}Cl_2CuN_{10}O_8S_2$ (652.93): calcd. C 23.5, H 2.3, N 19.6, S 9.0; found C 23.9, H 2.4, N 19.3, S 9.0. Selected IR data: $\tilde{\nu}_{max}$ = 3421–3189 (NH), 1619–1518 (C=N, C=C), 1118, 936, 632 [$\nu_3$, $\nu_1$, $\nu_4$ ($ClO_4$)], 1019 (NN), 847 (C=S), 488 (Cu–N2), 363 (Cu–S) cm$^{-1}$. FAB$^+$ MS [*m*/*z*, assignment]: 258, [Cu(HAm4DH)]. UV/Vis ($\lambda_{max}$, nm): 26364, 22655, 15593, 14290. EPR (X-band, solid sample): $g_{\parallel}$ = 2.19, $g_{\perp}$ = 2.04, $g_{av}$ = 2.08, $G$ = 4.75. $\mu_{eff}$ = 1.97 MB. Conductance ($\Lambda_m$/S·cm$^2$·mol$^{-1}$) in DMF: 152.4.

**Synthesis of [Cu(Am4DH)Cl]·0.5 EtOH (5):** A solution of HAm4DH (0.20 g, 1.02 mmol) in ethanol was added to a stirred solution of $CuCl_2 \cdot 2H_2O$ (0.18 g, 1.02 mmol) in ethanol (20 mL). After a few drops of triethylamine (0.14 mL, 1.02 mmol) were added, the mixture was stirred for 7 days, just to complete precipitation of a dark green solid which was filtered off, washed with ethanol, and dried. Yield: 0.30 g (92%). $C_8H_{11}ClCuN_5O_{0.5}S$ (316.27): calcd. C 30.4, H 3.5, N 22.1, S 10.1; found C 30.2, H 3.5, N 21.7, S, 9.4. Selected IR data: $\tilde{\nu}_{max}$ = 3473–3158 (NH), 1625–1515 (C=N, C=C), 1020 (NN), 783 (C=S), 467 (Cu–N2), 350 (Cu–S), 313 (Cu–Cl) cm$^{-1}$. FAB$^+$ MS [*m*/*z*, assignment]: 294, [Cu(H$_2$Am4DH)Cl]; 259, [Cu(H$_2$Am4DH)]. UV/Vis ($\lambda_{max}$, nm): 26385, 22989, 16247, 15662 cm$^{-1}$. EPR (X-band, solid sample): $g_{iso}$ = 2.08. $\mu_{eff}$ = 2.04 MB. Conductance ($\Lambda_m$/S·cm$^2$·mol$^{-1}$) in DMF: 47.8. Recrystallization from MeOH/$CCl_4$ or EtOH/$H_2O$ gave green prismatic crystals of [Cu(HAm4DH)Cl$_2$]$_2$ (**5a**) and green needles of $^1_\infty$[Cu(Am4DH)Cl] (**5b**), respectively, that were suitable for X-ray diffraction.

**Synthesis of [Cu(Am4DH)Br]·0.5 EtOH (6):** A solution of HAm4DH (0.20 g, 1.02 mmol) in ethanol (20 mL) was added to a solution of $CuBr_2$ (0.23 g, 1.02 mmol) in ethanol (20 mL). Triethylamine (0.14 mL, 1.02 mmol) was added and the mixture was stirred for one week. The resulting dark green solid was filtered off, washed with ethanol, and dried under vacuum. Yield: 0.31 g (84%). $C_8H_{11}BrCuN_5O_{0.5}S$ (360.72): calcd. C 26.6, H 3.1, N 19.4, S 8.9; found C 26.7, H 3.0, N 19.2, S 6.2. Selected IR data: $\tilde{\nu}_{max}$ = 3521–3159 (NH), 1613–1514 (C=N, C=C), 1017 (NN), 844 (C=S), 468 (Cu–N2), 329 (Cu–S), 255 (Cu–Br) cm$^{-1}$. FAB$^+$ MS [*m*/*z*, assignment]: 338, [Cu(Am4DH)Br]; 257, [Cu(Am4DH)]. UV/Vis ($\lambda_{max}$, nm): 26350, 23068, 16247, 15698 cm$^{-1}$. EPR (X-band, solid sample): $g_{iso}$ = 2.07. $\mu_{eff}$ = 1.98 MB. Conductance ($\Lambda_m$/S·cm$^2$·mol$^{-1}$) in DMF: 62.6. X-ray quality crystals of $^1_\infty$[Cu(Am4DH)Br] (**6a**) were obtained as blue prisms by recrystallization from MeOH/acetonitrile.

**Synthesis of [Cu(Am4DH)(OAc)] (7):** A solution of HAm4DH (0.20 g, 1.02 mmol) in ethanol (20 mL) was added to a solution of $Cu(CH_3OO)_2 \cdot H_2O$ (0.20 g, 1.02 mmol) in ethanol (20 mL) and triethylamine was added (0.14 mL, 1.02 mmol). The mixture was

 © 2006 Wiley-VCH Verlag GmbH & Co. KGaA, Weinheim 

stirred for 7 days and the resulting green solid was filtered off, washed with ethanol, and dried under vacuum. Yield: 0.26 g (80%). $C_9H_{11}CuN_5O_2S$ (316.83): calcd. C 34.1, H 3.5, N 22.1, S 10.1; found C 34.4, H 3.5, N 21.8, S 10.0. Selected IR data: $\tilde{\nu}_{max}$ = 3427–3183 (NH), 1596, 1515 (C=N, C=C, $CH_3COO$), 1407 ($CH_3COO$), 1018 (NN), 846 (C=S), 442 (Cu–N2), 409 (Cu–O), 351 (Cu–S) $cm^{-1}$. $FAB^+$ MS [*m*/*z*, assignment]: 257, [Cu(Am4DH)]. UV/Vis ($\lambda_{max}$, nm): 26399, 23364, 16155, 15662, 14358 $cm^{-1}$. EPR (X-band, solid sample): $g_{\parallel}$ = 2.20, $g_{\perp}$ = 2.04, $g_{av}$ = 2.06, $G$ = 5. $\mu_{eff}$ = 2.10 MB. Conductance ($\Lambda_m$/S·cm²·mol⁻¹) in DMF: 33.7.

**Synthesis of [Cu(Am4DH)(NO$_3$)]·0.5 EtOH (8):** A solution of HAm4DH (0.20 g, 1.02 mmol) in ethanol was added to a stirred solution of $Cu(NO_3)_2{\cdot}3H_2O$ (0.25 g, 1.02 mmol) in ethanol (20 mL). After adding a few drops of triethylamine (0.14 mL, 1.02 mmol), the mixture was stirred for 7 days and, a dark brown solid was isolated that was filtered off, washed with ethanol, and dried with calcium chloride. Yield: 0.27 g (77%). $C_8H_{13}CuN_6O_{3.5}S$ (342.82): calcd. C 28.0, H 3.2, N 24.5, S 9.4; found C 27.5, H 2.9, N 24.8, S 10.2. Selected IR data: $\tilde{\nu}_{max}$ = 3424–3172 (NH), 1598–1523 (C=N, C=C), 1384, 1101 ($NO_3$), 1016 (NN), 841 (C=S), 465 (Cu–N2), 333 (Cu–S) $cm^{-1}$. $FAB^+$ MS [*m*/*z*, assignment]: 320, [Cu(HAm4DH)($NO_3$)]; 257, [Cu(Am4DH)]. UV/Vis ($\lambda_{max}$, nm): 26406, 23474, 21186, 16353, 15785 $cm^{-1}$. EPR (X-band, solid sample): $g_{\parallel}$ = 2.20, $g_{\perp}$ = 2.04, $g_{av}$ = 2.05, $G$ = 5. $\mu_{eff}$ = 2.15 MB. Conductance ($\Lambda_m$/S·cm²·mol⁻¹) in DMF: 40.2.

**Synthesis of [Cu(Am4DH)(H$_2$O)](ClO$_4$) (9):** A solution of HAm4DH (0.20 g, 1.02 mmol) in ethanol was added to a stirred solution of $Cu(ClO_4)_2{\cdot}6H_2O$ (0.38 g, 1.02 mmol) in ethanol (20 mL). After adding a few drops of triethylamine (0.14 mL, 1.02 mmol), the mixture was stirred for 7 days and the brown solid formed was filtered off, washed with ethanol, and dried. Yield: 0.16 (43%). $C_7H_{10}ClCuN_5O_5S$ (375.25): calcd. C 22.4, H 2.7, N 18.7, S 8.5; found C 22.2, H 2.4, N 16.2, S 7.8. Selected IR data: $\tilde{\nu}_{max}$ = 3429–3175 (NH), 1608–1518 (C=N, C=C), 1109, 926, 627 [$\nu_3$, $\nu_1$, $\nu_4$ ($ClO_4$)], 1016 (NN), 791 (C=S), 466 (Cu–N), 350 (Cu–S) $cm^{-1}$. $FAB^+$ MS [*m*/*z*, assignment]: 255, [Cu(Am4DH-2 H)]. UV/Vis ($\lambda_{max}$, nm): 26716, 23252, 15964, 15431. $\mu_{eff}$ = 2.19 MB. Conductance ($\Lambda_m$/S·cm²·mol⁻¹) in DMF: 90.3. Dark green prismatic crystals of [Cu(HAm4DH)($H_2O$)($ClO_4$)$_2$]·MeOH·$H_2O$ (**9a**) suitable for X-ray diffractometry were obtained after a few days by slow evaporation of a mixture of MeOH/$CCl_4$ at room temperature.

**Synthesis of [Cu(Am4DH)$_2$]·4 H$_2$O (10):** $Cu(CH_3OO)_2{\cdot}H_2O$ (0.20 g, 1.02 mmol) and HAm4DH (0.4 g, 2.05 mmol) were dissolved in ethanol (20 mL); some triethylamine was added (0.28 mL, 2.05 mmol) and the mixture was stirred for a week. The dark green precipitate was filtered off, washed with ethanol, and dried under vacuum. Yield: 0.35 (42%). $C_{14}H_{24}CuN_{10}O_4S_2$ (524.08): calcd. C 32.1, H 4.6, N 26.7, S 11.2; found C 32.1, H 3.3, N 25.2, S 13.7. Selected IR data: $\tilde{\nu}_{max}$ = 3423–3174 (NH), 1598–1520 (C=N, C=C), 1016 (NN), 845 (C=S), 470 (Cu–N2), 337 (Cu–S) $cm^{-1}$. $FAB^+$ MS [*m*/*z*, assignment]: 452, [Cu(HAm4DH)(Am4DH)]; 257, [Cu(Am4DH)]. UV/Vis ($\lambda_{max}$, nm): 26724, 22624, 15649, 14409 $cm^{-1}$. EPR (X-band, solid sample): $g_{iso}$ = 2.08. $\mu_{eff}$ = 2.13 MB. Conductance ($\Lambda_m$/S·cm²·mol⁻¹) in DMF: 32.7.

**X-ray Crystallography:** Crystals were mounted on glass fibers and these samples were used for data collection. Data for **5b** and **6a** were collected with a Nonius CAD4 automatic diffractometer and for **5a** and **9a** with a Bruker SMART CCD 1000 diffractometer. Cell constants and an orientation matrix were obtained from data collection of $2.03 < \theta < 26.48°$ for **5a**, $15.69 < \theta < 45.59°$ for **5b**,

Table 6. Crystal data and structure refinement for **5a**, **5b**, **6a**, and **9a**.

| Compound | **5a** | **5b** | **6a** | **9a** |
|---|---|---|---|---|
| Empirical formula | $C_{14}H_{18}Cl_4Cu_2N_{10}S_2$ | $C_7H_8ClCuN_5S$ | $C_7H_8BrCuN_5S$ | $C_8H_{17}Cl_2CuN_5O_{11}S$ |
| Formula weight | 659.38 | 293.23 | 337.69 | 525.77 |
| Temperature [K] | 293(2) | 293(2) | 293(2) | 150(2) |
| Wavelength [Å] | 0.71073 | 1.54184 | 1.54184 | 0.71073 |
| Crystal system | monoclinic | orthorhombic | orthorhombic | triclinic |
| Space group | $P2_1/c$ (no. 14) | *Pbcn* (no. 60) | *Pbcn* (no. 60) | $P\bar{1}$ (no. 2) |
| *a* [Å] | 10.660(2) | 20.2564(8) | 19.8492(13) | 11.243(3) |
| *b* [Å] | 10.865(2) | 7.5598(3) | 7.7764(6) | 12.662(3) |
| *c* [Å] | 10.812(2) | 15.0873(7) | 15.2852(13) | 13.539(3) |
| *α* [°] | 90 | 90 | 90 | 80.230(3) |
| *β* [°] | 109.377(3) | 90 | 90 | 78.177(3) |
| *γ* [°] | 90 | 90 | 90 | 86.411(4) |
| Volume [Å$^{-3}$] | 1181.3(4) | 2310.4(2) | 2359.4(3) | 1858.4(8) |
| *Z* | 2 | 8 | 8 | 4 |
| $\rho_{calcd}$ [Mg·m$^{-3}$] | 1.854 | 1.686 | 1.901 | 1.879 |
| Abs. coefficient [mm$^{-1}$] | 2.456 | 6.295 | 8.050 | 1.641 |
| *F* (000) | 660 | 1176 | 1320 | 1068 |
| Crystal size | 0.51 × 0.47 × 0.27 | 0.48 × 0.12 × 0.02 | 0.48 × 0.24 × 0.08 | 0.58 × 0.49 × 0.17 |
| *θ* range [°] | 2.03–26.48 | 4.37–72.89 | 4.46–72.89 | 1.56–26.43 |
| Limiting indices *h*, *k*, *l* | –12/13, 0/13, –13/0 | 0/24, –9/0, –18/0 | –24/0, 0/9, 0/18 | –13/14, –15/15, 0/16 |
| Reflections collected | 9947 | 2975 | 3025 | 21117 |
| Unique reflections/$R_{int}$ | 2427/0.0203 | 2314/0.0553 | 2361/0.0532 | 7577/0.0188 |
| Absorp. correct. | SADABS | *Ψ*-scans | *Ψ*-scans | SADABS |
| Max./min. transmission | 0.5569/0.3673 | 0.8844/0.1521 | 0.5653/0.1131 | 0.7677/0.4494 |
| Data/parameters | 2427/145 | 2314/136 | 2361/136 | 7577/505 |
| Gof (for $F^2$) | 1.078 | 0.988 | 1.058 | 1.045 |
| Final *R* indices [$I > 2\sigma(I)$] | $R_1$ = 0.0268 | $R_1$ = 0.0699 | $R_1$ = 0.0481 | $R_1$ = 0.0425 |
| | $wR_2$ = 0.0714 | $wR_2$ = 0.1872 | $wR_2$ = 0.1400 | $wR_2$ = 0.1070 |
| *R* indices (all data) | $R_1$ = 0.0379 | $R_1$ = 0.1412 | $R_1$ = 0.1561 | $R_1$ = 0.0635 |
| | $wR_2$ = 0.0793 | $wR_2$ = 0.2064 | $wR_2$ = 0.1427 | $wR_2$ = 0.1239 |
| Larg. diff. peak/hole [e·Å$^{-3}$] | 0.560/–0.335 | 0.655/–0.637 | 0.904/–1.314 | 2.182/–1.292 |

 © 2006 Wiley-VCH Verlag GmbH & Co. KGaA, Weinheim 

$1.56 < \theta < 26.43°$ for **6a** and $4.37 < \theta < 72.98°$ for **9a**. The data for **5b** and **6a** were processed with SAINT[45] and corrected for absorption using SADABS.[46] The structures were solved by direct methods,[47] which revealed the position of all non-hydrogen atoms. These atoms were refined on $F^2$ by a full-matrix least-squares procedure using anisotropic displacement parameters.[48] The hydrogen atoms were located from difference syntheses or in their calculated positions (C–H, 0.93–0.97 Å), and were refined using a riding model. Atom scattering factors were taken from the International Tables for Crystallography.[49] Crystal and refinement data are listed in Table 6.

**Cleavage of pUV18 by Thiosemicarbazone/Copper:** The interaction of the copper(II) complexes with DNA was studied using the plasmid pUC18 in the presence of $H_2O_2$, with the resulting fragments analyzed by electrophoresis in agarose. Plasmid pUC18 has a size of 2686 base pairs at a concentration of 0.25 mg·mL$^{-1}$ in TE buffer (pH = 8, Tris 10 mM, EDTA 1 mM). The assay carried out involved digesting plasmid pUC18 with the copper complexes in the presence of a reducing agent. The copper(II) complexes are insoluble in the buffer solutions commonly used in DNA degradation processes. For this reason DMF was employed as a solvent and the method reported by Reddy[50] was used for studies in this solvent. A typical assay was carried out as follows: 7 μL of 0.1 M cacodylate buffer (pH = 6.0), 1 μL of DNA pUC18 (0.25 μg·μL$^{-1}$), 6 μL of a solution of the copper(II) complex (or copper) (40 or 80 μM) in 0.1 M cacodylate buffer (pH = 6.0), 3 μL of $H_2O_2$ (0.4 or 0.8 mM) in 0.1 M cacodylate buffer, and 3 μL ascorbate (0.4 or 0.8 mM). The samples were incubated at 37 °C for 60 min. After this time 3 μL of charge buffer (0.25% bromophenol, 0.25% xylene cyanol, and 30% glycerol) was added and the electrophoresis was carried out immediately at 80 V in 0.8% agarose gel [containing 2 μL/100 mL of a solution of ethidium bromide (10 mg·mL$^{-1}$)] using 0.5×TBE as a buffer (0.045 M Tris, 0.045 M boric acid, and 1 mM EDTA) for 2–2.5 h. The gel was photographed using a Gel printer Plus TDI system. Assays involving the various inhibitors were carried out in the same way as above but the agents under investigation were added as follows: *tert*-butyl alcohol (1 M) and DMSO (1 M) for their ability to scavenge OH· radicals, sodium azide (100 mM), and 2,2,6,6-tetramethyl-4-piperidone (100 mM), which are characterized by their ability to scavenge singlet oxygen; distamycin (8 mM), which intercalates between the nucleobases of the minor groove of the double helix of DNA and superoxide dismutase (15 units) for its ability to quench the superoxide radical. It is known that copper(II) shows nuclease activity in its own right and therefore comparative electrophoresis was carried out for a range of incubation times in order to determine whether the complex showed higher, lower or equivalent activity to the copper(II) salts.

CCDC-277157 (for $[Cu(HAm4DH)Cl_2]_2$), CCDC-277158 (for $^1_\infty[Cu(Am4DH)Cl]$), CCDC-277159 for ($^1_\infty[Cu(Am4DH)Br]$), and CCDC-277160 for ($[Cu(HAm4DH)(H_2O)(ClO_4)_2]$·MeOH·$H_2O$) contain the supplementary crystallographic data for this paper. These data can be obtained free of charge from The Cambridge Crystallographic Data Centre via www.ccdc.cam.ac.uk/data_request/cif.

## Acknowledgments

Financial support from ERDF (EU)-DGI-MCYT (Spain) (Projects BQU2002-04523-C02 and CTQ2004-03735) and the Xunta de Galicia (Project PGIDIT03PXIC20302PN) is gratefully acknowledged.

[1] a) D. X. West, A. E. Liberta, S. B. Padhye, R. C. Chikate, P. B. Sonawane, A. S. Kumbhar, R. G. Yerande, *Coord. Chem. Rev.* **1993**, *123*, 49–71; b) D. X. West, S. B. Padhye, P. B. Sonawane, *Struct. Bonding* **1991**, *76*, 1–50.
[2] P. J. Van Koningsbruggen, J. G. Haasnoot, R. A. G. de Graalf, J. Reedijk, *Inorg. Chim. Acta* **1995**, *234*, 87–94.
[3] J. García-Tojal, J. García-Jaca, R. Cortés, T. Rojo, M. K. Urtiaga, M. I. Arriortua, *Inorg. Chim. Acta* **1996**, *249*, 25–32.
[4] A. G. Bingham, H. Bögge, A. Müller, E. W. Ainscough, A. M. Brodie, *J. Chem. Soc., Dalton Trans.* **1987**, 493–499.
[5] E. W. Ainscough, A. M. Brodie, J. D. Ranford, J. M. Waters, *J. Chem. Soc., Dalton Trans.* **1991**, 1737–1742.
[6] E. W. Ainscough, A. M. Brodie, J. D. Ranford, J. M. Waters, K. S. Murray, *Inorg. Chim. Acta* **1992**, *197*, 107–115.
[7] J. García Tojal, M. K. Yrtiaga, R. Cortés, L. Lezama, M. I. Arriortua, T. Rojo, *J. Chem. Soc., Dalton Trans.* **1994**, 2233–2238.
[8] C. F. Bell, C. R. Theocharis, *Acta Crystallogr., Sect. C* **1987**, *43*, 26–29.
[9] A. Castiñeiras, I. García-Santos, E. Bermejo, D. X. West, *Z. Naturforsch., Teil B* **2000**, *B55*, 511–518.
[10] A. Castiñeiras, I. García-Santos, E. Bermejo, D. X. West, *Polyhedron* **2000**, *19*, 1873–1880.
[11] I. García-Santos, A. Hagenbach, U. Abram, *Dalton Trans.* **2004**, 677–682.
[12] I. García-Santos, U. Abram, R. Alberto, E. Vazquez-López, *Inorg. Chem.* **2004**, *43*, 1834–1836.
[13] D. X. West, J. K. Swearingen, J. Valdés-Martínez, S. Hernández-Ortega, A. K. El-Sawaf, F. van Meurs, A. Castiñeiras, I. García-Santos, E. Bermejo, *Polyhedron* **1999**, *18*, 2919–2929.
[14] I. García-Santos, E. Bermejo, A. K. El-Sawaf, A. Castiñeiras, D. X. West, *Polyhedron* **2002**, *21*, 729–737.
[15] E. Bermejo, A. Castiñeiras, L. M. Fostiak, I. García-Santos, A. L. Llamas-Saiz, J. K. Swearingen, D. X. West, *Z. Naturforsch. B* **2001**, *56*, 1297–1305.
[16] L. M. Fostiak, I. García-Santos, J. K. Swearingen, E. Bermejo, A. Castiñeiras, D. X. West, *Polyhedron* **2003**, *22*, 83–92.
[17] E. Bermejo, A. Castiñeiras, I. García-Santos, D. X. West, *Polyhedron* **2003**, *22*, 1147–1154.
[18] I. García-Santos, U. Abram, *Z. Anorg. Allg. Chem.* **2004**, *630*, 697–700.
[19] A. Castiñeiras, I. García-Santos, E. Bermejo, K. A. Ketcham, D. X. West, A. K. El-Sawaf, *Z. Anorg. Allg. Chem.* **2002**, *628*, 492–504.
[20] E. Bermejo, A. Castiñeiras, I. García-Santos, D. X. West, *Z. Allg. Anorg. Chem.* **2005**, *631*, 2011–2019.
[21] K. A. Ketcham, I. García-Santos, J. K. Swearingen, E. Bermejo, A. K. El-Sawaf, A. Castiñeiras, D. X. West, *Polyhedron* **2002**, *21*, 859–865.
[22] K. A. Ketcham, J. K. Swearingen, A. Castiñeiras, I. García-Santos, E. Bermejo, D. X. West, *Polyhedron* **2001**, *20*, 3265–3273.
[23] K. A. Ketcham, I. García-Santos, E. Bermejo, J. K. Swearingen, A. Castiñeiras, D. X. West, *Z. Anorg. Allg. Chem.* **2002**, *628*, 409–415.
[24] W. J. Geary, *Coord. Chem. Rev.* **1971**, *7*, 81–122.
[25] M. B. Ferrari, G. G. Fava, P. Tarasconi, C. Pelizzi, *J. Chem. Soc., Dalton Trans.* **1989**, 361–366.
[26] P. G. Beckingsale, A. T. Morcom, C. E. F. Rickard, T. N. Waters, *J. Chem. Soc., Dalton Trans.* **1977**, 2135–2138.
[27] P. De Meester, A. C. Skapski, *J. Chem. Soc., Dalton Trans.* **1972**, 2400–2404.
[28] a) E. D. Estes, W. E. Estes, W. E. Hatfield, D. J. Hodgson, *Inorg. Chem.* **1975**, *14*, 106–109; b) D. D. Swank, G. F. Needham, R. D. Willet, *Inorg. Chem.* **1979**, *18*, 761–765.
[29] D. X. West, J. K. Swearingen, T. J. Romack, I. S. Billeh, J. P. Jasinski, Y. Li, R. J. Staples, *J. Mol. Struct.* **2001**, *570*, 129–136.

 © 2006 Wiley-VCH Verlag GmbH & Co. KGaA, Weinheim 

[30] M. A. Ali, K. K. Dey, M. Nazimuddin, F. E. Smith, R. J. Butcher, J. P. Jasinski, J. M. Jasinski, *Polyhedron* **1996**, *15*, 3331–3339.
[31] W. E. Marsh, W. E. Hatfield, D. J. Hodgson, *Inorg. Chem.* **1982**, *21*, 2679–2684.
[32] D. J. Hodgson, P. K. Hale, W. E. Hatfield, *Inorg. Chem.* **1971**, *10*, 1061–1067.
[33] Y.-M. Lee, H.-W. Lee, Y.-I. Kim, *Polyhedron* **2005**, *24*, 377–382.
[34] A. W. Addison, T. N. Rao, J. Reedijk, J. V. Rijn, G. C. Verschoor, *J. Chem. Soc., Dalton Trans.* **1984**, 1349–1356.
[35] A. W. Addison, T. N. Rao, E. Sinn, *Inorg. Chem.* **1984**, *23*, 1957–1967.
[36] G. A. Lawrance, B. W. Skelton, A. H. White, *Aust. J. Chem.* **1986**, *39*, 1101–1108.
[37] S. C. Bhatia, A. K. Chatrath, P. C. Jain, *J. Indian Chem. Soc.* **1997**, *74*, 769–771.
[38] A. B. P. Lever, *Inorganic Electronic Spectroscopy*, 2nd ed., Elsevier, Amsterdam, **1986**.
[39] B. Bleaney, K. D. Bowers, *Proc. R. Soc. London, Ser. A* **1952**, *214*, 451–465.
[40] E. A. Boudreaux, L. N. Mulay, *Theory and Applications of Molecular Magnetism*, John Wiley & Sons, New York, **1976**.
[41] a) W. E. Hatfield, *Comments Inorg. Chem.* **1981**, *1*, 105–121; b) W. E. Marsh, K. C. Patel, W. I. Hatfield, D. J. Hodgson, *Inorg. Chem.* **1983**, *22*, 511–515; c) W. A. Alves, R. H. de Almeida Santos, A. Paduan-Filho, C. C. Becerra, A. C. Borin, A. M. Da Costa Ferreira, *Inorg. Chim. Acta* **2004**, *357*, 2269–2278.
[42] R. Rodríguez, A. Llobet, M. Corbello, A. E. Martell, J. Reibenspies, *Inorg. Chem.* **1999**, *38*, 2328–2334.
[43] P. Kapoor, A. Pathak, R. Kapoor, P. Venugopalan, M. Corbella, R. Rodríguez, J. Roblew, A. Llobet, *Inorg. Chem.* **2002**, *41*, 6153–6160.
[44] A. S. Kumbhar, S. S. Padhye, D. X. West, A. E. Liberta, *Transition Met. Chem.* **1991**, *16*, 276–279.
[45] Bruker, SMART and SAINT. *Area Detector Control Integration Software*, Bruker Analytical X-ray Instruments, Inc., Madison, WI, **1999**.
[46] G. M. Sheldrick, *SADABS, Program for Empirical Absorption Correction of Area Detector Data*, University of Göttingen, Germany, **1997**.
[47] G. M. Sheldrick, *Acta Crystallogr., Sect. A* **1990**, *46*, 467–473.
[48] G. M. Sheldrick, *SHELX-97, Program for the Refinement of Crystal Structures*, University of Göttingen, Germany, **1997**.
[49] A. J. C. Wilson (Ed.), *International Tables for Crystallography*, Kluwer Academic Publishers, Dordrecht, **1995**, vol. C.
[50] K. H. Reddy, P. S. Reddy, *Transition Met. Chem.* **2000**, *25*, 505–510.

Received: September 8, 2005
Published Online: January 19, 2006

 © 2006 Wiley-VCH Verlag GmbH & Co. KGaA, Weinheim 

DOI: 10.1002/ejic.200500822

# Novel Metallosupramolecular Networks Constructed from $Cu^{II}$, $Ni^{II}$, and $Cd^{II}$ with Mixed Ligands: Crystal Structures, Fluorescence, and Magnetism

**Miao Du,*[a] Xiu-Juan Jiang,[a] Xiao-Jun Zhao,[a] Hua Cai,[a] and Joan Ribas[b]**

**Keywords:** Coordination polymers / Inclusion complexes / Supramolecular chemistry / Noncovalent interactions

Reactions of mixed ligands succinic acid ($H_2$suc) and bent dipyridines, such as 2,5-bis(3-pyridyl)-1,3,4-oxadiazole (3-bpo) and its 4-*N*-donor analog (4-bpo), with inorganic $Cu^{II}$, $Ni^{II}$, and $Cd^{II}$ salts yield three new metal-organic coordination frameworks $\{[Cu(suc)(3\text{-bpo})(H_2O)_2]\cdot(H_2O)_{1.75}\}_n$ (**1**), $\{[Ni(suc)(4\text{-bpo})(H_2O)_2]\cdot(H_2O)_5\}_n$ (**3**), and $\{[Cd_2(suc)_2(3\text{-bpo})_2(H_2O)_2]\cdot(H_2O)_{6.75}\}_n$ (**4**), in which the metal centers are linked by bridging ligands 3-bpo/4-bpo and $suc^{2-}$ along two directions to form 2D infinite networks. The corrugated 2D nets of **1** and **4**, obtained under hydrothermal conditions, align in an interdigitated manner with the presence of significant aromatic-stacking interactions to result in similar 3D architectures. The 2D sheets in **3** are extended by interlayer hydrogen bonds to afford a 3D structure. However, when succinic acid is replaced by fumaric acid ($H_2$fum) in the reaction with 3-bpo and $Cu^{II}$ salt, a metallacyclophane $[Cu(Hfum)_2(3\text{-bpo})(H_2O)]_2\cdot(3\text{-bpo})_2\cdot(H_2O)_6$ (**2**) is generated. The binuclear coordinated motifs are hydrogen-bonded to the lattice water chains to furnish a unique 3D channel-like framework, in which the guest 3-bpo molecules are accommodated. The thermal stabilities of these new materials were investigated by thermogravimetric analysis (TGA) of mass loss. The magnetic coupling in complexes **1**–**3** is antiferromagnetic and very small, which is as expected considering the long organic bridges between the paramagnetic centers. The solid-state luminescence properties of **4** reveal an intense fluorescence emission at 378 nm.

(© Wiley-VCH Verlag GmbH & Co. KGaA, 69451 Weinheim, Germany, 2006)

## Introduction

Research on metal-organic supramolecular chemistry has rapidly developed to produce new materials with interesting structural features and potential applications, and is also one of the most active branches in current coordination chemistry.[1,2] By self-assembly of well-designed organic ligands and metal ions under appropriate conditions, a variety of novel metallosupramolecular architectures, such as coordination polymers and host-guest compounds, have been achieved so far.[1,2] Previous reports have revealed that bifunctional building blocks such as dicarboxylate and dipyridine can bind and bridge metal centers well,[3] and to some extent, it is now possible to predict the target materials based on such ligands containing specific structural and functional information. On the other hand, metal-carboxylate complexes are of great interest in several fields including bioinorganic chemistry,[4] molecular magnetism,[5] and crystal engineering.[6]

Nowadays, the combination of two or more predetermined organic building blocks within a structure has proven to be a powerful synthetic approach to generate functional metal-organic frameworks.[2b,7] Succinic acid ($H_2$suc) is an effective linking ligand that has been extensively used, together with 4,4′-bipyridine (bipy), to construct mixed-ligand polymeric arrays such as a 1D chain [Zn(suc)(bipy)],[8a] a 3D open framework $[Cu(suc)(bipy)(H_2O)_2]\cdot 2H_2O$,[8a] a 3D pillar-layered network $[Mn(suc)(bipy)(H_2O)]\cdot 0.5bipy$,[8b] a twofold interpenetrated 3D pillar-layered structure $[Cd(suc)(bipy)]\cdot 0.25H_2O$,[8c] and a unique twisting chiral net $[Co(suc)(bipy)(H_2O)_2]\cdot 2H_2O$.[8d] Recently, a dipyridyl *exo*-bidentate heterocyclic ligand, somewhat structurally similar to bipy but with a bent backbone, 2,5-bis(4-pyridyl)-1,3,4-oxadiazole (4-bpo) and its 3-*N*-donor analog (3-bpo) have been involved considerably in our investigations, and a series of interesting discrete/infinite coordination frameworks[9] and organic cocrystalline materials[10] have been generated utilizing their advantage as linking units with the potential ability for coordination, hydrogen-bonding, and/or aromatic-stacking interactions. As an extension of this research, our current work has been focused on simultaneous employment of such N-donor ligands in cooperation with dicarboxylates to assemble new coordination frameworks.[11] In this context, we describe here the preparation, crystal structures, and properties of the mixed-ligand systems $\{[Cu(suc)(3\text{-bpo})(H_2O)_2]\cdot(H_2O)_{1.75}\}_n$ (**1**), $[Cu(Hfum)_2(3\text{-bpo})(H_2O)]_2\cdot(3\text{-bpo})_2\cdot(H_2O)_6$ (**2**), $\{[Ni(suc)(4\text{-bpo})(H_2O)_2]\cdot(H_2O)_5\}_n$ (**3**), and $\{[Cd_2(suc)_2(3\text{-bpo})_2$-

[a] College of Chemistry and Life Science, Tianjin Normal University,
Tianjin 300074, P. R. China
Fax: +86-22-23540315
E-mail: dumiao@public.tpt.tj.cn
[b] Departament de Química Inorgànica, Universitat de Barcelona, Diagonal 647, 08028 Barcelona, Spain

 © 2006 Wiley-VCH Verlag GmbH & Co. KGaA, Weinheim 

$(H_2O)_2]\cdot(H_2O)_{6.75}\}_n$ (**4**), where $H_2$fum refers to fumaric acid. Complexes **1**, **3**, and **4** are 2D coordination polymers, while the dinuclear metallacyclophane **2** represents an unusual inclusion compound containing 1D water chains. The magnetic and fluorescence properties of these new materials were also studied.

## Results and Discussion

### Preparation and Thermal Stabilities of Complexes 1–4

Coordination polymers **1** and **4** were obtained by hydrothermal synthesis, and complexes **2** and **3** were prepared under ambient conditions. In the case of **3**, suitable crystals for X-ray diffraction were achieved by diffusion method in order to facilitate the slow growth of larger single crystals. During the preparation of coordination polymers **1**, **3**, and **4**, the pH environments of the reaction systems were adjusted by triethylamine to promote the complete deprotonation of succinic acid. As a consequence, in the resultant crystalline materials, the succinate dianions act as the bridging blocks to extend the 1D metal-bpo arrays to 2D infinite frameworks. Notably, in the dinuclear complex **2** with the unusual 3D inclusion architecture, the fumaric acid is found in its uncommon mono-deprotonation form and adopts the unprecedented terminal coordination mode with copper. This result is probably related to the fact that the reaction system leading to the generation of **2** does not include a sufficiently strong base. Presumably, the level of deprotonation of the dicarboxylic acid is of great relevance to the final structure of **2**. All complexes are air-stable and insoluble in common organic solvents and water, which is consistent with their polymeric and neutral nature. Thermogravimetric experiments were carried out to explore their thermal stabilities. The TGA curve of **1** shows an obvious weight loss of 6.33% in the range of 46–148 °C (peak: 123 °C), corresponding to the release of the lattice water molecules (calculated: 6.68%). The decomposition of the residuary $[Cu(suc)(3\text{-bpo})(H_2O)_2]$ moiety starts at 187 °C, and then there are three consecutive steps of weight losses ending at 396 °C (peaks: 253, 273, and 358 °C). Further heating to 800 °C reveals no weight loss. Complex **2** remains intact until heating to ca. 100 °C, and then there are three consecutive steps of weight losses (peaks: 182, 260, and 282 °C) concluding at 370 °C. Further heating to 800 °C reveals a continuous and slow weight loss. The TGA curve of **3** suggests that the first weight loss of 17.88% in the range 110–159 °C (peak: 133 °C) corresponds to the expulsion of the lattice water molecules (calculated: 17.14%). Then the coordination framework starts to decompose beyond 195 °C with a series of complicated weight losses, and does not end until heating to 800 °C. For complex **4**, the first step of weight loss (15.59%) in the 62–122 °C range correlates to the elimination of coordinated and lattice water molecules (calculated: 14.82%). The remaining substance does not lose weight upon further heating until two consecutive weight losses (peaks: 276 and 422 °C) occur in the temperature range of 196–478 °C. Further heating to 800 °C reveals no weight loss.

### Structural Analysis of Complexes 1–4

#### *{[Cu(suc)(3-bpo)(H$_2$O)$_2$]·(H$_2$O)$_{1.75}$}$_n$ (1)*

Single-crystal X-ray diffraction analysis reveals that complex **1** is a 2D metal-organic coordination network in which the metal centers are linked by bidentate $suc^{2-}$ and 3-bpo ligands. Each $Cu^{II}$ atom, located at an inversion center, has an octahedral geometry by virtue of two $suc^{2-}$ oxygen atoms, two 3-bpo nitrogen atoms, and two aqua ligands [Figure 1 (a)], and as expected, the geometry shows Jahn–Teller elongation with two $Cu–O_{water}$ bond distances

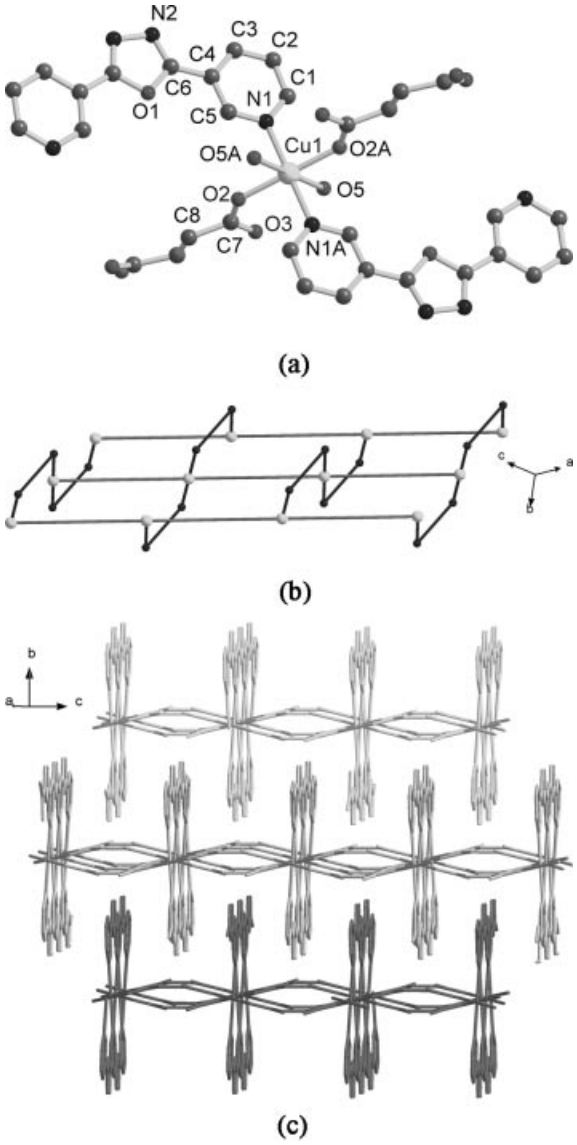


Figure 1. (a) A portion view of **1** with atom labeling of the asymmetric unit and the coordination sphere of copper (all hydrogen atoms are omitted for clarity). (b) A perspective view of the 2D $Cu^{II}$ network with mixed ligands $suc^{2-}$ and 3-bpo, which are simplified as rods and flexuous motifs, respectively. (c) A packing diagram of **1** showing the interdigitation of the 2D networks.

 © 2006 Wiley-VCH Verlag GmbH & Co. KGaA, Weinheim 

[2.621(7) Å] being significantly longer than those of the other four Cu–O/Cu–N bond lengths [1.947(2)/2.030(3) Å]. The carboxylate group is binding to copper through O(2) in a monodentate fashion, resulting in a longer bond length of C(7)–O(2) than that of C(7)–O(3). Detailed bond parameters are listed in Table 1. Both 3-bpo and $suc^{2-}$ bridging components adopt a *trans* arrangement around copper. As depicted in Figure 1 (b), the 3-bpo molecules connect the $Cu^{II}$ ions to produce a 1D sinusoidal chain, and a similar motif is also observed in $\{[Cu_2(3\text{-bpo})_2(H_2O)_6(SO_4)_2](H_2O)_6\}_n$.[9b] The adjacent chains are arranged in an A(-A) A(-A) sequence and are further interlinked by $suc^{2-}$ ligands in a *trans* bi-monodentate manner to generate a 2D (4,4) network. The distances between the $Cu^{II}$ centers separated by 3-bpo and $suc^{2-}$ are 8.302(3) and 9.499(2) Å, respectively. There also exist intralayer O–H···O hydrogen bonds [O(5)–H(5A)···O(3), H···O and O···O distances: 1.87 and 2.726(4) Å, O–H···O angle: 164°; O(5)–H(5B)···O(3)$^{i}$ (i = $-x + 3/2, -y + 1/2, -z + 1$), H···O and O···O distances: 2.06 and 2.904(5) Å; O–H···O angle: 158°], which further stabilize this framework.

Table 1. Selected bond lengths [Å] and angles [°] for complex **1**.[a]

| Bond lengths | | | |
|---|---|---|---|
| Cu(1)–O(2) | 1.947(2) | Cu(1)–N(1) | 2.030(3) |
| Cu(1)–O(5) | 2.621(7) | O(2)–C(7) | 1.277(4) |
| O(3)–C(7) | 1.231(4) | | |
| **Bond angles** | | | |
| O(2)–Cu(1)–N(1) | 89.29(10) | O(2)–Cu(1)–N(1A) | 90.71(10) |
| O(2)–Cu(1)–O(5) | 81.51(10) | O(2)–Cu(1)–O(5A) | 98.49(10) |
| N(1)–Cu(1)–O(5A) | 87.89(11) | N(1)–Cu(1)–O(5) | 92.11(11) |

[a] Symmetry codes: A: $-x + 3/2, -y + 1/2, -z$.

The most interesting structural feature of **1** is the packing mode of the 2D networks. As illustrated in Figure 1 (c), the 3-bpo segments lie up and down each 2D sheet, and as a consequence, these 2D arrays are interdigitated with the presence of interlayer π–π stacking interactions between the adjacent 3-bpo molecules. The center-to-center and center-to-plane distances of two antiparallel oxadiazole rings are 4.14 and 3.65 Å, respectively, and those for the pyridyl planes (with a dihedral angle of 4.7°) are 4.15 and 3.70/3.60 Å, respectively. Similar examples with such interdigitation alignment have been documented, which suggest that the stacking interactions can play an important role in extending the structural dimensionality of metallosupramolecular networks.[12]

### *[Cu(Hfum)$_2$(3-bpo)(H$_2$O)]$_2$·(3-bpo)$_2$·(H$_2$O)$_6$ (2)*

When succinic acid was replaced by the more rigid fumaric acid under different reaction conditions, a distinct complex **2** was produced. It consists of a centrosymmetrical binuclear unit $[Cu(Hfum)_2(3\text{-bpo})(H_2O)]_2$, two 3-bpo guests, and lattice water molecules. As shown in Figure 2 (a), in the binuclear entity, each $Cu^{II}$ atom is in a distorted square-pyramidal geometry with a $\tau$ parameter of 0.244.[13] Two 3-bpo nitrogen atoms and two carboxylate oxygen atoms of $Hfum^-$ occupy the basal plane, and a water ligand is located at the axial position with a significantly longer Cu–O bond distance of 2.219(3) Å. Selected bond lengths and angles for **2** are listed in Table 2. The two Cu atoms are linked by a pair of 3-bpo molecules to afford a bimetallic ring motif with an intramolecular Cu···Cu distance of 8.385(3) Å. Similar bimetallic macrocycles $[Cu_2(3\text{-bpo})_2(H_2O)_6](ClO_4)_4(H_2O)_4$ and $[Cu(3\text{-bpo})(NO_3)_2]_2(CH_3CN)_2$ were reported recently.[9b] Remarkably, the mono-deprotonated fumaric acid moieties coordinate to $Cu^{II}$ in a unidentate fashion and locate above and below the metallocycle plane. In most documented cases, fumaric acid serves as a dianionic fum bridge using both carboxylate groups,[14] and thus such a unidentate coordination mode of $Hfum^-$ and/or $fum^{2-}$ is quite unique.[15,16] In this structure, as expected, the C–O bonds of the carboxylate groups binding to copper

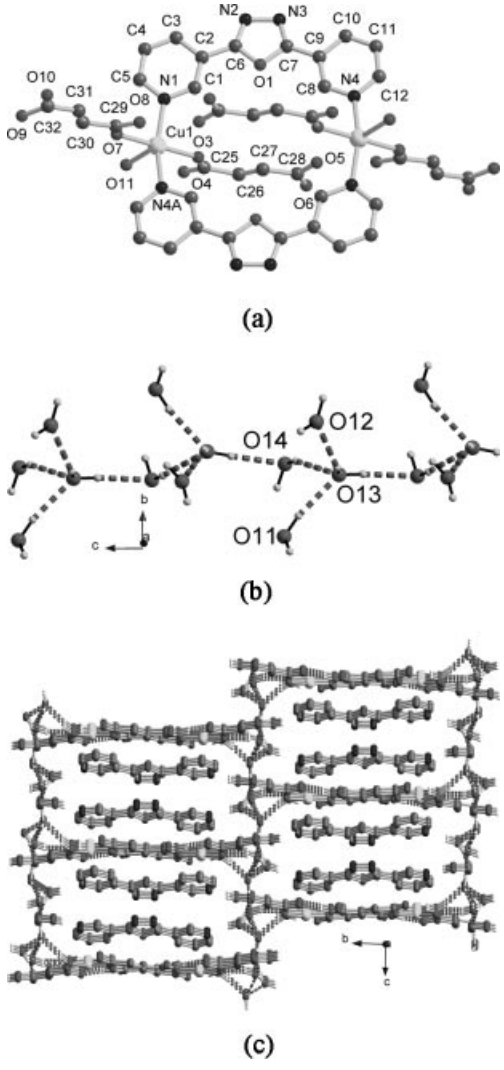


Figure 2. (a) Bimetallic macrocycle of **2** with atom labeling of the asymmetric unit and the coordination sphere of copper (all hydrogen atoms, guest 3-bpo, and lattice water molecules are omitted for clarity). (b) A representation of the 1D water chain linked by water-water interactions. (c) A perspective view of the 3D channel-like hydrogen-bonded network with the accommodation of guest 3-bpo molecules.

 © 2006 Wiley-VCH Verlag GmbH & Co. KGaA, Weinheim 

have longer lengths than those of the carboxylate groups not binding to copper, and the C–O bonds connecting with the hydrogen atoms of the carboxyl groups are also significant longer (see Table 2 for details). Another unique structural feature of **2** is that the 3-bpo molecules adopt the different *cisoid*-I and *cisoid*-II conformations[9a,17] when present as the bridging ligand and free guest molecule, respectively.

Table 2. Selected bond lengths [Å] and angles [°] for complex **2**.[a]

| Bond lengths | | | |
|---|---|---|---|
| Cu(1)–O(3) | 1.935(3) | Cu(1)–O(7) | 1.966(3) |
| Cu(1)–O(11) | 2.219(3) | Cu(1)–N(1) | 2.043(4) |
| Cu(1)–N(4A) | 2.034(4) | O(3)–C(25) | 1.263(5) |
| O(4)–C(25) | 1.231(5) | O(5)–C(28) | 1.315(5) |
| O(6)–C(28) | 1.198(5) | O(7)–C(29) | 1.263(6) |
| O(8)–C(29) | 1.233(6) | O(9)–C(32) | 1.301(6) |
| O(10)–C(32) | 1.204(6) | | |
| **Bond angles** | | | |
| O(3)–Cu(1)–O(7) | 176.15(13) | O(3)–Cu(1)–N(4A) | 85.93(13) |
| O(7)–Cu(1)–N(4A) | 92.03(13) | O(3)–Cu(1)–N(1) | 88.30(13) |
| O(7)–Cu(1)–N(1) | 92.65(13) | N(4A)–Cu(1)–N(1) | 161.51(14) |
| O(3)–Cu(1)–O(11) | 95.42(13) | O(7)–Cu(1)–O(11) | 88.07(13) |
| N(4A)–Cu(1)–O(11) | 97.64(14) | N(1)–Cu(1)–O(11) | 100.39(14) |

[a] Symmetry codes: A: $-x$, $1-y$, $1-z$.

Interestingly, the O(14)–H(14B)···O(13) and O(13)–H(13B)···O(14) hydrogen bonds between the lattice water molecules result in the formation of a 1D water chain along the *c* axis [see Figure 2 (b)], around which the lattice O(12) and coordinated O(11) water molecules are fixed by additional O(13)–H(13A)···O(12) and O(11)–H(11B)···O(13) interactions. Detailed hydrogen-bonding geometries are listed in Table 3. The binuclear subunits and the water chains are extended to a 2D layered structure along the crystallographic (011) plane by O(14)–H(14A)···O(7) and above water–water [O(11)···O(13)] interactions, and the structure is also stabilized by the O(11)–H(11A)···O(4) and O(5)–H(5)···O(8) bonds within each binuclear macrocycle. As shown in Figure 2 (c), these 2D arrays are further linked to afford a 3D channel-like network by interlayer O(12)–H(12B)···O(10) interactions, among which the guest 3-bpo entities are accommodated. Hydrogen-bonding interactions such as O(9)–H(9)···N(5) and O(12)–H(12A)···N(8) can be detected between the guest molecules and the host framework. Additionally, significant π–π stacking interactions exist between the adjacent 3-bpo moieties of the dimeric units within each 2D hydrogen-bonded layer, as well as between the neighboring guest 3-bpo molecules located in the cavities, with center-to-center and center-to-face separations of the aromatic rings in the range of 3.27–4.01 and 3.26–3.57 Å, respectively. Presumably, these supramolecular forces could consolidate this interesting host-guest inclusion system.

The significant structural difference between complexes **1** and **2** may be attributed to the intrinsic structural features of the $suc^{2-}$ and $Hfum^{-}$ ligands. We have clearly demonstrated that the structures of $Cu^{II}$ complexes with 3-bpo are solely dependent on the nature of the inorganic counteranions (for example, $ClO_4^-$, $NO_3^-$, $SO_4^{2-}$, and $OAc^-$),[9b] which afford two types of coordinated motifs such as the 1D sinusoidal chain and binuclear macrocycle (being similar to the cases of **1** and **2**, respectively) when 3-bpo takes the *cisoid*-I conformation. In this work, we can extend this conclusion to organic anions, which are also critical in determining the molecular assembly of the resultant polymeric networks.

### *{[Ni(suc)(4-bpo)(H$_2$O)$_2$]·(H$_2$O)$_5$}$_n$ (3)*

The 2D-layered polymeric network of complex **3** was revealed by X-ray single-crystal diffraction determination. As illustrated in Figure 3 (a), each $Ni^{II}$ center lies on an inversion site and is six-coordinate by binding to a pair of unidentate $suc^{2-}$ ligands, two aqua molecules, and two 4-bpo nitrogen atoms. Important bond lengths and angles are listed in Table 4. Two C–O bond lengths of the monodentate carboxylate group are similar, probably a result of the formation of hydrogen bonds as described later. The octahedral $Ni^{II}$ atoms are interconnected by 4-bpo ligands to afford a wavelike 1D chain running along the crystallographic [010] direction. Adjacent chains are further held together by *trans* bis-monodentate suc dianions, leading to the generation of a 2D undulating (4,4) layer, with the dimensions of the rectangle grid unit of $13.756(1)\times 8.934(1)$ Å$^2$ [see Figure 3 (b)]. As illustrated in Figure 3 (c), intralayer O(4)–H(4B)···O(3)$^{i}$ (i = $-x$, $-y+1$, $-z+1$) and interlayer O(4)–H(4A)···O(3)$^{ii}$ (ii = $-x+1/2$, $-y+1$, $z-1/2$) interactions between the aqua ligands and uncoordinated carboxylate oxygen atoms are observed.

Table 3. Hydrogen bond geometries in the crystal structure of complex **2**.

| D–H···A | D···A [Å] | H···A [Å] | D–H···A [°] | Symmetry codes |
|---|---|---|---|---|
| O(5)–H(5)···O(8) | 2.555(5) | 1.74 | 176 | $-x$, $-y+1$, $-z+1$ |
| O(9)–H(9)···N(5) | 2.627(5) | 1.81 | 171 | |
| O(11)–H(11A)···O(4) | 2.679(5) | 1.86 | 162 | |
| O(11)–H(11B)···O(13) | 2.796(6) | 1.96 | 169 | $x-1$, $y$, $z$ |
| O(12)–H(12A)···N(8) | 2.863(6) | 2.02 | 173 | $-x+1$, $-y+2$, $-z+1$ |
| O(12)–H(12B)···O(10) | 2.967(8) | 2.15 | 160 | |
| O(13)–H(13A)···O(12) | 2.697(7) | 1.99 | 140 | |
| O(13)–H(13B)···O(14) | 2.803(7) | 1.96 | 175 | $x$, $-y+3/2$, $z+1/2$ |
| O(14)–H(14A)···O(7) | 2.864(5) | 2.04 | 164 | $x+1$, $y$, $z$ |
| O(14)–H(14B)···O(13) | 2.815(6) | 2.04 | 152 | |

 © 2006 Wiley-VCH Verlag GmbH & Co. KGaA, Weinheim 

These afford two types of 6-membered and 13-membered hydrogen-bonded rings, with H···O/O···O distances of 1.85/2.659(4) and 1.87/2.711(4) Å, respectively, and O–H···O angles of 159 and 170°, respectively. Further analysis of the crystal packing indicates that these 2D waved layers take the parallel stacking mode with some offset, and are further linked to afford a 3D network by interlayer hydrogen bonds as stated earlier. Notably, allowing for the volume of the included disordered water molecules in this 3D open framework, there still remains 190.0 $Å^3$ of void space in the unit cell.[18]

Table 4. Selected bond lengths [Å] and angles [°] for complex **3**.[a]

| | | | |
|---|---|---|---|
| Bond lengths | | | |
| Ni(1)–O(2) | 2.024(4) | Ni(1)–O(4) | 2.068(3) |
| Ni(1)–N(1) | 2.107(3) | O(2)–C(7) | 1.250(5) |
| O(3)–C(7) | 1.244(5) | | |
| Bond angles | | | |
| O(2)–Ni(1)–O(4) | 87.48(9) | O(4)–Ni(1)–N(1) | 93.22(12) |
| O(2)–Ni(1)–N(1) | 88.63(12) | O(2)–Ni(1)–O(4A) | 92.52(9) |
| O(2)–Ni(1)–N(1A) | 91.37(12) | O(4)–Ni(1)–N(1A) | 86.78(12) |

[a] Symmetry codes: A: $-x$, $1-y$, $1-z$.

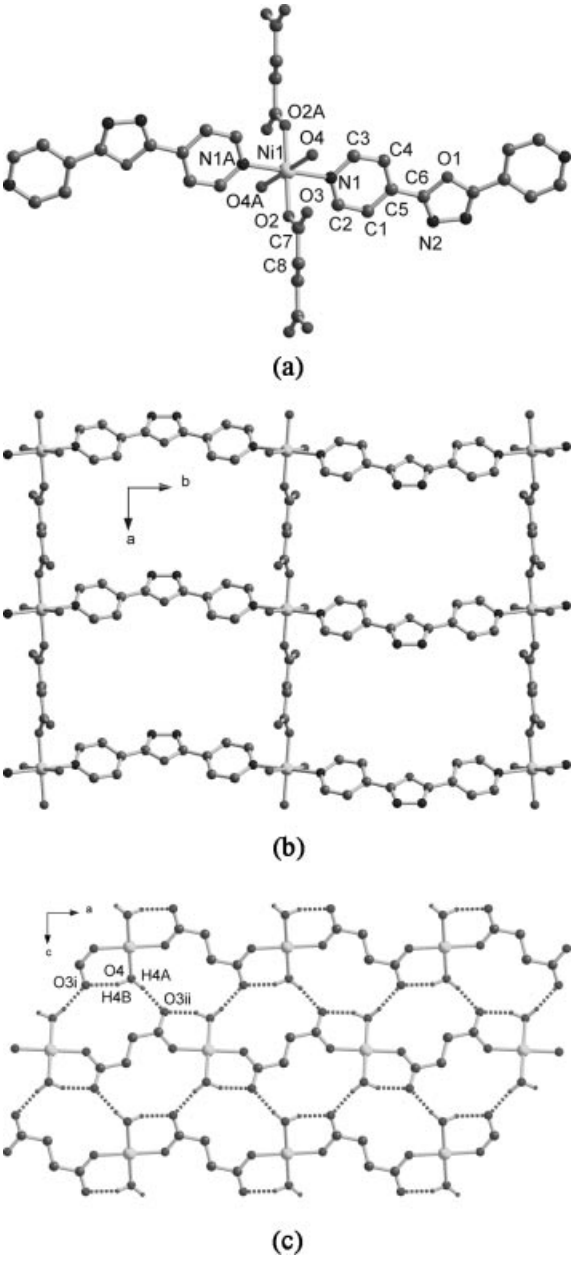


Figure 3. (a) A portion view of **3** with atom labeling of the asymmetric unit and the coordination sphere of nickel (all hydrogen atoms are omitted for clarity). (b) 2D metal-organic network constructed from $suc^{2-}$/4-bpo and $Ni^{II}$. (c) A view showing the interlayer and intralayer hydrogen bonds (4-bpo moieties are omitted for clarity).

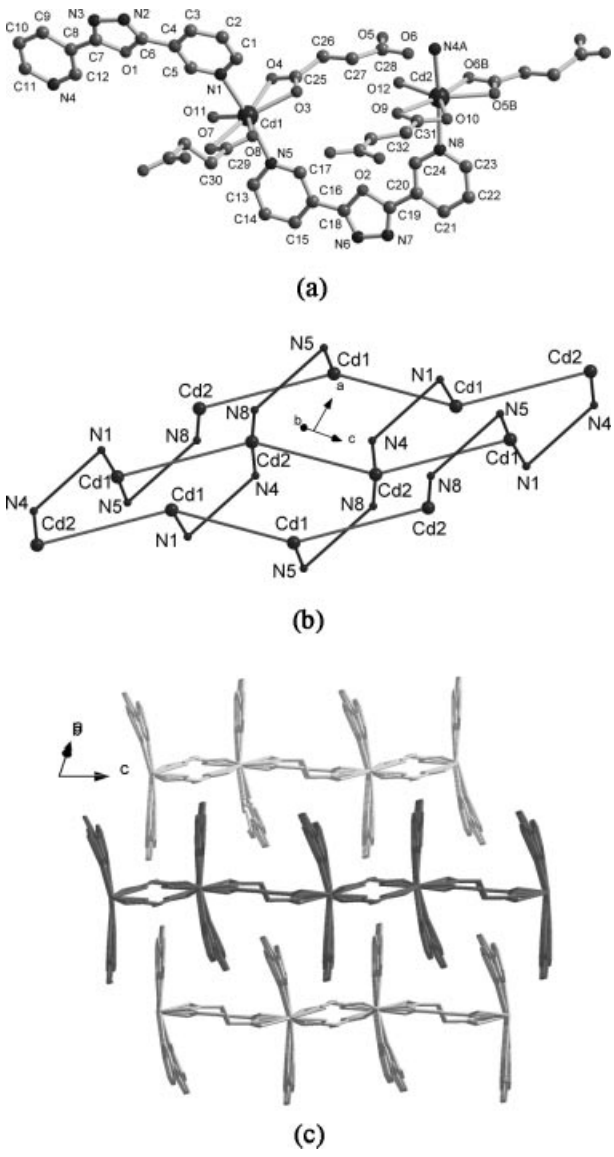


Figure 4. (a) A portion view of **4** with atom labeling of the asymmetric unit and the coordination spheres of cadmium (all hydrogen atoms are omitted for clarity). (b) A perspective view of the 2D $Cd^{II}$ network with mixed ligands $suc^{2-}$ and 3-bpo, which are simplified as rods and flexuous motifs, respectively. (c) A packing diagram of **3** showing the interdigitation of the 2D networks.

 © 2006 Wiley-VCH Verlag GmbH & Co. KGaA, Weinheim 

### *{[$Cd_2$(suc)$_2$(3-bpo)$_2$($H_2O$)$_2$]·($H_2O$)$_{6.75}$}$_n$ (4)*

Complex **4** is also a 2D network, constructed from $Cd^{II}$ and the mixed bridging ligands $suc^{2-}$ and 3-bpo. The local coordination environments around two crystallographically independent $Cd^{II}$ centers are similar, and can be best described as a pentagonal-bipyramidal geometry ($CdN_2O_5$). The equatorial plane is composed of two chelating carboxylate groups from a pair of $suc^{2-}$ ligands and one oxygen-donor aqua ligand [Cd–O: 2.259(6)–2.485(6) Å], and the axial positions are occupied by two 3-bpo nitrogen atoms [Cd–N: 2.345(8)–2.382(8) Å], as shown in Figure 4 (a). Important bonds lengths and angles are listed in Table 5. Most of the C–O bond lengths of the carboxylate groups are nearly equivalent as a result of their chelated coordination. Similar to the structure of complex **1**, the $Cd^{II}$ ions are connected by 3-bpo and $suc^{2-}$ ligands to furnish a 2D framework with common (4,4) topology [see Figure 4 (b)], and these 2D motifs interdigitate to result in a 3D crystal packing managed by aromatic stacking between 3-bpo moieties [see Figure 4 (c)]. The center-to-center and center-to-face distances between the neighboring 3-bpo molecules are in the range of 3.65–3.78 and 3.35–3.58 Å, respectively. Also, intralayer O(11)–H(11A)···O(4)$^i$ (i = $-x$ + 1, $-y$, $-z$ + 1) and O(12)–H(12B)···O(6) bonds [H···O/O···O distances: 1.95/2.795(9) and 1.89/2.732(8) Å, O–H···O angles: 169 and 172°] can be detected between the aqua ligands and carboxylate groups to further support this structure. However, the arrangement of 3-bpo in **4** is somewhat flexuous, rather than the complanate style as in **1** [see Figure 4 (c)]. This can be attributed to the dissimilar coordination tendency of bpo to $Cu^{II}$ and $Cd^{II}$ metal centers, reflected by the difference in N–M–N angles of 180° for **1** and 168.0(2)/168.1(3)° for **4**.

Table 5. Selected bond lengths [Å] and angles [°] for complex **4**.[a]

| Bond lengths | | | |
|---|---|---|---|
| Cd(1)–O(11) | 2.259(6) | Cd(1)–O(3) | 2.316(5) |
| Cd(1)–N(5) | 2.345(8) | Cd(1)–N(1) | 2.373(8) |
| Cd(1)–O(7) | 2.407(6) | Cd(1)–O(8) | 2.436(6) |
| Cd(1)–O(4) | 2.485(6) | Cd(2)–O(12) | 2.275(6) |
| Cd(2)–N(4A) | 2.382(8) | Cd(2)–O(5B) | 2.343(6) |
| Cd(2)–N(8) | 2.351(7) | Cd(2)–O(10) | 2.379(6) |
| Cd(2)–O(9) | 2.390(6) | Cd(2)–O(6B) | 2.445(6) |
| O(3)–C(25) | 1.255(9) | O(4)–C(25) | 1.251(10) |
| O(5)–C(28) | 1.255(10) | O(6)–C(28) | 1.270(10) |
| O(7)–C(29) | 1.251(12) | O(8)–C(29) | 1.220(12) |
| O(9)–C(31) | 1.255(11) | O(10)–C(31) | 1.266(11) |
| **Bond angles** | | | |
| O(11)–Cd(1)–O(3) | 131.1(2) | O(11)–Cd(1)–N(5) | 91.5(3) |
| O(3)–Cd(1)–N(5) | 91.8(2) | O(11)–Cd(1)–N(1) | 93.1(3) |
| O(3)–Cd(1)–N(1) | 93.5(3) | N(5)–Cd(1)–N(1) | 168.1(3) |
| O(11)–Cd(1)–O(7) | 85.7(2) | O(3)–Cd(1)–O(7) | 143.2(2) |
| N(5)–Cd(1)–O(7) | 85.7(2) | N(1)–Cd(1)–O(7) | 83.6(3) |
| O(11)–Cd(1)–O(8) | 138.7(2) | O(3)–Cd(1)–O(8) | 90.2(2) |
| N(5)–Cd(1)–O(8) | 86.8(3) | N(1)–Cd(1)–O(8) | 82.5(3) |
| O(7)–Cd(1)–O(8) | 53.0(2) | O(11)–Cd(1)–O(4) | 77.5(2) |
| O(3)–Cd(1)–O(4) | 53.90(19) | N(5)–Cd(1)–O(4) | 100.1(2) |
| N(1)–Cd(1)–O(4) | 91.7(3) | O(7)–Cd(1)–O(4) | 162.3(2) |
| O(8)–Cd(1)–O(4) | 143.4(2) | O(12)–Cd(2)–O(5B) | 133.3(2) |
| O(12)–Cd(2)–N(8) | 93.7(3) | O(5B)–Cd(2)–N(8) | 91.9(3) |
| O(12)–Cd(2)–N(4A) | 91.0(3) | O(5B)–Cd(2)–N(4A) | 92.9(3) |
| N(8)–Cd(2)–N(4A) | 168.0(2) | O(12)–Cd(2)–O(10) | 139.5(2) |
| O(5B)–Cd(2)–O(10) | 87.1(2) | N(8)–Cd(2)–O(10) | 86.6(2) |
| N(4A)–Cd(2)–O(10) | 82.7(3) | O(12)–Cd(2)–O(9) | 84.6(2) |
| O(5B)–Cd(2)–O(9) | 142.1(2) | N(8)–Cd(2)–O(9) | 87.0(3) |
| N(4A)–Cd(2)–O(9) | 82.5(3) | O(10)–Cd(2)–O(9) | 55.0(2) |
| O(12)–Cd(2)–O(6B) | 79.0(2) | O(5B)–Cd(2)–O(6B) | 54.4(2) |
| N(8)–Cd(2)–O(6B) | 93.0(2) | N(4A)–Cd(2)–O(6B) | 98.7(2) |
| O(10)–Cd(2)–O(6B) | 141.5(2) | O(9)–Cd(2)–O(6B) | 163.5(2) |

[a] Symmetry codes: A: $x$ – 1, $y$ + 1, $z$; B: $-x$, $-y$ + 1, $-z$ + 1.

A comparison of the three 2D suc/bpo-bridged coordination polymers **1**, **3**, and **4** also reveals the different alignment fashions of the 1D metal–bpo chains. As described earlier, such polymeric chains array in antiparallel [A(-A) A(-A), for **1**] and parallel [AAAA, for **3**] sequences in the resultant 2D networks by further linkage of suc dianions. However, the 1D structures take an A(-A)(-A′)A′ manner in the 2D framework of **4** [see Figure 4 (b)], due to its lower crystallographic symmetry.

### Magnetic Properties of Complexes 1–3

The magnetic properties of **1** are shown in Figure 5 (a). The $\chi_M T$ value ($\chi_M$ is the molar magnetic susceptibility for one $Cu^{II}$ ion) at 300 K is 0.40 $cm^3 mol^{-1} K$, which is as expected for one magnetically quasi-isolated spin doublet ($g > 2.00$). Starting from room temperature, $\chi_M T$ values smoothly decrease to 50 K and then quickly decrease to 0.09 $cm^3 mol^{-1} K$ at 2 K. The overall trend is characteristic of weak antiferromagnetic interactions. The reduced molar

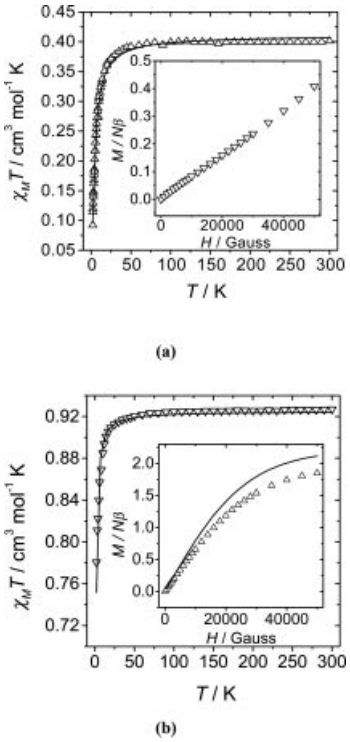


Figure 5. Plot of $\chi_M T$ vs. $T$ for (a) complex **1** and (b) complex **2**. Solid line represents the best fit. Inset: Plot of the reduced magnetization ($M/N\beta$) at 2 K for (a) complex **1** and (b) complex **2** (solid line represents the Brillouin function for $g$ = 2.22).

 © 2006 Wiley-VCH Verlag GmbH & Co. KGaA, Weinheim 

magnetization at 2 K [see inset in Figure 5 (a)] clearly indicates that the antiferromagnetic coupling is not negligible. The $M/N\beta$ value at 5 T is close to 0.5 electrons and the shape of the curve does not follow the Brillouin law.

Complex **1** is actually a 2D entity in which the $Cu^{II}$ ions are linked by $suc^{2-}$ and 3-bpo ligands. Both ligands are very long, and thus a small antiferromagnetic coupling is expected. Layers can be considered as pseudoquadratic. Considering these structural features, we have fitted the susceptibility data by the expression given by Rushbrooke and Wood for a Heisenberg square-planar system.[19] The expression was deduced by taking into account the $S = ½$ value for the $Cu^{II}$ ion, based on the spin Hamiltonian $H = -2J\Sigma_{ij}S_iS_j$.

$$\chi_M T = \frac{Ng^2\beta^2}{4k}\left[1-\frac{2}{x}+\frac{2}{x^2}-\frac{1.333}{x^3}+\frac{0.25}{x^4}+\frac{0.4833}{x^5}+\frac{0.003797}{x^6}\right]^{-1}$$

In this expression $x = kT/J$, and $N$, $\beta$, and $k$ have the usual meanings. The values obtained for the exchange parameters are $J = -1.06 \pm 0.01$ cm$^{-1}$, $g = 2.10 \pm 0.01$, and $R = 4 \times 10^{-5}$ ($R$ is the agreement factor defined as $\Sigma_i[(\chi_M T)_{obs} - (\chi_M T)_{calc}]^2/\Sigma[(\chi_M T)_{obs}]^2$ in this and the subsequent cases). This small $J$ value can be interpreted as a consequence of the weak overlap between the $Cu^{II}$ ions through the long organic ligands.

The magnetic properties of **2** as a $\chi_M T$ versus $T$ plot ($\chi_M$ is the molar magnetic susceptibility for two $Cu^{II}$ ions) and the reduced magnetization ($M/N\beta$ versus $H$, inset) are shown in Figure 5 (b). The value of $\chi_M T$ at 300 K is 0.93 cm$^3$ mol$^{-1}$ K, which is as expected for two isolated $Cu^{II}$ ions without coupling ($g > 2.00$). Starting from room temperature, $\chi_M T$ values are practically constant to 50 K, and below 50 K they quickly decrease to 0.78 cm$^3$ mol$^{-1}$ K at 2 K. This feature is characteristic of very weak antiferromagnetic interactions between the $Cu^{II}$ ions, which is also clearly corroborated by the reduced molar magnetization at 2 K. The $M/N\beta$ value at 5 T is close to 1.8 electrons and the curve is below the theoretical Brillouin function for $g = 2.22$. The fit of the susceptibility data of the dinuclear $Cu^{II}$ complex **2** was carried out by application of the Bleaney–Bowers formula.[20] The best-fit parameters obtained are $J = -0.90 \pm 0.01$ cm$^{-1}$, $g = 2.22 \pm 0.01$, and $R = 6.1 \times 10^{-5}$. The small $J$ value can be interpreted as a consequence of the almost nil overlap between the two $Cu^{II}$ ions through the long 3-bpo bridging ligand.[9]

On comparison of the $\chi_M T$ curves for complexes **1** and **2**, it is worth noting their quite different scales [see Figure 5 (a) and (b), respectively]. The $\chi_M T$ range (300–2 K) for **1** is approximately 0.4 to 0.1 cm$^3$ mol$^{-1}$ K, whereas the range for **2** is only 0.93 to 0.78 cm$^3$ mol$^{-1}$ K. This feature corresponds to the different behaviors of the reduced magnetization for both complexes, indicating that the antiferromagnetic coupling is smaller in complex **2**.

The plot of $\chi_M T$ versus $T$ for one $Ni^{II}$ ion (complex **3**) is shown in Figure 6 (a). From room temperature to 50 K, $\chi_M T$ values are constantly close to ca. 1.20 cm$^3$ mol$^{-1}$ K, which is typical for one isolated $Ni^{II}$ ion with $g > 2.00$. There is a small decrease down to 40 K, and then to 0.75 cm$^3$ mol$^{-1}$ K at 2 K, indicating a very small antiferromagnetic coupling or the logical existence of the zero-field splitting (ZFS) of $Ni^{II}$ ions. The plot of the reduced magnetization ($M/N\beta$) for **3** is also shown in the inset in Figure 6 (a). The expected value of reduced magnetization for two unpaired electrons at saturation would be 2.3 (assuming $g = 2.15$, which is the $g$ value obtained from magnetic measurements, see later). The experimental value is close to 1.8 electrons at 2 K and 50000 Gauss. In the same figure we have represented the Brillouin function for $S = 1$ and $g = 2.15$. The experimental data are below the theoretical curve, indicating either the presence of weak antiferromagnetic interactions or, most likely, the signature of single-ion ZFS ($D$) of $Ni^{II}$.

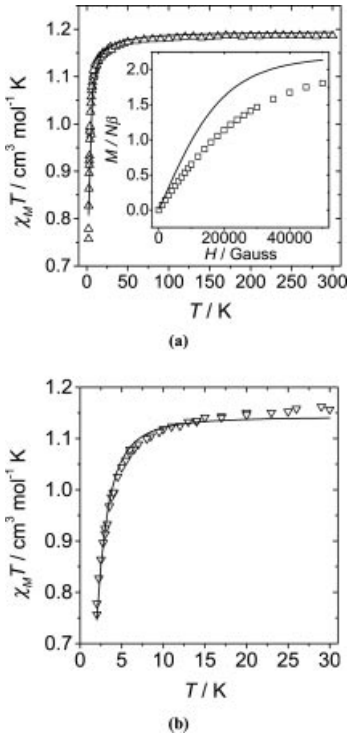


Figure 6. (a) Plot of $\chi_M T$ vs. $T$ for complex **3**. Solid line represents the best fit. Inset: Plot of the reduced magnetization ($M/N\beta$) at 2 K (solid line represents the Brillouin function at 2 K for $g = 2.15$). (b) Plot of the low temperature $\chi_M T$ region, assuming isolated $Ni^{II}$ ions with zero-field splitting ($D$ parameter). Solid line represents the best fit.

The structure of **3** is also a 2D case, which is difficult to fit, mainly due to small $J$ values. Therefore, in the first approach, we can assume that the long 3-bpo ligand does not create any coupling, and thus the small experimental coupling is due to the $suc^{2-}$ ligand. With this hypothesis, we can assume that complex **3** behaves as a 1D system. For systems of this kind, isotropic 1D $S = 1$, the temperature-dependence of the susceptibility extrapolated from calculations performed on ring systems of increasing length has been given by Weng,[21] which is valid only for antiferromagnetic coupling. Neither ZFS nor the Haldane gap effect[22] is taken into account in this expression. The best-fit parameters for **3** are $J = -0.38 \pm 0.01$ cm$^{-1}$, $g = 2.14 \pm 0.01$,

 © 2006 Wiley-VCH Verlag GmbH & Co. KGaA, Weinheim 

and $R = 2.0 \times 10^{-4}$. As indicated earlier, the small decrease in $\chi_M T$ values from 40 to 2 K could also be attributed to the typical single-ion ZFS for isolated $Ni^{II}$ ions, which is usually very great and of the order of 4–6 $cm^{-1}$.[23] For this reason we have also fitted the low temperature region assuming isolated $Ni^{II}$ ions (without any coupling), applying the formula given by Kahn for this $S = 1$ case.[20] It is important to emphasize that with this method it is only possible to calculate the absolute value of $D$, that is $|D|$, not its sign.[20] With this hypothesis, the best fit was obtained with the parameters $|D| = 3.9\ cm^{-1}$ and $g = 2.14$ [see Figure 6 (b)]. The calculated $D$ value lies in the order of magnitude typical for isolated $Ni^{II}$ ions, as indicated earlier.[23]

As a conclusion, we must emphasize that the two phenomena (small coupling and single-ion ZFS) may be active in this type of nickel complex. It is impossible to separate both components with these standard measurements. In any case, the antiferromagnetic coupling must be very small, as expected for the length of the bridging ligands.

### Luminescence Study of Complex 4

Solid-state luminescence properties of the polymeric $Cd^{II}$ ($d^{10}$ metal) complex **4** with the aromatic ligand 3-bpo were investigated ($\lambda_{ex} = 320$ nm). The free 3-bpo molecule displays an emission maximum at 364 nm, whereas a broad and intense emission band at 378 nm is observed for complex **4**. Hence, the fluorescence wavelength of 3-bpo is considerably affected by the incorporation of metal-coordination interactions. This significant red-shift phenomenon may be assigned to the ligand-to-metal charge transfer (LMCT). The intense fluorescence emission also shows that the coordination polymer **4** could have roles as potential photoactive inorganic-organic hybrid material.

## Conclusions

Three 2D metal-organic coordination polymers and a unique 3D metallosupramolecular inclusion complex have been achieved through self-assembly of metal ions and mixed organic ligands under different conditions. These new crystalline materials also display such useful properties as magnetism and fluorescence. This study clearly indicates that 3-bpo/4-bpo and $suc^{2-}$ ligands could act as excellent bridging spacers to construct programmed coordination polymers, and such a mixed-ligand synthetic strategy may further flourish this attractive chemistry. Further studies of the design and preparation of new metal-organic coordination frameworks with the bent *exo*-dipyridyl building blocks and other organic carboxylic acids (for example, the commonly used terephthalic, trimesic, and pyromellitic acids) are underway in our laboratory.

## Experimental Section

**General Materials and Methods:** All the reagents and solvents for synthesis and analysis were commercially available and used as received, except for 3-bpo and 4-bpo, which were prepared according to literature procedures.[24] FTIR spectra (KBr pellets) were recorded with an AVATAR-370 (Nicolet) spectrometer. Carbon, hydrogen, and nitrogen analyses were performed with a CE-440 (Leemanlabs) analyzer. TGA experiments were carried out with a Dupont thermal analyzer from room temp. to 800 °C under nitrogen at a heating rate of 10 °C/min. Fluorescence spectra were recorded with a Cary Eclipse spectrofluorimeter (Varian) equipped with a xenon lamp and quartz carrier at room temp.

**Magnetic Studies:** The variable-temp. magnetic susceptibilities were measured in the "Servei de Magnetoquímica (Universitat de Barcelona)" on polycrystalline samples (30 mg) with a Quantum Design SQUID MPMS-XL susceptometer, operating in the temp. range of 2–300 K and a magnetic field of 0.1 T. The diamagnetic corrections were evaluated from Pascal's constants for all constituent atoms.

**Syntheses of the Complexes**

**$\{[Cu(suc)(3\text{-bpo})(H_2O)_2]\cdot(H_2O)_{1.75}\}_n$ (1):** A mixture of succinic acid (17.2 mg, 0.15 mmol), $Cu(OAc)_2\cdot H_2O$ (23.5 mg, 0.12 mmol), 3-bpo (26.4 mg, 0.12 mmol), and triethylamine (0.2 mL) in water (10 mL) was sealed in a Teflon-lined stainless steel vessel (20 mL), which was heated at 140 °C for 5 d and then cooled to room temp. at a rate of 5 °C/h. Blue prism crystals were collected in 42% yield (24.0 mg, based on 3-bpo). $C_{16}H_{19.5}CuN_4O_{8.75}$ (471.40): calcd. C 40.76, H 4.17, N 11.88; found C 40.50, H 3.55, N 11.47. IR (KBr): $\tilde{\nu}$ = 3407 (br), 1616 (vs), 1556 (vs), 1482 (s), 1417 (vs), 1390 (vs), 1338 (s), 1284 (m), 1230 (s), 1194 (m), 1127 (m), 1083 (m), 1052 (m), 964 (m), 825 (s), 732 (s), 690 (vs) $cm^{-1}$.

**$[Cu(Hfum)_2(3\text{-bpo})(H_2O)]_2\cdot(3\text{-bpo})_2\cdot(H_2O)_6$ (2):** A mixture of fumaric acid (59.6 mg, 0.51 mmol) and $Cu(OAc)_2\cdot H_2O$ (38.9 mg, 0.19 mmol) in $CH_3OH/H_2O$ (10 mL, v:v = 1:1) was stirred for 10 min and the resultant blue precipitate was filtered. A solution of 3-bpo (23.6 mg, 0.10 mmol) in $CH_3OH$ (10 mL) was added to the filtrate with constant stirring for 30 min and then left to stand at room temp., producing blue block crystals after a period of 1 week in 12% yield (5.1 mg, based on 3-bpo). $C_{64}H_{60}Cu_2N_{16}O_{28}$ (1628.36): calcd. C 47.20, H 3.71, N 13.76; found C 47.42, H 3.84, N 13.72. IR (KBr): $\tilde{\nu}$ = 3432 (s), 3074 (s), 1720 (s), 1600 (vs), 1481 (m), 1413 (s), 1390 (vs), 1330 (s), 1282 (vs), 1251 (s), 1201 (s), 1164 (s), 1081 (m), 1042 (m), 975 (s), 829 (m), 730 (s), 695 (vs), 652 (s) $cm^{-1}$.

**$\{[Ni(suc)(4\text{-bpo})(H_2O)_2]\cdot(H_2O)_5\}_n$ (3):** The pH of a $CH_3OH/H_2O$ (5 mL, v:v = 1:1) solution containing succinic acid (14.5 mg, 0.12 mmol) and $Ni(ClO_4)_2\cdot 6H_2O$ (47.5 mg, 0.13 mmol) was adjusted to 7 with triethylamine. The resultant mixture was then carefully layered onto a buffer of glycol (2 mL), below which a solution of 4-bpo (23.4 mg, 0.11 mmol) in $CHCl_3$ (2 mL) was placed in a straight glass tube. Upon slow evaporation of the solvents over 2 weeks, green lamellar single crystals suitable for X-ray analysis were obtained in 26% yield (15.0 mg, based on 4-bpo). $C_{16}H_{26}N_4NiO_{12}$ (525.12): calcd. C 36.59, H 4.99, N 10.67; found: C 35.98, H 4.07, N 11.15. IR (KBr): $\tilde{\nu}$ = 3100 (br), 1546 (vs), 1489 (s), 1420 (vs), 1278 (w), 1224 (m), 1120 (w), 1063 (m), 1017 (w), 970 (w), 842 (s), 753 (s), 716 (s), 677 (s), 511 (m) $cm^{-1}$.

**$\{[Cd_2(suc)_2(3\text{-bpo})_2(H_2O)_2]\cdot(H_2O)_{6.75}\}_n$ (4):** The same hydrothermal procedure as for **1** was used except that $Cu(OAc)_2\cdot H_2O$ was replaced by $Cd(OAc)_2\cdot 2H_2O$, affording colorless block crystals of **4** in 58% yield (37.2 mg, based on 3-bpo). $C_{32}H_{41.5}Cd_2N_8O_{18.75}$ (1063.03): calcd. C 36.15, H 3.94, N 10.54; found: C 35.55, H 4.04, N 10.04. IR (KBr): $\tilde{\nu}$ = 3412 (br), 1581 (vs), 1548 (s), 1466 (m), 1415 (vs), 1292 (s), 1233 (w), 1192 (m), 1084 (m), 1029 (m), 900 (m), 815 (m), 732 (s), 692 (s), 639 (m) $cm^{-1}$.

 © 2006 Wiley-VCH Verlag GmbH & Co. KGaA, Weinheim 

Table 6. Crystallographic data and structure refinement summary for complexes **1**–**4**.

| | **1** | **2** | **3** | **4** |
|---|---|---|---|---|
| Empirical formula | $C_{16}H_{19.5}CuN_4O_{8.75}$ | $C_{64}H_{60}Cu_2N_{16}O_{28}$ | $C_{16}H_{26}N_4NiO_{12}$ | $C_{32}H_{41.5}Cd_2N_8O_{18.75}$ |
| *Mr* | 471.40 | 1628.36 | 525.12 | 1063.03 |
| Crystal size [mm] | 0.22×0.20×0.16 | 0.24×0.20×0.12 | 0.49×0.30×0.08 | 0.20×0.16×0.14 |
| Crystal system | monoclinic | monoclinic | orthorhombic | triclinic |
| Space group | *C*2/*c* | $P2_1/c$ | *Pnma* | $P\bar{1}$ |
| *a* [Å] | 16.031(6) | 12.576(4) | 8.9342(9) | 11.971(4) |
| *b* [Å] | 16.249(6) | 32.497(11) | 27.512(3) | 13.116(4) |
| *c* [Å] | 7.829(3) | 9.226(3) | 11.7133(12) | 15.075(5) |
| *α* [°] | 90 | 90 | 90 | 75.672(5) |
| *β* [°] | 99.777(6) | 107.843(6) | 90 | 77.826(5) |
| *γ* [°] | 90 | 90 | 90 | 88.422(6) |
| *V* [Å$^3$] | 2009.7(13) | 3589(2) | 2879.1(5) | 2241.0(13) |
| *Z* | 4 | 2 | 4 | 2 |
| $D_c$ [g cm$^{-3}$] | 1.558 | 1.507 | 1.211 | 1.575 |
| $\mu$ [mm$^{-1}$] | 1.142 | 0.689 | 0.728 | 1.028 |
| *F*(000) | 970 | 1676 | 1096 | 1071 |
| Total/independent Reflections | 5148/1783 | 18445/6309 | 14632/2601 | 11725/7874 |
| Parameters | 148 | 498 | 204 | 586 |
| $R_{int}$ | 0.0360 | 0.0673 | 0.0251 | 0.0393 |
| $R$,[a] $R_w$[b] | 0.0437, 0.0982 | 0.0575, 0.1272 | 0.0530, 0.1840 | 0.0536, 0.1328 |
| GOF[c] | 1.115 | 1.108 | 1.080 | 1.028 |
| Residuals [e Å$^{-3}$] | 0.374, –0.310 | 0.515, –0.396 | 0.761, –0.430 | 0.941, –0.555 |

[a] $R = \Sigma||F_o| - |F_c||/\Sigma|F_o|$. [b] $R_w = [\Sigma[w(F_o^2 - F_c^2)^2]/\Sigma w(F_o^2)^2]^{1/2}$. [c] GOF = $\{\Sigma[w(F_o^2 - F_c^2)^2]/(n - p)\}^{1/2}$.

***Caution!*** Perchlorate complexes of metal ions in the presence of organic ligands are potentially explosive. Only a small amount of material should be handled and with care.

**X-ray Crystallography:** Single-crystal X-ray diffraction data for complexes **1**–**4** were collected with a Bruker Apex II CCD diffractometer at 293(2) K with Mo-*Kα* radiation ($\lambda$ = 0.71073 Å) by $\omega$ scan mode. There was no evidence of crystal decay during data collection. A semiempirical absorption correction was applied using the SADABS program, and the program SAINT was used for integration of the diffraction profiles.[25] The structures were solved by direct methods using the SHELXS program of the SHELXTL package and refined with SHELXL.[26] The final refinement was performed by full-matrix least-squares methods with anisotropic thermal parameters for all non-hydrogen atoms on $F^2$. Hydrogen atoms bonded to carbon were placed geometrically and allowed to ride during subsequent refinement with an isotropic displacement parameter fixed at 1.2 times $U_{eq}$ of the parent atoms. Hydrogen atoms of the aqua ligands in all structures and the lattice water molecules in **2** were first located in difference Fourier maps, and then placed at calculated positions and included in the final refinement. The lattice water in the structures of **1**, **3**, and **4** were treated using the disordered model and their hydrogen atoms not located. Starting positions for carboxyl hydrogen atoms in the structure of **2** were located in difference syntheses, and refinement was performed using rigid O–H groups allowed to rotate but not tip, with the bond length of 0.82 Å. Further crystallographic data and structure refinement parameters of complexes **1**–**4** are summarized in Table 6.

CCDC-284066 to -284069 (for **1**–**4**, respectively) contain the supplementary crystallographic data for this paper. These data can be obtained free of charge from The Cambridge Crystallographic Data Centre via www.ccdc.cam.ac.uk/data_request/cif.

## Acknowledgments

This work was financially supported by the National Natural Science Foundation of China (No. 20401012), the Key Project of Tianjin Natural Science Foundation (No. 043804111), and Tianjin Normal University. J. R. acknowledges the financial support from the Spanish Government (Grant BQU2003/00539).

[1] a) M. W. Hosseini, *Acc. Chem. Res.* **2005**, *38*, 313–323; b) S. Kitagawa, R. Kitaura, S. Noro, *Angew. Chem. Int. Ed.* **2004**, *43*, 2334–2375; c) L. Carlucci, G. Ciani, D. M. Proserpio, *Coord. Chem. Rev.* **2003**, *246*, 247–289; d) O. R. Evans, W. B. Lin, *Acc. Chem. Res.* **2002**, *35*, 511–522; e) B. Moulton, M. J. Zaworotko, *Chem. Rev.* **2001**, *101*, 1629–1658.

[2] a) P. J. Steel, *Acc. Chem. Res.* **2005**, *38*, 243–250; b) B. H. Ye, M. L. Tong, X. M. Chen, *Coord. Chem. Rev.* **2005**, *249*, 545–565; c) L. Brammer, *Chem. Soc. Rev.* **2004**, *33*, 476– 489; d) C. Janiak, *Dalton Trans.* **2003**, 2781–2804; e) S. R. Seidel, P. J. Stang, *Acc. Chem. Res.* **2002**, *35*, 972–983; f) D. L. Caulder, K. N. Raymond, *Acc. Chem. Res.* **1999**, *32*, 975–982.

[3] a) Y. J. Kim, E. W. Lee, D.-Y. Jung, *Chem. Mater.* **2001**, *13*, 2684–2690; b) Y. J. Kim, M. K. Suh, D.-Y. Jung, *Inorg. Chem.* **2004**, *43*, 245–250; c) S. A. Barnett, N. R. Champness, *Coord. Chem. Rev.* **2003**, *246*, 145–168; d) S. Noro, R. Kitaura, M. Kondo, S. Kitagawa, T. Ishii, H. Matsuzaka, M. Yamashita, *J. Am. Chem. Soc.* **2002**, *124*, 2568–2583.

[4] a) D. Lee, B. Pierce, C. Krebs, M. P. Hendrich, B. H. Huynh, S. J. Lippard, *J. Am. Chem. Soc.* **2002**, *124*, 3993–4007; b) E. L. Hegg, R. Y. N. Ho, L. Que, Jr., *J. Am. Chem. Soc.* **1999**, *121*, 1972–1973; c) J. B. Vincent, G. L. Olivier-Lilley, B. A. Averill, *Chem. Rev.* **1990**, *90*, 1447–1467; d) G. Christou, *Acc. Chem. Res.* **1989**, *22*, 328–335.

[5] a) F. S. Delgado, J. Sanchiz, C. Ruiz-Perez, F. Lloret, M. Julve, *Inorg. Chem.* **2003**, *42*, 5938–5948; b) W. Wernsdorfer, N. Aliaga-Alcalde, D. N. Hendrickson, G. Christou, *Nature* **2002**, *416*, 406–409; c) J. T. Brockman, J. C. Huffman, G. Christou, *Angew. Chem. Int. Ed.* **2002**, *41*, 2506–2508; d) D. Gatteschi, A. Caneschi, L. Pardi, R. Sessoli, *Science* **1994**, *265*, 1054–1058.

[6] a) O. M. Yaghi, M. O'Keeffe, N. W. Ockwig, H. K. Chae, M. Eddaoudi, J. Kim, *Nature* **2003**, *423*, 705–714; b) C. N. R. Rao, S. Natarajan, R. Vaidhyanathan, *Angew. Chem. Int. Ed.* **2004**, *43*, 1466–1496.

[7] a) J. Tao, M. L. Tong, X. M. Chen, *J. Chem. Soc., Dalton Trans.* **2000**, 3669–3674; b) X. J. Li, R. Cao, D. F. Sun, W. H.

 © 2006 Wiley-VCH Verlag GmbH & Co. KGaA, Weinheim 

Bi, Y. Q. Wang, X. Li, M. C. Hong, *Cryst. Growth Des.* **2004**, *4*, 775–780; c) J. Tao, Y. Zhang, M. L. Tong, X. M. Chen, T. Yuen, C. L. Lin, X. Y. Huang, J. Li, *Chem. Commun.* **2002**, 1342–1343.

[8] a) S. M. Ying, J. G. Mao, Y. Q. Sun, H. Y. Zeng, Z. C. Dong, *Polyhedron* **2003**, *22*, 3097–3103; b) Y. Q. Zheng, J. L. Lin, Z. P. Kong, *Inorg. Chem.* **2004**, *43*, 2590–2596; c) J. Zhang, Z.-J. Li, Y.-H. Wen, Y. Kang, J.-K. Cheng, Y.-G. Yao, *Z. Anorg. Allg. Chem.* **2004**, *630*, 2731–2735; d) J. Zhang, Y. Kang, R.-B. Zhang, Z.-J. Li, J.-K. Cheng, Y.-G. Yao, *CrystEngCommun.* **2005**, *7*, 177–178.

[9] a) M. Du, X.-H. Bu, Y.-M. Guo, H. Liu, S. R. Batten, J. Ribas, T. C. W. Mak, *Inorg. Chem.* **2002**, *41*, 4904–4908; b) M. Du, X.-H. Bu, Z. Huang, S.-T. Chen, Y.-M. Guo, C. Diaz, J. Ribas, *Inorg. Chem.* **2003**, *42*, 552–559; c) M. Du, Y.-M. Guo, S.-T. Chen, X.-H. Bu, S. R. Batten, J. Ribas, S. Kitagawa, *Inorg. Chem.* **2004**, *43*, 1287–1293.

[10] a) M. Du, Z.-H. Zhang, X.-J. Zhao, *Cryst. Growth Des.* **2005**, *5*, 1199–1208; b) M. Du, Z.-H. Zhang, X.-J. Zhao, *Cryst. Growth Des.* **2005**, *5*, 1247–1254; c) M. Du, Z.-H. Zhang, X.-J. Zhao, H. Cai, *Cryst. Growth Des.* **2006**, *6*, 114–121.

[11] a) M. Du, H. Cai, X.-J. Zhao, *Inorg. Chim. Acta* **2005**, *358*, 4034–4038; b) M. Du, H. Cai, X.-J. Zhao, *Inorg. Chim. Acta* **2005**, 673–679.

[12] a) L. Y. Zhang, G. F. Liu, S. L. Zheng, B. H. Ye, X. M. Zhang, X. M. Chen, *Eur. J. Inorg. Chem.* **2003**, 2965–2971; b) D. Q. Chu, J. Q. Xu, L. M. Duan, T. G. Wang, A. Q. Tang, L. Ye, *Eur. J. Inorg. Chem.* **2001**, 1135–1137.

[13] A. W. Addison, T. N. Rao, J. Reedijk, J. Van Rijn, G. C. Verschoor, *J. Chem. Soc., Dalton Trans.* **1984**, 1349–1356.

[14] a) A. Michaelides, S. Skoulika, M. G. Siskos, *Chem. Commun.* **2004**, 2418–2419; b) S. Konar, E. Zangrando, N. R. Chaudhuri, *Inorg. Chim. Acta* **2003**, *355*, 264–271; c) A. Michaelides, S. Skoulika, M. G. Siskos, *Chem. Commun.* **2001**, 1346–1347; d) J. Tao, M. L. Tong, J. X. Shi, X. M. Chen, S. W. Ng, *Chem. Commun.* **2000**, 2043–2044.

[15] Unidentate coordination of $Hfum^-$ is unprecedented; for unidentate coordination of $Hmal^-$ (mal = maleate dianion) using its carboxylate oxygen see: a) A. Sequeira, H. Rajagopal, M. P. Gupta, F. Vanhouteghem, A. T. H. Lenstra, H. J. Geise, *Acta Crystallogr. Sect. C: Cryst. Struct. Commun.* **1992**, *48*, 1192–1197. For unidentate coordination of $Hmal^-$ using its carboxyl oxygen (notably, both cases are based on main group metals) see: b) Y.-Q. Zheng, Z.-P. Kong, J.-L. Lin, *Z. Kristallogr. - New Cryst. Struct.* **2001**, *216*, 355–356; c) V. V. Sharutin, O. K. Sharutina, A. P. Pakusina, V. K. Belsky, *J. Organomet. Chem.* **1997**, *536*, 87–92.

[16] For unidentate coordination of fum dianion see: a) K. L. Zhang, Z. Wang, H. Huang, Y. Zhu, X. Z. You, *J. Mol. Struct.* **2004**, *693*, 193–197. For unidentate coordination of mal dianion see: b) Y.-Q. Zheng, J.-L. Lin, Z.-P. Kong, B.-Y. Chen, *J. Chem. Crystallogr.* **2002**, *32*, 399–408; c) C.-G. Zhang, Y.-J. Leng, Z.-F. Ma, D.-Y. Yan, *J. Chem. Crystallogr.* **1999**, *29*, 1081–1084.

[17] M. Du, X.-J. Zhao, *J. Mol. Struct.* **2003**, *655*, 191–197.

[18] Computation of the channel space is performed using PLATON program, see: A. L. Spek, *J. Appl. Crystallogr.* **2003**, *36*, 7–13.

[19] G. S. Rushbrooke, P. Wood, *Mol. Phys.* **1963**, *6*, 409–421.

[20] O. Kahn, *Molecular Magnetism*, VCH Publishers, New York, **1993**.

[21] C. Y. Weng, Ph. D. Thesis, Carnegie Institute of Technology, **1968**.

[22] a) F. D. M. Haldane, *Phys. Rev. Lett.* **1983**, *50*, 1153–1156; b) F. D. M. Haldane, *Phys. Lett. A* **1983**, *93*, 464–468; c) J. P. Renard, M. Verdaguer, L. P. Regnault, W. A. C. Erkelens, J. Rossat-Mignon, W. G. Stirling, *Europhys. Lett.* **1987**, *3*, 945–951; d) J. P. Renard, M. Verdaguer, L. P. Regnault, W. A. C. Erkelens, J. Rossat-Mignon, J. Ribas, W. G. Stirling, C. J. Vettier, *Appl. Phys.* **1988**, *63*, 3538–3542.

[23] R. Boca, *Coord. Chem. Rev.* **2004**, *248*, 757–815 and references cited therein.

[24] F. Bentiss, M. Lagrenee, *J. Heterocycl. Chem.* **1999**, *36*, 1029–1032.

[25] Bruker AXS, *SAINT Software Reference Manual*, Madison, WI, **1998**.

[26] G. M. Sheldrick, *SHELXTL NT Version 5.1. Program for Solution and Refinement of Crystal Structures*, University of Göttingen, Germany, **1997**.

Received: September 15, 2005
Published Online: January 26, 2006

 © 2006 Wiley-VCH Verlag GmbH & Co. KGaA, Weinheim 

DOI: 10.1002/ejic.200500857

# Atmospheric Pressure Chemical Vapour Deposition of $NbSe_2$ Thin Films on Glass

Nicolas D. Boscher,[a] Claire J. Carmalt,[a] and Ivan P. Parkin*[a]

**Keywords:** Chemical vapour deposition / Metal selenide / Thin film

Atmospheric pressure chemical vapour deposition (APCVD) of niobium selenide films on glass substrates was achieved by reaction of di-*tert*-butyl selenide with $NbCl_5$ at 250–600 °C. X-ray diffraction showed that the $NbSe_2$ films were crystalline and of the $2H_a$ poly-type with cell constants close to those expected ($a$ = 3.44 Å; $c$ = 12.58 Å). Marked preferred orientation along either (101) or (200) was noted at higher deposition temperature and this unexpectedly varied depending on distance from the reactor inlet. The films produced at 600 °C showed exactly the Nb/Se ratio expected for $NbSe_2$ by energy dispersive analysis by X-rays. The films deposited at the substrate temperatures of 500 °C or less were selenium rich with a niobium to selenium ratio of 1:2.5. The films produced at 600 °C were dark-green, powdery and poorly adhesive. The films produced at 500 °C and below were dark-brown matte in appearance, they passed the Scotch tape test, but could be scratched with a steel scalpel. SEM showed that the films were composed of plate-like crystals, which become longer and thicker with increasing deposition temperature.
(© Wiley-VCH Verlag GmbH & Co. KGaA, 69451 Weinheim, Germany, 2006)

## 1. Introduction

Niobium diselenide ($NbSe_2$) is an important material because of its wide range of interesting physical properties, such as the presence of both a charge density wave transition and a superconducting transition. The structure of this low dimensionality layered material is hexagonal ($P6_{3/mmc}$) and composed of strongly bonded molecular layers stacked in a close-pack manner – with weak van der Waals interactions between the layers – which leads to highly anisotropic properties. Like all the layered group V transition-metal dichalcogenide, $NbSe_2$ has many different crystallographic poly-types, for example $2H_a$-, $2H_b$-, 3R-, $4H_a$-, $4H_{d1}$- and $4H_{d2}$-$NbSe_2$, depending on how the molecular layers stack-up and in turn the specific poly-type determines the physical properties of the materials. The poly-types $2H_a$- or $2H_b$-, and $4H_a$-$NbSe_2$ are superconducting with a transition temperature of $T_c$ = 7.2 K and $T_c$ = 6.3 K, respectively.[1,2] A charge-density wave is present in all the $NbSe_2$ polytypes. Moreover, an incommensurate charge-density wave is present in 2H-$NbSe_2$ below $T_c$ = 33.3 K. Its structure remains incommensurate through the superconducting transition.[3] Even though the phase diagram of the niobium–selenium system is not fully known, many forms of niobium selenide, apart from $NbSe_2$, have been observed, such as $Nb_5Se_4$, $Nb_3Se_4$, $NbSe_2$, $NbSe_3$ and $NbSe_4$.[2,4–6]

Similar to most of the transition-metal dichalcogenides, $NbSe_2$ has been cited for use as an electrical conductor and as a solid lubricant at high temperature. $NbSe_2$ is also a good intercalation host. It has been shown that the growth of hydrogen intercalated in $H_xNbSe_2$ results in changes in the conductivity type from metallic to semiconducting.[7] Therefore, due to this sensitivity to intercalated molecules, niobium diselenide films may, as titanium diselenide films, find application as hosts for sensor materials.

The most common method to grow crystals of $NbSe_2$ is the vapour-phase-transport of prereacted polycrystalline $NbSe_2$ with iodine as a transport agent. $NbSe_2$ thin films have been grown using van der Waals epitaxy (VDWE) and pulsed-laser deposition (PLD).[7,8] To the best of our knowledge a CVD route to $NbSe_2$ has not been reported to date.

Here we present the CVD of $NbSe_2$ thin films. The motivation for this work was to produce niobium selenide films on glass and to use precursors other than $H_2Se$. One interesting feature of this work was the unexpected variation in preferred orientation that was noted depending on the position of analysis on the substrate.

## 2. Results and Discussion

### Synthesis and Characterisation

Atmospheric pressure CVD reactions of $NbCl_5$ with $tBu_2Se$ were studied on glass substrates at 250–650 °C. The deposition was observed on both top plate and substrate. The extent of the film coverage was dependent on the deposition temperature. Only the six first centimetres of the substrate were coated for a deposition temperature of 600 °C,

[a] Department of Chemistry, University College London, 20 Gordon Street London, UK
E-mail: i.p.parkin@ucl.ac.uk

 © 2006 Wiley-VCH Verlag GmbH & Co. KGaA, Weinheim 

whilst the whole substrate was coated with uniform thickness at 300 °C. This indicates that the deposition is mass-transport-limited at the highest temperature, whereas the deposition is surface-reaction-limited at the lowest temperature. At a deposition temperature of 600 °C, the films produced from $t$Bu$_2$Se and NbCl$_5$ were dark-green and powdery. They failed the Scotch tape test and the scratch test but were insoluble in the common organic solvents, they only slowly decomposed in diluted nitric acid or diluted bleach, and were stable in air for over six months. At a deposition temperature at or below 500 °C, the films had a dark-black matt appearance; they passed the Scotch tape test, but were scratched with a steel scalpel.

Due to the porous nature of the films grown from NbCl$_5$ and $t$Bu$_2$Se at all the different reaction temperatures, the contact-angle measurement for water droplets was exceptionally small less than 10°. The films did not show photo-induced hydrophilic properties. This means that the surface of the niobium selenide films is unlikely to be oxide-terminated as niobium oxide shows a photo-induced reduction in the contact angle. Furthermore, this low contact-angle measurement means that water readily permeates the film and is related to high porosity.

The SEM images for the films deposited at the onset deposition temperature (300 °C) show ca. 0.2 μm plates in a perpendicular orientation to the substrate (Figure 1). The SEM images for the films deposited between 300 and 600 °C show a series of hexagonal platelets, which become longer and thicker with increasing deposition temperature. The average length of the platelets was 0.2 μm for the films deposited at 400 °C, up to 0.6 μm at 600 °C. This change in platelet size can be related to faster growth kinetics and smaller numbers of nucleation sites at the higher temperatures.

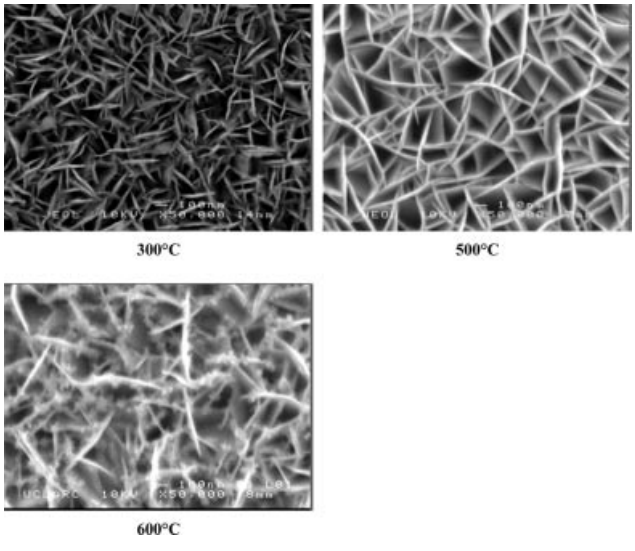


Figure 1. Scanning electron micrographs of the films produced from the APCVD of NbCl$_5$ and $t$Bu$_2$Se at substrate temperatures of 300, 500 °C and 600 °C.

The films produced at a deposition temperature of 600 °C showed exactly the Nb/Se ratio expected for NbSe$_2$ by EDAX [Nb$_{1.00(3)}$Se$_{2.00(3)}$]. No chlorine, carbon or other contamination was found by the EDAX in these films. The films deposited at substrate temperatures below 500 °C were selenium rich with a niobium to selenium ratio of 1:2.5 at 350, 450 and 500 °C. This could indicate the co-formation of NbSe$_3$ or NbSe$_4$ or elemental selenium which would raise the selenium content. No chlorine contamination was found in the films except those produced at the very lowest deposition temperature (300 °C), and then it was at trace levels ca. 1 atom%.

An X-ray photoelectron spectrum of the niobium 3d peak for the film from di-*tert*-butyl selenide and NbCl$_5$ revealed the presence of two different environments in the film (Figure 2). The peaks at 203.2 eV and 205.9 eV can be respectively assigned to the Nb 3d$_{5/2}$ and Nb 3d$_{3/2}$ peaks of the niobium diselenide. The peaks at 207.3 eV and 210.0 eV can be assigned to the Nb 3d$_{5/2}$ and Nb 3d$_{3/2}$ peaks of niobium oxide Nb$_2$O$_5$. This data suggest that the uppermost surface is partially oxidised. The XPS of the selenium 3d peak for the same NbSe$_2$ film shows that there are also three selenium environments present (Figure 3). The peaks at 52.9 eV and 53.8 eV can be respectively assigned to the Se 3d$_{5/2}$ and Se 3d$_{3/2}$ peaks of the niobium diselenide. The doublet peaks at 54.1 eV, 55.0 eV and 54.6 eV, 55.5 eV can be respectively assigned to selenium and selenium dioxide. These assignments are a little tentative because a range of different curve fittings could be employed.

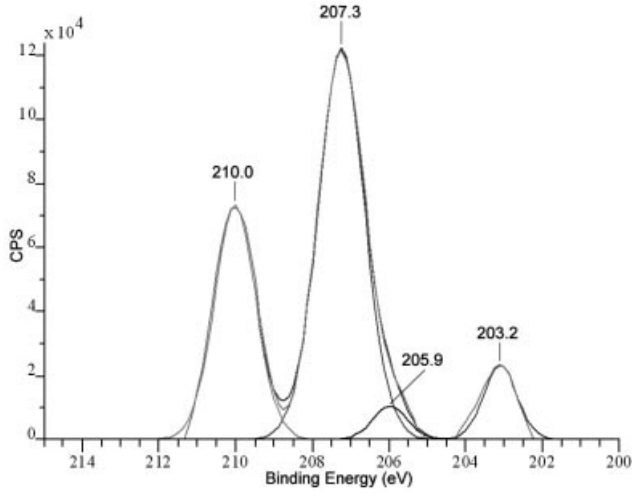


Figure 2. X-ray photoelectron spectrum of the Nb 3d peaks from the surface of a film deposited from the reaction of NbCl$_5$ and $t$Bu$_2$Se at 600 °C.

Glancing-angle X-ray powder diffraction of the films showed that the reflections matched the reference spectrum for 2H$_a$-NbSe$_2$ (JCPDS File No. 018–0923) (Figure 4). The films produced at 600 °C were highly crystalline. Interestingly, measuring the XRD pattern sequentially from the leading edge of the film until the back of the film showed that the preferred orientation became significantly more pronounced with distance from the reactor inlet. The preferential orientation in the first centimeter of the coating from the reactor inlet showed some (101) texturing, al-

 © 2006 Wiley-VCH Verlag GmbH & Co. KGaA, Weinheim 

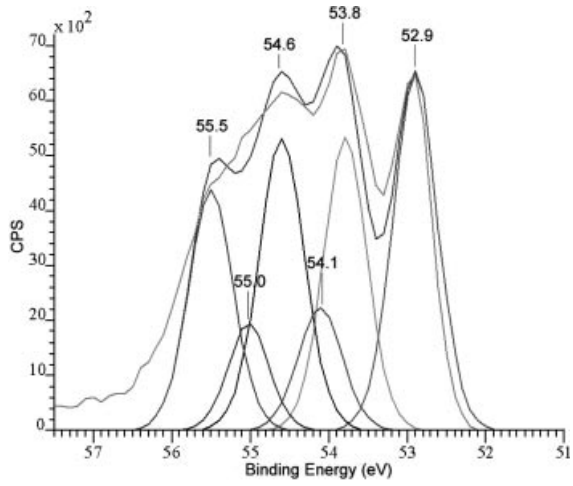


Figure 3. X-ray photoelectron spectrum of the Se 3d peaks from the surface of a film deposited from the reaction of $NbCl_5$ and $tBu_2Se$ at 600 °C. Outermost line is the actual data.

though the diffraction peaks were similar to the intensity stick pattern found in the literature. Very strong preferential growth along the (002) direction was shown in the next centimeter. Notably no preferential orientation was noticed in the films grown at lower substrate temperature. The indexed cell constants found for the films grown at 600 °C, $a$ = 3.44 Å and $c$ = 12.58 Å, compare well with the literature for hexagonal $NbSe_2$ $a$ = 3.44 Å and $c$ = 12.55 Å. The films grown at lower substrate temperatures all matched the literature diffraction patterns for 2H-$NbSe_2$ with the anticipated intensities and peak positions – however a detailed analysis of the cell constants indicated that they all tended to have slightly smaller $a$ values than stoichiometric $NbSe_2$.

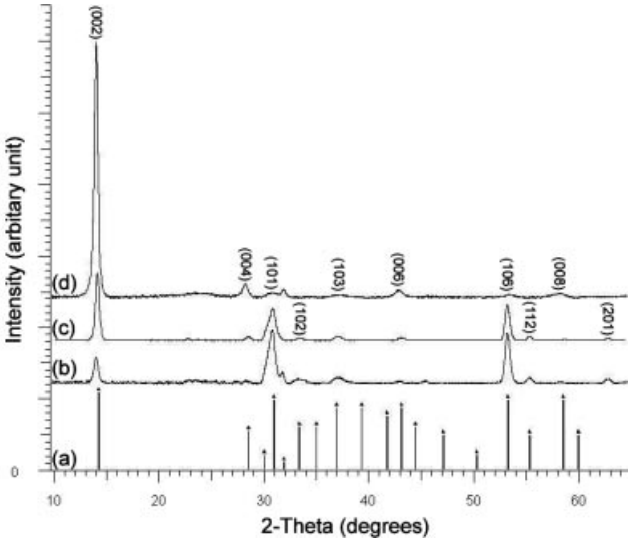


Figure 4. XRD pattern obtained for the film formed on glass from the APCVD of $NbCl_5$ and $tBu_2Se$ at 600 °C [(a) JCPDS reference file; (b) 0.5 cm, (c) 2 cm and (d) 4 cm from the front of the substrate].

Raman analysis of the films produced at 600 °C was identified as the distinctive 2H-$NbSe_2$ Raman pattern from the literature with a wide peak at 180 $cm^{-1}$ and a strong peak at 228 $cm^{-1}$ with a shoulder at 238 $cm^{-1}$ (Figure 5).[9–12] Raman analysis of the films produced at a substrate temperature of 500 °C or below show a similar Raman pattern with two strong bands around 182 $cm^{-1}$ and 245 $cm^{-1}$ and a smaller peak at 310 $cm^{-1}$ (Figure 6). This pattern is different to the one formed at higher temperature, the peaks are broader and an additional peak is seen at 309 $cm^{-1}$.

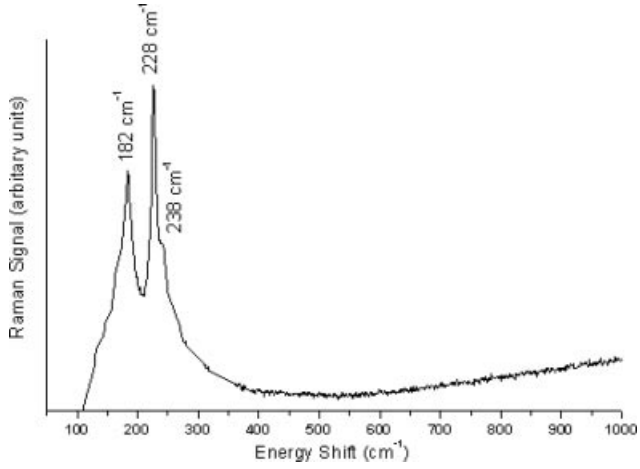


Figure 5. Raman pattern obtained for the film formed on glass from the APCVD of $NbCl_5$ and $tBu_2Se$ at 600 °C.

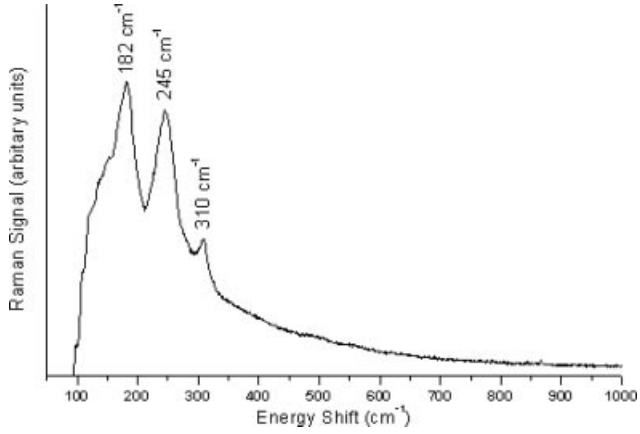


Figure 6. Raman pattern obtained for the film formed on glass from the APCVD of $NbCl_5$ and di-*tert*-butyl selenide at 300 °C.

### Preferred Orientation with Pathlength

The detection of changes in preferred orientation for the $NbSe_2$ thin film grown at 600 °C with deposition position along the substrate is highly unusual for a CVD process. The substrate was made of the same glass along its length and the substrate temperature was independently checked with an external thermocouple at different points on the glass and shown to be uniform. Thus the differences in preferred orientation cannot be attributed to temperature or substrate effects. Notably, the changes in preferred orientation only occurred at the highest deposition temperature and became more noticeable with distance along the sub-

 © 2006 Wiley-VCH Verlag GmbH & Co. KGaA, Weinheim 

strate. At 600 °C the deposition was only ca. 6 cm along the substrate, and the reaction had changed over from a surface-reaction-limited regime as seen at 500 °C, to a mass-transport-limited regime. Thus, along the length of the reactor the reaction becomes depleted in precursor. This depletion, therefore, has an effect on the growth of the crystallites – with growth in one particular direction being favoured under more dilute precursor conditions. Additionally, the diffusion effects of reactants and exhaust products through the boundary layer change with position along the reactor. This change over in preferred orientation is in part a consequence of the reactor design. A 'shower head' design reactor where multiple channels of reactants are used perpendicular to the substrate would be unlikely to show this effect.

### A New Superstoichiometric $NbSe_{2+x}$ Phase?

We have previously studied the analogous formation of $NbS_2$ films from the reaction of $NbCl_5$ and $tBu_2Se$ and *tert*-butylthiol.[13] In this case crystalline films were only found at substrate temperature above 500 °C, whereas the films formed in this study were crystalline at 300 °C and above. Furthermore, under some conditions EDX revealed that superstoichiometric $NbS_{2.4}$ was formed. This superstoichiometric material had similar principle Raman bands and intensity distribution (187, 242 and 298 $cm^{-1}$) to those formed in this study for the superstoichiometric $NbSe_2$ films.[14]

The films grown at substrate temperatures of 300–550 °C were all superstoichiometric – $NbSe_{2+x}$ ($x$ = 0.4–0.6) by EDX analysis. X-ray powder diffraction, Raman and spot EDX analysis did not detect any free selenium metal in these films. Furthermore, none of these techniques showed the presence of higher niobium phases such as $NbSe_3$ or $NbSe_4$. No other elements were found in the films – save for a slight surface oxidation (first few nanometres). As the films grown at 300–550 °C were all exceptionally similar if not the same as the 2H-$NbSe_2$ poly-type by X-ray diffraction, with the expected intensity pattern and peak positions, it is logical to assume that the excess selenium is embedded and intercalated within the structure, especially as these are layered structures with van der Waals interactions between neighbouring sheets. These films had a slightly different unit cell size with the *a* and *c* axis slightly smaller than the literature values, the difference is right at the margin for differentiation based on the 3σ criterion. Intuitively though one would expect a large increase in the cell parameters with excess selenium incorporation. A further explanation is that an amorphous phase is present with a higher selenium content that does not show up on the XRD, Raman or XPS analysis; however, given the breadth of analysis completed, this seems unlikely. Interestingly the Raman patterns were quite revealing and supportive of a similar structure type – having a slightly different pattern to that seen for the films grown at 600 °C – which matched exactly the literature pattern for 2H-$NbSe_2$. The Raman pattern of the films made at lower substrate temperatures most closely resembled that seen for our previous CVD studies of $NbS_{2.4}$.[13,14] Hence, the lower-temperature films were consistent with the formation of the 2H-$NbSe_2$ structure with some incorporated selenium. We have not found evidence of any literature reference on this type of material being reported previously.

## 3. Conclusion

Niobium selenide films were deposited on glass from the APCVD reaction of $NbCl_5$ and $tBu_2Se$. Between 300 and 500 °C, the films were crystalline and selenium rich with a niobium to selenium ratio of 1:2.5 at 350, 450 and 500 °C. The films produced at a deposition temperature of 600 °C showed exactly the Nb/Se ratio expected for $NbSe_2$. No chlorine, carbon or other contamination was found by the EDAX in these films. The films produced at 600 °C were highly crystalline with a preferential growth either along (101) or the (002) direction. The preferred orientation effects were more marked with distance from the reactor inlet and suggest that depletion in reagents leads to a slightly altered growth mechanism. The $NbSe_2$ films were stable in air, insoluble in the common organic solvents, and were only slowly decomposed in nitric acid. The films grown at 300–550 °C best fit the $2H_a$-$NbSe_2$ structural type with some excess intercalated selenium.

## 4. Experimental Section

***Caution:*** It should be noted that the CVD of $NbSe_2$ could produce $H_2Se$, which is highly toxic and malodorous. All the experiments should be conducted in a fume cupboard and the gas from the CVD process treated with bleach (with an associated copper sulfate indicator bubbler, to check the bleach is working) to destroy the possible presence of $H_2Se$. After the CVD synthesis the $NbSe_2$ films were treated as air sensitive although subsequent analysis showed that they were indefinitely air stable.

**Chemical Vapour Deposition Studies:** Depositions experiments were carried out under dinitrogen (99.99%) on glass substrates using a horizontal-bed cold-wall APCVD reactor. The glass substrate was a $SiO_2$-precoated (ca. 50 nm thick $SiO_2$ barrier layer) standard float glass (Pilkington, UK) 15 cm × 4 cm × 0.3 cm. The substrate was heated by a graphite block and the nitrogen carrier gas was preheated to 110 °C by being passed along 2 m lengths of coiled stainless-steel tubing inside a tube furnace.

Niobium pentachloride was obtained from Aldrich Chemical Co. and di-*tert*-butyl selenide was supplied by Epichem. They were both used without further purification. The di-*tert*-butyl selenide and $NbCl_5$ were placed into two different stainless-steel bubblers, which were both heated by a jacket. They were both introduced into the gas streams by passing hot $N_2$ through the bubblers. The bubbler temperatures and flow rates were kept constant to 90 °C and 0.5 L·$min^{-1}$ (67.4 mmol·$min^{-1}$) for the $tBu_2Se$ bubbler and to 210 °C and 2.0 L· $min^{-1}$ (47.8 mmol·$min^{-1}$) for the niobium pentachloride bubbler (Table 1). The flow rate through the mixing chamber was between 1.9 and 4.6 L·$min^{-1}$ for all depositions.

 © 2006 Wiley-VCH Verlag GmbH & Co. KGaA, Weinheim 

Table 1. EDAX, Raman and X-ray diffraction data for the films produced by APCVD reaction of $tBu_2Se$ with $NbCl_5$.

| Deposition temperature | XRD (lattice constant in Å+/– 0.01 Å) | Raman | EDAX |
|---|---|---|---|
| 250 °C | – | – | No film |
| 300 °C | 2H-$NbSe_2$; $a$ = 3.36, $c$ = 12.47 | 182 + 245 + 310 | $NbSe_{2.4}$ |
| 350 °C | 2H-$NbSe_2$; $a$ = 3.37, $c$ = 12.59 | 183 + 248 + 309 | $NbSe_{2.5}$ |
| 400 °C | 2H-$NbSe_2$; $a$ = 3.42, $c$ = 12.56 | 184 + 248 + 310 | $NbSe_{2.6}$ |
| 450 °C | 2H-$NbSe_2$; $a$ = 3.36, $c$ = 12.63 | 183 + 247 + 309 | $NbSe_{2.5}$ |
| 500 °C | 2H-$NbSe_2$; $a$ = 3.41, $c$ = 12.63 | 183 + 246 + 309 | $NbSe_{2.5}$ |
| 600 °C | 2H-$NbSe_2$; $a$ = 3.44, $c$ = 12.58 | 2H-$NbSe_2$ | $NbSe_2$ |

The reaction of $tBu_2Se$ and $NbCl_5$ was studied in the temperature range from 250–600 °C. The deposition time for all experiments was 1 min. At the end of the deposition, the bubbler line was closed and the substrate was cooled under nitrogen in the reactor. Then the substrates were handled briefly in air before storage under dry, oxygen-free nitrogen in a glove box. Analyses were performed for each sample on a 2 cm × 4 cm band cut 2 cm from the front of the substrate.

**Film Analysis:** X-ray diffraction patterns were measured with a Bruker X-pert diffractometer using monochromated Cu-$K_{\alpha 1}$ radiation ($K_{\alpha 1}$ = 1.5406 Å). The system had a focus and movable $x$-$y$ stage to analyse various portions of the film. The diffractometer used glancing incident radiation (1.5°). The samples were indexed using unit cell and compared to database standards. EDAX was obtained with a Philips XL30ESEM instrument and SEM was obtained with a JEOL 6301 instrument. UV/Vis-NIR spectra were recorded in the range 190–1100 nm using a Helios double-beam instrument. Reflectance and transmission spectra were recorded between 300 and 1200 nm with a Zeiss miniature spectrometer. Reflectance measurements were standardised relative to a rhodium mirror and transmission relative to air. Raman spectra were acquired with a Renishaw Raman System 1000 using a helium-neon laser of wavelength 632.8 nm. The Raman system was calibrated against the emission lines of neon. X-ray photoelectron spectroscopy was undertaken with a VG ESCALAB 220I XL instrument with focussed (300 μm spot) monochromatic Al-$K_\alpha$ radiation at a pass energy of 20 eV. Scans were acquired with steps of 50 meV. A flood gun was used to control charging. Binding energies were referenced to an adventitious C 1s peak at 284.6 eV (this peak is due to residual pump oil used in the XPS high vacuum system- but is removed on the first argon ion etching). Argon sputtering was used for approximately 1 minute in a rastering mode in order to remove surface contamination.

## Acknowledgments

Dr. G. Reid, Prof. W. Levason and Dr. A. Hector are thanked for useful discussions on related projects. The EPSRC is thanked for financial support.

[1] D. H. Galvan, S. Li, W. M. Yuhasz, J. H. Kim, M. B. Maple, E. Adem, *Physica C* **2003**, *398*, 147.
[2] T. Shimada, H. Nishikawa, A. Koma, Y. Furukawa, E. Arakawa, K. Takeshita, T. Matsushita, *Surf. Sci.* **1996**, *369*, 379.
[3] B. M. Murphy, J. Stettner, M. Traving, M. Sprung, I. Grotkopp, M. Muller, C. S. Oglesby, M. Tolan, W. Press, *Physica B* **2003**, *336*, 103.
[4] C. H. Du, W. J. Lin, Y. Su, B. K. Tanner, P. D. Hatton, D. Casa, B. Keimer, J. P. Hill, C. S. Oglesby, H. Hohl, *J. Phys.: Condens. Matter* **2000**, *12*, 5361.
[5] H. Haraldsen, *Angew. Chem. Int. Ed. Engl.* **1966**, *5*, 51.
[6] W. W. Fuller, T. M. Tritt, H. A. Hoff, *Phys. Rev. B* **1990**, *41*, 1671.
[7] L. M. Kulikov, A. A. Semjonov-Kobzar, M. M. Antonova, A. A. Chechovsky, L. G. Akselrud, R. V. Skolozdra, D. Fruchart, J. L. Soubeyroux, *J. Alloys Compd.* **1996**, *244*, 11.
[8] R. Vaidya, M. Dave, S. G. Patel, A. R. Jani, *Indian J. Phys.* **2005**, *79*, 85.
[9] A. Meerschaut, C. Deudon, *Mater. Res. Bull.* **2001**, *36*, 1721.
[10] J. C. Tsang, J. E. Smith, M. W. Shafer, *Phys. Rev. Lett.* **1976**, *37*, 1407.
[11] C. M. Pereira, W. Y. Liang, *J. Phys. C: Solid State Phys.* **1982**, *15*, L991.
[12] C. M. Pereira, W. Y. Liang, *J. Phys C: Solide State Phys.* **1985**, *18*, 6075.
[13] C. J. Carmalt, E. S. Peters, I. P. Parkin, T. D. Manning, A. L. Hector, *Eur. J. Inorg. Chem.* **2004**, *22*, 4470.
[14] E. S. Peters, Ph.D Thesis, **2004**, University of London.

Received: September 20, 2005
Published Online: February 2, 2006

 © 2006 Wiley-VCH Verlag GmbH & Co. KGaA, Weinheim 

DOI: 10.1002/ejic.200500881

# Counteranion-Induced Formation of *cis* and *trans* Singly and Doubly $H_2$biim-Bridged Di-, Hexa-, and Polymeric Ag–$H_2$biim Complexes

**Rui-Li Sang[a] and Li Xu*[a]**

**Keywords:** Crystal engineering / Luminescence / Metal–metal interactions / N ligands / Silver

A series of *cis* and *trans* singly and doubly $H_2$biim-bridged di-, hexa-, and polymeric complexes of silver(I) ($H_2$biim = 2,2′-biimidazole), namely $[Ag_2(\mu\text{-}H_2biim)_2]SO_4\cdot 2H_2O$ (**1**), $[Ag_2(\mu\text{-}H_2biim)_2(\mu\text{-ox})]_n$ (**2**), $[Ag_6(\mu\text{-}H_2biim)_5(H_2biim)_2](ClO_4)_4(CH_3CO_2)_2\cdot 2H_2O$ (**3**), and $[Ag(\mu\text{-}H_2biim)(nicotinate)]_n$ (**4**) have been synthesized and characterized by X-ray crystallography and IR and photoluminescence spectroscopy. The structural topology of the Ag–$H_2$biim system is determined by the charge of the counteranions. Thus, dianionic counterions facilitate the formation of dimeric structures driven by the charge-balance requirement, whereas a monoanionic counterion favors the formation of helical structures. Counteranions of larger size lead to either finite helical structures or a *trans* arrangement of the coordinating nitrogen atoms because of steric requirements. Organic counteranions with a strong coordination ability bind to the $Ag^+$ ions while inorganic counteranions are uncoordinated. The argentophilic attraction is not dominant in this system. Examination of the luminescent properties of $H_2$biim and compounds **1**–**4** indicates that the fluorescence emission of $H_2$biim is effectively shifted upon metal coordination.

(© Wiley-VCH Verlag GmbH & Co. KGaA, 69451 Weinheim, Germany, 2006)

## Introduction

The substitution reaction is one of the most important chemical reactions and is widely employed in the preparation of new chemical materials, especially supramolecular polymer materials. The general strategy is to use multifunctional organic ligands to replace inorganic ligands of simple starting metal complexes to build functional supramolecular architectures.[1–3] Crystal formation depends on many factors, including metal–ligand, metal–metal, ligand–ligands, hydrogen bonding, and π stacking interactions. Covalent metal–ligand interactions are the strongest and thus dominate crystal formation. Interactions between open metal ions, known as metal–metal bonds, are comparable in strength to metal–ligand bonds and are the driving force in the formation of metal clusters. However, interactions between closed metal ions, typically coinage ones, which are intermetallic attraction in nature,[4,5] are comparable to hydrogen bonds in strength. Thus, the aggregation of closed metal ions is flexible and depends on other factors, such as weak interactions and charge balance. Although metal coordination requirements are dominant in the global architecture, other auxiliary factors such as charge balance and weak, noncovalent requirements play a significant role due to the multiple bonding modes of the ligand and the variety of geometries available for some metal ions. Many metal complexes, especially those with neutral ligands, appear as cationic species and thus anionic counterparts are usually present for charge balance. The role of these counteranions has been the subject of several reports.[6–8] Recent research results have indicated that the coordinating ability, shape, and size of counteranions have a significant influence on the global structures through either metal coordination or crystal-packing effects when noncoordinated.[7,8] In the present work, we will describe the Ag–$H_2$biim system with various counteranions of different charge, size, and coordinating ability to compare their competitive power. $Ag^+$ is an appropriate probe as it has varied coordination geometries and is able to aggregate through argentophilic attractions.[6,7] 2,2′-Biimidazole is an evergreen ligand that has attracted constant interest in supramolecular chemistry,[9] biochemistry,[10] cluster science,[11] and antitumor drugs.[12] The Ag–$H_2$biim system is able to adopt multiple coordinating modes and a variety of geometries, and can thus serve as a probe to examine the role of the above counteranion characteristics in crystal-structure formation. Four new supramolecular complexes, namely $[Ag_2(\mu\text{-}H_2biim)_2]SO_4\cdot 2H_2O$ (**1**), $[Ag_2(\mu\text{-}H_2biim)_2(\mu\text{-ox})]_n$ (**2**), $[Ag_6(\mu\text{-}H_2biim)_5(H_2biim)_2](ClO_4)_4(CH_3CO_2)_2\cdot 4H_2O$ (**3**), and $[Ag(\mu\text{-}H_2biim)(nicotinate)]_n$ (**4**) have been synthesized and characterized and the influences of the competing counteranion characteristics (charge, coordinating ability, and size) in the crystal-structure formation will be discussed.

[a] State Key Laboratory of Structural Chemistry, Fujian Institute of Research on the Structure of Matter, Chinese Academy of Science,
Fuzhou, Fujian, 350002, China
Fax: +86-591-8370-5045
E-mail: xli@fjirsm.ac.cn

 InterScience © 2006 Wiley-VCH Verlag GmbH & Co. KGaA, Weinheim 

## Results and Discussion

### Syntheses of the Complexes

The syntheses of complexes **1**–**4** are summarized in Scheme 1. It is obvious that the complexation of $Ag^+$ and $H_2$biim depends on the charge, size, and coordination ability of the counteranions: organic counteranions of strong coordination ability, such as oxalate and nicotinate, become coordinated to produce the neutral reaction products **2** and **4**, whereas inorganic counteranions, such as $ClO_4^{2-}$ and $SO_4^{2-}$, are uncoordinated, yielding charged, polynuclear Ag–$H_2$biim complexes. It seems that dianionic counterions facilitate the formation of dimeric structures, presumably as a consequence of the charge-balance requirement, as suggested by the formation of the dimers **1** and **2**. In contrast, monoanionic counterions tend to favor the formation of helical structures, as suggested by **3**, **4**, and the previously reported complex $[Ag(\mu\text{-}H_2biim)]NO_3$.[10b] The use of larger $ClO_4^-$ instead of $NO_3^-$ leads to the formation of the finite helical complex **3**.

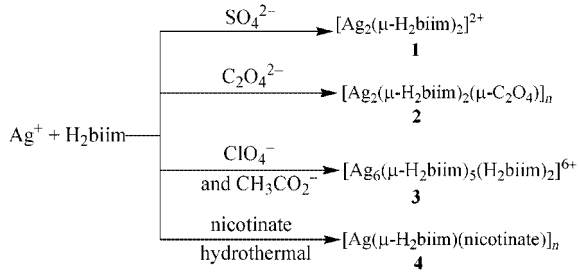


Scheme 1. Syntheses of compounds **1**–**4**.

### Crystal Structures

#### *$[Ag_2(\mu\text{-}H_2biim)_2]SO_4{\cdot}2H_2O$ (1)*

The structure of the dicationic dimer of **1** is given in Figure 1 (a). The two Ag atoms are doubly bridged by $H_2$biim, forming a dicationic dimeric structure. Such a dimeric structure facilitates the charge balance through an alternating arrangement of the dimer and $SO_4^{2-}$ in the resulting infinite chain (Figure 1, b). Each $Ag^+$ ion is coordinated to the two nitrogen atoms from the different $H_2$biim moieties [Ag–N1 = 2.149(6), Ag–N3 = 2.130(5) Å] in an almost linear arrangement [N1–Ag–N3 = 170.6(2)°] as in the case of $[\{Ru(pap)_2(Biim)\}_2Ag_2](ClO_4)_2$ (179°)[5a] and $[Ag_2(napy)_2](ClO_4)_2$ (168°).[5d] The distance between the two Ag atoms is 2.818(1) Å, slightly shorter than in the doubly bridged $[\{Ru(pap)_2(Biim)\}_2Ag_2](ClO_4)_2$ [2.890(2) Å],[5a] $[Ag_2(dpim)_2(CH_3CN)_2](ClO_4)_2$ [2.9932(9) Å],[5b] and $[Ag_2(Ph_2PCH_2SPh)_2](ClO_4)_2$ [2.9501(8) and 2.9732(9) Å][5c] but comparable to that in $[Ag_2(napy)_2](ClO_4)_2$[5d] [2.748(2) Å]. The $H_2$biim ligands are slightly twisted, with a dihedral angle of 14.6°. The two biimidazole ligands are nearly perpendicular to each other (the angle between their least-squares planes is 77.1°). The two neighboring $[Ag_2(H_2biim)_2]^{2+}$ units are linked together by weak Ag···$O_{sulfate}$ interactions into a one-dimensional chain with a pitch of 10.32 Å running along the *c* axis (Figure 1, b).

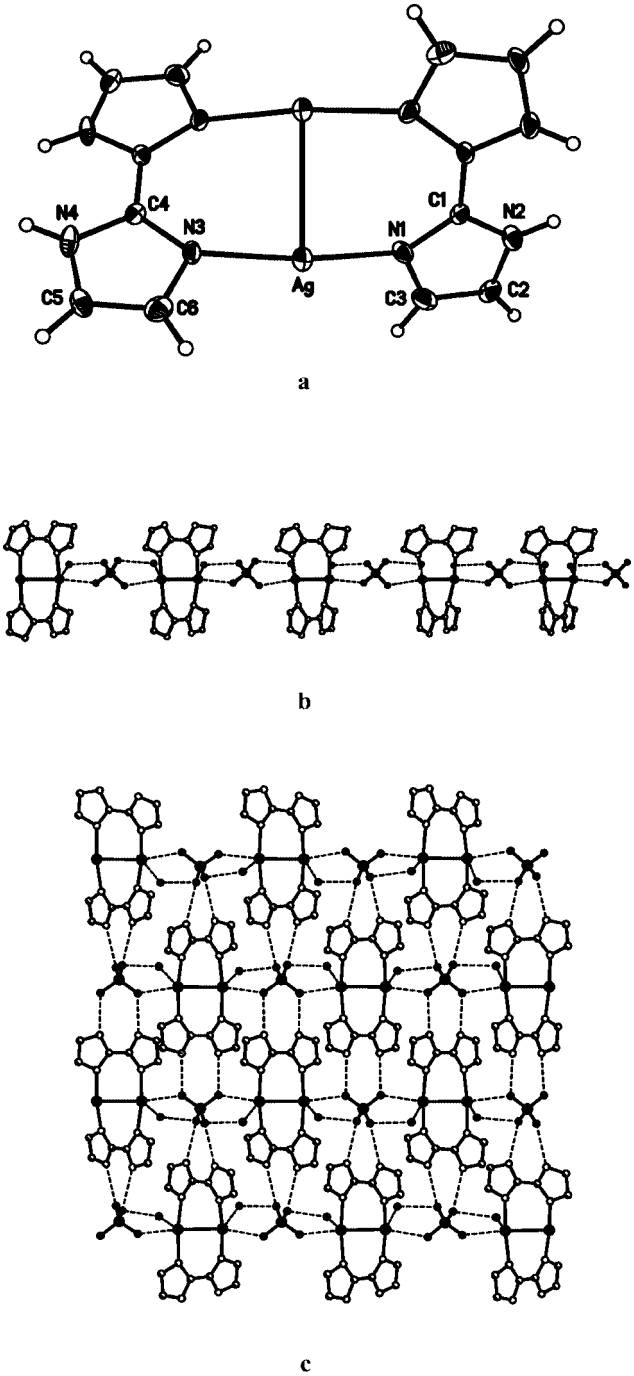


Figure 1. (a) ORTEP drawing of the $[Ag_2(H_2biim)_2]^{2+}$ moiety of **1** with 30% probability thermal ellipsoids. (b) Infinite chain showing $Ag^+$–$SO_4^{2-}$ and $Ag^+$–$H_2O$ interactions. (c) Hydrogen-bonded sheet structure.

The water molecules interact weakly with the Ag atoms [2.756(2) Å] and sulfate (2.861 Å). The staggered arrangement of $H_2$biim of the neighboring chains allows for the formation of interchain N–$H_{biim}$···$O_{sulfate}$ hydrogen bonds (N4···O1 = 2.722, N2···O2 = 2.770 Å) in the resultant sheet structure, as shown in part c of Figure 1.

 © 2006 Wiley-VCH Verlag GmbH & Co. KGaA, Weinheim 

### *[Ag$_2$(μ-H$_2$biim)$_2$(μ-ox)] (2)*

As shown in part a of Figure 2, compound **2** has a similar, doubly bridged dimeric structure to that of **1** although their counteranions are remarkably different in size, shape, and coordinating ability, thus indicating that the dimeric structure results from the charge, rather than the other characteristics such as coordinating ability, size, and shape, of the counteranions. Different from the inorganic counteranion $SO_4^{2-}$, the organic counteranion oxalate coordinates more strongly and acts as a didentate bridging ligand to link the dimers into an infinite chain [Ag–$O_{ox}$ = 2.392(4) Å; Figure 2, b]. The Ag–Ag separation [2.8437(9) Å] is not significantly changed by the oxalate coordination. Nevertheless, the binding of oxalate to $Ag^+$ apparently changes the geometric parameters of the dimer, as indicated by the considerably smaller N–Ag–N angle [132.95(16)°] and longer Ag–N distances [2.236(4) and 2.203(4) Å] than those in **1**.

Additionally, the direct coordination of oxalate also accounts for the absence of lattice water molecules in the crystals. The $H_2$biim ligands are slightly twisted, and their dihedral angle of 28.2° is larger than that (14.6°) in **1**. As opposed to **1**, the least-squares planes of the two biimidazole ligands are nearly parallel to each other. The atoms Ag, N1, N3, and O1 are nearly coplanar. In spite of these changes, the crystal structures of **1** and **2** are somewhat similar to each other: both have a one-dimensional, chain-like structure formed by either Ag–$O_{ox}$ bonds or Ag···$O_{sulfate}$ interactions and hydrogen-bonded sheet structures due to interchain N–H···$O_{sulfate}$ or N–H···$O_{ox}$ (2.722, 2.746 Å) hydrogen bonds, as indicated in Figures 1 (c) and 2 (b), respectively.

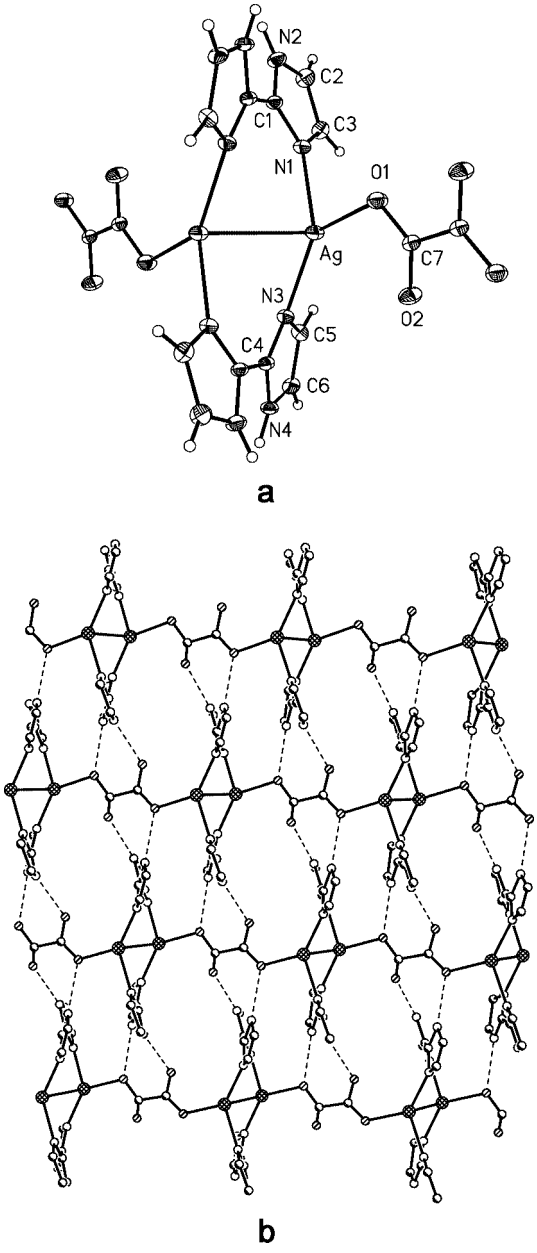


Figure 2. (a) ORTEP drawing of **2** with 30% probability thermal ellipsoids. (b) Sheet structure showing interchain $C_2O_4^{2-}$···$H_2$biim hydrogen bonds.

### *[Ag$_6$(μ-$_2$biim)$_5$(H$_2$biim)$_2$](ClO$_4$)$_4$(CH$_3$CO$_2$)$_2$·4H$_2$O (3)*

Complex **3** contains a mixture of monoanionic inorganic and organic anions and consequently adopts the hexanuclear helical structure $[Ag_6(\mu\text{-}H_2biim)_5(H_2biim)_2]^{6+}$, as shown in Figure 3 (a), instead of a dimeric structure, similar

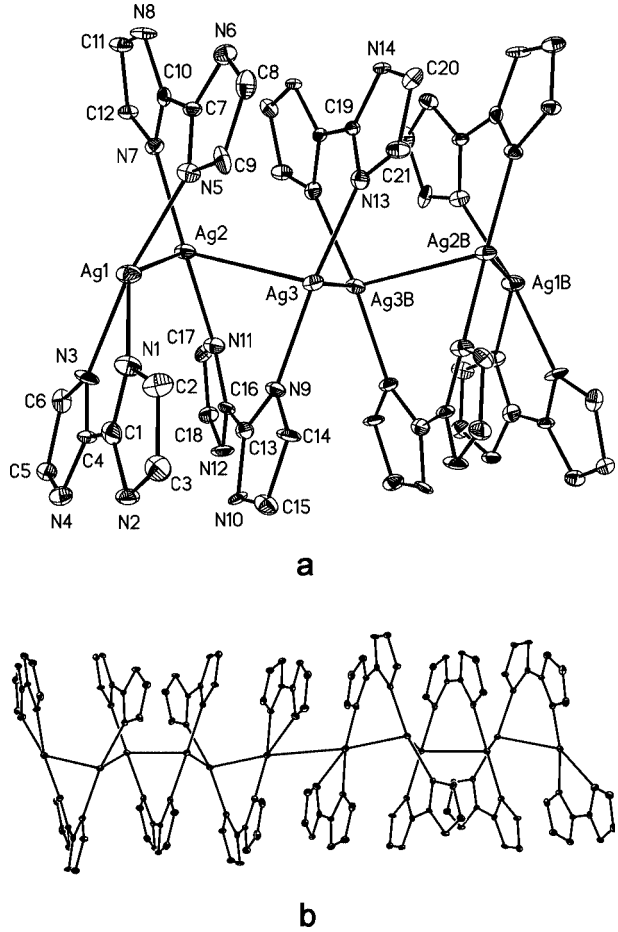


Figure 3. (a) ORTEP drawing of $[Ag_6(\mu\text{-}H_2biim)_5(H_2biim)_2]^{6+}$(**3**). (b) 1D Ag chain.

 © 2006 Wiley-VCH Verlag GmbH & Co. KGaA, Weinheim 

to that reported for [Ag($H_2$biim)$NO_3$].[10b] In this helical structure, the counteranion lies alongside the $Ag^+$ chain[10b] rather than between the $Ag^+$ ions to facilitate the charge balance. The hexameric structure has $C_2$ symmetry, with the twofold axis bisecting the Ag3–Ag3a bond. As opposed to **1** and **2**, the neighboring $Ag^+$ in **3** is singly bridged by the five $H_2$biim ligands through the *cis* nitrogen atoms, yielding a hexameric helix with Ag–N bonds ranging from 2.112(2) to 2.157(2) Å. The middle $Ag^+$ atoms (Ag2, Ag3) have an almost linear coordination geometry [N–Ag–N = 164.8(2)° and 172.6(2)°] that is stabilized by Ag···$O_{perchlorate}$ interactions (Ag2···O = 2.912, Ag3···O = 2.879 Å). The helix ends at Ag1 as it is chelated by $H_2$biim. It is notable that the Ag1–N1 distance of 2.543(7) Å is comparable to the above Ag···$O_{perchlorate}$ separations but considerably longer than the Ag1–N3 bond [2.163(5) Å], and is responsible for the almost linear N3–Ag1–N5 angle [170.4(2)°]. The Ag–Ag distances [Ag1–Ag2 = 2.9335(18), Ag2–Ag3 = 3.0093(16), Ag3–Ag3′ = 3.078(2) Å] are significantly longer than in **1** and **2** but similar to those reported previously.[10,11] Compound **3** adopts a hexameric helical structure rather than an infinite helical structure similar to the reported nitrate derivative[10b] as a consequence of the chelating instead of bridging $H_2$biim ligands that terminate the growth of the helix. This observation may be attributed to the steric requirement of perchlorate, which is larger than the nitrate in 1D [Ag(μ-$H_2$biim)]$NO_3$,[10b] and is thus unable to allow for the presence of counteranions surrounding the terminal Ag atoms (Ag1). This leads to the structural evolution whereby two sevenths of the bridging $H_2$biim ligands in the one-dimensional helical [Ag(μ-$H_2$biim)]$NO_3$[10b] become chelated in the present hexanuclear compound to compensate for the missing Ag1–O interaction that is needed to stabilize the linear coordination. The acetate groups are involved in hydrogen bonding with $H_2$biim (2.7–2.8 Å) and water (2.79 Å) rather than with the Ag atoms.

The preference of carboxylate groups to form hydrogen bonds with $H_2$biim rather than coordinate to metal ions has been demonstrated in the complexes [$M(H_2biim)_2(H_2O)_2$]-$(RCO_2)_2$.[9f] The chelating $H_2$biim is twisted to a lesser extent (the dihedral angle is 10.8°) than the bridging ones (22–25°). The helix is also characteristic of an approximately parallel arrangement of neighboring $H_2$biim ligands, with the dihedral angles and the distances between the ring atoms and the least-square planes ranging from 8–12° and 2.8–3.6 Å, respectively, due to π-stacking interactions between the aromatic imidazole rings. As shown in Figure 3 (b), the hexamers are connected by an unsupported Ag1–Ag1′ attraction [3.317(2) Å] and π-stacking interactions between the imidazole rings into a 1D Ag chain. The π-stacking interactions between the hexanuclear silver units are similar to those within the hexameric spiral. Other interactions in **2** are hydrogen bonds between lattice water molecules and uncoordinated nitrogen atoms, with separations between O and N of 2.722 (O1w–N10) and 2.728 Å (O2w–N6).

### *[Ag(μ-$H_2$biim)(nicotinate)]$_n$ (4)*

Compound **4** has a monoanionic, organic counterion that is believed to account for the formation of an infinite helical structure (Figure 4), as in the case of **3** and [Ag($H_2$-biim)]$NO_3$.[10b] Interestingly, unlike the nitrate analogue [Ag($H_2$biim)]$NO_3$,[10b] **4** has the coordinating nitrogen atoms *trans* to each other, which leads to a considerably longer Ag···Ag separation (ca. 6 Å) than in **3** and [Ag($H_2$-biim)]$NO_3$ (ca. 3 Å)[10b] due to the steric requirement of the bound nicotinate. This indicates that Ag–Ag attractions are not dominant in the Ag–$H_2$biim system. The Ag–$N_{nicotinate}$ distance [2.534(6) Å] is significantly longer than the Ag–$N_{biim}$ distance [av. 2.188(5) Å]. The three N atoms around $Ag^+$ are approximately in a T-shaped arrangement with the N–Ag–N angles being 159.3°, 110.3° and 89.4°, respectively. The bridging $H_2$biim is twisted, with a dihedral angle of about 30°. The helices are held together through Ag···$O_{nicotinate}$ interactions (Ag1···O1 = 2.843, Ag1···O2 = 2.957 Å) and N–H···$O_{nicotinate}$ hydrogen bonds (N2···O1 = 2.689 Å) to form a sheet structure, as illustrated in Figure 5. The pyridyl rings of two nicotinate groups separated by about 3.6 Å are almost parallel to each other, which suggests significant π-stacking interactions.

## Luminescent Properties

Metal complexes are promising luminescent materials for applications such as light-emitting materials owing to their ability to enhance, shift, and quench luminescent emission of organic ligands by metal coordination. Although numerous biimidazole complexes have been reported, their photophysical properties have been investigated only very re-

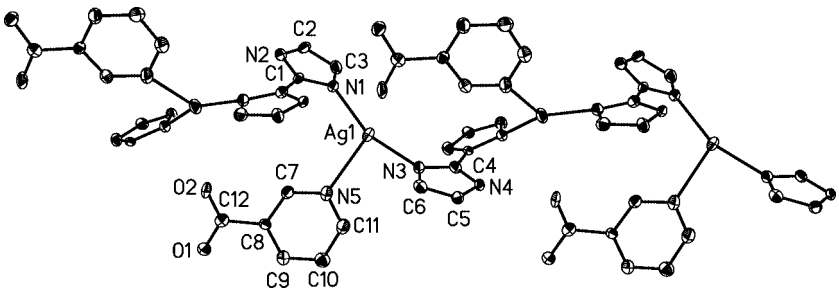


Figure 4. ORTEP drawing of [Ag($H_2$biim)$_2$(nicotinate)]$_n$ (**4**) with 30% probability thermal ellipsoids.

 © 2006 Wiley-VCH Verlag GmbH & Co. KGaA, Weinheim 

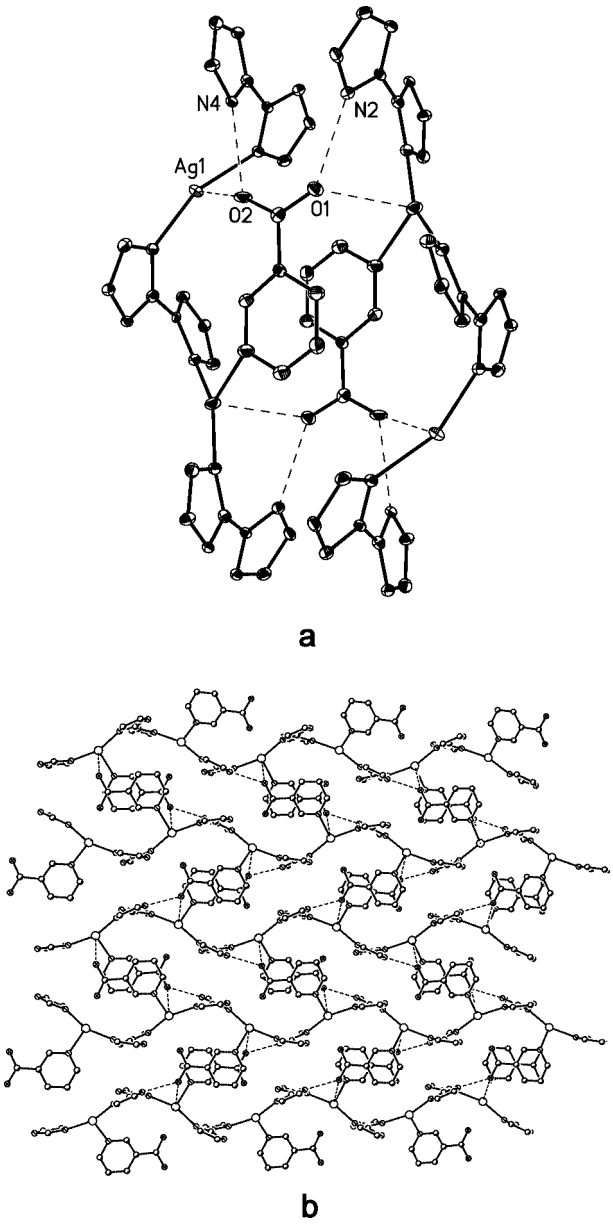


Figure 5. (a) Interhelix interactions and (b) multiple helices interconnected by nicotinate in **4**.

cently.[9a] The solid-state emission spectra of compounds **1**–**4** are shown in Figure 6. The free $H_2$biim ligand displays an emission maximum at 431 nm when excited at 334 nm in the solid state at ambient temperature. A violet-fluorescent emission band at 439 nm was observed for **1** upon excitation at 360 nm, attributable to the ligand-centered emission. Moreover, compound **1** exhibits violet-fluorescent emission bands at 346 nm and a yellowish-green radiation emission at lower energy (576 nm) upon excitation at 260 nm.

Upon excitation at a slightly longer wavelength (298 nm), compound **2** emits only one violet luminescence at 349 nm; the other one is probably quenched by oxalate. Excitation at 370 nm leads to greenish-blue photoluminescence with an emission maximum at 512 nm for **3**, similar to that in

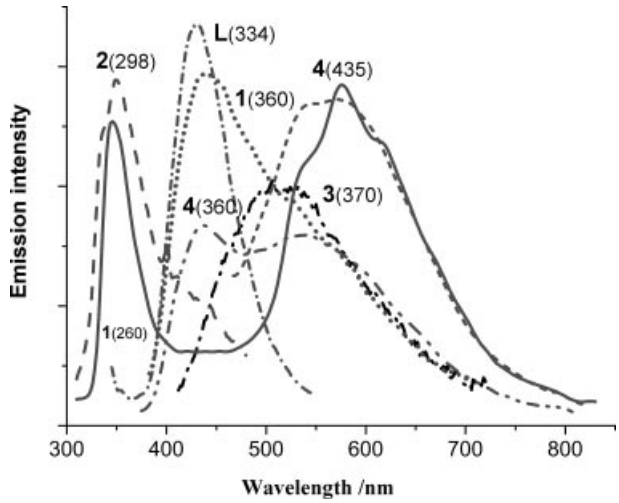


Figure 6. Luminescence emission spectra of **1**–**4** and **L** ($H_2$biim).

$[Ag(Me_2\text{-imy})_2][Ag\text{-}Cl_2]$ (544 nm), which possesses extended Ag–Ag interactions.[15] Compound **4** exhibits similar violet-fluorescent emission bands at 437 nm upon excitation at 360 nm. However, one more yellowish-green radiation emission of **4** was observed at 539 nm, presumably due to the aromatic nicotinate group. A similar yellowish-green fluorescent emission band at 571 nm was also observed for **4** upon excitation at 435 nm.

## Conclusion

The structural topology of the Ag–$H_2$biim system is determined by the charge of the counteranions. Thus, dianionic counterions facilitate the formation of dimeric structures driven by the charge-balance requirement, whereas a monoanionic counterion favors the formation of helical structures. Larger counteranions lead to either finite helical structures or a *trans* arrangement of the coordinating nitrogen atoms because of steric requirements. Organic counteranions with a strong coordination ability bind to the $Ag^+$ ions while inorganic counteranions remain uncoordinated. The argentophilic attraction is not dominant in the Ag–$H_2$biim system. The fluorescence emission of $H_2$biim is effectively shifted upon coordination of the ligand to $Ag^+$.

## Experimental Section

**General Remarks:** $H_2$biim was synthesized in accordance with a published procedure.[13] The reagents and solvents employed were commercially available and used as received without further purification. The C, H, and N microanalyses were carried out with a Vario EL III elemental analyzer. IR spectra were recorded with a Magna 750 FT-IR spectrometer photometer as KBr pellets in the range 4000–400 $cm^{-1}$. Fluorescent spectra were measured with an Edinburgh FLS920 analytical instrument.

***CAUTION**! Perchlorate salts are potentially explosive and should be handled with care and in small amounts.*

**$[Ag_2(H_2biim)_2]SO_4 \cdot 2H_2O$ (1):** $Ag_2O$ (0.056 g, 0.25 mmol) was dissolved in 20 mL of aqueous $H_2SO_4$ (0.05 M) and $H_2$biim (0.067 g,

 © 2006 Wiley-VCH Verlag GmbH & Co. KGaA, Weinheim 

0.5 mmol) in 10 mL of aqueous $H_2SO_4$ (0.05 M) was added to the resulting solution. The mixture was stirred at room temperature for two hours, then the resulting solution was filtered off and the filtrate was left in air to evaporate to form crystals of **1** after a few days. The crystals were collected by filtration, washed with ethanol, and dried in air (0.114 g, 74% yield based on Ag). $C_{12}H_{16}Ag_2N_8O_6S$ (616.13): calcd. C 23.39, H 2.62, N 18.19; found C 23.34, H 2.70, N 18.12. IR (KBr): $\tilde{\nu}$ = 3446 m $cm^{-1}$, 3074 m, 3001 m, 2896 m, 2806 m, 1631 w, 1546 s, 1435 m, 1406 s, 1385 m, 1334 m, 1218 m, 1105 vs, 939 s, 886 s, 761 w, 747 m, 689 m, 617 m.

**[$Ag_2$($H_2$biim)$_2$(μ-ox)] (2):** $AgNO_3$ (0.085 g, 0.5 mmol) was dissolved in 30 mL of $H_2O$ and $H_2$biim (0.067 g, 0.5 mmol) was added to the resulting solution. The mixture was stirred at room temperature for

Table 1. Crystallographic data for compounds **1**–**4**.

| Complex | **1** | **2** | **3** | **4** |
|---|---|---|---|---|
| Molecular formula | $C_{12}H_{16}Ag_2N_8O_6S$ | $C_{14}H_{12}Ag_2N_8O_4$ | $C_{46}H_{56}Ag_6Cl_4N_{28}O_{24}$ | $C_{12}H_{10}AgN_5O_2$ |
| Formula weight | 616.13 | 572.06 | 2174.21 | 364.12 |
| Crystal system | monoclinic | triclinic | monoclinic | monoclinic |
| Space group | *C*2/*c* | $P\bar{1}$ | *C*2/*c* | *C*2/*c* |
| *a* [Å] | 12.985(2) | 7.5550(12) | 25.857(17) | 16.5276(6) |
| *b* [Å] | 15.337(3) | 7.8391(12) | 14.424(8) | 13.2996(5) |
| *c* [Å] | 10.3207(17) | 8.4408(13) | 19.420(12) | 12.0687(2) |
| *α* [°] | 90 | 103.3800(10) | 90 | 90 |
| *β* [°] | 113.440(3) | 110.681(2) | 114.698(6) | 107.041(2) |
| *γ* [°] | 90 | 105.975(2) | 90 | 90 |
| Volume [$Å^3$] | 1885.8(5) | 418.54(11) | 6580(7) | 2536.35(14) |
| *Z* | 4 | 1 | 4 | 8 |
| $d_{calcd.}$ [$g\,cm^{-3}$] | 2.283 | 2.270 | 2.195 | 1.907 |
| *μ* [$cm^{-1}$] | 2.351 | 2.383 | 2.016 | 1.598 |
| *F*(000) | 1272 | 278 | 4280 | 1440 |
| Crystal size [mm] | 0.38 × 0.10 × 0.04 | 0.34 × 0.24 × 0.06 | 0.20 × 0.20 × 0.20 | 0.26 × 0.20 × 0.06 |
| Data/restraint/parameters | 1201/3/138 | 1440/0/127 | 5450/0/498 | 1777/0/181 |
| Reflns. collected | 2216 | 2195 | 18786 | 3223 |
| Unique reflns. | 1201 | 1440 | 5450 | 1777 |
| Goodness of fit | 1.134 | 1.582 | 1.206 | 1.390 |
| $R_1[I > 2\sigma(I)]$ | 0.0545 | 0.0416 | 0.0506 | 0.0640 |
| $\omega R_2[I>2\sigma(I)]$ | 0.1040 | 0.1203 | 0.0828 | 0.0886 |
| $R_1$ (all data) | 0.0812 | 0.0444 | 0.0685 | 0.0948 |
| $\omega R_2$(all data) | 0.1133 | 0.1232 | 0.0893 | 0.0953 |
| Residuals [$e\,Å^{-3}$] | 0.507, –0.527 | 0.845, –1.079 | 1.363, –0.836 | 0.427, –0.587 |

Table 2. Selected bond lengths [Å] and angles [°] for **1**–**4**.[a]

| | | | | | |
|---|---|---|---|---|---|
| Complex **1** | | | | | |
| Ag–N(1) | 2.149(6) | Ag–N(3) | 2.130(5) | Ag–Ag#1 | 2.8182(14) |
| N(3)–Ag–N(1) | 170.6(2) | N(3)–Ag–Ag#1 | 87.55(17) | N(1)–Ag–Ag#1 | 84.85(16) |
| Complex **2** | | | | | |
| Ag–N(1) | 2.236(4) | Ag–N(3) | 2.203(4) | Ag–O(1) | 2.392(4) |
| Ag–Ag#1 | 2.8437(9) | N(3)–Ag–N(1) | 132.95(16) | N(3)–Ag–O(1) | 131.28(14) |
| N(1)–Ag–O(1) | 95.76(14) | N(1)–Ag–Ag#1 | 91.71(12) | N(3)–Ag–Ag#1 | 79.42(11) |
| O(1)–Ag–Ag#1 | 103.91(10) | | | | |
| Complex **3** | | | | | |
| Ag(1)–N(1) | 2.549(5) | Ag(1)–N(3) | 2.163(5) | Ag(1)–N(5) | 2.160(5) |
| Ag(1)–Ag(2) | 2.9331(17) | Ag(1)–Ag(1)#1 | 3.3169(18) | Ag(2)–N(7) | 2.139(5) |
| Ag(2)–N(11) | 2.135(5) | Ag(2)–Ag(3) | 3.0091(15) | Ag(3)–N(9) | 2.111(5) |
| Ag(3)–N(13) | 2.122(5) | Ag(3)–Ag(3)#2 | 3.0767(19) | N(3)–Ag(1)–N(1) | 73.96(18) |
| N(5)–Ag(1)–N(1) | 108.77(17) | N(5)–Ag(1)–N(3) | 170.32(18) | N(3)–Ag(1)–Ag(2) | 87.75(13) |
| N(5)–Ag(1)–Ag(2) | 85.05(12) | N(1)–Ag(1)–Ag(2) | 144.91(11) | N(5)–Ag(1)–Ag(1)#1 | 104.98(13) |
| N(3)–Ag(1)–Ag(1)#1 | 84.30(13) | N(1)–Ag(1)–Ag(1)#1 | 55.78(12) | Ag(2)–Ag(1)–Ag(1)#1 | 153.14(3) |
| N(11)–Ag(2)–N(7) | 164.81(18) | N(11)–Ag(2)–Ag(1) | 109.47(13) | N(7)–Ag(2)–Ag(1) | 84.93(12) |
| N(11)–Ag(2)–Ag(3) | 80.69(14) | N(7)–Ag(2)–Ag(3) | 108.97(13) | Ag(1)–Ag(2)–Ag(3) | 73.30(5) |
| N(9)–Ag(3)–N(13) | 172.62(18) | N(9)–Ag(3)–Ag(2) | 88.47(13) | N(13)–Ag(3)–Ag(2) | 98.66(13) |
| N(9)–Ag(3)–Ag(3)#2 | 100.32(13) | N(13)–Ag(3)–Ag(3)#2 | 83.47(12) | Ag(2)–Ag(3)–Ag(3)#2 | 74.85(5) |
| Complex **4** | | | | | |
| Ag(1)–N(1) | 2.260(16) | Ag(1)–N(3) | 2.154(16) | Ag(1)–N(10) | 2.301(14) |
| Ag(2)–N(5) | 2.240(14) | Ag(2)–N(7) | 2.172(12) | N(3)–Ag(1)–N(1) | 157.7(6) |
| N(1)–Ag(1)–N(10) | 111.8(5) | N(3)–Ag(1)–N(10) | 90.3(6) | N(7)–Ag(2)–N(5) | 161.0(5) |

[a] Symmetry code for **1**: #1: –*x*, *y*, –*z* + 1/2; **2**: #1: –*x* + 1, –*y* + 1, –*z* + 2; **3**: #1: –*x* + 1/2, –*y* + 1/2, –*z* + 1; #2: –*x*, *y*, –*z* + 1/2.

 © 2006 Wiley-VCH Verlag GmbH & Co. KGaA, Weinheim 

half an hour then a water solution (20 mL) containing oxalic acid (0.032 g, 0.25 mmol) was added. The resulting solution was stirred at 80 °C for two hours and then filtered off. The filtrate was left in air to evaporate to form crystals of **2** after one day. The crystals were collected by filtration, washed with ethanol, and dried in air (0.093 g, 65% yield based on Ag). $C_{14}H_{12}Ag_2N_8O_4$ (572.06): calcd. C 29.39, H 2.12, N 19.59; found C 29.36, H 2.34, N 19.44. IR (KBr): $\tilde{\nu}$ = 3435 s $cm^{-1}$, 3142 w, 3076 m, 2999 m, 2898 m, 2807 m, 1597 s, 1545 s, 1435 w, 1406 s, 1384 m, 1334 w, 1310 s, 1218 w, 1105 s, 940 m, 886 m, 761 m, 747 m, 735 m, 689 m.

**$[Ag_6(\mu\text{-}H_2biim)_5(H_2biim)_2](ClO_4)_4(CH_3CO_2)_2\cdot 4H_2O$ (3):** An aqueous solution (10 mL) of $NaClO_4\cdot H_2O$ (0.70 g 0.5 mmol) was added to a well-stirred suspension of $H_2$biim (0.067 g, 0.5 mmol) and $Ag(CH_3COO)$ (0.083 g, 0.5 mmol) in 50 mL of water. The suspension was then refluxed for 2 h. After cooling, the resulting suspension was filtered off. The filtrate was left in air to evaporate the solvent and crystals were obtained after a few days. The product was collected by filtration, washed with ethanol, and dried in vacuo (0.078 g, 43% yield based on Ag). $C_{46}H_{56}Ag_6Cl_4N_{28}O_{24}$ (2174.2): calcd. C 25.41, H 2.60, N 18.04; found C 25.49, H 2.67, N 18.11. IR (KBr): $\tilde{\nu}$ = 3449 m $cm^{-1}$, 3176 w, 3143 w, 3076 m, 3002 m, 2898 m, 2807 m, 1631 w, 1546 m, 1436 w, 1406 m, 1384 s, 1333 m, 1218 w, 1144 m, 1121 s, 1106 s, 1084 s, 940 m, 887 m, 747 m, 689 m, 626 w.

**$[Ag_2(H_2biim)_2(nicotinate)_2]_n$ (4):** A mixture of $AgNO_3$ (0.042 g, 0.25 mmol), $H_2$biim (0.333 g, 0.25 mmol), and nicotinic acid (0.308 g, 0.25 mmol) in $H_2O$ (16 mL) was heated at 165 °C for 3 d under autogenous pressure. After cooling, the resulting solution was filtered off. The filtrate was left in air to evaporate the solvent and crystals were obtained after a few days. The product was collected by filtration, washed with ethanol, and dried in vacuo (0.042 g, 46% yield based on Ag). $C_{12}H_{10}AgN_5O_2$ (364.12): calcd. C 39.58, H 2.77, N 19.24; found C 39.53, H 2.85, N 19.16. IR (KBr): $\tilde{\nu}$ = 3435 m $cm^{-1}$, 3109 m, 3067 m, 2991 m, 2896 m, 2806 m, 1594 s, 1547 s, 1406 m, 1384 s, 1334 m, 1219 w, 1191 w, 1152 w, 1105 m, 1030 w, 993 w, 940 w, 915 w, 774 m, 749 mw, 691 m.

Table 3. Hydrogen bonds in **1**–**4**.[a]

| D–H···A | D–H | H···A | D–A | D–H–A |
|---|---|---|---|---|
| Complex **1** | | | | |
| N2–H2A···O2#1 | 0.86 | 1.94 | 2.774 | 162.4 |
| N4–H4A···O1#2 | 0.86 | 1.95 | 2.727 | 149.3 |
| O1W–H1WB···O2#3 | 0.87 | 2.00 | 2.869 | 178.6 |
| O1W–H1WA···O2#4 | 0.95 | 2.37 | 3.172 | 141.0 |
| Complex **2** | | | | |
| N2–H2A···O2#1 | 0.86 | 1.92 | 2.741 | 159.4 |
| N4–H4B···O1#2 | 0.86 | 1.89 | 2.724 | 164.2 |
| Complex **3** | | | | |
| N2–H2A···O4#1 | 0.86 | 2.49 | 2.973 | 116.1 |
| N2–H2A···O02 | 0.86 | 2.58 | 3.316 | 144.9 |
| N4–H4A···O02 | 0.86 | 2.28 | 3.099 | 160.5 |
| N4–H4A···O2#2 | 0.86 | 2.53 | 3.050 | 119.8 |
| N6–H6A···O2W#3 | 0.86 | 1.89 | 2.726 | 174.9 |
| N8–H8A···O02#4 | 0.86 | 2.36 | 3.078 | 140.9 |
| N10–H10A···O1W | 0.86 | 1.87 | 2.714 | 168.0 |
| N12–H12A···O1W | 0.86 | 2.34 | 3.017 | 135.4 |
| N12–H12A···O7#5 | 0.86 | 2.35 | 2.927 | 125.2 |
| N14–H14A···O01#6 | 0.86 | 1.87 | 2.722 | 172.7 |
| O1W–H1WA···O2#2 | 0.90 | 2.16 | 2.840 | 132.2 |
| O1W–H1WB···O01#7 | 0.90 | 1.96 | 2.796 | 153.9 |
| O1W–H1WB···O5#5 | 0.90 | 2.56 | 3.067 | 116.3 |
| O2W–H2WA···O02#8 | 0.91 | 2.19 | 3.034 | 153.3 |
| O2W–H2WB···O01#7 | 0.90 | 2.52 | 3.147 | 127.0 |
| Complex **4** | | | | |
| N2–H1···O1#1 | 0.85 | 1.85 | 2.688 | 167.3 |
| N4–H4···O2#2 | 0.93 | 1.80 | 2.694 | 161.0 |

[a] Symmetry codes for **1**: #1: $-x+1, -y+1, -z+1$; #2: $-x+1, -y, -z+1$; #3: $x, y, z-1$; #4: $-x+1/2, -y+1/2, -z+1$; **2**: #1: $x+1, y+1, z$; #2: $x, y, z+1$; **3**: #1: $x, -y+1, z+1/2$; #2: $-x+1/2, y+1/2, -z+1/2$; #3: $x, y-1, z$; #4: $-x+1/2, -y+1/2, -z+1$; #5: $x, -y+1, z-1/2$; #6: $x-1, y-1, z$; #7: $-x+1, y, -z+1/2$; #8: $-x+1/2, -y+3/2, -z+1$. **4**: #1: $-x+1/2, y-1/2, -z+3/2$; #2: $x, y, z-1$.

**X-ray Crystallographic Study:** Suitable single crystals of complexes **1**–**4** were mounted on a Siemens Smart CCD diffractometer equipped with a graphite-monochromated Mo-$K_\alpha$ radiation source ($\lambda$ = 0.71073 Å) at 298 K. All absorption corrections were performed with the SADABS program. All structures were solved by direct methods and refined by full-matrix least-squares fitting on $F^2$ with SHELXTL-97.[14] All non-hydrogen atoms were refined with anisotropic thermal parameters. Hydrogen atoms were located at geometrically calculated positions and treated as riding on their parent atoms. Crystallographic data and structural refinements for compounds **1**–**4** are summarized in Table 1. Selected bond lengths and hydrogen bonds are summarized in Tables 2 and 3, respectively. CCDC-285100 (**1**), -285101 (for **2**), -262860 (for **3**), and -285012 (for **4**) contain the supplementary crystallographic data for this paper. These data can be obtained free of charge from The Cambridge Crystallographic Data Center via www.ccdc.cam.ac.uk/data_request/cif.

## Acknowledgments

This work was supported by the National Science Foundation of China (grant no. 20473092) and the "One Hundred Talents Program" of the Chinese Academy of Science.

[1] a) *Comprehensive Supramolecular Chemistry* (Eds.: J. L. Atwood, J. E. D. Davies, J. M. Lehn, D. D. MacNicol, F. Vögtle), Pergamon, Oxford, **1996**; b) J.-M. Lehn, *Supramolecular Chemistry − Concepts and Perspectives*, VCH, Weinheim, **1995**.

[2] a) D. Philp, J. F. Stoddart, *Angew. Chem. Int. Ed. Engl.* **1996**, *35*, 1155–1196; b) O. M. Yaghi, H. Li, C. Davis, D. Richardson, T. L. Groy, *Acc. Chem. Res.* **1998**, *31*, 474–484; c) S. R. Batten, R. Robson, *Angew. Chem. Int. Ed.* **1998**, *37*, 1460–1494.

[3] a) S. Leininger, B. Olenyuk, P. J. Stang, *Chem. Rev.* **2000**, *100*, 853–891; b) M. Fujita, *Acc. Chem. Res.* **1999**, *32*, 53–61.

[4] a) P. Pyykkö, *Chem. Rev.* **1997**, *97*, 597–636; b) P. Pyykko, F. Mendizabal, *Chem. Eur. J.* **1997**, *3*, 1458–1465.

[5] a) P. Majumdar, K. K. Kamar, A. Castiñeiras, S. Goswami, *Chem. Commun.* **2001**, 1292–1293; b) V. J. Catalano, S. J. Horner, *Inorg. Chem.* **2003**, *42*, 8430–8438; c) E. J. Fernandez, J. M. Lopez de Luzuriaga, M. Monge, M. A. Rodriquez, O. Crespo, M. Concepcion, A. Laguna, P. G. Jones, *Inorg. Chem.* **1998**, *37*, 6002–6008; d) M. Munakata, M. Maekawa, S. Kitagawa, M. Adachi, H. Masuda, *Inorg. Chim. Acta* **1990**, *167*, 181–188.

[6] a) A. N. Khlobystov, A. J. Blake, N. R. Champness, D. A. Lemenovskii, A. G. Majouga, N. V. Zyk, M. Schroder, *Coord. Chem. Rev.* **2001**, *222*, 155–192; b) M. A. Withersby, A. J. Blake, N. R. Champness, P. Hubberstey, W. S. Li, M. Schroder, *Angew. Chem. Int. Ed. Engl.* **1997**, *36*, 2327–2329.

[7] a) M. J. Hannon, C. L. Painting, E. A. Plummer, L. J. Childs, N. W. Alco, *Chem. Eur. J.* **2002**, *8*, 2225–2238; b) S. Lopez, S. W. Keller, *Inorg. Chem.* **1999**, *38*, 1883–1888; c) K. A. Hirsch, S. R. Wilson, J. S. Moore, *Inorg. Chem.* **1997**, *36*, 2960–2968.

[8] a) B. Hasenknopf, J. M. Lehn, N. Boumediene, A. Dupont-Gervais, A. Van Dorsselaer, B. O. Kneisel, D. Fenske, *J. Am.*

 © 2006 Wiley-VCH Verlag GmbH & Co. KGaA, Weinheim 

*Chem. Soc.* **1997**, *119*, 10956–10962; b) R. D. Schnebeck, E. Freisinger, B. Lippert, *Angew. Chem. Int. Ed.* **1999**, *38*, 168–171; c) D. A. Mcmorran, P. J. Steel, *Angew. Chem. Int. Ed.* **1998**, *37*, 3295–3297; d) J. S. Fleming, K. L. V. Mann, C. A. Carraz, E. Psillakis, J. C. Jeffery, J. A. McCleverty, M. D. Ward, *Angew. Chem. Int. Ed.* **1998**, *37*, 1279–1281; e) P. C. Jones, K. J. Byrom, J. C. Jeffery, J. A. McCleverty, M. D. Ward, *Chem. Commun.* **1997**, 1361–1362.

[9] a) R.-L. Sang, L. Xu, *Inorg. Chem.* **2005**, *44*, 3731–3737; b) M. Tadokoro, K. Isober, H. Uekusa, Y. Ohashi, J. Toyoda, K. Tashiro, K. Nakasuji, *Angew. Chem. Int. Ed.* **1999**, *38*, 95–98; c) M. Tadocoro, H. Kanno, T. Kitajima, H. Shimada-Umemoto, N. Nakanishi, K. Isobe, K. Nakasuji, *Proc. Natl. Acad. Sci. USA* **2002**, *99*, 4950–4955; d) M. Tadocomo, T. Shiomi, K. Isobe, K. Nakasuji, *Inorg. Chem.* **2001**, *40*, 5476–5478; e) M. Tadomoro, K. Nakasuji, *Coord. Chem. Rev.* **2000**, *198*, 205–218; f) R. Atencio, M. Chacon, T. Gonzalez, A. Briceno, G. Agrifoglio, A. Sierraalta, *Dalton Trans.* **2004**, 505–513; g) W. E. Allen, C. J. Fowler, V. M. Lynch, J. L. Sessler, *Chem. Eur. J.* **2001**, *7*, 721–729; h) L. Ohrstrom, K. Larsson, S. Borg, S. T. Norberg, *Chem. Eur. J.* **2001**, *7*, 4805–4810.

[10] a) C. Kirchner, B. Krebs, *Inorg. Chem.* **1987**, *26*, 3569–3576; b) C. A. Hester, R. G. Baughman, H. L. Collier, *Polyhedron* **1997**, *16*, 2893–2895; c) A. S. Abushamleh, H. A. Goodwin, *Aust. J. Chem.* **1979**, *32*, 513–518; d) U. Sakaguchi, A. K. Addison, *J. Chem. Soc., Dalton Trans.* **1979**, 600–608; e) A. Bendini, F. Mani, *Inorg. Chim. Acta* **1988**, *154*, 215–219; f) S. Fortin, A. L. Beauchamp, *Inorg. Chem.* **2000**, *39*, 4886–4893; g) M. A. Lorente, F. Dahan, Y. Sanakis, V. Petrouleas, A. Boussedsou, J.-P. Tuchagues, *Inorg. Chem.* **1995**, *34*, 5346–5357; h) I. G. Dance, A. S. Abushamleh, H. A. Goodwin, *Inorg. Chim. Acta* **1980**, *43*, 217–221; i) A. D. Mighell, C. W. Reimann, F. A. Maucer, *Acta Crystallogr., Sect. B* **1969**, *25*, 60–66; j) J. Cancela, M. J. Gonzalez Garmendia, M. Qurios, *Inorg. Chim. Acta* **2001**, *313*, 156–159; k) B.-H. Ye, F. Xue, G.-Q. Xue, L.-N. Ji, T. C. W. Mak, *Polyhedron* **1999**, *18*, 1785–1790; l) R.-L. Sang, L. Xu, *Acta Crystallogr., Sect. E* **2005**, *61*, m793–m795.

[11] a) S. W. Kaiser, R. B. Saillant, W. M. Butler, P. G. Rasmussen, *Inorg. Chem.* **1976**, *15*, 2681–2687; b) S. W. Kaiser, R. B. Saillant, P. G. Rasmussen, *J. Am. Chem. Soc.* **1975**, *97*, 425–426; c) S. W. Kaiser, R. B. Saillant, W. M. Butler, P. G. Rasmussen, *Inorg. Chem.* **1976**, *15*, 2688–2694; d) M. S. Haddad, D. N. Hendrickson, *Inorg. Chem.* **1978**, *17*, 2622–2630; e) R. Usón, J. Gimeno, J. Forniés, F. Martínez, *Inorg. Chim. Acta* **1981**, *50*, 173–177; f) A. Maiboroda, G. Rheinwald, H. Lang, *Inorg. Chem. Commun.* **2001**, *4*, 381–383; g) P. Majumdar, S. M. Peng, S. Goswami, *J. Chem. Soc., Dalton Trans.* **1998**, 1569–1574; h) M. P. Garcia, A. M. López, M. A. Esteruelas, F. J. Lahoz, L. A. Oro, *J. Chem. Soc., Chem. Commun.* **1988**, 793 –795; i) R. Usón, L. A. Oro, J. Gimeno, M. A. Ciriano, J. A. Cabeza, *J. Chem. Soc., Dalton Trans.* **1983**, 233–330.

[12] a) J.-S. Casas, A. Castineiras, Y. Parajo, M.-L. Perez-Paralle, A. Sanchez, A. Sanchez-Gonzalez, J. Sordo, *Polyhedron* **2003**, *22*, 1113–1121; b) A. Sanchez-Gonzalez, J. S. Casas, J. Sordo, U. Russo, M. I. Lareo, B. J. Regueiro, *J. Inorg. Biochem.* **1990**, *39*, 227–235; c) C. Lopez, A. S. Gonzalez, M. E. Garcia, J. S. Casas, J. Sordo, R. Graziani, U. Casellato, *J. Organomet. Chem.* **1992**, *434*, 261–268; d) B. J. Holliday, C. A. Mirkin, *Angew. Chem. Int. Ed.* **2001**, *40*, 2023–2043; e) J. D. Watson, F. H. C. Crick, *Nature* **1953**, *171*, 737–738; f) P. A. Zoo, J. S. Casas, M. D. Couse, E. Freijanes, A. Furlani, V. Scarcial, J. Sordo, U. Russo, M. Varela, *Appl. Organomet. Chem.* **1997**, *11*, 963–968.

[13] R. P. Thummel, V. Goulle, B. Chen, *J. Org. Chem.* **1989**, *54*, 3057–3061.

[14] G. M. Sheldrick, *SHELXL-97, Program for Crystal Structure Solution*, University of Göttingen, Germany, **1997**.

[15] K. M. Lee, H. M. J. Wang, I. J. B. Lin, *J. Chem. Soc., Dalton Trans.* **2002**, 2852–2856.

Received: October 1, 2005
Published Online: February 2, 2006

 © 2006 Wiley-VCH Verlag GmbH & Co. KGaA, Weinheim 

DOI: 10.1002/ejic.200500888

# Synthesis, Structure and Stability of New $Pt^{II}$–Bis(N-Heterocyclic Carbene) Complexes

**Sebastian Ahrens,[a] Eberhardt Herdtweck,[b][‡] Sigrid Goutal,[a][‡‡] and Thomas Strassner*[a]**

**Keywords:** Carbene ligands / NMR spectroscopy / Platinum / Synthesis / Ligand design / Solid state structure

The use of metal acetates has allowed the synthesis of NHC complexes without isolation of the free carbene. This route is very useful in cases where the metal acetates are readily available and has been used, for example, for the synthesis of bis(N-heterocyclic carbene) complexes of palladium(II). In the case of platinum, however, the corresponding acetate is not commercially available and is difficult to synthesize. Previously published syntheses require either an external base (e.g. NaOAc or KO*t*Bu) or a transmetalation step. Here we present a new general synthetic pathway for platinum–bis(carbene) complexes using platinum(II) acetylacetonate as a commercially available metal precursor. Aromatic substituents greatly enhance the stability of the metal complexes against acidic media.
(© Wiley-VCH Verlag GmbH & Co. KGaA, 69451 Weinheim, Germany, 2006)

## Introduction

In the last decade N-heterocyclic carbene (NHC) complexes of transition metals have found applications in many fields of chemistry. Metal complexes of imidazoline-2-ylidenes have recently been shown to be extremely versatile and stable catalysts for a wide range of reactions, including C–C coupling reactions,[1,2] olefin metathesis,[3–6] hydroformylation,[7,8] and, most recently, CH activation.[9,10] The key for this development has been the number of improved synthetic methods for the preparation of NHC complexes, which have been summarized in recent reviews.[11–13]

Metal acetates allow the synthesis of NHC complexes without isolation of the free carbene. Palladium(II) acetate in wet dimethyl sulfoxide (DMSO) at elevated temperatures directly forms carbene complexes with imidazolium salts. Even methylene-bridged bis(imidazolium) salts can be converted into the corresponding bis(carbene) complexes in high yields (85–90%).[14–16] We and others have been particularly interested in these chelate ligands as a way of extending the area to more complex ligands and more stable complexes.[17–23] Here we present a new general synthetic pathway towards platinum–bis(carbene) complexes with aromatic substituents, which greatly enhance the stability of the corresponding platinum carbene complexes.

[a] Department Chemie – Physikalische Organische Chemie, Technische Universität Dresden,
Mommsenstr. 13, 01062 Dresden, Germany
Fax: +49-351-463-39679
E-mail: Thomas.Strassner@chemie.tu-dresden.de
[b] Department Chemie – Lehrstuhl für Anorganische Chemie, Technische Universität München,
Lichtenbergstr. 4, 85747 Garching b. München, Germany
Fax: +49-89-289-13473
[‡] Solid-state structure of compound **3b**.
[‡‡] Solid-state structure of compound **3d**.
Supporting information for this article is available on the WWW under http://www.eurjic.org or from the author.

## Results and Discussion

### Preparation of the Platinum(II)–Bis(carbene) Complexes

The previously reported syntheses of platinum–NHC complexes involve the preparation of either platinum precursors or free carbenes, which usually have to be handled under an inert gas atmosphere.[24–27] Since the acidic methylene protons in bis(imidazolium) salts might be attacked under common deprotonation conditions, a pathway via the free bis(carbenes) is only possible by using sterically demanding bases, but the yields are only moderate.[28,29] To circumvent the need for multi-step pathways we recently introduced a new synthetic route using the corresponding platinum(II) halide salts and sodium acetate as an external base for the synthesis of the metal complexes. However, the use of external bases like sodium acetate often leads to the formation of small amounts of platinum black, which produces lower yields in the reaction and is difficult to remove from the product.[22]

If platinum(II) acetylacetonate is used as metal precursor, no formation of platinum black is observed during the reaction. Like the platinum(II) halides used in our first protocol,[22] it is commercially available and can be handled in air. Furthermore, there are two major advantages for the use of platinum(II) acetylacetonate compared to platinum(II) halides. First, only platinum(II) halides with the same halides as the imidazolium salts can be used in the reaction to avoid anion scrambling in the complex, and platinum(II) halides are also much more expensive than platinum(II) acetylacetonate. Secondly, different from our

 InterScience © 2006 Wiley-VCH Verlag GmbH & Co. KGaA, Weinheim 

older procedure, no other external base has to be added since the basicity of the acetylacetonate anion is sufficient to deprotonate the imidazolium salt. When platinum(II) halides are used as metal precursors, sodium acetate has to be added to the reaction mixture, which leads to the formation of sodium halide salts during the reaction which have to be removed by washing the product with water several times.[22] In this case only pentan-2,4-dione emerges during the reaction, and this can be removed in vacuo along with the solvent. We were able to synthesize several new platinum–N-heterocyclic bis(carbene) complexes with different substituents at the aromatic ring following this method.

The synthesis of these new ligands can be accomplished in only two steps. First, the aromatic-substituted imidazoles were synthesized according to Scheme 1 from substituted anilines, which are commercially available in great diversity: 4-nitroaniline for **1a**, 4-chloroaniline for **1b**, 4-bromoaniline for **1c**, 4-methoxyaniline for **1d**, and ethyl 4-aminobenzoate for **1e**. The aromatic amine, glyoxal and formaldehyde are converted into an aromatic-substituted imidazole in a one-pot reaction. Additionally to the imidazoles prepared by Zhang et al.,[30] we extended this method to anilines substituted by different halogens. Both electron-donating and -withdrawing substituents are tolerated, although the yields of product are quite different (Table 1).

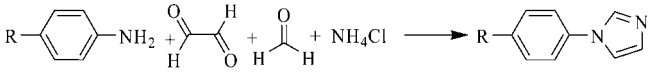

Scheme 1. Synthesis of imidazoles with different aromatic substituents [R = $NO_2$ (**1a**), R = Cl (**1b**), R = Br (**1c**), R = $OCH_3$ (**1d**), R = $COOCH_2CH_3$ (**1e**)].

Table 1. Isolated yields of **1a**–**1e**.

| | **1a** | **1b** | **1c** | **1d** | **1e** |
|---|---|---|---|---|---|
| Yield | 28.0% | 77.0% | 60.7% | 75.0% | 73.7% |

The low yield for **1a** can be explained by its lower solubility in organic solvents, so the extraction of the product is the limiting factor here. This reaction gives access to a wide range of N-substituted imidazoles with different functional groups at the aromatic ring, thereby allowing us to fine-tune the electronic situation in the N-heterocyclic carbene ligand.

These N-substituted imidazoles can be converted in good yields into the corresponding bis(imidazolium) salts by a nucleophilic substitution reaction with dibromomethane (Scheme 2). The reaction also works with diiodomethane,

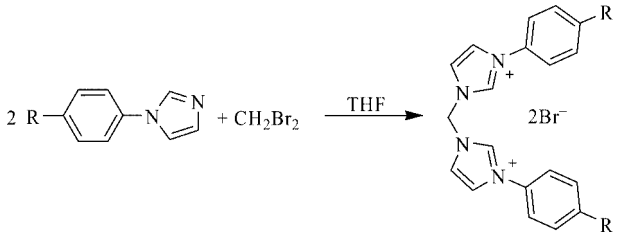

Scheme 2. Synthesis of the imidazolium salts [R = $NO_2$ (**2a**), R = Cl (**2b**), R = Br (**2c**), R = $OCH_3$ (**2d**), R = $COOCH_2CH_3$ (**2e**)].

as reported previously.[22] The preparation of the imidazoles and the following bridging step of two of these imidazoles with dibromomethane are compatible with a wide range of functional groups at the aromatic ring. Yields are given in Table 2.

Table 2. Isolated yields of **2a**–**2e**.

| | **2a** | **2b** | **2c** | **2d** | **2e** |
|---|---|---|---|---|---|
| Yield | 94.8% | 64.0% | 84.0% | 88.7% | 86.4% |

Finally, we succeeded in synthesizing the platinum–bis(carbene) complexes under very mild conditions, thus proving the application of our new compounds as suitable NHC ligands for late transition metals. In this case, the traditional metalation procedure involving deprotonation of the imidazolium precursor with strong bases produces unwanted side reactions because of the acidic protons in the bridging $CH_2$ group and in the functional groups at the aromatic ring.[31] Milder procedures were therefore needed that are compatible with more sensitive functionalities. Base-sensitive methylene-bridged bis(imidazolium) salts can be converted into the corresponding palladium–bis(carbene) complexes by treatment with $Pd(OAc)_2$ in wet dimethyl sulfoxide (DMSO) at elevated temperatures in high yields (Scheme 3).[14–16] This route is very useful in cases where the metal acetates are easily available. In the case of platinum, however, the corresponding acetate is not available and is difficult to synthesize.[32,33] So until now platinum(II) halides had to be used and sodium acetate had to be added to the reaction mixture as an external base, leading to the formation of sodium halides as by-products during the reaction.[22] Here we present a new synthetic approach that uses platinum(II) acetylacetonate as a commercially available metal precursor and base for the deprotonation of the imidazolium salt. The synthesis of the platinum complexes is illustrated in Scheme 4 and yields of the syntheses are given in Table 3.

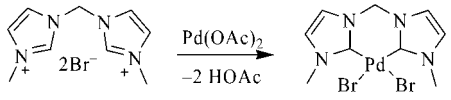

Scheme 3. Synthesis of bridged palladium complexes from imidazolium salts and palladium(II) acetate.

To obtain these complexes in good yields it is necessary to follow the synthetic protocol described below. It is crucial that the halide salt of the bis(imidazolium) compound is completely converted into the platinum–monocarbene species by slowly heating the reaction mixture over several hours first to 60 °C, thereby deprotonating only one of the imidazolium rings, otherwise a substantial amount of platinum black formation is observed.[22] The reaction mixture should then be heated up to 130 °C to deprotonate the second imidazolium ring. This is consistent with the earlier findings of Herrmann et al. regarding palladium–bis(carbene) complexes,[34] but had not been observed for platinum carbenes before.

 © 2006 Wiley-VCH Verlag GmbH & Co. KGaA, Weinheim 

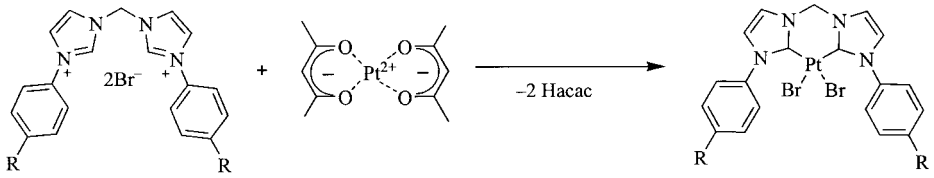


Scheme 4. Synthesis of the platinum complexes [R = $NO_2$ (**3a**), R = Cl (**3b**), R = Br (**3c**), R = $OCH_3$ (**3d**), R = $COOCH_2CH_3$ (**3e**)].

Table 3. Isolated yields of **3a**–**3e**.

| | 3a | 3b | 3c | 3d | 3e |
|---|---|---|---|---|---|
| Yield | 62.1% | 86.8% | 67.0% | 69.9% | 71.8% |

### Solid-State Structures and NMR Studies of the Platinum(II)–Bis(carbene) Complexes

Important geometrical parameters of the solid-state structures are shown in Table 4 and the Supporting Information. Details of the structure determinations are given in the Experimental Section.

Table 4. Selected bond lengths and bond and torsional angles of **3b**–**3e**.

| | 3b | 3c | 3d | 3e |
|---|---|---|---|---|
| Pt–C1 | 1.968(12)×2 | 1.968(5)×2 | 1.961(6) | 1.967(12) |
| Pt–C11 | | | 1.971(6) | 1.976(13) |
| Pt–Br1 | 2.4685(16)×2 | 2.4833(6)×2 | 2.4926(7) | 2.4746(13) |
| Pt–Br2 | | | 2.4831(7) | 2.4812(14) |
| C1–N1 | 1.366(16)×2 | 1.351(7)×2 | 1.349(8) | 1.377(15) |
| C11–N3 | | | 1.333(8) | 1.359(15) |
| C1–Pt–C1A/C11 | 86.4(5) | 84.9(2) | 84.4(3) | 85.6(5) |
| C1–Pt–Br1 | 92.2(4) | 92.75(15) | 92.34(18) | 93.1(4) |
| C1–N2–C5–C10 | 137.0(12) | –147.0(5) | 128.0(7) | –143.8(12) |

The molecular structures of complexes **3b**–**3e** are nearly identical with each other and with **4**; they contain a bowl-shaped NHC ligand. A DMSO solvent molecule, which covers the cavity, is found inside this bowl in all structures. The solid-state structure of complex **3d** is given in Figure 1 as an example, although the DMSO solvent molecule has been omitted for clarity. Pictures of the solid-state structures of the other complexes are given in the Supporting Information.

The Pt–carbene-C distances of the aromatic-substituted complexes **3b**–**3e** are equivalent within the margin of error. The biggest differences between these structures are found in the torsional angles of the plane of the aromatic rings towards the plane of the imidazole rings. Figure 2 shows a superposition of all four crystal structures; the DMSO and methanol solvent molecules found in the crystal structures have been omitted for clarity. The figure shows that the coordination environment of the metal center is highly preserved and so there are nearly no differences in the steric situation of the metal, even though the complexes crystallize in different space groups.

Although structurally quite similar these complexes have different electronic properties at the metal center, as can be seen from the $^{13}C$ NMR spectra. The effects of the different

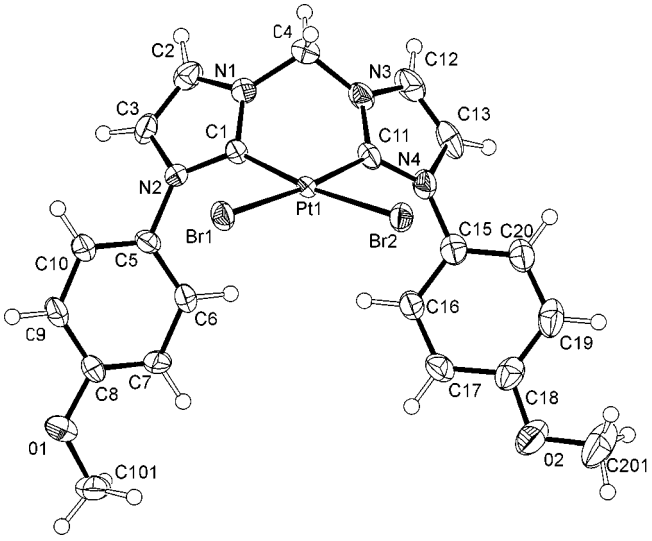


Figure 1. ORTEP-style plot of the solid-state structure of compound **3d**. Thermal ellipsoids are drawn at the 50% probability level. The disordered DMSO molecule in the crystal has been omitted for clarity.

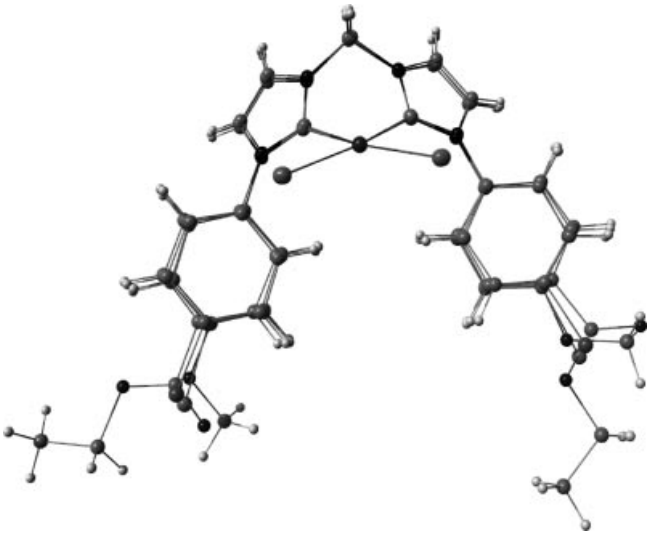

Figure 2. Superposition of the solid-state structures of **3b**–**3e**. Solvents omitted for clarity.

aromatic substituents $R_1$ on the $^{13}C$ chemical shifts for the carbene carbon atoms are shown in Figure 3. Therefore it is possible to fine-tune the electronic situation at the metal center by varying the functional groups at the aromatic ring. Electron-withdrawing groups like $NO_2$ or halogens at the aromatic ring lead to a shift of the $^{13}C$ signal of the

 © 2006 Wiley-VCH Verlag GmbH & Co. KGaA, Weinheim 

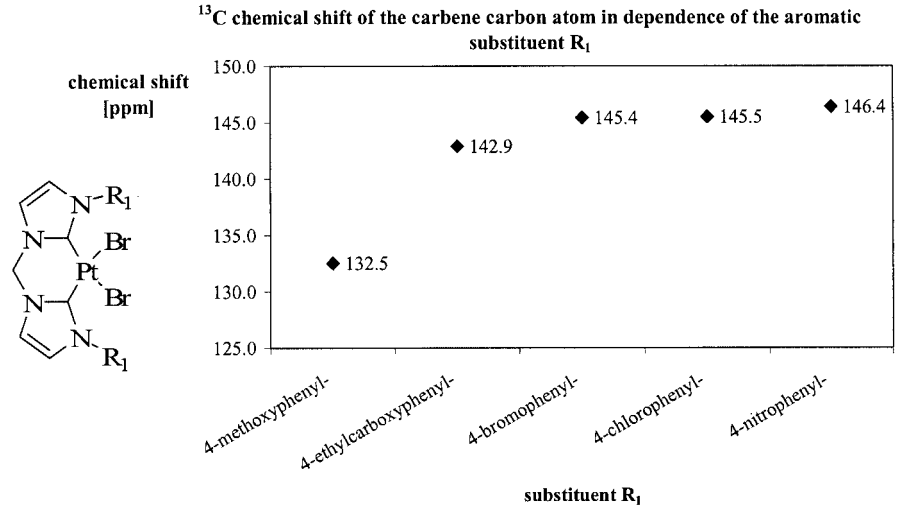


Figure 3. Dependence of the $^{13}C$ chemical shift of the carbene carbon atom on the aromatic substituents $R_1$.

carbene C to lower field, which is indicative of a higher partial negative charge at the carbene carbon atoms of the complex. As expected, the electron-withdrawing effects of a 4-chlorophenyl and a 4-bromophenyl group at the imidazole are nearly equivalent. On the other hand, electron-donating groups like the methoxy group at the aromatic ring lead to a high-field shift of the $^{13}C$ signal of the carbene carbon atom.

This type of complex also shows an unusually high thermal stability combined with a surprising resistance to acidic media. We have observed this stability previously for palladium(II)–NHC complexes like 1,1′-dimethyl-3,3′-methylene-4-diimidazoline-2,2′-diylidenepalladium(II) dibromide (**4**), which are catalysts for the activation of methane, while the analogous platinum(II)–NHC complex **5** decomposes quickly in trifluoroacetic acid (Figure 4).[9,10,22]

**4** **5**

Figure 4. Methyl-substituted bis-NHC complexes of palladium (**4**) and platinum (**5**).

With the introduction of aromatic ligands and the novel platinum(II) acetylacetonate synthesis presented here, we have been able to make several new platinum–bis(carbene) complexes with increased stability against strongly acidic conditions. While the analogous *N*-methyl-substituted complex **5** is stable towards air and moisture even at elevated temperatures, it decomposes within minutes to platinum black in trifluoroacetic acid.[9] However, the new complex **3b** does not decompose even after weeks in TFA or at elevated temperatures of up to 90 °C in the presence of strong oxidants like $K_2S_2O_8$. Complex **3e** can also be heated to 110 °C in 2 N HCl solution for 4 h with no change in the NMR spectrum. Neither reprotonation to the imidazolium salt nor hydrolysis of the ester functionality are observed under these conditions.

## Conclusion

We have shown that platinum(II)–bis(carbene) complexes with various aromatic substituents can be synthesized following our new protocol with platinum(II) acetylacetonate as metal precursor. Together with our new aromatic ligands with various substituents, acid-stable platinum(II)–bis(carbene) complexes are now synthetically available in great diversity. The electronic situation at the metal center can be fine-tuned by varying the functional groups at the aromatic ring without changing the steric situation of the metal center. This is important for future applications of these complexes in various catalytic reactions, since many known homogeneous catalytic processes depend on a particular electronic situation at the metal center.

## Experimental Section

**General Procedures:** Solvents of 99.5% purity were used throughout this study. Platinum(II) acetylacetonate (98%) was purchased from Acros. All other chemicals were obtained from common suppliers and used without further purification. Ligands **2a**–**2e** were prepared according to the procedures given in the Supporting Information. $^1H$ and $^{13}C$ NMR spectra were recorded with a Bruker AC 300 P, Jeol JNM GX-270, or Jeol JNM GX-400 spectrometer. As the $^1H$ and $^{13}C$ NMR spectra of one compound were not always measured on the same spectrometer, spectrometer frequencies of the measurements are given. The spectra were referenced internally to the resonances of the solvent ($^1H$, $^{13}C$). Elemental analyses were performed by the microanalytical laboratory at our institute using an EuroVektor Euro EA-300 Elemental Analyzer. Mass spectra were recorded with a Finnigan MAT 90 spectrometer.

**Synthesis of Platinum(II) Complex 3a:** 1,1′-Bis[1-(4-nitrophenyl)]-3,3′-methylenimidazolium dibromide (**2a**; 280.5 mg, 0.51 mmol) and platinum(II) acetylacetonate (200 mg, 0.51 mmol) were dissolved in 3 mL of dimethyl sulfoxide in a nitrogen-flushed Schlenk tube and heated for 2 h to 60 °C, 2 h to 80 °C, 2 h to 100 °C, and 1 h to 130 °C. At approximately 80 °C the reaction mixture became a clear, yellow solution. After removal of the solvent in vacuo the resulting residue was washed twice with 5 mL of diethyl ether and

 © 2006 Wiley-VCH Verlag GmbH & Co. KGaA, Weinheim 

5 mL of dichloromethane. The product was obtained as a yellow powder. Yield: 0.236 g (62.1%). $^1$H NMR (300 MHz, [D$_6$]DMSO): $\delta$ = 6.31 (d, $J$ = 14.4 Hz, 1 H, NC$H_2$N), 6.38 (d, $J$ = 14.4 Hz, 1 H, NC$H_2$N), 7.79 (d, $J$ = 9.0 Hz, 2 H, NC$H_2$CH$_2$N), 7.97–8.03 (m, 4 H, arom. H), 8.36 (d, $J$ = 9.0 Hz, 2 H, NCH$_2$C$H_2$N), 8.51–8.55 (m, 4 H, arom. H) ppm. $^{13}$C NMR (75 MHz, [D$_6$]DMSO): $\delta$ = 62.4 (N$C$H$_2$N), 121.0 (N$C$HCHN), 122.6 (NCH$C$HN), 124.5 (C2, C6 of C$_6$H$_4$NO$_2$), 125.5 (C3, C5 of C$_6$H$_4$NO$_2$), 126.4 (C1 of C$_6$H$_4$NO$_2$), 146.4 ($C$–Pt), 146.8 ($C$–NO$_2$). $C_{19}H_{14}Br_2N_6O_4Pt$·0.5DMSO (745.24 + 39.07): calcd. C 30.63, H 2.18, N 10.72; found C 30.94, H 2.46, N 10.79. MS (FAB): $m/z$ = 584.2 [M – 2Br]$^+$, 462.2 [M – 2Br – C$_6$H$_4$NO$_2$]$^+$, 341.2 [M – 2Br – 2C$_6$H$_4$NO$_2$]$^+$, 147.3 [M – 2Br – Pt – 2C$_6$H$_4$NO$_2$]$^+$.

**Synthesis of Platinum(II) Complex 3b:** 1,1-Bis[1-(4-chlorophenyl)]-3,3′-methylenimidazolium dibromide (**2b**; 500 mg, 0.94 mmol) and platinum(II) acetylacetonate (370 mg, 0.94 mmol) were dissolved in 10 mL of dimethyl sulfoxide in a nitrogen-flushed Schlenk tube and heated for 2 h to 40 °C, 2 h to 60 °C, 2 h to 80 °C, 2 h to 100 °C and 1 h to 130 °C. At 60 °C the reaction mixture became a clear, yellow solution. After removal of the solvent in vacuo the resulting residue was washed twice with 5 mL of ethanol. The product was obtained as a white powder. Yield: 0.591 g (86.8%). $^1$H NMR (300 MHz, [D$_6$]DMSO): $\delta$ = 6.10 (d, $J$ = 14.6 Hz, 1 H, NC$H_2$N), 6.31 (d, $J$ = 14.6 Hz, 1 H, NC$H_2$N), 7.64 (d, $J$ = 9.0 Hz, 4 H, arom. H), 7.73 (d, $J$ = 2.2 Hz, 2 H, NC$H$CHN), 7.77 (d, $J$ = 2.1 Hz, 2 H, NCHC$H$N), 7.81 (d, $J$ = 9.0 Hz, 4 H, arom. H) ppm. $^{13}$C NMR (75 MHz, [D$_6$]DMSO): $\delta$ = 67.0 (N$C$H$_2$N), 121.4 (N$C$HCHN), 122.2 (NCH$C$HN), 127.0 (C2, C6 of C$_6$H$_4$Cl), 128.6 (C3, C5 of C$_6$H$_4$Cl), 132.3 ($C$–Cl), 138.2 (C1 of C$_6$H$_4$Cl), 145.5 ($C$–Pt) ppm. $C_{19}H_{14}Br_2Cl_2N_4Pt$·DMSO (724.13 + 78.13): calcd. C 31.44, H 2.51, N 6.98, S 4.00; found C 31.16, H 2.51, N 6.65, S 4.00. MS (FAB): $m/z$ = 643.3 [M – Br]$^+$, 563.3 [M – 2Br]$^+$, 176.3 [C$_9$H$_6$N$_2$Cl$^+$].

**Synthesis of Platinum(II) Complex 3c:** 1,1-Bis[1-(4-bromophenyl)]-3,3′-methylenimidazolium dibromide (**2c**; 315.0 mg, 0.51 mmol) and platinum(II) acetylacetonate (200.0 mg, 0.51 mmol) were dissolved in 3 mL of dimethyl sulfoxide in a nitrogen-flushed Schlenk tube and stirred for 2 h at room temperature. The reaction mixture was then heated for 2 h to 60 °C, 1 h to 85 °C, and finally 1 h to 110 °C. The solvent was then removed in vacuo until only 0.5 mL of the solvent remained. After the addition of 3 mL of water a white solid precipitated. The aqueous solution was filtered off and the resulting residue was washed twice with 5 mL of dichloromethane. The product was obtained as a white powder. Yield: 0.278 g (67.0%). $^1$H NMR (270 MHz, [D$_6$]DMSO): $\delta$ = 6.10 (d, $J$ = 12.7 Hz, 1 H, NC$H_2$N), 6.31 (d, $J$ = 12.4 Hz, 1 H, NC$H_2$N), 7.53–7.95 (m, 12 H, remaining H) ppm. $^{13}$C NMR (67.9 MHz, [D$_6$] DMSO): $\delta$ = 62.5 (N$C$H$_2$N), 120.7 (N$C$HCHN), 121.5 ($C$–Br), 122.2 (NCH$C$HN), 127.3 (C2, C6 of C$_6$H$_4$Br), 131.6 (C3, C5 of C$_6$H$_4$Br), 138.8 (C1 of C$_6$H$_4$Br), 145.4 ($C$–Pt) ppm. MS (FAB): $m/z$ = 733.0 [M – Br]$^+$, 653.1 [M – 2Br]$^+$, 572.2 [M – 3Br]$^+$, 419.5 [M – 3Br – C$_6$H$_4$Br]$^+$.

**Synthesis of Platinum(II) Complex 3d:** 1,1-Bis[1-(4-methoxyphenyl)]-3,3′-methylenimidazolium dibromide (**2d**; 250.0 mg, 0.48 mmol) and platinum(II) acetylacetonate (188.3 mg, 0.48 mmol) were dissolved in 7 mL of dimethyl sulfoxide in a nitrogen-flushed Schlenk tube and stirred for 4 d at 60 °C. The solvent was then removed in vacuo and the product washed twice with 5 mL of water and twice with 5 mL of diethyl ether. The product was obtained as a white powder Yield: 0.240 g (69.9%). $^1$H NMR (300 MHz, [D$_6$] DMSO): $\delta$ = 3.86 (s, 6 H, OC$H_3$), 6.07 (d, $J$ = 14.6 Hz, 1 H, NC$H_2$N), 6.26 (d, $J$ = 14.6 Hz, 1 H, NC$H_2$N), 7.08 (m, 4 H, arom. H), 7.67 (s, 2 H, NC$H$CHN), 7.72 (s, 2 H, NCHC$H$N), 7.78 (m, 4 H, arom. H) ppm. $^{13}$C NMR (75 MHz, [D$_6$]DMSO): $\delta$ = 55.3 (O$C$H$_3$), 62.4 (N$C$H$_2$N), 113.7 (arom. $C$H), 122.5 (N$C$HCHN), 126.1 (arom. $C$H), 126.3 (NCH$C$HN), 126.7 (C1 of C$_6$H$_4$OMe), 132.5 (Pt–$C$), 158.8 ($C$–OMe) ppm. $C_{21}H_{20}Br_2N_4O_2Pt$ (715.30): calcd. C 35.26, H 2.81, N 7.86; found C 35.34, H 2.87, N 7.52. MS (FAB): $m/z$ = 635.1 [M – Br]$^+$, 554.3 [M – 2Br]$^+$, 448.2 [M – 2Br – C$_6$H$_4$OCH$_3$]$^+$, 341.3 [M – 2Br – 2C$_6$H$_4$OCH$_3$]$^+$.

**Synthesis of Platinum(II) Complex 3e:** 1,1-Bis[1-(4-ethylcarboxyphenyl)]-3,3′-methylenimidazolium dibromide (**3e**; 100.0 mg, 0.165 mmol) and platinum(II) acetylacetonate (64.9 mg, 0.165 mmol) were dissolved in 6 mL of dimethyl sulfoxide in a nitrogen-flushed Schlenk tube and stirred for 3 h at 40 °C, 2 h at 60 °C, 2 h at 70 °C, 2 h at 100 °C, and 1 h at 130 °C. The solvent was removed in vacuo and the product washed once with 5 mL of ethanol. The product was obtained as a white powder. Yield: 0.095 g (72%). $^1$H NMR (300 MHz, [D$_6$]DMSO): $\delta$ = 1.43 (t, $J$ = 7.0 Hz, 6 H, CH$_2$C$H_3$), 4.40 (q, $J$ = 7.0 Hz, 4 H, C$H_2$CH$_3$), 6.14 (d, $J$ = 13.2 Hz, 1 H, NC$H_2$N), 6.35 (d, $J$ = 13.2 Hz, 1 H, NC$H_2$N), 7.84 (d, $J$ = 2.7 Hz, 2 H, NC$H$CHN);7.91 (d, $J$ = 2.7 Hz, 2 H, NCHC$H$N), 7.98 (d, $J$ = 8.4 Hz, 4 H, arom. H), 8.19 (d, $J$ = 8.4 Hz, 4 H, arom. H) ppm. $^{13}$C NMR (75 MHz, [D$_6$]DMSO): $\delta$ = 14.1 (CH$_2$$C$H$_3$), 61.1 ($C$H$_2$CH$_3$), 62.7 (N$C$H$_2$N), 120.3 (arom. $C$H), 125.2 (N$C$HCHN), 129.8 (arom. $C$H), 130.7 (NCH$C$HN), 138.4 (C1 of C$_6$H$_4$COOEt), 139.1 (C4 of C$_6$H$_4$COOEt), 142.9 (Pt–$C$), 165.3 ($C$OOEt) ppm. $C_{25}H_{26}Br_2N_4O_2Pt$·0.5DMSO (799.37 + 39.07): calcd. C 37.25, H 3.25, N 6.68, S 1.91; found C 37.15, H 3.38, N 6.29, S 2.11.

**X-ray Crystal-Structure Determination for 3b–3e:** Crystals suitable for an X-ray investigation were obtained either by allowing methanol to condense into a saturated solution of the metal complex in DMSO (**3b**, **3c**) or by slowly cooling a hot, saturated solution of the complex in DMSO (**3d**, **3e**). The crystals were stored under perfluorinated ether, transferred to a Lindemann capillary, fixed, and sealed. Preliminary examination and data collection were carried out on an area-detection system (Kappa-CCD; Nonius) with graphite-monochromated Mo-$K_\alpha$ radiation ($\lambda$ = 0.71073 Å). Data collections were performed at 173 K (**3b**) or 198 K (**3c**–**3e**) in the $\Theta$ range 2.27° < $\Theta$ < 21.02° (**3b**) or 3.00° < $\Theta$ < 27.40° (**3c**–**3e**). The reflections were integrated, raw data were corrected for Lorentz, polarization, decay, and absorption effects. Due to the small size of the crystal the data set for **3d** was reduced to 25.00 and that of **3e** to 26.40. The absorption correction was applied using the PLATON DELABS algorithm for **3b** and SADABS for **3c**–**3e**. The independent reflections were used for all calculations after merging. The structures were solved by a combination of direct methods and difference Fourier syntheses. All non-hydrogen atoms were refined with anisotropic displacement parameters. All hydrogen atoms were calculated in ideal positions as riding on the parent carbon atoms. During the final stage of the refinements it becomes evident that the crystal of **3b** contains unresolvable solvent molecules. This problem was cured by using the PLATON CALC SQUEEZE procedure. All other solvent molecules in **3c**–**3e** could be fully resolved. Full-matrix least-squares refinements were carried out by minimizing $\Sigma w(F_o^2 - F_c^2)^2$ with SHELXL-97 weighting scheme and stopped at shift/err < 0.001. The final difference Fourier map showed high residual electron density peaks for **3b** (+1.610 and –2.096 e Å$^{-3}$) caused by the incomplete absorption correction and the incomplete removal of solvent molecules and **3c** (1.546 and –0.959 e Å$^{-3}$; distance to platinum 0.783 and 0.976 Å) caused by an incomplete absorption correction. Details of the structure determinations are given in Table 5. Neutral-atom scattering factors for all atoms and anomalous dispersion corrections for the non-hydrogen atoms were taken from the International Tables for Crystallography. All calcu-

 © 2006 Wiley-VCH Verlag GmbH & Co. KGaA, Weinheim 

Table 5. Selected parameters for the crystal-structure determination of **3b**–**3e**.

| | **3b** | **3c**·DMSO,·MeOH | **3d**·DMSO | **3e**·DMSO |
|---|---|---|---|---|
| Measured by | E.H. | S.A. | S.G. | S.A. |
| Crystal color and form | colorless needle | colorless needle | colorless needle | colorless fragment |
| Crystal size [$mm^3$] | 0.05 × 0.08 × 0.43 | 0.38 × 0.08 × 0.03 | 0.18 × 0.08 × 0.07 | 0.25 × 0.16 × 0.10 |
| Unit cell | orthorhombic | monoclinic | triclinic | monoclinic |
| Space group | *Pnma* (no. 62) | $P2_1/m$ (no. 11) | $P\bar{1}$ (no. 2) | $P2_1$ (no. 4) |
| $\Theta$ range [°] | 2.27–21.02 | 3.91–27.40 | 3.61–25.00 | 3.96–26.40 |
| $a$ [Å] | 13.2647(2) | 8.108(1) | 9.840(1) | 8.2480(3) |
| $b$ [Å] | 16.8268(3) | 17.395(1) | 10.050(1) | 17.8570(15) |
| $c$ [Å] | 10.6220(2) | 10.258(1) | 14.054(1) | 10.5310(7) |
| $\alpha$ [°] | | | 101.46(1) | |
| $\beta$ [°] | | 109.56(1) | 106.39(1) | 103.150(5) |
| $\gamma$ [°] | | | 95.43(1) | |
| $V$ [$Å^3$], $Z$ | 2370.86(7), 4 | 1363.3(2), 2 | 1289.9(2), 2 | 1510.38(17), 2 |
| $F_{000}$ | 1352 | 868 | 760 | 848 |
| Rflns. measured | 47273 | 18489 | 23987 | 20357 |
| Rflns. independent | 1336 | 3184 | 4533 | 6110 |
| Refined | 130-parameter full-matrix refinement | 168-parameter full-matrix refinement | 312-parameter full-matrix refinement | 373-parameter full-matrix refinement, 8 restraints (disordered solvent) |
| Refinement | least-squares refinement of 1336 reflections with Denzo/HKL | least-squares refinement of 3184 reflections with Collect/SADABS | least-squares refinement of 4533 reflections with Collect/SADABS | least-squares refinement of 6110 reflections with Collect/SADABS |
| Remaining electron density [e $Å^{-3}$] | +1.610, –2.096 (insuff. CALC SQEEZE) | +1.546, –0.959 (near platinum) | +0.668, –0.621 | +0.899, –0.596 |
| $R_1$[a] [$F_o > 4\sigma(F_o)$] | 0.0498 | 0.0283 | 0.0330 | 0.0379 |
| [all reflections] | 0.0530 | 0.0426 | 0.0568 | 0.0516 |
| $wR_2$[b] [$F_o > 4\sigma(F_o)$] | 0.1229 | 0.0560 | 0.0502 | 0.0741 |
| [all reflections] | 0.1252 | 0.0611 | 0.0537 | 0.0789 |
| GOF (on $F^2$)[a] | 1.172 | 1.137 | 0.995 | 1.065 |
| Diffractometer | Kappa CCD (Area Diffraction System; Nonius); Mo-$K_\alpha$; rotating anode | Kappa CCD (Area Diffraction System; Nonius); Mo-$K_\alpha$; sealed tube | Kappa CCD (Area Diffraction System; Nonius); Mo-$K_\alpha$; sealed tube | Kappa CCD (Area Diffraction System; Nonius); Mo-$K_\alpha$; sealed tube |

[a] $R_1 = \Sigma(||F_o| - |F_c||)/\Sigma|F_o|$. [b] $R_2 = [\Sigma w(F_o^2 - F_c^2)^2/\Sigma w(F_o^2)^2]^{1/2}$; GOF = $\{\Sigma[w(F_o^2 - F_c^2)^2]/(n - p)\}^{1/2}$.

lations were performed with the programs PLATON, SIR92, SHELXL-97, and SADABS.[35–38]

CCDC-287338 (**3b**), -287341 (**3c**), -287339 (**3d**), and -287340 (**3e**) contain the supplementary crystallographic data for this paper. These data can be obtained free of charge from The Cambridge Crystallographic Data Centre via www.ccdc.cam.ac.uk/data_request/cif.

**Supporting information** (see footnote on the first page of this article): Synthetic and analytical data of the aromatic substituted bis(carbene) ligands, as well as important data of the solid-state structures of **3b**–**3e**.

## Acknowledgments

We are grateful to the "Deutsche Forschungsgemeinschaft" (DFG) and the "Fonds der Chemischen Industrie" (FCI) for financial support. S.A. thanks the "Konrad-Adenauer-Stiftung" (KAS) for their support.

[1] V. P. W. Böhm, T. Weskamp, C. W. K. Gstöttmayr, W. A. Herrmann, *Angew. Chem. Int. Ed.* **2000**, *39*, 1602–1604.
[2] O. Navarro, H. Kaur, P. Mahjoor, S. P. Nolan, *J. Org. Chem.* **2004**, *69*, 3173–3180.
[3] T. Weskamp, W. C. Schattenmann, M. Spiegler, W. A. Herrmann, *Angew. Chem. Int. Ed.* **1998**, *37*, 2490–2493.
[4] T. Weskamp, F. J. Kohl, W. Hieringer, D. Gleich, W. A. Herrmann, *Angew. Chem. Int. Ed.* **1999**, *38*, 2416–2419.
[5] M. Scholl, S. Ding, C. W. Lee, R. H. Grubbs, *Org. Lett.* **1999**, *1*, 953–956.
[6] M. S. Sanford, J. A. Love, R. H. Grubbs, *J. Am. Chem. Soc.* **2001**, *123*, 6543–6554.
[7] W. A. Herrmann, J. A. Kulpe, W. Konkol, H. Bahrmann, *J. Organomet. Chem.* **1990**, *389*, 85–101.
[8] W. A. Herrmann, C. W. Kohlpaintner, *Angew. Chem. Int. Ed. Engl.* **1993**, *32*, 1524–1544.
[9] M. Muehlhofer, T. Strassner, W. A. Herrmann, *Angew. Chem. Int. Ed.* **2002**, *41*, 1745–1747.
[10] T. Strassner, M. Muehlhofer, A. Zeller, E. Herdtweck, W. A. Herrmann, *J. Organomet. Chem.* **2004**, *689*, 1418–1424.
[11] E. Peris, R. H. Crabtree, *Coord. Chem. Rev.* **2004**, *248*, 2239–2246.
[12] Y. Canac, M. Soleilhavoup, S. Conejero, G. Bertrand, *J. Organomet. Chem.* **2004**, *689*, 3857–3865.
[13] W. A. Herrmann, *Angew. Chem. Int. Ed.* **2002**, *41*, 1290–1309.
[14] M. G. Gardiner, W. A. Herrmann, C.-P. Reisinger, J. Schwarz, M. Spiegler, *J. Organomet. Chem.* **1999**, *572*, 239–247.
[15] J. Schwarz, E. Herdtweck, W. A. Herrmann, M. G. Gardiner, *Organometallics* **2000**, *19*, 3154–3160.
[16] J. Schwarz, V. P. W. Böhm, M. G. Gardiner, M. Grosche, W. A. Herrmann, W. Hieringer, G. Raudaschl-Sieber, *Chem. Eur. J.* **2000**, *6*, 1773–1780.
[17] C. A. Quezada, J. C. Garrison, M. J. Panzner, C. A. Tessier, W. J. Youngs, *Organometallics* **2004**, *23*, 4846–4848.

 © 2006 Wiley-VCH Verlag GmbH & Co. KGaA, Weinheim 

[18] H. M. Lee, C. Y. Lu, C. Y. Chen, W. L. Chen, H. C. Lin, P. L. Chiu, P. Y. Cheng, *Tetrahedron* **2004**, *60*, 5807–5825.
[19] H. V. Huynh, D. Le Van, F. E. Hahn, T. S. A. Hor, *J. Organomet. Chem.* **2004**, *689*, 1766–1770.
[20] J. A. Mata, A. R. Chianese, J. R. Miecznikowski, M. Poyatos, E. Peris, J. W. Faller, R. H. Crabtree, *Organometallics* **2004**, *23*, 1253–1263.
[21] M. Albrecht, J. R. Miecznikowski, A. Samuel, J. W. Faller, R. H. Crabtree, *Organometallics* **2002**, *21*, 3596–3604.
[22] M. Muehlhofer, T. Strassner, E. Herdtweck, W. A. Herrmann, *J. Organomet. Chem.* **2002**, *660*, 121–126.
[23] E. Herdtweck, M. Muehlhofer, T. Strassner, *Acta Crystallogr., Sect. E* **2003**, *59*, m970–m971.
[24] Q.-X. Liu, H.-B. Song, F.-B. Xu, Q.-S. Li, X.-S. Zeng, X.-B. Leng, Z.-Z. Zhang, *Polyhedron* **2003**, *22*, 1515–1521.
[25] M. A. Duin, N. D. Clement, K. J. Cavell, C. J. Elsevier, *Chem. Commun.* **2003**, *3*, 400–401.
[26] D. S. McGuinness, K. J. Cavell, B. F. Yates, B. W. Skelton, A. H. White, *J. Am. Chem. Soc.* **2001**, *123*, 8317–8328.
[27] A. J. Arduengo III, S. F. Gamper, J. C. Calabrese, F. Davidson, *J. Am. Chem. Soc.* **1994**, *116*, 4391–4394.
[28] R. E. Douthwaite, D. Hauessinger, M. L. H. Green, P. J. Silcock, P. T. Gomes, A. M. Martins, A. A. Danopoulos, *Organometallics* **1999**, *18*, 4584–4590.
[29] W. P. Fehlhammer, T. Bliss, U. Kernbach, I. Bruedgam, *J. Organomet. Chem.* **1995**, *490*, 149–153.
[30] J. Liu, J. Chen, J. Zhao, Y. Zhao, L. Li, H. Zhang, *Synthesis* **2003**, *17*, 2661–2666.
[31] W. A. Herrmann, C. Köcher, L. J. Goossen, G. R. J. Artus, *Chem. Eur. J.* **1996**, *2*, 1627–1636.
[32] D. Wright, Platinum(II) acetate and benzoate; patent nos.: 69-1948837, 1948837, 19690926, **1970**.
[33] B. W. Malerbi, *Chem. Ind. (London)* **1970**, *24*, 796.
[34] W. A. Herrmann, J. Schwarz, M. G. Gardiner, *Organometallics* **1999**, *18*, 4082–4089.
[35] A. L. Spek, *J. Appl. Crystallogr.* **2003**, *36*, 7–13.
[36] A. Altomare, G. Cascarano, C. Giacovazzo, A. Guagliardi, M. C. Burla, G. Polidori, M. Camalli, *J. Appl. Crystallogr.* **1994**, *27*, 435–436.
[37] G. M. Sheldrick, *SHELXL-97, Program for the Refinement of Crystal Structures*, University of Göttingen, Germany, **1997**.
[38] Bruker SADABS, Area Detector Absorbtion and Other Corrections, 2.03; Delft, Netherlands, **2002**.

Received: September 13, 2005
Published Online: January 31, 2006

 © 2006 Wiley-VCH Verlag GmbH & Co. KGaA, Weinheim 

DOI: 10.1002/ejic.200500979

# Amine-Functionalised Hexagonal Mesoporous Silica as Support for Copper(II) Acetylacetonate Catalyst

**Ana Rosa Silva,[a] Karen Wilson,[b] Adrian C. Whitwood,[c] James H. Clark,[b] and Cristina Freire*[a]**

**Keywords:** Copper / Anchoring / Mesoporous silica / EPR spectroscopy / Aziridination

Copper(II) acetylacetonate was anchored onto a hexagonal mesoporous silica (HMS) material using a two-step procedure: (i) functionalisation of the surface hydroxy groups with (3-aminopropyl)triethoxysilane (AMPTSi) and then (ii) anchoring of the copper(II) complex through Schiff condensation with free amine groups, using two different metal complex loadings. Upon the first step, nitrogen elemental analysis, XPS and DRIFT showed the presence of amine groups on the surface of the HMS material, and porosimetry indicated that the structure of the mesoporous material remained unchanged, although a slight decrease in surface area was observed. Atomic absorption, XPS and DRIFT showed that copper(II) acetylacetonate was anchored onto the amine-functionalised HMS by Schiff condensation between the free amine groups and the carbonyl groups of the copper(II) complex; using EPR an $NO_3$ coordination sphere was proposed for the anchored copper(II) complex. The new [Cu(acac)$_2$]-AMPTSi/HMS materials were tested in the aziridination of styrene at room temperature, using PhI=NTs as nitrogen source and acetonitrile as solvent. The styrene conversion and total TON of the heterogeneous phase reaction are higher than those of the same reaction catalysed in homogeneous phase by [Cu(acac)$_2$]; nevertheless, the initial activity decreases and the reaction time increases due to substrate and product diffusion limitations. The heterogeneous catalyst showed a successive slight decrease in catalytic activity when reused for two more times.

(© Wiley-VCH Verlag GmbH & Co. KGaA, 69451 Weinheim, Germany, 2006)

## Introduction

Currently, transition-metal complexes with Schiff-base ligands of the salen type are the object of intense research due to their high activity, chemoselectivity and enantioselectivity in a large range of catalytic processes.[1–3] One of the best-known examples are (salen)manganese(III) complexes, that catalyse the epoxidation of alkenes,[1–3] and lead (by direct atom transfer to olefins) to epoxides, which are of great utility in organic synthesis.[1–3,4] The equivalent nitrogen-atom-transfer process catalysed by transition-metal complexes has been less exploited,[4,5] despite aziridines being valuable products as intermediates in organic synthesis,[4–7] efficient chiral auxiliaries and ligands in asymmetric catalysis.[6] Evans et al. reported that copper(II) acetylacetonate is a very efficient homogeneous catalyst for the aziridination of alkenes using 4-methyl-*N*-(phenyl-$\lambda^3$-iodanylidene)benzenesulfonamide (PhI=NTs) as nitrogen source;[4] (salen)copper(II) complexes have also been applied as homogeneous catalysts for the alkene aziridination using the same nitrogen source.[7]

However, homogeneous catalysts can not be separated from the reaction media and, subsequently, can not be reused. Thus, one way to improve the homogeneous chemical processes, preventing the requirement for laborious and inefficient extraction processes, is to immobilise the (sometimes) expensive homogeneous catalyst on solid supports.[8] In fact, the last decade has witnessed a growing interest in the heterogenisation of homogeneous metal complexes using several types of supports and several immobilisation strategies.[9–13] Initially, the complexes were just ion-exchanged or adsorbed on the porous supports and, consequently, could be susceptible to leaching.[14,15] More recently, several grafting and tethering procedures have been developed to covalently attach transition-metal complexes to organic polymers,[13] silica, zeolites and other micro- and mesoporous inorganic materials.[9–12]

Copper(II) acetylacetonate has already been immobilised in a polymer[6] and activated carbon,[16,17] and the new materials have acted as recoverable and reusable heterogeneous catalysts for the aziridination of olefins using PhI=NTs as nitrogen source.[6,17] In the first case, the copper(II) complex was microencapsulated in polystyrene, and in the latter it was anchored onto an amine-functionalised activated car-

[a] REQUIMTE/Departamento de Química, Faculdade de Ciências, Universidade do Porto,
4169-007 Porto, Portugal
Fax: +351-226082959
E-mail: acfreire@fc.up.pt
[b] Department of Chemistry, Green Chemistry Group, University of York,
Heslington, York YO10 5DD, UK
[c] Department of Chemistry, University of York,
Heslington, York YO10 5DD, UK

 © 2006 Wiley-VCH Verlag GmbH & Co. KGaA, Weinheim 

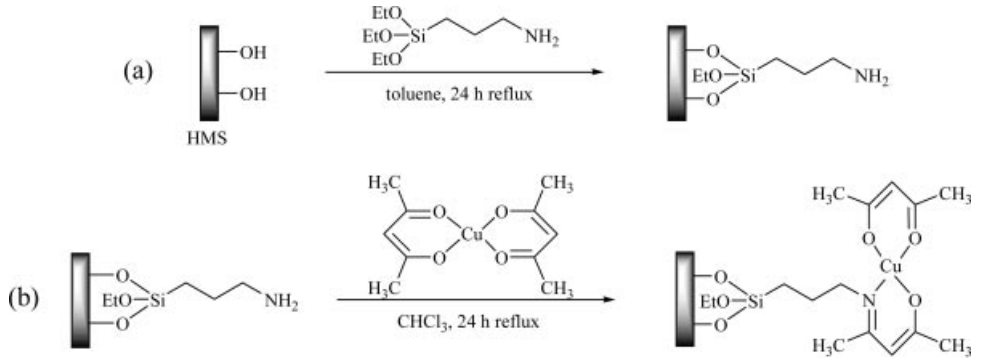


Scheme 1. Anchoring procedure: (a) functionalisation of the HMS with (3-aminopropyl)triethoxysilane and (b) anchoring copper(II) acetylacetonate onto AMPTSi-functionalised HMS.

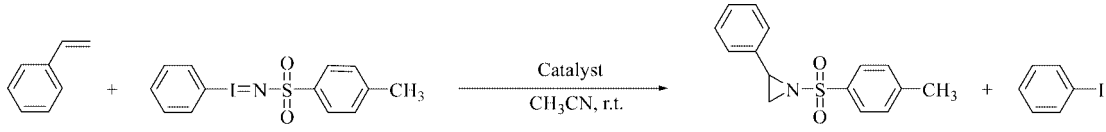


Scheme 2. Aziridination of styrene using PhI=NTs as nitrogen source.

bon,[16] through Schiff-base condensation between the free amine group, covalently attached to the activated carbon surface with the carbonyl groups of the acetylacetonate ligand coordinated to copper(II). Both heterogeneous catalysts presented similar catalytic parameters as those obtained in homogeneous-phase reaction using [Cu(acac)$_2$], under similar experimental conditions, and no significant metal complex leaching was observed after the catalytic reactions.[6,17] However, in the case where activated carbon was used as support, inherent diffusion limitations were observed due to the porous structure of the support, and thus a decrease in the initial activity (TOF), and an increase in the reaction time was observed.[17] Furthermore, the spectroscopic characterisation by DRIFT and UV spectroscopy of the new carbon-based heterogeneous catalysts proved to be difficult and impossible, respectively, due to the highly absorbing carbon matrix, which limited the gathering of information about the copper(II) complex formed on the surface of the amine-functionalised activated carbon. Immobilisation on several porous supports of (Schiff base)copper(II) complexes previously synthesised[18] or prepared in situ on the porous structure,[19,20] have also been reported in the literature.

The silica-based inorganic mesoporous materials which offer pore sizes in the range 20–100 Å, are more suitable for liquid-phase reactions, because they allow easy diffusion of reactants to the active sites.[8,21] Their surface silanol groups can also be easily functionalised by using trialkyloxysilanes, with amine, thiol, carboxylic acid, phenyl, cyano, sulfonic acid and vinyl groups, hence allowing subsequent chemical attachment of the catalytic active species, namely inorganic coordination compounds.[8,21] Furthermore, they can be easily characterised by several spectroscopic techniques. Despite of the hexagonal mesoporous silicas (HMS) being less ordered than MCM-41 and SBA-15 materials, they are much easier and straightforward to synthesise due to the use of a cheap and neutral template, which does not require the need of strongly acidic conditions.[22]

In the present work, a new and simpler route to obtain immobilised (Schiff base)copper(II) complexes is presented. A hexagonal mesoporous silica (HMS), organically functionalised with (3-aminopropyl)triethoxysilane, was chosen to anchor copper(II) acetylacetonate. The anchoring process was done through Schiff condensation between the free amine group, covalently attached to the HMS surface (Scheme 1), with the carbonyl groups of the acetylacetonate ligand, coordinated to copper(II), as depicted in Scheme 1. All the materials were characterised by nitrogen elemental analysis, FTIR-DRIFT, nitrogen isotherms at 77 K and XPS, and those with immobilised copper(II) complex were also characterised by copper atomic absorption, UV diffuse reflectance spectroscopy and EPR. The catalytic activity of this new materials in the aziridination of styrene at room temperature using PhI=NTs as nitrogen source was studied (Scheme 2).

## Results and Discussion

### Characterisation of the HMS and Amine Functionalisation

The nitrogen adsorption isotherm at 77 K of the calcined HMS material is of type IV (Figure 1), and therefore is typical of mesoporous materials, although the presence of micropores can be detected in the lower relative pressure region. The material has a BET surface area of 1158 $m^2 g^{-1}$ (Table 1).

The infrared spectrum of the calcined HMS shows the typical Si–O lattice vibrations: two broad bands between 2100 and 1750 $cm^{-1}$, with medium intensity, a strong and broad band with two peaks in the region 1450–900 $cm^{-1}$, and two strong bands between 900 and 500 $cm^{-1}$. Furthermore, a very broad band centred at 3450 $cm^{-1}$, due to the

 © 2006 Wiley-VCH Verlag GmbH & Co. KGaA, Weinheim 

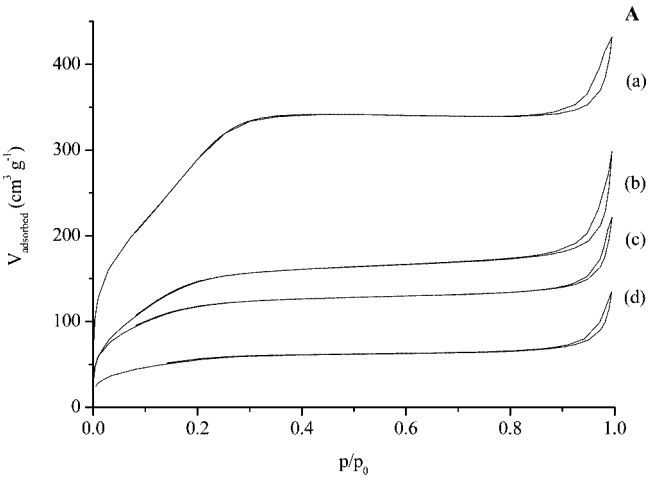


Figure 1. Nitrogen adsorption isotherms at 77 K of (a) calcined HMS, (b) AMPTSi/HMS, (c) [Cu(acac)$_2$]AMPTSi/HMS_A and (d) [Cu(acac)$_2$]AMPTSi/HMS_B.

Table 1. Selected characteristics of the modified HMS materials.

| Sample | Cu [mmol g$^{-1}$] | | N/Cu | | $A_{BET}$[b] |
|---|---|---|---|---|---|
| | AA | XPS[a] | EA/AA | XPS | [m$^2$ g$^{-1}$] |
| HMS | | | | | 1158 |
| AMPTSi/HMS | | | | | 561 |
| [Cu(acac)$_2$]AMPTSi/HMS_A | 0.362 | 0.269 | 3.9 | 4.6 | 436 |
| [Cu(acac)$_2$]AMPTSi/HMS_B | 0.068 | 0.036 | 23 | 27 | 201 |

[a] mol Cu/weight of HMS (from XPS data in Table 2) ≈ atom-% Cu/[atom-% C × Ar(C) + atom-% O × Ar(O) + atom-% N × Ar(N) + atom-% Si × Ar(Si) + atom-% Cu × Ar(Cu)]. [b] From the nitrogen adsorption isotherm at 77 K.

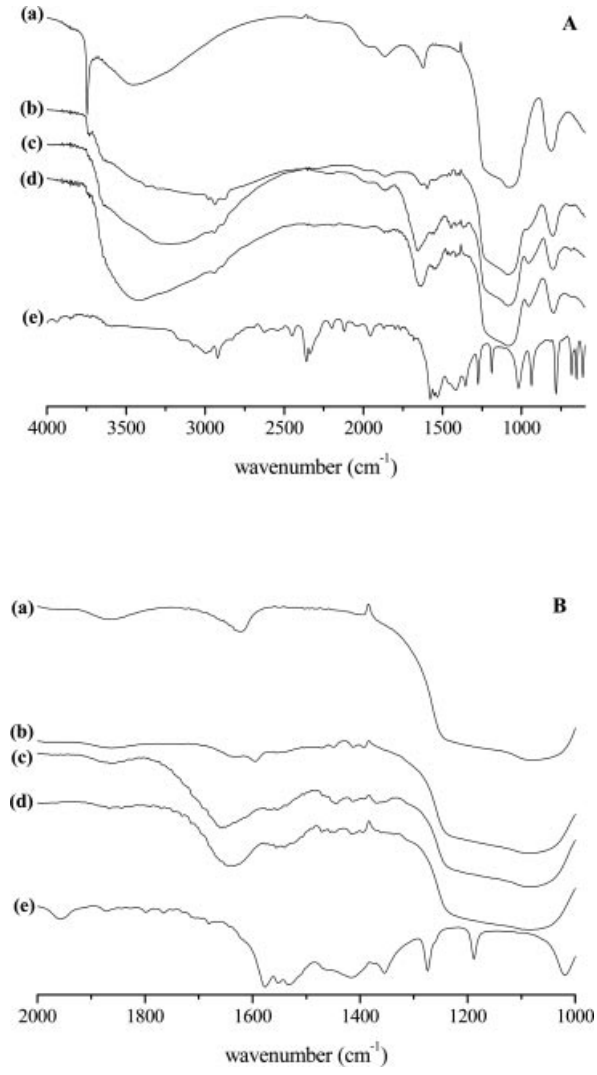


Figure 2. FTIR-DRIFT spectra of (a) calcined HMS, (b) AMPTSi/HMS, (c) [Cu(acac)$_2$]AMPTSi/HMS_A, (d) [Cu(acac)$_2$]AMPTSi/HMS_B and (e) [Cu(acac)$_2$] in the regions (A) 4000–500 cm$^{-1}$ and (B) 2000–1000 cm$^{-1}$.

Table 2. XPS elemental analysis [atom-%] of the modified HMS materials.

| Sample | C | O | N | Si | Cu |
|---|---|---|---|---|---|
| AMPTSi/HMS | 18.3 | 57.1 | 1.8 | 22.9 | – |
| [Cu(acac)$_2$]AMPTSi/HMS_A | 17.9 | 53.7 | 2.3 | 25.6 | 0.5 |
| [Cu(acac)$_2$]AMPTSi/HMS_B | 13.7 | 51.1 | 1.9 | 33.2 | 0.07 |
| [Cu(acac)$_2$] | 66.9 | 26.0 | – | – | 7.0 |

O–H stretching vibrations, and a very sharp band at 3745 cm$^{-1}$, with medium intensity, which is assigned to the stretching vibrations of isolated surface SiO–H groups, are observed. A band at 1622 cm$^{-1}$ is also observed in the spectrum and is attributed to the H–O–H bending vibrations of physisorbed water (Figure 2).

The HMS material was functionalised with (3-aminopropyl)triethoxysilane (AMPTSi) and both nitrogen elemental and XPS analyses show that nitrogen (Tables 1 and 2) was introduced on the surface of the material: 1.34 mmol g$^{-1}$ and 0.999 mmol g$^{-1}$, respectively. From the former value and taking into account the AMPTSi used in the functionalisation reaction (3.00 mmol g$^{-1}$), the anchoring efficiency of the amine derivative onto the support was 44.7%.

Upon amine functionalisation, a decrease in the intensity of the band at 3745 cm$^{-1}$ is observed (Figure 2A), indicating that the reaction between the isolated silanol groups of the surface of the HMS with the ethoxy groups of the silane derivative took place. The N–H and C–H stretching vibrations of AMPTSi are observed in the region 3400–3000 cm$^{-1}$ and 3000 cm$^{-1}$, respectively, and the corresponding H–N–H and H–C–H bending vibrations can also be observed in the regions 1700–1500 cm$^{-1}$ and 1500–1300 cm$^{-1}$, respectively, as weak intensity bands (Figure 1B).

No changes in the isotherm profile were observed upon surface functionalisation of HMS with AMPTSi, suggesting that the structure of the parent material was unaffected after this step (Figure 1); however, a decrease in the HMS surface area (Table 1), as well as some blockage of the micropores and a slight decrease in the mean mesopore size (Figure 1) are observed, as expected.

 © 2006 Wiley-VCH Verlag GmbH & Co. KGaA, Weinheim 

**Anchoring of Copper(II) Acetylacetonate onto the Amine-Functionalised HMS**

Two chloroform solutions containing different quantities of copper(II) acetylacetonate were refluxed for 24 h with the amine-functionalised HMS. Evidence for the effective anchorage of the copper(II) acetylacetonate complex onto the surface of AMPTSi/HMS was first provided by noting that (a) the blue colour of the complex solution disappears during the adsorption reaction, and (b) colourless solutions are obtained when the materials were purified by Soxhlet extraction.

Atomic absorption analysis (Table 1) of the materials revealed that the [Cu(acac)$_2$]AMPTSi/HMS_A material contains 362 μmol of copper/g of material and the [Cu(acac)$_2$]-AMPTSi/HMS_B material contains 68 μmol of copper/g. Relatively to the copper(II) complex quantity initially present in each solution, these values correspond to an anchoring efficiency of 73% and 82%, respectively, suggesting the presence of some diffusion control in the metal complex immobilisation reactions.

The N/Cu ratios obtained by elemental analysis and XPS have similar magnitudes (Table 1) suggesting that the anchored copper(II) species have the same chemical environment throughout the HMS matrix. Nevertheless, in both materials the spacer AMPTSi is always in excess relative to complex (larger excess in [Cu(acac)$_2$]AMPTSi/HMS_B).

No change in the isotherm profile was observed upon complex immobilisation (Figure 1), suggesting that the functionalised HMS structure was unaffected by complex anchoring; however, a further decrease in the material surface area (Table 1 and Figure 1), and a slight decrease in the mean mesopore size are observed, confirming indirectly the presence of the complex within the matrices. Surprisingly, the material with lower copper loading, [Cu(acac)$_2$]-AMPTSi/HMS_B, shows a larger decrease in the surface area, specially in the mesopore region, than the material with higher copper loading, [Cu(acac)$_2$]AMPTSi/HMS_A.

The IR spectra of [Cu(acac)$_2$AMPTSi]/HMS_A and [Cu-(acac)$_2$AMPTSi]/HMS_B show, with respect to the parent material, some changes in the regions where vibration from AMPTSi occur: 3500–3000 cm$^{-1}$ region, due to N–H stretching vibrations and 1700–1300 cm$^{-1}$, weak absorptions due to the H–N–H and H–C–H bending vibrations, suggesting that some molecular changes in the spacer took place. On the other hand, new broad bands are observed at about 1658 and 1555 cm$^{-1}$ (Figure 2), which may be attributed to a C=N stretching vibration and to the acetylacetonate ring vibrations of the metal complex, respectively. Furthermore, in the region between 1700 and 1300 cm$^{-1}$, where the fingerprint bands of [Cu(acac)$_2$] are usually detected, the DRIFT spectra of both [Cu(acac)$_2$AMPTSi]/HMS_A and [Cu(acac)$_2$AMPTSi]/HMS_B materials are different from that of free [Cu(acac)$_2$] (Figure 2), contrasting with a previous report for silica-supported [Cu(acac)$_2$], which shows a very similar DRIFT spectrum to that of the free complex.[23] These results clearly indicate that there was a Schiff condensation between the free amine groups on the surface of the HMS material and the oxygen atoms coordinated to copper(II), and that therefore the anchoring procedure occurred as depicted in Scheme 1.

The electronic spectrum of free [Cu(acac)$_2$] presents a large and asymmetric band with a maximum at $\lambda$ = 558 nm and a shoulder lying lower in energy at about $\lambda$ = 642 nm (Figure 3); this spectrum is typical of Cu$^{II}$ complexes with a square-planar geometry.[16] In this context the band at lower energy is assigned to the $d_{xy} \leftarrow d_{z^2}$ transition and the band at higher energies is attributed to the envelop of two other allowed d–d transitions: $d_{xy} \leftarrow d_{x^2-y^2}$ and $d_{xy} \leftarrow d_{xz} \approx d_{yz}$, which have very close energies.[24]

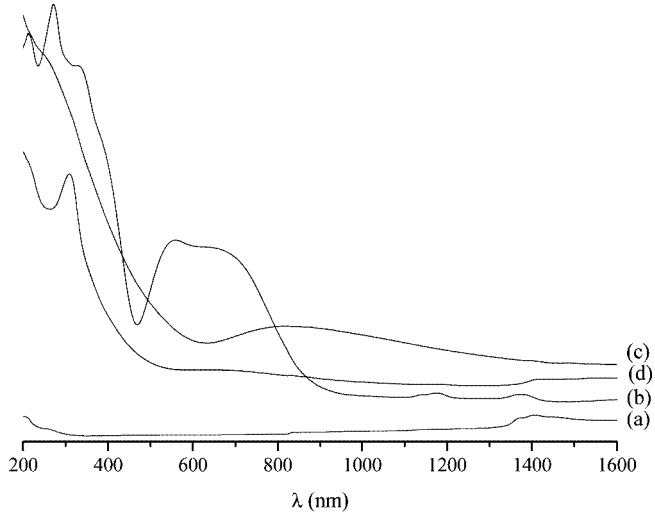


Figure 3. UV diffuse reflectance spectra of the HMS materials: (a) calcined HMS, (b) [Cu(acac)$_2$], (c) [Cu(acac)$_2$]AMPTSi/HMS_A and (d) [Cu(acac)$_2$]AMPTSi/HMS_B.

The electronic spectrum of the [Cu(acac)$_2$]AMPTSi/HMS_A material shows a broad asymmetric band at $\lambda$ = 823 nm tailoring to lower energies, which corresponds to the envelop of the three allowed d–d transitions ($d_{xy} \leftarrow d_{z^2}$, $d_{xy} \leftarrow d_{x^2-y^2}$ and $d_{xy} \leftarrow d_{xz} \approx d_{yz}$) with close energies. In comparison to the spectrum of free [Cu(acac)$_2$], the maximum of the band is shifted towards lower energy (Figure 3); this type of changes in the electronic spectrum of Cu$^{II}$ complexes can be interpreted as suggesting a tetrahedral distortion in the equatorial plane or axial coordination of a new ligand.[24] Although the first explanation could justify the proposed complex anchoring model, on the basis of electronic data alone, no choice between the two hypotheses can be made. The profile spectrum of [Cu(acac)$_2$]AMPTSi/HMS_B is similar to the previous one, but its low intensity, due to the lower copper content in this material, prevents any further interpretation (Figure 3).

Further insights into the copper(II) coordination sphere upon complex anchoring can be gathered from EPR spectroscopy. The EPR spectrum of [Cu(acac)$_2$]AMPTSi/HMS_B at 120 K, depicted in Figure 4 (b), is typical of copper(II) species: it is of the axial type and shows hyperfine couplings due to the interaction of the unpaired electron with the copper nucleus ($^{65}$Cu/$^{63}$Cu, $I$ = 3/2) in the low

 © 2006 Wiley-VCH Verlag GmbH & Co. KGaA, Weinheim 

magnetic field region (Figure 4b). The EPR spectrum of [Cu(acac)$_2$]AMPTSi/HMS_A (Figure 4a) shows band broadening due to the high local copper(II) concentration (2.30%, Table 1), which prevents any further analysis. In contrast, the EPR spectrum of the [Cu(acac)$_2$]AMPTSi/HMS_B shows smaller band-broadening effects, and thus could be analysed in detail.

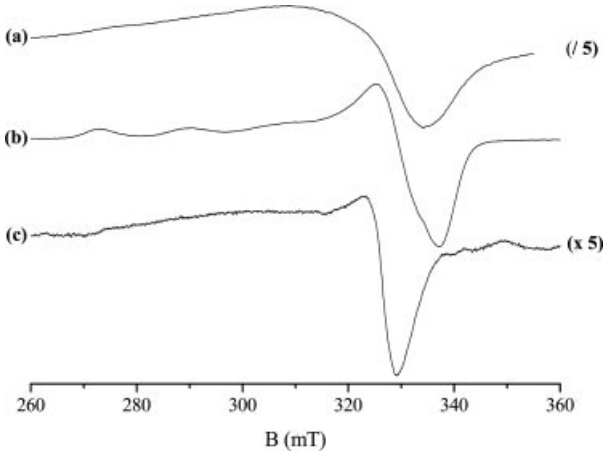


Figure 4. EPR spectra of the copper(II) acetylacetonate complexes, free and anchored onto HMS at 120 K: (a) [Cu(acac)$_2$]AMPTSi/HMS_A, (b) [Cu(acac)$_2$]AMPTSi/HMS_B and (c) [Cu(acac)$_2$]/HMS.

The EPR band profile of this material suggests that there is one major $Cu^{II}$ species within the HMS matrix[20] and its similarity with the EPR of analogous free $Cu^{II}$ complexes[18–20,25–28] allows the same orientation scheme for the tensor axes: $g_1 = g_2 = g_\perp$, $g_3 = g_\parallel$ (or $g_1 = g_x$, $g_2 = g_y$, $g_3 = g_z$), where $g_1$ and $g_3$ refer to the lowest and highest magnetic fields $g$ values (obviously, $A_1 = A_2 = A_\perp$, $A_3 = A_\parallel$ or $A_1 = A_x$, $A_2 = A_y$, and $A_3 = A_z$). In this context, as $g_x = g_y < g_z$ the ground state of $Cu^{II}$ in the immobilised complex has been kept and is $d_{xy}$; the values of the tensors $g$ and $A$ of the [Cu(acac)$_2$]AMPTSi/HMS_B were obtained by simulation and are compiled in Table 3, which also summarises the values for similar copper(II) acetylacetonate/salen-based complexes with $O_4$, $NO_3$ and $N_2O_2$ coordination spheres, as free complexes and immobilised onto other supports found in the literature.

Tetracoordinated copper(II) complexes with an equatorial $O_4$ coordination sphere generally possess higher $g_\parallel$ values (2.26–2.29)[26–28] relative to copper(II) complexes with an equatorial $N_2O_2$ coordination sphere (2.19–2.24),[18,29] because the introduction of nitrogen atoms into the equatorial plane increases the in-plane covalence. This can be confirmed by the data extracted from literature and compiled in Table 3. An $NO_3$ coordination sphere would give rise to intermediate $g$ values, with some overlap with the intervals given above, but confirmation with experimental data is quite difficult due not only to the failure of the preparation the free counterpart of the anchored complex (all synthetic attempts resulted in oils which we were unable to fully characterise), but also to the almost nonexistent EPR data for compounds with these coordinating atoms: only Murphy et al. reported a silica-anchored [Cu(salicylaldimine)] species with an $NO_3$ coordinating sphere, which showed a $g_\parallel$ = 2.29[20] and Talzi et al. reported $Cu^{II}$ complexes with an equatorial $NO_3$ coordination sphere with $g_\parallel$ = 2.27–2.28.[30] Nevertheless, some insights into the coordination sphere of the anchored complex can be gathered indirectly by comparison with $g$ and $A$ values of the parent copper complex and those with mixed $NO_3$ coordination spheres shown in Table 3.

Comparing the $g$ values of [Cu(acac)$_2$]AMPTSi/HMS_B with those of the free copper(II) acetylacetonate in a noncoordinating solvent ($CHCl_3$, Table 3) a decrease in $g_\parallel$ and $g_{\perp;}$ values, with consequent decrease in the $g_{av}$ value, is observed; these $g$ factors tendencies suggest that the anchored copper(II) complex has a different coordination sphere with higher equatorial covalence,[28] which is typical of the involvement of nitrogen atoms in the direct coordination with $Cu^{II}$.[20,28] As $g_\parallel$ = 2.275 is higher than the typical values observed for copper(II) complexes with an $N_2O_2$ coordinating sphere and similar to those observed by Talzi et al.,[30] we propose that the major Cu species immobilised in [Cu(acac)$_2$]AMPTSi/HMS_B have an $NO_3$ coordinating sphere as shown in Scheme 1 (other species, for example, with an $N_2O_2$ coordination sphere and present in low quantities, cannot be unambiguously excluded because of the solid-state broadening effects in the EPR spectra). Although

Table 3. EPR parameters of the free and immobilised [Cu(acac)$_2$].

| Sample (coordination sphere) | $g_\parallel$ | $g_\perp$ | $g_{av}$[a] | $\lvert A_\parallel \rvert$[b] | $\lvert A_\perp \rvert$[b] | Ref. |
|---|---|---|---|---|---|---|
| [Cu(acac)$_2$]AMPTSi/HMS_A[c,d] | [d] | [d] | [d] | [d] | [d] | |
| [Cu(acac)$_2$]AMPTSi/HMS_B[c] | 2.275 | 2.057 | 2.130 | 180.0 | 12.0 | [e] |
| [Cu(acac)$_2$]/$CHCl_3$ ($O_4$) | 2.285 | 2.060 | 2.135 | 180 | 12 | [25] |
| [Cu(acac)$_2$]/MeHO ($O_4$) | 2.290 | 2.067 | 2.141 | 165.0 | 15.4 | [19] |
| [Cu(salimine)]/$SiO_2$ ($NO_3$) | 2.290 | 2.065 | 2.140 | 155 | 13 | [20] |
| [Cu(salimine)]/$SiO_2$ ($N_2O_2$) | 2.243 | 2.065 | 2.124 | 183 | 13 | [20] |
| | | 2.062 | | | 16.8 | |
| [Cu(4-OHsalen)]/MeHO ($N_2O_2$) | 2.213 | | 2.111 | 192.2 | | [18] |
| | | 2.055 | | | 36.5 | |

[a] $g_{av} = 1/3(2 \times g_\perp + g_\parallel)$. [b] The values are expressed in $10^{-4}$ $cm^{-1}$. [c] At 120 K. [d] Not simulated due to band-broadening effects. [e] This work.

 © 2006 Wiley-VCH Verlag GmbH & Co. KGaA, Weinheim 

the spectrum was taken at low temperature, the bandwidths of the signals are still large to detect the nitrogen superhyperfine splittings (typically 14–25 G), due to the interaction between the copper unpaired spin and the nitrogen nuclear spin ($I$ = 1), hence hindering the direct confirmation of nitrogen atoms coordinated to the copper(II) centre in the equatorial plane. Further confirmation of the proposed $NO_3$ coordination sphere for Cu species in [Cu(acac)$_2$]-AMPTSi/HMS_B and the exclusion of complex immobilisation through axial coordination to the free amines of the support can be gathered from the $A_{\parallel}^{Cu}$ values. Axial coordination to a square-planar complex usually leads to a decrease of the metal hyperfine couplings:[26–29] in our case, upon immobilisation of the complex onto the support, no change in the $A_{\parallel}^{Cu}$ value was observed, suggesting that no effective axial coordination took place with the functionalised matrix.

Despite the band-broadening effects in the [Cu(acac)$_2$]-AMPTSi/HMS_A spectrum that prevented its simulation and detailed analysis, the same coordinating sphere is proposed, because the N/Cu ratio is much lower than in [Cu(acac)$_2$]AMPTSi/HMS_B (Table 1), and thus the in situ formation of an anchored copper(II) complex with an $N_2O_2$ coordinating sphere is less likely to occur.

It is noteworthy that in a control experiment, where a [Cu(acac)$_2$] solution in chloroform was refluxed with the unfunctionalised HMS for 24 h, a very low copper content (see Figure 4) was obtained after purification. This indicates that the functionalisation of the support with amine groups leads to higher metal loadings, as observed by us when activated carbon was used as the heterogeneous support.[16] The anchoring process of the copper(II) acetylacetonate onto the calcined HMS must occur through axial coordination of the $Cu^{II}$ centre to the isolated hydroxy groups of the HMS surface. The confirmation was achieved by the observation in the FTIR spectrum of a decrease in the intensity of the band at 3745 cm$^{-1}$, which is due to the isolated silanol groups. Taking into account that upon amine functionalisation of HMS there is a significant decrease in the intensity of this band (vide supra, Figure 2), it may be concluded that the axial coordination of the $Cu^{II}$ centre to the isolated hydroxy groups of the surface of the HMS is hindered in the amine-functionalised HMS material.

The EPR spectrum of this material, [Cu(acac)$_2$]/HMS, was also recorded and is shown in Figure 4c. Although the spectrum could not be simulated due to the low intensity of the signal, some qualitative information relating to the anchored complex can be gathered from the spectrum profile. With respect to the spectrum of [Cu(acac)$_2$]AMPTSi/HMS_B (Figure 4b), that of [Cu(acac)$_2$]/HMS shows the parallel region at higher magnetic field values as a broad band, which corresponds to the envelope of the unresolved four features due to the Cu hyperfine splittings. The main consequence of this is an increase in $g_{\parallel}$ and a decrease in $A_{\parallel}^{Cu}$. By using the data from analogous Cu complexes[26–29] and those referred to in Table 3, it can be clearly shown that in the unfunctionalised HMS, the Cu centre lies in an equatorial $O_4$ plane and possesses axial coordination to the matrix hydroxy groups. On the contrary, in the $NH_2$-functionalised HMS, the Cu centre has a coordination sphere which involves the nitrogen atoms of the modified matrix and no significant axial coordination takes place.

## Catalytic Experiments

The results obtained for the aziridination of styrene, catalysed by the [Cu(acac)$_2$] in homogeneous phase, and immobilised onto the amine-functionalised HMS are collected in Table 4, at room temperature, using PhI=NTs as nitrogen source.

Both [Cu(acac)$_2$]AMPTSi/HMS_A and [Cu(acac)$_2$]-AMPTSi/HMS_B materials acted as heterogeneous catalysts in the aziridination of styrene. As it was not possible to prepare the free counterparts of the anchored complexes, the catalytic activity of the heterogeneous copper complexes were compared with the parent free complex [Cu(acac)$_2$]. In this context, the former heterogeneous catalyst showed improved catalytic efficiency (styrene conversion and total TON, Figure 5) with respect to free [Cu(acac)$_2$] in the homogeneous phase, under similar experimental conditions. This is an important result, as the modification of the coordination sphere of the parent complex upon immobilisation

Table 4. Aziridination of styrene catalysed by the [Cu(acac)$_2$] in the homogeneous phase and heterogenised using PhI=NTs as nitrogen source.[a]

| Catalyst | Run | $t$ [h][b] | % C[c] | Total TON[d] | Initial TOF [h$^{-1}$][e] |
|---|---|---|---|---|---|
| [Cu(acac)$_2$] | | 0.5 | 69 | 11 | 21 |
| AMPTSi/HMS | | 24 | 21 | | |
| [Cu(acac)$_2$]AMPTSi/HMS_A | 1st | 4 | 92 | 21 | 8 |
| | 2nd | 24 | 79 | 24 | 7 |
| | 3rd | 24 | 40 | 14 | 5 |
| [Cu(acac)$_2$]AMPTSi/HMS_B | 1st | 24 | 15 | 3 | 0.5 |
| | 3rd | 24 | 12 | 13 | 0 |

[a] Catalyst/styrene/chlorobenzene (internal standard)/PhI=NTs (1:100:100:20), in $CH_3CN$, at room temperature. [b] Time needed for total consumption of PhI=NTs. [c] Corrected for limiting reagent (PhI=NTs). [d] TON = mmol converted styrene/mmol Cu. [e] Initial TOF calculated for 1 h of reaction.

 © 2006 Wiley-VCH Verlag GmbH & Co. KGaA, Weinheim 

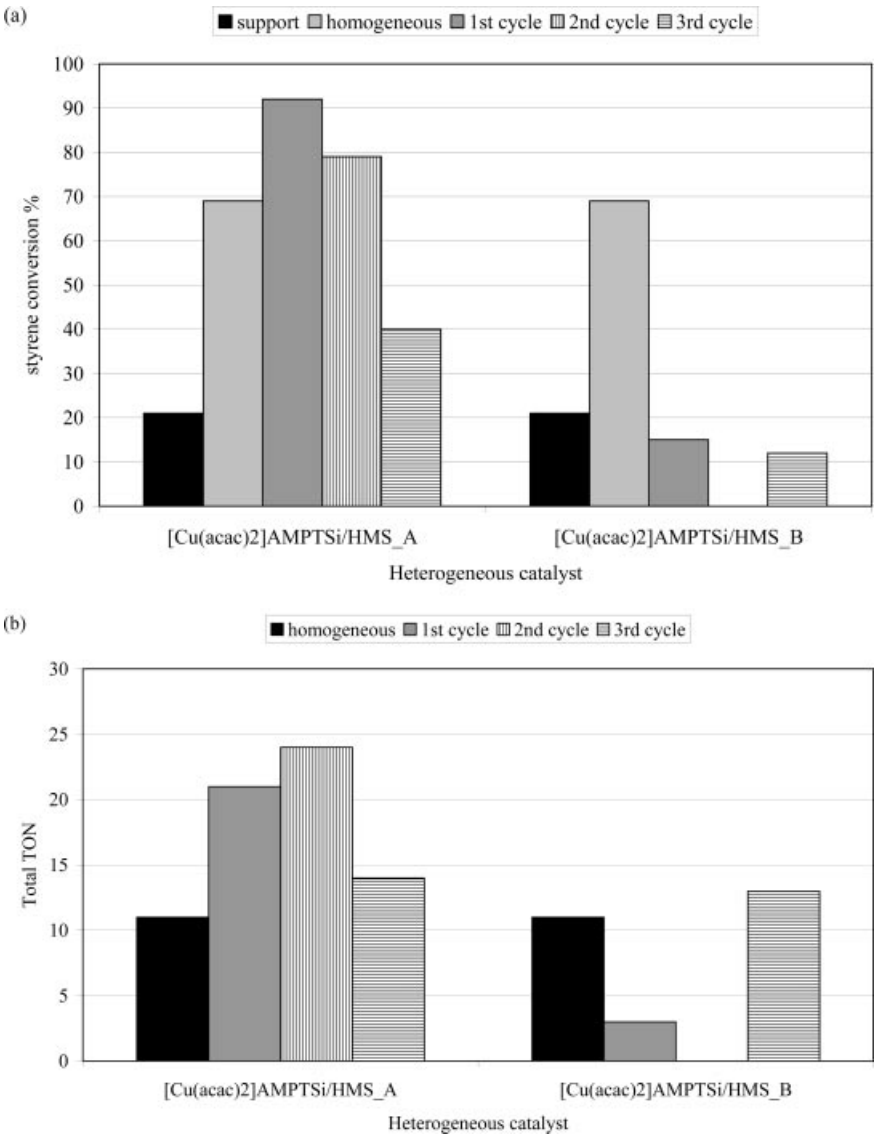


Figure 5. (a) Styrene conversion (%) and (b) total TON of the $[Cu(acac)_2]$ in the homogeneous phase and heterogenised onto an amine-functionalised HMS.

led to an increase in the catalytic activity, contrasting with usual decrease observed in the majority of the anchorage procedures, which involve the coordination sphere of the catalytic centres.

However, a decrease in the initial activity and increase in reaction time was observed, which may be due to the inherent diffusion limitations within the HMS porous structure, as the nitrogen source is a solid with limited solubility in acetonitrile, and its solubilisation is controlled by its rate of consumption.[4] Besides the formation of *p*-toluenesulfanamide, due to competitive homolytic cleavage of the PhI=NTs,[4] only very small amounts of benzaldehyde and epoxide were detected in the reaction media by gas chromatography.

The AMPTSi/HMS support also shows some catalytic activity in the conversion of styrene, but much smaller compared with the new heterogeneous catalysts. Nevertheless, the amount of the benzaldehyde by-product observed in the product mixture, can be related with residual catalytic activity of the support.

The materials could be reused at least in two other catalytic reactions with formation of aziridine. However, the catalyst $[Cu(acac)_2]$AMPTSi/HMS_A showed a loss of the catalytic activity with reuse, giving, nevertheless, better catalytic efficiency (total TON) than the reaction run in homogeneous phase with the $[Cu(acac)_2]$, under similar experimental conditions. The catalyst $[Cu(acac)_2]$AMPTSi/HMS_B showed improved catalytic efficiency in the 2nd reutilisation, and then a small drop in the 3rd cycle, which may be explained by a considerable decrease in the catalyst mass during the recycling procedure.

Nonetheless, the typical IR bands of the immobilised (Schiff base)copper(II) complex and silica backbone of both catalysts after the catalytic cycles remained unchanged, indicating the stability of the catalytic active species and support itself under the catalysis experimental conditions.

 © 2006 Wiley-VCH Verlag GmbH & Co. KGaA, Weinheim 

Hence, the loss of catalytic activity with reuse of the new heterogeneous catalyst may be due to slight leaching of active species, promoted by some degradation of the bond between the support and the spacer.

The [Cu(acac)$_2$]AMPTSi/HMS_A heterogeneous catalyst reported herein, which consists of copper(II) acetylacetonate anchored onto an amine-functionalised hexagonal mesoporous silica, presents higher catalytic activity in the aziridination of styrene, at room temperature, using PhI=NTs as nitrogen source, than [Cu(acac)$_2$] anchored onto a triamine-functionalised activated carbon.[17] However, it is not as stable and reusable as the latter heterogeneous catalyst, because this could be reused at least for 4 times with successive increase in styrene conversion, and thus in the total turnover number (TON) and initial activity (TOF).

## Conclusion

Copper(II) acetylacetonate was anchored onto an HMS material using a two-step procedure: (i) functionalisation of the surface hydroxy groups with (3-aminopropyl)triethoxysilane and then (ii) anchoring of the copper(II) complex through Schiff condensation with free amine groups, using two different metal loadings.

Nitrogen elemental analysis, XPS and DRIFT showed the presence of amine groups on the surface of the HMS material and porosimetry indicated that the structure of the mesoporous material remained unchanged after this step.

Atomic absorption and XPS data showed that the copper(II) acetylacetonate could be irreversibly immobilised onto the amine-functionalised HMS through Schiff condensation between the surface amine groups and the oxygen atoms of the copper(II) ligand, leading to an $NO_3$ coordination sphere for the anchored metal complex. This was confirmed by the combination of data extracted from FTIR and EPR spectra of the materials.

The new [Cu(acac)$_2$]AMPTSi/HMS materials were tested in the aziridination of styrene, using PhI=NTs as nitrogen source and acetonitrile as solvent, at room temperature. The styrene conversion and total TON of the heterogeneous phase reaction are higher than those of the same reaction catalysed in homogeneous phase by [Cu(acac)$_2$]; nevertheless, the initial activity decreases and reaction time increases due to substrate and product diffusion limitations. The heterogeneous catalyst showed a successive slight decrease in catalytic activity when reused for two more times.

## Experimental Section

**Materials and Reagents:** All reagents and solvents used in the preparation and modification of the hexagonal mesoporous silica (HMS) were used as received. Copper(II) acetylacetonate, 1-dodecylamine and (3-aminopropyl)triethoxysilane (AMPTSi) were from Aldrich; tetraethoxysilane was from Lancaster; toluene and other solvents used in the synthesis procedures were from Fischer Scientific (analytical reagent grade) and those used in the catalytic experiments and as eluents were from Romil or Fischer Scientific (HPLC grade). The nitrene donor 4-methyl-*N*-(phenyl-$\lambda^3$-iodanylidene)benzenesulfonamide (PhI=NTs) was synthesised using reported procedures.[31]

**Synthesis and Modification of Hexagonal Mesoporous Silica (HMS)**

**Synthesis of Hexagonal Mesoporous Silica (HMS):** The HMS was synthesised using a reported procedure;[22] tetraethoxysilane (37.0 mL, 0.166 mol) was added to a stirred solution of ethanol (88.1 mL, 1.51 mol), water (88.5 mL, 4.91 mol) and 1-dodecylamine (10.3 mL, 0.0448 mol). The mixture was stirred at room temperature for 24 h. The white precipitate obtained was vacuum-filtered, washed with deionised water (100 mL) and ethanol (100 mL). In order to remove the template (1-dodecylamine), the precipitate was calcined at 600 °C for 24 h.

**Functionalisation of the HMS with (3-Aminopropyl)triethoxysilane (AMPTSi/HMS):** A mixture of calcined HMS (3.00 g) in dry toluene (50.0 mL) and (3-aminopropyl)triethoxysilane (9.00 mmol, 2.10 mL) was refluxed for 24 h. The material was vacuum-filtered, washed with toluene (3 × 50 mL) and dried overnight in an oven at 85 °C.

**Anchoring of Copper(II) Acetylacetonate onto Amine-Functionalised HMS:** A solution of copper(II) acetylacetonate (0.1304 g, 498 μmol) in chloroform (100 mL, light blue solution) was refluxed with AMPTSi/HMS (1.02 g) for 24 h. At the end of the process, the colour of the solution was sligthtly blue. The solid was vacuum-filtered, washed with chloroform (3 × 20 mL), and then Soxhlet-extracted with chloroform for 6 h. Finally, the solid was dried overnight in an oven at 85 °C. This material will be referred to as [Cu(acac)$_2$]AMPTSi/HMS_A. Another material with lower complex loading was also prepared: [Cu(acac)$_2$]AMPTSi/HMS_B. In this case AMPTSi/HMS (0.35 g) was refluxed with copper(II) acetylacetonate (0.0077 g, 29 μmol) in chloroform (10 mL, light blue solution) for 24 h, after which an almost colourless solution was obtained after filtration of the material. The material was washed with chloroform (3 × 20 mL) and then Soxhlet-extracted with chloroform (150 mL) for 6 h. The blue solid was dried in an oven at 100 °C, after which it was light brown.

**Physico-Chemical Measurements:** Nitrogen elemental analysis and copper atomic absorption were performed by Microanalytical Services, University of Manchester, U. K. Surface area measurements were performed monitoring the $N_2$ adsorption isotherms at 77 K with a Micrometrics ASAP 2010 apparatus. Surface areas were calculated using the BET equation over the pressure range $p/p_0$ = 0.02–0.2. X-ray photoelectron spectroscopy was carried out with a Kratos AXIS His instrument equipped with a charge neutraliser and an Mg-$K_\alpha$ X-ray source. Spectra were recorded at normal emission with an analyser pass energy of 20 eV and an X-ray power of 225 W. The FTIR-DRIFT spectra of the powered materials were obtained with a Bruker Equinox 55 spectrophotometer in the region 400–4000 cm$^{-1}$. The UV diffuse reflectance spectra were obtained with a Shimadzu UV-3101 PC in the range 1600–200 nm, using barium sulfate as reference. EPR spectra were recorded with a Bruker ESP300 EPR spectrometer equipped with an X-band microwave bridge. Temperature control was achieved with a Bruker ER-4111 variable-temperature controller, the temperature at the centre of the EPR cavity was calibrated using a separate thermocouple. The spectra were taken at 120 K with the following typical experimental conditions: modulation frequency: 100 kHz; modulation amplitude: 5 G; microwave power: 1–5 mW. The EPR parameters were obtained by simulation using the program Win EPR Simfonia (Bruker) assuming axial or rhombic spin Hamiltonians. The reported values of $g_\perp$ (or $g_x$ and $g_y$) and $A_\perp$ (or $A_x$ and $A_y$) are less accurate because of their dependence on the used line

 © 2006 Wiley-VCH Verlag GmbH & Co. KGaA, Weinheim 

widths (50–60 G). GC-FID chromatograms were obtained with a Varian CP-3380 gas chromatograph using helium as carrier gas and a fused silica Varian Chrompack capillary column CP-Sil 8 CB Low Bleed/MS (30 m × 0.25 mm i.d.; 0.25 μm film thickness). Conditions: 60 °C (3 min), 5 °C $min^{-1}$, 170 °C (2 min), 20 °C $min^{-1}$, 200 °C (10 min); injector temperature: 200 °C; detector temperature: 300 °C. HPLC chromatograms were obtained with a Merck Hitachi Lachrom apparatus consisting of a pump L-7100, UV detector L-7400, interface D-7000, autosampler L-7200 and a column oven L-7300 equipped with a Phenomenex Luna 5u C18(2), 250 × 4.6 mm column. The eluent used was a mixture of 85% of acetonitrile and 15% of water with a flow rate of 1 mL $min^{-1}$.

**Catalysis Experiments:** The activity of the catalysts in the aziridination of styrene was studied at room temperature using a molar ratio of metal catalyst/alkene/chlorobenzene (internal standard)/PhI=NTs = 1:100:100:20 in acetonitrile (5.00 mL), whilst stirring. For the experiments with the catalyst $[Cu(acac)_2]$AMPTSi/HMS_A, styrene (1.22 mmol), chlorobenzene (1.22 mmol, internal standard), heterogeneous catalyst (0.0300 g) and PhI=NTs (0.244 mmol, nitrogen source) were used; for the experiments with catalyst $[Cu(acac)_2]$AMPTSi/HMS_B, styrene (0.20 mmol), chlorobenzene (0.20 mmol, internal standard), heterogeneous catalyst (0.0300 g) and PhI=NTs (0.041 mmol, nitrogen source) were used. During the experiment, 0.05-mL aliquots were taken from the solution with a hypodermic syringe, filtered through 0.2-μm PTFE syringe filters and directly analysed by GC-FID. When the entire PhI=NTs had disappeared from the solution and the ratio of the areas of iodobenzene and chlorobenzene in the chromatogram was constant, the solution was centrifuged at 3500 rpm for 15 min, and then to the decanted solution another portion of PhI=NTs (0.244 mmol) was added. This procedure checks the eventual existence of metal complex leaching to the reaction medium. The presence of the aziridine at the end of the reaction was confirmed by HPLC. The heterogeneous catalysts were then washed/centrifuged sequentially with acetonitrile (3 × 10 mL) and methanol (1 × 10 mL) and oven-dried at 90 °C overnight. These materials were reused for further two times using the same experimental procedure. To provide a framework for the results obtained using the heterogenised copper(II) complex, styrene aziridination was also carried out under experimental conditions comparable to those described above (a) in homogeneous media using the same amount of $[Cu(acac)_2]$ and (b) using the AMPTSi/HMS material, the precursor of both heterogeneous catalysts.

## Acknowledgments

A. R. S. thanks the "Fundação para a Ciência e Tecnologia" (Lisboa) and the European Social Fund for a Post-Doctoral fellowship. This work was funded by the Fundação para a Ciência e Tecnologia (Portugal) and the FEDER through project ref. POCTI/CTM/45449/2002.

[1] J. F. Larrow, E. N. Jacobsen, *Top. Organomet. Chem.* **2004**, *6*, 123–152.
[2] P. G. Cozzi, *Chem. Soc. Rev.* **2004**, *33*, 410–421.
[3] T. Katsuki, *Chem. Soc. Rev.* **2004**, *33*, 437–444.
[4] D. A. Evans, M. M. Faul, M. T. Bilodeau, *J. Org. Chem.* **1991**, *56*, 6744–6746.
[5] J. B. Sweeney, *Chem. Soc. Rev.* **2002**, *31*, 247–258.
[6] M. Lakshmi Kantam, B. Kavita, V. Neeraja, Y. Haritha, M. K. Chaudhuri, S. K. Dehury, *Tetrahedron Lett.* **2003**, *44*, 9029–9032.
[7] W. Sun, E. Herdtweck, F. E. Kühn, *New J. Chem.* **2005**, *29*, 1577–1580.
[8] P. M. Price, J. H. Clark, D. J. Macquarrie, *J. Chem. Soc., Dalton Trans.* **2000**, 101–110.
[9] Q.-H. Xia, H.-Q. Ge, C.-P. Ye, Z.-M. Liu, K.-X. Su, *Chem. Rev.* **2005**, *105*, 1603–1662.
[10] C. Li, *Catal. Rev.* **2004**, *46*, 419–492.
[11] Q.-H. Fan, Y.-M. Li, A. S. C. Chan, *Chem. Rev.* **2002**, *102*, 3385–3466.
[12] D. Brunel, N. Belloq, P. Sutra, A. Cauvel, M. Laspéras, P. Moreau, F. Di Renzo, A. Galarneau, F. Fajula, *Coord. Chem. Rev.* **1998**, *178–180*, 1085.
[13] N. E. Leadbeater, M. Marco, *Chem. Rev.* **2002**, *102*, 3217–3274.
[14] J. S. Rafelt, J. H. Clark, *Catal. Today* **2000**, *57*, 33–44.
[15] I. W. C. E. Arends, R. A. Sheldon, *Appl. Catal. A* **2001**, *212*, 175–187.
[16] A. R. Silva, M. Martins, M. M. A. Freitas, J. L. Figueiredo, C. Freire, B. de Castro, *Eur. J. Inorg. Chem.* **2004**, 2027–2035.
[17] A. R. Silva, J. L. Figueiredo, C. Freire, B. de Castro, *Catal. Today* **2005**, *102–103*, 154–159.
[18] A. R. Silva, C. Freire, B. de Castro, M. M. A. Freitas, J. L. Figueiredo, *Langmuir* **2002**, *18*, 8017–8024.
[19] R. Ferreira, M. Silva, C. Freire, B. de Castro, J. L. Figueiredo, *Microporous Mesoporous Mater.* **2000**, *38*, 391–401.
[20] E. F. Murphy, D. Ferri, A. Baiker, S. Van Doorslaer, A. Schweiger, *Inorg. Chem.* **2003**, *42*, 2559–2571.
[21] K. Wilson, A. F. Lee, D. J. Macquarrie, J. H. Clark, *Appl. Catal. A* **2002**, *228*, 127–133.
[22] P. T. Tanev, T. J. Pinnavaia, *Science* **1995**, *267*, 865–867.
[23] M. B. Mitchell, V. R. Chakravarthy, M. G. White, *Langmuir* **1994**, *10*, 4523–4529.
[24] A. B. P. Lever, *Inorganic Electronic Spectroscopy*, 2nd ed., Elsevier, Amesterdan, **1984**, vol. II, p. 554.
[25] J. V. Zanchetta, B. Deroide, B. Asri, J. C. Giuntini, *Microporous Mater.* **1995**, *4*, 187–193.
[26] H. R. Gersmann, J. D. Swalen, *J. Chem. Phys.* **1962**, *36*, 3221–3233.
[27] J. I. Zink, R. S. Drago, *J. Am. Chem. Soc.* **1972**, *94*, 4550–4554.
[28] H. Yokoi, A. W. Addison, *Inorg. Chem.* **1977**, *16*, 1341–1349.
[29] B. Jezowska-Trzebiatowska, J. Jezierska, *J. Mol. Struct.* **1973**, *19*, 627–634.
[30] E. P. Talzi, V. M. Nekipelov, K. I. Zamaraev, *Russ. J. Phys. Chem.* **1984**, *58*, 165.
[31] S. Taylor, J. Gullick, P. McMorn, D. Bethell, P. C. Bulman Page, F. E. Hancock, F. King, G. J. Hutchings, *J. Chem. Soc., Perkin Trans. 2* **2001**, 1714–1723.

Received: November 3, 2005
Published Online: January 26, 2006

 © 2006 Wiley-VCH Verlag GmbH & Co. KGaA, Weinheim 

DOI: 10.1002/ejic.200500986

# Methyl-Hydroxypyridinecarboxylic Acids as Possible Bidentate Chelating Agents for Aluminium(III): Synthesis and Metal–Ligand Solution Chemistry

Valerio B. Di Marco,*[a] Annalisa Dean,[a] Maria Grazia Ferlin,[b] Robert A. Yokel,[c] Haitao Li,[c][‡] Alfonso Venzo,[d] and G. Giorgio Bombi[a]

**Keywords:** Aluminium / Carboxylate ligands / Potentiometry / Chelation therapy

In view of a possible application to aluminium chelation therapy, 1-methyl-3-hydroxy-4-pyridinecarboxylic acid (1M3H4P) and 1-methyl-4-hydroxy-3-pyridinecarboxylic acid (1M4H3P) were synthesized, and their chemical interactions with aluminium(III) were investigated in aqueous 0.6 m (Na)Cl at 25 °C by means of potentiometric titrations. The qualitative and quantitative results obtained were confirmed by UV spectrophotometry and $^1$H NMR spectroscopy. For both ligands, the species $AlL^{2+}$, $AlL_2^+$, $AlL_3$, and $AlL_2H_{-1}$ were identified, with $\log\beta_{1,1,0} = 7.66$, $\log\beta_{1,2,0} = 14.27$, $\log\beta_{1,3,0} = 19.099$, and $\log\beta_{1,2,-1} = 7.00$ for 1M3H4P, $\log\beta_{1,1,0} = 7.21$, $\log\beta_{1,2,0} = 13.41$, $\log\beta_{1,3,0} = 18.15$, and $\log\beta_{1,2,-1} = 6.4$ for 1M4H3P. The chelation strength of 1M3H4P and 1M4H3P is lower than that of other available aluminium(III) chelators, e.g. deferiprone (pAl difference at physiological pH: ca. 3 log units). The octanol/aqueous partitioning values of 1M3H4P and 1M4H3P were 0.0054 and 0.0015, respectively, showing high hydrophilicity. The efficiencies of the ligands to chelate aluminium(III) were evaluated at physiological pH and ion strength "in vitro". 1M3H4P and 1M4H3P were more effective than their non-methylated analogs 3H4P and 4H3P.

(© Wiley-VCH Verlag GmbH & Co. KGaA, 69451 Weinheim, Germany, 2006)

## Introduction

The therapy for metal-overload pathologies usually involves the administration of suitable chelating agents to selectively remove the metal from the body. Regarding aluminium(III) and iron(III), there is a need for new, safe, inexpensive, efficient, and orally effective chelators,[1–3] because the existing ones, i.e. desferrioxamine and deferiprone, have a number of drawbacks, including oral inefficacy and the high cost for the former,[4–6] and several toxic side effects and controversial efficiency for the latter.[5–8]

In a previous work[9] we proposed hydroxypyridinecarboxylic acids (HPs) as new possible chelating agents for aluminium(III) in view of several promising properties such as their lack of toxicity (references in ref.[9]), their low molecular weight (which is required for oral activity), and their very low affinity towards essential metal ions like $Zn^{2+}$.[10] Our results showed that the unsubstituted derivatives, i.e. 3H4P and 4H3P, cannot be regarded as possible alternatives to desferrioxamine and deferiprone, because they do not adequately complex aluminium(III) at physiological pH. As a strategy to improve the $Al^{III}$ complexation ability, without affecting the positive properties, alkylation of the pyridinic ring was proposed, because the electron-donor properties of the alkyl substituents can be expected to increase the basicity of chelating oxygen atoms and therefore to increase the affinity towards hard metal ions, such as aluminium(III) and iron(III).

In this work, the *N*-methyl derivatives of 3H4P and 4H3P, i.e. 1-methyl-3-hydroxy-4-pyridinecarboxylic acid (1M3H4P) and 1-methyl-4-hydroxy-3-pyridinecarboxylic acid (1M4H3P) (Figure 1), have been synthesized, and the formation of complexes between the ligands and aluminium(III) studied in aqueous solutions by means of potentiometric titrations. The speciation data obtained has been confirmed by UV/Vis and $^1$H NMR measurements. The partitioning of the ligands in an octanol/aqueous system was determined with UV/Vis spectroscopy. The efficiency of the ligands to chelate aluminium(III) has been determined at physiological conditions (pH and ion strength) in vitro.

[a] Department of Chemical Sciences, University of Padova, Via Marzolo 1, 35131 Padova, Italy
E-Mail: valerio.dimarco@unipd.it
[b] Department of Pharmaceutical Sciences, University of Padova, Via Marzolo 5, 35131 Padova, Italy
[c] College of Pharmacy, 511C Pharmacy Building, University of Kentucky Medical Center, Rose Street, Lexington, KY 40536-0082, USA
[d] CNR, Institute of Sciences and Molecular Technologies, Via Marzolo 1, 35131 Padova, Italy
[‡] Current address: Dept. of Polymer Development, MediVas, LLC, 6275 Nancy Ridge Dr., San Diego, CA 92121, USA

## Results and Discussion

### Synthesis of the Ligands

To synthesize the new ligands, initially 3H4P and 4H3P (which are not commercially available) were prepared as de-

 © 2006 Wiley-VCH Verlag GmbH & Co. KGaA, Weinheim 

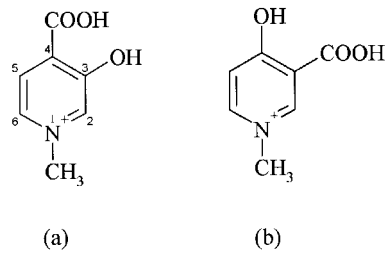


Figure 1. (**a**) 1-Methyl-3-hydroxy-4-pyridinecarboxylic acid (1M3H4P), (**b**) 1-methyl-4-hydroxy-3-pyridinecarboxylic acid (1M4H3P), both shown as the $H_2L^+$ forms.

scribed.[9] Next, the hydroxyacids were *N*-methylated by use of a conventional method ($CH_3I$ in dimethylformamide).[11]

## Solution Equilibria

### *Acidity Constants of the Ligands*

The potentiometric titration of the ligands alone allowed the computation of the p$K_a$ value for the HL form (for simplicity, charges will be generally omitted from the formulae, except in the Tables), corresponding to the deprotonation of the OH group (Table 1). Phenolic oxygen atoms in unsubstituted HPs, e.g. in 3H4P and 4H3P, generally have p$K_a$ values around 10–11:[9] the drastic ($10^4$–$10^5$-fold) increase of the acidity of this group in 1M3H4P and 1M4H3P can be explained by the strong inductive effect exerted by the positively charged nitrogen atom, and by the fact that the molecule is uncharged at the pH where OH deprotonates. In comparison, for 3H4P and 4H3P the nitrogen is neutral and the molecule is charged –1. For 1M4H3P the acidity is even higher because the positive charge of the nitrogen may exert also a resonance effect. To the best of our knowledge, a similar effect in a phenolic oxygen atom was observed only in a naphthyridine compound by Agafonova et al.:[12] for 8-hydroxy-1,6-naphthyridine the p$K_a$ was 8.33, whereas for 8-hydroxy-6-methyl-1,6-naphthyridinium it was 4.34.

Table 1. Acidic properties of 1M3H4P and 1M4H3P.[a]

| Species | **1M3H4P** | | **1M4H3P** | | Technique used to obtain the data |
|---|---|---|---|---|---|
| | $pK_a$ | $n$ | $pK_a$ | $n$ | |
| $H_2L^+$ | 0.28 ± 0.05 | 4 | 0.12 ± 0.02 | 2 | UV |
| HL | 6.6326 ± 0.0008 | 12 | 5.9578 ± 0.0006 | 8 | potentiometry |

[a] For potentiometric data, $n$ is the number of experiments from which the data were obtained. Values are shown as the mean and standard deviation of the mean. For UV data, $n$ is the number of wavelengths from which the data were obtained; a weighted mean and the corresponding weighted standard deviation were calculated from the data.

Accurate potentiometric measurements at pH values lower than ca. 1.5–2 cannot be executed, because in these conditions the pH modification is negligible because of the acid–base equilibria. Therefore, the more acidic pH region has been explored with UV measurements, which allowed the determination of the p$K_a$ value for the $H_2L$ form, corresponding to the deprotonation of the COOH group (Table 1). Its high acidity is in agreement with values previously observed for other HPs.[9]

### *Metal–Ligand Complexes – Potentiometric Results*

For both ligands, the potentiometric titrations of solutions containing the metal and the ligand allowed the identification of the complexes AlL, $AlL_2$, $AlL_3$, and $AlL_2H_{-1}$ (where HL represents either 1M3H4P or 1M4H3P in the neutral form). The values of their stability constants are reported in Table 2. The distribution diagrams for the two systems, as computed for a solution containing $10^{-3}$ m $Al^{III}$ and $4\cdot10^{-3}$ m ligand, are reported in Figure 2.

Table 2. Stability constants for Al–L complexes, at 25 °C in aqueous (Na)Cl 0.6 m (reactions: $m\,Al^{3+} + l\,L^- + h\,H^+ \rightleftharpoons Al_mL_lH_h^{3m-l+h}$; the p$K_a$ value refers to the equilibrium $AlL_2^+ \rightleftharpoons AlL_2H_{-1} + H^+$).

| Species | **1M3H4P** | | | **1M4H3P** | | |
|---|---|---|---|---|---|---|
| | log $\beta$ | p$K_a$ | $n$ | log $\beta$ | p$K_a$ | $n$ |
| $AlL^{2+}$ | 7.66 ± 0.03 | | 12 | 7.21 ± 0.06 | | 12 |
| $AlL_2^+$ | 14.27 ± 0.04 | 7.27 | 12 | 13.41 ± 0.03 | 7.0 | 12 |
| $AlL_2H_{-1}$ | 7.00 ± 0.07 | | 8 | 6.4 ± 0.1 | | 8 |
| $AlL_3$ | 19.099 ± 0.008 | | 8 | 18.15 ± 0.03 | | 8 |

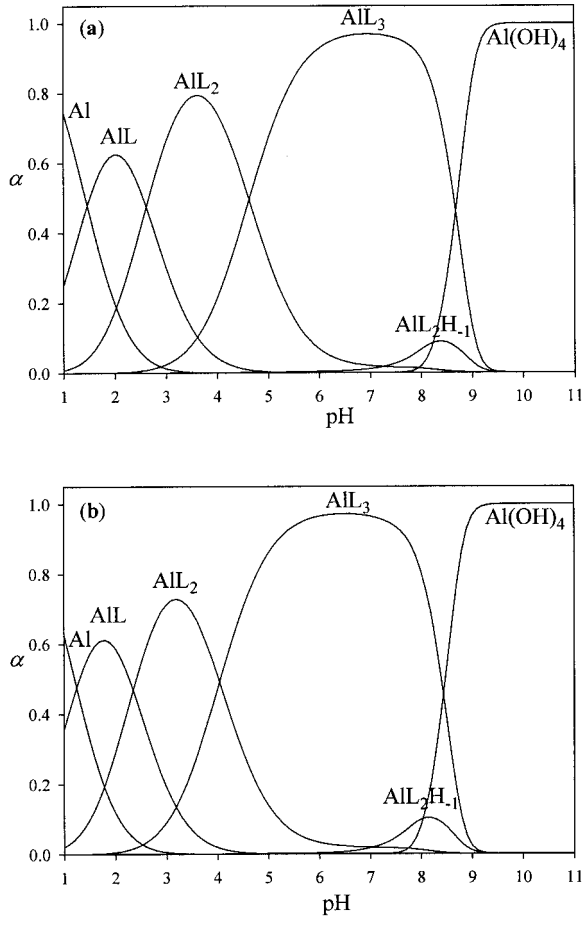


Figure 2. Distribution diagrams of the aluminium complexes in the presence of 1M3H4P (**a**) and 1M4H3P (**b**) in aqueous (Na)Cl 0.6 m, $T$ = 25 °C; $[Al]_0 = 10^{-3}$ m, $[ligand]_0 = 4\cdot10^{-3}$ m.

The free metal ion predominates only at very acidic pH values, i.e. below 1.5, wheras upon increasing the pH the

 © 2006 Wiley-VCH Verlag GmbH & Co. KGaA, Weinheim 

sequential formation of AlL, $AlL_2$ and $AlL_3$ is observed. A water molecule coordinated to the metal center in $AlL_2$ may deprotonate to form $AlL_2H_{-1}$. At basic pH values, all the complexes are destabilized owing to the formation of $Al(OH)_4$. In the investigated concentration range, the precipitation of aluminium hydroxide was not observed in either system in the presence of a threefold or higher excess ligand concentration, because of the high affinity of the ligands towards the metal ion.

The acidity of $AlL_2(H_2O)_2$ ($pK_a$ values around 7 for both ligands, see Table 2) is much lower than that of $Al(H_2O)_6$ ($pK_a = 5.52$[13]). This accounts for the negligible concentration of $AlL_2H_{-1}$ at acidic and neutral pH values. The lower acidity is due in part to statistical reasons [a smaller number of deprotonating water molecules in $AlL_2(H_2O)_2$ than in $Al(H_2O)_6$] and in part to a relatively high electronic density around the chelating oxygen atoms of the ligand, higher than that on the oxygen of water,[14] which destabilizes the deprotonation of the coordinated water molecules in $AlL_2(H_2O)_2$.

### *Metal–Ligand Complexes – UV Results*

Selected UV spectra for the Al/1M3H4P and the Al/1M4H3P solutions at acidic-to-neutral pH values are reported in Figure 3. All spectra show the typical absorption of substituted pyridinic rings. The increase of pH causes a bathochromic shift of the main peak and a general increase of the absorption coefficients. These effects are in agreement with the gradual formation of less positively charged, thus electron-richer, species ($AlL^{2+}$, $AlL_2^{+}$, $AlL_3$) at higher pH values.

In the elaboration of the UV data for both systems the formation constant of AlL was kept constant at the value determined from potentiometric titrations, as this species is already formed at the most acidic pH values investigated. The values for the stability constant of $AlL_2$ could be optimised: $\log \beta_{1,2,0} = 14.2 \pm 0.1$ for Al/1M3H4P, $\log \beta_{1,2,0} = 13.2 \pm 0.1$ for Al/1M4H3P. The $\log \beta$ values of $AlL_2$ compare reasonably well with the corresponding potentiometric ones ($\log \beta_{1,2,0} = 14.27 \pm 0.04$ and $13.41 \pm 0.03$, respectively). This agreement suggests the absence of systematic errors in the results.

### *Metal–Ligand Complexes – $^1$H NMR Results*

In the $^1$H NMR spectra of 1M3H4P in $D_2O$, the singlet of the $CH_3$ protons is at $\delta = 4.37$, and the signals due to the protons H(2), H(5), and H(6), are observed at $\delta = 8.52$ (s), $\delta = 8.28$ (d), and $\delta = 8.20$ (d), respectively. The signals do not show appreciable pD-dependent shift, at least in the investigated pD range (2–7). For 1M4H3P at acidic pD values (pD < 4), the singlet of the $CH_3$ protons appears at $\delta = 4.16$, and H(2), H(5), and H(6) are observed respectively at $\delta = 8.89$ (s), $\delta = 7.20$ (d), and $\delta = 8.31$ (d). At pD = 7.4, all signals appear at higher fields ($\delta = 3.94$, $\delta = 8.20$, $\delta = 6.70$, and $\delta = 7.89$, respectively), because of the deprotonation of the phenolic oxygen.

In the presence of aluminium(III), the peaks of the free ligands are observed only in acidic solutions, and new groups of peaks due to the complexes appear at all investigated pD values.

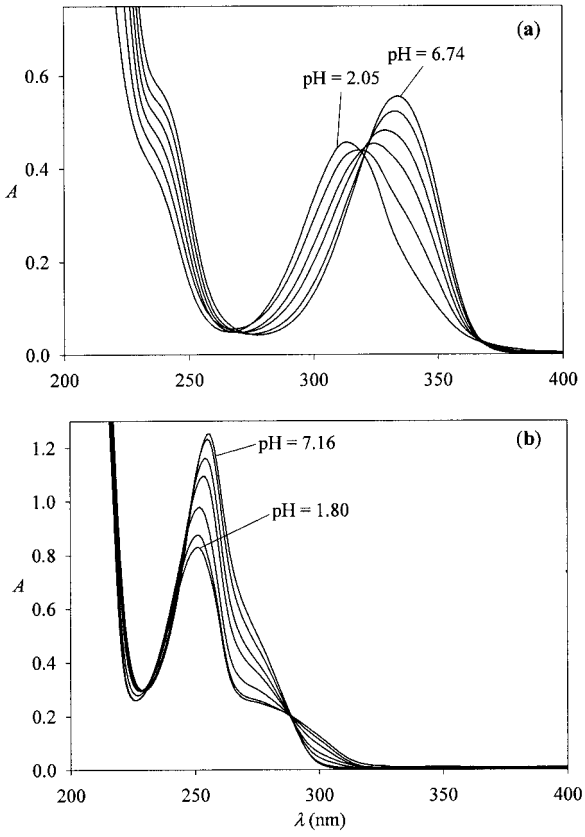


Figure 3. (a) UV spectra of Al/1M3H4P, (b) Al/1M4H3P at various pH values.

For Al/1M3H4P (Figure 4), at pD = 1.9 two additional peaks appear at $\delta = 4.30$ and $\delta = 4.28$, which represent the $CH_3$ protons of two complexes, i.e. AlL and $AlL_2$ according to the potentiometric data. The expected quantitative distribution suggests the attribution of the most intense signal ($\delta = 4.28$) to $AlL_2$. In the aromatic region AlL and $AlL_2$ give rise to two additional peaks, one more intense than the other, at $\delta = 8.05$ and $\delta = 8.00$, respectively, the other peaks of the complexes overlapping those of the free ligand. Upon increasing the pD to 4.0, the complexes give rise to four $CH_3$ signals at $\delta = 4.30$ (very low intensity, AlL), $\delta = 4.28$ ($AlL_2$), $\delta = 4.26$ and $\delta = 4.24$ ($AlL_3$, as discussed below). The peaks in the aromatic region show a complicated pattern in which only some peaks of the free ligand ($\delta = 8.52$ and 8.28 ppm) can be easily assigned. At pD = 6.5, even though only the species $AlL_3$ exists in solution in significant amount, four $CH_3$ signals are observed between 4.19 and 4.22 ppm, together with a fifth less intense peak at $\delta = 4.23$ ppm. This small signal is probably produced by $AlL_2$ and $AlL_2H_{-1}$, which at this pD value are about twenty times less concentrated than $AlL_3$. The other four signals can be explained considering that the ligand is not symmetrical and may chelate the metal, forming $AlL_3$, in two different spatial configurations (Figure 5). If the three ligands of $AlL_3$ chelate the metal ion in the same configurations, a

 © 2006 Wiley-VCH Verlag GmbH & Co. KGaA, Weinheim 

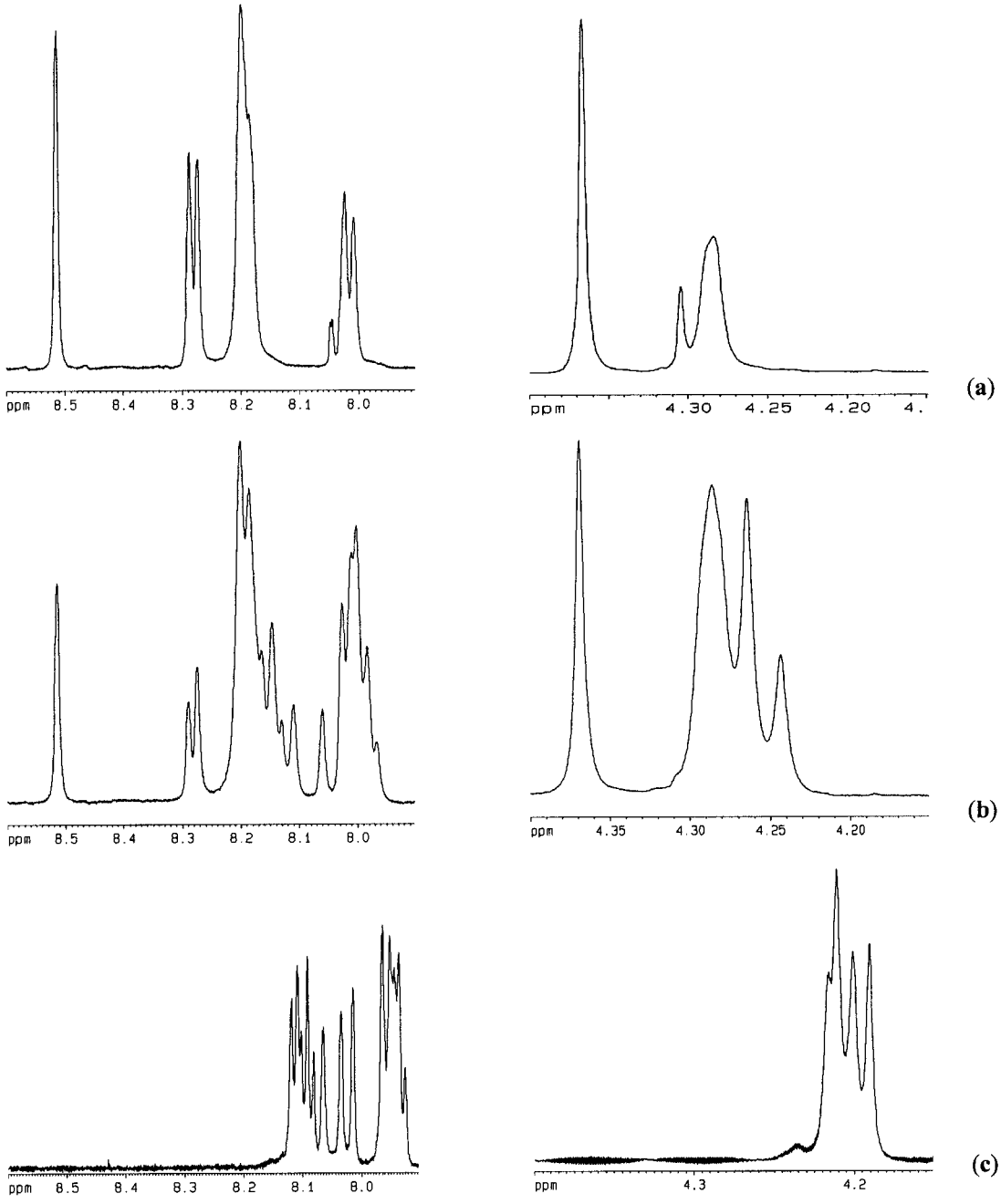


Figure 4. $^1H$ NMR spectra of $D_2O$ solutions containing $Al^{III}$ ($6.5 \cdot 10^{-3}$ m) and 1M3H4P ($1.9 \cdot 10^{-2}$ m), pD = 1.9 (a), 4.0 (b), 6.5 (c). For the spectrum at pD = 6.5, $v_0$ = 600 MHz. The sensitivity of spectra in the aromatic zone was enhanced by a factor 4.

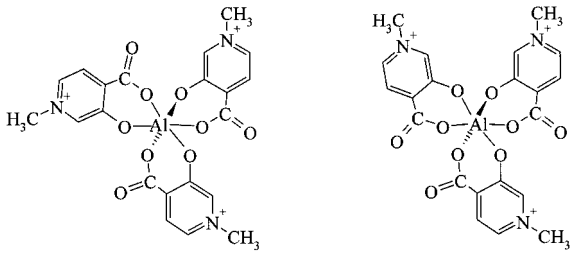

Figure 5. The two spatial diastereoisomers of $AlL_3$ (L = 1M3H4P).

symmetrical diastereoisomer ($AlL_{3-sym}$) forms, and the three $CH_3$ groups have the same NMR response. If one ligand chelates differently from the other two, an unsymmetrical diastereoisomer ($AlL_{3\text{-}unsym}$) forms, and the three $CH_3$ groups give rise to different signals in the NMR spectrum. In the aromatic region four signals are expected as well for each proton. The quite broad peaks at $\delta$ = 8.07, $\delta$ = 8.03, and $\delta$ = 8.01 do not show COSY couplings with other signals, and between them no reasonable coupling constant exists. Thus, they can be attributed to the H(2) protons of the two $AlL_3$ species. The fourth H(2) signal is

 © 2006 Wiley-VCH Verlag GmbH & Co. KGaA, Weinheim 

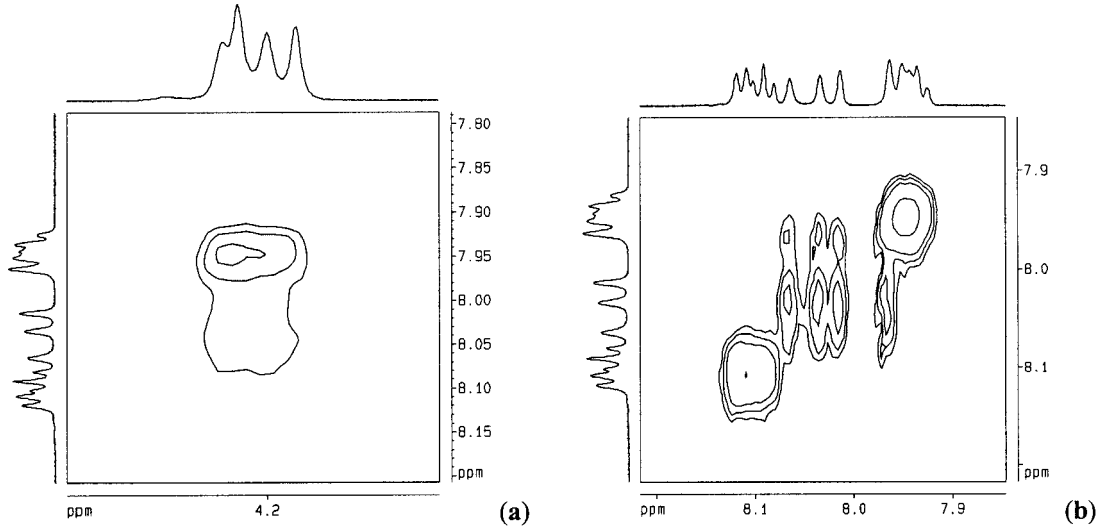


Figure 6. $^1H$ –$^1H$ phase sensitive NOESY spectra of a $D_2O$ solution containing $Al^{III}$ $6.5\cdot10^{-3}$ m and 1M3H4P $1.9\cdot10^{-2}$ m, pD = 6.46 ($\nu_o$, 600 MHz). (a) NOESY correlations between the aromatic (F1) and $CH_3$ (F2) protons. (b) *In phase* (exchange) correlations between the aromatic protons.

probably the singlet which appears at $\delta$ = 7.96 ppm. The four signals of H(5) and H(6) (centered at $\delta$ ca. 8.1 and $\delta$ ca. 7.95, respectively, COSY data) cannot be distinguished from each other due to strong overlap. The NOESY interactions between $CH_3$ and H(6) are significantly more intense than those between $CH_3$ and H(2) (Figure 6, a). This is in agreement with a distortion of the aromatic ring in the complex, which brings the $CH_3$ protons closer to H(6) than to H(2). In addition, NOESY spectra show strong correlation peaks between the aromatic protons which are in phase with the diagonal (Figure 6, b): this finding is in agreement with relatively fast chemical exchanges of the various ligand molecules in $AlL_3$.[15–17]

For Al/1M4H3P (Figure 7), at pD = 1.1 an additional $CH_3$ peak, and two H(5) and H(6) multiplets, are visible at higher fields. The pattern is in agreement with the formation of only one complex, which according to the potentiometric data is AlL [its H(2) signal overlaps with the corresponding signal of the free ligand at $\delta$ = 8.89 ppm]. In addition to the peaks of AlL and of the free ligand, at pD = 2.8 new broad signals of $CH_3$, H(2), H(5), and H(6) appear (e.g. at $\delta$ = 7.05 ppm) due to the formation of $AlL_2$. The broadness of these signals cannot be due to fast ligand exchanges, because the peaks of the free ligand are narrow. It may be explained as chemical-shift dispersion by the formation of four possible spatial isomers of $AlL_2$. At pD = 7.4, where only the species $AlL_3$ exists in solution in a significant amount, a complicated pattern is observed. The signal centered at $\delta$ = 6.95 ppm shows clearly four doublets having identical coupling constants ($^3J$ = 7.25 Hz), and as for Al/1M3H4P this pattern can be explained by assuming the formation of $AlL_{3\text{-sym}}$ and $AlL_{3\text{-unsym}}$. For this system it can be seen that the four doublets are equally intense, indicating that $[AlL_{3\text{-unsym}}] = 3\cdot[AlL_{3\text{-sym}}]$, as statistically expected. The independence of the relative intensities of these four doublets from pD was confirmed by another spectrum obtained at pD = 6.4 (not shown). The broad band at $\delta$ = 7.05 ppm, as well as the peak at 8.9 ppm, are produced by the minor species $AlL_2$ and $AlL_2H_{-1}$ (these two peaks do not couple with the peaks of $AlL_3$ centered at $\delta$ = 8.85, 8.20 and 6.95 ppm, as demonstrated by a COSY spectrum). The signals of the complexes, differently from those of the free ligand, do not show an appreciable pD-dependent shift, because they do not undergo any deprotonation (except $AlL_2$ to a small extent) in the entire pD range.

Generally, the use of $D_2O$ instead of $H_2O$ does not modify the qualitative results, i.e. the species existing in $H_2O$ should be present in $D_2O$ as well. However, heavy water introduces isotopic effects, which may modify the quantitative distribution of the species, especially of those bearing acidic protons.[18,19] In order to obtain NMR quantitative data directly comparable with the potentiometric results, the system Al/1M3H4P was investigated in $H_2O$. The spectra are identical to the corresponding ones in $D_2O$ (except that all peaks are broader). The integration values of the signals of the free ligand and of the complexes give the relative amount of free and complexed ligand. The results obtained are reported in Table 3, together with the corresponding values calculated from the stability constants reported in Table 1 and Table 2. The agreement between the two sets of data is very good at all pH values, suggesting the absence of systematic errors in the results.

### *Metal–Ligand Complexes – Comparison with Previous Results*

As previously mentioned, the methylation of the pyridinic ring is expected to increase the affinity of the ligand towards aluminium(III). To verify this, pAl plots[20] vs. pH for 1M3H4P, 1M4H3P, and their corresponding unmethylated compounds were computed (Figure 8): higher pAl values indicate stronger metal–ligand complexes. The plot for

 © 2006 Wiley-VCH Verlag GmbH & Co. KGaA, Weinheim 

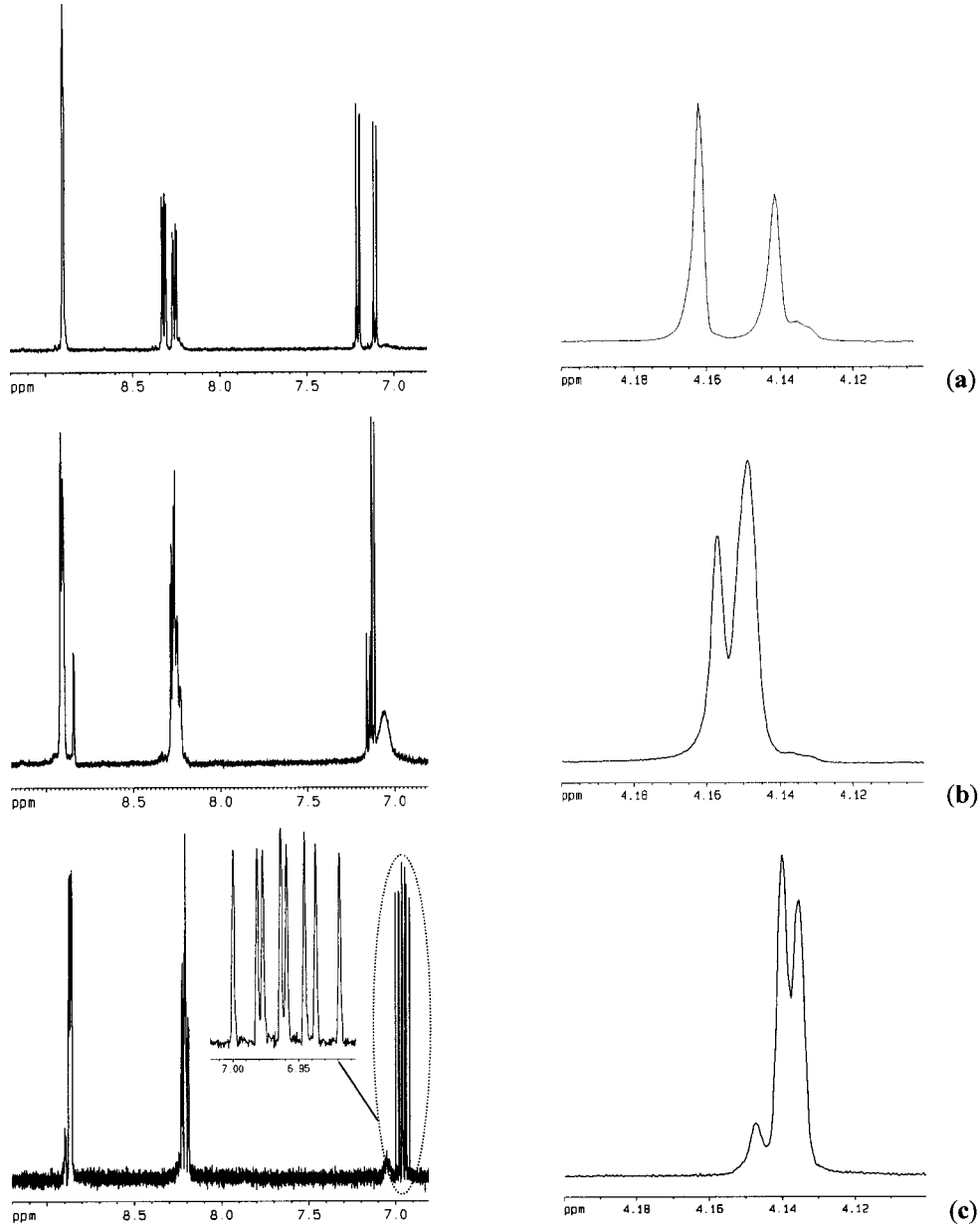


Figure 7. $^1H$ NMR spectra of $D_2O$ solutions containing $Al^{III}$ ($6.5 \cdot 10^{-3}$ m) and 1M4H3P ($1.1 \cdot 10^{-2}$ m), pD = 1.1 (a), 2.8 (b). Spectrum of $Al^{III}$ ($6.5 \cdot 10^{-3}$ m) + 1M3H4P ($2.0 \cdot 10^{-2}$ m), pD = 7.4 (c). The sensitivity of spectra in the aromatic zone was enhanced by a factor 4.

Table 3. Percentages of free and complexed ligand (Al/1M3H4P spectra in $H_2O$).

| pH | From NMR data | | From potentiometric results | |
|---|---|---|---|---|
| 2.08 | free ligand | 54.9 | $H_2L^+ + HL$ | 54.1 |
| | compl. ligand | 45.1 | $AlL^{2+} + 2\ AlL_2^+$ | 45.9 |
| 3.05 | free ligand | 40.1 | HL | 40.0 |
| | compl. ligand | 59.9 | $AlL^{2+} + 2\ AlL_2^+ + 3\ AlL_3$ | 60.0 |
| 4.04 | free ligand | 25.0 | HL | 26.2 |
| | compl. ligand | 75.0 | $AlL^{2+} + 2\ AlL_2^+ + 3\ AlL_3$ | 73.8 |
| 5.04 | free ligand | 12.0 | $HL + L^-$ | 14.7 |
| | compl. ligand | 88.0 | $2\ AlL_2^+ + 3\ AlL_3$ | 85.3 |
| 6.12 | free ligand | 8.6 | $HL + L^-$ | 8.5 |
| | compl. ligand | 91.4 | $2\ AlL_2^+ + 2\ AlL_2H_{-1} + 3\ AlL_3$ | 91.5 |

deferiprone (speciation data from ref.[21]) is reported for comparison. The HPs 3H4P, 4H3P, 1M3H4P, and 1M4H3P, are weaker aluminium(III) chelators than deferiprone at all pH values. However, it is important to note that 1M3H4P forms significantly more stable complexes with aluminium(III) than 3H4P does, especially at slightly acidic and neutral pH values: the pAl difference is up to two log units. On the other hand, the same methyl substitution in 4H3P did not produce any increase in chelation strength, as pAl values of 1M4H3P are almost identical to those of 4H3P. We do not yet have an explanation for the different effect of the *N*-methyl substitution in the two isomers. The

 © 2006 Wiley-VCH Verlag GmbH & Co. KGaA, Weinheim 

study of other alkylated HPs, now in progress, should better clarify this point.

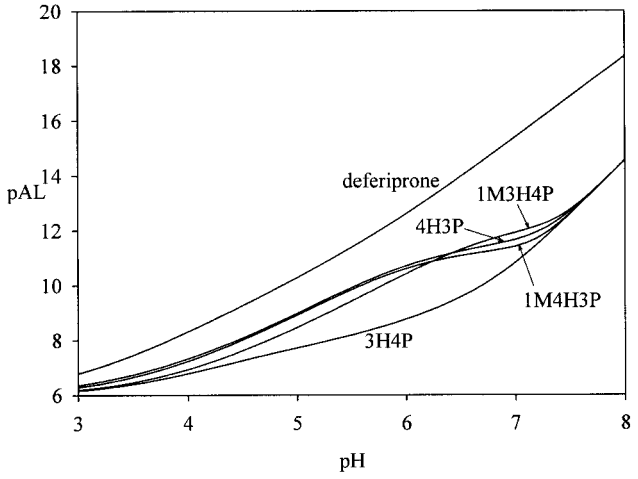


Figure 8. pAl for several ligands (see text); $[Al]_0 = 10^{-6}$ m, $[ligand]_0 = 5 \cdot 10^{-5}$ m.

### *n*-Octanol/Water Distribution and Chelation Efficacy

The octanol/water distribution coefficients of 1M3H4P, 1M4H3P and deferiprone were $0.0054 \pm 0.0042$, $0.0015 \pm 0.0013$, and $0.031 \pm 0.019$, respectively (mean ± standard deviation of 3 experiments, each conducted with duplicate observations), which shows the high hydrophilicity of these new ligands. In the presence of 1M3H4P and 1M4H3P, the concentration of Al in the octanol phase was very much lower than in the aqueous phase, which indicates very high hydrophilicity of the metal–ligand complexes. The results with deferiprone are reasonably similar to those previously published.[22]

The chelation-efficacy results obtained for deferiprone, 1M3H4P and 1M4H3P are summarized in Table 4. The efficiency of Al chelation of deferiprone (74%) is similar to that previously reported (65%).[22] As for 1M3H4P and 1M4H3P the results of the potentiometric studies show a 1:3 Al–ligand complex at pH 7.4 (Figure 2), the efficiency was calculated to show the percentage of ligand associated with aluminium in a 1:3 Al–ligand complex. Values for 3H4P and 4H3P are reported as well for comparison. An appreciable increase in efficiency can be observed for the 1-methyl derivatives. Statistical comparison of the efficiency of 3H4P, 4H3P, 1M3H4P and 1M4H3P by 1-way ANOVA followed by a Neuman–Keuls multiple comparison test shows a significant difference between 3H4P and 1M3H4P. Efficacy results are in agreement with thermodynamic data predictions at physiological pH, as the values at pH = 7.4 found in this study are in the same order as the pAl values are (Figure 8), i.e. 1M3H4P > 4H3P > 1M4H3P > 3H4P.

## Conclusions

Both 1M3H4P and 1M4H3P form strong complexes in solution with aluminium(III), so that in the investigated concentration range ($3 \cdot 10^{-4}$ m < $[Al]_0$ < $10^{-3}$ m, $10^{-3}$ m < $[L]_0$ < $4 \cdot 10^{-3}$ m) no metal hydroxide precipitates at neutral pH values in the presence of a threefold or higher ligand excess over aluminium(III). For both ligands the species AlL, $AlL_2$, $AlL_3$ and the minor species $AlL_2H_{-1}$ are formed in solution. UV spectra studies confirmed the stability constants for $AlL_2$ that were obtained in the potentiometric studies. $^1H$ NMR spectra in $D_2O$ at acidic pD values confirmed that several complexes coexist in solution. At neutral pD values the spectra allowed the detection of two different diastereoisomers of $AlL_3$, which could be quantified for 1M4H3P. For 1M3H4P the spectra indicated that in $AlL_3$ the aromatic ring of the ligand is distorted and that metal–ligand exchanges occur. For Al/1M3H4P, NMR spectra in $H_2O$ confirmed the quantitative ratio between free and complexed ligand at several pH values. The chelation efficiencies are quite high, and they are in agreement with thermodynamic data at physiological pH.

Table 4. $Al^{III}$ chelation efficiencies of some hydroxypyridinecarboxylic acids. The values for DFO and for deferiprone are reported for comparison. Values reported are mean ± standard deviation of three experiments with DFO, deferiprone, 3H4P and 4H3P, and six experiments with 1M3H4P and 1M4H3P, each conducted in duplicate.

| Ligand | Chelation efficiency (%) | Reference |
|---|---|---|
| DFO | 112 ± 29 | this work |
| deferiprone | 74 ± 6 | this work |
| 1M3H4P | 50 ± 16 | this work |
| 1M4H3P | 37 ± 15 | this work |
| 3H4P | 20 ± 2 | [9] |
| 4H3P | 43 ± 6 | [9] |

The metal–ligand complexes are very hydrophilic at physiological pH. This should be regarded as a positive property: although chelating agents having $D_{o/w}$ values around 0.2 were hypothesized to be best suitable,[23] in our evaluation of a series of 3,4-hydroxypyridinones we found that some very hydrophilic compounds were among the most orally bioavailable and effective chelators of Al.[24–26]

On the other hand, 1M3H4P and 1M4H3P form weaker complexes than deferiprone does at all pH values. Therefore, these derivatives are expected to not be as effective in vivo. The synthesis of HPs with stronger affinity towards aluminium(III) is advisable.

1M3H4P forms significantly stronger complexes with aluminium(III) than does 3H4P. This suggests that further alkylation of the pyridinic ring can be a good strategy towards the synthesis of stronger aluminium chelators. For 1M4H3P no increase of stability was observed with respect to 4H3P. It is therefore not clear whether the alkylation of the pyridinic ring can be effective for all HPs. Other derivatives should be investigated in order to clarify the effect of the alkyl substitution. In order not to affect significantly the high hydrophilicity of the complexes, the simple methyl derivatives seem to be more promising. Towards this goal, the syntheses of 2-methyl and 1,2-dimethyl derivatives of 3H4P and 4H3P, and the thermodynamic and in vitro studies of the complexation with aluminium(III), are now in progress.

 © 2006 Wiley-VCH Verlag GmbH & Co. KGaA, Weinheim 

## Experimental Section

### Synthesis of the Ligands

All chemicals and solvents were obtained from Aldrich Chimica, Lancaster or Acros. The identity and purity of the intermediates and of the final compounds were checked by melting point (m.p.) measurements (Gallenkamp MFB 595010 M/B capillary m.p. apparatus), $^1$H NMR spectra (Bruker 300 MHz), TLC (Merck silica gel 60F-254 glass plates), mass spectrometry (Mat, 112 Varian Mat Bremen mass spectrometer) and elemental analysis (Perkin–Elmer Elemental Analyzer Model 240B).

**1M3H4P:** 3H4P (0.5 g, 3.62 mmol) was dissolved in 30 mL DMF by adding NaOH 10% dropwise up to pH = 10, then $CH_3I$ (1.12 mL, $d$ = 2.280 g·cm$^{-3}$, 17.99 mmol) was added. The mixture was heated at 100 °C for 2 h and after cooling it was acidified with concd. HCl and the solvents evaporated to dryness. The residue was re-crystallized twice from ethanol and glacial $CH_3COOH$ giving 0.84 g (83% yield) of 1M3H4P·HI (*N*-methyl-3-hydroxy-4-carboxypyridinium iodide); m.p. 258 °C. $^1$H NMR ([D$_6$]DMSO): $\delta$ = 4.24 (s, 3 H, $CH_3$), 7.97 [d, $^3J_{5,6}$ = 5.92 Hz, 1 H, H(5)], 8.05 [dd, $^3J_{5,6}$ = 5.92 and $^4J_{6,2}$ = 0.95 Hz, 1 H, H(6)], 8.42 [d, $^4J_{2,6}$ = 0.95 Hz, 1 H, H(2)] ppm.

The iodide salt was transformed into the 3-hydroxy-*N*-methylpyridinium-4-carboxylate zwitterion (betaine). To this aim, the iodide salt (0.984 g) was dissolved in water (10 mL), acidified at pH = 2 with concd. HCl, and added to IRA-400-Cl amberlite resin (2.21 g, previously conditioned with HCl 1 M). The mixture was stirred for 2 h and then the resin was filtered off, the filtrate evaporated and the residue re-crystallized from glacial $CH_3COOH$. The collected precipitate was washed with acetone and dried (0.44 g, yield 83%). M.p. 252 °C (dec.). IR (KBr): $\tilde{\nu}$ = 3387, 2857, 2510, 1722 cm$^{-1}$. $^1$H NMR ([D$_6$]DMSO): $\delta$ = 4.19 (s, 3 H, $CH_3$), 8.02 [dd, $^3J_{5,6}$ = 5.8 Hz, 2 H, H(5) and H(6)], 8.44 [s, 1 H, H(2)] ppm. HR MS: $m/z$ = [MH]$^+$ 154.11. $C_7H_7NO_3$ (153.15): calcd. C 54.90, H 4.61, N 9.15; found C 54.85, H 4.62, N 9.10.

Finally, the betaine product was transformed into the corresponding chloride salt (1M3H4P·HCl), by dissolution in ethyl acetate and addition of concd. HCl. Then the resulting solution was evaporated to dryness (0.54 g, yield 100%). M.p. 220 °C. $^1$H NMR ($CD_3OD$): $\delta$ = 4.21 (s, 3 H, $CH_3$), 8.30 [d, $^3J_{5,6}$ = 6.3 Hz, 1 H, H(5)], 8.42 [d, $^3J_{5,6}$ = 6.4 Hz, 1 H, H(6)], 8.77 [s, 1 H, H(2)] ppm. HR MS : $m/z$ = [MH]$^+$ 155.23. $C_7H_8ClNO_3$ (189.60): calcd. C 44.34, H 4.25, N 7.39, Cl 18.70; found C 44.41, H 4.03, N 7.32, Cl 18.43. A 97.86% purity was obtained from potentiometric titrations.

**1M4H3P:** $CH_3I$ (4.25 mL, $d$ = 2.280 g·cm$^{-3}$, 68.26 mmol) was added to a 50-mL DMF solution containing 4H3P (1.89 g, 13.87 mmol). The mixture was heated to 100 °C for 2 h. The volatiles were then evaporated and the solid residue was re-crystallized from ethanol yielding a crystalline white product (2.10 g). Yield 99%; m.p. 248–249 °C. IR (KBr): $\tilde{\nu}$ = 3050, 1720, 1655 cm$^{-1}$. $^1$H NMR ([D$_6$]DMSO): $\delta$ = 3.73 (s, 3 H, $CH_3$), 6.75 [d, $^3J_{5,6}$ = 7.43 Hz, 1 H, H(5)], 8.06 [dd, $^3J_{5,6}$ = 7.43 and $^4J_{2,6}$ = 2.2 Hz, 1 H, H(6)], 8.69 [d, $^4J_{2,6}$ = 2.2 Hz, 1 H, H(2)], 16.36 (br. s, 1 H, COOH) ppm. HR MS: $m/z$ = [MH]$^+$ 154.11. $C_7H_7NO_3$ (153.14): calcd. C 54.9, H 4.61, N 9.15; found C 54.24, H 4.71, N 8.89. A 99.33% purity was obtained from potentiometric titrations.

### Solution Equilibria

The experimental apparatus, reagents and measurement methods were almost the same as reported previously.[27] In the following, a summary will be given; details are reported only when different from those already described.

**Apparatus:** All potentiometric measurements were performed with a Radiometer ABU93 Triburette apparatus. UV spectra were recorded with a Perkin–Elmer Lambda 25 spectrophotometer, $^1$H NMR spectra with Bruker DRX-400 and DRX-600 spectrometers operating at 400.13 and 600.09 MHz, respectively.

**Reagents:** All analyte concentrations were expressed in the molality scale (mol/kg of water). For potentiometric and UV measurements, working solutions of HCl (0.2 m), NaOH (0.2 m) and $AlCl_3$ (0.1 m, containing 0.3 m HCl) were prepared and standardised. 1M3H4P and 1M4H3P were used as synthesized to prepare respectively 0.14 m and 0.15 m working solutions. The ionic strength of all the solutions was adjusted to 0.6 m (0.594 M) (Na)Cl. Solutions for $^1$H NMR measurements were prepared by dissolving in $D_2O$ (Aldrich, 99.9 atoms% D), or in $H_2O$, weighed amounts of ligand, $AlCl_3$ (Fluka, ≥ 99%) and NaCl.

**Potentiometric Titrations:** Potentiometric titrations carried out in this work are summarized in Table 5. Temperature was 25.0 ± 0.1 °C. Duplicate potentiometric measurements were executed by using two different glass electrodes (Radiometer pHG201 and BDH 309/1015/02) and a Ag/AgCl/0.6 m NaCl reference electrode[28,29] with a J-shaped junction. Its acidic liquid junction potential has been determined previously[30] and it can be represented by the equation[29] $E_j = -S\cdot\log(1 + J\cdot[H^+])$, with $J$ = 3.69 ± 0.08.

Table 5. Potentiometric titrations (titrant: NaOH).

| Solutions | | Conditions $[Al]_0/10^{-3}$ m | $[L]_0/10^{-3}$ m | $[L]_0/[Al]_0$ | pH |
|---|---|---|---|---|---|
| 1. | 1M3H4P | – | 0.47–3.78 | – | 2.5–11.0 |
| | 1M4H3P | | 1.29–4.14 | | 2.6–11.0 |
| 2. | Al + 1M3H4P | 0.36–1.03 | 1.16–3.76 | 1, 2, 3, 4, 8 | 2.2–9.0 |
| | Al + 1M4H3P | 0.32–1.10 | 1.27–4.12 | | |

As a check of the accuracy of the entire experimental system, the p$K_w$ value for water in (Na)Cl 0.6 m was computed from HCl + NaOH titrations. The values obtained from two different series of experiments (p$K_w$ = 13.719 ± 0.002 and p$K_w$ = 13.710 ± 0.002) compare well with the literature value[31] in NaCl 0.6 M at 25 °C (13.727 ± 0.001).

All stability constants were calculated with the computer program PITMAP.[32] The hydroxo metal species reported by Öhman[13] have been considered and the corresponding log $\beta$ values kept fixed during the elaboration of the data.

After the addition of the metal and one of the two ligands to an acidic solution (pH < 3), the measured electromotive force drifted and reached a constant value only after ca. 1 hour, suggesting a low complex formation rate. The kinetics of the aluminium–ligand reaction became "normal" (equilibration after ca. 1 min) at pH values above 3. These findings are in agreement with previous results with other HPs.[9,14,33] Experimental details regarding the handling of the slow kinetics during the titrations are reported.[14]

**UV Measurements:** UV measurements (Table 6) were carried out for solutions containing the ligand alone, and for solutions containing the ligand and the metal ion, at various pH values (cell path 0.1 cm). When the pH of the solution was below 2, it was computed from the stoichiometric concentration of HCl, because the $[H^+]$ modifications produced by the other species were negligible under these conditions. In other cases the pH was measured with the same electrodes and procedures as for potentiometric titrations. The p$K_{a1}$ for both ligands and the log $\beta$ values for some aluminium–ligand complexes were computed by the program PITMAP.

 © 2006 Wiley-VCH Verlag GmbH & Co. KGaA, Weinheim 

Table 6. UV measurements.

| Solutions | Conditions $[Al]_0/10^{-3}$ m | $[L]_0/10^{-3}$ m | pH | $\lambda$ (nm) for calcd. |
|---|---|---|---|---|
| 1M3H4P | – | 0.98 | 0.25–2.00 | 217; 249; 324; 346 |
| 1M4H3P | – | 1.01 | 0.23–2.55 | 252; 290 |
| Al + 1M3H4P | 0.29 | 0.92 | 2.05–6.74 | 229; 303; 338 |
| Al + 1M4H3P | 0.30 | 0.93 | 1.80–7.16 | 256; 266; 298 |

**NMR Measurements:** $^1$H NMR spectra were obtained at 298 K. The chemical shift values are given in $\delta$ units with reference to internal $Me_4Si$. Suitable integral values for the proton spectra were obtained by a pre-scan delay of 10 s. The assignments of the proton resonances were performed by standard chemical shift correlations, COSY, TOCSY and NOESY experiments. $^1$H spectra were collected for both 1M4H3P and 1M3H4P at various pD values in $D_2O$ solutions containing only the free ligand or the ligand and the metal. For Al+1M3H4P, additional spectra were obtained in $H_2O$ (Table 7). For $D_2O$ solutions, the pH was measured with a glass electrode BDH 309/1025/02 previously calibrated in buffered solutions at pH = 4 and pH = 7, and 0.41 pH units were added to the pH meter readings to correct for isotopic and solvent effects,[34] i.e. pD rather than pH values were measured. For the $H_2O$ solutions, the pH was measured as described above for potentiometric titrations. Heavy water, necessary for the instrumental lock, was in a capillary concentric with the NMR tube.

### *n*-Octanol/Water Distribution and Chelation Efficacy

**Materials:** NaCl, KCl, $NaHCO_3$, $H_3BO_3$ and *n*-octanol were obtained from EM, Fisher, or Sigma; Al borate from Pfaltz and Bauer (Waterbury, CT) and an Al atomic absorption standard from Sigma. Polypropylene test tubes (10 mL) with polyethylene caps were purchased from VWR.

**Methods:** The distribution coefficients ($D_{o/w}$) of the ligands were determined as their concentration in the octanol phase/their concentration in the aqueous phase at equilibrium with a Shimadzu UV-2501PC UV/Vis recording spectrophotometer. UV absorbance was measured at $\lambda_{max}$, determined from a wavelength scan of the ligand.

A method to assess the aluminium chelation efficiency in vitro was used.[35] An octanol/aqueous system containing 125 mM NaCl, 25 mM $NaHCO_3$, 4.5 mM KCl and 100 mM borate at pH 7.4 was established. Equal volumes (4 mL) of the aqueous phase and 1-octanol were placed in a screw-cap polypropylene tube. The octanol phase was saturated with the aqueous solution before use to avoid distribution of hydrophilic compounds into the aqueous component of the octanol phase which would produce a falsely elevated value for octanol distribution. The opposite (i.e., the saturation of the aqueous phase with octanol) was not needed for our hydrophilic compounds.

For each experiment, duplicate tubes were prepared to contain 1) only the octanol and the aqueous phase, 2) as 1) plus 7 to 8 mg of aluminum borate to provide an excess of undissolved Al, saturating the aqueous phase and octanol with Al, 3) as 1) plus the ligand introduced into the aqueous phase at $1 \cdot 10^{-3}$ M, and 4) as 3) plus 7 to 8 mg of aluminum borate. The tubes were agitated overnight at room temperature to establish equilibrium.

**Aluminum Analysis:** The tubes were centrifuged (3400 g, 10 min), the aqueous phase was filtered through a filter with a 0.22 μm nylon membrane and then each phase analyzed by electrothermal atomic absorption spectroscopy (Perkin–Elmer 4100ZL) to determine the Al concentration. Aluminum recovery from the filtered aqueous phase was found to be 101% ± 6% (mean ± standard deviation of 12 observations), showing no loss of Al due to the filter.

**Chelator Efficiency:** The amount of Al in each liquid phase of tubes with added Al but no ligand, minus the amount of Al in tubes without added Al or ligand represented Al solubility from aluminum borate. The increase in Al in each liquid phase of tubes with Al plus ligand, over that seen in the absence of the ligand, was taken as complexation of Al by the ligand. In addition to 1M3H4P and 1M4H3P, values for the hexadentate ligand desferrioxamine (DFO) and the bidentate ligand deferiprone were obtained as positive controls to confirm the ability of the method to predict Al complexation (values close to 100% were expected). For DFO, where at pH = 7.4 a 1:1 aluminium/ligand complex was anticipated, the chelator efficiency was calculated by

$$\frac{[\text{sum of the M Al concentration in each phase}]}{1 \times 10^{-3}\ \text{M}}$$

For deferiprone, 1M3H4P and 1M4H3P, where at pH = 7.4 a 1:3 aluminium/ligand complex was anticipated (see, for example Figure 2), the chelator efficiency was calculated by

$$\frac{3[\text{sum of the M Al concentration in each phase}]}{1 \times 10^{-3}\ \text{M}}$$

## Acknowledgments

We thank professor Gianfranco Chiarelotto for helpful suggestions for the syntheses, and Paolo Rossi and Rebecca Florence for careful experimental work.

Table 7. NMR measurements.

| Solutions | Conditions $[Al]_0/10^{-3}$ m | $[L]_0/10^{-3}$ m | Solvent | pH/pD | Bidimensional spectra |
|---|---|---|---|---|---|
| 1M3H4P | – | 19 | $H_2O$ | 2.1; 3.0; 4.0; 5.0; 6.1 | – |
| 1M3H4P | – | 19 | $D_2O$ | 1.9; 4.0; 7.4 | – |
| 1M4H3P | – | 11 | $D_2O$ | 1.1; 2.8; 7.4 | – |
| Al + 1M3H4P | 6 | 19 | $H_2O$ | 2.1; 3.0; 4.0; 5.0; 6.1 | – |
| Al + 1M3H4P | 6 | 19 | $D_2O$ | 1.9 | COSY, TOCSY, NOESY |
| | | | | 4.0 | – |
| | | | | 6.5 | COSY, TOCSY, NOESY |
| Al + M4H3P | 6 | 11 | $D_2O$ | 1.1 | – |
| | | 11 | | 2.8 | – |
| | | 20 | | 6.4 | – |
| | | 20 | | 7.4 | COSY |

 © 2006 Wiley-VCH Verlag GmbH & Co. KGaA, Weinheim 

[1] C. Hershko (Guest Editor), *Sem. Hematol.* **2005**, *42* (Issue 2, Supplement 1).
[2] M. D. Cappellini, *Best Pract. Res. Clin. Haemat.* **2005**, *18*, 289–298.
[3] G. J. Kontoghiorghes, K. Pattichis, K. Neocleous, A. Kolnagou, *Curr. Med. Chem.* **2004**, *11*, 2161–2183.
[4] G. J. Kontoghiorghes, *Analyst* **1995**, *120*, 845–851.
[5] G. Faa, G. Crisponi, *Coord. Chem. Rev.* **1999**, *184*, 291–310.
[6] R. A. Yokel, P. Ackrill, E. Burgess, J. P. Day, J. L. Domingo, T. P. Flaten, J. Savory, *J. Toxicol. Environ. Health* **1996**, *48*, 667–683.
[7] M. L. Albina, M. Belles, D. J. Sanchez, J. L. Domingo, *Teratology* **2000**, *62*, 86–92.
[8] N. F. Olivieri, G. M. Brittenham, C. E. McLaren, D. M. Templeton, R. G. Cameron, R. A. McClelland, A. D. Burt, K. A. Fleming, *N. Engl. J. Med.* **1998**, *339*, 417–423.
[9] V. B. Di Marco, R. A. Yokel, M. G. Ferlin, A. Tapparo, G. G. Bombi, *Eur. J. Inorg. Chem.* **2002**, 2648–2655.
[10] V. B. Di Marco, A. Tapparo, A. Dolmella, G. G. Bombi, *Inorg. Chim. Acta* **2004**, *357*, 135–142.
[11] K. A. Wright, R. B. Cain, *Biochem. J.* **1971**, *128*, 543–559.
[12] A. Agafonova, I. Agafonov, *Zh. Fiz. Khim.* **1953**, *27*,1137, taken from ScQuery v.5.13, The Iupac stability constant database, Academic Software, Copyright 2001.
[13] L. O. Öhman, *Inorg. Chem.* **1988**, *27*, 2565–2570.
[14] V. B. Di Marco, A. Tapparo, G. G. Bombi, *Ann. Chim. (Rome, Italy)* **1999**, *89*, 535–546.
[15] C. L. Perrin, T. J. Dwyer, *Chem. Rev.* **1990**, *90*, 935–967.
[16] A. Venzo, A. Bisello, A. Ceccon, F. Manoli, S. Santi, *Inorg. Chem. Commun.* **2000**, *3*, 1–4.
[17] L. Pandolfo, R. Seraglia, A. Venzo, S. Gross, *Inorg. Chim. Acta* **2005**, *358*, 2739–2748.
[18] C. K. Rule, V. K. La Mer, *J. Am. Chem. Soc.* **1938**, *60*, 1974–1986.
[19] K. J. Laidler, Chemical kinetics. 3 edition., New York, Harper International, **1987**.
[20] T. Kiss, E. Farkas, *Perspec. Bioinorg. Chem.* **1996**, *3*, 199–250.
[21] E. T. Clarke, A. E. Martell, *Inorg. Chim. Acta* **1992**, *191*, 57–63.
[22] R. A. Yokel, A. K. Datta, E. G. Jackson, *J. Pharmacol. Exp. Ther.* **1991**, *257*, 100–106.
[23] J. B. Porter, E. R. Huehns, R. C. Hider, *Clin. Haematol.* **1989**, *2*, 257–292.
[24] R. A. Yokel, A. M. Fredenburg, K. A. Meurer, T. L. Skinner, *Drug Metab. Dispos.* **1995**, *23*, 1178–1180.
[25] R. A. Yokel, K. A. Meurer, T. L. Skinner, A. M. Fredenburg, *Drug Metab. Dispos.* **1996**, *24*, 105–111.
[26] R. A. Yokel, K. A. Meurer, C. B. Hong, K. M. Dickey, T. L. Skinner, A. M. Fredenburg, *Drug Metab. Dispos.* **1997**, *25*, 182–190.
[27] V. B. Di Marco, A. Tapparo, G. G. Bombi, *Ann. Chim. (Rome, Italy)* **1999**, *89*, 397–407.
[28] G. J. Janz, "*Silver – Silver Halide Electrodes*", in: *Reference Electrodes: Theory and Practice* (Eds.: D. J. G. Ives, G. J. Janz), New York – London, Academic Press, **1961**.
[29] G. Biedermann, L. G. Sillén, *Ark. Kemi* **1953**, *5*, 425–440.
[30] V. B. Di Marco, A. Tapparo, G. G. Bombi, *Ann. Chim. (Rome, Italy)* **2001**, *91*, 595–603.
[31] S. Sjöberg, Y. Hägglund, A. Nordin, N. Ingri, *Mar. Chem.* **1983**, *13*, 35–44.
[32] V. B. Di Marco, *Ph. D. Thesis*, University of Padova, **1998**.
[33] C. Baiocchi, E. Mentasti, *Ann. Chim. (Rome, Italy)* **1981**, *71*, 631–647.
[34] A. K. Covington, M. Paabo, R. A. Robinson, R. G. Bates, *Anal. Chem.* **1968**, *40*, 700–706.
[35] R. A. Yokel, H. B. Kostenbauder, *Toxicol. Appl. Pharmacol.* **1987**, *91*, 281–294.

Received: November 4, 2005
Published Online: January 26, 2006

 © 2006 Wiley-VCH Verlag GmbH & Co. KGaA, Weinheim 

DOI: 10.1002/ejic.200500843

# Complexes of Bidentate Phosphane Selenide Ligands with Mesitylenetellurenyl Iodide and with Tellurium Diiodide[‡]

Cristian G. Hrib,[a] Peter G. Jones,[a] Wolf-W. du Mont,*[a] Vito Lippolis,[b] and Francesco A. Devillanova[b]

**Keywords:** Phosphane selenides / Tellurium iodides / Heteronuclear NMR / Raman spectroscopy / Soft–soft interactions

Bis(diphenylphosphanyl)methane diselenide (dppm$Se_2$, **1**) and bis(diphenylphosphanyl)ethane diselenide (dppe$Se_2$, **2**) reacted with 2 equiv. $Br_2$ or $I_2$ to form the insoluble solid products, dppm$(SeX_2)_2$ (X = Br, **3**; X = I, **4**) and dppe$(SeX_2)_2$ (X = Br, **5**; X = I, **6**). However, using the iodine-like electrophile mesitylenetellurenyl iodide (MesTeI, **7**), fairly soluble complexes, dppm$Se_2$[Te(I)Mes]$_2$ (**8**) and dppe$Se_2$[Te(I)Mes]$_2$ (**9**), were obtained. Complexes **8** and **9** contain two T-shaped (10-Te-3) Se–Te(Mes)–I moieties bridged by dppm or dppe; solid **9** exhibits intermolecular *soft–soft* interactions between approximately linear Se–Te–I units. In a side reaction accompanying the crystallisation of complex **8**, or by the reaction of **1** with Te and $I_2$, a chelate complex dppm$Se_2TeI_2$ (**10**) was formed. Fortuitously, a crystal of the related compound dppe$Se_2TeI_2$ (**11**) was also obtained. In **10**, a square planar *cis*-$Se_2TeI_2$ group is part of a six-membered ring, and **11** is a coordination polymer with *trans*-$Se_2TeI_2$ moieties bridged by dppe. Averaged $^{31}$P- and $^{77}$Se NMR signals including $^{77}$Se–$^{31}$P couplings, together with broad $^{125}$Te NMR singlets indicate phosphane selenide ligand exchange in solution, that is, the kinetically labile behaviour of complexes **8** and **9**.

(© Wiley-VCH Verlag GmbH & Co. KGaA, 69451 Weinheim, Germany, 2006)

## Introduction

Phosphane chalcogenides $R_2R'P{=}Y$ (Y = S, Se) are known to act as donors towards dihalogen molecules.[2–5] Using phosphane selenides, which are stronger donors than the sulfides, a considerable number of 1:1 adducts $R_2R'PSeX_2$ have been isolated.[6–9] Iodine adducts exhibit type **A** (10-I-2) *molecular* structures $R_2R'PSeI_2$ (R, R′ = $C_6H_5$, $NMe_2$, $NEt_2$[7] and R = *t*Bu, R′ = I)[8] or type **C** (10-I-2) *ionic* structures $(R_3PSe)_2I^+I_3^-$,[6,10,11a] whereas bromination products exhibit type **B** (10-Se-3) T-shaped $PSeBr_2$ moieties in their structures (R, R′ = $NMe_2$, $C_6H_{11}$, *i*$C_3H_7$).[9,11a] With excess iodine, polyiodide salts featuring $R_3PSeI^+$ countercations (type **D**),[4,10,12] could be formed (Scheme 1). Many of these compounds are aggregated by further *soft–soft* contacts that lead to ion pairs, chains and extended networks.[3,4,6,8,9,11b,12] In particular, type **D**-like (iodoseleno)phosphonium cations behave as soft electrophiles by the iodine atom in the β position to the formally charged phosphorus atom (β-heteroatom Lewis acidity).[3,10,12]

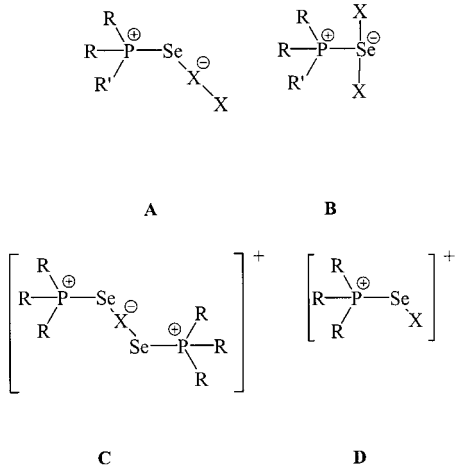


Scheme 1. Various Lewis-type structures of halogen adducts of phosphane selenides. These structures must be intended purely as a formal illustration of the various compounds with no implication as to the real distribution of charges. The same considerations apply to Scheme 2 and Scheme 3.

To stimulate the formation of supramolecular networks using the earlier mentioned types of soft–soft interactions, we are introducing *bifunctional* donor-acceptor systems into our studies. In a previous paper we described the self-assembly of iodophosphane selenides RR′P(=Se)I as bifunctional donor-acceptor molecules (selenium donor, iodine acceptor).[8] The bifunctional selenocarbonyl ligand 1,2-bis(3-methyl-4-imidazolin-2-selone)ethane was recently

[‡] Properties of Chalcogen–Chalcogen Bonds, 24. Part 23: Ref.[1]

[a] Institut für Anorganische und Analytische Chemie der Technischen Universität Braunschweig,
Postfach 3329, 38023 Braunschweig, Germany
Fax: +49-531-3915387
E-mail: w.du-mont@tu-bs.de
[b] Dipartimento di Chimica Inorganica ed Analitica, Complesso Universitario di Monserrato,
S. S. 554 Bivio per Sestu, 09042 Monserrato (CA), Italia
Fax: +39-070-6754456
E-mail: devilla@unica.it

 InterScience © 2006 Wiley-VCH Verlag GmbH & Co. KGaA, Weinheim 

shown to undergo $Br_2$[13] and IBr[14] oxidative addition at the Se atom of the >C=Se group, exhibiting a subtle interplay of soft–soft and hydrogen-bonding interactions in the solid.

In our present work we evaluate the use of bifunctional phosphane selenides, bis(diphenylphosphanyl)methane diselenide (dppm$Se_2$, **1**) and bis(diphenylphosphanyl)ethane diselenide (dppe$Se_2$, **2**), towards halogens ($Br_2$, $I_2$) and towards the halogen-like electrophile mesitylenetellurenyl iodide [MesTeI, **7**; Mes = 2,4,6-$(CH_3)_3C_6H_2$][15] with the intention of creating supramolecular soft–soft networks. Arenetellurenyl chlorides and bromides are known to give stable 1:1 complexes with triphenylphosphane selenide,[16a] tri(morpholine)phosphane selenide[16a,16b] and tris(dimethylamino)phosphane selenide.[17]

## Results and Discussion

### Formation of 1:2 Adducts of dppm$Se_2$ (1) and dppe$Se_2$ (2) with $Br_2$ and $I_2$

Addition of 2 equiv. $Br_2$ or $I_2$ to solutions of bidentate phosphane selenides (dppm$Se_2$, **1**, and dppe$Se_2$, **2**) led to precipitation of solids of the composition dppm$(SeX_2)_2$ (X = Br, **3**; X = I, **4**) and dppe$(SeX_2)_2$ (X = Br, **5**; X = I, **6**) (Scheme 2).

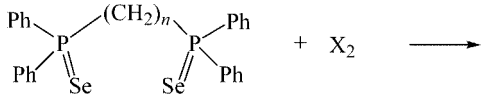


*n* = 1, dppm$Se_2$, **1**

*n* = 2, dppe$Se_2$, **2**

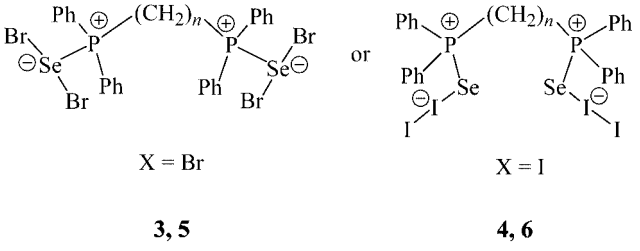


X = Br X = I

**3, 5** **4, 6**

Scheme 2. 1:2 Reactions of dppm$Se_2$ and dppe$Se_2$ with $Br_2$ and $I_2$. For an alternative structure of **4**, see vibrational spectra.

Since these materials are insoluble in aprotic-dipolar solvents and thus cannot be recrystallised, compounds **3**–**6** were not obtained as single crystals. In the absence of crystal data, only Raman spectra could be of help in investigating the structural features of the expected $PSeX_2$ functions of the compounds (see later). Reaction of dppe-diselenide **2** with only 1 equiv. $I_2$ also led to precipitation of the 1:2 product **6**; however, from $CH_2Cl_2$ solutions containing 1:1 mixtures of dppm-diselenide **1** with iodine, precipitation did not occur. The $^{31}P$ NMR spectrum of this solution shows only one resonance with a $^{77}Se,^{31}P$ satellite coupling that is smaller than that of the starting material. The $^{31}P$ NMR singlet may be due to a symmetric bonding mode of **1** with iodine, or, alternatively, to a rapid equilibration of coordinated and noncoordinated PSe functions (that is, signal averaging). In the $^{77}Se$ NMR spectra, titration-like addition of $I_2$ led to stepwise deshielding [**1**: $\delta^{77}Se$ = –240 ppm, **1**/$I_2$ (1:1 complex): $\delta^{77}Se$ = –68 ppm] and line broadening. This observation implies signal averaging at all stages of the iodine addition. Crystals of the 1:1 product were not obtained; precipitation by addition of pentane led to the solid 1:2 product **4**. Similarly, attempts to prepare 1:1 adducts of **1** and **2** with bromine led to formation of insoluble **5** and **6**.

### Reactions of dppm$Se_2$ (1) and dppe$Se_2$ (2) with MesTeI (7)

With the intention of exerting control over solubility properties and of introducing the NMR-active $^{125}Te$ nucleus as an additional probe for solution studies, we decided to include tellurenyl iodides in our study. Arenetellurenyl halides are known to exhibit electrophilic properties towards soft ligands; typically bromide, iodide and S-donor ligands lead to T-shaped complexes. A few phosphane selenide–tellurenyl bromide and chloride complexes have been crystallographically studied,[16,17] but neither a systematic structural study nor any heteronuclear NMR spectroscopic data has yet appeared in the literature. To favour aryl packing in the solid, we chose the in situ generated mesitylenetellurenyl iodide [MesTeI, **7**; Mes = 2,4,6-$(CH_3)_3C_6H_2$][15] as the iodine-related electrophile for coordination with **1** and **2**.

Addition of **1** or **2** to 2 equiv. **7**, prepared from $Mes_2Te_2$ with $I_2$, led to compounds **8** and **9**, which were isolated in moderate yields by crystallisation (Scheme 3). Complexes **8** and **9** were characterised by multinuclear NMR spectroscopy in solution, and a single crystal of the dppe$Se_2$ complex **9** was studied by X-ray crystallography.

Attempts to grow single crystals from crude solutions of **8** led to a few single crystals of an unexpected tellurium diiodide chelate complex **10**. Compound **10** was also isolated in small yield from reaction mixtures that were intended to produce a 1:1 complex of **1** with **7**. The $^{31}P$ NMR spectra of the 1:1 complexes of **1** and **2** with MesTeI show $^1J_{^{77}Se,^{31}P}$ coupling constants between those of **1**,**2** and **8**,**9** (Table 1). Compound **10** was also accessible by addition of elemental tellurium and iodine to dissolved **1** (Scheme 3). Fortuitously, upon crystallisation of compound **9**, a single crystal of the related tellurium diiodide complex **11** of ligand **2** was also isolated and studied by X-ray crystallography.

Formation of the $TeI_2$ complexes **10** and **11** from **7** involves breaking the Te–C bond, but the fate of the "lost" mesityl group remains unclear. Te–C bond cleavage with mesityl group transfer has previously been observed after a bromination/bromide abstraction sequence started with $Mes_2Te$ and led to $Mes_3Te^+$ $SbF_6^-$ and $Mes_5Te_2^+$ $SbF_6^-$.[1]

 © 2006 Wiley-VCH Verlag GmbH & Co. KGaA, Weinheim 

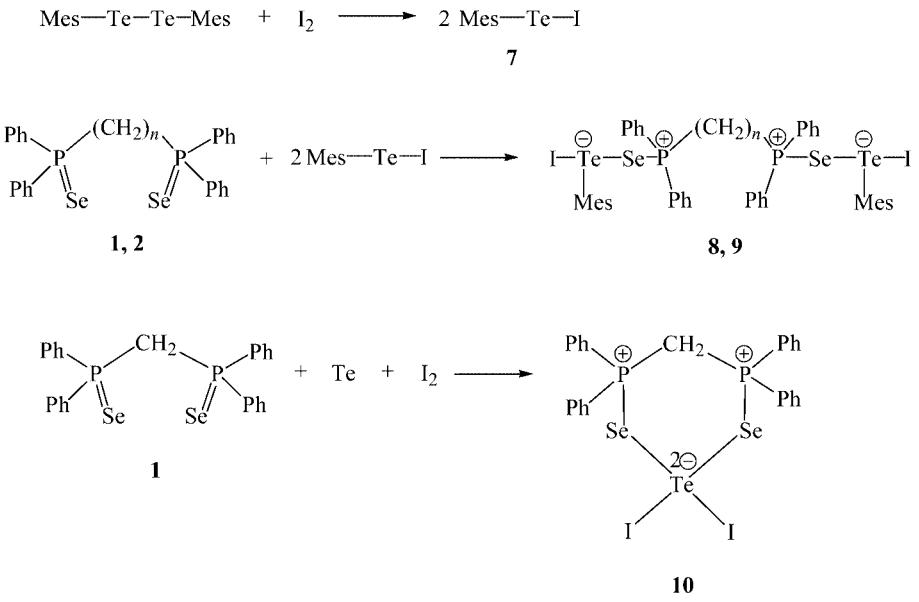


Scheme 3. Reactions of $dppmSe_2$ and $dppeSe_2$ with MesTeI.

Table 1. $^{31}P$-, $^{77}Se$- and $^{125}Te$ NMR spectroscopic data of ligands **1**,**2**, acceptor **7** and complexes **8**,**9**,**10** (solvent: $CD_2Cl_2$, *$CDCl_3$).

| | $\delta = {}^{31}P$ [ppm] | $^1J_{P,Se}$ [Hz] | $^nJ_{P,Se}$ [Hz] | $\delta = {}^{77}Se$ [ppm] | $\delta = {}^{125}Te$ [ppm] | $^nJ_{P,P}$ [Hz] |
|---|---|---|---|---|---|---|
| $dppmSe_2$ (**1**)[19,20] | 25.8 | 744.5 | 2.5 | –240.4 | – | 17.6 |
| $dppmSe_2[Te(I)Mes]_2$ (**8**) | 24.1 | 717.7 | – | –161 | 796 | 12.4 |
| $dppmSe_2TeI_2$ (**10**) | 21.8 | 682.3 | – | –93* | – | 8.9 |
| $dppeSe_2$ (**2**)[19] | 36.6 | 730.0 | 0.7 | –353.4 | – | 64.8 |
| $dppeSe_2[Te(I)Mes]_2$ (**9**) | 35.8 | 711.6 | 12.2 | –281 | 798 | 63.7 |
| MesTeI (**7**) | – | – | – | – | 867 | – |
| 1:1 complex (**1**:**7**)* | 24.2 | 727.5 | – | –170 | 727 | – |
| 1:1 complex (**2**:**7**)* | 35.6 | 720.8 | – | – | 614 | – |

Thermal decomposition of arenetellurenyl halides can also involve Te–C bond cleavage (loss of tellurium).[15]

## NMR Spectroscopic Investigation of Binuclear Complexes 8 and 9

The coordination of phosphane selenides with iodine or the oxidative addition of bromine to phosphane selenides is accompanied by a decrease in the NMR coupling constant $^1J_{^{31}P,^{77}Se}$.[7–10] The same observation is made when the bidentate phosphane selenide **1** reacts with 1 equiv. iodine, and when **1** or **2** coordinate with 2 equiv. mesitylenetellurenyl iodide **7**. Solutions containing **1** or **2** with fewer than 2 equiv. **7** do not give separate $^{31}P$ NMR signals for the different species in solution, instead averaged signals appear, which also show averaged $^{77}Se$ satellites. The averaged magnitudes of $^1J_{^{31}P,^{77}Se}$ decrease with increasing amounts of the electrophile **7**. The changes in the $^{77}Se$ NMR resonances of **1** and **2**[18,19] upon coordination with **7** (deshielding coordination shifts) are much larger than those of the $^{31}P$ NMR signals (Table 1). The $^{77}Se$ NMR resonances of **8** and **9** appear as (pseudo) doublets [X-parts of AA′X systems][18–20] due to $J_{^{77}Se,^{31}P}$, but they do not exhibit satellites from coupling with $^{125}Te$. Similarly, the broad $^{125}Te$ NMR signals do not allow the resolution of couplings with $^{31}P$: the kinetic lability (fast ligand exchange) of complexes **8** and **9** involves Se–Te bond breaking, whereas P–Se bonds stay intact. In relation to the signals of noncoordinated monomeric alkane- and arenetellurenyl halides [$(Me_3Si)_3CTeI$: $\delta^{125}Te$ = 1185 ppm,[21] 2,4,6-$iPr_3C_6H_2TeI$: $\delta^{125}Te$ = 842 ppm,[15] 2,4,6-$tBu_3C_6H_2TeI$: $\delta^{125}Te$ = 1162 ppm,[15] 2,4,6-$Me_3C_6H_2$-TeI: $\delta^{125}Te$ = 867 ppm], the $^{125}Te$ NMR signals of complexes **8** and **9** are deshielded by about 44–390 ppm. In the case of **8** and **9** and their mixtures with **1** and **2**, the exchange is apparently very fast on the NMR time scale.

## X-ray Crystallographic Studies

In solid $dppeSe_2[Te(I)Mes]_2$ (**9**), $dppeSe_2$ acts as a bridging bidentate ligand between two Te(I)Mes acceptor moieties (Figure 1a). The heavy-atom positions correspond to local inversion symmetry (rmsd = 6.6 pm; Figure 1b).

The molecules are packed in a way that allows side-on intermolecular soft–soft interactions between approximately linear Se–Te–I units, thus linking the molecules in chains parallel to the *x* axis (Figure 2).

The Te–I contacts are in the range of the sum of the relevant van der Waals radii. The "T"-type Se–Te(–C)–I

 © 2006 Wiley-VCH Verlag GmbH & Co. KGaA, Weinheim 

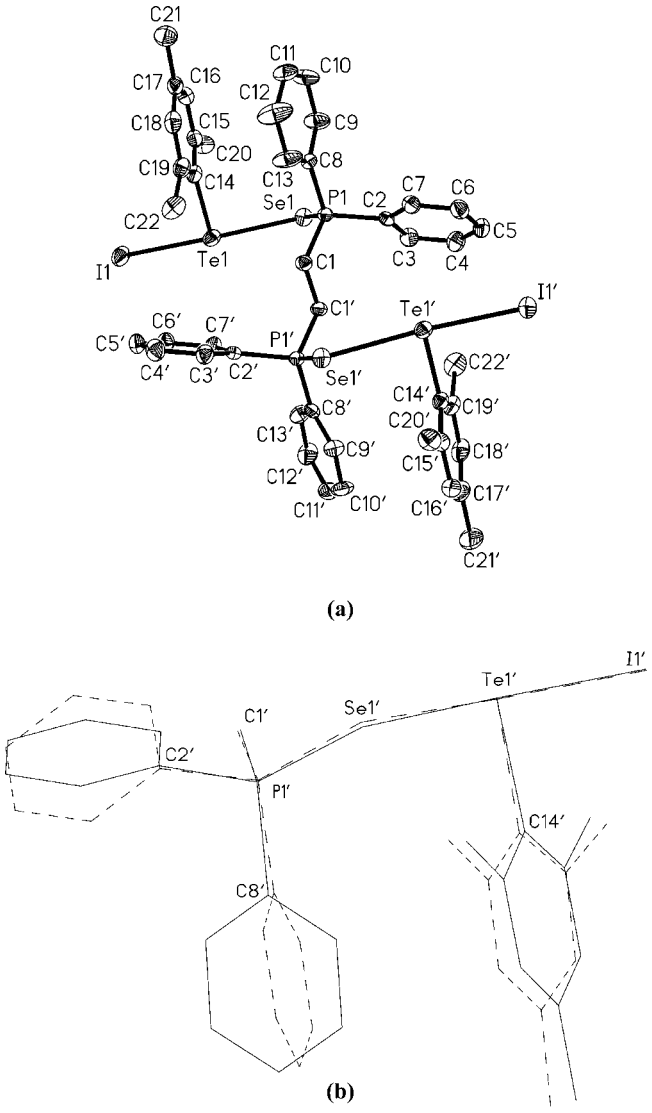


Figure 1. (**a**) Structure of $dppeSe_2[Te(I)Mes]_2$ (**9**); ellipsoid probability level 50%; all hydrogen atoms omitted for clarity; primes indicate atoms related by pseudosymmetry. (**b**) Least-squares fit of the two halves of molecule **9** (only heavy atoms and *ipso*-C fitted).

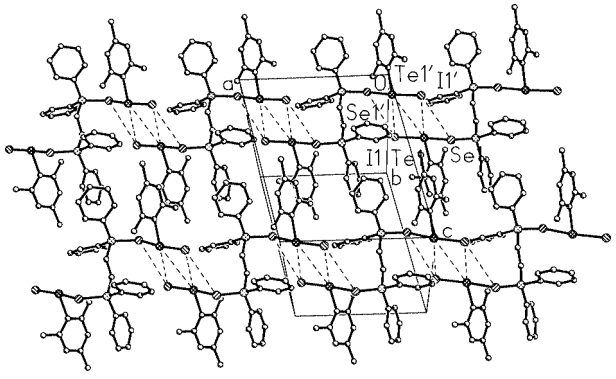


Figure 2. Intermolecular interactions in the packing diagram of **9**; selected contact distances [pm]: Se(1)–I(1′) 404.32(5), I(1′)–Te(1) 398.87(4), Te(1)–Te(1′) 415.83(3), I(1)–Te(1′) 400.35(4), Se(1′)–I(1) 414.30(5).

units deviate slightly from planarity (angles C–Te–Se 90°, C–Te–I 89°, Se–Te–I 173°; for standard deviations see Table 2); Se–Te and Te–I distances are in agreement with typical 3c-4e bonding (10-Te-3,[11] both bond orders are close to 0.5).[15,22,23]

Table 2. Bond lengths, interatomic contact distances [pm] and angles [°] of $dppeSe_2[Te(I)Mes]_2$ (**9**).[a]

| | | | |
|---|---|---|---|
| Te(1)–C(14) | 213.2(4) | C(1)–C(1′) | 151.8(4) |
| Te(1)–Se(1) | 287.75(4) | Te(1′)–C(14′) | 213.8(3) |
| Te(1)–I(1) | 289.61(4) | Te(1′)–I(1′) | 288.69(3) |
| Te(1)–Te(1′)#1 | 415.83(3) | Te(1′)–Se(1′) | 288.74(4) |
| I(1)–Te(1′)#1 | 400.35(4) | I(1′)–Te(1)#2 | 398.87(4) |
| Se(1)–P(1) | 215.13(9) | Se(1′)–P(1′) | 215.08(9) |
| Se(1)–I(1′)#1 | 404.32(5) | Se(1′)–I(1)#2 | 414.30(5) |
| | | | |
| C(14)–Te(1)–Se(1) | 91.5(1) | C(1)–P(1)–Se(1) | 113.4(1) |
| C(14)–Te(1)–I(1) | 89.85(9) | C(14′)–Te(1′)–I(1′) | 88.95(9) |
| Se(1)–Te(1)–I(1) | 172.96(1) | C(14′)–Te(1′)–Se(1′) | 89.96(9) |
| C(14)–Te(1)–Te(1′)#1 | 155.37(9) | I(1′)–Te(1′)–Se(1′) | 172.55(1) |
| Se(1)–Te(1)–Te(1′)#1 | 111.30(1) | Te(1′)–I(1′)–Te(1)#2 | 72.430(8) |
| I(1)–Te(1)–Te(1′)#1 | 66.379(8) | P(1′)–Se(1′)–Te(1′) | 107.05(3) |
| Te(1)–I(1)–Te(1′)#1 | 72.110(8) | P(1′)–Se(1′)–I(1)#2 | 119.70(3) |
| P(1)–Se(1)–Te(1) | 106.32(3) | Te(1′)–Se(1′)–I(1)#2 | 66.673(9) |
| P(1)–Se(1)–I(1′)#1 | 119.20(2) | C(8′)–P(1′)–Se(1′) | 113.4(1) |
| Te(1)–Se(1)–I(1′)#1 | 67.996(9) | C(2′)–P(1′)–Se(1′) | 110.0(1) |
| C(2)–P(1)–Se(1) | 110.2(1) | C(1′)–P(1′)–Se(1′) | 111.7(1) |
| C(8)–P(1)–Se(1) | 112.7(1) | | |

[a] Symmetry transformations used to generate equivalent atoms: #1: $x - 1, y, z$; #2: $x + 1, y, z$.

The Se–Te bonds in complex **9** are longer (Table 3) than those in chloro- and bromo-phenyl(trimorpholinophosphane selenide)tellurium(II)[16a,16b] and bromophenyl[tris(dimethylamino)phosphane selenide]tellurium(II),[17] and this correlates well with the weaker donor properties of alkyl-/arylphosphane selenides compared with aminophosphane selenides.[16a,16b,17,23] As expected, Se→Te donation is accompanied by P–Se bond expansion (ligand **2**: 209.4 pm,[18b] complex **9**: 215.1 pm).

Table 3. Important bond lengths (P–Se, Se–Te, Te–X) in solid phosphane selenides and phosphane selenidetellurenyl halogenides [pm].

| | P–Se | Se–Te | Te–X |
|---|---|---|---|
| $dppmSe_2$ (**1**)[18a] | 210.3(1) | – | – |
| $dppeSe_2$ (**2**)[18b] | 209.4(2) | – | – |
| $dppeSe_2[Te(I)Mes]_2$ (**9**) | 215.13(9) | 287.75(4) | 289.61(4) |
| | 215.08(9) | 288.74(4) | 288.69(3) |
| $dppmSe_2TeI_2$ (**10**) | 215.33(8) | 284.10(5) | 290.67(4) |
| | 214.47(8) | 283.00(4) | 291.42(4) |
| $dppeSe_2TeI_2$ (**11**) | 215.80(4) | 280.37(2) | 294.28(2) |
| $Mor_3PSeTe(Ph)Br$[16b] | 218.2(2) | 276.89(9) | 276.1(1) |
| $Mor_3PSeTe(Ph)Cl$[16b] | 217.6(2) | 278.27(9) | 260.0(2) |
| $[(CH_3)_2N]_3PSeTe(Ph)Br$[17] | 218.3(2) | 276.3(1) | 274.4(1) |

The chelate complex $dppmSe_2TeI_2$ (**10**) contains a distorted square planar *cis*-$Se_2TeI_2$ group (12-Te-4) as part of a puckered six-membered heterocycle with two different P–Se–Te angles (95.4 and 102.9°) (Figure 3, Table 4).

 © 2006 Wiley-VCH Verlag GmbH & Co. KGaA, Weinheim 

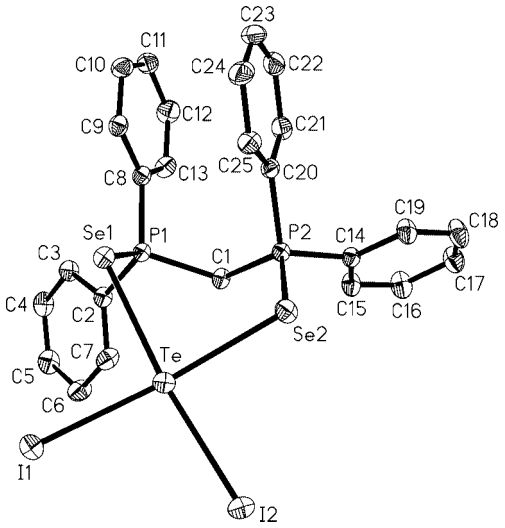


Figure 3. Structure of $dppmSe_2TeI_2$ (**10**); ellipsoid probability level 50%; all hydrogen atoms omitted for clarity.

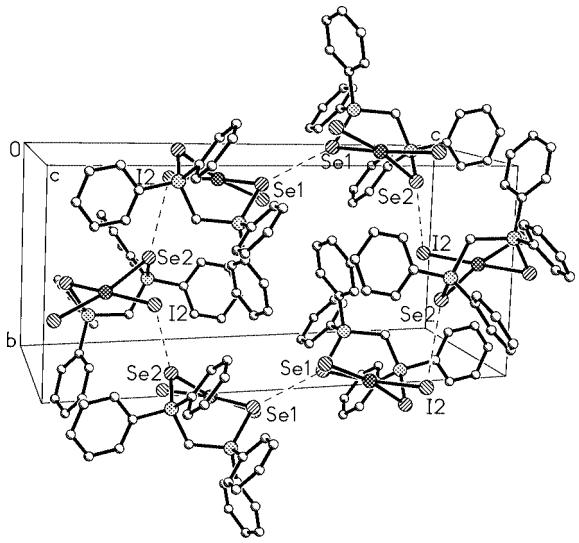


Figure 4. Intermolecular interactions in the packing diagram of **10**; selected contact distances [pm]: Se(1)–Se(1) 345.42(7), Se(2)–I(2) 414.98(6).

Table 4. Bond lengths, interatomic contact distances [pm] and angles [°] of $dppmSe_2TeI_2$ (**10**).[a]

| | | | |
|---|---|---|---|
| Te–Se(2) | 283.00(4) | Se(2)–I(2)#2 | 414.98(6) |
| Te–Se(1) | 284.10(5) | P(1)–C(8) | 179.7(3) |
| Te–I(1) | 290.67(4) | P(1)–C(2) | 179.9(3) |
| Te–I(2) | 291.42(4) | P(1)–C(1) | 182.7(3) |
| Se(1)–P(1) | 215.33(8) | P(2)–C(20) | 179.7(3) |
| Se(1)–Se(1)#1 | 345.42(7) | P(2)–C(14) | 179.9(3) |
| Se(2)–P(2) | 214.47(8) | P(2)–C(1) | 182.1(3) |
| | | | |
| Se(2)–Te–Se(1) | 86.53(1) | P(2)–Se(2)–I(2)#2 | 90.09(2) |
| Se(2)–Te–I(1) | 171.38(1) | Te–Se(2)–I(2)#2 | 147.28(1) |
| Se(1)–Te–I(1) | 90.19(1) | C(8)–P(1)–Se(1) | 110.9(1) |
| Se(2)–Te–I(2) | 88.18(1) | C(2)–P(1)–Se(1) | 115.4(1) |
| Se(1)–Te–I(2) | 172.01(1) | C(1)–P(1)–Se(1) | 112.77(9) |
| I(1)–Te–I(2) | 95.86(1) | C(20)–P(2)–Se(2) | 112.6(1) |
| P(1)–Se(1)–Te | 95.34(2) | C(14)–P(2)–Se(2) | 111.68(9) |
| P(1)–Se(1)–Se(1)#1 | 140.58(2) | C(1)–P(2)–Se(2) | 111.93(9) |
| Te–Se(1)–Se(1)#1 | 121.91(1) | P(2)–C(1)–P(1) | 118.6(2) |
| P(2)–Se(2)–Te | 102.86(2) | | |

[a] Symmetry transformations used to generate equivalent atoms: #1: $-x + 1, -y + 1, -z$; #2: $-x + , y - ½, -z + ½$.

A similar kind of distortion is documented in the chelate complexes $dppmS_2TeCl_4$,[24] $dppmSe_2HgI_2$,[25] $dppmSe_2HgBr_2$[25] and $dppmSe_2ZnBr_2$.[26] The distortion of the tellurium coordination spheres can be explained by the tendency of the ligands $dppmE_2$ (E = O, S, Se)[18a,27,28] to avoid intramolecular repulsion of the $P(=E)Ph_2$ groups (**1**: E = Se). In **10** the torsion angle Se(1)P(1)···P(2)Se(2) is 32°. The small bite angle Se(1)–Te–Se(2) (86.5°) is associated with a widening of the opposite angle I(1)–Te–I(2) (95.9°). Se–Te bond lengths in **10** are shorter than those of **9** because of the better acceptor properties of $TeI_2$ compared with MesTeI. Te–I distances [Te–I(1) 290.6 pm, Te–I(2) 291.4 pm] are slightly longer than those in **9** but shorter than those in the square planar $TeI_4^{2-}$ anion [298.5(2) pm].[29] In the case of bis[($\mu_2$-iodo)bis(ethyleneselenourea-Se)tellurium] diiodide[30] [Te–Se 261.8(1) pm] and *cis*-diiodobis(thiourea-S)tellurium,[31] Te–I distances

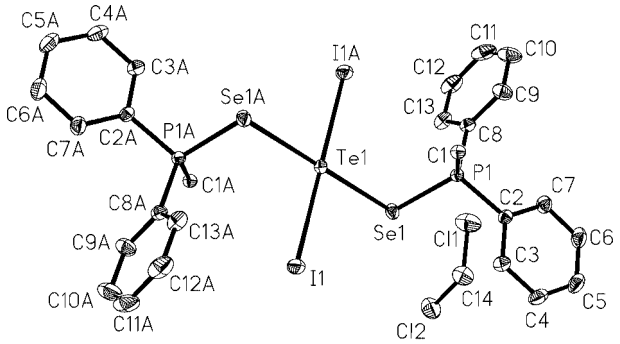


(a)

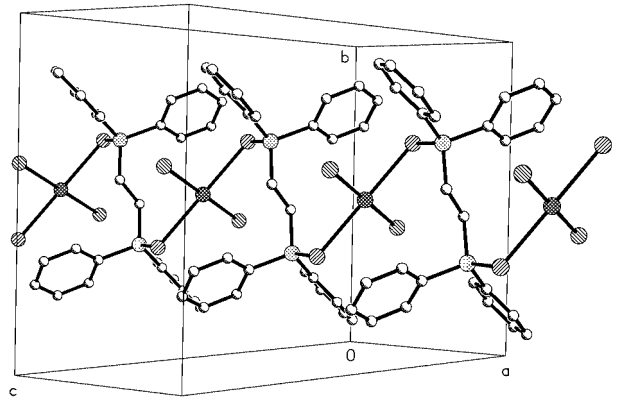


(b)

Figure 5. (**a**) Structure of $dppeSe_2TeI_2$ (**11**); asymmetric unit; ellipsoid probability level 50%; all hydrogen atoms omitted for clarity. (**b**) Polymeric structure of $dppeSe_2TeI_2$ (**11**). The chain direction is parallel to the *x* axis.

 © 2006 Wiley-VCH Verlag GmbH & Co. KGaA, Weinheim 

are very long [325.1(1) and 316.2(1) pm, respectively]. Complex **10** also exhibits intermolecular soft–soft interactions (Figure 4).

The Se(1)–Se(1′) interaction is shorter than the sum of the van der Waals radii and the Se(2)–I(1′) interaction is at the limit of the van der Waals radii. The selenium and iodine atoms exhibit borderline H···Se(I) intermolecular contacts (H···Se 316–334 pm, H···I 296–330 pm).

Complex **11** is a helical coordination polymer with centrosymmetric *trans*-$Se_2TeI_2$ moieties (12-Te-4) bridged by centrosymmetric dppe units (Figure 5, Table 5).

Table 5. Bond lengths [pm] and angles [°] of dppe$Se_2TeI_2$ (**11**).[a]

| | | | |
|---|---|---|---|
| Te(1)–Se(1) | 280.37(2) | P(1)–C(2) | 180.4(2) |
| Te(1)–I(1) | 294.28(2) | P(1)–C(1) | 182.4(2) |
| Se(1)–P(1) | 215.80(4) | C(1)–C(1)#2 | 153.0(3) |
| P(1)–C(8) | 179.9(2) | | |
| | | | |
| Se(1)–Te(1)–Se(1)#1 | 180.0 | I(1)–Te(1)–I(1)#1 | 180.0 |
| Se(1)–Te(1)–I(1) | 86.834(5) | P(1)–Se(1)–Te(1) | 102.74(1) |
| Se(1)#1–Te(1)–I(1) | 93.167(5) | C(8)–P(1)–Se(1) | 113.29(5) |
| Se(1)–Te(1)–I(1)#1 | 93.165(5) | C(2)–P(1)–Se(1) | 106.89(5) |
| Se(1)#1–Te(1)–I(1)#1 | 86.833(6) | C(1)–P(1)–Se(1) | 112.49(5) |

[a] Symmetry transformations used to generate equivalent atoms: #1: $-x + 1, -y, -z$; #2: $-x, -y, -z$.

The tellurium atom lies on the inversion centre ½, 0, 0 and the midpoint of the C1–C1′ bond lies on 0, 0, 0. Compared with the distorted chelate complex **10**, the coordination polymer **11** exhibits Se–Te bonds shorter by 3–4 pm and Te–I bonds longer by 3–4 pm. The coordination environment of Te in **11** deviates from square by expansion of the angle Se(1)–Te–I(1)#1 (93.2°) and compression of the angle Se(1)–Te–I(1) (86.8°). Among the three compounds **9**, **10** and **11**, the latter exhibits the shortest coordinative Se–Te bond (280.3 pm). The Te–I bond lengths are close to those in *trans*-diiodobis(tetramethylselenourea-Se)tellurium (*trans*-$Se_2TeI_2$ moieties) [295.4(1) pm][31] [Te–Se 282.1(1) pm], and are also similar to Te–I bonds in related *trans*-$S_2TeI_2$ moieties (293.3–298.2 pm).[32]

### Vibrational Spectra

FT-Raman spectroscopy is the main method of investigating the nature of the products obtained by the reactions of dihalogens/interhalogens with donor molecules containing 15- and 16-group elements in the absence of X-ray structural data.[33–38]

Among the compounds reported here, **3**–**6** are molecular adducts of dppm and dppe with $Br_2$ and $I_2$, while **8**–**11** are obtained by reacting the same ligands with MesTeI. No crystallographic data are available for **3**–**6**, but structural information can be obtained by comparing their FT-Raman spectra with those of several structurally characterised $I_2$ and $Br_2$ adducts with Se-donor molecules.[33–38] In contrast, no FT-Raman data are available from the literature for compounds similar to **8**–**11**, but the knowledge of the crystal structures of **9**–**11** allows a first tentative correlation between structural and FT-Raman data for these compounds.

Compounds **3** and **5** have similar FT-Raman spectra with two peaks at 144 and 195 $cm^{-1}$ for **3**, and at 157 and 191 $cm^{-1}$ for **5**, which agree with the presence of asymmetric Br–Se–Br groups in both compounds.[13,38,39]

The FT-Raman spectra of the corresponding adducts with $I_2$, **4** and **6**, differ from each other; compound **4** has a strong peak at 116 $cm^{-1}$ accompanied by a weaker peak at 145 $cm^{-1}$, whereas **6** has two well-defined peaks at 145 and 152 $cm^{-1}$ (see Figure 6).

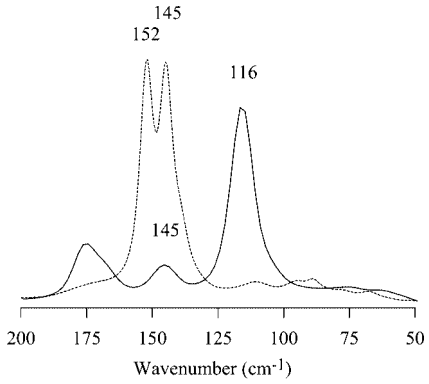


Figure 6. FT-Raman spectra of **4** (solid line) and **6** (dotted line).

The spectrum of **4** indicates the presence of asymmetric linear I–Se–I moieties,[35] whereas the spectrum of **6** is more consistent with a charge-transfer nature, characterised by the presence of linear Se–I–I groups. Strong $I_2$-charge-transfer adducts with selenium-donor molecules generally feature two bands in their FT-Raman spectra near 150 and 130 $cm^{-1}$ which are assigned to the antisymmetric and symmetric stretching modes, respectively, of the Se–I–I system.[34,35,37]

Complexes **8** and **9** have similar FT-Raman spectra with a strong peak at 126 $cm^{-1}$ accompanied by a weaker shoulder at 142 $cm^{-1}$ for **8**, and, correspondingly, at 129 and 146 $cm^{-1}$ for **9** (see Figure 7 for the FT-Raman spectrum of **8**).

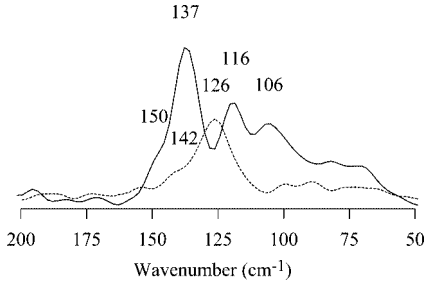


Figure 7. FT-Raman spectra of **8** (dotted line) and **10** (solid line).

On the basis of this similarity, it is possible to infer that the structural features of **8** are analogous to those of **9**; therefore, for both compounds the two FT-Raman peaks should be tentatively assigned to the symmetric and antisymmetric stretching vibrations of the Se–Te–I system. As already mentioned, these assignments cannot be supported by any data from the literature.[40] Significantly, the FT-Ra-

 © 2006 Wiley-VCH Verlag GmbH & Co. KGaA, Weinheim 

man peaks observed for **8** and **9** occur at frequencies close to those normally observed for the peaks typical of strong charge-transfer adducts featuring linear Se–I–I groups. Therefore, the two systems Se–Te–I and Se–I–I appear to have a similar vibrational behaviour.

The spectrum of **10** shows four peaks at 150 (shoulder), 137, 116 and 106 $cm^{-1}$ in good agreement with its structural features (see Figure 7). In fact, by approximating the local symmetry around the Te atom to the $C_{2v}$ point group, four Raman-active stretching vibration modes are to be expected. Therefore, on the basis of the different atomic weight of Se and I, the peaks at 106 and 116 $cm^{-1}$ should have a predominant contribution from the symmetric and antisymmetric stretching modes of the $TeI_2$ group, respectively, while the peaks at 137 and 150 $cm^{-1}$ should have a predominant contribution from the analogous vibrations of the $TeSe_2$ group.

The local symmetry around the Te atom in **11** can be approximated instead to the $D_{2h}$ point group, and only the $A_g$ vibrations for the linear I–Te–I and Se–Te–Se groups should be Raman-active. Indeed, the FT-Raman spectrum of **11** shows a very strong peak at 110 $cm^{-1}$ and a much weaker peak at around 150 $cm^{-1}$. Also in this case, the peak at lower frequency should have a predominant contribution from the symmetric stretching vibration of the I–Te–I moiety, whereas that at higher frequency should have a predominant contribution from the symmetric stretching vibration of the Se–Te–Se moiety. This assignment can be considered as reasonable since the symmetric I–Te–I and Se–Te–Se groups are structurally comparable to the symmetric $I_3^-$ and $IBr_2^-$, respectively. Indeed, $I_3^-$ and $IBr_2^-$, when symmetric, are characterised by only one Raman peak at around 110 and 160 $cm^{-1}$, respectively.[37,38,41]

Unfortunately, the quality of the FTIR spectra for all the compounds considered prevents any further discussion.

## Experimental Section

NMR spectra were recorded using Bruker spectrometers AC 200, Avance 200, Avance 400 and AMX 300, with 85% $H_3PO_4$, $(CH_3)_2Se$, $(CH_3)_2Te$ and $SiMe_4$ as external or internal standards.

FT-Raman spectra, in the range 500–50 $cm^{-1}$, were recorded with a resolution of 2 $cm^{-1}$ with a Bruker RFS100 FT-Raman spectrometer, fitted with an In-Ga-As detector (room temp.) operating with a Nd-YAG laser (excitation wavelength 1064 nm; 50–100 mW), with a 180° scattering geometry. The values in parentheses next to the wavenumber values reported for each compound represent the intensities of the peaks relating to the strongest, taken to be 10.

**3:** Diselenide **1** (1.08 g, 2.0 mmol) was dissolved in dichloromethane (20 mL) and a solution of bromine (0.63 g, 4.0 mmol) in dichloromethane (20 mL) was added. The reaction mixture was stirred at room temp. for 2 h, after which the raw product **3** was isolated by vacuum evaporation of the solvent, and purified by washing with pentane and drying under vacuum evaporation. An orange dppm$(SeBr_2)_2$ complex was obtained. Yield: 1.53 g, 89%; m.p. 133–134 °C. $C_{25}H_{22}Br_4P_2Se_2$ (861.93): calcd. C 34.84, H 2.57; found C 34.19, H 2.34. FT-Raman: $\tilde{\nu}$ = 195 (10), 144 (10) $cm^{-1}$.

**4:** Diselenide **1** (1.08 g, 2.0 mmol) was dissolved in dichloromethane (20 mL) and a solution of iodine (1.01 g, 4.0 mmol) in dichloromethane (20 mL) was added. The reaction mixture was stirred at room temp. for 3 h, after which the raw product **4** was isolated by vacuum evaporation of the solvent, and purified by washing with pentane and drying under vacuum evaporation. A red dppm$(SeI_2)_2$ complex was obtained. Yield: 1.93 g, 92%; m.p. 138–139 °C. $C_{25}H_{22}I_4P_2Se_2$ (1049.23): calcd. C 28.60, H 2.11; found C 28.57, H 2.06. FT-Raman: $\tilde{\nu}$ = 145 (2), 116 (10) $cm^{-1}$.

**5:** Diselenide **2** (1.11 g, 2.0 mmol) was dissolved in dichloromethane (20 mL) and a solution of bromine (0.63 g, 4.0 mmol) in dichloromethane (20 mL) was added. The reaction mixture was stirred at room temp. for 2 h, after which the raw product **5** was isolated by vacuum evaporation of the solvent, and purified by washing with pentane and drying under vacuum evaporation. A yellow dppe$(SeBr_2)_2$ complex was obtained. Yield: 1.66 g, 95%; m.p. 148–149 °C. $C_{26}H_{24}Br_4P_2Se_2$ (875.95): calcd. C 35.05, H 2.76; found C 34.98, H 2.98. FT-Raman: $\tilde{\nu}$ = 191 (9.5), 157 (10) $cm^{-1}$.

**6:** Diselenide **2** (1.11 g, 2.0 mmol) was dissolved in dichloromethane (20 mL) and a solution of iodine (1.01 g, 4.0 mmol) in dichloromethane (20 mL) was added. The reaction mixture was stirred at room temp. for 2.5 h, after which the raw product **6** was isolated by vacuum evaporation of the solvent, and purified by washing with pentane and drying under vacuum evaporation. A red dppe$(SeI_2)_2$ complex was obtained. Yield: 1.96 g, 92%; m.p. 197–198 °C. $C_{26}H_{24}I_4P_2Se_2$ (1063.95): calcd. C 29.35, H 2.27; found C 29.29, H 2.23. FT-Raman: $\tilde{\nu}$ = 152 (10), 145 (10) $cm^{-1}$.

**8:** Dimesityl ditelluride (0.99 g, 2.0 mmol) was dissolved in dichloromethane (20 mL) and a solution of iodine (0.51 g, 2.0 mmol) in dichloromethane (10 mL) was added. The reaction mixture was added to a solution of diselenide **1** (1.08 g, 2 mmol) in dichloromethane and was stirred for 24 h at room temp., after which the raw product **8** was isolated by vacuum evaporation of the solvent, and purified by washing with pentane, drying under vacuum evaporation and recrystallised by gas diffusion from dichloromethane/pentane. Yield: 1.93 g, 75%; m.p. 77–78 °C. $C_{43}H_{44}I_2P_2Se_2Te_2$ (1289.69): calcd. C 40.05, H 3.44; found C 39.80, H 3.44. $^{31}P$ NMR ($CD_2Cl_2$): $\delta$ = 24.1 (s, $^1J_{P,Se}$ = 717.7 Hz, $^2J_{P,P}$ = 12.4 Hz, 2 P) ppm. $^{77}Se$ NMR ($CD_2Cl_2$): $\delta$ = –161 (br. d, $^1J_{Se,P}$ = 750 ± 50 Hz) ppm. $^{125}Te$ NMR ($CD_2Cl_2$): $\delta$ = 796 (br. s) ppm. $^1H$ NMR ($CD_2Cl_2$): $\delta$ = 2.2 (s, 6 H), 2.5 (s, 12 H), 4.3 (t, $J_{H,P}$ = 13.1 Hz, 2 H), 6.9 (s, 4 H), 7.3 (m, 8 H), 7.4 (m, 4 H), 7.6 (m, 8 H) ppm. $^{13}C$ NMR ($CD_2Cl_2$): $\delta$ = 21.3 (s, 2 C), 31.2 (s, 4 C), 34.2 (s, 1 C), 117.5 (s, 2 C), 127.5 (s, 4 C), 127.8 (s, 4 C), 129.2 (t, $J_{C,P}$ = 6.6 Hz, 8 C), 132.8 (t, $J_{C,P}$ = 5.9 Hz, 8 C), 141.4 (s, 2 C), 147.2 (s, 4 C) ppm. FT-Raman: $\tilde{\nu}$ = 142 (5), 126 (10) $cm^{-1}$.

**9:** Dimesityl ditelluride (0.99 g, 2.0 mmol) was dissolved in dichloromethane (20 mL) and a solution of iodine (0.51 g, 2.0 mmol) in dichloromethane (10 mL) was added. The reaction mixture was added to a solution of diselenide **2** (1.11 g, 2 mmol) in dichloromethane and was stirred for 24 h at room temp., after which the raw product **9** was isolated by vacuum evaporation of the solvent, and purified by washing with pentane, drying under vacuum evaporation and recrystallised by gas diffusion from dichloromethane/pentane. Yield: 2.00 g, 77%; m.p. 158–159 °C. $C_{44}H_{46}I_2P_2Se_2Te_2$ (1303.67): calcd. C 40.54, H 3.56; found C 39.00, H 3.57. $^{31}P$ NMR ($CD_2Cl_2$): $\delta$ = 35.8 (s, $^1J_{P,Se}$ = 711.6 Hz, $^3J_{P,P}$ = 63.7 Hz, $^4J_{P,Se}$ = 12.2 Hz, 2 P) ppm. $^{77}Se$ NMR ($CD_2Cl_2$): $\delta$ = –281 (br. d, $^1J_{Se,P}$ = 690 ± 50 Hz) ppm. $^{125}Te$ NMR ($CD_2Cl_2$): $\delta$ = 798 (br. s) ppm. $^1H$ NMR ($CD_2Cl_2$): $\delta$ = 2.4 (s, 6 H), 2.7 (s, 12 H), 2.9 (d, $^2J_{H,P}$ = 2.3 Hz, 4 H), 7.03 (s, 4 H), 7.5 (m, 8 H), 7.6 (m, 4 H), 7.8 (m, 8 H) ppm. $^{13}C$ NMR ($CD_2Cl_2$): $\delta$ = 21.1 (s, 2 C), 25.3 (s, 2 C), 30.1 (s,

 © 2006 Wiley-VCH Verlag GmbH & Co. KGaA, Weinheim 

Table 6. Crystallographic data.

| Compound | **9** | **10** | **11** |
|---|---|---|---|
| Formula | $C_{44}H_{46}I_2P_2Se_2Te_2$ | $C_{25}H_{22}I_2P_2Se_2Te$ | $C_{28}H_{28}Cl_4I_2P_2Se_2Te$ |
| $M_r$ | 1303.67 | 923.69 | 1107.56 |
| Habit | red prism | red prism | red tablet |
| Crystal size [mm] | 0.3×0.2×0.2 | 0.3×0.2×0.2 | 0.6×0.5×0.18 |
| Crystal system | monoclinic | monoclinic | monoclinic |
| Space group | $P2_1$ | $P2_1/n$ | $P2_1/n$ |
| Cell constants | | | |
| $a$ [pm] | 1017.60(6) | 1309.0(2) | 757.13(4) |
| $b$ [pm] | 1917.2(1) | 979.0(1) | 1313.67(8) |
| $c$ [pm] | 1190.25(8) | 2254.7(3) | 1819.0(1) |
| $\beta$ [°] | 102.9(3) | 103.8(3) | 101.2(3) |
| $V$ [nm$^3$] | 2.2635(2) | 2.8054(7) | 1.7751(2) |
| $Z$ | 2 | 4 | 2 |
| $D_x$ [Mg m$^{-3}$] | 1.913 | 2.187 | 2.072 |
| $\mu$ [mm$^{-1}$] | 4.3 | 5.9 | 5.0 |
| $F$(000) | 1236 | 1712 | 1040 |
| $T$ [°C] | –140 | –140 | –140 |
| $2\theta_{max}$ | 60 | 60 | 61 |
| Reflections measured | 46435 | 52343 | 37457 |
| Reflections independent | 13698 | 8559 | 5410 |
| Transmissions | 0.829–0.928 | 0.555–0.928 | 0.714–0.928 |
| $R_{int}$ | 0.023 | 0.047 | 0.019 |
| Parameters | 476 | 289 | 178 |
| Restraints | 1 | 0 | 0 |
| $wR$ ($F_2$, all reflections) | 0.063 | 0.092 | 0.042 |
| $R$ [$F$, $>4\sigma(F)$] | 0.027 | 0.034 | 0.017 |
| $S$ | 0.99 | 1.06 | 1.07 |
| Max. $\Delta\rho$ [e nm$^{-3}$] | 1774 | 2464 | 975 |

4 C), 116.2 (s, 2 C), 127.4 (s, 4 C), 129.3 (t, $^2J_{C,P}$ = 6.1 Hz, 8 C), 129.4 (s, 4 C), 132.0 (t, $^3J_{C,P}$ = 5.6 Hz, 8 C), 142.1 (s, 2 C), 147.3 (s, 4 C) ppm. FT-Raman: $\tilde{\nu}$ = 146 (7.6), 129 (10) cm$^{-1}$.

**10:** Diselenide **1** (0.99 g, 2.0 mmol) was dissolved in dichloromethane (20 mL). Tellurium (0.26 g, 2 mmol) and iodine (0.51 g, 2.0 mmol) were added. The reaction mixture was stirred for 4 d at room temp., after which the raw product **10** was isolated by vacuum evaporation of the solvent, and purified by washing with pentane, drying under vacuum evaporation and recrystallised by gas diffusion from dichloromethane/hexane. Yield: 1.61 g, 85%; m.p. 192–193 °C. $C_{25}H_{22}I_2P_2Se_2Te$ (923.69): calcd. C 32.51, H 2.40; found C 32.07, H 2.40. $^{31}$P NMR ($CD_2Cl_2$): $\delta$ = 21.8 (s, $^1J_{P,Se}$ = 682.3 Hz, $^2J_{P,P}$ = 8.9 Hz) ppm. $^{77}$Se NMR ($CDCl_3$): $\delta$ = –93 (br. d, $^1J_{Se,P}$ = 653 ± 50 Hz) ppm. FT-Raman: $\tilde{\nu}$ = 150 (3, shoulder), 137 (10), 116 (6) and 106 (5) cm$^{-1}$.

**Structure Determinations:** Numerical details are presented in Table 6. All X-ray data were collected with monochromated Mo-$K_\alpha$ radiation ($\lambda$ = 0.71073 Å) on a Bruker SMART 1000 CCD area detector. Absorption corrections were based on multiple scans. The structures were solved by direct methods and refined anisotropically by full-matrix least-squares on $F^2$ (Program SHELXTL: Prof. G. M. Sheldrick, Univ. of Göttingen). Hydrogen atoms were included using a riding model (except methyl groups which were refined as rigid groups). Structure **9** was refined as a racemic twin. Structure **11** contains one ordered molecule of dichloromethane per asymmetric unit. CCDC-289068 (for **9**), -289069 (for **10**) and -289070 (for **11**) contain the supplementary crystallographic data for this paper. These data can be obtained free of charge from The Cambridge Crystallographic Data Centre via www.ccdc.cam.ac.uk/data_request/cif.


[1] J. Jeske, W.-W. du Mont, F. Ruthe, P. G. Jones, L. M. Mercuri, P. Deplano, *Eur. J. Inorg. Chem.* **2000**, 1591–1599.

[2] R. A. Zingaro, E. A. Meyers, *Inorg. Chem.* **1962**, *1*, 771–774; D. J. Williams, K. J. Wynne, *Inorg. Chem.* **1976**, *15*, 1449–1451.

[3] M. D. Rudd, S. V. Lindemann, S. Husebye, *Acta Chem. Scand. Ser. A* **1997**, *51*, 689–708.

[4] M. Arca, F. A. Devillanova, A. Garau, F. Isaia, V. Lippolis, G. Verani, F. Demartin, *Z. Anorg. Allg. Chem.* **1998**, *624*, 745–749; W. W. Schweikert, E. A. Meyers, *J. Phys. Chem. J. Phys. Chem.* **1968**, *72*, 1561–1565; D. C. Apperley, N. Bricklebank, S. L. Burns, D. E. Hibbs, M. B. Hursthouse, K. M. Abdul Malik, *J. Chem. Soc., Dalton Trans.* **1998**, 1289–1292.

[5] E. Krawczyk, A. Skowronska, *Phosphorus Sulfur Silicon* **1990**, *51*, 329.

[6] W.-W. du Mont, *Main Group Chem. News* **1994**, *2*(3), 18–26; M. Bätcher, Ph. D. thesis, University of Oldenburg, **1989**; J. Jeske, *Ph. D. thesis*, Techn. University of Braunschweig, **1997**.

[7] S. M. Godfrey, S. L. Jackson, C. A. McAuliffe, R. G. Pritchard, *J. Chem. Soc., Dalton Trans.* **1997**, 4499–4502.

[8] J. Jeske, W.-W. du Mont, P. G. Jones, *Chem. Eur. J.* **1999**, *5*, 385–389.

[9] S. M. Godfrey, S. L. Jackson, C. A. McAuliffe, R. G. Pritchard, *J. Chem. Soc., Dalton Trans.* **1998**, 4201–4204.

[10] E. Seppälä, F. Ruthe, W.-W. du Mont, P. G. Jones, *Chem. Commun.* **1999**, 1471–1472.

[11] a) [10-Se-3] means 10 valence electrons at the central Se atom, which has 3 substituents: C. W. Perkins, J. C. Martin, A. J. Arduengo III, W. Lau, A. Alegria, J. K. Kochi, *J. Am. Chem. Soc.* **1980**, *102*, 7753–7759; b) K.-y. Akiba, *Chemistry of Hypervalent Compounds*, Wiley-VCH, New York, N. Y., **1999**.

[12] W.-W. du Mont, A. Martens von Salzen, F. Ruthe, E. Seppälä, G. Mugesh, F. A. Devillanova, V. Lippolis, N. Kuhn, *J. Organomet. Chem.* **2001**, *623*, 14–28; W.-W. du Mont, A. Martens von Salzen, F. Ruthe, E. Seppälä, G. Mugesh, F. A. Devillanova, V. Lippolis, N. Kuhn, *J. Organomet. Chem.* **2001**, *628*, 280.

[13] F. Bigoli, P. Deplano, F. A. Devillanova, V. Lippolis, M. L. Mercuri, M. A. Pellinghelli, E. F. Trogu, *Eur. J. Inorg. Chem.* **1998**, 137–141.


 © 2006 Wiley-VCH Verlag GmbH & Co. KGaA, Weinheim 

[14] M. C. Aragoni, M. Arca, A. J. Blake, F. A. Devillanova, W.-W. du Mont, A. Garau, F. Isaia, V. Lippolis, G. Verani, C. Wilson, *Angew. Chem.* **2001**, *113*, 4359–4362; *Angew. Chem. Int. Ed.* **2001**, *40*, 4229–4232.
[15] W.-W. du Mont, H.-U. Meyer, S. Kubiniok, S. Pohl, W. Saak, *Chem. Ber.* **1992**, *125*, 761–766.
[16] a) S. Hauge, O. Vikane, *Acta Chem. Scand. Ser. A* **1973**, *27*, 3596–3599; b) S. Hauge, O. Vikane, *Acta Chem. Scand. Ser. A* **1985**, *39*, 553–562.
[17] M. D. Rudd, S. V. Lindemann, S. Husebye, *Acta Chem. Scand. Ser. A* **1996**, *50*, 759–774.
[18] a) P. J. Carroll, D. D. Titus, *J. Chem. Soc., Dalton Trans.* **1977**, 824–829; B. Ahrens, P. G. Jones, *Acta Crystallogr., Sect. C* **1997**, *53*, 1852–1854; b) D. H. Brown, R. J. Cross, P. R. Mallinson, D. D. MacNicol, *J. Chem. Soc., Perkin Trans. 2* **1980**, 993–998.
[19] S. W. Carr, R. Colton, *Aust. J. Chem.* **1981**, *34*, 35–44; I. J. Colquhoun, H. C. E. McFarlane, W. McFarlane, J. A. Nash, R. Keat, D. S. Rycroft, D. G. Thomson, *Org. Magnetic Resonance* **1979**, *12*, 473–475; P. A. W. Dean, *Can. J. Chem.* **1979**, *57*, 754–761.
[20] S. O. Grim, E. D. Walton, *Inorg. Chem.* **1980**, *19*, 1982–1987.
[21] K. Giselbrecht, B. Bildstein, F. Sladky, *Chem. Ber.* **1989**, *122*, 1255–1256.
[22] S. Hauge, O. Vikane, *Acta Chem. Scand. Ser. A* **1983**, *27*, 723–728.
[23] C. G. Hrib, Ph. D. thesis, Techn. University of Braunschweig, in preparation; C. G. Hrib, W.-W. du Mont, Halchem II International Meeting, Riviera Capitana (CA), 2004, Vol. of abstracts, p. 9.
[24] C. J. Carmalt, N. C. Norman, L. J. Farrugia, *Polyhedron* **1995**, *14*, 1405–1413.
[25] T. S. Lobana, R. Hundal, A. Singh, A. Sehdev, P. Turner, A. Castineiras, *J. Coord. Chem.* **2002**, *55*, 353–362.
[26] T. S. Lobana, R. Hundal, P. Turner, *J. Coord. Chem.* **2001**, *53*, 301–309.
[27] a) H. Schmidbaur, G. Reber, A. Schier, F. E. Wagner, G. Muller, *Inorg. Chim. Acta* **1988**, *147*, 143–150; b) M. Y. Antipin, Y. T. Struchkov, S. A. Pisareva, T. Y. Medved, M. I. Kabachnik, *Zh. Strukt. Khim. (Russ.) (J. Struct. Chem.)* **1980**, *21*, 101–107.
[28] C. J. Carmalt, A. H. Cowley, A. Decken, Y. G. Lawson, N. C. Norman, *Acta Crystallogr., Sect. C* **1996**, *52*, 931–933; D. C. Apperley, N. Bricklebank, M. B. Hursthouse, M. E. Light, S. J. Coles, *Polyhedron* **2001**, *20*, 1907–1913.
[29] S. Pohl, W. Saak, B. Krebs, *Z. Naturforsch., Teil B* **1985**, *40*, 251–257.
[30] O. Foss, R. Hermansen, K. Maroy, T. Moberg, *Acta Chem. Scand. Ser. A* **1987**, *41*, 130–138.
[31] O. Foss, K. Maartmann-Moe, *Acta Chem. Scand. Ser. A* **1987**, *41*, 121–129.
[32] S. Husebye, D. Mughannam, K. W. Tornroos, *Phosphorus, Sulfur, Silicon, Relat. Elem.* **2003**, *178*, 1825–1837; O. Foss, H. M. Kjoge, K. Maroey, *Acta Chem. Scand. Ser. A* **1965**, *19*, 2349–2360; O. Foss, K. Maartmann-Moe, K. Maroey, *Acta Chem. Scand. Ser. A* **1986**, *40*, 685–694; O. Foss, W. Johannessen, *Acta Chem. Scand. Ser. A* **1961**, *15*, 1941–1943; O. Foss, K. Maartmann-Moe, *Acta Chem. Scand. Ser. A* **1986**, *40*, 675–684.
[33] P. Deplano, F. A. Devillanova, J. R. Ferraro, F. Isaia, V. Lippolis, M. L. Mercuri, *Appl. Spectrosc.* **1992**, *46*, 1625–1629.
[34] F. Cristiani, F. Demartin, F. A. Devillanova, F. Isaia, V. Lippolis, G. Verani, *Inorg. Chem.* **1994**, *33*, 6315–6324.
[35] F. Bigoli, A. M. Pellinghelli, P. Deplano, F. A. Devillanova, V. Lippolis, M. L. Mercuri, E. F. Trogu, *Gazz. Chim. Ital.* **1994**, *124*, 445–454.
[36] F. Bigoli, F. Demartin, P. Deplano, F. A. Devillanova, F. Isaia, V. Lippolis, M. L. Mercuri, M. A. Pellinghelli, E. F. Trogu, *Inorg. Chem.* **1996**, *35*, 3194–3201.
[37] M. C. Aragoni, M. Arca, F. Demartin, F. A. Devillanova, A. Garau, F. Isaia, V. Lippolis, G. Verani, *Trends Inorg. Chem.* **1999**, *6*, 1–18.
[38] M. C. Aragoni, M. Arca, F. Demartin, F. A. Devillanova, A. Garau, F. Isaia, F. Lelj, V. Lippolis, G. Verani, *Chem. Eur. J.* **2001**, *7*, 3122–3133.
[39] M. C. Aragoni, M. Arca, F. Demartin, F. A. Devillanova, A. Garau, F. Isaia, V. Lippolis, G. Verani, *Dalton Trans.* **2005**, 2252–2258.
[40] P. Klaboe, O. Vikane, *Acta Chem. Scand. Ser. A* **1977**, *31*, 120–124.
[41] P. Deplano, F. A. Devillanova, J. R. Ferraro, V. Lippolis, M. L. Mercuri, E. F. Trogu, *Appl. Spectrosc.* **1994**, *48*, 1236–1241.

Received: September 21, 2005
Published Online: January 27, 2006

 © 2006 Wiley-VCH Verlag GmbH & Co. KGaA, Weinheim 

EurJIC
European Journal of Inorganic Chemistry

Issue 7/2006

Pages 1305–1528

*Papers available ahead of print in Early View at www.interscience.wiley.com*

*Earliest available Table of Contents:*
*Automatically, free of charge by e-mail through*
*www.interscience.wiley.com/alerts*

## COVER PICTURE

**The cover picture shows** the crystal structures of three related iron(II) complexes obtained with a triazine-based polypyridyl ligand, where minor structural changes result in very disparate magnetic properties, ranging from antiferromagnetic exchange through spin crossover to ferromagnetic coupling. These are clearly illustrated by the characteristic plots of the corresponding magnetic behaviours. The background map of Europe symbolizes the European collaboration responsible for the studies reported by P. Gamez, O. Roubeau, et al. on p. 1353 ff.

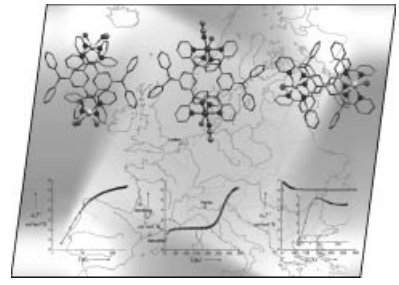

## MICROREVIEW

**Contents**

**1319** **S. Shimizu, A. Osuka***

Metalation Chemistry of *meso*-Aryl-Substituted Expanded Porphyrins

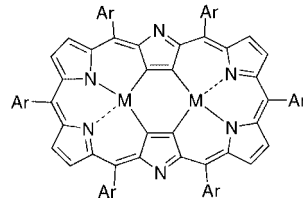

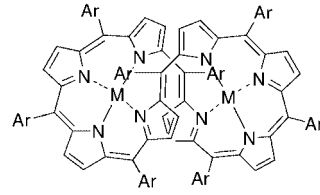

**Keywords:** Aromaticity / Conjugation / Macrocyclic ligands / Porphyrinoids

 © 2006 Wiley-VCH Verlag GmbH & Co. KGaA, Weinheim 

# SHORT COMMUNICATIONS


**1337** **C.-Z. Xie, Z.-F. Zhang, B.-F. Zhang, X.-Q. Wang,* R.-J. Wang, G.-Q. Shen, D.-Z. Shen, B. Ding**

A Novel 3D $Cu^{I}$ Metal−Organic Framework with Middle-Size Channels Despite the Sixfold $ThSi_2$ Interpenetrating Topological Structure

**Keywords:** Metal−organic framework / Interpenetration / 1D channels / Topological structure / Copper / X-ray diffraction


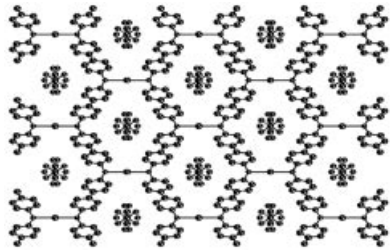


**1341** **S. K. Ghosh, P. K. Bharadwaj***

Decameric Water Clusters Shaped as Two Parallel Cyclic Pentamers with Staggered Conformation Stabilize Supramolecularly Bonded Infinite Chains of $H_2PO_4^-$ Ions

**Keywords:** Dibasic phosphate chain / Cryptands / Supramolecular chemistry / X-ray diffraction / Water cluster


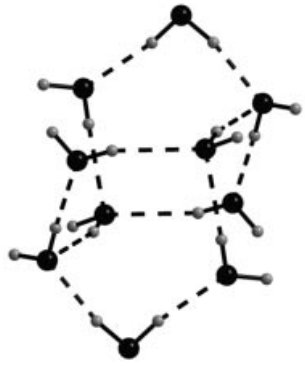


**1345** **P. Naumov,* K. Sakurai, T. Asaka, A. A. Belik, S. Adachi, J. Takahashi, S. Koshihara**

Photoinduced Phase Transition of the Coordinationally Unsaturated $d^9$ Metal Centers of Bis(*N*,*N*-diethylethylenediamine)copper(II) Perchlorate within the Thermal Hysteresis of the Spin-Exchange Interaction

**Keywords:** Photoinduced phase transitions / Jahn−Teller effect / Photodiffraction / Photochromism / Thermochromism


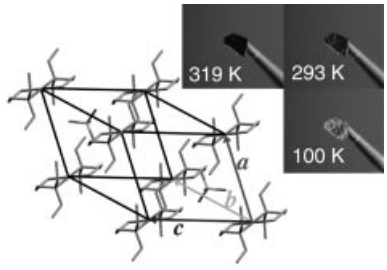



**1348** **R. Wolf, E. Hey-Hawkins***

Synthesis and Molecular Structure of [Cp*Ta(Ph)($P_6Ph_5$)]: A Terminal Phosphinidene Complex of the $(P_6Ph_5)^{3-}$ Ligand (Cp* = $C_5Me_5$)

**Keywords:** Tantalum / Phosphorus / P ligands / Oligophosphanes / Phosphinidene complexes


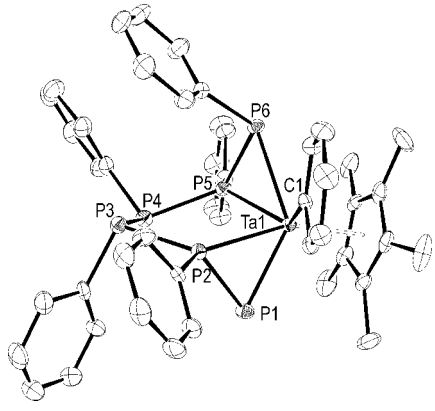


 © 2006 Wiley-VCH Verlag GmbH & Co. KGaA, Weinheim 

# FULL PAPERS


**1353** **M. Quesada, P. de Hoog, P. Gamez,* O. Roubeau,* G. Aromí, B. Donnadieu, C. Massera, M. Lutz, A. L. Spek, J. Reedijk**

Coordination Dependence of Magnetic Properties within a Family of Related [$Fe^{II}_2$] Complexes of a Triazine-Based Ligand

**Keywords:** Iron(II) complexes / Magnetic properties / Spin crossover / 1,3,5-Triazine / Polydentate ligands


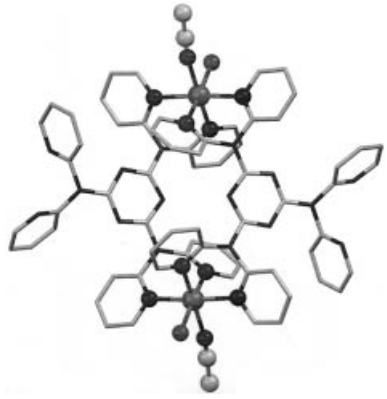


**1362** **L. Ortega-San Martín, J. P. Chapman, L. Lezama, J. Sánchez Marcos, J. Rodríguez-Fernández, M. I. Arriortua, T. Rojo***

Magnetic Properties of the Ordered Double Perovskite $Sr_2MnTeO_6$

**Keywords:** Perovskite phases / Magnetic structure / EPR spectroscopy / Neutron diffraction


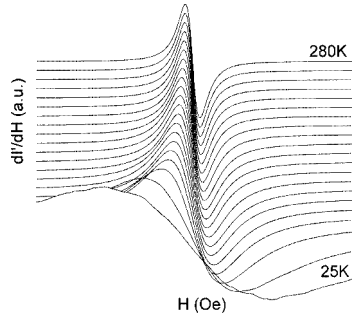



**1371** **B. Demerseman,* J.-L. Renaud, L. Toupet, C. Hubert, C. Bruneau**

Synthesis and Reactivity of [Ru(Cp*)(L)-$(MeCN)_2$][$PF_6$] (L = $Ph_2POMe$ or $Ph_2P$-*o*-tolyl) and {Ru(Cp*)[$Ph_2PCH_2C$(*t*Bu)=O](MeCN)}-[$PF_6$] Complexes, Their Involvement as Catalyst Precursors for Regioselective Allylic Substitution Reactions and Related [Ru(Cp*)Cl($Ph_2$-POMe)(RCHCHCH$_2$)][$PF_6$] $\eta^3$-Allyl Ruthenium(IV) Intermediates

**Keywords:** Allyl ligands / Allylation / Homogeneous catalysis / Regioselectivity / Ruthenium


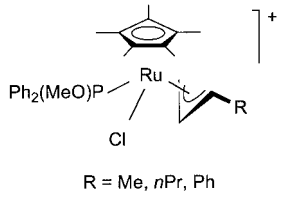


R = Me, *n*Pr, Ph


**1381** **T. Yi,* C. Ho-Chol, S. Gao, S. Kitagawa***

Tuning of the Spin States in Trinuclear Cobalt Compounds of Pyridazine by the Second Simple Bridging Ligand

**Keywords:** Pyridazine / Ligand tuning / Cobalt / Irregular spin states structure / Magnetic properties


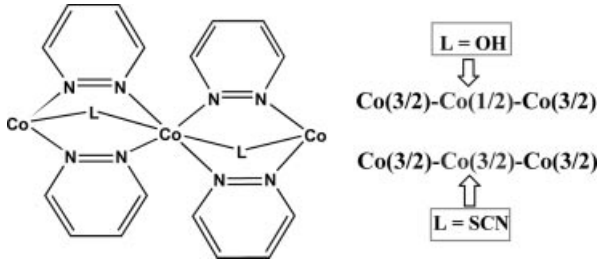




© 2006 Wiley-VCH Verlag GmbH & Co. KGaA, Weinheim

**1388** **P. Ortega, J. F. Bermejo, L. Chonco, E. de Jesus, F. J. de la Mata,* G. Fernández, J. C. Flores, R. Gómez,* M. J. Serramía, M. A. Muñoz-Fernandez***

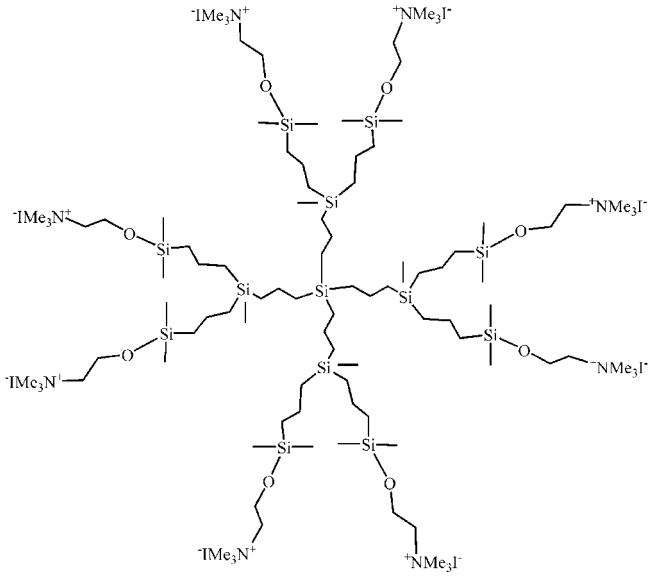

Novel Water-Soluble Carbosilane Dendrimers: Synthesis and Biocompatibility

**Keywords:** Bioinorganic chemistry / Dendrimers / Silicon / Drug delivery / Toxicity

**1397** **L. Hintermann,* F. Läng, P. Maire, A. Togni**

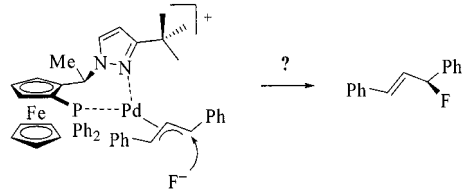

Interactions of Cationic Palladium(II)- and Platinum(II)-$\eta^3$-Allyl Complexes with Fluoride: Is Asymmetric Allylic Fluorination a Viable Reaction?

**Keywords:** Palladium / Platinum / Allyl ligands / Fluorination / Naked fluoride

**1413** **P. Werndrup, G. A. Seisenbaeva, G. Westin, I. Persson, V. G. Kessler***

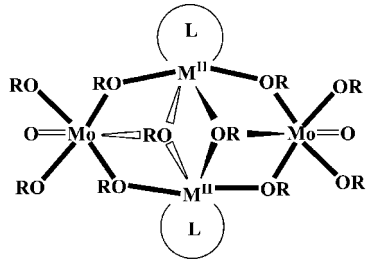

$M^{II}$ = Co, Ni, L = acac, $OCHMeCH_2NMe_2$

A Single-Source-Precursor Approach to Late Transition Metal Molybdate Materials: The Structural Role of Chelating Ligands in the Formation of Heterometallic Heteroleptic Alkoxide Complexes

**Keywords:** Cobalt molybdate / EXAFS / Heterogeneous catalysis / Materials / Nickel molybdate / Sol−gel processes

**1423** **M.-B. Zhang, Y.-M. Chen, S.-T. Zheng, G.-Y. Yang***

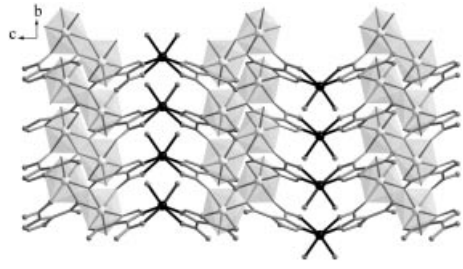

A 3D Manganese Coordination Polymer $[Mn_3(IMDC)_2(H_2O)_4]$ Constructed from $[Mn_2(IMDC)_2(H_2O)_2]$ Layers and $[Mn(H_2O)_2]$ Pillars (IMDC = 4,5-imidazoledicarboxylate)

**Keywords:** Carboxylate ligands / Coordination polymers / Hydrothermal synthesis / Manganese

 © 2006 Wiley-VCH Verlag GmbH & Co. KGaA, Weinheim 

**1429** **M. Alesi, S. Fantasia, M. Manassero,* A. Pasini***

The Role of Anions in Addressing the Outcome of the Reaction of Tetramethylthiourea with *cis*-$Pt^{II}(phos)_2$ Moieties (phos = $PPh_3$ or $^1/_2$dppe), Cyclometallation vs. Hydrolysis to Monothiocarbamato, and the Crystal Structure of *trans*-Bis(*N*-dimethylmonothiocarbamato)bis(triphenylphosphane)platinum(II)

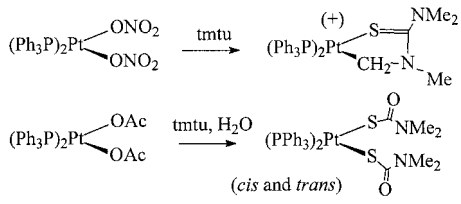


**Keywords:** Carboxylate ligands / Phosphane ligands / Ligands reactivity

**1436** **E. Urones-Garrote,* A. Gómez-Herrero, Á. R. Landa-Cánovas, L. C. Otero-Díaz**

An Electron Microscopy Study of New Chemically Twinned Phases in the MgS-$Yb_2S_3$ System

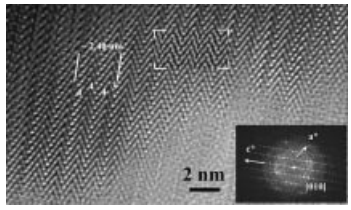


**Keywords:** Chemical twinning / Electron microscopy / Rare earths / Sulfides / Solid-state structures

**1444** **J. Notni, H. Görls, E. Anders***

Zinc Thiolate Complexes $[ZnL_n(SR)]^+$ with Azamacrocyclic Ligands: Synthesis and Structural Properties

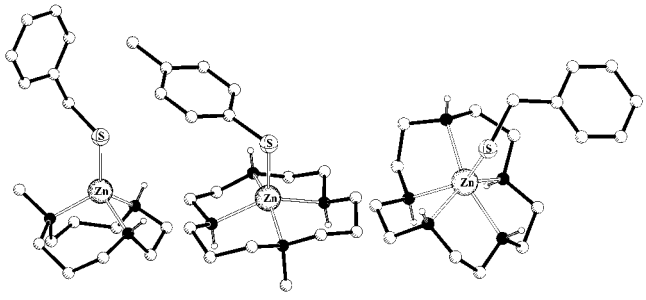


**Keywords:** Enzyme models / Macrocyclic ligands / S ligands / Solid-state structures / Zinc

**1456** **J. Ipaktschi,* P. Rooshenas, A. Dülmer**

Synthesis of $\eta^2$-Allene Complexes by the Reaction of a $\eta^1$-Vinylidene Tungsten Complex with Diazoalkanes

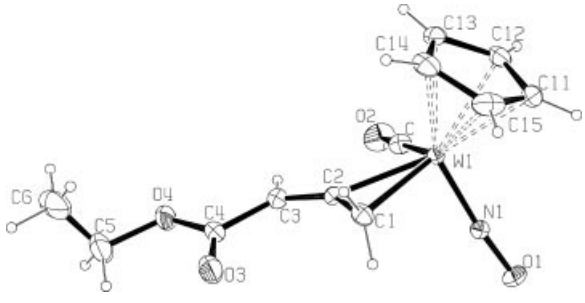


**Keywords:** Tungsten / Vinylidene ligands / Allene ligands / Diazoalkanes

**1460** **I. Mayer,* F. J. G. Cuisinier, I. Popov, Y. Schleich, S. Gdalya, O. Burghaus, D. Reinen**

Phase Relations Between β-Tricalcium Phosphate and Hydroxyapatite with Manganese(II): Structural and Spectroscopic Properties

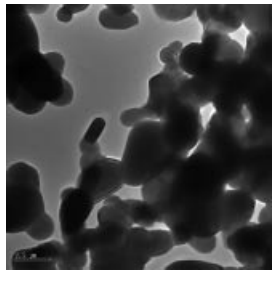

**Keywords:** Manganese / β-Tricalcium phosphate / EPR spectroscopy


 © 2006 Wiley-VCH Verlag GmbH & Co. KGaA, Weinheim 

**1466** **T. N. Parac-Vogt,* A. Pacco, P. Nockemann, Y.-F. Yuan, C. Görller-Walrand, K. Binnemans**

Mandelohydroxamic Acid as Ligand for Copper(II) 15-Metallacrown-5 Lanthanide(III) and Copper(II) 15-Metallacrown-5 Uranyl Complexes

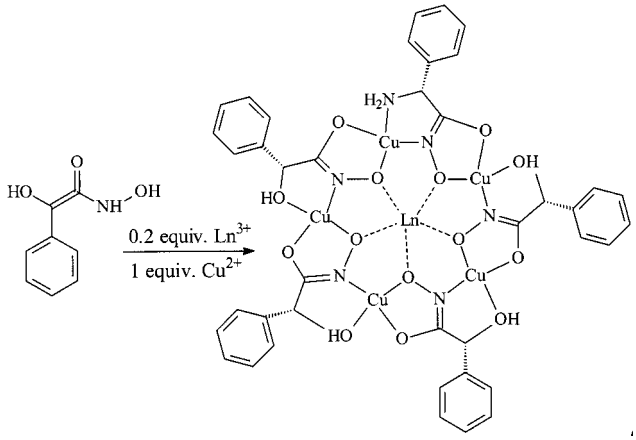


**Keywords:** Lanthanides / Hydroxamic acid / Metallacrowns / Rare earths / Uranium

**1475** **R. A. Varga, A. Rotar, M. Schürmann, K. Jurkschat, C. Silvestru***

Hypercoordinated Organotin(IV) Halides Containing 2-$(Me_2NCH_2)C_6H_4$ Groups: $\{2\text{-}(Me_2NCH_2)C_6H_4\}_2SnX_2$ (X = F, Cl, Br, I) and $\{2\text{-}(Me_2NCH_2)C_6H_4\}R_2SnX$ (R = Me, Ph; X = F, Cl, Br, I) and Their Solution Behaviour and Solid-State, Hydrogen-Bonding-Based Supramolecular Architecture

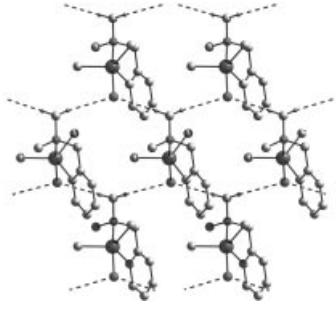

**Keywords:** Halides / Hydrogen bonding / Hypercoordination / Supramolecular chemistry / Tin

**1487** **G. S. Nunes, A. D. P. Alexiou, K. Araki, A. L. B. Formiga, R. C. Rocha,* H. E. Toma***

Proton-Coupled Redox Chemistry, Oxidative Reactivity, and Electronic Characterization of Aqua-, Hydroxo-, and Oxo-Triruthenium Clusters

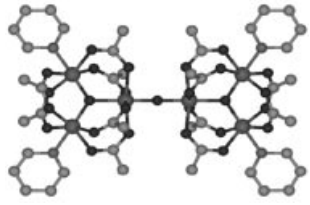

**Keywords:** Ruthenium−acetate clusters / Mixed-valence complexes / Oxygen-transfer catalysis / Proton-coupled electron transfer / Pourbaix diagram / Electrocatalysis / Spectroelectrochemistry

**1496** **B. Gaertner, A. Köhn, H.-J. Himmel***

The First End-On Bonded Superoxo Complexes of Ga and In: The Oxygen-Rich Compounds $GaO_4$ and $InO_4$

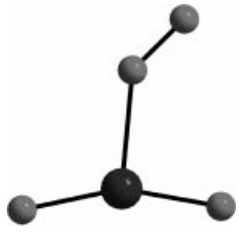

**Keywords:** Oxidation / Ga metal / Superoxo complex / Reaction mechanism / Matrix isolation / Vibrational spectrosopy

 © 2006 Wiley-VCH Verlag GmbH & Co. KGaA, Weinheim 

**1505** **V. Madhu, S. K. Das***

N−H···S Hydrogen Bonds in a New Family of Ion-Pair Complexes Between Cationic Nickel Tetraazabicyclononane and Anionic Metal Dithiolates: Synthesis, Characterization and Properties of $[Ni(C_9H_{22}N_6)][M(mnt)_2]$ ($M^{II}$ = Cu, Ni, Pd)

**Keywords:** Hydrogen bonds / Ion pairs / N ligands / Nickel / S ligands

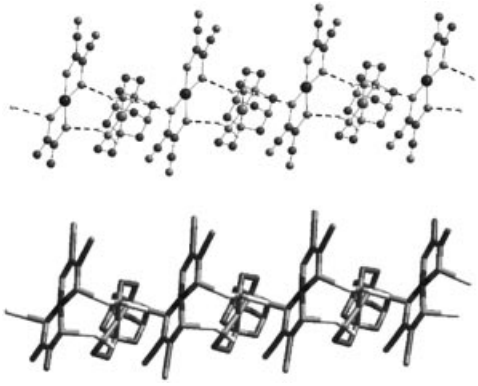

**1515** **P. Cabon, R. Rumin, J.-Y. Salaün,* H. des Abbayes, S. Triki**

Ring Closure of Alkoxycarbonyl(tetracarbonyl)-pyruvoyliron Complexes into Metallalactones Induced by Nucleophilic Attack of Carbanions

**Keywords:** Carbanions / Carbonyl ligands / Iron / Metallacycles / Nucleophilic addition

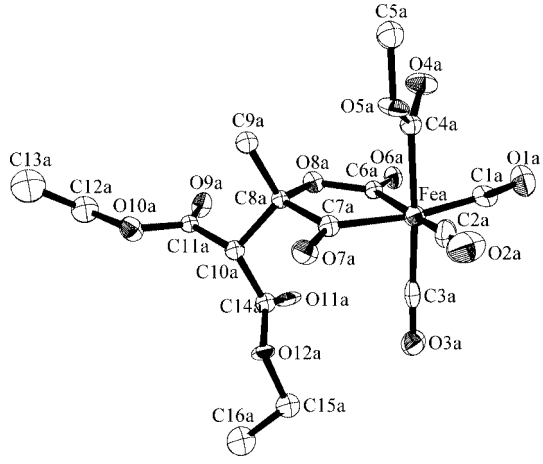

 © 2006 Wiley-VCH Verlag GmbH & Co. KGaA, Weinheim 

DOI: 10.1002/ejic.200501097

# Metalation Chemistry of *meso*-Aryl-Substituted Expanded Porphyrins

**Soji Shimizu[a] and Atsuhiro Osuka*[a]**

**Keywords:** Aromaticity / Conjugation / Macrocyclic ligands / Porphyrinoids

*meso*-Aryl-substituted expanded porphyrins are structural analogues of *meso*-aryl-substituted porphyrins. They exhibit rich and novel coordination behaviors, including multi-metal chelation due to the large cavities, spin–spin interaction arising from the proximity of metal centers, and large changes in their structural and electrochemical properties upon metalation. The recent discovery of a facile, one-pot synthesis of a series of *meso*-aryl-substituted expanded porphyrins enables us to investigate their metal-complexation chemistry. The aim of this Microreview is to highlight recent progress in the synthesis and characterization of metal complexes of *meso*-aryl-substituted expanded porphyrins.
(© Wiley-VCH Verlag GmbH & Co. KGaA, 69451 Weinheim, Germany, 2006)

## Introduction

Porphyrins, which play a key role in biological as well as artificial processes, are undoubtedly one of the most widely studied macrocycles and are characterized as 18π-electron aromatic ligands that can accommodate most metal ions to form 1:1 metal complexes.[1] In recent years, porphyrin analogues that include modified, confused, contracted, and expanded ones have attracted increasing attention owing to their intriguing properties, which are very difficult or impossible to achieve in porphyrins. Among these, expanded porphyrins bearing more than four pyrrole rings have been demonstrated to be quite promising due to their larger conjugation and diversity that allow remarkable absorption spectra ranging from the UV/visible to the near-IR region, variable oxidation states that are interconvertible among aromatic, antiaromatic, and nonaromatic systems, and multi-metal coordinating behaviors.[2–7] On account of these promising properties, they are in the spotlight in various fields, including receptors for anions,[8] ligands for several transition and lanthanoid metal ions, sensitizers for photodynamic therapy (PDT),[5,9] and magnetic resonance imaging (MRI) contrast agents.[10] In addition, they have re-

[a] Department of Chemistry, Graduate School of Science, Kyoto University, and Core Research for Evolutional Science and Technology (CREST), Japan Science and Technology Agency, Sakyo-ku, Kyoto 606-8502, Japan
Fax: +81-75-753-3970
E-mail: osuka@kuchem.kyoto-u.ac.jp

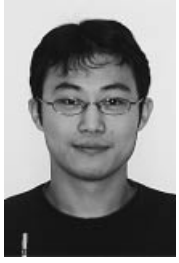

*Soji Shimizu was born in 1979 in Kyoto, Japan. He received his BSc and MSc degrees in 2002 and 2004, respectively, from Kyoto University. He is currently a PhD student with Professor Osuka at the same university, focusing on the synthesis and exploration of expanded porphyrins. During spring 2005, as a visiting fellow, he stayed at Professor Jonathan L. Sessler's laboratory in the Department of Chemistry and Biochemistry, the University of Texas at Austin. He was selected as a Research Fellow of the Japan Society for the Promotion of Science (JSPS) in 2004.*

*Atsuhiro Osuka was born in Gamagori, Aichi, in 1954. He received his PhD degree from Kyoto University in 1982 on the photochemistry of epoxyquinones. In 1979, he started his academic career at the Department of Chemistry, Ehime University as an assistant professor. In 1984, he moved to the Department of Chemistry, Kyoto University, where he became a professor of chemistry in 1996. He was awarded the CSJS Award for Young Chemists in 1988 and the Japanese Photochemistry Association Award in 1999. His research interests cover many aspects of synthetic approaches toward the artificial photosynthesis and development of porphyrin-related compounds with novel structures and functions. He was selected as a project leader of Core Research for Evolutional Science and Technology (CREST) of JST.*

**MICROREVIEWS:** This feature introduces the readers to the authors' research through a concise overview of the selected topic. Reference to important work from others in the field is included.

 © 2006 Wiley-VCH Verlag GmbH & Co. KGaA, Weinheim 

cently been shown to have potential as nonlinear optical materials owing to their large two-photon absorption (TPA) cross-sections, which will lead to a broad range of applications such as three-dimensional microfabrication, optical data storage, and optical limiting.[11,12] These promising attributes have encouraged diverse synthetic efforts towards various expanded porphyrins that differ in ring size, ring connectivity, peripheral substituents, and core modification.[5,13–21] Recently, we found that a modified Rothemund–Lindsey porphyrin synthesis leads to the formation of a series of *meso*-aryl-substituted expanded porphyrins that are all real porphyrin homologues in terms of a regularly alternating pyrrole and methine carbon arrangement (Scheme 1).[22] This synthesis requires aryl aldehyde substrates bearing electron-deficient and bulky substituents both at the 2- and 6-positions and 10 times higher concentrations of substrates (ca. 67 mM) than those optimized for the porphyrin synthesis. A series of fully fluorinated expanded porphyrins was prepared in a similar manner from the reaction of 3,4-difluoropyrrole and pentafluorobenzaldehyde (Scheme 2).[23] The ring-size-selective synthesis of expanded porphyrins has been achieved by using dipyrromethane and tripyrromethane as starting substrates under milder reaction conditions (Scheme 3).[24] This ring-size-selective synthesis has also allowed the preparation of hexaphyrins and octaphyrins bearing electron-rich *meso*-aryl substituents.[25]

The metalation chemistry of expanded porphyrins can be traced back to the 1980s. Representative examples are summarized in Figure 1. In 1983, Gossauer et al. reported the preparation of β-dodecaalkyl-substituted [26]hexaphyrins, which were converted into their bis-$Zn^{II}$ and bis-$Pd^{II}$ complexes.[26] Vogel and co-workers have synthesized a series of β-alkyl-substituted octaphyrins bearing twisted fig-

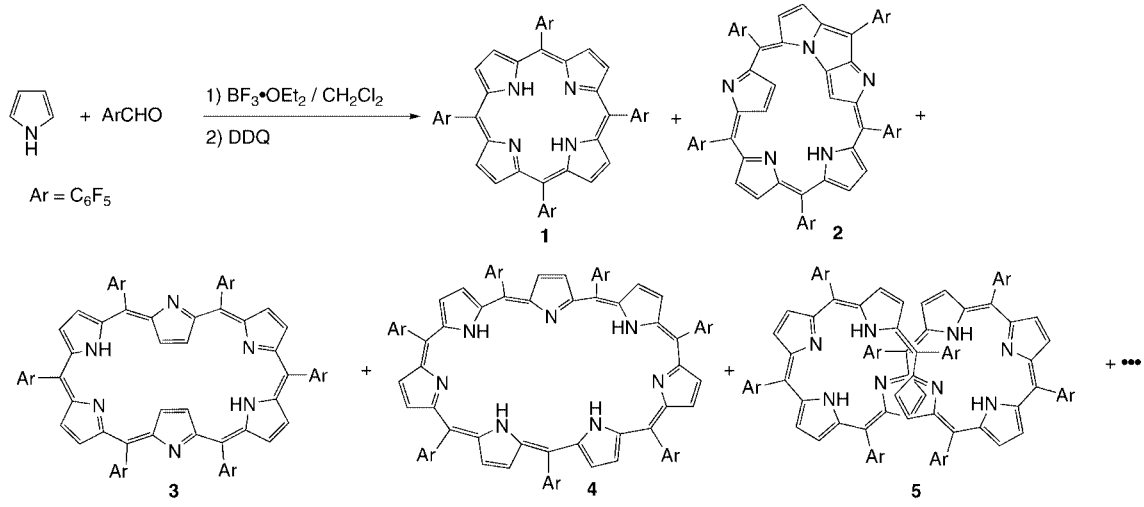


Scheme 1. Synthesis of *meso*-aryl-substituted expanded porphyrins.

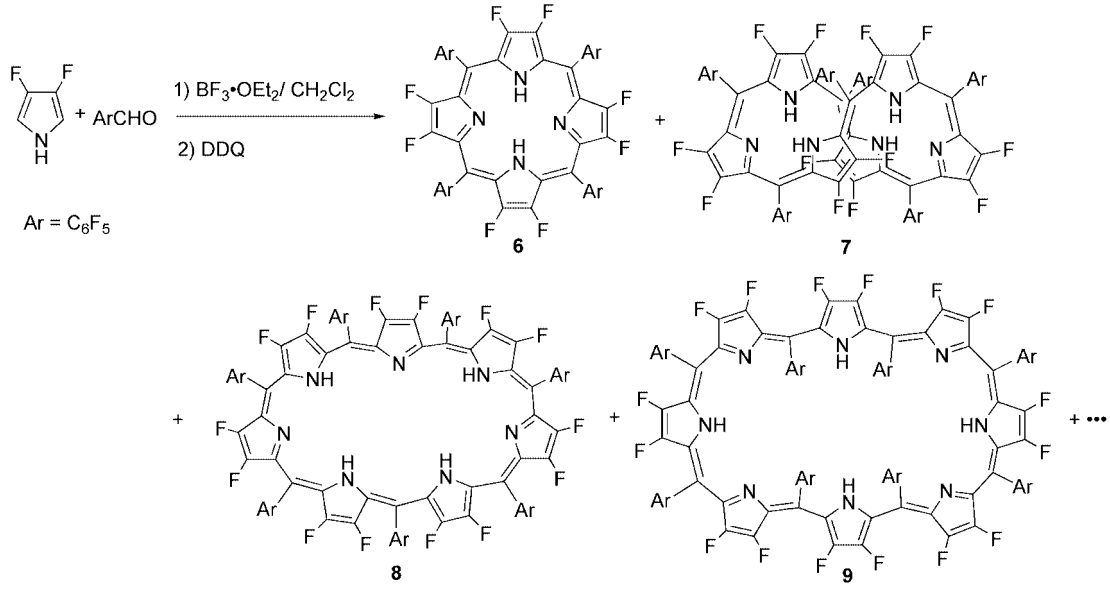


Scheme 2. Synthesis of perfluorinated expanded porphyrins.

 © 2006 Wiley-VCH Verlag GmbH & Co. KGaA, Weinheim 

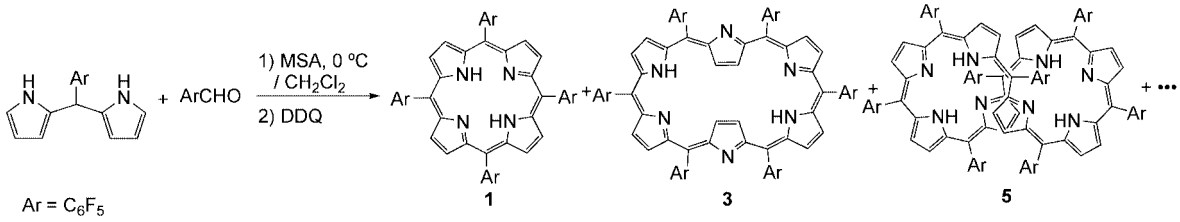


Scheme 3. Ring-size selective synthesis.

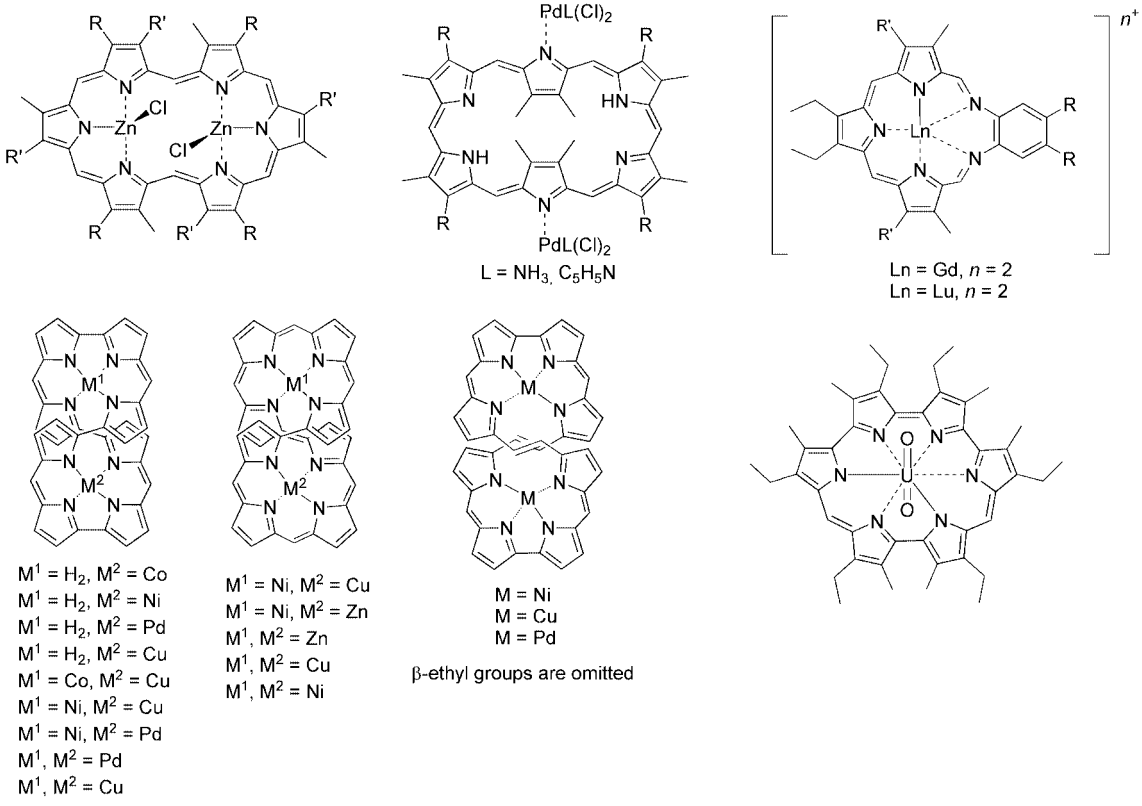


Figure 1. Representative examples of metal complexes of expanded porphyrins.

ure-eight conformations and revealed their facile complexation behaviors with several transition metal ions.[27] The figure-eight conformations were fixed upon complexation, which enabled optical separation of the metalated octaphyrins for the first time.[27a] Sessler et al. have investigated lanthanoid metal complexes of texaphyrins and medicinal applications of gadolinium texaphyrins as sensitizers for photodynamic therapy.[5,9] They synthesized the bis-$Cu^{II}$ complex of amethyrin and revealed the proximity of the metal centers and their antiferromagnetic behavior.[28] Recently, they have investigated the usage of expanded porphyrins as a colorimetric actinoid sensor.[29] Thus, expanded porphyrins are becoming increasingly important platforms for several metal ions and as promising materials in various fields. From this point of view, the *meso*-aryl-substituted expanded porphyrins can be regarded as another promising candidate to explore novel functional metal complexes since this facile, one-pot reaction affords a series of expanded porphyrins that differ in the number of the constituting pyrrolic subunits and thus in cavity size, conformational flexibility, and stable conformation.

In this Microreview we summarize our own contributions in the synthesis, characterization, and properties of metal complexes of *meso*-aryl-substituted expanded porphyrins, which are presented in order of their ring size. The compound names appearing in this review are partly based on a nomenclature put forward by Franck and Nonn for porphyrinic system.[30] The number in square brackets corresponds to the number of π-electrons in the shortest conjugation pathway and the core name represents the number of pyrroles.

## N-Fused Pentaphyrin ($NFP_5$)

### Structures and Properties of the Free Bases

*meso*-Pentafluorophenyl-substituted pentaphyrin was obtained as its N-fused form, whicht was found to exist as a

 © 2006 Wiley-VCH Verlag GmbH & Co. KGaA, Weinheim 

mixture of two oxidation states {[22]N-fused pentaphyrin ([22]$NFP_5$, **2a**) and [24]$NFP_5$ (**2b**); Figure 2} from the reaction shown in Scheme 1.[22,31] The yield of each compound varied depending on the oxidation time. Thus, **2a** was obtained after oxidation with an excess amount of DDQ for a long time (>15 h) in 18% yield as the sole pentapyrrolic product (Scheme 1).[31b] Alternatively, **2a** was prepared in 28% yield by an acid-catalyzed [3+2] condensation of tripyrrane and dipyrromethane (Scheme 4). Compound **2a** is easily reduced to **2b** with $NaBH_4$, which is quantitatively oxidized back to the original **2a** upon treatment with DDQ (Figure 2). An aromatic ring current effect arising from the 22π-electron conjugation is observed in the $^1H$ NMR spectrum of **2a**, while **2b** shows antiaromatic character due to its 24π-electron conjugation. According to X-ray diffraction analyses, both **2a** and **2b** possess a fused tripentacyclic ring (pyrroles A and B in Figure 3), an outward-pointing pyrrole ring (pyrrole C), and an inward-oriented dipyrromethene moiety (pyrroles D and E). The inverted pyrrole C is significantly tilted for each compound. Except for pyrrole C the entire structure of **2a** is planar, while that of **2b** is severely distorted.

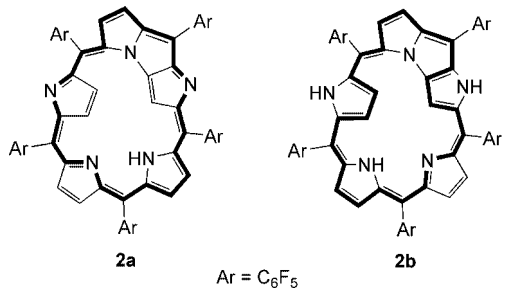


Figure 2. Redox behavior of $NFP_5$.

## Metal Complexes of $NFP_5$

Since both **2a** and **2b** possess a dipyrromethene moiety, we investigated complexation of $Rh^I$, which is known, in the coordination chemistry of porphyrinoids, to bind to one dipyrromethene ligand and two carbonyl ligands in a

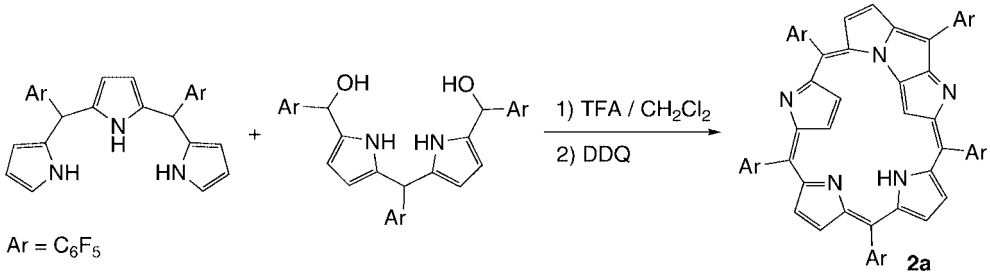


Scheme 4. Synthesis of **2a** by a [3+2] condensation reaction.

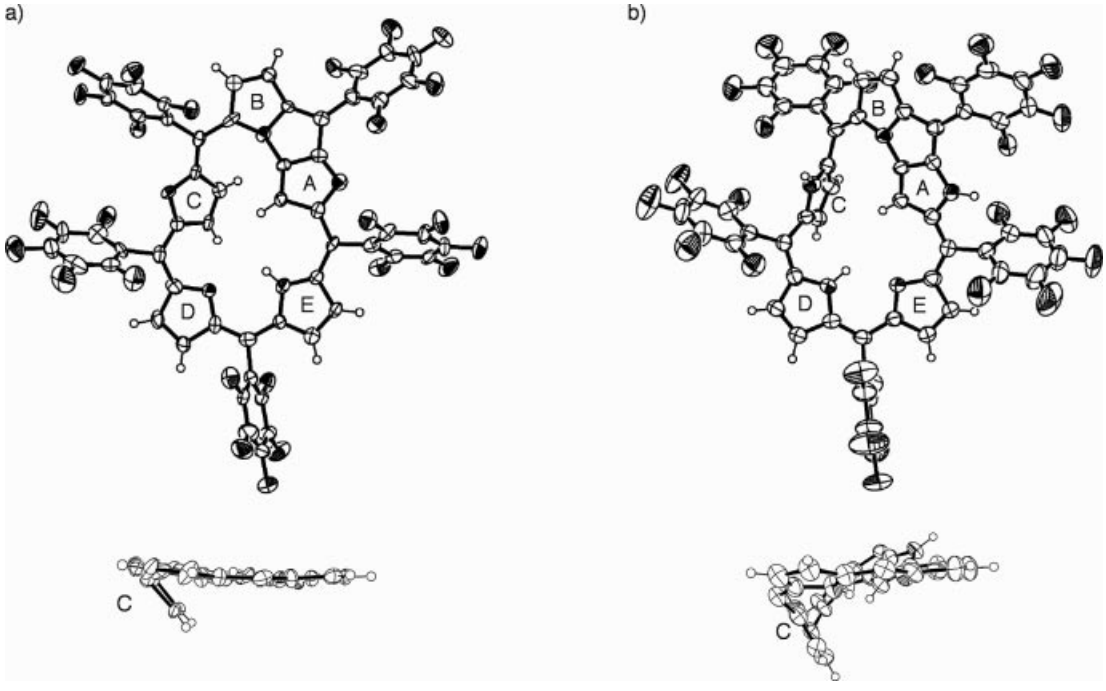


Figure 3. X-ray crystal structures of a) **2a** (preliminary) and b) **2b**; top views (top) and side views (bottom). *meso*-Aryl substituents have been omitted for clarity in the side views.

 © 2006 Wiley-VCH Verlag GmbH & Co. KGaA, Weinheim 

square-planar fashion.[32–34] Two rhodium complexes **10** and **11** were isolated in 2.4% and 23% yields, respectively, from the metalation of **2a** with two equivalents of $[RhCl(CO)_2]_2$ in $CH_2Cl_2$ in the presence of sodium acetate at room temperature for 4 h (Figure 4).[31b] The product ratio of **11** to **10** decreased as the reaction time increased. Under refluxing conditions the yield of **10** (42%) was distinctly higher than that of **11** (18%). These results suggest that **10** is the thermodynamic product of this reaction. On the contrary, the complexation of **2b** with $[RhCl(CO)_2]_2$ gave complex **11** as the sole product in 60% yield at room temperature after 1 h.

In the crystal structures, both **10** and **11** preserve basic $NFP_5$ skeletons with a 22π- and 24π-electron conjugation, respectively, in which the $Rh^I$ ion is bound above the center of the cavity by the dipyrromethene unit (pyrroles D and E for **10** and pyrroles C and D for **11**), with N–Rh distances of around 2.1 Å, and two carbonyl ligands in a square-planar fashion (Figure 5). The entire structure of **10** is relatively planar except for the pyrrole C. On the other hand, **11** has a severely distorted bent conformation despite the fully conjugated system. In accordance with these results, the $^1H$ NMR spectrum of **10** displays peaks for the inner β-CH protons of pyrroles A and C as a singlet at $\delta$ = 0.05 ppm and as a pair of doublets at $\delta$ = 1.62 and 1.16 ppm, respectively, and the outer β-CH protons as three pairs of doublets at $\delta$ = 9.23, 9.21, 8.61, 8.29, 8.21, and 8.13 ppm that indicate a diatropic ring-current effect arising from the planar structure and 22π-electron conjugation. In the $^1H$ NMR spectrum of **11**, however, resonances due to the inner and outer NH protons of pyrroles E and A are observed at $\delta$ = 0.68 and 9.44 ppm, respectively, indicating, to our surprise, a substantial diatropic ring current for **11**, which is also supported by the up- and downfield shifts of the peaks due to the inner and outer β-CH protons, respectively.

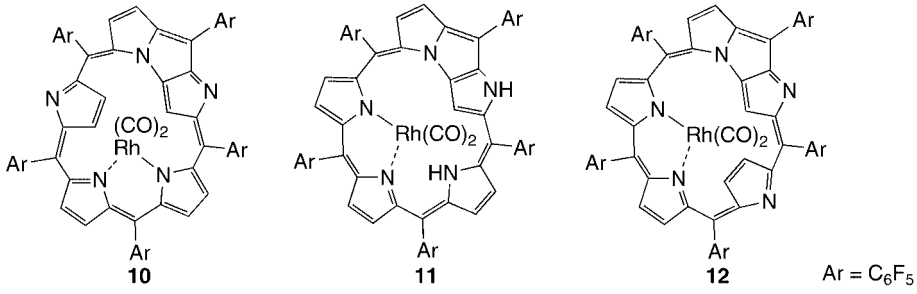


Figure 4. $Rh^I$ complexes of $NFP_5$.

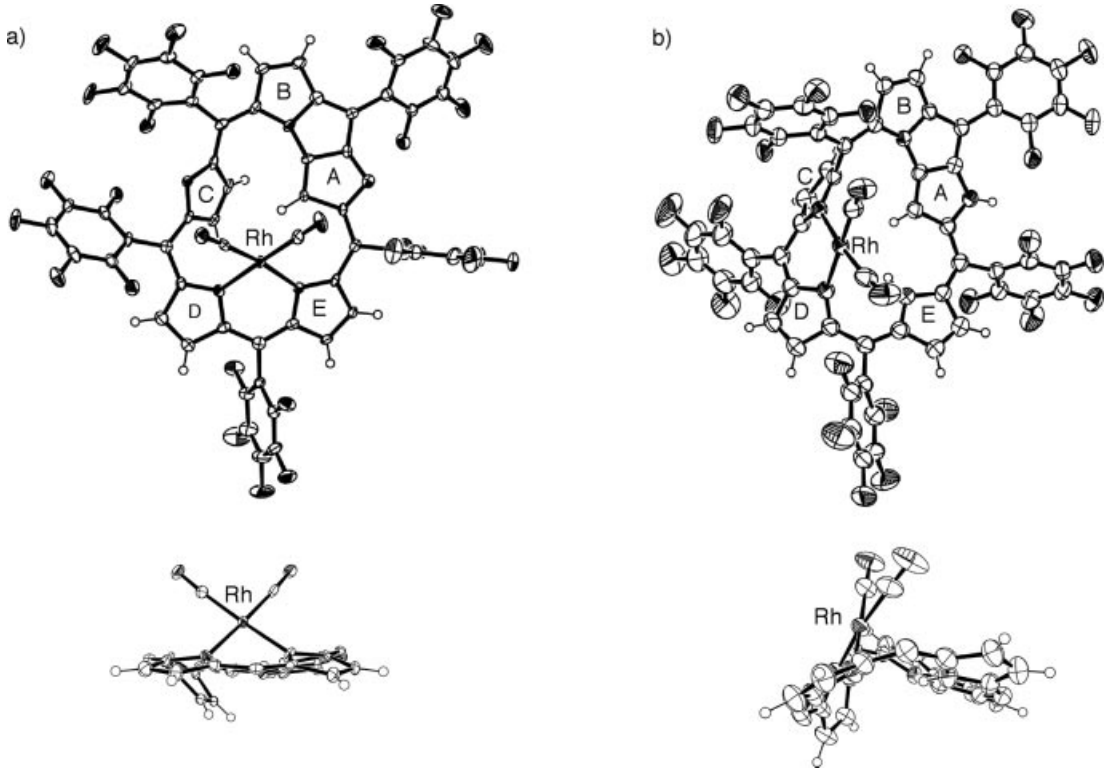


Figure 5. X-ray crystal structures of a) **10** and b) **11**; top views (top) and side views (bottom). *meso*-Aryl substituents have been omitted for clarity in the side views.

 © 2006 Wiley-VCH Verlag GmbH & Co. KGaA, Weinheim 

Since complex **10** is the major product at high temperature, thermal conversion of **11** to **10** was examined in refluxing $CH_2Cl_2$; this reaction turned out to be unsuccessful. Considering that the number of conjugated π electrons is 22 for **10** and 24 for **11**, interconversion between these complexes by two-electron oxidation and reduction should be feasible. Thus, treatment of **11** with DDQ at room temperature quantitatively converted it into complex **10** by a novel pivot-like-walk rearrangement of Rh. The details of this process were monitored by $^1$H NMR spectroscopy, in which an intermediate **12** (Figure 4) was detected before the final formation of **10**. In contrast, reduction of **10** with $NaBH_4$ caused demetalation to give **2b** without producing **11**.

## Hexaphyrin

### Structures and Properties of the Free Bases

Hexaphyrin **3**, which was first synthesized by Cavaleiro and co-workers,[35] was one of the major products from the modified Rothemund–Lindsey reaction and was obtained in 16–20% yield as an oxidized form with 26π electrons in its conjugation (Scheme 1).[22] The yield was improved by using the ring-size selective synthesis.[24] Upon treatment with $NaBH_4$, [26]hexaphyrin (**3a**) was easily reduced to [28]-hexaphyrin (**3b**), which could be quantitatively oxidized back to the original [26]hexaphyrin (Figure 6). In the solid, **3a** exhibits a planar rectangular structure with two inverted pyrrole rings (Figure 7, a).[35] Although a structural analysis of **3b** unfortunately has not yet been successful, the structure of an analogue of **3b** bearing alkylamino substituents at the *p* position of the pentafluorophenyl groups and exhibiting almost identical UV/Vis and NMR spectra to **3b** was revealed crystallographically to possess a similar conformation to that of **3a**.[36] In solution, **3a** exhibits aromatic character due to the 26π-electron conjugation and planar conformation. On the other hand, the $^1$H NMR spectrum of **3b** indicates aromatic rather than antiaromatic character. The explanation for this is uncertain at this stage.

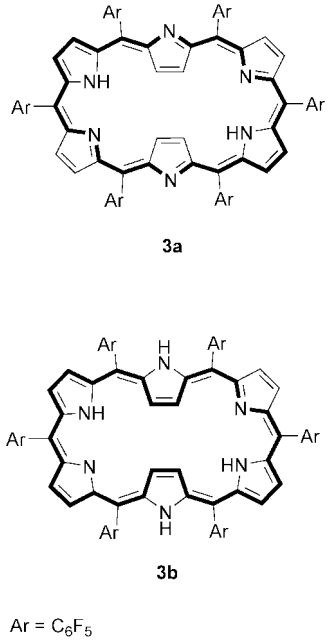


Figure 6. Redox behavior of hexaphyrin.

We have also investigated the synthesis of hexaphyrins bearing several substituents not only at the *meso* position but also at the β position. Perfluorinated [28]hexaphyrin (**7**) was isolated in 2–5% yield from a mixture of other perfluorinated expanded porphyrins obtained from the reaction of 3,4-difluoropyrrole with pentafluorobenzaldehyde.[23] In the solid state, **7** takes a figure-eight conformation and hence exhibits nonaromatic character (Figure 7, b). In addition to the coordination properties of these hexaphyrins, they are also drawing much attention as a near-IR absorbing dye.

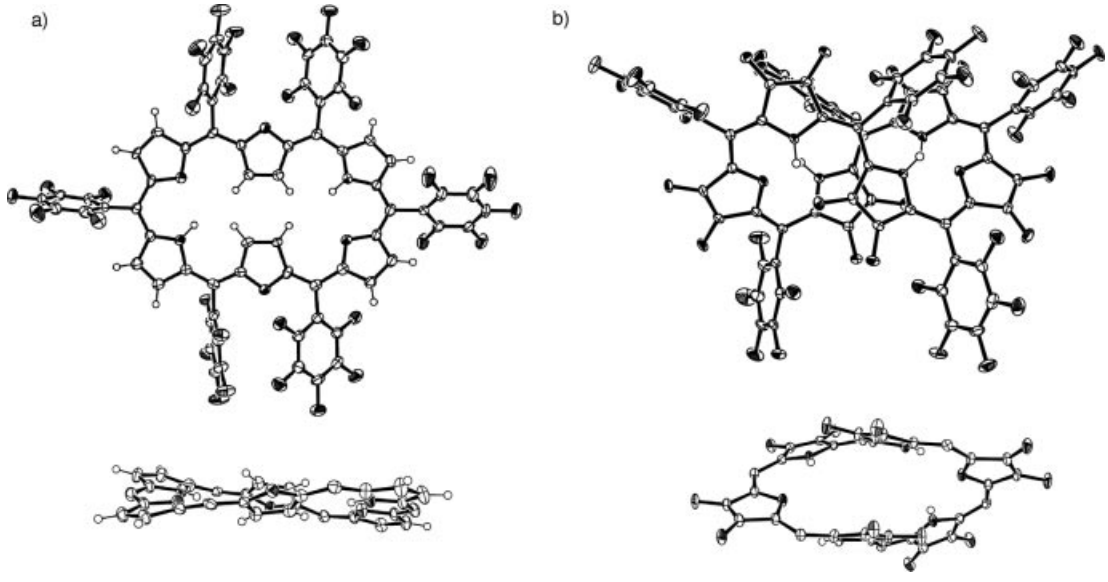


Figure 7. X-ray crystal structures of a) **3a** and b) **7**; top views (top) and side views (bottom). *meso*-Aryl substituents have been omitted for clarity in the side views.

 © 2006 Wiley-VCH Verlag GmbH & Co. KGaA, Weinheim 

The absorption spectrum of **3a** shows a Soret-like band at 568 nm and Q-like absorptions at 712, 898, and 1026 nm, and is formally similar to that of porphyrin although with substantial red-shifts owing to the extension of the π-conjugation.[11,35] Compound **3a** exhibits fluorescence emission at 1036 nm with a weak vibronic band at 1205 nm.[11] Recently, molecules having large two-photon absorption (TPA) cross-sections [$\sigma^{(2)}$] have been of great interest due to their potential applications in a variety of fields described in the previous section. Aromatic **3a** exhibits a large TPA cross-section value of about $10^4$ GM, which makes it quite attractive for further applications.[11]

### Copper Complexes of Hexaphyrins

The complexation reaction of **3a** with anhydrous $CuCl_2$ and NaOAc in $CH_2Cl_2$ gave the dicopper complex **13** in 84% yield.[37] Interestingly, metalation in the presence of anhydrous $Cu(OAc)_2$ and NaOAc led to isolation of a different dicopper complex **14** in 90% yield (Figure 8). Both structures were elucidated by X-ray single crystal analysis. The structure of **13** takes a gable structure with two semi-planar tripyrrolic planes in which each copper ion is bound to the bridging chloride atom, the oxygen atom attached at the *meso* position, and three nitrogen atoms of the tripyrrolic unit, in a square-pyramidal fashion (Figure 9, a). Compound **14** exhibits a similar gable structure with two copper ions, which are each bound to the *meso*-attached oxygen atom and three pyrrolic nitrogen atoms in a square-planar fashion (Figure 9, b). Contrary to complex **13**, there is no axial bridging in **14**.

Similar copper metalation was tested for perfluorinated [28]hexaphyrin (**7**). Complex **15** was obtained as the sole product (96% yield) from the reaction with $CuCl_2$, while metalation with $Cu(OAc)_2$ afforded a mixture of complex **15** and **16** in 26 and 56% yields, respectively (Figure 8). The structure of **15** is quite similar to that of **14**, while **16** takes a different structure in which the two copper ions are not directly bridged but are coordinated separately by the different tripyrrolic ligand and *meso*-attached oxygen atom (Figures 9, c and d). The oxygen ligands in **16** are from a tertiary alcohol and an alkoxide. Importantly, this structure leads to the assignment of **16** as a mixed-valence $Cu^I/Cu^{II}$ complex. The proximity of the two $Cu^{II}$ ions in **13**, **14**, and **15** allows antiferromagnetic couplings with exchange interaction values ($J$) of –8.27, –87.6, and –42.1 $cm^{-1}$, respectively. On the contrary, complex **16** has a temperature-independent $\chi_pT$ value (0.4229 emu K $mol^{-1}$) corresponding to an $S = 1/2$ state, in agreement with the $Cu^I/Cu^{II}$ mixed-valence state.

### Doubly N-confused [26]Hexaphyrin from [26]Hexaphyrin

In the course of their extensive investigations on N-confused porphyrinoids,[38] Furuta et al. have reported the synthesis of a doubly N-confused hexaphyrin (DNCH, **17**) bearing two oxygenated confused pyrrole rings, which offer efficient coordination sites for two transition metal ions such as $Cu^{II}$ **18** and $Ni^{II}$ **19** (Figure 10).[38c] Compound **17** and its bis-metal complexes are also attractive as near-IR-absorbing dyes due to their expanded π-electronic system but have been rather poorly explored, mainly due to the tedious, multi-step synthesis of the N-confused tripyrrane precursor.[38d] During our exploration of the metalation chemistry of hexaphyrin **3a**, we serendipitously found that treatment with $Cu^I$ under aerobic conditions in pyridine efficiently provided the bis-$Cu^{II}$ complex of DNCH (**18**; 24.4% yield), whose structure was confirmed by X-ray analysis (Figure 11, a).[39] Remarkably, both the inverted pyrrole rings of **3a** undergo simultaneous rearrangements to form N-confused pyrroles with concomitant oxygenation at the internal pyrrolic α positions. Although the reaction mechanism has not been elucidated yet, we anticipate the involvement of CuCl–pyridine–$O_2$ oxidation in this reaction on the basis of several experimental facts.

The bound copper ions are easily demetalated upon treatment with TFA in $CH_2Cl_2$ to give the free base **17**, which is a good ligand system for two divalent or trivalent metal ions ($Cu^{II}$ **18**, $Ni^{II}$ **19**, $Co^{II}$ **20**, $Zn^{II}$ **21**, $Mn^{III}$ **22**, and $Fe^{III}$ **23**; Figure 10). The $^1H$ NMR spectra of **17** and **21** display strong diatropic ring currents in line with their 26π aromatic conjugation. The absorption spectrum of **17** exhibits a Soret-like band at 566 nm with a shoulder at 586 nm and Q-like bands at 722, 793, 911, and 1047 nm. Interestingly, **17** shows fluorescence at 1058 nm, with a vibronic structure that has a very small Stokes shift. These observations suggest a rigid structure supported by multiple intramolecular hydrogen-bonding interactions.

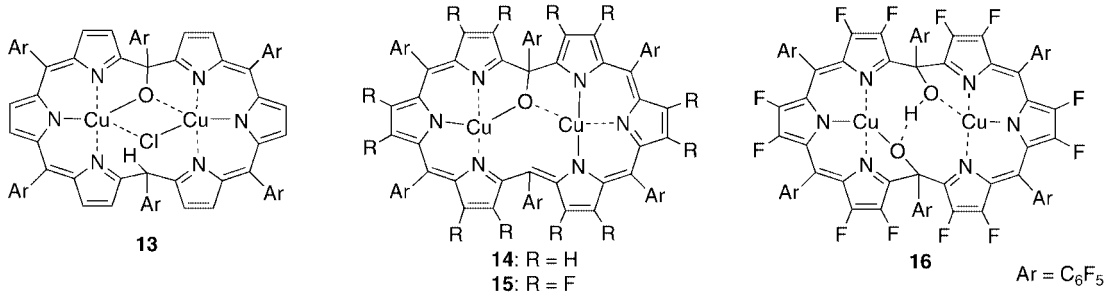


Figure 8. Bis-Cu complexes of hexaphyrins.

 © 2006 Wiley-VCH Verlag GmbH & Co. KGaA, Weinheim 

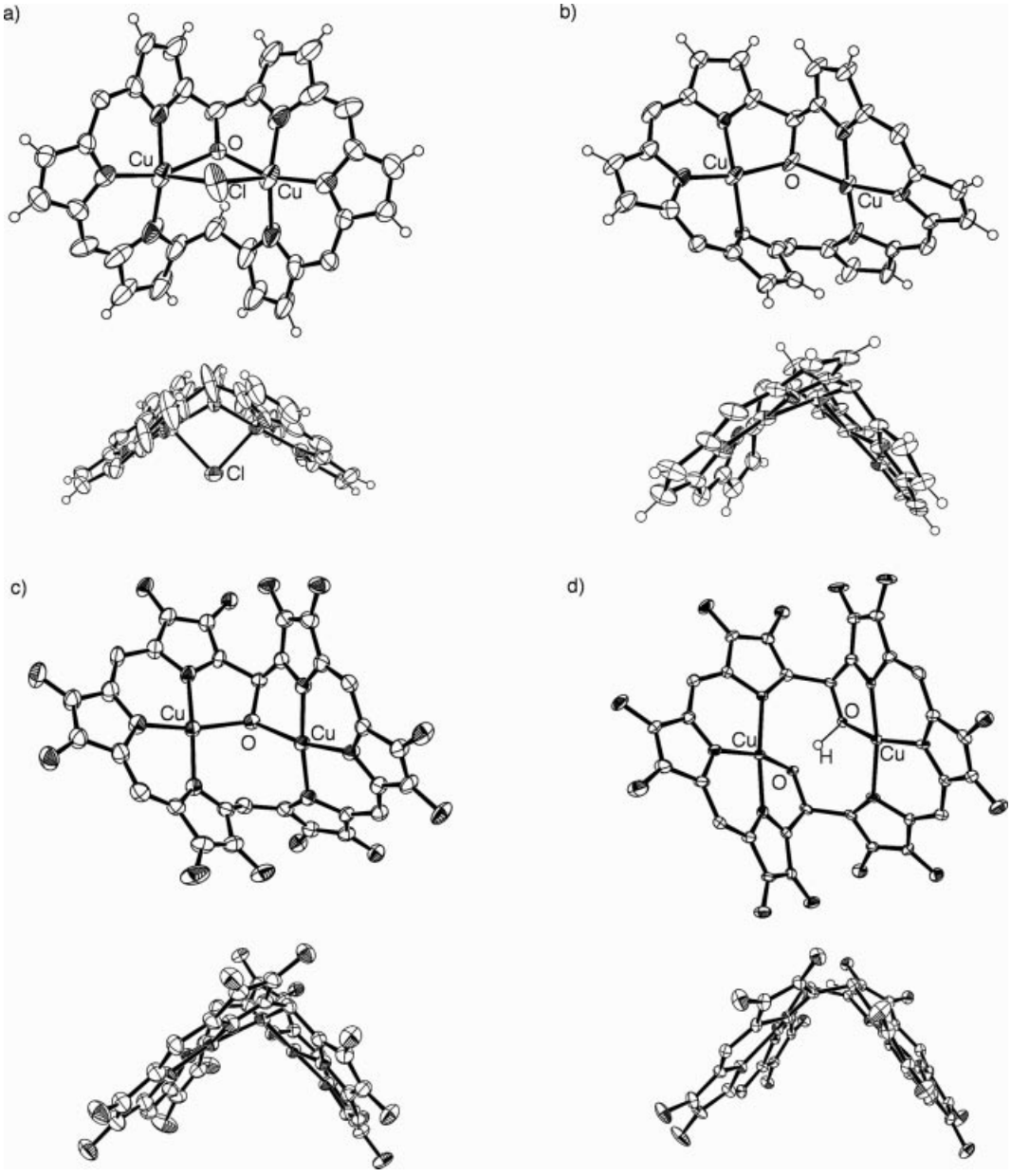


Figure 9. X-ray crystal structures of a) **13**, b) **14**, c) **15**, and d) **16**; top views (top) and side views (bottom). *meso*-Aryl substituents have been omitted for clarity.

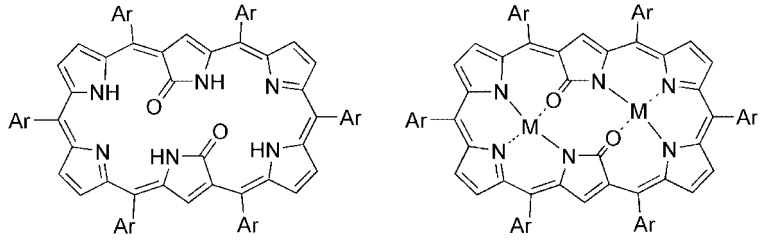


**17**

Ar = $C_6F_5$

**18**: M = Cu
**19**: M = Ni
**20**: M = Co
**21**: M = Zn
**22**: M = MnCl
**23**: M = FeCl

Figure 10. Doubly N-confused hexaphyrin and its metal complexes.

 © 2006 Wiley-VCH Verlag GmbH & Co. KGaA, Weinheim 

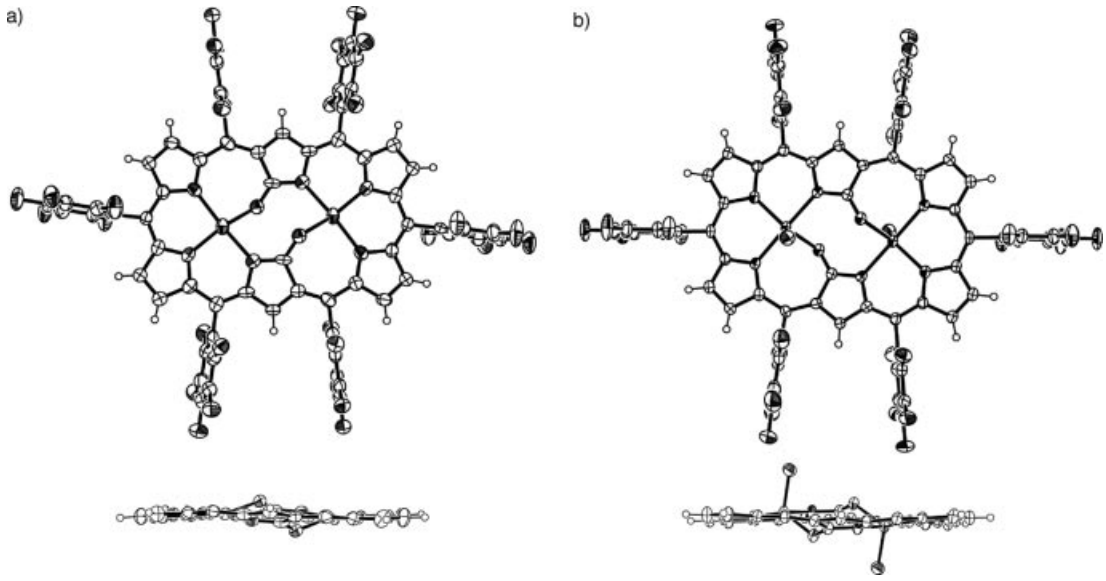


Figure 11. X-ray crystal structures of a) **18** and b) **20**; top views (top) and side views (bottom). *meso*-Aryl substituents have been omitted for clarity in the side views. Water molecules each coordinate to the axial position of the cobalt ion in **20**.

### Group 10 Metal Complexes of Hexaphyrin

The copper complexes described above exhibit large structural changes upon metalation. Next, we investigated the complexation of hexaphyrin with group 10 metal ions such as $Ni^{II}$, $Pd^{II}$, and $Pt^{II}$.[40] When a toluene solution of **3a** and $Ni(acac)_2$ was refluxed for one hour in the presence of sodium acetate under anaerobic conditions the mono-$Ni^{II}$ complex **24** was obtained in 50% yield. Similarly, the mono-$Pt^{II}$ complex **27** was obtained in 56% yield from the reaction of **3a** with $PtCl_2$ and NaOAc in refluxing $CH_2Cl_2$ under argon. Curiously, however, metalation with $PdCl_2$ in refluxing $CH_2Cl_2$ in the presence of NaOAc provided a mixture of mono-$Pd^{II}$ (**25**) and bis-$Pd^{II}$ (**26**) complexes, which were isolated in 50 and 9% yields, respectively (Figure 12). Single crystal analyses revealed that complexes **24**, **25**, and **27** possess a metal–carbon bond and have distorted structures (Figures 13, a–c). The $^1H$ NMR spectra of **24**, **25**, and **27** show nonaromatic character due to the nonplanar structures. In the crystal structure of **26** the two $Pd^{II}$ ions are bridged by the chloride atom. One $Pd^{II}$ ion is bound to three pyrrolic nitrogen atoms and the other is bound to two pyrrolic nitrogen atoms and a pyrrolic α-carbon, and an N-fusion reaction of the pyrrole E and the adjacent pentafluorophenyl group has taken place to form a planar pentacyclic ring (Figure 13, d). Thus, the internal β-pyrrolic CH bond of **3a** is activated to form a metal–carbon bond in the metalation reactions with group 10 metal ions.

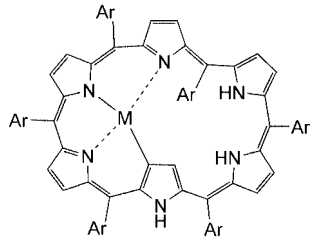


**24**: M = Ni
**25**: M = Pd
**27**: M = Pt

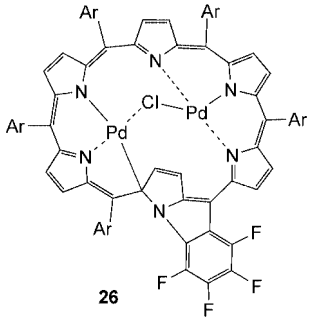


**26**

Ar = $C_6F_5$

Figure 12. Group 10 metal complexes of hexaphyrin.

### Gold Complexes of Hexaphyrin

Metal complexes of hexaphyrin preserving the original planar and rectangular shape are of great interest from the viewpoint of regulation of aromaticity and antiaromaticity. Towards this goal, metal ions with a strong C–H activation ability would be promising. During the exploration of the complexation chemistry of hexaphyrins, we fortunately found that gold metalation of **3a** accomplished this goal to provide mono-$Au^{III}$ and bis-$Au^{III}$ complexes.[41] A solution of **3a** and $NaAuCl_4$ in a 4:1 mixture of $CH_2Cl_2$ and methanol was stirred in the presence of sodium acetate at room temperature for three days. Separation on a silica gel column provided the mono-$Au^{III}$ (**28**) and bis-$Au^{III}$ (**29**) complexes in 16 and 14% yield, respectively, along with 15% of

 © 2006 Wiley-VCH Verlag GmbH & Co. KGaA, Weinheim 

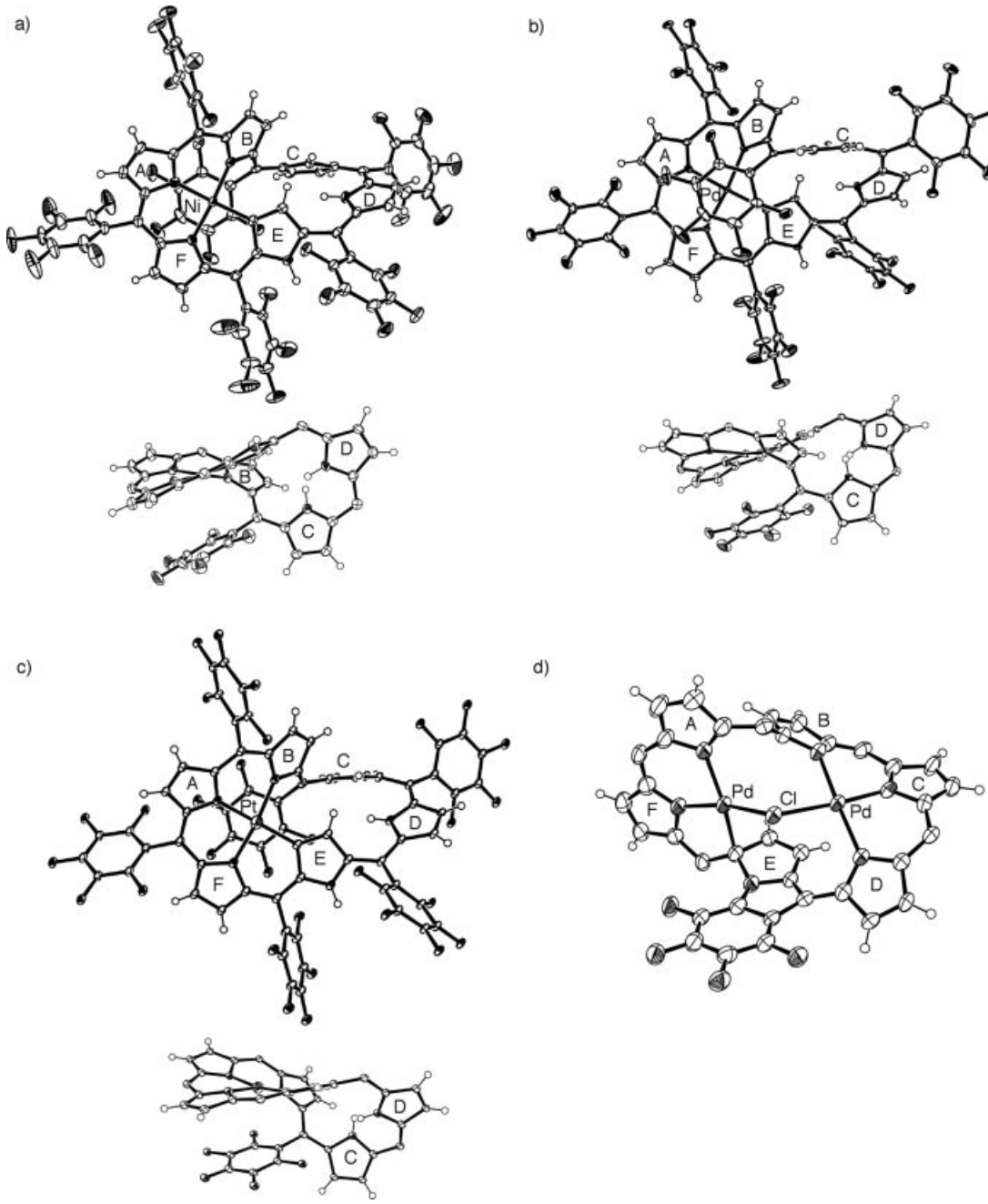


Figure 13. X-ray crystal structures of a) **24**, b) **25**, c) **27** (preliminary), and d) **26**; top views (top) and side views (bottom). *meso*-Aryl substituents have been partially omitted for clarity.

recovered **3a** (Figure 14). Curiously, in both crystal structures the inner β-CHs have been activated to form Au–C bonds and the $Au^{III}$ ions are coordinated to two pyrrolic nitrogen atoms and two pyrrolic β-carbon atoms within a flat [26]hexaphyrin core. The structure of **28** is planar in the coordinated moiety and rather distorted in the cavity, while **29** has a much more planar but overall bent structure (Figure 15). These structural differences can be explained by the steric congestion between the inner pyrrolic β-CHs. As anticipated from their crystal structures, aromaticity of these complexes was observed in their $^1$H NMR spectra. The outer β-CH protons of **28** appear downfield at $\delta$ = 9.51, 9.36, 9.35, and 9.03 ppm, and the inner β-CH and NH protons are seen at $\delta$ = –2.93 and –2.08 ppm, respectively, while for **29** the outer β-CH protons appear at $\delta$ = 9.66 and 9.51 ppm (Figures 16, a and b). Rigidification by Au coordination has been revealed to play a very important role in enhancing aromatic character, which, in turn, suggests a possible attainment of antiaromatic [28]hexaphyrin in the planar frame. Thus, complexes **28** and **29** were reduced with $NaBH_4$ to give complexes **30** and **31** without demetalation (Figure 14). The structures of **30** and **31** were both preliminarily revealed by X-ray analyses to keep the original rectangular structures but to have two NH hydrogen atoms at

 © 2006 Wiley-VCH Verlag GmbH & Co. KGaA, Weinheim 

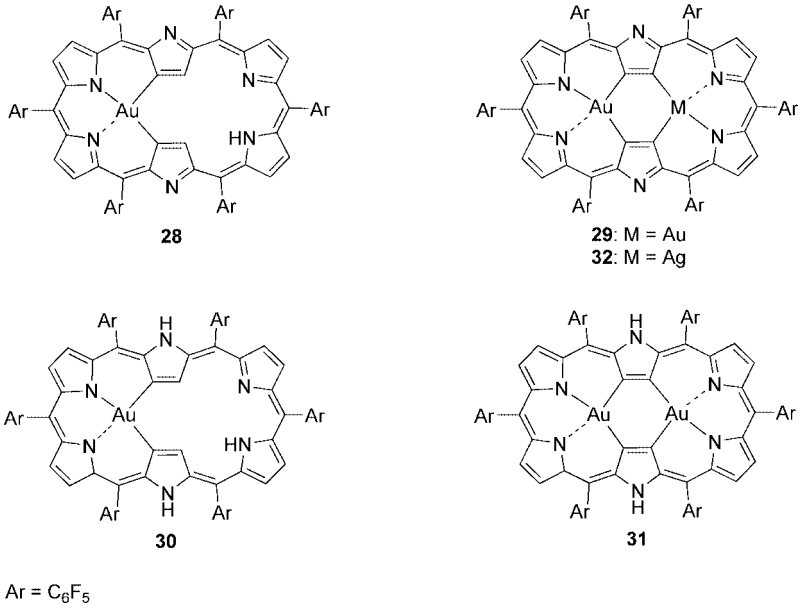


Figure 14. Gold complexes of hexaphyrin.

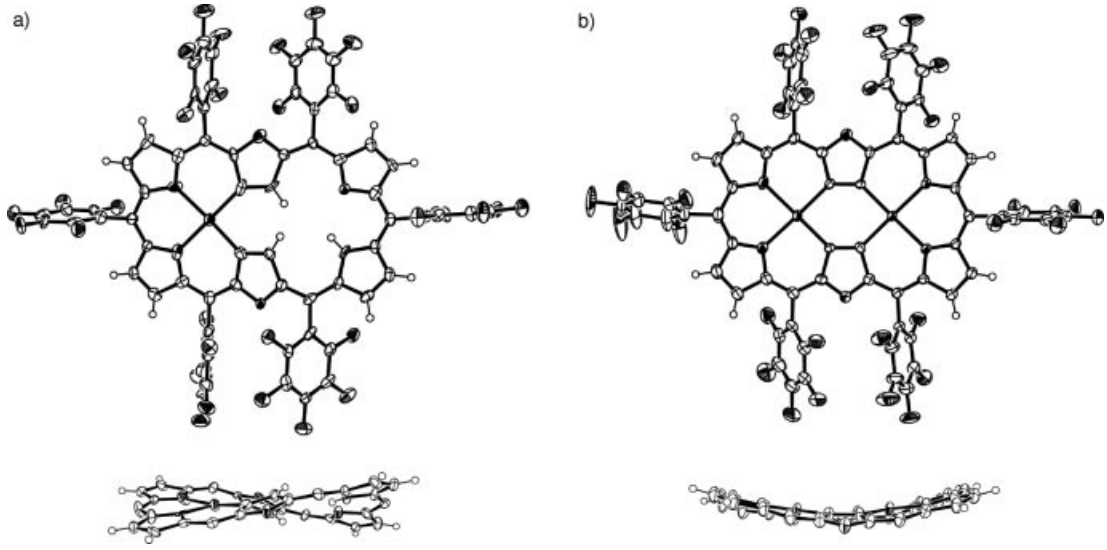


Figure 15. X-ray crystal structures of a) **28** and b) **29**; top views (top) and side views (bottom). *meso*-Aryl substituents have been omitted for clarity in the side views.

the inverted pyrroles. Very curiously, and consistent with Hückel's rule, the $^1$H NMR spectra of **30** and **31** show a paratropic ring-current effect (Figures 16, c and d). In the $^1$H NMR spectrum of **30**, the inner β-CH and NH protons are observed at $\delta$ = 19.39 and 24.57 ppm, respectively, while the outer β-CH protons appear as four doublets at $\delta$ = 5.02, 4.92, 4.32, and 4.07 ppm and the outer NH protons appear at $\delta$ = 4.10 ppm. Similarly, the $^1$H NMR spectrum of **31** exhibits the outer β-CH protons as a pair of doublets at $\delta$ = 3.16 and 3.10 ppm and the outer NH protons as a broad singlet at $\delta$ = 1.81 ppm. Considering the nonaromaticity of the group 10 metal complexes **24**, **25**, and **27**, firm rigidification of the planar conformation causes the strong antiaromatic character in [28]hexaphyrin.

Complex **28** still has a vacant cavity that may allow coordination of another metal ion. This possibility was examined by treating **28** with $CF_3COOAg$ to give the $Au^{III}/Ag^{III}$ hetero complex **32** in 58% yield with concomitant oxidation of $Ag^I$ to $Ag^{III}$ in order to fit into the core.

## Octaphyrin

### Structures and Properties of the Free Bases

Due to its large conjugation, *meso*-aryl-substituted octaphyrin is supposed to possess three different redox states with 34π-, 36π-, and 38π-electrons (**5b**, **5a**, and **5c**, respectively, in Figure 17). From the reaction shown in Scheme 1, octaphyrin was obtained as [36]octaphyrin (**5a**) in 5–6% yield. The yield of **5a** was improved by using the ring-size selective synthesis.[24] In the crystal structure, **5a** takes a twisted figure-eight conformation in which there are two

 © 2006 Wiley-VCH Verlag GmbH & Co. KGaA, Weinheim 

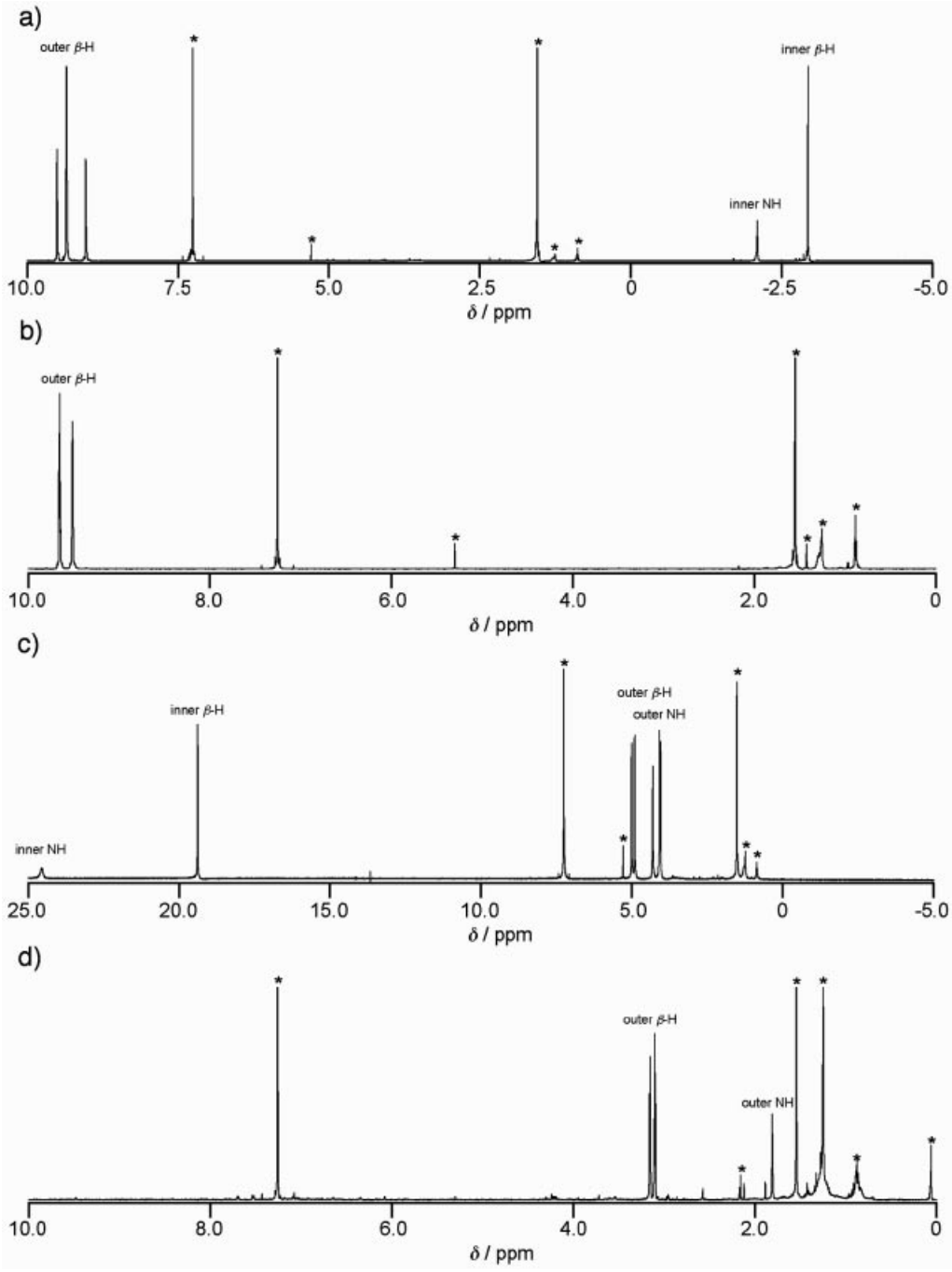


Figure 16. $^1$H NMR spectra of a) **28**, b) **29**, c) **30**, and d) **31** in $CDCl_3$. * indicates solvent and solvent impurities.

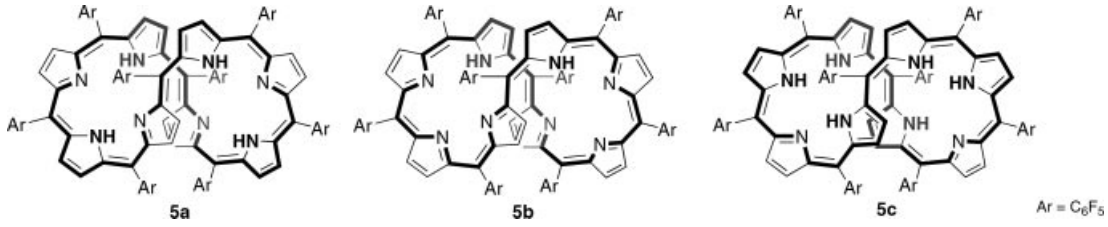


Figure 17. Redox behaviors of octaphyrin.

 © 2006 Wiley-VCH Verlag GmbH & Co. KGaA, Weinheim 

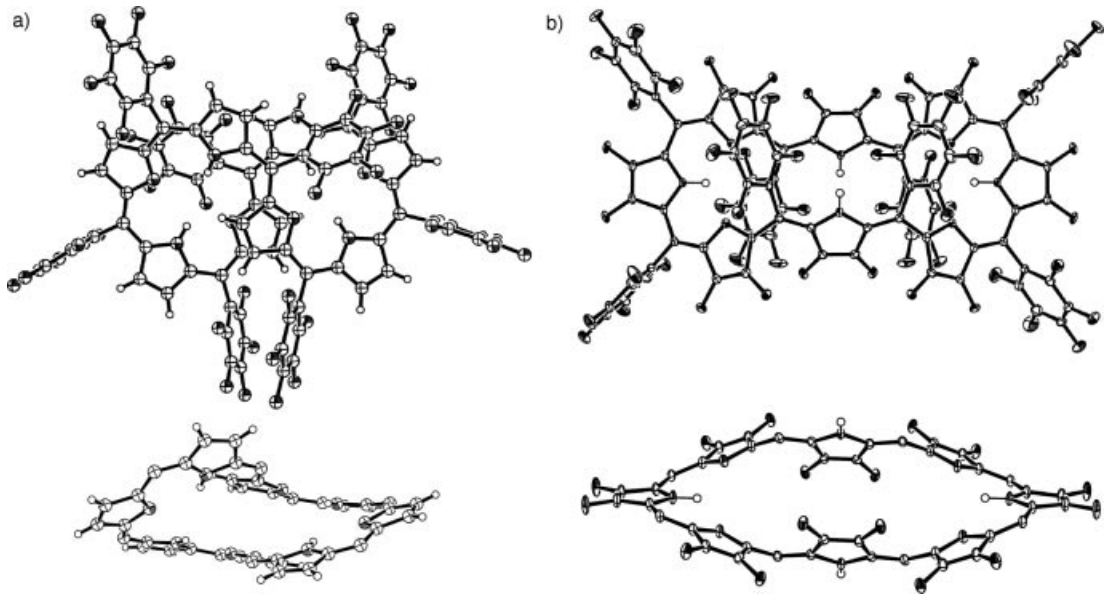


Figure 18. X-ray structures of a) **5a** and b) **9**; top views (top), and side views (bottom). *meso*-Aryl substituents have been omitted for clarity in the side views.

porphyrin-like teterapyrrolic hemimacrocycles; it thus has the potential to coordinate one metal ion in each cavity (Figure 18, a).[22] Upon reduction with $NaBH_4$, **5a** is quantitatively converted into [38]octaphyrin (**5c**), while oxidation of **5a** with $MnO_2$ gives [34]octaphyrin **5b**. Unfortunately, however, the structures of [34]- and [38]octaphyrin have not been determined yet, mainly due to the their instability under ambient conditions. On the other hand, perfluorinated [36]octaphyrin (**9**) was obtained in 4–7% yield from the reaction of 3,4-difluoropyrrole and pentafluorobenzaldehyde.[23] Interestingly, **9** takes a different conformation: it is not twisted figure-eight but has a round ellipsoidal structure (Figure 18, b). Mainly due to their nonplanar structures, these octaphyrins do not exhibit any aromatic or antiaromatic character.

### Copper Metalation of [36]Octaphyrin and Perfluorinated [36]Octaphyrin

A solution of **5a** in toluene was stirred at 50 °C in the presence of ten equivalents of $Cu(OAc)_2$ and five equivalents of NaOAc and the metalation process was monitored by UV/Vis absorption spectroscopy. Compound **5a** exhibits absorption bands at 410 and 643 nm, which change to absorption bands at 412 and 668 nm after 2 h and then to absorption bands at 351 and 522 nm after 4 h (Figure 19). These spectral changes were ascribed to sequential formation of mono-$Cu^{II}$ (**33**) and bis-$Cu^{II}$ (**34**) complexes by comparison with the absorption spectra of authentic samples (Figure 20).[42] On further heating the small, shoulder-like absorption at 408 nm in the spectrum increased and finally

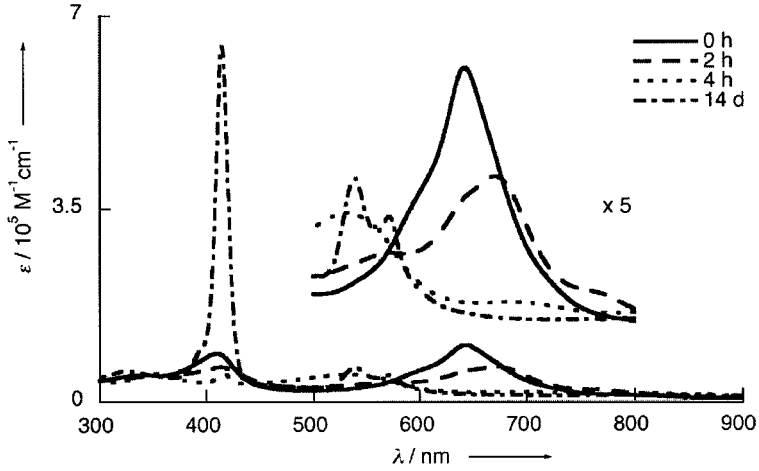


Figure 19. UV/Vis spectral changes recorded during metalation of **5a** with $Cu(OAc)_2$ at 50 °C in toluene.

 © 2006 Wiley-VCH Verlag GmbH & Co. KGaA, Weinheim 

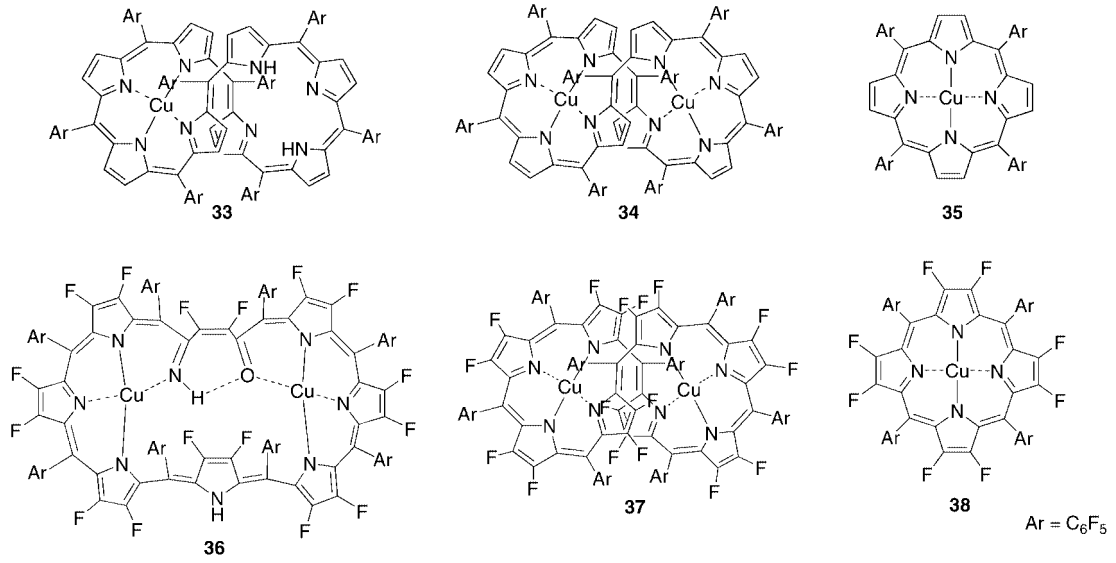


Figure 20. Copper complexes of octaphyrins and porphyrins.

the spectrum showed only the absorption at 408 nm with small bands at 535 and 570 nm after heating for two weeks (Figure 19). This final spectrum indicates the formation of the $Cu^{II}$ porphyrin **35** (Figure 20). The mono-$Cu^{II}$ complex **33** and the bis-$Cu^{II}$ complex **34** were prepared in 77 and 81% yields, respectively, under temperature-controlled conditions in a $CH_2Cl_2$ solution with a small amount of MeOH. In the solid state, **34** takes a similar twisted figure-eight conformation with two copper ions bound inside the porphyrin-like tetrapyrrolic cores. The coordination of the $Cu^{II}$ ions is severely distorted from square-planar coordination (Figure 21). Considering that neither free base **5a** nor **33** show splitting behavior, this structural feature suggests that the relief of strain in **34** may be the main driving force for this thermal splitting reaction.[42,43] We thus estimated the activation parameters of the splitting reaction by absorption spectroscopic analysis. The splitting reaction of **34** was found to be a unimolecular process with $\Delta H^{\ddagger}$ = 101 kJ mol$^{-1}$ and $\Delta S^{\ddagger}$ = –23.5 J K$^{-1}$ mol$^{-1}$. A possible mechanism of the splitting reaction may be a 2π + 2π cycloaddition process to give a spirocyclobutane intermediate, as shown in Scheme 5.

This thermal splitting reaction was also seen in the solid state. In the DSC experiment of **34**, a sharp exothermic re-

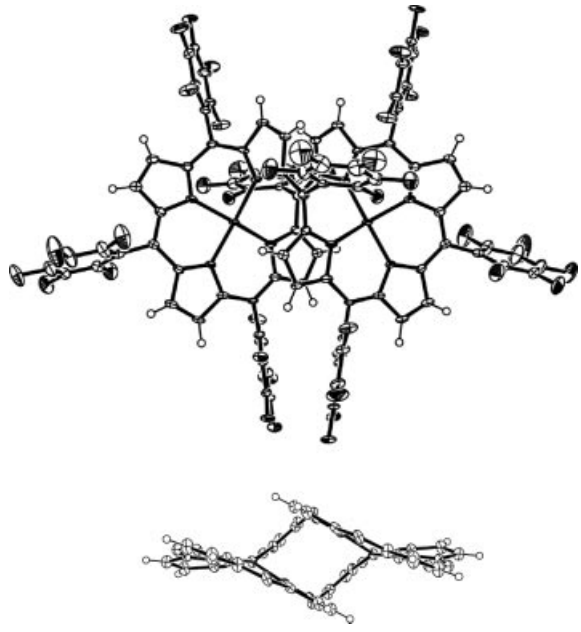

Figure 21. X-ray crystal structure of **34**; top view (top) and side-view (bottom). *meso*-Aryl substituents have been omitted for clarity in the side view.

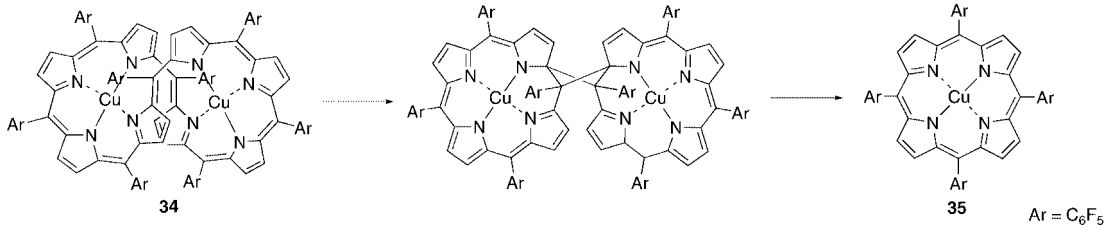


Scheme 5. A possible mechanism of the splitting reaction of **34**.

 © 2006 Wiley-VCH Verlag GmbH & Co. KGaA, Weinheim 

sponse was observed between 240 and 280 °C, and **35** was obtained in high yield from this thermolysis experiment. The present thermal splitting reaction may be attractive for application as a recording device in light of the dramatic spectral changes and the perfect material balance. Fortunately, **34** was found to form a good transparent film when spin-coated onto quartz. A preliminary thermolysis experiment with this film indicated the more robust nature of **34** in the film up to 140 °C, but clean splitting into **35** at 200 °C.

A similar copper metalation reaction of perfluorinated [36]octaphyrin **9** revealed the formation of two bis-$Cu^{II}$ metal complexes **36** and **37** in 58 and 14% yields, respectively, when treated with $Cu(OAc)_2$ and NaOAc in $CH_2Cl_2$ solution (Figure 20).[44] The crystal structure of **36** was determined by single-crystal X-ray analysis (Figure 22). It takes a bent, U-shaped, ellipsoidal conformation in which one pyrrole ring is hydrolytically cleaved to give a keto-imine moiety. One of the two copper ions is bound to the keto-carbonyl oxygen atom and the nitrogen atoms of the nearby tripyrrolic subunit, while the other copper ion is bound to the imine nitrogen atom and the nearby second tripyrrolic subunit. The minor product **37** exhibits an absorption spectrum that is quite similar to that of **34**, and the high-resolution ESI-TOF mass spectrum indicated the formation of the bis-$Cu^{II}$ complex of perfluorinated [36]octaphyrin (**37**; Figure 20). Although efforts to obtain suitable crystals of **37** have been unsuccessful, these data suggest that **37** is a bis-$Cu^{II}$ complex with a figure-eight structure similar to that of **34**. Thus, we tested the thermolysis reaction of **37** both in $CH_2Cl_2$ solution and in the solid state. Upon heating in solution it goes hydrolysis to give **36** with concomitant decomposition, whereas, interestingly, thermolysis in the solid state led to splitting into **38**. During the copper metalation of **9**, one possible route to **36** may be initial formation of **37** followed by subsequent hydrolytic ring opening of one pyrrole ring facilitated by the strongly electron-deficient nature of the perfluorinated macrocycle.

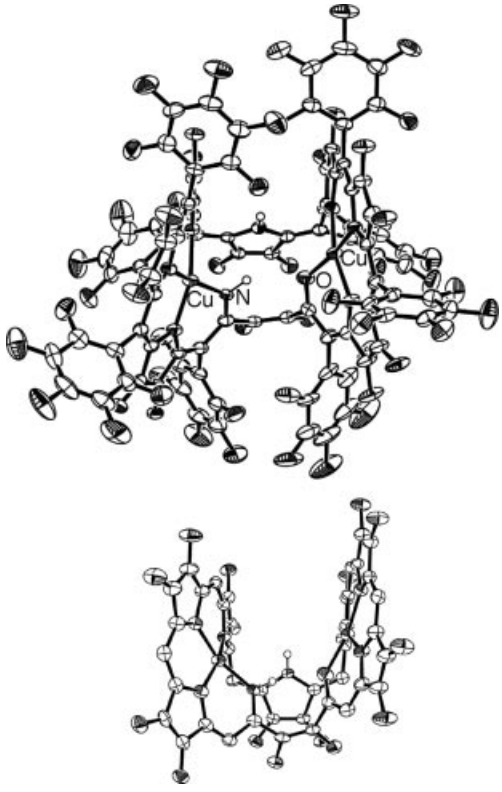


Figure 22. X-ray crystal structure of **36**; top view (top) and side view (bottom). *meso*-Aryl substituents have been omitted for clarity in the side view.

### Silver Metalation of [36]Octaphyrin and Perfluorinated [36]Octaphyrin

Among the transition metal ions tested, we found the complexation of **5a** and **9** with a salt of silver, a heavier congener of copper, proceeded smoothly without any skeletal rearrangement of the macrocyclic ring, in sharp contrast to the metalations with copper, to provide similar bis-silver complexes **39** and **40** almost quantitatively despite the different structures of the free base (Figure 23).[44] The bound silver ions are in the $Ag^{I}$ oxidation state judging from the coordination bond lengths and the diamagnetic nature of the complex observed in the $^1H$ NMR spectra, which indicates that [36]octaphyrin is oxidized to [34]octaphyrin by an excess amount of silver salt. The oxidized form acts as a divalent ligand to coordinate two $Ag^{I}$ ions. Both structures exhibit almost $C_2$-symmetric figure-eight conformations with two silver ions bound within porphyrin-like tetrapyrrolic cavities with Ag–N bond lengths in the range of 2.27–2.40 Å (Figure 24). Interestingly, pentafluorophenyl substituents at the crossing *meso* position lie just above the silver atoms in parallel with the tripyrrolic units, with interplanar distances of approximately 3.2 Å, while the β-substituents (hydrogen and fluorine atoms) of pyrroles D and H are placed below the silver ions with Ag–β-carbon distances of 2.89 and 2.87 Å for **39** and 3.14 and 3.16 Å for **40**. This proximity between the Ag ions and the substituents was supported by the additional through-space coupling with $Ag^{I}$ ($I$ = 1/2) observed in the $^1H$ and $^{19}F$ NMR spectra. Despite the figure-eight structures, which are similar to that of **34**, both **39** and **40** are thermally stable and do not exhibit the splitting reactivity observed for **34**. A major reason for this may be the 34π-electron system of **39** and **40**. Considering the instability of free base [34]octaphyrin

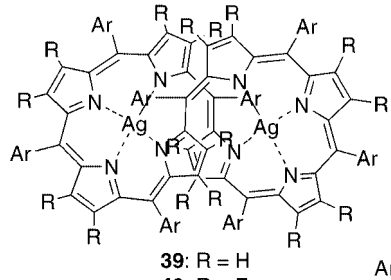


Figure 23. Bis-$Ag^{I}$ complexes of octaphyrins.

 © 2006 Wiley-VCH Verlag GmbH & Co. KGaA, Weinheim 

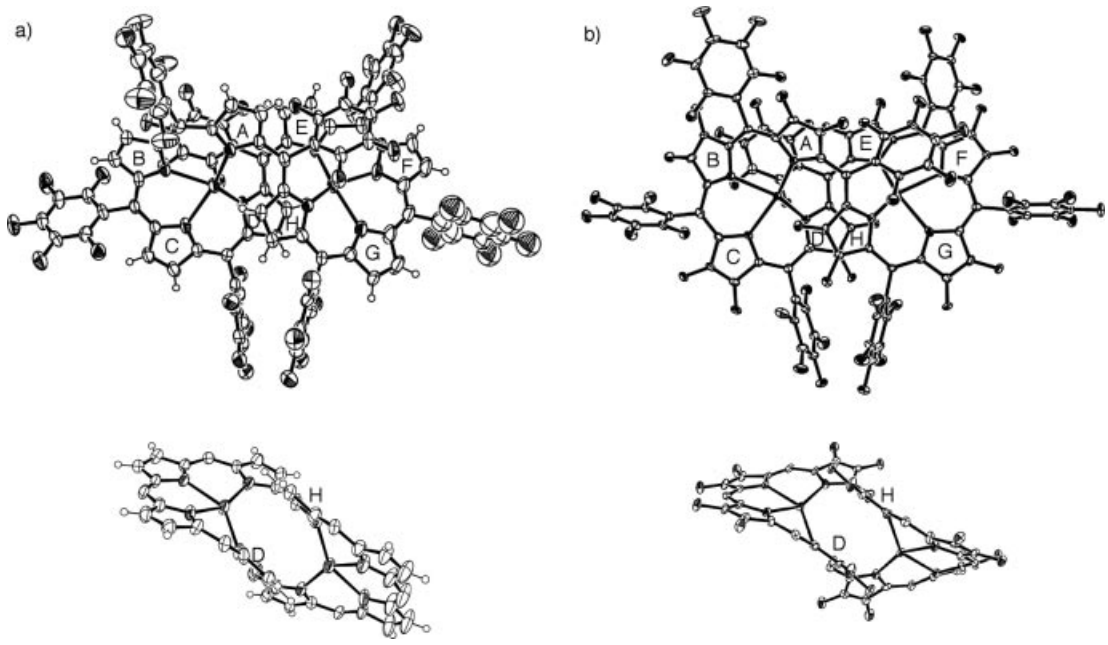


Figure 24. X-ray crystal structures of a) **39** and b) **40**; top views (top) and side views (bottom). *meso*-Aryl substituents have been omitted for clarity in the side views.

under ambient conditions, the oxidized octaphyrin ligands are stabilized by silver metalation. Despite the inertness of **39** and **40** upon heating, the Ag ions are easily removed upon reduction with $NaBH_4$ to provide the respective free base [38]octaphyrins.

## Summary and Outlook

The novel properties of the free bases and their metal complexes of expanded porphyrins have been revealed to be highly promising for various applications, including multimetal chelation, catalysis, receptors of anions and neutral molecules, PDT sensitizers, MRI contrast agents, and nonlinear optical materials. The serendipitous discovery of the facile, one-pot synthesis of *meso*-aryl-substituted expanded porphyrins has allowed the investigation of their fruitful coordination chemistry, which, however, still remains in its early stages. Investigation of their metal-complexation reactions and their fascinating properties for further applications is still in progress in our laboratory.

## Acknowledgments

This work was partly supported by Grants-in-Aid (B) (nos. 15350022 and 17350017) from the Ministry of Education, Culture, Sports, Science and Technology, Japan. S. S. thanks JSPS for a Research Fellowship for Young Scientists.

[1] *The Porphyrin Handbook*, Academic Press, San Diego, Volumes 1–10 (**2000**) and Volumes 11–20 (**2003**).
[2] A. Jasat, D. Dolphin, *Chem. Rev.* **1997**, *97*, 2267–2340.
[3] T. D. Lash, *Angew. Chem. Int. Ed.* **2000**, *39*, 1763–1767.
[4] H. Furuta, H. Maeda, A. Osuka, *Chem. Commun.* **2002**, 1795–1804.
[5] J. L. Sessler, D. Seidel, *Angew. Chem. Int. Ed.* **2003**, *42*, 5134–5175.
[6] T. K. Chandrashekar, S. Venkatraman, *Acc. Chem. Res.* **2003**, *36*, 676–691.
[7] A. Ghosh, *Angew. Chem. Int. Ed.* **2004**, *43*, 1918–1931.
[8] a) M. Shionoya, H. Furuta, V. Lynch, A. Harriman, J. L. Sessler, *J. Am. Chem. Soc.* **1992**, *114*, 5714–5722; b) J. L. Sessler, J. M. Davis, *Acc. Chem. Res.* **2001**, *34*, 989–997.
[9] a) A. Harriman, B. G. Maiya, T. Murai, G. Hemmi, J. L. Sessler, T. E. Mallouk, *J. Chem. Soc., Chem. Commun.* **1989**, 314–316; b) B. G. Maiya, A. Harriman, J. L. Sessler, G. Hemmi, T. Murai, T. E. Mallouk, *J. Phys. Chem.* **1989**, *93*, 8111–8115.
[10] J. L. Sessler, T. D. Mody, G. Hemmi, V. Lynch, S. W. Young, R. A. Miller, *J. Am. Chem. Soc.* **1993**, *115*, 10368–10369.
[11] T. K. Ahn, J. H. Kwon, D. Y. Kim, D. W. Cho, D. H. Jeong, S. K. Kim, M. Suzuki, S. Shimizu, A. Osuka, D. Kim, *J. Am. Chem. Soc.* **2005**, *127*, 12856–12861.
[12] H. Rath, J. Sankar, V. PrabhuRaja, T. K. Chandrashekar, A. Nag, D. Goswami, *J. Am. Chem. Soc.* **2005**, *127*, 11608–11609.
[13] V. J. Bauer, D. L. J. Clive, D. Dolphin, J. B. Paine III, F. L. Harris, M. M. King, J. Loder, S.-W. C. Wang, R. B. Woodward, *J. Am. Chem. Soc.* **1983**, *105*, 6429–6436.
[14] a) A. Gossauer, *Bull. Soc. Chim. Belg.* **1983**, *92*, 793–795; b) A. Gossauer, *Chimia* **1983**, *37*, 341–342; c) A. Gossauer, *Chimia* **1984**, *38*, 45–46.
[15] a) E. Vogel, M. Bröring, J. Fink, D. Rosen, H. Schmickler, J. Lex, K. W. K. Chan, Y.-D. Wu, D. A. Plattner, M. Nendel, K. N. Houk, *Angew. Chem. Int. Ed. Engl.* **1995**, *34*, 2511–2514; b) M. Bröring, J. Jendrny, L. Zander, H. Schmickler, J. Lex, Y.-D. Wu, M. Nendel, J. Chen, D. A. Plattner, K. N. Houk, E. Vogel, *Angew. Chem. Int. Ed. Engl.* **1995**, *34*, 2515–2517.
[16] a) D. Seidel, V. Lynch, J. L. Sessler, *Angew. Chem. Int. Ed.* **2002**, *41*, 1422–1425; b) T. Köhler, D. Seidel, V. Lynch, F. O. Arp, Z. Ou, K. M. Kadish, J. L. Sessler, *J. Am. Chem. Soc.* **2003**, *125*, 6872–6873.
[17] a) A. Srinivasan, V. M. Reddy, S. J. Narayanan, B. Sridevi, S. K. Pushpan, M. Ravikumar, T. K. Chandrashekar, *Angew. Chem. Int. Ed. Engl.* **1997**, *36*, 2598–2601; b) S. J. Narayanan, B. Sridevi, T. K. Chandrashekar, A. Vij, R. Roy, *Angew. Chem. Int. Ed.* **1998**, *37*, 3394–3397; c) S. J. Narayanan, B. Sridevi,

 © 2006 Wiley-VCH Verlag GmbH & Co. KGaA, Weinheim 

T. K. Chandrashekar, A. Vij, R. Roy, *J. Am. Chem. Soc.* **1999**, *121*, 9053–9068; d) V. G. Anand, S. K. Pushpan, S. Venkatraman, A. Dey, T. K. Chandrashekar, B. S. Joshi, R. Roy, W. Teng, K. Ruhlandt-Senge, *J. Am. Chem. Soc.* **2001**, *123*, 8620–8621.
[18] N. Sprutta, L. Latos-Grażyński, *Chem. Eur. J.* **2001**, *7*, 5099–5112.
[19] a) J.-i. Setsune, Y. Katakami, N. Iizuna, *J. Am. Chem. Soc.* **1999**, *121*, 8957–8958; b) J.-i. Setsune, S. Maeda, *J. Am. Chem. Soc.* **2000**, *122*, 12405–12406.
[20] A. Krivokapic, A. R. Cowley, H. L. Anderson, *J. Org. Chem.* **2003**, *68*, 1089–1096.
[21] C.-H. Hung, J.-P. Jong, M.-Y. Ho, G.-H. Lee, S.-M. Peng, *Chem. Eur. J.* **2002**, *8*, 4542–4548.
[22] J.-Y. Shin, H. Furuta, K. Yoza, S. Igarashi, A. Osuka, *J. Am. Chem. Soc.* **2001**, *123*, 7190–7191.
[23] S. Shimizu, J.-Y. Shin, H. Furuta, R. Ismael, A. Osuka, *Angew. Chem. Int. Ed.* **2003**, *42*, 78–82.
[24] R. Taniguchi, S. Shimizu, M. Suzuki, J.-Y. Shin, H. Furuta, A. Osuka, *Tetrahedron Lett.* **2003**, *44*, 2505–2507.
[25] M. Suzuki, A. Osuka, *Org. Lett.* **2003**, *5*, 3943–3946.
[26] R. Charrière, T. A. Jenny, H. Rexhausen, A. Gossauer, *Heterocycles* **1993**, *36*, 1561–1575.
[27] a) A. Werner, M. Michels, L. Zander, J. Lex, E. Vogel, *Angew. Chem. Int. Ed.* **1999**, *38*, 3650–3653; b) J.-P. Gisselbrecht, J. Bley-Escrich, M. Gross, L. Zander, M. Michels, E. Vogel, *J. Electroanalyt. Chem.* **1999**, *469*, 170–175; c) J. Bley-Escrich, J.-P. Gisselbrecht, E. Vogel, M. Gross, *Eur. J. Inorg. Chem.* **2002**, 2829–2837.
[28] S. J. Weghorn, J. L. Sessler, V. Lynch, T. F. Baumann, J. W. Silbert, *Inorg. Chem.* **1996**, *35*, 1089–1090.
[29] J. L. Sessler, P. J. Melfi, D. Seidel, A. E. V. Gorden, D. K. Ford, P. D. Palmer, C. D. Tait, *Tetrahedron* **2004**, *60*, 11089–11097.
[30] a) T. Wessel, B. Franck, M. Möller, U. Rodewald, M. Läge, *Angew. Chem. Int. Ed. Engl.* **1993**, *32*, 1148–1151; b) B. Franck, A. Nonn, *Angew. Chem. Int. Ed. Engl.* **1995**, *34*, 1795–1811.
[31] a) J.-Y. Shin, H. Furuta, A. Osuka, *Angew. Chem. Int. Ed.* **2001**, *40*, 619–621; b) S. Mori, J.-Y. Shin, S. Shimizu, F. Ishikawa, H. Furuta, A. Osuka, *Chem. Eur. J.* **2005**, *11*, 2417–2425.
[32] J. L. Sessler, A. Gebauer, A. Guba, M. Scherer, V. Lynch, *Inorg. Chem.* **1998**, *37*, 2073–2076.
[33] B. Sridevi, S. J. Nrayanan, R. Rao, T. K. Chandrashekar, U. Englich, K. Ruhlandt-Senge, *Inorg. Chem.* **2000**, *39*, 3669–3677.
[34] A. Srinivasan, H. Furuta, A. Osuka, *Chem. Commun.* **2001**, 1666–1667.
[35] M. G. P. M. S. Neves, R. M. Martins, A. C. Tomé, A. J. D. Silvestre, A. M. S. Silva, V. Félix, M. G. B. Drew, J. A. S. Cavaleiro, *Chem. Commun.* **1999**, 385–386.
[36] M. Suzuki, S. Shimizu, J.-Y. Shin, A. Osuka, *Tetrahedron Lett.* **2003**, *44*, 4597–4601.
[37] S. Shimizu, V. G. Anand, R. Taniguchi, K. Furukawa, T. Kato, T. Yokoyama, A. Osuka, *J. Am. Chem. Soc.* **2004**, *126*, 12280–12281.
[38] a) A. Srinivasan, T. Ishizuka, H. Furuta, *Angew. Chem. Int. Ed.* **2004**, *43*, 876–879; b) A. Srinivasan, T. Ishizuka, H. Maeda, H. Furuta, *Angew. Chem. Int. Ed.* **2004**, *43*, 2951–2955; c) A. Srinivasan, T. Ishizuka, A. Osuka, H. Furuta, *J. Am. Chem. Soc.* **2003**, *125*, 878–879; d) A. Srinivasan, H. Furuta, *Acc. Chem. Res.* **2005**, *38*, 10–20; e) J. H. Kwon, T. K. Ahn, M.-C. Yoon, D. Y. Kim, D. Kim, H. Furuta, M. Suzuki, A. Osuka, manuscript submitted to *J. Phys. Chem. A*.
[39] M. Suzuki, M.-C. Yoon, D. Y. Kim, J. H. Kwon, H. Furuta, D. Kim, A. Osuka, *Chem. Eur. J.*, in press; DOI: 10.1002/chem.200501061.
[40] S. Mori, S. Shimizu, R. Taniguchi, A. Osuka, *Inorg. Chem.* **2005**, *44*, 4127–4129.
[41] S. Mori, A. Osuka, *J. Am. Chem. Soc.* **2005**, *127*, 8030–8031.
[42] Y. Tanaka, W. Hoshino, S. Shimizu, K. Youfu, N. Aratani, N. Maruyama, S. Fujita, A. Osuka, *J. Am. Chem. Soc.* **2004**, *126*, 3046–3047.
[43] The unusual reactivity of bis-metal complexes of octaphyrins was recently highlighted: L. Latos-Grażyński, *Angew. Chem. Int. Ed.* **2004**, *43*, 5124–5128.
[44] S. Shimizu, Y. Tanaka, K. Youfu, A. Osuka, *Angew. Chem. Int. Ed.* **2005**, *44*, 3726–3729.

Received: December 7, 2005
Published Online: February 9, 2006

 © 2006 Wiley-VCH Verlag GmbH & Co. KGaA, Weinheim 

DOI: 10.1002/ejic.200500877

# A Novel 3D $Cu^{I}$ Metal–Organic Framework with Middle-Size Channels Despite the Sixfold $ThSi_2$ Interpenetrating Topological Structure

**Cheng-Zhi Xie,[a] Ze-Feng Zhang,[a] Bao-Feng Zhang,[a] Xiao-Qing Wang,*[a] Ru-Ji Wang,[a] Guang-Qiu Shen,[a] De-Zhong Shen,[a] and Bin Ding[b]**

**Keywords:** Metal–organic framework / Interpenetration / 1D channels / Topological structure / Copper / X-ray diffraction

A new univalent copper coordination polymer with an unusual asymmetric $ThSi_2$ topological structural network was synthesized and 1D middle-size channels were found despite the sixfold $ThSi_2$ interpenetrating topological structure.

(© Wiley-VCH Verlag GmbH & Co. KGaA, 69451 Weinheim, Germany, 2006)

Recently, the assembly of metal–organic open frameworks (MOFs) has attracted great attention; MOFs with various network topologies have been prepared by using metal ions and organic building blocks. MOFs with flexible or rigid microporous channels have potential applications in selective molecular recognition and separation, physical gas storage, chemical absorption, ion-exchange and heterogeneous catalysis. Structural interpenetration has been widely used to design intriguing topologies in inorganic chemistry and may enhance the stability of porous materials.[1] Despite the simple and common formula, the rigid ligand 4,4′-bpy has been used extensively to ligate metal ions into an open framework of diamond-like networks[2] or networks with rectangular channels.[3]

In previous literature the hydrothermal method has been shown to be a promising technique for preparing highly stable, infinite metal–ligand frameworks.[4] It has been found that many interesting phenomena such as ligand oxidative coupling, hydrolysis, substitution and redox reaction, can occur under the in-situ hydrothermal conditions.[5] These reactions represent new routes for constructing novel coordination polymers. Encouraged by several recent reports showing that $Cu^{II}$ could be reduced to $Cu^{I}$ under basic hydrothermal conditions,[6] we synthesized a new 3D MOF copper(I) coordination polymer $[Cu_2(4,4'\text{-bpy})_2Cl](ClO_4)$ (**1**). A simple one-step synthesis procedure has been schematically illustrated in Figure 1.

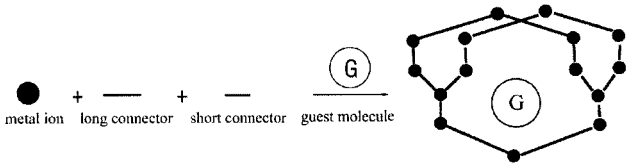


Figure 1. A schematic representation of the assembly of metal ions (dark spheres) and organic ligand connectors (dark rods: long connector; gray rods: short connector) to yield open frameworks with polygonal channels. The assembly is accompanied by the inclusion of a guest molecule G which occupies the void.

The hydrothermal reaction of $Cu(ClO_4)_2$ with 4,4′-bpy, pyrazine-2,3-dicarboxylic acid (or pyridine-2,6-dicarboxylic acid), and minor $CuCl_2$ led to the formation of a crystalline complex. The presence of the $Cu^{I}$ ion in the product indicates that the $Cu^{II}$ ion may act as an oxidant in a similar manner as shown in previous research in hydrothermal reactions.[6] Although the heterocycle carboxylic acids did not appear in the final complex **1**, they may change the pH value of the solution and therefore play a key role in the formation of the interpenetrating network. So it is quite different from the reported 2D structure of complex $[Cu_2Cl_2(bpy)]$.[5e] We synthesized the complex $[Cu_2Cl_2(bpy)]$ using a similar preparation procedure to complex **1** except that heterocycle multi-carboxylic acid is not involved in the starting material, and proved its structure by single-crystal X-ray diffraction.

X-ray single crystal analysis revealed that the actual crystal structure of complex **1** is a sixfold interpenetrating coordination network with a 3-connected $ThSi_2$ topological structure. This is in accordance with the fact that trigonal metal templates have a high tendency to form interpenetrated or self-inclusion compounds, if the cavities generated in this way are more than 50% of the crystal by volume.[7] In complex **1**, each $Cu^{I}$ ion in the 3D structure is

[a] Department of Chemistry, Tsinghua University, Beijing 100084, P. R. China
E-mail: xqwang@mail.tsinghua.edu.cn
[b] Department of Chemistry, Nankai University, Tianjin 300071, P. R. China

Supporting information for this article is available on the WWW under http://www.eurjic.org or from the author.

 © 2006 Wiley-VCH Verlag GmbH & Co. KGaA, Weinheim 

coordinated to two nitrogen atoms from two 4,4′-bpy ligands giving rise to a zigzag Cu–bpy chain. The chains are further connected to adjacent vertical chains via $\mu_2$-chlorine coordination bonds and extend into a 3D net as represented in Figure 2. The pyridyl rings and Cu atoms in the same chains are coplanar. The adjacent Cu–bpy–Cu chains are cross-linked in an almost perpendicular fashion (Cu1C···Cu1···Cu1A···Cu1D = 74.6°, as shown in Figure 3). The Cu–N and Cu–Cl distances [Cu1–N1 = 1.935(3) Å, Cu1–Cl1 = 2.3791(11) Å] are comparable with those found in [CuCl(bpy)],[8a] $[(CuCl)_2(C_{10}H_7N_3)]$,[8b] and $[Cu_2Cl_2(bpy)]$.[5e] The distances between the $Cu^I$ ions bridged by a Cl anion or by a 4,4′-bpy ligand are 4.758 and 10.968 Å, respectively. The shortest vector relating to adjacent nets equates to axis *a* (Cu···Cu inter-net distance of ca. 5.586 Å).

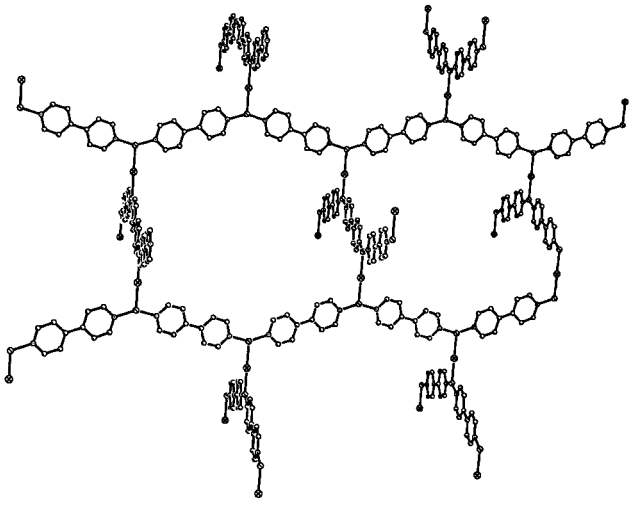

Figure 2. A view of a single framework of complex **1** with the perchlorate anion omitted.

Recent studies have shown the tendency of $Cu^I$ to form multi-dimensional structural units with halogen atoms and 4,4′-bpy under hydrothermal conditions. In these complexes the copper ions will always be four-coordinate and the structure will usually be 2D[5e,8–10] (except for complex [CuBr(bpy)][5e] that possesses a 3D structure formed by perpendicular interlocking 2D nets). To the best of our knowledge, no structurally characterized example of three-coordinate $Cu^I$ ions with bpy groups and hetero atoms has been documented to date. Compound **1** is a novel example of three-coordinate $Cu^I$ with bpy and $Cl^-$. It has a sixfold interpenetrating $ThSi_2$ topological structure of Class Ia with the interpenetration vector equating to axis *a*. This topological structure is rare, and the only known example is MOF $[Cu_2(4,4'\text{-bpy})_3](NO_3)_2(H_2O)_{1.25}$,[4a] but this has a different Class IIIa.

The most striking feature of complex **1** is that despite the sixfold interpenetrating 3D networks, complex **1** shows an unusual open framework containing middle-size hexagonal channels running along axis *a*, as shown in Figure 4 (the side lengths of the hexagonal channels are 4.16 and 6.66 Å, respectively). Guest perchlorate anions reside in the channels as counterions. The PLATON[11] programme reveals that the voids in complex **1** occupy 24.1% of the crystal volume (after the removal of the guest molecules). To compare the structural differences (especially in interpenetration) of complex **1** with $[Cu_2(4,4'\text{-bpy})_3](NO_3)_2(H_2O)_{1.25}$,[4a] we synthesized its isomorph $[Cu_2(4,4'\text{-bpy})_3](ClO_4)_2(H_2O)_2$ (**2**). From Figure 3, we can see that the interpenetration structures of the two polymers are different, while the latter possesses less channels as generally discussed in the literature.[4a] This is because of the two opposing rotations within the building unit of complex **2**: the pyridyl rings of two independent 4,4′-bpy rotate along the C–C single bond axis with dihedral angles of 33.3 and 40.1°; and the adjacent Cu–bpy–Cu chains are cross-linked with a lower angle (Cu1a···Cu1···Cu1c···Cu1e = 63.3°) compared to complex **1**.

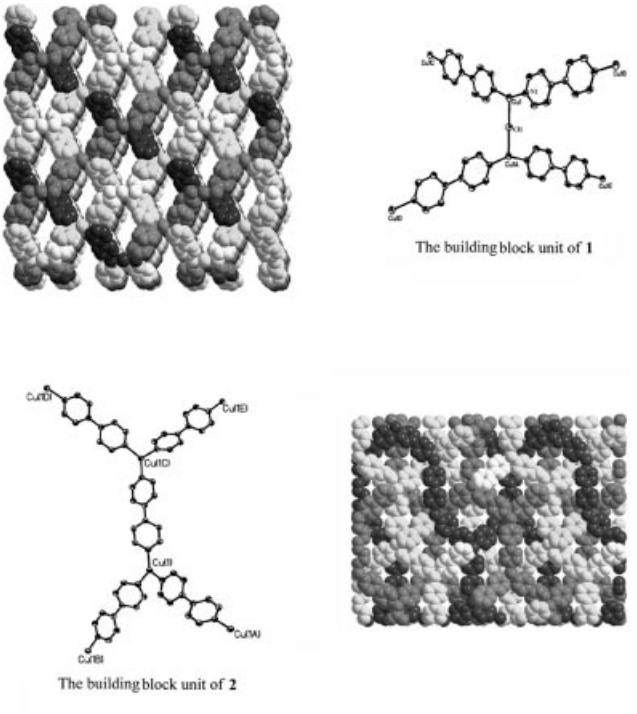


Figure 3. Schematic views of the 3D interpenetrating networks of complexes **1** (top) and **2** (bottom) along axis *a* showing the 1D channels.

Complex **1** is very stable in air at ambient temperature and is almost insoluble in common solvents such as water, alcohol, acetonitrile, chloroform, acetone, and toluene, being consistent with its polymeric nature. Thermal gravimetric analysis (TGA) from 80 to 500 °C indicates that complex **1** is thermally stable up to 240 °C (see Supporting Information, Figure S1). After heating a sample of complex **1** directly to 200 °C and keeping it for 1 h in an oven, the framework remains intact [monitored by X-ray powder diffraction (XRPD), see Supporting Information, Figure S2]. No signal was found in the ESR spectrum for complex **1**, which confirms that all the copper atoms in complex **1** are univalent.

In summary, a novel three-coordinate $Cu^I$ polymer possessing a sixfold interpenetrating 3D $ThSi_2$ topological

 © 2006 Wiley-VCH Verlag GmbH & Co. KGaA, Weinheim 

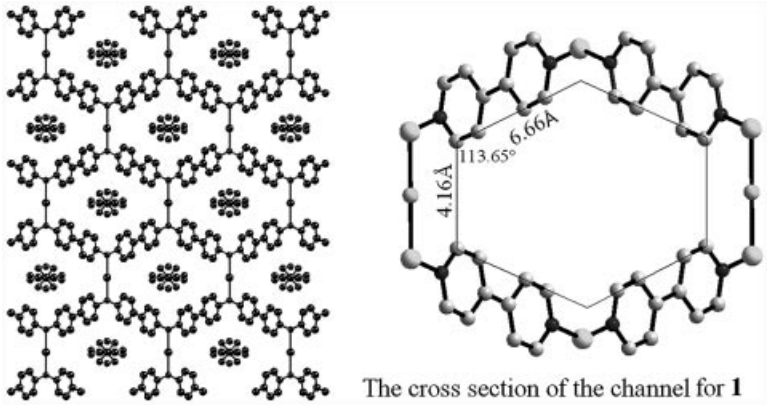


Figure 4. A ball and stick diagram of complex **1** showing the 1D channels formed by interpenetration.

structure was synthesized under hydrothermal conditions and characterized. Middle-size 1D channels were formed in the complex. To the best of our knowledge, there is no previous example of MOFs forming with mixed connectors containing the $ThSi_2$ topological structure.[12,13] The compound forms a 3-connected network with novel topology that has implications for understanding the relationship between related nets.

## Experimental Section

**General Remarks:** All chemicals were obtained from commercial sources and used as received. The C, H, N microanalyses were carried out with a Vario EL elemental analyzer. The IR spectra were recorded with a Magna-IR 750 spectrophotometer using the KBr pellet technique. Thermal gravimetric analysis (TGA) was carried out with a Perkin–Elmer TGA 7 thermogravimetric analyzer in $N_2$ condition with a heating rate of 10 °C min$^{-1}$. The electron paramagnetic resonance (EPR) powder spectrum was recorded at X-band with a Bruker ER 200B spectrometer. Powder XRD was performed with a Bruker D8 Advance X-ray diffractometer with monochromatized Cu-$K_\alpha$ radiation ($\lambda$ = 1.5418 Å).

### Preparations

**Synthesis of $[Cu_2(4,4'\text{-bpy})_2Cl](ClO_4)$ (1):** A mixture of $Cu(ClO_4)_2\cdot 6H_2O$ (0.186 g, 0.5 mmol), pyrazine-2,3-dicarboxylic acid (0.084 g, 0.5 mmol), 4,4′-bpy (0.096 g, 0.5 mmol), $CuCl_2$ (0.017 g, 0.1 mmol), and water (18.0 mL) in the molar ratio of 5:5:5:1:10000 was sealed in a 25-mL stainless steel reactor with Teflon liner, and heated directly to 180 °C. After being kept at 180 °C for 72 h, it was cooled slowly to 30 °C at a rate of 2 °C/h. From a large quantity of red deposit, the resulting orange block crystals of **1** were separated, washed, and dried in air (yield ca. 10% based on Cl). Replacing pyrazine-2,3-dicarboxylic acid by equivalent pyridine-2,6-dicarboxylic acid, the same crystals were obtained (yield ca. 5% based on Cl). $C_{10}H_8ClCuN_2O_2$ (287.17): calcd. C 41.83, H 2.81, N 9.76; found C 41.65, H 2.55, N 9.52. The pH value of the residuary solution is 4. IR (KBr): $\tilde{\nu}$ = 3441, 3070, 3042, 1635, 1601, 1526, 1482, 1408, 1326, 1215, 1109, 1084, 963, 817, 799, 724, 673, 625, 475.

**Synthesis of $[Cu_2(4,4'\text{-bpy})_3](ClO_4)_2(H_2O)_2$ (2):** A mixture of $Cu(ClO_4)_2\cdot 6H_2O$ (0.186 g, 0.5 mmol), 4,4′-bpy (0.096 g, 0.5 mmol), KI (0.083 g, 0.5 mmol), and water (18.0 mL) in the molar ratio of 1:1:1:1000 was sealed in a 25-mL stainless steel reactor with Teflon liner, and heated directly to 180 °C. After being kept at 180 °C for 72 h, it was cooled slowly to 30 °C at a rate of 2 °C/h. The resulting brown block crystals of complex **2** were washed and dried in air (yield ca. 15% based on Cu). $C_{15}H_{14}ClCuN_3O_5$ (830.56): calcd. C 43.34, H 3.37, N 10.11; found C 42.98, H 3.51, N 9.89. IR (KBr): $\tilde{\nu}$ = 3392, 3075, 3044, 1600, 1530, 1483, 1409, 1322, 1217, 1087, 818, 799, 673, 625, 473.

### X-ray Crystallography

**Crystal Data for Complex 1:** $C_{10}H_8ClCuN_2O_2$, $M$ = 287.17, orthorhombic, space group *Pnnn*, $a$ = 5.5864(18) Å, $b$ = 12.769(4) Å, $c$ = 15.621(5) Å, $V$ = 1114.3(6) Å$^3$, $Z$ = 4, $Dc$ = 1.712 g cm$^{-3}$, $\mu$ (Mo-$K_\alpha$) = 2.183 cm$^{-1}$, $F$(000) = 576, 1144 reflections measured, 829 [$I \geq 2\sigma(I)$] unique reflections were used in all calculations. The final $R_1$ = 0.0508, $wR_2$ = 0.1341, $S$ = 1.086.

**Crystal Data for Complex 2:** $C_{15}H_{14}ClCuN_3O_5$, $M$ = 415.28, orthorhombic, space group *Fddd*, $a$ = 18.747(2) Å, $b$ = 23.355(3) Å, $c$ = 30.404(4) Å, $V$ = 13312(3) Å$^3$, $Z$ = 16, $Dc$ = 1.658 g cm$^{-3}$, $\mu$ (Mo-$K_\alpha$) = 1.505 cm$^{-1}$, $F$(000) = 6752, 6258 reflections measured, 3839 [$I \geq 2\sigma(I)$] unique reflections were used in all calculations. The final $R_1$ = 0.0520, $wR_2$ = 0.1034, $S$ = 1.054. Data collections ($2.61 \leq \theta \leq 24.83°$ for complex **1**, $2.20 \leq \theta \leq 33.54°$ for complex **2**) were performed at 293 K with a Bruker SMART 1000 CCD diffractometer (Mo-$K_\alpha$, $\lambda$ = 0.71073 Å). The structures were solved with direct methods (SHELXS-97) and refined by full-matrix least-squares (SHELXL-97).

CCDC-227621 (for complex **1**) and -292359 (for complex **2**) contain the supplementary crystallographic data for this paper. These data can be obtained free of charge from The Cambridge Crystallographic Data Centre via www.ccdc.cam.ac.uk/data_request/cif.

**Supporting Information** (for details see the footnote on the first page of this article): TGA curve and X-ray powder diffration pattern of **1**.

## Acknowledgments

This work was supported by the NSFC (No. 50132010) and 985 Program of Tsinghua University.

[1] a) M. Eddaoudi, D. B. Moler, H. Li, B. Chen, T. M. Reineke, M. O'Keeffe, O. M. Yaghi, *Acc. Chem. Res.* **2001**, *34*, 319–330; b) S. R. Batten, R. Robson, *Angew. Chem. Int. Ed. Engl.* **1998**, *37*, 1460–1494; c) M. J. Zaworotko, *Angew. Chem. Int. Ed.* **2000**, *39*, 3052–3054; d) P. J. Hagrman, D. Hagrman, J. Zubi-

 © 2006 Wiley-VCH Verlag GmbH & Co. KGaA, Weinheim 

eta, *Angew. Chem. Int. Ed.* **1999**, *38*, 2638–2684; e) C. Janiak, *Angew. Chem. Int. Ed. Engl.* **1997**, *36*, 1431–1434; f) S. Kitagawa, R. Kitaura, S. Noro, *Angew. Chem. Int. Ed.* **2004**, *43*, 2334–2375.

[2] a) P. J. Stang, D. H. Cao, S. Saito, A. M. Arif, *J. Am. Chem. Soc.* **1995**, *117*, 6273–6283.; b) S. Subramanian, M. J. Zaworotko, *Angew. Chem. Int. Ed. Engl.* **1995**, *34*, 2127–2129; c) M. Fujita, Y. J. Kwon, S. Washizu, K. Ogura, *J. Am. Chem. Soc.* **1994**, *116*, 1151–1152.

[3] O. M. Yaghi, H. Li, *J. Am Chem. Soc.* **1996**, *118*, 295–296.

[4] a) O. M. Yaghi, H. Li, *J. Am. Chem. Soc.* **1995**, *117*, 10401–10402; b) S. O. H. Gutschke, M. Molinier, A. K. Powell, R. E. P. Winpenny, P. T. Wood, *Chem. Commun.* **1996**, 823–824; c) S. S. Y. Chui, S. M. F. Lo, J. P. H. Charament, A. G. Orpen, I. D. Williams, *Science* **1999**, *283*, 1148–1150; d) L. A. Gerrard, P. T. Wood, *Chem. Commun.* **2000**, 2107–2108.

[5] a) C. M. Liu, S. Gao, H. Z. Kou, *Chem. Commun.* **2001**, 1670–1671; b) S. O. H. Gutschke, D. J. Price, A. K. Powell, P. T. Wood, *Inorg. Chem.* **2000**, *39*, 3705–3707; c) W. B. Lin, Z. Y. Wang, L. Ma, *J. Am. Chem. Soc.* **1999**, *121*, 11249–11250; d) O. R. Evans, R. G. Xiong, Z. Y. Wang, G. K. Wong, W. B. Lin, *Angew. Chem. Int. Ed.* **1999**, *38*, 536–538; e) J. Y. Lu, B. R. Cabrera, R. J. Wang, J. Li, *Inorg. Chem.* **1999**, *38*, 4608–4611; f) S. M. F. Lo, S. S. Y. Chui, L. Y. Shek, Z. Lin, X. X. Zhang, G. H. Wen, I. D. Williams, *J. Am. Chem. Soc.* **2000**, *122*, 6293–6294.

[6] a) X. M. Zhang, M. L. Tong, X. M. Chen, *Angew. Chem. Int. Ed.* **2002**, *41*, 1029–1031; b) J. Tao, Y. Zhang, M. L. Tong, X. M. Chen, T. Yuen, C. L. Lin, X. Y. Huang, J. Li, *Chem. Commun.* **2002**, 1342–1343; c) X. M. Zhang, X. M. Chen, *Eur. J. Inorg. Chem.* **2003**, 413–417; d) M. L. Tong, L. J. Li, K. Mochizuki, H. C. Chang, X. M. Chen, Y. Li, S. Kitagawa, *Chem. Commun.* **2003**, 428–429; e) K. Jin, X. Y. Huang, L. Pang, J. Li, A. Appel, S. Wherland, *Chem. Commun.* **2002**, 2872–2873; f) J. P. Zhang, S. L. Zheng, X. C. Huang, X. M. Chen, *Angew. Chem. Int. Ed.* **2004**, *43*, 206–209; g) Y. Z. Zheng, M. L. Tong, X. M. Chen, *New J. Chem.* **2004**, *28*, 1412–1415.

[7] P. Losier, M. J. Zaworotko, *Angew. Chem. Int. Ed. Engl.* **1996**, *35*, 2779–2782.

[8] a) O. M. Yaghi, G. M. Li, *Angew. Chem. Int. Ed. Engl.* **1995**, *34*, 207–209; b) J. Y. Lu, B. R. Cabrera, R. J. Wang, J. Li, *Inorg. Chem.* **1998**, *37*, 4480–4481.

[9] a) D. Hagrman, R. P. Hammond, R. C. Haushalter, J. A. Zubieta, *Chem. Mater.* **1998**, *10*, 2091–2100; b) R. P. Hammond, M. Cavaluzzi, R. C. Haushalter, J. A. Zubieta, *Inorg. Chem.* **1999**, *38*, 1288–1292.

[10] B. R. Cabrera, R. J. Wang, J. Li, T Yuen, in *Solid State Chemistry of Inorganic Materials II*, Proceedings of the Symposium of the Materials Research Society, Boston, MA, November 30–December 4, **1998**; Materials Research Society, Warrendale, PA, **1999**, p. 493.

[11] A. L. Spek, *PLATON*, A Multipurpose Crystallographic Tool, Utrecht University, Utrecht, **1999**.

[12] V. A. Blatov, L. Carlucci, G. Ciani, D. M. Proserpio, *CrystEngComm* **2004**, *65*, 377–395.

[13] N. W. Ockwig, O. D. Friedrichs, M. O'Keeffe, O. M. Yaghi, *Acc. Chem. Res.* **2005**, *38*, 176–182.

Received: September 30, 2005
Published Online: February 24, 2006

 © 2006 Wiley-VCH Verlag GmbH & Co. KGaA, Weinheim 

DOI: 10.1002/ejic.200501055

# Decameric Water Clusters Shaped as Two Parallel Cyclic Pentamers with Staggered Conformation Stabilize Supramolecularly Bonded Infinite Chains of $H_2PO_4^-$ Ions

**Sujit K. Ghosh[a] and Parimal K. Bharadwaj*[a]**

**Keywords:** Dibasic phosphate chain / Cryptands / Supramolecular chemistry / X-ray diffraction / Water cluster

A laterally nonsymmetric aza-cryptand on acidification with $H_3PO_4$ affords an H-bonded infinite chain of $H_2PO_4^-$ ions. These chains are aligned parallel through H-bonding interactions with discreet decameric water clusters leaving large void spaces. Diprotonated cryptand molecules occupy these voids through supramolecular interactions. The crystal data for the compound are: triclinic space group $P\bar{1}$, $a$ = 12.765(5), $b$ = 13.254(2), $c$ = 13.817(4) Å, $V$ = 2137.3(14) Å$^3$, $Z$ = 2, $R1$ = 0.0582, $wR2$ = 0.1339, $S$ = 1.092.

(© Wiley-VCH Verlag GmbH & Co. KGaA, 69451 Weinheim, Germany, 2006)

## Introduction

The phosphate ion is an essential nutrient in biosystems and is transported by a phosphate-binding protein (PBP) that forms a strong H-bond with the mono- or dibasic form of phosphate.[1] Phosphate groups are frequently found with enzyme substrates or co-factors. It is not clear whether water plays any role in the translocation of inorganic phosphate across the cell membrane or in the formation of enzyme–substrate complexes. In DNA, water molecules are concentrated in six hydration sites per phosphate group and the positions as well as the occupancies of these sites are dependent on the conformation and nature of the nucleotide in addition to the type of DNA itself.[1] A water molecule exhibits uncertainty over the number of H-bonding interactions and their fluctuations with other water molecules−both of which are responsible for the anomalous behavior of bulk water. However, this diversity of H-bonding interactions is very important in the biological world as it can enforce a delicate balance among several possible conformations of an enzyme essential for its functional role(s). Recent years have witnessed both theoretical[2–5] and experimental[6–8] scrutiny of a number of small water clusters in different surroundings to investigate the development of properties of the condensed phase in a step-wise manner. We present here the structure of water decamers in the confinement of infinite H-bonded quasi-parallel chains of dibasic phosphates. Theoretical calculation[9] by Buck et al. had suggested that the minimum energy conformation for the decamer was as an octameric cube with two water molecules fused at one of the edges, while a more recent calculation showed two fused parallel pentamers to be energetically the most stable.[10] An ice-like diamondoid decamer[11] has been identified in a self-assembled metal-organic cage,[11d] while a water decamer in the form of two fused parallel cyclic pentamers with staggered conformation has been characterized[11c] in an organic host built from 5-hydroxyisophthalic acid and 18-crown-6. Supramolecular associations of water molecules forming a 3D structure with voids are potentially important for entrapment of molecules of interest if the water molecules can be removed without drastically altering the overall structure.

## Results and Discussion

Compound **1** is isolated as colorless crystals when an aza-cryptand (Scheme 1) is dissolved in water by dropwise addition of phosphoric acid. In the asymmetric unit (Figure 1), diprotonated cryptand, two $H_2PO_4^-$ anions, and seven water molecules are found. One of the water molecules (Ow7) is H-bonded inside the cryptand cavity, while another (Ow6) is H-bonded to the cryptand from outside. This molecule (Ow6) acts as an H-bond acceptor to one of the protonated amino nitrogen atoms of the cryptand arm with the N···O distance of 2.789 Å. This water molecule also forms an H-bond with $H_2PO_4^-$. The five remaining water molecules (Ow1–Ow5) describe a quasi-planar cyclic structure that eventually forms a decameric unit with five other centrosymmetrically related water molecules (Figure 2). The two pentameric cycles are oriented parallel to each other with a staggered conformation. Although this is a higher energy structure, it is stabilized by the environment. The $H_2PO_4^-$ anions form infinite H-bonded chains that run almost parallel to one another and the water deca-

[a] Department of Chemistry, Indian Institute of Technology Kanpur 208016, India
E-mail: pkb@iitk.ac.in

Supporting information for this article is available on the WWW under http://www.eurjic.org or from the author.

 © 2006 Wiley-VCH Verlag GmbH & Co. KGaA, Weinheim 

mers connect these chains through strong H-bonding interactions (Table 1) forming almost rectangular voids (approximate dimension 13.2×7.5 Å) that are occupied by cryptand molecules (Figure 3). The water molecule Ow4 of the cyclic pentamer acts as an H-bond acceptor to the cryptand, while the remaining four are H-bonded to the $H_2PO_4^-$ chains. The cryptand shows only weak interactions with the phosphate chains and the water molecules act as a glue holding together both the phosphate chains and the cryptands leading to the supramolecular assembly (Figure 4). The two parallel pentamers are connected at two positions

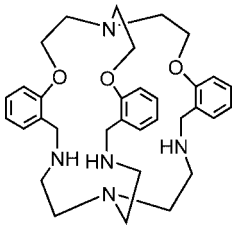


Scheme 1. Illustration of the laterally nonsymmetric aza-cryptand L.

Table 1. Hydrogen bond parameters in compound **1**.

| D–H···A | D–H [Å] | H···A [Å] | D···A [Å] | ∠D–H···A [°] |
|---|---|---|---|---|
| Ow1-H···Ow2 | 0.825(5) | 2.088(1) | 2.892(2) | 164.6(2) |
| Ow2-H···Ow5′ | 0.907(1) | 1.982(2) | 2.864(4) | 183.84(4) |
| Ow3-H···Ow2 | 0.815(2) | 2.082(3) | 2.894(1) | 174.14(5) |
| Ow4-H···Ow3 | 0.931(4) | 1.822(5) | 2.747(3) | 171.62(6) |
| Ow4-H···Ow5 | 0.923(3) | 1.822(3) | 2.728(4) | 166.67(5) |
| Ow5-H···Ow1 | 0.862(3) | 1.829(2) | 2.736(2) | 172.13(1) |
| Ow6-H···O4 | 0.817(1) | 1.996(3) | 2.809(4) | 173.24(5) |
| Ow7-H···N1 | 0.807(4) | 2.264(1) | 3.068(3) | 174.91(2) |
| Ow7-H···N5 | 0.929(5) | 1.857(4) | 2.782(4) | 173.12(5) |
| Ow1-H···O6 | 0.888(1) | 1.935(4) | 2.801(3) | 164.78(3) |
| Ow2-H···O9 | 0.897(3) | 1.936(2) | 2.806(1) | 162.83(6) |
| Ow3-H···O4 | 0.880(3) | 1.937(2) | 2.813(2) | 173.08(1) |
| Ow5-H···O11 | 0.815(4) | 1.939(3) | 2.744(4) | 169.35(5) |
| N3–H···Ow7 | 0.901(4) | 1.955(3) | 2.845(4) | 169.33(5) |
| N3–H···Ow4 | 0.900(1) | 1.856(4) | 2.682(1) | 151.57(2) |
| N4–H···Ow6 | 0.900(3) | 1.919(3) | 2.789(2) | 162.15(5) |
| N4–H···Ow7 | 0.900(4) | 1.895(2) | 2.782(4) | 168.12(3) |
| O5–H···O6 | 0.918(2) | 1.675(2) | 2.588(3) | 172.98(5) |
| O7–H···O11 | 0.788(4) | 1.809(3) | 2.595(1) | 174.48(2) |
| O8–H···O4 | 0.845(3) | 1.821(1) | 2.653(2) | 167.96(5) |
| O10–H···O9 | 0.888(4) | 1.692(3) | 2.572(4) | 170.42(5) |

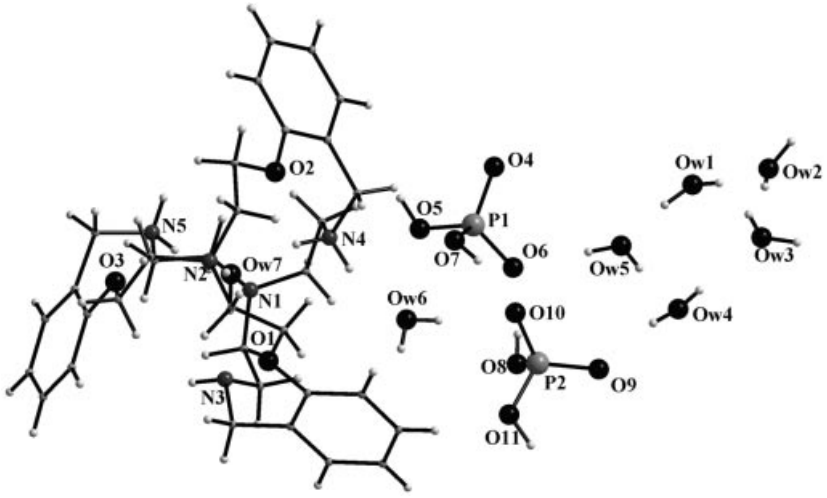


Figure 1. Asymmetric unit showing the diprotonated cryptand molecule with $H_2PO_4^-$ anions and seven water molecules.

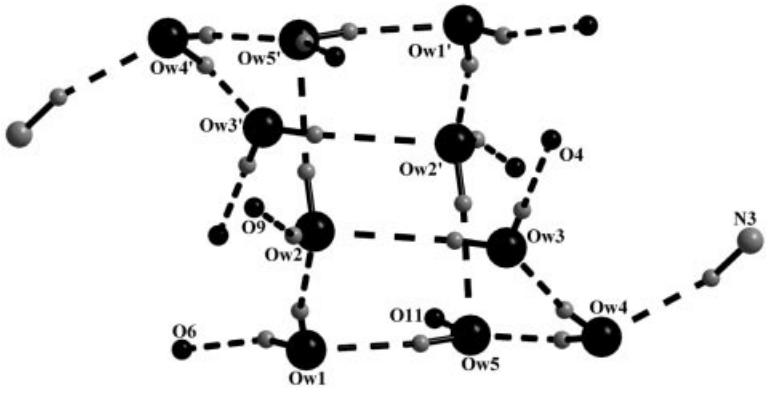


Figure 2. Perspective view of the $(H_2O)_{10}$ cluster showing the H-bonding interactions.

 © 2006 Wiley-VCH Verlag GmbH & Co. KGaA, Weinheim 

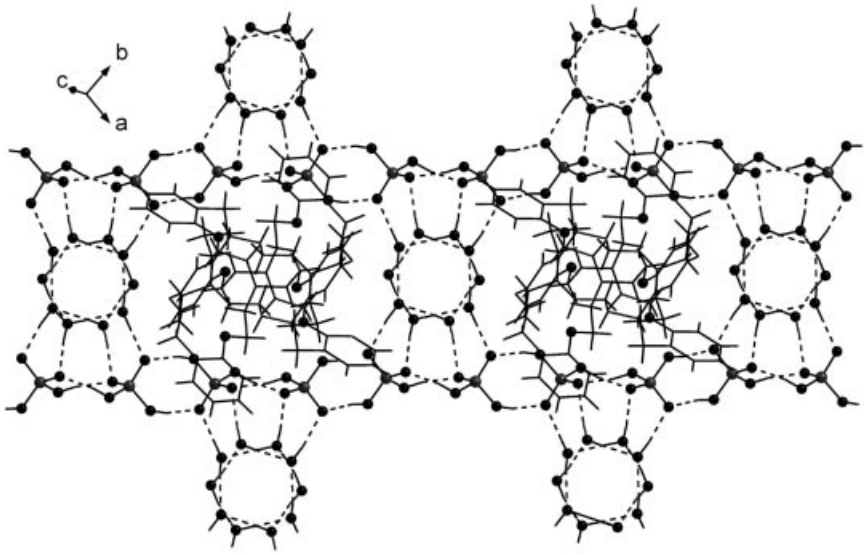


Figure 3. View showing chains of $H_2PO_4^-$ anions connected by water decamers with cryptand molecules occupying voids.

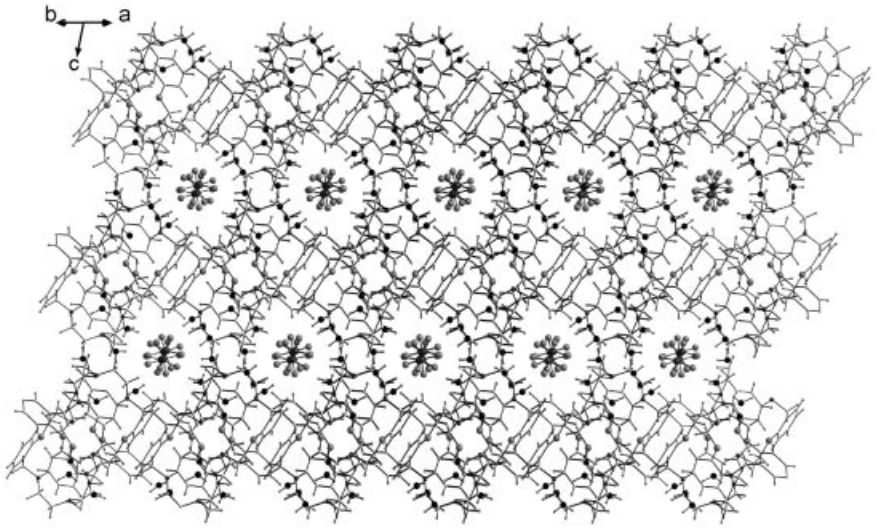


Figure 4. Self-assembled structure of compound **1** viewed along the phosphate chains.

through H-bonding and these four O atoms exhibit tetra-coordination while the rest are tri-coordinated. Such hydrogen-bond-deficient water molecules are, however, present[12,13] at the surface of liquid water or hexagonal ice. A wide range of O···O distances are observed (2.736–2.894 Å) in the present cluster as the water molecules adjust to the surroundings.

In the FTIR spectrum of compound **1**, a broad peak appears centering around 3420 $cm^{-1}$ attributable[14] to the water cluster. Thermal analysis of compound **1** shows that it begins to lose weight after ca. 50 °C without showing any plateau region.

## Conclusion

In conclusion, we have characterized a novel water decamer in the shape of two parallel five-membered staggered rings. These decamers glue quasi-parallel diphosphate chains resulting in large voids that are occupied by cryptand molecules.

## Experimental Section

**Materials:** All the reagent-grade chemicals were used without purification unless otherwise specified. Triethanolamine, salicylaldehyde, tris(2-aminoethyl)amine, and sodium borohydride were obtained from Aldrich. Sodium hydroxide, anhydrous sodium sulfate, phosphoric acid, and thionyl chloride were received from S. D. Fine Chemicals (India). Thionyl chloride and all the solvents were freshly distilled prior to use.

**Physical Measurements:** Spectroscopic data were collected as follows: IR (KBr disk, 400–4000 $cm^{-1}$): Perkin–Elmer Model 1320; thermogravimetric analysis (heating rate of 5 °C/min): Mettler Toledo Star System. Microanalysis data for the compound were obtained from CDRI, Lucknow.

 © 2006 Wiley-VCH Verlag GmbH & Co. KGaA, Weinheim 

**Synthesis of $[LH^{+2}{\cdot}2H_2PO_4^{-2}{\cdot}7H_2O]$ (1):** The cryptand L was synthesized as reported previously.[15] The cryptand was dissolved in water by dropwise addtion of phosphoric acid, and the resulting solution, upon slow concentration at room temperature, afforded pale yellow rectangular parallelepiped crystals of $[LH^{+2}{\cdot}2H_2PO_4^{-2}{\cdot}7H_2O]$ (**1**) in 60% (0.530 g) yield. $C_{33}H_{65}N_5O_{18}P_2$ (881.84): calcd. C 44.94, H 7.43, N 7.94; found C 44.91, H 7.52, N 8.01.

**X-ray Structural Studies:** The X-ray data were collected with a Bruker SMART APEX CCD diffractometer using graphite-monochromated Mo-$K_\alpha$ radiation (0.71069 Å). Data collection and its reduction were achieved with SMART (version 5.628) and SAINT (version 6.45). The structure was solved by direct methods and refined on $F^2$ using the SHELX-97 package.[16] All the H atoms bonded to water O were located in the difference Fourier maps. The non-hydrogen atoms were refined anisotropically. The H atoms were not refined. Crystal data for **1**: pale yellow, rectangular parallelepiped, crystal dimensions $0.19 \times 0.15 \times 0.12$ mm, triclinic, $P\bar{1}$, $Z = 2$, $a = 12.765(5)$, $b = 13.254(2)$, $c = 13.817(4)$ Å, $V = 2137.3(14)$ Å$^3$, $\rho_{cald.} = 1.37$ g cm$^{-3}$, $T = 100$ K, $\mu = 0.18$ mm$^{-1}$, $\theta_{max} = 28.32°$. A total of 14357 reflections collected, of which 7784 were unique, $R1 = 0.0582$, $wR2 = 0.1339$, GOOF = 1.092 for $I > 2\sigma(I)$, residual electron density: 0.512 and –0.548 e Å$^{-3}$. CCDC-287356 contains the supplementary crystallographic data for this paper. These data can be obtained from The Cambridge Crystallographic Data Centre via www.ccdc.cam.ac.uk/data_request/cif.

**Supporting Information** (see footnote on the first page of this article): Figure showing the water clusters viewed along the phosphate chains.

## Acknowledgments

We gratefully acknowledge the financial support received from the Department of Science and Technology, New Delhi, India (grant No.SR/S5/NM-38/2003 to P. K. B.) and an SRF from the CSIR to S. G.

[1] a) K. A. Denessiouk, M. S. Johnson, A. I. Denesyuk, *J. Mol. Biol.* **2005**, *345*, 611–629; b) L. L. E. Salins, S. K. Deo, S. Daunert, *Sens. Actuators, B* **2004**, *B97*, 81–89; c) H. Luecke, F. A. Quiocho, *Nature* **1990**, *347*, 402–405.
[2] K. D. Jordan, C. J. Tsai, *J. Phys. Chem.* **1993**, *97*, 5208–5210.
[3] T. S. Zwier, *Science* **2004**, *304*, 1119–1120.
[4] M. Miyazaki, A. Fujii, T. Ebata, N. Mikami, *Science* **2004**, *304*, 1134–1137.
[5] R. Ludwig, *ChemPhysChem* **2000**, *1*, 53–56.
[6] P. S. Lakshminarayanan, E. Suresh, P. Ghosh, *J. Am. Chem. Soc.* **2005**, *127*, 13132–13133.
[7] B.-Q. Ma, H.-L. Sun, S. Gao, *Chem. Commun.* **2005**, 2336–2338.
[8] Q.-Y. Liu, L. Xu, *CrystEngComm* **2005**, *7*, 87–89.
[9] U. Buck, F. Huisken, *Chem. Rev.* **2000**, *100*, 3863–3890.
[10] S. Maheswary, N. Patel, N. Sathyamurthy, A. D. Kulkarni, S. R. Gadre, *J. Phys. Chem. A* **2001**, *105*, 10525–10537.
[11] a) M. Yoshizawa, T. Kusukawa, M. Kawano, T. Ohhara, I. Tanaka, K. Kurihara, N. Nimura, M. Fujita, *J. Am. Chem. Soc.* **2005**, *127*, 2798–2799; b) R. D. Bergougnant, A. Y. Robin, K. M. Fromm, *Cryst. Growth Des.* **2005**, *5*, 1691–1694; c) O. Ermer, J. Neudörfl, *Chem. Eur. J.* **2001**, *7*, 4961–4980; d) L. J. Barbour, G. W. Orr, J. L. Atwood, *Nature* **1998**, *393*, 671–673.
[12] C. J. Gruenloh, J. R. Carney, C. A. Arrington, T. S. Zwier, S. Y. Fredericks, K. D. Jordan, *Science* **1997**, *276*, 1678–1681.
[13] R. Ludwig, *Angew. Chem. Int. Ed.* **2001**, *40*, 1808–1827.
[14] S. K. Ghosh, J. Ribas, M. S. E. Fallah, P. K. Bharadwaj, *Inorg. Chem.* **2005**, *44*, 3856–3862.
[15] D. K. Chand, K. Ragunathan, P. K. Bharadwaj, T. C. W. Mak, *J. Org. Chem.* **1996**, *61*, 1169–1171.
[16] G. M. Sheldrick, *SHELX-97, Program for the Solution and Refinement of Crystal Structures*, University of Göttingen, **1997**.
Received: November 25, 2005
Published Online: February 21, 2006

 © 2006 Wiley-VCH Verlag GmbH & Co. KGaA, Weinheim 

DOI: 10.1002/ejic.200501058

# Photoinduced Phase Transition of the Coordinationally Unsaturated $d^9$ Metal Centers of Bis(*N*,*N*-diethylethylenediamine)copper(II) Perchlorate within the Thermal Hysteresis of the Spin-Exchange Interaction

**Panče Naumov,*[a,b,c] Kenji Sakurai,[d] Toru Asaka,[e] Alexei A. Belik,[a] Shin-ichi Adachi,[c,f] Junichi Takahashi,[c,f] and Shin-ya Koshihara[c,f,g]**

**Keywords:** Photoinduced phase transitions / Jahn–Teller effect / Photodiffraction / Photochromism / Thermochromism

Diffraction evidence is presented that the structure of one-dimensional arrays of strained, coordinationally unsaturated $d^9$ pseudo-Jahn–Teller centers of bis(*N*,*N*-diethylethylenediamine)copper(II) perchlorate is affected by excitation of the LMCT bands within the hysteresis region of a low-temperature ferromagnetic-to-antiferromagnetic phase transition.
(© Wiley-VCH Verlag GmbH & Co. KGaA, 69451 Weinheim, Germany, 2006)

Novel materials with physical properties that can be efficiently controlled by light is one of the main goals of modern materials science.[1] Particularly interesting are the solid-to-solid phase transitions which can be induced by light, termed photoinduced phase transitions.

In some cases, such as the photoinduced metal–insulator phase transitions of organic one-dimensional molecular complexes,[2–4] the solid-state cooperativity enables very high efficiencies (more than one hundred molecules can be converted per absorbed photon through a domino-like mechanism), as well as ultra-fast photoresponses (picosecond scale). These two exotic properties are very prospective as a basis for the design of ultrafast devices that operate in the photon mode. Therefore, in addition to their importance for understanding fundamental solid-state phenomena, photoinduced phase transitions are very important for future applications in ultrafast photoelectronics. However, the number of known compounds undergoing photoinduced phase transitions is limited. The most studied are a group of iron complexes capable of light-induced spin-crossover[5,6] and organic molecular complexes similar to tetrathiafulvalene-chloranil which undergo light-induced intermolecular charge transfer followed by metal-to-insulator transition.[2–4] In this paper we report on a new strategy to build systems capable of photoinduced phase transition.

Nonlinear molecules with a partially filled set of degenerate orbitals are inherently Jahn–Teller (JT) unstable,[7] an effect which is considered to underpin important phenomena such as high-temperature superconductivity[8] and colossal magnetoresistance.[9] In this study, a pseudo-JT crystal composed of $d_{z^2}$ arrays of coordinationally unsaturated copper(II) ions was utilized as a potentially light-susceptible medium for which significant structural perturbations are expected upon excitation.

As a coordinationally unsaturated unit, the *trans*-square-planar bis(*N*,*N*-diethylethylenediamine)copper(II) cation in its perchlorate salt, $[Cu(dieten)_2](ClO_4)_2$, was selected (Figure 1A).[10] The bulky *gem*-dialkylamine ligands play multiple structural roles: first, they determine the square-planar geometry by shielding the apical metal valences from the approach of the anions beyond nonbonded distances; second, they effectively space out the metal ions, preventing dimerization; and third, they provide sufficient flexibility for distortions of the primary coordination sphere. The resulting instability can be compensated by pressure[11] or by heating above 317.6 K,[12] where the internal strain overweighs the energy gain from the electronic state ordering and the respective lattice distortions, resulting in spontaneous transition of the triclinic lattice ($P\bar{1}$, A) to a monoclinic one ($I2$, B) with doubled volume and tetrahedral distortion of the square-planar ligand plane (Figure 1).[13] Cooling of the crystal from ambient temperature results in a gradual change of the red color to orange, due to continuous change of the ligand field strength of the metal.[12]

[a] ICYS, National Institute for Materials Science,
1-1 Namiki, Tsukuba, Ibaraki 305-0044, Japan
Fax: +81-29-860-4706
E-mail: naumov.pance@nims.go.jp
[b] Institute of Chemistry, Faculty of Science, Sts. Cyril and Methodius University,
Arhimedova 5, P. O. B. 162, 1000 Skopje, Macedonia
[c] Exploratory Research for Advanced Technology (ERATO),
4-1-8 Honcho, Kawaguchi, Saitama 332-0012, Japan
[d] X-ray Physics Group, MEL, National Institute for Materials Science,
1-2-1 Sengen, Tsukuba, Ibaraki 305-0047, Japan
[e] HVEMS, National Institute for Materials Science,
1-1 Namiki, Tsukuba, Ibaraki 305-0044, Japan
[f] High Energy Accelerator Research Organization (KEK),
1-1 Oho, Tsukuba, Ibaraki 305-0801, Japan
[g] Department of Materials Science, Tokyo Institute of Technology,
1-12-1 O-okayama, Meguro, Tokyo 152-8551, Japan

 © 2006 Wiley-VCH Verlag GmbH & Co. KGaA, Weinheim 

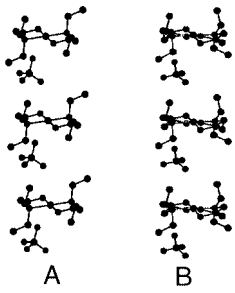


Figure 1. Structure of one-dimensional cationic chains in the low-temperature ordered (A) and high-temperature disordered (B) phases of $[Cu(dieten)_2](ClO_4)_2$ from single-crystal diffraction data.

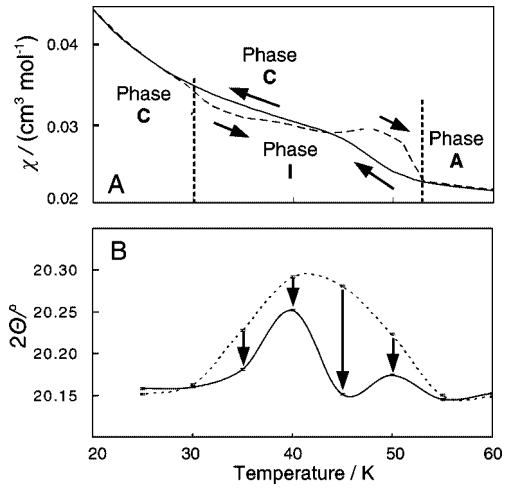


Figure 2. (A) Magnetic susceptibility recorded with the magnetic field vector $\perp\{100\}$ face of a $[Cu(dieten)_2](ClO_4)_2$ crystal cycled at low temperature (solid line: cooling, dashed line: heating). (B) Thermal profile of the position of the $(1\bar{1}0)$ reflection before (dotted line) and after (solid line) 1 s excitation with polychromatic UV light ($\lambda_{max}$ = 365 nm). The sample was annealed by heating to 300 K between each two temperatures. The abscissa is the same for both plots.

The magnetic susceptibility (see Experimental Section) of $[Cu(dieten)_2](ClO_4)_2$ single crystals cycled thermally in the dark below the phase transition A↔B (2–300 K) exhibits reproducible anomalies at low temperature (Figure 2A). On cooling ( ↓ ) from ambient temperature, a single-step transition occurs at 48 K ($T_\downarrow$), with onset at 60 K. During subsequent heating ( ↑ ) from 2 K to 300 K, the susceptibility is recovered in two steps between 25 and 57 K: at 30 ($T_{\uparrow,1}$) and 52 K ($T_{\uparrow,2}$). The hysteresis is reproducible by repeated thermal cycling with the magnetic field vector oriented perpendicular to each of the three crystal faces. The modified Curie–Weiss model[14] reveals a change of the weak-exchange interaction at $T_\downarrow$ from the high-temperature ferromagnetic regime I, phase A [80–290 K, $\Theta$ = 2.6(3) K, $\mu_{eff}$, $g$ = 1.743(3), 2.0126, $\chi_o$ = –3.36(3)·10$^{-4}$ cm$^3$/Cu-mol], to a low-temperature antiferromagnetic regime II, phase C [2–28 K, $\Theta$ = –0.467(15) K, $\mu_{eff}$, $g$ = 1.916(2), 2.2124, $\chi_o$ = –1.0(4)·10$^{-5}$ cm$^3$/Cu-mol], with hysteresis in the range 25–55 K. The two steps at $T_{\uparrow,1}$ and $T_{\uparrow,2}$ resolved on heating reveal that the one-step transition at $T_\downarrow$ on cooling from region I to region II involves two simultaneous processes. From the two steps on heating, the one at $T_{\uparrow,1}$ probably corresponds to switching of the exchange interaction of the antiferromagnetic phase C in region II to an intermediate phase in region III, which, by structural change of the lattice at $T_{\uparrow,2}$, is transformed back to the lattice A in region I.

From the combination of internal strain and the weak electronic coupling along the one-dimensional cationic chains, it is expected that local perturbations of this structure in the region of bistability are feasible and that they might influence the long-range structural order. In order to test this hypothesis, the effect of photoexcitation was examined with a specially designed system for temperature-controlled powder photodiffraction at laboratory scale (Figure 3).[15] Upon 365 nm flash-excitation of the ligand-to-metal-charge-transfer bands of $[Cu(dieten)_2](ClO_4)_2$ (200–400 nm), the strong reflections shift 0.04° on average, with various trends of change in the intensity and a remarkable change in color from bright orange to violet. The long time needed for data collection relative to the time of irradiation assured that the respective cell shrinkage was not due to heating effects but to the creation of a long-lived photoinduced ground state. From the peak shift, the overall effect of the excitation on the lattice is analogous to the cooling of the crystal. The temperature dependence of the photoinduced structural change, monitored by the position of the $(1\bar{1}0)$ reflection (Figure 3 and Figure 2B) showed that the photoexcitation strongly affects the lattice on cooling within the hysteresis region III, where phase C and the intermediate phase exist on cooling and heating, respectively. From the magnitude of the shift, it is concluded that the largest structural change occurs at 45 K, right after the transition of A to C has been completed (Figure 2B). This is an indication that the excitation induces transition from the low-temperature phase C, obtained in situ from cooled A, to the intermediate phase I between C and A, close to the transition point. Excitation below 30 K is less effective and results in qualitatively different structural changes, which was confirmed by comparison of the difference patterns in the $2\Theta$ region 5–60°. The photoinduced phase persists at 50 K, but it decays by thermal annealing at 300 K or by irradiation with visible light. Therefore, the diffraction experiments are conclusive that within and around the bistable region III, the photoexcitation significantly affects the crystal and electronic structure, particularly of the coupled cationic centers. Detailed structural studies are now underway.

In conclusion, the electronically coupled planar pseudo-JT cations in the one-dimensional cationic chains of $[Cu(dieten)_2](ClO_4)_2$ are subject to internal strain, balanced by a relatively strong, but moderately flexible ligand field. The lattice can withstand such strain only between 60 and 318 K; it can be collapsed by applying external pressure, or by altering the internal pressure by heating/cooling out of this temperature range. Above 318 K, the strain is released by tetrahedral distortion of the valence orbital orientation, enhanced ring puckering, disorder of the side ligand chains, and positional and rotational disorder of the counteranion.

 © 2006 Wiley-VCH Verlag GmbH & Co. KGaA, Weinheim 

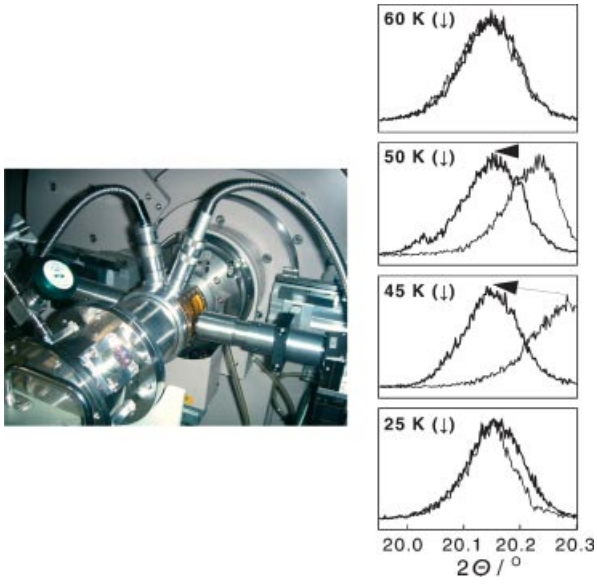


Figure 3. Left: Laboratory-built, low-temperature cryostat for powder X-ray photodiffraction. The double optical input on the top is connected to the UV output through a system of replaceable UV-transparent optics. The X-ray beam diffracts and is detected in horizontal $\Theta - 2\Theta$ geometry. Right: Temperature profile of the $(1\bar{1}0)$ reflection before (thin line) and after (thick line) flash excitation of cooled $[Cu(dieten)_2](ClO_4)_2$ powder. The ordinate represents intensity in arbitrary units. The sample was flash-excited at $\lambda_{max}$ = 365 nm, through biconvex fused-silica lenses and quartz windows, with polychromatic output from a high-pressure Hg lamp (SP-7, Ushio) and annealed at 300 K between the consecutive flashes.

Below 60 K, switching of the exchange interaction in virgin single crystals occurs from a ferromagnetic to an antiferromagnetic regime, with hysteresis between 25 and 55 K. In the region of low-temperature bistability, the phase transition can also be induced from the excited state by partial charge transfer, which results in overall shrinkage of the lattice. The possibility of employing the interplay between the JT instability and the ligand field strain, determined by a moderate flexibility of the primary coordination sphere, for triggering structural transitions by light, pressure, and temperature, paves the way to switching devices capable of multi-stimulus control.

## Experimental Section

Magnetic susceptibilities, $\chi = M/H$, were measured with a SQUID magnetometer (Quantum Design, MPMS) between 2 and 300 K in an applied field of 10 kOe [1 Oe = $(10^3/4\pi)$ A m$^{-1}$]. The temperature steps were 1 K between 2 and 100 K, and 5 K between 105 and 300 K. The heating/cooling rate was 10 K·min$^{-1}$ between the steps.

[1] a) O. Sato, *J. Photochem. Photobiol. C: Photochem. Rev.* **2004**, *5*, 203–223; b) P. Gütlich, Y. Garcia, T. Woike, *Coord. Chem. Rev.* **2001**, *219–221*, 839–879.
[2] E. Collet, M.-H. Lemée-Cailleau, M. Buron-Le Cointe, H. Cailleau, M. Wulff, T. Luty, S. Koshihara, M. Meyer, L. Toupet, P. Rabiller, S. Techert, *Science* **2003**, *300*, 612–615.
[3] L. Guérin, E. Collet, M.-H. Lemée-Cailleau, M. Buron-Le Cointe, H. Cailleau, A. Plech, M. Wulff, S. Koshihara, T. Luty, *Chem. Phys.* **2004**, *299*, 163–170.
[4] M. Chollet, L. Guerin, N. Uchida, S. Fukaya, H. Shimoda, T. Ishikawa, K. Matsuda, T. Hasegawa, A. Ota, H. Yamochi, G. Saito, R. Tazaki, S. Adachi, S. Koshihara, *Science* **2005**, *307*, 86–89.
[5] V. Legrand, C. Carbonera, S. Pillet, M. Souhassou, J. F. Létard, P. Guionneau, C. Lecomte, *J. Phys.: Conf. Ser.* **2005**, *21*, 73–80.
[6] J.-F. Létard, J. Sanchez Costa, S. Marcen, C. Carbonera, C. Desplanches, A. Kobayashi, N. Daro, P. Guionneau, J.-P. Ader, *J. Phys.: Conf. Ser.* **2005**, *21*, 23–29.
[7] L. R. Falvello, *J. Chem. Soc., Dalton Trans.* **1997**, 4463–4476.
[8] D. V. Fil, O. I. Tokar, A. L. Shelankov, W. Weber, *Phys. Rev. B* **1992**, *45*, 5633–5640.
[9] S. Jin, T. H. Tiefel, M. McCormack, R. A. Fastnacht, R. Ramesh, L. H. Chen, *Science* **1994**, *264*, 413–415.
[10] T. Yokoyama, K. Takahashi, O. Sato, *Phys. Rev. B* **2003**, *67*, 172104–172108.
[11] J. R. Ferraro, L. J. Basile, L. R. Garcia-Ineguez, P. Paoletti, L. Fabrizzi, *Inorg. Chem.* **1976**, *15*, 2342–2345.
[12] A. Nishimori, M. Sorai, E. A. Schmitt, D. A. Hendrickson, *J. Coord. Chem.* **1996**, *37*, 327–340.
[13] I. Grenthe, P. Paoletti, M. Sandström, S. Glikberg, *Inorg. Chem.* **1979**, *18*, 2687–2692.
[14] The modified Curie–Weiss law of the form $\chi(T) = \chi_o + (\mu_{eff})^2 N_A[3k_B(T - \theta)]^{-1}$ was used, where $\chi_o$ is the temperature-independent term, $\mu_{eff}$ is the effective magnetic moment, $N_A$ is Avogadro's number, $k_B$ is Boltzmann's constant, $\Theta$ is the Weiss constant, and $g$ is the g-value. Heating/cooling rate: 10 K·min$^{-1}$.
[15] There is one previous report on the formation of a light-induced "metastable state" in this compound: K. Takahashi, R. Nakajima, Z. Gu, H. Yoshiki, A. Fujishima, O. Sato, *Chem. Commun.* **2002**, 1578–1579.

Received: November 28, 2005
Published Online: February 21, 2006

 © 2006 Wiley-VCH Verlag GmbH & Co. KGaA, Weinheim 

DOI: 10.1002/ejic.200600084

# Synthesis and Molecular Structure of [Cp*Ta(Ph)($P_6Ph_5$)]: A Terminal Phosphinidene Complex of the $(P_6Ph_5)^{3-}$ Ligand (Cp* = $C_5Me_5$)

**Robert Wolf[a] and Evamarie Hey-Hawkins*[a]**

**Keywords:** Tantalum / Phosphorus / P ligands / Oligophosphanes / Phosphinidene complexes

The terminal phosphanyl phosphinidene complex [Cp*Ta(Ph)($P_6Ph_5$)] (**2**) has been isolated in 16% yield from the reaction of [Cp*$TaCl_4$] with 2 equiv. $Na_2(P_4Ph_4)$ and displays an $\eta^4$-bound $(P_6Ph_5)^{3-}$ ligand according to X-ray crystallography and $^{31}P$ NMR spectroscopy.

(© Wiley-VCH Verlag GmbH & Co. KGaA, 69451 Weinheim, Germany, 2006)

Terminal phosphinidene complexes [$L_nM(PR)$] are of much current interest due to their versatile reactivity and interesting bonding properties.[1,2] In this respect, phosphanyl phosphinidene complexes [$L_nM(PPR_2)$] are a particularly attractive subclass, as the phosphanyl group may or may not be involved in coordination.[3] The first representatives were described only recently.[4,5]

During our studies on the coordination chemistry of oligophosphanediide anions $(P_nR_n)^{2-}$ ($n$ = 2–4)[6–9] we could show that, in spite of its highly reducing nature,[9] the $(P_4Ph_4)^{2-}$ dianion remains intact in the transmetalation reaction of 2 equiv. of [$CuCl(PCyp_3)_2$] (Cyp = *cyclo*-$C_5H_9$) with $Na_2(P_4Ph_4)$ (**1**).[10] While this was an example of a successful transmetalation with a valence-electron-rich late-transition-metal halide,[11] we wished to extend the scope of this reaction to early transition-metal halides as well. Herein, we report the surprising result of the reaction of **1** with [Cp*$TaCl_4$] (Cp* = $C_5Me_5$). This led to the isolation of [Cp*Ta(Ph)($P_6Ph_5$)] (**2**), which not only contains an unprecedented oligophosphanide ligand $(P_6Ph_5)^{3-}$, but is also a rare example of a terminal phosphanyl phosphinidene complex of tantalum.

Complex **2** could be isolated in low, though reproducible, yield (16%) from the 2:1 reaction of **1** with [Cp*$TaCl_4$] (Scheme 1). An X-ray crystal structure analysis[12] of **2** revealed a mononuclear complex in which a trianionic $(P_6Ph_5)^{3-}$ ligand binds in an $\eta^4$ fashion to the metal center (Figure 1). The coordination sphere of tantalum is completed by an $\eta^5$-coordinated pentamethylcyclopentadienyl ligand and an $\eta^1$-bound phenyl ligand. Remarkably, the Ta–P bond of the "naked" phosphorus atom P1 is significantly shorter than the remaining Ta–P distances [$d$(Ta1–P1) = 2.416(2), $d$(Ta1–P2) = 2.528(2), $d$(Ta1–P5) = 2.561(2), $d$(Ta1–P6) = 2.659(2) Å], and this indicates multiple-bond character of the Ta–P1 bond. Nevertheless, it is longer than the Ta–P bonds in the phosphinidene-bridged Ta complexes [{Cp*TaCl(μ-PR)}$_2$] [R = Cy, *t*Bu, Ph, Mes, 2,4,6-*i*$Pr_3C_6H_2$; $d$(Ta–P) = 2.317(6)–2.358(3) Å][13,14] and the terminal phosphinidene complexes [N{$CH_2CH_2N(SiMe_3)$}$_3$Ta=PCy] [$d$(Ta–P) = 2.145(7) Å][2a] and [(*t*$Bu_3SiO)_3$Ta=PPh] [$d$(Ta–P) = 2.317(4) Å].[2b] The Ta–P distance of the other terminal phosphorus atom of the chain (P6) is much longer [$d$(Ta1–P6) = 2.659(2) Å]. It is in the upper range of the values found in other terminal phosphanido complexes of tantalum [$d$(Ta–P) = 2.390–2.595(3) Å].[14,15] The pyramidal coordination of P6 (sum of bond angles around P6: 301.3°) indicates that it acts as a one-electron donor to the metal center, which is also in accordance with the 18-electron rule (vide infra). The remaining Ta–P distances are in the known range for phosphane complexes of tantalum.[16,17] The Ta–C distance of the *ipso*-carbon atom of the $\eta^1$-coordinated phenyl ligand [$d$(Ta1–C1) = 2.230(7) Å] is similar to those found in other cyclopentadienyl-substituted phenyl complexes of tantalum.[18] While the P–P bond lengths of P2 to P6 are in the range of single bonds [$d$(P2–P3, P3–P4, P4–P5, P5–P6) = 2.133(3)–2.213(3) Å],[19] the P–P bond involving the naked phosphorus atom is distinctly shorter [$d$(P1–P2) = 2.096(3) Å]. Similarly short P–P bonds have been observed in other phosphanyl phosphinidene complexes[4] and also in diphosphene complexes.[20] In fact, the geometry of the (PPPh) unit in **2** closely resembles that in the recently described Nb phosphanyl phosphinidene complexes [Nb{N(R)$R^1$}$_3$($PPR^2_2$)] ($R^1$ = 3,5-$Me_2C_6H_3$, R = neopentyl, $R^2$ = Ph, *t*Bu).[4c]

Formally, compound **2** may be regarded as an 18-electron complex with a double bond between the metal center and the unsubstituted phosphorus atom (P1) and single bonds to the other coordinating P atoms (as depicted in Scheme 1). However, alternative descriptions of the bonding situation involving a multiply bonded PPPh fragment

[a] Institut für Anorganische Chemie der Universität Leipzig, Johannisallee 29, 04103 Leipzig, Germany
Fax: +49-341-9739319
E-mail: hey@rz.uni-leipzig.de

 WILEY InterScience DISCOVER SOMETHING GREAT © 2006 Wiley-VCH Verlag GmbH & Co. KGaA, Weinheim 

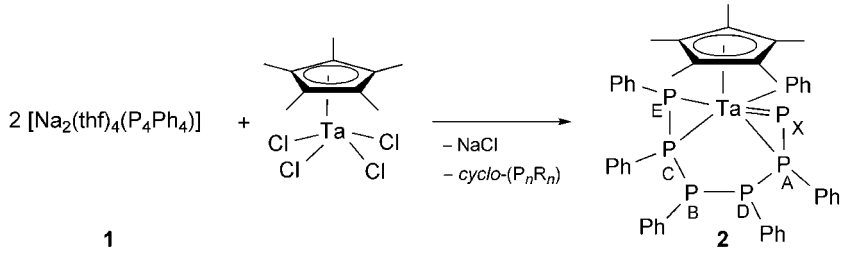


Scheme 1.

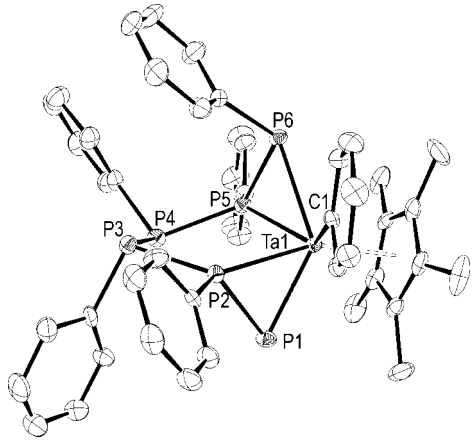


Figure 1. Solid-state molecular structure of **2**; H atoms omitted for clarity, ellipsoid probability: 30%. Selected bond lengths [Å] and angles [°]: Ta1–P1 2.416(2), Ta1–P2 2.528(2), Ta1–P5 2.561(2), Ta1–P6 2.659(2), Ta1–C1 2.230(7), av Ta–C in Cp* 2.451, P1–P2 2.096(3), P2–P3 2.213(3), P3–P4 2.185(3), P4–P5 2.211(3), P5–P6 2.133(3), C1–Ta1–P1 104.4(2), C1–Ta1–P2 78.6(2), C1–Ta1–P5 130.1(2), C1–Ta1–P6 89.6(2), P1–Ta1–P2 50.12(6), P1–Ta1–P5 93.61(7), P1–Ta1–P6 134.52(6), P2–Ta1–P5 78.55(6), P2–Ta1–P6 92.77(6), P5–Ta1–P6 48.20(6), P2–P1–Ta1 67.71(7), P5–P6–Ta1 63.50(7), P3–P2–Ta1 126.84(9), P4–P5–Ta1 118.84(9), P1–P2–P3 124.4(1), P2–P3–P4 95.7(1), P3–P4–P5 103.1(1), P4–P5–P6 129.4(1).

are equally plausible and may account for the relatively long Ta–P bond compared to other Ta phosphinidene complexes and the short bond between P1 and P2. Thus, the bonding situation is probably best described by a superposition of different mesomeric structures, as already suggested by Cummins and Pikies.[3,4,21]

The molecular composition of **2** was fully confirmed by IR spectroscopy, mass spectrometry, elemental analysis, and multinuclear NMR spectroscopy. Notably, no P–H stretch is observed in the IR spectrum. The $^1$H NMR spectrum shows multiplets in the region of 6.28 to 8.18 ppm for the phenyl groups and a singlet at $\delta$ = 1.81 ppm for the methyl resonances of the Cp* ligand. A characteristic low-field signal at +182.70 ppm is observed for the *ipso*-carbon atom of the Ta-bound phenyl group in the $^{13}C\{^1H,^{31}P\}$ NMR spectrum.[18,22] The $^{31}P\{^1H\}$ NMR spectrum displays a first-order ABCDEX spin system (Figure 2). No additional couplings are detected in the proton-coupled $^{31}$P NMR spectrum. Only the $^1J$(P–P) couplings could be assigned with certainty from the $^{31}P\{^1H\}$ NMR spectrum due to the line broadening caused by the interaction of four phosphorus nuclei ($P_X$, $P_A$, $P_C$, and $P_E$) with the $^{181}$Ta nucleus. Nevertheless, this observation permits the assignment of the individual resonances (cf. Scheme 1). The striking low-field shift of the two-coordinate, "naked" P atom $P_X$ ($\delta_X$ = +370.3, $^1J_{AX}$ = ±471 Hz) indicates multiple-bond character of the Ta–$P_X$ bond. Its chemical shift is comparable to those observed in the related Nb complexes [Nb{N(R)-$R^1$}$_3$($PPR^2_2$)] ($R^1$ = 3,5-$Me_2C_6H_3$, R = neopentyl; $R^2$ = Ph: $\delta$ = +401.3; $R^2$ = *t*Bu: $\delta$ = +405.5).[4c] The "phosphanyl moiety" ($P_E$ and $P_C$) displays a similarly large value for its $^1J$(P–P) coupling constant ($^1J_{CE}$ = ±444 Hz), but the resonance of its terminal P atom ($P_E$) is shifted to the typical high-field region observed for Ta phosphanides ($\delta_E$ = –127.7).[15] All in all, the $^{31}$P parameters confirm that the solid-state structure of **2** is retained in solution.

Besides the ABCDEX spin system of **2** a minor amount of *cyclo*-($P_4Ph_4$)[23] (ca. 4%) is observed in the $^{31}P\{^1H\}$

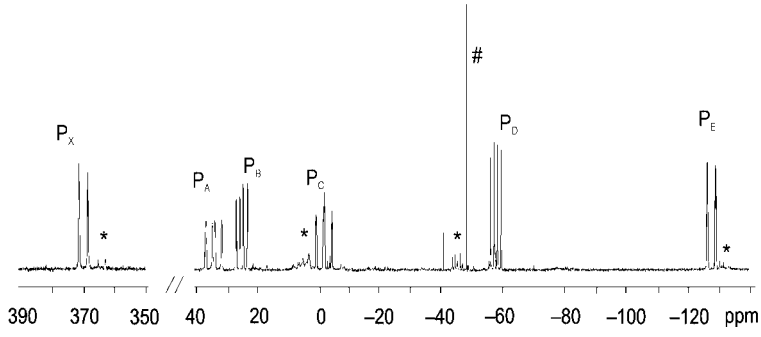


Figure 2. $^{31}P\{^1H\}$ NMR spectrum of **2** ($C_6D_6$, 161.97 MHz). The singlet of *cyclo*-($P_4Ph_4$)[23] is designated by #; * indicates signals of a further diastereomer of **2**. For the assignment of the individual multiplets, see Scheme 1.

 © 2006 Wiley-VCH Verlag GmbH & Co. KGaA, Weinheim 

NMR spectrum. Furthermore, a number of less intense multiplets are reproducibly observed, with rather similar chemical shifts to **2** (Figure 2). For example, a broad low-field doublet is detected at +364.3 ppm ($^1J_{PP}$ = ca. ±387 Hz). The unequivocal assignment of all signals was impaired by their low intensity (partly owing to the low solubility of **2** once isolated). Most likely, they can be attributed to the presence of a second diastereomer of **2** in solution, which may be formed by inversion of either of the uncoordinated P atoms ($P_B$ or $P_D$). It is well-known that catenated oligophosphanes have significantly reduced inversion barriers, as was observed, for example, in the heterocycles *cyclo*-1,4-$(BH_3)_2(P_4Ph_4CH_2)$[24] and [M{*cyclo*-$(P_4Cy_4As)$}] (M = Li, Na).[25]

While rearrangement of oligophosphanide ligands during transmetalation reactions has been observed in a few instances,[11,26] the mechanism of formation of **2** is obviously rather complex. Presumably, it involves the initial formation of a low-valent Ta intermediate. Subsequently, the phenyl group may be transferred by oxidative addition of the P–C bond to the reduced metal center. $^{31}$P NMR spectra of the reaction mixture show the formation of the cyclooligophosphanes *cyclo*-$(P_nPh_n)$ ($n$ = 4–6)[23,27] and the phosphinidene-bridged complex [{Cp*TaCl(μ-PPh)}$_2$][13] (identified by its characteristic low-field singlet at +402.3 ppm) as major products. In addition, numerous low-intensity multiplets are observed but could not be assigned. This seems to indicate the presence of a number of P–P bonded byproducts in the reaction mixture. No further tantalum-containing products could be isolated from the reaction. Attempts to obtain further insights by variation of the stoichiometry, the reaction conditions, and the starting materials have remained futile. Thus, the yield of **2** could not be increased by warming the reaction mixture to +80 °C. Furthermore, **2** could not be obtained from the reaction of 2 equiv. $K_2(P_3Ph_3)$ with [Cp*TaCl$_4$], from the reaction of [{Cp*TaCl(μ-PPh)}$_2$][13] with *cyclo*-$(P_5Ph_5)$ (warming to +100 °C for 2 h), or from the reaction of **1** with [{Cp*TaCl$_2$}$_2$][28] (2:1). Only the cyclophosphanes *cyclo*-$(P_nMes_n)$ ($n$ = 3, 4)[29] were isolated from the reaction of [Cp*TaCl$_4$] with 2 equiv. $[Na_2(THF)_4(P_4Mes_4)]$.[8a] Clearly, a more detailed understanding of the reaction mechanism will only be gained from future studies.

In conclusion, we have shown that the unprecedented $(P_6Ph_5)^{3-}$ ligand containing six catenated phosphorus atoms is stabilized in the Ta phosphinidene complex [Cp*Ta(Ph)$(P_6Ph_5)$] (**2**). This adds to the growing evidence that, although not always straightforward,[9,11] the transmetalation reaction of alkali metal oligophosphanediides with transition metal halides represents a viable route to phosphorus-rich metal complexes with unusual structures and reactivities.

## Experimental Section

All experiments were performed under an inert atmosphere. The NMR spectra were recorded with a Bruker AVANCE-DRX-400 spectrometer. $^1$H NMR (400.13 MHz): internal standard solvent, external standard TMS. $^{31}$P NMR (161.9 MHz): external standard 85% $H_3PO_4$. $^{13}$C NMR (100.16 MHz): internal standard solvent, external standard TMS. For the assignment of the phosphorus signals, see Scheme 1. The mass spectrum was recorded with a MASPEC II spectrometer (FAB-MS, matrix: 3-nitrobenzyl alcohol). The IR spectra were recorded with an FTIR spectrometer Perkin–Elmer System 2000 (KBr) in the range 350–4000 cm$^{-1}$. All solvents were purified by distillation, dried, saturated with argon, and stored over a potassium mirror. $[Na_2(THF)_4(P_4Ph_4)]$ (**1**)[8a] and [Cp*TaCl$_4$][30] were synthesized according to the literature procedures.

**2:** A solution of **1** (6.18 g, 8.1 mmol) in toluene (40 mL) was added dropwise to a suspension of [Cp*TaCl$_4$] (1.85 g, 4.0 mmol) in toluene (30 mL) at –80 °C. The mixture turned dark-brown immediately on addition. The dark suspension was slowly warmed to room temperature and stirred overnight. The solvent was reduced to ca. 30 mL and the mixture was filtered. The dark-brown residue was washed three times with 20 mL of toluene. Then the combined filtrates were reduced to ca. 20 mL and the clear, dark brown solution was layered with *n*-hexane (35 mL). Dark red crystals of **2** formed on storage at room temperature for several weeks. Yield: 0.61 g (16% ref. to [Cp*TaCl$_4$]); m.p. 180–181 °C (red oil). $^1$H NMR ($C_6D_6$): $\delta$ = 1.81 (s, 15 H, Cp*), 6.28–8.18 (m, 30 H, Ph) ppm. $^{13}$C{$^1$H,$^{31}$P} NMR ($C_6D_6$): $\delta$ = 12.10 (s, $C_5Me_5$), 113.49–147.63 (s, Ph, $C_5Me_5$), 182.70 (s, *ipso*-C of Ta–Ph) ppm. $^{31}$P{$^1$H} NMR ($C_6D_6$): ABCDEX spin system, $\delta_X$ = +370.3 (br. d, 1 P), $\delta_A$ = +34.0 (br. ddd, 1 P), $\delta_B$ = +24.9 (m, 1 P), $\delta_C$ = –1.8 (br. m, 1 P), $\delta_D$ = –57.6 (ddd, 1 P), $\delta_E$ = –127.7 (br. d, 1 P), $^1J_{AX}$ = ±471 Hz, $^1J_{BD}$ = ±204 Hz, $^1J_{BC}$ = ±391 Hz, $^1J_{AD}$ = ±355 Hz, $^1J_{CE}$ = ±444 Hz. IR (KBr, cm$^{-1}$): $\tilde{\nu}$ = 3135 (w), 3050 (m), 2986 (m), 2957 (m), 2898 (m), 2723 (w), 1953 (w), 1882 (w), 1807 (w), 1753 (w), 1649 (w), 1579 (m), 1567 (m), 1551 (m), 1476 (m), 1433 (s), 1374 (m), 1333 (w), 1303 (m), 1262 (m), 1237 (w), 1184 (w), 1152 (w), 1082 (m), 1068 (m), 1054 (m), 1023 (s), 998 (m), 909 (m), 842 (m), 803 (m), 733 (s), 689 (s), 617 (vw), 563 (m), 520 (w), 479 (m), 467 (m), 405 (m). MS (FAB): $m/z$ = 964.94 [M + H]$^+$; $C_{46}H_{45}P_6Ta$ (964.59): calcd. C 57.27, H 4.70; found C 57.36, H 4.59.

On one occasion, the product still contained some *cyclo*-$(P_5Ph_5)$ and a green, insoluble material as byproducts. In this case, the compound was purified by dissolving in toluene, filtration, and layering the clear filtrate with *n*-hexane.

## Acknowledgments

Financial support from the Studienstiftung des Deutschen Volkes (PhD grant for R. W.) and the Deutsche Forschungsgemeinschaft is gratefully acknowledged. We thank H. C. Starck GmbH & Co. KG for a generous donation of $TaCl_5$.

[1] a) A. H. Cowley, A. R. Barron, *Acc. Chem. Res.* **1988**, *21*, 81; b) A. H. Cowley, *Acc. Chem. Res.* **1997**, *30*, 445; c) K. B. Dillon, F. Mathey, J. F. Nixon, *Phosphorus: The Carbon Copy*, John Wiley & Sons, New York, chapter 3, **1998**; d) F. Mathey, N. H. T. Huy, A. Marinetti, *Helv. Chim. Acta* **2001**, *84*, 2938; e) K. Lammertsma, M. J. M. Vlaar, *Eur. J. Org. Chem.* **2002**, 1127; f) K. Lammertsma, *Phosphinidenes*, in: *Topics in Current Chemistry: New Aspects in Phosphorus Chemistry III* (Ed.: J.-P. Majoral), Springer, Berlin, Heidelberg, **2003**.

[2] Terminal phosphinidene complexes of Ta: a) C. C. Cummins, R. R. Schrock, W. M. Davis, *Angew. Chem.* **1993**, *105*, 758; *Angew. Chem. Int. Ed. Engl.* **1993**, *32*, 756; b) J. B. Bonanno, P. T. Wolczanski, E. B. Lobkovsky, *J. Am. Chem. Soc.* **1994**, *116*, 11159.

[3] Review: J. Olkowska-Oetzel, J. Pikies, *Appl. Organomet. Chem.* **2003**, *17*, 28.

 © 2006 Wiley-VCH Verlag GmbH & Co. KGaA, Weinheim 

[4] Complexes with an $\eta^2$-bound phosphanyl phosphinidene moiety ($PPR_2$): a) H. Krautscheid, E. Matern, I. Kovacs, G. Fritz, J. Pikies, *Z. Anorg. Allg. Chem.* **1997**, *623*, 1917; b) E. Matern, J. Pikies, G. Fritz, *Z. Anorg. Allg. Chem.* **2000**, *626*, 2136; c) J. S. Figueroa, C. C. Cummins, *Angew. Chem.* **2004**, *116*, 1002; *Angew. Chem. Int. Ed.* **2004**, *43*, 984.
[5] A complex with an $\eta^1$-bound phosphanyl phosphinidene moiety ($PPR_2$): J. Pikies, E. Baum, E. Matern, J. Chojnacki, R. Grubba, A. Robaszkiewicz, *Chem. Commun.* **2004**, 2478.
[6] a) K. Issleib, K. Krech, *Chem. Ber.* **1965**, *98*, 2545; b) K. Issleib, E. Fluck, *Z. Anorg. Allg. Chem.* **1965**, *339*, 274; c) K. Issleib, K. Krech, *Chem. Ber.* **1966**, *99*, 1310; d) K. Issleib, M. Hoffmann, *Chem. Ber.* **1966**, *99*, 1320; e) K. Issleib, Ch. Rockstroh, I. Duchek, E. Fluck, *Z. Anorg. Allg. Chem.* **1968**, *360*, 77; f) K. Issleib, K. Krech, *J. Prakt. Chem.* **1969**, *311*, 463.
[7] a) J. Geier, H. Rüegger, M. Wörle, H. Grützmacher, *Angew. Chem.* **2003**, *115* 4081; *Angew. Chem. Int. Ed.* **2003**, *42*, 3951; b) J. Geier, J. Harmer, H. Grützmacher, *Angew. Chem.* **2004**, *116*, 4185; *Angew. Chem. Int. Ed.* **2004**, *43*, 4093.
[8] a) R. Wolf, A. Schisler, P. Lönnecke, C. Jones, E. Hey-Hawkins, *Eur. J. Inorg. Chem.* **2004**, 3277; b) R. Wolf, E. Hey-Hawkins, *Z. Anorg. Allg. Chem*., in press; DOI: 10.1002/zaac.200500384.
[9] R. Wolf, PhD Thesis, University of Leipzig, **2005**.
[10] R. Wolf, E. Hey-Hawkins, *Angew. Chem.* **2005**, *117*, 6398; *Angew. Chem. Int. Ed.* **2005**, *44*, 6241.
[11] For other examples of transmetalation reactions of $M_2(P_nR_n)$ with transition-metal halides see: a) H. Köpf, R. Voigtländer, *Chem. Ber.* **1981**, *114*, 2731; b) R. A. Jones, M. H. Seeberger, B. R. Whittlesey, *J. Am. Chem. Soc.* **1985**, *107*, 6424.
[12] Structural data of **2**: $C_{46}H_{45}P_6Ta$, $M$ = 964.59, monoclinic, space group $P2_1/n$, $a$ = 9.701(5) Å, $b$ = 21.309(5) Å, $c$ = 20.476(5) Å, $\alpha$ = 90.0°, $\beta$ = 97.826(5)°, $\gamma$ = 90.0°, $V$ = 4193(3) Å$^3$, $Z$ = 4, $\rho_{calcd.}$ = 1.528 Mg·m$^{-3}$, $\mu$ = 2.882 mm$^{-1}$, $\theta_{max.}$ = 27.00°, $R$ = 0.0587, $Rw$ = 0.1178. The data were collected with a Siemens SMART CCD diffractometer [$\lambda_{Mo\text{-}K\alpha}$ = 0.71073 Å, $T$ = 213(2) K], 9123 independent reflections, 538 parameters, 0 restraints, max. residual electron density 1.209 e·Å$^{-3}$. An empirical absorption correction was carried out with SADABS (G. M. Sheldrick, SADABS – a Program for Empirical Absorption Correction, Göttingen, **1998**), and the structure solution with Patterson methods (G. M. Sheldrick, SHELXS-97, Program for Crystal Structure Solution, University of Göttingen, **1997**). Ta, P and C atoms were refined anisotropically (SHELXL-97: G. M. Sheldrick, SHELXL-97, Program for the Refinement of Crystal Structures, University of Göttingen, **1997**). CCDC-293167 contains the supplementary crystallographic data for this paper. These data can be obtained free of charge from the Cambridge Crystallographic Data Centre via www.ccdc.cam.ac.uk/data_request/cif.
[13] S. Blaurock, E. Hey-Hawkins, *Eur. J. Inorg. Chem.* **2002**, 2975.
[14] G. A. A. Hadi, K. Fromm, S. Blaurock, S. Jelonek, E. Hey-Hawkins, *Polyhedron* **1997**, *16*, 721.
[15] a) P. J. Domaille, B. M. Foxman, T. J. McNeese, S. S. Wreford, *J. Am. Chem. Soc.* **1980**, *102*, 4114; b) G. I. Nikonov, L. G. Kuzmina, P. Mountford, D. A. Lemenovskii, *Organometallics* **1995**, *14*, 3588.
[16] A search in the CSD (November **2003**) for tantalum complexes of tertiary phosphanes give 188 compounds (503 Ta–P distances) with a range of $d$(Ta–P) = 2.363–2.854 Å (av. 2.601 Å).
[17] S. Blaurock, E. Hey-Hawkins, *Z. Anorg. Allg. Chem.* **2002**, *628*, 2515.
[18] a) K. E. Stockman, K. L. Houseknecht, E. A. Boring, M. A. Sabat, M. G. Finn, R. N. Grimes, *Organometallics* **1995**, *14*, 3014; b) K. Mashima, Y. Tanaka, A. Nakamura, *Organometallics* **1995**, *14*, 5642; c) E. Boring, M. Sabat, M. G. Finn, G. N. Grimes, *Organometallics* **1997**, *16*, 3993.
[19] R. Blom, A. Haaland, *J. Mol. Struct.* **1985**, *128*, 21.
[20] L. Weber, *Chem. Rev.* **1992**, *92*, 1839.
[21] Recent calculations on the model compound [Nb($PPMe_2$)($NH_2$)$_3$] indicate that the multiply bonded character of the Nb–P bond is relatively small; cf. C. C. Cummins, *Angew. Chem.* **2006**, *118*, 876; *Angew. Chem. Int. Ed.* **2006**, *45*, 862.
[22] a) A. Castro, M. V. Galakhov, M. Gómez, P. Gómez-Sal, A. Martín, P. Royo, *J. Organomet. Chem.* **1998**, *554*, 185; b) P. Royo, J. Sánchez-Nieves, *J. Organomet. Chem.* **2000**, *597*, 61.
[23] M. Baudler, B. Carlsohn, W. Böhm, D. Reuschenbach, *Z. Naturforsch., Teil B* **1976**, *31*, 558.
[24] R. Wolf, M. Finger, C. Limburg, A. C. Willis, S. B. Wild, E. Hey-Hawkins, *Dalton Trans.* **2006**, 831.
[25] A. Bashall, F. Garcia, A. D. Hopkins, J. A. Wood, M. McPartlin, A. D. Woods, D. S. Wright, *Dalton Trans.* **2003**, 1143.
[26] a) A. Schisler, P. Lönnecke, T. Gelbrich, E. Hey-Hawkins, *Dalton Trans.* **2004**, 2895; b) A. Schisler, PhD Thesis, Universität Leipzig, **2003**.
[27] a) L. R. Smith, J. L. Mills, *J. Chem. Soc., Chem. Commun.* **1974**, 808; b) L. R. Smith, J. L. Mills, *J. Am. Chem. Soc.* **1976**, *98*, 3852; c) P. R. Hoffman, K. G. Caulton, *Inorg. Chem.* **1975**, *14*, 1997.
[28] C. Ting, N. C. Baenzinger, L. Messerle, *J. Chem. Soc., Chem. Commun.* **1988**, 1133.
[29] C. Frenzel, E. Hey-Hawkins, *Phosphorus Sulfur Silicon* **1998**, *143*, 1.
[30] R. D. Sanner, S. T. Carter, W. J. Bruton Jr, *J. Organomet. Chem.* **1982**, *240*, 157.

Received: January 25, 2006
Published Online: February 22, 2006

 © 2006 Wiley-VCH Verlag GmbH & Co. KGaA, Weinheim 

DOI: 10.1002/ejic.200501022

# Coordination Dependence of Magnetic Properties within a Family of Related [$Fe^{II}_2$] Complexes of a Triazine-Based Ligand

**Manuel Quesada,[a] Paul de Hoog,[a] Patrick Gamez,*[a] Olivier Roubeau,*[b] Guillem Aromí,[c] Bruno Donnadieu,[d] Chiara Massera,[e] Martin Lutz,[f] Anthony L. Spek,[f] and Jan Reedijk[a]**

**Keywords:** Iron(II) complexes / Magnetic properties / Spin crossover / 1,3,5-Triazine / Polydentate ligands

The coordination chemistry of the polydentate ligand 2,4,6-tris(dipyridin-2-ylamino)-1,3,5-triazine (dpyatriz) with $Fe^{II}$ has been explored, leading through variation of the counter-ion and the solvent system to the preparation of three different dinuclear complexes: $[Fe_2(dpyatriz)_2(H_2O)_2(CH_3CN)_2](ClO_4)_4$ (**1**), $[Fe_2(dpyatriz)_2(H_2O)_2(CH_3OH)_2](BF_4)_4$ (**2**) and $[Fe_2(dpyatriz)_2Cl_2](CF_3SO_3)_2$ (**3**). The X-ray structure of these compounds has revealed that besides the difference in the noncoordinated anion, complex **1** differs from complex **2** only in the nature of the terminal ligands. Bulk magnetisation studies and Mössbauer spectroscopy have shown that such a subtle difference produces a change to the crystal field on the metal atoms, originating an important disparity of the magnetic behaviour. Thus, complex **1** experiences a partial spin crossover centred at approximately 265 K, whereas complex **2** shows two uncoupled high-spin $Fe^{II}$ centres over most of the studied temperature range, experiencing the effect of very weak antiferromagnetic coupling and/or single-ion zero-field splitting at low temperature. By contrast, complex **3**, in which the triazine ring of dpyatriz is coordinated for the first time, displays (very uncommon) ferromagnetic coupling between both $Fe^{II}$ ions within the molecule, leading to an $S = 4$ spin ground state. A fit of the experimental data led to a value of the coupling constant of $J = +0.23\ cm^{-1}$ (using $H = -2JS_1S_2$ as the convention for the exchange Hamiltonian) and provided an estimation of $D = 0.63\ cm^{-1}$ for the ground-state axial zero-field splitting parameter.

(© Wiley-VCH Verlag GmbH & Co. KGaA, 69451 Weinheim, Germany, 2006)

## Introduction

The controlled design of molecule-based functional materials represents one of the research lines along which nanotechnological applications may develop. The area of coordination chemistry plays a primary role in this respect, as exemplified by the spectacular progress demonstrated in the context of molecular magnetism.[1] The search for molecular magnetic materials with specific functions is very often based on the use of ligands that will give rise to predictable chemical and physical properties. For instance, it is well known that azole-based ligands have the ability to generate the appropriate type of crystal field around $Fe^{II}$ ions, so as to prompt the appearance of the phenomenon of spin crossover (SC) within the metal atom.[2,3] Another example is the exploitation of the potential of certain ligand systems to propagate ferromagnetic interactions between paramagnetic metals with the aim of generating high-spin molecules or magnetically ordered materials. Among such ligand frameworks are (end-on) $N_3^-$ groups[4,5] and *m*-phenylene links (the latter usually facilitating ferromagnetism through a spin-polarisation mechanism).[6,7] Even more desirable in the preparation of versatile functional materials are systems capable of exhibiting different properties by introducing subtle changes of environment or of chemical nature.

With the aim of preparing novel coordination supramolecular architectures, some of us have recently synthesised and started to use the new multinucleating ligand 2,4,6-tris-(dipyridin-2-ylamino)-1,3,5-triazine (dpyatriz, Scheme 1)[8] in coordination chemistry reactions involving various metals. The versatility of this ligand has been demonstrated by the diversity of some of the coordination compounds obtained. Thus, the reaction with $Cu(NO_3)_2$ produces a magnetically exchanged 1D coordination polymer,[9] whereas a similar reaction involving $CuCl_2$ allows the characterisation

[a] Leiden Institute of Chemistry, Gorlaeus Laboratories, Leiden University,
P. O. Box 9502, 2300 RA Leiden, The Netherlands
Fax: +31-71-5274671
E-mail: p.gamez@chem.leidenuniv.nl
[b] Centre de Recherche Paul Pascal – CNRS UPR 8641,
115 avenue du dr. A. Schweitzer, 33600 Pessac, France
Fax: +33-556845600
E-mail: roubeau@crpp-bordeaux.cnrs.fr
[c] Departament de Química Inorgànica, Universitat de Barcelona, Diagonal 647, 08028 Barcelona, Spain
[d] Laboratoire de Chimie de Coordination CNRS – Université Paul Sabatier,
205 route de Narbonne, 31077 Toulouse Cedex 4, France
[e] Dipartimento di Chimica Generale ed Inorganica, Chimica Analitica, Chimica Fisica, Università degli Studi di Parma,
Parco Area delle Scienze 17/A, 43100 Parma, Italy
[f] Bijvoet Center for Biomolecular Research, Crystal and Structural Chemistry, Utrecht University,
Padualaan 8, 3584 CH Utrecht, The Netherlands

 © 2006 Wiley-VCH Verlag GmbH & Co. KGaA, Weinheim 

of the trinuclear discrete molecule $[(CuCl)_3(dpyatriz)_2][CuCl_4]Cl$.[10] The same process, using $Zn(NO_3)_2$, leads to the formation of the tetranuclear molecular species $[Zn_4(dpyatriz)_2(NO_3)_8]$.[11] In these products, the dpyatriz ligands have their three dipyridylamine (dpya) chelating units engaged in coordination. By contrast, the analogous reaction with $Co^{II}$ conduces to the dimeric complex $[Co_2(dpyatriz)_2(NO_3)_2(CH_3OH)_2](NO_3)_2$ in which each of the multidentate ligands maintains one of their dipyridyl chelating units uncoordinated. Very recently, we have discovered that using solvothermal conditions one can prepare compounds different than those formed from the corresponding reactions under normal conditions of temperature and pressure. In this manner, coordination polymers of $Cu^{II}$, $Zn^{II}$ and $Cd^{II}$ have been crystallographically characterised.[12] Despite the variety of coordination modes and structures observed, none of the complexes described so far shows the dpyatriz ligand using the N-donor of the triazine ring for coordination to a metal atom. It is conceivable that the versatility of dpyatriz can be exploited in the search of new supramolecular architectures exhibiting novel magnetic phenomena. With this aim, we engaged in exploring the reactivity of this ligand with various sources of $Fe^{II}$. We report herein on the ability of dpyatriz to form dinuclear complexes of magnetically exchanged $Fe^{II}$ ions in the form of the compounds $[Fe_2(dpyatriz)_2(H_2O)_2(CH_3CN)_2](ClO_4)_4$ (**1**), $[Fe_2(dpyatriz)_2(H_2O)_2(CH_3OH)_2](BF_4)_4$ (**2**) and $[Fe_2(dpyatriz)_2Cl_2](CF_3SO_3)_2$ (**3**), as revealed by single-crystal X-ray crystallography. The nature of the terminal ligands completing the coordination sites not occupied by dpyatriz affects either the ligand field around the metal ions or the coordination mode of the multinucleating ligand, leading thus to three related complexes with very disparate magnetic properties, ranging from spin crossover (**1**), antiferromagnetic exchange (**2**) or (very uncommon for Fe) ferromagnetic coupling (**3**). The synthesis of complexes **1**, **2** and **3** and their molecular structures are described, and the reasons for their very different magnetic behaviour discussed.

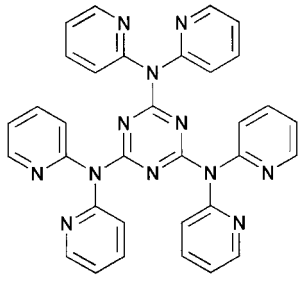

Scheme 1. Molecular structure of the ligand dpyatriz.

## Results

### Synthesis

In attempts to take advantage of the versatility of dpyatriz for the preparation of complexes with new and novel magnetic properties, reactions with different sources of $Fe^{II}$ in a variety of conditions have been conducted.

Mixing in acetonitrile $Fe(ClO_4)_2$ with dpyatriz close to the 1:2 molar ratio, and small amounts of ascorbic acid (in order to avoid aerial oxidation to $Fe^{III}$) led to a light pink solution from which crystals could be obtained by slow diffusion of $Et_2O$. The identity of this compound was established by X-ray crystallography (see below) as the dimeric discrete complex $[Fe_2(dpyatriz)_2(H_2O)_2(CH_3CN)_2](ClO_4)_4$ (**1**). Water in this compound originates from the hydrated iron salt, or from its adventitious presence in the solvent. Thus, the reaction leading to the formation of **1** can be described by a very simple chemical equation [Equation (1)].

$$2\ Fe(ClO_4)_2 + 2\ dpyatriz + 2\ H_2O + 2\ CH_3CN \rightarrow [Fe_2(dpyatriz)_2(H_2O)_2(CH_3CN)_2](ClO_4)_4\ (\mathbf{1}) \quad (1)$$

It was observed that crystals of **1**, crumbled upon exposure to air and turned into a yellowish crystalline material. Elemental analysis suggested the replacement of $CH_3CN$ molecules by $H_2O$, although no structural proof for the identity of the resulting material was obtained. Replacement of terminal $CH_3CN$ ligands by atmospheric water, while maintaining the core topology, is a very common process in coordination chemistry.[13] IR spectroscopy confirmed the absence of $CH_3CN$ in this new adduct, while the remaining spectral features were maintained.

The analogous reactivity was observed using $Fe(BF_4)_2$ and $CH_3OH$ as a solvent. Slow evaporation of the solvent from the reaction mixture resulted in the formation of light green crystals of a new complex, the formula of which was confirmed to be $[Fe_2(dpyatriz)_2(H_2O)_2(CH_3OH)_2](BF_4)_4$ (**2**) by single-crystal X-ray diffraction (see below) and elemental analysis. Thus, Equation (1) could serve to describe the formation of **2**, only replacing $CH_3CN$ and $ClO_4^-$ by $CH_3OH$ and $BF_4^-$, respectively. In contrast with **1**, however, this compound was found to be stable in air. The similarity of the synthesis and structure of **1** and **2** prompted us to test their interconversion. Indeed, when crystals of **1** are placed in $CH_3OH$, a slightly greenish powder is formed that does not turn purple when cooled to liquid $N_2$ temperature. Similarly, if crystals of **2** are immersed in $CH_3CN$, a slightly purple powder forms. Although this was not investigated further (mostly because the crystals crushed into powders), it seems that **1** and **2** can be converted into one another by simply changing their solvent environment.

Incorporation of $Cl^-$ into a system very similar to these described above gave comparable results, although with significant differences. Thus, dpyatriz and $Fe(CF_3SO_3)_2$ were mixed in benzyl cyanide in the presence of $Bu_4NCl$ and the solution brought to 100 °C inside a sealed pressure tube. Yellow crystals of the compound $[Fe_2(dpyatriz)_2Cl_2](CF_3SO_3)_2$ (**3**) formed under these conditions within a few days, according to the reaction described in Equation (2).

 © 2006 Wiley-VCH Verlag GmbH & Co. KGaA, Weinheim 

$$2\ Fe(CF_3SO_3)_2 + 2\ dpyatriz + 2\ Bu_4NCl \rightarrow [Fe_2(dpyatriz)_2Cl_2](CF_3SO_3)_2\ (\mathbf{3}) + 2\ Bu_4NCF_3SO_3 \quad (2)$$

The identity of compound **3** was unveiled by X-ray crystallography (see below), which revealed that the $Cl^-$ ions are coordinated to Fe and that dpyatriz uses N-donors from the triazine moiety to bind the metal atom, a fact observed for the first time and bearing important consequences with regard to the magnetic behaviour of the complex. It was observed that when stoichiometric amounts of the chloride salt were used, the yields obtained were inferior compared with reactions involving limiting amounts of this reagent. A possible reason is that increased amounts of $Bu_4NCl$ favour the formation of the dinuclear anion $[Fe_2OCl_6]^{2-}$ at the expense of complex **3**. This anion is very stable and quite ubiquitous in aerobic reactions involving $Fe^{II}$ and chloride.[14]

## Description of Structures

Crystallographic data for complexes **1**–**3** are collected in Table 4 whereas selected metric parameters are listed in Tables 1, 2 and 3.

Table 1. Selected interatomic distances [Å] and angles [°] for $[Fe_2(dpyatriz)_2(H_2O)_2(CH_3CN)_2](ClO_4)_4$ (**1**). Symmetry operation i: $1-x, 1-y, 1-z$.

| | | | |
|---|---|---|---|
| Fe1–O1W | 2.140(2) | N1–Fe1–N3 | 84.96(9) |
| Fe1–N1 | 2.160(3) | N1–Fe1–N4 | 100.00(9) |
| Fe1–N3 | 2.177(2) | N1–Fe1–N6 | 94.10(9) |
| Fe1–N4 | 2.159(2) | N1–Fe1–N13 | 171.01(10) |
| Fe1–N6 | 2.167(2) | N3–Fe1–N4 | 91.75(9) |
| Fe1–N13 | 2.151(3) | N3–Fe1–N6 | 175.51(9) |
| O1W–Fe1–N1 | 88.45(10) | N3–Fe1–N13 | 88.47(9) |
| O1W–Fe1–N3 | 90.87(10) | N4–Fe1–N6 | 84.08(9) |
| O1W–Fe1–N4 | 171.34(10) | N4–Fe1–N13 | 88.47(9) |
| O1W–Fe1–N6 | 93.50(10) | N6–Fe1–N13 | 89.74(10) |
| O1W–Fe1–N13 | 83.19(10) | Fe···Fe$^i$ | 9.232(2) |

Table 2. Selected interatomic distances [Å] and angles [°] for $[Fe_2(dpyatriz)_2(H_2O)_2(CH_3OH)_2](BF_4)_4$ (**2**). Symmetry operation i: $1-x, 1-y, 1-z$.

| | | | |
|---|---|---|---|
| Fe1–O2 | 2.1708(18) | O2–Fe1–N6 | 176.83(7) |
| Fe1–N1 | 2.167(2) | O1W–Fe1–N1 | 92.42(8) |
| Fe1–N6 | 2.176(2) | N1–Fe1–N4 | 177.02(8) |
| Fe1–O1W | 2.0846(18) | N3–Fe1–N6 | 97.54(7) |
| Fe1–N3 | 2.190(2) | N3–Fe1–N4 | 92.02(8) |
| Fe1–N4 | 2.152(2) | N6–Fe1–N4 | 86.02(8) |
| O2–Fe1–O1W | 88.07(8) | N1–Fe1–N3 | 87.04(8) |
| O2–Fe1–N3 | 85.57(7) | O1W–Fe1–N3 | 173.62(8) |
| O2–Fe1–N4 | 93.25(7) | Fe···Fe$^i$ | 9.2593(15) |
| O2–Fe1–N1 | 89.50(8) | | |

### *$[Fe_2(dpyatriz)_2(H_2O)_2(CH_3CN)_2](ClO_4)_4$ (1)*

Complex **1** is a centrosymmetric cationic dimer (Figure 1) comprising two octahedral $Fe^{II}$ ions bridged and chelated by two dpyatriz ligands through two of their dpya moieties, the third one remaining uncoordinated. The other two coordination sites on each metal atom are occupied in *cis* configuration by a molecule of $H_2O$ and one of $CH_3CN$, completing an $FeN_5O$ slightly distorted octahedral chromophore. The Fe–O and Fe–N($CH_3CN$) distances are 2.140(2) and 2.151(3) Å, respectively, whereas the Fe–N(dpyatriz) distances range from 2.159(2) to 2.177(2) Å. The Fe···Fe separation is 9.232(2) Å, while the shortest intermolecular Fe···Fe distance is 8.992 Å. Four perchlorate counteranions lie between the dinuclear units and exhibit disorder of their oxygen atoms. In addition, two lattice acetonitrile molecules are found in that space. No forces other than weak electrostatic and van der Waals interactions appear to operate within the crystal. The cation of **1** is structurally analogous to the equivalent complex with $Co^{II}$.[11]

Table 3. Selected interatomic distances [Å] and angles [°] for $[Fe_2(dpyatriz)_2Cl_2](CF_3SO_3)_2$ (**3**). Symmetry operation ′: $-x, 1-y, 1-z$.

| | | | |
|---|---|---|---|
| Fe1–Cl1 | 2.336(2) | N1–Fe1–N4 | 93.1(2) |
| Fe1–N1 | 2.229(3) | N1–Fe1–N7 | 76.6(1) |
| Fe1–N4 | 2.205(4) | N4–Fe1–N7 | 77.1(2) |
| Fe1–N7 | 2.220(4) | N1–Fe1–N11′ | 171.9(2) |
| Fe1–N11′ | 2.234(4) | N1–Fe1–N12′ | 91.8(2) |
| Fe1–N12′ | 2.215(4) | N4–Fe1–N11′ | 88.3(2) |
| Cl1–Fe1–N1 | 94.7(1) | N4–Fe1–N12′ | 168.4(2) |
| Cl1–Fe1–N4 | 97.2(1) | N7–Fe1–N11′ | 95.9(1) |
| Cl1–Fe1–N7 | 169.2(1) | N7–Fe1–N12′ | 93.9(2) |
| Cl1–Fe1–N11′ | 93.1(1) | N11–Fe1–N12′ | 85.5(2) |
| Cl1–Fe1–N12′ | 92.8(1) | Fe···Fe′ | 8.324(1) |

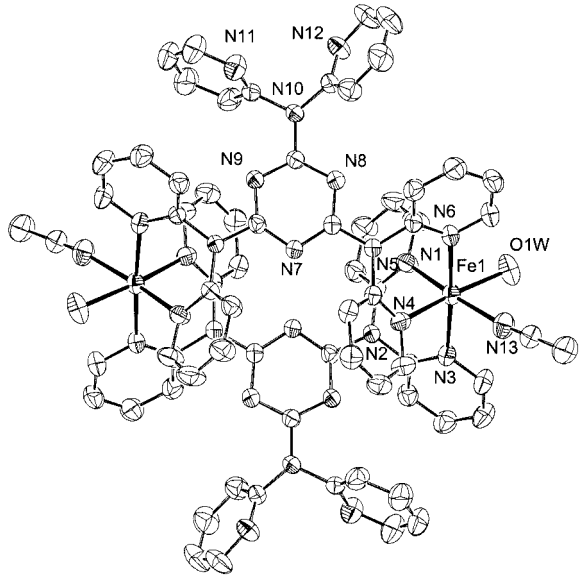


Figure 1. ORTEP representation at the 50% probability level of the cation of $[Fe_2(dpyatriz)_2(CH_3CN)_2(H_2O)_2](ClO_4)_4$ (**1**). Hydrogen atoms are not shown. Only unique non-carbon atoms are labelled.

### *$[Fe_2(dpyatriz)_2(H_2O)_2(CH_3OH)_2](BF_4)_4$ (2)*

The structure of **2** (Figure 2) is very similar to that of **1**. It also consists of centrosymmetric $Fe^{II}$ dinuclear entities held together by two dpyatriz ligands showing the same coordination mode. The only differences are the replacement of perchlorate by tetrafluoroborate and substitution of the $CH_3CN$ ligand by $CH_3OH$. The latter difference has important consequences for the magnetic properties of the system (see below). The geometric parameters also vary slightly;

 © 2006 Wiley-VCH Verlag GmbH & Co. KGaA, Weinheim 

thus, the Fe–N bond lengths range from 2.152(2) to 2.190(2), whereas the Fe–O distances are 2.1708(18) Å ($CH_3OH$) and 2.0846(18) Å ($H_2O$). The intradimer Fe···Fe vector measures 9.2593(15) Å and the shortest interdimer Fe···Fe distance is 8.3577(14) Å. The $BF_4^-$ ions are again located between the complex cations, whereas each of the two free dipyridylamine moieties accept hydrogen bonds from one $CH_3OH$ molecule of crystallisation, thus forming a bifurcated hydrogen bond [N···O distances 3.112(3) and 2.816(3) Å].

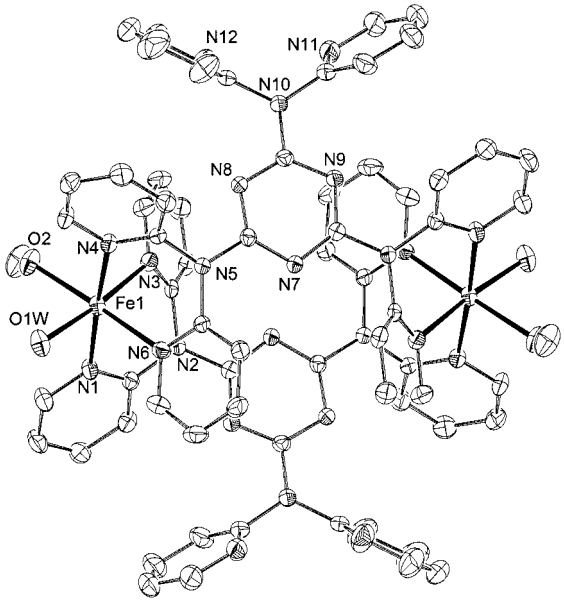


Figure 2. Labelled ORTEP representation at the 50% probability level of the cation of $[Fe_2(dpyatriz)_2(H_2O)_2(CH_3OH)_2](BF_4)_4$ (**2**). Hydrogen atoms are not shown. Only unique non-carbon atoms are labelled.

### *[Fe₂(dpyatriz)₂Cl₂](CF₃SO₃)₂ (3)*

Also the cationic complex **3** (Figure 3) consists of a centrosymmetric dimer in which two octahedral $Fe^{II}$ ions are connected by two dpyatriz ligands. In **3**, however, the binding mode of the multidentate ligand is very different from that observed in the two previous complexes. Here, each of the dpyatriz ligands chelates one iron cation through two nitrogen atoms from one dpya moiety and the other one with a N-donor from the triazine moiety and with two N atoms from dpya nonadjacent pyridyl rings. In this way two pyridyl rings in each dpyatriz ligand remain uncoordinated. Unlike in complexes **1** and **2**, the octahedral coordination around $Fe^{II}$ is not completed by solvent molecules, but by a terminal $Cl^-$ ion. The Fe1–Cl1 and Fe1–N7(triazine) distances are 2.336(2) and 2.220(4) Å respectively, while the other four Fe–N bonds involving the pyridyl groups vary from 2.205(4) to 2.234(4) Å (see Table 3). To the best of our knowledge complex **3** is the first crystallographically characterised compound where the central triazine moiety of dpyatriz is involved in coordination. The triazine rings of the two ligands lie mutually parallel although shifted with respect to each other, with a distance between the least-square planes passing through them of 3.584(1) Å. The intramolecular Fe···Fe [$-x$, $1-y$, $1-z$] separation is 8.324(1) Å, while the shortest intermolecular separation between two metal atoms is 9.041(2) Å. The two positive charges of the cationic complex $[Fe_2(dpyatriz)_2(Cl)_2]^{2+}$ are balanced by two disordered $CF_3SO_3^-$ anions located in the crystal lattice. Also two molecules of the solvent (benzyl cyanide) are present for each dimeric complex, orientated so that their CN groups point towards the triazine ring [the smallest distance of N1s to the least-squares plane passing through the ring being 3.038(9) Å].

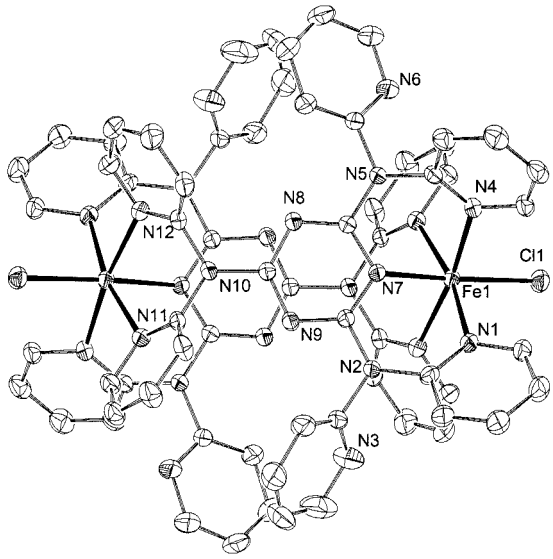


Figure 3. Labelled ORTEP representation at the 30% probability level of the cation of $[Fe_2(dpyatriz)_2Cl_2](CF_3SO_3)_2$ (**3**). Hydrogen atoms are not shown. Only unique non-carbon atoms are labelled.

### Magnetochemistry

The temperature dependence of the magnetisation of compounds **1**–**3** was studied on polycrystalline samples in the 2–350 K range. This is depicted in Figures 4, 7 and 8, for **1**, **2** and **3**, respectively, in the form of $\chi_m T$ versus $T$ plots, where $\chi_m$ is the molar paramagnetic susceptibility.

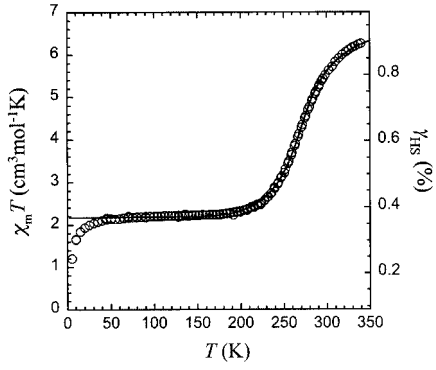


Figure 4. Plot of experimental $\chi_m T$ vs. $T$ for compound **1** (circles) collected with an applied field of 1000 Oe. The solid line is a fit to the regular solution theory model (see text for details), expressed as the HS fraction $\gamma_{HS}$.

 © 2006 Wiley-VCH Verlag GmbH & Co. KGaA, Weinheim 

For compound **1** (Figure 4), the $\chi_m T$ product at 340 K is 6.27 $cm^3 \cdot mol^{-1} \cdot K$, in the range expected for two noninteracting high-spin (HS, $S = 2$) $Fe^{II}$ centres (6 $cm^3 \cdot mol^{-1} \cdot K$, for $g = 2$). As the temperature decreases, the $\chi_m T$ value starts immediately to drop gradually to 2.2 $cm^3 \cdot mol^{-1} \cdot K$ in the vicinity of 200 K, where it remains constant upon further cooling. This is consistent with a process of SC by a fraction of the $Fe^{II}$ centres (calculated to be 63%, see below), from HS to low spin (LS, $S = 0$). Only at very low temperatures, a decrease of $\chi_m T$ is observed anew, resulting either from zero-field splitting (ZFS) of the remaining $Fe^{II}$ HS centres and/or from antiferromagnetic coupling of the remaining HS–HS pairs. Thus, compound **1** exhibits a gradual and incomplete SC, centred at around 265 K, but does not exhibit a plateau at $\chi_m T \approx 3.0$ (50% of $Fe^{II}$ centres LS), which is often observed for $Fe^{II}$ dimers undergoing a spin transition.[15,16] This indicates a lack of strong intermolecular interactions, which would stabilise domains of HS–LS pairs. In order to present a quantitative description of the process of spin transition, the Mössbauer spectra of **1** (Figure 5) were collected at 293 K (near the transition temperature) and 77 K. Signals from both the HS and LS states were detected at both temperatures. From these experiments the fraction of $Fe^{II}$ centres in the HS state at 77 K was calculated to be 37%.[17] The temperature dependence of the HS fraction deduced from susceptibility and Mössbauer data was then fit to an equation resulting from a regular solution model [Equation (3)],[18,19] where $\gamma_{HS}$ is the variable HS fraction, $\Gamma$ is the interaction parameter[3] and the other terms have their usual meaning. Although it represents a crude approximation, the calculated values were normalised to the fraction of species undergoing spin crossover.

$$\ln\left(\frac{1-\gamma_{HS}}{\gamma_{HS}}\right) = \frac{\Delta H + \Gamma(1-2\gamma_{HS})}{RT} - \frac{\Delta S}{R} \quad (3)$$

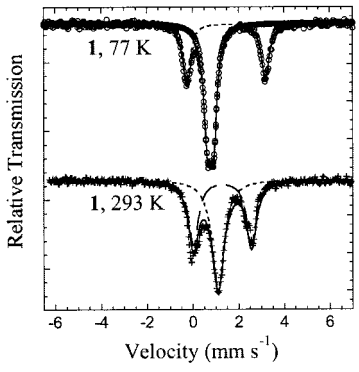


Figure 5. Mössbauer spectra of **1** at 77 and 293 K. Dashed lines represent subspectra used in the fitting procedure, while full lines are the overall fits to the experimental data.

The best fit provided (Figure 4, solid line) a value of $\Gamma$ = 2.9(2) $kJ \cdot mol^{-1}$ with $\Delta H$ = 11.0(1) $kJ \cdot mol^{-1}$ and $\Delta S$ = 40(1) $J \cdot mol^{-1} \cdot K^{-1}$. The cooperativity parameter $\Gamma$ is in agreement with the absence of strong interaction between the $Fe^{II}$ centres.[3] The entropy variation deduced is about three times that expected from the change in spin manifold ($R\ln 5$ = 13.4 $J \cdot mol^{-1} \cdot K^{-1}$), indicating, as usually observed, the presence of a vibrational contribution to the entropy variation. Both the transition entropy and enthalpy derived here are in agreement with the calorimetric characterisation of weakly cooperative SC systems.[20–23] The behaviour just described is retained only if the compound is kept sealed and/or in contact with acetonitrile. If complex **1** is left exposed to air, replacement of $CH_3CN$ by atmospheric water seems to take place (see above), the resulting material (**1a**) remaining HS throughout the whole range of temperatures.

The above results and spectroscopic evidence (see Figure 6 and below) show that the polydentate ligand dpyatriz constitutes a new member of the family of polypyridyl ligands capable of producing SC $Fe^{II}$ compounds in the presence of the right coligands.[24–26] The system shown here is peculiar in that it is dinuclear, unlike most previously reported examples. Also, it has the potential of acting as a building block in the formation of extended structures, a very attractive prospect, as high-dimensional SC systems are still rare.

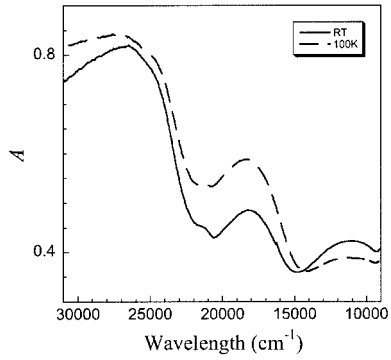


Figure 6. Absorption spectra of **1** at room temperature and about 100 K.

In contrast to complex **1**, the $\chi_m T$ product of **2** (Figure 7) remains practically constant at approximately 8.3 $cm^3 \cdot mol^{-1} \cdot K$ from room temperature to 50 K where it starts dropping to 2.65 $cm^3 \cdot mol^{-1} \cdot K$ at 2 K. This drop can

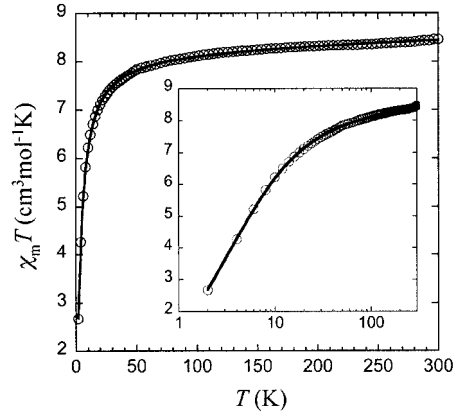


Figure 7. Plot of experimental $\chi_m T$ vs. $T$ for compound **2**. The inset is a semi-logarithmic form of that plot. The applied field was 1000 Oe. The full line corresponds to the best fit to a theoretical expression contemplating ZFS of $Fe^{II}$ ions (see text for details).

 © 2006 Wiley-VCH Verlag GmbH & Co. KGaA, Weinheim 

be ascribed either to antiferromagnetic exchange coupling within the dimeric units in **2** and/or to single-ion ZFS of the $Fe^{II}$ centres ($S = 2$). The absence of a maximum in the $\chi_m$ versus $T$ plot indicates that the exchange coupling is very weak. In such situations both effects, if present, are approximately of the same order and cannot be discerned. We have therefore reproduced the experimental data considering either exchange coupling [Equations (4) and (5)][18] or axial ZFS of individual $Fe^{II}$ ions [Equations (6) and (7)],[18] including in both cases a temperature-independent paramagnetism (TIP).

$$\hat{H} = -2J(\hat{S}_1 \cdot \hat{S}_2) \quad (4)$$

$$\chi_m = \frac{N_A g^2 \beta^2}{k_B T} \cdot \frac{2e^{2x} + 10e^{6x} + 28e^{12x} + 60e^{20x}}{1 + 3e^{2x} + 5e^{6x} + 7e^{12x} + 9e^{20x}} \quad (5)$$

$$\hat{H} = 2 \times D[\hat{S}_z^2 - S(S+1)] \quad (6)$$

$$\chi_m = 2 \times \frac{N_A g^2 \beta^2}{k_B T} \cdot \left[\frac{\frac{1}{3}(2e^{-x} + 8e^{-4x}) + \frac{2}{3}\{6(1 - e^{-x})/x + 4(e^{-x} - e^{-4x})/3x\}}{1 + 2e^{-x} + 2e^{-4x}}\right] \quad (7)$$

In these expressions, $D$ represents the single-ion ZFS parameter, $J$ is the exchange coupling constant between $Fe^{II}$ ions within the dinuclear entities, while $x$ is either $J/k_BT$ [Equation (5)] or $D/k_BT$ [Equation (7)]. The experimental data are indeed reproduced correctly with both models, yielding on the one hand $g = 2.32(1)$, $J/k_B = -0.54(1)$ K ($J = -0.37$ $cm^{-1}$) and TIP = $1.6 \times 10^{-3}$ $cm^3 \cdot mol^{-1} \cdot K$, and on the other hand $g = 2.41(1)$ and $D/k_B = 5.71(6)$ K ($D = 3.97$ $cm^{-1}$), with TIP = $1.17 \times 10^{-3}$ $cm^3 \cdot K \cdot mol^{-1}$. The latter fit has a better quality ($\chi^2$ of 0.1 compared to 0.5),[27] indicating that, although both effects are likely to be present, ZFS is probably the dominant one. The fact that the $Fe^{II}$ centres in **2** are very weakly coupled, if at all, is consistent with the long distance mediating between them (see above) and the absence of any magnetic superexchange pathway connecting the two. On the other hand, positive values of $D$ are often found in $Fe^{II}$ HS species.[28]

The magnetic properties of complex **3** differ dramatically from the behaviour of the above complexes (Figure 8). The value of $\chi_m T$ at 300 K is 7.05 $cm^3 \cdot mol^{-1} \cdot K$, close to that expected for two uncoupled $Fe^{II}$ HS centres, and remains practically constant to approximately 50 K. From that temperature, $\chi_m T$ starts to increase upon cooling to reach a maximum of 7.85 $cm^3 \cdot mol^{-1} \cdot K$ at $T = 10$ K and then suddenly drops to $\chi_m T = 4.74$ $cm^3 \cdot mol^{-1} \cdot K$ at 2 K. This behaviour is consistent with the presence of ferromagnetic exchange between the Fe centres of the dinuclear complex to form a spin ground state of $S = 4$, while the decrease of $\chi_m T$ at lower temperatures is most likely because of ZFS and not interactions between complexes, as no intermolecular exchange pathways were observed in the crystal lattice. In order to describe this behaviour quantitatively, the experimental data were fit to a $\chi_m = f(T)$ expression [Equation (8)] derived from the Van Vleck equation for two exchange $Fe^{II}$ centres ($S = 2$), including a term $D$ for the ZFS of the spin ground state ($S = 4$) of the dimer.[29]

$$\chi_m = \frac{N_A g^2 \beta^2}{k_B T} \cdot \frac{6e^{17x} + 24e^{8x} + 54e^{-7x} + 96e^{-28x} + 84e^{-8y} + 30e^{-14y} + 6e^{-18y}}{e^{20x} + 2e^{17x} + 2e^{8x} + 2e^{-7x} + 2e^{-28x} + 7e^{-8y} + 5e^{-14y} + 3e^{-18y}} \quad (8)$$

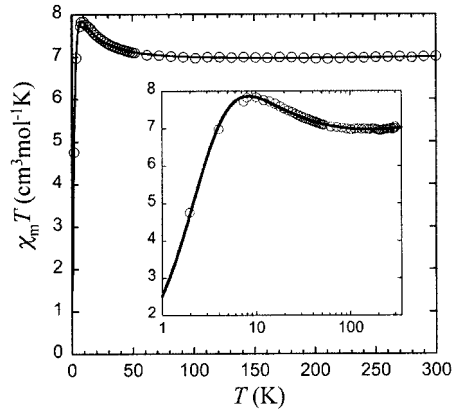


Figure 8. Plot of experimental $\chi_m T$ vs. $T$ for compound **3**. The inset is a semi-logarithmic form of that plot. The applied field was 1000 Oe. The full lines are best fits to the corresponding theoretical expression (see text for details).

In this equation, $x = D/3k_BT$ and $y = J/k_BT$. The best fit was obtained with $g = 2.12(1)$, $J/k_B = 0.33(1)$ K ($J = 0.23$ $cm^{-1}$) and $D/k_B = 0.91(2)$ K ($D = 0.63$ $cm^{-1}$). Ferromagnetic exchange coupling between $Fe^{II}$ centres is very uncommon.[30] A way of establishing this kind of interaction might be the mechanism of spin polarisation, by which the electronic cloud of species linking paramagnetic centres is polarised by the spin of the latter. For example, the alternation in the sign of the polarisation found within aromatic rings has allowed using them as linkers to induce predictably ferro- or antiferromagnetic interactions between spin carriers.[6] Complex **3** is the only one in the series of complexes reported here where the triazine rings are directly bound to $Fe^{II}$ and, thus, have chances of being polarised. It is possible that the weak ferromagnetic exchange occurs through the feeble π–π interaction between these two polarised rings, despite the fact that they are shifted with respect to each other. DFT calculations will be undertaken in order to establish the nature of the magnetic orbitals participating in this superexchange and rationalise the coupling.

### Solid-State Absorption Spectroscopy

Diffuse reflectance spectra of bulk **1** at 293 and about 100 K both display two very broad absorption bands centred around 11000 $cm^{-1}$ and 18200 $cm^{-1}$ (see Figure 6). These are typical for HS $^5T_2 \rightarrow {}^5E$ and LS $^1A_1 \rightarrow {}^1T_1$ transitions, respectively, in six-coordinate $Fe^{II}$ showing SC. The variation in relative intensities of these bands with temperature is in agreement with the spin crossover of **1** detected by magnetic susceptibility measurements. The corresponding ligand field parameter is derived as $10Dq^{HS}$ =

 © 2006 Wiley-VCH Verlag GmbH & Co. KGaA, Weinheim 

11000 $cm^{-1}$.[31] It is known that SC behaviour is to be expected for HS species having their $10Dq^{HS}$ in the range 10500–12000 $cm^{-1}$,[3] thus in agreement with the present observations. On the other hand, the $^5T_2 \rightarrow {}^5E$ transition in **2** is shifted towards higher energies, again in agreement with an HS ground state, and thus indicating that this compound does not show spin crossover behaviour.

## Conclusions

The reactivity of the polydentate ligand 2,4,6-tris(dipyridin-2-ylamino)-1,3,5-triazine with $Fe^{II}$ has been investigated for the first time. Small variations in reaction conditions have led to a new family of dinuclear complexes showing great diversity in magnetic behaviour. Changing solvents from $CH_3CN$ to $CH_3OH$ results in the change from SC behaviour in $[Fe_2(dpyatriz)_2(H_2O)_2(CH_3CN)_2](ClO_4)_4$ (**1**) to weak (or no) antiferromagnetic coupling within $[Fe_2(dpyatriz)_2(H_2O)_2(CH_3OH)_2](BF_4)_4$ (**2**). This effect is caused by the difference in crystal field produced by the solvent molecules, which in both cases act as terminal ligands. If a coordinating anion is included in the reaction, such as $Cl^-$, the complex $[Fe_2(dpyatriz)_2Cl_2](CF_3SO_3)_2$ (**3**) is obtained. In this case the structure of the complex differs significantly from before and $Fe^{II}$ is seen coordinated directly to N atoms from the triazine moiety. This results in a system exhibiting very rare ferromagnetic exchange between the metal atoms. These results suggest the possibility of fine-tuning important properties of the system by choosing the type of ligand occupying the peripheral positions of the dinuclear unit, or the prospect of preparing polymeric SC systems using the appropriate dimetallic moieties as a building block.

## Experimental Section

**Syntheses:** All reagents were used as received unless indicated otherwise. The ligand dpyatriz was prepared according to a previously published procedure.[8]

**$[Fe_2(dpyatriz)_2(CH_3CN)_2(H_2O)_2](ClO_4)_4$ (1):** dpyatriz (150 mg, 0.413 mmol) was added to a solution of $Fe(ClO_4)_2 \cdot 6H_2O$ (188 mg, 0.5 mmol) in acetonitrile (75 mL) and the mixture stirred. Slow diffusion of diethyl ether into this solution yielded pinkish parallelepiped crystals of $\mathbf{1} \cdot 2CH_3CN$ in 50% yield (185 mg). Complex **1** immediately lost $CH_3CN$ upon exposure to air, presumably to be replaced by water. The resulting species may be formulated as $[Fe_2(dpyatriz)_2(H_2O)_4](ClO_4)_4$ (**1a**) (see text). $\mathbf{1a} \cdot 4H_2O$ [$C_{66}H_{64}Cl_4Fe_2N_{24}O_{24}$ (1830.86)]: calcd. C 43.30, H 3.52, N 18.36; found C 42.94, H 3.05, N 17.95.

**$[Fe_2(dpyatriz)_2(H_2O)_2(CH_3OH)_2](BF_4)_4$ (2):** A solution of ligand dpyatriz (200 mg, 0.34 mmol) in methanol (20 mL) was mixed, whilst stirring, with a solution of $Fe(BF_4)_2 \cdot 6H_2O$ (344 mg, 1.01 mmol) and ascorbic acid (30 mg, 0.01 mmol) in methanol (10 mL) to give a green solution. After slow evaporation of the solvent in air at room temperature (3–4 d), green crystals of $\mathbf{2} \cdot 6H_2O$ were formed in 30% yield (90 mg), which were suitable for X-ray diffraction analysis. These crystals were collected by filtration, washed with methanol and dried in air. IR: $\tilde{\nu}$ = 1001.5, 1053.9, 1373.3, 3430, 3631.1 $cm^{-1}$. $\mathbf{2} \cdot 6CH_3OH$ [$C_{74}H_{84}B_4F_{16}Fe_2N_{24}O_{10}$ (1928.52)]: calcd. C 46.28, H 3.99, N 17.50; found C 45.75, H 4.06, N 17.99.

**$[Fe_2(dpyatriz)_2Cl_2](CF_3SO_3)_2$ (3):** A solution of ligand dpyatriz (230 g, 0.387 mmol) in benzyl cyanide (99%, 25 mL) was mixed, whilst stirring, with a solution of $Fe(CF_3SO_3)_2$ (230 mg, 0.581 mmol) in benzyl cyanide (99%, 10 mL) followed by addition of ascorbic acid (30 mg, 0.01 mmol). A solution of $Bu_4NCl$ (54 mg, 0.194 mmol) in benzyl cyanide (5 mL) was added to this mixture and the stirring maintained for several minutes. The resulting mixture was filtered and the filtrate placed into a pressure-sealed tube, which was then tightly closed and put in an oven at 100 °C. After 2 d at this temperature, yellow single crystals of $\mathbf{3} \cdot 2C_8H_7N$ suitable for X-ray diffraction were obtained. These crystals were collected and washed with methanol and diethyl ether. The yield was 15% (28 mg). IR: $\tilde{\nu}$ = 995.8, 1263.3, 1374.0 $cm^{-1}$. $\mathbf{3} \cdot 2C_8H_7N$ [$C_{84}H_{62}Cl_2F_6Fe_2N_{26}O_6S_2$ (1892.28)]: calcd. C 53.32, H 3.30, N 19.25; found C 53.03, H 3.54, N 19.55.

**Physical Measurements:** C,H,N analysis was performed with a Perkin–Elmer 2400 series. Infrared spectra (4000–300 $cm^{-1}$ range) were recorded with a Bruker 330V IR spectrophotometer equipped with a Golden Gate Diamond. The ligand field spectra of the solids (300–2000 $cm^{-1}$, diffuse reflectance) were taken with a Perkin–Elmer 330 spectrophotometer equipped with a home-made set-up to measure at low temperatures (down to about 100 K). Variable-temperature and field-magnetization measurements were carried out using Quantum Design MPMS-5S and MPMS-7XL SQUID magnetometers with fields up to 5 and 7 T, respectively, and in the temperature range 2–350 K. Corrections for diamagnetic contributions to the susceptibility of the sample, as deduced from Pascal's tables, and from the sample holder were applied. Mössbauer spectra were recorded in a constant acceleration mode using a $^{57}Co$ in Rh source. Isomer shifts are given relative to the sodium nitroprusside. Spectra were fitted with Lorentzian-shaped lines using a non-linear iterative minimisation routine. Accuracy for the isomer shift (I.S.) is 0.03 $mm \cdot s^{-1}$, for the electric quadrupole splitting (Q.S.) 0.05 $mm \cdot s^{-1}$ and for the spectral contribution (S.C.) 5%.

**X-ray Crystallographic Study:** The crystal structures were determined by single-crystal X-ray diffraction methods. Crystallographic and experimental details for the different structures are summarised in Table 4. **Compound 1:** Intensity data and cell parameters were recorded at 293(2) K with a Nonius Kappa CCD diffractometer with graphite-monochromated Mo-$K_\alpha$ radiation ($\lambda$ = 0.71073 Å). DENZO-SMN was used for data integration and SCALEPACK corrected data for Lorentz polarisation effects. Absorption corrections were applied for all data using the DIFABS program.[32] The SIR92 software package[33] and SHELXL 97, included in the WinGX package, were used for phase determination and structure refinement,respectively. Direct methods of phase determination followed by some subsequent difference Fourier maps led to an electron density map from which most of the non-hydrogen atoms were identified in the asymmetry unit of the unit cell. With subsequent isotropic refinement and Fourier difference synthesis, all of the non-hydrogen atoms were identified. Atomic coordinates, isotropic and anisotropic displacement parameters of all non-hydrogen atoms were refined by means of a full-matrix least-squares procedure on $F^2$. H atoms were included in the refinement in calculated positions, riding on the carbon atoms with an isotropic thermal parameter fixed 20% and 50% higher, respectively, than the $sp^2$- and $sp^3$-C atoms to which they are attached. **Compound 2:** Intensity data and cell parameters were recorded at 150 K. The structure was solved with direct methods[34] and refined with

 © 2006 Wiley-VCH Verlag GmbH & Co. KGaA, Weinheim 

Table 4. Crystallographic parameters of complexes **1**–**3**.

| | **1** | **2** | **3** |
|---|---|---|---|
| Empirical formula | $[C_{70}H_{58}Fe_2N_{26}O_2](ClO_4)_4 \cdot 2C_2H_3N$ | $[C_{68}H_{60}Fe_2N_{24}O_4](BF_4)_4 \cdot 6CH_3OH$ | $[C_{66}H_{48}Cl_2Fe_2N_{24}](CF_3O_3S)_2 \cdot 2C_9H_7N$ |
| Formula mass | 1887.03 | 1928.59 | 1892.32 |
| Diffractometer | Nonius KappaCCD | Nonius KappaCCD | Bruker AXS Smart 1000 |
| Wavelength [Å] | 0.71073 | 0.71073 | 0.71073 |
| $T$ [K] | 293(2) | 150(2) | 293(2) |
| Crystal size [mm] | $0.30 \times 0.20 \times 0.05$ | $0.54 \times 0.48 \times 0.12$ | $0.36 \times 0.30 \times 0.24$ |
| Crystal colour | colourless | yellow | yellow |
| Crystal system | triclinic | monoclinic | triclinic |
| Space group | $P\bar{1}$ (no. 2) | $P2_1/c$ (no. 14) | $P\bar{1}$ (no. 2) |
| $a$ [Å] | 11.417(2) | 13.282(2) | 13.250(2) |
| $b$ [Å] | 13.470(3) | 14.499(2) | 13.621(2) |
| $c$ [Å] | 14.100(3) | 22.6080(8) | 13.682(2) |
| $\alpha$ [°] | 109.80(3) | 90 | 64.419(3) |
| $\beta$ [°] | 93.60(3) | 91.703(5) | 70.521(3) |
| $\gamma$ [°] | 96.50(3) | 90 | 75.965(3) |
| $V$ [Å$^3$] | 2015.2(7) | 4351.8(9) | 2085.6(5) |
| $Z$ | 1 | 2 | 1 |
| $D_{calcd.}$ [g·cm$^{-3}$] | 1.558 | 1.472 | 1.507 |
| $\mu$ [mm$^{-1}$] | 0.582 | 0.438 | 0.547 |
| Measured reflections | 12334 | 68949 | 23330 |
| $(\sin\theta/\lambda)_{max}$ [Å$^{-1}$] | 0.62 | 0.65 | 0.66 |
| Abs. corr. | $\psi$-scans | multi-scan | multi-scan |
| Abs. corr. range | 0.87–0.97 | 0.79–0.92 | 0.87–1.00 |
| Unique reflections | 8121 | 9974 | 9310 |
| Parameters | 649 | 590 | 547 |
| Restraints | 278 | 0 | 4 |
| Extinction | 0.0269(19) | – | – |
| $R_1/wR_2$ [$I > 2\sigma(I)$] | 0.0467/0.1149 | 0.0506/0.1278 | 0.0781/0.2426 |
| $R_1/wR_2$ [all refl.] | 0.0604/0.1259 | 0.780/0.1438 | 0.1166/0.2726 |
| $S$ | 1.094 | 1.031 | 0.951 |
| $\rho_{min/max}$ [e·Å$^{-3}$] | –0.51/0.38 | –0.63/1.10 | –1.09/1.57 |

SHELXL-97[35] against $F^2$ of all reflections. All hydrogen atoms were located in the difference Fourier map. The OH hydrogen atoms were kept fixed at their located position; the other hydrogen atoms were refined as rigid groups. Drawings, geometry calculations and checking for higher symmetry were performed with the program PLATON.[36] **Compound 3:** Intensity data and cell parameters were recorded at room temperature (293 K) with a Bruker AXS Smart 1000 single-crystal diffractometer (Mo-$K_\alpha$ radiation) equipped with a CCD area detector. The data reductions were performed using the SAINT[37] and SADABS[38] programs. The structure was solved by direct methods using the SIR97 program[34] and refined on $F_o^2$ by full-matrix least-squares procedures using the SHELXL-97 program.[35] The non-hydrogen atoms were refined with anisotropic atomic displacements with the exception of the disordered triflate ion. The hydrogen atoms were included in the refinement at idealised geometries (C–H 0.95 Å) and refined "riding" on the corresponding parent atoms. The weighting scheme used in the last cycle of refinement was $w = 1/[\sigma^2(F_o^2) + (0.1687P)^2]$ (**3**), where $P = (F_o^2 + 2F_c^2)/3$. Molecular geometry calculations were carried out using the PARST97 program.[39] Drawings were obtained by ORTEP3 in the WinGX suite.[40] Calculations for **3** were carried out with a DIGITAL Alpha Station 255 computer. CCDC-224510 (**1**), -277598 (**2**) and -276288 (**3**) contain the supplementary crystallographic data for this paper. These data can be obtained free of charge from The Cambridge Crystallographic Data Centre via www.ccdc.cam.ac.uk/data_request/cif.

## Acknowledgments

The authors are greatly thankful to the Dutch WFMO (Werkgroep Fundamenteel-Materialen Onderzoek), CW (Foundation for the Chemical Sciences) and NWO (Organization for the Scientific Research), to the French CNRS (Centre National de la Recherche Scientifique), to the Conseil Général d'Aquitaine, to the Spanish Ministerio de Ciencia y Tecnología for a "Ramón y Cajal" contract and to the Ministero dell'Università e delle Ricerca Scientifica e Tecnologica. R. Clérac is gratefully acknowledged for helpful discussions and M. W. J. Crajé for Mössbauer measurements.

[1] J. S. Miller, M. Drillon (Eds.), *Magnetism: Molecules to Materials V*, Wiley-VCH, Weinheim, **2005**.
[2] P. J. van Koningsbruggen in *Spin Crossover in Transition Metal Compounds I*, *Topics in Current Chemistry* (Eds.: P. Gütlich, H. A. Goodwin), **2004**, vol. 233, p. 123.
[3] P. Gütlich, A. Hauser, H. Spiering, *Angew. Chem. Int. Ed. Engl.* **1994**, *33*, 2024.
[4] A. K. Boudalis, B. Donnadieu, V. Nastopoulos, J. Modesto Clemente-Juan, A. Mari, Y. Sanakis, J.-P. Tuchagues, S. P. Perlepes, *Angew. Chem. Int. Ed.* **2004**, *43*, 2266.
[5] T. K. Karmakar, B. K. Ghosh, A. Usman, H.-K. Fun, E. Rivière, T. Mallah, G. Aromí, S. K. Chandra, *Inorg. Chem.* **2005**, *44*, 2391.
[6] F. Lloret, G. De Munno, M. Julve, J. Cano, R. Ruiz, A. Caneschi, *Angew. Chem. Int. Ed.* **1998**, *37*, 135.
[7] I. Fernandez, R. Ruiz, J. Faus, M. Julve, F. Lloret, J. Cano, X. Ottenwaelder, Y. Journaux, M. C. Muñoz, *Angew. Chem. Int. Ed.* **2001**, *40*, 3039.
[8] P. de Hoog, P. Gamez, W. L. Driessen, J. Reedijk, *Tetrahedron Lett.* **2002**, *43*, 6783.
[9] P. Gamez, P. de Hoog, O. Roubeau, M. Lutz, W. L. Driessen, A. L. Spek, J. Reedijk, *Chem. Commun.* **2002**, 1488.
[10] S. Demeshko, S. Dechert, F. Meyer, *J. Am. Chem. Soc.* **2004**, *126*, 4508.

 © 2006 Wiley-VCH Verlag GmbH & Co. KGaA, Weinheim 

[11] P. Gamez, P. de Hoog, M. Lutz, W. L. Driessen, A. L. Spek, J. Reedijk, *Polyhedron* **2003**, *22*, 205.
[12] H. Casellas, C. Massera, P. Gamez, A. M. Manotti Lanfredi, J. Reedijk, *Eur. J. Inorg. Chem.* **2005**, 2902–2908.
[13] G. Aromí, O. Roubeau, M. Helliwell, S. J. Teat, R. E. P. Winpenny, *Dalton Trans.* **2003**, 3436.
[14] A. Machkour, D. Mandon, M. Lachkar, R. Welter, *Inorg. Chem.* **2004**, *43*, 1545.
[15] A. B. Gaspar, V. Ksenofontov, J. A. Real, P. Gütlich, *Chem. Phys. Lett.* **2003**, *373*, 385.
[16] J. A. Real, H. Bolvin, A. Bousseksou, A. Dworkin, O. Kahn, F. Varret, J. Zarembowitch, *J. Am. Chem. Soc.* **1992**, *114*, 4650.
[17] Complex **1** (77 K) presents an HS doublet with I.S. = 1.46, Q.S. = 3.45 and relative intensity = 37%, and an LS singlet with I.S. = 0.77, Q.S. = 0.26 and relative intensity = 63%.
[18] C. J. O'Connor, *Prog. Inorg. Chem.* **1982**, *29*, 203.
[19] Note that a normalisation of the data has been performed to take into account the residual fraction of 37% at 77 K, as measured by Mössbauer spectroscopy. Such a high residual fraction, although often ascribed to defaults, may arise from a thermal equilibrium between states of the same energy ($\Delta H = 0$) but with different degeneracies and thus degrees of freedom.
[20] O. Roubeau, M. de Vos, A. F. Stassen, R. Burriel, J. G. Haasnoot, J. Reedijk, *J. Phys. Chem. Solids* **2003**, *64*, 1003.
[21] M. Sorai, Y. Maeda, H. Oshio, *J. Phys. Chem. Solids* **1990**, *51*, 941.
[22] R. Jakobi, H. Romstedt, H. Spiering, P. Gütlich, *Angew. Chem. Int. Ed. Engl.* **1992**, *31*, 178.
[23] T. Nakamoto, Z. C. Tan, M. Sorai, *Inorg. Chem.* **2001**, *40*, 3805.
[24] H. Toftlund, *Coord. Chem. Rev.* **1989**, *94*, 67.
[25] N. Moliner, M. C. Muñoz, P. J. van Koningsbruggen, J. A. Real, *Inorg. Chim. Acta* **1998**, *274*, 1.
[26] K. H. Sugiyarto, D. C. Craig, A. D. Rae, H. A. Goodwin, *Aust. J. Chem.* **1994**, *47*, 869.
[27] This value is the sum of the squared error between the original data and the calculated curve fit. In general, the lower the $\chi^2$ value, the better the fit. The equation used to calculate $\chi^2$ is: $\chi^2 = \sum_i (\frac{y_i - x_i}{\sigma_i})^2$, where $\sigma_i$ is the weight, $y_i$ is the actual value and $x_i$ is the calculated value.
[28] R. L. Carlin, *Magnetochemistry*, Springer-Verlag, Berlin, **1985**.
[29] O. Kahn, *Molecular Magnetism*, VCH, New York, **1993**, p. 17.
[30] H. Oshio, N. Hoshino, T. Ito, M. Nakano, *J. Am. Chem. Soc.* **2004**, *126*, 8805.
[31] The ligand field strength $10Dq^{HS}$ can be determined directly from the ligand field spectrum, using the maximum of the $^5T_2 \rightarrow {}^5E$ transition. A good approximation to the ligand field strength of the low-spin state can be obtained from the corresponding spectrum using $10Dq^{LS} = E(^1T_1) - E(^1A_1) + [E(^1T_2) - E(^1T_1)]/4$. Unfortunately, the transition $^1A_1 \rightarrow {}^1T_2$ is not observed clearly in **1**, probably because of overlap with metal to ligand charge transfer.
[32] N. Walker, D. Stuart, *Acta Crystallogr. Sect. A* **1983**, *39*, 158.
[33] A. Altomare, G. G. Cascarano, C. Giacovazzo, A. Guagliardi, *J. Appl. Crystallogr.* **1993**, *26*, 343.
[34] A. Altomare, M. C. Burla, M. Camalli, G. L. Cascarano, C. Giacovazzo, A. Guagliardi, A. G. G. Moliterni, G. Polidori, R. Spagna, *J. Appl. Crystallogr.* **1999**, 115.
[35] G. M. Sheldrick, *SHELXL-97, Program for Crystal Structure Refinement*, University of Göttingen, **1997**.
[36] A. L. Spek, *J. Appl. Crystallogr.* **2003**, *36*, 7.
[37] *SAINT, Software Users Guide*, Bruker Analytical X-ray Systems, version 6.0, **1999**.
[38] G. M. Sheldrick, *SADABS: Area-Detector Absorption Correction*, version 2.03, University of Göttingen, **1999**.
[39] M. Nardelli, *J. Appl. Crystallogr.* **1996**, 296.
[40] L. J. Farrugia, *J. Appl. Crystallogr.* **1997**, *30*, 565.

Received: November 16, 2005
Published Online: February 6, 2006

 © 2006 Wiley-VCH Verlag GmbH & Co. KGaA, Weinheim 

DOI: 10.1002/ejic.200500880

# Magnetic Properties of the Ordered Double Perovskite $Sr_2MnTeO_6$

**Luis Ortega-San Martin,[a] Jon P. Chapman,[a] Luis Lezama,[a] Jorge Sánchez Marcos,[c] Jesús Rodríguez-Fernández,[c] María I. Arriortua,[b] and Teófilo Rojo*[a]**

**Keywords:** Perovskite phases / Magnetic structure / EPR spectroscopy / Neutron diffraction

The ordered double perovskite $Sr_2MnTeO_6$ was prepared by the freeze-drying method. The nuclear and magnetic structures were determined by both X-ray and neutron (D2B and D1B) powder diffraction. A distorted, double perovskite structure type described by the monoclinic $P12_1/n1$ space group is observed at room temperature and down to 4 K. The room temperature EPR spectrum shows an isotropic signal centered at a $g$ value of 1.998 indicating that manganese ions are in the +2 oxidation state. At low temperature the EPR signal broadens as the exchange and dipolar interactions between $Mn^{2+}$ cations increase. Below 25 K no signal is observed, indicating that the sample is magnetically ordered. The dc magnetic susceptibility shows the existence of antiferromagnetic interactions with an ordering temperature around 20 K. A sharp λ-type anomaly observed at 19 K in the specific heat curve and refinement of low-temperature neutron diffraction data confirm the presence of a three-dimensional, antiferromagnetic ordered structure with an ordering temperature of ca. 23 K. The propagation vector of the magnetic structure is $k = [0,0,0]$, yielding a type I antiferromagnetic ordering between $Mn^{2+}$ ($S = {}^5/_2$) cations. At 2 K, each manganese ion is antiferromagnetically aligned to 8 out of 12 nearest-neighbors at an approximate distance of 5.6 Å. This magnetic structure can be viewed as being composed of ferromagnetic arrangement of $Mn^{2+}$ moments in the $ab$ plane, coupled antiferromagnetically along the $c$ axis.
(© Wiley-VCH Verlag GmbH & Co. KGaA, 69451 Weinheim, Germany, 2006)

## Introduction

Ordered, double perovskites have been of technological interest since the early 1950s when the search for ferroelectric and piezoelectric materials, to be used mainly as capacitors, was extended from the common perovskite oxides, $ABO_3$ (A being Sr, Ba, Pb, or $Ln^{3+}$ cations and B transition metals), to more complex systems such as the ordered perovskites, $A_2BB'O_6$.[1] As a result, many double perovskites had been discovered and their dielectric properties determined by the mid 1970s.[2] The magnetic and other electrical properties of these ordered perovskites did not attract such interest until the discovery, by Kobayashi et al.[3] in 1998, of room temperature magnetoresistance in the half-metallic $Sr_2FeMoO_6$ oxide. The intense study in this class of materials carried out after this technologically important discovery has led to the observation of other potentially useful properties such as high temperature superconductivity in $Sr_2YRu_{0.85}Cu_{0.15}O_6$[4] and the coexistence of ferromagnetism and ferroelectricity in $Bi_2NiMnO_6$.[5]

The magnetic properties, and how the diverse magnetic behaviors depend on the constituent cations, continue to be one of the most important fields of study in these materials. $Sr_2FeB'O_6$ oxides ($B' = Mo^{5+}$ or $Re^{5+}$) are the best-known examples. These oxides show room temperature ferrimagnetic behavior which results from the incomplete cancellation of the localized Fe moments antiferromagnetically aligned with the delocalized Mo/Re moments, the latter being responsible for the half metallicity and magnetoresistance.[6] If Fe is substituted by Mn, magnetic and electrical behavior changes. $Sr(Mn_{0.5}Ru_{0.5})O_3$ is a partially disordered, ferrimagnetic perovskite with a $T_c$ of approximately 125 K, which also shows magnetoresistive effects. In this phase, however, magnetic exchange is complicated due to the mixed valences observed in the ionic pairs $Ru^{IV}/Ru^{V}$ and $Mn^{III}/Mn^{IV}$.[7] In other phases, manganese stabilizes as $Mn^{2+}$ leading to higher oxidation states of elements such as Re and Mo than in their Fe analogues, favoring an ordered arrangement of the B and B′ cations. $Sr_2MnReO_6$, for example, is also ferrimagnetic (arising from an antiferromagnetic coupling between ordered Re and Mn lattices) but has an ordering temperature of 100 K, a low electrical conductivity and shows a poor magnetoresistive effect.[8] $Sr_2MnMoO_6$ is, by contrast, an antiferromagnetic oxide with a low Néel temperature, of approximately 12 K.[9] In this case, $Mn^{2+}$ is the only paramagnetic cation present, producing a lengthening of the exchange pathways and a

[a] Departamento de Química Inorgánica, Facultad de Ciencia y Tecnología, Universidad del País Vasco (UPV/EHU), Apdo. 644,
48080 Bilbao, Spain
E-mail: teo.rojo@ehu.es
[b] Departamento de Mineralogía y Petrología, Facultad de Ciencia y Tecnología, Universidad del País Vasco (UPV/EHU), Apdo. 644,
48080 Bilbao, Spain
[c] CITIMAC, Facultad de Ciencias, Universidad de Cantabria, 39005 Santander, Spain
Supporting information for this article is available on the WWW under http://www.eurjic.org or from the author.

 InterScience © 2006 Wiley-VCH Verlag GmbH & Co. KGaA, Weinheim 

weakening of the predominantly antiferromagnetic interactions. Below the Néel temperature this phase shows three-dimensional antiferromagnetic order, the observed magnetic structure being of 'type II'.

In the absence of mixed valences and/or vacancy formation, complete cancellation of the antiferromagnetically aligned planes should occur, yielding conventional antiferromagnetic systems with no overall magnetic moment. The magnetic properties reported by Azad et al. for the $A_2MnWO_6$ (A = Ca, Ba, or Sr) phases,[10] expected to behave in a similar way to the analogous $Sr_2MnMoO_6$, did not fit, however, with this simple behavior. Low temperature magnetic susceptibility measurements showed the presence of two distinct maxima, the first at ca. 40 K, and the second at temperatures ranging from 9 (A = Ba) to 16 K (A = Ca). The first maximum was attributed to a disordered, canted antiferromagnetic state composed of various domains that, on further lowering of the temperature, undergo a magnetic transition to a three-dimensionally ordered antiferromagnetic phase, also of type II.

Subsequent variable temperature neutron diffraction experiments performed by Muñoz et al.[9a] in samples of the same oxides showed that the Ca and Sr phases are only three-dimensionally ordered below ca. 17 and ca. 14 K respectively, with no intermediate magnetically ordered state between 40 and 20 K. More recently, Lin et al.[11] reported a typical antiferromagnetic behavior for $Sr_2MnWO_6$ with a unique maximum at ca. 16 K in the magnetic susceptibility curve and no additional features around 40 K. The substitution of Sr cations by La, however, seems to induce in some samples the presence of a small shoulder in the magnetic susceptibility curve and irreversibility in the zero-field cooled/field-cooled susceptibilities also around 40 K.

This diversity of magnetic properties observed in such similar systems highlights the need for detailed studies of the structural and physical properties in related $A_2MnB'O_6$ (B′ = diamagnetic cation) double perovskites, such as those having B′ = Te. We have previously published the room temperature structure and high temperature phase transitions of $Sr_2MnTeO_6$.[12] In this paper we present the low temperature structure and magnetic properties of this material and establish correlations between structural features and magnetic behavior.

## Results and Discussion

### Crystal Structure

As previously reported, the room temperature crystal structure of the $Sr_2MnTeO_6$ ordered double perovskite, refined simultaneously from X-ray and D2B neutron diffraction data, is described by a monoclinic distortion of the ideal cubic cell, in space group $P12_1/n1$.[12] At high temperature, $Sr_2MnTeO_6$ undergoes three structural phase transitions at approximately 250, 550, and 675 °C, the sequence being $P12_1/n1 \rightarrow I12/m1 \rightarrow I4/m \rightarrow Fm\bar{3}m$, in good agreement with the schemes proposed by Howard and Stokes.[13]

Rietveld refinement of the low temperature crystal structure from high resolution D2B neutron powder diffraction data recorded at 4, 30, and 60 K, showed that the room temperature $P12_1/n1$ symmetry is maintained down to 4 K. The structural model was as previously reported at 298 K (reproduced in Table 1 for comparison), with all atomic positions and isotropic thermal factors freely refined. No mis-site disorder or vacancy formation was observed at 298 K and so was not refined at low temperature. Refined structural parameters are shown in Table 1 and selected bond lengths and angles in Table 2. The Rietveld fits to the 60 and 4 K data are shown in Figure 1. The structure consists of a framework of corner sharing $TeO_6$ and $MnO_6$ octahedra, with in phase (+) rotations around the *c* axis and *anti*-phase (–) rotations normal to the *c* axis. The expected increase in the magnitudes of the octahedral rotations and reduction in the cell volume on lowering the temperature are the only significant structural variations.

Table 1. Refined parameters and reliability factors for $Sr_2MnTeO_6$ from D2B powder diffraction data at different temperatures.

| *T* [K] | 298 | 60 | 30 | 4 |
|---|---|---|---|---|
| Symmetry | monoclinic | monoclinic | monoclinic | monoclinic |
| Space group | $P12_1/n1$ | $P12_1/n1$ | $P12_1/n1$ | $P12_1/n1$ |
| *a* [Å] | 5.7009(1) | 5.6887(1) | 5.6882(1) | 5.6897(1) |
| *b* [Å] | 5.6770(1) | 5.6704(1) | 5.6702(1) | 5.6719(1) |
| *c* [Å] | 8.0334(1) | 8.0207(1) | 8.0201(1) | 8.0177(1) |
| *β* [°] | 90.085(1) | 90.091(1) | 90.090(1) | 90.087(1) |
| *V* [Å$^3$] | 259.99(1) | 258.73(1) | 258.68(1) | 258.74(1) |
| Sr *x* | 0.5015(3) | 0.5034(4) | 0.5034(4) | 0.5035(4) |
| Sr *y* | 0.0153(2) | 0.0210(3) | 0.0212(3) | 0.0210(3) |
| Sr *z* | 0.2492(3) | 0.2508(4) | 0.2507(5) | 0.2492(5) |
| $U_{iso}$ (×100 Å$^2$) | 0.78(2) | 0.62(3) | 0.60(3) | 0.62(3) |
| Mn *x* = *y* = *z* | 0 | 0 | 0 | 0 |
| $U_{iso}$ (×100 Å$^2$) | 0.55(5) | 0.7(1) | 0.6(1) | 0.7(1) |
| Te *x* = *y* | 0 | 0 | 0 | 0 |
| Te *z* | 0.5 | 0.5 | 0.5 | 0.5 |
| $U_{iso}$ (×100 Å$^2$) | 0.38(3) | 0.51(6) | 0.52(6) | 0.57(6) |
| O1 *x* | 0.9453(4) | 0.9419(4) | 0.9418(4) | 0.9422(4) |
| O1 *y* | 0.0065(4) | 0.0076(3) | 0.0080(3) | 0.0086(4) |
| O1 *z* | 0.7350(3) | 0.7348(3) | 0.7349(3) | 0.7348(3) |
| $U_{iso}$ (×100 Å$^2$) | 0.83(5) | 0.46(6) | 0.47(6) | 0.51(7) |
| O2 *x* | 0.2906(4) | 0.2935(4) | 0.2933(4) | 0.2938(4) |
| O2 *y* | 0.2379(5) | 0.2348(5) | 0.2349(5) | 0.2344(5) |
| O2 *z* | 0.9713(4) | 0.9701(4) | 0.9700(4) | 0.9701(4) |
| $U_{iso}$ (×100 Å$^2$) | 0.91(6) | 0.61(6) | 0.60(6) | 0.74(6) |
| O3 *x* | 0.2591(4) | 0.2619(4) | 0.2617(4) | 0.2620(4) |
| O3 *y* | 0.2126(5) | 0.2112(5) | 0.2108(5) | 0.2096(5) |
| O3 *z* | 0.5283(4) | 0.5295(4) | 0.5296(4) | 0.5296(4) |
| $U_{iso}$ (×100 Å$^2$) | 1.14(6) | 0.87(6) | 0.82(6) | 0.74(6) |
| *M* (Mn)[a] | – | – | – | 4.55(2) |
| $R_{wp}$ [%] | 4.7 | 5.7 | 5.8 | 6.4 |
| $R_p$ [%] | 3.4 | 4.2 | 4.4 | 4.7 |
| $\chi^2$ | 2.1 | 2.0 | 2.1 | 2.4 |
| $R_F^2$ | 2.9 | 2.6 | 2.6 | 2.0 |
| $R_{mag}$ | – | – | – | 4.1 |

[a] $M_x = 4.55(2)$; $M_y = M_z = 0$.

The high degree of distortion of this phase with respect to the ideal cubic perovskite is a common feature of other similar $Sr_2MnB'O_6$ (B′ = $Mo^{6+}$, $W^{6+}$, and $Re^{6+}$) double perovskites, the structures of which are also described by the $P12_1/n1$ space group (see Table 3). This distortion type

 © 2006 Wiley-VCH Verlag GmbH & Co. KGaA, Weinheim 

Table 2. Selected bond lengths [Å] and angles [°] of $Sr_2MnTeO_6$ at various temperatures.

| $T$ [K] | 298 | 60 | 30 | 4 |
|---|---|---|---|---|
| Mn–O1 x2 | 2.151(3) | 2.153(2) | 2.152(2) | 2.152(2) |
| Mn–O2 x2 | 2.150(2) | 2.149(2) | 2.149(2) | 2.149(2) |
| Mn–O3 x2 | 2.145(2) | 2.139(2) | 2.141(2) | 2.146(2) |
| Mean | 2.149 | 2.147 | 2.147 | 2.149 |
| Calcd.[a] | *2.17* | | | |
| O1–Mn–O2 | 90.4(3) | 90.3(1) | 90.3(1) | 90.4(1) |
| O1–Mn–O3 | 90.0(2) | 90.1(1) | 90.2(1) | 90.2(1) |
| O2–Mn–O3 | 91.6(2) | 91.7(1) | 91.7(1) | 91.6(1) |
| Te–O1 x2 | 1.914(3) | 1.913(2) | 1.914(2) | 1.912(2) |
| Te–O2 x2 | 1.921(2) | 1.923(2) | 1.923(2) | 1.924(2) |
| Te–O3 x2 | 1.921(2) | 1.926(2) | 1.924(2) | 1.921(2) |
| Mean | 1.919 | 1.921 | 1.920 | 1.919 |
| Calcd.[a] | *1.91* | | | |
| O1–Te–O2 | 90.1(1) | 90.1(1) | 90.1(1) | 90.2(1) |
| O1–Te–O3 | 90.1(6) | 90.0(1) | 90.1(1) | 90.2(1) |
| O2–Te–O3 | 90.30(6) | 90.1(1) | 90.1(1) | 90.2(1) |
| Mn–O1–Te | 162.15(8) | 161.1(1) | 161.0(1) | 161.1(1) |
| Mn–O2–Te | 162.23(7) | 160.9(1) | 160.9(1) | 160.8(2) |
| Mn–O3–Te | 163.29(4) | 162.3(2) | 162.2(2) | 162.0(2) |

[a] According to ref.[14]

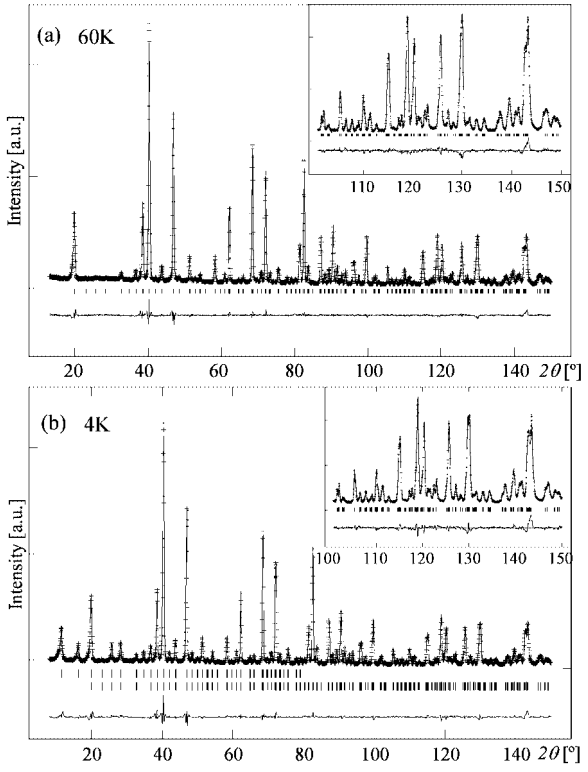


Figure 1. Rietveld fits to the D2B neutron diffraction data at (a) 60 K and (b) 4 K of $Sr_2MnTeO_6$ in space group $P12_1/n1$, showing observed, calculated and difference curves. Lower and upper reflection markers in (b) correspond to magnetic and nuclear structures, respectively. In each case, the fit to the high angle data is inset.

occurs when the A cation, $Sr^{2+}$ in this case, is too small to fill the space in the three-dimensional network of $B/B'O_6$ octahedra, the result of this mismatch being the tilting of these octahedra around the three axes of the primitive cubic perovskite.

### Electron Paramagnetic Resonance Measurements

The room temperature EPR data (see Figure 2, a) show a single, sharp resonance of Lorentzian shape with $\Delta H_{pp}$ = 80(1) Oe and a resonance field of 3375.3(2) Oe, corresponding to a $g$ value of 1.998(1). This value of the gyromagnetic factor confirms the oxidation state of Mn as +2 and the sharpness of the resonance is further evidence for the chemical and structural homogeneity of the octahedral Mn environment observed from X-ray and neutron diffraction.

Thermal evolution of the EPR signal was also studied in order to extract information regarding the magnetic and dipolar interactions in the sample. The area of the signal ($A_{EPR}$) and the peak-to-peak linewidth as a function of temperature are shown in part b of Figure 2. The peak-to-peak linewidth ($\Delta H_{pp}$) can be related to the $Mn^{2+}$ spins' relaxation time, $\tau$, in a way that $\Delta H_{pp}$ is proportional to the inverse of $\tau$.[19] As $\tau$ usually increases with decreasing temperature we should expect reduction of the signal broadening with lowering temperature. The exchange and dipolar interaction between manganese ions, however, act in the opposite sense. Figure 2 (b) shows that $\Delta H_{pp}$ is almost constant down to ca. 30 K indicating that both effects counteract one another. Below 30 K an exponential increase of $\Delta H_{pp}$ is observed which indicates that the effect of the exchange interactions between manganese cations is strong and dominates the EPR resonance process. The area of the signal, $A_{EPR}$, is related to the number of paramagnetic spins and is generally considered as the "EPR susceptibility". In order to avoid errors in the determination of the intensity because of the broadening of the signal into magnetic field regions not covered by the measurements, $A_{EPR}$ was calculated as $Y{\cdot}\Gamma{\cdot}\pi$, which results from double integration of the derivative equation that defines the resonance process for Lorentzian line-shapes.[19] In this expression, $Y$ is the height of the signal and $\Gamma$ the half-width at half-height, both of which were directly obtained from fits to the experimental data. As shown in part b of Figure 2 the value for $A_{EPR}$ increases monotonically as the temperature is reduced. In order to obtain further information about the type of magnetic interactions, the inverse of the $A_{EPR}$ curve was fitted at high temperatures by a Curie–Weiss law, $\chi = C_m/(T - \theta)$ [see inset (b) in Figure 2] which gave a Weiss constant of ca. –160 K, indicating the presence of antiferromagnetic interactions. Below 25 K, the EPR signal is no longer observed due to significant broadening and reduction in intensity; see the inset (a) in Figure 2. These effects are consistent with the existence of strong magnetic correlations between $Mn^{2+}$ spins below this temperature and the presence of a three dimensionally ordered state (see "Magnetic structure" below).

### Magnetic Susceptibility Measurements

Figure 3a shows the temperature dependence of the molar magnetic susceptibility ($\chi_m$) and inverse susceptibility ($1/\chi_m$) curves measured at 1 kOe after cooling without an applied field (ZFC). At high temperature, $T > 150$ K, the

 © 2006 Wiley-VCH Verlag GmbH & Co. KGaA, Weinheim 

Table 3. Selected structural and magnetic data for several $Mn^{2+}$-containing ordered perovskites.

| | S.G.[a] | $T_N$ | AST[b] | $\mu_{eff}$ ($\mu_B$) $T >> T_N$ | $M$ ($\mu_B$) $T \approx 4$ K[c] | Ref. |
|---|---|---|---|---|---|---|
| $Sr_2MnMoO_6$ | $P12_1/n1$ | 12–16 | II | $4.5 < \mu_{eff} < 6.28$ | 4.17(6) | [15,9a] |
| $Sr_2MnWO_6$ | $P12_1/n1$ | ≈14 | II | 5.6 | 4.54(5) | [9a,10a] |
| $Sr_2MnReO_6$ | $P12_1/n1$ | 120[d] | [e] | – | 4.49(8) | [16] |
| $Sr_2MnTeO_6$ | $P12_1/n1$ | 20 | I | 6.04 | 4.54(4) | this work |
| $Ca_2MnWO_6$ | $P12_1/n1$ | 16 | II | 6.19 | 4.9(1) | [10b] |
| $LaCaMnNbO_6$ | $P12_1/n1$ | 9 | II | 6.2 | 4.69(3) | [17] |
| $Ba_2MnTeO_6$ | R-3 | 9 | II | 6.05 | 4.75(4) | [18] |

[a] Space group. [b] Antiferromagnetic structure type. [c] Refined magnetic moment from neutron diffraction data. [d] In this case, the value refers to $T_C$. [e] Noncollinear ferromagnetic arrangement.

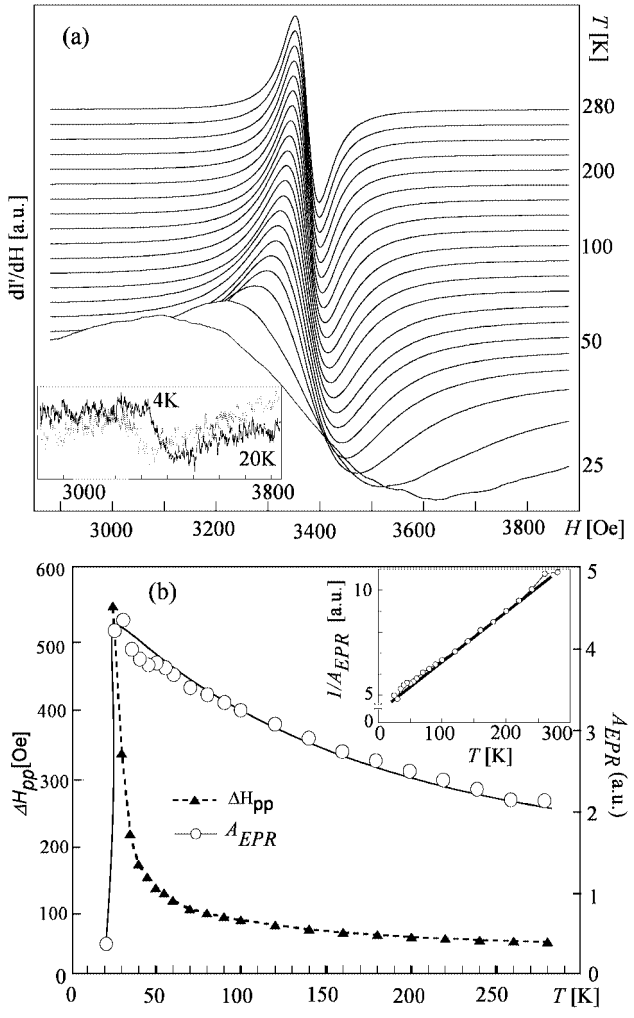


Figure 2. (a) Normalized EPR spectra between 280 and 25 K. The inset shows the weak EPR spectra observed at 4 and 20 K. (b) Thermal evolution of the signal area ($A_{EPR}$) and the peak-to-peak linewidth ($\Delta H_{pp}$).

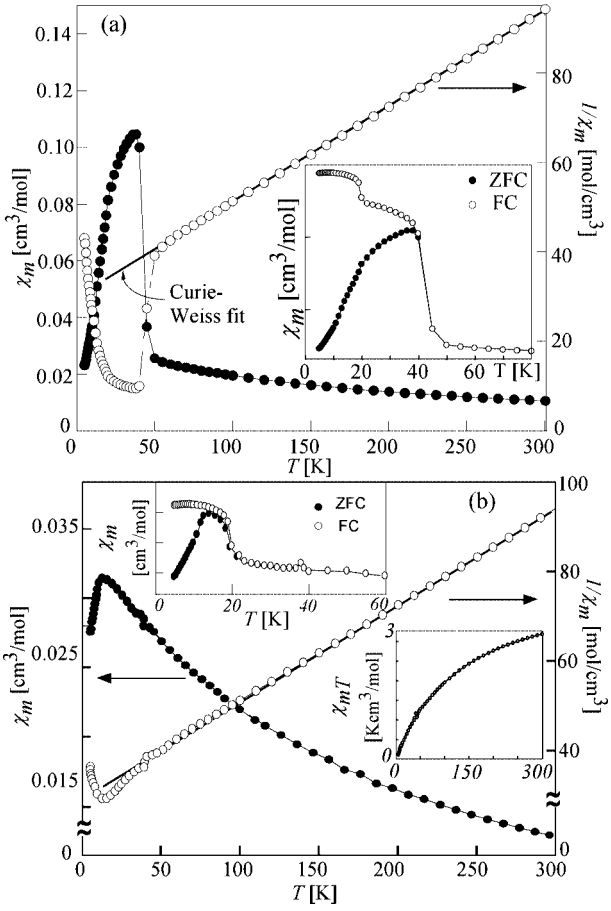


Figure 3. (a) Temperature dependence of the magnetic and reciprocal susceptibilities measured at 1 kOe. The inset shows low temperature details of the ZFC and FC modes of $\chi_m$. (b) Temperature dependence of the magnetic and reciprocal susceptibilities measured at 1 kOe after the subtraction of the component due to the presence of 1.5% by mass of $Mn_3O_4$. Inset are the corrected ZFC and FC modes and the corrected thermal evolution of the product $\chi_{mT}$.

thermal evolution of $\chi_m$ follows the classical Curie–Weiss law, with $C_m = 4.6$ cm$^3$·K/mol and $\theta = -136$ K indicating that the predominant interactions are of antiferromagnetic nature and in very good agreement with the values obtained from EPR. The effective magnetic moment ($\mu_{eff}$) calculated for the paramagnetic region well above the Néel temperature as $\mu_{eff} = 2.828\sqrt{C_m}$ gave the value of 6.05 $\mu_B$, very close to the theoretical value (5.91 $\mu_B$) obtained from $\mu_{eff} = g\sqrt{S(S+1)}$, considering high spin $S = {}^5/_2$ manganese cations with no orbital contribution.

The inset (a) in Figure 3 shows details of the low-temperature molar magnetic susceptibility ($\chi_m$) measured in ZFC and FC modes. Two distinct features, at approximately 40 and 20 K, can be observed in both modes. The most important characteristic of this low temperature behavior is that the maximum at ca. 40 K appears at the same tempera-

 © 2006 Wiley-VCH Verlag GmbH & Co. KGaA, Weinheim 

ture as that observed in all $A_2MnWO_6$ (A = Ca, Ba, Sr) phases studied by Azad et al.,[10] while the low temperature maximum appears at a different temperature in each sample. Similar characteristics have also been observed in phases of the $Sr_{2-x}La_xMnWO_6$ series.[11] It is worth noting that these features observed in some antiferromagnetic manganese-containing double perovskites are very similar to those reported for the ferrimagnetic $Mn_3O_4$, with a $T_c$ of 42 K.[20]

Field-dependent DC and AC susceptibility measurements, on both $Sr_2MnTeO_6$ and commercially available $Mn_3O_4$ (CAS number: 1317-35-7) showed very similar behavior, with the appearance of significant features around 40 K, the only difference being the appearance of a weak maximum in the DC susceptibility and in the real ($\chi'$) component of the AC susceptibility in the case of $Sr_2MnTeO_6$. These characteristics confirm that the maxima around 40 K correspond to $Mn_3O_4$ rather than originating from the magnetic behavior of $Sr_2MnTeO_6$. These observed DC susceptibility curves are similar to those reported for the similar double perovskite oxide $Ba_2MnWO_6$, in which the ferromagnetism observed below 40 K was attributed to a disordered canted antiferromagnetic state composed of various domains.[10c] Further details of the susceptibility study are available as supporting information to this article.

It is worth noting that the presence of undetected $Mn_3O_4$ has led to misinterpretation of the magnetic properties of many manganese-containing compounds. One of the first examples is the oxide MnO, which was considered to behave as a spin glass around 40 K, but the AC susceptibility revealed that the maximum observed in the DC susceptibility measurements at this temperature actually originated from an undetected fraction of $Mn_3O_4$.[21] Recently, Goff et al.[22] demonstrated that quantities as low as 1% of this oxide can completely mask the magnetic behavior of the majority phase. The magnetic behavior published for $A_2MnWO_6$ may be a further example of this type of undetected contamination with $Mn_3O_4$.[10] The DC susceptibility data for $Sr_2MnTeO_6$, corrected for an estimated 1.5% by mass of $Mn_3O_4$ are shown in Figure 3 (b). It is therefore clear that great care must be taken when analyzing the magnetic properties of manganese-containing compounds as manganese oxides exist with strong ferro/ferri-magnetic behavior that, well below the detection limit of other techniques, can completely dominate the magnetic properties of phases under investigation.

## Specific Heat Measurements

Figure 4 shows the observed total specific heat ($C_P$), the calculated contribution of lattice phonons to the specific heat, $C_{P(pho)}$, and the resulting magnetic specific heat, $C_{P(mag)}$. The total specific heat exhibits a three-dimensional ($\lambda$-type) magnetic ordering peak at 20 K, in agreement with the previous magnetic and neutron diffraction data. The contribution of the lattice vibrations to the specific heat capacity was calculated by fitting the experimental high temperature data (above the $\lambda$ anomaly) using a modified Debye model considering the existence of two phonon spectra. For a formula unit containing $N$ atoms, $n_1$ was assigned a Debye temperature $\theta_1$ and $n_2$, constrained such that $n_2 = N - n_1$, a Debye temperature $\theta_2$, yielding three independent variables to be refined, namely $\theta_1$, $\theta_2$, and $n_1$. Refined values indicate that, of the 10 atoms in the formula unit, 3.5 ($n_1$) have a Debye temperature of 217 K and 6.5 ($n_2 = N - n_1$) have a Debye temperature of 616.5 K. This result not only produces an excellent fit to the experimental data up to 300 K, but is also in good agreement with the chemical formula contents of 4 heavy atoms and 6 light atoms, the latter with a much higher Debye temperature. The magnetic specific heat, $C_{P(mag)}$, shown in Figure 4, being the result of subtracting the phonon component from the total specific heat ($C_P$).

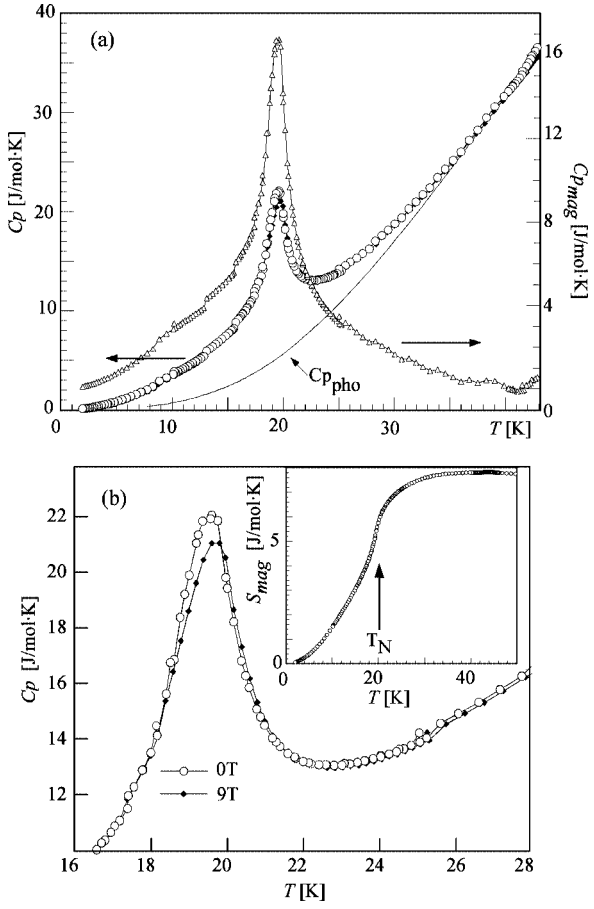


Figure 4. (a) Specific heat vs. temperature of $Sr_2MnTeO_6$ from 1.8 to 45 K showing total specific heat, $Cp$, the calculated phonon contribution, $Cp_{pho}$, and the resultant magnetic contribution, $Cp_{mag}$. (b) Comparison between the specific heat data measured at 0T and under an applied magnetic field of 9T. The inset shows the calculated magnetic entropy, $S_{mag}$.

The effect of a 9T magnetic field on the three-dimensional $\lambda$ peak in the heat capacity is shown in Figure 4 (b). In a pure antiferromagnetic sample, a small displacement of the peak to lower temperatures with increasing magnetic

 © 2006 Wiley-VCH Verlag GmbH & Co. KGaA, Weinheim 

field would be expected. It can be seen, however, that the peak is slightly displaced to higher temperature with the applied field, indicating a small ferromagnetic component. This ferromagnetic component may originate from a small canting in the antiferromagnetic structure as the small magnitude of the displacement is typical of highly anisotropic antiferromagnets. The thermal evolution of the magnetic entropy, $S_{mag}$, released in the ordering process for this phase is shown in the inset (b) of Figure 4. The total magnetic entropy, calculated from the $S_{mag}(T) = \int_0^T C_{mag}(T)/T \cdot dT$ expression, was found to be ≈8 J/mol·K above 20 K. This value is ≈60% of the theoretical value, $R \cdot \ln(2S + 1)$ = 14.9 J/mol·K, expected for the $S = {}^5/_2$ state of the $Mn^{2+}$ cation at low temperatures. This low value could be related to systematic errors in the subtraction of the lattice component around the observed maximum in the specific heat data or, as has been previously suggested, this deviation could indicate that some of the spins of the $Mn^{2+}$ ions are not correlated to the rest.[23] The latter explanation would, however, also imply a similar deviation of the low temperature magnetic moment of the $Mn^{2+}$ spins, an effect not observed in $Sr_2MnTeO_6$.

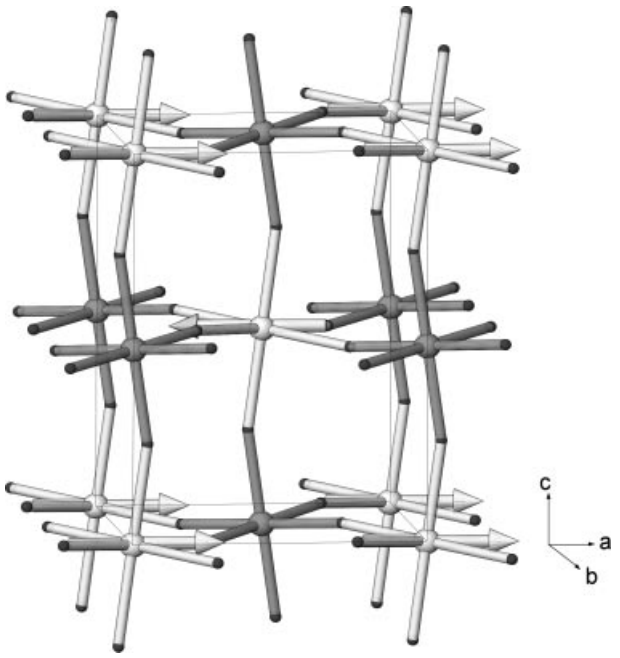


Figure 5. Type I antiferromagnetic structure of $Sr_2MnTeO_6$. Lighter spheres represent Mn and darker spheres Te. Sr atoms are omitted for clarity.

## Magnetic Structure

The 4 K neutron diffraction data show the presence of several additional peaks which arise from long-range magnetic order in the sample (see Figure 1, b). These reflections were not coincident with those of the nuclear structure indicating that this magnetic order is of antiferromagnetic nature. These peaks were indexed considering a magnetic cell with the same dimensions as that of the crystal cell (with parameters $\sqrt{2}a_p \times \sqrt{2}a_p \times 2a_p$, where $a_p$ is the primitive cubic perovskite parameter) in the $P1$ space group (refined neutron data are shown in Figure 1, b). The first two sharp magnetic peaks are, consequently, the unique (001) reflection and the unresolved doublet composed of the (010) and (100) reflections. The type I antiferromagnetic structure is the only collinear arrangement of magnetic ions compatible with these observed maxima. The strong (001) peak indicates that an important component of the magnetic moment is in the *ab* plane. The orientation of the magnetic moments in this plane could not be determined, because of the overlap of the (010) and (100) reflections. No significant component was observed in the *c*-direction. In the final model, magnetic moments of magnitude *M*, were fixed along *a* and –*a* in alternating planes in the *c*-direction. The refined structure at 4 K, showing the orientation of magnetic moments, is shown in Figure 5. In this magnetic structure each manganese cation is antiferromagnetically coupled by 90° superexchange interactions via diamagnetic –O–$Te^{6+}$–O– bridges to 8 out of 12 nearest-neighbors, NN, at an approximate distance of 5.6 Å. The six next nearest-neighbors, NNN, (at ca. 8.0 Å) are all ferromagnetically aligned via 180° –O–$Te^{6+}$–O– linkages.

Figure 6 shows the temperature-dependent D1B diffraction data. The thermal evolution of the refined magnetic moment ($M_x$) is represented in Figure 7. It can be observed that the three-dimensional magnetic order begins at 20 K. The $Mn^{2+}$ moment rapidly increases below 20 K, reaching saturation at approximately 10 K. The obtained value of $M_x$ = 4.55(5) $\mu_B$ is close to the theoretical value of 5 $\mu_B$ for high spin $S = {}^5/_2$ manganese at low temperature.

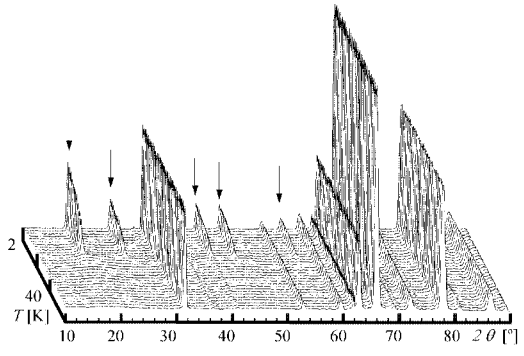


Figure 6. Temperature-dependent D1B neutron diffraction data from 2 to 60 K. Magnetic peaks are marked by arrows.

The temperature dependence of the refined lattice parameters and volume are shown in Figure 8. The thermal evolution of the lattice parameters is of particular interest. The *a* parameter exhibits almost no variation whereas the *b* and *c* parameters show different behaviors with temperature. Below 20 K, where three-dimensional magnetic order is observed, the parameters show no systematic change. At 20 K, a marked discontinuity is observed in both parameters with *c* increasing and *b* decreasing. Above 20 K, the *b* and *c* parameters are again virtually independent of tem-

 © 2006 Wiley-VCH Verlag GmbH & Co. KGaA, Weinheim 

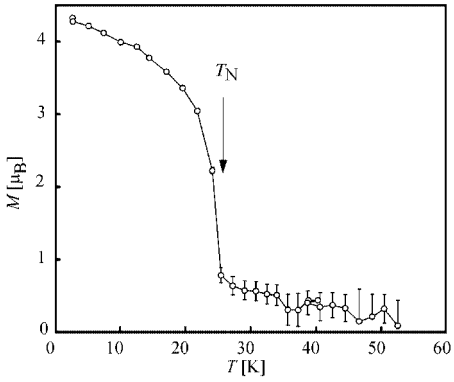


Figure 7. Temperature dependence of the magnitude of the magnetic moment refined from D1B neutron diffraction data from 2 to 60 K, with the Néel temperature, $T_N$ = 22 K, marked.

perature. The thermal evolution of the unit cell volume shows no change below 20 K and a small increase at higher temperatures.

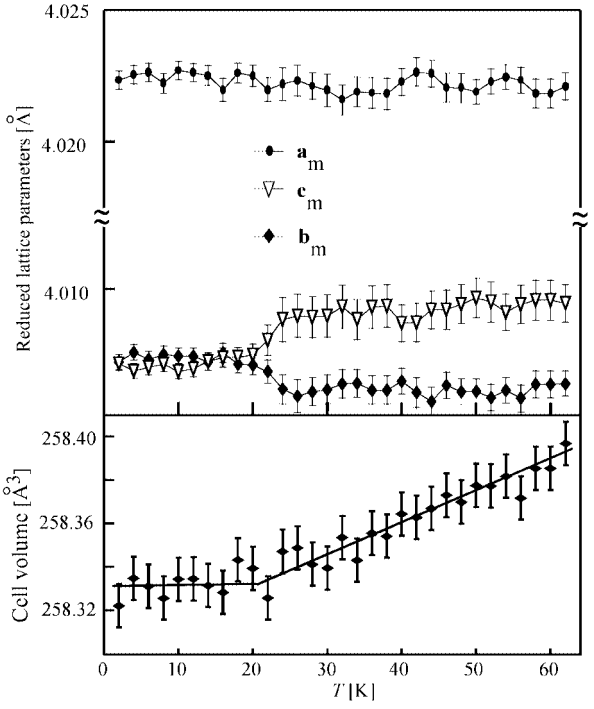


Figure 8. Temperature dependence of the reduced lattice parameters and cell volume refined from D1B neutron diffraction data from 2 to 60 K. Reduced lattice parameters were calculated as follows: $a_m = a/\sqrt{2}$, $b_m = b/\sqrt{2}$; cm = $c$/2.

The observed behavior could be associated to "spontaneous magnetostriction" resulting from a magnetically ordered state, in contrast to the "common magnetostriction" effect that results from the application of a magnetic field.[24] In $Sr_2MnTeO_6$, this effect can be viewed as the result of the nature of the magnetic order (see Figure 9), where moments perpendicular to the [001] direction attract one another, leading to a reduction of the $c$ parameter with the increase in $b$ parameter being the result of the repulsion between ferromagnetically aligned moments in the $ab$ plane. Similar, but more pronounced, spontaneous magnetostriction effects have also been recently observed in the ferromagnetic oxides $SrRu_{1-x}O_3$.[25a] Field-induced magnetostriction is common in other ferromagnetic perovskites, such as manganites and double perovskites,[25b–25c] but the observation of this spontaneous effect in this type of antiferromagnet is rare.

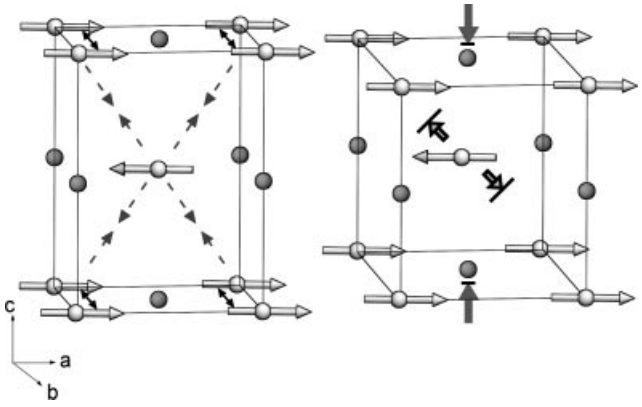


Figure 9. Origin of the spontaneous magnetostriction effect observed in $Sr_2MnTeO_6$. Dark spheres represent Te and light ones with arrows represent Mn with their magnetic moments. Also depicted are arrows indicating the compressions and elongations of the unit cell dimensions as a consequence of the magnetic ordering. Sr and O atoms are omitted for clarity.

## Conclusions

The ordered double perovskite $Sr_2MnTeO_6$ crystallizes at room temperature in space group $P12_1/n1$ and maintains its symmetry on cooling down to 4 K. Electron paramagnetic resonance spectroscopy shows the presence of a sharp resonance centred at a $g$ value of 1.998(2), indicating that manganese ions are in the +2 oxidation state. As the temperature is lowered and magnetic exchange interactions between $Mn^{2+}$ become stronger, the area of the resonance increases showing a maximum around 25 K. Below this temperature a large broadening of the signal occurs indicating that the sample is magnetically ordered.

Magnetic DC susceptibility follows the Curie–Weiss law at high temperatures, and a Weiss constant of –136 K indicates that the predominant interactions are of antiferromagnetic nature. The observed effective magnetic moment agrees well with a $S = {}^5/_2$ cation with no orbital contribution. The Néel temperature was estimated to be 20 K. At this same temperature the specific heat shows a $\lambda$-type anomaly typical of three-dimensionally ordered systems, which is slightly repressed on application of a field of 9T. Both effects are consistent with the observed anti-ferromagnetic ordering within the sample. Low temperature neutron diffraction indicates that the ordered antiferromagnetic state is of type I, in which planes perpendicular to the (001) direction contain $S = {}^5/_2$ $Mn^{2+}$ magnetic moments ferromagnetically coupled to one another within the plane via diamagnetic –O–$Te^{6+}$–O– bridges. These planes are coupled antiferromagnetically because of the stronger 90° Mn–

 © 2006 Wiley-VCH Verlag GmbH & Co. KGaA, Weinheim 

O···O–Mn linkages, producing the predominant antiferromagnetic inter-planar interactions. The observed magnetic moment per manganese ion of 4.5 $\mu_B$ indicates that virtually all the sample is magnetically ordered at this temperature. Discontinuities observed around the ordering temperature in the lattice parameters indicate that this phase also shows a small spontaneous magnetostriction effect.

## Experimental Section

Synthesis, room temperature structural refinement, and confirmation of nominal stoichiometry of the ordered double perovskite $Sr_2MnTeO_6$ have been reported previously.[12] Low temperature neutron powder diffraction data were collected at 4, 30, and 60 K on instrument D2B at the Institut Laue Langevin (I.L.L.), Grenoble, France. Neutrons of wavelength 1.595 Å were incident on 10 g of $Sr_2MnTeO_6$, contained in an 8-mm diameter vanadium can held in a liquid helium cryostat. Data were collected over the angular range $0 \leq 2\theta \leq 160°$, then normalized for subsequent refinement in GSAS.[26]

Temperature-dependent neutron powder diffraction data were collected on instrument D1B at the I.L.L. Neutrons of wavelength 2.52 Å were incident on 10 g of $Sr_2MnTeO_6$, contained in an 8-mm diameter vanadium can held in a liquid helium cryostat. Data were collected every 2 K from 2 to 60 K over the angular range $10 \leq 2\theta \leq 90°$. Evolution of lattice parameters and magnetic moment ($M_x$) with temperature were obtained by sequential refinement in FullProf[27] starting from the structural model refined with D2B data at 4 K.

X-band EPR spectra were recorded between 0 and 7 kOe from 300 to 5 K with a Bruker ESP 300 spectrometer. The temperature was controlled by an Oxford Instruments (ITC4) regulator. The magnetic field was measured with a Bruker BNM 200 gaussmeter and the frequency inside the cavity was determined using a Hewlett–Packard 5352B microwave frequency counter.

DC magnetic susceptibility measurements were performed using a Quantum Design MPMS-7 SQUID magnetometer whilst heating from 5 to 300 K in an applied field of 1 and 5 kOe. In both cases, data were collected after cooling either in the presence (field cooling –FC curve) or absence (zero-field cooling- ZFC curve) of the applied field. Magnetization as a function of applied field ($H$) was measured using the same MPMS-7 SQUID magnetometer after cooling the sample in zero field. Magnetization was also measured as a function of temperature between 5 and 80 K.

AC magnetic susceptibility measurements were made with a standard QD PPMS system with an alternate excitation field ($H_{ac}$) of 1 Oe at frequencies between $10^2$ and $10^4$ Hz. Data were recorded from 4 to 60 K as a function of both frequency and applied DC magnetic field.

Heat capacity measurements were carried out by a relaxation method using the same PPMS system. The sample was a plate of 0.3 mm thickness and 7 mg weight obtained by compressing the original powder. Data were collected with zero field (0T) and under an applied field of 9T from 1.8 to 300 K.

**Supporting Information** (for details see the footnote on the first page of this article): Further magnetic data are available as Supporting Information, due to the magnetic characterisation of $Sr_2MnTeO_6$ having been complicated by the presence of the ferromagnetic oxide, $Mn_3O_4$. Field-cooled and zero-field cooled DC susceptibilities at various applied fields and field- and frequency-dependent AC susceptibilities are presented for both the as-prepared $Sr_2MnTeO_6$ and commercially available $Mn_3O_4$. Also included is the field-dependence of the magnetization for $Sr_2MnTeO_6$.

## Acknowledgments

This work has been funded by the "Ministerio de Ciencia y Tecnología (MCyT)" (projects MAT2004-02425 and MAT2002-04178-C04-04). L.O.-S.M acknowledges MCyT for a Doctoral Fellowship and J.P.C. thanks MCyT for funding (MAT, 2001-0064). Prof. J.P. Attfield of the University of Edinburgh is acknowledged for fruitful magnetic discussions. The authors gratefully acknowledge Dr. G. Cuello for assistance with data collection at the I.L.L., Grenoble, France and the I.L.L. for provision of beam-time on instruments D2B and D1B.

[1] F. Galasso, *Perovskites and High Tc superconductors*, Gordon & Breach, New York, **1990**.
[2] M. T. Anderson, K. B. Greenwood, G. A. Taylor, K. R. Poeppelmeier, *Prog. Solid State Chem.* **1993**, *22*, 197–233.
[3] K.-I. Kobayashi, T. Kimura, H. Sawada, K. Terakura, Y. Tokura, *Nature* **1998**, *395*, 677–680.
[4] H. A. Blackstead, J. D. Dow, D. R. Harshman, W. B. Yelon, M. X. Chen, M. K. Wu, D. Y. Chen, F. Z. Chien, D. B. Pulling, *Phys. Rev. B* **2001**, *61*, 214412.
[5] M. Azuma, K. Takata, T. Saito, S. Ishiwata, Y. Shimakawa, M. Takano, *J. Am. Chem. Soc.* **2005**, *127*, 8889–8892.
[6] a) D. D. Sarma, *Curr. Opin. Solid State Mater. Science* **2001**, *5*, 261–268; b) O. Chmaissem, R. Kruk, B. Dabrowski, D. E. Brown, X. Xiong, S. Kolesnik, J. D. Jorgensen, W. C. Kimball, *Phys. Rev. B* **2000**, *62*, 14197–14206; c) H. Kato, T. Okuda, Y. Okimoto, T. Tomioka, K. Oikawa, T. Kamiyama, Y. Tokura, *Phys. Rev. B* **2004**, *69*, 184412.
[7] R. K. Sahu, S. Sundar-Manoharan, *J. Appl. Phys.* **2002**, *92*, 4831–4833.
[8] G. Popov, M. V. Lobanov, E. Tsiper, M. Greenblatt, E. Caspi, A. Borisov, V. Kiryukhin, J. Lin, *J. Appl. Phys.* **2004**, *16*, 135–145.
[9] a) A. Muñoz, J. A. Alonso, M. T. Casais, M. J. Martínez-Lope, M. T. Fernández-Díaz, *J. Phys.: Condens. Matter* **2002**, *14*, 8817–8830; b) M. Itoh, I. Ohta, Y. Inaguma, *Mater. Science Eng. B* **1996**, *41*, 55–58.
[10] a) A. K. Azad, S. A. Ivanov, S.-G. Eriksson, H. Rundölf, J. Eriksen, R. Mathieu, P. Svedlindh, *J. Mag. Mag. Mater.* **2001**, *237*, 124–134; b) A. K. Azad, S. A. Ivanov, S.-G. Eriksson, J. Eriksen, H. Rundölf, R. Mathieu, P. Svedlindh, *Mater. Res. Bull.* **2001**, *36*, 2485–2496; c) A. K. Azad, S. A. Ivanov, S.-G. Eriksson, J. Eriksen, H. Rundölf, R. Mathieu, P. Svedlindh, *Mater. Res. Bull.* **2001**, *36*, 2215–2228.
[11] Q. Lin, M. Greenblatt, M. Croft, *J. Solid State Chem.* **2005**, *178*, 1356–1366.
[12] L. Ortega-San Martín, J. P. Chapman, E. Hernández-Bocanegra, M. Insausti, M. I. Arriortua, T. Rojo, *J. Phys.: Condens. Matter* **2004**, *16*, 3879–3888.
[13] C. J. Howard, H. T. Stokes, *Acta Crystallogr. Sect. A* **2005**, *61*, 93–111.
[14] R. D. Shannon, *Acta Crystallog. A* **1976**, *32*, 751–767.
[15] A. K. Azad, S.-G. Erikson, S. A. Ivanov, R. Mathieu, P. Svendlindh, J. Eriksen, H. J. Rundölf, *J. Alloys Comp.* **2004**, *364*, 77–82.
[16] a) H. Kato, T. Okuda, Y. Okimoto, Y. Tomioka, K. Oikawa, T. Kamiyama, Y. Tokura, *Phys. Rev. B* **2004**, *69*, 184412; b) G. Popov, M. V. Lobanov, E. Tsiper, M. Greenblatt, E. Caspi, A. Borissov, V. Kiryukhin, J. Lynn, *J. Phys.: Condens. Matter* **2004**, *16*, 135–145.
[17] J.-W. G. Bos, J. P. Attfield, *Z. Anorg. Allg. Chem.* **2004**, *630*, 2248–2252.

 © 2006 Wiley-VCH Verlag GmbH & Co. KGaA, Weinheim 

[18] L. Ortega-San Martín, J. P. Chapman, L. Lezama, M. I. Arriortua, T. Rojo, *Abstracts of the Solid State Chemistry Conference (SSC2004)*, Academy of Science of the Czech Republic, Prague, September **2004**.
[19] a) F. E. Mabbs, D. Collison, *Electron Paramagnetic Resonance of d Transition Metal Compounds*, Elsevier, Amsterdam, **1992**; b) J. A. Weil, J. R Bolton, J. E. Wertz, *Electron Paramagnetic Resonance – Elementary Theory and Practical Applications*, John Wiley & Sons, New York, **1994**.
[20] W. S. Seo, H. H. Jo, K. Lee, B. Kim, S. J. Oh, J. T. Park, *Angew. Chem. Int. Ed.* **2004**, *43*, 1115–1117.
[21] J. J. Hauser, J. V. Waszczak, *Phys. Rev. B* **1984**, *30*, 5167–5171.
[22] R. J. Goff, A. J. Williams, J. P. Attfield, *Phys. Rev. B* **2004**, 014426.
[23] K. Boulahya, M. Parras, J. M. González Calbet, U. Amador, J. L. Martínez, M. T. Fernández-Díaz, *Phys. Rev. B* **2004**, *69*, 024418.
[24] A. del Moral, P. A. Algarabel, J. I. Arnaudas, L. Benito, M. Ciria, C. de la Fuente, B. García-Landa, M. R. Ibarra, C. Marquina, L. Morellón, J. M. de Teresa, *J. Magn. Magn. Mater.* **2002**, *242–245*, 788–796.
[25] a) B. Dabrowski, M. Avdeev, O. Chmaissem, S. Kolesnik, P. W. Klamut, M. Maxwell, J. D. Jorgensen, *Phys. Rev. B* **2005**, *71*, 104411; b) R. Mahendiran, M. R. Ibarra, C. Marquina, B. Garcia-Landa, L. Morellon, A. Maignan, B. Raveau, A. Arulraj, C. N. R. Rao, *Appl. Phys. Lett.* **2003**, *82*, 242–244; c) D. Serrate, J. M. De Teresa, P. A. Algarabel, C. Marquina, L. Morellon, J. Blasco, M. R. Ibarra, *J. Magn. Magn. Mater.* **2005**, *290–291*, 843–845.
[26] A. C. Larson, R. B. Von Dreele, "*GSAS*: General Structure Analysis System", Los Alamos National Laboratory Report LAUR 86–748, **1994**.
[27] J. Rodriguez-Carvajal, "*FULLPROF*: A Program for Rietveld Refinement and Pattern Matching Analysis", Abstracts of the Satellite Meeting on Powder Diffraction of the XV Congress of the IUCr, p. 127, Toulouse, France, **1990**.

Received: September 30, 2005
Published Online: February 6, 2006

 © 2006 Wiley-VCH Verlag GmbH & Co. KGaA, Weinheim 

DOI: 10.1002/ejic.200501051

# Synthesis and Reactivity of $[Ru(Cp^*)(L)(MeCN)_2][PF_6]$ (L = $Ph_2POMe$ or $Ph_2P$-*o*-tolyl) and $\{Ru(Cp^*)[Ph_2PCH_2C(tBu)=O](MeCN)\}[PF_6]$ Complexes, Their Involvement as Catalyst Precursors for Regioselective Allylic Substitution Reactions and Related $[Ru(Cp^*)Cl(Ph_2POMe)(RCHCHCH_2)][PF_6]$ $\eta^3$-Allyl Ruthenium(IV) Intermediates

**Bernard Demerseman,*[a] Jean-Luc Renaud,[a] Loïc Toupet,[a] Claudie Hubert,[a] and Christian Bruneau[a]**

**Keywords:** Allyl ligands / Allylation / Homogeneous catalysis / Regioselectivity / Ruthenium

The synthesis of the new complexes $[Ru(Cp^*)(L)(MeCN)_2][PF_6]$ (L = $Ph_2POMe$ or $Ph_2P$-*o*-tolyl) and $\{Ru(Cp^*)[Ph_2PCH_2C(tBu)=O](MeCN)\}[PF_6]$ (**2a–c**) is achieved starting from $[Ru(Cp^*)(MeCN)_3][PF_6]$. The acetonitrile ligands in complexes **2a–c** are labile, as emphasised by the easy formation of $\{Ru(Cp^*)(CO)_2[Ph_2PCH_2C(=O)tBu]\}[PF_6]$ (**3**). The keto-phosphane is used as a tool to convert **3** into $\{Ru(Cp^*)(CO)[Ph_2PCH_2C(tBu)=O]\}[PF_6]$ (**5**). Complex **5** reacts with 1,1-diphenyl-2-propyn-1-ol in methanol as solvent to afford the vinyl-carbene complex $\{Ru(Cp^*)(CO)[=C(OMe)CH=CPh_2][Ph_2PCH_2C(=O)tBu]\}[PF_6]$. The new $\eta^3$-allyl ruthenium(IV) derivatives $[Ru(Cp^*)Cl(Ph_2POMe)(CH_2CMeCH_2)][PF_6]$ and $[Ru(Cp^*)Cl(Ph_2POMe)(RCHCHCH_2)][PF_6]$ (R = Me; *n*Pr, **8d**; or Ph, **8e**) are obtained by reacting **2a** with the appropriate allylic halide. The X-ray crystal structure determination of the compounds **8d** and **8e** disclosed an *endo-trans*-$RCHCHCH_2$ $\eta^3$-allyl ligand. The formation of branched allyl aryl ethers is regioselectively favoured when complexes **2a–c** are involved as catalyst precursors for the etherification of cinnamyl chloride, chlorohexene and 3-chloro-4-phenylbut-1-ene with phenol, *p*-methoxyphenol, cresols and (*o* or *p*)-chlorophenols, in the presence of $K_2CO_3$.
(© Wiley-VCH Verlag GmbH & Co. KGaA, 69451 Weinheim, Germany, 2006)

## Introduction

Recently, the labile ruthenium(II) complex $[Ru(Cp^*)(MeCN)_3][PF_6]$ (**1**) (Cp* = pentamethylcyclopentadienyl) was disclosed as an efficient catalyst precursor for the allylation of phenols with cinnamyl derivatives according to stereospecific and regioselective processes.[1,2] Furthermore, enantioselective synthesis was also achieved in the additional presence of a chiral bis-oxazoline ligand.[3] Enantioselective allylic amination and alkylation involving related catalysts based on tethered Cp′ rings resulting in planar chirality at the ruthenium centre have also been reported.[4] From a mechanistic point of view, these catalytic reactions occur through transient formation of electrophilic $\eta^3$-allyl ruthenium(IV) species.[5] Indeed, complexes $[Ru(Cp^*)X(MeCN)(\eta^3\text{-}RCHCHCH_2)][PF_6]$ resulted from the oxidative addition of allylic halides to **1**, but have been disclosed to be a mixture of stereoisomers in solution, as enantiomeric pairs (see Scheme 1).[2] The recently reported tethered complexes $[Ru(Cp'\text{-}PR_2)Cl(\eta^3\text{-}CH_2CRCH_2)][PF_6]$ involved a symmetrical $\eta^3$-allyl ligand precluding analogous stereoisomerism arising from the presence of four distinct coordinating centres besides the cyclopentadienyl ligand.[6]

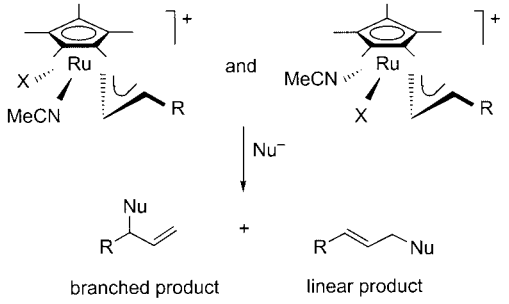


Scheme 1. Stereoisomerism and isomerism from unsymmetrical $\eta^3$-$CH_2CHCHR$ allyl ligand.

Therefore, no information was available concerning the relationship between the regioselectivity of the catalytic nucleophilic substitution and the stereoselective formation of the putative $\eta^3$-allyl ruthenium(IV) intermediate. Moreover, using such ruthenium catalysts, the regioselective formation of branched products by nucleophilic attack at an unsymmetrical $\eta^3$-$RCHCHCH_2$ allyl ligand, as depicted in Scheme 1, largely remained a challenge when R was an alkyl group instead of an aryl one arising from cinnamyl substrates. On the other hand, while the reactivity of

[a] Institut de Chimie de Rennes, UMR-CNRS 6509, Organométalliques et Catalyse, Université de Rennes 1,
35042 Rennes Cedex, France
Fax: +33-223236939
E-mail: bernard.demerseman@univ-rennes1.fr

 © 2006 Wiley-VCH Verlag GmbH & Co. KGaA, Weinheim 

$[Ru(Cp)(PR_3)(MeCN)_2][PF_6]$ complexes towards alkynes continued to stimulate studies,[7] little was known concerning their reactivity towards allylic organic substrates, although $[Ru(Cp)Br(PR_3)(\eta^3\text{-}CH_2CHCH_2)][PF_6]$ complexes have been synthesised.[8]

We wish to report herein (i) the reaction between $[Ru(Cp^*)(MeCN)_3][PF_6]$ and methyl diphenylphosphinite, *o*-tolyldiphenylphosphane or a hemilabile β-keto-phosphane, which provides an efficient tool for the building of new organometallic derivatives, (ii) the synthesis of $[Ru(Cp^*)X(Ph_2POMe)(RCHCHCH_2)][PF_6]$ $\eta^3$-allyl ruthenium(IV) complexes bearing an unsymmetrical monosubstituted allyl ligand and (iii) the involvement of these complexes as catalyst precursors for regioselective allylic etherification.

## Results and Discussion

### Synthesis of Complexes

With a procedure very similar to the reported synthesis of $[Ru(Cp^*)(PEt_3)(MeCN)_2][PF_6]$,[9] the reaction of $[Ru(Cp^*)(MeCN)_3][PF_6]$ (**1**) with one equiv. of methyl diphenylphosphinite or of the bulkier *o*-tolyldiphenylphosphane selectively resulted in the substitution of one acetonitrile ligand to afford the expected complexes $[Ru(Cp^*)(L)(MeCN)_2][PF_6]$ (L = $Ph_2POMe$, **2a** and L = $Ph_2P$-*o*-tolyl, **2b**), in 78% and 99% yield, respectively (Scheme 2).

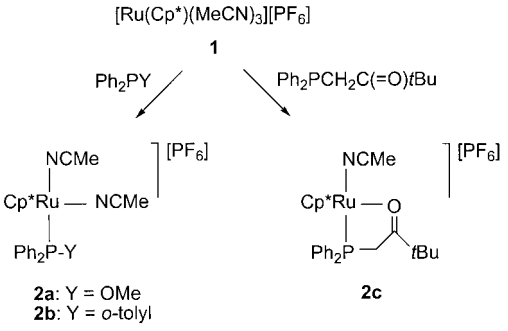


Scheme 2. Synthesis of the new complexes **2a**–**c**.

Distinctly, the reaction between **1** and the β-keto-phosphane $Ph_2PCH_2C(=O)tBu$ showed the substitution of two acetonitrile ligands to afford **2c** wherein the functional phosphane acted as a chelate, in 95% yield (Scheme 2). The new complexes **2a**–**c** were characterised by $^1H$, $^{13}C\{^1H\}$, $^{13}C$ DEPT and $^{31}P\{^1H\}$ NMR, IR spectroscopy and elemental analysis. The $^1H$ and $^{31}P\{^1H\}$ NMR spectra of **2a**–**c** unambiguously indicated the presence of coordinated acetonitrile and one phosphorus ligand besides the Cp* one. Additionally, IR spectroscopy provided evidence for the coordination of the keto function in **2c** ($\tilde{\nu}$ = 1611 $cm^{-1}$) as previously specified in the case of CpRu complexes.[10] Attempts of recrystallisation of **2b**,**c** invariably led to oils that transform to yellow solids under prolonged vacuum. By contrast, orange crystals of **2a** suitable for X-ray crystal structure determination easily formed according to diffusion of diethyl ether into a concentrated dichloromethane solution. An ORTEP drawing of **2a** is shown in Figure 1 and selected bond lengths and angles are given in the caption.

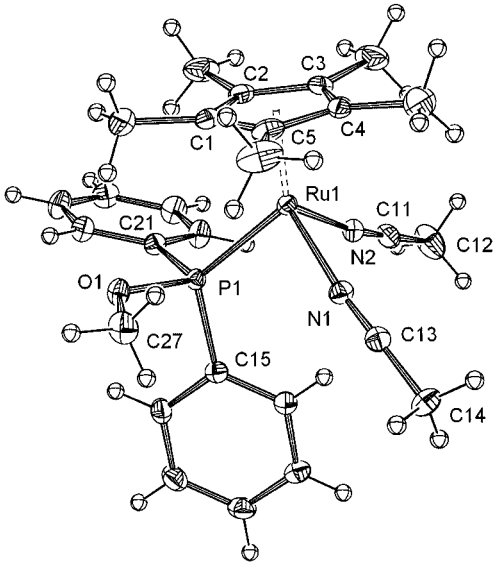


Figure 1. ORTEP drawing of **2a** showing 50% probability thermal ellipsoids. The $PF_6$ anion is omitted for clarity. Selected bond lengths [Å] and angles [°]: Ru1–N1 2.076(2), Ru1–N2 2.067(2), Ru1–P1 2.2894(6); N1–Ru1–N2 87.74(8), N1–Ru1–P1 94.55(6), N2–Ru1–P1 90.77(6).

The cation of **2a** showed the expected piano-stool geometry. The N–Ru–N and N–Ru–P angles are close to 90° and the structure of **2a** thus consisted of a pseudo-octahedron with the Cp* ligand occupying three facial coordination sites.

Complex **2c** retained two labile coordinating atoms, as indicated by its reaction with carbon monoxide, which occurred under mild conditions (1 atm, ambient temperature) to straightforwardly afford the dicarbonyl complex **3** (Scheme 3).

The formal selective substitution of the acetonitrile ligand in **2c** by carbon monoxide was indirectly achieved by reacting **3** with $Me_3NO{\cdot}2H_2O$ to form the enolato-phosphane derivative **4** (Scheme 3). The reaction consisted of the oxidation of one carbon monoxide ligand into carbon dioxide, thus also generating $NMe_3$, which subsequently deprotonated the keto-phosphane. The neutral complex **4** was then easily reprotonated with $HPF_6$ as its aqueous solution or with $HBF_4$ as its $Me_2O$ adduct, to obtain **5** and **5′**, respectively, in yields up to 81%. The protonation of **4** was also achieved with hydrochloric acid, but the additional coordination of the chloride anion resulted in the neutral chloro complex **6** (Scheme 3). These reactions emphasised the usefulness of hemilabile keto-phosphanes as a tool for the building of coordination compounds. Furthermore, the coordinated keto-function in **5** is labile enough to allow the coordination of alkynols such as 1,1-diphenyl-2-propyn-1-ol. Using methanol as solvent, the reaction led at room temperature to a red precipitate of the vinyl-carbene derivative

 © 2006 Wiley-VCH Verlag GmbH & Co. KGaA, Weinheim 

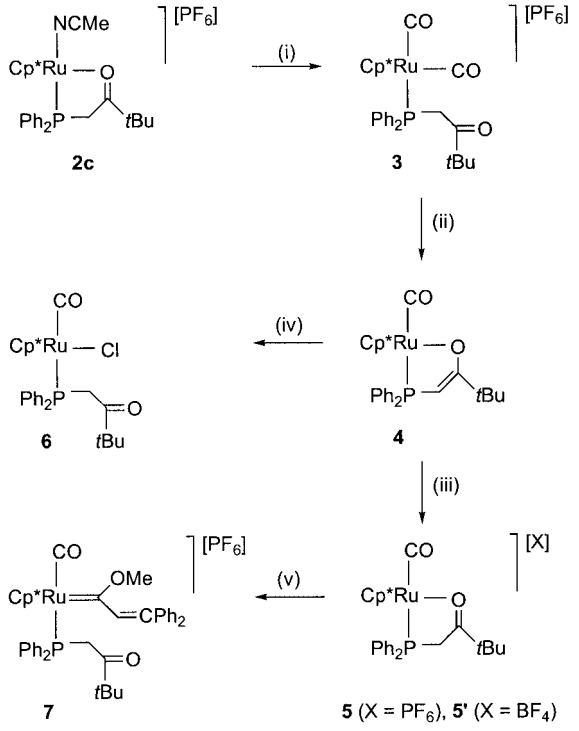


Scheme 3. Reactivity of complex **2c**: (i) CO, 1 atm; (ii) $Me_3NO{\cdot}2H_2O$; (iii) $HPF_6$ or $HBF_4$; (iv) HCl; (v) $Ph_2C(OH)C{\equiv}CH$, MeOH.

**7** (Scheme 3). The reaction might be conceived as an addition of methanol to a transient allenylidene species as previously investigated for $[Ru(Cp)(CO)(acetone)(P\textit{i}Pr_3)][BF_4]$.[11] Complexes **3**–**7** were characterised from a combination of $^1H$, $^{13}C\{^1H\}$, $^{13}C$ DEPT and $^{31}P\{^1H\}$ NMR, IR spectroscopy and elemental analysis. Owing to the chiral ruthenium centre, the two $PCH_2$ protons of the keto-phosphane were found to be diastereotopic in complexes **2c**, **5**, **5′**, **6** and **7**. Characteristic of the vinyl-carbene ligand in **7** is the observation by $^{13}C\{^1H\}$ NMR spectroscopy of a very low field resonance at $\delta$ = 303.7 ppm (d, $^2J_{PC}$ = 2.5 Hz) corresponding to the Ru=C carbon nucleus.[11] Some steric congestion in **7** is likely responsible for the broadness of both the $^{31}P\{^1H\}$ NMR resonance at $\delta$ = 38.8 ppm and the $^1H$ NMR resonance assigned to the OMe protons at $\delta$ = 4.05 ppm. IR spectroscopic data accounted for the presence of carbon monoxide as a ligand and for the coordination mode of the functional phosphane ($\tilde{\nu} \approx 1700\ cm^{-1}$, uncoordinated C=O, in **3**, **6** and **7**; $\tilde{\nu} \approx 1600\ cm^{-1}$, coordinated C=O, in **5** and **5′**; $\tilde{\nu} = 1500\ cm^{-1}$, C=CO, in **4**).[10]

Complexes **2a**–**c** were observed to react with allylic halides but crystallisable products were obtained only starting from **2a**. Using dichloromethane as solvent, the $\eta^3$-allyl ruthenium(IV) derivatives **8a**–**e** resulted from the reaction at room temperature between **2a** and 3-chloro-2-methylpropene, crotyl chloride or bromide, chlorohexene as a mixture of isomeric $n$PrCH=CHCH$_2$Cl and $n$PrCH(Cl)CH=CH$_2$, and cinnamyl chloride (Scheme 4). Complexes **8a**–**e** were isolated in high yield (62–85%) as yellow to red crystals that were observed to be stable in air. Of interest, the formation of complexes **8** was observed to be sluggish in acetonitrile as solvent. Thus, the addition of cinnamyl chloride (an excess) to a solution of **2a** in acetonitrile showed only about 10% of **2a** to be converted into **8e** after standing for two days at room temperature, as monitored by $^1H$ and $^{31}P\{^1H\}$ NMR spectroscopy. Indicating an irreversible formation, solutions of **8e** in acetonitrile were observed to be stable and unchanged after 8 days. Such an observation of a formation hindered by the presence of acetonitrile as coordinating solvent suggests a dissociative mechanism. The coordination of the olefinic bond of the allylic halide at a transient 16e-intermediate resulting from the loss of an acetonitrile ligand by **2a** would be a preliminary step allowing subsequent intramolecular oxidative addition.

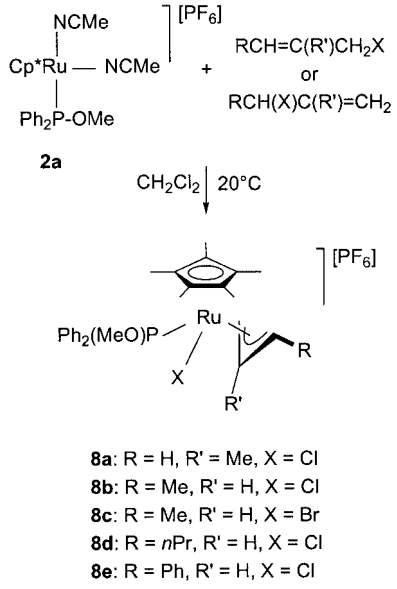


Scheme 4. Synthesis of the new $\eta^3$-allyl ruthenium(IV) complexes, **8a**–**e**.

Complexes **8a**–**e** were characterised by NMR spectroscopic techniques including $^1H\{^{31}P\}$ for **8c**,**d**, and elemental analysis. Of main interest, $CD_2Cl_2$ solutions of **8a**–**e** disclosed single species by $^1H$, $^{13}C\{^1H\}$ and $^{31}P\{^1H\}$ NMR spectroscopy. The characterisation of complexes **8a**–**e** was finally completed by an X-ray crystal structure determination of **8d** and **8e**. ORTEP drawings of cations of **8d** and **8e** are shown on Figure 2 and Figure 3, respectively. Selected bond lengths and angles are given in the captions of the figures.

Cations of **8d** and **8e** displayed a square-pyramidal structure with a chlorine, a phosphorus and the terminal carbon atoms of an *endo*-$\eta^3$-allyl ligand, at basal positions. Likely resulting from an increased steric demand, the Ru–P bond length in **8d** or **8e** [Ru1–P1 = 2.368(1) and 2.360(1) Å, respectively] is longer than in **2a** [Ru1–P1 = 2.2894(6) Å]. Moreover, the phosphorus atom in **8d** and **8e** is located in a *trans* position relative to the substituted allylic carbon and such an arrangement would minimise steric constraints between the allyl and the phosphorus ligands. The Ru–Cl bond lengths [2.406(1) Å in **8d**, 2.396(1) Å in **8e**] revealed

 © 2006 Wiley-VCH Verlag GmbH & Co. KGaA, Weinheim 

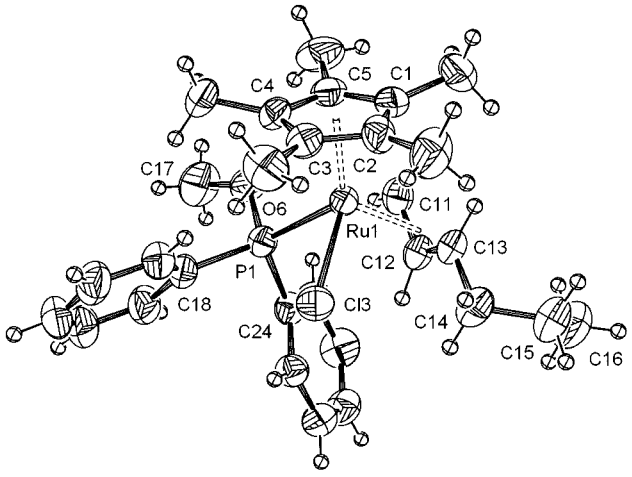


Figure 2. ORTEP drawing of **8d** showing 50% probability thermal ellipsoids. The $PF_6$ anion is omitted for clarity. Selected bond lengths [Å] and angles [°]: Ru1–C11 2.191(4), Ru1–C12 2.198(4), Ru1–C13 2.339(4), Ru1–P1 2.368(1), C11–C12 1.406(6), C12–C13 1.395(6), C13–C14 1.497(6), Ru1–P1 2.368(1); C11–C12–C13 119.1(4), C12–C13–C14 123.7(4).

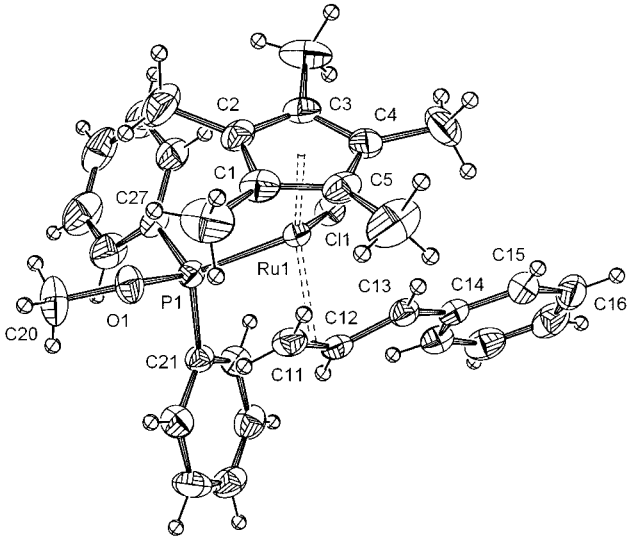


Figure 3. ORTEP drawing of **8e** showing 50% probability thermal ellipsoids. The $PF_6$ anion is omitted for clarity. Selected bond lengths [Å] and angles [°]: Ru1–C11 2.182(5), Ru1–C12 2.210(4), Ru1–C13 2.452(4), C11–C12 1.398(6), C12–C13 1.396(6), C13–C14 1.457(6), Ru1–P1 2.360(1); C11–C12–C13 119.5(4), C12–C13–C14 125.7(4).

no special feature and are very close to the values previously reported in the case of the related complexes $[Ru(Cp^*)Cl(MeCN)(\eta^3\text{-}PhCHCHCH_2)][PF_6]$ and $[Ru(Cp^*)Cl_2(\eta^3\text{-}PhCHCHCH_2)]$ [2.3998(7) and 2.398(3) Å, respectively].[5,13]

The only difference between **8d** and **8e** was an alkyl *n*-propyl group instead of a phenyl group, respectively, as the substituent linked to one terminal carbon of the $\eta^3$-allyl ligand. The Ru–C bond lengths involving the unsubstituted terminal allylic C11 carbon atom [2.191(4) Å in **8d** and 2.182(5) Å in **8e**] and the medium C12 carbon atom [2.198(4) Å in **8d** and 2.210(4) Å in **8e**] were close. The Ru–C13 bond length involving the substituted terminal carbon of the $\eta^3$-allyl ligand was significantly longer, especially in the case of **8e** [2.452(4) vs. 2.339(4) Å in **8d**]. These observations are in agreement with those arising from the study of the complexes $[Ru(Cp^*)(phenanthroline)(\eta^3\text{-cinnamyl})][PF_6]_2$,[12] $[Ru(Cp^*)Br(MeCN)(\eta^3\text{-crotyl})][PF_6]$[2] and $[Ru(Cp^*)Cl(MeCN)(\eta^3\text{-cinnamyl})][PF_6]$.[13]

A minor contribution from a formal $\eta^2$-olefinic $CH_2{=}CH{-}C^{(+)}HR$ coordination of the allyl ligand might intuitively account for both observation of a longer Ru–CHR bond and enhanced electrophilic reactivity at the substituted allylic carbon.[2,12,13] The comparison between the Ru–CHR bond lengths in **8d** and **8e** [2.339(4) and 2.452(4) Å, respectively] obviously suggested a reduced contribution from the formal $\eta^2$-olefinic coordination of the allyl ligand in **8d**. Therefore, high regioselectivities in favour of branched products might be expected to be more difficult to reach when starting from unsymmetrical alkyl-allylic substrates compared to cinnamyl derivatives.[2] However, the location of a bulky phosphane ligand close to the unsubstituted terminal allylic carbon atom, as displayed in **8d** and **8e**, might distinctly contribute to favour nucleophilic addition at the substituted one. To test these assumptions, the study of the potential of complexes **2a**–**c** as catalyst precursors for ruthenium-catalysed allylic substitution reactions was undertaken.

### Allylation Reactions Catalysed by Complexes 2a–c

The characterisation of an $\eta^3$-allyl ruthenium(IV) complex arising from an oxidative addition reaction between $[Ru(Cp^*)(MeCN)_3][PF_6]$ and *tert*-butyl cinnamyl carbonate recently provided further evidence for the key role of $\eta^3$-allyl ruthenium(IV) catalytic intermediates in ruthenium-catalysed nucleophilic allylic substitution reactions.[14] The activity of complexes **2a**–**c** as catalyst precursors for the allylation of dimethyl sodiomalonate with methyl cinnamyl carbonate was investigated. Thus, the addition of dimethyl sodiomalonate (1.2 equiv.) to a solution of methyl cinnamyl carbonate (0.5 mmol) in THF (3.0 mL) in the presence of **2a**–**c** (1.5 mol-%) at ambient temperature led to the monosubstituted dimethyl malonate **9** as a mixture of branched (B) and linear (L) isomers [Equation (1)], and disclosed a favoured formation of the branched isomer (Table 1).

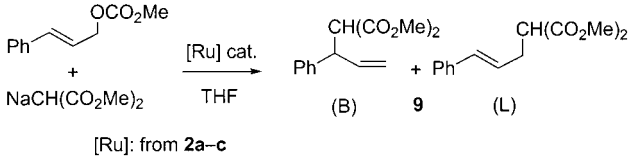


(1)

The results given in Table 1 clearly indicate that the three catalyst precursors **2a**–**c** provided complete conversion after 16 h of reaction. The regioselectivities in favour of the branched isomer of **9**, B/L ranging between 86:14 with **2c** and 92:8 with **2a**, were fairly good in comparison with those

 © 2006 Wiley-VCH Verlag GmbH & Co. KGaA, Weinheim 

Table 1. Comparison of complexes **2a**–**c** as catalyst precursors for the allylation of dimethyl sodiomalonate with methyl cinnamyl carbonate.[a]

| Entry | Catalyst | Conversion[b][c] | B/L ratio |
|---|---|---|---|
| 1 | **2a** | 100 | 92:8 |
| 2 | **2b** | 100 | 90:10 |
| 3 | **2c** | 100 | 86:14 |

[a] Conditions: 0.6 mmol of dimethyl sodiomalonate, 0.5 mmol of methyl cinnamyl carbonate, 0.0075 mmol of **2a** in 3 mL of THF, room temperature, 16 h. [b] Relative to methyl cinnamyl carbonate (%). [c] As determined by $^1$H NMR spectroscopy.

observed using **1** as the catalyst precursor.[1] However, complexes **2a**–**c**, as well as **1**,[2] were unable to catalyse this allylic alkylation without prior deprotonation of dimethyl malonate as achieved with [RuCp*(bipy)($CH_3CN$)][$PF_6$] precursors.[12]

The reaction of phenol with cinnamyl chloride in the presence of **2a** and potassium carbonate in dichloromethane as solvent was investigated also [Equation (2)]. The results are given in Table 2. Under experimental conditions analogous to those used with **1** as catalyst,[2] the reaction led to the formation of the allyl phenyl ether **10a** in a 85:15 branched to linear ratio (entry 1).

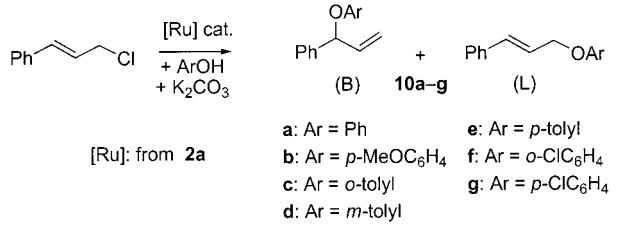


(2)

Table 2. Allylation of phenols ArOH with PhCH=$CHCH_2$Cl in the presence of **2a**.[a]

| Entry | Ar | Conversion[b][c] | Products | B/L ratio |
|---|---|---|---|---|
| 1 | Ph | 100 | **10a** | 85:15 |
| 2[d] | Ph | 0 | | |
| 3[e] | Ph | 0 | | |
| 4 | *p*-$MeOC_6H_4$ | 76 | **10b** | 92:8 |
| 5 | *o*-tolyl | 43 | **10c** | 88:12 |
| 6 | *m*-tolyl | 75 | **10d** | 73:27 |
| 7 | *p*-tolyl | 61 | **10e** | 88:12 |
| 8 | *o*-$ClC_6H_4$ | 52 | **10f** | 86:14 |
| 9 | *p*-$ClC_6H_4$ | 100 | **10g** | 50:50 |

[a] Conditions: 1.2 mmol of ArOH, 1.2 mmol of $K_2CO_3$, 1.0 mmol of cinnamyl chloride, 0.015 mmol of **2a** in 6 mL of $CH_2Cl_2$, room temperature, 16 h. [b] Relative to cinnamyl chloride (%). [c] As determined by $^1$H NMR spectroscopy. [d] THF as solvent. [e] Acetonitrile as solvent.

The regioselectivity was still fairly good although lower than that obtained with complex **1**.[2] Moreover, attempts to use THF or acetonitrile as solvent disclosed a lack of reactivity (entries 2, 3), whereas acetonitrile provided the best results in the case of catalyst **1**.[2] These observations suggested that the entrance of a phosphane ligand in complexes **2** would result in the strongest coordination of acetonitrile or THF, thus hindering the preliminary $\eta^2$-olefinic coordination of cinnamyl chloride as required for catalytic activity. The catalytic process proceeded smoothly for the allylation of various phenols in dichloromethane as solvent. Good regioselectivities were obtained starting from *p*-methoxyphenol (entry 4) and cresols (entries 5–7) as substituted phenols. Chlorophenols were also involved in the catalytic process (entries 8, 9) but only *o*-chlorophenol provided good regioselectivity.

Allyl aryl ethers arising from cinnamyl derivatives, valuable intermediates in organic chemistry, have drawn the main interest,[15] but another challenge is the development of efficient access to branched allyl aryl ethers starting from aliphatic allylic halides (vs. cinnamyl chloride-type substrates). The allylation of phenols with selected aliphatic or unconjugated allylic halides in the presence of **2a**–**c** as catalyst precursors was then investigated. Chlorohexene, synthesised as a 4:1 mixture of linear *n*PrCH=$CHCH_2$Cl and branched *n*PrCH(Cl)$CH=CH_2$ isomers starting from *trans*-2-hexen-1-ol and $PCl_3$,[16] reacted with various phenols to afford the allyl aryl ethers **11a**–**g**, as mixtures of branched *n*PrCH(OAr)$CH=CH_2$ and linear *n*PrCH=$CHCH_2$OAr isomers [Equation (3)]. The results are given in Table 3.

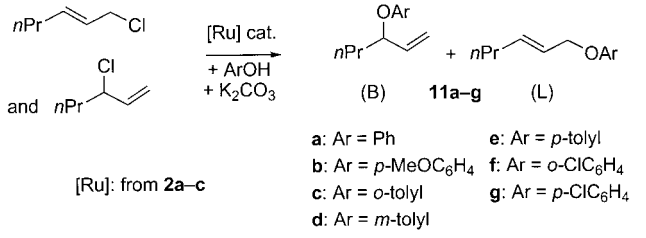


(3)

Table 3. Allylation of phenols ArOH with chlorohexene in the presence of **2a**–**c**.[a]

| Entry | Catalyst | Ar | Conversion[b][c] | Products | B/L ratio |
|---|---|---|---|---|---|
| 1 | **2a** | Ph | 100 | **11a** | 75:25 |
| 2[d] | **2a** | Ph | 100 | **11a** | 75:25 |
| 3[e] | **2a** | Ph | 100 | **11a** | 57:43 |
| 4 | **2b** | Ph | 94 | **11a** | 77:23 |
| 5 | **2c** | Ph | 100 | **11a** | 70:30 |
| 6 | **2a** | *p*-$MeOC_6H_4$ | 100 | **11b** | 61:39 |
| 7 | **2a** | *o*-tolyl | 74 | **11c** | 81:19 |
| 8 | **2a** | *m*-tolyl | 62 | **11d** | 75:25 |
| 9 | **2a** | *p*-tolyl | 88 | **11e** | 75:25 |
| 10 | **2a** | *o*-$ClC_6H_4$ | 62 | **11f** | 84:16 |
| 11 | **2a** | *p*-$ClC_6H_4$ | 99 | **11g** | 49:51 |

[a] Conditions: 1.2 mmol of ArOH, 1.5 mmol of $K_2CO_3$, 1.0 mmol of chlorohexene, 0.015 mmol of **2a**–**c** in 6 mL of THF, room temperature, 16 h. [b] Relative to chlorohexene (%). [c] As determined by $^1$H NMR spectroscopy. [d] Dichloromethane as solvent. [e] Acetonitrile as solvent.

In a typical run, the addition of phenol (1.2 equiv.) to chlorohexene (1.0 mmol) and $K_2CO_3$ (1.5 equiv.) in THF (6.0 mL) in the presence of **2a** (1.5 mol-%) for 16 h at ambient temperature resulted in the complete consumption of

 © 2006 Wiley-VCH Verlag GmbH & Co. KGaA, Weinheim 

chlorohexene and led to the formation of the allyl phenyl ether **11a** in a 75:25 B/L ratio (entry 1). Using complex **1** under similar catalytic conditions, chlorohexene was also converted into **11a**, but the regioselectivity was moderate, as emphasised by a B/L ratio of 60:40 in acetonitrile and 70:30 in acetone as solvent.[2] In the presence of complexes **2a**–**c**, the regioselectivity was slightly improved using THF or dichloromethane as solvent (entries 1, 2). As observed when starting from cinnamyl chloride, acetonitrile markedly disfavoured regioselectivity (entry 3). The involvement of **2b** and **2c** as catalysts (entries 4, 5) resulted in regioselectivities located in the same range as from **2a**. Complex **2a** was selected for the allylation of the substituted phenols. Using THF as solvent, satisfactory conversion and regioselectivity were reached with *p*-methoxyphenol and cresols (entries 6–9). The involvement of *p*-chlorophenol led to a 1:1 mixture of the branched and linear isomers of **11g** (entry 11), while *o*-chlorophenol was less reactive but provided a good B/L = 84:16 regioselectivity (entry 10). The low selectivity observed with *p*-chlorophenol might result from enhanced competition of the noncatalysed process, which contributed to the consumption of allylic halide but selectively led to the linear ether.

Readily available from benzyl bromide and allyl chloride,[17] 3-chloro-4-phenylbut-1-ene, $PhCH_2CH(Cl)CH=CH_2$, offered both the convenience of low volatility facilitating experimental work and an opportunity to test a pure branched allylic chloride under such catalytic conditions [Equation (4)]. The results are given in Table 4.

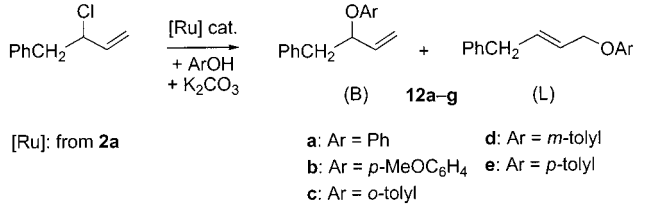


(4)

Table 4. Allylation of phenols ArOH with $PhCH_2CH(Cl)CH=CH_2$ catalysed by **2a**.[a]

| Entry | Ar | Conversion[b][c] | Products | B/L ratio |
|---|---|---|---|---|
| 1 | Ph | 87 | **12a** | 92:8 |
| 2[d] | Ph | 60 | **12a** | 73: 7 |
| 3[e] | Ph | 34 | **12a** | 50:50 |
| 4 | *p*-$MeOC_6H_4$ | 88 | **12b** | 96:4 |
| 5 | *o*-tolyl | 89 | **12c** | 92:8 |
| 6 | *m*-tolyl | 100 | **12d** | 96:4 |
| 7 | *p*-tolyl | 93 | **12e** | 91:9 |
| 8 | *o*-$ClC_6H_4$ | 0 | | |
| 9 | *p*-$ClC_6H_4$ | 0 | | |

[a] Conditions: 1.2 mmol of ArOH, 1.2 mmol of $K_2CO_3$, 1.0 mmol of allylic chloride, 0.015 mmol of **2a**–**c** in 6 mL of THF, room temperature, 16 h. [b] Relative to allylic chloride (%). [c] As determined by $^1H$ NMR spectroscopy. [d] Dichloromethane as solvent. [e] Acetonitrile as solvent.

Whereas the allylation of phenoxide anion in the presence of 3 mol-% of **1** afforded the ether **12a** with a rather poor B/L = 1.5:1 regioselectivity,[2] significantly increased regioselectivities up to B/L = 92:8 (entries 1, 2) were reached when catalyst **2a** was used. THF was an appropriate solvent but much lower conversion and regioselectivity were obtained in dichloromethane or acetonitrile (entries 1–3). It is worth noting the lack of reactivity when (*o*- or *p*-) chlorophenols were involved as the nucleophile (entries 8, 9), whereas good regioselectivities up to B/L = 96:4 were reached when *p*-methoxyphenol or (*o*-, *m*- or *p*-)cresols were involved as the nucleophile (entries 4–7).

## Conclusions

The reaction of one equiv. of phosphorus ligand with $[Ru(Cp^*)(MeCN)_3][PF_6]$ (**1**) allowed the selective substitution of one acetonitrile ligand, and the involvement of a hemilabile β-keto-phosphane provided a tool to selectively achieve the successive substitution of the three acetonitrile ligands by one phosphane, one carbon monoxide and one vinyl-carbene ligand. The products retaining acetonitrile as a ligand reacted with allylic halides to afford $\eta^3$-allyl ruthenium(IV) complexes and behave as catalyst precursors for allylic etherification of phenols with allylic chlorides in the presence of $K_2CO_3$, and alkylation of cinnamyl carbonate with dimethyl sodiomalonate under mild conditions. Although slightly less reactive than the unsubstituted parent complex **1**, the phosphane derivatives also favoured the formation of branched products when an unsymmetrical monosubstituted allylic substrate was involved, especially when starting from alkyl-substituted allylic substrates such as chlorohexene and 3-chloro-4-phenylbut-1-ene.

## Experimental Section

**General Comments:** The reactions were performed under inert argon according to Schlenk-type techniques. THF, diethyl ether and dichloromethane were distilled after drying according to conventional methods, whereas HPLC grade acetonitrile was straightforwardly used. NMR spectra were recorded at 297 K with AC 200 FT and AC 300 Bruker instruments and referenced internally to the solvent peak. IR spectra were recorded as Nujol mulls with Bruker IFS28. Elemental analyses were performed by the "Service de Microanalyse du CNRS" Vernaison, France. Complex **1** was synthesised according to the reported procedure.[2] Commercially available allylic halides were used without further purification whereas chlorohexene and 3-chloro-4-phenylbut-1-ene were prepared according to procedures described in the literature.[16,17]

**$[Ru(Cp^*)(Ph_2POMe)(MeCN)_2][PF_6]$ (2a):** Methyl diphenylphosphinite (2.0 mL, 9.98 mmol) was added to a cold solution (–80 °C) of **1** (5.04 g, 10.0 mmol) in a mixture of dichloromethane (70 mL) and acetonitrile (20 mL). After being stirred overnight at room temperature, the mixture was evaporated under vacuum. The crude product was dissolved in dichloromethane (80 mL) and the orange solution was covered with diethyl ether (200 mL). The natural diffusion of solvents resulted in the formation of orange crystals of **2a**. Yield: 5.30 g, 78%. $^1H$ NMR (200.13 MHz, $CD_2Cl_2$): $\delta$ = 1.57 (d, $^4J_{PH}$ = 2.0 Hz, 15 H, $C_5Me_5$), 2.27 (d, $^5J_{PH}$ = 1.3 Hz, 6 H, MeCN), 3.45 (d, $^3J_{PH}$ = 12.4 Hz, 3 H, OMe), 7.48–7.57 (m, 10 H, Ph) ppm. $^{13}C\{^1H\}$ NMR (50.32 MHz, $CD_2Cl_2$): $\delta$ = 4.2 (s, *Me*CN),

 © 2006 Wiley-VCH Verlag GmbH & Co. KGaA, Weinheim 

9.5 (s, $C_5Me_5$), 53.5 (d, $^2J$ = 5.7 Hz, OMe), 89.0 (d, $^2J$ = 2.2 Hz, $C_5Me_5$), 126.4 (s, Me*C*N), 128.7 (d, $^2J$ = 9.3 Hz, Ph, *ortho*), 130.8 (d, $^4J$ = 2.4 Hz, Ph, *para*), 131.8 (d, $^3J$ = 12.4 Hz, Ph, *meta*), 137.1 (d, $^1J$ = 37.3 Hz, Ph, *ipso*) ppm. $^{31}P\{^1H\}$ NMR (81.01 MHz, $CD_2Cl_2$): $\delta$ = 143.7 (s). $C_{27}H_{34}F_6N_2OP_2Ru$ (679.59): calcd. C 47.72, H 5.04, N 4.12, P 9.12; found C 47.56, H 5.12, N 4.06, P 9.17.

**[Ru(Cp*)(Ph$_2$P-*o*-tolyl)(MeCN)$_2$][PF$_6$] (2b):** Complex **2b** was similarly obtained by adding *o*-tolyldiphenylphosphane (1.68 g, 6.07 mmol) to a cold solution of **1** (3.06 g, 6.07 mmol) in a mixture of dichloromethane (70 mL) and acetonitrile (20 mL). After being stirred overnight at room temperature, the mixture was evaporated under vacuum to leave an oil that slowly crystallised. Diethyl ether (30 mL) was then added and the mixture was stirred to obtain a yellow powder that was collected by filtration and dried under vacuum. Yield: 4.45 g, 99%. $^1H$ NMR (200.13 MHz, $CD_2Cl_2$): $\delta$ = 1.42 (d, $^4J_{PH}$ = 1.6 Hz, 15 H, $C_5Me_5$), 2.11 (s, 3 H, Me), 2.20 (d, $^5J_{PH}$ = 1.5 Hz, 6 H, MeCN), 7.05–7.51 (m, 14 H, Ph) ppm. $^{13}C\{^1H\}$ NMR (50.32 MHz, $CD_2Cl_2$): $\delta$ = 4.2 (s, *Me*CN), 9.2 (s, $C_5Me_5$), 22.5 (d, $^3J$ = 7.0 Hz, Me), 87.1 (d, $^2J$ = 2.3 Hz, $C_5Me_5$), 126.4 (s, Me*C*N), 125.9–142.8 (m, $C_6$ rings) ppm. $^{31}P\{^1H\}$ NMR (81.01 MHz, $CD_2Cl_2$): $\delta$ = 46.2 (s) ppm. $C_{33}H_{38}F_6N_2P_2Ru$ (739.69): calcd. C 53.59, H 5.18, N 3.79, P 8.37; found C 52.98, H 5.22, N 3.71, P 8.33.

**{Ru(Cp*)[Ph$_2$PCH$_2$C(*t*Bu)=O](MeCN)}[PF$_6$] (2c):** A solution of $Ph_2PCH_2C(=O)tBu$ (2.58 g, 9.07 mmol) in dichloromethane (20 mL) was added to a cold solution (–80 °C) of **1** (4.58 g, 9.08 mmol) in a mixture of dichloromethane (60 mL) and acetonitrile (10 mL). After being stirred overnight at room temperature, the mixture was evaporated under vacuum. Methanol (30 mL) and diethyl ether (40 mL) were added to the residue and the mixture was stirred while an orange precipitate formed. The mixture was evaporated, then methanol (8 mL) and diethyl ether (60 mL) were added. The resulting orange crystalline precipitate was collected by filtration, then washed with diethyl ether and dried under vacuum. Yield: 6.06 g, 95%. IR: $\tilde{\nu}$ = 2269 cm$^{-1}$, C≡N; 1611 cm$^{-1}$, C=O. $^1H$ NMR (300.13 MHz, $CD_2Cl_2$): $\delta$ = 1.26 (s, 9 H, *t*Bu), 1.47 (d, $^4J_{PH}$ = 1.8 Hz, 15 H, $C_5Me_5$), 2.09 (d, $^5J_{PH}$ = 1.5 Hz, 3 H, MeCN), 2.94 (dd, $^2J_{HH}$ = 18.6, $^2J_{PH}$ = 7.5 Hz, 1 H, $PCH_2$, $H_a$), 4.24 (dd, $^2J_{HH}$ = 18.6, $^2J_{PH}$ = 10.1 Hz, 1 H, $PCH_2$, $H_b$), 6.85–7.65 (m, 10 H, Ph) ppm. $^{13}C\{^1H\}$ NMR (50.32 MHz, $CD_2Cl_2$): $\delta$ = 4.1 (s, *Me*CN), 9.9 (s, $C_5Me_5$), 27.0 (s, C$Me_3$), 45.8 (d, $^3J$ = 1.8 Hz, *C*Me$_3$), 46.5 (d, $^1J$ = 21.5 Hz, $PCH_2$), 85.7 (d, $^2J$ = 2.2 Hz, $C_5Me_5$), 127.7 (s, Me*C*N), 129.2 (d, $^2J$ = 10.3 Hz, Ph, *ortho*), 129.4 (d, $^1J$ = 42.1 Hz, Ph, *ipso*), 129.6 (d, $^2J$ = 10.2 Hz, Ph, *ortho*), 130.7 (d, $^3J$ = 10.9 Hz, Ph, *meta*), 130.7 (d, $^4J$ = 2.5 Hz, Ph, *para*), 132.1 (d, $^4J$ = 1.3 Hz, Ph, *para*), 134.9 (d, $^3J$ = 14.0 Hz, Ph, *meta*), 137.0 (d, $^1J$ = 39.3 Hz, Ph, *ipso*), 228.9 (d, $^2J$ = 7.1 Hz, C=O) ppm. $^{31}P\{^1H\}$ NMR (121.50 MHz, $CD_2Cl_2$): $\delta$ = 62.1 (s) ppm. $C_{30}H_{39}F_6NOP_2Ru$ (706.65): calcd. C 50.99, H 5.56, N 1.98, P 8.77; found C 50.37, H 5.64, N 1.89, P 8.79.

**{Ru(Cp*)(CO)$_2$[Ph$_2$PCH$_2$C(=O)*t*Bu]}[PF$_6$]·CH$_2$Cl$_2$ (3):** A solution of **2c** (6.06 g, 8.58 mmol) in a mixture of methanol (40 mL) and dichloromethane (40 mL) was stirred for 24 h under carbon monoxide and was then evaporated under vacuum. The residue was dissolved in dichloromethane (25 mL) and the solution was covered with methanol (5 mL) then diethyl ether (250 mL), to afford pale brown crystals. Yield: 6.03 g, 87%. Note that several recrystallisations are needed to obtain almost colourless crystals. $^1H$ NMR spectroscopy and elemental analysis provided evidence for the retention of one molecule of dichloromethane. However, a minor crystalline form free of dichloromethane was also detected. IR: $\tilde{\nu}$ = 2046, 2005 cm$^{-1}$, C≡O; 1701 cm$^{-1}$, C=O. $^1H$ NMR (300.13 MHz, $CD_2Cl_2$): $\delta$ = 0.97 (s, 9 H, *t*Bu), 1.72 (d, $^4J_{PH}$ = 2.0 Hz, 15 H, $C_5Me_5$), 3.83 (d, $^2J_{PH}$ = 9.6 Hz, 2 H, $PCH_2$), 7.33–7.56 (m, 10 H, Ph) ppm. $^{13}C\{^1H\}$ NMR (50.32 MHz, $CD_2Cl_2$): $\delta$ = 9.8 (s, $C_5Me_5$), 26.2 (s, C$Me_3$), 40.0 (d, $^1J$ = 36.8 Hz, $PCH_2$), 45.8 (d, $^3J$ = 2.2 Hz, *C*Me$_3$), 103.6 (s, $C_5Me_5$), 130.0 (d, $^1J$ = 50.2 Hz, Ph, *ipso*), 130.0 (d, $^2J$ = 11.1 Hz, Ph, *ortho*), 132.5 (d, $^3J$ = 11.6 Hz, Ph, *meta*), 132.6 (d, $^4J$ = 3.0 Hz, Ph, *para*), 198.8 (d, $^2J$ = 15.6 Hz, C≡O), 209.7 (d, $^2J$ = 4.0 Hz, C=O) ppm. $^{31}P\{^1H\}$ NMR (121.50 MHz, $CD_2Cl_2$): $\delta$ = 32.5 (s) ppm. $C_{30}H_{36}F_6O_3P_2Ru{\cdot}CH_2Cl_2$ (806.56): calcd. C 46.16, H 4.75, Cl 8.79, P 7.68; found C 46.47, H 4.68, Cl 7.35, P 7.67 (some presence of the minor form free of dichloromethane is likely responsible for the high carbon and low chlorine values).

**Ru(Cp*)(CO)[Ph$_2$PCH=C(*t*Bu)O] (4):** A mixture consisting of **3** (6.25 g, 7.75 mmol), $Me_3NO{\cdot}2H_2O$ (1.00 g, 9.00 mmol) and methanol (60 mL) was stirred overnight to afford a yellow slurry. Dissolution of the precipitate was subsequently obtained upon heating and completed by adding some dichloromethane (≈10 mL). The hot solution deposited yellow crystals of **4** upon cooling to –20 °C after partial removal of solvents (20 mL) under a stream of argon. Yield: 3.43 g, 81%. Note that further concentration of the solution led to a mixture of additional **4** and of ammonium salt. However, treatment of the mother liquor with an excess of $NH_4Cl$ allowed conversion of residual **4** into **6**, which may be subsequently separated according to selective dissolution in diethyl ether. IR: $\tilde{\nu}$ = 1933 cm$^{-1}$, C≡O; 1500 cm$^{-1}$, C=CO. $^1H$ NMR (300.13 MHz, $CD_2Cl_2$): $\delta$ = 1.19 (s, 9 H, *t*Bu), 1.53 (d, $^4J_{PH}$ = 1.5 Hz, 15 H, $C_5Me_5$), 4.59 (d, $^2J_{PH}$ = 2.9 Hz, 1 H, PCH=), 7.13–7.66 (m, 10 H, Ph) ppm. $^{13}C\{^1H\}$ NMR (50.32 MHz, $CD_2Cl_2$): $\delta$ = 9.7 (s, $C_5Me_5$), 30.0 (s, C$Me_3$), 38.5 (d, $^3J$ = 12.2 Hz, *C*Me$_3$), 74.5 (d, $^1J$ = 59.8 Hz, PCH), 95.3 (s, $C_5Me_5$), 128.2 (d, $^2J$ = 10.3 Hz, Ph, *ortho*), 128.4 (d, $^2J$ = 11.0 Hz, Ph, *ortho*), 128.9 (d, $^4J$ = 2.4 Hz, Ph, *para*), 129.8 (s, *para*), 131.7 (d, $^3J$ = 9.8 Hz, Ph, *meta*), 133.3 (d, $^3J$ = 11.0 Hz, Ph, *meta*), 138.5 (d, $^1J$ = 59.8 Hz, Ph, *ipso*), 140.2 (d, $^1J$ = 40.3 Hz, Ph, *ipso*), 200.8 (d, $^2J$ = 17.1 Hz, =CO), 206.0 (d, $^2J$ = 19.5 Hz, C≡O) ppm. $^{13}C$ NMR (50.32 MHz, $CD_2Cl_2$, selected values): $\delta$ = 74.5 (dd, $J_{HC}$ = 162.4, $J_{PC}$ = 58.6 Hz, PCH=) ppm. $^{31}P\{^1H\}$ NMR (121.50 MHz, $CD_2Cl_2$): $\delta$ = 55.3 (s) ppm. $C_{29}H_{35}O_2PRu$ (547.64): calcd. C 63.60, H 6.44, P 5.66; found C 63.65, H 6.39, P 5.98.

**{Ru(Cp*)(CO)[Ph$_2$PCH$_2$C(*t*Bu)=O]}[PF$_6$] (5):** A commercial 60% weight aqueous solution of $HPF_6$ (0.54 mL, 3.66 mmol) was added to a cold slurry (–80 °C) of **4** (2.00 g, 3.65 mmol) in methanol (40 mL). The mixture was warmed to room temperature and further stirred for 1 h. The resulting yellow solution was evaporated to dryness under vacuum and the residue was dissolved in dichloromethane (20 mL). The solution was covered with methanol (5 mL) then diethyl ether (140 mL) to afford orange needles. Yield: 2.05 g, 81%. IR: $\tilde{\nu}$ = 1975 cm$^{-1}$, C≡O; 1603 cm$^{-1}$, C=O. $^1H$ NMR (200.13 MHz, $CD_2Cl_2$): $\delta$ = 1.38 (s, 9 H, *t*Bu), 1.70 (d, $^4J_{PH}$ = 2.0 Hz, 15 H, $C_5Me_5$), 3.33 (dd, $^2J_{HH}$ = 18.5, $^2J_{PH}$ = 8.6 Hz, 1 H, $PCH_2$, $H_a$), 4.77 (dd, $^2J_{HH}$ = 18.4, $^2J_{PH}$ = 10.7 Hz, 1 H, $PCH_2$, $H_b$), 6.79–6.89 (m, 2 H, Ph), 7.48–7.72 (m, 8 H, Ph) ppm. $^{13}C\{^1H\}$ NMR (50.32 MHz, $CD_2Cl_2$): $\delta$ = 9.9 (s, $C_5Me_5$), 27.1 (s, C$Me_3$), 46.8 (d, $^3J$ = 2.3 Hz, *C*Me$_3$), 48.8 (d, $^1J$ = 29.2 Hz, $PCH_2$), 97.6 (d, $^2J$ = 1.6 Hz, $C_5Me_5$), 128.9 (d, $^1J$ = 57.1 Hz, Ph, *ipso*), 129.9 (d, $^2J$ = 10.2 Hz, Ph, *ortho*), 130.1 (d, $^2J$ = 11.7 Hz, Ph, *ortho*), 130.4 (d, $^3J$ = 11.0 Hz, Ph, *meta*), 132.1 (d, $^4J$ = 2.5 Hz, Ph, *para*), 132.6 (part of d, Ph, *ipso*), 133.3 (d, $^4J$ = 2.5 Hz, Ph, *para* and hidden part of d, Ph, *ipso*), 134.5 (d, $^3J$ = 12.5 Hz, Ph, *meta*), 202.8 (d, $^2J$ = 16.5 Hz, C≡O), 233.1 (d, $^2J$ = 4.0 Hz, C=O) ppm. $^{31}P\{^1H\}$ NMR (81.01 MHz, $CD_2Cl_2$): $\delta$ = 66.5 (s), –143.2 (sept, $PF_6$) ppm. $C_{29}H_{36}F_6O_2P_2Ru$ (693.61): calcd. C 50.22, H 5.23, P 8.93; found C 50.06, H 5.31, P 8.47.

 © 2006 Wiley-VCH Verlag GmbH & Co. KGaA, Weinheim 

**{Ru(Cp*)(CO)[$Ph_2PCH_2C(tBu)$=O]}[$BF_4$] (5′):** Large yellow-brown crystals of **5′** were similarly obtained in 80% yield after adding $HBF_4{\cdot}OMe_2$ (as a 0.7 M solution in methanol) to a cold slurry of **4** in methanol. IR: $\tilde{\nu}$ = 1957 $cm^{-1}$, C≡O; 1597 $cm^{-1}$, C=O. $^1H$ NMR (200.13 MHz, $CD_2Cl_2$): $\delta$ = 1.38 (s, 9 H, *t*Bu), 1.70 (d, $^4J_{PH}$ = 2.0 Hz, 15 H, $C_5Me_5$), 3.38 (dd, $^2J_{HH}$ = 18.7, $^2J_{PH}$ = 8.6 Hz, 1 H, $PCH_2$, $H_a$), 4.85 (dd, $^2J_{HH}$ = 18.6, $^2J_{PH}$ = 10.7 Hz, 1 H, $PCH_2$, $H_b$), 6.79–7.72 (m, 10 H, Ph) ppm. $^{13}C\{^1H\}$ NMR (50.32 MHz, $CD_2Cl_2$): $\delta$ = 9.9 (s, $C_5Me_5$), 27.1 (s, $CMe_3$), 46.8 (d, $^3J$ = 2.4 Hz, $CMe_3$), 48.7 (d, $^1J$ = 29.0 Hz, $PCH_2$), 97.5 (d, $^2J$ = 1.5 Hz, $C_5Me_5$), 129.0 (d, $^1J$ = 57.2 Hz, Ph, *ipso*), 129.8 (d, $^2J$ = 10.0 Hz, Ph, *ortho*), 130.0 (d, $^2J$ = 10.4 Hz, Ph, *ortho*), 130.4 (d, $^3J$ = 10.9 Hz, Ph, *meta*), 132.0 (d, $^4J$ = 2.2 Hz, Ph, *para*), 133.0 (d, $^1J$ = 39.8 Hz, Ph, *ipso*), 133.2 (d, $^4J$ = 3.0 Hz, Ph, *para*), 134.6 (d, $^3J$ = 12.7 Hz, Ph, *meta*), 202.9 (d, $^2J$ = 17.3 Hz, C≡O), 233.4 (d, $^2J$ = 4.9 Hz, C=O) ppm. $^{31}P\{^1H\}$ NMR (81.01 MHz, $CD_2Cl_2$): $\delta$ = 66.2 (s) ppm. $C_{29}H_{36}BF_4O_2PRu$ (635.45): calcd. C 54.81, H 5.71, P 4.87; found C 54.79, H 5.76, P 4.87.

**Ru(Cp*)Cl(CO)[$Ph_2PCH_2C$(=O)*t*Bu] (6):** 37% weight aqueous hydrochloric acid (0.30 mL, 3.65 mmol) was added to a cold slurry (–80 °C) of **4** (2.00 g, 3.65 mmol) in methanol (35 mL). The mixture was warmed to room temperature and further stirred for 1 h. The resulting solution was evaporated to dryness under vacuum and the residue was extracted with diethyl ether (30 mL). The solution was filtered and then slowly evaporated under vacuum to leave an orange-yellow solid. Yield: 2.04 g, 96%. IR: $\tilde{\nu}$ = 1916 $cm^{-1}$, C≡O; 1690 $cm^{-1}$, C=O. $^1H$ NMR (200.13 MHz, $CDCl_3$): $\delta$ = 0.82 (s, 9 H, *t*Bu), 1.48 (d, $^4J_{PH}$ = 1.9 Hz, 15 H, $C_5Me_5$), 3.90 (dd, $^2J_{HH}$ = 16.1, $^2J_{PH}$ = 6.6 Hz, 1 H, $PCH_2$, $H_a$), 4.08 (dd, $^2J_{HH}$ = 16.0, $^2J_{PH}$ = 8.5 Hz, 1 H, $PCH_2$, $H_b$), 7.39–7.43 (m, 6 H, Ph), 7.65–7.78 (m, 4 H, Ph) ppm. $^1H$ NMR (200.13 MHz, $CD_2Cl_2$): $\delta$ = 0.86 (s, 9 H, *t*Bu), 1.49 (d, $^4J_{PH}$ = 1.8 Hz, 15 H, $C_5Me_5$), 4.00 (d, $^2J_{PH}$ = 7.8 Hz, 2 H, $PCH_2$), 7.43–7.77 (m, 10 H, Ph) ppm. $^{13}C\{^1H\}$ NMR (50.32 MHz, $CD_2Cl_2$): $\delta$ = 9.9 (s, $C_5Me_5$), 26.5 (s, $CMe_3$), 38.0 (d, $^1J$ = 23.4 Hz, $PCH_2$), 46.2 (d, $^3J$ = 1.5 Hz, $CMe_3$), 96.9 (d, $^2J$ = 2.5 Hz, $C_5Me_5$), 128.6 (d, $^2J$ = 10.2 Hz, Ph, *ortho*), 128.8 (d, $^2J$ = 9.3 Hz, Ph, *ortho*), 130.9 (d, $^4J$ = 1.6 Hz, 2 C, Ph, *para*), 133.3 (d, $^1J$ = 40.0 Hz, Ph, *ipso*), 134.2 (d, $^3J$ = 11.0 Hz, Ph, *meta*), 134.3 (d, $^3J$ = 10.2 Hz, Ph, *meta*), 134.3 (d, $^1J$ = 46.9 Hz, Ph, *ipso*), 207.2 (d, $^2J$ = 21.2 Hz, C≡O), 210.8 (d, $^2J$ = 7.9 Hz, C=O) ppm. $^{31}P\{^1H\}$ NMR (81.01 MHz, $CD_2Cl_2$): $\delta$ = 41.9 (s) ppm. $C_{29}H_{36}ClO_2PRu$ (584.10): calcd. C 59.63, H 6.21, Cl 6.07, P 5.30; found C 60.09, H 6.38, Cl 6.30, P 5.20.

**{Ru(Cp*)(CO)[=C(OMe)CH=$CPh_2$][$Ph_2PCH_2C$(=O)*t*Bu]}[$PF_6$] (7):** A solution of **5** (1.00 g, 1.44 mmol) and of 1,1-diphenyl-2-propyn-1-ol (0.50 g, 2.40 mmol) in methanol (30 mL) was stirred at room temperature for 20 h. The resulting dark red precipitate was collected by filtration and washed with diethyl ether (20 mL), then dissolved in dichloromethane (25 mL). This solution was covered first with methanol (10 mL) then diethyl ether (120 mL) to afford orange-red crystals. Yield: 1.16 g, 88%. IR: $\tilde{\nu}$ = 1948 $cm^{-1}$, C≡O; 1709 $cm^{-1}$, C=O. $^1H$ NMR (200.13 MHz, $CD_2Cl_2$): $\delta$ = 1.06 (s, 9 H, *t*Bu), 1.56 (d, $^4J_{PH}$ = 1.7 Hz, 15 H, $C_5Me_5$), 3.76 (dd, $^2J_{HH}$ = 17.3, $^2J_{PH}$ = 7.2 Hz, 1 H, $PCH_2$, $H_a$), 3.86 (dd, $^2J_{HH}$ = 17.5, $^2J_{PH}$ = 8.1 Hz, 1 H, $PCH_2$, $H_b$), 4.05 (s, broad, 3 H, OMe), 6.15 (d, $^4J_{PH}$ = 1.8 Hz, 1 H, CH=), 6.99–7.59 (m, 20 H, Ph) ppm. $^{13}C\{^1H\}$ NMR (50.32 MHz, $CD_2Cl_2$): $\delta$ = 9.8 (s, $C_5Me_5$), 26.3 (s, $CMe_3$), 38.9 (d, $^1J$ = 31.9 Hz, $PCH_2$), 46.0 (s, $CMe_3$), 65.6 (s, $OCH_3$), 103.0 (s, $C_5Me_5$), 129.0–144.6 (m, CH= and Ph), 205.0 (d, $^2J$ = 17.1 Hz, C≡O), 209.0 (d, $^2J$ = 6.3 Hz, C=O), 303.7 (d, $^2J$ = 2.5 Hz, Ru=C) ppm. $^{31}P\{^1H\}$ NMR (81.01 MHz, $CD_2Cl_2$): $\delta$ = 38.8 (s, broad) ppm. $C_{45}H_{50}F_6O_3P_2Ru$ (915.90): calcd. C 59.01, H 5.50, P 6.76; found C 58.73, H 5.57, P 6.60.

**[Ru(Cp*)Cl($Ph_2POMe$)($CH_2CMeCH_2$)][$PF_6$] (8a):** An excess of 3-chloro-2-methylpropene (0.40 mL, 4.1 mmol) was added to a solution of **2a** (0.67 g, 0.99 mmol) in dichloromethane (25 mL). After being stirred overnight, the solution was covered with diethyl ether (100 mL) to afford orange-yellow crystals. Yield: 0.48 g, 70%. $^1H$ NMR (200.13 MHz, $CD_2Cl_2$): $\delta$ = 1.01 (s, 3 H, Me), 1.71 (d, $^4J_{PH}$ = 2.2 Hz, 15 H, $C_5Me_5$), 2.01 (broad s, 1 H, $CH_2$, *anti*), 3.07 (d, $^3J_{PH}$ = 3.8 Hz, 1 H, $CH_2$, *anti*), 3.41 (dd, $^4J_{HH} \approx {}^3J_{PH} \approx$ 2.3 Hz, 1 H, $CH_2$, *syn*), 3.60 (broad d, $^3J_{PH}$ = 11.0 Hz, 1 H, $CH_2$, *syn*), 3.79 (d, $^3J_{PH}$ = 11.0 Hz, 3 H, OMe), 7.45–7.70 (m, 10 H, Ph) ppm. $^{13}C\{^1H\}$ NMR (50.32 MHz, $CD_2Cl_2$): $\delta$ = 9.9 (s, $C_5Me_5$), 17.0 (s, Me, allyl), 53.4 (d, $^2J$ = 4.0 Hz, $CH_2$), 58.5 (d, $^2J$ = 14.8 Hz, OMe), 70.2 (d, $^2J$ = 6.2 Hz, $CH_2$), 107.2 (d, $^2J$ = 1.5 Hz, $C_5Me_5$), 116.1 (d, $^2J$ = 1.6 Hz, *C*Me, allyl), 128.5 (d, $^2J$ = 10.1 Hz, Ph, *ortho*), 128.6 (d, $^1J$ = 43.6 Hz, Ph, *ipso*), 129.4 (d, $^2J$ = 10.3 Hz, Ph, *ortho*), 131.9 (d, $^1J$ = 43.1 Hz, Ph, *ipso*), 133.2 (d, $^3J$ = 9.2 Hz, Ph, *meta*), 133.2 (d, $^4J$ = 3.8 Hz, Ph, *para*), 133.3 (d, $^4J$ = 2.5 Hz, Ph, *para*), 135.7 (d, $^3J$ = 11.0 Hz, Ph, *meta*) ppm. $^{31}P\{^1H\}$ NMR (81.01 MHz, $CD_2Cl_2$): $\delta$ = 124.5 (s) ppm. $C_{27}H_{35}ClF_6OP_2Ru$ (688.04): calcd. C 47.13, H 5.13, Cl 5.15, P 9.00; found C 47.11, H 5.02, Cl 5.27, P 8.70.

**[Ru(Cp*)Cl($Ph_2POMe$)($MeCHCHCH_2$)][$PF_6$] (8b):** An excess of 3-chloro-1-butene (0.50 mL, 5.0 mmol) was added to a solution of **2a** (0.84 g, 1.24 mmol) in dichloromethane (25 mL). After being stirred for 1 h, the solution was covered with diethyl ether (110 mL) to afford orange-yellow crystals. Yield: 0.72 g, 84%. $^1H$ NMR (200.13 MHz, $CD_2Cl_2$): $\delta$ = 1.27 (dd, $^3J_{HH}$ = 6.3, $^4J_{PH}$ = 1.4 Hz, 3 H, Me), 1.79 (d, $^4J_{PH}$ = 2.2 Hz, 15.5 H, $C_5Me_5$ and part of d, 0.5 H, $CH_2$, *anti*), 1.83 (part of d, 0.5 H, $CH_2$, *anti*), 3.29 (dddd, $^3J_{HHtrans} \approx$ 10.4, $^3J_{HHcis}$ = 6.0, $^3J_{PH}$ = 3.9 Hz, 1 H, CH), 3.67 (d, $^3J_{PH}$ = 11.0 Hz, 3 H, OMe), 3.72–3.83 (m, 2 H, C*H*Me and $CH_2$, *syn*), 7.41–7.71 (m, 10 H, Ph) ppm. $^{13}C\{^1H\}$ NMR (50.32 MHz, $CD_2Cl_2$): $\delta$ = 9.4 (s, $C_5Me_5$), 16.9 (d, $^3J$ = 1.5 Hz, CH*Me*), 52.8 (d, $^2J$ = 3.9 Hz, $CH_2$), 58.1 (d, $^2J$ = 14.7 Hz, OMe), 96.4 (d, $^2J \approx$ 3 Hz, *C*HMe) 96.4 (s, CH), 106.0 (d, $^2J$ = 1.6 Hz, $C_5Me_5$), 125.8 (d, $^1J$ = 49.4 Hz, Ph, *ipso*), 127.9 (d, $^2J$ = 10.9 Hz, Ph, *ortho*), 128.7 (d, $^2J$ = 10.4 Hz, Ph, *ortho*), 130.2 (d, $^1J$ = 44.5 Hz, Ph, *ipso*), 131.2 (d, $^3J$ = 9.2 Hz, Ph, *meta*), 132.2 (d, $^4J$ = 3.0 Hz, Ph, *para*), 132.9 (d, $^4J$ = 2.5 Hz, Ph, *para*), 135.8 (d, $^3J$ = 10.3 Hz, Ph, *meta*) ppm. $^{31}P\{^1H\}$ NMR (81.01 MHz, $CD_2Cl_2$): $\delta$ = 128.5 (s) ppm. $C_{27}H_{35}ClF_6OP_2Ru$ (688.04): calcd. C 47.13, H 5.13, Cl 5.15, P 9.00; found C 46.85, H 5.27, Cl 4.97, P 9.20.

**[Ru(Cp*)Br($Ph_2POMe$)($MeCHCHCH_2$)][$PF_6$] (8c):** An excess of crotyl bromide (0.40 mL, 3.9 mmol) was added to a solution of **2a** (0.86 g, 1.27 mmol) in dichloromethane (25 mL). After being stirred for 1 h, the solution was covered with diethyl ether (120 mL) to afford orange crystals. Yield: 0.72 g, 77%. $^1H$ NMR (200.13 MHz, $CD_2Cl_2$): $\delta$ = 1.53 (dd, $^3J_{HH}$ = 6.1, $^4J_{PH}$ = 1.5 Hz, 3 H, Me), 1.76 (broad d, $^3J_{HHtrans}$ = 10.0 Hz, 1 H, $CH_2$, *anti*), 1.87 (d, $^4J_{PH}$ = 2.0 Hz, 15 H, $C_5Me_5$), 3.21 (dddd, $^3J_{HHtrans}$ = 11.1 and 9.9, $^3J_{HHcis}$ = 5.9, $^3J_{PH}$ = 3.6 Hz, 1 H, CH), 3.59 (d, $^3J_{PH}$ = 11.0 Hz, 3 H, OMe), 3.71 (ddq, $^3J_{HHtrans}$ = 11.0, $^3J_{HH}$ = 6.2, $^3J_{PH}$ = 3.2 Hz, 1 H, C*H*Me), 3.85 (ddd, $^3J_{HHcis}$ = 6.0, $^2J_{HH}$ = 2.2, $^3J_{PH}$ = 8.4 Hz, 1 H, $CH_2$, *syn*), 7.38–7.72 (m, 10 H, Ph) ppm. $^1H\{^{31}P\}$ NMR (200.13 MHz, $CD_2Cl_2$, selected values): $\delta$ = 1.79 (d, $^3J_{HHtrans}$ = 10.2 Hz, 1 H, $CH_2$, *anti*), 3.22 (dt, $^3J_{HHtrans} \approx$ 10.5, $^3J_{HHcis}$ = 6.4 Hz, 1 H, CH), 3.71 (dq, $^3J_{HHtrans}$ = 11.7, $^3J_{HH}$ = 6.1 Hz, 1 H, C*H*Me), 3.87 (broad d, $^3J_{HHcis}$ = 4.3 Hz, 1 H, $CH_2$, *syn*) ppm. $^{13}C\{^1H\}$ NMR (50.32 MHz, $CD_2Cl_2$): $\delta$ = 10.5 (s, $C_5Me_5$), 15.1 (d, $^3J$ = 1.6 Hz, CH*Me*), 53.1 (d, $^2J$ = 4.4 Hz, $CH_2$), 58.8 (d, $^2J$ = 14.8 Hz, OMe), 96.3 (s, CH), 96.9 (d, $^2J$ = 4.8 Hz, *C*HMe), 106.5 (d, $^2J$ = 1.7 Hz, $C_5Me_5$), 127.5 (d, $^1J$ = 50.9 Hz, Ph, *ipso*), 128.6 (d, $^2J$ = 10.3 Hz, Ph, *ortho*), 129.5 (d, $^2J$ = 10.1 Hz, Ph, *ortho*),

 © 2006 Wiley-VCH Verlag GmbH & Co. KGaA, Weinheim 

130.8 (d, $^1J$ = 45.0 Hz, Ph, *ipso*), 132.1 (d, $^3J$ = 8.6 Hz, Ph, *meta*), 133.1 (d, $^4J$ = 2.1 Hz, Ph, *para*), 133.8 (d, $^4J$ = 2.2 Hz, Ph, *para*), 137.0 (d, $^3J$ = 11.1 Hz, Ph, *meta*) ppm. $^{31}P\{^1H\}$ NMR (81.01 MHz, $CD_2Cl_2$): $\delta$ = 128.7 (s) ppm. $C_{27}H_{35}BrF_6OP_2Ru$ (732.49): calcd. C 44.27, H 4.82, Br 10.91, P 8.46; found C 44.18, H 4.80, Br 10.57, P 7.96.

**[Ru(Cp*)Cl(Ph$_2$POMe)(*n*PrCHCHCH$_2$)][PF$_6$] (8d):** An excess of chlorohexene (0.80 mL of a 4:1 mixture of linear 1-chloro-2-hexene and branched 3-chloro-1-hexene) was added to a solution of **2a** (1.84 g, 2.71 mmol) in dichloromethane (25 mL). After being stirred for 1 h, the solution was covered with diethyl ether (150 mL) to afford orange-yellow crystals. Yield: 1.65 g, 85%. $^1H$ NMR (200.13 MHz, $CD_2Cl_2$): $\delta$ = 0.92 (m, broad, 3 H, Me), 1.49 (m, broad, 4 H, 2 $CH_2$), 1.78 (d, $^4J_{PH}$ = 2.2 Hz, 15 H, $C_5Me_5$ and overlapped: m, 1 H, $CH_2$, *anti*), 3.32 (m, 1 H, CH), 3.67 (d, $^3J_{PH}$ = 10.8 Hz, 3 H, OMe and overlapped: m, 1 H, *n*PrC*H*), 3.86 (ddd, $^3J_{HHcis}$ = 5.9, $^2J_{HH}$ = 2.2, $^3J_{PH}$ = 8.2 Hz, 1 H, $CH_2$, *syn*), 7.42–7.68 (m, 10 H, Ph) ppm. $^1H\{^{31}P\}$ NMR (200.13 MHz, $CD_2Cl_2$): $\delta$ = 0.94 (m, broad, 3 H, Me), 1.51 (m, broad, 4 H, 2 $CH_2$), 1.80 (s, 15 H, $C_5Me_5$ and overlapped: m, 1 H, $CH_2$, *anti*), 3.34 (ddd, $^3J_{HHtrans} \approx {}^3J_{H'Htrans} \approx$ 10.5, $^3J_{HHcis}$ = 6.1 Hz,1 H, CH), 3.69 (s, 3 H, OMe and overlapped: m, 1 H, *n*PrC*H*), 3.88 (dd, $^3J_{HHcis}$ = 6.1, $^2J_{HH}$ = 2.1 Hz, 1 H, $CH_2$, *syn*), 7.47–7.70 (m, 10 H, Ph) ppm. $^{13}C\{^1H\}$ NMR (50.32 MHz, $CD_2Cl_2$): $\delta$ = 9.9 (s, $C_5Me_5$), 14.0 (s, $CH_3$), 23.1 (s, $CH_2$), 33.9 (s, $CH_2$) 53.3 (s, =$CH_2$), 58.5 (d, $^2J$ = 15.0 Hz, OMe), 96.1 (s, CH), 100.4 (d, $^2J$ = 4.4 Hz, *n*Pr*C*H), 106.5 (d, $^2J$ = 1.8 Hz, $C_5Me_5$), 126.2 (d, $^1J$ = 49.1 Hz, Ph, *ipso*), 128.4 (d, $^2J$ = 10.7 Hz, Ph, *ortho*), 129.2 (d, $^2J$ = 9.9 Hz, Ph, *ortho*), 130.6 (d, $^1J$ = 45.1 Hz, Ph, *ipso*), 131.6 (d, $^3J$ = 8.5 Hz, Ph, *meta*), 132.7 (d, $^4J$ = 2.6 Hz, Ph, *para*), 133.3 (d, $^4J$ = 2.3 Hz, Ph, *para*), 136.2 (d, $^3J$ = 10.6 Hz, Ph, *meta*) ppm. $^{31}P\{^1H\}$ NMR (81.01 MHz, $CD_2Cl_2$): $\delta$ = 128.2 (s) ppm. $C_{29}H_{39}ClF_6OP_2Ru$ (716.09): calcd. C 48.64, H 5.49, Cl 4.95, P 8.65; found C 48.39, H 5.55, Cl 5.16, P 8.72.

**[Ru(Cp*)Cl(Ph$_2$POMe)(PhCHCHCH$_2$)][PF$_6$] (8e):** An excess of cinnamyl chloride (0.60 mL, 4.3 mmol) was added to a solution of **2a** (1.00 g, 1.47 mmol) in dichloromethane (25 mL). After being stirred for 20 h, the solution was covered first with methanol (15 mL), then diethyl ether (130 mL) to afford dark red crystals. Yield: 0.68 g, 62%. $^1H$ NMR (200.13 MHz, $CD_2Cl_2$): $\delta$ = 1.79 (d, $^4J_{PH}$ = 1.9 Hz, 15 H, $C_5Me_5$), 2.12 (d, broad, $^3J_{HH}$ = 9.2 Hz, 1 H, $CH_2$, *anti*), 3.71 (d, $^3J_{PH}$ = 11.0 Hz, 3 H, OMe), 3.79–3.93 (m, broad, 1 H, CH), 3.94–4.03 (m, 1 H, $CH_2$, *syn*), 4.73 (dd, $^3J_{HH}$ = 12.0, $^3J_{PH}$ = 3.1 Hz, 1 H, C*H*Ph), 6.94–7.70 (m, 15 H, Ph) ppm. $^{13}C\{^1H\}$ NMR (50.32 MHz, $CD_2Cl_2$): $\delta$ = 10.0 (s, $C_5Me_5$), 51.4 (d, $^2J$ = 5.0 Hz, $CH_2$), 58.5 (d, $^2J$ = 14.9 Hz, OMe), 91.0 (s, CH), 103.4 (d, $^2J$ = 4.7 Hz, *C*HPh), 106.3 (s, $C_5Me_5$), 127.0 (s, Ph, *ipso*), 128.4 (s, Ph, *ortho*), 128.4 (d, $^2J$ = 10.0 Hz, PhP, *ortho*), 129.3 (d, $^2J$ = 10.0 Hz, PhP, *ortho*), 131.2 (d, $^1J$ = 44.5 Hz, PhP, *ipso*), 131.5 (d, $^3J$ = 8.6 Hz, PhP, *meta*), 131.5 (s, Ph, *para*), 132.3 (s, Ph, *meta*), 132.5 (d, $^1J$ = 34.5 Hz, PhP, *ipso*), 133.0 (d, $^4J$ = 2.6 Hz, PhP, *para*), 133.4 (d, $^4J$ = 2.3 Hz, PhP, *para*), 136.0 (d, $^3J$ = 10.3 Hz, PhP, *meta*) ppm. $^{31}P\{^1H\}$ NMR (81.01 MHz, $CD_2Cl_2$): $\delta$ = 129.0 (s) ppm. $C_{32}H_{37}ClF_6OP_2Ru$ (750.11): calcd. C 51.24, H 4.97, Cl 4.73, P 8.26; found C 51.05, H 5.08, Cl 4.65, P 8.49.

**X-ray Crystallography:** The samples were studied with a NONIUS Kappa CCD (**2a**, **8d**) or Oxford Diffraction Xcalibur Saphir 3 (**8e**) diffractometer with graphite monochromator. Crystallographic

Table 5. Crystallographic data for complexes **2a**, **8d** and **8e**.[a]

| Complex | **2a** | **8d** | **8e** |
|---|---|---|---|
| Empirical formula | $C_{27}H_{34}F_6N_2OP_2Ru$ | $C_{29}H_{39}ClF_6OP_2Ru$ | $C_{32}H_{37}ClF_6OP_2Ru$ |
| Molecular weight [g mol$^{-1}$] | 679.57 | 716.06 | 750.08 |
| Crystal size [mm] | 0.30 × 0.30 × 0.28 | 0.22 × 0.22 × 0.22 | 0.24 × 0.22 × 0.20 |
| Crystal system | monoclinic | orthorhombic | orthorhombic |
| Space group | $P2_1/c$ | *Pbca* | *Pbca* |
| *a* [Å] | 14.8025(2) | 14.6192(2) | 14.8064(6) |
| *b* [Å] | 11.5147(1) | 20.5531(2) | 21.0835(8) |
| *c* [Å] | 17.0685(2) | 20.7975(2) | 20.6072(9) |
| $\beta$ [°] | 90.258(1) | | |
| Volume [Å$^3$] | 2909.23(6) | 6248.0(1) | 6433.0(5) |
| *Z* | 4 | 8 | 8 |
| Density [g cm$^{-3}$] | 1.552 | 1.522 | 1.549 |
| Temperature [K] | 130(1) | 293(2) | 293(2) |
| *F*(000) | 1384 | 2928 | 3056 |
| Mo-$K_\alpha$ radiation, $\lambda$ [Å] | 0.71073 | 0.71073 | 0.71073 |
| Absorption coefficient [mm$^{-1}$] | 0.711 | 0.747 | 0.730 |
| $\theta$ range [°] | 2.39–27.48 | 2.21–27.00 | 3.08–27.00 |
| Index ranges | $0 < h < 19$ | $0 < h < 18$ | $-12 < h < 12$ |
| | $0 < k < 14$ | $0 < k < 26$ | $-26 < k < 26$ |
| | $-22 < l < 22$ | $0 < l < 26$ | $-26 < l < 26$ |
| Reflections collected | 52105 | 105939 | 27593 |
| Independent reflections | 6652 ($R_{int}$ = 0.030) | 6811 ($R_{int}$ = 0.050) | 5899 ($R_{int}$ = 0.0519) |
| Reflections $I > 2\sigma(I)$ | 6121 | 5637 | 4981 |
| Refinement method | | Full-matrix least-squares on $F^2$ | |
| Data/restraints/parameters | 6652/0/371 | 6811/0/374 | 5899/0/389 |
| Goodness-of-fit on $F^2$ | 1.065 | 1.003 | 1.086 |
| Final *R* indices [$I > 2\sigma(I)$] | $R_1$ = 0.0374 | $R_1$ = 0.0492 | $R_1$ = 0.0545 |
| | $wR_2$ = 0.0968 | $wR_2$ = 0.1347 | $wR_2$ = 0.1411 |
| *R* indices (all data) | $R_1$ = 0.0408 | $R_1$ = 0.0612 | $R_1$ = 0.0642 |
| | $wR_2$ = 0.1004 | $wR_2$ = 0.1514 | $wR_2$ = 0.1507 |
| Largest diff. peak/hole [e Å$^{-3}$] | 1.005 and –0.797 | 0.709 and –0.734 | 0.982 and –0.786 |

[a] $w = 1/[\sigma^2(F_o^2) + (0.0518P)^2 + 6.0599P]$ (**2a**), $1/[\sigma^2(F_o^2) + (0.0843P)^2 + 11.8733P]$ (**8d**), $1/[\sigma^2(F_o^2) + (0.0754P)^2 + 15.1442P]$ (**8e**), where $P = (F_o^2 + 2F_c^2)/3$.

 © 2006 Wiley-VCH Verlag GmbH & Co. KGaA, Weinheim 

data are given in Table 5. The cell parameters were obtained with Denzo and Scalepack[18] (**2a**, **8d**) and data collection with NONIUS KappaCCD Software[19] (**2a**, **8d**) and CrysAlis RED[20] (**8e**). Data reduction was carried out with Denzo and Scalepack[18] (**2a**, **8d**) and CrysAlis RED[20] (**8e**). The structures were solved with SIR−97, which revealed the non-hydrogen atoms.[21] After anisotropic refinement, many hydrogen atoms were found with Fourier difference calculations. The whole structures were refined with SHELXL97 by full-matrix least-squares methods on $F^2$ ($x$, $y$, $z$, $\beta_{ij}$ for Ru, P, N, Cl, F, C and O atoms; $x$, $y$, $z$ in riding mode for H atoms).[22] ORTEP views were prepared with PLATON98.[23]

CCDC-261933 (for **2a**), -272359 (for **8d**) and -258428 (for **8e**) contain the supplementary crystallographic data for this paper. These data can be obtained free of charge from The Cambridge Crystallographic Data Centre via www.ccdc.cam.ac.uk/data_request/cif.

**Catalytic Experiments:** Organic compounds were identified from the comparison of $^1$H NMR spectra with available $^1$H NMR spectroscopic data.[24–26] In a typical experiment, a sample of phenol (1.2 mmol, 1.2 equiv.) was added to a stirred mixture consisting of allylic halide (1.0 mmol, 1.0 equiv.), catalyst precursor (0.015 mmol, 1.5 mol-%), $K_2CO_3$ (1.2–1.5 equiv.) and solvent (6.0 mL). The slurry was stirred at room temperature for 16 h and then was evaporated under vacuum. The residue was extracted with dichloromethane (20 mL) and the solution was filtered. The filtrate was evaporated to leave the crude product that was analysed by $^1$H NMR spectroscopy ($CDCl_3$) for conversion and regioselectivity determination.


[1] B. M. Trost, P. L. Fraisse, Z. T. Ball, *Angew. Chem. Int. Ed.* **2002**, *41*, 1059–1061.
[2] M. D. Mbaye, B. Demerseman, J.-L. Renaud, L. Toupet, C. Bruneau, *Adv. Synth. Catal.* **2004**, *346*, 835–841.
[3] M. D. Mbaye, J.-L. Renaud, B. Demerseman, C. Bruneau, *Chem. Commun.* **2004**, 1870–1871.
[4] Y. Matsushima, K. Onitsuka, T. Kondo, T. Mitsudo, S. Takahashi, *J. Am. Chem. Soc.* **2001**, *123*, 10405–10406.
[5] T. Kondo, H. Ono, N. Satabe, T. Mitsudo, Y. Watanabe, *Organometallics* **1995**, *14*, 1945–1953.
[6] Y. Matsushima, K. Onitsuka, S. Takahashi, *Organometallics* **2004**, *23*, 3763–3765.
[7] R. Schmid, K. Kirchner, *Eur. J. Inorg. Chem.* **2004**, 2609–2626.
[8] E. Rüba, W. Simanko, K. Mauthner, K. M. Soldouzi, C. Slugovc, K. Mereiter, R. Schmid, K. Kirchner, *Organometallics* **1999**, *18*, 3843–3850.
[9] E. Rüba, K. Mereiter, R. Schmid, K. Kirchner, E. Bustelo, M. C. Puerta, P. Valerga, *Organometallics* **2002**, *21*, 2912–2920.
[10] P. Crochet, B. Demerseman, M. I. Vallejo, M. P. Gamasa, J. Gimeno, J. Borge, S. García-Granda, *Organometallics* **1997**, *16*, 5406–5415.
[11] M. A. Esteruelas, A. V. Gómez, F. J. Lahoz, A. M. López, E. Oñate, L. A. Oro, *Organometallics* **1996**, *15*, 3423–3435.
[12] M. D. Mbaye, B. Demerseman, J.-L. Renaud, L. Toupet, C. Bruneau, *Angew. Chem. Int. Ed.* **2003**, *42*, 5066–5068.
[13] R. Hermatschweiler, I. Fernández, P. S. Pregosin, E. J. Watson, A. Albinati, S. Rizzato, L. F. Veiros, M. J. Calhorda, *Organometallics* **2005**, *24*, 1809–1812.
[14] R. Hermatschweiler, I. Fernández, F. Breher, P. S. Pregosin, L. F. Veiros, M. J. Calhorda, *Angew. Chem. Int. Ed.* **2005**, *44*, 4397–4400.
[15] B. M. Trost, M. L. Crawley, *Chem. Rev.* **2003**, *103*, 2921–2944.
[16] C. D. Hurd, R. W. McNamee, *J. Am. Chem. Soc.* **1932**, *54*, 1648–1651.
[17] M. Julia, J.-N. Verpeaux, T. Zahneisen, *Bull. Soc. Chim. Fr.* **1994**, *131*, 539–554.
[18] Processing of X-ray diffraction data collected in oscillation mode: Z. Otwinowski, W. Minor, *Methods Enzymol.* **1997**, *276*, 307–326.
[19] *NONIUS KappaCCD Software*, Nonius BV, Delft, The Netherlands, **1999**.
[20] Oxford Diffraction Ltd., Abingdon, Oxfordshire, UK, **2004**.
[21] *SIR-97* – a new tool for crystal structure determination and refinement: A. Altomare, M. C. Burla, M. Camalli, G. Cascarano, C. Giacovazzo, A. Guagliardi, A. G. G. Moliterni, G. Polidori, R. Spagna, *J. Appl. Crystallogr.* **1998**, *31*, 74–77.
[22] G. M. Sheldrick, *SHELXL97 – Program for the Refinement of Crystal Structures*, University of Göttingen, Germany, **1997**.
[23] A. L. Spek, *PLATON – A Multipurpose Crystallographic Tool*, University of Utrecht, The Netherlands, **1998**.
[24] F. Lopez, T. Ohmura, J. F. Hartwig, *J. Am. Chem. Soc.* **2003**, *125*, 3426–3427.
[25] T. Satoh, M. Ikeda, M. Miura, M. Nomura, *J. Org. Chem.* **1997**, *62*, 4877–4879.
[26] C. Goux, M. Massacret, P. Lhoste, D. Sinou, *Organometallics* **1995**, *14*, 4585–4593.


Received: November 24, 2005
Published Online: February 21, 2006

 © 2006 Wiley-VCH Verlag GmbH & Co. KGaA, Weinheim 

DOI: 10.1002/ejic.200500741

# Tuning of the Spin States in Trinuclear Cobalt Compounds of Pyridazine by the Second Simple Bridging Ligand

Tao Yi*[a,b] Chang Ho-Chol,[b] Song Gao,[c] and Susumu Kitagawa*[b]

**Keywords:** Pyridazine/ Ligand tuning / Cobalt / Irregular spin states structure / Magnetic properties

Three novel trinuclear cobalt(II) compounds of pyridazine, $[Co_3(\mu\text{-}OH)_2(\mu\text{-}pdz)_4(pdz)_2(NO_3)_2(H_2O)_2]\cdot(NO_3)_2\cdot(THF)\cdot 2(MeOH)$ (**1**), $[Co_3(\mu\text{-}OH)_2(\mu\text{-}pdz)_4(pdz)_4(NO_3)_2]\cdot[Co_3(\mu\text{-}OH)_2(\mu\text{-}pdz)_4(MeOH)_4(NO_3)_2]\cdot(NO_3)_4$ (**2**), and $[Co_3(\mu\text{-}pdz)_4(\mu\text{-}NCS)_2(pdz)_2(NCS)_4]\cdot 2MeOH$ (**3**) (pdz = pyridazine), have been synthesized and characterized. The structures of all three compounds consist of centrosymmetric trimer building blocks bridged by the two nitrogen atoms of the pyridazine ligands and the second small bridging anions (hydroxide in **1** and **2**, and end-on thiocyanate in **3**). The two-atom bridging modes of the pyridazine ligand in **1** and **2** are unusual: each bridging pyridazine ligand affords two nitrogen donors to two metal ions with different bond lengths. This results in two kinds of spin states for the cobalt(II) atoms in **1**. Magnetic measurements show a typical antiferromagnetic interaction between the high-spin metals in **3**, but an unusual magnetic coupling through two high- and one low-spin cobalt atoms within the trimer in **1**. An irregular spin states structure is also observed in **1** at low temperature.

(© Wiley-VCH Verlag GmbH & Co. KGaA, 69451 Weinheim, Germany, 2006)

## Introduction

Since the discovery of high-$T_c$ magnetic molecular materials based on 3D metal-cyano compounds and the occurrence of the room-temperature, spin-crossover phase transition in 1,2,4-trizol compounds, strong magnetic interactions between two metal ions have played an important role in magnetic material chemistry.[1–4] Compounds with five-membered heterocyclic ligands such as 1,2,4-trizol attract much interest because of their special magnetic behavior, such as spin crossover,[4c] while the magnetic properties of diazine ligands are rarely considered to be important. Only a few examples of polynuclear copper(II) compounds of pyridazine (pdz)[5] and related ligands[6,7] have been structurally and magnetically characterized. Magnetic data and MO calculations indicate that the magnetic coupling of two metal ions in binuclear compounds of pdz always involves antiferromagnetic interactions through a short two-atom pdz exchange pathway.[8,9] However, in the trinuclear nickel(II) compound $[Ni_3(pdz)_6(\mu\text{-}SCN)_6]$,[10] for which the quasi Curie law magnetic behavior was published, the antiferromagnetic interaction through double pdz bridges was compensated for by the ferromagnetic interaction through a single end-on thiocyanato bridge. At that time, it was conjectured that the magnetic properties of such polynuclear systems could be tuned by the second bridging ligand. The cobalt ion would be a better magnetic center for this objective, because it has two spin states (high and low), depending only on its coordination environment.[11–12] Control of the cobalt(II) spin states by the choice of the axial ligand in pdz-bridged dicobalt(II) macrocyclic compounds has recently been reported by S. Brooker et al.,[13] whereas tuning of the spin states of metal ions through the different contributions of the two nitrogen donors of the pdz ligand by introducing a second bridging ligand has not been published yet. In this study, three novel trinuclear compounds bridged by the pdz ligand and a second bridging anion ($-OH^-$ or $-NCS^-$), $[Co_3(\mu\text{-}OH)_2(\mu\text{-}pdz)_4(pdz)_2(NO_3)_2(H_2O)_2]\cdot(NO_3)_2\cdot(THF)\cdot 2(MeOH)$ (**1**), $[Co_3(\mu\text{-}OH)_2(\mu\text{-}pdz)_4(pdz)_4(NO_3)_2]\cdot[Co_3(\mu\text{-}OH)_2(\mu\text{-}pdz)_4(MeOH)_4(NO_3)_2]\cdot(NO_3)_4$ (**2**), and $[Co_3(\mu\text{-}pdz)_4(\mu\text{-}NCS)_2(pdz)_2(NCS)_4]\cdot 2MeOH$ (**3**), have been isolated and characterized. In **1**, both triplet and singlet states of cobalt ions coexist within a trimer; an irregular spin states structure is observed at low temperature. The dominant magnetic interaction in **3** is antiferromagnetic.

## Results and Discussion

### Crystal and Molecular Structure of 1–3

Single crystals suitable for X-ray analysis were obtained, and the structure was characterized. Selected bond lengths and angles for the cobalt compounds **1**–**3**, as well as their crystallographic data are given in Table 1 and Table 2, respectively.

[a] Laboratory of Advanced Materials, Fudan University, Shanghai 200433, China
[b] Department of Synthetic Chemistry and Biological Chemistry, Faculty of Engineering, Kyoto University, Kyoto 606–8501, Japan
[c] State Key Laboratory of Rare Earth Materials Chemistry and Applications, Peking University, Beijing 100871, China

 © 2006 Wiley-VCH Verlag GmbH & Co. KGaA, Weinheim 

Table 1. Selected bond lengths and angles in **1**, **2**, and **3**.

| Bond lengths [Å] of the central cobalt atom | | | | | | | |
|---|---|---|---|---|---|---|---|
| **1** | | **2** | | | | **3** | |
| | | Trimer A | | Trimer B | | | |
| Co2–O1 | 1.871(2) | Co1–O1 | 1.874(4) | Co4–O2 | 1.873(4) | Co1–N1 | 2.143(5) |
| Co2–N2 | 1.957(2) | Co1–N1 | 1.947(4) | Co4–N10 | 1.963(4) | Co1–N3 | 2.149(4) |
| Co2–N4 | 1.967(2) | Co1–N3 | 1.967(4) | Co4–N12 | 1.957(4) | Co1–N7 | 2.125(4) |
| Bond lengths [Å] of the terminal cobalt atoms | | | | | | | |
| **1** | | **2** | | | | **3** | |
| | | Trimer A | | Trimer B | | | |
| Co1–O1 | 1.968(2) | Co2–O1 | 1.996(4) | Co3–O2 | 1.970(4) | Co2–N2 | 2.192(4) |
| Co1–O2 | 2.098(3) | Co2–O5 | 2.092(4) | Co3–O3 | 2.093(4) | Co2–N4 | 2.195(5) |
| Co1–O3 | 2.061(2) | Co2–N2 | 2.139(5) | Co3–O4 | 2.104(6) | Co2–N5 | 2.174(6) |
| Co1–N1 | 2.130(2) | Co2–N4 | 2.176(4) | Co3–O8 | 2.039(7) | Co2–N7[d] | 2.197(5) |
| Co1–N3 | 2.206(3) | Co2–N5 | 2.144(5) | Co3–N9 | 2.159(5) | Co2–N8 | 2.056(7) |
| Co1–N5 | 2.137(3) | Co2–N7 | 2.143(5) | Co3–N11 | 2.206(5) | Co2–N9 | 2.041(5) |
| Co1···Co2 | 3.24 | Co1···Co2 | 3.24 | Co3···Co4 | 3.23 | Co1···Co2 | 3.45 |
| Bond angles [°] of the central cobalt atom | | | | | | | |
| **1** | | **2** | | | | **3** | |
| | | Trimer A | | Trimer B | | | |
| O1–Co2–N4[a] | 91.5(1) | O1–Co1–N1 | 88.1(2) | O2–Co4–N10 | 89.8(2) | N1–Co1–N3[d] | 88.0(2) |
| N2–Co2–N4 | 91.05(9) | O1–Co1–N1[b] | 91.9(2) | O2–Co4–N10[c] | 90.2(2) | N1–Co1–N7 | 94.1(2) |
| N2–Co2–N4[a] | 88.95(9) | O1–Co1–N3 | 89.0(2) | O2–Co4–N12 | 87.8(2) | N1–Co1–N7[d] | 85.9(2) |
| | | O1–Co1–N3[b] | 91.0(2) | O2–Co4–N12[c] | 92.2(2) | N3–Co1–N7 | 91.5(2) |
| | | N1–Co1–N3 | 92.7(2) | N10–Co4–N12 | 92.1(2) | N3–Co1–N7[d] | 88.5(2) |
| | | N1–Co1–N3[b] | 87.3(2) | N10–Co4–N12[c] | 87.9(2) | N1–Co1–N3 | 92.0(2) |
| Bond angles [°] of the terminal cobalt atoms | | | | | | | |
| **1** | | **2** | | | | **3** | |
| | | Trimer A | | Trimer B | | | |
| O1–Co1–N5 | 95.39(9) | O1–Co2–O5 | 174.3(2) | O2–Co3–O3 | 95.8(2) | N2–Co2–N4 | 88.8(2) |
| O2–Co1–O3 | 88.19(9) | O1–Co2–N2 | 81.6(2) | O2–Co3–O4 | 93.3(2) | N2–Co2–N5[d] | 94.0(2) |
| O2–Co1–N1 | 177.1(1) | O1–Co2–N4 | 81.5(2) | O2–Co3–O8 | 174.7(2) | N2–Co2–N7[d] | 83.5(2) |
| O2–Co1–N3 | 95.9(1) | O1–Co2–N5 | 97.5(2) | O2–Co3–N9 | 83.2(2) | N2–Co2–N8 | 89.9(2) |
| O2–Co1–N5 | 92.0(1) | O1–Co2–N7 | 94.0(2) | O2–Co3–N11 | 80.2(2) | N2–Co2–N9 | 174.3(3) |
| O3–Co1–N1 | 90.79(9) | O5–Co2–N2 | 99.5(2) | O3–Co3–O4 | 92.6(2) | N4–Co2–N7[d] | 86.0(2) |
| O3–Co1–N3 | 89.69(9) | O5–Co2–N4 | 93.0(2) | O3–Co3–O8 | 87.5(2) | N4–Co2–N8 | 89.7(2) |
| O3–Co1–N5 | 93.1(1) | O5–Co2–N5 | 88.1(2) | O3–Co3–N9 | 175.0(2) | N4–Co2–N9 | 88.0(2) |
| N1–Co1–N3 | 81.42(9) | O5–Co2–N7 | 85.1(2) | O3–Co3–N11 | 89.7(2) | N5–Co2–N7[d] | 95.3(2) |
| N1–Co1–N5 | 90.7(1) | N2–Co2–N4 | 85.0(2) | O4–Co3–O8 | 82.4(3) | N5–Co2–N9 | 89.3(2) |
| | | N2–Co2–N5 | 89.6(2) | O4–Co3–N9 | 92.3(2) | N7[d]–Co2–N8 | 172.2(2) |
| | | N2–Co2–N7 | 174.9(2) | O4–Co3–N11 | 173.3(2) | N7[d]–Co2–N9 | 91.6(2) |
| | | N4–Co2–N5 | 174.6(2) | O8–Co3–N9 | 93.8(2) | N8–Co2–N9 | 94.8(2) |
| | | N4–Co2–N7 | 97.0(2) | O8–Co3–N11 | 104.0(2) | N5–Co2–N7[d] | 95.3(2) |
| | | N5–Co2–N7 | 88.4(2) | N9–Co3–N11 | 85.3(2) | N5–Co2–N8 | 89.3(3) |
| Bond angles [°] of cobalt atoms with bridging OH, SCN, and pdz | | | | | | | |
| **1** | | **2** | | | | **3** | |
| | | Trimer A | | Trimer B | | | |
| Co1–O1–Co2 | 114.8(1) | Co1–O1–Co2 | 113.7(1) | Co3–O2–Co4 | 114.3(2) | Co1–N7–Co2[d] | 105.1(2) |
| Co1–N1–N2 | 119.9(2) | Co2–N2–N1 | 117.6(3) | Co3–N9–N10 | 116.2(3) | Co1–N1–N2 | 118.9(3) |
| Co2–N2–N1 | 117.6(2) | Co1–N1–N2 | 117.2(3) | Co4–N10–N9 | 118.1(3) | Co2–N2–N1 | 118.6(4) |
| Co1–N3–N4 | 115.8(2) | Co2–N4–N3 | 117.0(3) | Co3–N11–N12 | 116.4(3) | Co1–N3–N4 | 117.2(4) |
| Co2–N4–N3 | 118.0(2) | Co1–N3–N4 | 117.4(3) | Co4–N12–N11 | 117.3(3) | Co2[d]–N4–N3 | 120.3(3) |

[a] $1 - x, -y, 1 - z$. [b] $1 - x, 1 - y, 1 - z$. [c] $-x + 1/2, -y + 1/2, -z + 1/2$. [d] $-x, -y, -z$.

Compounds **1** and **2** (Figure 1 and Figure 2, respectively) have centrosymmetric linear structures. The central cobalt ion lies on a crystallographic inversion center of a generic octahedral coordination sphere. In **1**, there is only one kind of trimer, as observed in most trinuclear compounds, while in **2**, there are two different trimers (**2**A and **2**B). In every trimer of both compounds, the three cobalt atoms are linked together by four μ-pdz ligands and two μ-OH groups. The coordination environments of the central cobalt atoms are the same. The strong electronegativity of oxygen results in only 1.87 and 1.962 Å for the average lengths of the bonds between the central cobalt atom and its bridging OH and pdz ligands, respectively. Differing from the pdz compounds published previously,[5–9,13–15] the bridging pdz ligands in **1** and **2** afford two nitrogen donors to the two adjacent metal atoms with quite different bond lengths, an

 © 2006 Wiley-VCH Verlag GmbH & Co. KGaA, Weinheim 

average of 1.96 Å to the central and 2.17 Å to the terminal cobalt atoms. The bridging OH group also affords different bond lengths to the central (average 1.87 Å) and terminal cobalt atoms (average 1.98 Å). It is interesting that the average bond length of the central cobalt atom is 1.93 Å, which is shorter than that of the terminal cobalt atoms (2.09 Å), but similar to that of the low-spin-state cobalt(II) atoms in diazide derivatives.[13] A significant contribution to these differences comes from the two nitrogen donors of the bridging pdz ligands. All of the terminal cobalt atoms in **1** and **2** are coordinated with two bridging pdz ligands and one bridging OH group. The other three positions are occupied by one monodentate pdz ligand, one $NO_3^-$ ligand, and one water molecule in **1**, two terminal pdz ligands and one $NO_3^-$ ligand in **2**A, and one $NO_3^-$ ligand and two methanol molecules in **2**B. The angles subtended at the terminal cobalt(II) centers are 81.4(1)–95.9(1) in **1** and 81.5(2)–99.5(2) in **2**, whereas these angles are 88.95(9)–91.5(1) and 87.3(2)–92.7(2), very close to 90°, for the central cobalt(II) atoms of **1** and **2**, respectively, which indicates that the octahedral environment of the terminal cobalt centers is more distorted than that of the central one. The same situation was also observed when comparing the high-spin (HS) and low-spin (LS) cobalt compounds described in ref.[13]. By examining the structural information above, it can be postulated that the difference in the spin states of the central and terminal cobalt atoms is due to the varying strength of the ligand field around the two types of cobalt atoms. This is also proved by the magnetic data. The distance between the neighboring cobalt atoms in each trimer of both **1** and **2** is only 3.24 Å, much shorter than those in other pyridazine compounds.[13,14] The shortest intermolecular Co···Co distance is 7.04 Å. In **1**, there are two uncoordinated $NO_3^-$ groups per trimer in the structure. Each one affords two oxygen atoms to connect the terminally coordinated water molecules of two neighboring trimers by hydrogen bonds with the following distances and angles: 2.718(3) Å and 171(4)° (O2–H18···O6), and 2.782(4) Å and 170(4)° [O2–H19···O8# (#: $1 - x$, $-y$, $1 - z$)]. The trimers are connected together, forming a two-dimensional folded sheet structure through hydrogen bonds along the *bc* plane. Compound **2** contains three uncoordinated $NO_3^-$ counterions per trimer, but without intermolecular interactions. It should be noted that it is not common to have two different trimers in one crystal. The central cobalt atom in trimer **2**A occupies a central position of the cell, while that in trimer **2**B is at a corner position of the cell.

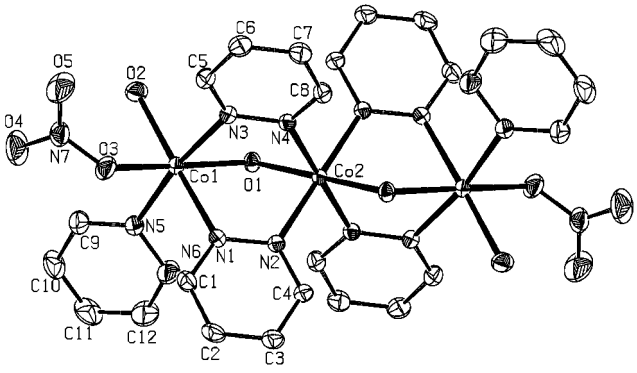


Figure 1. An ORTEP drawing of **1**, with the atom numbering scheme, showing 30% probability ellipsoids. Hydrogen atoms and solvent molecules are omitted for clarity.

In **3**, two monoatom bridged μ-SCN groups replace the OH groups in **1** and **2** to connect the three cobalt atoms (Figure 3). The lengths of the bonds of the central Co1 to the four centrosymmetric nitrogen atoms of pdz are 2.143(5) and 2.149(4) Å, and those to the two nitrogen atoms of μ-NCS are 2.125(4) Å. The terminal Co2 is coordinated to six nitrogen atoms: two from bridging pdz ligands, one from the μ-SCN group, one from the terminal pdz ligand, and another two from terminal NCS ligands. Differing from the close connections observed in **1** and **2**, the bond lengths of the cobalt atoms to the nitrogen atoms of the bridging NCS ligands are 2.125(4) (central Co) and 2.197(5) Å (terminal Co), which are longer than those to the terminal NCS ligands [2.056(7) and 2.041(5) Å, respectively]. The bridging pdz ligand in **3** affords two nitrogen donors with similar bond lengths [2.143(5) Å for Co1 and 2.192(4) Å for Co2] and angles [118.9(3) and 118.6(4)°] to

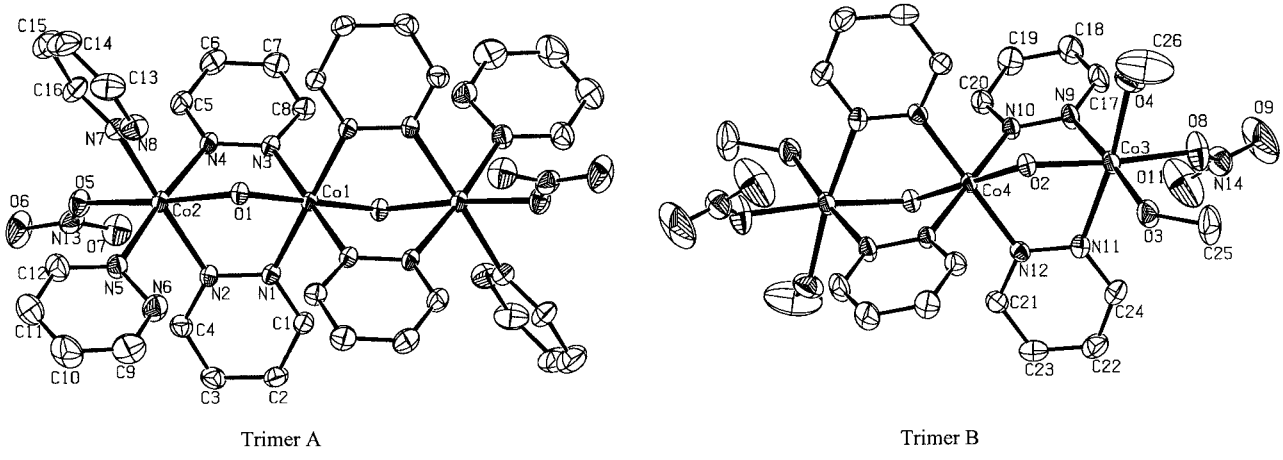


Figure 2. An ORTEP drawing of the two trimers in **2**, with the atom numbering scheme, showing 30% probability ellipsoids. Hydrogen atoms and uncoordinated anions are omitted for clarity.

 © 2006 Wiley-VCH Verlag GmbH & Co. KGaA, Weinheim 

the two adjacent metal atoms. The shortest intramolecular and intermolecular distances between the metal atoms are 3.43 and 8.55 Å, respectively, which are longer than those in **1** and **2**. Two uncoordinated methanol solvents are disordered in the molecular structure. A similar coordination sphere has been published for a nickel compound.[10]

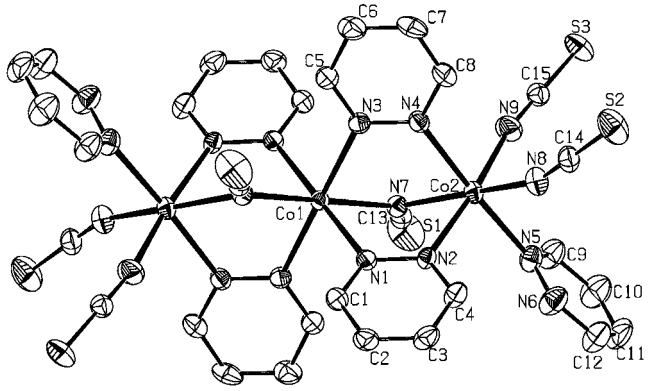


Figure 3. An ORTEP drawing of **3**, with the atom numbering scheme, showing 30% probability ellipsoids. Hydrogen atoms and solvent molecules are omitted for clarity.

As a bidentate bridging ligand, pdz can bond to different metal centers and display a variety of geometry and network motifs. The coordination modes of the pdz ligand could simply be summed up in three types according to the bridging methods. Type I is a typical monodentate mode as observed in the terminal ligands of multinuclear compounds, in which each pdz ligand only affords one nitrogen donor. The coordination type II is the typical bidentate bridging mode observed in **3** and other trinuclear or polymeric compounds,[5–9,13–15] in which the bridging pdz ligand affords two nitrogen donors symmetrically. Type III is the novel bridging mode first observed in **1** and **2**, in which the bond lengths between the two nitrogen atoms of the bridging pdz ligand and the two metal atoms are significantly different. It is obvious that the coordination mode of pdz is strongly affected by the second bridging ligand and the variety of bridging modes of pdz influences the magnetic properties of the compounds strongly.

## Magnetic Properties

All the samples used for magnetic measurements were pulverized crystals. The anisotropic magnetic measurement was not carried out, because the crystals lost their solvent molecules when they were powdered. The magnetic measurements of the thermal variation of the magnetic susceptibility for **1** and **3**, plotted as $\chi_M T$ vs. temperature in the temperature range 2–300 K (2–250 K for **3**) are shown in Figure 4 and Figure 5, respectively ($\chi_M$, the magnetic susceptibility per mole of trimer, was corrected for **1** by using the true molecular weight obtained from the elemental analysis). The $\chi_M T$ value for **1** at room temperature (5.19 $cm^3 \cdot K \cdot mol^{-1}$ at a magnetic field of 0.1 T) corresponds to that expected for two noninteracting high-spin cobalt atoms ($S$ = 3/2) and one low-spin cobalt atom ($S$ = 1/2), which is consistent with the results from the crystal structure data, in which the central Co atom is in a low-spin state with an average bond length of 1.93 Å, and the two terminal Co atoms are in a high-spin state with an average bond length of 2.09 Å. The $\chi_M T$ value remains practically unchanged down to 20 K, then decreases slightly, and finally increases quickly to 6.4 $cm^3 \cdot K \cdot mol^{-1}$ at 2 K under a magnetic field of 0.1 T, whereas at a magnetic field of 1 T, it goes through a maximum of 4.9 $cm^3 \cdot K \cdot mol^{-1}$ at 5.5 K and decreases again upon further cooling as a result of a field-saturation effect. The magnetic phenomenon in **1** can be explained by the irregular spin states structure, which has been reported in the $M^{II}Cu^{II}M^{II}$ (M = high-spin state of Mn, Co or Ni) system.[1,16] In the case of **1**, the interaction between Co(3/2) and Co(1/2) is weakly antiferromagnetic, the ground state is $E$(5/2, 3), above it there are $E$(7/2, 3), $E$(5/2, 2), $E$(3/2, 1), $E$(1/2, 0), $E$(1/2, 1), and $E$(3/2, 2). Such an irregular spin states structure exhibits quasi ferrimagnetic behavior in the $\chi_M T$ vs. $T$ plots as shown in Figure 4.

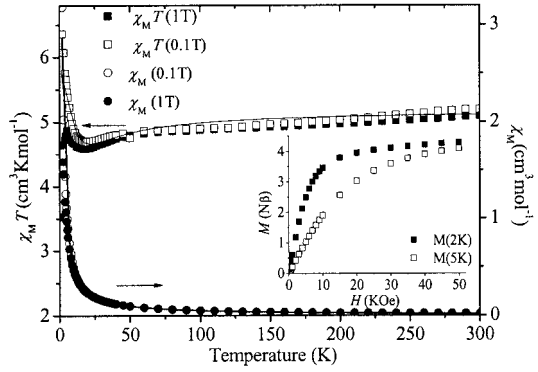


Figure 4. Thermal variation of $\chi_M T$ and $\chi_M$ for **1** at a magnetic field of 0.1 T (empty square and circle) and 1 T (filled square and circle), the solid line is the best fit for $\chi_M$ and $\chi_M T$ at 0.1 T using Equation (3). The inset is the magnetic field dependence of magnetization of **1** at temperatures of 2 and 5 K.

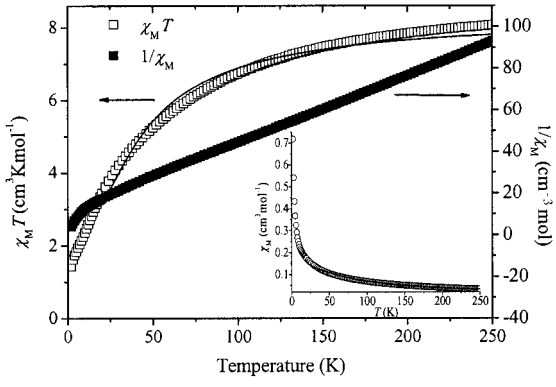


Figure 5. Thermal variations of $\chi_M T$ and $1/\chi_M$ for **3** at a magnetic field of 1 T. The inset is the curve of $\chi_M$ vs. $T$, and the solid line is the best fit for $\chi_M$and $\chi_M T$ using Equation (4).

To simulate the experimental magnetic behavior, the data of **1** and **3** are approximately fitted by the isotropic linear

 © 2006 Wiley-VCH Verlag GmbH & Co. KGaA, Weinheim 

trinuclear model.[1] The spin Hamiltonian and relative energies in the zero field are expressed as follows:

$$H = -J(S_{A1}.S_B + S_{A2}.S_B) \quad (1)$$

where $S_A = 3/2$, $S_B = 1/2$ for **1** and $S_A = S_B = 3/2$ for **3**.

$$E(S, S') = -(J/2)S(S+1) + (J/2)S'(S'+1);\ S' = S_{A1} + S_{A2},\ S = S' + S_B \quad (2)$$

The situation is always complicated for cobalt compounds. The exact expression of the Hamiltonian including spin-orbit coupling, axial and rhombic distortions, exchange, and Zeeman interactions[17] is not within the limits of our ability to calculate because of the very large size of the matrices. Therefore, the approximate fit for the average $\chi_M(T)$ [Equation (3)] was used for **1**, in which the orbital degeneracy on the distorted octahedral terminal $Co^{II}$ ($^4T_{1g}$) and the zero-field splitting effects were ignored.[1,13] Considering the phenomenon of an ascending $\chi_M T$ value at low temperature, both the antiferromagnetic exchange, $J$, between the neighboring HS and LS cobalt atoms and the weak ferromagnetic exchange, $J'$, between the two terminal cobalt atoms were included.

The best fit gives $g_A = 2.26$, $g_B = 2.04$, $J = -9.37\ cm^{-1}$, and $J' = 0.95\ cm^{-1}$ with $R = 3.9\cdot10^{-4}$ $\{R = \Sigma[(\chi_M T_{obs}) - (\chi_M T_{calc})]^2/\Sigma(\chi_M T_{obs}^2)\}$. The high values of $g_A$ for the terminal cobalt atoms reflect the spin-orbit coupling effects and the orbital degeneracy of octahedral HS $Co^{II}$.[13,18] The $J$ value is reasonably indicative of the exchange interactions across the pyridazine bridges.[13] The low-temperature limit of $\chi_M T$, $(\chi_M T)_{LT}$, is 5.736 $cm^3\cdot K\cdot mol^{-1}$, a little less than the value measured at 2 K (6.4 $cm^3\cdot K\cdot mol^{-1}$), which indicates an irregular spin states structure in **1** in the low-temperature range. If the temperature is low enough, the whole trimer is in the ground state with $S = 5/2$. The calculated saturation magnetization is 5.71 Nß at $g$ (5/2, 3) = 2.29. The measured magnetization of **1** as a function of field (0–5 T) gives a saturation magnetization value of 4.27 Nß at 2 K (Figure 4, inset), which is less than the value of $S = 5/2$, which also proves that the magnetic behavior at low temperature is a result of an irregular spin states structure.

The $\chi_M T$ value per trimer of **3** at 250 K is 8.07 $cm^3\cdot K\cdot mol^{-1}$ (Figure 5), which is larger than that for three noninteracting cobalt ions of $S = 3/2$ because of the orbital contribution. This value decreases gradually to 0.48 $cm^3\cdot K\cdot mol^{-1}$ from room temperature to 2 K. The $1/\chi_M$ value above 20 K fitted with the Curie–Weiss law gave $C$ = 3.016 $cm^3\cdot mol^{-1}$ and $\theta = -32.09$ K, which shows an intramolecular antiferromagnetic coupling of the adjacent cobalt atoms within the trimer. With the same approximations as in **1** and neglecting $J'$, the *Van Vleck* formula for **3** is expressed in Equation (4).

The best fit for temperatures greater than 20 K gives $g_A$ = 2.46, $g_B$ = 2.02, $J = -6.08\ cm^{-1}$ with $R = 9.5\cdot10^{-4}$. The larger value of $g_A$ indicates that the terminal cobalt atoms possess stronger anisotropy than the central one, which is consistent with the description of the molecular structure.

According to the theoretical calculations of magnetic interactions through bridged two-atom pdz and related compounds,[5,6,10,13] the magnetic coupling of the two cobalt atoms through pure bridging pdz ligands ($J \approx -10\ cm^{-1}$) are much weaker than that in the copper ($-J > 100\ cm^{-1}$) and nickel ($J \approx -30\ cm^{-1}$) compounds. It can be estimated that the contribution to the antiferromagnetic interaction between the adjacent cobalt atoms mainly comes from the bridging pdz ligands in **3**. End-on $NCS^-$ bridging may afford a weak ferromagnetic interaction, which compensates the antiferromagnetic interaction through the bridging pdz ligands to give a comparatively small value of $J$, as described for the corresponding nickel compound.[10] In the case of **1**, the entire magnetic interaction of the adjacent HS and LS cobalt atoms comes from the magnetic coupling through pdz and hydroxide, and the supra-exchange of the two metal ions. It can be deduced that the magnetic coupling through pdz must be an antiferromagnetic interaction

$$\chi_M = \frac{N\beta^2}{4kT} \times \frac{35g^2_{(5/2,3)} + 84g^2_{(7/2,3)}\exp(\frac{7J}{2kT}) + 35g^2_{(5/2,2)}\exp(\frac{3J-3J'}{kT}) + 10g^2_{(3/2,2)}\exp(\frac{J-6J'}{2kT}) + 10g^2_{(3/2,1)}\exp(\frac{5J-10J'}{2kT}) + g^2_{(1/2,1)}\exp(\frac{J-5J'}{kT}) + g^2_{(1/2,0)}\exp(\frac{2J-6J'}{kT})}{3 + 4\exp(\frac{7J}{2kT}) + 3\exp(\frac{3J-3J'}{kT}) + 2\exp(\frac{J-6J'}{2kT}) + 2\exp(\frac{5J-10J'}{2kT}) + \exp(\frac{J-5J'}{kT}) + \exp(\frac{2J-6J'}{kT})} \quad (3)$$

$$\chi_M = \frac{N\beta^2}{4kT} \times \frac{10g^2_{(3/2,3)} + 10g^2_{(3/2,0)}\exp(\frac{6J}{kT}) + g^2_{(1/2,1)}\exp(\frac{7J}{2kT}) + 35g^2_{(5/2,1)}\exp(\frac{15J}{2kT}) + g^2_{(1/2,2)}\exp(\frac{3J}{2kT}) + 84g^2_{(7/2,2)}\exp(\frac{9J}{kT}) + 165g^2_{(9/2,3)}\exp(\frac{21J}{2kT})}{2 + 2\exp(\frac{6J}{kT}) + \exp(\frac{7J}{2kT}) + 3\exp(\frac{15J}{2kT}) + \exp(\frac{3}{2}J/kT) + 4\exp(\frac{9J}{kT}) + 5\exp(\frac{21J}{2kT})} \quad (4)$$

 © 2006 Wiley-VCH Verlag GmbH & Co. KGaA, Weinheim 

because of spin polarization in the bridging ligand. The antiferromagnetic coupling between two neighboring cobalt atoms through the $OH^-$ group is very weak because of poor overlap between the $d_{x^2-y^2}$ and $d_{z^2}$ magnetic orbitals of the central low-spin cobalt(II) atom and the p-type orbitals of the oxygen atom from the $OH^-$ group. The different magnetic orbital contributions for the high- and low-spin states of the cobalt atoms also cause the overlap of the electron clouds of the two neighboring metal atoms to tend to zero and the spins of the two high-spin magnetic centers to tend to be positioned in the same direction, compensating for the antiferromagnetic interaction between neighboring cobalt atoms. The magnetic exchange for the two kinds of spin states of cobalt atoms within one molecule is rarely reported. The tuning of the spin states through a simple bridging ligand may afford a new method for the modification of magnetic properties at the molecular level.

In conclusion, three novel cobalt(II) trinuclear compounds bridged by the pdz ligand and a second small anion (hydroxide and end-on thiocyanate) were structurally and magnetically characterized in this paper. The two-atom bridging modes of the pdz ligand in **1** and **2** are unusual: each bridging pdz ligand affords two nitrogen donors to the two metal ions with different bond lengths. This results in a significant difference in the ligand fields between the central and terminal cobalt(II) coordination spheres in **1** and **2**. Both the structural analysis and magnetic data show that two spin states (HS and LS) of cobalt(II) atoms coexist in **1**. An irregular spin states structure was also observed in this compound at low temperature. This work provides a unique example of the modification of magnetic properties through a simple bridging group.

## Experimental Section

**Materials:** $Co(NO_3)_2{\cdot}6H_2O$ (>98%, Wako), pyridazine (98%, Tokyo Chemical), $NH_4SCN$ (99.5%, Wako) were used as obtained from commercial sources without further purification.

**Physical Measurements:** The powder infrared spectra were recorded with a Perkin–Elmer System 2000 instrument using KBr pellets. Magnetic susceptibility measurements were carried out using a Quantum Design SQUID magnetometer in the 2–300-K temperature range. Corrections for diamagnetism were applied by using Pascal's constants.[1a]

**Synthesis of $[Co_3(\mu\text{-}OH)_2(\mu\text{-}pdz)_4(pdz)_2(NO_3)_2(H_2O)_2]{\cdot}(NO_3)_2{\cdot}(THF){\cdot}2(MeOH)$ (1) and $[Co_3(\mu\text{-}OH)_2(\mu\text{-}pdz)_4(pdz)_4(NO_3)_2]{\cdot}[Co_3(\mu\text{-}OH)_2(\mu\text{-}pdz)_4(MeOH)_4(NO_3)_2]{\cdot}(NO_3)_4$ (2):** After mixing a THF solution (5 mL) of pdz (1.1 mmol) and a THF solution (15 mL) of $Co(NO_3)_2{\cdot}6H_2O$ (0.5 mmol), a red sediment was produced, which was dissolved by adding methanol (5 mL). Red-brown, cube-shaped single crystals of **1** were obtained from the prepared red solution by slow vaporization at room temperature. The crystals lost their solvent molecules and powdered slowly in air. $C_{30}H_{46}Co_3N_{16}O_{19}$ (**1**): calcd. C 32.39, H 4.14, N 20.15; found C 27.55, H 3.38, N 21.47. The experimental data is consistent with that of the molecule in which three organic solvent molecules are replaced by four water molecules. $C_{24}H_{38}Co_3N_{16}O_{20}$ (**1** – THF – 2MeOH + $4H_2O$): found C 27.52, H 3.66, N 21.40. Pyramid-shaped red crystals of **2** were isolated after one year from the same mother liquor of **1**. $C_{52}H_{64}Co_6N_{34}O_{38}$ (**2**): calcd. C 29.37, H 3.03, N 22.39; found C 29.58, H 3.25, N 22.13.

**Synthesis of $[Co_3(\mu\text{-}pdz)_4(\mu\text{-}NCS)_2(pdz)_2(NCS)_4]{\cdot}2MeOH$ (3):** Pyridazine (2.2 mmol) was added dropwise to a solution of $CoCl_2{\cdot}6H_2O$ (1 mmol) and $NH_4SCN$ (2.2 mmol) in methanol (20 mL) under continuous stirring. The prepared blue solution was filtered and allowed to evaporate slowly at room temperature to give red cube-shaped single crystals of **3** after two months. IR

Table 2. Crystallographic data for **1**, **2**, and **3**.

| | **1** | **2** | **3** |
|---|---|---|---|
| Formula | $C_{30}Co_3H_{46}N_{16}O_{19}$ | $C_{26}H_{32}Co_3N_{17}O_{19}$ | $C_{32}H_{30}Co_3N_{18}O_2S_6$ |
| Fw | 1111.56 | 1063.44 | 1067.87 |
| Dimensions [mm] | 0.25×0.20×0.15 | 0.3×0.20×0.1 | 0.25×0.20×0.1 |
| Crystal system | monoclinic | triclinic | monoclinic |
| Space group | *P*21/c | $P\bar{1}$ | *P*21/*n* |
| *a* [Å] | 10.115(1) | 12.8257(5) | 15.307(2) |
| *b* [Å] | 18.437(1) | 12.950(1) | 11.1583(5) |
| *c* [Å] | 12.573(1) | 13.5136(5) | 14.983(3) |
| *α* [°] | | 74.499(2) | |
| *β* [°] | 113.777(2) | 71.412(3) | 117.337(2) |
| *γ* [°] | | 85.829(2) | |
| *V* [Å$^3$] | 2145.6(3) | 2049.8(2) | 2273.3(5) |
| *Z* | 2 | 2 | 2 |
| $\rho_{cal\ d.}$ [g·cm$^{-3}$] | 1.714 | 1.723 | 1.560 |
| $\mu$ [cm$^{-1}$] | 12.43 | 12.98 | 14.10 |
| Temperature [°C] | 293 | 293 | 293 |
| No. of observations | 2464 | 7066 | 3759 |
| *h* | $-10 < h < 10$ | $-16 < h < 15$ | $-19 < h < 11$ |
| *k* | $-19 < k < 15$ | $-10 < k < 16$ | $-14 < k < 10$ |
| *l* | $-13 < l < 12$ | $-17 < l < 17$ | $-11 < l < 19$ |
| Residuals:[a] *R*,[b] $wR_2$ | 0.031, 0.077 | 0.07, 0.2123 | 0.0705, 0.2011 |
| GoF | 1.06 | 1.194 | 1.298 |
| Max. & min. peak in final diff. map (e$^-$ [Å$^3$]) | 0.45, –0.52 | 1.12 (0.72 Å from Co3), –0.78 | 0.62, –0.56 |

[a] $R = \Sigma||F_{obsd.}| - |F_{calcd.}||/\Sigma|F_{obsd.}|$ for $I > 2.0\sigma(I)$. [b] $Rw = [\Sigma w\,(|F_{obsd.}| - |F_{calcd.}|)^2/\Sigma w\,F_o^2]^{1/2}$.

 © 2006 Wiley-VCH Verlag GmbH & Co. KGaA, Weinheim 

(KBr): $\tilde{\nu}$ = 3388 (br., m), 3092 (br., w), 2079 (vs), 1989 (s), 1579 (m), 1415 (m), 1070 (m), 991 (w), 767 (m), 673 (w), 412 (w) $cm^{-1}$. $C_{32}H_{30}Co_3N_{18}O_2S_6$: calcd C 35.96, H 2.81, N 23.60, found C 35.35, H 2.87, N 23.67.

**X-ray Crystallography**

The single crystals of all the compounds were sealed into glass capillary tubes (0.7 mm, GLAS) containing a small amount of mother liquor and mounted on the crystal goniometer. The intensity data of all four samples were collected with the Rigaku Mercury CCD system using graphite monochromatic Mo-$K_\alpha$ radiation ($\lambda$ = 0.71069 Å) and the $\omega$ scan technique with a sample-to-detector distance of 35 mm at a temperature of 20 ± 1 °C (Table 2). The cell constants and orientation matrix were obtained from the reflections collected on the setting angles of six frames by changing $\omega$ by 0.5° for each frame.[19] Intensity data were collected in 480 frames with an $\omega$ scan width of 0.5° using two different $\psi$ settings (0 and 90°). The exposure time was 60, 90, and 150 s for **1**, **2**, and **3**, respectively. Empirical absorption corrections based on azimuthal scans were applied.[20] The data were also corrected for Lorentz and polarization effects.

All calculations were performed using the teXsan crystallographic software package[21] of the Molecular Structure Corporation. The structures were solved by direct methods and expanded using Fourier techniques.[22] The full-matrix least-squares refinement was performed by SHELXL-97[23] based on $F^2$. The non-hydrogen atoms were refined anisotropically. Hydrogen atoms were included but not refined. $R$ factor ($gt$) of the final full-matrix least-squares refinement was based on the observed data of $I > 2\sigma(I)$, while reflections of the weighted $R$ factor ($wR_2$) and GoF are based on all data. In **1** and **3**, the positions of the solvent molecules were disordered, while in **2**, the oxygen atoms of the terminally coordinated $NO_3^-$ were disordered. CCDC-276336 to 276338 contain the supplementary crystallographic data for this paper. These data can be obtained free of charge from The Cambridge Crystallographic Data Centre via www.ccdc.cam.ac.uk/data_request/cif.

## Acknowledgments

This work was supported by the Japanese Society for the Promotion of Science (JSPS) and the National Science Foundation of China (NSFC 20441006).

[1] a) O. Kahn, *Molecular Magnetism*, VCH, Weinheim, Germany, **1993**; b) *Magnetism: A Supramolecular Function*, ASI Kluwer Academic Publishers, **1995**.
[2] J. V. C. Rovira, D. B. Amabilino, *Supramolecular Engineering of Synthetic Metallic Materials*, Kluwer Academic Publishers, **1999**.
[3] K. Itoh, M. Kinoshita, *Molecular Magnetism-New Magnetic Material*, Gordon and Breach Science Publishers, **2000**.
[4] For example: a) S. Ferlay, T. Mallah, R. Ouahès, P. Veillet, M. Verdaguer, *Nature* **1995**, *378*, 701–703; b) O. Sato, T. Iyoda, A. Fijishma, K. Hashimoto, *Science* **1996**, *272*, 704–705; c) O. Kahn, C. Jay Martinez, *Science* **1998**, *279–282*, 44–48.
[5] a) L. Carlucci, G. Ciani, M. Moret, A. Sironi, *J. Chem. Soc., Dalton Trans.* **1994**, 2397–2403; b) T. Otieno, S. J. Rettig, R. C. Thompson, J. Trotter, *Inorg. Chem.* **1995**, *34*, 1718–1725.
[6] a) L.-Q. Chen, L. K. Thompson, J. N. Bridson, *Inorg. Chim. Acta* **1996**, *244*, 87–93; b) L. K. Thompson, S. K. Mandal, E. J. Gabe, F. L. Lee, A. W. Addison, *Inorg. Chem.* **1987**, *26*, 657–664; c) L. K. Thompson, A. W. Hanson, B. S. Ramaswamy, *Inorg. Chem.* **1984**, *23*, 2459–2465.
[7] a) J. Manzur, A. M. Garcia, R. Letelier, E. Spodine, O. Pena, D. Grandjean, M. M. Olmstead, B. C. Noll, *J. Chem. Soc., Dalton Trans.* **1993**, 905–911; b) Zh.-Q. Xu, L. K. Thompson, C. J. Matthews, D. O. Miller, A. E. Geota, C. Wilson, J. A. K. Howard, M. Ohba, H. Okawa, *J. Chem. Soc., Dalton Trans.* **2000**, 69–77.
[8] A. Escuer, R. Vicente, B. Mernari, A. El Gueddi, M. Pierrot, *Inorg. Chem.* **1997**, *36*, 2511–2516.
[9] T. Wen, L. K. Thompson, F. L. Lee, E. J. Gabe, *Inorg. Chem.* **1988**, *27*, 4190–4196.
[10] J. Cano, G. De Munno, F. Lloret, M. Julve, *Inorg. Chem.* **2000**, *39*, 1611–1614.
[11] F. A. Cotton, G. Wilkinson, *Advanced Inorganic Chemistry*, John Wiley & Sons, New York, **1988**.
[12] J. F. Berry, F. A. Cotton, C. Y. Liu, T. B. Lu, C. A. Murillo, B. S. Tsukerblat, D. Villagran, X. P. Wang, *J. Am. Chem. Soc.* **2005**, *127*, 4895–4902.
[13] a) S. Brooker, D. J. de Geest, R. J. Kelly, P. G. Plieger, B. Moubaraki, K. S. Murray, G. B. Jameson, *J. Chem. Soc., Dalton Trans.* **2002**, 2080–2087; b) U. Beckmann, S. Brooker, *Coord. Chem. Rev.* **2003**, *245*, 17–19.
[14] M. G. B. Drew, F. S. Esho, A. Lavery, S. M. Nelson, *J. Chem. Soc., Dalton Trans.* **1984**, 545–556.
[15] T. Yi, H.-Ch. Chang, S. Kitagawa, *Mol. Cryst. Liq. Cryst.* **2001**, *376*, 283–288.
[16] a) E. Q. Gao, J. K. Tang, D. Z. Liao, Z. H. Jiang, S. P. Yan, G. L. Wang, *Inorg. Chem.* **2001**, *40*, 3134–3140; b) P. Yu, J. Yves, O. Kahn, *Inorg. Chem.* **1988**, *27*, 399–404.
[17] a) R. Boca, *Coord. Chem. Rev.* **2004**, *248*, 757–815; b) A. V. Palii, B. S. Tsukerblat, E. Coronada, J. M. Clement-Juan, J. Borras-Almenar, *Inorg. Chem.* **2003**, *42*, 2455–2458; c) H. Sakiyama, R. Ito, H. Kumagai, K. Inoue, M. Sakamoto, Y. Nishida, M. Yamasaki, *Eur. J. Inorg. Chem.* **2001**, 2027–2032; H. Sakiyama, R. Ito, H. Kumagai, K. Inoue, M. Sakamoto, Y. Nishida, M. Yamasaki, *Eur. J. Inorg. Chem.* **2001**, 2705; d) K. Fink, C. Wang, V. Staemmler, *Inorg. Chem.* **1999**, *38*, 3847–3856.
[18] G. De Munno, M. Julve, F. Lloret, J. Faus, A. Caneschi, *J. Chem. Soc., Dalton Trans.* **1994**, 1175–1183.
[19] H.-Ch. Chang, H. Miyasaka, S. Kitagawa, *Inorg. Chem.* **2001**, *40*, 146–156.
[20] R. A. Jacobson, *REQABA Empirical Absorption Correction Version, 1.1–03101998*, Molecular Structure Corp., The Woodlands, TX, **1996–1998**.
[21] (*teXsan*): *Crystal Structure Analysis Package*, Molecular Structure Corporation, **1985** & **1999**.
[22] (*SIR92*): A. Altomare, M. C. Burla, M. Camalli, M. Cascarano, C. Giacovazzo, A. Guagliardi, G. Polidori, *J. Appl. Crystallogr.* **1994**, *27*, 435.
[23] G. M. Sheldrick, *SHELXL-97, An Integrated System for Solving and Refining Crystal Structures from Diffraction Data*, University of Göttingen, Germany, **1997**.

Received: August 22, 2005
Published Online: February 21, 2005

 © 2006 Wiley-VCH Verlag GmbH & Co. KGaA, Weinheim 

DOI: 10.1002/ejic.200500782

# Novel Water-Soluble Carbosilane Dendrimers: Synthesis and Biocompatibility

Paula Ortega,[a][‡] Jesus F. Bermejo,[b][‡] Louis Chonco,[b] Ernesto de Jesus,[a] F. Javier de la Mata,*[a] Gerónimo Fernández,[b] Juan Carlos Flores,[a] Rafael Gómez,*[a] M. Jesús Serramía,[b] and M. Angeles Muñoz-Fernandez*[b]

**Keywords:** Bioinorganic chemistry / Dendrimers / Silicon / Drug delivery / Toxicity

A synthetic strategy has been developed for the preparation of new peripheral amine- or ammonium-terminated carbosilane dendrimers of type *n*G-[Si($OCH_2CH_2NMe_2$)$_y$]$_x$ or *n*G-[Si($OCH_2CH_2NMe_3^+I^-$)$_y$]$_x$, respectively. It consists of the alcoholysis of well-known chlorosilane-terminated dendrimers with *N*,*N*-dimethylethanolamine and the subsequent quaternization with MeI. All these systems are susceptible to hydrolysis, although the decomposition depends on concentration and dendrimer generation. Evaluation of dendrimer toxicities by phase-contrast light microscopy and MTT assay were carried out, and evidence of dendrimer/oligonucleotide complex formation was carried out by gel electrophoresis.
(© Wiley-VCH Verlag GmbH & Co. KGaA, 69451 Weinheim, Germany, 2006)

## Introduction

There is currently significant interest in dendrimers as a result of their potential applications, including light harvesting and energy transfer, nanoscale catalysis, chemical sensors, unimolecular micelles, enzyme mimics, encapsulation of guest molecules, molecular recognition, diagnostic agents, and gene and drug delivery.[1]

The two common drug delivery systems are liposomes and polymers, although both present some problems.[2] Liposome-based systems have poor stability, difficulty targeting specific tissues, side effects like lung-inflammatory reactions, and in transfection, processes may fail in the presence of serum. The main drawbacks of the use of conventional degradable polymers as delivery agents are their polydispersity and thermodynamic instability that result in a short in vivo lifetime of the active species. Dendrimers represent an alternative approach to liposomes and polymeric systems for drug delivery. Their major advantages are the uniform structure, multiple sites of attachment, and the versatility to modify their skeletons and surfaces, allowing a precise characterization of the dendrimer/drug interaction. There are two general methods for the use of dendrimers as drug carriers, that is (i) encapsulation of drugs inside the dendritic skeleton[3] or (ii) formation of dendrimer-drug conjugates in which the drug is attached preferentially to its surface. For the latter method, two methodologies have been developed. The first technique consists of a covalent link between peripheral units of the dendrimer and the drug. For instance, methotrexate or folic acid have been attached to the exterior of polyarylether[4] dendrimers or conjugated in poly(amidoimine) (PAMAM)[5] dendrimers. The second approach is based on electrostatic interactions and has been mainly focused on the delivery of DNA drugs into the cell nucleus for gene or antisense therapy. Numerous reports have been published on the use of amino-terminated PAMAM dendrimers,[6] phosphorus-based dendrimers,[7] polypropylenimine (PPI)[8] or poly(lysine)[9] dendrimers as nonviral gene-transfer agents.

However, to the best of our knowledge, no studies concerning the use of water-soluble carbosilane-based dendrimers as potential drug carriers have been published, although an in vitro biocompatibility report was recently published on poly(ethylene oxide)-grafted carbosilane dendrimers.[10] Besides, a scarce number of polyionic silane dendrimers have been reported so far.[11–13]

Here we describe the synthesis and characterization of novel water-soluble carbosilane dendrimers up to the third generation, and the analysis of their biocompatibility in primary cell cultures of peripheral blood mononuclear cells (PBMCs).

## Results and Discussion

### Amine-Terminated Carbosilane Dendrimers

We have studied the synthesis of dendrimers containing peripheral amine groups. For this purpose, first-, second-,

[a] Departamento de Química Inorgánica, Universidad de Alcalá, Campus Universitario,
28871 Alcalá de Henares, Spain
Fax: +34-91-8854683
E-mail: Rafael.Gomez@uah.es
[b] Laboratorio de Inmunobiología Molecular, Hospital General Universitario Gregorio Marañón,
Madrid, Spain
[‡] Paula Ortega and Jesus F. Bermejo contributed equally to the development of this work.
Supporting information for this article is available on the WWW under http://www.eurjic.org or from the author.

 InterScience © 2006 Wiley-VCH Verlag GmbH & Co. KGaA, Weinheim 

and third-generation chlorosilane-terminated dendrimers were synthesized as previously reported.[14] Typically, we used tetraallylsilane or other allylsilane-terminated dendrimers as the initiator core and chlorodimethylsilane or dichloromethylsilane for the hydrosilylation step in the presence of a platinum catalyst (Karstedt catalyst),[15] to afford the well-known Cl–Si-terminated dendrimers 1G-$(SiCl)_4$, 1G-$(SiCl_2)_4$, 2G-$(SiCl)_8$, 2G-$(SiCl_2)_8$, 3G-$(SiCl)_{16}$, and 3G-$(SiCl_2)_{16}$. These formed the starting materials for the preparation of new dendrimers by alcoholysis reactions.

Treatment of dendrimer 1G-$(SiCl)_4$ with 4 equiv. of ethanolamine at room temperature in diethyl ether and in the presence of $NEt_3$ led to the formation of the corresponding amine-terminated dendrimer 1G-[$Si(OCH_2CH_2NH_2)]_4$ (**1**), which was isolated as a brown oil after separation from the precipitated ammonium salt $[HNEt_3]Cl$ and evaporation of the solvent (Scheme 1). In the absence of $NEt_3$, the dendrimer precipitated as a white solid material that we initially assigned to the self-quaternization of the amine groups in **1** because addition of $NEt_3$ to this white material in DMSO dissolved it to afford **1** again as the sole spectroscopic compound. However, when we tried to dissolve this material in water, an insoluble residue of polysiloxanes and the soluble ammonium salt of ethanolamine were separated. The data of the $^1H$ NMR spectrum performed in $D_2O$ are consistent with the hydrolysis of the Si–O bonds under these slight acidic conditions. Derivative **1** exhibits a multiplet in the $^1H$ NMR spectrum located at $\delta$ = 1.32 ppm, attributed to the middle methylene group of the branch –$SiCH_2CH_2CH_2Si$–, and the two signals at $\delta$ = 0.63 and 0.53 ppm are assigned to the methylene groups directly bonded to silicon. The outer branch gives two triplets at $\delta$ = 3.55 and 2.74 ppm, corresponding to –$CH_2O$– and –$CH_2N$–. The $^{13}C$ NMR spectroscopic data are consistent with this assignment. Water-solubilization of dendrimer **1** was attempted by quaternization of the terminal amine groups. Reaction of **1** with a diethyl ether solution of HCl produced the hydrolytic breaking of the Si–O bonds, in accordance with the reactivity mentioned earlier. The attempt to quaternize derivative **1** using MeI also failed because of the hydrolysis of the Si–O bonds caused by the HI generated by Me/H exchanges with the amine protons.[16]

To overcome these problems, chlorosilane-terminated dendrimers were treated with stoichiometric amounts of *N*,*N*-dimethylethanolamine in diethyl ether and in the presence of stoichiometric $NEt_3$, to afford the corresponding amine-terminated dendrimers 1G-[$Si(OCH_2CH_2NMe_2)]_4$ (**2**), 1G-[$Si(OCH_2CH_2NMe_2)_2]_4$ (**3**), 2G-[$Si(OCH_2CH_2NMe_2)]_8$ (**4**), 2G-[$Si(OCH_2CH_2NMe_2)_2]_8$ (**5**), 3G-[$Si(OCH_2CH_2NMe_2)]_{16}$ (**6**), and 3G-[$Si(OCH_2CH_2NMe_2)_2]_{16}$ (**7**) as brown oils in high yields (Scheme 2). All these derivatives are soluble in common organic solvents, but are insoluble in water.

The NMR spectroscopic and analytical data for derivatives **2**–**7** are consistent with their proposed structures (Scheme 2). The $^1H$ NMR spectra of the carbosilane framework for dendrimers **2**–**7** have almost identical chemical shifts for analogous nuclei in different generations, although broader and less structured resonances are present with increasing generation. These features have been ascribed to both a polymer-like structure with slightly different chemical environments for the nuclei in different generations and restricted mobility of the respective protons in the outer shells.[17,18] Five sets of signals attributed to the methylene groups are observed with the expected integration ratio. For the $SiCH_2CH_2CH_2Si$ branches, the middle methylenes are located at $\delta$ = 1.30 ppm, whilst the methylene groups bonded directly to silicon atoms are centered at $\delta$ = 0.61 and 0.51 ppm. We ascribed the resonances at $\delta$ = 0.61 ppm to the –$CH_2SiO$– groups and those at $\delta$ = 0.51 ppm to the rest of the methylene groups, based on the enlargement of the latter signal intensity with increasing dendrimer generation, and also on 1D $^1H$ TOCSY and NOESY experiments. Two triplets are observed for the $SiOCH_2CH_2N$ fragment, located at $\delta$ = 3.64 (for dendrimers **2**, **4**, and **6**) or 3.74 ppm (for dendrimers **3**, **5**, and **7**) attributed to the –$CH_2O$– groups, and $\delta$ = 2.43 ppm for the –$CH_2N$– groups; this observation is supported by data from NOESY experiments. Interestingly, the downfield shifts shown by dendrimers **3**, **5**, and **7** are consistent with the presence of two oxygen atoms bonded to the silicon atom, although this effect is negligible for the –$CH_2N$– groups. The $^{13}C$ NMR spectra for the methylene groups show two resonances located at $\delta$ = 61.4 (–$CH_2N$–) and 60.7 ppm (–$CH_2O$–) for the outer

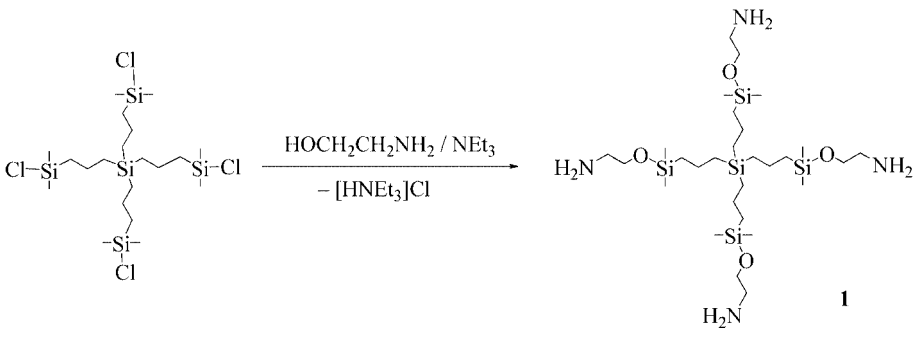


Scheme 1.

 © 2006 Wiley-VCH Verlag GmbH & Co. KGaA, Weinheim 

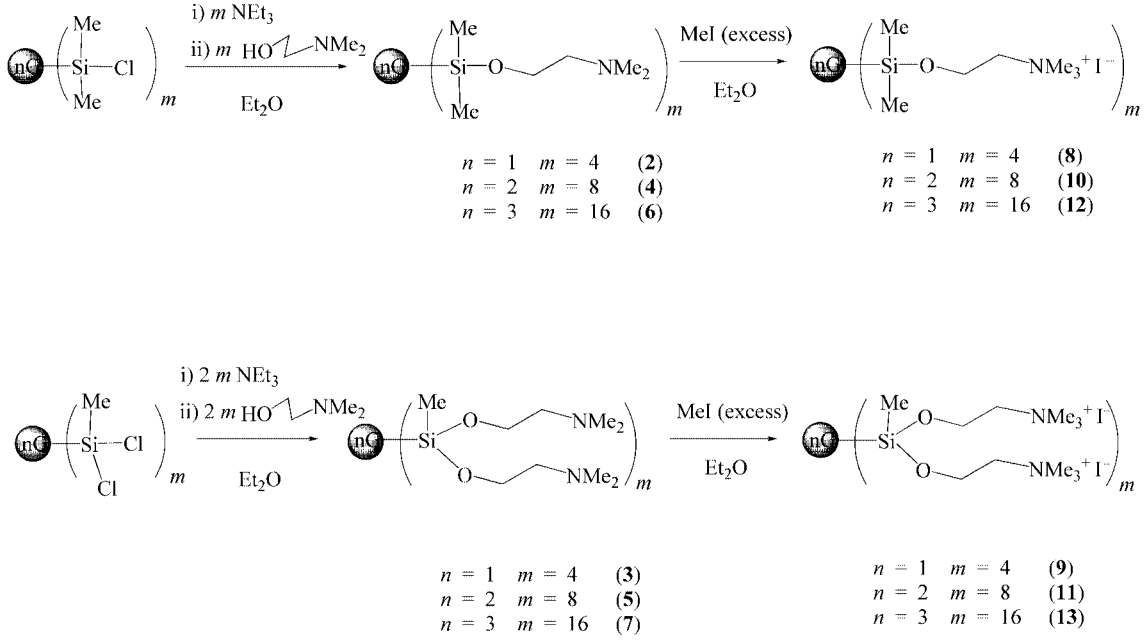


Scheme 2.

$SiOCH_2CH_2N$ branches, and for the inner $SiCH_2CH_2CH_2Si$ branches, signals in the range of $\delta$ = 21.3 to 17.4 ppm are observed. HMQC experiments were required to locate their resonances. For the N–Me groups, the signals in the $^1$H- and $^{13}$C NMR spectra show unchanged resonances at $\delta$ = 2.23 and 46.1 ppm, respectively. Both the $–SiMe_2–$ and –SiMe– fragments can be easily distinguished in all derivatives and generations (see Exp. Sect.). It is worth noting that for the outer –SiMe– groups the resonance appears about $\delta$ = –1.7 ppm in dendrimers **2**, **4**, and **6**, whilst it is located around $\delta$ = –4.4 ppm for dendrimers **3**, **5**, and **7**, as a consequence, again, of the presence of one or two silicon-bonded oxygen atoms, respectively. This feature is clearly observed in the $^{29}$Si NMR spectra, although the innermost silicon atom is only detected for the first generations.

Dendrimers were also analyzed by mass spectroscopy (electrospray or MALDI-TOF MS) using 1,8,9-trihydroxyanthracene (dithranol) as a matrix. However, the molecular peaks were not observed for the second and third generations, as described for many high-molecular-weight dendrimers.[19]

### Ammonium-Terminated Carbosilane Dendrimers

Attempts to quaternize the amine-terminated carbosilane dendrimers **2**–**7** with stoichiometric amounts or an excess of HCl failed because of hydrolysis of the Si–O bonds. However, treatment of the dendrimers with an excess of MeI in diethyl ether led to quantitative quaternization of the amine groups within 24–48 h, causing the precipitation of the ammonium iodide salts 1G-$[Si(OCH_2CH_2NMe_3^+I^-)]_4$ (**8**), 1G-$[Si(OCH_2CH_2NMe_3^+I^-)_2]_4$ (**9**), 2G-$[Si(OCH_2CH_2NMe_3^+I^-)]_8$ (**10**), 2G-$[Si(OCH_2CH_2NMe_3^+I^-)_2]_8$ (**11**), 3G-$[Si(OCH_2CH_2NMe_3^+I^-)]_{16}$ (**12**), and 3G-$[Si(OCH_2CH_2NMe_3^+I^-)_2]_{16}$ (**13**) in high yields as white hygroscopic solids (Scheme 2). In the case of the amine-terminated dendrimer **7**, some dimethylamine groups remained unquaternized. The $^1$H NMR spectrum revealed that roughly 29 of the 32 amine groups were quaternized, even if we used a large excess of MeI and prolonged reaction times. All the dendritic ionic derivatives are insoluble in normal organic solvents, but are soluble in DMSO, MeOH, and $H_2O$, although slow decomposition occurs in protic solvents (see later for decomposition behavior).

The NMR spectroscopic and analytical data of derivatives **8**–**13** are consistent with their proposed structures (Scheme 2 and Figure 1). The $^1$H NMR spectra were recorded in DMSO at room temperature, although in this solvent the line widths of these spectra tended to be broader than those of derivatives soluble in common organic solvents. The $^1$H- and $^{13}$C NMR spectra of the quaternized dendrimers **8**–**13** exhibit identical resonance patterns to those observed in their counterparts **2**–**7** for the carbosilane framework, although broader signals are seen with increasing generation (see Exp. Sect. and Supporting Information). Two broad multiplets are observed for the outer $SiOCH_2CH_2N$ grouping, centered at $\delta$ = 3.94 (for dendrimers **8**, **10**, and **12**) or 4.12 ppm (for dendrimers **9**, **11**, and **13**) for the $–CH_2O–$ groups, and $\delta$ = 3.45 (for dendrimers **8**, **10**, and **12**) or 3.56 ppm (for dendrimers **9**, **11**, and **13**) for the $–CH_2N–$ fragment. The quaternization of the amine groups resulted in a deshielding of the chemical shifts of the $–CH_2O–$ groups by 0.3–0.4 ppm, whereas for the $–CH_2N–$

 © 2006 Wiley-VCH Verlag GmbH & Co. KGaA, Weinheim 

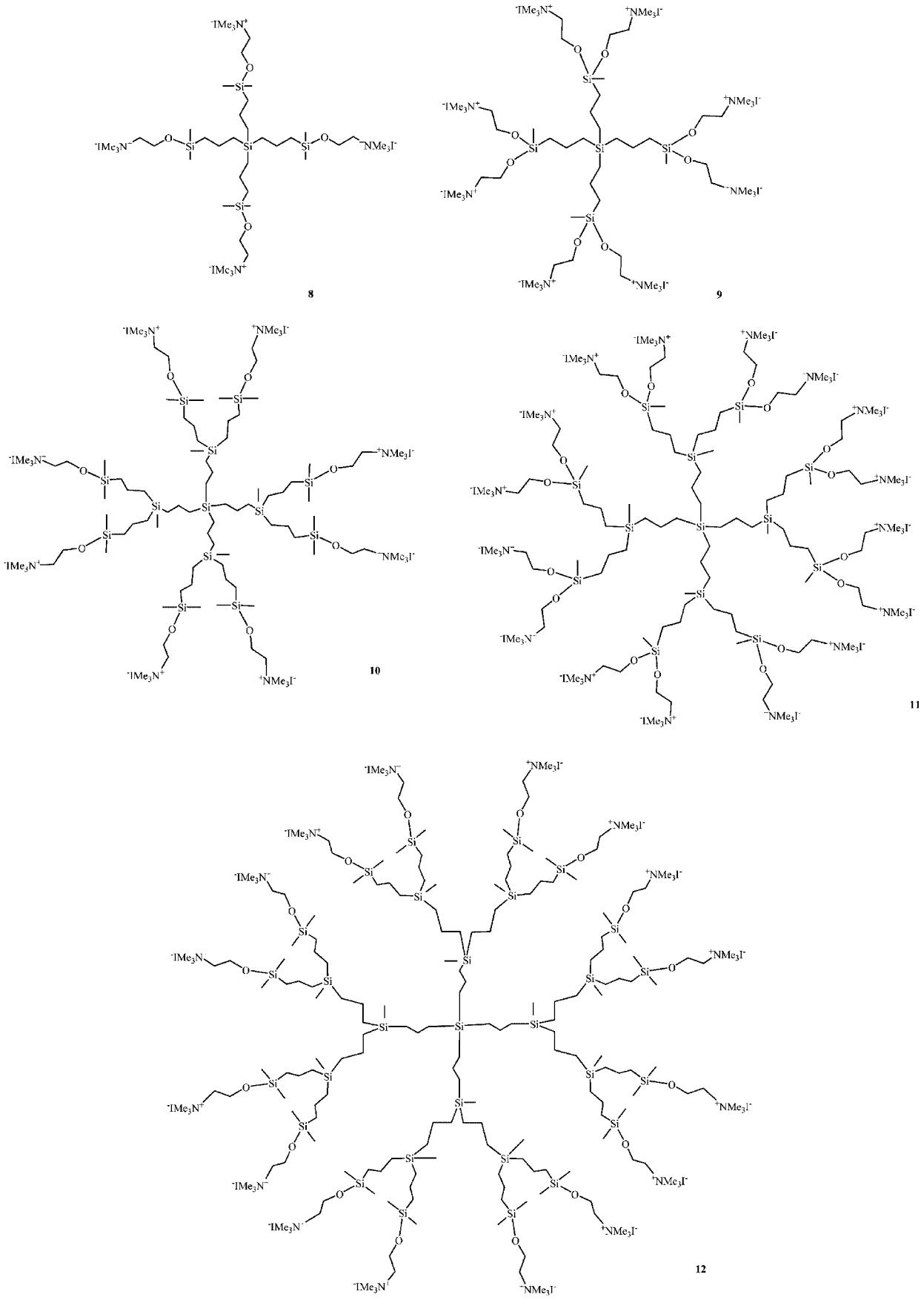


Figure 1. Molecular representations of the ammonium-terminated carbosilane dendrimers **8**–**12**.

 © 2006 Wiley-VCH Verlag GmbH & Co. KGaA, Weinheim 

methylene groups this shift was about 1 ppm, consistent with the presence of a positive charge on the nitrogen atom. Analogous shifts are observed for the carbon atoms in their $^{13}C$ NMR spectra. This behavior is also detected in the methyl groups, which appear in the $^{1}H$- and $^{13}C$ NMR spectra centered at $\delta$ = 3.18 and 52.6 ppm, respectively, downfield of those observed in the amine-terminated dendrimers **2**–**7**.

### Hydrolysis Behavior of Amine- and Ammonium-Terminated Dendrimers

As mentioned earlier, the amine-terminated dendrimers and the quaternized derivatives decompose in protic solvents. For instance, when dendrimers **3** or **9** are dissolved in methanol for several hours, after extraction with diethyl ether, a new dendrimer is formed, 1G-[Si(OMe)$_2$]$_4$, consistent with the alcoholysis of the Si–O bonds, the inclusion of methoxy groups,[20] and the respective formation of ethanolamine or its ammonium salt.

The hydrolysis of the second- and third-generation ammonium-terminated dendrimers **10** and **12** was studied in more detail. Both dendrimers degrade in deuterated water to form [DOCH$_2$CH$_2$NMe$_3^+$I$^-$] and an insoluble polymeric carbosiloxane material. The changes in dendrimer concentration were measured by $^{1}H$ NMR spectroscopy on the basis of the integration of both –OCH$_2$CH$_2$N– methylene proton resonances, which were always at pD = 7.2. A plot of ln[dendrimer] versus time showed an apparently first-order decomposition (see Figure 2). However, when the plot was performed using different initial dendrimer concentrations (see Supporting Information) the results showed that the rate constant decreases with increasing dendrimer concentration. The same decrease is observed on going from the second to the third generation when the hydrolytic processes were carried out at the same pD and initial concentrations in [Si–O] bonds, suggesting the existence of a dendritic effect (Figure 2). A plausible explanation for all these features may be the presence of interactions between branches in a cooperative effect that may decrease the rate of the process, making the decomposition a result of complex behavior.

### Evaluation of Dendrimer Toxicity

Quaternized second-generation carbosilane dendrimers **10** and **11** were tested on a primary cell culture of PBMCs (from healthy donors) as an initial screen for biocompatibility. Dendrimers of first generation were too water-sensitive for toxicity evaluation, while those of third generation were not tested because of solubility problems. As a primary cell culture, PBMCs are more sensitive to external challenge than immortalized cell lines; thus, they are good models in which to perform toxicity studies. Furthermore, there are a number of diseases that affect these cells (for example leukemia, viral infections such as HIV or HTLV, genetic disorders such as Severe Combined Immunodeficiency (SCID), and so on), and they are also a major target for immunomodulation. Additionally, PBMCs placed in the bloodstream are easily accessible to systemic drugs. In order to evaluate the range of biocompatibility of dendrimers **10** and **11**, PBMCs were incubated for 48 h with increased concentrations of free dendrimer (1, 5, 10, 20, and 100 μM). Untreated cells were used as a control for viability. After this period of incubation, cells were observed under a phase-contrast light microscope. In parallel, mitocondrial activity (MA) of cells challenged with dendrimers was evaluated by MTT test and compared with that shown by the control cells. MTT results demonstrated a similar MA in cells treated with both second-generation dendrimers **10** and **11** at the different concentrations tested (Figure 3). At the concentration of 1 μM, MA was around 80% of that shown by the control, while at 5 μM, MA decreased to 30%. Observation of cells under phase-contrast light microscopy showed that cells treated with concentrations from 1 to 5 μM of the dendrimers were alive, with no visible differences from control cells. Cells treated with concentrations of 10 μM or higher exhibited reduced membrane birefringence and a concentration-dependent increase in mortality, and even more, at these concentrations, formation of cell aggregates was observed with dendrimer **11**, probably caused by the presence of a higher cationic charge on its surface (not only dendrimers, but cationic macromolecules in general cause destabilization of the cell membrane).[1j–21] Overall, the results from the MTT test and the microscopic observa-

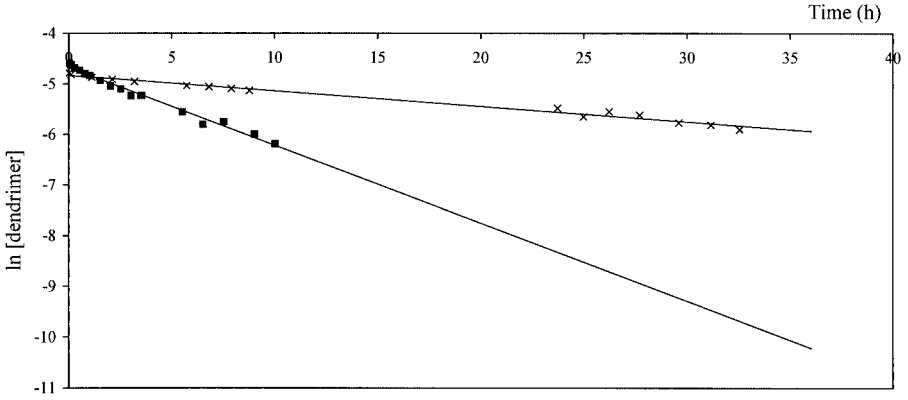


Figure 2. Plot of the hydrolysis process of the ammonium-terminated carbosilane dendrimers of second generation **10** (filled squares) and third generation **12** (crosses), at the same initial concentration.

 © 2006 Wiley-VCH Verlag GmbH & Co. KGaA, Weinheim 

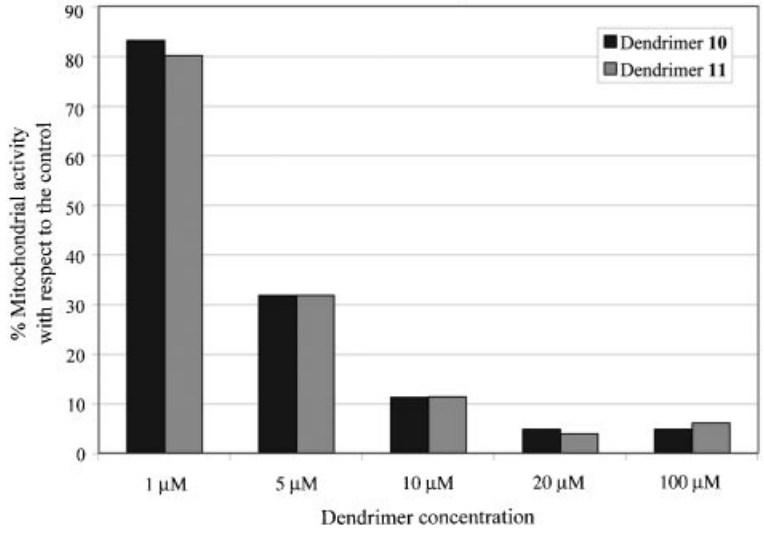


Figure 3. Quantification of mitochondrial activity of cells by MTT test after 48 h of incubation with different concentrations of the carbosilane dendrimers **10** and **11**.

tions lead to the conclusion that the biocompatible concentrations for both dendrimers are between 1 and 5 μM.

A preliminary study of the capacity of these dendrimers in the complexation with the nucleic material to give the so-called dendriplexes was performed by electrophoretic analysis. The technique was carried out in agarose gel using dendrimer **10** and a fluoresceinated phosphorothioate oligodeoxynucleotide (ODN) at different electrostatic charge ratios (+)/(–) (see Figure 4). The retardation of the ODN migration observed in the gel electrophoresis indicates that the ODN is associated with the dendrimer demonstrating a successful complex formation, even at 2:1 charge ratio in which the dendrimer concentration is in the range of biocompatibility mentioned earlier. Because of the hydrolytic problems shown by the carbosilane dendrimers with Si–O bonds, an experiment was performed to ensure that the quaternized dendrimers are responsible for the ODN retardation, rather than charged terminal functional groups detached from the dendritic structure. To this end, mixtures of ODN with the terminal groups [$HOCH_2CH_2NMe_3^+I^-$] alone were subjected to electrophoresis and retardation of the ODN assessed (see also Figure 4). The results clearly show that the terminal branches alone were not able to retard ODN migration, indicating that the whole functionalized dendrimer was necessary to form complexes with ODN. The dendriplexes released the ODN progressively between 6–24 h, which is adequate time for some biomedical applications.

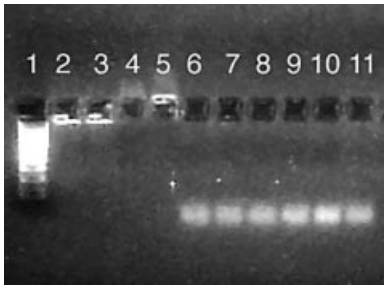


Figure 4. Electrophoresis of dendrimer **10** or [$HOCH_2CH_2NMe_3^+I^-$] and ODN on a 3% agarose gel: (1) a 100 bp DNA ladder as reference; (2) **10**/ODN ratio (+)/(–), 2:1; (3) **10**/ODN ratio (+)/(–), 4:1; (4) **10**/ODN ratio (+)/(–), 20:1; (5) **10**/ODN ratio (+)/(–), 40:1; (6) ODN only; (7) [$HOCH_2CH_2NMe_3^+I^-$]/ODN ratio (+)/(–), 2:1; (8) [$HOCH_2CH_2NMe_3^+I^-$]/ODN ratio (+)/(–), 4:1; (9) [$HOCH_2CH_2NMe_3^+I^-$]/ODN ratio (+)/(–), 20:1; (10) [$HOCH_2CH_2NMe_3^+I^-$]/ODN ratio (+)/(–), 40:1; (11) ODN only.

## Conclusion

A synthetic strategy has been developed for the preparation of new peripheral amine- or ammonium-terminated carbosilane dendrimers. It consists of the alcoholysis of well-known chlorosilane-terminated dendrimers with *N*,*N*-dimethylethanolamine and the subsequent quaternization reaction with MeI. This procedure was shown to be suitable for the growth of high generations, although partial quaternization was observed in the more crowded third-generation dendrimer **7**. Evaluation of dendrimer toxicity by phase-contrast light microscopy and MTT assay revealed that the second-generation dendrimers **10** and **11** show good toxicity profiles in primary cell culture models over extended periods for concentrations between 1 and 5 μM, making them attractive for potential use as biocompatible drug carriers. All these systems are sensitive towards hydrolysis by breaking of the Si–O bonds with the subsequent liberation of their peripheral units. This feature may have a detrimental effect on the dendrimer properties, however, such a process could be useful in the design of carriers for controlled release of drugs. In addition, the capacity of dendrimer/oligonucleotide complex formation was confirmed by electrophoresis. These experiments open the way to use these dendritic macromolecules as drug delivery systems by an electrostatic approach and their posterior release by means of the hydrolytic process. Further studies are in progress to modify the external ammonium motif of the carbosilane dendrimers in order to control their stability towards hydrolysis.

 © 2006 Wiley-VCH Verlag GmbH & Co. KGaA, Weinheim 

## Experimental Section

**General:** All manipulations of oxygen- or water-sensitive compounds were carried out under argon using standard Schlenk techniques or an argon-filled glovebox. Solvents were dried and freshly distilled under argon prior to use: hexane from sodium-potassium, toluene from sodium, tetrahydrofuran and diethyl ether from sodium benzophenone ketyl, and dichloromethane from $P_4O_{10}$. Unless otherwise stated, reagents were obtained from commercial sources and used as received. *n*G-$(SiCl_y)_x$ dendrimers were prepared according to reported methods.[14]

$^1$H-, $^{13}$C-, and $^{29}$Si NMR spectra were recorded with Varian Unity VXR-300 and Varian 500 Plus Instruments. Chemical shifts ($\delta$, ppm) were measured relative to residual $^1$H and $^{13}$C resonances for [$D_1$]chloroform and [$D_6$]dimethyl sulfoxide which were used as solvents, and $^{29}$Si chemical shifts were referenced to external $SiMe_4$ ($\delta$ = 0.00 ppm). The integral values of the signals in the $^1$H NMR spectra of dendrimer complexes represent only 25% of the total amount of hydrogen atoms. C, H, and N analyses were carried out with a Perkin–Elmer 240 C microanalyzer. MALDI-TOF MS samples were prepared in a 1,8,9-trihydroxyanthracene (dithranol) matrix, and spectra were recorded with a Bruker Reflex II spectrometer equipped with a nitrogen laser emitting at 337 nm and operated in the reflector mode at an accelerating voltage in the range 23000–25000 V.

**Synthesis of 1G-[Si(OCH$_2$CH$_2$NH$_2$)]$_4$ (1):** To a diethyl ether solution (50 mL) of the first-generation chloro-terminated dendrimer 1G-$(SiCl)_4$ (0.35 g, 0.61 mmol) were added a slight excess of $NEt_3$ (0.40 mL, 2.86 mmol) and ethanolamine (0.16 mL, 2.44 mmol). The reaction mixture was stirred for 12 h at room temp. and then evaporated to dryness to remove residual $NEt_3$. The residue was extracted with $Et_2O$ (50 mL) and filtered through Celite to remove the ammonium salt $NEt_3$·HCl. The resulting solution was evaporated under reduced pressure to give **1** as a brown oil (0.21 g, 51%). $^1$H NMR ($CDCl_3$): $\delta$ = 3.55 (t, 2 H, C$H_2$O), 2.74 (t, 2 H, C$H_2$N), 1.46 (s, 2 H, N$H_2$), 1.32 (m, 2 H, SiCH$_2$C$H_2$CH$_2$SiO), 0.63 (m, 2 H, C$H_2$SiO), 0.53 (m, 2 H, C$H_2$Si), 0.07 (s, 6 H, OSi$Me_2$) ppm. $^{13}$C{$^1$H} NMR ($CDCl_3$): $\delta$ = 64.8 (*C*H$_2$N), 44.3 (*C*H$_2$O), 21.3 (*C*H$_2$SiO), 17.9, 17.2 (Si*C*H$_2$*C*H$_2$CH$_2$SiO), –1.9 (OSi$Me_2$) ppm. $C_{28}H_{72}N_4O_4Si_5$ (668.4): calcd. C 50.27, H 10.77, N 8.38; found C 51.01, H 11.03, N 8.06.

**Synthesis of 1G-[Si(OCH$_2$CH$_2$NMe$_2$)]$_4$ (2):** To a diethyl ether (40 mL) solution of the first-generation chloro-terminated dendrimer 1G-$(SiCl)_4$ (0.85 g, 1.49 mmol) were added a slight excess of $NEt_3$ (0.86 mL, 6.2 mmol) and *N*,*N*-dimethylethanolamine (0.6 mL, 5.97 mmol). The reaction mixture was stirred for 1 h at room temp. and then evaporated to dryness to remove residual $NEt_3$. The residue was extracted with $Et_2O$ (30 mL) and filtered through Celite to remove the ammonium salt $NEt_3$·HCl. The resulting solution was evaporated under reduced pressure to give **2** as a pale yellow oil (0.98 g, 84%). $^1$H NMR ($CDCl_3$): $\delta$ = 3.64 (t, 2 H, C$H_2$O), 2.40 (t, 2 H, C$H_2$N), 2.22 (s, 6 H, N$Me_2$), 1.31 (m, 2 H, SiCH$_2$C$H_2$CH$_2$SiO), 0.60 (m, 2 H, C$H_2$SiO), 0.53 (m, 2 H, C$H_2$Si), 0.07 (s, 6 H, OSi$Me_2$) ppm. $^{13}$C{$^1$H} NMR ($CDCl_3$): $\delta$ = 61.5 (*C*H$_2$N), 60.8 (*C*H$_2$O), 46.1 (N*Me*$_2$), 21.3 (*C*H$_2$SiO), 18.1, 17.4 (Si*C*H$_2$*C*H$_2$CH$_2$SiO), –1.7 (OSi$Me_2$) ppm. $^{29}$Si{$^1$H} NMR ($CDCl_3$): $\delta$ = 0.49 ($G_0$-Si), 17.62 ($G_1$-Si) ppm. $C_{36}H_{88}N_4O_4Si_5$ (780.4): calcd. C 55.36, H 11.28, N 7.17; found C 55.16, H 11.22, N 7.06.

**Synthesis of 1G-[Si(OCH$_2$CH$_2$NMe$_2$)$_2$]$_4$ (3):** This dendrimer was prepared using a similar method to that described for **2**, starting from 1G-$(SiCl_2)_4$ (0.54 g, 0.87 mmol), *N*,*N*-dimethylethanolamine (0.7 mL, 6.94 mmol), and $NEt_3$ (1.0 mL, 7.2 mmol) to obtain compound **3** as a colorless oil (0.75 g, 80%). $^1$H NMR ($CDCl_3$): $\delta$ = 3.74 (t, 4 H, C$H_2$O), 2.43 (t, 4 H, C$H_2$N), 2.23 (s, 12 H, N$Me_2$), 1.31 (m, 2 H, SiCH$_2$C$H_2$CH$_2$SiO), 0.63 (m, 2 H, C$H_2$SiO), 0.52 (m, 2 H, C$H_2$Si), 0.09 (s, 3 H, OSi*Me*) ppm. $^{13}$C{$^1$H} NMR ($CDCl_3$): $\delta$ = 61.4 (*C*H$_2$N), 60.7 (*C*H$_2$O), 46.2 (N*Me*$_2$), 18.7 (*C*H$_2$SiO), 17.7, 17.2 (Si*C*H$_2$*C*H$_2$CH$_2$SiO), –4.4 (OSi*Me*) ppm. $^{29}$Si{$^1$H} NMR ($CDCl_3$): $\delta$ = 0.47 ($G_0$-Si), –3.65 ($G_1$-Si) ppm. $C_{48}H_{116}N_8O_8Si_5$ (1072.4): calcd. C 53.71, H 10.82, N 10.44; found C 53.54, H 11.33, N 10.06. MALDI-TOF MS: *m*/*z* 1095.8 [M + H]$^+$ (calcd. 1095.8).

**Synthesis of 2G-[Si(OCH$_2$CH$_2$NMe$_2$)]$_8$ (4):** This dendrimer was prepared using a similar method to that described for **2**, starting from 2G-$(SiCl)_8$ (0.27 g, 0.18 mmol), *N*,*N*-dimethylethanolamine (0.15 mL, 1.47 mmol), and $NEt_3$ (0.25 mL, 1.79 mmol) to obtain compound **4** as a pale yellow oil (0.31 g, 90%). $^1$H NMR ($CDCl_3$): $\delta$ = 3.64 (t, 4 H, C$H_2$O), 2.41 (t, 4 H, C$H_2$N), 2.23 (s, 12 H, N$Me_2$), 1.30 (m, 6 H, SiCH$_2$C$H_2$CH$_2$SiO and SiCH$_2$C$H_2$CH$_2$Si overlapping), 0.65 (m, 4 H, C$H_2$SiO), 0.53 (m, 8 H, rest of C$H_2$Si), 0.07 (s, 12 H, OSi$Me_2$), –0.09 (s, 3 H, Si*Me*) ppm. $^{13}$C{$^1$H} NMR ($CDCl_3$): $\delta$ = 61.5 (*C*H$_2$N), 60.8 (*C*H$_2$O), 46.1 (N*Me*$_2$), 21.1 (*C*H$_2$SiO), 18.6, 17.9 and overlapped signals (Si*C*H$_2$C*H*$_2$CH$_2$SiO and Si*C*H$_2$*C*H$_2$*C*H$_2$Si overlapping), –1.9 (OSi$Me_2$), –4.9 (Si*Me*) ppm. $^{29}$Si{$^1$H} NMR ($CDCl_3$): $\delta$ = 0.93 ($G_1$-Si), 17.60 ($G_2$-Si) ppm, $G_0$-Si was not observed. $C_{88}H_{212}N_8O_8Si_{13}$ (1873.0): calcd. C 56.38, H 11.32, N 5.98; found C 55.98, H 11.20, N 5.78.

**Synthesis of 2G-[Si(OCH$_2$CH$_2$NMe$_2$)$_2$]$_8$ (5):** This dendrimer was prepared using a similar method to that described for **2**, starting from 2G-$(SiCl_2)_8$ (0.48 g, 0.30 mmol), *N*,*N*-dimethylethanolamine (0.48 mL, 4.77 mmol), and $NEt_3$ (0.7 mL, 5.02 mmol) to obtain compound **5** as a colorless oil (0.66 g; 90%). $^1$H NMR ($CDCl_3$): $\delta$ = 3.75 (t, 8 H, C$H_2$O), 2.44 (t, 8 H, C$H_2$N), 2.24 (s, 24 H, N$Me_2$), 1.34 (m, 6 H, SiCH$_2$C$H_2$CH$_2$SiO and SiCH$_2$C$H_2$CH$_2$Si overlapping), 0.64 (m, 4 H, C$H_2$SiO), 0.51 (m, 8 H, rest of C$H_2$Si), 0.09 (s, 6 H, OSi*Me*), –0.10 (s, 3 H, Si*Me*) ppm. $^{13}$C{$^1$H} NMR ($CDCl_3$): $\delta$ = 61.4 (*C*H$_2$N), 60.7 (*C*H$_2$O), 46.2 (N*Me*$_2$), 18.6 (*C*H$_2$SiO), 17.7, 17.0 and overlapped signals (Si*C*H$_2$C*H*$_2$CH$_2$SiO and Si*C*H$_2$*C*H$_2$*C*H$_2$Si overlapping), –4.4 (OSi*Me*), –4.8 (Si*Me*) ppm. $^{29}$Si{$^1$H} NMR ($CDCl_3$): $\delta$ = 0.92 ($G_1$-Si), –3.54 ($G_2$-Si) ppm, $G_0$-Si was not observed. $C_{112}H_{268}N_{16}O_{16}Si_{13}$ (2457.0): calcd. C 54.70, H 10.91, N 9.12; found C 54.20, H 10.37, N 9.59.

**Synthesis of 3G-[Si(OCH$_2$CH$_2$NMe$_2$)]$_{16}$ (6):** This dendrimer was prepared using a similar method to that described for **2**, starting from 3G-$(SiCl)_{16}$ (0.20 g, 0.06 mmol), *N*,*N*-dimethylethanolamine (0.10 mL, 0.99 mmol), and $NEt_3$ (0.16 mL, 1.14 mmol) to obtain compound **6** as a pale yellow oil (0.18 g, 74%). $^1$H NMR ($CDCl_3$): $\delta$ = 3.65 (t, 8 H, C$H_2$O), 2.42 (t, 8 H, C$H_2$N), 2.24 (s, 24 H, N$Me_2$), 1.23 (m, 14 H, SiCH$_2$C$H_2$CH$_2$SiO and SiCH$_2$C$H_2$CH$_2$Si overlapping), 0.64 (m, 8 H, C$H_2$SiO), 0.53 (m, 20 H, rest of C$H_2$Si), 0.07 (s, 24 H, OSi$Me_2$), –0.10 (s, 9 H, Si*Me*) ppm. $^{13}$C{$^1$H} NMR ($CDCl_3$): $\delta$ = 61.5 (*C*H$_2$N), 60.8 (*C*H$_2$O), 46.1 (N*Me*$_2$), 21.1 (*C*H$_2$SiO), 18.6, 17.9 and overlapped signals (Si*C*H$_2$*C*H$_2$CH$_2$SiO and Si*C*H$_2$*C*H$_2$*C*H$_2$Si overlapping), –1.8 (OSi$Me_2$), –4.8 (Si*Me*) ppm. $^{29}$Si{$^1$H} NMR ($CDCl_3$): $\delta$ = 0.95 ($G_2$-Si), 17.95 ($G_3$-Si) ppm, $G_0$-Si and $G_1$-Si were not observed. $C_{192}H_{460}N_{16}O_{16}Si_{29}$ (4058.3): calcd. C 56.77, H 11.33, N 5.52; found C 56.17, H 11.28, N 5.34.

**Synthesis of 3G-[Si(OCH$_2$CH$_2$NMe$_2$)$_2$]$_{16}$ (7):** This dendrimer was prepared using a similar method to that described for **2**, starting from 3G-$(SiCl_2)_{16}$ (0.19 g, 0.05 mmol), *N*,*N*-dimethylethanolamine (0.17 mL, 1.68 mmol), and $NEt_3$ (0.24 mL, 1.79 mmol) to obtain compound **7** as a pale yellow oil (0.20 g, 72%). $^1$H NMR ($CDCl_3$): $\delta$ = 3.75 (t, 16 H, C$H_2$O), 2.44 (t, 16 H, C$H_2$N), 2.24 (s, 48 H, N$Me_2$), 1.32 (m, 14 H, SiCH$_2$C$H_2$CH$_2$SiO), 0.66 (m, 8 H,

 © 2006 Wiley-VCH Verlag GmbH & Co. KGaA, Weinheim 

$SiCH_2CH_2CH_2SiO$), 0.53 (m, 20 H, rest of $SiCH_2$), 0.07 (s, 12 H, $OSiMe$), –0.10 (s, 9 H, $SiMe$) ppm. $^{13}C\{^1H\}$ NMR ($CDCl_3$): $\delta$ = 61.4 ($CH_2N$), 60.7 ($CH_2O$), 46.1 ($NMe_2$), a range 18.4–17.4 and overlapped signals ($SiCH_2CH_2CH_2SiO$ and $SiCH_2CH_2CH_2Si$ overlapping), –4.7 ($OSiMe_2$), –5.2 ($SiMe$) ppm. $C_{240}H_{572}N_{32}O_{32}Si_{29}$ (5226.3): calcd. C 55.11, H 10.95, N 8.57; found C 56.11, H 11.89, N 8.13.

**Synthesis of 1G-[Si(OCH$_2$CH$_2$NMe$_3^+$I$^-$)]$_4$ (8):** To a diethyl ether (10 mL) solution of **2** (0.12 g, 0.15 mmol) was added a MeI solution (0.4 mL, 0.8 mmol, 2 M in $Et_2O$). The resulting solution was stirred for 48 h at room temp. and then evaporated under reduced pressure to remove residual MeI. The residue was washed with $Et_2O$ (2 × 5 mL) and dried under vacuum to give **8** as a white solid (0.20 g, 96%). $^1H$ NMR (DMSO): $\delta$ = 3.94 (m, 2 H, $CH_2O$), 3.43 (m, 2 H, $CH_2N$), 3.09 (s, 9 H, $NMe_3^+$), 1.29 (m, 2 H, $SiCH_2CH_2CH_2SiO$), 0.66 (m, 2 H, $CH_2SiO$), 0.56 (m, 2 H, $CH_2Si$), 0.11 (s, 6 H, $OSiMe_2$) ppm. $^{13}C\{^1H\}$ NMR (DMSO): $\delta$ = 65.8 ($CH_2N$), 55.8 ($CH_2O$), 52.6 ($NMe_3^+$), 19.7 ($CH_2SiO$), 16.9, 16.1 ($SiCH_2CH_2CH_2SiO$), –2.6 ($OSiMe_2$) ppm. $C_{40}H_{100}I_4N_4O_4Si_5$ (1348.0): calcd. C 35.61, H 7.42, N 4.15; found C 36.67, H 7.65, N 4.42.

**Synthesis of 1G-[Si(OCH$_2$CH$_2$NMe$_3^+$I$^-$)$_2$]$_4$ (9):** This first-generation dendrimer was prepared using a similar method to that described for **8**, starting from **3** (0.17 g, 0.16 mmol) and a MeI solution (0.80 mL, 1.6 mmol, 2 M in $Et_2O$). Compound **9** was isolated as a white solid (0.29 g, 86%). $^1H$ NMR (DMSO): $\delta$ = 4.12 (m, 4 H, $CH_2O$), 3.54 (m, 4 H, $CH_2N$), 3.17 (s, 18 H, $NMe_3^+$), 1.29 (m, 2 H, $SiCH_2CH_2CH_2SiO$), 0.75 (m, 2 H, $CH_2SiO$), 0.54 (m, 2 H, $CH_2Si$), 0.20 (s, 3 H, $OSiMe$) ppm. $^{13}C\{^1H\}$ NMR (DMSO): $\delta$ = 65.8 ($CH_2N$), 56.0 ($CH_2O$), 52.7 ($NMe_3^+$), 17.3 ($CH_2SiO$), 16.5, 15.9 ($SiCH_2CH_2CH_2SiO$), –5.3 ($OSiMe$) ppm. $C_{56}H_{140}I_8N_8O_8Si_5$ (2207.6): calcd. C 30.44, H 6.34, N, 5.07; found C 31.47, H 6.47, N, 5.19.

**Synthesis of 2G-[Si(OCH$_2$CH$_2$NMe$_3^+$I$^-$)]$_8$ (10):** This dendrimer was prepared using a similar method to that described for **8**, starting from **4** (0.25 g, 0.13 mmol) and a MeI solution (0.6 mL, 1.2 mmol, 2 M in $Et_2O$). Compound **10** was isolated as a white solid (0.35 g, 87%). $^1H$ NMR (DMSO): $\delta$ = 3.96 (m, 4 H, $CH_2O$), 3.45 (m, 4 H, $CH_2N$), 3.11 (s, 18 H, $NMe_3^+$), 1.29 (m, 6 H, $SiCH_2CH_2CH_2SiO$ and $SiCH_2CH_2CH_2Si$), 0.65 (m, 4 H, $SiCH_2CH_2CH_2SiO$), 0.52 (m, 8 H, rest of $SiCH_2$), 0.11 (s, 12 H, $OSiMe_2$), –0.10 (s, 3 H, $SiMe$) ppm. $^{13}C\{^1H\}$ NMR (DMSO): $\delta$ = 65.7 ($CH_2N$), 55.9 ($CH_2O$), 52.6 ($NMe_3^+$), 19.7, 17.5, 16.9 and overlapped signals ($SiCH_2CH_2CH_2SiO$ and $SiCH_2CH_2CH_2Si$), –2.5 ($OSiMe_2$), –5.3 ($SiMe$) ppm. $C_{96}H_{236}I_8N_8O_8Si_{13}$ (3008.2): calcd. C 38.29, H 7.85, N 3.72; found C 38.87, H 8.32, N, 3.79.

**Synthesis of 2G-[Si(OCH$_2$CH$_2$NMe$_3^+$I$^-$)$_2$]$_8$ (11):** This dendrimer was prepared using a similar method to that described for **8**, starting from **5** (0.10 g, 0.04 mmol) and a MeI solution (0.5 mL, 1.0 mmol, 2 M in $Et_2O$). Compound **11** was isolated as a white solid (0.17 g, 87%). $^1H$ NMR (DMSO): $\delta$ = 4.13 (m, 8 H, $CH_2O$), 3.56 (m, 8 H, $CH_2N$), 3.19 (s, 36 H, $NMe_3^+$), 1.28 (m, 6 H, $SiCH_2CH_2CH_2SiO$ and $SiCH_2CH_2CH_2Si$), 0.72 (m, 4 H, $SiCH_2CH_2CH_2SiO$), 0.55 (m, 8 H, rest of $SiCH_2$), 0.21 (s, 6 H, $OSiMe$), –0.08 (s, 3 H, $SiMe$) ppm. $^{13}C\{^1H\}$ NMR (DMSO): $\delta$ = 65.7 ($CH_2N$), 56.0 ($CH_2O$), 52.7 ($NMe_3^+$); 19.2, 17.2, 16.4 and overlapped signals ($SiCH_2CH_2CH_2SiO$ and $SiCH_2CH_2CH_2Si$), –5.2 ($OSiMe$), –5.6 ($SiMe$) ppm. $C_{128}H_{316}I_{16}N_{16}O_{16}Si_{13}$ (4727.4): calcd. C 32.49, H 6.68, N 4.74; found C 33.32, H 7.03, N, 4.72.

**Synthesis of 3G-[Si(OCH$_2$CH$_2$NMe$_3^+$I$^-$)]$_{16}$ (12):** This dendrimer was prepared using a similar method to that described for **8**, starting from **6** (0.12 g, 0.03 mmol) and a MeI solution (0.4 mL, 0.8 mmol, 2 M in $Et_2O$). Compound **12** was isolated as a white solid (0.16 g, 83%). $^1H$ NMR (DMSO): $\delta$ = 3.96 (m, 8 H, $CH_2O$), 3.47 (m, 8 H, $CH_2N$), 3.13 (s, 36 H, $NMe_3^+$), 1.28 (m, 14 H, $SiCH_2CH_2CH_2SiO$ and $SiCH_2CH_2CH_2Si$), 0.65 (m, 8 H, $SiCH_2CH_2CH_2SiO$), 0.52 (m, 20 H, rest of $SiCH_2$), 0.10 (s, 24 H, $OSiMe_2$), –0.08 (s, 9 H, $SiMe$) ppm. $^{13}C\{^1H\}$ NMR (DMSO): $\delta$ = 65.8 ($CH_2N$), 55.9 ($CH_2O$), 52.6 ($NMe_3^+$), 19.7, 17.2, 16.0 and overlapped signals ($SiCH_2CH_2CH_2SiO$ and $SiCH_2CH_2CH_2Si$), –2.7 ($OSiMe_2$), –5.5 ($SiMe$) ppm. $C_{208}H_{508}I_{16}N_{16}O_{16}Si_{29}$ (6328.7): calcd. C 39.43, H 8.03, N 3.54; found C 39.19, H 8.19, N, 3.68.

**Reaction of 3G-[Si(OCH$_2$CH$_2$NMe$_2$)$_2$]$_{16}$ (7) with MeI:** The reaction of **7** with MeI using a similar method to that described for **8** afforded the dendrimer 3G-[Si($OCH_2CH_2NMe_3^+I^-)_2$]$_{16}$ (**13**). However, the NMR analysis revealed that not all the amine groups were quaternized: roughly 29 groups were methylated, based on integration of the corresponding chemical shift of the outer –$OCH_2CH_2N$– branch for the amine or ammonium groups.

### Biocompatibility Studies

**Cells:** PBMC cells were derived from healthy voluntary donors, and obtained from leukophoresed blood by Ficoll™ gradient and elutriation centrifugation. Prior to challenge with dendrimers, PBMCs were stimulated for 48 h with phytohemagglutinin (2 μg/mL) and Interleukin 2 (IL-2, 100 IU/mL). On the day of the challenge, PBMCs were recovered and washed with Phosphate Buffered Saline (PBS), and then seeded in RPMI medium supplemented with 10% of fetal calf serum, 1% L-glutamine, antibiotics, and IL-2 (50 IU/mL), in a 5% $CO_2$ environment (100 000 cells per well in 96-well plates for the toxicity curve of dendrimer concentrations). The final volume in each well was 200 μL for the 96-well plates and 500 μL for the 24-well plates. For the toxicity curve of dendrimer concentrations, wells were coated with 20 μL of fibronectin/well at a concentration of 5 μg/mL. The intention was not to lose cells through pipetting during the MTT assay. In the case of the 24-well plates, stimulated cells were seeded in 340 μL of complete medium.

**Phase-Contrast Light Microscopy:** After incubation with dendrimers, changes in morphology and characteristics of PBMCs, such as cell membrane birefringence, were observed using a phase-contrast inverted microscope (Nikon TMS, Nikon, Japan) equipped with a 100X objective (Plan 10/0,30DL/Ph1, Nikon, Japan). Live PBMCs are bright, have a defined spherical shape, and float in the culture medium. Dead cells have a darker appearance, and are mostly present in the bottom of the well. In addition, we assessed the presence or absence of cell aggregation.

**MTT [3-(4,5-Dimethylthiazol-2-yl)-2,5-diphenyltetrazolium Bromide] Assay:** This method was selected to analyze detrimental intracellular effects on mitochondria and metabolic activity. The colorimetric MTT test, based on the selective ability of viable cells to reduce 3-(4,5-dimethylthiazol-2-yl)-2,5-diphenyltetrazolium bromide to purple formazan, relies on intact metabolic activity, and is frequently used for cytotoxicity screening. After 48 h of incubation of PBMCs with different concentrations of dendrimers in a 96-well plate, culture medium containing the dendrimers was replaced with serum-free Optimem (200 μL). Sterile filtered MTT (Sigma) stock solution (20 μL) in PBS pH = 7.4 (5 mg/mL) was added to each well to achieve a final concentration of 0.5 mg MTT/mL. After 4 h, unreacted dye was removed by aspiration, and the formazan crystals were dissolved in dimethyl sulfoxide (200 μL per well) (Merck, Darmstadt, Germany). The concentration of formazan was then determined spectrophotometrically in a plate reader at a wavelength of 570 nm (test) and 690 nm (reference). The spectrophotometer was calibrated to zero absorbance using Optimem medium without cells. The relative cell viability (%) related to control wells

 © 2006 Wiley-VCH Verlag GmbH & Co. KGaA, Weinheim 

(cells with no dendrimer) was calculated by [A] test/[A] control × 100. Each dendrimer concentration was tested in triplicate, according to ATCC directives.

**Formation of Dendrimer/Oligonucleotide Complexes:** The fluoresceinated phosphorothioate oligodeoxynucleotide (ODN) sequence was 25 bases long and corresponded to an antisense (complementary) sequence of the HIV Anti-Gag. Complex formation between dendrimer **10** or [$HOCH_2CH_2NMe_3^+I^-$] and ODN was performed using an electrostatic approach. Ratios of ODN to dendrimer were based on the calculation of the electrostatic charge present on each component, for example the number of phosphate groups in the ODN versus the number of terminal ammonium groups on the dendrimer. The dendrimer or [$HOCH_2CH_2NMe_3^+I^-$] was diluted in sterile distilled water at 2 mg/mL, and the ODN concentration for complexation with the carbosilane dendrimer was 0.88 μM (2.57 μg). All complexes or mixtures at different charge ratios were formed in serum-free RPMI medium (60 μL), with an incubation time of 20 min at room temp. Complex formation was assessed by evaluation of migration retardation of fluoresceinated ODN during electrophoresis on 3% agarose gel. A 100 bp DNA ladder was used as reference (Gibco BRL™).

**Supporting Information** (for details see the footnote on the first page of this article): Selected data as $^1$H-, $^{13}$C-, and $^{29}$Si NMR spectra of **1**, **3**–**6**, **9**–**11** (Figure S1–S3 and S6–S10), 2D HMQC and HMBC spectra of **4** (Figure S4–S5), and plots of the hydrolysis processes of **10** and **12** at different concentrations (Figure S11).

## Acknowledgments

We thank the Ministerio de Ciencia y Tecnología (Project BQU2001-1160), the DGI-Comunidad de Madrid (Project GR/MAT/0733/2004), the Plan Nacional de Salud (grant SAF-2004-06778, SAF-2003-09209), and the Red Temática Cooperativa de investigación en sida y genética (grant RIS G03/173 and grant RIG C03/07, respectively) of Fondos de Investigación Sanitaria (FIS) for financial support. J. F. B. is supported by a grant of Fondos de Investigación Sanitaria (BF03/00317) Madrid.

[1] a) M. Fischer, F. Vögtle, *Angew. Chem. Int. Ed.* **1999**, *38*, 884–905 and references cited therein; b) K. Inoue, *Prog. Polym. Sci.* **2000**, *25*, 453–571; c) J. M. Fréchet, D. A. Tomalia (Eds.), *Dendrimers and other dendritic polymers* (Wiley Series in Polymer Science), John Wiley & Sons, **2001**; d) G. R. Newkome, C. N. Moorefield, F. Vögtle (Eds.), *Dendrimers and Dendrons: Concepts, Syntheses, Applications*, Wiley-VCH, **2001**; e) G. E. Oosterom, J. N. H. Reek, P. C. J. Kamer, P. W. N. M. van Leeuwen, *Angew. Chem. Int. Ed.* **2001**, *40*, 1828–1849; f) D. Astruc, F. Chardac, *Chem. Rev.* **2001**, *101*, 2991–3023; g) S. M. Grayson, J. M. J. Fréchet, *Chem. Rev.* **2001**, *101*, 3819–3867; h) S. E. Stiriba, H. Frey, R. Haag, *Angew. Chem. Int. Ed.* **2002**, *41*, 1329–1334; i) F. Aulenta, W. Hayes, S. Rannard, *Eur. Polym. J.* **2003**, *39*, 1741–1771; j) U. Boas, P. M. H. Heegaard, *Chem. Soc. Rev.* **2004**, *33*, 43–63.

[2] a) R. Langer, *Nature* **1998**, *392*, 5–10; b) P. L. Felgner, T. R. Gadek, M. Holm, R. Roman, H. W. Chan, M. Wenz, J. P. Northrop, G. M. Ringold, M. Danielsen, *Proc. Natl. Acad. Sci. USA* **1987**, *84*, 7413–7417; c) G. McLachlan, B. J. Stevenson, D. J. Davidson, D. J. Porteous, *Gene Ther.* **2000**, *7*, 384–392; d) T. V. Chirila, P. E. Rakoczy, K. L. Garret, X. Lou, I. J. Constable, *Biomaterials* **2002**, *23*, 321–342.

[3] a) J. F. G. A. Jansen, E. M. M. de Brabander-van der Berg, E. W. Meijer, *Science* **1994**, *266*, 1226–1229; b) J. F. G. A. Jansen, E. W. Meijer, *J. Am. Chem. Soc.* **1995**, *117*, 4417–4418; c) C. Kojima, K. Kono, K. Maruyama, T. Takagishi, *Bioconjugate Chem.* **2000**, *11*, 910–917.

[4] a) K. Kono, M. Liu, J. M. J. Fréchet, *Bioconjugate Chem.* **1999**, *10*, 1115–1121; b) M. J. Liu, K. Kono, J. M. J. Fréchet, *J. Polym. Sci., Part A. Polym. Chem.* **1999**, *17*, 3492–3503.

[5] A. Quintana, E. Raczka, L. Piehler, I. Lee, A. Myc, I. Majoros, A. K. Patri, T. Thomas, J. Mulé, J. R. Baker Jr, *Pharm. Res.* **2002**, *19*, 1310–1316.

[6] a) J. Haensler, F. C. Szoka Jr, *Bioconjugate Chem.* **1993**, *4*, 372–379; b) A. U. Bielinska, C. Chen, J. Johnson, J. R. Baker Jr, *Bioconjugate Chem.* **1999**, *10*, 843–850; c) J. Dennig, E. Duncan, *Rev. Mol. Biotech.* **2002**, *90*, 339–347; d) J. Dennig, *Top. Curr. Chem.* **2003**, *228*, 227–236; e) C. L. Gebhart, A. V. Kabanov, *J. Control. Rel.* **2001**, *73*, 401–416.

[7] C. Loup, M. A. Zanta, A. M. Caminade, J. P. Majoral, B. Meunier, *Chem. Eur. J.* **1999**, *5*, 3644–3650.

[8] B. H. Zinselmeyer, S. P. Mackay, A. G. Schatzlein, I. F. Uchegbu, *Pharm. Res.* **2002**, *19*, 960–967.

[9] a) T. Nidome, M. Wakamatsu, A. Wada, T. Hirayama, H. Aoyagi, *J. Pept. Sci.* **2000**, 271–279; b) M. Ohsaki, T. Okuda, A. Wada, T. Hirayama, T. Nidome, H. Aoyagi, *Bioconjugate Chem.* **2002**, *13*, 510–517.

[10] N. Malik, R. Wiwattanapatapee, K. Klopsch, K. Lorenz, H. Frey, J. W. Weener, E. W. Meijer, W. Paulus, R. Duncan, *J. Controlled Release* **2000**, *65*, 133–148.

[11] S. W. Krska, D. Seyferth, *J. Am. Chem. Soc.* **1998**, *120*, 3604–3612.

[12] B. Luhmann, H. Lang, K. Bruning, *Phosphorus Sulfur Silicon Relat. Elem.* **2001**, *168*, 481–484.

[13] A. W. Kleij, R. van de Coevering, R. J. M. Klein Gebbink, A. M. Noordman, A. L. Spek, G. van Koten, *Chem. Eur. J.* **2001**, *7*, 181–192.

[14] a) A. W. van der Made, P. W. N. M. van Leeuwen, *J. Chem. Soc., Chem. Commun.* **1992**, 1400–1401; b) A. W. van der Made, P. W. N. M. van Leeuwen, J. C. de Wilde, R. A. C. Brandes, *Adv. Mater.* **1993**, *5*, 466–468; c) L. L. Zhou, J. Roovers, *Macromolecules* **1993**, *26*, 963–968; d) D. Seyferth, D. Y. Son, A. L. Rheingold, R. L. Ostrander, *Organometallics* **1994**, *13*, 2682–2690; e) I. Cuadrado, C. M. Casado, B. Alonso, M. Morán, J. Losada, V. Beloky, *J. Am. Chem. Soc.* **1997**, *119*, 7613–7614.

[15] B. D. Karstedt, U. S. Patent **1973**, 3, 775, 452.

[16] P. D. Bailey, K. M. Morgan, *Organonitrogen Chemistry* (Oxford Chemistry Primers), *38*, 6-31. ed., Oxford University Press, **1996**.

[17] K. Lorenz, R. Mülhaupt, H. Frey, U. Rapp, F. J. Mayer-Posner, *Macromolecules* **1995**, *28*, 6657–6661.

[18] K. T. Welch, S. Arévalo, J. F. C. Turner, R. Gómez, *Chem. Eur. J.* **2005**, *11*, 1217–1227.

[19] a) C. Kim, I. Jung, *J. Organomet. Chem.* **1999**, *588*, 9–19; b) I. Cuadrado, M. Morán, J. Losada, C. M. Casado, C. Pascual, B. Alonso, F. Lobete in *Advances in Dendritic Macromolecules*, vol. 3 (Ed.: G. R. Newkome), Jai Press, Greenwich, **1999**, pp. 151–191; c) M. Veith, R. Elsässer, R. P. Krüger, *Organometallics* **1999**, *18*, 656–661; d) C. Kim, I. Jung, *J. Organomet. Chem.* **2000**, *599*, 208–215; e) S. Arévalo, E. de Jesús, F. J. de la Mata, J. C. Flores, R. Gómez, *Organometallics* **2001**, *20*, 2583–2592.

[20] Selected $^1$H NMR spectroscopic data in $CDCl_3$ for 1G-[Si(-OMe)$_2$]$_4$: $\delta$ = 3.48 (s, 6 H, SiO*Me*), 1.36 (m, 2 H, $SiCH_2CH_2CH_2SiO$), 0.67, 0.56 (m, 4 H, $SiCH_2CH_2CH_2SiO$), 0.08 (s, 3H, $OSiMe_2$).

[21] K. Rittner, A. Benavante, S. Bompard, F. Heitz, G. Divita, R. Brasseur, E. Jacobs, *Mol. Ther.* **2002**, *5*, 104–114.

Received: September 5, 2005
Published Online: February 6, 2006

 © 2006 Wiley-VCH Verlag GmbH & Co. KGaA, Weinheim 

DOI: 10.1002/ejic.200500795

# Interactions of Cationic Palladium(II)- and Platinum(II)-$\eta^3$-Allyl Complexes with Fluoride: Is Asymmetric Allylic Fluorination a Viable Reaction?

**Lukas Hintermann,*[a,b] Florian Läng,[a] Pascal Maire,[a] and Antonio Togni[a]**

**Keywords:** Palladium / Platinum / Allyl ligands / Fluorination / Naked fluoride

The complex cations $[M(\eta^3\text{-}R_2All)(PPFPz\{3\text{-}t\text{Bu}\})]^+$ (M = $Pd^{II}$, $R_2$All = 1,3-diphenylallyl, 1,3-dicyclohexylallyl, indenyl; M = $Pt^{II}$, $R_2$All = 1,3-diphenylallyl; PPFPz-{3-*t*Bu} = 3-*tert*-butyl-1-{1-[2-diphenylphosphanyl-ferrocenyl]ethyl}-1*H*-pyrazole) have been prepared as salts with $PF_6^-$ or $SbF_6^-$. They have been characterized by NMR spectroscopy in solution and by X-ray crystallography in the solid state. Their reactions with sources of nucleophilic and "naked" fluoride have been investigated by multinuclear NMR spectroscopy. The $Pd^{II}$ complexes did not undergo any nucleophilic substitution with concomitant release of allyl fluorides. The dicyclohexylallyl fragment was released as a 1,3-diene by elimination, but with other allyl complexes nonspecific decomposition reactions predominated. The complex $[Pt(\eta^3\text{-}1,3\text{-}Ph_2C_3H_3)(PPFPz\{3\text{-}t\text{Bu}\})]PF_6$ underwent an anion exchange with $Me_4NF$ to give $[Pt(1,3\text{-}Ph_2C_3H_3)(PPFPz\{3\text{-}t\text{Bu}\})]F$ which existed as a mixture of interconverting allyl isomers in solution at ambient temperature. For the bromide salt, $[Pt(\eta^3\text{-}1,3\text{-}Ph_2C_3H_3)(PPFPz\{3\text{-}t\text{Bu}\})]Br$, allyl isomerization was slow at ambient temperature. Precursors of $Pt^0$ reacted with bromo-1,3-diphenylprop-2-ene to give $[Pt_2(\mu\text{-}Br)_2(\eta^3\text{-}1,3\text{-}Ph_2All)_2]$ and precursors of $Pd^0$ underwent oxidative additions with bromo- and fluoro-1,3-diphenyl-2-propene to give 1,3-diphenylallyl complexes of $Pd^{II}$. Therefore, the nucleophilic attack of fluoride on the allyl fragment of $Pd^{II}$ complexes is endergonic, and the high energy barrier of this step is difficult to overcome in a catalytic allylic fluorination reaction.

(© Wiley-VCH Verlag GmbH & Co. KGaA, 69451 Weinheim, Germany, 2006)

## Introduction

The organometallic and coordination chemistry of fluoride and the C–F bond have recently received much attention. Initial work centered around transition-metal fluoro complexes,[1–3] the coordination ability of the notoriously inert C–F bond[4] and its cleavage by means of electron-rich transition-metal centers using either stoichiometric[5] or catalytic methods.[6] Furthermore, "fluoride effects" have been discovered in homogeneous catalysis, which points to an important role of fluoride as a steering ligand in transition-metal-catalyzed reactions.[7,8] By contrast, the metal-catalyzed generation of C–F bonds (i.e. catalytic fluorination of organic compounds) has long been limited to industrial applications of the Swarts reaction[9] and some examples of the Pd-catalyzed fluorocarbonylations.[10,11] Research on the generation of fluoroarenes by reductive eliminations from aryl-fluoropalladium(II) complexes is actively pursued but not yet realized.[12] The neglect of transition-metal mediated fluorination methodologies comes as a surprise when the importance of fluorinated organic compounds in the chemical, agricultural, and pharmaceutical industry is considered. Here, selectively fluorinated organic compounds are in high demand for diverse applications.[13] In response to this situation, we have initiated a research program directed towards transition-metal catalyzed selective fluorination reactions at $sp^3$ centers. This has already resulted in a fluoro-$Ru^{II}$-complex-mediated halogen exchange reaction[14] and a titanium-catalyzed asymmetric catalytic α fluorination of β-keto esters.[15] Similar asymmetric fluorinations have been discovered by us and others using $Pd^{II}$,[16] $Cu^{II}$,[17–19] $Ni^{II}$,[18,20] and $Ru^{II}$[21] complexes as catalysts, all of them relying on electrophilic fluorination reagents. The present work involves a promising alternative strategy for asymmetric catalytic fluorination using fluoride nucleophiles. We were inspired by the observation that catalytic allylic substitution reactions enable the attachment of a variety of nucleophiles at allylic fragments with high enantioselectivity.[22] Consequently, we hoped to realize a palladium catalyzed allylic fluorination reaction starting from suitable allylic substrates and fluoride nucleophiles using chiral $Pd^{II}$ complexes as catalysts.[23] Since cationic $\eta^3$-allyl complexes of palladium(II) are well-established intermediates in asymmetric allylic substitution reactions,[24] we also wanted to investigate the interaction of such species with fluoride anions in order to clarify: (a) if nucleophilic attack of fluoride takes place; or (b) what other interactions (coordination, ion-pairing etc.) play a role. Analogous experiments with platinum(II) complexes were also planned

[a] Laboratory of Inorganic Chemistry, Swiss Federal Institute of Technology, ETH Hönggerberg, HCI, 8093 Zürich, Switzerland
[b] Institute of Organic Chemistry, RWTH Aachen University, Landoltweg 1, 52074 Aachen, Germany
E-mail: lukas.hintermann@oc.rwth-aachen.de

 © 2006 Wiley-VCH Verlag GmbH & Co. KGaA, Weinheim 

because the slower kinetics of $Pt^{II}$ relative to $Pd^{II}$ compounds should allow for the observation of short-lived intermediates with the added advantage of having $^{195}Pt$ NMR spectroscopy as a selective analytical tool.[25] Finally, we also hoped to clarify the issue of a "fluoride-effect" that we had observed earlier in the asymmetric amination of ethyl 1,3-diphenylallyl carbonate (**1**) catalyzed by $Pd^{II}$ with ligand **2a** (Scheme 1). The reaction gives the amination product **3** in either very high or low enantioselectivity, depending on the counterion ($F^-$ or $PF_6^-$) of the ammonium salt additive.[8]

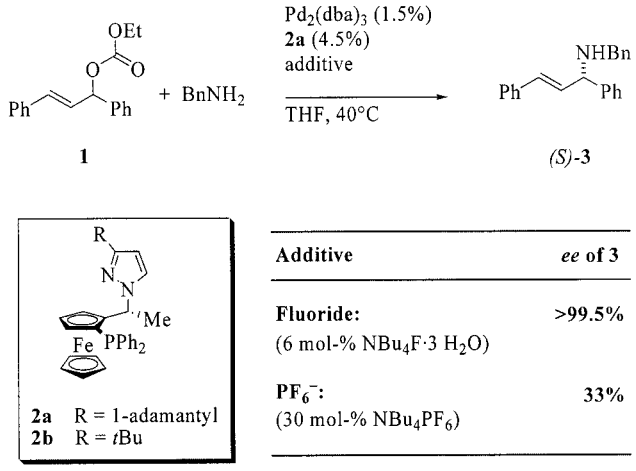


Scheme 1. The palladium-catalyzed asymmetric allylic amination is subject to astonishing anion effects on enantioselectivity.[8] dba = dibenzylidene acetone, Bn = benzyl.

## Results

The new phosphanyl-ferrocenyl pyrazole **2b**, (PPFPz-{3-*t*Bu}, 3-*tert*-butyl-1-{(*R*)-1-[2-($S_P$)-diphenylphosphanyl-ferrocenyl]ethyl}-1*H*-pyrazole), (Scheme 1) was prepared from 3(5)-*tert*-butylpyrazole[26] and (*R*,*S*)-PPFA[27] (PPFA = *N*,*N*-dimethyl-1-[2-diphenylphosphanyl-ferrocenyl]ethylamine) in high yield as a single regioisomer according to our standard method.[28] A test run with **2b** as the ligand in the palladium-catalyzed allylic amination reaction,[29] shown in Scheme 1, using cocatalytic $NBu_4F{\cdot}3H_2O$ (3 equiv. relative to [Pd]),[8] gave the amination product (*S*)-**3** with an *ee* > 99.5%. Thus, **2a** and **2b** behaved identically in this reaction, but **2b** was the preferred ligand for mechanistic studies because of the simplicity of the $^1H$ NMR-signal of the *tert*-butyl group over the adamantyl group. Using similar reaction conditions, we next attempted to perform catalytic allylic fluorination reactions with carbonate **1** (Scheme 2, a). The catalyst was generated in situ from $Pd(dba)_2$ and **2b**. The sources of nucleophilic fluoride that were tested are TBAT {$NBu_4[SiF_2Ph_3]$ (**4**)},[30] a nucleophilic non-basic fluoride transfer reagent, and $Me_4NF$ (**5**),[31] a "naked" fluoride[32] of high basicity. Anhydrous versions of these reagents are available and they also show considerable solubility in nonprotic organic solvents, which is an important characteristic because the nucleophilicity of fluoride is reduced by solvation in protic media or in the presence of trace water.[33] It should be noted that more traditional fluoride sources (such as KF, CsF, or $NBu_4F$) are either insoluble in nonprotic solvents or cannot be dried without decomposition.[34]

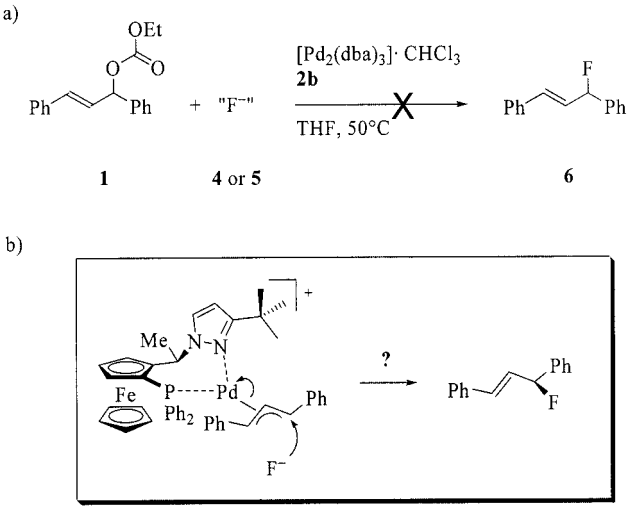


Scheme 2. Nucleophilic allylic fluorination of palladium complexes. (a) Attempted, but unsuccessful allylic fluorination with a $Pd^0$ catalyst. (b) The nucleophilic attack of fluoride on cationic allylpalladium(II) complexes is the key step in a postulated allylic fluorination reaction, as investigated in this work.

Analysis of reaction solutions from catalysis experiments using $^{19}F$ NMR spectroscopy did not show signals corresponding to 1,3-diphenylallyl fluoride (**6**),[14a,35] or any other organofluorine compound. Straightforward allylic fluorination in a catalytic manner is thus not feasible. We therefore proceeded to study the stoichiometric variant of this reaction, namely the attack of fluoride on isolated, fully-characterized cationic $\eta^3$-palladium(II) and -platinum(II) complexes (Scheme 2, b).

### Synthesis and Structure of Allylpalladium(II) and -platinum(II) Complexes

Several cationic palladium(II) allyl complexes incorporating the ligand **2b**, (PPFPz-{3-*t*Bu}), were synthesized in the usual manner[36] by reaction with the dinuclear allylpalladium(II) chlorides (**7**) followed by halide abstraction with either $TlPF_6$, $AgSbF_6$, or $(Et_3O)BF_4$ (Scheme 3 and Scheme 5). In some cases, we applied a new halide abstraction technique that relies on the combination of epichlorohydrine (or any other reactive epoxide) with an acid and a nonnucleophilic counterion, such as $HPF_6$. This method relies on the ability of epoxides to scavenge halide anions by nucleophilic-ring opening.

The diphenylallyl complex **8a** occurs predominantly as the *exo-syn-syn* isomer[37] (>98% by $^{31}P$ NMR spectroscopy) in $CDCl_3$ solution, in agreement with observations on complexes with similar ligands.[29] The same isomer is also present in the solid state, as shown by X-ray crystallography (vide infra, Figure 7). $\eta^3$-1,3-Dicyclohex-

 © 2006 Wiley-VCH Verlag GmbH & Co. KGaA, Weinheim 

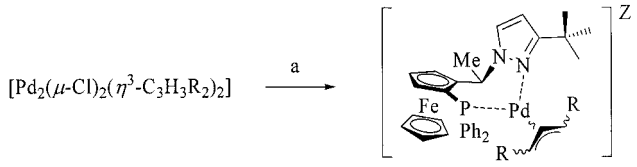


**7a** R = Ph
**7b** R = Cy
**7c** $R_2$ = 1,2-$C_6H_4$

**8a** R = Ph, Z = $PF_6$
**8b** R = Cy, Z = $PF_6$
**8c** $R_2$ = 1,2-$C_6H_4$, Z = $SbF_6$

Scheme 3. Synthesis of cationic allylpalladium(II) complexes. (a) **2b**, halide abstracting reagent (see Exp. Section). **8a**: 87%; **8b**: 96%; **8c**: 82%. Cy = cyclohexyl.

ylallyl complexes of palladium(II) are new. Our synthetic route (Scheme 4) started with an aldol addition of cyclohexyl methyl ketone (**9**) followed by elimination to the α,β-unsatuarated ketone and Luche reduction[38] to give dicyclohexylallyl alcohol (**10**). Fluorination with DAST [(diethylamino)sulfur(II) trifluoride][39] produced a reference sample of allyl fluoride **11**. According to a general procedure by Vitagliano et al.,[40] allyl trifluoroacetate (**12**) was treated with $Pd(dba)_2$ by oxidative addition to give the trifluoroacetate-bridged dimer **13**, and this complex underwent ligand exchange with LiCl to give the chloro-bridged dimer **7b**. Alternatively, and more conveniently, the last two steps could be performed in a single synthetic operation (**12**→**7b**).

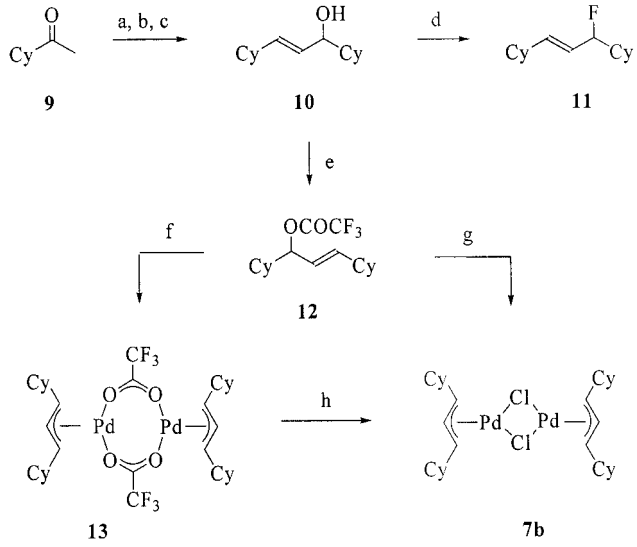


Scheme 4. Synthesis of (1,3-dicyclohexylallyl)palladium(II) complexes. (a) 1. LDA, THF, –78 °C; 2. CyCHO; 3. MsCl. (b) DBU, $Me_2CO$; 70% (from **9**). (c) $NaBH_4$, $CeCl_3 \cdot 7H_2O$, MeOH, room temp.; 77%. (d) DAST, $CH_2Cl_2$, –78 °C; quant. (e) TFAA, Py, 0 °C; 93%. (f) $Pd(dba)_2$, THF/MeCN (3:1), 40 °C; 93%.·(g) $Pd(dba)_2$, LiCl, THF/MeCN (3:1); 97%. (h) LiCl. LDA = lithium diisopropylamide, DBU = 1,8-diazabicyclo[5.4.0]undec-7-ene, TFAA = trifluoroacetic acid anhydride.

The bridged trifluoroacetate **13** showed interesting conformational isomerism in solution, similar to that reported for $[Pd_2(\mu\text{-}OAc)_2(\eta^3\text{-}R_2All)_2]$ complexes.[41] The VT $^1H$ NMR spectroscopic shifts (Table 1) were assigned to the $C_S$ symmetric isomer **A**, which has two sets of allylic protons, and the $C_{2v}$ symmetric isomer **B** (Figure 1). Interchange of **A** and **A′** was relatively slow up to a temperature of 273 K. Interchange of **A** with **B** was slow over the whole temperature range studied (253–298 K), but notable line broadening occurred at 298 K. The allyl units had the *syn-syn* configuration in both **A** and **B**, as deduced from the coupling [$^3J_{H,H}$ = 11 Hz] between the central and terminal allyl protons.

Table 1. $^1H$ NMR spectroscopic data for allyl hydrogen atoms within the conformational isomers of **13** at 253 K.

| Conformer | Central H | *anti* H |
|---|---|---|
| **A** | 5.39 ppm, t, $J$ = 11.1 | 3.48 ppm, dd, $J$ = 10.9, 5.1 |
| | 5.06 ppm, t, $J$ = 11.1 | 3.71 ppm, dd, $J$ = 10.9, 7.5 |
| **B** | 5.42 ppm, t, $J$ = 11.1 | 3.43 ppm, dd, $J$ = 11.0, 5.7 |

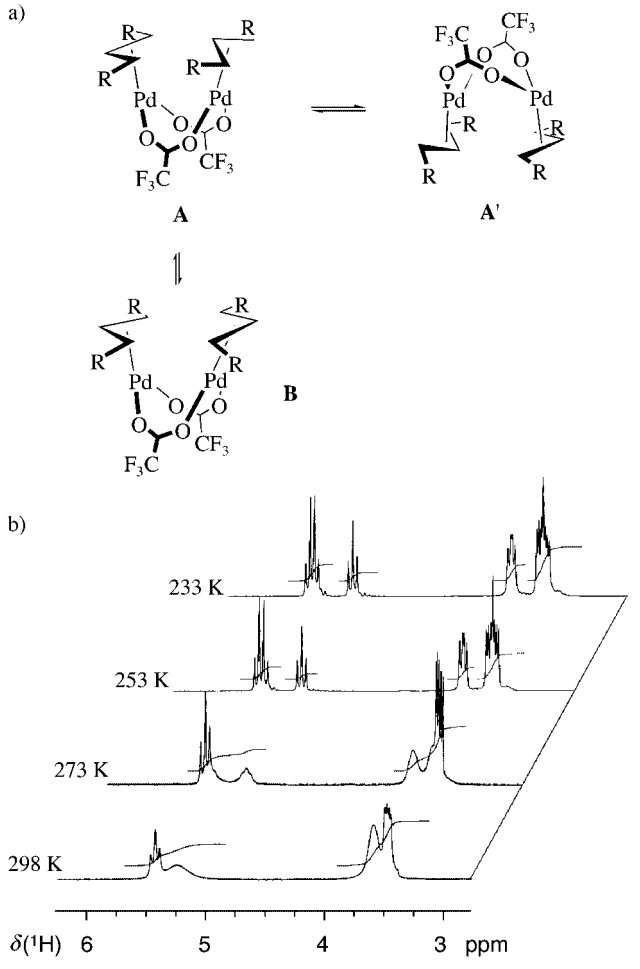


Figure 1. Conformational isomerism and VT $^1H$ NMR spectra of **13** ($CDCl_3$, 300 MHz). (a) Conformational isomerism and dynamic behavior of **13**. (b) VT-NMR: Signals of **A**/**A′** and **B** (compare in Table 1) are partially overlapping at all temperatures; the virtual quartet at 233 and 253 K is a superimposition of two triplets. At 298 K, the interconversion of **A** and **A′** approaches coalescence. Other processes such as conformational changes of the Cy substituents presumably add to the dynamics.

 © 2006 Wiley-VCH Verlag GmbH & Co. KGaA, Weinheim 

Incorporation of the (1,3-dicyclohexylallyl)palladium(II) fragment into a cationic complex with ligand **2b** (Scheme 3) yielded **8b**, initially as an 82:18 mixture of two allyl isomers. This ratio changed to about 1:1 (52:48) after recrystallization from hot methanol. On the basis of the $^1$H NMR coupling data, the *syn-syn* configuration was assigned to the main isomer, and the *syn-anti* (*anti* Cy group *trans* to N) configuration to the minor isomer, but the one-dimensional analysis did not give conclusive information about the *endo* or *exo* orientation. An X-ray crystal structure of **8b** supported the NMR spectroscopic assignment in a surprising way: the complex had crystallized as a statistical 1:1 mixture of allyl isomers possessing the *exo-syn-syn* and *endo-anti-syn* (*anti trans* to N) configurations, respectively (Figure 2). Apparently, both isomeric dicyclohexylallyl fragments had flexibly adapted to the coordination environment of the metal-ligand framework (Figure 2, **A** and **B**), which was kept as a common unit during the refinement of the structure. The bonding data for the dicyclohexylallyl fragments are not very accurate because of the disorder and will not be discussed.

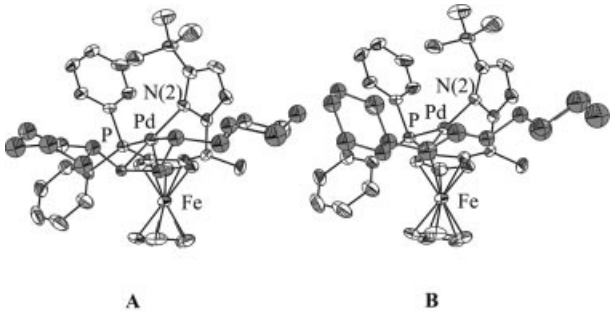


Figure 2. ORTEP representations (30% probability ellipsoids) of cationic fragments displaying configurational allyl isomerism in the solid-state structure of **8b**. $PF_6$ anions and hydrogen atoms are omitted for clarity, carbon atoms within the dicyclohexylallyl fragments are filled in as grey. **A**: *endo-syn-anti* isomer; **B**: *exo-syn-syn* isomer. Selected bond lengths [Å] and angles [°]: Pd–N(2) = 2.143(6), Pd–P 2.325(2); N(2)–Pd–P = 89.16(18). As a result of the disorder, values for the allyl fragments are not accurate.

The dark-red indenyl complex **8c** was prepared from $\{PdCl(Ind)\}_n$ (**7c**)[42] in the usual way (Scheme 3). Unlike most other cationic complexes described here, the indenyl compound was somewhat air-sensitive, with solutions of it slowly decomposing in air. A mixture of *exo* and *endo* isomers was present in solution, with *exo*-**8c** as the major species, as shown by H,H NOESY cross peaks of the central allyl hydrogen and the *tert*-butyl group. In the solid state only the *exo* isomer is present (Figure 3). The X-ray crystal structure also shows that the indenyl fragment is $\eta^3$-bonded, rather than $\eta^5$.

Unlike the much studied (1,3-diphenylallyl)palladium(II) complexes,[29,43,44] the corresponding platinum compounds are unknown, even though platinum-catalyzed allylic alkylation (including that of 1,3-diphenylallyl substrates) has been studied and the intermediacy of cationic $\eta^3$-allyl complexes have been invoked in analogy to Pd chemistry.[45,46] We have found that the addition of 1,3-diphenylallyl bromide (**15**)[47] to a Karstedt complex solution (**16**)[48,49] readily produces a yellow precipitate of the allylplatinum(II) bromide (**17**) (Scheme 5). $Pt_2(dba)_3$[50] also underwent this oxidative addition, but the resulting product was less pure due to metallic platinum residues in the precursor complex. Reaction of **17** with **2b** gave the complex **18·Br**, which was converted to **18·PF$_6$** using the new $HPF_6$/epichlorohydrine reagent (Scheme 5).

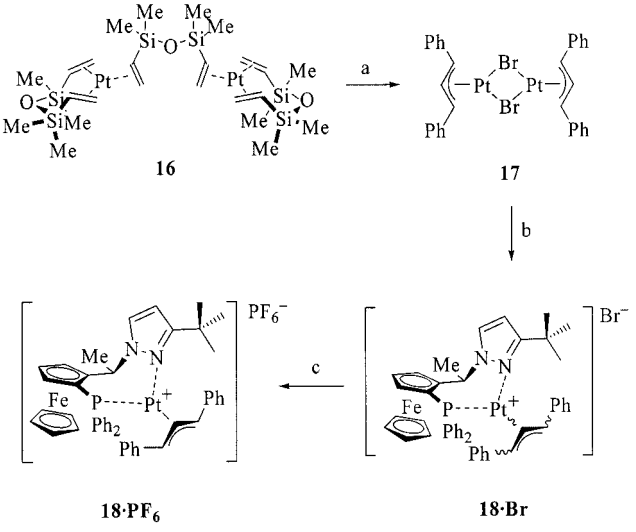


Scheme 5. Synthesis of (1,3-diphenylallyl)platinum(II) complexes. (a) PhCH=CHCH(Br)Ph (**15**), *t*BuOMe, 0 °C; 77%. (b) **2b**, THF; 97%. (c) 1. epichlorohydrine, $HPF_6$, $Me_2CO$; 2. crystallization from $CH_2Cl_2$/MeOH; 73% (from **17**).

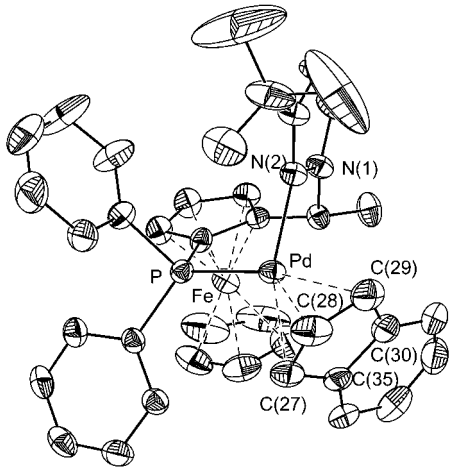


Figure 3. ORTEP plot (30% probability ellipsoids) of **8c·$CH_2Cl_2$**. Hydrogen atoms, $CH_2Cl_2$, and $SbF_6$ anion are omitted for clarity. Selected bond lengths [Å] and angles [°]: Pd–P = 2.303(2), Pd–N(2) = 2.122(6), Pd–C(27) = 2.191(8), Pd–C(28) = 2.225(9), Pd–C(29) = 2.260(10), Pd–C(30) = 2.570(9), Pd–C(35) = 2.576(8), C(27)–C(28) = 1.397(14), C(27)–C(35) = 1.460(13), C(28)–C(29) = 1.424(17), C(29)–C(30) = 1.421(17), C(30)–C(35) = 1.431(12); N(2)–Pd–P(1) = 92.32(18), C(27)–C(28)–C(29) = 106.4(10).

Comparative spectroscopic data for the platinum compounds was collected from a range of reference complexes

 © 2006 Wiley-VCH Verlag GmbH & Co. KGaA, Weinheim 

whose synthesis is displayed in Scheme 6. Pregosin's bis(styrene)platinum(II) chloride[51] served as the most suitable precursor for dichloro complex **19** under mild conditions. The diphenyl complex **20** resulted from reaction of **19** with excess Grignard reagent. Interestingly, the substance crystallized with one equivalent of phenol, which originated from a partially oxidized PhMgBr solution. The X-ray crystal structure of **20·PhOH** is shown in Figure 4. The phenolic OH group is presumably involved in a weak hydrogen bond with the electron-rich $Pt^{II}$ center.[52] The phenol is arranged with the OH group pointing towards the Pt center and the O–Pt distance is 4.21 Å. By comparison, O–Pd distances of 3.2–3.7 Å have been observed for related interactions between $Pd^0$ and aliphatic alcohols.[53]

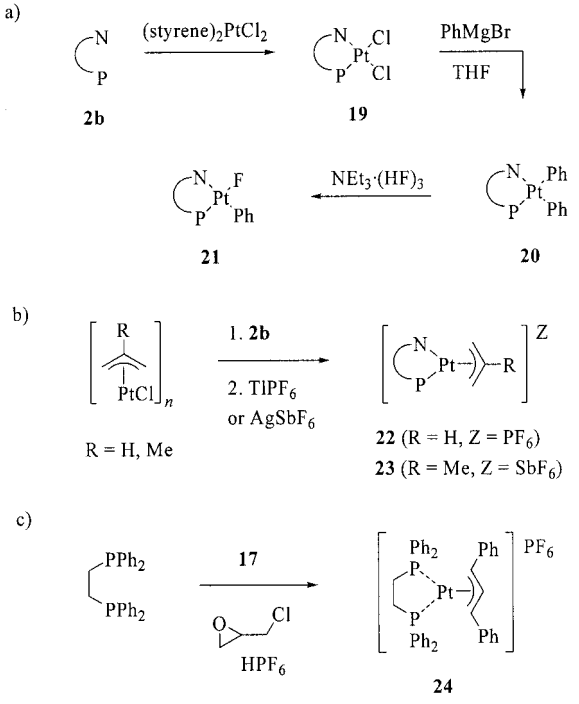


Scheme 6. Syntheses of platinum(II) complexes incorporating ligand **2b** and/or an allyl ligand.

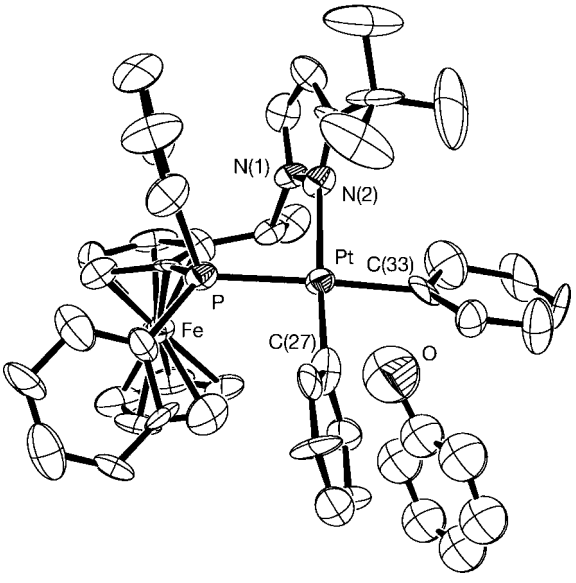


Figure 4. ORTEP plot (50% probability ellipsoids) of **20·PhOH**. Hydrogen atoms are omitted for clarity. Selected bond lengths [Å] and angles [°]: Pt–P = 2.33(2), Pt–N(2) = 2.18(5), Pt–C(27) = 1.97(5), Pt–C(33) = 2.08(3); P–Pt–N(2) = 88.7(16), C(27)–Pt–C(33) = 86.8(19), P–Pt–C(27) = 93.1(12), P–Pt–C(33) = 175.4(5), N(2)–Pt–C(33) = 91.8(13), N(2)–Pt–C(27) = 174.6(9).

The fluoro complex **21** was obtained in situ in an NMR tube by protonolysis of the diphenylplatinum complex **20** with $NEt_3$·$(HF)_3$. Only one bond was cleaved even though an excess of reagent was added. The presence of a Pt–F bond in this complex is evident from the coupling patterns in the $^{19}F$ NMR spectrum (doublet with platinum satellites) and the $^{31}P$ NMR spectrum (doublet with platinum satellites) (Figure 5). Any complex containing a covalent Pt–F bond in our study would have similar NMR characteristics, whereas ionic $Pt^+/F^-$ interactions would not be expected to result in such $^{19}F$ NMR signals or coupling characteristics.

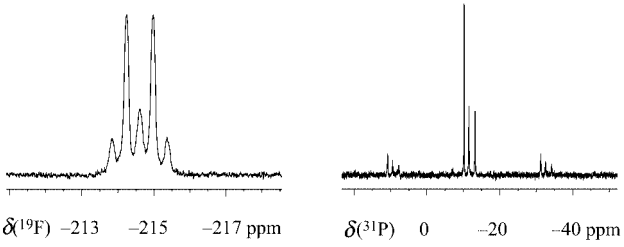


Figure 5. NMR spectra of fluoro complex **21**. (a) $^{19}F$ NMR (282.4 MHz, $CDCl_3$), the signal at $\delta$ = –214.6 ppm ($^2J_{P,F}$ = 207, $^1J_{Pt,F}$ = 210 Hz) is due to the platinum bound fluoro ligand. (b) $^{31}P$ NMR (121.5 MHz, $CDCl_3$), the signal at $\delta$ = –11.8 ppm (d, $J_{P,F}$ = 207, $J_{Pt,P}$ = 5104 Hz) is due to the fluoro complex, while the signal at $\delta$ = –9.6 ppm (s, $J_{Pt,P}$ = 5107 Hz) belongs to an unidentified side product.

The allyl complex **22** and the methallyl derivative **23** were obtained by the usual method (Scheme 6, b). They formed equilibrium mixtures of *exo* and *endo* isomers in solution, with the larger methallyl group inducing a slightly higher amount of the *exo* isomer (Table 2).

### Solution Structure of (1,3-Diphenylallyl)platinum(II) Complexes

The $\eta^3$-allyl complex **18·PF$_6$** occurs predominantly as the *exo-syn-syn* isomer in either [$D_8$]THF or $CDCl_3$ solution in the same manner as its Pd-counterpart **8a** (Figure 6).

In contrast, the bromide **18·Br** exists as a mixture of four main isomers in $CDCl_3$ solution (Table 2) and the isomeric ratio remained unchanged on refluxing a solution of the complex in toluene. The allyl isomers of **18·Br** could be of the cationic $\eta^3$-type (eight possible diastereomers) or the neutral $\eta^1$-type with coordinated bromide (four possible diastereomers), or mixtures thereof. The $J_{Pt,P}$ coupling constants of the **18·Br** isomers were in the range of 4700 to 5100 Hz (Table 2), which is close to the value for the $\eta^3$-allyl complex **18·PF$_6$**, but rather high compared to the value of [$PtBr_2$(**2a**)].[55] The low frequency $^{195}Pt$ NMR chemical shifts of **18·Br** also point towards a cationic $\eta^3$-configuration. However, the most important notion is that the nature

 © 2006 Wiley-VCH Verlag GmbH & Co. KGaA, Weinheim 

Table 2. NMR data and isomer equilibrium composition of the platinum complexes. $^{31}$P NMR spectroscopy at 101.3 or 121.5 MHz, $^{195}$Pt NMR spectroscopy at 64.3 or 86 MHz. All data at room temp. in $CDCl_3$, besides **18·PF$_6$** ([D$_8$]THF), **18·F** ([D$_8$]toluene at 213 K).

| Complex | Isomer | Abundance | $^{31}$P NMR [$\delta$/ppm] | $^{195}$Pt NMR [$\delta$/ppm] | $J_{Pt,P}$ [Hz] |
|---|---|---|---|---|---|
| **18·PF$_6$** | *exo* | >98% | 10.4 | –4453 | 5029 |
| **18·Br** | **A** | 12% | 7.5 | –4565 | 5056 |
| | **B** | 20% | 9.2 | –4790 | 4697 |
| | **C** | 44% | 12.6 | –4897 | 5130 |
| | **D** | 23% | 13.5 | –4903 | 4760 |
| **18·F** | **A** | 7% | 1.1 | n.d. | 3903 |
| | **B** | 9% | 1.8 | n.d. | 3890 |
| | **C** | 17% | 3.1 | n.d. | 4098 |
| | **D** | 63% | 7.5 | n.d. | 3925 |
| | **E** | 5% | 10.7 | n.d. | 3818 |
| [Pt($\eta^3$-C$_3$H$_5$)(2b)]PF$_6$ (**22**) | *exo* | 78% | 12.5 | n.d. | 4413 |
| | *endo* | 22% | 12.6 | n.d. | n.d. |
| [Pt($\eta^3$-C$_4$H$_7$)(2b)]PF$_6$ (**23**) | *exo* | 81% | 11.5 | n.d. | 4291 |
| | *endo* | 19% | 11.9 | n.d. | 4010 |
| [Pt(Ph$_2$All)(dppe)]PF$_6$ (**24**) | | 100% | 44.7 | –5521 | 3847 |
| [PtCl$_2$(2b)] (**19**) | | – | –16.1 | –3700 | 3783 |
| [PtBr$_2$(2a)][a] | | – | –14.6 | n.d. | 3713 |
| [PtPh$_2$(2b)] (**20**) | | – | 5.3 | n.d. | 1688 |
| [Pt(Ph)F(2b)] (**21**)[b] | | – | –11.8 | n.d. | 5104 |

[a] Ref.[55] [b] F is *trans* to P, deduced from the large values of $^1J_{Pt,P}$ or $^2J_{P,F}$.[54]

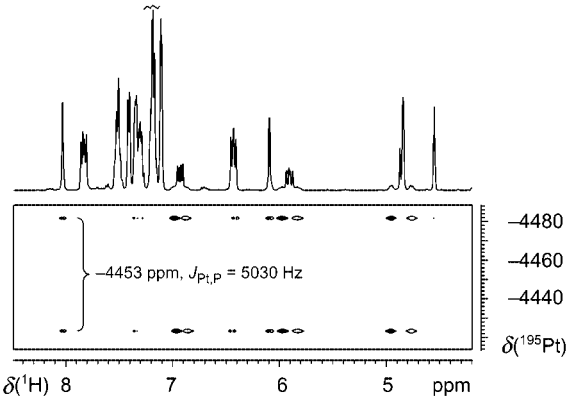


Figure 6. $^{195}$Pt,$^1$H HMQC of **18·PF$_6$** in [D$_8$]THF. The crosspeaks lie below the positions of the $^{195}$Pt satellites in the $^1$H NMR spectrum and are split vertically into a doublet ($J_{Pt,P}$ = 5030 Hz). Intense crosspeaks are observed for allylic protons ($\delta$ = 4.9, 5.9, and 6.9 ppm), whereas weaker coupling is observed with two sets of *ortho*-hydrogen atoms of phenyl groups ($\delta$ = 6.4, 7.4 ppm) and with the pyrazole hydrogen 4-H at 8.0 ppm.

of the anion directly and strongly influences the equilibrium composition of the allyl isomer mixture.

### Solid-State Structures of (1,3-Diphenylallyl)platinum(II) Complexes

Crystals of **18·PF$_6$** were easily obtained and the result of the X-ray structural analysis is shown in Figure 7 (a) along with a structure comparison generated by overlaying the structure of the palladium analog **8a** (Figure 7, b). These complexes are almost perfectly isostructural within differences in bond lengths of less than 2%. The interplane angle between the allyl plane and the coordination plane (defined by P, Pt, N) in these structures is 64.8°, and the rotation of the allyl vector normal plane [approximated by the plane C(27)–Pt/Pd–C(29)] out of the coordination plane is 14°. This numerical value serves as a measure of the asymmetry induced on the allyl fragment by the chiral ligand.[29] The $^{31}$P NMR chemical shifts of **8a** and **18·PF$_6$** also match closely (Table 2). These results justify, once more, the approach of using kinetically more inert platinum complexes as analogs for the corresponding palladium species in mechanistic research. In fact, **18·PF$_6$** is also a catalyst for the allylic alkylation of ethyl 1,3-diphenylallyl carbonate (**1**) with dimethyl malonate, giving the product of allylic alkylation in 74% *ee* in a slow reaction,[56,65] whereas analogous Pd complexes (with ligand **2a**) react much faster to give the alkylation product in 91% *ee*.[55] Asymmetric allylic alkylation of 1,3-diphenylallyl substrates using Pt complexes has been studied in detail by Williams and coworkers.[46]

Another example of a cationic (1,3-diphenylallyl)platinum(II) complex is the DIPHOS derivative **24**, which was also structurally characterized as the *syn-syn* isomer in both the $CD_2Cl_2$ solution and in the solid state (Figure 7, c). The bite angle P–Pt–P in this complex is 86.4° instead of the 94.5° for **18·PF$_6$**. The interplane angle defined by C(1)–C(2)–C(3)/P(1)–Pt–P(2) is 67° in this complex and the rotation of the allyl fragment vector normal plane (approximated by C(1)–Pt–C(3)), out of the idealized perpendicularity to the coordination plane [defined by P(1)–Pt–P(2)], is only 1°, a very low value despite the local chiral $C_2$ symmetry that the DIPHOS ligand adopts in its solid-state conformation.

### Reactions of Cationic Allyl Complexes with Fluoride

In the first series of experiments, one of the complexes **8a**, **8b**, or **8c** and one of the fluoride sources TBAT (**4**), Me$_4$NF (**5**), or Schwesinger's phosphazenium fluoride P$_2$F (**25**)[57] were mixed in deuterated solvents ($CDCl_3$ or [D$_3$]-

 © 2006 Wiley-VCH Verlag GmbH & Co. KGaA, Weinheim 

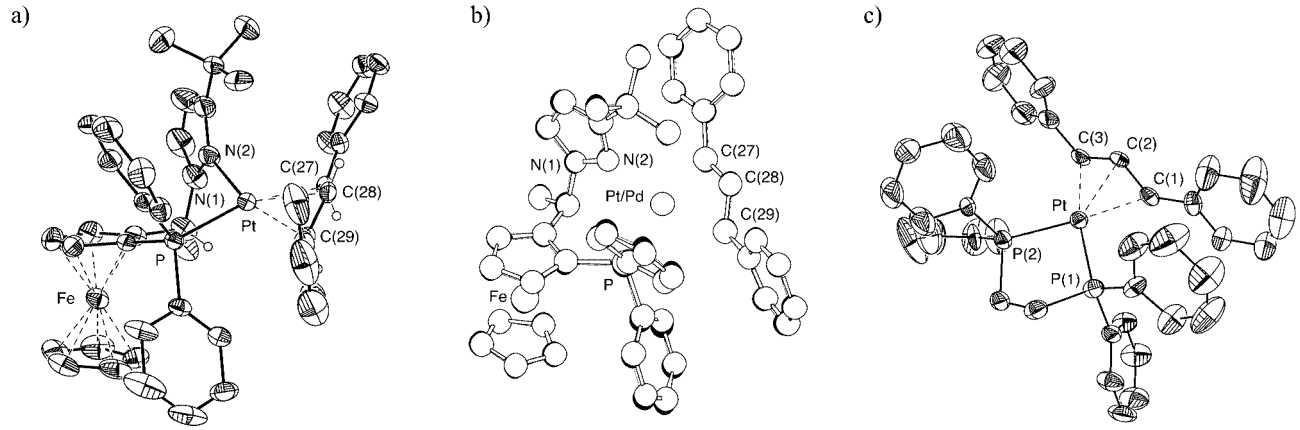


Figure 7. X-ray crystal structures of the cationic 1,3-diphenylallyl complexes **18·PF$_6$**, **8a**, and **24**. (a) ORTEP plot (30% probability ellipsoids) of platinum complex **18·PF$_6$**. The anion and most hydrogens are omitted for clarity. Selected data (bond lengths [Å]; bond angles [°]): Pt–P = 2.265(2), Pt–N(2) = 2.121(5), Pt–C(27) = 2.283(6) =, Pt–C(28) = 2.195(6), Pt–C(29) = 2.113(6); N(2)–Pt–P = 94.5(2). (b) Alignment of ball and stick representations of the complex cations of **8a** (grey filled atoms, below) and **18·PF$_6$** (white filled atoms, on top). The structures of the complexes match closely. Selected data for **8a**: Pd–P = 2.3123(8), Pd–N(2) = 2.159(3), Pd–C(27) = 2.283(3), Pd–C(28) = 2.193(3), Pd–C(29) = 2.137(3); N(2)–Pd–P = 94.49(8). The atom numbering has been adapted here to match that from the structure of **18·PF$_6$**, but is different in the CSD CIF file. (c) ORTEP plot (30% probability ellipsoids) of platinum complex **24**, anion and hydrogen atoms are omitted for clarity. Selected data: Pt–C(1) = 2.233(8), Pt–C(2) = 2.168(7), Pt–C(3) = 2.233(8), Pt–P(1) = 2.258(2), Pt–P(2) = 2.270(2); P(1)–Pt–P(2) = 86.37(8).

MeCN for **4**, [D$_3$]MeCN for **5**, $C_6D_6$ for **25**) and the samples were then monitored using $^1$H, $^{19}$F, and $^{31}$P NMR spectroscopy over a suitable range of time. If no change was observed at room temperature the samples were warmed to 50 °C. The appearance of peaks arising from allyl fluorides was carefully checked by $^{19}$F NMR spectroscopy (**6**: $\delta\{^{19}F\}$ = –165.4 ppm;[14a] **11**: –175.2 ppm; indenyl fluoride: –201.24 ppm[58]), but these signals were not detected. In experiments with $Me_4NF$ (**5**) and 1,3-diphenylallyl complex **8a**, the main fluorinated species observed was $DF_2^-$, resulting from deprotonation of [D$_3$]MeCN by naked fluoride.[31] A specific reaction pattern was only observed with complex **8b** and the naked fluorides $Me_4NF$ (**5**, in [D$_3$]-MeCN) and $P_2F$ (**25**, in $C_6D_6$), where diene **26**[59] was released in an elimination reaction (Scheme 7). Other reactant combinations resulted in no reaction at all or unspecific decomposition with precipitation of palladium metal on heating.[60]

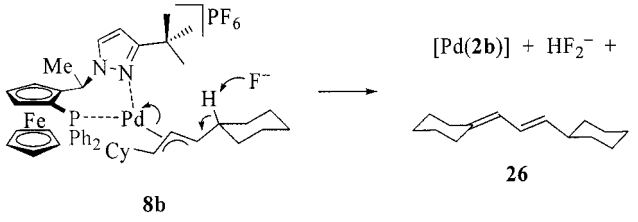


Scheme 7. Fluoride-mediated elimination of diene **26** from dicyclohexylallyl complex **8b**.

We then turned our attention to the reaction of cationic allylplatinum complex **18·PF$_6$** with naked fluoride $Me_4NF$ (**5**). A suspension of the reactants in toluene was stirred at ambient temperature, which resulted in a slow but clean anion exchange reaction to give a yellow solution of **18·F** and a colorless precipitate of $Me_4NPF_6$. Evaporation of the filtered solution gave **18·F** as an amorphous yellow powder, which was soluble in most organic solvents. The $^{19}$F NMR spectrum of **18·F** in $CDCl_3$ consisted of a broad signal at $\delta$ = –139.8 ppm ($\Delta_{1/2}$ = 15 Hz), a value which is close to that given by Grushin[61] ($\delta$ = –141 ppm, $\Delta_{1/2}$ = 9 Hz) for an in situ generated naked fluoride in $CDCl_3$. In [D$_8$]toluene solution the $^{19}$F NMR peak for fluoride disappeared in background noise that was generated from fluorinated polymers within the NMR probe head. The $^{31}$P NMR spectrum

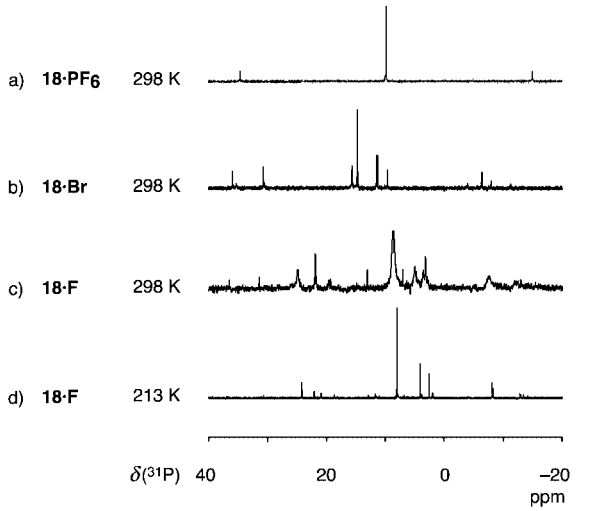


Figure 8. $^{31}$P NMR spectra of **18·PF$_6$**, **18·Br**, and **18·F**. (a) 101.3 MHz, [D$_8$]THF. **18·PF$_6$** is exclusively present as the *exo-syn-syn* isomer. Note the $^{195}$Pt satellites ($J_{Pt,P}$ = 5029 Hz). (b) 121.5 MHz, $CDCl_3$. **18·Br** forms a mixture of four allyl isomers. (c) 121.5 MHz, [D$_8$]toluene. **18·F** forms a mixture of allyl isomers whose lines are broadened due to exchange. (d) As in (c), but at 213 K (–60 °C). The interconversion of allyl isomers of **18·F** is "frozen" at low temperature, resulting in a spectrum similar to that of **18·Br** at room temperature. Splitting due to $J_{P,F}$ is absent.

 © 2006 Wiley-VCH Verlag GmbH & Co. KGaA, Weinheim 

consists of one main broad peak and smaller additional signals (Figure 8, c). On cooling to 213 K, the spectrum becomes clearer and a set of at least five lines (each with platinum satellites), corresponding to allyl isomers, appear (see d in Figure 8 and Table 2). Again, no peak was detected by $^{19}F$ NMR spectroscopy, but this should be seen in connection with experimental difficulties (mentioned above) and the low concentration of the sample. The absence of $^{31}P/^{19}F$ couplings (which are so clearly visible for **21**) shows that no inert covalent Pt–F bond is present in **18·F**. When combined these pieces of evidence suggest that **18·F** consists of a mixture of isomeric allyl cations $[Pt(\mathbf{2b})(\eta^3\text{-}Ph_2All)]^+$ in solution, which form lipophilic contact ion pairs with fluoride. The fluoride anions themselves are involved in a fast exchange between the ion pairs. At room temperature there is notable interconversion of configurationally isomeric allyl cations within **18·F** (broad lines in the $^{31}P$ NMR spectrum, Figure 8, c), but slow interconversion among the allyl isomers of **18·Br** (separate, sharp lines in the $^{31}P$ NMR spectrum, Figure 8, b). This important finding directly relates the nature of the counterion of a cationic allyl complex to the kinetics of its allyl isomerization.

### Oxidative Addition of $Pd^0$ with $Ph_2AllF$ (6) and $Ph_2AllBr$ (15)

The failure to observe any allylic substitution products resulting from attack of fluoride on cationic allyl complexes indicates that this reaction is thermodynamically unfavorable.[62] To test this assumption, we investigated whether the reverse reaction, namely the oxidative addition of allyl fluorides to $Pd^0$, would proceed instead. The addition of a solution of **6**[14a] to either $Pd(dba)_2$ or mixtures of $Pd(dba)_2$ and phosphanyl pyrazole (**2c**) (Scheme 8) did, in fact, result in oxidative addition and the formation of $\eta^3$-allylpalladium(II) compounds **27·F** or **28·F**, respectively. Identification of these compounds was based on the characteristic $^1H$ NMR and $^{31}P$ NMR spectra of the cationic units since a well-defined complex did not crystallize from solutions of **27·F**. The properties and spectroscopic data of **28·F** match closely those of the hydrated fluoride salts of cationic palladium complexes investigated earlier in our laboratory.[8] The analogous oxidative addition of 1,3-diphenylallyl bromide (**15**) with $Pd(dba)_2$ gave the $\eta^3$-allyl bromide **27·Br** (Scheme 8).

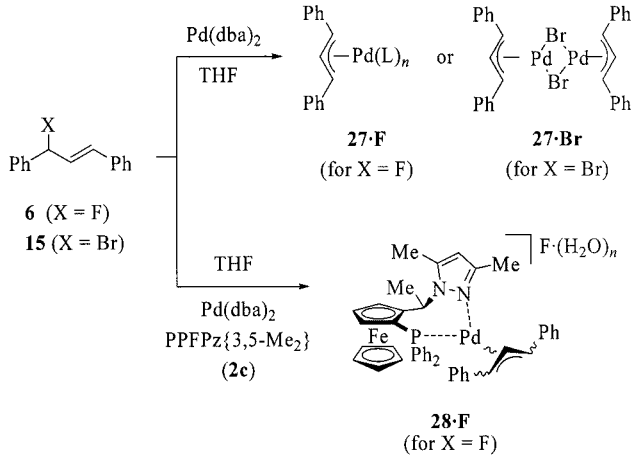


Scheme 8. The oxidative addition of 1,3-diphenylallyl fluoride and bromide to $Pd^0$ complexes is a spontaneous reaction that leads to products containing the cationic allylpalladium(II) fragment. L = F or solvent molecules.

The $^1H$ NMR spectroscopic data of **27·F** and **27·Br** in DMSO are very similar to those of the known chloro analog **27·Cl**.[44b]

## Discussion

### Fluoride Effects in Asymmetric Allylation Reactions

We have identified two modes in the reaction of "naked" or nucleophilic fluorides with cationic allyl complexes of palladium(II) and platinum(II): Allyl complexes bearing hydrogens α to the allyl group can either undergo base-mediated elimination (see Scheme 7) or a simple anion exchange can take place, which gives cationic allyl complexes as contact ion pairs with fluoride as the counterion. NMR spectroscopic studies of the platinum complexes **18·PF$_6$**, **18·Br**, and **18·F** revealed that the counterion in these ion pairs dramatically influences: (a) the allyl isomer composition at equilibrium; and (b) the kinetics of exchange between these isomers. In the presence of fluoride, allyl isomers interconvert at room temperature (cf. Figure 8, c) whereas this process is slow for the bromide salt (Figure 8, b) and probably even slower for the hexafluorophosphate (Figure 8, a). This evidence, obtained from a platinum model system, supports our earlier proposal of an anion effect in the catalytic asymmetric amination reaction (cf. Scheme 1):[8] Addition of fluoride accelerates the isomerization of allyl isomers and therefore effectively deletes the "memory of chirality"[63] stored within the configuration of the allyl isomers. However, addition of $PF_6^-$ has an inverse effect by slowing down isomerization. This assumption has now been justified by experimental results.

### The Viability of an (Asymmetric) Catalytic Allylic Fluorination

The reaction of cationic allyl complexes of palladium(II) and platinum(II) with naked or nucleophilic fluorides does not produce allyl fluorides. On the contrary, the oxidative addition of allyl fluoride **6** to $Pd^0$ proceeds with ease. This finding is in agreement with calculations by Hagelin et al. who have found that the attack of fluoride on the allylpalladium(II) cation is energetically favorable in the gas phase, but becomes unfavorable in the polar condensed phase because of the solvation of the fluoride anion.[64] Despite this thermodynamically unfavorable step, an overall catalytic allylic fluorination reaction should still be exergonic, as long as energetically high lying (reactive) sources of fluoride are used. Nevertheless, the presence of an energetically low-lying, nonreactive intermediate (such as **18·F**) in the reaction

 © 2006 Wiley-VCH Verlag GmbH & Co. KGaA, Weinheim 

pathway presents a severe obstacle for catalysis for kinetic reasons. If possible, alternative pathways will be followed (cf. release of **26** from **8b**, Scheme 7) and $Pd^0$ will eventually precipitate. These factors appear to cause the failure of the desired palladium-catalyzed asymmetric allylic fluorination reaction when it is carried out in analogy to known asymmetric allylic substitutions.

## Conclusion

We have reported the synthesis of new cationic allyl complexes of palladium(II) and platinum(II), among them the previously unknown (1,3-diphenylallyl)platinum(II) complexes. The reactivity of these complexes towards naked and nucleophilic sources of fluoride has been investigated. Stoichiometric allylic fluorination was shown to be thermodynamically unfeasible, and catalytic reactions are probably also unfeasible due to a kinetic barrier in the reaction pathway. It was shown that the counterions of cationic allylplatinum(II) complexes determine both the exchange kinetics between allyl isomers and the isomer composition at equilibrium. This finding has been used to rationalize a "fluoride anion effect" observed earlier in palladium-catalyzed asymmetric allylic amination reactions.

## Experimental Section

**General Remarks:** Syntheses of, and with, sensitive products were performed using Schlenk and glovebox techniques. Naked fluorides were handled exclusively in a glovebox. NMR spectroscopy: $^1$H NMR shifts relative to internal TMS, $^{13}$C NMR shifts relative to TMS, but referenced by solvent signals, notably $\delta(CDCl_3)$ = 77.0 ppm. $^{19}$F NMR shifts relative to external $CFCl_3$, $^{31}$P NMR shifts relative to external $H_3PO_4$ (85%), $^{195}$Pt NMR shifts relative to external $Na_2[PtCl_6]$ (aq). General techniques for NMR structure elucidation were the same as in ref.[29] For additional $^{13}$C NMR and IR data, see ref.[65]

**Abbreviations and Substances:** All = allyl ($C_3H_5$), $Ph_2All$ = 1,3-diphenylallyl etc., CC = column chromatography on $SiO_2$, HV = high vacuum (<0.01 mbar), Ms = methylsulfonyl, Pz = pyrazole, *t*BuOMe = *tert*-butyl methyl ether. The following substances were prepared according to literature procedures: (*R*,$S_P$)-PPFA[27] (recrystallized twice from EtOH to ensure high enantiomeric purity), anhydrous $Me_4NF$ (**4**),[31] TBAT [tetrabutylammonium difluorotriphenylsilicate(II)] (**5**),[30] 3-*tert*-butylpyrazole,[26] $[Pt_2(dba)_3]$,[50] $[Pd_2(dba)_3]\cdot CHCl_3$ or $Pd(dba)_2$,[66] $[\{PdCl(Ph_2All)\}_2]$ (**7a**),[44b] $[\{PdCl(Ind)\}_n]$ (**7c**),[42] 1,3-diphenylallyl bromide (**15**),[47] Karstedt catalyst (**16**).[49b] Schwesinger's phosphazenium fluoride $P_2F$ (**25**)[57] was obtained from Fluka.

**3-*tert*-Butyl-1-{(*R*)-1-[($S_P$)-2-(diphenylphosphanyl)ferrocenyl]ethyl}-1*H*-pyrazole (PPFPz{3-*t*Bu}, 2b):** Degassed HOAc (5 mL), (*R*,*S*)-PPFA (2.047 g, 4.628 mmol) and 3-*tert*-butylpyrazole (862 mg, 6.94 mmol) were stirred for 1 d at 70 °C. After workup with water and extraction with $CH_2Cl_2$, CC (*t*BuOMe/pentane, 1:20, and 3% $NEt_3$) gave 2.022 g (84%) as orange crystals. $[\alpha]_D$ = –281.7 (*c* = 0.88, MeOH). M.p. 130 °C. $^1$H NMR (250 MHz, $CDCl_3$): $\delta$ = 1.06 (s, 9 H, *t*Bu), 1.83 (d, *J* = 6.9 Hz, 3 H, *Me*CH), 3.87 (m, 1 H-Cp), 3.99 (s, 5 H, Cp′), 4.34 (t, *J* = 2.5 Hz, 1 H-Cp), 4.64 (br. s, 1 H-Cp), 5.52 (d, *J* = 2.3 Hz, 4-H, Pz), 5.77 (qd, *J* = 6.9 Hz, 3.2 Hz, 1 H, *H*CMe), 6.67–6.75 (m, 2 H, aryl), 6.82 (d, *J* = 2.3 Hz, 5-H, Pz), 6.92–7.02 (m, 3 H, aryl), 7.28–7.33 (m, 3 H, aryl), 7.49–7.56 (m, 2 H, aryl) ppm. $^{31}$P NMR (101.3 MHz, $CDCl_3$): $\delta$ = –24.5 (s) ppm. MS (EI): *m*/*z* (%) = 520 (100) [$M^+$], 455 (25), 396 (20), 331 (59). $C_{31}H_{33}FeN_2P$ (520.44): calcd. C 71.54, H 6.39, N 5.38; found C 71.60, H 6.47, N 5.33.

**Bis(μ-chloro)-bis(η³-1,3-dicyclohexylallyl)dipalladium(II) (7b):** A suspension of $Pd(dba)_2$ (658.7 mg, 1.146 mmol), **12** (403 mg, 1.266 mmol), and LiCl (1.203 mmol 1.05 equiv.) in THF (15 mL) and MeCN (5 mL) was stirred for 15 min at 30 °C. The greenish reaction mixture was evaporated to dryness, taken up in $CH_2Cl_2$ and filtered through $SiO_2$. Evaporation yielded 385.5 mg (97%) of a light yellow powder. M.p. 174 °C. $^1$H NMR (300 MHz, $CDCl_3$): $\delta$ = 1.02–1.36 (m, 20 H-Cy), 1.53–1.87 (m, 20 H-Cy), 2.02–2.07 (m, 4 H-Cy), 3.62 (dd, *J* = 11.2 Hz, 5.2 Hz, 4 H, 1-H/1′-H, 3-H/3′-H), 5.14 (t, *J* = 11.2 Hz, 2 H, 2-H/2′-H) ppm. $^{13}$C NMR ($CDCl_3$): $\delta$ = 26.1 ($CH_2$), 26.2 ($CH_2$), 31.7 ($CH_2$), 32.8 ($CH_2$), 39.5 (CH), 88.2 (CH), 103.43 (CH) ppm. MS (FAB): *m*/*z* (%) = 659 (100) [M – Cl]$^+$. $C_{30}H_{50}Cl_2Pd_2$ (694.47): calcd. C 51.89, H 7.26; found C 51.77, H 7.09.

**Indenylpalladium(II) Chloride (7c):** In our hands, only the method reported by Lin and Boudjouk gave a pure product.[42] Others have made similar observations.[42b] We note that the use of 94% EtOH in the synthesis is important because residual water favors the reaction.

**[Pd(η³-$Ph_2$All)(2b)]$PF_6$ (8a):** $[Pd_2(\mu\text{-}Cl)_2(\eta^3\text{-}Ph_2All)_2]$ (226.8 mg, 0.338 mmol) was added to **2b** (352.2 mg, 0.677 mmol) in acetone (40 mL) and the mixture was stirred until dissolution occurred (3 min). $TlPF_6$ (236.4 mg, 0.677 mmol) was added and the resulting suspension stirred for 1 h. Filtration through Celite, evaporation to dryness, and precipitation from $CH_2Cl_2$/pentane gave 570.4 mg (87%) of an orange powder. $[\alpha]_D$ = –278 (*c* = 0.50, $CHCl_3$). M.p. dec. from 190 °C. $^1$H NMR (250 MHz, $CDCl_3$): $\delta$ = 0.48 (s, 9 H, *t*Bu), 2.35 (d, *J* = 6.9 Hz, 3 H, *Me*CH), 3.90 (s, 5 H, Cp′), 3.97–4.01 (m, 1 H-Cp), 4.41 (t, *J* = 2.6 Hz, 1 H-Cp), 4.54–4.58 (m, 1 H-Cp), 5.25 (d, *J* = 10.0 Hz, allyl H, *anti*, *trans* N), 5.91 (d, *J* = 2.7 Hz, 4-H, Pz), 6.21 (dd, *J* = 14.1 Hz, 9.9 Hz, allyl H, *central*), 6.08–6.16 (m, 2 H, aryl), 7.01–7.32 (m, 15 H, 13 H, aryl + allyl H, *anti*, *trans* P + C*H*Me), 7.45–7.55 (m, 3 H, aryl), 7.58 (d, *J* = 2.7 Hz, 5-H, Pz), 7.70–7.89 (m, 2 H, aryl) ppm. $^{13}$C NMR (62.9 MHz, $CDCl_3$): $\delta$ = 18.4 ($CH_3$), 29.6 ($CH_3$), 31.8 (C), 58.4 (d, $J_{P,C}$ = 5 Hz, CH, *C*HMe), 66.0 (d, $J_{P,C}$ = 3 Hz, CH, Cp), 66.1 (d, $J_{P,C}$ = 1 Hz, allyl CH, *trans* N), 70.6 (d, $J_{P,C}$ = 6 Hz, Cp-CH), 71.3 (CH, Cp′), 73.0 (CH, Cp), 74.9 [d, $J_{P,C}$ = 42 Hz, C(1)-Cp], 93.8 [d, $J_{P,C}$ = 20, C(2)-Cp], 107.1 [CH, C(4) Pz], 107.1 (d, $J_{P,C}$ = 19 Hz, allyl CH, *trans* P), 112.4 (d, $J_{P,C}$ = 4 Hz, allyl CH, *central*), 127.3 (d, $J_{P,C}$ = 2 Hz, CH), 127.9 (d, $J_{P,C}$ = 3, CH), 128.1 (d, $J_{P,C}$ = 9 Hz, CH), 128.3–129.4 (several CH), 130.7 (d, $J_{P,C}$ = 48 Hz, C), 130.9 (d, $J_{P,C}$ = 2 Hz, CH), 131.4 (d, $J_{P,C}$ = 11 Hz, CH), 133.1 (d, $J_{P,C}$ = 44 Hz, C), 134.3 (d, $J_{P,C}$ = 14 Hz, CH), 135.4 (d, $J_{P,C}$ = 5 Hz, C), 138.9 (d, $J_{P,C}$ = 3 Hz, C), 162.7 [C, C(3) Pz] ppm. $^{31}$P NMR (101.3 MHz, $CDCl_3$): $\delta$ = –142 (sept, $J_{PF}$ = 695 Hz, $PF_6^-$), 10.5 (s) ppm. IR (KBr): $\tilde{\nu}$ = 842 (s), 696 (m), 558 (m) cm$^{-1}$. MS (FAB): *m*/*z* (%) = 1783 (3) [2 M – $PF_6$]$^+$, 819 (100) [M – $PF_6$]$^+$, 625 (12) [M – $PF_6$ – $Ph_2All$]$^+$. $C_{46}H_{46}F_6FeN_2P_2Pd$ (965.07): calcd. C 57.25, H 4.80, N 2.90; found C 57.08, H 4.95, N 2.94.

**[Pd(η³-$Cy_2$All)(2b)]$PF_6$ (8b): 7b** (179.5 mg, 0.258 mmol) was added to a solution of **2b** (269.1 mg, 0.517 mmol) in acetone (35 mL) and the mixture was stirred until dissolution was complete (15 min). After addition of $TlPF_6$ (180.6 mg, 0.517 mmol) and stirring for 1.5 h, the suspension was filtered through Celite and the filtrate evaporated to dryness. Precipitation from $CH_2Cl_2$/pentane gave

 © 2006 Wiley-VCH Verlag GmbH & Co. KGaA, Weinheim 

484 mg (96%) of a yellow powder. M.p. 221° (dec.). $^1$H NMR (250 MHz, $CDCl_3$). Major isomer: $\delta$ = 0.43–0.52 (m, 1 H-Cy), 0.82 (s, 9 H, *t*Bu), 0.76–1.85 (m, 21 H-Cy), 2.17 (d, $J$ = 7.0 Hz, 3 H, CH*Me*), 3.94–3.98 (m, 1 H-Cp), 3.96 (s, 5 H, Cp′), 4.30 (dd, $J$ = 10.4 Hz, 2.3 Hz, allyl H, *anti*, *trans* N), 4.46 (t, $J$ = 2.6 Hz, 1 H-Cp), 4.65–4.69 (m, 1 H-Cp), 5.27 (dd, $J$ = 13.4 Hz, 10.0 Hz, allyl H, *central*), 5.56 (dt, $J$ = 13.3 Hz, 8.3 Hz, allyl H, *trans* P), 6.14 (d, $J$ = 2.6 Hz, 4-H, Pz), 6.51–6.62 (m, 2 H, aryl), 6.67 (q, $J$ = 7.0 Hz, C*H*Me), 7.14 –7.33 (m, 3 H, aryl), 7.58–7.66 (m, 3 H, aryl), 7.59 (d, $J$ = 2.7 Hz, 5-H, Pz), 7.76–7.85 (m, 2 H, aryl); minor isomer): $\delta$ = 0.76–1.80 (m, 22 H-Cy), 0.91 (s, 9 H, *t*Bu), 2.04 (d, $J$ = 7.0 Hz, 3 H, CH*Me*), 3.75–3.79 (m, 1 H-Cp), 3.90 (s, 5 H, Cp′), 4.42 (t, $J$ = 2.6 Hz, 1 H-Cp), 4.58 (ddd, $J$ = 13.7 Hz, 11.1 Hz, 5.5 Hz, allyl H, *anti*, *trans* P), 4.76–4.80 (m, 1 H-Cp), 5.44 (t, $J \approx$ 8.5 Hz, allyl H, *trans* N) 5.94 (dd, $J$ = 13.5 Hz, 7.8 Hz, allyl H, *central*), 6.21 (d, $J$ = 2.7 Hz, 4-H, Pz), 6.34 (q, $J$ = 7.0 Hz, C*H*Me), 6.45–6.60 (m, 2 H, aryl), 7.14–7.33 (m, 3 H, aryl), 7.58–7.66 (m, 3 H, aryl), 7.68 (d, $J$ = 2.7 Hz, 5-H, Pz), 7.76–7.85 (m, 2 H, aryl) ppm. $^{31}$P NMR (101.3 MHz, $CDCl_3$): $\delta$ = –144.3 Hz (sept, $J_{P,F}$ = 698, $PF_6^-$), 10.9 (s, major isomer), 11.9 (s, minor isomer) ppm. MS (FAB): *m*/*z* (%) = 1809.5 (2) $[2\ M - PF_6]^+$, 831.4 (100) $[M - PF_6]^+$, 710 (6) $[M - PF_6 - Cy_2All]^+$, 627 (74). $C_{46}H_{58}F_6FeN_2P_2Pd$ (977.18): calcd. C 56.54, H 5.98, N 2.87; found C 56.48, H 5.91, N 2.82.

**[Pd(η$^3$-Ind)(2b)]SbF$_6$ (8c):** A mixture of **2b** (320 mg, 0.62 mmol) and **7c** (155 mg, 0.30 mmol) was stirred in THF (5 mL) until dissolution was complete (20 min). $AgSbF_6$ (206 mg, 0.60 mmol) was added to the dark red solution, and the resulting suspension was stirred for 1 h. After filtration through Celite and evaporation, the residue was precipitated from $CH_2Cl_2$/*t*BuOMe to give a dark red powder, which was redissolved in $CH_2Cl_2$ and set aside for slow diffusion against hexane at –20 °C. Within 2 d dark red crystals (also used for X-ray) of a $CH_2Cl_2$ solvate were formed. The yield of solvent-free compound after drying is 483 mg (82%). It is stable as a solid, but slow decomposition occurs in solution and in air. $^1$H NMR (400 MHz, [D$_3$]MeCN, *exo* isomer): $\delta$ = 0.80 (s, 9 H, *t*Bu), 1.74 (d, $J$ = 7.1 Hz, 3 H, CH*Me*), 3.85 (s, 5 H, Cp′), 4.08–4.10 (m, 5-H, Cp), 4.54 (t, $J$ = 2.7 Hz, 4-H, Cp), 4.74–4.77 (m, 3-H, Cp), 5.52 (qd, $J$ = 7.1 Hz, 1.2 Hz, 1 H, C*H*Me), 6.28 (d, $J$ = 2.7 Hz, 4-H, Pz), 6.44–6.50 (m, 2 $H_{ortho,axial}$), 6.60 (t, $J$ = 2.5 Hz, 3-H, Ind), 6.76 (dddd, $J$ = 9.2 Hz, 3.5 Hz, 2.0 Hz, 0.8 Hz, 1-H, Ind), 6.82 (ddd, $J$ = 3.5 Hz, 3.0 Hz, 0.6 Hz, 2-H, Ind), 7.14–7.19 (*m*, 2 $H_{meta,axial}$), 7.26, (obscured, 6-H, Ind), 7.28 (obscured, 7-H, Ind), 7.30 (obscured, 1 $H_{para,axial}$), 7.35, (obscured, 5-H, Ind), 7.68–7.75 (m, 2 $H_{meta,equ}$ + 1 $H_{para,equ}$), 7.70, (obscured, 4-H, Ind), 7.71 [d, $J$ = 2.7 Hz, 5-H, Pz (obscured)]. 7.88–7.96 (m, 2 $H_{ortho,equ}$) ppm; assignments from HH COSY and long-range $^1$H,$^{13}$C HMQC. $^1$H NMR (300 MHz, $CDCl_3$, minor isomer, selected peaks): $\delta$ = 0.49 (s, 9 H, *t*Bu), 2.13 (d, $J$ = 7.0 Hz, 3 H, MeCH), 4.00 (m, 1 H-Cp), 4.04 (s, 5 H, Cp′), 5.84 (t, $J$ = 2.4 Hz, 1 H-Cp), 6.09 (d, $J$ = 2.8 Hz, 1 H-Pz), 6.97 (m, CHMe), 7.59 (d, $J$ = 2.8 Hz, 1 H-Pz) ppm. Isomer ratio in $CDCl_3$ *exo*/*endo* = 11:1, in [D$_3$]MeCN = 16:1. $^1$H{$^{31}$P} NMR (250 MHz, [D$_3$]MeCN, $^{31}$P-decoupling at $\delta$ = 12.2 ppm, selected peaks): $\delta$ = 4.08 (dd, $J$ = 2.7 Hz, 1.3 Hz, 5-H, Cp), 4.54 (dt, $J$ = 2.7 Hz, 0.6 Hz, 4-H, Cp), 4.75 (ddd, $J$ = 2.7 Hz, 1.3 Hz, 0.5 Hz, 3-H, Cp), 6.27 (dd, $J$ = 2.8 Hz, 0.6 Hz, 5-H, Pz), 6.44–6.49 (m, 2 H, H, aryl *ortho*), 6.60 (ddd, $J$ = 3.1 Hz, 2.0 Hz, 0.5 Hz, 3-H, Ind), 6.75 (ddd, $J$ = 3.5 Hz, 2.0 Hz, 0.8 Hz, 1-H, Ind), 6.82 (dd, $J$ = 3.5 Hz, 3.1 Hz, 2-H, Ind) ppm. $^{13}$C NMR (100 MHz, [D$_3$]MeCN): selected signals, $\delta$ = 77.3 [d, $J_{P,C}$ = 4 Hz, C(3) Ind], 99.0 (d, $J_{P,C}$ = 21 Hz, C(1) Ind), 115.9 [d, $J_{P,C}$ = 6 Hz, C(2) Ind] ppm, C(1) defined as *trans* to P. $^{19}$F NMR (282.4 MHz, [D$_3$]MeCN): $\delta$ = –124.3 (6 lines, $J_{121Sb,19F}$ = 1935 Hz, and 8 lines, $J_{123Sb,19F}$ = 1060 Hz) ppm. $^{31}$P NMR (121.5 MHz, [D$_3$]MeCN): $\delta$ = 12.2 (s, *exo* isomer), 12.4 (s, *endo* isomer) ppm. $^{121}$Sb NMR ([Ξ] = 71.8223640 MHz, [D$_3$]-MeCN): 93.1 (sept, $J_{Sb,F}$ = 1936 Hz) ppm. MS (FAB): *m*/*z* (%) = 741.3 (100) $[M - SbF_6]^+$, 626.2 (33) $[M - Ind - SbF_6]^+$. $C_{40}H_{40}F_6N_2PFePdSb$ (977.74): calcd. C 49.14, H 4.12, N 2.87; found C 48.84, H 4.17, N 2.80.

**(*E*)-1,3-Dicyclohexylprop-2-en-1-ol (10): (a) (*E*)-1,3-Dicyclohexylpropenone:** Acetylcyclohexane (**9**) (6.9 mL, 50 mmol) was slowly dropped into a stirred solution of LDA (31 mL, 2 M in hexanes, 62 mmol) in THF (80 mL) at –78 °C. After 1 h, CyCHO (6.9 mL, 57.1 mmol) was slowly added and the reaction mixture stirred for 4 h at –78 °C. MsCl (9.7 mL, 125 mmol) was added dropwise. After 1 h the reaction mixture was warmed to room temp., quenched with sat. $NaHCO_3$ solution (50 mL) and extracted with *t*BuOMe. The organic phases were dried ($Na_2SO_4$) and the solvents evaporated. DBU (12.4 mL, 83.3 mmol) was added dropwise at 0 °C to the residue in acetone (100 mL). After 1 h stirring, workup ($NH_4Cl$ sat/*t*BuOMe) gave an oil which was purified by CC (*t*BuOMe/hexanes, 1:20) to give 7.707 g (70%) of a colorless liquid. $^1$H NMR (300 MHz, $CDCl_3$): $\delta$ = 1.08–1.82 (m, 20 H-Cy), 2.08–2.19 (m, 1 H-Cy), 2.50–2.60 (m, 1 H-Cy), 6.10 (dd, $J$ = 15.9 Hz, 1.4 Hz, 2-H), 6.80 (dd, $J$ = 15.9 Hz, 6.8 Hz, 3-H) ppm. $^{13}$C NMR (62.9 MHz, $CDCl_3$): $\delta$ = 25.7 ($CH_2$), 25.7 ($CH_2$), 25.9 ($CH_2$), 25.9 ($CH_2$), 28.7 ($CH_2$), 31.8 ($CH_2$), 40.6 (CH), 48.6 (CH), 126.0 [CH, C(3)], 151.9 [CH, C(2)], 203.9 [C(1)] ppm. MS (CI): *m*/*z* (%) = 221 (100) $[M + H]^+$, 165 (3), 137 (61) $[C_9H_{13}O]^+$, 83 (11), $[C_6H_{11}]^+$, 55 (15). IR ($CHCl_3$): $\tilde{\nu}$ = 1684 (m, C=O), 1655 (m), 1620 (m, C=C) cm$^{-1}$. $C_{15}H_{24}O$ (220.35): calcd. C 81.76, H 10.98; found C 82.02, H 11.03.

**(b) (*E*)-1,3-Dicyclohexyl-2-propen-1-ol (10):** $NaBH_4$ (167 mg, 4.41 mmol) was added to a solution of 1,3-dicyclohexylpropenone (973 mg, 4.41 mmol) and $CeCl_3 \cdot 7H_2O$ (1646 mg, 4.41 mmol) in MeOH (12 mL) at room temp. The mixture was stirred for 10 min and worked up with aq. HCl (2.5 M, 3 mL), $H_2O$ and *t*BuOMe. Purification by CC (*t*BuOMe/hexanes, 1:10) gave 758 mg (77%) of a colorless liquid. $^1$H NMR ($CDCl_3$): $\delta$ = 0.85–1.42 (m, 11 H-Cy), 1.45 (d, $J$ = 3.0 Hz, OH), 1.63–1.74 (m, 9 H-Cy), 2.01–1.81 (m, 2 H-Cy), 3.75 (ddd, $J$ = 6.9 Hz, 6.9 Hz, 3.1 Hz, 3-H), 5.39 (ddd, $J$ = 15.5 Hz, 7.2 Hz, 0.9 Hz, 2-H), 5.56 (dd, $J$ = 15.5 Hz, 6.5 Hz, 1-H) ppm. Known compound, CAS number 79605-63-3.

**(*E*)-1,3-Dicyclohexylallyl Fluoride (11):** DAST (101.8 mg, 0.63 mmol) was added at –78 °C to a solution of **10** (126.6 mg, 0.569 mmol) in $CH_2Cl_2$ (11 mL) while stirring. The temperature was raised to 0 °C and the mixture stirred for another 10 min. Quenching with aq. $NaHCO_3$ (10 mL), followed by extraction with three portions of *t*BuOMe (20 mL) gave, after drying ($MgSO_4$) and evaporation, 130 mg (quant.) of a yellowish oil. Kugelrohr distillation (90 °C/0.01 mbar) gave a colorless oil. $^1$H NMR (250 MHz, $CDCl_3$): $\delta$ = 0.9–2.1 (m, 22 H-Cy), 4.49 (dt, $J$ = 48.6 Hz, 7.2 Hz, 1-H), 5.44 (dddd, $J$ = 15.6 Hz, 9.8 Hz, 7.6 Hz, 1.3 Hz, 2-H), 5.67 (ddd, $J$ = 15.6 Hz, 6.4 Hz, 4.6 Hz, 3-H) ppm. $^{13}$C NMR (62.9 MHz, $CDCl_3$): $\delta$ = 25.7 ($CH_2$), 25.9 ($CH_2$), 25.9 ($CH_2$), 26.1 ($CH_2$), 26.4 ($CH_2$), 28.1 (d, $J_{F,C}$ = 5, $CH_2$), 28.2 (d, $J_{F,C}$ = 5 Hz, $CH_2$), 32.5 (d, $J_{F,C}$ = 2 Hz, $CH_2$), 32.7 (d, $J_{F,C}$ = 2 Hz, $CH_2$), 40.3 (CH), 42.5 (d, $J_{F,C}$ = 22 Hz, CH), 98.5 [d, $J_{F,C}$ = 164 Hz, CH, C(1)], 124.5 [d, $J_{F,C}$ = 20 Hz, CH, C(2)], 141.8 [d, $J_{F,C}$ = 12 Hz, CH, C(3)] ppm. $^{19}$F NMR (282.4 MHz, $CDCl_3$): $\delta$ = –175.2 (dddt, $J_{F,H} \approx$ 48.5 Hz, 13.9 Hz, 9.8 Hz, 5 Hz) ppm.

**(*E*)-1,3-Dicyclohexylallyl Trifluoroacetate (12):** TFAA (0.634 mL, 4.56 mmol) was slowly added to **10** (506.8 mg, 2.28 mmol) in pyridine (8.6 mL) at 0 °C and the reaction mixture stirred for 1 h. Workup with *t*BuOMe and washing of the organic phase (aq. HCl, aq. sat. $NaHCO_3$, $H_2O$) gave, after drying ($Na_2SO_4$) and evaporation, 680 mg (93%) of a colorless liquid. An analytical sample was

 © 2006 Wiley-VCH Verlag GmbH & Co. KGaA, Weinheim 

purified by Kugelrohr distillation (90 °C/0.005 mbar). The substance decomposed within a few days at room temp. $^1$H NMR (250 MHz, $CDCl_3$): $\delta$ = 0.92–1.31 (m, 10 H-Cy). 1.60–1.77 (m, 10 H-Cy), 1.92–2.04 (m, 2 H-Cy), 5.10 (dd, $J$ = 8.1 Hz, 7.2 Hz, 1-H), 5.34 (ddd, $J$ = 15.5 Hz, 8.4 Hz, 1.3 Hz, 2-H), 7.75 (dd, $J$ = 15.5 Hz, 6.6 Hz, 3-H) ppm. $^{13}$C NMR (62.9 MHz, $CDCl_3$): $\delta$ = 25.6 ($CH_2$), 25.7 ($CH_2$), 25.8 ($CH_2$), 26.0 ($CH_2$), 26.2 ($CH_2$), 28.4 ($CH_2$), 32.4 ($CH_2$), 40.3 (CH), 41.3 (CH), 84.7 (CH), 122.1 (CH), 143.8 (CH) ppm. IR ($CHCl_3$): $\tilde{\nu}$ = 1777 (s), 1450 (s), 1272 (s) cm$^{-1}$. $C_{17}H_{25}F_3O_2$ (318.38): calcd. C 64.13, H 7.91; found C 63.94, H 8.07.

**Bis(μ-trifluoroacetato)-bis(η³-1,3-dicyclohexylallyl)dipalladium(II) (13):** A suspension of $Pd(dba)_2$ (756 mg, 1.32 mmol) and **12** (461 mg, 1.45 mmol) in THF (12 mL) and MeCN (3 mL) was stirred for 1 h at room temp. , followed by 10 min at 40 °C. The resulting solution was evaporated to dryness and repeatedly extracted with MeCN/$H_2O$ (70:30). The extract was evaporated to a yellow powder, which was purified by precipitation from $Et_2O$/pentane to give 520 mg (93%) of yellow crystals. M.p. 82 °C (dec.). $^1$H NMR (250 MHz, $C_6D_6$ + 10% [$D_3$]MeCN): $\delta$ = 1.00–1.98 (m, 44 H-Cy), 3.43 (dd, $J$ = 11.6 Hz, 4.9 Hz, 4 H, 1-H, 1′-H, 3-H, 3′-H), 5.10 (t, $J$ = 11.6 Hz, 2 H, 2-H, 2′-H) ppm. VT NMR: see Scheme 5 and Table 1. $^{13}$C NMR (75.5 MHz, $CDCl_3$/[$D_3$]MeCN 3:1): $\delta$ = 25.5 ($CH_2$), 25.6 ($CH_2$), 25.6 ($CH_2$), 31.6 ($CH_2$), 32.0 ($CH_2$), 39.1 (CH), 88.2 (br., CH), 106.5 (br., CH) ppm. MS (FAB): *m/z* (%) = 1084 (9), 737 (47) [M – $OCOCF_3$]$^+$, 311 (100) [Pd($Cy_2$All)]$^+$. $C_{34}H_{50}F_6O_4Pd$ (849.60): calcd. C 48.99, H 6.05; found C 48.09, H 5.92.

**Di-μ-bromo-bis(η³-1,3-diphenylallyl)diplatinum(II) (17):** (a) A Karstedt complex solution (corresponding to 4 mmol of Pt) was added dropwise to a solution of **15** (1.37 g, 5.0 mmol) in *t*BuOMe (30 mL) at 0 °C while stirring. A vanilla-yellow powder precipitated. After stirring for 2 h at 0 °C, filtration and washing with MeOH, a fine, bright yellow powder (1.440 g, 77%) was obtained that was hardly soluble in any solvents, except for DMSO and pyridine. (b) A suspension of $Pt_2(dba)_3$ (109 mg, 0.1 mmol) and **15** (58 mg, 0.21 mmol) in acetone (2 mL) and THF (2 mL) was stirred for 1 d at room temp. The reaction mixture was evaporated to dryness and the solid was suspended in MeOH (2 mL) and filtered. Washing with MeOH and acetone gave 66 mg (70%) of a greyish yellow powder. The discoloration was caused by finely divided $Pt^0$ already present in $Pt_2(dba)_3$. M.p. 159 °C (dec.). $^1$H NMR (250 MHz, [$D_6$]-DMSO): $\delta$ = 4.46 (d, $J$ = 11.0 Hz, $J_{Pt,H} \approx$ 56 Hz, 4 H, 1-H, 3-H), 6.05 (t, $J$ = 11.0 Hz, $J_{Pt,H} \approx$ 76 Hz, 2 H, 2-H), 7.10–7.70 (m, 20 H, aryl) ppm. $^{13}$C NMR (62.9 MHz, [$D_6$]DMSO): $\delta$ = 74.6 (br.), 104.7, 130.7, 131.3, 131.8, 141.4 ppm. IR (KBr): $\tilde{\nu}$ = 755 (s), 698 (s) cm$^{-1}$. $C_{30}H_{26}Br_2Pt_2$ (936.50): calcd. C 38.48, H 2.80; found C 38.54, H 2.89.

**[Pt(η³-$Ph_2$All)(2b)]$PF_6$ (18·$PF_6$):** Ligand **2b** (515 mg, 0.99 mmol) and **17** (463 mg, 0.494 mmol) were stirred in acetone (10 mL) until they had completely dissolved. Epichlorohydrine (1.0 mL, 12.8 mmol) and $HPF_6$ (1 M, 1.1 mL, 1.1 mmol, freshly prepared from 75% aq. $HPF_6$ and EtOH) were added, and the mixture stirred for 20 min and then evaporated to dryness. The residue was thoroughly dried under HV, washed with *t*BuOMe and then dissolved in $CH_2Cl_2$ (5 mL) and the solution filtered through a cotton plug into MeOH (10 mL). On standing in the fridge (4 °C), dark orange crystals formed (763 mg, 73%). $^1$H NMR (400 MHz, [$D_8$]-THF): $\delta$ = 0.51 (s, 9 H, *t*Bu), 2.37 (d, $J$ = 6.9 Hz, 3 H, *Me*CH), 3.94 (s, 5 H, Cp′), 4.05–4.08 (m, 1 H-Cp), 4.51 (t, $J$ = 2.3 Hz, 1 H-Cp), 4.79–4.80 (m, 1 Cp-H), 4.81 (d, $J$ = 9.2 Hz, $J_{Pt,H}$ = 77 Hz, allyl H, *anti*, *trans* N), 5.86 (ddd, $J$ = 13.9 Hz, 9.1 Hz, 2.1 Hz, $J_{Pt,H}$ = 56, allyl H, *central*), 6.05 (d, $J$ = 2.9 Hz, $J_{Pt,H} \approx$ 11 Hz, 4-H, Pz), 6.35–6.43 (m, 2 H, aryl), 6.89 (dd, $J$ = 13.8 Hz, 7.0 Hz, $J_{Pt,H}$ = 49 Hz, allyl H, *anti*, *trans* P), 7.04–7.08 (m, 3 H, aryl), 7.10–7.18 (5 H, aryl), 7.22–7.32 (m, 3 H, aryl), 7.25 (q, $J$ = 6.9 Hz, C*H*Me), 7.34–7.39 (m, 2 H, aryl), 7.42–7.50 (m, 3 H, aryl), 7.75–7.82 (m, 2 H, aryl), 7.98 (d, $J$ = 2.9 Hz, 5-H, Pz) ppm. $^{13}$C NMR (62.9 MHz, [$D_8$]THF): $\delta$ = 18.2 ($CH_3$), 30.8 (s, $J_{Pt,C}$ = 7 Hz, $CH_3$), 33.1 (C), 51.4 (s, $J_{Pt,C}$ = 318 Hz, allyl CH, *trans* N), 59.5 (d, $J_{P,C}$ = 3 Hz, *C*HMe), 67.9 [d, $J_{P,C}$ = 7 Hz, CH, C(3) Cp], 71.9 [d, $J_{P,C}$ = 7 Hz, CH, C(4) Cp], 72.3 (CH, Cp′), 74.4 [d, $J_{P,C}$ = 3 Hz, $J_{Pt,C}$ = 40 Hz, CH, C(5′) Cp], 75.4 (d, $J_{P,C}$ = 58 Hz, C), 94.8 (d, $J_{P,C}$ = 17 Hz, C), 100.7 (d, $J_{P,C}$ = 19 Hz, CH, All *trans* P), 108.9 [s, $J_{Pt,C}$ = 34 Hz, CH, C(4) Pz], 109.8 (s, $J_{Pt,C}$ = 33 Hz, allyl CH, *central*), 127.2 (CH), 128.8 (CH), 129.1 (d, $J_{P,C}$ = 10 Hz, CH) 129.1 (d, $J_{P,C}$ = 2 Hz, CH), 129.3 (CH), 129.4 (d, $J_{P,C}$ = 1 Hz, CH), 129.5 (d, $J_{P,C}$ = 1 Hz, CH), 129.6 (d, $J_{P,C}$ = 1 Hz, CH), 130.9 (CH), 130.9 [CH, C(5) Pz], 131.1 (d, $J_{P,C}$ = 65 Hz, C), 131.8 (d, $J_{P,C}$ = 3 Hz, CH), 132.9 (d, $J_{P,C}$ = 10 Hz, CH, *ortho*-PPh axial), 134.2 (d, $J_{P,C}$ = 57 Hz, C), 135.4 (d, $J_{P,C}$ = 13 Hz, CH, *ortho*-PPh equatorial), 136.8 (d, $J_{P,C}$ = 4 Hz, C), 142.0 (d, $J_{P,C}$ = 1 Hz, C), 163.2 [C, C(3) Pz] ppm. $^{31}$P NMR (161.9 MHz, [$D_8$]THF): $\delta$ = –142.7 (sept, $J_{PF}$ = 714 Hz, $PF_6^-$), 10.4 (s, $J_{Pt,P}$ = 5029 Hz), 9.2 (s, minor isomer, <2%). $^{195}$Pt NMR (86.0 MHz, HMQC, [$D_8$]THF): $\delta$ = –4453 (d, $J_{Pt,P}$ = 5030 Hz) ppm. $C_{46}H_{46}F_6FeN_2P_2Pt$ (1053.75): calcd. C 52.43, H 4.40, N 2.66; found C 52.38, H 4.44, N 2.63.

**[Pt(η³-$Ph_2$All)(2b)]Br (18·Br):** A combination of **2b** (30 mg, 58 mmol) and **17** (27 mg, 29 mmol) in THF (2 mL), followed by filtration and evaporation gave a yellow residue. Crystallization from $CH_2Cl_2$/pentane at 5 °C (over layering) produced fine yellow needles (43.5 mg, 76%). Additional material was crystallized from the mother liquors (12 mg, total 97%). M.p. 141–147 °C. $^{31}$P NMR (101.3 MHz, $CDCl_3$) and $^{195}$Pt NMR (HMQC, 64.3 MHz, $CDCl_3$): see Table 2. MS (FAB): *m/z* (%) = 908.4 (73) [M – Br]$^+$, 715.3 (100) [M – Br – $Ph_2$All]$^+$. $C_{46}H_{46}BrFeN_2PPt$ (988.69): calcd. C 55.88, H 4.69, N 2.83; found C 55.99, H 4.74, N 2.75.

**[Pt(η³-$Ph_2$All)(2b)]F (18·F):** (a) $Me_4NF$ (17 mg, 0.18 mmol) was added to a solution of **18·$PF_6$** (128 mg, 0.12 mmol) in THF (1 mL) and the resulting suspension stirred at room temp. Samples of the supernatant solution were taken and $C_6D_6$ was added for locking purposes, and the NMR spectra recorded. After 1 d, some $PF_6^-$ remained in the solution ($^{19}$F NMR, $^{31}$P NMR), but after 2 d such signals had disappeared. The reaction mixture was filtered and the filtrate evaporated under HV. A yellow solid remained which was soluble in benzene. $^{19}$F NMR (282.4 MHz, $CDCl_3$): $\delta$ = –139.8 (br. s, $\Delta_{1/2}$ = 15 Hz, $F^-$) ppm. $^{31}$P NMR (121.5 MHz, $CDCl_3$): $\delta$ = 2.2 (s, $J_{Pt,P}$ = 3903 Hz), 3.5 (s, $J_{Pt,P}$ = 4094 Hz), 7.0 (br. s, $J_{Pt,P}$ = 3947 Hz) ppm.

(b) Reaction in toluene: **18·$PF_6$** (115 mg) and $Me_4NF$ (15 mg) were stirred for 2 d in [$D_8$]toluene (3 mL). The sample was filtered into a J. Young NMR tube. $^{19}$F NMR (282 MHz, [$D_8$]toluene, 298 K): $\delta$ = –116 (br. s) ppm. Note that the signal is within a region of heavy artifacts (due to fluoropolymers within the NMR probe head). $^{31}$P NMR (121.5 MHz, [$D_8$]toluene, 298 K): $\delta$ = 2.4 (s, $J_{Pt,P}$ = 3908 Hz), 4.1 (br. s, $J_{Pt,P}$ = 4070 Hz), 7.8 (br. s, $J_{Pt,P}$ = 3938 Hz) ppm. VT $^{31}$P NMR (121.5 MHz, [$D_8$]toluene, 213 K): see Table 2.

**[$PtCl_2$(2b)] (19):** Bis(styrene)platinum(II) chloride (0.475 g, 1.00 mmol) and **2b** (0.5377 g, 1.03 mmol) were stirred in $CH_2Cl_2$ (10 mL) for 1 d at 40 °C. Filtration through Celite, evaporation to 2 mL and addition of pentane gave an orange precipitate. This was dissolved in a little $CH_2Cl_2$ and over layered with EtOAc. Slow evaporation in the fume hood gave orange-red crystals containing

 © 2006 Wiley-VCH Verlag GmbH & Co. KGaA, Weinheim 

the solvent of crystallization. Yield as $[PtCl_2(\mathbf{2b})]\cdot 0.35\ CH_2Cl_2\cdot 0.25$ AcOEt: 0.716 g (87%). An analytical sample was dried to remove solvents of crystallization. M.p. 215 °C (dec.). $^1$H NMR (300 MHz, $CDCl_3$): $\delta$ = 1.18 (s, 9 H, *t*Bu), 2.12 (d, $J$ = 7.2 Hz, 3 H, CH*Me*), 3.75–3.79 (m, 1 H-Cp), 4.16 (s, 5 H, Cp′), 4.41 (t, $J$ = 2.5 Hz, 1 H-Cp), 4.74–4.79 (m, 1 H-Cp), 6.05 (d, $J$ = 2.9 Hz, 4-H, Pz), 6.68–6.78 (m, 2 H, aryl), 7.14–7.23 (dt, $J$ = 8 Hz, 3 Hz, 2 H, aryl), 7.29–7.36 (m, 1 H, aryl), 7.42–7.58 (m, 3 H, aryl), 7.52 (d, $J$ = 2.9 Hz, 5-H, Pz), 8.08 (q, $J$ = 7.2 Hz, C*H*Me), 8.11–8.20 (m, 2 H, aryl) ppm. $^{13}$C NMR (62.9 MHz, $CDCl_3$): $\delta$ = 17.3 ($CH_3$, CH*Me*), 31.3 ($CH_3$, *t*Bu), 33.3 (C, *t*Bu), 57.5 (CH, *C*HMe), 68.0 (d, $J_{P,C}$ = 8 Hz, CH, Cp), 70.7 (d, $J_{P,C}$ = 7 Hz, CH, Cp), 71.1 [d, $J_{P,C}$ = 67 Hz, C, C(1)-Cp], 71.3 (CH, Cp′), 73.8 (d, $J_{P,C}$ = 4 Hz, CH, Cp), 92.4 [d, $J_{P,C}$ = 15 Hz, C, C(2)-Cp], 107.8 [CH, C(4)-Pz], 127.4 (d, $J_{P,C}$ = 11 Hz, CH), 127.5 (d, $J_{P,C}$ = 68 Hz, C), 127.6 [CH, C(5)-Pz], 128.3 (d, $J_{P,C}$ = 10 Hz, CH), 130.1 (d, $J_{P,C}$ = 3 Hz, CH), 131.3 (d, $J_{P,C}$ = 3 Hz, CH), 131.6 (d, $J_{P,C}$ = 10 Hz, CH), 132.7 (d, $J_{P,C}$ = 61 Hz, C), 135.7 (d, $J_{P,C}$ = 10 Hz, CH), 162.7 [C, C(3)-Pz] ppm. $^{31}$P NMR (125.5 MHz, $CDCl_3$): $\delta$ = –16.1 (s, $J_{Pt,P}$ = 3783 Hz) ppm. $^{195}$Pt NMR (HMQC, 64.525 MHz, $CDCl_3$): $\delta$ = –3700 (d, $J_{Pt,P}$ = 3790 Hz) ppm. MS (FAB): *m*/*z* (%) = 1537 (50) [2 M – Cl]$^+$, 786 (27) M$^+$, 750 (92) [M – Cl]$^+$, 714 (100) [M – 2 Cl]$^+$, 630 (74). $C_{31}H_{33}Cl_2FeN_2PPt$ (786.42): calcd. C 47.35, H 4.23, N 3.56; found C 47.43, H 4.45, N 3.61.

**[PtPh$_2$(2b)] (20):** (a) Complex **19** (100 mg, 0.127 mmol) was added to a 10–20 fold excess of PhMgBr in THF (ca. 2 mL) and stirred for 1 d at 50 °C. Quenching with aq. $NH_4Cl$ and extraction with *t*BuOMe, followed by drying of the organic phase ($MgSO_4$) and evaporation gave a yellow semisolid. This was crystallized from heptane/$CH_2Cl_2$ by slow evaporation at 4 °C to give orange-yellow crystals (81 mg, 73%).

(b) An aged solution of PhMgBr (2 mL, 2 M, 4 mmol) was added dropwise to **19** (0.21 mmol) in THF (7 mL). After stirring for 1 d at 50 °C the reaction was quenched with water and extracted with *t*BuOMe. Drying over $MgSO_4$ and evaporation gave an orange oil that was filtered through $SiO_2$ using *t*BuOMe/hexane (1:10). The yellow fractions were collected and the solvents evaporated. Heptane (3 mL) was added to the residue and enough $CH_2Cl_2$ to dissolve all solids. Diffusion against heptane at –20 °C gave 160 mg (79%) of orange crystals of the phenol adduct (**20·PhOH**, $M_r$ = 963.82). The PhOH was apparently an impurity arising from the Grignard reagent used. Analytical data for the solvate-free compound: M.p. 185–189 °C (dec.). $^1$H NMR (250 MHz, $CDCl_3$): $\delta$ = 0.66 (s, 9 H, *t*Bu), 2.21 (d, $J$ = 7.3 Hz, 3 H, *Me*CH), 3.66–3.71 (m, 1 H-Cp), 3.97 (s, 5 H, Cp′), 4.30 (t, $J$ = 2.6 Hz, 1 H-Cp), 4.66–4.71 (m, 1 H-Cp), 5.95 (d, $J$ = 2.7 Hz, 4-H,Pz), 6.49–6.59 (m, 2 H, aryl), 6.69–7.38 (m, 16 H, aryl), 7.49 (d, $J$ = 2.7 Hz, 5-H, Pz), 7.52–7.91 (br. m, 2 H, aryl), 8.82 (q, $J$ = 7.2 Hz, C*H*Me) ppm. $^{13}$C NMR (62.9 MHz, $CDCl_3$): $\delta$ = 18.4 ($CH_3$), 30.2 ($CH_3$), 31.9 (C), 56.8 (d, $J_{P,C}$ = 1 Hz, $CH_3$), 67.3 (d, $J_{P,C}$ = 6 Hz, CH), 70.3 (d, $J_{P,C}$ = 4 Hz, CH), 70.4 (CH, Cp′), 73.6 (CH), 74.9 (d, $J_{P,C}$ = 42 Hz, C, Cp), 93.5 (d, $J_{P,C}$ = 18 Hz, C, Cp), 106.0 (CH), 120.9 (d, $J_{P,C}$ = 1.5 Hz), 122.0 (d, $J_{P,C}$ = 1.0 Hz), 125.8 (CH), 126.2 (d, $J_{P,C}$ = 7 Hz, CH), 127.0 (d, $J_{P,C}$ = 9 Hz, CH), 127.5 (d, $J_{P,C}$ = 9 Hz, CH), 128.0 (d, $J_{P,C}$ = 2 Hz, CH), 128.5 (CH), 129.2 (d, $J_{P,C}$ = 56 Hz, C), 129.5 (d, $J_{P,C}$ = 2 Hz, CH), 131.3 (d, $J_{P,C}$ = 10 Hz, CH), 131.6 (d, $J_{P,C}$ = 44 Hz, C), 135.9 (d, $J_{P,C}$ = 10 Hz, CH), 137.7 ($J_{Pt,C}$ = 38 Hz), 138.7 (C), 138.9 (br.), 139.3 (C), 139.5 (br.), 143.0, 143.2, 144.6, 158.9, 160.8 ppm. Some of the signals were not detected due to line broadening, which arose from hindered rotation of the phenyl groups. $^{31}$P NMR (101.3 MHz, $CDCl_3$): $\delta$ = 5.3 (s, $J_{Pt,P}$ = 1688 Hz) ppm. MS (FAB): *m*/*z* (%) = 1584.8 (14) [2 M – 2 Ph]$^+$, 868.4 (5) [M]$^+$, 791.3 (12) [M – Ph]$^+$, 715.3 (100) [M – 2 Ph]$^+$. $C_{43}H_{43}FeN_2PPt$ (869.73): calcd. C 59.38, H 4.98, N 3.22; found C 59.38, H 5.05, N 3.21.

**[Pt(Ph)F(2b)] (21):** In an NMR tube, **20** (10 mg) in $CDCl_3$ (0.5 mL) was mixed with 2 drops of $NEt_3\cdot(HF)_3$. NMR analysis revealed two species (ratio 1.4:1) with similar $^1$H NMR spectra. The major species was the fluoro complex and the minor species remains unknown. No attempt was made to isolate the compounds. $^1$H NMR (300 MHz, $CDCl_3$), selected signal: $\delta$ = 7.36 (s, 6 H, benzene) ppm. $^{19}$F NMR (282.4 MHz, $CDCl_3$): $\delta$ = –214.6 (d, $J_{P,F}$ = 207 Hz, $J_{Pt,F}$ = 210 Hz), –129.7 (br. s, $Et_3NH^+/F^-$, excess reagent), –165.0 (br. s, $HF/HF_2^-$) ppm. $^{31}$P NMR (121.5 MHz, $CDCl_3$): $\delta$ = –9.6 (s, $J_{Pt,P}$ = 5107 Hz), –11.8 (d, $J_{PF}$ = 207, $J_{Pt,P}$ = 5104 Hz) ppm.

**[Pt($\eta^3$-All)(2b)]SbF$_6$ (22):** $[\{PtCl(C_3H_5)\}_4]$[67] (103 mg, 0.095 mmol) and **2b** (203 mg, 0.39 mmol) were stirred in acetone (3 mL) and $CH_2Cl_2$ (3 mL) until a homogeneous solution was obtained. $AgSbF_6$ (135 mg, 0.39 mmol) was added and the resulting suspension stirred for 30 min. After filtration through Celite and evaporation, the residue was purified by precipitation from acetone/hexane to give 284 mg (71%) of orange crystals containing 0.5 equiv. acetone. $^{31}$P NMR (81.0 MHz, $CDCl_3$): $\delta$ = 12.5 (s, $J_{Pt,P}$ = 4413 Hz, *exo* isomer), 12.6 (s, *endo* isomer) ppm. MS (FAB): *m*/*z* (%) = 1276.8 (16) [2 M – $PF_6$]$^+$, 756.4 (100) [M – $PF_6$]$^+$, 715.4 (25), [M – $PF_6$ – $C_3H_5$]$^+$. $C_{34}H_{38}F_6FeN_2PPtSb\cdot 0.5\,C_3H_6O$ (1021.36): calcd. C 41.75, H 4.05, N 2.74; found C 41.83, H 4.00, N 2.83.

**[Pt($\eta^3$-2-MeAll)(2b)]PF$_6$ (23):** Ligand **2b** (193 mg, 0.37 mmol) and $[Pt_2(\mu\text{-}Cl)_2(2\text{-}MeAll)_2]$[68] (98.6 mg, 0.17 mmol) were stirred at room temp. for 2 h in $CH_2Cl_2$ (3 mL). $AgPF_6$ (94 mg, 0.37 mmol) in MeOH (3 mL) was added and the resulting suspension was stirred for 30 min, then filtered through Celite. The solution was evaporated to dryness and the residue crystallized from $CH_2Cl_2$/*t*BuOMe (slow diffusion) to give 254 mg (81%) of orange crystals. $^{31}$P NMR (81.0 MHz, $CDCl_3$): $\delta$ = –143.5 (sept, $J_{PF}$ = 713 Hz, $PF_6^-$), 11.5 (s, $J_{Pt,P}$ = 4291 Hz, major isomer); 11.9 (s, $J_{Pt,P}$ = 4010 Hz, minor isomer) ppm. MS (FAB): *m*/*z* (%) = 770.4 (100) [M – $PF_6$]$^+$. $C_{35}H_{40}F_6FeN_2P_2Pt$ (915.57): calcd. C 45.91, H 4.40, N 3.06; found C 45.97, H 4.61, N 3.03.

**[Pt($\eta^3$-Ph$_2$All)(dppe)]PF$_6$ (24):** A mixture of **17** (51.5 mg, 0.055 mmol) and 1,2-bis(diphenylphosphanyl)ethane (43.8 mg, 0.11 mmol) in acetone (1 mL) and $CH_2Cl_2$ (1 mL) was stirred until completely dissolved. Epichlorohydrine (0.1 mL, 1.28 mmol) and $HPF_6$ solution [0.1 mL, 0.114 mmol; freshly prepared from 0.6 mL $HPF_6$ (75%) and EtOH up to 5.0 mL total volume] were then added dropwise. After 30 min stirring, the reaction mixture was evaporated to dryness and the residue dried under HV. The yellow solid was dissolved in $CH_2Cl_2$ (2 mL), the solution filtered through Celite, and the filtrate reduced to a volume of 1 mL. Addition of butanone (1 mL) followed by slow evaporation in the fume hood gave yellow, rhombic crystals (67 mg, 65%), suitable for X-ray analysis. $^1$H NMR (250 MHz, $CD_2Cl_2$): $\delta$ = 2.28–2.62 (m, $J_{Pt,H}$ = 34 Hz, 4 H, $CH_2CH_2$), 4.80 (m, AA′ of AA′BXX′, $J_{AB}$ = $J_{A'B}$ = 12.8 Hz, $J_{AX}$ + $J_{AX'}$ = 22.1 Hz, $J_{Pt,H}$ = 45.3 Hz, 2 allyl H, *anti*), 6.14 (t, B of AA′BXX′, $J$ = 12.8 Hz, $J_{Pt,H}$ = 45 Hz, 1 allyl H, *central*), 7.80–6.80 (m, 30 H, aryl) ppm. $^{13}$C NMR (62.9 MHz, $CD_2Cl_2$): $\delta$ = 31.0 (AMM′, ψ-dd, $J$ = 41 Hz, 9 Hz, $J_{Pt,C}$ = 56 Hz, $CH_2$), 83.5 [AMM′, ψ-d, $J$ = 27 Hz, $J_{Pt,C}$ = 55 Hz, CH, All-C(1,3)], 110.9 [A of $AM_2$, t, $J_{P,C}$ = 4 Hz, $J_{Pt,C} \approx$ 17 Hz, CH, All–C(2)], 126.8 (AMM′, ψ-dd, $J$ = 57 Hz, 0.8 Hz, $J_{Pt,C}$ = 49 Hz, C, PPh-*ipso*-C), 128.4 (AMM′, ψ-quint, $J$ = 2 Hz, CH), 128.7 (AMM′, ψ-dd, $J$ = 56 Hz, 0.6 Hz, $J_{Pt,C}$ = 38 Hz, C, PPh-*ipso*-C), 129.3 (AMM′, ψ-t, $J$ = 1.5 Hz, CH), 130.3 (AMM′, ψ-t, $J$ = 1.3 Hz, CH), 131.1–131.6 (m, 2 CH), 133.7 (AMM′, CH), 133.8 (AMM′, $J_{Pt,C}$ = 24 Hz, CH), 134.5 (AMM′, CH), 134.9 (AMM′, $J_{Pt,C}$ =

 © 2006 Wiley-VCH Verlag GmbH & Co. KGaA, Weinheim 

25 Hz, CH), 137.7 (AMM′, C) ppm. Spin system nomenclature: A corresponds to the carbon atom in question, M and M′ correspond to the $^{31}$P nuclei. $^{31}$P NMR (101.3 MHz, $CD_2Cl_2$): $\delta$ = –143.7 (sept, $J_{P,F}$ = 711 Hz, $PF_6^-$), 44.7 (s, $J_{Pt,Pt}$ = 3847 Hz) ppm. $^{195}$Pt NMR (HMQC, 64.2 MHz, $CD_2Cl_2$): $\delta$ = –5521 (t, $J_{Pt,P} \approx$ 3830 Hz) ppm. MS (FAB): *m*/*z* (%) = 1717 (9) $[2\ M - PF_6]^+$, 786 (100) $[M - PF_6]^+$, 592 (10) $[M - PF_6 - Ph_2All]^+$. $C_{41}H_{37}F_6P_3Pt$ (931.72): calcd. C 52.85, H 4.00; found C 52.83, H 4.14.

**(*E*)-1-Cyclohexyl-3-cyclohexylidenepropene (26):** (a) The substance was formed, in NMR experiments, from **8b** and an excess of either $Me_4NF$ (in $[D_3]$MeCN) or Schwesinger's $P_2F$[57] (in $C_6D_6$). (b) A reference sample was obtained as follows: MsCl (56.0 mg, 0.488 mmol) was added dropwise at –78 °C to a solution of **10** (98.8 mg, 0.444 mmol) and *i*$Pr_2$NEt (0.091 mL, 0.533 mmol) in THF (5 mL). After stirring for 45 min and another addition of *i*$Pr_2$NEt (0.18 mL, 1.06 mmol) and MsCl (120 mg, 1 mmol) the reaction mixture was warmed to room temp. and stirred for 2 h. Workup with $H_2O$/*t*BuOMe gave, after drying ($MgSO_4$) and evaporation to dryness, a residue that was filtered through $SiO_2$ (*t*BuOMe) to yield 38.7 mg (42%) of a colorless oil. $^1$H NMR (250 MHz, $CDCl_3$): $\delta$ = 0.75–2.30 (m, 21 H-Cy), 5.54 (dd, *J* = 15.2 Hz, 7.0 Hz, 1-H), 5.73 (dd, *J* = 10.9 Hz, 0.7 Hz, 3-H), 6.25 (ddd, *J* = 15.2 Hz, 10.8 Hz, 1.2 Hz, 2-H) ppm. $^{13}$C NMR (62.9 MHz, $CDCl_3$): $\delta$ = 26.1 ($CH_2$), 26.2 ($CH_2$), 26.8 ($CH_2$), 27.6 ($CH_2$), 28.4 ($CH_2$), 29.2 ($CH_2$), 33.1 ($CH_2$), 37.2 ($CH_2$), 41.0 (CH), 122.1 (CH), 123.2 (CH), 138.3 (CH), 141.2 (C) ppm. IR ($CHCl_3$): $\tilde{\nu}$ = 2930 (s), 2853 (m), 1616 (w), 1448 (m), 1344 (w), 968 (m) cm$^{-1}$. MS (EI): *m*/*z* = 204 $[M]^+$.

**Oxidative Addition of $Ph_2$AllF (6) to Pd(dba)$_2$ (→27·F):** Pd(dba)$_2$ (170 mg, 0.29 mmol) and $Ph_2$AllF (**6**)[14a] (76 mg, 0.36 mmol, solution in 7 mL hexane) were stirred in THF (10 mL). Within 15 min, the color changed from violet to yellow, and a yellow solid precipitated. After filtration, the solid was dried under HV. The product could not be further purified and was only analyzed spectroscopically for the presence of the (1,3-diphenylallyl)palladium(II) fragment. $^1$H NMR ($[D_6]$DMSO): $\delta$ = 5.29 [d, *J* = 12.0 Hz, 4 H, C(2),C(3)], 6.98 [t, *J* = 11.8 Hz, 2 H, C(2)], 7.39 (br. m, 12 H, aryl), 7.78 (br. m, 8 H, aryl) ppm. $^{19}$F NMR: no signal detected.

**Di-μ-bromobis($\eta^3$-1,3-diphenylallyl)dipalladium(II) (27·Br):** Pd(dba)$_2$ (40 mg, 0.070 mmol) and **15** (22.8 mg, 0.083 mmol) were stirred in THF (20 mL) at room temp. The color of the violet suspension became brighter within 20 min and a yellow precipitate was deposited. The solid was isolated by filtration and dried under HV. No further purification was attempted due to the small scale of the reaction. $^1$H NMR ($[D_6]$DMSO): $\delta$ = 5.19 (d, *J* = 11.7 Hz, 4 H, allyl H, *anti*), 6.80 (t, *J* = 11.7 Hz, 2 H, allyl H, *central*), 7.30–7.27 (m, 12 H, aryl), 7.66–7.69 (m, 8 H, aryl) ppm. $C_{30}H_{26}Br_2Pd_2$ (759.18): calcd. C 47.46, H 3.45; found C 46.87, H 3.48.

**Oxidative Addition of $Ph_2$AllF (6) to Pd(dba)$_2$ in the Presence of PPFPz{3,5-Me$_2$} {→[Pd($\eta^3$-$Ph_2$All)(PPFPz{3,5-Me$_2$})]F·($H_2O$)$_n$ (28·F)}:** PPFPz{3,5-$Me_2$} (**2c**)[28] (54.2 mg, 0.11 mmol) and Pd(dba)$_2$ (57.5 mg, 0.10 mmol) were stirred in THF (10 mL) at 40 °C for 30 min to give an orange-brown solution. $Ph_2$AllF (**6**)[14a] (2 mL, 75 mM in *N*,*N*-dimethylformamide, 0.15 mmol), was added and the reaction mixture, which quickly turned yellow, was stirred for 1 h at room temp. Solvents were removed under HV and the residue purified by precipitation (in air) from $CH_2Cl_2$/pentane. $^1$H NMR (250 MHz, $CDCl_3$): $\delta$ = 0.71 (s, 3 H, Me-Pz), 1.67 (s, ca. 4 H, $H_2O$), 2.29 (d, *J* = 7.4 Hz, 3 H, CH*Me*), 2.31 (s, 3 H, Me–Pz), 3.75 (s, 1 H-Cp), 4.18 (s, 5 H, Cp′); 4.35–4.37 (m, 1 H-Cp), 4.65 (s, 1 H-Cp), 5.30 (s, 1 H-Pz), 6.12–6.19 (m, 3 H, 1 allyl H,, 2 H, aryl), 6.43–6.52 (m, 1 allyl H,), 6.98–8.03 (m, 19 H, 1 allyl H,, 18 H, aryl) ppm,

Table 3. Crystallographic data for **8a**, **8b**, and **8c·$CH_2Cl_2$**.

| | **8a** | **8b** | **8c·$CH_2Cl_2$** |
|---|---|---|---|
| CCDC number | 279485 | 279484 | 279489 |
| Formula | $C_{46}H_{46}F_6FeN_2P_2Pd$ | $C_{46}H_{58}F_6FeN_2P_2Pd$ | $C_{41}H_{42}Cl_2F_6FeN_2P$ Pd Sb |
| $M_r$ | 965.07 | 977.13 | 1062.64 |
| Crystal system | orthorhombic | orthorhombic | triclinic |
| Space group | $P2_12_12_1$ | $P2_12_12_1$ | $P_{1r}$ |
| *a* [Å] | 10.677(2) | 10.3481(16) | 10.281(7) |
| *b* [Å] | 19.505(3) | 17.276(3) | 15.338(10) |
| *c* [Å] | 20.809(3) | 25.231(4) | 13.684(9) |
| *α* [°] | 90 | 90 | 90.0100(10) |
| *β* [°] | 90 | 90 | 92.1260(10) |
| *V* [Å$^3$] | 4333.5(11) | 4510.7(12) | 2156(2) |
| *Z* | 4 | 4 | 2 |
| Density calcd. [Mg·m$^{-3}$] | 1.479 | 1.439 | 1.637 |
| *μ* [mm$^{-1}$] | 0.884 | 0.850 | 1.584 |
| *F*(000) | 1968 | 2016 | 1056 |
| Crystal size [mm$^3$] | 0.94 × 0.34 × 0.16 | 0.50 × 0.44 × 0.28 | 0.80 × 0.54 × 0.26 |
| *θ* range (°) | 1.43–28.31 | 1.43–24.78 | 1.33–29.69 |
| Index ranges | $-14 \le h \le 14$ | $-12 \le h \le 11$ | $-14 \le h \le 12$ |
| | $-25 \le k \le 26$ | $-20 \le k \le 20$ | $-18 \le k \le 21$ |
| | $-17 \le l \le 27$ | $-29 \le l \le 19$ | $-18 \le l \le 16$ |
| Reflections collected/used | 36689/10782 | 25274/7719 | 15564/12425 |
| | [$R_{int}$ = 0.0672] | [$R_{int}$ = 0.1009] | [$R_{int}$ = 0.0365] |
| Data/restraints/parameters | 10782/0/523 | 7719/42/509 | 12425/3/994 |
| Goodness-of-fit on $F^2$ | 0.964 | 0.949 | 1.062 |
| *R* indices | $R_1$ = 0.0349 | $R_1$ = 0.0589 | $R_1$ = 0.0457 |
| [$I > 2\sigma(I)$] | $wR_2$ = 0.0767 | $wR_2$ = 0.1324 | $wR_2$ = 0.1232 |
| (all data) | $R_1$ = 0.0538 | $R_1$ = 0.0983 | $R_1$ = 0.0514 |
| | $wR_2$ = 0.0837 | $wR_2$ = 0.1489 | $wR_2$ = 0.1338 |
| Abs. struct. parameter | –0.04(2) | –0.05(4) | –0.02(2) |
| Largest diff. peak/hole [e·Å$^{-3}$] | 0.490/–0.572 | 1.643/–0.750 | 0.829/–0.857 |

 © 2006 Wiley-VCH Verlag GmbH & Co. KGaA, Weinheim 

Table 4. Crystallographic data for **18·PF$_6$**, **20·PhOH**, and **24**.

| | **18·PF$_6$** | **20·PhOH** | **24** |
|---|---|---|---|
| CCDC number | 279486 | 279488 | 279487 |
| Formula | $C_{46}H_{46}F_6FeN_2P_2Pt$ | $C_{49}H_{49}FeN_2OPPt$ | $C_{41}H_{37}F_6P_3Pt$ |
| $M_r$ | 1053.73 | 963.85 | 931.71 |
| Crystal system | orthorhombic | monoclinic | orthorhombic |
| Space group | $P2_12_12_1$ | $P2_1$ | *Pbca* |
| *a* [Å] | 10.709(2) | 11.591(14) | 18.525(7) |
| *b* [Å] | 19.566(3) | 10.998(9) | 18.644(9) |
| *c* [Å] | 20.832(3) | 16.464(3) | 22.108(9) |
| $\alpha$ [°] | 90 | 90 | 90 |
| $\beta$ [°] | 90 | 94.72(9) | 90 |
| *V* [Å$^3$] | 4376.3(3) | 2092(4) | 7636(6) |
| *Z* | 4 | 2 | 8 |
| Density calcd. [Mg·m$^{-3}$] | 1.599 | 1.530 | 1.621 |
| $\mu$ [mm$^{-1}$] | 3.658 | 3.764 | 3.859 |
| *F*(000) | 2096 | 968 | 3680 |
| Crystal size [mm$^3$] | 0.95 × 0.3 × 0.3 | 0.5 × 0.3 × 0.2 | 0.2 × 0.17 × 0.13 |
| $\theta$ range (°) | 1.43–29.96 | 1.76–20.04 | 1.80–20.15 |
| Index ranges | $-14 \le h \le 14$ | $-11 \le h \le 11$ | $0 \le h \le 17$ |
| | $-18 \le k \le 27$ | $-10 \le k \le 10$ | $0 \le k \le 17$ |
| | $-28 \le l \le 28$ | $-15 \le l \le 15$ | $0 \le l \le 21$ |
| Reflections collected/used | 32667/11386 | 3931/1989 | 3553/3553 |
| | [$R_{int}$ = 0.0683] | – | [$R_{int}$ = 0.0000] |
| Data/restraints/parameters | 11386/0/524 | 1989/0/461 | 3553/0/461 |
| Goodness-of-fit on $F^2$ | 0.945 | 1.825 | 0.903 |
| *R* indices | $R_1$ = 0.0405 | $R_1$ = 0.036 | $R_1$ = 0.0304 |
| [$I > 2\sigma(I)$] | $wR_2$ = 0.0759 | $wR_2$ = 0.033 | $wR_2$ = 0.0752 |
| (all data) | $R_1$ = 0.0925 | $R_1$ = 0.037 | $R_1$ = 0.0455 |
| | $wR_2$ = 0.0897 | $wR_2$ = 0.033 | $wR_2$ = 0.0788 |
| Abs. struct. parameter | –0.031(6) | – | – |
| Largest diff. peak/hole [e·Å$^{-3}$] | 1.164/–1.020 | 0.754/–1.179 | 0.561/–0.637 |

peaks broadened. $^{19}$F NMR (282.4 MHz, $CDCl_3$): no signal detected. $^{31}$P NMR ($CDCl_3$): $\delta$ = 12.1 (br. s) ppm. $C_{44}H_{42}FFeN_2PPd + 3H_2O$ (865.10): calcd. C 61.09, H 5.59, N 3.24; found C 61.02, H 5.09, N 2.77.

**X-ray Crystallography:** Data were collected at 293 K with a Siemens SMART CCD diffractometer (graphite-monochromated Mo-$K_\alpha$ radiation, $\lambda$ = 0.71073 Å, ω-scan technique), except for **20·PhOH** and **24**, for which the data was collected with a Syntex P21 4-circle diffractometer. The structures were solved by direct methods using SHELXS-97.[69] A full matrix least-squares refinement on $F^2$ was performed with SHELXL-97.[70] Allyl fragments in **8b** and the phenol solvate in **20·PhOH** were refined isotropically, all other non-hydrogen atoms were refined anisotropically. The hydrogen atoms were placed in calculated positions and assigned using an isotropic displacement parameter of 0.08 Å$^2$. SADABS[71] was used to perform area-detector scaling and absorption corrections. No absorption correction was applied for **20·PhOH** and **24**.

CCDC-279484 to -279489 (cf. Table 3 and Table 4) contain the supplementary crystallographic data for this paper. This data can be obtained free of charge from The Cambridge Crystallographic Data Centre via www.ccdc.cam.ac.uk/data_request/cif.

## Acknowledgments

L. H. thanks Solvias AG, Basel, for a Ph.D. grant, the Deutsche Forschungsgemeinschaft for current support with an Emmy Noether Programm, and Prof. C. Bolm for continued support. Credit for crystallographic measurements, preliminary structure solutions, data shuffling, and final solutions goes to Diego Broggini, Ulli Englert, Céline Gambs, Volker Gramlich, Arianna Martelletti, Gerhard Raabe, Michael Wörle, and Stefan Zürcher. Daniel Whelligan is thanked for eliminating English glitches.

[1] M. N. Doherty, N. W. Hoffmann, *Chem. Rev.* **1991**, *91*, 553.
[2] E. F. Murphy, H. W. Roesky, *Chem. Rev.* **1997**, *97*, 3425.
[3] S. Thrasher, S. H. Strauss, *Inorganic Fluorine Chemistry towards the 21st Century*, American Chemical Society, Washington, DC, **1994**.
[4] H. Plenio, *Chem. Rev.* **1997**, *97*, 3363.
[5] J. L. Kiplinger, T. G. Richmond, C. E. Osterberg, *Chem. Rev.* **1994**, *94*, 373.
[6] a) J. Burdeniuc, B. Jedlicka, R. H. Crabtree, *Chem. Ber./Recueil* **1997**, *130*, 145; b) M. Aizenberg, D. Milstein, *Science* **1994**, *265*, 359.
[7] a) K. Fagnou, M. Lautens, *Angew. Chem.* **2002**, *114*, 26; *Angew. Chem. Int. Ed.* **2002**, *41*, 26; b) B. L. Pagenkopf, E. M. Carreira, *Chem. Eur. J.* **1999**, *5*, 3437.
[8] U. Burckhardt, M. Baumann, A. Togni, *Tetrahedron: Asymmetry* **1997**, *8*, 155.
[9] a) A. L. Henne, T. H. Newby, *J. Am. Chem. Soc.* **1948**, *70*, 130; b) A. L. Henne, A. M. Whaley, J. K. Stevenson, *J. Am. Chem. Soc.* **1941**, *63*, 3478; c) A. L. Henne, *Org. React.* **1944**, *2*, 49.
[10] Fluorocarbonylations: a) T. Okano, N. Harada, J. Kiji, *Chem. Lett.* **1994**, 1057; b) T. Okano, N. Harada, J. Kiji, *Bull. Chem. Soc. Jpn.* **1992**, *65*, 1741; c) T. Sakakura, M. Chaisupakitsin, T. Hayashi, M. Tanaka, *J. Organomet. Chem.* **1987**, *334*, 205.
[11] Additional examples of transition-metal catalyzed or mediated fluorinations: a) R. D. Chambers, J. Hutchinson, *J. Fluorine Chem.* **1998**, *92*, 45; b) S. Bruns, G. Haufe, *J. Fluorine Chem.* **2000**, *104*, 247.
[12] V. V. Grushin, *Chem. Eur. J.* **2002**, *8*, 1006.
[13] a) M. Shimizu, T. Hiyama, *Angew. Chem.* **2005**, *117*, 218; *Angew. Chem. Int. Ed.* **2005**, *44*, 214; b) P. Kirsch, *Modern Fluoroorganic Chemistry*, Wiley-VCH, Weinheim, **2004**; c) T. Hi-

 © 2006 Wiley-VCH Verlag GmbH & Co. KGaA, Weinheim 

yama, *Organofluorine Compounds*, Springer, Berlin, **2000**; d) V. A. Soloshonok, *Enantiocontrolled Synthesis of Fluoro-Organic Compounds*, Wiley, Chichester, **1999**; e) M. Hudlicky, A. E. Pavlath, *Chemistry of Organic Fluorine Comounds II*, American Chemical Society, Washington, DC, **1995**; f) J. T. Welch, *Selective Fluorination in Organic and Bioinorganic Chemistry*, American Chemical Society, Washington, DC, **1991**.

[14] a) P. Barthazy, L. Hintermann, R. M. Stoop, M. Wörle, A. Mezzetti, A. Togni, *Helv. Chim. Acta* **1999**, *82*, 2448; b) P. Barthazy, A. Togni, A. Mezzetti, *Organometallics* **2001**, *20*, 3472.

[15] L. Hintermann, A. Togni, *Angew. Chem.* **2000**, *112*, 4530; *Angew. Chem. Int. Ed.* **2000**, *39*, 4359.

[16] Y. Hamashima, K. Yagi, H. Takano, L. Tamás, M. Sodeoka, *J. Am. Chem. Soc.* **2002**, *124*, 14530.

[17] J. Ma, D. Cahard, *Tetrahedron: Asymmetry* **2004**, *15*, 1007.

[18] N. Shibata, T. Ishimaru, T. Nagai, J. Kohno, T. Toru, *Synlett* **2004**, 1703.

[19] M. Sanna, PhD Dissertation, ETH Nr. 15191, Zürich, **2003**.

[20] N. Shibata, J. Kohno, K. Takai, T. Ishimaru, S. Nakamura, T. Toru, S. Kanemasa, *Angew. Chem.* **2005**, *117*, 4276; *Angew. Chem. Int. Ed.* **2005**, *44*, 4204.

[21] H. Ibrahim, A. Togni, *Chem. Commun.* **2004**, 1147.

[22] B. M. Trost, M. L. Crawley, *Chem. Rev.* **2003**, *103*, 2921.

[23] Preliminary communication: A. Togni, A. Mezzetti, P. Barthazy, C. Becker, I. Devillers, R. Frantz, L. Hintermann, M. Perseghini, M. Sanna, *Chimia* **2001**, *55*, 801.

[24] G. Helmchen, A. Pfaltz, *Acc. Chem. Res.* **2000**, *33*, 336.

[25] Example: H. C. Clark, M. J. Hampden-Smith, H. Ruegger, *Organometallics* **1988**, *7*, 2087.

[26] J. Elguero, E. Gonzalez, R. Jacquier, *Bull. Soc. Chim. Fr.* **1968**, 707.

[27] a) T. Hayashi, T. Mise, M. Fukushima, M. Kagotani, N. Nagashima, Y. Hamada, A. Matsumoto, S. Kawakami, M. Konishi, K. Yamamoto, M. Kumada, *Bull. Chem. Soc. Jpn.* **1980**, *53*, 1138; b) Improved procedure for preparing PPFA: S. Gischig, A. Togni, *Organometallics* **2004**, *23*, 2479.

[28] a) A. Schnyder, L. Hintermann, A. Togni, *Angew. Chem.* **1995**, *107*, 996; *Angew. Chem. Int. Ed. Engl.* **1995**, *34*, 931; b) U. Burckhardt, L. Hintermann, A. Schnyder, A. Togni, *Organometallics* **1995**, *14*, 5415.

[29] A. Togni, U. Burckhardt, V. Gramlich, P. S. Pregosin, R. Salzmann, *J. Am. Chem. Soc.* **1996**, *118*, 1031.

[30] A. S. Pilcher, H. L. Ammon, P. DeShong, *J. Am. Chem. Soc.* **1995**, *117*, 5166.

[31] K. O. Christe, W. W. Wilson, R. D. Wilson, R. F. Bau, J. A. Feng, *J. Am. Chem. Soc.* **1990**, *112*, 7619.

[32] K. Seppelt, *Angew. Chem.* **1992**, *104*, 299; *Angew. Chem. Int. Ed. Engl.* **1992**, *31*, 292.

[33] D. Landini, A. Maia, A. Rampoldi, *J. Org. Chem.* **1989**, *54*, 328.

[34] a) R. K. Sharma, J. L. Fry, *J. Org. Chem.* **1983**, *48*, 2112; b) However, preparation of truly dry TBAF has just been claimed: H. Sun, S. G. DiMagno, *J. Am. Chem. Soc.* **2005**, *127*, 2050.

[35] Compound **6** is characterized by $\delta(^{19}F) = -165.4$ ppm.[14a]

[36] a) J. A. Davies, in: *Comprehensive Organometallic Chemistry II* (Ed.: R. J. Puddephatt), Elsevier *Science* Oxford, **1995**, Vol. 9, p. 291; b) P. M. Maitlis, P. Espinet, M. J. H. Russell, in: *Comprehensive Organometallic Chemistry* (Ed.: G. Wilkinson), Pergamon, Oxford, **1982**, vol. 6, p. 385.

[37] *exo*: the arrow head defined by the three allyl carbons points away from the lower Cp ring of the ferrocene unit; *endo*: the allyl vector points towards the lower Cp ring. The nomenclature is used as in ref.[29]

[38] A. L. Gemal, J. Luche, *J. Am. Chem. Soc.* **1981**, *103*, 5454.

[39] W. J. Middleton, *J. Org. Chem.* **1975**, *40*, 574.

[40] A. Vitagliano, B. Åkermark, S. Hansson, *Organometallics* **1991**, *10*, 2592.

[41] a) R. G. Brown, R. V. Chaudhari, J. M. Davidson, *J. Chem. Soc., Dalton Trans.* **1977**, 176; b) J. Powell, *J. Am. Chem. Soc.* **1969**, *91*, 4311.

[42] a) S. Lin, P. Boudjouk, *J. Chin. Chem. Soc. (Taipei)* **1989**, *36*, 35; b) C. Sui-Seng, G. D. Enright, D. Zargarian, *Organometallics* **2004**, *23*, 1236.

[43] Recent examples: a) C. Amatore, A. A. Bahsoun, A. Jutand, L. Mensah, G. Meyer, L. Ricard, *Organometallics* **2005**, *24*, 1569; b) G. Malaise, S. Ramdeehul, J. A. Osborn, L. Barloy, N. Kyritsakas, R. Graff, *Eur. J. Inorg. Chem.* **2004**, 3987; c) P. B. Armstrong, L. M. Bennett, R. N. Ryan, J. L. Fields, J. P. Jasinski, R. J. Staples, R. C. Bunt, *Tetrahedron Lett.* **2005**, *46*, 1441.

[44] a) P. S. Pregosin, R. Salzmann, *Coord. Chem. Rev.* **1996**, *155*, 35; b) P. von Matt, G. C. Lloyd-Jones, A. B. E. Minidis, A. Pfaltz, L. Macko, M. Neuburger, M. Zehnder, H. Rüegger, P. S. Pregosin, *Helv. Chim. Acta* **1995**, *78*, 265; c) P. Barbaro, P. S. Pregosin, R. Salzmann, A. Albinatti, R. Kunz, *Organometallics* **1995**, *14*, 5160.

[45] a) J. M. Brown, J. E. MacIntyre, *J. Chem. Soc., Perkin Trans. 2* **1985**, 961; b) H. Kurosawa, *J. Chem. Soc., Dalton Trans.* **1979**, 939.

[46] Asymmetric catalytic allylation with platinum: a) A. J. Blacker, M. L. Clarke, M. S. Loft, M. F. Mahon, M. E. Humphries, J. M. J. Williams, *Chem. Eur. J.* **2000**, *6*, 353; b) A. J. Blacker, M. L. Clark, J. M. J. Williams, M. S. Loft, *Chem. Commun.* **1999**, 913.

[47] R. Lespieau, R. L. Wakeman, *Bull. Soc. Chim. Fr.* **1932**, *51*, 384.

[48] The Karstedt catalyst solution is used industrially and is commercially available.

[49] a) M. F. Lappert, F. P. A. Scott, *J. Organomet. Chem.* **1995**, *492*, C11; b) P. B. Hitchcock, M. F. Lappert, N. J. W. Warhurst, *Angew. Chem.* **1991**, *103*, 439; *Angew. Chem. Int. Ed. Engl.* **1991**, *30*, 438; c) B. D. Karstedt, U. S. Patent 3775452, **1973**.

[50] L. N. Lewis, T. A. Krafft, J. C. Huffman, *Inorg. Chem.* **1992**, *31*, 3555.

[51] A. Albinati, W. R. Caseri, P. S. Pregosin, *Organometallics* **1987**, *6*, 788.

[52] L. Brammer, D. Zhao, F. T. Ladipo, J. Braddock-Wilking, *Acta Crystallogr. Sect. B* **1995**, *51*, 632.

[53] K. Hallman, A. Frölander, T. Wondimagegn, M. Svensson, C. Moberg, *PNAS* **2004**, *101*, 5400.

[54] a) P–Pt–F *trans* complexes: A. Yahav, I. Goldberg, A. Vigalok, *J. Am. Chem. Soc.* **2003**, *125*, 13634; b) P–Pt–F *cis* complexes: A. Yahav, I. Goldberg, A. Vigalok, *Inorg. Chem.* **2005**, *44*, 1547.

[55] U. Burckhardt, PhD Dissertation, ETH Nr. 12167, Zürich, **1997**.

[56] L. Hintermann, A. Togni, result presented at the *XVIII$^{th}$ International Conference on Organometallic Chemistry*, Munich, **1998**.

[57] R. Schwesinger, R. Link, G. Thiele, H. Rotter, D. Honert, H. H. Limbach, F. Männle, *Angew. Chem.* **1991**, *103*, 1376; *Angew. Chem. Int. Ed.* **1991**, *30*, 1372.

[58] W. E. Barnette, *J. Am. Chem. Soc.* **1984**, *106*, 452.

[59] Diene **26** was identified by comparison with a reference sample, see Exp. Section.

[60] The decomposition of phosphane complexes of $Pd^{II}$ induced by fluoride is known: P. A. McLaughlin, J. G. Verkade, *Organometallics* **1998**, *17*, 5937.

[61] V. V. Grushin, *Angew. Chem.* **1998**, *110*, 1042; *Angew. Chem. Int. Ed.* **1998**, *37*, 994.

[62] We exclude a high kinetic barrier in allylic substitutions by using a small and reactive nucleophile-like "naked" fluoride.

[63] G. C. Lloyd-Jones, S. C. Stephen, M. Murray, C. P. Butts, S. Vyskocil, P. Kocovsky, *Chem. Eur. J.* **2000**, *6*, 4348.

[64] H. Hagelin, B. Åkermark, P. Norrby, *Chem. Eur. J.* **1999**, *5*, 902.

[65] L. Hintermann, PhD Dissertation, ETH Nr. 13892, Zürich, **2000**.

 © 2006 Wiley-VCH Verlag GmbH & Co. KGaA, Weinheim 

[66] M. F. Rettig, P. M. Maitlis, *Inorg. Synth.* **1990**, *28*, 110.
[67] J. Lukas, *Inorg. Synth.* **1974**, *15*, 75.
[68] D. J. Mabbott, B. E. Mann, P. M. Maitlis, *J. Chem. Soc., Dalton Trans.* **1977**, 294.
[69] G. M. Sheldrick, *SHELXS-97 Program for the Solution of Crystal Structures*, University of Göttingen, **1990**.
[70] G. M. Sheldrick, *SHELXL-97 Program for the Refinement of Crystal Structures*, University of Göttingen, **1997**.
[71] G. M. Sheldrick, *SADABS Program for Empirical Absorption Correction of Area Detector Data*, University of Göttingen, **1996**.

Received: September 8, 2005
Published Online: February 9, 2006

 © 2006 Wiley-VCH Verlag GmbH & Co. KGaA, Weinheim 

DOI: 10.1002/ejic.200500811

# A Single-Source-Precursor Approach to Late Transition Metal Molybdate Materials: The Structural Role of Chelating Ligands in the Formation of Heterometallic Heteroleptic Alkoxide Complexes

**Pia Werndrup,[a] Gulaim A. Seisenbaeva,[a] Gunnar Westin,[b] Ingmar Persson,[a] and Vadim G. Kessler*[a]**

**Keywords:** Cobalt molybdate / EXAFS / Heterogeneous catalysis / Materials / Nickel molybdate / Sol–gel processes

The synthesis and structural determination of three new heterometallic molybdenum complexes, one with cobalt and two with nickel and two of these with β-diketonate ligands and one with amino alcohol ligands, are presented. The reaction of cobalt acetylacetonate with $[MoO(OMe)_4]$ provides $[Co_2Mo_2O_2(acac)_2(OMe)_{10}]$ (**1**) and $[MoO(acac)(OMe)_3]$ (**4**), and the reaction of nickel acetylacetonate with $[MoO(OMe)_4]$ provides $[Ni_2Mo_2O_2(acac)_2(OMe)_{10}]$ (**2**) and **4**. The reaction of $[Ni(OR^N)_2]$ ($R^N$ = $CHMeCH_2NMe_2$) with $[MoO(OMe)_4]$ yields $[Ni_2Mo_2O_2(OR^N)_2(OMe)_{10}]$ (**3**). The two new oxomolybdenum complexes undergo ether elimination upon storage to give the corresponding dioxo complexes $[MoO_2(acac)(OMe)]_2$ (**5**) and $[MoO_2(OR^N)(OMe)]_2$ (**6**). Compounds **3** and **4** could also be obtained from the reaction of stoichiometric amounts of Hacac with $[MoO(OMe)_4]$ and $[MoO_2(OMe)_2]$, respectively. The local structure around the nickel atom in compound **2** in solution and compound **3** in the solid state and in toluene/hexane solution has been determined by means of EXAFS spectroscopy. The complexes are intended to be used as single-source precursors, which are attractive in coatings and for the preparation of mesoporous materials; its application for the synthesis of nickel molybdate by sol–gel processing is therefore reported. The oxide material obtained from **3** displays a uniform grain size and a large surface area. (© Wiley-VCH Verlag GmbH & Co. KGaA, 69451 Weinheim, Germany, 2006)

## Introduction

The development of low-temperature routes to late transition metal molybdates with small grain size and a high active surface is today one of the most intensively explored fields in materials science related to heterogeneous catalysis. Cobalt and nickel molybdates have been reported to be efficient catalysts in such reactions as oxidative dehydrogenation of alkanes[1] and disproportionation of carbon monoxide with formation of single-walled carbon nanotubes.[2] Nitridation and sulfidation of the initially prepared oxide materials has provided efficient catalysts for higher productivity ammonia synthesis[3] and hydrodesulfurisation reactions,[4] respectively. A great deal of attention has been paid to the properties of the final catalyst in relation to the preparation conditions, especially the pH during the synthesis in aqueous media,[5] and also to the effects of different chemical impurities, both in the original material and introduced by reactants, on the activity and stability of the catalysts.[6] Cobalt and nickel molybdates are usually applied as coatings on different supports, most commonly alumina ($\gamma$-$Al_2O_3$)[6] or activated carbon.[7] Application of these catalysts deposited on niobia for hydrodesulfurisation applications and comparison of the influence of different oxide substrates has been reported.[8] A common approach to late transition metal molybdates is a high-temperature decomposition of a salt mixture, such as $Co(NO_3)_2{\cdot}6H_2O$ and $(NH_4)_6Mo_7O_{24}$, leading to the formation of a molybdate powder.[7,9] Great efforts have been made to enhance homogenisation of the components in the course of preparation of these materials by using approaches such as freeze-drying,[10] impregnation of porous supports by water solutions of salts stabilized by chelating ligands, such as, for example, nitrilotriacetates[11] or ethylenediamine in combination with hydrothermal treatment,[12] and electrodeposition in sulfate-citrate medium.[13] Very recently, a special focus in this research field has been the development of sol–gel approaches to this class of materials, applying silica[14] or non-ionic[15] or block-copolymer zwitterionic surfactants[16,17] to ensure the chemical homogeneity and development of desired morphological features. It would be advantageous to be able to deposit a $M^{II}MoO_4$ phase selectively on substrates from solutions. Single-source precursors have been very successfully used in coatings and the preparation of mesoporous materials. It is very simple, once the precursor has beens prepared, to use sol–gel techniques for spin- or dip-coating of surfaces or to hydrolyse and condense the precursors in

[a] Department of Chemistry, SLU,
P. O. Box 7015, 750 07 Uppsala, Sweden
E-mail: Vadim.Kessler@kemi.slu.se
[b] Department of Materials Chemistry, Ångström Laboratory, Uppsala University,
Box 538, 75121 Uppsala, Sweden
Supporting information for this article is available on the WWW under http://www.eurjic.org or from the author.

 © 2006 Wiley-VCH Verlag GmbH & Co. KGaA, Weinheim 

the solution in order to make a gel, which will become a mesoporous powder after calcination, often at a lower temperature than that used in solid-state reactions.[18] This mesoporous coating will be formed on a chosen substrate, which represents an additional advantage for this procedure.

Heterometallic alkoxide complexes of late and heavy transition metals are of interest as single-source precursors for catalytically active materials. The synthetic approaches to heterometallic compounds are restricted, however, because alkoxides of late transition metals are insoluble and unreactive. A promising pathway to heterometallic complexes is provided by the reaction between a metal alkoxide and a β-diketonate complex of another metal atom. This approach has been pioneered by Mosset et al., who observed formation of cobalt-zirconium[19] and iron-zirconium[20] alkoxide complexes in minor yields in alcoholic media. We have previously[21,22] investigated in detail the interaction of divalent metal β-diketonate complexes and tantalum or niobium alkoxides. The main products of this reaction − a new class of heterometallic heteroleptic alkoxide complexes $[M^{II}_2M^{V}_2(acac)_2(OR)_{12}]$ ($M^{II}$ = Co, Ni, Zn, Mg, R = Me, Et, and $M^{V}$ = Ta, Nb) − are formed quantitatively in hydrocarbon solvents according to Equation (1).

$$[M^{II}(acac)_2] + 2[M^{V}(OR)_5] \rightarrow \tfrac{1}{2}[M^{II}_2M^{V}_2(acac)_2(OR)_{12}] + [M^{V}(acac)(OR)_4 \quad (1)$$

If the late transition metal complex contains a different chelating ligand, the reaction with an alkoxide can provide heterometallic heteroleptic alkoxide complexes with different solubility and reactivity than the homoleptic alkoxide. This will alter the hydrolytic properties and provide a tool to control the sol–gel preparation of materials for catalysis. We present here the synthesis, structure determination and sol–gel processing of three new heterometallic molybdenum complexes, one with cobalt and two with nickel, and two of these with β-diketonate ligands and one with amino alcohol ligands.

## Results and Discussion

### Synthesis of Precursor Compounds

In order to develop the concept of molecular structure design for a synthetic approach to single-source precursors suitable for production of inorganic materials[23] we wanted to use the synthetic strategy formulated with the syntheses of the heterometallic heteroleptic complexes $[M^{II}_2M^{V}_2(acac)_2(OMe)_{12}]$ ($M^{II}$ = Co, Ni, Zn, Mg, and $M^{V}$ = Ta, Nb).[21] These reactions use the β-diketonate metal complexes to provide stability in the solution (due to the chelating effects of the β-diketonate ligands) and the methoxide complexes as Lewis bases. The complexes are formed when the initial $M^{II}/M^{V}$ ratio is lower than 1:2; we tested ratios between 1:2.1 and 1:3.5 and the syntheses were successful. Extending the synthetic strategy to molybdenum and late transition metal complexes, we used cobalt acetylacetonate in the reaction with molybdenum oxomethoxide $[MoO(OMe)_4]$. The reaction was successful and provided $[Co_2Mo_2O_2(acac)_2(OMe)_{10}]$ (**1**) [Figure 1 and Equation (2)] in high yields at Co/Mo ratios less than or equal to 1:2.

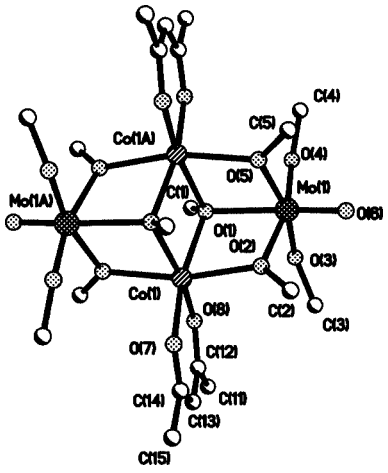


Figure 1. Molecular structure of $[Co_2Mo_2O_2(acac)_2(OMe)_{10}]$ (**1**).

$$[Co(acac)_2] + 2[MoO(OMe)_4] \rightarrow \tfrac{1}{2}[Co_2Mo_2O_2(acac)_2(OMe)_{10}]\ (\mathbf{1}) + [MoO(acac)(OMe)_3]\ (\mathbf{4}) \quad (2)$$

The use of nickel acetylacetonate in hexane instead of cobalt acetylacetonate in the reaction with $[MoO(OMe)_4]$ provided $[Ni_2Mo_2O_2(acac)_2(OMe)_{10}]$ (**2**). The compositions of the reaction products indicate the same reaction pathway [Equation (2)] for both nickel and cobalt acac derivatives, analogous to the one observed earlier for the formation of bimetallic complexes of niobium and tantalum[21,22] [Equation (1)]. Both new cobalt-molybdenum and nickel-molybdenum complexes have much lower solubility in toluene than the corresponding tantalum or niobium ones. In order to improve this low solubility we altered the reaction pathway [Equation (3)] by using an amino alcohol complex, in hexane, instead of the acetylacetonate one.

The use of $Ni(OR^N)_2$ ($R^N$ = $CHMeCH_2NMe_2$) in the reaction with $[MoO(OMe)_4]$ provided the nickel-molybdenum complex $[Ni_2Mo_2O_2(OR^N)_2(OMe)_{10}]$ (**3**). A ligand-exchange reaction occurs when $Ni(L)_2$ (L = acac or $OR^N$) and $[MoO(OMe)_4]$ react in hexane, which gives two new heterometallic heteroleptic alkoxide complexes (**2**, **3**) along with new molybdenum complexes containing the chelating ligand [Equation (3)]. The structure of the by-product com-

$$\begin{array}{l} Ni(L)_2 + 2\ MoO(OMe)_4 \rightarrow \tfrac{1}{2}\ Ni_2Mo_2O_2(L)_2(OMe)_{10}\ (L = acac\ \mathbf{2},\ OR^N\ \mathbf{3}) + MoO(L)(OMe)_3\ (L = acac\ \mathbf{4}) \\ \qquad\qquad\qquad\qquad\qquad\qquad\qquad\qquad \downarrow - Me_2O \\ \qquad\qquad\qquad\qquad\qquad\qquad\qquad\qquad \tfrac{1}{2}\ [MoO_2(L)(OMe)]_2\ (L = acac\ \mathbf{5},\ OR^N\ \mathbf{6}) \end{array} \quad (3)$$

 © 2006 Wiley-VCH Verlag GmbH & Co. KGaA, Weinheim 

plex containing the acac ligand [MoO(acac)$(OMe)_3$] (**4**) (Figure 2, A) was determined by a single-crystal X-ray study. The two new $M^{II}$-molybdenum complexes undergo ether elimination upon storage [Equation (3)] to give the corresponding dioxo complexes [$MoO_2$(acac)$(OMe)]_2$ (**5**) and [$MoO_2(OR^N)(OMe)]_2$ (**6**). The structures of **5** and **6** were also determined by single-crystal X-ray diffraction studies [Figures 2, B and C, respectively]. The presence of dimethyl ether was detected in both mother liquors by the GC-MS technique. Compound **4** was also successfully prepared by the reaction between [$MoO(OMe)_4$] and Hacac. Compound **5** is formed from **4** very slowly at room temperature. An attempt to accelerate this process by refluxing the solutions of **4** led to quick development of a reddish-brown colour associated with reduction of $Mo^{VI}$ to $Mo^{V}$. The mother liquor in this case contained the dimethyl acetal of formaldehyde [$CH_2(OMe)_2$], which is the organic by-product of this reduction reaction.[24] The same kind of reduction associated with ligand redistribution turned out to be major obstacle in the synthesis of **5**, and especially **6**, by the reaction of insoluble [$MoO_2(OMe)_2$] with acetylacetone or (dimethylamino)propanol. The white [$MoO_2(OMe)_2$] turns blue on refluxing with these reagents in toluene, while the solution becomes reddish brown. GC-MS indicated that the solution contained $CH_2(OMe)_2$ in both cases. Compound **5** was isolated in minor yield from the mother liquor by crystallisation, but the solution derived from molybdenum dioxomethoxide and (dimethylamino)propanol did not provide any isolable product.

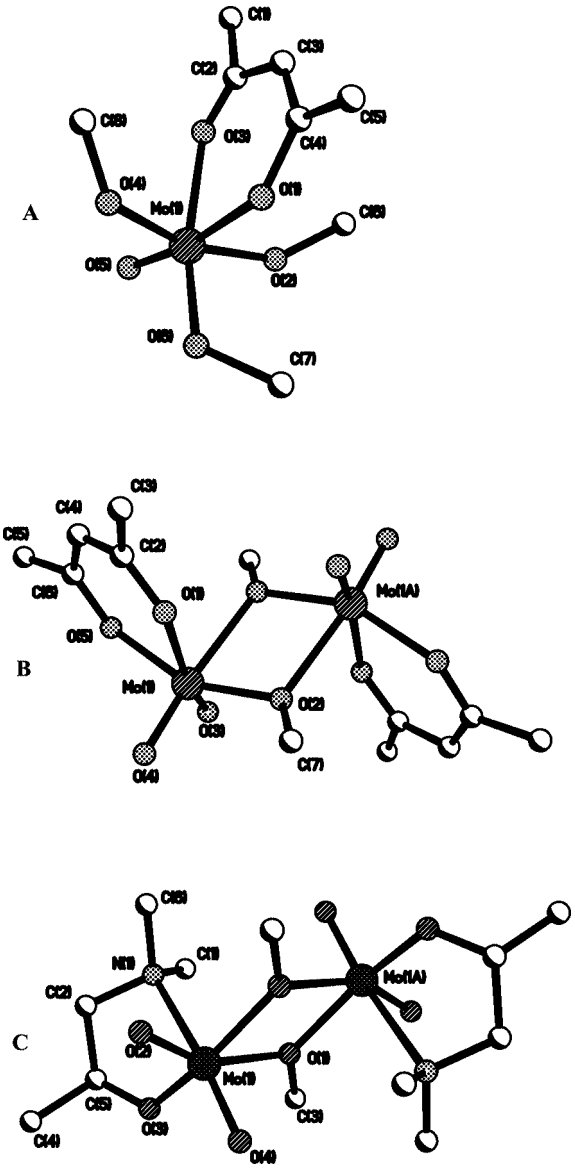


Figure 2. Molecular structure of [MoO(acac)$(OMe)_3$] (**4**; A), [$MoO_2$(acac)$(OMe)]_2$ (**5**; B) and [$MoO_2(OR^N)(OMe)]_2$ (**6**; C).

## Structure Determinations

The molecular structure of the cobalt-molybdenum complex **1** follows the well-known [$Ti_4(OMe)_{16}$] structural type.[25] The structure of **1** was determined by a single-crystal X-ray study (Figure 1 and Table 1). The octahedron surrounding the Co atoms is distorted because of the two types of oxygen atoms from the μ- and $\mu_3$-OR groups in the complex; the *trans* O–Co–O angles are 165.74(14)–166.81(14)°. The acac ring does not distort the octahedron − the O–Co–O angle in the ring is 90.61(16)°. The Co–O distances in **1** are 2.019(4)–2.135(3) Å, depending on the bonding mode of the oxygen atoms. The ionic radii of the cobalt(II) (high spin) and nickel ions in octahedral configuration are 0.745 and 0.690 Å, respectively,[26] and, along with the radius of the water-oxygen-bound di- and trivalent metal ion (1.34 Å),[27] this gives expected Co–O and Ni–O bond lengths of 2.09 Å and 2.03 Å, respectively. The shortest Co–O distances in **1** are to the oxygen atoms in the acac ring (both terminal and chelating) and the longest ones are for the $\mu_3$-oxygens in the complex. In **1**, the Co···C distances in the acac ring are calculated to be 2.995(5) and 2.996(5) Å for the two carbon atoms connected to an oxygen atom in the acac ring, and 3.281(5) Å for the one in the centre of the ring. The molybdenum atom has a distorted octahedral coordination environment with six oxygen atoms. None of the *trans* O–Mo–O angles have ideal 180° angles; they vary between 162.00(17) ° and 165.67(16)°. It is the angle between the two Mo-μ-O bonds that distorts the octahedron the most; it is only 85.59(15)°. The Mo–O bonds for the two terminal methoxide groups [1.857(4) and 1.834(4) Å] are in agreement with the corresponding bonds in complexes such as [$Mo(OMe)_6$][28] and [$Mo_2O_2(OMe)_8$],[29] and very close to those in [$Mg_2Mo_2O_2(OMe)_{10}(MeOH)_4$],[30] a close structural analogue of **1**, where they vary between 1.862(4) and 1.909(4) Å. The two Mo–μ-O bonds are longer [1.998(3) and 1.998(4) Å, respectively] and the Mo–$\mu_3$-O bond is even longer [2.187(3) Å] as this kind of bonding, with an atom shared with one or two other atoms, normally results in a significant increase of bond lengths. The Mo=O bond also causes a deviation from a perfect octahedron. The length of the double bond [1.683(4) Å] is in agreement with the length of the same kind of bond in [$MoO(OMe)_4$] [1.672(5) Å].[29] It is interesting to note that **1** is only the

 © 2006 Wiley-VCH Verlag GmbH & Co. KGaA, Weinheim 

second cobalt-molybdenum alkoxide complex reported in the literature after [{$Mo_2$(DAniF)$_3$}$_2$Co(OMe)$_4$] (DAniF = *N*,*N*′-di-*p*-anisylformamidinate).[31,32]

Table 1. Selected bond lengths [Å] and angles [°] for [$Co_2Mo_2O_2$(acac)$_2$(OMe)$_8$] (**1**).[a]

| | |
|---|---|
| Mo(1)–O(6) | 1.683(4) |
| Mo(1)–O(4) | 1.834(4) |
| Mo(1)–O(3) | 1.857(4) |
| Mo(1)–O(2) | 1.988(3) |
| Mo(1)–O(5) | 1.998(4) |
| Mo(1)–O(1) | 2.187(3) |
| Co(1)–O(8) | 2.019(4) |
| Co(1)–O(7) | 2.026(3) |
| Co(1)–O(2) | 2.123(4) |
| Co(1)–O(5)#1 | 2.126(4) |
| Co(1)–O(1)#1 | 2.130(4) |
| Co(1)–O(1) | 2.135(3) |
| O(6)–Mo(1)–O(4) | 103.5(2) |
| O(6)–Mo(1)–O(3) | 100.8(2) |
| O(4)–Mo(1)–O(3) | 92.35(18) |
| O(6)–Mo(1)–O(2) | 91.44(18) |
| O(4)–Mo(1)–O(2) | 164.69(16) |
| O(3)–Mo(1)–O(2) | 88.00(16) |
| O(6)–Mo(1)–O(5) | 92.15(19) |
| O(4)–Mo(1)–O(5) | 90.50(17) |
| O(3)–Mo(1)–O(5) | 165.67(16) |
| O(2)–Mo(1)–O(5) | 85.59(15) |
| O(6)–Mo(1)–O(1) | 162.00(17) |
| O(4)–Mo(1)–O(1) | 89.68(15) |
| O(3)–Mo(1)–O(1) | 90.65(15) |
| O(2)–Mo(1)–O(1) | 75.00(12) |
| O(5)–Mo(1)–O(1) | 75.31(14) |
| O(8)–Co(1)–O(7) | 90.61(16) |
| O(8)–Co(1)–O(2) | 97.57(15) |
| O(7)–Co(1)–O(2) | 93.49(14) |
| O(8)–Co(1)–O(5)#1 | 93.26(16) |
| O(7)–Co(1)–O(5)#1 | 94.83(15) |
| O(2)–Co(1)–O(5)#1 | 166.25(15) |
| O(8)–Co(1)–O(1)#1 | 165.74(14) |
| O(7)–Co(1)–O(1)#1 | 96.71(14) |
| O(2)–Co(1)–O(1)#1 | 94.19(14) |
| O(5)#1–Co(1)–O(1)#1 | 73.99(14) |
| O(8)–Co(1)–O(1) | 93.18(14) |
| O(7)–Co(1)–O(1) | 166.81(14) |
| O(2)–Co(1)–O(1) | 73.49(12) |
| O(5)#1–Co(1)–O(1) | 97.56(13) |
| O(1)#1–Co(1)–O(1) | 82.44(13) |

[a] Symmetry transformations used to generate equivalent atoms: #1 –*x*, – *y* + 1, –*z* + 2.

The acac ring in compound **4** (part A in Figure 2 and Table 2) distorts the octahedral surrounding of the Mo atom along with the other four oxygens surrounding the Mo atom. The O–Mo–O angle in the acac ring is 80.5(2)° and influences the other O–Mo–O angles such that all four of the O=Mo–O angles are larger than 90° [they vary between 92.0(6)° and 100.6(3)°]. The *trans* O–Mo–O angles are in the range 162.29(19)–171.1(6)°. The Mo–O bond length for the three terminal methoxide groups is 1.846(15)–1.861(4) Å, in agreement with the lengths of the same kind of bonds in [Mo(OMe)$_6$]. The Mo=O bond is also the shortest one in **4** [1.683(14) Å], and the Mo–O bonds to the oxygen in the acac ring are 2.080(10)–2.182(10) Å.

After ether elimination from the two new $M^{II}$-molybdenum complexes [Equation (3)] two new dioxo complexes

Table 2. Selected bond lengths [Å] and angles [°] for [MoO(OMe)$_3$(acac)] (**4**).

| | |
|---|---|
| Mo(1)–O(5) | 1.683(14) |
| Mo(1)–O(6) | 1.846(15) |
| Mo(1)–O(4) | 1.855(4) |
| Mo(1)–O(2) | 1.861(4) |
| Mo(1)–O(1) | 2.080(12) |
| Mo(1)–O(3) | 2.182(10) |
| O(5)–Mo(1)–O(6) | 100.6(3) |
| O(5)–Mo(1)–O(4) | 96.5(7) |
| O(6)–Mo(1)–O(4) | 96.5(6) |
| O(5)–Mo(1)–O(2) | 96.1(7) |
| O(6)–Mo(1)–O(2) | 93.3(6) |
| O(4)–Mo(1)–O(2) | 162.29(19) |
| O(5)–Mo(1)–O(1) | 171.1(6) |
| O(6)–Mo(1)–O(1) | 87.4(5) |
| O(4)–Mo(1)–O(1) | 78.6(5) |
| O(2)–Mo(1)–O(1) | 87.1(5) |
| O(5)–Mo(1)–O(3) | 92.0(6) |
| O(6)–Mo(1)–O(3) | 166.3(5) |
| O(4)–Mo(1)–O(3) | 87.3(5) |
| O(2)–Mo(1)–O(3) | 79.9(4) |
| O(1)–Mo(1)–O(3) | 80.5(2) |

were isolated. The structures of these complexes – [$MoO_2$(acac)(OMe)]$_2$ (**5**) and [$MoO_2$($OR^N$)(OMe)]$_2$ (**6**) – were determined by single-crystal X-ray diffraction studies (Figures 2, B and C, respectively). The molybdenum atoms all have distorted octahedral surroundings in these two complexes. In **5**, the octahedron contains only oxygen atoms, with *trans* O–Mo–O angles in the range 155.02(12)–163.83(15)° (Table 3). The acac ring distorts the octahedron to give an O–Mo–O angle of 80.02(12)°. The Mo–O bonds in the ring are 2.004(3) and 2.166(3) Å, respectively, in good agreement with the same kind of bond in **4**. As with all Mo=O bonds discussed previously, they are the shortest Mo–O bonds in this complex [1.696(3) and 1.697(3) Å, respectively]. In **6**, the octahedron surrounding the Mo atom is composed of five oxygen atoms and one nitrogen atom. The ring distorts the octahedron such that the *trans* N–Mo–O(4) angle is 167.4(3)° and the two *trans* O–Mo–O angles are 153.2(2)° and 155.1(3)° (Table 4). The N–Mo–O(3) angle in the ring is 72.4(2)° and the (μ-O)–Mo–(μ-O) angle is 67.4(2)°. The Mo=O bonds are also the shortest Mo–O ones in **6**, at 1.688(6) and 1.690(6) Å, respectively, and the longest are the Mo–(μ-O) bonds [2.053(6) and 2.175(5) Å]; the Mo–N bond is 2.485(7) Å. The bonding within the aminoalkoxide ring is considerably different from that in the known complexes of $Mo^{VI}$ with triethanolamine, where the presence of several fused chelating cycles results in considerably shortened Mo–N distance, such as 2.342(6) Å in, for example, [$HMoO_2(OC_2H_4)_3N$].[33]

Single crystals of the heterometallic complexes [$Ni_2Mo_2O_2(L)_2(OMe)_{10}$] (**2** and **3**), large enough for single-crystal X-ray studies, have not yet been isolated. The cobalt and nickel atoms are of similar size, and therefore occupy approximately the same volume in a molecule, with nickel being the smaller one (see above). Cobalt atoms have a higher preference to ideal octahedral angles in the inner sphere than nickel. On the other hand, the distortion of the inner sphere of a nickel atom can be severe, and the O–Ni–

 © 2006 Wiley-VCH Verlag GmbH & Co. KGaA, Weinheim 

Table 3. Selected bond lengths [Å] and angles [°] for $[MoO_2(acac)(OMe)]_2$ (**5**).[a]

| | |
|---|---|
| Mo(1)–O(3) | 1.696(3) |
| Mo(1)–O(4) | 1.697(3) |
| Mo(1)–O(2) | 1.991(3) |
| Mo(1)–O(5) | 2.004(3) |
| Mo(1)–O(1) | 2.166(3) |
| Mo(1)–O(2)#1 | 2.264(3) |
| O(3)–Mo(1)–O(4) | 104.19(18) |
| O(3)–Mo(1)–O(2) | 100.58(15) |
| O(4)–Mo(1)–O(2) | 95.15(15) |
| O(3)–Mo(1)–O(5) | 91.48(15) |
| O(4)–Mo(1)–O(5) | 103.05(16) |
| O(2)–Mo(1)–O(5) | 155.02(12) |
| O(3)–Mo(1)–O(1) | 163.83(15) |
| O(4)–Mo(1)–O(1) | 91.18(16) |
| O(2)–Mo(1)–O(1) | 82.67(12) |
| O(5)–Mo(1)–O(1) | 80.02(12) |
| O(3)–Mo(1)–O(2)#1 | 88.71(14) |
| O(4)–Mo(1)–O(2)#1 | 163.06(14) |
| O(2)–Mo(1)–O(2)#1 | 71.37(13) |
| O(5)–Mo(1)–O(2)#1 | 87.27(12) |
| O(1)–Mo(1)–O(2)#1 | 77.25(12) |

[a] Symmetry transformations used to generate equivalent atoms: #1 $-x, -y + 1, -z$.

Table 4. Selected bond lengths [Å] and angles [°] for $[MoO_2(OR^N)OMe]_2$ (**6**).[a]

| | |
|---|---|
| Mo(1)–O(4) | 1.688(6) |
| Mo(1)–O(2) | 1.690(6) |
| Mo(1)–O(3) | 1.895(6) |
| Mo(1)–O(1)#1 | 2.053(6) |
| Mo(1)–O(1) | 2.175(5) |
| Mo(1)–N(1) | 2.485(7) |
| O(4)–Mo(1)–O(2) | 104.6(3) |
| O(4)–Mo(1)–O(3) | 96.3(3) |
| O(2)–Mo(1)–O(3) | 103.6(3) |
| O(4)–Mo(1)–O(1)#1 | 101.5(3) |
| O(2)–Mo(1)–O(1)#1 | 91.1(3) |
| O(3)–Mo(1)–O(1)#1 | 153.2(2) |
| O(4)–Mo(1)–O(1) | 92.4(3) |
| O(2)–Mo(1)–O(1) | 155.1(3) |
| O(3)–Mo(1)–O(1) | 92.2(2) |
| O(1)#1–Mo(1)–O(1) | 67.4(2) |
| O(4)–Mo(1)–N(1) | 167.4(3) |
| O(2)–Mo(1)–N(1) | 83.8(3) |
| O(3)–Mo(1)–N(1) | 72.4(2) |
| O(1)#1–Mo(1)–N(1) | 87.5(2) |
| O(1)–Mo(1)–N(1) | 82.9(2) |

[a] Symmetry transformations used to generate equivalent atoms: #1 $-x, -y, -z + 1$.

O angles are shifted instead of differentiating the Ni–O bond lengths in the octahedron. Despite this difference in inner-sphere flexibility, we propose the structure of **1** as a model for the description of the nickel-molybdenum complexes **2** and **3**.

A powder of the acac complex **2** was studied by Ni-EXAFS (part A in Figure 3 and Table 5), which gave a mean Ni–O distance of 2.024(2) Å (Figure 4, A). This distance is significantly shorter than the same kind of distances in the model, obtained from the X-ray single-crystal experiment, of the cobalt analogue **1** with a range of 2.123(4)–2.135(3) Å for the Co–(μ-O) and Co–($\mu_3$-O) distances. No Ni···C distances could be determined from the EXAFS experiment. The Ni···Ni distance in **2** is 3.150(11) Å and the Ni···Mo distance is 3.311(2) Å, both in agreement with the observed distances in **1** (3.208 Å for Co···Co and 3.348 Å for Co···Mo) taking into account the smaller ionic radius of nickel.

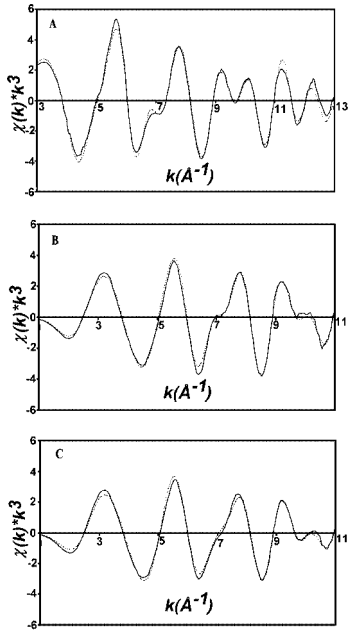


Figure 3. EXAFS spectra of $[Ni_2Mo_2O_2(acac)_2(OMe)_{10}]$ (**2** as a powder; **A**) and $[Ni_2Mo_2O_2(OR^N)_2(OMe)_{10}]$ [**3** as a powder (**B**) and in solution (C)]. Solid lines represent experimental data and dotted lines calculated data.

Table 5. EXAFS model parameters[a] for **2** (in solution) and **3** (powder and in solution).

| Interaction | *N* | *d* [Å] | $\sigma^2$ [Å$^2$] | $E_o$ [eV] | $S_o^2$ |
|---|---|---|---|---|---|
| **2** solution | | | | | |
| Ni–O | 6 | 2.024(2) | 0.0076(2) | 8330.0(3) | 0.83(2) |
| Ni···Ni | 1 | 3.150(11) | 0.015(2) | | |
| Ni···Mo | | 2 | 3.311(2) | 0.0060(1) | |
| **3** powder | | | | | |
| Ni–O | 5 | 2.058(2) | 0.0065(3) | 8329.9(3) | 0.86(3) |
| Ni–N | 1 | 2.336(13) | 0.0088(15) | | |
| Ni···Ni | 1 | 3.144(2) | 0.0040(2) | | |
| Ni···Mo | 2 | 3.297(2) | 0.027(4) | | |
| **3** solution | | | | | |
| Ni–O | 5 | 2.033(3) | 0.0073(6) | 8327.7(4) | 0.69(2) |
| Ni–N | 1 | 2.133(9) | 0.0010(6) | | |
| Ni···Ni | 1 | 3.127(2) | 0.0036(2) | | |
| Ni···Mo | 2 | 3.120(21) | 0.029(4) | | |

[a] The parameters are the number of interactions (*N*), bond length (*d*), Debye–Waller factor ($\sigma^2$), threshold energy ($E_0$) and amplitude reduction factor ($S_0^2$).

A powder and a toluene/hexane solution of **3** were also studied by Ni-EXAFS (B and C in Figures 3 and Table 5). The heterometallic complex is preserved in solution, as can be seen by the similarity of the EXAFS curves. Fourier transforms of the EXAFS curves (Figures 4, B and C) provide similar Ni–O distances in the powder and in solution [2.058(2) Å and 2.033(3) Å, respectively]. The Ni–N bond

 © 2006 Wiley-VCH Verlag GmbH & Co. KGaA, Weinheim 

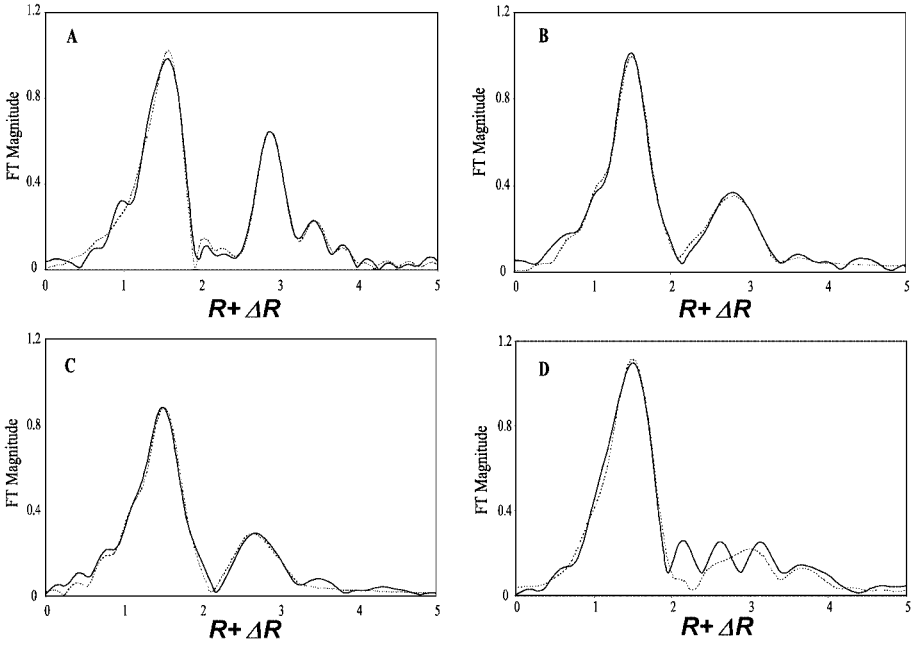


Figure 4. Fourier transforms of $[Ni_2Mo_2O_2(acac)_2(OMe)_{10}]$ (**2** as a powder; **A**), $[Ni_2Mo_2O_2(OR^N)_2(OMe)_{10}]$ [**3** as a powder (**B**) and in solution (**C**)] and $[Co_2Nb_2(acac)_2(OMe)_{12}]$ (powder; D). Solid lines represent experimental data and dotted lines calculated data.

in **3** was determined to be 2.336(13) Å for the powder and 2.133(9) Å for the solution, which is close to the Mo–N bond in **6**. Also for **3** the Ni···Ni distances were refined to 3.144(2) Å for the powder and 3.127(2) Å for the solution. The Ni···Mo distances were refined to 3.297(2) Å for the powder and 3.120(21) Å for the solution, which is in good agreement with the observed distances in **2** and the molecular structure of **1**.

Similarities in the results from the EXAFS experiment of complexes **2** and **3** indicate similarities in the molecular structures of these compounds, the nature of the chelating ligands being the only difference between them. The molecular structures of these heterometallic complexes are therefore analogous and follow the model found in the X-ray single-crystal study well. The Fourier transform of the EXAFS curve for the powder of $[Co_2Nb_2(acac)_2(OMe)_{12}]$ is included for comparison in Figure 4 (see part D).[21] This Co–Nb complex is also a tetranuclear molecule belonging to the $[Ti_4(OMe)_{16}]$ structural type, with Co–O distances of 2.096(11) Å for the four longest bonds and 1.963(14) Å for the two shortest ones, and with Co···Co and Co···Nb distances close to 3.30 Å.

## Sol–Gel Preparation

The sol–gel technique is a useful and attractive means of obtaining nanocomposite materials due to its easy handling

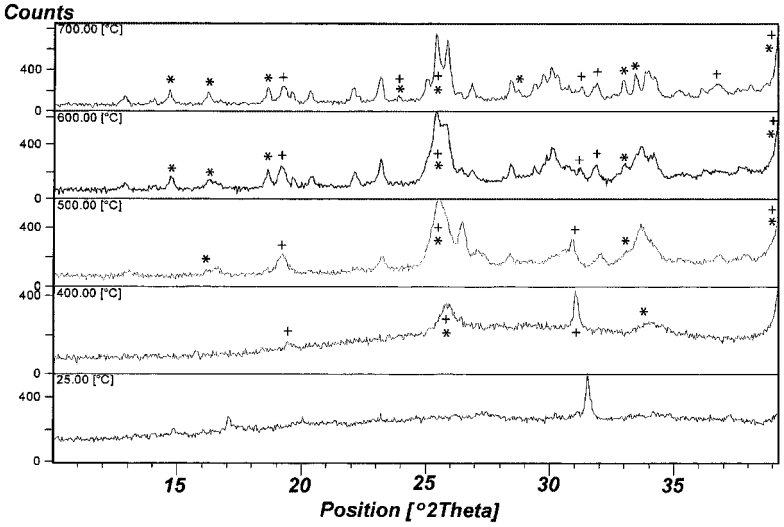


Figure 5. Powder X-ray diffraction of **3** at different temperatures. +: monoclinic (*P*2/*c*) $NiMoO_4$ [16-0291];[34] *: monoclinic (*I*2/*m*) $NiMoO_4$ [33-0948].[34]

 © 2006 Wiley-VCH Verlag GmbH & Co. KGaA, Weinheim 

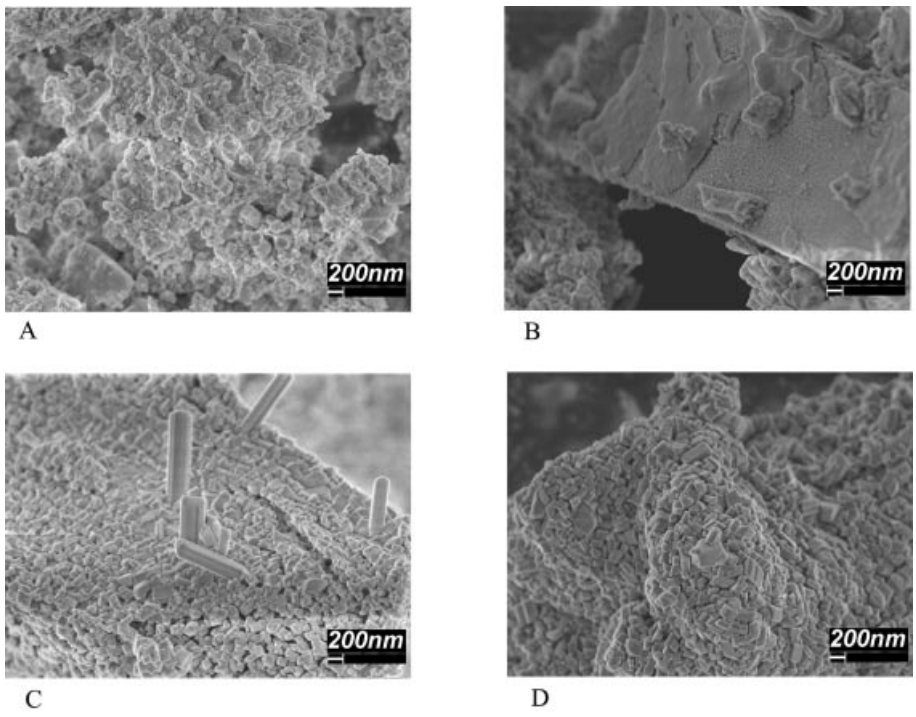


Figure 6. SEM images of the xerogel from **3** annealed at 300 °C (A), 400 °C (B), 500 °C (C) and 700 °C (D).

and low annealing temperatures. Complex **3** was used to obtain xerogel powders. The hydrolysed complex was checked by TGA to confirm the annealing temperatures used. At 315 °C the curve shows a sharp decrease in weight until 420 °C, and at 535 °C the decomposition ends, with only minor weight loss at higher temperatures. Powder X-ray diffraction of the xerogel shows the incipient crystallisation of $NiMoO_4$ [16-0291][34] at 400 °C (Figure 5). At 700 °C, the crystallisation of the monoclinic (*P*2/*c*) oxide $NiMoO_4$ is more pronounced and a monoclinic (*I*2/*m*) $NiMoO_4$ phase [33-0948][34] is seen as well. Scanning electron microscopy of the annealed xerogels confirmed the results from the powder X-ray diffraction analysis. At 300 °C, the gel is porous with a low degree of crystallinity; no sharp edges on the grains can be seen (Figure 6, A). Annealing at 400 °C started the crystallisation and the grains become larger but are still porous (Figure 6, B). The crystallisation process is well underway at 500 °C. The grains are uniform in size (75–100 nm) and well packed with a large surface area (Figure 6, C). Small rods of crystallised oxide can be seen. At 700 °C, the grains are even larger (175–250 nm; Figure 6, D), and rods of crystallised oxide with a diameter of 1 μm are uniformly spread over the sample. The grains have lost the porosity visible at 300 °C, and they are well packed with a large surface area, leaving the material well suited for catalysis experiments.

## Conclusions

The two chelating ligands used appear to play analogous structural roles leading, in both cases studied, to the formation of complexes belonging to the $[Ti_4(OMe)_{16}]$ structural type. The structure of the Co–Mo complex determined by X-ray single-crystal study has been used successfully as a prototype for different Ni–Mo structures studied by EXAFS spectroscopy. The preparation of oxide material from the new nickel-molybdenum amino alcohol complex was successful, with the materials annealed at 500 °C showing uniform grain size and a large surface area.

## Experimental Section

**Reagents and General Procedures:** All experimental procedures were carried out under a dry nitrogen atmosphere using Schlenk techniques or a dry box. $[Ni(OR^N)_2]$ ($R^N$ = $CHMeCH_2NMe_2$), $[MoO(OMe)_4]$ and $[MoO_2(OMe)_2]$ were prepared as described elsewhere.[29,35,36] $[Ni(acac)_2]$ and $[Co(acac)_2]$ (acac = acetylacetonate) (Aldrich, p.a.) were dried by vacuum sublimation.[21] Toluene (Merck, p.a.) and hexane (Merck, p.a.) were dried by distillation over $LiAlH_4$. The IR spectra of nujol mulls were recorded with a Perkin–Elmer FT-IR spectrometer 1720 X. $^1H$ NMR spectra were obtained for solutions in anhydrous $CDCl_3$ with a Bruker 400 MHz spectrometer. SEM was performed with a LEO 1550 high-resolution scanning electron microscope at an accelerating voltage of 20 kV. X-ray powder diffraction was performed with a Phillips SR5056 temperature-programmed diffractometer. Thermogravimetric analysis (TGA) was performed with a Setaram Setsystem 16/18 coupled to a TGA/DSC instrument. The GC-MS analysis was carried out with a JEOL JMS-SX/SX-102A mass spectrometer for fractions of mother liquors distilled in vacuo. The metal ratio in the samples was determined by the Arrhenius Laboratory, Stockholm University, Sweden, with a JEOL-820 scanning electron microscope (SEM) fitted with a Link AN-10000 energy dispersive spectrometer (EDS). The microanalysis data for C, H, N content were obtained at the Laboratory of Organic Analysis at the Moscow State University, Russia, and at MikroKemi AB, Sweden.

 © 2006 Wiley-VCH Verlag GmbH & Co. KGaA, Weinheim 

**Preparation of $[Co_2Mo_2O_2(acac)_2(OMe)_{10}]$ (1):** $[MoO(OMe)_4]$ (1.2477 g, 5.285 mmol) was dissolved in dry toluene (5 mL). $[Co(acac)_2]$ (0.6594 g, 2.567 mmol) was then added (molar ratio Co/Mo = 1:2.1) and the solution was refluxed for 30 min. The solution was cooled and purple crystals of $[Co_2Mo_2O_2(acac)_2(OMe)_{10}]$ (**1**) precipitated at 4 °C overnight. Yield: 1.53 g (1.80 mmol, 70%). $C_{20}H_{44}Co_2Mo_2O_{16}$ (850.29): calcd. C 28.3, H 5.2; found C 27.7, H 4.9. Co/Mo ≈ 1:1 by EDS. IR: $\tilde{\nu}$ = 2932 s cm$^{-1}$, 2857 s, 2726 s, 2672 sh, 2362 w, 2343 w, 2027 br, 1571 s, 1461 s, 1377 s, 1304 s, 1090 s, 970 w, 941 w, 891 w, 847 w, 768 sh, 627 s, 565 br.

**Preparation of $[Ni_2Mo_2O_2(acac)_2(OMe)_{10}]$ (2):** $[MoO(OMe)_4]$ (0.2276 g, 0.964 mmol) was dissolved in dry hexane (6 mL). $[Ni(acac)_2]$ (0.1238 g, 0.482 mmol) was then added (molar ratio Ni/Mo = 1:2) and the solution was refluxed for 30 min. After cooling, dry toluene (1 mL) was added and the solution was refluxed again for 15 min. Small greenish crystals of $[Ni_2Mo_2O_2(acac)_2(OMe)_{10}]$ (**2**) precipitated at 4 °C overnight. Yield: 0.246 g (0.289 mmol, 60%). $C_{20}H_{44}Mo_2Ni_2O_{16}$ (849.80): calcd. C 28.2, H 5.2; found C 27.8, H 5. In 100% metal content Ni = 52.7% and Mo = 47.3% by EDS. IR: $\tilde{\nu}$ = 2921 s cm$^{-1}$, 2726 s, 2672 w, 2363 w, 1576 s, 1518 s, 1456 s, 1376 s, 1307 sh, 1260 sh, 1196 sh, 1151 w, 1088 s, 1044 w, 1016 sh, 987 w, 934 w, 920 w, 897 w, 767 s, 627 s, 553 br. After several weeks at –30 °C crystals of $[MoO(acac)(OMe)_3]$ (**4**) and $[MoO_2(acac)(OMe)]_2$ (**5**) (identified by their single-crystal X-ray unit-cell parameters) were obtained in minor yields from the decanted solution.

**Isolation and Direct Synthesis of $[MoO(acac)(OMe)_3]$ (4) and $[MoO_2(acac)(OMe)]_2$ (5):** $[MoO(acac)(OMe)_3]$ (**4**) was obtained in a practically quantitative yield by addition of a stoichiometric amount of Hacac to $[MoO(OMe)_4]$. Thus, $[MoO(OMe)_4]$ (0.2168 g, 0.918 mmol) was dissolved in hexane (4 mL) at room temperature and Hacac (0.09 mL) was added with a syringe. The slightly brownish-yellow solution was evaporated in vacuo and the brownish-yellow powder obtained was identified as **4** by microanalysis and spectroscopic data (quantitative yields). $C_8H_{16}MoO_6$ (304.15): calcd. C 31.6, H 5.3; found C 30.7, H 5.5. IR: $\tilde{\nu}$ = 1595 br cm$^{-1}$, 1521 s, 1461 s, 1377 s, 1307 w, 1271 s, 1090 s, 941 s, 817 w, 771 w, 656 w, 627 s, 567 br. $^1$H NMR ($CDCl_3$): $\delta$ = 5.75 (1 H, acac-C*H*), 4.71 {3 H, C$H_3$-[O(6)Me]}, 4.41 {6 H, C$H_3$-[O(2 and 4)Me]}, 2.11 [6 H, C$H_3$-(acac-Me)] ppm. $[MoO_2(acac)(OMe)]_2$ (**5**) was obtained in moderate yields (25–30%), although always contaminated with minor amounts of $[MoO_2(acac)_2]$, by treatment of $[MoO_2(OMe)_2]$ with sub-stoichiometric amounts of Hacac in hexane at reflux. In a typical procedure, $[MoO_2(OMe)_2]$ (0.8162 g, 4.3 mmol) was mixed with 5 mL of hexane and Hacac (0.21 mL, 2.1 mmol) and refluxed for 30 min. The light yellow mother liquor was separated by decantation and the solvents evaporated to dryness. The resulting yellowish residue was recrystallised from 1 mL of hexane. Yield: 0.1409 g (26% in relation to Hacac). $C_{12}H_{20}Mo_2O_{10}$ (516.16): calcd. C 27.9, H 3.9; found C 27.6, H 3.8. IR: $\tilde{\nu}$ = 1591 s cm$^{-1}$, 1527 s, 1461 s, 1377 s, 1305 w, 1275 s, 1091 s, 1031 m, 982 s, 931 s, 819 w, 769 sh, 628 s, 565 br. $^1$H NMR ($CDCl_3$): $\delta$ = 5.84 (1 H, acac-C*H*), 3.50 {3 H, C$H_3$-[O(6)Me]}, 2.14 [3 H, C$H_3$-(acac-Me)], 216 [3 H, C$H_3$-(acac-Me)] ppm.

Preparation of both **4** and **5** can also be carried out with toluene as solvent but provides only a few single crystals of these compounds, probably due to their much higher solubility in this solvent. The yields could be increased by subsequent recrystallisation from hexane, but application of the latter for the whole synthetic procedure appears more attractive.

**Preparation of $[Ni_2Mo_2O_2(OR^N)_2(OMe)_{10}]$ (3):** $[MoO(OMe)_4]$ (0.3815 g, 1.616 mmol) was dissolved in dry hexane (4 mL). $[Ni(OR^N)_2]$ (0.2828 g, 0.7963 mmol) was then added (molar ratio Ni/Mo = 1:2) and the solution was refluxed for 30 min. After cooling, dry toluene (1 mL) was added and the solution was refluxed again for 15 min. Small greenish crystals of $[Ni_2Mo_2O_2(OR^N)_2(OMe)_{10}]$ (**3**) precipitated at 4 °C overnight. Yield: 0.375 g (0.438 mmol, 55%). $C_{20}H_{54}Mo_2N_2Ni_2O_{14}$ (855.91): calcd. C 28.0, H 6.3, N 3.3; found C 29.1, H 6.4, N 3.5. In 100% metal content Ni = 55.2% and Mo = 44.8% by EDS. IR: $\tilde{\nu}$ = 3354 br cm$^{-1}$, 3191 sh, 2921 s, 2852 s, 2726 s, 1603 s, 1461 s, 1377 s, 1309 w, 1279 w, 1136 s, 1088 s, 1032 s, 942 s, 902 s, 860 s, 835 s, 722 s, 627 s, 595 s, 532 s, 509 w, 476 w. The decanted solution was stored at –30 °C for several weeks and $[MoO_2(OR^N)(OMe)]_2$ (**6**) precipitated (minor yield).

**X-ray Structure Determinations:** Data collection was performed using a Bruker SMART CCD 1 K diffractometer, at 295(2) K, with Mo-$K_\alpha$ radiation ($\lambda$ = 0.71073 Å; see Table 6 for details). The SAINT PLUS and the SHELXTL-NT program packages were used for data reduction and computations.[37] Empirical absorption correction was applied using the Bruker SADABS program package. The structures were solved by direct methods. The coordinates of the heavy atoms were taken from the initial solution and the non-hydrogen atoms were located in subsequent Fourier syntheses.

Table 6. Crystallographic data for **1**, **4**, **5** and **6**.

| | **1** | **4** | **5** | **6** |
|---|---|---|---|---|
| Identification code | como1m | mooacn1m | mooac1m | nimo220 |
| Empirical formula | $C_{20}H_{44}Co_2Mo_2O_{16}$ | $C_8H_{16}MoO_6$ | $C_{12}H_{20}Mo_2O_{10}$ | $C_{12}H_{30}Mo_2N_2O_8$ |
| Formula weight | 850.29 | 304.15 | 516.16 | 522.26 |
| Space group | $P\bar{1}$ | $P2_1$ | *Pbca* | $P2_1/n$ |
| *a* [Å] | 8.136(4) Å | 7.2455(19) | 8.109(3) | 7.152(4) |
| *b* [Å] | 10.596(6) Å | 12.124(3) | 13.392(5) | 12.154(7) |
| *c* [Å] | 10.951(6) Å | 7.3576(19) | 16.074(5) | 11.240(6) |
| *α* [°] | 112.390(9) | 90 | 90 | 90 |
| *β* [°] | 90.983(10) | 112.922(4) | 90 | 91.959(13) |
| *γ* [°] | 112.259(10) | 90 | 90 | 90 |
| Volume [Å$^3$] | 793.4(7) | 595.3(3) | 1745.6(10) | 976.5(9) |
| *Z* | 1 | 2 | 4 | 2 |
| $d_{calcd.}$ [Mg m$^{-3}$] | 1.780 | 1.697 | 1.964 | 1.776 |
| Absorption coeff. [mm$^{-1}$] | 1.865 | 1.108 | 1.484 | 1.322 |
| Reflections collected | 4070 | 2867 | 10211 | 1357 |
| Independent reflections | 2766 [*R*(int) = 0.0274] | 1922 [*R*(int) = 0.0278] | 2151 [*R*(int) = 0.1431] | 889 [*R*(int) = 0.0281] |
| Final *R* indices [$I > 2\sigma(I)$] | *R*1 = 0.0389, *wR*2 = 0.0816 | *R*1 = 0.0358, *wR*2 = 0.0735 | *R*1 = 0.0412, *wR*2 = 0.0883 | *R*1 = 0.0412, *wR*2 = 0.0983 |
| *R* indices (all data) | *R*1 = 0.0703, *wR*2 = 0.0861 | *R*1 = 0.0503, *wR*2 = 0.0762 | *R*1 = 0.0879, *wR*2 = 0.1021 | *R*1 = 0.0547, *wR*2 = 0.1030 |

 © 2006 Wiley-VCH Verlag GmbH & Co. KGaA, Weinheim 

The structures were refined by full-matrix least-squares techniques in an isotropic and then finally in an anisotropic approximation.

CCDC-283731 to -283734 (for **1**, **4**, **5** and **6**, respectively) contain the supplementary crystallographic data for this paper. These data can be obtained free of charge from The Cambridge Crystallographic Data Centre via www.ccdc.cam.ac.uk/data_request/cif.

**EXAFS Data Collection and Data Treatment:** Nickel and cobalt K-edge X-ray absorption spectra were recorded at the wiggler beam line 4-1 at the Stanford Synchrotron Radiation Laboratory (SSRL), Stanford, USA. SSRL operates at 3.0 GeV and at a maximum current of 100 mA. The EXAFS station was equipped with a Si[220] double crystal monochromator. Data collection was performed in transmission and fluorescence mode simultaneously at ambient temperature. Higher-order harmonics were reduced by detuning the second monochromator to 50% of the maximum intensity at the end of the scans. The solid compounds were diluted with boron nitride to give an edge step of about one unit in the logarithmic intensity ratio, and the sample cells were made of 1-mm brass frames and Mylar tape windows. The toluene/hexane solution was measured in a sample cell with a 2-mm Vitone spacer and Kapton tape windows. The energy scales of the X-ray absorption spectra were calibrated by assigning the first inflection points of the K edges of a nickel foil to 8331.6 eV and a cobalt foil to 7709.5 eV.[38] For each sample 2–3 scans were averaged, giving satisfactory data ($k^3$-weighted) up to $k = 14$ Å$^{-1}$. The EXAFSPAK program package was used for all data treatment and refinement.[39] The EXAFS oscillations were obtained after performing standard procedures for pre-edge subtraction, normalisation and spline removal. The $k^3$-weighted model functions were calculated using ab initio calculated phase and amplitude parameters obtained by the FEFF7 program package (version 7.01).[40] The given errors of the calculated bond lengths in Table 5 originate from the EXAFSPAK algorithms. The errors given are the statistical ones and the true errors of the bond lengths are usually a few times larger.

**Hydrolysis and Heat-Treatment:** Hydrolysis of **3** was performed in toluene by adding an equimolar amount of water with respect to the number of alkoxy groups in **3** and stirring. The sol was poured into a dish and the solvent evaporated to leave a fine powder. The thermal evolution of the powder was investigated by TGA in air at a rate of 10 °C min$^{-1}$ between 23 and 800 °C. Oxide formation of the hydrolysed **3** was performed by heating the powder in air at a rate of 10 °C min$^{-1}$ to the annealing temperature (300–700 °C) for 60 min in a Comecta SA 3L furnace. Scanning electron microscopy (SEM) was performed on the samples in order to study their morphology. X-ray powder diffraction was used to establish the nature of the obtained phases.

**Supporting Information** (see footnote on the first page of this article): $^1$H NMR spectra of [MoO(acac)(OMe)$_3$] (**4**) and [MoO$_2$(acac)(OMe)]$_2$ (**5**) in Figure S1.

## Acknowledgments

Financial support from the Swedish Research Council (VR) is gratefully acknowledged. Mr. Anders Johansson at the Department of Materials Chemistry Ångström Laboratory, Uppsala University, Sweden, is acknowledged for running the SEM analysis. Mr. Gerald Spijksma, Inorganic Materials Science Group, University of Twente, The Netherlands, is acknowledged for help with TGA and XRD analyses. Mr. Rolf Andersson, SLU, is acknowledged for help with the NMR studies. Portions of this research were carried out at the Stanford Synchrotron Radiation Laboratory, a national user facility operated by Stanford University on behalf of the U.S. Department of Energy, Office of Basic Energy Sciences. The SSRL Structural Molecular Biology Program is supported by the Department of Energy, Office of Biological and Environmental Research, and by the National Institutes of Health, National Centre for Research Resources, Biomedical Technology Program.

[1] M. M. Barsan, F. C. Thyrion, *Catal. Today* **2003**, *81*, 159–170.
[2] J. E. Herrera, L. Balzano, A. Borgna, W. E. Alwarez, D. E. Resasco, *J. Catal.* **2001**, *204*, 129–145.
[3] R. Kojima, K. Aika, *Appl. Catal. A* **2001**, *215*, 149–160.
[4] H. Nakamura, M. Amemiya, K. Ishida, *J. Jpn. Petrol. Inst.* **2005**, *48*, 281–289.
[5] M. Barsan, A. Maione, F. C. Thyrion, *Stud. Surf. Sci. Catal.* **2002**, *143*, 1063–1072.
[6] M. N. Kwini, J. M. Botha, *Appl. Catal. A* **2005**, *280*, 199–208.
[7] M. Ferrari, B. Delmon, P. Grange, *Microporous Mesoporous Mater.* **2002**, *56*, 279–290.
[8] A. C. Faro, P. Grange, A. C. B. dos Santos, *Phys. Chem. Chem. Phys.* **2002**, *4*, 2997–4007.
[9] S. A. Halawy, *Monatsh. Chem.* **2003**, *134*, 371–380.
[10] D. Vie, E. Martinez, F. Sapina, J. V. Folgado, A. Beltran, R. X. Valenzuela, V. Cortes-Corberan, *Chem. Mater.* **2004**, *16*, 1697–1703.
[11] A. J. van Dillen, R. J. A. M. Terörde, D. J. Lensveld, J. W. Geus, K. P. de Jong, *J. Catal.* **2003**, *216*, 257–264.
[12] L. A. Palacio, A. Echavarría, S. Sierra, E. A. Lombardo, *Catal. Today* **2005**, *107–108*, 338–345.
[13] E. Gomez, E. Pellicer, E. Valles, *J. Electroanal. Chem.* **2005**, *580*, 222–230.
[14] A. Maione, M. Devillers, *J. Solid State Chem.* **2004**, *177*, 2339–2349.
[15] D. Genuit, P. Afanasiev, M. Vrinat, *J. Catal.* **2005**, *235*, 302–317.
[16] F. Rullens, M. Devillers, A. Laschewsky, *J. Mater. Chem.* **2004**, *14*, 3421–3426.
[17] F. Rullens, N. Deligne, A. Laschewsky, M. Devillers, *J. Mater. Chem.* **2005**, *15*, 1668–1676.
[18] L. G. Hubert-Pfalzgraf, *J. Mater. Chem.* **2004**, *14*, 3113–3123.
[19] R. Schmid, A. Mosset, J. Galy, *Inorg. Chim. Acta* **1991**, *179*, 167–170.
[20] R. Schmid, H. Ahamdane, A. Mosset, *Inorg. Chim. Acta* **1991**, *190*, 237–240.
[21] P. Werndrup, V. G. Kessler, *J. Chem. Soc., Dalton Trans.* **2001**, 574–579.
[22] P. Werndrup, M. Verdenelli, F. Chassagneux, S. Parola, V. G. Kessler, *J. Mater. Chem.* **2004**, *14*, 344–350.
[23] V. G. Kessler, *Chem. Commun.* **2003**, 1213–1222.
[24] V. G. Kessler, K. V. Nikitin, A. I. Belokon', *Polyhedron* **1998**, *17*, 2309–2311.
[25] D. A. Wright, D. A. Williams, *Acta Crystallogr., Sect. B* **1968**, *24*, 1107–1114.
[26] R. D. Shannon, *Acta Crystallogr., Sect. A* **1976**, *32*, 751–767.
[27] J. K. Beattie, S. P. Best, B. W. Skelton, A. H. White, *J. Chem. Soc., Dalton Trans.* **1981**, 2105–2111.
[28] G. A. Seisenbaeva, L. Kloo, P. Werndrup, V. G. Kessler, *Inorg. Chem.* **2001**, *40*, 3815–3818.
[29] V. G. Kessler, A. V. Mironov, N. Y. Turova, A. I. Yanovsky, Y. T. Struchkov, *Polyhedron* **1993**, *12*, 1573–1576.
[30] M. Antipin, Y. Struchkov, A. Shilov, A. Shilova, *Gazz. Chim. Ital.* **1993**, *123*, 265–270.
[31] F. A. Cotton, N. S. Dalal, C. Y. Liu, C. A. Murillo, M. J. North, X. Wang, *J. Am. Chem. Soc.* **2003**, *125*, 12945–12952.
[32] F. A. Cotton, C. Y. Liu, C. A. Murillo, X. Wang, *Inorg. Chem.* **2003**, *42*, 4619–4623.
[33] S. C. Liu, L. D. Ma, D. McGowty, J. Zubieta, *Polyhedron* **1990**, *9*, 1541–1553.

 © 2006 Wiley-VCH Verlag GmbH & Co. KGaA, Weinheim 

[34] JCPDS Powder Diffraction Database, File card number, International Centre for Diffraction Data, Newtown Square, PA, USA, **1997**.
[35] P. Werndrup, S. Gohil, V. G. Kessler, M. Kritikos, L. G. Hubert-Pfalzgraf, *Polyhedron* **2001**, *20*, 2163–2169.
[36] N. Y. Turova, V. G. Kessler, S. I. Kucheiko, *Polyhedron* **1991**, *10*, 2617–2628.
[37] SHELXTL 5.3 Reference Manual, Bruker AXS, Madison, WI, USA, **1997**.
[38] A. Thompson, D. Attwood, E. Gullikson, M. Howells, K.-J. Kim, J. Kirz, J. Kortright, I. Lindau, P. Pianatta, A. Robinson, J. Scofield, J. Underwood, D. Vaughan, G. Williams, H. Winick, *X-ray Data Booklet*, Lawrence Berkeley National Laboratory, **2001**.
[39] G. N. George, I. J. Pickering, *EXAFSPAK − A Suite of Computer Programs for Analysis of X-ray Absorption Spectra* (Eds.: G. N. George, I. J. Pickering), SSRL, Stanford, CA, **1993**.
[40] a) S. I. Zabinsky, J. J. Rehr, A. Ankudinov, R. C. Albers, M. J. Eller, *Phys. Rev. B* **1995**, *52*, 2995–3009; b) A. Ankudinov, Ph. D. Thesis, University of Washington, **1996**; c) The FEFF program is available from: http://Feff.phys.washington.edu/feff.

Received: September 14, 2005
Published Online: February 9, 2006

 © 2006 Wiley-VCH Verlag GmbH & Co. KGaA, Weinheim 

DOI: 10.1002/ejic.200500883

# A 3D Manganese Coordination Polymer $[Mn_3(IMDC)_2(H_2O)_4]$ Constructed from $[Mn_2(IMDC)_2(H_2O)_2]$ Layers and $[Mn(H_2O)_2]$ Pillars (IMDC = 4,5-imidazoledicarboxylate)

**Man-Bo Zhang,[a] Yong-Mei Chen,[b] Shou-Tian Zheng,[a] and Guo-Yu Yang*[a]**

**Keywords:** Carboxylate ligands / Coordination polymers / Hydrothermal synthesis / Manganese

A novel three-dimensional coordination polymer $[Mn_3(IMDC)_2(H_2O)_4]$ (**1**) (IMDC = 4,5-imidazoledicarboxylate), consisting of $[Mn_2(IMDC)_2(H_2O)_2]$ layers and $[Mn(H_2O)_2]$ pillars, was synthesized hydrothermally and characterized by IR spectroscopy, elemental analysis, TGA, and magnetic measurements. It is the first example of a 3D framework containing 4,5-imidazoledicarboxylate in the family of manganese complexes. Variable-temperature magnetic susceptibility measurements show a weak antiferromagnetic coupling interaction between the $Mn^{II}$ ions of the dimeric units.
(© Wiley-VCH Verlag GmbH & Co. KGaA, 69451 Weinheim, Germany, 2006)

## Introduction

Extended solids containing manganese and bridging ligands have been investigated widely in the past decades, mainly for use as molecule-based magnets in both fundamental and potential applications, especially those that exhibit spontaneous magnetization,[1,2] and in the synthesis of manganese metalloenzyme mimics in some biological redox-active systems,[3] as well as the intriguing varieties of architectures and topologies displayed by these compounds.[4,5] In the research area of metalloenzyme mimics, carboxylate-bridged systems are the focus of investigation. To date, many manganese complexes of carboxylic acids with six-membered heterocycles, such as 2,3-pyrazinedicarboxylic acid,[6] 2-pyrazinecarboxylic acid,[7] pyridine-2,6-dicarboxylic acid,[4,5] and pyridine-3,4-dicarboxylic acid[8] have been reported. However, the coordination chemistry of manganese and carboxylic acids with five-membered heterocycle is less developed. 4,5-Imidazoledicarboxylic acid ($H_3IMDC$) exhibits several interesting characteristics: a) it can be partially or completely deprotonated to generate $H_2IMDC^-$, $HIMDC^{2-}$, and $IMDC^{3-}$ by controlling the pH carefully, which allows 4,5-imidazoledicarboxylate anions to display various coordination modes;[9] b) the departure of carboxyl groups from the plane of the imidazole ring may allow 4,5-imidazoledicarboxylate to be used for the construction of helical structures; c) its six potential coordination donors allow the formation of interesting higher-dimensional structure. To the best of our knowledge, transition metal complexes of 4,5-imidazoledicarboxylate are usually either mononuclear,[10,11] dinuclear,[12] a 1D chain,[13,14] or a 2D layered network;[15] no 3D open framework is known. The typical coordination modes of 4,5-imidazoledicarboxylate anions are summarized in Scheme 1 (a–i). Herein, we report the synthesis, crystal structure, and magnetic properties of the first 3D coordination polymer of manganese with multidentate IMDC as ligand and linker, namely $[Mn_3(IMDC)_2(H_2O)_4]$ (**1**).

[a] State Key Laboratory of Structural Chemistry, Fujian Institute of Research on the Structure of Matter, Chinese Academy of Sciences,
Fuzhou, Fujian 350002, China
[b] Department of Applied Chemistry, Faculty of Science, Beijing University of Chemical Technology,
Beijing 100029, China
E-mail: ygy@fjirsm.ac.cn
Supporting information for this article is available on the WWW under http://www.eurjic.org or from the author.

## Results and Discussion

### Synthesis and Structure

As a few high dimensional coordination polymers of 4,5-imidazoledicarboxylic acid ($H_3IMDC$) have already been documented, we aimed to assemble the IMDC ligands and manganese ions into polymers with an open framework. In general, $H_3IMDC$ is insoluble in water under neutral or acidic conditions at room temperature and is difficult to deprotonate under acidic conditions, which makes the construction of high-dimensional complexes difficult. In addition, although the sodium salt of 4,5-imidazoledicarboxylate is soluble in water, it easily forms precipitates, rather than crystals, in the presence of manganese ions. Taking into account the above two aspects, we chose the insoluble manganese salt $MnCO_3$ as starting material, with an $H_3IMDC/MnCO_3$ molar ratio of 2:1, and heated the mixture hydrothermally at 175 °C for 15 days, expecting that the insoluble $MnCO_3$ should slow the reaction down and allow the $H_3IMDC$ time to deprotonate. We also carried

 © 2006 Wiley-VCH Verlag GmbH & Co. KGaA, Weinheim 

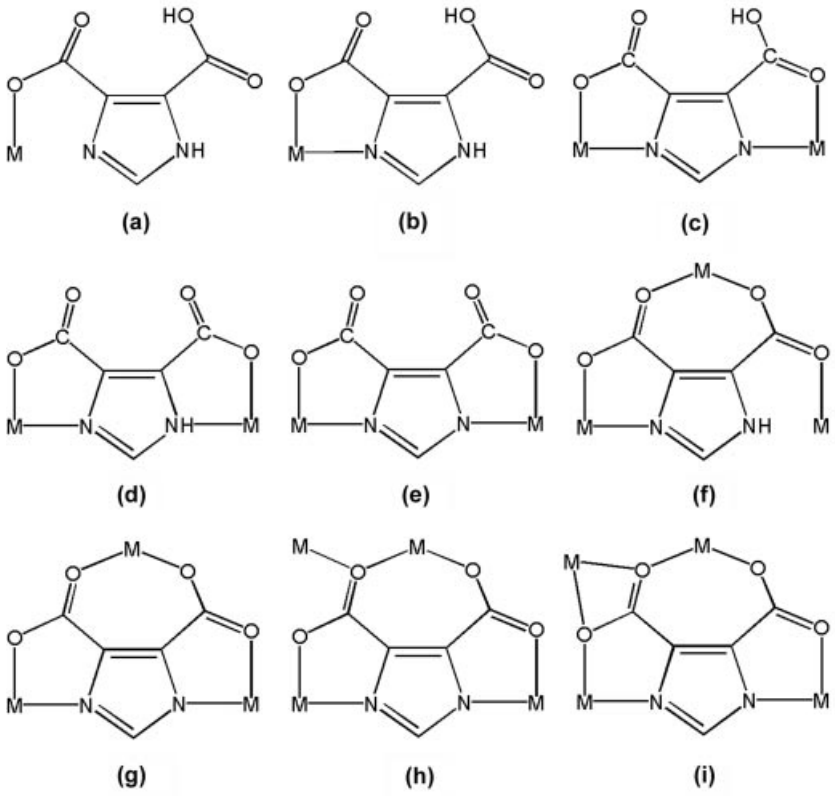


Scheme 1. Typical coordination modes of the IMDC ligand.

out the same reaction in a period shorter than 10 days, but no crystals were obtained. Thus, the slower rate and longer time may be crucial factors for the crystallization of **1**.

X-ray analysis revealed that the asymmetric unit consists of two crystallographically independent $Mn^{2+}$ centers, one IMDC ligand, and two coordinated water molecules (Figure S1, see Supporting Information). The coordination mode of the IMDC in **1** is illustrated in Scheme 1 (h) and Figure S2 in the Supporting Information. The coordination environments of the Mn(1) and Mn(2) atoms and the IMDC ligand in the symmetric unit are presented in Figure 1. Both Mn(1) and Mn(2) are six coordinated to form two octahedra, $Mn(1)NO_4(H_2O)$ and $Mn(2)N_2O_2(H_2O)_2$. In the $Mn(1)NO_4(H_2O)$ moiety the six donors are one N atom of an imidazole ring, one water molecule, and four O atoms of four carboxylate groups, with one in mode A, two in mode B, and one in mode C (Scheme 1), while in $Mn(2)N_2O_2(H_2O)_2$ the donors are two N atoms from two IMDC ligands, two water molecules, and two O atoms of two carboxylate groups (mode A). As for the IMDC ligand, the carboxyl groups bonds to four Mn atoms in four different coordination modes:[16] a $\mu_2$-carboxylato-*syn-anti* mode for Mn(1)–O(1)–C(1)–O(2)–Mn(1d), a $\mu_2$-carboxylato-*anti-anti* mode for Mn(1)–O(1)–C(1)–O(2)–Mn(1e), a $\mu_2$-carboxylato-*anti-anti* mode for Mn(2)–O(4)–C(4)–O(3)–Mn(1e), and a bis($\mu_2$,$\eta^1$-carboxylato) mode for Mn(1d)–O(2)–Mn(1e) (see Figure S2).

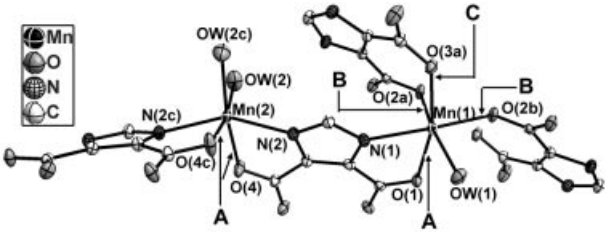


Figure 1. ORTEP drawing (ellipsoids at 50% probability) with the atom-labeling scheme for the symmetric unit of complex **1**. The labels "a" or "b" refer to symmetry-generated atoms and the labels "A", "B", and "C" refer to the different binding modes of the carboxylate groups of then IMDC ligand.

Although both Mn(1) and Mn(2) are six-coordinate, the different coordination environments around them result in an Mn(1) dimer and Mn(2) monomer (Figure S3). In the dimer, the O(2) atom from a mode-B carboxylate group bonds two Mn(1) centers to form the dimeric unit $Mn_2(IMDC)_2(H_2O)_2$ [Mn(1)–O(2) = 2.169 Å] whose Mn···Mn distance is 3.477 Å; the O–Mn–O angle in the $Mn_2O_2$ ring is 75.46°, while the Mn–O–Mn angle is 104.54°. These values fall in the range of similar dinuclear manganese complexes.[17–19] In the structure, each $Mn_2(IMDC)_2(H_2O)_2$ dimer further connects to adjacent dimeric units through O(1) from a mode-A carboxylate group and N(1) atoms to form a 2D layer in the *ab* plane (Figures 2 and 3).

 © 2006 Wiley-VCH Verlag GmbH & Co. KGaA, Weinheim 

It is worth noting the presence of left- and right-handed helical chains consisting of repeating –Mn(1)–O(2)–C(1)–O(1)– linkages in the layer along the [100] direction (Figures 3 and S4). O(4) from a mode-A carboxylate group and the N(2) atoms coordinate to the Mn(2) center to give rise to the 3D open framework (Figures 4 and S5). In other words, the Mn(1) centers mainly contribute to constructing the layers together with IMDC ligand, while the Mn(2) centers act as pillars between the layers.

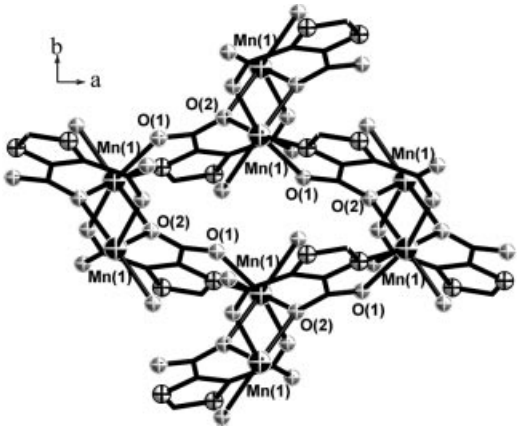


Figure 2. Layer containing $Mn_2(IMDC)_2(H_2O)_2$ dimers.

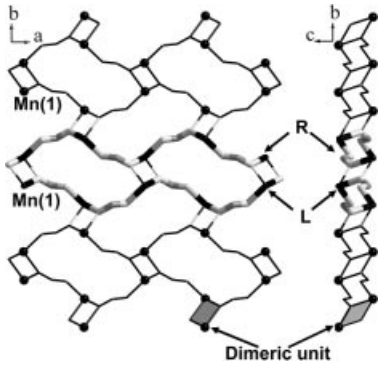


Figure 3. View of the layer constructed by $Mn_2(IMDC)_2(H_2O)_2$ dimers along the *c* and *a* axis; the imidazole rings of IMDC ligands have been omitted for clarity; L and R indicate the left- and right-handed helical chains. The thick, two-colored line represents the helical chains in the *ab* plane.

The $H_3IMDC$ is completely deprotonated in compound **1**, and all six potential donor atoms coordinate to four Mn centers through coordination mode h of Scheme 1, which plays a key role in constructing the 3D framework of **1** (Figure S1). The previously reported coordination modes of the IMDC ligand, i.e. modes a and b of Scheme 1, can only coordinate to one metal center, thus monomers are the favorable entity to accommodate them.[10,11] As for coordination modes c, d, and e, they can link two metal centers through two chelating five-membered rings on the opposite side of the imidazole group to form a linear bridge. For example, if the IMDC ligands connect the metal centers along one direction, chain-like structures are formed as in [Mn(phen)(HIMDC)][13] and $[Cd(HIMDC)(H_2O)_2]$[14] (Figure S6a), whereas if the ligands connect the metal

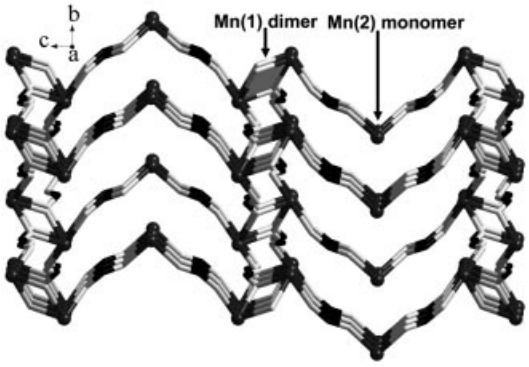


Figure 4. View of the 3D framework constructed by 2D layers containing Mn(1) atoms and pillars consisting of Mn(2) atoms.

centers perpendicularly, a square tetramer, as in $[Na_2\{Co^{II}_2Co^{III}_2(IMDC)_4(bipy)_4\}]\cdot 12H_2O$[20] (Figure S6b) or a cubane-like $[Ni_8(HIMDC)_{12}]^{8-}$ cluster unit, as in $[Ni_8(HIMDC)_{12}(H_2TMDP)_4(DMF)_4(EtOH)_4(H_2O)_6]$[21] (Figure S6c) are formed. Mode f in Scheme 1 tends to yield a 2D layered network.[15] In the structures of a series of lanthanide complexes $[Ln_2(IMDC)_2(H_2O)_3]\cdot nH_2O$,[9] the IMDC ligands displays modes g and i: in the g mode they connect three lanthanide atoms to form a 1D helical channel, while in the i mode they contribute to connecting the helical channels to form a 3D framework. From the above discussion, we can conclude that multidentate modes of the IMDC ligand, such as g, h, and i, benefit the formation of higher-dimensional frameworks.

### IR Spectrum and Thermal Stability Analysis

The absence of any strong bands around 1700 $cm^{-1}$ in the IR spectrum of **1** indicates that 4,5-imidazoledicarboxylic acid has been completely deprotonated to generate $IMDC^{3-}$ anions. The sharp bands in the region 1581–1541 $cm^{-1}$ may be attributed to the $COO^-$ asymmetric stretching modes, and the bands at 1384 $cm^{-1}$ are characteristic of the symmetric stretching modes of $COO^-$ (Figure S7). The value of the difference $\Delta(\nu_{as} - \nu_s)$ between the two stretching modes is about 197 $cm^{-1}$, which indicates strong coordination of the carboxylate oxygen to the manganese center. In contrast to **1**, the presence of a medium intensity band in the region 1730–1710 $cm^{-1}$ in the IR spectrum of *cis*-$[Ru(PPh_3)_2(L^3H_2)_2]$ ($L^3H_2 = H_2IMDC$) suggests that the 4,5-imidazoledicarboxylic acid is only partially deprotonated.[22]

The TG curve shows that the structure is stable up to 210 °C, and the weight loss of complex **1** can be divided into three steps in the range 210–1000 °C (Figure S8). The weight loss of 13.5 % during the first step from 210 to 350 °C corresponds to the loss of four coordinated water molecules (calcd. 13.3 %). On further heating, the material loses weight continuously during the second and the third steps, with the combined weight loss of 47.3% (calcd. 47.5%) corresponding to decomposition of the IMDC ligand. Assuming the residue is MnO, the observed weight

 © 2006 Wiley-VCH Verlag GmbH & Co. KGaA, Weinheim 

(38.8%) is in good agreement with the calculated value (39.2%).

### Magnetic Properties

Temperature-dependent magnetic susceptibility measurements for complex **1** were performed over a temperature range from 5 to 300 K at 5 kOe. The magnetic susceptibility above 6 K obeys the Curie–Weiss law and gives a Curie constant, $C$, of 13.6 $cm^3 K mol^{-1}$ and a Weiss constant, $\theta$, of –14.1 K. The value of $C$ is in agreement with that expected for three magnetically isolated $Mn^{2+}$ ions with $S = 5/2$ (13.1 $cm^3 K mol^{-1}$; $g = 2$). Upon cooling, the value of $\chi_M T$ decreases monotonically, attaining a value of 3.0 $cm^3 K mol^{-1}$ at 5 K. Such behavior is characteristic of the presence of weak antiferromagnetic interactions between the neighboring $Mn^{2+}$ ions (Figure 5).

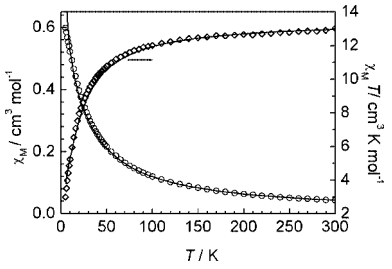


Figure 5. Plot of the $\chi_M T$ product and $\chi_M$ versus $T$ for complex **1**. The solid lines represent the best fit to the model with inclusion of the ZFS term.

From the known structural data, there are four types of Mn···Mn exchange pathways via the carboxylate groups in the structure (Figure S2). As the Mn···Mn distance of 3.477 Å within the bis($\mu_2$,$\eta^1$-carboxylato)-bridged bimetallic $Mn_2O_2$ core is much shorter than the Mn···Mn separations of 5.60–6.52 Å through $\mu_2$-1,3-carboxylato modes (in *anti-anti*/*syn-anti*) or an IMDC bridge, and the latter is generally less capable of transmitting magnetic interactions,[13,23–26] we can simplify the coupling interaction system as a doubly $\mu_2$,$\eta^1$-carboxylato-bridged dimeric manganese combining an isolated $Mn(2)^{2+}$ ion. The magnetic behavior of the compound is therefore approximated by the sum of the contributions of one $Mn^{2+}$ dimer (Bleaney–Bowers-like equation based on the isotropic Heisenberg model $H = -2JS_1 \cdot S_2$)[27] and one isolated $Mn^{2+}$ ion, in which a Weiss constant, $\theta'$, is included to describe the interdimer interactions and the exchange coupling between Mn1 and Mn2 is neglected. The corresponding analytical expression for the $\chi_M T$ product is given as follows [Equations (1), (2), and (3)].

$$\chi_M T = \chi_{dimer} T + \chi_{mono} T \quad (1)$$

where

$$\chi_{dimer} = \frac{2Ng^2\beta^2}{k(T-\theta)} \times \left[ \frac{e^x + 5e^{3x} + 14e^{6x} + 30e^{10x} + 55e^{15x}}{1 + 3e^x + 5e^{3x} + 7e^{6x} + 9e^{10x} + 11e^{15x}} \right]$$

$$x = 2J/kT \quad (2)$$

and

$$\chi_{mono} = \frac{Ng^2\beta^2 S(S+1)}{3kT} \quad (3)$$

in which $N$, $g$, $k$, and $\beta$ have their usual meanings, and $J$ is the exchange coupling constant between the doubly $\mu_2$,$\eta^1$-carboxylato-bridged manganese ions. The fitting using Equation (1) gave a satisfactory result above 10 K with the superexchange parameters $J = -1.34\ cm^{-1}$, $\theta' = -7.40$ K, and $g = 2.03$. The agreement factor $R$, defined as $\Sigma[(\chi_M T)_{obs} - (\chi_M T)_{calc}]^2/\Sigma(\chi_M T^2_{obs})$ is equal to $1.85 \times 10^{-3}$. These values confirm the antiferromagnetic character of the magnetic interaction between the $Mn^{2+}$ ions via double $\mu_2$,$\eta^1$-carboxylato bridges. The deviation below 10 K may arise from the neglect of the coupling interactions involving the Mn(2) ion or its zero-field splitting (ZFS).

When the zero-field splitting ($D$) of the Mn(2) ions is considered by using the theoretical expression[28] for an $S = 5/2$ spin instead of Equation (3), a better agreement between the observed and calculated $\chi_M T$ value at low temperature is found with the four-parameter fits than with the three-parameter fit. However, the parameters $D$ and $\theta'$ are strongly dependent on each other, therefore it is difficult to calculate these values with reasonable accuracy. If the values of $J$, $g$, and $\theta'$ are constrained to the value obtained by the simplified expression based on Equations (2) and (3), the best fitting based on the model with inclusion of ZFS term yields $D = 7.89\ cm^{-1}$ with $R = 5.4 \times 10^{-4}$. The $D$ value is obviously larger than those observed in similar systems,[29,30] suggesting that there are still some disparities between the present magnetic model and the actual magnetic interaction system. The small $J$ value ($-1.34\ cm^{-1}$) indicates weak antiferromagnetic coupling in the dimeric units of complex **1**, which is comparable to the values found in the doubly $\mu_2$,$\eta^1$-carboxylato-bridged manganese complexes ($-0.631$ to $-0.942\ cm^{-1}$).[19,25] Due to a shorter Mn···Mn distance (3.477 Å), the $J$ value of **1** is slightly larger than those of the above mentioned manganese complexes (3.67–3.73 Å).

## Conclusion

In summary, we have synthesized a novel 3D Mn-IMDC coordination polymer under hydrothermal conditions. The structure is constructed from $[Mn(H_2O)_2]$ pillars and $[Mn_2(IMDC)_2(H_2O)_2]$ layers containing left- and right-handed helical chains. The 4,5-imidazoledicarboxylic acids are completely deprotonated and adopt coordination mode h of Scheme 1. Compared with the coordination modes shown in this scheme, mode h allows the 4,5-imidazoledicarboxylate ligand to form a high dimensional framework. The TG curve shows **1** is very stable below 210 °C and the magnetic measurement of **1** indicates the presence of weak antiferromagnetic exchange interactions.

 © 2006 Wiley-VCH Verlag GmbH & Co. KGaA, Weinheim 

## Experimental Section

**General Remarks:** 4,5-Imidazoledicarboxylic acid ($H_3IMDC$) and $MnCO_3$ were purchased from commercial sources and used as received. Elemental analysis (C,H,N) was carried out with a Vario EL III elemental analyzer. IR spectra (400–4000 $cm^{-1}$) were recorded from KBr pellets on an ABB Bomem IR MB102 series spectrophotometer. The thermogravimetric analysis was performed with a Mettler Toledo TGA/SDTA 851e analyzer in $N_2$ with a heating rate of 10 °C $min^{-1}$ from 30 to 1000 °C. The variable-temperature magnetic susceptibility measurement of a crystalline sample was performed in a field of 5 kOe with a Quantum Design MPMS-7 magnetometer; the susceptibility of the sample holder and diamagnetic contribution were subtracted from the raw data for the complexes.

**Synthesis and Initial Characterization:** A mixture of $H_3IMDC$ (0.2341 g, 1.5 mmol), $MnCO_3$ (0.0862 g, 0.75 mmol), and $H_2O$ (5 mL; $MnCO_3/H_3IMDC/H_2O$ molar ratio of 1:2:370) was stirred under ambient conditions. The resulting mixture with a pH of 4 was sealed in a 25-mL Teflon-lined steel autoclave and heated at 175 °C for 15 d under autogenous pressure. After cooling to room temperature, the colorless prismatic crystals of **1** were filtered off, washed with distilled water, and dried at ambient temperature (39 mg, yield 28.7% based on $MnCO_3$). $C_{10}H_{10}Mn_3N_4O_{12}$ (543.04): calcd. C 22.12, H 1.86, N 10.33; found C 22.20, H 2.01, N 10.35. IR (KBr pellet): $\tilde{\nu}$ = 3542 (s) $cm^{-1}$, 3280 (s), 1662 (m), 1581 (s), 1515 (vs), 1409 (vs), 1384 (vs), 1276 (m), 1241 (s), 1107 (m), 1099 (m), 803 (m), 671 (m).

**X-ray Crystallographic Study:** A crystal of dimensions $0.35 \times 0.18 \times 0.15$ $mm^3$ was used for data collection on a Siemens Smart CCD diffractometer with graphite-monochromated Mo-$K_\alpha$ radiation ($\lambda$ = 0.71073 Å). Of the 8895 reflections ($2\theta_{max}$ = 50.04°), 1422 were independent ($R_{int}$ = 0.0199) and 1396 reflections with $I > 2\sigma(I)$. The structure of **1** was solved by direct methods and all calculations were performe with the SHELXL program and refined by full-matrix, least-squares minimizations of $(F_o - F_c)^2$ with anisotropic thermal parameters for all non-hydrogen atoms. The position of the hydrogen atoms were found in the difference Fourier maps and refined isotropically. The last successful full-matrix least-squares refinement with anisotropic thermal parameters for all non-hydrogen atoms converged to $R_1$ = 0.0226, $wR_2$ = 0.0640. Experimental details for X-ray data collection of **1** are presented in Table 1, while selected bond lengths and angles are listed in Table 2.

Table 1. Crystal data and structure refinement for complex **1**.

| | |
|---|---|
| Empirical formula | $C_{10}H_{10}Mn_3N_4O_{12}$ |
| Formula weight | 543.04 |
| Crystal system | orthorhombic |
| Space group | *Pbcn* |
| *a* [Å] | 9.386 |
| *b* [Å] | 7.351 |
| *c* [Å] | 23.3442(17) |
| *V* [Å$^3$] | 1610.78(12) |
| Z | 4 |
| $\mu$(Mo-$K_\alpha$) [$mm^{-1}$] | 2.396 |
| *T* [K] | 293(2) |
| $\rho_{calc}$ [g $cm^{-3}$] | 2.239 |
| $\lambda$ [Å] | 0.71073 |
| *F*(000) | 1076 |
| $\theta$ range for data collection | 1.74–25.02° |
| Reflections collected/unique | 8895/1422 [*R*(int) = 0.0199] |
| Goodness-of-fit on $F^2$ | 1.016 |
| Final *R* indices [$I > 2\sigma(I)$] | $R1$ = 0.0226[a]<br>$wR2$ = 0.0640[b] |
| *R* indices (all data) | $R1$ = 0.0252, $wR2$ = 0.0922 |
| Largest diff. peak and hole [e Å$^{-3}$] | 0.369 and –0.332 |

[a] $R1 = \Sigma(||F_o| - |F_c||)/\Sigma|F_o|$. [b] $wR2 = \{\Sigma[w(F_o^2 - F_c^2)^2]/\Sigma[w(F_o^2)^2]\}^{1/2}$, where $w = 1/[\sigma^2(F_o)^2 + (0.0506P)^2 + 5.0080P]$ where $P = (F_o^2 + 2F_c^2)/3$.

Table 2. Selected bond lengths [Å] and angles [°] for complex **1**.[a]

| | | | |
|---|---|---|---|
| Mn(1)–O(3A) | 2.126(2) | Mn(2)–N(2C) | 2.181(2) |
| Mn(1)–O(2B) | 2.169(2) | Mn(2)–N(2) | 2.181(2) |
| Mn(1)–OW1 | 2.180(2) | Mn(2)–OW(2C) | 2.215(3) |
| Mn(1)–O(1) | 2.205(2) | Mn(2)–OW(2) | 2.215(3) |
| Mn(1)–N(1) | 2.213(2) | Mn(2)–O(4) | 2.241(2) |
| Mn(1)–O(2A) | 2.228(2) | Mn(2)–O(4C) | 2.241(2) |
| | | | |
| O(3A)–Mn(1)–O(2B) | 90.3(1) | O(1)–Mn(1)–O(2A) | 85.8(1) |
| O(3A)–Mn(1)–OW(1) | 107.8(1) | N(1)–Mn(1)–O(2A) | 93.7(1) |
| O(2B)–Mn(1)–OW(1) | 92.7(1) | N(2C)–Mn(2)–N(2) | 150.6(1) |
| O(3A)–Mn(1)–O(1) | 163.6(1) | N(2)–Mn(2)–OW(2C) | 102.7(1) |
| O(2B)–Mn(1)–O(1) | 98.7(1) | OW(2C)–Mn(2)–OW(2) | 85.1(2) |
| OW(1)–Mn(1)–O(1) | 85.6(1) | N(2C)–Mn(2)–O(4) | 88.8(1) |
| O(3A)–Mn(1)–N(1) | 93.3(1) | N(2)–Mn(2)–O(4) | 73.7(1) |
| O(2B)–Mn(1)–N(1) | 168.2(1) | OW(2C)–Mn(2)–O(4) | 168.0(1) |
| OW(1)–Mn(1)–N(1) | 96.9(1) | OW(2)–Mn(2)–O(4) | 84.2(1) |
| O(1)–Mn(1)–N(1) | 75.3(1) | N(2C)–Mn(2)–O(4C) | 73.7(1) |
| O(3A)–Mn(1)–O(2A) | 83.2(1) | N(2)–Mn(2)–O(4C) | 88.9(1) |
| O(2B)–Mn(1)–O(2A) | 75.5(1) | N(2)–Mn(2)–OW(2) | 98.8(1) |
| OW(1)–Mn(1)–O(2A) | 164.2(1) | O(4)–Mn(2)–O(4C) | 107.0(1) |

[a] Symmetry transformations used to generate equivalent atoms: A: $-x - 3/2$, $y - 1/2$, $z$; B: $x + 1/2$, $-y + 1/2$, $-z + 1$; C: $-x - 2$, $y$, $-z + 1/2$.

CCDC-258312 contains the supplementary crystallographic data for this paper. These data can be obtained free of charge from The Cambridge Crystallographic Data Centre via www.ccdc.cam.ac.uk/data_request/cif.

**Supporting Information** (see footnote on the first page of this article): Eight additional figures including the IR spectrum and TG curve are available.

## Acknowledgments

This work was supported by the National Natural Science Foundation of China (grant nos. 20271050 and 20473093), the Talents Program of the Chinese Academy of Sciences, and the Natural Science Foundation of Fujian Province (grant nos. E0510030 and E0210029).

[1] S. Wang, G. Yang, D. Liao, L. Li, *Inorg. Chem.* **2004**, *43*, 852–854.
[2] H.-J. Chen, Z.-W. Mao, S. Gao, X.-M. Chen, *Chem. Commun.* **2001**, 2320–2321.
[3] G. C. Dismukes, *Chem. Rev.* **1996**, *96*, 2909–2926.
[4] B. Zhao, P. Cheng, Y. Dai, C. Cheng, D. Liao, S. Yan, Z. Jiang, G. Wang, *Angew. Chem. Int. Ed.* **2003**, *42*, 934–936.
[5] B. Zhao, P. Cheng, X. Chen, C. Cheng, W. Shi, D. Liao, S. Yan, Z. Jiang, *J. Am. Chem. Soc.* **2004**, *126*, 3012–3013.
[6] J.-Z. Zou, Z. Xu, W. Chen, K.-M. Lo, X.-Z. You, *Polyhedron* **1999**, *18*, 1507–1512.
[7] J. Limburg, G. W. Brudvig, R. H. Crabtree, *J. Am. Chem. Soc.* **1997**, *119*, 2761–2762.
[8] W. Chen, Q. Yue, C. Chen, H. M. Yuan, W. Xu, J. S. Chen, S. N. Wang, *Dalton Trans.* **2003**, 28–30.
[9] Y.-Q. Sun, J. Zhang, Y.-M. Chen, G.-Y. Yang, *Angew. Chem. Int. Ed.* **2005**, *44*, 5814–5817.
[10] C. Ma, F. Chen, C. Chen, Q. Liu, *Acta Crystallogr., Sect. C* **2003**, *59*, m516–m518.

 © 2006 Wiley-VCH Verlag GmbH & Co. KGaA, Weinheim 

[11] Y. L. Wang, R. Cao, W. H. Bi, *Acta Crystallogr., Sect. C* **2004**, *60*, m609–m611.
[12] M. T. Caudle, J. W. Kampf, M. L. Kirk, P. G. Rasmussen, V. L. Pecoraro, *J. Am. Chem. Soc.* **1997**, *119*, 9297–9298.
[13] X. Zhang, D. Huang, F. Chen, C. Chen, Q. Liu, *Inorg. Chem. Commun.* **2004**, *7*, 662–665.
[14] Y.-Q. Sun, J. Zhang, G.-Y. Yang, *Acta Crystallogr., Sect. C* **2004**, *60*, m590–m591.
[15] S. Gao, L. Huo, H. Zhao, J. Liu, *Acta Crystallogr., Sect. E* **2005**, *61*, m155–m157.
[16] R. L. Rardin, W. B. Tolman, S. J. Lippard, *New J. Chem.* **1991**, *15*, 417–430.
[17] C. Policar, S. Durot, F. Lambert, M. Cesario, F. Ramiandrasoa, I. Morgenstern-Badarau, *Eur. J. Inorg. Chem.* **2001**, *40*, 1807–1818.
[18] C. Ma, C. Chen, Q. Liu, D. Liao, L. Li, *Eur. J. Inorg. Chem.* **2003**, *42*, 1227–1231.
[19] H. Iikura, T. Nagata, *Inorg. Chem.* **1998**, *37*, 4702–4711.
[20] C. F. Wang, E. Q. Gao, Z. He, C. H. Yan, *Chem. Commun.* **2004**, 720–721.
[21] Y. Liu, V. Kravtsov, R. D. Walsh, P. Poddar, H. Srikanth, M. Eddaoudi, *Chem. Commun.* **2004**, 2806–2807.
[22] P. Sengupta, R. Dinda, S. Ghosh, W. S. Sheldrick, *Polyhedron* **2001**, *20*, 3349–3354.
[23] E. Colacio, J. M. Domínguez-Vera, M. Ghazi, R. Kivekäs, M. Klinga, J. M. Moreno, *Eur. J. Inorg. Chem.* **1999**, 441–445.
[24] C. Policar, F. Lambert, M. Cesario, I. Morgenstern-Badarau, *Eur. J. Inorg. Chem.* **1999**, 2201–2207.
[25] S. Durot, C. Policar, G. Pelosi, F. Bisceglie, T. Mallah, J. Mahy, *Inorg. Chem.* **2003**, *42*, 8072– 8080.
[26] H. Oshio, E. Ino, I. Magi, T. Ito, *Inorg. Chem.* **1993**, *32*, 5697–5703.
[27] E.-Q. Gao, L.-H. Yin, J.-K. Tang, P. Cheng, D.-Z. Liao, Z.-H. Jiang, S.-P. Yan, *Polyhedron* **2001**, *20*, 669–673.
[28] O. Kahn, *Molecular Magnetism*, VCH Publishers, New York, **1993**, p. 24.
[29] J. Cui, P. Cheng, D. Liao, Z. Jiang, S. Yan, G. Wang, X. Huang, *Polyhedron* **1998**, *17*, 2517–2522.
[30] R. Boća, *Coord. Chem. Rev.* **2004**, *248*, 757–815.

Received: October 2, 2005
Published Online: February 21, 2006

 © 2006 Wiley-VCH Verlag GmbH & Co. KGaA, Weinheim 

DOI: 10.1002/ejic.200500892

# The Role of Anions in Addressing the Outcome of the Reaction of Tetramethylthiourea with *cis*-$Pt^{II}(phos)_2$ Moieties (phos = $PPh_3$ or ½dppe), Cyclometallation vs. Hydrolysis to Monothiocarbamato, and the Crystal Structure of *trans*-Bis(*N*-dimethylmonothiocarbamato)bis(triphenylphosphane)-platinum(II)

**Maria Alesi,[a] Serena Fantasia,[a] Mario Manassero,*[b] and Alessandro Pasini*[a]**

**Keywords:** Carboxylate ligands / Phosphane ligands / Ligands reactivity

The product of the reaction between tetramethylthiourea (tmtu) and *cis*-$Pt^{II}(phos)_2$ moieties (phos = $PPh_3$, or ½ dppe) depends on the anionic species present. With $NO_3^-$, $CF_3CO_2^-$, $CF_3SO_3^-$ and $BF_4^-$, the cyclometallate cationic complex $[Pt(phos)_2(tmtu^*\text{-}C,S)]^+$ is obtained (tmtu* is tmtu deprotonated at one methyl group). The acetato and malonato complexes are inactive towards such deprotonation, but, in the presence of water, promote tmtu hydrolysis with formation of *N*-dimethylmonothiocarbamato (mtc) complexes in which mtc is *S*-coordinated. *cis*-$[Pt(PPh_3)_2(mtc)_2]$ isomerises slowly to the *trans* isomer, whose crystal structure is reported.

(© Wiley-VCH Verlag GmbH & Co. KGaA, 69451 Weinheim, Germany, 2006)

## Introduction

A knowledge of the factors that influence the reactivity of coordinated ligands is of great importance in coordination and organometallic chemistry. Here we wish to report that the proper choice of anionic ligands may affect the outcome of the reaction between tetramethylthiourea (tmtu) and *cis*-$Pt^{II}(phos)_2$ moieties (phos = $PPh_3$ or ½ dppe).

We have recently found that the reaction of *cis*-$[Pt(PPh_3)_2(NO_3)_2]$ (**1**) with tmtu does not give the disubstituted product *cis*-$[Pt(PPh_3)_2(tmtu)_2]^{2+}$, but that the initially formed *cis*-$[Pt(PPh_3)_2(NO_3)(tmtu)](NO_3)$ (**2**) transforms into the cyclometallated complex $[Pt(PPh_3)_2(tmtu^*\text{-}C,S)](NO_3)$ (**3**) [tmtu*, tetramethylthiourea deprotonated at one methyl group], with formation of nitric acid (Scheme 1).[1] This reaction, performed at room temperature in either chloroform or $CH_2Cl_2$, was found to be unaffected by both air and water, which, in some experiments, was purposely added to extract the nitric acid formed during the reaction.[1]

Such facile cyclometallation is clearly favoured by the lability of the nitrate ion *cis* to tmtu in **2**; detachment of this ionic ligand produces a vacant coordination site which can interact with a C–H bond of a methyl group of tmtu, activating the bond towards deprotonation.[2,3] The proton is then captured by a "free" (i.e. uncomplexed) $NO_3^-$ ion to give nitric acid.[1] In order to better understand the role of the anion either as a ligand, or as a base, we decided to investigate the reaction of tmtu with a series of other *cis*-$Pt^{II}(PPh_3)_2$ complexes with various anionic ligands and we found that the product of the reaction depends on the nature of the anions present. Thus, while cyclometallation also occurs with *cis*-$[Pt(PPh_3)_2(CF_3CO_2)_2]$ (**4**) and *cis*-$[Pt(PPh_3)_2(CH_3CN)_2]X_2$ (**5a**, X = $BF_4^-$; **5b**, X = $CF_3SO_3^-$, TfO), the reaction of tmtu with *cis*-$[Pt(PPh_3)_2(AcO)_2]$ (**6**) and $[Pt(PPh_3)_2(malonato)]$ (**7**) follows a completely different route: these anionic ligands promote tmtu hydrolysis, giving rise to the dimethylmonothiocarbamato (mtc) complexes

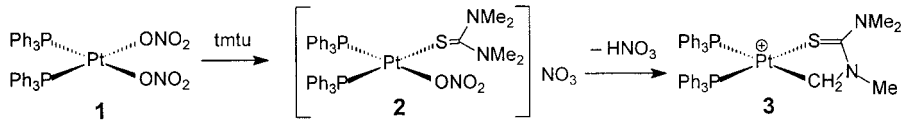


Scheme 1.

[a] Università di Milano, Dipartimento di Chimica Inorganica, Metallorganica e Analitica,
Via Venezian 21, 20133, Milano, Italy
E-mail: alessandro.pasini@unimi.it
[b] Università di Milano, Dipartimento di Chimica Strutturale e Stereochimica Inorganica,
Via Venezian 21, 20133 Milano, Italy
E-mail: mario.manassero@unimi.it

 © 2006 Wiley-VCH Verlag GmbH & Co. KGaA, Weinheim 

*cis*-[Pt(PPh$_3$)$_2$(mtc)$_2$] (**8**) and *trans*-[Pt(PPh$_3$)$_2$(mtc)$_2$] (**9**). The Pt$^{II}$(dppe) complexes behave similarly. We report here these studies, as well as the X-ray structure of *trans*-[Pt(PPh$_3$)$_2$(mtc)$_2$] (**9**). Although the structure of a phosphane-Pd$^{II}$ complex of mtc has been reported,[4] to the best of our knowledge this is the first X-ray structure of a Pt-mtc derivative. Dialkyldithiocarbamato-Pt complexes are well known,[5] but there are very few reports on Pt-mtc complexes,[4,6] and indeed mtc complexes have been little studied,[7] a possible reason being the unpleasant synthesis of the mtc$^-$ ligand, which requires the use of carbonyl sulfide.[6] The hydrolysis reaction reported here may therefore represent an easy route to Pt-mtc complexes.

## Results and Discussion

### Cyclometallation versus Hydrolysis: the Role of the Anions

While *cis*-[Pt(PPh$_3$)$_2$(CF$_3$CO$_2$)$_2$] (**4**) is a known compound,[8] $BF_4^-$ and $TfO^-$ have a rather poor complexing ability, therefore we have synthesised the salts of these anions with *cis*-[Pt(PPh$_3$)$_2$(CH$_3$CN)$_2$]$^{2+}$, **5a** and **5b**, respectively. Reactions of tmtu with these three complexes, in $CH_2Cl_2$ solutions, give the corresponding salts of the cationic cyclometallated complex **3**, which were characterised by elemental analyses and by comparison of their NMR spectra with those of the already described nitrate derivative.[1] When the reactions between tmtu and compounds **5** were followed by $^{31}$P NMR spectroscopy, we observed, in both cases, the fast formation of a species **10**, which shows two doublets (Table 1), consistent with one phosphane *trans* to an S ligand ($\delta$ = 13.7 ppm; $J_{Pt-P}$ = 2890 Hz, compared with, for instance, ref.[9]) and one *trans* to $CH_3CN$ ($\delta$ = 7.6 ppm; $J_{Pt-P}$ = 3839 Hz, compared with the data for **5**). The $^1$H NMR spectrum displays a peak at $\delta$ = 3.30 ppm, which integrates for 12 protons, and a singlet at $\delta$ = 2.00 ppm (three protons). We therefore conclude that **10** is *cis*-[Pt(PPh$_3$)$_2$(CH$_3$CN)(tmtu)]$^{2+}$. The TfO salt of this intermediate evolves to **3**(TfO) in a few hours, whereas such a conversion is much slower for the $BF_4$ derivative (>24 h). A fast conversion of **10**($BF_4$) to **3**($BF_4$) can be achieved by heating the solution at 40 °C or, rather interestingly, also at room temperature by addition of $(Et_4N)NO_3$ to the solution, which shows the high activity of nitrate anions in the cyclometallation reaction (Scheme 2).

When we investigated *cis*-[Pt(PPh$_3$)$_2$(AcO)$_2$] (**6**) in the initial runs, we did not use anhydrous conditions, since, as explained in the Introduction, cyclometallation of tmtu is not affected by the presence of water.[1] However, to our surprise, the reaction of **6** with tmtu did not afford **3**, but a mixture, which, according to $^{31}$P NMR spectroscopy (Table 1), contains essentially two products **8** and **9** (minor component), with no detectable signal from **3**. Slow diffusion of hexane into a $CH_2Cl_2$ solution of this mixture gave crystals, which were found to be *trans*-[Pt(PPh$_3$)$_2$(mtc)$_2$] through X-ray analysis, see below. A $CDCl_3$ solution of these crystals produced a $^{31}$P NMR spectrum consistent with that of **9**.

Compounds **8** and **9** were also obtained by reaction of tmtu with the malonato complex **7**.

Table 1. $^{31}$P and relevant $^1$H NMR spectroscopic data.[a]

| Compound | $^{31}$P NMR | $^1$H NMR |
|---|---|---|
| *cis*-[Pt(PPh$_3$)$_2$(NO$_3$)$_2$], **1**[b] | 3.62 (4010) | |
| *cis*-[Pt(PPh$_3$)$_2$(NO$_3$)(tmtu)]$^+$, **2**[b] | 1.70 (3830), 18.95 (3225) ($J_{P-P}$ 19.5) | 3.17 (s, 12 H) |
| *cis*-[Pt(PPh$_3$)$_2$(tmtu*)]$^+$, **3**[b] | 17.14 (2022), 22.22 (3462) ($J_{P-P}$ 22.8) | 3.02 (s, 6 H), 3.08 (s, 3 H), 3.52 (mt, $J_{Pt-H}$ 60, 2 H) |
| *cis*-[Pt(PPh$_3$)$_2$(CF$_3$CO$_2$)$_2$], **4**[c] | 4.38 (3933) | |
| *cis*-[Pt(PPh$_3$)$_2$(CH$_3$CN)$_2$]$^{2+}$, **5** | 3.27 (3683) | 2.00 (s, 3 H) |
| *cis*-[Pt(PPh$_3$)$_2$(AcO)$_2$], **6** | 5.72 (3826) | 1.34 (s) |
| [Pt(PPh$_3$)$_2$(malonato)], **7** | 7.9 (3757) | 3.42 (s, 2 H) |
| *cis*-[Pt(PPh$_3$)$_2$(mtc)$_2$], **8**[d] | 15.7 (3277) | 3.21 (s, 12 H) |
| *trans*-[Pt(PPh$_3$)$_2$(mtc)$_2$], **9** | 14.9 (3676) | 3.20 (s, 12 H) |
| *cis*-[Pt(PPh$_3$)$_2$(CH$_3$CN)(tmtu)]$^{2+}$, **10**[d] | 7.6 (3839), 13.7 (2890) ($J_{P-P}$ 17.0) | 3.30 (12 H), 2.00(3 H) |
| *cis*-[Pt(PPh$_3$)$_2$(AcO)(tmtu)]$^+$, **11**[d] | 6.82 (3979), 17.2 (3246) ($J_{P-P}$ 19) | 2.71 (s, 12 H), 2.22 (s, 3 H) |
| *cis*-[Pt(PPh$_3$)$_2$(AcO)(NO$_3$)], **12**[d] | 6.60 (4250), 8.15 (3921)[e] | 1.31 (br., 3 H) |
| [Pt(dppe)(NO$_3$)$_2$], **13**[f] | 32.94 (3942) | |
| [Pt(dppe)(tmtu*)]$^+$, **14** | 45.4 (3259), 45.9 (1900) ($J_{P-P}$ 7.7) | 4.00 (dd, $J_{Pt-P}$ 54.4, 2 H), 3.23 (s, 3 H), 3.14 (s, 6 H) |
| [Pt(dppe)(AcO)$_2$], **15** | 30.99 (3785) | 1.71 (s, 6 H) |
| [Pt(dppe)(mtc)$_2$], **16** | 43.04 (3157) | 3.37 (s, 12 H) |

[a] $CDCl_3$ solutions, $\delta$ values in ppm from external $H_3PO_4$ and $Me_4Si$. $J$ in Hz. $^1$H integrations are based on the peaks of the phosphane moieties. [b] Compare ref.[1]. [c] Compare ref.[8]. [d] Recorded in $CH_2Cl_2/CDCl_3$, 1:1. [e] These peaks were too broad to allow a reliable determination of the P–P coupling constant. [f] Compare ref.[9]

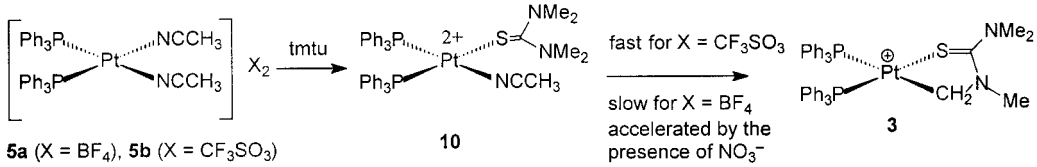


Scheme 2.

 © 2006 Wiley-VCH Verlag GmbH & Co. KGaA, Weinheim 

### Structure and Characterization of *trans*-[$Pt(PPh_3)_2(mtc)_2$] (9)

The structure consists of the packing of [$Pt(PPh_3)_2(mtc)_2$] molecules with normal van der Waals contacts. An ORTEP[10] view of the complex is shown in Figure 1, while selected bond lengths and angles are reported in Table 2. The metal ion is four-coordinate square planar, with two mutually *trans* phosphane groups and two *trans* mtc anions that are monodentate and coordinated through their sulfur atoms. The planarity around Pt is rigorous, since this atom lies on a crystallographic inversion centre. The mtc ligand is essentially planar, with maximum deviations from the least-squares plane of +0.033(1) Å for S and –0.037(3) Å for C(3). The Pt–P bond length [2.316(1) Å] is comparable with values found in other *trans*-$Pt(PPh_3)_2$ complexes.[11,12] To the best of our knowledge, no Pt-mtc complex has ever been structurally characterised, however, we note that the Pt–S bond length in **9** is in the range of those found in the few instances of monodentate dialkyldithiocarbamate complexes of $Pt^{II}$.[13] In particular, a compound analogous to **8**, *trans*-[$Pt(PMe_2Ph)_2$(dttc-*S*)$_2$], displays a very similar Pt–S distance [2.335(2) Å].[14] The dihedral angle between the mtc best plane and the metal coordination plane is 68.0(5)° and can be compared with that of the analogous *trans*-[$Pd(PPh_3)_2$(*N*-dipropylmonothiocarbamato)$_2$].[4] Bond lengths within the thiocarbamato ligand are also similar.[4]

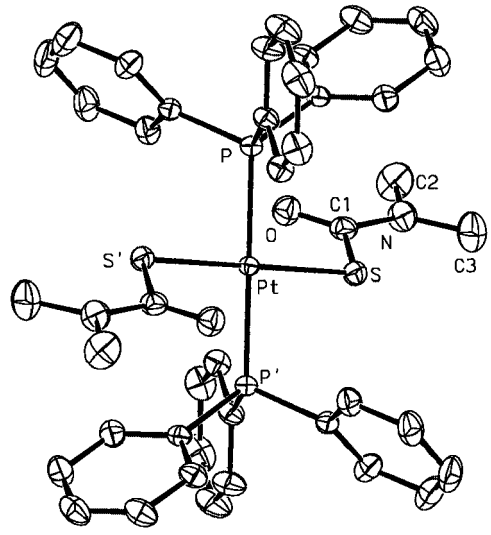


Figure 1. ORTEP view of complex**9**. Ellipsoids are drawn at the 30% probability level.

The NMR spectroscopic data of **9** are reported in Table 1. Note the rather high Pt–P coupling constant, which in *trans*-$Pt^{II}(PPh_3)_2$ complexes is usually in the 2500–3000 Hz range; higher values have, however, also been reported.[12,15] The $FAB^+$ mass spectrum of **9** (see Experimental section) shows only a weak peak (ca. 5%) corresponding to $[M]^+$; the most abundant peaks are due to $[Pt(PPh_3)_2(SCO)_2]^+$ and $[Pt(PPh_3)_2(mtc)]^+$. This behaviour seems characteristic of these phosphane mtc complexes.

Table 2. Selected bond lengths [Å] and angles [°] for **9**, with estimated standard deviations in parentheses.

| | | | |
|---|---|---|---|
| Pt–S | 2.336(1) | Pt–P | 2.316(1) |
| S–C(1) | 1.777(2) | O–C(1) | 1.222(3) |
| N–C(1) | 1.375(3) | N–C(2) | 1.460(3) |
| N–C(3) | 1.450(4) | | |
| S–Pt–S′ | 180 | S–Pt–P | 94.1(1) |
| S–Pt–P′ | 85.9(1) | P–Pt–P′ | 180 |
| Pt–S–C(1) | 105.2(1) | C(1)–N–C(2) | 117.6(2) |
| C(1)–N–C(3) | 125.0(2) | C(2)–N–C(3) | 117.3(3) |
| S–C(1)–O | 123.1(2) | S–C(1)–N | 115.6(2) |
| O–C(1)–N | 121.2(2) | | |

### Mechanistic Studies

When the reaction between tmtu and **6** was followed by $^{31}P$ NMR spectroscopy, we observed the fast formation of two main species, **8** and **11**. The resonances due to **11** diminish with time, and after 4 hours at room-temperature, the spectrum shows only peaks from **8** and **9**. The concentration of **9** increases on standing, although at a very slow rate (weeks); it is therefore likely that isomerisation occurs after hydrolysis. Isolation of the *trans* isomer **9** as a pure sample is due to its lower solubility in the crystallisation procedure.

As for the intermediate **11**, NMR spectroscopic data (see Table 1) suggest the formula *cis*-[$Pt(PPh_3)_2$(AcO)(tmtu)](AcO). In fact, tmtu is still present as such (i.e. not yet hydrolysed), as shown by the presence in the $^1H$ NMR spectrum of a peak at $\delta$ = 2.71 ppm, which integrates for 12 protons. As for the $^{31}P$ NMR spectrum, the Pt–P coupling constant of the doublet at $\delta$ = 17.2 ppm (3246 Hz) is in accordance with a P atom *trans* to an S ligand,[1,9] while the doublet at $\delta$ = 6.82 ppm ($J_{Pt-P}$ = 3979 Hz) is assigned to P *trans* to the acetato moiety (compared with $\delta$ = 5.72 ppm, $J_{Pt-P}$ = 3826 Hz in **6**). In order to prove the assignment of **11**, we performed the following experiment. We mixed, in $CH_2Cl_2$, equimolar quantities of **1** and **6**, obtaining the fast equilibration of these two materials with a new species **12** in the ratio 1:1:3. The two doublets shown in the $^{31}P$ NMR spectrum of this new species are in agreement with two phosphane groups *trans* to the $NO_3$ and AcO ligands (Table 1, $\delta$ and $J_{Pt-P}$ values of **12** compared with those of **1** and **6**). Since no other ligand is present, **12** must be *cis*-[$Pt(PPh_3)_2$(AcO)($NO_3$)]. Upon addition of one mole of tmtu per mole of Pt, we obtained a compound with the same NMR parameters as **11**, as the only species in solution (Scheme 3).

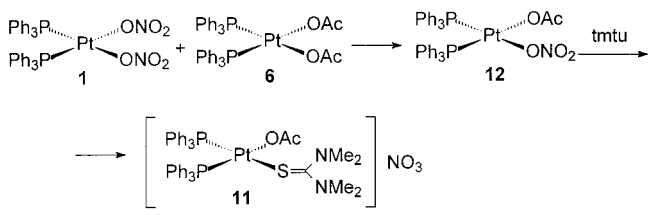


Scheme 3.

 © 2006 Wiley-VCH Verlag GmbH & Co. KGaA, Weinheim 

The latter solution is stable (>1 day), i.e. no hydrolysis was observed, even in wet $CH_2Cl_2$. Because no "free" (i.e. uncomplexed) acetate is present, it is concluded that it is this ion that triggers the hydrolysis reaction. It must be noted that in this experiment, **11** was obtained as the nitrate salt, but no cyclometallation was observed, despite the presence of free $NO_3^-$, which, according to the results described in a previous section, should promote such a reaction. However, the C–H activation step of the cyclometallation process requires a labile ligand that is *cis* to tmtu.[1–3] In **11**, this position is occupied by an acetato group that is *trans* to a phosphane group, a situation that, because of the antisymbiosis effect,[16] renders a carboxylato ligand rather inert to substitution,[17] as we have recently observed.[18]

Characterisation of **8** presents the problem that it could not be isolated in a pure form, as a result of contamination with **9**. Only after repeated crystallisations could a few milligrams of a pure sample of **8** be obtained, which is just enough for mass and NMR spectroscopy. The $^{31}P$ NMR parameters of **8** [a singlet with Pt–P coupling constant in the 3200 Hz range (Table 1)] are indicative of a *cis*-$PtP_2S_2$ coordination set, i.e. two equivalent phosphane groups *trans* to sulfur ligands.[9] Moreover, the peak at $\delta$ = 3.21 ppm in the proton spectrum integrates for 12 protons. These facts suggest the formula *cis*-[$Pt(PPh_3)_2(mtc)_2$] for **8**. A final confirmation of its stoichiometry was obtained by a high resolution $ESI^+$ spectrum, which showed a peak that corresponds to $[M + Na]^+$ (100%) and whose position differs by only 1 ppm from that computed. Fragmentation is similar to that of **9** (see Experimental Section).

In conclusion, the course of the hydrolysis reaction is summarised in Scheme 4.

Because **8** was always contaminated with the *trans* isomer, and to avoid the problem of *cis–trans* isomerisation, we decided to investigate the dppe derivatives.

First of all we wanted to check whether reaction of [$Pt(dppe)(NO_3)_2$] (**13**) with tmtu gives, in analogy with **1**, the cyclometallated product [Pt(dppe)(tmtu*)]($NO_3$) (**14**). This was indeed obtained, although at a much slower rate than in the case of **1**. Compound **14** was isolated and characterised by elemental analysis, $^1H$ and $^{31}P$ NMR spectroscopy (see Table 1). Not only are the Pt–P coupling constants in agreement with a P atom *trans* to a carbon atom and a P atom *trans* to an S ligand, but, more importantly, in the $^1H$ NMR spectrum, the resonances resulting from tmtu* are also very similar to those of **3**. In particular, the signal centred at 4 ppm, which integrates for 2 protons and displays Pt–H coupling (54.4 Hz), is assigned to Pt–$CH_2$ (Scheme 5).

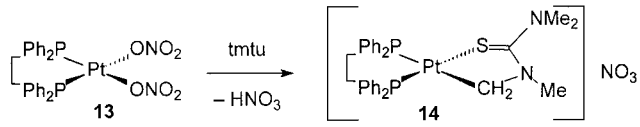


Scheme 5.

We then moved on to [$Pt(dppe)(AcO)_2$] (**15**). Reaction of this compound with tmtu led to the isolation of [$Pt(dppe)(mtc)_2$] (**16**) as a pure product. Besides elemental analysis and mass spectroscopy (see Experimental Section), its identification is confirmed by NMR spectroscopy (Table 1): a $^1H$ singlet which integrates for 12 protons and one $^{31}P$ singlet with $J_{Pt-P}$ in accordance with a P atom *trans* to an S atom. On the basis of comparing the Pt–P coupling constants, and by remembering that in the case of the dppe derivatives such constants are usually about 100 Hz lower than those of the analogous $PPh_3$ complexes,[19] we can confirm the assignment of the structure *cis*-[$Pt(PPh_3)_2(mtu)_2$] to **8**.

The above results show that the course of the reaction between these Pt–phosphane complexes and tmtu depends on the nature of the anion and the lability of the ligand in the position *cis* to tmtu. Thus, even in the presence of water, no hydrolysis of tmtu was observed with the nitrato and trifluoroacetato complexes as well as with compounds **5a** and **5b**; the only product is the cyclometallated species. On the contrary, with the acetato and malonato derivatives, cyclometallation seems to be inhibited, and, in the presence of water, tmtu is hydrolysed and the mtc complexes **8**, **9** and **16** are formed. To better clarify these points we performed the following experiments.

First, under strictly anhydrous conditions, no reaction was observed between tmtu and **6**, which was recovered unchanged after 4 hours. Addition of water, or allowing humidity to enter the reaction vessel by opening it, produced the monothiocarbamato complexes **8** and **9**, showing that water not only hydrolyses tmtu, but also, rather interestingly, that it has an active role in labilising the Pt–acetato bonds.

Second, again under anhydrous conditions, we mixed, in $CH_2Cl_2$, **1**, tmtu and NaAcO in the molar ratio 1:2:10. This led to the precipitation of $NaNO_3$ and to the formation of a 1:7 mixture of **6** and the acetato salt of **2** (Scheme 6).

The formation of **2** was easily recognised by NMR spectroscopy, since its nitrate salt is already known, as it was the intermediate species that was detected during the cyclometallation reaction of tmtu with **1**.[1] While this mixture is stable for more than one day, it slowly transforms into **11**.

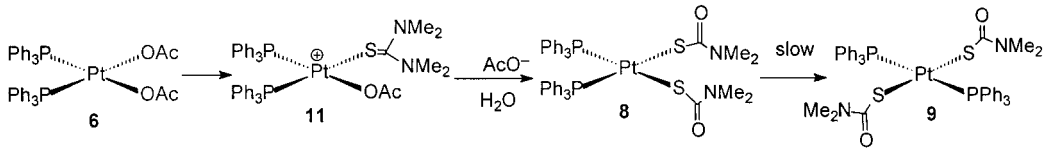


Scheme 4.

 © 2006 Wiley-VCH Verlag GmbH & Co. KGaA, Weinheim 

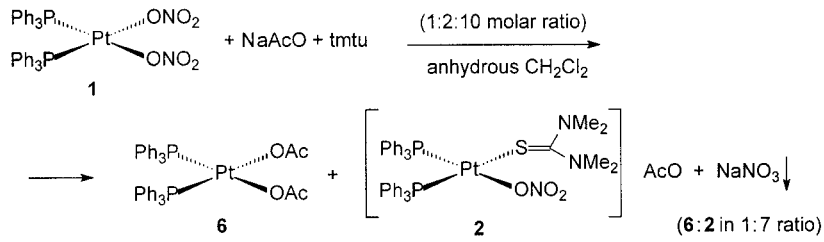


Scheme 6.

However, before such a transformation takes place, not only does no hydrolysis occur (no water is present), but also no cyclometallation is observed. This experiment confirms that the latter reaction is promoted by the presence of "free" nitrate and not by acetate; the promotion by free nitrate must be ruled out under these conditions as $NaNO_3$ is insoluble in $CH_2Cl_2$. When this experiment was repeated using wet $CH_2Cl_2$, tmtu was hydrolysed, as expected.

## Conclusions

We have shown that the interaction of tmtu with the *cis*-$Pt^{II}(phos)_2$ moieties can follow two different reaction paths according to the nature of the anions present. Thus $NO_3^-$, $CF_3CO_2^-$, $BF_4^-$ and $TfO^-$ lead to the cyclometallated products **3** or **14**, whereas $AcO^-$ and malonate are inactive and, in the presence of water, promote tmtu hydrolysis to give the mtc complexes **8**, **9** and **16**. The two reaction routes are not competitive: no hydrolysis occurs with the former anions and no cyclometallation is observed with the acetato and malonato complexes. As to the origin of the different behaviour, we note the following points.

Cyclometallation requires intermediate cationic complexes, such as **2** or **10**, in which *S*-coordinated tmtu is *cis* to a labile ligand (here $NO_3$, $CF_3CO_2$, $CH_3CN$). Dissociation of these ligands gives rise to a vacant coordination site in the position *cis* to tmtu, which through a σ C–H interaction with the metal centre is a key step in the C–H activation process.[2,3] On the contrary, an acetato group *cis* to tmtu and *trans* to a phosphane group, as in **11**, is less prone to substitution because of the antisymbiosis effect.[16–18] In the latter cationic complex, a methyl group of *S*-coordinated tmtu cannot interact with Pt and tmtu is activated towards nucleophilic attack. However, the function of the "free" anion is less clear; in particular, it is not obvious why deprotonation of a tmtu methyl group (whatever its intimate mechanism) is easily accomplished by $NO_3^-$ and not by $AcO^-$ (see the stability of the acetate salt of **2** in Scheme 6). We propose two possible explanations. First, the relative strengths of protic acids in $CHCl_3$ or $CH_2Cl_2$ cannot be compared with those in aqueous solutions. For instance, spectroscopic evidence suggests that $HNO_3$ is a weak acid (and hence $NO_3^-$ a strong base) in chlorinated solvents, even in the presence of water.[20] Thus $NO_3^-$ can easily capture a proton, favouring deprotonation of a $CH_3$ group. However, the reason why "free" $NO_3^-$ does not induce hydrolysis in the presence of water remains unclear. A second point is that in non-ionising solvents, such as $CHCl_3$ and $CH_2Cl_2$, the anions are not "free", but presumably strongly associated with the cationic complexes that are the intermediate species in both C–H activation (**2**) and hydrolysis (**11**). The different reaction routes reported here may also depend on the degree and the nature of these ion pairs, which, at the present stage, are difficult to rationalise.

Formation of the *trans* isomer **9** deserves a final comment. In all the hydrolysis runs of tmtu with either **6** or **7**, the *cis* isomer **8** was found to be more abundant, but a small amount of **9** was always present. Formation of such *trans* isomers is not surprising. Not only has the analogous Pd complex this geometry,[4] but also it has been reported that complexes with a somewhat similar coordination set, i.e. $[Pt(phos)_2(ER)_2]$ (E = S, Se, Te), crystallise with a *trans* geometry[21] or the initially obtained *cis* complex slowly rearranges to the *trans* isomer, which has been calculated to be more stable.[22] It is tempting to think that the formation of **9** may be associated with the rather large $J_{Pt-P}$ value, an indication of a large σ contribution to the Pt–P interaction, which probably originates from the poor σ-donor ability of S-coordinated mtc groups. Thus, formation of this isomer may arise from a subtle balance between the *trans* and *cis* influence.

## Experimental Section

Elemental analyses were performed at the Microanalytical Laboratory, the University of Milano. $^1H$ and $^{31}P\{^1H\}$ NMR spectra (Table 1) were recorded on a Bruker Advance DRX 300 at 300 and 121 MHz respectively; $\delta$ values (ppm) are vs. external $Me_4Si$ and $H_3PO_4$. Mass spectra were recorded with a VCA Analytical 7070 EQ ($FAB^+$, from nitrobenzyl alcohol, with xenon as the FAB source) and with an ICR-FTMS APEX II with a 4.7-T magnet, Bruker Daltonics ($ESI^+$, $CH_2Cl_2$/methanol, 1:1). Isotope cluster abundance was checked by computer simulation.

All chemicals were reagent grade. Except where otherwise stated, solvents were used as received.

The syntheses of $[Pt(phos)_2(NO_3)_2]$ have been described previously.[5] *cis*-$[Pt(PPh_3)_2(CH_3CN)_2](BF_4)_2$, *cis*-$[Pt(PPh_3)_2(CH_3CN)_2](CF_3SO_3)_2$ and *cis*-$[Pt(PPh_3)_2(CF_3CO_2)_2]$ have been prepared according to literature procedures.[9,23] cis-$Pt[(PPh_3)_2(AcO)_2]$ (**6**), $[Pt(PPh_3)_2(malonato)]$ (**7**) and $[Pt(dppe)(AcO)_2]$ (**15**) were obtained in 75% yields, by a modification of literature methods,[8] using excess sodium acetate or malonate instead of the corresponding silver salts.

 © 2006 Wiley-VCH Verlag GmbH & Co. KGaA, Weinheim 

**Cyclometallation of tmtu with the Acetonitrile Complexes**

**3($BF_4$):** A $CH_2Cl_2$ solution (20 mL) of **5a** (0.120 g, 0.123 mmol) and tmtu (0.016 g, 0.123 mmol) was refluxed for 4 h. The solution was concentrated to 2 mL under reduced pressure, and addition of ethyl acetate gave 0.087 g of the product (75%). $C_{41}H_{41}BF_4N_2P_2PtS$ (937.68): calcd. C 52.5, H 4.4, N 3.0%; found C 52.8, H 4.7, N 3.2%.

**3(TfO):** This was obtained in a manner similar to that described above from **5a** (0.155 g) and tmtu (0.019 g), but the reaction was performed at room temperature. Yield: 69.4% (0.110 g). $C_{42}H_{41}F_3N_2O_3P_2PtS_2$ (999.94): calcd. C 50.5, H 4.1, N 2.8%; found C 50.2, H 4.3, N 3.0%.

***cis*-[Pt($PPh_3$)$_2$(AcO)(tmtu)]$^+$ (11):** An equimolar amount of tmtu (0.006 g) was added to a solution of [Pt($PPh_3$)$_2$($NO_3$)$_2$] (0.035 g, 0.041 mmol) and [Pt($PPh_3$)$_2$(AcO)$_2$] (0.035 g, 0.041 mmol) in $CH_2Cl_2$ (20 mL). After 6 h at room temperature, the solution was concentrated under reduced pressure. Addition of diisopropyl ether gave a white product. Yield: 0.053 g (65.3%). $C_{43}H_{45}N_3O_5P_2PtS$ (972.93): calcd. C 53.1, H 4.7, N 4.3%; found C 52.8, H 4.6, N 4.3%. The presence of coordinated acetate and ionic nitrate was confirmed by IR spectroscopy (KBr pellets): $\tilde{\nu}$ = 1595 ($\nu_{asym}$ coordinated carboxylate), 1384 (sharp, ionic $NO_3^-$) $cm^{-1}$.

***trans*-[Pt($PPh_3$)$_2$(mtc)$_2$] (9):** A $CH_2Cl_2$ solution (20 mL) of [Pt($PPh_3$)$_2$(AcO)$_2$] (0.060 g, 0.0717 mmol) and tmtu (0.019 g, 0.144 mmol) was left at room temperature for 6 h. After two weeks diffusion of *n*-hexane gave crystals (10 mg) suitable for X-ray investigation. FAB-MS: *m*/*z* (%) = 927 (5) $[M]^+$, 839 (50) $[M - 2\ NMe_2]^+$, 823 (100) $[M - mtc]^+$, 719 (100) $[M - 2\ mtc]^+$.

***cis*-[Pt($PPh_3$)$_2$(mtc)$_2$] (8):** The $CH_2Cl_2$/hexane solution obtained above, after filtration of **9**, was evaporated to 2 mL and filtered. Addition of diisopropyl ether to the filtrate gave a white precipitate, which was found by $^{31}P$ NMR spectroscopy to consist of **9** with an impurity of **8**. Repeated crystallizations gave a few milligrams of pure **8** ($^{31}P$ NMR evidence). FAB-MS: *m*/*z* (%) = 927 (5) $[M]^+$, 839 (80) $[M - 2\ NMe_2]^+$, 823 (80) $[M - mtc]^+$, 719 (100) $[M - 2\ mtc]^+$. ESI-MS: *m*/*z* (%) = 950 (100) $[M + Na]^+$, 928 (5) $[M + 1]^+$, 839 (5) $[M - 2\ NMe_2]^+$, 823 (5) $[M - mtc]^+$. High resolution ESI-MS: calcd. 950.1706 $[M + Na]^+$; found 950.1712.

**[Pt(dppe)(tmtu*)]$NO_3$ (14):** This compound was obtained by refluxing a solution of [Pt(dppe)($NO_3$)$_2$] (0.050 g, 0.07 mmol) and tmtu (0.009 g, 0.07 mmol) for two days. The white product was obtained by addition of diisopropyl ether. Yield: 0.033 g (60%). $C_{31}H_{35}N_3O_3P_2PtS$ (786.72): calcd. C 47.3, H 4.5, N 5.3%; found C 47.0, H 4.9, N 5.6%. FAB-MS: *m*/*z* = 724 $[M - NO_3]^+$.

**[Pt(dppe)(mtc)$_2$] (16):** A solution of [Pt(dppe)(AcO)$_2$] (0.055 g, 0.077 mmol) in $CH_2Cl_2$ (20 mL) and tmtu (0.021 g, 0.155 mmol) was left at room temperature for 4 h and concentrated under reduced pressure. The product was obtained by addition of diisopropyl ether. Yield: 0.054 g (86.8%). $C_{32}H_{36}N_2O_2P_2PtS_2$ (801.80): calcd. C 47.9, H 4.5, N 3.5%; found C 47.5, H 4.3, N 3.8%. FAB-MS: *m*/*z* (%) = 713 (100) $[M - 2\ NMe_2]^+$, 697 (20) $[M - mtc]^+$, 591 (5) $[M - 2\ mtc]^+$. ESI-MS: *m*/*z* (%) = 824 (5) $[M + Na]^+$, 713 (100) $[M - 2\ NMe_2]^+$, 697 (50) $[M - mtc]^+$.

**Reaction of 1 with tmtu and Sodium Acetate:** Sodium acetate (0.039 g 0.476 mmol) was added to a solution of [Pt($PPh_3$)$_2$($NO_3$)$_2$] (0.040 g, 0.048 mmol) and tmtu (0.013 g, 0.055 mmol) in $CH_2Cl_2$ (20 mL). The resulting slurry was vigorously stirred for 4 h at room temperature, and the solvent was evaporated completely under reduced pressure. The $^{31}P$ NMR spectrum of a $CDCl_3$ solution of the residue showed the presence of the monothiocarbamato complexes.

**Reactions under Anhydrous Conditions:** The following reactions were performed under an atmosphere of dry nitrogen, using reagents which had been dried under vacuum for 24 h. $CH_2Cl_2$ was distilled over $CaH_2$ immediately before use.

**Reaction of *cis*-[Pt($PPh_3$)$_2$(AcO)$_2$] (6) with tmtu:** tmtu (0.013 g, 0.10 mmol) was added to a solution of **6** (0.042 g, 0.05 mmol) in anhydrous $CH_2Cl_2$ (20 mL). The solution was left for 6 h at room temperature under a nitrogen atmosphere. The solvent was evaporated to dryness under vacuum and redissolved in $CDCl_3$. $^{31}P$ NMR spectroscopy showed the presence of only the starting material.

**Reactivity of 1 with tmtu and Sodium Acetate:** Dry sodium acetate (0.042 g, 0.512 mmol) was added to a $CH_2Cl_2$ solution (20 mL) of [Pt($PPh_3$)$_2$($NO_3$)$_2$] (0.043 g, 0.051 mmol) and tmtu (0.0134 g, 0.103 mmol). The slurry was stirred vigorously for 4 h at room temperature under a nitrogen atmosphere, and the solvent was then evaporated completely under vacuum. $^{31}P$ NMR spectroscopy of a $CDCl_3$ solution of the residue showed the presence of a mixture of [Pt($PPh_3$)$_2$(AcO)$_2$] (**6**) and [Pt($PPh_3$)$_2$($NO_3$)(tmtu)]$^+$ (**2**).

**X-ray Data Collection and Structure Determination:** Crystal data are summarised in Table 3. The diffraction experiment was carried out with a Bruker SMART CCD area-detector diffractometer at 296 K, using Mo-$K_\alpha$ radiation ($\lambda$ = 0.71073) with a graphite crystal monochromator in the incident beam. No crystal decay was ob-

Table 3. Crystallographic data.

| | |
|---|---|
| Compound | **9** |
| Formula | $C_{42}H_{42}N_2O_2P_2PtS_2$ |
| *M* | 927.98 |
| Colour | colourless |
| Crystal system | triclinic |
| Space group | $P\bar{1}$ |
| *a* [Å] | 10.087(1) |
| *b* [Å] | 10.411(1) |
| *c* [Å] | 11.455(1) |
| *α* [°] | 99.12(1) |
| *β* [°] | 114.88(1) |
| *γ* [°] | 104.04(1) |
| *U* [Å$^3$] | 1011.3(2) |
| *Z* | 1 |
| *F*(000) | 464 |
| $D_c$ [g cm$^{-3}$] | 1.524 |
| *T* [K] | 296 |
| Crystal dimensions [mm] | 0.28 × 0.32 × 0.41 |
| *μ* (Mo-*Kα*) [cm$^{-1}$] | 37.2 |
| Min. and max. transmission Factors | 0.754–1.000 |
| Scan mode | *ω* |
| Frame width [°] | 0.30 |
| Time per frame [sec] | 10 |
| No. of frames | 4900 |
| Detector-sample distance [cm] | 4.00 |
| *θ* range | 3–27 |
| Reciprocal space explored | full sphere |
| No. of reflections (total; independent) | 23827, 4411 |
| $R_{int}$ | 0.0213 |
| Final $R_2$ and $R_{2w}$ indices[a] ($F^2$, all reflections) | 0.030, 0.038 |
| Conventional $R_1$ index [$I>2\sigma(I)$] | 0.015 |
| Reflections with $I>2\sigma(I)$ | 4323 |
| No. of variables | 232 |
| Goodness of fit[b] | 0.94 |

[a] $R_2 = [\Sigma(|F_o^2 - kF_c^2|)/\Sigma F_o^2]$, $R_{2w} = [\Sigma w/(F_o^2 - kF_c^2)^2/\Sigma w(F_o^2)^2]^{1/2}$. [b] $[\Sigma w(F_o^2 - kF_c^2)^2/(N_o - N_v)]^{1/2}$, where $w = 4F_o^2/\sigma(F_o^2)^2$, $\sigma(F_o^2) = [\sigma^2(F_o^2) + (pF_o^2)^2]^{1/2}$, $N_o$ is the number of observations, $N_v$ the number of variables, and *p*, the ignorance factor, = 0.02.

 © 2006 Wiley-VCH Verlag GmbH & Co. KGaA, Weinheim 

served, therefore no time-decay correction was needed. The collected frames were processed with the software SAINT,[24] and an empirical absorption correction was applied (SADABS)[25] to the collected reflections. Calculations were performed using the Personal Structure Determination Package,[26] and the physical constants tabulated therein.[27] The structure was solved by direct methods (SHELXS)[28] and refined by full-matrix least-squares using all reflections and minimising the function $\Sigma w(F_o^2 - kF_c^2)^2$ (refinement on $F^2$). All the non-hydrogen atoms were refined with anisotropic thermal factors. The hydrogen atoms were placed in their ideal positions (C–H = 0.97 Å), with the thermal parameter *B* 1.10 times that of the carbon atom to which they are attached, and were not refined. In the final Fourier map, the maximum residual was 0.76(6) e Å$^{-3}$ at 0.82 Å from Pt. CCDC-272407 contains the supplementary crystallographic data for this paper. These data can be obtained free of charge from The Cambridge Crystallographic Data Centre via www.ccdc.cam.ac.uk/data_request/cif.

## Acknowledgments

This work has been supported by MIUR. We thank Dr. E. Caneva for the ESI mass spectra and Dr. E. S. Stoyanov for a helpful discussion on the acid strengths in chlorinated solvents.

[1] S. Fantasia, M. Manassero, A. Pasini, *Inorg. Chem. Commun.* **2004**, *7*, 97–100.
[2] U. Fekland, K. I. Goldberg, *Adv. Inorg. Chem.* **2003**, *54*, 259–320.
[3] R. H. Crabtree, *J. Organomet. Chem.* **2004**, *689*, 4083–4091.
[4] G. Besenyei, E. Herdtweck, S. Holly, D. Maennig, H. Noerth, L. I. Simandi, P. Viski, *Inorg. Chem.* **1988**, *27*, 3201–3201.
[5] For instance: a) R. Colton, T. A. Stephenson, *Polyhedron* **1984**, *3*, 231–234; b) G. Exarchos, S. D. Robinson, J. W. Steed, *Polyhedron* **2001**, *20*, 2951–2963; c) R. Colton, J. Ebner, *Inorg. Chem.* **1989**, *28*, 1559–1563.
[6] a) E. M. Krankovits, R. J. Magee, M. J. O'Connor, *Aust. J. Chem.* **1973**, *26*, 1645–1652; b) K. R. M. Springsteen, D. L. Greene, B. J. McCormick, *Inorg. Chim. Acta* **1977**, *23*, 13–18.
[7] a) J. G. M. van der Linden, W. Blommerde, A. H. Dix, F. W. Pijpers, *Inorg. Chim. Acta* **1977**, *24*, 261–267; b) R. D. Bereman, D. M. Baird, J. R. Dorfman, J. Bordner, *Inorg. Chem.* **1982**, *21*, 2365–2368; c) B. J. McCormick, R. Bereman, D. Baird, *Coord. Chem. Rev.* **1984**, *54*, 99–130.
[8] A. L. Tan, P. M. N. Low, Z.-Y. Zhou, W. Zheng, B.-M. Wu, T. C. W. Mak, T. S. A. Hor, *J. Chem. Soc., Dalton Trans.* **1996**, 2207–2214.
[9] A. Pasini, S. Rizzato, D. De Cillis, *Inorg. Chim. Acta* **2001**, *315*, 196–204.
[10] C. K. Johnson, *ORTEP*, Report ORNL-5138, Oak Ridge National Laboratory, Oak Ridge, Tn, **1976**.
[11] For instance: a) N. M. Boag, K. Mohan Rao, N. J. Terril, *Acta Crystallogr., Sect. C* **1991**, *47*, 1064–1065; b) A. C. Dema, C. M. Lukehart, *Inorg. Chim. Acta* **1997**, *264*, 193–198; c) D. Steinborn, S. Becke, C. Bruhn, F. W. Heinemann, *J. Organomet. Chem.* **1998**, *556*, 189–196; d) M. Basato, A. Biffis, G. Martinati, C. Tubaro, A. Venzo, P. Ganis, F. Benetollo, *Inorg. Chim. Acta* **2003**, *355*, 399–403.
[12] a) N. Mintcheva, Y. Nishihara, A. Mori, K. Osakada, *J. Organomet. Chem.* **2001**, *629*, 61–67; b) U. Abram, D. Belli Dell′Amico, F. Calderazzo, L. Marchetti, J. Straehle, *J. Chem. Soc., Dalton Trans.* **1999**, 4093–4098; c) W. V. Konze, B. L. Scott, G. J. Kubas, *Chem. Commun.* **1999**, 1807–1808.
[13] a) P. C. Christidis, P. J. Rentzeperis, *Acta Crystallogr., Sect. B* **1979**, *35*, 2543–2547; b) R. Colton, M. F. Mackay, V. Tedesco, *Inorg. Chim. Acta* **1993**, *207*, 227–232.
[14] I. J. B. Lin, H. W. Chen, J. P. Fackler Jr, *Inorg. Chem.* **1978**, *17*, 394–401.
[15] E. Enzmann, M. Eckert, W. Ponikwar, K. Polborn, S. Schneiderbauer, M. Beller, W. Beck, *Eur. J. Inorg. Chem.* **2004**, 1330–1340.
[16] J. Kuyper, *Inorg. Chem.* **1979**, *18*, 1484–1489.
[17] a) L. Battan, S. Fantasia, M. Manassero, A. Pasini, M. Sansoni, *Inorg. Chim. Acta* **2005**, *358*, 555–564 and references cited therein; b) L. Battan, M. Manassero, A. Pasini, *Inorg. Chem. Commun.* **2001**, *4*, 606–609.
[18] R. G. Pearson, *Chemical Hardness*, Wiley VCH, **1977**, p. 15.
[19] P. S. Pregosin, R. W. Kunz, *$^{31}P$ and $^{13}C$ NMR of Transition Metal Complexes*, Springer-Verlag, **1979**.
[20] a) E. S. Stoyanov, T. P. Vorob′yova, I. V. Smirnov, *J. Struct. Chem.* **2003**, *44*, 365–375; b) E. S. Stoyanov, personal communication.
[21] a) T. B. Rauchfuss, J. S. Shu, D. M. Roundhill, *Inorg. Chem.* **1976**, *15*, 2096–2101; b) V. K. Jain, S. Kannan, E. R. T. Tiekink, *J. Chem. Res. (S)* **1994**, 85; V. K. Jain, S. Kannan, E. R. T. Tiekink, *J. Chem. Res. (M)* **1994**, 501.
[22] M. S. Hannu-Kuure, J. Komulainen, R. Oilunkaniemi, R. S. Laitinen, R. Suontamo, M. Ahlgren, *J. Organomet. Chem.* **2003**, *666*, 111–120.
[23] a) R. Bertani, R. A. Michelin, M. Mozzon, A. Sassi, M. Basato, A. Biffis, G. Martinati, M. Zecca, *Inorg. Chem. Commun.* **2001**, *4*, 281–284; b) R. Bertani, M. Biasiolo, K. Darini, R. A. Michelin, M. Mozzon, F. Visentin, L. Zanotto, *J. Organomet. Chem.* **2002**, *642*, 32–39.
[24] SAINT Reference manual, Siemens Energy and Automation, Madison, W1, **1994–1996**.
[25] G. M. Sheldrick, *SADABS, Empirical Absorption Correction Program*, University of Göttingen, **1997**.
[26] B. A. Frenz, *Comput. Phys.* **1988**, *2*, 42–47.
[27] *Crystallographic Computing 5*, Oxford University Press, Oxford, U. K., **1991**, ch. 11, p. 126.
[28] G. M. Sheldrick, *SHELXS 86, Program for the Solution of Crystal Structures*, University of Göttingen, Germany, **1985**.

Received: October 6, 2005
Published Online: February 9, 2006

 © 2006 Wiley-VCH Verlag GmbH & Co. KGaA, Weinheim 

DOI: 10.1002/ejic.200500943

# An Electron Microscopy Study of New Chemically Twinned Phases in the $MgS$-$Yb_2S_3$ System

**Esteban Urones-Garrote,*[a] Adrián Gómez-Herrero,[b] Ángel R. Landa-Cánovas,[c] and L. Carlos Otero-Díaz[a,b]**

**Keywords:** Chemical twinning / Electron microscopy / Rare earths / Sulfides / Solid-state structures

Four new phases in the $MgS$-$Yb_2S_3$ system have been identified and characterised by means of transmission electron microscopy and associated techniques, such as microdiffraction and X-ray energy dispersive spectroscopy analysis. The observed stoichiometries are: $MgYb_2S_4$ [$a$ = 0.3752(2), $b$ = 1.259(1), $c$ = 1.268(2) nm] and $Mg_2Yb_6S_{11}$ [$a$ = 0.37297(4), $b$ = 1.2592(2), $c$ = 3.4853(3) nm] with orthorhombic symmetry (space group $Cmcm$) and $Mg_3Yb_8S_{15}$ [$a$ = 1.2637(1), $b$ = 0.37176(5), $c$ = 2.4132(2) nm; $\beta$ = 100.40(1)°] and $MgYb_4S_7$ [$a$ = 1.2578(2), $b$ = 0.3735(3), $c$ = 1.1417(7) nm; $\beta$ = 104.88(6)°] with monoclinic symmetry (space group $C2/m$). Their structures can be described and derived from the NaCl-type by the crystallographic operation of chemical twinning at the unit-cell level along the $\{113\}_{NaCl}$ planes. The $a$ and $b$ lattice parameters are common in all the structures while the $c$ parameter depends on the total extension of the twin slabs' sequence, $n$, such that $c \approx n \times d(113)_{MgS}$ (for orthorhombic phases) or $d(001) \approx n \times d(113)_{MgS}$ (for monoclinic phases). All the unit-cell parameters were refined from the X-ray powder diffraction data after the unit-cell symmetries had been deduced from electron microscopy data.

(© Wiley-VCH Verlag GmbH & Co. KGaA, 69451 Weinheim, Germany, 2006)

## Introduction

The crystallographic operation termed "chemical twinning at the unit-cell level" by Hyde and Andersson[1,2] is very useful for understanding, describing and clarifying many crystal structures as this concept allows the building of apparently complex structures from simple units. The regular and repeated reflection twinning on the {113} planes of the NaCl-type parent structure produces a series of homologous ordered phases in an important number of systems, including sulfides, sulfo salts and oxides.[1,2] Ferraris et al.[3] denote it as a "lillianite homologous series", after the structure of $Pb_3Bi_2S_6$.[4] The twinning operation generates trigonal prisms in the composition planes perpendicular to $[113]_{NaCl}$ that share their triangular faces. The frequency of these composition (or twin) planes is responsible for the stoichiometry. They are separated by blocks of NaCl-type structure whose thickness and ordering reflect the $c$ unit-cell parameter. The block thickness can be denoted by the number of atom layers parallel to the twin planes.[1] The members of the homologous series present equal $a$ and $b$ crystal parameters while the $c$ parameter varies with the total twin slabs' sequence and is proportional to $d(113)_{NaCl}$.

Several phases derived from the NaCl-type by chemical twinning have been reported in the Pb-Bi-S system, such as natural sulfo salts[3] and synthetic samples,[5,6] including $PbBi_4S_7$, with a $Y_5S_7$-type structure,[7] which presents a ...(4,3)... twin sequence. Other phases with more complex twin slab sequences have also been found, such as $Pb_2Bi_6S_{11}$ [...(4,4,3,4,4,3)...] and $Pb_3Bi_{10}S_{18}$ [...(4,4,3,4,3,4,4,3,4,3)...]. Bakker and Hyde were the first to study these structures by means of transmission electron microscopy (TEM), especially several phases in the Mn-Y-S system,[8] including the phase $MnY_2S_4$, which has a $CaTi_2O_4$-type structure[9] with a ...(4,4)... twin sequence. Some other phases were observed and predicted between $MnY_2S_4$ and $MnY_4S_7$ stoichiometries, such as $Mn_3Y_8S_{15}$ and $Mn_2Y_6S_{11}$, whose structure can be considered as an ordered intergrowth between the former phases.

The Cr-Er-S system has been extensively studied, mainly by X-ray powder diffraction (XRPD) data, by Tomas et al.,[10–12] who reported several different phases, such as $CrEr_2S_4$, $Cr_2Er_6S_{11}$ and $CrEr_4S_7$. The structure of $CrEr_2S_4$ is reported to be a twofold superstructure of $MnY_2S_4$ along the short axis due to the Jahn–Teller effect on $Cr^{2+}$-centred octahedra. The $Cr_2Er_6S_{11}$ phase presents the orthorhombic space group $Cmc2_1$, whereas some other phases with the same stoichiometry present the $Cmcm$ space group, including $Fe_2Yb_6S_{11}$[13] and the binary sulfide $Tm_8S_{11}$.[14] Phases derived from an NaCl-type structure by the operation of

[a] Dpto. Química Inorgánica, Fac. CC. Químicas, Universidad Complutense,
28040, Madrid, Spain
[b] Centro de Microscopía, Universidad Complutense,
28040, Madrid, Spain
[c] Inst. Ciencia de Materiales de Madrid, CSIC,
28049, Madrid, Spain
E-mail: esteban@brunilda.sme.ucm.es

 © 2006 Wiley-VCH Verlag GmbH & Co. KGaA, Weinheim 

chemical twinning have also been found in the Mn-Er-S series. For example, Tomas et al. have studied the $Mn_{0.4}Er_{4.6}S_7$ phase[15] from single-crystal X-ray diffraction data, and a more detailed characterisation of the system was carried out by TEM.[16,17] Disordered intergrowths of $Mn_2Er_6S_{11}$ and $Mn_3Er_8S_{15}$ along the *c* axis of the structures were also found, along with well-ordered crystals. The transformation of the $MnEr_2S_4$ sulfospinel into different chemically twinned (CT) phases and into NaCl-type structure was observed in this system[18] due to irradiation damage effects under the electron microscope beam (intermediate acceleration voltage of 400 kV). The Ca-Tl-O system presents several CT phases belonging to the homologous series $Ca_nTl_2O_{n+3}$.[19,20] The structure of each phase was further studied by means of neutron diffraction by Berastegui et al.[21]

Some other CT phases have the same stoichiometry as $CaTi_2O_4$ but with a twin sequence that is different to ...(4,4)..., as is the case of $HgBi_2S_4$[22] and $CdBi_2S_4$,[23] which are monoclinic phases with a ...(5,3)... twin slabs' sequence, denoted as a pavonite homologous series by Ferraris et al.[3]

The formation of NaCl-type MS-$RE_2S_3$ solid solutions (M = divalent metal; RE = rare-earth element) is well documented,[24] mainly by characterisation with XRPD data. When M = Mg, Mn and Ca extensive solid solutions with NaCl-type structure are generated for the heavy rare-earth elements and for Y. Some orthorhombic and monoclinic phases have also been reported in these systems from XRPD data,[25,26] although none was isolated with M = Mg and RE = Yb. TEM studies carried out in the Mg-Yb-S system[27] indicate that a transition from an NaCl-type to a spinel-type structure occurs through short-range order phenomena and segregation of extended defects. In this work, we present the preparation and characterisation of four new CT phases derived from the NaCl-type structure in this ternary system, as determined by TEM and associated techniques [microdiffraction and X-ray energy dispersive spectroscopy (XEDS) analysis]. XRPD information is employed to refine the crystal parameters of each phase once their unit-cell symmetries have been determined from the electron diffraction data.

## Results and Discussion

The XRPD patterns of each sample are complex, with a large number of maxima (about 40) in the range $5° \leq 2\theta \leq 70°$ due to the presence of different phases with large unit cells. The diffraction maxima are also broad, which indicates the existence of defects. All these observations were confirmed by the study of the samples by TEM and associated techniques. The phases present in each of the samples were first identified from their selected-area electron diffraction (SAED) patterns, from which the approximate unit-cell dimensions can be obtained and then refined from XRPD data. Four CT ordered phases were observed, with the average stoichiometries indicated in Table 1 and discussed below.

### $MgYb_2S_4$

The XRPD pattern indicates the presence of the cubic spinel-type phase $MgYb_2S_4$ [$a$ = 1.0951(2) nm], which has been described previously,[27] as well as other phases. An ordered major phase was identified by means of TEM observations. An orthorhombic unit cell could be assigned to these crystals from SAED patterns taken along different orientations (see Figure 1). The approximate crystal parameters are: $a \approx 0.37$, $b \approx 1.25$, $c \approx 1.26$ nm.

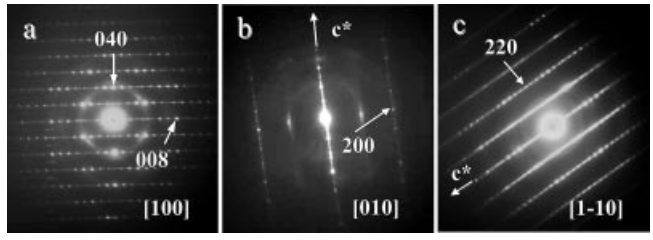


Figure 1. SAED patterns along different orientations, belonging to three different crystals of the sample with a nominal Mg:Yb ratio of 1:2. Note the streaking of the reflections along *c**, which is indicative of the presence of plane defects and/or disorder perpendicular to *c*.

The one-dimensional (1D) intensity streaking of the diffraction maxima along *c** in some of the diffraction patterns indicates the presence of disordered planar defects perpendicular to *c*. The cation ratio was semi-quantitatively measured by XEDS (ten crystals were analysed) with an average result of Mg/Yb = 0.46 [$Mg_{0.93(4)}Yb_{2.03(4)}S_4$], which is very close to a 1:2 stoichiometry. There are several possible orthorhombic structure-types with a similar $AB_2S_4$ ideal stoichiometry, such as the $CaFe_2O_4$ type[7] ($a$ = 0.9230, $b$ = 0.3024, $c$ = 1.0705 nm; space group *Pnma*), the $CaTi_2O_4$ type[9] ($a$ = 0.3136, $b$ = 0.9727, $c$ = 0.9976 nm; space group *Cmcm*) and the $Yb_3S_4$ type[28] ($a$ = 1.2777, $b$ = 0.3837,

Table 1. Crystal parameters of the different CT phases previously described, refined from XRPD data. The space group and the twin slabs' sequences inside the unit cell are included in each case.

| Phase | XEDS analysis | S/(Mg+Yb) ratio | Space group | Lattice parameters [nm] | $Z$ | Twin sequence |
|---|---|---|---|---|---|---|
| $MgYb_2S_4$ | $Mg_{0.93(4)}Yb_{2.03(4)}S_4$ | 1.333 | *Cmcm* | $a$ = 0.3752(2), $b$ = 1.259(1), $c$ = 1.268(2) | 4 | (4,4) |
| $Mg_3Yb_8S_{15}$ | $Mg_{3.04(9)}Yb_{7.97(6)}S_{15}$ | 1.363 | *C*2/*m* | $a$ = 1.2637(1), $b$ = 0.37176(5), $c$ = 2.4132(2); $\beta$ = 100.40(1)° | 2 | (4,4,4,3) |
| $Mg_2Yb_6S_{11}$ | $Mg_{1.96(7)}Yb_{6.03(5)}S_{11}$ | 1.375 | *Cmcm* | $a$ = 0.37297(4), $b$ = 1.2592(2), $c$ = 3.4853(3) | 4 | (4,4,3,4,4,3) |
| $MgYb_4S_7$ | $Mg_{1.03(6)}Yb_{3.98(4)}S_7$ | 1.400 | *C*2/*m* | $a$ = 1.2578(2), $b$ = 0.3735(3), $c$ = 1.1417(7); $\beta$ = 104.88(6)° | 2 | (4,3) |

 © 2006 Wiley-VCH Verlag GmbH & Co. KGaA, Weinheim 

$c$ = 1.2926 nm; space group *Pnma*). The measured unit-cell parameters do not allow us to differentiate between them. The actual space group can be identified by means of the microdiffraction technique[29,30] by studying the "ideal symmetry" of the microdiffraction patterns, which is determined by the position and relative intensity of the reflections, either on the zero-order Laue zone (ZOLZ) or in the whole pattern (WP), which includes high-order Laue zones (HOLZ). The difference of periodicity and the shifts between the Laue zones give information about the presence of glide planes and screw axes and about the centring of the lattice, respectively. A microdiffraction pattern along the [010] zone axis, where a shift of the FOLZ and the ZOLZ along $c^*$ can be observed, is shown in Figure 2 (a). The $h0l$ reflections with $h = 2n + 1$ are absent in the ZOLZ but the $h1l$ ones with $h = 2n + 1$ are present in the FOLZ (first-order Laue zone). Furthermore, $00l$ ($l = 2n + 1$) reflections are observed in the ZOLZ but the $01l$ reflections are absent in the FOLZ. This shift of the Laue zones along $c^*$ due to the indicated extinctions is indicative of the C-centring of the lattice, according to the extinction condition $hkl$: $h + k = 2n + 1$. Two possible orthorhombic space groups have the same extinction conditions for compounds with the stoichiometry $AB_2S_4$: *Cmcm* and $Cmc2_1$. The tilted pattern of Figure 2 (b) shows the presence of an *m*-plane perpendicular to *c*, and the [110] ZOLZ microdiffraction pattern of Figure 2 (c) shows (2*mm*) "ideal" symmetry, which confirms, together with the information obtained from the other patterns, that this phase presents the *Cmcm* space group.[29,30] The $Cmc2_1$ space group would have shown (*m*) "ideal" symmetry along the [110] zone axis. Therefore, the major well-ordered phase found in this sample [XEDS: $Mg_{0.93(4)}Yb_{2.03(4)}S_4$] can be considered to be isostructural with a $CaTi_2O_4$-type structure, in other words it can be described as a ...(4,4)... CT structure according to the nomenclature proposed by Hyde and Andersson.[1] An idealised model of this CT-$MgYb_2S_4$ structure, viewed along the [100] direction, is included in Figure 3. $Mg^{2+}$ cations are located in octahedral coordination sites and the $Yb^{3+}$ cations lie in the remaining octahedral sites (50%) and in the bicapped trigonal prisms present in the twin planes. Both cations occur randomly in the octahedral sites.

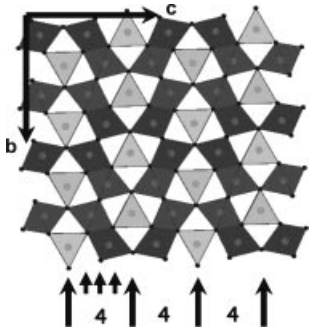


Figure 3. Idealized model of the ...(4,4)... CT structure of the $MgYb_2S_4$ phase ($Z$ = 4). The $\{(Mg,Yb)S_6\}$ octahedra are represented in dark grey and the $\{YbS_{6+2}\}$ bicapped trigonal prisms are represented in light grey. The caps have been excluded from the model for clarity. The twin slabs' sequence in the unit cell is clearly visible.

In order to confirm the proposed structure model, HRTEM (high-resolution TEM) images were taken along the short axis (in this case the *a* axis), which best reflects the CT structure. Figure 4 shows an HRTEM Fourier-filtered image of the CT-$MgYb_2S_4$ phase along [100], and the corresponding fast Fourier transform (FFT) is included as an inset. Simulated images were obtained at several microscope defocus and crystal thickness values, using the ideal $CaTi_2O_4$-type atomic positions and the experimentally refined crystal parameters from XRPD patterns. The best fit with

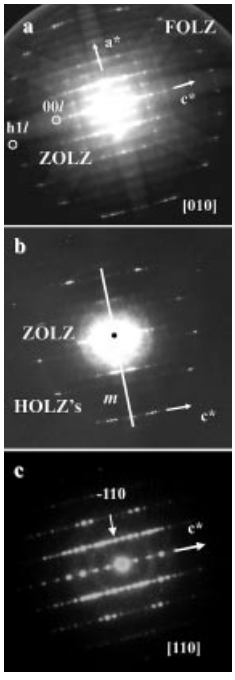


Figure 2. Microdiffraction patterns corresponding to a crystal with a Mg:Yb ratio of 1:2. Information about the centring of the lattice (C) and the actual space group (*Cmcm*) are deduced from them (see the text for details). The pattern in (b) is tilted off-axis in order to observe the HOLZ reflections.

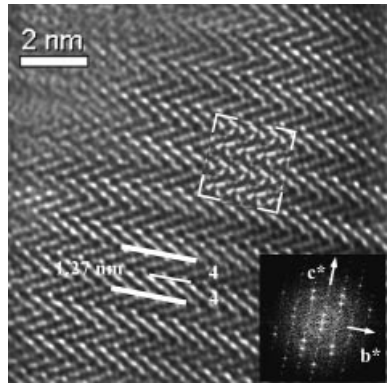


Figure 4. Fourier-filtered HRTEM image of an $MgYb_2S_4$ crystal taken along the short-axis of the CT structure. The corresponding FFT is included in the lower right part as an inset. The simulated image (defocus, $\Delta f$ = –40 nm; thickness, $t$ = 8 nm) agrees well with the experimental one.

 © 2006 Wiley-VCH Verlag GmbH & Co. KGaA, Weinheim 

the experimental image is superimposed in Figure 4 and shows a good correspondence with the experimental image, which indicates that the observed phase presents the Ca-$Ti_2O_4$-type structure.[9]

### $MgYb_4S_7$

Detailed TEM observations of the sample with a nominal Mg/Yb ratio of 1:4 showed the existence of a major, well-ordered phase as well as a minor $MgYb_2S_4$ spinel phase (which was not observed in the XRPD pattern) and crystals with disordered lattice planes. The SAED patterns of the major phase (see Figure 5) can be assigned to a monoclinic phase with the approximate unit cell parameters $a \approx 1.26$, $b \approx 0.37$ and $c \approx 1.15$ nm, and $\beta \approx 105°$.

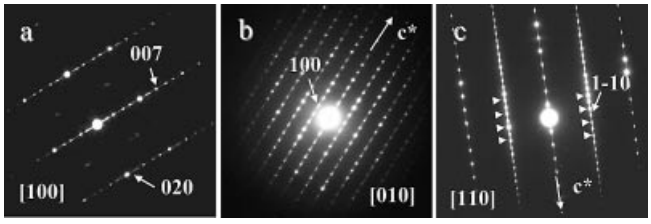


Figure 5. SAED patterns along different orientations, belonging to different crystals of the sample with a nominal Mg:Yb ratio of 1:4. Note the intensity streaking of the reflections along $c^*$, which is indicative of the presence of defects and/or disorder.

XEDS analyses of 10 crystals provided the average cation ratio Mg/Yb $\approx$ 0.26 [$Mg_{1.03(6)}Yb_{3.98(4)}S_7$], which is very close to 1:4 ratio. A possible structure type with $AB_4S_7$ stoichiometry is $Y_5S_7$,[7] whose structure can be described as a ...(4,3)... CT phase.

The actual space group can be identified by means of microdiffraction patterns. Thus, the [100] microdiffraction pattern of Figure 6 (a) shows that the ZOLZ reflections are shifted by $1/2\,b^*$ with respect to the FOLZ ones. The $0kl$ reflections turn into $1kl$ reflections in the FOLZ, and are absent when $1 + k = 2n + 1$. The shift provoked by these extinctions is indicative of the C-centring of the lattice. The [110] ZOLZ microdiffraction pattern in Figure 6 (b) presents (*2*) "ideal" symmetry, which agrees with the *C*2/*m* space group,[29,30] whereas *C*2 and *Cm* space groups, which present the same extinction conditions, would display (*1*) "ideal" symmetry along the same zone axis. Therefore, microdiffraction results support the *C*2/*m* space group rather than *C*2 or *Cm*, and the observed phase can be described as a ..(4,3)... CT phase, with an ideal $MgYb_4S_7$ stoichiometry [XEDS: $Mg_{1.03(6)}Yb_{3.98(4)}S_7$] and a $Y_5S_7$-type structure.

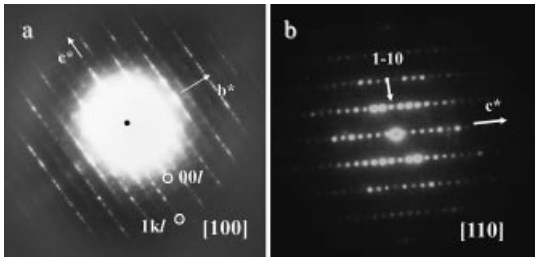


Figure 6. Microdiffraction patterns corresponding to the major ordered phase in the sample with a nominal Mg:Yb ratio of 1:4. The C-centring of the lattice is deduced from (a) and the "ideal" symmetry of the ZOLZ pattern in (b) − (*2*) − indicates that the phase presents the *C*2/*m* space group. See text for details.

Note that some intensity streaking is observed in the diffraction maxima along $c^*$ in the SAED patterns of Figure 5, which is indicative of plane defects perpendicular to *c*. Furthermore, in the [110] SAED pattern of Figure 5 (c), extra maxima are present (marked with arrows) due to the presence of macroscopic twin planes in the crystal, parallel to (001), which can be attributed to unit-cell twin sequences of the type ...4,3,4,3,4/4,3,4,3,4...

An idealised model of the CT-$MgYb_4S_7$ structure, along [010], is shown in Figure 7, where $Mg^{2+}$ and half of the $Yb^{3+}$ cations lie in octahedral sites at random and the other half of the $Yb^{3+}$ cations lie in the trigonal prisms at the composition planes.

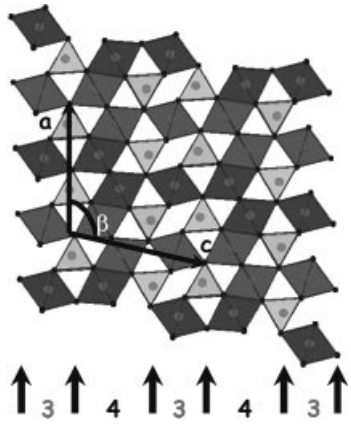


Figure 7. Idealized model of the ...(4,3)... CT structure of the $MgYb_4S_7$ phase (isostructural with $Y_5S_7$). The {(Mg,Yb)$S_6$} octahedra are represented in dark grey, and the {$YbS_6$} trigonal prisms are represented in light grey.

HRTEM images were obtained along the short axis of the structure to confirm the proposed model. Image simulations were calculated from the ideal atomic positions of the $Y_5S_7$-type structure and the refined crystal parameters from the XRPD pattern. The correspondence of the experimental images and the simulated ones is quite good, as shown in Figure 8, thus confirming the proposed structure model.

### $Mg_3Yb_8S_{15}$ and $Mg_2Yb_6S_{11}$ Phases

TEM observations from the crystals previously described as $MgYb_2S_4$ and $MgYb_4S_7$ showed the existence of disorder along $c^*$ due to the presence of both phases intergrown in a disordered manner. The ordered crystals found in this system had 3:8 and 1:3 Mg/Yb ratios, so two new samples were prepared with these nominal chemical compositions.

In the first case the XEDS analyses of ten crystals indicated a Mg/Yb ratio of about 0.38, close to an ideal $A_3B_8S_{15}$ stoichiometry [$Mg_{3.04(9)}Yb_{7.97(6)}S_{15}$], as reported before in the Mn-Er-S system[16,17] mentioned above. This phase is monoclinic, with the following approximate lattice

 © 2006 Wiley-VCH Verlag GmbH & Co. KGaA, Weinheim 

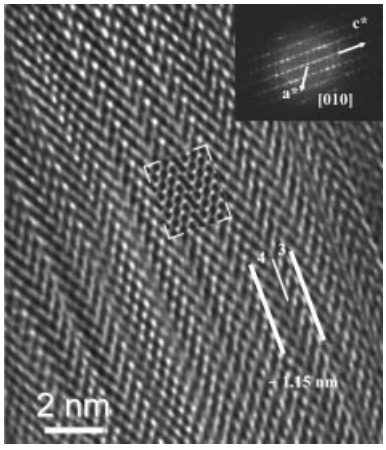


Figure 8. Fourier-filtered HRTEM image along the short axis of a CT-$MgYb_4S_7$ crystal ([010] direction). The corresponding FFT is included as an inset. The simulated image ($\Delta f$ = –50 nm; $t$ = 2 nm) agrees well with the experimental one.

parameters measured from SAED patterns (see Figure 9): $a \approx 1.26$, $b \approx 0.37$, $c \approx 2.40$ nm; $\beta \approx 100°$.

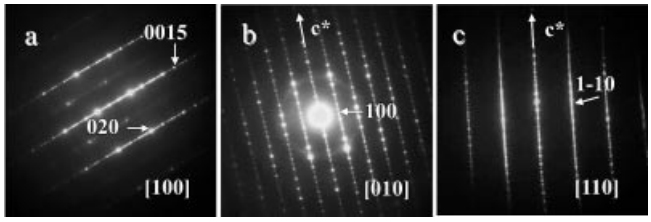


Figure 9. SAED patterns along different orientations, belonging to different crystals of the sample with a nominal Mg:Yb ratio of 3:8.

Most of the observed CT-$Mg_3Yb_8S_{15}$ crystals present streaking along $c$*, so the identification of its actual space group by means of microdiffraction patterns was problematic. However, the C-centring of the lattice was observed in the [100] microdiffraction pattern due to the shift of the ZOLZ and FOLZ reflections.

HRTEM images along the short axis of the structure (see Figure 10) indicated a ...(4,4,4,3)... twin slabs' sequence. The simulated image that showed the best fit among different defocus and thickness values is shown as the inset in Figure 10. The calculations were performed with the ideal atomic positions directly obtained from the ...(4,4,4,3)... model and the HRTEM image (*C*2/*m* space group), and with the crystal parameters refined from XRPD data. Therefore, according to this model, the CT-$Mg_3Yb_8S_{15}$ structure presents a ...(4,4,4,3)... twin sequence, with $Mg^{2+}$ and half of the $Yb^{3+}$ cations in octahedra (at random) and the other half in trigonal prisms at the composition planes (see Figure 11).

In the case of the sample with a 1:3 cation ratio, the previously described CT phases were observed, together with the sulfospinel $MgYb_2S_4$. An orthorhombic ordered phase was also found, with the following approximate crystal parameters obtained from SAED patterns: $a \approx 0.37$, $b \approx 1.26$, $c \approx 3.50$ nm.

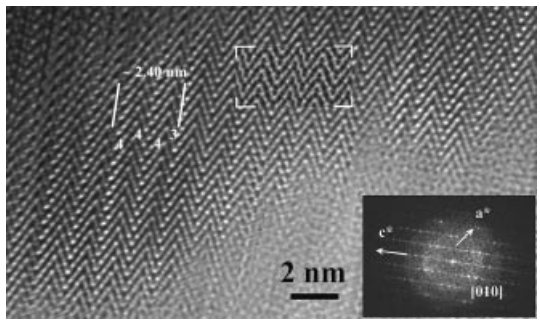


Figure 10. Fourier-filtered HRTEM image along the short axis of a CT-$Mg_3Yb_8S_{15}$ crystal ([010] direction). The corresponding FFT is included as an inset. The simulated image ($\Delta f$ = –50 nm; $t$ = 2 nm) agrees well with the experimental one. It was calculated by employing the preliminary crystal parameters measured from SAED patterns (*C*2/*m* space group) and the atomic parameters directly obtained from the ideal model and from the image.

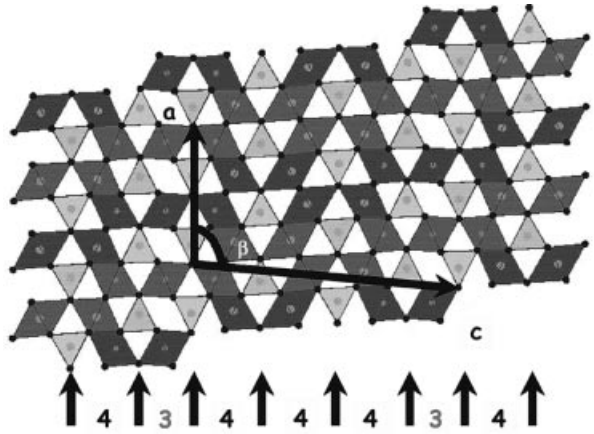


Figure 11. Idealized model of the CT-$Mg_3Yb_8S_{15}$ phase ($Z$ = 2). The twin slabs' sequence is ...(4,4,4,3)... in this case. The {(Mg,Yb)-$S_6$} octahedra are represented in dark grey, and the {$YbS_6$} trigonal prisms are represented in light grey.

The measured XEDS (six crystals) Mg/Yb ratio was about 0.32, which corresponds to a 1:3 cation stoichiometry. The chemical composition and lattice parameters are similar to the previously described $Tm_8S_{11}$ and $Mn_2Er_6S_{11}$ structures,[14,17] so that the average XEDS analysis can be formulated as $Mg_{1.96(7)}Yb_{6.03(5)}S_{11}$. The crystals belonging to this CT phase are usually disordered along $c$* (1D intensity streaking of the diffraction spots along that direction, as observed in the SAED patterns; see Figure 12). The model was confirmed by HRTEM images, such as the one shown in Figure 13 along the [110] orientation. The experimental image agrees quite well with the simulated one (inset) calculated with the ideal $Fe_2Yb_6S_{11}$ atomic positions (*Cmcm* space group) and with the crystal parameters refined from the XRPD data. Therefore, the observed $Mg_2Yb_6S_{11}$ structure is a new phase and can be described as a ...(4,4,3,4,4,3)... CT one. As in the previously described phases, $Mg^{2+}$ and half of the $Yb^{3+}$ cations occupy octahedral positions at random, whereas the other half of the $Yb^{3+}$ cations lie in the trigonal prisms at the composition planes, as shown in the structural model in Figure 14.

 © 2006 Wiley-VCH Verlag GmbH & Co. KGaA, Weinheim 

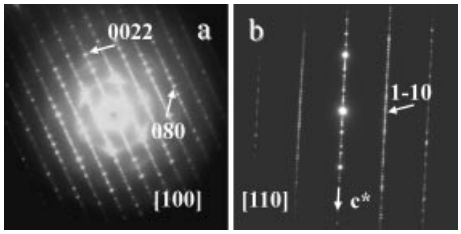


Figure 12. SAED patterns along different crystal orientations, belonging to the sample with a nominal Mg:Yb ratio of 1:3. Intensity streaking along the $c^*$ reflections can be observed due to the presence of plane defects perpendicular to $c$.

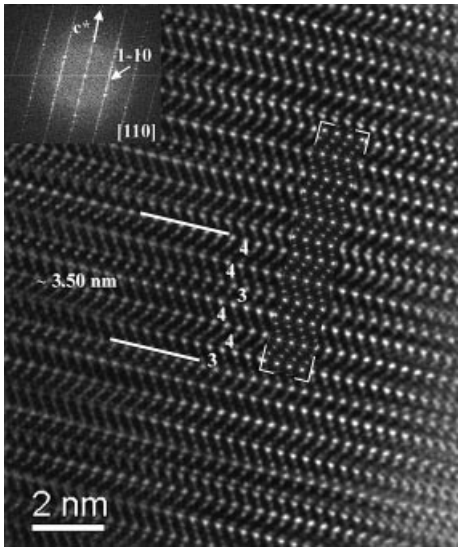


Figure 13. Fourier-filtered HRTEM image of the CT-$Mg_2Yb_6S_{11}$ phase along the [110] direction. The corresponding FFT is included as an inset. The simulated image ($\Delta f$ = –50 nm; $t$ = 6 nm) agrees well with the experimental one and reflects the twin slabs' sequence in the unit cell.

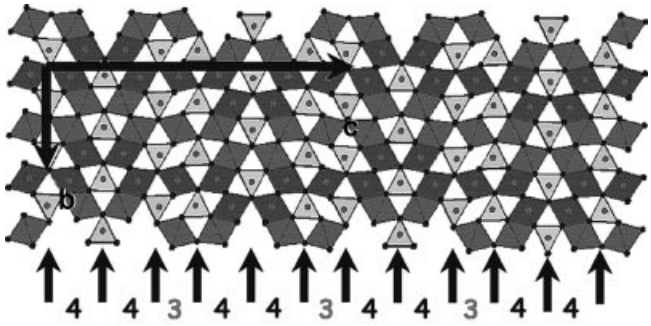


Figure 14. Idealized model of the ...(4,4,3,4,4,3)... structure of the CT-$Mg_2Yb_6S_{11}$ phase. It presents the $Fe_2Yb_6S_{11}$-type structure (*Cmcm* space group and $Z$ = 4). The {(Mg,Yb)$S_6$} octahedra are represented in dark grey, and the {$YbS_{6+1}$} mono-capped trigonal prisms are represented in light grey (the caps have been excluded for clarity).

Disorder perpendicular to $c$ is common in these phases, as was previously observed in the SAED patterns (1D streaking). Intergrowths were also found in many crystals, as can be seen in the HRTEM image included in Figure 15, where slabs of $Mg_2Yb_6S_{11}$ and $Mg_3Yb_8S_{15}$ alternate along $c$, apparently at random.

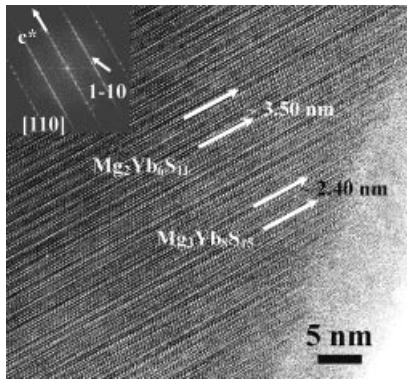


Figure 15. HRTEM image of a crystal from the sample with nominal composition $Mg_2Yb_6S_{11}$, showing a disordered intergrowth of the CT-$Mg_3Yb_8S_{15}$ and CT-$Mg_2Yb_6S_{11}$ structures along $c$. The corresponding FFT is included as an inset.

In the phases derived from the NaCl-type structure by chemical twinning the $c$ parameter accounts for the twin blocks periodicity [$c \approx n \times d(113)_{MgS}$ for orthorhombic phases and $d(001) \approx n \times d(113)_{MgS}$ for monoclinic ones], i.e., it indicates the stoichiometry of the phase. The value of $n$, which stands for the total extension of the NaCl-type slabs between the twin planes included in the unit cell, can be derived from the superstructure periodicity along $[113]^*_{NaCl}$ (or $c^*$). Figure 16 includes an enlargement of the $c^*$ rows belonging to the four CT phases described in this work, with $n$ = 8 for CT-$MgYb_2S_4$, $n$ = 15 for CT-$Mg_3Yb_8S_{15}$, $n$ = 22 for CT-$Mg_2Yb_6S_{11}$ and $n$ = 7 for CT-$MgYb_4S_7$ (see Table 1).

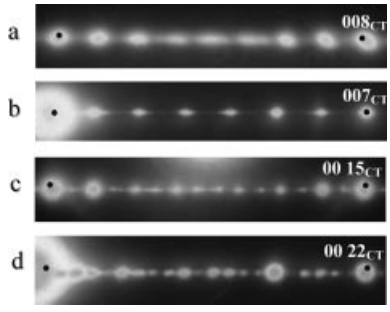


Figure 16. Detail of the 00l reflections row ($c^*$) of the four CT phases described in this work. The superstructure periodicity inside $113_{NaCl}$ is directly related to the twinning sequence ($n$). a) $MgYb_2S_4$, with $n$ = 8 and twin sequence ...(4,4)...; b) $MgYb_4S_7$, $n$ = 7 and ...(4,3)...; c) $Mg_3Yb_8S_{15}$, $n$ = 15 and ...(4,4,4,3)...; d) $Mg_2Yb_6S_{11}$, $n$ = 22 and ...(4,4,3,4,4,3)...

## XRPD Studies

Once the four observed phases had been identified and characterised by means of TEM and associated techniques, the lattice parameters were refined from XRPD data. The results are summarised in Table 1, including the twin slabs' sequences.

 © 2006 Wiley-VCH Verlag GmbH & Co. KGaA, Weinheim 

Since the origin of these CT structures is the regular and repeated twinning on $\{113\}_{NaCl}$ planes, the variation of $d(113)_{NaCl}$ vs. composition has been studied in the MgS-$Yb_2S_3$ system, including samples with NaCl and spinel structures reported previously,[27] with lower $Yb^{3+}$ content than the CT phases described in this work. The change in $d(113)_{NaCl}$ with the Yb/Mg ratio is represented in Figure 17. This parameter increases in the NaCl-type structure samples as the $Yb^{3+}$ concentration is increased, since the ionic radius of $Yb^{3+}$ in sixfold coordination (0.1008 nm) is bigger than in the case of $Mg^{2+}$ (0.0710 nm).[31] The introduction of $Yb^{3+}$ into the matrix of MgS generates cation vacancies.[27] When a spinel-type phase is formed with higher $Yb^{3+}$ content, there is a sudden variation in $d(113)_{NaCl}$ [$\approx 1/2 \times d(113)_{spinel}$], which is related to the structure change, with ordering of vacancies. It remains constant with slight composition variations since the unit-cell enlargement due to the increase of vacancies and $Mg^{2+}$ substitution by $Yb^{3+}$ must be compensated by the occupancy of tetrahedral positions.[27] When considering the CT phases described in this work, the $d(113)_{NaCl}$ value, which is directly related to the $d(001)_{CT}$, as mentioned before, decreases significantly and abruptly with respect to the spinel phase values due to the elimination of all the cation vacancies by the chemical twinning operation. The $d(113)_{NaCl}$ value decreases slightly (see Figure 17) as the relative number of composition planes in the unit cell of each CT phase increases, i.e., from $MgYb_2S_4$ [two composition planes every eight $(113)_{NaCl}$ planes] to $MgYb_4S_7$ [two composition planes every seven $(113)_{NaCl}$ planes].

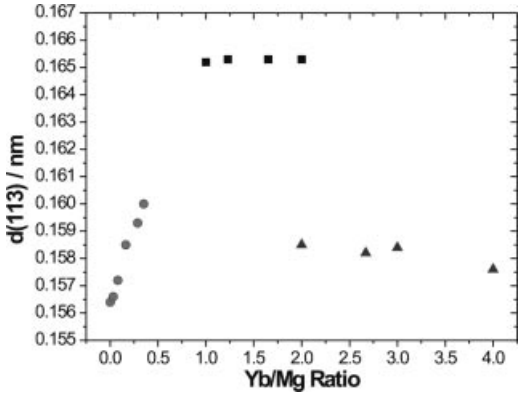


Figure 17. Variation of $d(113)_{NaCl}$ with the Yb/Mg ratio. The grey circles correspond to phases with an NaCl structure,[27] the black squares correspond to phases with a spinel-type structure with cationic excess[27] and the grey triangles correspond to the CTP phases described in this work.

## Conclusions

As can be observed in Table 1, the phases described in this work present common *a* and *b* crystal parameters while the *c* axis changes according to the composition. It was mentioned previously that the composition variations in the phases derived from the NaCl-type structure by the chemical twinning operation are accommodated through the twin slabs' sequence and periodicity, i.e., the generation of twin (composition) planes. These CT structures can be considered as members of a homologous series, with the two different symmetries (orthorhombic and monoclinic) depending on the twin slabs' sequence within the unit cell and with variation of the *c* axis with the stoichiometry.

As the twin sequence gets more complicated, i.e. the *c* axis gets larger, the difficulty of long-range ordering increases, as was observed in the $Mg_3Yb_8S_{15}$ and $Mg_2Yb_6S_{11}$ phases, which very often present intergrowths between CT structures. These two phases, whose Mg/Yb ratio lies between $MgYb_2S_4$ and $MgYb_4S_7$, are regular intergrowths of the ...(4,4)... and the ...(4,3)... sequences. Therefore, within this composition range, some other ordered phases could be expected, as predicted by Bakker et al.[8] in the Mn-Y-S system or as observed in other related systems,[5,11,13,14] which are actually built up from the $MgYb_2S_4$ and $MgYb_4S_7$ "units". In the system studied in this work, no more ordered CT phases were observed.

The co-existence of the CT-$MgYb_2S_4$ and the normal spinel with the same nominal stoichiometry is an interesting case of polymorphism, which extends to the high-pressure polymorph with $Th_3P_4$-type structure.[32] We have not been able to relate this polymorphism with temperature (annealing at 1373 K does not give any change in the relative abundance of the phases). However, slight but significant composition differences have been found between them, as measured by XEDS analysis. The CT-$MgYb_2S_4$ phase presents an excess of $Yb^{3+}$ with respect to the Mg/Yb ratio of 0.50, while the spinel phase has an excess of $Mg^{2+}$ [XEDS: $Mg_{1.1(1)}Yb_{1.92(7)}S_4$]. Therefore, although the $AB_2S_4$ composition is the ideal one for both phases, it seems to be the separating line between them.

## Experimental Section

**Preparation of the Samples:** Several mixtures of nitrates $Mg(NO_3)_2 \cdot 6H_2O$ and $Yb(NO_3)_3 \cdot 5H_2O$ were placed in graphite boats inside a tubular furnace and heated under a flow of $H_2S$ (10%)/Ar (50 mL/min) and Ar (20 mL/min) (bubbling in $CS_2$). The samples with nominal cation ratio (Mg/Yb) 1:2 and 1:4 were prepared at 1273 K for 10 h, whereas the other ones (3:8 and 1:3) were treated first at 798 K for 4 h and then at 1273 K for four more hours. The gas flow was maintained while raising the temperature. Each sample was cooled down to room temperature by switching off the furnace and maintaining a flow of Ar to avoid oxidation. The gases at the exit of the furnace were neutralised in a concentrated NaOH solution.

**Characterisation of the Samples:** Specimens for TEM observations were obtained from suspensions ultrasonically dispersed in butanol. A drop of each corresponding suspension was placed on a copper grid covered with a holey carbon film. A JEM 2000FX electron microscope, equipped with a LINK ISIS 300 XEDS analysis system, was employed to explore the reciprocal lattice of the samples (double-tilt specimen holder: ±45°) and to analyse the chemical composition. A Philips CM200 FEG (field emission gun) electron microscope, equipped with an EDAX DX4 XEDS analysis system was employed for the microdiffraction studies. HRTEM images were taken with a JEM 3000F (point resolution: 0.17 nm)

 © 2006 Wiley-VCH Verlag GmbH & Co. KGaA, Weinheim 

electron microscope. Due to the preferential cleavage of the crystals, the short axis of the structures under study could not be observed because they were beyond the tilt capacities of the JEM 3000F microscope (double-tilt specimen holder: ±20°). Therefore, the samples were embedded in epoxy resin and thin slices were obtained with an ultramicrotome for TEM observations. Crystals close to the short-axis orientation could be found in this way.

The as-prepared sulfides were studied by XRPD, using a Philips X'pert Diffractometer (Cu-$K_{\alpha 1}$ radiation) to refine the lattice parameters.

## Acknowledgements

The authors acknowledge the financial support from the MCYT to the project with reference MAT2003-08465-C02-01.

[1] S. Andersson, B. G. Hyde, *J. Solid State Chem.* **1974**, *9*, 92–101.
[2] B. G. Hyde, S. Andersson, M. Bakker, C. M. Plug, M. O'Keeffe, *Prog. Solid State Chem.* **1979**, *12*, 273–327.
[3] G. Ferraris, E. Makovicky, S. Merlino, *Crystallography of Modular Materials*, Oxford University Press, Oxford, **2004**.
[4] J. Takagi, Y. Takéuchi, *Acta Crystallogr., Sect. B* **1972**, *28*, 649–651.
[5] D. Colaïtis, D. Van Dyck, S. Amelinckx, *Phys. Status Solidi A* **1981**, *68*, 419–438.
[6] A. Prodan, M. Bakker, M. Versteegh, B. G. Hyde, *Phys. Chem. Miner.* **1982**, *8*, 188–192.
[7] B. G. Hyde, S. Andersson, *Inorganic Crystal Structures*, Wiley, New York, **1989**.
[8] M. Bakker, B. G. Hyde, *Philos. Mag. A* **1978**, *38*, 615–628.
[9] E. F. Bertaut, P. Blum, *Acta Crystallogr.* **1956**, *9*, 121–126.
[10] A. Tomas, R. Chevalier, P. Laruelle, B. Bachet, *Acta Crystallogr., Sect. B* **1976**, *32*, 3287–3289.
[11] A. Tomas, J. Rigoult, M. Guittard, P. Laruelle, *Acta Crystallogr., Sect. B* **1980**, *36*, 1987–1989.
[12] A. Tomas, M. Guittard, *Mater. Res. Bull.* **1980**, *15*, 1547–1556.
[13] S. M. Chaqour, A. Tomas, P. Lemoine, *Acta Crystallogr., Sect. C* **1994**, *50*, 1655–1657.
[14] Y. Zhang, H. F. Franzen, B. Harbrecht, *J. Less-Common Met.* **1990**, *166*, 135–140.
[15] A. Tomas, M. Robert, C. Adolphe, M. Guittard, *Mater. Res. Bull.* **1984**, *19*, 1643–1646.
[16] J. Arce de la Plaza, L. C. Otero-Díaz, *J. Less-Common Met.* **1985**, *110*, 371–374.
[17] A. R. Landa-Cánovas, L. C. Otero-Díaz, *Aust. J. Chem.* **1992**, *45*, 1473–1487.
[18] A. R. Landa-Cánovas, L. C. Otero-Díaz, *Solid State Ionics* **1993**, *63–65*, 378–387.
[19] F. Goutenoire, V. Caignaert, M. Hervieu, C. Michel, B. Raveau, *J. Solid State Chem.* **1995**, *114*, 428–435.
[20] F. Goutenoire, V. Caignaert, M. Hervieu, B. Raveau, *J. Solid State Chem.* **1995**, *119*, 134–141.
[21] P. Berastegui, S. Eriksson, S. Hull, F. J. García-García, J. Eriksen, *Solid State Sci.* **2004**, *6*, 433–441.
[22] W. G. Mumme, J. A. Watts, *Acta Crystallogr., Sect. B* **1980**, *36*, 1300–1304.
[23] W. Choe, S. Lee, P. O'Connell, A. Covey, *Chem. Mater.* **1997**, *9*, 2025–2030.
[24] J. Flahaut, in *Handbook on the Physics and Chemistry of Rare Earths*, vol. 4 (Ed.: K. Gschneider, L. Eyring), North Holland, Amsterdam, **1979**, 1.
[25] M. Patrie, J. Flahaut, *C. R. Acad. Sci. Paris* **1967**, *264*, 395–398.
[26] C. Adolphe, P. Laruelle, *Bull. Soc. Fr. Minéral. Cristallogr.* **1968**, *91*, 219–232.
[27] E. Urones-Garrote, A. Gómez-Herrero, A. R. Landa-Cánovas, R. L. Withers, L. C. Otero-Díaz, *Chem. Mater.* **2005**, *17*, 3524–3531.
[28] L. C. Otero-Díaz, A. R. Landa-Cánovas, B. G. Hyde, *J. Solid State Chem.* **1990**, *89*, 237–259.
[29] J. P. Morniroli, J. W. Steeds, *Ultramicroscopy* **1992**, *45*, 219–239.
[30] M. Tanaka, M. Terauchi, *Convergent-Beam Electron Diffraction*, Jeol-Maruzen, Tokyo, **1985**.
[31] R. D. Shannon, *Acta Crystallogr., Sect. A* **1976**, *32*, 751–767.
[32] K. Hirota, N. Kinomura, S. Kume, M. Koizumi, *Mater. Res. Bull.* **1976**, *11*, 227–232.

Received: October 25, 2005
Published Online: February 15, 2006

 © 2006 Wiley-VCH Verlag GmbH & Co. KGaA, Weinheim 

DOI: 10.1002/ejic.200500947

# Zinc Thiolate Complexes $[ZnL_n(SR)]^+$ with Azamacrocyclic Ligands: Synthesis and Structural Properties

Johannes Notni,[a] Helmar Görls,[b] and Ernst Anders*[a]

**Keywords:** Enzyme models / Macrocyclic ligands / S ligands / Solid-state structures / Zinc

A series of 24 novel zinc thiolate complexes containing saturated macrocyclic polyamine ligands with the general formula $[Zn(L_n)(SR)]ClO_4$ ($L_n$: *n*-dentate azamacrocyclic ligand) has been synthesized. Two different thiolate ligands (R = phenyl, benzyl) and 12 macrocyclic ligands with ring sizes varying from 11 to 16 atoms and containing three, four, and five nitrogen donors (including a new macrocyclic triamine ligand, 8-methyl-[11]ane$N_3$) have been used. The solid-state structures of 20 of the 24 complexes have been characterized by X-ray diffraction. The crystal lattice of all compounds is comprised exclusively of monomers. The tetracoordinate $N_3S$ compounds exhibit Zn–S bond lengths ranging from 2.2259(5) to 2.2492(9) Å and the pentacoordinate $N_4S$ systems from 2.266(2) to 2.3200(7) Å. In addition, two complexes with the very rare $N_5S$ coordination environment for zinc have been found. They exhibit Zn–S bond lengths of 2.3782(7) and 2.42 Å (mean value of two independent molecules). The thiolate complexes are suitable model systems for the precursor proteins of matrix metalloproteases (proMMPs) as well as for thiolate alkylating enzymes such as cobalamine-dependent/independent methionine synthases, farnesyl transferase, and the Ada repair protein.
(© Wiley-VCH Verlag GmbH & Co. KGaA, 69451 Weinheim, Germany, 2006)

## Introduction

Zinc thiolate complexes have received considerable attention in the past decade. This interest derives from the fact that many enzymes feature the alkylation (methylation) of a zinc–thiolate bond.[1,2] The most prominent among them are the Ada repair protein,[3] cobalamine-dependent/independent methionine synthases,[4,5] and farnesyl transferase.[6] The studies focusing on zinc thiolate complexes have thus paid special attention to the mechanism of the alkylation of thiols. Two different possible reaction modes are discussed. On the one hand, the alkylation may occur intramolecularly and the thiol is alkylated in the zinc-bound state, whereas the reaction could also start with an initial heterolytic dissociation, followed by a reaction of free thiolate. Wilker and Lippard have employed the anionic tetrathiolate $[Zn(SPh)_4]^{2-}$ as a functional model for Ada.[7] They found a methylation of the complex by $(MeO)_3PO$ to yield PhSMe and postulated a dissociative reaction mechanism. Vahrenkamp et al. have studied the methylation of [tris(pyrazolyl)borato]zinc thiolates ($Tp^{R,R}ZnSR$) and have provided strong evidence (gained from kinetic measurements) that these reactions occur intramolecularly and feature a four-center transition structure.[8–10] A similar interpretation has been provided by Carrano et al., who have investigated the methylation of a series of (scorpionato)zinc thiolates.[11–13] Darensbourg et al. have investigated the alkylation of a zinc complex with a bis(thiolate) $[N_2S_2]^{2-}$ chelate ligand.[14] They also obtained the thioether derivatives, but did not discuss the mechanism.

The above (incomplete and arbitrary) list of examples provides insight into some established applications of zinc thiolate complexes as enzyme models. They also resemble, however, the catalytic domain of another important class of enzymes, the matrix metalloproteases (MMPs or matrixins). These play an important role in the degradation of extracellular matrix components, such as collagen.[15,16] The enzymes are secreted into the extracellular space in a latent (inactive) form, the so-called proMMPs, therefore an additional activation step is required to induce protease activity. This is a sensitive process, since the active form can digest its own framework and thus the timing of activation is critical. Furthermore, an imbalance of the active enzyme and its inhibited form is implicated in the pathology of diseases such as arthritis, cancer, multiple sclerosis, and cardiovascular diseases.[17] Thus, it is vitally important to gain a detailed understanding of the activation mechanism.[18]

The catalytic zinc(II) ion in the latent enzymes − the MMP precursor proteins (proMMPs) − is bound to the deprotonated sulfhydryl group of a cysteine and to three histidine residues.[19,20] In vitro experiments have shown that an activation can be achieved with a variety of reagents, but the initial step is always a hydrolytic cleavage of the zinc–sulfur linkage.[21] The coordination sphere of the zinc ion is then completed by a water molecule to form the catalytically active $His_3ZnOH$ motif.[22] A model reaction for this

[a] Institut für Organische Chemie und Makromolekulare Chemie, Humboldtstr. 10, 07743 Jena, Germany
E-mail: ernst.anders@uni-jena.de
[b] Institut für Anorganische und Analytische Chemie, Lessingstr. 8, 07743 Jena, Germany.

 InterScience © 2006 Wiley-VCH Verlag GmbH & Co. KGaA, Weinheim 

process has been reported by Parkin et al., who performed the hydrolytic cleavage of a tripodal $S_3Zn$–SR complex and obtained free thiolate.[23] To the best of our knowledge, no model complex that resembles the $His_3Zn$–Cys coordination motif of the inactive enzyme has been used for these investigations so far. Our complexes might thus prove to be useful in this field of research.

Furthermore, recent investigations have suggested that carbonic anhydrase[24,25] plays a pivotal role in the fixation of carbonyl sulfide according to the equation $L_nZnOH + COS \rightarrow L_nZnSH + CO_2$.[26] Quantum mechanical calculations have revealed that a zinc hydrosulfide moiety $His_3Zn$–SH is formed in the course of this interconversion.[27] A suitable structural model − the neutral hydrosulfide complex $Tp^{Ph,Me}ZnSH$ − has been found by Vahrenkamp et al.[28,29] Our efforts to obtain an equivalent zinc hydrosulfide complex with an azamacrocyclic ligand were not successful because these compounds are not stable. Nevertheless, due to their positive overall charge, our thiolate complexes also could be regarded as suitable model systems for this species.

In this article we focus on the solid-state structures of cationic zinc monothiolates bearing a polyazamacrocyclic ligand. Azamacrocyclic ligands are available with many ring sizes and different numbers of donor atoms, therefore they allow a wide range of complexes to be synthesized with different electronic properties and steric demands. Thus, one can study the influence of the "protein-imitating" ligand on the binding mode and reactivity of a zinc-bound thiolate in great detail. With regard to future investigations or possible synthetic applications, it is convenient to choose the most suitable thiolate complex out of a large pool of substances with different reactivities and solubilities. We cover complexes formed with a wide range of azamacrocycles and reveal insights into both zinc thiolate coordination chemistry and coordination geometries of polyazamacrocyclic ligands on zinc centers. In subsequent articles, we will report on the reactions that these thiolates are capable of undergoing.

## Results and Discussion

### Starting Materials

Figure 1 illustrates the macrocyclic ligands that we used for complexation experiments. They feature ring sizes varying from 9 to 16 atoms and contain three, four, or five nitrogen donors. In addition, we report the synthesis of a new azamacrocycle, 8-methyl-[11]aneN$_3$ (**4**). All azamacrocycles were prepared using a slightly modified Richman–Atkins procedure.[30]

### Complexation Experiments

Zinc monothiolates with macrocyclic amine ligands are a novel class of compounds, and only two such examples are documented in the literature. Koike, Kimura et al.[31] postulated the formation of a complex of $[Zn(cyclen)]^{2+}$ with captopril, a hypertensive drug containing a thiolate function, but they did not characterize this substance. Their work illustrates, however, the biological significance of this type of compounds. In addition, Addison and Sinn have reported the complex *trans*-$[Zn(cyclam)(SC_6F_5)_2]$, which bears two pentafluorothiophenolate ligands.[32] Initially, we prepared our complexes in a similar way by treating equimolar amounts of the macrocyclic ligand with zinc perchlorate in methanol. This was followed by addition of an equimolar amount of sodium thiolate in methanol. The desired compounds $[Zn(L_n)(SR)]ClO_4$ precipitated with good yields. The reaction mode is outlined in Equation (1).

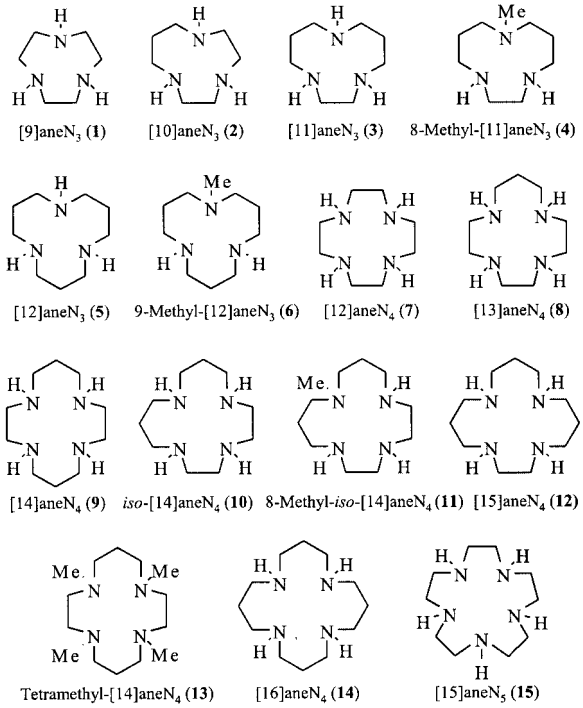


Figure 1. Macrocyclic polyamine ligands used for complexation experiments.

$$L_n + Zn(ClO_4)_2 + NaSR \rightarrow [Zn(L_n)(SR)]ClO_4 + NaClO_4 \quad (1)$$

A higher purity and better yields were achieved with potassium thiolates since the precipitation of potassium perchlorate forces the equilibrium towards the desired products.

However, this synthesis has its limits. The nature of the thiolate has a marked influence on this reaction: only arene- and phenylmethanethiolates yield the desired thiolate complexes. This is in contrast to the [tris(pyrazolyl)borato]zinc thiolates, for which aryl- *and* alkyl derivatives are available.[9] Alkyl thiolates (e.g. MeSH, EtSH, *t*BuSH) only afford the zinc bis(thiolates) $Zn(SR)_2$ and the bis(perchlorate) complexes $[Zn(L_n)](ClO_4)_2$.

Restrictions are also encountered when the ligand does not possess the proper ring size and the right type and number of nitrogen donor sites. If the macrocycle is smaller than 11 atoms (ligands **1** and **2**), the synthesis again yields only the bis(thiolate) salts $Zn(SR)_2$ and complexes of the

 © 2006 Wiley-VCH Verlag GmbH & Co. KGaA, Weinheim 

composition $[Zn(L_3)_2](ClO_4)_2$. The reason is that small ring systems form extremely stable metal complexes[33] that are much more stable than complexes with larger rings.[34] In addition, 9- and 10-membered cyclic triamines do not react according to a 1:1 stoichiometry with zinc ions, which prevents the coordination of an additional monodentate ligand. Instead, a 1:2 complex precipitates from solutions, thus leaving behind noncomplexed zinc(II), which then forms a bis(thiolate) salt. A similar observation was made in the case of $L_4$ (tetramethylcyclam, **13**). This ligand always exhibits an unfavorable steric arrangement in its complexes with zinc as well as with other metal ions [it normally adopts the (+ + + +) configuration;[35] see below for details]. These complexes are generally less stable than complexes of its unsubstituted analogue, cyclam (**8**).[36] In the present case, the zinc(II) ion is removed from the macrocycle by formation of the more stable bis(thiolate) of zinc, releasing the free ligand.

## Structures

As already mentioned, of all the mercaptans tested only phenylmethane- and arenethiols form the desired complexes. Therefore we synthesized two series of isomeric complexes $[Zn(L_n)(SR)]ClO_4$ employing phenylmethanethiol (**a**; R = $CH_2C_6H_5$) and 4-methylbenzenethiol (**b**; R = $C_6H_4CH_3$). Twenty four novel thiolate complexes were obtained, of which 20 were characterized by single-crystal X-ray diffraction. (In the structure representations, the hydrogen atoms on carbon atoms and the perchlorate ions have been omitted for clarity.)

### *[Zn(3)(SR)]ClO$_4$ (17) and [Zn(4)(SR)]ClO$_4$ (18)*

The complexes derived from the 11-membered ring ligands **3** and **4** are remarkably similar regarding their individual structural parameters. The $N_3ZnS$ unit exhibits a slightly distorted tetrahedral coordination geometry (Figure 2), and all four Zn–S bond lengths are in the very narrow range of 2.2295(5)–2.2394(6) Å. The Zn–N bonds have distances between 2.037(2) and 2.076(2) Å. There is no significant correlation with the nature of the N donor, i.e. secondary or tertiary. The IR spectra show a single N–H band

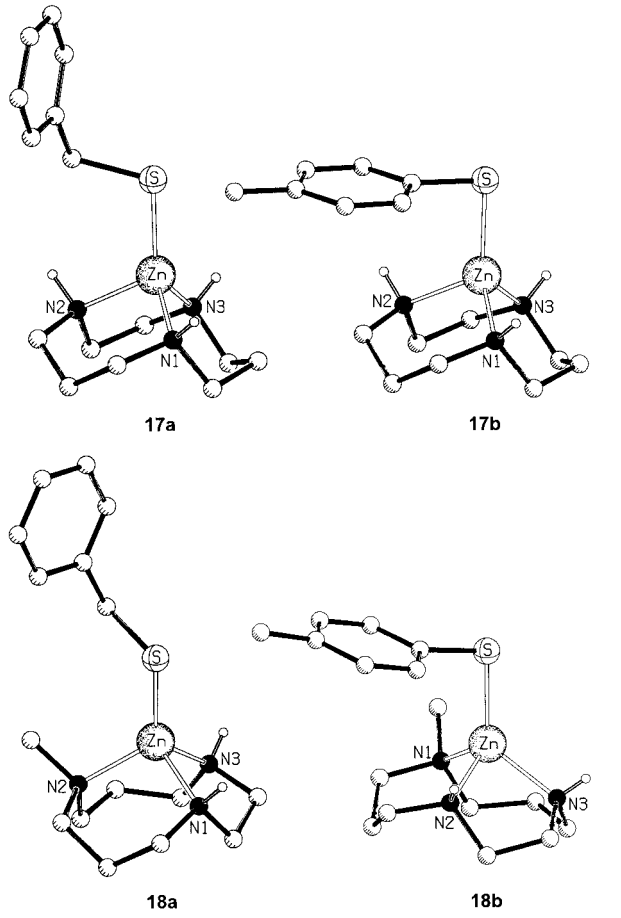


Figure 2. Molecular structures of **17a**, **17b**, **18a**, and **18b**. Selected bond lengths [Å]: **17a**: Zn–S 2.2353(9), Zn–N1 2.044(3), Zn–N2 2.047(3), Zn–N3 2.073(7); **17b**: Zn–S 2.2394(6), Zn–N1 2.056(2), Zn–N2 2.066(4), Zn–N3 2.048(2); **18a**: Zn–S 2.2295(5), Zn–N1 2.076(2), Zn–N2 2.060(2), Zn–N3 2.066(2); **18b**: Zn–S 2.2358(5), Zn–N1 2.068(2), Zn–N2 2.065(2), Zn–N3 2.037(2).

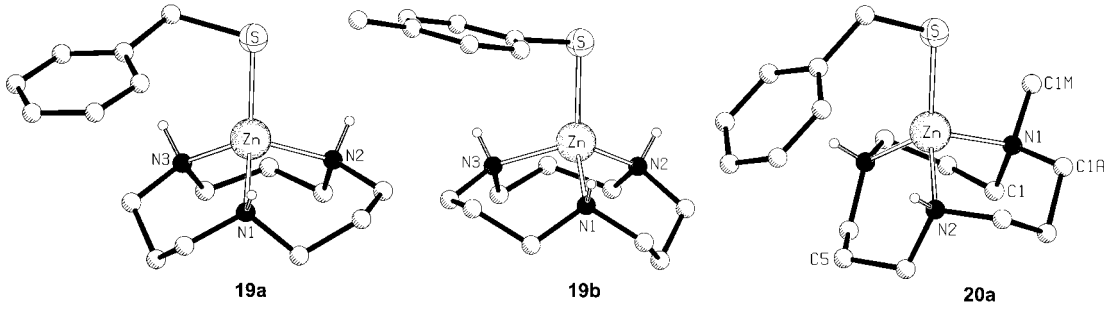


Figure 3. Molecular structures of **19a**, **19b**, and **20a**. Selected bond lengths [Å]: **19a**: Zn–S 2.245(2), Zn–N1 2.046(3), Zn–N2 2.056(3), Zn–N3 2.052(3); **19b**: Zn–S 2.2492(9), Zn–N1 2.036(3), Zn–N2 2.032(3), Zn–N3 2.052(3); **20a**: Zn–S 2.2367(7), Zn–N1 2.075(2), Zn–N2 2.050(2).

 © 2006 Wiley-VCH Verlag GmbH & Co. KGaA, Weinheim 

in the range of 3261–3271 $cm^{-1}$, which is broadened to a varying extent. This indicates the high degree of chemical analogy of these hydrogen atoms. Interestingly, the ligand's methyl substitution in **18a** has a marked effect on its solubility; it is readily soluble in dichloromethane, while the unsubstituted analogue, **17a**, is not.

### *[Zn(5)(SR)]$ClO_4$ (19) and [Zn(6)(SR)]$ClO_4$ (20)*

The three structurally characterized compounds **19a**, **19b**, and **20a** (Figure 3), synthesized with ligands **5** and **6**, show the same geometrical equivalence as observed for the complexes **17** and **18**. Slightly longer Zn–S bonds than in the case of the 11-membered cycles are encountered. However, the values for the Zn–N bonds are found in the same range. The IR spectra again show single bands in the region between 3252 and 3259 $cm^{-1}$. If the complex is asymmetric, they are broadened as mentioned above. Compound **20a** is symmetric along the C5–Zn–S plane (apart from a disorder of the atoms C1, C1A, N1, and C1M); therefore, the two hydrogen atoms attached to N2 and N2A are identical and give rise to a single, very narrow IR absorption. This shows the usefulness of IR absorption bands of N–H groups in determining the symmetry properties of macrocyclic amine complexes, a concept which will be referred to again later. Complex **20b** also exhibits a single band at almost the same value as **20a**, but it is noticeably broadened. This indicates the absence of a strict symmetry here. However, the structure is likely to follow the same motif. Similar to **18a**, the additional methyl group induces a solubility of **20a** in dichloromethane.

## Coordination Geometries in $N_4$ Complexes

Whether a five-coordinate complex belongs to the trigonal-bipyramidal or the tetragonal-pyramidal type is a question which is tricky to answer in the present case. Justifying an answer solely by the values of the bond angles, and thus seeking a more or less distorted trigonal bipyramidal axis, does not suffice. Upon first inspection, all the structures would appear to be a form of distorted square pyramid (see Figures 4–7 below). One thus needs to pay closer attention to the Zn–N bond lengths. In some cases (**23a**, **23b**, and to a lesser extent **27a**), the Zn–N bonds have almost the same lengths and the coordination polyhedra should therefore be regarded as being tetragonal-pyramidal with the sulfur atom in the apical position. The other complexes exhibit strongly differing values for pairs of opposing Zn–N bonds. They can therefore be classified as trigonal-bipyramidal. In these cases the thiolate ligand assumes an equatorial position. This effect is most strongly pronounced in complex **26a** (Figure 7): the mean deviation between adjacent Zn–N bond lengths is nearly twice as large (0.14 Å) as the difference between the *average* Zn–N and Zn–S bond length (0.08 Å). The species **21a** and **21b** must be classified as being "in between", since they exhibit neither a peculiar "axis" nor sufficiently small deviations in the Zn–N bond lengths.

The nitrogen atoms in these complexes are chiral in nature and we describe their actual configuration using established conventions.[37,38] The positions of hydrogen atoms or methyl groups are denoted relative to a plane (or near-plane) defined by the nitrogen atoms. If the N-bound residues are found on the side of the complex that bears the thiolate, their position is indicated with a (+). N-bound residues opposite the thiolate side are denoted with a (–). It is obvious that the configuration of the $N_3$ complexes is always (+ + +), as is expected for ligands whose cavities are too small for the respective metal ion.[37]

### *[Zn(7)(SR)]$ClO_4$ (21) and [Zn(8)(SR)]$ClO_4$ (22)*

The ring size of ligands **7** and **8** is rather small and all four structures accordingly exhibit the (+ + + +) configuration (Figure 4). Although compounds **21** both have a pair of opposing "long" and "short" bonds, the difference of both "axes" is too small to consider the geometries as being

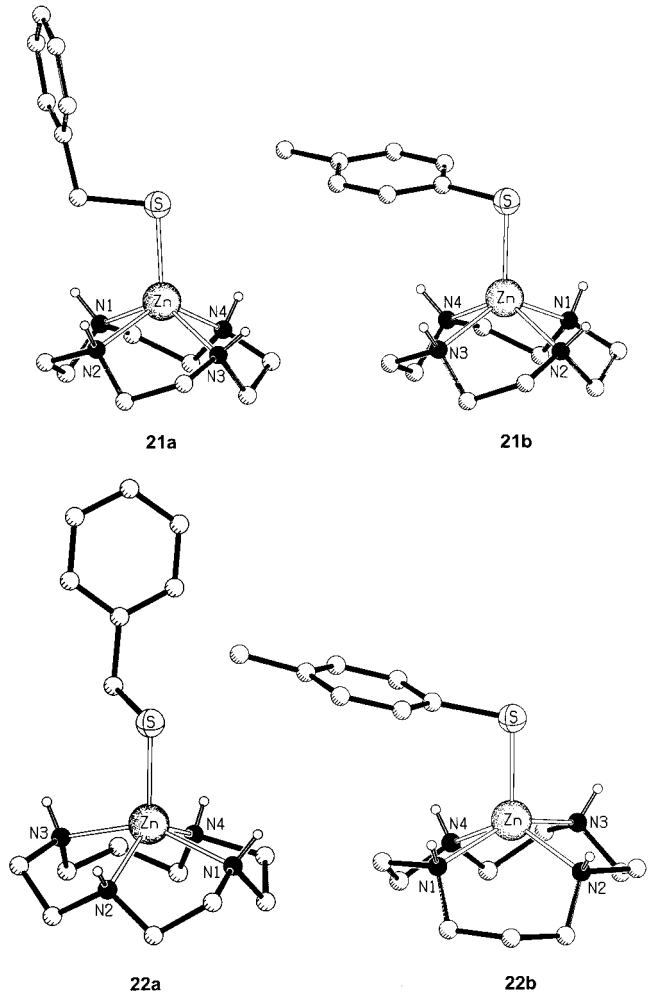


Figure 4. Molecular structures of **21a**, **21b**, **22a**, and **22b**. Selected bond lengths [Å]: **21a**: Zn–S 2.266(2), Zn–N1 2.159(4), Zn–N2 2.205(5), Zn–N3 2.151(4), Zn–N4 2.176(4); **21b**: Zn–S 2.2796(7), Zn–N1 2.175(2), Zn–N2 2.143(3), Zn–N3 2.201(3), Zn–N4 2.162(2); **22a**: Zn–S 2.2853(9), Zn–N1 2.218(3), Zn–N2 2.127(3), Zn–N3 2.187(3), Zn–N4 2.114(4); **22b**: Zn–S 2.2957(5), Zn–N1 2.200(2), Zn–N2 2.109(2), Zn–N3 2.208(2), Zn–N4 2.138(2).

 © 2006 Wiley-VCH Verlag GmbH & Co. KGaA, Weinheim 

trigonal-bipyramidal. The reason for this distortion is the small ring size of the ligand **7**, which enforces a marked rigidity in the coordination polyhedron. Although the system obviously strives for bipyramidality, steric constraints imposed by the ring force a tetragonal-pyramidal structure. In the case of complexes **22**, the ring is considerably larger and allows the formation of a (severely distorted) trigonal bipyramid. In agreement with this assignment, the IR spectra show a single N–H stretching band for complexes **21a** (3292 $cm^{-1}$) and **21b** (3301 $cm^{-1}$), emphasizing the degree of equivalence of the nitrogen atoms. In contrast to this, the N–H protons of compounds **22** are chemically inequivalent and three stretching bands are observed for both **22a** (3276, 3288, and 3306 $cm^{-1}$) and **22b** (3272, 3289, and 3322 $cm^{-1}$).

### *[Zn(9)(SR)]ClO$_4$ (23)*

With regard to the other [$N_4$] ligands, cyclam (**9**) yields an unusual result as complexes of **9** are the only ones which exhibit an almost perfect square-pyramidal geometry (Figure 5). This is particularly surprising since the ligand is clearly large enough to allow the formation of a trigonal bipyramid. The influence of the thiolate ligand on the conformation is minimal. All the Zn–N bond lengths are almost identical, with their maximum deviation being less than 0.02 Å for **23a** and 0.01 Å for **23b**. The two Zn–S bond lengths are identical within experimental error. Both complexes exhibit a (+ + – –) configuration which has been reported as being generally the most stable geometry.[39] Of the investigated complexes, **23b** is the only one which possesses a rigorous molecular symmetry ($C_s$) in the solid state, with the plane of symmetry being defined by C1, Zn, and S. The IR spectrum of **23b** thus exhibits two extraordinarily sharp N–H stretching bands at 3270 and 3259 $cm^{-1}$ with exactly the same intensity. In contrast, the absorptions of **23a** at 3272 and 3259 $cm^{-1}$ are not as sharp and their intensities show a marked difference.

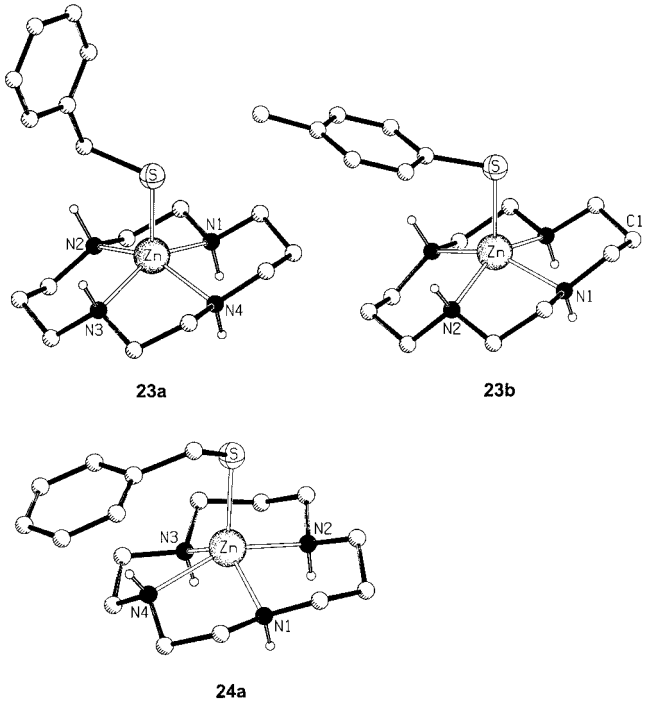


Figure 5. Molecular structures of **23a**, **23b**, and **24a**. Selected bond lengths [Å]: **23a**: Zn–S 2.3161(7), Zn–N1 2.155(2), Zn–N2 2.151(2), Zn–N3 2.149(2), Zn–N4 2.139(2); **23b**: Zn–S 2.3174(8), Zn–N1 2.139(2), Zn–N2 2.147(2); **24a**: Zn–S 2.2902(6), Zn–N1 2.112(2), Zn–N2 2.187(2), Zn–N3 2.123(2), Zn–N4 2.218(2).

### *[Zn(10)(SR)]ClO$_4$ (24)*

Complex **24a** possesses a (+ – – –) configuration which complies with the structural symmetry of the ligand (Figure 5). The symmetry of **24a** results in essentially two amine bands in its IR spectrum. One is located at 3268 $cm^{-1}$ (br., N1–H, N2–H, N3–H) and apparently consists of two closely overlapping bands, and the second band at 3309 $cm^{-1}$ is quite sharp (N4–H). The IR spectrum of **24b** is very similar. It also exhibits two bands at 3248 and 3305 $cm^{-1}$. We therefore assume that **24b** is very likely to have the same configuration.

### *[Zn(11)(SR)]ClO$_4$ (25)*

The most significant difference between the two compounds derived from ligand **11** is the configuration of the tertiary nitrogen atom, which is found to be (+) in complex **25a** and (–) in **25b**. This results in differing symmetries for the complexes (Figure 6). A related observation has been reported by Alcock et al.,[40] who have determined from $^1$H NMR spectroscopic data that a $D_2O$ solution of [Zn(**11**)]$(NO_3)_2$ contains two isomers, one of which is symmetric and the other asymmetric. In the present case, this effect can be observed in the $^1$H NMR spectrum of **25a** but not for **25b** due to the lack of an isolated signal. The benzylic methylene protons of **25a** yield two peaks at $\delta$ = 3.80 and 3.76 ppm with a relative intensity of 5:1. Its $^{13}$C NMR spectrum shows a predominant set of signals with five ring methylene peaks. For **25b**, two different $^{13}$C NMR spectroscopic data sets could be detected for the methylene carbon atoms of the macrocycle, a major set with five peaks and a

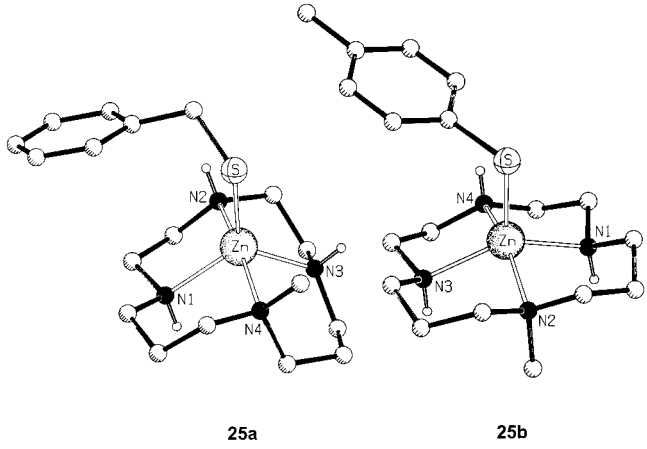


Figure 6. Molecular structures of **25a** and **25b**. Selected bond lengths [Å] and angles [°]: **25a**: Zn–S 2.3200(7), Zn–N1 2.118(2), Zn–N2 2.235(2), Zn–N3 2.133(2), Zn–N4 2.202(2); N2–Zn–N4 165.81(9); **25b**: Zn–S 2.3182(9), Zn–N1 2.106(3), Zn–N2 2.171(3), Zn–N3 2.105(3), Zn–N4 2.191(3); N2–Zn–N4 154.3(2).

 © 2006 Wiley-VCH Verlag GmbH & Co. KGaA, Weinheim 

minor set consisting of ten peaks. We thus assume that in both cases the predominant species is of the same symmetric configuration as found in the solid-state structure of **25b**. The minor component is of an asymmetric configuration, analogous to the solid-state structure of **25a**.

The fact that the crystal lattices of **25a** and **25b** contain different configurational isomers is also reflected in their IR spectra. Three N–H bands at 3239, 3308 and 3346 $cm^{-1}$ are present in the case of the unsymmetrically configured **25a** and only two at 3246 (br.) and 3293 $cm^{-1}$ for the symmetric ligand configuration found in **25b**.

### *[Zn(12)(SR)]$ClO_4$ (26)*

As mentioned above, **26a** (synthesized from ligand **12**) has the largest deviations in its Zn–N bond lengths. It clearly adopts a trigonal-bipyramidal geometry and a (+ – – –) configuration of the nitrogen atoms (denoted in the order N1–N2–N3–N4; see Figure 7). Similar to **25a**, the NMR spectra reveal that a chloroform solution of complex **26a** contains two isomers. The $^{13}C$ NMR spectrum exhibits 11 methylene carbon peaks for the main component and seven for the minor component. The major component possesses an asymmetric configuration of the chiral nitrogen atoms, which is very likely identical to the solid-state structure of this compound. The symmetric configuration of the minor component might be (+ – – +) or all-(–), but this question could not be answered from the routine NMR spectroscopic data. The $^1H$ NMR spectrum shows a multiplet for the benzylic methylene protons. Upon closer inspection, this multiplet consists of a singlet at $\delta$ = 3.85 ppm (minor component, 15% of total integral value of benzyl protons) overlapping with an AB spin system at $\delta$ = 3.81 ppm (main component, $J$ = 14.3 Hz, $\Delta\delta$ = 9.7 Hz). This observation fits perfectly, since the asymmetric configuration of the nitrogen atoms ensures a chiral zinc atom. The benzyl protons are thus in a diastereotopic environment, which causes the multiplicity of their NMR signal. (Why this is only observed for **25a** and not for the other complexes of asymmetric configuration remains a mystery. A possible explanation could be found in different velocities of configurational change, which might cause enhanced line-widths for the other complexes and render the detection of signal multiplicities impossible. However, we are not sure about this.) The IR spectrum shows only three bands at 3251, 3266, and 3286 $cm^{-1}$, which is not surprising since the structural environments of N2 and N4 are very similar. For compound **26b**, only one structural motif could be obtained by X-ray crystallography. It reveals, however, that the configuration of the ligand is the same as found in **26a**.

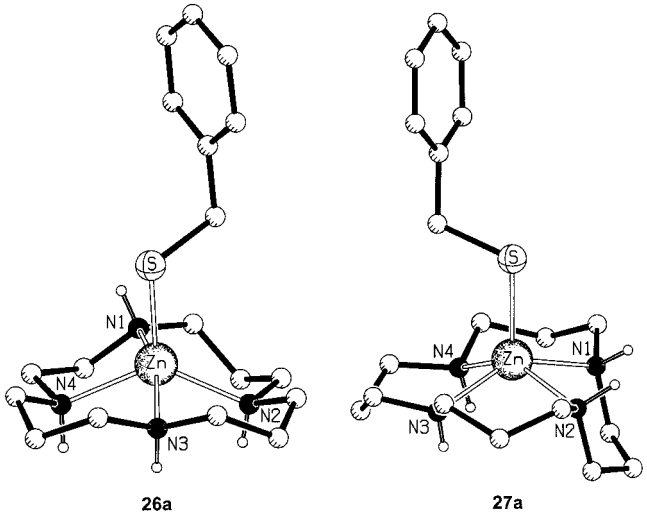


Figure 7. Molecular structures of **26a** and **27a**. Selected bond lengths [Å]: **26a**: Zn–S 2.28(2), Zn–N1 2.271(3), Zn–N2 2.115(3), Zn–N3 2.256(3), Zn–N4 2.123(3); **27a**: Zn–S 2.299(2), Zn–N1 2.208(3), Zn–N2 2.182(3), Zn–N3 2.194(3), Zn–N4 2.189(3).

### *[Zn(14)(SR)]$ClO_4$ (27)*

Ligand **14** is known to form complexes that are less stable than complexes formed from smaller macrocycles. A detailed study has shown that the steric strain in the six-membered chelate rings is responsible for this.[37] Zinc(II) tends to form the complex [Zn(**14**)]$(ClO_4)_2$ with a (+ – + –) configuration. Its stability stems from the fact that the metal ion's size and the Zn–N bond length ensure a chair conformation in each of the four chelate rings. A mixture of this compound with **27a** was obtained when sodium thiolate was used for synthesis; only the potassium salt afforded the pure thiolate complex. In the case of **27a**, the central $Zn^{2+}$ ion is pentacoordinate (Figure 7), which obviously does not allow the nitrogen atoms to arrange in a tetrahedral manner. However, the ligand folds in such a way that only chelate rings with a chair conformation are formed. The N–Zn–N angles of the adjacent nitrogen atoms vary between 78 and 89°. Obviously, ring strain is low enough to render the complex more stable than [Zn(**14**)]$(ClO_4)_2$. In accordance with the observed molecular symmetry, the IR spectrum of **27a** shows only one N–H absorption at 3249 $cm^{-1}$. Two IR bands were observed for compound **27b**, which comply with two pairs of chemically nonequivalent hydrogen atoms. This does not, however, necessarily indicate the presence of another configuration.

### *[Zn(15)(SR)]$ClO_4$ (28)*

When sodium thiolate was used to synthesize complex **28a**, the sulfur-free complex [Zn(**15**)]$(ClO_4)_2$ (**16**) was obtained instead (Figure 8). Only the use of the potassium salt afforded complex **28a**, while **28b** was also obtained with sodium *p*-methylbenzenethiolate. These compounds and complex **16** are the first reported zinc complexes of the ligand [15]ane$N_5$ (**15**). They all show a high degree of structural equivalence regarding the configuration of the macrocycle. The unit cell of **28b** contains two independent molecules with almost superimposable coordination polyhedra, although noticeable deviations in the bond lengths are encountered. Since the two molecules have nearly the same appearance, only one of them is depicted in Figure 8.

These hexacoordinate zinc complexes with the rare $N_5S$ coordination environment (only one structurally charac-

 © 2006 Wiley-VCH Verlag GmbH & Co. KGaA, Weinheim 

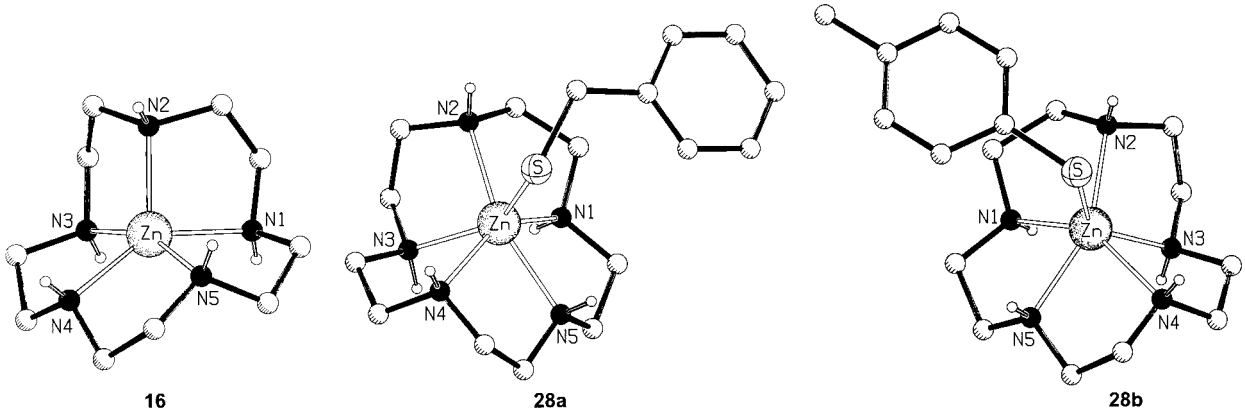


Figure 8. Molecular structures of **16**, **28a**, and **28b**. Selected bond lengths [Å]: **16**: Zn–N1 2.100(2), Zn–N2 2.067(2), Zn–N3 2.170(2), Zn–N4 2.179(2), Zn–N5 2.168(2); **28a**: Zn–S 2.3782(7), Zn–N1 2.199(3), Zn–N2 2.366(3), Zn–N3 2.192(3), Zn–N4 2.368(3), Zn–N5 2.221(3); **28b** (molecule A): Zn–S 2.405(2), Zn–N1 2.206(7), Zn–N2 2.331(6), Zn–N3 2.152(5), Zn–N4 2.385(6), Zn–N5 2.194(5); (molecule B, not depicted): Zn–S 2.435(2), Zn–N1 2.265(5), Zn–N2 2.309(6), Zn–N3 2.199(5), Zn–N4 2.307(6), Zn–N5 2.205(5).

terized example has been reported until now[41]) do not have much in common with the other complexes discussed in this work. Their coordination polyhedra cannot be assigned to a specific structure type. Of the complexes discussed in this study, **28a** reveals the largest mean Zn–N bond length (2.267 Å), and **28b** shows the largest deviation within a single molecule (0.23 Å). However, the most significant characteristics are probably the zinc–sulfur bond lengths, which are 2.3782(7) Å for **28a** and 2.405(2) and 2.435(2) Å for **28b**, respectively. These are extraordinarily long Zn–S bonds compared to the average bond length of 2.29 Å for terminal zinc thiolates listed in the Cambridge Structural Database.[1] This makes complexes **28** somewhat equivalent to the zinc tetrathiolate *anion* $[Zn(SPh)_4]^{2-}$, which has a Zn–SPh bond length of 2.36 Å,[42,43] and accentuates their exceptional structural properties.

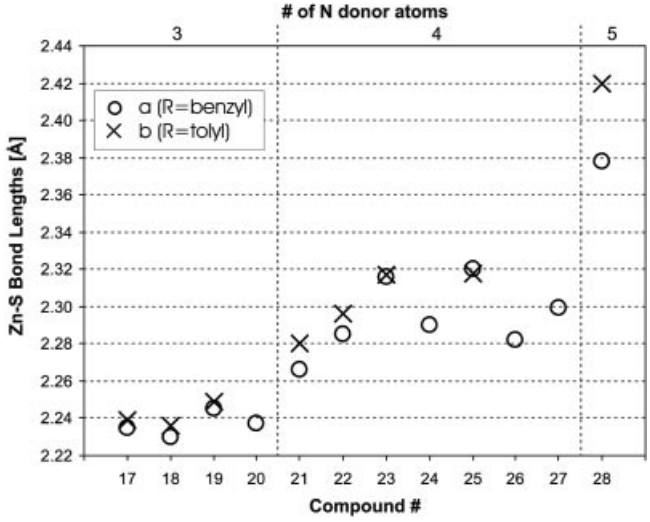


Figure 9. Zn–S bond lengths [Å] (mean value for **28b**).

## Comparative Considerations

Figure 9 shows that the Zn–S bond lengths depend on the number or the nature of the nitrogen donor sites in only a loose way. It is much more obvious that there is a certain correlation with the ring size: as it increases from 11 to 13 atoms, the Zn–S bond lengths increase from approx. 2.23 to 2.29 Å. The Zn–S bonds in complexes with 14-membered or larger rings (compounds **23** to **27**) seem to scatter around a "standard" length of approx. 2.3 Å, which is close to the average zinc thiolate linkage of 2.29 Å as mentioned above. The fact that compounds **28** are much less stable than the other complexes is reflected in their extremely long Zn–S bonds.

In contrast to the previous case, it is not the ring size of the macrocyclic ligand but rather the number of nitrogen donors that seems to have the pivotal influence on the average Zn–N bond lengths. The plot depicted in Figure 10 reveals three distinct groups of compounds, corresponding to the number of nitrogen atoms involved. Their secondary or tertiary nature does not contribute to a Zn–N bond length alteration in a noticeable way. As far as can be

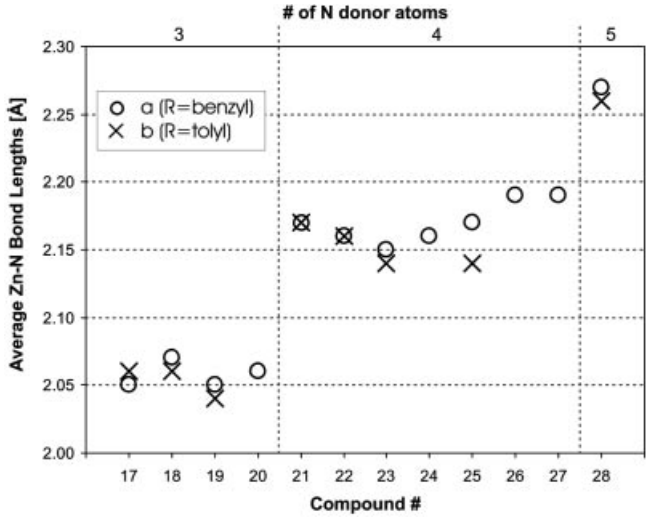


Figure 10. Average Zn–N bond lengths [Å].

 © 2006 Wiley-VCH Verlag GmbH & Co. KGaA, Weinheim 

judged from this incomplete data (four structures are missing), the type of thiolate has no significant influence either.

### NMR Spectra

The $^1$H NMR spectra generally show only nonspecific multiplets and broadened peaks for the hydrogen atoms attached to the macrocycle. This is very likely caused by dynamic effects. Measurements of gradually diluted solutions with concentrations ranging from 0.1 to 4 mM yield unaltered spectra. This allows the conclusion that there is no distinct contribution of intermolecular interactions. Only the benzyl methylene, the tolyl methyl groups, and the aromatic hydrogen atoms exhibit the usual line shape. However, their shifts show only very little dependence on macrocycle substitution. Nevertheless, these signals are suitable for reaction monitoring.

The $^{13}$C NMR spectra are resolved much better, even though they sometimes exhibit considerably increased linewidths for the methylene carbon atoms of the macrocyclic ligands. For all complexes but **26**, the number of detected methylene peaks is smaller than the number of methylene carbon atoms of the macrocycle and correlates directly with the valence symmetry of the macrocyclic ligand. This allows the conclusion that either the complexes adopt a symmetrical structure in solution or the dynamic conformational changes proceed quickly enough to override the asymmetry of the macrocycle that originates in the conformation enforced by the metal coordination. Nevertheless, compounds **19**, **20b**, **22**, **23a**, **25b**, and **26** exhibit additional signals of small intensities for the carbon atoms of the macrocycle. This indicates the presence of at least one additional isomer. In case of the more rigid systems **19**, **20b**, and **22** it is possible that conformational changes in the bridging ethylene and propylene units require comparably high energy barriers and hence are slow on the NMR timescale, thus allowing the detection of the conformers as separate signal sets. Another possible interconversion between species in solution is the configuration inversion of a chiral nitrogen atom. This seems to hold for **23a**, **26**, and particularly for **25b** (see discussion of structures above).

### Mass Spectra

Mass spectra, recorded in ESI mode with a mixture of MeOH and MeCN as solvents, provide valuable information on the stability of the Zn–S bond. The weaker the thiolate is bound, the more species are detected with the monodentate thiolate ligand being replaced by $HO^-$, $MeO^-$, or MeCN, or simply without the ligand. Thus, the intensity of these signals as compared to the molecular peak $[Zn(L_n)(SR)]^+$ may be considered as an indicator of complex stability.

According to this approach, the mass spectra reveal the complexes containing small macrocyclic ligands to be the most stable. All complexes with rings of up to 12 atoms (**17**–**21**) show none or only small amounts (up to 10% intensity) of the mentioned degradation products. For the compounds with 13- to 16-membered rings (**28** not considered), the peak intensities of the solvent complexes increase with the ring size, reaching a maximum for compounds **27**. In addition, the aromatic thiolate yields complexes of considerably higher stability than phenylmethanethiolate. This agrees with the observations made during the preparation of **27a** and **28a**. The "overcrowded" complexes **28** are the least stable ones. In the case of the phenylmethanethiolate complex **28a**, the molecular peak could not even be detected. In no case was any evidence for a dissociation of the macrocycle from the zinc center found.

## Conclusions

Azamacrocycles have been found to be suitable ligands to obtain stable, soluble thiolate complexes of $Zn^{II}$. In retrospect, this cannot be taken as a matter of course. The fact that only certain ring sizes and thiolates yield the desired complexes illustrates how sensitive these systems are to steric and electronic influences. (It is worth mentioning that substituted arene- and phenylmethanethiolates are generally suitable for these syntheses, as some additional experiments have shown. However, a more detailed investigation of the issue has not been performed because we did not expect it to provide any fundamentally enhanced insight into the matter.) It is surprising that the crystal lattices of all complexes comprise only monomeric structures. We assume that the steric demand of the benzyl and aryl residues of the thiolate ligands is a substantial factor behind this behavior. Less sterically hindered thiolates such as $MeS^-$ would presumably promote the formation of dimers or oligomers. However, this will probably remain speculation because these compounds are elusive and our efforts to develop alternative synthetic routes were not successful.

The main advantage of this class of complexes is its structural diversity. A large number of thiolate–zinc linkages that differ in length, stability, and bond order can be studied. With the exception of **28**, their solubility in non- and semipolar organic solvents allows the investigation of reactions under conditions that resemble the hydrophobic cavities of enzyme proteins. In addition, there are two characteristics that make them ideally suited for studies combining experimental work and computational methods. First, their molecular structure data are, except for a few examples, available with high accuracy. Second, they contain a comparably small number of non-hydrogen atoms. Thus, quantum mechanical calculations of these compounds can actually be performed at sufficiently high levels of theory to gain insight into reaction mechanisms. Finally, their easy accessibility, long-term stability, and the variety of characterized compounds renders this class of complexes useful for biomimetic studies wherever zinc thiolates are involved.

## Experimental Section

**Materials and Methods:** All reagents used were of analytical purity. Solvents were not dried prior to use, except where indicated. NMR

 © 2006 Wiley-VCH Verlag GmbH & Co. KGaA, Weinheim 

spectra were recorded using a Bruker AC 250 spectrometer at a temperature of 30 °C. IR spectra were recorded from the neat substances using a Nicolet Avatar 320 FT-IR spectrometer. Elemental analyses were performed using a Heraeus Vario EL III system. Melting points were determined with a Büchi Melting Point B 545 apparatus and are uncorrected. Mass spectra were recorded using a Finnigan MAT SSQ 710 or a Finnigan MAT 900XL TRAP.

**Preparation of the Azamacrocycles:** The preparation essentially followed a published procedure.[30] Small alterations were made to the reaction conditions of the cyclization (2–3 h at 125 °C) and the workup procedure of the deprotected amine. The preparation of 8-methyl-[11]ane$N_3$ (**4**) serves as an example.

**Preparation of 8-Methyl-1,4,8-triazacycloundecane (8-Methyl-[11]ane$N_3$) (4):** A solution of the disodium salt[30] of *N*,*N*-bis[3-(*p*-tolylsulfonyl)aminopropyl]methylamine[44] (88 mmol) and 1,2-bis(*p*-tolylsulfonyloxy)ethane (88 mmol) in dry DMF (1.5 L) was stirred at 140 °C for 3 h. Three-quarters of the solvent was then distilled off in vacuo and the mixture was poured into 1 L of an ice/water mixture. The product was filtered off, washed with plenty of water, and recrystallized from ethanol to yield 56% of 8-methyl-1,4-bis(*p*-toluenesulfonyl)-1,4,8-triazacycloundecane as a colorless solid. M.p. 161 °C. $^1$H NMR (250 MHz, $CDCl_3$): $\delta$ = 1.78 (q, $J$ = 5.65 Hz, 4 H, C$H_2$), 2.19 (s, 3 H, N–C$H_3$), 2.45 (s, 6 H, Ph–C$H_3$), 2.58 (t, $J$ = 6.25 Hz, 4 H, C$H_2$), 3.16 (t, $J$ = 5.73 Hz, 4 H, C$H_2$), 3.37 (s, 4 H, C$H_2$), 7.30 and 7.69 (d, $J$ = 6.56 Hz, 4 H each, Ph–*H*) ppm. $^{13}$C NMR (62.9 MHz, $CDCl_3$): $\delta$ = 21.5, 24.4, 42.4, 48.5, 50.8, 52.5, 127.5, 129.7, 134.9, 143.4 ppm. $C_{23}H_{33}N_3S_2O_4$ (479.67): calcd. C 57.59, H 6.39, N 8.76, S 13.37; found C 57.32, H 7.17, N 8.60, S 13.24. For detosylation, the solid was heated in concd.

Table 1. Analytical data for compounds **17**–**28**.

| Complex | Composition calcd. [%] | | | | | Complex | Composition found [%] | | | | | Yield | M.p.[a] |
|---|---|---|---|---|---|---|---|---|---|---|---|---|---|
| | C | H | Cl | N | S | | C | H | Cl | N | S | [%] | [°C] |
| **17** | 40.46 | 5.98 | 7.96 | 9.44 | 7.20 | **17a** | 40.47 | 6.24 | 8.00 | 9.48 | 6.95 | 37 | 228–230 |
| | | | | | | **17b** | 40.31 | 5.86 | 7.82 | 9.36 | 6.72 | 53 | 310 d |
| **18**, **19** | 41.84 | 6.14 | 7.72 | 9.15 | 6.98 | **18a** | 41.78 | 6.19 | 7.94 | 9.09 | 6.55 | 53 | 162–164 |
| | | | | | | **18b** | 41.77 | 6.16 | 7.99 | 9.09 | 6.53 | 21 | 228–229 |
| | | | | | | **19a** | 41.67 | 6.17 | 7.83 | 9.02 | 6.50 | 46 | 187–190 |
| | | | | | | **19b** | 41.75 | 6.05 | 7.54 | 9.07 | 6.61 | 65 | 309 d |
| **20** | 43.39 | 6.39 | 7.49 | 8.87 | 6.77 | **20a** | 43.03 | 6.45 | 7.30 | 8.82 | 6.51 | 53 | 158–160 |
| | | | | | | **20b** | 43.00 | 6.33 | 7.69 | 8.78 | 6.32 | 49 | 218–220 |
| **21** | 39.41 | 5.91 | 7.70 | 12.17 | 6.97 | **21a** | 39.01 | 5.88 | 7.54 | 12.10 | 6.44 | 35 | 253–256 |
| | | | | | | **21b** | 39.05 | 6.98 | 7.41 | 12.16 | 6.66 | 73 | 310d |
| **22** | 40.52 | 6.16 | 7.47 | 11.81 | 6.76 | **22a** | 40.36 | 6.25 | 7.50 | 11.82 | 6.28 | 31 | 216–218 |
| | | | | | | **22b** | 40.41 | 6.23 | 7.51 | 11.90 | 6.45 | 50 | 292 d |
| **23**, **24** | 41.81 | 6.4 | 7.26 | 11.47 | 6.57 | **23a** | 41.66 | 6.32 | 7.01 | 11.49 | 6.17 | 61 | 204–206 |
| | | | | | | **23b** | 41.66 | 6.36 | 6.99 | 11.39 | 6.22 | 79 | 276 d |
| | | | | | | **24a** | 41.80 | 6.16 | 7.05 | 11.49 | 6.40 | 60 | 221–223 |
| | | | | | | **24b** | 41.64 | 6.47 | 7.01 | 11.33 | 6.09 | 67 | 275 d |
| **25**, **26** | 43.03 | 6.62 | 7.06 | 11.15 | 6.38 | **25a** | 42.88 | 6.58 | 6.88 | 11.14 | 6.04 | 41 | 211–213 |
| | | | | | | **25b** | 42.90 | 6.77 | 6.96 | 11.24 | 6.09 | 56 | 230–232 |
| | | | | | | **26a** | 42.95 | 7.19 | 7.40 | 11.15 | 6.12 | 38 | 193–195 |
| | | | | | | **26b** | 42.67 | 6.73 | 6.77 | 11.15 | 5.75 | 47 | 272 d |
| **27a** | 43.80 | 7.17 | 6.46 | 10.21 | 5.85 | **27a** | 43.58 | 7.22 | 6.58 | 10.21 | 5.60 | 60 | 173–175 |
| **27b** | 44.19 | 6.83 | 6.86 | 10.84 | 6.21 | **27b** | 44.07 | 6.98 | 6.96 | 10.85 | 6.10 | 54 | 270 d |
| **28** | 40.56 | 6.41 | 7.04 | 13.91 | 6.37 | **28a** | 40.21 | 6.31 | 7.36 | 13.97 | 6.00 | 20 | 182–183 |
| | | | | | | **28b** | 40.48 | 6.53 | 7.25 | 13.92 | 6.06 | 66 | 248 d |

[a] d: decomposition.

Table 2. Spectroscopic data for compounds **17**–**28**.

| Complex | MS [*m*/*z* (%)][a] | IR [cm$^{-1}$][b] | Complex | MS [*m*/*z* (%)][a] | IR [cm$^{-1}$][b] |
|---|---|---|---|---|---|
| **17a** | 344 (100) | 3271 | **23a** | 387 (100), 281 (94) | 3272, 3259 |
| **17b** | 344 (100) | 3246 | **23b** | 387 (100), 281 (35) | 3270, 3259 |
| **18a** | 358 (100) | 3268 | **24a** | 387 (100), 281 (64) | 3309, 3268 |
| **18b** | 358 (100) | 3261 | **24b** | 387 (100), 281 (34) | 3305, 3248 |
| **19a** | 358 (100) | 3254 | **25a** | 401 (100), 295 (46) | 3346, 3308, 3239 |
| **19b** | 358 (100) | 3259 | **25b** | 401 (100), 295 (54) | 3293, 3246 |
| **20a** | 372 (100) | 3256 | **26a** | 401[c] (75), 295 (100) | 3286, 3266, 3251 |
| **20b** | 372 (100) | 3252 | **26b** | 401 (100), 295 (63) | 3275, 3244 |
| **21a** | 359 (100) | 3292 | **27a** | 415[c] (33), 309 (100) | 3249, (3199, O–H) |
| **21b** | 359 (100) | 3301 | **27b** | 415 (100), 309 (87) | 3274, 3226 |
| **22a** | 373 (100), 267 (20) | 3306, 3288, 3276 | **28a** | 278 (100),[d] 139 (46) | 3353, 3338, 3278 |
| **22b** | 373 (100), 267 (16) | 3322, 3289, 3272 | **28b** | 402[c] (29), 278 (100) | 3352, 3329, 3306, 3268 |

[a] Only the molecular peak and the peak of the main degradation product $[Zn(L)(OH)]^+$ are given. [b] Only the data of the N–H absorptions are denoted. [c] Molecular peak (where different from base peak). [d] No molecular peak detected.

 © 2006 Wiley-VCH Verlag GmbH & Co. KGaA, Weinheim 

$H_2SO_4$ (100 mL) for 72 h. A saturated NaOH solution was used to neutralize the $H_2SO_4$ until a pH of 12 was reached. The amine was extracted with chloroform (5×100 mL), the combined extracts were dried with $Na_2SO_4$, the solvent was evaporated, and the crude product distilled using a kugelrohr apparatus (b.p. 100 °C, 0.1 mbar) to give 2.75 g (32%) of **4** as a colorless oil. IR: $\tilde{\nu}$ = 3289 m (NH), 2918 s, 2833 ($CH_2$), 2869 s, 2789 s ($CH_3$), 1677 m, 1456 s, 1144 s, 1119 s, 1058 s, 737 s $cm^{-1}$. $^1H$ NMR (250 MHz, $CDCl_3$): $\delta$ = 1.48 (q, $J$ = 5.26 Hz, 4 H, $CH_2$–C$H_2$–$CH_2$), 2.09 (s, 3 H, N–C$H_3$), 2.42 (t, $J$ = 5.43 Hz, 4 H, MeN–C$H_2$), 2.63 (s, 4 H, C$H_2$–C$H_2$), 2.68 (t, $J$ = 5.29 Hz, 4 H, HN–C$H_2$) ppm. $^{13}C$ NMR (62.9 MHz, $CDCl_3$): $\delta$ = 25.65, 41.76, 47.43, 48.13, 57.36 ppm. $C_9H_{21}N_3$ (171.26): calcd. C 62.74, H 12.87, N 24.39; found C 59.28, H 12.19, N 22.83 (hygroscopic material; no exact determination of sample weight possible).

**Preparation of [Zn([15]aneN$_5$)](ClO$_4$)$_2$ (16):** [15]aneN$_5$ (**15**; 1 mmol) was added to a 0.1 M solution of $Zn(ClO_4)_2 \cdot 6H_2O$ (10 mL) in $H_2O$. After heating for 10 min, the mixture was cooled. A colorless precipitate separated within several hours. The crystals were filtered off, washed twice with ethanol, and dried in vacuo to give 179 mg of **16** (37%) as colorless crystals, m.p. 182–184 °C. $C_{10}H_{25}Cl_2N_5O_8Zn$ (479.36): calcd. C 25.04, H 5.25, Cl 14.78, N 14.60; found C 24.95, H 5.18, Cl 14.60, N 14.65. MS: $m/z$ (%) = 378 (100), 278 (28), 160 (18), 140 (31). $^1H$ NMR (250 MHz, DMSO): $\delta$ = 2.1–2.65 (m, 10 H), 2.65–3.15 (m, 10 H), 3.4–3.9 (br. m, 5 H,

Table 3. $^1H$ NMR spectroscopic data for compounds **17**–**28** ($\delta$ [ppm], 250 MHz, 30 °C). Due to dynamic effects only unspecific multiplets are obtained for the hydrogen atoms of the macrocyclic ligand. Thus, only the data of the protons of the thiolate ligands are given.

| Complex | $C_6H_5CH_2$ | $C_6H_5CH_2$ | Complex | $C_6H_5CH_2$ | $C_6H_5CH_2$ |
|---|---|---|---|---|---|
| **17a**[a] | 3.71 (s) | 7.21 (t), 7.33 (t), 7.47 (d) | **17b**[a] | 2.25 (s) | 6.98 (d), 7.29 (d) |
| **18a**[a] | 3.70 (s) | 7.21 (t), 7.33 (t), 7.43 (d) | **18b**[a] | 2.25 (s) | 6.98 (d), 7.27 (d) |
| **19a**[a] | 3.73 (s) | 7.22 (t), 7.33 (t), 7.45 (d) | **19b**[a] | 2.25 (s) | 6.98 (d), 7.31 (d) |
| **20a**[a] | 3.73 (s) | 7.21 (t), 7.34 (t), 7.45 (d) | **20b**[a] | 2.25 (s) | 6.99 (d), 7.33 (d) |
| **21a**[a] | 3.65 (s) | 7.22 (t), 7.30 (t), 7.43 (d) | **21b**[a] | 2.24 (s) | 6.94 (d), 7.24 (d) |
| **22a**[a] | 3.66 (s) | 7.19 (t), 7.31 (t), 7.44 (d) | **22b**[a] | 2.24 (s) | 6.95 (d), 7.26 (d) |
| **23a**[b] | 3.79 (s) | 7.19 (t), 7.31 (t), 7.48 (d) | **23b**[b] | 2.26 (s) | 6.99 (d), 7.28 (d) |
| **24a**[b] | 3.73 (s) | 7.15 (t), 7.23 (t), 7.41 (d) | **24b**[b] | 2.26 (s) | 6.95 (d), 7.33 (d) |
| **25a**[b] | 3.80 (s), 3.76 (s) (20%)[d] | 7.17–7.33 (m), 7.40–7.48 (m) | **25b**[b] | 2.25 (s) | 6.95 (d), 7.29 (d) |
| **26a**[b] | 3.81,[e] 3.85 (s) (15%)[d] | 7.15–7.32 (m), 7.41–7.50 (m) | **26b**[b] | 2.26 (s) | 6.89–7.43 (m) |
| **27a**[b] | 3.84 (s) | 7.15 (t), 7.22 (t), 7.29 (d) | **27b**[b] | 2.25 (s) | 6.90 (d), 7.42 (d) |
| **28a**[c] | 3.57 (s) | 7.09 (t), 7.22 (t), 7.29 (d) | **28b**[c] | 2.15 (s) | 6.82 (d), 7.21 (d) |

[a] In $CD_3CN$. [b] In $CDCl_3$. [c] In [$D_6$]DMSO. [d] Multiple peaks detected, percentage of minor peak given in brackets. [e] AB spin system, $J$ = 14.3 Hz, $\Delta\delta$ = 9.7 Hz.

Table 4. $^{13}C$ NMR spectroscopic data (62.3 MHz, 30 °C) for compounds **17**–**28**.

| Complex | Solvent | $\delta$ [ppm] |
|---|---|---|
| **17a** | $CD_3CN$ | 23.5, 28.6, 45.1, 48.3, 126.0, 127.9, 128.3, 146.1 |
| **18a** | $CD_3CN$ | 22.6, 28.6, 45.0, 48.0, 48.2, 58.4, 126.0, 127.9, 128.3, 146.0 |
| **19a**[a] | $CD_3CN$ | 126.0, 127.9, 128.2, 146.0 |
| **20a** | $CD_3CN$ | 23.4, 23.9, 27.1, 28.6, 45.9, 48.0, 48.8, 126.0, 127.9, 128.3, 146.0 |
| **21a** | $CD_3CN$ | 29.0, 43.7, 125.6, 127.9, 128.0, 146.3 |
| **22a**[b] | $CD_3CN$ | 27.2, 29.0, 43.5, 45.5, 47.7, 49.5, 125.6, 127.9, 128.0, 146.3 |
| **23a**[b] | $CDCl_3$ | 27.9, 28.2, 30.3, 47.4, 48.7, 49.1, 51.1, 126.6, 128.5, 128.6, 145.9 |
| **24a** | $CDCl_3$ | 28.1, 30.2, 48.2, 49.4, 50.2, 51.6, 126.4, 128.3, 128.4, 145.8 |
| **25a** | $CDCl_3$ | 24.6, 30.7, 39.9, 47.3, 49.7, 50.1, 60.1, 126.6, 128.4, 128.5, 145.4 |
| **26a**[b] | $CDCl_3$ | 24.8, 28.1, 28.2, 30.2, 47.0, 49.2, 50.2, 51.6, 52.0, 54.0, 54.6, 126.4, 128.1, 128.4, 145.6 |
| **27a** | $CDCl_3$ | 27.4,[c] 30.3, 53.8,[c] 126.2, 128.1, 128.6, 145.2 |
| **28a** | [$D_6$]DMSO | 29.7, 45.9,[c] 125.1, 127.7, 128.2, 146.3 |
| **17b** | $CD_3CN$ | 19.6, 23.6, 45.2, 48.2, 48.4, 129.1, 133.3, 133.4, 135.0 |
| **18b** | $CD_3CN$ | 19.6, 22.7, 45.1, 47.8, 48.2, 58.6, 129.2, 133.3, 133.4, 134.9 |
| **19b**[b] | $CD_3CN$ | 19.6, 24.1, 49.2, 129.2, 133.4, 133.6, 135.3 |
| **20b**[b,d] | $CD_3CN$ | 19.6, 21.7, 24.1, 46.4, 48.0, 48.2, 57.6, 129.2, 133.5, 133.7 |
| **21b** | $CD_3CN$ | 19.6, 43.7, 128.9, 132.5, 133.4, 137.9 |
| **22b**[b] | $CD_3CN$ | 19.6, 27.2, 43.5, 45.4, 47.7, 49.6, 129.0, 132.6, 133.6, 138.2 |
| **23b** | $CDCl_3$ | 20.8, 24.9, 27.8, 47.8–51.1,[c] 130.0, 133.8, 134.6, 138.2 |
| **24b** | $CDCl_3$ | 20.8, 28.1, 48.0, 49.3, 50.2, 51.7, 129.5, 133.8, 135.0, 137.5 |
| **25b**[e] | $CDCl_3$ | 20.8, 24.6, 39.7, 47.3, 49.6, 50.0, 60.2, 129.7, 133.9, 135.0, 137.4<br>24.0, 24.5, 45.1, 46.0 (2 C), 47.3, 49.0, 50.3, 51.2, 56.2, 62.6 |
| **26b**[b] | $CDCl_3$ | 20.8, 24.8, 28.2, 47.0, 49.5, 50.5, 51.6, 52.1, 52.9, 54.0, 54.7, 129.5, 133.7, 134.8, 137.5 |
| **27b** | $CDCl_3$ | 20.8, 27.3,[c], 53.7,[c] 129.0, 133.5, 135.1, 136.8 |
| **28b** | [$D_6$]DMSO | 20.4, 45.5,[c] 128.6, 130.5, 133.8, 142.2 |

[a] Due to dynamic effects, too many signals were detected for the ring methylene carbon atoms; therefore, only aromatic signals are given. [b] Multiple conformers present; only signals of main component given. [c] br. [d] One aromatic signal not detected due to dynamic processes. [e] Two components due to configuration inversion; ring ligand shifts of the second species (approx. 20%) shown in the second line.

 © 2006 Wiley-VCH Verlag GmbH & Co. KGaA, Weinheim 

N–*H*) ppm. $^{13}$C NMR (62.9 MHz, DMSO): $\delta$ = 44.6, 44.8, 45.3, 46.0 ppm. IR: $\tilde{\nu}$ = 3298 m, 2944 m, 2887 m, 1467 m, 1342 w, 1071 vs, 973 s, 945 s, 798 s, 621 vs cm$^{-1}$.

**Preparation of the Thiolate Complexes:** The ligand (4 mmol) was added with stirring to 40 mL of a hot 0.1 M solution of $Zn(ClO_4)_2 \cdot 6H_2O$ in methanol. Stirring and heating were continued for an additional 15 min. Depending on the ligand, some precipitation occurred. A solution of 4 mmol of the thiol in 8 mL of 0.5 M KOH was then added dropwise, whereupon potassium perchlorate precipitated. The solution was filtered and, after a varying amount of time, colorless crystals separated spontaneously. The precipitates were filtered off and, if necessary, recrystallized from methanol. All complexes revealed a 1:1:1:1 composition of zinc/macrocyclic amine/thiolate/perchlorate, consistent with the general formula $[Zn(L)(SR)]ClO_4$.

**Note:** It is important that the precipitation starts as quickly as possible. Prolonged standing of concentrated solutions lowers the yields and the purity of the products considerably, most likely due to oxidation processes. Thus, it is best to induce the formation of crystals by adding a seed crystal or by ultrasound treatment. If the precipitation of the complex occurs instantly upon addition of the potassium thiolate, which is not normally the case, separation from the solid potassium perchlorate is difficult. In such cases, the synthesis should be carried out using a sodium thiolate solution. The desired complex will then be obtained in a good yield, although without the removal of the alkali metal perchlorate.

**General Properties and Solubility:** All thiolate complexes **17**–**28** form colorless crystalline solids. Substances featuring macrocycles with ring sizes from 14 to 16 atoms and four nitrogen atoms (i.e. **23**–**27**) are readily soluble in chloroform. All complexes, with the exception of **28**, are soluble in acetonitrile and nitromethane, but only partially in methanol. Compounds **28** show only low solubility in all solvents mentioned, but are soluble in DMSO. Other data [elemental analytical data, melting points, and yields (Table 1), IR and mass spectroscopic data (Table 2), and $^1$H (Table 3) and $^{13}$C NMR (Table 4) data] are given in the respective tables.

**Crystal Structure Determination:**[45] The intensity data for compound **23b** were collected with a Nonius CAD4 diffractometer and for the other compounds with a Nonius KappaCCD diffractometer, using graphite-monochromated Mo-$K_\alpha$ radiation. Data were corrected for Lorentz and polarization effects, but not for absorption.[46–48] The structures were solved by direct methods (SHELXS[49]) and refined by full-matrix least-squares techniques against $F_o^2$ (SHELXL-97[50]). For all compounds except for **17b**, **19a**, **20a**, and **21b**, the hydrogen atoms of the amine groups were located by difference Fourier synthesis and refined isotropically. All other hydrogen atoms were included at calculated positions with fixed thermal parameters. All non-hydrogen atoms were refined anisotropically.[50] The absolute structures of compounds **16**, **19a**, **21a**, and **28b** could not be determined because they show racemic twinning. XP (SIEMENS Analytical X-ray Instruments, Inc.) was used for structure representations. The drawings in this paper were generated using PLATON.[51]

## Acknowledgments

Financial support of this work by the Deutsche Forschungsgemeinschaft (SFB 436: "Metal-Mediated Reactions Modeled After Nature") is gratefully acknowledged.

[1] G. Parkin, *Chem. Rev.* **2004**, *104*, 699–767.
[2] E. Kimura, T. Koike, *Adv. Inorg. Chem.* **1997**, *44*, 229–261.
[3] L. C. Myers, M. P. Terranova, A. E. Ferentz, G. Wagner, G.-L. Verdine, *Science* **1993**, *261*, 1164.
[4] R. G. Matthews, C. W. Goulding, *Curr. Opin. Chem. Biol.* **1997**, *1*, 332–339.
[5] K. Peariso, Z. S. Zhou, A. E. Smith, R. G. Matthews, J. E. Penner-Hahn, *Biochemistry* **2001**, *40*, 987–993.
[6] H.-W. Park, S. R. Boduluri, J. F. Moomaw, P. J. Casey, L. S. Beese, *Science* **1997**, *275*, 1800–1805.
[7] J. J. Wilker, S. J. Lippard, *Inorg. Chem.* **1997**, *36*, 969–978.
[8] R. Burth, H. Vahrenkamp, *Z. Anorg. Allg. Chem.* **1998**, *624*, 381–385.
[9] U. Brand, M. Rombach, J. Seebacher, H. Vahrenkamp, *Inorg. Chem.* **2001**, *40*, 6151–6157.
[10] M. Ji, B. Benkmil, H. Vahrenkamp, *Inorg. Chem.* **2005**, *44*, 3518–3523.
[11] B. S. Hammes, C. J. Carrano, *Inorg. Chem.* **1999**, *38*, 4593–4600.
[12] B. S. Hammes, C. J. Carrano, *Inorg. Chem.* **2001**, *40*, 919–927.
[13] J. N. Smith, Z. Shirin, C. J. Carrano, *J. Am. Chem. Soc.* **2003**, *125*, 868–869.
[14] C. A. Grapperhaus, T. Tuntulani, J. H. Reibenspies, M. Y. Darensbourg, *Inorg. Chem.* **1998**, *37*, 4052–4058.
[15] J. F. Woessner Jr, *FASEB J.* **1991**, *5*, 2145–2154.
[16] H. Nagase, J. F. Woessner Jr, *J. Biol. Chem.* **1999**, *274*, 21491–21494.
[17] H. Matter, M. Schudok, *Curr. Opin. Drug Discovery Dev.* **2004**, *7*, 513–535.
[18] N. Borkakoti, *Biochem. Soc. Trans.* **2004**, *32*, 17–20.
[19] S. P. Salowe, A. I. Marcy, G. C. Cuca, C. K. Smith, I. E. Kopka, W. K. Hagmann, J. D. Hermes, *Biochemistry* **1992**, *31*, 4535–4540.
[20] R. C. Holz, S. P. Salowe, C. K. Smith, G. C. Cuca, L. Que Jr, *J. Am. Chem. Soc.* **1992**, *114*, 9611–9614.
[21] E. B. Springman, E. L. Angleton, H. Birkedahl-Hansen, H. E. Van Wart, *Proc. Natl. Acad. Sci. USA* **1990**, *87*, 364–368.
[22] H. E. Van Wart, H. Birkedahl-Hansen, *Proc. Natl. Acad. Sci. USA* **1990**, *87*, 5578–5582.
[23] B. M. Bridgewater, T. Fillebeen, R. A. Friesner, G. Parkin, *J. Chem. Soc., Dalton Trans.* **2000**, 4494–4496.
[24] D.-W. Christianson, C. A. Fierke, *Acc. Chem. Res.* **1996**, *29*, 331–339.
[25] T. Wingo, C. Tu, P. J. Laipis, D. N. Silverman, *Biochem. Biophys. Res. Commun.* **2001**, *288*, 666–669.
[26] G. Protoschill-Krebs, C. Wilhelm, J. Kesselmeier, *Atmos. Environ.* **1996**, *30*, 3151–3156.
[27] S. Schenk, J. Kesselmeier, E. Anders, *Chem. Eur. J.* **2004**, *10*, 3091–3105.
[28] M. Bräuer, E. Anders, S. Sinnecker, W. Koch, M. Rombach, H. Brombacher, H. Vahrenkamp, *Chem. Commun.* **2000**, 647–648.
[29] M. Rombach, H. Vahrenkamp, *Inorg. Chem.* **2001**, *40*, 6144–6150.
[30] J. E. Richman, T. J. Atkins, *J. Am. Chem. Soc.* **1974**, *96*, 2268–2270.
[31] T. Koike, M. Takamura, E. Kimura, *J. Am. Chem. Soc.* **1994**, *116*, 8443–8449.
[32] A.-W. Addison, E. Sinn, *Inorg. Chem.* **1983**, *22*, 1225–1228.
[33] R. Yang, L.-L. Zompa, *Inorg. Chem.* **1976**, *15*, 1499–1502.
[34] L.-L. Zompa, *Inorg. Chem.* **1978**, *17*, 2531–2536.
[35] M. T. S. Amorim, S. Chave, R. Delgado, J. J. R. F. da Silva, *J. Chem. Soc., Dalton Trans.* **1991**, 3065–3072.
[36] E. K. Barefield, F. Wagner, *Inorg. Chem.* **1973**, *12*, 2435–2439.
[37] R. Luckay, T. E. Chantson, J. H. Reibenspies, R. D. Hancock, *J. Chem. Soc., Dalton Trans.* **1995**, 1363–1367.
[38] F. Wagner, M. T. Mocella, M. J. D'Aniello Jr, A. H.-J. Wang, E. K. Barefield, *J. Am. Chem. Soc.* **1974**, *96*, 2625–2627.
[39] B. Bosnich, C. K. Poon, M. L. Tobe, *Inorg. Chem.* **1965**, *4*, 1102–1108.

 © 2006 Wiley-VCH Verlag GmbH & Co. KGaA, Weinheim 

[40] N. W. Alcock, P. Moore, C. Pierpoint, *J. Chem. Soc., Dalton Trans.* **1984**, 2371–2376.
[41] J. Marek, P. Kopel, Z. Travnicek, *Acta Crystallogr., Sect. C* **2003**, *59*, 558–560.
[42] D. Swenson, N. C. Baenziger, D. Coucouvanis, *J. Am. Chem. Soc.* **1978**, *100*, 1932–1934.
[43] N. Ueyama, T. Sugawara, K. Sasaki, A. Nakamura, S. Yamashita, Y. Wakatsuki, H. Yamazaki, N. Yasuoka, *Inorg. Chem.* **1988**, *27*, 741–747.
[44] A. Bencini, M. I. Burguete, E. Garcia-Espana, S. V. Luis, J. F. Miravet, C. Soriano, *J. Org. Chem.* **1993**, *58*, 4749–4753.
[45] CCDC-257864 to -257884 contain the supplementary crystallographic data for this paper. These data can be obtained free of charge from The Cambridge Crystallographic Data Centre via http://www.ccdc.cam.ac.uk/data_request/cif.
[46] *MOLEN, An Interactive Structure Solution Procedure*, Enraf–Nonius, Delft, The Netherlands, **1999**.
[47] *COLLECT, Data Collection Software*, Nonius B.V., The Netherlands, **1998**.
[48] Z. Otwinowski, W. Minor, in *Methods in Enzymology* (Eds.: C. Carter, R. Sweet), Academic Press, New York, **1997**, pp. 307–326.
[49] G. Sheldrick, *Acta Crystallogr., Sect. A* **1990**, *46*, 467–473.
[50] G. Sheldrick, *SHELXL-97*, Release 97-2, University of Göttingen, Germany, **1997**.
[51] A. L. Spek, *PLATON, A Multipurpose Crystallographic Tool*, Utrecht University, Utrecht, The Netherlands, **2004** (http://www.cryst.chem.uu.nl/platon).

Received: October 26, 2005
Published Online: February 21, 2006

 © 2006 Wiley-VCH Verlag GmbH & Co. KGaA, Weinheim 

DOI: 10.1002/ejic.200500958

# Synthesis of $\eta^2$-Allene Complexes by the Reaction of a $\eta^1$-Vinylidene Tungsten Complex with Diazoalkanes

**Junes Ipaktschi,*[a] Parham Rooshenas,[a] and Ansgar Dülmer[a]**

**Keywords:** Tungsten / Vinylidene ligands / Allene ligands / Diazoalkanes

The reaction of the $\eta^1$-vinylidene complex Cp(CO)(NO)-W=C=$CH_2$ (**5**) with diazomethane, to give complex **8**, as well as with ethyl diazoacetate, to give complexes **10** and **11**, is described. The crystal structures of these complexes are reported.

(© Wiley-VCH Verlag GmbH & Co. KGaA, 69451 Weinheim, Germany, 2006)

## Introduction

In recent years we have investigated the chemistry of tungsten and molybdenum $\eta^1$-acetylide complexes **3** and the corresponding $\eta^1$-vinylidene complexes **4**.[1] A broad range of differently substituted derivatives of **3** and **4** are prepared by the reaction of the corresponding lithium acetylide **2** with the carbonyl complex **1** in THF at –30 °C, which gives rise to the $\eta^1$-acetylide **3**, and by subsequent addition of electrophiles such as dilute acids, alkylating reagents like alkyltriflates, or iminium salts, which leads to the $\eta^1$-vinylidene complexes **4** (Scheme 1).

Because of the limited accessibility of propyne and also the low solubility of Li–C≡C–$CH_3$, the corresponding complexes **3** and **4** with R = methyl that are prepared by this procedure have low yields. In order to avoid using propyne we have also reported the preparation of **3** and **4** by the reaction of in situ prepared propynyllithium, generated by dehydrobromination of 2-bromopropene, with **1** and concomitant protonation.[2]

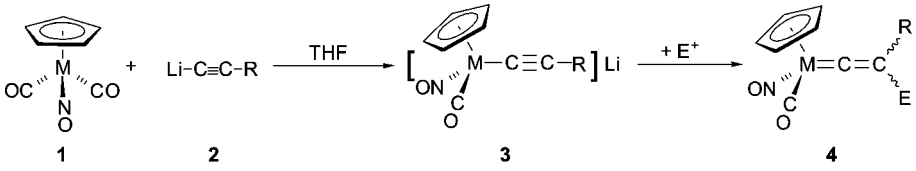


Scheme 1.

Owing to the high C–H acidity on the β-carbon atom of the $\eta^1$-vinylidene complexes[3] and in order to obtain complex **7** in good yield, we tested the reaction of $\eta^1$-vinylidene complex **5** with diazomethane. Contrary to the results obtained for the methylation of ruthenium $\eta^1$-vinylidene complexes with diazomethane,[4] we obtained the $\eta^2$-allene derivative **8** instead of complex **7**.[5] In this paper we describe the results of the reaction of diazomethane and ethyl diazoacetate with the $\eta^1$-vinylidene complex **5** (Scheme 2).

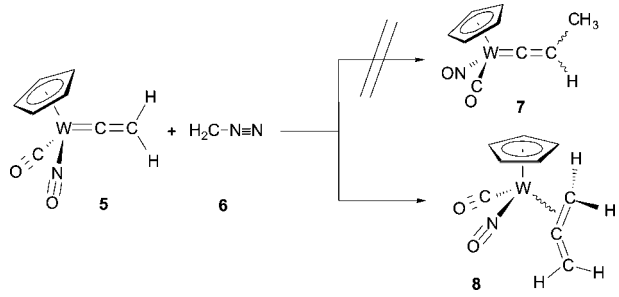


Scheme 2.

## Results and Discussion

The reaction of diazomethane with the $\eta^1$-vinylidene complex **5** was carried out in THF/ether at –30 °C (Scheme 2). The progress of the reaction was followed by IR spectroscopy, and after the starting material had disappeared, the solvent was evaporated and the product was

[a] Institute of Organic Chemistry, Justus-Liebig University, Heinrich-Buff-Ring 58, 35392 Giessen, Germany
Fax: +49-641-9934309
E-mail: junes.ipaktschi@org.chemie.uni-giessen.de


InterScience
© 2006 Wiley-VCH Verlag GmbH & Co. KGaA, Weinheim

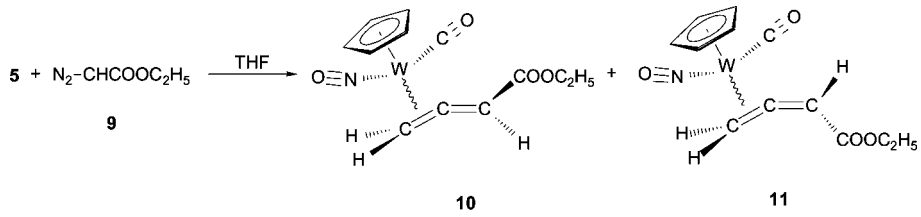


Scheme 3.

purified by chromatography on a short silica column. Complex **8** was isolated in high yields as bright yellow air-stable crystals, which are soluble in most organic solvents. On the basis of the NMR spectroscopic data, it was found that the compound consists of two rotamers in a ratio of 2:1. The structure of **8** was fully characterized by spectroscopic methods (see Exp. Sect.)[6] and by single-crystal X-ray analysis of one of the rotamers. The variable-temperature measurement NMR spectroscopic studies ([$D_6$]DMSO) show that both rotamers of **8** interconvert to one another. The singlet for the Cp protons at $\delta$ = 6.0 and 5.9 ppm broadens at higher temperatures and finally collapses because of the fast equilibration of both rotamers. The free activation energy for this process, calculated from the coalescence temperature (77 kJ·mol$^{-1}$), is higher than the reported energies for allene complexes such as dicarbonyl $\eta^5$-cyclopentadienyl($\eta^2$-tetramethylallene)iron.[7]

Similarly, treatment of the $\eta^1$-vinylidene complex **5** at 40 °C in THF with excess ethyl diazoacetate (**9**) resulted in the formation of the stereoisomers **10** and **11** in 87% yield (Scheme 3). According to the $^1$H NMR spectrum, the crude product consists of a mixture of **10** and **11** in a ratio of 1:5. Complex **10** consists of two rotamers in a ratio of 3:5 depending on the relative orientation of the NO and CO ligands. Complexes **10** (mixture of rotamers) and **11** were isolated by HPLC and characterized by means of elemental analysis, spectroscopic methods (see Experimental Section), and single-crystal X-ray analysis. The significant difference between the structures of **10** and **11** is the relative orientation of the ester group toward the tungsten center (*E* or *Z*). While in the minor component **10** the orientation of the ester group and the tungsten atom is *Z* relative to each other, the orientation of these groups in complex **11** is *E*.

### Molecular Structure of Complexes 8, 10, and 11

Suitable crystals for a single-crystal X-ray diffraction analysis of complexes **8** and **10** were grown from pentane and crystals of **11** from an ether solution at 4 °C. The molecular structures are shown in Figure 1, Figure 2, and Figure 3, respectively, and relevant crystal data are included in Table 1. The crystal structures of these complexes consist of a well-spaced array of molecular units, and the intermolecular contacts correspond to normal van der Waals distances and the angles are as expected. Complexes **8**, **10**, and **11** all display a piano-stool coordination geometry about the metal atom. The allene ligand is bent in a manner that is generally found in $\eta^2$-allene complexes: the C1–C2–C3

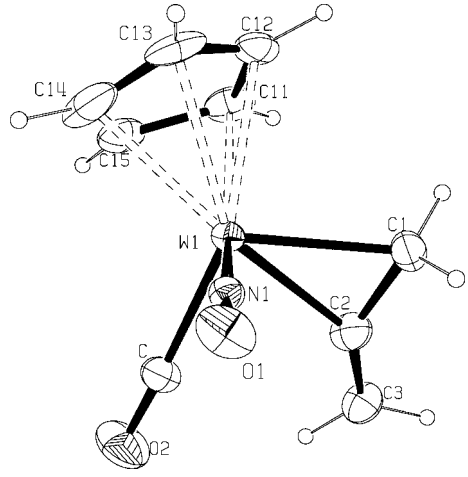


Figure 1. Molecular structure and atom-numbering scheme for complex **8**. Thermal ellipsoids are shown at the 20% probability level. Selected bond lengths [Å] and angles [°] (with standard deviations): W1–N1 1.767(10), W1–C 2.027(14), W1–C2 2.185(14), W1–C1 2.188(14), C1–C2 1.46(2), C2–C3 1.31(2), O1–N1 1.234(13), C–O2 1.096(18), N1–W1–C 91.3(5), N1–W1–C2 103.8(5), C–W1–C2 70.6(6), N1–W1–C1 93.1(5), C–W1–C1 108.1(6), C2–W1–C1 38.9(6), C2–C1–W1 70.4(8), C3–C2–C1 144.9(15), C3–C2–W1 144.3(14), C1–C2–W1 70.7(8), O1–N1–W1 176.1(9), O2–C–W1 177.5(16).

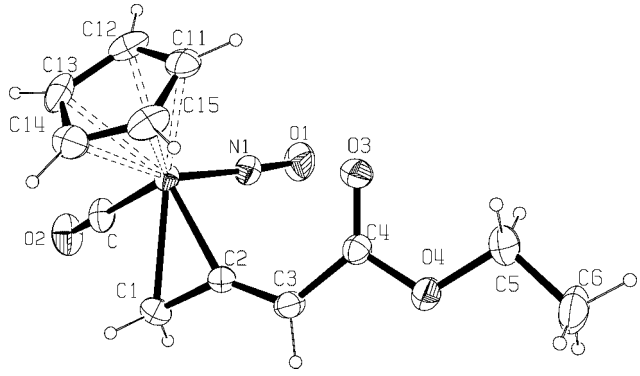


Figure 2. Molecular structure and atom-numbering scheme for complex **10**. Thermal ellipsoids are shown at the 20% probability level. Selected bond lengths [Å] and angles [°] (with standard deviations): W1–N1 1.795(5), W1–C 2.009(5), W1–C2 2.112(5), W1–C1 2.250(6), N1–O1 1.188(6), C–O2 1.121(6), C1–C2 1.402(7), C2–C3 1.330(7), C3–C4 1.454(7), C4–O3 1.203(6), N1–W1–C 90.7(2), N1–W1–C2 90.0(2), C–W1–C2 108.9(2), N1–W1–C1 102.2(2), C–W1–C1 73.6(2), C2–W1–C1 37.3(2), O1–N1–W1 176.7(5), O2–C–W1 179.4(5), C2–C1–W1 66.0(3), C3–C2–C1 139.7(5), C3–C2–W1 143.0(4), C1–C2–W1 76.7(3), C2–C3–C4 124.2(5).

 © 2006 Wiley-VCH Verlag GmbH & Co. KGaA, Weinheim 

angle is 144.9(15)° in complex **8**, 139.7(5)° in complex **10**, and 142.1(6)° in complex **11**.[8] The length of the coordinated double bond in **8** [C1=C2, 1.46(2) Å] is significantly longer than that of the uncoordinated bond [C2=C3, 1.330(7) Å]. However, relative to the C1–C2 bond in **8**, the coordinated double bonds in complexes **10** and **11** are slightly shorter: 1.402(7) Å in **10** and 1.393(8) Å in **11**. The length of the C4–O3 bond of the acyl function falls into the expected average value range for an α-β unsaturated ketone: 1.203(6) Å in **10** and 1.215(0) Å in **11**.[9] The distance from the metal to the central carbon atom of the allene ligand (W–C2) is slightly shorter than the distance from the metal to the terminal carbon atom (W–C1). This difference is 0.138 Å in complex **11** and 0.45 Å in **10**.[10] The overlap between a filled d orbital on the metal and both of the unoccupied orthogonal π* orbitals of the central carbon atom contribute to this difference.[11] However, this interaction seems to be unpronounced in complex **8**.

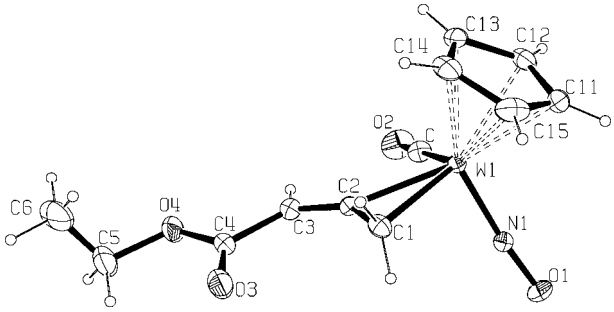


Figure 3. Molecular structure and atom-numbering scheme for complex **11**. Thermal ellipsoids are shown at the 20% probability level. Selected bond lengths [Å] and angles [°] (with standard deviations): W1–N1 1.783(5), W1–C 1.964(7), W1–C2 2.175(5), W1–C1 2.220(6), C1–C2 1.393(8), C2–C3 1.314(8), C3–C4 1.478(9), N1–O1 1.212(6), N1–W1–C 92.6(3), N1–W1–C2 99.5(2), C–W1–C2 74.9(3), N1–W1–C1 92.0(2), C–W1–C1 111.4(3), C2–W1–C1 37.0(2), C2–C1–W1 69.8(3), C3–C2–C1 142.1(6), C3–C2–W1 144.5(5), C1–C2–W1 73.3(3), C2–C3–C4 122.4(7), O1–N1–W1 173.8(4), O2–C–W1 178.1(7).

## Experimental Section

**General Considerations:** All reactions were carried out under an argon atmosphere (99.99%, by Messer-Griesheim). Solvents were purified by standard methods and distilled under argon prior to use. Literature methods were used to prepare [($\eta^5C_5H_5$)(CO)(NO)W=C=$CH_2$] (**5**),[12] $CH_2N_2$,[13] and $N_2CHCO_2CH_3$[14]. All other compounds were commercially available. NMR spectra were obtained with Bruker AM 400 and AC 200 spectrometers. Proton and

Table 1. Crystal data and structure refinements of **8**, **10**, and **11**.

| | **8** | **10** | **11** |
|---|---|---|---|
| Formula | $C_9H_9NO_2W$ | $C_{12}H_{13}NO_4W$ | $C_{12}H_{13}NO_4W$ |
| $M_r$ [g·mol$^{-1}$] | 347.02 | 419.08 | 419.08 |
| Color and habit | | yellow | |
| Crystal system | | monoclinic | |
| Space group | $P2_1/n$ | $P2_1/a$ | $P2_1/n$ |
| $a$ [Å] | 7.3511(7) | 6.7864(5) | 11.1820(13) |
| $b$ [Å] | 6.1294(6) | 21.0383(18) | 10.6952(12) |
| $c$ [Å] | 21.249(3) | 9.2890(8) | 11.6848(12) |
| $\beta$ [°] | 97.683(13) | 97.671(10) | 111.296(12) |
| $V$ [Å$^3$] | 948.8517 | 1314.36(19) | 1302.0(2) |
| $Z$ | 2 | 4 | 4 |
| $\rho_{calcd.}$ [g·cm$^{-3}$] | 2.429 | 2.118 | 2.138 |
| Linear absorption coefficient [cm$^{-1}$] | 121.38 | 8.794 | 8.877 |
| Diffractometer | | Stoe IPDS | |
| Radiation | | Mo-$K_\alpha$ ($\lambda$ = 0.71069 Å) | |
| Monochromator | | graphite | |
| Scan range [°] | $4.29 \le \theta \le 25.90$ | $2.21 \le \theta \le 25.97$ | $2.67 \le \theta \le 27.50$ |
| | $-8 \le h \le 8$ | $-8 \le h \le 8$ | $-14 \le h \le 14$ |
| | $-7 \le k \le 7$ | $-25 \le k \le 25$ | $-13 \le k \le 13$ |
| | $-25 \le l \le 26$ | $-11 \le l \le 11$ | $-15 \le l \le 14$ |
| Reflections collected | 6223 | 9598 | 11083 |
| $R_{int}$ | 0.0210 | 0.0524 | 0.0396 |
| Independent reflections | 1712 | 2388 | 2976 |
| Applied corrections | | Lorentz and polarization coefficients | |
| Structure determination and refinement | | $W$ positional parameters from Patterson synthesis (program SHELXS-86)[a] | |
| Data/restraints/parameters | 1712/0/119 | 2388/0/163 | 2976/ 0/163 |
| Goodness-of-fit on $F_2$ | 1.356 | 1.029 | 1.076 |
| Final $R$ indices [$I > 2\sigma(I)$] | $R_1$ = 0.0343 | $R_1$ = 0.0235 | $R_1$ = 0.0303 |
| | $wR_2$ = 0.0999 | $wR_2$ = 0.0625 | $wR_2$ = 0.0729 |
| $R$ indices (all data) | $R_1$ = 0.0385 | $R_1$ = 0300 | $R_1$ = 0.0353 |
| | $wR_2$ = 0.1234 | $wR_2$ = 0.0652 | $wR_2$ = 0.0747 |

[a] G. M. Sheldrick, SHELXS-86; Program for the Solution of Crystal Structures, University of Göttingen, **1986**); further atoms from F-synthesis (program SHELXL-93: G. M. Sheldrick, SHELXL-93; Program for Crystal Structure Refinement, University of Göttingen, **1993**); structure refinement by the anisotropic full-matrix least-squares procedure for all non-hydrogen atoms. Atomic scattering factors from: Int. Tables for Crystallography, vol. C (Ed.: A. J. C. Wilson), Kluwer Academic Publishers, Dordrecht, **1992**.

 © 2006 Wiley-VCH Verlag GmbH & Co. KGaA, Weinheim 

carbon chemical shifts were referenced to tetramethylsilane. MS measurements (70 eV) were performed with a Varian MAT 311-A. IR spectra were recorded with a Bruker FT-IR IFS 85. Microanalyses were done on a Carlo–Erba 1104 elemental analyzer.

**Preparation of [($\eta^5$-$C_5H_5$)(CO)(NO)W($\eta^2$-$H_2C{=}C{=}CH_2$)] (8):** A solution of $CH_2N_2$ (0.14 M, 230 mL) in diethyl ether (33.3 mmol) was slowly added to a solution of **5** (990 mg, 3.3 mmol) in THF (10 mL) at –30 °C, and the progress of the reaction was monitored by IR Spectroscopy. After 6 h, the solvent was removed under vacuum, and the crude product was purified by chromatography on silica gel with a pentane/ether mixture (1:1). The yellow compound was recrystallized from an ether/pentane solution to give 700 mg of complex **8** (61% yield), which consists of two isomers with a diasteriomeric ratio of 2:1, determined from $^1$H NMR spectroscopic data. $C_9H_9O_2NW$ (347.01): calcd. C 31.15, H 2.61, N 4.04; found: C 31.52, H 2.28, N 3.89. $^1$H NMR (400 MHz, $CDCl_3$): $\delta$ = 6.91 and 6.86 (t, $^4J_{H,H}$ = 3.5 Hz for both rotamers, 1 H, C3) and 6.09 and 5.81 (t, $^4J_{H,H}$ = 3.5 Hz for both rotamers, 1 H, C3), 5.71 and 5.66 (Cp), 1.86 and 2.19 and 1.77 (the major component: t, $^4J_{H,H}$ = 3.5 Hz; the minor component: two dt, $^2J_{H,H}$ = 11 Hz, $^4J_{H,H}$ = 3.5 Hz, 2 H, C1) ppm.$^{13}$C NMR (100 MHz, $CDCl_3$): $\delta$ = 213.7 and 215.0 (CO), 161.3 and 160.2 (C2), 110.3 and 107.1 (C3), 95.9 and 95.5 (Cp), 7.2 and –4.1 (C1) ppm. IR (KBr): $\tilde{\nu}$ = 1988 (C≡O), 1599 (N≡O) cm$^{-1}$.

**Preparation of (*E*/*Z*)-{($\eta^5$-$C_5H_5$)(CO)(NO)W[$\eta^2$(2,3)-$H_2C{=}C{=}CH$-$C(O)OCH_2CH_3$]} (10 and 11):** A solution of ethyl diazoacetate (464 mg, 4 mmol) in THF (10 mL) was added to a solution of the vinylidene complex **5** (1 mmol, 333 mg) in THF (10 mL) at a rate of 1 ml per hour at 45 °C. The reaction mixture was monitored by IR Spectroscopy, and the reaction reached completion after 12 h. The solvent was removed under vacuum. The crude product was redissolved in pentane and purified by chromatography on a silica column. The yellow band was eluted with $CH_2Cl_2$/pentane (1:2), which resulted in 182 mg of a mixture of two stereoisomers **11** and **10** (87% yield), in a ratio of 5:1. The isomers were separated by HPLC, with TBME/hexane as the eluent mixture on a Diol-Phase. $C_{12}H_{13}O_4NW$ (405.07): calcd. C 34.39, H 3.13, N 3.34; found C 34.34, H 3.15, N 3.31.

**(*Z*)-{($\eta^5$-$C_5H_5$)(CO)(NO)W[$\eta^2$(2,3)-$H_2C{=}C{=}CHC(O)OCH_2CH_3$]} (10):** $^1$H NMR (400 MHz, $CDCl_3$): $\delta$ = 7.43 (t, X part of an ABX spin system, 1 H, C3), 5.80 (s, 5 H, Cp), 4.24 (m, 2 H, C5); 2.07 (dd, $^2J_{H,H}$ = 12.1, $^4J_{H,H}$ = 2.7 Hz, B part of the ABX system, 1 H, C1), 1.77 (dd, $^2J_{H,H}$ = 12.1 Hz, $^4J_{H,H}$ = 3.2 Hz, A part of the ABX system, 1 H, C1), 1.33 (t, 3 H, C6) ppm. $^{13}$C NMR (100 MHz, $CDCl_3$): $\delta$ = 212.9 (*C*O), 180.0 (C4), 167.8 (C2), 117.0 (C3), 96.7 (Cp), 59.6 (C5), 14.5 (C6), 3.9 (C1) ppm. IR (KBr): $\tilde{\nu}$ = 2030 (W–*C*≡*O*), 1703 (C=O ester), 1625 and 1671 (N≡O) cm$^{-1}$.

**(*E*)-{($\eta^5$-$C_5H_5$)(CO)(NO)W[$\eta^2$(2,3)-$H_2C{=}C{=}CHC(O)OCH_2CH_3$]} (11):** The major component was recrystallized from an ether/pentane solution and consisted of two rotamers in a ratio of 3:5. $^1$H NMR (400 MHz, $CDCl_3$): $\delta$ = 6.67 and 6.47 (t, $^4J_{H,H}$ = 3.0 Hz, $^4J_{H,H}$ = 3.6 Hz, C3, X part of ABX spin-system, 1 H), 5.72 and 5.70 (s, 5 H, Cp), 4.24 (m, 2 H, C4); 2.58 and 2.29, (dd, AB part, $^2J_{H,H}$ = 12.8 Hz, $^4J_{H,H}$ = 3.0 Hz, 1 H, C1 with the first order approximation), 2.24 and 2.17 (dd, $^2J_{H,H}$ = 12.8 Hz, $^4J_{H,H}$ = 3.0 Hz, 1 H, C1 with the first order approximation), 1.31 (t, $^3J_{H,H}$ = 6.9 Hz, 3 H, C6) ppm. $^{13}$C NMR (100 MHz, $CDCl_3$): $\delta$ = 213.0 and 210.8 (C*O*), 179.1 and 176.4 (C4), 165.9 and 164.9 (C2), 118.9 and 115.7 (C3), 96.0 and 95.6 (Cp), 60.2 and 60.6 (C5), 14.4 and 14.3 (C6), 10.4 and –0.2 (C1) ppm. IR (KBr): $\tilde{\nu}$ = 2006 (W–*C*≡O), 1717 (C=O ester), 1681 and 1598 (N≡O) cm$^{-1}$.

CCDC-288085 to -288087 contain the supplementary crystallographic data for this paper. These data can be obtained free of charge from The Cambridge Crystallographic Data Centre via www.ccdc.cam.ac.uk/data_request/cif.

## Acknowledgments

This work was supported by the Deutsche Forschungsgemeinschaft (IP 7/5-2; IP 7/5-3).

[1] a) J. Ipaktschi, P. Rooshenas, A. Dülmer, *Organometallics* **2005**, *24*, 6239–6243; b) J. Ipaktschi, F. Munz, T. Klotzbach, *Organometallics* **2005**, *24*, 206–213; c) J. Ipaktschi, J. Mohseni-Ala, A. Dülmer, S. Steffens, C. Wittenburg, J. Heck, *Organometallics* **2004**; *23*, 4902–4909; d) J. Ipaktschi, J. Mohsseni-ala, S. Uhlig, *Eur. J. Inorg. Chem.* **2004**, 4313–4320; e) J. Ipaktschi, K. Reimann, M. Serafin, A. Dülmer, *J. Organomet. Chem.* **2003**, *670*, 66–74; f) J. Ipaktschi, F. Munz, *Organometallics* **2002**, *21*, 977–981; g) J. Ipaktschi, S. Uhlig, A. Dülmer, *Organometallics* **2001**, *20*, 4840–4846; h) J. Ipaktschi, F. Mirzaei, K. Reimann, J. Beck, M. Serafin, *Organometallics* **1998**, *17*, 5086–5090; i) J. Ipaktschi, G. J. Demuth-Eberle, B. G. Mirzaei, F. Mueller, J. Beck, M. Serafin, *Organometallics* **1995**, *14*, 3335–3341; j) J. Ipaktschi, B. G. Mueller, R. Glaum, *Organometallics* **1994**, *13*, 1044–1046.

[2] J. Ipaktschi, T. Klotzbach, A. Dülmer, *Organometallics* **2000**, *19*, 5281–5286.

[3] a) V. Cadierno, M. P. Gamasa, J. Gimeno, C. Gonzalez-Bernardo, E. Perez-Carreno, S. Garcia-Granda, *Organometallics* **2001**, *20*, 5177–5188; b) C. Bianchini, P. Innocenti, A. Meli, M. Peruzzini, F. Zanobini, P. Zanello, *Organometallics* **1990**, *9*, 2514–2522; c) J. Ipaktschi, F. Mirzaei, B. G. Mueller, J. Beck, M. Serafin, *J. Organomet. Chem.* **1996**, *526*, 363–370; d) J. Ipaktschi, F. Mirzaei, G. J. Demuth-Eberle, J. Beck, M. Serafin, *Organometallics* **1997**, *16*, 3965–3972.

[4] G. Consiglio, R. Schwab, F. Morandini, *Chem. Commun. (Cambridge, U. K.)* **1988**, 25–26.

[5] a) H. Werner, M. Laubender, R. Wiedemann, B. Windmüller, *Angew. Chem.* **1996**, *108*, 1330–1331; b) J. Wolf, R. Zolk, U. Schubert, H. Werner, *J. Organomet. Chem.* **1988**, *340*, 161–178.

[6] For spectroscopic data of allene complexes see: a) J. M. Zhuang, D. Sutton, *Organometallics* **1991**, *10*, 1516–1527; b) A. M. J. Pu, T. S. Peng, A. M. Arif, J. A. Gladysz, *Organometallics* **1992**, *11*, 3232–3237; c) E. G. Lundquist, K. Folting, W. E. Streib, J. C. Huffman, O. Eisenstein, K. G. Caulton, *J. Am. Chem. Soc.* **1990**, *112*, 855–863; d) J. Zhuang, D. Sutton, *Organometallics* **1991**, *10*, 1516–1527; e) S. T. Chacon, M. H. Chisholm, K. Folting, J. C. Huffman, M. J. Hampden Smith, *Organometallics* **1991**, *10*, 3722–3735.

[7] B. M. Foxman, D. Marten, A. Rosan, S. Raghu, M. Rosenblum, *J. Am. Chem. Soc.* **1977**, *99*, 2160–2165.

[8] a) B. M. Foxman, *J. Chem. Soc. Chem. Commun.* **1975**, 221–222; b) D. L. Hughes, A. J. L. Pombeiro, C. J. Pickett, R. L. Richards, *J. Chem. Soc. Chem. Commun.* **1984**, 992–993; c) D. Lentz, S. Willemsen, *Organometallics* **1999**, *18*, 3962–3964; d) L. Lee, I. Wu, Y. Lin, G. Lee, Y. Wang, *Organometallics* **1994**, *13*, 2521–2526.

[9] a) K. S. Huang, D. Britton, M. C. Etter, *Acta Crystallogr., Cryst. Struct. Commun. Sect. C* **1995**, *51*, 1661–1663; b) S. Ji, Z. Shen, D. Gu, S. Wang, *J. Organomet. Chem.* **2004**, *689*, 1843–1848; c) T. Murai, Y. Mutoh, S. Kato, *Org. Lett.* **2001**, *3*, 1993–1995.

[10] The observed value for allenes is 0.05 to 0.19 Å.

[11] T. J. Hewitt, J. DeBoer, *J. Chem. Soc. A* **1971**, 817–822.

[12] J. Ipaktschi, P. Rooshenas, T. Klotzbach, A. Dulmer, E. Huseynova, *Organometallics* **2005**, *24*, 1351–1354.

[13] Th. J. De Boer, H. J. Backer, *Org. Synth. Coll. Vol.4* **1963**, 250–253.

[14] N. E. Searle, *Org. Synth. Coll. Vol.4,* **1963**, 424–427.

Received: October 28, 2005
Published Online: February 21, 2006

 © 2006 Wiley-VCH Verlag GmbH & Co. KGaA, Weinheim 

DOI: 10.1002/ejic.200501009

# Phase Relations Between β-Tricalcium Phosphate and Hydroxyapatite with Manganese(II): Structural and Spectroscopic Properties

Isaac Mayer,*[a] Frederic J. G. Cuisinier,[b] Ina Popov,[c] Yechezkel Schleich,[a] Sarit Gdalya,[a] Olaf Burghaus,[d] and Dirk Reinen[d]

**Keywords:** Manganese / β-Tricalcium phosphate / EPR spectroscopy

The preparation of Mn-containing β-tricalcium phosphate (β-TCP) samples was achieved in two ways: a) transformation of precipitated Mn-containing calcium hydroxyapatite (HA) to β-TCP by heating at 1100 °C, and b) preparation by solid-state reaction of a mixture of $CaCO_3$, $(NH_4)_2HPO_4$, and $Mn(NO_3)_2$ at 1100 °C. Powder X-ray diffraction (XRD) analyses of the samples, obtained by both methods, show well-defined patterns with structural data of the rhombohedral R3c, β-TCP phase. The calculated lattice constants are smaller than those known for β-$Ca_3(PO_4)_2$ because of substitution of $Ca^{2+}$ by $Mn^{2+}$. EPR spectroscopy indeed reveals that manganese is divalent in the samples. Apparently, the Ca(5) site in the β-TCP structure is occupied by $Mn^{2+}$. The distribution of $Mn^{2+}$ between the β-TCP and the HA phase in the case of preparation (b) was studied by EPR spectroscopy, and a pronounced preference for the former lattice was found. Micron- and submicron-sized crystals with visible faces were observed by TEM in the case of β-TCP prepared by solid-state reaction, and large micron-sized, droplike-shaped crystals, sensitive to beam radiation, were found in the case of samples prepared by heating HA at elevated temperatures.

(© Wiley-VCH Verlag GmbH & Co. KGaA, 69451 Weinheim, Germany, 2006)

## Introduction

Calcium hydroxyapatite (HA), the main constituent of bones and teeth, is biocompatible and widely used in dentistry and orthopedics to repair bone defects and substitution, and as coating material for metallic implants. β-Tricalcium phosphate is also known as a biocompatible material and is found in many cases to be advantageous as compared with HA.[1–3] It is also used as a host when doped with Mg, Zn, and Cd ions.[4,5]

In previous work,[6] HA samples containing $Mn^{2+}$ were prepared by a precipitation method. The motivation for the addition of $Mn^{2+}$ ions to HA was due to the fact that divalent $Mn^{2+}$ has been linked to the activation of integrins,[7] a family of receptors that mediate cellular interactions with extracellular matrix and cell surface ligands. In the presence of $Mn^{2+}$ ions the ligand affinity of integrin increases and cell adhesion is promoted. High-temperature treatment of the precipitated samples showed that samples with low carbonate content transform partially or completely to β-TCP. EPR spectroscopy proved that manganese is divalent also in the heated samples and is found to partly occupy $Ca^{2+}$ sites in the β-TCP structure.[6] In further work,[8] human osteoblasts were cultured on the surfaces of Mn-doped HA thin films deposited on etched Ti substrates. Biological tests demonstrated that the Mn-doped HA coatings favor osteoblasts proliferation, activation of their metabolism, and differentiation.

The aim of the present work was to prepare Mn-doped β-TCP samples and to determine the $Mn^{2+}/Ca^{2+}$ miscibility limit. Two preparation methods were applied: a) transformation of Mn-containing HA to β-TCP, and b) preparation of β-TCP by high-temperature solid-state reaction of stoichiometric mixtures of $CaCO_3$, $(NH_4)_2HPO_4$, and $Mn(NO_3)_2$.

## Results

### β-TCP Prepared by Heating Precipitated HAMn

HAMn samples were prepared with a broad range of Mn content (0.1–4.0%). In Table 1, Mn content and Ca/P molar ratios of the samples are listed. The Ca/P values of the original HAMn samples were always lower than 1.67, indicating nonstoichiometric HA, and these values decreased with increased Mn content. The powder XRD patterns of the precipitated HAMn samples had reflections solely of the hexagonal apatite structure. The XRD patterns of the samples after heating to 400 °C showed no change in their crystal structure. At 600 °C the XRD patterns already contained

[a] Department of Inorganic and Analytical Chemistry, Hebrew University,
Jerusalem 91904, Israel
[b] INSERM U 424, Centre de Recherches Odontologique,
1 Place de l'Hospital, 6700 Strasbourg, France
[c] Unit Nanoscopic Characterization, Hebrew University,
Jerusalem 91904, Israel
[d] Fachbereich Chemie und Zentrum für Materialwissenschaften, Philipps Universität,
35032 Marburg, Germany

 © 2006 Wiley-VCH Verlag GmbH & Co. KGaA, Weinheim 

Table 1. β-Tricalcium phosphate phases obtained by heating HAMn samples to 800–1000 °C. Lattice constants and unit cell volumes, Mn content, Ca/P molar ratios (in the initial HA phase), and estimated rates of transformation to β-TCP.

| Sample | Mn (1)[a] molar content | Lattice constants [Å] *a* | *c* | Lattice volume [Å$^3$] | Ca/P molar ratios | Transformation to β-TCP [%] |
|---|---|---|---|---|---|---|
| $Ca_3(PO_4)_2$ | – | 10.43 | 37.38 | 3522 | 1.50 | – |
| HAMn28 | 0.030 | 10.42 | 37.37 | 3510 | 1.54 | 65 |
| HAMn5b | 0.035 | 10.42 | 37.35 | 3510 | 1.49 | 85 |
| HAMn147 | 0.070 | 10.41 | 37.33 | 3505 | 1.48 | 65 |
| HAMn142 | 0.105 | 10.40 | 37.29 | 3494 | 1.48 | 70 |
| HAMn145 | 0.117 | 10.39 | 37.25 | 3482 | 1.51 | 75 |
| HAMn146 | 0.130 | 10.39 | 37.20 | 3478 | 1.45 | 75 |
| HAMn149 | 0.150 | 10.39 | 37.24 | 3483 | 1.41 | 75 |
| HAMn158 | 0.165 | 10.30 | 37.29 | 3473 | 1.41 | 75 |

[a] (1) in β-TCP, if complete transformation would occur.

reflections of two crystal phases: reflections of the original hexagonal HA phase[9] and reflections of the rhombohedric β-TCP.[10] In the 800–1000 °C region, most of the HA (around 75%) transformed to β-TCP. The degree of transformation of HA to β-TCP was roughly estimated by the relative peak heights of the strongest HA (211) and β-TCP (0.2.10) reflections. These findings suggest that the hexagonal apatite structure of the nonstoichiometric HA samples is stable even at very low Ca/P ratios and transforms to the rhombohedral structure only on heating. The structural data of the rhombohedral phases are listed in Table 1.

### β-TCP Prepared by Solid-State Reaction

Samples with a general composition of $Ca_{3-x}Mn_x(PO_4)_2$ were prepared with different $x$ values in the range of 0.1–1.0 in intervals of 0.1 and appear in Table 2. The XRD patterns of the obtained samples revealed that these samples crystallize in the R3c rhombohedral structure characteristic of β-TCP. No reflections of a different impurity phase were present up to the composition $Ca_{2.4}Mn_{0.6}(PO_4)_2$. Above this composition the XRD pattern contained peaks of a second unknown crystal phase. Apparently, about 20 mol-% of $Mn^{2+}$ can be substituted for $Ca^{2+}$ in β-TCP.

Table 2. Structural data of β-$Ca_{3-x}Mn_x(PO_4)_2$ solid solutions obtained by solid-state reaction.

| Lattice constants [Å] *c* | *a* | Lattice volume [Å$^3$] | Composition | Samples |
|---|---|---|---|---|
| 37.38 | 10.431 | 3522 | $Ca_3(PO_4)_2$ | TCP |
| 37.37 | 10.424 | 3517 | $Ca_{2.9}Mn_{0.1}(PO_4)_2$ | TCPMn1 |
| 37.32 | 10.404 | 3498 | $Ca_{2.8}Mn_{0.2}(PO_4)_2$ | TCPMn2 |
| 37.32 | 10.376 | 3480 | $Ca_{2.7}Mn_{0.3}(PO_4)_2$ | TCPMn3 |
| 37.31 | 10.395 | 3491 | $Ca_{2.6}Mn_{0.4}(PO_4)_2$ | TCPMn4 |
| 37.26 | 10.366 | 3465 | $Ca_{2.5}Mn_{0.5}(PO_4)_2$ | TCPMn5 |
| 37.22 | 10.351 | 3453 | $Ca_{2.4}Mn_{0.6}(PO_4)_2$ | TCPMn6 |

All samples listed in Table 1 and Table 2 were pink at high Mn concentrations and were white at low Mn concentrations. This is in agreement with a +2 oxidation state and hence with the presence of only very weak Laporte- and spin-forbidden transitions in the d-d spectrum of the visible region.

### EPR Analysis

Our previously published EPR spectroscopic data showed that precipitated HAMn[6] contains $Mn^{II}$ in the cubic or nearly cubic environment of an impurity phase, presumably $MnCO_3$ or $Mn(OH)_2$. The EPR spectra in Figure 1 show the characteristic six-line hyperfine structure with $A \approx 90$ G ($\approx 0.0085$ cm$^{-1}$) at Q-band frequency, without any indication of a zero-field splitting also in the X-band, thus excluding the presence of $Mn^{2+}$ in $Ca^{2+}$ positions. On heating to 600 and 800 °C the samples behaved differently, depending on their carbonate content: carbonate-rich (CR) samples retained the apatite structure, while carbonate-poor (CP) samples transformed partly or fully to the β-TCP type.

The Q-band spectrum of $Mn^{2+}$-doped β-TCP prepared by high-temperature solid-state reaction is shown, together with a simulated spectrum with a zero-field splitting of $D$ = 0.047 cm$^{-1}$ (500 G), in Figure 2 (bottom). Besides the partly resolved central signal, whose hyperfine splitting is not accounted for in the simulation ($A$ = 0), the agreement is fairly good, suggesting that the chosen $D$-parameter is near to the one of the experimental spectrum. Inspecting the crystal structure of β-TCP[11] with its five different Ca positions, it is most likely that $Mn^{2+}$ is substituted into the Ca(5) site. The coordination number (CN) is six, the polyhedron geometry is a slightly hexagonally distorted octahedron with $C_3$ point symmetry, and Ca–O bond lengths of 2.263(25) Å are much shorter than the average distances in the other polyhedra with CNs between seven and nine (>2.4 Å). The reported Ca(5)–O bond lengths are surprisingly even smaller than those in CaO (2.40 Å) and rather close to those in MnO (2.22 Å),[13] which both crystallize in the NaCl type. Because the symmetry of the $Ca(5)O_6$ polyhedron is axial, a vanishing (orthorhombic) $E$-parameter is indeed expected in the case of isomorphous substitution of $Ca^{2+}$ by $Mn^{2+}$. Figure 2 (top) shows, in small size, the spectrum of a CP sample with β-TCP structure as well, but obtained from solution by subsequent heating to 800 °C. It is identical with the bottom spectrum, though less resolved because of a poorer sample crystallinity. It can be concluded, therefore, that Mn is present as $Mn^{II}$ in a $Ca^{2+}$ position of the β-TCP host. The X-band measurement on the same two samples confirms this result (Figure 3). The spec-

 © 2006 Wiley-VCH Verlag GmbH & Co. KGaA, Weinheim 

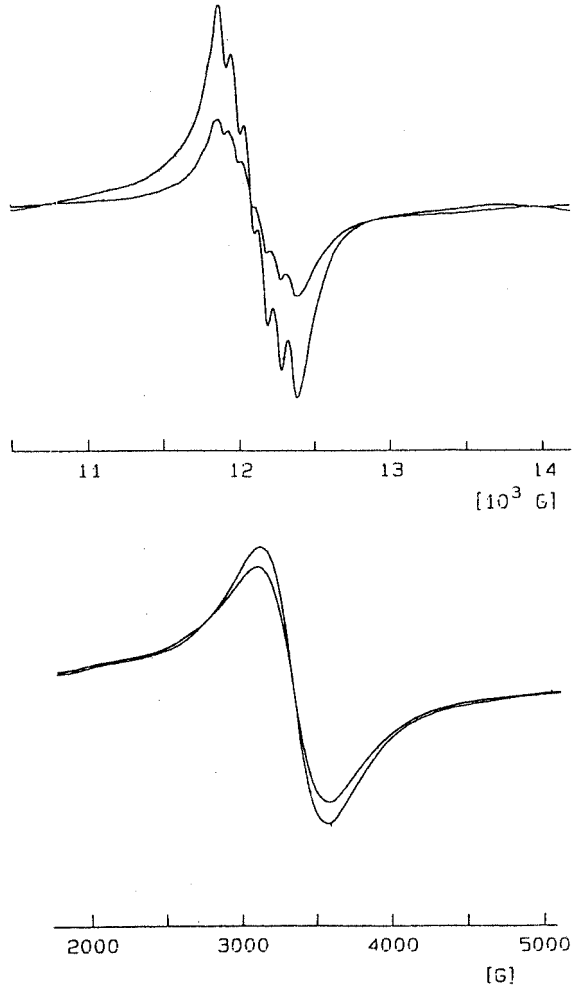


Figure 1. Typical Q- (33.93 GHz) and X-band (9.26 GHz) spectra of precipitated calcium hydroxyapatites in the presence of Mn (298 K).

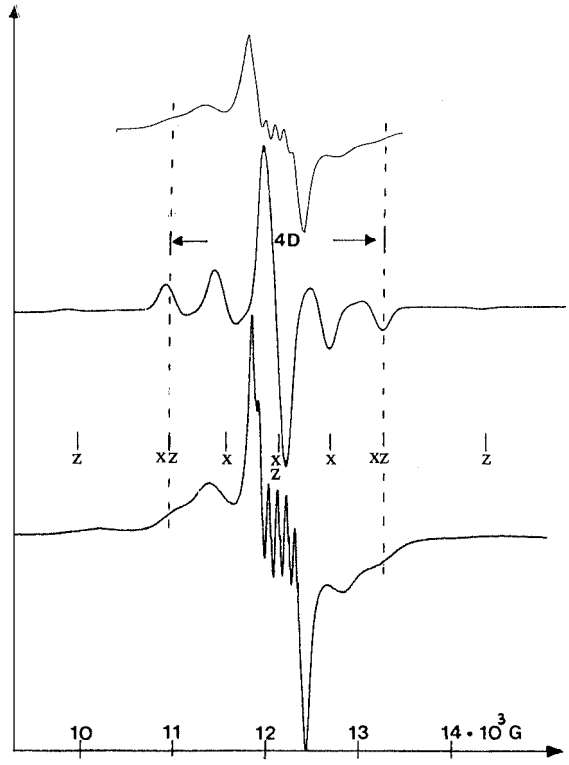


Figure 2. EPR Q-band spectra (34.0 GHz) of $Mn^{2+}$-doped β-TCP obtained by solid-state reaction (TCPMn1; 126 K, bottom) and from solution after subsequent heating to 800 °C with nearly complete transformation to β-TCP (298 K, top), as compared with a simulated spectrum with $D = 0.047\ cm^{-1}$, $A = 0$ (adopted from ref.[12]). The transition parallel ($z$) and perpendicular ($x = y$) to the preferred axial direction are indicated.

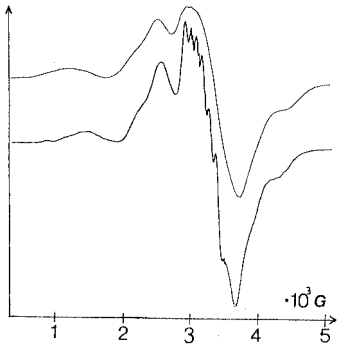


Figure 3. X-band spectra (9.22 GHz; 298 K) of $Mn^{2+}$-doped β-TCP by solid-state reaction (TCPMn1; bottom) and of a CP sample from solution after subsequent heating to 800 °C (top).

tra are identical, but again with a partly resolved hyperfine structure in the case of the sample obtained by solid-state reaction.

The Q-band EPR spectra (Figure 4) of heated Mn-doped CR samples have a completely different appearance from the one in Figure 2 (top). Each hyperfine line in the central part of these spectra undergoes an increasingly pronounced splitting when raising the temperature; this is obviously mainly caused by better resolution due to an improved sample crystallinity at higher heating temperatures. It corresponds to a tiny zero-field $D$-parameter of about 0.002 $cm^{-1}$ (≈ 20 G). It is distinctly smaller than $A$ and by far too small to indicate substitution into a $Ca^{2+}$ site in the lattice. The solids turned blue after heating above 400 °C. Very weak features between 8000 and 17000 G (not shown here) and the well-resolved half-field signal (Figure 4, inset) are indicative of this color effect, caused by the formation of $Mn^{V}$ in the tetrahedral $P^{V}$ position of the apatite host, as was substantiated by optical spectroscopy.[6] A rough assignment of the latter resonances is possible with the parameters $D \approx 0.40\ cm^{-1}$, $E \approx 0.05\ cm^{-1}$, and a $g$-factor of ca. 1.96, values which are near to those of $Mn^{V}$-doped $Sr_5(PO_4)_3$-Cl.[14] The obvious reason that $Mn^{2+}$ is not substituted into the $Ca^{2+}$ site of the apatite lattice, even after heating to 800 °C, is the weak tendency to occupy $Ca^{2+}$ positions of CNs seven and nine in this structure, at least at moderate heating temperatures. Apparently, the preference of $Mn^{2+}$ to enter a $Ca^{2+}$ position in the two alternative host lattices is much stronger in the case of β-TCP and is supported by ionic size considerations.

 © 2006 Wiley-VCH Verlag GmbH & Co. KGaA, Weinheim 

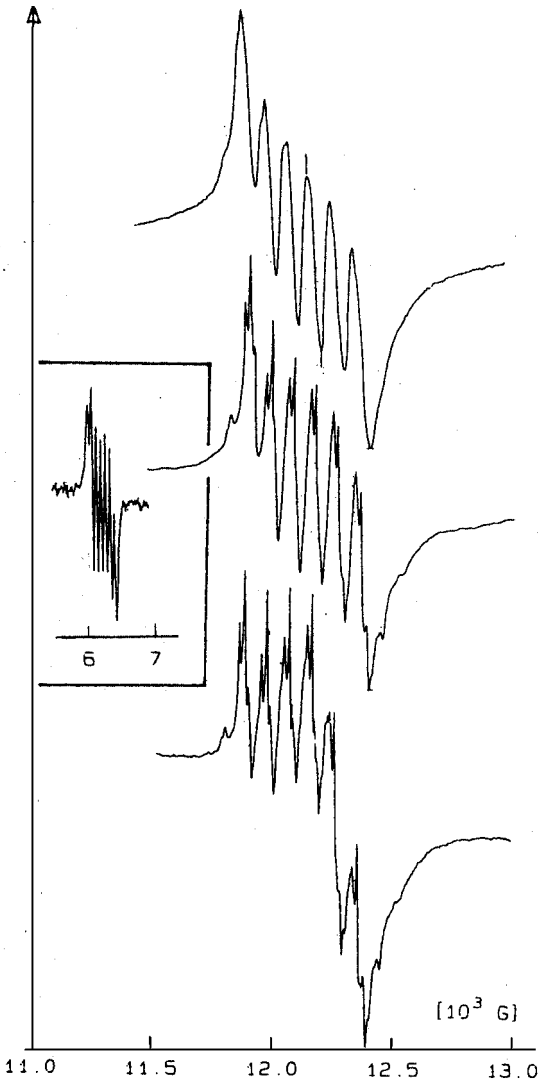


Figure 4. Q-band spectra (34.0 GHz; 298 K) of a CR sample from solution in the presence of Mn, when subsequently heated to 400 °C (top), 600 °C, and 800 °C (bottom). The (enlarged) half-field signal (inset), is due to $Mn^{V}$.

Considering TCP samples with increased Mn content, the X-band spectrum of TCPMn3 (Table 2, Figure 5) or the very similar spectrum of sample HAMn146 after the heat treatment at 800 °C (Table 1), still show the essential features of TCPMn1 (Figure 3), though the increase in the $Mn^{2+}$ concentration has partly narrowed the signal, as a result of exchange interactions between the $d^5$ cations in the lattice. However, a striking feature is that a further increase in the Mn concentration far beyond the one which corresponds to the full occupation of the Ca(5) site ($Mn_{0.286}$), completely removes the features characterizing the zero-field splitting (TCPMn6 in Figure 5). This result might be the consequence of the substitution of further $Ca^{2+}$ sites in such a way that neighbored polyhedra to $Mn(5)O_6$ (which lie isolated in the lattice) with common oxygen ligand atoms are involved, inducing intense exchange narrowing in the EPR spectra.

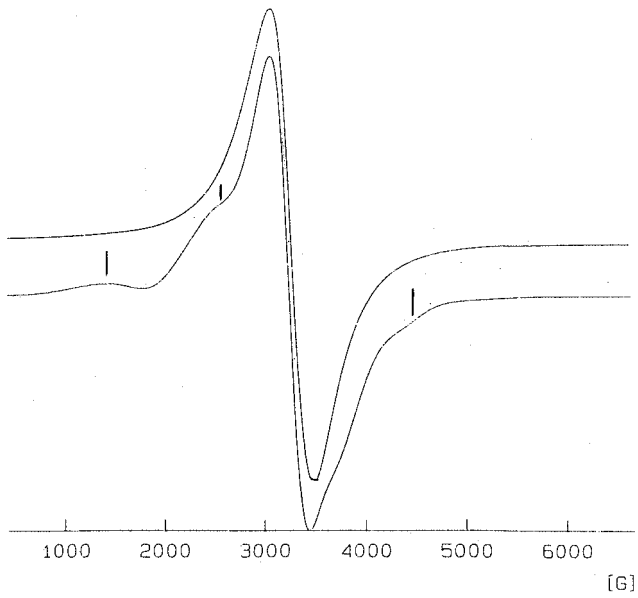


Figure 5. X-band spectra (9.11 GHz; 298 K) of solids TCPMn3 (bottom; the zero-field splitting is marked, see Figure 3) and TCPMn6 (top), with high Mn concentrations (Table 2).

## TEM

Two β-TCP samples were analyzed by TEM methods: a sample prepared after heating sample HAMn147, and $Ca_{2.7}Mn_{0.3}(PO_4)_2$ prepared by solid-state synthesis.

The HAMn147 crystals were 3D, rounded, and droplike-shaped (Figure 6). The smallest crystals were 100 nm in size, but in general they were larger, up to tens of microns. The small crystals had a polyhedral shape in most cases, while small round crystals were also observed. The crystals were not transparent enough to see their lattice, but several good

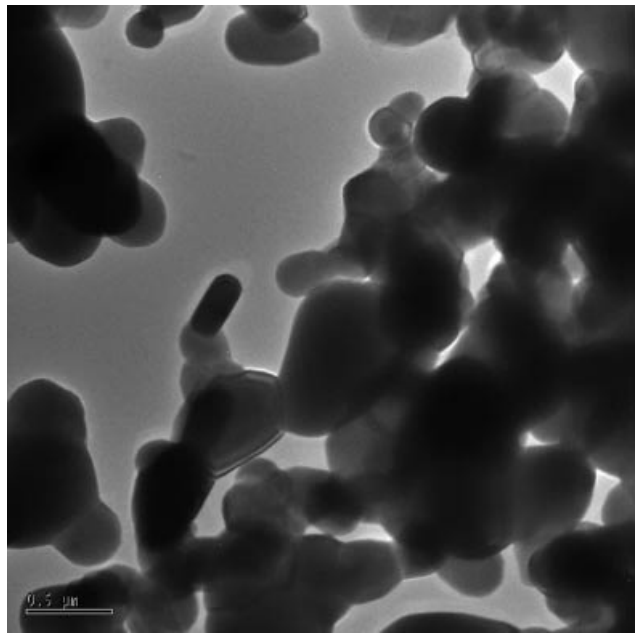

Figure 6. Droplike-shaped crystal of sample HAMn147 after heating to 800 °C.

 © 2006 Wiley-VCH Verlag GmbH & Co. KGaA, Weinheim 

images of their lattice were still observed. The crystals were extremely sensitive to radiation damage; holes were formed in the crystallites. This most probably indicated that the material was composed of nanometer-sized crystalline flakes, which lost their mutual order under the radiation but did not disappear. Comparison of these results with the TEM results of parent HA[6] shows that after heat treatment the morphology changed from thin platelike polygons to 3D crystals.

In the case of $Ca_{2.7}Mn_{0.3}(PO_4)_2$ two groups of crystallites were observed: 2D polygonal flakes of crystallites of nanometer size (nonstable under radiation) (Figure 7) and large, hundreds of nanometers in size, 3D crystallites which were more stable under radiation. Good lattice images and at least one good electron-diffraction pattern from the big crystallites were obtained.

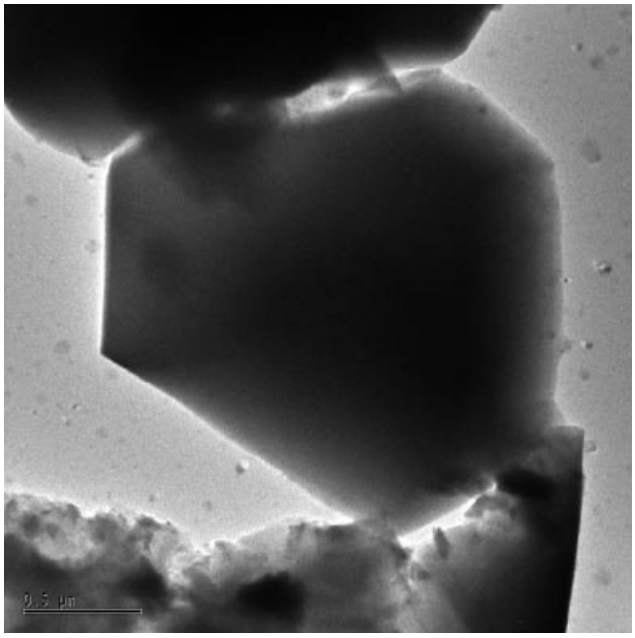


Figure 7. Large 3D crystal of $Ca_{2.7}Mn_{0.3}(PO_4)_2$.

## Discussion

The aim of the present work was to prepare Mn-doped β-TCP samples which can be considered as improved biocompatible coating materials for metallic implants. The results of this study reveal that these materials can be prepared either by heating precipitated Mn-containing HA samples above 600 °C, or by solid-state reaction. The low observed Ca/P ratios for the samples with relatively high Mn concentration (Table 1) indicate an enhanced substitution of $HPO_4^{2-}$ anions into the HA lattice, thus generating $Ca^{2+}$ vacancies. This might be caused by the release of $H^+$ as the consequence of precipitation of some amorphous $MnCO_3$ or $Mn(OH)_2$. Ca/P ratios even below 1.5 favor the transformation to β-TCP in the presence of larger percentages of Mn with the ability to occupy $Ca^{2+}$ positions (see Table 2).

XRD analyses prove that the samples obtained by both methods crystallize in the rhombohedric β-TCP structure; the lattice constants and volumes (hexagonal setting) listed in Table 1 and Table 2 show a slight but continuous decrease with the increase in Mn content. This indicates the formation of solid solutions by partial replacement of $Ca^{2+}$ by the smaller $Mn^{2+}$ ions in the β-TCP lattice. In the case of the precipitated samples, transformation of HA to β-TCP is partial, and a mixture of HA and β-TCP is always obtained; the maximum transformation, about 75%, is reached at 800 °C. Such mixtures are actually often recommended for coating purposes. In the solid-state reaction, the product is of the rhombohedric β-TCP crystal phase only, with maximum Mn content of the composition $Ca_{2.4}Mn_{0.6}(PO_4)_2$.

The unit cell parameters of the $Ca_{3-x}Mn_x(PO_4)_2$ series indicate a discontinuity around $x = 0.3$, which is in well agreement with EPR spectroscopic findings. The full occupation of the Ca(5) site in the β-TCP structure would correspond to $x = 0.286$. The rather high preparation temperature of 1000 °C apparently allows the substitution into further sites with larger CN and bond lengths: preferably Ca(1) with CN = 7 (≈ 2.4 Å) + 1 (≈ 3.0 Å) and/or Ca(2) with CN = 6 (≈ 2.4 Å) + 2 (≈ 2.7 Å). These sites have oxygen atoms with Ca(5) in common, which may well explain the mentioned discontinuity through geometric rearrangements between the interconnected polyhedra. EPR spectroscopy is indicative of such interconnections as well, where exchange narrowing along O–Mn–O bridgings occurs.

Finally, one might speculate about the improvement of biocompatibility of HA by Mn in light of these results. Possibly, the local formation of intermediary β-TCP phases plays a certain role in the respective mechanisms. As shown in this contribution, the phase effect becomes very distinct at higher concentrations of the manganese dopant.

## Experimental Section

### Synthesis of β-TCP from Mn-Containing HA Samples

Samples of HA with Mn (0.1–4.0%) and with carbonate (1.0–3.0%) and without carbonate were prepared by a precipitation method described in more detail elsewhere.[15] A phosphate solution [$(NH_4)_2HPO_4$ (3.7 g) in triple distilled water (TDW) (200 mL)] was added dropwise to a calcium solution [$Ca(NO_3)_2{\cdot}4H_2O$ (9.47 g) in TDW (200 mL)]. Carbonate (5.0 and 10.0 mL) was added from a $NaHCO_3$ stock solution (1 M). These additions were designed to give 2.5–3.5% carbonate in the final sample. The amount of Mn added was 0, 2.5, 5.0, 10, 15.0, 20.0, and 25.0 mL per sample from a $MnCl_2$ solution (0.025 M).

HA samples with $Mn^{2+}$ were prepared at pH = 5.8–6.0. The pH was maintained constant during precipitation by addition of NaOH solution using a Mettler pH-stat automatic titrator. The precipitation was carried out over 2 h, and following this, the temp. was raised to the boiling point and the system was refluxed for 2 h. The sample was then washed with TDW and dried overnight in air at 120 °C.

 © 2006 Wiley-VCH Verlag GmbH & Co. KGaA, Weinheim 

The Ca, P, and Mn contents of the samples were determined by ICP-atomic emission spectroscopy with a precision of ±0.1, ±0.5, and ±0.3% for Ca, P, and Mn, respectively.

The subsequent heating, over 5 h, was carried out in porcelain crucibles in an electric furnace, from 600 °C to 1000 °C in 200 °C intervals.

**Synthesis of β-TCP by High-Temperature Solid-State Reaction**

Stoichiometric amounts of $CaCO_3$, $(NH_4)_2HPO_4$, and $Mn(NO_3)_2$ were thoroughly crushed and mixed in an agate mortar and heated in an alumina crucible at 300 °C for 3 h, recrushed, mixed and then heated at 1000 °C overnight. The samples with higher Mn content had a reddish-purple color.

**Characterization Methods**

XRD was used for crystal phase and lattice constant determination. The X-ray diffraction analyses were made by a Philips Automatic Diffractometer using Cu-$K_\alpha$ radiation. The samples were scanned in the $2\theta$ range of 20–55°. The lattice parameters were calculated by a least-square computer program. Maximum deviation of the lattice constants was ±0.003 Å.

The characterization of the samples by infrared (IR) spectroscopy was performed by a Nicolet FTIR spectrometer. Samples (approx. 1 mg) were pressed into pellets with KBr (approx. 150 mg). The carbonate content of the samples was estimated by IR analysis using the extinction ratio of the carbonate (1420 $cm^{-1}$) and phosphate (575 $cm^{-1}$) bands. Carbonate is determined by this method with an accuracy of ±5%.[16]

EPR measurements were performed at X- and Q-band frequencies between 300 and 80 K with a Bruker ESP-300 spectrometer. UV/Vis spectra were recorded using the powder diffuse reflection technique with a Zeiss PMQII.

Samples were also examined by TEM. For this purpose they were ground and sonicated in ethanol. The obtained suspension was deposited onto a honeycomb carbon-coated grid. All of the study was done using the transmission electron microscope Tecnai F20 $G^2$ (FEI Company) operated at 200 kV and equipped with STEM HAADF detector and EDAX EDS detector.

[1] M. Vallet-Regi, *J. Chem. Soc., Dalton Trans.* **2001**, 97–108.
[2] A. Ogose, T. Hotta, H. Kawashima, N. Kondo, W. Gu, T. Kamura, N. Endo, *J. Biomed. Mater. Res., Part B, Appl. Biomater.* **2005**, *72*, 94–101.
[3] M. Aizawa, K. Itatani, I. Okada, *J. Ceram. Soc. Japan* **2005**, *113*, 245–251.
[4] A. Bigi, E. Foresti, M. Gazzano, A. Ripamonti, N. Roveri, *J. Chem. Research (S)* **1986**, 170–171.
[5] E. Jallot, J. L. Irigaray, H. Quadadesse, V. Brun, G. Weber, P. Frayssiner, *Eur. Phys. J. Appl. Phys.* **1999**, *6*, 205–215.
[6] I. Mayer, O. Jacobsohn, T. Niazov, J. Werckman, M. Iliescu, M. Richard-Plouet, O. Burghaus, D. Reinen, *Eur. J. Inorg. Chem.* **2003**, 1445–1451.
[7] A. Armulik, G. Svineng, K. Wennerberg, R. Faessler, S. Johansson, *Experimental Cell Res.* **2000**, *254*, 55–63.
[8] A. Bigi, B. Bracci, F. Cuisinier, R. Elkaim, M. Fini, I. Mayer, I. N. Mihailescu, G. Socol, L. Sturba, P. Torricelli, *Biomaterials* **2005**, *26*, 2381–2389.
[9] International Centre for Diffraction Data. Powder Diffraction File **2000**, 09–0432.
[10] International Centre for Diffraction Data. Powder Diffraction File **2001**, 09–0169 (2001).
[11] B. Dickens, L. W. Schroeder, W. E. Brown, *J. Solid State Chem.* **1974**, *10*, 232–248.
[12] F. E. Mabbs, D. Collison, in *Studies in Inorganic Chemistry* vol. 16 (Electron Paramagnetic Resonance of d Transition Metal Compounds), Elsevier, **1992**.
[13] D. Reinen, G. Schwab, W. Günzler, *Z. Anorg. Allg. Chem.* **1984**, *516*, 140–152.
[14] D. Reinen, H. Lachwa, R. Allmann, *Z. Anorg. Allg. Chem.* **1986**, *542*, 71–88; D. Reinen, W. Rauw, U. Kesper, M. Atanasov, H. U. Güdel, M. Hazenkamp, U. Oetliker, *J. Alloys Comp.* **1997**, *246*, 193–208.
[15] J. D. B. Featherstone, I. Mayer, F. C. M. Driessens, R. M. H. Verbeeck, M. Heijligers, *Calcif. Tissue Int.* **1983**, *35*, 169–171.
[16] J. D. B. Featherstone, S. Pearson, R. Z. LeGeros, *Caries Res.* **1984**, *18*, 63.

Received: November 14, 2005
Published Online: February 15, 2006

 © 2006 Wiley-VCH Verlag GmbH & Co. KGaA, Weinheim 

DOI: 10.1002/ejic.200501015

# Mandelohydroxamic Acid as Ligand for Copper(II) 15-Metallacrown-5 Lanthanide(III) and Copper(II) 15-Metallacrown-5 Uranyl Complexes

**Tatjana N. Parac-Vogt,*[a] Antoine Pacco,[a] Peter Nockemann,[a] Yao-Feng Yuan,[a] Christiane Görller-Walrand,[a] and Koen Binnemans[a]**

**Keywords:** Lanthanides / Hydroxamic acid / Metallacrowns / Rare earths / Uranium

The formation of pentanuclear copper(II) complexes with the mandelohydroxamic ligand was studied in solution by electrospray ionization mass spectrometry (ESI-MS), absorption spectrophotometry, circular dichroism and $^1$H NMR spectroscopy. The presence of lanthanide(III) or uranyl ions is essential for the self-assembly of the 15-metallacrown-5 compounds. The negative mode ESI-MS spectra of solutions containing copper(II), mandelohydroxamic acid and lanthanide(III) ions (Ln = La, Ce, Nd, Eu, Gd, Dy, Er, Tm, Lu, Y) or uranyl in the ratio 5:5:1 showed only the peaks that could be unambiguously assigned to the following intact molecular ions: $\{Ln(NO_3)_2[15\text{-}MC_{Cu^{II}N(MHA)}\text{-}5]^{2-}\}^-$ and $\{Ln(NO_3)[15\text{-}MC_{Cu^{II}N(MHA)}\text{-}5]^{3-}\}^-$, where MHA represents doubly deprotonated mandelohydroxamic acid. The NMR spectra of the pentanuclear species revealed only one set of peaks indicating a fivefold symmetry of the complex. The pentanuclear complexes synthesized with the enantiomerically pure *R*- or *S*-forms of mandelohydroxamic acid ligand, showed circular dichroism spectra which were mirror images of each other. The pentanuclear complex made from the racemic form of the ligand showed no signals in the CD spectrum. The UV/Vis titration experiments revealed that the order in which the metal salts are added to the solution of the mandelohydroxamic acid ligand is crucial for the formation of metallacrown complexes. The addition of copper(II) to the solutions containing mandelohydroxamic acid and neodymium(III) in a 5:1 ratio lead to the formation of a pentanuclear complex in solution. In contrary, titration of lanthanide(III) salt to the solution containing copper(II) and mandelohydroxamic acid did not show any evidence for the formation of pentanuclear species. (© Wiley-VCH Verlag GmbH & Co. KGaA, 69451 Weinheim, Germany, 2006)

## Introduction

Hydroxamic acids, whether naturally occurring or synthetic, are an important family of organic bioligands.[1] One of the first biomedical applications of hydroxamic acids was associated with the uptake or removal of iron from the body.[2] In recent years it has become evident that these weak acids possess other types of biological activities.[3–7] Their role as potent and selective inhibitors of a range of metalloenzymes has been of special interest to inorganic chemists, because the biological activities of hydroxamic acids have been mainly attributed to their complexing properties toward transition-metal ions.[8] As a result, the transition-metal complexes of hydroxamic acids are frequently used as bioinorganic model compounds to investigate the enzymatic interactions and binding properties of these bioligands.

Hydroxamic acid ligands can exhibit different possible chelation modes, and this results in a rich variety of metal complex structures.[9,10] By far the most common mode of metal binding is the bidentate coordination mode through the deprotonated hydroxamate and carbonyl oxygen atoms, resulting in the formation of simple mononuclear complexes. The introduction of secondary coordinating groups can significantly modify the coordination behavior of hydroxamate ligands. For instance, aminohydroxamic acids can coordinate to metals through (*O*,*O*) as a singly deprotonated hydroxamate, through (*N*,*N*) of the amino and the deprotonated hydroxamic nitrogen, or as a (*N*,*N*)-(*O*,*O*) bridging bis-chelating ligand. Very often, the complexation to metal ions leads to formation of oligomeric or polymeric complexes.[9] However, under certain conditions, the formation of metallacrowns, types of compounds which are analogous to crown ethers in both structure and function, has been observed.[11–13] For example, a pentanuclear [12-metallacrown-4]copper(II) complex is self-assembled from solutions of copper(II) and β-alaninehydroxamic acid (Scheme 1, a). Besides the β-aminohydroxamic acids several other ligands like salicylhydroxamic acid (Scheme 1, b), 2-aminophenylhydroxamic acid, 2-pyridylacetohydroxamic acid and 3-naphthohydroxamic acid have also been used in the 12-metallacrown-4 synthesis.[14] In addition to the [12-metallacrown-4]copper(II) complexes, 12-metallacrown-4 complexes containing other ring metals such as manganese(II), manganese(III), iron(III), oxovanadium(IV) and gallium(III) have been synthesized.[15–21]

[a] Katholieke Universiteit Leuven, Department of Chemistry, Celestijnenlaan 200F, 3001 Leuven, Belgium
Fax: +32-16-327992
E-mail: Tatjana.Vogt@chem.kuleuven.be

 InterScience® © 2006 Wiley-VCH Verlag GmbH & Co. KGaA, Weinheim 

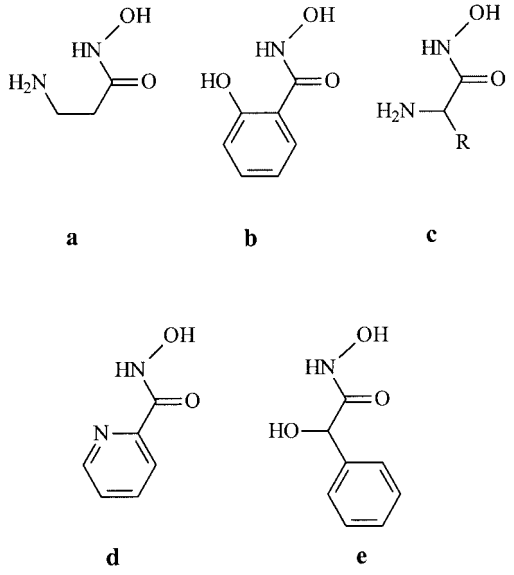


Scheme 1. Precursor ligands used for the synthesis of metallacrown complexes. (a) β-Alaninehydroxamic acid; (b) salicylhydroxamic acid; (c) α-aminohydroxamic acid; (d) picolinehydroxamic acid; (e) mandelohydroxamic acid.

In contrast to the numerous 12-metallacrown-4 structures reported so far, there are only very few examples of ligands capable of forming planar rings of the larger 15-metallacrown-5 structure type. Up to now, only α-aminohydroxamic acids and picolinehydroxamic acid (Scheme 1, c–d) have been found to form planar 15-metallacrown-5 complexes. The key property of these two ligand scaffolds is that they are able to form two fused five-membered chelate rings, which allows five metals and five ligands to form a planar 15-metallacrown-5 structure.[22,23] The planar 15-metallacrown-5 complexes formed in this way are capable to incorporate in their central cavity cations with a larger ionic radius and with a higher coordination number than 12-metallacrown-4 complexes. As a result, lanthanide(III)[24–28] and uranyl ($UO_2^{2+}$)[23,28,29] ions have been incorporated in the center of a 15-metallacrown-5 ring.

The limited number of ligands that are reported to form planar 15-metallacrown-5 complexes creates a challenge for the predesigned synthesis of these structural motifs. The geometry of a particular ligand and its known interaction with a metal ion should contain all the information required for the successful self-assembly of the metallacrown compounds. Therefore, when planning the synthesis of metallacrowns, the general choice of ligand type, ligand geometry, metal type and reaction conditions have to be considered. Although many metal complexes of hydroxamic acids and their derivatives have been studied in detail, the coordination chemistry of mandelohydroxamic acid (Scheme 1, e) is virtually unexplored. A few complexes of divalent cations have been prepared through precipitation in aqueous solution,[30,31] and the metal-ligand stability constants for some mononuclear complexes have been reported.[32] However, no structural data are available for this type of metal complexes.

In this paper, we show that in the presence of copper(II) and lanthanide(III) ions, mandelohydroxamic acid forms stable 15-metallacrown-5 complexes in solution by self-assembly. The copper(II) ion was chosen as the ring metal, as it can form complexes of square-planar geometry, and because its relatively labile metal–ligand bonds should allow the rearrangement of initially formed kinetic products into the thermodynamically stable product. The role of lanthanide(III) and uranyl ions as central templating ions for the self-assembly was examined, as well as conditions which are necessary for the formation of 15-metallacrown-5 complexes.

## Results and Discussion

### Complexation of Mandelohydroxamic Acid to Copper(II)

Mandelohydroxamic acid (MHA) was synthesized from mandelic acid according to Scheme 2. The racemic DL and the enantiomerically pure (*S*)-(+) and (*R*)-(–) forms of the MHA ligand were obtained depending on the stereochemistry of the starting material. Our intention to use mandelohydroxamic acid (MHA) as the ligand for the formation of 15-metallacrown-5 complexes was based on the fact that this ligand possesses a secondary coordinating hydroxy group, and that bidentate coordination through this hydroxy group and the hydroxamate nitrogen would form five-membered chelate rings. The additional coordination by two oxygen atoms can lead to the formation of two five-membered chelate rings (Scheme 3), with an angle of 108° between the two metal atoms. This is, according to the rational design, a geometrical prerequisite for the formation of the 15-metallacrown-5 structure.[21]

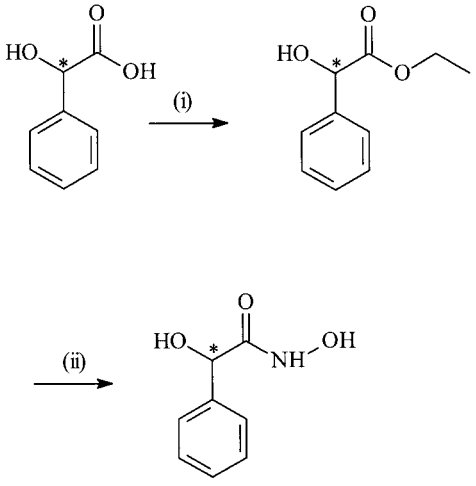


Scheme 2. Synthesis of mandelohydroxamic acid. Conditions: (i) ethanol, $H_2SO_4$, (ii) $NH_2OH{\cdot}HCl$, KOH, methanol.

Previous studies of the mandelohydroxamic acid (MHA) ligand have shown that in the presence of divalent metal ions 1:1 and 2:1 complexes are formed, in which the coordination of the MHA occurs by the formation of five-membered chelates through the deprotonated hydroxamate and carbonyl oxygen atoms.[30–32] The coordination of the hy-

 © 2006 Wiley-VCH Verlag GmbH & Co. KGaA, Weinheim 

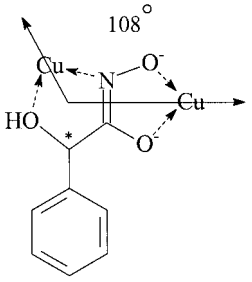


Scheme 3. Rationale for the formation of planar 15-metallacrown-5 complexes.

droximato nitrogen and hydroxy oxygen to the metal ions has not been observed.

Mixing of copper(II) and the enantiomerically pure *R*- or *S*-form of MHA in aqueous solutions resulted in the formation of a green solid after few hours of stirring. Similar reactions occurred when methanol or ethanol were used as solvents. The elemental analyses carried out for the precipitate isolated from methanolic or ethanolic solutions indicated the formation of a complex with the stoichiometry [CuL]. However, the insolubility of this solid in all conventional solvents suggests a polymeric nature of the complex. Polymeric complexes of hydroxamic acids which possess a secondary coordinating group have been previously reported.[33]

When racemic DL-mandelohydroxamic acid was used instead of the enantiomerically pure *S*- or *R*-form, the equimolar mixture of $Cu(OAc)_2$ and MHA in methanol or ethanol remained clear during the course of several weeks. The UV/Vis spectrum of the green solution exhibits an absorption maximum at 650 nm, which is equal to the values observed in [Cu(acetohydroxamate)$_2$] ($\lambda_{max}$ = 653 nm)[34] and other copper(II) complexes with deprotonated hydroxamate and carbonyl oxygen donors.[35] The ESI-MS spectra did not show any evidence for the presence of metallacrown species, so it is likely that the complex formed in solution is the mononuclear $Cu(MHA)_2$ complex in which the coordination to copper(II) occurs by the deprotonated hydroxamate and carbonyl oxygen donors. This finding is in sharp contrast to the analogous reaction between α-aminohydroxamic acids and copper(II), in which exclusively the $[Cu_5(\alpha\text{-aha})_4]^{2+}$ (aha = aminohydroxamic acid) 12-metallacrown-4 complex is formed in solution.[12] In that metallacrown complex the coordination of aminohydroxamic acid occurs also by the deprotonated hydroxamate and carbonyl oxygen atoms; however, the second five-membered ring is also formed through the coordination of hydroximato nitrogen and amino nitrogen to copper(II). This leads to the formation of a puckered structure with four copper(II) ions in the backbone of the metallacrown and a cavity which accommodates the fifth copper(II) ion.

Although the coordination geometries of α-aminohydroxamic acids and mandelohydroxamic acid are almost identical, the main difference between these two ligands is that mandelohydroxamic acid possesses a hydroxy group instead of the amino group of α-aminohydroxamic acids. The presence of the hydroxy group, which is a weaker ligating group for copper(II) ions, probably prevents the formation of the second chelating ring, and thus the formation of a 12-metallacrown-4 metallacrown structure.

### Formation of 15-Metallacrown-5 Complex Monitored by ESI-MS

Our previous studies have shown that lanthanide(III) and uranyl ions have a large influence on the structure of the metallacrown complexes based on α-aminohydroxamic acid and copper(II) ion.[29,36,37] The addition of lanthanide(III) and uranyl ions to $[Cu_5(\alpha\text{-aha})_4]^{2+}$ induces a complete reassembly of the 12-metallacrown-4 structure to the 15-metallacrown-5 structure, in which lanthanide(III) or uranyl ions occupy the central cavity of the planar ring. Although lanthanide(III) ions seem to be essential for the synthesis of 15-metallacrown-5 complexes, their exact role has never been examined.[24] Previously, it has been suggested that lanthanide(III) ions are being merely recognized end-encapsulated by the 15-metallacrown-5 ring, and that this inclusion may contribute to the stability of the whole metallacrown structure. These findings prompted us to exploit lanthanide(III) and uranyl ion as possible templates for the formation of metallacrown complexes based on mandelohydroxamic acid and copper(II). When 0.25 equiv. of neodymium(III) were present in an equimolar solution of copper(II) and (*S*)-mandelohydroxamic acid, the color of the solution gradually changed from blue to green. The addition of sodium formate or sodium acetate salts resulted in the formation of a microcrystalline solid (see Exp. Section). Unfortunately, all attempts to isolate crystals of quality good enough for X-ray single crystal analysis were unsuccessful, but the elemental analysis results were consistent with the stoichiometry $Nd[Cu_5(MHA)_5]\cdot 3(HCOO)\cdot 3(H_2O)$ and $Nd[Cu_5(MHA)_5]\cdot 3(CH_3COO)\cdot (H_2O)$, where MHA represents the doubly deprotonated mandelohydroxamic acid. Crystallization techniques, such as evaporation of the solvent, diffusion techniques (vapor and liquid), and various co-crystallants were used on all three types of metallacrown complexes containing racemic DL and the enantimerically pure *S*-(+)and *R*-(–) forms of the mandelohydroxamate ligand. The only few crystals that were obtained were of insufficient quality for X-ray diffraction studies. The only reflections that could be observed were weak reflections in the small-angle region and were not suitable for the determination of the crystallographic unit cell. The solutions containing equimolar amounts of (*S*)-mandelohydroxamic acid and copper(II) acetate, in which 0.2 mol equivalents of different trivalent rare-earth ions (Ln = La, Ce, Nd, Eu, Gd, Dy, Er, Tm, Lu, Y) or uranyl ions ($UO_2^{2+}$) were present, have been further analyzed by electrospray ionization mass spectrometry (ESI-MS). In recent years, ESI-MS has been proven very useful for the analysis of self-assembled clusters. The results obtained by ESI-MS have been often regarded as indicative for the solution behavior of a species rather than for its gas-phase behavior.[38] The method has

 © 2006 Wiley-VCH Verlag GmbH & Co. KGaA, Weinheim 

also been proven as very useful for confirming the integrity of metallacrown complexes in solution.[14] Several studies indicate that the results obtained by ESI-MS correlate very well with those obtained by other techniques, such as NMR and X-ray diffractometry.[38,39] Nonetheless, ESI-MS studies of large self-assembled metal complexes remain nontrivial and often require thorough optimization of the experimental parameters. All peaks detected in the mass spectra of $Cu^{II}$/MHA/$Ln^{III}$ and $Cu^{II}$/MHA/$UO_2^{2+}$ solutions appear as cluster peaks, because of the different copper(II) and lanthanide(III) isotopes in the detected complexes. Species with different degrees of protonation were detected in the ESI-MS spectra. This may be due to the deprotonation or protonation during the ionization process, or may be due to the different degree of protonation of mandeloxydroxamate ligand. It is possible that the deprotonation of the mandelohydroxamate ligand occurs not only on the hydroxamate nitrogen and oxygen atoms, like it was reported for other hydroxamate ligands that form 15-metalacrown-5,[24–29] but that the hydroxyl group may also be deprotonated. Both protonated and deprotonated forms of the hydroxyl group can bind to copper(II), and moreover, the Lewis acidity of the copper(II) may cause the deprotonation of the hydroxyl group upon binding. The peaks that were observed in the ESI-MS spectra are summarized in Table 1 and Table 2. The reported *m*/*z* values are the maxima of the cluster peaks. All the peaks detected in the negative mode (Table 1) could be unambiguously assigned to the following two intact molecular ions: $\{Ln(NO_3)_2[15\text{-}MC_{Cu^{II}N(MHA)}\text{-}5]^{2-}\}^-$ and $\{Ln(NO_3)[15\text{-}MC_{Cu^{II}N(MHA)}\text{-}5]^{3-}\}^-$, where MHA represents doubly deprotonated mandelohydroxamic acid (mandelohydroximate) (Figure 1). If the neodymium(III) perchlorate was used instead of neodynium(III) nitrate, peaks corresponding to $\{Nd(ClO_4)_2[15\text{-}MC_{Cu^{II}N(MHA)}\text{-}5]^{2-}\}^-$ and $\{Nd(ClO_4)_3[15\text{-}MC_{Cu^{II}N(MHA)}\text{-}5]^{2-}\}^{2-}$ species with two and three perchlorate counterions were observed. Thus, the positive charge of the central lanthanide(III) ions is always compensated by the negative charge of the ring and by nitrate or perchlorate anions present in the solution.

Table 1. Negative-ion ESI-MS data for 15-metallacrown-5 complexes derived from (*S*)-(+)-mandelohydroxamic acid, copper(II) ions as the ring metal and with different central cavity metals(M).

| Species M | $\{M(NO_3)_2[15\text{-}MC\text{-}5]^{2-}\}^-$ *m*/*z* exp. | *m*/*z* calcd. | $\{M(NO_3)[15\text{-}MC\text{-}5]^{3-}\}^-$ *m*/*z* exp. | *m*/*z* calcd. |
|---|---|---|---|---|
| $Y^{III}$ | 1354.6 | 1354.3 | 1291.9 | 1291.3 |
| $La^{III}$ | 1404.6 | 1404.4 | 1341.9 | 1341.4 |
| $Ce^{III}$ | 1405.6 | 1405.6 | 1342.9 | 1342.5 |
| $Nd^{III}$ | 1409.5 | 1409.6 | 1346.9 | 1346.6 |
| $Eu^{III}$ | 1417.5 | 1417.4 | 1353.9 | 1354.4 |
| $Gd^{III}$ | 1422.6 | 1422.7 | 1358.9 | 1359.7 |
| $Dy^{III}$ | 1427.6 | 1427.9 | 1363.9 | 1364.9 |
| $Er^{III}$ | 1432.6 | 1432.7 | 1369.0 | 1369.7 |
| $Tm^{III}$ | 1434.6 | 1434.4 | 1371.7 | 1371.4 |
| $Lu^{III}$ | 1440.6 | 1440.4 | – | – |
| $UO_2^{2+}$ | – | – | 1410.9 | 1410.5[a] |

[a] Value calculated for $\{M[15\text{-}MC\text{-}5]^{3-}\}^-$.

When lutetium(III) or thulium(III) were used as central cavity ions, additional peaks, that could not be attributed to a 15-metallacrown-5 species with a lanthanide(III) ion in the central cavity, were observed in the ESI-MS spectra. In both cases, a peak at *m*/*z* = 1222 was detected which corresponds to a 15-metallacrown-5 species with copper(II) ion in the central cavity: $\{Cu(OH)[15\text{-}MC_{Cu^{II}N(MHA)}\text{-}5]^{2-}\}^-$. Another peak at *m*/*z* = 993 could be assigned to $\{Cu(OH)[12\text{-}MC\text{-}4]^{2-}\}^-$. As thulium(III) and lutetium(III) are lanthanide ions with a small ionic radius (87 and 85 pm, respectively), this probably leads to less effective encapsulation into the central cavity and thus to a reduced stability of the 15-metallacrown-5 complexes.

Table 2. Positive-ion mode ESI-MS data for 15-metallacrown-5 complexes derived from (*S*)-(+)-mandelohydroxamic acid, copper(II) ions as the ring metal and with different central cavity metals (M).

| Species M | $\{M(NO_3)[15\text{-}MC\text{-}5]\}^{2+}$ *m*/*z* exp. | *m*/*z* calcd. | $\{M(NO_3)[15\text{-}MC\text{-}5]^-\}^+$ *m*/*z* exp. | *m*/*z* calcd. |
|---|---|---|---|---|
| $Y^{III}$ | 645.3 | 645.3 | – | – |
| $La^{III}$ | 672.2 | 672.2 | 1342.5 | 1343.4 |
| $Ce^{III}$ | 672.7 | 672.8 | 1343.9 | 1344.6 |
| $Nd^{III}$ | 674.5 | 674.8 | 1347.6 | 1348.7 |
| $Eu^{III}$ | 678.3 | 678.7 | 1355.7 | 1356.4 |
| $Gd^{III}$ | 681.8 | 681.3 | 1361.7 | 1361.7 |
| $Dy^{III}$ | 683.5 | 683.9 | 1366.1 | 1366.9 |
| $Er^{III}$ | 685.7 | 686.3 | 1371.5 | 1371.1 |
| $Tm^{III}$ | 686.3 | 687.2 | – | – |
| $Lu^{III}$ | 689.2 | 690.2 | – | – |
| $UO_2^{2+}$ | 706.4 | 706.8[a] | 1412.7 | 1412.5[a] |

[a] Values calculated for $\{M[15\text{-}MC\text{-}5]\}^{2+}$ and $\{M[15\text{-}MC\text{-}5]^-\}^+$.

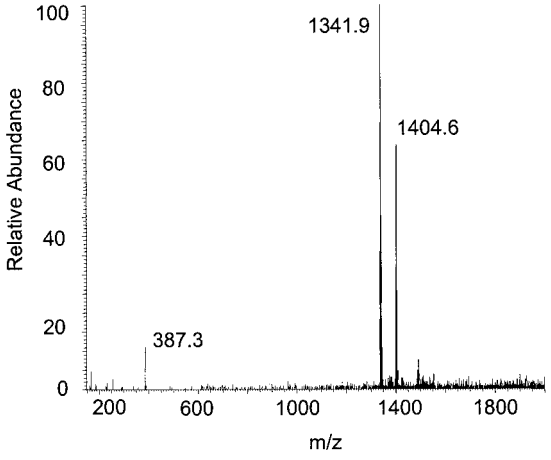


Figure 1. Negative-ion mode ESI-MS spectra of the methanolic solutions containing $Cu^{II}$/MHA/$La^{III}$ in 5:5:1 ratio.

The ESI-MS spectra in the positive mode also gave strong evidence for the existence of 15-metallacrown-5 complexes (Table 2). The peak with the highest intensity corresponds to the doubly charged $\{Ln(NO_3)[15\text{-}MC_{Cu^{II}N(MHA)}\text{-}5]\}^{2+}$ species. Another peak with approx. 10% of the intensity of the former was detected in all the spectra and could be assigned to the $\{Ln(NO_3)[15\text{-}MC_{Cu^{II}N(MHA)}\text{-}5]^-\}^+$ molecular ion.

Only one peak at *m*/*z* = 1410 was observed in the ESI-MS spectra taken in the negative mode for the solution containing the uranyl ion. The mass of this peak could be un-

 © 2006 Wiley-VCH Verlag GmbH & Co. KGaA, Weinheim 

ambiguously assigned to the intact $\{UO_2[15\text{-}MC_{Cu^{II}N(MHA)}\text{-}5]^{3-}\}^{-}$ molecular ion. The axial coordination of two oxygen atoms in the uranyl ion does not allow for additional binding of counterions, and the first coordination sphere of the uranyl ion is completed by five equatorial oxygen atoms from the metallacrown ring. In the positive mode ESI-MS spectra of the solution containing the uranyl ion, two peaks at $m/z$ = 706 and 1412 were detected (Figure 2). They correspond to the $\{UO_2[15\text{-}MC_{Cu^{II}N(MHA)}\text{-}5]\}^{2+}$ and $\{UO_2[15\text{-}MC_{Cu^{II}N(MHA-)}\text{-}5]^{-}\}^{+}$ pentanuclear species, respectively. The peak at $m/z$ = 1412.7 corresponds to a 15-metallacrown-5 species in which the hydroxyl group in one of the ligands is deprotonated, and the peak at $m/z$ = 706.4 corresponds to a metallacrown species in which all five hydroxyl groups are protonated.

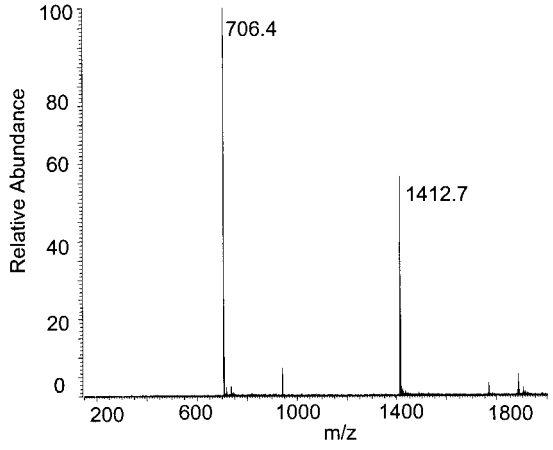


Figure 2. Positive-ion mode ESI-MS spectra of the methanolic solutions containing $Cu^{II}$/MHA/$UO_2^{2+}$ in 5:5:1 ratio.

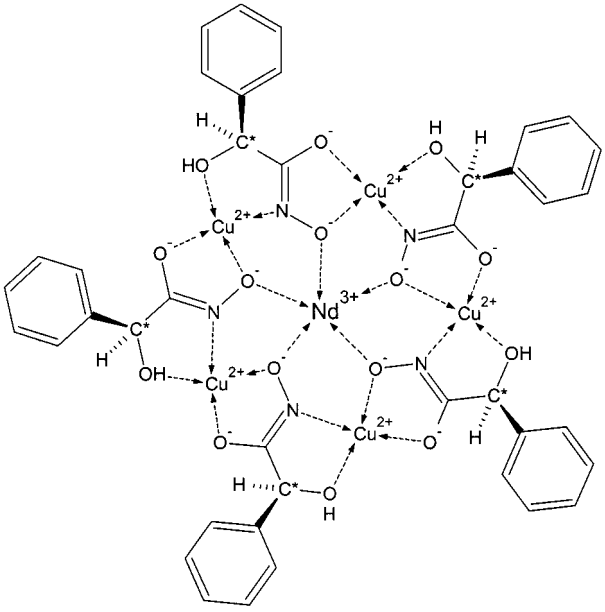


Figure 3. Proposed structure of the pentanuclear Nd[15-$MC_{Cu^{II}N[(S)\text{-}MHA]}$-5] metallacrown complex in solution. The coordination sphere of neodymium(III) ion is completed by nitrate or water ligands.

The spectra of solutions containing racemic DL-mandelohydroxamic acid, copper(II) and neodymium(III) or uranyl were also recorded, and the $m/z$ values observed in those spectra were identical to the $m/z$ values observed when (*S*)-mandelohydroxamic acid was used as coordinating ligand.

The presented ESI-MS data indicate that solutions containing copper(II) salt, mandelohydroxamic acid [DL- or (*S*)-] and a central templating ion in methanolic and ethanolic solutions are forming pentanuclear species. The only species detected for the solutions prepared with M = Y, La, Ce, Nd, Eu, Gd, Dy, Er, and $UO_2$ correspond to the intact M[15-$MC_{Cu^{II}N(MHA)}$-5] pentanuclear species. On the basis of the previously mentioned geometric considerations, it is very likely that the structure of the pentanuclear species corresponds to the structure of the planar 15-metallacrown-5 ring, in which lanthanide(III) ions or uranyl ions are encapsulated in the central cavity (Figure 3).

### Complexation of Mandelohydroxamic Acid Monitored by UV/Vis Spectroscopy

Titration experiments were performed in order to gain insight into the formation of the metallacrown complexes. Surprisingly, these experiments revealed that the order in which the metal salts are added to the MHA solution is crucial for the formation of metallacrown complexes. Titration of $Cu^{II}$/DL-MHA solution with neodymium(III) and uranyl in steps of 0.04 equivalents caused a slight decrease in the intensity of the broad shoulder between 300 nm and 450 nm and also the decrease of the d–d transition band at 687 nm. Even after the reaction mixture was let to react for 24 hours, no appearance of new peaks and shifting of the ligand field or d–d bands was observed. The ESI-MS spectra of these solutions were recorded and they did not show any evidence for the existence of pentanuclear species.

On the contrary, the titration of copper(II) to the solutions containing DL-MHA and neodymium(III) in a 5:1 ratio caused significant changes in the UV/Vis spectra. New bands at 330 nm and 638 nm (Figure 4) appeared, and their intensity increased until 5 equivalents of copper(II) were added, and it leveled off upon addition of 6 equivalents of copper(II). The molar absorptivity of the copper(II) ligand field band observed at a Cu/Ln ratio of 5:1 was consistent with the isolated 15-metallacrown-5 sample, dissolved in MeOH. The plot of the ratio of concentrations of neodymium(III) to copper(II) vs. the molar absorptivity at 330 nm and 638 nm is shown in Figure 5. The composition of the sample in which the ratio of Nd/MHA/Cu was 1:5:5 is consistent with the formula Nd[15-$MC_{Cu^{II}N(MHA)}$-5]. With the further increase of lanthanide concentration, no changes in the copper(II) ligand field band were observed, indicating that the presence of excess of lanthanide or uranyl ions does not disturb the metallacrown structures. Indeed, the ESI-MS spectra of the final solution showed exclusively cluster peaks which could be unambiguously assigned to the 15-metallacrown-5 species. The UV/Vis spectrum of Nd[15-$MC_{Cu^{II}N(MHA)}$-5] resembles the UV/Vis spectra of other

 © 2006 Wiley-VCH Verlag GmbH & Co. KGaA, Weinheim 

pentanuclear complexes with lanthanide(III) ions. The band at 330 nm is in agreement with the band at 336 nm observed in the 15-metallacrown-5 complexes with tryptophanhydroxamic acid.[40] This band contains most likely contributions of $N^-–O^-_{(nitrogen)}$ and $N^-–O^-_{(oxygen)}$ to copper(II) charge-transfer transitions.

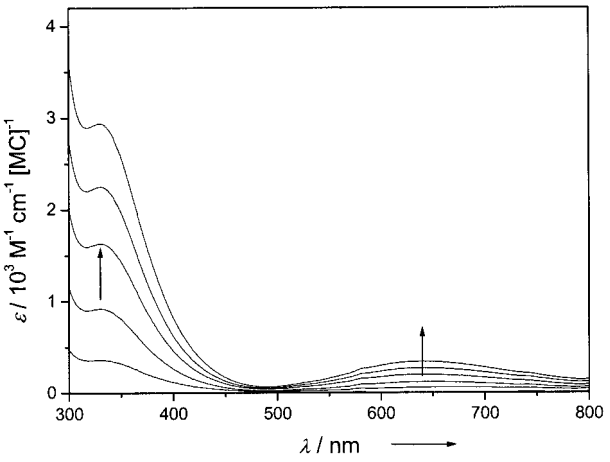


Figure 4. Changes in the UV/Vis absorption spectra of $Nd^{III}$/MHA solutions in methanol, upon addition of copper(II) ions. Copper(II) ions were added in 0.2 equiv. increments, until the final ratio of $Nd^{III}$/MHA/$Cu^{II}$ reached 1:5:5 ratio.

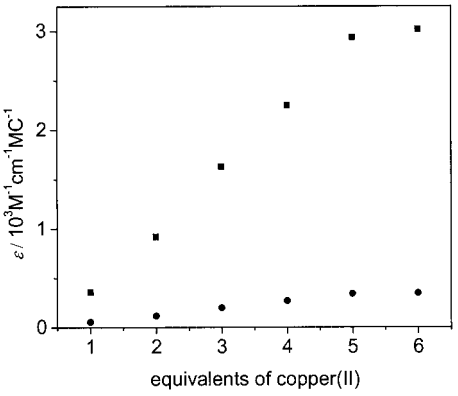


Figure 5. Change of molar absorptivity at 330 nm (squares) and 638 nm (circles) of the $Nd^{III}$/MHA/$Cu^{II}$ solution as a function of number of copper(II) equivalents.

The complex formation of lanthanide(III) with mandelohydroxamic acid has not been reported before, and no information about the stability of such complexes is available. The X-ray single-crystal structure of the complex formed between europium(III) and analogous α-alaninehydroxamic acid has shown that the hydroxamate group of α-alaninehydroxamate ligands forms a bridge between two europium(III) ions, so that a binuclear complex is formed.[41] However, it has been shown that the addition of copper(II) to solutions of lanthanide(III) and α-aminohydroxamic acid leads to the formation of the 15-metallacrown-5 structure.[37] Obviously, the high lability of the lanthanide(III) ligand bonds may allow for the initially formed products to rearrange into the 15-metallacrown-5 structure upon addition of copper(II) ion.

However, it must be mentioned that factors, such as the acidity of the solution and the different protonation states of the ligand, may be responsible for the fact that the order in which the metal salts are added to the MHA solution is crucial for the formation of the metallacrown complex. The determination of the degree of protonation of the ligand in the presence of copper(II) and lanthanide(III) ions would require thorough potentiometric titrations and evaluation of many possible equilibria involved in the ternary $H^+$/MHA/$Cu^{2+}$/$Ln^{3+}$ system.

### CD Spectroscopy of 15-Metallacrown-5 Complexes

Because the *R*- and *S*-enantiomeric forms of the MHA are chiral, their copper(II) complexes are expected to be optically active as well. The chirality of the 15-metallacrown-5 complexes formed with *R*- and *S*-enantiomeric forms of the MHA has been studied by circular dichroism (CD) spectroscopy. The ESI-MS spectra of all the solutions used for the spectrophotometric measurements were recorded, and the species observed were consistent with the Ln[15-$MC_{Cu^{II}N(MHA)}$-5] structure as described earlier in the mass spectrometric results. The CD spectrum of methanolic solutions of (*S*)-MHA/$Cu^{II}$/$Nd^{III}$ (ratio: 1:1:0.2), shows a positive Cotton effect at 342 nm ($\Delta\varepsilon$ = 2.86 mol·$L^{-1}$ $cm^{-1}$) and two negative Cotton effects at 603 ($\Delta\varepsilon$ = –1.2 mol·$L^{-1}$ $cm^{-1}$) and 733 nm ($\Delta\varepsilon$ = –1.08 mol·$L^{-1}$ $cm^{-1}$). If (*R*)-MHA was used as the ligand, the CD spectrum of the resulting complex was the mirror image of the spectrum of the complex of (*S*)-MHA. As expected, the 15-metallacrown-5 complex made from the racemic MHA showed no signal in the CD spectrum (Figure 6).

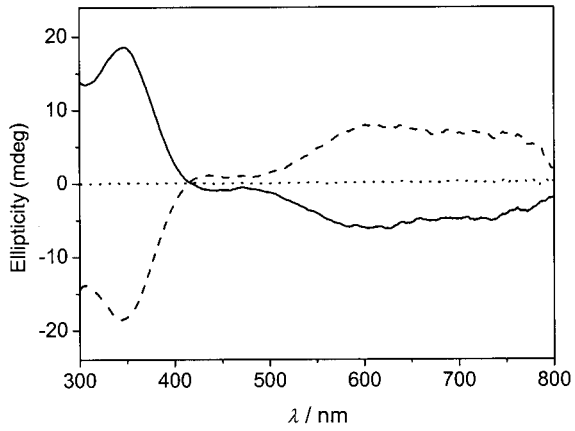


Figure 6. CD absorption spectra of Nd[15-$MC_{Cu^{II}N[(S)\text{-MHA}]}$-5] (full line), Nd[15-$MC_{Cu^{II}N[(R)\text{-MHA}]}$-5] (dotted line) and Nd[15-$MC_{Cu^{II}N(DL\text{-MHA})}$-5] (dashed line) in methanol.

The chirality of the 15-metallacrown-5 complex implies that all five phenyl groups of the MHA ligand have to be positioned upon the same face of the metallacrown. This side-chain orientation is enforced by the directionality of the metal–nitrogen–oxygen bonds, as it was previously reported in other chiral 15-metallacrown-5 complexes.[22,24]

 © 2006 Wiley-VCH Verlag GmbH & Co. KGaA, Weinheim 

### Proton NMR of of 15-Metallacrown-5 Complexes

Proton NMR signals of nuclei close to paramagnetic metal ions are usually very broad and the extent of paramagnetically induced line broadening depends on the electronic relaxation time of the metal centers.[42] Complexes with paramagnetic copper(II) ions usually exhibit broad NMR signals because of the relatively long electronic relaxation times of copper(II) ($\tau_s$ = $1 \cdot 10^{-9}$ s to $5 \cdot 10^{-9}$ s). However, a shortening of the electronic relaxation times can occur because of the magnetic coupling between the metal ions.[42] Previous studies have shown that the copper(II) ions in the 15-metallacrown-5 are antiferromagnetically coupled,[22,24] so that the $\tau_s$ value of those metallacrowns is shorter than it would be in the absence of magnetic coupling. This could allow the detection of relatively narrow peaks in high-resolution NMR experiments.

The $^1$H NMR spectrum of the Nd[15-MC$_{Cu^{II}N[(R)\text{-MHA}}$-5] complex in [D$_4$]MeOH showed three peaks at $\delta$ = 5.85, 6.58, and 7.75 ppm (Figure 7). The α-proton of the ligand could not be observed, most likely because it was too broad. It has been shown that the protons to the closest proximity to the paramagnetic center are showing the greatest line broadening.[43] The assignment of the peaks was done with the help of two-dimensional proton correlation spectroscopy (COSY). The comparison with the proton NMR spectrum of the previously reported Nd[15-MC$_{Cu^{II}N(L\text{-tyrha})}$-5] complex revealed that the aromatic protons of the mandelohydroxamate ligand appear in the same region as the signals of the aromatic protons of the tyrosinehydroxamate ligand. The simplicity of the spectra, i.e. the presence of only one set of resonances indicates the fivefold pseudosymmetry of the molecule. The NMR results are consistent with those of the previously studied lanthanide(III) containing 15-metallacrown-5 copper(II) complexes, which also showed only one set of ligand resonances.[24]

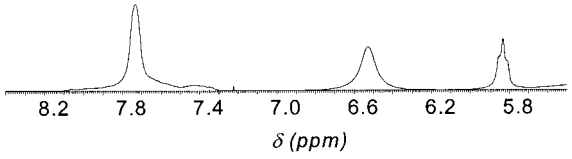


Figure 7. Proton NMR spectrum of Nd[15-MC$_{Cu^{II}N[(R)\text{-MHA}]}$-5] complex in [D$_4$]MeOH solution.

It is noteworthy to emphasize the fact that whereas the NMR signals were observable for the 15-metallacrown-5 complex in which several highly paramagnetic ions are present, no NMR spectrum could be obtained for the complexes formed in the absence of lanthanide(III) ions. Obviously, there are significant differences in the relaxation times of copper(II) ions in these two types of complexes. The absence of any protons in the NMR spectrum recorded in the absence of lanthanide(III) is consistent with the presence of mononuclear copper(II) complexes.

## Conclusions

In this paper we explore the strategy that leads to the formation of pentanuclear copper(II) complexes with the mandelohydroxamic ligand. The results of ESI-MS, UV/Vis, CD, and NMR studies are consistent with the formation of 15-metallacrown-5 complexes. The mandelohydroxamic ligand as novel scaffold for the 15-metallacrown-5 complex fulfils the geometric requirements which bring five metal ions into a plane, enforcing an angle of 108° between adjacent metal ions, and thus enforcing the formation of a planar, pentagonal ring. Our study shows that for the self-assembly of the 15-metallacrown-5, the presence of lanthanide(III) or uranyl ions is essential, as it has been demonstrated before. As it has been suggested before that lanthanide(III) ions are being recognized and encapsulated by 15-metallacrown-5 complexes, this study shows that lanthanide(III) ions may have a templating effect and could play a crucial role in the early stages of 15-metallacrown-5 formation.

## Experimental Section

**Synthesis of the Ligands:** The ligands, (*R*)-(–)-mandelohydroxamic acid, (*S*)-(+)-mandelohydroxamic acid and DL-mandelohydroxamic acid were synthesized from the corresponding ethyl ester. The preparation method for (*S*)-(+)-mandelohydroxamic acid and DL-mandelohydroxamic acid is identical to that of the synthesis of (*R*)-(–)-mandelohydroxamic acid that is described below.

**Synthesis of Ethyl (*R*)-(–)-Mandelate:** To a solution of (*R*)-(–)-mandelic acid (100 mmol, 15.2 g) in ethanol (170 mL) was added $H_2SO_4$ (5 mL) as the catalyst. The reaction mixture was heated at reflux temperature for 4 h. After the reaction mixture was cooled to room temperature, the solvent was evaporated under reduced pressure. Then, after addition of dichloromethane, the organic layer was neutralized by a saturated $NaHCO_3$ solution and dried with $MgSO_4$. Dichloromethane was removed under reduced pressure. Yield: 91% (16.41 g). $^1$H NMR ([D$_6$]DMSO, 300 MHz, ppm): $\delta$ = 1.13 (t, 3 H, $CH_3$), 4.07 (t, 2 H, $OCH_2$), 5.11 (d, 1 H, CH), 6.04 (d, 1 H, OH), 7.40 (m, 5 H, H-aromatic).

**Synthesis of (*R*)-(–)-Mandelohydroxamic Acid:** To a solution of $NH_2OH \cdot HCl$ (2 equiv., 182 mmol, 12.65 g) in methanol (110 mL), potassium hydroxide (3 equiv., 273 mmol, 15.29 g) dissolved in methanol (42 mL) was added under nitrogen. The hydroxylamine solution was cooled to 0 °C and KCl was removed by filtration. The solution was added to (*R*)-(–)-mandelic ethyl ester (1 equiv., 91 mmol, 16.41 g) and stirred at room temperature during 12 h. The white precipitate of the potassium salt was filtered off and dried (10.53 g, 51 mmol, 56% yield). To a suspension of the potassium salt in methanol was added 12 M HCl (51 mmol, 4.25 mL). Potassium chloride precipitated and was filtered off. The solvent of the filtrate was partially removed under reduced pressure and water was added to the solution. The solution was left to stand at 4 °C to allow the final product to crystallize. Yield: 51% (4.35 g). $^1$H NMR ([D$_6$]DMSO, 300 MHz, ppm): $\delta$ = 4.89 (d, 1 H, CH), 5.95 (d, 1 H, OH), 7.40 (m, 5 H, H-aromatic), 8.77 (s, 1 H, NH), 10.72 (s, 1 H, $OH_{hydr.}$). $C_8H_9NO_3$ (167 g/mol): calcd. C 57.48, H 5.43, N 8.38; found C 57.16, H 5.49, N 8.32.

**Synthesis of the Metallacrowns**

**(1) Nd[15-MC-5]·3(HCOO)·3($H_2O$):** $Nd(NO_3)_3 \cdot 6H_2O$ (109 mg, 0.25 mmol) was dissolved into methanol (50 mL) and (*R*)-MHA (167 mg, 1 mmol) was added. The solution was stirred for 10 min, then sodium methoxide (108 mg, 2 mmol) was added to the reaction mixture. After another 10 min, anhydrous copper(II) chloride

 © 2006 Wiley-VCH Verlag GmbH & Co. KGaA, Weinheim 

(170 mg, 1 mmol) was added. The mixture was stirred for 2 h until the solution became green. Finally sodium formate (68 mg, 1 mmol) was added, and the blue-green precipitate was filtered, washed with water to remove sodium chloride and dried under vacuum. $C_{43}H_{44}Cu_5N_5NdO_{24}$ (1476.8 g/mol): calcd. C 34.97, H 3.00, N 4.74; found C 35.15, H 3.57, N 4.81.

**(2) Nd[15-MC-5]·3($CH_3COO$)·($H_2O$):** $Nd(NO_3)_3·6H_2O$ (109 mg, 0.25 mmol) was dissolved into methanol (50 mL) and (*R*)-MHA (167 mg, 1 mmol) was added. The solution was stirred for 10 min, then sodium methoxide (108 mg, 2 mmol) was added to the reaction mixture. After another 10 min, anhydrous copper(II) chloride (170 mg, 1 mmol) was added. The mixture was stirred for 2 h until the solution became green. Finally the sodium acetate (82 mg, 1 mmol) was added, and the blue-green precipitate was filtered, washed with water to remove sodium chloride and dried under vacuum. $C_{46}H_{46}Cu_5N_5NdO_{22}$ (1518.9 g/mol): calcd. C 37.26, H 3.13, N 4.72; found C 37.41, H 3.13, N 4.69.

**UV/Vis and CD Spectrophotometry:** UV/Vis absorption spectra were recorded with a Shimadzu UV-1601PC spectrophotometer using quartz cells of 1-cm path length. Circular dichroism spectra were recorded with a JASCO J-810 spectropolarimeter using quartz cells of 2-cm path length. The spectra were measured between 200 nm and 900 nm. The concentration of the copper(II) and mandelohydroxamic acid in methanol was always 0.5 mM. A neodymium(III) nitrate stock solution (0.25 mM). was prepared in methanol for the UV/Vis titration experiment. Different amounts of this solution were added to the copper(II)/mandelohydroxamic solution in order to obtain different ratios of $Nd^{III}/Cu^{II}$. The solutions were left to stir overnight before measurement. The $Nd^{III}/Cu^{II}$ ratio was varied in steps of 0.04 from 0 to 0.28.

**ESI-MS Method:** Electrospray ionization mass spectra were recorded with a Q-TOF 2 mass spectrometer (Micromass, Manchester, UK). Some of a ethanolic metallacrown solution, prepared with 1 mmol of the copper(II) and mandelohydroxamic acid and 0.2 mmol of the central metal ion, was injected in the apparatus at a flow rate of 5 μL/min.

**Proton NMR:** Proton nuclear magnetic resonance spectra were recorded in deuterated methanol solutions with a Bruker Avance 300 spectrometer operating at 300 MHz. A 500 μL solution of [$D_4$]MeOH containing equimolar amounts of $Cu(OAc)_2$ and (*R*)-(–)-mandelohydroxamic acid (0.1 M) was added 1.0 equiv. of $Nd(NO_3)_3$. This was achieved by adding 60 μL of a neodymium(III) nitrate [$D_4$]MeOH solution (0.166 M).

## Acknowledgments

T. N. P.-V. and K. B. thank the K. U. Leuven (VIS/01/006.01/20002-06/2004 and GOA 03/03) and the F. W. O. Flanders (Belgium) (project G.01117.03) for financial support. T. N. P.-V. acknowledges the F. W. O. Flanders for a Postdoctoral Fellowship. Financial support by the IWT-Vlaanderen to A. P. is gratefully acknowledged. The authors thank Prof. Thierry Verbiest (K. U. Leuven) for access to his CD spectrometer. ESI-MS spectra were recorded by Ms. Leen Van Nerum. CHN analyses were performed by Ms. Petra Bloemen.

[1] K. Kehl (Ed.), *Chemistry and Biology of Hydroxamic Acids*, Karger, New York, **1982**.
[2] K. N. Raymond, *Coord. Chem. Rev.* **1990**, *105*, 135–153.
[3] S. S. C. Tam, D. H. S. Lee, E. Y. Wang, D. G. Munroe, C. Y. Lau, *J. Biol. Chem.* **1995**, *270*, 13948–13955.
[4] M. Arnold, D. A. Brown, O. Degg, W. Errington, W. Haase, K. Herlihy, T. J. Kemp, H. Nimir, R. Werner, *Inorg. Chem.* **1998**, *37*, 2920–2925.
[5] I. Botos, L. Scapozza, D. Zhang, L. A. Liotta, E. F. Meyer, *Proc. Natl. Acad. Sci. USA* **1996**, *93*, 2749–2754.
[6] R. Zamora, A. Grzesiok, H. Weber, M. Feelisch, *Biochem. J.* **1995**, *312*, 333–339.
[7] M. J. Miller, *Chem. Rev.* **1989**, *89*, 1563–1579, and references therein.
[8] C. J. Marmion, D. Griffith, K. B. Nolan, *Eur. J. Inorg. Chem.* **2004**, 3003–3016.
[9] B. Kurzak, H. Kozlowski, E. Farkas, *Coord. Chem. Rev.* **1992**, *114*, 169–200.
[10] B. Chatterjee, *Coord. Chem. Rev.* **1978**, *26*, 281–303.
[11] B. Kurzak, E. Farkas, T. Glowiak, H. Kozlowski, *J. Chem. Soc., Dalton Trans.* **1991**, 163–167.
[12] M. Careri, F. Dallavalle, M. Tegoni, I. Zagoni, *J. Inorg. Biochem.* **2003**, *93*, 174–180.
[13] J. A. Halfen, J. J. Bodwin, V. L. Pecoraro, *Inorg. Chem.* **1998**, *37*, 5416–5417.
[14] B. R. Gibney, D. P. Kessissoglou, J. W. Kampf, V. L. Pecoraro, *Inorg. Chem.* **1994**, *33*, 4840–4849.
[15] M. S. Lah, V. L. Pecoraro, *Inorg. Chem.* **1991**, *30*, 878–880.
[16] M. S. Lah, M. L. Kirk, W. Hatfield, V. L. Pecoraro, *J. Chem. Soc., Chem. Commun.* **1989**, 1606–1608.
[17] M. S. Lah, V. L. Pecoraro, *J. Am. Chem. Soc.* **1989**, *111*, 7258–7259.
[18] V. L. Pecoraro, *Inorg. Chim. Acta* **1989**,*155*, 171–173.
[19] M. S. Lah, B. R. Gibney, D. L. Tierney, J. E. Penner-Hahn, V. L. Pecoraro, *J. Am. Chem. Soc.* **1993**, *115*, 5857–5858.
[20] B. R. Gibney, A. J. Stemmler, S. Pilotek, J. W. Kampf, V. L. Pecoraro, *Inorg. Chem.* **1993**, *32*, 6008–6015.
[21] V. L. Pecoraro, A. J. Stemmler, B. R. Gibney, J. J. Bodwin, H. Wang, J. W. Kampf, A. Barwinski, *Prog. Inorg. Chem.* **1997**, *45*, 83–177.
[22] A. J. Stemmler, A. Barwinski, M. J. Baldwin, V. Young, V. L. Pecoraro, *J. Am. Chem. Soc.* **1996**, *118*, 11962–11963.
[23] A. J. Stemmler, J. W. Kampf, V. L. Pecoraro, *Angew. Chem. Int. Ed. Engl.* **1996**, *35*, 2841–2843.
[24] A. J. Stemmler, J. W. Kampf, M. L. Kirk, B. H. Atasi, V. L. Pecoraro, *Inorg. Chem.* **1999**, *38*, 2807–2817.
[25] A. D. Cutland, R. G. Malkani, J. W. Kampf, V. L. Pecoraro, *Angew. Chem. Int. Ed.* **2000**, *39*, 2689–2691.
[26] J. J. Bodwin, A. D. Cutland, R. G. Malkani, V. L. Pecoraro, *Coord. Chem. Rev.* **2001**, *216*, 489–512.
[27] A. D. Cutland-Van Noord, J. W. Kampf, V. L. Pecoraro, *Angew. Chem. Int. Ed.* **2002**, *41*, 4667–4670.
[28] A. J. Stemmler, V. L. Pecoraro, *Inorg. Synth.* **2002**, *33*, 67–70.
[29] T. N. Parac-Vogt, A. Pacco, C. Görller-Walrand, K. Binnemans, *J. Inorg. Biochem.* **2005**, *99*, 497–504.
[30] F. Salinas, J. L. Martinez-Vidal, A. R. Fernandez-Alba, *Ann. Quim.* **1989**, *86*, 266–270.
[31] F. Salinas, *Thermochim. Acta* **1988**, *127*, 285–293.
[32] F. Salinas, *Bull. Soc. Chim. Belg.* **1989**, *98*, 371–373.
[33] E. Farkas, E. A. Enyedy, H. A. Csoka, *Polyhedron* **1999**, *18*, 2391–2398.
[34] E. Farkas, E. Kozma, T. Kiss, I. Tóth, B. Kurzak, *J. Chem. Soc., Dalton Trans.* **1995**, 477–481.
[35] É. A. Enyedy, I. Pósci, E. Ferkas, *J. Inorg. Biochem.* **2004**, *98*, 1957–1966.
[36] A. Pacco, T. N. Parac-Vogt, E. van Besien, K. Pierloot, C. Görller-Walrand, K. Binnemans, *Eur. J. Inorg. Chem.* **2005**, 3303–3310.
[37] T. N. Parac-Vogt, A. Pacco, P. Nockemann, S. Laurent, L. Van der Elst, R. N. Muller, M. Wickleder, G. Meyer, K. Binnemans, *Chem. Eur. J.* **2006**, *11*, 204–210.
[38] For examples of ESI analysis of oligonuclear metal complexes see: a) A. Marquis-Rigault, A. Dupont-Gervais, P. N. W. Baxter, A. Van Dorsselaer, J.-M. Lehn, *Inorg. Chem.* **1996**, *35*, 2307–2310; b) S. Blanc, P. Yakirevitch, E. Leize, M. Meyer, J.

 © 2006 Wiley-VCH Verlag GmbH & Co. KGaA, Weinheim 

Libman, A. van Dorsselaer, A.-M. Albrecht-Gary, A. Shanzer, *J. Am. Chem. Soc.* **1997**, *119*, 4934–4944.
[39] D. L. Caulder, M. C. Bruckner, R. E. Powers, C. Konig, T. N. Parac, J. A. Leary, K. N. Raymond, *J. Am. Chem. Soc.* **2001**, *123*, 8923–8938.
[40] F. Dallavalle, M. Tegoni, *Polyhedron* **2001**, *20*, 2697–2704.
[41] E. Galdecka, Z. Galdecki, P. Gawryszewska, J. Legendziewicz, *New J. Chem.* **1998**, *22*, 941–945.
[42] I. Bertini, C. Luchinat, S. Aime, *Coord. Chem. Rev.* **1996**, *150*, 131–161.
[43] I. Bertini, C. Luchinat. *Physical Methods for Chemists*, 2nd ed.; Saunders College Publishing: Philadelphia, PA, **1992**; p. 500.
Received: November 15, 2005
Published Online: February 9, 2006

 © 2006 Wiley-VCH Verlag GmbH & Co. KGaA, Weinheim 

DOI: 10.1002/ejic.200501018

# Hypercoordinated Organotin(IV) Halides Containing 2-($Me_2NCH_2$)$C_6H_4$ Groups: {2-($Me_2NCH_2$)$C_6H_4$}$_2SnX_2$ (X = F, Cl, Br, I) and {2-($Me_2NCH_2$)-$C_6H_4$}$R_2SnX$ (R = Me, Ph; X = F, Cl, Br, I) and Their Solution Behaviour and Solid-State, Hydrogen-Bonding-Based Supramolecular Architecture

**Richard A. Varga,[a] Adina Rotar,[a] Markus Schürmann,[b] Klaus Jurkschat,[b] and Cristian Silvestru*[a]**

**Keywords:** Halides / Hydrogen bonding / Hypercoordination / Supramolecular chemistry / Tin

The hypercoordinated di- and triorganotin(IV) chlorides [{2-($Me_2NCH_2$)$C_6H_4$}$_2SnCl_2$] (**1a**) and [{2-($Me_2NCH_2$)$C_6H_4$}-$R_2SnCl$] [R = Me (**2a**), Ph (**3a**)] were prepared by treating $SnCl_4$ or $R_2SnCl_2$ with [Li{2-($Me_2NCH_2$)$C_6H_4$}]. Halide-exchange reactions between the organotin(IV) chlorides and the appropriate potassium halides gave [{2-($Me_2NCH_2$)-$C_6H_4$}$_2SnX_2$] [X = F (**1b**), I (**1d**)], [{2-($Me_2NCH_2$)$C_6H_4$}-$Me_2SnX$] [X = F (**2b**), Br (**2c**), I (**2d**)] and [{2-($Me_2NCH_2$)-$C_6H_4$}$Ph_2SnX$] [X = F (**3b**), I (**3d**)]. Their solution behaviour was investigated by multinuclear ($^1H$, $^{13}C$, $^{19}F$ and $^{119}Sn$) NMR spectroscopy, including variable-temperature studies. Single-crystal X-ray diffraction analyses revealed that the strong intramolecular coordination of the nitrogen atom from the pendant $CH_2NMe_2$ group to tin induces chirality. The influence of the identity and the number of the halogen atoms and the organic substituents at tin is discussed in relation with the hydrogen-bonding network, which results in different supramolecular architectures in the crystal.
(© Wiley-VCH Verlag GmbH & Co. KGaA, 69451 Weinheim, Germany, 2006)

## Introduction

Several organotin(IV) halides containing the [2-($Me_2NCH_2$)$C_6H_4$] group or related organic ligands have been investigated so far both in solution and the solid state. Single crystal X-ray diffraction studies have revealed, in all cases, hypercoordinated structures obtained as a result of strong intramolecular N→Sn interactions.[1–27] On the basis of NMR spectroscopic data, octahedrally and trigonal bipyramidally configured tin atoms were suggested in solution for the intramolecularly coordinated diorganotin dihalides [{2-($Me_2NCH_2$)$C_6H_4$}$_2SnX_2$] and triorganotin halides [{2-($Me_2NCH_2$)$C_6H_4$}$R_2SnX$] (X = halogen), respectively. Single-crystal X-ray diffraction studies have confirmed the hypercoordinated nature of [{2-($Me_2NCH_2$)$C_6H_4$}-$Me_2SnCl$] (**2a**)[17] and [{2-($Me_2NCH_2$)$C_6H_4$}$Ph_2SnX$] [X = Cl (**3a′**),[20] Br (**3c**)[3]), but no crystallographic data are available for the diorganotin(IV) derivatives [{2-($Me_2$-$NCH_2$)$C_6H_4$}$_2SnX_2$], and no studies on the influence of the identity and number of halogen atoms and organic substituents on the association through hydrogen bonds in the solid state have been reported. On the other hand, it has been shown previously that intramolecular coordination of the nitrogen atom to a metal atom in compounds containing a [2-($Me_2NCH_2$)$C_6H_4$]M moiety induces chirality at the metal centre,[27–31] and therefore the crystals usually contain 1:1 mixtures of (*R*) and (*S*) isomers [with the C(1)–C(6) aromatic ring and the N(1) atom as chiral plane and pilot atom, respectively].[32] While this work was in progress the molecular structures of the fluorides [{2-($Me_2NCH_2$)-$C_6H_4$}$R_2SnF$] [R = Me (**2b′**), Ph (**3b′**)], which crystallise in different space groups,[26] were reported, but no details concerning the planar chirality induced by the intramolecular N→Sn interaction and the hydrogen-bond network in the crystal were mentioned.

Here we report the synthesis and spectroscopic characterisation of some organotin(IV) halides, as well as the crystal and molecular structures of [{2-($Me_2NCH_2$)-$C_6H_4$}$_2SnX_2$] [X = Cl (**1a**), F (**1b**), I (**1d**)], [{2-($Me_2NCH_2$)-$C_6H_4$}$Me_2SnX$] [X = Cl (**2a**), F (**2b**), Br (**2c**), I (**2d**)] and [{2-($Me_2NCH_2$)$C_6H_4$}$Ph_2SnX$] [X = F (**3b**), I (**3d**)]. The discussion of the solid-state structure is focused on the hydrogen-bonding-based network between the isomers, which results in different supramolecular architectures in the crystal.

[a] Facultatea de Chimie si Inginerie Chimica, Universitatea Babes-Bolyai,
Str. Arany Janos Nr. 11, 400028 Cluj-Napoca, Romania,
Fax: +40-264-590-818
E-mail: cristi@chem.ubbcluj.ro
[b] Lehrstuhl für Anorganische Chemie II der Universität Dortmund,
44227 Dortmund, Germany,
Fax: +49-231-755-5048
E-mail: klaus.jurkschat@uni-dortmund.de
Supporting information for this article is available on the WWW under http://www.eurjic.org or from the author.

 © 2006 Wiley-VCH Verlag GmbH & Co. KGaA, Weinheim 

## Results and Discussion

The diorganotin(IV) dihalides were prepared according to Scheme 1. The ligand-redistribution reaction between [{2-($Me_2NCH_2$)$C_6H_4$}$_4$Sn] and $SnCl_4$ in the absence of a solvent has proved to be an excellent alternative to the direct synthesis from [Li{2-($Me_2NCH_2$)$C_6H_4$}] and $SnCl_4$ for the preparation of **1a** as it allows a better control of the stoichiometry of the reagents. The halide-exchange reactions between the organotin(IV) chlorides and the appropriate potassium halides (Schemes 1 and 2) were performed according to a modified literature procedure[33] in a two-layer solvent system ($H_2O$/MeOH/$CH_2Cl_2$).

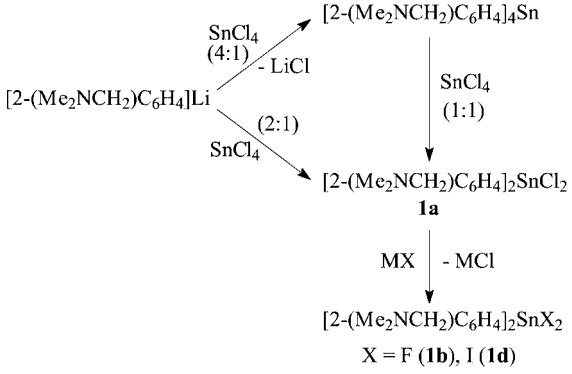


Scheme 1. Synthesis of compounds **1a**–**1d**.

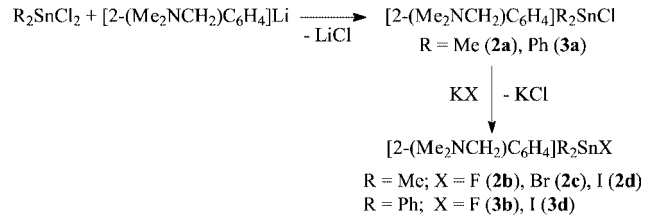


Scheme 2. Synthesis of compounds **2a**–**2d**, **3a**, **3b** and **3d**.

All compounds were isolated as air-stable, colourless, crystalline products. They are soluble in common organic solvents, such as chloroform, methylene dichloride or benzene.

### Solution Behaviour

All compounds were investigated by multinuclear ($^1$H, $^{13}$C, $^{119}$Sn) NMR spectroscopy in solution at room temperature. For the organotin fluorides, the $^{19}$F NMR spectra were also recorded.

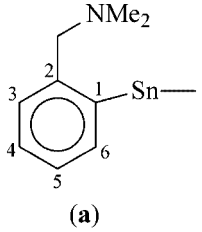


**(a)**

The assignments of the $^1$H and $^{13}$C resonances according to the numbering scheme above were based on 2D experiments and tin–carbon coupling constants, and were confirmed for several compounds by simulation of the aromatic region of the $^1$H NMR spectra using the gNMR program (see Supporting Information).

The low-temperature $^1$H NMR spectra of the diorganotin derivatives [{2-($Me_2NCH_2$)$C_6H_4$}$_2$$SnX_2$] [X = Cl (**1a**), F (**1b**) and I (**1d**)] are very similar (see Supporting Information) to that reported for the dibromide analogue **1c**,[6] i.e. an AB system and two singlet resonances in the aliphatic region for the diastereotopic $CH_2$ protons and the $CH_3$ groups at nitrogen, respectively. This is consistent with a *trans* arrangement of the organic ligands and a *cis* arrangement of the two coordinated nitrogen atoms and halogen atoms in solution,[6] as subsequently proved by single-crystal X-ray diffraction for compounds **1a**, **1b** and **1d** (see below). When the temperature is raised, the diorganotin dichloride **1a** and the diorganotin diiodide **1d** exhibit a similar behaviour to the diorganotin dibromide **1c**.[6,22] The two singlets for the methyl protons of the $NMe_2$ group coalesce at 20 °C for **1a** ($\Delta G^{\ddagger}$ = 13.8 kcal mol$^{-1}$) and 0 °C for **1d** ($\Delta G^{\ddagger}$ = 12.6 kcal mol$^{-1}$) in $CDCl_3$. This coalescence indicates that the process involving N→Sn dissociation/recoordination, with inversion at a three-coordinate nitrogen atom and rotation of the $C_{methylene}$–N bond, becomes fast on the NMR timescale. The AB pattern for the methylene protons is retained even at 60 °C, thus indicating configurational stability of the tin atom in the [{2-($Me_2NCH_2$)$C_6H_4$}$_2$$SnX_2$] derivatives containing heavier halogens. In contrast, coalescence of both the two resonances of the $NMe_2$ group ($\Delta G^{\ddagger}$ = 14.2 kcal mol$^{-1}$) and the AB pattern of the $CH_2$ group ($\Delta G^{\ddagger}$ = 14.3 kcal mol$^{-1}$) is observed at 10 °C for the diorganotin difluoride **1b** in $CDCl_3$. This suggests that exchange of the chloride by fluoride results in a considerable decrease of the configurational stability of the tin atom in **1b** compared to **1a**. There is no indication for a *cis–trans* equilibrium in solution such as that observed for [{$Me_2N(CH_2)_3$}$_2$$SnF_2$]·2$H_2O$.[34]

The magnitudes of the $^{119}$Sn chemical shifts for the diorganotin halides **1a** (s, $\delta$ = –260.7 ppm), **1b** (t, $\delta$ = –386.7 ppm) and **1d** ($\delta$ = –346.9 ppm) at room temperature are typical for six-coordinate diorganotin(IV) species in solution [cf. [{$Me_2N(CH_2)_3$}$_2$$SnF_2$]·2$H_2O$[34] ($\delta$ = –292.0 ppm in $CD_2Cl_2$) and [(8-$Me_2NC_{10}H_6$)$_2$$SnI_2$][11] ($\delta$ = –361.9 ppm in $C_6D_5CD_3$)]. The equivalence of the fluoride atoms in **1b** is reflected in a singlet $^{19}$F resonance surrounded by tin satellites ($\delta$ = –181.5 ppm, $^1J_{F,Sn}$ = 2567/2683 Hz) and a triplet $^{119}$Sn resonance ($\delta$ = –386.7 ppm, $^1J_{F,Sn}$ = 2663 Hz).

The $^1$H and $^{13}$C NMR spectra for the triorganotin halides [{2-($Me_2NCH_2$)$C_6H_4$}$Me_2$SnX] [X = Cl (**2a**), F (**2b**), Br (**2c**), I (**2d**)] and [{2-($Me_2NCH_2$)$C_6H_4$}$Ph_2$SnX] [X = F (**3b**), I (**3d**)] are very similar to those of benzyldimethylamine, regardless of the nature of the halogen and the other organic groups attached to tin. Two singlet resonances are observed in the aliphatic region for the methylene and the methyl protons, respectively, which is compatible either with a tetrahedral or with a pentacoordinate structure (assuming a fast conformational change of the five-membered $SnC_3N$ nonplanar chelate ring in solution, which gives averaged $^1$H NMR signals). The $^{13}$C NMR spectrum contains two sing-

 © 2006 Wiley-VCH Verlag GmbH & Co. KGaA, Weinheim 

Table 1. Comparison of the solution NMR spectroscopic data for triorganotin(IV) compounds ($\delta$ in ppm, $J$ in Hz).[a]

| Compound | $^{119}$Sn | $^{19}$F |
|---|---|---|
| [{2-($Me_2NCH_2$)$C_6H_4$}$_2$$SnF_2$] (**1b**) | –386.7 (t)[b] | –181.5 (s) |
| | ($^1J_{F,Sn}$ = 2663) | ($^1J_{F,Sn}$ = 2567/2683) |
| [{2-($Me_2NCH_2$)$C_6H_4$}$_2$$SnCl_2$] (**1a**) | –260.7 (s)[b] | |
| [$Ph_2SnCl_2$][35] | –26.7 (s) | |
| [{2-($Me_2NCH_2$)$C_6H_4$}$_2$$SnI_2$] (**1d**) | –346.9 (s) | |
| [$Ph_2SnI_2$][35] | –241.1 (s) | |
| [{2-($Me_2NCH_2$)$C_6H_4$}$Me_2SnF$] (**2b**)[c] | –52.7 (d) | –178.4 (s) |
| | ($^1J_{F,Sn}$ = 2039.3) | ($^1J_{F,Sn}$ = 1944.2/2034.6) |
| [$Me_2PhSnF$][33] | –52.3 (t) | –137.4 (s) |
| | ($^1J_{F,Sn}$ = 1340) | ($^1J_{F,Sn}$ = 1255) |
| | –53.0 (t, br)[d] | –139.0 (s)[d] |
| | ($^1J_{F,Sn}$ = 1334) | ($^1J_{F,Sn}$ = 1260) |
| | –49.5 (t)[e] | |
| | ($^1J_{F,Sn}$ = 1235) | |
| [{2-($Me_2NCH_2$)$C_6H_4$}$Me_2SnCl$] (**2a**) | –48.7 (s)[b] | |
| [$Me_2PhSnCl$][36] | 48.3 (s) | |
| [{2-($Me_2NCH_2$)$C_6H_4$}$Me_2SnBr$] (**2c**) | –55.5 (s) | |
| [{2-($Me_2NCH_2$)$C_6H_4$}$Me_2SnI$] (**2d**) | –72.8 (s) | |
| [$Me_2PhSnI$][37] | –17.9 (s) | |
| [{2-($Me_2NCH_2$)$C_6H_4$}$Ph_2SnF$] (**3b**)[f] | –197.6 (d) | –182.4 (s) |
| | ($^1J_{F,Sn}$ = 2157) | ($^1J_{F,Sn}$ = 2058.3/2154.0) |
| [$Ph_3SnF$][38] | –211.9 (t)[e] | |
| | ($^1J_{F,Sn}$ = 1530) | |
| [{2-($Me_2NCH_2$)$C_6H_4$}$Ph_2SnCl$] (**3a**)[20] | –176.9 (s) | |
| [$Ph_3SnCl$][39] | –44.8 (s) | |
| [{2-($Me_2NCH_2$)$C_6H_4$}$Ph_2SnI$] (**3d**) | –199.5 (s) | |
| [$Ph_3SnI$][39] | –113.4 (s) | |

[a] Spectra recorded in $CDCl_3$ at room temperature. [b] In $CH_2Cl_2$/[D$_6$]acetone. [c] Ref.[26]: $\delta_{^{119}Sn}$ = –53.8 ppm ($^1J_{F,Sn}$ = 2023 Hz), $\delta_{^{19}F}$ = –178.8 ppm. [d] In $C_6D_5CD_3$. [e] $^{119}$Sn MAS NMR spectroscopic data. [f] Ref.[26]: $\delta_{^{119}Sn}$ = –198.6 ppm ($^1J_{F,Sn}$ = 2141 Hz), $\delta_{^{19}F}$ = –182.3 ppm.

let signals for the methylene and the methyl carbon atoms, respectively, but the tin satellites are well resolved only for the former; the magnitude of the $^2J_{C,Sn}$ (ca. 28–30 Hz) couplings is consistent with the presence of an intramolecular N→Sn coordination, i.e. a trigonal bipyramidal (*C*,*N*)-$C_2SnX$ core. The major difference noted in the $^1$H NMR spectra of the two series of compounds is the downfield shift of the resonance for the aromatic H-6 proton, which is a result of the intramolecular interaction of this proton with the halogen atom.

The increase in the H-6 chemical shift follows the order F < Cl < Br < I ($\delta$ = 7.97, 8.17, 8.26 and 8.31 ppm for the triaryltin halides **2b**, **2a**, **2c** and **2d**, respectively). In addition to the resonances assigned to the 2-($Me_2NCH_2$)$C_6H_4$ ligand, the $^1$H and $^{13}$C NMR spectra for the [{2-($Me_2NCH_2$)-$C_6H_4$}$R_2SnX$] derivatives also contain signals corresponding to equivalent methyl and phenyl groups, respectively.

A comparison of the $^{19}$F and $^{119}$Sn NMR parameters for the diorganotin dihalides [{2-($Me_2NCH_2$)$C_6H_4$}$_2$$SnX_2$] and the triorganotin halides [{2-($Me_2NCH_2$)$C_6H_4$}$R_2SnX$] described in this work and the related [$Ph_2SnX_2$], [$Me_2PhSnX$] and [$Ph_3SnX$] derivatives is given in Table 1. The increase of the coordination number at the metal atom in solution to six and five, respectively, is supported by the upfield shift of the $^{119}$Sn chemical shift in the 2-($Me_2NCH_2$)$C_6H_4$-containing derivatives (X = Cl, Br, I) with respect to the corresponding monomeric, tetrahedral [$Ph_2SnX_2$], [$Me_2PhSnX$] and [$Ph_3SnX$] compounds.

In conclusion, the NMR spectroscopic data indicate that both [{2-($Me_2NCH_2$)$C_6H_4$}$_2$$SnX_2$] and [{2-($Me_2NCH_2$)-$C_6H_4$}$R_2SnX$] compounds exhibit intramolecular N→Sn coordination in solution, which results in similar coordination geometries to those found in the solid state (see below).

## Solid-State Structures

The crystal and molecular structures of **1a**, **1b**, **1b**·$CH_2Cl_2$, **1d**, **2a**, **2a′**, **2b**–**2d**, **3a**, **3b** and **3d** were determined by single-crystal X-ray diffraction. Crystals suitable for X-ray diffraction analysis were generally grown by solvent diffusion from dichloromethane and *n*-hexane. Crystals of the dichloromethane solvate of the diorganotin difluoride [{2-($Me_2NCH_2$)$C_6H_4$}$_2$$SnF_2$], namely **1b**·$CH_2Cl_2$, were obtained from a $CH_2Cl_2$/*n*-hexane (approximately 1:3) mixture, and were measured immediately after removal from solution. The crystal was stable enough for a sufficiently good measurement, but they turned opaque within two days in the air due to loss of the crystallisation solvent, as proved by $^1$H NMR spectroscopy. Crystals of [{2-($Me_2NCH_2$)$C_6H_4$}$_2$$SnF_2$] (**1b**), free of crystallisation solvent, were also obtained by slow crystallisation from a $CH_2Cl_2$/*n*-hexane (approximately 1:5) mixture. The triorganotin chloride [{2-($Me_2NCH_2$)$C_6H_4$}$Me_2SnCl$] crystallises in different forms from ethanol (**2a**; orthorhombic, space group *Pbca*) and *n*-hexane (**2a′**; orthorhombic, space group $Pna2_1$. This form has also been reported by Rippstein et al.[17] for crystals grown from $CHCl_3$). Monoclinic crystals (space group $P2_1/n$) with different unit-cell parameters were obtained for [{2-($Me_2NCH_2$)$C_6H_4$}-$Ph_2SnCl$] when the compound was crystallised from tolu-

 © 2006 Wiley-VCH Verlag GmbH & Co. KGaA, Weinheim 

ene[20] or $CH_2Cl_2$/*n*-hexane (**3a**); the first form contains one molecule in the unit cell[20] while the second one contains two independent molecules. The crystals of [{2-($Me_2NCH_2$)-$C_6H_4$}$Ph_2SnF$] (**3b**; monoclinic, space group $P2_1/n$, which is different from the reported space group $P2_1/c$[26]) also contain two independent molecules in the unit cell.

Selected molecular parameters are given in Tables 2, 3 and 4, and the molecular structures of representative compounds **1b** and **3d**, with the atom numbering schemes, are shown in Figures 1 and 2, respectively. The molecules of all compounds investigated in this work feature a metal atom strongly coordinated by two or one nitrogen atoms of the pendant arms *trans* to an Sn–halogen bond in diorganotin(IV) and triorganotin(IV) halides, respectively [the Sn–N distance exceeds the sum of the covalent radii for the corresponding atoms, $\Sigma_{cov}$(Sn,N) = 2.1 Å[40]]. This results in different coordination environments of the metal atom, i.e. octahedral $(C,N)_2SnX_2$ for **1a**, **1b** and **1d**, and trigonal bipyramidal $(C,N)C_2SnX$ configurations for **2a**–**2d**, **3b** and **3d**.

The $(C,N)_2SnX_2$ core in the [{2-($Me_2NCH_2$)-$C_6H_4$}$_2SnX_2$] derivatives shows a *trans*-$SnC_2$ fragment, while the N and X atoms are *cis* (Figure 1). This contrasts with the molecular structure reported for the related [{$Me_2N(CH_2)_3$}$_2SnF_2$]·$2H_2O$,[34] which exhibits an all-*trans* octahedral $(C,N)_2SnX_2$ configuration. The difference in the configuration of the octahedral environment of tin is reflected in the lengthening and shortening of the Sn–F and Sn–N bond lengths, respectively, in **2b** [Sn(1)–F(1) = 1.9726(14), Sn(1)–F(2) = 1.9774(13), Sn(1)–N(1) = 2.5083(19) and Sn(1)–N(2) = 2.6064(18) Å] in comparison

Table 2. Selected bond lengths [Å] and angles [°] for [{2-($Me_2NCH_2$)$C_6H_4$}$_2SnX_2$] compounds.

| | **1a**[a] (X = Cl) | **1b** (X = F) | **1b**·$CH_2Cl_2$ (X = F) | **1d** (X = I) |
|---|---|---|---|---|
| Sn(1)–C(1) | 2.1278(17) | 2.119(2) | 2.109(6) | 2.142(6) |
| Sn(1)–C(10) | | 2.113(2) | 2.130(5) | 2.128(5) |
| Sn(1)–X(1) | 2.4394(5) | 1.9726(14) | 1.988(3) | 2.8371(7) |
| Sn(1)–X(2) | | 1.9774(13) | 1.988(3) | 2.8315(7) |
| Sn(1)–N(1) | 2.6199(16) | 2.5083(19) | 2.601(5) | 2.572(5) |
| Sn(1)–N(2) | | 2.6064(18) | 2.469(5) | 2.677(6) |
| C(1)–Sn(1)–C(10) | 152.22(9) | 154.86(8) | 154.8(2) | 156.3(2) |
| X(1)–Sn(1)–N(1) | 166.25(4) | 166.79(6) | 168.00(16) | 170.95(14) |
| X(2)–Sn(1)–N(2) | | 167.53(6) | 166.83(16) | 170.62(12) |
| C(1)–Sn(1)–N(1) | 73.77(6) | 74.99(7) | 73.7(2) | 74.3(2) |
| C(10)–Sn(1)–N(2) | | 73.54(7) | 75.26(19) | 73.1(2) |
| N(1)–Sn(1)–N(2) | 108.54(7) | 103.86(6) | 105.40(17) | 102.39(18) |
| X(1)–Sn(1)–X(2) | 89.79(3) | 89.87(7) | 88.30(18) | 89.55(2) |

[a] C(10) = C(1a), X(2) = X(1a), N(2) = N(1a); symmetry equivalent positions (–*x*, *y*, –*z* + 1/2) are indicated by an "a".

Table 3. Selected bond lengths [Å] and angles [°] for [{2-($Me_2NCH_2$)$C_6H_4$}$Me_2SnX$] compounds.

| | **2a**[a] (X = Cl) | **2a′**[b] (X = Cl) | **2b** (X = F) | **2c** (X = Br) | **2d** (X = I) |
|---|---|---|---|---|---|
| Sn(1)–C(1) | 2.129(3) | 2.127(4) | 2.123(3) | 2.132(3) | 2.135(4) |
| Sn(1)–C(10) | 2.124(4) | 2.144(5) | 2.118(3) | 2.110(4) | 2.120(4) |
| Sn(1)–C(11) | 2.115(4) | 2.121(4) | 2.120(3) | 2.106(4) | 2.133(5) |
| Sn(1)–X(1) | 2.5250(16) | 2.5371(9) | 2.0187(17) | 2.6839(5) | 2.9367(5) |
| Sn(1)–N(1) | 2.485(3) | 2.488(3) | 2.509(2) | 2.445(3) | 2.442(4) |
| X(1)–Sn(1)–N(1) | 168.11(7) | 170.79(8) | 167.45(9) | 168.62(7) | 170.45(9) |
| C(1)–Sn(1)–N(1) | 74.17(11) | 75.55(13) | 74.08(11) | 74.76(12) | 75.99(15) |
| C(1)–Sn(1)–C(10) | 123.73(14) | 119.92(16) | 118.91(13) | 124.67(16) | 129.5(2) |
| C(1)–Sn(1)–C(11) | 116.94(15) | 116.13(18) | 123.55(13) | 116.02(17) | 111.66(18) |
| C(10)–Sn(1)–C(11) | 117.71(16) | 122.55(19) | 115.75(15) | 118.17(19) | 117.2(2) |

[a] Crystals from ethanol. [b] Crystals from *n*-hexane.

Table 4. Selected bond lengths [Å] and angles [°] for [{2-($Me_2NCH_2$)$C_6H_4$}$Ph_2SnX$] compounds.

| | **3a**[a,b] (X = Cl) | | **3b**[b] (X = F) | | **3d** (X = I) |
|---|---|---|---|---|---|
| Sn(1)–C(1) | 2.118(4) | 2.134(4) | 2.105(5) | 2.128(5) | 2.135(5) |
| Sn(1)–C(10) | 2.130(4) | 2.126(4) | 2.121(4) | 2.132(5) | 2.132(5) |
| Sn(1)–C(16) | 2.134(4) | 2.132(4) | 2.129(4) | 2.132(4) | 2.135(4) |
| Sn(1)–X(1) | 2.4944(11) | 2.4872(12) | 2.008(3) | 2.006(4) | 2.8631(6) |
| Sn(1)–N(1) | 2.538(4) | 2.509(3) | 2.560(4) | 2.521(4) | 2.496(4) |
| X(1)–Sn(1)–N(1) | 169.73(10) | 168.68(8) | 167.53(14) | 168.34(14) | 171.56(10) |
| C(1)–Sn(1)–N(1) | 75.46(15) | 74.86(14) | 74.74(17) | 74.88(18) | 75.36(18) |
| C(1)–Sn(1)–C(10) | 116.85(16) | 113.58(15) | 117.34(18) | 126.98(19) | 114.09(19) |
| C(1)–Sn(1)–C(16) | 124.23(15) | 126.56(16) | 122.80(17) | 112.10(17) | 122.55(17) |
| C(10)–Sn(1)–C(16) | 116.28(16) | 117.42(17) | 117.61(18) | 118.45(18) | 121.29(19) |

[a] Crystals from $CH_2Cl_2$/*n*-hexane. [b] Two independent molecules are present in the unit cell.

 © 2006 Wiley-VCH Verlag GmbH & Co. KGaA, Weinheim 

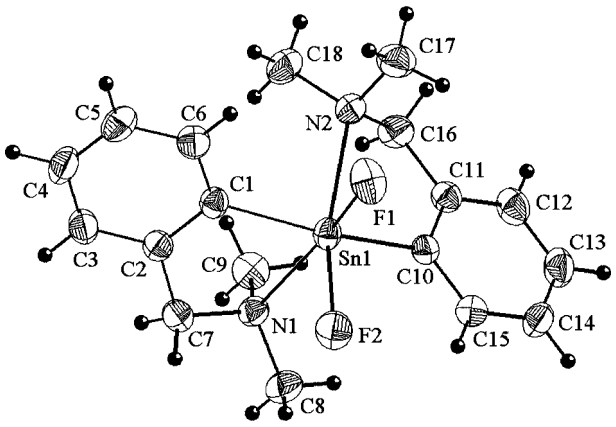


Figure 1. ORTEP representation at 50% probability and atom-numbering scheme for the isomer ($R_{N1}$,$S_{N2}$)-**1b**.

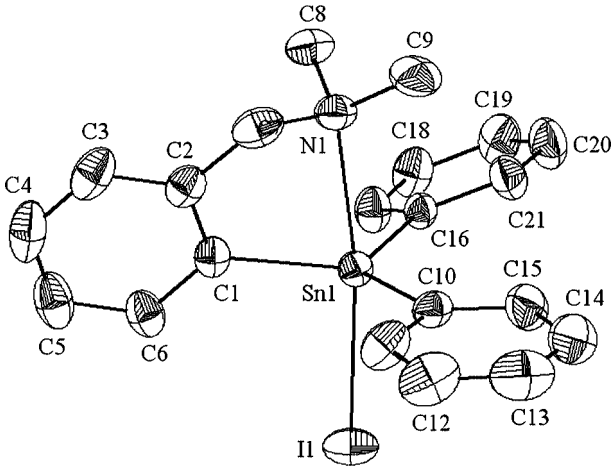


Figure 2. ORTEP representation at 30% probability and atom-numbering scheme for the isomer (*S*)-**3d**. Hydrogens have been omitted for clarity.

with [{$Me_2N(CH_2)_3$}$_2$$SnF_2$]·$2H_2O$ [Sn(1)–F(1) = 2.084(6) and Sn(1)–N(1) = 2.366(8) Å].[34]

The molecular structures of the triorganotin halides [{2-($Me_2NCH_2$)$C_6H_4$}$R_2$SnX] (**2a**–**2d**, **3b** and **3d**) are very similar. One representative is shown in Figure 2. The tin–nitrogen distances are not dramatically affected by the identity of the halogen atom *trans* to the nitrogen atom. The Sn(1) atom is displaced from the equatorial plane defined by C(1), C(10) and C(16) (Figure 2) in the direction of the X(1) atom, which means that the X–Sn–C angles are larger than the N–Sn–C angles.

As a result of the intramolecular coordination of the nitrogen to the tin atom a five-membered $SnC_3N$ ring is formed. This ring is not planar but is folded along the Sn(1)···$C_{methylene}$ axis, with the nitrogen atom lying above the best plane defined by Sn(1), C(1), C(2) and C(methylene). This induces planar chirality at the metal atom,[27–31] and all compounds reported here crystallise as racemates. The crystals of the triorganotin(IV) derivatives (**2a**, **2a′**, **2b**–**2d**, **3a**, **3a′**, **3b**, **3b′** and **3d**) contain 1:1 mixtures of (*R*) and (*S*) isomers, with the C(1)–C(6) aromatic ring and the N(1) atom as chiral plane and pilot atom, respectively.[32] The crystals of the diorganotin(IV) derivatives contain either ($S_{N1}$,$R_{N2}$) and ($R_{N1}$,$S_{N2}$) isomers (for **1b**) or ($S_{N1}$,$S_{N2}$) and ($R_{N1}$,$R_{N2}$) isomers (for **1a** and **1d**) with respect to the two chelate rings in a molecular unit. The discrete monomeric molecular units are separated by normal van der Waals distances between heavy atoms.

However, a closer check of the crystal structures revealed several intermolecular hydrogen-bonding interactions shorter than the sum of the corresponding van der Waals radii [i.e. $\Sigma_{vdW}$(F,H) ≈ 2.55, $\Sigma_{vdW}$(Cl,H) ≈ 3.0, $\Sigma_{vdW}$(Br,H) ≈ 3.15 and $\Sigma_{vdW}$(I,H) ≈ 3.35 Å].[40] This results in different supramolecular architectures that are presented in the subsequent discussion taking into account the increasing degree of association, with the common patterns summarised in Table 5 (further details are available in the Supporting Information). Thus, in the crystal of the fluoride **3b** (space group $P2_1/n$) pairs of isomers (*S*,*S* or *R*,*R*) of the two independent molecules are associated through F(1)···H(34)$_{aryl}$ contacts (2.50 Å). The short interatomic distance (2.56 Å) between the F(2) atom and a methyl hydrogen of a neighbouring dinuclear unit of the same type is at the limit of a van der Waals contact. The crystal of **3b′** (space group $P2_1/c$[26]) contains polymeric chains of (*S*) and (*R*) isomers, respectively, built through F(1)···H(17Ba)$_{methylene}$ interactions (2.37 Å). Similar polymeric chains of (*S*) and (*R*) isomers, respectively, were also found in the crystals of the triorganotin chlorides **3a**, **3a′**[20] and the triorganotin iodide **3d**. In contrast to the phenyl derivatives, the crystals of the methyl analogues **2a** (space group *Pbca*) and **2b** contains chains of alternating (*S*) and (*R*) isomers. There are no further halogen–hydrogen contacts between the parallel polymeric chains.

For compound **1b**·$CH_2Cl_2$, alternating ($R_{N1}$,$S_{N2}$)- and ($S_{N1}$,$R_{N2}$)-**1b** isomers are connected through F(2)···H-(7Ab)$_{methylene}$ interactions (2.52 Å) and further bridged by $CH_2Cl_2$ molecules [F(1)···H(19A)$_{solvent}$ = 2.37, Cl(2a)···H-(8A)$_{methyl}$ = 2.94 Å], resulting in ribbon-like chains (Figure 3), with no further inter-chain halogen–hydrogen contacts.

Polymeric chains of (*S*) and (*R*) isomers, respectively, built through I(1)···H(7Ba)$_{methylene}$ interactions (3.16 Å), are also found in the crystal of the triorganotin iodide **2d**, but in this case additional I(1)···H(10Ac)$_{Sn–methyl}$ contacts (3.29 Å) between chains of the same isomers result in a 2D supramolecular architecture. The crystal consists of layers alternating in the sequence -*R*-*R*-*S*-*S*-*R*-*R*-*S*-*S*-, with no further inter-layer contacts. The triorganotin chloride **2a′** (space group $Pna2_1$) and the triorganotin bromide **2c** also form polymeric chains, but in this case they are built from alternating (*S*) and (*R*) isomers [Cl(1)···H(8Bb)$_{N–methyl}$ = 2.81 Å for **2a′**; Br(1)···H(9Bb)$_{N–methyl}$ = 3.02 Å for **2c**]. For **2a′**, weak inter-chain contacts [Cl(1)···H(8Cc)$_{N–methyl}$ = 2.98 Å] result in a 2D network with a honeycomb motif (Figure 4, a) in which each molecule is linked to four neighbouring molecules (two isomers of a different type for the polymeric chain and two isomers of the same type for the parallel chains). For **2c**, the weak inter-chain contacts between the halogen and an aromatic hydrogen atom [Br(1)···

 © 2006 Wiley-VCH Verlag GmbH & Co. KGaA, Weinheim 

Table 5. Structural patterns of the hydrogen-bonding-based supramolecular architectures in the crystals of [{2-($Me_2NCH_2$)$C_6H_4$}$_2SnX_2$] and [{2-($Me_2NCH_2$)$C_6H_4$}$R_2SnX$].

| Compound [R = 2-($Me_2NCH_2$)$C_6H_4$] | Supramolecular architecture patterns | X···H [Å] | | |
|---|---|---|---|---|
| 1D architectures | | | | |
| [$RPh_2SnF$] (**3b**) | dinuclear associations between isomers of the same type of two independent molecules; no further intermolecular contacts | intermolecular | F(1)–H(34)$_{aryl}$ | 2.50 |
| [$RPh_2SnF$] (**3b′**)[26] | chains of (*S*) and (*R*) isomers no inter-chain contacts | intra-chain | F(1)–H(17Ba)$_{methylene}$ | 2.37 |
| [$RPh_2SnCl$] (**3a**) | chains of (*S*) and (*R*) isomers | intra-chain | Cl(1)–H(34b)$_{aryl}$ | 2.88 |
| | (with alternating independent molecules 1 and 2); no inter-chain contacts | intra-chain | Cl(2a)–H(9A)$_{methyl}$ | 2.92 |
| [$RPh_2SnCl$] (**3a′**)[20] | chains of (*S*) and (*R*) isomers no inter-chain contacts | intra-chain | Cl(1)–H(20a)$_{aryl}$ | 2.89 |
| [$RPh_2SnI$] (**3d**) | chains of (*S*) and (*R*) isomers no inter-chain contacts | intra-chain | I(1)–H(19a)$_{aryl}$ | 3.11 |
| [$RMe_2SnCl$] (**2a**) | chains of alternating (*S*) and (*R*) isomers; no inter-chain contacts | intra-chain | Cl(1)–H(9Cb)$_{N–methyl}$ | 2.95 |
| [$RMe_2SnF$] (**2b**) | chains of alternating (*S*) and (*R*) isomers; | intra-chain | F(1)–H(10Bb)$_{Sn–methyl}$ | 2.47 |
| | no inter-chain contacts | intra-chain | F(1)–H(9Ab)$_{N–methyl}$ | 2.52 |
| [$R_2SnF_2$]·$CH_2Cl_2$ | ribbon-like chains of alternating | intra-chain | F(2)–H(7Ab)$_{methylene}$ | 2.52 |
| (**1b**·$CH_2Cl_2$) | ($R_{N1}$,$S_{N2}$)- and ($S_{N1}$,$R_{N2}$) isomers, | intra-chain | F(1)–H(19A)$_{solvent}$ | 2.37 |
| | connected through $CH_2Cl_2$ molecules; no inter-chain contacts | intra-chain | Cl(2a)–H(8A)$_{methyl}$ | 2.94 |
| 2D Architectures | | | | |
| [$RMe_2SnI$] (**2d**) | chains of (*S*) and (*R*) isomers | intra-chain | I(1)–H(7Ba)$_{methylene}$ | 3.16 |
| | contacts between parallel chains, resulting in a layer network; | inter-chain | I(1)–H(10Ac)$_{Sn–methyl}$ | 3.29 |
| | no inter-layer contacts | | | |
| [$R_2SnF_2$] (**1b**) | chains of ($R_{N1}$,$S_{N2}$) and ($S_{N1}$,$R_{N2}$) | intra-chain | F(2)–H(12a)$_{aryl}$ | 2.38 |
| | isomers | inter-chain | F(1)–H(7Ad)$_{methylene}$ | 2.47 |
| | contacts between parallel chains, resulting in a layer network; | | | |
| | no inter-layer contacts | | | |
| [$RMe_2SnCl$] (**2a′**) | chain of alternating (*S*) and (*R*) isomers; | intra-chain | Cl(1)–H(8Bb)$_{N–methyl}$ | 2.81 |
| | contacts between parallel chains, resulting in a layer network; | inter-chain | Cl(1)–H(8Cc)$_{N–methyl}$ | 2.98 |
| | no inter-layer contacts | | | |
| [$RMe_2SnBr$] (**2c**) | chain of alternating (*S*) and (*R*) isomers; | intra-chain | Br(1)–H(9Bb)$_{N–methyl}$ | 3.02 |
| | contacts between parallel chains, resulting in a layer network; | inter-chain | Br(1)–H(4d)$_{aryl}$ | 3.15 |
| | no inter-layer contacts | | | |
| 3D architectures | | | | |
| [$R_2SnCl_2$] (**1a**) | alternating layers of ($S_{N1}$,$S_{N2}$) and | intra-layer | Cl(1)–H(4a′)$_{aryl}$ | 2.81 |
| | ($R_{N1}$,$R_{N2}$) isomers, respectively; | inter-layer | Cl(1)–H(6f′)$_{aryl}$ | 2.94 |
| | inter-layer contacts leading to a 3D supramolecular architecture | | | |
| [$R_2SnI_2$] (**1d**) | chain of alternating ($S_{N1}$,$S_{N2}$) and | intra-chain | I(2)–H(9Ca)$_{methyl}$ | 3.15 |
| | ($R_{N1}$,$R_{N2}$) isomers; | inter-chain | I(2)–H(8Ac)$_{methyl}$ | 3.26 |
| | contacts between parallel chains, resulting in a layer network; | inter-layer | I(1)–H(14f)$_{aryl}$ | 3.32 |
| | inter-layer contacts leading to a 3D supramolecular architecture | | | |

H(4d)$_{aryl}$ = 3.15 Å, at the limit of a van der Waals contact] lead to a different two-dimensional motif, with rings built from two molecules [(*R*)- and (*S*)-**2c** isomers] and four molecules [(*R*)-(*R*)-(*S*)-(*S*)-**2c** isomers], respectively (Figure 4, b). In both cases there are no further contacts between the parallel layers.

In contrast to **1b**·$CH_2Cl_2$, the crystal structure of the diorganotin difluoride **1b** consists of layers in which alternating polymeric chains of ($R_{N1}$,$S_{N2}$)- and ($S_{N1}$,$R_{N2}$)-**1b** isomers [F(2)–H(12a)$_{aryl}$ = 2.38 Å] are connected through F(1)–H(7Ad)$_{methylene}$ (2.47 Å) interactions. The overall layer network resembles that observed in the crystal of the triorganotin iodide **2d**, with both fluorine atoms being involved in weak hydrogen-bonding interactions.

Three-dimensional supramolecular architectures (Table 5) were found for the diorganotin dihalides **1a** and **1d**. Thus, in the crystal of the diorganotin diiodide **1d** there are parallel chains built from alternating ($S_{N1}$,$S_{N2}$) and

 © 2006 Wiley-VCH Verlag GmbH & Co. KGaA, Weinheim 

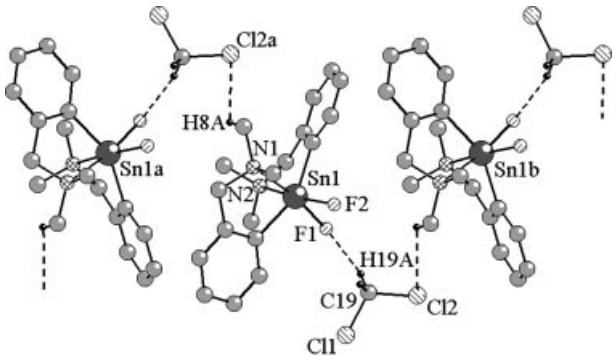


Figure 3. Polymeric associations in the crystal of compound **1b**·$CH_2Cl_2$ based on halogen–hydrogen contacts (only hydrogens involved in such contacts are shown) [symmetry-equivalent atoms ($x$, 2 – $y$, 0.5 + $z$) and ($x$, 2 – $y$, –0.5 + $z$) are labelled as "a" and "b"].

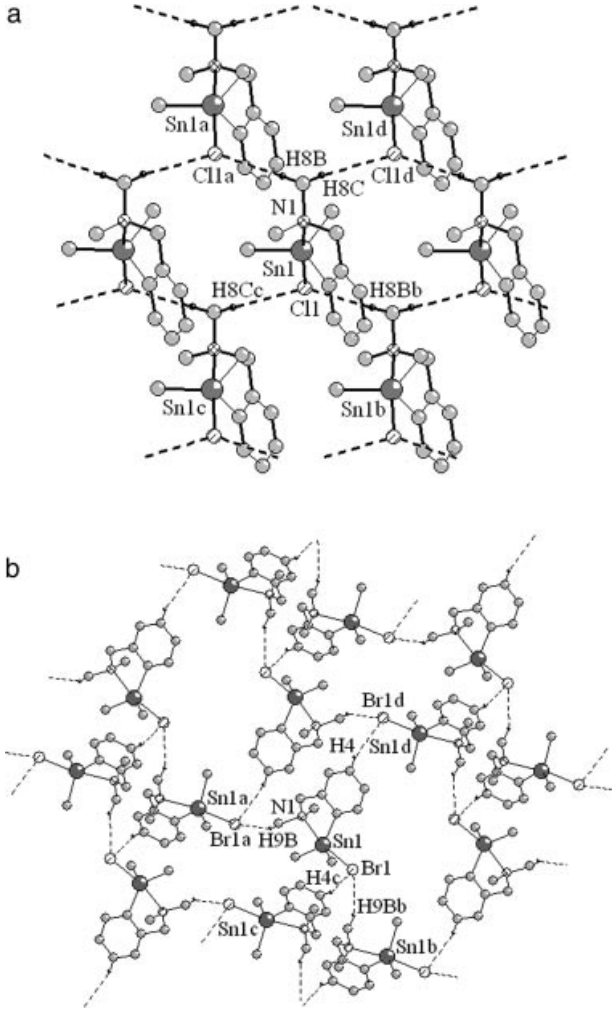


Figure 4. View of the layer network based on intermolecular hydrogen bonding (only hydrogens involved in intermolecular interactions are shown) in the crystals of (a) **2a**′ [symmetry-equivalent atoms (1.5 – $x$, 0.5 + $y$, 0.5 + $z$), (1.5 – $x$, –0.5 + $y$, –0.5 + $z$), (1.5 – $x$, –0.5 + $y$, 0.5 + $z$) and (1.5 – $x$, 0.5 + $y$, –0.5 + $z$) are labelled "a", "b", "c" and "d", respectively] and (b) **2c** [symmetry-equivalent atoms (–0.5 + $x$, $y$, 0.5 – $z$), (0.5 + $x$, $y$, 0.5 – $z$), (0.5 – $x$, –$y$, 0.5 + $z$) and (0.5 – $x$, –$y$, –0.5 + $z$) are labelled "a", "b", "c" and "d", respectively].

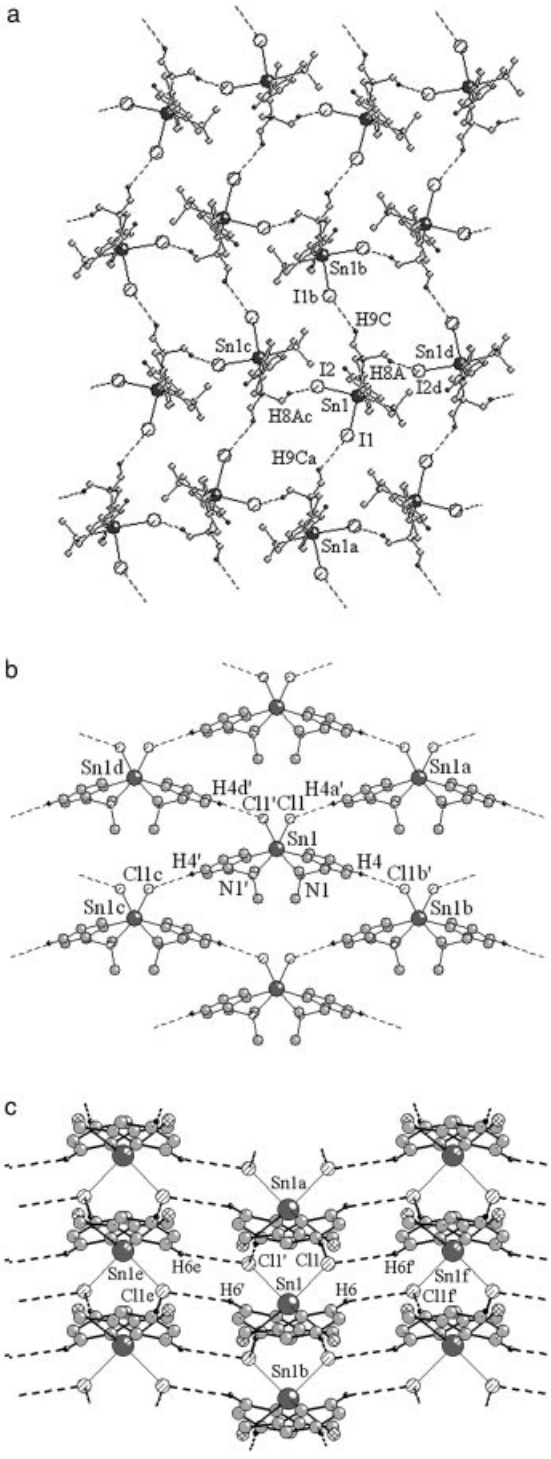


Figure 5. View of supramolecular architectures based on hydrogen bonding (only hydrogen atoms involved in intermolecular interactions are shown): (a) the layer network of ($S_{N1}$,$S_{N2}$) and ($R_{N1}$,$R_{N2}$) isomers in the crystal of **1d** [symmetry equivalent atoms (–0.5 + $x$, 1.5 – $y$, 0.5 + $z$), (0.5 + $x$, 1.5 – $y$, –0.5 + $z$), (0.5 – $x$, –0.5 + $y$, 1.5 – $z$) and (0.5 – $x$, 0.5 + $y$, 1.5 – $z$) are labelled as "a", "b", "c" and "d", respectively]; (b) the layer network of ($S_{N1}$,$S_{N2}$) isomers in the crystal of **1a** [symmetry equivalent atoms (0.5 + $x$, 0.5 + $y$, $z$), (0.5 + $x$, –0.5 + $y$, $z$), (–0.5 + $x$, –0.5 + $y$, $z$) and (–0.5 + $x$, 0.5 + $y$, $z$) are labelled as "a", "b", "c" and "d", respectively]; (c) 3D supramolecular structure in the crystal of **1a** [symmetry equivalent atoms (–$x$, 1 – $y$, 1 – $z$) and (0.5 – $x$, 0.5 – $y$, –$z$) are labelled as "e" and "f", respectively].

 © 2006 Wiley-VCH Verlag GmbH & Co. KGaA, Weinheim 

($R_{N1}$,$R_{N2}$) isomers through I···$H_{methyl}$ contacts [I(2)–H-(9Ca)$_{methyl}$ = 3.15 Å]. Inter-chain contacts [I(2)···H-(8Ac)$_{methyl}$ = 3.26 Å] result in a similar layer network to that observed for **2a′** (Figure 5, a). Additional weak, inter-layer contacts between I(1) and an aromatic proton [I(1)···H(14f)$_{aryl}$ = 3.32 Å] lead to a 3D network. By contrast, in the crystal of the diorganotin dichloride **1a** only aromatic protons are involved in hydrogen bonding. The molecules are associated into layers built of the same type of isomer [Cl(1)···H(4a′)$_{aryl}$ = 2.81 Å] (Figure 5, b) and alternating parallel layers of ($S_{N1}$,$S_{N2}$) or ($R_{N1}$,$R_{N2}$) isomers are bridged through weak Cl(1)···H(6f′)$_{aryl}$ (2.94 Å) interactions (Figure 5, c).

## Conclusion

The hypercoordinated di- and triorganotin(IV) halides [{2-($Me_2NCH_2$)$C_6H_4$}$_2$$SnX_2$], [{2-($Me_2NCH_2$)$C_6H_4$}-$Me_2$SnX] and [{2-($Me_2NCH_2$)$C_6H_4$}$Ph_2$SnX] (X = F, Cl, Br, I) have been prepared and their solutions investigated by multinuclear NMR spectroscopy, including variable-temperature studies. Single-crystal X-ray structure analyses have revealed that the strong intramolecular coordination of the nitrogen atom from the pendant $CH_2NMe_2$ group to tin induces planar chirality and the compounds crystallise as racemates. The influence of the identity and number of halogen atoms and organic substituents attached to the tin atoms is reflected in different supramolecular architectures based on hydrogen-bonding networks.

## Experimental Section

**General Remarks:** All manipulations were carried out under argon using dried solvents freshly distilled prior to use. The $^1$H and $^{13}$C NMR spectra were recorded with Bruker Avance DRX 400 (including 2D experiments), Bruker Avance 300 and Bruker DPX 200 instruments. The $^{19}$F NMR were recorded with Bruker Avance DRX 400 and Bruker DPX 300, and $^{119}$Sn NMR were obtained using Bruker DPX 400 and Varian Unity 300 instruments. Variable-temperature $^1$H NMR studies were performed with a Varian Unity 300 (compound **1a**) and a Varian Gemini 300S (compound **1b**). The chemical shifts are reported in ppm relative to the residual peak of solvent ($CHCl_3$; $\delta_{^1H}$ = 7.26, $\delta_{^{13}C}$ = 77.0 ppm for $^1$H and $^{13}$C, $CFCl_3$ for $^{19}$F and neat $SnMe_4$ for $^{119}$Sn). Starting materials such as $SnCl_4$, $BuSnCl_3$, $Ph_2SnCl_2$, $Me_2SnCl_2$ KX (X = F, Br, I), *N*,*N*-dimethylbenzylamine and *n*-butyllithium were commercially available. The compounds [Li{2-($Me_2NCH_2$)$C_6H_4$}],[41] [{2-($Me_2NCH_2$)$C_6H_4$}$_4$Sn][17] and [{2-($Me_2NCH_2$)$C_6H_4$}$Ph_2$SnCl] (**3a**)[20] were prepared according to the literature methods.

**Synthesis of [{2-($Me_2NCH_2$)$C_6H_4$}$_2$$SnCl_2$] (1a). Procedure 1:** A suspension of [Li{2-($Me_2NCH_2$)$C_6H_4$}] [prepared as above from *n*BuLi in *n*-hexane (24.6 mL, 1.6 M, 20% excess) and $Me_2NCH_2C_6H_5$ (4.43 g, 32.8 mmol) in 200 mL of anhydrous *n*-hexane] in anhydrous toluene (150 mL) was added dropwise, whilst stirring, to a cooled (–78 °C) solution of $SnCl_4$ (4.27 g, 16.4 mmol) in 300 mL of toluene (300 mL). After all the suspension had been added, the reaction mixture was stirred for 1 h at –78 °C, and then allowed to reach room temperature overnight. The reaction mixture was filtered under inert atmosphere and the solvent of the filtrate was removed in vacuo. The solid residue was recrystallised from $CH_2Cl_2$/*n*-hexane to give 6.1 g (81%) of the title compound as colourless crystals.

**Procedure 2:** $SnCl_4$ (0.437 g, 1.68 mmol) was added to [{2-($Me_2NCH_2$)$C_6H_4$}$_4$Sn] (1.1 g, 1.68 mmol) under inert atmosphere and the mixture was slowly heated whilst stirring until a homogeneous melt was obtained. The heating was maintained for 15 min and then the reaction mixture was cooled to room temperature. Recrystallisation from a $CH_2Cl_2$/*n*-hexane mixture (approximately 1:4) provided 1.2 g (78%) of **1a** as colourless crystals (m.p. 257–259 °C). $^1$H NMR ($CDCl_3$, 300 MHz, 20 °C): $\delta$ = 2.22 (br. s, 12 H, $NCH_3$), AB spin system with $\delta_A$ = 3.37 and $\delta_B$ = 4.07 ($^2J_{H,H}$ = 14.1 Hz, 4 H, $CH_2N$), 7.18 (m, 2 H, 3-H), 7.41 (m, 4 H, 4,5-H), 8.22 (m, $^3J_{H,Sn}$ = 108 Hz, 2 H, 6-H) ppm. $^1$H NMR ($CDCl_3$, 300 MHz, 60 °C): $\delta$ = 2.21 (br. s, 12 H, $NCH_3$), AB spin system with $\delta_A$ = 3.38 and $\delta_B$ = 4.04 (br. s, 4 H, $CH_2N$), 7.17 (d, $^3J_{H,H}$ = 6.9 Hz, 2 H, 3-H), 7.52 (m, 4 H, 4,5-H), 8.25 (d, $^3J_{H,H}$ = 6.3, $^3J_{H,Sn}$ = 108 Hz, 2 H, 6-H) ppm. $^1$H NMR (300 MHz, $CDCl_3$, –60 °C): $\delta$ = 2.05 (s, $^3J_{H,Sn}$ = 39 Hz, 6 H, $NCH_3$), 2.55 (s, $^3J_{H,Sn}$ = 39 Hz, 6 H, $NCH_3$), AB spin system with $\delta_A$ = 3.39 and $\delta_B$ = 4.14 ($^2J_{H,H}$ = 14.2, $^3J_{H,Sn}$ = 39 Hz, 4 H, $CH_2N$), 7.19 (d, $^3J_{H,H}$ = 6.6 Hz, 2 H, 3-H), 7.41 (m, 4 H, 4,5-H), 8.19 (d, $^3J_{H,H}$ = 6.8, $^3J_{H,Sn}$ = 110 Hz, 2 H, 6-H) ppm. $^{13}$C NMR ($CDCl_3$, 100.6 MHz, 20 °C): $\delta$ = 46.78 (br. s, $NCH_3$), 63.80 (s, $^2J_{C,Sn}$ = 42.8 Hz, $CH_2N$), 127.85 (s, $^3J_{C,Sn}$ = 97.1/99.3 Hz, C-3), 128.18 (s, $^3J_{C,Sn}$ = 104.8/107.6 Hz, C-5), 130.16 (s, $^4J_{C,Sn}$ = 19.1 Hz, C-4), 135.47 (s, $^2J_{C,Sn}$ = 61.3 Hz, C-6), 140.79 (s, $^2J_{C,Sn}$ = 62.8 Hz, C-2; $^1J_{C,Sn}$ = 1167.1/1221.3 Hz, C-1) ppm. $^{119}$Sn NMR ($CH_2Cl_2$/[D$_6$]acetone, 149.2 MHz, 20 °C): $\delta$ = –260.7 ppm (s). $C_{18}H_{24}Cl_2N_2Sn$ (458.00): calcd. C 47.21, H 5.28, N 6.12; found C 47.34, H 5.43, N 5.84.

**Synthesis of [{2-($Me_2NCH_2$)$C_6H_4$}$_2$$SnF_2$] (1b):** Dichloromethane was added to a suspension of **1a** (0.3 g, 0.65 mmol) in MeOH (20 mL) until the solid compound dissolved. An aqueous solution of KF (0.2 g, 3.44 mmol) was then added and the mixture was stirred for 3 h at room temperature. The organic layer was separated and the water solution was washed twice with 5 mL of $CH_2Cl_2$. The combined organic layers were dried with anhydrous $Na_2SO_4$. The latter was filtered, the solvent was removed in vacuo and the obtained white solid residue was recrystallised from a $CH_2Cl_2$/*n*-hexane mixture to give **1b** (0.25 g, 90%; m.p. 213–215 °C). Colourless crystals suitable for single-crystal X-ray diffraction were obtained by slow crystallisation from a $CH_2Cl_2$/*n*-hexane (approximately 1:5) mixture. $^1$H NMR ($CDCl_3$, 400 MHz, 20 °C): $\delta$ = 2.24 (br. s, 12 H, $NCH_3$), 3.66 (br. s, 4 H, $CH_2N$), 7.16 (m, 2 H, 3-H), 7.38 (m, 4 H, 4,5-H), 8.08 (m, $^3J_{H,Sn}$ = 92.2 Hz, 2 H, 6-H) ppm. $^1$H NMR ($CDCl_3$, 300 MHz, 55 °C): $\delta$ = 2.24 (s, 12 H, $NCH_3$), 3.66 (s, 4 H, $CH_2N$), 7.17 (m, 2 H, 3-H), 7.39 (m, 4 H, 4,5-H), 8.09 (m, $^3J_{H,Sn}$ = 91.5 Hz, 2 H, 6-H) ppm. $^1$H NMR ($CDCl_3$, 300 MHz, –55 °C): $\delta$ = 2.10 (s, 6 H, $NCH_3$), 2.42 (s, 6 H, $NCH_3$), AB spin system with $\delta_A$ = 3.53 and $\delta_B$ = 3.82 ($^2J_{H,H}$ = 14.3 Hz, 4 H, $CH_2N$), 7.17 (m, 2 H, 3-H), 7.38 (m, 4 H, 4,5-H), 8.05 (m, $^3J_{H,Sn}$ = 93.3 Hz, 2 H, 6-H) ppm. $^{13}$C NMR ($CDCl_3$, 100.6 MHz, 20 °C): $\delta$ = 46.09 (br. s, $NCH_3$), 64.10 (s, $^2J_{C,Sn}$ = 48.4 Hz, $CH_2N$), 127.31 (s, $^3J_{C,Sn}$ = 96.7 Hz, C-3), 127.93 (s, $^3J_{C,Sn}$ = 99.3 Hz, C-5), 129.97 (s, $^4J_{C,Sn}$ = 17.6 Hz, C-4), 136.30 (s, $^2J_{C,Sn}$ = 49.5 Hz, C-6), 139.23 (t, $^3J_{C,F}$ = 22.5 Hz, C-1), 141.04 (s, $^2J_{C,Sn}$ = 66.7 Hz, C-2) ppm. $^{19}$F NMR ($CDCl_3$, 282.38 MHz, 20 °C): $\delta$ = –181.5 ppm (s, $^1J_{F,Sn}$ = 2567/2683 Hz). $^{119}$Sn NMR ($CH_2Cl_2$/[D$_6$]acetone, 149.2 MHz, 20 °C): $\delta$ = –386.7 ppm (t, $^1J_{F,Sn}$ = 2663 Hz). $C_{18}H_{24}F_2N_2Sn$ (425.09): calcd. C 50.86, H 5.69, N 6.59; found C 50.58, H 5.33, N 6.37.

**Synthesis of [{2-($Me_2NCH_2$)$C_6H_4$}$_2$$SnI_2$] (1d):** A saturated aqueous solution of $NH_4I$ (20 mL) was added to a solution of **1a** (0.79 g,

 © 2006 Wiley-VCH Verlag GmbH & Co. KGaA, Weinheim 

1.73 mmol) in $CH_2Cl_2$ (20 mL)/EtOH (4 mL) and the reaction mixture was stirred for 10 h at room temperature. The organic layer was separated and the water solution was washed twice with 5 mL of $CH_2Cl_2$. The organic solution was separated and dried with anhydrous $Na_2SO_4$. The latter was filtered, the solvent was removed in vacuo and the solid residue was recrystallised from a $CH_2Cl_2$/*n*-hexane mixture to give **1d** as colourless crystals (0.66 g, 60%; m.p. 238 °C). $^1$H NMR ($CDCl_3$, 300 MHz, 20 °C): $\delta$ = 2.23 (br. s, 12 H, $NCH_3$), AB spin system with $\delta_A$ = 3.19 and $\delta_B$ = 4.22 ($^2J_{H,H}$ = 12.7 Hz, 4 H, $CH_2N$), 7.13 (d, $^3J_{H,H}$ = 6.9 Hz, 2 H, 3-H), 7.37 (dd, $^3J_{H,H}$ = 7.4 Hz, 2 H, 4-H), 7.47 (dd, $^3J_{H,H}$ = 7.5 Hz, 2 H, 5-H), 8.19 (d, $^3J_{H,H}$ = 7.2, $^3J_{H,Sn}$ = 111.9 Hz, 2 H, 6-H) ppm. $^1$H NMR ($CDCl_3$, 300 MHz, 50 °C): $\delta$ = 2.21 (s, $^3J_{H,Sn}$ = 39.1 Hz, 12 H, $NCH_3$), AB spin system with $\delta_A$ = 3.24 and $\delta_B$ = 4.16 (br. s, 4 H, $CH_2N$), 7.12 (d, $^3J_{H,H}$ = 7.3 Hz, 2 H, 3-H), 7.37 (dd, $^3J_{H,H}$ = 7.4 Hz, 2 H, 4-H), 7.47 (dd, $^3J_{H,H}$ = 7.5 Hz, 2 H, 5-H), 8.21 (d, $^3J_{H,H}$ = 7.3, $^3J_{H,Sn}$ = 111.9 Hz, 2 H, 6-H) ppm. $^1$H NMR (300 MHz, $CDCl_3$, –50 °C): $\delta$ = 1.96 (s, $^3J_{H,Sn}$ = 39.2 Hz, 6 H, $NCH_3$), 2.63 (s, $^3J_{H,Sn}$ = 38.8 Hz, 6 H, $NCH_3$), AB spin system with $\delta_A$ = 3.17 and $\delta_B$ = 4.30 ($^2J_{H,H}$ = 14.2 Hz, 4 H, $CH_2N$), 7.13 (d, $^3J_{H,H}$ = 7.2 Hz, 2 H, 3-H), 7.37 (dd, $^3J_{H,H}$ = 7.4 Hz, 2 H, 4-H), 7.46 (dd, $^3J_{H,H}$ = 7.4 Hz, 2 H, 5-H), 8.15 (d, $^3J_{H,H}$ = 7.4, $^3J_{H,Sn}$ = 115.3 Hz, 2 H, 6-H) ppm. $^{13}$C NMR ($CDCl_3$, 100.6 MHz, 20 °C): $\delta$ = 46.90 (br. s, $NCH_3$), 62.80 (s, $^2J_{C,Sn}$ = 35.6 Hz, $CH_2N$), 128.02 (s, $^3J_{C,Sn}$ = 104.1 Hz, C-5), 128.22 (s, $^3J_{C,Sn}$ = 90.8 Hz, C-3), 130.29 (s, $^4J_{C,Sn}$ = 18.2 Hz, C-4), 135.73 (s, $^2J_{C,Sn}$ = 67.1 Hz, C-6), 138.17 (s, C-1), 140.51 (s, C-2) ppm. $^{119}$Sn NMR ($CDCl_3$, 111.9 MHz, 20 °C): $\delta$ = –346.9 ppm (s). $C_{18}H_{24}I_2N_2Sn$ (640.90): calcd. C 33.73, H 3.77, N 4.37; found C 33.42, H 3.53, N 4.12.

**Synthesis of [{2-($Me_2NCH_2$)$C_6H_4$}$Me_2SnCl$] (2a):** A suspension of [Li{2-($Me_2NCH_2$)$C_6H_4$}] [prepared as above from *n*BuLi in *n*-hexane (17.6 mL, 1.6 M, 20% excess) and $Me_2NCH_2C_6H_5$ (3.18 g, 23.5 mmol) in 50 mL of anhydrous *n*-hexane] in anhydrous toluene (50 mL) was added dropwise, whilst stirring, to a cooled (–78 °C) solution of $Me_2SnCl_2$ (5.17 g, 23.5 mmol) in 150 mL of toluene (300 mL). After all the suspension had been added the reaction mixture was stirred for 1 h at –78 °C, and then allowed to reach room temperature overnight. The reaction mixture was filtered under inert atmosphere and the solvent was removed in vacuo. The white solid residue was recrystallised from $CH_2Cl_2$/*n*-hexane to give **2a** (5.2 g, 69%) as colourless crystals (m.p. 119–121 °C; ref.[12] 120–123 °C). $^1$H NMR ($CDCl_3$, 200 MHz, 20 °C): $\delta$ = 0.73 (s, $^2J_{H,Sn}$ = 64.1/67.0 Hz, 6 H, $SnCH_3$), 2.29 (s, 6 H, $NCH_3$), 3.62 (s, 2 H, $CH_2N$), 7.12 (m, 1 H, 3-H), 7.32 (m, 2 H, 4,5-H), 8.17 (m, $^3J_{H,Sn}$ = 67.2 Hz, 1 H, 6-H) ppm. $^{13}$C NMR ($CDCl_3$, 50.3 MHz, 20 °C): $\delta$ = –0.28 (s, $^1J_{C,Sn}$ = 492.4/515.4 Hz, $SnCH_3$), 45.15 (s, $NCH_3$), 64.78 (s, $^2J_{C,Sn}$ = 28.8 Hz, $CH_2N$), 126.46 (s, $^3J_{C,Sn}$ = 59.1 Hz, C-3), 127.88 (s, $^3J_{C,Sn}$ = 67.2 Hz, C-5), 129.32 (s, $^4J_{C,Sn}$ = 13.2 Hz, C-4), 137.60 (s, $^2J_{C,Sn}$ = 42.9 Hz, C-6), 140.28 (s, C-1), 141.78 (s, $^2J_{C,Sn}$ = 38.6 Hz, C-2) ppm. $^{119}$Sn NMR ($CH_2Cl_2$/[$D_6$]acetone, 149.2 MHz, 20 °C): $\delta$ = –48.7 ppm (s). $C_{11}H_{18}ClNSn$ (318.41): calcd. C 41.49, H 5.70, N 4.40; found C 41.23, H 5.61, N 4.53.

**Synthesis of [{2-($Me_2NCH_2$)$C_6H_4$}$Me_2SnF$] (2b):** Same procedure as for **1b**, using **2a** (0.25 g, 0.78 mmol) and KF (0.228 g, 3.92 mmol). Recrystallisation from $CH_2Cl_2$/*n*-hexane (approximately 1:3) mixture gave **2b** (0.21 g, 89%) as colourless crystals (m.p. 92–94 °C). $^1$H NMR ($CDCl_3$, 400 MHz, 20 °C): $\delta$ = 0.56 (d, $^3J_{H,F}$ = 3.7, $^2J_{H,Sn}$ = 64.8/67.2 Hz, 6 H, $SnCH_3$), 2.28 (s, 6 H, $NCH_3$), 3.59 (s, 2 H, $CH_2N$), 7.12 (m, 1 H, 3-H), 7.32 (m, 2 H, 4,5-H), 7.97 (m, $^3J_{H,Sn}$ = 60.4 Hz, 1 H, 6-H) ppm. $^{13}$C NMR ($CDCl_3$, 100.6 MHz, 20 °C): $\delta$ = –3.67 (d, $^2J_{C,F}$ = 16.7, $^1J_{C,Sn}$ = 507.7/531.3 Hz, $SnCH_3$), 45.16 (s, $NCH_3$), 64.91 (s, $^2J_{C,Sn}$ = 30.3 Hz, $CH_2N$), 126.47 (s, $^3J_{C,Sn}$ = 58.3 Hz, C-3), 127.83 (s, $^3J_{C,Sn}$ = 64.6 Hz, C-5), 129.24 (s, $^4J_{C,Sn}$ = 12.8 Hz, C-4), 137.19 (s, $^2J_{C,Sn}$ = 38.2 Hz, C-6), 141.32 (d, $^3J_{C,F}$ = 21.7 Hz, C-1), 142.04 (s, $^2J_{C,Sn}$ = 39.4 Hz, C-2) ppm. $^{19}$F NMR ($CDCl_3$, 376.5 MHz, 20 °C): $\delta$ = –178.4 ppm (s, $^1J_{F,Sn}$ = 1944.2/2034.6 Hz). $^{119}$Sn NMR ($CDCl_3$, 111.9 MHz, 20 °C): $\delta$ = –52.7 ppm (d, $^1J_{F,Sn}$ = 2039.3 Hz). $C_{11}H_{18}FNSn$ (301.96): calcd. C 43.75, H 6.01, N 4.64; found C 43.41, H 5.79, N 4.41.

**Synthesis of [{2-($Me_2NCH_2$)$C_6H_4$}$Me_2SnBr$] (2c):** An aqueous solution of KBr (0.93 g, 7.85 mmol) was added to a solution of **2a** (0.5 g, 1.57 mmol) in $CH_2Cl_2$ (30 mL) and the reaction mixture was stirred for 3 h at room temperature. The organic layer was separated and the water solution was washed twice with 10 mL of $CH_2Cl_2$. The organic solution was dried with anhydrous $Na_2SO_4$. The solvent was removed in vacuo and the obtained pale brown-red residue was recrystallised from a $CH_2Cl_2$/*n*-hexane mixture to give **2c** (0.52 g, 91%) [m.p. 136–138 °C (dec); ref.[2] white solid, 136–137 °C]. Colourless crystals suitable for single-crystal X-ray diffraction were obtained from a $CH_2Cl_2$/*n*-hexane (approximately 1:4) solution. $^1$H NMR ($CDCl_3$, 200 MHz, 20 °C): $\delta$ = 0.87 (s, $^2J_{H,Sn}$ = 63.5/66.4 Hz, 6 H, $SnCH_3$), 2.32 (s, 6 H, $NCH_3$), 3.64 (s, 2 H, $CH_2N$), 7.12 (m, 1 H, 3-H), 7.35 (m, 2 H, 4,5-H), 8.26 (m, $^3J_{H,Sn}$ = 68.5 Hz, 1 H, 6-H) ppm. $^{13}$C NMR ($CDCl_3$, 50.3 MHz, 20 °C): $\delta$ = 1.02 (s, $^1J_{C,Sn}$ = 483.1/505.1 Hz, $SnCH_3$), 45.22 (s, $NCH_3$), 64.74 (s, $^2J_{C,Sn}$ = 28.1 Hz, $CH_2N$), 126.46 (s, $^3J_{C,Sn}$ = 58.9 Hz, C-3), 127.89 (s, $^3J_{C,Sn}$ = 67.6 Hz, C-5), 129.39 (s, C-4), 138.22 (s, $^2J_{C,Sn}$ = 44.7 Hz, C-6), 139.54 (s, C-1), 141.58 (s, $^2J_{C,Sn}$ = 37 Hz, C-2). $^{119}$Sn NMR ($CDCl_3$, 149.2 MHz, 20 °C): $\delta$ = –55.5 ppm (s). $C_{11}H_{18}BrNSn$ (362.86): calcd. C 36.41, H 5.00, N 3.86; found C 36.11, H 5.21, N 3.67.

**Synthesis of [{2-($Me_2NCH_2$)$C_6H_4$}$Me_2SnI$] (2d):** Same procedure as for **1b**, using **2a** (0.2 g, 0.63 mmol) and KI (0.52 g, 3.14 mmol). Recrystallisation from a $CH_2Cl_2$/*n*-hexane (approximately 1:3) mixture gave **2d** (0.21 g, 82%) as pale-yellow crystals (m.p. 105–107 °C). $^1$H NMR ($CDCl_3$, 300 MHz, 20 °C): $\delta$ = 1.05 (s, $^2J_{H,Sn}$ = 63.2/65.0 Hz, 6 H, $SnCH_3$), 2.34 (s, 6 H, $NCH_3$), 3.65 (s, 2 H, $CH_2N$), 7.11 (d, $^3J_{H,H}$ = 7.0 Hz, 1 H, 3-H), 7.35 (m, 2 H, 4,5-H), 8.30 (d, $^3J_{H,H}$ = 6.6, $^3J_{H,Sn}$ = 71.2 Hz, 1 H, 6-H) ppm. $^{13}$C NMR ($CDCl_3$, 75.5 MHz, 20 °C): $\delta$ = 3.18 (s, $^1J_{C,Sn}$ = 470.1/492.0 Hz, $SnCH_3$), 45.42 (s, $NCH_3$), 64.84 (s, $^2J_{C,Sn}$ = 26.9 Hz, $CH_2N$), 126.54 (s, $^3J_{C,Sn}$ = 58.9 Hz, C-3), 128.03 (s, $^3J_{C,Sn}$ = 69.4 Hz, C-5), 129.58 (s, $^3J_{C,Sn}$ = 13.7 Hz, C-4), 138.26 (s, $^1J_{C,Sn}$ = 664.0/694.8 Hz, C-1), 139.62 (s, $^2J_{C,Sn}$ = 46.2 Hz, C-6), 141.40 (s, $^2J_{C,Sn}$ = 35.8 Hz, C-2) ppm. $^{119}$Sn NMR ($CDCl_3$, 111.9 MHz, 20 °C): $\delta$ = –72.8 ppm (s). $C_{11}H_{18}INSn$ (409.87): calcd. C 32.24, H 4.43, N 3.42; found C 32.11, H 4.25, N 3.33.

**Synthesis of [{2-($Me_2NCH_2$)$C_6H_4$}$Ph_2SnF$] (3b):** Same procedure as for **1b**, using **3a** (0.25 g, 0.56 mmol) and KF (0.164 g, 2.82 mmol). Recrystallisation from a $CH_2Cl_2$/*n*-hexane (approximately 1:3) mixture gave **3b** (0.21 g, 87%) as colourless crystals (m.p. 161–163 °C). $^1$H NMR ($CDCl_3$, 400 MHz, 20 °C): $\delta$ = 1.97 (s, 6 H, $NCH_3$), 3.56 (s, 2 H, $CH_2N$), 7.20 (d, $^3J_{H,H}$ = 7.2 Hz, 1 H, 3-H), 7.44 (m, 8 H, 4,5-H + $C_6H_5$-*meta*,*para*), 7.72 (m, $^3J_{H,Sn}$ = 61.1 Hz, 4 H, $C_6H_5$-*ortho*), 8.31 (d, $^3J_{H,H}$ = 7.0, $^3J_{H,Sn}$ = 64.4 Hz, 1 H, 6-H) ppm. $^{13}$C NMR ($CDCl_3$, 100.6 MHz, 20 °C): $\delta$ = 45.76 (s, $NCH_3$), 64.82 (s, $^2J_{C,Sn}$ = 31.2 Hz, $CH_2N$), 127.03 (s, $^3J_{C,Sn}$ = 64.6 Hz, C-3), 128.05 (s, $^3J_{C,Sn}$ = 68.7 Hz, C-5), 128.75 (s, $^3J_{C,Sn}$ = 67.5 Hz, $C_6H_5$-*meta*), 129.53 (s, $^4J_{C,Sn}$ = 13.5 Hz, $C_6H_5$-*para*), 129.93 (s, $^4J_{C,Sn}$ = 13.1 Hz, C-4), 136.03 (s, $^2J_{C,Sn}$ = 44.8 Hz, $C_6H_5$-*ortho*), 138.34 (s, $^2J_{C,Sn}$ = 39.1 Hz, C-6), 140.29 (d, $^3J_{C,F}$ = 15.5 Hz, $C_6H_5$-*ipso*), 142.88 (s, $^2J_{C,Sn}$ = 44.3 Hz, C-2) ppm; the resonance for C-1 is overlapped by the resonance of C-6. $^{19}$F NMR ($CDCl_3$, 376.5 MHz, 20 °C): $\delta$ = –182.4 ppm (s, $^1J_{F,Sn}$ = 2058.3/2154.0 Hz). $^{119}$Sn NMR ($CDCl_3$,

 © 2006 Wiley-VCH Verlag GmbH & Co. KGaA, Weinheim 

111.9 MHz, 20 °C): $\delta$ = –197.6 ppm (d, $^1J_{F,Sn}$ = 2157 Hz). $C_{21}H_{22}FNSn$ (426.10): calcd. C 59.20, H 5.20, N 3.29; found C 58.96, H 5.05, N 3.07.

**Synthesis of [{2-($Me_2NCH_2$)$C_6H_4$}$Ph_2SnI$] (3d):** Same procedure as for **1b**, using **3a** (0.2 g, 0.45 mmol) and KI (0.375 g, 2.26 mmol). Recrystallisation from a $CH_2Cl_2$/*n*-hexane (approximately 1:4) mixture gave **3d** (0.22 g, 91%) as pale-yellow crystals (m.p. 235–236 °C). $^1$H NMR ($CDCl_3$, 300 MHz, 20 °C): $\delta$ = 1.87 (s, 6 H, $NCH_3$), 3.56 (s, 2 H, $CH_2N$), 7.18 (d, $^3J_{H,H}$ = 7.3 Hz, 1 H, 3-H), 7.40 (m, 7 H, 4-H + $C_6H_5$-*meta*,*para*), 7.53 (dd, $^3J_{H,H}$ = 7.5 Hz, 1 H, 5-H), 7.72 (m, $^3J_{H,Sn}$ = 65.3 Hz, 4 H, $C_6H_5$-*ortho*), 8.60 (d, $^3J_{H,H}$ = 7.1, $^3J_{H,Sn}$ = 75.1 Hz, 1 H, 6-H) ppm. $^{13}$C NMR ($CDCl_3$, 75.4 MHz, 20 °C): $\delta$ = 45.84 (s, $NCH_3$), 64.64 (s, $^2J_{C,Sn}$ = 25.8 Hz, $CH_2N$), 127.19 (s, $^3J_{C,Sn}$ = 62.1 Hz, C-3), 128.29 (s, $^3J_{C,Sn}$ = 74.2 Hz, C-5), 128.85 (s, $^3J_{C,Sn}$ = 69.3 Hz, $C_6H_5$-*meta*), 129.35 (s,

Table 6. Crystallographic data for compounds **1a**, **1b**, **1b**·$CH_2Cl_2$ and **1d**.

| | **1a** | **1b** | **1b**·$CH_2Cl_2$ | **1d** |
|---|---|---|---|---|
| Empirical formula | $C_{18}H_{24}Cl_2N_2Sn$ | $C_{18}H_{24}F_2N_2Sn$ | $C_{18}H_{24}F_2N_2Sn{\cdot}CH_2Cl_2$ | $C_{18}H_{24}I_2N_2Sn$ |
| Formula mass | 457.98 | 425.08 | 510.01 | 640.88 |
| Crystal system | monoclinic | monoclinic | monoclinic | monoclinic |
| Space group | *C*2/*c* | $P2_1/n$ | *Cc* | $P2_1/n$ |
| *a* [Å] | 16.9910(4) | 9.4178(13) | 12.9347(16) | 10.0711(10) |
| *b* [Å] | 8.0759(1) | 16.101(2) | 12.7973(16) | 13.7642(14) |
| *c* [Å] | 14.5798(4) | 12.2211(17) | 13.4533(17) | 15.1918(15) |
| *α* [°] | 90 | 90 | 90 | 90 |
| *β* [°] | 105.9252(11) | 111.560(2) | 102.312(2) | 96.531(2) |
| *γ* [°] | 90 | 90 | 90 | 90 |
| *V* [Å$^3$] | 1980.0(3) | 1723.6(4) | 2175.7(5) | 2092.2(4) |
| *Z* | 4 | 4 | 4 | 4 |
| $D_{calcd.}$ [g cm$^{-3}$] | 1.581 | 1.638 | 1.557 | 2.035 |
| *F*(000) | 920 | 856 | 1024 | 1208 |
| Crystal size [mm] | 0.25 × 0.15 × 0.13 | 0.40 × 0.31 × 0.18 | 0.32 × 0.20 × 0.10 | 0.44 × 0.20 × 0.20 |
| $\mu$(Mo-$K_\alpha$) [mm$^{-1}$] | 1.607 | 1.503 | 1.442 | 4.174 |
| $\theta$ range [°] | 3.79–27.45 | 2.19–27.10 | 2.26–26.37 | 2.00–26.37 |
| No. of reflections collected | 8700 | 10414 | 8549 | 16388 |
| No. of independent reflections | 2201 ($R_{int}$ = 0.0330) | 3778 ($R_{int}$ = 0.0201) | 4259 ($R_{int}$ = 0.0349) | 4274 ($R_{int}$ = 0.0392) |
| No. of parameters | 107 | 213 | 239 | 212 |
| Absorption correction | none | multi-scan (Bruker SAINT) | multi-scan (SAINT) | multi-scan (SAINT) |
| $R_1$ [$I > 2\sigma(I)$] | 0.0211 | 0.0240 | 0.0381 | 0.0465 |
| $wR_2$ | 0.0452 | 0.0529 | 0.0816 | 0.1068 |
| GOF on $F^2$ | 1.006 | 1.080 | 1.023 | 1.157 |
| Residual electron density [e Å$^{-3}$] | 0.370/–0.601 | 0.408/–0.334 | 0.767/–0.700 | 1.277/–1.382 |

Table 7. Crystallographic data for compounds **2a**, **2a′** and **2b**–**2d**.

| | **2a** | **2a′** | **2b** | **2c** | **2d** |
|---|---|---|---|---|---|
| Empirical formula | $C_{11}H_{18}ClNSn$ | $C_{11}H_{18}ClNSn$ | $C_{11}H_{18}FNSn$ | $C_{11}H_{18}BrNSn$ | $C_{11}H_{18}INSn$ |
| Formula mass | 318.40 | 318.40 | 301.97 | 362.86 | 409.85 |
| Crystal system | orthorhombic | orthorhombic | monoclinic | orthorhombic | monoclinic |
| Space group | *Pbca* | $Pna2_1$ | $P2_1/n$ | *Pbca* | $P2_1/n$ |
| *a* [Å] | 13.993(9) | 17.155(3) | 9.5956(8) | 14.1705(13) | 7.1685(10) |
| *b* [Å] | 12.973(9) | 11.2080(19) | 12.7844(12) | 13.0368(12) | 7.5197(11) |
| *c* [Å] | 14.687(10) | 7.0150(12) | 11.3157(10) | 14.6525(14) | 26.236(4) |
| *α* [°] | 90 | 90 | 90 | 90 | 90 |
| *β* [°] | 90 | 90 | 111.521(2) | 90 | 90.067(2) |
| *γ* [°] | 90 | 90 | 90 | 90 | 90 |
| *V* [Å$^3$] | 2666(3) | 1348.8(4) | 1291.4(2) | 2706.9(4) | 1414.3(4) |
| *Z* | 8 | 4 | 4 | 8 | 4 |
| $D_{calcd.}$ [g cm$^{-3}$] | 1.586 | 1.568 | 1.553 | 1.781 | 1.925 |
| *F*(000) | 1264 | 632 | 600 | 1408 | 776 |
| Crystal size [mm] | 0.13 × 0.21 × 0.23 | 0.42 × 0.37 × 0.17 | 0.24 × 0.29 × 0.53 | 0.25 × 0.22 × 0.17 | 0.37 × 0.21 × 0.08 |
| $\mu$(Mo-$K_\alpha$) [mm$^{-1}$] | 2.084 | 2.084 | 1.957 | 4.808 | 3.959 |
| $\theta$ range [°] | 2.55–26.37 | 2.17–26.37 | 2.4–26.4 | 2.54–26.37 | 1.55–26.37 |
| No. of reflections collected | 19522 | 10378 | 7352 | 20438 | 10856 |
| No. of independent reflections | 2716 ($R_{int}$ = 0.0372) | 2727 ($R_{int}$ = 0.0220) | 2623 ($R_{int}$ = 0.0174) | 2763 ($R_{int}$ = 0.0362) | 2876 ($R_{int}$ = 0.0519) |
| No. of parameters | 131 | 131 | 131 | 131 | 132 |
| Absorption correction | multi-scan (SAINT) | multi-scan (SAINT) | multi-scan (SAINT) | multi-scan (SAINT) | multi-scan (SAINT) |
| $R_1$ [$I > 2\sigma(I)$] | 0.0315 | 0.0217 | 0.0260 | 0.0317 | 0.0354 |
| $wR_2$ | 0.0620 | 0.0447 | 0.0588 | 0.0715 | 0.0752 |
| GOF on $F^2$ | 1.100 | 1.092 | 1.060 | 1.101 | 1.116 |
| Residual electron density [e Å$^{-3}$] | 0.522/–0.470 | 0.218/–0.408 | 0.476/–0.202 | 0.534/–0.602 | 0.701/–0.762 |

 © 2006 Wiley-VCH Verlag GmbH & Co. KGaA, Weinheim 

Table 8. Crystallographic data for compounds **3a**, **3b** and **3d**.

| | **3a** | **3b** | **3d** |
|---|---|---|---|
| Empirical formula | $C_{21}H_{22}ClNSn$ | $C_{21}H_{22}FNSn$ | $C_{21}H_{22}INSn$ |
| Formula mass | 442.54 | 426.09 | 533.99 |
| Crystal system | monoclinic | monoclinic | monoclinic |
| Space group | $P2_1/n$ | $P2_1/n$ | $P2_1/n$ |
| $a$ [Å] | 9.2370(15) | 9.2868(7) | 8.8090(15) |
| $b$ [Å] | 24.215(4) | 23.5553(17) | 15.875(3) |
| $c$ [Å] | 17.832(3) | 17.8373(13) | 15.058(3) |
| $\alpha$ [°] | 90 | 90 | 90 |
| $\beta$ [°] | 97.558(3) | 99.7480(10) | 92.636(3) |
| $\gamma$ [°] | 90 | 90 | 90 |
| $V$ [Å$^3$] | 3954.1(11) | 3845.6(5) | 2103.5(6) |
| $Z$ | 8 | 8 | 4 |
| $D_{calcd.}$ [g cm$^{-3}$] | 1.487 | 1.472 | 1.686 |
| $F(000)$ | 1776 | 1712 | 1032 |
| Crystal size [mm] | 0.24 × 0.23 × 0.18 | 0.20 × 0.19 × 0.04 | 0.22 × 0.15 × 0.14 |
| $\mu$(Mo-$K_\alpha$) [mm$^{-1}$] | 1.429 | 1.339 | 2.684 |
| $\theta$ range [°] | 1.43–26.35 | 1.45–26.38 | 1.87–26.37 |
| No. of reflections collected | 31134 | 30497 | 16667 |
| No. of independent reflections | 8068 ($R_{int}$ = 0.0424) | 7877 ($R_{int}$ = 0.0411) | 4292 ($R_{int}$ = 0.0438) |
| No. of parameters | 220 | 437 | 219 |
| Absorption correction | multi-scan (SAINT) | multi-scan (SAINT) | multi-scan (SAINT) |
| $R_1$ [$I > 2\sigma(I)$] | 0.0444 | 0.0457 | 0.0425 |
| $wR_2$ | 0.0933 | 0.1091 | 0.0830 |
| GOF on $F^2$ | 1.195 | 1.026 | 1.058 |
| Residual electron density [e Å$^{-3}$] | 1.161/–0.509 | 2.576/–0.921 | 0.797/–0.874 |

$^4J_{C,Sn}$ = 13.7 Hz, $C_6H_5$-*para*), 130.20 (s, $^4J_{C,Sn}$ = 14.2 Hz, C-4), 135.18 (s, $^2J_{C,Sn}$ = 45.8 Hz, $C_6H_5$-*ortho*), 135.23 (s, C-1), 140.80 (s, $^2J_{C,Sn}$ = 50.3 Hz, C-6), 142.32 (s, $^2J_{C,Sn}$ = 38.4 Hz, C-2), 142.36 (s, $^1J_{C,Sn}$ = 705.1/737.9 Hz, $C_6H_5$-*ipso*). $^{119}$Sn NMR ($CDCl_3$, 111.9 MHz, 20 °C): $\delta$ = –199.5 ppm (s). $C_{21}H_{22}INSn$ (534.01): calcd. C 47.23, H 4.15, N 2.62; found C 47.01, H 3.88, N 2.45.

**X-ray Crystallographic Study:** The crystal structure measurement and refinement data for **1a**, **1b**, **1b**·$CH_2Cl_2$, **1d**, **2a**, **2a′**, **2b**–**2d**, **3a**, **3b** and **3d** are given in Tables 6, 7 and 8. Data for **1a** were collected with a Nonius KappaCCD diffractometer (University of Dortmund) at 291 K. For all the other compounds the data were collected using a SMART APEX diffractometer ("Babes-Boyai" University) at 297 K. In both cases a graphite monochromator was used to produce a wavelength (Mo-$K_\alpha$) of 0.71073 Å. The structures were solved by direct methods (full-matrix least-squares on $F^2$). All non-hydrogen atoms were refined with anisotropic thermal parameters. For structure solving and refinement the SHELX-97 software package was used.[42] The drawings were created with the Diamond program by Crystal Impact GbR.[43]

CCDC-231308 (for **1a**), -230620 (for **1b**), -230621 (for **1b**·$CH_2Cl_2$), -285103 (for **1d**), -215229 (for **2a**), -215230 (for **2a′**), -215224 (for **2b**), -230622 (for **2c**), -215380 (for **2d**), -215228 (for **3a**), -215226 (for **3b**) and -215227 (for **3d**) contain the supplementary crystallographic data for this paper. These data can be obtained free of charge from The Cambridge Crystallographic Data Centre via www.ccdc.cam.ac.uk/data_request/cif.

**Supporting Information Available** (for details see the footnote on the first page of this article): Figure S1 (variable-temperature $^1$H NMR spectra for **1a** and **1b**, in $CDCl_3$ solution), Figures S2–S8 (simulation of the aromatic region of the $^1$H NMR spectra for **1a**, **1b**, **2a**–**2d** and **4b**, respectively) and Figures S9–S43 (details of the different supramolecular architectures based on hydrogen-bonding networks in the crystals of investigated compounds).

## Acknowledgments

This work was supported by the National University Research Council of Romania [a CNCSIS grant ($A_T$-23/552/2004) and a CERES Project (contract no. 32/12.11.2004). We thank the National Center for X-ray Diffraction ("Babes-Bolyai" University, Cluj-Napoca) for performing the single-crystal X-ray diffraction studies.

[1] J. T. B. H. Jastrzebski, G. van Koten, *Adv. Organomet. Chem.* **1993**, *35*, 241–294.
[2] G. van Koten, C. A. Schaap, J. G. Noltes, *J. Organomet. Chem.* **1975**, *99*, 157–170.
[3] G. van Koten, J. G. Noltes, A. L. Spek, *J. Organomet. Chem.* **1976**, *118*, 183–189.
[4] G. van Koten, J. T. B. H. Jastrzebski, J. G. Noltes, W. M. G. F. Pontenagel, J. Kroon, A. L. Spek, *J. Am. Chem. Soc.* **1978**, *100*, 5021–5028.
[5] G. van Koten, J. T. B. H. Jastrzebski, J. G. Noltes, A. L. Spek, J. C. Schoone, *J. Organomet. Chem.* **1978**, *148*, 233–245.
[6] G. van Koten, J. T. B. H. Jastrzebski, J. G. Noltes, *J. Organomet. Chem.* **1979**, *177*, 283–292.
[7] R. Barbieri, A. Silvestri, G. van Koten, J. G. Noltes, *Inorg. Chim. Acta* **1980**, *40*, 267–271.
[8] J. T. B. H. Jastrzebski, P. A. van der Schaaf, J. Boersma, G. van Koten, M. C. Zoutberg, D. Heijdenrijk, *Organometallics* **1989**, *8*, 1373–1375.
[9] J. T. B. H. Jastrzebski, P. A. van der Schaaf, J. Boersma, M. de Wit, Y. Wang, D. Heijdenrijk, C. H. Stam, *J. Organomet. Chem.* **1991**, *407*, 301–311.
[10] J. T. B. H. Jastrzebski, J. Boersma, G. van Koten, *J. Organomet. Chem.* **1991**, *413*, 43–53.
[11] J. T. B. H. Jastrzebski, D. M. Grove, J. Boersma, G. van Koten, J.-M. Ernsting, *Magn. Reson. Chem.* **1991**, *29*, S25–S30.
[12] E. Vedejs, S. M. Duncan, A. R. Haight, *J. Org. Chem.* **1993**, *58*, 3046–3050.

 © 2006 Wiley-VCH Verlag GmbH & Co. KGaA, Weinheim 

[13] P. Steenwinkel, J. T. B. H. Jastrzebski, B.-J. Deelman, D. M. Grove, H. Kooijman, N. Veldman, W. J. J. Smeets, A. L. Spek, G. van Koten, *Organometallics* **1997**, *16*, 5486–5498.
[14] A. Růžička, V. Pejchal, J. Holeček, A. Lyčka, K. Jacob, *Collect. Czech. Chem. Commun.* **1998**, *63*, 977–989.
[15] K. Schwarzkopf, M. Blumenstein, A. Hayen, J. O. Metzger, *Eur. J. Org. Chem.* **1998**, 177–181.
[16] R. Rippstein, G. Kickelbick, U. Schubert, *Inorg. Chim. Acta* **1999**, *290*, 100–104.
[17] R. Rippstein, G. Kickelbick, U. Schubert, *Monatsh. Chem.* **1999**, *130*, 385–399.
[18] A. Růžička, R. Jambor, J. Brus, I. Cisařová, J. Holeček, *Inorg. Chim. Acta* **2001**, *323*, 163–170.
[19] R. Jambor, A. Růžička, J. Brus, I. Cisařová, J. Holeček, *Inorg. Chem. Commun.* **2001**, *4*, 257–260.
[20] R. A. Varga, M. Schürmann, C. Silvestru, *J. Organomet. Chem.* **2001**, *623*, 161–167.
[21] A. Růžička, A. Dostál, R. Jambor, V. Buchta, J. Brus, I. Cisařová, M. Holčapek, J. Holeček, *Appl. Organomet. Chem.* **2002**, *16*, 315–322.
[22] M. Biesemans, J. C. Martins, R. Willem, A. Lyčka, A. Růžička, J. Holeček, *Magn. Reson. Chem.* **2002**, *40*, 65–69.
[23] A. Růžička, A. Lyčka, R. Jambor, P. Novák, I. Cisařová, M. Holčapek, M. Erben, J. Holeček, *Appl. Organomet. Chem.* **2003**, *17*, 168–174.
[24] A. Růžička, R. Jambor, I. Cisařová, J. Holeček, *Chem. Eur. J.* **2003**, *9*, 2411–2418.
[25] P. Novák, I. Cisařová, R. Jambor, A. Růžička, J. Holeček, *Appl. Organomet. Chem.* **2004**, *18*, 241–243.
[26] J. Bareš, P. Novák, M. Nádvorník, R. Jambor, T. Lébl, I. Cisařová, A. Růžička, J. Holeček, *Organometallics* **2004**, *23*, 2967–2971.
[27] R. A. Varga, C. Silvestru, C. Deleanu, *Appl. Organomet. Chem.* **2005**, *19*, 153–160.
[28] L. M. Opris, A. Silvestru, C. Silvestru, H. J. Breunig, E. Lork, *Dalton Trans.* **2003**, 4367–4374.
[29] O. Bumbu, C. Silvestru, M. C. Gimeno, A. Laguna, *J. Organomet. Chem.* **2004**, *689*, 1172–1179.
[30] L. M. Opris, A. Silvestru, C. Silvestru, H. J. Breunig, E. Lork, *Dalton Trans.* **2004**, 3575–3585.
[31] M. Kulcsar, A. Silvestru, C. Silvestru, J. E. Drake, C. L. B. Macdonald, M. E. Hursthouse, M. E. Light, *J. Organomet. Chem.* **2005**, *690*, 3217–3228.
[32] *IUPAC Nomenclature of Organic Chemistry*, Pergamon Press, Oxford, **1979**.
[33] J. Beckmann, D. Horn, K. Jurkschat, F. Rosche, M. Schürmann, U. Zachwieja, D. Dakternieks, A. Duthie, A. E. K. Lim, *Eur. J. Inorg. Chem.* **2003**, 164–174.
[34] N. Pieper, C. Klaus-Mrestani, M. Schürmann, K. Jurkschat, M. Biesemans, I. Verbruggen, J. Martins, R. Willem, *Organometallics* **1997**, *16*, 1043–1052.
[35] J. Holeček, A. Lyčka, K. Handlíř, M. Nádvorník, *Collect. Czech, J. Chem. Soc., Chem. Commun.* **1990**, *55*, 1193–1207.
[36] H. Weichmann, C. Schmoll, *Z. Chem.* **1984**, *24*, 390–391.
[37] P. J. Cox, S. J. Garden, R. A. Howie, O. A. Melvin, J. L. Wardell, *J. Organomet. Chem.* **1996**, *516*, 213–224.
[38] H. Bai, R. K. Harris, H. Reuter, *J. Organomet. Chem.* **1991**, *408*, 167–172.
[39] I. Wharf, A.-M. Lebuis, G. A. Roper, *Inorg. Chim. Acta* **1999**, *294*, 224–231.
[40] J. Emsley, *Die Elemente*, Walter de Gruyter, Berlin, **1994**.
[41] A. Meller, H. Hoppe, W. Maringgele, A. Haase, M. Noltemeyer, *Organometallics* **1998**, *17*, 123–124.
[42] G. M. Sheldrick, *SHELXTL-97*, University of Göttingen, Germany, 1997.
[43] DIAMOND – Visual Crystal Structure Information System, CRYSTAL IMPACT: P. O. Box 1251, 53002 Bonn, Germany, **2001**.

Received: November 15, 2005
Published Online: February 6, 2006

 © 2006 Wiley-VCH Verlag GmbH & Co. KGaA, Weinheim 

DOI: 10.1002/ejic.200501089

# Proton-Coupled Redox Chemistry, Oxidative Reactivity, and Electronic Characterization of Aqua-, Hydroxo-, and Oxo-Triruthenium Clusters

**Genebaldo S. Nunes,[a] Anamaria D. P. Alexiou,[a] Koiti Araki,[a] André L. B. Formiga,[a] Reginaldo C. Rocha,*[b] and Henrique E. Toma*[a]**

**Keywords:** Ruthenium–acetate clusters / Mixed-valence complexes / Oxygen-transfer catalysis / Proton-coupled electron transfer / Pourbaix diagram / Electrocatalysis / Spectroelectrochemistry

The pH-dependent electronic and electrochemical properties of a series of triangular $\mu_3$-oxo-centered trinuclear clusters of the type $[Ru_3O(Ac)_6(py)_2(OH_x)]^n$ (Ac = acetate; py = pyridine; $x$ = 0, 1, or 2; where the formal oxidation states on the metal ions range from +II to +IV) have been investigated with emphasis on the elucidation of the successive proton-coupled redox processes spanning the interconvertible aqua- ($x$ = 2), hydroxo- ($x$ = 1), and oxo- ($x$ = 0) forms, from which the complete Pourbaix diagram has been proposed. From the spontaneous slow coupling reaction of the monomeric cluster in its deprotonated (oxo) form at high pH, the μ-oxo-bridged cluster dimer (i.e. $\{(py)_2(Ac)_6ORu_3\}$-O-$\{Ru_3O(Ac)_6(py)_2\}$) has been isolated and fully characterized by spectroelectrochemistry as well. A further understanding of the underlying electronic interactions across the various oxidation and protonation states, and the role of such phenomena in the activation of the Ru–O bonding system in oxygen-transfer catalysis, have also been explored.
(© Wiley-VCH Verlag GmbH & Co. KGaA, 69451 Weinheim, Germany, 2006)

## Introduction

The chemistry of water as a ligand in coordination compounds can be rather puzzling when the metal ions display many successive oxidation states.[1] That is mostly because, in such systems, the ligand acid–base behavior and metal-centered redox properties are coupled and, therefore, proton and electron transfer can simultaneously occur in connection with chemical and electronic transformations in the complex. The consequences of this type of dynamic synergism called proton-coupled electron transfer (PCET) are, in many different aspects, widespread in synthetic and natural systems (e.g. from sol-gel processes in materials chemistry to photosynthetic oxygen evolution in green plants).[2,3]

In the particular context of model systems towards (electro)catalytic oxidation of organics, a remarkable series of (polypyridyl)ruthenium complexes involving oxidation-state/pH-dependent equilibrium PCET reactions of the type $H_2O$–$Ru^{II} \rightleftharpoons$ HO–$Ru^{III} \rightleftharpoons$ O=$Ru^{IV}$ (i.e. aqua, hydroxo, and oxo forms, respectively), has been largely investigated by Meyer and co-workers.[4] In the light of those studies, an extraordinary chemistry has been revealed from the apparently simple Ru–O structure. In addition to the complexity introduced by the multiple ligand-based protonation states coexisting with the metal-based oxidation states, a detailed understanding of the underlying metal–ligand interactions can be especially challenging when metal–metal electronic coupling is also involved, as in the case of the triangular μ-oxo-centered triruthenium clusters $[Ru_3O(Ac)_6(py)_2(OH_x)]^n$ (Ac = acetate ion, py = pyridine), focused herein (Scheme 1, a).

The trinuclear ruthenium complexes of the type $[Ru_3O(Ac)_6(L)_3]^n$ and $[Ru_3O(Ac)_6(L)_2(L')]^n$ (where L is usually a pyridyl ligand) have been extensively investigated[5] since the seminal work by Wilkinson[6,7] and Meyer[8,9] and co-workers, on the mixed-valence properties of the $Ru_3O$ cluster core. In addition to the metal–metal bonding, the triangular center is strongly held by six acetate bridges and a central oxygen atom (oxo) that is capable of interacting with up to three empty Ru $d_\pi$ orbitals. When L′ is $H_2O$, its acid–base properties are expected to be sensitive to the redox states of the Ru ions and, to some extent, the electronic coupling within the trinuclear cluster core. There is also the possibility of forming oxo-bridged dimers (Scheme 1, b), expanding the influence of the mixed-valence interactions over the entire polymetallic system. All these aspects have been investigated in this work, with especial emphasis on the elucidation of the proton-coupled redox processes by electrochemical and spectroelectrochemical methods. Further, the role of intermetallic electronic interactions in the activation of the Ru–O bonding structure in oxygen-transfer catalysis has also been explored.

[a] Instituto de Química, Universidade de São Paulo, C.P. 26077, CEP 05513-970, São Paulo, SP, Brazil
E-mail: henetoma@iq.usp.br
[b] Los Alamos National Laboratory, Mail Stop G755, Los Alamos, NM 87545, USA
E-mail: rcrocha@lanl.gov

 © 2006 Wiley-VCH Verlag GmbH & Co. KGaA, Weinheim 

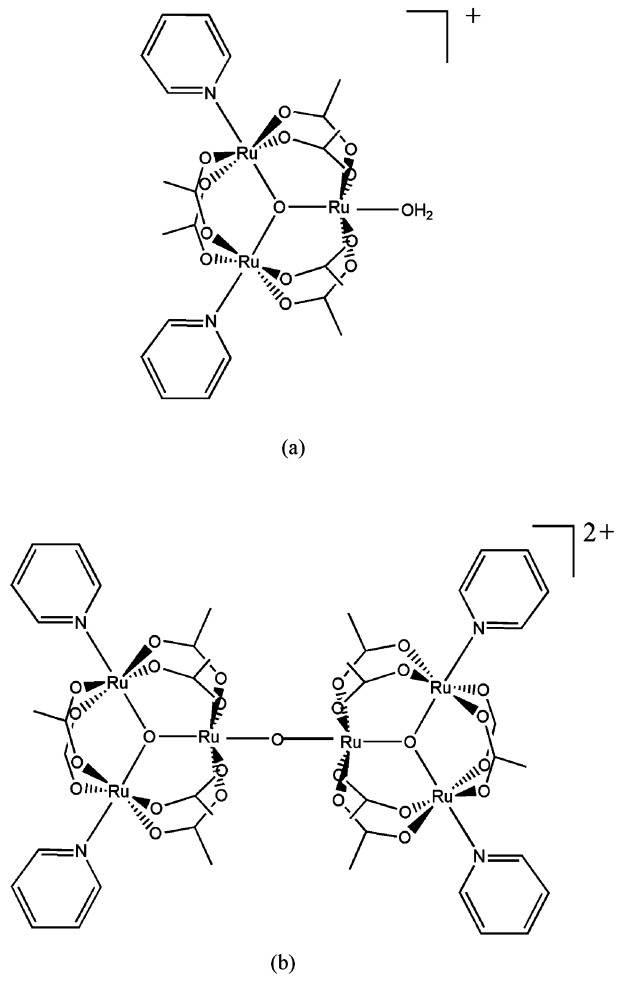


Scheme 1. Structural formulas of (a) the cluster $[Ru_3O(Ac)_6(py)_2(H_2O)]^+$ and (b) the oxo-bridged cluster dimer $[\{Ru_3O(Ac)_6(py)_2\}_2(\mu\text{-}O)]^{2+}$.

## Results and Discussion

### Electronic Absorption Spectra

The electronic spectra of the $[Ru_3^{III,III,III}O(Ac)_6(py)_2(H_2O)]^+$ complex in aqueous solution, at various pH values, are shown in Figure 1. In general, a characteristic set of absorption bands is observed at 498 ($\varepsilon$ = 1630), 607 ($\varepsilon$ = 3390), and 683 nm ($\varepsilon$ = 4300), in addition to a shoulder near 390 nm. The main visible absorption envelope and the higher-energy shoulder have been associated to intracluster (IC) metal–metal electronic transitions and $Ru_3O(d_\pi)\rightarrow py(\pi^*)$ charge-transfer (CT) transitions, respectively, on the basis of previous detailed assignments.[5,9–11]

As shown in Figure 1, no spectral change is observed in the pH range of 1.9–6.5. Above pH 6.5, a systematic spectral shift of the IC bands to 592, 702, and ≈808 nm occurs, accompanied by two isosbestic points at 577 and 712 nm. In the pH range of 6.5–11.5, the process is essentially reversible, corresponding to the acid–base equilibrium of Equation (1).

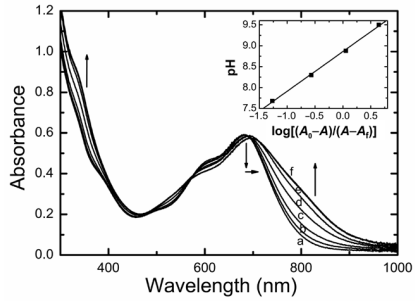


Figure 1. Eletronic spectra of $[Ru_3O(Ac)_6(py)_2(H_2O)]^+$ ($1.4\cdot10^{-4}$ M) in BR buffer at various pH values: (a) 1.9–6.5; (b) 7.7; (c) 8.3; (d) 8.9; (e) 9.5; and (f) 11.1 and 12.0. Inset: pH vs. $\log[(A_0 - A)/(A - A_f)]$, where A is the measured absorbance at any given pH, $A_0$ is the starting absorbance at the lowest pH, and $A_f$ is the final absorbance at the highest pH.

$$[Ru_3^{III,III,III}O(Ac)_6(py)_2(H_2O)]^+ \rightleftharpoons [Ru_3^{III,III,III}O(Ac)_6(py)_2(OH)] + H^+ \quad (1)$$

From the linear plot of pH vs. $\log[(A_0 - A)/(A - A_f)]$ (Figure 1; inset), the $pK_a$ for the process given in Equation (1) was calculated to be 8.86 (±0.02). It is interesting to notice that the $K_a$ of the aqua ligand in the $[Ru_3^{III,III,III}O(Ac)_6(py)_2(H_2O)]^+$ species herein is about four orders of magnitude smaller than that previously reported for the $[Ru_3^{III,III,III}O(Ac)_6(OH)_2(H_2O)]^-$ species ($pK_a$ > 12).[5,6] This observation reflects the influence of the π-backbonding ability of the pyridine ligands, in contrast with the hydroxo ligands. Also, considering that the $pK_a$ of the $[Ru(bpy)_2(py)(H_2O)]^{3+}$ complex is 0.85,[12] the dominant role of the metal–metal interactions in the trinuclear $Ru^{III}$ cluster becomes quite evident. Actually, the presence of the strong bonding and delocalization within the $Ru_3O$ core provides an electronic environment that closely resembles that of mononuclear $Ru^{II}$ complexes such as $[Ru(bpy)_2(py)(H_2O)]^{2+}$ and *trans*-$[Ru(bpydip)(H_2O)_2]^{2+}$ [where bpy is 2,2′-bipyridine, and bpydip is a tetradentate Schiff base ligand, *N*,*N*′-bis(7-methyl-2-pyridylmethylene)-1,3-diiminopropane], as deduced from their $pK_a$ of 10.6 and 8.9, respectively.[4,13]

By monitoring the electronic spectra of the hydroxo, neutral $[Ru_3^{III,III,III}O(Ac)_6(py)_2(OH)]$ species as a function of time (Figure 2), it was observed that the systematic decrease of the absorption band around 700 nm occurs simultaneously with the rise of a broad band around 900 nm, which is characteristic of the aqua cluster $[Ru_3^{III,III,II}O(Ac)_6(py)_2(H_2O)]$ (as demonstrated below by spectroelectrochemistry). Therefore, as shown in Equation (2), the hydroxo-[III,III,III] species slowly disproportionates, at high pH, generating the corresponding protonated/reduced (aqua-[III,III,II]) and deprotonated/oxidized (oxo-[IV,III,III]) forms.

Figure 2 (b) shows the corresponding kinetics for the disproportionation reaction of Equation (2). The initial rates measured at 700 nm $(1.04\pm0.02)\cdot10^{-5}$ $s^{-1}$ and 900 nm $(1.98\pm0.03)\cdot10^{-5}$ $s^{-1}$, were in excellent agreement with the theoretical relationship of Equation (3).

 © 2006 Wiley-VCH Verlag GmbH & Co. KGaA, Weinheim 

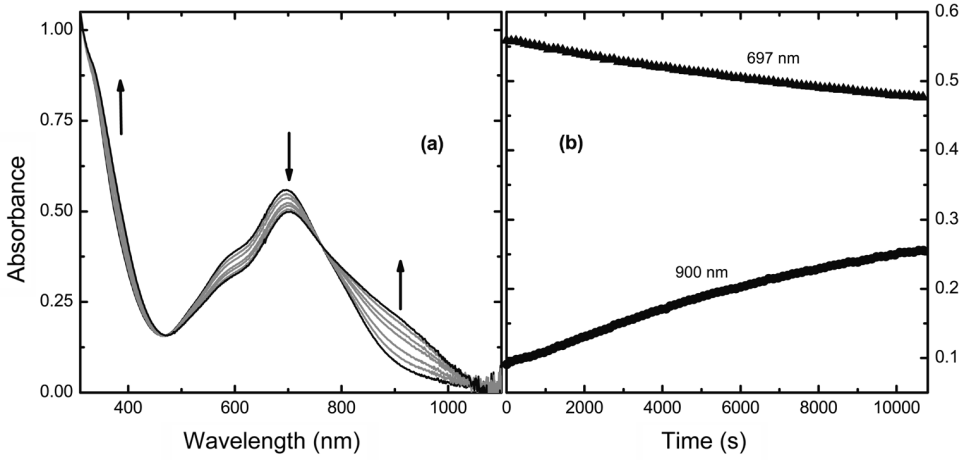


Figure 2. (a) Spectral changes of $[Ru_3O(Ac)_6(py)_2(H_2O)]^+$ ($1.4 \cdot 10^{-4}$ M) in BR buffer at pH 11.4, as a function of time; (b) absorbance changes at 697 and 900 nm as a function of time.

$$2\ [Ru_3^{III,III,III}O(Ac)_6(py)_2(OH)] \rightleftharpoons [Ru_3^{III,III,II}O(Ac)_6(py)_2(OH_2)] + [Ru_3^{IV,III,III}O(Ac)_6(py)_2(O)] \quad (2)$$

$$-(1/2)\ d[Ru_3^{III,III,III}(OH)]/dt = d[Ru_3^{III,III,II}(OH_2)]/dt \quad (3)$$

In order to evaluate the end point of the reaction, the sample undergoing disproportionation was kept in the dark for 24 h and, then, the spectra were measured again at several pH values (Figure 3). The major differences (relative to the spectra of Figure 2, a) were observed above pH 11; i.e., the main absorption band was shifted from 683 nm to 702 nm, and there was an enhancement of the absorption at 343 nm. In addition, the lack of isosbestic points indicates the occurrence of further reactions following the disproportionation process.

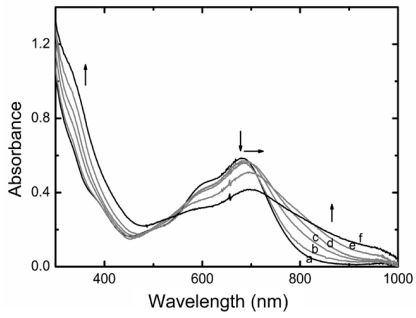


Figure 3. Eletronic spectra of $[Ru_3O(Ac)_6(py)_2(H_2O)]^+$ ($1.4 \cdot 10^{-4}$ M) in BR buffer at various pH values: (a) 1.9; (b) 8.3; (c) 8.9; (d) 9.5; (e) 11.1; (f) 12.0. The sample solution was prepared 24 h prior to the measurements.

By treating the solution (aged for 24 h at pH 12) with diethyl ether, only the neutral aqua cluster, i.e. $[Ru_3^{III,III,II}O(Ac)_6(py)_2(OH_2)]$, could be detected in the organic fraction, as shown in Figure 4, a (see below for detailed assignments).

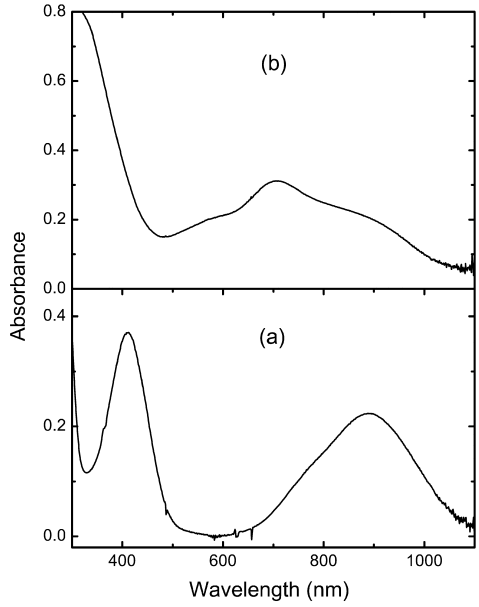


Figure 4. Electronic spectra of (a) the diethyl ether fraction containing the reduced aqua species, $[Ru_3^{III,III,II}O(Ac)_6(py)_2(OH_2)]$, and (b) the remaining, previously ether-treated aqueous solution at pH 12.0 (BR buffer, 0.1 M).

The spectrum of the ether-treated aqueous solution (Figure 4, b) exhibits absorption bands at 893, 712, 566 and 343 nm. In principle, according to the disproportionation reaction of Equation (2), before the extraction with ether the reaction mixture should also contain the oxo species, $[Ru_3^{IV,III,III}O(Ac)_6(py)_2(O)]$, and perhaps some remainder of the starting hydroxo species, $[Ru_3^{III,III,III}O(Ac)_6(py)_2(OH)]$. However, although these are both electrically neutral species, none of these forms could be detected in the extracted organic phase containing the aqua counterpart. A plausible explanation for this observation is that, after aging for 24 h at pH > 11, the $[Ru_3^{IV,III,III}O(Ac)_6(py)_2(O)]$ species would dimerize into $[\{Ru_3^{IV,III,III}O(Ac)_6(py)_2\}_2(O)]^{2+}$

 © 2006 Wiley-VCH Verlag GmbH & Co. KGaA, Weinheim 

[Equation (4)], analogously to the previously reported for the $[Ru(bpy)_2(py)(O)]^{2+}$ complex.[14]

$$2\ [Ru_3^{IV,III,III}O(Ac)_6(py)_2(O)] + H_2O \rightleftharpoons [\{Ru_3^{IV,III,III}O(Ac)_6(py)_2\}_2(O)]^{2+} + 2\ OH^- \quad (4)$$

Alternatively, the oxo-[IV,III,III] species could react with any remaining amount of the cluster in the hydroxo-[III,III,III] form to yield the mixed-valent dimer, as shown in Equation (5).

$$[Ru_3^{IV,III,III}O(Ac)_6(py)_2(O)] + [Ru_3^{III,III,III}O(Ac)_6(py)_2(OH)] \rightleftharpoons [(py)_2(Ac)_6ORu_3^{IV,III,III}(O)Ru_3^{III,III,III}O(Ac)_6(py)_2]^+ + OH^- \quad (5)$$

In order to obtain additional evidence on the formation of such dimeric species, the final product was further isolated and characterized as follows. The starting $[Ru_3^{III,III,III}O(Ac)_6(py)_2(H_2O)]Cl$ compound was dissolved in a minimum volume of water and treated with an equimolar amount of NaOH. After 24 h, the one-electron reduced, neutral species ($H_2O$-[III,III,II]) was extracted from the mixture with diethyl ether (as above), and the treated aqueous solution was evaporated to dryness. Mass spectra (ESI-MS; see Exp. Sect. for details) of the product, in methanol, exhibited a main peak at $m/z = 1751$, consistent with the $[\{Ru_3O(Ac)_6(py)_2\}_2(O)]Cl_2^+$ formulation ($m/z = 1751$) which, therefore, corresponds to the μ-oxo-bridged mixed-valent [IV,IV,III–IV,III,III] cluster dimer after ionization in gas phase. It is worth noting that the chloride ions were present as counterions because the cluster dimer was generated from the starting $[Ru_3O(Ac)_6(py)_2(H_2O)]Cl$ complex. Isolation of the dimeric species in pure form (using conventional liquid chromatography) has not yet been accomplished because such species seems to undergo facile interconversion between the mixed-valence states, as confirmed by the ESI-MS experiments.

## Electrochemical Behavior

Typical cyclic voltammograms of the $[Ru_3O(Ac)_6(py)_2(H_2O)]^+$ cluster in aqueous solution, at three representative pH values, are shown in Figure 5. A characteristic reversible wave, assigned to the Ru-centered III,III,III/III,III,II redox couple, was observed with $E_{1/2} = 0.20$ V (vs. SHE); Equation (6). Above pH 8, the process exhibits a pH-dependent, Nernstian behavior with $E^o$ (V vs. SHE) = 0.20 – 0.059·pH. The $pK_a$ associated with the equilibrium of Equation (7) was evaluated from the Pourbaix ($E_{1/2}$ vs. pH) plot shown in Figure 6, with the determined value of 8.7 in agreement with that obtained by spectrophotometry (8.86) as above.

$$[Ru_3^{III,III,III}(H_2O)]^+ + e \rightleftharpoons [Ru_3^{III,III,II}(H_2O)] \quad E_{1/2} = 0.20\ V \quad (6)$$

$$[Ru_3^{III,III,III}(H_2O)]^+ \rightleftharpoons [Ru_3^{III,III,III}(OH)] + H^+ \quad pK_a = 8.8 \quad (7)$$

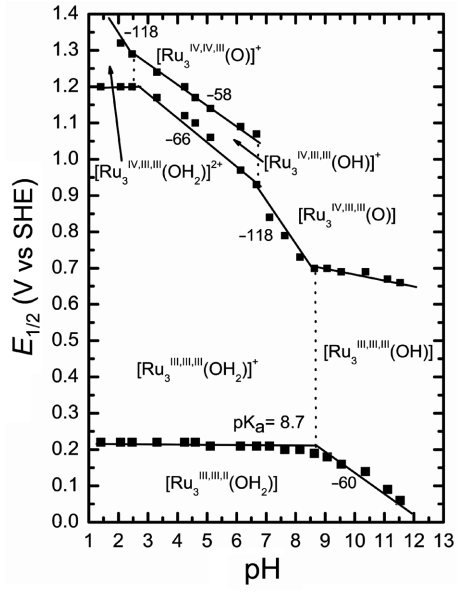


Figure 6. Pourbaix diagrams for $[Ru_3O(Ac)_6(py)_2(OH_x)]^n$ in aqueous solution; $pK_a$ values and slopes (given in mV) are also noted in the Figure. At pH > 9 and $E^o > 1.0$ V, the dimeric species (not shown) predominate; see text for details.

The corresponding spectral changes accompanying the above redox transformations are shown in Figure 7. The electrochemical III,III,III/III,III,II reduction of the aqua cluster at pH 6.7 proceeds reversibly, generating the characteristic cluster-core IC bands with $\lambda_{max}$ around 890 nm and the $Ru_3O(d_\pi) \rightarrow py(p_\pi^*)$ CT band at 364 nm.

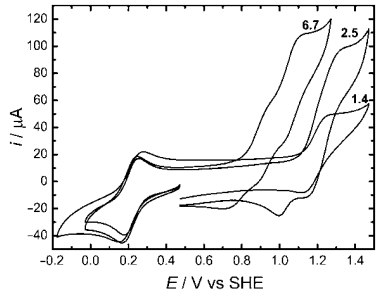


Figure 5. Cyclic voltammograms (at 50 mV $s^{-1}$) of $[Ru_3O(Ac)_6(py)_2(H_2O)]^+$ ($1.3 \cdot 10^{-3}$ M) in BR buffer/NaTFA (0.1 M) at pH 1.4, 2.5, and 6.7.

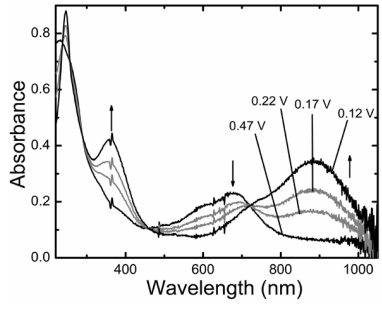


Figure 7. Spectroelectrochemical changes in a solution of $[Ru_3O(Ac)_6(py)_2(H_2O)]^n$ ($1.9 \cdot 10^{-3}$ M), at pH 6.7 [BR buffer/NaTFA (0.1 M)], in the potential range of 0.47 V ($Ru_3^{III,III,III}$; $n = 1+$) to 0.12 V ($Ru_3^{III,III,II}$; $n = 0$).

 © 2006 Wiley-VCH Verlag GmbH & Co. KGaA, Weinheim 

At pH 1.4, the cyclic voltammograms display another reversible wave at 1.2 V (Figure 5), corresponding to the IV,III,III/III,III,III redox couple [Equation (8)], which is dramatically sensitive to pH changes. The Pourbaix plots (Figure 6) exhibit two breaking points at pH 2.5 and 6.7, which correspond to the p$K_a$'s of the equilibria in Equation (9) and Equation (10), respectively.

$$[Ru_3^{IV,III,III}(H_2O)]^{2+} + e \rightleftharpoons [Ru_3^{III,III,III}(H_2O)]^{+} \quad E_{1/2} = 1.20\ V \quad (8)$$

$$[Ru_3^{IV,III,III}(H_2O)]^{2+} \rightleftharpoons [Ru_3^{IV,III,III}(OH)]^{+} + H^{+} \quad pK_a = 2.5 \quad (9)$$

$$[Ru_3^{IV,III,III}(OH)]^{+} \rightleftharpoons [Ru_3^{IV,III,III}(O)] + H^{+} \quad pK_a = 6.7 \quad (10)$$

Because the required potentials for the oxidation of the $[Ru_3^{III,III,III}O(Ac)_6(py)_2(H_2O)]^+$ species were near the working limits of water, the formation of the IV,III,III redox state could not be monitored spectroelectrochemically. Instead, a spectrophotometric redox titration was carried out in $HClO_4$ (0.1 M) using $Ce^{IV}$ as a chemical oxidant. As shown in Figure 8 (b), the redox titration was consistent with a 1:1 stoichiometry. The oxidized $[Ru_3^{IV,III,III}O(Ac)_6(py)_2(H_2O)]^{2+}$ species exhibits two characteristic IC bands at 565 and 776 nm, as shown in Figure 8 (a).

At pH 2.5, an additional oxidation wave was discernible at 1.3 V, overlapping the existing reversible wave with $E_{1/2}$ = 1.2 V. The intensity of the resulting convoluted wave was two times that of a monoelectronic process. The new cathodic wave is pH-dependent and was assigned to the 1-$H^+$ or 2-$H^+$ proton-coupled IV,IV,III/IV,III,III redox process of Equation (11) or Equation (12), respectively, depending on the pH region (Figure 6).

$$[Ru_3^{IV,IV,III}(O)]^{+} + 2\,H^{+} + e^{-} \rightleftharpoons [Ru_3^{IV,III,III}(OH_2)]^{2+} \quad pH < 2.5 \quad (11)$$

$$[Ru_3^{IV,IV,III}(O)]^{+} + H^{+} + e^{-} \rightleftharpoons [Ru_3^{IV,III,III}(OH)]^{+} \quad pH > 2.5 \quad (12)$$

The overall redox processes discussed above have been collected in the Pourbaix diagrams of Figure 6.

It should be noted that at pH 6.7 the spectroelectrochemical oxidation (Figure 9) of $[Ru_3^{III,III,III}O(Ac)_6(py)_2(H_2O)]^+$, starting from 0.47 V, actually involves two overlapping successive redox processes. At 0.97 V, the hydroxo species $[Ru_3^{IV,III,III}O(Ac)_6(py)_2(OH)]^+$ should be predominantly formed; at 1.12 V, the product of oxidation (coupled to deprotonation) is expected to be $[Ru_3^{IV,IV,III}O(Ac)_6(py)_2(O)]^+$. A new band at 418 nm was observed for the latter, in addition to a broad band around 850 nm. On the other hand, the vestiges of the initial band around 700 nm may be an indication of some partial regeneration of the starting complex, perhaps by a parallel catalytic process involving the decomposition of water by the highly oxidized, oxo-[IV,IV,III] species (a point that will be discussed below).

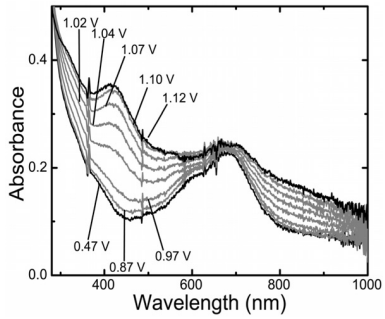


Figure 9. Spectroelectrochemical changes in a solution of $[Ru_3O(Ac)_6(py)_2(OH_x)]^+$ ($1.9\cdot10^{-3}$ M), at pH 6.7 [BR buffer/NaTFA (0.1 M)], in the potential range of 0.47 V (aqua-$Ru_3^{III,III,III}$) to 0.97 V (hydroxo-$Ru_3^{IV,III,III}$), and then to 1.12 V (oxo-$Ru_3^{IV,IV,III}$).

At pH 9.5 a different electrochemical pattern is observed (Figure 10), with three oxidation waves in the 0.7–1.2 V range. The anodic process at 0.73 V seems to follow a regular pattern when it is inserted into the Pourbaix diagram (Figure 6), and is consistent with the proton-coupled redox process of Equation (13).

$$[Ru_3^{III,III,III}(OH)] + OH^{-} \rightarrow [Ru_3^{IV,III,III}(O)] + H_2O + e^{-} \quad (13)$$

The remaining anodic peaks around 1.0 V exhibit relative intensities strongly dependent on the potential scan rates, indicating the occurrence of chemical reactions coupled with the oxidation of the $[Ru_3^{IV,III,III}O(Ac)_6(py)_2(O)]$ species (into $[Ru_3^{IV,IV,III}O(Ac)_6(py)_2(O)]^+$). A possibility is the decomposition of water by the oxo-[IV,IV,III] species [Equation (14)], which accounts for the catalytic peak mani-

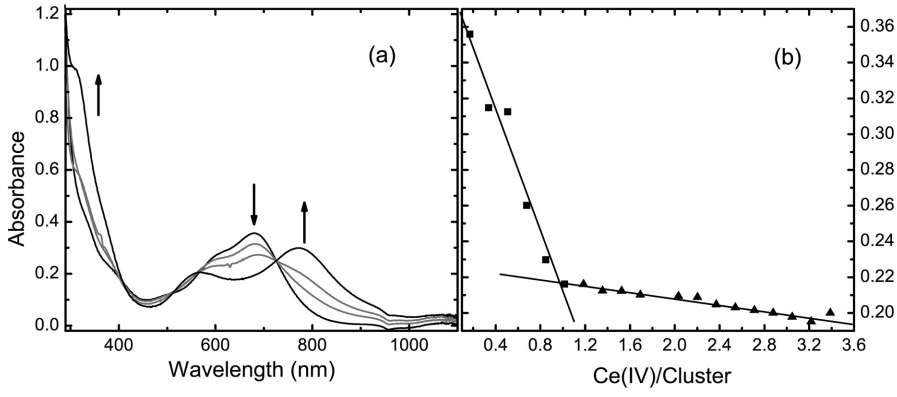


Figure 8. (a) Spectrophotometric redox titration of $[Ru_3O(Ac)_6(py)_2(H_2O)]^+$ ($1.0\cdot10^{-4}$ M) in $HClO_4$ (0.1 M) with Ce(IV) in $H_2SO_4$ (1.0 M). (b) Plot of absorbance (at 683 nm) vs. Ce(IV)/cluster molar ratio.

 © 2006 Wiley-VCH Verlag GmbH & Co. KGaA, Weinheim 

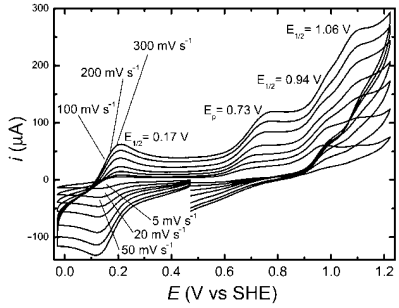


Figure 10. Cyclic voltammograms, at several scan rates, of $[Ru_3O(Ac)_6(py)_2(H_2O)]^+$ ($1.3\cdot10^{-3}$ M) in BR buffer/NaTFA (0.1 M) at pH 9.5.

fested near 1.0 V at low scan rates (Figure 10). This reaction regenerates the starting aqua-[III,III,III] species, thus explaining the lack of cathodic waves in the reverse scan.

$$2\ [Ru_3^{IV,IV,III}(O)]^+ + 2\ H_2O \rightarrow 2\ [Ru_3^{III,III,III}(H_2O)]^+ + O_2 \qquad (14)$$

By increasing the scan rates, two inflections can be noted around 0.95 and 1.15 V, in addition to the catalytic wave. As shown below, these signals can be assigned to the presence of small amounts of dimeric species. In fact, cyclic voltammograms of the product isolated from the disproportionation reaction discussed above, in acetonitrile (Figure 11), are consistent with the existence of dimeric species.

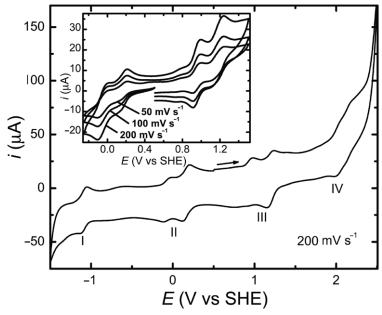


Figure 11. Cyclic voltammograms of the cluster dimer $[\{Ru_3O(Ac)_6(py)_2\}_2(O)]^{2+}$ ($1.9\cdot10^{-3}$ M) in acetonitrile/TEAP (0.1 M).

The voltammograms of the cluster dimer in acetonitrile exhibit essentially the characteristic waves for the cluster monomer "in duplicate". Table 1 summarizes the corresponding processes in four distinct regions: (I) –1.09 V; (II) –0.07 and 0.16 V; (III) 0.95 and 1.17 V; (IV) 2.01 and 2.14 V (see also Figure 11).

Table 1. Redox potentials for the oxo-bridged cluster dimer, $[\{Ru_3O(Ac)_6(py)_2\}_2(O)]^n$, in acetonitrile/TEAP (0.1 M).

| Redox couple ($Ru_3$–$Ru_3$) | $E_{1/2}$ (V vs. SHE) |
|---|---|
| [III,III,II]–[III,III,II]/2[III,II,II] | –1.09 |
| [III,III,III]–[III,III,II]/[III,III,II]–[III,III,II] | –0.07 |
| [III,III,III]–[III,III,III]/[III,III,III]–[III,III,II] | 0.16 |
| [IV,III,III]–[III,III,III]/[III,III,III]–[III,III,III] | 0.95 |
| [IV,III,III]–[IV,III,III]/[IV,III,III]–[III,III,III] | 1.17 |
| [IV,IV,III]–[IV,III,III]/[IV,III,III]–[IV,III,III] | 2.01 |
| [IV,IV,III]–[IV,IV,III]/[IV,IV,III]–[IV,III,III] | 2.14 |

The reversible waves observed at 0.95 and 1.17 V are consistent with those obtained in aqueous solution at pH 9. From the splitting of the redox couples involving mixed-valent states, the comproportionation constant for the $[Ru_3–Ru_3]^n + [Ru_3–Ru_3]^{n+2} \rightleftharpoons 2\times[Ru_3–Ru_3]^{n+1}$ equilibrium can be calculated as $K_c = \exp[(\Delta E\cdot F)/RT]$,[15] where $\Delta E$ is the potential separation between the $[Ru_3–Ru_3]^{n+2}/[Ru_3–Ru_3]^{n+1}$ and $[Ru_3–Ru_3]^{n+1}/[Ru_3–Ru_3]^n$ redox couples (i.e., $\Delta E_{1/2}$). In this way, the obtained values for regions II–IV are: $7.7\cdot10^3$ ($\Delta E$ = 230 mV; region II), $5.2\cdot10^3$ ($\Delta E$ = 220 mV; region III) and $1.6\cdot10^2$ ($\Delta E$ = 130 mV; region IV). As comproportionation constants can be related to the stabilization promoted by the electronic delocalization in the mixed-valence states,[15] according to this evaluation of $K_c$ based on the closely-spaced redox potentials, the electronic coupling between the two cluster units does not appear to be particularly strong within the oxidation-state range studied and reported herein. Consistent with these findings are also preliminary results of ongoing theoretical calculations of molecular and electronic structures, which provide additional evidence for the moderate extent of cluster-to-cluster electronic communication (despite the obvious metal–ligand mixing and delocalization within each cluster).

Attempts to detect the existence of cluster-to-cluster intervalence charge-transfer (IVCT) bands in the mixed-valence states of the cluster dimer were conducted by means of Vis/near-IR spectroelectrochemistry in acetonitrile, in the potential range of –1.0 to 1.2 V. Unfortunately, the results were not conclusive, resembling those of the monomeric species. No evidence of such IVCT transitions was found, most likely due to weak absorptivity or convolution with the broad IC bands.

## Electrocatalytic Activity in the Oxidation of Benzyl Alcohol

Oxo–metal complexes are of great interest in the catalytic oxidation of organic substrates[16–31] because of their ability to promote selective oxygen-transfer reactions, without the participation of less specific oxygen-free radical agents.[24,29,30] For this reason, we extended the study on the redox properties of the oxo–ruthenium clusters to include their electrocatalytic behavior in the oxidation of benzyl alcohol in aqueous solution.

Figure 12 shows typical cyclic voltammograms of the $[Ru_3^{III,III,III}O(Ac)_6(py)_2(H_2O)]^+$ complex in aqueous solution, at pH 3.0, in the presence of increasing amounts of benzyl alcohol. A linear increase of the amperometric current is observed at 1.2 V, which coincides with the convoluted waves assigned above to the proton-coupled oxidation of $[Ru_3^{III,III,III}O(Ac)_6(py)_2(H_2O)]^+$ into $[Ru_3^{IV,III,III}{}_3O(Ac)_6(py)_2(OH)]^+$ and $[Ru_3^{IV,IV,III}O(Ac)_6(py)_2(O)]^+$. The lack of redox response from the benzyl alcohol up to 1.4 V, and the absence of the cathodic waves from the oxidized clusters in the reverse scan, are consistent with the electrocatalytic oxidation of benzyl alcohol.

 © 2006 Wiley-VCH Verlag GmbH & Co. KGaA, Weinheim 

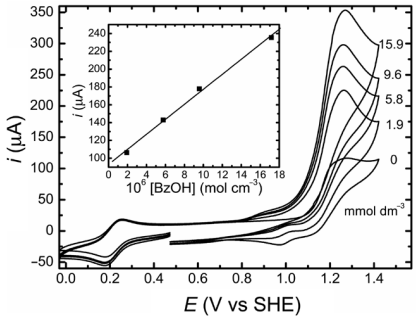


Figure 12. Cyclic voltammograms (at 50 mV $s^{-1}$) of $[Ru_3O(Ac)_6(py)_2(H_2O)]^+$ ($1.3\cdot10^{-3}$ M) in BR buffer/NaTFA (0.1 M), at pH 3.0, in the presence of various amounts of benzyl alcohol. The inset shows the linear dependence of the anodic peak current above 1.2 V vs. the concentration of benzyl alcohol.

Additional insight into the electrocatalytic oxidation of benzyl alcohol was obtained from the cyclic voltammograms of similar sample solutions at pH 6.7 (Figure 13). In this case, the pH-dependent reduction potential of the hydroxo-[IV,III,III]/aqua-[III,III,III] redox/protonation couple was shifted to 0.9 V. From the current increase at 1.1 V,

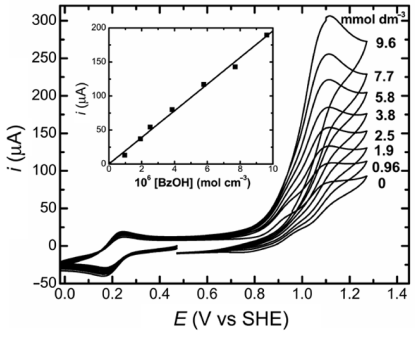


Figure 13. Cyclic voltammograms (at 50 mV $s^{-1}$) of $[Ru_3O(Ac)_6(py)_2(H_2O)]^+$ ($1.3\cdot10^{-3}$ M) in BR buffer/NaTFA (0.1 M), at pH 6.7, in the presence of various amounts of benzyl alcohol. The inset shows the linear dependence of the anodic peak current around 1.1 V vs. the concentration of benzyl alcohol.

the catalytic wave can be readily associated with participation of the oxo-[IV,IV,III]/hydroxo-[IV,III,III] couple.

The electrocatalytic scheme in this case corresponds to that categorized by Nicholson and Shain[32] as type VII, which involves a reversible electron transfer followed by a reaction regenerating the starting complex [Equation(15)].

$$R \rightleftharpoons O + ne^- \quad (15a)$$

$$O + Z \rightarrow R\ (k'_f) \quad (15b)$$

For this scheme, assuming a diffusional process for the catalytic reaction, Sawyer[33] has shown that, when the scan rates increase by an order of magnitude, the peak potential ($E_p$) is shifted by approximately 0.030 V, as expressed by Equation (16) (where α is the electron-transfer coefficient, $n_\alpha$ is the number of electrons involved in the process, and $v$ is the potential scan rate). From the slope of the linear plot in Figure 14 (a), $\alpha\cdot n_\alpha = 0.91$. Similarly, by combining this value into Equation (17)[32,33] (where $i_p$ is the oxidation peak current, $A$ is the electrode area, $C_0$ is the substrate concentration, and the diffusion coefficient, $D_0 = 7.1\cdot10^{-6}$ $cm^2 s^{-1}$, was estimated from the Stokes-Einstein[25] equation: $D = k_B T/6\pi r\eta$, $k_B$ = Boltzmann's constant, $T$ = temperature, $r$ = solvodynamic radius, and $\eta$ = viscosity), the number of electrons $n$ was calculated to be 2.04 from the slope of the corresponding linear plot shown in Figure 14 (b). Therefore, the oxidation of benzyl alcohol proceeds by a two-electron-transfer process to generate benzaldehyde, as also confirmed by standard tests with (2,4-dinitrophenyl)hydrazine.

$$E_p = K + (0.03/\alpha\cdot n_\alpha)\log(v) \quad (16)$$

$$i_p = 2.99\cdot10^5\, n\, (\alpha\cdot n_\alpha)^{1/2}\, A\cdot C_0\cdot D_0^{1/2}\cdot v^{1/2} \quad (17)$$

The catalytic kinetic constant ($k_f$) can be determined from the working plot of $i_k/i_d$ vs. $\psi^{1/2}$ (where $i_k$ is the catalytic current, $i_d$ is the diffusion current, $\psi = k_f/a$ and $a = nFv/RT$), as described by Nicholson and Shain[32] (Figure 15, a). The catalytic current, in this case, was measured in the presence of benzyl alcohol under pseudo-first-order conditions ($C = 9.6\cdot10^{-3}$ M). The diffusion current was given

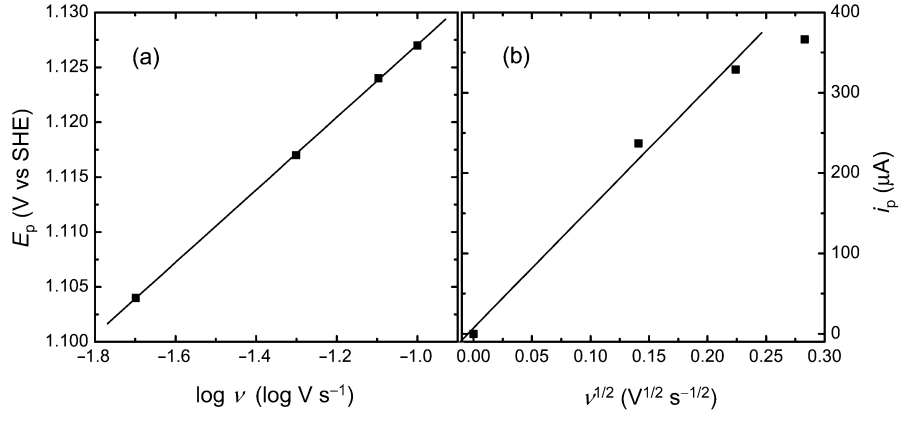


Figure 14. Plots of the catalytic potential peak vs. log$v$ (a) or catalytic current peak vs. $v^{1/2}$ (b), for the oxidation of benzyl alcohol ($3.85\cdot10^{-3}$ M) by the cluster ($1.3\cdot10^{-3}$ M) at pH 6.7 [BR buffer/NaTFA (0.1 M)].

 © 2006 Wiley-VCH Verlag GmbH & Co. KGaA, Weinheim 

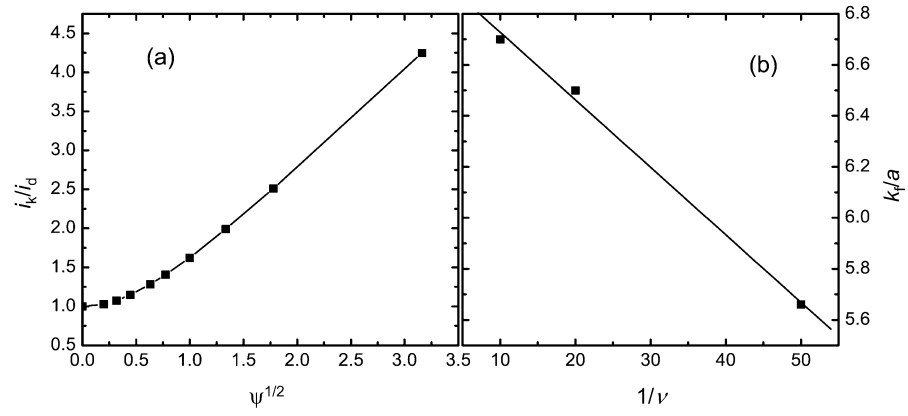


Figure 15. Plots of (a) $i_k/i_d$ vs. $\psi^{1/2}$, and (b) $k_f/a$ vs. $1/\nu$ (see text for details).

by the same measurement in the absence of the substrate. The calculated $k_f/_a$ values are then plotted against $1/\nu$ and, from the slope, $k_f/(nF/RT)$ is obtained. In this way, $k_f$ was determined to be 2.1 $s^{-1}$ and, the corresponding second-order rate constant, $k'_f = k_f/[\text{substrate}]$, is $2.2 \cdot 10^2$ $M^{-1}$ $s^{-1}$.

It is interesting to notice that the kinetic constant for the oxidation of benzyl alcohol by the cluster is significantly higher than those reported[34] for the complexes $[Ru^{IV}(tpy)(bpy)(O)]^{2+}$, at pH 13, ($k'_f$ = 36.1 $M^{-1}$ $s^{-1}$) or $[Ru^{IV}(tpy)(bpz)(O)]^{2+}$ ($k'_f$ = 23.0 $M^{-1}$ $s^{-1}$), at pH 11 (tpy = 2,2′′:6,2′′-terpyridine; bpz = 2,2′-bipyrazine). Considering the redox potentials for these complexes (0.86 V and 0.90 V, respectively),[34,35] the comparatively enhanced catalytic activity of the $[Ru_3^{IV,IV,III}O(Ac)_6(py)_2(O)]^+$ cluster may arise from its stronger oxidizing character ($E^o$ = 1.1 V at pH 6.7).

## Conclusion

In summary, the trinuclear ruthenium clusters of the type $[Ru_3O(Ac)_6(py)_2(OH_x)]^n$ exhibit a very rich proton-coupled redox chemistry in aqueous solution. On the basis of cyclic voltammetry and spectroelectrochemical measurements as a function of pH, the various protonation/oxidation states have been characterized and the complete Pourbaix diagram has been proposed for the system, which comprises all reversible one-proton/one-electron transformations involving the aqua- ($x$ = 2), hydroxo- ($x$ = 1), and oxo- ($x$ = 0) forms with the increasing oxidation states of the triangular redox center. An enhanced catalytic activity for the $[Ru_3^{IV,IV,III}O(Ac)_6(py)_2(O)]^+$ oxo species has been demonstrated in the oxidation of benzyl alcohol, evidencing the activation of the $Ru^{IV}$–O bonding in oxygen-transfer reactions. Moreover, the new μ-oxo-bridged cluster dimer $[\{(py)_2(Ac)_6ORu_3\}\text{-}O\text{-}\{Ru_3O(Ac)_6(py)_2\}]^n$ has been isolated and characterized, and the combined electrochemical and spectroscopic results indicate only moderate electronic coupling between the two triangular cluster units through the oxo bridge. Next, additional understanding of the molecular and electronic structures of these systems will also be pursued by means of theoretical quantum chemical calculations, which should be of invaluable assistance in providing a comprehensive view of the electronic interactions across the various oxidation/protonation states as well as the wealth of useful properties arising from the proton-coupled redox chemistry of these *apparently* simple triruthenium clusters.

## Experimental Section

**Chemical Preparations:** The precursor complex $[Ru_3O(Ac)_6(py)_2(CH_3OH)]PF_6$ was prepared according to reported procedures.[5] All other reagents and solvents were of analytical grade and used as supplied. Britton–Robinson (BR) buffer solution (0.1 M) was employed in the pH-controlled experiments (pH 4–12). Sodium trifluoroacetate (NaTFA) or tetraethylammonium perchlorate (TEAP) was used as supporting electrolyte ($I$ = 0.1 M) in sample solutions for (spectro)electrochemical measurements in water or acetonitrile, respectively.

$[Ru_3O(Ac)_6(py)_2(H_2O)]Cl$ was obtained by treating $[Ru_3O(Ac)_6(py)_2(CH_3OH)]PF_6$ (400 mg; 0.40 mmol) with $[AsPh_4]Cl$ (170 mg; 0.40 mmol) dissolved in water (30 mL), whilst stirring, for at least 2 h. The resulting white precipitate of $[AsPh_4]PF_6$ was collected on a fine filter containing microcrystalline cellulose, and the filtrate was roto-evaporated to dryness. The solid product was stored under vacuum. Yield: 230 mg (65%). $C_{22}H_{30}ClN_2O_{14}Ru_3$ (885.1): calcd. C 29.85, H 3.42, N 3.16; found C 28.77, H 3.35, N 3.29. IR (KBr, $cm^{-1}$): $\tilde{\nu}$ = 1556 m ($\upsilon_{as,}$ $CO_2$) , 1418 s ($\upsilon_s$, $CO_2$) , 1607 m ($\upsilon_{ring}$, py), 1485 m, and 1448 sh.

**Physical Methods:** Electronic spectra were recorded with either a HP 8453 diode-array spectrophotometer (UV/Vis) or a Guided Wave 260 fiber-optic instrument (near-IR). Cyclic voltammetry measurements were carried out with an Autolab PGSTAT 30 potentiostat/galvanostat and a conventional three-electrode cell containing a glassy-carbon working electrode ($A$ = 0.196 $cm^2$), a platinum-wire auxiliary electrode, and an Ag/AgCl (1.0 M KCl, $E^0$ = 0.222 V vs. SHE) or $Ag/AgNO_3$ (0.010 M, $E^0$ = 0.503 V vs. SHE) reference minielectrodes in aqueous or acetonitrile solutions, respectively. A three-electrode system, arranged in a rectangular quartz cell ($l$ = 0.25 mm), was used for the spectroelectrochemical measurements. In this case, a gold minigrid as a transparent working electrode was used with the above mentioned auxiliary and reference minielectrodes. All measurements were performed at room temperature (25 °C). Electrospray mass spectra were recorded with

 © 2006 Wiley-VCH Verlag GmbH & Co. KGaA, Weinheim 

a Micromass Q-Tof mass spectrometer with a quadrupole (Qq) and high-resolution orthogonal time of flight (o-TOF) configuration. Samples dissolved in pure methanol were injected using a syringe pump (Harvard Apparatus, Pump 11, 10 μL/min) through an uncoated fused-silica capillary. The ESI-MS mass spectra were acquired using an ESI capillary voltage of 3 kV and a cone voltage of 10 V.

## Acknowledgments

The support from FAPESP, CNPq, RENAMI, IM2C, and CAPES/PICD is gratefully acknowledged.

[1] J. Burgess, *Metal Ions in Solution*, John Wiley & Sons, New York, **1978**.
[2] R. I. Cukier, D. G. Nocera, *Annu. Rev. Phys. Chem.* **1998**, *49*, 337–369.
[3] J. M. Mayer, *Annu. Rev. Phys. Chem.* **2004**, *55*, 363–390.
[4] T. J. Meyer, M. H. V. Huynh, *Inorg. Chem.* **2003**, *42*, 8140–8160.
[5] H. E. Toma, K. Araki, A. D. P. Alexiou, S. Nikolaou, S. Dovidauskas, *Coord. Chem. Rev.* **2001**, *219–221*, 187–234.
[6] A. Spencer, G. Wilkinson, *J. Chem. Soc., Dalton Trans.* **1972**, 1570–1577.
[7] A. Spencer, G. Wilkinson, *J. Chem. Soc., Dalton Trans.* **1974**, 786–792.
[8] S. T. Wilson, R. F. Bondurant, T. J. Meyer, D. J. Salmon, *J. Am. Chem. Soc.* **1975**, *97*, 2285–2287.
[9] J. A. Baumann, D. J. Salmon, S. T. Wilson, T. J. Meyer, W. E. Hatfield, *Inorg. Chem.* **1978**, *17*, 3342–3350.
[10] H. E. Toma, C. Cipriano, *J. Electroanal. Chem.* **1989**, *263*, 313–322.
[11] H. E. Toma, C. J. Cunha, *Can. J. Chem.* **1989**, *67*, 1632–1635.
[12] B. A. Moyer, T. J. Meyer, *Inorg. Chem.* **1981**, *20*, 436–444.
[13] V. R. Souza, G. S. Nunes, R. C. Rocha, H. E. Toma, *Inorg. Chim. Acta* **2003**, *348*, 50–56.
[14] E. L. Lebeau, S. A. Adeyemi, T. J. Meyer, *Inorg. Chem.* **1998**, *37*, 6476–6484.
[15] R. C. Rocha, H. E. Toma, *Quim. Nova* **2002**, *25*, 624–638.
[16] B. A. Moyer, M. S. Thompson, T. J. Meyer, *J. Am. Chem. Soc.* **1980**, *102*, 2310–2312.
[17] M. S. Thompson, W. F. Degiovani, B. A. Moyer, T. J. Meyer, *J. Org. Chem.* **1984**, *49*, 4972–4977.
[18] J. C. Dobson, W. K. Seok, T. J. Meyer, *Inorg. Chem.* **1986**, *25*, 1513–1514.
[19] K. Y. Wong, C. M. Che, F. C. Anson, *Inorg. Chem.* **1987**, *26*, 737–741.
[20] L. Roecker, T. J. Meyer, *J. Am. Chem. Soc.* **1987**, *109*, 746–754.
[21] C. M. Che, V. W. W. Yam, *J. Am. Chem. Soc.* **1987**, *109*, 1262–1263.
[22] M. E. Marmion, K. J. Takeuchi, *J. Am. Chem. Soc.* **1988**, *110*, 1472–1480.
[23] C. M. Che, W. T. Tang, W. T. Wong, T. F. Lai, *J. Am. Chem. Soc.* **1989**, *111*, 9048–9056.
[24] C. M. Che, V. W. W. Yam, T. C. W. Mak, *J. Am. Chem. Soc.* **1990**, *112*, 2284–2291.
[25] C. M. Che, C. Ho, T. C. Lau, *J. Chem. Soc., Dalton Trans.* **1991**, 1901–1907.
[26] C. M. Che, W. T. Tang, W. O. Lee, K. Y. Wong, T. C. Lau, *J. Chem. Soc., Dalton Trans.* **1992**, 1551–1556.
[27] Y. K. Lai, K. Y. Wong, *Electrochim. Acta* **1993**, *38*, 1015–1021.
[28] A. S. Kanmani, S. Vancheesan, *J. Mol. Catal. A* **1997**, *125*, 127–134.
[29] M. Navarro, W. F. Degiovani, J. R. Romero, *J. Mol. Catal. A* **1998**, *135*, 249–256.
[30] E. L. Lebeau, T. J. Meyer, *Inorg. Chem.* **1999**, *38*, 2174–2181.
[31] D. Chatterjee, A. Mitra, R. E. Shepherd, *Inorg. Chim. Acta* **2004**, *357*, 980–990.
[32] R. S. Nicholson, I. Shain, *Anal. Chem.* **1964**, *36*, 706–722.
[33] D. T. Sawyer, A. Sobkowiak, J. L. Roberts Jr, *Electrochemistry for Chemists*, John Wiley & Sons, New York, **1995**.
[34] A. Gerli, J. Reedijk, M. T. Lakin, A. L. Spek, *Inorg. Chem.* **1995**, *34*, 1836–1843.
[35] K. J. Takeuchi, M. S. Thompson, D. W. Pipes, T. J. Meyer, *Inorg. Chem.* **1984**, *23*, 1845–1851.

Received: December 6, 2005
Published Online: February 15, 2006

 © 2006 Wiley-VCH Verlag GmbH & Co. KGaA, Weinheim 

DOI: 10.1002/ejic.200501116

# The First End-On Bonded Superoxo Complexes of Ga and In: The Oxygen-Rich Compounds $GaO_4$ and $InO_4$

**Benjamin Gaertner,[a] Andreas Köhn,[b] and Hans-Jörg Himmel*[a]**

*Dedicated to Prof. Hansgeorg Schnöckel on the occasion of his 65th birthday*

**Keywords:** Oxidation / Ga metal / Superoxo complex / Reaction mechanism / Matrix isolation / Vibrational spectrosopy

We report the first sighting and characterization of the oxygen-rich molecules $GaO_4$ and $InO_4$, being the products of a three-step process taking place in an Ar matrix. This process includes (i) reaction of Ga or In atoms (M) with one dioxygen molecule to give the cyclic superoxo complex $MO_2$, (ii) photoisomerization into linear OMO by the action of UV light, and (iii) reaction of linear OMO with an additional $O_2$ molcule. The molecules can be described as end-on bonded superoxo complexes $OMO(O_2)$. On the basis of the observed isotopic data the O–Ga–O angle can be estimated to be ca. 165°. In addition to the experimental studies, quantum chemical calculations were performed to achieve a more complete characterization of these interesting new and unusual molecules, representing the first ever found examples of end-on bonded superoxo complexes of Ga and In.

(© Wiley-VCH Verlag GmbH & Co. KGaA, 69451 Weinheim, Germany, 2006)

## Introduction

Oxidation of a metal is an important but very complex process. To shed more light on this process, the interaction of $O_2$ with a number of metals was studied intensively in the past decades.[1] The matrix isolation technique offers the possibility to study in detail the reactivity of metal atoms and small clusters towards dioxygen. E.g. Co atoms react upon photolysis with $O_2$ to give firstly the linear OCoO molecule with a $^2\Sigma_g^-$ electronic ground state.[2,3] Reaction of this species with a second $O_2$ molcule leads to an end-on bonded OCoO(OO) complex,[4] which in the matrix slowly undergoes conversion into a side-on bonded complex. According to quantum chemical calculations, the electronic ground state, $^2A_2$, of this complex is indeed the side-on bonded form. The calculations predict a decrease of the OCoO angle from 180° to 116° in the course of complexation. However, a $^4A'$ electronic state with an end-on bonded $O_2$ unit is only about 35 kJ·mol$^{-1}$ higher in energy. The experimental results show that the excited $^4A'$ state is firstly formed and that the product then relaxes in a spin-forbidden process [Equation (1)] from the end-on bonded complex to the side-on bonded complex. The excited state lifetime amounts to ca. 23 min in Ar and 15 min in Ne. In an Ar matrix, the $\nu$(O–O) mode of the ligated $O_2$ unit shows at 1286.2 cm$^{-1}$ in the case of the end-on bonded complex and at 950.6 cm$^{-1}$ for the side-on bonded form.

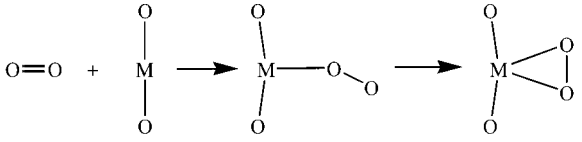


(1)

Very recently it has been shown that Al atoms can bind up to three $O_2$ units, leading to the oxygen-rich tris-superoxo complex $Al(O_2)_3$.[5] The species $Al(O_2)_2$ was also sighted, being a radical (one unpaired electron) featuring $D_{2d}$ symmetry. It was also shown that photolytically activated AlX (X = F, Cl, Br) molecules react with $O_2$ to give the peroxo complex $XAlO_2$,[6] or, with an excess of $O_2$, the bis-superoxo complex $XAl(O_2)_2$.[7] These examples show that group 13 elements and subvalent compounds undergo interesting and complex reactions with $O_2$.

The reaction of Ga atoms with one $O_2$ molcule leading to $GaO_2$ has now been studied in some detail both in inert gas matrices[8–10] and in the gas phase.[11] First the cyclic superoxo complex $GaO_2$ is formed in the course of a spontaneous reaction in the absence of any significant reaction barrier. The quantum chemical results indicate that the electron is transferred from the Ga atom to the $O_2$ unit at a distance of ca. 270 pm between Ga and the $O_2$ centroid. Cyclic $GaO_2$ in its $^2A_2$ electronic ground state is characterised by an O–Ga–O bond angle of 39° and an O–O bond length of 136 pm. This molecule can be photoconverted

[a] Inorganic Chemistry Laboratory
South Parks Road, Oxford, OX1 3QR, Great Britain
E-mail: hans-jorg.himmel@chem.ox.ac.uk
[b] Department of Chemistry, University of Aarhus
Langelandsgade 140, 8000 Aarhus, Denmark


© 2006 Wiley-VCH Verlag GmbH & Co. KGaA, Weinheim

into the linear isomer OGaO [see Equation (2)], which is formally valence isoelectronic to the $[OCO]^+$ cation, by the action of UV light ($\lambda_{max}$ = 254 nm).[10] Isomerization only by thermal means is opposed to a massive barrier in the order of ca. 300 kJ·mol$^{-1}$. Quantum chemical calculations on linear OGaO proved to be extremely difficult. Only if highly correlated methods are applied, it can be shown that linear OGaO in its $^2\Pi_g$ electronic ground state is ca. 18 kJ·mol$^{-1}$ more stable than cyclic $GaO_2$ ($^2A_2$ electronic ground state). As discussed in detail in a previous publication, calculations on the vibrational properties are hampered due to singlet instabilities of the ROHF wavefunction.[10] The analogous reaction between In atoms and $O_2$ has also been studied.

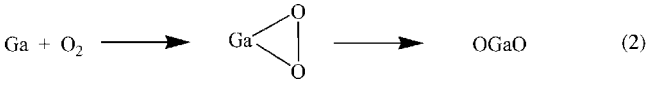


(2)

Here we will show that the linear OGaO and OInO molecules are capable of binding to an $O_2$ molcule leading to a species with the overall formula $GaO_4$ and $InO_4$, respectively. The vibrational (IR as well as Raman) spectra were used to characterize these interesting species. The results of quantum chemical calculations are also discussed. In the light of the problems with the calculations in the case of OGaO it does not come as surprise that the $O_2$ complex of this species turned also out to be difficult to calculate.

## Results and Discussion

In the following, the results for the reactions of Ga and In atoms with $O_2$ using IR and Raman spectroscopy will be reported in turn.

### Ga + $O_2$

**IR.** In experiments in which Ga atoms were codeposited together with 1% of $^{16}O_2$ in Ar, bands were observed in the IR spectrum at 1089.3, 380.5/378.9, and 283.2 cm$^{-1}$ which were already sighted previously and shown to belong to the cyclic superoxo complex $GaO_2$, **1a**. An increase of the $O_2$ concentration brought about an increase of the band intensities in a way characteristic for a species containing two O atoms. However, even in a pure $O_2$ matrix the spectra showed no sign of any product of a spontaneous reaction of Ga with more than one $O_2$ molcule. Thus, under the conditions of our experiments, Ga spontaneously takes up not more than one dioxygen molecule. Subsequently the matrix was subjected to a 15 min period of photolysis with UV light ($\lambda_{max}$ = 254 nm). The IR spectrum taken after this photolysis treatment (see Figure 1) displayed two families of bands, which both were absent in the spectra taken before photolysis. At the same time, the bands due to the cyclic superoxo complex $GaO_2$, **1a**, decreased significantly in intensity. The first family showed at 912.6/908.5 and 204.9/204.0 cm$^{-1}$. The absorber responsible for these bands was already identified to be the linear molecule OGaO, **2a**, formed via photoisomerization of cyclic $GaO_2$, **1a**.[10] The second group of bands belongs to a different species **3a**, which has not yet been identified. A very intense absorption of **3a** was observed with its maximum of intensity at 568.7 cm$^{-1}$. Figure 2 shows that this band can be fitted satisfactorily with two pairs of Lorenzian-type curves having their maxima at 568.7/566.2 and 565.9/563.6 cm$^{-1}$. The relative intensities within each of the pairs amount to 60.1:39.9, reflecting the natural abundances of $^{69}$Ga and $^{71}$Ga in a species containing only one Ga atom. Thus it is likely that **3a** contains one Ga atom. Convincing support comes from the inspection of the two weaker bands at lower wavenumbers (174.8/174.1 and 165.6/164.9 cm$^{-1}$), which both clearly show the isotopic pattern ($^{69}$Ga/$^{71}$Ga) characteristic for a species containing one Ga atom. The bands of **3a** at 1264.2/1261.8 cm$^{-1}$ come in a region in which ν(O–O) modes of end-on coordinated $O_2$ groups are expected to show [cf. Fe(OO) 1204.5,[12] OCoO(OO) 1286.2 cm$^{-1}$ [4]]. Bands at 1824.7/1820.0, 1816.7/1811.7 cm$^{-1}$ are most likely due to a combination mode between the modes showing near 568 and near 1264 cm$^{-1}$ (the presence of four maxima of absorption is then caused by matrix splitting of the fundamentals).

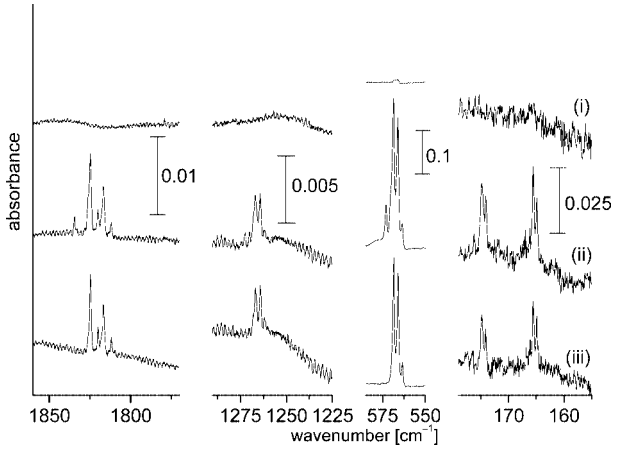


Figure 1. Some regions of the IR spectra recorded for a matrix containing Ga atoms and 0.3% $O_2$. (i) following deposition, (ii) upon UV photolysis ($\lambda_{max}$ = 254 nm), and (iii) annealing of the matrix to 30 K.

The experiments were repeated with different concentrations of Ga and $O_2$ in the matrix. Figure 3 compares two regions of the IR spectra taken for a matrix containing Ga and a) 0.3% and b) 1.0% $O_2$ in Ar. These two regions show bands characteristic for cyclic $GaO_2$, **1a**, which appear directly upon deposition and are virtually extinguished upon UV photolysis, and for linear OGaO, **2a**, and species **3a**, which both grow in upon UV photolysis and decrease in intensity upon annealing. For the low concentration of 0.3% of $O_2$ in the matrix the bands due to linear OGaO are much more intense than the ones due to **3a**. For higher concentrations of $O_2$ in the matrix (1%), the bands due to **3a** gain in relative intensity. This variation in the relative intensities indicates that two $O_2$ molcules are involved in the formation of **3a**, arguing for a species with the overall formula $GaO_4$. Using similar arguments experiments with

 © 2006 Wiley-VCH Verlag GmbH & Co. KGaA, Weinheim 

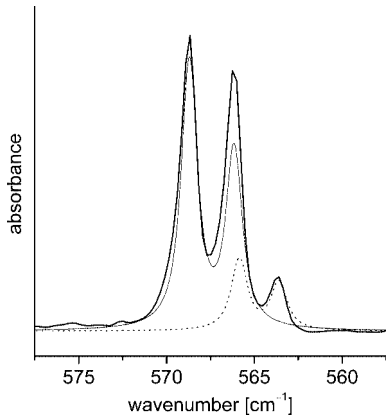


Figure 2. High-resolution IR spectrum showing the structure of the band near 570 cm$^{-1}$. The band structure can be fitted with two pairs of Lorenzian curves with intensities within each pair in agreement to the natural abundance of the $^{69}$Ga and $^{71}$Ga isotopomers.

different Ga concentrations are in agreement with the presence of only one Ga atom in **3a**, in line with the observed isotopic pattern.

Subsequently, experiments were carried out in a solid $O_2$ matrix (see Figure 4). In these experiments, the bands due to cyclic $GaO_2$, **1a**, were observed in the spectrum recorded immediately after deposition, in analogy to the situation in an $O_2$-doped Ar matrix. The bands decreased in intensity upon UV photolysis. However, there was no sign of the bands attributable to linear OGaO, **2a**, after photolysis. Instead, the spectra showed massive bands in close energetic proximity to those measured for **3a** in an Ar matrix (at 1853.5/1845.4, 1842.5/1834.3, 1286.0/1283.8, 1279.3/1276.3, 580.5/577.8, 575.9/573.3, 178.2, and 163.3 cm$^{-1}$). No bands belonging to another product of the reaction between Ga and $O_2$ were observed. Thus we conclude that $GaO_4$ can not take up another $O_2$ molcule. This is in clear difference to Al, which has been shown to form the tris-superoxo complex $Al(O_2)_3$, but in line with the general finding that Ga prefers lower coordination numbers than Al.

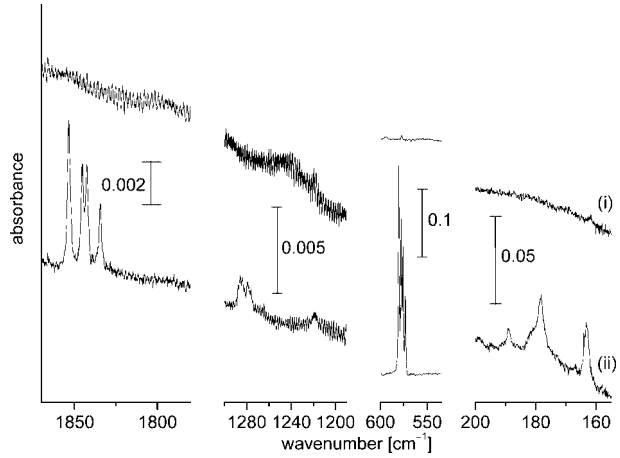


Figure 4. IR spectrum taken for an $O_2$ matrix containing Ga atoms. (i) upon deposition. (ii) upon UV radiation ($\lambda_{max}$ = 254 nm).

Finally, the experiments were repeated with different $O_2$ isotopomers. Figure 5 shows the regions of the IR spectra which contain bands due to **3a** for $^{16}O_2$, $^{18}O_2$, equimolar mixtures of $^{16}O_2$ and $^{18}O_2$ and 1:2:1 mixtures of $^{16}O_2$, $^{16}O^{18}O$, and $^{18}O_2$. Note that the spectra in the low (600–30 cm$^{-1}$) and high (2000–600 cm$^{-1}$) wavenumber region had to be recorded for different matrices using a Bolometer for the low and an MCT detector for the high wavenumber region (since we had to change the material of the windows of our high-vacuum apparatus from CsI for measurements with the MCT detector to polyethylene for measurements with the bolometer). It can be seen that all bands due to **3a** are red-shifted if $^{16}O_2$ is replaced by $^{18}O_2$. The IR spectra taken in the case of equimolar mixtures of $^{16}O_2$ and $^{18}O_2$ in the matrix virtually are the superposition of the IR spectra taken for $^{16}O_2$ and $^{18}O_2$ alone. The only difference is a

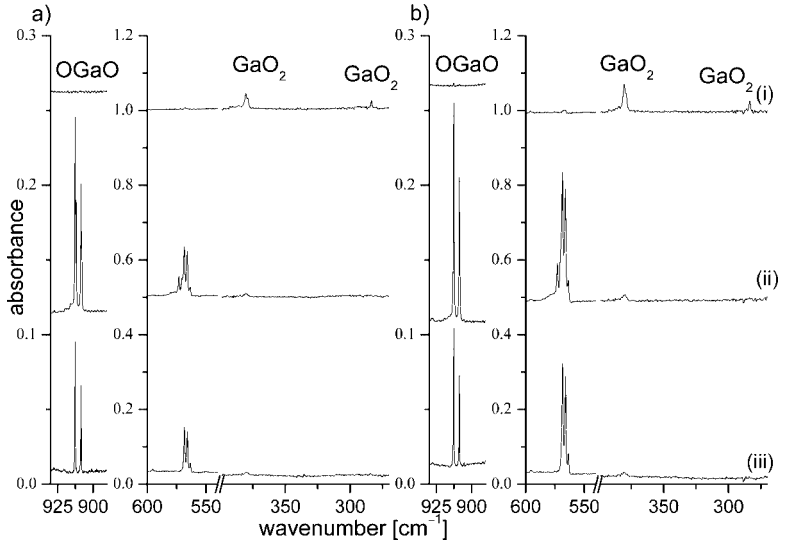


Figure 3. IR spectra taken for an Ar matrix containing Ga atoms (emitted from an oven kept at 1000 °C) and a) 0.3% and b) 1% $O_2$. (i) after deposition at 10 K, (ii) after UV photolysis ($\lambda_{max}$ = 254 nm), and (iii) after annealing to 30 K.

 © 2006 Wiley-VCH Verlag GmbH & Co. KGaA, Weinheim 

slight but nevertheless significant (see Discussion) broadening of the bands, especially those around 1266 and 1824 $cm^{-1}$ and the corresponding bands observed for the $^{18}O$ counterpart. This broadening is significant and will be shown to be consistent with the formulation of **3a** as an end-on bonded OGaO(OO) complex. The spectra taken with 1:2:1 mixtures of $^{16}O_2/^{16}O^{18}O/^{18}O_2$ give evidence for extra bands with wavenumbers between those measured for $^{16}O_2$ and $^{18}O_2$. The wavenumbers of all bands are included in Table 1.

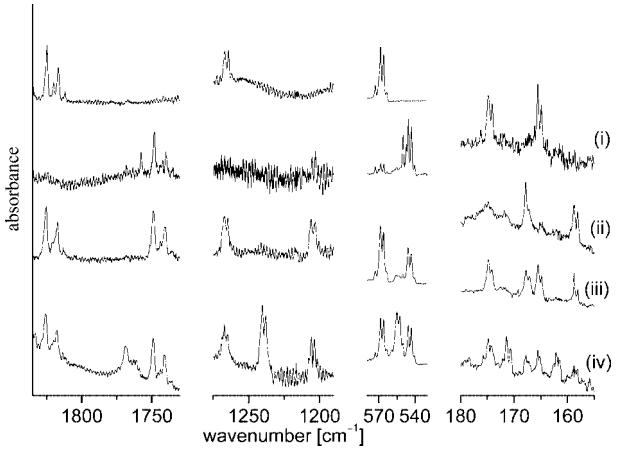


Figure 5. IR spectra taken after UV photolysis ($\lambda_{max}$ = 254 nm) of Ar matrices containing Ga atoms and (i) $^{16}O_2$, (ii) $^{18}O_2$, (iii) an equimolar mixture of $^{16}O_2$ and $^{18}O_2$, and (iv) a 1:2:1 mixture of $^{16}O_2/^{16}O^{18}O/^{18}O_2$.

Table 1. Wavenumbers observed for the reaction between Ga atoms and $O_2$ in Ar and pure solid $O_2$ matrices following photolysis at $\lambda_{max}$ = 254 nm.

| | Ga/$O_2$/Ar | | | Ga/$O_2$ | |
|---|---|---|---|---|---|
| | $^{16}O_2$ | $^{16}O^{18}O$ | $^{18}O_2$ | $^{16}O_2$ | $^{18}O_2$ |
| $GaO_2$, **1a** | 1089.3 | 1059.0 | 1027.9 | 1087.4 | 1026.0 |
| | 380.5/378.9 | 373.6/372.2 | 365.9/364.5 | 380.2 | 364.9 |
| | 283.2 | 275.3 | 268.1 | 288.8 | 273.1 |
| OGaO, **2a** | 912.6/908.5 | 897.4/893.4 | 877.6/873.4 | – | – |
| | 204.9/204.0 | 201.1/200.1 | 197.3/196.3 | – | – |
| $GaO_4$, **3a** | 1824.7 | 1769.1 | 1748.0 | 1853.5 | 1775.4 |
| | 1820.0 | | 1743.3 | 1845.4 | – |
| | 1816.7 | 1761.4 | 1739.8 | 1842.5 | 1765.5 |
| | 1811.7 | | 1735.2 | 1834.3 | – |
| | 1266.9 | 1240.4 | 1205.1 | 1286.0 | – |
| | 1264.2 | 1238.1 | 1202.5 | 1279.3 | – |
| | 716.2[a] | 676.0[a] | 697.6[a] | | |
| | 568.7 | 555.2 | 545.5 | 580.5 | 556.8 |
| | 565.9 | 552.5 | 543.1 | 577.8 | 553.9 |
| | 563.6 | 550.1 | 540.7 | 575.9 | 552.7 |
| | | | | 573.3 | 549.9 |
| | 174.8/174.1 | 171.4/170.6 | 167.8/167.1 | 178.2 | – |
| | 165.6/164.9 | 162.2/161.5 | 158.8/158.1 | 163.3 | – |

[a] Observed in the Raman experiments.

**Raman.** The Raman spectrum of a matrix containing Ga and $^{16}O_2$ showed an intense signal at 716.2 $cm^{-1}$ (Figure 6, i). This signal is already present directly after deposition, and shows no significant alterations in intensity upon radiation with UV light. On the basis of experiments in which the concentration of $O_2$ and Ga in the matrix was varied, it is likely that species **3a** is the author of this signal. Since the experiments have shown that photolysis is necessary to generate **3a**, the only reasonable explanation for the appearance of the band directly upon deposition is that **3a** is generated by the laser light used to excite the Raman spectra. In Figure 6, the Raman spectra taken for $^{16}O_2$, $^{18}O_2$, 1:1 mixtures of $^{16}O_2$ and $^{18}O_2$, and 1:2:1 mixtures of $^{16}O_2$, $^{16}O^{18}O$, and $^{18}O_2$ are compared. Again, the spectrum measured for a 1:1 mixture of $^{16}O_2$ and $^{18}O_2$ is not significantly different to the superposition of the spectra taken for $^{16}O_2$ and $^{18}O_2$ alone, thus showing two signals at 716.2 and 676.0 $cm^{-1}$. An extra signal at 697.6 $cm^{-1}$ appeared in the spectra taken for a 1:2:1 mixture of $^{16}O_2$, $^{16}O^{18}O$, and $^{18}O_2$. The wavenumbers are included in Table 1. Experiments were also carried out with Ga isolated in a solid $O_2$ matrix. These experiments give evidence for a signal at 723.0 $cm^{-1}$, slightly blue shifted with respect to the signal detected in an Ar matrix.

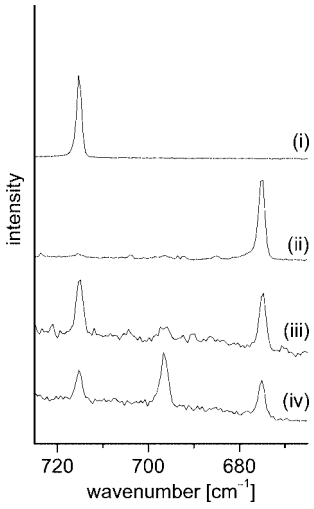


Figure 6. Raman spectra upon deposition for an Ar matrix containing Ga atoms and (i) $^{16}O_2$, (ii) $^{18}O_2$, (iii) an equimolar mixture of $^{16}O_2$ and $^{18}O_2$, and (iv) a 1:2:1 mixture of $^{16}O_2/^{16}O^{18}O/^{18}O_2$.

## In + $O_2$

**IR.** The IR spectra taken for an Ar matrix containing In atoms and $^{16}O_2$ are displayed in Figure 7. The spectrum taken immediately upon deposition contains sharp absorptions at 1084.2, 331.7 and 276.5 $cm^{-1}$ which were already previously assigned to cyclic $InO_2$, **1b**.[9,10] The effect of photolysis of the matrix with UV radiation ($\lambda_{max}$ = 254 nm) is the decrease of the bands due to **1b**. At the same time, two families of absorptions grow in. One family shows at 754.6 and 159.7 $cm^{-1}$ and belongs to linear OInO, **2b**.[10] The other family shows at 1498.8/1493.4, 1067.6/1063.8, 462.1/459.2, 151.3, and 146.5 $cm^{-1}$ and can be assigned to a new species **3b**. The conditions of its appearance indicate that **3b** is the In analogue to **3a**. In analogy to the experiments with Ga, the response of the bands due to **3b** to different concentrations of In and $O_2$ in the matrix are in agreement with the presence of one In atom and four O

 © 2006 Wiley-VCH Verlag GmbH & Co. KGaA, Weinheim 

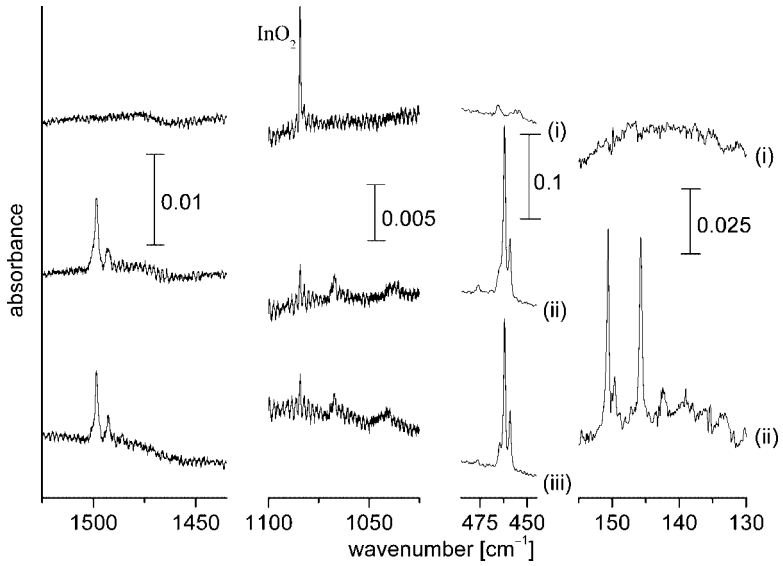


Figure 7. IR spectra of an Ar matrix containing Ga atoms and $^{16}O_2$. (i) upon deposition, (ii) upon UV photolysis ($\lambda_{max}$ = 254 nm), (iii) upon annealing to 30 K.

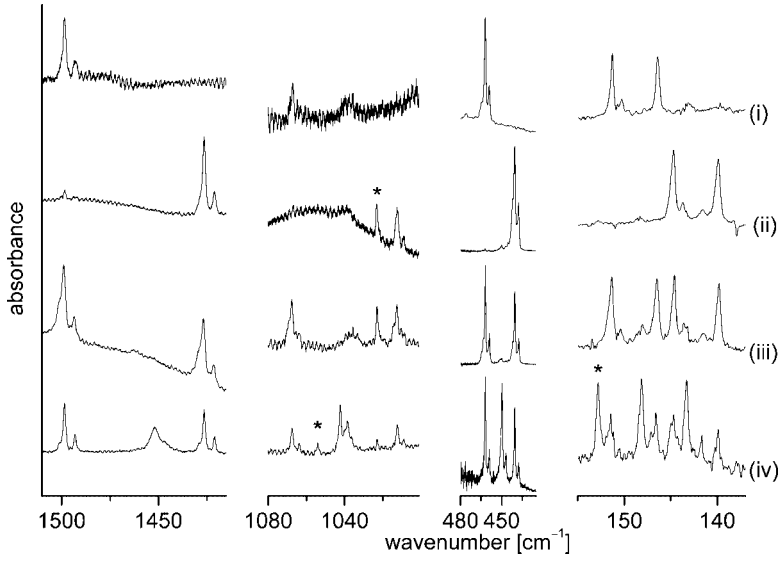


Figure 8. IR spectra taken after UV photolysis ($\lambda_{max}$ = 254 nm) of an Ar matrices containing Ga atoms and (i) $^{16}O_2$, (ii) $^{18}O_2$, (iii) an equimolar mixture of $^{16}O_2$ and $^{18}O_2$, and (iv) a 1:2:1 mixture of $^{16}O_2/^{16}O^{18}O/^{18}O_2$. Bands marked by an asteriks are due to $InO_2$.

atoms in the molecule. Figure 8 compares the spectra measured in experiments using different $O_2$ isotopomers ($^{16}O_2$, $^{18}O_2$, equimolar mixtures of $^{16}O_2$ and $^{18}O_2$, and 1:2:1 mixtures of $^{16}O_2/^{16}O^{18}O/^{18}O_2$). The band at 1498.8/1493.4 cm$^{-1}$ in the experiments with $^{16}O_2$ shifts to 1426.8/1421.5 cm$^{-1}$ with $^{18}O_2$. The band at 1067.6/1063.8 cm$^{-1}$ experienced a red-shift to 1012.6/1009.1 cm$^{-1}$ [$\nu(^{16}O):\nu(^{18}O)$ = 1.054]. The intense absorption at 462.1/459.2 cm$^{-1}$ shifts to 440.5/437.7 cm$^{-1}$ [$\nu(^{16}O):\nu(^{18}O)$ = 1.049]. The two bands which occur at 151.3 and 146.5 cm$^{-1}$ in the experiments with $^{16}O_2$ show at 144.6 and 139.8 cm$^{-1}$ with $^{18}O_2$. All bands are included in Table 2.

**Raman.** In difference to the reaction with Ga, the Raman spectra taken immediately upon deposition of In with $O_2$ shows the signals characteristic of cyclic $InO_2$, **1b** (see Figure 9). These signals decrease in intensity if the matrix is subjected to UV photolysis ($\lambda_{max}$ = 254 nm). At the same time a new intense signal appears at 621.0 cm$^{-1}$. Its response to photolysis and annealing and to variations in the concentrations of In and $O_2$ in the matrix indicates that this signal belongs to species **3b**. In experiments in which $^{16}O_2$ was replaced by $^{18}O_2$, the signal shifts to 586.6 cm$^{-1}$.

## Identification and Characterization

The identification of **3a** and **3b** can be made on the basis of (i) the $^{69}Ga/^{71}Ga$ isotopic shifts and the effects observed in experiments in which $^{16}O^{18}O$ and $^{18}O_2$ were used in place for $^{16}O_2$, (ii) the effects of varying the concentration of Ga or In and $O_2$ in the matrix and of annealing on the IR

 © 2006 Wiley-VCH Verlag GmbH & Co. KGaA, Weinheim 

Table 2. Wavenumbers observed for the reaction between In atoms and $O_2$ in Ar and pure solid $O_2$ matrices following photolysis at $\lambda_{max}$ = 254 nm.

| | In/$O_2$/Ar $^{16}O_2$ | $^{16}O^{18}O$ | $^{18}O_2$ | In/$O_2$ $^{16}O_2$ |
|---|---|---|---|---|
| $InO_2$, **1a** | 1084.2 | 1054.0 | 1022.9 | 1082.8 |
| | 331.7 | 325.2 | 317.2 | 331.7 |
| | 276.5 | 267.8 | 261.3 | 283.5 |
| OInO, **2a** | 754.6 | 741.4 | 721.7 | – |
| | 159.7 | 156.3 | 152.8 | – |
| $InO_4$, **3a** | 1498.8 | 1452.0 | 1426.8 | 1522.1 |
| | 1493.4 | 1447.1 | 1421.5 | – |
| | 1067.6 | 1042.2 | 1012.6 | – |
| | 1063.8 | 1038.4 | 1009.1 | – |
| | 621.0[a] | – | 586.6[a] | – |
| | 462.1 | 449.8 | 440.5 | 471.8 |
| | 459.2 | 447.0 | 437.7 | 468.4 |
| | 151.3 | 148.2 | 144.6 | – |
| | 146.5 | 143.3 | 139.8 | – |

[a] Observed in the Raman experiments.

and Raman intensities, (iv) the conditions of formation and consumption of the bands due to **3a** and **3b**, and (v) the IR and Raman intensities. It will be shown that **3a** and **3b** can be described as dioxygen complexes to OGaO and OInO, respectively. The discussion in this work will predominantly concentrate on the Ga reaction, because that of In atoms follows a similar pattern.

The experiments indicate that product **3a** contains one Ga atom and four O atoms. They also suggest that it is formed by reaction of linear OGaO and $O_2$. As already mentioned, the band at 1266.9/1264.2 $cm^{-1}$ can be assigned to the ν(O–O) mode of an $O_2$ unit, which is weakened by coordination. The wavenumber of the ν(O–O) mode can be compared e.g. with that observed for the end-on bonded complexes FeOO (1204.5 $cm^{-1}$)[13] or $O_2Co(O_2)$ (1286.2 $cm^{-1}$).[4] Of course, the electronic situation in these transition metal dioxygen complexes is different, but the coupling between the O–O coordinate and the other coordinates in the molecule is in all cases fairly weak. This gets also evident when the isotopic data are considered. The ν(O–O) mode of the coordinated $O_2$ unit of $^{18}O_2Co(^{16}O_2)$ occurs virtually at the same wavenumber as that of $^{16}O_2Co(^{16}O_2)$. Similarly, the O–O coordinate of the ligated $O_2$ unit in **3a** (and **3b**) is not significantly coupled to the other Ga–O coordinates. The only sign of weak coupling is a slight increase of the halfwidth of some of the bands in the experiments with $^{16}O_2/^{18}O_2$ mixtures with respect to those with $^{16}O_2$ or $^{18}O_2$ alone (see the bands around 1266 and 1824 $cm^{-1}$). In the case of the end-on bonded complex FeOO, the wavenumber measured for the ν(O–O) band is almost identical for the two versions $Fe^{16}O^{18}O$ and $Fe^{18}O^{16}O$ (1173.0 and 1170.4 $cm^{-1}$). The same is the case for $O_2Co(O_2)$ and also for **3a** and **3b**. The mode at 568.7/565.9/563.6 $cm^{-1}$ exhibits a smaller isotopic shift than the one at 1266.9/1264.2 $cm^{-1}$ when $^{16}O_2$ is replaced by $^{18}O_2$ (about –23 $cm^{-1}$). The obvious inference is that it belongs to a ν(Ga–O) mode, this time involving motion of the other O atoms in **3a**. The observed Ga isotopic splitting is in agreement with this assignment. From these considerations we conclude that **3a** is a complex between OGaO and $O_2$. The mode at 568.7/565.9/563.6 $cm^{-1}$ is then the antisymmetric Ga–O stretch, $\nu_{as}$(Ga–O), of the OGaO unit. This mode is IR-active, but virtually Raman silent. The corresponding symmetric Ga–O stretch, $\nu_s$(Ga–O), on the other hand, is visible at 716.2 $cm^{-1}$ in the Raman spectra, but more or less IR silent. Because the Ga atom is not involved in the motion, this signal exhibits no observable Ga isotopic splitting. The fact that no detectable band appears at 716.2 $cm^{-1}$ in the IR spectra indicates that the O–Ga–O bond angle of the OGaO unit is still close to 180° after coordination of $O_2$. The isotopic pattern observed for the antisymmetric stretch is in good agreement to this assumption. Thus the

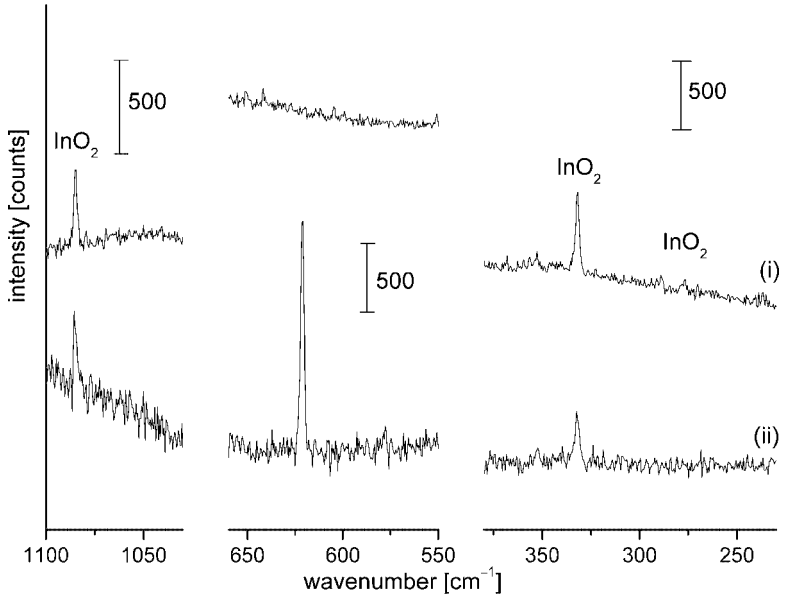


Figure 9. Raman spectra of an Ar matrix containing In atoms and $^{16}O_2$. (i) upon deposition. (ii) upon UV photolysis ($\lambda_{max}$ = 254 nm).

 © 2006 Wiley-VCH Verlag GmbH & Co. KGaA, Weinheim 

mode occurs at 568.7 $cm^{-1}$ for the $O^{69}GaO$ unit and at 566.2 $cm^{-1}$ for the $O^{71}GaO$ unit. From this isotopic shift the O–Ga–O angle can be estimated to be 165°. Strong support for this assignment comes also from the wavenumbers as measured for the $\nu_{as}$(Ga–O) and $\nu_s$(Ga–O) modes of the $^{16}OGa^{18}O(O_2)$ version of **3a**. The band due to the $\nu_{as}$(Ga–O) mode is slightly red shifted with respect to the center of the bands measured for the $^{16}O_2$ and $^{18}O_2$ isotopomers. On the other hand, the band due to the $\nu_s$(Ga–O) mode is slightly blue shifted with respect to the corresponding center. This shift is a consequence of the coupling of the symmetric and antisymmetric stretch in the $^{16}OGa^{18}O(O_2)$ isotopomer. The bands at 1824.7, 1820.0, 1816.7, and 1811.7 $cm^{-1}$ can be assigned to the combination $\nu$(O–O) + $\nu_{as}$(Ga–O). The sum of the wavenumbers measured for the two modes is between 1835.6 and 1827.8 $cm^{-1}$. The bands at 174.8/174.1 and 165.6/164.9 $cm^{-1}$ most likely belong to deformation modes involving some degree of motion of the Ga atoms as evidenced by the isotopic pattern. Thus our experiments hit on five fundamentals and one combinational mode of $GaO_4$.

In a previous publication, the band at 568.7 $cm^{-1}$ has been assigned to the $[OGaO]^-$ anion.[9] However, on the basis of our new experiments it can be immediately concluded that this identification cannot be correct, since it is impossible to produce a charged species in our experimental setup. Of course, **3a** cannot be this species also because the number of fundamentals detected for **3a** in our experiments exeeds the number of fundamentals a threeatomic molecule exhibits. Nevertheless, we have performed quantum chemical calculations on this species. The linear $[OGaO]^-$ molecule exhibits a $^1\Sigma_g^+$ electronic state. Applying CASSCF/TZVPPext, the following vibrational modes were calculated (in $cm^{-1}$, with IR intensities in km $mol^{-1}$ given in parenthesis): 752.5 (0, $\sigma_g$), 224.0 (114, $\pi_u$), 909.4 (145, $\sigma_u$). Thus no mode should be visible in the region around 570 $cm^{-1}$. A cyclic form $[OGaO]^-$, exhibiting a $^1A_1$ electronic state, is 131 kJ·$mol^{-1}$ higher in energy (including vibrational zero-point energy corrections). It is characterized by Ga–O and O–O bond lengths of 189.9 and 160.9 pm, respectively, and an O–Ga–O bond angle of 50.1°. The vibrational properties (in $cm^{-1}$, with IR intensities in km $mol^{-1}$ given in parenthesis) were calculated to be: 743.8(33), 513.0(74), and 461.9(22). We also performed calculations on the cationic species $GaO_2^+$. If the $OGaO(O_2)$ complex can be regarded as a superoxo complex, the OGaO unit should carry a formal charge of +1. As anticipated and in difference to the situation with $GaO_2^-$, a bent structure ($^3A_2$) is more stable in the case of the cation. Cyclic $[GaO_2]^+$ is by ca. 73 kJ·$mol^{-1}$ (according to CASSCF/TZVPPext) more stable than linear $[OGaO]^+$. Its vibrational fundamentals are calculated to show at the following wavenumbers (in $cm^{-1}$, with IR intensities in km·$mol^{-1}$ given in parenthesis): 998.6(2), 573.4(47), and 420.2(0). Thus there is indeed a strong fundamental in the region around 570 $cm^{-1}$. The calculated isotopic shifts –22.4 $cm^{-1}$ for $Ga(^{18}O)_2$ and –10.5 $cm^{-1}$ for $Ga(^{16}O^{18}O)$ are also close to those observed in the experiments. According to the calculations, the Ga–O and O–O bond lengths are 190.4 and 141.3 pm and the O–Ga–O bond angle is 43.5°.

Because of the fact that the electronic situation in linear OGaO is already very complicated and extremely difficult to calculate,[10] it might not come as surprise that $GaO(O_2)$ turned out to be difficult to calculate. Nevertheless, using the BP86 method and an SVP basis set, we succeeded in finding an energy minimum which should be close to the correct structure.[14] According to these calculations, the coordination of the $O_2$ molcule to the OGaO unit results in a decrease of the O–Ga–O angle to a value of 157.8°. This value is not too far away from the 168° estimated from the experimental results. The coordinating $O_2$ molcule features an O–O distance of 125.6 pm and is thus significantly elongated with respect to the distance in free $O_2$ (121.6 pm as calculated using the same method and basis set). In line with this elongation the $\nu$(O–O) mode (a′ symmetry) is calculated to occur at 1304.7 $cm^{-1}$. This wavenumber compares with an experimental one of 1264.2/1261.8 $cm^{-1}$. Two vibrations at very low wavenumbers and with sufficient IR intensity are calculated to show at 189.9 (a′) and 151.0 (a″) $cm^{-1}$. In the experiments, two bands show at 174.8/174.1 and 165.6/164.9 $cm^{-1}$. As already experienced in the case of linear OGaO, calculations on the symmetric and antisymmetric $GaO_2$ stretches of the OGaO unit are not very reliable. While the calculated 662.7 $cm^{-1}$ for the symmetric $GaO_2$ stretch (a′) is in fair agreement with the observed 716.2 $cm^{-1}$, the calculated 732.3 $cm^{-1}$ for the antisymmetric stretch (also a′) is not in good agreement with the observed 568.7 $cm^{-1}$. Other calculated wavenumbers are 705.5 (a″), 258.7 (a′), 108.6 (a′), and 81.7 (a′); however, all these bands are predicted to have only very small IR intensities. In summary the calculations, although there are inconsistencies, are in line with the description of $GaO_4$ as an end-on bonded $O_2$ complex to OGaO. Using the observed wavenumbers the valence force constant *f*(Ga–O) of the OGaO unit in $GaO_4$ can be estimated to be 350 N·$m^{-1}$. Thus the force constant is significantly smaller than that of OGaO prior to $O_2$ complexation (586 N·$m^{-1}$). This decrease is not surprising since the donation of electron density from the OGaO unit into the ligated $O_2$ leads to a partial depopulation of one of the bonding $\pi_g$ orbitals.

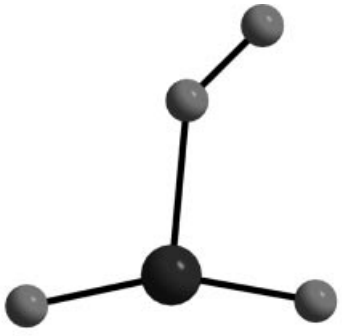

Model of the $GaO_4$ molecule, **3a**

Thus the geometry of $GaO_4$ is very different to that reported for the $AlO_4$ molcule.[5] $AlO_4$ in its energy minimum

 © 2006 Wiley-VCH Verlag GmbH & Co. KGaA, Weinheim 

form exhibits $D_{2d}$ symmetry and is characterized by O–O and Al–O distances of 148 and 175 pm, respectively. The distances of the $O_2$ groups are both equal and the unpaired electron is located in parts on both groups. This means that the $O_2$ groups can be described as being in between superoxo- and peroxo groups. In the case of $GaO_4$, the $D_{2d}$ symmetric structure defines not an energy minimum on the potential energy hypersurface. For the doublet electronic state we calculated O–O and Ga–O bond lengths of 148 and 184 pm, respectively. According to B3LYP/TZVPP calculations, its energy is 89 kJ·mol$^{-1}$ higher than that of separated OGaO and $O_2$.

There are all indications that $InO_4$, **3b**, has a structure similar to that of $GaO_4$. The ν(O–O) mode of the ligated $O_2$ unit shows now at 1067.6/1063.8 cm$^{-1}$. This wavenumber is close to that adopted e.g. in the end-on bonded superoxo complex CuOO (1089.6 cm$^{-1}$).[15] In line with this assignment, the ν($^{16}$O)/ν($^{18}$O) ratio is relatively large (1.054). The $\nu_{as}$(In–O) mode and the $\nu_s$(In–O) mode of the OInO unit in $InO_4$ show at 462.1/459.2 and 621.0 cm$^{-1}$.[16] The fact that one is IR active and the other Raman active indicates that the O–In–O angle is, in similarity with the Ga homologue, close to 180°. DFT (BP86) calculations yielded a structure for this complex with In–O and O–O bond lengths of 192.3 and 127.7 pm, respectively, and O–In–O and In–O–O bond angles of 147.8° and 137.8°, respectively. The ν(O–O) mode of the ligated $O_2$ unit was calculated to show at 1220.8 cm$^{-1}$. Thus, the calculations predict the wavenumber to be lower than the corresponding one of the Ga homologue. This trend is in agreement with the experimental results (1264.2/1261.8 cm$^{-1}$ for $GaO_4$ and 1067.6/1063.8 cm$^{-1}$ for $InO_4$), although the deviation between experiment and calculation is quite high. The $\nu_{as}$(In–O) mode of the OInO unit is calculated to show at 578.0 cm$^{-1}$. This value compares with an observed one of 462.1/459.2 cm$^{-1}$. Like in the case of $GaO_4$, the calculations predict a too low wavenumber for the $\nu_s$(In–O) mode of the O–In–O unit (calculated: 551.9 cm$^{-1}$, measured: 621.0 cm$^{-1}$). Two modes calculated at 204.9 cm$^{-1}$ (a″) and 175.3 cm$^{-1}$ (a′) can be assigned to observed ones at 151.3 and 146.5 cm$^{-1}$. Other weak modes, which were not detected in our experiments, were calculated to show at 303.5 (a′), 113.9 (a″), 91.9 (a′), and 77.5 (a′) cm$^{-1}$.

## Conclusions

The reactions of Ga and In atoms in Ar matrices with $O_2$ lead spontaneously to the cyclic $GaO_2$ and $InO_2$ molcules, respectively. These species can be photoconverted into linear OGaO and OInO. Reaction of linear OGaO and OInO with a second $O_2$ molcule leads to the new end-on bonded superoxo complexes $OGaO(O_2)$ [see Equation (3)] and $OInO(O_2)$. These molecules represent the first ever experimentally verified end-on bonded superoxo complexes of Ga and In. Our experimental findings show that the group 13 elements Ga and In are capable to bind up to four O atoms. The experimental results indicate that the O–Ga–O angle in this complex is ca. 165°. Quantum chemical calculations provide further details of the structure of the new molecules, which differs remarkably from that of the $D_{2d}$ symmetric $Al(O_2)_2$ complex. The characterization of these oxidation processes is of relevance to the mechanism of metal oxidation in general and thus contributes to a more detailed understanding of this very important but complex class of reactions.

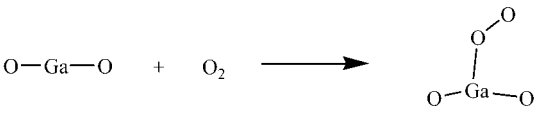


(3)

## Experimental Section and Calculational Details

In a vacuum apparatus, thermally evaporated gallium or gallium metal was deposited together with dioxygen in an excess of Ar onto a freshly polished Cu block kept at 12 K with the aid of a closed-cycle refrigerator (Leybold LB115). The experiment was repeated with different dioxygen isotopomers. $^{16}O_2$ was used as delivered from Messer (purity 99.9998%). $^{18}O_2$ was purchased from Linde (isotopic purity 99.0%). For experiments with a 1:2:1 mixture of $^{16}O_2$/$^{16}O^{18}O$/$^{18}O_2$, an equimolar mixture of $^{16}O_2$ and $^{18}O_2$ in a glass bulb was subjected for several hours to an electric discharge. The resulting $O_3$ molcules were trapped in a cold finger at 77 K. Subsequently the cold finger was warmed up again to room temperature and decomposition of the $O_3$ molcules results in the statistical 1:2:1 mixture of $^{16}O_2$/$^{1}O^{18}O$/$^{18}O_2$. Experiments in solid $O_2$ matrices were also carried out. Further details of the matrix isolation technique can be found elsewhere.[17]

IR spectra were recorded on a Bruker 113v FT-IR spectrometer equipped with a DTGS and an MCT detector for measurements in the spectral regions 4000–200 cm$^{-1}$, respectively, and a bolometer for measurements between 700 and 30 cm$^{-1}$.

Raman spectra were measured on a XY800 spectrometer from Jobin Yvon Horiba, equipped with a CCD camera (Wright Instruments). The spectra were excited with an $Ar^+$ ion laser. Both the 488.0 nm and 514.5 nm lines were used.

Quantum chemical (DFT) calculations using the B3LYP[18] and the BP86[19] functionals were performed with the aid of the TURBOMOLE[20] programme and using either an SVP[21] or a TZVPPext[22] basis set. The Dalton programme code[23] was used for CASSCF calculations. All valence orbitals were included into the active space.

## Acknowledgments

The authors gratefully acknowledge support from the Deutsche Forschungsgemeinschaft and Fonds der Chemischen Industrie.

[1] See, for example: a) E. I. Solomon, P. Chen, M. Metz, S.-K. Leo, A. E. Palmer, *Angew. Chem. Int. Ed.* **2001**, *40*, 4570; b) S. Fukuzumi, H. Ohtsu, K. Ohkubo, S. Itoh, H. Imahori, *Coord. Chem. Rev.* **2002**, *226*, 71; c) A. Bakac, *Adv. Inorg. Chem.* **2004**, *55*, 1.

[2] G. V. Chertihin, A. Citra, L. Andrews, C. W. Bauschlicher Jr, *J. Phys. Chem. A* **1997**, *101*, 8793.

 © 2006 Wiley-VCH Verlag GmbH & Co. KGaA, Weinheim 

[3] D. Danset, M. E. Alikhani, L. Manceron, *J. Phys. Chem. A* **2005**, *109*, 97.
[4] D. Danset, M. E. Alikhani, L. Manceron, *J. Phys. Chem. A* **2005**, *109*, 105.
[5] G. Stößer, H. Schnöckel, *Angew. Chem.* **2005**, *117*, 4334; *Angew. Chem. Int. Ed.* **2005**, *44*, 4261.
[6] a) J. Bahlo, H.-J. Himmel, H. Schnöckel, *Inorg. Chem.* **2002**, *41*, 2678.
[7] a) J. Bahlo, H.-J. Himmel, H. Schnöckel, *Angew. Chem.* **2001**, *113*, 4820; *Angew. Chem. Int. Ed.* **2001**, *40*, 4696; b) J. Bahlo, H.-J. Himmel, H. Schnöckel, *Inorg. Chem.* **2002**, *41*, 4488.
[8] a) M. J. Zehe, D. A. Lynch Jr, B. J. Kelsall, K. D. Carlson, *J. Phys. Chem.* **1979**, *83*, 656; b) L. V. Serebrennikov, S. B. Ozin, A. A. Maltsev, *J. Mol. Struct.* **1982**, *81*, 25.
[9] a) T. R. Burkholder, J. T. Yustein, L. Andrews, *J. Phys. Chem.* **1992**, *96*, 10189; b) L. Andrews, G. P. Kushto, J. T. Yustein, E. Archibong, R. Sullivan, J. Leszczynski, *J. Phys. Chem. A* **1997**, *101*, 9077.
[10] A. Köhn, B. Gaertner, H.-J. Himmel, *Chem. Eur. J.* **2005**, *11*, 5575.
[11] G. Meloni, S. M. Sheehan, D. M. Neumark, *J. Chem. Phys.* **2005**, *122*, 074317
[12] L. Andrews, G. V. Chertihin, A. Ricca, C. W. Bauschlicher Jr, *J. Am. Chem. Soc.* **1996**, *118*, 467.
[13] a) L. Andrews, G. V. Chertihin, A. Ricca, C. W. Bauschlicher Jr, *J. Am. Chem. Soc.* **1996**, *118*, 467; b) G. V. Chertihin, W. Saffel, J. T. Yustein, L. Andrews, M. Neurock, A. Ricca, C. W. Bauschlicher Jr, *J. Phys. Chem.* **1996**, *100*, 5261.
[14] In this structure ($^2A'$ electronic state), the Ga–O and O–O distances were calculated to be 174.3 and 125.6 pm, respectively. The bond angle Ga–O–O from the Ga metal to the ligated $O_2$ unit and the O–Ga–O bond angle of the OGaO unit came out to be 140.1 and 157.8°. It should be mentioned that calculations using the B3LYP methods did not find a corresponding minimum structure.
[15] G. V. Chertihin, L. Andrews, C. W. Bauschlicher Jr, *J. Phys. Chem. A* **1997**, *101*, 4026.
[16] The splitting of the $\nu_{as}$(In–O) mode is due to a matrix site effect. It is in the same order as that observed for the Ga homologue, **3a**.
[17] See, for example: H.-J. Himmel, A. J. Downs, T. M. Greene, *Chem. Rev.* **2002**, *102*, 4191.
[18] a) A. D. P. Becke, *Phys. Rev. A* **1988**, *38*, 3098; b) C. Lee, W. Yang, R. G. Parr, *Phys. Rev. B* **1988**, *37*, 785; c) A. D. Becke, *J. Chem. Phys.* **1993**, *98*, 5648.
[19] a) J. P. Perdew, *Phys. Rev. B* **1986**, *33*, 8822; b) A. D. P. Becke, *Phys. Rev. A* **1988**, *38*, 3098.
[20] a) R. Ahlrichs, M. Bär, M. Häser, H. Horn, C. Kölmel, *Chem. Phys. Lett.* **1989**, *162*, 165; b) K. Eichkorn, O. Treutler, H. Öhm, M. Häser, R. Ahlrichs, *Chem. Phys. Lett.* **1995**, *240*, 283; c) K. Eichkorn, O. Treutler, H. Öhm, M. Häser, R. Ahlrichs, *Chem. Phys. Lett.* **1995**, *242*, 652; d) K. Eichkorn, F. Weigend, O. Treutler, R. Ahlrichs, *Theor. Chem. Acc.* **1997**, *97*, 119; e) F. Weigend, M. Häser, *Theor. Chem. Acc.* **1997**, *97*, 331; f) F. Weigend, M. Häser, H. Patzelt, R. Ahlrichs, *Chem. Phys. Lett.* **1998**, *294*, 143.
[21] A. Schäfer, H. Horn, R. Ahlrichs, *J. Chem. Phys.* **1992**, *97*, 2571.
[22] A. Köhn, H.-J. Himmel, B. Gaertner, *Chem. Eur. J.* **2003**, *9*, 3909.
[23] T. Helgaker, H. J. A. Jensen, P. Jørgensen, J. Olsen, K. Ruud, H. Ågren, A. A. Auer, K. L. Bak, V. Bakken, O. Christiansen, S. Coriani, P. Dahle, E. K. Dalskov, T. Enevoldsen, B. Fernandez, C. Hättig, K. Hald, A. Halkier, H. Heiberg, H. Hettema, D. Jonsson, S. Kirpekar, R. Kobayashi, H. Koch, K. V. Mikkelsen, P. Norman, M. J. Packer, T. B. Pedersen, T. A. Ruden, A. Sanchez, T. Saue, S. P. A. Sauer, B. Schimmelpfennig, K. O. Sylvester-Hvid, P. R. Taylor, O. Vahtras; *DALTON* – an electronic structure program, release 1.2, **2001**.

Received: December 14, 2005
Published Online: February 21, 2006

 © 2006 Wiley-VCH Verlag GmbH & Co. KGaA, Weinheim 

DOI: 10.1002/ejic.200500751

# N–H···S Hydrogen Bonds in a New Family of Ion-Pair Complexes Between Cationic Nickel Tetraazabicyclononane and Anionic Metal Dithiolates: Synthesis, Characterization and Properties of $[Ni(C_9H_{22}N_6)][M(mnt)_2]$ ($M^{II}$ = Cu, Ni, Pd)

**Vedichi Madhu[a] and Samar K. Das*[a]**

**Keywords:** Hydrogen bonds / Ion pairs / N ligands / Nickel / S ligands

The ion-pair complexes $[Ni(C_9H_{22}N_6)][Cu(mnt)_2]$ (**1**), $[Ni(C_9H_{22}N_6)][Ni(mnt)_2]$ (**2**), and $[Ni(C_9H_{22}N_6)][Pd(mnt)_2]$ (**3**; $mnt^{2-}$ = 1,2-dicyanoethylenedithiolate, $C_9H_{22}N_6$ = 3,7-bis(2-aminoethyl)-1,3,5,7-tetraazabicyclo[3.3.1]nonane) have been synthesized and characterized by elemental analysis, IR, UV/Vis, and $^1H$ NMR spectroscopy, X-ray powder diffraction, and electrochemical studies, and unambiguously by single-crystal X-ray crystallography. All three complexes are isostructural and crystallize in the monoclinic space group $P2_1/n$. The N–H···S-type hydrogen-bonding capabilities of the classical sulfur-containing complex anions $[M^{II}(mnt)_2]^{2-}$ (A; M = Cu, Ni and Pd) have been explored using amine groups containing the nickel complex cation $[Ni(C_9H_{22}N_6)]^{2+}$ (C) in the ion-pair compounds **1**, **2**, and **3**. In the crystal, the cation interacts with two different anions through three N–H···S hydrogen bonds and, likewise, the anion is hydrogen-bonded to two different cations through three hydrogen bonds, resulting in the formation of a chain-like arrangement. The average N–H···S hydrogen-bond lengths are 3.498(3), 3.505(3), and 3.490(5) Å for compounds **1**, **2**, and **3**, respectively. Another crystallographic feature is the presence of CC–AA–CC–AA-type packing with short S···Ni contacts in the crystal structures. Besides crystallography, the existence of these N–H···S hydrogen bonds between cation $[Ni(C_9H_{22}N_6)]^{2+}$ (C) and anion $[M^{II}(mnt)_2]^{2-}$ (A) is strongly supported by the IR and $^1H$ NMR studies. The stability of the $[Ni(C_9H_{22}N_6)]^{2+}$ (C) moiety in compounds **1**, **2**, and **3** is discussed in light of electrochemical studies performed on these compounds and $[Ni(C_9H_{22}N_6)](ClO_4)_2$. Complex **1** exhibits a well-resolved ESR signal corresponding to a $Cu^{2+}$ ($d^9$) system at liquid-nitrogen temperature.

(© Wiley-VCH Verlag GmbH & Co. KGaA, 69451 Weinheim, Germany, 2006)

## Introduction

The assembly of cationic and anionic components into ion-pair-containing supramolecular systems in which the positive and negative partners interact through noncovalent hydrogen bonding and/or π–π interactions is a challenging task in modern chemistry.[1] Bis(1,2-dithiolene)–transition metal complexes have been extensively studied as one of the ion-pair components because of their importance as functional materials, for example as near-infrared (NIR) laser dyes,[2] conducting[3] and magnetic materials,[4] and in nonlinear optics.[5] The molecular-conductor-type ion-pair charge-transfer (IPCT) complexes $[A^{2+}\{ML_2\}^{2-}]$ [$A^{2+}$ = bipyridinium dication derivative, $[ML]^{2-}$ = metal bis(dithiolate), $M^{2+}$ = Ni, Pd, Pt, and Cu] exhibit an IPCT transition in the solid state due to a supramolecular electronic interaction between the cation and anion.[6] A class of ion-pair complexes has been obtained with a combination of uncharged organic components and, in this case, the ion pairing is achieved by a radical mechanism.[7] Although charge-transfer (CT) complexes of metal dithiolenes with organic cations as acceptors have been investigated quite well, including their structural characterization, ion-pair complexes of metal dithiolenes with transition metal inorganic complexes as cations are rare.[8] We have been working on ion-pair supramolecular systems in order to explore the noncovalent, hydrogen-bonding interactions between cationic and anionic components by choosing appropriate H-bond donor and acceptor sites. We have recently reported the NIR absorption due to a supramolecular electronic interaction between an anion and cation in a three-dimensional hydrogen-bonded networking material, namely [4,4′-$H_2$bpy][$Cu(mnt)_2$], emphasizing the N–H···N-type hydrogen bonding between cation and anion.[9] Now we extend this study to an inorganic transition metal complex, $NiL^{2+}$ {L = $C_9H_{22}N_6$ = 3,7-bis(2-aminoethyl)-1,3,5,7-tetraazabiclo[3.3.1]nonane} as a cation and $[M^{II}(mnt)_2]^{2-}$ (M = Cu, Ni and Pd; $mnt^{2-}$ = 1,2-dicyanoethylenedithiolate) as anions in ion-pair complexes (Scheme 1).

[a] School of Chemistry, University of Hyderabad, Hyderabad 500 046, India
Fax: +91-40-2301-2460
E-mail: skdsc@uohyd.ernet.in

Supporting information for this article is available on the WWW under http://www.eurjic.org or from the author.

 © 2006 Wiley-VCH Verlag GmbH & Co. KGaA, Weinheim 

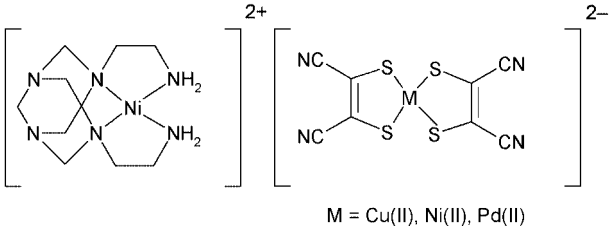


Scheme 1.

In this group of ion-pair complexes the nickel complex cation has coordinated $NH_2$ groups. The aim of this work was to examine whether these amine hydrogens form N–H···S-type hydrogen bonds with the thiolate sulfur of the mnt ligands of the anions. Living systems contain several important sulfur-containing molecules, such as cysteine and methionine, and hydrogen bonding between amide groups and the cysteine sulfur is a common feature of all iron-sulfur proteins.[10] For example, the formation of N–H···S hydrogen bonds plays a crucial role in the function of many proteins, including *Pasteurella aerogenes* ferredoxin and *Clostridium pasteurianum* rubredoxin.[11] Much of the importance of the N–H···S hydrogen-bonding interaction derives from the fact that it may modulate the redox potentials of several of these proteins.[10,12] Therefore, the study of N–H···S hydrogen bonds using simple inorganic compounds may have fundamental importance in understanding the chemical functions of those metal-associated proteins in which the negative metal–sulfur cluster is hydrogen-bonded to the surrounding amide groups of peptides/proteins. Various metal thiolate complexes have been synthesized and structurally characterized as model compounds of these natural proteins.[13] In many of these model studies, intramolecular N–H···S hydrogen-bonding interactions are observed because the ligand coordinated to the metal center has amide-type functional groups. Intermolecular amide–thiolate hydrogen-bonding interactions have been described[14] for the complex $[(CH_3)_3NCH_2CONH_2]_2[Co(SC_6H_5)_4]$ and the metal-free compound $[(CH_3)_3NCH_2CONH_2][SC_6H_5]$. Herein we describe the synthesis, crystal structures, and properties of a new family of ion-pair complexes, namely $[Ni(C_9H_{22}N_6)][Cu(mnt)_2]$ (**1**), $[Ni(C_9H_{22}N_6)][Ni(mnt)_2]$ (**2**), and $[Ni(C_9H_{22}N_6)][Pd(mnt)_2]$ (**3**), all of which contain N–H···S hydrogen bonds between the cation and anion in their ion pairs. Our results show a systematic decrease in $M–S_H$ bond lengths with respect to the $M–S_N$ bond length ($M = Cu^{2+}$, $Ni^{2+}$ and $Pd^{2+}$; $S_H$ is the sulfur atom involved in hydrogen bonding and $S_N$ that which is not involved in hydrogen bonding). We explain this trend in terms of N–H···S hydrogen-bonding interactions. We also describe detailed IR and $^1H$ NMR studies that support the existence of N–H···S hydrogen bonds between the cation (C) and anion (A).

## Results and Discussion

### Synthesis

The reaction of $[Ni^{II}(C_9H_{22}N_6)](ClO_4)_2$ with $[Bu_4N]_2[M^{II}(mnt)_2]$ (M = Cu, Ni, and Pd) in MeCN solution leads to the isolation of the ion-pair complexes $[Ni(C_9H_{22}N_6)][M(mnt)_2]$. The relevant reactions can be described according to Equation (1).

$$[Ni^{II}(C_9H_{22}N_6)](ClO_4)_2 + [Bu_4N]_2[M^{II}(mnt)_2] \rightarrow [Ni^{II}(C_9H_{22}N_6)][M^{II}(mnt)_2] + 2\,Bu_4NClO_4 \quad (1)$$

Crystals of compounds **1** (M = Cu), **2** (M = Ni), and **3** (M = Pd) gave satisfactory elemental analyses. The numbers of Cu and Ni sites in compound **1** and of Pd and Ni sites in compound **3**, as revealed by single-crystal X-ray structure analyses, are consistent with the results of EDAX analyses, which gave an average Ni/Cu value of around 1:1 for compound **1** and a Ni/Pd value of about 1:1 for compound **3**. All three compounds were obtained in high yield. However, these high-yield procedures produced microcrystalline products instead of the single crystals required for crystal-structure determination. Single crystals were obtained by a slow-diffusion technique, as described in the Experimental Section.

### X-ray Powder-Diffraction Studies

X-ray powder-diffraction patterns of microcrystalline compounds **1**–**3** were recorded. The simulated patterns were generated from the single-crystal X-ray data of the appropriate compounds obtained by the slow-diffusion technique. The simulated patterns match the respective experimentally observed powder-diffraction patterns very well, as shown in SI-Figure 38 (see Supporting Information). This confirms the homogeneity and the purity of the bulk samples **1**–**3**.

### Description of the Structures

Complexes **1**–**3** crystallize in the monoclinic space group $P2_1/n$. A thermal ellipsoidal plot of the non-hydrogen atoms is presented in Figure 1. This shows the presence of $[Ni(C_9H_{22}N_6)]^{2+}$ as a cation and $[M(mnt)_2]^{2-}$ as an anion. The four nitrogen donor atoms in the $[Ni(C_9H_{22}N_6)]^{2+}$ cation form a plane with a maximum deviation of 0.0022 Å. The nickel ion is displaced by 0.040(1) Å from the least-squares plane. The average Ni–N bond length is $1.913 \pm 0.002$ Å, which is about 0.01 Å longer than those in the crystal structure of the previously reported[15] compound $[Ni(C_9H_{22}N_6)](ClO_4)_2$, which contains the same cation. However, the quality of the crystal of this complex was too poor to be refined aniosotropically (disorder problem of the whole cation in addition to disordered perchlorate anions).[15] This is reflected in some of the C–N bond lengths, which are either unreasonably short or unreasonably long. In the present study, we were able to overcome this disorder problem of the $[Ni(C_9H_{22}N_6)]^{2+}$ cations in complexes **1**–**3**. There are 14 N–C single bonds in the ligand $C_9H_{22}N_6$ (Figure 1). Depending on the environments of the nitrogen atoms in the $[Ni(C_9H_{22}N_6)]^{2+}$ cation, the N–C bond lengths show systematic variations ranging from 1.433 to 1.522 Å for compound **1**. There are four tertiary nitrogen atoms, namely N(7), N(8), N(9), and N(10). The six bonds

 © 2006 Wiley-VCH Verlag GmbH & Co. KGaA, Weinheim 

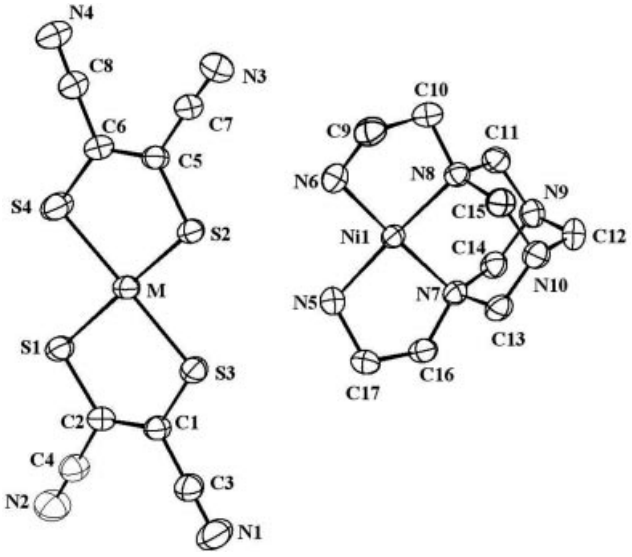


Figure 1. Thermal ellipsoidal plot (50% probability) of compounds $[Ni(C_9H_{22}N_6)][M(mnt)_2]$ (M = $Cu^{2+}$, $Ni^{2+}$ and $Pd^{2+}$). Hydrogen atoms have been omitted for clarity.

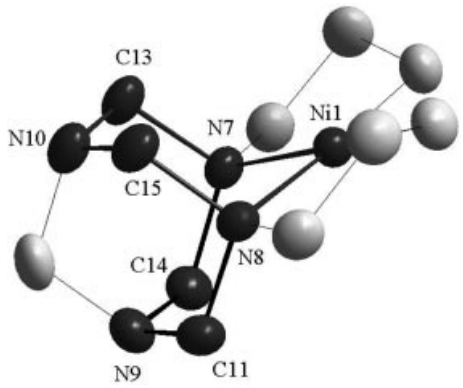


Figure 2. The molecular structure of $[Ni(C_9H_{22}N_6)]^{2+}$ in **1**–**3** showing the chair form of the six-membered chelate ring [Ni(1)–N(7)–C(14)–N(9)–C(11)–N(8)] and the chair form of the other six-membered chelate ring [N(10)–C(13)–N(7)–Ni(1)–N(8)–C(15)] formed between the bicyclononane rings and the nickel ion. The six-membered chelate rings (chair forms) are shown in dark grar. Hydrogen atoms have been omitted for clarity.

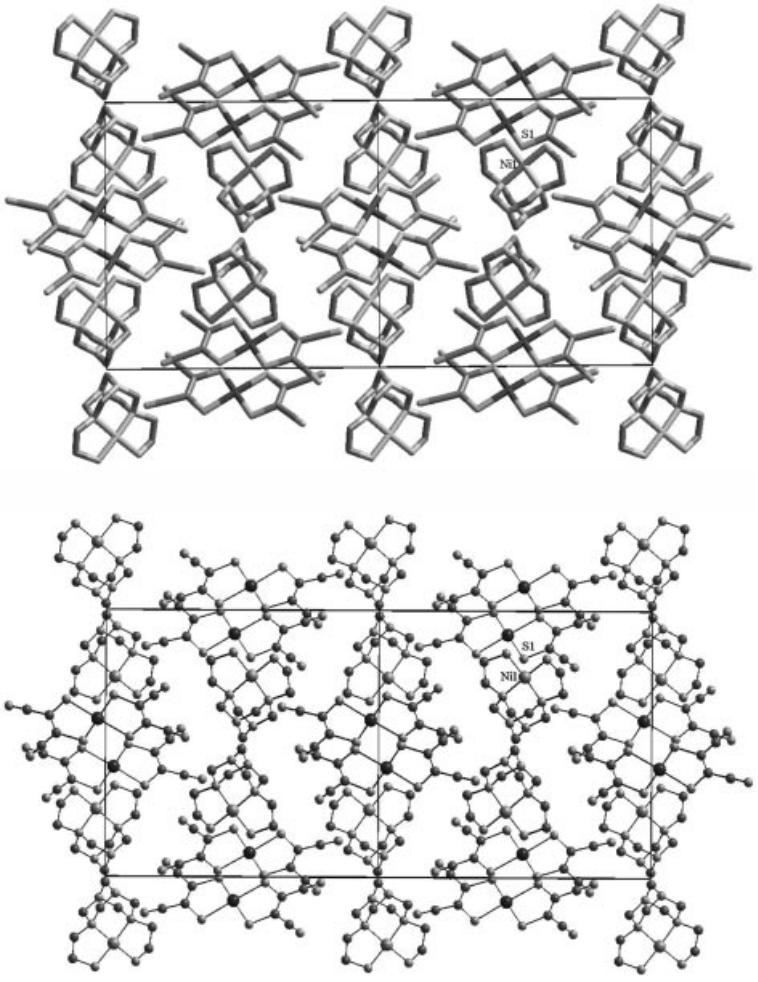

Figure 3. Packing diagram (4×4 cells) of $[Ni(C_9H_{22}N_6)][M(mnt)_2]$ (M = $Cu^{2+}$, $Ni^{2+}$, and $Pd^{2+}$): wire-frame representation (top) and ball-and-stick representation (bottom) showing the mixed-stacked CC–AA–CC–AA-type arrangement along the crystallographic *c* axis (C = cation and A = anion). Hydrogen atoms have been omitted for clarity.

 © 2006 Wiley-VCH Verlag GmbH & Co. KGaA, Weinheim 

from N(7) and N(8) to their immediate carbon atoms are the longest, with an average distance of 1.507 ± 0.003 Å. This is considerably longer than the average N–C bond lengths (1.445 ± 0.004 Å) observed for the other six bonds from N(9) and N(10) to their immediate carbon atoms. The lengthening of these N–C bonds is consistent with the fact that N(7) and N(8) are coordinated to the nickel ion and N(9) and N(10) are not.

The N(5)–Ni(1)–N(7) bite angle in one of the five-membered chelate rings [Ni(1)–N(5)–C(17)–C(16)–N(7)] in the cation of **1** is 87.45(10)° and the N(6)–Ni(1)–N(8) bite angle of the other five-membered ring [Ni(1)–N(8)–C(10)–C(9)–N(6)] is 87.35(10)°. The respective bite distances are 2.647 and 2.642 Å (Figure 1). These values are consistent with those in the five-membered rings of other $Ni^{II}$ macrocyclic complexes,[16–19] including the tetraazabicyclononane–$Ni^{II}$ complex $[Ni(C_{12}H_{27}N_7)](ClO_4)_2$.[15] The N(5)–Ni(1)–N(6) angle, which is not constrained by any ring closure (Figure 1), is 94.99(11)° and the length between the N(5) and N(6) atoms is 2.817 Å. Interestingly, the N(7)–Ni(1)–N(8) bite angle of 90.11(10)° and the N(7)–N(8) bite distance of 2.713 Å involving two six-membered rings in bicyclononane are considerably smaller than those for the open side of the cation. This N(7)–N(8) separation, in principle, should be determined by the intracyclic valence angles at the C(11), C(15), C(13), C(14), N(9), and N(10) centers of the bicyclononane ring (Figure 1). These angles, which range from 111.7° to 114.6°, are already larger than the normal values of 107° for N($sp^3$) and 109.5° for C($sp^3$). Therefore, there is no chance for a lengthening of the bite distance between atoms N(7) and N(8).

There are four six-membered and two five-membered rings in the cation. The two six-membered rings [C(12)–N(9)–C(14)–N(7)–C(13)–N(10) and C(12)–N(9)–C(11)–N(8)–C(15)–N(10)] in the bicyclononane ring assume a stable chair conformation with average intracyclic torsion angles of 58° and 57.44° in the cation of compound **1** (see Figure 1). The two six-membered chelate rings formed between the bicyclononane ring and the nickel ion also assume a chair conformation. These rings are Ni(1)–N(7)–C(14)–N(9)–C(11)–N(8) and N(10)–C(13)–N(7)–Ni(1)–N(8)–C(15) in the cation of compounds **1**–**3**, as shown in Figure 2.

The anion $[Cu(mnt)_2]^{2-}$ has a planar structure, in good agreement with other relevant literature data.[20] The anion (A) and the cation (C) are arranged face to face, forming a mixed-stacked CC–AA-CC–AA-type arrangement along the crystallographic *a* axis (Figure 3). The angle between the planes of the cation and anion, defined by Ni(1)–N(5)–N(7)–N(8)–N(6) and Cu(1)–S(1)–S(3)–S(2)–S(4), is 38.28(6)° (Figure 1) for compound **1**, which comes under the category of noncoplanar structures among ion-pair compounds. The closest intra-stack distance of 3.947 Å is found between Ni(1) and S(1) in the case of compound **1** (Figure 3).

The single-crystal X-ray diffraction analyses revealed that compounds **2** and **3** are isostructural with **1** and therefore the unit-cell dimensions, volumes, and other related data for the structure determinations of all three compounds vary only slightly (see table in Experimental Section). Selected bond lengths and angles for compounds **1**–**3** are presented in Table 1.

Table 1. Selected bond lengths [Å] and angles [°] for compounds **1**–**3** (see Figure 1).[a]

| | | | |
|---|---|---|---|
| Compound **1** | | | |
| Ni(1)–N(5)* | 1.909(2) | Ni(1)–N(6)* | 1.911(2) |
| Ni(1)–N(7) | 1.920(2) | Ni(1)–N(8) | 1.914(2) |
| Cu(1)–S(1)* | 2.2574(10) | Cu(1)–S(2)* | 2.2624(10) |
| Cu(1)–S(3)* | 2.2766(10) | Cu(1)–S(4) | 2.2793(10) |
| S(1)–C(2) | 1.732(3) | N(3)–C(7) | 1.137(4) |
| N(5)*–C(17) | 1.476(4) | N(6)*–C(9) | 1.477(4) |
| N(5)–Ni(1)–N(6) | 94.99(11) | N(6)–Ni(1)–N(8) | 87.35(10) |
| N(5)–Ni(1)–N(7) | 87.45(10) | S(1)–Cu(1)–S(2) | 175.21(3) |
| S(1)–Cu(1)–S(3) | 90.74(4) | C(1)–S(3)–Cu(1) | 101.86(10) |
| Compound **2** | | | |
| Ni(1)–N(5)* | 1.901(2) | Ni(1)–N(6)* | 1.905(2) |
| Ni(1)–N(7) | 1.914(2) | Ni(1)–N(8) | 1.915(2) |
| Ni(2)–S(2)* | 2.1660(11) | Ni(2)–S(1)* | 2.1672(11) |
| Ni(2)–S(3)* | 2.1769(9) | Ni(2)–S(4) | 2.1817(9) |
| S(1)–C(2) | 1.734(3) | N(3)–C(7) | 1.140(4) |
| N(5)*–C(17) | 1.479(3) | N(6)*–C(9) | 1.480(3) |
| N(5)–Ni(1)–N(6) | 95.06(10) | N(5)–Ni(1)–N(7) | 87.44(9) |
| N(6)–Ni(1)–N(7) | 176.16(9) | N(6)–Ni(1)–N(8) | 87.28(9) |
| N(7)–Ni(1)–N(8) | 90.12(9) | S(1)–Ni(2)–S(3) | 92.00(4) |
| C(1)–S(3)–Ni(2) | 103.41(9) | C(6)–S(4)–Ni(2) | 102.64(10) |
| Compound **3** | | | |
| Ni(1)–N(6)* | 1.903(4) | Ni(1)–N(5)* | 1.908(4) |
| Ni(1)–N(7) | 1.909(4) | Ni(1)–N(8) | 1.909(4) |
| Pd(1)–S(2)* | 2.2836(15) | Pd(1)–S(1)* | 2.2866(15) |
| Pd(1)–S(3)* | 2.2924(12) | Pd(1)–S(4) | 2.2955(13) |
| S(1)–C(2) | 1.740(5) | N(3)–C(7) | 1.135(6) |
| N(5)*–C(17) | 1.477(6) | N(6)*–C(9) | 1.471(6) |
| N(6)–Ni(1)–N(5) | 94.95(16) | N(5)–Ni(1)–N(7) | 87.44(16) |
| N(6)–Ni(1)–N(8) | 87.28(16) | N(7)–Ni(1)–N(8) | 90.24(15) |
| S(2)–Pd(1)–S(1) | 179.35(4) | S(2)–Pd(1)–S(3) | 89.41(4) |
| C(1)–S(3)–Pd(1) | 102.10(16) | | |

[a] Atoms marked with an asterisk * are involved in N–H···S hydrogen-bonding interactions.

### N–H···S Hydrogen Bonds Between the Cation and Anion

The inorganic transition metal complex $NiL^{2+}$ (L = $C_9H_{22}N_6$ = 3,7-bis(2-aminoethyl)-1,3,5,7-tetraazabiclo-[3.3.1]nonane) was chosen as a cation since the nickel-coordinated $NH_2$ groups can provide potential points of organization for the formation of N–H···S hydrogen bonds with the thiolate sulfur atoms of the anions $[M(mnt)_2]^{2-}$ (M = $Cu^{2+}$, $Ni^{2+}$, $Pd^{2+}$). Even though the electronegativity difference between H and S ($\delta$ = 0.38, Pauling scale) is very small compared to those between H and X (X = Cl, N, O), and therefore the hydrogen bonds involving H and S will necessarily be weak due to the poorer match between the hard proton and soft sulfur, N–H···S hydrogen bonds have been observed in crystals of sulfur-containing organic molecules,[21] inorganic coordination complexes,[13,22] and metalloproteins.[10–12] In many cases, N–H···S hydrogen bonds play important roles, for example, the arrangement of proteins having amide and amine functional groups

 © 2006 Wiley-VCH Verlag GmbH & Co. KGaA, Weinheim 

around Fe–S clusters in *Pasteurella aerogenes* ferredoxin and *Clostridium pasteurianum* rubredoxin has been suggested to contribute to the stabilization of the negatively charged cluster by providing possible hydrogen-bond donors in forming N–H···S hydrogen bonds.[11]

The N–H···S bonds involving the amine nitrogen atoms of the cation $[Ni(C_9H_{22}N_6)]^{2+}$ and the dithiolate sulfur atoms of $[M(mnt)_2]^{2-}$ (M = $Cu^{2+}$, $Ni^{2+}$, $Pd^{2+}$) are illustrated in Figure 4; the geometrical parameters of these hydrogen bonds are presented in Table 2. As shown in Figure 4, the cation interacts with two different anions through three N–H···S hydrogen bonds (two H-bonds with one anion and one H-bond with another anion). Similarly, the anion is hydrogen bonded to two different cations through three hydrogen bonds. This results in the formation of a chain-like arrangement consisting of alternating cations and anions, as shown in Figure 5. The N···S and H···S distances are 3.485–3.512 and 2.65–2.73 Å, respectively, for compound **1**. The same distances in **2** are 3.468–3.527 and 2.63–2.76 Å and in **3** are 3.471–3.500 and 2.64–2.74 Å (see Table 2). The N–H···S bond angles in these compounds range from 142.3° to 159.6° and show a direct correlation whereby a decreasing bond angle results in a lengthening, and therefore weakening, of the hydrogen bond (Table 2). These N–H···S hydrogen-bond parameters are similar to those observed in the crystal structure of *Clostridium pasteurianum* rubredoxin protein.[11]

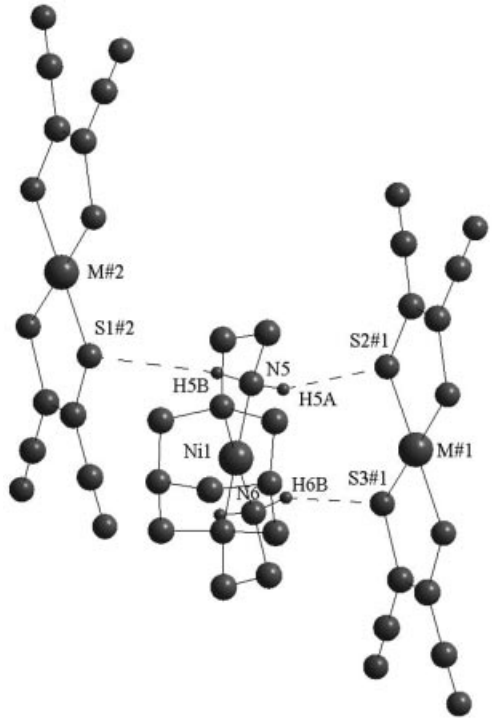


Figure 4. Crystal structure of compounds $[Ni(C_9H_{22}N_6)][M(mnt)_2]$ (M = $Cu^{2+}$, $Ni^{2+}$, and $Pd^{2+}$) showing intermolecular N–H···S hydrogen bonding between the cation and anion. Dotted lines indicate the N–H···S hydrogen bonds. Methylene hydrogen atoms have been omitted for clarity. Atoms with additional labels #1 and #2 are related to each other by the following symmetry operations: #1 1 – *x*, –*y*, 1 – *z*; #2 –*x*, –*y*, 1 – *z*.

Table 2. Hydrogen bonds for compounds **1**–**3** (see Figure 4).[a]

| D–H···A | *d*(D···H) | *d*(H···A) | *d*(D···A) | <(DHA) |
|---|---|---|---|---|
| Compound **1** | | | | |
| N5–H5A···S2 #1 | 0.90 | 2.65 | 3.499(3) | 158.3 |
| N5–H5B···S1 #2 | 0.90 | 2.73 | 3.485(3) | 142.3 |
| N6–H6B···S3 #1 | 0.90 | 2.68 | 3.512(3) | 155.0 |
| Compound **2** | | | | |
| N5–H5A···S2 #1 | 0.90 | 2.66 | 3.520(3) | 159.6 |
| N5–H5B···S1 #2 | 0.90 | 2.76 | 3.527(3) | 144.1 |
| N6–H6B···S3 #1 | 0.90 | 2.63 | 3.468(3) | 156.0 |
| Compound **3** | | | | |
| N5–H5A···S2 #1 | 0.90 | 2.65 | 3.499(5) | 157.5 |
| N5–H5B···S1#2 | 0.90 | 2.74 | 3.500(5) | 142.8 |
| N6–H6B···S3 #1 | 0.90 | 2.64 | 3.471(5) | 154.3 |

[a] Atoms with additional labels #1 and #2 are related to each other by symmetry operations: #1 1 –*x*, –*y*, 1 – *z*; #2 –*x*, –*y*, 1 – *z*.

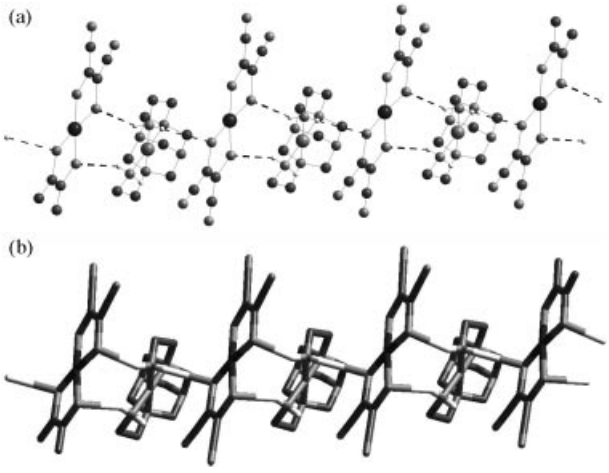


Figure 5. Chain-like arrangement consisting of alternating $[Ni(C_9H_{22}N_6)]^{2+}$ (cation) and $[M(mnt)_2]^{2-}$ (anion) formed by N–H···S hydrogen bonds in the crystal structure of $[Ni(C_9H_{22}N_6)][M(mnt)_2]$ (M = $Cu^{2+}$, $Ni^{2+}$, and $Pd^{2+}$): (a) ball-and-stick representation and (b) wire-frame representation. Methylene hydrogen atoms have been omitted for clarity.

The average Cu–$S_H$ bond length in **1** involving hydrogen-bonded sulfur ($S_H$) is 2.265(1) Å, which is 0.014 Å shorter than the Cu–$S_N$ bond length [2.279(1) Å], in which $S_N$ is not involved in hydrogen-bonding interactions. In the case of compound **2**, the average Ni–$S_H$ bond length [2.170(1) Å] is 0.012 Å shorter than the Ni–$S_N$ bond length [2.182(1) Å]. Compound **3** also follows the same trend but with a smaller difference [average Pd–$S_H$ = 2.287(1) and Pd–$S_N$ = 2.295(1) Å]. The shortening of the M–$S_H$ (M = $Cu^{2+}$, $Ni^{2+}$, $Pd^{2+}$) bonds compared to the M–$S_N$ bond can be explained by a molecular orbitals approach. Thiolate sulfurs are σ- and π-electron donors and the π orbitals that are occupied by a lone pair of electrons interact with the occupied p and d orbitals on the metal ion $M^{2+}$. The occupation of these metal orbitals, which have antibonding character, results in the weakening of the M–S interaction.[23] However, in the present case, it can be expected that the N–H···S hydrogen bonding stabilizes the sulfur π-donor orbitals and thereby diminishes the M–S antibonding interaction. This results in

 © 2006 Wiley-VCH Verlag GmbH & Co. KGaA, Weinheim 

a slight shortening of the M–$S_H$ (M = $Cu^{2+}$, $Ni^{2+}$, $Pd^{2+}$) bonds compared to the M–$S_N$ bonds.

In concert with the metal–sulfur bond length changes in the anion $[M(mnt)_2]^{2-}$, it is expected that the N–H bonds would be lengthened by the N–H···S hydrogen-bonding interaction, while the C–$N_H$ and Ni–$N_H$ bonds ($N_H$ = hydrogen-bonded nitrogen) in the cation $[Ni(C_9H_{22}N_6)]^{2+}$ would be shortened.[24,25] In the present study, the N–H bond lengths cannot be considered because the amine hydrogens were assigned positions on the basis of geometrical considerations in the crystal-structure determination. On the other hand, and in contrast to our expectations, a trend of increasing C–$N_H$ and Ni–$N_H$ bond lengths in the $[Ni(C_9H_{22}N_6)]^{2+}$ cations of **1**, **2**, and **3** is evident when comparing them with those in the crystal structure of $[Ni(C_9H_{22}N_6)](ClO_4)_2$. The average C–N and Ni–N bond lengths (adjacent to amine groups) in $[Ni(C_9H_{22}N_6)](ClO_4)_2$ are 1.37(5) and 1.90(3) Å, respectively.[15] The corresponding average C–$N_H$ and Ni–$N_H$ distances in the cations of **1**–**3** are 1.476(4) and 1.910(2) Å for **1**, 1.479(2) and 1.903(2) Å for **2**, and 1.474(6) and 1.905(2) Å for **3**. The shortening of the Ni–$N_H$ bond lengths compared to the Ni–$N_N$ ($N_N$ = non-hydrogen-bonded nitrogen) bond lengths in the cations of **1**–**3** [average Ni–$N_N$ bond lengths are 1.917(2), 1.914(2), and 1.909(4) Å for **1**–**3**, respectively] is consistent with the fact that the $N_H$ atoms are involved in N–H···S hydrogen-bonding interactions.

## IR Spectra

The N–H···S hydrogen-bonding interactions described above are also reflected in the IR spectra of compounds **1**–**3**. The perchlorate salt of the cation, $[Ni(C_9H_{22}N_6)](ClO_4)_2$ exhibits two NH bands at 3342 and 3296 $cm^{-1}$ in its IR spectrum (Figure 6, a). In the IR spectra of compounds **1**–**3** these bands shift to about 3260 and 3200 $cm^{-1}$, respectively (Figure 6, b–d). This large shift of the NH bands suggests that compounds **1**–**3** have intermolecular N–H···S hydrogen bonds involving cation and anion. The CN bands of the anions $[M(mnt)_2]^{2-}$ (M = $Cu^{2+}$, $Ni^{2+}$, $Pd^{2+}$) in compounds **1**–**3** appear at around 2195 $cm^{-1}$ and the corresponding C=C bands are observed at 1465, 1485, and 1485 $cm^{-1}$, respectively, for **1**–**3** (for IR spectra, see Supporting Information).

## $^1$H NMR Spectra

The $^1$H NMR spectra of $[Ni(C_9H_{22}N_6)](ClO_4)_2$ and compound **2** were recorded in [$D_6$]DMSO (see SI-Figure 6 in the Supporting Information). The protons of the two $NH_2$ groups are observed at $\delta$ = 5.75 and 6.97 ppm, respectively, in the spectrum of $[Ni(C_9H_{22}N_6)](ClO_4)_2$. These two peaks are shifted downfield, appearing at $\delta$ = 7.18 and 8.42 ppm, respectively, in the spectrum of **2**, which also shows the $CH_2$ protons in the range $\delta$ = 2 to 6 ppm. The downfield shift of the $NH_2$ protons from $[Ni(C_9H_{22}N_6)](ClO_4)_2$ to **2** can be ascribed to the existence of the N–H···S hydrogen-bonding

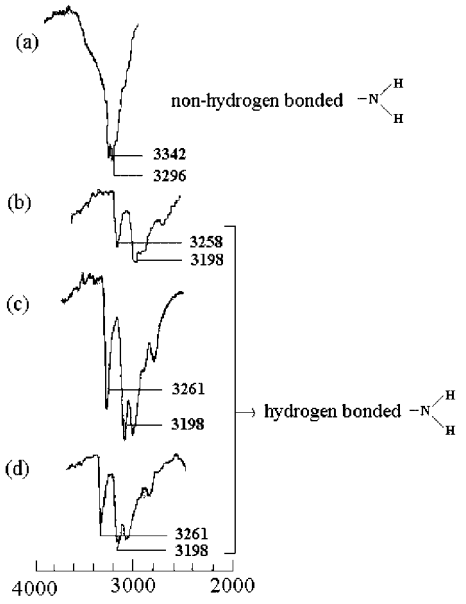


Figure 6. Selected IR bands in the $NH_2$ region of (a) $[Ni(C_9H_{22}N_6)](ClO_4)_2$, (b) $[Ni(C_9H_{22}N_6)][Cu(mnt)_2]$ (**1**), (c) $[Ni(C_9H_{22}N_6)][Ni(mnt)_2]$ (**2**), and (d) $[Ni(C_9H_{22}N_6)][Pd(mnt)_2]$ (**3**) in the solid state (KBr pellets).

interactions between cation and anion (hydrogen bonding decreases the electron density around proton). A similar downfield shift of the amide NH signal was observed in the $^1$H NMR spectrum of the compound $(NEt_4)_2[Hg(S\text{-}2\text{-}CH_3NHCOC_6H_4)_4]$ compared with the bis(carbamoylthiophenoate) complex in [$D_6$]DMSO due to the formation of intramolecular N–H···S hydrogen bonds in the mercury complex.[26]

When the initial concentration of **2** is increased a steady chemical-shift change is observed for the $NH_2$ protons involved in N–H···S hydrogen-bonding interactions. This demonstrates that the percentage of hydrogen-bonded species increases with increasing initial concentrations of **2**. At a concentration of $1 \times 10^{-3}$ M no shift of the $NH_2$ protons with respect to that of $[Ni(C_9H_{22}N_6)](ClO_4)_2$ was observed. However, at higher concentrations (in the range of 0.013 to 0.034 M) a downfield shift of the $NH_2$ protons from $[Ni(C_9H_{22}N_6)](ClO_4)_2$ to **2** was observed (see Figure 7 in the Supporting Information for concentration-dependent NMR spectra). The $^1$H NMR spectra of $[Ni(C_9H_{22}N_6)](ClO_4)_2$ were recorded in the same concentration range used for compound **2**; the peak positions for the $NH_2$ group remained essentially same.

## Electrochemistry

The cationic complex $[Ni(C_9H_{22}N_6)](ClO_4)_2$ shows a quasi-reversible oxidation at +1.24 V vs. SCE and a quasi-reversible reduction at –1.34 V vs. SCE in MeCN solution.[15] However, its ion-pair compounds **1**–**3** are not soluble in MeCN, therefore we performed the electrochemical studies in DMF. In DMF, the reversible oxidation and reduction are observed at +1.00 V vs. SCE and at –1.30 V vs.

 © 2006 Wiley-VCH Verlag GmbH & Co. KGaA, Weinheim 

SCE, respectively, for $[Ni(C_9H_{22}N_6)](ClO_4)_2$ (see Supporting Information). Cyclic voltammograms of **1**–**3** are shown in Figure 7. Compounds **2** and **3** show similar features in their cyclic voltammograms. The reversible reductions at around –1.30 V (vs. SCE) for $[Ni(C_9H_{22}N_6)](ClO_4)_2$ become quasi-reversible in its ion-pair compounds and the oxidative response at around +1.00 V (vs. SCE) for $[Ni(C_9H_{22}N_6)](ClO_4)_2$ is not clearly observed in the ion-pair compounds. Instead, all three cyclic voltammograms (Figure 7) exhibit a strong irreversible oxidation at around +1.16 V (vs. SCE) whose shape is rather complicated. This can be assigned to the oxidation of the dithiolate sulfurs of the mnt ligands (by comparing the cyclic voltammograms of $[Bu_4N]_2[M(mnt)_2]$). This complicated feature might also include the oxidative response of $[Ni(C_9H_{22}N_6)]^{2+}$ at a shifted (higher) potential, which is in agreement with the small bump observed around +1.25 V for all complexes. These data indicate that the oxidation of $[Ni(C_9H_{22}N_6)]^{2+}$ becomes somewhat more difficult in the ion-pair compounds **1**–**3** than in the perchlorate complex $[Ni(C_9H_{22}N_6)](ClO_4)_2$ and the reduced complex $[Ni(C_9H_{22}N_6)]^{+}$ becomes more unstable in the ion-pair compounds than in the perchlorate complex (on the cyclic voltammetric timescale). This implies that the stability of $[Ni(C_9H_{22}N_6)]^{2+}$ in its ion-pair compounds would make the transition from $Ni^{II}$ to $Ni^{III}$ or $Ni^{I}$ more unfavorable than in its perchlorate salt. Compound **1** shows an additional irreversible reduction at around –0.75 V vs. SCE (Figure 7, a) that is not observed in the case of compounds **2** and **3** (Figures 7, parts b and c, respectively). We assign this reductive response to the $[Cu(mnt)_2]^{2-}/[Cu(mnt)_2]^{3-}$ couple based on relevant literature data.[27] Compounds **1**–**3** exhibit a reversible oxidation that corresponds to the couple $[M(mnt)_2]^{-}/[M(mnt)_2]^{2-}$ (M = $Cu^{2+}$, $Ni^{2+}$ and $Pd^{2+}$; 0.33 V vs. SCE for **1**, 0.33 V vs. SCE for **2** and 0.54 V vs. SCE for **3** in DMF).

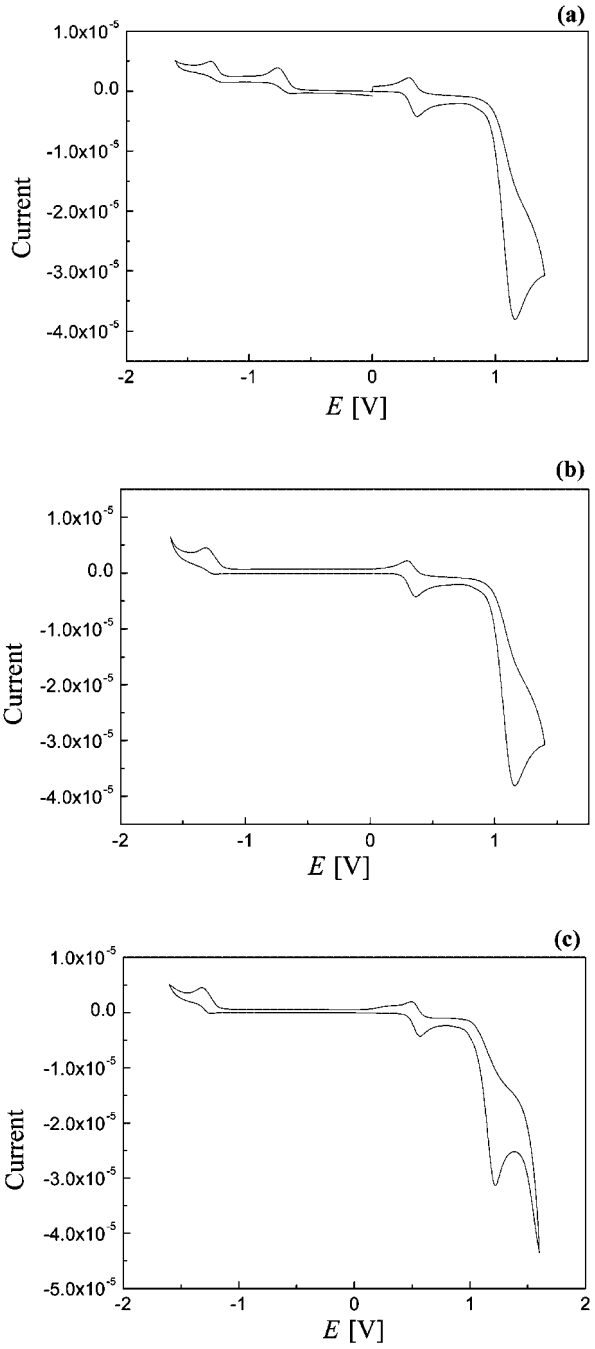


Figure 7. Cyclic voltammograms of a 1.0 mM solution of (a) $[Ni(C_9H_{22}N_6)][Cu(mnt)_2]$ (**1**), (b) $[Ni(C_9H_{22}N_6)][Ni(mnt)_2]$ (**2**), and (c) $[Ni(C_9H_{22}N_6)][Pd(mnt)_2]$ (**3**) in DMF at room temperature. Scan rate: 100 mV $s^{-1}$. Current given in A.

## UV/Vis-NIR Spectra

The UV/Vis spectra of compounds **1**–**3** were measured both in solution and the solid state at room temperature. The perchlorate salt of the cation $[Ni(C_9H_{22}N_6)](ClO_4)_2$ exhibits a d-d band at around 450 nm in the solid state and at 440 nm in solution ($\varepsilon$ = 80 $M^{-1}cm^{-1}$ in MeCN), which is the characteristic absorption for a square-planar $Ni^{II}$-$N_4$ chromophore (Figures 18 and 19 in the Supporting Information). The d-d band of $[Ni(C_9H_{22}N_6)]^{2+}$ at 440 nm is obscured by the intense MLCT charge-transfer bands for the metal–dithiolene moieties in the ion-pair complexes (at around 430 nm for **1**, 470 nm for **2**, and 430 nm for **3**). The d-d bands at around 1100 (for **1**), 860 (for **2**), and 630 nm (for **3**) are characteristic features of $[Cu(mnt)_2]^{2-}$, $[Ni(mnt)_2]^{2-}$, and $[Pd(mnt)_2]^{2-}$ respectively (see SI-Figure 20 in the Supporting Information).

## ESR Spectroscopy

The ESR spectrum of compound **1** in DMF at liquid-nitrogen temperature was also measured. It exhibits hyperfine structure due to $^{63,65}Cu$ nuclei. Interestingly, both $g_{\|}$ and $g_{\perp}$ features are resolved due to $^{63,65}Cu$ hyperfine coupling, which is very rarely observed in metal–dithiolene complexes. The average value of the hyperfine coupling parameters (determined from $|A_{\|}|$ = 15.3 mT and $|A_{\perp}|$ = 4.8 mT) is 8.3 mT, which is not identical to that (7.4 mT) of the solution ESR spectrum at room temperature (see SI-Figures

 © 2006 Wiley-VCH Verlag GmbH & Co. KGaA, Weinheim 

21–23 in the Supporting Information). This is consistent with the NMR studies.

## Conclusion

Numerous model compounds of sulfur-containing metallo-proteins have been reported that emphasize the importance of N–H···S hydrogen bonds in stabilizing the negatively charged metal–sulfur cluster (the active site) of the relevant protein. Intramolecular N–H···S hydrogen bonding was observed in many of these model studies and, in a few cases, intermolecular hydrogen bonding was also identified. We have introduced, for the first time, this N–H···S hydrogen-bonding interaction between a novel cationic inorganic complex $[Ni(C_9H_{22}N_6)]^{2+}$ (that has H-bond donor sites) and the classical inorganic anionic complexes $[M(mnt)_2]^{2-}$ ($M = Cu^{2+}$, $Ni^{2+}$ and $Pd^{2+}$) with dithiolato sulfur anions as H-bond acceptor sites. The existence of such supramolecular intermolecular N–H···S interactions in this new family of ion-pair compounds is additionally supported by IR, $^1H$ NMR, and ESR spectral studies. The complex cation $[Ni(C_9H_{22}N_6)]^{2+}$ was reported earlier as its perchlorate salt, although its crystal structure was not discussed in detail because of disorder problems. We have succeeded in resolving this disorder problem in the crystal structures of the ion-pair compounds **1**–**3**.

## Experimental Section

**General:** Microanalytical (C, H, N, S) data were obtained with a FLASH EA 1112 Series CHNS Analyzer. IR spectra were recorded for KBr pellets with a JASCO FT/IR-5300 spectrometer in the region 400–4000 $cm^{-1}$. Electronic spectra were recorded with a UV-3101PC/UV/Vis-NIR spectrophotometer (Shimadzu) equipped with a diffuse reflectance accessory (reflectance spectra were recorded for KBr pellets). The diffuse reflectance spectra obtained were then Kubelka–Munk corrected. The ESR spectra were recorded with a (JEOL) JES-FA200 ESR spectrometer. A Cypress model CS-1090/CS-1087 electroanalytical system was used for cyclic voltammetric experiments. The electrochemical experiments were measured in DMF containing $Bu_4NClO_4$ as a supporting electrolyte, using a conventional cell consisting of two platinum wires as working and counter electrodes, and a saturated calomel electrode (SCE) as reference. The potentials reported here are uncorrected for junction contributions. Some electrochemical measurements were performed on a BAS i Epsilon-EC Bioanalytical System Inc. using Ag/AgCl reference electrode and glassy carbon as a working electrode. Powder X-ray diffraction data were collected on Phillips PW 3710 diffractometer. EDAX analyses were performed using Philips XL 30 SEM equipment.

**Materials:** All commercially available chemicals were of reagent grade and were used as received without further purification. The solvents were dried and distilled according to standard procedures for the electrochemical and spectroscopy experiments. The acyclic $Ni^{II}$ complex of 3,7-bis(2-aminoethyl)-1,3,5,7-tetraazabiclo[3.3.1]-nonane was synthesized as its perchlorate salt according to a reported method.[15] The salts $[Bu_4N]_2[M(mnt)_2]$ ($M = Ni^{2+}$, $Pd^{2+}$, and $Cu^{2+}$) were prepared according to a literature procedure.[28] Disodium maleonitriledithiolate [the disodium salt of 1,2-dicyanoethylenedithiolate ($Na_2mnt$)] was prepared following a synthetic procedure described in the same paper.[28]

**Synthesis of $[Ni(C_9H_{22}N_6)][Cu(mnt)_2]$ (1):** $[Ni(C_9H_{22}N_6)](ClO_4)_2$ (0.047 g, 0.10 mmol) was dissolved in 10 mL of MeCN by mild heating in a water bath. The resulting clear, yellow solution was treated with $[Bu_4N]_2[Cu(mnt)_2]$ (0.082 g, 0.1 mmol) dissolved in 15 mL of MeCN. The final reaction mixture was then heated to about 50 °C in an oil bath for 10 min with stirring, whereby the dark microcrystalline compound **1** precipitated out within a day. The crystals of **1** were filtered, washed with diethyl ether, and dried at room temperature. Yield: 0.045 g (74% based on Cu). $C_{17}H_{22}CuN_{10}NiS_4$ (616.94): calcd. C 33.09, H 3.59, N 22.70, S 20.79; found C 33.29, H 3.48, N 22.59, S 21.01. IR (KBr): $\tilde{\nu}$ = 3258 (w), 3192 (m), 2191 (s), 1570 (w), 1464 (s), 1281 (w), 1150 (m), 1086 (s), 992 (w), 941 (m), 908 (w), 856 (s), 814 (s), 716 (w), 607 (m), 586 (w), 511 (s) $cm^{-1}$. UV/Vis/NIR (DMF): $\lambda_{max}$ ($\varepsilon$) = 321 nm (36360 $M^{-1}cm^{-1}$), 372 (23230), 426 (12120), 485 (10100), 1200 (74).

Single crystals suitable for an X-ray structure determination were grown in a $\lambda$-shaped glass tube with two terminals. $[Ni(C_9H_{22}N_6)](ClO_4)_2$ was dissolved in 10 mL of MeCN in a 20-mL round-bottomed flask and this was fixed to one terminal of the tube; the other terminal of the tube was connected to a 20-mL round-bottomed flask containing 10 mL of an MeCN solution of $[Bu_4N]_2[Cu(mnt)_2]$. Finally, the empty part of the tube was slowly filled with MeCN (from the top) and sealed. The crystals collected after 25 days from the top of the tube were identified as **1**.

**Synthesis of $[Ni(C_9H_{22}N_6)][Ni(mnt)_2]$ (2):** This compound was synthesized by stirring an MeCN solution (10 mL) of $[Ni(C_9H_{22}N_6)](ClO_4)_2$ (0.047 g, 0.10 mmol) with an MeCN solution (15 mL) of $[Bu_4N]_2[Ni(mnt)_2]$ (0.082 g, 0.1 mmol) at room temperature for half an hour. The red microcrystals of **2** were separated by filtration, washed with diethyl ether, and dried at room temperature. Yield: 0.05 g (82% based on Ni). $C_{17}H_{22}N_{10}Ni_2S_4$ (612.11): calcd. C 33.36, H 3.62, N 22.88, S 20.95; found C 33.58, H 3.53, N 22.78, S 21.06. IR (KBr): $\tilde{\nu}$ = 3264 (w), 3196 (m), 2195 (s), 1570 (w), 1485 (s), 1280 (w), 1233 (m), 1149 (s), 1086 (s), 1055 (m), 990 (m), 943 (w), 909 (w), 856 (s), 814 (s), 713 (w), 605 (s), 546 (w), 509 (s) $cm^{-1}$. UV/Vis/NIR (DMF): $\lambda_{max}$ ($\varepsilon$) = 317 nm (41410 $M^{-1}cm^{-1}$), 387 (10100), 482 (6060), 510 (3131), 770 (53).

Single crystals suitable for an X-ray crystal structure determination were grown as described for compound **1**.

**Synthesis of $[Ni(C_9H_{22}N_6)][Pd(mnt)_2]$ (3):** This compound was synthesized by the same procedure as described for compound **2**, starting from MeCN solutions of $[Ni(C_9H_{22}N_6)](ClO_4)_2$ (0.047 g, 0.1 mmol) and $[Bu_4N]_2[Pd(mnt)_2]$ (0.087 g, 0.1 mmol). Yield: 0.041 g (63% based on Pd). $C_{17}H_{22}N_{10}NiPdS_4$ (659.80): calcd. C 30.94, H 3.36, N 21.23, S 19.44; found C 31.06, H 3.31, N 21.34, S 19.66. IR (KBr): $\tilde{\nu}$ = 3262 (w), 3198 (m), 2195 (s), 1568 (w), 1485 (s), 1338 (m), 1279 (w), 1232 (w), 1202 (w), 1178 (w), 1146 (s), 1086 (s), 1043 (w), 990 (w), 943 (w), 909 (w), 854 (s), 815 (s), 713 (w), 605 (m), 507 (s) $cm^{-1}$. UV/Vis (DMF): $\lambda_{max}$ ($\varepsilon$) = 367 nm (2121 $M^{-1}cm^{-1}$), 429 (5050), 450 (5454), 637 (110).

***Caution!*** *Perchlorate salts are potentially explosive and should be handled in small quantities with caution.*

**X-ray Crystallography:** Crystal data were collected with an Enraf–Nonius CAD4 diffractometer at 25 °C equipped with a graphite-monochromated Mo-$K_\alpha$ ($\lambda$ = 0.71073 Å) radiation source. An empirical absorption correction based on a series of $\psi$ scans was applied. The structures were solved by direct methods (SHELXS-97)[29] and refined by full-matrix least-squares on $F^2$ (SHELXL-97).[30] All non-hydrogen atoms were refined anisotropi-

 © 2006 Wiley-VCH Verlag GmbH & Co. KGaA, Weinheim 

Table 3. Crystal data and structural refinement for compounds **1**, **2** and **3**.

| | **1** | **2** | **3** |
|---|---|---|---|
| Empirical formula | $C_{17}H_{22}CuN_{10}NiS_4$ | $C_{17}H_{22}N_{10}Ni_2S_4$ | $C_{17}H_{22}N_{10}NiPdS_4$ |
| Formula weight | 616.94 | 612.11 | 659.80 |
| $T$ [K] | 298(2) | 298(2) | 298(2) |
| $\lambda$ [Å] | 0.71073 | 0.71073 | 0.71073 A |
| Crystal system | monoclinic | monoclinic | monoclinic |
| Space group | $P2_1/n$ | $P2_1/n$ | $P2_1/n$ |
| $a$ [Å] | 8.493(2) | 8.481(5) | 8.489(8) |
| $b$ [Å] | 16.897(5) | 16.753(4) | 16.904(3) |
| $c$ [Å] | 16.863(8) | 16.857(8) | 16.898(4) |
| $\beta$ [°] | 101.77(3) | 101.27(4) | 101.68(4) |
| $V$ [Å$^3$] | 2369.1(14) | 2348.9(19) | 2374(2) |
| $Z$ | 4 | 4 | 4 |
| $D_{calcd.}$ [Mg m$^{-3}$] | 1.730 | 1.731 | 1.846 |
| $\mu$ [mm$^{-1}$] | 2.074 | 1.988 | 1.931 |
| F[000] | 1260 | 1256 | 1328 |
| Crystal size [mm$^3$] | 0.68 × 0.64 × 0.48 | 0.68 × 0.60 × 0.56 | 0.68 × 0.36 × 0.32 |
| $\theta$ range for Data collection [°] | 1.72 to 27.47 | 1.73 to 27.46 | 1.72 to 24.97 |
| Reflections collected/unique | 5409/5409 | 5363/5363 | 4178/4178 |
| Refinement method | Full-matrix least-squares on $F^2$ | | |
| Data/restraints /parameters | 5409/0/298 | 5363/0/298 | 4178/0/298 |
| Goodness-of-fit on $F^2$ | 1.132 | 1.132 | 1.291 |
| $R_1/wR_2$ [$I > 2\sigma(I)$] | 0.0306/0.0816 | 0.0306/0.0790 | 0.0322/0.1054 |
| $R_1/wR_2$ (all data) | 0.0437/0.0986 | 0.0463/0.0915 | 0.0459/0.1110 |
| Largest diff. Peak/hole [e·Å$^3$] | 1.031/–0.417 | 0.608/–0.503 | 1.239/–0.465 |

cally. Hydrogen atoms were introduced at calculated positions and included in the refinement as riding on their respective parent atoms. The crystallographic data and the parameters of structure refinement for compounds **1**–**3** are summarized in Table 3.
CCDC-273272 (for **1**), -273273 (for **2**), and -273274 (for **3**) contain the supplementary crystallographic data for this paper. These data can be obtained free of charge from The Cambridge Crystallographic Data Center via www.ccdc.cam.ac.uk/data_request/cif.

**Supporting Information** available (for details see the footnote on the first page of this article): Figures related to crystal structures for compounds **1**, **2** and **3**; $^1$H NMR spectrum for compound **2** and $^1$H NMR spectra for concentration-dependent NMR studies; IR spectra for compounds **1**, **2** and **3**; cyclic voltammograms for compounds **1**, **2** and **3**; solution and solid-state electronic spectra for compounds **1**, **2** and **3**; ESR spectra for compound **1**; X-ray powder diffraction patterns (simulated and observed).

## Acknowledgments

We thank CSIR, Government of India, for financial support [Project No.: 01(1737)/02/EMR-II]. The National X-ray Diffractometer facility at University of Hyderabad by the Department of Science and Technology, Government of India, is gratefully acknowledged. We are grateful to UGC, New Delhi, for providing infrastructure facility at University of Hyderabad under UPE grant. The authors thank Professor S. Pal for providing electrochemical data for this work. We also thank Professor Sabyasachi Sarkar and Mr. Kuntal Pal (Department of Chemistry, IIT Kanpur, India) for helping us by providing some electrochemical data at the revision stage of this work. V. M. thanks CSIR, New Delhi, for a fellowship.

[1] V. Balzani, F. Scandola, *Supramolecular Photochemistry*, Horwood, Chichester, **1991**.
[2] U. T. Mueller-Westerhoff, B. Vance, D. I. Yoon, *Tetrahedron* **1991**, *47*, 909–932.
[3] H. Tanaka, Y. Okano, H. Kobayashi, W. Suzuki, A. Kobayashi, *Science* **2001**, *291*, 285–287.
[4] A. T. Coomber, D. Beljonne, R. H. Friend, J. K. Bredas, A. Charlton, N. Robertson, A. E. Underhill, M. Kurmoo, P. Day, *Nature* **1996**, *380*, 144–146.
[5] C.-T. Chen, S.-Y. Liao, K.-J. Lin, L.-L. Lai, *Adv. Mater.* **1998**, *3*, 334–338.
[6] a) I. Nunn, B. Eisen, R. Benedix, H. Kisch, *Inorg. Chem.* **1994**, *33*, 5079–5085; b) C. Handrosch, R. Dinnebier, G. Bondarenko, E. Bothe, F. Heinemann, H. Kisch, *Eur. J. Inorg. Chem.* **1999**, 1259–1269; c) G. Schmauch, F. Knoch, H. Kisch, *Chem. Ber.* **1994**, *127*, 287–294; d) W. Dümler, H. Kisch, *New J. Chem.* **1991**, *15*, 649–656; e) H. Kisch, B. Eisen, R. Dinnebier, K. Shankland, W. I. F. David, F. Knoch, *Chem. Eur. J.* **2001**, *7*, 738–748.
[7] R. C. Wheland, *J. Am. Chem. Soc.* **1976**, *98*, 3926–3930.
[8] a) H. Kisch, *Coord. Chem. Rev.* **1997**, *159*, 385–396; b) A. Vogler, H. Kunkely, *J. Chem. Soc. Chem. Commun.* **1986**, 1616–1617; c) G. Schmauch, T. Chihara, K. Wakatsuki, M. Hagiwara, H. Kisch, *Bull. Chem. Soc. Jpn.* **1996**, *69*, 2573–2579; d) F. Bigoli, P. Deplano, M. L. Mercuri, M. A. Pellinghelli, L. Pilia, G. Pintus, A. Serpe, E. F. Trogu, *Inorg. Chem.* **2002**, *41*, 5241–5248.
[9] V. Madhu, S. K. Das, *Polyhedron* **2004**, *23*, 1235–1242.
[10] E. T. Adman, *Biochim. Biophys. Acta* **1979**, *549*, 107–144.
[11] E. Adman, K. D. Watenpaugh, L. H. Jensen, *Proc. Natl. Acad. Sci. U. S. A* **1975**, *72*, 4854–4858.
[12] A. Nakamura, N. Ueyama, in *Metal Clusters in Proteins* (Ed.: L. Que), American Chemical Society, Washington, DC, **1998**, chapter 14.
[13] a) N. Ueyama, T. Okamura, A. Nakamura, *J. Am. Chem. Soc.* **1992**, *114*, 8129–8137; b) N. Ueyama, T. Okamura, A. Nakamura, *J. Chem. Soc. Chem. Commun.* **1992**, 1019–1020; c) T. Okamura, N. Ueyama, A. Nakamura, E. W. Ainscough, A. M. Brodie, J. M. Waters, *J. Chem. Soc. Chem. Commun.* **1993**, 1658–1660; d) N. Ueyama, N. Nishikawa, Y. Yamada, T. Oka-

 © 2006 Wiley-VCH Verlag GmbH & Co. KGaA, Weinheim 

mura, A. Nakamura, *J. Am. Chem. Soc.* **1996**, *118*, 12826–12827; e) N. Ueyama, Y. Yamada, T. Okamura, S. Kimura, A. Nakamura, *Inorg. Chem.* **1996**, *35*, 6473–6484; f) T. Okamura, S. Takamizawa, N. Ueyama, A. Nakamura, *Inorg. Chem.* **1998**, *37*, 18–28; g) N. Ueyama, N. Nishikawa, Y. Yamada, T. Okamura, S. Oka, H. Sakurai, A. Nakamura, *Inorg. Chem.* **1998**, *37*, 2415–2421; h) M. A. Walters, C. L. Roche, A. L. Rheingold, S. W. Kassel, *Inorg. Chem.* **2005**, *44*, 3777–3779; i) M. Kato, T. Okamura, H. Yamamoto, N. Ueyama, *Inorg. Chem.* **2005**, *44*, 1966–1972.

[14] M. A. Walters, J. C. Dewan, C. Min, S. Pinto, *Inorg. Chem.* **1991**, *30*, 2656–2662.

[15] M. P. Suh, W. Shin, H. Kim, C. H. Koo, *Inorg. Chem.* **1987**, *26*, 1846–1852.

[16] T. Ito, K. Toriumi, *Acta Crystallogr. Sect. B* **1981**, *37*, 88–92.

[17] R. Murray-Rust, J. Murray-Rust, *Acta Crystallogr. Sect. B* **1979**, *35*, 1704–1706.

[18] G. Ferguson, R. J. Restivo, R. W. Hay, *Acta Crystallogr. Sect. B* **1979**, *35*, 159–162.

[19] M. F. Bailey, I. E. Maxwell, *J. Chem. Soc., Dalton Trans.* **1972**, 938–944.

[20] a) P. Kuppusamy, B. L. Ramakrishna, P. T. Manoharan, *Inorg. Chem.* **1984**, *23*, 3886–3892; b) S. S. Staniland, W. Fujita, Y. Umezono, K. Awaga, P. J. Camp, S. J. Clark, N. Robertson, *Inorg. Chem.* **2005**, *44*, 546–551.

[21] a) M. K. Krepps, S. Parkin, D. A. Atwood, *Cryst. Growth Des.* **2001**, *1*, 291–297; b) K. C. Kumara Swamy, S. Kumara Swamy, S. Raja, K. S. Kumar, *J. Chem. Crystallogr.* **2001**, *31*, 51–56.

[22] a) N. Ueyama, K. Taniuchi, T. Okamura, T. Nakamura, H. Maeda, S. Emura, *Inorg. Chem.* **1996**, *35*, 1945–1951; b) B. R. Srinivasan, S. N. Dhuri, C. Näther, W. Bensch, *Acta Crystallogr., Sect. E* **2002**, *58*, m622–m624; c) B. R. Srinivasan, S. N. Dhuri, C. Näther, W. Bensch, *Acta Crystallogr. Sect. C* **2003**, *59*, m124–m127; d) B. R. Srinivasan, M. Poisot, C. Näther, W. Bensch, *Acta Crystallogr., Sect. E* **2004**, *60*, i136–i138; e) B. R. Srinivasan, S. N. Dhuri, M. Poisot, C. Näther, W. Z. Bensch, *Naturforsch., Teil B* **2004**, *59*, 1083–1092; f) B. R. Srinivasan, S. N. Dhuri, M. Poisot, C. Näther, W. Bensch, *Z. Anorg. Allg. Chem.* **2005**, *631*, 1087–1094.

[23] S. Harris, *Polyhedron* **1989**, *8*, 2843–2882.

[24] V. Gutmann, G. Resch, W. Linert, *Coord. Chem. Rev.* **1982**, *43*, 133–164 and references cited therein.

[25] M. Kitano, K. Kuchitsu, *Bull. Chem. Soc. Jpn.* **1973**, *46*, 3048–3051.

[26] M. Kato, K. Kojima, T. Okamura, H. Yamamoto, T. Yamamura, N. Ueyama, *Inorg. Chem.* **2005**, *44*, 4037–4044.

[27] S. P. Best, S. A. Ciniawsky, R. J. H. Clark, R. C. S. McQueen, *J. Chem. Soc. Dalton Trans.* **1993**, 2267–2271.

[28] A. Davison, R. H. Holm, *Inorg. Synth.* **1967**, *10*, 8–26.

[29] G. M. Sheldrick, *SHELXS-97*, *A Program for Structure Solution*, University of Göttingen, Göttingen, Germany, **1997**.

[30] G. M. Sheldrick, *SHELXL-97*, *A Program for Structure Refinement*, University of Göttingen: Göttingen, Germany, **1997**.

Received: August 26, 2005
Published Online: February 15, 2006

 © 2006 Wiley-VCH Verlag GmbH & Co. KGaA, Weinheim 

DOI: 10.1002/ejic.200500997

# Ring Closure of Alkoxycarbonyl(tetracarbonyl)pyruvoyliron Complexes into Metallalactones Induced by Nucleophilic Attack of Carbanions

**Patrice Cabon,[a] René Rumin,[a] Jean-Yves Salaün,*[a] Hervé des Abbayes,[a] and Smail Triki[a]**

**Keywords:** Carbanions / Carbonyl ligands / Iron / Metallacycles / Nucleophilic addition

The reaction of carbanions with the pyruvoyl-substituted iron complex $[(CO)_4Fe(CO_2CH_3)\{C(O)C(O)CH_3\}]$ (**1**) affords the anionic trifunctionalized metallalactones $[(CO)_3Fe\{C(O)C(CH_3)(CRR'R'')OC^4(O)(Fe–C^4)\}(CO_2CH_3)]^-$ (**3**), whose formation results from the addition of the nucleophile to the β carbonyl of the pyruvoyl moiety, followed by attack of the oxygen of this β carbonyl on a terminal carbonyl ligand. These anionic lactones react, at low temperature, with HCl to give rise to the neutral lactones $[(CO)_4Fe\{C(O)C(CH_3)(CRR'R'')OC^4(O)(Fe–C^4)\}]$ (**2**), which were previously obtained by addition of NuH nucleophiles to **1**. Complex **3(3)**, whose lactonic ring formation has been performed using the diethyl malonate anion (R = R′ = $CO_2C_2H_5$; R′′ = H), and the dimethyl-substituted neutral lactone **2(1)** (R = R′ = R′′ = H) have been characterized by X-ray diffraction studies.

(© Wiley-VCH Verlag GmbH & Co. KGaA, 69451 Weinheim, Germany, 2006)

## Introduction

Nucleophilic attacks upon organic ligands coordinated to transition metals are important processes in the formation of new reactive organometallic intermediates that are useful in organic synthesis. Although it is possible to assess the reactivity of various ligands toward nucleophiles, it is more difficult to predict the site of nucleophilic attack on polyfunctional complexes. Thus, while nucleophiles react very easily with terminal carbonyls of metal–carbonyl compounds to afford acyl, aroyl, alkoxycarbonyl, or carbamoyl ligands, the same reaction occurs regiospecifically at the α-carbon of a carbene ligand,[1] at the α- and γ-carbons of an allenylidene,[2,3] and at the β-carbon of an allenyl ligand[4] of analogous complexes. It has also been shown that acyl ligands are less electrophilic than terminal carbonyl ligands.[5] In the course of a study of complexes considered as possible models for double or polycarbonylation reactions, we investigated the reactivity of compounds displaying a ligand with a C(O)C(O)R chain toward nucleophilic reagents. Indeed, addition of nucleophiles at $C_\alpha$ of this type of ligand has been proposed to account for the formation of phenylpyruvic esters by dicarbonylation of organic halides catalyzed by $[Co(CO)_4]^-$.[6] The very few nucleophilic additions performed on cationic (Fe[7] Pt[8]) or neutral complexes (Fe[9]) displaying an M–C(O)–C(O)–R chain have been shown to occur at a terminal carbonyl ligand of the molecule. We recently observed the original behavior of the complex *cis*-$[(CO)_4Fe\{C(O)C(O)CH_3\}(CO_2CH_3)]$ (**1**), which afforded its cyclic isomer **2** quantitatively, at 15 °C, in a reaction involving the formation of a metallalactone ring by addition of the oxygen of the β carbonyl of the pyruvoyl to the alkoxycarbonyl ligand and a migration of the methoxy group of this latter ligand to the β carbon of the pyruvoyl (Scheme 1, a).[10]

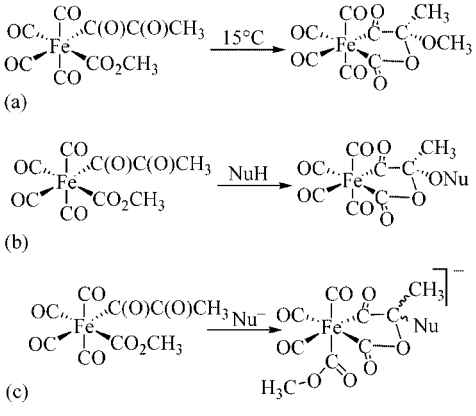


Scheme 1.

This reaction appeared very similar to the ring-chain isomerism observed for organic γ-keto esters.[11] Indeed, as the alkoxycarbonylpyruvoyliron complex **1** can be considered as a γ-keto ester with a metal inserted into the chain linking its two organic functions, a parallel between the organic reaction and the organometallic process can be drawn. When performed in the presence of an excess of pronucleophilic reagents (Nu–H), the reaction affords Nu-sub-

[a] Laboratoire de Chimie, Electrochimie Moléculaires et Chimie Analytique, UMR CNRS-Université de Bretagne Occidentale 6521, UFR Sciences et Techniques,
6 Avenue le Gorgeu, CS 93837, 29238 Brest Cédex, France
E-mail: jean-yves.salaun@univ-brest.fr

 © 2006 Wiley-VCH Verlag GmbH & Co. KGaA, Weinheim 

stituted metallalactones (Scheme 1, b) which are formed, under these conditions, by an addition of the nucleophile to the β carbonyl of the pyruvoyl followed by metallalactone ring formation due to attack of the oxygen of this β carbonyl on the alkoxycarbonyl ligand and elimination of the methoxy group of this latter ligand.[7] To the best of our knowledge, prior to our study, only one example of nucleophilic addition at a carbonyl carbon of a ligand displaying a double C(O) chain had been described in the literature. In this paper, hydride was reported to attack the β carbonyl of a ligand of $[(CO)_5Mn\{C(O)C(O)C_6H_5)\}]$ to afford an anionic metallalactone by cyclization of the phenylglyoxyl with a terminal carbonyl.[12] These results prompted us to perform the cyclization of **1** with anionic nucleophiles ($RO^-$, $RS^-$, or $R_2P^-$).[13] These reactions, as they only afford two isomers of the anionic trifunctionalized metallalactone **3** (Scheme 1, c), also suggested that the formation of the metallalactonic ring could indeed proceed by addition to a terminal carbonyl rather than to the alkoxycarbonyl ligand. However, as the structure of these trifunctionalized anions **3** was not firmly established, we tried to perform analogous reactions using C–H nucleophiles and carbanions of various nucleophilicity and of different steric effects. The results of this study will be the topic of this paper.

## Results and Discussion

### Reaction of 1 with Activated C–H Bonds or Carbanions as Nucleophiles

Although often used as nucleophiles,[14] pronucleophiles displaying activated methylenes, such as diethyl malonate (1 equiv.) or malononitrile (20 equiv.), were found to be unreactive towards **1** at –10 °C. This lack of reactivity is not too surprising as **1** only reacts slowly with $CH_3OH$, $C_2H_5SH$, $HP(C_6H_5)_2$, or $HP(C_6H_{11})_2$.[7] On the other hand, as shown by IR monitoring, **1** reacts very rapidly with carbanionic reagents such as MeLi, *n*BuLi, $NaCH(CO_2C_2H_5)_2$, $NaCH(C{\equiv}N)_2$, $NaCH[C(O)CH_3]_2$, $NaCH[C(O)CH_3](CO_2CH_3)$, $NaCH(CO_2C_2H_5)(C{\equiv}N)$, $NaC(CH_3)(CO_2C_2H_5)_2$, or $NaC(CH_2CH{=}CH_2)(CO_2C_2H_5)_2$ to afford instantaneously, even at –70 °C, new complexes displaying a set of three ν(C≡O) bands between 2084 and 1970 $cm^{-1}$. These frequencies are similar to those observed for the product of the reaction between **1** and $RO^-$, $RS^-$, or $R_2P^-$ anions,[13] and are intermediate between the ν(C≡O) of the monofunctionalized anion $[Fe(CO)_4(CO_2R)]^-$ (three bands around 1910 $cm^{-1}$)[15] and those of their homologues of the neutral complex *cis*-$[Fe(CO)_4(CO_2R)_2]$ (four bands between 2130 and 2050 $cm^{-1}$).[16] They fall within the range of those of trifunctionalized mono anions such as *fac*-$[(CO)_3Fe(CO_2R)_3]^-$ (two bands at 2080 and 2015 $cm^{-1}$), which are themselves obtained by addition of $RO^-$ to a terminal carbonyl of $[(CO)_4Fe(CO_2R)_2]$.[9] These values measured for ν(C≡O) are therefore consistent with a moderate increase of the electron density on the metal. The observation of three ν(C≡O) bands instead of the two required by $C_{3v}$ symmetry could result from the presence of a metallacycle in the complex. These results suggest the *fac* trifunctionalized metallalactone structure **3** for the products of these reactions (see Scheme 2).

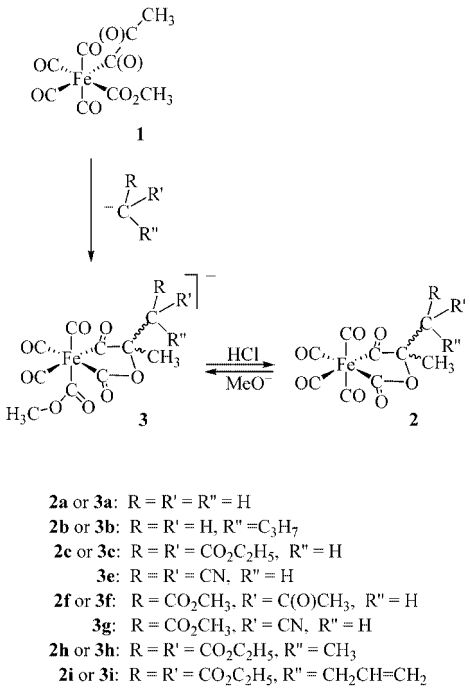


**2a** or **3a**: R = R' = R'' = H
**2b** or **3b**: R = R' = H, R'' = $C_3H_7$
**2c** or **3c**: R = R' = $CO_2C_2H_5$, R'' = H
**3e**: R = R' = CN, R'' = H
**2f** or **3f**: R = $CO_2CH_3$, R' = $C(O)CH_3$, R'' = H
**3g**: R = $CO_2CH_3$, R' = CN, R'' = H
**2h** or **3h**: R = R' = $CO_2C_2H_5$, R'' = $CH_3$
**2i** or **3i**: R = R' = $CO_2C_2H_5$, R'' = $CH_2CH{=}CH_2$

Scheme 2.

This assumption was confirmed by the $^{13}C$ NMR spectroscopic data of these compounds. Although most of these complexes were found to be sparingly soluble in organic solvents, the $^{13}C$ NMR spectra of these compounds could be obtained in $[D_8]$THF (see Exp. Sect.). The anionic structure of complexes **3** was indicated by a shift of the signals of the carbonyls linked to the metal toward lower fields relative to their homologues **1** ($\Delta\delta$ = 10 ppm for the terminal carbonyls and 15 ppm for the carbon of the alkoxycarbonyl).[13] However, the negative charge is very probably delocalized over the three carbonylated substituents of the complex as the chemical shifts of the terminal carbonyls of **3** (from $\delta$ = 205 to 212 ppm) fall between those observed for **1** ($\delta$ = 200 ppm)[13] and those of $[(CO)_4Fe(CO_2R)]^-$ ($\delta$ = 220 ppm).[15] The electron density of the metal center of **3** is therefore intermediate between that observed for neutral complexes and for the monofunctionalized anion. The formation of a metallacycle in complexes **3** is shown by the signal of their disubstituted cyclic quaternary carbon atom between $\delta$ = 86.5 and 96.9 ppm. This value is not very different from those observed for similar carbons substituted by OR ($\delta$ = 111 ppm), SR ($\delta$ = 95.5 ppm), or $PR_2$ ($\delta$ = 90 ppm) groups.[13] As **3(1)** displays two methyl substituents on this cyclic quaternary carbon, it only exists as one isomer. The formation of this single isomer is shown in the $^{13}C$ NMR spectrum by the observation of one signal for each carbon of this complex. The nonequivalency of these two methyls, shown by two signals at $\delta$ = 15.8 and 8.4 ppm, results from the *fac* position of the alkoxycarbonyl ligand. Reaction of **1** with *n*BuLi afforded

 © 2006 Wiley-VCH Verlag GmbH & Co. KGaA, Weinheim 

a similar complex. This compound, which has both *n*-butyl and methyl substituents on the quaternary carbon of its metallalactone [R = R′ = H; R′′ = $C_3H_7$; **3(2)**], was formed as a 50:50 mixture of two isomers. The presence of these two isomers is shown by the observation of two signals of equal intensities at $\delta$ = 274.1 and 271.5 ppm for the C=O acyl, at $\delta$ = 96.9 and 96.7 ppm for the cyclic $sp^3$ carbon, and at $\delta$ = 60.5 and 59.9 ppm for the $OCH_3$ group of the alkoxycarbonyl ligand. Surprisingly, the same reaction performed with $NaCH(CO_2C_2H_5)_2$ afforded only one isomer of the anion **3(3)** (R = R′ = $CO_2C_2H_5$; R′′ = H). Indeed, the $^{13}C$ NMR spectrum of this compound only displays one signal at $\delta$ = 269.3 ppm for the acyl C=O, at $\delta$ = 94.3 ppm for the cyclic $sp^3$ carbon, at $\delta$ = 50.9 ppm for the methoxy of the methoxycarbonyl ligand, and at $\delta$ = 21.7 ppm for the methyl located on the cyclic $sp^3$ carbon. On the other hand, due to the asymmetry of the metallalactone ring, the two ethoxycarbonyls of the malonyl group are not equivalent and appear as two signals at $\delta$ = 168.7 and 167.3 ppm, 62.65 and 62.55 ppm, and 13.6 and 13.7 ppm for the carbonyl, the $CH_2$, and the $CH_3$ carbon atoms, respectively, while the central carbon of this malonyl group only displays a single resonance at $\delta$ = 55.25 ppm. The solubility of **3(3)** is significantly better than **3(1)** and **3(2)**.

When **1** was treated with the anions obtained from 2,4-pentanedione or malononitrile, **3(4)** [R = R′ = $C(O)CH_3$, R′′ = H] and **3(5)** (R = R′ = CN, R′′ = H) were formed, respectively. As shown by their $^{13}C$ NMR spectra (see Exp. Sect.), they are obtained as mixtures of two isomers (70:30 and 60:40, respectively). As observed for **3(3)**, the $CH_3C(O)$ and CN groups of each isomer of these complexes are not equivalent. Thus, **3(4)** displays four $CH_3$ resonances at $\delta$ = 32.9, 32.7, 32.3, and 32.1 ppm (the signals for the C=O groups of the terminal carbonyls are not detectable) and **3(5)** four CN resonances at $\delta$ = 113.7, 113.45, 112.6, and 112.5 ppm while two peaks are observed for the central carbon of the malononitrile group of **3(5)** at $\delta$ = 31.1 and 30.8 ppm [the resonance of the homologue carbon atom of **3(4)** is probably hidden by the signal of the THF]. Asymmetric nucleophiles such as $NaCH[C(O)CH_3](CO_2CH_3)$ or $NaCH(CO_2C_2H_5)(CN)$ also afforded anions of type **3**. The formed complexes **3(6)** (R = $CO_2CH_3$, R′ = $C(O)CH_3$, R′′ = H) or **3(7)** (R = $CO_2CH_3$, R′ = CN, R′′ = H) were again obtained as two *cis*/*trans* isomers (50:50) but, due to the asymmetry of their metallacycle and of the central carbon of their nucleophile group, each of these isomers is observed as two diastereoisomers. For this reason, the $^{13}C$ NMR spectra of **3(6)** and **3(7)** exhibit four signals for each of their carbon atoms. For example, **3(6)** displays four acyl CO signals at $\delta$ = 268.5, 267.4, 267.0, and 266.8 ppm, four peaks for the cyclic quaternary carbon at $\delta$ = 94.2, 93.1, 92.6, and 92.1 ppm, and four signals for the resonance of the central carbon atom of the nucleophilic group at $\delta$ = 62.5, 62.2, 61.9, and 61.2 ppm. In the same way, the $^{13}C$ NMR spectrum of **3(7)** shows four CO signals at $\delta$ = 267.5, 266.8, 266.5, and 266.2 ppm, four CN signals at $\delta$ = 118.0, 117.5, 117.3, and 116.8 ppm, four resonances for the cyclic quaternary carbon at $\delta$ = 93.0, 92.5, 91.5, and 91.0 ppm, and four signals for the central carbon of the nucleophile at $\delta$ = 44.5, 43.5, 42.5, and 42.0 ppm.

As shown by IR monitoring, the reaction of **1** with the bulky nucleophiles $NaC(CH_3)(CO_2C_2H_5)_2$ or $NaC(CH_2CH{=}CH_2)(CO_2C_2H_5)_2$ also affords trifunctionalized anionic metallalactones. However, the $^{13}C$ NMR spectra of the thus formed compounds **3(8)** (R = R′ = $CO_2C_2H_5$, R′′ = $CH_3$) and **3(9)** (R = R′ = $CO_2C_2H_5$, R′′ = $CH_2CH{=}CH_2$) are found to display broad signals whose chemical shifts are in good agreement with those expected for anionic metallalactones (see Exp. Sect.). The detection of at least three signals for the resonances of the acyl CO or for their cyclic quaternary carbon suggests the presence of at least three isomers for these two complexes. The broadness of the observed signals probably results from slow interconversion between the observed species. However, no change was observed in the spectra of these compounds when they were recorded at different temperatures (from 20 °C to –50 °C). The only isomer of **3(3)** was obtained as single crystals suitable for an X-ray diffraction study.

### Structural Study of Complex 3(3)

Single crystals of **3(3)**, with $K^+$ as counterion, were grown from a hexanes/dichloromethane mixture (90:10) at –30 °C. An ORTEP diagram of the anion is displayed in Figure 1, crystallographic data are given in the Exp. Sect., and selected bond lengths and angles are gathered in Table 1 and Table 2, respectively.

The crystal structure confirms the proposed anionic, metallacyclic, trifunctionalized geometry for **3(3)**. The structure can be described as being composed of four crystallographically different (Figure 1, a) trifunctionalized entities linked to four potassium ions (Figure 1, b). As these anions exhibit slight differences in their bond lengths and angles, the values measured for each of these entities (a, b, c, and d) will be mentioned in the following discussion. The crystal structure study establishes that the only formed complex is the isomer with the alkoxycarbonyl ligand and the malonyl group *trans* to each other on the metallacycle (Figure 1, a). This complex, which is sterically less hindered than the corresponding *cis* isomer, is probably the species observed in solution. The coordination polyhedron at the metal center is a distorted octahedron built of three terminal carbonyl ligands, an alkoxycarbonyl, and the chelating carbonylated ligand. As observed for neutral metallalactones[7,10,12,13] and for five-membered iron metallacycles,[17] the bite angle of the chelate C(7)–Fe–C(6) [82.3(5)–83.4(5)°] is smaller than the angle measured between the two organic carbonylated ligands of the noncyclic *cis*-bis(alkoxycarbonyl)iron complex $[(CO)_4Fe(CO_2tBu)_2]$ [88.5(2)°].[18] Therefore, its opposite angle on the metal [C(1)–Fe–C(2)] displays a larger value than that expected for an octahedral geometry [96.0(6)–100.2(5)°]. The axial alkoxycarbonyl ligand is bent toward the metallacycle [C(4)–Fe–C(6) from 81.3(5)° to 84.6 (5)° and C(4)–Fe–C(7) from 84.8(5)° to 89.0(5)°]. The other angles around the metal are normal,

 © 2006 Wiley-VCH Verlag GmbH & Co. KGaA, Weinheim 

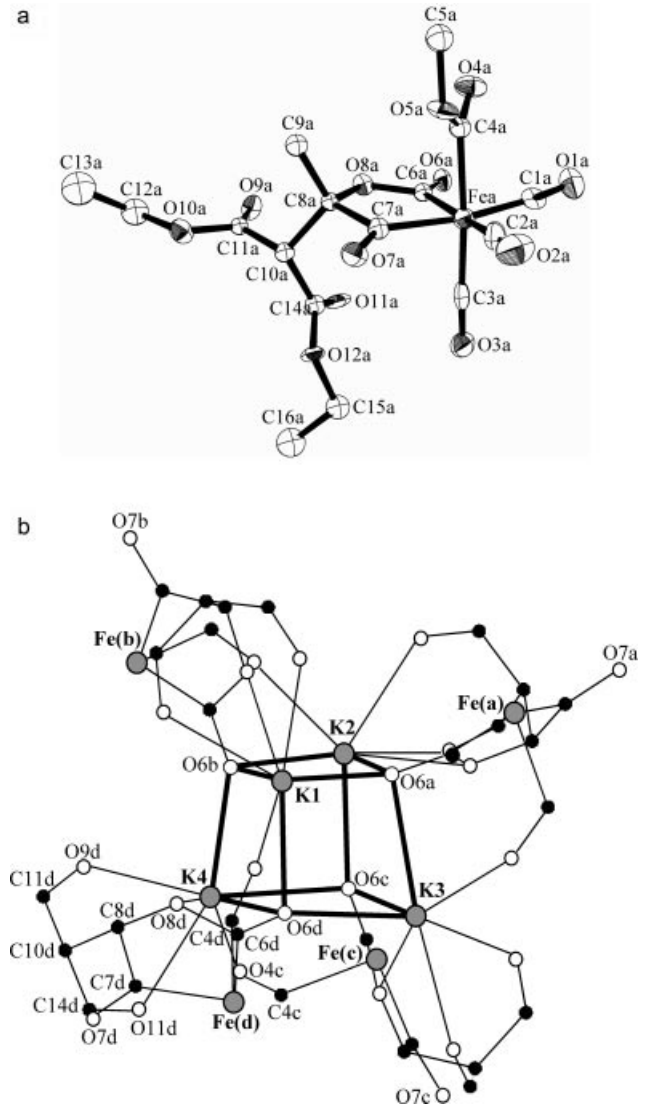


Figure 1. Structure of **3(3)**. Part a: ORTEP view of the anionic complex **a** (50% probability ellipsoids); anions **b**, **c**, and **d** are similar. Part b: Perspective view showing the potassium ions' environment.

with values close to 90°. The Fe–terminal carbonyl distances [1.79(1)–1.90(1) Å] are similar to those in the homologous trifunctionalized iron monoanion[9] or to the neutral complex $[(CO)_4Fe(CO_2tBu)_2]$[18] but are longer than the Fe–C≡O distance observed in a monofunctionalized iron anion.[19] These data confirm a reduced electron density on the metal due to the delocalization of the negative charge of the complex on the carbonylated organic ligands. The short Fe–cyclic(C=O)O distances [Fe–C(6) from 1.93(1) to 1.97(1) Å] associated with long C(6)–O(6) bonds [from 1.21(1) to 1.23(1) Å] show the enolate character of this group whose C=O oxygen is bound to three potassium ions (see below). Such a lengthening of the C=O double bond is not observed for C(4)=O(4), C(11)=O(9), or C(14)=O(11), whose oxygens are only bound to one potassium, or for C(7)=O(7), which does not interact with this metal. The other bond lengths or angles of the complex are analogous

Table 1. Bond lengths [Å] and angles [°] measured for the four (**a**, **b**, **c**, and **d**) anionic forms of **3(3)**.

| | **a** | **b** | **c** | **d** |
|---|---|---|---|---|
| Fe–C1 | 1.83(1) | 1.86(1) | 1.79(1) | 1.87(1) |
| Fe–C2 | 1.78(1) | 1.81(1) | 1.90(1) | 1.85(1) |
| Fe–C3 | 1.79(1) | 1.79(1) | 1.82(1) | 1.84(1) |
| Fe–C4 | 1.99(1) | 2.00(1) | 2.05(1) | 2.01(1) |
| Fe–C6 | 1.93(1) | 1.94(1) | 1.97(1) | 1.94(1) |
| Fe–C7 | 1.94(1) | 1.96(1) | 1.97(1) | 1.98(1) |
| O4–C4 | 1.24(1) | 1.22(2) | 1.14(2) | 1.22(1) |
| O6–C6 | 1.23(1) | 1.22(2) | 1.21(2) | 1.22(1) |
| O7–C7 | 1.21(1) | 1.22(2) | 1.20(2) | 1.21(1) |
| O8–C6 | 1.38(1) | 1.38(1) | 1.36(1) | 1.41(2) |
| O8–C8 | 1.40(1) | 1.42(2) | 1.43(2) | 1.44(1) |
| O9–C11 | 1.17(1) | 1.20(2) | 1.18(2) | 1.23(1) |
| O11–C14 | 1.20(2) | 1.19(2) | 1.22(2) | 1.21(2) |
| C7–C8 | 1.60(1) | 1.56(2) | 1.58(1) | 1.55(2) |
| C1–Fe–C2 | 99.3(5) | 98.5(6) | 100.2(5) | 96.0(6) |
| C1–Fe–C3 | 97.1(6) | 94.8(6) | 94.7(6) | 95.4(6) |
| C1–Fe–C4 | 85.1(6) | 87.6(5) | 87.1(5) | 85.8(6) |
| C1–Fe–C6 | 88.4(5) | 88.9(6) | 87.8(5) | 88.7(5) |
| C1–Fe–C7 | 89.2(5) | 89.4(6) | 88.7(5) | 91.2(6) |
| C3–Fe–C6 | 93.0(5) | 91.1(5) | 93.5(5) | 89.9(5) |
| C3–Fe–C7 | 88.3(5) | 89.7(5) | 88.6(6) | 93.3(6) |
| C4–Fe–C6 | 83.3(5) | 83.4(5) | 81.3(5) | 84.6(5) |
| C4–Fe–C7 | 89.0(5) | 87.2(5) | 88.9(5) | 84.8(5) |
| C6–Fe–C7 | 82.3(5) | 82.6(5) | 82.9(5) | 83.4(5) |
| C6–O8–C8 | 117.8(9) | 117.7(9) | 117.2(8) | 116.0(8) |
| Fe–C6–O6 | 130.1(8) | 129.8(8) | 129.4(9) | 130(1) |
| Fe–C6–O8 | 117.6(8) | 116.6(9) | 116.8(9) | 116.7(9) |
| O6–C6–O8 | 112.3(9) | 113(1) | 113.8(9) | 112(1) |
| Fe–C7–O7 | 131.1(8) | 128.5(8) | 129.8(8) | 130.5(9) |
| Fe–C7–C8 | 113.9(8) | 114.0(9) | 112.1(9) | 112.5(8) |
| O7–C7–C8 | 115.0(9) | 117(1) | 118(1) | 117(1) |
| O8–C8–C7 | 107.6(8) | 108.6(9) | 110(1) | 110(1) |

Table 2. Interionic K–O distances [Å] and angles [°] in the cubane-like structure of **3(3)** (see Figure 1, part b).

| | | | | | | | |
|---|---|---|---|---|---|---|---|
| K1–O4d | 2.688(8) | K2–O4b | 2.650(9) | K3–O4a | 2.611(8) | K4–O4c | 2.675(9) |
| K1–O6b | 2.886(7) | K2–O6b | 2.787(8) | K3–O6c | 2.839(7) | K4–O6b | 2.742(9) |
| K1–O6d | 2.859(9) | K2–O6c | 2.709(9) | K3–O6d | 2.709(9) | K4–O6c | 2.799(8) |
| K1–O6a | 2.721(8) | K2–O6a | 2.873(7) | K3–O6a | 2.876(9) | K4–O6d | 2.868(7) |
| K1–O8b | 2.758(8) | K2–O8a | 2.760(8) | K3–O8c | 2.708(7) | K4–O8d | 2.827(7) |
| K1–O9b | 2.741(9) | K2–O9a | 2.697(8) | K3–O9c | 2.79(1) | K4–O9d | 2.726(9) |
| K1–O11b | 2.81(1) | K2–O11a | 2.744(8) | K3–O11 | 2.804(9) | K4–O11d | 2.824(9) |
| O6b–K1–O6d | 75.3(2) | O6b–K2–O6c | 83.5(2) | O6c–K3–O6d | 73.3(2) | O6b–K4–O6c | 82.6(3) |
| O6b–K1–O6a | 75.1(2) | O6b–K2–O6a | 74.3(2) | O6c–K3–O6a | 75.2(2) | O6b–K4–O6d | 77.4(2) |
| O6d–K1–O6a | 79.0(2) | O6c–K2–O6a | 77.2(2) | O6d–K3–O6a | 78.9(2) | O6c–K4–O6d | 71.5(2) |
| K1–O6b–K2 | 104.1(3) | K1–O6d–K3 | 96.8(2) | K1–O6b–K4 | 104.1(3) | K1–O6d–K4 | 101.6(3) |
| K2–O6b–K4 | 92.0(3) | K3–O6d–K4 | 108.3(3) | K2–O6c–K3 | 105.6(2) | K1–O6a–K2 | 106.2(3) |
| K2–O6c–K4 | 92.4(3) | K1–O6a–K3 | 96.1(2) | K3–O6c–K4 | 106.6(2) | K2–O6a–K3 | 100.5(2) |

 © 2006 Wiley-VCH Verlag GmbH & Co. KGaA, Weinheim 

to those measured for neutral metallalactones.[7,10,13] As shown by the deviations of O(8) (+0.13 and +0.18 Å) and C(8) (+0.11 and +0.20 Å) from the plane defined by C(6)–Fe–C(7), the metallalactone ring of **3(3)** is not rigorously planar. It is worth noting that C(8) and O(8) are located on the same side of this plane. The steric effect of the malonyl group induces a pseudo axial position of the methyl substituent of the metallacycle, as shown by deviations of C(9) from the C(6)–Fe–C(7) plane of between 1.42 and 1.53 Å; deviations of between 0.91 and 1.09 Å are observed for C(10), which is the central atom of the malonyl group. As mentioned above, **3(3)** is composed of four slightly different entities in the solid state that display their four potassium ions and four cyclic ester carbonyl oxygens [O(6)] alternately at the corners of a distorted cube (see Figure 1, b). This cube displays small O–K–O angles (71.5–83.5°) and larger K–O–K angles (92.0–108.3°). Each potassium is linked to seven oxygen atoms; for example, K(4) interacts with O(6d) and O(8d), which are the two oxygen atoms of the cyclic ester group of d, with the oxygen atoms [O(9d) and O(11d)] of the two carbonyl oxygens of the malonyl group of d, with the oxygen atoms of the carbonyl of the cyclic esters of molecules b and c [O(6b) and O(6c)], and with the carbonyl oxygen of the alkoxycarbonyl ligand of complex c [O(4c)]. Short K–O(4) distances (2.61–2.68 Å) are observed between the potassium and the oxygen of this latter ligand. Recall that O(6) − the carbonyl oxygen of the cyclic ester group of each anion − interacts with three potassium ions, which induces a lengthening of the C(6)–O(6) bond (1.23 vs. 1.19 Å observed for neutral lactones[7,10,13]) and a shortening of the Fe–C(6) distance (1.93 vs. 1.99 Å). The complexation of O(6) with a potassium ion [K(4)] that is itself bound to O(8), O(9), and O(11) of the same molecule brings about a reduction of the O(6)–C(6)–O(8) $sp^2$ angle from 112(1)° to 113.8 (9)°. The absence of complexation of the cyclic acyl oxygen O(7) must also be noted.

This crystallographic work confirms without any doubt the structure attributed to this series of anionic trifunctionalized metallalactones **3**. However, a clear relation between the nature of the nucleophile and the *trans*/*cis* ratio observed for the different complexes **3** (from 100% to 50% of the *trans* isomer) has not been established. For example, the steric hindrance of $KCH(CO_2C_2H_5)_2$ cannot justify the specific formation of the *trans* isomer of **3(3)** except if the possible formation of aggregates of the anionic nucleophile is considered. Such a hypothesis has already been taken into account to explain the stereospecific nucleophilic additions on organic ketones. The formation of anionic compounds **3** when the transformation of **1** is induced by anionic nucleophiles raises the question of the specific formation of neutral lactones **2** by reaction of **1** with pronucleophiles Nu–H. An answer to this question is given by the reaction of complexes **3** with anhydrous HCl.

### Reaction of Anionic Lactones 3 with HCl

As shown by IR monitoring of the process, the reaction of complexes **3(1)**, **3(2)**, **3(3)**, **3(4)**, **3(6)**, **3(8)**, and **3(9)** with one equivalent of anhydrous HCl at –80 °C instantaneously affords new compounds displaying four ν(C≡O) bands between 2131 and 2041 $cm^{-1}$. The presence of these four IR bands and their frequencies suggested the formation of neutral *cis* disubstituted complexes. Under the same reaction conditions an analogous process was observed for **3(5)** and **3(7)**, although the formed complexes rapidly evolved into $Fe(CO)_5$ and organic compounds. Complexes **2(1)**, **2(2)**, **2(3)**, **2(4)**, **2(6)**, **2(8)**, and **2(9)**, formed by reaction of **3(1)**, **3(2)**, **3(3)**, **3(4)**, **3(6)**, **3(8)**, and **3(9)** with HCl, respectively, were obtained as pale-yellow crystals from a hexanes/$CH_2Cl_2$ (95:5) mixture at –30 °C. Their $^{13}C$ NMR spectra confirm their neutral character as they display terminal C≡O resonances between $\delta$ = 202.75 and 196.2 ppm (vs. $\delta$ = 212.5–201.0 ppm for the starting complexes). Their other resonances are very close to those exhibited by neutral metallalactones: a C=O cyclic acyl between $\delta$ = 249.9 and 254.1 ppm (vs. $\delta$ = 274.1 and 262.3 ppm for the anionic lactones) and a cyclic C=O ester indiscernible from the terminal C≡O. The presence of a metallacycle in these complexes is shown by the observation of signals corresponding to cyclic quaternary carbons between $\delta$ = 92.3 and 98.4 ppm. All these characteristics are in good agreement with the formation of neutral metallalactones of type **2** (Scheme 2). Complex **2(1)**, whose quaternary cyclic carbon is substituted by two methyl groups, displays a single signal for its two axial terminal carbonyl ligands at $\delta$ = 200.2 ppm. This equivalence may result either from the quasi planarity of the metallacycle or from rapid interconversion between different conformations of the metallacycle. Other complexes **2** whose cyclic quaternary carbons are substituted by two different groups exhibit two signals for their axial carbonyl ligands. For example, five peaks are observed for the four terminal C≡O groups and the C=O of the cyclic ester of **2(2)** between $\delta$ = 200.5 and 196.5 ppm. Due to the asymmetry of the lactone ring, the two ethoxycarbonyl groups of the malonyl substituent of **2(3)** are not equivalent (two peaks are observed for the C=O at $\delta$ = 168.74 and 168.70 ppm, for the $CH_2$ at $\delta$ = 62.2 and 62.15 ppm, and for the $CH_3$ at $\delta$ = 13.9 and 13.75 ppm, whereas a single signal at $\delta$ = 58.6 ppm corresponds to the CH). A similar spectrum should be obtained for **2(4)**. However, as its acetyl C=O signals are hidden by those of the terminal C≡O, the presence of two different acetyl groups is only shown by the two peaks of their methyl groups at $\delta$ = 31.05 and 30.2 ppm. Complex **3(6)**, which displays an acetomethyl acetate and a methyl group on its cyclic quaternary carbon, affords, upon reaction with HCl, the neutral complex **2(6)**. Owing to the presence of the asymmetric central carbon of the acetoacetate group and to the asymmetry of the metallacycle itself, **2(6)** is obtained as an equimolecular mixture of two diastereoisomers. The presence of these two isomers is shown in the $^{13}C$ NMR spectrum by two C=O acyl resonances at $\delta$ = 251.32 and 251.22 ppm, by numerous signals between $\delta$ = 202.06 and 196.29 ppm [terminal carbonyls, cyclic ester group and organic C(O) acetyl], and by the splitting in two of the other signals: the organic C=O ester at $\delta$ = 169.9 and 169.4, the cyclic quaternary carbon at $\delta$ = 92.78 and

 © 2006 Wiley-VCH Verlag GmbH & Co. KGaA, Weinheim 

92.32 ppm, the CH at $\delta$ = 65.86 and 65.35 ppm, the $OCH_3$ at $\delta$ = 53.30 and 53.08 ppm, the acetyl $CH_3$ at $\delta$ = 30.11 and 29.42 ppm, and the other $CH_3$ at $\delta$ = 22.19 and 22.15 ppm. Recall that anions **3(8)** and **3(9)**, whose metallacycle is substituted by the crowded diethyl methyl- or allylmalonate groups, exhibit broad signals in their $^{13}C$ NMR spectra. Their reaction with HCl also affords complexes of type **2**, whose formation confirms the structure attributed to these anions. Contrary to their precursors, **2(8)** and **2(9)** give very well resolved $^{13}C$ NMR spectra. The characteristics of these spectra are very close to those of **2(3)**, which bears an unsubstituted malonyl, as they display two nonequivalent ethoxycarbonyls on their substituted malonyl group. This is shown by a splitting in two of the signals of the carbons of these ethoxycarbonyl groups, whereas the resonances of the third substituent and of the central quaternary carbon of the malonyl are found as singlets (see Exp. Sect.). Among this series of neutral complexes **2**, crystals suitable for a structural study were obtained for **2(1)**.

### Crystallographic Study of Complex 2(1)

Single crystals of **2(1)** suitable for an X-ray diffraction study were obtained from a hexanes/dichloromethane mixture (95:5) at –30 °C. Figure 2 displays an ORTEP drawing of the molecule; selected bond lengths and angles are listed in Table 3, and further crystallographic data can be found in the Exp. Sect.

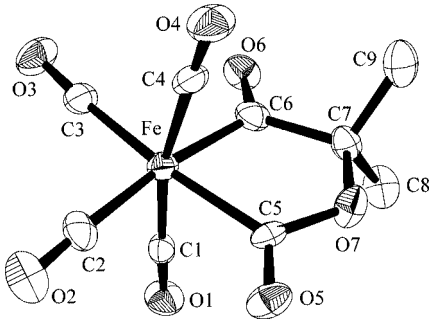


Figure 2. ORTEP view of **2(1)** (50% probability ellipsoids).

As observed for **3(3)**, the coordination around the iron atom in this complex can be described as a distorted octahedron with a reduced metallacyclic angle [C(6)–Fe–C(5) = 82.6(3)°, vs. an average of 82.8° for **3c**] and a larger value for its opposite angle C(3)–Fe–C(2) of 96.8(2)° due to the presence of the metallacycle. As already described by us for other neutral metallalactones,[7,10,13] the two axial terminal carbonyls of **2(1)** are bent toward the metallacycle [C(1)–Fe–C(4) = 167.7(2)°; C(4)–Fe–C(6) = 88.1(2)°; C(4)–Fe–C(5) = 83.8(2)°; C(1)–Fe–C(6) = 84.2(2)°; C(1)–Fe–C(5) = 85.7(2)]°. The Fe–cyclic ester bond [Fe–C(5)] of 1.991(5) Å and the C=O bond of this organic function [C(5)–O(5) = 1.199 (6) Å] are respectively longer and shorter than their homologues in **3(3)** (average of 1.95 Å for the first and 1.22 Å for the second). These bond lengths, which are similar to those measured for neutral metallalactones,[7,10,13] are indicative of an absence of enolate character of this function, whose oxygens are linked to the counterion in **3(3)**. The metallacycle is quasi planar, as shown by the torsion angles C(5)–Fe–C(6)–C(7) [–4.6(4)°] and C(6)–Fe–C(5)–O(7) [+6.2(4)°]. However, contrary to **3(3)**, O(7) and C(7) are no longer located on the same side of the C(6)–Fe–C(5) plane. The rapid evolution of complexes **3** into neutral metallalactones **2** when treated with HCl sheds new light on the direct formation of **2** by reaction of **1** with Nu–H nucleophiles. These observations suggest that the formation of **2** could result from a cyclization of the pyruvoyl and a terminal carbonyl ligand (and not, as considered earlier, the alkoxycarbonyl ligand) that affords an anionic, trifunctionalized metallalactone **3**. This intermediate, which would have $H^+$ as counterion, would then instantaneously evolve into **2**. The formation of complexes **2** by cyclization of the pyruvoyl and the alkoxycarbonyl ligand is therefore not necessarily involved in the process of anionic lactone formation. The reaction of **2** with NaOMe will confirm that this compound is not an intermediate of the reaction of formation of **3** by cyclization of **1** by anionic reagents.

Table 3. Bond lengths [Å] and angles [°]for compound **2(1)**.

| | | | |
|---|---|---|---|
| Fe–C4 | 1.796(7) | O1–C1 | 1.143(6) |
| Fe–C1 | 1.811(7) | O3–C3 | 1.130(6) |
| Fe–C2 | 1.849(8) | O5–C5 | 1.199(6) |
| Fe–C3 | 1.856(6) | O2–C2 | 1.146(7) |
| Fe–C6 | 1.975(6) | O4–C4 | 1.137(5) |
| Fe–C5 | 1.991(5) | C9–C7 | 1.524(9) |
| O6–C6 | 1.205(6) | C7–C8 | 1.508(8) |
| O7–C5 | 1.371(6) | C7–C6 | 1.539(7) |
| O7–C7 | 1.451(6) | | |
| C4–Fe–C1 | 167.7(2) | O1–C1–Fe | 177.3(5) |
| C4–Fe–C2 | 93.6(2) | O3–C3–Fe | 176.1(5) |
| C1–Fe–C2 | 92.8(2) | O5–C5–O7 | 117.4(5) |
| C4–Fe–C3 | 95.1(2) | O5–C5–Fe | 127.1(5) |
| C1–Fe–C3 | 94.6(2) | O7–C5–Fe | 115.4(5) |
| C2–Fe–C3 | 96.8(2) | O7–C7–C8 | 107.2(5) |
| C4–Fe–C6 | 88.1(2) | O7–C7–C9 | 105.7(5) |
| C1–Fe–C6 | 84.2(2) | C8–C7–C9 | 112.8(6) |
| C2–Fe–C6 | 172.6(3) | O7–C7–C6 | 109.5(4) |
| C3–Fe–C6 | 90.3(2) | C8–C7–C6 | 112.0(5) |
| C4–Fe–C5 | 83.8(2) | C9–C7–C6 | 109.3(5) |
| C1–Fe–C5 | 85.7(2) | O2–C2–Fe | 177.6(6) |
| C2–Fe–C5 | 90.4(3) | O4–C4–Fe | 176.4(5) |
| C3–Fe–C5 | 172.8(3) | O6–C6–C7 | 117.8(5) |
| C6–Fe–C5 | 82.6(3) | O6–C6–Fe | 128.2(4) |
| C5–O7–C7 | 117.8(5) | C7–C6–Fe | 114.0(4) |

### Reactions of Neutral Lactones 2 with NaOMe

The formation of anionic trifunctionalized metallalactones **3** by nucleophilic addition of $CH_3O^-$ to a terminal carbonyl of complexes **2** was performed with **2(1)** (R = R′ = $CH_3$; R′′ = H), **2(3)** (R = R′ = $CO_2C_2H_5$; R′′ = H), and **2(8)** (R = R′ = $CO_2C_2H_5$; R′′ = $CH_3$). As shown by the IR, $^1H$, and $^{13}C$ NMR spectra of the formed complexes, **2(1)** affords **3(1)** while **2(3)** gives rise to **3(3)**, again as a single isomer. The product formed by reaction of **2(8)** with NaOMe also displays the IR spectrum of a trifunctionalized anionic lactone. Its $^{13}C$ NMR spectrum is similar to that of **3(8)** obtained by cyclization of **1** performed with

 © 2006 Wiley-VCH Verlag GmbH & Co. KGaA, Weinheim 

$CH(CH_3)(CO_2C_2H_5)_2$ and exhibits broad signals that again reveal the formation of at least three isomers of this compound. Upon reaction with HCl at low temperature this latter compound, which is very probably **3(8)**, was again found to evolve into **2(8)**. The yield of complexes **3(1)**, **3(3)** and **3(8)**, upon addition of NaOMe to a terminal carbonyl of neutral lactones, remains low (from 30 to 35%), and careful IR monitoring of the process showed that their formation is always concomitant with the detection of another product displaying the IR spectrum of a monofunctionalized anion (three bands around 1900 $cm^{-1}$). Unfortunately, the low stability of this complex did not allow its characterization.

## Conclusion

This work has allowed us to show that in complex **1**, which displays an alkoxycarbonyl, a pyruvoyl, and terminal carbonyl ligands, the β carbonyl of the pyruvoyl is the most electrophilic site of the molecule. Addition of various nucleophiles to this site affords anionic trifunctionalized metallalactones **3** whose metallalactone ring is formed by addition of the oxygen of this β carbonyl to a terminal carbonyl. When treated with HCl, the rapid evolution of these complexes **3** into neutral metallalactones **2** explains the direct formation of **2** when the cyclization of **1** is performed with pronucleophiles (Nu–H). Recall that, starting from complex **1**, the formation of **3** could also be performed by the intermediate formation of **2** obtained by cyclization of the pyruvoyl ligand of **1** with the alkoxycarbonyl moiety of the same complex and release of $CH_3O^-$. The rapid addition of this $CH_3O^-$ to a terminal carbonyl of **2** was then supposed to afford **3**. This work allowed us to dismiss this hypothesis as the reaction of complex **2** with $CH_3O^-$ was only found to afford **3** in very low yield. However, two aspects of this work remain unclear: i) the formation of a single isomer of **3(3)** from the cyclization of **1** with the anion of diethyl malonate, and ii) the broadness of the NMR signals of **3(8)** and **3(9)** associated with the high number of isomers observed for the complexes bearing a diethyl methylmalonate or a diethyl allylmalonate as substituent. Further experiments are under progress to find an answer these questions.

## Experimental Section

**General Remarks:** All reactions were carried out with Schlenk techniques under dry, oxygen-free argon. All solvents were purified by preliminary distillation from an appropriate drying agent.[20] $CD_2Cl_2$ and [$D_8$]THF were stored over molecular sieves under inert atmosphere until needed. Infrared spectra were recorded in the range 2300–1600 $cm^{-1}$ in solution in hexanes, $CH_2Cl_2$, or THF with a FT-IR NEXUS NICOLET spectrometer. $^1H$ and $^{13}C$ NMR spectra were recorded at 0 °C in $CD_2Cl_2$ or [$D_8$]THF with a Bruker AMX-3 300 or Bruker DRX 400 spectrometer. NMR HMQC, HMBC, and COSY spectra were recorded with a Bruker DRX 500. Chemical shifts are reported in $\delta$ units (ppm) downfield from tetramethylsilane. Elemental analyses were performed by the Service Central d'Analyses du CNRS. $Fe(CO)_5$, NaOMe, $CH_3Li$ (1.6 M in diethyl ether), *n*BuLi (1.6 M in hexanes), $CH_2(CO_2C_2H_5)_2$, $CH_2[C(O)CH_3]_2$, $CH_2(CN)_2$, $CH(CH_3)(CO_2C_2H_5)_2$, $CH_2(CO_2C_2H_5)$-$[C(O)CH_3]$, and $CH_2(CO_2C_2H_5)(CN)$ were purchased from commercial sources and used as received. $CH(CH_2CH{=}CH_2)$-$(CO_2C_2H_5)_2$ was prepared as described in the literature[21] by reaction of $ClCH_2CH{=}CH_2$ with $NaCH(CO_2C_2H_5)_2$[21–23] and purified by distillation (b.p. 105 °C, 15 Torr). Complex **1** was obtained as described elsewhere[13] by reaction of $ClC(O)C(O)CH_3$[24] with $[(CO)_4Fe(CO_2CH_3)]^-$.[15]

**General Procedure for the Preparation of Stabilized Carbanions:** These anions were prepared as described in the literature.[21,23] The substrate (1.5 mmol) in solution in THF (5 mL) was added dropwise, over a period of 10 min, to a suspension of NaH (36 mg, 1.5 mmol obtained from a 40% dispersion in mineral oil washed with 5 × 5 mL of hexanes before use) in THF (10 mL) at room temperature. $H_2$ gas evolution was observed. The solution obtained was stirred for 10 min and used without further purification.

**Reaction of $[(CO)_4Fe\{C(O)C(O)CH_3\}(CO_2CH_3)]$ (1) with Carbanions. General Procedure for the Preparation of the Trifunctionalized Anionic Complexes 3:** The carbanion (1.5 mmol; 0.94 mL of a 1.6 M solution of $CH_3Li$ in diethyl ether, 0.6 mL of a 2.5 M solution of *n*BuLi in hexanes, or the solution of the stabilized carbanion prepared as described above) was added, with stirring, to a solution of **1** (450 mg, 1.5 mmol) in THF (30 mL) at –70 °C. As shown by IR monitoring, the reaction was very fast as three new bands were rapidly observed in the ν(CO) region. The temperature was then raised to –10 °C and the solvent evaporated to dryness. The residue was washed with hexanes at –20 °C (3 × 5 mL) to afford a white powder, which was generally found to be insoluble in most organic solvents, with the exception of the complexes obtained with $(CO_2C_2H_5)_2C(R)^-$ (R = H, $CH_3$ or allyl) and $(CO_2C_2H_5)[C(O)$-$CH_3]C(H)^-$, which could be extracted with a hexanes/$CH_2Cl_2$ mixture (75:25) at 0 °C (3 × 30 mL) and recrystallized from this mixture at –40 °C. We were unable to obtain correct analysis of these rather unstable anionic complexes **3**.

**Reaction of 1 with $CH_3Li$:** According to the general procedure for this reaction, **1** (450 mg, 1.5 mmol) was treated with $CH_3Li$ (950 μL of a 1.6 M solution in diethyl ether) to give **3(1)** (385 mg, 80% yield). IR (THF): ν(C≡O) = 2070 (w), 1995 (s), 1970 $cm^{-1}$ (s); ν(C=O) = 1680 (br), 1635 (br), 1605 (br). $^1H$ NMR (400 MHz, [$D_8$]THF, 273 K): $\delta$ = 3.3 (br. s, 3 H, $OCH_3$), 1.1 (br. s, 6 H, $CH_3$) ppm. $^{13}C\{^1H\}$ NMR (400 MHz, THF, 273 K): $\delta$ = 262.3 (C=O), 225.4 [cyclic C(O)O-], 209.7, 208.3, 207.2 and 206.3 [CO and C(O)-O-], 94.3 (cyclic quaternary carbon), 50.3 ($OCH_3$), 15.8 ($CH_3$), 8.4 ppm ($CH_3$).

**Reaction of 1 with *n*BuLi:** The reaction of **1** (1.5 mmol, 450 mg) with *n*BuLi (600 μL of a 2.5 M solution in hexanes) was found to afford white crystals of **3(2)** (270 mg, 50% yield). IR (THF): ν(C≡O) = 2068 (m), 2002 (s), 1982 $cm^{-1}$ (s); ν(C=O) = 1660 (sh), 1636 (m), 1610 (m). $^1H$ NMR (400 MHz, [$D_8$]THF, 273 K): $\delta$ = 3.4 (br. s, 1.5 H, $OCH_3$), 3.2 (br. s, 1.5 H, $OCH_3$), 1.7–0.8 (br. m, 12 H, *n*Bu and $CH_3$) ppm. $^{13}C\{^1H\}$ NMR [400 MHz, THF, 273 K; two isomers (50:50)]: $\delta$ = 274.1, 271.5 (C=O), 229.5, 228.8 [cyclic C(O)O-], 212.5–208.0 [numerous signals for CO and C(O)O], 96.9, 96.7 (cyclic quaternary carbon), 60.5, 59.9 ($OCH_3$), 50.3, 50.1, 38.2, 37.7, 23.1, 22.2 ($CH_2$), 22.5, 22.1, 14.7, 14.5 ppm ($CH_3$).

**Reaction of 1 with $NaC(H)(CO_2C_2H_5)_2$:** Complex **1** (450 mg, 1.5 mmol) was treated at –70 °C with a solution of $NaC(H)$-$(CO_2C_2H_5)_2$ (1.5 mmol, prepared as described above) in THF (10 mL). The product of the reaction, obtained as a white powder, was extracted at –10 °C with a hexanes/$CH_2Cl_2$ (60:40) mixture

 © 2006 Wiley-VCH Verlag GmbH & Co. KGaA, Weinheim 

(3 × 30 mL) and recrystallized at –40 °C from this solution to give white crystals of **3(3)** (650 mg, 90% yield). IR ($CH_2Cl_2$): ν(C≡O) = 2082 (s), 2022 (s), 2000 $cm^{-1}$ (s); ν(C=O) = 1747 (s), 1624 (s). $^1H$ NMR (400 MHz, $CD_2Cl_2$, 273 K): $\delta$ = 4.26 (dq, $J$ = 7, $J'$ = 3 Hz, 1 H, $OCH_2$), 4.09 (dq, $J$ = 7, $J'$ = 3 Hz, 1 H, $OCH_2$), 3.88 (dq, $J$ = 7, $J'$ = 3 Hz, 1 H, $OCH_2$), 3.74 (dq, $J$ = 7, $J'$ = 3 Hz, 1 H, $OCH_2$), 3.74 (s, 1 H, CH), 3.24 (s, 3 H, $OCH_3$), 1.21 (t, $J$ = 7 Hz, 3 H, C$H_3$$CH_2$), 1.09 (t, $J$ = 7 Hz, 3 H, C$H_3$$CH_2$), 1.06 (s, 3 H, C$H_3$C) ppm. $^{13}C\{^1H\}$ NMR (400 MHz, $CD_2Cl_2$, 273 K): $\delta$ = 269.3 (C=O), 229.5 [cyclic C(O)O-], 207.1, 206.9, 206.4 and 204.4 [CO and C(O)O], 168.7 (C=O ester),; 167.3 (C=O ester), 92.0 (cyclic quaternary carbon), 62.65 ($OCH_2$), 62.55 ($OCH_2$), 55.25 (CH), 50.9 ($OCH_3$), 21.7 (C$CH_3$), 13.7 ($CH_2CH_3$), 13.6 ($CH_2CH_3$) ppm. The different signals were allocated to each carbon by HMBC and HMQC sequences.

**Reaction of 1 with NaC(H)[C(O)CH$_3$]$_2$:** As described in the general procedure, **1** (450 mg 1.5 mmol) was added at –70 °C to a suspension of NaC(H)[C(O)$CH_3$]$_2$ (1.5 mmol) in THF (10 mL) to give **3(4)** as a white powder (475 mg, 75% yield) that was found to be insoluble in most organic solvents. IR (THF): ν(C≡O) = 2071 (s), 2011 (s), 1985 $cm^{-1}$ (s); ν(C=O) = 1726 (w), 1697 (w), 1651 (s), 1598 (w). $^1H$ NMR (400 MHz, [$D_8$]THF, 273 K): $\delta$ = 3.54 (s, 1 H, CH), 3.39 (s, 3 H, $OCH_3$), 2.20 (s, 3 H, $CCH_3$), 2.06 [s, 6 H, C(O)$CH_3$] ppm. $^{13}C\{^1H\}$ NMR [400 MHz, [$D_8$]THF, 273 K; 2 isomers (70:30)]: $\delta$ = 268.8 (C=O), 267.5 (C=O), 220.9 [cyclic C(O)O], 207.7, 207.1, 206.3, 205.1, 204.6, 203.5, 203.15, 202.6, and 201.6 [CO, C(O)O, and $C$(O)$CH_3$], 94.0 (cyclic quaternary carbon), 69.2 [$C${C(O)$CH_3$}$_2$], 51.85, 50.45 ($OCH_3$), 34.05, 33.88, 33.05,32.05 [C(O)$CH_3$], 21.95, 20.3 ($CH_3$) ppm.

**Reaction of 1 with NaC(H)(C≡N)$_2$:** As described in the general procedure, **1** (450 mg, 1.5 mmol) was added at –70 °C to a solution of NaC(H)(C≡N)$_2$ (1.5 mmol) in THF (10 mL). The yellow powder of **3(5)** which was obtained (375 mg, 65% yield) was insoluble in most organic solvents. IR (THF): ν(C≡N) = 2253 $cm^{-1}$ (w); ν(C≡O) = 2075 (s), 2015 (s), 1987 (s); ν(C=O) = 1658 (s), 1622 (sh), 1601 (sh). $^1H$ NMR [400 MHz, [$D_8$]THF, 273 K; 2 isomers (60:40)]: $\delta$ = 4.98 (s, 0.6 H, CH), 4.61 (s, 0.4 H, CH), 3.34 (s, 1.8 H, $OCH_3$), 3.30 (s, 1.2 H, $OCH_3$), 1.39 (s, 1.8 H, $CH_3$), 1.15 (s, 1.2 H, $CH_3$) ppm. $^{13}C\{^1H\}$ NMR (400 MHz, [$D_8$]THF, 273 K): $\delta$ = 267.6 (C=O), 264.5 (C=O), 220.4, 219.25 [cyclic C(O)O], 208.7, 207.8, 207.35, 207.2, 206.9, 206.65 (CO), 206.2, 205.25 [s, C(O)$OCH_3$], 113.7, 113.45, 112.6, 112.5 (C≡N), 90.5, 88.5 (cyclic quaternary carbon), 51.5, 50.65 ($OCH_3$), 31.1, 30.8 [$C$(C≡N)$_2$], 22.15, 21.0 (C$CH_3$) ppm.

**Reaction of 1 with NaC(H)(CO$_2$CH$_3$)[C(O)CH$_3$]:** Following the general procedure, **1** (450 mg, 1.5 mmol) was allowed to react with a solution of NaC(H)($CO_2CH_3$)[C(O)$CH_3$] (1.5 mmol) in THF (10 mL) at –70 °C to give **3(6)** as a yellow powder (490 mg, 75% yield) after extraction with a 60:40 hexanes/$CH_2Cl_2$ mixture (3 × 15 mL) at 0 °C and crystallization from this mixture at –40 °C. IR ($CH_2Cl_2$): ν(C≡O) = 2071 (s), 2011 (s), 1984 $cm^{-1}$ (s); ν(C=O) = 1744 (s), 1655 (sh), 1621 (s). $^1H$ NMR (400 MHz, $CD_2Cl_2$, 273 K; 4 isomers): $\delta$ = 4.2 (s, 1 H, CH), 3.65 (s, 3 H, $OCH_3$), 3.4 (s, 1.5 H, $OCH_3$), 3.25 (s, 1.5 H, $OCH_3$), 2.3 [s, 1.5 H, C(O)$CH_3$], 2.1 (s, 1.5 H, C(O)$CH_3$], 1.2 (s, 1.5 H, $CCH_3$), 1.1 (s, 1.5 H, $CCH_3$) ppm. $^{13}C\{^1H\}$ NMR (400 MHz, [$D_8$]THF, 273 K): $\delta$ = 268.5, 267.4, 267.1, 267.0 (C=O), 221.9, 221.3, 220.6, 220.4 [cyclic C(O)O], 211.7, 209.6, 208.5, 208.4, 208.3, 208.1, 207.7, 207.2, 207.1, 203.5, 203.3, 202.7, 201.0 [CO, $C$(O)$OCH_3$, and $C$(O)$CH_3$], 169.6, 169.2 (2), 168.7 [organic C(O)$OCH_3$], 93.9, 93.1, 92.6, 92.3 (cyclic quaternary carbon), 62.5, 62.2, 61.9, 61.2 (CH), 52.7, 52.5, 52.2, 50.8 (2), 50.5, 50.3, 49.9 ($OCH_3$), 32.9, 32.7, 32.3, 32.1 [$CH_3$ C(O), 24.1, 23.7, 23.2, 22.9 (C$CH_3$) ppm.

**Reaction of 1 with NaC(H)(CO$_2$C$_2$H$_5$)(C≡N):** Complex **1** (450 mg, 1.5 mmol) was treated with a solution of NaC(H)-($CO_2C_2H_5$)(C≡N) (1.5 mmol) in THF (10 mL) at –70 °C. After evaporation of the solvent, the yellow oily residue was washed with hexanes (3 × 15 mL) at 0 °C to afford **3(7)** as a brown powder (350 mg; 59% yield). IR (THF): ν(C≡N) = 2246 $cm^{-1}$ (w); ν(C≡O) = 2073 (s), 2012 (s), 1987 (s), ν(C=O) = 1749 (m), 1652 (s). $^1H$ NMR (400 MHz, [$D_8$]THF, 273 K): $\delta$ = 4.45 (s, 1 H, CH), 4.10 (m, 2 H, $OCH_2$), 3.30 (s, 3 H, $OCH_3$), 1.10 (m, 3 H, $CH_2CH_3$), 1.05 (s, 3 H, C$CH_3$) ppm.$^{13}C\{^1H\}$ NMR (400 MHz, [$D_8$]THF, 273 K; four isomers): $\delta$ = 267.5, 266.8, 266.5, 266.2 (C=O), 222.5–202.0 [numerous peaks for CO, $C$(O)$OCH_3$, and cyclic $C$(O)O], 167.0, 166.2, 165.5, 164.0 [organic $C$(O)$OC_2H_5$], 118.0, 117.5, 117.3, 116.8 (C≡N), 93.0, 92.5, 91.5, 91.0 (cyclic quaternary carbon), 60–52 (numerous peaks for $OCH_3$ and $OCH_2$), 14–10 (numerous resonances for C$CH_3$ and $CH_2CH_3$) ppm.

**Reaction of 1 with Substituted Malonate Anions NaC(R)(CO$_2$C$_2$H$_5$)$_2$ (R = CH$_3$ or allyl):** Compound **1** (450 mg 1.5 mmol) was treated at –70 °C with NaC(R)($CO_2C_2H_5$)$_2$ [1.5 mmol in solution in THF (10 mL) prepared as described above: 300 mg for R = $CH_3$ or 330 mg for R = allyl]. The product of the reaction, obtained as a white powder, was extracted at 0 °C with a hexanes/$CH_2Cl_2$ (60:30) mixture (3 × 30 mL) but, despite several attempts, we were unable to get crystals from these solutions. The solvent was removed to give 550 mg (R = $CH_3$; 75% yield) or 505 mg (R = allyl; 65% yield) of a white powder which was probably composed of several isomers of **3(8)** (R = $CH_3$) or **3(9)** (R = allyl).

**3(8):** IR ($CH_2Cl_2$): ν(C≡O) = 2084 (s), 2023 (s), 2000 $cm^{-1}$ (s); ν(C=O) = 1721 (s), 1606 (s); (THF): ν(C≡O) = 2069 (s), 2006 (s), 1995 $cm^{-1}$ (s); ν(C=O) = 1735 (s), 1637 (s). $^1H$ NMR (400 MHz, $CD_2Cl_2$, 273 K): $\delta$ = 4.20 (br. m, 4 H, $OCH_2$), 3.41 (br. s, 3 H, $OCH_3$), 1.46 (br. s, 3 H, $CH_3$), 1.40 (br. s, 3 H, $CH_3$), 1.23 (br. m, 6 H, $CH_3$) ppm. $^{13}C\{^1H\}$ NMR (400 MHz, $CD_2Cl_2$, 273 K): $\delta$ = 262.3, 266.2, 265.8 (C=O), 237.8, 236.3 [cyclic C(O)O], 210.9, 210.6, 209.4, 208.9, 206.3, 205.6, 205.2 [CO and C(O)O], 173.7, 168.2 (C=O ester), 96.3, 96.2, 95.4, 95.0 (cyclic quaternary carbon), 62.9, 62.3, 62.2, 62.1, 59.6, 59.2 ($OCH_2$), 52.0, 51.8, 51.5 [O$CH_3$, $C$($CH_3$)], 22.4, 21.6, 20.2, 19.3, 18.4, 13.9, 13.8 ($CH_3$) ppm.

**3(9):** IR ($CH_2Cl_2$): ν(C≡O) = 2070 (s), 2010 (s), 1983 $cm^{-1}$ (s); ν(C=O) = 1749 (s), 1610 (s). $^1H$ NMR (400 MHz, $CD_2Cl_2$, 273 K): $\delta$ = 5.74 (br. m, 1 H, CH allyl), 5.30 (br. m, 2 H, $CH_2$ allyl), 4.16, 4.05 (br. m, 4 H, $OCH_2$), 3.36 (br. s, 3 H, $OCH_3$), 2.61, 2.19 (br. m, 2 H, $CH_2$ allyl), 1.36 (br. s, 3 H, $CH_3$), 1.15 (br. s, 6 H, $CH_3$) ppm. $^{13}C\{^1H\}$ NMR (400 MHz, $CD_2Cl_2$, 273 K): $\delta$ = 272 (br., C=O), 237.5 [br., cyclic C(O)O], 210.0, 206.7, 206.3 [br., CO and C(O)O], 171.3, 167.6 (C=O ester), 134.4, 133.8, 132.4 (allylic CH), 119.3, 118.2, 117.3 (allylic $CH_2$), 95.6, 93.9, 92.2 (cyclic quaternary carbon), 64.5 (malonyl quaternary carbon), 62.1, 61.7 ($OCH_2$), 51.6, 51.3 ($OCH_3$), 36.5, 35.3, 34.5 (allylic $CH_2$), 25.5, 22.8 (C$CH_3$), 13.6 ($CH_3$) ppm.

**Reaction of the Anionic Trifunctionalized Metallalactones 3 with HCl. General Procedure for Preparation of Neutral Alkyl-Substituted Lactones 2:** A 1 M solution of HCl in diethyl ether (1 mL) was added to a slurry of anionic lactones **3** (1 mmol) in THF (40 mL) at –70 °C. As shown by IR monitoring of the reaction, the reaction was very fast. After 15 min at this temperature the ν(CO) bands of neutral complexes **2** at 2120, 2070, 2060, and 2040 $cm^{-1}$ were found to have totally replaced those of the starting complexes **3** at 2080, 2020, and 2000 $cm^{-1}$. The temperature was then raised to –10 °C and the solvent removed to dryness. The residue was extracted at –10 °C with a hexanes/$CH_2Cl_2$ (95:5) mixture (5 × 25 mL). This

 © 2006 Wiley-VCH Verlag GmbH & Co. KGaA, Weinheim 

solution was reduced to 10 mL at –40 °C to afford pure crystals of complexes **2**.

**Reaction of 3(1) with HCl: Preparation of 2(1):** Following the general procedure, **3(1)** (385 mg, 1.20 mmol) was treated with HCl (1.2 mL of a 1 M solution in diethyl ether) to afford **2(1)** (219 mg 65% yield). IR (hexanes): ν(C≡O) = 2125 (m), 2073 (sh), 2064 (m), 2042 $cm^{-1}$ (s); ν(C=O) = 1780 (m), 1685 (sh). $^1H$ NMR (400 MHz, $CD_2Cl_2$, 273 K): $\delta$ = 1.3 (s, 6 H, $CH_3$) ppm. $^{13}C\{^1H\}$ NMR (400 MHz, $CD_2Cl_2$, 273 K): $\delta$ = 254.1 (C=O), 200.2 (2 C, axial C≡O), 198.4, 196.6, 196.3 [CO and cyclic C(O)O], 96.2 (cyclic quaternary carbon), 24.1 ($CH_3$) ppm. $C_9H_6FeO_7$ (281.95): calcd. C 38.33, H 2.14, Fe 19.80; found C 38.21, H 2.12, Fe 19.73.

**Reaction of 3(2) with HCl. Preparation of 2(2):** The reaction of **3(2)** (270 mg, 0.75 mmol) with HCl (750 μL of a 1 M solution in diethyl ether) gave rise to **2(2)** (134 mg, 55% yield). IR (hexanes): ν(C≡O) = 2124 (s), 2072 (sh), 2063 (s), 2041 $cm^{-1}$ (s); ν(C=O) = 1738 (w), 1704 (s). $^1H$ NMR (400 MHz, $CD_2Cl_2$, 273 K): $\delta$ = 1.5–1.2 (br. m, 9 H, *n*Bu), 0.85 (br. s, 3 H, $CH_3$) ppm. $^{13}C\{^1H\}$ NMR (400 MHz, $CD_2Cl_2$, 273 K): $\delta$ = 254.1 (C=O), 200.5, 200.3, 198.4, 196.6, 196.5 [CO and cyclic C(O)O], 98.4 (cyclic quaternary carbon), 36.9, 26.9, 25.6, 23.0, 21.9 ($CH_2$ and $CH_3$) ppm. $C_{12}H_{12}FeO_7$ (324.03): calcd. C 44.48, H 3.73, Fe 17.23; found C 44.62, H 3.92, Fe 17.15.

**Reaction of 3(3) with HCl. Preparation of 2(3):** Complex **3(3)** (480 mg, 1 mmol) and HCl (1 mL of a 1 M solution in diethyl ether) were reacted to afford **2(3)** (255 mg, 60% yield). IR (hexanes): ν(C≡O) = 2131 (s), 2083 (m), 2064 (s), 2047 $cm^{-1}$ (s); ν(C=O) = 1734 (m), 1689 (s). $^1H$ NMR (400 MHz, $CD_2Cl_2$, 273 K): $\delta$ = 4.13 (m, 4 H, $OCH_2$), 3.70 [s, 1 H, C(*H*)$(CO_2C_2H_5)_2$], 1.34 (s, 3 H, CC*H*$_3$), 1.22 (m, 6 H, $CH_2CH_3$) ppm. $^{13}C\{^1H\}$ NMR (400 MHz, $CD_2Cl_2$, 273 K): $\delta$ = 251.8 (C=O), 202.0, 199.4, 199.05 (2 C), 196.3 [CO and cyclic C(O)O], 166.3, 166.1 ($CO_2C_2H_5$), 92.6 (cyclic quaternary carbon), 62.2, 62.15 ($OCH_2$), 58.6 (CH), 22.2 (C*C*H$_3$), 13.9, 13.75 ppm ($CH_2CH_3$). $C_{15}H_{14}FeO_{11}$ (426.12): calcd. C 42.28, H 3.31, Fe 13.11; found C 42.46, H 3.35, Fe 13.05.

**Reaction of 3(4) with HCl. Preparation of 2(4):** Complex **3(4)** (1 mmol 420 mg) was reacted at –50 °C with HCl (1 mL of a 1 M solution in diethyl ether) to afford **2(4)** (200 mg, 55% yield). IR (hexanes): ν(C≡O) = 2131 (s), 2085 (m), 2064 (s), 2047 $cm^{-1}$ (s); ν(C=O) = 1720 (sh), 1705 (s), 1690 (sh). $^1H$ NMR (400 MHz, $CD_2Cl_2$, 273 K): $\delta$ = 2.15 (s, 3 H, C*C*H$_3$), 2.02 [s, 6 H, C(O)C*H*$_3$] ppm. $^{13}C\{^1H\}$ NMR (400 MHz, $CD_2Cl_2$, 273 K): $\delta$ = 251.65 (C=O), 202.1, 201.8, 201.3, 199.3 (2 C), 197.85, 196.2 [CO, cyclic C(O)O and *C*(O)$CH_3$], 92.65 (cyclic quaternary carbon), 74.0 (CH), 31.05, 30.2 [*C*H$_3$C(O)], 22.2 (C*C*H$_3$) ppm. $C_{13}H_{10}FeO_9$ (366.064): calcd. C 42.65, H 2.75, Fe 15.26; found C 42.78, H 2.85, Fe 15.22.

**Reaction of 3(6) with HCl. Preparation of 2(6):** The reaction of **3(6)** (500 mg, 1.15 mmol) with HCl (1.15 mL of a 1 M solution in diethyl ether) at –50 °C was found to afford **2(6)** (285 mg 65% yield). IR (hexanes): ν(C≡O) = 2131 (m), 2085 (m), 2064 (s), 2047 $cm^{-1}$ (s); ν(C=O) = 1755 (w), 1721 (sh), 1703 (m). $^1H$ NMR (400 MHz, $CD_2Cl_2$, 273 K; two isomers: $\delta$ = 3.98 (s, 0.6 H, CH), 3.92 (s, 0.4 H, CH), 3.78 (s, 1.8 H, $OCH_3$), 3.66 (s, 1.2 H, $OCH_3$), 2.25 [s, 1.2 H, C(O)C*H*$_3$], 2.12 [s, 1.8 H, C(O)C*H*$_3$], 1.28 (s, 1.8 H, CC*H*$_3$), 1.25 (s, 1.2 H, CC*H*$_3$) ppm. $^{13}C\{^1H\}$ NMR (400 MHz, $CD_2Cl_2$, 273 K): $\delta$ = 251.32, 251.22 (C=O), 202.06, 201.94, 200.72, 200.01, 198.41, 198.31, 198.15, 198.08, 198.02, 196.29 [CO, cyclic C(O)O and *C*(O)$CH_3$], 167.70, 167.18 ($CO_2CH_3$), 92.78, 92.32 (cyclic quaternary carbon), 65.86, 65.35 (CH), 53.30, 53.08 ($OCH_3$), 30.11, 29.42 [C(O)C*H*$_3$], 22.19, 22.15 (C*C*H$_3$) ppm. $C_{13}H_{10}FeO_{10}$ (382.063): calcd. C 40.87, H 2.64, Fe 14.62; found C 41.05, H 2.63, Fe 14.52.

**Reaction of Complexes 3(5) or 3(7) with HCl:** The reactions of these complexes, which contain one or two C≡N groups, with 1 equiv. of HCl was found, even at low temperature (–80 °C), to lead to their decomposition into $Fe(CO)_5$ and organic compounds.

**Reaction of the Mixture of Isomers of 3(8) or 3(9) Bearing Bulky Substituents with HCl. Preparation of 2(8) and 2(9):** The reaction of **3(8)** or **3(9)** [1 mmol, 500 mg for **3(8)** (R = $CH_3$) or 520 mg for **3(9)** (R = allyl)] with HCl (1 mL of a 1 M solution in diethyl ether) at –50 °C afforded **2(8)** (310 mg, 70% yield) or **2(9)** (233 mg, 50% yield), respectively, as white powders after crystallization from hexanes at –40 °C.

**2(8):** IR (hexanes): ν(C≡O) = 2131 (s), 2084 (m), 2052 (m), 2050 $cm^{-1}$ (s); ν(C=O) = 1727 (m), 1695 (s). $^1H$ NMR (400 MHz, $CD_2Cl_2$, 273 K): $\delta$ = 4.11 (q, *J* = 7 Hz, 4 H, $OCH_2$), 1.58 (s, 3 H, $CH_3$), 1.44 (s, 3 H, $CH_3$), 1.20 (t, *J* = 7 Hz, 6 H, $CH_2CH_3$) ppm. $^{13}C\{^1H\}$ NMR (400 MHz, $CD_2Cl_2$, 273 K): $\delta$ = 249.9 (C=O), 202.6, 199.55 (3 C), 196.35 [CO and cyclic C(O)O], 169.9, 169.4 ($CO_2C_2H_5$), 95.25 (cyclic quaternary carbon), 62.1, 61.8 [quaternary malonic carbon and $OCH_2$ (2 C)]; 20.1 ($CH_3$), 18.95 ($CH_3$), 13.8 [$CH_2CH_3$ (2 C)] ppm. $C_{16}H_{16}FeO_{11}$ (440.143): calcd. C 43.66, H 3.66, Fe 12.67; found C 43.85, H 3.63, Fe 12.62.

**2(9):** IR (hexanes): ν(C≡O) = 2128 (s), 2083 (m), 2059 (m), 2041 $cm^{-1}$ (s); ν(C=O) = 1750 (m). 1737 (m), $^1H$ NMR (400 MHz, $CD_2Cl_2$, 273 K): $\delta$ = 5.8 (m, 1 H, =CH), 5.1 (m, 2 H, $=CH_2$), 4.15 (m, 4 H, $OCH_2$), 2.8 (d, *J* = 5 Hz, 2 H, allylic $CH_2$), 1.49 (s, 3 H, $CH_3$), 1.22 (t, *J* = 7 Hz, 6 H, $CH_2CH_3$) ppm. $^{13}C\{^1H\}$ NMR (400 MHz, $CD_2Cl_2$, 273 K): $\delta$ = 249.84 (C=O), 202.75, 198.48, 198.34, 197.98, 196.41 [CO and cyclic C(O)O-], 168.74, 168.70 ($CO_2C_2H_5$), 133.94 (=CH), 118.16 ($=CH_2$), 95.60 (cyclic quaternary carbon), 65.71 (quaternary malonic carbon), 62.19, 62.07 ($OCH_2$), 37.59 (allylic $CH_2$), 19.90 ($CH_3$), 13.94, 13.80 ($CH_2CH_3$) ppm. $C_{18}H_{18}FeO_{11}$ (466.181): calcd. C 46.38, H 3.89, Fe 11.98; found C 46.52, H 3.93, Fe 11.97.

**Reaction of 2(1) (R = R′ = R′′ = H), 2(3) (R = R′ = $CO_2C_2H_5$; R′′ = H), and 2(8) (R = R′ = $CO_2C_2H_5$; R′′ = $CH_3$) with NaOMe. Formation of 3(1), 3(3), and 3(8):** Complex **2** [0.5 mmol; 140 mg of **2(1)**, 210 mg of **2(3)**, or 220 mg of **2(8)**] in solution in THF (30 mL) at 0 °C was added to a suspension of 28 mg of NaOMe in THF. The reaction was monitored by IR spectroscopy. After 90 min the solvent was removed to dryness. The residue of the reaction performed with **2(1)** was washed with $CH_2Cl_2$ (3 × 5 mL) at 0 °C. The residues obtained from **2(3)** and **2(8)** were washed with hexanes (3 × 5 mL) and extracted with a hexanes/$CH_2Cl_2$ (60:40, 3 × 10 mL) mixture and crystallized from this solution at –40 °C. The $^{13}C$ NMR spectra of the obtained products were found to be similar to those of **3(1)**, **3(3)**, and **3(8)**, respectively. These reactions were found to afford 60 mg of **3(1)** (35% yield), 70 mg of **3(3)** (30% yield), or 75 mg of **3(8)** (30% yield).

**X-ray Crystallographic Studies:** Data for compounds **2(1)** and **3(3)** were collected on a Xcalibur 1 diffractometer (Oxford Diffraction) at 150 and 100 K, respectively. The very low stability of compound **3(3)** made a correct X-ray data collection difficult. In this case we had only a few seconds to select a correct single crystal which was very quickly mounted on the goniometer head of the diffractometer at 100 K. After several attempts we succeeded in finding a correct single crystal of **3(3)** suitable for the data collection. Both structures were solved by direct methods and successive Fourier difference syntheses, and were refined by weighted anisotropic full-matrix least-squares methods.[25] The hydrogen atoms of compound **2(1)** were located by difference Fourier techniques and were refined isotropically; while those of compound **3(3)** were calculated [*d*(C–H) = 0.95 Å]; their thermal parameters were taken as $U_{iso}$ = 1.3·$U_{equ}$(C) and therefore included as isotropic fixed contributors to $F_c$. Scattering factors and corrections for anomalous dispersion

 © 2006 Wiley-VCH Verlag GmbH & Co. KGaA, Weinheim 

Table 4. Crystal data and structural refinement details for **2(1)** and **3(3)**.

| | **2(1)** | **3(3)** |
|---|---|---|
| Empirical formula | $C_9H_6FeO_7$ | $C_{67}H_{74}Cl_6Fe_4K_4O_{48}$ |
| Molecular weight | 281.99 | 2239.82 |
| Space group | $P\bar{4}2_1c$ | $P\bar{1}$ |
| $a$ [Å] | 17.824(2) | 14.892(1) |
| $b$ [Å] | 17.824(2) | 17.082(1) |
| $c$ [Å] | 7.1894(5) | 20.093(2) |
| $\alpha$ [°] | 90 | 75.553(7) |
| $\beta$ [°] | 90 | 84.644(7) |
| $\gamma$ [°] | 90 | 77.615(6) |
| $V$ [Å$^3$] | 2284.0(4) | 4830.3(9) |
| $Z$ | 8 | 2 |
| $\rho_{calcd.}$ [g cm$^{-3}$] | 1.64 | 1.54 |
| Temperature | 150(2) | 100 |
| $\mu$ [cm$^{-1}$] | 13.30 | 10.16 |
| $F(000)$ | 1136 | 2284 |
| Reflections measured | 7474 | 16359 |
| $2\theta$ range | 7.22–43.70 | 5.0–44.10 |
| Reflections unique/$R_{int}$ | 952/0.049 | 7262/0.042 |
| Reflections with $I > 2\sigma(I)$ | 881 | 5125 |
| $N_v$ | 178 | 837 |
| $R_1$,[a] $wR_2$[b] | 0.0262/0.0556 | 0.065/0.082 |
| *GooF*[c] | 1.064 | 1.619 |
| Flack parameter | –0.01(3) | |
| $\Delta\rho_{max.,min.}$ [e Å$^{-3}$] | +0.209, –0.159 | +0.771, –0.223 |

[a] $R_1 = \Sigma|F_o - F_c|/F_o$. [b] $wR_2 = \{\Sigma[w(F_o^2 - F_c^2)^2]/\Sigma[w(F_o^2)^2]\}^{1/2}$. [c] GooF = $S = \{\Sigma[w(F_o^2 - F_c^2)^2]/(N_{obsd} - N_{var})\}^{1/2}$.

were taken from the International Tables for X-ray Crystallography.[26] The thermal ellipsoid drawings were made with the ORTEP program.[27] Pertinent crystal data and selected bond lengths and bond angles of **2(1)** and **3(3)** are listed in Tables 1–4.

CCDC-286043 [for **2(1)**] and -270916 [for **3(3)**] contain the supplementary crystallographic data for this paper. These data can be obtained free of charge from The Cambridge Crystallographic Data Center via www.ccdc.cam.ac.uk/data_request/cif.


[1] J. P. Collman, L. S. Hegedus, J. R. Norton, R. G. Finke, *Principles and Applications of Organotransition Metal Chemistry*, University Science Books, Mill Valley, CA, **1987**.

[2] a) M. I. Bruce, *Chem. Rev.* **1998**, *98*, 2797–2858; b) D. Touchard, P. H. Dixneuf, *Coord. Chem. Rev.* **1998**, *178–180*, 409–429; c) H. Werner, *Chem. Commun.* **1997**, 903–910; d) V. Cadierno, M. P. Cornasa, J. Gimeno, *Eur. J. Inorg. Chem.* **2001**, 571–591.

[3] a) B. E. R. Schilling, R. Hoffmann, D. L. Lichtenberger, *J. Am. Chem. Soc.* **1979**, *101*, 585–591; b) A. Sgamelotti, C. Floriani, *Organometallics* **2000**, *19*, 1115–1122; c) M. Baya, P. Crochet, M. A. Esteruelas, E. Gutierez-Puebla, A. M. Lopez, J. Modrego, E. Onate, N. Vela, *Organometallics* **2000**, *19*, 2585–2596.

[4] J. T. Chen, *Coord. Chem. Rev.* **1999**, *190–192*, 1143–1168.

[5] H. des Abbayes, J. Y. Salaün, *Dalton Trans.* **2003**, 1041–1052 and references cited therein.

[6] a) H. des Abbayes, A. Buloup, *J. Chem. Soc., Chem. Commun.* **1978**, 1090–1091; b) F. Francalanci, L. Gardano, T. Abis, T. Fiorani, M. Foa, *J. Organomet. Chem.* **1983**, *243*, 87–94; c) F. Francalanci, M. Foa, *J. Organomet. Chem.* **1982**, *232*, 59–70; d) L. Cassar, *Ann. N. Y. Acad. Sci.* **1980**, *333*, 208–224.

[7] P. Cabon, M. Sellin, J. Y. Salaün, V. Patinec, H. des Abbayes, M. M. Kubicki, *Organometallics* **2002**, *21*, 2196–2202.

[8] T. M. Huang, Y. J. You, C. S. Yang, W. H. Tzeng, J. T. Chen, M. C. Cheng, Y. Wang, *Organometallics* **1991**, *10*, 1020–1026.

[9] M. Sellin, D. Luart, J. Y. Salaün, P. Laurent, L. Toupet, H. des Abbayes, *Organometallics* **1996**, *15*, 521–526.

[10] M. Sellin, D. Luart, J. Y. Salaün, P. Laurent, L. Toupet, H. des Abbayes, *Chem. Commun.* **1996**, 857–858.

[11] R. E. Valters, W. Flitsch, *Ring–Chain Tautomerism*, Plenum, New York **1985**.

[12] J. C. Selover, G. D. Vaughn, C. E. Strouse, J. A. Gladysz, *J. Am. Chem. Soc.* **1986**, *108*, 1455–1462.

[13] P. Cabon, R. Rumin, J. Y. Salaün, S. Triki, H. des Abbayes, *Organometallics* **2005**, *24*, 1709–1717.

[14] See, for example: a) M. Picquet, C. Bruneau, P. H. Dixneuf, *Tetrahedron* **1999**, *55*, 3937–3948; b) N. Tsukada, A. Shibuya, I. Nakamura, H. Kitahara, Y. Yamamoto, *Tetrahedron* **1999**, *55*, 8833–8844; c) I. Kadota, A. Shbuya, H. C. Gyoung, Y. Yamamoto, *J. Am. Chem. Soc.* **1998**, *120*, 10262–10263; d) Y. Yamamoto, U. Radhakrishnan, *Chem. Soc. Rev.* **1999**, *28*, 199–207.

[15] J. L. McLean, *Ph.D. Thesis*, New York University, **1974**.

[16] J. Y. Salaün, G. le Gall, P. Laurent, H. des Abbayes, *J. Organomet. Chem.* **1992**, *441*, 99–108.

[17] a) R. C. Pettersen, J. L. Cihonski, F. R. Young, R. A. Levenson, *J. Chem. Soc., Chem. Commun.* **1975**, 370–371; b) K. Hoffmann, E. Weiss, *J. Organomet. Chem.* **1977**, *128*, 389–398; c) S. Aime, L. Milone, E. Sappa, A. Tiripicchio, A. M. Manotti Lanfredi, *J. Chem. Soc., Dalton Trans.* **1979**, 1664–1670; d) K. J. Karel, T. H. Tulip, S. D. Ittel, *Organometallics* **1990**, *9*, 1276–1282.

[18] D. Luart, N. le Gall, J. Y. Salaün, L. Toupet, H. des Abbayes, *Inorg. Chim. Acta* **1999**, *291*, 166–177.

[19] R. H. Dotz, U. Wenicker, G. Muller, H. G. Alt, D. Seyferth, *Organometallics* **1986**, *5*, 2570–2572.

[20] D. D. Perrin, W. L. F. Armarego, D. R. Perrin, *Purification of Laboratory Chemicals*, Pergamon Press, New York, **1980**.

[21] L. S. Hegedus, Y. Inoue, *J. Am. Chem. Soc.* **1982**, *104*, 4917–4921.

[22] R. T. Arnold, M. DeMoura-Campos, K. L. Lindsay, *J. Chem. Soc.* **1953**, *75*, 1044–1047.

[23] J. Chen, V. G. Young, R. J. Angelici, *Organometallics* **1996**, *15*, 325–331.

[24] H. C. J. Ottenheijm, M. W. Tijhuis, *Org. Synth.* **1983**, *61*, 1–4.

[25] a) C. K. Fair, *MolEN, An Interactive Intelligent System for Crystal Structure Analysis*, User Manual, Enraf–Nonius, Delft, The Netherlands, **1985**; b) G. M. Sheldrick, *SHELX-97, Programs for Crystal Structure Analysis*, **1997**, University of Göttingen, Germany.

[26] *International Tables for X-ray Crystallography*, vol. 4, Kynoch Press, Birmingham, **1975**.

[27] C. K. Johnson, *ORTEP*, Rep. ONL-3794, Delft, The Netherlands, **1985**.


Received: November 9, 2005
Published Online: February 21, 2006

 © 2006 Wiley-VCH Verlag GmbH & Co. KGaA, Weinheim 

EurJIC
European Journal of Inorganic Chemistry

Issue 8/2006

Pages 1529–1708

Papers available ahead of print in Early View at www.interscience.wiley.com

*Earliest available Table of Contents:*
*Automatically, free of charge by e-mail through*
*www.interscience.wiley.com/alerts*

## COVER PICTURE

**The cover picture shows** the honeycomb structure formed by π-π stacking of homoleptic octahedral $Ni^{II}$ complexes of the "large-surface" ligand 1,12-diazaperylene (dap), $[Ni(dap)_3](BF_4)_2$ (Ni red, N green, C dark yellow, B blue, F light yellow). The $[Ni(dap)_3]^{2+}$ cation and one of the $BF_4^-$ counterions form parallel nanosized channels (ca. 9.60 Å in diameter), which run along the crystallographic *c* axis and are filled with the other disordered $BF_4^-$ counterion (omitted for clarity). The $C_3$ symmetry of $[Ni(dap)_3]^{2+}$ is a prerequisite for forming the highly symmetrical supramolecular assembly. Details are discussed in the article by H.-J. Holdt et al. on p. 1547 ff.

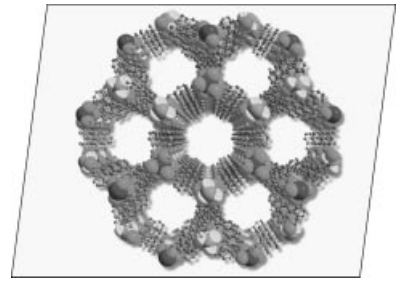

## SHORT COMMUNICATION

Contents

**1543** **L.-P. Zhang, P. A. Tanner,* T. C. W. Mak**

Two Novel 5f–3d Bimetallic Cyano-Bridged Complexes

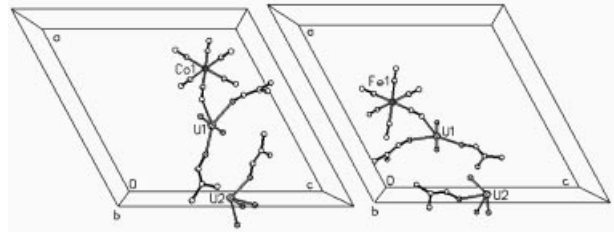


**Keywords:** Cyano bridge / Transition metal / Uranium / Electronic structure

 © 2006 Wiley-VCH Verlag GmbH & Co. KGaA, Weinheim 

# FULL PAPERS


**1547** **S. Kammer, H. Müller, N. Grunwald, A. Bellin, A. Kelling, U. Schilde, W. Mickler, C. Dosche, H.-J. Holdt***

Supramolecular Assemblies with Honeycomb Structures by π-π Stacking of Octahedral Metal Complexes of 1,12-Diazaperylene

**Keywords:** Nickel / Iron / N ligands / π Interactions / Self-assembly

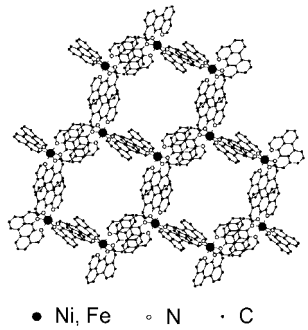


**1552** **A. Belous,* O. Gavrilenko, O. Pashkova, C. Galven, O. Bohnké**

Peculiarities of the Synthesis of Lithium Ion Conducting Lanthanum Tantalate by Solid-State Reaction and Precipitation from Solutions

**Keywords:** Tantalates / Solid-state reactions / Precipitation from solution / Microstructure / Ionic conductivity

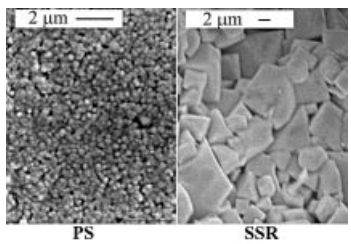


**1561** **H.-J. Deiseroth,* K. Aleksandrov, C. Reiner, L. Kienle, R. K. Kremer**

$Fe_3GeTe_2$ and $Ni_3GeTe_2$: Two New Layered Transition-Metal Compounds: Crystal Structures, HRTEM Investigations, and Magnetic and Electrical Properties

**Keywords:** Layered compounds / Crystal structures / Iron germanium telluride / Magnetism / Electron microscopy / Conductivity

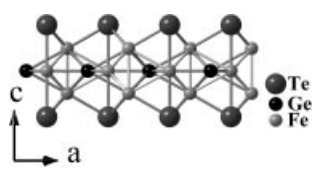


**1568** **P. K. Chan, W. K. Leong,* K. I. Krummel, M. V. Garland***

Aminoethyl-Functionalized Cyclopentadienyliridium Complexes: Photochemical C−H Activation and Carbonylation of Cycloalkanes

**Keywords:** Carbonylation / C−H activation / Cyclopentadienyl ligands / Iridium / Photochemistry

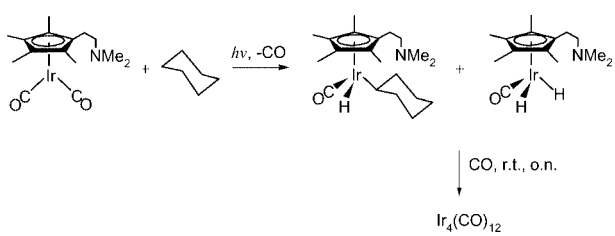



 © 2006 Wiley-VCH Verlag GmbH & Co. KGaA, Weinheim 

**1573** **B. Demerseman,* L. Toupet**

Enolate-Phosphane Ligands Providing a Tool for the Selective Substitution of Triphenylphosphane by Carbon Monoxide or Trimethylphosphane in Complex {Ru(Cp)[$\eta^2$-*P*,*O*-$Ph_2PCH_2C(tBu)=O](PPh_3)$}[$PF_6$], and Subsequent Reactivity Towards Terminal Alkynes

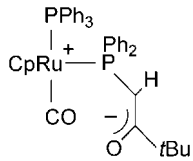


**Keywords:** Cyclopentadienyl ligands / Metallacycles / Phosphane ligands / Ruthenium / Vinylidene ligands

**1582** **F. Li, T.-H. Li, W. Su, S.-Y. Gao, R. Cao***

Formation of Two 1D Polymeric Water Morphologies

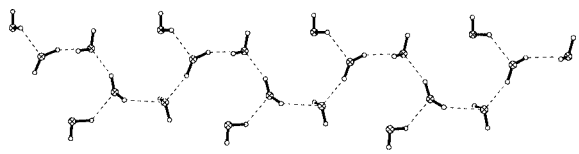

**Keywords:** Hosts / Water morphologies / Chains / Tapes

**1588** **V. Schmid, R. Linder, C. M. Marian***

The UV/Vis Spectrum of Potassium Heptacyanovanadate(III): A Theoretical Multi-Reference Configuration Interaction Study Combined with Low-Temperature Experiments

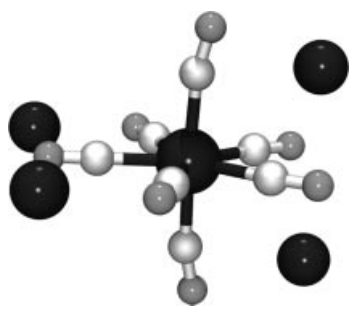

**Keywords:** Cyanide ligands / Electronic structure / Quantum chemistry / UV/Vis spectroscopy / Vanadium

**1594** **H. Han, S. Zhang, H. Hou,* Y. Fan, Y. Zhu**

Fe(Cu)-Containing Coordination Polymers: Syntheses, Crystal Structures, and Applications as Benzyl Alcohol Oxidation Catalysts

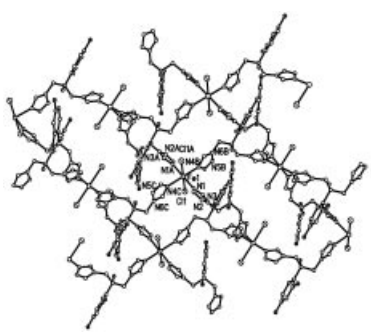

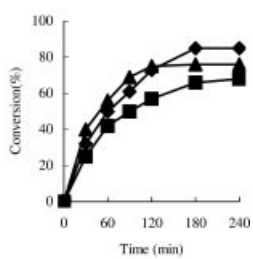


**Keywords:** Fe(Cu)-coordination polymers / Benzyl alcohol oxidation / Catalysts

 © 2006 Wiley-VCH Verlag GmbH & Co. KGaA, Weinheim 

**1601** **J.-Y. Xu, J. Astner, O. Walter, F. W. Heinemann, S. Schindler,* M. Merkel, B. Krebs***

Iron(III) Complexes with the Ligand *N*′,*N*′-Bis[(2-pyridyl)methyl]ethylenediamine (uns-penp) and Its Amide Derivative *N*-Acetyl-*N*′,*N*′-bis[(2-pyridyl)methyl]ethylenediamine (acetyl-uns-penp)

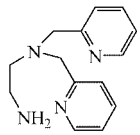


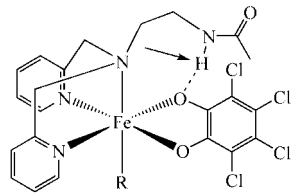

**Keywords:** Iron / Tripodal ligands / Catechol dioxygenase / Amide hydrogen bonding / Carboxamide coordination

**1611** **C. Binkowski-Machut, M. Canipelle, H. Bricout, S. Tilloy, F. Hapiot, E. Monflier***

Supramolecular Trapping of Phosphanes by Cyclodextrins: A General Approach to Generate Phosphane Coordinatively Unsaturated Organometallic Complexes

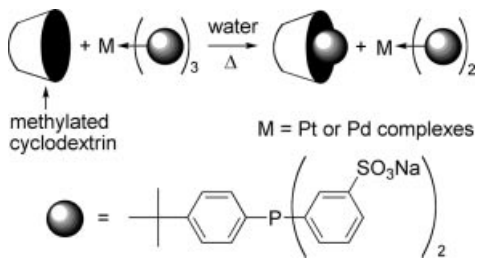


**Keywords:** Phosphane ligands / Cyclodextrins / Molecular recognition / Palladium / Platinum

**1620** **Q.-Y. Liu, L. Xu***

Synthesis, Crystal Structures, and Photophysical Properties of Two Novel Lead(II)−SIP Coordination Polymers ($NaH_2SIP$ = 5-Sulfoisophthalic Acid Monosodium Salt) Containing Tetranuclear Lead(II) Units

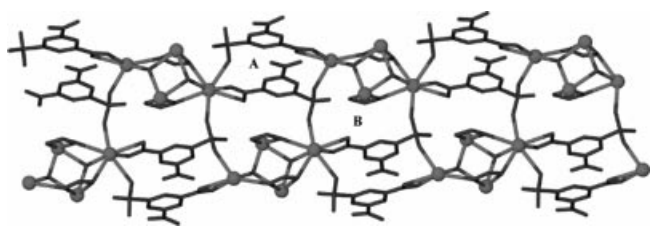


**Keywords:** Tetranuclear lead / Hydrothermal synthesis / Crystal structures / Photophysical properties

**1629** **W. Lu, Y. Zhang, J. Dai*, Q.-Y. Zhu, G.-Q. Bian, D.-Q. Zhang**

A Radical-Radical and Metal−Metal Coupling Tetrathiafulvalene Derivative in which Organic Radicals Directly Coordinate to $Cu^{II}$ Ions

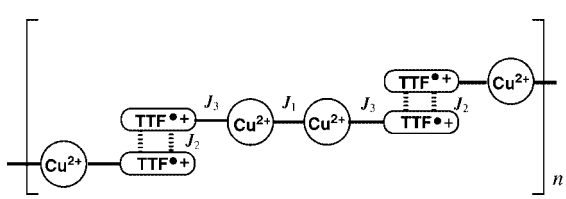


**Keywords:** Tetrathiafulvalenes / Copper(II) complexes / Magnetic coupling

 © 2006 Wiley-VCH Verlag GmbH & Co. KGaA, Weinheim 

**1635** **R. Z. Pellicani, F. P. Intini, L. Maresca, E. Mesto, C. Pacifico, G. Natile***

The First Example of a Dinuclear Platinum(III) Complex with Three Bridging Ligands

**Keywords:** Bridging ligands / Hydrogen bonds / Metal−metal interactions / N ligands / Platinum(III)

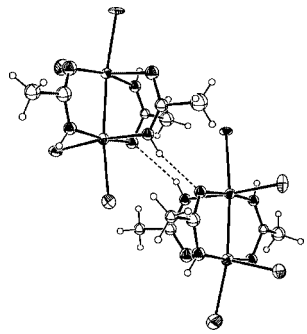

**1643** **Q. R. Zhao, Y. Gao, X. Bai, C. Z. Wu, Y. Xie***

Facile Synthesis of $SnO_2$ Hollow Nanospheres and Applications in Gas Sensors and Electrocatalysts

**Keywords:** Tin oxides / Room-temperature sensitivity / Electrocatalysts

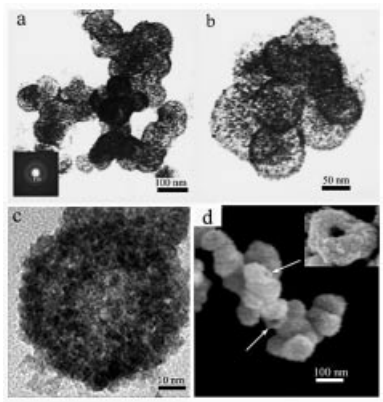


**1649** **R.-H. Wang, D.-Q. Yuan, F.-L. Jiang, L. Han, S. Gao, M. Hong***

Syntheses, Structures, and Characterization of Two Manganese(II)-Aminobenzoic Complexes

**Keywords:** Manganese / Aminobenzoic acid / Magnetic properties

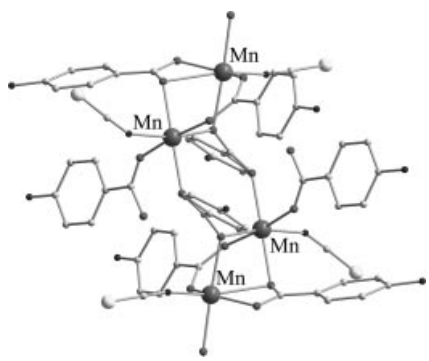


**1657** **C. von Hänisch,* O. Rubner**

Synthesis and Metallation of the Diphosphanylsilane $i$Pr$_2$Si(PHMe)$_2$

**Keywords:** Clusters / Phosphorus / Silicon / Tin / Zinc

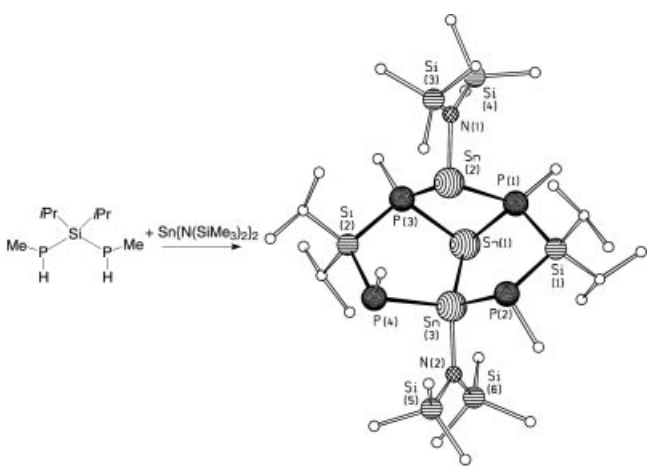


 © 2006 Wiley-VCH Verlag GmbH & Co. KGaA, Weinheim 

**1662** **S. S. Braga, F. A. Almeida Paz, M. Pillinger, J. D. Seixas, C. C. Romão,* I. S. Gonçalves***

Structural Studies of β-Cyclodextrin and Permethylated β-Cyclodextrin Inclusion Compounds of Cyclopentadienyl Metal Carbonyl Complexes

**Keywords:** Ab initio calculations / Cyclodextrins / Inclusion compounds / Iron / Molybdenum / Sandwich complexes

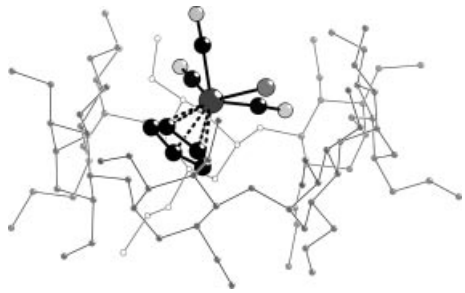

**1670** **S.-Y. Hou, Z.-H. Zhou,* T.-R. Lin, H.-L. Wan**

Peroxotungstates and Their Citrate and Tartrate Derivatives

**Keywords:** Bioinorganic chemistry / Peroxo ligands / Polyoxometalates / Tungsten

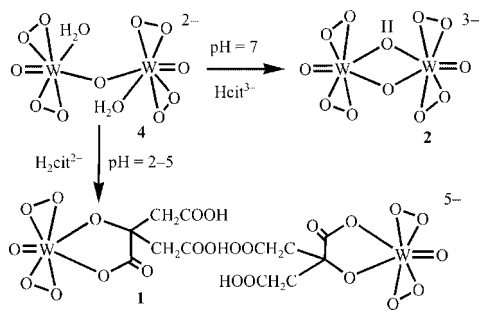


**1678** **A. Pañella, J. Pons,* J. García-Antón, X. Solans, M. Font-Bardia, J. Ros***

Synthesis of New Palladium(II) Complexes Containing Hemilabile *N*-(Alkylamino)pyrazole Ligands: Spectroscopic Analysis and Crystal Structure of [PdCl(ddae)]Cl·$H_2O$ {ddae = Bis[2-(3,5-dimethyl-1-pyrazolyl)ethyl]ethylamine}

**Keywords:** Hemilabile ligands / N ligands / Palladium

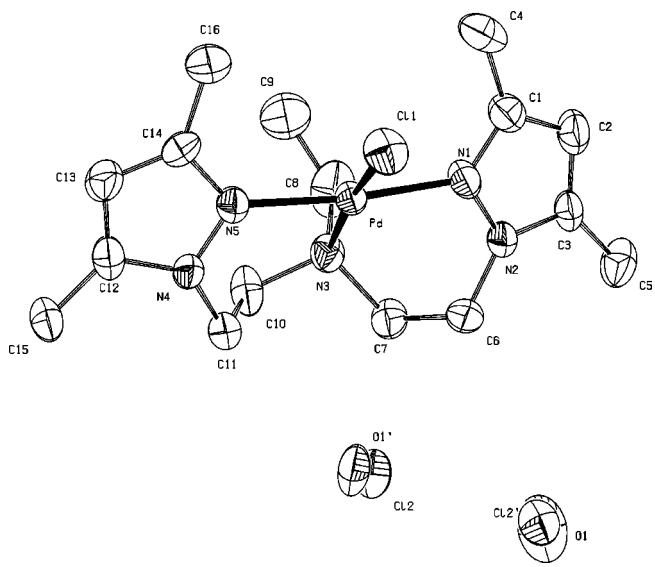


**1686** **A. Shibli, M. Srebnik***

Synthesis of Novel α-Aminoboronate Complexes of Aminoboranes and Aminocyanoboranes

**Keywords:** Amines / Aminoboranes / Aminocyanoboranes / Boranes / Lewis acids

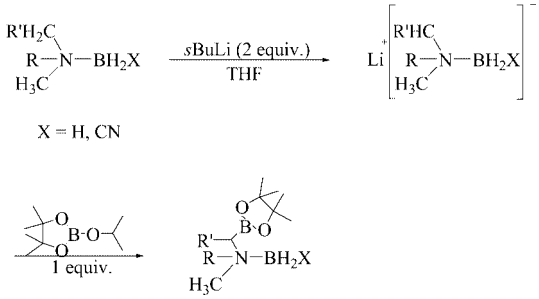


 © 2006 Wiley-VCH Verlag GmbH & Co. KGaA, Weinheim 

**1690** **I. M. Malkowsky, R. Fröhlich, U. Griesbach, H. Pütter, S. R. Waldvogel***

Facile and Reliable Synthesis of Tetraphenoxyborates and Their Properties

**Keywords:** Borates / Sodium / Anions / Phenolates

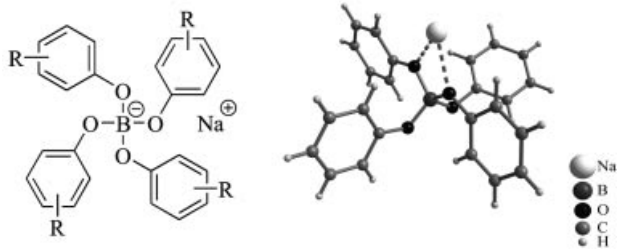


**1698** **B.-C. Tzeng,* Y.-M. Lu, G.-H. Lee, S.-M. Peng**

Self-Assembly of *N*,*N*′,*N*″,*N*‴-Tetra(pyridin-4-yl)-1,4,7,10-tetraazacyclododecane-1,4,7,10-tetracarboxamide with $Zn^{2+}$ or $Cd^{2+}$ Ions

**Keywords:** Charge transfer / Luminescence / Metallomacrocycles / Self-assembly / Supramolecular chemistry

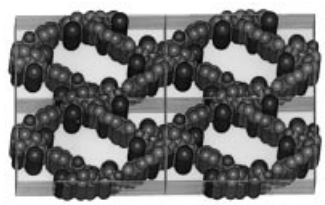

 © 2006 Wiley-VCH Verlag GmbH & Co. KGaA, Weinheim 

DOI: 10.1002/ejic.200600029

# Two Novel 5f–3d Bimetallic Cyano-Bridged Complexes

**Lin-Ping Zhang,[a,b] Peter A. Tanner,*[c] and Thomas C. W. Mak[a]**

**Keywords:** Cyano bridge / Transition metal / Uranium / Electronic structure

Bimetallic cyano-bridged uranyl Co and uranyl Fe compounds crystallize in the same space group but are not isomorphous and each comprises two different types of uranyl ion. The spectroscopic consequences with regard to band intensities and positions for the transitions at these different uranyl ion sites are novel and are rationalized.
(© Wiley-VCH Verlag GmbH & Co. KGaA, 69451 Weinheim, Germany, 2006)

## Introduction

There has been considerable interest in 3d–4f bimetallic cyano-bridged complexes due to their catalytic, semiconductive and magnetic properties.[1] Du et al.[2] have listed another 15 applications. Although there have been several reports of 3d–5f complexes,[3] attention has not been directed towards cyano-bridged 3d–5f complexes, so that we decided to synthesize such complexes comprising the uranyl ion, because the electronic structure and spectroscopy of this actinide ion are well-documented.[4] Two novel complexes involving also the coordination of dimethylformamide (dmf) and aqua ligands to $U^{VI}$ are reported herein: $[UO_2(H_2O)_4(dmf)_2]_{0.5}\cdot\{UO_2[M(CN)_6](dmf)_2\}$, M = Co (**1**), Fe (**2**) and their spectroscopic properties have been investigated.

## Results and Discussion

### Crystal Structures

Compound **1** comprises two ionic components (Figure 1, a). The anionic component is a cyano-bridged infinite layer in which the $U^{VI}$ cation is seven-coordinate in a pentagonal-bipyramidal geometry, bonding to two oxygen atoms [U1–O1, 1.727(7) Å, U1–O2, 1.761(7) Å], two dmf molecules [U1–O3, 2.325(6) Å, U1–O4, 2.359(5) Å], and three cyanide groups from different $[Co(CN)_6]^{3-}$ ions [U1–N1, 2.494(6) Å, U1–N2a, 2.499(6) Å, U1–N5b, 2.492(6) Å]. The $Co^{III}$ cation is octahedrally coordinated by six cyanide groups (Co–C, 1.884–1.904 Å), with three of them connecting three different $U^{VI}$ cations. The $U^{VI}$ ions bridge other $[Co(CN)_6]^{3-}$ ions through cyanide groups, forming an infinite two-dimensional anionic layer parallel to the *bc* plane (Figure 2, a). The cationic component comprises discrete centrosymmetric $[UO_2(H_2O)_4(dmf)_2]^{2+}$ cations, situated above and below the anionic layer, each forming O–H···N interactions with it. This $U^{VI}$ cation is eight-coordinate in a hexagonal bipyramidal geometry, being coordinated by

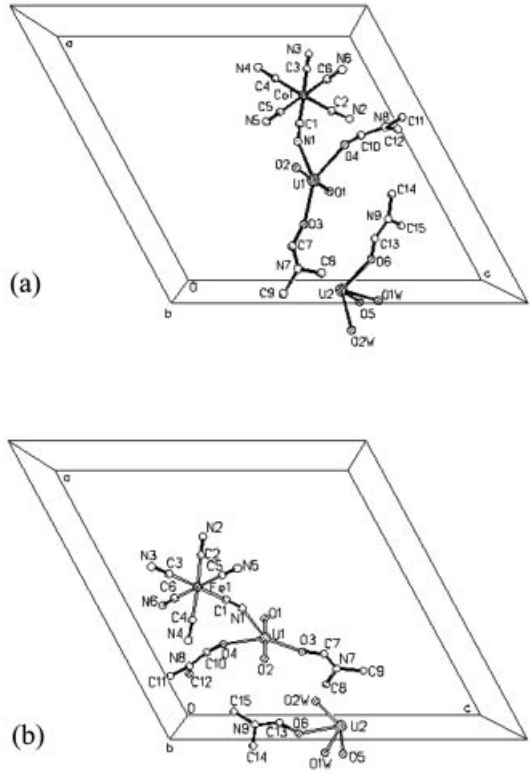


Figure 1. Atom labeling in the asymmetric unit: (a) $[UO_2(H_2O)_4(dmf)_2]_{0.5}\cdot\{UO_2[Co(CN)_6](dmf)_2\}$ (**1**); (b) $[UO_2(H_2O)_4(dmf)_2]_{0.5}\cdot\{UO_2[Fe(CN)_6](dmf)_2\}$(**2**) .

[a] The Department of Chemistry, The Chinese University of Hong Kong, Shatin, New Territories,
Hong Kong S.A.R., P. R. China
[b] College of Chemistry and Chemical Engineering, Donghua University,
West Yan-an Road 1882, Shanghai 20051, P. R. China
[c] Department of Biology and Chemistry, City University of Hong Kong,
Tat Chee Avenue, Kowloon, Hong Kong S.A.R., P. R. China
Fax: +852-2788-7406
E-mail: bhtan@cityu.edu.hk
Supporting information for this article is available on the WWW under http://www.eurjic.org or from the author.

 © 2006 Wiley-VCH Verlag GmbH & Co. KGaA, Weinheim 

two oxo groups [U2–O5 = U2–O5c, 1.750(7) Å], two dmf molecules [U2–O6 = U2–O6c, 2.27(2) Å], and four aqua ligands [U2–O1W = U2–O1Wc, 2.58(2) Å;U2–O2W = U2–O2Wc, 2.39(2) Å]. The latter form O–H···N hydrogen bonds with the non-bridging cyanide group of the anionic layers, linking them into a three-dimensional network.

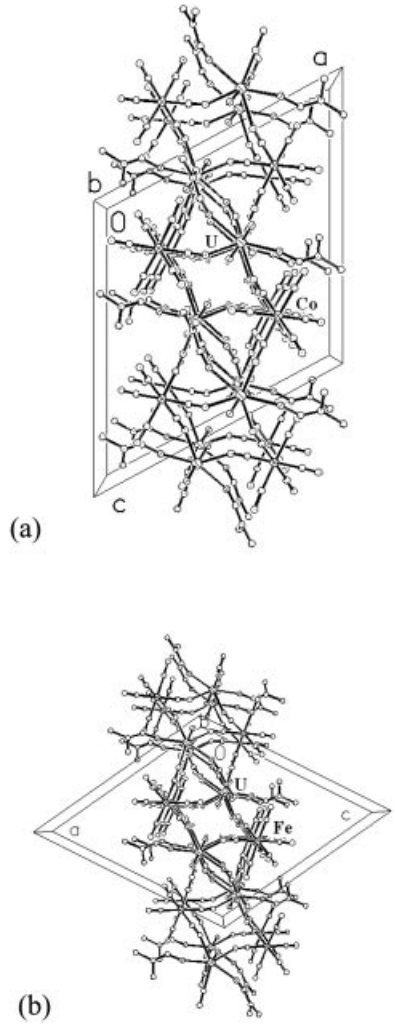


Figure 2. (a) Anionic layer viewed along the [010] direction in **1**; (b) **2**.

Although **1** and **2** both crystallize in the same space group $P2_1/c$ with very similar unit-cell dimensions, they are not isomorphous as the atoms take different positions in the unit cell (see parts a and b in Figure 1). However, compound **2** is isostructural to compound **1** in all respects, and the only difference is that the anionic layer in **2** runs parallel to the plane (1,–1,0), rather than parallel to the *bc* plane as in the case of **1** (see Figure 2, a and b).

### Spectroscopic Properties of 1 and 2

The IR and Raman spectra of **1** and **2** exhibit at least four bands between 2120 and 2180 $cm^{-1}$, corresponding to terminal and bridging CN vibrations, with the energies for **1** being slightly higher than those for **2**, just as in $Cs_2LiM(CN)_6$ (M = Co, Fe).[5] The spectroscopic properties of **1** and **2** are interesting because they each contain uranium atoms in two types of coordination geometry: seven-coordinate U1 situated at a $C_1$ site and eight-coordinate U2 at a $C_i$ site. Besides this, there are two U1 atoms for every U2 atom in the unit cell. Sixfold equatorial coordination of the uranyl ion exhibits rather different spectral characteristics as compared to fivefold, and drastic differences also occur for noncentrosymmetric vs. centrosymmetric uranyl ions.[4] Thus, as well as vibrations due to dmf and aqua ligands in the IR spectrum of **2**, two strong bands due to antisymmetric stretch of the uranyl ion are observed, at 933 and 949 $cm^{-1}$. The higher energy band is associated with sixfold equatorial coordination [c.f. $MUO_2(NO_3)_3$ M = Rb 962 $cm^{-1}$, M = Cs 956 $cm^{-1}$], whereas that at lower energy is due to fivefold coordinated $UO_2^{2+}$ [c.f. $UO_2(H_2PO_2)_2{\cdot}H_2O$ 909 $cm^{-1}$].[4] Also, the relative intensities of the 933, 949 $cm^{-1}$ bands are in the ratio 2:1, being consistent with the atom ratio U1:U2.

The 10-K absorption spectrum of **1** is shown in Figure 3. The lowest energy absorption bands of the uranyl ion correspond to the $\Sigma_g^+ \rightarrow \Pi_g$ ($D_{\infty h}$) electronic transition, and because this involves a large increase in bond length, a strong progression in the totally symmetric uranyl stretching mode, $\nu_s$(OUO) is based upon the electronic origin. Now, for lower than fourfold symmetry of the uranyl ion the final state is not degenerate, and whereas the transition is magnetic dipole-allowed for centrosymmetric uranyl ions, additional electric dipole intensity is present when this is not the case. Finally, it has been found that a blue-shift occurs when the equatorial coordination number increases from 5 to 6.[4] With these facts in mind, the intense bands at lowest energy are marked and assigned to the electronic origins of uranyl ions U1 and U2, with that of the noncentrosymmetric U1 being more intense and at lower energy. The $\nu_s$(OUO) progression frequency based upon the U1 origin (724 $cm^{-1}$) is about 10 $cm^{-1}$ lower than the corresponding one for U2. The resolution of the absorption spectrum does not permit a clear, detailed interpretation but the intense

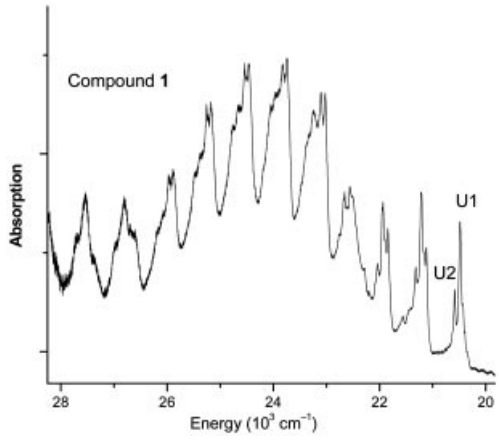


Figure 3. 10-K absorption spectrum of a crystal of **1** between 20000–28000 $cm^{-1}$.

 © 2006 Wiley-VCH Verlag GmbH & Co. KGaA, Weinheim 

bands commencing at 23021, 23102 $cm^{-1}$ mark the beginning of a new progression, presumably of U1.

The 10 K luminescence spectrum of **1** is also dominated by the transitions from the lowest energy site U1. The symmetric and antisymmetric OUO stretching frquencies are $857 \pm 5\ cm^{-1}$ and $943\ cm^{-1}$, respectively, and the progressions are observed up to 5 members.

## Conclusions

In summary, two cyano-bridged 3d–5f complexes **1** and **2** have been synthesized with three-dimensional structures comprising uranyl groups arranged in cationic and anionic layers. Although both compounds crystallize in space group $P2_1/c$ with very similar unit-cell dimensions, they are not isomorphous. The electronic absorption and emission spectra of the uranyl ions in **1** are dominated by the uranyl ions of site symmetry $C_1$, which are subjected to less restrictive optical selection rules and more numerous than those of site symmetry $C_i$.

## Experimental Section

**Physical Methods:** Electronic absorption spectra were obtained between 300 and 10 K at the resolution 2 $cm^{-1}$ by a Biorad FTS-60A spectrometer equipped with a photomultiplier tube detector. The sample was placed in an Oxford Instruments closed-cycle cryostat. Emission spectra were recorded at temperatures down to 10 K using a tunable pulsed laser (Panther OPO system pumped by the third harmonic of a Surelite Nd:YAG). The signal was collected at 90° by an 0.5 m Acton monochromator, with gratings blazed at 250 nm (1800 grooves/mm), 500 nm (1200 groove/mm), and 750 nm (600 groove/mm), respectively, and a back-illuminated SpectruMM CCD detector. Infrared and Raman spectra were recorded with a Perkin–Elmer 2000 FTIR spectrometer equipped with a Raman unit.

**Materials and Synthesis of Compounds 1 and 2:** For compound **1**, $UO_2(NO_3)_2{\cdot}6H_2O$ (0.151 g; 0.3 mmol; Strem 99.99%) was dissolved in 10 $cm^3$ water (solution A). Yellow $K_3Co(CN)_6$ (0.067 g; 0.2 mmol; Acros 95%) was dissolved in 10 $cm^3$ dmf, to which solution A was added dropwise with continuous stirring, and the resulting solution was stirred for another 30 min in the dark and filtered. The filtrate was allowed to stand for several weeks in the dark at room temperature for crystallization. Compound **2** was prepared analogously using a molar ratio $UO_2(NO_3)_2{\cdot}6H_2O$: $K_3Fe(CN)_6$ of 3:2. **1:** $C_{15}H_{25}CoN_9O_8U_{1.5}$ (875.41): calcd. C 20.58, H 2.88, N 14.40; found C 20.36, H 1.93, N 14.17. **2:** $C_{15}H_{25}FeN_9O_8U_{1.5}$ (872.34): calcd. C 20.65, H 2.87, N 14.45; found C 20.24, H 1.61, N 14.38. IR of **2** ($cm^{-1}$): $\tilde{\nu}$ = 3339 w ($H_2O$), 2131 sh, 2137 s, 2147 sh, 2157 m CN, 1651 ms (C=O), 949 m, 933 s ($UO_2$ asymm.), 872 vw, 856 vw ($UO_2$ symm.). Raman of **1** ($cm^{-1}$): 2178 s, 2161 m, 2151 m, 2146 sh CN, 862 vs. ($UO_2$ symm.), 2951 m, 1657 vw, 1440 m, 1427 vs, 687 m dmf.

**X-ray Crystallography:** Intensity data of compounds **1** and **2** were collected with a Bruker SMART 1000 CCD diffractometer with graphite-monochromatized Mo-$K_\alpha$ radiation ($\lambda$ = 0.71073 Å) at 293 K. The structures were solved by direct methods and refined by full-matrix least-squares based on $F^2$ using the SHELXTL program package. All the non-hydrogen atoms were refined anisotropically, and the hydrogen atoms were generated geometrically except for those of the water molecules, which were located from the $\Delta F$ maps. The crystallographic data of the complexes **1** and **2** are summarized in Table S1, and selected bond lengths and angles are given in Table S2 (see Supporting Information; for details see the footnote on the first page of this article). Complex **1**, $C_{15}H_{25}CoN_9O_8U_{1.5}$: $P2_1/c$, $a$ = 16.066(2) Å, $b$ = 11.365(1) Å, $c$ = 16.884(2) Å, $\alpha$ = 90°, $\beta$ = 118.323(2)°, $\gamma$ = 90°, $Z$ = 4, $R_1$ = 0.0456. Complex **2**, $C_{15}H_{25}FeN_9O_8U_{1.5}$: $a$ = 16.154(2) Å, $b$ = 11.373(1) Å, $c$ = 16.975(2) Å, $\alpha$ = 90°, $\beta$ = 118.651(2)°, $\gamma$ = 90°, $Z$ = 4, $R_1$ = 0.0441.

CCDC-281906 and -281907 contain the supplementary crystallographic data for this paper. These data can be obtained free of charge from The Cambridge Crystallographic Data Centre via www.ccdc.cam.ac.uk/data_request/cif.

**Supporting Information** (see also the footnote on the first page of this article): Crystal data and structure refinement parameters, bond lengths and angles, hydrogen bonds, descriptions of structure; Raman, infrared and emission spectra are available from the authors.

## Acknowledgments

We thank C.S. K. Mak and W. L. Cheung for their contributions to the early part of this study and acknowledge funding from the Hong Kong University Research Grants Council under CERG Research Grant CityU 1115/02P.

[1] J. A. Kautz, D. F. Mullica, B. P. Cunningham, R. A. Combs, J. A. Farmer, *J. Mol. Struct.* **2000**, *523*, 175–182; S. Tanase, M. Andruh, A. Müller, M. Schmidtmann, C. Mathonière, G. Rombaut, *Chem. Commun.* **2001**, 1084–1085; M. Ohba, H. Okawa, *Coord. Chem. Rev.* **2000**, *198*, 313–328; J. Liu, E. A. Meyers, S. G. Shore, *Inorg. Chem.* **1998**, *37*, 5410–5411.

[2] B. Du, E. A. Meyers, S. G. Shore, *Inorg. Chem.* **2000**, *39*, 4639–4645.

[3] M. Frisch, C. L. Cahill, *Dalton Trans.* **2005**, *8*, 1518–1523; G. H. John, I. May, M. J. Sarsfield, H. M. Steele, D. Collison, M. Helliwell, J. D. McKinney, *Dalton Trans.* **2004**, *5*, 734–740; Z.-T. Yu, Z.-L. Liao, Y.-S. Jiang, G.-H. Li, G.-D. Li, J.-S. Chen, *Chem. Commun.* **2004**, *16*, 1814–1815; L. Salmon, P. Thuéry, M. Ephritikhine, *Polyhedron* **2003**, *22*, 2683–2688; L. Salmon, P. Thuéry, E. Rivière, J.-J. Girerd, M. Ephritikhine, *Dalton Trans.* **2003**, *14*, 2872–2880; W. Chen, H.-M. Yuan, J.-Y. Wang, Z.-Y. Liu, J.-J. Xu, M. Yang, J.-S. Chen, *J. Am. Chem. Soc.* **2003**, *125*, 9266–9267.

[4] R. G. Denning, *Struct. Bonding (Berlin)* **1992**, *79*, 215–276; C. D. Flint, P. Sharma, P. A. Tanner, *J. Phys. Chem.* **1982**, *86*, 1921–1922; P. A. Tanner, T. C. W. Mak, *Inorg. Chem.* **1999**, *38*, 6024–6031; C. D. Flint, P. A. Tanner, *Molec. Phys.* **1981**, *43*, 933–944.

[5] B. I. Swanson, L. H. Jones, *Inorg. Chem.* **1974**, *13*, 313–316.

Received: January 12, 2006
Published Online: March 15, 2006

 © 2006 Wiley-VCH Verlag GmbH & Co. KGaA, Weinheim 

DOI: 10.1002/ejic.200600092

# Supramolecular Assemblies with Honeycomb Structures by π-π Stacking of Octahedral Metal Complexes of 1,12-Diazaperylene

**Stefan Kammer,[a] Holger Müller,[a] Nicolas Grunwald,[a] Anja Bellin,[a] Alexandra Kelling,[a] Uwe Schilde,[a] Wulfhard Mickler,[a] Carsten Dosche,[b] and Hans-Jürgen Holdt*[a]**

**Keywords:** Nickel / Iron / N ligands / π Interactions / Self-assembly

Homoleptic $Ni^{II}$ and $Fe^{II}$ complexes of the "large-surface" phenanthroline-type ligand 1,12-diazaperylene (dap), $[Ni(dap)_3](BF_4)_2$ (**1**) and $[Fe(dap)_3](PF_6)_2$ (**2**), respectively, were synthesized. In the crystal structure the complex cation $[M(dap)_3]^{2+}$ (M = Ni, Fe) exhibits $C_3$ symmetry and interacts with three other cations by π-π stacking. It forms a new metalla-supramolecular assembly with a honeycomb structure containing nanochannels running parallel to the crystallographic *c* axis. Aggregation by π-π stacking between metal complexes of "large-surface" ligands should give new perspectives for inorganic supramolecular chemistry.

(© Wiley-VCH Verlag GmbH & Co. KGaA, 69451 Weinheim, Germany, 2006)

## Introduction

The design and construction of nanoporous supramolecular systems has recently become one of the most active research subjects in modern coordination chemistry.[1] It is well known that weak intermolecular noncovalent interactions such as hydrogen bonds[2] and aromatic π-π stacking interactions[3] play important roles in supramolecular systems. The understanding and utilization of all noncovalent interactions, including π-π stacking, is of fundamental importance for the further development of inorganic supramolecular chemistry and the tuning and prediction of crystal structures.[3c]

In particular, π-π stacking interactions have been reported to exist between metal complexes with aromatic nitrogen-containing ligands, such as bipyridine- and 1,10-phenanthroline-based ligands.

Aggregation by π-π stacking becomes increasingly favorable with an increasing number of arene rings connected to the aromatic nitrogen-containing ligands. Dipyrido[3,2-*a*:2′,3′-*c*]phenazine[4] (dppz), eilatin[5] (eil), and 1,12-diazaperylene[6] (dap) (Scheme 1) are such ligands with increased π-surfaces (called "large-surface" ligands[7]).

In the planar dichloro(dipyridophenazine)platinum(II) complex $[PtCl_2(dppz)]$, both ligand-ligand and platinum-platinum π-π interactions lead to aggregation of this complex in the crystal, forming two infinite stacks with an interplanar distance of about 3.45 Å between the dipyridophenazine moieties.[8] The octahedral mono(eilatin) $Ru^{II}$ and $Os^{II}$ complexes $[M(L–L)_2(eil)]^{2+}$ (M = Ru, Os; L–L = bipyridyl-type ligands) dimerize by π-π stacking between the eilatin moieties in the solid state and in solution.[9] In all solid-state structures a well-defined discrete dimer is observed, in which the eilatin surfaces are about 3.4 Å apart, a typical distance for systems held by π-π stacking interactions.[3c,10]

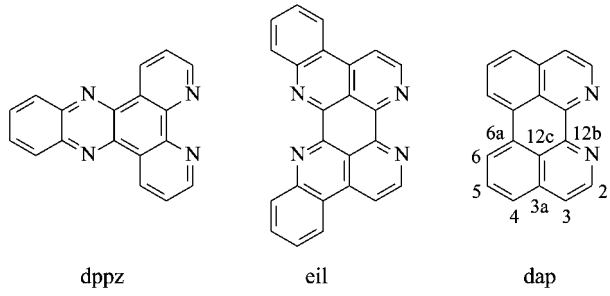


Scheme 1. "Large-surface" phenanthroline-type ligands.

Homoleptic octahedral complexes with three "large-surface" phenanthroline-type ligands are rare[11] because the steric requirements for coordination at the metal center are greater than those of the parent 1,10-phenanthroline. However, such complexes provide the opportunity for optimal π-π interactions by three "large surface" ligands. They are potential rigid building blocks for the self-assembly into well-defined supramolecular architectures mediated by effective π-π interactions.

Recently Chouai et al. synthesized the $Ru^{II}$ complex of 1,12-diazaperylene, $[Ru(dap)_3](PF_6)_2$.[11a] In the crystal structure the asymmetric unit of $[Ru(dap)_3](PF_6)_2$ contains two $[Ru(dap)_3]^{2+}$ cations which exhibit large distortions

[a] Institut für Chemie, Anorganische Chemie, Universität Potsdam,
Karl-Liebknecht-Straße 24–25, 14476 Golm, Germany
Fax: +49-331-977-5055
E-mail: holdt@chem.uni-potsdam.de
[b] Institut für Physik, Universität Potsdam
Am Neuen Palais 10, 14469 Potsdam, Germany

 © 2006 Wiley-VCH Verlag GmbH & Co. KGaA, Weinheim 

from the expected $D_3$ symmetry. π-π Interactions are observed between two dap ligands between both complex cations of the asymmetric unit. The distance between the two approximately parallel planes that separate the two dap ligands is 3.42 Å. No other π-π interactions are observed. To utilize the π-π interaction opportunities of all three "large surface" ligands of an octahedral metal complex in order to form a supramolecular assembly, a symmetrically octahedral complex is probably necessary.

It is well known that complexes of first row transition metals can show more regular geometries than those of second row transition metals. To investigate the π-π interaction opportunities of first row transition octahedral metal complexes with "large surface" ligands, we synthesized the dap complexes of $Ni^{II}$ and $Fe^{II}$, $[Ni(dap)_3](BF_4)_2$ (**1**) and $[Fe(dap)_3](PF_6)_2$ (**2**), respectively. In the solid state, **1** and **2** form honeycomb structures built by π-π stacking.

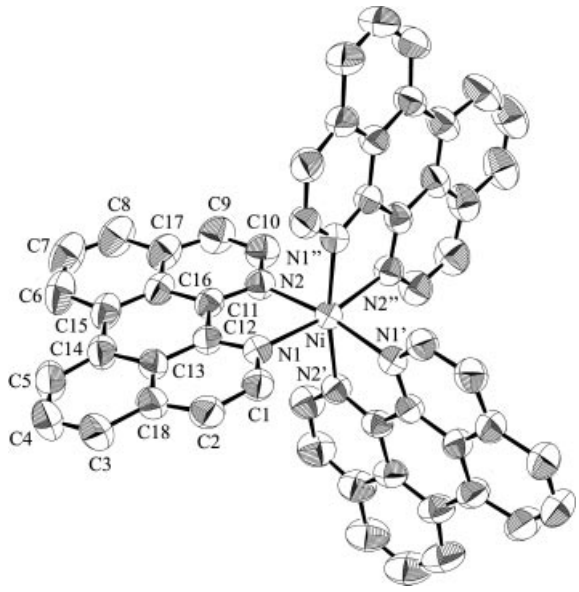


Figure 1. Structure of $[Ni(dap)_3]^{2+}$ in **1** with 50% ellipsoids. Hydrogen atoms have been omitted for clarity.

## Results and Discussion

Homoleptic 1,12-diazaperylene complexes of $Ni^{II}$ and $Fe^{II}$ are best prepared under microwave heating. **1** was synthesized by the reaction of $Ni(BF_4)_2{\cdot}6H_2O$ with dap in ethanol and **2** by the reaction of $Fe(NH_4)_2(SO_4)_2{\cdot}6H_2O$ with dap in water and subsequent addition of $NH_4PF_6$.

Crystals suitable for the X-ray structure determinations were obtained by slow evaporation of a solution of **1** in acetone and by diffusion of ethanol into a solution of **2** in a solvent mixture of acetone, acetonitrile, and chloroform.

In the crystal structure, the complex cation $[Ni(dap)_3]^{2+}$ of **1** exhibits $C_3$ symmetry. Figure 1 shows the structure of the cation along the threefold axis which coincides with the crystallographic *c* axis. The asymmetric unit of $[Ni(dap)_3](BF_4)_2$ (**1**) contains one third of $[Ni(dap)_3]^{2+}$ and also one third of one $B(1)F_4^-$ anion. One of the fluorine atoms of $B(1)F_4^-$ is partially disordered. $[Ni(dap)_3]^{2+}$ and $B(1)F_4^-$ are located alternately along the crystallographic *c* axis.

The bond lengths of Ni–N1 [2.105(2) Å], Ni–N2 [2.109(2) Å] and the bite angle of N1–Ni–N2 [78.54(8)°] are similar to the corresponding values of $[Ni(phen)_3]^{2+}$.[12] The diazaperylene ligand is coplanar to within 0.1617(36) Å. The dap ligands are almost perpendicular to each other, with a dihedral angle of 87.36 °.

Each complex cation $[Ni(dap)_3]^{2+}$ interacts with three other cations by π-π stacking, using all three dap ligands (see Figure 2, a). It forms a honeycomb structure containing channels running parallel to the crystallographic *c* axis (see Figure 2, b). If the van der Waals radii of the atoms are taken into account the resulting channels are approximately 9.60 Å in diameter. The channels contain the second anion, $B(2)F_4^-$, which shows a strong degree of disorder.

The $[Fe(dap)_3](PF_6)_2$ (**2**) compound is isostructural with **1**. The resulting channels in the honeycomb structure of **1** are 0.15 Å greater in diameter (ca. 9.75 Å). The Fe–N bond lengths amount to 1.9826(19) Å and 1.9779(18) Å. The N1–Fe–N2 bite angle is 81.71(7)°. These data are similar to the corresponding values of $[Fe(phen)_3]^{2+}$.[13]

The π-π stacking between two dap ligands of two $[Ni(dap)_3]^{2+}$ moieties in **1** are shown in Figure 3. The distance between the two approximately parallel planes that separate the 1,12-diazaperylene ligands is 3.341 Å (**2**: 3.456 Å). Only one arene ring of each dap is involved in π-π stacking. They interact in an offset or parallel-displaced mode.[3c] The centroid-centroid distance is 3.663 Å (**2**: 3.633 Å) and the displacement angle is 24.2° (**2**: 17.96°).

To the best of our knowledge, supramolecular assemblies with honeycomb structures were not, until now, built by π-π stacking of a metal complex.

In addition to the single-crystal X-ray structure analysis, high resolution transmission electron microscopy (HRTEM) was performed on samples of **2** to further characterize the structure of the compound. Unfortunately, the crystals of **2** were very sensitive to electron-beam-induced damage, even at low temperature (–180 °C).

The nickel(II) complex was found to be paramagnetic, with a value of 2.77 ± 0.02 B.M., as expected for a typical $d^8$ system. The $^1H$ NMR spectrum of complex **2** in $[D_6]$-acetone exhibits five signals, consistent with the expected $D_3$ symmetry of $[Fe(dap)_3]^{2+}$ in solution.

The absorption spectra for complexes **1**, **2**, and dap are illustrated in Figure 4. The free dap resembles perylene, showing a strong well-resolved π-π* transition at 442 nm. This same transition is evident in the $Ni^{II}$ and $Fe^{II}$ complexes, but is shifted to a longer wavelength by 36 and 41 nm, respectively. Moreover, the spectrum of the $Fe^{II}$ complex **2** shows the expected MLCT transition at 684 nm. This value is the lowest-energy absorption for a tris(diimin)-iron(II) complex that has been observed. As already observed for the phenanthroline $Fe^{II}$ complex[14] **2** shows no phosphorescence or CT emission even if cooled to 10 K.

Cyclic voltammetry experiments in $CH_3CN$ revealed that the $Fe^{II}$ complex **2** and the reference complex $[Fe(phen)_3]$-

 © 2006 Wiley-VCH Verlag GmbH & Co. KGaA, Weinheim 

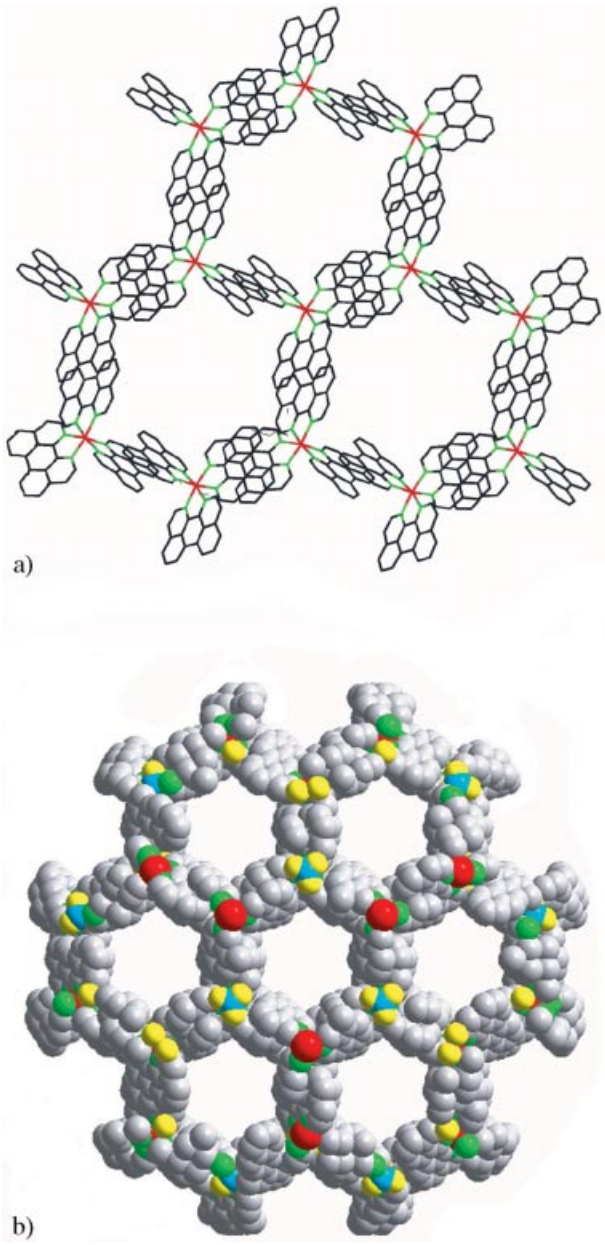


Figure 2. (a) Aggregation by π-π stacking between $[Ni(dap)_3]^{2+}$ moieties in $[Ni(dap)_3](BF_4)_2$ (**1**), viewed along the crystallographic *c* axis. Hydrogen atoms have been omitted for clarity. (b) Honeycomb structural motif in **1** (view down c) as a space-filling representation. $[Ni(dap)_3]^{2+}$ and one $B(1)F_4^-$ ion form parallel nanosized channels, which run along the crystallographic *c* axis and are filled with the second disordered $B(2)F_4^-$ counterion (omitted for clarity). Red: Ni, pink: B, yellow: F, green: N, grey: C.

$(PF_6)_2$ are oxidized at +0,69 V (rev., vs. $Fc/Fc^+$). These metal-centered oxidations indicate that the iron d orbitals are not influenced by complexation with dap as compared with that of phen. The reduction processes for the $Fe^{II}$ complex **2**, as well as the $Ni^{II}$ complex **1**, occur at the same potential (–1.08 V, irr.), probably because reduction is ligand-centered. The $Ni^{II}$ complex **1** is oxidized at 1.34 V (irr.) and $[Ni(phen)_3](BF_4)_2$ at 1.58 V (irr.).

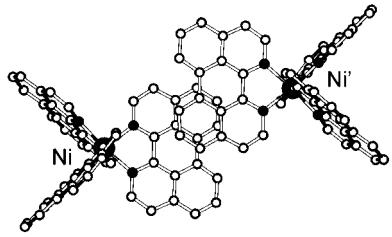


Figure 3. Aggregation by π-π stacking between two dap ligands of two $[Ni(dap)_3]^{2+}$ moieties in **1**. Hydrogen atoms have been omitted for clarity.

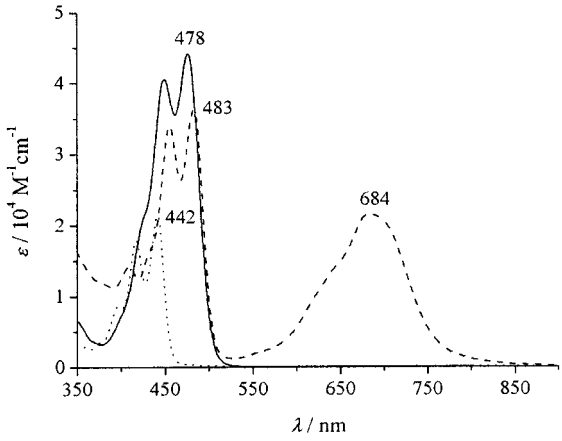


Figure 4. Absorption spectra of the complexes **1** (——) and **2** (– – – –), and of dap (·····), recorded in acetonitrile ($c = 10^{-5}$ mol/L).

## Conclusions

In conclusion, we have shown that homoleptic octahedral metal complexes of 1,12-diazaperylene are able to form supramolecular assemblies with honeycomb structures by π-π stacking when the complex cation, $[M(dap)_3]^{2+}$ (M = Ni, Fe), adopts a $C_3$ symmetry and the anions are $BF_4^-$ or $PF_6^-$. Further studies with other metal complexes of 1,12-diazaperylene and derivatives of dap using π-π stacking for self-assembly are in progress. Aggregation by π-π stacking between metal complexes of "large surface ligands" should give new perspectives for the development of inorganic supramolecular chemistry.

## Experimental Section

**General:** All reactions were carried out in dry solvents under an argon atmosphere. 1,12-Diazaperylene was prepared according to a known procedure.[6] Reference complexes $[Ni(phen)_3](BF_4)_2$ and $[Fe(phen)_3](PF_6)_2$ were synthesized following the methods described for complexes **1** and **2**, respectively. NMR spectra were recorded using an Avance 300 spectrometer. IR spectra were recorded with a Thermo Nicolet NEXUS FTIR instrument. UV/Vis measurements were carried out with an Analytik Jena Specord S 100 spectrophotometer using sealed quartz cuvettes. The ESI spectra were recorded using a Micromass Q-$TOF_{micro}$ mass spectrometer in positive electrospray mode. Elemental analyses (C, H, N) were performed with an Elementar Vario EL elemental analyzer. For phosphorescence emission measurements, the samples were pro-

 © 2006 Wiley-VCH Verlag GmbH & Co. KGaA, Weinheim 

vided as solids on quartz substrates. The samples were cooled to 10 K with a helium cryostat (Optistat CF, Oxford Instruments, Wiesbaden, Germany). For excitation, 2 mJ pulses from an optical parametric oscillator (VisIR 2/120, GWU, Erfstadt, Germany), which was pumped at 355 nm with a Q-switched Nd-YAG laser (SL 400, GWU), were used. The samples were excited in the ligand π-π* band at 440 nm. Electrochemical measurements were performed with a BAS 100B system using a platinum working and auxiliary electrode, and a $Ag/AgNO_3$ reference electrode. The experiments were conducted using degassed MeCN solutions using 0.1 M [$n$Bu$_4$N$^+$][$PF_6^-$] as the supporting electrolyte, and the Ferrocene/Ferrocinium ($Fc/Fc^+$) couple as a reference. Magnetic studies were performed at room temp. on a vibration sample magnetometer V.S.M. 3001.

**[Ni(dap)$_3$](BF$_4$)$_2$ (1):** A suspension of 1,12-diazaperylene (228.9 mg, 0.9 mmol) in ethanol (3 mL) was added to a solution of $Ni(BF_4)_2 \cdot H_2O$ (102.1 mg, 0.3 mmol) in ethanol (4 mL). The mixture was heated in a CEM-Discover microwave oven for 15 min (temp.: 85 °C, pressure: 17 bar). After cooling the mixture the precipitate was filtered. Dichloromethane (10 mL) and diethyl ether (100 mL) were added to the crude product, the solid was filtered and dried under vacuum to yield an orange powder (245 mg, 0.25 mmol, 82%). M.p. > 360 °C. IR (KBr): $\tilde{\nu}$ = 1051 (s, B–F) $cm^{-1}$. UV/Vis ($CH_3CN$): $\lambda_{max}$ ($\varepsilon$) = 478 (42700), 451 (39400), 426 (20300) sh, 352 (6400) sh nm. ESI(HR)-MS: $m/z$ calcd. for $[M - 2BF_4]^{2+}$ ($[C_{54}H_{30}NiN_6]^{2+}$) 410.0942, found 410.0915. $C_{54}H_{30}B_2F_8N_6Ni$ (995.17): C 65.17, H 3.04, N 8.44; found C 64,92, H 3.10, N 8.37.

**[Fe(dap)$_3$](PF$_6$)$_2$ (2):** A suspension of 1,12-diazaperylene (255 mg, 1 mmol) and $Fe(NH_4)_2(SO_4)_2 \cdot 6H_2O$ (98.04 mg, 0.25 mmol) in water (8 mL) was heated in a CEM-Discover microwave oven for 10 min (temp.: 120 °C, pressure: 15 bar). After cooling the solution, $NH_4PF_6$ (122.3 mg, 0.75 mmol) was added to precipitate **2**. The raw product was filtered and dissolved in acetone (25 mL). The desired product was precipitated by addition of diethyl ether (100 mL), filtered, and dried under vacuum to yield a dark green powder (270 mg, 0.24 mmol, 97%). M.p. > 360 °C. $^1$H NMR (300 MHz, [D$_6$]acetone): $\delta$ = 8.83 (dd, $^3J_{H,H}$ = 7.4, $^4J_{H,H}$ = 0.6 Hz, 2 H, 6-H), 8.09 (d, $^3J_{H,H}$ = 7.8 Hz, 2 H, 4-H), 8.01 (t, $^3J_{H,H}$ = 7.4 Hz, 2 H, 5-H] 7.87 (d, $^3J_{H,H}$ = 6.4 Hz, 2 H, 3-H), 7.60 (d, $^3J_{H,H}$ = 6.4 Hz, 2 H, 2-H) ppm. $^{13}$C NMR (300 MHz, [D$_6$]acetone): $\delta$ = 159.2 (C12b), 148.1 (C2), 138.2 (C3a), 135.3 (C5), 131.4 (C6a), 129.9 (C4), 127.6 (C3), 127.3 (C12c), 127.1 (C6) ppm. IR (KBr): $\tilde{\nu}$ = 838 (s, P–F), 558 (m, P–F) $cm^{-1}$. UV/Vis($CH_3CN$): $\lambda_{max}$ ($\varepsilon$) = 684 (21900), 483 (36700), 456 (34400), 433 (16500) sh, 410 (14500), 346 (16900) nm. ESI(HR)-MS: $m/z$ calcd. for $[M - 2PF_6]^{2+}$ ($[C_{54}H_{30}FeN_6]^{2+}$) 409.0940, found 409.0908. $C_{54}H_{30}F_{12}FeN_6P_2$ (1108.65): C 58.50, H 2.73, N 7.58; found C 58.27, H 2.80, N 7.50.

**Crystallographic Data:** Data were collected with a STOE IPDS-2 diffractometer at 210(2) K using graphite-monochromated Mo-$K_\alpha$ radiation ($\lambda$ = 0.71073 Å). Spherical absorption corrections were applied. Structure solution by direct methods (SHELXS-97)[15] and full-matrix refinement against $F^2$ (SHELXL-97).[16] Non-hydrogen atoms were refined with anisotropic temperature factors.

CCDC-290982 (for **1**) and -290981 (for **2**) contain the supplementary crystallographic data for this paper. These data can be obtained free of charge from The Cambridge Crystallographic Data Centre via www.ccdc.cam.ac.uk/data_request/cif.

**1:** $C_{54}H_{30}B_2F_8NiN_6$, 995.16 g·mol$^{-1}$, orange prism 0.62 × 0.31 × 0.14 mm, trigonal, $P\bar{3}$, $a = b$ = 18.126(3), $c$ = 11.1481(13) Å, $V$ = 3171.9(7) Å$^3$, $Z$ = 2, $F$(000) = 930, $\rho_{calc}$ = 0.961 g·cm$^{-3}$, $\mu$(Mo-$K_\alpha$) = 0.35 mm$^{-1}$, 26875 reflections measured ($2\Theta_{max}$ = 50.0°), of which 3728 were unique ($R_{int}$ = 0.0482). 253 parameters, $wR_2$ = 0.1355, $S$ = 0.974 (all data), $R_1$ [2806 data with $I > 2\sigma(I)$] = 0.0463, max./min. residual electron density: 0.259/–0.185 e·A$^{-3}$. Either of the tetrafluorborate anions, B(1)$F_4^-$, are located on the threefold axis, of which the F atoms are disordered over a mixture of full and partial occupancy sites. The second $BF_4^-$ counterion, B(2)$F_4^-$, is accommodated inside the channel. Because of its strong disordered positions, a suitable refinement model could not be found. Therefore this ion was disregarded by the SQUEEZE instruction of the program PLATON[17] and not accounted for in the final refinement cycles.

**2:** $C_{54}H_{30}F_{12}FeN_6P_2$, 1108.63 g·mol$^{-1}$, green prism 0.6 × 0.35 × 0.32 mm, trigonal, $P\bar{3}$, $a = b$ = 18.3658(14), $c$ = 11.5512(8) Å, $V$ = 3374.2(4) Å$^3$, $Z$ = 2, $F$(000) = 1120, $\rho_{calc}$ = 1.091 g·cm$^{-3}$, $\mu$(Mo-$K_\alpha$) = 0.34 mm$^{-1}$, 21742 reflections measured ($2\Theta_{max}$ = 50.0°), of which 3956 were unique ($R_{int}$ = 0.0555). 206 parameters, $wR_2$ = 0.1258, $S$ = 0.898 (all data), $R_1$ [2801 data with $I > 2\sigma(I)$] = 0.0448, max./min. residual electron density: 0.255/–0.214 e·A$^{-3}$. The first $PF_6^-$ counterion, P(1)$F_6^-$, could be found with certainty from the Fourier map, located on the threefold axis. The second counterion, P(2)$F_6^-$, as well as solvent molecules, fill the channels. The extremely diffuse electron density indicates severely disordered occupancies. Because it was not possible to assign atoms, the observed structure factors were corrected by subtracting the electron density in this region using the SQUEEZE instruction of PLATON.

## Acknowledgments

We thank Dr. N. Pinna (Martin-Luther-University of Halle-Wittenberg) for the HRTEM studies.

[1] a) S. S. Y. Chui, S. M. F. Lo, J. P. H. Charmant, A. G. Orpen, I. D. Williams, *Science* **1999**, *283*, 1148–1150; b) E. Coronado, J. R. Galan-Mascaros, C. J. Gomez-Garcia, C. Laukhin, *Nature* **2000**, *408*, 447–449; c) W. Schmitt, J. P. Hill, M. P. Juanico, A. Caneschi, F. Costantino, C. E. Anson, A. K. Powell, *Angew. Chem.* **2005**, *117*, 4259–4264; *Angew. Chem. Int. Ed.* **2005**, *44*, 4187–4192.

[2] a) G. R. Desiraju, *Acc. Chem. Res.* **2002**, *35*, 565–573; b) J.-M. Lehn, in: *Supramolecular Polymers* (Ed.: A. Ciferi), Dekker: New York, **2000**, 615–641; c) E. A. Archer, H. Gong, M. J. Krische, *Tetrahedron* **2001**, *57*, 1139–1159.

[3] a) C. Schmuck, *Angew. Chem.* **2003**, *115*, 2552–2556; *Angew. Chem. Int. Ed.* **2003**, *42*, 2448–2451; b) K. Oh, K.-S. Jeong, J. S. Moore, *Nature* **2001**, *414*, 889–893; c) C. Janiak, *J. Chem. Soc., Dalton Trans.* **2000**, 3885–3896.

[4] J. E. Dickeson, L. A. Summers, *Austral. J. Chem.* **1970**, *23*, 1023–1027.

[5] G. Gellerman, A. Rudi, Y. Kashman, *Tetrahedron* **1994**, *50*, 12959–12972.

[6] O. Schmelz, A. Mews, T. Basche, A. Hermann, K. Müllen, *Langmuir* **2001**, *17*, 2861–2865.

[7] E. C. Glazer, Y. Tor, *Angew. Chem.* **2002**, *114*, 4194–4198; *Angew. Chem. Int. Ed.* **2002**, *41*, 4022–4026.

[8] M. Kato, C. Kosuge, S. Yano, M. Kimura, *Acta Crystallogr., Sect. C* **1998**, *54*, 621–623.

[9] D. Gut, A. Rudi, J. Kopilov, I. Goldberg, M. Kol, *J. Am. Chem. Soc.* **2002**, *124*, 5449–5456.

[10] a) C. A. Hunter, J. K. Sanders, *J. Am. Chem. Soc.* **1990**, *112*, 5525–5534; b) C. A. Hunter, K. R. Lawson, J. Perkins, C. J. Urch, *J. Chem. Soc., Perkin Trans. 2* **2001**, *2*, 651–669.

[11] a) A. Chouai, S. E. Wicke, C. Turro, J. Bacsa, K. R. Dunbar, D. Wang, R. P. Thummel, *Inorg. Chem.* **2005**, *44*, 5996–6003; b) S. D. Bergman, D. Gut, M. Kol, C. Sabatini, A. Barbieri, F. Bargelletti, *Inorg. Chem.* **2005**, *44*, 7943–7950.

[12] B. A. Frenz, J. A. Ibers, *Inorg. Chem.* **1972**, *11*, 1109–1116.

 © 2006 Wiley-VCH Verlag GmbH & Co. KGaA, Weinheim 

[13] L. L. Koh, Y. Xu, A. K. Hsieh, *Acta Crystallogr., Sect. C* **1994**, *50*, 884–886.
[14] D. W. Fink, W. E. Ohnesorge, *J. Am. Chem. Soc.* **1969**, *91*, 4995–4998.
[15] G. M. Sheldrick, *SHELXS-97. Program for Crystal Structure Solution*, Göttingen **1997**.
[16] G. M. Sheldrick, *SHELXL-97. Program for Crystal Structure Refinement*, Göttingen **1997**.
[17] A. L. Spek, *PLATON. A Multipurpose Crystallographic Tool*, Utrecht **2005**.

Received: January 6, 2006
Published Online: March 9, 2006

 © 2006 Wiley-VCH Verlag GmbH & Co. KGaA, Weinheim 

DOI: 10.1002/ejic.200500667

# Peculiarities of the Synthesis of Lithium Ion Conducting Lanthanum Tantalate by Solid-State Reaction and Precipitation from Solutions

**Anatolii Belous,*[a] Oksana Gavrilenko,[a] Olena Pashkova,[a] Cyrille Galven,[b] and Odile Bohnké[b]**

**Keywords:** Tantalates / Solid-state reactions / Precipitation from solution / Microstructure / Ionic conductivity

Synthesis of lithium ion conducting tantalates has been carried out by conventional solid-state reaction (SSR) techniques and by precipitation from solutions (PS). It is shown that the latter chemical route leads to the formation of a pure perovskite phase, made up of nanosized particles, and uses milder conditions when compared with the solid-state reaction technique. Thermal analyses, X-ray powder diffraction (XRD) and infrared (IR) spectroscopy are used to investigate the phase transformations that occur during the preparation of these tantalates from powder precursors. After sintering, the nanosized particles of the powder obtained by the (PS) route are preserved and pellets with good compactness (89 %) are obtained. The electrical properties of the sintered ceramics have been investigated by ac impedance spectroscopy. These experiments showed that the total ionic conductivity (bulk and grain boundaries) of the (PS) pellet is slightly lower than that of the (SSR) pellet. This decrease of conductivity is attributed to an enhancement of the blocking effect of the grain boundaries resulting from the microstructure of the fine-grain ceramics. The bulk conductivity is not affected by the synthetic route.

(© Wiley-VCH Verlag GmbH & Co. KGaA, 69451 Weinheim, Germany, 2006)

## Introduction

Much attention is given to the investigation of solid-state lithium ion conductors because of their potential use in electrochemical devices as solid electrolytes, electrodes or ion-selective membranes. The lithium containing lanthanum titanates, which have a defect perovskite structure $(Li_{3x}La_{4/3-x}v_{2/3-2x})Ti_2O_6$ (v = vacancy), have deserved much attention these last years because of their high ionic conductivity of $10^{-3}$ S·cm$^{-1}$ at 300 K.[1–3] Apart from the titanate perovskites, the lithium-containing lanthanum tantalates, which also display a defect perovskite structure $(Li_{3x}La_{2/3-x}v_{4/3-2x})Ta_2O_6$ with a large number of vacancies, show an ionic conductivity of $10^{-4}$ S·cm$^{-1}$ at 300 K, only one order of magnitude smaller than the ionic conductivity of the titanates. The crystallographic structure and transport properties of these tantalates prepared by solid-state reactions have already been studied.[4–8] However, the details and peculiarities of the different chemical reactions and phase transformation occurring during the synthesis of the lanthanum tantalate $(La_{2/3}v_{4/3})Ta_2O_6$ and the lithium-containing lanthanum tantalates $(Li_{3x}La_{2/3-x}v_{4/3-2x})Ta_2O_6$ have never been considered. This is the main purpose of this work. Furthermore, since it is clearly established that the method of synthesis affects the microstructure and consequently the properties of the oxides, we investigated two different methods of synthesis: the precipitation from solution (PS) and the more conventional solid-state reaction (SSR) methods. An advantage of the (PS) method is the possibility to greatly reduce the synthesis temperature and also to produce nanosized particles.[9]

The aim of the present work is then to investigate the phase transformations occurring during the synthesis of lithium-containing lanthanum tantalate $(Li_{3x}La_{2/3-x}v_{4/3-2x})Ta_2O_6$ either by the solid-state reaction (SSR) technique or by precipitation from solution (PS), and to study the effect of the synthetic method on the microstructure and the electrophysical properties of these tantalates.

## Results And Discussion

### Synthesis

#### *Solid-State Reaction (SSR) Method*

According to the results of the XRD analysis, the mixture of the original reagents after a mild homogenisation consists of monoclinic $Li_2CO_3$ (for lithium-containing samples), hexagonal $La(OH)_3$ and orthorhombic $Ta_2O_5$. Figure 1 (a) shows DTA, DTG and TG curves for four mixtures of the original reagents with different lithium contents: $3x = 0$ (curve 1), 0.50 (curve 2), 1.10 (curve 3) and

[a] V.I.Vernadskii Institute of General and Inorganic Chemistry, 32/34 Palladina Avenue, 03680 Kyiv, 142 Ukraine
Fax: +380-42-42-211
E-mail: a.belous@list.ru
[b] Institut de Recherche en Ingénierie Moléculaire et Matériaux Fonctionnels FR CNRS 2575, Laboratoire des Oxydes et Fluorures (UMR, 6010 CNRS), Université du Maine, Avenue O. Messiaen, 72085 Le Mans Cedex 9, France

 © 2006 Wiley-VCH Verlag GmbH & Co. KGaA, Weinheim 

1.85 (curve 4). The DTG curves display four loss peaks, which are accompanied by endothermic reactions, as shown in the DTA. The first peak at 620–650 K (A), which decreases with $x$ content and disappears in curve 4 when La is almost absent, can be attributed to $La(OH)_3$ dehydration. The second one at 910–990 K (B), which does not appear in curve 1 when Li is absent and that increases with $x$ content, is attributed to $Li_2CO_3$ thermolysis. As the $Li_2CO_3$ content increases (curves 2 to 4), the initial $Li_2CO_3$ decomposition temperature range increases and the decomposition rate increases. For instance, for $(Li_{3x}La_{2/3-x}v_{4/3-2x})Ta_2O_6$ samples at $3x = 0.50$, 1.10 and 1.85, the $Li_2CO_3$ decomposition temperature range becomes wider: from 820–990 K to 770–990 K and finally to 720–990 K, respectively. Finally, the two other peaks, marked as (∗) and (o) on the curves, can be attributed to the partial (700–800 K) and complete (1050–1075 K) $La_2O_2CO_3$ decarbonation. The appearance of lanthanum dioxomonocarbonate has been proved by XRD analysis on samples calcined at 770 K. The complete decomposition temperature of lanthanum dioxomonocarbonate decarbonation in lithium-containing samples shifts towards higher temperatures as compared with the basic $La_{2/3}Ta_2O_6$ sample. This is accounted for by the fact that the thermal decomposition of dioxomonocarbonate slows down in an atmosphere rich in $CO_2$.[10]

Figure 1 (b) shows IR spectra, recorded at room temperature, of raw materials $Ta_2O_5$ (curve 1), $La_2O_3$ (curve 2), $Li_2CO_3$ (curve 3) and of their homogenised mixtures (curves 4–7). The IR spectra of the mixtures (curves 4–7) are characterised by a superposition of absorption bands, which are typical of the spectra of original reagents. However, small shifts can be observed. The stretching vibration band of the CO groups, observed at 1480 $cm^{-1}$ in pure $Li_2CO_3$, shifts slightly towards higher frequencies.[11] Furthermore, the deformation vibration $\delta$ band and stretching vibration $v$ band of Ta–O observed at 355 $cm^{-1}$ and 555 $cm^{-1}$, respectively, in pure $Ta_2O_5$, shift to higher and lower frequencies, respectively. The shifts depend on the Li content ($3x$). For instance, the Ta–O vibration frequencies of samples at $3x = 0$, 0.50, 1.10, 1.85 are observed at 355 and 555 $cm^{-1}$, 368 and 545 $cm^{-1}$, 375 and 525 $cm^{-1}$, 380 and 510 $cm^{-1}$, respectively. From these results, it can be inferred that the system obtained after homogenising milling differs from a simple mixing of the original reagents.

Powder XRD spectra have been recorded at room temperature on powders as a function of composition and firing temperature, in the temperature range from 370 K to 1770 K. The results are summarised in Table 1. From these results, it is evident that during the formation of the lanthanum metatantalate with a defect perovskite structure of the composition $La_{2/3}Ta_2O_6$ ($3x = 0$) the reaction between lanthanum oxide and tantalum oxide begins at 1320 K, and carries on actively at temperatures above 1470 K. According to the XRD spectra analysis, the synthesis proceeds via the formation of intermediate phases: monoclinic lanthanum orthotantalate ($LaTaO_4$), orthorhombic lanthanum heptatantalate ($LaTa_7O_{19}$) and pentatantalate ($LaTa_5O_{14}$).[12] Lanthanum metatantalate as the main phase

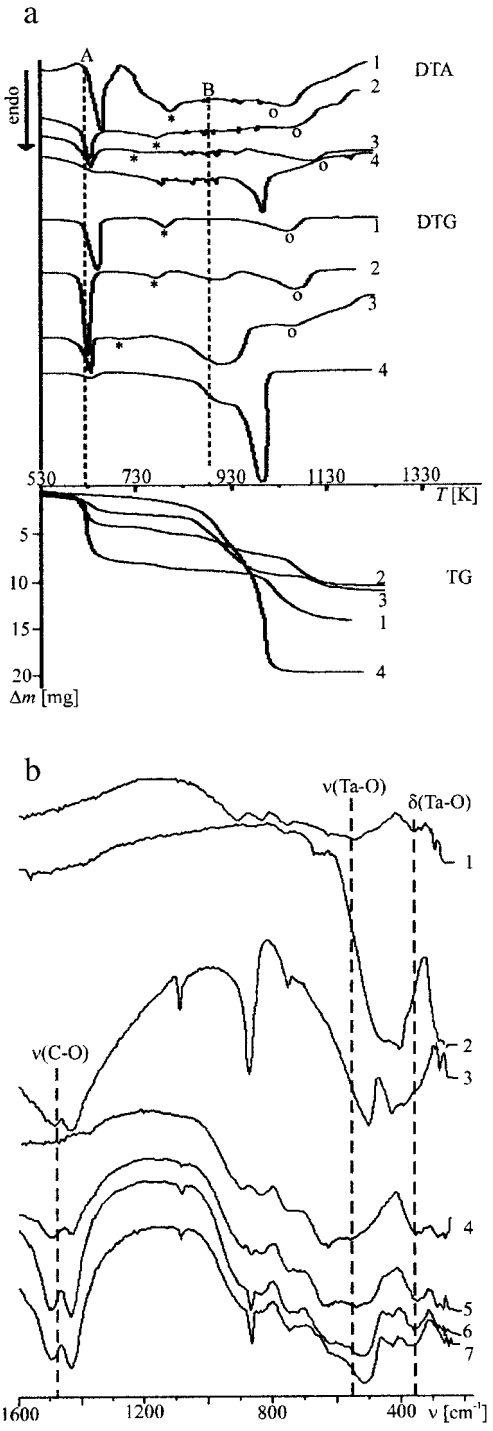


Figure 1. (a) Thermal analyses of the mixture of original reagents, with different lithium contents, for the synthesis by the (SSR) route of $(Li_{3x}La_{2/3-x}v_{4/3-2x})Ta_2O_6$: (1) $3x = 0$, (2) $3x = 0.50$, (3) $3x = 1.10$, (4) $3x = 1.85$. (b) IR spectra, recorded at room temperature, of the original reagents (1) $Ta_2O_5$, (2) $La_2O_3$, (3) $Li_2CO_3$ and of their homogenised mixtures, with different lithium contents, for the synthesis by the (SSR) route of $(Li_{3x}La_{2/3-x}v_{4/3-2x})Ta_2O_6$: (4) $3x = 0$, (5) $3x = 0.50$, (6) $3x = 1.10$, (7) $3x = 1.85$.

was found in the samples calcined at 1570 K. At 1770 K, the yield of the phase with the perovskite structure is 95% (Table 1). It is obvious that a higher temperature is required for the complete reaction of formation of $La_{2/3}Ta_2O_6$ by the

 © 2006 Wiley-VCH Verlag GmbH & Co. KGaA, Weinheim 

Table 1. Phase composition of the $(Li_{3x}La_{2/3-x}v_{4/3-2x})Ta_2O_6$ powder prepared by the (SSR) route as a function of lithium content, $3x$, and firing temperature, $T$ (the firing time is 1 h). The different phases are given in the order of their decreasing amount.

| $T$ [K] | $3x = 0$ | $3x = 0.50$ | $3x = 0.62$ | $3x = 0.74$ | $3x = 1.10$ |
|---|---|---|---|---|---|
| 370 | $Ta_2O_5$<br>$La(OH)_3$ | $Ta_2O_5$<br>$La(OH)_3$<br>$Li_2CO_3$ | $Ta_2O_5$<br>$La(OH)_3$<br>$Li_2CO_3$ | $Ta_2O_5$<br>$La(OH)_3$<br>$Li_2CO_3$ | $Ta_2O_5$<br>$La(OH)_3$<br>$Li_2CO_3$ |
| 770 | $Ta_2O_5$<br>$La(OH)_3$<br>$La_2O_2CO_3$ | $Ta_2O_5$<br>$La_2O_2CO_3$<br>$LiTaO_3$ | $Ta_2O_5$<br>$La_2O_2CO_3$<br>$LiTaO_3$ | $Ta_2O_5$<br>$La_2O_2CO_3$<br>$LiTaO_3$ | $Ta_2O_5$<br>$LiTaO_3$<br>$Li_2CO_3$<br>$La_2O_2CO_3$ |
| 970 | $Ta_2O_5$<br>$La_2O_3$ | $Ta_2O_5$<br>$LiTaO_3$<br>$La_2O_3$<br>$La_3TaO_7$ | $Ta_2O_5$<br>$LiTaO_3$<br>$La_2O_3$<br>$La_3TaO_7$ | $LiTaO_3$<br>$Ta_2O_5$<br>$La_2O_3$<br>$La_3TaO_7$ | $LiTaO_3$<br>$Ta_2O_5$<br>$La_2O_3$<br>$La_3TaO_7$ |
| 1220 | $Ta_2O_5$<br>$La_2O_3$ | $Ta_2O_5$<br>$LiTaO_3$<br>$La_2O_3$<br>$LiTa_3O_8$<br>perovskite<br>$LaTaO_4$ | $LiTaO_3$<br>$Ta_2O_5$<br>$LiTa_3O_8$<br>$La_2O_3$<br>perovskite<br>$LaTaO_4$ | $LiTaO_3$<br>$Ta_2O_5$<br>$LiTa_3O_8$<br>$La_2O_3$<br>perovskite<br>$LaTaO_4$ | – |
| 1320 | $Ta_2O_5$<br>$LaTa_7O_{19}$<br>perovskite<br>$LaTa_5O_{14}$<br>$LaTaO_4$ | $Ta_2O_5$<br>$LiTaO_3$<br>perovskite<br>$LiTa_3O_8$<br>$LaTaO_4$<br>$LaTa_5O_{14}$ | $LiTaO_3$<br>$Ta_2O_5$<br>perovskite<br>$LiTa_3O_8$<br>$LaTa_5O_{14}$<br>$LaTaO_4$ | $LiTaO_3$<br>$Ta_2O_5$<br>$LiTa_3O_8$<br>perovskite<br>$LaTa_5O_{14}$<br>$LaTaO_4$ | $LiTaO_3$<br>$Ta_2O_5$<br>$LiTa_3O_8$<br>perovskite<br>$LaTa_5O_{14}$<br>$LaTaO_4$ |
| 1420 | $Ta_2O_5$<br>perovskite<br>$LaTa_7O_{19}$<br>$LaTa_5O_{14}$<br>$LaTaO_4$ | $LiTa_3O_8$<br>$Ta_2O_5$<br>perovskite<br>$LiTaO_3$<br>$LaTaO_4$<br>$LaTa_5O_{14}$ | $LiTaO_3$<br>$LiTa_3O_8$<br>$Ta_2O_5$<br>perovskite<br>$LaTa_5O_{14}$<br>$LaTaO_4$ | | |
| 1570 | perovskite<br>$Ta_2O_5$<br>$LaTa_5O_{14}$<br>$LaTaO_4$ | perovskite<br>$LiTa_3O_8$<br>$LiTaO_3$<br>$LaTaO_4$<br>$Ta_2O_5$ | $LiTaO_3$<br>$LiTa_3O_8$<br>$Ta_2O_5$<br>perovskite<br>$LaTa_5O_{14}$<br>$LaTaO_4$ | $LiTaO_3$<br>$Ta_2O_5$<br>$LiTa_3O_8$<br>perovskite<br>$LaTaO_4$<br>$LaTa_5O_{14}$ | $LiTaO_3$<br>perovskite |
| 1770 | perovskite<br>$LaTa_5O_{14}$<br>(4.8%) | perovskite<br>$LaTa_5O_{14}$<br>(7.7%) | perovskite<br>$LaTa_5O_{14}$<br>(3.3%) | perovskite<br>$LiTaO_3$<br>(4%) | perovskite<br>$LiTaO_3$<br>(37%) |

SSR method. According to Portnoi et al. this temperature is 1870 K.[13] On the basis of the analysis of the phase composition and phase ratio as a function of firing temperature (Table 1) and taking into account the literature data,[14,15] the process of formation of lanthanum metatantalate, $La_{2/3}Ta_2O_6$ ($LaTa_3O_9$), with a defect perovskite structure of the tetragonal system, may be represented by Equations (1), (2), (3), (4) and (5).

$$La_2O_3 + Ta_2O_5 \xrightarrow{1320-1570\ K} 2\ LaTaO_4 \quad (1)$$

$$LaTaO_4 + Ta_2O_5 \xrightarrow{1320-1570\ K} LaTa_3O_9 \quad (2)$$

$$LaTa_3O_9 + Ta_2O_5 \xrightarrow{1320-1420\ K} LaTa_5O_{14} \quad (3)$$

For lithium-containing samples $(Li_{3x}La_{2/3-x}v_{4/3-2x})Ta_2O_6$, the primary phase that appears in the process of

$$LaTa_5O_{14} + Ta_2O_5 \underset{1470-1570\ K}{\overset{1320-1420\ K}{\rightleftharpoons}} LaTa_7O_{19} \quad (4)$$

$$LaTa_5O_{14} + LaTaO_4 \xrightarrow{1320-1770\ K} 2\ LaTa_3O_9 \quad (5)$$

heat treatment of a homogenised mixture of original reagents is lithium metatantalate ($LiTaO_3$) of the rhombohedral system, which appears in diffractograms of samples fired at 770 K [Equation (6)].

$$Li_2O + Ta_2O_5 \xrightarrow{770-1320\ K} 2\ LiTaO_3 \quad (6)$$

When the temperature is raised to 1170 K, the amount of $LiTaO_3$ increases and an orthorhombic lanthanum paratantalate ($La_3TaO_7$) phase appears [Equation (7)].

$$3\ La_2O_3 + Ta_2O_5 \xrightarrow{770-1170\ K} 2\ La_3TaO_7 \quad (7)$$

The $La_3TaO_7$ phase transforms into the lanthanum orthotantalate ($LaTaO_4$) for the temperature range 1170–1220 K. During the synthesis of $La_{2/3}Ta_2O_6$ ($3x = 0$), $LaTaO_4$ is formed at 1320 K (Table 1). Therefore, its appearance at a lower temperature (1220 K) in lithium-containing samples is probably due to the decomposition of $La_3TaO_7$ as expressed by Equation (8).[14]

$$La_3TaO_7 \xrightarrow{1170-1220\ K} La_2O_3 + LaTaO_4 \quad (8)$$

At 1220 K, $LiTaO_3$ from Equation (6) as well as $La_2O_3$ and $LaTaO_4$ from Equation (8) can react partially with the remaining $Ta_2O_5$ to form the monoclinic phase of lithium polytantalate $LiTa_3O_8$, $LaTaO_4$ and $LaTa_3O_9$, respectively, according to the following reactions, Equations (9), (10) and (11).

$$LiTaO_3 + Ta_2O_5 \underset{1450-1600\ K}{\overset{1220-1420\ K}{\rightleftharpoons}} LiTa_3O_8 \quad (9)$$

$$La_2O_3 + Ta_2O_5 \xrightarrow{1220-1320\ K} 2\ LaTaO_4 \quad (10)$$

$$LaTaO_4 + Ta_2O_5 \xrightarrow{1220-1570\ K} LaTa_3O_9 \quad (11)$$

At the same time, $LiTaO_3$ and $LaTa_3O_9$ react to form the lithium-containing metatantalates (P) with the perovskite structure.

When the temperature is raised to 1320 K, the $LaTa_5O_{14}$ phase begins to form in addition to the above-mentioned phases [Equation (12)].

$$LaTa_3O_9 + Ta_2O_5 \xrightarrow{1320-1770\ K} LaTa_5O_{14} \quad (12)$$

 © 2006 Wiley-VCH Verlag GmbH & Co. KGaA, Weinheim 

This phase can react with $LaTaO_4$ to form $LaTa_3O_9$ [Equation (13)].

$$LaTa_5O_{14} + LaTaO_4 \xrightarrow{1320–1770\ K} 2\ LaTa_3O_9 \quad (13)$$

It should be noted that in the diffractograms of all the samples fired at 1320 K and higher, the diffraction lines typical of the high-temperature modification (F1) of tantalum(v) oxide appear in addition to the lines resulting from the low-temperature modification (F) of $Ta_2O_5$[12] (Figure 2, a). The appearance of a defect-perovskite structure in lithium-containing samples is observed at 1220 K, which is 100 K lower than the initial formation temperature in the synthesis of $La_{2/3}Ta_2O_6$ ($3x = 0$). As generally observed in Ca tantalates[16] or La titanates,[17] the addition of lithium greatly decreases the required synthesis temperature of the perovskite compounds.

Figure 2 (a) shows diffractograms recorded at room temperature in the $2\theta$ range from 20° to 40° of $Li_{0.5}La_{0.5}Ta_2O_6$ ($3x = 0.5$) samples fired at and above 1320 K. As discussed previously, at 1320 K the formation of the perovskite phase (P) can be observed by the appearance of the diffraction line at $2\theta = 32.5°$. All the other phases are present: $Ta_2O_5$ (F and F1), $LiTaO_3$ (B), $LaTaO_4$ (C), the monoclinic form of $LiTa_3O_8$ (G1) and $LaTa_5O_{14}$ (D) in a small amount. As temperature increases, the amount of perovskite (P) increases. The formation of lithium-containing metatantalates (P) is accompanied by a consumption of the phases $Ta_2O_5$ (F1), $LiTaO_3$ (B), $LaTaO_4$ (C) and $LiTa_3O_8$ (G1 and G2). At 1770 K, a $Li_{0.5}La_{0.5}Ta_2O_6$ sample containing 92.3% of the perovskite phase is obtained with 7.7% of the $LaTa_5O_{14}$ phase. It is obvious that the temperature of 1770 K is not sufficient for the completion of the reaction, as in the case of the synthesis of lithium-free lanthanum metatantalate. A higher yield of 96–97% of the perovskite phase (P) can be achieved for higher lithium content ($0.5 < 3x < 1$). As $3x$ increases, the impurity phase observed at 1770 K changes from $LaTa_5O_{14}$ to $LiTaO_3$. This is clearly shown in Figure 2 (b), which shows fragments of diffractograms of $La_{0.3}Li_{1.1}Ta_2O_6$ ($3x = 1.1$) samples fired at 1320, 1570 and 1770 K. The presence of $LaTa_5O_{14}$ as the impurity can be explained by the existence of a partial reaction [Equation (13)] when $3x$ is small. At 1320 K, the formation of the perovskite phase (P) is observed with the presence of all the above-mentioned phases (F), (B) in a greater amount, (C), (G1) and (D). A two-phase sample (perovskite and $LiTaO_3$) is obtained at 1570 K. An increase in the amount of the perovskite phase (P) accompanied by a decrease in the amount of $LiTaO_3$ (B) in the two-phase sample, over the temperature range 1570–1770 K, demonstrates unambiguously that lithium metatantalate ($LiTaO_3$) is involved in the reaction.

The end reaction of lanthanum-lithium metatantalate formation may proceed according to Equation (14).

$$(2/3\text{-}x)\ LaTa_3O_9 + 3x\ LiTaO_3 \xrightarrow{1220–1770\ K} Li_{3x}La_{2/3\text{-}x}Ta_2O_6 \quad (14)$$

Thus, it has been found that the processes of formation of lanthanum metatantalate and lithium-containing lanthanum metatantalate proceed via the formation of the intermediate phases $LaTaO_4$, $LaTa_5O_{14}$, $LaTa_7O_{19}$ and $LiTaO_3$, $LiTa_3O_8$, $LaTaO_4$, $LaTa_3O_9$, $LaTa_5O_{14}$, respectively. This complex multistep mechanism of the formation of $(Li_{3x}La_{2/3-x}v_{4/3-2x})Ta_2O_6$ by the SSR method predetermines the micro heterogeneity of the obtained materials and calls for prolonged soaking at high temperature.

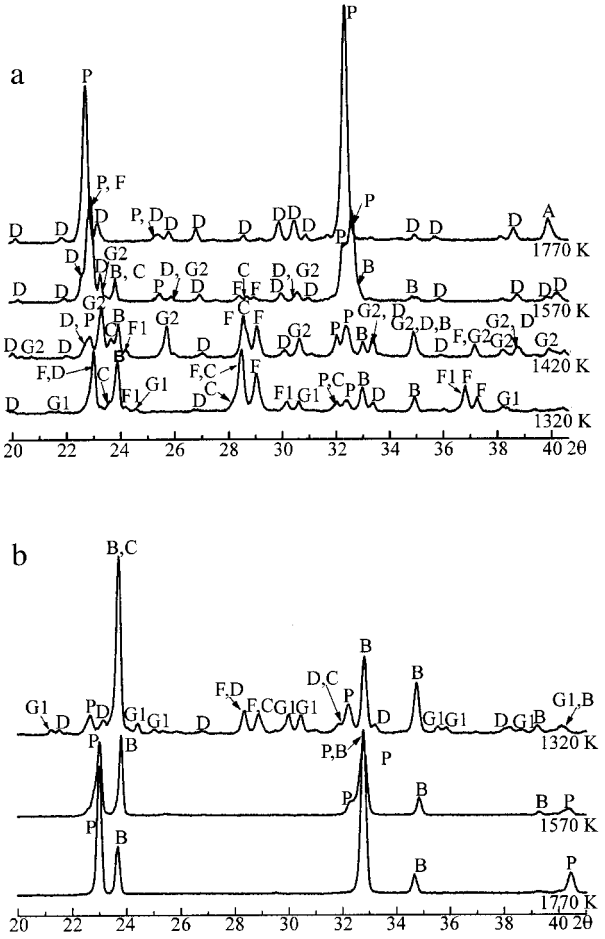


Figure 2. (a) Powder XRD spectra, recorded at room temperature, of $Li_{0.5}La_{0.5}Ta_2O_6$ prepared by the (SSR) technique and fired at different temperatures. P = perovskite, B = $LiTaO_3$, C = $LaTaO_4$, D = $LaTa_5O_{14}$, F = $Ta_2O_5$ (low temperature form), F1 = $Ta_2O_5$ (high temperature form), G1 = $LiTa_3O_8$ (monoclinic), G2 = $LiTa_3O_8$ (orthorhombic). (b) Powder XRD spectra, recorded at room temperature, of $Li_{0.3}La_{1.1}Ta_2O_6$ prepared by the (SSR) technique and fired at different temperatures. P = perovskite, B = $LiTaO_3$, C = $LaTaO_4$, D = $LaTa_5O_{14}$, F = $Ta_2O_5$ (low temperature form), G1 = $LiTa_3O_8$ (monoclinic).

### *Precipitation from Solution (PS) Method*

The results of the thermal investigation (DTA) of lanthanum and tantalum hydroxides and the product of their co-precipitation after addition of a stoichiometric amount of lithium hydroxide $(LLTaO)_{PS}$ are presented in Figure 3 (a). An examination of the heating curves for $(LLTaO)_{PS}$ (curve 3) showed the absence of thermoeffects inherent for individual hydroxides. Therefore it was suggested from thermal analysis that when the (PS) method is used the starting

 © 2006 Wiley-VCH Verlag GmbH & Co. KGaA, Weinheim 

powder of precursors $(LLTaO)_{PS}$ is not a mechanical mixture of hydroxides. The dehydration and decarbonation processes, which are accompanied by endothermic peaks observed in the thermogram of $(LLTaO)_{PS}$, occur until the crystallisation of the mixture and separation of a lithium metatantalate phase takes place (exothermic peak at 920 K) (see part a in Figure 3 and Table 2). In this case, the most intensive decrease in weight, resulting from the loss of $CO_2$ and $H_2O$, is accompanied by a broad endothermic peak with a maximum at 390 K. It should be noted that the $(LLTaO)_{PS}$ dehydration and decarbonation temperatures are lower than those for hydroxides [410 K and 450 K for $La(OH)_3{\cdot}nH_2O$ and $Ta_2O_5{\cdot}nH_2O$, respectively, Figure 3 (a)], which is apparently accounted for by the peculiar nature of the product obtained.

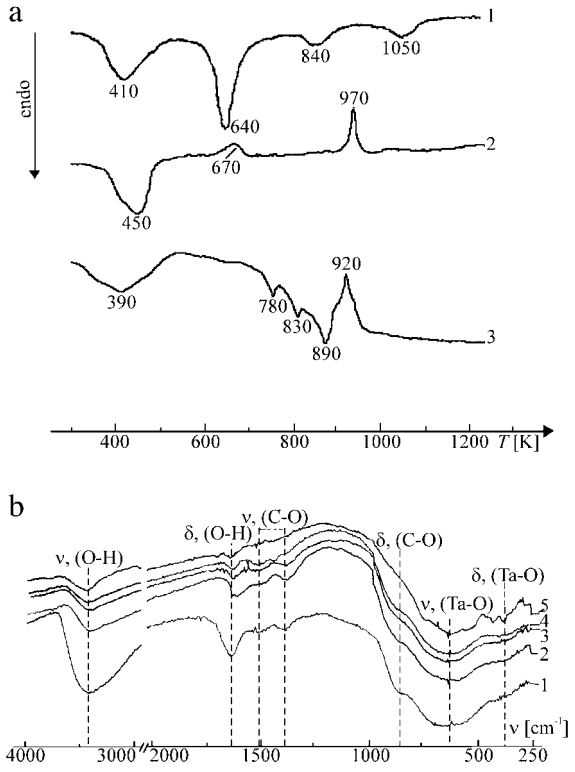


Figure 3. (a) Thermal analyses (DTA) of samples of (1) $La(OH)_3{\cdot}nH_2O$, (2) $Ta_2O_5{\cdot}nH_2O$ and (3) $Li_{0.5}La_{0.5}Ta_2O_6$, prepared by the (PS) route [$(LLTaO)_{PS}$]. (b) IR spectra, recorded at room temperature, of $Li_{0.5}La_{0.5}Ta_2O_6$ prepared by the (PS) route [$(LLTaO)_{PS}$] and fired at different temperatures: (1) 370 K, (2) 470 K, (3) 570 K, (4) 670 K and (5) 1020 K for 1 h.

The results of the IR spectroscopy of $(LLTaO)_{PS}$ over a wide-temperature range indicate the absence of the absorption bands that are characteristic of lanthanum and tantalum hydroxides,[18,19] which confirms the formation of new compounds during precipitation (Figure 3, b). The presence of a broad and intense absorption band with a maximum at 630 $cm^{-1}$, which corresponds to the Ta–O stretching vibration $\nu$ and shifts to 660 $cm^{-1}$ with increasing firing temperature, is typical of the octahedral coordination of Ta atoms and indicates the presence of O–Ta–O bridge bonds of the polymeric type.[20] The band of the Ta–O deformation vibration $\delta$ at 350–380 $cm^{-1}$ is poorly defined at low temperatures (part b of Figure 3, curves 1–4) but is well defined at 1020 K (part b of Figure 3, curve 5), which is the onset temperature for the formation of the defect perovskite structure (Table 2). The IR spectra of $(LLTaO)_{PS}$ are characterised by the presence of intense absorption bands at 3400–3440 $cm^{-1}$ and 1600–1640 $cm^{-1}$, which correspond to stretching and deformation vibrations of $H_2O$ molecules, respectively. Their frequencies depend weakly on the degree of hydration of samples, indicating that the bond energy of $H_2O$ molecules in $(LLTaO)_{PS}$ does not vary (Figure 3, b). The high adsorption power of this system with respect to $CO_2$ is corroborated by the existence of stretching vibrations ($\nu$) of the CO bond, at 1380–1520 $cm^{-1}$, and a shoulder at 850 $cm^{-1}$, which relates to deformation vibrations ($\delta$) of CO groups and undergoes a considerable high-frequency shift (to 930 $cm^{-1}$) in the crystalline sample containing the perovskite phase (part b of Figure 3, curve 5).

Table 2. Phase composition of the $Li_{0.5}La_{0.5}Ta_2O_6$ powder prepared by the (PS) route $(LLTaO)_{PS}$ as a function of firing temperature, $T$ (the firing time is 1 h). The different phases are given in the order of their decreasing amount.

| $T$ [K] | Phase composition |
|---|---|
| 770 | X-ray amorphous state |
| 920 | $LiTaO_3$ |
| | X-ray amorphous phase |
| 1020 | $LiTaO_3$ |
| | perovskite |
| | $LiTa_3O_8$ |
| | X-ray amorphous phase |
| 1070 | $LiTaO_3$ |
| | perovskite |
| | $LiTa_3O_8$ |
| 1120 | perovskite |
| | $LiTaO_3$ |
| | $LiTa_3O_8$ |
| 1170 | perovskite |
| | $LiTaO_3$ |
| | $LiTa_3O_8$ |
| 1270 | perovskite |
| | $LiTaO_3$ |
| 1320 | perovskite |
| | $LiTaO_3$ |
| 1370 | perovskite |
| | $LiTaO_3$ |
| 1570 | perovskite |
| | $LiTaO_3$ |
| 1670 | perovskite |

Thus on the basis of the results of the thermal analysis and IR spectroscopy it was concluded that when the PS method is used, the starting powder of precursors $(LLTaO)_{PS}$ obtained for the synthesis of lithium-containing lanthanum tantalate differs from the mechanical mixture of individual hydroxides and is an aquacomplex-type "inorganic polymer".[18]

The analysis of the XRD patterns of the $(LLTaO)_{PS}$ powders, fired at different temperatures (Figure 4 and Table 2), showed that the crystallization of the mixture, involving the formation of a lithium metatantalate phase, takes place at

 © 2006 Wiley-VCH Verlag GmbH & Co. KGaA, Weinheim 

920 K (Table 2). Several differences can be noted between the two synthetic methods. When the (PS) method is used, (i) the onset temperature of the defect-perovskite phase formation, from $(LLTaO)_{PS}$ powder, is 1020 K, which is 200 K lower than in the case for the synthesis by the SSR method (Table 1), (ii) the perovskite phase becomes predominant at 1120 K, instead of 1570 K for the (SSR) synthesis, (iii) the final firing temperature of the $Li_{0.5}La_{0.5}Ta_2O_6$ powder (1670 K) is decreased by 100 K (Table 1 and Table 2), (iv) the product obtained has a single phase, whereas the sample obtained by the SSR method contains a $LaTa_5O_{14}$ phase in addition to the perovskite (Table 1, Table 2; part a of Figure 2 and Figure 4). The observed considerable increase in the rate of chemical processes, when using the (PS) synthesis method, is because of the larger surface energy of the $(LLTaO)_{PS}$ powder and hence to a greater reactivity of the precursors.

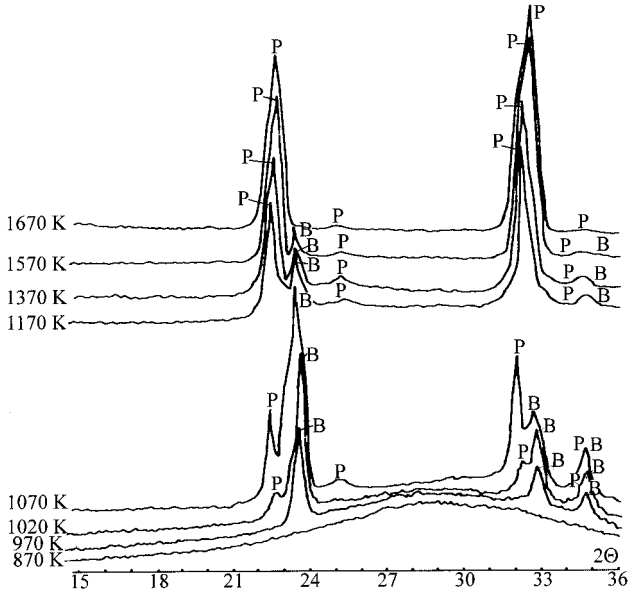


Figure 4. Powder XRD spectra, recorded at room temperature, of $Li_{0.5}La_{0.5}Ta_2O_6$ prepared by the (PS) route ($(LLTaO)_{PS}$) and fired at different temperatures. P = perovskite, B = $LiTaO_3$.

The Fullprof Rietveld analysis of the patterns collected from (SSR)[21] as well as from (PS) sintering samples indicated the formation of the defect-perovskite structure with tetragonal symmetry and the lattice parameters: $a = b = 3.903$ Å, $c = 7.831$ Å, $V = 119.29$ Å$^3$ and $a = b = 3.896$ Å, $c = 7.826$ Å, $V = 118.79$ Å$^3$, respectively.

## Microstructure

Figure 5 (a) shows TEM micrographs of the $(LLTaO)_{PS}$ powders fired at different temperatures for 1 h. In the temperature range corresponding to the amorphous region ($T < 900$ K) particles of about 5 nm in size form aggregates, as shown in Figure 5 (a). In the crystallization region ($970\ K < T < 1570$ K) the particle size increases from 15 nm to 140 nm (Figure 5, a). Part b of Figure 5 shows that the size increases linearly with firing temperature. The dilatometric curve shown in Figure 5 (c) reveals that the sintering process occurs at the same time when the grain growth takes place. Sintering begins at 1300 K leading to the shinkage of the pellet and to its compactness. The highest compactness (89%) has been achieved after a sintering at 1570 K for 2 h. Figure 6 shows a TEM image of a ceramic sintered at 1570 K for 2 h and the corresponding electron diffraction pattern. It confirms the good crystallinity of the sample and the absence of an amorphous phase. The powder is made up of grains of 150–200 nm in size with domains due to the cell-parameter values ($a_p$, $a_p$, $2a_p$).

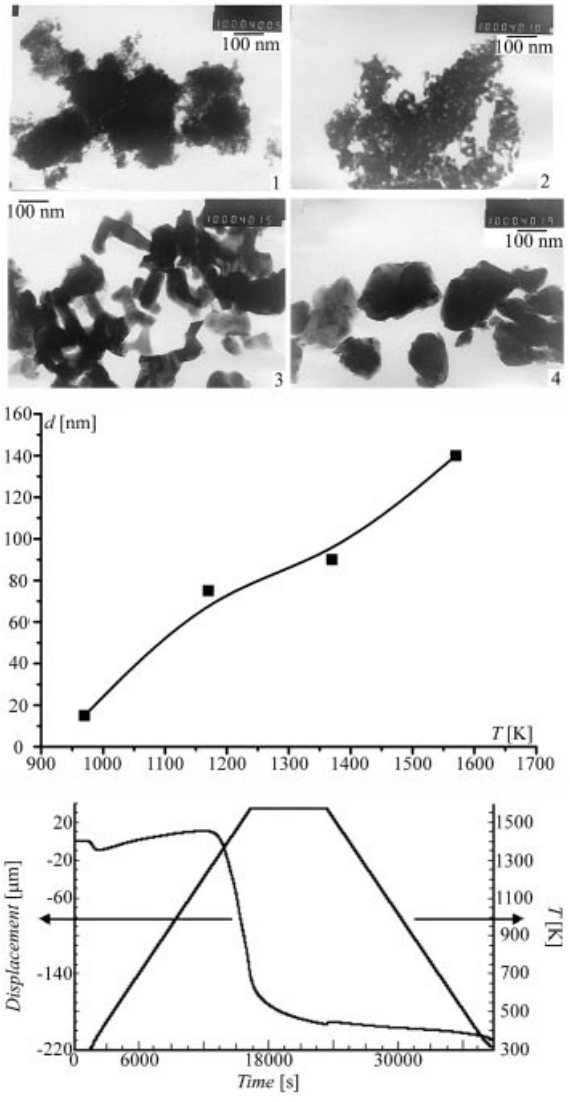


Figure 5. (a) TEM micrographs of the $Li_{0.5}La_{0.5}Ta_2O_6$ powder prepared by the (PS) route [$(LLTaO)_{PS}$)] and fired at different temperatures: (1) 370 K, (2) 970 K, (3) 1170 K, (4) 1570 K for 1 h. (b) Particle average size of the $Li_{0.5}La_{0.5}Ta_2O_6$ powder prepared by the (PS) route [$(LLTaO)_{PS}$] as a function of firing temperatures. (c) Dilatometric curve of a pellet of the $Li_{0.5}La_{0.5}Ta_2O_6$ powder prepared by the (PS) route [$(LLTaO)_{PS}$].

The peculiarities of the precipitation method employed in the synthesis of ceramic materials are known to enable preparation of a mixture of starting reagents at a "molecular level", which facilitates the formation of fine-grained ce-

 © 2006 Wiley-VCH Verlag GmbH & Co. KGaA, Weinheim 

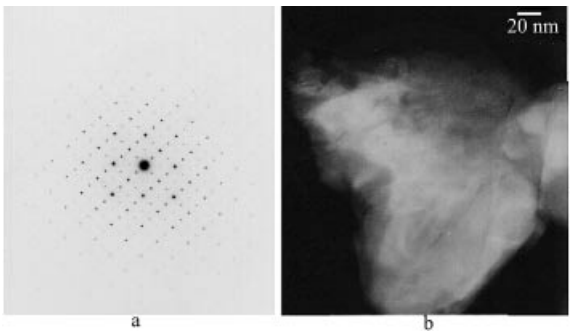


Figure 6. Electron diffraction pattern (a) and the corresponding TEM picture (b) of the $Li_{0.5}La_{0.5}Ta_2O_6$ powder prepared by the (PS) route [$(LLTaO)_{PS}$] fired at 1570 K for 2 h and ground.

ramics. A comparison can be made in Figure 7 that shows the microstructure of $Li_{0.5}La_{0.5}Ta_2O_6$ ceramics obtained by both synthetic methods. Figure 7 (a) shows the microstructure of a ceramic pellet obtained from powders prepared by the (PS) route and sintered at 1570 K for 2 h. It is characterised by a particle size of the order of 200 nm. Figure 7 (b) shows the microstructure of a ceramic pellet obtained by the (SSR) route and sintered at 1770 K for 1 h. A bigger grain size of about 6 μm is observed. Without doubt this result confirms the advantage of the precipitation method to prepare fine-grained ceramics.

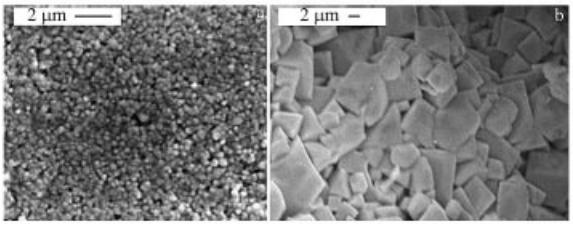


Figure 7. SEM micrographs of a sintered pellet of $Li_{0.5}La_{0.5}Ta_2O_6$ prepared (a) by the (PS) route and fired at 1570 K for 2 h and (b) by the (SSR) route and fired at 1770 K for 1 h.

## Electrical Properties of the Sintered Tantalates

For many electrochemical applications the resistance of the grain boundaries as well as the compactness of the sample are important parameters. The resistance of the grain boundaries generally limits the performance of an electrochemical device. To minimise the resistance of the grain boundaries and to increase the compactness of the pellet, sintering has been performed at 1570 K for 2 h for the pellet prepared by the (PS) method and at 1770 K for 1 h for the pellet prepared by the (SSR) route. It is obvious that such different sintering conditions will lead to different grain boundary properties. The electrical properties of these sintered ceramics have been studied by the impedance spectroscopy technique. Figure 8 shows typical impedance spectra obtained at 300 K under dry $N_2$, for both pellets. In order for comparisons to be made, the real and imaginary parts of the impedance have been normalised according to the geometric factor of the sample (l/s, l = thickness and s = geometric area). The high frequency part of the diagrams ($f > 10$ or 1 kHz) is attributed without doubt to the ionic relaxation in the bulk and the grain boundaries of the oxide. The low frequency part, which appears as a straight line, is attributed to the electrode polarisation. From Figure 8 it can be clearly observed that the total ionic impedance of the PS sample is higher than that for the SSR sample. This overall behaviour is observed for all the temperatures investigated. Figure 9 presents the total ionic conductivity (bulk and grain boundaries) as a function of temperature of sintered samples obtained from either the (SSR) or (PS) route. We attribute the deterioration of the transport properties of the fine-grained sample, prepared by the (PS) method, to an increase of the grain boundary impedance contribution, as previously observed with the 200 nm grain size $Li_{0.30}Ca_{0.35}TaO_3$ synthesised by a polymerised complex route.[20]

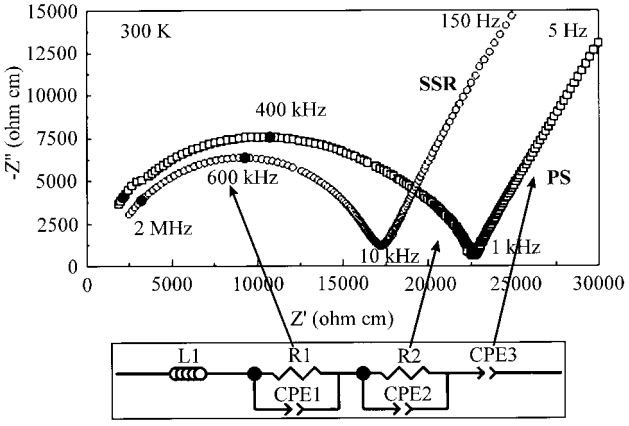


Figure 8. Normalised impedance spectra, recorded at 300 K, of $Li_{0.5}La_{0.5}Ta_2O_6$ prepared by the (PS) route and fired at 1570 K for 2 h and by the (SSR) route and fired at 1770 K for 1 h with the equivalent electrical circuit used for spectra refinement. The normalising factor is the pellet geometric factor (s/l).

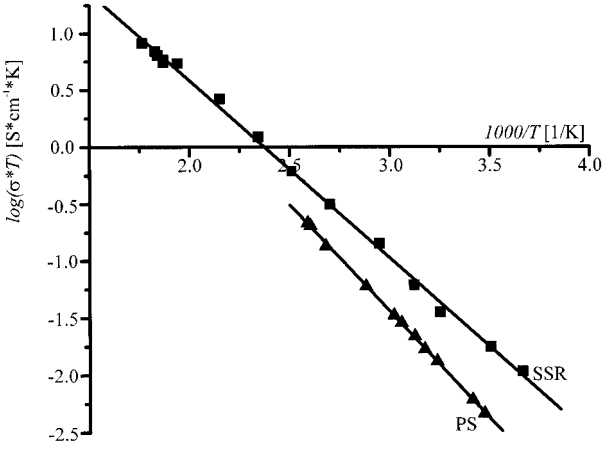


Figure 9. Arrhenius plots of the total ionic conductivity of sintered pellets of $Li_{0.5}La_{0.5}Ta_2O_6$ prepared by the (PS) route and fired at 1570 K for 2 h and by the (SSR) route and fired at 1770 K for 1 h.

In order to evaluate the importance of the grain boundary impedance of the sintered sample obtained by the (PS)

 © 2006 Wiley-VCH Verlag GmbH & Co. KGaA, Weinheim 

method, we performed the analysis of the impedance diagrams by means of an electrical model. Several possible electrical models were used, which were made up of series and parallel circuits. The model shown in Figure 8, below the impedance diagram, is the one which enabled us to fit all the impedance diagrams in the 175 K to 600 K temperature range. The analysis shows that two relaxations are necessary to fit the "semicircle" of the (PS) sample above room temperature, instead of only one for the (SSR) route. The high frequency relaxation is attributed to the ionic motion of $Li^+$ inside the grains and the low frequency relaxation to the ionic motion from grain to grain. The bulk conductivity of the sample is easily determined by using the high-frequency resistance $R_{Hf}$. Figure 10 shows the bulk conductivity, plotted in an Arrhenius fashion for both the (PS) and (SSR) sintered pellets. As found for the titanates,[22] the bulk conductivity is the same for both tantalates confirming that neither the synthesis method nor the grain size influence the nature and consequently the electrical properties of the oxide. On the other hand, the grain boundary resistance varies with the synthetic route. It is negligible when the sample is prepared by the (SSR) route and sintered at 1770 K for 1 h, whereas it becomes important when the sample is prepared by the (PS) route, sintered at 1570 K for 2 h and made up of particles of the order of 200 nm in size. It has to be noted that below room temperature thee relaxations are needed to fit the impedance data of the (PS) sample showing the presence of another electrical barrier that can be attributed to a boundary between the aggregates. The presence of this complex microstructure leads to an increase in the blocking effect and therefore to an increase in the total impedance of the (PS) pellet. This phenomenon has already been observed in $Li_{0.30}Ca_{0.35}TaO_3$[20] and in $Li_{3x}La_{2/3-x}TiO_3$[23] perovskites obtained by the sol-gel route, where both display a microstructure made up of grains and aggregates.

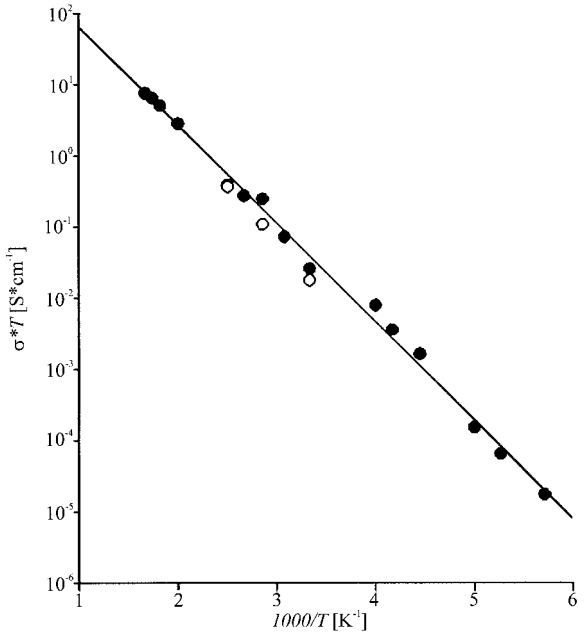


Figure 10. Arrhenius plots of the bulk conductivity of the (PS) ceramic sintered at 1570 K for 2 h (black dots) and of the (SSR) ceramic sintered at 1770 K for 1 h (white dots).

## Conclusion

The peculiarities of the preparation of lithium-containing lanthanum tantalates with a defect-perovskite structure using different synthetic methods have been studied. For the solid-state reaction (SSR) method it has been found that the formation of lanthanum metatantalate and lithium-containing lanthanum metatantalates proceeds via the formation of the intermediate phases $LaTaO_4$, $LaTa_5O_{14}$, $LaTa_7O_{19}$ and $LiTaO_3$, $LiTa_3O_8$, $LaTaO_4$, $LaTa_3O_9$, $LaTa_5O_{14}$, respectively. When using the precipitation from solution (PS) route, it has been shown that the precipitate formed is an aquacomplex of the polymeric type. The specific features of the (PS) method enabled the perovskite-phase formation temperature (1020 K) and the sintering temperature (1570 K) to be reduced by 200 K, as compared with the solid-state reaction method (1220 K and 1770 K, respectively). Furthermore, this chemical route facilitates the formation of fine-grained ceramics, even after sintering ($d \approx 200$ nm). The analysis of the impedance data reveals that the $Li^+$ motion inside the grains is not affected by the synthetic route. However, the complex microstructure of the ceramic obtained by the (PS) route, made up of fine grains and aggregates, leads to an increase of the grain- and aggregate-boundary blocking effect and to a slight decrease of the overall ionic conductivity.

## Experimental Section

Extra pure oxides and carbonates, $La_2O_3$, $Ta_2O_5$ and $Li_2CO_3$, were used as original reagents in the synthesis of $(Li_{3x}La_{2/3-x}v_{4/3-2x})$-$Ta_2O_6$ ($3x$ = 0, 0.50, 0.62, 0.74, 1.10, 1.85) by the SSR method. The synthesis and pellet sintering procedures have been described previously in detail.[7,8]

To synthesize $(Li_{3x}La_{2/3-x}v_{4/3-2x})Ta_2O_6$ ($3x$ = 0.5) by the PS method, alcoholic solutions of extra pure $La(NO_3)_3$ and $TaCl_5$ and aqueous solutions of LiOH and $NH_4OH$ were used. The $NH_4OH$ solution was added, at pH 9, to the mixture of $La(NO_3)_3$ and $TaCl_5$ solutions, taken in a stoichiometric ratio. The obtained precipitate was washed with a 2-propanol/distilled water mixture. The LiOH solution was then added to the precipitate, whilst stirring, and the solvents were evaporated. The obtained powder, hereafter named $(LLTaO)_{PS}$, was subjected to thermal treatment over a temperature range 770–1670 K for 1 h.

Differential thermal analysis (DTA), differential thermal gravimetry (DTG) and thermal gravimetry (TG) were performed with a Q-1000 OD-102 device at a heating rate of 10 K·min$^{-1}$, under dynamic conditions in air, using a Pt crucible. The infrared (IR) spectra were recorded with a Specord-M80 spectrometer over the 200–4000 cm$^{-1}$ frequency range. Samples used for the investigation were prepared as pellets with KBr. Powder X-ray diffraction (XRD) experiments were carried out with a DRON-4-07 diffractometer at room temperature using Cu-$K_\alpha$ radiation (40 kV, 18 mA). The data were recorded using a step-scanning mode in the $2\theta$ range from 10° to

 © 2006 Wiley-VCH Verlag GmbH & Co. KGaA, Weinheim 

150°, with a step size of 0.02° and an exposure time of 10 s for each point. $SiO_2$ ($2\theta$ standard) and NIST SRM1976-$Al_2O_3$ (certified intensity standard) were used as external standards.[24] The crystal parameters were refined using the Fullprof Rietveld analysis.

Microstructure studies were performed by scanning electron microscopy (SEM) using a JEM 10CX II (JEOL) electron microcope. Transmission Electron Microscopy (TEM) was also performed. Thin specimens for the TEM study were obtained by ultrasonically dispersing particles in ethanol and depositing one drop of the resulting suspension onto a Cu grid covered with a holey carbon film. After drying, the grid was fixed in a side-entry ±30° double-tilt specimen holder and introduced into a JEOL-2010 electron microscope operating at 200 kV.

A dilatometric experiment was performed with a vertical dilatometer (Setsys Evolution 1750 TMA equipment from Setaram). The dilatometer follows the continuous axial shinkage of the studied pellet as a function of temperature. Experiments were carried out in air with a 5 K·min$^{-1}$ sweep rate, from ambient temperature to 1570 K. This constant temperature was maintained for 2 h and then cooling to room temperature was performed at the same sweep rate as above. The probe used was that of an aluminium hemisphere. The density of the sintered pellets was estimated from the mass and the geometric dimensions of the sample. The compactness after sintering was then evaluated from the density, the molar mass and the cell parameters of the compound.

The electrophysical properties of the ceramic samples after sintering were investigated by complex impedance spectroscopy in the frequency range 1–10 MHz using a 1260 Frequency Response Analyzer and a 1296 Dielectric Interface from Solartron. The measurements were performed over the temperature range 135–600 K under vacuum at low temperature in a cryogenerator and under dry $N_2$ above room temperature in an oven (Dataline). We checked that the electrochemical system remains linear up to 1 V (rms), and therefore the applied ac voltage was 400 mV (rms).

The pellets were obtained from powders resulting from either the solid-state reaction or precipitation from the solution. The powders obtained from the (SSR) technique were pressed into pellets and then sintered for 1 h at 1700–1770 K in air. The powder obtained from the (PS) route [$(LLTaO)_{PS}$] was first mixed with an organic binder (Rhodoviol®) to prevent the breaking of the pellet owing to the presence of very fine grains. Pellets were then prepared by first pressing the powder uniaxially at ≈250 MPa and later pressing it isostatically at ≈500 MPa. The pellet was then heated at 670 K for 12 h in air to decompose the organic binder and then sintered for 2 h at 1570 K (with a sweeping rate of 5 K min$^{-1}$). Sputtered Pt films were deposited onto the pellets and used as ion-blocking electrodes in the measurement of the ionic conductivity. The same electrical model as described in ref.[22] was used to determine the bulk conductivity and the grain boundary conductance.

## Acknowledgments

We thank M.-P. Crosnier-Lopez for the help with the TEM micrograph and electron diffraction pattern of Figure 6.

[1] A. Belous, G. Novitskaya, S. Polianetskaya, Y. Gornikov, *Izv. Akad. Nauk SSSR. Neorg Mater.* **1987**, *23*, 470–472.
[2] Y. ınaguma, C. Liquan, M. Itoh, T. Nakamura, T. Uchida, H. Ikuta, M. Wakihara, *Solid State Commun.* **1993**, *86*, 689–695.
[3] O. Bohnké, J. Emery, J. L. Fouquet, J. Badot, *Recent Research Developments in Solid State Ionics* (Ed.: S. G. Pandalai), Transworld Research Network Publishers, ISBN 81–7895-069-3, **2003**, *1*, 47.
[4] A. Belous, I. Didukh, E. Novosadova, Y. Pashkova, *Phys. Solid State* **1986**, *28*, 3230–3232 (in Russian).
[5] K. Mirumoto, S. Hayashi, *J. Ceram. Soc. Jpn.* **1998**, *106*, 369–371.
[6] K. Mirumoto, S. Hayashi, *Solid State Ionics* **1999**, *116*, 263–269.
[7] O. Gavrilenko, A. Belous, Y. Pashkova, V. Mirnyi, *Neorg. Mater.* **2002**, *38*, 1126–1130.
[8] A. Belous, Y. Pashkova, O. Gavrilenko, O. V'yunov, L. Kovalenko, *Intern. Journal of Ionics* **2003**, *9*, 21–27.
[9] I. Vasserman, *Chem. (Leningrad)* **1980**, 207 (in Russian).
[10] L. Komissarova, V. Shatskii, G. Pushkina, *Nauka (Moscow)* **1984**, 234 (in Russian).
[11] K. Nakamoto, *Mir (Moscow)* **1991**, 320 (in Russian).
[12] Powder Diffraction File **1997**: PDF-2, *Database Sets*, 47.
[13] K. Portnoi, N. Timofeeva, S. Salibekov, *Neorg. Mater.* **1970**, *6*, 289–293.
[14] P. Arsenyev, V. Glushkova, A. Yevdokimov, *Nauka (Moscow)* **1985**, 261 (in Russian).
[15] Y. Isupova, R. Pomes, Y. Savchenko, E. Keler, *Neorg. Mater.* **1975**, *11*, 384–386.
[16] Q. Pham, C. Bohnké, J. Emery, O. Bohnké, F. Le Berre, M. Crosnier-Lopez, J. Fourquet, P. Florian, *Solid State Ionics* **2005**, *176*, 495.
[17] J. Fourquet, H. Duroy, M. Crosnier-Lopez, *J. Solid State Chem.* **1996**, *127*, 283–294.
[18] A. Sych, T. Novik, L. Yeryomenko, V. Kushkov, *Ukr. Khim. Zhurn.* **1978**, *44*, 794–798.
[19] T. Panova, E. Keler, *Zhurn. Neorg. Khim.* **1975**, *XXI*, 815–820.
[20] Q. Pham, M. Vijayakumar, C. Bohnké, O. Bohnké, *J. Solid State Chem.* **2005**, *178*, 1915–1924.
[21] A. Belous, E. Pashkova, O. Gavrilenko, O. V'yunov, L. Kovalenko, *Ionics* **2003**, *9*, 21–27.
[22] A. Belous, O. Yanchevskiy, O. V′yunov, O. Bohnke, C. Bohnke, F. Le Berre, J. Fourquet, *Chem. Mater.* **2004**, *16*, 407–417.
[23] M. Vijayakumar, O. Bohnké, *J. Eur. Ceram. Soc.*, in press.
[24] Certificate of Analysis, Standard Reference Material **1976**, Instrument Sensitivity Standard for X-ray Powder Diffraction, National Institute of Standards & Technology, Gaithersburg, **1991**, 4.

Received: July 26, 2005
Published Online: March 1, 2006

 © 2006 Wiley-VCH Verlag GmbH & Co. KGaA, Weinheim 

DOI: 10.1002/ejic.200501020

# $Fe_3GeTe_2$ and $Ni_3GeTe_2$ – Two New Layered Transition-Metal Compounds: Crystal Structures, HRTEM Investigations, and Magnetic and Electrical Properties

**Hans-Jörg Deiseroth,*[a] Krasimir Aleksandrov,[a] Christof Reiner,[a] Lorenz Kienle,[b] and Reinhard K. Kremer[b]**

*Dedicated to Prof. Dr. Hanskarl Müller-Buschbaum on the occasion of his 75th birthday*

**Keywords:** Layered compounds / Crystal structures / Iron germanium telluride / Magnetism / Electron microscopy / Conductivity

$Fe_3GeTe_2$ and $Ni_3GeTe_2$ are two new air-stable, black-metallic solids. They were characterized by single-crystal X-ray crystallography, high resolution transmission electron microscopy (HRTEM), and preliminary magnetic measurements. Both compounds crystallize in the hexagonal system [$P6_3/mmc$, $Z = 2$; $Fe_3GeTe_2$: $a = 399.1(1)$ pm, $c = 1633(3)$ pm; $Ni_3GeTe_2$: $a = 391.1(1)$ pm, $c = 1602.0(3)$ pm], and represent a new structure type with a pronounced macroscopic and microscopic layer character. They show close structural relationships to iron/nickel germanium alloys. Each layer in the title compounds represents a sandwich structure with two layers of tellurium atoms covering a triple-layer $Fe_3Ge$ ($Ni_3Ge$) substructure on both sides. Assuming full occupancies for the Fe and Ni sites, a mixed-valence formulation for the transition-metal atoms according to $(M^{2+})(M^{3+})_2(Ge^{4-})(Te^{2-})_2$ (M = Fe, Ni) may be concluded. A slightly reduced occupancy for one Fe/Ni position, however, indicates a more complicated local structural situation. This is confirmed by weak residual electron density in the van der Waals gap and by the results of detailed HRTEM and electron-diffraction experiments for $Ni_3GeTe_2$. The latter results show variations in the arrangement of Ni atoms, as well as vacancies and a misfit of in-plane disordered hexagonal layers. $Fe_3GeTe_2$ shows Curie–Weiss behavior above and ferromagnetism below 230 K, while $Ni_3GeTe_2$ exhibits temperature-independent paramagnetism in the measured temperature range and a metallic behavior of the electrical resistance.

(© Wiley-VCH Verlag GmbH & Co. KGaA, 69451 Weinheim, Germany, 2006)

## Introduction

The title compounds represent two unexpected new solids. They were obtained from a series of experiments aimed at the syntheses of new mixed-valence compounds with *transition metals* related to those compounds with *main group elements* investigated in our group.[1,2]

$Fe_3GeTe_2$ is possibly identical to a solid obtained earlier[3] that could not, however, be structurally characterized. $Ni_3GeTe_2$ has not been reported previously. The crystal structures of both compounds exhibit a pronounced layer character with layered $Fe_3Ge$ ($Ni_3Ge$) substructures sandwiched by two layers of Te atoms and a van der Waals gap between adjacent Te layers. The $Fe_3Ge$ and $Ni_3Ge$ substructures are closely related to layered sections of the structures of alloys with the compositions $Fe_{1.67}Ge$[4] and $Ni_{1.67}Ge$.[5] From a general topological viewpoint, a close relationship with respect to the sandwich character is also obvious to a group of layered metal-rich Nb, Ta, and Hf chalcogenides and to $Pd_5AlI_2$ characterized earlier by different authors.[6–9] The latter solid is the earliest example to fit into this group of unconventional layer structures. In all these solids, at least three layers of metal atoms (or mixed-metal and semimetal atoms) are sandwiched between two layers of chalcogen (or halogen) atoms.

For both compounds there seems to be a simple mixed-valence formulation like $M_3GeTe_2 = (M^{2+})(M^{3+})_2(Ge^{4-})(Te^{2-})_2$, which is strongly supported by the crystallographic multiplicity of the respective atomic sites. However, disorder phenomena and structural inhomogeneity, in combination with the general properties of the new solids, make a simple formulation as type 1 mixed-valence solids[10] with clearly distinguishable oxidation states most unlikely, and complicate a concise description of these new compounds.

[a] Anorganische Chemie, Universität Siegen,
Adolf-Reichwein-Straße, 57068 Siegen, Germany
Fax: +49-271-7402555
E-mail: deiseroth@chemie.uni-siegen.de
[b] Max-Planck-Institut für Festkörperforschung,
Heisenbergstraße 1, 70569 Stuttgart, Germany
Fax: +49-711-689-1091
E-mail: L.Kienle@fkf.mpg.de

 © 2006 Wiley-VCH Verlag GmbH & Co. KGaA, Weinheim 

Table 1. Summary of the data collection and refinement details for $Fe_3GeTe_2$ and $Ni_3GeTe_2$.

| Name | Triiron germanide ditelluride | Trinickel germanide ditelluride |
|---|---|---|
| Chemical formula | $Fe_3GeTe_2$ | $Ni_3GeTe_2$ |
| Molecular mass [g/mol] | 495.34 | 503.9 |
| Temperature [K] | 293(2) | 293(2) |
| Wavelength [pm] | Mo-$K_\alpha$, $\lambda$ = 71.073 | Mo-$K_\alpha$, $\lambda$ = 71.073 |
| Crystal system, space group | hexagonal, $P6_3/mmc$ (No. 194) | hexagonal, $P6_3/mmc$ (No. 194) |
| Cell dimensions [pm] | $a$ = 399.1(1), $c$ = 1633(3) | $a$ = 391.1(1), $c$ = 1602.0(3) |
| Volume [$10^6$ pm$^3$] | 225.34(9) | 212.10(9) |
| $Z$, X-ray crystal density [g/cm$^3$] | 2, 7.3 | 2, 7.89 |
| Absorption coefficient [mm$^{-1}$] | 28.552 | 33.389 |
| $F$(000) | 428 | 440 |
| Diffractometer | IPDS (Stoe) | IPDS (Stoe) |
| Scan type | $\varphi$ | $\varphi$ |
| Crystal size [mm] | 0.15×0.15×0.01 | 0.08×0.08×0.03 |
| Measured range ($\theta$) [°] | 2.49–25.79 | 6.02–30.31 |
| Index ranges | $-4 \le h \le 4$ | $-4 \le h \le 5$ |
| | $-4 \le k \le 4$ | $-5 \le k \le 5$ |
| | $-20 \le l \le 20$ | $-22 \le l \le 17$ |
| Measured reflections; unique; significant | 1566; 113; 112 | 1182; 156; 120 |
| $R_{int}$, $R_\sigma$ | 0.0535, 0.0225 | 0.0484, 0.0239 |
| Completeness to ($\theta$) [°] | 93.8% (25.79) | 91.1% (30.31) |
| $T_{min.}$, $T_{max.}$ | 0.0048, 0.5039 | 0.029, 0.073 |
| Structure solution | direct methods[a] | direct methods[a] |
| Structure refinement | full-matrix least-squares on $F^2$ [b] | full-matrix least-squares on $F^2$ [b] |
| Data/restraints/parameter | 113/0/15 | 156/0/16 |
| $S(F_2)$ | 1.547 | 1.061 |
| Absorption correction | numerical[c] | numerical[c] |
| $R_1$, w$R_2$ [$I > 2\sigma(I)$] | 0.0328, 0.0731 | 0.0282, 0.0608 |
| $R_1$, w$R_2$ (all data) | 0.0330, 0.0731 | 0.0396, 0.0628 |
| Extinction coefficient | 0.069(7) | 0.007(1) |
| $\rho_{min}$, $\rho_{max}$ | –1.9(5), 1.6(5) | –1.5(4), 1.5(4) |

[a] G. M. Sheldrick, SHELXS-97, Program for the Solution of Crystal Structures, University of Göttingen, 1997. [b] G. M. Sheldrick, SHELXL-97, Program for Structure Refinement, University of Göttingen, Germany, 1997. [c] STOE & CIE, X-SHAPE 1.06, Darmstadt, 1999.

Here we present information about the preparation conditions and the crystal structures obtained by X-ray single-crystal and powder diffraction studies. Detailed discussions of the real structure based on results from HRTEM and SAED (Selected Area Electron Diffraction) studies of $Ni_3GeTe_2$ are also provided. In addition, preliminary temperature-dependent measurements of the magnetic susceptibility for powder samples of both compounds are presented.

## Results and Discussion

Tables 1, 2, and 3 contain the relevant crystallographic and crystal chemical results for the title compounds.

Table 2. Atomic coordinates, Wyckoff notations, site occupation factors, and equivalent isotropic displacement parameters $U_{eq}$ [$10^4$ pm$^2$] for $Fe_3GeTe_2$ and $Ni_3GeTe_2$ (printed in *italics*). $U_{eq}$ is defined as one-third of the trace of the orthogonalized $U_{ij}$ tensor.

| Atom | Wyckoff | $x$ | $y$ | $z$ | $U_{eq}$ | *s.o.f.* |
|---|---|---|---|---|---|---|
| Fe1 | 4e | 0 | 0 | 0.6718(1) | 0.0086(7) | 1.0(1) |
| *Ni1* | *4e* | *0* | *0* | *0.6670(1)* | *0.0097(5)* | *1* |
| Fe2 | 2c | 0.6667 | 0.3333 | 0.75 | 0.0077(2) | 0.83(2) |
| *Ni2* | *2c* | *0.6667* | *0.3333* | *0.75* | *0.007(1)* | *0.70(1)* |
| *Ni3* | *2a* | *0* | *0* | *0.5* | *0.010(3)* | *0.25(1)* |
| Ge | 2d | 0.3333 | 0.6667 | 0.75 | 0.021(1) | 0.99(2) |
| *Ge* | *2d* | *0.3333* | *0.6667* | *0.75* | *0.0218(6)* | *1* |
| Te | 4f | 0.6667 | 0.3333 | 0.59018(6) | 0.0096(7) | 1 |
| *Te* | *4f* | *0.6667* | *0.3333* | *0.58852(6)* | *0.0079(4)* | *1* |

### $Fe_3GeTe_2$

Figure 1 shows a projection of the crystal structure of $Fe_3GeTe_2$, emphasizing that layers of Te atoms sandwich 2D structural sections built from Fe and Ge atoms. The shortest distance $d$(Te–Te) between adjacent layers amounts to 374 pm. In order to illustrate the Fe/Ge substructure in more detail, the three atomic layers consisting of Fe, Fe/Ge, and Fe atoms are projected along [001] in part b of Figure 1. A comparison with structural data given in the literature for $Fe_{1.67}Ge$ (see earlier) reveals that this alloy contains similar hexagonal layers of Fe and Fe/Ge atoms, however, it forms a compact, isotropic 3D structure without any macroscopic layer character. It should be noted that the chemical composition as obtained by refinement of the crystallographic occupational parameters based on single-crystal X-ray data gives $Fe_{2.83}GeTe_2$ instead of $Fe_3GeTe_2$ (Table 2). This minor but significant difference was repeatedly found for different crystals. It stems from an occupational deficiency of the Fe2 site (forming a common layer with Ge), however, it differs from results obtained by analytical scanning electron microscopy for a variety of crys-

 © 2006 Wiley-VCH Verlag GmbH & Co. KGaA, Weinheim 

Table 3. Selected interatomic distances *d* [pm] for $Fe_3GeTe_2$ and $Ni_3GeTe_2$.

| | | $Fe_3GeTe_2$ | $Ni_3GeTe_2$ |
|---|---|---|---|
| Ge | –Fe2/Ni2 (3×) | 230.42(6) | 225.74(6) |
| | –Fe1/Ni1 (6×) | 263.4(1) | 261.9(1) |
| Fe1/Ni1 | –Fe1/Ni1 | 255.4(4) | 265.6(4) |
| | –Fe2/Ni2 (3×) | 263.4(1) | 261.9(1) |
| | –Ge (3×) | 263.4(1) | 261.9(1) |
| | –Te (3×) | 266.2(1) | 258.5(1) |
| | –Ni3 | – | 267.7(2) |
| Fe2/Ni2 | –Ge (3×) | 230.42(6) | 225.74(6) |
| | –Te (2×) | 261.1(1) | 266.59(7) |
| | –Fe1/Ni1 (6×) | 263.4(1) | 261.9(1) |
| Ni3 | –Te (6×) | – | 266.59(7) |
| | –Ni1 (2×) | – | 267.7(2) |

tals. These strongly support the composition $Fe_3GeTe_2$ for the series of tested crystals. A possible solution for this contradiction assumes a marginal fraction of 0.17 Fe atoms (per formula unit) statistically distributed over atomic positions in the van der Waals gap. This problem is even more pronounced for the corresponding Ni atoms in $Ni_3GeTe_2$, and is therefore discussed together with the character of the coordination polyhedra and further structural details later.

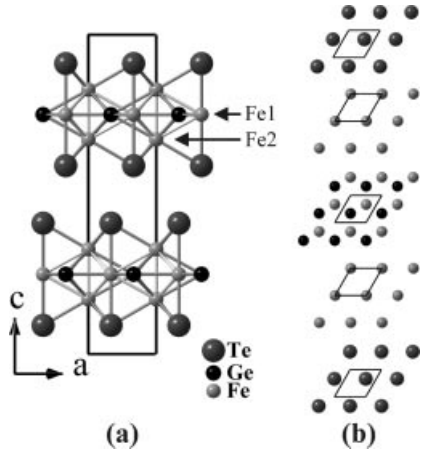


Figure 1. (a) Projection of the crystal structure of $Fe_3GeTe_2$ along [010]. (b) [001] projections of the single Te, Fe, and mixed Fe/Ge layers of the upper layer package.

## $Ni_3GeTe_2$

Figure 2 (a) shows a projection of the crystal structure of $Ni_3GeTe_2$ along [010], which is basically isotypic to $Fe_3GeTe_2$. Even more pronounced than for $Fe_3GeTe_2$, a significant residual electron density in the van der Waals gap is observed in the refinement of the single-crystal X-ray diffraction data. The reliability factor of the refinement significantly improves if we assume partial occupancy (0.25) of the Ni3 site located in the van der Waals gap between adjacent Te layers.

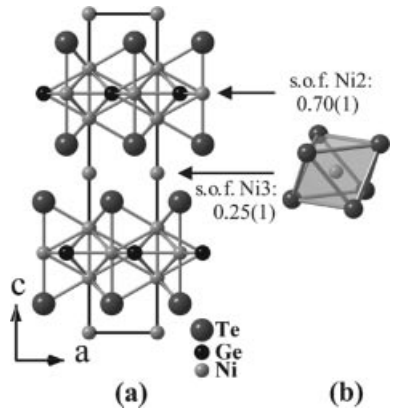


Figure 2. (a) Projection of the crystal structure of $Ni_3GeTe_2$ along [010]. (b) The octahedral coordination polyhedron for Ni3 (this Ni-position is located in the van der Waals gap with an approximate occupancy of 0.25).

In Figure 2 (b), the coordination polyhedron for Ni3 is displayed. It is similar to the coordination polyhedron found, for example, for Ni in $NiTe_2$ ($CdI_2$ type[11]). This Ni3–Te partial structure can be treated as a 2D section of a Ni-deficient $NiTe_2$ structure. Together with the reduced occupancy of Ni2 (Table 2), the occupancy of Ni3 completes the chemical composition to give $(Ni3)_{0.25}(Ni2)_{0.7}(Ni1)_2GeTe_2 = Ni_{2.95}GeTe_2$.

From the inspection of SEM images (Figure 3), it is most likely that the presence of Ni3 in the van der Waals gap causes a stronger cohesion between adjacent layers, and may be responsible for the more compact and less pronounced layer character of the $Ni_3GeTe_2$ sample in comparison with $Fe_3GeTe_2$.

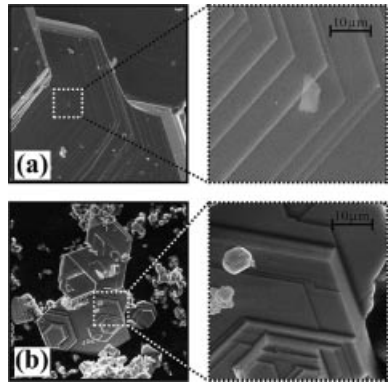


Figure 3. A comparison between SEM images of (a) $Fe_3GeTe_2$ and (b) $Ni_3GeTe_2$ showing the hexagonal platelets which are characteristic for both compounds. The platelets formed by the Ni compound are thicker and more compact.

## Further Crystal Chemical Aspects

The individual coordination polyhedra shown in Figure 4 for $Fe_3GeTe_2$ clearly demonstrate that there is no typical coordination geometry (for example, tetrahedral) around the germanium atoms that would formally allow a +4 oxidation number to be ascribed to the Ge atoms. In-

 © 2006 Wiley-VCH Verlag GmbH & Co. KGaA, Weinheim 

stead, the germanium atoms are surrounded by iron atoms exclusively in their first coordination sphere, whereas tellurium atoms are typical constituents of the second coordination sphere [the shortest *d*(Ge–Te) = 348 pm in comparison with the shortest *d*(Ge–Fe) = 230 pm]. On the other hand, both types of iron atoms (Fe1 and Fe2) are coordinated by Ge, Fe, *and* Te atoms in their first coordination sphere (Figure 4), suggesting in particular significant Fe–Fe interactions [the shortest *d*(Fe–Fe) = 255 pm in comparison to *d*(Fe–Fe) = 250 pm in alpha-Fe]. At first glance, these structural details partly seem to support the earlier mentioned simple ionic description of $Fe_3GeTe_2$ as $(Fe^{2+})$-$(Fe^{3+})_2(Ge^{4-})(Te^{2-})_2$.

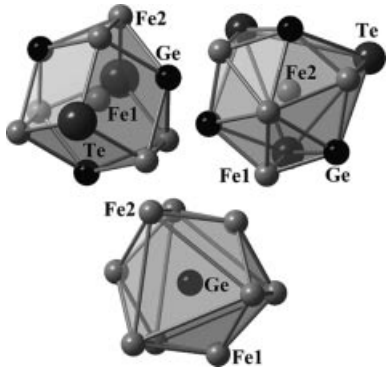


Figure 4. Coordination polyhedra around Fe1, Fe2, and Ge in $Fe_3GeTe_2$.

If we omit the enclosing Te atom layers and the Ni atoms located in the van der Waals gap, we can clearly see from Figure 5 that the Fe/Ge and Ni/Ge atoms form a 2D system of trigonal prisms $GeFe(2)_{6/3}$ interconnected by additional Fe(1) atoms, or alternatively as a system of trigonal prisms $Fe(1)Fe(2)_{6/3}$ interconnected by Ge atoms. The first view is reminiscent of the aspect that the 2D partial structure represented in this way can be interpreted as a stuffed 2D NiAs structure.

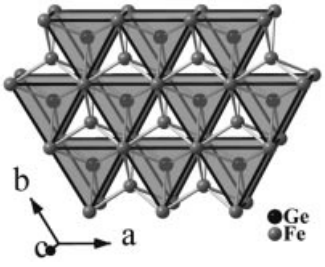


Figure 5. The 2D $Fe_3Ge$ ($Ni_3Ge$) partial structure of $Fe_3GeTe_2$ ($Ni_3GeTe_2$) visualized as a 2D arrangement of trigonal prismatic $GeFe_{6/3}$ units interconnected by Fe atoms or as a 2D system of trigonal prismatic $FeFe_{6/3}$ units interconnected by Ge atoms.

A comparison of $Fe_3GeTe_2$ and $Ni_3GeTe_2$ based on the statements given earlier shows that the most important difference between their crystal structures concerns the partially occupied atomic position Ni3 (0.25 Ni per formula unit) located in the van der Waals gap. In the case of the iron compound this position does not show any significant residual electron density. A supporting argument comes from the experimental observation that $NiTe_2$ crystallizes in the $CdI_2$ structure type[12] with Ni in a similar coordination as Ni3 in $Ni_3GeTe_2$. $FeTe_2$ on the other hand does *not* crystallize in this structure type. Instead, only a marcasite modification of $FeTe_2$ is known.[12] Thus, the crystal structure of $Ni_3GeTe_2$ can actually be treated as an intergrowth species between the two Ni-deficient constituting phases $Ni_xTe_2$ and $Ni_{1-x}Ni_2GeTe_2$ with $x = 0.25$.

In order to clarify the structural situation, it must be mentioned at this point that a completely *ordered* distribution of Ni3 (hypothetical Fe3) would require multiple lengths of *a* and *b* (not *c*). A fully (or partially) *ordered* distribution of Ni3 on the other hand would result in additional (diffuse) superstructure reflections. It was found that more detailed information on this subtle problem could only be derived from HRTEM and SAED investigations with $Ni_3GeTe_2$ (see later), and not from the X-ray structure analyses.

## HRTEM and SAED Investigations of $Ni_3GeTe_2$

Our study was specifically focused on the degree of structural disorder on the nanometer scale, and in particular on the examination of the Ni and Ge atomic disorder. Disorder phenomena resulting from X-ray analyses in many cases have been artificially generated by a superposition of ordered real structure components, like domains or stacks of layers with ordered structure. In fact, some peculiarities of the morphology could be addressed to layered components: see the well-defined microstructure in the bright field images of Figure 6 (part a, zone axis [001] and part b). Electron-diffraction patterns along zone axes [*uv*0] demonstrate that all stacks are strictly parallel to (001). Figure 6 (b) was recorded along zone axis [100], and hence displays the (001) stacks edge on. The lower limit of their thickness is in the range of several nanometers. The stacks separate at the outermost rims of the crystals, while they match perfectly at coherent boundaries in thicker areas. HRTEM proves that the stacks are not significantly shifted to each other; therefore, they are not part of a classical polytypic structure. EDX linescans indicate no noticeable changes in the average composition of adjacent stacks, particularly not of the Ni/Ge ratio. At first glance, SAED patterns (tilting experiments) are in good agreement with patterns simulated on the basis of the average structure. However, closer inspection reveals two kinds of intensities in addition to the main structure reflections. Both phenomena indicate marginal deviations of the real structure from the disordered average structure.

The first one includes weak diffuse rods parallel to [001]* intersecting all positions $^{h}/_{3}{}^{h}/_{3}0$ and $^{2h}/_{3}{}^{2h}/_{3}0$ of the reciprocal space which are equivalent for the hexagonal system. The rods are shown as diffuse lines in patterns containing [001]* (see for instance zone axis [210] in Figure 6, c), while they are cut into intersection points in [001] patterns (Figure 6, d). The diffuse intensity observed in different areas of the same crystallite is variable, as demonstrated by the

 © 2006 Wiley-VCH Verlag GmbH & Co. KGaA, Weinheim 

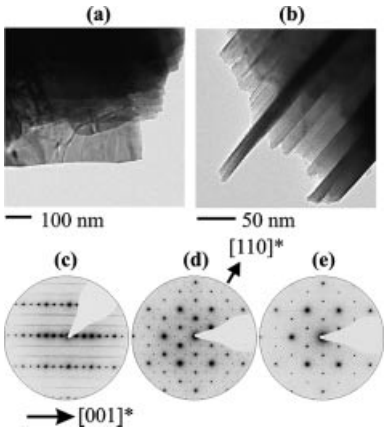


Figure 6. Bright field images of compact crystals, (a) zone axis [001] and (b) zone axis [100]. Electron-diffraction patterns with diffuse intensities, (c) for [210], and intersection points, (d) [001]. Pattern (e) was recorded on another selected area of the same crystal as (d).

existence or absence of intersection points, cf. Figure 6 (parts d and e). In some cases, we observed [001] patterns without any diffuse scattering in the precise zone axis orientation, however, when tilting the diffuse intensities became significant (see later).

Taking into account the high sensitivity of electron-diffraction experiments and the exceptionally weak diffuse intensity observed, the lack of such intensities in X-ray diffraction patterns can be rationalized. It was challenging to image the deviation from the average structure, especially because of the beam sensitivity of the sample under the conditions of HRTEM. However, with selection of low dose modes, we were at least able to record [001] micrographs with significant intersection points in the Fourier transforms. An interpretation of the scattering phenomena in real space is complicated as a result of moiré effects (see later). However, a basic interpretation is straightforward, that is, the existence of diffuse rods in reciprocal space correlates with the evolution of structural order within layers of direct space. For the modeling of such in-plane ordering, ordered arrangements of Ni atoms and vacancies in the Ni and (Ni, Ge) layers were introduced. Additionally, the occupancy factors were fixed to the average values. Prototypes for such ordering can be derived from the structures of (Ni, Ge) intermetallics. Those compounds show related disorder phenomena to those observed for $Ni_3GeTe_2$. A top view of a mixed (Ni, Ge) layer of $Ni_5Ge_3$[13] is characterized by an ordered vacancy distribution (see Figure 7).

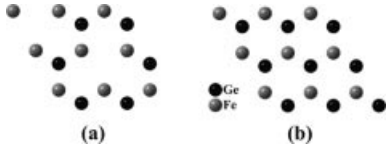


Figure 7. (a) Top view of the ordered (Ni, Ge) layer of $Ni_5Ge_3$. (b) Top view of the disordered (Ni, Ge) layer in $Ni_3GeTe_2$.

The composition of this layer is the same as that of the mixed and disordered (Ni2, Ge) layer in $Ni_3GeTe_2$. The ordered vacancies can be introduced in large supercells, which serve for simulation. The simulated [001] SAED pattern shows, like the experimental patterns, intensities in addition to the main structure reflections on all positions $^{h}/_{3}{}^{h}/_{3}0$ and $^{2h}/_{3}{}^{2h}/_{3}0$. The occurrence of diffuse scattering in the experimental patterns could be interconnected with a nonperiodic sequence of the ordered layers, for example by applying rotations of adjacent layers. In the case of disorder, the intensity distribution within the diffuse rods depends on the degree of structural order within the analyzed area. If the structure appears to be randomly arranged along [001], for instance by assuming equal numbers of ordered layers with 0°, ±60°, and ±120° rotation (rotation axis [001]), we expect no intersection points in the zero-order Laue zone of [001] patterns. However, diffuse intensity should be present in layers slightly above (001)*; hence, the formation of intersection points by tilting slightly from precise [001] zone axis orientation is rationalized. As shown by simulated micrographs, the significance of ordered vacancies in HRTEM micrographs is marginal, in particular for real structures containing a disorder of layers. Therefore, future projects are focusing on HRTEM on long-term annealed samples which may be long-range ordered crystals.

The second type of diffracted intensity, in addition to the main structure reflections, can be assigned to moiré effects based on a misfit of hexagonal layers (see later). In this case, no diffuse intensities were observed as evidence of an in-plane disordered arrangement of Ni atoms and vacancies. Along [001], the misfit produces characteristic patterns of double diffraction (see Figure 8).

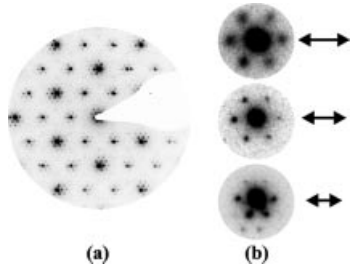


Figure 8. Double diffraction patterns in [001], (a) typical example and (b) enlarged sections of patterns, displaying distinct difference vectors ($\Delta d$, see arrows).

No multiple twinning (triplets) of stacks with a lower symmetry than hexagonal (for example, orthorhombic *C*) is shown. All [001] patterns as well as Fourier transforms of HRTEM images show perfect hexagonal symmetry and no splitting of the main structure reflections. As a rule, a translational moiré effect is observed, which is based on hexagonal layers with parallel orientation of all lattice vectors but with significant variations of the in-plane (*a*) lattice parameter. The changes of the lattice could be interconnected with strain, for example because of in-plane aggregation of Ni atoms on Ni2 and Ni3 positions within adjacent (001) stacks. The lattice mismatch varies from crystal to crystal: see the arrows in Figure 8 (b) which highlight the distinct

 © 2006 Wiley-VCH Verlag GmbH & Co. KGaA, Weinheim 

difference vectors of both lattices. Slight variations of the mismatch are also evident within the same crystallite. The in-plane aggregation could be interconnected with variations in the density of the Ni atoms in consecutive (001) layers containing Ni2 and Ni3 positions. To check for such real structures, the average density of the Ni atoms was split in terms of more or less occupied Ni2 and Ni3 positions within consecutive (001) layers. The significance of such separation in HRTEM micrographs is demonstrated for [100] in Figure 9 (a). The simulations were calculated close to Scherzer defocus. The black contrasts correspond to atoms (high projected potential), and the white contrasts correspond to cavities (low projected potential), with both superimposed in rows along [100]. The black and gray arrows highlight the layers containing Ni2 and Ni3 positions edge on. Starting from a ratio of occupied positions Ni2/Ni3 = 100:0, the average occupation of Ni2 layers was decreased while that of Ni3 was increased in steps of the same value. The series of simulations clearly demonstrates that the significance of HRTEM is limited to full separation which has never been experimentally observed, not even by selection of different focusing conditions (see Figure 9, b). On the contrary, all experimental images are in good agreement with the simulated images based on the average structure. The occupation of the position Ni3, for example, is in accordance to the average structure low, and a separation in layers with full and nonoccupied positions Ni3 can be excluded. Hence, the mismatch must be based on in-plane aggregations of Ni atoms without significant changes to the average occupancy factors.

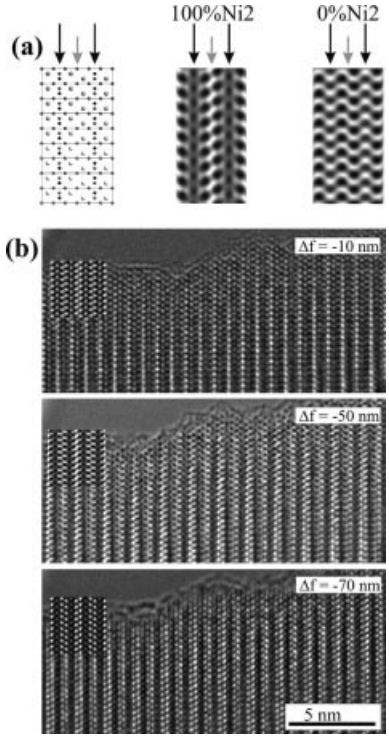


Figure 9. (a) Simulated micrographs for Scherzer defocus (zone axis [100]) with different densities on positions Ni2, Ni3; see text. (b) Defocus series with inserted simulations ([100], thickness: 3.2 nm).

To conclude, the ordering of Ni atoms and vacancies in the real structure is never complete. Two scattering phenomena demonstrate variations in the arrangement of Ni atoms and vacancies. The first one (diffuse intensities) indicates in-plane ordering, while the second one (double diffraction) is characterized by a misfit of in-plane disordered hexagonal layers.

### Magnetism of $Fe_3GeTe_2$ and $Ni_3GeTe_2$ and Electrical Conductivity of $Fe_3GeTe_2$

Preliminary measurements of the temperature dependence of the magnetic susceptibility reveal a spontaneous magnetization below 230 K, indicating ferro- or ferrimagnetic behavior of $Fe_3GeTe_2$ (Figure 10, a). The splitting of the zero-field cooled (zfc) and field-cooled (fc) susceptibility measured in an external field of 0.1 T below about 200 K closes for larger external fields (1 and 5 T). We ascribe the splitting of the fc-zfc susceptibilities to irreversible effects due to domain ordering. The inset in Figure 10a displays the magnetization of $Fe_3GeTe_2$ at 10 K. Saturation is observed for external fields above 5 T with a moment of about 1.2 $\mu_{Bohr}$ per Fe atom, about half of the saturated moment of elementary iron.

$Ni_3GeTe_2$ shows no indication of spontaneous magnetization. Rather, a weak temperature-independent susceptibility is observed above 100 K (Figure 10, b). The increase of the susceptibilities below 50 K can be understood as caused by traces of a paramagnetic impurity, and the field dependence of the susceptibilities as caused by traces of a ferromagnetic impurity.

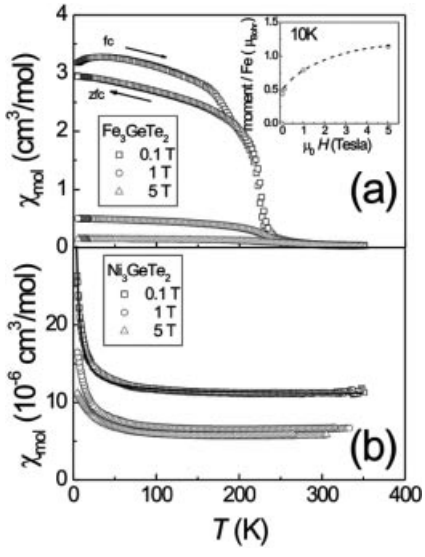


Figure 10. (a) Magnetic susceptibility for $Fe_3GeTe_2$ as a function of temperature and magnetic field. The inset displays the magnetic moment per Fe atom at 10 K. (b) Magnetic susceptibility for $Ni_3GeTe_2$ as a function of temperature and magnetic field. The solid line represents a fit of a modified Curie law (see text) to the susceptibility of $Ni_3GeTe_2$ measured in a field of 0.1 T. The increase in the susceptibility at low temperatures can be ascribed to a temperature-dependent paramagnetic impurity with a concentration of about 0.2% assuming $S = {}^1/_2$ entities with an effective moment of 1.73 $\mu_B$.

 © 2006 Wiley-VCH Verlag GmbH & Co. KGaA, Weinheim 

The observed field dependence of the magnetic susceptibilities follows if the sample ($m$ = 135 mg) is assumed to contain about 400 μg of elementary ferromagnetic Ni (saturation magnetization 0.62 $\mu_{Bohr}$[14]).

The magnitude and temperature dependence of the electrical resistance (Figure 11) prove $Fe_3GeTe_2$ is a metal. The magnetic transition shows up as a kinklike anomaly at about 225 K (see inset in Figure 11) because of spin-flip scattering.

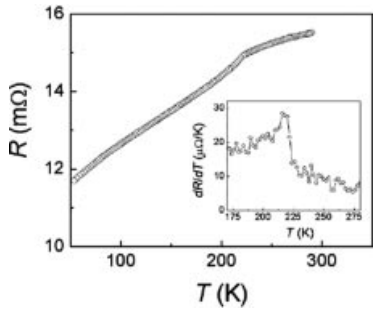


Figure 11. Temperature dependence of the in-plane electrical resistance of a small crystal (approximately $1 \times 1 \times 0.05$ mm$^3$) of $Fe_3GeTe_2$. The inset displays the derivative of the in-plane resistance with respect to temperature. A clear maximum of the derivative is seen at the magnetic ordering temperature.

In order to clarify the earlier mentioned valence problems of iron, more detailed magnetic measurements together with Moessbauer investigations are currently in progress.

## Experimental Section

$Fe_3GeTe_2$ was prepared by a direct solid-state reaction starting from an intimate mixture of the pure elements in the molar ratio 3:1:2 (Fe: 99.9%, powder, Heraeus; Ge: 99.99%, powder 250 μm, Chempur; Te: 99.999%, pieces, Chempur). The mixture of the starting materials was filled into a dry quartz glass ampoule, which was evacuated and sealed, heated up to 625 °C, and kept at this temp. for two weeks. The homogeneous gray, air-stable product did not show any impurities in standard X-ray diagrams, melted incongruently at 837 °C, and formed crystals with the shape of small hexagonal plates suitable for X-ray single-crystal experiments. Polycrystalline $Ni_3GeTe_2$ was prepared in an analogous way (Ni: 99.9%, powder, Heraeus). Bulk material and crystals, viewed under a light microscope, looked very similar to $Fe_3GeTe_2$, and melted incongruently at 879 °C. However, a more compact and less pronounced layer character of small crystals of the nickel compound became obvious in the scanning electron microscope. Standard powder X-ray diagrams for $Ni_3GeTe_2$ did not show any contaminations. Further details of the crystal structure investigation for $Fe_3GeTe_2$ and $Ni_3GeTe_2$ may be obtained from the Fachinformationszentrum Karlsruhe, 76344 Eggenstein-Leopoldshafen (Germany), on quoting the depository numbers CSD 415616 or CSD 415617, respectively.

For the HRTEM investigations, crystals of $Ni_3GeTe_2$ were crushed and suspended in *n*-butanol (HRTEM measurements of $Fe_3GeTe_2$ were not possible because of unexpectedly emerging ferromagnetism already at ambient temp.). One drop of the *n*-butanol suspension was transferred to a perforated carbon/copper net which served as support of the crystallites after drying. HRTEM and SAED investigations were performed with a Philips CM30ST (300 kV, $LaB_6$ cathode, $C_S$ = 1.15 mm). Computer simulations of the HRTEM images (multislice formalism) and SAED patterns (kinematical approximation) were carried out with the EMS program package[15] (spread of defocus: 70 Å, illumination semiangle: 1.2 mrad). All images were collected with a Multiscan CCD Camera [software Digital Micrograph 3.6.1 (Gatan)]. EDX spectroscopy was performed in the scanning- and nanoprobe mode of CM30ST with a Si/Li-EDX detector (Noran, Vantage System).

Magnetic measurements for both compounds were carried out with the SQUID magnetometer (MPMS, Quantum Design, Dan Diego, USA) of the Max-Planck-Institut für Festkörperforschung (Stuttgart). The in-plane electrical resistance of $Fe_3GeTe_2$ was measured on a platelet-shaped crystal with dimensions $\approx 1 \times 1 \times 0.05$ mm$^3$ in the temp. range 50–300 K. Electrical contacts were made by four parallel Cr/Au stripe contacts which had been evaporated on a (110) face of the crystal.

## Acknowledgments

The authors would like to thank Mrs. V. Duppel for practical TEM work and Prof. Dr. Dr. h. c. mult. A. Simon for enabling the TEM experiments. The authors are grateful to the "Deutsche Forschungsgemeinschaft" and the "Fonds der Chemischen Industrie" for their financial support.

[1] H. J. Deiseroth, C. Reiner, M. Schlosser, L. Kienle, *Z. Anorg. Allg. Chem.* **2002**, *628*, 1641–1647.
[2] J. Schlirf, H. J. Deiseroth, *Z. Kristallogr.- NCS* **2001**, *216*, 27–28.
[3] N. Kh. Abrikosov, L. A. Bagaeva, LD. Dudkin, L. I. Pertova, V. M. Sokolova, *Izv. Akad. Nauk. SSSR, Neorg. Mater.* **1985**, *21*, 1680.
[4] A. K. Yasukochi, K. Kanematsu, T. Ohoyama, *J. Phys. Soc., Jpn.* **1961**, *16*, 429–433.
[5] M. Ellner, *J. Less-Common Met.* **1976**, *48*, 21–52.
[6] R. L. Abdon, T. Hughbanks, *Angew. Chem.* **1994**, *106*, 2414–2416.
[7] B. Harbrecht, T. Degen, M. Conrad, *J. Alloys Compd.* **1997**, *246*, 37–50.
[8] S. Debus, B. Harbrecht, *Z. Anorg. Allg. Chem.* **2000**, *626*, 173–179.
[9] H.-B. Merker, H. Schäfer, B. Krebs, *Z. Anorg. Allg. Chem.* **1980**, *462*, 49–56.
[10] M. B. Robin, P. Day, *Adv. Inorg. Chem. Radiochem.* **1967**, *10*, 247–422.
[11] S. Furuseth, K. Selte, A. Kjekshus, *Acta Chem. Scand.* **1965**, *19*, 257–258.
[12] G. Brostigen, A. Kjekshus, *Acta Chem. Scand.* **1970**, *24*, 1925–1940.
[13] M. Ellner, T. Goedecke, K. Schubert, *J. Less-Common Met.* **1971**, *24*, 23–400.
[14] D. R. Lide, *CRC Handbook of Chemistry and Physics*, 79th ed., CRC Press, **1998**, pp. 12–117.
[15] P. A. Stadelmann, *Ultramicroscopy* **1987**, *21*, 131–146.

Received: November 16, 2005
Published Online: March 1, 2006

 © 2006 Wiley-VCH Verlag GmbH & Co. KGaA, Weinheim 

DOI: 10.1002/ejic.200501049

# Aminoethyl-Functionalized Cyclopentadienyliridium Complexes: Photochemical C–H Activation and Carbonylation of Cycloalkanes

**Pek Ke Chan,[a] Weng Kee Leong,*[a] Karl I. Krummel,[b] and Marc V. Garland*[b]**

**Keywords:** Carbonylation / C–H activation / Cyclopentadienyl ligands / Iridium / Photochemistry

The photochemical C–H activation of cycloalkanes by aminoethyl-functionalized cyclopentadienyliridium complexes proceeds in a broadly similar way to that for their unfunctionalized analogues. In a carbon monoxide atmosphere, there is evidence that carbonylation to form the carboxaldehyde occurred with both systems. In situ infrared spectroscopic studies on these reactions allow the identification of several species present in low concentrations in the reaction mixture. (© Wiley-VCH Verlag GmbH & Co. KGaA, 69451 Weinheim, Germany, 2006)

## Introduction

UV initiated photodissociation of CO or $H_2$ from group-9 organometallic compounds of the type [CpMLL′] or [Cp*MLL′] (M = Ir, Rh; L = CO, $PMe_3$; L′ = CO, $H_2$) have been known to generate intermediates that are capable of activating the otherwise inert C–H bonds in hydrocarbon solvents.[1] This has stimulated much interest due to the plentiful supply of alkanes and the potential of using alkanes as chemical feedstocks for catalytic syntheses of organic molecules. Over the last two decades there have been several studies on the mechanism, kinetics, and thermodynamics of this activation process in solution, the gas phase, low-temperature matrices, and liquid noble gases.[1d,2] For $[Cp^XM(CO)_2]$ ($Cp^X$ = Cp or Cp*; M = Ir or Rh), spectroscopic measurements have shown that the primary photoproduct is a coordinatively unsaturated 16-electron species $[Cp^XM(CO)]$ obtained by dissociation of a CO ligand. This species is extremely reactive and forms a solvent adduct complex $[Cp^XM(CO)\cdots S]$ before undergoing C–H activation to give the hydridoalkyl species $[Cp^XM(CO)(R)(H)]$.[2b,3]

Many functionalized cyclopentadienyl ligands containing side-chain donor groups (OR, NRR′, PRR′, $CH{=}CH_2$) are beginning to appear in the literature. In particular, we were interested in aminoethyl-functionalized cyclopentadienyl ligands because of their "hard-soft" combination of electron donors; the cyclopentadienyl ligand is known to stabilize transition metals in high as well as low oxidation states whereas the amino group favors coordination to metals in high oxidation states. Only weak interactions are anticipated to metals in low oxidation states, although these may be strengthened by the chelate effect.[4] As a result, aminoethyl-functionalized cyclopentadienyl ligands may be expected to behave as hemilabile ligands; under the conditions for the activation of hydrocarbons, the nitrogen donor on the side-arm of the aminoethyl-functionalized cyclopentadienyliridium complex may coordinate to the iridium center. This reversible coordination to a reactive metal center is of general interest in catalysis as it may stabilize a highly reactive, electronically and sterically unsaturated intermediate by weakly occupying the vacant coordination site until the actual substrate coordinates and replaces the amino group.[5] In this paper, we present the results of our study on the photolysis of $[Cp^*Ir(CO)_2]$ (**1b**), as well as its aminoethyl-functionalized analogue, in vacuo or under an argon or carbon monoxide atmosphere.

## Results and Discussion

The aminoethyl-functionalized cyclopentadienyliridium complexes $[Cp^{\wedge}Ir(CO)_2]$ (**1c**) and $[Cp^{*\wedge}Ir(CO)_2]$ (**1d**; $Cp^{\wedge}$ = $C_5H_4CH_2CH_2NMe_2$ and $Cp^{*\wedge}$ = $C_5Me_4CH_2CH_2NMe_2$) were synthesized by an analogous route to that reported for $[CpIr(CO)_2]$ (**1a**; Scheme 1).[6]

The UV absorption spectrum of **1d** shows absorption maxima at about 210 and 280 nm. Upon UV irradiation of a degassed solution of **1d** in cyclohexane, the solution darkened slowly from yellow to orange-brown. Monitoring the photolysis by infrared spectroscopy showed initial formation only of the corresponding hydridoalkyl species **2d** ($\nu_{CO}$ = 1981 $cm^{-1}$), the CO stretching vibration of which is essentially identical to that of the [Cp*IrCO(Cy)(H)] analogue ($\nu_{CO}$ = 1981 $cm^{-1}$ in cyclohexane).[7] As the photolysis progressed, a new species showing a carbonyl stretch at 1996 $cm^{-1}$ in the infrared spectrum and a hydride resonance at $\delta$ = –15.7 ppm ([$D_8$]toluene) in the $^1H$ NMR spectrum was formed (Scheme 2). This was assigned to the dihydride

[a] Department of Chemistry, National University of Singapore, 3 Science Drive 3, Singapore 117543, Singapore
[b] Department of Chemical and Biomolecular Engineering, National University of Singapore, 4 Engineering Drive 4, Singapore 119260, Singapore

 © 2006 Wiley-VCH Verlag GmbH & Co. KGaA, Weinheim 

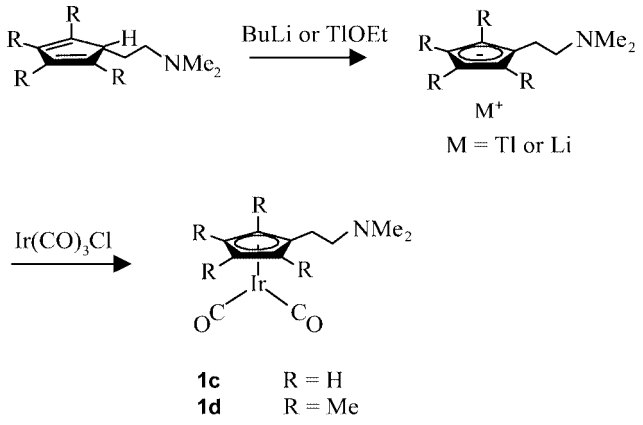


Scheme 1.

complex **3** by comparison of its spectroscopic data with the analogue [Cp*Ir(CO)$H_2$] ($\nu_{CO}$ = 1996 $cm^{-1}$ in cyclohexane; $\delta$ = –15.8 ppm in $C_6D_6$);[7,8] the latter was reported to form when **1b** was irradiated under a hydrogen atmosphere.[7]

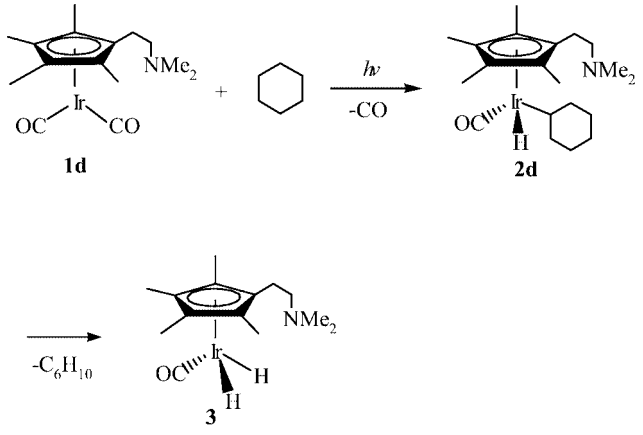


Scheme 2.

Since our irradiation experiment was carried out in the absence of hydrogen gas, the formation of **3** may have resulted from β-hydrogen elimination of cyclohexene from **2d**. Indeed, cyclohexene was detected by GC-MS analysis of the reaction solution. Similar irradiation of **1c** in cyclohexane also resulted in the formation of the corresponding dihydride species, although in this case there appeared to be some decomposition during irradiation. Similar results could also be achieved in a shorter time by irradiation with a 266-nm laser; for **1c**, the ratio of **1c**/**2c**, as determined by the relative intensities of the CO absorbance, was 3.3 after 6 h of UV irradiation, while the ratio was 2.0 after irradiation with the laser for 45 minutes. We also found that with [($C_5H_4CH_2Ph$)Ir($CO)_2$] (**1e**), which has a benzyl group as the side-arm, a dihydride species was also obtained. It therefore appears that photolysis of the complexes carrying a side-arm results in the formation of dihydride complexes; this has not been reported to occur with [Cp*Ir($CO)_2$] itself. The $^1$H NMR spectrum of the reaction mixture also shows another hydride resonance at $\delta$ = –17.5 ppm, which could be due to intramolecular C–H activation of the amine group on the Cp ligand or CO insertion into the Ir–C bond to give the acyl species [Cp*^Ir(CO)(H)($COC_6H_{11}$)].

Under a CO atmosphere (1 bar), the activation of **1d** in cyclohexane to form **2d** was slower and occurred with lower yield; the ratio of the absorbance of the CO stretch for **2d**/**1d** was 0.43 after 5 h under a CO atmosphere, and 1.4 after 2 h in vacuo. The same difference in ratios was observed for the activation of **1b** in cyclohexane to form **2b**; the ratio of (absorbance of) **2b**/**1b** was essentially constant at 0.65 after 30 min under a CO atmosphere, while it increased steadily from 1.03 at 30 min to 1.61 at 60 min in vacuo, although there were signs of decomposition in the latter on prolonged photolysis. Instead of **3**, the cluster [$Ir_4(CO)_{12}$] (**4**; $\nu_{CO}$ = 2029, 2069 $cm^{-1}$) was obtained together with **2d**; cluster **4** was also obtained from **1b** under similar conditions. Cluster **4** was not formed when a cyclohexane solution of **1d** was stirred under a CO atmosphere without irradiation. However, if the cyclohexane solution of **1d** was first irradiated, and then a CO atmosphere introduced, a mixture of **1d**, **2d**, and **4** was obtained; the changes in the relative intensities in the infrared spectra suggest that **3** is completely converted into **4** while **2d** is only partially converted into **4**. If this mixture was degassed and then subjected to irradiation, a mixture of **1d**, **2d**, and **3** was obtained. All these are summarized by the scheme and spectra given in Figure 1, and suggest that **4** is formed by the decomposition of **2d** and **3**, and that this is reversible.

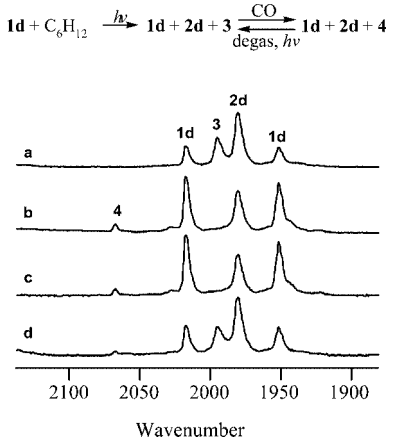


Figure 1. IR spectra of **1d** taken in cyclohexane: (a) after UV irradiation in vacuo for 6 h, followed by (b) stirring overnight under 1 atm of CO, (c) degassing and stirring overnight in vacuo, and (d) UV irradiation in vacuo for 3 h.

We confirmed the identity of **4** by an independent synthesis,[9] and also found that upon irradiation, a degassed suspension of **4** in cyclohexane in the presence of Cp*H or Cp*^H gave partial conversion to **1b** or **1d**, respectively, as identified by IR spectroscopy. Further irradiation of the reaction mixture containing **1b** and the starting materials resulted in the formation of the corresponding hydridoalkyl species **2b**; the yield of **2d** for the corresponding reaction was low. At the end of the 5 h irradiation, suspension of **4** in the reaction mixture was still observed, thus the low conversion rates may be attributed to the low solubility of **4** in cyclohexane.

 © 2006 Wiley-VCH Verlag GmbH & Co. KGaA, Weinheim 

In line with earlier findings that smaller rings show higher reactivity toward C–H activation,[1c,10] we found that the C–H activation of cyclopentane by **1d** was indeed more facile; the ratio of **2e**/**1d** (by absorbance) was 2.22 after 10 min, compared to a **2d**/**1d** ratio of 1.94 after the same period. These figures also indicate that the activation of **1d** is faster than that of **1b**. On stirring the resultant solution overnight under a CO atmosphere, both **2e** and **3** converted completely into **4** (Figure 2).

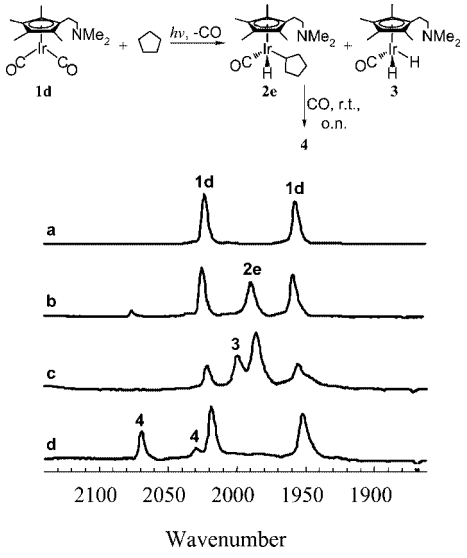


Figure 2. IR spectrum of **1d** in cyclopentane: (a) after stirring for 2 h under CO, followed by (b) 3 h UV irradiation under CO, (c) degassing and irradiation for 3 h in vacuo, and finally (d) stirring overnight under 1 atm of CO.

To gain further insight into the process, particularly with respect to the detection of compounds that we have hitherto not isolated or identified, we carried out in situ IR measurements on the C–H activation of cyclohexane, and used the band-targeted entropy minimization (BTEM) technique that one of us has developed for deconvolution of the data matrix.[11] The BTEM algorithm has been proven to be useful for picking up signals due to species that are present in low concentration, have low absorbance, are unstable, or have peaks that overlap with those due to other species.[11] The schematic diagram for the set-up used for the in situ IR measurements is shown below (Figure 3).

Measurements were made for both **1b** and **1d**; for each complex, spectra were collected at 5 min intervals, and a total of 232 spectra were collected.[12] For **1b**, the individual IR spectra of **1b**, **2b**, and **4**, in the CO stretching region (1650–2250 $cm^{-1}$) were recovered, together with the C=O stretch for cyclohexanecarboxaldehyde (Figure 4). Further confirmation of the aldehyde identity was obtained by NMR and GC-MS characterization. Formation of the corresponding carboxaldehyde in reactions carried out with cyclopentane was also observed by NMR spectroscopy. The carboxaldehyde could have been formed by carbonylation

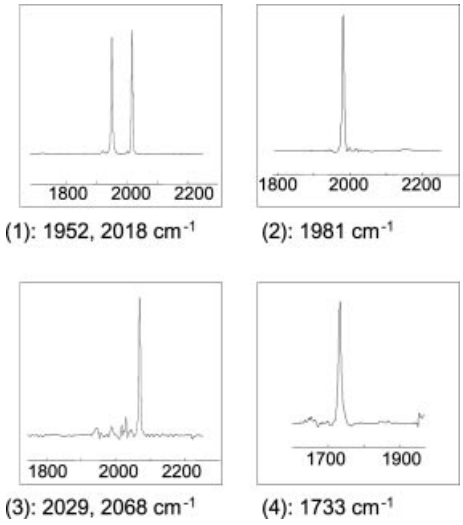


Figure 4. Pure component IR spectra of individual species recovered from deconvolution of the IR spectra of the reaction mixture: (1) $[Cp^*Ir(CO)_2]$ (**1b**), (2) $[Cp^*Ir(CO)(H)(C_6H_{11})]$ (**2b**), (3) $[Ir_4(CO)_{12}]$ (**4**), and (4) $C_6H_{11}CHO$.

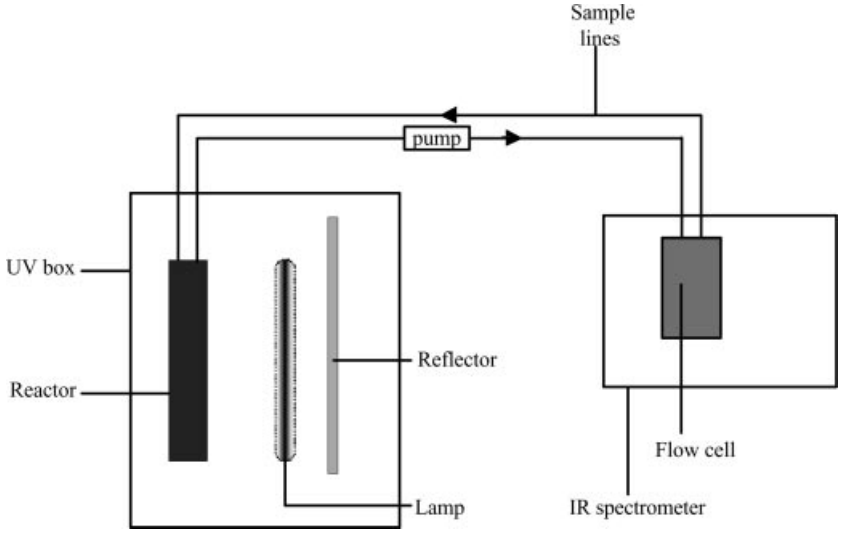


Figure 3. Schematic diagram of the set-up used for in situ IR measurements.

 © 2006 Wiley-VCH Verlag GmbH & Co. KGaA, Weinheim 

of the hydridoalkyl species followed by reductive elimination. Carbonylation of hydrocarbons catalyzed by group-9 transition metal complexes such as $[RhCl(CO)(PMe_3)_3]$ under UV irradiation has been reported,[13] but 18-electron Cp*Ir complexes have not been known to carbonylate hydrocarbons as it was believed that coordination of an incoming CO ligand would result in dissociation of the hydrocarbon.[14] A FAB-MS analysis of the reaction mixture yielded a fragment at *m*/*z* 267 in the positive-ion mode, and the $^{13}C$ NMR spectrum also shows a resonance at $\delta$ = 210.54 ppm, both of which suggest the presence of an acyl species, which may be the intermediate in the carbonylation reaction, although we have yet to confirm its identity.

We analyzed the yield of carboxaldehyde by GC-FID and found that UV irradiation of **1b** in cyclohexane in vacuo for one hour (absence of external CO source) afforded 0.9% of cyclohexanecarboxaldehyde (wrt [Ir]). When the photolysis was carried out under CO (1 bar) for the same length of time, the yield of aldehyde was 71.8%. So far, however, the yield is still far from catalytic. A high CO pressure may inhibit the initial CO dissociation from the dicarbonyliridium complex while favoring the insertion of CO into the Ir–C bond to form the putative $[Cp^*Ir(CO)(COC_6H_{11})(H)]$ acyl intermediate. Photolysis at various CO pressures (1.3 to 7.4 bars) was carried out but we did not find any significant trend in the aldehyde yield with CO pressure.

## Conclusions

We have found that dicarbonylcyclopentadienyliridium complexes in which there is a side-arm carrying an amino group undergo photochemical C–H activation of alkanes in much the same way as the parent complexes without the side-arm. By employing in situ IR measurements and using iterative band-targeted entropy minimization to analyze the spectra, however, we have been able to detect the presence of many hitherto undetected products and intermediates in the C–H activation reaction of such iridium species, including a carboxaldehyde. The formation of the carboxaldehyde represents the first evidence that the cyclopentadienyliridium system can be photochemically activated to promote the carbonylation of alkanes.

## Experimental Section

**General:** All operations were carried out using standard Schlenk techniques under an inert argon atmosphere unless otherwise stated. Cyclopentane (99+%), cyclohexane (99.9%), and hexane were distilled under nitrogen from sodium/benzophenone ketyl. Chlorotricarbonyliridium (Strem) was purchased and used without further purification.

NMR spectra were recorded with either a Bruker ACF 300 MHz or Bruker DPX 300 MHz spectrometer. Chemical shifts are reported with respect to residual solvent peaks. UV absorption spectra of starting complexes were recorded in cyclohexane with a Shimadzu 160 spectrometer. Gas chromatography (GC) analyses were performed with a HP 6890 gas chromatograph equipped with an HP 5973 mass-selective detector and a ZB-1 (30 m × 0.25 mm × 0.25 μm) capillary column, or with an HP5890 Series II plus equipped with an FID detector and a DB-5 (30 m × 0.32 mm × 0.25 μm) capillary column. Photolyses were carried out with either a Hanovia 450-W UV lamp with a nominal $\lambda_{max}$ of 254 nm, or a continuum Surelite III 10-ns-pulse Nd-YAG laser operating at 3 mJ per pulse with 266-nm radiation.

IR spectra for routine analysis were recorded with a Bio-Rad FTS 165, a Digilab Excalibur Series FTS 3000MX, or a Shimadzu IR Prestige-21 FTIR-8400S FT-IR spectrometer at a resolution of 1 $cm^{-1}$ using a solution IR cell with NaCl windows and a path length of 0.1 mm. IR spectra for in situ studies under ambient pressure were recorded with a Perkin–Elmer 2000 FTIR spectrometer at a resolution of 4 $cm^{-1}$ using a high-pressure heatable liquid cell with ZnSe windows and a path length of 0.1 mm from Specac. IR spectra for high-pressure studies were taken in a thermostatted high-pressure cell constructed of 316 stainless steel and AMTIR windows with a path length of 0.5 mm; details of the design will be described elsewhere.[15] Only carbonyl stretches in the 1600–2200 $cm^{-1}$ region are reported.

The compounds Cp^H,[16] Cp*^H,[17] $C_5H_5CH_2Ph$ ($Cp^{Bz}H$),[18] and $[Cp^*Ir(CO)_2]$ (**1b**)[19] were prepared following published procedures. Thallium salts were prepared following a literature method.[20] The complexes $[Cp^{\wedge}Ir(CO)_2]$ (**1c**), $[Cp^{*\wedge}Ir(CO)_2]$ (**1d**), and $[Cp^{Bz}Ir(CO)_2]$ (**1e**) were synthesized by a procedure analogous to that used for the synthesis of $[CpIr(CO)_2]$ (**1a**).[6]

**Preparation of [Cp*^Ir(CO)$_2$]:** Cp*^Li was prepared in situ from Cp*^H (98.2 mg, 0.509 mmol) and *n*BuLi (0.3 mL of a 2.2 M solution, 0.66 mmol) in hexane. The suspension was cannula transferred into a suspension of $[Ir(CO)_3Cl]$ (102 mg, 0.327 mmol) in hexane (10 mL) in a Carius tube. The mixture was degassed and heated at 70 °C for 2 d. The resultant mixture was cooled and filtered through celite to remove unreacted starting materials. The yellow filtrate was vacuum-dried to give **1d** as a yellow oil. IR (cyclohexane): $\tilde{\nu}$ = 1954, 2020 $cm^{-1}$. $^1H$ NMR ($CDCl_3$): $\delta$ = 2.60–2.54 (m, 2 H, $CH_2$-N) 2.27 (s, 6 H, N-$CH_3$), 2.26–2.19 (m, 2 H, $CH_2$), 2.15 (s, 6 H, ring $CH_3$), 2.16 (s, 6 H, ring $CH_3$) ppm. The $^1H$ NMR spectroscopic data matched the literature values.[21,22]

**Preparation of [Cp$^{Bz}$Ir(CO)$_2$]:** A degassed suspension of $Cp^{Bz}Tl$ (55 mg, 0.154 mmol) and $[Ir(CO)_3Cl]$ (21.2 mg, 0.068 mmol) in hexane (20 mL) was heated in a Carius tube at 80 °C for 2 d. The resultant mixture was cooled and filtered through celite to remove unreacted starting materials. The yellow filtrate was vacuum-dried to give **1e** as a yellow oil. IR (cyclohexane): $\tilde{\nu}$ = 1969, 2036 $cm^{-1}$. $^1H$ NMR ($CDCl_3$): $\delta$ = 7.23 (m, 5 H, $C_6H_5$), 5.45 (m, 2 H, $C_5H_4$), 5.37 (m, 2 H, $C_5H_4$), 3.77 (s, 2 H, $CH_2$) ppm. The IR data matched the literature values.[20]

Complex **1c** was prepared from Cp^Tl (432 mg, 1.265 mmol) and $[Ir(CO)_3Cl]$ (217 mg, 0.696 mmol) in an analogous manner. IR (cyclohexane): $\tilde{\nu}$ = 1967, 2034 $cm^{-1}$. $^1H$ NMR ($CDCl_3$): $\delta$ = 5.52 (m, 2 H, $C_5H_4$), 5.37 (m, 2 H, $C_5H_4$), 2.58–2.36 (m, 4 H, $CH_2CH_2$), 2.26 (s, 6 H, N-$CH_3$) ppm. The $^1H$ NMR spectroscopic data matched the literature values.[20]

**Preparative Photolysis:** A solution of the metal complex in the hydrocarbon solvent (1 mg $mL^{-1}$) was placed in a closed quartz tube, degassed by three cycles of freeze-pump-thaw, and then irradiated with a 450-W water-cooled, medium-pressure mercury lamp placed approximately 15 cm away whilst being continuously stirred. For reaction under CO atmosphere, the quartz tube was refilled with 1 atm of CO from the Schlenk line after degassing. For the laser irradiation, dichroic mirrors were used to direct the pulses; cooling by water circulation was not necessary.

 © 2006 Wiley-VCH Verlag GmbH & Co. KGaA, Weinheim 

**In situ IR Measurements:** For measurements at ambient pressure, a well-stirred solution of **1b** or **1d** in cyclohexane was circulated between the quartz reactor and a ZnSe cell through Vitron (internal diameter 2.06 mm) and Tygon tubing using a peristaltic pump (MASTERflex C/L 5910 pump systems model 77120–62). UV irradiation was carried out through the quartz reactor. The reactor was fan-cooled and the temperature was not controlled. The atmosphere was either argon or carbon monoxide.

For the high-pressure measurements, a solution of **1b** in cyclohexane was circulated between a 100-mL stainless-steel autoclave type reactor, a high-pressure cell of original design (AMTIR windows), and an industrial sapphire tube (Almaz Optics, Inc., Marlton, New Jersey) of 5 mm internal diameter (I.D.) via stainless steel tubing of 1/16 inch i.d. under various CO pressures. UV irradiation was carried out through the sapphire tube. The temperature was kept at 20 °C by cryostatic control.

## Acknowledgments

This work was supported by an A*STAR grant (research grant no. 012 101 0035), and K. I. K. and P. K. C. would like to thank the University for research scholarships.

[1] a) A. H. Janowicz, R. G. Bergman, *J. Am. Chem. Soc.* **1982**, *104*, 352–354; b) J. K. Hoyano, W. A. G. Graham, *J. Am. Chem. Soc.* **1982**, *104*, 3723–3725; c) A. H. Janowicz, R. A. Periana, J. M. Buchanan, C. A. Kovac, J. M. Stryker, M. J. Wax, R. G. Bergman, *Pure Appl. Chem.* **1984**, *56*, 13–23; d) S. T. Belt, F. W. Grevels, W. E. Klotzbucher, A. McCamley, R. N. Perutz, *J. Am. Chem. Soc.* **1989**, *111*, 8373–8382; e) A. A. Bengali, R. H. Schultz, C. B. Moore, R. G. Bergman, *J. Am. Chem. Soc.* **1994**, *116*, 9585–9589.

[2] a) J. M. Buchanan, J. M. Stryker, R. G. Bergman, *J. Am. Chem. Soc.* **1986**, *108*, 1537–1550; b) S. E. Bromberg, T. Lian, R. G. Bergman, C. B. Harris, *J. Am. Chem. Soc.* **1996**, *118*, 2069–2072; c) N. Dunwoody, S. Sun, A. J. Lees, *Inorg. Chem.* **2000**, *39*, 4442–4451.

[3] A. J. Lees, *J. Organomet. Chem.* **1998**, *554*, 1–11.

[4] C. Muller, D. Vos, P. Jutzi, *J. Organomet. Chem.* **2000**, *600*, 127–143.

[5] P. Jutzi, T. Redeker, *Eur. J. Inorg. Chem.* **1998**, 663–674.

[6] S. A. Gardner, P. S. Andrews, M. D. Rausch, *Inorg. Chem.* **1973**, *12*, 2396–2402.

[7] W. A. G. Graham, *J. Organomet. Chem.* **1986**, *300*, 81–91.

[8] D. M. Heinekey, D. A. Fine, T. G. P. Harper, S. T. Michel, *Can. J. Chem.* **1995**, *73*, 1116–1125.

[9] F. P. Pruchnik, K. Waijda-Hermanowicz, M. Koralewicz, *J. Organomet. Chem.* **1990**, *384*, 381–383.

[10] R. G. Bergman, *Science* **1984**, *223*, 902–908.

[11] a) W. Chew, E. Widjaja, M. Garland, *Organometallics* **2002**, *21*, 1982–1990; b) E. Widjaja, C. Li, M. Garland, *Organometallics* **2002**, *21*, 1991–1997.

[12] We observed no significant difference in product distribution for the experiments carried out at ambient pressure using Vitron tubing and those carried out under CO pressure using stainless-steel tubing.

[13] a) T. Sakakura, T. Sodeyama, K. Sasaki, K. Wada, M. Tanaka, *J. Am. Chem. Soc.* **1990**, *112*, 7221–7229; b) G. P. Rosini, K. M. Zhu, A. S. Goldman, *J. Organomet. Chem.* **1995**, *504*, 115–121; c) G. P. Rosini, W. T. Boese, A. S. Goldman, *J. Am. Chem. Soc.* **1994**, *116*, 9498–9505.

[14] M. Tanaka, T. Sakukara, in *Homogeneous Transition Metal Catalyzed Reactions* (Eds.: W. R. Moser, D. W. Slocum); Advances in Chemistry Series 230; American Chemical Society: Washington, DC, **1992**, chapter 12, pp 181–196.

[15] F. Gao, K. P. Ng, C. Li, K. I. Krummel, A. D. Allian, M. A. Garland, *J. Catal*. **2006**, *237*, 49–57.

[16] T. F. Wang, T. Y. Lee, *J. Organomet. Chem.* **1992**, *423*, 31–38.

[17] P. Jutzi, J. Dahlhaus, *Synthesis* **1993**, *7*, 684–686.

[18] P. Singh, M. D. Rausch, *J. Organomet. Chem.* **1988**, *352*, 273–282.

[19] R. G. Ball, W. A. G. Graham, D. M. Heinekey, J. K. Hoyano, A. D. McMaster, B. M. Mattson, S. T. Michel, *Inorg. Chem.* **1990**, *29*, 2023–2025.

[20] M. S. Blais, J. C. W. Chien, M. D. Raush, *Organometallics* **1998**, *17*, 3775–3783.

[21] M. S. Blais, M. D. Rausch, *J. Organomet. Chem.* **1995**, *502*, 1–8.

[22] P. Jutzi, M. O. Kristen, B. Neumann, H. G. Stammler, *Organometallics* **1994**, *13*, 3854–3861.

Received: November 24, 2005
Published Online: February 28, 2006

 © 2006 Wiley-VCH Verlag GmbH & Co. KGaA, Weinheim 

DOI: 10.1002/ejic.200501073

# Enolate-Phosphane Ligands Providing a Tool for the Selective Substitution of Triphenylphosphane by Carbon Monoxide or Trimethylphosphane in Complex {Ru(Cp)[$\eta^2$-*P*,*O*-$Ph_2PCH_2C(t$Bu)=O](PPh$_3$)}[$PF_6$], and Subsequent Reactivity Towards Terminal Alkynes

**Bernard Demerseman*[a] and Loïc Toupet[a]**

**Keywords:** Cyclopentadienyl ligands / Metallacycles / Phosphane ligands / Ruthenium / Vinylidene ligands

The deprotonation under basic conditions of the keto-phosphane ligand in complexes {Ru(Cp)[$\eta^1$-*P*-$Ph_2PCH_2C$(=O)-*t*Bu](PPh$_3$)(L)}[$PF_6$] (L = CO or $PMe_3$) that arise from the addition of L to {Ru(Cp)[$\eta^2$-*P*,*O*-$Ph_2PCH_2C(t$Bu)=O](PPh$_3$)}[$PF_6$] generates {$Ru^+$(Cp)[$\eta^1$-*P*-$Ph_2PCH$=C(*t*Bu)$O^-$](PPh$_3$)(L)} zwitterionic species, as shown by an X-ray crystal structure determination (L = CO). The removal of the triphenylphosphane ligand is subsequently achieved under thermal activation to afford the neutral derivatives Ru(Cp)[$\eta^2$-*P*,*O*-$Ph_2PCH$=C-(*t*Bu)O](L). A further protonation step is sufficient to complete the formation of the new complex {Ru(Cp)[$\eta^2$-*P*,*O*-$Ph_2PCH_2C(t$Bu)=O](PMe$_3$)}[$PF_6$], which reacts in methanol at reflux with 1,1-diphenyl-2-propyn-1-ol to afford the six-membered metallacyclic derivative {Ru(Cp)[$\eta^2$-*C*,*P*:C(CH=$CPh_2$)OC(*t*Bu)=CH–$PPh_2$](PMe$_3$)}[$PF_6$], as shown by an X-ray single crystal analysis. The synthesis of related $\eta^5$-indenyl ruthenium complexes and of {Ru(Cp)-(=C=$CH_2$)[$Ph_2PCH_2C$(=O)*t*Bu](PR$_3$)}[$PF_6$] ($PR_3$ = $PPh_3$ or $PMe_3$) vinylidene complexes is also reported.

(© Wiley-VCH Verlag GmbH & Co. KGaA, 69451 Weinheim, Germany, 2006)

## Introduction

Enolato-phosphane chelates derived from β-keto-phosphanes associate an ancillary phosphorus coordinating centre with a strongly coordinating but reactive enolate moiety. Thus, the enolato function had been shown to interfere in the 1-alkyne to vinylidene rearrangement when coordination of 1-alkynes at a ruthenium centre was additionally instigated. As depicted on Scheme 1, carbon–carbon bond formation occurred and resulted in cationic metallacyclic derivatives **A** and **B**.[1–3]

On the other hand, protonation of the enolato function under acidic conditions converted the chelate into a hemilabile β-keto-phosphane one, where the oxygen atom might compare to a weakly coordinating ketone.[4–6] Taking advantage of the hemilabile property of β-keto-phosphanes in related cyclopentadienyl ruthenium complexes, the synthesis of allenylidene ruthenium derivatives had been achieved (Scheme 1).[7] A further deprotonation of the $\eta^1$-*P*-coordinated keto-phosphane still resulted in a formal carbon–carbon coupling reaction between an enolate moiety and the allenylidene ligand to afford a neutral ruthenaphosphacyclobutane derivative (**C**).

These results emphasised the nucleophilic character of the enolate moiety from functional enolato-phosphane chelate, or generated in situ under basic conditions from $\eta^1$-*P*-coordinated keto-phosphane. We wish to report now (i) an unusual $\eta^1$-*P* coordination mode of an enolate-phosphane ligand in new zwitterionic cyclopentadienyl ruthenium complexes, (ii) the reactivity of the uncoordinated anionic enolate moiety, which provides a new tool to cleanly achieve ligand-exchange reactions, and (iii) the formation of a ruthenaoxophosphacyclohexadiene ring, which may be formally summarised as an oxygen–carbon coupling reaction between an allenylidene ligand and an $\eta^1$-*P*-coordinated enol-phosphane.

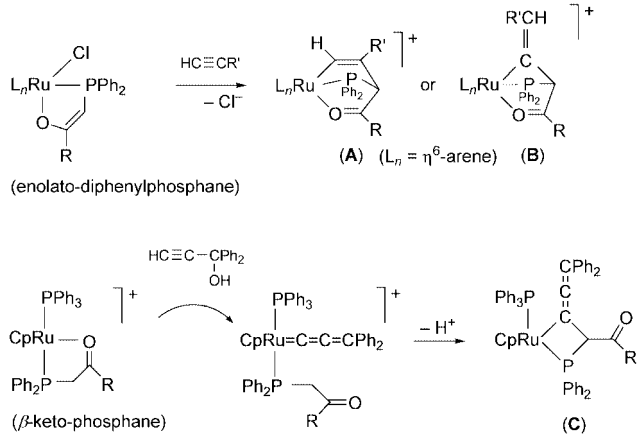


Scheme 1. Carbon–carbon coupling reactions leading to ruthenacycles **A**–**C**.

[a] Institut de Chimie de Rennes, UMR-CNRS 6509, Organométalliques et Catalyse, Université de Rennes 1,
35042 Rennes Cedex, France
Fax: +33-223236939
E-mail: bernard.demerseman@univ-rennes1.fr

 © 2006 Wiley-VCH Verlag GmbH & Co. KGaA, Weinheim 

## Results and Discussion

The hemilabile property of the β-keto-phosphane in the cyclopentadienyl ruthenium complex {Ru(Cp)[η²-*P*,*O*-$Ph_2PCH_2C(tBu)$=O](PPh₃)}[PF₆] (**1a**) allowed the entrance not only of 1-alkynols or carbon monoxide as reported previously,[7] but also of phosphorus ligands such as trimethylphosphane or trimethyl phosphite [Equation (1)].

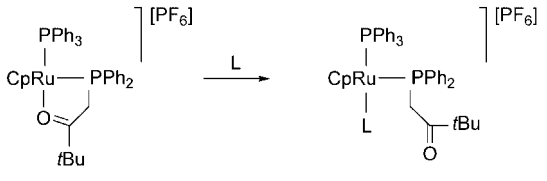


(1)

The new complexes **2c**,**d** were thus isolated as yellow solids in a nearly quantitative yield and were characterised by a combination of $^1H$, $^{13}C\{^1H\}$, $^{13}C$ and $^{31}P\{^1H\}$ NMR, IR spectroscopy, and elemental analysis. The $^1H$ and $^{31}P\{^1H\}$ NMR spectra accounted for the coordination of the phosphorus ligands besides the cyclopentadienyl one while IR spectroscopy indicated the η¹-*P*-coordination mode of the keto-phosphane.[7] Attempts to achieve a similar entrance of triphenylphosphane failed. Indeed, steric congestion in the putative expected complex {Ru(Cp)[η¹-*P*-$Ph_2PCH_2C(=O)tBu$](PPh₃)₂}[PF₆] was believed to be responsible for the easy synthesis of **1a**, by reacting the keto-phosphane $Ph_2PCH_2C(=O)tBu$ with RuCl(Cp)(PPh₃)₂ and $NH_4PF_6$ in methanol as solvent.[7] The loss of steric constraints in complexes **2b**–**d** provided thermal stability and complexes **2b**–**d** remained unchanged when they were heated in toluene at reflux. Unfortunately, such thermal stability precluded a removal of the triphenylphosphane ligand in **2b**–**d** and thus an easy recovery of the chelate coordination mode of the keto-phosphane.

The generation of an enolate anion might be expected to enhance the reactivity of the oxygen atom from the keto-phosphane when involved as an η¹-*P*-coordinated ligand, but such a formation would require basic conditions. No reaction was detected when an excess of KOH was added to a stirred solution of **2b** in methanol. However, a subsequent complete removal of volatiles under prolonged vacuum at room temperature resulted in the formation of the new enolate-phosphane complex **3b** [Equation (2)].

Complex **3b** was isolated in 79% yield as orange crystals that were found to be stable in air and could be kept at room temperature. IR spectroscopy indicated the retention of a carbon monoxide ligand ($\tilde{\nu}$ = 1959 cm⁻¹) and the conversion of the keto-function into an enolate one ($\tilde{\nu}$ = 1489 cm⁻¹). The $^{31}P\{^1H\}$ NMR spectrum of **3b** indicated the coordination of two phosphorus atoms with a normal coupling constant value ($^2J_{PP}$ = 26.7 Hz). More noteworthy was the observation by $^1H$ NMR spectroscopy of a doublet at $\delta$ = 3.66 ppm exhibiting a high $^2J_{PH}$ coupling constant

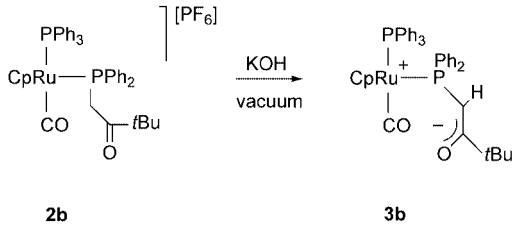


(2)

value of 27.1 Hz and assigned to the PCH= proton, whereas the $^{13}C\{^1H\}$ NMR resonance of the corresponding carbon nucleus displayed usual features ($\delta$ = 60.6 ppm, $^1J_{PC}$ = 70.9 Hz). Further characterisation of **3b** was obtained from an X-ray crystal structure determination. An ORTEP drawing of **3b** is shown in Figure 1, and selected bond lengths and angles are given in the caption.

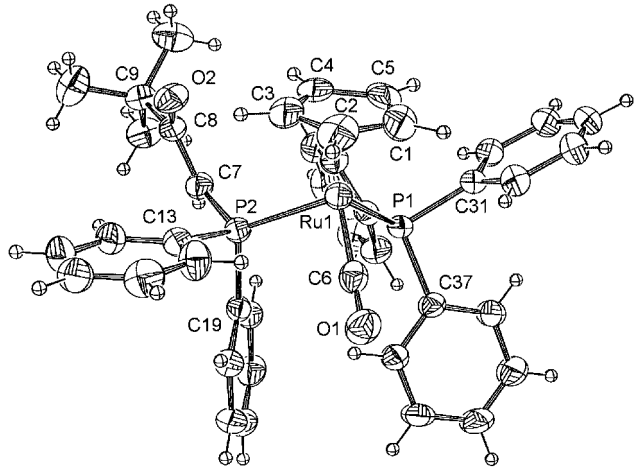


Figure 1. ORTEP drawing of **3b**·$CH_2Cl_2$ showing 50% probability thermal ellipsoids. The $CH_2Cl_2$ molecule is omitted for clarity. Selected bond lengths [Å] and angles [°]: Ru1–C6 1.858(5), Ru1–P1 2.339(1), Ru1–P2 2.370(1), C7–C8 1.379(5), C8–C9 1.561(6), C8–O2 1.271(5), P2–C7 1.759(4); C7–C8–C9 120.1(4), C7–C8–O2 124.1(4), C8–C7–P2 123.7(3), C9–C8–O2 115.8(4), C7–P2–Ru1 120.7(1), C6–Ru1–P1 90.5(1), C6–Ru1–P2 91.3(1), P1–Ru1–P2 99.19(4).

Complex **3b** disclosed a classical piano-stool geometry involving an η⁵-cyclopentadienyl ruthenium moiety. One carbon monoxide ligand and two phosphorus atoms complete the coordination of a formal $Ru^+$ centre. Moreover, the two Ru–P bond lengths are close [Ru1–P1: 2.339(1), Ru1–P2: 2.370(1) Å], thus providing straightforward evidence for a normal coordination of the functionalised phosphane. The C7–C8 and C8–O2 bond lengths [1.379(5) and 1.271(5) Å, respectively] clearly indicated a marked double bond character, as expected for an anionic enolate fragment. Therefore, complex **3b** is best described as a zwitterionic compound. Remarkably, the O2 oxygen atom lies in a *cis* position relative to the P2 phosphorus atom, thus in a favourable position for a subsequent coordination of the oxygen atom.

The removal of the triphenylphosphane ligand in **3b** was achieved by heating at reflux a solution of **3b** in THF monitored by $^{31}P\{^1H\}$ NMR spectroscopy as having a new sing-

 © 2006 Wiley-VCH Verlag GmbH & Co. KGaA, Weinheim 

let resonance at $\delta$ = 61.4 ppm, besides a singlet resonance, as might be expected from the presence of free triphenylphosphane [Equation (3)].

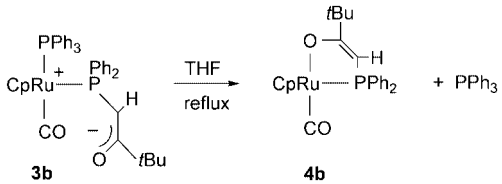


**3b** **4b** (3)

Attempts to separate the enolato-phosphane derivative **4b** from free triphenylphosphane by generating under acidic conditions a less soluble cationic $\{Ru(Cp)[Ph_2PCH_2C(tBu)=O](CO)\}^+$ species immediately showed the additional coordination of triphenylphosphane leading to the recovery of cationic **2b**. The addition of $ICH_3$ to convert the free phosphane into the corresponding phosphonium salt was more successful. The neutral complex **4b** was then selectively extracted with diethyl ether and isolated as orange-yellow crystals in 72% yield. Of interest is the comparison of the $^1H$ and $^{13}C\{^1H\}$ NMR spectra of **4b** and **3b**, which showed in the case of **4b** the PCH= proton resonance as a doublet at $\delta$ = 4.85 ppm with a normal $^2J_{PH}$ coupling constant value of 4.1 Hz, while the corresponding $^{13}C\{^1H\}$ NMR resonance ($\delta$ = 74.0 ppm, $^1J_{PC}$ = 61.9 Hz) appeared moderately low-field shifted, relative to **3b**.

The study of the reaction between **2c** (L = $PMe_3$) and KOH in methanol as solvent under similar experimental conditions was disappointing, as the $^{31}P\{^1H\}$ NMR spectrum of the crude product showed a major presence of unreacted **2c**. However, a new set of resonances might indicate a partial formation of the expected zwitterionic intermediate and thus suggested that more drastic experimental conditions would allow completion of the reaction. Indeed, the enolato-diphenylphosphane complex **4c** was straightforwardly obtained when NaH was used as a base in THF at reflux [Equation (4)]. A subsequent treatment under acidic conditions (addition of anhydrous HCl and $NH_4PF_6$ in methanol as solvent) led to the new cationic derivative $\{Ru(Cp)[Ph_2PCH_2C(tBu)=O](PMe_3)\}[PF_6]$ (**1c**) [Equation (4)].

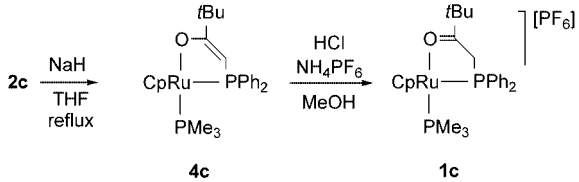


**4c** **1c** (4)

With the addition of trimethylphosphane to **1a** to generate **2c**, as a supplementary step, the whole process achieved the selective substitution of the triphenylphosphane ligand in **1a** by a trimethylphosphane one, to afford **1c** in 73% yield. NMR and IR spectroscopy, and elemental analysis accounted for the structure of the stable complexes **4c** and **1c**.

Further emphasising the usefulness of the hemilabile property of the keto-phosphane ligand to conveniently allow the entrance of an additional ligand, complexes **1a**,**c** reacted with ethyne under very mild conditions (1 atm, room temperature) to afford the new vinylidene complexes **5a**,**c** [Equation (5)].

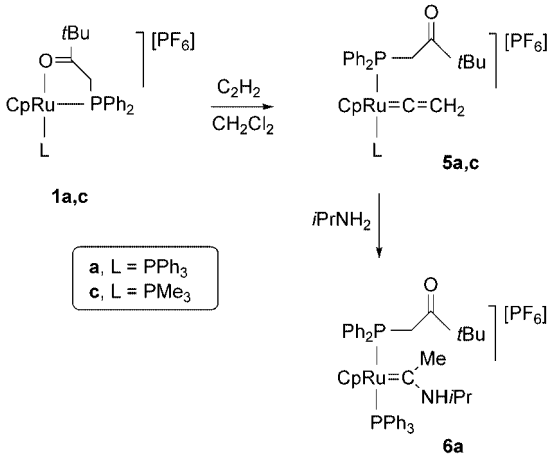


**1a,c** **5a,c** **6a** (5)

Complexes **5a**,**c** were isolated as yellow-brown crystals in 93% and 92% yield, respectively, and fully characterised by $^1H$, $^{13}C\{^1H\}$, $^{13}C$ and $^{31}P\{^1H\}$ NMR spectroscopy, and elemental analysis. Several unsubstituted vinylidene ruthenium complexes have been reported previously,[8] but the almost quantitative formation of **5a**,**c** using ethyne under mild conditions, and avoiding any formation of by-product, is noteworthy. Under the same experimental conditions, the parent complex $RuCl(Cp)(PMe_2Ph)_2$ reacted with ethyne in the presence of $TlBF_4$ to afford the $\eta^2$-ethyne complex $Ru(Cp)(\eta^2\text{-}C_2H_2)(PMe_2Ph)_2$, from which the 1-alkyne to vinylidene rearrangement needed a thermal activation to occur.[9] Similar observations were made starting from $RuCl(Cp)(PMe_3)_2$,[10] and the mechanism of the isomerisation has been fully investigated.[11] The $^{13}C\{^1H\}$ NMR spectra of **5a**,**c** showed a very low-field resonance at $\delta$ = 346.6 and 345.5 ppm, respectively, and thus unambiguously provided evidence for the presence of a vinylidene ligand. Furthermore, complexes **5a**,**c** easily added primary amines such as isopropylamine to afford amino-carbene derivatives, as emphasised by the formation of complex **6a** [Equation (5)]. Like the vinylidene ruthenium complexes **5a**,**c**, the amino-carbene derivative **6a** was a robust compound, which could be kept in air at room temperature.

The labile keto-oxygen ligand in complexes **1a**,**c** also allowed the entrance of 1-alkynols and the synthesis of the allenylidene derivative $\{Ru(Cp)(=C=C=CPh_2)[Ph_2PCH_2C(=O)tBu](PPh_3)\}[PF_6]$ by reacting **1a** with 1,1-diphenyl-2-propyn-1-ol in methanol at reflux has already been reported.[7] By contrast, a distinct complex **7c** was selectively formed when the same alkynol was treated with **1c** under similar experimental conditions (Scheme 2).

 © 2006 Wiley-VCH Verlag GmbH & Co. KGaA, Weinheim 

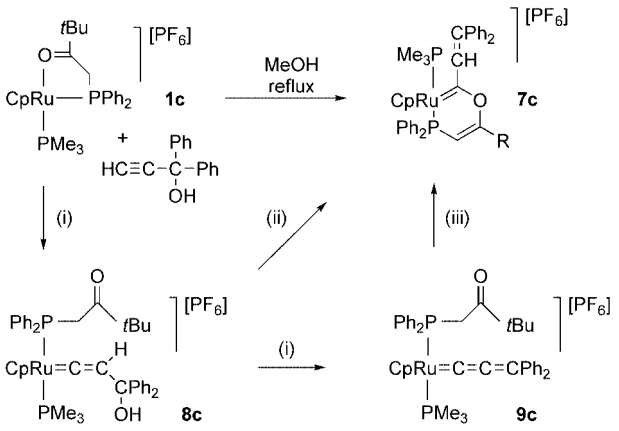


Scheme 2. Reactivity of complex **1c** towards 1,1-diphenyl-2-propyn-1-ol: (i) in $CH_2Cl_2$ as solvent, (ii) in MeOH as solvent (room temperature), (iii) in $CH_2Cl_2$ as solvent and in the presence of aqueous $K_2CO_3$.

Such a formation of **7c** in methanol also occurred at room temperature but the completion of the reaction needed 10 days instead of 1 h under reflux conditions. The stable complex **7c** was isolated in 69% yield as dark-red crystals. The $^{31}P\{^1H\}$ NMR spectrum of **7c** indicated the retention of two coordinating phosphorus centres, while $^1H$ NMR and IR spectroscopy both indicated the transformation of the keto-phosphane into an enolate-phosphane. Furthermore, the $^{13}C\{^1H\}$ NMR spectrum of **7c** exhibited a very low-field resonance at $\delta$ = 286.1 ppm and thus suggested that a carbene ligand completed the coordination of the ruthenium centre. Finally, an X-ray crystal structure determination of **7c** showed a vinyl-carbene ligand to formally arise from an addition at the $C_\alpha$ position of an allenylidene ligand of the enol form of an $\eta^1$-*P*-coordinated keto-phosphane. An ORTEP drawing of **7c** is shown in Figure 2, and selected bond lengths and angles are given in the caption.

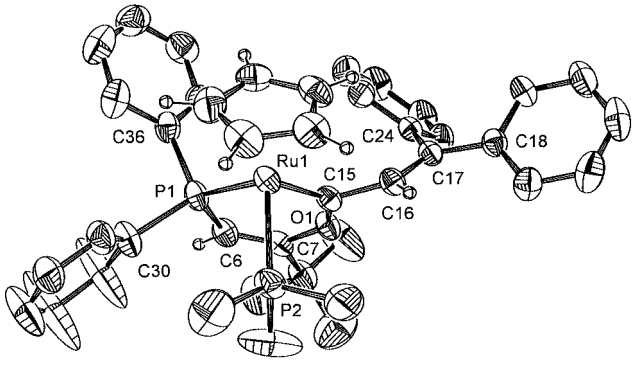


Figure 2. ORTEP drawing of **7c** showing 50% probability thermal ellipsoids. The hydrogen atoms and the $PF_6$ anion are omitted for clarity. Selected bond lengths [Å] and angles [°]: Ru1–C15 1.924(3), Ru1–P1 2.2497(7), Ru1–P2 2.3197(8), C6–C7 1.319(4), C7–O1 1.393(3), P1–C6 1.776(3), C15–C16 1.472(4), C16–C17 1.354(4); C6–P1–Ru1 113.2(1), C7–C6–P1 125.6(2), C6–C7–O1 125.7(3), C7–O1–C15 128.1(2), O1–C15–Ru1 134.3(2), C15–Ru1–P1 90.21(8), C15–Ru1–P2 89.62(8), P1–Ru1–P2 95.57(3), Ru1–C15–C16 119.1(2), C15–C16–C17 129.0(3).

Figure 2 displays a piano-stool geometry where a carbene and two phosphorus ligands complete the coordination of a formal cationic $\eta^5$-cyclopentadienyl ruthenium fragment. One phosphorus and the (carbene)-carbon atoms are involved in a six-membered metallacycle that is closely planar, as monitored by a sum of internal angles of 717.1°, close to 720°. Furthermore, the ruthenacycle compares with a 1,4-cyclohexadiene ring wherein the Ru1–P1–C6 and C7–O1–C15 fragments are linked through two short C6–C7 and Ru1–C15 double bonds [1.319(4) and 1.924(3) Å, respectively].

The formation of **7c** was strongly dependent on the nature of the solvent and became almost negligible when the reaction between **1c** and 1,1-diphenyl-2-propyn-1-ol was conducted in dichloromethane at room temperature. As monitored by $^{31}P\{^1H\}$ NMR spectroscopy, the complete consumption of **1c** in dichloromethane as solvent was virtually achieved after 20 h and the reaction mixture disclosed a major presence (ca. 85% as determined by $^1H$ NMR spectroscopy) of the hydroxy-vinylidene complex **8c** (Scheme 2). Complex **8c** then gradually disappeared, leaving the allenylidene ruthenium complex **9c** as the final product after 3 days; no further change was detected after 10 days. Complex **9c** can be rapidly synthesised by reacting **1c** and the alkynol in THF at reflux. The structure of complexes **8c** and **9c** was inferred from $^1H$, $^{13}C\{^1H\}$, $^{13}C$ and $^{31}P\{^1H\}$ NMR spectroscopic studies. Thus, the $^1H$ NMR spectrum of **8c** showed two additional resonances relative to the spectrum of **9c**, at $\delta$ = 3.19 (s) and 5.25 (dd, $^4J_{PH}$ = 2.5 and 1.6 Hz) ppm, which might reasonably be assigned to the OH and Ru=C=CH protons, respectively.[12,13] The formation of the allenylidene complex $[Ru(Cp)(=C=C=CPh_2)(PMe_3)_2][PF_6]$ similarly involved a hydroxy-vinylidene intermediate when $RuCl(Cp)(PMe_3)_2$ was treated with 1,1-diphenyl-2-propyn-1-ol.[14] Moreover, several hydroxy-vinylidene complexes have been later isolated and characterised as pentamethylcyclopentadienyl ruthenium derivatives.[12,13]

The formation of the isomeric complexes **7c** and **9c**, in methanol and in dichloromethane as solvent, respectively, was intriguing. Two supplementary experiments were significantly informative. First, a mixture of **8c** and **9c** in an approximately 1:1 molar ratio was formed in dichloromethane and the solvent was evaporated under vacuum. The residue was dissolved in methanol and the solution was stirred at room temperature for 20 h. The examination of the resulting solution by $^{31}P\{^1H\}$ NMR spectroscopy surprisingly disclosed a mixture of **7c** and **9c**, indicating a conversion of **8c** into **7c** but also a passiveness of the allenylidene complex **9c** (Scheme 2). However, a very slow isomerisation of **9c** into **7c**, needing 10 days to complete, was observed to occur in methanol at ambient temperature.

In the second experiment, a small amount of a 0.07 M $K_2CO_3$ aqueous solution was added to a solution of **9c** in dichloromethane. On stirring, the colour of the solution rapidly (<1 h) turned from violet to red and although a deprotonation of the keto-phosphane in **9c** under such mild heterogeneous conditions was unlikely, **7c** was observed to

 © 2006 Wiley-VCH Verlag GmbH & Co. KGaA, Weinheim 

be quantitatively formed by $^{31}P\{^1H\}$ NMR spectroscopy (Scheme 2).

These observations suggested that the coupling process leading to **7c** preliminarily required the formation of an intermediate that would arise either from **8c** in methanol or from the addition of hydroxide anion to **9c**. As depicted in Scheme 3, a plausible candidate consisted of a neutral alkynyl complex arising from a deprotonation (requiring a solvent with proton-acceptor ability such as methanol) of the vinylidene ligand in **8c**, or from the addition of hydroxide anion at the γ position of the allenylidene ligand in **9c**. A subsequent proton migration from the keto-fragment to the alkynyl ligand would subsequently lead to **7c**. Finally, the presence of a bulkier triphenylphosphane ligand in **1a** might sufficiently hinder closeness between the keto function and the alkynyl chain to preclude a similar coupling process.

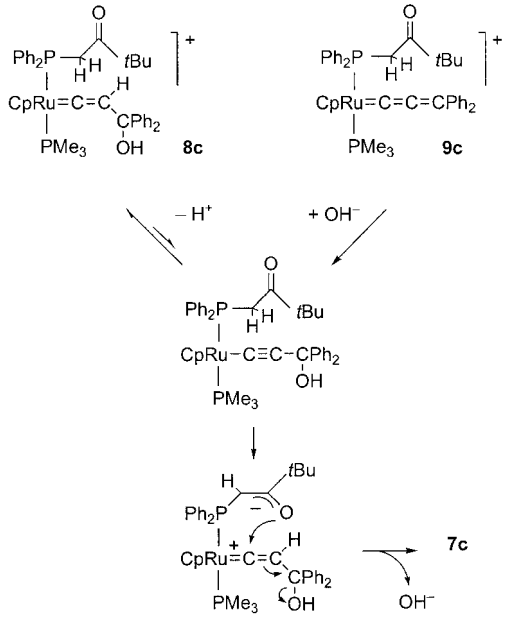


Scheme 3. Rationale accounting (i) for the formation of **7c** in methanol and (ii) for the isomerisation of **9c** into **7c** catalysed by hydroxide anions.

The reactions allowing the synthesis of the trimethylphosphane derivatives **2c**, **1c** and **7c** tolerated the presence of an indenyl ligand instead of the cyclopentadienyl one. As summarised in Scheme 4, the indenyl ruthenium precursor complex {Ru(Ind)[$\eta^2$-*P*,*O*-$Ph_2PCH_2C(tBu)$=O](PPh$_3$)}[PF$_6$] (**1′a**) (Ind = $\eta^5$-$C_9H_7$)[7] easily added trimethylphosphane to afford **2′c**, which was isolated as orange-red crystals, in 89% yield. Treatment of **2′c** with NaH in THF under reflux and subsequent work under acidic conditions (HCl + $NH_4PF_6$) led to **1′c**, which was isolated as orange crystals, in 77% yield. Finally, complex **1′c** reacted with 1,1-diphenyl-2-propyn-1-ol in methanol at reflux to afford **7′c** isolated as deep-red crystals, in 71% yield. The $^1H$, $^{13}C\{^1H\}$, $^{13}C$ and $^{31}P\{^1H\}$ NMR spectroscopic data collected for **7′c** unambiguously indicated a similar structure relative to complex **7c**.

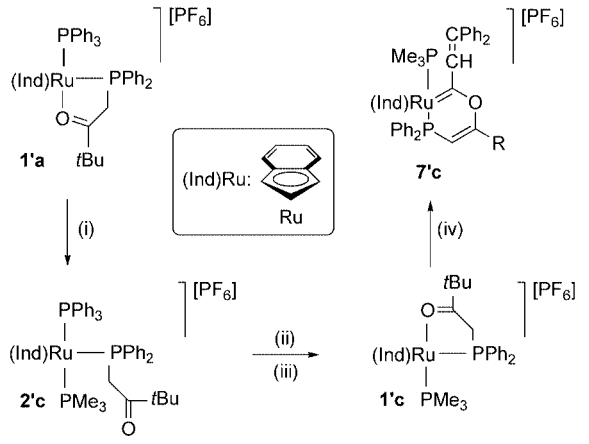


Scheme 4. Synthesis of the new complexes **2′c**, **1′c** and **7′c**: (i) $PMe_3$, $CH_2Cl_2$, (ii) NaH, THF, reflux, (iii) HCl, $NH_4PF_6$, MeOH, (iv) HC≡CC(OH)$Ph_2$, MeOH, reflux.

## Conclusions

The deprotonation of an $\eta^1$-*P*-coordinated β-keto-phosphane in cyclopentadienyl or indenyl ruthenium complexes was achieved under basic conditions and was observed to enhance the affinity of the oxygen atom to coordinate the metal centre. Subsequent removal of a triphenylphosphane ligand was facilitated and allowed the chelate coordination mode of the functionalised phosphane. Thus, using the β-keto-phosphane as a tool, the substitution of a triphenylphosphane ligand by a less sterically demanding ligand such as carbon monoxide or trimethylphosphane was achieved. Furthermore, such a synthesis offered an opportunity to compare two analogous complexes but with distinct steric constraints. The presence of the hemilabile β-keto-phosphane not only allowed an easy additional coordination of ethyne but also facilitated further rearrangement into vinylidene derivatives. The coordination of 1-alkynols similarly led to allenylidene complexes, but the presence of a reactive functionalised phosphane might interfere in the process to afford new metallacyclic complexes.

## Experimental Section

**General Comments:** The reactions were performed under inert argon according to Schlenk-type techniques. THF, diethyl ether and dichloromethane were distilled after drying according to conventional methods. NMR spectra were recorded at 297 K with an AC 300 Bruker instrument and referenced internally to the solvent peak. IR spectra were recorded as Nujol mulls with Bruker IFS28. Elemental analyses were performed by the "Service de Microanalyse du CNRS", Vernaison, France. Complexes **1a** (as its dichloromethane adduct) and **1′a** were prepared as described previously.[7]

**{Ru(Cp)[$Ph_2PCH_2C$(=O)*t*Bu](PPh$_3$)(CO)}[PF$_6$] (2b):** In a 125 mL stainless steel vessel, a solution of **1a** (13.8 g, 14.6 mmol) in dichloromethane (70 mL) was stirred for 3 days at room temperature under carbon monoxide pressure (65 atm). The resulting solution was concentrated under vacuum (≈40 mL) before being covered with methanol (10 mL) and then diethyl ether (160 mL), to afford lemon-yellow crystals. Yield: 11.9 g, 92%. $^{13}C\{^1H\}$ NMR (75.47 MHz, $CD_2Cl_2$): $\delta$ = 25.7 (s, $CMe_3$), 35.9 (d, $^1J$ = 29.4 Hz,

 © 2006 Wiley-VCH Verlag GmbH & Co. KGaA, Weinheim 

$PCH_2$), 45.5 (d, $^3J$ = 1.5 Hz, $CMe_3$), 90.9 (s, Cp), 129.0–135.1 (m, 5 Ph groups), 202.5 (t, $^2J \approx 17.8$ Hz, C≡O), 207.6 (d, $^2J$ = 8.2 Hz, C=O) ppm. $^1H$ and $^{31}P\{^1H\}$ NMR, and IR spectroscopic data were given elsewhere.[7]

**{Ru(Cp)[$Ph_2PCH_2C$(=O)*t*Bu](PPh$_3$)(PMe$_3$)}[PF$_6$] (2c):** A 1.0 M solution of trimethylphosphane in THF (8.0 mL, 8.0 mmol) was added to a stirred solution of **1a** (7.04 g, 7.47 mmol) in THF (40 mL). The mixture was further stirred overnight to obtain a yellow precipitate, which was collected by filtration, then washed with diethyl ether and dried under vacuum. Yield: 7.00 g, 100%. IR: $\tilde{\nu}$ = 1699 cm$^{-1}$, C=O. $^1H$ NMR (300.13 MHz, $CD_2Cl_2$): $\delta$ = 0.64 (s, 9 H, *t*Bu), 1.45 (d, $^2J_{PH}$ = 8.6 Hz, 9 H, $PMe_3$), 2.99 (dd, $^2J_{HH}$ = 16.4, $^2J_{PH}$ = 8.5 Hz, 1 H, $PCH_2$, $H_a$), 3.16 (dd, $^2J_{HH}$ = 16.4, $^2J_{PH}$ = 4.0 Hz, 1 H, $PCH_2$, $H_b$), 4.68 (s, 5 H, Cp), 6.80–7.47 (m, 25 H, Ph) ppm. $^{31}P\{^1H\}$ NMR (121.50 MHz, $CD_2Cl_2$): $\delta$ = –10.4 (t, $^2J_{PP} \approx {}^2J_{PP'} \approx$ 38 Hz, PMe), 36.9 (t, $^2J_{PP} \approx {}^2J_{PP'} \approx$ 38 Hz), 43.9 (t, $^2J_{PP} \approx {}^2J_{PP'} \approx$ 38 Hz) ppm. $C_{44}H_{50}F_6OP_4Ru$ (933.84): calcd. C 56.59, H 5.40; found C 56.66, H 5.87.

**{Ru(Cp)[$Ph_2PCH_2C$(=O)*t*Bu](PPh$_3$)[P(OMe)$_3$]}[PF$_6$] (2d):** Trimethyl phosphite (0.80 mL, 6.78 mmol) was added to a solution of **1a** (3.00 g, 3.18 mmol) in dichloromethane (50 mL). After being stirred overnight, the solution was evaporated to dryness to leave the crude product. Recrystallisation from dichloromethane (20 mL) and diethyl ether (110 mL) afforded thin yellow needles that were collected by filtration. Yield: 3.05 g, 98%. IR: $\tilde{\nu}$ = 1703 cm$^{-1}$, C=O. $^1H$ NMR (300.13 MHz, $CDCl_3$): $\delta$ = 0.55 (s, 9 H, *t*Bu), 2.43 (dd, $^2J_{HH}$ = 16.1, $^2J_{PH}$ = 10.8 Hz, 1 H, $PCH_2$, $H_a$), 3.71 (d, $^3J_{PH}$ = 10.8 Hz, 10 H, POMe and hidden $PCH_2$, $H_b$), 4.71 (d, $^2J_{PH}$ = 0.7 Hz, 5 H, Cp), 6.92–7.61 (m, 25 H, Ph) ppm. $^{31}P\{^1H\}$ NMR (121.50 MHz, $CDCl_3$): $\delta$ = 41.9 (dd, $^2J_{PP}$ = 63 and 32 Hz, PPh), 45.9 (dd, $^2J_{PP}$ = 63 and 32 Hz, PPh), 144.3 (t, $^2J_{PP} \approx {}^2J_{PP'} \approx$ 63 Hz, POMe) ppm. $C_{44}H_{50}F_6O_4P_4Ru$ (981.84): calcd. C 53.83, H 5.13, P 12.62; found C 53.73, H 5.10, P 12.34.

**Ru$^+$(Cp)[$\eta^1$-*P*-$Ph_2PCH$=C(*t*Bu)O$^-$](PPh$_3$)(CO)·$CH_2Cl_2$ (3b):** A mixture consisting of a sample of **2b** (3.00 g, 3.39 mmol), KOH (0.31 g, 5.54 mmol) and methanol (50 mL) was stirred for 3 days at room temperature. The resulting pale-yellow slurry was evaporated under vacuum until an orange colour was observed, and the residue was extracted with dichloromethane (20 mL). The solution was filtered and the orange filtrate was covered with diethyl ether (100 mL). The subsequent diffusion of solvents was conducted at –20 °C to avoid decomposition, and afforded large orange crystals, which were washed with hexane (20 mL). Yield: 2.20 g, 79%. IR: $\tilde{\nu}$ = 1489 cm$^{-1}$, C=CO; 1959 cm$^{-1}$, C≡O. $^1H$ NMR (300.13 MHz, $CD_2Cl_2$): $\delta$ = 1.10 (s, 9 H, *t*Bu), 3.66 (d, $^2J_{PH}$ = 27.1 Hz, 1 H, PCH=), 4.98 (s, 5 H, Cp), 7.00–7.65 (m, 25 H, Ph) ppm. $^{13}C\{^1H\}$ NMR (75.47 MHz, $CD_2Cl_2$): $\delta$ = 29.6 (s, $CMe_3$), 40.7 (d, $^3J$ = 10.7 Hz, $CMe_3$), 60.6 (d, $^1J$ = 70.9 Hz, PCH=), 90.4 (s, Cp), 127.8 (d, $^2J$ = 9.9 Hz, PPh, *ortho*), 127.8 (d, $^2J$ = 10.8 Hz, PPh, *ortho*), 128.1 (d, $^4J$ = 2.7 Hz, PPh, *para*), 128.5 (d, $^2J$ = 9.9 Hz, $PPh_3$, *ortho*), 128.7 (d, $^4J$ = 2.7 Hz, PPh, *para*), 130.6 (d, $^4J$ = 1.8 Hz, $PPh_3$, *para*), 131.7 (d, $^3J$ = 9.0 Hz, PPh, *meta*), 132.6 (d, $^3J$ = 10.8 Hz, PPh, *meta*), 134.0 (d, $^3J$ = 10.8 Hz, $PPh_3$, *meta*), 135.3 (d, $^1J$ = 48.5 Hz, $PPh_3$, *ipso*), 140.8 (d, $^1J$ = 53.0 Hz, PPh, *ipso*), 141.7 (d, $^1J$ = 50.3 Hz, PPh, *ipso*), 191.9 (s, =CO), 205.6 (dd, $^2J$ = 19.3 and 15.7 Hz, C≡O) ppm. $^{13}C$ NMR (75.47 MHz, $CD_2Cl_2$, selected values): $\delta$ = 60.6 (dd, $^1J_{HC}$ = 158, $^1J_{PC}$ = 70.5 Hz, PCH=) ppm. $^{31}P\{^1H\}$ NMR (121.50 MHz, $CD_2Cl_2$): $\delta$ = 19.5 (d, $^2J_{PP}$ = 27 Hz), 47.9 (d, $^2J_{PP}$ = 27 Hz). $C_{42}H_{40}O_2P_2Ru$·$CH_2Cl_2$ (824.73): calcd. C 62.62, H 5.13, Cl 8.60, P 7.51; found C 62.36, H 5.10, Cl 7.36, P 7.51.

**Ru$^+$(Cp)[$\eta^1$-*P*-$Ph_2PCH$=C(*t*Bu)O$^-$](PPh$_3$)(PMe$_3$):** A similar treatment of **2c** with KOH in methanol was attempted, but examination of the crude product after evaporation of the resulting dichloromethane solution by $^1H$ and $^{31}P\{^1H\}$ NMR spectroscopy disclosed resonances corresponding to unreacted **2c** as well as a new set of resonances arising from the presence of the assumed zwitterionic complex. $^1H$ NMR (300.13 MHz, $CDCl_3$, available values): $\delta$ = 1.01 (s, 9 H, *t*Bu), 1.44 (d, $^2J_{PH}$ = 8.6 Hz, 9 H, $PMe_3$), 4.35 (s, 5 H, Cp) ppm. $^{31}P\{^1H\}$ NMR (121.50 MHz, $CDCl_3$, the additional presence of **2c** is omitted): $\delta$ = –5.3 (t, $^2J_{PP} \approx {}^2J_{PP'} \approx$ 42 Hz, PMe), 18.7 (dd, $^2J_{PP}$ = 42 and 35 Hz), 46.8 (dd, $^2J_{PP}$ = 42 and 35 Hz) ppm.

**Ru(Cp)[$\eta^2$-*P*,*O*-$Ph_2PCH$=C(*t*Bu)O](CO) (4b):** Crude **3b** was obtained from evaporation of the dichloromethane solution as described above starting from **2b** (13.0 g, 14.7 mmol), and then dissolved in THF (70 mL). The solution was heated at reflux for 20 h and then evaporated. Dichloromethane (60 mL) then methyl iodide (2.0 mL, 32.1 mmol, an excess) were added and this mixture was stirred overnight, then evaporated. The residue was extracted with diethyl ether (100 mL). The solution was filtered and the filtrate was evaporated to leave crude **4b**. Yield: 5.03 g, 72%. Heptane (60 mL) was added to a solution of crude **4b** in dichloromethane (30 mL) and this solution was slowly concentrated under vacuum to yield pure **4b** as a crystalline yellow powder. Orange-yellow crystals were also obtained by recrystallisation from hot hexane. IR: $\tilde{\nu}$ = 1494 cm$^{-1}$, C=CO; 1940 cm$^{-1}$, C≡O. $^1H$ NMR (300.13 MHz, $C_6D_6$): $\delta$ = 1.40 (s, 9 H, *t*Bu), 4.45 (s, 5 H, Cp), 4.85 (d, $^2J_{PH}$ = 4.1 Hz, 1 H, PCH=), 6.99–7.79 (m, 10 H, Ph) ppm. $^{13}C\{^1H\}$ NMR (75.47 MHz, $CD_2Cl_2$): $\delta$ = 29.8 (s, $CMe_3$), 39.3 (d, $^3J$ = 12.1 Hz, $CMe_3$), 74.0 (d, $^1J$ = 61.9 Hz, PCH=), 84.5 (d, $^2J$ = 1.6 Hz, Cp), 128.6 (d, $^2J$ = 10.5 Hz, PPh, *ortho*), 128.6 (d, $^2J$ = 10.8 Hz, PPh, *ortho*), 129.2 (d, $^4J$ = 2.6 Hz, PPh, *para*), 130.3 (d, $^4J$ = 2.5 Hz, PPh, *para*), 130.7 (d, $^3J$ = 11.3 Hz, PPh, *meta*), 133.3 (d, $^3J$ = 10.8 Hz, PPh, *meta*), 136.9 (d, $^1J$ = 62.0 Hz, PPh, *ipso*), 143.4 (d, $^1J$ = 46.8 Hz, PPh, *ipso*), 202.7 (d, $^2J$ = 15.5 Hz, =CO), 203.6 (d, $^2J$ = 18.9 Hz, C≡O) ppm. $^{31}P\{^1H\}$ NMR (121.50 MHz, $C_6D_6$): $\delta$ = 61.4 (s) ppm. $C_{24}H_{25}O_2PRu$ (477.51): calcd. C 60.37, H 5.28; found C 60.54, H 5.28.

**Ru(Cp)[$\eta^2$-*P*,*O*-$Ph_2PCH$=C(*t*Bu)O](PMe$_3$) (4):** The slow concentration under vacuum of a solution of crude **4c** in methanol, the preparation of which is detailed below (see synthesis of **1c**), allowed the formation of orange crystals of analytical purity. IR: $\tilde{\nu}$ = 1492 cm$^{-1}$, C=CO. $^1H$ NMR (300.13 MHz, $C_6D_6$): $\delta$ = 0.91 (d, $^2J_{PH}$ = 9.0 Hz, 9 H, $PMe_3$), 1.42 (s, 9 H, *t*Bu), 4.21 (s, 5 H, Cp), 4.95 (d, $^2J_{PH}$ = 1.3 Hz, 1 H, PCH=), 6.98–7.74 (m, 10 H, Ph) ppm. $^{31}P\{^1H\}$ NMR (121.50 MHz, $C_6D_6$): $\delta$ = 6.8 (d, $^2J_{PP}$ = 42 Hz, PMe), 64.8 (d, $^2J_{PP}$ = 42 Hz, PPh) ppm. $C_{26}H_{34}OP_2Ru$ (525.58): calcd. C 59.42, H 6.52, P 11.79; found C 59.72, H 6.71, P 12.12.

**{Ru(Cp)[$Ph_2PCH_2C$(*t*Bu)=O](PMe$_3$)}[PF$_6$] (1):** A mixture consisting of a sample of **2c** (6.13 g, 6.56 mmol), an excess of NaH (0.89 g, 37.1 mmol) and THF (80 mL) was heated at reflux for 20 h. The resulting mixture was filtered and the orange-yellow filtrate was evaporated to dryness to leave crude **4c** as a solid. The solid was dissolved in hot methanol (50 mL) to obtain an orange solution that was filtered. $NH_4PF_6$ (1.34 g, 8.22 mmol) and a 6 M solution of HCl in diethyl ether (2.0 mL, 12.0 mmol) were added to the filtrate, and the mixture was further stirred for 10 min. The resulting yellow precipitate was collected by filtration and washed with diethyl ether (50 mL), and then extracted with dichloromethane (60 mL). The solution was filtered and the filtrate was covered with methanol (20 mL) then diethyl ether (160 mL) to afford yellow crystals. Yield: 3.20 g, 73%. IR: $\tilde{\nu}$ = 1603 cm$^{-1}$, C=O. $^1H$ NMR (300.13 MHz, $CD_2Cl_2$): $\delta$ = 1.16 (d, $^2J_{PH}$ = 9.1 Hz, 9 H, $PMe_3$), 1.26 (s, 9 H, *t*Bu), 3.32 (dd, $^2J_{HH}$ = 19.3, $^2J_{PH}$ = 7.2 Hz, 1 H, $PCH_2$,

 © 2006 Wiley-VCH Verlag GmbH & Co. KGaA, Weinheim 

$H_a$), 4.23 (dd, $^2J_{HH}$ = 19.3, $^2J_{PH}$ = 10.7 Hz, 1 H, $PCH_2$, $H_b$), 4.55 (s, 5 H, Cp), 6.87–7.64 (m, 10 H, Ph) ppm. $^{31}P\{^1H\}$ NMR (121.50 MHz, $CD_2Cl_2$): $\delta$ = 2.3 (d, $^2J_{PP}$ = 39 Hz, PMe), 67.3 (d, $^2J_{PP}$ = 39 Hz, PPh) ppm. $C_{26}H_{35}F_6OP_3Ru$ (671.55): calcd. C 46.50, H 5.25, P 13.84; found C 46.18, H 5.28, P 13.84.

**{Ru(Cp)(=C=CH$_2$)[Ph$_2$PCH$_2$C(=O)*t*Bu](PPh$_3$)}[PF$_6$]·1/6CH$_2$Cl$_2$ (5a):** A solution of **1a** (3.90 g, 4.14 mmol) in dichloromethane (40 mL) was stirred for 2 days under ethyne. The resulting solution was then covered with diethyl ether (120 mL) to afford orange-brown crystals. Yield: 3.45 g, 93%. IR: $\tilde{\nu}$ = 1632 cm$^{-1}$, =C=CH$_2$; 1703 cm$^{-1}$, C=O. $^1H$ NMR (300.13 MHz, $CD_2Cl_2$): $\delta$ = 0.60 (s, 9 H, *t*Bu), 2.04 (dd, $^2J_{HH}$ = 17.6, $^2J_{PH}$ = 11.5 Hz, 1 H, $PCH_2$, $H_a$), 3.76 (dd, $^2J_{HH}$ = 17.2, $^2J_{PH}$ = 2.4 Hz, 1 H, $PCH_2$, $H_b$), 4.33 (dd, $^4J_{PH}$ = 3.1 and 1.7 Hz, 2 H, =$CH_2$), 5.06 (s, 5 H, Cp), 6.98–7.76 (m, 25 H, Ph) ppm. $^{13}C\{^1H\}$ NMR (75.47 MHz, $CD_2Cl_2$): $\delta$ = 25.8 (s, C*Me*$_3$), 32.5 (d, $^1J$ = 29.7 Hz, $PCH_2$), 45.8 (d, $^3J$ = 1.8 Hz, *C*Me$_3$), 94.9 (s, Cp), 97.5 (s, =$CH_2$), 128.7–134.9 (m, Ph resonances), 207.4 (d, $^2J$ = 9.9 Hz, C=O), 346.6 (t, $^2J \approx$ 15.7 Hz, Ru=C) ppm. $^{13}C$ NMR (75.47 MHz, $CD_2Cl_2$, selected values): $\delta$ = 97.5 (t, $^1J_{HC}$ = 165 Hz, =$CH_2$) ppm. $^{31}P\{^1H\}$ NMR (121.50 MHz, $CD_2Cl_2$): $\delta$ = 38.8 (d, $^2J_{PP}$ = 27 Hz), 45.7 (d, $^2J_{PP}$ = 27 Hz) ppm. $C_{43}H_{43}F_6OP_3Ru$·1/6$CH_2Cl_2$ (897.95): calcd. C 57.74, H 4.86, Cl 1.32, P 10.35; found C 57.44, H 4.87, Cl 1.13, P 10.06.

**{Ru(Cp)(=C=CH$_2$)[Ph$_2$PCH$_2$C(=O)*t*Bu](PMe$_3$)}[PF$_6$] (5c):** A solution of **1c** (2.07 g, 3.08 mmol) in dichloromethane (60 mL) was stirred for 2 days under ethyne. The resulting solution was then covered with diethyl ether (130 mL) to afford yellow-brown crystals. Yield: 1.97 g, 92%. IR: $\tilde{\nu}$ = 1630 cm$^{-1}$, =C=CH$_2$; 1706 cm$^{-1}$, C=O. $^1H$ NMR (300.13 MHz, $CD_2Cl_2$): $\delta$ = 1.00 (s, 9 H, *t*Bu), 1.22 (d, $^2J_{PH}$ = 10.5 Hz, 9 H, $PMe_3$), 3.80 (dd, $^2J_{HH}$ = 17.6, $^2J_{PH}$ = 9.7 Hz, 1 H, $PCH_2$, $H_a$), 4.02 (dd, $^4J_{PH}$ = 2.7 and 2.0 Hz, 2 H, =$CH_2$), 4.07 (dd, $^2J_{HH}$ = 17.6, $^2J_{PH}$ = 5.8 Hz, 1 H, $PCH_2$, $H_b$), 5.35 (s, 5 H, Cp), 7.26–7.52 (m, 10 H, Ph) ppm. $^{13}C\{^1H\}$ NMR (75.47 MHz, $CD_2Cl_2$): $\delta$ = 21.2 (d, $^1J$ = 35.9 Hz, $PMe_3$), 26.4 (s, C*Me*$_3$), 39.9 (d, $^1J$ = 33.1 Hz, $PCH_2$), 46.1 (d, $^3J$ = 2.5 Hz, *C*Me$_3$), 92.8 (s, Cp), 95.1 (s, =$CH_2$), 129.1 (d, $^2J$ = 10.8 Hz, PPh, *ortho*), 129.4 (d, $^2J$ = 10.8 Hz, PPh, *ortho*), 131.5 (d, $^4J$ = 2.7 Hz, PPh, *para*), 131.7 (d, $^4J$ = 2.7 Hz, PPh, *para*), 132.6 (d, $^3J$ = 10.8 Hz, PPh, *meta*), 132.9 (d, $^3J$ = 10.8 Hz, PPh, *meta*), 133.9 (dd, $^1J$ = 51.2, $^3J$ = 1.8 Hz, PPh, *ipso*), 135.4 (d, $^1J$ = 50.3 Hz, PPh, *ipso*), 209.0 (d, $^2J$ = 6.9 Hz, C=O), 345.5 (t, $^2J \approx$ 15.3 Hz, Ru=C) ppm. $^{13}C$ NMR (75.47 MHz, $CD_2Cl_2$, selected values): $\delta$ = 95.1 (t, $^1J_{HC}$ = 164 Hz, =$CH_2$) ppm. $^{31}P\{^1H\}$ NMR (121.50 MHz, $CD_2Cl_2$): $\delta$ = 7.4 (d, $^2J_{PP}$ = 31 Hz, PMe), 38.0 (d, $^2J_{PP}$ = 31 Hz, PPh) ppm. $C_{28}H_{37}F_6OP_3Ru$ (697.58): calcd. C 48.21, H 5.35, P 13.32; found C 48.00, H 5.46, P 13.08.

**{Ru(Cp)(=CMeNH*i*Pr)[Ph$_2$PCH$_2$C(=O)*t*Bu](PPh$_3$)}[PF$_6$] (6a):** Isopropylamine (1.00 mL, 11.7 mmol) was added to a solution of **5a** (3.02 g, 3.36 mmol) in dichloromethane (40 mL) and the mixture was stirred for 20 h. The resulting green solution was evaporated under vacuum. The residue was dissolved in dichloromethane (30 mL) and the solution was covered with diethyl ether (140 mL) to afford yellow crystals. Yield: 2.85 g, 90%. $^1H$ NMR (300.13 MHz, $CD_2Cl_2$): $\delta$ = 0.80 (s, 9 H, *t*Bu), 1.10 (d, $^3J_{HH}$ = 6.8 Hz, 3 H, CH*Me*), 1.13 (d, $^3J_{HH}$ = 6.5 Hz, 3 H, CH*Me*), 2.36 (s, 3 H, RuCMe), 2.53 (dd, $^2J_{HH}$ = 17.9, $^2J_{PH}$ = 4.4 Hz, 1 H, $PCH_2$, $H_a$), 3.64 (dd, $^2J_{HH}$ = 17.9, $^2J_{PH}$ = 12.3 Hz, 1 H, $PCH_2$, $H_b$), 4.15 (m, 1 H, C*H*Me$_2$), 4.46 (s, 5 H, Cp), 6.69–7.48 (m, 25 H, Ph), 10.4 (broad s, 1 H, NH) ppm. $^{13}C\{^1H\}$ NMR (75.47 MHz, $CD_2Cl_2$): $\delta$ = 21.3 (s, CH*Me*), 21.6 (s, CH*Me*), 26.7 (s, C*Me*$_3$), 38.0 (s, RuC*Me*), 42.3 (d, $^1J$ = 17.5 Hz, $PCH_2$), 45.4 (s, *C*Me$_3$), 51.6 (s, *C*HMe$_2$), 88.0 (s, Cp), 128.5–145.8 (m, Ph), 215.0 (d, $^2J$ = 4.5 Hz, C=O), 247.3 (dd, $^2J$ = 16.2 and 11.7 Hz, Ru=C) ppm. $^{31}P\{^1H\}$ NMR (121.50 MHz, $CD_2Cl_2$): $\delta$ = 33.9 (d, $^2J_{PP}$ = 34 Hz), 51.2 (d, $^2J_{PP}$ = 34 Hz) ppm. $C_{46}H_{52}F_6NOP_3Ru$ (942.91): calcd. C 58.60, H 5.56, N 1.49, P 9.85; found C 58.41, H 5.58, N 1.64, P 9.42.

**{Ru(Cp)[η$^2$-*C*,*P*-:C(CH=CPh$_2$)OC(*t*Bu)=CH–PPh$_2$](PMe$_3$)}[PF$_6$] (7c):** A solution of **1c** (1.52 g, 2.26 mmol) and 1,1-diphenyl-2-propyn-1-ol (0.60 g, 2.88 mmol) in methanol (30 mL) was heated at reflux for 1 h. The resulting dark-red mixture was evaporated under vacuum and the residue was dissolved in dichloromethane (35 mL). The solution was filtered and the filtrate was covered with methanol (15 mL), then diethyl ether (130 mL) to afford dark-red crystals. Yield: 1.34 g, 69%. IR: $\tilde{\nu}$ = 1556 cm$^{-1}$, C=CO; 1611 cm$^{-1}$, C=C$Ph_2$. $^1H$ NMR (300.13 MHz, $CD_2Cl_2$): $\delta$ = 0.84 (s, 9 H, *t*Bu), 1.19 (d, $^2J_{PH}$ = 10.1 Hz, 9 H, $PMe_3$), 5.24 (s, 5 H, Cp), 5.83 (d, $^2J_{PH}$ = 0.8 Hz, 1 H, PCH=), 6.87 (s, 1 H, C*H*=C$Ph_2$), 7.08–7.62 (m, 20 H, Ph) ppm. $^{13}C\{^1H\}$ NMR (75.47 MHz, $CD_2Cl_2$): $\delta$ = 21.5 (d, $^1J$ = 34.6 Hz, $PMe_3$), 27.6 (s, C*Me*$_3$), 39.0 (d, $^3J$ = 7.1 Hz, *C*Me$_3$), 85.9 (d, $^1J$ = 55.0 Hz, PCH=), 93.4 (s, Cp), 129.1–133.1 (m, set of Ph resonances), 138.4 (s, *C*$Ph_2$), 140.2 and 142.1 (2 s, C*Ph*$_2$, *ipso*), 142.2 (dd, $^1J$ = 53.9, $^3J$ = 2.7 Hz, PPh, *ipso*), 142.3 (s, *C*HC$Ph_2$), 178.3 (d, $^2J$ = 4.5 Hz, O*Ct*Bu), 286.1 (dd, $^2J$ = 15.7 and 13.9 Hz, Ru=C) ppm. $^{13}C$ NMR (75.47 MHz, $CD_2Cl_2$, selected values): $\delta$ = 85.9 (dd, $^1J_{HC}$ = 160, $^1J_{PC}$ = 55.0 Hz, PCH=), 138.4 (d, $^2J_{HC}$ = 2.7 Hz, *C*$Ph_2$), 142.3 (d, $^1J_{HC}$ = 160 Hz, *C*HC$Ph_2$) ppm. $^{31}P\{^1H\}$ NMR (121.50 MHz, $CD_2Cl_2$): $\delta$ = 5.9 (d, $^2J_{PP}$ = 36 Hz, PMe), 35.5 (d, $^2J_{PP}$ = 36 Hz, PPh) ppm. $C_{41}H_{47}F_6OP_3Ru$ (863.81): calcd. C 57.01, H 5.48, P 10.76; found C 56.88, H 5.37, P 10.37.

**{Ru(Cp)[=C=CHC(OH)Ph$_2$][Ph$_2$PCH$_2$C(=O)*t*Bu](PMe$_3$)}[PF$_6$] (8c):** An equimolar mixture of **1c** and 1,1-diphenyl-2-propyn-1-ol was dissolved in $CD_2Cl_2$ in an NMR tube and the solution was kept at room temperature. $^1H$ and $^{31}P\{^1H\}$ NMR spectra were recorded after 20 h and showed **8c** to be the major compound (≈85%). $^1H$ NMR (300.13 MHz, $CD_2Cl_2$, the presence of residual **1c** and of **9c** is omitted): $\delta$ = 0.93 (s, 9 H, *t*Bu), 1.10 (d, $^2J_{PH}$ = 10.6 Hz, 9 H, $PMe_3$), 3.19 (s, 1 H, OH), 3.81 (dd, $^2J_{HH}$ = 17.8, $^2J_{PH}$ = 9.1 Hz, 1 H, $PCH_2$, $H_a$), 4.21 (dd, $^2J_{HH}$ = 17.8, $^2J_{PH}$ = 6.1 Hz, 1 H, $PCH_2$, $H_b$), 5.25 (dd, $^4J_{PH}$ = 2.5 and 1.6 Hz, 1 H, =CH), 5.35 (s, 5 H, Cp), 7.26–7.61 (m, 20 H, Ph) ppm. $^{31}P\{^1H\}$ NMR (121.50 MHz, $CD_2Cl_2$): $\delta$ = 8.9 (d, $^2J_{PP}$ = 33 Hz, PMe), 38.4 (d, $^2J_{PP}$ = 33 Hz, PPh) ppm. The conversion of **8c** into **9c** was almost complete after 75 h.

**{Ru(Cp)(=C=C=CPh$_2$)[Ph$_2$PCH$_2$C(=O)*t*Bu](PMe$_3$)}[PF$_6$] (9c):** A solution of **1c** (2.51 g, 3.74 mmol) and 1,1-diphenyl-2-propyn-1-ol (1.15 g, 5.52 mmol) in THF (40 mL) was heated at reflux for 2 h. The resulting solution was evaporated under vacuum and the residue was washed with diethyl ether to obtain a violet powder. Recrystallisation from dichloromethane (40 mL) and diethyl ether (130 mL) afforded a dark-green crystalline powder, but an obvious minor presence of orange crystals (presumably **7c**) precluded elemental analysis. Yield: 2.68 g, ≈83%. $^1H$ NMR (300.13 MHz, $CD_2Cl_2$): $\delta$ = 0.74 (s, 9 H, *t*Bu), 1.25 (d, $^2J_{PH}$ = 10.3 Hz, 9 H, $PMe_3$), 3.65 (dd, $^2J_{HH}$ = 17.6, $^2J_{PH}$ = 9.7 Hz, 1 H, $PCH_2$, $H_a$), 3.96 (dd, $^2J_{HH}$ = 17.6, $^2J_{PH}$ = 4.4 Hz, 1 H, $PCH_2$, $H_b$), 5.37 (s, 5 H, Cp), 7.22–7.81 (m, 20 H, Ph) ppm. $^{13}C\{^1H\}$ NMR (75.47 MHz, $CD_2Cl_2$): $\delta$ = 22.1 (d, $^1J$ = 34.5 Hz, $PMe_3$), 26.1 (s, C*Me*$_3$), 40.7 (d, $^1J$ = 30.9 Hz, $PCH_2$), 45.6 (d, $^3J$ = 1.7 Hz, *C*Me$_3$), 92.1 (s, Cp), 128.9 (d, $^2J$ = 10.8 Hz, PPh, *ortho*), 129.2 (d, $^2J$ = 10.8 Hz, PPh, *ortho*), 129.7 (s, =C*Ph*$_2$, *ortho*), 130.7 (s, =C*Ph*$_2$, *meta*), 131.1 (d, $^4J$ = 2.7 Hz, PPh, *para*), 131.5 (d, $^4J$ = 2.7 Hz, PPh, *para*), ≈132.3 and 132.2 (d, PPh, *meta*, and s, =C*Ph*$_2$, *para*), 132.9 (d, $^3J$ = 9.9 Hz, PPh, *meta*), 134.1 (dd, $^1J$ = 49.4, $^3J$ = 1.8 Hz, PPh, *ipso*), 136.1 (d, $^1J$ = 47.6 Hz, PPh, *ipso*), 144.3 (s, =C*Ph*$_2$, *ipso*), 158.4 (t, $^4J \approx$

 © 2006 Wiley-VCH Verlag GmbH & Co. KGaA, Weinheim 

0.9 Hz, =*C*Ph$_2$), 208.8 (dd, $^3J$ = 2.7 and 1.3 Hz, Ru=C=*C*), 208.9 (d, $^2J$ = 7.2 Hz, C=O), 293.2 (dd, $^2J$ = 18.4 and 16.6 Hz, Ru=C) ppm. $^{31}$P{$^1$H} NMR (121.50 MHz, $CD_2Cl_2$): $\delta$ = 9.6 (d, $^2J_{PP}$ = 36 Hz, PMe), 41.2 (d, $^2J_{PP}$ = 36 Hz, PPh).

**Isomerisation of 9c into 7c:** A solution of a sample of **9c** in methanol was stirred at room temperature and the isomerisation of **9c** into **7c** was monitored by $^{31}$P{$^1$H} NMR spectroscopy. Completion of the reaction was reached after 15 days. A 0.07 M aqueous solution of $K_2CO_3$ (2.0 mL, 0.14 mmol) was added to a solution of **9c** (1.80 g, 2.08 mmol) in dichloromethane (40 mL) and the mixture was stirred for 1 h. Examination of the resulting orange-red solution by $^{31}$P{$^1$H} NMR spectroscopy showed the isomerisation of **9c** into **7c** to be complete.

**{Ru(Ind)[Ph$_2$PCH$_2$C(=O)*t*Bu](PPh$_3$)(PMe$_3$)}[PF$_6$] (2′c):** A 1.0 M solution of trimethylphosphane in THF (8.0 mL, 8.0 mmol) was added to a solution of {Ru(Ind)[Ph$_2$PCH$_2$C(*t*Bu)=O](PPh$_3$)}[PF$_6$] (**1′a**) (6.00 g, 6.61 mmol) in dichloromethane (50 mL). The mixture was stirred overnight and then evaporated to dryness to leave the crude product that was recrystallised from dichloromethane (35 mL) and diethyl ether (140 mL) to afford orange-red crystals. Yield: 5.78 g, 89%. IR: $\tilde{\nu}$ = 1705 cm$^{-1}$, C=O. $^1$H NMR (300.13 MHz, $CD_2Cl_2$): $\delta$ = 0.63 (s, 9 H, *t*Bu), 1.46 (d, $^2J_{PH}$ = 8.5 Hz, 9 H, PMe$_3$), 3.11 (m, 2 H, PCH$_2$), 4.51 (s, broad, 1 H, Ind), 5.44 (s, broad, 1 H, Ind), 5.57 (m, 1 H, Ind), 6.80–7.45 (m, 29 H, Ph and Ind) ppm. $^{31}$P{$^1$H} NMR (121.50 MHz, $CD_2Cl_2$): $\delta$ = –10.5. (t, $^2J_{PP} \approx {}^2J_{PP'} \approx$ 33 Hz, PMe), 42.8 (t, $^2J_{PP} \approx {}^2J_{PP'} \approx$ 33 Hz), 45.0 (t, $^2J_{PP} \approx {}^2J_{PP'} \approx$ 33 Hz) ppm. $C_{48}H_{52}F_6OP_4Ru$ (983.90): calcd. C 58.60, H 5.33, P 12.59; found C 58.51, H 5.34, P 12.64.

**{Ru(Ind)[Ph$_2$PCH$_2$C(*t*Bu)=O](PMe$_3$)}[PF$_6$] (1′c):** A mixture consisting of a sample of **2′c** (3.00 g, 3.05 mmol), an excess of NaH (0.78 g, 32.5 mmol) and THF (60 mL) was heated at reflux for 20 h. The resulting mixture was filtered and the dark-orange filtrate was evaporated to dryness. Methanol (50 mL) was added to the residue and this mixture was stirred to obtain a red-orange slurry. $NH_4PF_6$ (0.60 g, 3.68 mmol) and then a 6 M solution of HCl in diethyl ether (2.0 mL, 12 mmol) were added to the slurry. The mixture was stirred for 10 min and the resulting orange precipitate was collected by filtration and washed with diethyl ether (50 mL). The solid was extracted with dichloromethane (25 mL), the solution was filtered and the filtrate was covered with methanol (10 mL) then diethyl ether (120 mL) to afford orange crystals. Yield: 1.70 g, 77%. IR: $\tilde{\nu}$ = 1607 cm$^{-1}$, C=O. $^1$H NMR (300.13 MHz, $CD_2Cl_2$): $\delta$ = 0.94 (d, $^2J_{PH}$ = 9.0 Hz, 9 H, PMe$_3$), 1.19 (s, 9 H, *t*Bu), 3.34 (dd, $^2J_{HH}$ = 19.4, $^2J_{PH}$ = 7.6 Hz, 1 H, PCH$_2$, H$_a$), 4.10 (dd, $^2J_{HH}$ = 19.4, $^2J_{PH}$ = 10.9 Hz, 1 H, PCH$_2$, H$_b$), 4.28 (m, 1 H, Ind), 4.61 (m, 1 H, Ind), 4.73 (m, 1 H, Ind), 6.82–7.62 (m, 14 H, Ph and Ind) ppm. $^{31}$P{$^1$H} NMR (121.50 MHz, $CD_2Cl_2$): $\delta$ = 0.9 (d, $^2J_{PP}$ = 38 Hz, PMe), 75.2 (d, $^2J_{PP}$ = 38 Hz, PPh) ppm. $C_{30}H_{37}F_6OP_3Ru$ (721.61): calcd. C 49.93, H 5.17, P 12.88; found C 50.20, H 5.20, P 12.84.

**{Ru(Ind)[η$^2$-*C*,*P*-:C(CH=CPh$_2$)OC(*t*Bu)=CH–PPh$_2$](PMe$_3$)}[PF$_6$] (7′c):** Starting from **1′c** instead of **1c**, the procedure detailed for the synthesis of **7c** was used and similarly yielded **7′c** as dark-purple crystals (71%). $^1$H NMR (300.13 MHz, $CD_2Cl_2$): $\delta$ = 0.70 (s, 9 H, *t*Bu), 1.11 (d, $^2J_{PH}$ = 10.0 Hz, 9 H, PMe$_3$), 4.46 (d, $^2J_{PH}$ = 1.6 Hz, 1 H, PCH=), 4.57 (m, 1 H, Ind), 5.68 (m, 1 H, Ind), 5.72 (s, 1 H, C*H*=CPh$_2$), 5.90 (m, 1 H, Ind), 6.29–7.61 (m, 24 H, Ph and Ind) ppm. $^{13}$C{$^1$H} NMR (75.47 MHz, $CD_2Cl_2$): $\delta$ = 20.1 (d, $^1J$ = 34.1 Hz, PMe$_3$), 27.4 (s, C*Me*$_3$), 38.8 (d, $^3J$ = 7.1 Hz, *C*Me$_3$), 80.0 (s, Ind), 85.1 (d, $^1J$ = 58.5 Hz, PCH=), 87.0 (s, Ind), 96.7 (s, Ind), 109.4 (d, $^2J$ = 6.3 Hz, Ind), 120.2 (s, Ind), 120.7–133.3 (m, set of Ph and Ind resonances), 137.9 (d, $^4J$ = 2.7 Hz, *C*HCPh$_2$), 139.3 (s,

Table 1. Crystallographic data for complexes **3b**·$CH_2Cl_2$ and **7c**.

| Complex | **3b**·$CH_2Cl_2$ | **7c** |
|---|---|---|
| Empirical formula | $C_{43}H_{42}Cl_2O_2P_2Ru$ | $C_{41}H_{45}F_6OP_3Ru$ |
| Molecular weight [g mol$^{-1}$] | 824.68 | 861.75 |
| Crystal size [mm] | 0.48 × 0.35 × 0.32 | 0.45 × 0.35 × 0.35 |
| Crystal system | monoclinic | monoclinic |
| Space group | $P2_1/c$ | $P2_1/n$ |
| *a* [Å] | 10.7595(1) | 11.8729(1) |
| *b* [Å] | 28.0871(3) | 25.8064(2) |
| *c* [Å] | 13.6725(2) | 13.2105(1) |
| β [°] | 109.5282(5) | 96.4906(3) |
| *V* [Å$^3$] | 3894.19(8) | 4021.71(6) |
| *Z* | 4 | 4 |
| Density [g cm$^{-3}$] | 1.407 | 1.423 |
| Temperature [K] | 293(2) | 293(2) |
| *F*(000) | 1696 | 1768 |
| Mo-$K_\alpha$ radiation, λ [Å] | 0.71073 | 0.71073 |
| Absorption coefficient [mm$^{-1}$] | 0.658 | 0.568 |
| θ range [°] | 1.74–27.48 | 2.70–27.48 |
| Index ranges | $0 < h < 13$ | $0 < h < 15$ |
| | $0 < k < 36$ | $0 < k < 33$ |
| | $-17 < l < 16$ | $-17 < l < 17$ |
| Reflections collected | 33970 | 54682 |
| Independent reflections | 8841 ($R_{int}$ = 0.033) | 9180 ($R_{int}$ = 0.035) |
| Reflections $I > 2\sigma(I)$ | 6496 | 7134 |
| Data/restraints/parameters | 8841/0/447 | 9180/0/470 |
| Goodness-of-fit on $F^2$ | 1.014 | 1.019 |
| Final *R* indices [$I > 2\sigma(I)$] | $R_1$ = 0.0593 | $R_1$ = 0.0437 |
| | $wR_2$ = 0.1581 | $wR_2$ = 0.1140 |
| *R* indices (all data) | $R_1$ = 0.0851 | $R_1$ = 0.0614 |
| | $wR_2$ = 0.1769 | $wR_2$ = 0.1250 |
| Largest diff. peak/hole [e Å$^{-3}$] | 1.786 and –1.618 | 0.869 and –0.840 |

$w = 1/[\sigma^2(F_o^2) + (0.0949P)^2 + 5.7242P]$ (**3b**), $1/[\sigma^2(F_o^2) + (0.0680P)^2 + 2.4890P]$ (**7c**), where $P = (F_o^2 + 2F_c^2)/3$

 © 2006 Wiley-VCH Verlag GmbH & Co. KGaA, Weinheim 

*C*$Ph_2$), 140.2 and 140.6 (2 s, C*Ph*$_2$, *ipso*), 141.8 (dd, $^1J$ = 55.7, $^3J$ = 2.7 Hz, PPh, *ipso*), 178.1 (d, $^2J$ = 3.6 Hz, O*C*tBu), 285.4 (dd, $^2J$ = 16.2 and 12.6 Hz, Ru=C) ppm. $^{13}$C NMR (75.47 MHz, $CD_2Cl_2$, selected values): $\delta$ = 85.1 (dd, $^1J_{HC}$ = 160, $^1J_{PC}$ = 58.5 Hz, PCH=), 137.9 (d, $^1J_{HC}$ = 160 Hz, *C*HCPh$_2$), 139.3 (d, $^2J_{HC}$ = 2.7 Hz, *C*Ph$_2$) ppm. $^{31}$P{$^1$H} NMR (121.50 MHz, $CD_2Cl_2$): $\delta$ = 1.6 (d, $^2J_{PP}$ = 31 Hz, PMe), 42.5 (d, $^2J_{PP}$ = 31 Hz, PPh) ppm. $C_{45}H_{49}F_6OP_3Ru$ (913.87): calcd. C 59.14, H 5.40, P 10.17; found C 58.29, H 5.17, Cl 0.73, P 10.34. The presence of chlorine indicated a slight retention of dichloromethane, which is likely responsible for the low carbon value.

**X-ray Crystallography:** Selected crystals of **3b**·$CH_2Cl_2$ and **7c** were studied with a NONIUS Kappa CCD diffractometer with graphite monochromator. Crystallographic data are given in Table 1. The cell parameters were obtained with Denzo and Scalepack,[15] and data collection with NONIUS KappaCCD Software.[16] Data reduction was carried out with Denzo and Scalepack.[15] The structures were solved with SIR-97, which revealed the non-hydrogen atoms.[17] After anisotropic refinement, many hydrogen atoms may be found with Fourier difference calculations. The whole structures were refined with SHELXL97 by full-matrix least-squares methods on $F^2$ ($x$, $y$, $z$, $\beta_{ij}$ for Ru, P, Cl, O and C atoms; $x$, $y$, $z$ in riding mode for H atoms).[18] ORTEP views were prepared with PLATON98.[19] Thermal ellipsoids for some atoms in the C30 ring in **7c** might suggest a disorder problem. Calculations to split these atoms in two positions to improve the structural model were unsuccessful, probably because this defect is not symmetrical relative to the phenyl ring axis.

CCDC-291347 (for **3b**) and -291348 (for **7c**) contain the supplementary crystallographic data for this paper. These data can be obtained free of charge from The Cambridge Crystallographic Data Centre via www.ccdc.cam.ac.uk/data_request/cif.

[1] P. Crochet, B. Demerseman, *Organometallics* **1995**, *14*, 2173–2176.
[2] B. Demerseman, B. Guilbert, C. Renouard, M. Gonzalez, P. H. Dixneuf, D. Masi, C. Mealli, *Organometallics* **1993**, *12*, 3906–3917.
[3] B. Guilbert, B. Demerseman, P. H. Dixneuf, C. Mealli, *J. Chem. Soc., Chem. Commun.* **1989**, 1035–1037.
[4] P. Braunstein, F. Naud, *Angew. Chem. Int. Ed.* **2001**, *40*, 680–699.
[5] A. Bader, E. Lindner, *Coord. Chem. Rev.* **1991**, *108*, 27–110.
[6] J. C. Jeffrey, T. B. Rauchfuss, *Inorg. Chem.* **1979**, *18*, 2658–2666.
[7] P. Crochet, B. Demerseman, M. I. Vallejo, M. P. Gamasa, J. Gimeno, J. Borge, S. García-Granda, *Organometallics* **1997**, *16*, 5406–5415.
[8] M. C. Puerta, P. Valerga, *Coord. Chem. Rev.* **1999**, *193–195*, 977–1025.
[9] J. R. Lomprey, J. P. Selegue, *J. Am. Chem. Soc.* **1992**, *114*, 5518–5523.
[10] R. M. Bullock, *J. Chem. Soc., Chem. Commun.* **1989**, 165–166.
[11] I. de los Ríos, M. J. Tenorio, M. C. Puerta, P. Valerga, *J. Am. Chem. Soc.* **1997**, *119*, 6529–6538.
[12] E. Bustelo, M. Jiménez-Tenorio, M. C. Puerta, P. Valerga, *Organometallics* **1999**, *18*, 4563–4573.
[13] E. Bustelo, M. Jiménez-Tenorio, M. C. Puerta, P. Valerga, *Organometallics* **1999**, *18*, 950–951.
[14] J. P. Selegue, *Organometallics* **1982**, *1*, 217–218.
[15] Processing of X-ray diffraction data collected in oscillation mode: Z. Otwinowski, W. Minor, *Macromol. Crystallogr. A* **1997**, *276*, 307–326.
[16] *NONIUS KappaCCD Software*, Nonius BV, Delft, The Netherlands, **1999**.
[17] *SIR-97 – A New Tool for Crystal Structure Determination and Refinement*: A. Altomare, M. C. Burla, M. Camalli, G. Cascarano, C. Giacovazzo, A. Guagliardi, A. G. G. Moliterni, G. Polidori, R. Spagna, *J. Appl. Crystallogr.* **1998**, *31*, 74–77.
[18] G. M. Sheldrick, *SHELXL97 – Program for the Refinement of Crystal Structures*, University of Göttingen, Germany, **1997**.
[19] A. L. Spek, *PLATON – A Multipurpose Crystallographic Tool*, University of Utrecht, The Netherlands, **1998**.

Received: December 1, 2005
Published Online: February 21, 2006

 © 2006 Wiley-VCH Verlag GmbH & Co. KGaA, Weinheim 

DOI: 10.1002/ejic.200501077

# Formation of Two 1D Polymeric Water Morphologies

Feng Li,[a] Tao-Hai Li,[a] Wei Su,[a] Shui-Ying Gao,[a] and Rong Cao*[a]

**Keywords:** Hosts / Water morphologies / Chains / Tapes

Two complexes with double- or triple-stranded chain structures, $\{[Cd(pg)(phen)]\cdot 3H_2O\}_n$ (**1**) and $\{[Cd_3(cpg)_3(phen)_2]\cdot 3H_2O\}_n$ (**2**), have been hydrothermally synthesized [$H_2pg$ = 3-phenylglutaric acid, $H_2cpg$ = 3-(4-chlorophenyl)glutaric acid, phen = 1,10-phenanthroline]. In the crystal lattices of **1** and **2**, two 1D polymeric water morphologies are observed (a treelike chain for **1** and a staircaselike tape for **2**), both of which contain $(H_2O)_6$ subunits. The geometrical parameters of water chains and tapes are similar to those in ice, $I_h$, and liquid water, respectively.
(© Wiley-VCH Verlag GmbH & Co. KGaA, 69451 Weinheim, Germany, 2006)

## Introduction

The fundamental importance of water in physical, biological, and chemical processes has prompted intensive research efforts, however, some properties of water still remain "anomalous".[1–4] The structural information of discrete water clusters is the first step to understanding the behavior of water.[5] In recent years, extensive structural studies on discrete water clusters have significantly advanced our preliminary comprehension of water.[6] A comparison between the physical properties of discrete water clusters and polymeric clusters, which structurally lie between small water clusters and bulk water/ice, shows that the properties of polymeric clusters are more closely associated with those of bulk water. Thus, studies involving polymeric water clusters are a further step towards understanding water. With the development of polymeric water clusters, three morphologies of polymeric water clusters[7] including infinite 1D-chain,[8] tape,[9] and 2D-layer[10] structures, have been observed. Among the three morphologies, 1D water chains and tapes are of great interest since many fundamental biological processes[11] and properties of materials[12] appear to depend on the unique properties of 1D water morphologies. Structural studies have shown that 1D water morphologies exist in gramicidin A membrane channels,[13] bacteriorhodopsin,[14] and α-amylase[15] for the rapid transport of protons and act as "proton wires". Thus, it is essential that 1D water morphologies can be rationally and predictably designed. However, most water clusters are obtained occasionally, and the rational design of such water morphologies still remains a challenge.

[a] State Key Laboratory of Structural Chemistry, Fujian Institute of Research on the Structure of Matter, The Chinese Academy of Sciences,
Fuzhou, Fujian, 350002, P. R. China
Fax: +86-591-371-4946
E-mail: rcao@ms.fjirsm.ac.cn

The lattices of crystal hosts offer environments for stabilizing various topologies of water clusters, which play important roles in the formation of different water morphologies. To obtain 1D water morphologies, it is necessary to construct suitable host frameworks for water molecules extending into chains or tapes. Without a doubt, a host channel, which can encapsulate the water chains or tapes, generated by organic or inorganic moieties is a good choice.[16] If a host chain can provide hydrogen-bond donors and/or acceptors, it may induce the free water molecules or discrete water clusters to extend with itself, and finally lead to 1D water morphologies. A metal–organic chain may be another good choice. In this paper, we report on two complexes, $[Cd_3(cpg)_3(phen)_2]\cdot 3H_2O$ (**1**) and $[Cd(cpg)(phen)]\cdot 3H_2O$ (**2**) [$H_2pg$ = 3-phenylglutaric acid, $H_2cpg$ = 3-(4-chlorophenyl) glutaric acid, phen = 1,10-phenanthroline], which both have 1D host frameworks and result in 1D water chains and tapes, respectively.

## Results and Discussion

Carboxyl groups can provide hydrogen-bond donors and/or acceptors, so we have chosen two similar benzoic carboxylates ($H_2pg$ and $H_2cpg$) as organic ligands to construct the host frameworks. In order to obtain 1D metal–organic chains, we selected 1,10-phen as a secondary ligand. The induction of the terminal ligand can prevent the chain from extending to intricate 2D and 3D architectures.

### Crystal Structure of $\{[Cd(pg)(1,10\text{-}Phen)]\cdot 3H_2O\}_n$ (1)

Single-crystal X-ray analysis reveals that **1** is a 1D double-stranded chain. As shown in Figure 1, each central cadmium ion is coordinated by two oxygen atoms from two monatomic bridging carboxylate groups (Scheme 1a), two

 InterScience © 2006 Wiley-VCH Verlag GmbH & Co. KGaA, Weinheim 

oxygen atoms from one chelating carboxylate group (Scheme 1b) and two nitrogen atoms from one 1,10-phen molecule. Two $pg^{2-}$ ligands link two cadmium ions forming a metal–organic ring, and these are bridged into a double-stranded chain through the monatomic bridging carboxylate groups (Figure 2).

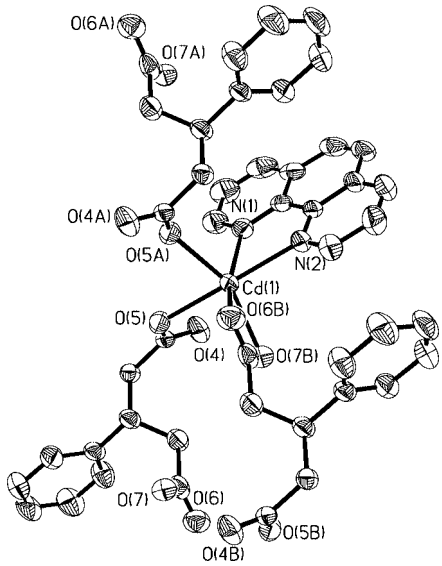


Figure 1. The coordination environment of cadmium ions in **1** with the thermal ellipsoids at the 50% probability level (all H atoms were omitted for clarity). Symmetry codes: #A: $-x + 1, -y + 1, -z$; #B: $-x + 1, -y + 2, -z$.

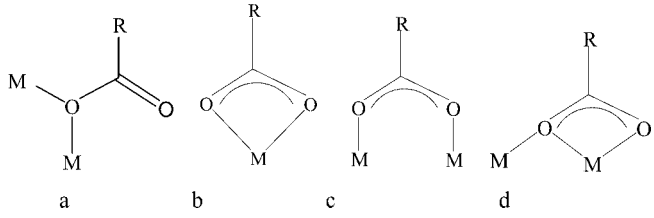


Scheme 1. The coordination modes assumed by the carboxylate ligands.

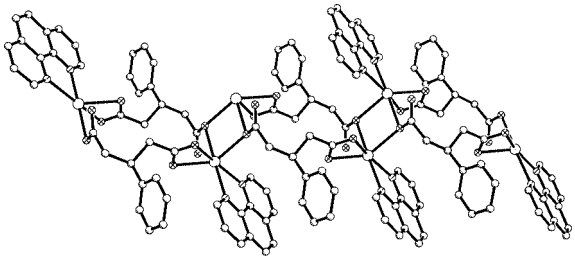

Figure 2. The double-stranded host chain of **1**.

In the crystal lattice of **1**, three crystallographically independent water molecules (O1w, O2w, and O3w) are observed, which are associated by hydrogen bonds to form a water trimer. The water trimer is hydrogen bonded to its equivalent, derived by the crystallographic $2_1$ axis along the [010] direction, forming a $(H_2O)_6$ unit. The geometric parameters of the hexamers are summarized in Table 1. The $2_1$ axis in symmetry operations of generating $(H_2O)_6$ clusters leads to a water hexamer with an opening structure. Such an open structure is different from any hexamer conformation revealed by theoretical calculations (ring, book, bag, cage, and prism).[19,20,6a] With O1w and equivalent molecules dangling at two sides, the hexamers are self-assembled into treelike chains along the [010] direction (Figure 3). The average O···O distance of 2.796 Å is very close to the corresponding value of 2.759 Å in ice, $I_h$, at –90 °C.[1] However, there is a wide variation in the O–O–O angles with an average of 131.2°, which deviates considerably from the corresponding value found in ice, $I_h$. The water chains link adjacent double-stranded metal–organic chains into a 2D network through the O1w–H···O6 and O3w–H···O4 hydrogen bonds. Neighbor layers are extended into a three-dimensional architecture through π–π interactions (3.367 Å) between two phenanthroline rings of the 1,10-phen ligand.

Table 1. Hydrogen-bonding parameters ([Å] and [°]) for $\{[Cd(pg)(phen)]\cdot 3H_2O\}_n$ (**1**) and $\{[Cd_3(cpg)_3(phen)_2]\cdot 3H_2O\}_n$ (**2**).[a]

| O–H···O | O–H | O···O | H···O | O–H···O |
|---|---|---|---|---|
| **1** | | | | |
| O6–H(6WA)···O7$^{\#1}$ | 0.96(5) | 2.763(6) | 1.87(6) | 154.7(7) |
| O7–H(7WB)···O1$^{\#2}$ | 1.02(8) | 2.816(4) | 1.80(8) | 174.8(2) |
| O6–H(6WB)···O7 | 1.01(2) | 2.857(8) | 2.19(9) | 122.0(5) |
| O5–H(5WA)···O3$^{\#2}$ | 0.92(5) | 2.728(4) | 1.82(5) | 172.1(5) |
| O5–H(5WB)···O6 | 1.21(3) | 2.769(6) | 1.99(3) | 117.9(3) |
| **2** | | | | |
| O(1)–H(1WA)···O3$^{\#3}$ | 0.74(9) | 2.765(1) | 2.08(1) | 153(1) |
| O(1)–H(1WB) ···O2 | 0.75(9) | 2.812(2) | 2.10(1) | 161(1) |
| O(2)–H(2WB)···O4 | 0.67(9) | 2.853(1) | 2.18(9) | 175(1) |
| O(2)–H(2WA)···O3 | 0.79(9) | 2.997(2) | 2.23(9) | 165(1) |
| O(3)–H(3WB)··· O6$^{\#4}$ | 0.80(9) | 2.755(1) | 1.96(9) | 175(9) |
| O(3)–H(3WA)···O1$^{\#5}$ | 1.07(9) | 2.875(2) | 1.84(9) | 164(7) |

[a] Symmetry codes: #1: $-x, y + 1/2, -z + 1/2$; #2: $-x + 1, y - 1/2, -z + 1/2$; #3: $-x + 1, -y, -z + 2$; #4: $x + 1, y, z$; #5: $x + 1, y, z$.

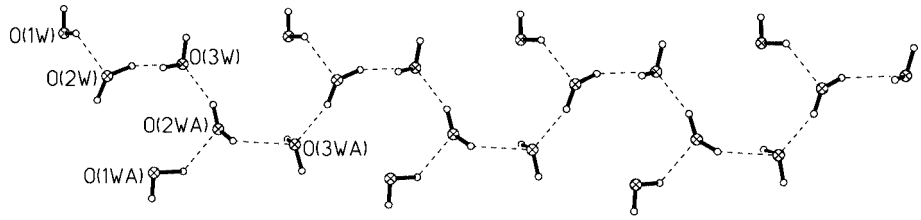


Figure 3. The 1D treelike water chain with dangling molecules in **1**.

 © 2006 Wiley-VCH Verlag GmbH & Co. KGaA, Weinheim 

### Crystal Structure of $\{[Cd_3(cpg)_3(1,10\text{-Phen})_2]\cdot 3H_2O\}_n$ (2)

In the asymmetric unit of **2**, there are three crystallographically independent $Cd^{II}$ ions, three $cpg^{2-}$ ligands, two 1,10-phen ligands, and three water molecules, as revealed by X-ray crystallography. The coordination environments around the three $Cd^{II}$ ions are different, however, they all exhibit an octahedral-coordination geometry (Figure 4). Cd(1) is coordinated by two nitrogen atoms from one 1,10-phen ligand, one oxygen atom from one *syn*,*syn*-$\eta^1$:$\eta^1$:$\mu_2$ bridging carboxylate group (Scheme 1c), one oxygen atom from one monatomic bridging carboxylate group (Scheme 1a), and two oxygen atoms from one chelate bridging carboxylate group (Scheme 1d). Cd(2) is coordinated by two nitrogen atoms from one 1,10-phen ligand, two oxygen atoms from two *syn*,*syn*-$\eta^1$:$\eta^1$:$\mu_2$ bridging carboxylate groups (Scheme 1c), and two oxygen atoms from one chelate bridging carboxylate group (Scheme 1d). Cd(3) is coordinated by three oxygen atoms from three *syn*,*syn*-$\eta^1$:$\eta^1$:$\mu_2$ bridging carboxylate groups (Scheme 1c), two oxygen atoms from one chelate bridging carboxylate group (Scheme 1d), and one oxygen atom from one monatomic bridging carboxylate group (Scheme 1a). As a result of the coordination diversity of carboxylate groups, three $Cd^{II}$ ions are connected to form a trinuclear cluster. As a basic building unit, the trinuclear clusters are fused to an infinite triple-stranded chain bridged by the carboxylate groups of the $cpg^{2-}$ ligands. To accommodate the role of the bridging trinuclear clusters, the alkyl chain of the $cpg^{2-}$ ligands rotates from the most stable *anti* form to the gauche form, which is higher in energy. The rotation of the flexible $cpg^{2-}$ ligand allows each strand to twist in order to form a helical chain. By sharing cadmium ions, the three strands are attached to produce a novel triple-stranded helical chain (Figure 5). In the case of the infinite double and higher order helices there are two kinds of possibilities: (i) The strands of the helix are independent infinite chains held together by noncovalent forces, analogous to the situation in DNA;[21] and (ii) The strands are not independent, but are attached through coordinative bonds to a column of metal atoms, which form the axis of the helix. To the best of our knowledge, complex **1** is the first infinite triple-stranded helical chain of type (ii).

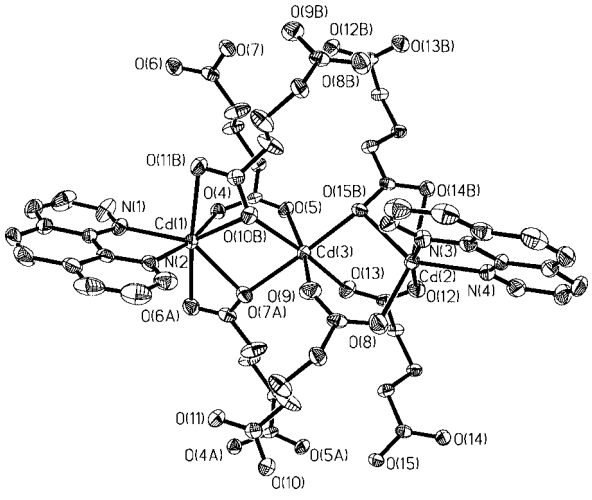


Figure 4. The coordination environment of cadmium ions in **2** with the thermal ellipsoids at the 30% probability level (all hydrogen atoms and the chlorophenyl groups of the $cpg^{2-}$ ligand were omitted for clarity). Symmetry codes: #A: $x + 1$, $y$, $z$; #B: $x - 1$, $y$, $z$.

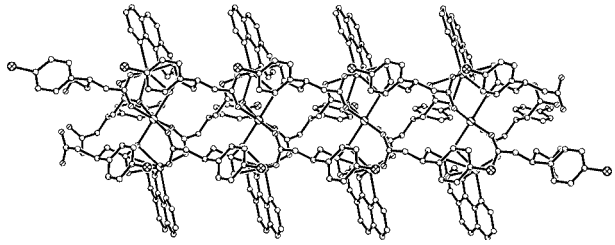

Figure 5. The triple-stranded host chain of **2**.

Similar to **1**, there are three crystallographically independent free water molecules in the crystal lattice of complex **2**. These three water molecules and their equivalents, generated by a crystallographic inversion center, are associated by O–H···O hydrogen bonds in a cyclic centrosymmetric hexamer. The mean deviation of the three atoms from the plane is 0.0088 Å, which shows that these atoms are almost located on the same plane and the hexamer ring exists as a planar conformation. The geometric parameters of the hexamers are summarized in Table 1. The average O···O distance of 2.858 Å is longer than the value of 2.759 Å in ice, $I_h$,[1] but very similar to the O···O distance of 2.85 Å in liquid water.[22] The average value of the O–O–O angles is 119.3°, which deviates considerably from the corresponding value found in liquid water. The hexamers are self-assembled by O3w–H···O1w hydrogen bonds into extended water tapes along the [100] direction, consisting of fused four- and six-membered water rings (Figure 6). The dihedral angle between four- and six-membered rings is 44.1°, which makes the water tape "staircase"-like. The interhexamer O1···O3B distance of 2.892 Å is also close to the corresponding O···O distance in liquid water. Additional O2w–H···O4 and O3w–H···O6 hydrogen bonds anchor the water tapes to two adjacent metal–organic chains, resulting in triple helical chain pairs. The triple chain pairs are extended

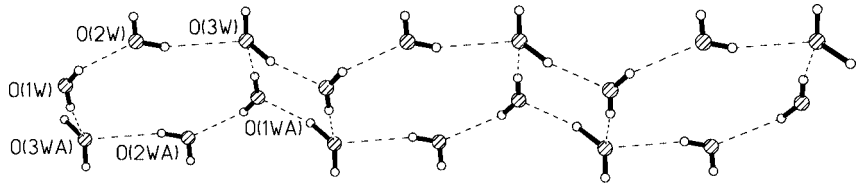


Figure 6. The staircaselike water tape in **2**.

 © 2006 Wiley-VCH Verlag GmbH & Co. KGaA, Weinheim 

into a three-dimensional architecture through π–π interactions (3.779 Å) between two phenanthroline rings of 1,10-phen ligands from neighboring chains.

### Thermal Analysis and X-ray Powder Diffraction

Samples of **1** and **2** were examined by TGA, which show similar TGA curves (Figure 7). TGA analyses of **1** show a 4.11% weight loss from 63 to 108 °C, which corresponds to 1.26 of the 3 free water molecules. The remaining water molecules are eventually lost at 345 °C. For **2**, the weight loss of 1.92% from 61 to 91 °C is equivalent to the loss of 1.57 of the three free water molecules. The remaining water molecules are lost slowly until a temperature of 268 °C is reached. After all the free water molecules were released from the structure the metal–organic host chains started to decompose. To confirm the TGA, the original samples and dehydrated samples of **1** and **2** were characterized by X-ray Powder diffraction (XRPD) at room temperature (Figure 8 and Figure 9). The patterns that were simulated from the single-crystal X-ray data of **1** and **2** were in good agreement with those that were observed. However, after water molecules were lost as a result of heat, total changes in the pattern were observed, suggesting decomposition of the metal–organic framework. This is expected, as the water chain or tape acts as a "glue" to assemble the overall structure.

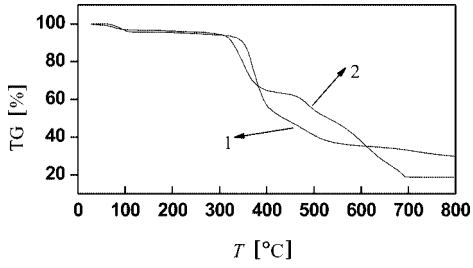


Figure 7. TGA curves for **1** and **2**.

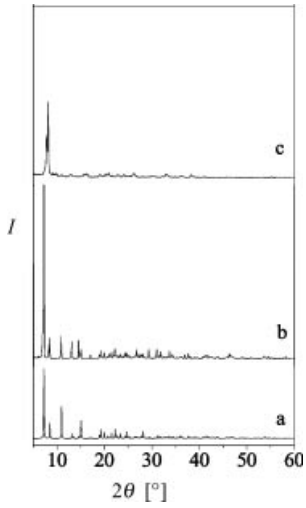


Figure 8. XRPD patterns for **1**: (a) calculated from single-crystal X-ray data; (b) taken at room temperature; (c) after heating at 350 °C for 2 h.

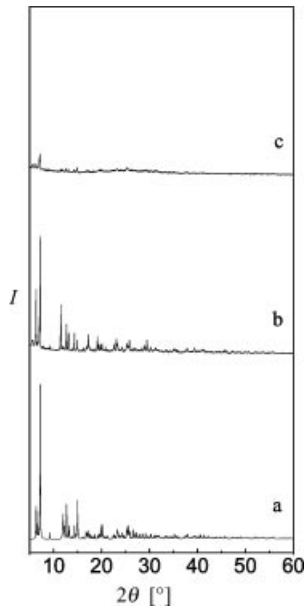


Figure 9. XRPD patterns for **2**: (a) calculated from single-crystal X-ray data; (b) taken at room temperature; (c) after heating at 300 °C for 2 h.

### Vibrational Spectra

The FT-IR spectroscopy of **1** shows strong bands at 1574 and 1428 $cm^{-1}$ due to the $\upsilon_{asym}(CO_2)$ and $\upsilon_{sym}(CO_2)$ stretching vibrations, respectively. For **2**, the $\upsilon_{asym}(CO_2)$ and $\upsilon_{sym}(CO_2)$ stretching vibrations appear at 1585 $cm^{-1}$ and 1402 $cm^{-1}$, respectively. The spectra of **1** and **2** exhibit broad bands centered around 3375 and 3406 $cm^{-1}$, respectively. The O–H stretching vibration for the quasiplanar water hexamer appears[23] as a broad band centered around 3400 $cm^{-1}$; the O–H stretching vibration for the same cluster in a helium droplet appears at 3325 $cm^{-1}$.[6b] In comparison, this vibration of the planar hexamers in the ice I and II phases occurs at 3220 $cm^{-1}$.[1] After removing the water from the crystal lattices of **1** and **2** by heating, the bands centered around 3375 and 3406 $cm^{-1}$ disappear. Therefore, in the case of **1** and **2**, these bands are attributable to the O–H stretching frequency of the $(H_2O)_6$ core structure. The difference in the stretching vibration may arise from their different conformations and environments. Deliberate exposure to water vapor for 3 d does not lead to reabsorption of water into the lattice as monitored by FTIR spectroscopy.

## Conclusions

In conclusion, two complexes with metal–organic host chains have been synthesized successfully, in which two 1D water morphologies are observed. When the host chains change from double stranded to triple stranded, the water morphologies are observed as treelike chains and staircaselike tapes, respectively, which contain $(H_2O)_6$ subunits with different conformations. The water morphologies act as building blocks extending the host frameworks into a higher dimensionality. In this sense, the water chains and

 © 2006 Wiley-VCH Verlag GmbH & Co. KGaA, Weinheim 

tapes are different from other 1D water morphologies encapsulated in the host channels generated by organic or inorganic moieties. We propose that the metal–organic chain, with selected hydrophilic groups, may be a good host framework to induce the formation of 1D water morphologies. This discovery may be helpful in the rational design of 1D water morphologies.

## Experimental Section

**General Methods:** All chemicals were obtained commercially and used without further purification. Elemental analyses were carried out with an Elementar Vario EL III analyzer. Infrared (IR) spectra were recorded with a PerkinElmer Spectrum One as KBr pellets in the range 4000–400 $cm^{-1}$. Thermogravimetric analyses were carried out with a NETZSCH STA 449C unit at a heating rate of 10 °C $min^{-1}$ under nitrogen. X-ray Powder diffraction measurements were recorded with a RIGAKU DMAX2500PC diffractometer using Cu-$K_\alpha$ radiation.

**Preparation of Complexes**

**{[Cd(pg)(1,10-Phen)]·3H$_2$O}$_n$ (1):** A mixture of $H_2$pg (0.021 g, 0.1 mmol), 1,10-phen (0.020 g, 0.1 mmol), and $Cd(NO_3)_2$·4$H_2O$ (0.031 g, 0.1 mmol) in distilled water (15 mL) was sealed in a Teflon-lined Stainless autoclave and heated at 165 °C for 3 d under autogenous pressure and then cooled to room temperature for 2 d. Colorless crystals (26 mg) were isolated in 47% yield and washed with distilled water. $C_{23}H_{24}N_2O_7Cd$ (552.84): calcd. C 49.81, H 4.37, N 5.05; found C 49.80, H 4.38, N 5.06. IR (KBr): $\tilde{\nu}$ = 3375 (m), 3063 (w), 1574 (vs), 1515 (s), 1428 (vs), 1251 (w), 1103(w), 973(w), 864 (s), 854 (vs), 775 (m), 729 (s) $cm^{-1}$.

**{[Cd$_3$(cpg)$_3$(1,10-Phen)$_2$]·3H$_2$O}$_n$ (2):** A mixture of $H_2$cpg (0.024 g, 0.1 mmol), 1,10-phen (0.020 g, 0.1 mmol), and $Cd(NO_3)_2$·4$H_2O$ (0.031 g, 0.1 mmol) in distilled water (15 mL) was sealed in a Teflon-lined Stainless autoclave and heated at 165 °C for 3 d under autogenous pressure and then cooled to room temperature for 2 d. Yellow prism-like crystals (47 mg) suitable for X-ray analysis were isolated in 32% yield and washed with distilled water. $C_{57}H_{49}N_4O_{15}Cl_3Cd_3$ (1473.55): calcd. C 46.46, H 3.35, N 3.80; found C 46.48, H 3.34, N 3.81. IR (KBr): $\tilde{\nu}$ = 3406 (m), 1581 (vs), 1518 (m), 1493 (m), 1402 (s), 1281 (w), 1092 (w), 1014 (w), 976 (w), 866 (m), 831 (m), 729 (s) $cm^{-1}$.

Table 2. Selected bond lengths [Å] and angles [°] for {[Cd(pg)(phen)]·3$H_2O$}$_n$ (**1**)[a] and {[Cd$_3$(cpg)$_3$(phen)$_2$]·3$H_2O$}$_n$ (**2**).[a]

| | | | |
|---|---|---|---|
| **1** | | | |
| Cd(1)–N(1) | 2.299(2) | Cd(1)–O(7)$^{\#1}$ | 2.310(2) |
| Cd(1)–N(2) | 2.385(2) | Cd(1)–O(5)$^{\#2}$ | 2.3294(19) |
| Cd(1)–O(5) | 2.3035(19) | Cd(1)–O(6)$^{\#1}$ | 2.438(2) |
| O(7)$^{\#1}$–Cd(1)–O(6)$^{\#1}$ | 54.94(8) | N(1)–Cd(1)–O(7)$^{\#1}$ | 136.06(8) |
| N(1)–Cd(1)–O(5)$^{\#2}$ | 88.86(8) | O(5)–Cd(1)–N(2) | 174.75(7) |
| O(5)$^{\#2}$–Cd(1)–O(6)$^{\#1}$ | 83.32(8) | | |
| **2** | | | |
| Cd(1)–N(1) | 2.316(7) | Cd(2)–N(3) | 2.363(8) |
| Cd(1)–N(2) | 2.331(7) | Cd(2)–N(4) | 2.301(7) |
| Cd(1)–O(4) | 2.264(6) | Cd(2)–O(14)$^{\#4}$ | 2.454(6) |
| Cd(1)–O(6)$^{\#3}$ | 2.513(6) | Cd(3)–O(5) | 2.286(6) |
| Cd(1)–O(7)$^{\#3}$ | 2.351(7) | Cd(3)–O(7)$^{\#3}$ | 2.309(6) |
| Cd(2)–O(8) | 2.247(7) | Cd(3)–O(9) | 2.281(7) |
| Cd(1)–O(10)$^{\#4}$ | 2.368(7) | Cd(3)–O(10)$^{\#4}$ | 2.280(7) |
| Cd(1)–O(11)$^{\#4}$ | 2.609(8) | Cd(3)–O(13) | 2.228(6) |
| Cd(2)–O(12) | 2.220(6) | Cd(3)–O(15)$^{\#4}$ | 2.265(5) |
| Cd(2)–O(15)$^{\#4}$ | 2.296(6) | | |

[a] Symmetry transformations used to generate equivalent atoms: #1: $-x+1, -y+2, -z$; #2: $-x+1, -y+1, -z$; #3: $x+1, y, -z$; #4: $x-1, y, z$.

Table 3. Crystallographic data for {[Cd(pg)(phen)]·3$H_2O$}$_n$ (**1**) and {[Cd$_3$(cpg)$_3$(phen)$_2$]·3$H_2O$}$_n$ (**2**).

| | **1** | **2** |
|---|---|---|
| Empirical formula | $C_{23}H_{24}N_2O_7Cd$ | $C_{57}H_{49}N_4O_{15}Cl_3Cd_3$ |
| Formula mass [g $mol^{-1}$] | 552.84 | 1473.55 |
| Crystal system | Monoclinic | Monoclinic |
| Space group | $P2_1/c$ | $P2_1/n$ |
| $a$ [Å] | 11.1744(6) | 7.674(3) |
| $b$ [Å] | 8.5230(5) | 27.815(9) |
| $c$ [Å] | 26.1459(14) | 26.611(9) |
| $\alpha$ [°] | 90 | 90 |
| $\beta$ [°] | 111.879(3) | 94.640(7) |
| $\gamma$ [°] | 90 | 90 |
| $V$ [Å$^3$] | 2310.8(2) | 5661(3) |
| $Z$ | 4 | 4 |
| $\rho_{calcd.}$ [mg $m^{-3}$] | 1.589 | 1.729 |
| $\mu$ (Mo-$K_\alpha$) [$mm^{-1}$] | 0.991 | 1.330 |
| No. of data collected | 17114 | 35940 |
| No. of unique data (all) | 5296 [$R$(int) = 0.0195] | 9979 [$R$(int) = 0.0663] |
| No. of obsd. data [$F > 2(\sigma F)$] | 4912 | 8329 |
| Parameters | 304 | 763 |
| $R_1$,[a] $wR_2$[b] [$I > 2\sigma(I)$] | 0.0327, 0.0873 | 0.0777, 0.1719 |
| $R_1$,[a] $wR_2$[b] (all data) | 0.0362, 0.0902 | 0.0972, 0.1823 |
| GOF | 1.005 | 1.162 |

[a] $R = \Sigma||F_o| - |F_c|| / \Sigma|F_o|$. [b] $wR(F^2) = [\Sigma w(F_o^2 - F_c^2)^2 / \Sigma w(F_o^2)^2]^{1/2}$. $w = 1/[\sigma^2(F_o^2) + (0.0530P)^2 + 1.6272P]$, where $P = (F_o^2 + 2F_c^2)/3$ for **1**. $w = 1/[\sigma^2(F_o^2) + (0.0550P)^2 + 18.1927P]$, where $P = (F_o^2 + 2F_c^2)/3$ for **2**.

 © 2006 Wiley-VCH Verlag GmbH & Co. KGaA, Weinheim 

**X-ray Crystallography**

X-ray diffraction data were collected with a Rigaku diffractometer with a Mercury CCD area detector (Mo-$K_\alpha$; $\lambda$ = 0.71073 Å) for **1** and **2** at 173(2) K. Empirical absorption corrections were applied to the data using the CrystalClear program.[17] The structures were solved by the direct method and refined by the full-matrix least-squares on $F^2$ using the SHELXTL-97 program.[18] The hydrogen atoms on the organic ligands were generated by the riding mode (C–H = 0.95 Å), and hydrogen atoms on water molecules were located from difference maps. Bond lengths and bond angles are listed in Table 2. Crystallographic data and other pertinent information for **1** and **2** are summarized in Table 3.

CCDC-289131 and CCDC-281815 contain the supplementary crystallographic data for this paper. These data can be obtained free of charge from The Cambridge Crystallographic Data Centre via www.ccdc.cam.ac.uk/data_request/cif.

## Acknowledgments

We thank the National Natural Science Foundation of China for financial support (90206040, 20325106, 20333070), the Natural Science Foundition of Fujian Province (E0520003), and the "one-hundred Talent" Project from CAS.

[1] D. Eisenberg, W. Kauzmann, *The Structure and Properties of Water*, Oxford University Press, New York, **1969**.
[2] R. Ludwig, *Angew. Chem. Int. Ed.* **2001**, *40*, 1808–1827.
[3] F. N. Keutsch, R. J. Saykally, *Proc. Natl. Acad. Sci. USA* **2001**, *98*, 10533–10540.
[4] R. Ludwig, *Angew. Chem. Int. Ed.* **2003**, *42*, 3458–3460.
[5] B.-Q. Ma, H.-L. Sun, S. Gao, *Angew. Chem. Int. Ed.* **2004**, *43*, 1374–1376.
[6] a) K. Liu, M. G. Brown, C. Carter, R. J. Saykally, J. K. Gregory, D. C. Clary, *Nature* **1996**, *381*, 501–503; b) K. Nauta, R. E. Miller, *Science* **2000**, *287*, 293–295; c) J. M. Ugalde, I. Alkorta, J. Elguero, *Angew. Chem. Int. Ed.* **2000**, *39*, 717–721.
[7] a) L. Infantes, S. Motherwell, *CrystEngComm* **2002**, *4*, 454–461; b) L. Infantes, J. Chisholm, S. Motherwell, *CrystEngComm* **2003**, *5*, 480–486.
[8] L. E. Cheruzel, M. S. Pometun, M. R. Cecil, M. S. Mashuta, R. J. Wittebort, R. M. Buchanan, *Angew. Chem. Int. Ed.* **2003**, *42*, 5452–5455.
[9] a) S. Pal, N. B. Sankaran, A. Samanta, *Angew. Chem. Int. Ed.* **2003**, *42*, 1741–1743; b) C. Y. Guo, M. B. Hickey, E. R. Guggenheim, V. Enkelmannb, B. M. Foxman, *Chem. Commun.* **2005**, 2220–2222; c) B. Venkataramanan, W. L. G. James, J. J. Vittal, V. Suresh, *Cryst. Growth Des.* **2004**, *3*, 553–561; d) R. Custelcean, C. Afloroaei, M. Vlassa, M. Polverejan, *Angew. Chem. Int. Ed.* **2000**, *39*, 3094–3096.
[10] P. S. Lakshminarayanan, E. Suresh, P. Ghosh, *J. Am. Chem. Soc.* **2005**, *127*, 13132–13133.
[11] a) K. M. Jude, S. K. Wright, C. Tu, D. N. Silverman, R. E. Viola, D. W. Christianson, *Biochemistry* **2002**, *41*, 2485–2491; b) Y. S. Lee, M. Krauss, *J. Am. Chem. Soc.* **2004**, *126*, 2225–2230.
[12] a) G. Hummer, J. C. Rasaiah, J. P. Noworyta, *Nature* **2001**, *414*, 188–190; b) K. Koga, G. T. Gao, X. C. Zeng, *Nature* **2001**, *412*, 802–805.
[13] F. Kovacs, J. Quine, T. A. Cross, *Proc. Natl. Acad. Sci. USA* **1999**, *96*, 7910–7915.
[14] Y.-S. Lee, M. Krauss, *J. Mol. Struct.* **2004**, *700*, 243–246.
[15] N. Ramasubbu, K. Sundar, C. Ragunath, M. M. Rafi, *Arch. Biochem. Biophys.* **2004**, *421*, 115–124.
[16] X. M. Zhang, R. Q. Fang, H. S. Wu, *Cryst. Growth Des.* **2005**, *5*, 1335–1337.
[17] G. M. Sheldrick, *SADABS*; University of Göttingen: Göttingen, Germany, **1996**.
[18] *SHELXTL* (version 5.10); Siemens Analytical X-ray Instruments Inc.: Madison, WI, **1994**.
[19] C. J. Tsai, K. D. Jordan, *Chem. Phys. Lett.* **1993**, *213*, 181–188.
[20] K. Kim, K. D. Jordan, T. S. Zwier, *J. Am. Chem. Soc.* **1994**, *116*, 11568–11569.
[21] a) L. Carlucci, G. Ciani, D. W. V. Gudenberg, D. M. Proserpio, *Inorg. Chem.* **1997**, *36*, 3812–3813; b) O. Mamula, A. V. Zelewsky, T. Bark, G. Bernardinelli, *Angew. Chem. Int. Ed.* **1999**, *38*, 2945–2948.
[22] A. H. Narten, W. E. Thiessen, L. Blum, *Science* **1982**, *217*, 1033–1034.
[23] J. N. Moorthy, R. Natarajan, P. Venugopalan, *Angew. Chem. Int. Ed.* **2002**, *41*, 3417–3420.

Received: December 2, 2005
Published Online: March 1, 2006

 © 2006 Wiley-VCH Verlag GmbH & Co. KGaA, Weinheim 

DOI: 10.1002/ejic.200500712

# The UV/Vis Spectrum of Potassium Heptacyanovanadate(III): A Theoretical Multi-Reference Configuration Interaction Study Combined with Low-Temperature Experiments

Volker Schmid,[a] Rolf Linder,[a] and Christel M. Marian*[a]

**Keywords:** Cyanide ligands / Electronic structure / Quantum chemistry / UV/Vis spectroscopy / Vanadium

The electronic spectrum of $K_4[V(CN)_7]$ has been calculated by means of a combined quantum chemical density functional and multi-reference configuration interaction scheme. In addition to the states known so far, our calculations predict the existence of two low-lying triplet electronic states with excitation energies of 13600 and 13700 $cm^{-1}$, respectively. Both result from $d_{e''_1} \rightarrow d_{e'_2}$ excitations in the slightly distorted pentagonal-bipyramidal ligand field. To validate these theoretical results we measured a UV/Vis spectrum at low temperatures. In the wavelength range between 800 and 500 nm we observed a broad band with vibrational substructure (peak positions: 13661, 14450, 15243, 16051, and 16807 $cm^{-1}$). The origin transition at 13661 $cm^{-1}$ is in excellent agreement with our theoretical predictions.
(© Wiley-VCH Verlag GmbH & Co. KGaA, 69451 Weinheim, Germany, 2006)

## Introduction

Six- and fourfold coordination of a central atom by ligands is the most common coordination scheme observed in transition metal complexes. Ligand-field parameters have been derived from experimental d–d spectra for a variety of these complexes.[1–3] To be able to adjust ligand parameters in a meaningful way, the character of a spectral band observed in absorption or emission has to be assigned properly. In some instances, the assignment, and thus also the parameter adjustment, is hampered because electronic d–d transitions in highly symmetric complexes are dipole forbidden and thus tend to be weak.

In the past decade, quantum chemical methods have made enormous progress, such that the properties of molecular ground states, for example the electronic structure or the molecular geometry, can be computed routinely with high confidence. In contrast, electronically excited states pose a much harder challenge, particularly for large molecules. Here, only a few methods are applicable. Among the ab initio approaches, presently the most common one is time-dependent density functional theory (TDDFT)[4] because of its computational efficiency. However, its has been shown recently that TDDFT, when used with standard functionals, may give dramatic failures for charge-transfer (CT) states.[5,6] The reliable prediction of the electronic excitation spectra of transition metal complexes has come into reach through the development of multi-reference second-order perturbation theory methods, such as CASPT2[7] and MRMP2,[8] as well as variational procedures that combine density functional theory and multi-reference configuration interaction schemes such as the DFT/MRCI approach.[9] These methods do not suffer from the flaws of TDDFT and offer the possibility to compute absorption spectra of transition metal complexes and thus help assign fragmentary experimental data.

Vanadium is one of the few transition metals that forms hexa- as well as heptacoordinate complexes, although knowledge of the heptacoordinate vanadates is patchy. Until recently, only two d–d transitions at 20600 and 22800 $cm^{-1}$ had been observed in a solid-state spectrum of $K_4[V(CN)_7]\cdot 2H_2O$,[10] although Bennett and Nicholls have prepared crystals with the approximate chemical composition $K_4[V(CN)_7]\cdot H_2O$ for which they found d–d transitions at 22300 and 28900 $cm^{-1}$.[11] Bands at approximately 14700 $cm^{-1}$ have also been seen in aqueous solutions of $K_4[V(CN)_7]$.[12,13] However, $[V(CN)_7]^{4-}$ ions are known to disproportionate in water and the bands were assigned to originate either from a spin-forbidden transition in $[V(CN)_6]^{4-}$[13] or to $VO(CN)_5^{4-}$ complexes.[11] Thus, the assignment of the 14700 $cm^{-1}$ band to a heptacyanovanadate(III) complex in water was rather uncertain. Bands at 36400 $cm^{-1}$ and higher energies have been ascribed to CT transitions in crystals of $K_4[V(CN)_7]\cdot H_2O$.[11]

The $d^2$ configuration of the $V^{3+}$ ion yields nine singlets and six triplets for the free complex in $D_{5h}$ symmetry, i.e., the symmetry point-group of a pentagonal bipyramid. From EPR spectra, the electronic ground state of $K_4[V(CN)_7]$ is known to be a high-spin state,[11] therefore only triplet states are considered here. In the solid state, the

[a] Institute of Theoretical and Computational Chemistry, Heinrich-Heine-University,
Universitätsstr. 1, 40225 Düsseldorf, Germany,
Fax: +49-211-811-3466,
E-mail: christel.marian@uni-duesseldorf.de

 © 2006 Wiley-VCH Verlag GmbH & Co. KGaA, Weinheim 

Table 1. Triplet states resulting from a $d^2$ occupancy in a pentagonal-bipyramidal ligand field and distorted towards $C_{2v}$ symmetry.

| $D_{5h}$ Symmetry Orbital product | Electronic state(s) | $C_{2v}$ Symmetry Electronic state(s) |
|---|---|---|
| $d_{e_1''} \otimes d_{e_1''}$ | $^3A_2'$ | $^3B_2$ |
| $d_{e_1''} \otimes d_{e_2'}$ | $^3E_1'' \oplus {}^3E_2''$ | $2\,{}^3A_2 \oplus 2\,{}^3B_1$ |
| $d_{e_1''} \otimes d_{a_1'}$ | $^3E_1''$ | $^3A_2 \oplus {}^3B_1$ |
| $d_{e_2'} \otimes d_{e_2'}$ | $^3A_2'$ | $^3B_2$ |
| $d_{e_2'} \otimes d_{a_1'}$ | $^3E_2'$ | $^3A_1 \oplus {}^3B_2$ |

high symmetry of the ligand field is distorted because of the tetrahedral arrangement of potassium counterions in the unit cell.[14] This reduction to $C_{2v}$ symmetry results in a splitting of degenerate electronic energies to yield 10 nondegenerate triplet states. The electronic configurations originating from a $d^2$ configuration and their irreducible representations in the $D_{5h}$ and $C_{2v}$ molecular point-groups are displayed in Table 1. In addition to these states, CT states will occur at higher energies in the electronic spectrum.

## Results and Discussion

The optimized complex geometry (OptGeo) corresponds to a slightly distorted pentagonal bipyramid with nearly equal axial and equatorial ligand bond lengths (see Figure 1). Crystal water that is present in the unit cell of $K_4[V(CN)_7]\cdot 2H_2O$[10] has been ignored in the calculations. The computed vanadium–carbon distances range from 218 to 220 pm, in fair agreement with the X-ray diffraction data (213–216 pm).[10] The CN ligand bonds are slightly longer in the optimized structure (116–117 pm) than in the experimental one (114–115 pm). In the fully optimized structure, the bond angles between equatorial ligands range between 70.6° and 73.5°. These values agree with the experimentally derived data within ±1°. The C–V–C angle of the two axial ligands, on the other hand, comes out somewhat too large. For this angle we compute a value of 177° compared to 171° in the X-ray structure. The energetic splitting of electronic states that are degenerate in the ideal $D_{5h}$ symmetry might therefore be somewhat underestimated in our calculations.

Although the $[V(CN)_7]^{4-}$ moiety is nearly $C_{2v}$ symmetric, the overall symmetry of the experimental X-ray structure is $C_1$ because two of the potassium counterions are slightly distorted out of the equatorial plane by the crystal water. In our calculations, we find the two equatorial $K^+$ ions at a distance of 462 pm from the central vanadium compared to values of 479 or 480 pm from the X-ray data. The two $K^+$ ions located below and above the equatorial plane, respectively, are separated from the vanadium nucleus by 393 pm according to our calculations, whereas these distances are 442 and 445 pm in the crystal.

To get an idea of the influence of the nuclear geometry on the electronic excitation energies, we performed two additional calculations. In the first one, $C_{2v}$ symmetry was retained but the C–V–C angle of the two axial ligands was set to the experimental value of 171°. The corresponding V–C–N angles were set to 173°. The coordinates of the potassium ions and the equatorial ligands were left unchanged with respect to the optimized geometry. This structure will be denoted as (AxLGeo). The second nuclear arrangement (ExpGeo) exhibits no symmetry at all. Here, the coordinates of all $CN^-$ ligands and the potassium counterions were fixed at their experimental X-ray positions.[14] It differs from the experimental unit-cell only by the lack of crystal water.

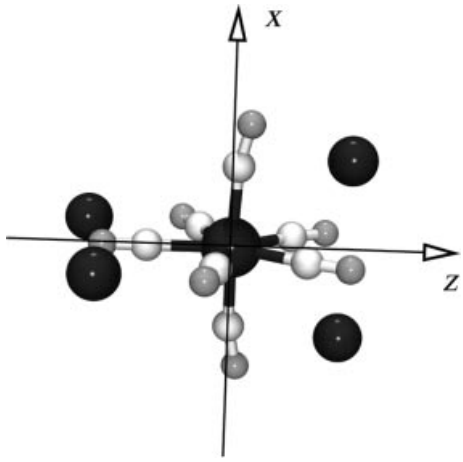


Figure 1. Optimized structure of the free potassium heptacyanovanadate(III) complex and orientation of the Cartesian coordinate system. The *y*-axis points toward the viewer.

The electronic ground-state corresponds to a configuration in which the d orbital of $e_1''$ symmetry is doubly occupied. As the *z*-axis has been chosen to coincide with the $C_2$ rotation axis of the $C_{2v}$ subgroup, $d_{e_1''}$ correlates with the Cartesian $d_{xz}$ and $d_{xy}$ orbitals. According to Table 1, this occupation gives rise to a triplet state of $A_2'$ symmetry in the undistorted pentagonal bipyramid or a $^3B_2$ state in the actual $C_{2v}$ point group.

A collection of measured and computed spectroscopic data is displayed in Table 2. Theoretical values correspond to vertical excitation energies at the optimized geometry (OptGeo). UTDDFT entries are not displayed in energetical order but are identified according to their symmetry labels and have been sorted to match the order of the corresponding DFT/MRCI entries. The lowest excited triplet states arise from d–d single excitations and combinations thereof. The first two states with DFT/MRCI excitation energies around 14000 $cm^{-1}$ are derived from the $d_{e_1''} \rightarrow d_{e_2'}$ ($^3E_2''$) state in $D_{5h}$ point-group symmetry. The lower one, $1\,{}^3A_2$, exhibits a $d^1_{xz}\,d^1_{yz}$ occupation, while its nearly degenerate partner state of $B_1$ symmetry has a leading configura-

 © 2006 Wiley-VCH Verlag GmbH & Co. KGaA, Weinheim 

tion with $d_{xz}$ and $d_{y^2-z^2}$ open shells. The electronic structures of the states originating from the two $^3E_1''$ states are considerably more involved because their $d^1_{e_1''}\,d^1_{e_2'}$ and $d^1_{e_1''}\,d^1_{a_1'}$ configurations are allowed to interact even in a perfect pentagonal-bipyramidal arrangement. A simple molecular orbital picture is therefore not appropriate in this case. In addition to d–d single excitations, we find some contributions from excitations into vanadium p and ligand σ orbitals. As a result, we observe a marked energetic splitting of the $^3E_1''$ components due to the $C_{2v}$-symmetric ligand field. The four members belonging to this group of states span an energy range from approximately 20600 cm$^{-1}$, where the second $^3B_1$ state is located, to the fourth $^3A_2$ state at about 31400 cm$^{-1}$. In between, and extending well above this energy regime, we find several CT states. The third, fifth, and sixth $^3A_2$ states, the fourth to seventh $^3B_1$ states, all $^3A_1$ as well as the second and third $^3B_2$ states correspond to CT excitations from a vanadium d orbital to a $CN^-$ ligand π* orbital. The seventh $^3A_2$ state also exhibits CT character, but in a reversed sense. Here, the excitation originates from the highest occupied $a_1$ ligand-orbital and the electron is placed in the $d_{e_1''}$ orbital of vanadium. No indication for states arising from double excitations within the d shell (corresponding to the orbital products $d_{e_2'} \otimes d_{e_2'}$ and $d_{e_2'} \otimes d_{a_1'}$, respectively) are found in the energy regime below 40000 cm$^{-1}$.

When we started the present investigation, the lowest experimentally known band was located at about 20600 cm$^{-1}$.[10] In our theoretical spectrum, we find a transition exactly at this wavenumber. However, this band corresponds to the third excited electronic state (2 $^3B_1$). Since the dipole moments of the d–d excited states are all very similar (see Table 2), we do not expect considerable solvent shifts. Could our computed excitation energies of the $K_4[V(CN)_7]$ complex be so erroneous? In order to answer this question, a UV/Vis spectrum of $K_4[V(CN)_7]$ was recorded at liquid helium temperatures. This spectrum is shown in Figure 2. In the wavelength range between 800 and 500 nm we observe a broad band with substructure (peak positions: 13661, 14450, 15243, 16051, and 16807 cm$^{-1}$). Our calculations predict two electronic transitions ($^3B_2 \rightarrow {}^3A_2$ and $^3B_2 \rightarrow {}^3B_1$) in this spectral area. Their small crystal-field splitting presumably prevents the resolution of these electronic transitions in the experimental spectrum. The regular spacing of the substructure (approx. 800 cm$^{-1}$) leads us to the conclusion that it is caused by a vibrational progression,

Table 2. Electronic triplet states of $K_4[V(CN)_7]$. Excitation energies $\Delta E$ are given in wavenumber units and dipole moments, $\mu$, in Debye units. Oscillator strengths $f(r)$ were computed in the length form and are dimensionless.

| | | Exp.[a] | Exp.[b] | Exp.[c] | Exp.[d] | DFT/MRCI | | | | | UTDDFT[e] | |
|---|---|---|---|---|---|---|---|---|---|---|---|---|
| | | | | | | (AxLGeo) | (OptGeo) | | | | (OptGeo) | |
| No. | State | $\Delta E$ | | | | | | $\mu$ | $f(r)$ | character | $\Delta E$ | $f(r)$ |
| 1 | $1^3B_2$ | – | – | – | – | 0 | 0 | 7.6 | – | | 0 | |
| 2 | $1^3A_2$ | – | – | – | 13661 | 13485 | 13611 | 8.6 | $<10^{-5}$ | $d_{e_1''} \rightarrow d_{e_2'}$ | 17894 | $1\cdot10^{-5}$ |
| 3 | $1^3B_1$ | – | – | – | – | 13809 | 13712 | 6.7 | – | $d_{e_1''} \rightarrow d_{e_2'}$ | 17914 | – |
| 4 | $2^3B_1$ | 20600 | – | – | – | 21210 | 20613 | 7.9 | – | $d_{e_1''} \rightarrow \{d_{a_1'}, d_{e_2'}\}$ | 22034 | – |
| 5 | $2^3A_2$ | 22800 | 22300 | 22200 | – | 23644 | 24078 | 6.7 | $2\cdot10^{-5}$ | $d_{e_1''} \rightarrow \{d_{e_2'}, d_{a_1'}\}$ | 20873 | $5\cdot10^{-5}$ |
| 6 | $3^3B_1$ | – | – | – | – | 25708 | 25399 | 7.0 | – | $d_{e_1''} \rightarrow \{d_{e_2'}, d_{a_1'}\}$ | 26776 | – |
| 7 | $4^3B_1$ | – | – | – | – | 27280 | 27303 | 16.3 | – | CT ($d \rightarrow L$) | 27869 | – |
| 8 | $3^3A_2$ | – | 28900 | 28300 | – | 29083 | 29168 | 15.8 | $7\cdot10^{-4}$ | CT ($d \rightarrow L$) | 27964 | $3\cdot10^{-4}$ |
| 9 | $5^3B_1$ | – | – | – | – | 31209 | 31310 | 29.3 | – | CT ($d \rightarrow L$) | 29950 | – |
| 10 | $4^3A_2$ | – | – | – | – | 31162 | 31378 | 7.4 | $6\cdot10^{-5}$ | $d_{e_1''} \rightarrow \{d_{a_1'}, d_{e_2'}\}$ | 28996 | $6\cdot10^{-5}$ |
| 11 | $1^3A_1$ | – | – | – | – | 33232 | 33133 | 25.4 | $3\cdot10^{-4}$ | CT ($d \rightarrow L$) | 33512 | $1\cdot10^{-3}$ |
| 12 | $2^3A_1$ | – | 36400 | – | – | 34647 | 34757 | 10.8 | $3\cdot10^{-3}$ | CT ($d \rightarrow L$) | 34846 | $1\cdot10^{-3}$ |
| 13 | $6^3B_1$ | – | – | – | – | 36046 | 36137 | 12.7 | – | CT ($d \rightarrow L$) | 31830 | – |
| 14 | $2^3B_2$ | | | | | 37870 | 37939 | 11.0 | $6\cdot10^{-3}$ | CT ($d \rightarrow L$) | 34254 | $5\cdot10^{-3}$ |
| 15 | $7^3B_1$ | – | 38100 | – | – | – | 37944 | 17.7 | – | CT ($d \rightarrow L$) | 35900 | – |
| 16 | $5^3A_2$ | | | | | – | 38381 | 14.0 | $1\cdot10^{-3}$ | CT ($d \rightarrow L$) | 29645 | $6\cdot10^{-4}$ |
| 17 | $6^3A_2$ | – | – | – | – | – | 38252 | 12.0 | $3\cdot10^{-4}$ | CT ($d \rightarrow L$) | 32539 | $2\cdot10^{-3}$ |
| 18 | $7^3A_2$ | – | – | 40000 | – | – | 39611 | 6.1 | $5\cdot10^{-3}$ | CT ($L \rightarrow d_{e_1''}$) | – | – |
| 19 | $3^3B_2$ | | | | | – | 40389 | 22.6 | $1\cdot10^{-3}$ | CT ($d \rightarrow L$) | 35649 | $1\cdot10^{-3}$ |

[a] Spectrum of $K_4[V(CN)_7]\cdot 2H_2O$ in a Nujol mull recorded at liquid nitrogen temperature.[10] [b] Solid-state reflectance spectrum of $K_4[V(CN)_7]\cdot H_2O$.[11] [c] Solution spectrum (4 M KCN) of $K_4[V(CN)_7]\cdot H_2O$.[11] [d] Spectrum of $K_4[V(CN)_7]\cdot 2H_2O$ dispersed in silicon paste and measured at 5 K (this work). [e] Order of states complies with symmetry labels.

 © 2006 Wiley-VCH Verlag GmbH & Co. KGaA, Weinheim 

and the first peak at 13661 $cm^{-1}$ is assumed to be the origin of the electronic transition. Its position is in excellent agreement with our predictions. In view of the typical error bars of the DFT/MRCI method (approx. ±2000 $cm^{-1}$)[9] such a close match must be considered somewhat fortuitous. The fourth electronically excited state ($2\ ^3A_2$) in our theoretical spectrum is located 1300–1900 $cm^{-1}$ above the corresponding experimental band, depending on the reference.

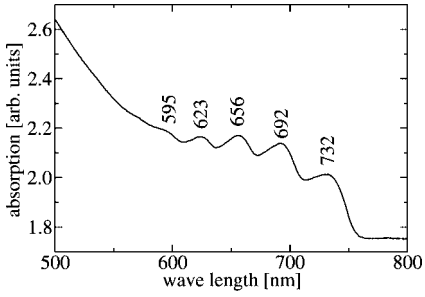


Figure 2. UV/Vis spectrum of $K_4[V(CN)_7]\cdot 2H_2O$ dispersed in silicon paste and recorded at 5 K.

The assignment of the higher-lying d–d states is less certain. In a solid-state spectrum of the (possibly eightfold coordinated) $K_4[V(CN)_7]\cdot H_2O$, Bennett and Nicholls[11] found a band with d–d character at 28900 $cm^{-1}$. In our theoretical spectrum, we only obtain a CT state with moderate oscillator strength in this energy regime. The d–d excited third $^3B_1$ state lies about 3000 $cm^{-1}$ below this transition. However, since the pure electronic transition is dipole forbidden, this state might be difficult to locate.

The DFT/MRCI calculations yield many more CT states than experimentally observed bands. However, this is not thought to be an artifact of our quantum chemical method. The MRCI treatment includes the nonlocal exchange interaction that is required for a correct asymptotic behavior of CT states.[6] The experimental spectra exhibit broad, poorly resolved bands. As the theoretical density of states is very high, we refrained from specifying the particular orbital excitations and labeled these states either as CT (d→L) or CT (L→d), depending on the direction of the charge transfer. Our assignment can only be tentative as it rests on the observation that the extinction coefficients of the CT bands in a solution spectrum (4 M KCN)[11] are larger than those of the d–d bands by two orders of magnitude.

It is difficult to judge the quality of the UTDDFT results. Overall, UTDDFT in combination with the B3LYP functional performs quite well for the d–d transitions, although it appears that the interaction between electronic configurations with a $d_{e_1''} \otimes d_{e_2'}$ open-shell structure is somewhat underestimated. This becomes apparent in the smaller splitting between the corresponding $^3E_2''$ and $^3E_1''$ states compared to the DFT/MRCI results and in the higher excitation energies of the first two excited states. CT states that involve predominantly ligand orbitals of $a_2$, $b_1$, or $b_2$ symmetries are located at comparable excitation energies in the UTDDFT and DFT/MRCI treatments, whereas excitations into totally symmetric ligand orbitals appear at considerably lower energies in the UTDDFT spectrum. The largest energy difference (more than 8000 $cm^{-1}$) is found for the $5\ ^3A_2$ state. This state is dominated by a single excitation from the vanadium $d_{e_1''}$ ($b_1$) orbital to unoccupied $a_1$ ligand orbitals. To a lesser extent, similar observations are made for other $A_2$ and $B_2$ CT states. We suppose that this difference is related to the above-mentioned wrong asymptotic behavior of the local exchange correlation functional and the fact that B3LYP contains only 20% exact exchange, although we cannot prove this hypothesis.

DFT/MRCI excitation energies obtained at the (AxLGeo) geometry, where the deflection of the axial ligands from the $z$ axis is identical to the X-ray structure, differ by, at most, 600 $cm^{-1}$ from the corresponding (OptGeo) values (see Table 2). The splitting between the $^3A_2$ and $^3B_1$ components of the lowest $^3E_2''$ and $^3E_1''$ states increase only slightly when proceeding from (OptGeo) to (AxLGeo). The oscillator strengths have the same order of magnitude at the two geometries and are therefore not listed. The energetic location of the CT states remains nearly unchanged. However, dramatic changes are observed in the spectrum if the electrostatic interaction with the counterions is not optimized (ExpGeo). In this case, diffuse electron-density distributions are stabilized to an extent that the first CT transitions appear already at about 20000 $cm^{-1}$, whereas all d–d transitions are blue-shifted. The first two d–d transitions are found at 18029 and 18995 $cm^{-1}$, respectively, in this DFT/MRCI calculation, followed by four CT states before the next d–d transition appears at 26351 $cm^{-1}$. This situation is aggravated if the counterions are moved even further out, eventually leading to an electron detachment from the central $[V(CN)_7]^{4-}$ unit. In that case, the solutions become heavily dependent on the AO basis set and are meaningless.

## Summary and Conclusions

We have computed the electronic spectrum of $K_4[V(CN)_7]$ by means of the DFT/MRCI method, which is a combined density functional and multi-reference configuration interaction approach. In addition to the states known so far from experiment, our quantum chemical calculations predict the existence of two low-lying excited electronic states that result from single excitations within the vanadium d shell. The configurations of the higher d–d excitations are considerably mixed so that a simple molecular orbital picture is not applicable.

The theoretical prediction of additional low-lying d–d states is confirmed by low-temperature optical spectroscopy measurements. For $K_4[V(CN)_7]\cdot 2H_2O$, a broad band with vibrational substructure in the wavelength range between approximately 750 and 600 nm is observed for the first time.

Concerning the excitation energies, we obtain excellent agreement between theory and experiment. Taking all measured transitions into account, the root mean square deviation (RMSD) from experiment amounts to merely 600 $cm^{-1}$. These findings suggest that the DFT/MRCI method, which was originally devised for organic molecules,

 © 2006 Wiley-VCH Verlag GmbH & Co. KGaA, Weinheim 

can equally well be applied to determine the electronic spectra of transition metal complexes. The theoretical prediction of d–d excitations has thus become a valuable complement to the measurement of these weak bands.

We have shown that d–d transitions of transition metal coordination compounds in the solid state can be modeled successfully by calculations on isolated clusters. However, at least for highly negatively charged coordination complexes such us $[V(CN)_7]^{4-}$, single-point calculations at the experimental geometry of the unit cell are not sufficient. Before the vertical spectrum can be computed, it is necessary to relax the geometry of the complex, including the counterions, thus optimizing the electrostatic interactions of the surrounding.

## Experimental Section

**Theoretical Methods:** The geometry of the free $K_4[V(CN)_7]$ complex was optimized utilizing the B3LYP density functional[15,16] as implemented in the TURBOMOLE package.[17,18] The search for a minimum on the potential-energy surface started from the experimentally known X-ray structure[14] of the crystalline unit cell, i.e., a slightly distorted pentagonal bipyramid of $[V(CN)_7]^{4-}$ tetrahedrally surrounded by four potassium ions. Carbon and nitrogen atomic orbitals (AOs) were described by the TZVPP basis (valence triple zeta plus 2d1f polarization) of the TURBOMOLE library. For vanadium, we employed a 13-electron relativistic effective core potential.[19] The corresponding valence basis was augmented with two f functions with exponents 1.14 and 0.52, optimized in scalar relativistic calculations[20] on $V^+(^5D_g)$ for the description of s–d and d–d correlation effects, respectively. We chose to represent even the potassium ions by (large-core) pseudopotentials[21] instead of point charges to prevent an artificial drain of electrons from the fourfold negatively charged complex.

The electronic spectrum was computed by means of the DFT/MRCI method by Grimme and Waletzke.[9] For comparison, a spin-unrestricted time-dependent DFT (UTDDFT) calculation was carried out at the optimized geometry. For this task we utilized the ESCF module of TURBOMOLE[22] employing the B3LYP density functional. In the DFT/MRCI approach, major parts of dynamic electron correlation are included by density functional theory whereas moderate multi-reference configuration interaction expansions take account of static correlation effects. To this end, the determinants in the CI expansion are built up from Kohn–Sham (KS) orbitals and an effective Hamiltonian is employed that contains five empirical parameters. Optimized parameter sets are currently available in combination with the BHLYP[16,23] functional. Double counting of electron correlation is obviated by scaling off-diagonal CI matrix elements with a factor that depends exponentially on the energy difference between the diagonal energies of the two configuration state functions. For further technical details we refer to the original publication.[9]

The DFT/MRCI calculations were carried out in a somewhat reduced AO basis set: we employed a TZVP basis (valence triple zeta plus 1d polarization) for carbon and nitrogen while keeping the vanadium and potassium basis sets unchanged. KS orbitals were optimized for the lowest lying closed-shell determinant, which served also as a starting point for the automated generation of the CI reference space. A common set of reference configurations was used for all spatial symmetries. The first set comprised all single and double excitations involving eight electrons in the four energetically highest-lying occupied orbitals and the four lowest unoccupied orbitals. In $C_{2v}$ symmetry, CI energies and vectors were determined for the three lowest triplet states in the $A_1$ and $B_2$ irreducible representations, respectively. As many of the low-lying triplet states exhibit $A_2$ or $B_1$ symmetry, seven roots were computed for these irreducible representations. The CI expansion was kept moderate by extensive configuration selection: all excitations into MO with orbital energies above 8 $E_H$ (anti-core) and all configurations with energies 0.75 $E_H$ above the energy of the highest reference vector were discarded. The original reference space was then iteratively improved (two times) by adding all configurations contributing at least 0.001 to the norm of any of the CI vectors. This procedure resulted in a final reference set of 543 configurations and CI expansion lengths of approximately 1.1 million configuration state functions per irreducible representation. In $C_1$ symmetry, the number of roots was confined to 12 due to the lack of symmetry blocking.

**Experimental Details:** The compound was prepared at the Institute of Inorganic Chemistry of the Heinrich Heine University following the procedure of Müller et al.[24] The elemental analysis confirmed the chemical composition of $K_4[V(CN)_7]\cdot 2H_2O$.

The optical spectra were recorded with a Cary 4E instrument containing a tungsten lamp as light source, a 25-cm double monochromator, and a photomultiplier with an S20 photocathode as detector. The substance was dispersed in silicon paste and applied to a sapphire sample carrier. The samples were cooled by immersion in superfluid helium using a Konti bathcryostat type Spectro C of CryoVac.

## Acknowledgments

We are grateful to the Institute of Inorganic Chemistry of the Heinrich Heine University (Prof. Kläui) for the preparation of the potassium heptacyanovanadate complex. Volker Schmid cordially thanks Georg Jansen (University of Essen-Duisburg) and Reinhold Fink (Ruhr-University Bochum) for helpful discussions.

[1] C. K. Jørgensen, *Absorption Spectra and Chemical Bonding in Complexes*, **1962**, Pergamon Press, Cambridge.
[2] M. Gerloch, R. C. Slade, *Ligand-Field Parameters*, **1973**, Cambridge University Press, Cambridge.
[3] *Comprehensive Coordination Chemistry II* (Ed.: B. Lever), **2003**, vol. 1, Elsevier, Amsterdam.
[4] M. E. Casida, *Recent Advances in Density Functional Methods*, **1973** World Scientific, Singapore.
[5] S. Grimme, M. Parac, *ChemPhysChem.* **2003**, *4*, 292.
[6] A. Dreuw, J. L. Weisman, M. Head-Gordon, *J. Chem. Phys.* **2003**, *119*, 2943.
[7] K. Andersson, P. Å. Malmqvist, B. O. Roos, A. J. Sadley, K. Wolinski, *J. Phys. Chem.* **1990**, *94*, 5483.
[8] S. Grimme, M. Waletzke, *Phys. Chem. Chem. Phys.* **2000**, *2*, 2075.
[9] S. Grimme, M. Waletzke, *J. Chem. Phys.* **1999**, *111*, 5645.
[10] R. A. Levenson, R. J. G. Dominguez, *Inorg. Chem.* **1973**, *12*, 2342.
[11] B. G. Bennett, D. Nicholls, *J. Chem. Soc. A* **1971**, 1204.
[12] J. R. Perumareddi, A. D. Liehr, A. W. Adamson, *J. Am. Chem. Soc.* **1963**, *85*, 249.
[13] J. J. Alexander, H. B. Gray, *J. Am. Chem. Soc.* **1968**, *90*, 4260.
[14] R. A. Levenson, L. R. Towns, *Inorg. Chem.* **1974**, *13*, 105.
[15] A. D. Becke, *Phys. Rev. A* **1988**, *38*, 3098.
[16] C. Lee, W. Yang, R. G. Parr, *Phys. Rev. B* **1988**, *37*, 785.
[17] R. Ahlrichs, M. Bär, M. Häser, H. Horn, C. Kölmel, *Chem. Phys. Lett.* **1989**, *162*, 165.
[18] O. Treutler, R. Ahlrichs, *J. Chem. Phys.* **1995**, *102*, 346.

 © 2006 Wiley-VCH Verlag GmbH & Co. KGaA, Weinheim 

[19] M. Dolg, U. Wedig, H. Stoll, H. Preuss, *J. Chem. Phys.* **1987**, *86*, 866.
[20] S. J. Hutter, *Methodologische Aspekte der Behandlung der Spin-Bahn-Kopplung zweiatomiger Moleküle*, Dissertation, University of Bonn, **1994**.
[21] A. Bergner, M. Dolg, W. Küchle, H. Stoll, H. Preuss, *J. Mol. Phys.* **1993**, *80*, 1431.
[22] F. Furche, R. Ahlrichs, *J. Chem. Phys.* **2002**, *117*, 7433.
[23] A. D. Becke, *J. Chem. Phys.* **1993**, *98*, 1372.
[24] A. Müller, P. J. Aymonino, P. Werle, E. Diemann, *Chem. Ber.* **1972**, *105*, 2419

Received: August 9, 2005
Published Online: March 1, 2006

 © 2006 Wiley-VCH Verlag GmbH & Co. KGaA, Weinheim 

DOI: 10.1002/ejic.200500808

# Fe(Cu)-Containing Coordination Polymers: Syntheses, Crystal Structures, and Applications as Benzyl Alcohol Oxidation Catalysts

**Huayun Han,[a] Sujuan Zhang,[a] Hongwei Hou,*[a] Yaoting Fan,[a] and Yu Zhu[a]**

**Keywords:** Fe(Cu)-coordination polymers / Benzyl alcohol oxidation / Catalysts

In this paper three coordination polymers, $\{[Fe(fcz)_2Cl_2]\cdot 2CH_3OH\}_n$ (**1**), $\{[Cu(fcz)_2(H_2O)]\cdot SO_4\cdot DMF\cdot 2CH_3OH\cdot 2H_2O\}_n$ (**2**), and $\{[Cu(fcz)_2Cl_2]\cdot 2CH_3OH\}_n$ (**3**) {fcz = 1-(2,4-difluorophenyl)-1,1-bis[(1*H*-1,2,4-triazol-l-yl)methyl]ethanol}, were synthesized. Crystallographic analysis reveals that polymer **1** exhibits a 2-D rhombohedral grid structure with (4, 4) nets, while polymer **2** has a 1-D double-chain framework. The structure of polymer **3** is similar to that of **1**. We found that polymers **1**–**3** could effectively catalyze the oxidation of benzyl alcohol to benzaldehyde with $H_2O_2$ (30 mass-%) as oxidant in aqueous medium. Various reaction conditions were studied, and optimal reaction conditions were obtained. Under the optimal conditions, the selectivity to benzaldehyde was almost up to 100 % and the conversion of benzyl alcohol was 87 % for **1**, 79 % for **2**, and 68 % for **3**. The results of the recycling test showed that the catalytic activity decreased by only about 7 % after three consecutive reaction cycles. However, under similar conditions, when we used the corresponding metal salt instead of the polymer as catalyst, or replaced the water with acetonitrile as solvent, neither the selectivity nor the conversion was the same.

(© Wiley-VCH Verlag GmbH & Co. KGaA, 69451 Weinheim, Germany, 2006)

## Introduction

In the past decade, the investigation of coordination polymers has been intensified because of their promising perspectives toward the development of new functional materials with various structural features and properties for applications in such areas as magnetic and optical materials, gas storage, molecular recognition devices, and so on.[1–6] However, little attention has been paid to their catalytic activities.[7–9] In principle, coordination polymers would be expected to be one of the new candidates for catalysts.[10–12] First, the success of metal complexes in catalysis is largely dependent on their structures and electronic properties.[13–15] Coordination polymers offer a variety of molecular structures and electronic properties that can be obtained by changing the metal ions, ligands, anions, coordination modes, etc. For example, the d orbitals of some transition metals may interact with organic π electrons to provide a localized electronic system within a polymer.[16–19] This diversity should give one an opportunity to tune the electronic properties of the molecules, and hence to tune the catalytic activity. On the other hand, the high stability and large number of active metal centers of coordination polymers are advantageous for practical applications as catalysts.[20] Meanwhile, the structures of the catalysts should be characterized in order to fine-tune both catalytic activity and selectivity; however, the structures of the traditional heterogeneous catalysts are usually not very clear.

Benzaldehyde is a very important raw material and intermediate which is used in the perfumery, pharmaceutical, dyestuff, and agrochemical industry, and the market demands have been steadily increasing over the last years.[21–22] The selective oxidation of benzyl alcohol to benzaldehyde is one of the most fundamental reactions both for laboratory-scale experiments and in the manufacturing processes. Up to now, catalytic vapor-phase oxidation of benzyl alcohol to benzaldehyde has been widely investigated.[23–25] The few studies on the liquid-phase oxidation of benzyl alcohol mainly focus on expensive metals, such as Ru, Pd, or Pd–Ag,[26–27] heteropolyacids[28] and some Cu, Fe, and Mn complexes.[29–34] In addition, the traditional reactions are often performed in environmentally undesirable solvents.[35–36]

On the basis of the above considerations, we synthesized three coordination polymers, $\{[Fe(fcz)_2Cl_2]\cdot 2CH_3OH\}_n$ (**1**), $\{[Cu(fcz)_2(H_2O)]\cdot SO_4\cdot DMF\cdot 2CH_3OH\cdot 2H_2O\}_n$ (**2**), and $\{[Cu(fcz)_2Cl_2]\cdot 2CH_3OH\}_n$ (**3**) {fcz = 1-(2,4-difluorophenyl)-1,1-bis[(1*H*-1,2,4-triazol-l-yl)methyl]ethanol}, Scheme 1], and characterized their structures as well as their catalytic activities in the oxidation of benzyl alcohol with $H_2O_2$ as oxidant in aqueous medium. The results show that the selectivity to benzaldehyde was almost 100% for the three polymers, and the conversion of benzyl alcohol was 87% for **1**, 79% for **2**, and 68% for **3**. When we used the corresponding metal salts as catalysts, or acetonitrile as solvent, neither the selectivity nor the conversion was the same.

[a] Department of Chemistry, Zhengzhou University, Henan 450052, P. R. China
Fax: + 86-371-67761744
E-mail: houhongw@zzu.edu.cn

 © 2006 Wiley-VCH Verlag GmbH & Co. KGaA, Weinheim 

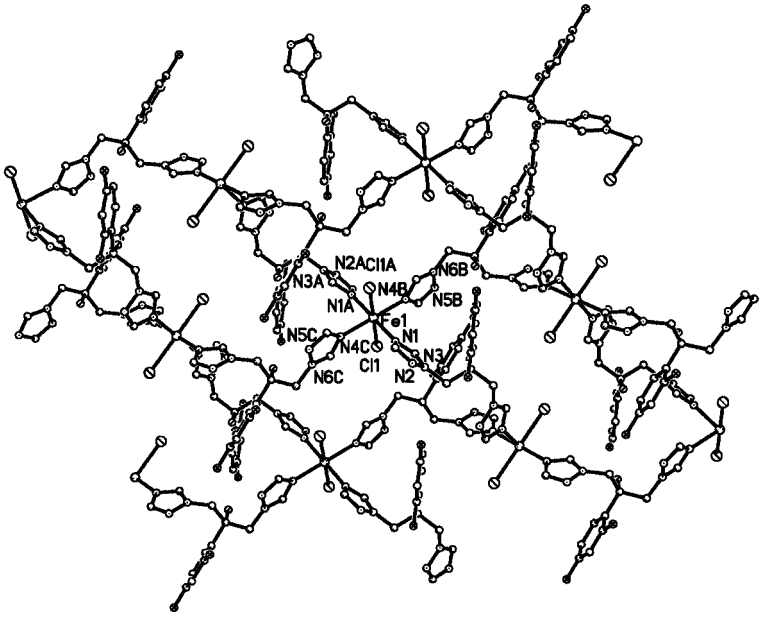


Figure 1. The two-dimensional rhombohedral grid structure of polymer **1**. Hydrogen atoms and solvent molecules have been omitted for clarity.

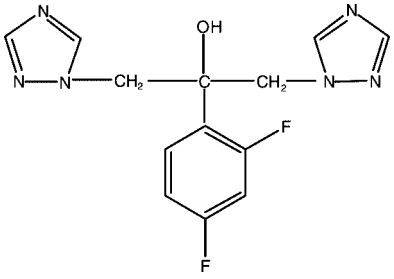


Scheme 1.

## Results and Discussion

### Crystal Structure of Polymer $\{[Fe(fcz)_2Cl_2]\cdot 2CH_3OH\}_n$ (1)

Coordination polymer **1** crystallizes in the monoclinic space group *C*2/*c* and exhibits a 2-D rhombohedral grid network structure with (4, 4) nets. Each $Fe^{II}$ ion is located at the center of an elongated octahedron. Two chlorine anions occupy the axial positions. Four nitrogen atoms from four fcz ligands occupy the equatorial positions (Figure 1). The axial Fe–Cl bond lengths [2.560(2) Å] are substantially longer than the equatorial Fe–N bond lengths (average: 2.174 Å). The bond angles around the $Fe^{II}$ ion are 180° (Cl1A–Fe1–Cl1, N4B–Fe1–N4C, N1A–Fe1–N1) or close to 90° (N1A–Fe1–Cl1A, N1A–Fe1–N4B, Cl1A–Fe1–N4C, etc.).

In the structure, all fcz ligands are equivalent. Every fcz ligand binds with two $Fe^{II}$ ions leading to a rhombohedral grid unit. Each grid consists of a 40-membered ring, $Fe_4(fcz)_4$, the four $Fe^{II}$ ions serving as four nodes and the four fcz groups acting as four sides. The rhombohedral grids have the dimensions 11.210 Å × 11.210 Å, the diagonal distances 9.430 Å × 20.337 Å, and the interior angles 49.8° and 130.2°. Two methanol molecules occupy the cavity of the (4, 4) network. Moreover, the solid-state structure of polymer **1** exhibits the layered packing mode.

### Crystal Structure of Polymer $\{[Cu(fcz)_2(H_2O)]\cdot SO_4\cdot DMF\cdot 2CH_3OH\cdot 2H_2O\}_n$ (2)

Crystallographic analysis reveals that polymer **2** crystallizes in the monoclinic space group $P2_1/n$ and exhibits a 1-D polymeric double-chain structure as shown in Figure 2. Each $Cu^{II}$ ion is at the center of a distorted tetragonal pyramid. Four nitrogen atoms from four fcz ligands occupy the basal sites, and one oxygen atom from a terminally coordinated water molecule fills the apical position. The Cu–O bond length of 2.365(4) Å is longer than the average Cu–N bond length (2.032 Å). The bond angles around the $Cu^{II}$ ion deviate from 180° or 90° (172.6 –177.1° or 86.9–96.8°), which differs from the structure of **1**.

In contrast to polymer **1**, in polymer **2** there are two kinds of fcz ligands, fcz1 and fcz2. In fcz1, the dihedral angle between two triazole rings is 107.0°, and the dihedral angle between the triazole ring and the phenyl ring is 59.1° or 48.9°. In fcz2, the corresponding dihedral angles are 112.2° and 56.1° or 56.3°, respectively. The dihedral angle between the two benzyl rings from two different fcz ligands is 6.8°. These ligands twist to meet the requirement of steric exclusion. The torsion angles are 179.2(3) Å for N3A–C3A–C4A–C11A and 177.4(3) Å for C3A–C4A–C11A–N4A in fcz1, and 163.0(3) Å for N9A–C16A–C17A–C24A and –177.6(3) Å for C16A–C17A–C24A–N10A in fcz2.

The twisted fcz ligands link two $Cu^{II}$ ions, resulting in a bimetallic ring as building block in which the Cu···Cu distance is 10.958 Å. The bimetallic rings are extended

 © 2006 Wiley-VCH Verlag GmbH & Co. KGaA, Weinheim 

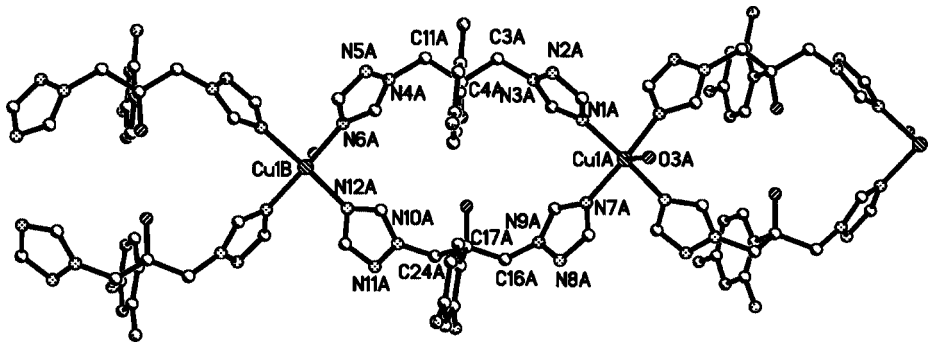


Figure 2. The double-chain structure of polymer **2** (cation part). Hydrogen atoms and solvent molecules have been omitted for clarity.

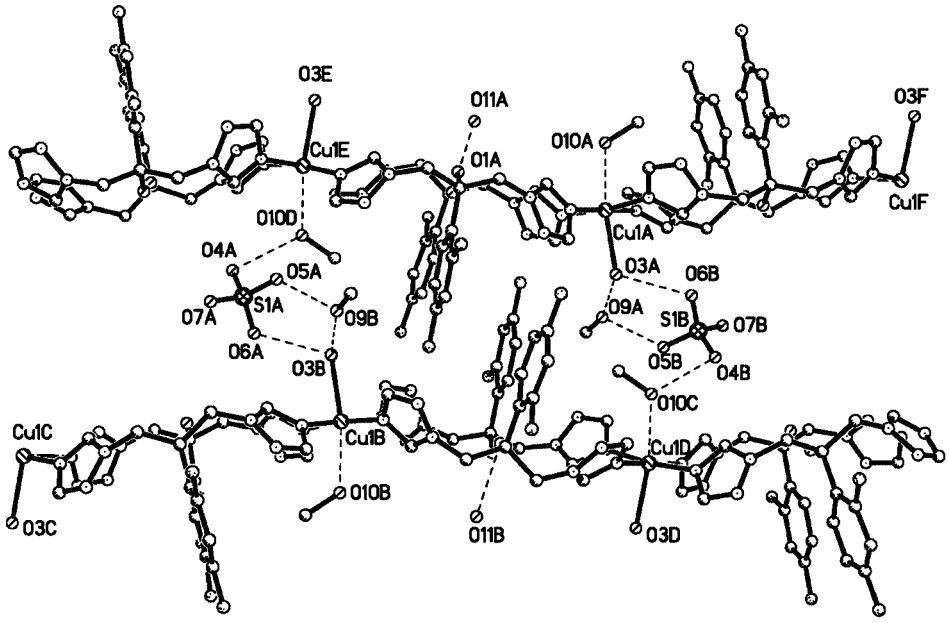


Figure 3. The crystal-packing diagram of polymer **2** with hydrogen bonds.

through co-$Cu^{II}$ to generate an infinite double chain. These chains are further connected through intermolecular hydrogen bonds and π–π stacking interactions of the phenyl rings, as shown in Figure 3. The sulfate anions and solvent molecules are located at the vacancy among the 1-D chains and hold the cationic chains together to generate a layered architecture. In this architecture, the shortest Cu···Cu distance between adjacent chains is 9.242 Å

The structure of polymer **3**[37] is similar to that of **1**. However, the average Cu–N bond length (2.032 Å) in **3** is shorter than that of Fe–N in **1**, and the Cu–Cl bond lengths [2.793(4) Å] are longer than those of Fe–Cl because of the Jahn–Teller effect.

### Catalytic Activities of the Polymers

To evaluate the catalytic properties of coordination polymers **1**–**3**, we selected the oxidation of benzyl alcohol as a probe reaction. The crystal polymers (1 mg/FW of **1** = $1.25 \cdot 10^{-3}$ mmol, 1 mg/FW of **2** = $2.08 \cdot 10^{-3}$ mmol, and 1 mg/FW of **3** = $1.23 \cdot 10^{-3}$ mmol[20]) were ground well into appropriate sizes. The effects of various reaction conditions such as temperature and amount of catalyst and oxidant $H_2O_2$ were investigated in detail by fixing the amount of benzyl alcohol at 4.6 mmol in 10 mL aqueous medium.

Figure 4 shows the effect of temperature on the oxidation with polymer **1**. It can be seen that the conversion of benzyl alcohol increases with increasing temperature. Especially when the temperature was raised from 30 to 40 °C, there was a significant increase in the conversion. At higher temperatures, rapid decomposition of hydrogen peroxide may take place and selectivity to benzaldehyde will decline, which are undesirable. Therefore, the optimal reaction temperature is 40 °C.

Figure 5 shows the effect of the amount of polymer **1**. When 0.005 mmol polymer **1** was employed in the reaction system, about 48% conversion of benzyl alcohol was achieved in 4 h. However, when the catalyst amount was increased to 0.01 mmol, the conversion was greatly improved and reached about 51% in 1 h and 87% in 4 h. A steady state of the catalytic reaction was observed after 4 h. Further increase in the amount of catalyst could not im-

 © 2006 Wiley-VCH Verlag GmbH & Co. KGaA, Weinheim 

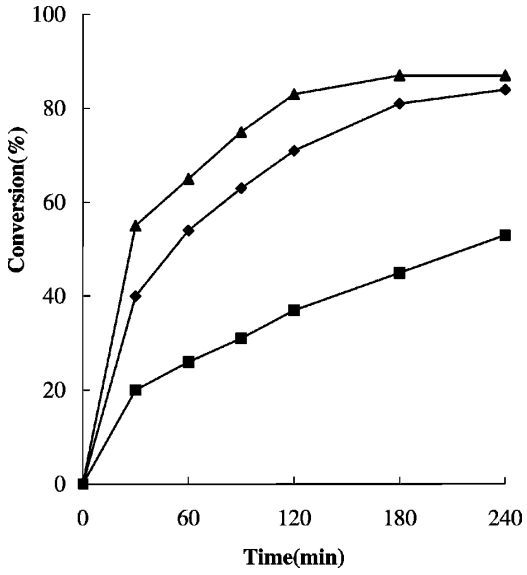


Figure 4. Effect of reaction temperature on conversion with polymer **1**: (■) 30 °C, (♦) 40 °C, (▲) 50 °C with fixed amounts of benzyl alcohol (4.6 mmol), $H_2O_2$ (6.0 mmol), and catalyst (0.01 mmol).

prove the conversion of benzyl alcohol significantly. The trend for polymer **2** or **3** as a catalyst was similar to that for **1**.

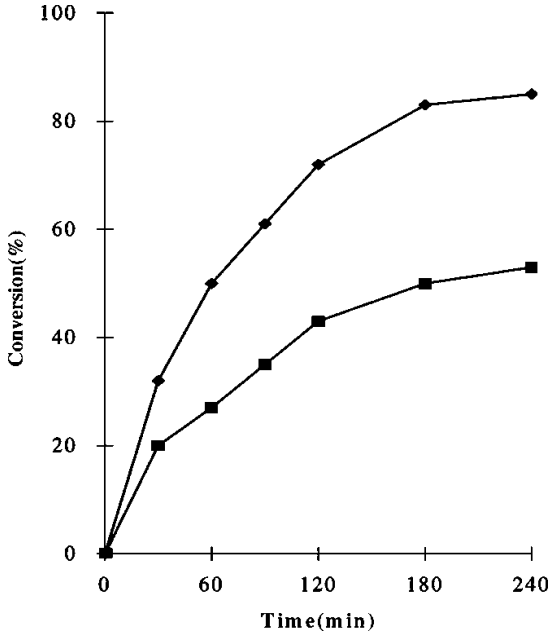


Figure 5. Effect of the amount of polymer **1** on benzyl alcohol oxidation: (■) 0.005 mmol, (♦) 0.01 mmol, with fixed amounts of benzyl alcohol (4.6 mmol) and $H_2O_2$ (6.0 mmol) at 40 °C in aqueous medium.

Moreover, the effect of the amount of oxidant was studied by using different concentrations of $H_2O_2$, viz. 4.6, 6.0, and 6.9 mmol (the molar ratio of $H_2O_2$ to benzyl alcohol was 1:1, 1:1.3, and 1:1.5). When the amount of $H_2O_2$ was increased from 4.6 to 6.9 mmol, the conversion of benzyl alcohol increased. Although excess $H_2O_2$ can increase the conversion, we chose 6.0 mmol $H_2O_2$ as the oxidant in order to avoid the formation of byproducts. In addition, the solvent was also taken into consideration for the oxidation of benzyl alcohol. The selectivity and conversion are better in aqueous medium than in acetonitrile, as shown in Table 1. The results are consistent with those in the literature,[38] in which benzyl alcohol was used as the substrate for the oxidation in a triphase using water with about sevenfold increase in conversion as compared with that obtained in a biphase using acetonitrile as solvent with titanium silicate catalyst.

Table 1. Results of oxidation of benzyl alcohol to benzaldehyde.[a]

| Catalysts | Solvent | Conversion (%) | Selectivity (%) |
|---|---|---|---|
| Polymer **1** | $H_2O$ | 87[a] | 100 |
| | | 85[b] | 100 |
| | | 81[c] | 100 |
| | $CH_3CN$ | 38 | 62 |
| Polymer **2** | $H_2O$ | 79[a] | 100 |
| | | 77[b] | 100 |
| | | 73[c] | 100 |
| | $CH_3CN$ | 29 | 56 |
| Polymer **3** | $H_2O$ | 68[a] | 100 |
| | | 66[b] | 100 |
| | | 63[c] | 100 |
| | $CH_3CN$ | 36 | 59 |
| $FeCl_2 \cdot 4H_2O$ | $H_2O$ | 32 | 85 |
| $CuCl_2 \cdot 2H_2O$ | $H_2O$ | 34 | 82 |
| $CuSO_4 \cdot 5H_2O$ | $H_2O$ | 35 | 84 |

[a] The superscripts "a, b, c" show the results of recycling from the first (fresh), to the second, and third runs, respectively.

Finally, the recycling of the catalysts was investigated. The organic phase was separated when the oxidation of benzyl alcohol was over. The aqueous phase and catalysts were reused for the subsequent oxidation reaction. The conversion of benzyl alcohol decreased by only about 7% after three consecutive cycles (Table 1). In order to prove that the Fe(Cu)-containing coordination polymers were heterogeneous catalysts, we filtered the catalysts and allowed the filtered catalysts and the filtrate to catalyze other benzyl alcohol oxidations. About 80–85% of the original conversion was achieved by using the filtered catalyst, while the filtrate showed only 10–15% conversion under similar conditions. This result suggests that the dominant reactive species is the heterogeneous catalyst.

Figure 6 presents the conversions of benzyl alcohol using polymers **1**–**3** as catalysts under optimized conditions. Obviously, polymer **2** exhibits the best catalytic activity in the first 2 h. However, the catalytic activity of polymer **1** improves later and surpasses that of polymer **2**. All relevant data, i.e. the conversion of benzyl alcohol and the selectivity to benzaldehyde, are collected in Table 1. We can find that the catalytic activities of these polymers are better than those of the corresponding salts. For example, the selectivity of polymer **1** to benzaldehyde was almost 100%, while the selectivity with $FeCl_2$ reached only 85%. This may be explained by the stabilizing effect of the fcz ligands. On the other hand, free metal ions resulted in rapid decomposition

 © 2006 Wiley-VCH Verlag GmbH & Co. KGaA, Weinheim 

of hydrogen peroxide, and poor selectivity was observed. Also, it can be seen that the conversion of benzyl alcohol using Fe-containing polymer **1** as catalyst is higher than those using Cu-containing polymers, and the Cu-containing polymers **2** and **3** exhibit different catalytic activities, which can be ascribed to the difference in the coordination environment of their $Cu^{II}$ centers. The results suggest that both the central metals and the structures of the polymers have great influence on their catalytic activities.

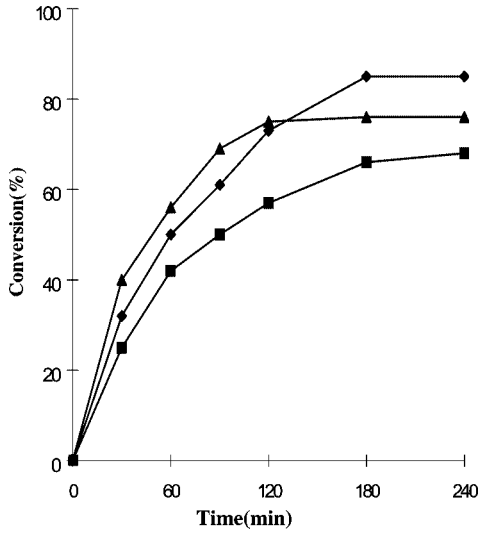


Figure 6. Dependence of the conversion of benzyl alcohol on the reaction time with different polymers: (♦) polymer **1**, (▲) polymer **2**, (■) polymer **3**, under the optimized conditions with fixed amounts of benzyl alcohol (4.6 mmol), $H_2O_2$ (6.0 mmol), and catalyst (0.01 mmol) at 40 °C in aqueous medium.

## Conclusions

The present study shows that polymers **1**–**3** are potential catalysts for the oxidation of benzyl alcohol to benzaldehyde. In addition, central metals and structures of the polymers have great influence on their catalytic activities.

## Experimental Section

**Materials and General Details:** Fcz was supplied by Zhongshuai Pharmaceutical Sci. & Tech. Development Co. Ltd., Henan Province, China. All the solvents and chemicals were used without further purification. IR spectroscopy was performed with a PE 1710 spectrophotometer in the 400–4000-$cm^{-1}$ region. Carbon, hydrogen, and nitrogen analysis were performed with a Carlo–Erba 1106 elemental analyzer.

**Synthesis of Polymer $\{[Fe(fcz)_2Cl_2]\cdot 2CH_3OH\}_n$ (1):** A methanol solution of fcz (0.2 mmol, 6 mL) was added dropwise into an aqueous solution of $FeCl_2\cdot 4H_2O$ (0.1 mmol, 1 mL) to give a clear solution. The resulting solution was allowed to stand at room temperature for two weeks. Yellow crystals formed; yield 56 mg (ca. 70%). The crystals are insoluble in water and most organic solvents. $C_{28}H_{32}Cl_2F_4FeN_{12}O_4$ (803.41): calcd. C 41.84, H 3.98, N 20.92; found C 41.72, H 4.07, N 20.76. IR (KBr): $\tilde{\nu}$ = 3446 (s), 1619 (s), 1502 (s), 1277 (s), 1129 (s), 967 (m), 677 (m) $cm^{-1}$.

**Synthesis of Polymer $\{[Cu(fcz)_2(H_2O)]\cdot SO_4\cdot DMF\cdot 2CH_3OH\cdot 2H_2O\}_n$ (2):** A mixture of methanol and DMF solution of fcz (0.2 mmol, 6 mL) was slowly added into an aqueous solution of $CuSO_4\cdot 5H_2O$ (0.1 mmol, 1 mL) to give a clear solution. The resulting solution was allowed to stand at room temperature for two weeks. Blue crystals formed; yield 30 mg (ca. 60%). The crystals are insoluble in water and most organic solvents. $C_{31}H_{45}CuF_4N_{13}O_{12}S$ (963.40): calcd. C 38.61, H 4.67, N 18.89; found C 38.52, H 4.67, N 18.76. IR (KBr): $\tilde{\nu}$ = 3445 (s), 3131 (s), 1620 (s), 1500 (m), 1279 (m), 1130 (s), 675 (m) $cm^{-1}$.

Table 2. Crystal data and structure refinement for polymers **1** and **2**.

| | **1** | **2** |
|---|---|---|
| Empirical formula | $C_{28}H_{32}Cl_2F_4FeN_{12}O_4$ | $C_{15.5}H_{22.5}Cu_{0.5}F_2N_{6.5}O_6S_{0.5}$ |
| Formula weight | 803.41 | 481.70 |
| Temperature [K] | 291(2) | 291(2) |
| Radiation | Mo-$K_\alpha$ | Mo-$K_\alpha$ |
| Wavelength [Å] | 0.71073 | 0.71073 |
| Crystal system | monoclinic | monoclinic |
| Space group | *C*2/*c* | $P2_1/n$ |
| Crystal dimensions [$mm^3$] | 0.20×0.18×0.18 | 0.20×0.18×0.18 |
| *a* [Å] | 23.423(5) | 12.006(2) |
| *b* [Å] | 9.4356(19) | 18.014(4) |
| *c* [Å] | 20.826(4) | 18.953(4) |
| $\alpha$ [°] | 90 | 90 |
| $\beta$ [°] | 125.66(3) | 93.81(3) |
| $\gamma$ [°] | 90 | 90 |
| *V* [$Å^3$] | 3739.8(13) | 4092.2(14) |
| *Z* | 4 | 8 |
| *F*(000) | 1648 | 1996 |
| $\rho$ [g $cm^{-3}$] | 1.427 | 1.564 |
| $\mu$ [$mm^{-1}$] | 0.616 | 0.679 |
| Data/restrains/parameters | 2375/0/235 | 7548/0/599 |
| Goodness-of-fit on $F^2$ | 0.966 | 1.047 |
| $R_1 = [I > 2\sigma(I)]$ | 0.0792 | 0.0553 |
| $wR_2$ (all data) | 0.2008 | 0.1292 |

 © 2006 Wiley-VCH Verlag GmbH & Co. KGaA, Weinheim 

**Synthesis of Polymer $\{[Cu(fcz)_2Cl_2]\cdot 2CH_3OH\}_n$ (3):** Polymer **3** was synthesized according to the literature[37] as blue crystals; yield 50 mg (ca. 60%). The crystals are insoluble in water and most organic solvents. $C_{28}H_{32}CuCl_2F_4N_{12}O_4$ (811.10): C 41.43, H 3.95, N 20.72; found C 41.49, H 3.90, N 20.74. IR (KBr): $\tilde{\nu}$ = 3448 (s), 1619 (s), 1501 (s), 1278 (s), 992 (m), 673 (m) $cm^{-1}$.

**Crystal-Structure Determination:** Crystallographic data for the polymers **1** and **2** were collected with a Rigaku R-AXIS-IV image plate area detector with graphite-monochromatized Mo-$K_\alpha$ *X*-radiation ($\lambda$ = 0.71073 Å). The data were corrected for Lorentz and polarization effects and for absorption by using empirical scan data. All calculations were performed using the SHELXL-97 crystallographic software package,[39] and refined by full-matrix least-squares methods based on $F^2$ with isotropic thermal parameters for the non-hydrogen atoms. The hydrogen atoms were located theoretically. Processing parameters and the crystal data for polymers **1** and **2** are summarized in Table 2, and selected bond lengths and bond angles are listed in Table 3.

Table 3. Selected bond lengths [Å] and angles [°] for polymers **1** and **2**.[a]

| Polymer **1** | | | |
|---|---|---|---|
| Fe(1)–N(1) | 2.162(6) | Fe(1)–N(4)#2 | 2.185(7) |
| Fe(1)–Cl(1) | 2.560(2) | N(1)–Fe(1)–N(1)#1 | 180.0(3) |
| N(4)#2–Fe(1)–N(4)#3 | 180.000(1) | N(1)–Fe(1)–N(4)#2 | 90.7(2) |
| N(1)#1–Fe(1)–N(4)#2 | 89.3(2) | N(1)–Fe(1)–Cl(1) | 90.61(17) |
| N(1)#1–Fe(1)–Cl(1) | 89.39(17) | N(4)#2–Fe(1)–Cl(1) | 90.32(18) |
| N(4)#3–Fe(1)–Cl(1) | 89.68(18) | Cl(1)–Fe(1)–Cl(1)#1 | 180.00(9) |
| Polymer **2** | | | |
| Cu(1)–N(7) | 2.022(3) | Cu(1)–N(12)#1 | 2.031(3) |
| Cu(1)–N(6)#1 | 2.032(3) | Cu(1)–N(1) | 2.043(3) |
| Cu(1)–O(3) | 2.365(4) | N(7)–Cu(1)–N(12)#1 | 86.94(12) |
| N(7)–Cu(1)–N(6)#1 | 172.64(13) | N(12)#1–Cu(1)–N(6)#1 | 95.53(12) |
| N(7)–Cu(1)–N(1) | 90.19(12) | N(12)#1–Cu(1)–N(1) | 177.12(12) |
| N(6)#1–Cu(1)–N(1) | 87.34(12) | N(7)–Cu(1)–O(3) | 96.81(15) |
| N(12)#1–Cu(1)–O(3) | 90.60(13) | N(6)#1–Cu(1)–O(3) | 90.11(14) |
| N(1)–Cu(1)–O(3) | 89.58(13) | | |

[a] Symmetry transformations used to generate equivalent atoms: Polymer **1** # 1 – *x*, –*y* + 2, –*z*; #2 –*x* – 1/2, –*y* + 3/2, *z* – 1/2; #3 – *x* + 1/2, *y* + 1/2, –*z* + 1/2; Polymer **2** #1 *x* + 1/2, –*y* + 3/2, *z* + 1/2.

CCDC-262170 and -262172, for polymers **1** and **2**, respectively, contain the supplementary crystallographic data for this paper. These data can be obtained free of charge from The Cambridge Crystallographic Data Centre via www.ccdc.cam.ac.uk/data_request/cif.

**Catalytic Experiments:** Catalytic experiments were carried out in a 50-mL, three-necked, round-bottom reaction flask fitted with a water condenser. One neck of the flask was equipped with a mercury thermometer for measuring the reaction temperature. The crystal polymer catalysts were ground well into appropriate sizes to increase the surface area, but not too small for a convenient filtration. Benzyl alcohol and water were mixed in the reactor with a magnetic stirrer and heated to a given temperature. Then, hydrogen peroxide (concentration determined by iodometric titration before use) was added to the reaction system. Samples of 0.2 mL were removed every 30 min and diluted (1:10) with $CH_3OH$ to be analyzed by HPLC (HP 1100 high-pressure liquid chromatogram analyzer). A reversed-phase Eclipse×DB-C8 (4.6×150 mm) column was used at ambient temperature, and a methanol/water mixture (70:30 vol-%, 0.5 mL·$min^{-1}$) was used as the eluent. The UV detector was employed at 253 nm. All reactions were run at least in triplicate, and the data reported represent the average of these reactions. Commercial products were used for all chromatographic standardizations.

## Acknowledgments

We gratefully acknowledge the financial support of the National Science Foundation of China (Nos. 20001006 and 20371042) and the Henan Province.

[1] H. W. Hou, Y. L. Song, H. Xu, Y. L. Wei, Y. T. Fan, Y. Zhu, C. X. Du, *Macromolecules* **2003**, *36*, 999–1008.
[2] X. R. Meng, G. Li, H. W. How, H. Y. Han, Y. T. Fan, Y. Zhu, C. X. Du, *J. Organomet. Chem.* **2003**, *679*, 153–161.
[3] S. A. Boume, J. Lu, A. Mondal, B. Moulton, M. J. Zaworotko, *Angew. Chem. Int. Ed.* **2001**, *40*, 2111–2113.
[4] M. J. Zaworotko, *Chem. Commun.* **2001**, 1–10.
[5] X.-M. Zhang, M.-L. Tong, X.-M. Chen, *Angew. Chem. Int. Ed.* **2002**, *41*, 1029–1031.
[6] S. W. Keller, S. Lopez, *J. Am. Chem. Soc.* **1999**, *121*, 6306–6307.
[7] M. Fujita, Y. J. Kwon, S. Washizu, K. Ogura, *J. Am. Chem. Soc.* **1994**, *116*, 1151–1152.
[8] J. S. Seo, D. Whang, H. Lee, S. I. Jun, J. Oh, Y. J. Jeon, K. Kim, *Nature.* **2000**, *404*, 982–986.
[9] T. Sawaki, T. Dewa, Y. Acyama, *J. Am. Chem. Soc.* **1998**, *120*, 8539–8540.
[10] C. Janiak, *Dalton Trans.* **2003**, 2781–2804.
[11] M. Fujita, K. Umemota, M. Yoshizawa, N. Fujita, T. Kusukawa, K. Biradha, *Chem. Commun.* **2001**, 509–518.
[12] S. K. Yoo, J. Y. Ryu, J. Y. Lee, C. Kim, S.-J. Kim, Y. Kim, *Dalton Trans.* **2003**, 1454–1456.
[13] M. Abrantes, A. Valente, M. Pillinger, I. S. Goncalves, J. Rocha, C. C. Romao, *J. Catal.* **2002**, *209*, 237–244.
[14] A. Togni, L. M. Venanzi, *Angew. Chem. Int. Ed. Engl.* **1994**, *33*, 497–526.
[15] F. Fache, B. Dunjic, P. Gamez, M. Lemaire, *Top. Catal.* **1997**, *4*, 201–209.
[16] Y. Garcia, P. J. Van Koningsbruggen, H. Kooijman, A. L. Spek, J. G. Haasnoot, O. Kahn, *Eur. J. Inorg. Chem.* **2000**, 307–314.
[17] Effendy, F. Marchetti, C. Pettinari, R. Pettinari, B. W. Skelton, A. H. White, *Inorg. Chem.* **2003**, *42*, 112–117.
[18] G. A. van Albada, R. C. Guijt, J. G. Haasnoot, M. Lutz, A. L. Spek, J. Reedijk, *Eur. J. Inorg. Chem.* **2000**, 121–126.
[19] T. Hirao, *Coord. Chem. Rev.* **2002**, *226*, 81–91.
[20] S. J. Hong, J. Y. Ryu, J. Y. Lee, C. Kim, S. J. Kim, Y. Kim, *Dalton Trans.* **2004**, 2697–2701.
[21] D. V. McGrath, R. H. Grubbs, J. W. Ziller, *J. Am. Chem. Soc.* **1991**, *113*, 3611–3613.
[22] D. A. Knight, T. L. Schull, *Synth. Commun.* **2003**, *33*, 827–831.
[23] J. Farkas, S. Békássy, J. Madarász, F. Figueras, *New J. Chem.* **2002**, *26*, 750–754.
[24] M. Arai, S. Nishiyama, S. Tsuruya, M. Masai, *J. Chem. Soc., Faraday Trans.* **1996**, *92*, 2631–2636.
[25] S. Sueto, S. Nishiyama, S. Tsuruya, M. Masai, *J. Chem. Soc., Faraday Trans.* **1997**, *93*, 659–664.
[26] L. F. Liotta, A. M. Venezia, G. Deganello, A. Longo, A. Martorana, Z. Schay, L. Guczi, *Catal. Today* **2001**, *66*, 271–276.
[27] R. Sumathi, K. Johnson, B. Vishwanathan, T. K. Varadarajan, *Appl. Catal. A: Gen.* **1998**, *172*, 15–22.
[28] G. D. Yadav, C. K. Mistry, *J. Mol. Catal. A: Chem.* **2001**, *172*, 135–149.
[29] N. Idaka, S. Nishiyama, S. Tsuruya, *Phys. Chem. Chem. Phys.* **2001**, *3*, 1918–1924.
[30] C. H. Jun, H. S. Hong, C. W. Hun, *Tetrahedron Lett.* **1999**, *40*, 8897–8900.
[31] S. Das, T. Punniyamurthy, *Tetrahedron Lett.* **2003**, *44*, 6033–6035.

 © 2006 Wiley-VCH Verlag GmbH & Co. KGaA, Weinheim 

[32] P. Gamez, I. W. C. E. Arends, J. Reedijk, R. A. Sheldon, *Chem. Commun.* **2003**, 2414–2415 and references cited therein.
[33] A. Dijksman, I. W. C. E. Arends, R. A. Sheldon, *Org. Biomol. Chem.* **2003**, *1*, 3232–3237.
[34] I. E. Marko, P. R. Giles, M. Tsukazaki, I. Chelle-Regnaut, A. Gautier, S. M. Brown, C. J. Urch, *J. Org. Chem.* **1999**, *64*, 2433.
[35] P. Gallezot, *Catal. Today* **1997**, *37*, 405–418.
[36] B. M. Trost, R. J. Kulawiec, *J. Am. Chem. Soc.* **1993**, *115*, 2027–2036.
[37] H. Y. Han, Y. L Song, H. W. Hou, Y. T. Fan, Y. Zhu, *Dalton Trans.* **2006**, ASAP article.
[38] R. Kumar, A. Bhaumik, *Microporous Mesoporous Mater.* **1998**, *21*, 497–526.
[39] G. M. Sheldrick, *SHELXTL-97*, *Program for Refinement of Crystal Structures*, University of Göttingen, Germany, **1997**.
Received: September 13, 2005
Published Online: February 23, 2006

 © 2006 Wiley-VCH Verlag GmbH & Co. KGaA, Weinheim 

DOI: 10.1002/ejic.200500902

# Iron(III) Complexes with the Ligand *N*′,*N*′-Bis[(2-pyridyl)-methyl]ethylenediamine (uns-penp) and Its Amide Derivative *N*-Acetyl-*N*′,*N*′-bis[(2-pyridyl)methyl]ethylenediamine (acetyl-uns-penp)

**Jing-Yuan Xu,[a,b] Jörg Astner,[b] Olaf Walter,[c] Frank W. Heinemann,[d] Siegfried Schindler,*[b] Michael Merkel,[e] and Bernt Krebs*[e]**

**Keywords:** Iron / Tripodal ligands / Catechol dioxygenase / Amide hydrogen bonding / Carboxamide coordination

Synthesis and structural characterization of the iron(III) complexes of the tripodal ligands *N*′,*N*′-bis[(2-pyridyl)methyl]-ethylenediamine (uns-penp), $[Fe(uns\text{-}penp)Cl_2]ClO_4 \cdot CH_3CN$, $[\{Fe(uns\text{-}penp)Cl\}_2O](ClO_4)_2 \cdot 2CH_3CN$ and the amide derivative *N*-Acetyl-*N*′,*N*′-bis[(2-pyridyl)methyl]ethylenediamine (acetyl-uns-penp), $[Fe_2(acetyl\text{-}uns\text{-}penp)_2O](ClO_4)_2 \cdot H_2O$, $[Fe(acetyl\text{-}uns\text{-}penp)(tcc)Br] \cdot (C_2H_5)_2O$ (tcc = tetrachlorocatecholate), and $[\{Fe(acetyl\text{-}uns\text{-}penp)(tcc)\}_2O] \cdot (C_2H_5)_2O \cdot CH_3OH$ are reported. Catechol dioxygenase reactivity of in situ prepared complex solutions was tested and showed that all complexes reacted slower compared with the iron tmpa system described in the literature.
(© Wiley-VCH Verlag GmbH & Co. KGaA, 69451 Weinheim, Germany, 2006)

## Introduction

Tripodal ligands such as tris[(2-pyridyl)methyl]amine (tmpa, also abbreviated as tpa in the literature) as well as derivatives, e.g. N4Py (Scheme 1), have been used successfully in experimental studies to model copper and iron enzymes.[1–5] Iron(II) complexes of the related ligand Rtpen (R = Me, Bz etc.) were shown to react with an excess of hydrogen peroxide to form an end-on hydroperoxo complex that can convert to a side-on peroxo complex at higher pH values.[6–10] More recently it was demonstrated that iron complexes with the ligand Bztpen as well as N4Py can form an iron(IV) oxo species that is able to oxidise alkanes such as cyclohexane.[11]

Rtpen can be prepared in two different synthetic procedures. The first described previously starts from a monosubstituted ethylendiamine that is reacted with picolylchloride.[6–8] The second takes advantage of the amine *N*′,*N*′-bis[(2-pyridyl)methyl]ethylenediamine (uns-penp; Scheme 1), a versatile tripodal ligand described previously,[12,13] as a starting material. Interestingly, so far only an iron(II) complex of uns-penp has been described in the literature that has been investigated with regard to its spin crossover properties.[14] Furthermore, very recently an iron(II) complex of a derivative of uns-penp was described.[15] However, so far no iron(III) complexes have been described in the literature. Therefore, we decided to study the appropriate iron(III) complexes of this ligand as well as of its acetyl derivative *N*-acetyl-*N*′,*N*′-bis[(2-pyridyl)methyl]ethylenediamine (acetyl-uns-penp; Scheme 1), an amide that was obtained during the synthesis of uns-penp.

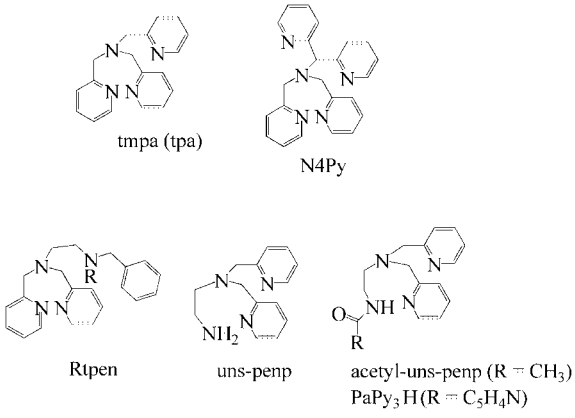


Scheme 1. The ligands discussed in the text.

## Results and Discussion

Only recently have different research groups started to use uns-penp as a versatile ligand in different areas of coor-

[a] Pharmacy College, Tianjin Medical University, 300070 Tianjin, China
[b] Institut für Anorganische und Analytische Chemie der Justus-Liebig-Universität Gießen, Heinrich-Buff-Ring 58, 35392 Gießen, Germany
Fax: +49-641-9934149
E-mail: Siegfried.Schindler@chemie.uni-giessen.de
[c] Institut für Technische Chemie – Chemisch-Physikalische Verfahren (ITC-CPV), Forschungszentrum Karlsruhe, Postfach 3640, 76021 Karlsruhe, Germany
[d] Institut für Anorganische Chemie der Friedrich-Alexander-Universität Erlangen-Nürnberg, Egerlandstraße 1, 91058 Erlangen, Germany
[e] Institut für Anorganische und Analytische Chemie der Westfälischen Wilhelms-Universität, Wilhelm-Klemm-Straße 8, 48149 Münster, Germany
Fax: +49-251-83-38366
E-mail: krebs@uni-muenster.de

 © 2006 Wiley-VCH Verlag GmbH & Co. KGaA, Weinheim 

dination chemistry and different synthetic procedures have been described.[12,13,15–19] However, most of the authors unfortunately do not refer to the original synthesis of this ligand by Mandel and co-workers[12] and in one case it is presented a second time and described incorrectly as a new compound (ten years later in the same journal).[14] Some of us have used this ligand previously in studies within the field of copper chemistry and have improved its preparation.[13] During the two-step synthesis of uns-penp its protected form, *N*-Acetyl-*N*′,*N*′-bis[(2-pyridyl)methyl]ethylenediamine (acetyl-uns-penp), was easily obtained in pure form in high yields. Recrystallisation from petroleum ethers afforded single crystals that were suitable for X-ray diffraction studies. Acteyl-uns-penp crystallises with two molecules per unit cell. Those are dimerised by hydrogen bonding between the carboxamido group and one of the pyridine groups. The molecular structure of one of these dimers is presented in Figure 1 (see Table 2 for a summary of the crystallographic data and refinement parameters). Besides the hydrogen bonding, the crystal structure shows no extraordinary features.

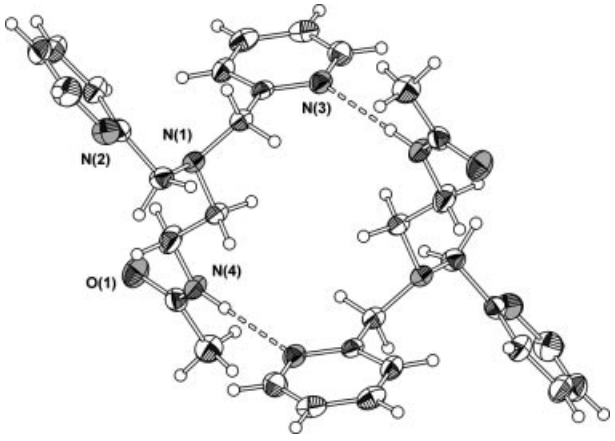


Figure 1. Thermal ellipsoid plot of an acetyl-uns-penp dimer (50% probability).

Furthermore, iron complexation with carboxamide ligands has attracted the interest of inorganic chemists to gain better understanding of metal–peptide bond coordination chemistry in life sciences[20] and to use such complexes as model compounds for the anti-tumor drug bleomycin[21,22] or nitrile hydratase.[23–25] Important in that regard are the results reported by Mascharak and co-workers, who have investigated in detail the structures and properties of $Fe^{II}/Fe^{III}$ complexes of a number of carboxamide ligands, several based on a pyridine-2-carboxamide framework, e.g. *N*-{[bis(2-pyridylmethyl)amino]ethyl}pyridine-2-carboxamide ($PaPy_3H$).[22,25–31] The ligand $PaPy_3H$ (Scheme 1) is related to acetyl-uns-penp; instead of the methyl group in acetyl-uns-penp it contains an additional coordinating pyridyl unit.

### $[Fe_2(acetyl\text{-}uns\text{-}penp)_2O](ClO_4)_2\cdot H_2O$ (1)

Acetyl-uns-penp has so far only been used to synthesise and characterise a copper(II) complex with this ligand. Herein the amide is not deprotonated, however, the carboxamido function of acetyl-uns-penp is no longer truly $sp^2$ hybridised and the nitrogen atom undergoes a weak interaction with the metal centre.[13] The copper complex of $PaPy_3H$ forms a dimer in which the oxygen atom of the amide is coordinated to the copper(II) ion.[32] In contrast, the iron amide complexes of $PaPy_3H$ described by Mascharak and co-workers contained the deprotonated ligand form.[27,30,32,33] However, our own efforts to synthesise the mononuclear deprotonated iron(III) complex [Fe(acetyl-uns-penp)]$(ClO_4)_2$ were only partially successful. Instead of the mononuclear species we obtained the dinuclear complex $[Fe_2(acetyl\text{-}uns\text{-}penp)_2O](ClO_4)_2\cdot H_2O$ (**1**). It is interesting to note at this point that the stoichiometrically identical compound $[Fe_2(PaPy_3H)_2O](ClO_4)_2$ (containing additional ethanol solvent molecules) derived through oxidation of the iron(II) complex is structurally completely different from **1**.[30] In this complex the oxo-bridge assembles two mononuclear amide complexes (with coordinated deprotonated amide nitrogen atoms while the oxygen atoms are not coordinated) to form the dimer (as one would expect). In contrast and as discussed below, in **1** the ligand acetyl-uns-penp additionally bridges the two iron(III) ions and involves the amide nitrogen as well as the oxygen atom in the coordination.

Crystals of **1** were at first obtained from the reaction of $Fe(ClO_4)_3$, acetyl-uns-penp and $NaN_3$ in methanol followed by recrystallisation of the precipitate in acetonitrile. In contrast to our expectations no azide complex was formed but instead deprotonation of the amide occurred under these conditions and because of the presence of water the oxo-bridged dinuclear complex **1** was obtained. Taking this result into account it was furthermore possible to crystallise **1** successfully by replacing the $NaN_3$ by $Et_3N$ or NaOH as the deprotonating agent. The cation of **1**, as depicted in Figure 2, shows that the crystallographically equivalent iron(III) centres are triply bridged by one oxo and two carboxamido groups from two acetyl-uns-penp ligands, respectively, leading to an intramolecular Fe–Fe distance of 2.992 Å and an Fe–O–Fe angle of 113.1°. A summary of the crystallographic data and refinement parameters for the structures is presented in Table 2. Selected bond lengths and angles for the iron(III) complexes are reported in Table 1.

It is interesting to note that in **1**, the acetyl-uns-penp ligand shows an unusual pentadentate coordination mode displaying deprotonated carboxamido NCO bridging groups ($\eta^2$, $\mu_2$) involving the delocalisation of π-bonding [*d*(C–O) = 1.283, *d*(C–N) = 1.306 Å], which is in agreement with the values of a related ($\eta^2$, $\mu_2$) NCO-bridged iron complex reported previously.[34] However, in contrast, structural properties of **1** are quite different to a related iron(III) complex with a bridging urea anion.[35] Compared to other di-iron(III) complexes with three bridging ligands, of which at least one is a μ-oxo unit, **1** exhibits some unique structural features. The Fe–Fe separation is significantly shorter than those of other μ-oxo-tribridged diiron(III) complexes (range 3.048–3.335 Å) and the Fe–O–Fe angle is among the smallest of them all (range 113.8–134.7°).[36] Each iron(III) ion

 © 2006 Wiley-VCH Verlag GmbH & Co. KGaA, Weinheim 

Table 1. Selected distances [Å] and angles [°] in **1**–**5**.[a]

| Atoms | **1** | Atoms | **2** | **3** | Atoms | **4** | Atoms | **5** |
|---|---|---|---|---|---|---|---|---|
| Fe(1)–O(1) | 1.792(2) | Fe(1)–X | 2.4813(9) | 1.7929(5) | Fe(1)–N(1) | 2.127(2) | Fe(1)–O(1) | 1.798(1) |
| Fe(1)–O(2A) | 2.013(2) | Fe(1)–O(2) | 1.961(3) | 2.012(2) | Fe(1)–N(3) | 2.136(2) | Fe(1)–N(3) | 2.141(2) |
| Fe(1)–N(4) | 2.100(2) | Fe(1)–O(3) | 1.969(3) | 2.008(2) | Fe(1)–N(4) | 2.172(2) | Fe(1)–N(1) | 2.147(2) |
| Fe(1)–N(2) | 2.157(2) | Fe(1)–N(1) | 2.266(4) | 2.366(3) | Fe(1)–N(2) | 2.214(2) | Fe(1)–N(2) | 2.213(2) |
| Fe(1)–N(3) | 2.162(2) | Fe(1)–N(2) | 2.191(4) | 2.170(3) | Fe(1)–Cl(1) | 2.2622(5) | Fe(1)–N(4) | 2.235(2) |
| Fe(1)–N(1) | 2.245(2) | Fe(1)–N(3) | 2.159(4) | 2.175(2) | Fe(1)–Cl(2) | 2.3081(6) | Fe(1)–Cl(1) | 2.3166(4) |
| O(1)–Fe(1A) | 1.792(2) | Fe(1)···Fe(1A) | | 3.586 | | | O(1)–Fe(1A) | 1.798(1) |
| O(2)–Fe(1A) | 2.013(2) | Fe(1)···N(4) | | 3.692(3) | | | Fe(1)···Fe(1A) | 3.596(1) |
| Fe(1)···Fe(1A) | 2.992(1) | O(2)···N(4) | | 2.755(3) | | | | |
| | | | | | | | | |
| O(1)–Fe(1)–O(2A) | 98.35(5) | X–Fe(1)–O(2) | 96.2(2) | 98.25(6) | N(1)–Fe(1)–N(3) | 153.61(6) | O(1)–Fe(1)–N(3) | 93.26(3) |
| O(1)–Fe(1)–N(4) | 103.62(6) | X–Fe(1)–O(3) | 99.8(2) | 106.26(7) | N(1)–Fe(1)–N(4) | 83.51(6) | O(1)–Fe(1)–N(1) | 90.95(3) |
| O(2A)–Fe(1)–N(4) | 93.13(7) | X–Fe(1)–N(1) | 165.6(2) | 161.78(7) | N(3)–Fe(1)–N(4) | 90.55(6) | N(3)–Fe(1)–N(1) | 153.72(5) |
| O(1)–Fe(1)–N(2) | 102.11(6) | X–Fe(1)–N(2) | 93.5(2) | 95.87(7) | N(1)–Fe(1)–N(2) | 78.07(6) | O(1)–Fe(1)–N(2) | 93.08(3) |
| O(2A)–Fe(1)–N(2) | 85.80(6) | X–Fe(1)–N(3) | 95.4(2) | 92.24(7) | N(3)–Fe(1)–N(2) | 75.55(6) | N(3)–Fe(1)–N(2) | 76.04(4) |
| N(4)–Fe(1)–N(2) | 154.12(7) | O(2)–Fe(1)–O(3) | 82.9(2) | 81.31(8) | N(4)–Fe(1)–N(2) | 79.08(6) | N(1)–Fe(1)–N(2) | 77.84(4) |
| O(1)–Fe(1)–N(3) | 96.96(5) | O(2)–Fe(1)–N(1) | 95.4(2) | 95.28(9) | N(1)–Fe(1)–Cl(1) | 105.57(4) | O(1)–Fe(1)–N(4) | 170.11(3) |
| O(2A)–Fe(1)–N(3) | 164.53(6) | O(2)–Fe(1)–N(2) | 168.1(2) | 160.74(9) | N(3)–Fe(1)–Cl(1) | 100.04(4) | N(3)–Fe(1)–N(4) | 88.86(4) |
| N(4)–Fe(1)–N(3) | 85.43(7) | O(2)–Fe(1)–N(3) | 86.5(2) | 96.38(9) | N(4)–Fe(1)–Cl(1) | 89.42(4) | N(1)–Fe(1)–N(4) | 82.98(4) |
| N(2)–Fe(1)–N(3) | 88.81(6) | O(3)–Fe(1)–N(1) | 90.1(2) | 87.77(9) | N(2)–Fe(1)–Cl(1) | 167.56(5) | N(2)–Fe(1)–N(4) | 78.04(4) |
| O(1)–Fe(1)–N(1) | 173.14(7) | O(3)–Fe(1)–N(2) | 88.7(2) | 82.20(9) | N(1)–Fe(1)–Cl(2) | 89.33(5) | O(1)–Fe(1)–Cl(1) | 102.82(2) |
| O(2A)–Fe(1)–N(1) | 87.39(7) | O(3)–Fe(1)–N(3) | 162.3(2) | 161.50(9) | N(3)–Fe(1)–Cl(2) | 92.30(5) | N(3)–Fe(1)–Cl(1) | 100.45(3) |
| N(4)–Fe(1)–N(1) | 79.68(7) | N(1)–Fe(1)–N(2) | 76.2(2) | 74.16(9) | N(4)–Fe(1)–Cl(2) | 169.15(4) | N(1)–Fe(1)–Cl(1) | 103.87(3) |
| N(2)–Fe(1)–N(1) | 74.44(7) | N(1)–Fe(1)–N(3) | 76.8(2) | 74.12(9) | N(2)–Fe(1)–Cl(2) | 91.49(4) | N(2)–Fe(1)–Cl(1) | 163.93(3) |
| N(3)–Fe(1)–N(1) | 77.19(7) | N(2)–Fe(1)–N(3) | 99.5(2) | 96.10(9) | Cl(1)–Fe(1)–Cl(2) | 100.38(2) | N(4)–Fe(1)–Cl(1) | 86.26(3) |
| Fe(1A)–O(1)–Fe(1) | 113.1(2) | Fe(1A)–O(1)–Fe(1) | | 180 | | | Fe(1A)–O(1)–Fe(1) | 180 |

[a] X = Br(1) in **2** or O(4) in **3** A: *x*, *y*, –*z* + 1/2 (for **1**); –*x*, –*y*, –*z* (for **5**).

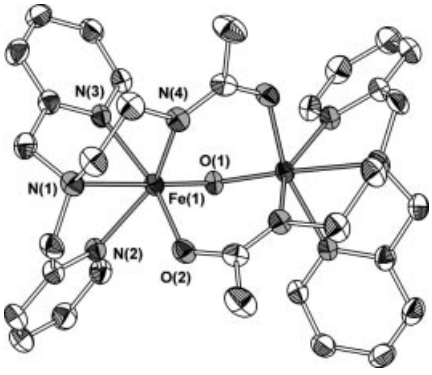


Figure 2. Thermal ellipsoid plot of the dinuclear complex in **1** (50% probability; hydrogen atoms omitted for clarity).

adopts a distorted octahedron coordination geometry by a $N_4O_2$ donor set, in which two pyridine nitrogen atoms (N2 and N3), one carboxamido nitrogen atom (N4) and a carboxamide oxygen atom (O2A) from the second acetyl-uns-penp ligand reside in the equatorial plane while oxo-bridged O(1) and the tertiary amino N(1) atoms occupy the axial positions. The negative charge of the μ-oxo-bridge leads to a rather short Fe(1)–O(1) bond [1.792(2) Å] and likewise because of the *trans* effect, the opposing Fe(1)–N(1) bond is weakened with a distance of 2.245(2) Å. All *cis* angles around O(1) are larger than the ideal 90°, with values of 98.35(5)° for O(1)–Fe(1)–O(2A), 102.11(6)° for O(1)–Fe(1)–N(2), 96.96(5)° for O(1)–Fe(1)–N(3) and 103.62(6)° for O(1)–Fe(1)–N(4). Obviously, deprotonation of the carboxamide groups facilitates the increase of bond lengths around the $Fe^{III}$ ions (Table 1).

### Model Complexes for Intradiol Catechol Dioxygenases

One reason for our efforts to obtain the mononuclear iron(III) complex with the deprotonated acetyl-uns-penp as ligand was our hope that this complex might be an excellent functional model for intradiol catechol dioxygenases. These mononuclear nonheme iron enzymes catalyse the oxidative cleavage of catechol derivatives by insertion of both atoms of dioxygen into the substrate—a key step in the degradation of aromatic compounds.[4,37,38]

Since Funabiki et al. reported the first functional models for catechol dioxygenases, increased efforts have been made by bioinorganic chemists to mimic the structure and function of these enzymes.[4,37–42] Besides macrocyclic ligands,[43–45] especially tetradentate tripodal ligands have shown considerable abilities to regulate the properties of model complexes, indicating that dioxygenase activity strongly depends on the nature of the ligand. The most effective biomimetic catalyst to date is the iron(III) tmpa (tpa) complex that was first reported by Que and co-workers.[4,46] Furthermore, several other systems with tripodal $N_4$ donor ligands showed considerable catechol dioxygenase activity.[47,48] Complexes with enzyme-analogous $N_2O_2$ donor sets represent good structural and spectroscopic model compounds, however, they are poor functional models so far.[49–56] Our recent efforts to reach higher activities than

 © 2006 Wiley-VCH Verlag GmbH & Co. KGaA, Weinheim 

the iron(III) tmpa complex by increasing or decreasing the chelate ring sizes in this system were unsuccessful.[57]

The substrate-binding process in the reaction cycle of the catechol cleavage involves protonation of two ligands at the active site, Tyr447 and a hydroxide.[58,59] These two proton acceptors dissociate from the metal ion and thereby enable the proton donor molecule, the catechol, to coordinate in its dianionic form (see Scheme 2).

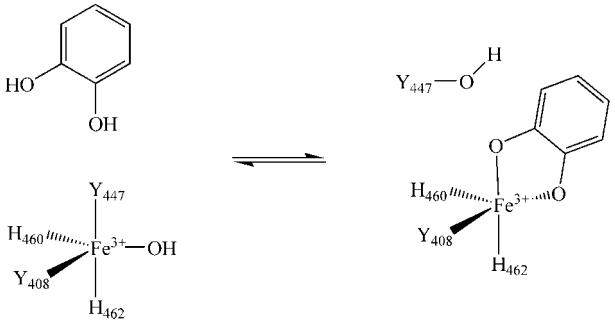


Scheme 2. Proposed substrate-binding process in catechol-1,2-dioxygenases.

The special electronic properties of the leaving Tyr447 group have been studied extensively using spectroscopic methods and seem to influence the reactivity of the enzyme to a large extent.[60] In previous work some of us used a tmpa-derived ligand [(6-bromo-2-pyridyl)methyl]bis[(2-pyridyl)methyl]amine (brtpa) to mimic the weak bonding of one of the donor groups, however, again it was observed that catechol dioxygenase reactivity decreased compared to the iron tmpa system, most likely because of steric hindrance.[61]

Replacing one pyridyl moiety of the tmpa ligand with a deprotonated carboxamide function we had hoped to finally increase reaction rates of the oxidation of catecholates compared to the tmpa system. However, as discussed below we did not reach this goal and furthermore, in contrast to the synthesis of complex **1**, we did not succeed in the preparation of deprotonated amide complexes when using acetyl-uns-penp, catecholates and base.

### [Fe(acetyl-uns-penp)(tcc)Br]·$(C_2H_5)_2O$ (2)

When iron(III) bromide, acetyl-uns-penp, tetrachlorocatechol and triethylamine were mixed in acetone the complex [Fe(acetyl-uns-penp)(tcc)Br]·$(C_2H_5)_2O$ (**2**) was obtained. Slow diffusion of diethyl ether into the complex solutions allowed the precipitation of single crystals that were suitable for X-ray diffraction studies. Four complex molecules and four diethyl ether molecules form the unit cell of compound **2**. The diethyl ether molecules are attached to the complex via hydrogen bonding to the noncoordinating carboxamide function of the ligand. The structure of **2** is depicted in Figure 3 (the solvate molecule has been omitted for clarity; crystallographic data are presented in Table 2 and Table 1).

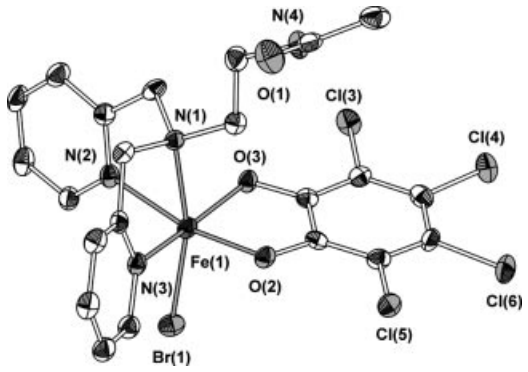


Figure 3. Thermal ellipsoid plot of the iron(III) complex in **2** (50% probability; hydrogen atoms omitted for clarity).

The iron(III) core is ligated by three nitrogen atoms, two catecholate oxygen atoms and one bromide atom. The longest bonds formed by iron and its donor atoms are found for Fe(1)–Br(1) and Fe(1)–N(1) with 2.4813(9) and 2.266(4) Å, respectively. This causes stretching of the coordination octahedron along the Br(1)–Fe(1)–N(1) axis. The *cis* angles around the bromide ion are widened to an average angle of 96.2°. On the other hand, the formation of five-membered chelate rings leads to small values for the N(1)–Fe(1)–N(2) and N(1)–Fe(1)–N(3) angles of 76.2(2) and 76.8(2)°, respectively.

### [{Fe(acetyl-uns-penp)(tcc)}$_2$O]·$(C_2H_5)_2O$·$CH_3OH$ (3)

Interestingly, applying the same experimental conditions as for the synthesis of **2**, though using a slightly larger amount of base, the dinuclear oxo-bridged complex [{Fe(acetyl-uns-penp)(tcc)}$_2$O]·$(C_2H_5)_2O$·$CH_3OH$ (**3**) was obtained (the syntheses of **2** and **3** could be reproduced applying these conditions). The molecular structure of the cation of **3** is shown in Figure 4 (crystallographic data are presented in Table 2 and Table 1).

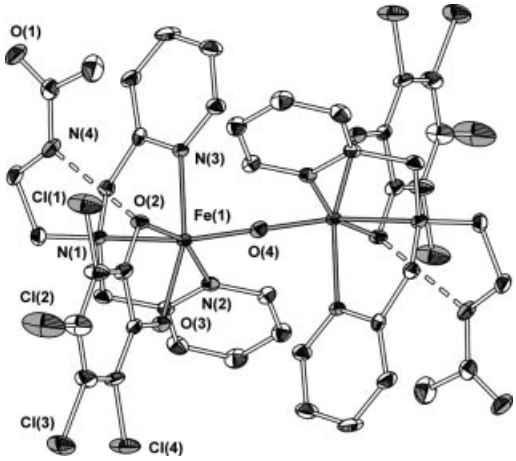


Figure 4. Thermal ellipsoid plot of the dinuclear complex in **3** (50% probability; hydrogen atoms omitted for clarity).

The unit cell contains two complexes as well as four diethyl ether and two disordered methanol molecules. Since

 © 2006 Wiley-VCH Verlag GmbH & Co. KGaA, Weinheim 

the bridging oxygen atom O(4) is located on a symmetry centre, one half of the dinuclear complex is generated by inversion. The metal–metal distance is 3.586 Å and both iron ions are surrounded by an $N_3O_3$ donor set. The nitrogen donor atoms are provided by the ligand acetyl-uns-penp, whereas the oxygen atoms belong to the dianionic tetrachlorocatecholate ligand and the μ-oxo-bridge. The coordination sphere of the iron centre has a distorted octahedral geometry. The negative charge of the μ-oxo-bridge leads to a rather short Fe(1)–O(4) bond (1.793 Å) and because of a *trans* effect, the opposing Fe(1)–N(1) bond is weakened. All *cis* angles around O(4) are larger than the ideal 90°. Especially those to the catecholate oxygen atoms are widened, since this effect can be attributed to electrostatic repulsion. The negative charge of O(2) is reduced by the intramolecular hydrogen bond and therefore the corresponding O(2)–Fe(1)–O(4) angle has a value of only 98.25(6)° compared to 106.29(9)° for O(3)–Fe(1)–O(4).

The most striking feature of **3** is the intramolecular hydrogen bond between the carboxamide nitrogen N(4) and O(2) of the catecholate. The donor acceptor distance has a typical value of 2.755(3) Å and the distance between Fe(1) and N(4) is 3.692 Å. This is in good agreement with similar intramolecular hydrogen bonding reported recently.[61] In a way this hydrogen bonding indicates a possible pathway for the deprotonation of the catechol similar to the enzyme reaction shown in Scheme 1.

### Spectrophotometric Titrations

To gain a better understanding of the influence of the base and furthermore to achieve optimised conditions for catechol cleavage by molecular dioxygen it is necessary to provide a high concentration of the mononuclear iron complex with one coordinated catecholate dianion ([Fe(L)(3,5-dbc)]$^+$). To determine these ideal conditions for the catechol cleavage experiments, spectrophotometric titrations were performed (see Figure 5 and Exp. Sect.) as described previously for related systems.[61]

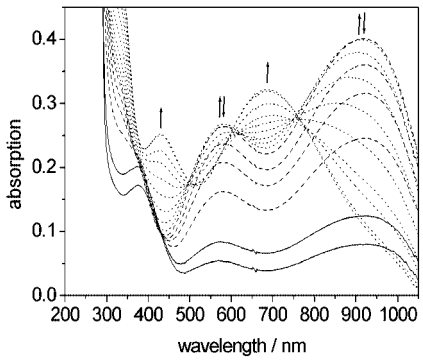


Figure 5. Spectrophotometric titration of a solution of iron(III) perchlorate hydrate, acetyl-uns-penp and 3,5-dbc against piperidine; solid lines: 0.0 and 0.5 equiv.; dashed lines: 1.0–1.6 equiv.; dotted lines: 1.8–4.0 equiv..

This analysis allowed us to gain insight into the species distribution in solution depending on the amount of external base that was added to a mixture of iron salt, the ligand and the substrate 3,5-dbc. At the beginning of the titration (0.0–0.5 equiv. of piperidine; piperidine was used for comparison with previous studies, however triethylamine works in the same way) an absorption band at 375 nm can be observed that is assigned to an oxo-iron(III)-CT transition.

We suggest that the main species in solution is a μ-oxo-bridged dinuclear compound without coordinated substrate. Such dinuclear complexes are thermodynamically favoured in the presence of water and many examples have been reported in the literature.[62–72] With regard to previous results it is possible that the carboxamido group of the ligand already undergoes a very weak interaction with the metal centre and is not truly $sp^2$ hybridised, however is not yet deprotonated.[13] Furthermore, two weak transitions occur at 580 and 920 nm which are typical for catecholate-iron(III)-CT transitions and indicate the presence of a low concentration of the desired mononuclear substrate adduct. Upon further addition of base (1.0–1.6 equiv.) these two absorption bands rise dramatically and so does the concentration of the mononuclear substrate adduct. In the last part of the titration (1.8–4.0 equiv.) the bands at 580 and 920 nm disappear and two new bands are seen at 430 and 690 nm that are also assigned to catecholate-iron(III)-CT transitions. The shift to higher energies indicates a higher electron density on the iron(III) core that makes the charge transfer from the catecholate more difficult. In accordance to the crystal structure of **3** we suggest that a dinuclear μ-oxo-bridged substrate adduct is formed in which the large electron density of the oxo-group is partially transferred to the metal ions and one ligand arm is detached. Finally, the amount of base that is necessary to reach optimal reaction conditions for the catechol cleavage was determined from a plot of the absorption of the lower energy CT band vs. the amount of base added (see Figure 6). The maximum of this plot is located at 1.7 equiv..

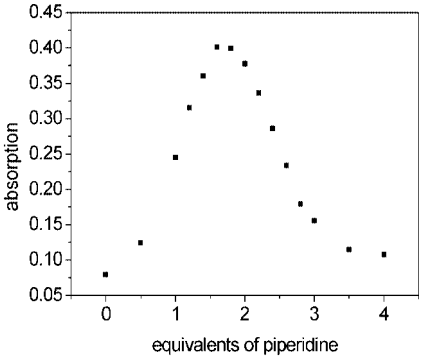


Figure 6. Absorbance vs. base equivalents plot ( $\lambda$ = 980 nm).

### Catechol 1,2-Dioxygenase Activity

An in situ prepared complex solution containing equimolar amounts of iron(III) perchlorate hydrate and acetyl-uns-penp was treated with 1 equiv. of 3,5-dbc and 1.7 equiv. of piperidine. The decrease in the lower energy LMCT band

 © 2006 Wiley-VCH Verlag GmbH & Co. KGaA, Weinheim 

was monitored by UV/Vis-spectroscopy. The reaction was performed in air-saturated methanol, resulting in a more than tenfold excess of dioxygen that ensures pseudo-first-order kinetics for the complete reaction. From the slope of the ln(absorbance) vs. time plot, the reaction rate was determined to be 0.05 $M^{-1}s^{-1}$, which is more than two orders of magnitude lower than that reported for the iron-tmpa system under similar reaction conditions.[46] Because of this low reactivity no further experiments were performed with this system.

### [Fe(uns-penp)$Cl_2$]$ClO_4$·$CH_3CN$ (4)

The ligand uns-penp was obtained in good yields according to the procedures described in the literature. Mixing uns-penp together with iron(III) salts in methanol afforded a yellow material that could be recrystallised from acetonitrile by ether diffusion to yield crystals suitable for X-ray structural analysis. The ORTEP representation of [Fe(uns-penp)$Cl_2$]$^+$ is shown in Figure 7.

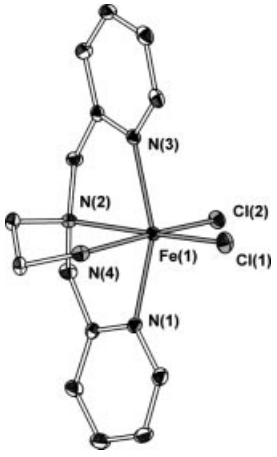


Figure 7. Thermal ellipsoid plot of the cation of **4** (50% probability; hydrogen atoms omitted for clarity).

The structure of the cation of **4** shows a distorted octahedral geometry coordinated with four N atoms of the uns-penp ligand and two chloride ions, as represented by the *trans* ligand angles of 153.61(6)° for N(1)–Fe(1)–N(3), 167.56(5)° for N(2)–Fe(1)–Cl(1), and 169.15(4)° for N(4)–Fe(1)–Cl(2). Moreover, the angle for Cl(1)–Fe(1)–Cl(2) is 100.38(2)°, which is significantly larger than 90°. As is often the case with a tripodal ligand that forms five-membered chelate rings, the coordination geometry is distorted toward the tertiary amino group (average $N_{amine}$–Fe–$N_{py/amine}$ = 77.55°). The Fe–$N_{py}$ bonds (av. 2.132 Å) are shorter than the Fe–N(amine) bond (av. 2.193 Å), which are comparable to the values of $Fe^{III}$ tmpa complexes.[46,73,74] Consequently the Fe(1)–Cl(1) bond which is *trans* to the tertiary amino group [2.2622(5) Å] is shorter than the Fe(1)–Cl(2) bond *trans* to a primary amino nitrogen [2.3081(6) Å].

### {[Fe(uns-penp)Cl]$_2$O}$(ClO_4)_2$·$2CH_3CN$ (5)

It is well known that a general problem in iron(III) chemistry is the formation of oxo-bridged dimers during the synthesis of the complexes such as for example the iron(III) tmpa complex or the acetyl-uns-penp ligand system described above. Addition of base can accelerate this reaction and therefore when base was added during the synthesis of **4** the dinuclear oxo-bridged complex **5** was obtained instead. The thermal ellipsoid representation of the cation of **5** is shown in Figure 8. The molecular structure is composed of centrosymmetric dimeric cations with a linear Fe–O–Fe unit. Each iron centre is in a distorted octahedral environment ligated by the two pyridine nitrogen atoms, the primary and tertiary amine nitrogen atoms, as well as the oxygen atom which is bound to the second iron centre. The Fe–O bond length of 1.798(1) Å is in keeping with the mean values of 1.79(6) (with a range of 1.73–1.82 Å) for such bond lengths in oxo-bridged iron(III) complexes.[75] The Fe–$N_{py}$ bonds of 2.141(2) Å and 2.147(2) Å are considerably shorter than the Fe–$N_{amine}$ bonds [2.213(2) and 2.235(2) Å]. This is analogous to the structures of the respective (μ-oxo) diiron(III) complexes of tmpa. The chloride ligands coordinate *trans* to the tertiary amine nitrogen on each iron centre and *anti* to each other relative to the Fe–O–Fe axis. The Fe–Cl bond lengths of 2.3166(4) Å are slightly longer than the values of **4** arising from steric hindrance in the dimer. The Fe–Fe distance of 3.596 Å is typical for complexes with singly bridged Fe–O–Fe cores, which are usually in the range 3.4–3.6 Å, whereby the longer distances are associated with Fe–O–Fe angles that are linear or close to linearity.

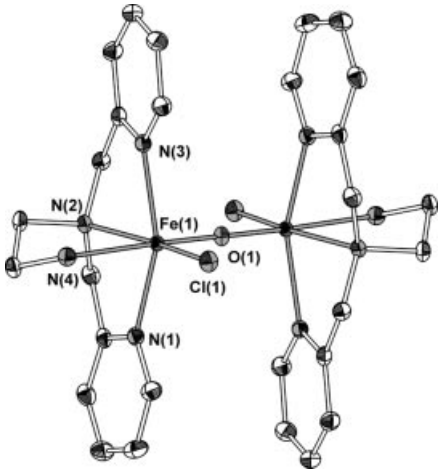


Figure 8. Thermal ellipsoid plot of the cation of **5** (50% probability; hydrogen atoms omitted for clarity).

### Catechol 1,2-Dioxygenase Activity of the Iron(III)-uns-penp System

The iron(III)-uns-penp complex was investigated under the same conditions used previously for the iron(III) tmpa catecholate (3,5-dbc) system.[57] Stopped-flow kinetic investigations revealed again that the rate of the reaction of the iron tmpa system is faster under these conditions, however, at least the iron-uns-penp complex was only slower by a factor of 20. No further detailed kinetic studies were

 © 2006 Wiley-VCH Verlag GmbH & Co. KGaA, Weinheim 

performed on this system because of the fact that the rate could not be increased and that no reactive intermediates could be detected spectroscopically.

## Conclusion

Acetyl-uns-penp has not been used in coordination chemistry so far despite its interesting ligand properties and in contrast to related ligands (in which additional pyridine or phenol donor groups are present) that have attracted a lot of interest in amide chemistry recently.[18,27–33,76–78] A copper(II) complex was recently reported, where the carboxamido function of acetyl-uns-penp is no longer truly $sp^2$ hybridised and the nitrogen atom undergoes a weak interaction with the metal centre.[13] In our present work, we demonstrated that acetyl-uns-penp is capable of influencing coordination chemistry by building hydrogen bonds with hydrogen acceptors in the vicinity of the carboxamido function. The intramolecular hydrogen bond between one arm of the tripodal ligand and a coordinated substrate molecule in **3** suggests a pathway for the second substrate deprotonation step in the reaction cycle of intradiol cleaving catechol dioxygenases according to Scheme 2. Taking into account that the carboxamide can also undergo strong binding interactions with a metal centre upon deprotonation, as demonstrated in **1**, acetyl-uns-penp is a very versatile ligand. Furthermore, structural characterization of two iron(III) complexes of the ligand uns-penp and its catechol dioxygenase reactivity provided additional information on the chemistry of this interesting ligand.

## Experimental Section

**Materials:** All chemicals were obtained from commercial sources and used without further purification.

***Caution!*** *The syntheses and procedures described below involve compounds that contain perchlorate and azide ions, which can detonate explosively and without warning. Although we have not encountered any problems with the compounds used in this study, they should be handled with extreme care.*

**Physical Measurements:** UV/Vis spectroscopy was performed with a Hewlett–Packard 8453 diode array spectrometer. Elemental analyses were carried out with an Elementar Vario EL III analyzer at the University of Münster.

### Syntheses

**Ligand Syntheses:** The ligand acetyl-uns-penp as well as uns-penp were prepared according to literature procedures.[13]

**$[Fe_2$(acetyl-uns-penp)$_2O](ClO_4)_2\cdot H_2O$ (1):** Iron(III) perchlorate hexadrate (177 mg, 0.5 mmol) and acetyl-uns-penp (142 mg, 0.5 mmol) were combined in methanol (10 mL). After 10 min of stirring, to the resulting brown solution $NaN_3$ (49 mg, 0.75 mmol) was added, immediately leading to a very dark red suspension. After 2 h a brown precipitate was filtered off, washed with methanol and diethyl ether, and dried under vacuum. Dark brown prism crystals, air stable and suitable for X-ray diffraction analysis, were obtained by slow evaporation of an acetonitrile solution after 1 week (69 mg, 0.03 mmol, 30%). $C_{16}H_{20}ClFeN_4O_6$ (455.66): calcd. C 42.2, H 4.4, N 12.3; found C 42.6, H 4.2, N 12.7.

**1** could also be prepared analogously to the former synthesis except that $Et_3N$ (101 mg, 1.0 mmol) or NaOH (40 mg, 1.0 mmol) were used instead of $NaN_3$.

**[Fe(acetyl-uns-penp)(tcc)Br]$\cdot(C_2H_5)_2O$ (2):** Anhydrous iron(III) bromide (30 mg, 0.1 mmol) and acetyl-uns-penp (28 mg, 0.1 mmol) were dissolved in acetone (7 mL). After addition of tetrachlorocatechol hydrate (27 mg, 0.1 mmol) and triethylamine (24 μL, 17 mg, 0.17 mmol) the reaction mixture was stirred for 10 min and filtered. Vapor diffusion of diethyl ether into the complex solution yielded single crystals of **2** (58 mg, 0.09 mmol, 90%), m.p. 181 °C (decomposition). $C_{22}H_{20}BrCl_4FeN_4O_3$ (without solvent, 666.0): calcd. C 39.7, H 3.0, N 8.4; found C 39.0, H 3.9, N 7.9.

**[{Fe(acetyl-uns-penp)(tcc)}$_2$O]$\cdot(C_2H_5)_2O\cdot CH_3OH$ (3):** The synthetic procedure is identical to the preparation of **2** with the only difference being that a slightly larger amount of triethylamine (28 μL, 20 mg, 0.2 mmol) was used. Vapor diffusion of diethyl ether into the complex solution yielded single crystals of **3** (37 mg, 0.03 mmol, 60%), m.p. 223 °C (decomposition). $C_{44}H_{40}Cl_8Fe_2N_8O_7$ (without solvent, 1188.2): calcd. C 44.5, H 3.4, N 9.4; found C 43.8, H 3.7, N 9.1.

**[Fe(uns-penp)Cl$_2$]$\cdot ClO_4\cdot CH_3CN$ (4):** To a solution of uns-penp (219 mg, 0.9 mmol) in methanol (10 mL) was added a solution of $Fe(ClO_4)_3\cdot xH_2O$ (139 mg, 0.3 mmol) and $FeCl_3$ (109 mg, 0.6 mmol) in methanol (10 mL). The resulting brown solution was stirred for 1 h at room temperature during which time a greenish yellow solid precipitated, which was then filtered. The precipitate was washed with methanol and diethyl ether, and dried under vacuum. Yellow prism crystals for crystallographic studies were obtained by vapor diffusion of diethyl ether into the acetonitrile solution. Yield: 221 mg (ca. 50%). $C_{16}H_{21}Cl_3FeN_5O_4$ (509.58): calcd. C 37.71, H 4.15, N 13.75; found C 37.59, H 4.13, N 13.68.

**[{Fe(uns-penp)Cl}$_2$O]$\cdot(ClO_4)_2\cdot 2CH_3CN$ (5):** To a methanol suspension (15 mL) of $Fe(ClO_4)_3\cdot xH_2O$ (115 mg, 0.25 mmol), $FeCl_3$ (41 mg, 0.25 mmol) and uns-penp ligand (122 mg, 0.5 mmol) was added $Et_3N$ (51 mg, 0.5 mmol) in methanol (5 mL) whilst stirring. After 1 h, the resulting greenish brown slurry was filtered and the precipitate was washed with methanol and diethyl ether. Dark brown cubic crystals suitable for X-ray diffraction analysis were obtained by slow evaporation of an acetonitrile solution about 1 week. Yield: 200 mg (ca. 42%). $C_{32}H_{42}Cl_4Fe_2N_{10}O_9$ (964.26): calcd. C 39.86, H 4.39, N 14.53; found C 39.62, H 4.24, N 14.41.

**X-ray Crystallographic Studies:** Intensity data for **1** were collected with a Siemens SMART CCD 1000 diffractometer using graphite monochromated Mo-$K_\alpha$ radiation ($\lambda$ = 0.71073 Å) by the ω-scan technique. The collected reflections were corrected for absorption effects.[79] The structure was solved by direct methods and refined by least-squares techniques using the SHELX97 programme package.[80] Further data collection parameters are summarised in Table 2.

Intensity data for acetyl-uns-penp, **2** and **3** were collected with a Bruker AXS SMART 6000 CCD diffractometer (Cu-$K_\alpha$, $\lambda$ = 1.54178 Å, Göbel mirror) using the ω-scan technique. The collected reflections were corrected for absorption effects.[79] The structure was solved by direct methods and refined by full-matrix least-squares methods on $F^2$.[80] Further data collection parameters are summarised in Table 2.

Intensity data for **4** and **5** were collected at a temperature of 100 K with a Bruker-Nonius KappaCCD diffractometer with graphite-monochromated Mo-$K_\alpha$ radiation ($\lambda$ = 0.71073 Å). Data were corrected for Lorentz and polarization effects. Absorption effects were corrected numerically[81] for **4** and by semi-empirical methods

 © 2006 Wiley-VCH Verlag GmbH & Co. KGaA, Weinheim 

Table 2. Crystallographic data and experimental details.

| Compound | Acetyl-uns-penp | **1** | **2** | **3** | **4** | **5** |
|---|---|---|---|---|---|---|
| Empirical formula | $C_{16}H_{20}N_4O$ | $C_{32}H_{40}Cl_2Fe_2N_8O_{12}$ | $C_{26}H_{30}BrCl_4FeN_4O_4$ | $C_{53}H_{64}Cl_8Fe_2N_8O_{10}$ | $C_{16}H_{21}Cl_3FeN_5O_4$ | $C_{32}H_{42}Cl_4Fe_2N_{10}O_9$ |
| $M_r$ | 284.36 | 455.66 | 740.10 | 1368.42 | 509.58 | 964.26 |
| Temperature [K] | 140(2) | 200(2) | 100(2) K | 150(2) | 100(2) | 100(2) |
| Radiation ($\lambda$ [Å]) | Cu-$K_\alpha$, 1.54178 | Mo-$K_\alpha$, 0.71073 | Cu-$K_\alpha$, 1.54178 | Cu-$K_\alpha$, 1.54178 | Mo-$K_\alpha$, 0.71073 | Mo-$K_\alpha$, 0.71073 |
| Crystal colour and shape | colourless, cuboid | brown, prism | red, plate | brown, cuboid | yellow, prism | brown, irregular |
| Crystal size [mm] | 0.20 × 0.14 × 0.10 | 2.00 × 0.40 × 0.50 | 0.13 × 0.12 × 0.03 | 0.31 × 0.29 × 0.29 | 0.24 × 0.15 × 0.12 | 0.23 × 0.22 × 0.12 |
| Crystal system | triclinic | monoclinic | monoclinic | monoclinic | monoclinic | triclinic |
| Space group | $P\bar{1}$ (No. 2) | $C2/c$ (No. 15) | $P2_1/c$ (No. 14) | $P2_1/n$ (No. 14) | $P2_1/n$ (No 14) | $P\bar{1}$ (No 2) |
| $a$ [Å] | 9.3758(2) | 16.2248(17) | 12.4448(5) | 10.4477(3) | 11.241(1) | 8.4308(5) |
| $b$ [Å] | 9.6178(2) | 12.8536(13) | 13.4022(6) | 20.9973(7) | 7.8366(6) | 11.2769(6) |
| $c$ [Å] | 10.2342(3) | 19.653(2) | 18.1585(8) | 13.9166(5) | 24.330(2) | 11.8246(8) |
| $\alpha$ [°] | 82.807(2) | | | | | 71.583(4) |
| $\beta$ [°] | 68.351(2) | 112.910(1) | 92.758(3) | 94.824(2) | 91.443(7) | 76.621(5) |
| $\gamma$ [°] | 62.401(2) | | | | | 80.422(4) |
| $V$ [Å$^3$] | 751.10(3) | 3775.2(7) | 3025.1(2) | 3042.1(2) | 2142.6(3) | 1032.4(2) |
| $Z$ | 2 | 4 | 4 | 2 | 4 | 1 |
| $\rho_{calcd.}$ [g·cm$^{-3}$] | 1.257 | 1.603 | 1.625 | 1.494 | 1.580 | 1.551 |
| $\mu$ [mm$^{-1}$] | 0.652 | 0.983 | 9.127 | 7.570 | 1.111 | 1.024 |
| $F$(000) | 304 | 1880 | 1500 | 1412 | 1044 | 496 |
| $\theta$ range [°] | 4.66 to 71.30 | 2.09 to 28.28 | 3.56 to 71.35 | 3.82 to 71.44 | 3.14 to 27.88 | 3.30 to 27.87 |
| Index ranges | $-10 \le h \le 11$ | $-16 \le h \le 21$ | $-14 \le h \le 14$ | $-11 \le h \le 12$ | $-14 \le h \le 14$ | $-11 \le h \le 10$ |
| | $-10 \le k \le 11$ | $-17 \le k \le 16$ | $-15 \le k \le 16$ | $-22 \le k \le 24$ | $-10 \le k \le 10$ | $-14 \le k \le 14$ |
| | $-11 \le l \le 12$ | $-26 \le l \le 26$ | $-20 \le l \le 22$ | $-15 \le l \le 17$ | $-32 \le l \le 32$ | $-15 \le l \le 15$ |
| Reflections collected | 4369 | 13663 | 16266 | 17174 | 32406 | 27493 |
| Unique reflections | 2521 | 4476 | 5631 | 5614 | 5103 | 4910 |
| $R_{int}$ | 0.0285 | 0.0263 | 0.0766 | 0.0650 | 0.0792 | 0.0272 |
| Data/restraints/parameters | 2521/0/195 | 4476/0/266 | 5631/0/368 | 5614/0/380 | 5103/0/263 | 4910/0/260 |
| Goodness-of-fit on $F^2$ | 1.099 | 1.040 | 0.888 | 0.954 | 1.032 | 1.065 |
| Final $R$ indices [$I > 2\sigma(I)$] | $R1$ = 0.0490 | $R1$ = 0.0365 | $R1$ = 0.0492 | $R1$ = 0.0463 | $R1$ = 0.0330 | $R1$ = 0.0240 |
| | $wR2$ = 0.1381 | $wR2$ = 0.0954 | $wR2$ = 0.0981 | $wR2$ = 0.1065 | $wR2$ = 0.0671 | $wR2$ = 0.0580 |
| $R$ indices (all data) | $R1$ = 0.0553 | $R1$ = 0.0428 | $R1$ = 0.0864 | $R1$ = 0.0683 | $R1$ = 0.0568 | $R1$ = 0.0323 |
| | $wR2$ = 0.1443 | $wR2$ = 0.1000 | $wR2$ = 0.1082 | $wR2$ = 0.1118 | $wR2$ = 0.0721 | $wR2$ = 0.0606 |
| Largest diff. peak/hole [e·Å$^{-3}$] | 0.210/–0.325 | 0.937/–0.644 | 1.458/–0.501 | 0.400/–0.692 | 0.401/–0.525 | 0.434/–0.442 |

based on multiple scans[79] for **5**. The structures were solved by direct methods; full-matrix least-squares refinement was carried out on $F^2$ using SHELXTL NT 6.12.[82] All non-hydrogen atoms were refined anisotropically. All hydrogen atoms were geometrically positioned; their isotropic displacement parameters were tied to those of their corresponding carrier atoms by a factor of 1.2 or 1.5.

CCDC-266956 (acetyl-uns-penp), -263645 (for **1**), -266957 (for **2**), -266958 (for **3**), -283894 (for **4**), and -283895 (for **5**) contain the supplementary crystallographic data for this paper. These data can be obtained free of charge from The Cambridge Crystallographic Data Centre via www.ccdc.cam.ac.uk/data_request/cif.

**Determination of the Catechol 1,2-Dioxygenase Activity:** The catechol cleaving activity of an in situ prepared complex solution was tested using piperidine as an external base as described previously.[61] The amount of base needed to reach the highest reaction rates was determined according to the spectrophotometric titration method described below. To 2 mL of a $2\cdot10^{-4}$ M methanolic solution of $Fe(ClO_4)_3\cdot H_2O$ and the ligand was added a $2\cdot10^{-2}$ M (1 equiv.) solution of 3,5-$H_2$dbc (0.02 mL). The proper amount of base was added to the reaction mixture from a $2\cdot10^{-2}$ M stock solution. To limit errors, the oxidation of the complex was followed three times by UV/Vis spectroscopy. It is important to note that during these studies iron salts with noncoordinating ions (such as perchlorate or triflate) were used and besides the catecholate ligand no additional coordinating ions (such as bromide used in the crystallographic studies) were present.

**Spectrophotometric Titrations:** The spectrophotometric titrations were carried out with the same solutions as described above for the activity determinations. To avoid cleavage of the substrate, all manipulations were carried out under argon. A sample of the 3,5-$H_2$dbc solution (0.1 mL) was added to the complex solution (10 mL). The resulting mixture was titrated with piperidine and the UV/Vis-spectra were monitored using a flow cell (1 cm).

## Acknowledgments

We thank the Deutsche Forschungsgemeinschaft (SPP 1118 and SFB 424) and the Fonds der Chemischen Industrie for financial support. M. M. thanks the University of Münster and the International Graduate College "Template Directed Chemical Synthesis" for graduate fellowships.

[1] E. A. Lewis, W. B. Tolman, *Chem. Rev.* **2004**, *104*, 1047–1076.
[2] L. M. Mirica, X. Ottenwaelder, T. D. P. Stack, *Chem. Rev.* **2004**, *104*, 1013–1045.
[3] S. Schindler, *Eur. J. Inorg. Chem.* **2000**, 2311–2326.
[4] M. Costas, M. P. Mehn, M. P. Jensen, L. Que Jr, *Chem. Rev.* **2004**, *104*, 939–986.
[5] S. V. Kryatov, E. V. Rybak-Akimova, S. Schindler, *Chem. Rev.* **2005**, *105*, 2175–2226.
[6] I. Bernal, I. M. Jensen, K. B. Jensen, C. J. McKenzie, H. Toftlund, J.-P. Tuchagues, *J. Chem. Soc., Dalton Trans.* **1995**, 3667–3675.
[7] L. Duelund, R. Hazell, C. J. McKenzie, L. Preuss Nielsen, H. Toftlund, *J. Chem. Soc., Dalton Trans.* **2001**, 152–156.
[8] A. Hazell, C. J. McKenzie, L. P. Nielsen, S. Schindler, M. Weitzer, *J. Chem. Soc., Dalton Trans.* **2002**, 310–317.

 © 2006 Wiley-VCH Verlag GmbH & Co. KGaA, Weinheim 

[9] A. J. Simaan, F. Banse, P. Mialane, A. Boussac, S. Un, T. Kargar-Grisel, G. Bouchoux, J.-J. Girerd, *Eur. J. Inorg. Chem.* **1999**, 993–996.
[10] A. J. Simaan, S. Dopner, F. Banse, S. Bourcier, G. Bouchoux, A. Boussac, P. Hildebrandt, J.-J. Girerd, *Eur. J. Inorg. Chem.* **2000**, 1627–1633.
[11] J. Kaizer, E. J. Klinker, N. Y. Oh, J.-U. Rohde, W. J. Song, A. Stubna, J. Kim, E. Münck, W. Nam, L. Que Jr, *J. Am. Chem. Soc.* **2004**, *126*, 472–473.
[12] J. Mandel, C. Maricondi, B. Douglas, *Inorg. Chem.* **1988**, *27*, 2990–2996.
[13] M. Schatz, M. Leibold, S. P. Foxon, M. Weitzer, F. W. Heinemann, F. Hampel, O. Walter, S. Schindler, *Dalton Trans.* **2003**, 1480–1487.
[14] G. S. Matouzenko, A. Bousseksou, S. Lecocq, P. J. van Koningsbruggen, M. Perrin, O. Kahn, A. Collet, *Inorg. Chem.* **1997**, *36*, 2975–2981.
[15] C. J. Davies, J. Fawcett, R. Shutt, G. A. Solan, *Dalton Trans.* **2005**, 2630–2640.
[16] J. Mandel, B. Douglas, *Inorg. Chim. Acta* **1989**, *155*, 55–69.
[17] O. Horner, M.-F. Charlot, A. Boussac, S. Un, T. Kargar-Grisel, G. Bouchoux, J.-J. Girerd, *Inorg. Chem.* **1999**, *38*, 1222–1232.
[18] C. Incarvito, M. Lam, B. Rhatigan, A. L. Rheingold, C. J. Quin, A. L. Gavrilova, B. Bosnich, *J. Chem. Soc., Dalton Trans.* **2001**, 3478–3488.
[19] K. Hanaoka, K. Kikuchi, Y. Urano, T. Nagano, *J. Chem. Soc., Perkin Trans. 2* **2001**, *2*, 1840–1843.
[20] H. Sigel, R. B. Martin, *Chem. Rev.* **1982**, *82*, 385–426.
[21] D. S. Marlin, P. K. Mascharak, *Chem. Soc. Rev.* **2000**, *29*, 69–74.
[22] R. J. Guajardo, S. E. Hudson, S. J. Brown, P. K. Mascharak, *J. Am. Chem. Soc.* **1993**, *115*, 7971–7977.
[23] S. Nagashima, M. Nakasako, N. Dohmae, M. Tsujimura, K. Takio, M. Odaka, M. Yohda, N. Kamiya, I. Endo, *Nat. Struct. Biol.* **1998**, *5*, 347–351.
[24] W. Huang, J. Jia, J. Cummings, M. Nelson, G. Schneider, Y. Lindqvist, *Structure* **1997**, *5*, 691–699.
[25] J. C. Noveron, M. M. Olmstead, P. K. Mascharak, *J. Am. Chem. Soc.* **2001**, *123*, 3247–3259.
[26] R. J. Guajardo, F. Chavez, E. T. Farinas, P. K. Mascharak, *J. Am. Chem. Soc.* **1995**, *117*, 3883–3884.
[27] A. K. Patra, R. K. Afshar, M. M. Olmstead, P. K. Mascharak, *Angew. Chem. Int. Ed.* **2002**, *41*, 2512–2515.
[28] D. S. Marlin, M. M. Olmstead, P. K. Mascharak, *Eur. J. Inorg. Chem.* **2002**, 859–865.
[29] A. K. Patra, J. M. Rowland, D. S. Marlin, E. Bill, M. M. Olmstead, P. K. Mascharak, *Inorg. Chem.* **2003**, *42*, 6812–6823.
[30] A. K. Patra, R. K. Afshar, J. M. Rowland, M. M. Olmstead, P. K. Mascharak, *Angew. Chem. Int. Ed.* **2003**, *42*, 4517–4521.
[31] R. K. Afshar, A. K. Patra, M. M. Olmstead, P. K. Mascharak, *Inorg. Chem.* **2004**, *43*, 5736–5743.
[32] J. M. Rowland, M. M. Olmstead, P. K. Mascharak, *Inorg. Chim. Acta* **2002**, *332*, 37–40.
[33] A. K. Patra, P. K. Mascharak, *Inorg. Chem.* **2003**, *42*, 7363–7365.
[34] H. Müller, W. Seidel, H. Görls, *J. Organomet. Chem.* **1994**, *472*, 215–220.
[35] S. V. Kryatov, A. Nazarenko, P. D. Robinson, E. V. Rybak-Akimova, *Chem. Commun.* **2000**, 921–922.
[36] D. M. Kurtz Jr, *Chem. Rev.* **1990**, *90*, 585–606.
[37] T. D. H. Bugg, C. J. Winfield, *Nat. Prod. Rep.* **1998**, *15*, 513–530.
[38] L. Que Jr, R. Y. N. Ho, *Chem. Rev.* **1996**, *96*, 2607–2624.
[39] T. Funabiki, H. Sakamoto, S. Yoshida, L. Tamara, *J. Chem. Soc., Chem. Commun.* **1979**, 754–755.
[40] T. Funabiki, A. Mizoguchi, T. Sugimoto, S. Tada, M. Tsuji, H. Sakamoto, S. Yoshida, *J. Am. Chem. Soc.* **1986**, *108*, 2921–2932.
[41] R. Yamahara, S. Ogo, H. Masuda, Y. Watanabe, *J. Inorg. Biochem.* **2002**, *91*, 151–158.
[42] T. D. H. Bugg, G. Lin, *Chem. Commun.* **2001**, 941–952.
[43] N. Raffard, R. Carina, A. J. Simaan, J. Sainton, E. Riviere, L. Tchertanov, S. Bourcier, G. Bouchoux, M. Delroisse, F. Banse, J.-J. Girerd, *Eur. J. Inorg. Chem.* **2001**, 2249–2254.
[44] W. O. Koch, H.-J. Krüger, *Angew. Chem.* **1995**, *107*, 2928–2931; *Angew. Chem. Int. Ed. Engl.* **1995**, *34*, 2671–2674.
[45] D.-H. Jo, L. Que Jr, *Angew. Chem. Int. Ed.* **2000**, *39*, 4284–4287.
[46] H. G. Jang, D. D. Cox, L. Que Jr, *J. Am. Chem. Soc.* **1991**, *113*, 9200–9204.
[47] M. Pascaly, M. Duda, F. Schweppe, K. Zurlinden, F. K. Müller, B. Krebs, *J. Chem. Soc., Dalton Trans.* **2001**, 828–838.
[48] M. Duda, M. Pascaly, B. Krebs, *Chem. Commun.* **1997**, 835–836.
[49] R. H. Heistand II, R. B. Lauffer, E. Fikrig, L. Que Jr, *J. Am. Chem. Soc.* **1982**, *104*, 2789–2796.
[50] R. H. Heistand II, L. A. Roe, L. Que Jr, *Inorg. Chem.* **1982**, *21*, 676–681.
[51] K. Spartalian, C. J. Carrano, *Inorg. Chem.* **1989**, *28*, 19–24.
[52] P. Mialane, E. Anxolabéhère-Mallart, G. Blondin, A. Nivorojkine, J. Guilhem, L. Tchertanova, M. Cesario, N. Ravi, E. Bominaar, J.-J. Girerd, E. Münck, *Inorg. Chim. Acta* **1997**, *263*, 367–378.
[53] M. Merkel, F. K. Müller, B. Krebs, *Inorg. Chim. Acta* **2002**, *337*, 308–316.
[54] R. Viswanathan, M. Palaniandavar, T. Balasubramanian, T. P. Muthiah, *Inorg. Chem.* **1998**, *37*, 2943–2951.
[55] H. Fujii, Y. Funahashi, *Angew. Chem. Int. Ed.* **2002**, *41*, 3638–3641.
[56] M. Velusamy, M. Palaniandavar, *Inorg. Chem.* **2003**, *42*, 8283–8293.
[57] M. Merkel, M. Pascaly, B. Krebs, J. Astner, S. P. Foxon, S. Schindler, *Inorg. Chem.* **2005**, *44*, 7582–7589.
[58] A. M. Orville, J. D. Lipscomb, D. H. Ohlendorf, *Biochemistry* **1997**, *36*, 10052–10066.
[59] M. W. Vetting, D. A. D'Argenio, L. N. Ornston, D. H. Ohlendorf, *Biochemistry* **2000**, *39*, 7943–7955.
[60] M. I. Davis, A. M. Orville, F. Neese, J. M. Zaleski, J. D. Lipscomb, E. I. Solomon, *J. Am. Chem. Soc.* **2002**, *124*, 602–614.
[61] M. Merkel, D. Schnieders, S. M. Baldeau, B. Krebs, *Eur. J. Inorg. Chem.* **2004**, 783–790.
[62] Y. Dong, H. Fujii, M. P. Hendrich, R. A. Leising, G. Pan, C. R. Randall, E. C. Wilkinson, Y. Zang, L. Que Jr, *J. Am. Chem. Soc.* **1995**, *117*, 2778–2792.
[63] R. M. Buchanan, S. Chen, J. F. Richardson, M. Bressan, L. Forti, A. Morvillo, R. H. Fish, *Inorg. Chem.* **1994**, *33*, 3208–3209.
[64] A. Hazell, K. B. Jensen, C. J. McKenzie, H. Toftlund, *Inorg. Chem.* **1994**, *33*, 3127–3134.
[65] S. Ito, T. Okuno, H. Matsushima, T. Tokii, Y. Nishida, *J. Chem. Soc., Dalton Trans.* **1996**, 4479–4484.
[66] T. Kojima, R. A. Leising, Y. Shiping, L. Que Jr, *J. Am. Chem. Soc.* **1993**, *115*, 11328–11335.
[67] B. R. Whittlesey, Z. Pang, R. A. Holwerda, *Inorg. Chim. Acta* **1999**, *284*, 124–126.
[68] B. Kwak, K. W. Cho, M. Pyo, M. S. Lah, *Inorg. Chim. Acta* **1999**, *290*, 21–27.
[69] E. C. Wilkinson, Y. Dong, L. Que Jr, *J. Am. Chem. Soc.* **1994**, *116*, 8394–8395.
[70] Y. Nishida, T. Okuno, S. Ito, A. Harada, S. Ohba, H. Matsushima, T. Tokii, *Chem. Lett.* **1995**, 885–886.
[71] M. Pascaly, M. Duda, A. Rompel, B. H. Sift, W. Meyer-Klaucke, B. Krebs, *Inorg. Chim. Acta* **1999**, *291*, 289–299.
[72] D. Moon, M. S. Lah, R. E. D. Sesto, J. S. Miller, *Inorg. Chem.* **2002**, *41*, 4708–4714.
[73] S. Yan, D. D. Cox, L. L. Pearce, C. Juarez-Garcia, L. Que Jr, J. H. Zhang, C. J. O'Connor, *Inorg. Chem.* **1989**, *28*, 2507–2509.
[74] R. E. Norman, S. Yan, L. Que Jr, G. Backes, J. Ling, J. Sanders-Loehr, J. H. Zhang, C. J. O'Connor, *J. Am. Chem. Soc.* **1990**, *112*, 1554–1562.

 © 2006 Wiley-VCH Verlag GmbH & Co. KGaA, Weinheim 

[75] G. Musie, C.-H. Lai, J. H. Reibenspies, L. W. Sumner, M. Y. Darensbourg, *Inorg. Chem.* **1998**, *37*, 4086–4093.
[76] K. Ghosh, A. A. Eroy-Reveles, B. Avila, T. R. Holman, M. M. Olmstead, P. K. Mascharak, *Inorg. Chem.* **2004**, *43*, 2988–2997.
[77] K. Hanaoka, K. Kikuchi, H. Kojima, Y. Urano, T. Nagano, *Angew. Chem. Int. Ed.* **2003**, *42*, 2996–2999.
[78] J. M. Rowland, M. M. Olmstead, P. K. Mascharak, *Inorg. Chem.* **2001**, *40*, 2810–2817.
[79] *SADABS*, Siemens Area Detector Absorption Correction, Siemens.
[80] G. M. Sheldrick, *SHELX-97*, University of Göttingen, **1997**.
[81] P. Coppens in *Crystallographic Computing* (Eds.: F. R. Ahmed, S. R. Hall, C. P. Huber), Munksgard, Copenhagen, **1970**, 255–270.
[82] G. M. Sheldrick, *SHELXTL NT*, Bruker Analytical Instruments, Madison, Version 6.12, **2002**.

Received: October 10, 2005
Published Online: March 1, 2006

 © 2006 Wiley-VCH Verlag GmbH & Co. KGaA, Weinheim 

DOI: 10.1002/ejic.200500925

# Supramolecular Trapping of Phosphanes by Cyclodextrins: A General Approach to Generate Phosphane Coordinatively Unsaturated Organometallic Complexes

**Cécile Binkowski-Machut,[a] Michaël Canipelle,[a] Hervé Bricout,[a] Sébastien Tilloy,[a] Frédéric Hapiot,[a] and Eric Monflier*[a]**

**Keywords:** Phosphane ligands / Cyclodextrins / Molecular recognition / Palladium / Platinum

As shown by $^{31}P\{^1H\}$ NMR spectroscopy, addition of the native β-cyclodextrin or randomly methylated β-cyclodextrin to an aqueous solution of $Cl[Pt\{(p\text{-}tBuC_6H_4)P(m\text{-}C_6H_4SO_3Na)_2\}_3Cl]$ or $[Pd\{(p\text{-}tBuC_6H_4)P(m\text{-}C_6H_4SO_3Na)_2\}_3]$ allows us to generate the phosphane coordinatively unsaturated $[Pt\{(p\text{-}tBuC_6H_4)P(m\text{-}C_6H_4SO_3Na)_2\}_2Cl_2]$ or $[Pd\{(p\text{-}tBuC_6H_4)P(m\text{-}C_6H_4SO_3Na)_2\}_2]$ complexes, respectively. The existence of second-sphere coordination adducts between the organometallic complex and the cyclodextrin, in which the local bulkiness around the metallic centre is high, appears to be the essential prerequisite for the dissociation of one $(p\text{-}tBuC_6H_4)P(m\text{-}C_6H_4SO_3Na)_2$ phosphane ligand from the metal centre. (© Wiley-VCH Verlag GmbH & Co. KGaA, 69451 Weinheim, Germany, 2006)

## Introduction

One of the most challenging aspects of organometallic catalysis is to generate phosphane unsaturated species. Indeed, these complexes are generally accepted as the catalytically active species in numerous transition-metal-catalysed reactions.[1] An efficient strategy that favours the formation of such compounds consists of using hindered phosphanes. Actually, because of the bulkiness generated around the metallic centre, coordination of numerous ligands to the metal is prohibited and low-coordinated species are obtained. Thus, the use of hindered phosphane has proved to be efficient in generating coordinatively unsaturated complexes that are well known as active catalysts in hydroformylation[2] and carbon–carbon or carbon–heteroatom bond formation.[3] Unfortunately, these catalytic entities have often remained experimentally inaccessible in large amounts because of their low stability, and have required the synthesis of elaborate phosphanes.

We have recently put forward the remarkable properties of cyclodextrins to form inclusion complexes with water-soluble phosphane ligands used to dissolve the organometallic catalyst in water.[4] In particular, the native β-cyclodextrin (β-CD, Scheme 1) and the randomly methylated β-cyclodextrin (RAME-β-CD, Scheme 1) have proved to strongly interact with the disodium bis(3-sulfonatophenyl)(4-*tert*-butylphenyl)phosphane $[(p\text{-}tBuC_6H_4)P(m\text{-}C_6H_4SO_3Na)_2$ (**1**) ] (Scheme 1) as a result of the well-known ability of the *tert*-butylphenyl group to fit tightly into the β-CD cavity.[5] Thus, the association constants for the β-

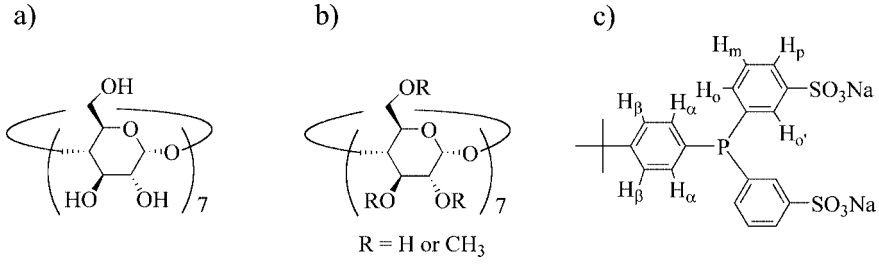


Scheme 1. (a) Native β-cyclodextrin (β-CD), (b) randomly methylated β-cyclodextrin (RAME-β-CD), (c) disodium bis(3-sulfonatophenyl)(4-*tert*-butylphenyl)phosphane $[(p\text{-}tBuC_6H_4)P(m\text{-}C_6H_4SO_3Na)_2]$ (**1**).

[a] Université d'Artois, Laboratoire de Physico-Chimie des Interfaces et Applications, FRE CNRS 2485, Faculté des Sciences Jean Perrin, Rue Jean Souvraz,
SP 18-62307 Lens Cédex, France
Fax: +33-3-21791755
E-mail: monflier@univ-artois.fr

Supporting information for this article is available on the WWW under http://www.eurjic.org or from the author.

 © 2006 Wiley-VCH Verlag GmbH & Co. KGaA, Weinheim 

CD/**1** and RAME-β-CD/**1** inclusion complexes were found to be notably higher than those measured for the inclusion complexes formed with trisulfonated triphenylphosphane (TPPTS); a phosphane currently used in aqueous organometallic catalysis (400000 and 250000 $M^{-1}$ at 25 °C for β-CD/**1** and RAME-β-CD/**1** inclusion complexes, respectively; 1200 and 1000 $M^{-1}$ at 25 °C for β-CD/TPPTS and RAME-β-CD/TPPTS inclusion complexes, respectively).

Interestingly, the strong interaction between **1** and CD derivatives can be used to generate phosphane low-coordinated rhodium species.[5] Indeed, we have demonstrated that $[HRh(CO)(\mathbf{1})_3]$ can be partially converted in the presence of β-CD or RAME-β-CD into the hydroxy complex $[HORh(CO)(\mathbf{1})_2]$ under nitrogen, or into the hydrido complex $[HRh(CO)_2(\mathbf{1})_2]$ under carbon monoxide.

In this paper, we would like to demonstrate that the use of a hydrosoluble phosphane, very strongly interacting with CDs such as **1**, could be a general approach to generate phosphane coordinatively unsaturated complexes under mild conditions. The feasibility of our approach was exam-

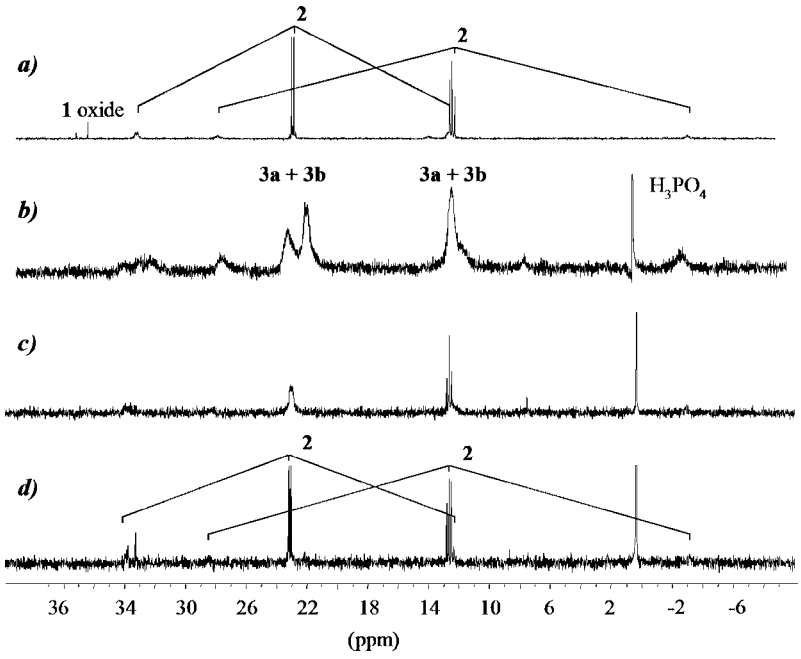


Figure 1. $^{31}P\{^1H\}$ NMR spectra of the platinum complex $Cl[ClPt((p\text{-}tBuC_6H_4)P(m\text{-}C_6H_4SO_3Na)_2)_3]$ (**2**) (10 mM) in $D_2O$ (a) without cyclodextrin at 25 °C; after addition of 1 equiv. β-CD with respect to the platinum at (b) 25 °C; (c) 60 °C; (d) 85 °C.

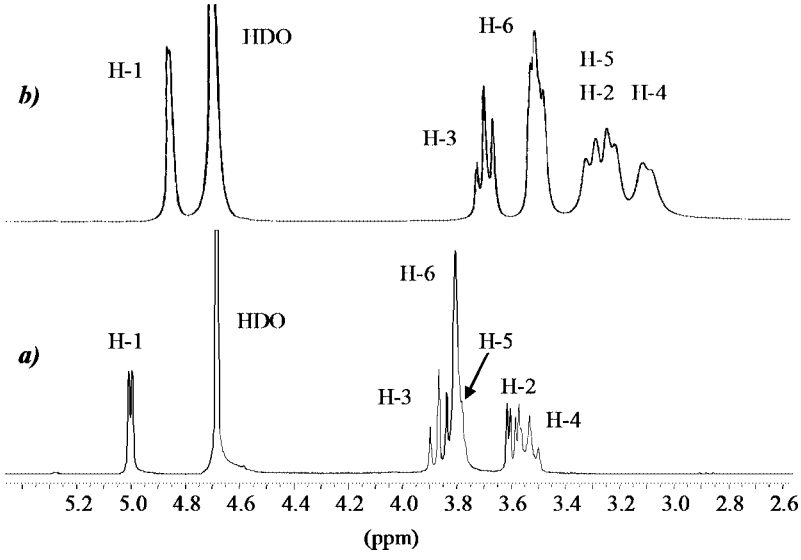


Figure 2. $^1H$ NMR spectra at 25 °C in $D_2O$ of (a) β-CD alone (10 mM); (b) β-CD after addition of 1 equiv. $Cl[ClPt((p\text{-}tBuC_6H_4)P(m\text{-}C_6H_4SO_3Na)_2)_3]$ (2) (10 mM).

 © 2006 Wiley-VCH Verlag GmbH & Co. KGaA, Weinheim 

ined using platinum or palladium complexes of **1** and β-CD or RAME-β-CD as phosphane trapping agents.

## Results and Discussion

Initial experiments were performed using β-CD whose well-defined $^1$H NMR signals are easier to read than the signals of RAME-β-CD, where the overlapped resonances are often noninterpretable. The Cl[Pt(**1**)$_3$Cl] platinum complex (**2**) was prepared by mixing $K_2PtCl_4$ with 3 equiv. of **1** according to a procedure previously described in the literature for the synthesis of the analogous complex Cl[Pt(TPPTS)$_3$Cl].[6] Figure 1 shows the $^{31}P\{^1H\}$ NMR spectra relative to **2** without β-CD (Figure 1, a) and in the presence of 1 equiv. of β-CD at 25 °C (Figure 1, b), 60 °C (Figure 1, c) and 85 °C (Figure 1, d).

Since only one third of the platinum ($^{195}$Pt) has a spin of 1/2, the phosphorus of the square-planar structure of **2** exhibits a 1:4:1 triplet of doublets centred at $\delta$ = 23.0 ppm ($^1J_{Pcis–Pt}$ = 2494 Hz; $^2J_{Pcis–Ptrans}$ = 18.6 Hz) corresponding to the two phosphorus atoms *cis* to the chloride and a 1:4:1 triplet of triplets centred at $\delta$ = 12.4 ppm ($^1J_{Ptrans–Pt}$ = 3718 Hz; $^2J_{Pcis–Ptrans}$ = 18.6 Hz) corresponding to the phosphorus atom *trans* to the chloride (Figure 1, a). At 25 °C, addition of β-CD leads to the appearance of new resonances and a broadening of all signals (Figure 1, b). No peak is detected in the chemical shift region of the free or CD-included phosphane (from 0 ppm to –12 ppm). This can be explained by assuming that β-CD interacts with **2** without inducing the dissociation of phosphane **1** from the metal. The nature of the interactions between both species **1** and **2** with β-CD has been established by $^1$H NMR spectroscopic measurements. Figure 2 shows the $^1$H NMR spectra of β-CD, both alone and also as a stoichiometric β-CD/**2** mixture (Figure 2).

Upon addition of **2** to the β-CD solution, strong upfield chemical shifts are observed for the internal 3-H and 5-H CD protons suggesting the formation of inclusion complexes between **2** and β-CD. It should be noted that the other protons of the CD are also shielded upfield by the presence of **2**, indicating that they are also affected by the inclusion process. The formation of inclusion complexes between **2** and β-CD was unambiguously demonstrated by a 2D NMR T-ROESY spectrum of a 1:1 mixture of **2** and β-CD, which revealed intense cross-peaks between the *t*Bu group of the phosphane and the internal CD protons 3-H, 5-H and 6-H (Figure 3).

Nevertheless, the absence of correlations between the 3-H, 5-H or 6-H protons and $H_\alpha$ shows that the penetration of the phosphane into the CD cavity was not deep (Scheme 2).

This observation is opposite to what has previously been established for the β-CD/**1** inclusion complex. Indeed, a detailed study has clearly demonstrated that phosphane **1** was

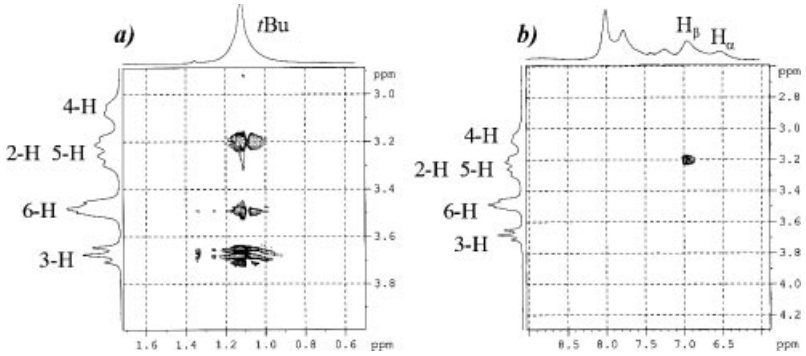


Figure 3. Partial contour plot of the T-ROESY spectrum of a solution containing β-CD (10 mM) and **2** (10 mM) in $D_2O$ at 25 °C with a 300 ms mixing time. (a) Cross-peaks between the β-CD protons and protons of the *tert*-butyl group. (b) Cross-peaks between the β-CD protons and the aromatic protons of phosphane **1**.

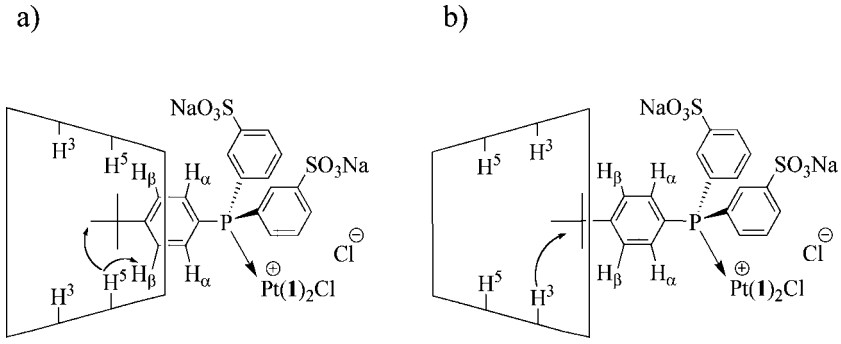


Scheme 2. Second-sphere coordination adducts between β-CD and **2** with a recognition process (a) at the primary face and (b) at the secondary face. The interactions observed in the T-ROESY spectrum between the different protons and the deduced orientation of the phosphane **1** in the CD cavity are also shown.

 © 2006 Wiley-VCH Verlag GmbH & Co. KGaA, Weinheim 

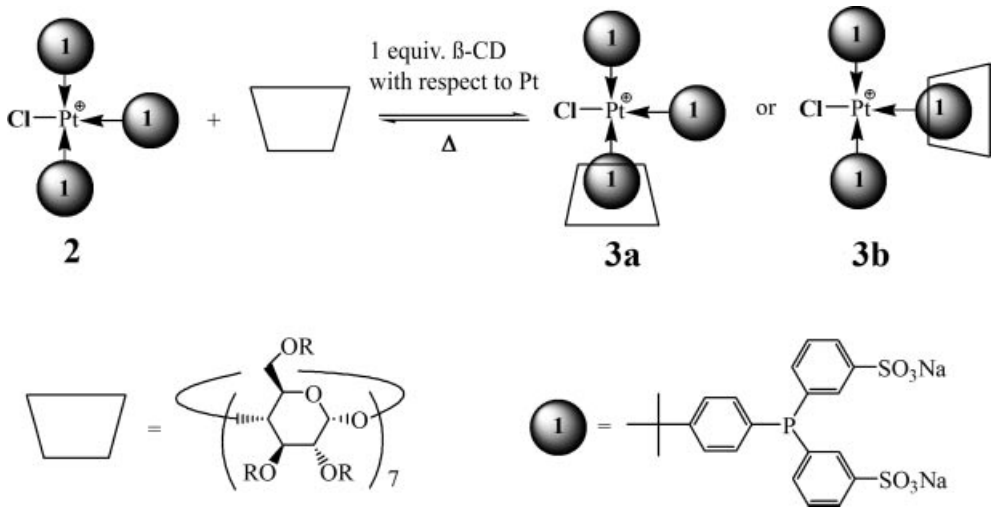


Scheme 3. Equilibrium between the platinum complexes of **1** in the presence of 1 equiv. β-CD (inclusion of **1** at the secondary face is also possible).

deeply included in the β-CD cavity at the primary face (intense cross-peaks between $H_\alpha$ and 5-H or 6-H, see Supporting Information). Therefore, **1** interacted very differently with β-CD when free in solution and when coordinated to the platinum complex. Furthermore, the presence of intense cross-peaks between the *t*Bu group of the phosphane and the 3-H, 5-H and 6-H CD protons strongly suggests that inclusion occurred at the primary face (Scheme 2, a) but also at the secondary face of the β-CD (Scheme 2, b). Indeed, a low-deep inclusion of **2** at the primary face of the β-CD cannot rationalise the intense cross-peak observed between the *t*Bu and 3-H proton. Finally, it must be pointed out that the inclusion of the phosphane **1** into the cavity at the secondary face was so small that no contact was detected between the 3-H and $H_\beta$ (or a fortiori $H_\alpha$) protons.

Knowing that **2** and β-CD were supramolecularly interacting, the splitting and broadening of the peaks of Figure 1 (b) are attributed to the existence of two possible inclusions of **2** in β-CD (Scheme 3), either by one of the two ligands **1** *cis* to the chloride (species **3a**) or by the ligand **1** *trans* to the chloride (species **3b**). Although inclusion of **2** at the secondary face also occurred, only the structures obtained with an inclusion at the primary face have been represented for clarity in Scheme 3.

Interestingly, the splitting of the signal at $\delta$ = 23.0 ppm, corresponding to the two phosphorus atoms *cis* to the chloride, into two broad signals in the 25–20 ppm region in the presence of β-CD (see parts a and b in Figure 1) indicates that the coordinated *cis* phosphanes **1** become inequivalent when β-CD binds to complex **2**. As only 1 equiv. of β-CD was added to a solution of **2**, this phenomenon probably finds its origin in the fact that when one of the two *cis* phosphanes **1** is included into the β-CD cavity, the other remains nonincluded. Finally, the important and unusual upfield shifts observed in the $^1$H NMR spectrum for the external protons of the CD (1-H, 2-H and 4-H) might be explained by the closeness in species **3** of nonincluded coordinated ligands **1** with the edges of a β-CD bound to a coordinated ligand **1**, suggesting an overcrowded environment at the periphery of the CD.

Consequently, at room temperature, it appears that β-CD acts as a host for a ligand that was directly coordinated to the platinum. Although the formation of second-sphere coordination adducts between CD derivatives and organometallic complexes is a well-known phenomenon,[7] it is worth mentioning that the formation of such adducts between CD and organometallic complexes bearing phosphane ligands has rarely been observed. Indeed, to the best

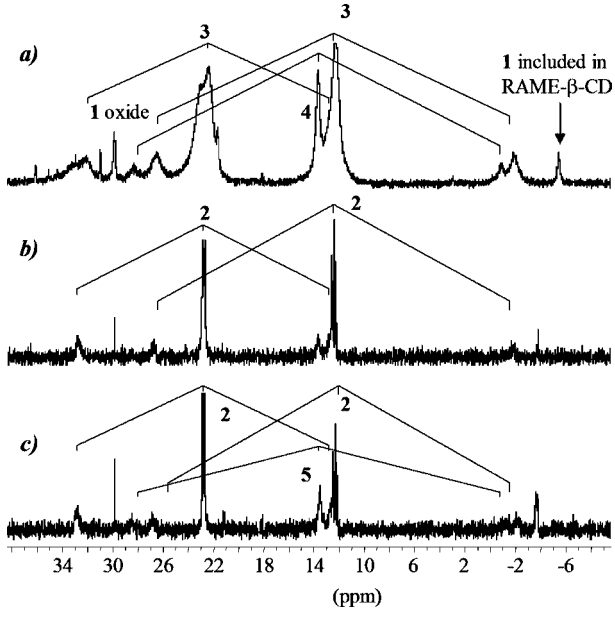


Figure 4. $^{31}$P{$^1$H} NMR spectra of the platinum complex Cl[ClPt((*p*-*t*BuC$_6$H$_4$)P(*m*-C$_6$H$_4$SO$_3$Na)$_2$)$_3$] (**2**) (10 mM) in $D_2O$ with 12 equiv. RAME-β-CD with respect to the platinum at (a) 25 °C; (b) 60 °C; (c) 85 °C.

 © 2006 Wiley-VCH Verlag GmbH & Co. KGaA, Weinheim 

of our knowledge, there are only four reports in the literature on the formation of such adducts in organic or aqueous media.[8]

Information concerning the thermal stability of second-sphere coordination adducts **3** was obtained by carefully examining the $^{31}P\{^{1}H\}$ NMR spectra recorded at various temperatures. Increasing the temperature to 60 and 85 °C gave more resolved spectra (see parts c and d in Figure 1). In particular, the $^{31}P\{^{1}H\}$ NMR spectrum recorded at 85 °C (Figure 1, d) strongly resembles that recorded at 25 °C (Figure 1, a), indicating that the second-sphere coordination adducts **3a** and **3b** disappeared when the temperature was increased. Actually, an increase in the temperature decreased the association constant between β-CD and **1**, which found expression in a dissociation of β-CD from the organometallic complex. Interestingly, the spectrum recorded at 60 °C suggests that the β-CD interacted more strongly with the *cis* ligands than with the *trans* ligand. Indeed, the signal at $\delta$ = 12.4 ppm corresponding to the *trans* phosphane is well resolved whereas the signal corresponding to the *cis* phosphanes remains broad at 60 °C. This result can easily be rationalised by considering that the steric

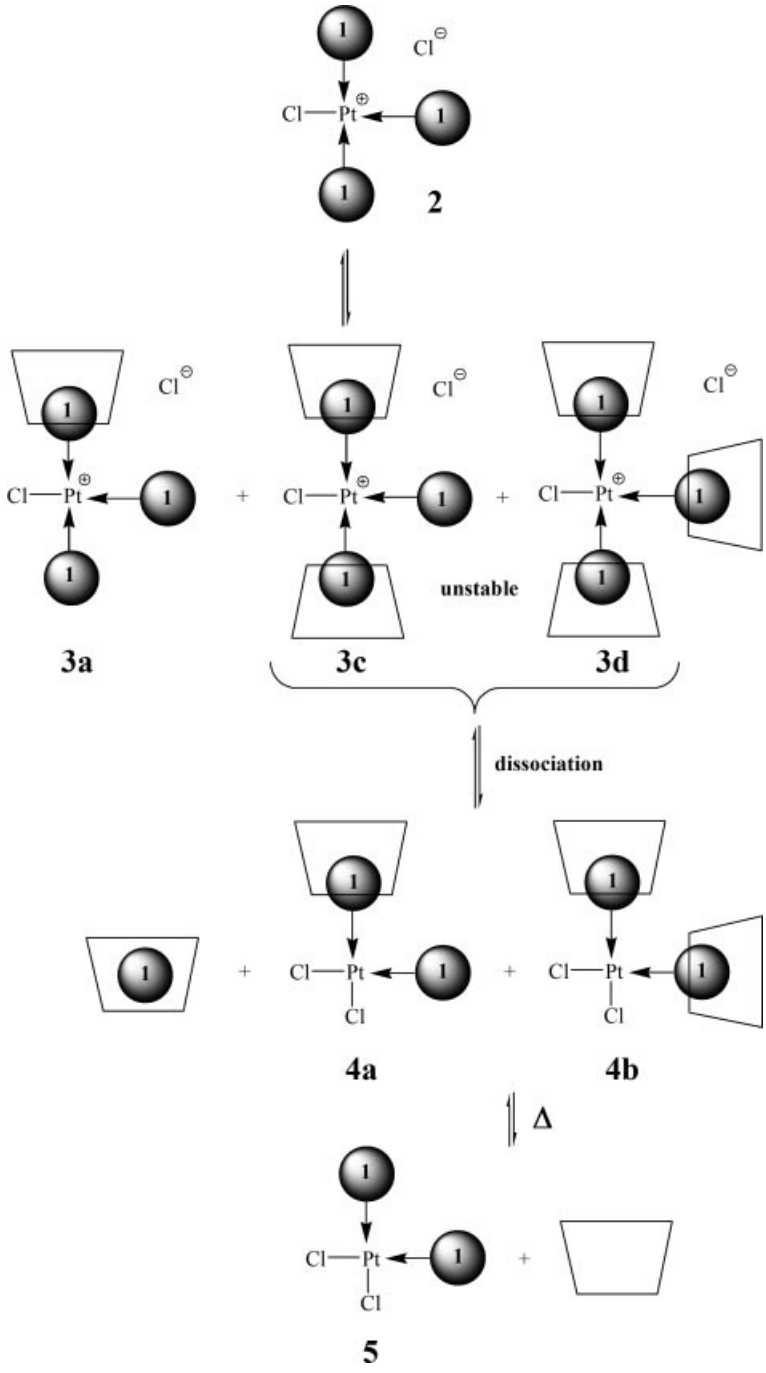


Scheme 4. Equilibria between the platinum complexes of **1** in the presence of 12 equiv. RAME-β-CD (inclusion of **1** at the secondary face is also possible). Some second-sphere coordination adducts are not represented for clarity.

 © 2006 Wiley-VCH Verlag GmbH & Co. KGaA, Weinheim 

congestion around the *trans* ligand is more important than it is around the *cis* ligand.

The stability of the second-sphere adducts in the presence of various amounts of β-CD or RAME-β-CD was also investigated. Similar results were obtained with 3 equiv. β-CD and with 1 or 3 equiv. RAME-β-CD. However, the results were very different when 12 equiv. RAME-β-CD was used. Indeed, along with the numerous changes already observed above, the $^{31}P\{^{1}H\}$ NMR spectrum also revealed a broad 1:4:1 triplet centred at $\delta$ = 13.8 ppm ($^{1}J_{P,Pt}$ = 3700 Hz) assigned to a new platinum species (**4**) and a resonance characteristic of an inclusion complex between **1** and the RAME-β-CD at $\delta$ = –5.5 ppm (Figure 4, a).

This new platinum species **4** was identified by comparing its chemical shift and platinum-phosphorus coupling constant values with those for the known water-soluble platinum complexes and by integration of the $^{31}P$ NMR signals. Actually, we found that the spectroscopic data of **4** are very similar to those of [*cis*-Pt(TPPTS)$_2$Cl$_2$][6] and that the intensity of the $^{31}P$ NMR signal of the species **4** was twice as high as the intensity of the signal relative to the RAME-β-CD/**1** inclusion complex. These two findings led us to assume that the new platinum species **4** corresponds to second-sphere coordination adducts between [Pt(**1**)$_2$Cl$_2$] and the RAME-β-CD obtained by dissociation of **1** from adducts **3** according to Scheme 4.

As previously observed with adducts **3** (vide infra), dissociation of RAME-β-CD from platinum species **4** occurred at high temperatures, leading to nonincluded [Pt(**1**)$_2$Cl$_2$] (**5**). Indeed, increasing the temperature led to the destabilisation of the second-sphere coordination adducts (well-defined peaks at 60 and 85 °C) and additionally to a larger proportion of the signal corresponding to free phosphane **1** in interaction with RAME-β-CD (Figure 4, parts b and c) (Scheme 4). As the intensity of the signal relative to the RAME-β-CD/**1** inclusion complex is directly proportional to the $^{31}P$ NMR signal of the new species **4** and **5**, the percentage (**4** and **5**) could be determined starting from the integration of the peak assigned to the free phosphane **1** that is included into RAME-β-CD (see Supporting Information). At 85 °C, an amount of 22% (**4** and **5**) was calculated.

In order to confirm that the formation of the phosphane coordinatively unsaturated platinum complexes **4** and **5** was a result of the RAME-β-CD similar experiments have been performed with methyl-α-D-glucopyranoside, which constitutes the monomeric "building block" of RAME-β-CD. No modification of the spectra could be observed in this case, proving that the molecular recognition ability of RAME-β-CD plays a fundamental role in the formation of **4** and **5**.

Throughout these experiments, it was clear that an excess of RAME-β-CD was necessary to generate the phosphane coordinatively unsaturated platinum complexes. The explanation of such a phenomenon not only lies in the strength of the RAME-β-CD/**2** interaction, but also in the steric hindrance generated by the presence of RAME-β-CD on the first-sphere ligands. Indeed, below 3 equiv. of RAME-β-CD with respect to the amount of platinum, it is reasonable to assume that the equilibrium between the nonincluded and included **2** remained possible as the steric hindrance around the metallic centre should not be very important when one CD is bound to a coordinated phosphane **1** (Scheme 3). By contrast, when a large amount of RAME-β-CD was added, the equilibrium was displaced towards the second-sphere coordination adducts containing two and three CDs. The local bulkiness around the metallic centre of the obtained supramolecular adducts probably became too high and a steric decongestion by dissociation of the phosphane/CD inclusion complex from the platinum occurred leading to phosphane low-coordinated complexes **4** or **5**, depending on the temperature (Scheme 4). These observations are perfectly consistent with those already made above with β-CD for which a hindered structure for the β-CD/**2** complex has been thought of (vide infra). So, the existence of second-sphere coordination adducts in which the local bulkiness around the metallic centre is high appears to be an intermediate step in the formation of phosphane coordinatively unsaturated complexes.

The NMR study has been widened to the palladium complex [Pd{(*p*-*t*BuC$_6$H$_4$)P(*m*-C$_6$H$_4$SO$_3$Na)$_2$}$_3$] (**6**) whose $^{31}P\{^{1}H\}$ NMR spectrum is depicted in Figure 5 (a).

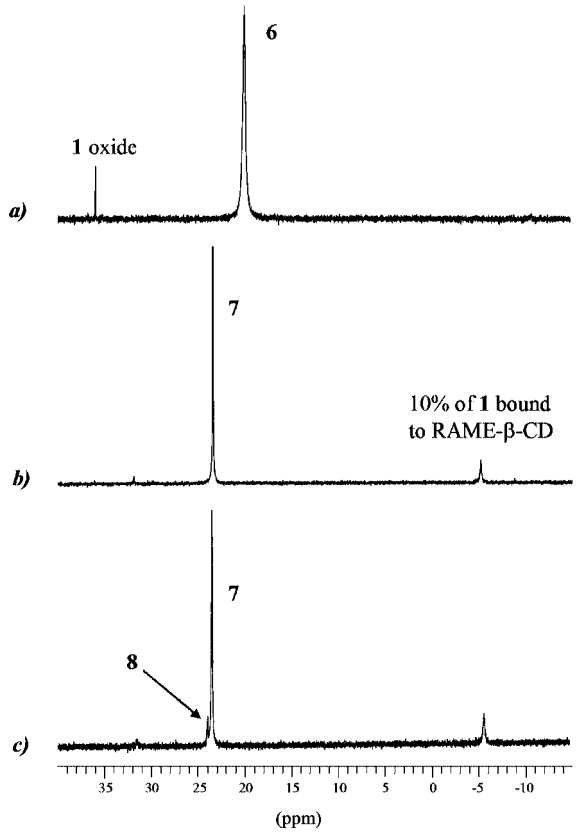


Figure 5. $^{31}P\{^{1}H\}$ NMR spectra of palladium complex [Pd((*p*-*t*BuC$_6$H$_4$)P(*m*-C$_6$H$_4$SO$_3$Na)$_2$)$_3$] (**6**) (20 mM) in D$_2$O at 25 °C (a) without cyclodextrin; (b) after addition of 3 equiv. RAME-β-CD with respect to palladium; (c) after addition of 12 equiv. RAME-β-CD with respect to palladium.

Besides the minor resonance of the phosphane oxide impurity ($\delta$ = 36 ppm), a broad signal was detected at $\delta$ =

 © 2006 Wiley-VCH Verlag GmbH & Co. KGaA, Weinheim 

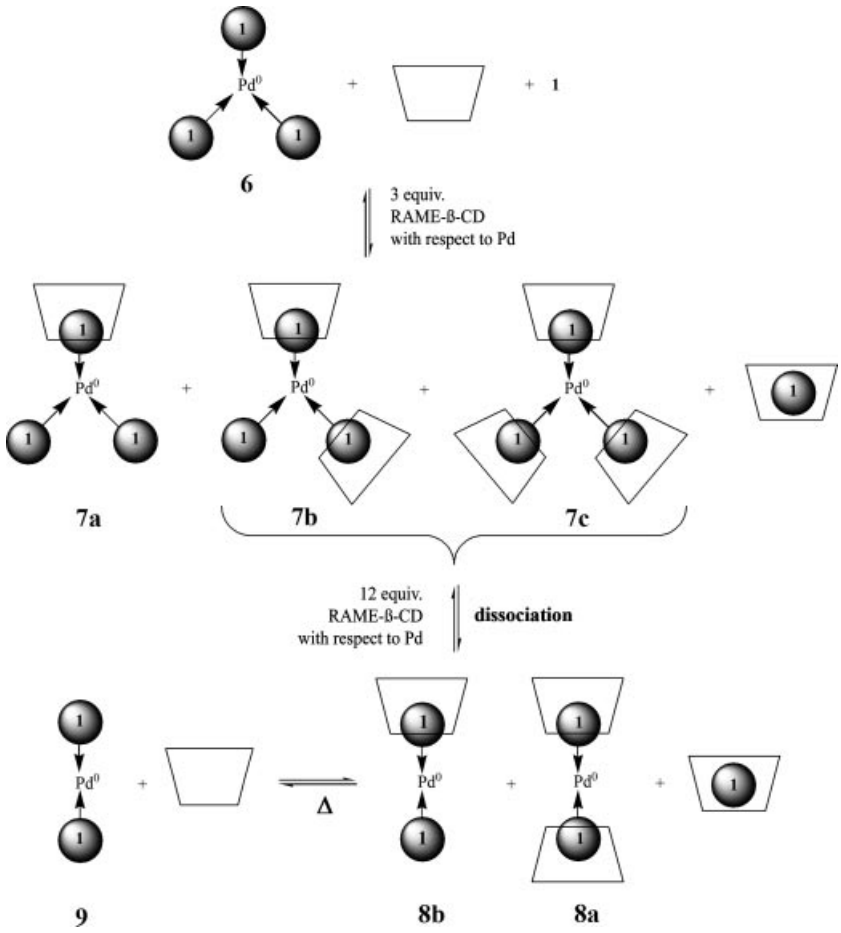


Scheme 5. Equilibria between the palladium complexes of **1** in the presence of various amounts of RAME-β-CD (inclusion of **1** at the secondary face is also possible).

20.1 ppm. As an excess of phosphane **1** was present in the medium (10%, see Exp. Sect.), this broad peak is an average signal resulting from the fast equilibrium between free phosphane **1** and the palladium complex **6**.[9] By addition of 3 equiv. of RAME-β-CD with respect to **6**, two distinct signals are observed at $\delta$ = 24 and $\delta$ = –5.5 ppm (Figure 5, b). Integration of the $^{31}$P NMR signals at $\delta$ = –5.5 ppm shows that the amount of noncoordinated **1** is 10%, which corresponds to the excess of phosphane **1** initially present in the medium. This last result indicates that 3 equiv. of RAME-β-CD were insufficient to induce the formation of the phosphane coordinatively unsaturated species. Consequently, the signal at $\delta$ = 24 ppm has been assigned to the second-sphere coordination adducts of the palladium complex **6** with the RAME-β-CD (species **7**) and the signal at $\delta$ = –5.5 ppm to the phosphane **1** in interaction with RAME-β-CD (Scheme 5). Moreover, it can be concluded that RAME-β-CD decreased the exchange rate between phosphane **1** and the palladium species since the excess of the phosphane **1** complex is visible.

Much more interesting were the results obtained when 12 equiv. of RAME-β-CD, with respect to the palladium complex, were added to an aqueous solution of **6** (Figure 5, c). Indeed, a new species at $\delta$ = 24.5 ppm (**8**) was observed and the amount of phosphane **1** bound to RAME-β-CD was higher than the previous one (16% compared with 10%). Furthermore, calculations showed that the intensity of the $^{31}$P NMR signal of the new species **8** was twice as high as the intensity of the phosphane **1** signal that appeared. By analogy with the platinum complexes, this outstanding result led us to assume that **8** was the palladium species [(**1**)$_2$Pd$^0$] containing two phosphane ligands included in the RAME-β-CD cavities. As observed for platinum species **4** and **5**, the steric hindrance generated by two or three CDs around the metallic centre of **6** could be invoked to explain the formation of the phosphane low-coordinated palladium species **8** (Scheme 5).

Here again, the amounts of included phosphane **1** and complex **8** were found to be dependent on the temperature. Indeed, when the solution containing 12 equiv. of RAME-β-CD with respect to **6** was heated at 40 °C (Figure 6, b) and 60 °C (Figure 6, c), the signals corresponding to the palladium complex **8** and phosphane **1** included into RAME-β-CD notably increased. Although no evidence has been obtained contrary to that for the platinum species, it is reasonable to think that, at higher temperatures, dissociation of the second-sphere adducts **8** could lead to the formation of species [(**1**)$_2$Pd$^0$] (species **9**, Scheme 5).

Calculations revealed that the amount of phosphane **1** that appeared was directly connected to the amount of spe-

 © 2006 Wiley-VCH Verlag GmbH & Co. KGaA, Weinheim 

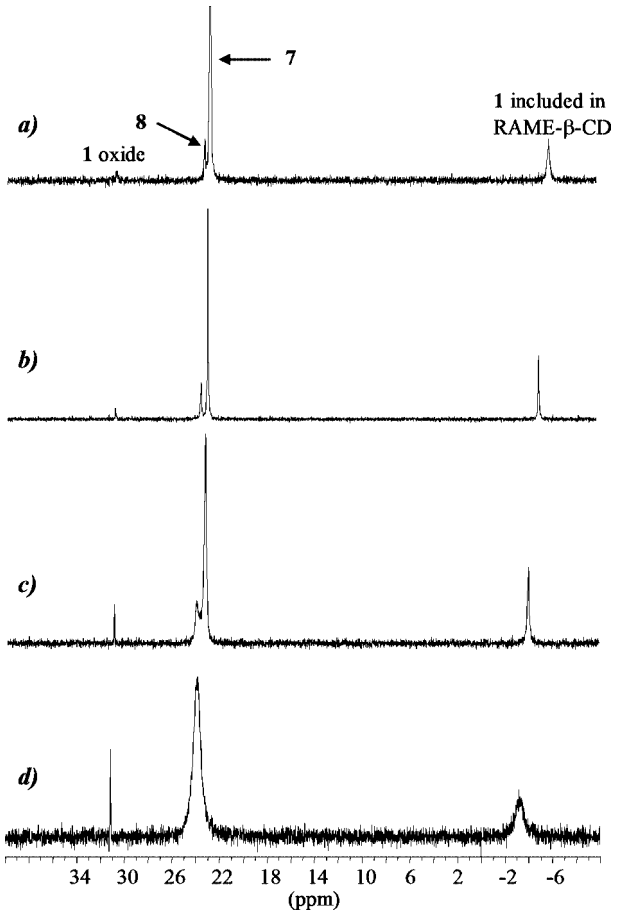


Figure 6. $^{31}P\{^{1}H\}$ NMR spectra of a mixture of [Pd((*p*-*t*BuC$_6$H$_4$)P(*m*-C$_6$H$_4$SO$_3$Na)$_2$)$_3$] (**6**) (20 mM) and RAME-β-CD (240 mM) in $D_2O$ at various temperatures: (a) 25 °C; (b) 40 °C; (c) 60 °C; (d) 85 °C.

cies **8** and **9** (see Supporting information). The percentage of **8** and **9** relative to the total amount of palladium could reach 40% at 85 °C (Figure 7).

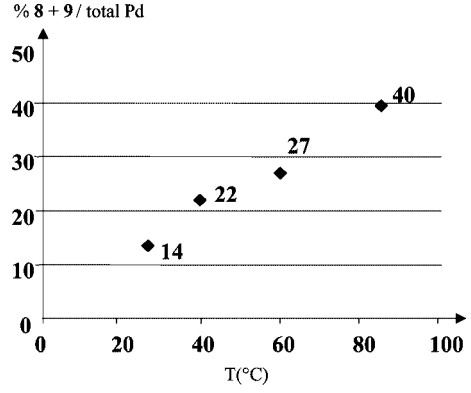


Figure 7. Percentage of palladium species (**8** and **9**) relative to the total palladium amount [% complex (**8** and **9**)/total Pd] as a function of the temperature [Pd((*p*-*t*BuC$_6$H$_4$)P(*m*-C$_6$H$_4$SO$_3$Na)$_2$)$_3$ (20 mM) and RAME-β-CD (240 mM)].

Finally, it must be pointed out that the above phenomena were reversible since a new $^{31}P\{^{1}H\}$ NMR spectrum recorded at 27 °C, after the heating period, was identical to that observed before heating the sample.

To confirm that the formation of the phosphane coordinatively unsaturated palladium complexes **8** and **9** was due to RAME-β-CD, similar experiments were also performed with methyl-α-D-glucopyranoside. As previously reported with the platinum species, no modification of the spectra could be observed in this case, proving that the molecular recognition ability of RAME-β-CD plays a fundamental role in the formation of **8** and **9**.

## Conclusion

This work has clearly demonstrated that the strong interaction between RAME-β-CD and the especially designed phosphane **1** can be used for generating phosphane coordinatively unsaturated platinum and palladium complexes, which are spectroscopically evidenced by $^{31}P$ NMR measurements. This constitutes the first example of the existence of low-coordinated palladium species in water. The existence of second-sphere coordination adducts in which the local bulkiness around the metallic centre is high appeared to be the essential prerequisite leading to the dissociation of the sulfonated ligand from the metal. Studies are currently underway in our laboratory to examine the catalytic activity of these supramolecularly generated species.

## Experimental Section

**General Remarks:** The $^{1}H$ and $^{31}P\{^{1}H\}$ NMR spectra were recorded with a Bruker Avance 300 DPX instrument at 300.13 and 75.46 MHz, respectively. The 2D T-ROESY experiments were run using the software supplied by Bruker. Mixing times for T-ROESY experiments were set at 300 ms. The data matrix for the T-ROESY was made from 512 free induction decays, 1 K points each, resulting from the coaddition of 32 scans. The real resolution was 1.5–6.0 Hz/point in the F2 and F1 dimensions. They were transformed in the nonphase, sensitive mode after QSINE window processing. Palladium acetate, potassium chloro-platinate and randomly methylated β-cyclodextrin (RAME-β-CD) were purchased from Aldrich. RAME-β-CD was a native β-CD partially methylated; statistically 1.8 OH groups per glucopyranose unit were modified. The synthesis of the disodium bis(3-sulfonatophenyl)(4-*tert*-butylphenyl)phosphane [(*p*-*t*BuC$_6$H$_4$)P(*m*-C$_6$H$_4$SO$_3$Na)$_2$ (**1**)] was described in one of our previous publications.[10]

**$^{31}P\{^{1}H\}$ NMR Study on the Complex Cl[Pt{(*p*-*t*BuC$_6$H$_4$)P(*m*-C$_6$H$_4$SO$_3$Na)$_2$}$_3$Cl] (2):** $K_2Pt_2Cl_4$ (21 mg, 0.05 mmol) was dissolved in degassed deuterated water (5 mL). Three equiv. of **1** (7.9 mg, 0.15 mmol) were added to the solution, which was then stirred for 30 min at room temperature under nitrogen. Complex **2** was quantitatively obtained. Studies in the presence of β-CD or RAME-β-CD were conducted as follows: the required amount of cyclodextrin was introduced into 1 mL of the above solution. After 15 min. of stirring the solution was transferred into a 5 mm NMR tube.

**$^{31}P\{^{1}H\}$ NMR Study on the Complex [Pd{(*p*-*t*BuC$_6$H$_4$)P(*m*-C$_6$H$_4$SO$_3$Na)$_2$}$_3$] (4):** [Pd{(*p*-*t*BuC$_6$H$_4$)P(*m*-C$_6$H$_4$SO$_3$Na)$_2$}$_3$] in a $D_2O$ solution was synthesized according to a modified literature procedure.[9a] Pd(PPh$_3$)$_4$ (412 mg, 0.36 mmol) was dissolved in degassed toluene (8 g) in a Schlenk tube under nitrogen. (*p*-*t*BuC$_6$H$_4$)-

 © 2006 Wiley-VCH Verlag GmbH & Co. KGaA, Weinheim 

P(*m*-$C_6H_4SO_3Na)_2$ (277 mg, 0.53 mmol) was dissolved in $D_2O$ (8 g) and cannulated into the palladium solution. The mixture was stirred for 30 min at room temperature. After decantation, the aqueous phase was recovered. The obtained [Pd{(*p*-*t*Bu$C_6H_4$)P(*m*-$C_6H_4SO_3Na)_2$}$_3$] solution was then used for the $^{31}P\{^1H\}$ NMR spectroscopic study. This solution contained the expected palladium complex [Pd{(*p*-*t*Bu$C_6H_4$)P(*m*-$C_6H_4SO_3Na)_2$}$_3$] and an excess of about 10% of free (*p*-*t*Bu$C_6H_4$)P(*m*-$C_6H_4SO_3Na)_2$ {with regard to the initial amount of (*p*-*t*Bu$C_6H_4$)P(*m*-$C_6H_4SO_3Na)_2$}. A study in the presence of RAME-β-CD was conducted as follows: the required amount of RAME-β-CD was introduced, under nitrogen, to 1 mL of the above [Pd{(*p*-*t*Bu$C_6H_4$)P(*m*-$C_6H_4SO_3Na)_2$}$_3$] solution. After 15 min. of stirring, the solution was transferred via a cannula into a nitrogen pressurized 5 mm NMR tube.

**Supporting Information** (for details see the footnote on the first page of this article): Spectroscopic study of the β-CD/**1** complex. Determination of the percentage of platinum complex [$Cl_2PtL_2$] relative to the total platinum amount. Determination of the percentage of palladium complex [$PdL_2$] relative to the total palladium amount.


[1] a) M. Beller, C. Bolm, *Transition Metals for Organic Synthesis*, Wiley-VCH, Weinheim, **1998**; b) B. Cornils, W. A. Herrmann, *Applied Homogeneous Catalysis with Organometallic Compounds*, Wiley-VCH, Weinheim, **1996**, vol. 1 and 2.

[2] a) P. C. J. Kamer, J. N. H. Reek, P. W. N. M. van Leeuwen, in *Rhodium Catalyzed Hydroformylation* (Eds.: P. W. N. M. van Leeuween, C. Claver), Kluwer, Dordrecht, **2000** pp. 35–62; b) V. F. Slagt, P. C. J. Kamer, P. W. N. M. van Leeuwen, J. N. H. Reek, *J. Am. Chem. Soc.* **2004**, *126*, 1526–1536.

[3] a) Q. S. Hu, Y. Lu, Z.-Y. Tang, H.-B. Yu, *J. Am. Chem. Soc.* **2003**, *125*, 2856–2857; b) A. F. Littke, G. C. Fu, *Angew. Chem. Int. Ed.* **1998**, *37*, 3387–3388; c) J. F. Hartwig, *Angew. Chem. Int. Ed.* **1998**, *37*, 2046–2067.

[4] a) E. Monflier, S. Tilloy, C. Méliet, A. Mortreux, S. Fourmentin, D. Landy, G. Surpateanu, *New J. Chem.* **1999**, *23*, 469–472; b) E. Monflier, S. Tilloy, L. Caron, J. M. Wieruszeski, G. Lippens, S. Fourmentin, D. Landy, G. Surpateanu, *J. Inclusion Phenom. Macrocyclic Chem.* **2000**, *38*, 361–379; c) T. Mathivet, C. Méliet, Y. Castanet, A. Mortreux, L. Caron, S. Tilloy, E. Monflier, *J. Mol. Catal. A: Chem.* **2001**, *176*, 105–116; d) L. Caron, C. Christine, S. Tilloy, E. Monflier, D. Landy, S. Fourmentin, G. Surpateanu, *Supramol. Chem.* **2002**, *14*, 11–20; e) M. Canipelle, L. Caron, C. Caline, S. Tilloy, E. Monflier, *Carbohydr. Res.* **2002**, *337*, 281–287; f) M. Canipelle, S. Tilloy, A. Ponchel, H. Bricout, E. Monflier, *J. Inclusion Phenom. Macrocyclic Chem. J. Inclusion Phenom.* **2005**, *51*, 79–85.

[5] L. Caron, M. Canipelle, S. Tilloy, H. Bricout, E. Monflier, *Eur. J. Inorg. Chem.* **2003**, 595–599.

[6] L. W. Francisco, D. A. Moreno, J. D. Atwood, *Organometallics* **2001**, *20*, 4237–4245.

[7] a) J. F. Stoddart, R. Zarzycki, *Recl. Trav. Chim. Pays-Bas* **1988**, *107*, 515–528; b) E. Fenyvesi, L. Szente, N. Russell, M. McNamara, Specific Guest Types, in *Cyclodextrins* (Eds.: J. L. Atwood, J. E. D Davies, D. D. MacNicol, F. Vögtle), Comprehensive Supramolecular Chemistry. Vol. 3, Pergamon: Oxford, **1996**, pp 305–366; c) H. M. Colquhoun, J. F. Stoddart, D. J. Williams, *Angew. Chem. Int. Ed. Engl.* **1986**, *25*, 487–507; d) T. Joh, A. Harada, S. Takahashi, *Mem. Inst. Sci. Ind. Res., Osaka Univ.* **1989**, *46*, 37–50e) F. Hapiot, S. Tilloy, E. Monflier, *Chem. Rev.* **2006**, in press, DOI: 10.1021/cr050576c.

[8] a) D. R. Alston, A. M. Z. Slawin, J. F. Stoddart, D. J. Williams, *Angew. Chem. Int. Ed. Engl.* **1989**, *27*, 1184–1185; b) D. Hesek, G. A. Hembury, M. G. B. Drew, V. V. Borovkov, Y. Inoue, *J. Am. Chem. Soc.* **2001**, *123*, 12232–12237; c) L. Caron, H. Bricout, S. Tilloy, D. Landy, S. Fourmentin, E. Monflier, *Adv. Synth. Catal.* **2004**, *346*, 1449–1456; d) A. Harada, *Preparation, Properties and Stereochemical Aspects of Inclusion Compounds of Organometallic Complexes with Cyclodextrins*, in *Chain, Clusters, Inclusion Compounds, Paramagnetic Labels and Organic Rings* (Ed.: P. Zanello), Stereochemistry of organometallic and inorganic compounds, vol 5; Elsevier: Amsterdam, **1994**, pp. 411–455.

[9] a) W. A. Herrmann, J. Kellner, H. Riepl, *J. Organomet. Chem.* **1990**, *389*, 103–128; b) F. Monteil, P. Kalck, *J. Organomet. Chem.* **1994**, *482*, 45–51; c) E. G. Kuntz, O. M. Vittori, *J. Mol. Catal. A: Chem.* **1998**, *129*, 159–171.

[10] L. Caron, M. Canipelle, S. Tilloy, H. Bricout, E. Monflier, *Tetrahedron Lett.* **2001**, *42*, 8837–8840.


Received: October 19, 2005
Published Online: February 21, 2006

 © 2006 Wiley-VCH Verlag GmbH & Co. KGaA, Weinheim 

DOI: 10.1002/ejic.200500939

# Synthesis, Crystal Structures, and Photophysical Properties of Two Novel Lead(II)–SIP Coordination Polymers ($NaH_2SIP$ = 5-Sulfoisophthalic Acid Monosodium Salt) Containing Tetranuclear Lead(II) Units

**Qing-Yan Liu[a,b] and Li Xu*[a]**

**Keywords:** Tetranuclear lead / Hydrothermal synthesis / Crystal structures / Photophysical properties

Two new $Pb^{II}$–SIP coordination polymers, $\{[Pb_4(OH)_2(SIP)_2(H_2O)](H_2O)_5\}_n$ (**1**) and $[Pb_3(SIP)_2(H_2O)_5]_n$ (**2**), have been synthesized by hydrothermal reactions of $Pb(OH)_2$ or $Pb(NO_3)_2$ and 5-sulfoisophthalic acid monosodium salt ($NaH_2SIP$) at 160 °C, respectively. Single-crystal X-ray diffraction reveals that compound **1** has a 2D brick-wall-like architecture constructed from 1D tapes containing the basketlike tetranuclear $[Pb_4(\mu_3\text{-}OH)_2(COO)_2]$. Compound **2** has a 2D-layered structure, which is constructed from a 1D-ladder structure composed of the cyclic $[Pb_4(SIP)_2(COO)_2]$ grid with the four Pb atoms nearly coplanar. In the solid state, compound **1** exhibits blue photoluminescence with the maximum emission intensity at 436 nm upon excitation at 335 nm. Compound **2** shows phosphorescence with the maximum emission intensity at 603 nm upon excitation at 426 nm. Both compounds have also been characterized by elemental analysis, IR spectra, TG analysis, and powder X-ray diffraction.

(© Wiley-VCH Verlag GmbH & Co. KGaA, 69451 Weinheim, Germany, 2006)

## Introduction

The design and construction of coordination polymers is one of the most active areas of materials research. The intense interest in these materials is driven by both their interesting network topologies and potential applications such as catalysis, molecular magnets, sensors, ion exchange, adsorption, and phase separation.[1–4] Many of the efforts have so far been devoted to the study of transition-metal-based coordination polymers.[5–7] However, relatively little attention has been paid to the coordination polymers of main group metal ions despite their important applications in electroluminescent devices or organic light-emitting diode (OLED) technology.[8–11] $Pb^{2+}$ is employed in the present work for several reasons: (1) it has a $6s^2$ outer electron configuration and large radius, which can lead to interesting topological arrangements;[12–14] (2) the absence of crystal field stabilization energy effects allows the $Pb^{2+}$ ion to adopt varied coordination geometries including octahedra, tetrahedra, or square planes amongst others, which give rise to novel coordination networks;[15–17] and (3) it has interesting photochemical and photophysical properties.[18–21] On the other hand, the SIP ligand, with three functional groups, exhibits multiple coordinating modes facilitating the formation of multi-dimensional structures and diversified topologies.[22–24] Recently, we have reported a series of lanthanide–SIP coordination polymers wherein SIP proves to be a sensitive probe in examining the role of the lanthanide contraction effect in crystal structure formation.[25] In this contribution, SIP will serve as a probe to examine the coordination polymer chemistry of $Pb^{2+}$, and the two novel polymeric materials with $Pb_4$ secondary building blocks, $\{[Pb_4(OH)_2(SIP)_2(H_2O)](H_2O)_5\}_n$ (**1**) and $[Pb_3(SIP)_2(H_2O)_5]_n$ (**2**), will be described with regard to syntheses, crystal structures, TG analysis, powder X-ray diffraction, IR spectra, and photoluminescent properties. An unprecedented coordinating mode of SIP (Scheme 1, b) is observed in polymer **1**.

## Results and Discussion

### Preparation of the Complexes

Hydrothermal synthesis is widely employed to produce new structures, but is still a kind of "black box". This method can minimize the problems associated with ligand solubility and enhance the reactivity of reactants in favor of efficient molecular building during the crystallization process. The two $Pb^{II}$–SIP polymers, $\{[Pb_4(OH)_2(SIP)_2(H_2O)](H_2O)_5\}_n$ (**1**) and $[Pb_3(SIP)_2(H_2O)_5]_n$ (**2**), are obtained from hydrothermal reactions of the lead(II) salts and $NaH_2SIP$ in aqueous solution. The preparative reactions

[a] State Key Laboratory of Structural Chemistry, Fujian Institute of Research on the Structure of Matter, Chinese Academy of Sciences,
Fuzhou, Fujian, 350002, P. R. China
Fax: +86-591-83705045
E-mail: xli@fjirsm.ac.cn
[b] Graduate School of the Chinese Academy of Sciences,
Beijing 100039, P. R. China
Fax: +86-591-83705045
E-mail: qyliu@fjirsm.ac.cn

Supporting information for this article is available on the WWW under http://www.eurjic.org or from the author.

 © 2006 Wiley-VCH Verlag GmbH & Co. KGaA, Weinheim 

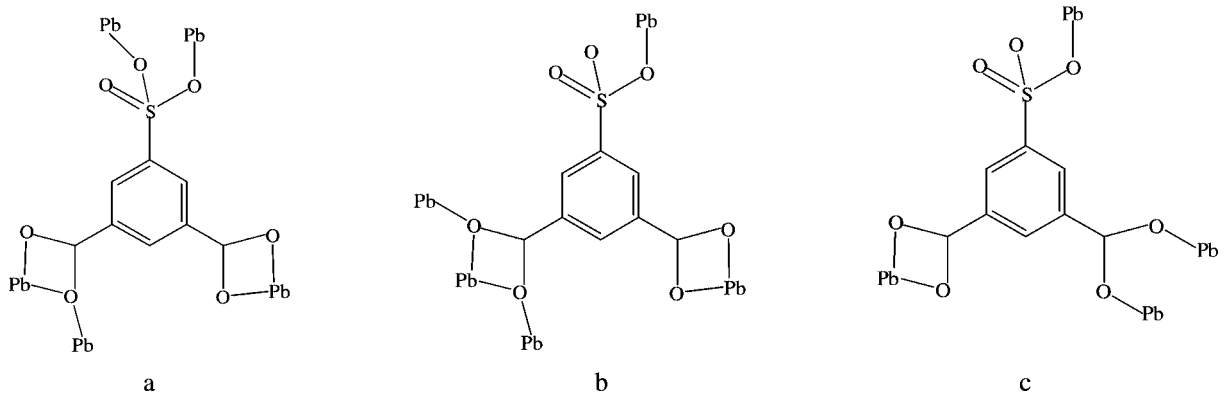


Scheme 1. Coordination modes of SIP observed in compound **1** and **2**.

were carried out under different temperatures (140, 160, and 180 °C) to examine the temperature-dependence of their solid structures. X-ray diffraction analyses of the reaction products indicate that the same results were obtained under these reaction temperatures although the purity and yields are slightly different, indicative of the thermodynamic nature of the hydrothermal reactions. Compounds **1** and **2** cannot be obtained from the reaction of the corresponding lead(II) salts and $NaH_2SIP$ in aqueous solution at room temperature (in contrast to hydrothermal conditions), indicating the kinetic nature of this conventional method. The dramatic difference in reaction products between conventional and hydrothermal reactions is attributable to their different reaction mechanisms that are shifted from a kinetic domain for conventional solution reactions to a thermodynamic domain for hydrothermal reactions.[26–28]

### Crystal Structure of $\{[Pb_4(OH)_2(SIP)_2(H_2O)](H_2O)_5\}_n$ (1)

Compound **1** features a two-dimensional brick-wall-like architecture constructed from unusual tetranuclear lead(II) motifs as a secondary building block. As depicted in Figure 1 (a), the asymmetric unit of **1** contains four crystallographically independent lead(II) ions. Pb(1) is surrounded by six oxygen atoms, of which four are from three surrounding SIP ligands, one is from a water molecule, and one is from a $\mu_3$-hydroxy group. The coordination geometry of Pb(1) can be described as a distorted pentagonal bipyramid with the seventh coordination site occupied by its lone pair of electrons. The atoms O(17) and O(6B) (B: $-x + 1$, $y + 1/2$, $-z + 2/3$) occupy the axial positions (Figure 1, a). The Pb(1)–O distances range from 2.469(8) to 2.714(8) Å, comparable to those observed in the related lead(II) compounds.[7–9] The Pb(3) atom has a similar coordination geometry to that of Pb(1) with the two apical positions occupied by the carboxylate and hydroxy oxygen atoms [O(2E) (E: $-x + 1$, $y - 1/2$, $-z + 3/2$) and O(16)], and they both have similar Pb–O distances [Pb–O = 2.425(8)–2.752(8) Å]. Pb(2) has a distorted [:PbO4] tetragonal-pyramid geometry with the four basal positions occupied by a chelating carboxylate group and two $\mu_3$-hydroxy groups and the apical position occupied by the lone pair of electrons. The Pb(2)–O distances [2.328(8)–2.612(9) Å] are slightly shorter than those around the six-coordinate Pb(1) center. The Pb(4) atom has a similar coordination geometry to that of Pb(2) as illustrated in Figure 1 (a). As shown in Figure 1 (b), the four $Pb^{2+}$ ions are capped by two $\mu_3$-hydroxy groups generating a butterfly $[Pb_4(\mu_3\text{-}OH)_2]$ cluster. The Pb(1)Pb(2) Pb(3) and Pb(1)Pb(4)Pb(3) triangles are each capped by an additional carboxylate group to form a basketlike structure with a weak Pb(1)–O(4) (3.18 Å) interaction. The basal plane [Pb(2), Pb(4), O(15), and O(16)] of the basket is almost planar with the Pb(4)–O(15)–Pb(2) and Pb(4)–O(16)–Pb(2) angles of 104.6(3) and 103.1(3)°, respectively (Table 1). The Pb(2)···Pb(4) separation of about 3.8 Å is longer than the sum of the van der Waals radii (3.20 Å).[29] The dihedral angles between the side faces and the basal plane are 67.8(2), 97.2(1), 112.8(2), 106.1(1), 88.2(1), and 64.8(3)°, respectively. Interestingly, the basketlike structure of the tetranuclear cluster $[Pb_4(\mu_3\text{-}OH)_2(COO)_2]$ core resembles many cubanelike structures that are commonly found in many other compounds. However, in the current compound the carboxylate groups make the cluster more open instead of the bridging oxygen atoms.[30–31] Several complexes containing $[Pb_4(\mu_3\text{-}OH)_2]$ have been documented, but the $[Pb_4(\mu_3\text{-}OH)_2]$ cluster has a chair structure with the two Pb atoms above and below the $[Pb_2(\mu_3\text{-}OH)_2]$ plane.[32–34] Therefore, this is a rare example concerning lead(II) complexes.

As shown in Figure 1 (a), the two independent SIP ligands exhibit different coordinating modes. SIP(a) acts as a pentadentate ligand (Scheme 1, a) with the bidentate sulfonate group, one chelating carboxylate group, and one $\mu_2$-$\eta^2$:$\eta^1$ carboxylate group (one oxygen atom bridges two metal atoms, the other connects one metal atom, and the carboxylate group coordinates to two metal atoms). The unprecedented coordinating mode of SIP(b) is depicted in Scheme 1 (b) wherein one carboxylate group chelates to one $Pb^{2+}$ ion and the other displays an unusual $\mu_3$-$\eta^2$:$\eta^2$ coordinating mode (each oxygen atom coordinates to two metal atoms and the carboxylate group coordinates to three metal atoms). To the best of our knowledge, this type of coordinating mode of the SIP ligand is not observed in the previously reported SIP complexes. Unlike that of SIP(a), the sulfonate group of the SIP(b) ligand is unidentate.

 © 2006 Wiley-VCH Verlag GmbH & Co. KGaA, Weinheim 

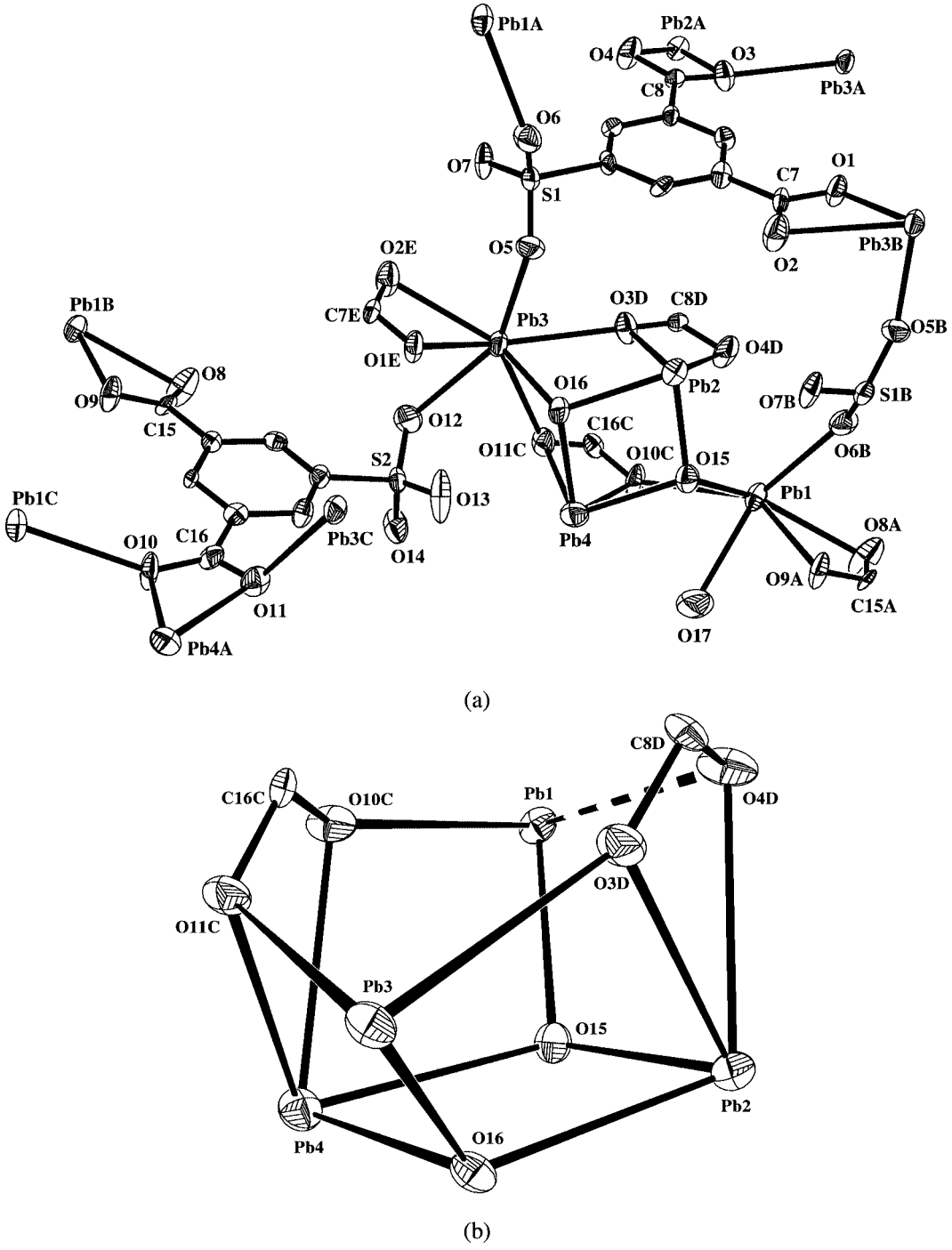


Figure 1. (a) Molecular structure of compound **1**. (b) The basketlike tetranuclear $[Pb_4(\mu_3\text{-}OH)_2(COO)_2]$ cluster as a secondary building block.

The $[Pb_4(\mu_3\text{-}OH)_2(COO)_2]$ secondary building blocks are interconnected into a one-dimensional tape structure propagating along the crystallographic *b* axis (Figure 2) by the SIP ligand through the chelating carboxylate and sulfonate groups. Two types of 16-membered rings are observed in the 1D tape; ring A is composed of two SIP ligands and two Pb atoms and ring B consists of one $[Pb_4(\mu_3\text{-}OH)_2(COO)_2]$, one Pb atom, one SIP ligand, and one sulfonate group. Such cyclic structures are characteristic of the SIP coordination polymers.[25] The separation between the two neighboring $Pb_4$ units, linked by ring A, is 15.3 Å, comparable to the length of the *b* axis. As described above, the two independent SIP ligands use four of their six functional groups to form a 1D tape. The remaining two carboxylate groups link the 1D tapes along the *c* axis into a 2D brick-wall-like layered structure where the cavities have an approximate dimension of 12.8×6.5 Å, as depicted in Figure 3. The layers are parallel and do not slip in the crystal

 © 2006 Wiley-VCH Verlag GmbH & Co. KGaA, Weinheim 

Table 1. Selected bond lengths [Å] and bond angles [°] of **1**.

| | | | |
|---|---|---|---|
| Pb(1)–O(8A) | 2.676(9) | Pb(1)–O(9A) | 2.482(8) |
| Pb(1)–O(10C) | 2.714(8) | Pb(1)–O(15) | 2.469(8) |
| Pb(1)–O(17) | 2.623(11) | Pb(1)–O(6B) | 2.574(8) |
| Pb(2)–O(3D) | 2.525(8) | Pb(2)–O(4D) | 2.612(9) |
| Pb(2)–O(15) | 2.328(8) | Pb(2)–O(16) | 2.500(8) |
| Pb(3)–O(1E) | 2.440(8) | Pb(3)–O(2E) | 2.715(9) |
| Pb(3)–O(3) | 2.752(8) | Pb(3)–O(5) | 2.579(8) |
| Pb(3)–O(11C) | 2.687(8) | Pb(3)–O(12) | 2.730(10) |
| Pb(3)–O(16) | 2.425(8) | Pb(4)–O(10C) | 2.567(8) |
| Pb(4)–O(11C) | 2.490(8) | Pb(4)–O(15) | 2.513(8) |
| Pb(4)–O(16) | 2.393(8) | | |
| O(15)–Pb(1)–O(9A) | 83.5(3) | O(15)–Pb(1)–O(6B) | 91.2(3) |
| O(15)–Pb(1)–O(10C) | 67.8(3) | O(15)–Pb(1)–O(17) | 81.6(4) |
| O(8A)–Pb(1)–O(9A) | 50.1(3) | O(8A)–Pb(1)–O(10C) | 149.2(3) |
| O(17)–Pb(1)–O(9A) | 74.8(4) | O(17)–Pb(1)–O(8A) | 90.8(4) |
| O(17)–Pb(1)–O(10C) | 67.9(3) | O(9A)–Pb(1)–O(6B) | 77.4(3) |
| O(8A)–Pb(1)–O(6B) | 74.3(3) | O(10C)–Pb(1)–O(6B) | 134.0(3) |
| O(17)–Pb(1)–O(6B) | 151.9(4) | O(3D)–Pb(2)–O(4D) | 50.1(3) |
| O(3D)–Pb(2)–O(16) | 69.1(3) | O(15)–Pb(2)–O(16) | 76.7(3) |
| O(15)–Pb(2)–O(4D) | 80.1(3) | O(4D)–Pb(2)–O(16) | 110.1(3) |
| O(3D)–Pb(2)–O(15) | 97.4(3) | O(1E)–Pb(3)–O(2E) | 50.1(3) |
| O(3D)–Pb(3)–O(2E) | 142.7(3) | O(1E)–Pb(3)–O(12) | 74.8(3) |
| O(2E)–Pb(3)–O(12) | 73.2(3) | O(16)–Pb(3)–O(1E) | 84.1(3) |
| O(11C)–Pb(3)–O(12) | 67.1(3) | O(16)–Pb(3)–O(3D) | 66.5(2) |
| O(3D)–Pb(3)–O(11C) | 72.6(3) | O(16)–Pb(3)–O(11C) | 70.6(3) |
| O(5)–Pb(3)–O(2E) | 78.2(3) | O(5)–Pb(3)–O(1E) | 77.5(3) |
| O(5)–Pb(3)–O(16) | 85.7(3) | O(5)–Pb(3)–O(3D) | 72.1(3) |
| O(11C)–Pb(4)–O(16) | 74.6(3) | O(15)–Pb(4)–O(16) | 75.3(3) |
| O(11C)–Pb(4)–O(15) | 104.5(3) | O(16)–Pb(4)–O(10C) | 100.4(3) |
| O(11C)–Pb(4)–O(10C) | 51.0(2) | O(10C)–Pb(4)–O(15) | 69.5(3) |
| Pb(1)–O(15)–Pb(2) | 119.5(3) | Pb(4)–O(15)–Pb(2) | 104.6(3) |
| Pb(1)–O(15)–Pb(4) | 110.3(3) | Pb(4)–O(16)–Pb(3) | 110.6(3) |
| Pb(4)–O(16)–Pb(2) | 103.1(3) | Pb(3)–O(16)–Pb(2) | 114.6(3) |

Symmetry transformation for equivalent atoms: A: $x$, $y + 1$, $z$; B; $-x + 1$, $y + 1/2$, $-z + 3/2$; C: $x$, $y - 1$, $z$; D: $-x + 1$, $-y$, $-z + 1$; E: $-x + 1$, $y - 1/2$, $-z + 3/2$

packing. So, the intralayer pores form a channel along the *a* axis. The lattice water molecules occupying the voids of the 2D layered structure serve as receptors or donors of the extensive O–H···O hydrogen bonds with O···O distances of 2.701(1)–3.096(3) Å. The layers are further held together by π-stacking interactions between the parallel neighboring phenyl rings with a face-to-face distance of 3.337(3) Å, and the neighboring phenyl rings have a dihedral angle of 8.2(1)° with a centroid–centroid distance of 3.728(4) Å. Similar π–π stacking interactions have also been reported in a number of cadmium– and copper–SIP complexes.[35,36]

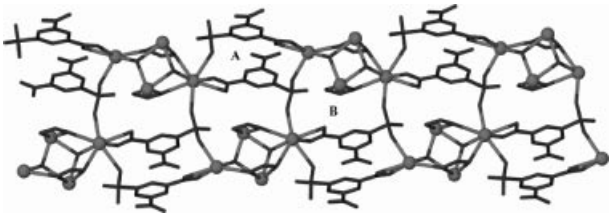


Figure 2. View of the tetranuclear $[Pb_4(\mu_3\text{-}OH)_2(COO)_2]$ bridged by SIP to form a one-dimensional tape structure propagating along the *b* axis (Pb atoms are represented as balls).

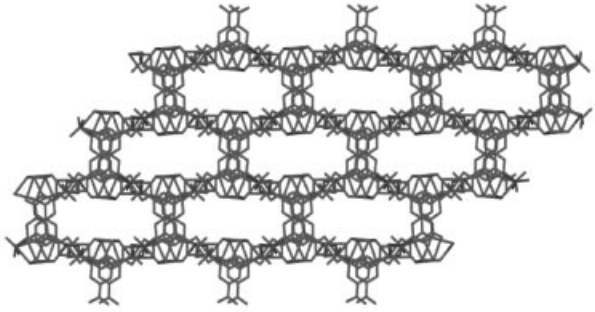

Figure 3. View of the two-dimensional brick-wall-like architecture of **1** along the *bc* plane.

### Crystal Structure of $[Pb_3(SIP)_2(H_2O)_5]_n$ (2)

Compound **2** has a 2D-layered structure with the tetranuclear $[Pb_4(SIP)_2(H_2O)_6]$ unit. As shown in Figure 4, the asymmetric unit of **2** consists of three $Pb^{2+}$ ions, two SIP ligands, and five coordinating water molecules. The Pb(1) atom coordinates to three carboxylate oxygen atoms from two SIP ligands and two water molecules, with Pb(1)–O distances of 2.460(15)–2.680(14) Å. The coordination geometry of Pb(1) can be described as a distorted pentagonal

 © 2006 Wiley-VCH Verlag GmbH & Co. KGaA, Weinheim 

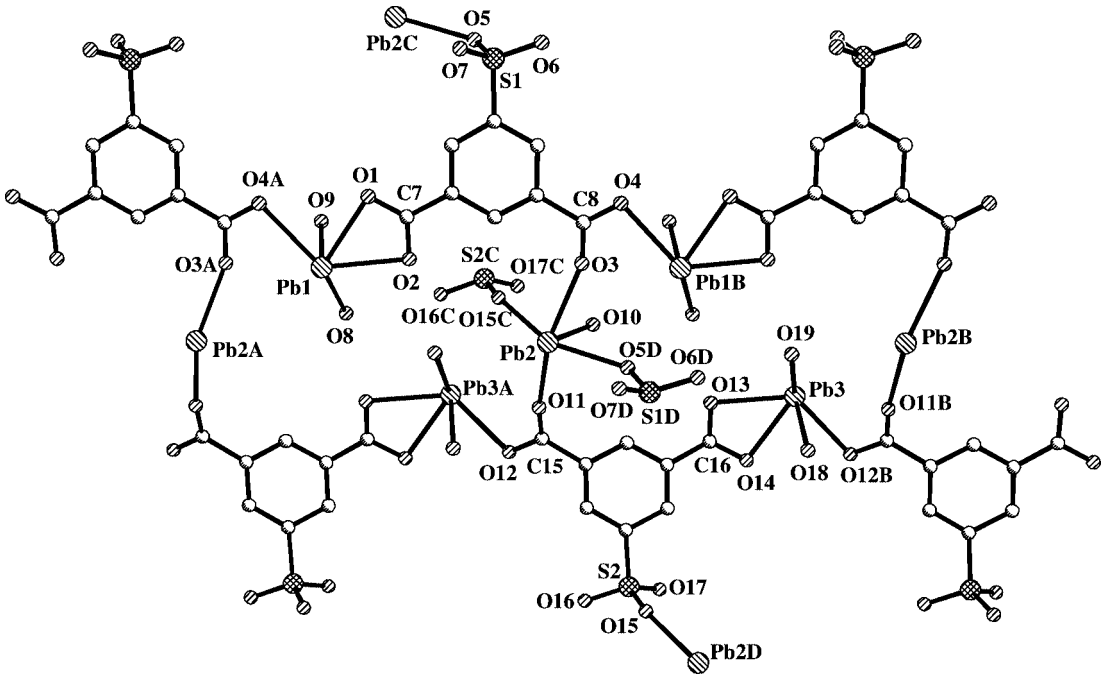


Figure 4. Crystal structure of compound **2**.

pyramid with the lone pair of electrons completing the pentagonal plane and the water molecule [O(9)] lying at the apical position. Pb(3) is crystallographically independent but geometrically similar to Pb(1) with the apical position occupied by the O(18) atom of the water molecule. The Pb(3)–O distances of 2.437(13)–2.715(15) Å are similar to those around Pb(1). Pb(2) has a distorted [:PbO5] octahedral coordination geometry with equatorial positions occupied by two carboxylate and two sulfonate oxygen atoms, and the apical positions taken up by one water molecule and the lone pair of electrons. The Pb(2)–O distances [2.26(2)–2.562(13) Å] are within the normal experimental limitation (Table 3)[12,13] but slightly shorter than those around the seven-coordinate Pb(1) and Pb(3) atoms. The two independent SIP ligands have similar coordinating modes as illustrated in Scheme 1 (c).

As illustrated in Figure 5, the $Pb^{2+}$ ions are interconnected by the SIP ligands into a 1D-ladder structure featuring the cyclic $[Pb_4(SIP)_2(COO)_2]$ with an approximate dimension of $10.2 \times 5.8$ Å$^2$. The four Pb ions [Pb(1), Pb(2), Pb(3A), and Pb(2A), A: $x$, $y + 1$, $z$] are nearly coplanar with a maximum deviation of 0.377(1) Å for [Pb(1)] and a mean deviation of 0.344(1) Å. This type of coplanar $Pb_4$ unit is, to the best our knowledge, uncommon. The 1D ladder can also conveniently be regarded as resulting from two 1D $[Pb(SIP)(H_2O)_2]_n$ single chains bridged by Pb(2) (Figure 5). As mentioned above, the SIP ligands use the carboxylate groups to form the 1D ladder. The remaining sulfonate groups further link the 1D ladders into a 2D layer through Pb(2)–sulfonate bonding [Pb(2)–O(5D), 2.452(15); Pb(2)–O(15C), 2.511(14) Å; C: $x$, $y - 1$, $z$, D: $x$, $y + 1$, $z$] (see Figure 6). The stacking of the 1D ladders is clearly affected by π interactions between the SIP ligands. The phenyl rings between the ladders are almost parallel and closely stacked [the dihedral angle is 1.5(1)° and the centroid–centroid distance is 3.559(1) Å]. The coordinating water molecules fill the cavities of the neighboring ladders preventing interpenetration.

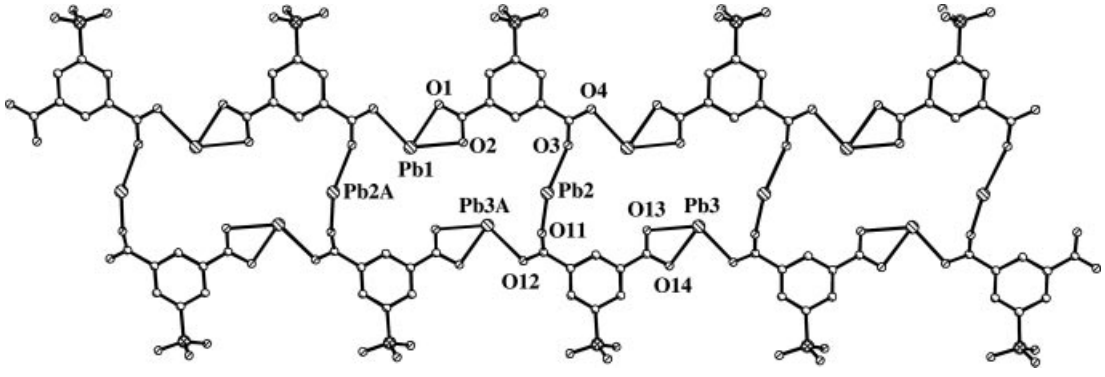


Figure 5. View of the 1D ladder of compound **2** along the *a* axis (water molecules are omitted for clarity).

 © 2006 Wiley-VCH Verlag GmbH & Co. KGaA, Weinheim 

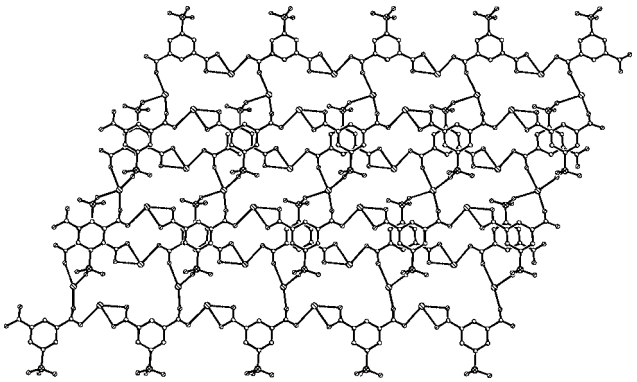

Figure 6. View of the 2D layered structure of **2** in the *ab* plane (water molecules are omitted for clarity).

### FT-IR Spectra, Thermogravimetric Analyses, and Powder X-ray Diffraction

The FT-IR spectra of **1** and **2** exhibit broad absorptions centered at 3390 and 3410 $cm^{-1}$ for **1** and **2**, respectively, occurring because of the existence of water molecules in the structures. The IR spectrum of **1** shows the typical asymmetric (1597 $cm^{-1}$) and symmetric (1542 and 1431 $cm^{-1}$) stretching bands of carboxylate groups. The respective values of [$\nu_{as}(CO_2) - \nu_s(CO_2)$] clearly indicate the presence of chelating (55 $cm^{-1}$) and bridging (166 $cm^{-1}$) coordination modes of the carboxylate groups in **1**.[37] The strong bands at 1598 $cm^{-1}$, and 1522 and 1434 $cm^{-1}$, respectively, correspond to the asymmetric and symmetric stretching bands of the carboxylate groups in the IR spectrum of **2**. Similar to those in **1**, the values of [$\nu_{as}(CO_2) - \nu_s(CO_2)$] are 76 $cm^{-1}$ and 164 $cm^{-1}$ in **2**, which supports the presence of chelating and bridging coordination modes of the carboxylate groups. The absorptions in the region 1000–1200 $cm^{-1}$ for the two complexes are typical of the sulfonate group. The strong absorption bands at 621 and 623 $cm^{-1}$ for **1** and **2**, respectively, are because of the $\nu_{S-O}$ stretching.

To examine the thermal stability of the two compounds and their structural variation as a function of the temperature, thermogravimetric analyses (TGA) were performed on single-phase polycrystalline samples of these materials (see Figure S1 in the Supporting Information). Results from the TGA measurements of **1** exhibit two distinct weight loss steps. The first weight loss occurs between 60 and 290 °C because of the release of all water molecules (weight loss: measured 7.2%, theoretical 7.4%). The need for such an unusually high temperature for the removal of the water molecules is because of the hydrogen bonding with the carboxylate or sulfonate oxygen atoms. The second weight loss in the temperature range 410–800 °C corresponds to the decomposition of the SIP ligand. The thermogravimetric analysis of **2** shows that the initial weight loss occurs in the temperature range 110–240 °C, attributable to the release of all coordinating water molecules (observed, 7.3%, calculated 7.5%). Increasing the temperature led to the decomposition of the SIP ligand at 420 °C.

The X-ray powder diffraction patterns (XRPD) of both compounds are illustrated in Figure S2 and S3. The different structures of compounds **1** and **2** have also been indicated by their different XRPD patterns. Their XRPD patterns are in good agreement with those simulated from single crystal structural data, thus both compounds **1** and **2** were obtained as a single phase.

### Photoluminescent Properties

Photoluminescent properties of $s^2$-metal complexes are not well studied as compared with those of $d^{10}$-metal complexes, although there are reports on the photoluminescent properties of lead-containing materials.[38–41] The photoluminescence properties of **1** and **2**, as well as the free ligand, were examined in the solid state at room temperature. The free $Na_2HSIP$ displays photoluminescent emission at 320 nm under 286 nm radiation.[42] Compound **1** exhibits intense photoluminescent emission with a maximum at 436 nm upon excitation at 335 nm (Figure 7). In the case of **2**, photoluminescence with a maximum emission at 603 nm upon excitation at 426 nm is observed. The emission wavelength of **1** (436 nm) is much longer than that of the free SIP ligand (320 nm) and similar to those of the reported $s^2$-metal cluster complexes.[43–46] Therefore, this emission can be assigned to the lead(II) cluster complex. A remarkable bathochromic shift is also observed in compound **2**. As seen from Figure 7, the emission of **2** occurs at a much lower energy of 603 nm with a large Stokes shift. The low-energy emissions associated with large Stokes shifts have been commonly observed for other $s^2$-metal complexes, which can be assigned to a metal-centered transition involving the s and p metal orbital as proposed by Vogler.[39,43,47] With these concerns in mind, the emission band at 603 nm of **2** can be assigned to a metal-centered s → p transition. The large Stokes shift is caused by the elimination of the ground-state distortion in the excited state.[39] The further lifetime measurements at room temperature of each emission maximum give the results of 2.43 ns for **1** and 3.47 μs for **2**. The long emission lifetime of **2** can be assigned to phosphorescence, which is consistent with the general idea that the appearance of a room-temperature phosphorescence requires the presence of a heavy metal ion, which re-

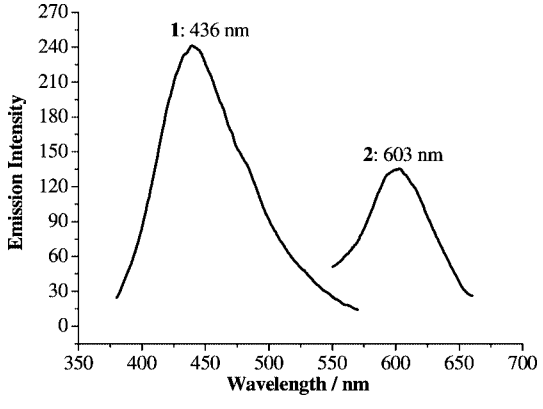


Figure 7. The solid-state emission photoluminescent spectra of **1** ($\lambda_{ex}$ = 335 nm) and **2** ($\lambda_{ex}$ = 426 nm) at room temperature.

 © 2006 Wiley-VCH Verlag GmbH & Co. KGaA, Weinheim 

duces the radiative lifetime of triplets by increased spin-orbit coupling.[21] As described above, we can conclude that the different emission spectra of **1** and **2** can be significantly influenced by their crystal structures.

## Conclusion

In conclusion, the self-assembly of the lead(II) ions with SIP affords two novel $Pb^{II}$–SIP coordination polymers **1** and **2** containing tetranuclear lead(II) motifs. Because of the diversity of the SIP ligand in bridging metal ions, the metal–SIP complexes are expected to show various novel, interesting structures and desired properties. In the present case, compounds **1** and **2**, obtained with the same SIP ligand and under almost the same synthetic procedures, are distinct from each other, with regard to composition, topology, and photoluminescent properties. Compound **1** displays a 2D brick-wall-like structure featuring a unique basketlike tetranuclear $[Pb_4(\mu_3\text{-}OH)_2(COO)_2]$ motif. Compound **2** has a 2D layered structure containing 1D ladders characteristic of the cyclic $[Pb_4(SIP)_2(COO)_2]$ unit. Therefore, the multiple coordinating modes of the SIP ligand, together with the varied coordination geometry of $Pb^{2+}$, exhibit diverse structural topologies of the $Pb^{II}$–SIP system. In addition, the lone pair of electrons usually leads to the asymmetric coordination geometry of $Pb^{II}$, which probably disfavors the formation of high-dimensional structures. So, lead(II) materials usually have low-dimensional structures. Compound **1** displays fluorescent emission and **2** shows phosphorescence emission at room temperature, indicating structure-dependent photoluminescent properties of the Pb–SIP coordination polymers, and revealing potential for application in OLED technology.

## Experimental Section

**General Remarks:** 5-Sulfoisophthalic acid monosodium salt (Alfa) was purchased commercially and used without further purication. Elemental analyses were carried out with an Elementar Vario EL III analyzer and IR spectra (KBr pellets) were recorded with a PerkinElmer Spectrum One. Fluorescent spectra were measured at room temperature with an Edinburgh FL-FS90 TCSPC system. The thermogravimetric measurements were performed with a Netzsch STA449C apparatus under a nitrogen atmosphere with a heating rate of 10 °C/min from 25 to 800 °C. X-ray powder diffraction patterns were performed with a RIGAKU DMAX2500PC diffractometer using Cu-$K_\alpha$ radiation. All complexes were synthesized by the hydrothermal method under autogenous pressure.

**Synthsis of $\{[Pb_4(OH)_2(SIP)_2(H_2O)](H_2O)_5\}_n$ (1):** A mixture of $Pb(OH)_2$ (0.048 g, 0.2 mmol) and 5-sulfoisophthalic acid monosodium salt (0.027 g, 0.1 mmol) in a 2:1 molar ratio in $H_2O$ (18 mL) was introduced into a Parr Teon-lined stainless steel vessel (30 mL). The vessel was sealed and heated to 160 °C. This temperature was kept for 5 d and then the mixture was cooled at a rate of 5 °C/h to form colorless crystals of **1**. A pale yellow crystalline product was filtered, washed with distilled water, and dried at ambient temperature (yield: 0.47 g, 64% on the basis of Pb). $C_{16}H_{20}O_{22}S_2Pb_4$ (1457.20): calcd. C 13.18, H 1.37; found C 13.11, H 1.33. IR (KBr): $\tilde{\nu}$ = 3390 (s), 1597 (vs), 1542 (vs), 1431(s), 1355 (vs), 1197 (s), 1149 (s), 1107 (s), 1036 (s), 925 (w), 872 (w), 771 (m), 719(s), 677 (w), 621 (s), 447 (m) $cm^{-1}$.

**Synthsis of $[Pb_3(SIP)_2(H_2O)_5]_n$ (2):** A mixture of $Pb(NO_3)_2$ (0.033 g, 0.1 mmol), 5-sulfoisophthalic acid monosodium salt (0.041 g, 0.15 mmol), and triethyl amine (0.1 mL) in a 2:3:6 molar ratio in $H_2O$ (18 mL) was introduced into a Parr Teon-lined stainless steel vessel (30 mL). The vessel was sealed and heated to 160 °C. This temperature was kept for 5 d and then the mixture was cooled at a rate of 5 °C/h to form colorless crystals of **1**. A pale yellow crystalline product was filtered, washed with distilled water, and dried at ambient temperature (yield: 0.40 g, 56% on the basis of Pb). $C_{16}H_{16}O_{19}S_2Pb_3$ (1197.98): calcd. C 16.04, H 1.35; found C 16.01, H 1.34. IR (KBr): $\tilde{\nu}$ = 3410 (s), 1598 (vs), 1522 (vs),

Table 2. Selected bond lengths [Å] and bond angles [°] of **2**.

| | | | |
|---|---|---|---|
| Pb(1)–O(1) | 2.468(14) | Pb(1)–O(2) | 2.501(14) |
| Pb(1)–O(8) | 2.680(14) | Pb(1)–O(9) | 2.460(15) |
| Pb(1)–O(4A) | 2.558(13) | Pb(2)–O(3) | 2.562(13) |
| Pb(2)–O(10) | 2.26(2) | Pb(2)–O(11) | 2.521(13) |
| Pb(2)–O(5D) | 2.452(15) | Pb(2)–O(15C) | 2.511(14) |
| Pb(3)–O(14) | 2.437(13) | Pb(3)–O(13) | 2.524(15) |
| Pb(3)–O(18) | 2.469(15) | Pb(3)–O(19) | 2.715(15) |
| Pb(2)–O(12B) | 2.553(14) | | |
| O(1)–Pb(1)–O(2) | 52.2(4) | O(2)–Pb(1)–O(8) | 78.7(5) |
| O(1)–Pb(1)–O(4A) | 75.5(4) | O(4A)–Pb(1)–O(8) | 132.0(5) |
| O(9)–Pb(1)–O(1) | 74.7(5) | O(2)–Pb(1)–O(9) | 88.3(5) |
| O(9)–Pb(1)–O(8) | 66.6(5) | O(9)–Pb(1)–O(4A) | 74.3(5) |
| O(10)–Pb(2)–O(5D) | 73.0(5) | O(10)–Pb(2)–O(15C) | 74.7(5) |
| O(15C)–Pb(2)–O(5D) | 147.0(5) | O(3)–Pb(2)–O(11) | 154.3(5) |
| O(3)–Pb(2)–O(10) | 78.8(5) | O(3)–Pb(2)–O(5D) | 81.0(4) |
| O(3)–Pb(2)–O(15C) | 86.5(5) | O(10)–Pb(2)–O(11) | 75.4(6) |
| O(11)–Pb(2)–O(5D) | 90.9(5) | O(11)–Pb(2)–O(15C) | 87.2(5) |
| O(13)–Pb(3)–O(14) | 53.0(5) | O(13)–Pb(3)–O(19) | 79.8(5) |
| O(19)–Pb(3)–O(12B) | 129.4(5) | O(14)–Pb(3)–O(12B) | 77.4(5) |
| O(18)–Pb(3)–O(14) | 74.0(5) | O(13)–Pb(3)–O(18) | 86.8(5) |
| O(18)–Pb(3)–O(19) | 66.7(5) | O(18)–Pb(3)–O(12B) | 74.8(5) |

Symmetry transformation for equivalent atoms: A: $x-1, y, z$; B: $x+1, y, z$; C: $x, y-1, z$; D: $x, y+1, z$

 © 2006 Wiley-VCH Verlag GmbH & Co. KGaA, Weinheim 

1434 (vs), 1361 (vs), 1219 (s), 1197 (s), 1142 (s), 1107 (s), 1029 (s), 994 (w), 925 (m), 767 (s), 719 (s), 677 (w), 623 (s), 575 (w), 511 (w), 440 (m) $cm^{-1}$.

**X-ray Crystallographic Study:** X-ray diffraction data of compound **1** and **2** were collected with a Rigaku Mercury CCD diffractometer equipped with a graphite-monochromated Mo-$K_\alpha$ radiation ($\lambda$ = 0.71073 Å). The CrystalClear software was used for data reduction and empirical absorption corrections.[48] The structures were solved by direct methods and successive Fourier difference syntheses, and refined by the full-matrix least-squares method on $F^2$ (SHELXTL Version 5.1[49]). All non-hydrogen atoms except for the carbon atoms of compound **2** were refined with anisotropic thermal parameters. Aromatic hydrogen atoms were assigned to calculated positions with isotropic thermal parameters fixed at 1.2 times that of the attached carbon atom. Hydrogen atoms attached to oxygen atoms for compound **1** were located from difference maps and refined with O–H distances restrained to 0.90 Å, and isotropic thermal parameters fixed at 1.5 times that of the respective oxygen atom. Water hydrogen atoms for compound **2** could not be located in the difference Fourier map. The final Fourier map had a maximum and a minimum electron density of 2.153/–1.675 e·Å$^{-3}$, 2.438/–3.797 e·Å$^{-3}$ for compound **1** and **2**, respectively, and are within 1.0 Å of the lead atoms. The $R_1$ values are defined as $R_1 = \Sigma||F_o| - |F_c|| / \Sigma|F_o|$ and $wR_2 = \{\Sigma[w(F_o^2 - F_c^2)^2]/\Sigma[w(F_o^2)^2]\}^{1/2}$. The selected bond lengths and bond angles are listed in Table 2 and details of the crystal parameters, data collection, and refinement are summarized in Table 3.

Table 3. Crystallographic data for compounds **1** and **2**.

| | **1** | **2** |
|---|---|---|
| Empirical formula | $C_{16}H_{20}O_{22}S_2Pb_4$ | $C_{16}H_{16}O_{19}S_2Pb_3$ |
| Formula mass [g·mol$^{-1}$] | 1457.20 | 1197.98 |
| Temperature [K] | 293(2) | 293(2) |
| Crystal size [mm] | 0.12×0.12×0.10 | 0.24×0.20×0.18 |
| Crystal system | monoclinic | triclinic |
| Space group | $P2_1/c$ | $P\bar{1}$ |
| $Z$ | 4 | 2 |
| $a$ [Å] | 13.4123(1) | 10.2218(1) |
| $b$ [Å] | 15.2719(1) | 10.3214(1) |
| $c$ [Å] | 13.6859(8) | 13.315(2) |
| $\alpha$ [deg] | 90 | 71.866(1) |
| $\beta$ [deg] | 91.274(3) | 71.366(1) |
| $\gamma$ [deg] | 90 | 65.06 |
| $V$ [Å$^3$] | 2802.6(3) | 1678.07(15) |
| $D_c$ [g·cm$^{-3}$] | 3.454 | 3.368 |
| $\mu$ [mm$^{-1}$] | 24.203 | 21.6 |
| Measured reflections | 21466 | 6173 |
| Independent reflections | 6398 | 4144 |
| Observed reflections, [$I > 2\sigma(I)$] | 5375 | 3516 |
| Parameters | 436 | 281 |
| $F$(000) | 2608 | 1084 |
| Completeness [%] | 99.6 | 98.9 |
| 2$\theta$ range [°] | 3.04 to 27.47 | 1.65 to 25.04 |
| $h/k/l$ ranges | –16/17 | –12/11 |
| | –19/14 | –11/12 |
| | –17/17 | –15/15 |
| $R$ [int] | 0.0524 | 0.0434 |
| $R_1$ [obsd. refl.] | 0.0495 | 0.0658 |
| $wR_2$ [all refl.] | 0.0958 | 0.1523 |
| Largest diff. peak/hole [e·Å$^{-3}$] | 2.153/–1.675 | 2.438/–3.797 |

CCDC-285784 (for **1**) and -285785 (for **2**) contain the supplementary crystallographic data for this paper. These data can be obtained free of charge from The Cambridge Crystallographic Data Centre via www.ccdc.cam.ac.uk/data_request/cif.

**Supporting Information** (for details see the footnote on the first page of this article): This contains the TG curves and X-ray powder diffraction patterns of both compounds.

## Acknowledgments

We gratefully acknowledge the financial support of the "One Hundred Talents Program" of the Chinese Academy of Sciences and National Science Foundation of China (Grant No. 20473092).

[1] B. Moulton, M. J. Zaworotko, *Chem. Rev.* **2001**, *101*, 1629–1658.
[2] O. R. Evans, R. Xiong, Z. Wang, G. K. Wong, W. Lin, *Angew. Chem.* **1999**, *111*, 557–559; *Angew. Chem. Int. Ed.* **1999**, *38*, 536–538.
[3] T. Bein, *Supramolecular Architecture*, Am. Chem. Soc. Washington, DC, **1992**.
[4] O. Sato, T. Iyoda, A. Fujishima, K. Hashimoto, *Science* **1996**, *271*, 49–51.
[5] S. K. Ghosh, R. Joan, P. K. Bharadwaj, *Cryst. Growth Des.* **2005**, *5*, 623–629.
[6] D. S. Kim, P. M. Forster, R. L. Toquin, A. K. Cheetham, *Chem. Commun.* **2004**, 2148–2149.
[7] Y. P. Yuan, J. G. Mao, J. L. Song, *J. Solid State Chem.* **2004**, *177*, 922–927.
[8] T. Tsuboi, P. Sifsten, *Phys. Rev. B* **1991**, *43*, 1777–1780.
[9] A. A. Bol, A. Meijerink, *Phys. Chem.* **2001**, *3*, 2105–2112.
[10] P. Singh, M. M. Richter, *Inorg. Chim. Acta* **2004**, *357*, 1589–1592.
[11] S. Miyata, H. S. Nalwa (Eds.), *Organic Electroluminescent Materials and Devices*, Gordon and Breach, New York, **1997**.
[12] C. S. Weinert, I. A. Guzei, A. L. Rheingold, L. R. Sita, *Organometallics* **1998**, *17*, 498–500.
[13] M. H. Jack, M. Saeed, A. S. Ali, *Inorg. Chem.* **2004**, *43*, 1810–1812.
[14] Y. J. Shi, L. H. Li, Y. Z. Li, X. T. Chen, Z. L. Xue, X. Z. You, *Polyhedron* **2003**, *22*, 917–923.
[15] M. R. S. J. Foreman, T. Gelbrich, M. B. Hursthouse, M. J. Plater, *Inorg. Chem. Commun.* **2000**, *3*, 234–238.
[16] R. A. Varga, J. E. Drake, C. Silvestru, *J. Organomet. Chem.* **2003**, *675*, 48–56.
[17] S. M. Ying, J. G. Mao, *Eur. J. Inorg. Chem.* **2004**, 1270–1276.
[18] H. Nikol, A. Vogler, *J. Am. Chem. Soc.* **1991**, *113*, 8988–8990.
[19] R. Ballardini, G. Varani, M. T. Indelli, F. Scandola, *Inorg. Chem.* **1986**, *25*, 3858–3865.
[20] A. Strasser, A. Vogler, *J. Photochem. Photobiol. A* **2004**, *165*, 115–118.
[21] A. Strasser, A. Vogler, *Inorg. Chem. Commun.* **2004**, *7*, 528–530.
[22] D. F. Sun, R. Cao, Y. Q. Sun, X. Li, W. H. Bi, M. C. Hong, Y. J. Zhao, *Eur. J. Inorg. Chem.* **2003**, 94–98.
[23] J. Tao, X. Yin, Z. B. Wei, R. B. Huang, L. S. Zheng, *Eur. J. Inorg. Chem.* **2004**, 125–133.
[24] Z. M. Sun, J. G. Mao, Y. Q. Sun, H. Y. Zeng, A. Clearfield, *Inorg. Chem.* **2004**, *43*, 336–341.
[25] Q. Y. Liu, L. Xu, *Eur. J. Inorg. Chem.* **2005**, 3458–3466.
[26] R. M. Barrer, *Hydrothermal Chemistry of Zeolites*, Academic Press, London, **1982**.
[27] G. Bemazeau, *J. Mater. Chem.* **1999**, *9*, 15–18.
[28] S. H. Feng, R. R. Xu, *Acc. Chem. Res.* **2001**, *34*, 239–247.
[29] F. A. Cotton, G. Wilkinson, *Advanced Inorganic Chemistry*, John Wiley & Sons, New York, **1988**.
[30] T. J. Boyle, T. M. Alam, K. P. Peters, M. A. Rodriguez, *Inorg. Chem.* **2001**, *40*, 6281–6286.
[31] A. Tsohos, S. Dionyssopoulou, C. P. Raptopoulou, A. Terzis, E. G. Bakalbassis, S. P. Perlepes, *Angew. Chem. Int. Ed.* **1999**, *38*, 983–985.
[32] A. V. Sienkiewicz, V. N. Kokozay, *Z. Naturforsch., Teil B* **1994**, *49*, 615–617.

 © 2006 Wiley-VCH Verlag GmbH & Co. KGaA, Weinheim 

[33] A. V. Sienkiewicz, V. N. Kokozay, *Polyhedron* **1994**, *13*, 1431–1437.
[34] C. D. Brandt, P. G. Pliege, R. J. Kelly, D. J. de Geest, D. K. Kennepohl, S. S. Iremonger, S. Brooker, *Inorg. Chim. Acta* **2004**, *357*, 4265–4272.
[35] Q. Y. Liu, L. Xu, *Inorg. Chem. Commun.* **2005**, *8*, 401–405.
[36] Q. Y. Liu, L. Xu, *Acta Crystallogr., Sect. E* **2005**, *61*, m1972–1974.
[37] G. B. Deacon, R. J. Pihllips, *Coord. Chem. Rev.* **1980**, *33*, 227–250.
[38] S. Deo, H. A. Godwin, *J. Am. Chem. Soc.* **2000**, *122*, 174–175.
[39] P. C. Ford, A. Vogler, *Acc. Chem. Res.*. **1993**, *26*, 220–226.
[40] H. Y. Duan, X. P. Ai, Z. K. He, *Spectrochim. Acta A* **2003**, *60*, 1447–1451.
[41] Y. Q. Xu, D. Q. Yuan, L. Han, E. Ma, M. Y. Wu, Z. Z. Lin, M. C. Hong, *Eur. J. Inorg. Chem.* **2005**, 2054–2059.
[42] Q. Y. Liu, L. Xu, *CrystEngComm* **2005**, *7*, 87–89.
[43] A. Vogler, A. Paukner, H. Kunkely, *Coord. Chem. Rev.* **1980**, *33*, 227–250.
[44] S. K. Dutta, M. W. Perkovic, *Inorg. Chem.* **2002**, *41*, 6938–6940.
[45] H. Kunkely, A. Vogler, *Chem. Phys. Lett.* **1991**, *187*, 609–612.
[46] S. K. Dutta, M. W. Perkovic, *Inorg. Chem.* **2002**, *41*, 6938–6940.
[47] H. Nikol, A. Becht, A. Vogler, *Inorg. Chem.* **1992**, *31*, 3277–3279.
[48] *CrystalClear version 1.3*, Rigaku Corp. **2000**.
[49] G. M. Sheldrick, *SHELXS 97*, *Program for Crystal Structure Solution*, University of Göttingen, **1997**.

Received: October 24, 2005
Published Online: February 24, 2006

 © 2006 Wiley-VCH Verlag GmbH & Co. KGaA, Weinheim 

DOI: 10.1002/ejic.200500945

# A Radical-Radical and Metal–Metal Coupling Tetrathiafulvalene Derivative in which Organic Radicals Directly Coordinate to $Cu^{II}$ Ions

**Wen Lu,[a] Yong Zhang,[a] Jie Dai,*[a,b] Qin-Yu Zhu,[a] and Guo-Qing Bian,[a] and De-Qing Zhang[b]**

**Keywords:** Tetrathiafulvalenes / Copper(II) complexes / Magnetic coupling

A new dinuclear metal complex including tetrathiafulvalene (TTF) radicals as ligands has been prepared and characterized, $[\{DMT\text{-}TTF(CONH_2)_2\}_2Cu_2Cl_6]$ (**1**), DMT-$TTF(CONH_2)_2$ = *o*-bis(amido)-appended dimethylthio-tetrathiafulvalene. The compound is an uncommon example in which TTF radicals directly coordinate to the copper(II) halide by the amido group. Crystal structure analysis shows that it is a unique coordination bond/H-bond/S···S stacking cooperative system with two radicals and two paramagnetic transition metal ions, $TTF^{+\cdot}$–$Cu^{II}$–$Cu^{II}$–$TTF^{+\cdot}$. In the structure of **1**, the DMT-TTF units form dimers with very strong S···S interactions. The $Cu^{II}$–O(amide) distance of the coordination bond is 2.271(2) Å and the S···S stacking distances between the radicals are in the range 3.345–3.489 Å. The metal–metal ions are mildly antiferromagnetically coupled ($2J_1$ = –58.4 $cm^{-1}$), while the radical pairs are strongly antiferromagnetically coupled ($2J_2 > -1000$ $cm^{-1}$).

(© Wiley-VCH Verlag GmbH & Co. KGaA, 69451 Weinheim, Germany, 2006)

## Introduction

Until the end of the twentieth century, the work on tetrathiafulvalene (TTF) chemistry was mostly concerned with the radical salts of magnetic molecular conductors.[1–5] In the crystals of these salts, the organic radicals and paramagnetic inorganic counterions are discretely arranged. Therefore, the interaction between them could only occur through space by weak intermolecular interactions, such as hydrogen bonding and stacking of atoms. With increasing light being shed on the interactions of TTFs with transition metals, recent interests of inorganic chemists are devoted to organic–inorganic hybrid TTF materials in which the synergy between organic and inorganic parts are through stronger covalent or coordination bonds. The incorporation of TTF units into dithiolate ligands ($TTFS_4^{4-}$ and $TTFS_2^{2-}$) is one of the successful strategies, and systems of single molecular complexes with d–π interactions have been reported.[6–10] Another strategy that has been popular is the design and synthesis of TTF derivatives that are substituted with heteroatom-based groups capable of coordinating to a metallic center, such as thioethers,[11–14] phosphanes,[15–18] pyridines,[19–24] alkylsilyls,[25] and stibines.[26] The corresponding coordination compounds have also been reported. The metal coordination of complexes with the TTF ligand offers a novel perspective on the modulation of the architecture and collective properties of molecular solids. However, to the best of our knowledge, the TTF moieties in most of the reported complexes are in the neutral state. Therefore, their direct applications as electronic or magnetic materials are limited. Very recently, an important step was reached by the synthesis and characterization of a radical electron/d electron directly cooperative complex, $[Cu^{II}(hfac)_2(TTF\text{-}py)_2][PF_6]\cdot 2CH_2Cl_2$, which has metal–radical and radical-radical couplings.[22] Besides the metal coordination, hydrogen bonds are also one of the successful strategies used to promote the properties of molecular solids. Some amide-functionalized TTFs have been prepared and their radical salts involving N–H···Cl/O hydrogen bonds were studied.[27–31]

What follows is a report on the preparation, crystal structure, and magnetic properties of a new TTF-amide derivative with two radicals and two paramagnetic transition metal ions, $[\{DMT\text{-}TTF(CONH_2)_2\}_2Cu_2Cl_6]$ (**1**), DMT-$TTF(CONH_2)_2$ = *o*-bis(amide)-appended dimethylthio-tetrathiafulvalene. Complex **1** is a new dinuclear $TTF^{+\cdot}$–$Cu^{II}$–$Cu^{II}$–$TTF^{+\cdot}$ system with coordination bonds, H-bonds and S···S stacking, which is different from $[Cu^{II}(hfac)_2(TTF\text{-}py)_2][PF_6]\cdot{}_2CH_2Cl_2$, which has a mono-nuclear TTF–$Cu^{II}$–$TTF^{+\cdot}$ coordination system. The radical-radical and metal–metal magnetic couplings are also discussed.

## Results and Discussion

### Synthesis and General Discussion

The TTF derivative DMT-$TTF(CONH_2)_2$ was synthesized by a similar procedure described in the literature.[27]

[a] Department of Chemistry, Suzhou University, P. O. Box 174, Suzhou 215123, P. R. China
E-mail: daijie@suda.edu.cn
[b] Laboratory of Organic Solids, Center for Molecular Sciences, Institute of Chemistry, Chinese Academy of Sciences, Beijing 100080, P. R. China

 © 2006 Wiley-VCH Verlag GmbH & Co. KGaA, Weinheim 

Compound **1** was prepared by the reaction of the TTF precursor with excess $CuCl_2$ using a diffusing method in ambient conditions (Scheme 1). The details are given in the experimental section. During the reaction the ligands are oxidized by $Cu^{II}$ ions forming the radical cations and, hence, the charge distribution of **1** might be deduced as [{DMT-TTF$(CONH_2)_2^{+\cdot}$}$_2(Cu_2Cl_6)^{2-}$].

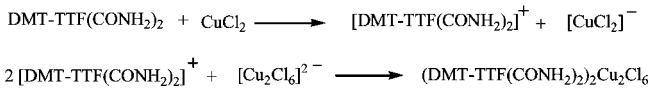


Scheme 1.

Copper(II) halides readily oxidize the TTF derivatives, providing a variety of charge-transfer (CT) salts that have conductive or semiconductive properties. Although a number of TTF CT compounds with copper(II) halides have been prepared, no cation-anion coordinated model has been found.[32–37] Due to the weak coordination of the TTF radicals with the $Cu^{II}$ center (by the thioether or alkylthio group), the paramagnetic copper(II) halides, such as the familiar $Cu_2Cl_6^{2-}$ anion, are arranged discretely as counterions. However, anions of copper(I) halides, which can be formed from the reduction of $Cu^{II}$ halides, are easily coordinated by the alkylthio group of the TTFs or its radicals. Some copper(I) halide-TTF complexes[11–14] or CT compounds[38–40] having S–$Cu^{I}$ coordination bonds have been obtained. Compound **1** is an uncommon example where direct coordination of the copper(II) halide with the TTF radical occurs. In the case of **1** the TTF moieties are appended by two amido groups, which enable the $Cu^{II}$ center to be bonded by the oxygen atom of the amide group.

## Description of the Structures

The single crystal structure of **1** was solved by direct methods. A summary of the experimental details and crystal data for compound **1** is given in Table 1. Selected bond lengths, contact distances, bond angles, and torsion angles are listed in Table 2. The ligand, DMT-TTF$(CONH_2)_2$, in **1** adopts a conformation with an intramolecular hydrogen bond [N(1)–H···O(2), Figure 1], which has been observed for several TTF amides and their radical salts.[27–31] As a consequence of the intramolecular hydrogen bond, the two *ortho*-amido groups are fixed and form a seven-membered ring fused with the TTF moiety, which enables the conjugated π system to extend to the oxygen atoms of the amide groups.

Table 1. Crystallographic data for compound **1**.

| Compound | **1** |
|---|---|
| Empirical formula | $C_{20}H_{20}Cl_6Cu_2N_4O_4S_{12}$ |
| Formula mass | 1104.90 |
| Color, Habit | black, platelet |
| Crystal system | triclinic |
| Crystal size [mm] | 0.3 × 0.2 × 0.02 |
| Space group | $P\bar{1}$ (No. 2) |
| $a$ [Å] | 8.4564(12) |
| $b$ [Å] | 10.8253(19) |
| $c$ [Å] | 10.8817(18) |
| $\alpha$ [°] | 111.302(4) |
| $\beta$ [°] | 90.645(4) |
| $\gamma$ [°] | 91.970(3) |
| $Z$ | 1 |
| $T$ [K] | 193(2) |
| $V$ [Å$^3$] | 927.2(3) |
| $D_{calcd.}$ [g·cm$^{-3}$] | 1.979 |
| $\mu$ [mm$^{-1}$] | 4.090 |
| $F(000)$ | 552 |
| Reflections collected | 9242 |
| Unique reflections | 3371 |
| Observations [$I > 2\sigma(I)$] | 2996 |
| Variables | 220 |
| $R1$ [$I > 2\sigma(I)$] | 0.0308 |
| $wR_2$ | 0.0754 |
| Goodness of fit indicator | 1.040 |

$R_1 = \Sigma||F_o| - |F_c|| / \Sigma|F_o|$ and $wR_2 = \{\Sigma[w(F_o^2 - F_c^2)^2] / \Sigma[w(F_o^2)^2]\}^{1/2}$

Table 2. Selected bond lengths, angles, torsion angles, contact distances, and hydrogen bonds.

| | | | |
|---|---|---|---|
| Bond lengths [Å] | | | |
| Cu(1)–Cl(1) | 2.3042(8) | Cu(1)–Cl(2) | 2.2845(8) |
| Cu(1)–Cl(3) | 2.2540(8) | Cu(1)–Cl(1$^{i}$) | 2.3346(9) |
| Cu(1)–O(1) | 2.271(2) | C(5)–C(6) | 1.379(4) |
| Bond angles [°] | | | |
| Cu(1)–Cl(1)–Cu(1$^{i}$) | 97.12(3) | O(1)–Cu(1)–Cl(1) | 92.97(6) |
| O(1)–Cu(1)–Cl(1$^{i}$) | 90.83(6) | O(1)–Cu(1)–Cl(2) | 92.50(6) |
| O(1)–Cu(1)–Cl(3) | 98.56(6) | | |
| Torsion angles [°] | | | |
| N(1)–C(1)–C(3)–C(4) | 22.8(5) | N(2)–C(2)–C(4)–C(3) | 157.9(3) |
| Contact distances [Å] | | | |
| Cu(1)–Cu(1$^{i}$) | 3.478 | O(2)–S(6$^{ii}$) | 3.317 |
| S(1)–S(6$^{iii}$) | 3.345 | S(2)–S(5$^{iii}$) | 3.489 |
| S(3)–S(4$^{iii}$) | 3.409 | | |
| Hydrogen bonds [Å, °] | | | |
| D–H···A | distance H···A | distance D···A | angle D–H···A |
| N(1)–H···O(2) | 1.92 | 2.709(3) | 148.7 |
| N(1)–H···S(5$^{ii}$) | 2.92 | 3.524(2) | 127.1 |
| N(2)–H···Cl(2$^{v}$) | 2.63 | 3.443(3) | 154.6 |
| N(2)–H···Cl(2$^{iv}$) | 2.42 | 3.288(2) | 171.1 |

i: $-x + 1, -y, -z + 1$; ii: $x - 1, y - 1, z$; iii: $-x + 1, -y, -z$; iv: $-x + 1, -y - 1, -z$; v: $x, y, z - 1$

 © 2006 Wiley-VCH Verlag GmbH & Co. KGaA, Weinheim 

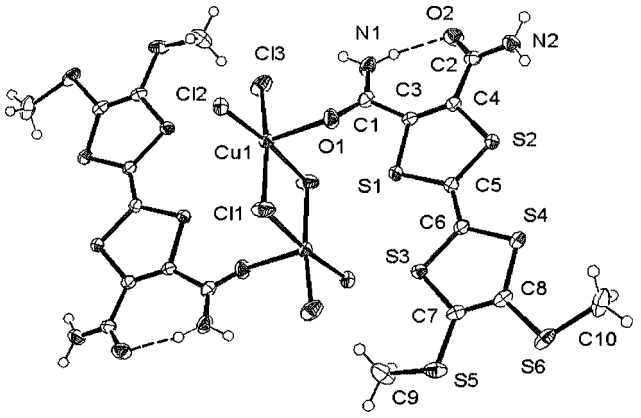


Figure 1. ORTEP view of **1**, showing the atom-labeling scheme. Displacement ellipsoids are drawn at the 50% probability level.

The center of **1** is a dinuclear moiety of $Cu_2Cl_6^{2-}$, in which the $Cu^{II}$ ions take on a quasi-square coordination and the two squares share a common edge of Cl(1)–Cl(1$^i$). The Cu–Cl distances are in the range 2.254–2.335 Å, and are comparable to those reported for the $Cu_2Cl_6^{2-}$ ion. However, the Cu(1)–Cl(1)–Cu(1$^i$) angle of 97.12(3)° is located at the top of the angle range compared with those of the corresponding compounds.[36,41,42] In addition to the coordination of chloride ions, the DMT-TTF$(CONH_2)_2$ coordinates to the $Cu^{II}$ ions by the amide oxygen atom O(1), perpendicular to the square planes of the $CuCl_4$ moieties (see Figure 1). The 2.271(2) Å distance of Cu(1)–O(1) undoubtedly shows the formation of a strong coordination bond, which forces the $Cu_2Cl_6^{2-}$ ion to take on a quasi-planar geometry [atom Cl(3) is somewhat out of the square plane]. In contrast, the discrete $Cu_2Cl_6^{2-}$ ion adopts a structure with two distorted tetrahedra sharing a common edge.[36,43,44] The central C=C distance of the TTF moiety [C(5)–C(6), 1.379(4) Å], however, is longer than that found in the neutral TTF compounds (1.331 Å) but in accordance with that of the $TTF^{+\cdot}$ radicals (1.373–1.383 Å).[27]

All of the TTF units form dimers in the crystal structure **1** with very strong S···S stacking [Figure 2 (a)]. There are six S···S interactions between the TTF units of the dimer, in which the shortest one is 3.345 Å and the longest is 3.489 Å (average 3.414 Å, Table 2). The S···S interactions are considerably shorter than the sum of the van der Waals radii (3.60–3.70 Å), and they are related to the strong antiferromagnetic coupling of the organic radical dimer (vide infra).

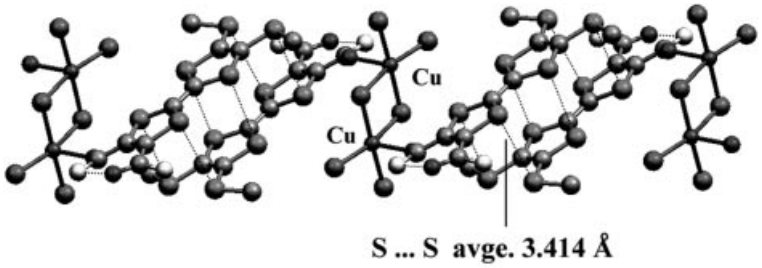


(a)

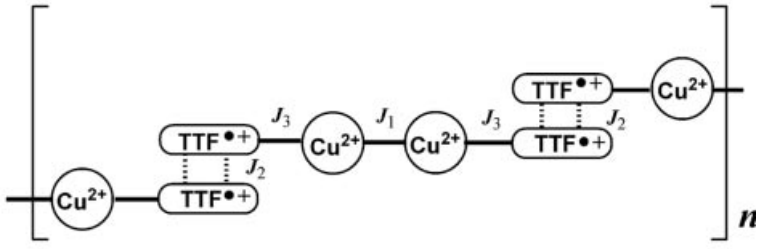


(b)

Figure 2. (a) One-dimensional structure of the molecules assembled by S···S stacking and metal coordination. (b) Schematic diagram of the two TTF radicals with the $Cu^{II}$ system and the magnetic coupling constants.

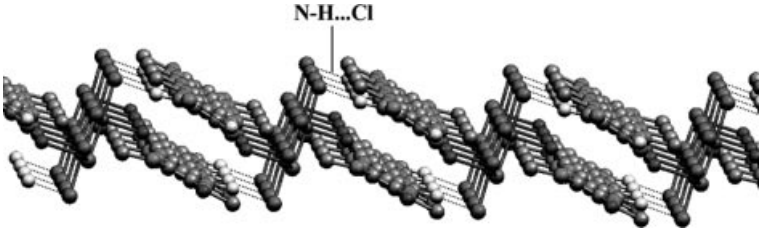


Figure 3. The inter-chain N(2)–H···Cl(2) (3.288 Å) hydrogen bonds of the assembled two-dimensional structure of the title compound.

 © 2006 Wiley-VCH Verlag GmbH & Co. KGaA, Weinheim 

Assembled by S···S stacking and Cu–O metal coordination, compound **1** forms an infinite chain propagating in the [101] direction. The crystal structure of **1** is further stabilized by inter-chain N(2)–H···Cl(2) hydrogen bonds (3.288 Å) and S(6)···O(2) contacts (3.317 Å), which assemble the molecules into two-dimensional slabs parallel to the plane (1–11) (Figure 3). It has been shown that the hydrogen-bond network is correlated with the density of states at the Fermi level and the spin susceptibility behavior.[31]

### Magnetic Properties

Until now, work on TTF-containing π–d-type magnetic compounds has mostly been concerned with radical salts, except for the example reported recently by Ouahab et al., which has a mono-nuclear TTF–$Cu^{II}$–$TTF^{+\cdot}$ coordination system.[22] Compound **1**, reported here, has a new dinuclear $TTF^{+\cdot}$–$Cu^{II}$–$Cu^{II}$–$TTF^{+\cdot}$ coordination system [Figure 2 (b)]. The magnetic properties of **1** were measured with a SQUID magnetometer in the range 4–260 K (Figure 4). The magnetic moment (2.40 B. M. at room temperature) is considerably lower than the spin-only value, 6.92 B. M., for a noncoupling four-spin system (1.73 B. M. × 4), but the value of 2.40 B. M. corresponds to the value which is expected for a two-spin ($S$ = 1/2) system with antiferromagnetic (AF) coupling (3.46 B. M. for a noncoupling two-spin system).

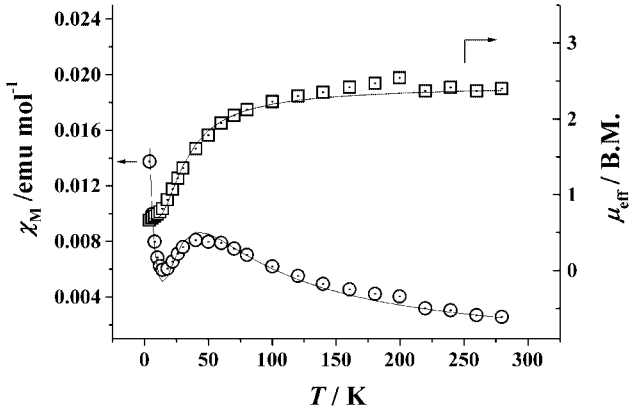


Figure 4. Variable-temperature magnetic susceptibility data and effective magnetic moments of **1** collected by a SQUID magnetometer in the range 4–260 K. The solid lines were calculated based on a singlet-triplet model.

A solid-state EPR spectrum (polycrystalline sample), which strongly supports the speculation, was measured at 110 K (Figure 5). Because the organic radicals are dimerized with very short S···S stacking and are strongly antiferromagnetically coupled no sharp radical signal is observed in the EPR spectrum. The spectrum only shows a parallel and perpendicular split of $Cu^{II}$ character with $g$ values of 2.045 and 2.246 for $g_{\|}$ and $g_{\perp}$, respectively. This result means that the two TTF radicals are AF coupled with $2J_2 > -1000\ cm^{-1}$. In addition, because the spin density of the radical is mainly located on the central TTF core and the amide oxygen atom of **1** coordinates to the $Cu^{II}$ center of the $Cu_2Cl_6$ plane along the axial position, the interaction of the radicals with the metal ions should be very weak. Therefore, the $J_3$ coupling can be neglected in the fitting procedure. Consequently, this compound can be described as a system that has a strongly coupled $TTF^{+\cdot}$ ($J_2$) dimer and a mildly coupled $Cu_2Cl_6$ ($J_1$) dimer with very weak radical-metal interaction ($J_3$) [Figure 2 (b)]. From a simplified calculation, considering the antiferromagnetic coupling intensity, the magnetic susceptibility of compound **1** can be fitted by a $Cu_2Cl_6$ dimer model with spin-exchange Hamiltonian $\hat{H} = -2J_1\hat{S}_{Cu1}\hat{S}_{Cu2}$, where $J_1$ is the spin-exchange coupling constant between the two $Cu^{II}$ ions (Figure 4). The susceptibility data were fitted using Equation (1) containing the paramagnetic impurity term ρ. The best least-squares fit gave $J_1 = -29.2\ cm^{-1}$, $g = 2.08$, $\rho = 0.08$ and the consistent factor $R = \Sigma(\chi_{obsd} - \chi_{calcd})^2/\Sigma\chi_{obsd}^2 = 3.85 \times 10^{-3}$. The structural-magnetic correlation for the $Cu_2Cl_6^{2-}$ ion has been intensively discussed elsewhere.[45,46] The present result of $2J_1 = -58.4\ cm^{-1}$ supports the structure in which the copper(II) center adopts a square-planar geometry.

$$\chi_M = \frac{2Ng^2\beta^2}{KT}\left[\frac{1}{3+\exp(-2J_1/KT)}\right](1-\rho) + \frac{Ng^2\beta^2}{2KT}\rho + N_\alpha \quad (1)$$

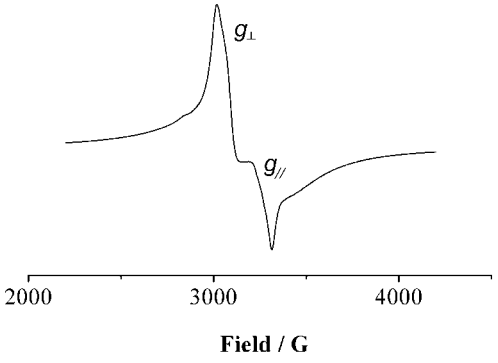


Figure 5. Solid-state EPR spectrum of the title compound measured at 110 K.

## Conclusion

Prior to the report of Ouahab et al., where the TTF radicals directly coordinate to the paramagnetic ions,[22] the charge transfer TTF compounds containing paramagnetic inorganic ions were radical salts in which the cations and anions are discretely arranged. The compound **1** reported here is a new example in which the TTF radicals directly coordinate to the paramagnetic ions. Crystal structure analysis showed that it is a unique coordination bond/H-bond/S···S stacking cooperative system with two radicals and two paramagnetic transition metal ions, $TTF^{+\cdot}$–$Cu^{II}$–$Cu^{II}$–$TTF^{+\cdot}$. Although the direct coordination of the $TTF(CONH_2)_2^{+\cdot}$ radical to the paramagnetic transition metal anion, $(Cu_2Cl_6)^{2-}$, does not improve the interaction of the radical electrons and the d electrons in this case, because

 © 2006 Wiley-VCH Verlag GmbH & Co. KGaA, Weinheim 

of the strong antiferromagnetic coupling within the radical pairs (TTF radical couples) the preparation of materials with direct coordination of TTF radicals to transition metal anions is still an attractive strategy for chemists in molecular design.

## Experimental Section

**General Remarks:** All analytical grade chemicals were obtained commercially and used for synthesis directly without further purification. Elemental analyses of C, H, and N were performed using an MOD 1106 elemental analyzer. The IR spectra were recorded as KBr discs with a Nicolet Magma 550 FT-IR spectrometer. Solid-state EPR spectra were recorded with an EMX-10/12 spectrometer at 110 K and at a frequency of 9.4852 GHz. The magnetic properties were measured with a SQUID magnetometer (Quantum Desigen, MPMS-2) in the range 3.99–278 K, with an applied field of 10000 gauss.

**Synthesis of Compounds**

**DMT-TTF(CONH$_2$)$_2$ (Ligand):** The ligand was synthesized by a similar procedure described in the literature.[27] A purple powder was obtained (yield 79%). $C_{10}H_{10}N_2O_2S_6$ (382.56): calcd. C 31.24, H 2.64, N 7.33; found C 32.09, H 2.87, N 6.60. IR (KBr): $\tilde{\nu}$ = 3375–3189 ($NH_2$), 1675–1662 (C=O) cm$^{-1}$.

**(C$_{10}$H$_{10}$N$_2$O$_2$S$_6$)$_2$Cu$_2$Cl$_6$ (1):** Well-defined black platelet crystals of **1** were obtained by a diffusing method with an acetonitrile solution of $CuCl_2$ ($4 \times 10^{-2}$ M) and a THF solution of the ligand ($5 \times 10^{-3}$ M). $C_{20}H_{20}Cl_6Cu_2N_4O_4S_{12}$ (1104.93): calcd. C 21.83, H 1.83, N 5.09; found C 21.56, H 2.05, N 4.89. IR (KBr): $\tilde{\nu}$ = 3329–3149 ($NH_2$), 1671–1660 (C=O) cm$^{-1}$.

**X-ray Crystallographic Study:** All measurements were carried out with a Rigaku Mercury CCD diffractometer at 193 K with graphite-monochromated Mo-$K_\alpha$ ($\lambda$ = 0.71073 Å) radiation. X-ray Crystallographic data of compounds **1** were collected and processed using CrystalClear (Rigaku).[47] The structures were solved by direct methods with SHELXS-97[48] and the refinements against all reflections of the compound were performed using SHELXL-97.[49] The non-hydrogen atoms were refined anisotropically and hydrogen atoms were refined using the theoretical riding model. The final cycle of full-matrix least-squares refinement was done on the basis of 3371 independent reflections and 220 variable parameters. The weighted $R$ factor ($wR$) and goodness of fit ($S$) were obtained on the basis of 2996 [$I > 2\sigma(I)$] reflections. The calculations were performed using the CrystalStructure software package.[50]

CCDC-268681 contains the supplementary crystallographic data for this paper. These data can be obtained free of charge from The Cambridge Crystallographic Data Centre via www.ccdc.cam.ac.uk/data_request/cif.

## Acknowledgments

This work was supported by the NNS Foundation (20071024, 20371033), P. R. China, and the Key Laboratory of Organic Synthesis of Jiangsu Province, Suzhou University. The authors are also grateful to Prof. T. Kuroda-Sowa and M. Munakata (Kinki Univ., Japan) for a SQUID measurement, and Dr. Q. Wang and Prof. S. Yan (Nankai Univ., China) for assistance with the determination of the magnetic properties.

[1] E. Coronado, C. J. Gómez-García, *Chem. Rev.* **1998**, *98*, 273–296.
[2] M. B. Nielsen, C. Lomholt, J. Becher, *Chem. Soc. Rev.* **2000**, *29*, 153–164.
[3] E. Coronado, P. Day, *Chem. Rev.* **2004**, *104*, 5419–5448.
[4] T. Enoki, A. Miyazaki, *Chem. Rev.* **2004**, *104*, 5449–5478.
[5] P. Day, M. Kurmoo, *J. Mater. Chem.* **1997**, *7*, 1291–1295.
[6] H. Tanaka, Y. Okano, H. Kobayashi, W. Suzuki, A. Kobayashi, *Science* **2001**, *291*, 285–287.
[7] E. Fujiwara, A. Kobayashi, H. Fujiwara, H. Kobayashi, *Inorg. Chem.* **2004**, *43*, 1122–1129.
[8] W. Suzuki, E. Fujiwara, A. Kobayashi, Y. Fujishiro, E. Nishibori, M. Takata, M. Sakata, H. Fujiwara, H. Kobayashi, *J. Am. Chem. Soc.* **2003**, *125*, 1486–1487.
[9] H. Tanaka, H. Kobayashi, A. Kobayashi, *J. Am. Chem. Soc.* **2002**, *124*, 10002–10003.
[10] A. Kobayashi, E. Fujiwara, H. Kobayashi, *Chem. Rev.* **2004**, *104*, 5243–5264.
[11] M. Munakata, T. Kuroda-Sawa, M. Maekawa, A. Hirota, S. Kitagawa, *Inorg. Chem.* **1995**, *34*, 2705–2710.
[12] L. P. Wu, J. Dai, M. Munakata, T. Kuroda-Sowa, M. Maekawa, Y. Suenaga, Y. Ohno, *J. Chem. Soc., Dalton Trans.* **1998**, 3255–3261.
[13] J. C. Zhong, Y. Misaki, M. Munakata, T. Kuroda-Sawa, M. Maekawa, Y. Suenaga, H. Konaka, *Inorg. Chem.* **2001**, *40*, 7096–7098.
[14] J. Ramos, V. M. Yartsev, S. Golhen, L. Ouahab, P. Delhaés, *J. Mater. Chem.* **1997**, *7*, 1313–1319.
[15] M. Fourmigué, P. Batail, *Bull. Soc. Chim. Fr.* **1992**, *129*, 29–36.
[16] M. Fourmigué, C. E. Uzelmeier, K. Boubekeur, S. L. Bartley, K. R. Dunbar, *J. Organomet. Chem.* **1997**, *529*, 343–350.
[17] E. Cerrada, C. Diaz, M. C. Diaz, M. B. Hursthouse, M. Laguna, M. E. Light, *J. Chem. Soc., Dalton Trans.* **2002**, 1104–1109.
[18] N. Avarvari, D. Martin, M. Fourmigué, *J. Organomet. Chem.* **2002**, *643/644*, 292–300.
[19] F. Iwahori, S. Golhen, L. Ouahab, R. Carlier, J.-P. Sutter, *Inorg. Chem.* **2001**, *40*, 6541–6542.
[20] S.-X. Liu, S. Dolder, M. Pilkington, S. Decurtins, *J. Org. Chem.* **2002**, *67*, 3160–3162.
[21] S.-X. Liu, S. Dolder, P. Franz, A. Neels, H. Stoeckli-Evans, S. Decurtins, *Inorg. Chem.* **2003**, *42*, 4801–4803.
[22] F. Setifi, L. Ouahab, S. Golhen, Y. Yoshida, G. Saito, *Inorg. Chem.* **2003**, *42*, 1791–1793.
[23] L. Ouahab, F. Iwahori, S. Golhen, R. Carlier, J.-P. Sutter, *Synth. Met.* **2003**, *133–134*, 505–507.
[24] T. Devic, N. Avarvari, P. Batail, *Chem. Eur. J.* **2004**, *10*, 3697–3707.
[25] M. J. Jayaswal, H. N. Peindy, F. Guyon, M. Knorr, N. Avarvari, M. Fourmigué, *Eur. J. Inorg. Chem.* **2004**, 2646–2651.
[26] S. S. Kuduva, N. Avarvari, M. Fourmigué, *J. Chem. Soc. Dalton Trans.* **2002**, 3686–3690.
[27] S. A. Baudron, N. Avarvari, P. Batail, C. Coulon, R. Clerac, E. Canadell, P. Auban-Senzier, *J. Am. Chem. Soc.* **2003**, *125*, 11583–11590.
[28] K. Heuze, C. Meziere, M. Fourmigue, P. Batail, C. Coulon, E. Canadell, P. Auban-Senzier, D. Jerome, *Chem. Mater.* **2000**, *12*, 1898–1904.
[29] T. Devic, N. Avarvari, P. Batail, *Chem. Eur. J.* **2004**, *10*, 3697–3707.
[30] S. A. Baudron, N. Avarvari, E. Canadell, P. Auban-Senzier, P. Batail, *Chem. Eur. J.* **2004**, *10*, 4498–4511.
[31] M. Fourmigué, P. Batail, *Chem. Rev.* **2004**, *104*, 5379–5418.
[32] P. Day, M. Kurmoo, T. Mallah, I. R. Marsden, R. H. Friend, F. L. Pratt, W. Hayes, D. Chasseau, J. Gaultier, G. Bravic, L. Ducasse, *J. Am. Chem. Soc.* **1992**, *114*, 10722–10729.
[33] M. Inoue, M. B. Inoue, C. Cruz-Vazque, S. Roberts, Q. Fernando, *Synth. Met.* **1987**, *19*, 641–642.

 © 2006 Wiley-VCH Verlag GmbH & Co. KGaA, Weinheim 

[34] S. G. Liu, S. P.-J. Wu, D. B. Zhu, *Synth. Met.* **1997**, *86*, 2031–2032.
[35] S. Le Moustarder, N. Mercier, P. Hudhomme, A. Gorgues, A. Riou, *Synth. Met.* **1999**, *102*, 1671–1672.
[36] L.-P. Wu, X. M. Gan, M. Munakata, T. Kuroda-Sowa, M. Maekawa, Y. Suenaga, *Mol. Cryst. Liq. Cryst. Sci. Technol. Sect A* **1996**, *285*, 75–82.
[37] T. Mori, F. Sakai, G. Saito, H. Inokuchi, *Chem. Lett.* **1987**, 927–928.
[38] M. B. Inoue, M. Inoue, M. A. Bruck, Q. J. Fernando, *J. Chem. Soc., Chem. Commun.* **1992**, 515–516.
[39] R. Kanehama, M. Umemiya, F. Iwahori, H. Miyasaka, K.-I. Sugiura, M. Yamashita, Y. Yokochi, H. Ito, S.-I. Kuroda, H. Kishida, H. Okamoto, *Inorg. Chem.* **2003**, *42*, 7173–7181.
[40] J. Ramos, V. M. Yartsev, S. Golhen, L. Ouahab, P. Delhaes, *J. Mater. Chem.* **1997**, *7*, 1313–1319.
[41] A. Bencini, D. Gatteschi, C. Zanchini, *Inorg. Chem.* **1985**, *24*, 704–708.
[42] A. Colombo, L. Menabue, A. Motori, G. C. Pellacani, W. Porzio, F. Sandrolini, R. D. Willett, *Inorg. Chem.* **1985**, *24*, 2900–2905.
[43] R. D. Willett, C. Chow, *Acta Crystallogr., Sect. B* **1974**, *30*, 207.
[44] M. Textor, E. Dubler, H. R. Oswald, *Inorg. Chem.* **1974**, *13*, 1361–1365.
[45] D. B. Brown, J. W. Hall, M. F. Scott, W. E. Hatfield, *Inorg. Chem.* **1977**, *16*, 1813–1814.
[46] A. Bencini, D. Gatteschi, *J. Am. Chem. Soc.* **1986**, *108*, 5763–5771.
[47] Rigaku Corporation, **1999**, *CrystalClear Software User's Guide, Molecular Structure Corporation* **2000**; J. W. Pflugrath, *Acta Crystallogr., Sect. D* **1999**, *55*, 1718–1725.
[48] G. M. Sheldrick, *SHELXS-97, Program for structure solution*, University of Göttingen, Germany, **1997**.
[49] G. M. Sheldrick, *SHELXL-97, Program for structure refinement*, University of Göttingen, Germany, **1997**.
[50] *Crystal Structure Analysis Package*, Rigaku and Rigaku/MSC, **2000**–**2002**.

Received: October 26, 2005
Published Online: February 21, 2006

 © 2006 Wiley-VCH Verlag GmbH & Co. KGaA, Weinheim 

DOI: 10.1002/ejic.200500952

# The First Example of a Dinuclear Platinum(III) Complex with Three Bridging Ligands

**Raffaella Z. Pellicani,[a] Francesco P. Intini,[a] Luciana Maresca,[a] Ernesto Mesto,[b] Concetta Pacifico,[a] and Giovanni Natile*[a]**

**Keywords:** Bridging ligands / Hydrogen bonds / Metal–metal interactions / N ligands / Platinum(III)

The first triply bridged dinuclear platinum(III) compound with acetamidate ligands, $X[Pt_2Cl_4\{N(H)C(CH_3)O\}_3]$ ($X = K^+$ or $AsPh_4^+$), has been isolated in the solid state and characterized by one- and two-dimensional NMR spectroscopy and X-ray crystallography. Owing to the asymmetry of the bridging acetamidate ligands, three isomers can be formed (HHH, HHT, and HTH), although only two are found in the crude reaction product: HHT and HTH. The HTH species is thermodynamically less stable and slowly (half life of around two days at room temperature) isomerizes into the HHT form. The more stable and less symmetric HHT isomer crystallizes from chloroform/pentane ($AsPh_4^+$ counter ion). The two $[Pt_2Cl_4\{N(H)C(CH_3)O\}_3]^-$ anions of the unit cell are linked by two strong N–H···O H-bonds while contiguous anions of adjacent cells are linked together by two, slightly weaker N–H···Cl H-bonds. The result is a chain of anions running along the *a* direction. The crystal packing allows for the formation of one-dimensional pore channels, also running along the *a* direction, which are filled with disordered pentane molecules.

(© Wiley-VCH Verlag GmbH & Co. KGaA, 69451 Weinheim, Germany, 2006)

## Introduction

The chemistry and reactivity of platinum(III) compounds has not yet been explored to the same extent as those of platinum(II) and platinum(IV) species. The majority of platinum(III) complexes have dinuclear structures supported by two[1–3] or four[4–6] bridging ligands. The chelating chain is usually made up of three atoms of the type NCO, NCS, NCN, POP, or OYO (Y = C, S, P), with these three atoms forming a five-membered metallacycle with the two metal centers.[7–9] A few examples of mononuclear platinum(III) species[10] and dinuclear complexes unsupported by covalent bridges have also been reported.[11–13]

Very recently, further interest in dinuclear compounds of platinum(III) has arisen from their potential use as catalysts for the oxidation of olefins.[14–18] This property is fostered by the unusual reactivity of the axial ligands. The axial metal–ligand distances are longer than those found in octahedral platinum(IV) and square-planar platinum(II) complexes but much shorter than distances sometimes found for ligands interacting with platinum(II) species from axial sites.[1]

In spite of the large number of platinum(III) dimers with two or four bridging ligands, very few reports have so far dealt with platinum(III) dimers supported by three covalent bridges. In two NMR investigations, it was shown that species with three acetate bridging ligands can be formed as intermediates in the synthesis of quadruply bridged complexes[19] or as decomposition products of the latter compounds in water,[20] however such species were not isolated or fully characterized.

In this paper, we report the synthesis, NMR characterization, and X-ray structure of the first example of a triply bridged platinum(III) compound with acetamidate ligands, namely $X[Pt_2Cl_4\{N(H)C(CH_3)O\}_3]$ ($X = K^+$ or $AsPh_4^+$).

## Results and Discussion

### Synthesis and Spectroscopic Characterization

When $K_2PtCl_4$ and $K_2PtCl_6$ (1:1 ratio) are allowed to react with a large excess of free amide at high temperature (90 °C) and for a long time (5 h), quadruply bridged dimeric lantern-type complexes are formed. These complexes are insoluble in water and precipitate soon after formation. Full accounts of their synthesis and characterization have already been published.[5,6]

In order to obtain platinum(III) dimers with a smaller number of bridging ligands, we used the same procedure but shortened the reaction time until incipient precipitation of the quadruply bridged species (one instead of five hours). The reaction solution was then filtered and the solvent evaporated to dryness to leave an orange residue. Purification of the crude reaction product was performed by washing with chloroform to remove the excess of acetamide li-

[a] Dipartimento Farmaco-Chimico, Università degli Studi di Bari, Via E. Orabona 4, 70125 Bari, Italy
Fax: +39-080-544-2230
E-mail: natile@farmchim.uniba.it
[b] Dipartimento Geomineralogico, Università degli Studi di Bari, Via E. Orabona 4, 70125 Bari, Italy

 © 2006 Wiley-VCH Verlag GmbH & Co. KGaA, Weinheim 

gand, extraction with methanol to remove insoluble KCl and trace amounts of unreacted platinum(II) and platinum(IV) species, and finally precipitation with diethyl ether. The orange precipitate was characterized by elemental analysis and IR and NMR spectroscopy, and was found to be the triply bridged species $K[Pt_2Cl_4\{N(H)C(CH_3)O\}_3]$ (**1a**). The corresponding tetraphenylarsonium salt, $(AsPh_4)[Pt_2Cl_4\{N(H)C(CH_3)O\}_3]$ (**1b**), which is soluble in chloroform − **1a** is only soluble in protic solvents such as water and methanol − and precipitates as well-shaped orange crystals from a mixture of chloroform and pentane (1:1, v/v), was also prepared and characterized by elemental analysis, NMR spectroscopy, and X-ray crystallography.

The reaction conditions (90 °C and 1 h reaction time) appear to be critical to maximize the yield of triply bridged species. Longer reaction times result in greater formation of undesired quadruply bridged complexes, while shorter reaction times (0.5 h) leave significant amounts of unreacted platinum(II) and platinum(IV) species. Moreover, if the temperature is lowered the reaction becomes slower and at room temperature does not appear to take place at all.

Since the reaction can lead to formation of several interconverting isomers of the same species (for instance the triply bridged species can be present in three isomeric forms depending upon the relative orientations of the three amidates: HHH, HHT, and HTH), we analyzed the reaction products before and after purification. The latter will be described first.

A solution of **1b** in $CDCl_3$ gives a $^1H$ NMR spectrum characterized by the presence of two sets of three signals. One set falls in the region of amidic protons ($\delta$ = 6.5–5.5 ppm), while the second set falls in the region of aliphatic protons ($\delta$ = 2.5–2.0 ppm). The three signals have equal intensities within each set, and the relative intensities of the two sets is 1:3.

The correlations between the two sets of signals were established by a 2D NOESY experiment, which shows a cross peak between the less-shielded amidic proton signal at $\delta$ = 6.41 ppm (A) and the less-shielded methyl proton signal at $\delta$ = 2.29 ppm (D) and two overlapping cross peaks between the amidic proton signals at $\delta$ = 5.75 (B) and 5.73 (C) ppm and the methyl proton signals at $\delta$ = 2.03 (F) and 2.05 (E) ppm, respectively (Figure 1).

Three isomers are possible for a dinuclear species with three acetamidate bridging ligands (Figure 2). Two of them, HHH and HTH, have magnetically equivalent acetamidate bridges in *trans* positions, while the third isomer, HHT, has all three acetamidate bridges in different magnetic environments. Since the $^1H$ NMR spectrum exhibits distinct signals for each of the three acetamidate ligands, we can conclude that the isolated product has an HHT configuration.

The $^{195}Pt$ NMR spectrum of compound **1b** in $CDCl_3$ reveals the presence of two platinum resonances, one at $\delta$ = 241 ppm and the other at $\delta$ = –437 ppm. Each resonance is flanked by $^{195}Pt$ satellites with a $^1J_{Pt,Pt}$ coupling of 6660 Hz (Figure 3).[14,21,22]

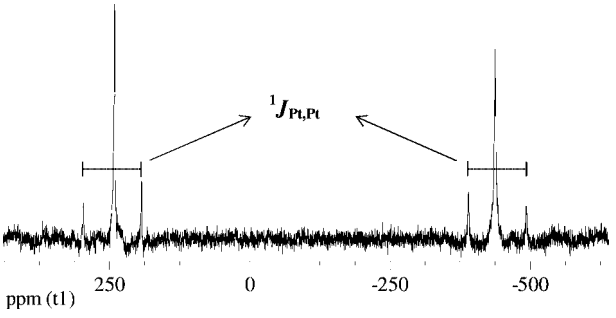


Figure 3. $^{195}Pt$ NMR spectrum of $(AsPh_4)[Pt_2Cl_4\{N(H)C(CH_3)O\}_3]$ in $CDCl_3$ ($4.6\times10^{-3}$ M) at 295 K.

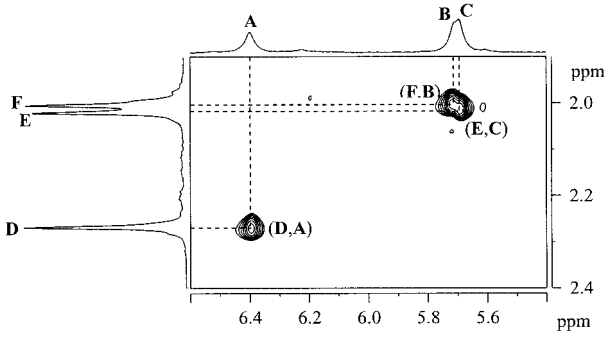


Figure 1. 2D NOESY spectrum of $(AsPh_4)[Pt_2Cl_4\{N(H)C(CH_3)O\}_3]$ in $CDCl_3$ ($4.6\times10^{-3}$ M) at 295 K.

On the basis of the established correlations between $^{195}Pt$ chemical shifts and electronegativities of the donor atoms,[23] the less-shielded signal, at $\delta$ = 241 ppm, can be assigned to the Pt atom with $Cl_2NO_2$ set of donor atoms while the most-shielded signal, at $\delta$ = –437 ppm, can be assigned to the Pt atom with $Cl_2N_2O$ set of donor atoms. This assignment is also supported by the broader profile of the peak at $\delta$ = –437 ppm as compared to that at $\delta$ = 241 ppm. Such a broadening is caused by the N donors, which

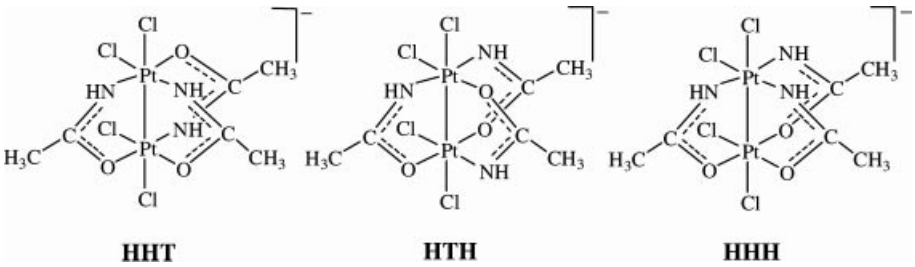


Figure 2. The three possible isomers for the complex $[Pt_2Cl_4\{N(H)C(CH_3)O\}_3]^-$. HH and HT stand for equal (head-to-head) or opposite (head-to-tail) orientation of adjacent amidates, respectively.

 © 2006 Wiley-VCH Verlag GmbH & Co. KGaA, Weinheim 

number two for the platinum resonating at $\delta$ = –437 ppm and only one for the platinum resonating at $\delta$ = 241 ppm. It is worth noting that, differently from the present case, where only a broadening of the signals has been observed, the Pt–N couplings are well resolved in some mononuclear complexes with terminal amides.[24]

Compounds **1a** and **1b** in aqueous solution (**1a** is not soluble in $CDCl_3$) give identical $^{195}Pt$ NMR spectra, with resonances at $\delta$ = 220 and –430 ppm indicating that the two compounds contain the same complex anion.

The presence of only one isomer in the purified product indicates that this isomer is the end product of the purification procedure but not necessarily that it is the only product formed in the reaction. For this reason we performed an NMR investigation on the crude reaction product obtained by evaporation of the aqueous reaction solution to dryness. The $^{195}Pt$ NMR spectrum (due to the presence of a very large excess of free amide the $^1H$ NMR spectrum is not informative; moreover, water was used as solvent in order to ensure complete dissolution of the raw material) showed the presence of two sets of signals: one corresponding to that of the purified product (signals at $\delta$ = 220 and –430 ppm) and the other (signals at $\delta$ = 161 and –86 ppm) indicating the presence of a second isomer. The intensity of this second set of signals was initially similar to that of the other isomer (about 0.7 times its intensity). However, on standing in solution at room temperature its intensity decreased and after eight days became negligible (Figure 4). Therefore, we can conclude that two major dinuclear species are initially formed and that with time, under the experimental conditions used for this investigation (water solution of the raw material still containing a large excess of free acetamide), one isomer converts into the other.

It has already been demonstrated that the thermodynamically favored isomer has an HHT configuration, therefore the second isomer observed in the crude reaction product can have either an HTH or an HHH configuration. For the HTH isomer the chemical-shift difference between the two platinum atoms and the peak profiles are expected to be similar to those observed for the HHT isomer since both have similar sets of donor atoms for platinum ($Cl_2NO_2$ and $Cl_2N_2O$). In contrast, for the HHH isomer the chemical-shift difference between the two platinum atoms is expected to be greater than for the HHT and HTH isomers due to the greater difference between the sets of donor atoms ($Cl_2N_3$ and $Cl_2O_3$). Furthermore, the peak profile is expected to be much broader for $Pt(Cl_2N_3)$ than for $Pt(Cl_2O_3)$. Since the chemical-shift difference between the two platinum atoms and the peak profiles for the second isomer present in the raw material are very similar to those observed for the HHT isomer, we propose that this second isomer has HTH configuration.

## X-ray Diffraction Analysis of $(AsPh_4)[Pt_2Cl_4\{N(H)C(CH_3)O\}_3]$

### *Bond Lengths and Angles*

Orange crystals of $\{(AsPh_4)[Pt_2Cl_4\{N(H)C(CH_3)O\}_3]\}_2 \cdot C_5H_{12}$ were obtained by crystallization from $CHCl_3$/pentane (1:1, v/v). The asymmetric unit comprises two independent complex molecules **A** and **B**. The two $[Pt_2Cl_4\{N(H)C(CH_3)O\}_3]^-$ ions are very close to one another, implying the formation of hydrogen bonds between the NH groups of one anion and the O atoms of the second anion. Since the amidate groups in each independent anion are in an HHT arrangement, four different models can be drawn for the pair of independent anions in the asymmetric unit: Z1, Z2, Z3, and Z4 (Scheme 1). The four models converged to $R_1$ = 0.0375 and $wR_2$ = 0.0772 for Z1, $R_1$ = 0.0376 and

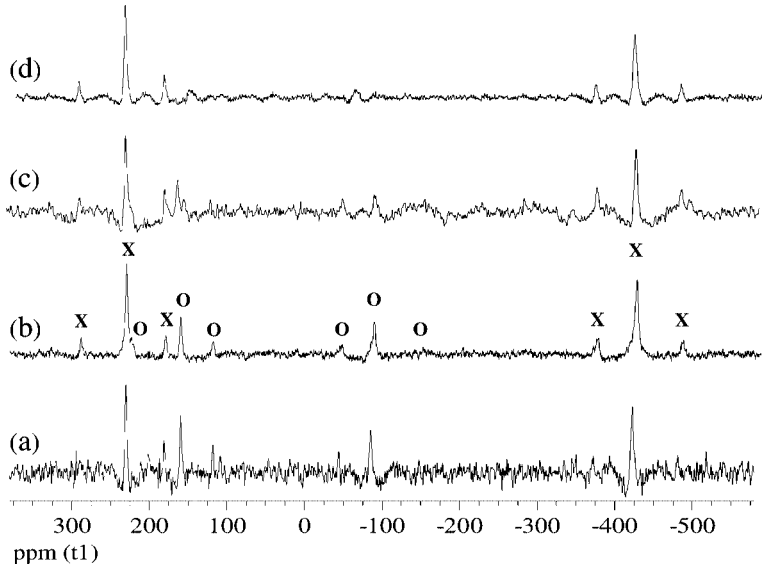


Figure 4. $^{195}Pt$ NMR spectrum of the crude reaction product dissolved in $D_2O$ and kept at 295 K. The spectra were registered soon after dissolution (a) and after one (b), three (c), and eight (d) days. Resonances of the HHT and HTH isomers are labeled with x and o, respectively.

 © 2006 Wiley-VCH Verlag GmbH & Co. KGaA, Weinheim 

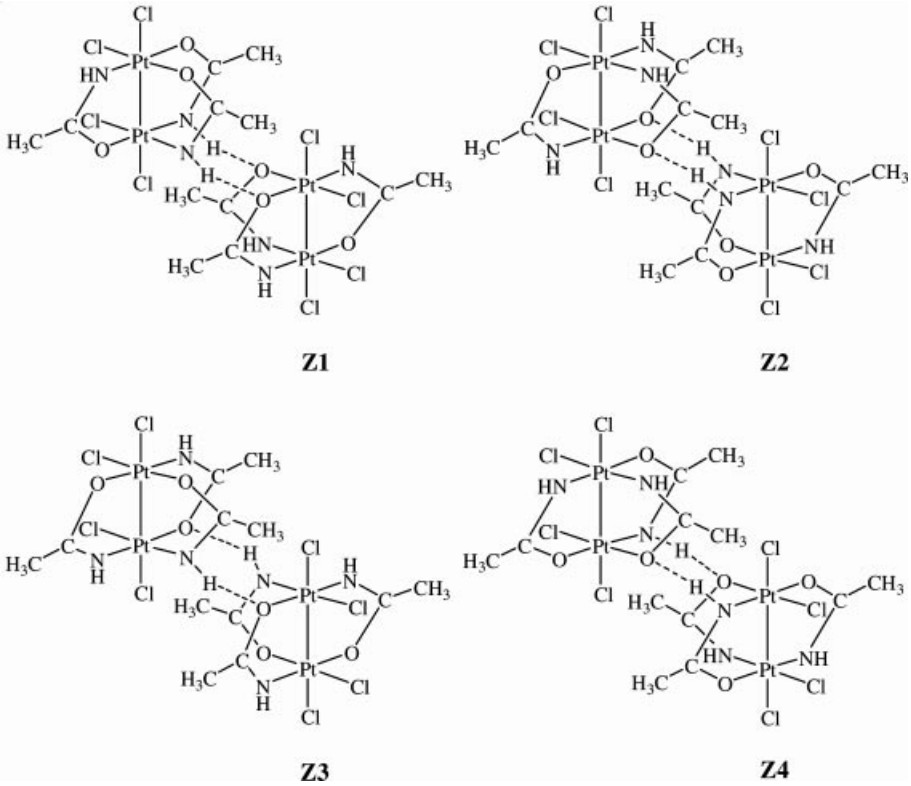


Scheme 1.

$wR_2$ = 0.0778 for Z2, $R_1$ = 0.0374 and $wR_2$ = 0.0766 for Z3, and $R_1$ = 0.0383 and $wR_2$ = 0.0811 for Z4. Among these four models, Z3 has the lowest value of $wR_2$, the best values of thermal parameters for all the N and O atoms of the acetamidate bridging ligands, and the best geometry for the hydrogen bonds between NH and O groups of the two independent anions within the unit cell. On this basis, Z3 was chosen as the correct model. However, clear-cut evidence in favor of Z3 came from analysis of the short contacts between anions of adjacent unit cells. While the Z3 model leads to short (<3.5 Å) N···Cl contacts, indicative of N–H···Cl H-bond interactions, all other models lead to short O···Cl distances, which imply unfavorable electrostatic repulsion between the two electron-rich atoms (see following discussion on intermolecular interactions).

Within a dinuclear complex molecule, each platinum(III) atom has a distorted octahedral geometry with three amidates and a chloride ligand in equatorial positions and a chloride ligand and the second platinum atom in axial positions (Figure 5). Selected bond lengths and angles are reported in Table 1.

The equatorial Pt–Cl [2.27(1)–2.35(1) Å], Pt–N [1.97(2)–2.07(2) Å], and Pt–O distances [2.03(2)–2.08(2) Å] are in the range of those reported for doubly and quadruply bridged dinuclear platinum(III),[5,6,25,26] four-coordinate platinum(II), and six-coordinate platinum(IV) complexes.[11] The axial Pt–Cl distances [2.43(1)–2.47(1) Å] are significantly longer (ca. 0.14 Å) than the equatorial Pt–Cl distances and are comparable to those already reported for axial Pt–Cl distances in dinuclear complexes of platinum(III) (average Pt–Cl distance of 2.44 Å).[5,25–27] The Pt–Pt distances [2.533(2) and 2.527(2) Å] are in between the Pt–Pt distances observed for

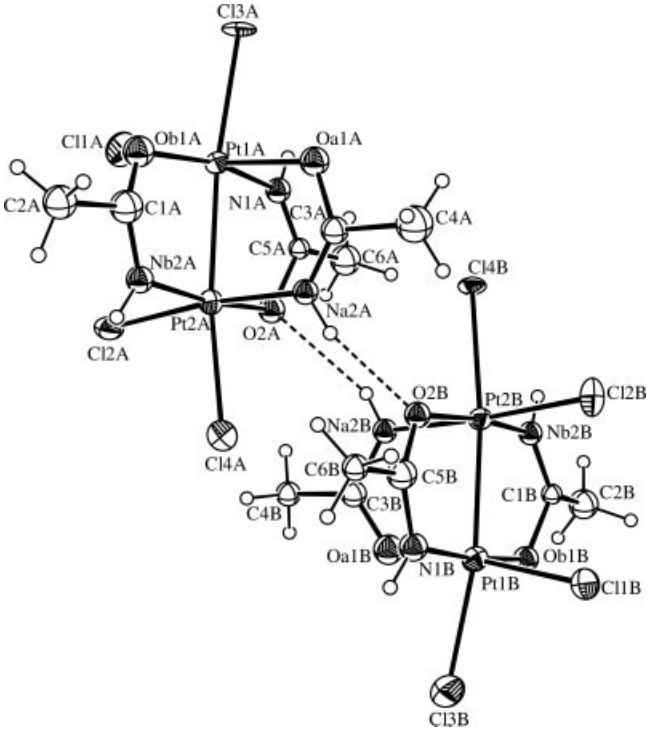


Figure 5. ORTEP view, with labelling scheme, of the two independent $[Pt_2Cl_4\{N(H)C(CH_3)O\}_3]^-$ ions within the unit cell. Ellipsoids enclose 30% probability.

 © 2006 Wiley-VCH Verlag GmbH & Co. KGaA, Weinheim 

Table 1. Selected bond lengths [Å] and angles [°] for the molecules **A** and **B** of $\{(AsPh_4)[Pt_2Cl_4\{N(H)C(CH_3)O\}_3]\}_2 \cdot C_5H_{12}$.

| **A** | | **B** | |
|---|---|---|---|
| Pt(1A)–Pt(2A) | 2.527(2) | Pt(1B)–Pt(2B) | 2.533(2) |
| Pt(1A)–N(1A) | 2.037(19) | Pt(1B)–N(1B) | 1.96(2) |
| Pt(1A)–O(a1A) | 2.058(12) | Pt(1B)–O(a1B) | 2.030(13) |
| Pt(1A)–O(b1A) | 2.071(14) | Pt(1B)–O(b1B) | 2.051(13) |
| Pt(1A)–Cl(1A) | 2.273(10) | Pt(1B)–Cl(1B) | 2.302(10) |
| Pt(1A)–Cl(3A) | 2.455(7) | Pt(1B)–Cl(3B) | 2.429(10) |
| Pt(2A)–N(a2A) | 1.970(17) | Pt(2B)–N(b2B) | 1.99(2) |
| Pt(2A)–N(b2A) | 2.00(2) | Pt(2B)–N(a2B) | 2.074(17) |
| Pt(2A)–O(2A) | 2.083(16) | Pt(2B)–O(2B) | 2.040(15) |
| Pt(2A)–Cl(2A) | 2.346(10) | Pt(2B)–Cl(2B) | 2.309(10) |
| Pt(2A)–Cl(4A) | 2.448(10) | Pt(2B)–Cl(4B) | 2.470(7) |
| N(1A)–Pt(1A)–O(a1A) | 89.0(6) | N(1B)–Pt(1B)–O(a1B) | 93.4(6) |
| O(a1A)–Pt(1A)–O(b1A) | 97.5(5) | O(a1B)–Pt(1B)–O(b1B) | 80.1(5) |
| O(b1A)–Pt(1A)–Cl(1A) | 86.9(5) | O(b1B)–Pt(1B)–Cl(1B) | 93.9(5) |
| Cl(1A)–Pt(1A)–N(1A) | 87.9(6) | Cl(1B)–Pt(1B)–N(1B) | 93.1(6) |
| N(1A)–Pt(1A)–Cl(3A) | 93.9(6) | N(1B)–Pt(1B)–Cl(3B) | 91.4(7) |
| O(b1A)–Pt(1A)–Cl(3A) | 95.5(4) | O(b1B)–Pt(1B)–Cl(3B) | 93.4(5) |
| O(a1A)–Pt(1A)–Cl(3A) | 84.9(4) | O(a1B)–Pt(1B)–Cl(3B) | 84.0(5) |
| Cl(1A)–Pt(1A)–Cl(3A) | 87.2(4) | Cl(1B)–Pt(1B)–Cl(3B) | 90.5(4) |
| N(1A)–Pt(1A)–Pt(2A) | 84.5(6) | N(1B)–Pt(1B)–Pt(2B) | 85.7(6) |
| O(b1A)–Pt(1A)–Pt(2A) | 86.9(4) | O(b1B)–Pt(1B)–Pt(2B) | 88.4(4) |
| O(a1A)–Pt(1A)–Pt(2A) | 88.1(4) | O(a1B)–Pt(1B)–Pt(2B) | 86.6(4) |
| Cl(1A)–Pt(1A)–Pt(2A) | 99.6(3) | Cl(1B)–Pt(1B)–Pt(2B) | 99.2(3) |
| Cl(3A)–Pt(1A)–Pt(2A) | 172.9(2) | Cl(3B)–Pt(1B)–Pt(2B) | 170.0(3) |
| N(a2A)–Pt(2A)–N(b2A) | 95.7(7) | N(a2B)–Pt(2B)–N(b2B) | 86.6(7) |
| N(b2A)–Pt(2A)–Cl(2A) | 89.1(6) | N(b2B)–Pt(2B)–Cl(2B) | 92.9(6) |
| Cl(2A)–Pt(2A)–O(2A) | 87.0(5) | Cl(2B)–Pt(2B)–O(2B) | 92.2(5) |
| O(2A)–Pt(2A)–N(a2A) | 89.0(6) | O(2B)–Pt(2B)–N(a2B) | 88.7(6) |
| N(a2A)–Pt(2A)–Cl(4A) | 83.8(6) | N(a2B)–Pt(2B)–Cl(4B) | 88.3(6) |
| N(b2A)–Pt(2A)–Cl(4A) | 93.1(7) | N(b2B)–Pt(2B)–Cl(4B) | 91.1(7) |
| O(2A)–Pt(2A)–Cl(4A) | 95.3(5) | O(2B)–Pt(2B)–Cl(4B) | 94.0(5) |
| Cl(2A)–Pt(2A)–Cl(4A) | 90.3(3) | Cl(2B)–Pt(2B)–Cl(4B) | 88.2(3) |
| N(a2A)–Pt(2A)–Pt(1A) | 85.6(5) | N(a2B)–Pt(2B)–Pt(1B) | 83.9(5) |
| N(b2A)–Pt(2A)–Pt(1A) | 85.1(6) | N(b2B)–Pt(2B)–Pt(1B) | 86.5(6) |
| O(2A)–Pt(2A)–Pt(1A) | 87.4(5) | O(2B)–Pt(2B)–Pt(1B) | 87.8(4) |
| Cl(2A)–Pt(2A)–Pt(1A) | 100.5(2) | Cl(2B)–Pt(2B)–Pt(1B) | 99.6(3) |
| Cl(4A)–Pt(2A)–Pt(1A) | 169.0(3) | Cl(4B)–Pt(2B)–Pt(1B) | 171.9(2) |

doubly bridged (ca. 2.58 Å)[25–27] and quadruply bridged platinum(III) complexes [2.448(2) Å][5] having bridging amidates and terminal Cl ligands.

The dihedral angles between equatorial planes are 15.3(4)° for molecule **A** and 15.9(4)° for molecule **B**. The bow-like distortion of the Cl3–Pt1–Pt2–Cl4 axis, as indicated by the sum of the deviations from 180° of the angles Cl3–Pt1–Pt2 and Pt1–Pt2–Cl4, is 18.1(4)° for both molecules **A** and **B** and corresponds roughly to the dihedral angle between the equatorial planes. It should be noted that the dihedral angle between the equatorial planes in triply bridged acetamidate species is smaller than in the corresponding doubly bridged species (ca. 20°).[25,26]

### *Intermolecular Interactions*

Compound **1b** crystallizes with one molecule of pentane per asymmetric unit. The molecules of solvent are located in pores of the crystal lattice running along the *a* direction, which appear to be specific for this solvent. For a better understanding of how these pores are formed a detailed description of the crystal packing is given in this section. As already anticipated, two strong H-bonds link the two independent anions (**A** and **B**) within the asymmetric unit. The atoms involved in H-bonding are the nitrogen Na2 and the oxygen O2 [Na2A···O2B = 2.92(2), (Na2A)H···O2B = 2.09(1) Å, Na2A–H···O2B = 162(1)°; Na2B···O2A = 3.09(2), (Na2B)H···O2A = 2.36(2) Å, Na2B–H···O2A = 142(1)°].

Anions **A** and **B** of one cell are hydrogen-bonded with anions of adjacent cells. These H-bonds involve the Cl4 and Nb2 atoms of anion **A** of one cell and the Nb2 and Cl4 atoms of anion **B** of the adjacent cell [Nb2A···Cl4B($x$ + 1, +$y$, +$z$) = 3.49(2), (Nb2A)H···Cl4B($x$ + 1, +$y$, +$z$) = 2.664(7) Å, Nb2A–H···Cl4B($x$ + 1, +$y$, +$z$) = 162(1)°; Nb2B···Cl4A($x$ – 1, +$y$, +$z$) = 3.46(2), (Nb2B)H···Cl4A($x$ – 1, +$y$, +$z$) = 2.615(9) Å, Nb2B–H···Cl4A($x$ – 1, +$y$, +$z$) = 170(1)°].

As already anticipated, all the models other than Z3 reported in Scheme 1 (Z1, Z2, and Z4) would result in very short O···Cl nonbonding distances between contiguous **A** and **B** anions of adjacent cells. The resulting O···Cl distances (ca. 3.46 Å) would be very close to the sum of the van der Waals radii for oxygen and chlorine atoms and would lead to unfavorable electrostatic repulsion between

 © 2006 Wiley-VCH Verlag GmbH & Co. KGaA, Weinheim 

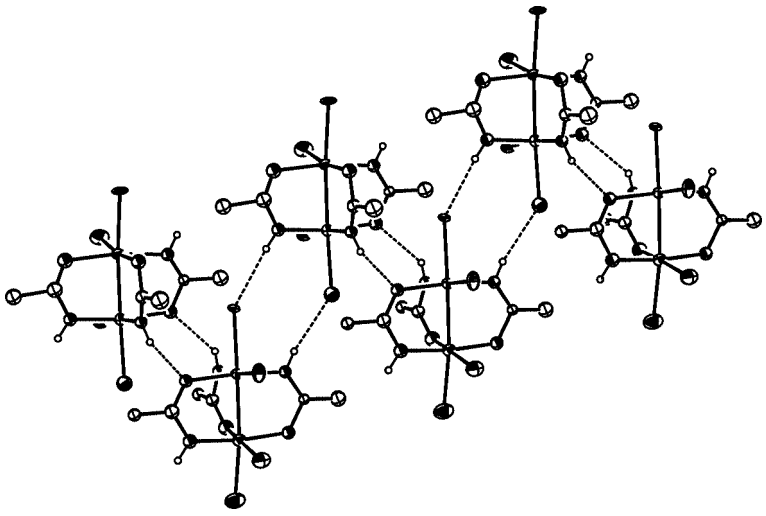

Figure 6. View of the hydrogen-bonding network.

the two electron-rich atoms. This observation gives strong support to the choice of model Z3 for describing the positioning of the two anions within the unit cell.

The N–H···O hydrogen bonds linking the **A** and **B** molecules within the same cell and the N–H···Cl bonds linking the **A** molecule of one cell with the **B** molecule of the adjacent cell make a chain of $[Pt_2Cl_4\{N(H)C(CH_3)O\}_3]^-$ anions extending along the *a* axis (Figure 6).

The tetraphenylarsonium cations are located between the chains of anions extending along the *a* direction, which results in columns running parallel to the chains of anions. There are no direct interactions between these cations, however there are H-bonds between the Cl atoms of the chains of anions and the H atoms of the cations [Cl1A···C20A = 3.46(2), Cl1A···H(C20A) = 2.72(1) Å, Cl1A···H–C20A = 137(1)°; Cl1A···C29B($x-1, y-1, z-1$) = 3.77(2), Cl1A···H(C29B)($x-1, y-1, z-1$) = 3.00(1) Å, Cl1A···H–C29B($x-1, y-1, z-1$) = 141(1)°; Cl2A···C11A = 3.55(2), Cl2A···H(C11A) = 2.79(1) Å, Cl2A···H–C11A = 140(1)°; Cl2A···C27A($x+1, y, z$) = 3.60(2), Cl2A···H(C27A)($x+1, y, z$) = 2.72(1) Å, Cl2A···H–C27A($x+1, y, z$) = 158(1)°; Cl3A···C30B($x-1, y-1, z-1$) = 3.46(2), Cl3A···H(C30B)($x-1, y-1, z-1$) = 2.77(1) Å, Cl3A···H–C30B($x-1, y-1, z-1$) = 132(1)°; Cl4A···C15B($x, y, z-1$) = 3.63(2), Cl4A···H(C15B)($x, y, z-1$) = 2.73(1) Å, Cl4A···H–C15B($x, y, z-1$) = 162(1)°; Cl1B···C8B = 3.55(2), Cl1B···H(C8B) = 2.72(1) Å, Cl1B···H–C8B = 149(1)°; Cl2B···C15A($x, y, z+1$) = 3.56(2), Cl2B···H(C15A)($x, y, z+1$) = 2.70(1) Å, Cl2B···H–C15A($x, y, z+1$) = 153(1)°; Cl3B···C30A($x+1, y+1, z+1$) = 3.67(2), Cl3B···H(C30A)($x+1, y+1, z+1$) = 2.99(1) Å, Cl3B···H–C30A($x+1, y+1, z+1$) = 132(1)°; Cl4B···C27B($x-1, y, z$) = 3.80(2), Cl4B···H(C27B)($x-1, y, z$) = 2.99(1) Å, Cl4B···H–C27B($x-1, y, z$) = 146(1)°; Cl4B···C14A($x, y, z+1$) = 3.67(2), Cl4B···H(C14A)($x, y, z+1$) = 2.95(1) Å, Cl4B···H–C14A($x, y, z+1$) = 135(1)°]. The packing of the chains of anions and columns of cations extending along the *a* direction leaves some channels, which also extend along the *a* direction; the pentane molecules of crystallization are located in these channels (Figure 7).

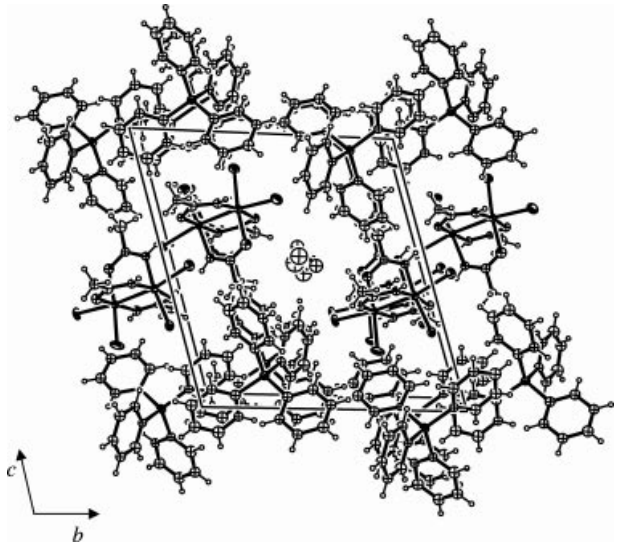


Figure 7. Crystal packing of $\{(AsPh_4)[Pt_2Cl_4\{N(H)C(CH_3)O\}_3]\}_2 \cdot C_5H_{12}$, showing the location of the solvent molecules in the pores of the crystal lattice.

## Conclusions

Dimeric platinum(III) complexes supported by three covalent bridges between the two metal centers have generally been considered as transient species in the reaction leading to quadruply bridged species starting from a 1:1 mixture of $Pt^{II}$ and $Pt^{IV}$ chloro species and excess bridging ligand. We have proven that, by reducing the reaction time, the triply bridged compound can become the major reaction product.

Due to the asymmetry of the acetamide ligand, three isomers can be formed (HHH, HHT, and HTH), although only two major species were found in the crude reaction product: HHT and HTH. Moreover, the HTH species is

 © 2006 Wiley-VCH Verlag GmbH & Co. KGaA, Weinheim 

thermodynamically less stable and slowly (half life of about two days at room temperature) isomerizes into the HHT form. A possible explanation for the observed preference is the more homogeneous sets of donor atoms for the two platinum atoms provided by the HHT and HTH isomers ($Cl_2N_2O$ and $Cl_2NO_2$) as compared to the HHH isomer ($Cl_2N_3$ and $Cl_2O_3$). The HHT isomer is favored over the HTH isomer by a statistical factor of two. It should be noted that the greater stability of the HHT isomer is also in agreement with the configurations found in the quadruply bridged dimers prepared by a similar reaction procedure.[5] The preferred configurations were usually found to be HHTH and HHTT. These two configurations can both be generated from the triply bridged HHT species by addition of a fourth bridge in an H or T orientation. In contrast, the HTH isomer can generate, upon the addition of a fourth bridge, only one observed configuration (HTHH) and a second, never observed, configuration (HTHT).

The crystal structure of the more stable and less symmetric HHT isomer is made up of chains of $[Pt_2Cl_4\{N(H)C(CH_3)O\}_3]^-$ ions running along the *a* direction and columns of tetraphenylarsonium cations also running along the *a* direction. A curious aspect of the crystal packing is the presence of one-dimensional pore channels filled with disordered pentane molecules. The dimension of the pore is probably such that only molecules of *n*-pentane can be accommodated, leaving out completely the molecules of chloroform which, in principle, should give stronger interactions (H bonds) with the aromatic protons on the surface of the pores.

## Experimental Section

**Physical Measurements:** Elemental analyses were obtained with an Elementar Analyser mod. 1106 Carlo Erba instrument. $^1H$ and $^{195}Pt$ NMR spectra were recorded with a Bruker Avance DPX 300 WB spectrometer. $^1H$ chemical shifts are referenced to TMS and $^{195}Pt$ chemical shifts to $K_2PtCl_4$ (1 M in water, $\delta$ = –1614 ppm).

**Preparation of $K[Pt_2Cl_4\{N(H)C(CH_3)O\}_3]$ (1a):** $K_2PtCl_4$ (500 mg, 1.2 mmol) and $K_2PtCl_6$ (585 mg, 1.2 mmol) were dissolved in water (25 mL) and treated with an excess of acetamide (2.8 g, 48 mmol). The reaction mixture was stirred for 1 h at 90 °C. The resulting red solution was cooled to room temperature and then taken to dryness under reduced pressure. The orange solid residue was washed several times with small portions of chloroform in order to remove the excess of acetamide and then extracted with methanol, which solubilizes only the desired compound (**1a**) while leaving KCl and unreacted $K_2PtCl_6$ and $K_2PtCl_4$ as insoluble residue. Orange microcrystals of $K[Pt_2Cl_4\{N(H)C(CH_3)O\}_3]$ precipitated from the methanolic solution upon addition of diethyl ether. Yield: 45% (400 mg). $K[Pt_2Cl_4\{N(H)C(CH_3)O\}_3]\cdot 2H_2O$, $C_6H_{16}Cl_4KN_3O_5Pt_2$ (780.9): calcd. C 9.21, H 2.05, N 5.38; found C 8.83, H 1.83, N 5.54. $^{195}Pt$ NMR (64.3 MHz, $D_2O$, 22 °C): $\delta$ = –430 ($PtCl_2N_2O$) and 220 ($PtCl_2NO_2$) ppm ($^1J_{Pt,Pt}$ = 7020 Hz).

**Preparation of $(AsPh_4)[Pt_2Cl_4\{N(H)C(CH_3)O\}_3]$ (1b):** $K[Pt_2Cl_4\{N(H)C(CH_3)O\}_3]$ (400 mg, 0.54 mmol) and $AsPh_4Cl$ (339 mg, 0.81 mmol) were dissolved in chloroform (70 mL) and stirred for a few minutes. The white precipitate of KCl was removed while the filtered mother liquor was concentrated to a smaller volume (10 mL) and then layered with pentane (10 mL). Under these conditions, orange crystals of the desired product $(AsPh_4)[Pt_2Cl_4\{N(H)C(CH_3)O\}_3]$ separated from solution. Yield: 23% (135 mg). $\{(AsPh_4)[Pt_2Cl_4\{N(H)C(CH_3)O\}_3]\}_2\cdot C_5H_{12}$, $C_{65}H_{76}Cl_8N_6O_6Pt_4As_2$ (2249.4): calcd. C 34.69, H 3.40, N 3.73; found C 34.78, H 3.27, N 3.50. $^1H$ NMR (300 MHz, $CDCl_3$, 22 °C): $\delta$ = 2.03 (s, 3 H, $CH_3$), 2.05 (s, 3 H, $CH_3$), 2.29 (s, 3 H, $CH_3$), 5.73 (s, 1 H, NH), 5.75 (s, 1 H, NH), 6.41 (s, 1 H, NH) ppm. $^{195}Pt$ NMR (64.3 MHz, $CDCl_3$, 22 °C): $\delta$ = –437 ($PtCl_2N_2O$) and 241 ($PtCl_2NO_2$) ppm ($^1J_{Pt,Pt}$ = 6660 Hz).

**X-ray Crystal Structure Determination of $\{(AsPh_4)[Pt_2Cl_4\{N(H)C(CH_3)O\}_3]\}_2\cdot C_5H_{12}$:** Compound **1b**, which crystallizes from $CHCl_3$/pentane with half a molecule of pentane per molecule of compound, was investigated by X-ray diffraction analysis. X-ray data were collected on a BrukerAXS X8 APEX CCD system equipped with a four-circle Kappa goniometer and a 4 K CCD detector (Mo-$K_\alpha$ radiation). A Miracol fiber optics capillary collimator (0.3 mm) was used to enhance the intensity of the Mo-$K_\alpha$ radiation and to reduce X-ray beam divergence. The diameter of the active imaging area was 90 mm and the data were collected at a resolution of 512 × 512 pixels. The crystal-to-detector distance was 40 mm. The SAINT-IRIX package was employed for data reduction and unit-cell refinement.[28]

A total of 53118 reflections ($\Theta_{max}$ = 25.00°) were indexed, integrated, and corrected for Lorentz, polarization, and absorption effects using the program SADABS.[29] The number of independent reflections was 12139. The unit-cell dimensions were calculated from all reflections. The structure was solved by direct methods technique in the *P*1 space group. A pseudo center of inversion is present between the two dinuclear independent molecules **A** and **B**, which is reminiscent of a virtual $P\bar{1}$ space group, although attempts to refine in this group were unsuccessful.

Table 2. Crystal data and structure-refinement parameters for $\{(AsPh_4)[Pt_2Cl_4\{N(H)C(CH_3)O\}_3]\}_2\cdot C_5H_{12}$.

| | |
|---|---|
| Empirical formula | $C_{65}H_{76}As_2Cl_8N_6O_6Pt_4$ |
| Formula mass | 2315.12 |
| Temperature | 293(2) K |
| Wavelength | 0.71073 Å |
| Crystal system | triclinic |
| Space group | *P*1 |
| Unit-cell dimensions | *a* = 8.6244(3) Å $\alpha$ = 104.322(2)° |
| | *b* = 14.6244(5) Å $\beta$ = 97.420(2)° |
| | *c* = 15.3213(5) Å $\gamma$ = 105.320(2)° |
| *V* | 1766.28(10) Å$^3$ |
| *Z* | 1 (A + B) |
| $D_{calcd.}$ | 2.177 g cm$^{-3}$ |
| $\mu$ | 9.190 mm$^{-1}$ |
| *F*(000) | 1102 |
| Crystal size | 0.036 × 0.224 × 0.010 mm |
| $\theta$ range | 1.40–25.00° |
| Index ranges | $-10 \le h \le 10$ |
| | $-17 \le k \le 17$ |
| | $-18 \le l \le 18$ |
| Reflections collected | 53153 |
| Independent reflections | 12146 [*R*(int) = 0.0721] |
| Absorption correction | SADABS (Sheldrick, 1996) |
| Refinement method | Full-matrix least-squares on $F^2$ |
| Data/restraints/parameters | 12146/3/349 |
| Goodness-of-fit on $F^2$ | 1.012 |
| Final *R* indices [$I > 2\sigma(I)$] | $R_1$ = 0.0374, $wR_2$ = 0.0766 |
| *R* indices (all data) | $R_1$ = 0.0676, $wR_2$ = 0.0873 |
| Absolute structure parameter | 0.00(1) |
| Largest diff. peak and hole | 0.966 and –0.659 e Å$^{-3}$ |

 © 2006 Wiley-VCH Verlag GmbH & Co. KGaA, Weinheim 

The model was refined by full-matrix least-square methods. Only the Pt, Cl, and As atoms were refined anisotropically; the remaining atoms needed isotropic treatment in order to maintain satisfactory thermal displacement parameters. Furthermore, the phenyl groups were treated as rigid, idealized hexagons. Hydrogen atoms were placed at calculated positions and refined given isotropic parameters equivalent to 1.2-times (for phenyl groups) or 1.5-times (for methyl groups) those of the atom to which they are attached.

The pentane solvent molecule of crystallization was disordered. The final difference-Fourier map showed electron density peaks (up to 0.966 e $Å^{-3}$) lying near the Pt atoms. All calculations and molecular graphics were carried out using the SIR2002,[30] SHELXL97,[31] PARST97,[32] WinGX,[33] or ORTEP-3 for Windows packages.[34] The crystallographic data are listed in Table 2.

CCDC-288044 contains the supplementary crystallographic data for this paper. These data can be obtained free of charge from The Cambridge Crystallographic Data Center via www.ccdc.cam.ac.uk/data_request/cif.

## Acknowledgments

The authors thank the Università degli Studi di Bari (ex. 60% funds), the Italian "Ministero dell'Istruzione, Università e Ricerca (MIUR)" (PRIN 2004 no. 2004059078_006), and the EC (COST Chemistry projects D20/0001/2000 and D20/0003/01) for support.

[1] K. Matsumoto, K. Sakai, *Adv. Inorg. Chem.* **1999**, *49*, 375–427.
[2] W. Chen, K. Matsumoto, *Inorg. Chim. Acta* **2003**, *342*, 88–96.
[3] B. Lippert, *Coord. Chem. Rev.* **1999**, *181*, 263–295.
[4] T. N. Fedotova, L. K. Minacheva, G. N. Kuznetsova, V. G. Sakharova, M. I. Gel'fman, I. B. Baranovskii, *Russ. J. Inorg. Chem.* **1997**, *42*, 1838–1846.
[5] A. Dolmella, F. P. Intini, C. Pacifico, G. Padovano, G. Natile, *Polyhedron* **2002**, *21*, 275–280.
[6] G. Bandoli, A. Dolmella, F. P. Intini, C. Pacifico, G. Natile, *Inorg. Chim. Acta* **2003**, *346*, 143–150.
[7] G. Natile, F. P. Intini, C. Pacifico, in *Cisplatin*: *Chemistry and Biochemistry of a Leading Anticancer Drug* (Ed.: B. Lippert), Verlag Helvetica Chimica Acta Zürich, Switzerland, and Wiley-VCH, Weinheim, Germany, **1999**; p. 429–453.
[8] K. Umakoshi, Y. Sasaki, *Adv. Inorg. Chem.* **1993**, *40*, 187–239.
[9] G. Kampf, M. Willermann, E. Zangrando, L. Randaccio, B. Lippert, *Chem. Commun.* **2001**, 747–748.
[10] a) T. V. O'Halloran, S. J. Lippard, *Isr. J. Chem.* **1985**, *25*, 130–137; b) O. Renn, A. Albinati, B. Lippert, *Angew. Chem. Int. Ed. Engl.* **1990**, *29*, 84–85; c) M. Kurmoo, R. J. Clark, *Inorg. Chem.* **1985**, *24*, 4420–4425; d) C. S. Glennon, T. D. Hand, A. G. Sykes, *J. Chem. Soc., Dalton Trans.* **1980**, 19–23; e) K. K. S. Gupta, P. K. Sen, S. S. Gupta, *Inorg. Chem.* **1977**, *16*, 1396–1399; f) J. Halpern, M. Pribanic, *J. Am. Chem. Soc.* **1968**, *90*, 5942–5943; g) C. V. Chan, L. K. Cheng, C.-M. Che, *Coord. Chem. Rev.* **1994**, *132*, 87–97; h) J. Forniés, B. Menjon, R. M. Sanz-Carrillo, M. Tomas, N. G. Connelly, J. G. Crossley, A. G. Orpen, *J. Am. Chem. Soc.* **1995**, *117*, 4295–4304.
[11] R. Cini, F. P. Fanizzi, F. P. Intini, G. Natile, *J. Am. Chem. Soc.* **1991**, *113*, 7805–7806.
[12] R. Cini, F. P. Fanizzi, F. P. Intini, L. Maresca, G. Natile, *J. Am. Chem. Soc.* **1993**, *115*, 5123–5131.
[13] G. Bandoli, P. A. Caputo, F. P. Intini, M. F. Sivo, G. Natile, *J. Am. Chem. Soc.* **1997**, *119*, 10370–10376.
[14] K. Matsumoto, J. Matsunami, K. Mizuno, H. Uemura, *J. Am. Chem. Soc.* **1996**, *118*, 8959–8960.
[15] K. Matsumoto, Y. Nagai, J. Matsunami, K. Mizuno, T. Abe, R. Somazawa, J. Kinoshita, H. Shimura, *J. Am. Chem. Soc.* **1998**, *120*, 2900–2907.
[16] Y. Lin, S. Takeda, K. Matsumoto, *Organometallics* **1999**, *18*, 4897–4899.
[17] N. Saeki, N. Nakamura, T. Ishibashi, M. Arime, H. Sekiya, K. Ishihara, K. Matsumoto, *J. Am. Chem. Soc.* **2003**, *125*, 3605–3616.
[18] M. Ochiai, Y. Lin, J. Yamada, H. Misawa, S. Arai, K. Matsumoto, *J. Am. Chem. Soc.* **2004**, *126*, 2536–2545.
[19] T. G. Appleton, K. A. Byriel, J. M. Garrett, J. R. Hall, C. H. L. Kennard, M. T. Mathieson, R. Stranger, *Inorg. Chem.* **1995**, *34*, 5646–5655.
[20] T. G. Appleton, K. A. Byriel, J. R. Hall, C. H. L. Kennard, M. T. Mathieson, *J. Am. Chem. Soc.* **1992**, *114*, 7305–7307.
[21] T. G. Appleton, J. R. Hall, D. W. Neale, S. F. Ralph, *Inorg. Chim. Acta* **1983**, *77*, L149–L151.
[22] T. G. Appleton, J. R. Hall, D. W. Neale, *Inorg. Chim. Acta* **1985**, *104*, 19–31.
[23] P. S. Pregosin, "Platinum NMR Spectroscopy", *Annu. Rep. NMR Spectrosc.* **1986**, *17*, 285–349.
[24] R. Cini, F. P. Fanizzi, F. P. Intini, G. Natile, C. Pacifico, *Inorg. Chim. Acta* **1996**, *251*, 111–118.
[25] B. Lippert, H. Scholhorn, U. Thewalt, *Inorg. Chem.* **1986**, *25*, 407–408.
[26] L. S. Hollis, M. M. Roberts, S. J. Lippard, *Inorg. Chem.* **1983**, *22*, 3637–3644.
[27] K. Sakai, Y. Tanaka, Y. Tsuchiya, K. Hirata, T. Tsubomura, S. Iijima, A. Bhattacharjee, *J. Am. Chem. Soc.* **1998**, *120*, 8366–8379.
[28] Bruker: SAINT-IRIX. Bruker AXS Inc., Madison, Wisconsin, USA, **2003**.
[29] G. M. Sheldrick, *SADABS, Program for Empirical Absorption Correction of Area Detector Data*, University of Göttingen, Germany, **1996**.
[30] Sir2002: M. C. Burla, M. Camalli, B. Carrozzini, G. L. Cascarano, C. Giacovazzo, G. Polidori, R. Spagna, *J. Appl. Crystallogr.* **2003**, *36*, 1103.
[31] *Programs for Crystal Structure Analysis (release 97-2)*, G. M. Sheldrick, Institut für Anorganische Chemie der Universität, Tammanstrasse 4, 37077 Göttingen, Germany, **1998**.
[32] a) M. Nardelli, *Comput. Chem.* **1983**, *7*, 95–97; b) M. Nardelli, *J. Appl. Crystallogr.* **1995**, *28*, 659.
[33] L. J. Farrugia, *J. Appl. Crystallogr.* **1999**, *32*, 837–838.
[34] L. J. Farrugia, *J. Appl. Crystallogr.* **1997**, *30*, 565.

Received: October 27, 2005
Published Online: March 1, 2006

 © 2006 Wiley-VCH Verlag GmbH & Co. KGaA, Weinheim 

DOI: 10.1002/ejic.200500975

# Facile Synthesis of $SnO_2$ Hollow Nanospheres and Applications in Gas Sensors and Electrocatalysts

Qingrui Zhao,[a] Yang Gao,[a] Xue Bai,[a] Changzheng Wu,[a] and Yi Xie*[a]

**Keywords:** Tin oxides / Room-temperature sensitivity / Electrocatalysts

Tin oxide ($SnO_2$) hollow nanospheres have been successfully synthesized from mixed ethanol and water systems containing the surfactants sodium dodecyl benzenesulfonate (SDBS) and terephthalic acid. Systematic studies reveal that terephthalic acid plays pivotal roles in the formation of hollow nanospheres. In the present work, the as-synthesized $SnO_2$ hollow nanospheres exhibit excellent room-temperature ethanol sensitivity and potential catalytic ability towards the electrooxidation of ethanol, and thus are expected to be economical alternative catalysts and useful in industrial applications such as room-temperature gas sensors.

(© Wiley-VCH Verlag GmbH & Co. KGaA, 69451 Weinheim, Germany, 2006)

## Introduction

Tin oxide ($SnO_2$), an n-type semiconductor with a wide bandgap ($E_g$ = 3.62 eV), is a key functional material, which has attracted a lot of interest as an excellent candidate for optoelectronic devices,[1] gas sensors,[2] transparent conducting electrodes,[3] and catalyst supports.[4] With specific morphologies, the hollow structures are more desirable because of their potential for encapsulation of large quantities of guest molecules or large-sized guests within the empty core domain.[5] For example, hollow $SnO_2$ microspheres offer enhancement in sensitivity to methanol, carbon monoxide, benzene, and water over compact chemical vapor deposition (CVD) films at high temperatures.[6] On the basis of this, hollow spheres of $SnO_2$ have been produced with sizes ranging in the submicrometer regime. For example, Xia et al. used polystyrene particles as templates to fabricate mesoscale hollow spheres of $SnO_2$ with an average diameter of 400 nm.[7] Qian et al. synthesized $SnO_2$ hollow microspheres with a diameter of several micrometers by hydrolysis of $SnCl_4$ in alkaline media.[8]

Although various types of gas sensors have been investigated, great effort has focused on exploring the high temperature sensitivity of sensors.[9] However, the sensors working at lower temperatures, especially room temperature, no doubt have wider and more practical applications such as in the detection of drunk drivers by measuring ethanol concentrations of their breath. Therefore, it becomes more important to explore the room-temperature sensitivity of $SnO_2$. One useful strategy for increasing the poor sensitivity of tin oxide at room temperature may be realized by controlling the morphology as well as decreasing the size of the sensor materials. However, little work has been reported on the production of hollow $SnO_2$ nanospheres, which are expected to show superior properties. Thus, the exploration of a simple and easily scaled-up route to hollow nanostructures is still a great challenge so far.

Tin oxide materials have been known for a long time to display good catalytic activity towards the synthesis of vinyl ketone,[10] oxidation of methanol,[11] and so on. Recently, the demands for alternative energy sources such as fuel cells have attracted great interest in the studies on nanostructured materials. Among various candidates for catalysts of ethanol fuel cells, carbon-supported $PtSnO_2$ catalysts have exhibited excellent catalytic activity for ethanol electrooxidation, in which $SnO_2$ can enhance the catalytic activity for alcohol electrooxidation.[11] Therefore, nanomaterials with $SnO_2$ alone are believed to display potential catalytic activity for ethanol electrooxidation. In this paper, the electrochemical properties of the prepared hollow $SnO_2$ nanospheres for ethanol electrooxidation were examined.

Among many preparative methods for hollow nano- and mesoscaled structures, template-assisted synthesis is an effective approach in which hard templates[12,13] and soft templates[14] have been utilized. Surfactants tend to self-assemble to form micelles with desired structures and have been widely used as soft templates.[15] However, in many systems, the aggregated micelles may be very sensitive to the solvents and become unstable, which may not facilitate their use as templates in the microreactors. Thus, the complex surfactant systems are introduced to fabricate hollow structures.[16,17] For example, Qi et al. reported the synthesis of micrometer-sized hollow $CaCO_3$ spheres by using the complex surfactant of poly(ethylene oxide)-*block*-poly(methacrylic acid)–sodium dodecylsulfate (PEO-*b*-PMAA-

[a] Nano-materials and Nano-chemistry, Hefei National Laboratory for Physical Sciences at Microscale, University of Science & Technology of China,
Hefei, Anhui 230026, P. R. China
Fax: +86-551-3603987
E-mail: yxielab@ustc.edu.cn

 © 2006 Wiley-VCH Verlag GmbH & Co. KGaA, Weinheim 

SDS) micelles as templates,[16] in which the additive of PEO-*b*-PMAA could hold $Ca^{2+}$ ions and assisted with the precipitation of $CaCO_3$. However, the large steric hindrance of the surfactant polymer PEO-*b*-PMAA-SDS made it difficult to restrict the size to the nanometer regime. Here, we suppose a simple coordination agent, which can hold metal ions without the large steric hindrance, may help to increase the stability of the soft template and thus further increase the formation of the hollow nanospheres. $SnO_2$ hollow nanospheres are successfully synthesized from a micelle system that is made up of the surfactants terephthalic acid along with sodium dodecyl benzenesulfonate (SDBS) in an ethanol and water (volume ratio 1:1) solution. Terephthalic acid can hold $Sn^{2+}$ ions without a large steric hindrance, which is helpful for the growth of $SnO_2$ hollow nanospheres. We found that the as-synthesized $SnO_2$ hollow nanospheres show good room-temperature sensitivity to ethanol vapors and potential catalytic activity for electrooxidation of ethanol, which offers promising applications in the fields involving sensors and catalysts.

## Results and Discussion

The phase and purity of the sample was determined by X-ray powder diffraction (XRD), and the typical diffraction pattern is shown in Figure 1. All the peaks were readily indexed to the tetragonal phase of $SnO_2$ (JCPDS card No. 41-1445), with lattice constants of $a$ = 4.738 Å and $c$ = 3.187 Å. No characteristic peaks were observed for the other impurities.

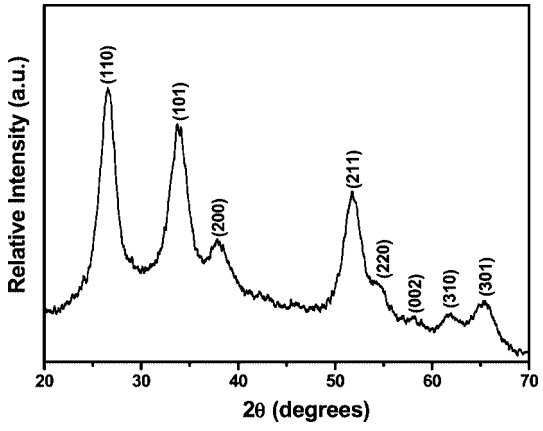


Figure 1. XRD pattern of the $SnO_2$ hollow nanospheres.

To further characterize the product, XPS was carried out to investigate the surface compositions and chemical state of the as-prepared products, and the results are shown in Figure 2. The binding energies obtained in the XPS analysis were corrected for specimen charging by referencing $C_{1s}$ to 284.75 eV. The sample appeared as a spin-orbit doublet at ca. 486.85 eV ($3d_{5/2}$) and ca. 495.25 eV ($3d_{3/2}$) (Figure 2, a), which is in agreement with the reported value in the literature.[18] The $O_{1s}$ binding energy of 531.00 eV (Figure 2, b) indicates that the oxygen atoms exist as $O^{2-}$ species in the compounds. Quantification gave the atomic ratio of O and Sn elements as 1.93 on the basis of the areas of the O and Sn peaks within experimental error. Consequently, from the results of the XRD and XPS measurements the as-synthesized products could be determined as $SnO_2$.

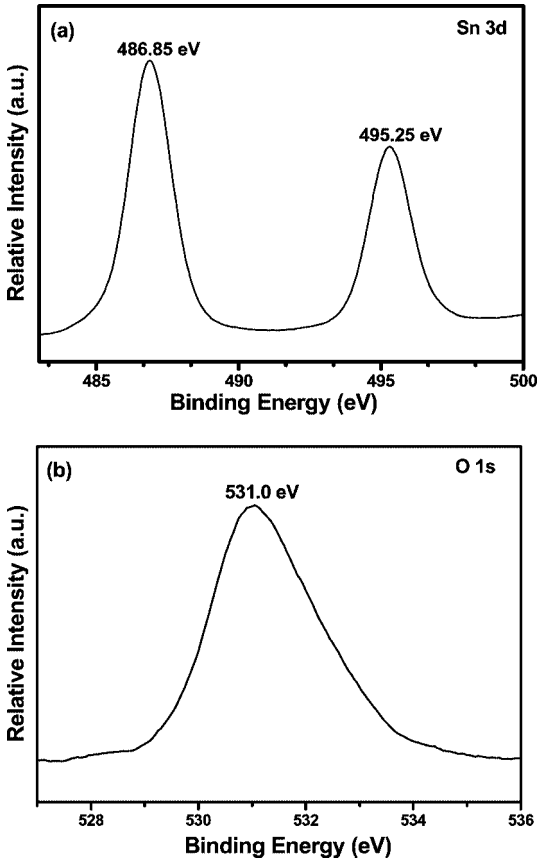


Figure 2. XPS spectra of the $SnO_2$ hollow nanospheres: (a) Sn region; (b) O region.

The structure and morphology of these hollow $SnO_2$ nanostructures were investigated by TEM. From the panoramic morphology shown in Figure 3 (a), a bright contrast (dark/bright) between the boundary and the center of the spheres is seen, confirming their hollow nature. The external diameter of the hollow spheres is 80–120 nm and the thickness of the shell is ca. 10–20 nm. The inset in Figure 3 (a) corresponds to the SAED pattern performed on the shell, and the circular character indicates the polycrystalline $SnO_2$ shell. The structural details were investigated from a high-magnification TEM image (Figure 3, b), revealing that the shells of hollow $SnO_2$ nanospheres seem to be rough and consist of nanoparticles with sizes in the range of 3–5 nm. The high-resolution transmission electron microscopy (HRTEM) images (Figure 3, c) further confirm the hollow nanostructures. FE-SEM observations also revealed that the $SnO_2$ nanospheres are hollow, which was learned from the broken regions of the spheres, as indicated by the arrows (see part d of Figure 3 and the inset).

It is known that SDBS is an anionic surfactant, which tends to self-assemble to form aggregates and further lead to the formation of microemulsions with desired structures because of its bulky hydrophobic tail compared with the

 © 2006 Wiley-VCH Verlag GmbH & Co. KGaA, Weinheim 

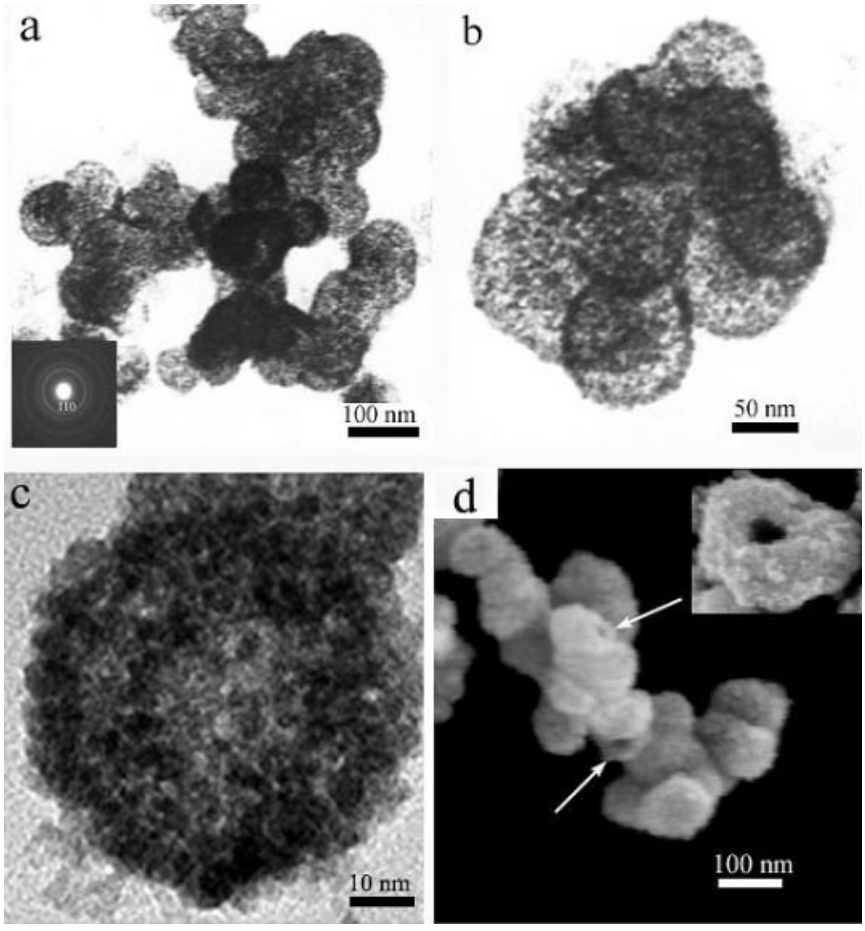


Figure 3. Electron microscopy images of the $SnO_2$ nanostructures. (a) TEM images. The inset in (a) is the corresponding ED pattern; (b) High-magnification TEM image; (c) HRTEM image of an individual $SnO_2$ hollow nanosphere; (d) FESEM image. The upper inset is the FESEM image of the 'opened' structure of a hollow sphere.

hydrophilic group.[19] However, in many systems SDBS micelles become unstable. Thus, terephthalic acid is added to play the important role of facilitating the formation of more stable aggregates to provide chemical microenviroments. Previous investigations of the interaction between SDS, poly(ethylene glycol) (PEG), and poly(methacrylic acid) (PMAA) showed that ionic headgroups of SDS repelled the charged PMAA chains and only hydrocarbon chains of SDS partitioned into the PEG core of the polymer aggregates. Then PMAA as a shell may be adsorbed onto the surface of the core, which is made up of PEG and SDS, through the interaction between the PMAA and PEG.[20] Thus, we could speculate that the mixture of SDBS and terephthalic acid in the mixed ethanol and water solutions could form complex micelles similar to that of the PEG-PMAA-SDS complex. In this case, ethanol with ethyl and ethylene oxide groups could interact with anionic SDBS to form micelles.[21] Terephthalic acid as a shell might be adsorbed onto the surface of the micelles through the interaction between ethanol and terephthalic acid. Such micelles would function as soft templates and provide the microenviroment in which nucleation and growth of $SnO_2$ could occur. In this approach, $SnO_2$ was synthesized by the chemical reaction of $SnCl_2$ and $KClO_3$ in ethanol and water solutions of terephthalic acid and SDBS, on the basis of the following equation:

$$3\,Sn^{2+} + ClO_3^- + 3\,H_2O \rightarrow 3\,SnO_2 + Cl^- + 6\,H^+$$

Terephthalic acid provides the nucleation sites for the crystallization of $SnO_2$ owing to the interaction of terephthalic acid and $Sn^{2+}$, which leads to a high local supersaturation of $Sn^{2+}$ over the micelle periphery.[20] The crystallization of $SnO_2$ started from these nucleation sites on the surface of the micelles and the crystals developed outwards until they collided with each other, leading to the final hollow structures. A schematic pattern of the formation process was shown in Scheme 1. It is worth noting that the $SnO_2$ hollow nanospheres, which are attributed to the simple coordination agent terephthalic acid that can hold $Sn^{2+}$ ions, formed without a large steric hindrance.

The complex surfactant system was critical in the formation of hollow nanospheres. If the reaction was carried out in the absence of terephthalic acid the products were found to be large amounts of $SnO_2$ nanoparticles and a few hollow nanospheres; whereas if the experiment was carried out without SDBS under similar conditions, only $SnO_2$ nanoparticles were obtained. The results above indicate that single SDBS-micelles as soft templates ae unstable, but the presence of terephthalic acid favored the formation of stable

 © 2006 Wiley-VCH Verlag GmbH & Co. KGaA, Weinheim 

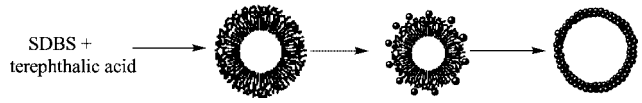


Scheme 1. Schematic illustration of the formation process of $SnO_2$ hollow nanospheres: a mixture of SDBS and terephthalic acid complexes in the system → complex micelles were formed → $SnO_2$ particles formed on the surface of the micelles → $SnO_2$ hollow nanospheres emerged as the final product.

micelles, and thus further helped the growth of the $SnO_2$ hollow nanospheres. The synergistic effect of terephthalic acid and SDBS as the soft templates in the formation of $SnO_2$ hollow nanospheres has been confirmed.

It is known that the solvent composition has a great effect on the formation of the micelle structures.[15] The solvent composition influences the difference in solubility of the hydrophilic head and hydrophobic tail of the surfactant, thus affecting the formation and aggregation of the micelles. To investigate the effect of the solvent composition, a series of comparative experiments were carried out. When keeping other experimental conditions unchanged, the absence of ethanol would only produce irregular $SnO_2$ particles. When trace ethanol was introduced into the system, a few hollow nanospheres appeared in the products. If the volume ratio of ethanol and water was increased to 1:1 all the samples had a hollow nanosphere morphology. These results demonstrate that ethanol seems to perform the function of bridging the SDBS and terephthalic acid, which is consistent with the proposed mechanism above. Moreover, the addition of ethanol could have increased the solubility of terephthalic acid in this approach, which facilitated the formation of micelles and was necessary for the formation of $SnO_2$ hollow nanospheres. However, at a high percentage of the ethanol solvent only a few $SnO_2$ hollow nanospheres formed. This may be caused by the lower solubility of $KClO_3$ at a high ethanol percentage, leading to incomplete reaction.

The room-temperature PL spectrum of hollow $SnO_2$ nanospheres, as shown in Figure 4, was obtained with an excitation wavelength of 340 nm. It can be seen that the spectrum of the sample is characterized by one strong emission band at 410 nm. Earlier reports indicated that $SnO_2$ thin films exhibit a broad dominant peak near 396 nm (3.1 eV),[22] and that $SnO_2$ nanoribbons synthesized by self-catalyst growth have a strong emission band centered at ca. 500 nm because of other luminescence centers, such as crystal defects.[23] The newly observed peaks at 410 nm might result from other luminescence centers, such as oxygen vacancies or tin interstitials in the obtained hollow $SnO_2$ nanospheres.

The hollow structure of the $SnO_2$ hollow nanospheres was expected to offer advantages in fabricating gas sensors at room temperature. The room-temperature sensitivity of the obtained $SnO_2$ hollow nanospheres in response to $C_2H_5OH$ was investigated, which is shown in Figure 5 (a). The gas sensitivity, $S_g$, was defined as $R_{air}/R_{gas}$, where $R_{air}$ and $R_{gas}$ are the electrical resistances for the sensor in air and in gas.[24] It can be seen from Figure 5 (a) that the sensitivity of the $SnO_2$ hollow nanospheres gradually increases with an increase in ethanol gas concentration. To evaluate the sensitivity of the $SnO_2$ hollow nanospheres, solid $SnO_2$ nanoparticles with a diameter of 5 nm were fabricated according to ref.[25] The room-temperature sensitivity of 5 nm $SnO_2$ nanoparticles is displayed in Figure 5 (b) and compared with that of the hollow nanospheres. As shown in Figure 5, the sensitivity of the $SnO_2$ hollow nanospheres versus ethanol concentration was much greater than that for the $SnO_2$ nanoparticles under the same conditions. For the sensors, we believe that the higher sensitivity might be attributed to the hollow structures of the sample, which has more chance to adsorb and desorb the gas molecules.[24] In addition, in order to test the reversibility of the sample, the measurements were repeated more than 10 times and no major changes in the signals were observed.

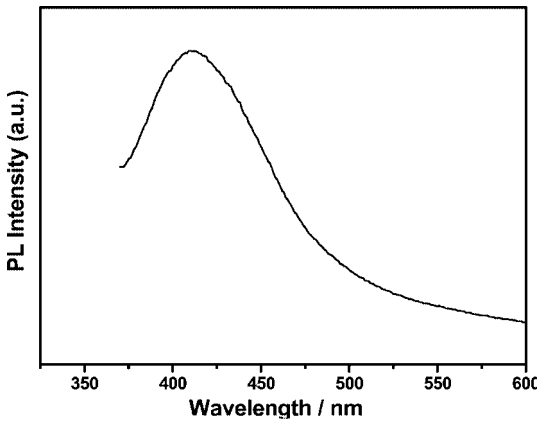


Figure 4. PL spectrum of the $SnO_2$ hollow nanospheres.

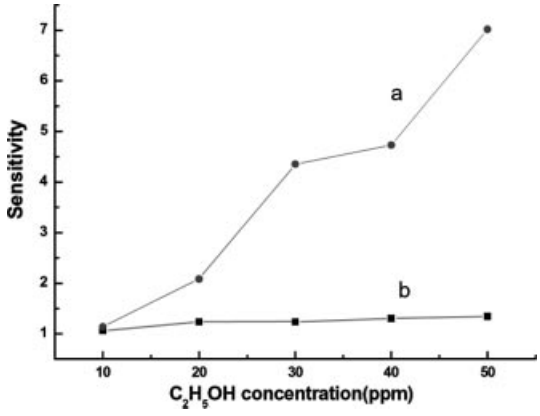


Figure 5. Room-temperature sensor sensitivity to ethanol of (a) the as-prepared $SnO_2$ hollow nanospheres and (b) nanoparticles.

Brunauer–Emmett–Teller (BET) nitrogen adsorption-desorption measurements showed that the surface area of the hollow $SnO_2$ nanospheres is 44 $m^2 g^{-1}$, whereas the surface area of $SnO_2$ nanoparticles is 31 $m^2 g^{-1}$. The small difference between the BET surface area of the $SnO_2$ hollow nanospheres and the nanoparticles may be attributed to the fact that the surface of the $SnO_2$ hollow nanospheres is composed of compact nanoparticles. The superior sensing properties of the obtained hollow $SnO_2$ nanospheres could

 © 2006 Wiley-VCH Verlag GmbH & Co. KGaA, Weinheim 

be because of its porous structure associated with the small grain size,[6] which enables ethanol gas to access almost all of the surfaces of the hollow $SnO_2$ nanospheres contained in the sensing unit. Therefore, hollow $SnO_2$ nanospheres with a higher surface area have more chances to adsorb and desorb ethanol gas molecules, which leads to higher sensitivity at room temperature.

In previous reports, $SnO_2$ nanoparticles were employed to synthesize the carbon-supported $PtSnO_2$ catalyst, which promoted catalytic activity of the ethanol electrooxidation in fuel cells.[11] However, a critical problem with Pt-based catalysts is their prohibitive cost. Therefore, economical and effective alternative catalysts are required. Thus, in the current work the electrooxidation of ethanol of $SnO_2$ hollow nanospheres was investigated without Pt, using a well-used electrochemical reaction in a solution of $H_2SO_4$,[26] and the result indicated that $SnO_2$ hollow nanospheres exhibit a good electrocatalytic performance for the electrooxidation of ethanol. Figure 6 shows the cyclic voltammetric responses of the bare glass carbon electrode (GCE) (a) and also the $SnO_2$ hollow nanospheres on the glass carbon electrode surface (b) in the presence of ethanol. From the voltammograms in Figure 6 (b), it can be seen that $SnO_2$ hollow nanospheres show catalytic behavior for electrooxidation of ethanol by the appearance of an oxidation current in the positive potential region. The peak potentials for the oxidation of ethanol were approximately 0.46 V, in agreement with the literature values of ethanol oxidation for the formation of acetaldehyde.[27,28] The electrochemical reaction can be described by the following equations:

$$SnO_2(CH_3CH_2OH)_{ads} \rightarrow SnO_2(CH_3CHO)_{ads} + 2\,H^+ + 2\,e^-$$

$$SnO_2(CH_3CHO)_{ads} \rightarrow CH_3CHO + SnO_2$$

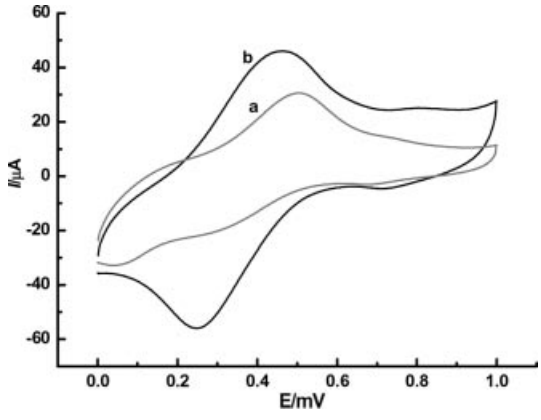


Figure 6. Cyclic voltammograms of the (a) bare glass carbon electrode and (b) $SnO_2$ hollow nanospheres on the glass carbon electrode surface in $H_2SO_4$ (0.5 M) and ethanol (0.6 M). Scan rate = 50 mV $s^{-1}$.

The scission of the alcohol bond occurred at the tin dioxide site with the breaking of the C–H bonds. The potential was about 40 mV more negative than the oxidation peak at the bare GCE. The peak currents of the hollow nanospheres loading onto the bare GCE and the bare GCE are 46 μA and 31 μA, respectively. The reduction of potential and the enhancement of the peak current indicates that the modified electrode can effectively catalyze the electrooxidation of ethanol. Most probably, the catalytic performance may be ascribed to the hollow structures. More chemicals (ions) can be stored in the hollow structures of the sample with a greater chance of participating in the reactions, thus greatly improving the catalytic efficiency of the obtained nanostructures. To test the recycling performance of the sample, two runs were reperformed under the same conditions. It was found that the catalytic efficiency in the third cycle was still the same, revealing its excellent recycling performance. Therefore, the $SnO_2$ hollow nanospheres exhibited potential catalytic behavior for the electrooxidation of ethanol.

## Conclusions

The present study describes a micelle system for the preparation of $SnO_2$ hollow nanospheres on a large scale, which is made up of SDBS and terephthalic acid in mixed ethanol and water solutions. Their cooperative functions contribute to the final morphology of the $SnO_2$ hollow nanospheres. Such a system may represent a promising microreactor for the synthesis of other inorganic materials with unique properties. The obtained $SnO_2$ hollow nanospheres exhibit not only good room-temperature sensitivity to ethanol, but also potential electrocatalytic activity towards electrooxidation of ethanol, which may be useful in industrial applications including catalytic nanoreactors and gas sensors.

## Experimental Section

In a typical experimental process, sodium dodecyl benzenesulfonate (SDBS) (1.4 g, 4 mmol) in distilled water (25 mL) and terephthalic acid (0.3 g, 2 mmol) in ethanol (25 mL) were loaded into a 60 mL Teflon-lined stainless steel autoclave, which was stirred for half an hour. Then $SnCl_2$ (0.45 g, 2 mmol) and $KClO_3$ (0.49 g, 4 mmol) were added under constant stirring to the solution to form a homogeneous solution, which was maintained at 180 °C for 12 h. After the reaction was completed, the white products were collected from solution, rinsed several times with distilled water and absolute ethanol, and then dried under vacuum at 40 °C for 4 h.

The samples were characterized by X-ray powder diffraction (XRD) with a Japan Rigaku D/max rA X-ray diffractometer equipped with graphite-monochromatized high-intensity Cu-$K_\alpha$ radiation ($\lambda$ = 1.54178 Å), recorded with $2\theta$ ranging from 10 to 70°. The transmission electron microscopy (TEM) images and electron diffraction (ED) patterns were performed with a Hitachi Model H-800 instrument with a tungsten filament, using an accelerating voltage of 200 kV. High-resolution transmission electron microscopy (HRTEM) images were carried out with a JEOL-2010 TEM at an acceleration voltage of 200 kV. The field emission scanning electron microscopy (FE-SEM) images were taken with a FEI Sirion-200 SEM. XPS was performed with a ESCALAB MKII with Mg-$K_\alpha$ ($h\nu$ = 1253.6 eV) as the excitation source. The binding energies obtained from the XPS spectral analysis were corrected for specimen charging by referencing $C_{1s}$ to 284.75 eV. The room-temperature photoluminescence (PL) spectra were performed with a Jobin Yvon-Labram Steady-State/Lifetime Spectrofluorometer with a He-Cd laser. Gas-sensing measurements were performed with a

 © 2006 Wiley-VCH Verlag GmbH & Co. KGaA, Weinheim 

*WS-30A* system (Weisheng Instruments Co., Zhengzhou, China). Brunauer–Emmett–Teller (BET) surface area measurements was performed with a Micromeritics ASAP-2000 nitrogen adsorption apparatus. The as-prepared samples were cast as a thin film spanning across the two gold electrodes for test. Electrochemical measurements were performed with a CHI 832 electrochemical station (ChenHua Instruments Co., Shanghai, China). A conventional three-electrode system was used, consisting of a glassy carbon (4 mm diameter) working electrode (GCE), platinum wire auxiliary electrode, and a saturated calomel reference electrode (SCE). The working electrode was polished with $Al_2O_3$ paste and washed ultrasonically in distilled water, loading 0.3 mg cm$^{-2}$. Electrocatalytic oxidation measurements were carried out in a solution of $H_2SO_4$ (0.5 M) and ethanol (0.6 M).

## Acknowledgments

This work was supported by the National Natural Science Foundation of China and Chinese Ministry of Education.

[1] J. S. Lee, S. K. Sim, B. Min, K. Cho, S. W. Kim, S. Kim, *J. Crystal. Growth* **2004**, *267*, 145–149.
[2] a) G. Faglia, C. Baratto, G. Sberveglieri, *Appl. Phys. Lett.* **2005**, *86*, 11923; b) G. Xu, Y. W. Zhang, X. Sun, C. L. Xu, C. H. Yan, *J. Phys. Chem. B* **2005**, *109*, 3269–3278.
[3] a) Y. Wang, J. Y. Lee, *J. Phys. Chem. B* **2004**, *108*, 17832–17837; b) H. Sugimoto, H. Tsukube, K. Tanaka, *Eur. J. Inorg. Chem.* **2004**, 4550–4553.
[4] N. Q. Jia, Q. Zhou, L. Liu, M. M. Yan, Z. Y. Jiang, *J. Electroanal. Chem.* **2005**, *580*, 213–221.
[5] Y. Xie, J. X. Huang, B. Li, Y. Liu, Y. T. Qian, *Adv. Mater.* **2000**, *12*, 1523–1526.
[6] C. J. Martinez, B. Hockey, C. B. Montgomery, S. Semancik, *Langmuir* **2005**, *21*, 7937–7944.
[7] Z. Y. Zhong, Y. D. Yin, B. Gates, Y. N. Xia, *Adv. Mater.* **2000**, *12*, 206–209.
[8] W. P. Shao, Z. H. Wang, Y. G. Zhang, J. H. Cui, W. C. Yu, Y. T. Qian, *Chem. Lett.* **2005**, *34*, 556–557.
[9] Z. A. Ansari, T. G. Ko, J. H. Oh, *IEEE Sensors J.* **2005**, *5*, 817–824.
[10] N. L. V. Carreno, H. V. Fajardo, A. P. Maciel, A. Valentini, F. M. Pontes, L. F. D. Probst, E. R. Lrite, E. Longo, *J. Molecular Catalysis A: Chem.* **2004**, *207*, 89–94.
[11] L. H. Jiang, G. Q. Sun, Z. H. Zhou, S. G. Sun, Q. Wang, S. Y. Yan, H. Q. Li, J. Tian, J. S. Guo, B. Zhou, Q. Xin, *J. Phys. Chem. B* **2005**, *109*, 8774–8778.
[12] a) M. L. Breen, A. D. Dinsmore, R. H. Pink, S. B. Qadri, B. R. Ratna, *Langmuir* **2001**, *17*, 903–907; b) Z. Yang, Z. Niu, Y. Lu, Z. Hu, C. C. Han, *Angew. Chem. Int. Ed.* **2003**, *42*, 1943–1945.
[13] a) Z. Dai, L. Dahne, H. Mohwald, B. Tiersch, *Angew. Chem. Int. Ed.* **2002**, *41*, 4019–4022; b) K. P. Velikov, A. van Blaaderen, *Langmuir* **2001**, *17*, 4779–4786.
[14] a) Y. J. Xiong, Y. Xie, J. Yang, R. Zhang, C. Z. Wu, G. A. Du, *J. Mater. Chem.* **2002**, *12*, 3712–3716; b) H. G. Yang, H. C. Zeng, *Angew. Chem. Int. Ed.* **2004**, *43*, 5206–5209.
[15] D. Chen, G. Z. Shen, K. B. Tang, Z. H. Liang, H. G. Zheng, *J. Phys. Chem. B* **2004**, *108*, 11280–11284.
[16] L. M. Qi, J. Li, J. M. Ma, *Adv. Mater.* **2002**, *14*, 300–303.
[17] D. B. Zhang, L. M. Qi, J. M. Ma, H. M. Cheng, *Adv. Mater.* **2002**, *14*, 1499–1502.
[18] H. J. Ahn, H. C. Choi, K. W. Park, S. B. Kim, Y. E. Sun, *J. Phys. Chem. B* **2004**, *108*, 9815–9820.
[19] T. Namani, P. Walde, *Langmuir* **2005**, *21*, 6210–6219.
[20] S. G. Deng, J. M. Cao, J. Feng, J. Guo, B. Q. Fang, M. B. Zheng, J. Tao, *J. Phys. Chem. B* **2005**, *109*, 11473–11477.
[21] G. Wang, G. Olofsson, *J. Phys. Chem. B* **1998**, *102*, 9276–9283.
[22] T. W. Kim, D. U. Lee, Y. S. Yoon, *J. Appl. Phys.* **2000**, *88*, 3759–3761.
[23] a) J. Q. Hu, Y. Bando, Q. L. Liu, D. Golberg, *Chem. Phys. Lett.* **2003**, *372*, 758–762; b) J. Q. Hu, Y. Bando, Q. L. Liu, D. Golberg, *Adv. Funct. Mater.* **2003**, *13*, 493–496.
[24] J. Chen, L. N. Xu, W. Y. Li, X. H. Gou, *Adv. Mater.* **2005**, *17*, 582–586.
[25] J. J. Zhu, Z. H. Lu, S. T. Aruna, D. Aurbach, A. Gedanken, *Chem. Mater.* **2000**, *12*, 2557–2566.
[26] H. P. Liang, H. M. Zhang, J. S. Hu, Y. G. Guo, L. J. Wan, C. L. Bai, *Angew. Chem. Int. Ed.* **2004**, *43*, 1540–1543.
[27] L. H. Jiang, G. Q. Sun, Z. H. Zhou, W. J. Zhou, Q. Xin, *Catalysis Today* **2004**, *93–95*, 665–670.
[28] J. M. Leger, *Electrochim. Acta* **2005**, *50*, 3123–3129.

Received: November 3, 2005
Published Online: February 21, 2006

 © 2006 Wiley-VCH Verlag GmbH & Co. KGaA, Weinheim 

DOI: 10.1002/ejic.200500985

# Syntheses, Structures, and Characterization of Two Manganese(II)-Aminobenzoic Complexes

**Ruihu Wang,[a] Daqiang Yuan,[a] Feilong Jiang,[a] Lei Han,[a] Song Gao,[b] and Maochun Hong*[a]**

**Keywords:** Manganese / Aminobenzoic acid / Magnetic properties

A discrete tetranuclear manganese(II) complex, $\{(H_3O)_2Mn_4(4\text{-Haba})_2(4\text{-aba})_6(SCN)_4(H_2O)_2\}$ (**1**) and a two-dimensional coordination polymer $[Mn(3\text{-aba})_2]_n$ (**2**) (4-Haba = 4-aminobenzoic acid, 3-Haba = 3-aminobenzoic acid), have been synthesized and characterized by elemental analyses, IR, X-ray crystallography, and magnetic susceptibility. In complex **1**, 4-aba in three types of coordination modes connects $Mn^{II}$ centers to form a discrete tetranuclear anionic molecule. Hydrogen bonding interaction links the tetranuclear units to generate a one-dimensional supramolecular chain. In complex **2**, 3-aba in an *exo*-tridentate mode bridges six-coordinate $Mn^{II}$ centers forming a two-dimensional coordination architecture. Studies of the magnetic susceptibilities of **1** and **2** reveal weak antiferromagnetic exchange interactions between adjacent $Mn^{II}$ centers.

(© Wiley-VCH Verlag GmbH & Co. KGaA, 69451 Weinheim, Germany, 2006)

## Introduction

A significant amount of research has been dedicated to the study of the magnetic behavior of discrete polynuclear entities and molecule-based coordination polymers with extended structures.[1–3] The increasing interest in this field is justified not only by the intellectual challenge of understanding the fundamental relationship between structures and magnetic properties, but also by the development of new types of functional molecule-based magnetic materials.[4–7] In this context, one of the points to be seriously considered for the preparation of these magnetic solids is the choice of appropriate bridging ligands, since they mediate superexchange interactions between the paramagnetic metal centers. The type, size, shape, flexibility, conformation, and symmetry of the ligands along with their connective patterns are all important parameters, affecting the type and magnitude of the magnetic exchange interaction.[5–8] In the course of formation of desirable magnetic complexes, certain features of the organic ligands connecting paramagnetic metal centers can be utilized and tuned. For example, the carboxyl group can not only bridge two or more metal centers to produce a wide variety of complexes ranging from zero-dimensional discrete molecules to three-dimensional architectures, but also can adopt various types of bridging conformation modes, such as the so-called *syn-syn*, *syn-anti*, and *anti-anti* modes (Scheme 4). The magnetic properties are closely related to the bridging modes adopted by the carboxyl group in these complexes.[9,10] Thus, in terms of constructing the extended structural motifs, either di- and muti-carboxyl ligands, or multifunctional carboxyl-containing ligands incorporating other coordination groups, such as N, and S, have been employed;[5,11,12] the N or S donor atoms coordinating to metal centers can result in fascinating extended complexes with beautiful aesthetics and useful functional properties.[13,14c] However, owing to the presence of many subtle factors in the assembly process and the difficulty in predicting the final architectures, the rational design of coordination complexes from multifunctional organic ligands and metal ions is still a challenge to chemists, and a great deal of work is required to extend the knowledge of relevant magnetic solids and establish proper synthetic strategies leading to desirable architectures and useful properties.

As a part of our work towards rational design and preparation of functional supramolecular complexes with intriguing structures and potential applications in optics, electrical conductivity, magnetism, and host-guest chemistry,[14,15] we have successfully prepared a series of $Cd^{II}$ and $Ag^{I}$ complexes from the multifunctional organic ligands 4-aminobenzoic acid (4-Haba) and 3-aminobenzoic acid (3-Haba) through combination of their amino and carboxyl groups.[15b,15c] It is known that high-spin manganese(II) contains five unpaired electrons and is quite oxophilic, and

[a] State Key Laboratory of Structural Chemistry, Fujian Institute of the Research on the Structure of Matter, Chinese Academy of Sciences,
Fuzhou, Fujian, 350002, China
Fax: +86-591-8371-4946
E-mail: hmc@ms.fjirsm.ac.cn
[b] State Key Laboratory of Rare Materials Chemistry and Applications, College of Chemistry and Molecular Engineering, Peking University,
Beijing, 100871, China

Supporting information for this article is available on the WWW under http://www.eurjic.org or from the author.

 © 2006 Wiley-VCH Verlag GmbH & Co. KGaA, Weinheim 

that the assembly of manganese(II) with organic ligands containing the carboxyl group is inclined to the formation of larger clusters and extended solids.[16] Moreover, carboxyl-bridged manganese(II) complexes have been known to exist at the active centers of some $Mn^{II}$-containing enzymes.[17] Recently, we have reported a three-dimensional manganese(II) complex from 4-Haba exhibiting ferrimagnetic and metamagnetic behavior.[15a] Considering the versatile bridging modes of the carboxyl group and efficient mediation of magnetic coupling in 4-aba and 3-aba, herein, we wish to report the syntheses and characterization of a discrete tetranuclear manganese(II) complex $\{(H_3O)_2[Mn_4(4\text{-Haba})_2(4\text{-aba})_6(SCN)_4(H_2O)_2]\}$ (**1**) and a two-dimensional coordination architecture $[Mn(3\text{-aba})_2]_n$ (**2**).

## Result and Discussion

### Synthesis and Characterization

Reaction of $MnCl_2{\cdot}4H_2O$, 4-Haba, and $NaN_3$ at room temperature produced a three-dimensional complex $[Mn_3(4\text{-aba})_6]_n$ (**3**),[15a] in which $N_3^-$ is not involved in coordination to the $Mn^{II}$ ion and acts as a base to deprotonate 4-Haba. Previous research demonstrates that the assembly process of 4-Haba and transitional metal ions has been highly influenced by counter anions, pH value, solvent system, and metal-to-ligand ratio besides the coordination nature of the metal ions.[15,18] In some cases, a subtle alteration in any of these factors can result in new complexes with different structural topologies and different functions. The successful isolation of **3** prompted us to prepare other $Mn^{II}$ complexes from 4-Haba and 3-Haba through altering reaction-influencing factors. Instead of $N_3^-$, the use of $SCN^-$ in the presence of NaOH led to a tetranuclear $Mn^{II}$ complex (**1**), and the reaction of 3-Haba and $MnCl_2{\cdot}4H_2O$ in the presence of either $NaN_3$ or $NH_4SCN$ and NaOH afforded the complex **2**. In the preparation of compounds **1**–**3**, the counter anions obviously have an important effect on their assembly process even if they are not present in the complexes. We presume that these counter anions coordinate to a part of the metal ions in solution and remain soluble species, whereas only the insoluble crystalline material can be isolated and identified. It is possible therefore, that the presence of these counter anions is important for the equilibrium that leads eventually to the isolation of the polynuclear carboxylates. It is well known that the relative orientation of the coordination sites in organic ligands is also one of the most important factors in controlling the construction of supramolecular architectures.[19] The assembly of organic ligands with different orientations of coordination sites and metal ions can produce different structural frameworks. Thus, the difference between complex **2** and complex **1** and **3** can be ascribed to the different stereochemistry of the ligands.

The C≡N stretching vibration of the thiocyanate group in **1** appears as a single strong peak at 2085 $cm^{-1}$, which is consistent with the occurrence of thiocyanate-N coordination.[20] The characteristic bands of the carboxyl group of 4-aba are shown at 1608 $cm^{-1}$ for antisymmetric stretching and at 1406 and 1396 $cm^{-1}$ for symmetric stretching. The separations ($\Delta$) between $\nu_{asym}$(–COO) and $\nu_{sym}$(–COO) are 202 and 212 $cm^{-1}$, respectively, revealing that the carboxyl group of 4-aba functions in different bridging modes. The IR spectrum of complex **2** shows typical antisymmetric and symmetric stretching bands of the carboxyl group at 1579 and 1394 $cm^{-1}$, respectively, the $\Delta$ value is 185 $cm^{-1}$.

### Structural Description

**$\{(H_3O)_2[Mn_4(4\text{-Haba})_2(4\text{-aba})_6(SCN)_4(H_2O)_2]\}$ (1):** Single-crystal X-ray diffraction analysis reveals that **1** consists of a tetranuclear $[Mn_4(4\text{-Haba})_2(4\text{-aba})_6(SCN)_4(H_2O)_2]^{2-}$ anion and two lattice water molecules; the two lattice water molecules or two of the total eight amino groups of the tetranuclear unit are required to be protonated to achieve overall charge balance. These protons were not located crystallographically and could reside on any of the eight amino groups or two lattice water molecules. Since the amino group is more basic than the water molecule, the protonation likely occurs at the amino groups of some ligands. As shown in Figure 1 (a), there are two crystallographically independent $Mn^{II}$ centers in the tetranuclear anionic framework. Mn(1) is coordinated by two carboxyl oxygen atoms and one chelating carboxyl group from three different 4-aba, one water molecule, and one nitrogen atom of the terminal $SCN^-$. However, Mn(2) is coordinated by four carboxyl oxygen atoms from different 4-aba, one carboxyl oxygen atom from 4-Haba, and one nitrogen atom of the terminal $SCN^-$. Thus, Mn(1) and Mn(2) are in a highly distorted octahedral geometry. Mn(1)–O(21)–Mn(2) and Mn(1)–O(41)–Mn(2) bond angles are 94.30(14) and 98.59(15)°, respectively. The $SCN^-$ groups are almost linear with the N(1)–C(1)–S(1) and N(2)–C(2)–S(2) bond angles being 177.8(6) and 179.0(8)°, respectively. The connections between $Mn^{II}$ and $SCN^-$ groups are slightly bent with the C(1)–N(1)–Mn(2) and C(2)–N(2)–Mn(1) bond angles being 151.5(5) and 168.4(6)°, respectively. 4-Haba acts as a monodentate ligand through one carboxylic oxygen atom coordinating to Mn(2) (Scheme 1, a). However, 4-aba has three distinctly different coordination modes, in which the amino nitrogen atom is not involved in coordination with $Mn^{II}$: one behaves in a $\mu_2$-$\eta^2$-carboxyl bridging mode (Scheme 1, b); the second adopts a $\mu_2$-chelating/bridging mode (Scheme 1, c); and the third acts as a $\mu_3$-carboxyl bridge (Scheme 1, d). Thus, Mn(1) and Mn(2) are linked together by three different types of 4-aba through one *syn-syn* μ-carboxyl bridge (Scheme 1, b), two μ-O atoms from the $\mu_2$-chelating/bridging carboxyl group (Scheme 1, c), and the $\mu_3$-carboxyl group (Scheme 1, d), respectively. The separation of Mn(1)···Mn(2) is 3.407 Å. A similar molecular geometry to this kind of connection has been found in $[Mn_3(HCOO)_6]$, where the Mn–Mn connectivity is 3.625 Å.[21] The other oxygen atom in the $\mu_3$-carboxyl group of 4-aba (Scheme 1, d) coordinates to Mn(2) and further links the two independent $Mn^{II}$ into a tetranuclear $Mn^{II}$

 © 2006 Wiley-VCH Verlag GmbH & Co. KGaA, Weinheim 

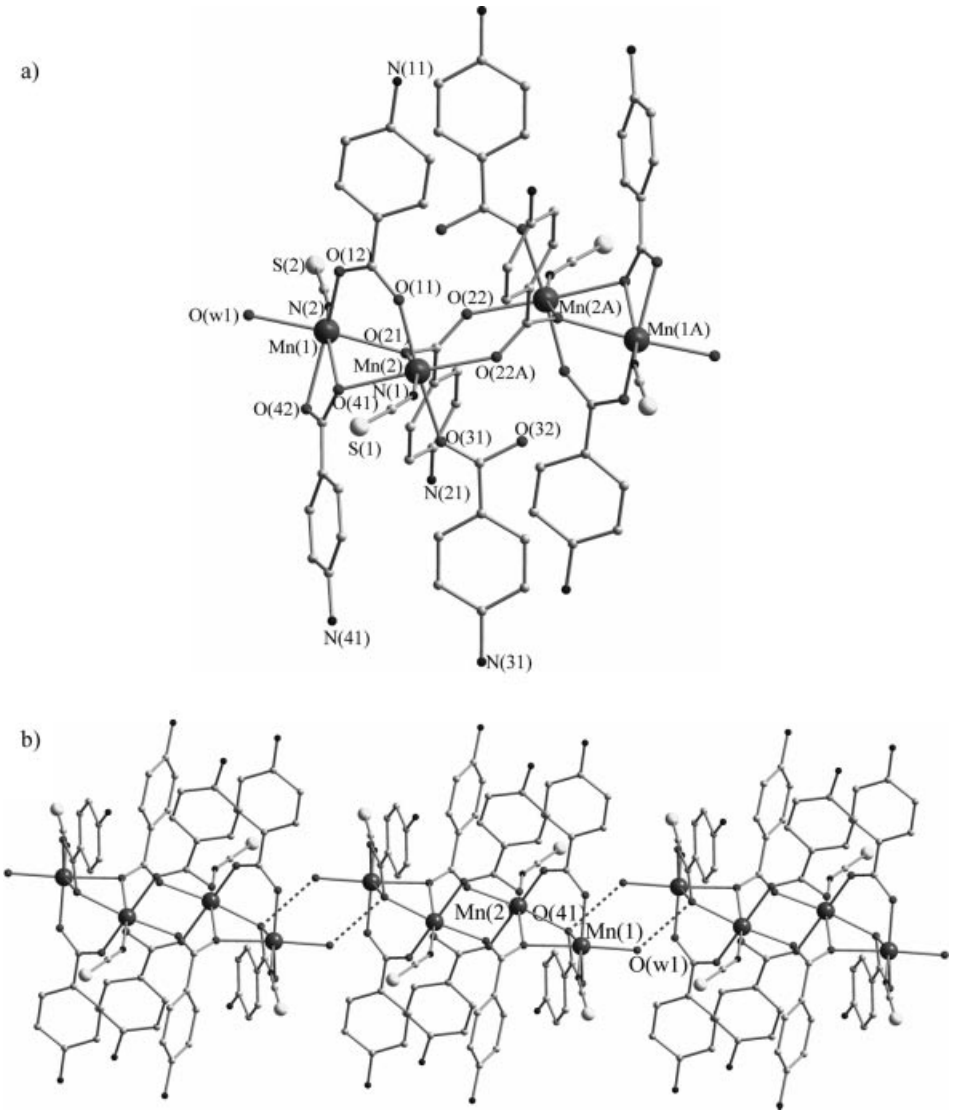


Figure 1. (a) View of the tetranuclear $Mn^{II}$ anionic framework in **1**. (A) $2 - x$, $1 - y$, $1 - z$. (b) View of a one-dimensional hydrogen bonding chain consisting of tetranuclear $Mn^{II}$ anions in **1**.

cluster, in which the Mn(2)···Mn(2A) and Mn(1)···Mn(2A) separations bridged by the carboxyl group of 4-aba are 5.058 and 6.150 Å, respectively. The topology of the rhombic tetranuclear $Mn^{II}$ cluster is rather unusual, and it has an unprecedented $[Mn_4(\mu_3\text{-4-aba})_2(\mu_2\text{-}\eta^2\text{-4-aba})_2]$ core, which is different to several rhombic or butterfly-like tetranuclear Mn clusters with an $[Mn_4(\mu\text{-carboxylic})]$ or $[Mn_4(\mu_3\text{-phth})_2]$ core that have been reported.[22] The hydrogen bonding interaction between the coordinated water molecule and the μ-O atom in the $\mu_3$-carboxyl of 4-aba [OW1–H(1)···O(41)$^i$ 2.854(7) Å; symmetry code (i) $-x + 1$, $-y + 1$, $-z + 1$] cross-links the tetramers into a one-dimensional supramolecular chain. The closest Mn···Mn distance between adjacent tetramers in the chain is 4.994 Å (Figure 1, b).

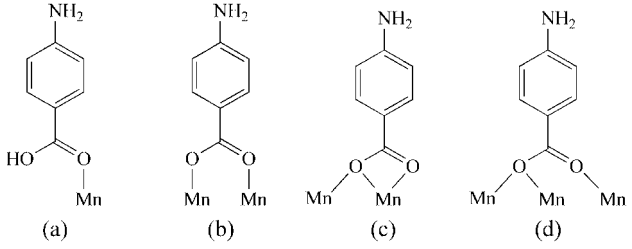


Scheme 1. Coordination modes of 4-Haba and 4-aba in **1**.

**$[Mn(3\text{-aba})_2]_n$ (2):** Complex **2** is a two-dimensional coordination polymer based on infinite Mn–O–C–O chains. As shown in Figure 2 (a), Mn(1) is in a slightly distorted octahedral coordination environment and is coordinated by four carboxyl oxygen atoms and two nitrogen atoms from six different 3-aba. Four carboxyl oxygen atoms comprise the equatorial plane and $Mn^{II}$ is coplanar with the mean plane of four equatorial carboxyl oxygen atoms, and the two amino nitrogen atoms occupy the axial positions. The bond angles between the *cis* donors around $Mn^{II}$ range from

 © 2006 Wiley-VCH Verlag GmbH & Co. KGaA, Weinheim 

85.27(17) to 94.73(17)°. The Mn–N bond length of 2.290(5) Å is slightly longer then the Mn–O bond lengths of 2.150(4) and 2.201(4) Å, suggesting an elongated octahedron. In addition, 3-aba acts as an *exo*-tridentate bridge through the amino nitrogen atom and $\mu_2$-$\eta^2$-carboxyl group (Scheme 2). The carboxyl group is slightly distorted with respect to the phenyl ring with the dihedral angle between them being 11.8°. The double *syn-syn* mode $\mu_{1,3}$-carboxyl bridges coming from two different 3-aba ligands exist between neighboring $Mn^{II}$ ions forming an infinite Mn–O–C–O chain with the C–O–Mn bond angles being 124.6(3) and 133.8(3)°. The closest Mn···Mn distance within the chain is 4.607 Å. As shown in Figure 2 (b), the chains are cross-linked into a two-dimensional layer structure through the amino nitrogen atom of 3-aba coordinating to the remaining coordination sites of $Mn^{II}$. The shortest inter-chain Mn···Mn distance is 8.129 Å. There are no other short contacts or noteworthy aryl-aryl interactions between the adjacent two-dimensional layers.

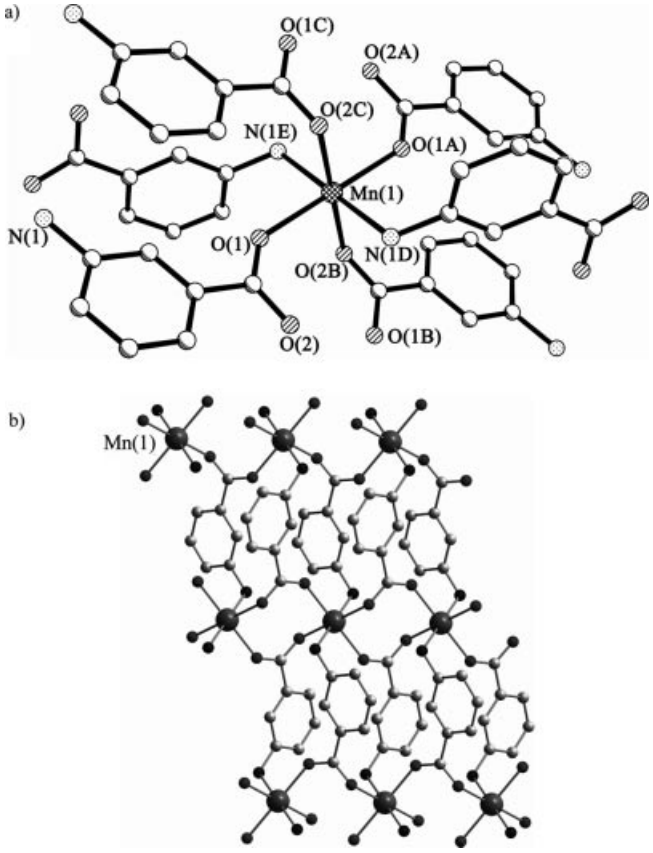


Figure 2. (a) View of the coordination environment around $Mn^{II}$ in **2**. (A) 1 – *x*, –*y*, 1 – *z*; (B) 1 – *x*, –*y* – 1, 1 – *z*; (C) *x*, 1 + *y*, *z*; (D) *x* – 1/2, –*y* – 1/2, *z* – 1/2; (E) 3/2 – *x*, 1/2 + *y*, 3/2 – *z*. (b) View of a pack diagram along the *a* axis showing the two-dimensional network in **2**.

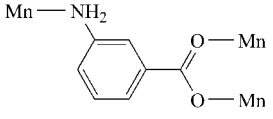


Scheme 2. Coordination mode of 3-aba in **2**.

## Magnetic Properties

The magnetic susceptibilities of complexes **1** and **2** were measured in the 2–300 K temperature range and are shown in Figure 3 and Figure 4, respectively. The experimental $\chi_m T$ values of **1** and **2** at room temperature are 4.66 and 4.24 $cm^3 \cdot mol^{-1} \cdot K$ per $Mn^{II}$, respectively, close to the spin-only value expected for an uncoupled high-spin $Mn^{II}$ ion (4.38 $cm^3 \cdot mol^{-1} \cdot K$). As the temperature is lowered to 2 K, the $\chi_m T$ products decrease first slowly and then rapidly. The behavior suggests that antiferromagnetic interactions are operative in the two complexes. The temperature dependence of the reciprocal susceptibilities ($1/\chi_m$) obeys the Curie–Weiss law above 5 K for **1** and 15 K for **2** with $\theta$ = –8.9 and –13.9 K for **1** and **2**, respectively. The negative $\theta$ values support the presence of overall antiferromagnetic interactions in the two complexes.

The crystallographic data of **1** suggest that there are three different types of superexchange pathways within the tetranuclear unit, which can be schematized as shown in Scheme 3. Therefore, the magnetic data of **1** should be analyzed by an analytical expression based on the Hamiltonian in Equation (1).

$$H = -2J_1S_1S_2 - 2J_2(S_1S_3 + S_2S_4) - 2J_3(S_1S_4 + S_2S_3) \quad (1)$$

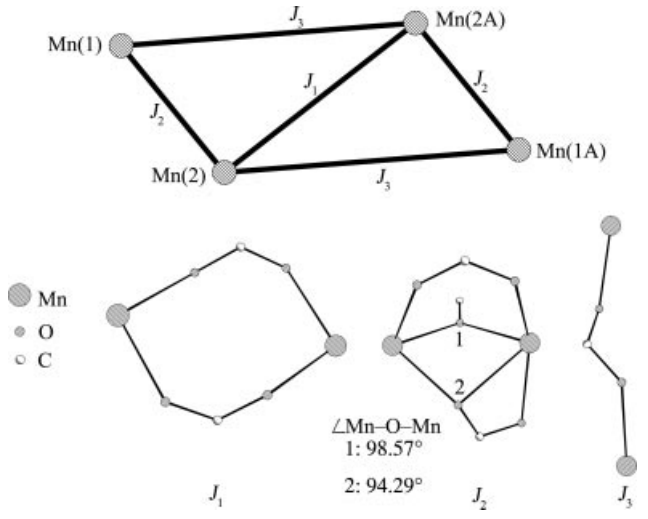


Scheme 3. Spin topology for **1** assuming three different *J* values.

Calculations were performed with the magnetism package MAGPACK.[23] The best-fit parameters obtained were $J_1$ = –1.84(1) $cm^{-1}$, $J_2$ = –0.18(2) $cm^{-1}$, $J_3$ = 0.02(1) $cm^{-1}$, $g$ = 2.090(2) and $R = 2.6 \cdot 10^{-4}$ ($R = \Sigma[(\chi_m T)_{obs}^2 - (\chi_m T)_{calc}^2]/\Sigma[(\chi_m T)_{obs}^2]$). As expected from the structural parameters depicted in Scheme 3, the results show the presence of two antiferromagnetic and one very weak ferromagnetic interaction. The difference in the magnetic exchange interactions found for **1** can be satisfactorily explained in terms of the conformation modes of the carboxyl bridge. The exchange

 © 2006 Wiley-VCH Verlag GmbH & Co. KGaA, Weinheim 

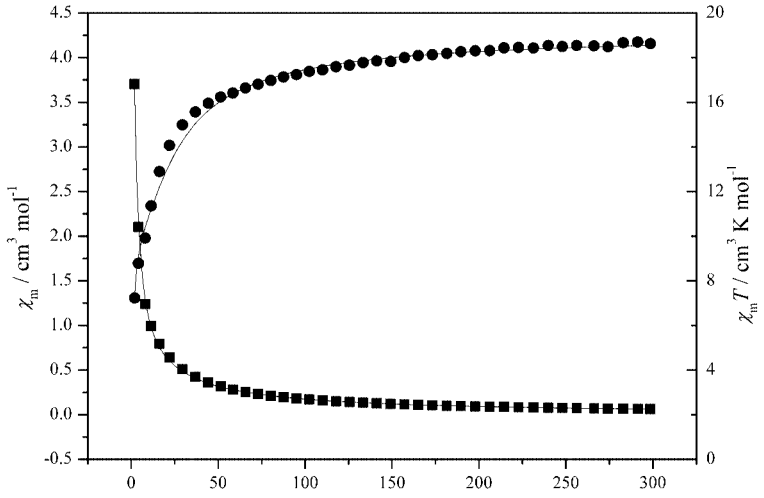


Figure 3. Temperature dependence of $\chi_m$ (■) and $\chi_m T$ (●) values for complex **1**. The solid lines correspond to the best-fit curves using the parameters described in the text.

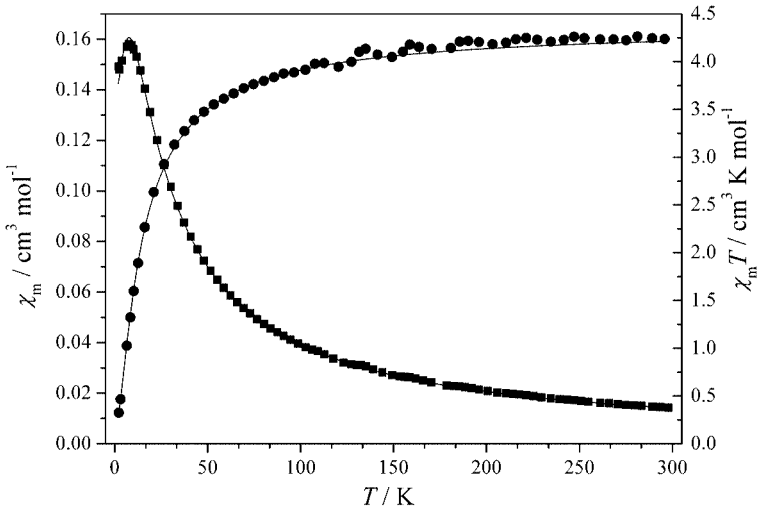


Figure 4. Temperature dependence of $\chi_m$ (■) and $\chi_m T$ (●) values for complex **2**. The solid lines correspond to the best-fit curves using the parameters described in the text.

coupling through the carboxyl bridge is highly dependent on the conformation modes (Scheme 4) of the bridge between the metal centers.[16b] The *syn-syn* mode provides small metal–metal distances and a good overlap of magnetic orbitals, which usually induces antiferromagnetic coupling in $Mn^{II}$ polynuclear complexes.[24] The *syn-anti* mode induces much smaller $J$ values because of the expanded metal center and a mismatch in the orientation of magnetic orbitals.[8b,9] The few examples involving the *anti-anti* mode indicated that this coupling is weakly ferromagnetic or antiferromagnetic.[9,25] Coupling $J_1$ arises from the double *syn-syn* carboxyl bridge and gives a weak antiferromagnetic coupling in this case, but coupling $J_3$ through the single *anti-anti* carboxyl bridge gives very weak ferromagnetic coupling. The $J_1$ value is larger than the $J_3$ value, which shows that the *syn-syn* carboxyl bridge is more favorable than the *anti-anti* mode for transmission of the magnetic coupling interaction.[9,26] In the coupling $J_2$, the effect of the two carboxyl bridges in *syn-syn* and *syn-anti* configuration is antiferromagnetic, but the two μ–O bridges with Mn–O–Mn angles of 98.59° and 94.30° may show weak ferromagnetic coupling and will reduce the antiferromagnetic contribution.[27]

The situation for **2** is much simpler. Magnetically, **2** is a uniform chain, in which there is only one type of superexchange pathway: the double *syn-syn* mode carboxyl bridge. The interchain magnetic interactions should be much weaker. The magnetic interaction within the chain can be expressed by the isotropic Hamiltonian $H = -2J\Sigma S_i S_{i+1}$, where $J$ is the coupling constant between neighboring metal ions. To simulate the experimental magnetic behavior, we used the analytical expression derived by Fisher[28] for a one-dimensional Heisenberg chain of classical spins [$S = 5/2$, Equation (2)].

$$\chi_{chain} = [Ng^2\beta^2 S(S + 1)/(3kT)][(1 + u)/(1 - u)] \quad (2)$$

where $N$ is Avogadro's number, $\beta$ is Bohr's magneton, $k$ is Boltzmann's constant, and $u$ is the well-known Langevin

 © 2006 Wiley-VCH Verlag GmbH & Co. KGaA, Weinheim 

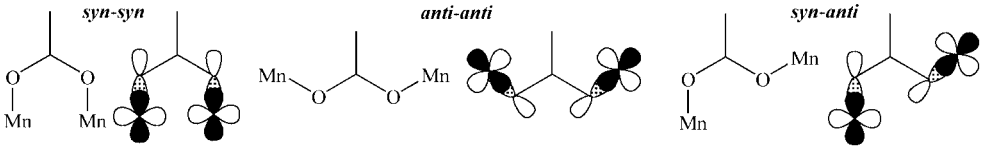


Scheme 4. Schematic representations of the coordination modes for the carboxylate bridges and the overlap of *d-p* magnetic orbitals.

function: $u = \coth[2JS(S + 1)/kT] - kT/[2JS(S + 1)]$. To take into account the interchain interaction, we applied the molecular field approximation [Equation (3)].[29]

$$\chi = \chi_{chain}/[1 - (2zJ'/Ng^2\beta^2)\chi_{chain}] \quad (3)$$

The best least-squares fit of the theoretical equation to experimental data leads to $J = -0.640(3)\ cm^{-1}$, $2zJ' = 0.070(1)\ cm^{-1}$, and $g = 2.000(2)$. The $J$ value suggests that a weak antiferromagnetic interaction between neighboring $Mn^{II}$ ions is mediated through the double *syn-syn* mode $\mu_2$-carboxyl bridges. It is comparable to those reported for other $Mn^{II}$ species with similar double carboxyl bridges.[16c]

## Conclusions

One tetranuclear manganese(II) complex and one two-dimensional coordination polymer based on infinite Mn–O–C–O chains from 4-Haba and 3-Haba, respectively, have been synthesized and characterized crystallographically and magnetically. The structural difference between **1** and **2** is ascribed to the relatively different orientation of coordination sites of 4-aba and 3-aba. The analysis of the magnetic properties of **1** and **2** suggests weak antiferromagnetic interactions. Three types of magnetic interaction operative in complex **1** result in an overall antiferromagnetic behavior, as indicated by the temperature dependence of the magnetic susceptibility. Complex **2** exhibits weak antiferromagnetic interactions through double $\mu_2$-$\eta^2$-carboxyl bridges within the chain.

## Experimental Section

**General:** All reagents were commercially available and used as purchased. The IR spectra (KBr disk) were recorded with a Magna 750 FT-IR spectrophotometer. C, H, and N elemental analyses were determined with an Elementary Vario ELIII elemental analyzer. Variable-temperature magnetic susceptibilities were measured with a Quantum Design MPMS SQUID magnetometer equipped with a 5 kOe magnet in the temperature range 2–300 K. The observed susceptibility data were corrected for underlying diamagnetism by using Pascal's constants.[1b]

**Synthesis of $\{(H_3O)_2[Mn_4(4\text{-Haba})_2(4\text{-aba})_6(SCN)_4(H_2O)_2]\}$ (1):** A solution of $MnCl_2{\cdot}4H_2O$ (0.10 g, 0.5 mmol) and $NH_4SCN$ (0.08 g, 1.0 mmol) in $H_2O$ (10 mL) was added slowly to a solution of 4-aminobenzoic acid (0.07 g, 0.5 mmol) in ethanol (10 mL) under stirring, then 0.1 mol·$L^{-1}$ NaOH aqueous solution was added dropwise to the reaction mixture until a small amount of precipitate was formed (pH = 4.0–4.5). The precipitate was filtered off and the filtrate was allowed to stand at room temperature for about 2 weeks, yellow crystals were produced. Yield: 0.13 g (61%). $C_{30}H_{30}Mn_2N_6O_{10}S_2$ (808.60): calcd. C 44.56, H 3.71, N 10.39; found C 44.51, H 3.67, N 10.35. IR (KBr): $\tilde{\nu}$ = 3460 (w), 3365 (s), 3271 (m), 2085 (s), 1608 (s), 1574 (w), 1528 (s), 1508 (s), 1406 (vs), 1396 (vs), 1327 (w), 1292 (w), 1261 (w), 1184 (w), 1174 (w), 1128 (vw), 1093 (vw), 1014 (vw), 978 (w), 957 (vw), 850 (vw), 789 (m), 700 (vw), 621 (w), 552 (vw), 492 (vw) $cm^{-1}$.

**Synthesis of $[Mn(3\text{-aba})_2]_n$ (2):** The procedure is similar to the synthesis of **1** except that 3-aminobenzoic acid (0.07 g, 0.5 mmol) was used instead of 4-aminobenzoic acid. Yield: 0.09 g (55%). $C_{14}H_{12}MnN_2O_4$ (327.2): calcd. C 51.39, H 3.67, N 8.56; found C 51.35, H 3.61, N 8.53. IR (KBr): $\tilde{\nu}$ = 3358 (m), 3284 (w), 1579 (m), 1547 (s), 1454 (m), 1394 (s), 1311 (vw), 1246 (w), 1120 (vw), 1074 (vw), 976 (m), 924 (w), 912 (w), 901 (w), 787 (m), 775 (s), 690 (vw), 669 (vw), 565 (vw), 546 (vw), 517 (vw) $cm^{-1}$. Compound **2** can also be obtained through the directed reaction of 3-Haba, $MnCl_2{\cdot}4H_2O$, and $NaN_3$ in EtOH/$H_2O$ at room temperature.

Table 1. Selected bond lengths [Å] and angles [°] for **1** and **2**.

| | | | |
|---|---|---|---|
| Complex **1** | | | |
| Mn(1)–O(12) | 2.093(4) | Mn(1)–N(2) | 2.122(7) |
| Mn(1)–O(W1) | 2.184(4) | Mn(1)–O(42) | 2.220(4) |
| Mn(1)–O(21) | 2.257(4) | Mn(1)–O(41) | 2.401(4) |
| Mn(2)–O(11) | 2.095(4) | Mn(2)–N(1) | 2.164(6) |
| Mn(2)–O(31) | 2.186(4) | Mn(2)–O(22A) | 2.198(4) |
| Mn(2)–O(21) | 2.238(4) | Mn(2)–O(41) | 2.244(4) |
| | | | |
| O(12)–Mn(1)–N(2) | 108.2(2) | O(12)–Mn(1)–O(W1) | 89.28(17) |
| N(2)–Mn(1)–OW1 | 89.6(2) | O(12)–Mn(1)–O(42) | 148.26(18) |
| N(2)–Mn(1)–O(42) | 103.4(2) | O(W1)–Mn(1)–O(42) | 87.34(18) |
| O(12)–Mn(1)–O(21) | 94.53(16) | N(2)–Mn(1)–O(21) | 90.4(2) |
| O(W1)–Mn(1)–O(21) | 176.00(17) | O(42)–Mn(1)–O(21) | 88.78(15) |
| O(12)–Mn(1)–O(41) | 93.94(16) | N(2)–Mn(1)–O(41) | 154.1(2) |
| O(W1)–Mn(1)–O(41) | 104.41(17) | O(42)–Mn(1)–O(41) | 56.64(15) |
| O(21)–Mn(1)–O(41) | 74.16(14) | O(11)–Mn(2)–N(1) | 92.83(19) |
| O(11)–Mn(2)–O(31) | 171.89(18) | N(1)–Mn(2)–O(31) | 94.87(19) |
| O(11)–Mn(2)–O(22A) | 93.59(16) | N(1)–Mn(2)–O(22A) | 94.5(2) |
| O(31)–Mn(2)–O(22A) | 83.31(16) | O(11)–Mn(2)–O(21) | 89.19(16) |
| N(1)–Mn(2)–O(21) | 167.71(19) | O(31)–Mn(2)–O(21) | 83.81(16) |
| O(22A)–Mn(2)–O(21) | 97.51(16) | O(11)–Mn(2)–O(41) | 90.35(16) |
| N(1)–Mn(2)–O(41) | 90.17(19) | O(31)–Mn(2)–O(41) | 92.14(15) |
| O(22A)–Mn(2)–O(41) | 173.76(16) | O(21)–Mn(2)–O(41) | 77.69(15) |
| Complex **2** | | | |
| Mn–O(1) | 2.150(4) | Mn–O(2B) | 2.201(4) |
| Mn–N(1D) | 2.290(5) | | |
| | | | |
| O(1)–Mn–O(2C) | 88.94(15) | O(1)–Mn–O(2B) | 91.06(15) |
| O(1)–Mn–N(1D) | 90.41(16) | O(1A)–Mn–O(2C) | 91.06(15) |
| O(2C)–Mn–N(1D) | 94.73(17) | O(2B)–Mn–N(1D) | 85.27(17) |
| O(1A)–Mn–N(1E) | 90.41(16) | O(1)–Mn–N(1E) | 89.59(16) |
| O(2C)–Mn–N(1E) | 85.27(17) | O(2B)–Mn–N(1E) | 94.73(17) |

Symmetry code: **1** (A) $-x + 2, -y + 1, -z + 1$; **2** (A) $-x + 1, -y, -z + 1$; (B) $-x + 1, -y - 1, -z + 1$; (C) $x, y + 1, z$; (D) $x - 1/2, -y - 1/2, z - 1/2$; (E) $-x + 3/2, y + 1/2, -z + 3/2$

 © 2006 Wiley-VCH Verlag GmbH & Co. KGaA, Weinheim 

**X-ray Crystallography:** Intensity data for **1** and **2** were measured with a Siemens Smart CCD diffractometer with graphite-monochromated Mo-$K_\alpha$ radiation ($\lambda$ = 0.71073 Å) at room temperature. All empirical absorption corrections were applied using the SADABS program.[30] The structures were solved by direct methods[31] and refined on $F^2$ by full-matrix least-squares using the SHELXL-97 program package.[32] The positions of H atoms were generated geometrically (C–H bond fixed at 0.96 Å), assigned isotropic thermal parameters, and allowed to ride on their parent carbon atoms before the final cycle of refinement. No attempt was made to locate the hydrogen atoms of water. The selected bond lengths and angles for **1** and **2** are listed in Table 1.

**Crystal Data for 1:** $C_{30}H_{30}Mn_2N_6O_{10}S_2$, $Mr$ = 808.60, 0.46 × 0.34 × 0.26 mm, triclinic, space group $P\bar{1}$ (No. 2), $a$ = 12.2553(2), $b$ = 12.28000(10), $c$ = 12.2833(2) Å, $\alpha$ = 80.774(1), $\beta$ = 85.798(1), $\gamma$ = 67.587(1)°, $V$ = 1686.68(4) Å$^3$, $Z$ = 2, $D_c$ = 1.592 g/cm$^3$, $F$(000) = 828, Mo-$K_\alpha$ radiation, $\lambda$ = 0.71073 Å, $T$ = 173(2) K, $2\theta_{max}$ = 50.1°, 8783 reflections collected, 5900 unique ($R_{int}$ = 0.0320). Final $GooF$ = 1.088, $R1$ = 0.0738, $wR2$ = 0.1414, $R$ indices based on 4667 reflections with $I > 2\sigma(I)$ (refinement on $F^2$), 455 parameters, $\mu$ = 0.938 mm$^{-1}$.

**Crystal Data for 2:** $C_{14}H_{12}MnN_2O_4$, $Mr$ = 327.20, 0.30 × 0.26 × 0.20 mm, monoclinic, space group $P2_1/n$ (No. 14), $a$ = 8.8522(17), $b$ = 4.6071(9), $c$ = 15.377(3) Å, $\beta$ = 105.279(3)°, $V$ = 604.9(2) Å$^3$, $Z$ = 2, $D_c$ = 1.796 g/cm$^3$, $F$(000) = 334, Mo-$K_\alpha$ radiation, $\lambda$ = 0.71073 Å, $T$ = 293(2) K, $2\theta_{max}$ = 50.2°, 1785 reflections collected, 1054 unique ($R_{int}$ = 0.0400). Final $GooF$ = 1.247, $R1$ = 0.0603, $wR2$ = 0.1243, $R$ indices based on 866 reflections with $I > 2\sigma(I)$ (refinement on $F^2$), 121 parameters, $\mu$ = 1.110 mm$^{-1}$.

CCDC-288647 and -288648 (for **1** and **2**) contain the supplementary crystallographic data for this paper. These data can be obtained free of charge from The Cambridge Crystallographic Data Centre via www.ccdc.cam.ac.uk/data_request/cif.

**Supporting Information** (for details see the footnote on the first page of this article): Figure S1, packing diagram of **1** along the $c$ axis and Figure S2, packing diagram of **2** along the $b$ axis.

## Acknowledgments

This work was supported by the National Nature Science Foundation of China (No. 20231020) and Nature Science Foundation of Fujian Province.

[1] a) J. S. Miller, M. Drilon, *Magnetism: Molecules to Materials*, Wiley-VCH, Weinheim, **2002**, vol. 3; b) O. Kahn, *Molecular Magnetism*, VCH, Weinheim, **1993**.

[2] J. Ribas, A. Escuer, M. Monfort, R. Vicente, R. Cortes, L. Lezama, T. Rojo, *Coord. Chem. Rev.* **1999**, *195*, 1027–1068 and references therein.

[3] a) J. Larionova, R. Clerac, J. Sanchiz, O. Kahn, S. Golhen, L. Ouahab, *J. Am. Chem. Soc.* **1998**, *120*, 13088–13095; b) C. Boskovic, E. K. Brechin, W. E. Streib, K. Folting, D. N. Hendrickson, G. Christou, *Chem. Commun.* **2001**, 467–468.

[4] C. Janiak, *Dalton Trans.* **2003**, 2781–2804.

[5] a) K. Barthelet, J. Marrot, D. Riou, G. Ferey, *Angew. Chem. Int. Ed.* **2002**, *41*, 281–284; b) N. Guillou, S. Pastre, C. Livage, G. Ferey, *Chem. Commun.* **2002**, 2358–2359.

[6] a) E. Q. Gao, S. Q. Bai, Z. M. Wang, C. H. Yan, *J. Am. Chem. Soc.* **2003**, *125*, 4984–4985; b) M. Minguet, D. Luneau, E. Lhotel, V. Villar, C. Paulsen, D. B. Amabilino, J. Veciana, *Angew. Chem. Int. Ed.* **2002**, *41*, 586–589; c) B. O. Patrick, W. M. Reiff, V. Sanchez, A. Storr, R. C. Thompson, *Inorg. Chem.* **2004**, *43*, 2330–2339.

[7] a) J. R. Galan-Mascaros, K. R. Dunbar, *Angew. Chem. Int. Ed.* **2003**, *42*, 2289–2293; b) H. L. Sun, B. Q. Ma, S. Gao, G. Su, *Chem. Commun.* **2001**, 2586–2587; c) M. Kurmoo, H. Kumagai, M. A. Green, B. W. Lovett, S. J. Blundell, A. Ardavan, J. Singleton, *J. Solid State Chem.* **2001**, *159*, 343–351.

[8] a) K. Okada, O. Nagao, H. Mori, M. Kozaki, D. Shiomi, K. Sato, T. Takui, Y. Kitagawa, K. Yamaguchi, *Inorg. Chem.* **2003**, *42*, 3221–3228; b) C. Policar, F. Lambert, M. Cesario, I. Morgenstern-Badarau, *Eur. J. Inorg. Chem.* **1999**, 2201–2207.

[9] E. Colacio, J. M. Domínguez-Vera, M. Ghazi, R. Kivekäs, M. Klinga, J. M. Moreno, *Eur. J. Inorg. Chem.* **1999**, 441–445 and references cited therein.

[10] a) P. King, R. Clerac, C. E. Anson, C. Coulon, A. K. Powell, *Inorg. Chem.* **2003**, *42*, 3492–3500; b) D. Schulz, T. Weyhermüller, K. Wieghardt, C. Butzlaff, A. X. Trautwein, *Inorg. Chim. Acta* **1996**, *246*, 387–394.

[11] a) S. Konar, P. S. Mukherjee, E. Zangrando, F. Lloret, N. R. Chaudhuri, *Angew. Chem. Int. Ed.* **2002**, *41*, 1561–1563; b) H. J. Chen, Z. W. Mao, S. Gao, X. M. Chen, *Chem. Commun.* **2001**, 2320–2321.

[12] a) P. M. Forster, A. K. Cheetham, *Angew. Chem. Int. Ed.* **2002**, *41*, 457–459; b) Z. L. Huang, M. Drillon, N. Masciocchi, A. Sironi, J. T. Zhao, P. Rabu, P. Panissod, *Chem. Mater.* **2000**, *12*, 2805–2812; c) J. M. Rueff, S. Pillet, N. Claiser, G. Bonaventure, M. Souhassou, P. Rabu, *Eur. J. Inorg. Chem.* **2002**, 895–900.

[13] a) D. Cave, J. M. Gascon, A. D. Bond, S. J. Teat, P. T. Wood, *Chem. Commun.* **2002**, 1050–1051; b) W. B. Lin, O. R. Evans, G. T. Yee, *J. Solid State Chem.* **2000**, *152*, 152–158; c) S. M. Humphrey, R. A. Mole, J. M. Rawson, P. T. Wood, *Dalton Trans.* **2004**, 1670–1678.

[14] a) M. C. Hong, Y. J. Zhao, W. P. Su, R. Cao, M. Fujita, Z. Y. Zhou, A. S. C. Chan, *J. Am. Chem. Soc.* **2000**, *122*, 4819–4820; b) W. P. Su, M. C. Hong, J. B. Weng, R. Cao, S. F. Lu, *Angew. Chem. Int. Ed.* **2000**, *39*, 2911–2914; c) Y. J. Zhao, M. C. Hong, Y. C. Liang, R. Cao, W. J. Li, J. B. Weng, S. F. Lu, *Chem. Commun.* **2001**, 1020–1021.

[15] a) R. H. Wang, E. Q. Gao, M. C. Hong, S. Gao, J. H. Luo, Z. Z. Lin, L. Han, R. Cao, *Inorg. Chem.* **2003**, *42*, 5486–5488; b) R. H. Wang, M. C. Hong, J. H. Luo, R. Cao, Q. Shi, J. B. Weng, *Eur. J. Inorg. Chem.* **2002**, 2904–2912; c) R. H. Wang, M. C. Hong, J. H. Luo, F. L. Jiang, L. Han, Z. Z. Lin, R. Cao, *Inorg. Chim. Acta* **2004**, *357*, 103–114.

[16] a) J. D. Martin, R. F. Hess, *Chem. Commun.* **1996**, 2419–2420; b) T. K. Maji, S. Sain, G. Mostafa, T. H. Lu, J. Ribas, M. Monfort, N. R. Chaudhuri, *Inorg. Chem.* **2003**, *42*, 709–716; c) W. Chen, Q. Yue, C. Chen, H. M. Yuan, W. Xu, J. S. Chen, S. N. Wang, *Dalton Trans.* **2003**, 28–30; d) H. H. Zhao, C. P. Berlinguette, J. Bacsa, A. V. Prosvirin, J. K. Bera, S. E. Tichy, E. J. Schelter, K. R. Dunbar, *Inorg. Chem.* **2004**, *43*, 1359–1369.

[17] a) V. L. Pecoraro, *Manganese Redox Enzymes*, VCH, Weinheim, **1992**; b) R. L. Rardin, P. Poganiuch, A. Bino, D. P. Goldberg, W. B. Tolman, S. C. Liu, S. J. Lippard, *J. Am. Chem. Soc.* **1992**, *114*, 5240–5249; c) K. F. Hsu, S. L. Wang, *Inorg. Chem.* **2000**, *39*, 1773–1778.

[18] a) P. J. Smith, R. O. Day, V. Chandrasekhar, J. M. Holmes, R. Holmes, *Inorg. Chem.* **1986**, *25*, 2495–2499; b) L. P. Battaglia, A. C. Bonamartini, S. Ianelli, M. A. Zoroddu, G. Sanna, *J. Chem. Soc., Faraday Trans.* **1991**, *87*, 3863–3867; c) M. R. Sundberg, J. K. Koskimies, J. Matikainen, H. Tylli, *Inorg. Chim. Acta* **1998**, *268*, 21–30; d) H. J. Chen, X. M. Chen, *Inorg. Chim. Acta* **2002**, *329*, 13–21; e) G. Smith, K. A. Byriel, C. H. L. Kennard, *Aust. J. Chem.* **1999**, *52*, 325–327.

[19] Z. He, Z. M. Wang, C. H. Yan, *CrystEngComm* **2005**, *7*, 143–150.

[20] a) Q. H. Zhao, H. F. Li, X. F. Wang, Z. D. Chen, *New J. Chem.* **2002**, *26*, 1709–1710; b) G. A. Van Albada, R. C. Guijt, J. G. Haasnoot, M. Lutz, A. L. Spek, J. Reedijk, *Eur. J. Inorg. Chem.* **2000**, 121–126.

[21] a) Z. M. Wang, B. Zhang, H. Fujiwara, H. Kobayashi, M. Kurmoo, *Chem. Commun.* **2004**, 416–417; b) R. D. Poulsen, A.

 © 2006 Wiley-VCH Verlag GmbH & Co. KGaA, Weinheim 

Bentien, M. Chevalier, B. B. Iversen, *J. Am. Chem. Soc.* **2005**, *127*, 9156–9166.
[22] a) C. B. Ma, W. G. Wang, X. F. Zhang, C. N. Chen, Q. T. Liu, H. P. Zhu, D. Z. Liao, L. C. Li, *Eur. J. Inorg. Chem.* **2004**, 3522–3532; b) G. Aromi, S. M. J. Aubin, M. A. Bolcar, G. Christou, H. J. Eppley, K. Folting, D. N. Hendrickson, J. C. Huffman, R. C. Squire, H.-L. Tsai, S. Wang, M. W. Wemple, *Polyhedron* **1998**, *17*, 3005–3020; c) G. Aromi, M. W. Wemple, S. M. J. Aubin, K. Folting, D. N. Hendrickson, G. Christou, *J. Am. Chem. Soc.* **1998**, *120*, 5850–5851; d) R. J. Kulawiec, R. H. Crabtree, G. W. Brudvig, G. K. Schulte, *Inorg. Chem.* **1988**, *27*, 1309–1311; e) E. Libby, J. K. McCusker, E. A. Schmitt, K. Folting, D. N. Hendrickson, G. Christou, *Inorg. Chem.* **1991**, *30*, 3486–3495; f) S. Wang, K. Folting, W. E. Streib, E. A. Schmitt, J. K. McCusker, D. N. Hendrickson, G. Christou, *Angew. Chem. Int. Ed. Engl.* **1991**, *30*, 304–306.
[23] a) J. J. Borrás-Almenar, J. M. Clemente-Juan, E. Coronado, B. Tsukerblat, *Inorg. Chem.* **1999**, *38*, 6081–6088; b) J. J. Borrás-Almenar, J. M. Clemente-Juan, E. Coronado, B. S. Tsukerblat, *J. Comput. Chem.* **2001**, *22*, 985–991.
[24] X. S. Tan, D. F. Xiang, W. X. Tang, J. Sun, *Polyhedron* **1997**, *16*, 689–694.
[25] C. Ruiz-perez, M. Hernandez-Molina, P. Lorenzo-luis, F. Lloret, J. Cano, M. Julve, *Inorg. Chem.* **2000**, *39*, 3845–3852.
[26] a) Z.-N. Chen, S.-X. Liu, T. Qiu, Z.-M. Wang, J.-L. Huang, W.-X. Tang, *J. Chem. Soc., Dalton Trans.* **1994**, 2989–2993; b) C. B. Ma, C. N. Chen, Q. T. Liu, F. Chen, D. Z. Liao, L. C. Li, L. C. Sun, *Eur. J. Inorg. Chem.* **2003**, 2872–2879.
[27] a) M. Wesolek, D. Meyer, J. A. Osborn, A. Decian, J. Fischer, A. Derory, P. Legoll, M. Drillon, *Angew. Chem. Int. Ed. Engl.* **1994**, *33*, 1592–1594; b) S. L. Lambert, D. N. Hendrickson, *Inorg. Chem.* **1979**, *18*, 2683–2686; c) H. Chang, S. K. Larsen, P. D. W. Boyd, C. G. Pierpont, D. N. Hendrickson, *J. Am. Chem. Soc.* **1988**, *110*, 4565–4576; d) K. K. Nanda, L. K. Thompson, J. N. Bridson, K. Nag, *J. Chem. Soc., Chem. Commun.* **1994**, 1337–1338.
[28] M. E. Fisher, *Am. J. Phys.* **1964**, *32*, 343–346.
[29] C. J. O'Connor, *Prog. Inorg. Chem.* **1982**, *29*, 203–283.
[30] G. W. Sheldrick, *SADABS*, Program for Empirical Absorption Correction of Area Detector Data, University of Göttingen, **1996**.
[31] G. W. Sheldrick, *SHELXS 97*, Program for Crystal Structure Solution, University of Göttingen, **1997**.
[32] G. W. Sheldrick, *SHELXL 97*, Program for Crystal Structure Refinement, University of Göttingen, **1997**.

Received: November 4, 2005
Published Online: February 24, 2006

 © 2006 Wiley-VCH Verlag GmbH & Co. KGaA, Weinheim 

DOI: 10.1002/ejic.200500995

# Synthesis and Metallation of the Diphosphanylsilane $i$Pr$_2$Si(PHMe)$_2$

Carsten von Hänisch*[a] and Oliver Rubner[b]

**Keywords:** Clusters / Phosphorus / Silicon / Tin / Zinc

The reaction of [LiAl(PHMe)$_4$] with $i$Pr$_2$SiCl$_2$ yields the dialkyldiphosphanylsilane $i$Pr$_2$Si(PHMe)$_2$ (**1**). This compound is formed as a diastereomeric mixture and was identified by NMR spectroscopy and mass spectrometry. Silane **1** reacts with [Sn{N(SiMe$_3$)$_2$}$_2$] and [Zn{N(SiMe$_3$)$_2$}$_2$] to form the polycyclic compounds [Sn{SnN(SiMe$_3$)$_2$}$_2${$i$Pr$_2$Si(PMe)$_2$}$_2$] (**2**) and [{ZnN(SiMe$_3$)$_2$}$_3${$i$Pr$_2$Si(PMe)$_2$}$_2$H] (**3**), respectively. The tricyclic compound **2** possesses one Sn–Sn bond and contains tin atoms in the formal oxidation states +1, +2 and +3. The central structural motif of the zinc–phosphorus cluster **3** is a Zn$_3$P$_4$Si$_2$ cage. The compounds [$i$Pr$_2$Si{P(Me)MEt$_2$}$_2$]$_2$ (**4**: M = Al; **5**: M = Ga), which feature an adamantane-like cage formed by four metal, four phosphorus and two silicon atoms can be obtained by the reaction of **1** with MEt$_3$ (M = Al, Ga).
(© Wiley-VCH Verlag GmbH & Co. KGaA, 69451 Weinheim, Germany, 2006)

## Introduction

In the last few years reactions of primary silylphosphanes or -arsanes (R$_3$SiEH$_2$; E = P, As) with amide or alkyl compounds of different main- and subgroup metals have been applied several times to synthesise metal–phosphorus and metal–arsenic compounds.[1–3] Cyclic and cage-like species were obtained by these reactions. The molecular structures of the reaction products can be influenced by the silyl groups attached to the P or As atom. The reactions of [Sn{N(SiMe$_3$)$_2$}$_2$] with R$_3$SiEH$_2$ (E = P, As) serve as an example. Thus, the hexagonal-prismatic compounds [SnESi$i$Pr$_3$]$_6$ (E = P, As) are formed starting from $i$Pr$_3$SiEH$_2$, whereas the reaction of $t$Bu$_3$SiPH$_2$ with [Sn{N(SiMe$_3$)$_2$}$_2$] yields the heterocubane [SnPSi$t$Bu$_3$]$_4$.[2] Recently, it was shown that the diisopropyldiphosphanylsilane $i$Pr$_2$Si(PH$_2$)$_2$ is a very promising starting compound for the formation of novel ternary clusters. For example, it reacts with MEt$_3$ (M = Al, Ga, In) to form the ternary compounds [$i$Pr$_2$Si{P(H)MEt$_2$}$_2$]$_2$ (M = Al, Ga, In), which exhibit an M$_4$P$_4$Si$_2$ adamantane cage as the central structural motif.[3] In this paper, the synthesis of the new diphosphanylsilane $i$Pr$_2$Si(PHMe)$_2$ and its reactions with the metal amides [Sn{N(SiMe$_3$)$_2$}$_2$] and [Zn{N(SiMe$_3$)$_2$}$_2$], as well as with the alkyl compounds AlEt$_3$ and GaEt$_3$, are described.

[a] Forschungszentrum Karlsruhe GmbH, Institut für Nanotechnologie,
Postfach 3640, 76021 Karlsruhe
Fax: +49-7247-826-368
E-mail: carsten.vonhaenisch@int.fzk.de
[b] Institut für Physikalische Chemie, Universität Münster,
Corrensstr. 30/3, 48149 Münster
E-mail: oliver.rubner@uni-muenster.de
Supporting information for this article is available on the WWW under http://www.eurjic.org or from the author.

## Results and Discussion

A solution of [LiAl(PHMe)$_4$] in DME was treated with $i$Pr$_2$SiCl$_2$ and furnished the dialkyldiphosphanylsilane $i$Pr$_2$Si(PHMe)$_2$ (**1**) in about 30% yield. Because of the high inversion barrier of the phosphorus atoms, compound **1** forms as a diastereomeric mixture. Therefore, the $^{31}$P{$^1$H} NMR spectrum of **1** shows two singlet signals at $\delta$ = –190.2 and –193.1 ppm. Two triplets at $\delta$ = 19.3 and 21.3 ppm, with $^1J_{Si,P}$ coupling constants of 44 and 45 Hz, can be observed in the $^{29}$Si{$^1$H} NMR spectrum. In the $^1$H NMR spectrum, the signals of the diastereomers are superposed. One can observe a multiplet for the methyl groups at $\delta$ = 0.93 ppm, a multiplet for the isopropyl groups at $\delta$ = 1.06 ppm, and a quadruplet of doublets for the PH protons at $\delta$ = 2.20 ppm. The phosphorus-decoupled $^1$H NMR spectrum shows two doublets at $\delta$ = 0.94 and 0.93 ppm for the methyl groups, with $^3J_{H,H}$ coupling constants of 7.4 Hz. The mass spectrum of **1** shows the molecular peak at $m/z$ = 208, as well as peaks for the fragments [M$^+$ – Me], [M$^+$ – PHMe] and [M$^+$ – C$_3$H$_6$].

Compound **1** reacts with [Sn{N(SiMe$_3$)$_2$}$_2$] in heptane to give a red solution from which orange crystals can be obtained at –35 °C. An X-ray crystal structure determination revealed that [Sn{SnN(SiMe$_3$)$_2$}$_2${$i$Pr$_2$Si(PMe)$_2$}$_2$] (**2**) (Figure 1) has been formed.[4] This compound shows a polycyclic Sn$_3$P$_4$Si$_2$ core structure, which is formed by two Sn$_2$P$_2$Si rings and one Sn$_2$P$_2$ ring. Two of the tin atoms bear one N(SiMe$_3$)$_2$ substituent each, whereas the central tin atom has no exocyclic ligands. Remarkably, a tin–tin bond [Sn(1)–Sn(3)] appears in the molecular structure of **2**, hence compound **2** contains three electronically different tin atoms.[5] The $^{119}$Sn Mössbauer spectrum (recorded at 77 K with a BaSnO$_3$ source) could be fitted with six Lorentzian lineshape components at 4.0, 3.3, 2.5, 2.1, 1.6, and

 © 2006 Wiley-VCH Verlag GmbH & Co. KGaA, Weinheim 

1.3 mm s$^{-1}$ with approximately equal intensities. The linewidths of these components (0.8 mm s$^{-1}$) are close to the expected natural linewidth. These six Lorentzians most likely comprise three spectral components that are split into doublets by nuclear electronic quadrupolar interactions with the spin 3/2 nuclear excited state of $^{119}$Sn, consistent with the expectation of three distinct crystallographic sites. As there is currently no body of suitable reference data, we cannot identify the specific sets of lines making up these three quadrupolar doublets with certainty. In view of the crystallographic information, it appears plausible, however, to group these six lines into one doublet centred near 1.5 mm s$^{-1}$, characterised by a rather small quadrupolar splitting [this doublet is most likely assignable to the four-coordinate Sn(3) site], and two doublets having relatively large quadrupolar splittings, which are assigned to the three-coordinate Sn(1) and Sn(2) sites. While we cannot specify isomeric shifts and quadrupolar splitting parameters of Sn(1), Sn(2) and Sn(3) beyond doubt at the present time, we can nevertheless conclude that the Mössbauer spectrum is consistent with the proposed structure.

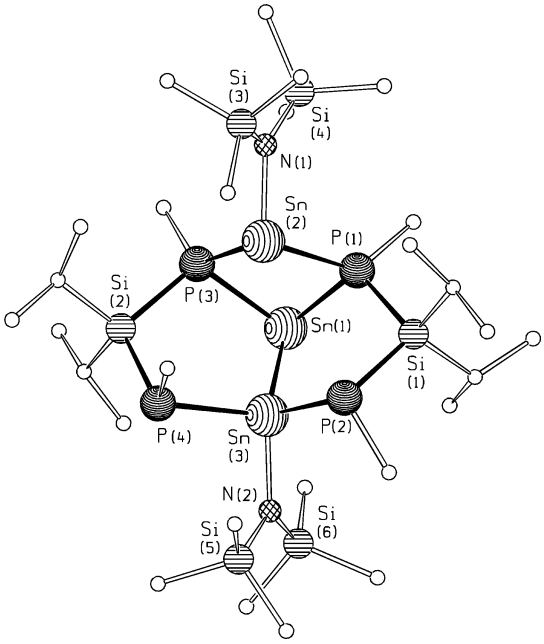


Figure 1. Molecular structure of **2**. Selected bond lengths [pm] and angles [°]: Sn(1)–Sn(3) 288.1(1), Sn(1)–P(1) 263.2(1), Sn(1)–P(3) 261.5(1), Sn(2)–N(1) 210.6(4), Sn(2)–P(1) 266.9(1), Sn(2)–P(3) 270.1(1), Sn(3)–N(2) 210.4(3), Sn(3)–P(2) 256.1(1), Sn(3)–P(4) 256.9(1), Si(1)–P(1) 226.4(1), Si(1)–P(2) 226.8(1), Si(2)–P(3) 226.8(2), Si(2)–P(4) 224.8(2); P(1)–Sn(1)–Sn(3) 84.66(3), P(3)–Sn(1)–Sn(3) 86.03(3), P(1)–Sn(1)–P(3) 84.47(3), P(2)–Sn(3)–P(4) 107.93(4), P(2)–Sn(3)–Sn(1) 111.26(3), P(4)–Sn(3)–Sn(1) 110.33(3), P(1)–Sn(2)–P(3) 82.12(4), P(1)–Si(1)–P(2) 105.73(5), P(3)–Si(2)–P(4) 111.33(3), Sn(1)–P(1)–Sn(2) 93.46(4), Si(1)–P(2)–Sn(3) 101.16(5), Sn(1)–P(3)–Sn(2) 93.09(3), Si(2)–P(4)–Sn(3) 100.13(5).

In the $^{31}P\{^1H\}$ NMR spectrum of **2** one signal with one pair of Sn satellites at $\delta$ = –181.5 ppm ($^1J_{P,Sn}$ = 948 Hz), which corresponds to P(2) and P(4), and another signal with two pairs of Sn satellites at $\delta$ = –176.6 ppm ($^1J_{P,Sn}$ = 1105 and 935 Hz), which corresponds to P(1) and P(3), can be observed. The $^{117}$Sn NMR spectrum shows three broad signals with a triplet structure at $\delta$ = 39, 172 and 290 ppm.

The Sn(1)–Sn(3) bond length of 288.1 pm is within the usual range for Sn–Sn single bonds; the Sn–P bonds in compound **2** are between 256.1 and 266.9 pm. In the mixed-valence Sn/P cluster $[Sn_8(PSi\textit{i}Pr_3)_6Cl_2]$ described recently, the Sn–Sn bonds are in the range 283.4–288.8 pm and the Sn–P bonds are in the range 253.8–272.8 pm.[6]

The reaction of **1** with the zinc amide $[Zn\{N(SiMe_3)_2\}_2]$ in heptane yields a colourless solution from which crystals of $[\{ZnN(SiMe_3)_2\}_3\{\textit{i}Pr_2Si(PMe)_2\}_2H]$ (**3**) can be obtained. Compound **3** crystallises in the orthorhombic space group $Pna2_1$ and was refined as an inversion twin (Figure 2). The molecular structure contains a heavily folded six-membered $Zn_3P_3$ ring. Each zinc atom binds to one exocyclic $N(SiMe_3)_2$ substituent, and each phosphorus atom bears one methyl group. Two of the phosphorus atoms [P(1) and P(2)] of this ring are further connected by an Si*i*Pr$_2$ group to form a four-membered $ZnP_2Si$ ring. The third phosphorus atom [P(3)] binds to an Si*i*Pr$_2$PHMe fragment. The phosphorus atom of this PHMe group [P(4)] coordinates the opposite zinc atom of the ring [Zn(1)]. Therefore, Zn(1) has a coordination number of four, whereas Zn(2) and Zn(3) have a trigonal-planar coordination. Due to the lower coordination, the Zn–P and Zn–N bonds at Zn(2) and Zn(3) are significantly shorter than to Zn(1) [Zn(1)–P = 246.6–250.1 ppm, Zn(1)–N = 192.3 pm, Zn(2,3)–P = 234.9–241.2 ppm, Zn(2,3)–N = 189.8 and 189.2 pm]. In the zinc–phosphorus ring compound $[MeZn\{\mu\text{-}P(SiMe_3)_2\}]_3$, in which the coordination of all Zn atoms is trigonal-planar, the Zn–P bonds are, on average, 238 pm long.[7] The ring compound $[Zn_2Cl_2\{\mu\text{-}P(SiMe_3)_2\}_2(P\textit{n}Pr_3)_2]$ shows Zn atoms with coordination number four due to the coordination of additional phosphane ligands. In this compound, the Zn–P($\mu_2$) bonds are 242.6 to 244.7 pm long, whereas the terminal Zn–P bonds amount to 240.8–243.0 pm.[8] The hydrogen atom at P(4) could not be satisfactorily fitted in the difference map; however, the $^1$H and $^{31}$P NMR spectra of **3** give clear evidence for the presence of a hydrogen atom. Beside the signals of the PMe, $SiMe_3$ and Si*i*Pr$_2$ groups, the $^1$H NMR spectrum shows a weak doublet of multiplets with a $^1J_{P,H}$ coupling constant of 270 Hz; in the $^1H\{^{31}P\}$ NMR spectrum this signal appears as a quadruplet with a $^3J_{H,H}$ coupling constant of 7.5 Hz. In the $^{31}P\{^1H\}$ NMR spectrum four multiplets for the four different phosphorus atoms in **3** can be observed in the range from $\delta$ = –150 to –200 ppm (ABCD spin system). In the $^{31}$P NMR spectrum the signal at $\delta$ = –155 ppm is further split by a $^1J_{P,H}$ coupling (see Figure 3a,b), therefore this signal can be assigned to P(4). Quantum chemical calculations with the Turbomole program package were applied to allocate the three remaining multiplets to specific P atoms. The method applied was DFT with the BP86 functional and a TZVPP basis set for all atoms;[9,10] for performance reasons the resolution-of-identity (RI) approximation was used.[11] The reference for the chemical shifts was $H_3PO_4$, computed with the same parameters as were used for the cluster. Those calculations that gave chemical shifts closest to the experimental values

 © 2006 Wiley-VCH Verlag GmbH & Co. KGaA, Weinheim 

were performed as single-point calculations with the geometry obtained from the X-ray structure analysis. As the position of the hydrogen atom at P(4) could not be determined by the experiment, its distance to the phosphorus atom was varied systematically. Geometry optimisations with different basis sets led to deviations from the experimental values of about $\delta$ = 15–30 ppm, although the order of peaks for P(1), P(2) and P(3) was always retained. For a given geometry of the cluster, the shift of P(4) is extremely sensitive to the P–H distance and the H–P–C bond angle. Thus, the correct combination of distance and angle could not definitely be fixed. The best agreements were achieved for a distance of about 150 pm at an angle of 100°. The resulting chemical shifts are given in Table 1.

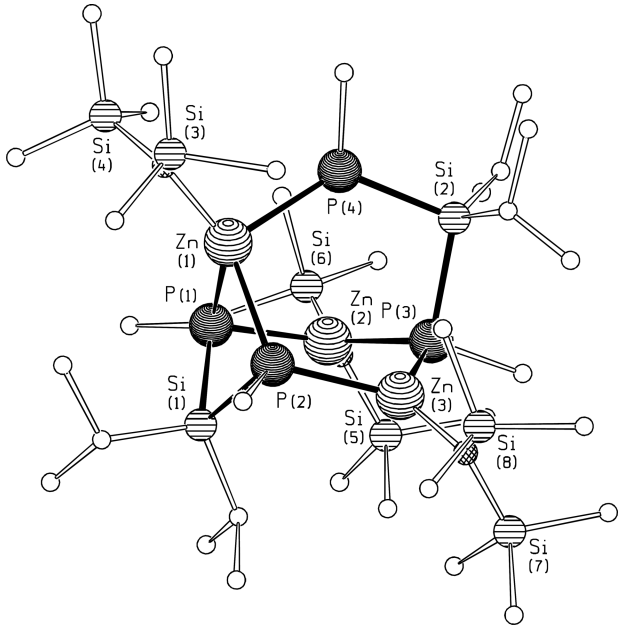


Figure 2. Molecular structure of **3**. Selected bond lengths [pm] and angles [°]: Zn(1)–P(1) 250.1(2), Zn(1)–P(2) 246.6(3), Zn(1)–P(4) 249.5(4), Zn(1)–N(1) 192.3(7), Zn(2)–P(1) 236.7(2), Zn(2)–P(2) 241.2(2), Zn(2)–N(2) 189.8(6), Zn(3)–P(2) 234.9(3), Zn(3)–P(3) 238.8(2), Zn(3)–N(3) 189.2(6), P(1)–Si(1) 224.6(4), P(2)–Si(1) 227.4(4), P(3)–Si(2) 224.2(3), P(4)–Si(2) 219.5(5); P(1)–Zn(1)–P(2) 81.13(8), P(1)–Zn(1)–P(4) 95.47(13), P(2)–Zn(1)–P(4) 109.15(12), P(1)–Zn(2)–P(3) 109.66(8), P(2)–Zn(3)–P(3) 106.56(8), Si(1)–P(1)–Zn(2) 106.42(12), Si(1)–P(1)–Zn(1) 87.65(10), Si(1)–P(2)–Zn(3) 107.44(12), Si(1)–P(2)–Zn(1) 87.88(11), Si(2)–P(3)–Zn(3) 103.96(11), Si(2)–P(4)–Zn(1) 124.61(18), P(1)–Si(1)–P(2) 91.21(12), P(3)–Si(2)–P(4) 102.54(14).

A complete analysis of the $^{31}$P NMR spectrum by an iterative optimisation of the coupling constants yielded the values $J_{P1,P2}$ = 302.4, $J_{P1,P3}$ = 202.4, $J_{P1,P4}$ = 168.8, $J_{P2,P3}$ = 217.3, $J_{P2,P4}$ = 134.1, $J_{P3,P4}$ = 93.2 Hz and $^1J_{P4,H}$ = 272.7 Hz; the simulated spectrum is shown in Figure 3c.[12]

Compound **1** reacts with $MEt_3$ (M = Al, Ga) in heptane at ambient temperature with elimination of ethane. Recrystallisation from benzene yielded colourless crystals of the composition [$i$Pr$_2$Si{P(Me)MEt$_2$}$_2$]$_2$·2C$_6$H$_6$ (**4**: M = Al; **5**: M = Ga). The molecular structures of **4** and **5** (Figure 4) are almost identical to the compounds [$i$Pr$_2$Si{P(H)-MEt$_2$}$_2$]$_2$ (M = Al, Ga, In), described recently, but with methyl groups bound to the phosphorus atoms instead of hydrogen atoms.[3] The central structural motif is an adamantane-like cage of four aluminium or gallium atoms, four phosphorus and two silicon atoms. The phosphorus atoms are in the bridgehead positions and the metal and silicon atoms are in the secondary positions. This results in an eight-membered M$_4$P$_4$ (M = Al, Ga) ring where the opposite phosphorus atoms [P(1), P(3) and P(2), P(4)] are bridged by $i$Pr$_2$Si groups on different sides of the ring. The M$_4$P$_4$ ring is therefore strongly distorted and shows a boat-like conformation. The observed P–M and P–Si bond lengths are in the typical range for single bonds between these elements [**4**: Al–P = 242.8(1)–244.3(1), P–Si = 228.5(1)–228.8(1) pm; **5**: Ga–P = 241.5(1)–243.5(1), P–Si = 228.2(2)–229.3(2) pm]. Each of the metal atoms is bound to two exocyclic ethyl groups, and the silicon atoms possess two isopropyl groups each.

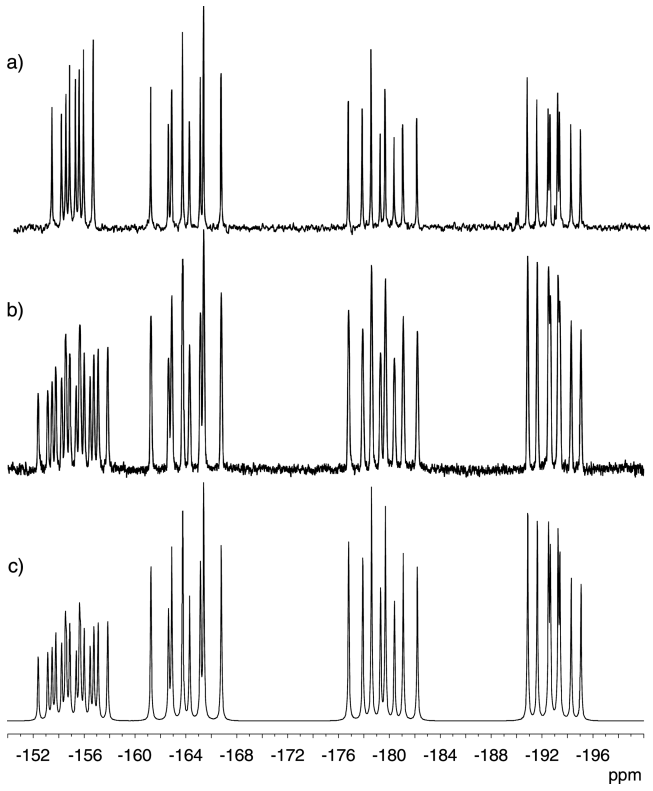


Figure 3. $^{31}$P NMR spectra of **3** (C$_6$D$_6$): a) experimental $^{31}$P{$^1$H} NMR spectrum; b) experimental $^{31}$P NMR spectrum; c) simulated $^{31}$P NMR spectrum.

Table 1. Calculated and experimental $^{31}$P chemical shifts for compound **3**.

| | P(1) | P(2) | P(3) | P(4) |
|---|---|---|---|---|
| Calculated | –157 | –171 | –190 | –151 |
| Experimental | –164 | –179 | –193 | –155 |

 © 2006 Wiley-VCH Verlag GmbH & Co. KGaA, Weinheim 

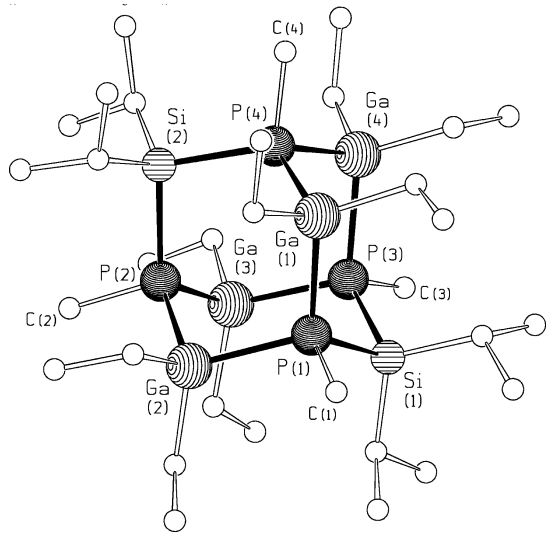


Figure 4. Molecular structure of **5**. Selected bond lengths [pm] and angles [°]: Ga(1)–P(1) 243.5(1), Ga(1)–P(4) 241.5(1), Ga(2)–P(1) 242.1(1), Ga(2)–P(2) 242.2(1), Ga(3)–P(2) 242.0(1), Ga(3)–P(1) 241.5(1), Ga(4)–P(3) 242.4(1), Ga(4)–P(4) 241.5(1), P(1)–Si(1) 228.7, P(3)–Si(1) 228.9(2), P(2)–Si(2) 229.3(2), P(4)–Si(2) 228.2(2); Si–P–Ga 114.23(6)–115.63(6), Ga–P–Ga 109.32(5)–110.28(5), P–Ga–P 110.47(5)–101.24(4).

## Experimental Section

**General:** All manipulations were performed under nitrogen, with rigorous exclusion of oxygen and moisture, using a Schlenk line. Solvents were dried and freshly distilled before use. NMR spectra were recorded with a Bruker DPX Avance 300 or with a Bruker AC 250 instrument. $[LiAl(PHMe)_4]$ and $GaEt_3$ were prepared according to the literature.[13] $AlEt_3$, $[Sn\{N(SiMe_3)_2\}_2]$ and $[Zn\{N(SiMe_3)_2\}_2]$ were obtained from Aldrich and used as received. Crystallographic data of **2**–**5** are shown in Table 2.[4]

**1:** $i Pr_2SiCl_2$ (3.0 g, 0.016 mol) was added to 50 mL of a 0.16 M solution of $[LiAl(PHMe)_4]$ in DME at 0 °C. The reaction mixture was warmed to room temperature and stirred for 16 h. Subsequently, pentane (50 mL) was added and the yellow precipitate was removed by filtration. Finally, the solvent was distilled off under reduced pressure at room temperature and the residue was distilled under vacuum. Compound **1** was obtained as a colourless liquid at 40 °C ($10^{-3}$ mbar). Yield: 1.0 g (32%). $^1H\{^{31}P\}$ NMR ($C_6D_6$): $\delta$ = 0.93 (d, $^3J_{H,H}$ = 7.4 Hz, 6 H, P–Me), 0.94 (d, $^3J_{H,H}$ = 7.4 Hz, 6 H, P–Me), 1.15 (m, 14 H, *i*Pr), 2.20 (qd, $^3J_{H,H}$ = 7.4, $^1J_{P,H} \approx$ 194 Hz, 2 H, P–H) ppm. $^{13}C\{^1H\}$ NMR ($C_6D_6$): $\delta$ = –3.2 (m, P–Me), 14.0 [m, $CH(CH_3)_2$], 19.4 [s, $CH(CH_3)_2$] ppm. $^{29}Si\{^1H\}$ NMR ($C_6D_6$): $\delta$ = 19.3 (t, $^1J_{P,Si}$ = 44 Hz), 21.3 (t, $^1J_{P,Si}$ = 45 Hz) ppm. $^{31}P$ NMR ($C_6D_6$): $\delta$ = –190.2 (d, $^1J_{P,H}$ = 194 Hz), –193.1 (d, $^1J_{P,H}$ = 195 Hz) ppm. MS (EI, 70 eV): *m*/*z* (%) = 208 (90) [$M^+$], 193 (10) [$M^+$ – Me], 161 (80) [$M^+$ – PHMe], 119 (100) [$M^+ - C_3H_6$], 43 (60) [$iPr^+$].

**2:** $[Sn\{N(SiMe_3)_2\}_2]$ (0.51 g, 1.15 mmol) was added to a solution of $iPr_2Si(PHMe)_2$ (0.12 g, 0.58 mmol) in heptane (5 mL) at 0 °C. The reaction mixture was warmed to room temperature and stirred for 16 h. During this time the colour of the solution changed from orange to red, and small amounts of a precipitate appeared. After filtration, the solution was cooled to –35 °C. Orange crystals of compound **2** appeared within 2 d. Yield: 0.25 g (79%). $C_{28}H_{76}N_2P_4Si_6Sn_3$ (1089.4): calcd. C 30.87, H 7.03, N 2.57; found C 30.91, H 7.05, N 2.44. $^1H$ NMR ($C_6D_6$): $\delta$ = 0.51 [s, 18 H, $N(SiMe_3)_2$], 0.58 (s, 9 H, $SiMe_3$), 0.80 (s, 9 H, $SiMe_3$), 1.07–1.33 (m, 28 H, *i*Pr), 1.83 (d, $^2J_{P,H}$ = 5.0 Hz, 6 H, PMe), 1.96 (d, $^2J_{P,H}$ = 8.1 Hz, 6 H, PMe) ppm. $^{31}P\{^1H\}$ NMR ([D$_8$]toluene, 50 °C): $\delta$ = –176.6 (br.), –181.5 (br.) ppm. $^{117}Sn\{^1H\}$ NMR ($C_6D_6$): $\delta$ = 39 (t, $^1J_{Sn,P} \approx$ 1000 Hz), 172 (t, $^1J_{Sn,P} \approx$ 935 Hz), 290 (t, $^1J_{Sn,P} \approx$ 1340 Hz) ppm.

**3:** $[Zn\{N(SiMe_3)_2\}_2]$ (0.22 g, 0.57 mmol) was added to a solution of $iPr_2Si(PHMe)_2$ (0.06 g, 0.29 mmol) in 5 mL of heptane at 0 °C. The reaction mixture was warmed to room temperature and stirred for 3 h. The solution was then cooled to 6 °C. Colourless crystals of **3** appeared after 2 d. Yield: 0.13 g (62%). $C_{34}H_{95}N_3P_4Si_8Zn_3$ (1090.9): calcd. C 37.44, H 8.78, N 3.85; found C 37.10, H 8.51, N 3.69. $^1H\{^{31}P\}$ NMR ([D$_8$]toluene): $\delta$ = 0.27 [s, 18 H, $Si(CH_3)_3$],

Table 2. Crystallographic data of **2**–**5**.[4]

| Compound | **2** | **3** | **4** | **5** |
|---|---|---|---|---|
| Empirical formula | $C_{28}H_{76}N_2P_4Si_6Sn_3$ | $C_{34}H_{94}N_3P_4Si_2Zn_3$ | $C_{32}H_{80}P_4Al_4Si_2{\cdot}2C_6H_6$ | $C_{32}H_{80}P_4Ga_4Si_2{\cdot}2C_6H_6$ |
| Space group | $P2_1/n$ | $Pna2$ | $P\bar{1}$ | $P\bar{1}$ |
| Formula units | 4 | 4 | 2 | 2 |
| Temperature [K] | 200 | 200 | 200 | 200 |
| *a* [pm] | 1259.4(3) | 2861.1(6) | 1119.1(2) | 1120.1(2) |
| *b* [pm] | 1591.0(3) | 1584.0(3) | 1354.3(3) | 1357.2(3) |
| *c* [pm] | 2529.3(5) | 1335.2(3) | 1864.5(4) | 1868.3(4) |
| $\alpha$ [°] | 90 | 90 | 81.83(2) | 81.86(3) |
| $\beta$ [°] | 98.28(3) | 90 | 86.41(3) | 86.28(3) |
| $\gamma$ [°] | 90 | 90 | 86.52(4) | 86.79(3) |
| Volume [$10^6$ pm$^3$] | 5015.1(7) | 6051(2) | 2787.9(10) | 2802.5(10) |
| Density [g cm$^{-3}$] | 1.443 | 1.196 | 1.083 | 1.280 |
| $2\Theta$ range [°] | 3–52 | 4–45 | 3–50 | 3–54 |
| Reflections measured | 22665 | 24840 | 11927 | 14814 |
| Independent reflections | 9721 ($R_{int}$ = 0.0422) | 7875 ($R_{int}$ = 0.0362) | 8231 ($R_{int}$ = 0.0545) | 10439 ($R_{int}$ = 0.0708) |
| Independent reflections with $F_o > 4\sigma(F_o)$ | 8409 | 7166 | 5835 | 7432 |
| Parameters | 388 | 470 | 487 | 487 |
| $\mu$(Mo-$K_\alpha$) [mm$^{-1}$] | 1.774 | 1.468 | 0.268 | 2.086 |
| Flack parameter | – | 0.514 | – | – |
| $R_1$ | 0.0373 | 0.0574 | 0.0555 | 0.0657 |
| $wR_2$ (all data) | 0.1073 | 0.1603 | 0.1601 | 0.1792 |
| Residual electron density [e/Å$^3$] | 2.170 | 1.446 | 0.378 | 0.647 |

 © 2006 Wiley-VCH Verlag GmbH & Co. KGaA, Weinheim 

0.31 [s, 36 H, Si(C$H_3$)$_3$], 1.19 (d, $^3J_{H,H}$ = 7.3 Hz, 3 H, C$H_3$PH), 1.20–1.35 (m, 28 H, Si$iPr_2$), 1.46 (s, 3 H, C$H_3$P), 1.50 (s, 3 H, C$H_3$P), 151 (s, 3 H, C$H_3$P), 3.03 (q, $^3J_{H,H}$ = 7.3 Hz, 1 H, CH$_3$P$H$) ppm. $^{29}$Si{$^1$H} NMR ([D$_8$]toluene): $\delta$ = –4.9 (s, SiMe$_3$), –4.5 (s, SiMe$_3$), –3.9 (s, SiMe$_3$), 2.1 (s, Si$i$Pr$_2$) ppm. $^{31}$P{$^1$H} NMR ([D$_8$]-toluene): $\delta$ = –154 (m), –164 (m), –179 (m), –193 (m) ppm. Raman: $\tilde{\nu}$ = 2950 (s), 2918 (s), 2899 (vs), 2342 (w), 1461 (w), 1230 (w), 879 (w), 681 (m), 627 (m), 467 (w), 397 (m), 180 (m), 114 (m) cm$^{-1}$.

**4:** A solution of AlEt$_3$ (1.2 mL, 1.0 M) in hexane (1.2 mmol) was added, with stirring, to a solution of $i$Pr$_2$Si(PHMe)$_2$ (0.13 g, 0.60 mmol) in heptane (5 mL). After 16 h, all volatile compounds were removed under vacuum. Recrystallisation of the residue from 2 mL of benzene yielded **4**·2C$_6$H$_6$ as large, colourless crystals within 3 d. Yield: 0.18 g (66%). $C_{32}H_{80}Al_4P_4Si_2$ (909.16): calcd. C 51.04, H 10.71; found C 50.03, H 10.58. $^1$H NMR (C$_6$D$_6$): $\delta$ = 0.73 (q, $^3J_{H,H}$ = 7.8 Hz, 16 H, C$H_2$CH$_3$), 1.33 [d, $^3J_{H,H}$ = 7.5 Hz, 24 H, CH(C$H_3$)$_2$], 1.56 (m, 36 H, CH$_2$C$H_3$, PC$H_3$), 1.70 [sept, $^3J_{H,H}$ = 7.5 Hz, 4 H, C$H$(CH$_3$)$_2$] ppm. $^{31}$P NMR (C$_6$D$_6$): $\delta$ = –181.3 (s) ppm.

**5:** GaEt$_3$ (0.18 g, 1.16 mmol) was added, with stirring, to a solution of $i$Pr$_2$Si(PHMe)$_2$ (0.123 g, 0.58 mmol) in heptane (5 mL). After 16 h, all volatile compounds were removed under vacuum. Recrystallisation of the residue from 2 mL of benzene yielded **5**·2C$_6$H$_6$ as large, colourless crystals within 3 d. Yield: 0.20 g (64%). $C_{32}H_{80}Ga_4P_4Si_2$ (1080.1): calcd. C 41.60, H 8.73; found C 42.67, H 8.92. $^1$H NMR (C$_6$D$_6$): $\delta$ = 1.15 (q, $^3J_{H,H}$ = 7.2 Hz, 16 H, C$H_2$CH$_3$), 1.36 [d, $^3J_{H,H}$ = 7.5 Hz, 24 H, CH(C$H_3$)$_2$], 1.60 (m, 36 H, CH$_2$C$H_3$, PC$H_3$), 2.20 [sept, $^3J_{H,H}$ = 7.5 Hz, 4 H, C$H$(CH$_3$)$_2$] ppm. $^{31}$P NMR (C$_6$D$_6$): $\delta$ = –167.2 (s) ppm.

**Supporting Information** (see footnote on the first page of this article): Details about the $^{119}$Sn Mössbauer spectrum of compound **2**.

## Acknowledgments

C. v. H. thanks Dr. E. Matern (Institut für Anorganische Chemie, Universität Karlsruhe) for his valuable help with the NMR experiments and simulations and Dr. B. Mosel (Institut für Physikalische Chemie, Westfälische Wilhelms-Universität Münster) for recording the $^{119}$Sn Mössbauer spectrum.

[1] M. Driess, *Adv. Inorg. Chem.* **2000**, *50*, 235–284.
[2] a) M. Driess, S. Martin, K. Merz, V. Pintchouk, H. Pritzkow, H. Grützmacher, M. Kaupp, *Angew. Chem.* **1997**, *109*, 1982–1985; *Angew. Chem. Int. Ed. Engl.* **1997**, *36*, 1894–1897; b) M. Westerhausen, M. Krofta, N. Wiberg, H. Nöth, A. Pfitzner, *Z. Naturforsch., Teil B* **1998**, *53*, 1489–1493; c) M. Westerhausen, N. Makropoulos, H. Piotrowski, M. Warchhold, H. Nöth, *J. Organomet. Chem* **2000**, *614–615*, 70–73; d) M. Westerhausen, M. Krofta, S. Schneiderbauer, H. Piotrowski, *Z. Anorg. Allg. Chem.* **2005**, *631*, 1391–1396.
[3] C. von Hänisch, *Eur. J. Inorg. Chem.* **2003**, 2955–2958.
[4] STOE-IPDS2 (Mo-$K_\alpha$ radiation, $\lambda$ = 0.71073 Å). The structure was solved by direct methods and refined by full-matrix least-squares techniques against $F^2$ (Sn, Zn, Ga, Al, P, Si, C refined anisotropically, H atoms at the phosphorus atoms refined isotropically, all other H atoms calculated at ideal positions). CCDC-285122 (**2**), -285123 (**3**), -285120 (**4**) and -285121 (**5**) contain the supplementary crystallographic data for this paper. These data can be obtained free of charge from The Cambridge Crystallographic Data Centre via www.ccdc.cam.ac.uk/data_request/cif.
[5] Formal oxidation states are: +1 for Sn(1), +2 for Sn(2) and +3 for Sn(3).
[6] D. Nikolova, C. von Hänisch, A. Adolf, *Eur. J. Inorg. Chem.* **2004**, 2321–2325.
[7] B. Rademacher, W. Schwarz, M. Westerhausen, *Z. Anorg. Allg. Chem.* **1995**, *621*, 287–300.
[8] O. Fuhr, D. Fenske, *Z. Anorg. Allg. Chem.* **1999**, *625*, 1229–1236.
[9] O. Treutler, R. Ahlrichs, *J. Chem. Phys.* **1995**, *102*, 346–354.
[10] M. Häser, R. Ahlrichs, H. P. Baron, P. Weis, H. Horn, *Theor. Chim. Acta* **1992**, *83*, 455–470.
[11] K. Eichkorn, F. Weigend, O. Treutler, R. Ahlrichs, *Theor. Chem. Acc.* **1997**, *97*, 119.
[12] Programs *WinNMR* and *WinDaisy*, Bruker Daltonik, Bremen, **1999**; G. Hägele, M. Engelhardt, W. Boenigk, *Simulation und automatisierte Analyse von NMR-Spektren*, VCH, Weinheim, **1987**.
[13] a) N. Muller, A. L. Otermat, *Inorg. Chem.* **1965**, *4*, 296–299; b) G. Fritz, H. Schäfer, *Z. Anorg. Allg. Chem.* **1971**, *385*, 243–255.

Received: November 8, 2005
Published Online: February 22, 2006

 © 2006 Wiley-VCH Verlag GmbH & Co. KGaA, Weinheim 

DOI: 10.1002/ejic.200501006

# Structural Studies of β-Cyclodextrin and Permethylated β-Cyclodextrin Inclusion Compounds of Cyclopentadienyl Metal Carbonyl Complexes

**Susana S. Braga,[a] Filipe A. Almeida Paz,[a] Martyn Pillinger,[a] João D. Seixas,[b,c] Carlos C. Romão,*[b,c] and Isabel S. Gonçalves*[a]**

**Keywords:** Ab initio calculations / Cyclodextrins / Inclusion compounds / Iron / Molybdenum / Sandwich complexes

[CpM(CO)$_n$Cl] complexes with M = Fe ($n$ = 2) and Mo ($n$ = 3) have been immobilised in plain β-cyclodextrin (β-CD) and permethylated β-CD (TRIMEB) by methods tailored according to the stabilities and solubilities of the individual components. Four adducts were obtained with a 1:1 host/guest stoichiometry. The compounds were studied by powder X-ray diffraction (XRD), thermogravimetric analysis (TGA), $^{13}C\{^1H\}$ CP/MAS NMR and FTIR spectroscopy. A comparison of the experimental powder XRD data for the TRIMEB/[CpMo(CO)$_3$Cl] inclusion compound with reference patterns revealed that the crystal packing is very similar to that reported previously for a TRIMEB/ethyl laurate inclusion compound. The unit-cell parameters refined to $a$ = 14.731, $b$ = 22.476, $c$ = 27.714 Å (volume = 9176.3 Å$^3$), and the space group was confirmed as $P2_12_12_1$. A hypothetical structural model of the inclusion compound was subsequently obtained by global optimisation using simulated annealing.

(© Wiley-VCH Verlag GmbH & Co. KGaA, 69451 Weinheim, Germany, 2006)

## Introduction

Cyclodextrins (CDs) are water-soluble cyclic oligosaccharides that are capable of forming inclusion compounds with a wide range of organic molecules, inorganic ions and metallo-organic species.[1] Suitable guests include transition metal complexes and organometallic compounds bearing hydrophobic ligands such as cyclopentadienyl (Cp = $\eta^5$-$C_5H_5$) and $\eta^6$-arene groups.[2] With these ligands, the weaker categories of non-covalent bonding, such as van der Waals and charge-transfer interactions, assume considerable importance. CDs are known to bind ferrocene and its derivatives,[3] metallocene dihalides,[4] aromatic ruthenium complexes,[5] mixed-sandwich complexes such as [($\eta^5$-$C_5H_5$)Fe($\eta^6$-$C_6H_6$)]($PF_6$),[6] and half-sandwich complexes such as [CpFe(CO)$_2$X] (X = Cl, Me, CN),[7] [CpFe(CO)$_2$-$NH_3$]($PF_6$),[8] [CpMn(CO)$_3$],[9] [($\eta^6$-$C_6H_6$)Cr(CO)$_3$],[10] [Cp′Mo($\eta^3$-$C_3H_5$)(CO)$_2$],[11] [Cp′Mo($\eta^3$-$C_6H_7$)(CO)$_2$] and [Cp′Mo($\eta^4$-$C_6H_8$)(CO)$_2$]($BF_4$) (Cp′ = Cp, Ind).[12] Encapsulated metallo-organic complexes often exhibit markedly different physical and chemical characteristics compared to the bulk material, for example in their nonlinear optical properties,[13] electrochemical behaviour,[3b,3g,3i,3j,14] ligand substitution/insertion reactions,[7a,7b] and catalysis.[15] In the present work, we describe the synthesis and solid-state characterisation of inclusion compounds formed between the cyclopentadienyl metal carbonyl complexes [CpFe(CO)$_2$Cl] (**1**) and [CpMo(CO)$_3$Cl] (**2**) (Figure 1) and unmodified β-cyclodextrin and 2,3,6-tri-*O*-methyl-β-CD (TRIMEB). The encapsulation of the tricarbonylmolybdenum complex is of particular interest because this molecule is a precursor to the dioxomolybdenum(VI) complex [CpMoO$_2$Cl], which has been shown to be a very effective catalyst for the epoxidation of olefins using *tert*-butyl hydroperoxide as the oxidising agent.[16]

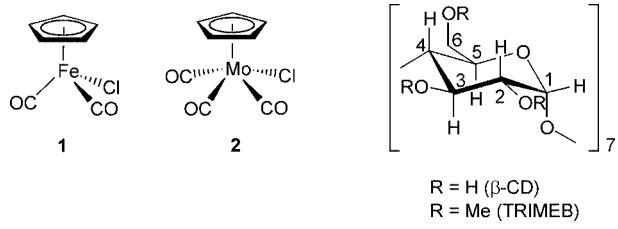


Figure 1. Guests and hosts used in this work.

Among the organometallic–cyclodextrin inclusion compounds described in the literature, only a few have been successfully characterised by single-crystal X-ray diffraction,[3e,3f,5,6] mainly because of the difficulty in preparing crystals of appropriate size that exhibit stability under the X-ray beam over the period of data collection. Useful structural information can, however, be obtained through a combination of other techniques such as powder XRD and NMR spectroscopy.[17–19] In particular, Caira described a

[a] Department of Chemistry, CICECO, University of Aveiro, 3810-193 Aveiro, Portugal
Fax: +351-234-370084
E-mail: igoncalves@dq.ua.pt
[b] Instituto de Tecnologia Química e Biológica da Universidade Nova de Lisboa,
Quinta do Marquês, EAN, Apt. 127, 2781-901 Oeiras, Portugal
[c] Alfama, Research and Development of Pharmaceutical Drugs, Ltd.,
IBET, Apartado 12, 2781-901 Oeiras, Portugal

 © 2006 Wiley-VCH Verlag GmbH & Co. KGaA, Weinheim 

few years ago a reliable empirical technique based on the visual comparison of X-ray powder patterns, which can almost unambiguously identify the type of crystal-packing arrangement of CD molecules in a typical host–guest inclusion compound.[17] This method can be envisaged as a "manual" (in some cases not very effective) direct-space approach to finding a hypothetical structural model. Even though it gives a rather reasonable first approach, this technique is also limited in its essence as it cannot explore all of the possible combinations in direct space. In this paper, we use conventional powder X-ray data, in combination with the technique proposed by Caira, to produce a hypothetical structural model of the inclusion compound TRIMEB·[CpMo(CO)$_3$Cl], obtained by global optimisation using simulated annealing. The calculations were performed using the recently developed FOX program,[20,21] which has proven to be a reliable, fast and robust software package for the solution of many different types of compounds.[22–26] This kind of ab initio model idealisation is unusual among compounds typically composed of light atoms (such as carbon, hydrogen and oxygen), and, to the best of our knowledge, is completely unprecedented among cyclodextrin inclusion compounds.

## Results and Discussion

The relative solubilities of β-CD, TRIMEB, and the complexes [CpFe(CO)$_2$Cl] (**1**) and [CpMo(CO)$_3$Cl] (**2**) determined the method used for the preparation of the respective inclusion compounds. An initial CD/complex molar ratio of 1:1 was always used. The iron complex **1** is slightly water soluble, and so the encapsulations were carried out using a mixture of water and ethanol. The compound β-CD·[CpFe(CO)$_2$Cl] (**3**) precipitated as an orange microcrystalline solid upon slow cooling of a hot water/ethanol solution. The high solubility of the modified cyclodextrin TRIMEB meant that the corresponding adduct, TRIMEB·[CpFe(CO)$_2$Cl] (**4**), could only be isolated by complete evaporation of the solvents. For the molybdenum complex **2**, dichloromethane had to be used to solubilise the guest. β-CD inclusion was achieved by mixing a dichloromethane solution of **2** with an aqueous solution of β-CD. After stirring at 40 °C for 2 h, a microcrystalline brick-red precipitate formed at the interface between the two solutions, designated as β-CD·[CpMo(CO)$_3$Cl] (**5**). Inclusion of the molybdenum complex **2** in TRIMEB was performed by dissolving the guest in a dichloromethane solution of the host followed by vacuum-drying to isolate TRIMEB·[CpMo(CO)$_3$Cl] (**6**). This uncommon technique works particularly well for the methylated cyclodextrin TRIMEB due to its high solubility in organic solvents. In fact, the same method has been successfully used by some of us in previous work.[27] Elemental analysis of compounds **3**–**6** confirmed that the final host/guest molar ratios were close to 1:1.

X-ray diffraction studies allow the identification of true inclusion complexes of cyclodextrins, mainly based on the empirical evidence that the powder XRD patterns of these complexes should be clearly distinct from those obtained by the superimposition of the diffractograms of each individual component.[1b] Figure 2 shows the patterns for complexes **1** and **2**, β-CD, and the adducts **3** and **5**. The diffractograms for the adducts are clearly different from the sum of the individual patterns of β-CD and either the iron complex **1** or the molybdenum complex **2**. For compound **3**, the overall pattern matches reasonably well with the reference pattern reported by Caira for the isostructural series characterised by channel-type packing of β-CD dimers ($C_2$ space group).[17] This type of packing has been previously identified in several β-CD inclusion complexes of organometallic molecules, such as ferrocene derivatives,[3k] mixed-sandwich complexes,[6] and half-sandwich molybdenum carbonyl complexes.[11,12] Most of the reflections in the powder XRD pattern of compound **5** match those present in the corresponding pattern for the parent β-CD hydrate, even though substantial changes in relative intensities are markedly visible along with some slight displacements in the 2$\theta$ values. The reflection centred at about 4.5° 2$\theta$ is characteristic of cage-type packing, as observed for β-CD hydrate or β-CD inclusion complexes of relatively small guests.[17] The existence of this type of crystal packing for compound **5** would therefore be surprising, although it is known that a molecule at least as large as benzyl alcohol can be accommodated by the host without a change in the packing arrangement.[17]

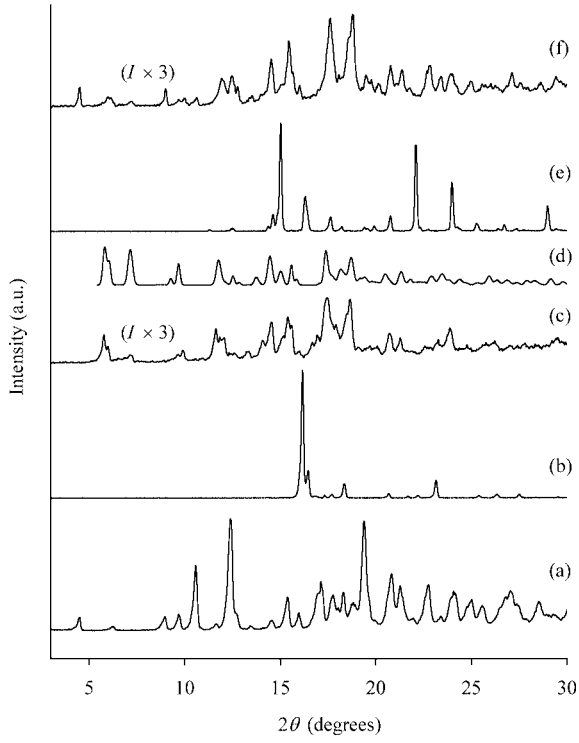


Figure 2. Powder XRD patterns of (a) β-CD hydrate, (b) [CpFe(CO)$_2$Cl] (**1**), (c) the inclusion compound β-CD·[CpFe(CO)$_2$Cl] (**3**), (d) a channel model,[16] (e) [CpMo(CO)$_3$Cl] (**2**) and (f) the inclusion compound β-CD·[CpMo(CO)$_3$Cl] (**5**).

 © 2006 Wiley-VCH Verlag GmbH & Co. KGaA, Weinheim 

Figure 3 shows the powder XRD patterns for complexes **1** and **2**, TRIMEB, and adducts **4** and **6**. Compound **4** is poorly crystalline, making it difficult to deduce the type of crystal packing arrangement. Nevertheless, a comparison of this pattern with those for the iron complex **1** and the parent TRIMEB indicates that a true inclusion compound has been isolated. The adduct TRIMEB·[CpMo(CO)$_3$Cl] (**6**) exhibits a better defined diffractogram, which could also be attributed to a new phase corresponding to a true inclusion compound. A careful inspection of this pattern suggests that the crystal packing should share close similarities with that found by Mentzafos et al. for a 1:1 inclusion compound comprising TRIMEB and ethyl laurate (in which the macrocycles are arranged along the *b* axis in a zigzag mode to form a distorted column structure).[28] This allowed us to perform a more in-depth structural evaluation using ab initio calculations. As typically observed for this type of compounds, the overall crystallinity of TRIMEB·[CpMo(CO)$_3$Cl] (**6**) is low due to structural orientation disorder of the host and/or the guest molecules, and the existence of several solvent molecules also highly affected by thermal disorder. Compound **6** diffracts very weakly at high angles and the diffractogram is generally characterised by poorly resolved lines (with large full-width-at-half-maximum). This creates, a priori, several limitations for a typical ab initio structural determination, and several approximations based on empirical evidence had to be taken into account (see below).

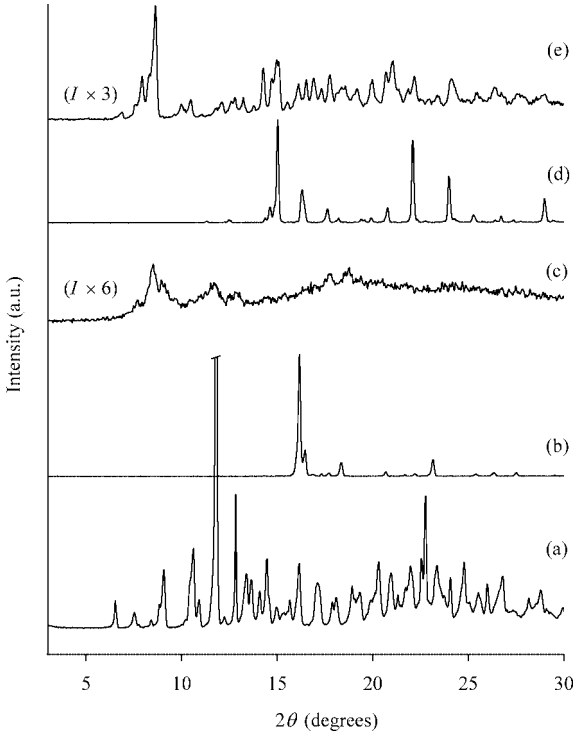


Figure 3. Powder XRD patterns of (a) TRIMEB, (b) [CpFe(CO)$_2$Cl] (**1**), (c) the inclusion compound TRIMEB·[CpFe(CO)$_2$Cl] (**4**), (d) [CpMo(CO)$_3$Cl] (**2**) and (e) the inclusion compound TRIMEB·[CpMo(CO)$_3$Cl] (**6**).

The ab initio determination of a hypothetical structural model for the inclusion compound TRIMEB·[CpMo(CO)$_3$Cl] (**6**) started by comparing the experimental data with the TRIMEB/ethyl laurate model compound, which has the Cambridge Structural Database (CSD)[29,30] refcode PINMAA [crystal data: $a$ = 14.796(2), $b$ = 22.444(6), $c$ = 27.720(8) Å, $V$ = 9205.03 Å$^3$, and space group $P2_12_12_1$]. Collected data were examined using the software package CHECKCELL,[31] and the unit-cell parameters refined to $a$ = 14.731, $b$ = 22.476, and $c$ = 27.714 Å (volume = 9176.3 Å$^3$), using 33 reflections for the CELREF subroutines.[32] By cross-examining the collected powder XRD pattern with the refined cell parameters, the space group of $P2_12_12_1$ for the inclusion compound **6** was unambiguously confirmed using CHECKCELL.

The modelling of compound **6** using FOX[20,21] started by assuming that the interactions between the guest [CpMo(CO)$_3$Cl] and the host TRIMEB molecules are mainly weak (van der Waals and hydrogen-bonding interactions) and mediated by close-packing principles. We assumed that the molecular geometries of the individual molecules remain relatively unchanged upon interaction to form the inclusion complex. In this case, FOX is particularly robust as individual molecules can be added as mathematical objects in the form of a Fenske–Hall Z-matrix, thus retaining some tacit knowledge of their geometry for the optimisation algorithm. Moreover, as the guest molecule contains a heavy atom (Mo), whose electron density contrasts well with the smeared-out density coming from the organic component, we assumed that the crystallographic position of [CpMo(CO)$_3$Cl] would be easily determined from the powder XRD pattern.

Firstly, the atomic coordinates of [CpMo(CO)$_3$Cl] were taken from the structure reported by Bueno et al. (deposited in the CSD with the refcode CPDMOC01),[33] and a Fenske–Hall Z-matrix (without hydrogen atoms) was created using BABEL.[34] The pivot atom was selected to be the central Mo in order to facilitate the mobility of the rigid molecule inside the unit cell. A Monte Carlo optimisation (using the optimised parallel tempering algorithm), in which the parameters of the Z-matrix were fixed (i.e., the molecule was treated as a rigid body), was launched in FOX and, after nearly 1,300,000 movements, the initial location of the crystallographically independent [CpMo(CO)$_3$Cl] complex was found (calculated weighted residual of $R_{wp}$ = 0.412). Starting from random initial positions, individual optimisations converged to nearly the same final crystallographic location, with comparable $R_{wp}$ factors. Figure 4 (b) shows the simulated powder XRD pattern for the hypothetical unit cell containing just the [CpMo(CO)$_3$Cl] complexes.

In the next stage of the global optimisation, the position of the [CpMo(CO)$_3$Cl] moieties was fixed and a second crystallographic object composed of a Fenske–Hall Z-matrix (also without hydrogen atoms) of the cyclodextrin TRIMEB, as reported by Mentzafos et al.,[28] was added to the unit cell. In the subsequent Monte Carlo optimisation steps using FOX (once again using the more efficient parallel tempering algorithm), the PINMAA residue was allowed to

 © 2006 Wiley-VCH Verlag GmbH & Co. KGaA, Weinheim 

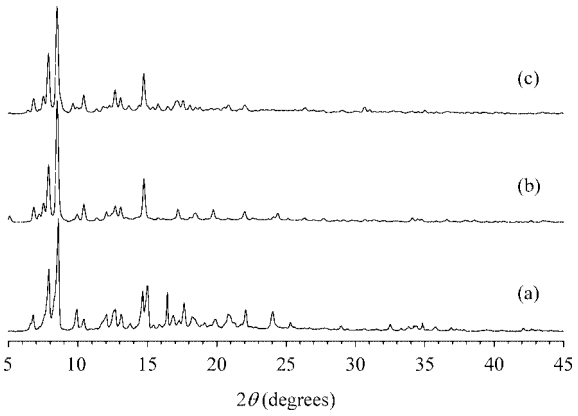


Figure 4. Powder XRD patterns of: (a) the as-synthesised inclusion compound TRIMEB·[$CpMo(CO)_3Cl$] (**6**), (b) the unit cell containing just the individual [$CpMo(CO)_3Cl$] complexes and (c) the hypothetical structural model for the inclusion compound **6**.

freely move as a rigid body and, after just four million moves, the model converged to that shown in Figure 5. Figure 4 (c) shows the simulated powder XRD pattern with a calculated weighted residual of $R_{wp}$ = 0.386. Apart from the general low crystallinity of the inclusion complex, the powder pattern is also affected by textural effects such as preferred orientation. To minimise such effects a refineable March–Dollase correction[35,36] was applied in FOX. The model obtained using the Monte Carlo optimisation clearly proves the existence of a true inclusion complex, with the final convergence being achieved without the use of any antibump restraints. Since this model was obtained by treating the molecules as rigid entities, some groups of atoms are closer together than they would be in a real crystal structure. This is particularly evident for the methyl groups of TRIMEB, which, in some cases, nearly overlap. Such "structural errors" could be eliminated by performing a Rietveld refinement in the present model. However, as high-resolution powder XRD data were not available due to the low crystallinity of the material, and probably could only be obtained using synchrotron radiation, preliminary studies using FULLPROF[37] did not produce the expected results (data not shown).

Thermogravimetric analysis was also useful for the recognition of inclusion complex formation in compounds **3**–**6** (Figure 6). The β-CD adducts β-CD·[$CpFe(CO)_2Cl$] (**3**) and β-CD·[$CpMo(CO)_3Cl$] (**5**) exhibit a step from room temperature up to about 65 °C, assigned to the removal of water molecules located in the β-CD cavities, and also in the interstices between the macrocycles. The corresponding weight losses are 10.7% for **3** and 6.2% for **5**, which are in agreement with the microanalysis results and indicate that the approximate number of water molecules per β-CD molecule in **3** and **5** are eight and six, respectively. For comparison, plain β-CD hydrate shows a similar well-defined step from room temperature up to about 80 °C (not shown), with a mass loss of 14.6% (11 water molecules per β-CD molecule). The reduction in the number of water molecules

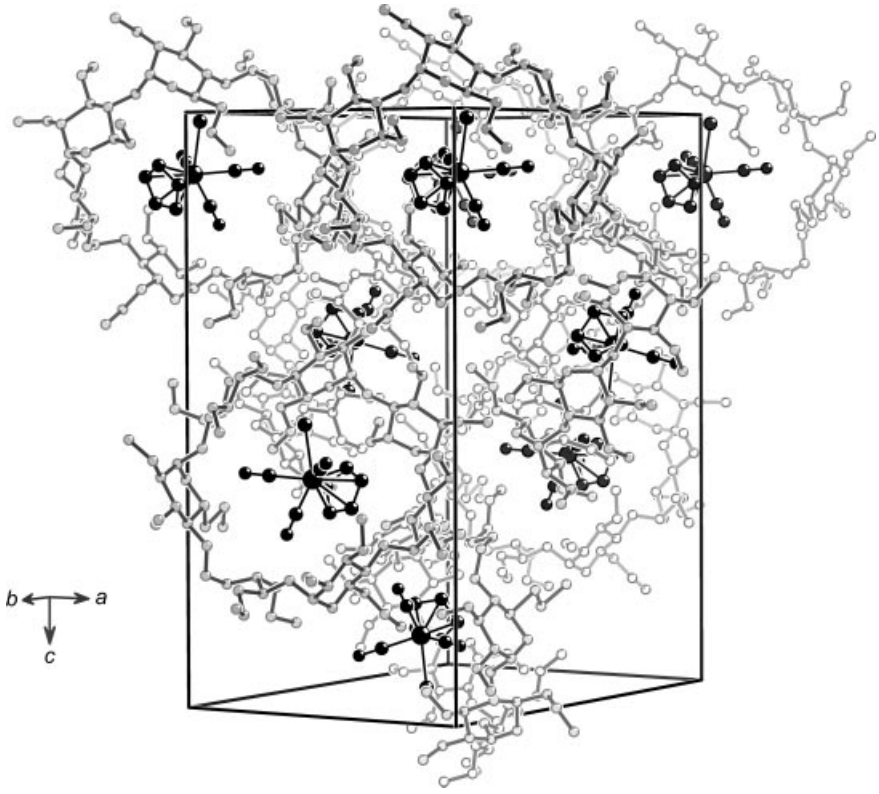


Figure 5. Unit cell contents, viewed in perspective towards the (1 7 0) plane, of the Monte Carlo optimised structural model of the inclusion compound TRIMEB·[$CpMo(CO)_3Cl$] (**6**). TRIMEB and [$CpMo(CO)_3Cl$] residues are represented with grey- and black-filled bonds, respectively.

 © 2006 Wiley-VCH Verlag GmbH & Co. KGaA, Weinheim 

per β-CD molecule in the inclusion compounds is consistent with at least partial occupation of the β-CD cavities by the hydrophobic organometallic guests. After the dehydration step, the TG curves for **3** and **5** are very similar. There is a gradual mass loss in the temperature range of 65–200 °C (7.8% for **3** and 9.8% for **5**), attributed to the loss of CO and/or Cl ligands from the included guest molecules (since plain β-CD hydrate exhibits insignificant mass loss in the temperature range of 80–200 °C). The corresponding steps for the non-included complexes **1** and **2** are much more abrupt (not shown): 16.3% between 90 and 120 °C for **1**, and 23.6% between 100 and 160 °C for **2**. Finally, the host molecules in the two inclusion compounds start to decompose at about 205 °C, while plain β-CD hydrate starts to decompose around 270 °C. This difference is attributed to the promoting effects of iron and molybdenum on the decomposition of β-cyclodextrin, and is further evidence for the existence of a significant host–guest interaction in the inclusion compounds.[10] A similar result was obtained for the TRIMEB inclusion compounds TRIMEB·[CpFe(CO)$_2$Cl] (**4**) and TRIMEB·[CpMo(CO)$_3$Cl] (**6**). Thus, while pure TRIMEB starts to melt and decompose at about 175 °C (not shown), compounds **4** and **6** start at 135 and 150 °C, respectively (Figure 6). In the low-temperature range of the thermogram compound **6** exhibits a weight loss between 75 and 130 °C (2.8%), presumably due to the partial loss of CO and/or Cl ligands from the included guest molecules. No such step is evident for compound **4**, and only a minor mass loss of about 1% is observed from room temperature up to the onset of decomposition. Finally, it is worth noting that the residual masses at 500 °C are 6.1% for the inclusion compounds containing the Fe complex and 9.5% for the compounds containing the Mo complex.

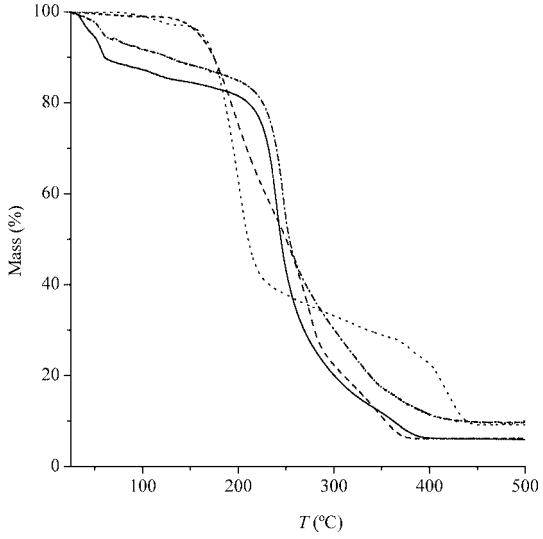


Figure 6. TGA curves of the inclusions compounds β-CD·[CpFe(CO)$_2$Cl] (**3**) (——), TRIMEB·[CpFe(CO)$_2$Cl] (**4**) (– – –), β-CD·[CpMo(CO)$_3$Cl] (**5**) (– · – ·), and TRIMEB·[CpMo(CO)$_3$Cl] (**6**) (· · · · ·).

The $^{13}C\{^1H\}$ CP/MAS NMR spectra of complexes **1** and **2**, and their corresponding inclusion compounds with β-CD and TRIMEB, are shown in Figure 7 for the [CpFe(CO)$_2$Cl] series and in Figure 8 for the [CpMo(CO)$_3$Cl] series. Plain β-CD hydrate exhibits a complex $^{13}C\{^1H\}$ CP/MAS NMR spectrum (not shown), with multiple sharp resonances for each type of carbon atom. These features have been correlated with different torsion angles about the α(1→4) linkages,[38] and with torsion angles describing the orientation of the hydroxy groups.[39] Upon inclusion to give β-CD·[CpFe(CO)$_2$Cl] (**3**) and β-CD·[CpMo(CO)$_3$Cl] (**5**), the resonances due to the C1, C4, C2,3,5, and C6 host carbon atoms (Figure 1) appear mainly as single broad peaks, with little or no structure, centred around $\delta$ = 104, 81, 73, and 61 ppm, respectively. Furthermore, the dispersion in the chemical shift for each signal (i.e., the chemical-shift range that comprises all of the resonances from the same carbon atom in distinct glycosidic units) decreases with respect to the β-CD spectrum. These observations are typically attributed to a symmetrisation of the β-CD macrocycle, that is, the encapsulation of the guest molecule induces the ring to adopt a less distorted conformation, with each glucose unit in a more similar environment.[3k,3l,4b,7d,11,12,40] For the inclusion compound **3** (Figure 7), the Cp carbon atoms of the guest molecule give rise to one weak resonance at $\delta$ = 89.2 ppm, which is shifted downfield by 2.5 ppm relative to the resonance for non-included [CpFe(CO)$_2$Cl] (**1**). The Cp carbon atoms of the mo-

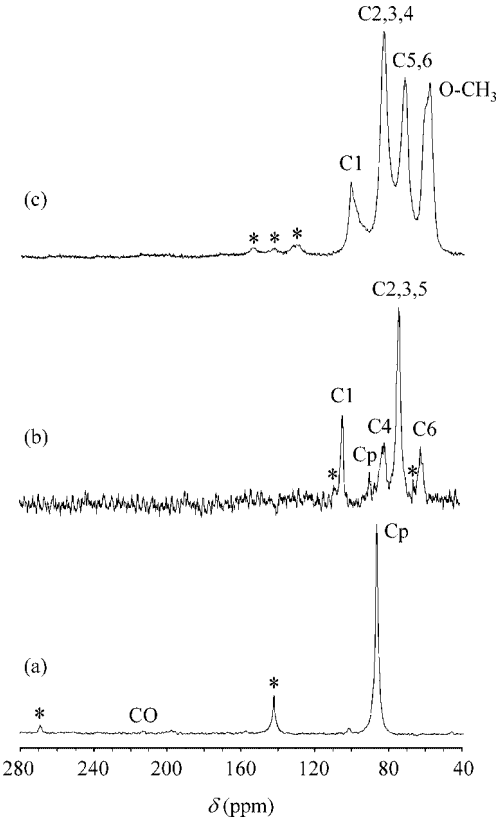


Figure 7. Solid-state $^{13}C\{^1H\}$ CP/MAS NMR spectra of (a) [CpFe(CO)$_2$Cl] (**1**), (b) the inclusion compound β-CD·[CpFe(CO)$_2$Cl] (**3**) and (c) the inclusion compound TRIMEB·[CpFe(CO)$_2$Cl] (**4**). Spinning sidebands are denoted by asterisks.

 © 2006 Wiley-VCH Verlag GmbH & Co. KGaA, Weinheim 

lybdenum complex in **5** give rise to two resolved peaks at $\delta$ = 94.8 and 96.1 ppm, which are shifted slightly upfield relative to the sharp line exhibited by non-included [$CpMo(CO)_3Cl$] (**2**) (Figure 8). The presence of two peaks may mean that there are two distinct inclusion modes for the guest molecule, comprising, for example, different orientations of the guest relative to the host and/or different degrees of penetration of the guest in the host cavity.

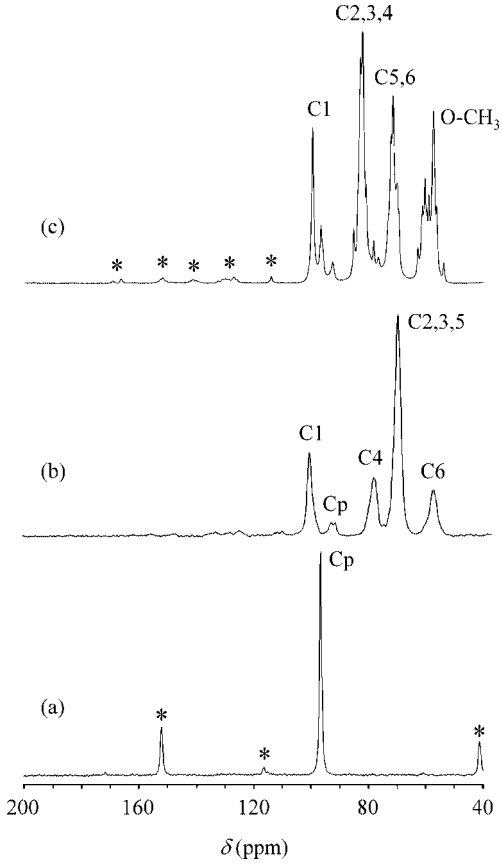


Figure 8. Solid-state $^{13}C\{^1H\}$ CP/MAS NMR spectra of (a) [$CpMo(CO)_3Cl$] (**2**), (b) the inclusion compound β-CD·[$CpMo(CO)_3Cl$] (**5**) and (c) the inclusion compound TRIMEB·[$CpMo(CO)_3Cl$] (**6**). Spinning sidebands are denoted by asterisks.

Like plain β-CD hydrate, the $^{13}C\{^1H\}$ CP/MAS NMR spectrum of TRIMEB also shows multiple resonances for each type of carbon atom (not shown).[27] This is because the host assumes a severely collapsed conformation in the solid state, which minimises the hydrophobic cavity in the absence of a hydrophobic guest. This multiplicity is lost for the inclusion compound TRIMEB·[$CpFe(CO)_2Cl$] (**4**) and only broad peaks are observed, indicating a change in the conformation of the host macrocycle (Figure 7).[27,41] The spectrum for the inclusion compound TRIMEB·[$CpMo(CO)_3Cl$] (**6**) is slightly different, exhibiting several resolved lines for each type of carbon atom (Figure 8). This could be related to the fact that the overall crystallinity of compound **6** is higher than that for compound **4**, as evidenced by powder XRD. For compound **6**, at least seven resonances are discernible for the methyl carbon atoms, indicating that these groups exist in several different well-defined environments. The expected Cp resonances for the guest molecules in compounds **4** and **6** cannot be confidently assigned due to overlap with the resonances for the C1 carbon atoms of the host. Also, for all of the inclusion compounds studied, even with a contact time of 2 ms, it was not possible to clearly identify the resonances (masked in the background) for the CO groups of the guest molecules. The presence of these groups was confirmed by IR spectroscopy. Thus, in addition to the intense and typical bands of the cyclodextrin hosts, the spectra contain strong bands in the CO stretching region (1940–2060 $cm^{-1}$). As expected, two bands are observed for compounds **3** and **4**, while three bands were identified for compounds **5** and **6**. These are slightly shifted relative to the corresponding bands for the non-included complexes **1** and **2** in the solid state. The spectra for the inclusion compounds also contain bands in the range 800–850 $cm^{-1}$ (out-of-plane CH deformation of the Cp ring) and 1420–1430 $cm^{-1}$ (C–C stretching vibration of the Cp ring).

## Concluding Remarks

Inclusion compounds comprising cyclodextrins and half-sandwich complexes of iron and molybdenum have been prepared with a 1:1 host-to-guest stoichiometry and characterised in the solid state by various techniques. The results support the existence of true inclusion compounds. By reference to previous molecular modelling and crystallographic studies of related organometallic–cyclodextrin adducts, it is reasonable to conclude that the interaction geometries in the studied compounds probably involve insertion of the Cp ligands inside the host cavities. The ab initio determination of a hypothetical structural model for the inclusion compound TRIMEB·[$CpMo(CO)_3Cl$] using X-ray studies in direct space has afforded a reliable structural model which is, on the one hand, in good agreement with the results obtained using the other techniques (such as TGA and solid-state NMR) and, on the other, a systematic implementation of the empirical technique previously described by Caira.[17] The low crystallinity of the sample under study, largely reflected in the generally poorly resolved powder XRD pattern, prevents a more precise structural refinement. However, we are currently applying the strategies described in this manuscript to other more crystalline cyclodextrin inclusion compounds. As mentioned in the introduction, oxidative decarbonylation of [$CpMo(CO)_3Cl$] yields a dioxomolybdenum(VI) complex which is an active catalyst for the epoxidation of olefins. We are investigating the effect that CD encapsulation has on the reactivity of the tricarbonyl complex towards oxidative decarbonylation, that is, the possibility of forming a CD·[$CpMoO_2Cl$] complex. Molecular encapsulation of the tricarbonyl complex with TRIMEB may be advantageous in several ways from a catalytic point of view, such as enhancing the solubility of the pre-catalyst in different solvents, and improving the stability of the resultant dioxomolybdenum(VI) complex.

 © 2006 Wiley-VCH Verlag GmbH & Co. KGaA, Weinheim 

## Experimental Section

**General Remarks:** β-CD was kindly donated by Laboratoires La Roquette (France), and heptakis-2,3,6-tri-*O*-methyl-β-CD was obtained from Fluka. All air-sensitive operations were carried out using standard Schlenk techniques under nitrogen. Solvents were dried by standard procedures, distilled under nitrogen or argon, and kept over 4-Å molecular sieves. Microanalyses for CHN were performed at the ITQB, Oeiras, Portugal (by C. Almeida), and Fe/Mo were determined by ICP-OES at the Central Laboratory for Analysis, University of Aveiro (by E. Soares). TGA studies were carried out using a Shimadzu TGA-50 system at a heating rate of 5 °C min$^{-1}$ under air. Powder XRD data were collected at ambient temperature on an X′Pert MPD Philips diffractometer (Cu-$K_\alpha$ X-radiation) with a curved graphite monochromator. Routine examination of compounds **1**–**6** was performed with quick scans with variable slit opening (Figures 2 and 3). Data for the structure optimisation (Figure 4) were collected with a fixed divergence slit of 1/8°, and a flat plate sample holder, in a Bragg–Brentano parafocusing optics configuration. Intensity data were collected by the step counting method (step 0.03° and time 35 s) in the $5° \leq 2\theta \leq 45°$ range. Infrared spectra were recorded with a Unican Mattson Mod 7000 FTIR spectrophotometer. $^{13}C\{^1H\}$ CP/MAS NMR spectra were recorded at 125.72 MHz on a (11.7 T) Bruker Avance 500 spectrometer, with an optimised π/2 pulse for $^1H$ of 4.5 μs, 2-ms contact time, a spinning rate of 7 kHz and 12-s recycle delays. Chemical shifts are quoted in parts per million from tetramethylsilane. The complexes $[CpFe(CO)_2Cl]$ (**1**) and $[CpMo(CO)_3Cl]$ (**2**) were prepared as described in the literature,[42] and characterised by elemental analysis and FTIR spectroscopy.

**β-CD·[CpFe(CO)$_2$Cl] (3):** A solution of β-CD (110 mg, 0.09 mmol) in water (2 mL) at 70 °C was added dropwise to a solution of $[CpFe(CO)_2Cl]$ (**1**; 20 mg, 0.09 mmol) in ethanol (1 mL), and the resultant brick-red solution was stirred for 30 min. After cooling slowly inside a Dewar flask, an orange microcrystalline precipitate was formed, which was separated from the mother liquor and dried. $(C_{42}H_{70}O_{35})\cdot(C_7H_5ClFeO_2)\cdot 8H_2O$ (1491.5): calcd. C 39.46, H 6.15, Fe 3.74; found C 39.52, H 6.54, Fe 3.31. TGA up to 65 °C revealed a sample weight loss of 10.7% (calcd: for loss of 8 $H_2O$, 9.7%). FTIR (KBr): $\tilde{\nu}$ = 3375 cm$^{-1}$ vs, 2967 sh, 2925 m, 2040 s, 1995 s, 1639 m, 1429 m, 1370 m, 1334 m, 1305 m, 1245 w, 1206 w, 1157 s, 1103 s, 1080 s, 1054 vs, 1027 vs, 1003 vs, 945 m, 937 m, 860 m, 841 m, 836 m, 757 m, 703 m, 669 m, 606 m, 635 m, 592 m, 576 m, 542 sh, 504 w, 476 m, 442 w, 412 m, 355 w. $^{13}C\{^1H\}$ CP/MAS NMR: $\delta$ = 104.2 (β-CD, C1), 89.2 (guest, Cp), 81.0 (β-CD, C4), 73.0 (β-CD, C2,3,5), 61.3 ppm (β-CD, C6).

**TRIMEB·[CpFe(CO)$_2$Cl] (4):** A solution of TRIMEB (1.55 g, 1.08 mmol) and $[CpFe(CO)_2Cl]$ (**1**; 230 mg, 1.08 mmol) in a mixture of water and ethanol (10 + 10 mL) was stirred for 1 h. The solution was then evaporated to dryness to give an orange solid. $(C_{63}H_{112}O_{35})\cdot(C_7H_5ClFeO_2)\cdot 2H_2O$ (1678.0): calcd. C 50.11, H 7.27, Fe 3.33; found C 50.00, H 6.08, Fe 3.34. FTIR (KBr): $\tilde{\nu}$ = 3480 cm$^{-1}$ m, 2984 s, 2931 s, 2841 m, 2050 s, 2004 s, 1792 w, 1751 w, 1717 m, 1623 m, 1418 sh, 1460 m, 1404 sh, 1368 m, 1324 m, 1304 m, 1196 sh, 1164 vs, 1141 vs, 1107 vs, 1087 vs, 1071 vs, 1035 vs, 968 s, 950 sh, 937 s, 907 m, 857 m, 785 vw, 755 m, 706 m, 605 m, 596 w, 567 m, 548 m, 470 vw, 376 vw, 348 m. $^{13}C\{^1H\}$ CP/MAS NMR: $\delta$ = 99.7 (TRIMEB, C1), 82.4 (TRIMEB, C2,3,4 and overlapping guest Cp), 71.3 (TRIMEB, C5,6), 58.1 ppm (TRIMEB, O-$CH_3$).

**β-CD·[CpMo(CO)$_3$Cl] (5):** A solution of $[CpMo(CO)_3Cl]$ (**2**; 32 mg, 0.12 mmol) in dichloromethane (1 mL) was added to a solution of β-CD (150 mg, 0.12 mmol) in water (4 mL) at 40 °C, and the resultant biphasic mixture was stirred for 2 h. During this period, a pale brick-red precipitate formed at the interface between the two solutions. The solid was recovered, washed with dichloromethane (2 mL) and water (10 mL), and dried. $(C_{42}H_{70}O_{35})\cdot(C_8H_5MoO_3Cl)\cdot 6H_2O$ (1523.6): calcd. C 39.42, H 5.76, Mo 6.30; found C 39.50, H 6.03, Mo 5.45. TGA up to 65 °C revealed a sample weight loss of 6.2% (calcd: for loss of 6$H_2O$, 7.1%). FTIR (KBr): $\tilde{\nu}$ = 3345 cm$^{-1}$ vs, 2923 s, 2853 sh, 2044 s, 1968 s, 1944 s, 1642 m, 1426 m, 1380 m, 1369 m, 1334 m, 1248 m, 1202 m, 1157 s, 1104 s, 1082 s, 1055 vs, 1028 vs, 1004 s, 945 m, 937 m, 860 m, 837 sh, 827 w, 759 m, 703 m, 606 m, 594 m, 576 m, 528 m, 499 vw, 474 w, 445 w, 435 w, 407 m, 404 sh, 378 vw, 359 m, 358 sh. $^{13}C\{^1H\}$ CP/MAS NMR: $\delta$ = 104.0 (β-CD, C1), 96.1, 94.8 (guest, Cp), 81.5 (β-CD, C4), 73.0 (β-CD, C2,3,5), 60.6 ppm (β-CD, C6).

**TRIMEB·[CpMo(CO)$_3$Cl] (6):** $[CpMo(CO)_3Cl]$ (**2**; 29.4 mg, 0.12 mmol) was added stepwise to a solution of TRIMEB (150 mg, 0.12 mmol) in dichloromethane (3 mL), allowing each fraction to dissolve before adding the next. The mixture was stirred for 2 h and then evaporated to dryness under reduced pressure to obtain a bright brick-red solid product. $(C_{63}H_{112}O_{35})\cdot(C_8H_5MoO_3Cl)\cdot 5H_2O$ (1800.1): calcd. C 47.37, H 7.11, Mo 5.33; found C 47.93, H 7.55, Mo 5.36. FTIR (KBr): $\tilde{\nu}$ = 3112 cm$^{-1}$ m, 3101 m, 3094 m, 2979 vs, 2929 vs, 2831 s, 2050 vs, 1962 vs, 1941 vs, 1641 m, 1464 s, 1420 sh, 1404 m, 1368 m, 1322 m, 1303 m, 1258 sh, 1194 vs, 1161 vs, 1143 vs, 1109 vs, 1090 vs, 1073 vs, 1041 vs, 970 vs, 951 s, 910 m, 877 sh, 856 m, 838 w, 824 m, 785 w, 754 m, 736 m, 704 m, 658 w, 602 m, 564 s, 524 s, 470 m, 432 w, 419 sh, 407 m, 399 sh, 377 w, 357 w, 350 w. $^{13}C\{^1H\}$ CP/MAS NMR: $\delta$ = 99.8, 96.9, 92.8 (TRIMEB, C1), 85.5, 83.1, 82.3, 81.0, 78.6, 76.8 (TRIMEB, C2,3,4), 73.6, 72.6, 71.8, 70.6, 70.3, 69.8 (TRIMEB, C5,6), 63.2, 61.6, 60.9, 60.1, 59.3, 57.8, 56.7, 54.1 ppm (TRIMEB, O-$CH_3$).

## Acknowledgments

This work was partly funded by the FCT, POCTI, and FEDER (project POCTI/CTM/46780/2002). We wish to thank Prof. João Rocha for access to research facilities and Paula Esculcas for assistance with the solid-state NMR experiments. We are also grateful to Celeste Azevedo for carrying out the TGA experiments and to Rosário Soares for collection of the powder diffraction data.

[1] a) J. Szejtli, *Chem. Rev.* **1998**, *98*, 1743–1754; b) W. Saenger, *Angew. Chem. Int. Ed. Engl.* **1980**, *19*, 344–362.

[2] a) W. Sliwa, T. Girek, *Heterocycles* **2003**, *60*, 2147–2183; b) E. Fenyvesi, L. Szente, N. R. Russel, M. McNamara, in *Comprehensive Supramolecular Chemistry* (Eds.: J. Szejtli, T. Osa), Pergamon, Oxford, **1996**, vol. 3, pp. 305–366; c) H. M. Colquhoun, J. F. Stoddart, D. J. Williams, *Angew. Chem. Int. Ed. Engl.* **1986**, *25*, 487–507.

[3] a) R. Breslow, G. Trainor, A. Ueno, *J. Am. Chem. Soc.* **1983**, *105*, 2739–2744; b) T. Matsue, D. H. Evans, T. Osa, N. Kobayashi, *J. Am. Chem. Soc.* **1985**, *107*, 3411–3417; c) A. Harada, S. Takahashi, *J. Chem. Soc., Chem. Commun.* **1984**, 645–648; d) A. Harada, Y. Hu, S. Yamamoto, S. Takahashi, *J. Chem. Soc., Dalton Trans.* **1988**, 729–732; e) Y. Odagaki, K. Hirotsu, T. Higuchi, A. Harada, S. Takahashi, *J. Chem. Soc., Perkin Trans. 1* **1990**, 1230–1231; f) Y. Liu, R.-Q. Zhong, H.-Y. Zhang, H.-B. Song, *Chem. Commun.* **2005**, 2211–2213; g) H. Ju, D. Leech, *Langmuir* **1998**, *14*, 300–306; h) A. E. Kaifer, *Acc. Chem. Res.* **1999**, *32*, 62–71; i) E. Coutouli-Argyropoulou, A. Kelaidopoulou, C. Sideris, G. Kokkinidis, *J. Electroanal. Chem.* **1999**, *477*, 130–139; j) D. Osella, A. Carretta, C. Nervi, M. Ravera, R. Gobetto, *Organometallics* **2000**, *19*, 2791–2797; k) J. A. Fernandes, S. Lima, S. S. Braga, P. Ribeiro-Claro, J. E. Rodriguez-

 © 2006 Wiley-VCH Verlag GmbH & Co. KGaA, Weinheim 

Borges, C. Teixeira, M. Pillinger, J. J. C. Teixeira-Dias, I. S. Gonçalves, *J. Organomet. Chem.* **2005**, *690*, 4801–4808; l) J. A. Fernandes, S. Lima, S. S. Braga, M. Pillinger, J. E. Rodríguez-Borges, P. Ribeiro-Claro, J. J. C. Teixeira-Dias, I. S. Gonçalves, *Eur. J. Inorg. Chem.* **2005**, 4729–4734; m) J. A. Fernandes, S. Lima, S. S. Braga, M. Pillinger, P. Ribeiro-Claro, J. E. Rodriguez-Borges, A. D. Lopes, J. J. C. Teixeira-Dias, I. S. Gonçalves, *Organometallics* **2005**, *24*, 5673–5677.

[4] a) I. Turel, A. Demšar, J. Košmrlj, *J. Inclusion Phenom.* **1999**, *35*, 595–604; b) S. S. Braga, I. S. Gonçalves, M. Pillinger, P. Ribeiro-Claro, J. J. C. Teixeira-Dias, *J. Organomet. Chem.* **2001**, *632*, 11–16; c) S. S. Braga, M. P. M. Marques, J. B. Sousa, M. Pillinger, J. J. C. Teixeira-Dias, I. S. Gonçalves, *J. Organomet. Chem.* **2005**, *690*, 2905–2912; d) J. Vinklárek, J. Honzícek, J. Holubová, *Central Eur. J. Chem.* **2005**, *3*, 72–81.

[5] G. Meister, H. Stoeckli-Evans, G. Süss-Fink, *J. Organomet. Chem.* **1993**, *453*, 249–253.

[6] B. Klingert, G. Rihs, *J. Chem. Soc., Dalton Trans.* **1991**, 2749–2760.

[7] a) M. Shimada, A. Harada, S. Takahashi, *J. Chem. Soc., Chem. Commun.* **1991**, 263–264; b) P. P. Patel, M. E. Welker, *J. Organomet. Chem.* **1997**, *547*, 103–112; c) C. Díaz, A. Arancibia, *J. Inclusion Phenom.* **1998**, *30*, 127–141; d) S. S. Braga, I. S. Gonçalves, P. Ribeiro-Claro, A. D. Lopes, M. Pillinger, J. J. C. Teixeira-Dias, J. Rocha, C. C. Romão, *Supramol. Chem.* **2002**, *14*, 359–366.

[8] D. R. Alston, A. M. Z. Slawin, J. F. Stoddart, D. J. Williams, *Angew. Chem. Int. Ed. Engl.* **1985**, *24*, 786–787.

[9] L. Song, Q. Meng, X. You, *J. Organomet. Chem.* **1995**, *498*, C1–C5.

[10] A. Harada, K. Saeki, S. Takahashi, *Organometallics* **1989**, *8*, 730–733.

[11] S. S. Braga, I. S. Gonçalves, A. D. Lopes, M. Pillinger, J. Rocha, C. C. Romão, J. J. C. Teixeira-Dias, *J. Chem. Soc., Dalton Trans.* **2000**, 2964–2968.

[12] S. Lima, I. S. Gonçalves, P. Ribeiro-Claro, M. Pillinger, A. D. Lopes, P. Ferreira, J. J. C. Teixeira-Dias, J. Rocha, C. C. Romão, *Organometallics* **2001**, *20*, 2191–2197.

[13] a) D. F. Eaton, A. G. Anderson, W. Tam, Y. Wang, *J. Am. Chem. Soc.* **1987**, *109*, 1886–1888; b) A. R. Dias, M. H. Garcia, M. P. Robalo, A. P. S. Tekheira, L. A. Bulygina, V. I. Sokolov, *Russ. J. Org. Chem.* **2001**, *37*, 620–623.

[14] P. M. Bersier, J. Bersier, B. Klingert, *Electroanalysis* **1991**, *3*, 443–455.

[15] L. Caron, H. Bricout, S. Tilloy, A. Ponchel, D. Landy, S. Fourmentin, E. Monflier, *Adv. Synth. Catal.* **2004**, *346*, 1449–1456.

[16] a) M. Abrantes, A. M. Santos, J. Mink, F. E. Kühn, C. C. Romão, *Organometallics* **2003**, *22*, 2112–2118; b) A. A. Valente, J. D. Seixas, I. S. Gonçalves, M. Abrantes, M. Pillinger, C. C. Romão, *Catal. Lett.* **2005**, *101*, 127–130.

[17] M. R. Caira, *Rev. Roumaine Chim.* **2001**, *46*, 371–386.

[18] H.-J. Schneider, F. Hacket, V. Rüdiger, H. Ikeda, *Chem. Rev.* **1998**, *98*, 1755–1785.

[19] a) L. Caron, C. Christine, S. Tilloy, E. Monflier, D. Landy, S. Fourmentin, G. Surpateanu, *Supramol. Chem.* **2002**, *14*, 11–20; b) L. Caron, S. Tilloy, E. Monflier, J. M. Wieruszeski, G. Lippens, D. Landy, S. Fourmentin, G. Surpateanu, *J. Inclusion Phenom.* **2000**, *38*, 361–379.

[20] V. Favre-Nicolin, R. Cerný, *J. Appl. Crystallogr.* **2002**, *35*, 734–743.

[21] V. Favre-Nicolin, R. Cerný, *FOX* – A Program for ab initio Structure Solution from Powder Diffraction Data, Program Developed for the Swiss National Science Foundation, University of Geneva, Switzerland, **2000**.

[22] M. Baranska, W. Łasocha, H. Kozłowski, L. M. Proniewicz, *J. Inorg. Biochem.* **2004**, *98*, 995–1001.

[23] R. Cerný, G. Renaudin, V. Favre-Nicolin, V. Hlukhyy, R. Pöttgen, *Acta Crystallogr., Sect. B* **2004**, *60*, 272–281.

[24] L. M. González-Méndez, F. L. Cumbrera, M. C. García-Cuesta, F. Sánchez-Bajo, A. L. Ortiz, F. J. Higes-Rolando, F. Luna-Giles, *Mater. Lett.* **2004**, *58*, 672–678.

[25] A. Grzechnik, V. Dmitriev, H.-P. Weber, J.-Y. Gesland, S. van Smaalen, *J. Phys.: Condens. Matter* **2004**, *16*, 1033–1043.

[26] E. M. Opozda, W. Łasocha, B. Włodarczyk-Gajda, *Z. Anorg. Allg. Chem.* **2004**, *630*, 597–603.

[27] a) Ž. Petrovski, S. S. Braga, S. S. Rodrigues, C. C. L. Pereira, I. S. Gonçalves, M. Pillinger, C. Freire, C. C. Romão, *New J. Chem.* **2005**, *29*, 347–354; b) Ž. Petrovski, S. S. Braga, A. M. Santos, S. S. Rodrigues, I. S. Gonçalves, M. Pillinger, F. E. Kühn, C. C. Romão, *Inorg. Chim. Acta* **2005**, *358*, 981–988.

[28] D. Mentzafos, I. M. Mavridis, H. Schenk, *Carbohydr. Res.* **1994**, *253*, 39–50.

[29] F. H. Allen, *Acta Crystallogr., Sect. B* **2002**, *58*, 380–388.

[30] F. H. Allen, W. D. S. Motherwell, *Acta Crystallogr., Sect. B* **2002**, *58*, 407–422.

[31] J. Laugier, B. Bochu, *CHECKCELL* – A Software Performing Automatic Cell/Space Group Determination, Collaborative Computational Project Number 14 (CCP14), Laboratoire des Matériaux et du Génie Physique de l'Ecole Supérieure de Physique de Grenoble (INPG), France, **2000**.

[32] J. Laugier, B. Bochu, *CELREF Version 3* – Cell Parameters Refinement Program from Powder Diffraction Diagram, Collaborative Computational Project Number 14 (CCP14), Laboratoire des Matériaux et du Génie Physique de l'Ecole Supérieure de Physique de Grenoble (INPG), France, **2000**.

[33] C. Bueno, M. R. Churchill, *Inorg. Chem.* **1981**, *20*, 2197–2202.

[34] P. Walters, M. Stahl, *BABEL Version 1.3* – A Program for the Interconversion of File Formats Used in Molecular Modelling, Department of Chemistry, University of Arizona, Tucson, AZ 85721, US, **1996**.

[35] A. March, *Z. Kristallogr.* **1932**, *81*, 285.

[36] W. A. Dollase, *J. Appl. Crystallogr.* **1986**, *19*, 267–272.

[37] J. Rodriguez-Carvajal, *FULLPROF* – A Program for Rietveld Refinement and Pattern Matching Analysis, Abstract of the Satellite Meeting on Powder Diffraction of the XV Congress of the IUCR, Toulouse, France, **1990**, p. 127.

[38] a) M. J. Gidley, S. M. Bociek, *J. Am. Chem. Soc.* **1988**, *110*, 3820–3829; b) S. J. Heyes, N. J. Clayden, C. M. Dobson, *Carbohydr. Res.* **1992**, *233*, 1–14.

[39] R. P. Veregin, C. A. Fyfe, R. H. Marchessault, M. G. Tayler, *Carbohydr. Res.* **1987**, *160*, 41–56.

[40] L. Cunha-Silva, J. J. C. Teixeira-Dias, *New J. Chem.* **2005**, *29*, 1335–1341.

[41] G. R. Brown, M. R. Caira, L. R. Nassimbeni, B. van Oudtshoorn, *J. Inclusion Phenom.* **1996**, *26*, 281–294.

[42] J. K. P. Ariyaratne, A. M. Bierrum, M. L. H. Green, M. Ishaq, C. K. Prout, M. G. Swanwick, *J. Chem. Soc. A* **1969**, 1309.

Received: November 11, 2005
Published Online: February 28, 2006

 © 2006 Wiley-VCH Verlag GmbH & Co. KGaA, Weinheim 

DOI: 10.1002/ejic.200501008

# Peroxotungstates and Their Citrate and Tartrate Derivatives

Shu-Ya Hou,[a,b] Zhao-Hui Zhou,*[a] Tao-Ran Lin,[a] and Hui-Lin Wan[a]

**Keywords:** Bioinorganic chemistry / Peroxo ligands / Polyoxometalates / Tungsten

The reaction of potassium tungstate with the biologically relevant ligands citric and tartaric acid, in the presence of hydrogen peroxide, was investigated to discover the effect of pH variation on the product pattern. The reaction with citric acid led to the formation of the dimer $K_5[WO(O_2)_2(Hcit)H(Hcit)(O_2)_2OW]\cdot 6H_2O$ (**1**; $H_4cit$ = citric acid) due to carboxyl-carboxylic acid hydrogen bonding in the pH range 2–5; this complex can also be obtained by an exchange reaction between the oxo ligands of the dimeric hydrogencitrate tungstate $K_4[W_2O_5(Hcit)_2]\cdot 4H_2O$ (**6**) and $H_2O_2$. Interestingly, a novel dimeric peroxotungstate $K_3[W_2O_3(O_2)_4(OH)]\cdot H_2O$ (**2**), without the coordination of citrate ligands, was isolated in the pH range 7–9, as confirmed by $^{17}O$ NMR solution studies. The reaction of potassium tungstate with (*R*,*R*)-tartaric acid afforded the tartratoperoxotungstate $K_4[W_2O_2(O_2)_4\{(R,R)\text{-tart}\}]\cdot 3H_2O$ [**3**; $H_4tart$ = (*R*,*R*)-tartaric acid] in the pH range 1–3. The dimeric peroxotungstate $K_2[W_2O_3(O_2)_4(H_2O)_2]\cdot 2H_2O$ (**4**) was found to react with citric or tartaric acid at pH 2–5 or 2–3, respectively, to give species **1** and **3**. Evidence that **1** exists as a dimer in solution is presented. The three complexes were characterized by elemental analysis, IR and NMR spectroscopy, and X-ray structural analyses. The formation of these complexes is dictated by pH, and the thermal stabilities of **1** and **3** vary with the coordinated ligands.
(© Wiley-VCH Verlag GmbH & Co. KGaA, 69451 Weinheim, Germany, 2006)

## Introduction

Due to their catalytic activity and specialized redox behavior, peroxotungstates have received special attention in a variety of industrial, pharmaceutical, and biological processes as they can be regarded as an environmentally friendly alternative to traditional oxidation reactions that represents an improvement in terms of pollution prevention.[1] They are widely used in stoichiometric as well as catalytic oxidation in organic chemistry,[2] for example in the oxidation of alcohols,[3,4] internal alkenes,[5] amines,[6] sulfides,[4,7,8] isobutyraldehyde,[9] hydroquinones,[2] bromide,[10] benzyl chlorides,[11] epoxidation of chiral allylic alcohols,[12] geraniol, linalool[13] and also in olefin epoxidations,[14–17] such as cyclohexene,[18] propylene,[19] alkene,[20] and *cis*-1-propenylphosphonic acid.[21] To better understand these catalytic processes, a more detailed characterization of peroxotungstates is necessary. It appears that $[W(O_2)_4]^{2-}$ predominates at high pH (>7) and in the presence of excess $H_2O_2$,[22] whereas at intermediate pH (1.3–7.0) the dimer $[W_2O_3(O_2)_4(H_2O)_2]^{2-}$ is the major species,[23] and at lower pH the solution become unstable and lose oxygen.[24] Although other peroxotungstates have also been observed in the solid state[25–27] and solution,[28,29] the key to stabilizing peroxotungstates is to incorporate a ligand that can effectively coordinate to tungsten. The reactivity of peroxo complexes also depends on both the number and nature of the auxiliary ligands.

A variety of peroxotungstates with oxygen and nitrogen donors have been studied in solution and in the solid state.[28–39] However, unlike peroxomolybdates(VI), which have been investigated extensively,[40–47] fewer peroxotungstate species with other ligands have been structurally reported. Known compounds include dimeric oxalate and tetranuclear carbonate complexes such as $M_2[WO(O_2)_2(C_2O_4)]$ (M = $K^+$, $NH_4^+$)[48,49] $[(n\text{-}C_4H_9)_4N]_2[W_2O_2(O_2)_4(C_2O_4)]$,[50] $K_6[W_4O_8(O_2)_6(CO_3)]\cdot 6H_2O$,[51] or isoperoxotungstates like $K_2[W(O_2)_4]$,[22] $K_2[W_2O_3(O_2)_2(H_2O)_2]\cdot 2H_2O$,[23] $(Me_3CNH_3)_4[W_4O_{12}(O_2)_2]$,[25] $[(n\text{-}C_4H_9)_4N]_2[W_4O_6(O_2)_6(OH)_2(H_2O)_2]\cdot H_2O$,[26] and $Cs_2(CN_3H_6)_3[(C_2H_5)_2NH_2][W_7O_{22}(O_2)_2]\cdot 3H_2O$.[27]

Citrate ions are present in most plant and animal tissues where they regulate various fundamental physiological processes and are intermediates in carbohydrate metabolism, such as in the Krebs cycle. (*R*,*R*)-Tartaric acid, which is also widely distributed in nature and is classified as a fruit acid, is another example of an α-hydroxycarboxylic acid that is involved in many biochemical processes. Our study in this field has been undertaken in order to answer one fundamental question, namely whether a pH variation can act as the sole factor to induce structural changes in isolable peroxotungstates in a hydrogen peroxide solution containing both tungstate and citrate or tartrate ions. It should be

[a] Department of Chemistry, College of Chemistry and Chemical Engineering and State Key Laboratory of Physical Chemistry of Solid State Surfaces, Xiamen University, Xiamen 361005, China
[b] College of Chemistry and Chemical Engineering, Donghua University, Shanghai 201620, China
Fax: +86-592-218-3047
E-mail: zhzhou@xmu.edu.cn
Supporting information for this article is available on the WWW under http://www.eurjic.org or from the author.

 InterScience® © 2006 Wiley-VCH Verlag GmbH & Co. KGaA, Weinheim 

noted that peroxotungstates are much more unstable and their isolation is more difficult than their peroxomolybdate homologs.

Here we report the isolation and characterization of the dimeric citrato and tartrato peroxotungstates $K_5[WO(O_2)_2(Hcit)H(Hcit)(O_2)_2OW]\cdot 6H_2O$ (**1**) and $K_4[W_2O_2(O_2)_4\{(R,R)\text{-tart}\}]\cdot 3H_2O$ (**3**). The hydroxy-bridged dinuclear peroxotungstate $K_3[W_2O_3(O_2)_4(OH)]\cdot H_2O$ (**2**) was also isolated serendipitously from a weakly basic solution and is the first example of an isolated dimeric $W_2O_3(O_2)_4(OH)$ skeleton.

## Results and Discussion

Scheme 1 shows the different pathways that lead to peroxo compounds **1**–**4**. The compound numbers shown correspond both to the potassium salts and the anions of the complexes, which are used interchangeably in this description. It appears that pH acts as a decisive factor in dictating the structural features of the isolated complexes. When the pH of an aqueous solution containing potassium tungstate, potassium citrate, and excess hydrogen peroxide was adjusted to 2–5, the dimer **1** was isolated, and this compound could also be isolated by the treatment of **4** with citric acid under comparable conditions. The dimeric peroxotungstate **4** is in equilibrium with the monomeric species in aqueous solution,[29] and it is possible that the monomeric species reacts directly with the citrate or tartrate to form **1** or **3**. Alternatively, complex **1** was prepared at pH 4 by the reaction of $H_2O_2$ with the dimeric hydrogencitratodioxotungstate $K_4[W_2O_5(Hcit)_2]\cdot 4H_2O$ (**6**), which was isolated from a solution of potassium tungstate and citric acid at pH 3.0–3.5. This is a clear demonstration that the β-carboxylate in complex **6** is relative weakly coordinated and can be detached by a peroxo group, which results in the formation of a more stable didentate citrate peroxotungstate at pH 2–5.

It is significant that **1** is a centrosymmetric dimer formed through the linear hydrogen bonding of a β-carboxy to a β-carboxylic acid group [O···O = 2.502(8) Å]. In view of the intramolecular hydrogen-bonding distance [O···O = 2.636(7) Å] in salicylic acid,[52] and the ordinary OH bond of 0.96 Å, the hydrogen bonding in **1** must be very strong as an intramolecular mode. This, in turn, reveals the stability of dimer **1**. In light of its low solubility and its $^{13}C$ and $^{1}H$ NMR signals, which will be discussed later, **1** probably exists as a dimer both in the crystalline state and in solution due to this strong hydrogen bonding.

When the pH of the same solution that formed **1** was changed to 7–8, it slowly deposited $K_2[W_2O_3(O_2)_4(OH)]\cdot H_2O$ (**2**) instead of the molybdate(VI) analog $[WO(O_2)_2(cit)]^{4-}$ (**5**).[45] Here, citric acid acts as both reactant and buffer

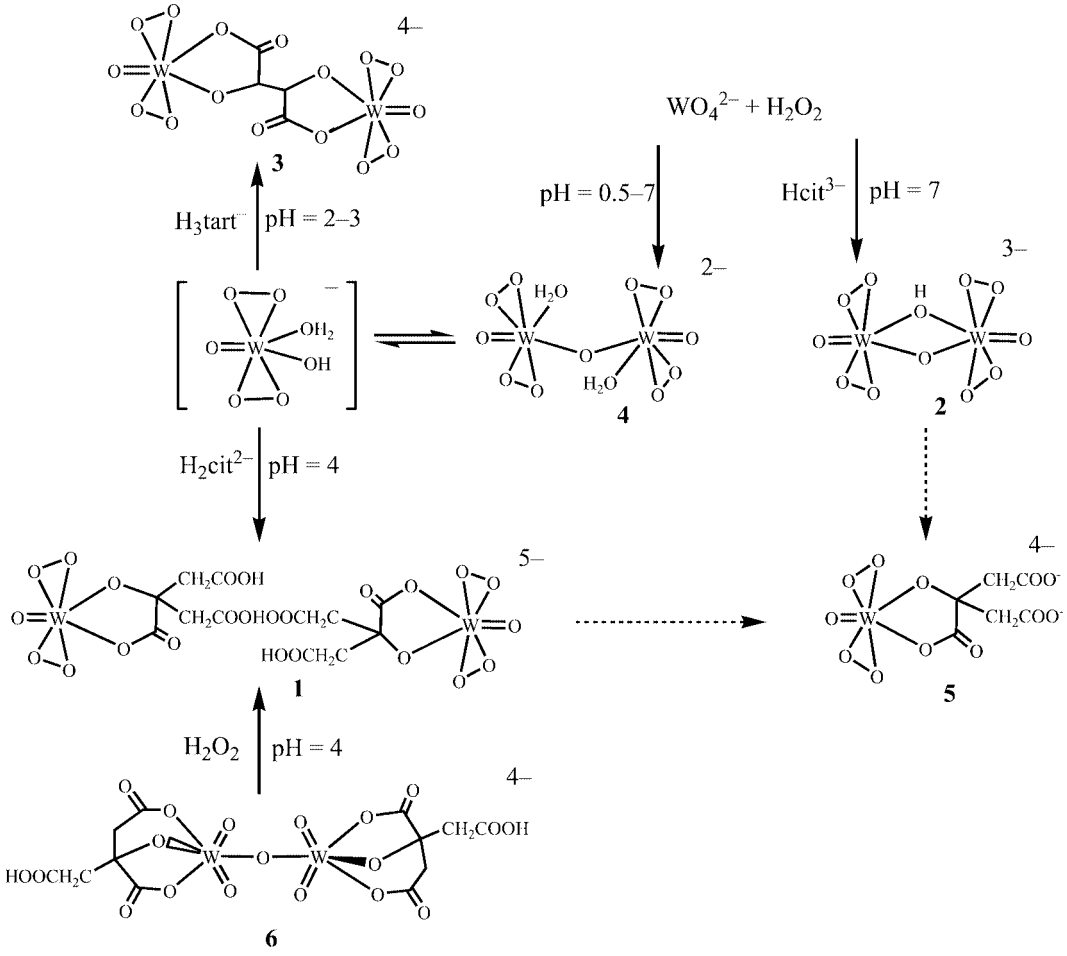


Scheme 1. Synthesis and transformation of citrato- and tartratoperoxotungstates.

 © 2006 Wiley-VCH Verlag GmbH & Co. KGaA, Weinheim 

agent to capture this species. As the pH value increases, the coordination ability of citrate with peroxotungstate decreases and therefore complex **5** is not isolated. Reversible dimerization and dissociation do not occur. It is known that the monomeric species $[W(O_2)_4]^{2-}$ is the principal species at high pH (7–9) in the presence of excess $H_2O_2$,[22] while the dimeric anion $[W_2O_3(O_2)_4(H_2O)_2]^{2-}$ (**4**) is the major species at intermediate pH (1.3–7.0). Complex **2** could be an intermediate between the two peroxotungstates mentioned above, and it can also be considered as the product of deprotonation of the coordinated water molecule in $K_2[W_2O_3(O_2)_4(H_2O)_2]\cdot 2H_2O$ (**4**). Complex **4** exhibits high catalytic activity for the epoxidation of various allylic alcohols using hydrogen peroxide in water.[53]

The pH is also critical in the formation of the tartratoperoxotungstate **3**. The reaction of potassium tungstate, (*R*,*R*)-tartaric acid, and excess hydrogen peroxide in aqueous solution at pH 2–3 gave **3**, which can also be obtained by treating **4** with (*R*,*R*)-tartaric acid under comparable conditions via the monomeric peroxo species. The higher pH only led to the formation of potassium tartrate. Complex **3** is efflorescent, and can easily be converted into a powder by dehydration.

An equilibrium between dimeric and monomeric peroxotungstate species like $[WO(O_2)_2(OH_2)]$ and $[W_2O_3(O_2)_4(H_2O)_2]^{2-}$ has been proposed,[28,29] therefore it does not seem necessary that **1** and **3** are directly formed from **4**. Although the detailed structures of the monomeric peroxotungstates remain controversial,[32] some monomeric species like $[WO(O_2)_2(OH_2)_2]$, $[WO(O_2)_2(OH)(OH_2)]^-$, $[WO(O_2)_2(OH)_2]^{2-}$, and $[WO(O_2)(OH)_3(OH_2)]$ are suggested.

Selected bond lengths and angles for the three compounds are summarized in Table 1, and further crystallographic data can be found in the Experimental Section. The structure of the anion in complex **1** is shown in Figure 1. Each tungsten atom is seven-coordinate with a pentagonal-bipyramidal geometry. The axial positions are occupied by the oxo ligand and the oxygen atom from an α-carboxy group. The equatorial positions are occupied by the two bonded peroxo groups and a deprotonated α-alkoxy group. The didentate ($\eta^2$-$O_2^{2-}$) ligand is a π-donor-like oxo ligand,[30] thus each peroxo and oxo ligand in this complex are in the *cis* configuration and interact with different metal orbitals. The citrate ion acts as a didentate ligand with the α-alkoxy and α-carboxy oxygen coordinated to the tungsten atom, while one of the β-carboxy groups is free to bind as a centrosymmetric dimer through a linear $[CO_2^-\cdots HO_2C]$ hydrogen bond, that is, one of the β-carboxylates of the citrate unit is bonded to the β-carboxylic acid group of the other unit.

Table 1. Selected bond lengths [Å] and angles [°] for $K_5[WO(O_2)_2(Hcit)H(Hcit)(O_2)_2OW]\cdot 6H_2O$ (**1**), $K_3[W_2O_3(O_2)_4(OH)]\cdot H_2O$ (**2**), and $K_4[W_2O_2(O_2)_4\{(R,R)\text{-tart}\}]\cdot 3H_2O$ (**3**).

| | | | | | |
|---|---|---|---|---|---|
| Complex **1** | | | | | |
| W(1)–O(1) | 2.015(3) | W(1)–O(2) | 2.190(4) | W(1)–O(8) | 1.707(4) |
| W(1)–O(9) | 1.971(4) | W(1)–O(10) | 1.926(4) | W(1)–O(11) | 1.927(4) |
| O(1)–W(1)–O(2) | 74.2(1) | O(1)–W(1)–O(8) | 92.0(2) | O(1)–W(1)–O(9) | 89.9(2) |
| O(1)–W(1)–O(10) | 133.7(2) | O(1)–W(1)–O(11) | 134.0(2) | O(1)–W(1)–O(12) | 89.9(2) |
| O(2)–W(1)–O(8) | 166.2(2) | O(2)–W(1)–O(9) | 81.7(2) | O(2)–W(1)–O(10) | 87.2(2) |
| O(2)–W(1)–O(11) | 87.3(2) | O(2)–W(1)–O(12) | 81.2(2) | O(8)–W(1)–O(9) | 99.1(2) |
| O(8)–W(1)–O(10) | 103.2(2) | O(8)–W(1)–O(11) | 102.4(2) | O(8)–W(1)–O(12) | 98.6(2) |
| O(9)–W(1)–O(10) | 44.9(2) | O(9)–W(1)–O(11) | 129.3(2) | O(9)–W(1)–O(12) | 162.3(2) |
| O(10)–W(1)–O(11) | 85.4(2) | O(10)–W(1)–O(12) | 129.3(2) | O(11)–W(1)–O(12) | 45.1(2) |
| O(6)···O(6)[a] | 2.502(8) | | | | |
| Complex **2** | | | | | |
| W(1)–O(1) | 1.964(9) | W(1)–O(2) | 1.933(8) | W(1)–O(3) | 1.980(8) |
| W(1)–O(4) | 1.947(7) | W(1)–O(5) | 1.730(8) | W(1)–O(6) | 2.219(6) |
| O(1)–W(1)–O(2) | 45.3(3) | O(1)–W(1)–O(3) | 163.0(3) | O(1)–W(1)–O(4) | 131.0(3) |
| O(1)–W(1)–O(5) | 98.6(4) | O(1)–W(1)–O(6) | 81.7(3) | O(1)–W(1)–O(7) | 90.6(4) |
| O(2)–W(1)–O(3) | 129.8(3) | O(2)–W(1)–O(4) | 86.5(3) | O(2)–W(1)–O(5) | 102.1(4) |
| O(2)–W(1)–O(6) | 86.3(3) | O(2)–W(1)–O(7) | 134.5(4) | O(3)–W(1)–O(4) | 44.6(3) |
| O(3)–W(1)–O(5) | 98.4(4) | O(3)–W(1)–O(6) | 81.7(3) | O(3)–W(1)–O(7) | 88.3(4) |
| O(4)–W(1)–O(5) | 100.5(4) | O(4)–W(1)–O(6) | 87.6(3) | O(4)–W(1)–O(7) | 131.9(4) |
| O(5)–W(1)–O(6) | 168.5(3) | O(5)–W(1)–O(7) | 94.2(4) | O(6)–W(1)–O(7) | 74.3(3) |
| Complex **3** | | | | | |
| W(1)–O(1) | 1.964(7) | W(1)–O(2) | 2.224(8) | W(1)–O(4) | 1.969(7) |
| W(1)–O(5) | 1.928(8) | W(1)–O(6) | 1.919(9) | W(1)–O(7) | 1.996(9) |
| O(1)–W(1)–O(2) | 76.1(3) | O(1)–W(1)–O(4) | 89.7(3) | O(1)–W(1)–O(5) | 132.1(4) |
| O(1)–W(1)–O(6) | 134.8(4) | O(1)–W(1)–O(7) | 90.0(4) | O(1)–W(1)–O(8) | 95.9(4) |
| O(2)–W(1)–O(4) | 82.3(4) | O(2)–W(1)–O(5) | 85.3(4) | O(2)–W(1)–O(6) | 86.0(4) |
| O(2)–W(1)–O(7) | 80.5(4) | O(2)–W(1)–O(8) | 171.9(4) | O(4)–W(1)–O(5) | 43.8(4) |
| O(4)–W(1)–O(6) | 129.0(4) | O(4)–W(1)–O(7) | 162.4(4) | O(4)–W(1)–O(8) | 98.7(5) |
| O(5)–W(1)–O(6) | 86.0(4) | O(5)–W(1)–O(7) | 130.2(4) | O(5)–W(1)–O(8) | 101.0(4) |
| O(7)–W(1)–O(8) | 98.8(5) | O(6)–W(1)–O(7) | 45.8(4) | O(6)–W(1)–O(8) | 99.4(5) |

[a] Symmetry transformation: $1-x$, $1-y$, $-z$.

 © 2006 Wiley-VCH Verlag GmbH & Co. KGaA, Weinheim 

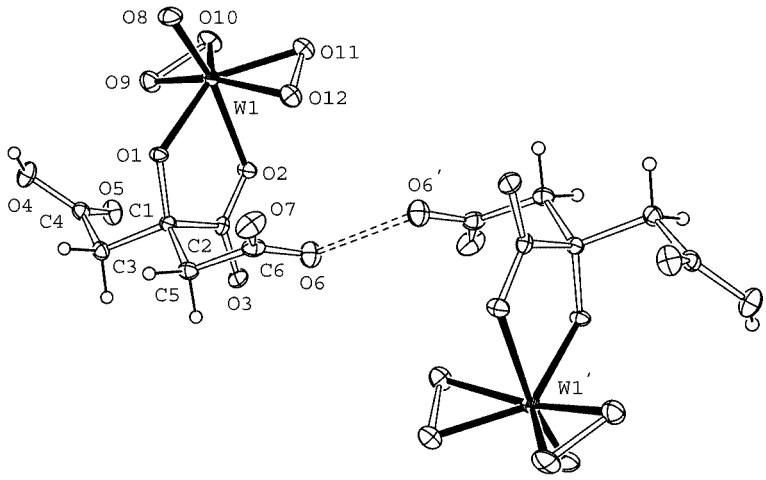


Figure 1. Perspective view of the anion structure of $K_5[WO(O_2)_2(Hcit)H(Hcit)(O_2)_2OW]\cdot 6H_2O$ (**1**).

As shown in Table 1, the W–O distances in complex **1** vary systematically. The distance of the W=O double bond is 1.707(4) Å, and the W–O(peroxo) bond lengths are in the range 1.927(4)–1.976(4) Å, which suggests that they are bonded asymmetrically. The slightly shorter W–O(alkoxy) bond [2.015(3) Å] indicates the deprotonation of the hydroxy group. The W–O(carboxy) bond is the longest [2.190(4) Å] due to the strong *trans* influence of the terminal oxo group.

An ORTEP diagram of the anion of **2** is shown in Figure 2. The dimeric complex **2** has a *cis* configuration and is bridged by two oxygen atoms. The existence of such a dimeric anion has been predicted previously by an $^{17}O$ NMR study.[28,29] The structure of **2** shows that one of the two bridged oxygen atoms is protonated, which represents a new isolated structural example of peroxotungstates. The coordination about the tungsten is essentially pentagonal bipyramidal. The equatorial place is defined by the five oxygen atoms corresponding to the two peroxo groups and one bridging oxygen atom. None of the atoms deviate more than 0.08 Å from the mean plane, and the tungsten atom is placed 0.23 Å above this plane. The axial positions are occupied by the oxo ligand and the hydroxy group. As shown in Table 1, the W–O6(hydroxy) bond [2.219(6) Å] is longer than the W–O7 bridge bond. The ligand binding is inferred to be significantly weaker at the axial position than the equatorial position due to the *trans* influence of the terminal oxygen.

The X-ray structure of the (*R*,*R*)-tartratoperoxotungstate **3** consists of discrete anions, potassium cations, and water molecules. As shown in Figure 3, the two $WO(O_2)_2$ moieties are spanned by a tartrato ligand that is didentate at each end, giving a pentagonal-bipyramidal coordination at the tungsten atoms. The tungsten is bound by a terminal oxo group, two didentate peroxo groups, and a didentate tartrate ligand that binds through its α-alkoxy and α-carboxy groups. The axial positions are occupied by the terminal oxo ligand [W–O = 1.707(9) Å] and an oxygen atom from the deprotonated carboxy group [W–O(2) = 2.224(8) Å]. The equatorial positions are occupied by the two slightly

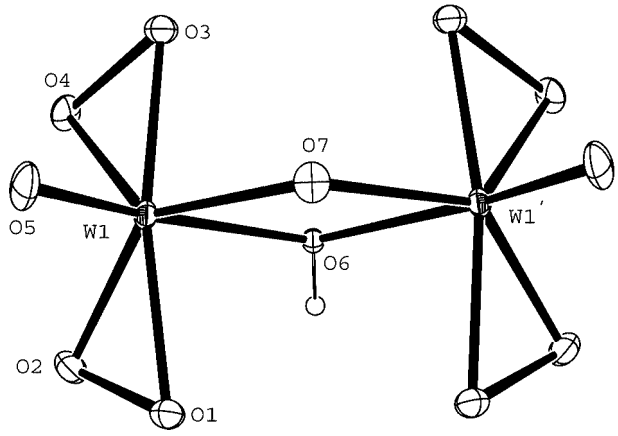


Figure 2. Perspective view of the anion structure of $K_3[W_2O_3(O_2)_4(OH)]\cdot H_2O$ (**2**).

asymmetrically bound peroxo ligands, while the α-alkoxy group of the tartrate makes up the distorted pentagon [W–O = 1.964(7) Å]. It appears that the α-alkoxy group assumes the equatorial rather than the axial position so as to form a strong bond. The W–O(peroxo) distances in **3** vary only slightly. The W–$O_2$, W=O, and O–O distances in the peroxo groups are all within the range of distances previously observed for this class of peroxo complexes. Moreover, the potassium ions in complexes **1**–**3** are coordinated by water molecules, the oxygen atoms of the peroxo groups, and citrate or tartrate ligands. The coordination numbers of the potassium ions are between 7 and 9 and the coordination bond lengths of K–O between 2.65–3.30 Å. These ions are important for the stabilities of the overall structures: replacing the counterion with $Na^+$ results in no isolation of peroxotungstates **1**–**3**, which suggests that the sodium salt is more soluble in water than the potassium salt.

Table 2 shows a comparison of Mo–O and W–O distances. The W–O distances of α-alkoxy group in the peroxotungstates are longer than those in their molybdate homologs, although the W–O distances of the α-carboxy groups are shorter than the Mo–O distances of the α-carboxy group.

 © 2006 Wiley-VCH Verlag GmbH & Co. KGaA, Weinheim 

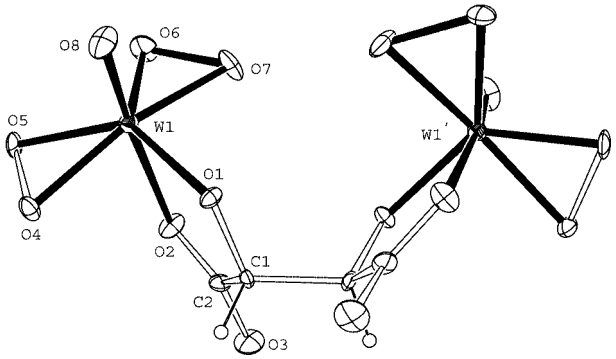


Figure 3. Perspective view of the anion structure of $K_4[W_2O_2(O_2)_4\{(R,R)\text{-tart}\}]\cdot 3H_2O$ (**3**).

O–O bond activation is a major feature of the reactivity of peroxo complexes, therefore it is instructive to compare the O–O distances in peroxotungstates and peroxomolybdates. The peroxo bonds in tungstates are slightly longer than those in molybdates, which indicates that activation of the peroxo group is much more effective with the peroxotungstates.

Complexes **1** and **3** display characteristic features of the coordinated citrate or tartrate ligand in their IR spectra. The coordinated carboxy frequencies are shifted to lower values compared to those of the free ligands. Specifically, absorptions for the antisymmetric stretching carboxy vibrations $\nu_{as}$(COOH) and/or $\nu_{as}$(COO) appear at 1731 and 1654 $cm^{-1}$ for **1** and 1642 and 1612 $cm^{-1}$ for **3**, and those of the symmetric stretching vibrations $\nu_s$(COO) appear at 1440–1330 $cm^{-1}$. For the peroxotungstates without a carboxy ligand there is an obvious band at 703 or 763 $cm^{-1}$, which is assigned to the W–O–W vibration for **2** or **4**, respectively. The W=O vibrations appear as strong bands at 950/970, 928, and 947 $cm^{-1}$ for **1**–**3**, respectively. The ν(O–O) vibration appears as a clearly defined strong band at around 840 $cm^{-1}$, which is a higher frequency than in the spectra of simple peroxide salts (800 $cm^{-1}$). Additional bands in the range 650–560 $cm^{-1}$ belong to $\nu_{as}$W(O–O) and $\nu_s$W(O–O).

Owing to their dissociation on dissolution in $H_2O$ ($D_2O$) the NMR spectra of **1** and **3** show additional peaks, although the major peaks could be interpreted. The $^{13}C$ NMR spectrum of $K_5[WO(O_2)_2(Hcit)H(Hcit)(O_2)_2OW]\cdot 6H_2O$ (**1**) displays four groups of resonance, with two close signals for each group. Complex **1** shows large low-field shifts of some $^{13}C$ resonances upon coordination relative to the corresponding carbons in the $KH_3cit$ ion at a similar pH (3.4). For example, the shifts of the α-alkoxy carbons at $\delta$ = 88.1 and 85.6 ppm are 14.5 and 12 ppm, respectively, and those of the α-carboxy carbons at $\delta$ = 189.0, 187.4 ppm are 11.4 and 9.8 ppm, respectively (Figure 4). It also shows several AB quartets for the methylene protons of the coordinated citrate ligand in the $^1H$ NMR spectrum. The proton of the methylene belonging to the β-carboxy that forms hydrogen bonds is shifted to lower field than the others. These data do not conflict with the existence of **1** as a dimer in solution.

In the tartrate complex $K_4[W_2O_2(O_2)_4((R,R)\text{-tart})]\cdot 3H_2O$ (**3**), two singlets appear at around $\delta$ = 186 and 88 ppm in the $^{13}C$ NMR spectrum due to the α-carboxy and α-alkoxy groups. These low-field shifts relative to (*R*,*R*)-tartaric acid ($\delta$ = 177.1 and 72.0 ppm) imply the involvement of coordination (Figure 5). These results prove that the tartrate serves as a tetradentate ligand to form a dinuclear complex. The $^1H$ NMR spectrum of **3** shows multiple signals around $\delta$ = 5.3 ppm. These shifts occur at lower fields than in the free ligand. When these complexes are dissolved in $D_2O$ they emit bubbles, thus the $^1H$ and $^{13}C$ NMR spectra display several additional peaks derived from the liberated ligand in addition to the signals of the complexes themselves.

Thermogravimetric (TG) and differential thermal analysis (DTA) were carried out for **1**–**4** under $N_2$; they indicated that the different ligands in the peroxo complexes give dif-

Table 2. A comparison of M–O (M = Mo, W) and O–O distances [Å] of peroxomolybdates and peroxotungstates.

| Complex | M–O(α-alkoxy) | M–O(α-carboxy) | M–$O_{av}$ (peroxo) | O–O (peroxo) | Ref. |
|---|---|---|---|---|---|
| $K_2[MoO(O_2)_2(glyc)]\cdot 2H_2O$ | 1.991(5) | 2.239(6) | | | [42] |
| $(NH_4)_2[MoO(O_2)_2(glyc)]\cdot 0.5EtOH$ | 1.974(2), 2.011(2) | 2.211(2), 2.310(2) | 1.962(2) | 1.484(2) | [45] |
| $K_2[MoO(O_2)_2(H_2cit)]\cdot 3H_2O\cdot 0.5H_2O_2$ | 2.011(7) | 2.220(8) | 1.951(9) | 1.48(1) | [41] |
| $K_2[MoO(O_2)_2(S\text{-Hmal})]\cdot H_2O$ | 2.013(5) | 2.281(4) | 1.956(4) | 1.492(7)av | [46] |
| $K_4[MoO(O_2)_2(cit)]\cdot 4H_2O$ | 1.971(2) | 2.228(2) | 1.959(2) | 1.478(3) | [46] |
| $K_4[Mo_2O_2(O_2)_4\{(R,R)\text{-tart}\}]\cdot 4H_2O$ | 1.962(7) | 2.248(7) | 1.956(8) | 1.48(1) | [43] |
| $K_4[W_2O_2(O_2)_4\{(R,R)\text{-tart}\}]\cdot 3H_2O$ | 1.964(7) | 2.224(8) | 1.953(9) | 1.49(1)av | [a] |
| $K_5[MoO(O_2)_2(Hcit)H(Hcit)(O_2)_2OMo]\cdot 6H_2O$ | 2.033(5) | 2.196(3) | 1.953(3) | 1.480(4) | [46] |
| $K_5[WO(O_2)_2(Hcit)H(Hcit)(O_2)_2OW]\cdot 6H_2O$ | 2.015(3) | 2.190(4) | 1.950(4) | 1.494(6) | [a] |
| $K_6[W_4O_8(O_2)_6(CO_3)]\cdot 6H_2O$ | | 2.18(2) | 1.95(3) | 1.48(5) | [51] |
| $(NH_4)_2[MoO(O_2)_2(C_2O_4)]$ | | 2.045(3),2.261(3) | 1.937(5) | 1.475(4) | [45] |
| $[(n\text{-}C_4H_9)_4N]_2[WO(O)_2(C_2O_4)WO(O_2)_2]$ | | 2.09(2), 2.40(1) | 1.92(1) | 1.48(2) | [50] |
| $K_2[MoO(O_2)_2(C_2O_4)]$ | | 2.17(1) | 1.95(1) | 1.46(2) | [40] |
| $K_2[WO(O_2)_2(C_2O_4)]$ | | 2.033(6), 2.245(6) | 1.951(8) | 1.51(1) | [48] |
| $K_2[Mo_2O_3(O_2)_4(H_2O)_2]\cdot 2H_2O$ | | | 1.968(1) | 1.48(2) | [55] |
| $K_2[W_2O_3(O_2)_4(H_2O)_2]\cdot 2H_2O$ | | | 1.96 | 1.50 | [23] |
| $K_2[W_2O_3(O_2)_4(OH)]\cdot H_2O$ | | | 1.956(9) | 1.50(1) | [a] |
| $(Me_3CNH_3)_4[Mo_4O_{12}(O_2)_2]$ | | | 2.224(3) | 1.473(4) | [25] |
| $(Me_3CNH_3)_4[W_4O_{12}(O_2)_2]$ | | | 2.233(6) | 1.47(1) | [25] |

[a] This work.

 © 2006 Wiley-VCH Verlag GmbH & Co. KGaA, Weinheim 

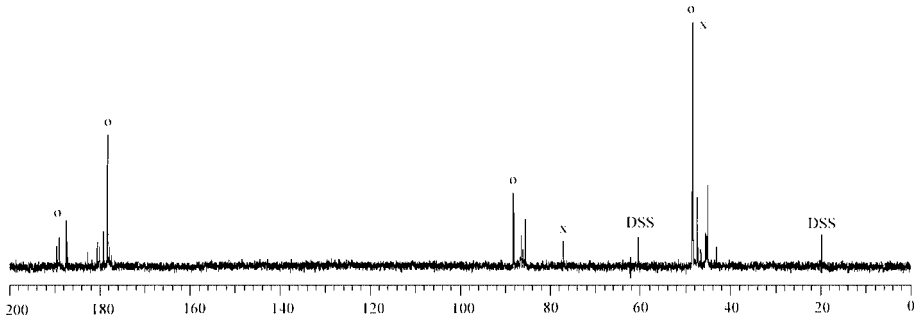


Figure 4. $^{13}C$ NMR spectra of the citratoperoxotungstate $K_5[WO(O_2)_2(Hcit)H(Hcit)(O_2)_2OW]\cdot 6H_2O$ (**1**). Labels: (x) free citrate; (o) coordinated citrate complex.

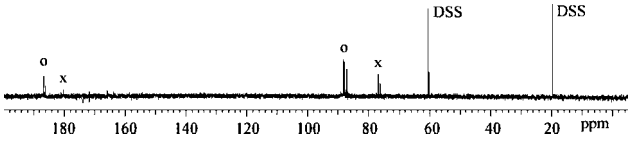


Figure 5. $^{13}C$ NMR spectra of the tartratoperoxotungstate $K_4[W_2O_2(O_2)_4\{(R,R)\text{-tart}\}]\cdot 3H_2O$(**3**). Labels: (x) free tartrate; (o) coordinated tartrate complex.

ferent thermal stability. The first decomposition in $K_5[WO(O_2)_2(Hcit)H(Hcit)(O_2)_2OW]\cdot 6H_2O$ (**1**), which is an endothermic process occurring at 112 °C, is believed to be associated with the loss of three $H_2O$ molecules, and is followed by the loss of another three $H_2O$ and peroxo groups at 166 °C. It is probable that **1** undergoes complete dehydration at this temperature and that this is followed by the rearrangement of the crystal lattice through an exothermic process, as confirmed by the TG and DTA plots, to form an anhydrous species such as $K_5[WO_3(Hcit)H(Hcit)O_3W]$. It then undergoes extensive decomposition at 301 °C to form potassium tungstate and carbonaceous matter due to the combustion of the citrate groups. The observed decomposition temperatures for the dehydration and decomposition of the peroxo groups of **1** are lower than for the corresponding Mo analogues, which may be related to the electrostatic interaction between $M^{6+}$ and $O_2^{2-}$.

The dimeric peroxotungstate $K_2[W_2O_3(O_2)_4(OH)]\cdot H_2O$ (**2**) dehydrates in air and no water-loss step is observed. It is stable up to 158 °C, where it loses two peroxo groups. $K_4[W_2O_2(O_2)_4((R,R)\text{-tart})]\cdot 3H_2O$ (**3**) is not particularly stable and decomposes at 108 and 138 °C in exothermic processes that correspond to the loss of three water molecules and the loss of peroxo groups, respectively. $K_2[W_2O_3(O_2)_4(H_2O)_2]\cdot 2H_2O$ (**4**) first loses $H_2O$ at 114 °C and then begins to lose its peroxo groups at 145 °C. These four complexes all showed rearrangement with exothermic process around 380 – 390 °C. From the data above, it is concluded that complexes **1** and **2** are much stable.

## Experimental Section

**Physical Measurements:** Infrared spectra were recorded as Nujol mulls between KBr plates with a Nicolet 360 FT-IR spectrometer. Elemental analyses were performed with an EA 1110 elemental analyzer. $^1H$ and $^{13}C$ NMR spectra were recorded in $D_2O$ on a Varian UNITY 500 NMR spectrometer using DSS (sodium 2,2-dimethyl-2-silapentane-5-sulfonate) as the internal reference. Thermogravimetric (TG) and differential thermal analysis (DTA) were carried out using a Netzsch Sta 449C thermal analyzer.

All experiments were carried out in the open air. All chemicals were analytical-grade reagents and were used without further purification. Nanopure-quality water was used throughout this work.

**Preparation of $K_5[WO(O_2)_2(Hcit)H(Hcit)(O_2)_2OW]\cdot 6H_2O$ (1):** Potassium tungstate, prepared from the reaction of tungsten trioxide (0.92 g, 4.0 mmol) and potassium hydroxide (2 M, 9 mL), was added dropwise to a solution containing citric acid (0.93 g, 4.4 mmol) and an excess of 30% hydrogen peroxide (1 mL). The resulting reaction mixture was adjusted to pH 4 with hydrochloric acid solution (1 M) in an ice-bath. Colorless crystals deposited gradually from the solution after several days in a refrigerator. They were collected and washed with ethanol to give **1** (0.87 g, 36%) as a white solid. $C_{12}H_{23}K_5O_{30}W_2$ (1210.5): calcd. C 12.3, H 1.7; found C 11.9, H 1.9. IR (KBr): $\nu_{as}$(C=O) = 1731 s, 1654 vs; $\nu_s$(C=O) = 1437 m, 1387 s, 1335 m; ν(W=O) = 950 s; ν(O–O) = 837 s; $\nu_{as}$W(O–O) = 637 s; $\nu_s$W(O–O) = 571 m $cm^{-1}$. $^1H$ NMR (500 MHz): $\delta$ = 2.86 (d, $J$ = 15.0 Hz, 1 H, $CH_2$), 2.83 (d, $J$ = 15.0 Hz, 1 H, $CH_2$), 2.76 (d, $J$ = 16.5 Hz, 1 H, $CH_2$), 2.72 (d, $J$ = 15.5 Hz, 1 H, $CH_2$) ppm. $^{13}C$ NMR (125 MHz): $\delta$ = 189.0, 187.4 $(CO_2)_\alpha$, 179.3, 178.4 $(CO_2)_\beta$, 88.1, 85.6 (≡CO), 48.5, 47.3 (=$CH_2$) ppm.

**Preparation of $K_3[W_2O_3(O_2)_4(OH)]\cdot H_2O$ (2):** Potassium tungstate (4 mmol), prepared in situ as above, and citric acid (0.92 g, 4.4 mmol) were dissolved in 5 mL of water and an excess of 30% hydrogen peroxide (1 mL) was added dropwise in an ice-bath. Potassium hydroxide was added to give a light-yellow solution of pH 7. Colorless crystals were obtained from EtOH/$H_2O$ solution after cooling in a refrigerator for several weeks and these were washed with ethanol to give **2** (8.2 mg, 0.5%) as a white solid. IR (KBr): ν(OH) = 3641 vs, 3409 vs; ν(W=O) = 970 s, 928 vs; ν(O–O) = 841 vs; ν(W–O–W) = 703 s; $\nu_{as}$W(O–O) = 605 s; $\nu_s$W(O–O) = 564 s $cm^{-1}$.

**Preparation of $K_4[W_2O_2(O_2)_4\{(R,R)\text{-tart}\}]\cdot 3H_2O$ (3):** An aqueous solution of (*R*,*R*)-tartaric acid (0.36 g, 2.4 mmol) and an excess of 30% hydrogen peroxide (1 mL) were added slowly to a stirred solution of potassium tungstate (4.0 mmol) in an ice-bath. Hydrochloric acid was then added to adjust the solution to pH 3. To induce precipitation, 95% ethanol solution was added dropwise until a permanent turbidity was obtained. The ethanol solution was kept in a refrigerator for several days to give colorless crystals, which were filtered and washed with ethanol to give **3** (0.60 g, 34%) as a white solid. $C_4H_8K_4O_{19}W_2$ (884.2): calcd. C 5.4, H 0.9; found C 5.0, H 0.7. IR (KBr): $\nu_{as}$(C=O) = 1642 vs, 1612 vs; $\nu_s$(C=O) = 1382 s; ν(W=O) = 926 s; ν(O–O) = 844 m; $\nu_{as}$W(O–O) = 627 m; $\nu_s$W(O–

 © 2006 Wiley-VCH Verlag GmbH & Co. KGaA, Weinheim 

Table 3. Crystal data and structure refinement for $K_5[WO(O_2)_2(Hcit)H(Hcit)(O_2)_2OW]\cdot 6H_2O$ (**1**), $K_3[W_2O_3(O_2)_4(OH)]\cdot H_2O$ (**2**), and $K_4[W_2O_2(O_2)_4\{(R,R)\text{-tart}\}]\cdot 3H_2O$ (**3**).

| | | | |
|---|---|---|---|
| Empirical formula | $C_{12}H_{23}O_{30}K_5W_2$ | $H_3O_{13}K_3W_2$ | $C_4H_8O_{19}K_4W_2$ |
| Formula mass | 1210.5 | 696.2 | 884.2 |
| Crystal color, habit | | colorless, needle | |
| Crystal size [mm] | 0.45 × 0.09 × 0.07 | 0.15 × 0.04 × 0.04 | 0.20 × 0.05 × 0.05 |
| *a* [Å] | 7.9107(4) | 8.2899(4) | 15.9030(7) |
| *b* [Å] | 9.4857(5) | 13.7073(6) | |
| *c* [Å] | 11.3471(6) | 21.308(1) | 7.8151(4) |
| *α* [°] | 72.517(1) | 21.308(1) | 7.8151(4) |
| *β* [°] | 77.767(1) | 21.308(1) | 7.8151(4) |
| *γ* [°] | 71.983(1) | 21.308(1) | 7.8151(4) |
| *V* [°] | 765.64(7) | 2421.3(2) | 1976.5(1) |
| *Z* | 1 | 8 | 4 |
| $D_{calcd.}$ [g cm$^{-3}$] | 2.625 | 3.819 | 2.971 |
| *F*(000) | 578 | 2496 | 1640 |
| Diffractometer | | Smart Apex CCD | |
| Radiation | | Mo-$K_\alpha$ ($\lambda$ = 0.7107 Å) | |
| Temp. [°C] | | 23 | |
| Flack parameter[54] | | | 0.03(3) |
| GOF on $F^2$ | 1.02 | 1.14 | 1.17 |
| $R_1$ [$I > 2\sigma(I)$] | 0.037 | 0.049 | 0.044 |
| $R_1$ (all data) | 0.038 | 0.051 | 0.047 |

O) = 577 m cm$^{-1}$. $^1$H NMR (500 MHz): $\delta$ = 4.456 (s, 2 H, CH) ppm. $^{13}$C NMR (125 MHz): $\delta$ = 186.6, 186.2 $(CO_2)_\alpha$, 88.2, 87.0 (≡CO) ppm.

**Transformation of $K_2[W_2O_3(O_2)_4(H_2O)_2]\cdot 2H_2O$ (4) into 1:** The dimeric peroxotungstate **4** (0.50 g, 0.7 mmol), prepared by the published method,[23] was dissolved in 5 mL of water. Citric acid (0.34 g, 1.5 mmol) was added to this solution followed by a small amount of 30% $H_2O_2$. The resulting mixture was stirred and the pH adjusted to 4 with potassium hydroxide (1 M). Colorless crystals of **1** (0.28 g, 33%) were obtained after one day in the refrigerator.

**Transformation of 4 into 3:** Peroxotungstate **4** (0.65 g, 0.94 mmol) in water was added to (*R*,*R*)-tartaric acid (0.15 g, 0.56 mmol) in an ice-bath. Hydrochloric acid was added followed by a small amount of 30% $H_2O_2$ to get a solution of pH 3. The solution was kept in a refrigerator for two days to give colorless crystals of **3** (0.092 g, 11%).

**Transformation of $K_4[W_2O_5(Hcit)_2]\cdot 4H_2O$ (6) into 1:** A solution of dimeric hydrogendioxocitratotungstate (**6**; 1.79 g, 1.4 mmol), prepared as reported previously,[56] in water was added to excess 30% hydrogen peroxide (1 mL) to give a solution of pH 4. The solution was kept in a refrigerator for two days to afford yellow crystals of **1** (0.94 g, 55%).

**X-ray Structure Determination:** Diffraction data were collected on a Bruker Smart Apex CCD diffractometer with graphite-monochromated Mo-$K_\alpha$ radiation at 296 K. Further details can be found in Table 3. The structures were solved with SHELXS-97 and refined by full-matrix least-squares procedures with anisotropic thermal parameters for all the non-hydrogen atoms. H-atoms were located from a difference Fourier map. All calculations were performed with the programs SHELXL-97 and SHELXS-97.[57,58]

CCDC-284258 to -284260 contain the supplementary crystallographic data for this paper. These data can be obtained free of charge from The Cambridge Crystallographic Data Centre via www.ccdc.cam.ac.uk/data_request/cif.

**Supporting Information** (for details see the footnote on the first page of this article): Details of IR spectra, $^1$H NMR spectra, and thermogravimetric analyses.

## Acknowledgments

We thank the Ministry of Science & Technology (2005CB221408, 2001CB108906) and the National Natural Science Foundation of China (20571061, 20021002, 20423002) for their generous support of this research.

[1] K. Sato, M. Aoki, R. Noyori, *Science* **1998**, *281*, 1646–1647.
[2] B. Tamami, H. Yeganeh, *React. Funct. Polym.* **2002**, *50*, 101–106.
[3] S. E. Jacobson, D. A. Muccigrosso, F. Mares, *J. Org. Chem.* **1979**, *44*, 921–924.
[4] R. Noyori, M. Aoki, K. Sato, *Chem. Commun.* **2003**, 1977–1986.
[5] Y. Ishii, Y. Sakata, *J. Org. Chem.* **1990**, *55*, 5545–5547.
[6] A. J. Bailey, W. P. Griffith, B. C. Parkin, *J. Chem. Soc., Dalton Trans.* **1995**, 1833–1837.
[7] A. Arcoria, F. P. Ballisteri, G. A. Tomaselli, F. D. Furia, G. Modena, *J. Mol. Catal.* **1983**, *18*, 177–188.
[8] A. Arcoria, F. P. Ballisteri, G. A. Tomaselli, *J. Mol. Catal.* **1984**, *24*, 189–196.
[9] J. Hu, R. C. Burns, *J. Mol. Catal. A: Chem.* **2002**, *184*, 451–464.
[10] M. S. Reynolds, K. J. Babinski, M. C. Bouteneff, J. L. Brown, R. E. Campbell, M. A. Cowan, M. R. Durwin, T. Foss, P. O'Brien, H. R. Penn, *Inorg. Chim. Acta* **1997**, *263*, 225–230.
[11] M. Shi, Y. S. Feng, *J. Org. Chem.* **2001**, *66*, 3235–3237.
[12] W. Adam, P. L. Alsters, R. Neumann, C. R. Saha-Möller, D. Sloboda-Rozner, R. Zhang, *J. Org. Chem.* **2003**, *68*, 1721–1728.
[13] A. Arcoria, F. P. Ballistreri, G. A. Tomaselli, *J. Org. Chem.* **1986**, *51*, 2374–2376.
[14] D. V. Deubel, J. Sundermeyer, G. Frenking, *Eur. J. Inorg. Chem.* **2001**, 1819–1827.
[15] C. D. Valentin, P. Gisdakis, I. V. Yudanov, N. Rösch, *J. Org. Chem.* **2000**, *65*, 2996–3004.
[16] C. Aubry, G. Chottard, N. Plazzer, J. M. Brégeault, R. Thouvenot, F. Chauvea, C. Huet, H. Ledon, *Inorg. Chem.* **1991**, *30*, 4409–4415.
[17] K. A. Jørgensen, *Chem. Rev.* **1989**, *89*, 431–458.
[18] G. Gelbard, F. Breton, M. Quenard, D. C. Sherrington, *J. Mol. Catal. A: Chem.* **2000**, *153*, 7–18.
[19] Z. W. Xi, N. Zhou, Y. Sun, K. L. Li, *Science* **2001**, *292*, 1139–1141.

 © 2006 Wiley-VCH Verlag GmbH & Co. KGaA, Weinheim 

[20] P. U. Maheswari, P. de Hoog, R. Hage, P. Gamez, J. Reedijk, *Adv. Synth. Catal.* **2005**, *347*, 1759–1764.
[21] X. Y. Wang, H. C. Shi, S. Y. Xu, *J. Mol. Catal. A: Chem.* **2003**, *206*, 213–223.
[22] R. Stomberg, *J. Less-Common Metals* **1988**, *143*, 363–371.
[23] F. W. B. Einstein, B. R. Penfold, *Acta Crystallogr.* **1964**, *17*, 1127–1133.
[24] N. J. Campbell, A. C. Dengel, C. J. Edwards, W. P. Griffith, *J. Chem. Soc., Dalton Trans.* **1989**, 1203–1208.
[25] T. Ozeki, T. Yamase, *Bull. Chem. Soc. Jpn.* **1997**, *70*, 2101–2105.
[26] W. P. Griffith, B. C. Parkin, A. J. P. White, D. J. Williams, *J. Chem. Soc., Dalton Trans.* **1995**, 3131–3138.
[27] H. Suzuki, M. Hashimoto, S. Okeya, *Eur. J. Inorg. Chem.* **2004**, 2632–2634.
[28] *Polyoxometalate Chemistry* (Eds.: M. T. Pope, A. Müller), Kluwer Academic Publishers, **2001**, pp. 145–149.
[29] O. W. Howarth, *Dalton Trans.* **2004**, 476–481.
[30] M. H. Dickman, M. T. Pope, *Chem. Rev.* **1994**, *94*, 569–584.
[31] D. Chakraborty, M. Bhattacharjee, R. Krätzner, R. Siefken, H. W. Roesky, I. Usón, H. G. Schmidt, *Organometallics* **1999**, *18*, 106–108.
[32] B. Pecquenard, S. Castro-Garcia, J. Livage, P. Y. Zavalij, M. S. Whittingham, R. Thouvenot, *Chem. Mater.* **1998**, *10*, 1882–1888.
[33] W. P. Griffithm, A. M. Z. Slawin, K. M. Thompson, D. J. Williams, *J. Chem. Soc., Chem. Commun.* **1994**, 569–570.
[34] N. M. Gresley, W. P. Griffith, B. C. Parkin, A. J. P. White, D. J. Williams, *J. Chem. Soc., Dalton Trans.* **1996**, 2039–2045.
[35] J. Y. Piquemal, C. Bois, J. M. Brégeault, *Chem. Commun.* **1997**, 473–474.
[36] M. L. Ramos, M. M. Pereira, A. M. Beja, M. R. Silva, J. A. Paixão, V. M. S. Gil, *J. Chem. Soc., Dalton Trans.* **2002**, 2126–2231.
[37] M. L. Ramos, M. M. Calderia, V. M. S. Gil, *J. Chem. Soc., Dalton Trans.* **2000**, 2099–2103.
[38] T. T. Bhengu, D. K. Sanyal, *Thermochim. Acta* **2003**, *397*, 181–197.
[39] M. R. Maurya, M. N. Jayaswal, *J. Chem. Res.* **1988**, 446–447.
[40] R. Stomberg, *Acta Chem. Scand. A* **1970**, *24*, 2024–2036.
[41] J. Flanagan, W. P. Griffith, A. C. Skapski, R. W. Wiggins, *Inorg. Chim. Acta* **1985**, *96*, L23–L24.
[42] A. C. Dengel, W. P. Griffith, R. D. Powell, A. C. Skapski, *J. Chem. Soc., Dalton Trans.* **1987**, 991–995.
[43] A. C. Dengel, W. P. Griffith, R. D. Powell, A. C. Skapski, *J. Chem. Soc., Chem. Commun.* **1986**, 555–556.
[44] H. Glas, M. Spiegler, W. R. Thiel, *Eur. J. Inorg. Chem.* **1998**, 275–281.
[45] D. Bayot, B. Tinant, M. Devillers, *Inorg. Chim. Acta* **2004**, *357*, 809–816.
[46] Z. H. Zhou, S. Y. Hou, H. L. Wan, *Dalton Trans.* **2004**, 1393–1399.
[47] J. A. Brito, M. Gómez, G. Muller, H. Teruel, J. C. Clinet, E. Duňach, M. A. Maestro, *Eur. J. Inorg. Chem.* **2004**, 4278–4285.
[48] R. Stomberg, S. Olson, *Acta Chem. Scand. A* **1985**, *39*, 79–83.
[49] X. B. Shi, C. G. Li, S. H. Wu, J. Chen, G. Y. Xie, *Chin. Sci. Bull.* **1994**, *39*, 1886–1889.
[50] M. Hashimoto, T. Ozeki, H. Ichida, Y. Sasaki, K. Matsumoto, T. Kudo, *Chem. Lett.* **1987**, 1873–1876.
[51] R. Stomberg, *Acta Chem. Scand. A* **1985**, *39*, 507–514.
[52] G. E. Bacon, R. J. Jude, *Z. Kristallogr.* **1973**, *138*, 19–40.
[53] K. Kamata, K. Yamaguchi, S. Hikichi, N. Mizuno, *Adv. Synth. Catal.* **2003**, *345*, 1193–1196.
[54] H. D. Flack, *Acta Crystallogr., Sect. A* **1983**, *39*, 876–881.
[55] R. Stomberg, *Acta Chem. Scand.* **1968**, *22*, 1072–1090.
[56] H. Zhang, H. Zhao, Y. Q. Jiang, S. Y. Hou, Z. H. Zhou, H. L. Wan, *Inorg. Chim. Acta* **2003**, *351*, 311–318.
[57] L. J. Farrugia, *J. Appl. Crystallogr.* **1999**, *32*, 837–838.
[58] G. M. Sheldrick, *SHELXL97 and SHELXS97*, University of Göttingen, Germany, **1997**.

Received: November 13, 2005
Published Online: February 28, 2006

 © 2006 Wiley-VCH Verlag GmbH & Co. KGaA, Weinheim 

DOI: 10.1002/ejic.200501056

# Synthesis of New Palladium(II) Complexes Containing Hemilabile *N*-(Alkylamino)pyrazole Ligands: Spectroscopic Analysis and Crystal Structure of [PdCl(ddae)]Cl·$H_2O$ {ddae = Bis[2-(3,5-dimethyl-1-pyrazolyl)ethyl]ethylamine}

**Anna Pañella,[a] Josefina Pons,*[a] Jordi García-Antón,[a] Xavier Solans,[b] Mercè Font-Bardia,[b] and Josep Ros*[a]**

**Keywords:** Hemilabile ligands / N ligands / Palladium

Treatment of the tridentate (*NN′N*) *N*-alkylaminopyrazole ligands bis[2-(3,5-dimethyl-1-pyrazolyl)ethyl]ethylamine (ddae), bis[2-(3,5-dimethyl-1-pyrazolyl)ethyl]isopropylamine (ddai) and bis[2-(3,5-dimethyl-1-pyrazolyl)ethyl]*tert*-butylamine (ddat) with [$PdCl_2(CH_3CN)_2$] in a 1:1 M/L ratio in $CH_2Cl_2$ produces [$PdCl_2$(*NN′N*)]. Treatment of the corresponding ligand with [$PdCl_2(CH_3CN)_2$] in a 1:2 M/L ratio in the presence of $AgBF_4$ in $CH_2Cl_2$/methanol (6:1) gives [PdCl(*NN′N*)]($BF_4$). The complexes [$PdCl_2$(*NN′N*)] were again obtained when the complexes [PdCl(*NN′N*)]($BF_4$) were heated under reflux in a solution of $NEt_4Cl$ in acetonitrile, which means that ligands ddae, ddai and ddat in complexes **1**–**6** are hemilabile. These $Pd^{II}$ complexes have been characterised by elemental analyses, conductivity measurements and IR and $^1H$ and $^{13}C\{^1H\}$ NMR spectroscopy. The $^1H$ NMR spectroscopic studies for compounds [$PdCl_2$(*NN′N*)] give evidence of $\kappa^2(N_{pz},N_{pz})$ coordination in acetonitrile and $\kappa^3(N_{pz},N_{amino},N_{pz})$ coordination in methanol. The X-ray structure of the complex [PdCl(ddae)]Cl·$H_2O$ has been determined. The $Pd^{II}$ is coordinated to the ddae ligand by two nitrogen atoms of the pyrazolyl groups and one nitrogen atom of the amine, along with one chlorine atom, in a slightly distorted square-planar geometry.

(© Wiley-VCH Verlag GmbH & Co. KGaA, 69451 Weinheim, Germany, 2006)

## Introduction

In the course of a study of pyrazole-derived ligands we have studied and reported the synthesis and characterisation of ligands combining a pyrazolyl group with some other functions containing O (alcohol or ether),[1] S (thiol or thioether),[2] P (phosphane or phosphinite)[3] or N (amine)[4] as donor atoms. The synthesis of pyrazolyl-N(amine) ligands has been developed by Driessen et al. and, so far, the study of their coordinating ability has been mainly focused on the design of chelating systems to mimic metalloenzymes.[5]

In our group, we have investigated the reactivity of bi- (*NN′*) and tridentate (*NN′N*) *N*-(alkylamino)pyrazole ligands {1-[2-(ethylamino)ethyl]-3,5-dimethylpyrazole, 1-[2-(isopropylamino)ethyl]-3,5-dimethylpyrazole and bis[(3,5-dimethylpyrazolyl)methyl]ethylamine} with $Rh^I$ and obtained the complexes [$Rh_2Cl_2(COD)_2$(*NN′*)],[4b] [Rh(COD)(*NN′*)]($BF_4$)[4e] and [$Rh(CO)_2$(*NN′N*)]($BF_4$), [4c] respectively. In a recent publication some of us have shown that bis[(3,5-dimethylpyrazolyl)methyl]ethylamine is a very flexible ligand with $\kappa^2(N,N)$ or $\kappa^3(N,N',N)$ bonding modes depending on the electronic configuration and the steric constrains around the metal.[4c] The hemilabile centre of the ligand is the nitrogen atom of the amine function.

Recently, we have synthesised the new $Pd^{II}$ complexes [$PdCl_2$(*NN′*)],[6] and [$Pd(NN')_2$]($BF_4$)$_2$[7] {*NN′* = 1-[2-(ethylamino)ethyl]-3,5-dimethylpyrazole, 1-[2-(isopropylamino)-ethyl]-3,5-dimethylpyrazole and 1-[2-(*tert*-butylamino)-ethyl]-3,5-dimethylpyrazole}; the NMR studies of the complexes have shown the rigid conformation of the ligands when they are complexed.

This paper extends this work to a new family of *NN′N* ligands with $Pd^{II}$. We report the synthesis of the ligands bis[2-(3,5-dimethyl-1-pyrazolyl)ethyl]ethylamine (ddae), bis[2-(3,5-dimethyl-1-pyrazolyl)ethyl]isopropylamine (ddai) and bis[2-(3,5-dimethyl-1-pyrazolyl)ethyl]*tert*-butylamine (ddat), and the study of their reactivity with $Pd^{II}$. The ligands contain two pyrazole nitrogens and one amine nitrogen as potential N-donor atoms (Scheme 1).

[a] Departament de Química, Unitat de Química Inorgànica, Universitat Autònoma de Barcelona,
08193 Bellaterra, Barcelona, Spain
Fax: +34-93-581-3101
E-mail: Josefina.Pons@uab.es
[b] Cristallografia, Mineralogia i Dipòsits Minerals, Universitat de Barcelona,
Martí i Franquès s/n, 08028 Barcelona, Spain

## Results and Discussion

### Synthesis and Spectroscopic Properties

Although bis[2-(3,5-dimethyl-1-pyrazolyl)ethyl]ethylamine (ddae) has already been described,[5g] an alternative

 © 2006 Wiley-VCH Verlag GmbH & Co. KGaA, Weinheim 

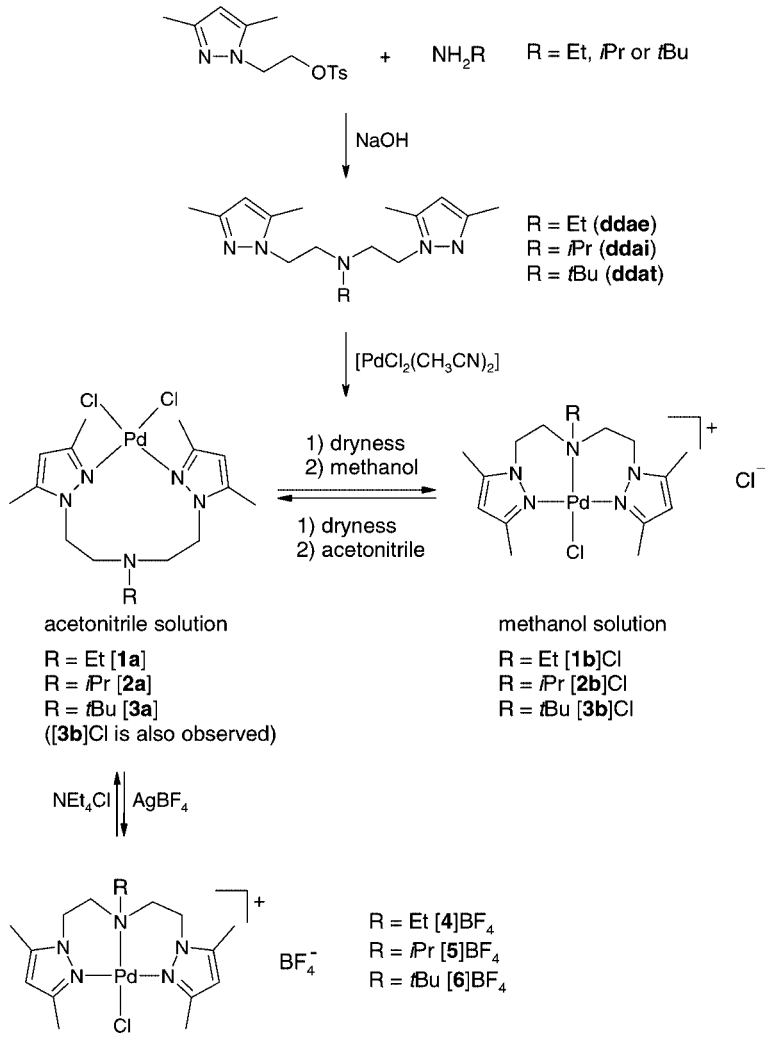


Scheme 1.

pathway for its synthesis is presented here. This new method is also useful to develop two new ligands that had not been described previously: bis[2-(3,5-dimethyl-1-pyrazolyl)ethyl]-isopropylamino (ddai) and bis[2-(3,5-dimethyl-1-pyrazolyl)-ethyl]*tert*-butylamino (ddat), neither of which could be synthesised by the same method that was used in the literature for ddae.

Synthesis of the three ligands consists of the treatment of 3,5-dimethyl-1-(2-toluene-*p*-sulfonyloxyethyl)pyrazole[8] with the appropriate primary amine (ddae: ethylamine; ddai: isopropylamine; ddat: *tert*-butylamine) in the presence of sodium hydroxide in water.

Each product was obtained as a yellow oil. This oil consists of a mixture of the mono- and bis(pyrazolyl)alkylamine ligands. The ligands were further purified by chromatography (silica gel 60) with ethyl acetate as eluent. The proportions of the bis(pyrazolyl)alkylamine/mono(pyrazolyl)alkylamine were 3:1 for ddae, 1:1 for ddai and 4:1 for ddat.

The ligands were characterised by elemental analysis, mass spectrometry and IR, $^1$H and $^{13}$C{$^1$H} NMR spectroscopy. The NMR signals were assigned by reference to the literature[9] and from DEPT, COSY and HMQC NMR experiments.

Complexes [$PdCl_2(NN'N)$] [$NN'N$ = ddae (**1**), ddai (**2**) and ddat (**3**)] were obtained by treatment of the corresponding ligand with [$PdCl_2(CH_3CN)_2$] in a 1:1 M/L ratio in $CH_2Cl_2$. Complexes [$PdCl(NN'N)$]($BF_4$) [$NN'N$ = ddae (**4**), ddai (**5**) and ddat (**6**)] were obtained by reaction of the corresponding ligand with [$PdCl_2(CH_3CN)_2$] in a 1:1 M/L ratio in the presence of $AgBF_4$ in $CH_2Cl_2$/methanol (6:1). When complexes **4**–**6** were heated under reflux in a solution of $Et_4NCl$ in $CH_3CN$ for 24 h complexes **1**–**3** were again obtained. The elemental analyses of products **1**–**3** are consistent with the formula [$PdCl_2(NN'N)$] and those for compounds **4**–**6** with [$PdCl(NN'N)$]($BF_4$).

Depending on the solvent used, different values of conductivity were found for complexes **1**–**3**. The conductivity values in methanol are 83–95 $\Omega^{-1}cm^2mol^{-1}$ (consistent with a 1:1 electrolyte), whereas those in acetonitrile are 78–80 $\Omega^{-1}cm^2mol^{-1}$ for **1** and **2** (in agreement with the non-electrolyte nature of the complexes) and 118 $\Omega^{-1}cm^2mol^{-1}$ for **3** (higher than for **1** and **2** due to the presence of a mixture of neutral and cationic isomers, as seen in the

 © 2006 Wiley-VCH Verlag GmbH & Co. KGaA, Weinheim 

NMR section). The conductivity values for complexes **4**–**6** in acetonitrile and methanol are in agreement with 1:1 electrolytes. The reported values for $10^{-3}$ M solutions of non-electrolyte complexes are lower than 120 $\Omega^{-1}cm^2mol^{-1}$ or 80 $\Omega^{-1}cm^2mol^{-1}$ in acetonitrile or methanol, respectively, while the range of conductivity values for $10^{-3}$ M solutions of 1:1 electrolyte compounds in methanol is between 80–115 $\Omega^{-1}cm^2mol^{-1}$ and in acetonitrile between 120 and 160 $\Omega^{-1}cm^2mol^{-1}$.[10]

The IR spectra of all complexes are similar to those of the ligands, the most characteristic bands being those attributable to the pyrazolyl group: ν(C=C) and ν(C=N) between 1556 and 1554 $cm^{-1}$ and $\delta(C–H)_{oop}$ between 820 and 801 $cm^{-1}$. The ν(B–F) band between 1060–1053 $cm^{-1}$ is characteristic for **4**–**6**.

The IR spectra of the complexes in the 500–100 $cm^{-1}$ region were also recorded and show a well-defined band corresponding to ν(Pd–Cl) between 342 and 335 $cm^{-1}$. The number and energy of the bands is consistent with the presence of terminal chlorine. Bands attributable to ν(Pd–N) between 460 and 426 $cm^{-1}$ are also present.[11]

The $^1H$ NMR, $^{13}C\{^1H\}$ NMR, HMQC and NOESY spectra were recorded in $CD_3CN$ and methanol for **1**–**3**, and $CD_3CN$ for **4**–**6**, and show the signals of the ligands (ddae, ddai, and ddat). NMR spectroscopic data are reported in the Exp. Sect.

The $^1H$ NMR spectra of **1** and **2** in acetonitrile at room temperature show the presence of one isomer (**1a** and **2a**, respectively), whereas the spectrum of **3** shows the presence of two isomers (**3a** and **3b**$^+$) in a 1:3 ratio (Scheme 1). The $^1H$ NMR spectra of **1**–**3** in methanol at room temperature show the presence of one isomer (**1b**$^+$, **2b**$^+$ and **3b**$^+$, respectively). The most significant feature for probing structural difference is provided by the $N_{pz}CH_2CH_2N_{amine}$ resonances: the $CH_2$ signals of the isomers **1b**$^+$–**3b**$^+$ are more deshielded than those of **1a**–**3a**. This observation suggests that the nitrogen of the amine group is bonded to palladium in **1b**$^+$–**3b**$^+$. For isomers **1a**–**3a**, at 298 K, the methylene protons appear as four poorly defined broad bands. This led us to record variable-temperature spectra for **1** in acetonitrile. At higher temperatures (313 K) only one signal can be observed for each $CH_2$ of the $N_{pz}CH_2CH_2N_{amine}$ chain, whereas lowering of the temperature induces a progressive broadening and splitting of the two signals corresponding to each $CH_2$. At 283 K, four well-defined bands are observed at $\delta$ = 4.95, 4.31, 3.09 and 2.72 ppm. This suggests that at 313 K there is a fluxional process in which, with ring-flipping, the two hydrogens of each $CH_2$ are interconverted and only one signal can be observed. This process would take place with a $\Delta G^{\ddagger}$ value of about 60 $kJ\,mol^{-1}$, as deduced from the coalescence behaviour of the methylene resonances.[12]

The $^1H$ NMR spectra at room temperature for **4**–**6** complexes in acetonitrile show the presence of one isomer (**4b**$^+$, **5b**$^+$ and **6b**$^+$, respectively).

The NMR spectra of complexes **1**–**3** in methanol and **4**–**6** in acetonitrile were studied in detail. Treatment of the $N_{pz}CH_2CH_2N_{amino}$ fragment as an AA′XX′ system gave a set of coupling constants for each compound. These constants are consistent with the simulated spectra for compounds **1**–**6** obtained with the aid of the *g* NMR program.[13] All these results are reported in Tables 1 and 2. Figures 1 and 2 show the experimentally determined and simulated spectra for **2** and **5**, respectively. HMQC spectra were used to assign the signals of protons H-6 and H-7. The two protons of each $CH_2$ group in a $N_{pz}CH_2$-$CH_2N_{amino}$ chain are diastereotopic and thus give rise to four groups of signals, each attributable to a single hydrogen atom of one $N_{pz}CH_2CH_2N_{amino}$ chain. Each group of signals can be assigned as a doublet of doublets of doublets for H-6 and H-7.

Table 1. Chemical shifts [ppm] and $^1H$-$^1H$ coupling constants [Hz] for **1b**$^+$–**3b**$^+$ in methanol.

| Compound | [**1b**]$^+$ | [**2b**]$^+$ | [**3b**]$^+$ |
|---|---|---|---|
| $\delta_H$ (6a) | 4.68 | 4.71 | 4.71 |
| $\delta_H$ (6b) | 5.21 | 5.30 | 5.44 |
| $\delta_H$ (7a) | 3.26 | 3.22 | 3.19 |
| $\delta_H$ (7b) | 2.87 | 2.96 | 3.30 |
| $^2J$(6a,6b) | 15.71 | 15.75 | 15.82 |
| $^2J$(7a,7b) | 14.22 | 14.47 | 14.89 |
| $^3J$(6a,7a) | 3.33 | 3.78 | 3.80 |
| $^3J$(6b,7b) | 11.19 | 11.03 | 10.54 |
| $^3J$(6a,7b) | 2.54 | 2.04 | 1.60 |
| $^3J$(6b,7a) | 2.25 | 1.84 | 1.25 |

Table 2. Chemical shifts [ppm] and $^1H$-$^1H$ coupling constants [Hz] for **4b**$^+$–**6b**$^+$ in $CD_3CN$.

| Compound | [**4b**]$^+$ | [**5b**]$^+$ | [**6b**]$^+$ |
|---|---|---|---|
| $\delta_H$ (6a) | 4.54 | 4.55 | 4.58 |
| $\delta_H$ (6b) | 5.10 | 5.17 | 5.22 |
| $\delta_H$ (7a) | 3.16 | 3.07 | 2.97 |
| $\delta_H$ (7b) | 2.78 | 2.85 | 3.08 |
| $^2J$(6a,6b) | 15.84 | 15.74 | 15.98 |
| $^2J$(7a,7b) | 14.30 | 14.01 | 14.86 |
| $^3J$(6a,7a) | 3.18 | 3.42 | 3.75 |
| $^3J$(6b,7b) | 11.22 | 11.01 | 11.22 |
| $^3J$(6a,7b) | 2.47 | 1.97 | 1.60 |
| $^3J$(6b,7a) | 2.63 | 1.60 | 1.25 |

In the NOESY spectra of compounds **1**–**3** in methanol and **4**–**6** in acetonitrile, it was observed that the methyl linked to the pyrazole at $\delta$ = 2.66 (**1b**$^+$), 2.63 (**2b**$^+$) 2.58 (**3b**$^+$), 2.63 (**4b**$^+$), 2.61 (**5b**$^+$) and 2.58 ppm (**6b**$^+$) shows an NOE with the doublet of doublets of doublets at $\delta$ = 4.58, 4.71, 4.71, 4.54, 4.55 and 4.48 ppm (**1b**$^+$–**6b**$^+$, respectively), but not with the ones at $\delta$ = 5.21, 5.30, 5.44, 5.10, 5.17 and 5.22 ppm (**1b**$^+$–**6b**$^+$, respectively). This allowed us to assign H-6a to the first set of doublet of doublets of doublets. From the NOESY spectra it can also be observed that the methyl groups from the ethylamino [$\delta$ = 1.65 (**1b**$^+$), 1.57 ppm (**4b**$^+$)], isopropylamino [$\delta$ = 1.55 (**2b**$^+$), 1.47 ppm (**5b**$^+$)] and *tert*-butylamino [$\delta$ = 1.22 (**3b**$^+$), 1.17 (**6b**$^+$)] moieties show NOEs with the doublet of doublets of doublets at $\delta$ = 2.87 (**1b**$^+$), 2.96 (**2b**$^+$), 3.30 (**3b**$^+$), 2.78 (**4b**$^+$), 2.85 (**5b**$^+$) and 3.08 ppm (**6b**$^+$). This information allowed us to assign H-7b to these signals. These assignments were possible thanks to the X-ray crystal structure of (**1b**)Cl·$H_2O$ (Fig-

 © 2006 Wiley-VCH Verlag GmbH & Co. KGaA, Weinheim 

**IONIC FORM WITH Cl⁻**

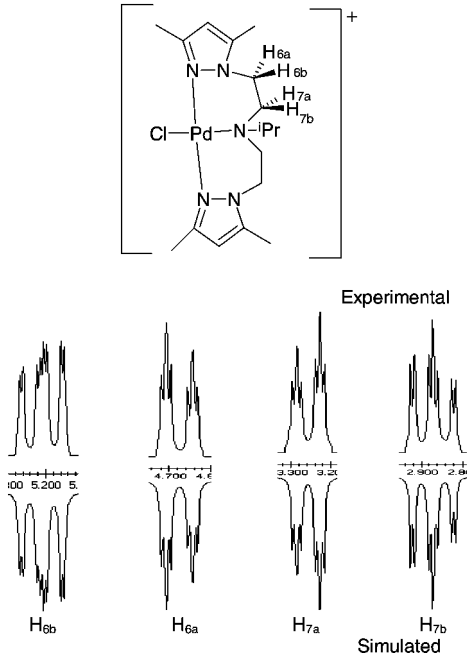


Figure 1. The experimental (250 MHz) and simulated (*g* NMR) $^1$H NMR spectra for the H-6 and H-7 protons of the $N_{pz}CH_2$-$CH_2N_{amino}$ fragment of [PdCl(ddai)]Cl ([**2b**]Cl).

**IONIC FORM WITH $BF_4^-$**

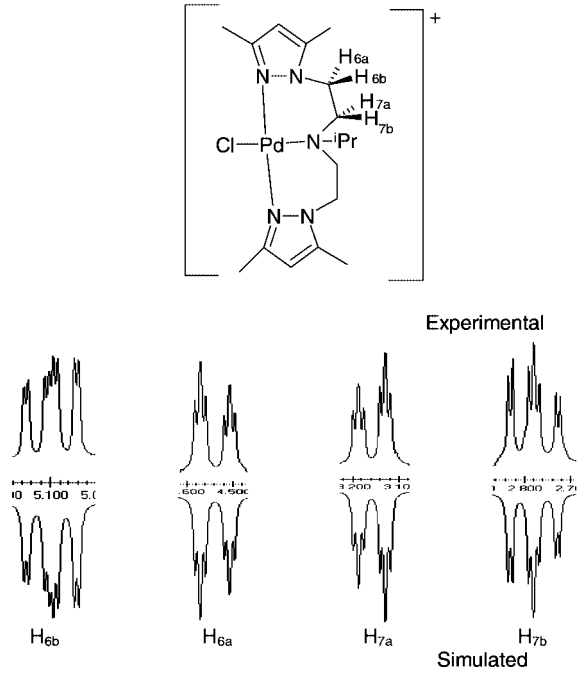


Figure 2. The experimental (250 MHz) and simulated (*g* NMR) $^1$H NMR spectra for the H-6 and H-7 protons of the $N_{pz}CH_2$-$CH_2N_{amino}$ fragment of [PdCl(ddai)]$BF_4$ ([**5b**]$BF_4$).

ure 3), which shows that the shortest distances are between the methyl linked to the pyrazole at $\delta$ = 2.66 ppm and the doublet of doublets of doublets at $\delta$ = 4.67 ppm (H6b···H5a = 2.03, H11a···H15a = 2.01 Å) and between the methyl group from the ethylamino group and H-7b (H10b···H9c = 2.09 Å).

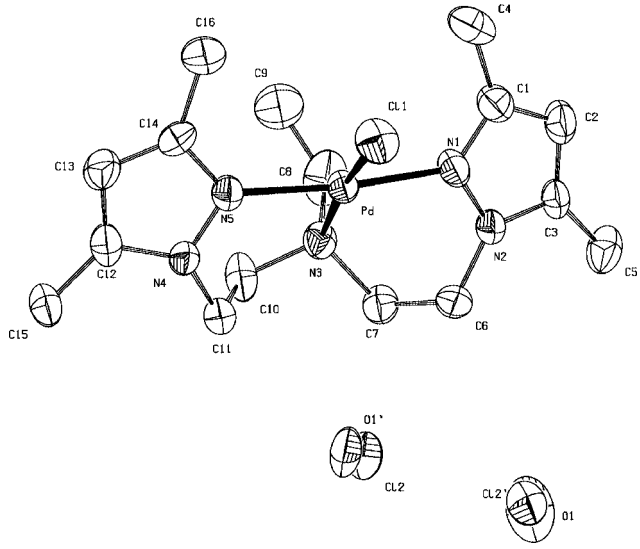

Figure 3. ORTEP drawing of [PdCl(ddae)]Cl·$H_2O$, showing all non-hydrogen atoms and the atom-numbering scheme; 50% probability amplitude displacement ellipsoids are shown.

### Crystal Structure of [PdCl(ddae)]Cl·$H_2O$

The crystal structure consists of discrete $[PdCl(ddae)]^+$ units, chloride anions and solvent molecules ($H_2O$) (Figure 3). The $H_2O$ and chloride ions are disordered.

The cation complex is mononuclear, and the $Pd^{II}$ is coordinated to the ddae ligand by its three donor atoms (two nitrogen atoms of the pyrazolyl group and one nitrogen atom of the amine moiety), along with one chlorine atom, in a slightly distorted square-planar geometry. The tetrahedral distortion can be observed from the bond angles and from the mean separation (0.0045 Å) of the atoms coordinated to the Pd atom in relation to the mean plane that contains these four atoms and the Pd atom. The dihedral angle between the planes N5–Pd–N3 and N1–Pd–N3 is 37.1(3)°. The ddae ligand acts as a tridentate chelate and forms two six-membered rings, with a boat conformation for Pd–N1–N2–C6–C7–N3 and a twist-boat conformation for Pd–N5–N4–C11–C10–N3, which share an edge (Pd–$N_{amino}$). The boat distortions in the six-membered rings are $\Delta C_s[(N3–C7)] = \Delta C_s[(N1–N2)] = 19.4(6)°$ for Pd–N1–N2–C6–C7–N3 and $\Delta C_s[(N3–C10)] = \Delta C_s[(N5–N4)] = 52.2(6)°$ for Pd–N5–N4–C11–C10–N3.

A $PdN_3Cl$ core is present in 89 complexes in the literature.[14] Some selected bond lengths and bond angles for this complex are listed in Table 3. The Pd–$N_{pz}$ bond lengths [2.019(6) and 2.027(6) Å], the Pd–$N_{amino}$ bond length [2.113(5) Å] and the Pd–Cl bond length [2.2991(18) Å] can be regarded as normal compared with the distances found

 © 2006 Wiley-VCH Verlag GmbH & Co. KGaA, Weinheim 

in the literature. For Pd–$N_{pz}$, the literature describes values between 1.979 and 2.141 Å,[1a,1b,1f,2a–2d,2g,6,15] for Pd–$N_{amino}$ between 2.017 and 2.280 Å,[16] and for Pd–Cl between 2.280 and 2.341 Å.[1a,1b,1f,2a–2d,6,15b,15c]

Table 3. Selected bond lengths [Å] and angles [°] for [PdCl(ddae)]Cl·$H_2O$.

| | | | |
|---|---|---|---|
| Pd–N(1) | 2.019(6) | Pd–N(3) | 2.113(5) |
| Pd–N(5) | 2.027(6) | Pd–Cl(1) | 2.2991(18) |
| N(1)–Pd–N(5) | 172.3(2) | N(1)–Pd–Cl(1) | 90.44 (17) |
| N(1)–Pd–N(3) | 87.3(2) | N(5)–Pd–Cl(1) | 92.30(17) |
| N(5)–Pd–N(3) | 90.8(2) | N(3)–Pd–Cl(1) | 173.15(15) |

The $N_{pyrazole}$–$N_{amino}$ bite angles of the ligand are 87.3(2)° and 90.8(2)°, respectively, and are similar to the corresponding bite angles in the complexes [$PdCl_2$(*NN′*)] [*NN′* = deae, deat; 89.3(2)° and 88.16(18)°, respectively][6] and [Pd(*NN′*)$_2$]($BF_4$)$_2$ [*NN′* = deat; 87.3(2)°].[7]

## Conclusion

The *N*-alkylaminopyrazole ligands ddae, ddai, and ddat can coordinate $Pd^{II}$ centres in different ways. In complexes **1**–**3** these ligands show didentate coordination (*NN*) in acetonitrile and tridentate coordination (*NN′N*) in methanol. Furthermore, we have demonstrated the hemilabile properties of these ligands when coordinated to $Pd^{II}$.

Complexes **4**–**6**, where the ligand uses *NN′N* coordination, are obtained from **1**–**3** by treatment with $AgBF_4$. When complexes **4**–**6** are heated under reflux in a solution of $Et_4NCl$ in $CH_3CN$, **1**–**3** are obtained once again. This could be considered as type-III hemilability.[17]

## Experimental Section

**General Details:** The reactions were carried out under nitrogen using vacuum-line and Schlenk techniques. Solvents were dried and distilled according to standard procedures and stored under nitrogen. Elemental analyses (C, H, N) were carried out by the staff of the Chemical Analyses Service of the Universitat Autònoma de Barcelona on a Carlo Erba CHNS EA-1108 instrument. Conductivity measurements were performed at room temperature in $10^{-3}$ M acetonitrile and methanol, employing a CyberScan CON 500 (Euthech Instruments) conductimeter. Infrared spectra were run on a Perkin–Elmer FT spectrophotometer, series 2000 $cm^{-1}$ as NaCl pellets, KBr pellets or polyethylene films in the range 4000–100 $cm^{-1}$. $^1H$, $^{13}C\{^1H\}$, DEPT, COSY, HMQC, and NOESY NMR spectra were recorded with an NMR-FT Bruker 250 MHz spectrometer in $CDCl_3$, $CD_3CN$ or [$D_4$]methanol solutions at room temperature. All chemical-shift values ($\delta$) are given in ppm. Mass spectra were obtained with an Esquire 3000 ion-trap mass spectrometer from Bruker Daltonics. The complex [$PdCl_2(CH_3CN)_2$][18] was synthesised according to published methods. The precursor 3,5-dimethyl-1-[2-(*p*-tosyloxy)ethyl]pyrazole was prepared as described in the literature.[8]

**Synthesis of the Ligands Bis[2-(3,5-dimethyl-1-pyrazolyl)ethyl]ethylamine (ddae), Bis[2-(3,5-dimethyl-1-pyrazolyl)ethyl]isopropylamine (ddai) and Bis[2-(3,5-dimethyl-1-pyrazolyl)ethyl]-*tert*-butylamine (ddat):** The synthesis consists of the reaction between 3,5-dimethyl-1-[2-(*p*-tosyloxy)ethyl]pyrazole (6.17 g, 21 mmol), 11 mmol of the appropriate primary amine (ddae: 0.88 mL of 70% ethylamine; ddai: 0.98 mL of 97% isopropylamine; ddat: 1.18 mL of 98% *tert*-butylamine), and sodium hydroxide (0.96 g, 24 mmol). The reaction was carried out in 20 mL of water with continuous stirring at reflux for 4 h. The mixture was then cooled down to room temperature and extracted three times with 6 mL of $CH_3Cl$. The organic phase was collected and dried overnight with anhydrous $MgSO_4$. The solution was filtered off and the solvent removed under vacuum. Each product was obtained as a yellow oil. This oil consisted of a mixture of the mono- and bis(pyrazolylalkyl)amine ligands. The proportions of the bis(pyrazolylalkyl)amine and the mono(pyrazolylalkyl)amine were 3:1 for ddae, 1:1 for ddai and 1:4 for ddat.

In order to separate the two ligands, a silica gel column with ethyl acetate as eluent was used. The mono(pyrazolylalkyl)amine ligand stayed on top of the column whereas the bis(pyrazolylalkyl)amine ligand eluted. The solvent was removed under vacuum to give ddae as a pale-yellow oil, ddai as a pale-yellow solid (m.p. 25 °C) and ddat as a white solid (m.p. 30 °C).

**ddae:** Yield: 24% (0.76 g). $C_{16}H_{27}N_5$ (289.5): calcd. C 66.44, H 9.34, N 24.22; found C 66.01, H 9.35, N 24.50. MS (ESI): *m*/*z* (%) = 312.2(31) [$MNa^+$], 290.2 (100) [$MH^+$]. IR (NaCl): $\tilde{\nu}$ = 3120 $cm^{-1}$ $\nu$(C–H)$_{ar,}$ 2968, 2928 $\nu$(C–H)$_{al}$, 1552 [$\nu$(C=C), $\nu$(C=N)]$_{ar}$, 1462, 1424 [$\delta$(C=C), $\delta$(C=N)]$_{ar}$, 1092 $\delta$(C–H)$_{ip}$, 774 $\delta$(C–H)$_{oop}$. $^1H$ NMR ($CDCl_3$, 250 MHz): $\delta$ = 5.66 [s, 2 H, C*H*(pz)], 3.77 (t, $^3J$ = 6.8 Hz, 4 H, $N_{pz}CH_2CH_2N$), 2.75 (t, $^3J$ = 6.8 Hz, 4 H, $N_{pz}CH_2CH_2N$), 2.50 (q, $^3J$ = 7.2 Hz, 2 H, $NCH_2CH_3$), 2.12 [s, 12 H, $CH_3$(pz)], 0.92 (t, $^3J$ = 7.2 Hz, 3 H, $NCH_2CH_3$) ppm. $^{13}C$ NMR ($CDCl_3$, 63 MHz): $\delta$ = 147.7 (*C*$CH_3$), 139.5 (*C*$CH_3$), 105.1 [*C*H(pz)], 54.8 ($N_{pz}CH_2CH_2N$), 49.1 ($NCH_2CH_3$), 47.8 ($N_{pz}CH_2CH_2N$), 13.8 (C*C*$H_3$), 12.5 ($NCH_2CH_3$), 11.4 (C*C*$H_3$) ppm.

**ddai:** Yield: 23% (0.77 g). $C_{17}H_{29}N_5$ (303.5): calcd. C 67.33, H 9.57, N 23.10; found C 67.09, H 9.76, N 22.80. MS (ESI): *m*/*z* (%) = 304.2 (100) [$MH^+$], 208.1 (5) [$MH^+$ – 3,5-dmpz]. IR (KBr): $\tilde{\nu}$ = 3114 $cm^{-1}$ $\nu$(C–H)$_{ar,}$ 2959, 2926 $\nu$(C–H)$_{al}$, 1552 [$\nu$(C=C), $\nu$(C=N)]$_{ar}$, 1460, 1425 [$\delta$(C=C), $\delta$(C=N)]$_{ar}$, 1089 $\delta$(C–H)$_{ip}$, 777 $\delta$(C–H)$_{oop}$. $^1H$ NMR ($CDCl_3$, 250 MHz): $\delta$ = 5.66 [s, 2 H, C*H*(pz)], 3.66 (t, $^3J$ = 6.7 Hz, 4 H, $N_{pz}CH_2CH_2N$), 2.78 [sp, $^3J$ = 6.5 Hz, 1 H, $NCH(CH_3)_2$], 2.70 (t, $^3J$ = 6.7 Hz, 4 H, $N_{pz}CH_2CH_2N$), 2.12 [s, 12 H, $CH_3$(pz)], 0.90 [d, $^3J$ = 6.5 Hz, 6 H, $NCH(CH_3)_2$] ppm. $^{13}C$ NMR ($CDCl_3$, 63 MHz): $\delta$ = 147.7 (*C*$CH_3$), 139.6 (*C*$CH_3$), 105.0 [*C*H(pz)], 52.3 [N*C*H$(CH_3)_2$], 51.9 ($N_{pz}CH_2CH_2N$), 48.9 ($N_{pz}CH_2CH_2N$), 18.6 [NCH(*C*$H_3)_2$], 13.9 (C*C*$H_3$), 11.5 (C*C*$H_3$) ppm.

**ddat:** Yield: 21% (0.73 g). $C_{18}H_{31}N_5$ (317.5): calcd. C 68.14, H 9.78, N 22.08; found C 68.08, H 9.43, N 22.02. MS (ESI): *m*/*z* (%) = 340.2 (2) [$MNa^+$], 318.3 (100) [$MH^+$], 262.1 (76) [$MH^+$ – *t*Bu]. IR (KBr): $\tilde{\nu}$ = 3114 $cm^{-1}$ $\nu$(C–H)$_{ar,}$ 2975, 2915 $\nu$(C–H)$_{al}$, 1553 [$\nu$(C=C), $\nu$(C=N)]$_{ar}$, 1462, 1425 [$\delta$(C=C), $\delta$(C=N)]$_{ar}$, 1097 $\delta$(C–H)$_{ip}$, 776 $\delta$(C–H)$_{oop}$. $^1H$ NMR ($CDCl_3$, 250 MHz): $\delta$ = 5.66 [s, 2 H, C*H*(pz)], 3.61 (t, $^3J$ = 6.4 Hz, 4 H, $N_{pz}CH_2CH_2N$), 2.79 (t, $^3J$ = 6.4 Hz, 4 H, $N_{pz}CH_2CH_2N$), 2.15 [s, 6 H, $CH_3$(pz)], 2.11 [s, 6 H, $CH_3$(pz)], 1.02 [s, 9 H, C(*C*$H_3)_3$] ppm. $^{13}C$ NMR ($CDCl_3$, 63 MHz): $\delta$ = 147.7 (*C*$CH_3$), 139.6 (*C*$CH_3$), 105.1 [*C*H(pz)], 55.8 [N*C*$(CH_3)_3$], 52.8 ($N_{pz}CH_2CH_2N$), 50.3 ($N_{pz}CH_2CH_2N$), 27.4 [NC(*C*$H_3)_3$], 13.9 (C*C*$H_3$), 11.6 (C*C*$H_3$).

**Synthesis of the Complexes [$PdCl_2$(*NN′N*)] [*NN′N* = ddae (1), ddai (2), ddat (3)]:** A solution of 0.27 mmol of the corresponding ligand (ddea: 0.078 g; ddai: 0.082 g; and ddat: 0.086 g) in 5 mL of dry $CH_2Cl_2$ was added to a solution of [$PdCl_2(CH_3CN)_2$] (0.070 g, 0.27 mmol) in 10 mL of dry $CH_2Cl_2$. After the mixture had been stirred for 12 h, most of the solvent was removed under vacuum. Diethyl ether (5 mL) was then added dropwise to induce precipi-

 © 2006 Wiley-VCH Verlag GmbH & Co. KGaA, Weinheim 

tation. The orange solids were filtered off, washed twice with 5 mL of diethyl ether, and recrystallised from a dichloromethane/diethyl ether (1:1) mixture.

Key coupling constants for **1b**$^+$–**3b**$^+$ in methanol are given in Table 1.

**1:** Yield: 53% (0.067 g). $C_{16}H_{27}Cl_2N_5Pd$ (466.8): calcd. C 41.17, H 5.79, N 15.01; found C 41.05, H 5.94, N 14.86%. Conductivity ($8.57\times10^{-4}$ M in acetonitrile): 78 $\Omega^{-1}cm^2mol^{-1}$; ($8.72\times10^{-4}$ M in methanol): 95 $\Omega^{-1}cm^2mol^{-1}$. IR (KBr): $\tilde{\nu}$ = 3129, 3085 $cm^{-1}$ $\nu$(C–H)$_{ar}$, 2965, 2915 $\nu$(C–H)$_{al}$, 1554 [$\nu$(C=C), $\nu$(C=N)]$_{ar}$, 1465, 1422 [$\delta$(C=C), $\delta$(C=N)]$_{ar}$, 1093 $\delta$(C–H)$_{ip}$, 801 $\delta$(C–H)$_{oop}$; (polyethylene): $\tilde{\nu}$ = 458 $cm^{-1}$ $\nu$(Pd–N), 336 $\nu$(Pd–Cl). $^1$H NMR for isomer **1a** ($CD_3CN$, 250 MHz): $\delta$ = 6.12 [s, 2 H, C*H*(pz)], 5.02 (m, 2 H, $N_{pz}CHHCH_2N$), 4.68 (m, 2 H, $N_{pz}CHHCH_2N$), 3.16 (m, 2 H, $N_{pz}CH_2CHHN$), 2.88 (m, 2 H, $N_{pz}CH_2CHHN$), 2.63 [s, 6 H, C$H_3$(pz)], 2.38 [s, 6 H, C$H_3$(pz)], 2.17 (q, 2 H, C$H_2$CH$_3$), 1.57 (t, 3 H, CH$_2$C$H_3$) ppm; isomer **1b**$^+$ ([D$_4$]methanol, 250 MHz): $\delta$ = 6.16 [s, 2 H, C*H*(pz)], 5.21 (ddd, 2 H, $N_{pz}CHHCH_2N$), 4.67 (ddd, 2 H, $N_{pz}CHHCH_2N$), 3.26 (ddd, 2 H, $N_{pz}CH_2CHHN$), 2.87 (ddd, 2 H, $N_{pz}CH_2CHHN$), 2.66 [s, 6 H, C$H_3$(pz)], 2.42 [s, 6 H, C$H_3$(pz)], 2.18 (q, 2 H, C$H_2$CH$_3$), 1.65 (t, 3 H, CH$_2$C$H_3$) ppm. $^{13}$C NMR for isomer **1a** ($CD_3CN$, 63 MHz): $\delta$ = 153.3 (*C*CH$_3$), 145.0 (*C*CH$_3$), 108.8 [*C*H(pz)], 60.8 (N*C*H$_2$CH$_3$), 60.6 ($N_{pz}CH_2CH_2N$), 48.6 ($N_{pz}CH_2CH_2N$), 14.8 (C*C*H$_3$), 14.2 (NCH$_2$*C*H$_3$), 11.2 (C*C*H$_3$) ppm; isomer **1b**$^+$ ([D$_4$]methanol, 63 MHz): $\delta$ = 153.5 (*C*CH$_3$), 144.8 (*C*CH$_3$), 108.7 [*C*H(pz)], 60.9 (N*C*H$_2$CH$_3$), 60.6 ($N_{pz}CH_2CH_2N$), 48.2 ($N_{pz}CH_2CH_2N$), 14.2 (C*C*H$_3$), 13.8 (NCH$_2$*C*H$_3$), 10.3 (C*C*H$_3$) ppm.

**2:** Yield: 46% (0.060 g). $C_{17}H_{29}Cl_2N_5Pd$ (480.8): calcd. C 42.47, H 6.04, N 14.57; found C 42.58, H 6.09, N 14.69. Conductivity ($6.24\times10^{-4}$ M in acetonitrile): 80 $\Omega^{-1}cm^2mol^{-1}$; ($9.05\times10^{-4}$ M in methanol): 83 $\Omega^{-1}cm^2mol^{-1}$. IR (KBr): $\tilde{\nu}$ = 3125, 3077 $cm^{-1}$ $\nu$(C–H)$_{ar}$, 2963, 2922 $\nu$(C–H)$_{al}$, 1554 [$\nu$(C=C), $\nu$(C=N)]$_{ar}$, 1468, 1424 [$\delta$(C=C), $\delta$(C=N)]$_{ar}$, 1093 $\delta$(C–H)$_{ip}$, 807 $\delta$(C–H)$_{oop}$; (polyethylene): $\tilde{\nu}$ = 460 $cm^{-1}$ $\nu$(Pd–N), 335 $\nu$(Pd–Cl). $^1$H NMR for isomer **2a** ($CD_3CN$, 250 MHz): $\delta$ = 6.11 [s, 2 H, C*H*(pz)], 5.13 (m, 2 H, $N_{pz}CHHCH_2N$), 4.60 (m, 2 H, $N_{pz}CHHCH_2N$), 3.15 (m, 2 H, $N_{pz}CH_2CHHN$), 2.87 (m, 2 H, $N_{pz}CH_2CHHN$), 2.61 [s, 6 H, C$H_3$(pz)], 2.38 [s, 6 H, C$H_3$(pz)], 2.27 [sp, 1 H, C*H*(CH$_3$)$_2$], 1.47 [d, 6 H, CH(C$H_3$)$_2$] ppm; isomer **2b**$^+$ ([D$_4$]methanol, 250 MHz): $\delta$ = 6.15 [s, 2 H, C*H*(pz)], 5.29 (ddd, 2 H, $N_{pz}CHHCH_2N$), 4.70 (ddd, 2 H, $N_{pz}CHHCH_2N$), 3.22 (ddd, 2 H, $N_{pz}CH_2CHHN$), 2.96 (ddd, 2 H, $N_{pz}CH_2CHHN$), 2.63 [s, 6 H, C$H_3$(pz)], 2.42 [s, 6 H, C$H_3$(pz)], 2.32 [sp, 1 H, C*H*(CH$_3$)$_2$], 1.55 [d, 6 H, CH(C$H_3$)$_2$] ppm. $^{13}$C NMR for isomer **2a** ($CD_3CN$, 63 MHz): $\delta$ = 153.2 (*C*CH$_3$), 144.9 (*C*CH$_3$), 108.7 [*C*H(pz)], 65.5 [N*C*H(CH$_3$)$_2$], 58.3 ($N_{pz}CH_2CH_2N$), 48.7 ($N_{pz}CH_2CH_2N$), 19.5 [NCH(*C*H$_3$)$_2$], 14.6 (C*C*H$_3$), 14.2 (NCH$_2$*C*H$_3$), 11.2 (C*C*H$_3$) ppm; isomer **2b**$^+$ ([D$_4$]methanol, 63 MHz): $\delta$ = 153.3 (*C*CH$_3$), 144.6 (*C*CH$_3$), 108.6 [*C*H(pz)], 65.8 [N*C*H(CH$_3$)$_2$], 58.5 ($N_{pz}CH_2CH_2N$), 48.2 ($N_{pz}CH_2CH_2N$), 19.0 [NCH(*C*H$_3$)$_2$], 14.1 (C*C*H$_3$), 10.4 (C*C*H$_3$) ppm.

**3**: Yield: 22% (0.029 g). $C_{18}H_{31}Cl_2N_5Pd$ (494.8): calcd. C 43.70, H 6.27, N 14.16; found C 43.91, H 6.24, N 13.81. Conductivity ($1.12\times10^{-3}$ M in acetonitrile): 118 $\Omega^{-1}cm^2mol^{-1}$; ($6.07\times10^{-4}$ M in methanol): 89 $\Omega^{-1}cm^2mol^{-1}$. IR (KBr): $\tilde{\nu}$ = 3122, 3077 $cm^{-1}$ $\nu$(C–H)$_{ar}$, 2971, 2922 $\nu$(C–H)$_{al}$, 1556 [$\nu$(C=C), $\nu$(C=N)]$_{ar}$, 1471, 1424 [$\delta$(C=C), $\delta$(C=N)]$_{ar}$, 1093 $\delta$(C–H)$_{ip}$, 802 $\delta$(C–H)$_{oop}$; (polyethylene): $\tilde{\nu}$ = 457 $cm^{-1}$ $\nu$(Pd–N), 336 $\nu$(Pd–Cl). $^1$H NMR for isomer **3a** ($CD_3CN$, 250 MHz): $\delta$ = 6.01 [s, 2 H, C*H*(pz)], 5.15 (m, 2 H, $N_{pz}CHHCH_2N$), 4.91 (m, 2 H, $N_{pz}CHHCH_2N$), 3.60 (m, 2 H, $N_{pz}CH_2CHHN$), 3.12 (m, 2 H, $N_{pz}CH_2CHHN$), 2.56 [s, 6 H, C$H_3$(pz)], 2.36 [s, 6 H, C$H_3$(pz)], 1.15 [s, 9 H, C(C$H_3$)$_3$] ppm; isomer **3b**$^+$: $\delta$ = 6.07 [s, 2 H, C*H*(pz)], 5.32 (ddd, 2 H, $N_{pz}CHHCH_2N$), 4.68 (ddd, 2 H, $N_{pz}CHHCH_2N$), 3.17 (ddd, 2 H, $N_{pz}CH_2CHHN$), 3.10 (ddd, 2 H, $N_{pz}CH_2CHHN$), 2.56 [s, 6 H, C$H_3$(pz)], 2.36 [s, 6 H, C$H_3$(pz)], 1.15 [s, 9 H, C(C$H_3$)$_3$] ppm; isomer **3b**$^+$ ([D$_4$]methanol, 250 MHz): $\delta$ = 6.10 [s, 2 H, C*H*(pz)], 5.44 (ddd, 2 H, $N_{pz}CHHCH_2N$), 4.71 (ddd, 2 H, $N_{pz}CHHCH_2N$), 3.30 (ddd, 2 H, $N_{pz}CH_2CHHN$), 3.19 (ddd, 2 H, $N_{pz}CH_2CHHN$), 2.58 [s, 6 H, C$H_3$(pz)], 2.41 [s, 6 H, C$H_3$(pz)], 1.22 [s, 9 H, C(C$H_3$)$_3$] ppm. $^{13}$C NMR for isomer **3a** ($CD_3CN$, 63 MHz): $\delta$ = 152.7 (*C*CH$_3$), 144.5 (*C*CH$_3$), 108.5 [*C*H(pz)], 69.3 [N*C*(CH$_3$)$_3$], 60.6 ($N_{pz}CH_2CH_2N$), 49.2 ($N_{pz}CH_2CH_2N$), 19.2 [NC(*C*H$_3$)$_3$], 14.3 (C*C*H$_3$), 10.8 (C*C*H$_3$) ppm; isomer **3b**$^+$: $\delta$ = 153.1 (*C*CH$_3$), 144.8 (*C*CH$_3$), 108.7 [*C*H(pz)], 69.4 [N*C*(CH$_3$)$_3$], 60.9 ($N_{pz}CH_2CH_2N$), 49.4 ($N_{pz}CH_2CH_2N$), 19.5 [NC(*C*H$_3$)$_3$], 14.5 (C*C*H$_3$), 11.0 (C*C*H$_3$) ppm; isomer **3b**$^+$ ([D$_4$]-methanol, 63 MHz): $\delta$ = 153.1 (*C*CH$_3$), 144.6 (*C*CH$_3$), 108.5 [*C*H(pz)], 69.7 [N*C*(CH$_3$)$_3$], 60.9 ($N_{pz}CH_2CH_2N$), 49.4 ($N_{pz}CH_2CH_2N$), 19.0 [NC(*C*H$_3$)$_3$], 14.0 (C*C*H$_3$), 10.3 (C*C*H$_3$) ppm.

**Synthesis of the Complexes [PdCl(*NN′N*)](BF$_4$) [*NN′N* = ddae (4), ddai (5), ddat (6)]:** $AgBF_4$ (0.052 g, 0.27 mmol) in 5 mL of methanol and 0.27 mmol of the corresponding ligand (ddae: 0.078 g; ddai: 0.082 g; ddat: 0.086 g) in 5 mL of dry $CH_2Cl_2$ were added to a solution of [$PdCl_2(CH_3CN)_2$] (0.070 g, 0.27 mmol) in 10 mL of dry $CH_2Cl_2$. The mixture was protected from the light and stirred at room temp. for 1 h. The yellow solution was then filtered through a pad of Celite. The solution was stirred for 30 min and then most of the solvent was removed under vacuum. Diethyl ether (5 mL) was then added dropwise to induce precipitation. The yellow solid was filtered off, washed twice with 5 mL of diethyl ether and dried under vacuum.

Key coupling constants for **4b**$^+$–**6b**$^+$ in $CD_3CN$ are given in Table 2.

**4:** Yield: 81% (0.11 g). $C_{16}H_{27}BClF_4N_5Pd$ (517.7): calcd. C 37.09, H 5.22, N 13.52; found C 37.41, H 5.11, N 13.48. Conductivity ($7.73\times10^{-4}$ M in acetonitrile): 156 $\Omega^{-1}cm^2mol^{-1}$; ($8.01\times10^{-4}$ M in methanol): 93 $\Omega^{-1}cm^2mol^{-1}$. IR (KBr): $\tilde{\nu}$ = 3132, 3078 $cm^{-1}$ $\nu$(C–H)$_{ar,}$ 2975, 2938 $\nu$(C–H)$_{al}$, 1555 [$\nu$(C=C), $\nu$(C=N)]$_{ar}$, 1466, 1422 [$\delta$(C=C), $\delta$(C=N)]$_{ar}$, 1053 $\nu$(B–F), 820 $\delta$(C–H)$_{oop}$; (polyethylene): $\tilde{\nu}$ = 426 $cm^{-1}$ $\nu$(Pd–N), 341 $\nu$(Pd–Cl). $^1$H NMR ($CD_3CN$, 250 MHz): $\delta$ = 6.12 [s, 2 H, C*H*(pz)], 5.10 (ddd, 2 H, $N_{pz}CHHCH_2N$), 4.54 (ddd, 2 H, $N_{pz}CHHCH_2N$), 3.16 (ddd, 2 H, $N_{pz}CH_2CHHN$), 2.78 (ddd, 2 H, $N_{pz}CH_2CHHN$), 2.63 [s, 6 H, C$H_3$(pz)], 2.36 [s, 6 H, C$H_3$(pz)], 2.14 (q, $^3J$ = 7.2 Hz, 2 H, NC$H_2$CH$_3$), 1.57 (t, $^3J$ = 7.2 Hz, 3 H, NCH$_2$C$H_3$) ppm. $^{13}$C NMR ($CD_3CN$, 63 MHz): $\delta$ = 153.4 (*C*CH$_3$), 145.0 (*C*CH$_3$), 108.8 [*C*H(pz)], 60.8 (N*C*H$_2$CH$_3$), 60.7 ($N_{pz}CH_2CH_2N$), 48.1 ($N_{pz}CH_2CH_2N$), 14.7 (C*C*H$_3$), 14.1 (NCH$_2$*C*H$_3$), 11.0 (C*C*H$_3$) ppm.

**5:** Yield: 78% (0.11 g). $C_{17}H_{29}BClF_4N_5Pd$ (531.7): calcd. C 38.37, H 5.45, N 13.16; found C 38.38, H 4.77, N 12.56. Conductivity ($7.52\times10^{-4}$ M in acetonitrile): 154 $\Omega^{-1}cm^2mol^{-1}$; ($9.28\times10^{-4}$ M in methanol): 92 $\Omega^{-1}cm^2mol^{-1}$. IR (KBr): $\tilde{\nu}$ = 3128, 3077 $cm^{-1}$ $\nu$(C–H)$_{ar,}$ 2966, 2920 $\nu$(C–H)$_{al}$, 1555 [$\nu$(C=C), $\nu$(C=N)]$_{ar}$, 1466, 1422 [$\delta$(C=C), $\delta$(C=N)]$_{ar}$, 1060 $\nu$(B–F), 809 $\delta$(C–H)$_{oop}$) ; (polyethylene): $\tilde{\nu}$ = 459 $cm^{-1}$ $\nu$(Pd–N), 342 $\nu$(Pd–Cl). $^1$H NMR ($CD_3CN$, 250 MHz): $\delta$ = 6.11 [s, 2 H, C*H*(pz)], 5.17 (ddd, 2 H, $N_{pz}CHHCH_2N$), 4.55 (ddd, 2 H, $N_{pz}CHHCH_2N$), 3.07 (ddd, 2 H, $N_{pz}CH_2CHHN$), 2.85 (ddd, 2 H, $N_{pz}CH_2CHHN$), 2.61 [s, 6 H, C$H_3$(pz)], 2.37 [s, 6 H, C$H_3$(pz)], 2.28 [sp, $^3J$ = 6.6 Hz, 1 H, C*H*(CH$_3$)$_2$], 1.47 [d, $^3J$ = 6.6 Hz, 6 H, CH(C$H_3$)$_2$] ppm. $^{13}$C NMR ($CD_3CN$, 63 MHz): $\delta$ = 153.2 (*C*CH$_3$), 144.9 (*C*CH$_3$), 108.7 [*C*H(pz)], 65.6 [N*C*H(CH$_3$)$_2$], 58.3 ($N_{pz}CH_2CH_2N$), 48.5 ($N_{pz}CH_2CH_2N$), 19.4 [NCH(*C*H$_3$)$_2$], 14.6 (C*C*H$_3$), 11.0 (C*C*H$_3$) ppm.

 © 2006 Wiley-VCH Verlag GmbH & Co. KGaA, Weinheim 

**6:** Yield: 73% (0.11 g). $C_{18}H_{31}BClF_4N_5Pd$ (545.7): calcd. C 39.58, H 5.68, N 12.83; found C 39.31, H 5.49, N 13.13. Conductivity ($7.73\times10^{-4}$ M in acetonitrile): 153 $\Omega^{-1}cm^2mol^{-1}$; ($6.32\times10^{-4}$ M in methanol): 92 $\Omega^{-1}cm^2mol^{-1}$. IR (KBr): $\tilde{\nu}$ = 3122, 3085 $cm^{-1}$ $\nu$(C–H)$_{ar}$, 2981, 2922 $\nu$(C–H)$_{al}$, 1555 [$\nu$(C=C), $\nu$(C=N)]$_{ar}$, 1473, 1424 [$\delta$(C=C), $\delta$(C=N)]$_{ar}$, 1060 $\nu$(B–F), 809 $\delta$(C–H)$_{oop}$; (polyethylene): $\tilde{\nu}$ = 458 $cm^{-1}$ $\nu$(Pd–N), 335 $\nu$(Pd–Cl). $^1$H NMR ($CD_3CN$, 250 MHz): $\delta$ = 6.09 [s, 2 H, C*H*(pz)], 5.33 (ddd, 2 H, $N_{pz}CHHCH_2N$), 4.58 (ddd, 2 H, $N_{pz}CHHCH_2N$), 3.17 (ddd, 2 H, $N_{pz}CH_2CHHN$), 3.07 (ddd, 2 H, $N_{pz}CH_2CHHN$), 2.58 [s, 6 H, $CH_3$(pz)], 2.38 [s, 6 H, $CH_3$(pz)], 1.17 [s, 9 H, $C(CH_3)_3$] ppm. $^{13}$C NMR ($CD_3CN$, 63 MHz): $\delta$ = 153.1 ($CCH_3$), 144.8 ($CCH_3$), 108.7 [*C*H(pz)], 69.5 [$NC(CH_3)_3$], 60.9 ($N_{pz}CH_2CH_2N$), 49.4 ($N_{pz}CH_2CH_2N$), 19.5 [$NC(CH_3)_3$], 14.5 ($CCH_3$), 11.0 ($CCH_3$) ppm.

**X-ray Crystal Structure for Compound [PdCl(ddae)]Cl·$H_2O$:** Crystals suitable for X-ray diffraction were obtained by crystallisation from methanol. A prismatic crystal was selected and mounted on a Enraf–Nonius CAD4 four-circle diffractometer. Unit-cell parameters were determined from automatic centring of 25 reflections ($12 < \theta < 21°$) and refined by least-squares method. Intensities were collected with graphite-monochromated Mo-$K_\alpha$ radiation using the $\omega/2\theta$ scan technique. 6425 Reflections were measured in the range $2.41 \le \theta \le 29.96°$, 6085 reflections of which were non-equivalent by symmetry [$R_{int}$(on $I$) = 0.031]. 4431 Reflections were assumed as observed by applying the condition $I > 2\sigma(I)$. Three reflections were measured every two hours as orientation and intensity control; significant intensity decay was not observed. Lorentz-polarisation but no absorption corrections were made. The structure was solved by direct methods using the SHELXS computer program,[19] and refined by full-matrix least-squares method with SHELX-97 [20] using 6425 reflections (very negative intensities were not assumed). The function minimised was $\Sigma w||F_o|^2 - |F_c|^2|^2$ where $\omega = [\sigma^2(I) + (0.0818P)^2 + 10.1890\ P]^{-1}$, and $P = (|F_o|^2 + 2|F_c|^2)/3$. All H-atoms were computed and refined using a riding model, with an overall temperature factor equal to 1.2-times the equivalent temperature factor of the atom to which they are linked. The final $R(F)$ factor and $R_w(F^2)$ values, as well as the number of parameters and other details concerning the refinement of the crystal structure, are gathered in Table 4.

Table 4. Crystallographic data for [PdCl(ddae)]Cl·$H_2O$.

| | |
|---|---|
| Formula | $C_{16}H_{29}Cl_2N_5OPd$ |
| $M$ | 484.74 |
| Temperature [K] | 293(2) |
| Crystal System | monoclinic |
| Space group | $P2_1/a$ |
| $a$ [Å] | 7.893(4) |
| $b$ [Å] | 31.437(5) |
| $c$ [Å] | 8.861(12) |
| $\alpha$ [°] | 90 |
| $\beta$ [°] | 107.31(7) |
| $\gamma$ [°] | 90 |
| $Z$ | 4 |
| $D_{calc}$ [g $cm^{-3}$] | 1.534 |
| $\mu$ [$mm^{-1}$] | 1.153 |
| $F$(000) | 992 |
| Crystal size [mm] | $0.2\times0.1\times0.1$ |
| $\theta$ range [°] | 2.41 to 29.96 |
| Index range | $-11 \le h \le 10$, $0 \le k \le 44$, $0 \le l \le 12$ |
| Reflexions collected/unique | 6425/6085 [$R$(int) = 0.0313] |
| Completeness to $\theta$ [%] | 99.9 |
| Absorption correction | none |
| Data/restraints/parameters | 6085/0/245 |
| Goodness-of-fit | 1.080 |
| Final $R_1$, $\omega R_2$ | 0.0472, 0.1541 |
| $R_1$ (all data), $\omega R_2$ | 0.0864, 0.1898 |
| Extinction coefficient | 0.0020(2) |
| Residual electron density [e $Å^{-3}$] | 0.858 and –0.737 |

CCDC-290469 contains the supplementary crystallographic data for this paper. These data can be obtained free of charge from The Cambridge Crystallographic Data Centre via www.ccdc.cam.ac.uk/data_request/cif.

## Acknowledgments

Support by the Spanish Ministerio de Educación y Cultura (project BQU2003–03582) is gratefully acknowledged.

[1] a) A. Boixassa, J. Pons, A. Virgili, X. Solans, M. Font-Bardía, J. Ros, *Inorg. Chim. Acta* **2002**, *340*, 49; b) A. Boixassa, J. Pons, X. Solans, M. Font-Bardía, J. Ros, *Inorg. Chim. Acta* **2003**, *346*, 151; c) A. Boixassa, R. Mathieu, N. Lugan, J. Pons, J. Ros, *Acta Crystallogr., Sect. E* **2003**, *59*, m658; d) A. Boixassa, J. Pons, J. Ros, R. Mathieu, N. Lugan, *J. Organomet. Chem.* **2003**, *682*, 233; e) A. Boixassa, J. Pons, X. Solans, M. Font-Bardía, J. Ros, *Inorg. Chim. Acta* **2003**, *355*, 254; f) A. Boixassa, J. Pons, X. Solans, M. Font-Bardía, J. Ros, *Inorg. Chim. Acta* **2004**, *357*, 733; g) A. Boixassa, J. Pons, X. Solans, M. Font-Bardía, J. Ros, *Inorg. Chim. Acta* **2004**, *357*, 827.

[2] a) J. García-Antón, J. Pons, X. Solans, M. Font-Bardía, J. Ros, *Eur. J. Inorg. Chem.* **2002**, 3319; b) J. García-Antón, J. Pons, X. Solans, M. Font-Bardía, J. Ros, *Eur. J. Inorg. Chem.* **2003**, 2992; c) J. García-Antón, J. Pons, X. Solans, M. Font-Bardía, J. Ros, *Eur. J. Inorg. Chem.* **2003**, 3952; d) J. García-Antón, J. Pons, X. Solans, M. Font-Bardía, J. Ros, *Inorg. Chim. Acta* **2003**, *355*, 87; e) J. García-Antón, J. Pons, X. Solans, M. Font-Bardía, J. Ros, *Inorg. Chim. Acta* **2004**, *357*, 571; f) J. García-Antón, R. Mathieu, N. Lugan, J. Pons, J. Ros, *J. Organomet. Chem.* **2004**, *689*, 1599; g) J. García-Antón, J. Pons, J. Ros, X. Solans, M. Font-Bardía, *Acta Crystallogr., Sect. E* **2004**, *60*, m1087.

[3] a) R. Tribó, J. Pons, R. Yáñez, J. F. Piniella, A. Alvarez-Larena, J. Ros, *Inorg. Chem. Commun.* **2000**, *3*, 545; b) G. Esquius, J. Pons, R. Yáñez, J. Ros, R. Mathieu, B. Donnadieu, N. Lugan, *Eur. J. Inorg. Chem.* **2002**, 2999; c) G. Esquius, J. Pons, R. Yáñez, J. Ros, R. Mathieu, N. Lugan, B. Donnadieu, *J. Organomet. Chem.* **2003**, *667*, 126; d) R. Tribó, J. Ros, J. Pons, R. Yáñez, A. Alvarez-Larena, J. F. Piniella, *J. Organomet. Chem.* **2003**, *676*, 38; e) R. Tribó, S. Muñoz, J. Pons, R. Yáñez, A. Alvarez-Larena, J. F. Piniella, J. Ros, *J. Organomet. Chem.* **2005**, *690*, 4072.

[4] a) G. Esquius, J. Pons, R. Yáñez, J. Ros, X. Solans, M. Font-Bardía, *J. Organomet. Chem.* **2000**, *605*, 226; b) G. Esquius, J. Pons, J. Ros, R. Yáñez, *J. Organomet. Chem.* **2001**, *619*, 14; c) R. Mathieu, G. Esquius, N. Lugan, J. Pons, J. Ros, *Eur. J. Inorg. Chem.* **2001**, 2683; d) G. Esquius, J. Pons, R. Yáñez, J. Ros, *Acta Crystallogr., Sect. C* **2002**, *58*, m133; e) G. Esquius, J. Pons, R. Yáñez, J. Ros, R. Mathieu, B. Donnadieu, N. Lugan, *Eur. J. Inorg. Chem.* **2002**, 2999; f) G. Zamora, J. Pons, X. Solans, M. Font-Bardía, J. Ros, *J. Organomet. Chem.* **2004**, *689*, 980; g) G. Zamora, J. Pons, J. Ros, *Inorg. Chim. Acta* **2004**, *357*, 2899; h) G. Aullón, G. Esquius, A. Lledós, F. Maseras, J. Pons, J. Ros, *Organometallics* **2004**, *23*, 5530.

[5] a) W. L. Driessen, R. M. de Vos, A. Etz, J. Reedijk, *Inorg. Chim. Acta* **1995**, *235*, 127; b) H. L. Blonk, W. L. Driessen, J. Reedijk, *J. Chem. Soc., Dalton Trans.* **1985**, 1699; c) J. B. Veldhuis, W. L. Driessen, J. Reedijk, *J. Chem. Soc., Dalton Trans.* **1986**, 537; d) M. R. Malachowski, M. G. Davidson, *Inorg. Chim. Acta* **1989**, *162*, 199; e) J. W. F. M. Schoonhoven, W. L. Driessen, J. Reedijk, G. C. Verschoor, *J. Chem. Soc., Dalton Trans.* **1989**, 1053; f) R. T. Stibrany, S. Knapp, J. A. Potenza,

 © 2006 Wiley-VCH Verlag GmbH & Co. KGaA, Weinheim 

H. J. Schugar, *Inorg. Chem.* **1999**, *38*, 132; g) W. L. Driessen, *Recl. Trav. Chim. Pays-Bas* **1982**, *101*, 441; h) Y. C. M. Pennings, W. L. Driessen, J. Reedijk, *Polyhedron* **1988**, *7*, 2583.
[6] A. Pañella, J. Pons, J. García-Antón, X. Solans, M. Font-Bardía, J. Ros, *Inorg. Chim. Acta*, in press.
[7] A. Pañella, J. Pons, J. García-Antón, X. Solans, M. Font-Bardía, J. Ros, *Inorg. Chim. Acta*, in press.
[8] W. G. Haanstra, W. L. Driessen, J. Reedijk, U. Tupeinen, R. Hämäläinen, *J. Chem. Soc., Dalton Trans.* **1989**, 2309.
[9] a) E. Pretsch, T. Clerc, J. Seibl, W. Simon, *Tables of Determination of Organic Compounds. $^{13}C$ NMR, $^{1}H$ NMR, IR, MS, UV/Vis, Chemical Laboratory Practice*, Springer Verlag, Berlin, Germany, **1989**; b) D. H. Williams, I. Fleming, *Spectroscopic Methods in Organic Chemistry*, McGraw-Hill, London, UK, **1995**; c) M. Hesse, M. Maier, B. Zeeh, *Spectroscopic Methods in Organic Chemistry*, Thieme Verlag, Berlin, Germany, **1987**.
[10] a) W. J. Geary, *Coord. Chem. Rev.* **1971**, *7*, 81; b) L. K. Thompson, F. L. Lee, E. J. Gabe, *Inorg. Chem.* **1988**, *27*, 39.
[11] K. Nakamoto, *Infrared and Raman Spectra of Inorganic and Coordination Compounds*, fourth ed., Wiley, New York, USA, **1986**.
[12] H. Günther, *NMR Spectroscopy*, Wiley, New York, **1980**.
[13] P. H. M. Budzelaar, *g* NMR – *version 4.0*. IvorySoft, Cherwell Scientific, Oxford, UK, **1997**.
[14] F. A. Allen, O. Kennard, *Chem. Des. Autom. News* **1993**, *8*, 31.
[15] a) A. Boixassa, J. Pons, X. Solans, M. Font-Bardía, J. Ros, *Inorg. Chem. Commun.* **2003**, *6*, 922; b) J. A. Pérez, J. Pons, X. Solans, M. Font-Bardía, J. Ros, *Inorg. Chim. Acta* **2005**, *358*, 617; c) V. Montoya, J. Pons, X. Solans, M. Font-Bardía, J. Ros, *Inorg. Chim. Acta* **2005**, *358*, 2312.
[16] a) R. P. Hughes, M. A. Meyer, M. D. Tawa, A. J. Ward, A. Williamson, A. L. Rheingold, L. N. Zakharov, *Inorg. Chem.* **2004**, *43*, 747; b) S. Dey, V. K. Jain, A. Knoedler, W. Kaim, *Anal. Sci.* **2004**, *20*, x127; c) K. I. Gasanov, A. S. Antsyshkina, G. G. Sadikov, N. A. Ivanova, D. I. Mirzai, I. A. Efimenko, V. S. Sergienko, *Crystallogr. Rep.* **2002**, *47*, 603; d) L. Pech, Yu. Boukousky, A. Kemme, E. Silina, J. Ashaks, A. Sturis, *Latuijos Kimijas Zurnals* **2000**, *4*, 19; e) G. Zhao, H. Lin, P. Yu, H. Sun, S. Zhu, X. Su, Y. Chen, *J. Inorg. Biochem.* **1999**, *73*, 14; f) E. C. Alyea, S. A. Dias, G. Ferguson, A. J. McAlees, R. McCrindle, P. J. Roberts, *J. Am. Chem. Soc.* **1977**, *99*, 4985.
[17] P. Braunstein, F. Naud, *Angew. Chem. Int. Ed.* **2001**, *40*, 680.
[18] S. Komiya, *Synthesis of Organometallic Compounds: A Practice Guide*, John Wiley & Sons, New York, USA, **1997**.
[19] G. M. Sheldrick, *SHELXS-97, Program for Crystal Structure Determination*, University of Göttingen, Germany **1997**.
[20] G. M. Sheldrick, *SHELXL-97, Program for Crystal Structure Refinement*, University of Göttingen, Germany **1997**.

Received: November 25, 2005
Published Online: February 21, 2006

 © 2006 Wiley-VCH Verlag GmbH & Co. KGaA, Weinheim 

DOI: 10.1002/ejic.200501085

# Synthesis of Novel α-Aminoboronate Complexes of Aminoboranes and Aminocyanoboranes

Amal Shibli[a] and Morris Srebnik*[a]

**Keywords:** Amines / Aminoboranes / Aminocyanoboranes / Boranes / Lewis acids

Tertiary amines activated either by borane ($BH_3$) or cyanoborane ($BH_2CN$) groups were α-C lithiated with *s*BuLi (2 equiv.) and then treated with 2-isopropoxy-4,4,5,5-tetramethyl-1,3,2-dioxaborolane to produce the α-aminoboronate complexes of aminoboranes and aminocyanoboranes **2**–**7** in 70–85 % yields.
(© Wiley-VCH Verlag GmbH & Co. KGaA, 69451 Weinheim, Germany, 2006)

## Introduction

During the last 30 years much effort has been focused in the area of pharmaceutical chemistry on the synthesis and biological activity studies of boron analogues of α-amino acids (α-aminoboronic acids **1**), in which the carboxylic acid moiety is replaced by a boronic acid moiety, as they are highly effective inhibitors of serine proteases.[1] In addition, α-aminoboronic acids have been shown to be inhibitors for proteosomes, arginase, NOS,[2] and cysteine enzymes.[3] The incorporation of a Lewis basic amine and a Lewis acidic boronic acid functionality into the same molecule is a notoriously difficult procedure, and synthetic routes to these compounds are scarce. It is known that primary and secondary derivatives of α-aminoboronic acids are not stable in their neutral form; however, they can be stabilized either by forming their hydrochloride salts or by converting the molecules into their amide derivatives.[4–6] In this context, new effective methods to prepare amino and related boron compounds will have a tremendous impact on synthetic, bioinorganic, and pharmaceutical chemistry.[7–12] The first synthesis of an α-amidoboronic ester was reported by Matteson et al.,[13] and remains the standard method for synthesis of α-aminoboronic acids; however, it is a multistep method and is time consuming.

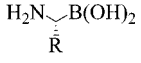

**1**

Deprotonation of tertiary amines can be promoted by a Lewis acid, since on forming a complex a positive charge develops on the nitrogen to inductively facilitate the removal of a proton from the α-C position. This concept of tertiary amine activation using Lewis acid activators was introduced by Kessar and co-workers in 1991. These authors used $BF_3$ as an activator that facilitated the α-metalation of several tertiary amine complexes.[14] Based on these results, in 1995 Ebden and co-workers applied a similar approach to aminoborane complexes, which underwent interesting metalation reactions.[15]

Trimethylaminocyanoboranes can also be easily α-deprotonated at the α-carbon and treated with various electrophiles to give more complicated aminocyanoboranes, as was recently reported by Takrouri et al.[16] The biological and pharmaceutical activities of aminocyanoboranes ($A{\cdot}BH_2CN$) and aminocarboxyboranes ($A{\cdot}BH_2COOH$) and their amide, ester, peptide, and transition metal derivatives have been investigated;[17] they have been shown to possess anticancer,[18] antiosteoporotic,[19] antiinflammatory,[20] and hypolipidemic properties.[20b,21] These molecules have also been mentioned as possible boron carriers to tumor cells for boron neutron capture therapy (BNCT).[22]

Based on the above results, we have now applied these methods with a more complex electrophile. Thus, the boron-containing electrophile 2-isopropoxy-4,4,5,5-tetramethyl-1,3,2-dioxaborolane was mainly used to give the α-aminoboronic ester attached to the cyano ($BH_2CN$) or borane ($BH_3$) groups on the same molecule. In this work, we report a novel, short, simple, and direct method to prepare novel α-aminoboronate complexes of aminoboranes and aminocyanoboranes in very good yields. Our method starts from tertiary amines that are activated either by borane or cyanoborane groups. This, in turn, leads to selective α-deprotonation. Reaction of the lithiated complexes with a boron-containing electrophile gives the title compounds.

## Results and Discussion

### Preparation of Aminoborane Derivatives

We initially focused on 2-isopropoxy-4,4,5,5-tetramethyl-1,3,2-dioxaborolane as an electrophile in our study. Treat-

[a] Department of Medicinal Chemistry & Natural Products, School of Pharmacy, Hebrew University in Jerusalem, P. O. Box 12065, Jerusalem 91120, Israel
E-mail: msrebni@md.huji.ac.il

 InterScience © 2006 Wiley-VCH Verlag GmbH & Co. KGaA, Weinheim 

ment of the borane adduct with two equivalents of *s*BuLi in THF at –78 °C, warming to the room temperature, followed by recooling to –78 °C and addition of the electrophile gave good yields of the desired α-aminoboronic acid products **2** and **3** (Scheme 1, Table 1).

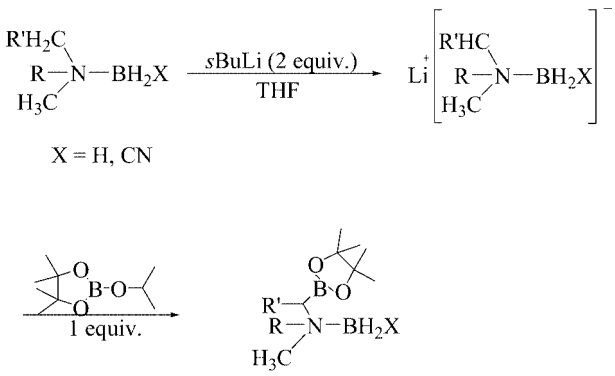


Scheme 1. Synthesis of α-aminoboronate complexes of aminoboranes and aminocyanoboranes.

Table 1. α-Aminoboronic acid derivatives **2**–**7** prepared from aminoboranes or aminocyanoboranes.

| Product | X | R′ | R | Yield [%][a] |
|---|---|---|---|---|
| **2** | H | Ph | $CH_3$ | 85 |
| **3** | H | 2-naph | $CH_3$ | 84 |
| **4** | CN | H | $CH_3$ | 83 |
| **5** | CN | H | $C_4H_9$ | 70 |
| **6** | CN | H | $C_9H_{19}$ | 80 |
| **7** | CN | H | $C_{12}H_{25}$ | 70 |

[a] Yields after column chromatography.

The use of an excess of *s*BuLi is necessary to get high yields, as using a lower amount of *s*BuLi resulted in reduced conversion to product and recovery of unreacted starting material. We suspect that this may be due to the known instability of organolithium reagents in THF.[23] It is also possible that some limited destruction of the borane complexes occurs by nucleophilic attack of *s*BuLi, resulting in partial consumption of the base. Adventitious water may also be involved.[15]

The products were stable enough to be purified on silica gel and were isolated as solids. However, these products should be stored at low temperature, otherwise they decompose slowly to give back the starting material.

### Preparation of Aminocyanoborane Derivatives

In an analogous manner, trialkylaminocyanoboranes were lithiated with *s*BuLi and then treated with 2-isopropoxy-4,4,5,5-tetramethyl-1,3,2-dioxaborolane to give the oily alkyl α-aminoboronic acid derivatives **4**–**7**. The desired products were purified on silica gel in high yields and in high purity (Scheme 1, Table 1).

Products **2**–**7** were fully characterized by $^1H$, $^{13}C$, and $^{11}B$ NMR spectroscopy, GC/MS, FT-IR spectroscopy, and elemental analysis. In the borane products **2** and **3** a new stereogenic center is created in the benzylic position, which means that the methyl groups attached to the nitrogen become diastereotopic and peaks for each group are evident in both the $^1H$ and $^{13}C$ NMR spectra. The methyl groups on the pinacol are also diastereotopic and peaks for each of the two methyls appear in the $^1H$ and $^{13}C$ NMR spectra.

The 4,4,5,5-tetramethyl-1,3,2-dioxaborolane group causes a high-field shift of the benzylic proton in the $^1H$ NMR spectra in products **2** and **3** and also for the methylenic protons in products **4**–**7** in comparison with the starting materials. In the $^{13}C$ NMR spectra of all products typical pinacol peaks are observed at $\delta$ = 24 [C($CH_3$)$_2$] and 84 ppm [$C$(CH$_3$)$_2$]. No peaks are observed for the carbon in the α-position to the boron due to the rapid relaxation of this boron-bound carbon.[24] Two peaks are observed in the $^{11}B$ NMR spectra of all the products: a positive boron chemical shift appears as a singlet at $\delta$ = 29–30 ppm, which is typical for a boron substituted with two oxygens, and a negative boron chemical shift, which is typically associated with tetracoordinate boron, appears as a quartet for products **2** and **3** at $\delta$ = –9 ppm or as a triplet for products **4**–**7** at $\delta$ = –14 ppm. These results agree with results published in the literature.[25] Typical peaks are also observed in the FT-IR spectra [2236–2407 (B–H), 2196–2199 (C≡N), 653–752 cm$^{-1}$ (B–N)].

## Conclusions

A series of novel α-aminoboronic acids **2**–**7** that also bear a borane or cyanoborane group have been prepared in a one-pot reaction in very good yields. This method involves short reaction times and is applicable to prepare diverse α-aminoboronic acids.

## Experimental Section

**Materials and Instrumentation:** Solvents were dried with sodium/benzophenone and freshly distilled before use. All reactions were carried out under dry nitrogen in oven-dried glassware. Melting points were determined on a Fisher scientific melting point apparatus. Infrared spectra were run for samples as neat films for liquids and in KBr disks for solids on a Bruker Vector 22 FT-IR spectrophotometer. $^1H$, $^{13}C$, and $^{11}B$ NMR spectra were recorded with a Varian Unity spectrometer (300, 75, and 96 MHz, respectively). Elemental analysis was performed in-house at the Hebrew University Microanalysis laboratory. Chemical shifts were recorded relative to an internal standard ($SiMe_4$) for $^1H$ and $^{13}C$ NMR and an external standard ($Et_2O{\cdot}BF_3$) for $^{11}B$ NMR spectroscopy. Liquid chromatography was performed by column chromatography with the indicated solvent system on Merck silica gel 60 (0.040–0.063 mm).

**Synthesis:** All aminoboranes complexes were prepared from borane methylsulfide and the corresponding amine using the literature method.[15] Trimethylaminocyanoborane was prepared from trimethylamine hydrochloride and sodium cyanoborohydride using the literature method.[26] All other cyanoboranes were prepared analogously as in the literature.[16] The electrophile 2-isopropoxy-4,4,5,5-tetramethyl-1,3,2-dioxaborolane was prepared using the literature method.[27] All other chemicals were obtained from Sigma–Aldrich and used as received without any further purification.

 © 2006 Wiley-VCH Verlag GmbH & Co. KGaA, Weinheim 

**General Procedure. Synthesis of 2:** A solution of *s*BuLi in cyclohexane (1.3 M, 2 mmol) was added dropwise to a solution of (dimethylbenzylamino)borane (0.149 g, 1 mmol) in THF (2.5 mL) at –78 °C. The solution was stirred for 30 min at –78 °C, then it was warmed up to room temperature for 30 min, before cooling down to –78 °C again and addition of 2-isopropoxy-4,4,5,5-tetramethyl-1,3,2-dioxaborolane (0.186 g, 1 mmol) in one portion. After 2 min the cooling bath was removed, and the reaction mixture was stirred for 30 min at room temperature. A saturated $NaHCO_3$ solution (10 mL) was then added, the layers were separated, and the aqueous layer was extracted with diethyl ether (2 × 10 mL); the combined organic layers were dried with sodium sulfate. After evaporation of all the volatiles the residue was purified by column chromatography on silica gel (2.5% EtOAc in petroleum ether) to give *N*,*N*-dimethyl-*N*-[phenyl(4,4,5,5-tetramethyl-1,3,2-dioxaborolan-2-yl)methyl]aminoborane (**2**) as a white solid, m.p. 93–95 °C, (0.235 g; yield: 85%). $^1$H NMR ($CDCl_3$, 25 °C): $\delta$ = 1.22 [s, 6 H, $C(CH_3)_2$], 1.28 [s, 6 H, $C(CH_3)_2$], 2.36 (s, 3 H, $NCH_3$), 2.70 (s, 3 H, $NCH_3$), 3.83 (s, 1 H, PhC*H*), 7.35 (m, 5 H, Ph) ppm; BH could not be detected. $^{11}$B NMR ($CDCl_3$, 25 °C): $\delta$ = –9.1 (q, $J$ = 96.25 Hz), 29.4 ppm (s). $^{13}C\{^1H\}$ NMR ($CDCl_3$, 25 °C): $\delta$ = 24.7, 24.8, 47.0, 52.1, 84.3, 128.6, 129.0, 132.5, 132.9 ppm; BC could not be detected. IR (KBr): $\tilde{\nu}$ = 2363 cm$^{-1}$ (B–H), 2321 (B–H), 2270 (B–H), 1469 (C–N) 664 (B–N) ppm. MS (EI): *m*/*z* = 275 [M$^+$], 261, 246, 231, 217, 202, 187, 172, 157, 132, 127. $C_{15}H_{27}B_2NO_2$ (275): calcd. C 65.45, H 9.81, N 5.09; found C 66.25, H 9.80, N 5.12.

**Preparation of *N*,*N*-Dimethyl-*N*-[naphthalen-2-yl(4,4,5,5-tetramethyl-1,3,2-dioxaborolan-2-yl)methyl]aminoborane (3):** White solid, m.p. 108–110 °C, (0.275 g; yield 84%). $^1$H NMR ($CDCl_3$, 25 °C): $\delta$ = 1.23 [s, 6 H, $C(CH_3)_2$], 1.30[s, 6 H, $C(CH_3)_2$], 2.42 (s, 3 H, $NCH_3$), 2.78 (s, 3 H, $NCH_3$), 4.01 (s, 1 H, PhC*H*), 7.54 (m, 4 H), 7.84 (m, 2 H), 7.95 (s, 1 H) ppm; BH could not be detected. $^{11}$B NMR ($CDCl_3$, 25 °C): $\delta$ = –9.0 (q, $J$ = 94.38 Hz), 29.1 ppm (s). $^{13}C\{^1H\}$ NMR ($CDCl_3$, 25 °C): $\delta$ = 24.5, 24.6, 46.9, 52.0, 84.1, 126.3, 126.7, 127.5, 127.9, 128.1, 129.91, 129.95, 132.4, 133.0, 133.1 ppm; BC could not be detected. IR (KBr): $\tilde{\nu}$ = 2361 cm$^{-1}$ (B–H), 2311 (B–H), 2269 (B–H), 1468 (C–N), 632 (B–N) ppm. MS (EI): *m*/*z* = 327 [M$^+$], 313, 298, 283, 269, 254, 239, 224, 209, 184, 129, 127. $C_{19}H_{31}B_2NO_2$ (327): calcd. C 69.72, H 9.48, N 4.28; found C 70.27, H 9.37, N 4.30.

**Preparation of *N*,*N*-Dimethyl-*N*-[(4,4,5,5-tetramethyl-1,3,2-dioxaborolan-2-yl)methyl]aminocyanoborane (4):** The crude product was purified by column chromatography with 20% of EtOAc in petroleum ether as eluent to give a yellow oil (0.186 g; yield 83%). $^1$H NMR ($CDCl_3$, 25 °C): $\delta$ = 1.27 {s, 12 H, $[C(CH_3)_2]_2$}, 2.68 (s, 2 H, $NCH_2B$), 2.79 [s, 6 H, $N(CH_3)_2$] ppm; BH could not be detected. $^{11}$B NMR ($CDCl_3$, 25 °C): $\delta$ = –14.1 (t, $J$ = 103.12 Hz), 29.6 ppm (s). $^{13}C\{^1H\}$ NMR ($CDCl_3$, 25 °C): $\delta$ = 24.6, 52.0, 84.5 ppm; BC could not be detected. IR (neat): $\tilde{\nu}$ = 2354 cm$^{-1}$ (B–H), 2330 (B–H), 2199 (C≡N), 1470 (C–N), 752 (B–N) ppm. MS (EI): *m*/*z* = 224 [M$^+$], 209, 194, 184, 170, 155, 127. $C_{10}H_{22}B_2N_2O_2$ (224): calcd. C 53.57, H 9.82, N 12.50; found C 54.01, H 9.69, N 12.70.

**Preparation of *N*-Methyl-*N*-[(4,4,5,5-tetramethyl-1,3,2-dioxaborolan-2-yl)methyl]butylaminocyanoborane (5):** The crude product was purified by column chromatography with 20% of EtOAc in petroleum ether as eluent to give a yellow oil (0.186 g; yield 70%). $^1$H NMR ($CDCl_3$, 25 °C): $\delta$ = 0.95 (t, $J_{H,H}$ = 15 Hz, 3 H, $CH_2CH_3$), 1.26 {s, 12 H, $[C(CH_3)_2]_2$}, 1.68 [m, 4 H, $CH_3(CH_2)_2$], 2.60 (s, 2 H, $NCH_2B$), 2.74 (s, 3 H, $NCH_3$), 2.99 (m, 2 H, $NCH_2CH_2$) ppm; BH could not be detected. $^{11}$B NMR ($CDCl_3$, 25 °C): $\delta$ = –15.5 (t, $J$ = 103.5 Hz), 29.5 ppm (s). $^{13}C\{^1H\}$ NMR ($CDCl_3$, 25 °C): $\delta$ = 13.7, 20.1, 24.6, 25.4, 49.9, 62.6, 84.4 ppm; BC could not be detected. IR (neat): $\tilde{\nu}$ = 2407 cm$^{-1}$ (B–H), 2338 (B–H), 2197 (C≡N), 1467 (C–N), 653 (B–N) ppm. MS (EI): *m*/*z* = 266 [M$^+$], 251, 227, 212, 198, 184, 169, 154. $C_{13}H_{28}B_2N_2O_2$ (266): calcd. C 58.64, H 10.52, N 10.52; found C 58.75, H 10.33, N 10.32.

**Preparation of *N*-Methyl-*N*-[(4,4,5,5-tetramethyl-1,3,2-dioxaborolan-2-yl)methyl]nonylaminocyanoborane (6):** The crude product was purified by column chromatography with 20% of EtOAc in petroleum ether as eluent to give a yellow oil (0.269 g, yield 80%). $^1$H NMR ($CDCl_3$, 25 °C): $\delta$ = 0.87 (t, $J_{H,H}$ = 13.2 Hz, 3 H, $CH_2CH_3$), 1.26 {br. s, 22 H, $[C(CH_3)_2]_2$ + $(CH_2)_5$}, 1.66 (m, 4 H, $NCH_2CH_2CH_2$), 2.59 (s, 2 H, $NCH_2B$), 2.74 (s, 3 H, $NCH_3$), 2.98 (m, 2 H, $NCH_2CH_2$) ppm; BH could not be detected. $^{11}$B NMR ($CDCl_3$, 25 °C): $\delta$ = –14.6 (t, $J$ = 104.0 Hz), 30.2 ppm (s). $^{13}C\{^1H\}$ NMR ($CDCl_3$, 25 °C): $\delta$ = 14.0, 22.6, 23.3, 24.6, 26.8, 29.12, 29.17, 29.3, 31.7, 49.8, 62.9, 84.4 ppm; BC could not be detected. IR (neat): $\tilde{\nu}$ = 2337 cm$^{-1}$ (B–H), 2236 (B–H), 2197 (C≡N), 1466 (C–N), 663 (B–N) ppm. MS (EI): *m*/*z* = 336 [M$^+$], 297, 282, 254, 240, 185, 170, 156, 142, 128, 114, 100, 84. $C_{18}H_{38}B_2N_2O_2$ (336): calcd. C 64.28, H 11.30, N 8.33; found C 63.55, H 11.21, N 8.37.

**Preparation of *N*-Methyl-*N*-[(4,4,5,5-tetramethyl-1,3,2-dioxaborolan-2-yl)methyl]dodecylaminocyanoborane (7):** The crude product was purified by column chromatography with 20% of EtOAc in petroleum ether to give a yellow oil (0.255 g; yield 70%). $^1$H NMR ($CDCl_3$, 25 °C): $\delta$ = 0.87 (t, $J_{H,H}$ = 13.2 Hz, 3 H, $CH_2CH_3$), 1.26 {br. s, 28 H, $[C(CH_3)_2]_2$ + $(CH_2)_8$}, 1.72 (m, 4 H, $CH_3CH_2CH_2$), 2.59 (s, 2 H, $NCH_2B$), 2.74 (s, 3 H, $NCH_3$), 3.00 (m, 2 H, $NCH_2CH_2$) ppm; BH could not be detected. $^{11}$B NMR ($CDCl_3$, 25 °C): $\delta$ = –15.3 (t, $J$ = 104.23 Hz), 29.6 ppm (s). $^{13}C\{^1H\}$ NMR ($CDCl_3$, 25 °C): $\delta$ = 14.0, 22.6, 23.3, 24.6, 26.8, 29.1, 29.2, 29.42, 29.47, 29.5, 31.8, 43.3, 49.8, 62.9, 84.4 ppm; BC could not be detected. IR (neat): $\tilde{\nu}$ = 2362 cm$^{-1}$ (B–H), 2339 (B–H), 2196 (C≡N), 1465 (C–N), 667 (B–N) ppm. MS (EI): *m*/*z* = 378 [M$^+$], 339, 324, 310, 296, 282, 268, 254, 240, 226, 212, 198, 184, 170, 156, 141, 126, 111, 96. $C_{21}H_{44}B_2N_2O_2$ (378): calcd. C 66.66, H 11.64, N 7.40; found C 65.77, H 11.48, N 7.54.

## Acknowledgments

The authors thank the Hebrew University Internal Funds for support of this work.

[1] J. C. Power, J. Harper, *Inhibitors of Serine Proteases*, Elsevier Science Publishing Co., New York, **1986**, vol. 12.
[2] C. Lebarbier, B. Carreaux, J. L. Boucher, *Bioorg. Med. Chem. Lett.* **1998**, *8*, 2573–2576.
[3] A. Urbani, E. Bianchi, F. Narjes, A. Tramontana, R. De Francesco, C. Steinkuhler, A. Pessi, *J. Biol. Chem.* **1997**, *272*, 9204–9209.
[4] D. S. Matteson, K. M. Sadhu, *Organometallics* **1984**, *3*, 614–618.
[5] P. Amiri, R. N. Lindquist, D. S. Matteson, K. M. Sadhu, *Arch. Biochem. Biophys.* **1984**, *234*, 531–536.
[6] K. Duncan, S. W. Faraci, D. S. Matteson, C. T. Walsh, *Biochemistry* **1989**, *28*, 3541.
[7] *Enzymes in Synthetic Organic Chemistry* (Eds.: C. H. Wong, G. M. Whitesides), Pergamon Publishers, New York, **1994**.
[8] C. L. M. J. Verlinde, W. G. J. Hol, *Structure* **1994**, *2*, 577–587.
[9] I. V. Kurinov, R. W. Harrison, *Nat. Struct. Biol.* **1994**, *1*, 735.
[10] M. G. Grutter, J. P. Priestle, J. Rahuel, H. Grossenbacher, H. Bode, J. Hofsteenge, S. R. Stone, *EMBO J.* **1990**, *9*, 2361–2365.
[11] T. R. Hynes, M. Randal, L. A. Kennedy, E. Eigenbrot, A. A. Kossiakoff, *Biochemistry* **1990**, *29*, 10018–10022.
[12] M. Yakamoto, R. Sawaya, S. Mohanam, V. H. Rao, J. Bruner, G. L. Nicholson, K. Ohshima, J. S. Rao, *J. Neurooncol.* **1994**, *22*, 139.

 © 2006 Wiley-VCH Verlag GmbH & Co. KGaA, Weinheim 

[13] D. S. Matteson, K. M. Sadhu, G. E. Lienhard, *J. Am. Chem. Soc.* **1981**, *103*, 5241–5242.
[14] S. V. Kessar, P. Singh, R. Vohar, N. P. Kaur, K. N. Singh, *J. Chem. Soc., Chem. Commun.* **1991**, 568–570.
[15] M. R. Ebden, N. S. Simpkins, D. N. A. Fox, *Tetrahedron* **1998**, *54*, 12923–12952.
[16] K. Takrouri, J. Katzhendler, M. Srebnik, *Organometallics* **2004**, *23*, 2817–2820.
[17] B. Györi, Z. Berente, R. Király, I. Lázár, *J. Chem. Soc., Perkin Trans. 1* **2002**, *3*, 300–303.
[18] a) B. S. Burnham, S. Y. Chen, A. Sood, B. F. Spievogel, I. H. Hall, *Pharmazie* **1995**, *50*, 779–783; b) I. H. Hall, A. Elkins, A. Sood, J. Tomasz, B. F. Spievogel, *Anticancer Res.* **1996**, *16*, 3709–3714; c) M. C. Miller III, A. Sood, B. F. Spievogel, I. H. Hall, *Anticancer Res.* **1997**, *17*, 3299.
[19] K. G. Rajendran, S. Y. Chen, A. Sood, B. F. Spievogel, I. H. Hall, *Biomed. Pharmacother.* **1995**, *49*, 131–140.
[20] a) B. F. Spievogel, A. Sood, I. H. Hall, WO Patent 9,309,123, **1993**; b) M. C. Miller III, A. Sood, B. F. Spievogel, R. P. Shrewsbury, I. H. Hall, *Met-Based Drugs* **1996**, *3*, 219–226.
[21] A. T. McPhail, B. F. Spievogel, I. H. Hall, US Patent 4,550,186, **1985**.
[22] M. Takagaki, W. Powell, A. Sood, B. F. Spievogel, N. S. Hosmane, M. Kirihata, K. Ono, S. I. Masunaga, Y. Kinashi, S. I. Miyatake, N. Hashimoto, *Radiat. Res.* **2001**, *156*, 118–122.
[23] a) H. Gilamn, B. Gaj, *J. Org. Chem.* **1957**, *22*, 1165–1168; b) A. Rembaum, S. P. Siao, N. Indictor, *J. Polym. Sci.* **1962**, *56*, S17–S19; c) A. Maercker, *Angew. Chem. Int. Ed. Engl.* **1987**, *26*, 972–989.
[24] M, K. Das, S. N. Bandyopadhyay, *Inorg. Chem.* **1994**, *33*, 5358–5359.
[25] a) H. Nöth, H. Vahrenkamp, *Chem. Ber.* **1966**, *99*, 1049; b) L. H. Toporcer, R. E. Dessy, S. I. E. Green, *Inorg. Chem.* **1965**, *4*, 1649–1655.
[26] P. Wisian-Neilson, M. K. Das, B. F. Spielvogel, *Inorg. Chem.* **1978**, *17*, 2327–2329.
[27] R. Smoum, A. Rubinstein, M. Srebnik, *Bioorg. Chem.* **2003**, *31*, 464–474.

Received: December 5, 2005
Published Online: March 1, 2006

 © 2006 Wiley-VCH Verlag GmbH & Co. KGaA, Weinheim 

DOI: 10.1002/ejic.200600074

# Facile and Reliable Synthesis of Tetraphenoxyborates and Their Properties

Itamar M. Malkowsky,[a] Roland Fröhlich,[b] Ulrich Griesbach,[c] Hermann Pütter,[c] and Siegfried R. Waldvogel*[a]

**Keywords:** Borates / Sodium / Anions / Phenolates

Tetraphenoxyborates are reliably prepared in a two-step sequence, exploiting less corrosive reagents like boric acid and the corresponding phenols. The broad scope of this transformation is demonstrated in 22 examples. Several solid-state structures reveal the preferential conformation of the phenoxy moieties allowing cation interaction. Furthermore, a novel architecture of a phenoxy-substituted tetraborate was found. Surprisingly, the tetraphenoxyborates exhibit a good stability in neutral and basic media.

(© Wiley-VCH Verlag GmbH & Co. KGaA, 69451 Weinheim, Germany, 2006)

## Introduction

Tetracoordinated borates play an important role in nature.[1] In particular, these natural products are involved in the communication among bacterial microorganisms.[2] Size, oxophilic nature, and a maximum coordination number of four predestine boron for templating alkoxy or phenoxy moieties in an efficient manner. The synthesis and properties of tetracoordinated borates are well established, whereas the corresponding tetraphenoxy derivatives are only little explored. Tetraphenoxyborates are commonly used as bulky and inert counterions for catalysts[3] or as electrolytes in batteries.[4]

The formation of such tetragonal-coordinated compounds involves the reaction of Lewis acidic boron species with a nucleophilic phenoxy system. If very electron-deficient boranes are applied with no additional base, a tetragonal boron derivative is observed, incorporating an unusual tautomeric form of the phenolate.[5] Treatment of the corresponding phenol with boron trichloride in the presence of a nitrogen base leads to the triphenoxyborane by a direct displacement of chlorine and subsequently to the anionic tetragonal derivative. This approach requires very electron-deficient phenols and a highly corrosive boron reagent.[6] When employing sodium tetrahydridoborate as boron source in the reaction with phenol a variety of different borates is observed. Herein the counterion plays a crucial role, because the sodium cations link the borate subunits to infinite polymeric structures.[7] The stepwise formation of tetraphenoxyborates requires the prior construction of the triesters of boric acid followed by the conversion with phenolates. In order to obtain soluble phenolate equivalents of divalent cations like barium, sophisticated reagent mixtures were applied.[8] However, the direct use of barium metal ameliorated the process to barium-linked dimeric borates.[9]

We present a reliable protocol for the synthesis of a wide scope of tetraphenoxyborates. The simple two-step sequence can be performed in a one-pot process and is feasible for large quantities of the desired tetragonal boron compound.

## Results and Discussion

The synthesis of tetraphenoxyborates began with the esterification of the corresponding phenol with boric acid (Scheme 1). The transformation was performed in refluxing toluene with the use of a Dean–Stark trap. With the removal of water the reaction mixture became homogeneous. The amount of water received was slightly lower than anticipated from a stoichiometric condensation reaction.

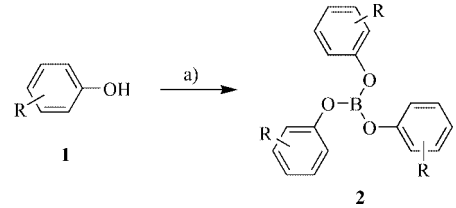


Scheme 1. a) $B(OH)_3$, toluene, 12 h reflux with a Dean–Stark trap.

Removal of the solvent under reduced pressure yielded a mixture of phenyl esters of boric acid. Mass spectrometric investigation of the crude product indicated the presence of several trigonal boron species as depicted in Figure 1.

[a] Kekulé-Institut für Organische Chemie und Biochemie, Gerhard-Domagk-Str. 1, 53121 Bonn, Germany
Fax: +49-228-73-9608
E-mail: waldvogel@uni-bonn.de
[b] Westfälische Wilhelms-Universität Münster, Organisch-Chemisches Institut, Corrensstr. 40, 48149 Münster, Germany
[c] BASF Aktiengesellschaft, GCI/E-M311, 67056 Ludwigshafen, Germany

 InterScience © 2006 Wiley-VCH Verlag GmbH & Co. KGaA, Weinheim 

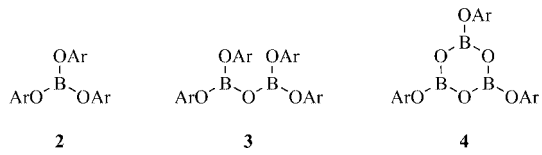

2 3 4

Figure 1. Major products by the condensation reaction of **1** with boric acid.

The presence of abundant **1** gives rise to a fast equilibrium among the ester species **2**–**4**.[10] When the crude material was carefully distilled under high vacuum ($10^{-4}$–$10^{-5}$ mbar), the pure triester **2** could be obtained. However, this step turned out to be time-consuming. Furthermore, it was only feasible on smaller quantities, limited to substrates of low molecular weight and involved an unacceptable loss of material. Therefore, the crude mixture was directly subjected to the corresponding phenolate in THF (Scheme 2).

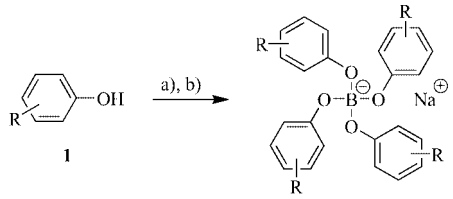

1 5

Scheme 2. a) $B(OH)_3$, toluene, 12 h reflux with a Dean–Stark trap; b) Na, **1**, THF, room temp.

THF proved to be the appropriate solvent for this particular transformation including the reaction of phenol with sodium as well as the formation of the desired tetraphenoxyborate **5**, which precipitated and could easily be isolated by simple filtration. The formation of anionic borates results in a fast equilibrium of the corresponding trigonal compounds **2**–**4** and strongly favours the formation of the mononuclear borate species **5**. Noteworthy, performing the transformation at high concentration led almost exclusively to **5**. However, application of 4-methoxyphenol in this reaction sequence yielded the desired borate **9** besides the tetranuclear borate **28** as by-product in very low yields. Fortunately, a suitable single crystal for X-ray analysis was obtained (Figure 2). Further spectroscopic investigation was not possible because not sufficient pure material of **28** was available.

Compound **28** represents an intermediate in the formation of **5** from higher aggregates similar to **3** or **4**. The molecular structure reveals a mixed tetraborate. In the centre, a trigonal boric anhydride unit is connected to three tetragonal anionic borate moieties. The tetrahedral symmetry of the borates is distorted and shows two pairs of angles

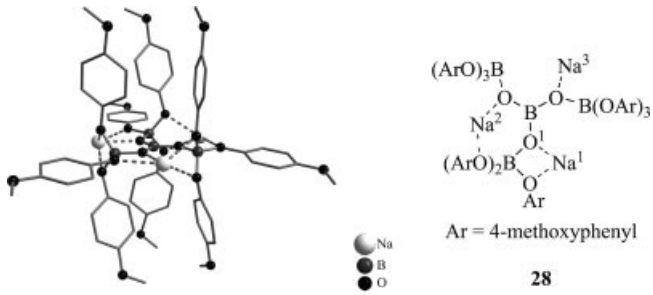

Figure 2. Left: X-ray structure of the tetraborate **28**; right: coordination pattern.

(Table 1). Three sodium cations link the borate fragments through the phenol oxygen atoms and compensate the negative charge. In addition, each sodium cation is coordinated by two THF molecules, which are omitted in Figure 2 for clarity. The architecture of the depicted tetraborate **28** is unique. Remarkably, **28** exhibits no $C_3$ symmetry, due to the deviated orientation of the methoxy substituents in its periphery.

As shown in Table 2, the parent phenol (Entry 1) as well as mono-, di- and trisubstituted substrates were applied in the synthesis of their tetraphenoxyborates in moderate to excellent yields. The reaction outcome is determined by the steric demand and electronic nature of the individual phenol derivative. The conversion of *para*- and *ortho*-cresol to the corresponding borates **7** and **14**, respectively, shows a lower yield for the latter one, due to the steric demand close to the borate centre (Entries 2 and 9). This trend is reflected in the conversion of almost all *ortho*-alkyl-substituted phenols compared to the congeners with free *ortho* positions. Interestingly, thymol and 4-chlorothymol, both exhibiting an isopropyl group at C-2, provide the borates **16** and **26** in high yields (Entries 11 and 21).

Phenols with a single *tert*-butyl substituent were successfully subjected to the condensation reaction with boric acid followed by salt formation to yield **8**, **17**, **19** or **25** in good yields (Entries 3, 12, 14 and 20), whereas two *tert*-butyl groups dramatically disfavour the arrangement of four phenolates around the boron centre (Entry 13). Furthermore, electronic effects can lower the nucleophilicity of the intermediate sodium phenolate, resulting in a lower yield for the desired borate. Therefore, substrates like 4-fluorophenol, 4-chlorophenol and 2-bromo-4-methylphenol were converted into the corresponding borates **10**, **11** and **20**, respectively, in moderate yields (Entries 5, 6 and 15). In contrast, tetraphenoxyborates of electron-rich phenols were obtained in good to excellent yields (Entries 4, 7 and 17).

Table 1. Selected geometric parameters [Å, °] for a subunit of **28**.

| | | | |
|---|---|---|---|
| $B^{trig}$–$O^1$ | 1.3624(1) | O–$B^{trig}$–O | 119.542(5) |
| $B^{tetr}$–O(Ar) | 1.4630(1), 1.4647(1), 1.4888(1) | $B^{trig}$–$O^1$–$B^{tetr}$ | 126.218(10) |
| $B^{tetr}$–$O^1$ | 1.4610(1) | $O^1$–$B^{tetr}$–O($Na^1$) | 102.450(8) |
| $Na^1$–$O^1$ | 2.3255(2) | ($Na^2$)O–$B^{tetr}$–O($Na^2$) | 99.389(12) |
| $Na^1$–O(Ar) | 2.6439(2) | ($Na^1$)O–$B^{tetr}$–O($Na^2$) | 113.274(5), 115.317(5) |
| $Na^2$–O(Ar) | 2.4078(2), 2.4635(2) | | |

 © 2006 Wiley-VCH Verlag GmbH & Co. KGaA, Weinheim 

Table 2. Substrates for the synthesis of tetraphenoxyborates.

| Entry | Phenol | Yield borate | Entry | Phenol | Yield borate |
|---|---|---|---|---|---|
| 1 | 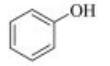 | 82% (**6b**) | 12 | 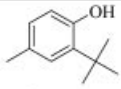 | 63% (**17**) |
| 2 | 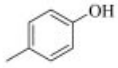 | 84% (**7**) | 13 | 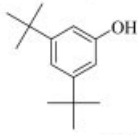 | 37% (**18**) |
| 3 | 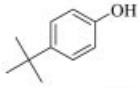 | 57% (**8**) | 14 | 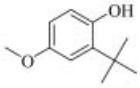 | 57% (**19**) |
| 4 | 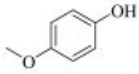 | 66% (**9**) | 15 | 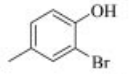 | 43% (**20**) |
| 5 | 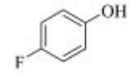 | 37% (**10**) | 16 | 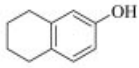 | 62% (**21**) |
| 6 | 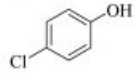 | 41% (**11**) | 17 | 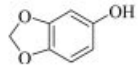 | 82% (**22**) |
| 7 | 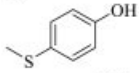 | 99% (**12**) | 18 | 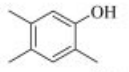 | 71% (**23**) |
| 8 | 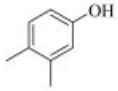 | 83% (**13**) | 19 | 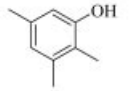 | 68% (**24**) |
| 9 | 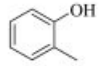 | 64% (**14**) | 20 | 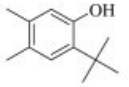 | 64% (**25**) |
| 10 | 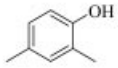 | 75% (**15**) | 21 | 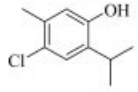 | 93% (**26**) |
| 11 | 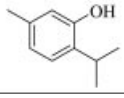 | 90% (**16**) | 22 | 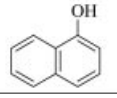 | 57% (**27**) |

Phenols with two *ortho* substituents smoothly undergo the condensation reaction to the triphenoxyborane, whereas the subsequent formation of the tetraphenoxyborates was not observed (Scheme 3).

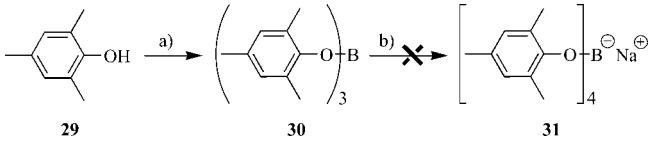


**29** **30** **31**

Scheme 3. a) $B(OH)_3$, toluene, 24 h reflux with a Dean–Stark trap; b) **29**, NaH, THF.

The conversion of 2,4,6-trimethylphenol (**29**) with sodium metal was sluggish, therefore sodium hydride was employed for deprotonation. Still, the addition of **30** to the phenolate of **29** gave no indication for the formation of the sodium tetraphenoxyborate **31**. The reaction mixture was analyzed by $^{11}B$ NMR spectroscopy, as the signals for a trigonal and a tetragonal boron atom clearly differ from each other. Only a broad signal at $\delta$ = 15.89 ppm was observed, indicating the triphenoxyborane **30**. Remarkably, compound **30** could easily be separated from the phenolate of **29** by chilling the reaction mixture. Compound **30** was filtered off and obtained as pure colourless solid. Thus, triphenoxyboranes of phenol derivatives exhibiting two alkyl substituents in the *ortho* positions are far too shielded to undergo addition with a further phenolate equivalent.

Because suitable crystals for X-ray analysis of both, triphenoxyborane (**6a**) and the corresponding tetraphenoxyborate (**6b**) were available, a direct comparison of the structural features was possible (Figure 3). The obtained geometric data are representative for most analogues.

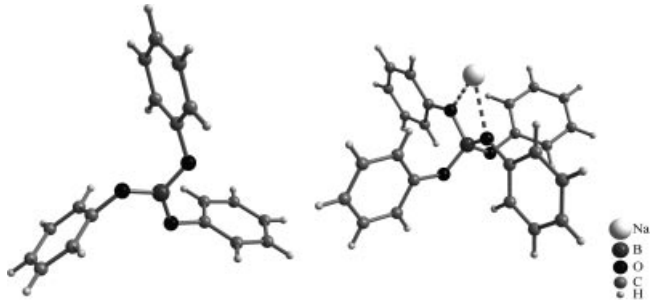


**6a** **6b**

Figure 3. Molecular structure of triphenoxyborane (**6a**) and the tetraphenoxyborate (**6b**) determined by X-ray analysis.

Triphenoxyborane (**6a**) exhibits a trigonal-planar boron centre with three phenyl units symmetrically arranged around the boron atom. The planes of the aromatic rings are oriented almost perpendicular to the $BO_3$ plane, resulting in a water-wheel-shaped molecule. Three almost similar distances of about 2.35 Å between the oxygen atoms of **6a** emphasise the expected $C_3$ symmetry of **6a**. In contrast, the tetraphenoxyborate (**6b**) reveals a slight deviation from the tetrahedral symmetry by elongation in one direction. The pair of oxygen atoms bridged by the sodium cation forms the shorter side of the tetrahedron and exhibits an interatomic distance of about 2.26 Å. Interestingly, the opposite side shows the same oxygen–oxygen distance without a coordinating counterion. The corresponding interatomic distances on the longer side are in the range of 2.44–2.48 Å. Compared to **6a**, neighboured *ortho*-carbon atoms come closer to each other up to 4.28 Å. The sodium cation in **6b** has in fact a coordination number of five. Two positions are held by phenoxy oxygen atoms, represented in Figure 3 by dashed lines. The remaining three ligands are THF molecules, which are omitted for clarity. Almost the same assembly can be found in the X-ray structure of tetraphenoxyborate **10** as shown in Figure 4. Again, THF molecules are not depicted for clarity.

The tetraphenoxyborate **10** exhibits very similar structural features compared to **6b** according to geometry and complexation of the sodium cation by the substrate and three THF molecules. In contrast, the tetranaphthoxyborate **27** (Figure 4) is no longer able to coordinate to the sodium cation itself, due to the highly crowded boron centre. Therefore, the cation is coordinated by five THF molecules

 © 2006 Wiley-VCH Verlag GmbH & Co. KGaA, Weinheim 

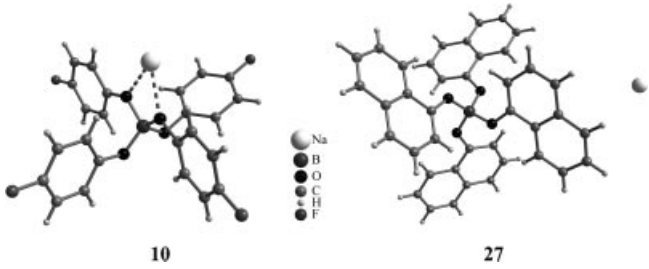


Figure 4. Molecular structures of tetraphenoxyborates **10** and **27** determined byX-ray analysis.

and reveals a boron–sodium distance of 8.97 Å, which is about 3 times longer than for **6b** or **10**. The boron–oxygen bond lengths in **27** are comparable with those observed for **6b** and **10**, whereas the distance between the phenoxy carbon atoms increases by 6% (Table 3). The oxygen atoms in **27** are almost equidistant, resulting in a consistent tetrahedral symmetry of the $BO_4$ unit.

Table 3. Selected geometric parameters [Å (shortest), ° (largest)] for **6a**, **6b**, **10** and **27**.

| | **6a** | **6b** | **10** | **27** |
|---|---|---|---|---|
| B–O | 1.3570(1) | 1.4505(1) | 1.4500(1) | 1.4595(1) |
| O–Na | – | 2.3422(2) | 2.3469(2) | 8.1432(5) |
| $C^1$–$C^{1'}$ | 4.1062(4) | 3.5017(2) | 3.4752(2) | 3.6991(2) |
| O–B–O | 120.454(20) | 98.510(4)[a] | 99.052(4)[a] | 114.254(4) |
| | | 102.130(4)[b] | 103.291(4)[b] | |
| | | 115.489(5) | 114.775(4) | |
| B–O–$C^1$ | 122.382(15) | 126.445(4) | 126.102(4) | 126.247(4) |

[a] Sodium-bridged pair of oxygen atoms. [b] Non-bridged pair of oxygen atoms.

The geometric data for the described sodium tetraphenoxyborates correspond to earlier reports on complex architectures of sodium hydrido(phenoxy)borates concerning oxygen–boron and oxygen–sodium bond lengths as well as the angle for the sodium-chelating oxygen–boron–oxygen cleft at about 100°.[7] In contrast to sodium borates, the non-coordinating oxygen atoms in barium-linked dimeric borates span a significantly wider oxygen–boron–oxygen angle than the opposite angle between the cation-bridged oxygen atoms.[9]

It turned out that tetraphenoxyborates are much less prone to hydrolysis than the corresponding trigonal triphenoxyborane species. Consequently, **5** can be handled for short times at ambient conditions,[11] whereas the triphenyl ester of boric acid is almost immediately affected by moisture. The enhanced stability of the tetragonal boron systems is based on the saturated coordination sphere of the boron centre. However, protic media or strongly coordinating solvents like methanol or acetonitrile might affect the stability of **5**. In this context, $^{11}$B NMR studies proved to be a versatile tool. Besides the chemical shift as an indicator for the electronic properties, the line full width at half maximum can individually characterize the structure of a specific borate derivative. The comparison of different triphenoxyboranes is not facile to accomplish, due to extremely broad signals. However, triphenoxyboranes and tetraphenoxyborates can easily be distinguished as presented in Figure 5.

The $^{11}$B NMR spectrum of triphenoxyborane in chloroform (Figure 5, top) shows a broad signal at $\delta \approx 15$ ppm with a line full width at half maximum of 320 Hz, which represents a typical value for a trigonal boron species. When the same substrate is recorded in methanol, a shift to $\delta \approx 18$ ppm is observed accompanied by a significantly decreased line full width at half maximum of 85 Hz. Methanol is a particular solvent since an adduct formation with the ester of boric acid can occur.[12] Thus, the electrophilic boron centre experiences a tetragonal environment which is clearly supported by the NMR spectroscopic data. Interestingly, only a single species is detected revealing that no exchange of the phenolate groups occurs. When recording the corresponding tetraphenoxyborate in methanol, the protic and nucleophilic properties have no significant impact on the NMR spectroscopic data. The chemical shift as well as the line width of the signal correspond to the data collected for a THF solution. Furthermore, the typical line full width at half maximum for a tetraphenoxyborate of 20–40 Hz in THF or MeOH was also observed in acetonitrile (Figure 5, bottom).

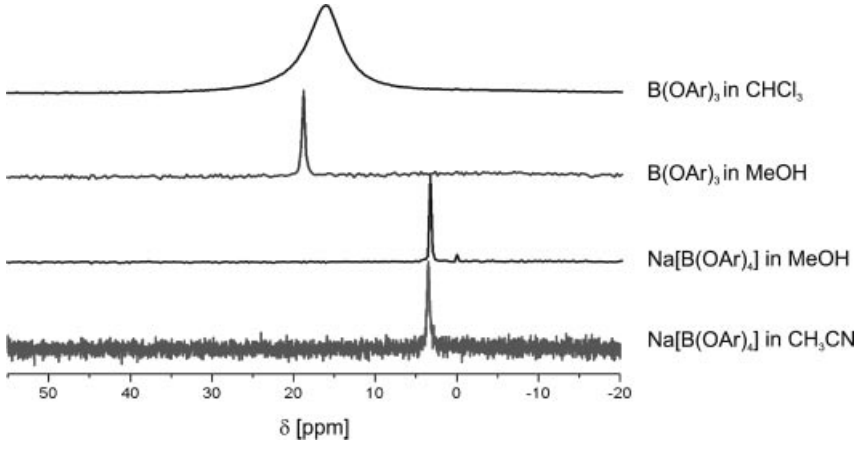


Figure 5. $^{11}$B NMR studies of trigonal and tetragonal boron species (Ar = 2,4-dimethylphenyl).

 © 2006 Wiley-VCH Verlag GmbH & Co. KGaA, Weinheim 

## Conclusion

A reliable and easy to perform two-step-one-pot sequence for the synthesis of tetraphenoxyborates was elaborated. The protocol is applicable to a broad scope of phenols and useful for larger scale as well. Interestingly, the tetraphenoxyborates exhibit a much higher stability than the trigonal congeners. Consequently, tetraphenoxyborates can be handled in methanol, THF and acetonitrile.

Furthermore, a novel tetranuclear borate system was found, consisting of trigonal and tetragonal boron moieties. The structural comparison of the corresponding tetraphenoxyborates and triphenyl esters of boric acid reveals that the tetragonal arrangement yields in a superb organisation of the *ortho* positions in the aryl moieties. Oxidative coupling reactions of these boron-templated phenolates are currently studied and will be reported in due course.

## Experimental Section

**General Remarks:** All reagents were used in analytical grades. Solvents were desiccated if necessary by standard methods. Microanalyses were performed with a Vario EL III (Elementar-Analysensysteme, Hanau, D). $^1$H and $^{13}$C NMR spectra were recorded at 25 °C with a Bruker ARX 300, AM 360 or AMX 400. Chemical shifts ($\delta$) are reported in parts per million (ppm) relative to traces of $CHCl_3$, [$D_7$]THF or $CD_2HCN$ in the corresponding deuterated solvents. $^{11}$B NMR spectra were recorded at 25 °C with a Bruker AC 200 by external calibration. Mass spectra were obtained with a Quattro LC (Waters-Micromass) or Micro TOF (Bruker) by employing ESI and HRMS (negative mode).

**Triphenoxyborane (6a):** Phenol (9.4 g, 0.10 mol) and boric acid (2.1 g, 0.03 mol) were suspended in toluene (50 mL) and the reaction mixture was heated for a period of 12 h (Dean–Stark trap). Toluene was removed under reduced pressure and the crude product was purified by distillation to yield a colourless oil, which solidified upon cooling; yield 5.8 g, 67%. B.p. 150 °C, $5\cdot10^{-6}$ mbar; m.p. 82 °C. $^1$H NMR (300 MHz, $CDCl_3$): $\delta$ = 6.94–6.99 (m, 3 H, 4-H), 7.00–7.04 (m, 6 H, 2-H), 7.15–7.21 (m, 6 H, 3-H) ppm. $^{13}$C NMR (75 MHz, $CDCl_3$): $\delta$ = 120.20 (C-2), 123.50 (C-4), 129.26 (C-3), 152.85 (C-1) ppm. $^{11}$B NMR (64 MHz, $CDCl_3$): $\delta$ = 15.65 ppm. MS (EI = 70 eV): *m/z* (%) = 290.0 (100) $[M]^{+\cdot}$, 197.0 (44) $[M - C_6H_5O]^{+\cdot}$, 94.0 (75) $[C_6H_5O]^{+\cdot}$, 77.0 (81) $[C_6H_5]^{+\cdot}$.

**General Procedure for the Preparation of Sodium Tetraphenoxyborates:** A suspension of the corresponding phenol derivative (0.32 mol) and boric acid (0.10 mol) in toluene (200 mL) was heated for a period of 12 h (Dean–Stark trap). Toluene was removed under reduced pressure and the excess of phenol was removed by distillation, solid phenols were removed by sublimation. The crude product was dissolved in THF (40 mL) and added dropwise to a solution of the sodium phenolate, which was prepared by deprotonation of the corresponding phenol (0.09 mol) with 1 equiv. of sodium (0.09 mol) in THF (70 mL). After stirring for additional 1–12 h, the precipitated product was filtered off and washed subsequently with diethyl ether (40 mL) and pentane (40 mL). The filtrate was stored at 4 °C for another 12 h and a second crop was isolated as described above. Drying under high vacuum provided the desired products as colourless solids that were stored under inert conditions at ambient temperature. For **10**, **11**, **12**, **17**, **20**, **21** and **26** the scale of the protocol was reduced by a factor of three. All borates decomposed at temperatures above 200 °C under change of colour. The obtained tetraphenoxyborates exhibit good stability. However, the microanalyses of most borates show slight deviations from ±0.4% and therefore, HRMS data are given.[13]

**Sodium Tetraphenoxyborate (6b):** 33.3 g, 82%. $^1$H NMR (300 MHz, $CD_3CN$): $\delta$ = 6.64–6.70 (m, 4 H, 4-H), 7.06–7.08 (m, 16 H, 2-H, 3-H) ppm. $^{13}$C NMR (75 MHz, $CD_3CN$): $\delta$ = 119.26 (C-4), 120.14 (C-2), 129.64 (C-3), 158.93 (C-1) ppm. $^{11}$B NMR (64 MHz, $CD_3CN$): $\delta$ = 2.79 ppm. HRMS: calcd. for $C_{24}H_{20}BO_4$ 383.1453 $[M - Na^+]^-$; found 383.1417.

**Sodium Tetrakis(4-methylphenoxy)borate (7):** 38.8 g, 84%. $^1$H NMR (400 MHz, [$D_8$]THF): $\delta$ = 2.14 (s, 12 H, $CH_3$), 6.74–6.78 (m, 8 H, 2-H), 6.87–6.91 (m, 8 H, 3-H) ppm. $^{13}$C NMR (75 MHz, [$D_8$]-THF): $\delta$ = 20.76 ($CH_3$), 120.62 (C-2), 127.56 (C-4), 129.53 (C-3), 156.62 (C-1) ppm. $^{11}$B NMR (64 MHz, $CD_3CN$): $\delta$ = 2.34 ppm. HRMS: calcd. for $C_{28}H_{28}BO_4$ 439.2080 $[M - Na^+]^-$; found 439.2066.

**Sodium Tetrakis(4-*tert*-butylphenoxy)borate (8):** 35.9 g, 57%. $^1$H NMR (300 MHz, [$D_8$]THF): $\delta$ = 1.22 (s, 36 H, $CH_3$), 6.90–6.93 (m, 8 H, 2-H), 6.99–7.02 (m, 8 H, 3-H) ppm. $^{13}$C NMR (75 MHz, [$D_8$]-THF): $\delta$ = 32.16 ($CH_3$), 34.45 [$C(CH_3)_3$], 120.27 (C-2), 125.64 (C-3), 141.07 (C-4), 156.67 (C-1) ppm. $^{11}$B NMR (64 MHz, [$D_8$]-THF): $\delta$ = 2.04 ppm. HRMS: calcd. for $C_{40}H_{52}BO_4$ 607.3971 $[M - Na^+]^-$; found 607.3979.

**Sodium Tetrakis(4-methoxyphenoxy)borate (9):** 34.7 g, 66%. $^1$H NMR (300 MHz, $CD_3CN$): $\delta$ = 3.79 (s, 12 H, $OCH_3$), 6.75–6.78 (m, 8 H, arom. H), 7.07–7.10 (m, 8 H, arom. H) ppm. $^{13}$C NMR (75 MHz, $CD_3CN$): $\delta$ = 56.16 ($OCH_3$), 114.92, 120.65 (C-2, C-3), 152.69, 153.33 (C-1, C-4) ppm. $^{11}$B NMR (64 MHz, $CD_3CN$): $\delta$ = 2.30 ppm. MS (ESI): *m/z* (%) = 503 (100) $[M - Na^+]^-$. $C_{28}H_{28}BNaO_8$ (526.2): calcd. C 63.90, H 5.36; found C 63.60, H 5.26.

**Sodium Tetrakis(4-fluorophenoxy)borate (10):** 5.9 g, 37%. $^1$H NMR (300 MHz, $CD_3CN$): $\delta$ = 6.77–6.83 (m, 8 H, 2-H), 6.97–7.02 (m, 8 H, 3-H) ppm. $^{13}$C NMR (75 MHz, $CD_3CN$): $\delta$ = 115.61 [d, $^2J$(F,C) = 24.8 Hz, C-3], 120.79 [d, $^3J$(F,C) = 7.9 Hz, C-2], 155.20 (C-1), 156.85 [d, $^1J$(F,C) = 247.4 Hz, C-4] ppm. $^{11}$B NMR (64 MHz, $CD_3CN$): $\delta$ = 2.66 ppm. HRMS: calcd. for $C_{24}H_{16}BF_4O_4$ 455.1072 $[M - Na^+]^-$; found 455.1103.

**Sodium Tetrakis(4-chlorophenoxy)borate (11):** 7.4 g, 41%. $^1$H NMR (300 MHz, $CD_3CN$): $\delta$ = 6.98–7.06 (m, 16 H, 2-H, 3-H) ppm. $^{13}$C NMR (75 MHz, $CD_3CN$): $\delta$ = 121.51 (C-2), 123.41 (C-4), 129.38 (C-3), 157.75 (C-1) ppm. $^{11}$B NMR (64 MHz, $CD_3CN$): $\delta$ = 2.57 ppm. HRMS: calcd. for $C_{24}H_{16}BCl_4O_4$ 517.9927 $[M - Na^+]^-$; found 517.9906.

**Sodium Tetrakis(4-methylthiophenoxy)borate (12):** 19.5 g, 99%. $^1$H NMR (400 MHz, $CD_3CN$): $\delta$ = 2.05 (s, 12 H, $SCH_3$), 6.64–6.70 (m, 16 H, 2-H, 3-H) ppm. $^{13}$C NMR (100 MHz, $CD_3CN$): $\delta$ = 18.37 ($SCH_3$), 120.85 (C-2), 126.78 (C-3), 130.66 (C-4), 157.09 (C-1) ppm. $^{11}$B NMR (128 MHz, $CD_3CN$): $\delta$ = 4.07 ppm. HRMS: calcd. for $C_{28}H_{28}BO_4S_4$ 567.0969 $[M - Na^+]^-$; found 567.0955.

**Sodium Tetrakis(3,4-dimethylphenoxy)borate (13):** 43.0 g, 83%. $^1$H NMR (300 MHz, $CD_3CN$): $\delta$ = 2.04 (s, 12 H, 4-$CH_3$), 2.07 (s, 12 H, 3-$CH_3$), 6.72–6.76 (m, 8 H, 5-H, 6-H), 6.78 (s, 4 H, 2-H) ppm. $^{13}$C NMR (75 MHz, $CD_3CN$): $\delta$ = 18.84 (3-$CH_3$), 20.18 (4-$CH_3$), 117.27 (C-6), 121.35 (C-2), 126.54 (C-4), 130.49 (C-5), 137.19 (C-3), 156.94 (C-1) ppm. $^{11}$B NMR (64 MHz, $CD_3CN$): $\delta$ = 2.60 ppm. HRMS: calcd. for $C_{32}H_{36}BO_4$ 495.2718 $[M - Na^+]^-$; found 495.2720.

**Sodium Tetrakis(2-methylphenoxy)borate (14):** 29.6 g, 64%. $^1$H NMR (400 MHz, [$D_8$]THF): $\delta$ = 2.10 (s, 12 H, $CH_3$), 6.51 [dd,

 © 2006 Wiley-VCH Verlag GmbH & Co. KGaA, Weinheim 

$^3J_{3,4}$(H,H) = $^3J_{4,5}$(H,H) = 7.4 Hz, 4 H, 4-H], 6.76 [ddd, $^3J_{4,5}$(H,H) = 7.4 Hz, $^3J_{5,6}$(H,H) = 8.4 Hz, $^4J_{3,5}$ = 1.6 Hz, 4 H, 5-H], 6.87 [d, $^3J_{3,4}$(H,H) = 7.4 Hz, 4 H, 3-H], 7.19 [d, $^3J_{5,6}$(H,H) = 8.4 Hz, 4 H, 6-H] ppm. $^{13}$C NMR (100 MHz, [D$_8$]THF): $\delta$ = 17.78 ($CH_3$), 118.86 (C-4), 120.59 (C-6), 126.38 (C-5), 129.11 (C-2), 130.19 (C-3), 157.55 (C-1) ppm. $^{11}$B NMR (64 MHz, $CD_3CN$): $\delta$ = 2.92 ppm. HRMS: calcd. for $C_{28}H_{28}BO_4$ 439.2080 [M – Na$^+$]$^-$; found 439.2065.

**Sodium Tetrakis(2,4-dimethylphenoxy)borate (15):** 38.9 g, 75%. $^1$H NMR (360 MHz, [D$_8$]THF): $\delta$ = 2.03 (s, 12 H, 2-$CH_3$), 2.10 (s, 12 H, 4-$CH_3$), 6.55 [dd, $^3J_{5,6}$(H,H) = 8.3 Hz, $^4J_{3,5}$(H,H) = 1.8 Hz, 4 H, 5-H], 6.68 [d, $^4J_{3,5}$(H,H) = 1.8 Hz, 4 H, 3-H], 6.98 [d, $^3J_{5,6}$(H,H) = 8.3 Hz, 4 H, 6-H] ppm. $^{13}$C NMR (75 MHz, $CD_3CN$): $\delta$ = 17.56 (2-$CH_3$), 20.57 (4-$CH_3$), 119.06 (C-6), 126.49 (C-5), 127.02 (C-2), 127.94 (C-4), 131.05 (C-3), 155.62 (C-1) ppm. $^{11}$B NMR (64 MHz, $CD_3CN$): $\delta$ = 3.21 ppm. HRMS: calcd. for $C_{32}H_{36}BO_4$ 494.2737 [M – Na$^+$]$^-$; found 494.2785.

**Sodium Tetrakis[5-methyl-2-(1-methylethyl)phenoxy]borate (16):** 56.8 g, 90%. $^1$H NMR (400 MHz, $CD_3CN$): $\delta$ = 1.35 [d, $^3J$(H,H) = 6.9 Hz, 24 H, CH(C$H_3$)$_2$], 2.23 (s, 12 H, 5-$CH_3$), 3.64 [sept, $^3J$(H,H) = 6.9 Hz, 4 H, C$H$($CH_3$)$_2$], 6.48 [d, $^3J_{3,4}$(H,H) = 7.8 Hz, 4 H, 4-H], 6.99 [d, $^3J_{3,4}$(H,H) = 7.5 Hz, 4 H, 3-H], 7.52 (s, 4 H, 6-H) ppm. $^{13}$C NMR (100 MHz, $CD_3CN$): $\delta$ = 21.62 [$C$H($CH_3$)$_2$], 23.79 [CH($C$H$_3$)$_2$], 27.98 (5-$CH_3$), 118.24 (C-6), 120.22 (C-4), 125.64 (C-3), 135.16 (C-2), 135.55 (C-5), 156.98 (C-1) ppm. $^{11}$B NMR (64 MHz, $CD_3CN$): $\delta$ = 3.22 ppm. HRMS: calcd. for $C_{40}H_{52}BO_4$ 607.3971 [M – Na$^+$]$^-$; found 607.3981.

**Sodium Tetrakis(2-*tert*-butyl-4-methylphenoxy)borate (17):** 14.4 g, 63%. $^1$H NMR (400 MHz, [D$_8$]THF): $\delta$ = 1.58 [s, 36 H, C($CH_3$)$_3$], 2.04 (s, 12 H, $CH_3$), 6.40 [dd, $^3J_{5,6}$(H,H) = 8.6 Hz, $^4J_{3,5}$(H,H) = 2.1 Hz, 4 H, 5-H], 6.70 [d, $^4J_{3,5}$(H,H) = 2.1 Hz, 4 H, 3-H], 7.64 [d, $^3J_{5,6}$(H,H) = 8.6 Hz, 4 H, 6-H] ppm. $^{13}$C NMR (100 MHz, [D$_8$]-THF): $\delta$ = 21.20 ($CH_3$), 31.47 [C($C$H$_3$)$_3$], 35.42 [$C$(CH$_3$)$_3$], 120.21 (C-6), 123.29 (C-3), 125.98 (C-5), 126.62 (C-4), 136.99 (C-2), 156.04 (C-1) ppm. $^{11}$B NMR (128 MHz, [D$_8$]THF): $\delta$ = 4.87 ppm. HRMS: calcd. for $C_{44}H_{60}BO_4$ 663.4590 [M – Na$^+$]$^-$; found 663.4571.

**Sodium Tetrakis(3,5-di-*tert*-butylphenoxy)borate (18):** 31.6 g, 37%. $^1$H NMR (300 MHz, $CD_3CN$): $\delta$ = 1.21 [s, 72 H, C($CH_3$)$_3$], 6.71 [d, $^4J_{2,4}$(H,H) = 1.5 Hz, 4 H, 4-H], 6.98 [d, $^4J_{2,4}$(H,H) = 1.5 Hz, 8 H, 2-H] ppm. $^{13}$C NMR (75 MHz, $CD_3CN$): $\delta$ = 32.13 [C($C$H$_3$)$_3$], 35.47 [$C$(CH$_3$)$_3$], 112.63 (C-2), 114.86 (C-4), 151.49 (C-3), 159.14 (C-1) ppm. $^{11}$B NMR (64 MHz, $CD_3CN$): $\delta$ = 2.75 ppm. HRMS: calcd. for $C_{56}H_{84}BO_4$ 831.6468 [M – Na$^+$]$^-$; found 831.6431.

**Sodium Tetrakis(2-*tert*-butyl-4-methoxyphenoxy)borate (19):** 42.8 g, 57%. $^1$H NMR (400 MHz, $CD_3CN$): $\delta$ = 1.57 [s, 36 H, C($CH_3$)$_3$], 3.56 (s, 12 H, $OCH_3$), 6.29 [dd, $^3J_{5,6}$(H,H) = 8.8 Hz, $^4J_{3,5}$(H,H) = 2.6 Hz, 4 H, 5-H], 6.64 [d, $^4J_{3,5}$(H,H) = 2.6 Hz, 4 H, 3-H], 7.64 [d, $^3J_{5,6}$(H,H) = 8.8 Hz, 4 H, 6-H] ppm. $^{13}$C NMR (100 MHz, $CD_3CN$): $\delta$ = 31.15 [C($C$H$_3$)$_3$], 35.91 ($OCH_3$), 56.45 [$C$(CH$_3$)$_3$], 110.77 (C-5), 113.98 (C-6), 120.18 (C-3), 139.29 (C-2), 151.73 (C-1), 152.34 (C-4) ppm. $^{11}$B NMR (128 MHz, $CD_3CN$): $\delta$ = 2.99 ppm. HRMS: calcd. for $C_{44}H_{60}BO_8$ 727.4387 [M – Na$^+$]$^-$; found 727.4364.

**Sodium Tetrakis(2-bromo-4-methylphenoxy)borate (20):** 11.1 g, 43%. $^1$H NMR (400 MHz, [D$_8$]THF): $\delta$ = 2.12 (s, 12 H, $CH_3$), 6.78 [dd, $^3J_{5,6}$(H,H) = 8.4 Hz, $^4J_{3,5}$(H,H) = 1.7 Hz, 4 H, 5-H], 7.13 [d, $^4J_{3,5}$(H,H) = 1.7 Hz, 4 H, 3-H], 7.46 [d, $^3J_{5,6}$(H,H) = 8.4 Hz, 4 H, 6-H] ppm. $^{13}$C NMR (100 MHz, [D$_8$]THF): $\delta$ = 20.26 ($CH_3$), 114.29 (C-2), 120.95(C-6), 129.29 (C-5), 129.82 (C-4), 132.96 (C-3), 152.24 (C-1) ppm. $^{11}$B NMR (128 MHz, [D$_8$]THF): $\delta$ = 2.12 ppm. HRMS: calcd. for $C_{28}H_{24}BBr_4O_4$ 750.8507 [M – Na$^+$]$^-$; found 750.8503.

**Sodium Tetrakis(5,6,7,8-tetrahydro-2-naphthoxy)borate (21):** 12.9 g, 62%. $^1$H NMR (400 MHz, [D$_8$]THF): $\delta$ = 1.79 (m, 16 H, 7-H, 6-H), 2.67 (m, 16 H, 8-H, 5-H), 6.54 [d, $^4J_{1,3}$(H,H) = 1.7 Hz, 4 H, 1-H], 6.75 [dd, $^3J_{3,4}$(H,H) = 8.4 Hz, $^4J_{1,3}$(H,H) = 1.7 Hz, 4 H, 3-H], 6.88 [d, $^3J_{3,4}$(H,H) = 8.4 Hz, 4 H, 4-H] ppm. $^{13}$C NMR (100 MHz, [D$_8$]THF): $\delta$ = 26.68, 29.72 (C-6, C-7), 29.83, 30.76 (C-5, C-8), 118.84 (C-3), 121.26 (C-1), 127.11 (C-4), 129.53 (C-4a), 137.06 (C-8a), 156.88 (C-2) ppm. $^{11}$B NMR (100 MHz, [D$_8$]THF): $\delta$ = 3.99 ppm. HRMS: calcd. for $C_{40}H_{44}BO_4$ 599.3338 [M – Na$^+$]$^-$; found 599.3312.

**Sodium Tetrakis(1,3-benzodioxol-5-yloxy)borate (22):** 47.7 g, 82%. $^1$H NMR (400 MHz, [D$_8$]THF): $\delta$ = 5.83 (s, 8 H, $OCH_2O$), 6.48 [dd, $^3J_{6,7}$(H,H) = 8.4 Hz, $^4J_{4,6}$(H,H) = 2.2 Hz, 4 H, 6-H], 6.55 [d, $^3J_{6,7}$(H,H) = 8.4 Hz, 4 H, 7-H], 6.74 [d, $^4J_{4,6}$(H,H) = 2.2 Hz, 4 H, 4-H] ppm. $^{13}$C NMR (100 MHz, [D$_8$]THF): $\delta$ = 101.39 ($OCH_2O$), 102.96 (C-4), 107.88 (C-6), 112.00 (C-7), 141.09 (C-7a), 148.50 (C-3a), 153.88 (C-5) ppm. $^{11}$B NMR (128 MHz, [D$_8$]THF): $\delta$ = 4.03 ppm. HRMS: calcd. for $C_{28}H_{20}BO_{12}$ 559.1053 [M – Na$^+$]$^-$; found 559.1033.

**Sodium Tetrakis(2,4,5-trimethylphenoxy)borate (23):** 40.8 g, 71%. $^1$H NMR (300 MHz, $CD_3CN$): $\delta$ = 2.03 (s, 12 H, 5-$CH_3$), 2.04 (s, 12 H, 4-$CH_3$), 2.09 (s, 12 H, 2-$CH_3$), 6.67 (s, 4 H, 3-H), 7.19 (s, 4 H, 6-H) ppm. $^{13}$C NMR (75 MHz, $CD_3CN$): $\delta$ = 17.22 (2-$CH_3$), 18.94 (4-$CH_3$), 19.99 (5-$CH_3$), 121.08 (C-6), 125.16 (C-4), 124.43 (C-2), 131.72 (C-3), 133.88 (C-5), 155.99 (C-1) ppm. $^{11}$B NMR (64 MHz, $CD_3CN$): $\delta$ = 2.85 ppm. HRMS: calcd. for $C_{36}H_{44}BO_4$ 551.3344 [M – Na$^+$]$^-$; found 551.3342.

**Sodium Tetrakis(2,3,5-trimethylphenoxy)borate (24):** 39.1 g, 68%. $^1$H NMR (300 MHz, $CD_3CN$): $\delta$ = 2.06 (s, 12 H, 5-$CH_3$), 2.07 (s, 12 H, 3-$CH_3$), 2.11 (s, 12 H, 2-$CH_3$), 6.25 (s, 4 H, 6-H), 7.14 (s, 4 H, 4-H) ppm. $^{13}$C NMR (75 MHz, $CD_3CN$): $\delta$ = 12.54 (2-$CH_3$), 20.63 (3-$CH_3$), 21.59 (5-$CH_3$), 118.11 (C-6), 120.43 (C-4), 123.61 (C-2), 134.67 (C-3), 136.67 (C-5), 157.95 (C-1) ppm. $^{11}$B NMR (64 MHz, $CD_3CN$): $\delta$ = 2.99 ppm. HRMS: calcd. for $C_{36}H_{44}BO_4$ 551.3344 [M – Na$^+$]$^-$; found 551.3352.

**Sodium Tetrakis(2-*tert*-butyl-4,5-dimethylphenoxy)borate (25):** 47.5 g, 64%. $^1$H NMR (400 MHz, [D$_8$]THF): $\delta$ = 1.63 [s, 36 H, C($CH_3$)$_3$], 1.91 (s, 12 H, 5-$CH_3$), 1.93 (s, 12 H, 4-$CH_3$), 6.63 (s, 4 H, 3-H), 7.61 (s, 4 H, 6-H) ppm. $^{13}$C NMR (100 MHz, [D$_8$]THF): $\delta$ = 19.08 (5-$CH_3$), 19.33 (4-$CH_3$), 31.80 [C($C$H$_3$)$_3$], 35.24 [$C$-(CH$_3$)$_3$], 121.70 (C-6), 121.76 (C-5), 126.70 (C-3), 132.81 (C-4), 134.81 (C-2), 156.17 (C-1) ppm. $^{11}$B NMR (64 MHz, [D$_8$]THF): $\delta$ = 2.75 ppm. HRMS: calcd. for $C_{48}H_{68}BO_4$ 719.5205 [M – Na$^+$]$^-$; found 719.5225.

**Sodium Tetrakis[4-chloro-5-methyl-2-(1-methylethyl)phenoxy]borate (26):** 23.8 g, 93%. $^1$H NMR (300 MHz, [D$_8$]THF): $\delta$ = 1.18 [d, $^3J$(H,H) = 6.9 Hz, 24 H, CH(C$H_3$)$_2$], 2.09 (s, 12 H, 5-$CH_3$), 3.47 [sept, $^3J$(H,H) = 6.9 Hz, 4 H, C$H$($CH_3$)$_2$], 6.80 (s, 4 H, 3-H), 7.42 (s, 4 H, 6-H) ppm. $^{13}$C NMR (75 MHz, [D$_8$]THF): $\delta$ = 20.00 (5-$CH_3$), 22.93 [CH($C$H$_3$)$_2$], 28.09 [$C$H(CH$_3$)$_2$], 121.76 (C-6), 121.82 (C-4), 125.58 (C-3), 132.05 (C-2), 137.62 (C-5), 155.53 (C-1) ppm. $^{11}$B NMR (64 MHz, [D$_8$]THF): $\delta$ = 2.54 ppm. HRMS: calcd. for $C_{40}H_{48}BCl_4O_4$ 743.2405 [M – Na$^+$]$^-$; found 743.2378.

**Sodium Tetrakis(1-naphthoxy)borate (27):** Boric acid (0.62 g, 0.01 mol) was added to a solution of 1-naphthol (4.61 g, 0.032 mol) in toluene (40 mL) and the reaction mixture was heated for 12 h (Dean–Stark trap). Toluene was removed under reduced pressure and the crude product was dissolved in THF (15 mL). First, 1-naphthol (1.33 g, 0.9 mol) and then sodium hydride (0.37 g, 60% suspension in paraffin, 0.9 mol) was added to the solution at 0 °C. After completion of the reaction, the solution was stored at 4 °C

 © 2006 Wiley-VCH Verlag GmbH & Co. KGaA, Weinheim 

for 12 h. The precipitated product was isolated by filtration and subsequent washing with diethyl ether (5 mL) and pentane (5 mL); yield: 3.4 g, 57%. $^1$H NMR (400 MHz, $CD_3CN$): $\delta$ = 7.13–7.18 (m, 8 H, 7-H and 8-H), 7.36–7.41 (m, 8 H, 4-H and 5-H), 7.67–7.72 (m, 8 H, 2-H and 6-H), 8.55–8.57 (m, 4 H, 3-H) ppm. $^{13}$C NMR (100 MHz, $CD_3CN$): $\delta$ = 112.28 (C-2), 117.60 (C-8), 124.58 (C-3), 124.74 (C-5), 126.30 (C-4), 127.74 (C-7 and C-8a), 128.14 (C-6), 135.92 (C-4a), 155.63 (C-1) ppm. $^{11}$B NMR (64 MHz, $CD_3CN$): $\delta$ = 4.05 ppm. HRMS: calcd. for $C_{40}H_{28}BO_4$ 583.2086 $[M - Na^+]^-$; found 583.2090.

**Tris(2,4,6-trimethylphenoxy)borane (30):** 2,4,6-Trimethylphenol (**29**) (15 g, 0.11 mol) and boric acid (2.1 g, 0.03 mol) were suspended in toluene (100 mL) and the reaction mixture was heated for a period of 24 h (Dean–Stark trap). Toluene was distilled off under reduced pressure and excess of **29** was removed by sublimation. The crude product was purified by crystallisation in toluene to yield a colourless solid; yield 9.1 g, 64%; m.p. 245 °C (toluene). $^1$H NMR (300 MHz, $CDCl_3$): $\delta$ = 2.20 (s, 9 H, 4-$CH_3$), 2.28 (s, 18 H, 2-$CH_3$ and 6-$CH_3$), 6.80 (s, 6 H, 3-H and 5-H) ppm. $^{13}$C NMR (75 MHz, $CDCl_3$): $\delta$ = 16.95 (2-$CH_3$ and 6-$CH_3$), 20.59 (4-$CH_3$), 127.71 (C-2 and C-6), 129.15 (C-3 and C-5), 132.45 (C-4), 148.26 (C-1) ppm. $^{11}$B NMR (64 MHz, $CDCl_3$): $\delta$ = 15.89. MS (EI = 70 eV): *m*/*z* (%) = 416.2 (100) $[M]^{+\cdot}$, 281.2 (12) $[M - (CH_3)_3C_6H_2O]^{+\cdot}$.

**X-ray Crystal Structure Analysis for 6a:** $C_{18}H_{15}BO_3$ (290.11), colourless crystal 0.30 × 0.25 × 0.15 mm, $a$ = 11.650(1), $b$ = 15.897(2), $c$ = 19.724(2) Å, $\alpha$ = 113.31(1), $\beta$ = 106.59(1), $\gamma$ = 90.19(1)°, $V$ = 3186.9(6) Å$^3$, $\rho_{calcd.}$ = 1.209 g cm$^{-3}$, $\mu$ = 0.648 mm$^{-1}$, empirical absorption correction based on $\psi$ scan data (0.829 ≤ $T$ ≤ 0.909), $Z$ = 8, triclinic, space group $P\bar{1}$ (no. 2), $\lambda$ = 1.54178 Å, $T$ = 223 K, $\omega$/2$\theta$ scans, 13476 reflections collected (±$h$, +$k$, ±$l$), [(sin$\theta$)/$\lambda$] = 0.62 Å$^{-1}$, 12986 independent ($R_{int}$ = 0.043) and 8143 observed reflections [$I \geq 2\sigma(I)$], 794 refined parameters, $R$ = 0.049, $wR_2$ = 0.143, max. residual electron density 0.23 (–0.27) e·Å$^{-3}$, four almost identical independent molecules in the asymmetric unit, hydrogen atoms calculated and refined as riding atoms.

**X-ray Crystal Structure Analysis for 6b:** $C_{36}H_{44}BNaO_7$ (622.51), colourless crystal 0.70 × 0.50 × 0.30 mm, $a$ = 18.299(1), $b$ = 9.803(1), $c$ = 19.287(1) Å, $\beta$ = 100.09(1)°, $V$ = 3406.3(4) Å$^3$, $\rho_{calcd.}$ = 1.214 g cm$^{-3}$, $\mu$ = 0.772 mm$^{-1}$, empirical absorption correction (0.614 ≤ $T$ ≤ 0.801), $Z$ = 4, monoclinic, space group $P2_1/c$ (no. 14), $\lambda$ = 1.54178 Å, $T$ = 223 K, $\omega$ and $\varphi$ scans, 25313 reflections collected (±$h$, ±$k$, ±$l$), [(sin$\theta$)/$\lambda$] = 0.59 Å$^{-1}$, 5816 independent ($R_{int}$ = 0.055) and 4546 observed reflections [$I \geq 2\sigma(I)$], 481 refined parameters, $R$ = 0.051, $wR_2$ = 0.153, max. residual electron density 0.30 (–0.27) e·Å$^{-3}$, two of the three THF solvent molecules are disordered and refined with split positions, hydrogen atoms calculated and refined as riding atoms.

**X-ray Crystal Structure Analysis for 10:** $C_{36}H_{40}BF_4NaO_7$ (694.48), colourless crystal 0.60 × 0.60 × 0.45 mm, $a$ = 12.955(1), $b$ = 17.126(1), $c$ = 16.242(1) Å, $\beta$ = 99.17(1)°, $V$ = 3557.5(4) Å$^3$, $\rho_{calcd.}$ = 1.297 g cm$^{-3}$, $\mu$ = 0.963 mm$^{-1}$, empirical absorption correction (0.596 ≤ $T$ ≤ 0.671), $Z$ = 4, monoclinic, space group $P2_1/n$ (no. 14), $\lambda$ = 1.54178 Å, $T$ = 223 K, $\omega$ and $\varphi$ scans, 10815 reflections collected (±$h$, ±$k$, ±$l$), [(sin$\theta$)/$\lambda$] = 0.59 Å$^{-1}$, 6038 independent ($R_{int}$ = 0.026) and 4264 observed reflections [$I \geq 2\sigma(I)$], 443 refined parameters, $R$ = 0.053, $wR_2$ = 0.163, max. residual electron density 0.38 (–0.32) e· Å$^{-3}$, the THF solvent molecules are partly disordered, refinement with split positions did not improve the model, hydrogen atoms calculated and refined as riding atoms.

**X-ray Crystallography Study:** Data sets were collected with Enraf Nonius CAD4 and Nonius KappaCCD diffractometers. For the programs used see ref.[14] CCDC-285239 to -285243 contain the supplementary crystallographic data for this paper. These data can be obtained free of charge from The Cambridge Crystallographic Data Centre via www.ccdc.cam.ac.uk/data_request/cif.

**X-ray Crystal Structure Analysis for 27:** $C_{60}H_{68}BNaO_9$ (966.94), colourless crystal 0.30 × 0.25 × 0.15 mm, $a$ = 17.904(1), $b$ = 17.710(1), $c$ = 16.789(1) Å, $\beta$ = 91.69(1)°, $V$ = 5321.1(5) Å$^3$, $\rho_{calcd.}$ = 1.207 g cm$^{-3}$, $\mu$ = 0.703 mm$^{-1}$, empirical absorption correction (0.817 ≤ $T$ ≤ 0.902), $Z$ = 4, monoclinic, space group $C2/c$ (no. 15), $\lambda$ = 1.54178 Å, $T$ = 223 K, $\omega$ and $\varphi$ scans, 16055 reflections collected (±$h$, ±$k$, ±$l$), [(sin$\theta$)/$\lambda$] = 0.59 Å$^{-1}$, 4362 independent ($R_{int}$ = 0.034) and 2748 observed reflections [$I \geq 2\sigma(I)$], 323 refined parameters, $R$ = 0.075, $wR_2$ = 0.258, max. residual electron density 0.56 (–0.28) e·Å$^{-3}$, the THF solvent molecules are heavily disordered, refinement with split positions did not improve the model, hydrogen atoms calculated and refined as riding atoms.

**X-ray Crystal Structure Analysis for 28:** $C_{87}H_{111}B_4Na_3O_{27}$ (1700.97), colourless crystal 0.40 × 0.30 × 0.30 mm, $a$ = 14.658(1), $b$ = 16.913(1), $c$ = 19.312(1) Å, $\alpha$ = 85.15(1), $\beta$ = 87.80(1), $\gamma$ = 70.01(1)°, $V$ = 4482.9(5) Å$^3$, $\rho_{calcd.}$ = 1.260 g cm$^{-3}$, $\mu$ = 0.878 mm$^{-1}$, empirical absorption correction (0.720 ≤ $T$ ≤ 0.779), $Z$ = 2, triclinic, space group $P\bar{1}$ (no. 2), $\lambda$ = 1.54178 Å, $T$ = 223 K, $\omega$ and $\varphi$ scans, 17206 reflections collected (±$h$, ±$k$, ±$l$), [(sin$\theta$)/$\lambda$] = 0.59 Å$^{-1}$, 14334 independent ($R_{int}$ = 0.040) and 10777 observed reflections [$I \geq 2\sigma(I)$], 1156 refined parameters, $R$ = 0.055, $wR_2$ = 0.164, max. residual electron density 0.33 (–0.25) e· Å$^{-3}$, C67 and THF molecule O211–C215 disordered and refined with split positions, hydrogen atoms calculated and refined as riding atoms.

## Acknowledgments

Financial support by the BASF AG and the International Graduate College "Template-Directed Chemical Synthesis" (DFG) is highly appreciated.

[1] A. Ricardo, M. A. Carrigan, A. N. Olcott, S. A. Benner, *Science* **2004**, *303*, 196 and literature cited therein.
[2] M. F. Semmelhack, S. R. Campagna, C. Hwa, M. J. Federle, B. L. Bassler, *Org. Lett.* **2004**, *6*, 2635–2637 and literature cited therein; M. Berger, J. Mulzer, *J. Am. Chem. Soc.* **1999**, *121*, 8393–8394.
[3] W. Funakoshi, K. Sasaki, M. Abe, Japan Patent No. 07207017, **1995**.
[4] S. Yoshimura, T. Noma, I. Yonetsu, Japan Patent No. 2000243437, **2000**.
[5] D. Vagedes, R. Fröhlich, G. Erker, *Angew. Chem.* **1999**, *111*, 3561–3565; *Angew. Chem. Int. Ed.* **1999**, *38*, 3362–3365.
[6] F. A. R. Kaul, G. T. Puchta, H. Schneider, M. Grosche, D. Mihalios, W. A. Herrmann, *J. Organomet. Chem.* **2001**, *621*, 184–189.
[7] M. Bishop, S. G. Bott, A. R. Barron, *J. Chem. Soc., Dalton Trans.* **2000**, 3100–3105.
[8] K. G. Caulton, M. H. Chisholm, S. R. Drake, K. Folting, J. C. Huffman, W. Streib, *Inorg. Chem.* **1993**, *32*, 1970–1976.
[9] R. J. Errington, M. Tombul, G. L. P. Walker, W. Clegg, S. L. Heath, L. Horsburgh, *J. Chem. Soc., Dalton Trans.* **1999**, 3533–3534.
[10] Maldi-TOF analysis of the crude product. $^{11}$B NMR studies turned out to be less useful since the equilibration is fast on the NMR timescale and the particular shifts are very similar.
[11] For longer times and storage purposes, an anhydrous environment is recommended to avoid hydrolysis.
[12] H. I. Schlesinger, H. C. Brown, D. L. Mayfield, J. R. Gilbreath, *J. Am. Chem. Soc.* **1953**, *75*, 213–215.
[13] NMR spectroscopic data gave no indication of impurities such as remaining solvent molecules or other borate species. Since

 © 2006 Wiley-VCH Verlag GmbH & Co. KGaA, Weinheim 

these compounds are considered to be very moisture-sensitive no elemental analyses can be given (compare: T. Alaviuhkola, J. Bobacka, M. Nissinen, K. Rissanen, A. Ivaska, J. Pursiainen, *Chem. Eur. J.* **2005**, *11*, 2071–2080).

[14] Data collection EXPRESS (Nonius B.V., **1994**) and COLLECT (Nonius B.V., **1998**), data reduction MolEN (K. Fair, Enraf–Nonius B.V., **1990**) and Denzo-SMN (Z. Otwinowski, W. Minor, *Methods Enzymol.* **1997**, *276*, 307–326), absorption correction for CCD data SORTAV (R. H. Blessing, *Acta Crystallogr., Sect. A* **1995**, *51*, 33–37; R. H. Blessing, *J. Appl. Crystallogr.* **1997**, *30*, 421–426) and Denzo (Z. Otwinowski, D. Borek, W. Majewski, W. Minor, *Acta Crystallogr., Sect. A* **2003**, *59*, 228–234), structure solution SHELXS-97 (G. M. Sheldrick, *Acta Crystallogr., Sect. A* **1990**, *46*, 467–473), structure refinement SHELXL-97 (G. M. Sheldrick, University of Göttingen, **1997**), graphics DIAMOND 3.0d (Crystal Impact GbR, Bonn, Germany).

Received: January 24, 2006
Published Online: February 28, 2006

 © 2006 Wiley-VCH Verlag GmbH & Co. KGaA, Weinheim 

DOI: 10.1002/ejic.200501060

# Self-Assembly of *N*,*N*′,*N*′′,*N*′′′-Tetra(pyridin-4-yl)-1,4,7,10-tetraazacyclododecane-1,4,7,10-tetracarboxamide with $Zn^{2+}$ or $Cd^{2+}$ Ions

**Biing-Chiau Tzeng,*[a] Yun-Mei Lu,[a] Gene-Hsiang Lee,[b] and Shie-Ming Peng[b]**

**Keywords:** Charge transfer / Luminescence / Metallomacrocycles / Self-assembly / Supramolecular chemistry

We report the design and synthesis of *N*,*N*′,*N*′′,*N*′′′-tetra(pyridin-4-yl)-1,4,7,10-tetraazacyclododecane-1,4,7,10-tetracarboxamide (**L**), which contains four *N*-(pyridin-4-yl)carboxamide groups as functional appendages, as well as the structural and luminescence properties of its $Zn^{2+}$ and $Cd^{2+}$ complexes. The reaction of $ZnBr_2$ with **L** forms the two-dimensional coordination polymer $[ZnBr_2(\mathbf{L})_{1/2}]_n$ (**1**). In the two-dimensional domain, the 68-membered metallomacrocycles as well as 12-membered 1,4,7,10-tetraazacyclododecane (cyclen) units propagate into two-dimensional extended structures. Interestingly, the metallomacrocycles are stacked to form one-dimensional parallelogram channels in the solid state. In addition, the reaction of $CdX_2$ (X = Br, I) with **L** forms the isomorphous, three-dimensional coordination networks $[CdX_2(\mathbf{L})]_n$ [X = Br (**2**), I (**3**)], which have tubular channels in the solid state. **L** in **1**–**3** is tetradentate and acts as a versatile connector in the construction of supramolecular coordination networks. The 34-membered metallomacrocycles and 12-membered cyclen macrocycles of **2** and **3** also propagate into three-dimensional extended structures. Unlike those of **1** and **2**, the emission maximum at around 439 nm in the iodo compound **3** can be assigned to a ligand-to-metal charge-transfer (LMCT) transition as the excited state upon photoexcitation.

(© Wiley-VCH Verlag GmbH & Co. KGaA, 69451 Weinheim, Germany, 2006)

## Introduction

The widespread use of the coordinative-bond approach in the construction of supramolecular coordination compounds by self-assembly is well established.[1] So far, a variety of one-, two-, and three-dimensional infinite solid-state coordination architectures[2] as well as discrete molecular structures have been isolated and structurally characterized.[1] Applications, including chemical sieving, sensing, and catalysis based on the supramolecular coordination compounds have been discovered, and some have shown really exciting and valuable progress.[3] Surprisingly, the ligands used in the assembly of materials are generally didentate, with some tridentate ones;[1,2] tetradentate ligands are relatively scarce.[4] A macrocyclic ligand with a tetraaza macrocycle seems a good candidate in this regard since macrocyclic compounds have long attracted great interest owing to their intriguing structural and spectroscopic properties as well as host–guest chemistry.[5] In addition, tetraaza macrocycles can be easily functionalized by several groups, such as alkynyl,[6] phosphanylmethyl,[7] carboxyl,[8] and pyridyl[9] on their secondary N-sites to produce some novel properties in coordination, electro- and photoluminescent, and catalytic chemistry.

We have previously reported a study of metal-containing cyclic amides based on a didentate *N*-pyridylcarboxamide ligand – *N*,*N*′-bis(4-methylpyridyl)oxalamide – where interesting solid-state frameworks featuring cyclic peptides are constructed from hydrogen bonding/π···π interactions.[10]

Organic amides have proved to be very useful in self-assembly through hydrogen bonding, and the assembled products often have relevance to biological systems. Most remarkably, cyclic oligoamides can give rise to interesting nanotube frameworks through inter-ring NH···O=C hydrogen bonding, as reported by Ghadiri et al.[11] A new *N*-pyridylcarboxamide ligand (**L**) is used here as a tetradentate ligand for a crystal-engineering study. We report the design and synthesis of *N*,*N*′,*N*′′,*N*′′′-tetra(pyridin-4-yl)-1,4,7,10-tetraazacyclododecane-1,4,7,10-tetracarboxamide (**L**), which contains four *N*-(pyridin-4-yl)carboxamide groups as functional appendages, as well as the structural and luminescence properties of its $Zn^{2+}$ and $Cd^{2+}$ complexes.

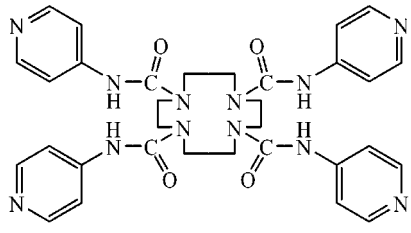

**L**

[a] Department of Chemistry and Biochemistry, National Chung Cheng University,
168, University Rd., Min-Hsiung, Chia-Yi, Taiwan 621
[b] Department of Chemistry, National Taiwan University,
1, Sec. 4, Roosevelt Road, Taipei, Taiwan 106

 © 2006 Wiley-VCH Verlag GmbH & Co. KGaA, Weinheim 

## Results and Discussion

Hosseini and co-workers[4c] have recently reported an interesting porphyrinic ligand with four *N*-pyridylcarboxamides as appendages for the construction of one- and two-dimensional $Cu^{2+}$-containing coordination networks as an example of supramolecular isomerism. Another new type of tetraaza macrocycle that contains four *N*-(pyridin-4-yl)-carboxamide groups as functional appendages for the construction of supramolecular coordination frameworks has also been designed and synthesized in this study. Unlike most of the literature studies, the tetradentate ligand (**L**) studied here is a rare example of a tetradentate ligand in a crystal-engineering study. A methanolic solution of $ZnBr_2$ and $CdX_2$ (X = Br, I) was carefully layered on top of a DMSO solution of **L** to give pale-yellow crystals of **1**·DMSO·4$CH_3OH$ or colorless crystals of **2**·4DMSO and **3**·4DMSO, respectively, in good yield (70–80%) within a couple of days. The compounds are all air stable and photoluminescent in the solid state.

### Description of the Crystal Structures

Complexes **1**–**3** were isolated and their molecular structures determined by an X-ray diffraction study, which confirmed the formation of coordination polymers in the solid state. The molecular structure of **1** (Figure 1, a) displays a two-dimensional coordination polymer where **L** acts as a tetradentate ligand. The cyclen macrocycle contains four *N*-pyridylcarboxamide appendages, each of which coordinates to tetrahedral $Zn^{2+}$ ions; the $Zn^{2+}$ ions coordinate to two bromides and another *N*-pyridylcarboxamide appendage. In the two-dimensional domain, the 68-membered metallomacrocycles built from four **L** and four $ZnBr_2$ units, as well as the 12-membered macrocycles of the cyclen units, propagate into two-dimensional extended structures. Interestingly, the metallomacrocycles are stacked to form one-dimensional parallelogram channels (as viewed along the *a* axis) in the solid state, as shown in Figure 1 (b); the diagonal distances of these parallelogram channels are 26.59 and 15.73 Å. In addition, doubly hydrogen-bonding interactions [N(3)–H(3A)···O(3): N(3)···O(3) = 3.041(7) Å, N(3)–H(3A)···O(3) = 159.95°; N(5)–H(5A)···O(3): N(5)···O(3) = 2.913(9) Å, N(5)–H(5A)···O(3) 167.09°] between the solvated DMSO molecules and amide groups are observed in the solid state; the channels are also filled with methanol molecules. Although **1** has a high *R* value due to the fast loss of solvated solvents, there is no doubt that the structural framework of **1** can be still corroborated by the X-ray diffraction study.

Both **2** and **3** are essentially isomorphous, therefore the molecular structure and the extended structural framework of **3** are shown in Figure 2, parts a and b, respectively, as a representative example. Unlike the two-dimensional coordination network of **1**, **2** and **3** both form three-dimensional coordination networks with octahedral $Cd^{2+}$ ions coordinating to two anionic (Br, I) and four bridging **L** ligands,

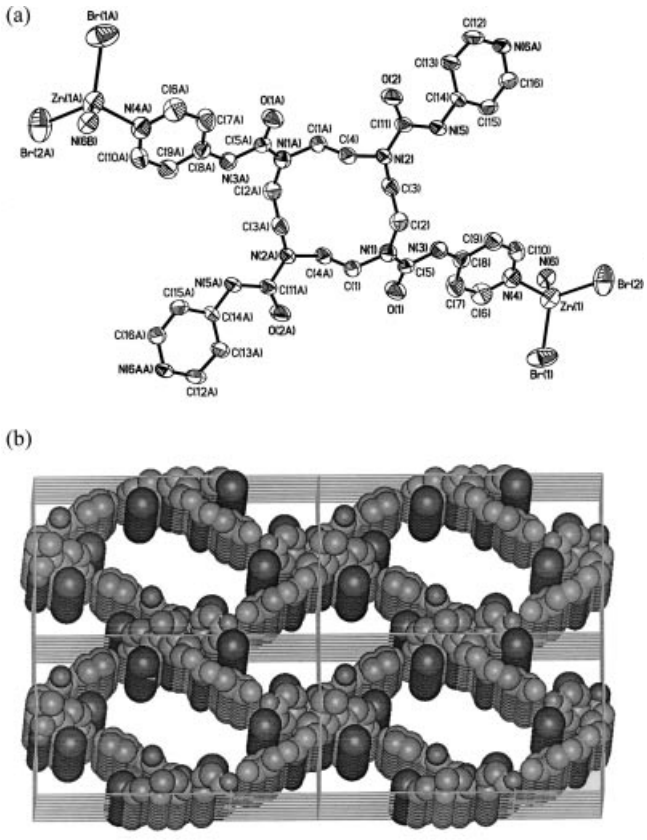


Figure 1. (a) Molecular structure of **1**·DMSO. ORTEP diagram shows 50% probability ellipsoids, and (b) its two-dimensional extended framework showing a 1-D channel structure with solvates omitted (viewing through the a axis) in the solid state.

as shown in part a of Figure 2. In more detail, the four *N*-pyridylcarboxamide appendages of the cyclen macrocycle each coordinate to octahedral $Cd^{2+}$ ions, which also coordinate to two bromides and another three N-pyridylcarboxamides. The cyclen plane is approximately perpendicular to that of the $CdN_4$ (pyridyl) unit, with two pyridyl groups (at positions 1 and 7) roughly coplanar with the cyclen plane and the other two (at positions 4 and 10) above and below the plane. This different orientation of **L** results in the formation of interesting three-dimensional coordination networks. Furthermore, the metallomacrocycles with 34-membered rings built from two $CdBr_2$ and two **L** units are packed into columns that form interesting tubular channels (viewed along the *b* axis) in the solid state, as shown in Figure 2 (b). Thus, the metallamacrocycles and cyclen macrocycles also propagate into three-dimensional extended structures. Hydrogen-bonding interactions [N(6)–H(6A)···O(4): N(6)···O(4) = 2.955(7) Å, N(6)–H(6A)···O(4) = 153.31°] between the solvated DMSO molecules and amide groups are observed in the solid state, and the channels are also filled with DMSO molecules. Upon changing the anion from $Br^-$ to $I^-$, the *trans*-$CdN_4X_2$ geometry remains unchanged, and thus the structural frameworks also retain a similar structural motif.

 © 2006 Wiley-VCH Verlag GmbH & Co. KGaA, Weinheim 

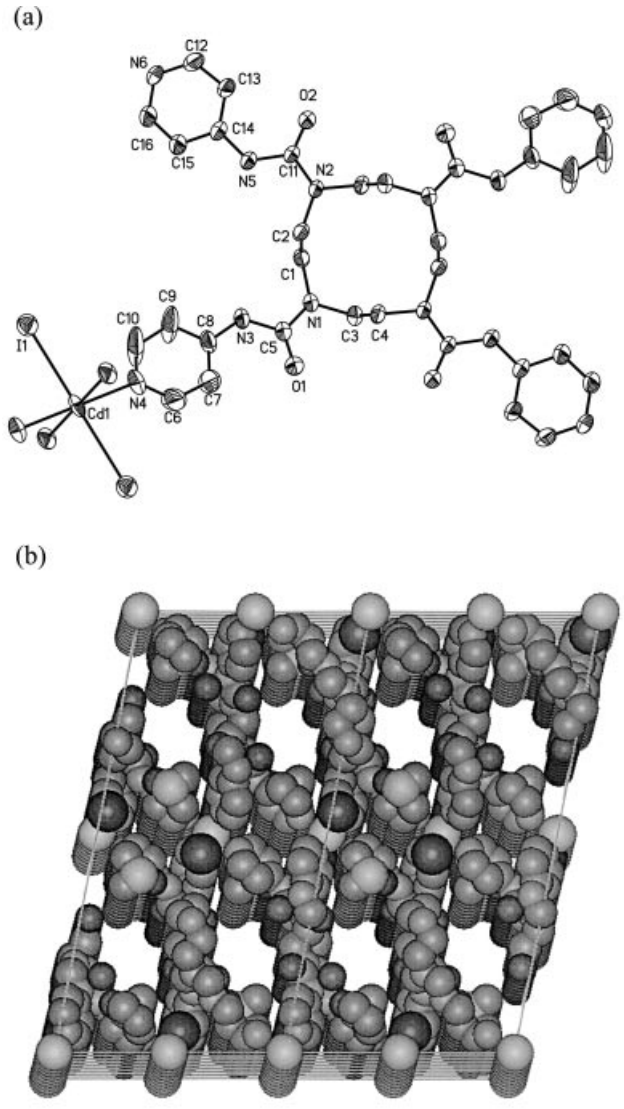


Figure 2. (a) Molecular structure of **3**. ORTEP diagram shows 30% probability ellipsoids, and (b) its three-dimensional extended framework showing a 1-D channel structure with solvates omitted (viewing through the b axis) in the solid state.

Very recently, Cao et al.[4a] reported a cyclam (1,4,8,11-tetraazacyclotetradecane)-based tetradentate ligand containing pyridylmethyl groups as appendages as well as the structural study of its two novel $Cd^{2+}$ polymeric metallomacrocyclic complexes, where the ligand adopts $\mu_2$- or $\mu_4$-coordination modes in the structural framework. Indeed, the different coordination modes that co-exist in the same structure result in the formation of interesting three-dimensional coordination networks. In this study, it is interesting to find that given the same bridging ligands (**L**) and only one coordination mode ($\mu_4$) in the system, the structural motif changes dramatically and the supramolecular complexity increases upon changing the metal ions from tetrahedral (four-coordinate) $Zn^{2+}$ to octahedral (six-coordinate) $Cd^{2+}$ ions. Unlike the structures reported by Cao et al.,[4a] which contain two coordination modes for the ligands in the same framework, the structures of **2** and **3** also form three-dimensional networks with tubular channels only due to the different orientation of the *N*-pyridylcarboxamide appendages of the cyclen moieties. In this context, **L** has been shown to be a tetradentate ligand that acts as a versatile connector in the construction of interesting supramolecular coordination networks. Unfortunately, crystals of **1**–**3** easily lose solvent, which causes the crystal lattices to collapse instantaneously and thus prevents further studies by TGA and powder XRD analysis that might allow us to gain some insight into the channel structures.

### Solid-State Emission Spectra

**L** and **1**–**3** are all luminescent in the solid state, as shown in Figure 3 (a), at room temperature. Upon photoexcitation at 325 nm, **1** shows a broad emission with a maximum at around 412 nm, whereas **L** displays a similar emission at around 403 nm. Given the high similarity between these emissions, they were tentatively assigned to an intraligand (IL) transition. The solid-state emission of **2** (Figure 3, b) at room temperature has an emission maximum at around

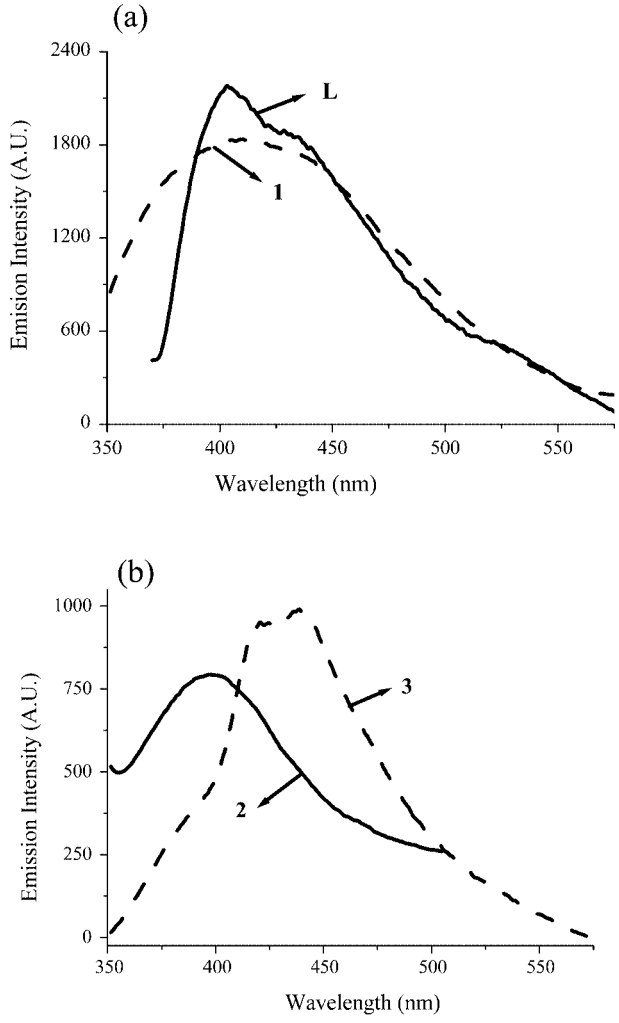


Figure 3. (a) The solid-state emission spectra of **L** and **1**, and (b) the solid-state emission spectra of **2** and **3** measured at room temperature with an excitation wavelength at 325 nm.

 © 2006 Wiley-VCH Verlag GmbH & Co. KGaA, Weinheim 

398 nm, which is also comparable to those of **L** and **1**. Thus, it seems reasonable that the excited state responsible for the emission for **2** is also an IL transition. Most importantly, **3** shows a solid-state emission with an emission maximum at around 439 nm, which is red-shifted with respect to those of **1** and **2**. In light of previous studies[10,12] and the red-shift in emission energy on going from the bromo to the iodo complex, this emission can tentatively be assigned to a ligand-to-metal charge-transfer (LMCT) transition, although intraligand transition mixing with LMCT cannot be excluded. Intraligand transitions as excited states are not uncommon for $Zn^{2+}$ and $Cd^{2+}$ complexes, but charge-transfer excited states are so far still rare.[13]

## Conclusion

A new type of tetraaza macrocycle (**L**) containing four *N*-pyridylcarboxamide groups as functional appendages has been designed and synthesized in this study, which is a rare example of the use of a tetradentate ligand in a crystal-engineering study. Complex **1** can be isolated as a two-dimensional coordination polymer upon reaction of $ZnBr_2$ with **L**. In the two-dimensional domain, the 68-membered metallomacrocycles built from four **L** and four $ZnBr_2$ units, as well as the 12-membered macrocycles of cyclen, propagate into two-dimensional extended structures. Interestingly, the metallomacrocycles are stacked to form one-dimensional parallelogram channels in the solid state. In addition, reaction of $CdX_2$ (X = Br, I) with **L** leads to the formation of **2** and **3**, respectively, which form isomorphous three-dimensional coordination networks with tubular channels due to the different orientation of the *N*-pyridylcarboxamide appendages of the cyclen moieties. Again, the 34-membered metallomacrocycles built from two $CdX_2$ and two **L** units, as well as the 12-membered macrocycles of the cyclen units, propagate into three-dimensional extended structures in **2** and **3**. Unlike those of **1** and **2**, the emission maximum of the iodo compound **3** at around 439 nm can be tentatively assigned to a ligand-to-metal charge-transfer transition upon photoexcitation. The channel structure, as well as the luminescence properties, of these tetraaza-macrocycle-based materials may be anticipated to hold potential for use as luminescent sensors. Moreover, the cyclen moiety acts as a versatile connector in the construction of supramolecular coordination networks, and is also capable of functioning as a receptor site for recognition events.

## Experimental Section

**General Information:** All solvents for syntheses (analytical grade), which were used without further purification, and metal salts [$ZnBr_2$, $CdX_2$ (X = Br, I)] are commercially available. *N*,*N*′,*N*″,*N*‴-Tetra(pyridin-4-yl)-1,4,7,10-tetraazacyclododecane-1,4,7,10-tetracarboxamide (**L**) was prepared following literature methods.[14] MS: positive-ion FAB mass spectra were recorded with a Finnigan MAT95 mass spectrometer. Steady-state emission spectra were recorded with a SPEX Fluorolog-2 spectrophotometer.

**Synthesis of *N*,*N*′,*N*″,*N*‴-Tetra(pyridin-4-yl)-1,4,7,10-tetraazacyclododecane-1,4,7,10-tetracarboxamide (L):** Isonicotinic acid (2.00 g, 16.24 mmol) was put into a 250-mL, two-necked flask with toluene (100 mL), under an atmosphere of nitrogen, and the mixture was stirred for ten minutes after addition of triethylamine (2.72 mL, 19.49 mmol). After addition of phosphorazidic acid diphenyl ester (3.15 mL, 14.62 nm) the solution was stirred for one hour; it gradually became colorless. The solution was later refluxed for three hours at 90 °C (it became yellow) and was then cooled to room temperature. 1,4,7,10-Tetraazacyclododecane (0.56 g, 3.25 mmol) dissolved in 100 mL of toluene was slowly and carefully transferred into the above two-necked flask to give a pale-yellow precipitate after stirring for two days at room temperature. The toluene was then removed under vacuum and the ligand was recrystallized from 200 mL of methanol to give a pure and white solid (0.64 g, 0.975 mmol) in 30% yield. MS (FAB): *m*/*z* (%) = 654 (35) [$M^+$]. $^1$H NMR (400 MHz, [$D_6$]DMSO, 25 °C): $\delta$ = 3.69 (s, 4 H, $CH_2$), 7.48 (d, 2 H, $NCH_2CH_2$], 8.32 (d, 2 H, $NCH_2$), 8.88 (s, 1 H, N*H*) ppm. $^{13}$C NMR (400 MHz, [$D_6$]DMSO, 25 °C): $\delta$ = 47.67,

Table 1. Crystallographic data for **1**·DMSO·4$CH_3OH$, **2**·4DMSO and **3**·4DMSO.

| | **1**·DMSO·4CH3OH | **2**·4DMSO | **3**·4DMSO |
|---|---|---|---|
| Empirical formula | $C_{22}H_{40}Br_2N_6O_7SZn$ | $C_{40}H_{60}Br_2CdN_{12}O_8S_4$ | $C_{40}H_{60}CdI_2N_{12}O_8S_4$ |
| Formula mass | 757.85 | 1237.46 | 1331.46 |
| Crystal system | monoclinic | monoclinic | monoclinic |
| Space group (No.) | $P2_1/c$ | $C2/c$ | $C2/c$ |
| *a* [Å] | 10.5783(5) | 32.643(2) | 33.074(3) |
| *b* [Å] | 26.5867(12) | 9.9817(6) | 9.8463(7) |
| *c* [Å] | 15.7293(7) | 16.6382(11) | 16.8512(12) |
| $\beta$ [°] | 108.604(2) | 101.032(2) | 101.712(2) |
| *V* [Å$^3$], *Z* | 4192.6(3), 4 | 5321.2(6), 4 | 5373.5(7), 4 |
| *F*(000) (e) | 1544 | 2520 | 2656 |
| $\mu$ (Mo-*K*$\alpha$) [mm$^{-1}$] | 2.577 | 2.127 | 1.769 |
| *T* [K] | 295(2) | 295(2) | 295(2) |
| Reflections collected | 41668 | 30975 | 31119 |
| Independent reflections [$F_o \geq 2\sigma(F_o)$] | 9627 ($R_{int}$ = 0.070) | 6495 ($R_{int}$ = 0.055) | 6553 ($R_{int}$ = 0.032) |
| Refined parameters | 367 | 308 | 307 |
| Goodness-of-fit on $F^2$ | 1.039 | 1.032 | 1.072 |
| $R^{[a]}$, $R_w^{[b]}$ [$I \geq 2\sigma(I)$] | 0.096, 0.283 | 0.072, 0.178 | 0.055, 0.150 |
| $R^{[a]}$, $R_w^{[b]}$ (all data) | 0.162, 0.344 | 0.102, 0.200 | 0.068, 0.163 |

[a] $R = \Sigma||F_o| - |F_c||/\Sigma|F_o|$. [b] $wR_2 = \{[\Sigma w(F_o^2 - F_c^2)^2]/\Sigma[w(F_o^2)^2]\}^{1/2}$.

 © 2006 Wiley-VCH Verlag GmbH & Co. KGaA, Weinheim 

113.71, 147.46, 150.03, 155.48 ppm. FT-IR (KBr): $\nu_{NH}$ = 3358 and $\nu_{C=O}$ = 1654 $cm^{-1}$. $C_{32}H_{36}N_{12}O_4$ (652.71): calcd. C 58.88, H 5.56, N 25.75; found C 59.05, H 5.78, N 25.67.

**Synthesis of $[ZnBr_2(L)_{1/2}]_n$ (1) and $[CdX_2(L)]_n$ [X = Br (2), I (3)]**

**1:** $ZnBr_2$ (30 mg, 0.14 mmol) dissolved in 2 mL $CH_3OH$ was carefully layered onto a DMSO solution of **L** [90 mg (0.14 mmol), dissolved in 2 mL of DMSO]. The pale-yellow crystals were obtained in two days with a ca. 70% yield. FT-IR (KBr): $\nu_{NH}$ = 3300 and $\nu_{C=O}$ = 1681 $cm^{-1}$. $C_{16}H_{18}Br_2N_6O_2Zn$ (551.55): calcd. C 34.84, H 3.29, N 15.24; found C 34.58, H 3.48, N 15.09.

**2:** $CdBr_2$ [30 mg, 0.11 mmol] dissolved in 2 mL $CH_3OH$ was carefully layered onto a DMSO solution of **L** [70 mg (0.11 mmol), dissolved in 2 mL of DMSO]. The colorless crystals were obtained in three days with a ca. 80% yield. FT-IR (KBr): $\nu_{NH}$ = 3313 and $\nu_{C=O}$ = 1669 $cm^{-1}$. $C_{32}H_{36}Br_2CdN_{12}O_4$ (924.93): calcd. C 41.55, H 3.92, N 17.28; found (%): calcd. C 41.18, H 3.78, N 17.09. **3**: It was prepared in a similar method as **2** except using $CdI_2$ instead of $CdBr_2$ and the colorless crystals were obtained in a ca. 80% yield. FT-IR (KBr): $\nu_{NH}$ = 3300 and $\nu_{C=O}$ = 1681 $cm^{-1}$. $C_{32}H_{36}CdI_2N_{12}O_4$ (1018.93): calcd. C 37.72, H 3.56, N 16.50; found C 37.35, H 3.78, N 16.69.

**X-ray Crystallography:** Suitable single crystals of **1**·DMSO·4$CH_3OH$, **2**·4DMSO, and **3**·4DMSO were mounted on a glass capillary respectively, and data collection was carried out on a Bruker SMART CCD diffractometer with Mo radiation (0.71073 Å) at 295(2) K. A preliminary orientation matrix and unit cell parameters were determined from 3 runs of 15 frames each, each frame corresponding to 0.3° scan in 15 s, followed by spot integration and least-square refinement. Data were measured using an $\omega$ scan of 0.3° per frame for 20 s until a complete hemisphere had been collected. Cell parameters were retrieved using SMART[15] software and refined with SAINT[16] on all observed reflections. Data reduction was performed with the SAINT software and corrected for Lorentz and polarization effects. Absorption corrections were applied with the program SADABS.[17] The structure was solved by direct methods with the SHELX93[18] program and refined by full-matrix least-squares methods on $F^2$ with SHEXLTL–PC V 5.03.[18] All non-hydrogen atomic positions were located in difference Fourier maps and refined anisotropically. The hydrogen atoms were placed in their geometrically generated positions. Detailed data collection and refinement of the four complexes are summarized in Table 1. Selected bond lengths and angles in the structures are summarized in Table 2, and hydrogen bonds are given in Table 3, respectively.

CCDC-282733 to -282735 (for complexes **1**, **2**, and **3**) contain the supplementary crystallographic data for this paper. These data can be obtained free of charge from The Cambridge Crystallographic Data Centre via www.ccdc.cam.ac.uk/data_request/cif.

Table 2. Selected bond lengths [Å] and angles [°] for **1**, **2**, and **3**.

| | | | | |
|---|---|---|---|---|
| **1** | Zn(1)–N(4) | 2.039(6) | Zn(1)–N(6) | 2.012(5) |
| | Zn(1)–Br(1) | 2.352(2) | Zn(1)–Br(2) | 2.350(2) |
| | N(6)–Zn(1)–N(4) | 107.2(2) | N(6)–Zn(1)–Br(2) | 107.6(2) |
| | N(4)–Zn(1)–Br(2) | 107.9(2) | N(6)–Zn(1)–Br(1) | 109.8(2) |
| | N(4)–Zn(1)–Br(1) | 108.0(2) | Br(2)–Zn(1)–Br(1) | 116.0(1) |
| **2** | Cd(1)–N(1) | 2.385(5) | Cd(1)–Br(1) | 2.890(1) |
| | N(1)–Cd(1)–Br(1) | 92.1(2) | C(1)–N(1)–Cd(1) | 119.9(5) |
| | C(5)–N(1)–Cd(1) | 125.8(5) | | |
| **3** | Cd(1)–N(4) | 2.421(4) | Cd(1)–I(1) | 3.080(1) |
| | N(4)–Cd(1)–I(1) | 91.9(1) | C(10)–N(4)–Cd(1) | 119.8(5) |
| | C(6)–N(4)–Cd(1) | 126.9(5) | | |

## Acknowledgments

We thank the National Science Council and National Chung Cheng University of the Republic of China for financial support.

[1] a) M. Fujita, *Chem. Soc. Rev.* **1998**, *27*, 417–425; b) S. Leininger, B. Olenyuk, P. J. Stang, *Chem. Rev.* **2000**, *100*, 853–908; c) B. J. Holliday, C. A. Mirkin, *Angew. Chem. Int. Ed.* **2001**, *40*, 2022–2043; d) O. M. Yaghi, H. L. Li, C. Davis, D. Richardson, T. L. Groy, *Acc. Chem. Res.* **1998**, *31*, 474–484; e) P. H. Dinolfom, J. T. Hupp, *Chem. Mater.* **2001**, *13*, 3113–3125.

[2] a) C. Janiak, *Dalton Trans.* **2003**, 2781–2804; b) S. L. James, *Chem. Soc. Rev.* **2003**, *32*, 276–288; c) S. Kitagawa, R. Kitaura, S.-I. Noro, *Angew. Chem. Int. Ed.* **2004**, *43*, 2334–2375; d) M. Eddaoudi, J. Kim, D. Vodak, A. Sudik, J. Wachter, M. O'Keeffe, O. M. Yaghi, *Proc. Natl. Acad. Sci. USA* **2002**, *99*, 4900–4904; e) S.-L. Zheng, X.-M. Chen, *Aust. J. Chem.* **2004**, *57*, 703–712; f) D. Maspoch, D. Ruiz-Molina, J. Veciana, *J. Mater. Chem.* **2004**, *14*, 2713–2723; g) S. R. Batten, K. S. Murray, *Coord. Chem. Rev.* **2003**, *246*, 103–130; h) L. Carlucci, G. Ciani, D. Proserpio, *Coord. Chem. Rev.* **2003**, *246*, 247–289.

[3] a) S. Bélanger, J. T. Hupp, C. L. Stern, R. V. Slone, D. F. Watson, T. M. Carrell, *J. Am. Chem. Soc.* **1999**, *121*, 557–563; b) S. Bélanger, J. T. Hupp, *Angew. Chem. Int. Ed.* **1999**, *38*, 2222–2224; c) G. A. Mines, B.-C. Tzeng, K. J. Stevenson, J. Li, J. T. Hupp, *Angew. Chem. Int. Ed.* **2001**, *41*, 154–157; d) M. H. Keefe, R. V. Slone, J. T. Hupp, K. F. Czaplewski, R. Q. Snurr, C. L. Stern, *Langmuir* **2000**, *16*, 3964–3970; e) M. L. Merlau, M. d. P. Mejia, S. T. Nguyen, J. T. Hupp, *Angew. Chem. Int. Ed.* **2001**, *40*, 4239–4242; f) S. S. Sun, A. J. Lees, *J. Am. Chem. Soc.* **2000**, *122*, 8956–8967; g) S. Tashiro, M. Tominaga, M. Kawano, B. Therrien, T. Ozeki, M. Fujita, *J. Am. Chem. Soc.* **2005**, *127*, 4546–4547; h) M. Yoshizawa, Y. Takeyama, T. Okano, M. Fujita, *J. Am. Chem. Soc.* **2003**, *125*, 3243–3244.

[4] a) Z. Ma, Z. Chen, R. Cao, *Eur. J. Inorg. Chem.* **2005**, 2978–2981; b) M. Tadokoro, S. Mizugaki, M. Kozaki, K. Okada, *Chem. Commun.* **2005**, 1140–1141; c) B. Zimmer, V. Bulach, M. W. Hosseini, A. D. Cian, N. Kyritsakas, *Eur. J. Inorg. Chem.* **2002**, 3079–3082; d) C. Kleina, E. Graf, M. W. Hosseini, A. D. Cian, J. Fischer, *Chem. Commun.* **2000**, 239–240.

[5] a) P. D. Beer, N. G. Berry, A. R. Cowley, E. J. Hayes, E. C. Oates, W. W. H. Wong, *Chem. Commun.* **2003**, 2408–2409; b) C. Bucher, R. S. Zimmerman, V. Lynch, J. L. Sessler, *Chem. Commun.* **2003**, 1646–1647; c) M. Albrecht, S. Schmid, M. deGroot, P. Weis, R. Fröhlich, *Chem. Commun.* **2003**, 2526–2527; d) J. Farkas Jr, S. J. Stoudt, E. M. Hanawalt, A. D. Pajerski, H. G. Richey Jr, *Organometallics* **2004**, *23*, 423–427; e) J. Nel-

Table 3. Hydrogen bonds in the structures for **1**·DMSO·4$CH_3OH$, **2**·4DMSO, and **3**·4DMSO.[a]

| Complex | D–H···A [Å] | D–H [Å] | H···A [Å] | D···A [Å] | D–H···A [°] |
|---|---|---|---|---|---|
| **1**·DMSO·4$CH_3OH$ | N(3)–H(3A)···O(3) | 0.860 | 2.219 | 3.041(7) | 159.95 |
| | N(5)–H(5A)···O(3) | 0.860 | 2.068 | 2.913(9) | 167.09 |
| **2**·4DMSO | N(6)–H(6A)···O(4) | 0.860 | 2.161 | 2.955(7) | 153.31 |
| **3**·4DMSO | N(5)–H(5A)···O(3)[a] | 0.860 | 2.136 | 2.940(7) | 155.52 |

[a] Symmetry positions of atoms: (a) 1 –*x*, *y*, 1/2 – *z*.

 © 2006 Wiley-VCH Verlag GmbH & Co. KGaA, Weinheim 

son, M. Nieuwenhuyzen, I. Pál, R. M. Town, *Dalton Trans.* **2004**, 229–235; f) B. Bag, P. K. Bharadwaj, *Inorg. Chem.* **2004**, *43*, 4626–4630.
[6] M. V. Baker, D. H. Brown, B. W. Skelton, A. H. White, *J. Chem. Soc., Dalton Trans.* **2000**, 4607–4616.
[7] a) B.-C. Tzeng, W.-C. Lo, C.-M. Che, S.-M. Peng, *Chem. Commun.* **1996**, 181–182; b) P. Planinic, D. Matkovic-Calogovic, H. Meider, *J. Chem. Soc., Dalton Trans.* **1997**, 3445–3451.
[8] L. Burai, É. Tóth, G. Moreau, A. Sour, R. Scopelliti, A. E. Merbach, *Chem. Eur. J.* **2003**, *9*, 1394–2404.
[9] a) M. E. Padilla-Tosta, J. M. Lloris, R. Martonez-Manez, A. Benito, J. Soto, T. Pardo, M. A. Miranda, M. D. Marcos, *Eur. J. Inorg. Chem.* **2000**, 741–748; b) N. W. Alcock, K. P. Balakrishnan, P. Moore, *J. Chem. Soc., Dalton Trans.* **1986**, 743–749.
[10] B.-C. Tzeng, B.-S. Chen, S.-Y. Lee, W.-H. Liu, G.-H. Lee, S.-M. Peng, *New J. Chem.* **2005**, *29*, 1254–1257.
[11] a) J. D. Hartgerink, T. D. Clark, M. R. Ghadiri, *Chem. Eur. J.* **1998**, *4*, 1367–1372; b) M. R. Ghadiri, K. Kobayashi, J. R. Granja, R. K. Chadha, D. E. McRee, *Angew. Chem. Int. Ed. Engl.* **1995**, *34*, 93–95.
[12] M. Linhard, M. Weigel, *Z. Anorg. Chem.* **1951**, *266*, 49–72.
[13] a) L.-Y. Zhang, G.-F. Liu, S.-L. Zheng, B.-H. Ye, X.-M. Zhang, X.-M. Chen, *Eur. J. Inorg. Chem.* **2003**, 2965–2971; b) J.-H. Luo, M.-C. Hong, R.-H. Wang, R. Cao, L. Han, Z.-Z. Lin, *Eur. J. Inorg. Chem.* **2003**, 2705–2710; c) B.-C. Tzeng, H.-T. Yeh, *Z. Naturforsch., Teil B* **2004**, *59*, 1320–1324.
[14] a) F. Charbonnier, A. Marsura, K. Roussel, J. Kovács, I. Pintér, *Helv. Chim. Acta* **2001**, *84*, 535–551; b) S. Sunami, T. Sagara, M. Ohkubo, H. Morishima, *Tetrahedron Lett.* **1999**, *40*, 1721–1724.
[15] *SMART V 4.043, Software for the CCD Detector System*; Siemens Analytical Instruments Division: Madison, WI, **1995**.
[16] *SAINT V 4.035, Software for the CCD Detector System*; Siemens Analytical Instruments Division: Madison, WI, **1995**.
[17] Sheldrick, G. M. *SHELXL-93, Program for the Refinement of Crystal Structures*; University of Göttingen: Göttingen, Germany, **1993**.
[18] SHELXTL 5.03 (PC-Version), Program Liberary for Structure Solution and Molecular Graphics; Siemens Analytical Instruments Division: Madison, WI, **1995**.

Received: November 28, 2005
Published Online: February 28, 2006

 © 2006 Wiley-VCH Verlag GmbH & Co. KGaA, Weinheim 

EurJIC
European Journal of Inorganic Chemistry

Issue 9/2006

Pages 1709–1900

*Papers available ahead of print in Early View at www.interscience.wiley.com*

*Earliest available Table of Contents:*
*Automatically, free of charge by e-mail through*
*www.interscience.wiley.com/alerts*

## COVER PICTURE

**The cover picture shows** the isomerization sequence of cobaltatricarbollides $(C_4Me_4)Co(C_3B_8H_{11})$ prepared by using convenient synthons of the $(C_4Me_4)Co$ fragment. The isomerization is associated with progressive space separation of the negatively charged carbon atoms and correlates well with the calculated relative stabilities of non-methylated analogs. Introduction of an amino substituent at the cage carbon atom dramatically reduces the rearrangement barrier and changes the pathway of the process. Details are discussed in the article by A. R. Kudinov et al. on p. 1737 ff.

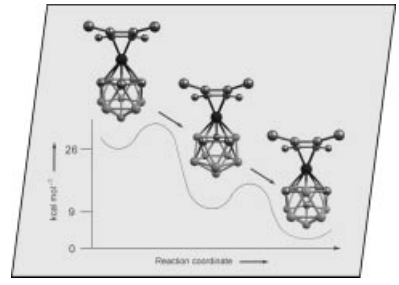


## MICROREVIEW

Contents

**1723** **J. J. Schneider,* J. Engstler**

Carbon and Polymer Filaments in Nanoporous Alumina

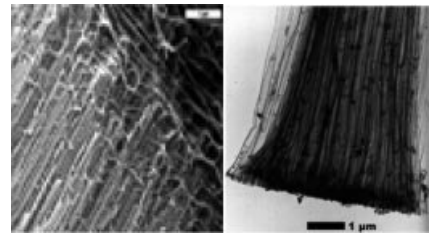


**Keywords:** Alumina / Porous templates / Nanotubes / Carbon / Nanochemistry

 © 2006 Wiley-VCH Verlag GmbH & Co. KGaA, Weinheim 

# FULL PAPERS


**1737** **E. V. Mutseneck, D. S. Perekalin, J. Holub, K. A. Lyssenko, P. V. Petrovskii, B. Štíbr, A. R. Kudinov***

(Tetramethylcyclobutadiene)cobalt Complexes with Tricarbollide Ligands

**Keywords:** Boron / Cobalt / Metallacarboranes / Cyclobutadiene

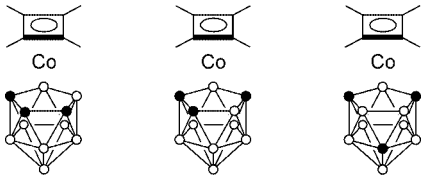


**1743** **T. Morotti, M. Pizzotti,* R. Ugo, S. Quici, M. Bruschi, P. Mussini, S. Righetto**

Electronic Characterisation and Significant Second-Order NLO Response of 10,20-Diphenylporphyrins and Their $Zn^{II}$ Complexes Substituted in the *meso* Position with π-Delocalised Linkers Carrying Push or Pull Groups

**Keywords:** Nonlinear optics / Porphyrins / Cyclic voltammetry / UV/Vis spectroscopy

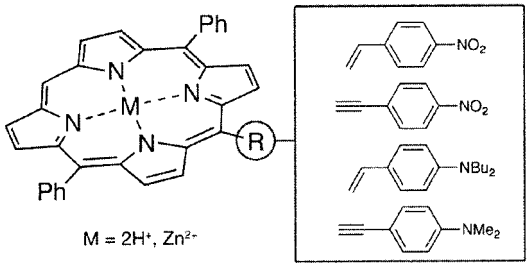


**1758** **A. Caballero, M. Cruz-Yusta, J. Morales, J. Santos-Peña,* E. Rodríguez-Castellón**

A New and Fast Synthesis of Nanosized $LiFePO_4$ Electrode Materials

**Keywords:** Copper / Lithium ion batteries / Materials science / Nanostructures / Phosphates

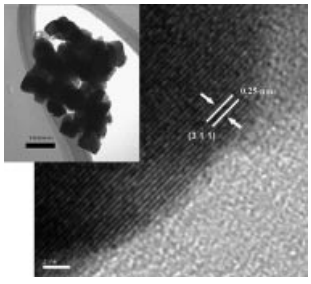

**1765** **T. Kajiwara,* T. Kobashi, R. Shinagawa, T. Ito, S. Takaishi, M. Yamashita, N. Iki***

Highly Symmetrical Tetranuclear Cluster Complexes Supported by *p-tert*-Butylsulfonylcalix[4]arene as a Cluster-Forming Ligand

**Keywords:** Cluster compounds / Calixarenes / Magnetic properties / Ligand exchange

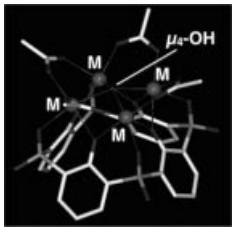


**1771** **D. Ray, P. K. Bharadwaj***

Alteration in the Binding Property of a Laterally Nonsymmetric Aza Cryptand toward $Cu^{II}$, $Ag^{I}$, and $Tl^{I}$ Ions upon Derivatization with a Cyanomethyl Group

**Keywords:** Cryptands / Coordination chemistry / Metal cryptate / Silver / Copper / Thallium

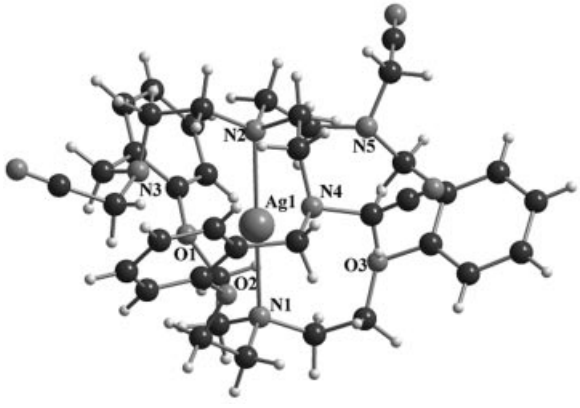



 © 2006 Wiley-VCH Verlag GmbH & Co. KGaA, Weinheim 

**1777** **F. Dornhaus, M. Bolte, H.-W. Lerner, M. Wagner***

Phosphanylborohydrides: First Assessment of the Relative Lewis Basicities of $[BH_3PPh_2]^-$, $CH_3PPh_2$, and $HPPh_2$

**Keywords:** P Ligands / Phosphanylborohydride / Ligand design / Donor–acceptor systems / Isoelectronic analogues

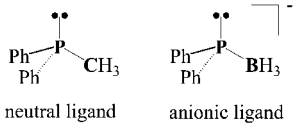


**1786** **R. H. Herber,* A. R. Kudinov, P. Zanello, I. Nowik, D. S. Perekalin, V. I. Meshcheryakov, K. A. Lyssenko, M. Corsini, S. Fedi**

Synthesis, Structure, Electrochemistry, and Metal-Atom Dynamics of Cyclopentadienyl Ferracarboranes

**Keywords:** Cyclopentadienyl ferracarboranes / Electrochemistry / X-ray diffraction / Mössbauer spectroscopy

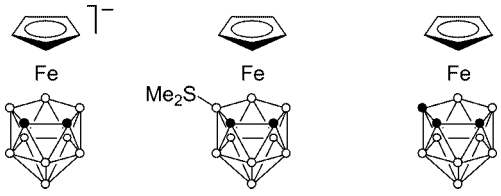


**1796** **R. Weiss, Y. Guo, S. Vukojević, L. Khodeir, R. Boese, F. Schüth, M. Muhler, M. Epple***

Catalytic Activity of Copper Oxide/Zinc Oxide Composites Prepared by Thermolysis of Crystallographically Defined Bimetallic Coordination Compounds

**Keywords:** Heterogeneous catalysis / Copper / Zinc / Thermochemistry / Structural chemistry

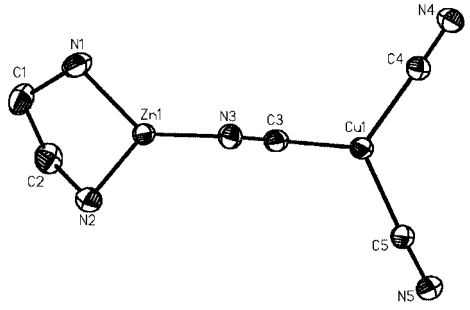


**1803** **R. Malacea, E. Manoury,* L. Routaboul, J.-C. Daran, R. Poli, J. P. Dunne, A. C. Withwood, C. Godard, S. B. Duckett**

Coordination Chemistry and Diphenylacetylene Hydrogenation Catalysis of Planar Chiral Ferrocenylphosphane-Thioether Ligands with Cyclooctadieneiridium(I)

**Keywords:** Ferrocenylphosphane ligands / Hemilability / Hydrogenation / Iridium / Planar chirality / Thioether ligands

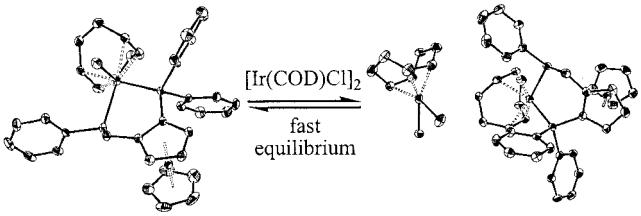


**1817** **W. Uhl,* A. El-Hamdan, K. P. Schindler**

Investigations into the Reactivity of Organoelement Gallium Subhalides – Syntheses of Bifunctional Digallium Carboxylate Iodides Possessing Bridged Ga–Ga Bonds and Terminal Iodine Atoms

**Keywords:** Gallium / Subvalent compounds / Subhalides / Metal–metal bonds / Carboxylato ligands

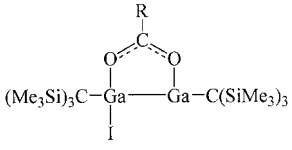



 © 2006 Wiley-VCH Verlag GmbH & Co. KGaA, Weinheim 

**1824** **A. Mondal, S. Basak, S. Sarkar, D. Chopra, R. Das, K. K. Rajak***

Binuclear Mixed Valence Oxovanadium(IV/V) Complexes Containing a $[OV^{IV}(\mu\text{-}O_{oxo})(\mu\text{-}O_{phen})V^{V}O]^{2+}$ Core: Synthesis, EPR Spectra, Molecular and Electronic Structure

**Keywords:** Vanadium / Oxovanadium complexes / Mixed valence

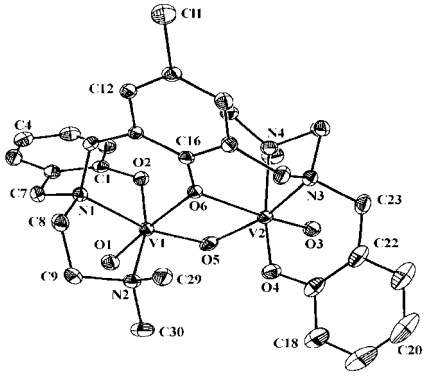


**1830** **D.-K. Cao, J. Xiao, Y.-Z. Li, J. M. Clemente-Juan, E. Coronado, L.-M. Zheng***

Metal Phosphonates Based on {[(Benzimidazol-2-ylmethyl)imino]bis(methylene)}bis(phosphonic Acid): Syntheses, Structures and Magnetic Properties of the Chain Compounds $[M\{(C_7H_5N_2)CH_2N(CH_2PO_3H)_2\}]$ (M = Mn, Fe, Co, Cu, Cd)

**Keywords:** Chain structures / Magnetic properties / N,O ligands / Organic−inorganic hybrid composites / Transition metals

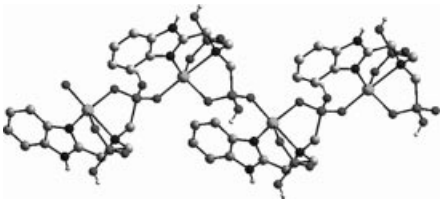

**1838** **Q. X. Wang, K. Jiao,* W. Sun, F. F. Jian, X. Hu**

Binding of an Oxo-Bridged Dinuclear Iron(III) Complex $\{[Fe(phen)(H_2O)_3]_2O\}(SO_4)_2$ to DNA and Its Recognition of Single- and Double-Stranded DNA As Determined by Electrochemical Studies

**Keywords:** Oxo-bridged diiron(III) complex / Crystallography / DNA recognition / Voltammetry

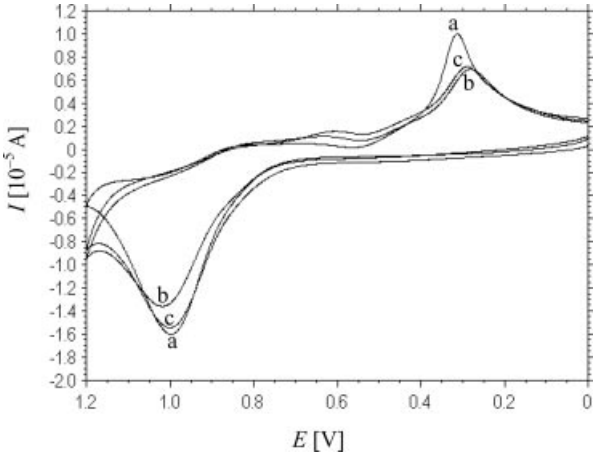


**1846** **A. Figuerola, J. Ribas, X. Solans, M. Font-Bardía, M. Maestro, C. Diaz***

One Dimensional 3d−4f Heterometallic Compounds: Synthesis, Structure and Magnetic Properties

**Keywords:** Lanthanides / Chromium / Cyanide / Magnetic properties

 © 2006 Wiley-VCH Verlag GmbH & Co. KGaA, Weinheim 

**1853** **D. Ávila-Brande,* L. C. Otero-Díaz, Á. R. Landa-Cánovas, S. Bals, G. Van Tendeloo**

A New $Bi_4Mn_{1/3}W_{2/3}O_8Cl$ Sillén−Aurivillius Intergrowth: Synthesis and Structural Characterisation by Quantitative Transmission Electron Microscopy

**Keywords:** Sillén−Aurivillius intergrowths / Layered oxyhalide / Electron microscopy / Exit-wave reconstruction / Bismuth

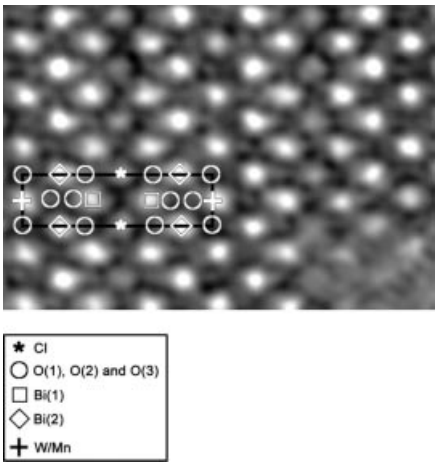


**1859** **A. Mondry,* P. Starynowicz**

Ten-Coordinate Neodymium(III) Complexes with Triethylenetetraaminehexaacetic Acid

**Keywords:** Chelates / Lanthanides / N ligands / Neodymium / UV/Vis spectroscopy

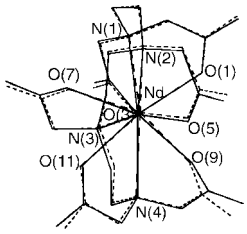


**1868** **M. R. C. Couri, M. V. de Almeida, A. P. S. Fontes,* J. D'Arc S. Chaves, E. T. Cesar, R. J. Alves, E. C. Pereira-Maia, A. Garnier-Suillerot**

Synthesis of Polyamines from Ethylenediamine and Their Platinum(II) Complexes, Potential Antitumor Agents

**Keywords:** Amines / Platinum / Antitumor agents

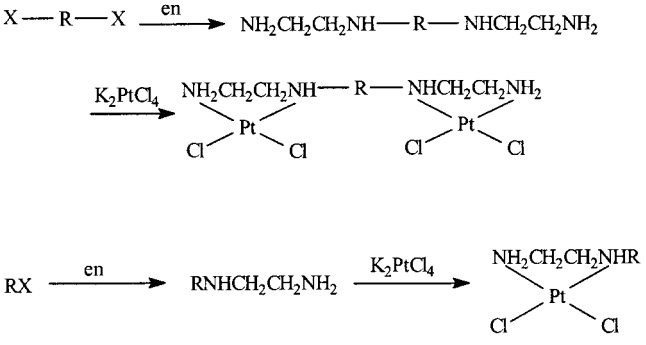


**1875** **E. Fördös, N. Ungvári, T. Kégl, F. Ungváry***

Reactions of $^{13}CO$ with Ethoxycarbonylcarbene-Bridged Dicobalt Carbonyl Complexes: [$\mu_2$-{Ethoxycarbonyl(methylene)}-$\mu_2$-(carbonyl)bis(tricarbonylcobalt)(*Co*−*Co*)] and [Di-$\mu_2$-{ethoxycarbonyl(methylene)}bis(tricarbonylcobalt)(*Co*−*Co*)]

**Keywords:** Isotopic labeling / C−C coupling / Carbene and carbonyl ligands / Cobalt / Fluxionality

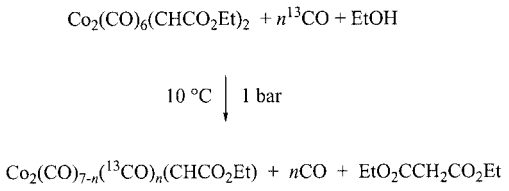


 © 2006 Wiley-VCH Verlag GmbH & Co. KGaA, Weinheim 

**1881** **D. V. Konarev,* A. Y. Kovalevsky, S. S. Khasanov, G. Saito, D. V. Lopatin, A. V. Umrikhin, A. Otsuka, R. N. Lyubovskaya**

Synthesis, Crystal Structures, Magnetic Properties and Photoconductivity of $C_{60}$ and $C_{70}$ Complexes with Metal Dialkyldithiocarbamates $M(R_2dtc)_x$, where M = $Cu^{II}$, $Cu^{I}$, $Ag^{I}$, $Zn^{II}$, $Cd^{II}$, $Hg^{II}$, $Mn^{II}$, $Ni^{II}$, and $Pt^{II}$; R = Me, Et, and *n*Pr

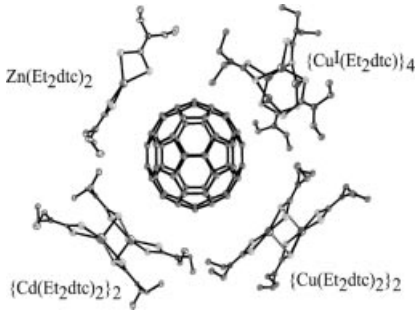


**Keywords:** Crystal engineering / Fullerenes / Metal dialkyldithiocarbamates / Magnetic properties / Photoconductivity

DOI: 10.1002/ejic.200501145

# Carbon and Polymer Filaments in Nanoporous Alumina

Jörg J. Schneider*[a] and Jörg Engstler[a]

**Keywords:** Alumina / Porous templates / Nanotubes / Carbon / Nanochemistry

Nanoporous alumina membranes represent templates for the synthesis and alignment of filamentous nanostructured materials. Porous aluminium oxide (PAOX) membranes are ideal for high-temperature synthesis. They are transparent, flexible, freestanding and thermally robust. Their pore sizes can be varied over a wide range. The membrane backside seems suited for structuring processes on the nanoscale, for which it may serve as a master. After introducing the formation process of PAOX membranes, synthesis of carbon nanotubes (CNTs) with different morphologies, their electrical field emission properties, and the formation of polymeric filaments and structured polymer surfaces with the aid of PAOX are reported in this microreview.

(© Wiley-VCH Verlag GmbH & Co. KGaA, 69451 Weinheim, Germany, 2006)

## 1. Introduction

Nanotubes derived from various carbon sources, doped with non-carbon atoms[1] or pure inorganic tubes[2] such as $MoS_2$,[3] $WS_2$,[4] BN,[5] are intensively studied over the last years because of their unique material properties. Besides the challenge towards the synthesis of such materials, there is also the need to arrange such materials in an organized manner. One important research goal is to synthesize and organize nanomaterials in a single process step that allows for their 1D, 2D, or even 3D arrangement. A common and widely used technique for 2D structuring of nanomaterials is the template process, in which a given form acts as a structure-directing shape to organize individual building blocks in a 2D arrangement. Inorganic templates are typically solid phases; they can be crystalline or amorphous. They are stable with respect to a geometrically defined structure and usually up to higher temperatures. Zeolites are prominent examples of such template types. They enable the organization of matter in a 1D or 3D fashion. Unordered inorganic porous structures bearing multiple voids

[a] Fachbereich Chemie, Eduard-Zintl-Institut für Anorganische und Physikalische Chemie, Technische Universität Darmstadt, Petersenstraße 18, 64287 Darmstadt, Germany
Fax: +49-6151-16-3470
E-Mail: joerg.schneider@ac.chemie.tu-darmstadt.de

*Jörg J. Schneider obtained his diploma and doctoral degree in chemistry at the Philipps-Universität Marburg in 1986, both in the group of Ch. Elschenbroich. After a one-year post doctoral stay in the group of K. J. Klabunde, USA, he joined the Max-Planck-Institut für Kohlenforschung, Mülheim an der Ruhr, in 1988. In 1994 he moved to the University of Essen as lecturer and Heisenberg fellow of the Deutsche Forschungsgemeinschaft. In 2000 he accepted a call as professor of inorganic chemistry at the Karl-Franzens-Universität, Graz, Austria. In 2003 he moved to his current position as professor of inorganic chemistry at the University of Technology, Darmstadt. His research interests are currently oriented towards interdisciplinary aspects of materials synthesis as well as organometallic chemistry. Examples include synthesis and properties of carbon tubes, porous materials, multinuclear metal complexes of condensed aromatics, as well as metal vapour synthesis as a synthetic tool in organometallic and materials chemistry.*

*Jörg Engstler was born in 1973. He studied chemistry at the University of Essen, Germany and obtained his diploma degree in 2000 in the field of synthesis and arrangement of carbon nanotubes. In the same year he moved to the Karl-Franzens-Universität, Graz, Austria, for pursuing his Ph.D. studies in the group of J. J. Schneider. His research activity was focussed on the synthesis and enhancement of field-emission properties of carbon nanotubes in and on porous alumina. In 2003 he received a Dr. rer nat. from the University of Essen. Since 2003, he is a post doc in the group of J. J. Schneider at TU Darmstadt, Germany. His research interests are in the area of porous nanomaterials, CVD and microscopic characterization techniques.*

**MICROREVIEWS:** This feature introduces the readers to the authors' research through a concise overview of the selected topic. Reference to important work from others in the field is included.

 © 2006 Wiley-VCH Verlag GmbH & Co. KGaA, Weinheim 

and pores of nonuniform diameters that are randomly distributed in the material are another kind of such a template. Those materials can typically not be used for the controlled organization of matter in 2D or 3D dimensions, because their pores appear unordered.

For creating filamentous nanomaterials with functional properties, for example for optics or electronics applications, a defined 1D orientation of materials and therefore of the pore structure of the template is essential. Zeolite-based templates like MCM 41, as well as organic-based templates, for example polycarbonate membranes, are useful in this regard. However, membrane templates based on organic materials are often temperature-sensitive, and therefore high-temperature processes within the membranes often employed for the synthesis of inorganic nanostructures are impossible with these templates.

Anodic porous aluminium oxide (PAOX) is a valuable template material for high-temperature processes. It is widely used in the scientific community as a template for synthesis and organization of nanomaterials.[6] Recently Schmid has reviewed the synthesis and properties of various nanoparticle compositions in PAOX.[7] Synthesis, arrangement and properties of different rod-shaped magnetic materials in PAOX have been reviewed by Wade.[8] Our contribution presented herein is focussed on the generation, properties and 2D arrangement of CNTs and filamentous polymeric structures, both made by gas-phase processes in and on the surface of PAOX.

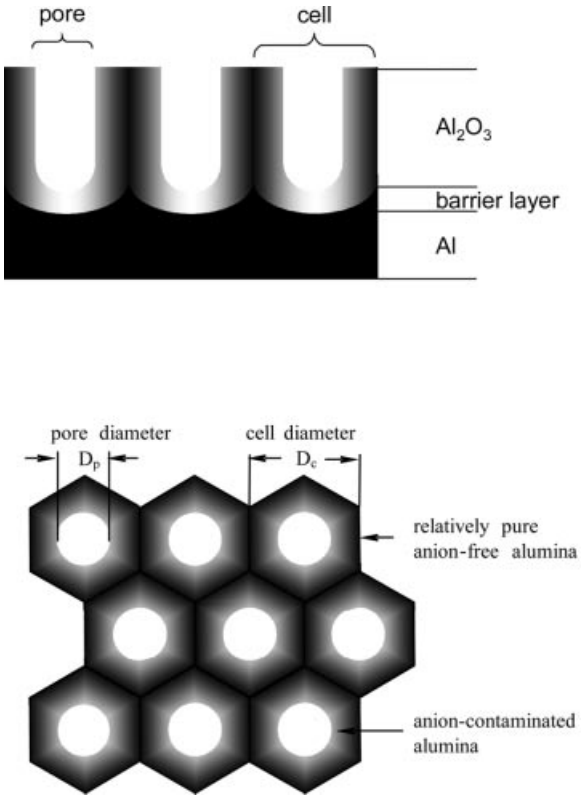


Figure 1. Schematic drawing of PAOX with idealized hexagonal ordered cells (diameter $D_c$) with a pore (diameter $D_p$) in the centre of each cell; cross-section (top), view from the top of the pore arrangement (bottom).

## 2. Nanoporous Anodic Aluminium Oxide as Template for Nanofilament Arrangement

The process of electrolytic oxidation of aluminium has a long-standing technological relevance and is commercially used for surface processing of aluminium for many decades. The pore system of alumina is formed by potentiostatic anodization, which is characterized by a constant voltage with a current change due to increased resistance in the growing oxide. The morphology of PAOX films synthesized in sulfuric acid has been investigated by Keller et al. already in 1953.[9] Early studies on the growth mechanism were performed by O'Sullivan and Wood in 1970.[10]

### *Formation and Structure of PAOX*

Figure 1 shows a schematic drawing of a PAOX membrane with a hexagonally ordered pore system.

The membrane consists of hexagonally ordered cells with one centred pore in each cell. Each cell has a unidirectional shape orthogonal to the membrane surface. The bottom of the pores is sealed by the so-called barrier layer, which connects the PAOX membrane with the aluminium metal base from which the porous membrane grows in a self-organized manner during an ongoing electrochemical oxidation process. This barrier layer is compact, however it has numerous defects due to the permanent dissolution by the electrolyte. These defects (channels, pits, voids) are the starting points for regular pore formation in latter stages of the electrochemical oxidation. Thus redissolving alumina and ongoing aluminium oxidation are competitive processes (see below). The finally resulting highly ordered PAOX membrane has a porosity of up to 10% with pore densities of up to $10^{11}$ pores per $cm^2$.[11] When a disordered growth is observed, the overall porosity can be significantly lower or higher.[12] The pore walls of the cells consist of two different types of alumina.[12] One type is a relatively pure, anion-free, dense alumina (dark grey regions in Figure 1, bottom). It builds up the hexagonal body of the cell. This material is not in direct contact with the open pore space. The inner cell region of the pores consists of a less dense alumina (light grey regions in Figure 1, bottom) contaminated with electrolyte anions ($PO_4^{3-}$ $SO_4^{2-}$, $C_2O_4^{2-}$), which forms the pore wall and therefore is in direct contact with the electrolyte during the electrochemical process. By controlled selective etching of the backside barrier layer, PAOX membranes with complete trough-hole pore morphology can be obtained.

The diameter of the pores ($D_p$) and the cells ($D_c$) of a PAOX membrane are dependent on the anodization potential applied in the electrolytic process.[6h,13] Additional experimental parameters governing the pore size are temperature and current density. The latter is influenced by the concentration and the type of electrolyte used.[11]

PAOX membrane pore diameters between ca. 5–300 nm are so far experimentally accessible. As a rule of thumb, a voltage of 1 V corresponds to a pore growth of ca.

 © 2006 Wiley-VCH Verlag GmbH & Co. KGaA, Weinheim 

1.2 nm.[10] This value depends on anodization conditions and electrolyte concentration. Figure 2 shows examples of electron micrographs of PAOX membranes with varying pore diameters (Figure 2).

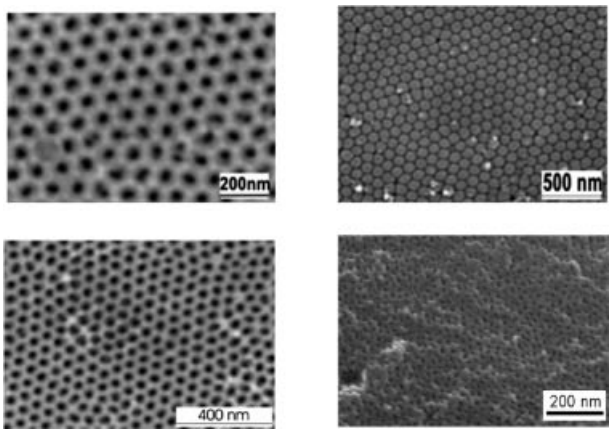


Figure 2. SEM images of freestanding PAOX membranes. From upper left to lower right: open front side of a PAOX membrane generated at 40 V, back side of a PAOX membrane generated at 40 V, open front side of a PAOX membrane generated at 25 V, open front side of a PAOX membrane generated at 8 V.

To obtain PAOX templates with different pore size regimes, different electrolytes are used. From 150 to 300 nm $H_3PO_4$, from 30 to 70 nm oxalic acid and below 20 nm $H_2SO_4$ give reproducible results with respect to pore-size diameters.[8] This electrolyte dependence of pore size distribution is mainly due to the fact that the pore diameter is affected strongly by the dissolution velocity of alumina in the electrolyte chosen. The dependence of pore size on electrolyte type is, however, complex and involves the dissociation behaviour (pH value, acid/conjugate base equilibrium) and concentration of the electrolyte (e.g. changing the electrolyte concentration changes the pH) as the foremost parameters.

The basic membrane-film-forming reaction is dissolution of the base metal according to

$$Al(s) \rightarrow Al^{3+} + 3e^-$$

$Al_2O_3$ is then formed by reaction with $O^{2-}$ ions which are generated in the acidic electrolyte medium by the reaction

$$3/2\ H_2O \rightarrow 3\ H^+ + 3/2\ O^{2-}$$

The formation process of the alumina is accompanied by a local dissolution of the formed alumina due to agitation by protons

$$1/2\ Al_2O_3(s) + 3\ H^+(aq) \rightarrow Al^{3+}(aq) + 3/2\ H_2O(l)$$

The latter reaction preferentially occurs at the bottom of the formed pores where the electrical field is highest. This reaction obviously does not play an important role during the initial formation of the compact base oxide layer lying underneath the porous layer.

During electrolyte anion incorporation into the growing membrane, the following reactions occur:[6h]

$$H_3PO_4\ (aq) \rightarrow H_2PO_4^{2-} + H^+$$

$$H_2PO_4^-\ (aq) \rightarrow HPO_4^{2-} + H^+$$

The conjugate divalent base anion $HPO_4^{2-}$ can replace $O^{2-}$ in the oxide forming reaction, thus leading to a contamination in the growing film. Therefore 6–8 wt.-% $PO_4^{3-}$ incorporation of the membranes is typically observed when phosphoric acid is used the electrolyte. Similar percentages of incorporation are observed for other electrolyte anions ($SO_4^{2-}$, $C_2O_4^{2-}$). In contrast, electrolytes which do not form protonated conjugate bases lead to contamination of free PAOX membranes (e.g. chromic acid[6h]).

The electrochemical process of controlling and downsizing the pore diameter by adjusting the anodization voltage as one of the crucial parameters works well down to pore sizes of around 15 nm in the strong electrolyte $H_2SO_4$. There is an interest in such nanoporous self-supporting template materials due to their application as nanovessels for synthesis and organization of matter on the nanoscale. In the size regime below 15 nm, quantum size effects start to become important for many materials, and a self-supporting porous template should make it possible to study anisotropic effects of such structure-confined materials. However, reports on self-supporting PAOX membranes with a pore size below ca. 15 nm are scarce. Highly unordered PAOX films deposited on glass substrates with small pore diameters (<10 nm) are known.[14–16] We have studied pore-size growth of PAOX at anodization voltages down to 8 V. Formation of a porous alumina with a pore diameter of about 10 nm results. Handling these PAOX membranes as freestanding templates, however, becomes increasingly difficult: for example, such membrane templates tend to be brittle and are mechanically fragile. In contrast, PAOX membranes with pore sizes between 20 and several 100 nm exhibit good mechanical stability. They are not very fragile and can withstand even moderate mechanical torsion, for example bending. The reason for this is their cellular structure. It is well known that if pores in a given cellular structure are hexagonally oriented, the mechanical stiffness of such a cellular arrangement decreases roughly by a factor of 50 compared to a similar compact structure.[17] This finding is based on the variation of the *E*-module which is dramatically affected when comparing a compact with a porous structure. In a first approximation, this is regardless of the individual material composition of such a structure.

Thus, the high tensile strength of the as-prepared PAOX template relative to a dense, compact alumina film of the same composition seems mainly due to its mechanical flexibility imparted by its regular open porous nature relative to the dense material of same composition.

## 3. Carbon Nanotubes and Polymer Fibres in PAOX

### 3.1 Carbon Nanotubes in PAOX

#### *CNTs Synthesized in PAOX without Catalyst*

Spatially arranged CNTs provide a promising material for applications in e.g. Li-ion batteries,[18] chemical filters,[19] capacitors,[20] cold field emitting sources[21] or tran-

 © 2006 Wiley-VCH Verlag GmbH & Co. KGaA, Weinheim 

sistors.[22] PAOX is ideally suited as a template for CNT synthesis by CVD, a process which typically operates above 700 °C.[23–25] The diameter of the CNTs formed inside the PAOX template pores during CVD should be the same as the PAOX pore diameter. Hence, a general feature of PAOX, its versatility to control the diameter of the CNTs, becomes apparent.

In a typical experiment, a gaseous precursor like propylene or acetylene transported by a carrier gas is decomposed within a hot-wall tube reactor in which the open membrane is inserted vertically in a flow-through geometry.[26] The pores of the membrane are then completely filled with CNTs during the CVD process. Figure 3 shows a SEM image of such a CNT/PAOX membrane composite.

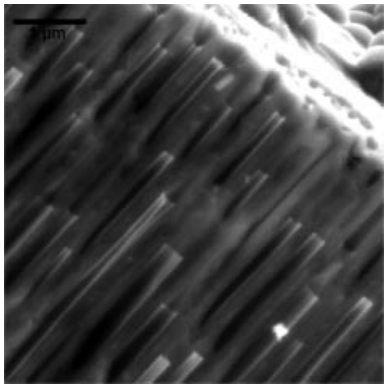

Figure 3. SEM image of a CNT/PAOX membrane composite showing a broken edge from which the CNTs protrude out of the pores of the PAOX.

Typical synthesis conditions for our CNT formation process are 900 °C, propylene flow between 1 mL and 14 mL per minute depending on the reaction time (5 min to 40 min). After the CVD process, the PAOX surface is usually covered with residual carbon materials. These can be "burned away" under controlled and mild oxidative conditions without destroying the CNTs.[26]

### *CNTs Synthesized in PAOX Loaded with Catalyst*

PAOX templates can be loaded with appropriate catalyst precursors like inorganic Fe salts prior to CNT growth, for example simply by dip filling.[27,28] Under reducing conditions, flowing $H_2$ is used for this purpose; the active catalyst can then be generated in nanoparticle form.[29] The effect of the catalyst particles on CNT growth is twofold. On the one hand, the use of catalyst particles reduce the synthesis temperature for CNT growth, on the other hand, CNT graphitization can be achieved already at lower temperatures relative to an uncatalyzed CVD process.

Impregnation of PAOX membranes with a catalyst prior to CNT synthesis leads to a CNT/PAOX composite material. The CNT/PAOX composite material can be freed from the PAOX template by dissolving it in diluted HF. The resulting carbon filaments have a fibre-like compact structure as revealed by transmission electron microscopy (TEM). At a higher magnification, a tube-in-tube morphology ("carbon nanotube bags") can be identified by TEM (Figure 4).[29,30] The smaller inner tubes display helicoidal structures and are almost densely packed within the outer "carbon nanotube bags". The compact fibre-like material therefore contains two different carbon tube morphologies of different size. The outer, larger tubes are produced by the deposition of carbonaceous precursor species derived from the molecular precursor gas source (e.g. propylene). These CNTs are formed on the inner walls of the PAOX membrane during the CVD process. Their diameter is determined by the pore dimensions of the template. In this process, the inner walls of the PAOX template are cast.

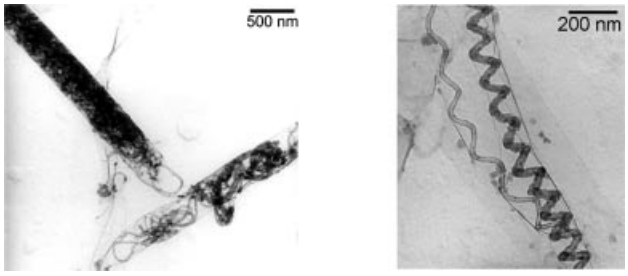


Figure 4. TEM image of "nanotube bags" freed from the PAOX template; left: the inner helicoidal CNTs are surrounded by the outer, larger CNT; right: helicoidal morphology of a single interior CNT.

The PAOX template pore walls represent a surface with high morphological roughness. This roughness is reflected in the morphology of the CNT walls, which show no ideal straight alignment but a rather high degree of dislocation of the carbon tube walls (Figure 5).

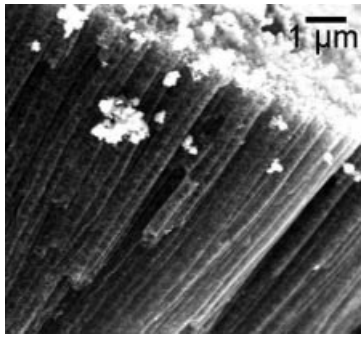


Figure 5. SEM micrograph showing PAOX-freed CNTs in typical parallel block arrangement.

The dense filling of the larger carbon tubes with the smaller helicoidal CNTs in their interior is due to a catalytic process. It is mediated by the iron particles which are derived from the catalyst precursor introduced into the PAOX by the impregnation step.[27] The diameter of the helicoidal inner CNTs is about 20 nm and corresponds well with the size of the catalyst particles which are mainly found at the end of the tubes (Figure 6).

In addition, TEM and AFM investigations[29] reveal that the diameter of the large outer CNTs is enlarged when freed from the template, relative to what is expected from the given size of the template pores in which they are formed. This fact can be understood by the only partially graphi-

 © 2006 Wiley-VCH Verlag GmbH & Co. KGaA, Weinheim 

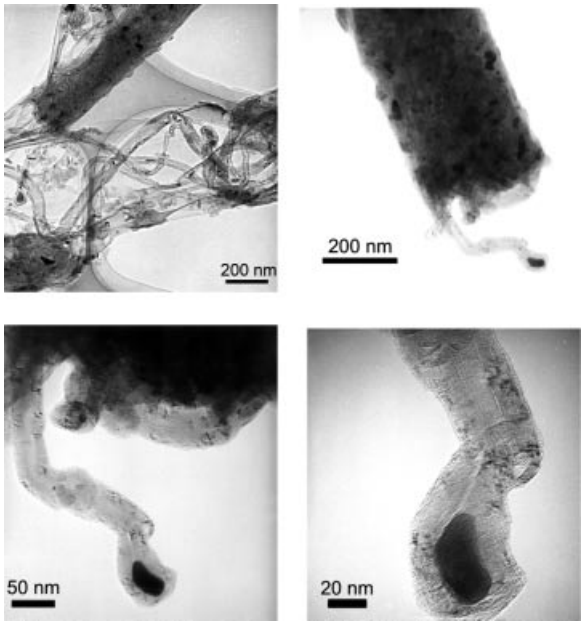


Figure 6. TEM images of CNT bags filled with small CNTs derived from catalyst impregnation. From upper left to lower right: overview of small CNTs with catalytic particles located at the end of the smaller inner tubes; different magnifications of CNT inner tubes with catalytic particles at the end of the small CNTs.

tized structure of the tube walls of the outer CNTs as it is revealed by high resolution TEM (HRTEM) investigations (Figure 7).

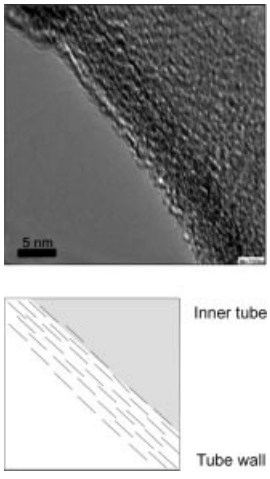


Figure 7. Top: HRTEM image of a "CNT bag" wall structure showing the partially graphitized wall structure; bottom: corresponding schematic model of the outer CNT wall structure.

The schematic model, which is in accord with the experimentally observed morphology found in the HRTEM, is shown in Figure 7. Relatively short multilayered, intermingled graphene sheets are characteristic for the CNT wall structure. This graphene sheet structure is flexible and allows the outer tubes to widen their diameter significantly when an inner pressure is exerted upon the walls. As long as the CNTs are embedded in the PAOX template, their diameter is fixed. However, when the CNTs are freed from the template, a dense filling of the CNTs may lead to a significant expansion of their diameter. This is a kind of "breathing process" which releases inner pressure from the CNT walls imposed on them by the dense filling with the small helicoidal tubes. Obviously, such a widening process can even lead to a rupture of the walls of the large CNTs and to the liberation of the entrapped small helicoidal tubes (Figure 8).

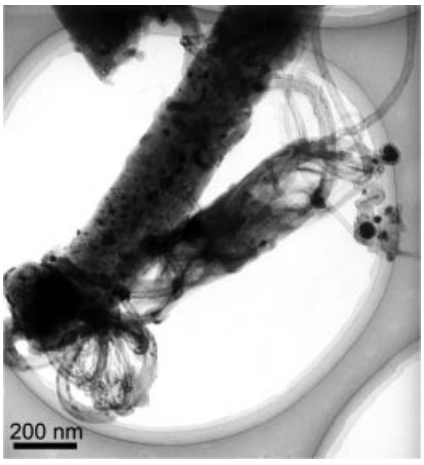


Figure 8. TEM of a compact CNT bag. After breaking the outer CNT wall, the inner CNTs swell out of their surrounding shell (bottom left).

We have studied the elastic properties of the carbon nanotube bags by AFM with the nanoindentation technique.[31–33] A Berkovitch-type indentation probe (100-nm

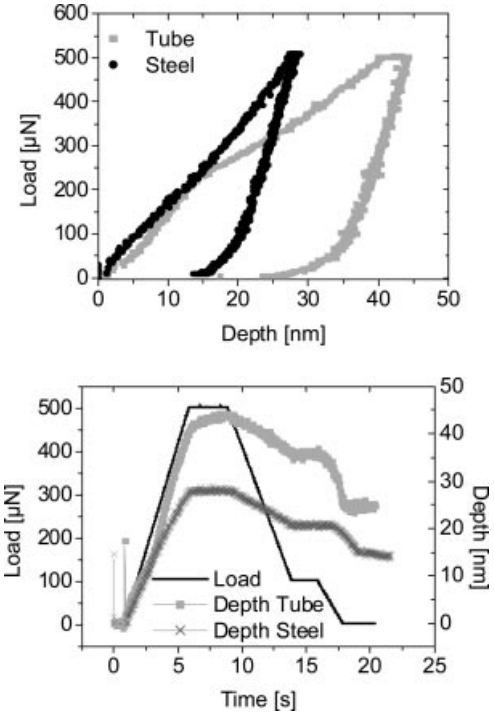


Figure 9. Nanoindentation loads (up to 500 μN) vs. indentation depth applied to a single filled carbon nanotube bag.

 © 2006 Wiley-VCH Verlag GmbH & Co. KGaA, Weinheim 

tip radius) was placed in the middle of a single carbon nanotube bag. Experiments were conducted with up to 500-μN loads on the tip (Figure 9, top). Up to loads of 220 μN, the indentation depth increased linearly with increasing load. In the low-load regime (up to ca. 60 μN) the CNT displayed viscoelastic behaviour with nearly no residual plastic deformation (<1 nm). When the final indentation load was increased to 500 μN, the depth of impression on the carbon nanotube bag structure increased considerably to 35 nm. However, at a load of 230 μN a sudden deviation from a linear behaviour was found (Figure 9, top).

After release of the maximum load a residual depth of impression of 27 nm remained in the material (Figure 9, bottom). Compared with the low-load regime, where a maximum load of 60 μN was applied, this dramatically different behaviour at higher loads may be attributed to a sudden rupture of the CNT wall structure. In the low-load regime, the filled CNT nanotubes show viscoelastic behaviour typically observed for soft matter (e.g. polymers), whereas high enough compression loads lead to the destruction of the outer CNTs (see Figure 8).

### *CNTs in PAOX Derived from Single-Source Precursor Molecules*

There have been several reports on the synthesis of CNTs using single-source precursors.[34] Examples for such precursors are organometallic compounds like metallocenes or coordination compounds like iron(II)phthalocyanine.[35,36] In these precursors, there exists a fixed, stoichiometrically defined metal-to-carbon ratio. Ferrocene is a prominent precursor for CNT synthesis by CVD techniques.

Figure 10 displays a typical TEM image of CNTs derived from ferrocene as the sole CNT precursor. In these experiments, the CNTs have been first synthesized and then deposited freely on a freshly cleaved mica surface. Due to the low carbon-to-iron-catalyst ratio (10:1) when employing ferrocene, the CNTs are mostly filled with iron metal.[37]

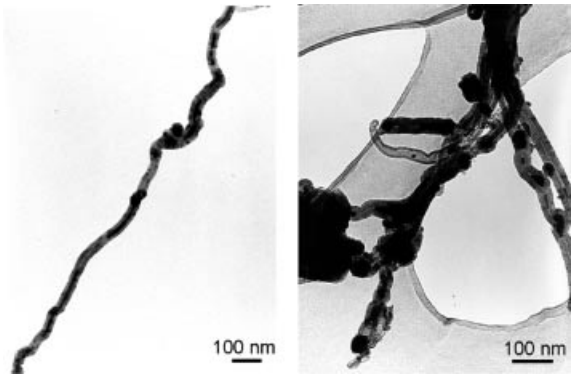


Figure 10. TEM images of CNTs synthesized via CVD of ferrocene on a native mica support at different magnifications.

When the carbon-to-iron ratio is increased by a factor of 7, CNTs with a much lower iron content are formed, and subsequently no formation of compact iron rods is observed inside the CNTs. Instead, particles are formed in the CNTs (Figure 11). An increase in the carbon-to-iron ratio was achieved by adding an additional carbon source to the ferrocene precursor.[38] We used the polycondensed aromatic hydrocarbon decacyclene $C_{36}H_{18}$ as the additional carbon source.[26,39,40]

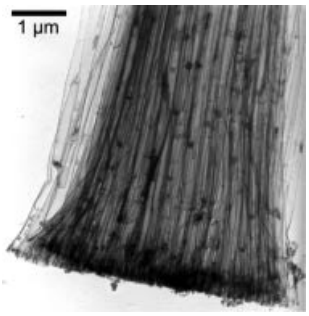


Figure 11. TEM micrograph of a CNT bundle synthesized by deposition of a mixture of decacyclene/ferrocene (70:1 at.-%) in PAOX (template removed).

Bundle-like arrangements of CNTs are found after dissolution of the PAOX template. Metal particles are distributed within these CNT bundles.

When using chromocene, $[(\eta^5\text{-}C_5H_5)_2Cr]$, a precursor with the same carbon-to-metal ratio as that in ferrocene, CNTs are formed under similar conditions (Figure 12). However, in contrast to the CNT material obtained from the ferrocene precursor, no metallic wires are formed within the tubes. The CNTs contain particles distributed alongside the CNTs, although the carbon-to-metal ratio is identical to that in ferrocene. Obviously, not only the stoichiometric carbon-to-metal ratio, but also the nature of the catalytic metal or the precursor are important for the filling of the CNTs, either with metallic rods or particles.

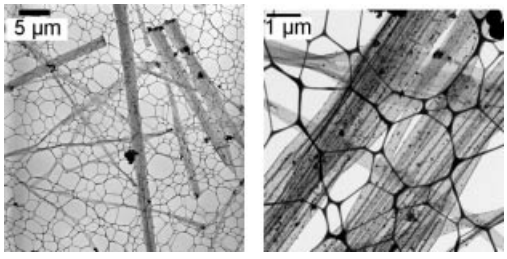


Figure 12. TEM micrographs of template-freed CNTs synthesized by deposition of chromocene in PAOX. A characteristic parallel-block arrangement of CNTs derived from PAOX is maintained (template removed).

Comparison of the results for CNT synthesis performed by the single-source strategy without a structure-directing template and those for the template-steered synthesis by using PAOX shows that the resulting CNT materials have different morphologies. CNTs prepared by the template technique display a parallel alignment of CNTs, with overall straight tube body morphology and defined tube radii. In contrast, CNTs prepared by a template-free CVD process by using a single-source strategy have a poorer straightness, a significant deviation in tube diameter and a random distribution of their metal filling.

 © 2006 Wiley-VCH Verlag GmbH & Co. KGaA, Weinheim 

Element-filtered TEM (EFTEM) has provided detailed information about the elemental distribution of CNT materials. In general, EFTEM enables the recording of two-dimensional distributions of chemical elements (Li to U) with a resolution down to about 1 nm. Chemical and structural heterogeneities may thus be imaged by recording elemental distributions. Applying this technique supplies an enormous amount of information relative to conventional bright-field TEM. In Figure 13, the results of such an EFTEM investigation of a single CNT synthesized by CVD by using chromocene as precursor and PAOX as template are shown.

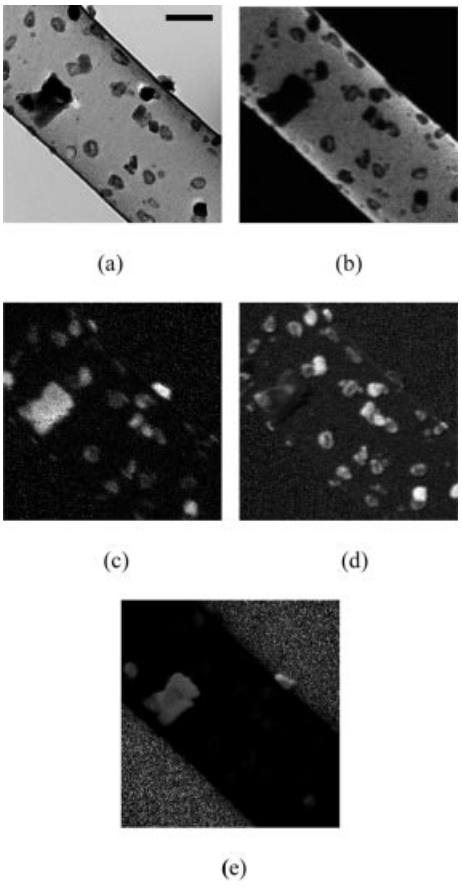


Figure 13. EFTEM investigations on a single CNT (precursor: chromocene): (a) bright-field image of a single CNT with incorporated particles; images of single-element distributions with elements displayed in lower contrast, (b) carbon, (c) oxygen, (d) chromium, (e) aluminium; (scalebar for all images: 100 nm).

The selective elemental mapping gives the spatial distribution along the CNT (Figure 13b–e). Obviously, chromium is a main constituent. Besides the elements chromium and carbon, oxygen is also present in the irregularly shaped particles, which have a diameter between 20 and 30 nm (shown in Figure 13c). Thus, the formation of chromium oxide particles seems reasonable. The formation of these oxide particles is yet unclear since the CVD process proceeds under otherwise inert conditions.

The origin of the detected alumina particles (Figure 13c,e: O and Al elemental maps) can be attributed to the incomplete dissolution process of the PAOX template during sample preparation, leaving minor amounts of residual alumina in the sample.

Similar experimental and EFTEM analytical results were obtained for the synthesis of CNTs by using metallocenes of Ni and Co as single-source precursors. In both cases, CNTs with diameters corresponding to the PAOX template were found. The CNTs again contained metal particles inside the tubes. Ultrathin samples of these CNTs, still embedded in the PAOX template, were studied by TEM (Figure 14).

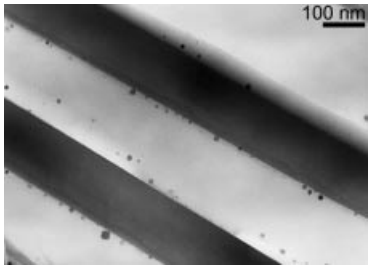


Figure 14. TEM image of an ultrathin sample of CNTs embedded in PAOX, obtained by microtoming (CVD precursor nickelocene). Dense regions which appear with a dark contrast display the PAOX template walls. Alongside the PAOX tube walls, small nickel particles are deposited. Some appear to be partly embedded in an amorphous carbon shell.

Particles with a high nickel content, which are found alongside the pore walls of the CNTs and/or the PAOX template, can be detected by EFTEM analysis of such samples. As for the chromocene case, oxygen is present, however its origin cannot be unambiguously determined, now because of the close proximity of the Ni particles to the surrounding alumina pore walls.

### *Field Emission from CNT Arrays*

An interesting electrical property of CNTs is their field-emission (FE) behaviour. Because of their small diameter, the electronic working function of CNTs is dramatically reduced. Thus, a tunnelling effect of electrons can occur, and consequently theoretical and experimental studies on the electron emission of CNTs have been in the focus of research already for more than one decade.[39,41] Multiwalled CNTs (MWCNTs) are mechanically more robust and are also less prone to electrical degradation than single-walled CNTs (SWCNTs). The emission from MWCNTs shows metal-like behaviour, as deduced from electron spectroscopic studies.[42] For MWCNTs, characteristic parameters in FE, such as the onset field for emission, current density and electrical field enhancement factors β,[43] are drastically improved[44,45] relative to other relevant FE materials like diamond tips,[46] Si[47] and GaN,[48] which were studied intensively over the past years.

For isolated, single CNTs, ten times higher field enhancing factors β are observed relative to CNT films containing bundles of unordered tubes.[49] Thus, different strategies can be followed to obtain good field-emitting devices based on SWCNTs or MWCNTs. One general strategy seeks the most perfect two-dimensional arrangement of CNTs in order to

 © 2006 Wiley-VCH Verlag GmbH & Co. KGaA, Weinheim 

arrange as many emitters as possible on a substrate.[50] This assures that a huge number of high aspect ratio structures are produced and are available for FE. Another synthetic strategy arranges CNT emitters in defined areas with a high enough distance to each other, thus fulfilling the theoretical requirement that the distance between single emitters is about the height of an individual emitter to obtain long-term FE stability.[51] By realizing the latter approach, the inter-emitter field penetration due to charging and electrical degradation is significantly reduced relative to arrangements where a higher emitter density is achieved (Figure 15).

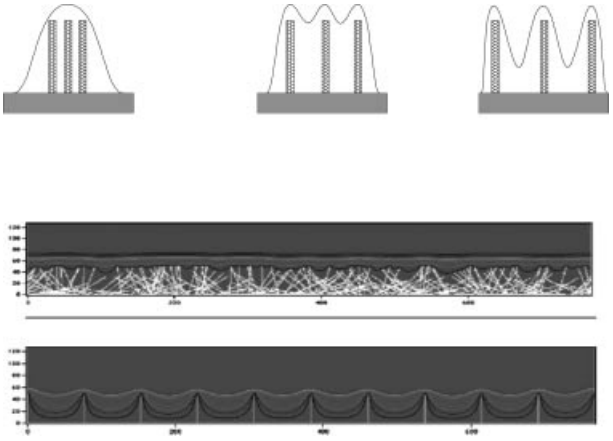

Figure 15. Schematics showing the dependence of the individual electrical field penetration of CNT emitters as a function of the emitter distance. Idealized model (top), model of a realistic CNT surface with high emitter surface coverage (bottom).

Densely populated CNT cathodes therefore have definite disadvantages in their FE behaviour at low fields due to mutual shielding effects (Figure 15).[51] Well-separated CNTs with still high enough densities per area and homogeneous FE characteristics, however, need synthesis techniques other than the former.[44] Up to this date, successful studies have been reported to optimize the FE performance for aligned CNTs.[41e,45,50,52–54] We used PAOX as a templating material for CNTs and investigated the resulting FE properties.[55] In these experiments, additional positive influences of PAOX on the FE behaviour could be detected: for example, electrical insulation of the CNT emitters due to their embedding in the dielectric matrix of PAOX seems advantageous in avoiding destructive degradation by field effects.[51] On the other hand, it has been observed that an outgrow of CNTs over the PAOX surface promotes FE properties.[56] For CNTs which are overgrowing the PAOX template structure, low onset fields for emission of 3–4 V $\mu m^{-1}$ are found. In contrast to these results, CNTs which are totally embedded in PAOX and do not surmount the surface at all, have ten times higher onset fields for FE.[55]

Our work in the area of synthesis and arrangement of CNTs for FE applications has so far focussed on metallocenes or mixtures of metallocenes with polycondensed aromatics as precursors for CNT synthesis.[29,44,57–59] Growing of CNTs by using metallocene precursors was achieved in and on the surface of PAOX membranes and led to an unordered growth on the PAOX surface. Good FE characteristics for such materials were observed when alumina particles were first deposited by CVD from a precursor [source: aluminium tris(sec-butoxide)] on the PAOX surface prior to CNT deposition by CVD (precursor: ferrocene). Then, CNT growth preferentially occurred on the deposited alumina islands (Figure 16).[44,58–60]

FE measurements on this material where performed in a diode configuration. The emission picture was obtained after sample conditioning by current processing.[58,59] Sample conditioning is a standard procedure in FE studies and is necessary because the FE effect and especially the long-term stability of the emitters are very sensitive to any surface and gaseous atmospheric impurity.[58–60] Integral FE measurements on such samples have yielded current densities up to 32 mA $cm^{-2}$ at 7.2 V $\mu m^{-1}$.[59] These values are based on a uniform emitter distribution and an emitter number density of 10000 $cm^{-2}$. This is so far a superior result compared with current values from other studies.[52–54]

Single-emitter investigations on the material revealed stable Fowler-Nordheim-like I–V curves.[58] Despite the observation of some short-term current fluctuations, the alumina-based CNT cathodes provide already reasonable long-term current stability (>18 h) as shown in Figure 17 and Figure 18.

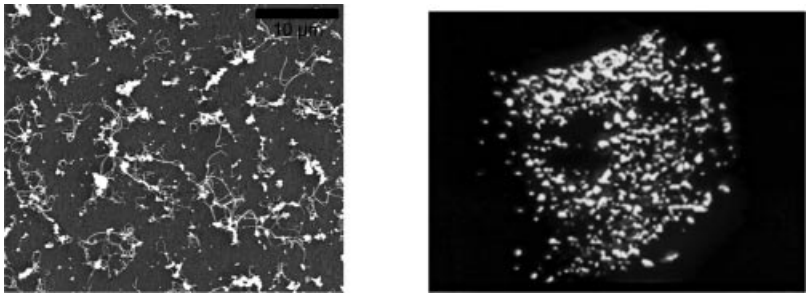


Figure 16. Typical SEM image of isolated CNTs grown on the surface of the PAOX membrane by CVD for FE investigations. The CNTs responsible for FE are linked to the surface of the PAOX by CVD deposition on predeposited alumina islands; right: emission picture of such a sample (size 28 $mm^2$) after conditioning (see text).[59]

 © 2006 Wiley-VCH Verlag GmbH & Co. KGaA, Weinheim 

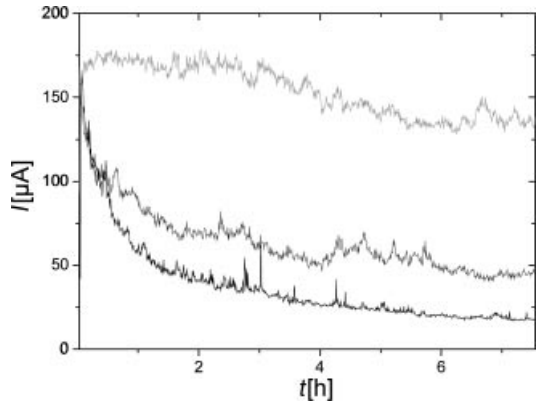


Figure 17. Long-term current stability of a 28-mm$^2$ sample on PAOX at various pressures/fields: $2\times10^{-6}$ mbar at 4.6 V µm$^{-1}$ (upper trace); $5\times10^{-5}$ mbar at 5.3 V µm$^{-1}$ (middle trace); $5\times10^{-4}$ mbar at 6.5 V µm$^{-1}$ (lower trace).[59]

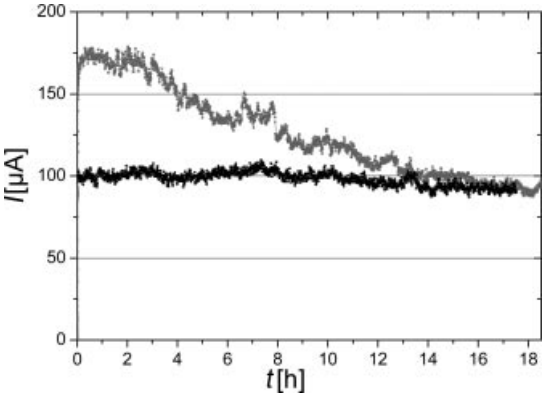


Figure 18. Comparison of the typical long-term current stability of a CNT cathode measured at $10^{-6}$ mbar at 4.6 V µm$^{-1}$ before (upper trace) and after processing (lower trace) up to 700 µA.[59]

Nevertheless, developing stable CNT field emitters with high performance characteristics is an important task in this research area (long-term stability ≥ 10000 h). Furthermore, an aligned and directed growth of CNTs has to be realized in order to obtain well-separated nanotubes. Such an alignment of emitter structures is so far only realized in Spindt type configurations, which are up to now still the only industrially viable field emitter structures.

### 3.2 Polymeric Structures in and on PAOX

#### *Synthesis and Alignment of Polymeric Poly(p-xylene) (PPX) Filaments Derived from PAOX*

The first reports on the synthesis of polymer tubes and cylinders in PAOX templates appeared in the mid 1990s.[61–63] A recently explored technique uses the controlled wetting of ordered pores of PAOX to generate polymer nanotubes.[64,65] In this approach, the high-energy surface of a PAOX membrane is wetted by a low-energy organic polymer to fill the pores and mould the PAOX template structure. This results in formation of polymeric nanotubes after removal of the template. With this technique, 2D arranged polystyrene, polytetrafluoroethylene (PTFE), polymethyl methacrylate (PMMA) or palladium/polymer composite materials are accessible in filamentous form, either embedded in the template or freed from the template.[64,65] 2D confinement studies of symmetric and asymmetric block copolymers in PAOX templates have been reported recently.[66,67] Formation of polymer or block copolymer nanorods is driven by capillary forces which force the polymer[66] or copolymer melt[67] into the cylindrical nanopores of the PAOX template. These studies show that microphase separated copolymers are formed within the nanochannels of PAOX. The observed polymer structures are not only triggered by the pore size of the template but also by the specific interaction of pore wall with polymer, leading to phase-segregated copolymer rods in which for example styrene or polybutadiene forms the central core.[67,68]

Gas phase processes have been studied recently to form tube- or wire-like structures of other technically important polymers, like poly(*p*-xylene), PPX, in PAOX.[68] PPX films have very good electrical insulation and barrier properties, excellent solvent and hydrolytic resistance, biocompatibility, transparency and thermomechanical properties. PPX is formed by evaporation and vapour-phase pyrolysis of [2.2]-paracyclophanes as precursors. 1,4-Quinodimethanes are formed as intermediates, acting as monomers (Scheme 1). The in situ formed quinodimethanes polymerize spontaneously on nearly any given substrate upon vapour phase deposition at temperatures equal to or below 30 °C by formation of conformal highly adhesive PPX films.[69]

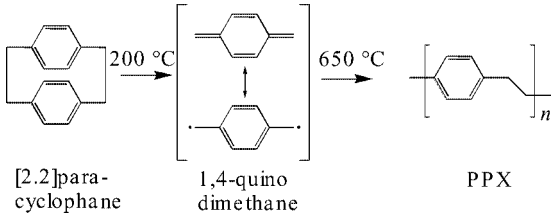


Scheme 1. Formation of PPX polymer starting from [2.2]paracyclophane precursor via intermediate 1,4-quinodimethane.

Within PAOX, PPX can be synthesized in a fibre morphology by chemical vapour deposition polymerization. Figure 19 shows a top and side view of a PPX film formed on PAOX after CVD polymerization deposition. PPX forms a closed film on top of the template, covering its surface completely.

PPX fibres are formed within the pores of the template (Figure 19). The compact PPX films on top of the template can be detached from the surface mechanically or by chemical techniques.

The ordered backside of PAOX membranes can be used for patterning a polymer such as PPX in a straightforward technique by moulding the backside when using it as a master form. This master backside with desired nanodimensions can be prepared by electrochemical oxidation of aluminium metal and detachment of the film from the metal base. This simple technique avoids complicated physical structuring processes like e-beam lithography for shaping a

 © 2006 Wiley-VCH Verlag GmbH & Co. KGaA, Weinheim 

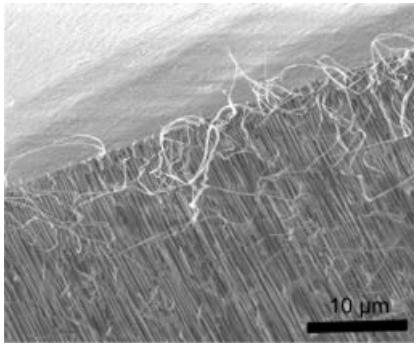


Figure 19. SEM image of a PAOX/PPX composite surface. Fibrous PPX structures protude out of the pores of the PAOX template.

master form, which can then be used in the moulding process. Instead, the self-organization process of forming the nanostructured alumina cells is used to produce the master form. The barrier layer of PAOX provides a nanostructured surface with regular hexagonally ordered concave domes (Figure 20). A replication of the backside PAOX structure with a polymer film may thus represent a straightforward way to nanostructured polymer surfaces with an inverse morphology when detached from the master.

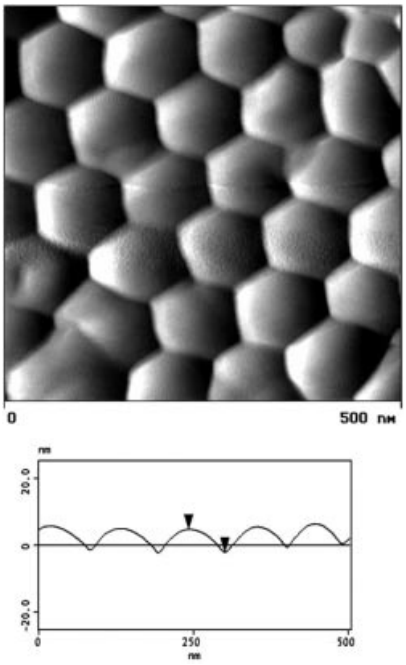


Figure 20. AFM image of a closed PAOX backside with hexagonal pore order used as master in moulding experiments with PPX; bottom: corresponding height profile.

The coating of the PAOX backside template with a thin PPX film can be done in a CVD reactor consisting of a quartz reactor tube in which a three-zone heating can be realized. A temperature gradient from 170° to 700 °C is suitable for sublimation and for initiating the in situ CVD polymerization. After CVD polymerization, the PPX film on the backside of the membrane can either be lifted off mechanically or detached chemically from the resulting PPX/PAOX composite to give a structured PPX film. This process is shown schematically in Figure 21.

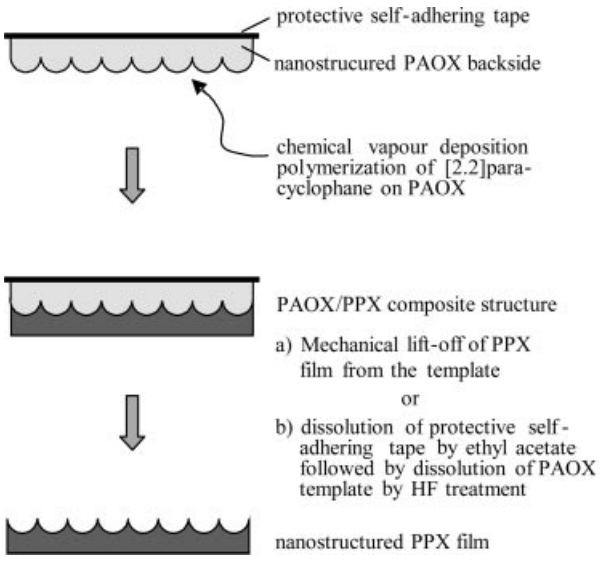


Figure 21. Schematic drawing showing the steps involved in the moulding of a PAOX backside to yield a PPX polymer as well as its detachment to obtain a freestanding nanostructured PPX film.

Figure 22 compares the appearance of a structured PPX film after mechanical lift-off with that after chemical detachment from the PAOX template. The breaking of the film by mechanical stress during the detachment results in the formation of fibrous structures. In contrast, the morphology of the structured PPX film can be retained intact over wide areas by chemical detachment from the master. The film then shows a regular concave structure, in which the small dimples mirror an almost ideal replication of the convex dome-like PAOX backside structure.

Such nanostructured surfaces may show a drastically altered wetting behaviour. Measuring the contact angle at a solid/liquid/gas interface is a very sensitive surface analytical method. It probes the outer atomic layers of a surface and enables the study of chemical as well as morphological surface changes.[70,71]

The hydrophilicity/hydrophobicity of a surface can be determined by measuring the contact angle $\Theta$ between water and the surface (Figure 23). A contact angle of 0° relates to a flat monomolecular water film on a surface of a solid. At a contact angle of 180°, a drop of water, for example, is in contact with the surface only at a single point (superhydrophobic). Between these extremes, surfaces are termed hydrophilic (<90°) or hydrophobic (>90°).

The contact angle of water on a flat PPX surface is 86° (weak hydrophilic behaviour). This compares with an angle of 14° for water on a flat glass surface (roughness ≤ 0.5 nm, piranha-solution-cleaned glass), which is classified as superhydrophilic.[72] The nanostructured PPX film (see Figure 22) which represents a rough surface, shows a drastically reduced water contact angle of only 24° compared to

 © 2006 Wiley-VCH Verlag GmbH & Co. KGaA, Weinheim 

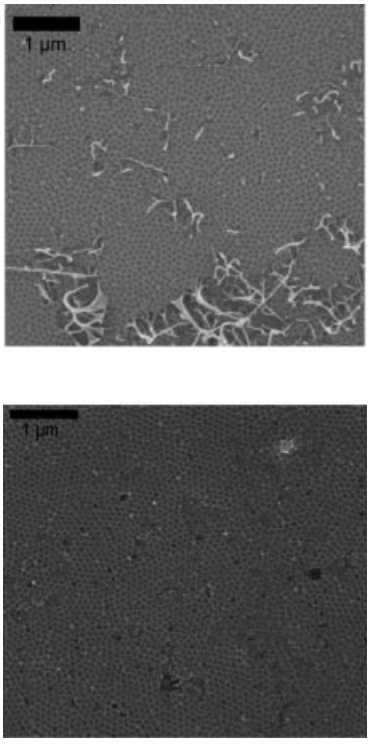


Figure 22. Top: SEM image of a PPX film obtained after deposition on the backside of a PAOX membrane. The fibrous structures result from the destruction of the PAOX film during the mechanical detachment process; bottom: SEM image of a PPX film detached chemically from the PAOX backside by HF dissolution.

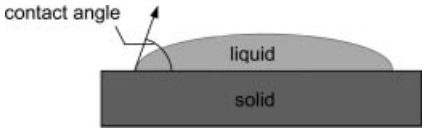


Figure 23. Definition of the contact angle $\Theta$ of a liquid on a solid surface.

a flat unstructured PPX film with a contact angle of 86°. This difference of more than 60° is caused by the structuring of the PPX surface with the regular nanopattern. A possible explanation for the reinforcement of the hydrophilicity of the structured PPX relative to the flat PPX surface can be given when considering the model developed by Wenzel, who has theoretically treated liquid wetting of small-scale rough surfaces (Figure 24).[73] A further refined model for superhydrophilic surfaces (superwetting) was developed recently by Quéré.[74]

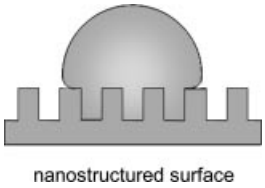


Figure 24. Schematic model of roughness filling of a nanostructured surface by water according to the Wenzel theory.[73]

In the Wenzel model, the space between the protrusions (Figure 24) is filled by a liquid (water), and the theory predicts that both hydrophilicity and hydrophobicity are reinforced by this surface roughness according to the relation:[73]

$\cos\Theta_w = r \cos\Theta_t$

Here $\Theta_w$ is the apparent angle on the rough surface (e.g. structured PPX, Figure 22), $\Theta_t$ is the contact angle of water on a smooth surface of identical chemical composition (e.g. unstructured PPX film), $r$ is a roughness factor, which is defined as the ratio of the actual surface area over the projected area.

As a result, the contact angle $\Theta$ of a surface can be tuned by its surface roughness in the hydrophilic region ($\Theta < 90°$) much in the same way as it can be done in the hydrophobic region ($\Theta > 90°$).[74,75] Thus, a structural change in the surface morphology of the polymeric PPX film is able to tailor the surface wetting of this material from weakly hydrophilic to strongly hydrophilic (Figure 25).

## 4. Conclusions

Nanoporous alumina is an extraordinary material for synthesis and alignment of nanomaterials. Its straightforward synthetic access, its availability in different sizes and shapes, and most important, its high porosity with a massive number of pores running parallel through the transparent material makes this oxidic structure a unique candidate for nanochemistry.

Consequently a wide variety of materials have been synthesized within the pore system of PAOX over the years in a number of different groups. Its high thermal and structural

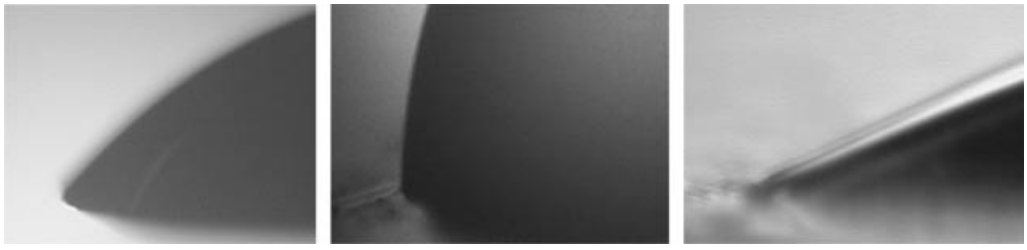

Figure 25. Photographs of the wetting behaviour of water. From left to right: water drop on cleaned glass surface, water drop on flat PPX film surface, water drop on nanostructured PPX film surface (see Figure 22). All contact angles were measured by the sessile drop method.

 © 2006 Wiley-VCH Verlag GmbH & Co. KGaA, Weinheim 

stability makes PAOX also useful as template in gas-phase CVD processes.

Herein we have described the formation, alignment and FE properties of CNTs inside the pores and on the surface of PAOX. Various single-source precursors were studied and led to the formation of CNTs with and without metal filling of their interior.

In field emission, we found that PAOX has a significant influence on the emission characteristics, which is proven by the highest dc current density so far measured for CNT structures, for example. Moreover long current stabilities of up to 18 h were obtained for these materials after cathode conditioning was employed.

Polymer wires are accessible by a gas-phase route by polymerizing reactive polymer precursors inside the pores of PAOX. Besides the polymerization inside porous alumina, PAOX can be used as a mould to emboss organic polymers. PPX films with a resulting concave surface structure can be deposited on the dome-shaped backside of PAOX and afterwards securely detached from it. This leads to a nanostructured polymer surface, which shows an increased hydrophilicity relative to an unstructured flat PPX polymer film. This may be attributed to an enhanced wetting behaviour of the regular nanopatterned structure relative to a smooth unstructured PPX surface.

The future for even more synthetic as well as technological applications of porous alumina membranes is worth being explored in more detail. Research areas like catalysis, for which its mesopores can be tailored and chemically modified, have been barely touched so far.[76–78] Nanoreactors based on PAOX membranes could be an interesting extension of the already well-established microreactor technique.

Biomolecules are ideal candidates for immobilization inside the pore volume of PAOX because of the variable template pore size in the mesoporous range. Biosensor action is a possible target application that can be realized with such systems.[79] The sector of medical applications of these inorganic membranes is also under current study.[80]

## Acknowledgments

Our work was supported by the DFG and the Volkswagenstiftung. The authors gratefully acknowledge the fruitful cooperation in collaborations with FELMI, Graz (EFTEM, Prof. Dr. F. Hofer, TU Graz), with the Erich Schmid Institute of the Austrian Academy of Science, Leoben (Dr. T. Schöberl), both in Austria, and with Prof. Dr. G. Müller, Physics Department, Wuppertal University.

[1] a) M. Terrones, R. Kamalukaran, T. Seeger, M. Rühle, *Chem. Commun.* **2000**, 2335–2336; b) E.-G. Wang, *Adv. Mater.* **1999**, *11*, 1129–1133; c) M. Terrones, P. Redlich, N. Grobert, S. Trasobares, W. K. Hsu, H. Terrones, Y. Q. Zhu, J. P. Hare, C. L. Reeves, A. K. Cheetham, M. Rühle, H. W. Kroto, D. R. M. Walton, *Adv. Mater.* **1999**, *11*, 655–658; d) N. Grobert, M. Terrones, S. Trasobares, K. Kordatos, H. Terrones, J. Olivares, J. P. Zhang, P. Redlicj, W. K. Hsu, C. L. Reeves, D. J. Wallis, Y. Q. Zhu, J. P. Hare, A. J. Pidduck, H. W. Kroto, D. R. M. Walton, *Appl. Phys. A* **2000**, *70*, 175–183.

[2] W. Tremel, *Angew. Chem.* **1999**, *111*, 2311–2315; *Angew. Chem. Int. Ed.* **1999**,*38*, 2175–2179.

[3] a) M. Remskar, Z. Skraba, F. Cleton, R. Sangines, F. Levy, *Appl. Phys. Lett.* **1996**, *69*, 351–353; b) C. M. Zelenski, P. K. Porhout, *J. Am. Chem. Soc.* **1998**, *120*, 734–742; c) L. Margulis, G. Salitra, R. Tenne, M. Taliankar, *Nature* **1993**, *365*, 113–114; d) Y. Feldmann, E. Wassermann, D. J. Srolovitz, R. Tenne, *Science* **1995**, *267*, 222–225.

[4] a) R. L. O. Whitby, W. K. Hsu, C. B. Boothroyd, P. K. Fearon, H. W. Kroto, D. R. M. Walton, *ChemPhysChem* **2001**, *2*, 620–623; b) E. B. Macki, D. H. Galvan, E. Adam, S. Talapatra, G. Yang, A. D. Migone, *Adv. Mater.* **2000**, *12*, 495–498; c) R. Tenne, L. Margulis, M. Genet, G. Hodes, *Nature* **1992**, *360*, 444–446.

[5] a) W. Mickelson, S. Aloni, Wei-Qiang Han, J. Cummings, A. Zettl, *Science* **2003**, *300*, 467–469; b) E. J. M. Hamilton, S. E. Dalton, C. M. Mann, H. O. Cilija, C. A. McDonald, S. G. Shore, *Science* **1993**, *260*, 659–661; c) R. Ma, Y. Bando, T. Sato, K. Kurashima, *Chem. Mater.* **2001**, *13*, 2965–2971.

[6] a) R. B. Wehrspohn, J. Schilling, *MRS Bull.* **2002**, *8*, 263; b) M. S. Sander, A. L. Prieto, R. Gronsky, T. Sands, A. M. Stacy, *Adv. Mater.* **2002**, *14*, 665–667; c) S.-Z. Chu, K. Wada, S. Inoue, M. Isogai, A. Yasumori, *Adv. Mater.* **2005**, *17*, 2115–2119; d) P. P. Mardilovich, A. N. Govyadinov, N. I. Mazurenko, R. Paterson, *J. Membr. Sci.* **1995**, *98*, 143–155; e) N. Itoh, K. Kato, T. Tsuij, M. Hongo, *J. Membr. Sci.* **1996**, *117*, 189–196; f) A. T. Shawaqfeh, R. E. Baltus, *J. Membr. Sci.* **1999**, *157*, 147–158; g) J. H. Yuan, F. Y. He, D. C. Sun, X. H. Xia, *Chem. Mater.* **2004**, *16*, 1841–1844; h) F. Li, L. Zhang, R. Metzger, *Chem. Mater.* **1998**, *10*, 2470–2480; i) A. Michailowski, D. Al-Mawlawi, G. Cheng, M. Moskovits, *Chem. Phys. Lett.* **2001**, *349*, 1–5; j) Y. Wang, J. Y. Lee, H. C. Zjeng, *Chem. Mater.* **2005**, *17*, 3899–3903; k) K. B. Shelimov, M. Moskovits, *Chem. Mater.* **2000**, *12*, 250–254; l) F. Li, J. He, W. L. Zhou, J. B. Wiley, *J. Am. Chem. Soc.* **2003**, *125*, 16166–16167; m) B. A. Hernandez, K. S. Chang, E. R. Fisher, P. K. Dorhout, *Chem. Mater.* **2002**, *14*, 480–482; n) C. Y. Kuo, S. Y. Lu, T.-Y. Wei, *J. Cryst. Growth* **2005**, *285*, 400–407.

[7] G. Schmid, *J. Mater. Chem.* **2002**, *12*, 1231–1238.

[8] T. L. Wade, J.-E. Wegrove, *Eur. Phys. J. Appl. Phys.* **2005**, *29*, 3–22.

[9] F. Keller, M. S. Hunter, D. L. Robinson, *J. Electrochem. Soc.* **1953**, *100*, 411–419.

[10] G. C. Wood, J. P. O'Sullivan, *Proc. R. Soc.* **1970**, *A317*, 511–543.

[11] K. Nielsch, J. Choi, K. Schwirn, R. B. Wehrspohn, U. Gösele, *Nano Lett.* **2002**, *2*, 677–680.

[12] a) S. Ono, N. Masuko, *Corros. Sci.* **1992**, *33*, 503–505; b) S. Ono, H. Ichinose, N. Masuko, *Corros. Sci.* **1992**, *33*, 841–850.

[13] V. P. Parkhuitik, V. I. Shershulsky, *J. Phys.* **1992**, *D25*, 1258–1263.

[14] S. Z. Chu, K. Wada, S. Inoue, S.-I. Todoroki, *Chem. Mater.* **2002**, *14*, 4595–4602.

[15] M. Tian, S. Xu, J. Wang, N. Kumar, E. Wertz, Q. Li, P. M. Campbell, M. H. W. Chan, T. E. Mallouk, *Nano Lett.* **2005**, *5*, 697–703.

[16] H. de L. Lira, R. Paterson, *J. Membr. Sci.* **2002**, *206*, 375–387.

[17] L. J. Gibson, M. F. Ashby, *Cellular Solids: Structure and Properties*, Pergamon Press,**1988**.

[18] a) M. Wada, Y. Kitano, S. Tanase, O. Kajita, T. Sakai, *J. Electrochem. Soc.* **2005**, *152*, A1341–A1346; b) P. T. Kumar, R. Ramesh, Y. Y. Lin, G. T. K. Fey, *Electrochem. Commun.* **2004**, *6*, 520–525.

[19] M. Valcarcel, B. M. Simonet, S. Cardenas, B. Suarez, *Anal. Bioanal. Chem.* **2005**, *382*, 1783–1790.

[20] a) F. Pico, J. M. Rojo, M. L. Sanjuan, A. Anson, A. M. Benito, M. A. Callejas, W. K. Maser, M. T. Martinez, *J. Electrochem. Soc.* **2004**, *151*, A831–837; b) J. H. Chen, W. Z. Li, D. Z. Wang, S. X. Yang, J. G. Wen, Z. F. Ren, *Carbon* **2002**, *40*, 1193–1197;

 © 2006 Wiley-VCH Verlag GmbH & Co. KGaA, Weinheim 

c) G. Seifert, T. Kohler, T. Frauenheim, *Appl. Phys. Lett.* **2000**, *77*, 1313–1315.
[21] a) S. H. Jeong, H. Y. Hwang, K. H. Lee, Y. Jeong, *Appl. Phys. Lett.* **2001**, *78*, 2052–2054; b) Y. Zhang, J. Liu, X. Li, *Proc. XIV IVMC* **2001**, 13.
[22] a) C. Kocabas, S. H. Hur, A. Gaur, M. A. Meitl, M. Shim, J. A. Rogers, *Small* **2005**, *1*, 1110–1116; b) Z. B. Zhang, J. Cardenas, E. E. B. Campbell, S. L. Zhang, *Appl. Phys. Lett.* **2005**, *87*, 043110/1–043110/3; c) T. Shimada, T. Sugai, Y. Ohno, S. Kishimoto, T. Mizutani, H. Yoshida, T. Okazaki, H. Shinohara, *Appl. Phys. Lett.* **2004**, *84*, 2412–2414.
[23] T. Kyotani, L.-F. Tsai, A. Tomita, *Chem. Mater.* **1996**, *8*, 2109–2113.
[24] T. Yanagishita, M. Sasaki, K. Nishio, H. Masuda, *Adv. Mater.* **2004**, *16*, 429–432.
[25] N. I. Maksimova, J. Engstler, J. J. Schneider, *Nato ASCI Series* **2006**, in press.
[26] J. J. Schneider, N. I. Maksimova, J. Engstler, R. Schierholz, *New. J. Chem.* **2006**, submitted.
[27] P. C. P. Watts, W. K. Hsu, D. P. Randell, V. Kotzeva, G. Z. Chen, *Chem. Mater.* **2002**, *14*, 4505–4508.
[28] H. Hou, A. K. Schaper, F. Weller, A. Greiner, *Chem. Mater.* **2002**, *14*, 3994–3999.
[29] J. J. Schneider, J. Engstler, S. Franzka, K. Hofmann, B. Albert, J. Ensling, P. Gütlich, P. Hildebrandt, S. Döpner, W. Pfleging, B. Günther, G. Müller, *Chem. Eur. J.* **2001**, *7*, 2888–2895.
[30] G. Che, B. B. Lakshmi, E. R. Fisher, C. R. Martin, *Nature* **1998**, *393*, 346–349.
[31] W. Guo, C. Z. Zhu, T. X. Yu, H. Woo, B. Hang, Y. T. Dai, *Phys. Rev. Lett.* **2004**, *93*, 245502/1–245502/4.
[32] H. J. Qi, K. B. K. Teo, K. K. S. Lau, M. C. Boyce, W. I. Milne, J. Robertson, K. K. Gleason, *J. Mech. Phys. Solids* **2003**, *51*, 2213–2237.
[33] Y. R. Jeng, P. C. Tsai, T. H. Fang, *J. Chem. Phys.* **2005**, *122*, 224713/1–224713/8.
[34] C. N. R. Rao, A. Govindaraj, *Acc. Chem. Res.* **2002**, *35*, 998–1007 and references cited therein.
[35] J. Wu, B. E. Hamaoui, J. Li, L. Zhi, U. Kolb, K. Müllen, *Small* **2005**, *1*, 210–212.
[36] L. Zhi, T. Gorelik, R. Friedlein, J. Wu, U. Kolb, W. R. Salaneck, K. Müllen, *Small* **2005**, *1*, 798–801.
[37] See also: a) C. N. R. Rao, B. Satishkumar, A. Govindarai, M. Nath, *ChemPhysChem* **2001**, *2*, 78–105; b) C. N. R. Rao, R. Sen, B. C. Satishkumar, A. Govindarai, *Chem. Commun.* **1998**, 1525; c) C. N. R. Rao, A. Govindaraj, *Acc. Chem. Res.* **2002**, *35*, 998–1007.
[38] a) A. R. Harutyunyan, G. Chen, P. C. Eklund, *Appl. Phys. Lett.* **2003**, *82*, 4794–4796.
[39] A. R. Harutyunyan, G. Chen, P. C. Eklund, *Appl. Phys. Lett.* **2003**, *82*, 4794–4796.
[40] Y. Saito, S. Uemura, *Carbon* **2000**, *38*, 169–182.
[41] a) P. M. Ajayan, O. Stephan, C. Colliex, D. Trauth, *Science* **1994**, *265*; 1212–1214; b) J. I. Sohn, S. Lee, *Mat. Res. Soc., Symp. Proc.* **2001**, *63A*, 14.9.1–14.9.6; c) Y.-H. Lee, Y.-T. Jang, D.-H. Kim, J.-H. Ahn, B. K. Ju, *Adv. Mater.* **2001**, *13*, 479–482; d) X. Xu, G. R. Brandes, *Mat. Res., Symp. Proc.* **1998**, *509*, 107; e) L. A. de Heer, D. Ugarte, A. Chatelain, *Science* **1995**, *270*, 1179–1180.
[42] a) M. J. Fransen, T. L. van Rooy, P. Kruit, *Appl. Surf. Sci.* **1999**, *146*, 312–327; b) J. W. Gadzuk, E. W. Plummer, *Rev. Mod. Phys.* **1973**, *45*, 487.
[43] β is the electrical field enhancement factor of an external electrical field applied to an emitting structure. It is greatly influenced (aside from other factors) by a high aspect ratio of the emitting structure. β is a measure of the lowering of the onset field of FE which is typically between $E$ = 1–10 V μm$^{-1}$ for CNTs. β for MWCNTs can be determined from a Fowler-Nordheim plot assuming a work function of 4.6 eV for graphite.
[44] B. Günther, A. Göhl, G. Müller, J. Engstler, J. J. Schneider, *Proc. 13th IVMC* **2001**, *207*, 2000.
[45] M. Stammler, J. Ristein, T. Habermann, A. Göhl, K. Janoschowsky, D. Nau, G. Müller, L. Ley, *Diam. Relat. Mater.* **1999**, *8*, 792–792.
[46] a) T. Habermann, A. Göhl, D. Nau, M. Wedel, G. Müller, M. Christ, M. Schreck, B. Stritzker, *J. Vac. Sci. Technol.* **1998**, *B16*, 693–696; b) A. Göhl, T. Habermann, G. Müller, D. Nau, M. Wedel, G. Müller, M. Christ, M. Schreck, B. Stritzker, *Diam. Relat. Mater.* **1998**, *7*, 666–670.
[47] a) F. M. Charbonnier, W. A. Mackie, T. Xie, P. R. Davis, *Ultramicroscopy* **1999**, *79*, 73–82; b) S. Kanemaru, T. Hirano, H. Tanoue, J. Itoh, *J. Vac. Sci. Techn.* **1996**, *B14*, 1885–1888; c) M. S. Chung, B.-G. Yoon, J. M. Park, K.-Y. Ha, *Appl. Surf. Sci.* **1999**, *146*, 138–142.
[48] a) N. N. Chubun, A. G. Chakhovskoi, M. Hajra, C. E. Hunt, *J. Vac. Sci. Technol. B* **2003**, *21*, 483–485; b) M. Hajra, N. N. Chubun, A. G. Chakhovskoi, C. E. Hunt, K. Liu, A. Murali, S. H. Risbud, T. Tyler, V. Zhirnov, *J. Vac. Sci. Technol. B* **2003**, *21*, 458–463; c) B. R. Chalamala, R. H. Reuss, K. A. Dean, *Appl. Phys. Lett.* **2001**, *78*, 2375–2377.
[49] J. M. Kim, W. B. Choi, N. S. Lee, J. E. Jung, *Diam. Relat. Mater.* **2000**, *9*, 1184–1189.
[50] O. Gröning, O. M. Küttel, C. Emmenger, P. Gröning, L. Schlappbach, *J. Vac. Sci. Technol.* **2000**, *B18*, 665–678.
[51] L. Nilsson, O. Groenning, C. Emmengger, O. Kuettel, E. Schaller, L. Schlappach, H. Kind, J.-M. Bonard, K. Kern, *Appl. Phys. Lett.* **2000**, *76*, 2071–2073.
[52] J. L. Kwo, M. Yokoyama, W. C. Wang, F. Y. Chuang, I. N. Lin, *Diam. Relat. Mater.* **2000**, *9*, 1270–1274.
[53] S. Kanemaru, T. Hirano, H. Tanoue, J. Itoh, *Appl. Surf. Sci.* **1997**, *111*, 218–223.
[54] J. I. Sohn, S. Lee, Y.-H. Song, S.-Y. Choi, K.-I. Cho, K. S. Nam, *Curr. Appl. Phys.* **2001**, *1*, 61–65.
[55] D. N. Davydov, P. A. Sattari, D. AlMawlawi, A. Osika, T. L. Daslett, M. Moskovits, *J. Appl. Phys.* **1999**, *86*, 3983–3987.
[56] a) J. S. Suh, K. S. Jeong, J. S. Lee, I. Han, *Appl. Phys. Lett.* **2002**, *80*, 2392–2394; b) S. H. Jeong, H. Y. Hwang, K. H. Lee, Y. Jeong, *Appl. Phys. Lett.* **2001**, *78*, 2052–2054; c) Z. H. Yuan, H. Huang, Y. Dang, J. E. Cao, B. H. Hu, S. S. Fan, *Appl. Phys. Lett.* **2001**, *78*, 3127–3129.
[57] F. Kaldasch, B. Günther, G. Müller, J. Engstler, J. J. Schneider, *Proc. IVMC* **2001**, *01TH8586*, 25.
[58] J. Engstler, dissertation University Duisburg-Essen, Essen, **2003**.
[59] D. Lysenkov, H. Abbas, G. Müller, J. Engstler, K. P. Budna, J. J. Schneider, *J. Vac. Sci. Technol. B* **2005**, *23*, 809–813.
[60] B. Günther, dissertation, University Wuppertal, WUB Diss.02-8, **2002**.
[61] H. Masuda, K. Nishio, N. Baba, *Jpn. J. Appl. Phys.* **1992**, *31*, 1775–1777.
[62] H. Masuda, K. Fukuda, *Science* **1995**, *268*, 1466–1468.
[63] C. Goh, K. M. Coakley, M. D. McGehee, *Nano Lett.* **2005**, *5*, 1545–1549.
[64] M. Steinhart, J. H. Wendorff, A. Greiner, R. B. Wehrspon, K. Nielsch, J. Schilling, J. Choi, U. Gösele, *Science* **2002**, *296*, 1997.
[65] A. H. Greiner, J. H. Wendorf, M. Steinhart, *Nachr. Chem.* **2004**, *52*, 426–431.
[66] S. I. Moon, T. J. McCarthy, *Macromolecules* **2003**, *36*, 4253–4255.
[67] H. Xiang, K. Shin, T. Kim, S. I. Moon, T. J. McCarthy, T. P. Rusell, *Macromolecules* **2004**, *37*, 5660–5664.
[68] Ph. Hanefeld, O. Kriha, J. Engstler, M. Steinhart, U. Gösele, J. H. Wendorff, A. Greiner, J. J. Schneider, *Chem. Mater.* **2006**, in press.
[69] W. F. Gorham, *J. Polym. Sci. Part A-1* **1966**, *4*, 3027–3039.
[70] J. Böing, Diss., RWTH Aachen, **2003**.

 © 2006 Wiley-VCH Verlag GmbH & Co. KGaA, Weinheim 

[71] E. Martines, K. Seunarine, H. Morgan, N. Gadegaard, C. D. W. Wilkinson, M. O. Riehle, *Nano Lett.* **2005**, *5*, 2097–2103.
[72] D. Klee, J. Böing, H. Höcker, *Mater.-wiss. u. Werkstofftech.* **2004**, *35*, 186–191.
[73] R. N. Wenzel, *Ind. Eng. Chem.* **1936**, *28*, 988–994.
[74] D. Quéré, *Phys. A* **2002**, *313*, 32–46.
[75] S. Shibuichi, T. Onda, N. Satoh, K. Tsujii, *J. Phys. Chem.* **1996**, *100*, 19512–19517.
[76] H.-P. Kormann, G. Schmid, K. Pelzer, K. Philippot, B. Chaudret, *Z. Anorg. Allg. Chem.* **2004**, *630*, 1913–1918.
[77] a) D. Höneke, *Appl. Catal.* **1983**, *5*, 179–198; b) D. Höneke, *J. Catal.* **1987**, *105*, 10–18.
[78] D. Höneke, G. Wießmeier, *Ind. Eng. Chem. Res.* **1996**, *35*, 4412–4416.
[79] a) S. Hou, J. Wang, C. R. Martin, *J. Am. Chem. Soc.* **2005**, *127*, 8586–8587; b) P. Kunit, C. R. Martin, *Curr. Pharm. Biotechnol.* **2005**, *6*, 35–467; c) F. Matsumoto, K. Nishio, H. Masuda, *Adv. Mater.* **2004**, *16*, 2105–2108; d) F. Matsumoto, M. Kamiyama, N. Kazuyuki, H. Masuda, *Jpn. J. Appl. Phys. Part 2* **2005**, *44*, L355–L358; e) M. Herrmann, *Chem. Mater.* **2005**, *17*, 4577–4593; f) V. Benoit, A. Steel, M. Torres, Y.-Y. Yu, H. Yang, J. Cooper, *Anal. Chem*. **2001**, *73*, 2412–2420; g) B. J. Cheek, A. B. Steel, M. P. Torres, Y.-Y. Yu, H. Yang, *Anal. Chem*. **2001**, *73*, 5777–578.
[80] a) Patents: DE 1985542i, C2, **2001**; DE 199910188, 4–45, **2001**; DE 19948783 C2, **2001**; b) E. P. Briggs, M. Karlsson, A. R. Walpole, E. Palsgard, P. R. Wilshaw, *J. Mater. Sci. Mater. Med.* **2004**, *15*, 1–9; c) M. Karlsoon, E. Palsgard, P. R. Wilshaw, L. Di Silvio, *Biomaterials* **2003**, *24*, 3039–3046; d) M. Karlsson, A. Johansson, L. Tang, M. Boman, *Microsc. Res. Technol.* **2004**, *63*, 259–265; e) R. van Beuningen, H. van Damme, P. Boeneder, N. Bastiaensen, A. Chan, T. Kievits, *Clin. Chem.* **2001**, *47*, 1931–1933; f) F. Matsumoto, K. Nishio, H. Masuda, *Adv. Mater.* **2004**, *16*, 2105–2107.

Received: December 23, 2005
Published Online: April 3, 2006

 © 2006 Wiley-VCH Verlag GmbH & Co. KGaA, Weinheim 

DOI: 10.1002/ejic.200600051

# (Tetramethylcyclobutadiene)cobalt Complexes with Tricarbollide Ligands[‡]

**Elena V. Mutseneck,[a] Dmitry S. Perekalin,[a] Josef Holub,[b] Konstantin A. Lyssenko,[a] Pavel V. Petrovskii,[a] Bohumil Štíbr,[b] and Alexander R. Kudinov*[a]**

**Keywords:** Boron / Cobalt / Metallacarboranes / Cyclobutadiene

Reactions of the 11-vertex *nido*-tricarbollide anions [7,8,9-$C_3B_8H_{11}]^-$ (**2a**) and [7,8,10-$C_3B_8H_{11}]^-$ (**3**) with [Cb*Co-$(MeCN)_3]^+$ or [Cb*Co$(C_6H_6)]^+$ (Cb* = $C_4Me_4$) afford the expected cobaltatricarbollides 1-Cb*-1,2,3,4-$CoC_3B_8H_{11}$ (**4a**) and 1-Cb*-1,2,3,5-$CoC_3B_8H_{11}$ (**5**), respectively. A similar reaction of the amino-substituted anion [7-*t*BuNH-7,8,9-$C_3B_8H_{10}]^-$ (**2b**) is accompanied by polyhedral rearrangement even at room temperature, giving 1-Cb*-12-*t*BuNH-1,2,4,12-$CoC_3B_8H_{10}$ (**7b**). Complex **4a** rearranges to the isomeric complex **5** at 110 °C and further to 1-Cb*-1,2,4,10-$CoC_3B_8H_{11}$ (**6a**) at 160 °C. The amino-substituted derivative 1-Cb*-10-*t*BuNH-1,2,4,10-$CoC_3B_8H_{10}$ (**6b**) was obtained by isomerization of **7b** at 160 °C. The observed rearrangement sequence for Cb*$CoC_3B_8H_{11}$ correlates well with the relative stabilities of nonmethylated analogs estimated by DFT calculations. The structures of **4a** and **7b** were determined by X-ray diffraction.

(© Wiley-VCH Verlag GmbH & Co. KGaA, 69451 Weinheim, Germany, 2006)

## Introduction

Recently, we have developed two methods for the preparation of (tetramethylcyclobutadiene)cobalt complexes containing cyclopentadienyl, phospholyl, and pyrrolyl ligands, Cb*Co($C_4R_4E$) (Cb* = $C_4Me_4$; E = CR, P, and N).[2,3] One method is based on the reaction of the (carbonyl)iodide complex Cb*Co$(CO)_2I$ with the corresponding anions, while another one uses the acetonitrile complex [Cb*Co-$(MeCN)_3]^+$ as a starting material. The second method is more general, allowing Cb*Co($C_4R_4E$) compounds to be synthesized in higher yields under milder conditions. The same approaches proved to be useful in metallacarborane chemistry, which was clearly demonstrated by the synthesis of Cb*Co complexes with charge-compensated dicarbollide ligands [9-L-7,8-$C_2B_9H_{10}]^-$ (**1**).[1,4] The *nido*-tricarbollide anions **2** and **3**,[5] similar to **1**, have a five-membered face and a single negative charge, which makes them analogous to $Cp^-$ in their coordinating ability. In contrast to dicarbollide derivatives, the presence of the third carbon atom hampers the prediction of the product structure owing to the ease of cluster rearrangement.[6–8] The chemistry of ferratricarbollides is well studied.[9] However, only one example of a cobalt derivative was described.[10] Herein we report the preparation of Cb*Co complexes of anions **2** and **3** and their further rearrangements.

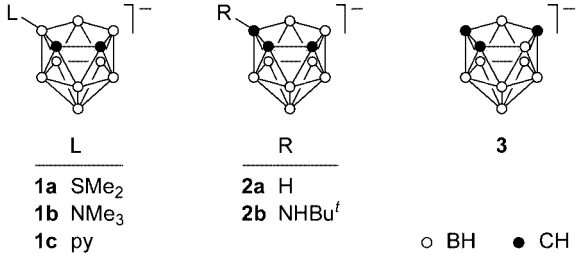


## Results and Discussion

### Synthesis and Rearrangements of Cobaltatricarbollides

We found that the room-temperature reaction of the tricarbollide anion [7,8,9-$C_3B_8H_{11}]^-$ (**2a**) with the acetonitrile complex [Cb*Co$(MeCN)_3]^+$ in THF gives cobaltatricarbollide 1-Cb*-1,2,3,4-$CoC_3B_8H_{11}$ (**4a**)[11] (Scheme 1). The same compound was prepared by photochemical reaction of **2a** with the benzene complex [Cb*Co$(C_6H_6)]^+$ in $CH_2Cl_2$.[12] The second method is more favorable as it avoids preliminary preparation of [Cb*Co-$(MeCN)_3]^+$ by irradiation of [Cb*Co$(C_6H_6)]^+$ in MeCN.[13] As shown recently, the related iron complex 1-Cp-1,2,3,4-$FeC_3B_8H_{11}$ is formed by a similar photochemical reaction of **2a** with [CpFe$(C_6H_6)]^+$.[8] The arrangement of the carbon atoms in the cobalt and iron complexes is the same as in the starting anion **2a**. In contrast, the room-temperature reaction of **2a** with $[Cp^*RuCl]_4$ is accompanied by polyhedral rearrangement to afford 1-Cp*-1,2,3,5-$RuC_3B_8H_{11}$,[8] indicating that the ease of the process depends on the nature of the metal.

[‡] (Tetramethylcyclobutadiene)cobalt Complexes, 4. Part 3: Ref.[1]

[a] A. N. Nesmeyanov Institute of Organoelement Compounds, 28 ul. Vavilova, 119991 Moscow, GSP-1, Russian Federation
Fax: +7-495-135-5085
E-mail: arkudinov@ineos.ac.ru
[b] Institute of Inorganic Chemistry, Academy of Sciences of the Czech Republic, 250 68 Řež, Czech Republic

Supporting information for this article is available on the WWW under http://www.eurjic.org or from the author.

 © 2006 Wiley-VCH Verlag GmbH & Co. KGaA, Weinheim 

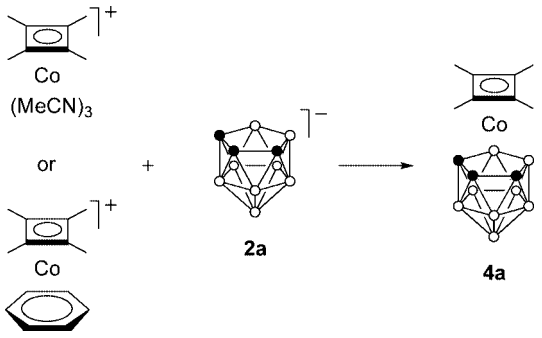


Scheme 1. Synthesis of cobaltatricarbollide **4a**.

The isomeric tricarbollide anion [7,8,10-$C_3B_8H_{11}$]$^-$ (**3**) reacts with [Cb*Co(MeCN)$_3$]$^+$ to give cobaltatricarbollide 1-Cb*-1,2,3,5-$CoC_3B_8H_{11}$ (**5**) (Scheme 2). CpFe and Cp*Ru analogs have been prepared recently by reactions of **3** with [CpFe($C_6H_6$)]$^+$ and [Cp*RuCl]$_4$.[8] No rearrangement has been observed in these reactions.

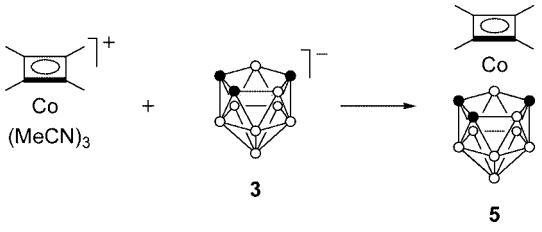


Scheme 2. Synthesis of cobaltatricarbollide **5**.

Complex **4a** rapidly rearranges into **5** in refluxing toluene (Scheme 3). Refluxing of **4a** or **5** in diglyme results in selective formation of isomer 1-Cb*-1,2,4,10-$CoC_3B_8H_{11}$ (**6a**) with mutual *m*-disposition of cage carbon atoms. The same isomerization sequence was observed earlier for the iron and ruthenium analogs.[8] This sequence is associated with progressive space separation of the CH vertices and is consistent with a diamond-square-diamond mechanism.[14]

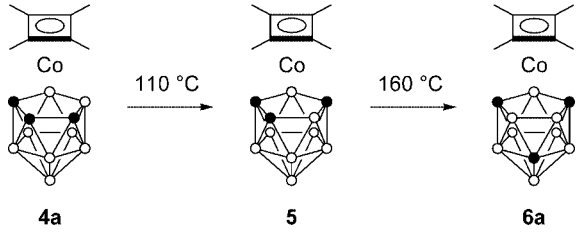


Scheme 3. Thermal rearrangements of **4a** and **5**.

Unlike the parent anion **2a**, the room-temperature reaction of the amino-substituted derivative [7-*t*BuNH-7,8,9-$C_3B_8H_{10}$]$^-$ (**2b**) with [Cb*Co(MeCN)$_3$]$^+$ (THF) or [Cb*Co($C_6H_6$)]$^+$ ($CH_2Cl_2$, *hv*) affords the rearranged *p*-substituted complex 1-Cb*-12-*t*BuNH-1,2,4,12-$CoC_3B_8H_{10}$ (**7b**) instead of the expected isomer 1-Cb*-2-*t*BuNH-1,2,3,4-$CoC_3B_8H_{10}$ (**4b**) (Scheme 4). Interestingly, treatment of **2b** with the less reactive (carbonyl)iodide complex Cb*Co(CO)$_2$I (THF, 65 °C) also gives **7b**, in contrast to an analogous reaction with **2a**, which does not lead to any isolable complexes. This suggests the higher nucleophilicity of **2b** compared with the parent anion **2a**, in accordance with a strong donor effect of the amino group. It should be added that reactions of anion **2b** with CpFe(CO)$_2$I and [Cp*RuCl]$_4$ also afford metallatricarbollides of the same cluster configuration.[7,15] Refluxing of the *p*-substituted compound **7b** in diglyme results in the formation of *m*-isomer 1-Cb*-10-*t*BuNH-1,2,4,10-$CoC_3B_8H_{10}$ (**6b**). Analogous transformation has been observed earlier for amino-substituted ferra- and ruthenatricarbollides.[7,16]

It can be concluded that the introduction of an amino substituent dramatically reduces the rearrangement barrier of the initial complexation product **4**.[17] Moreover, the substitution changes its rearrangement direction. Nevertheless, the final product has the same polyhedral structure in both cases (cf. Scheme 3 and Scheme 4).

## X-ray Diffraction Study

Structures of the tricarbollide complexes **4a** and **7b** were confirmed by X-ray diffraction (Figure 1 and Figure 2). The Cb* ring is nearly an ideal square with a mean side length 1.453–1.457 Å, which approximates those found for the Cb*Co complexes with charge-compensated carborane ligands: 1.456 Å for Cb*Co[**1a**] and 1.452 Å for Cb*Co[**1c**].[1] The carbon atoms of the Cb* methyl groups are deviated for 0.10–0.20 Å from the ring plane away from the cobalt atom. The metal-bonding ligand planes are essentially coplanar, the dihedral angles being 1.2–2.9°.

The Co···Cb* distances in complexes **4a** (1.696 Å) and **7b** (1.703 Å) are slightly longer than that in Cb*Co(η-$C_5H_4$COMe) (1.683 Å)[3] but shorter than in Cb*Co[**1a**] (1.712 Å) and Cb*Co[**1c**] (1.711 Å),[1] suggesting that the tricarbollide ligands **2a** and [1-*t*BuNH-1,7,9-$C_3B_8H_{10}$]$^-$ are weaker donors than acetylcyclopentadienide but stronger donors than the charge-compensated dicarbollide ligands

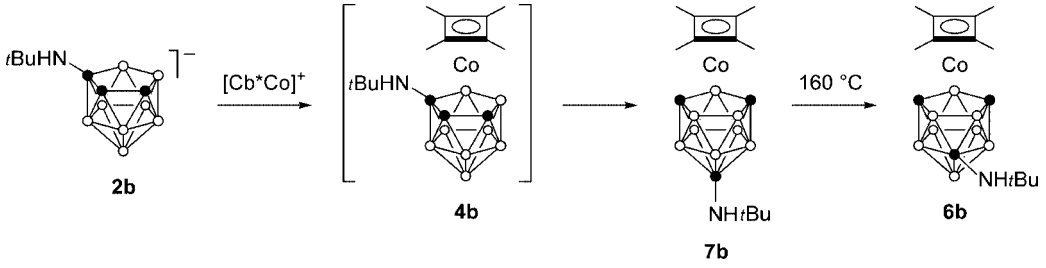


Scheme 4. Synthesis and thermal rearrangement of **7b**.

 © 2006 Wiley-VCH Verlag GmbH & Co. KGaA, Weinheim 

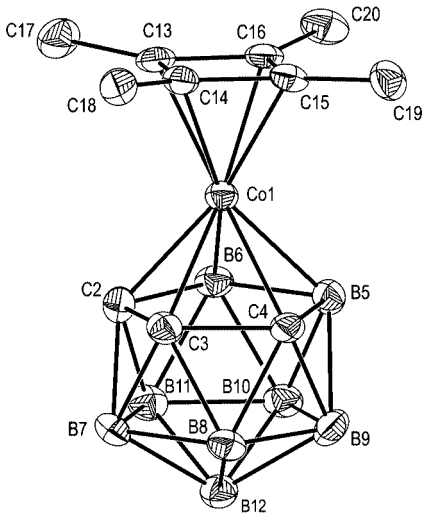


Figure 1. The molecular structure of 1-Cb*-1,2,3,4-$CoC_3B_8H_{11}$ (**4a**). Ellipsoids are shown at the 50% level. Selected bond lengths [Å] and angles [°]: Molecule 1: Co1–C2 2.052(3), Co1–C3 2.031(3), Co1–C4 2.051(3), Co1–B5 2.088(4), Co1–B6 2.092(4), C2–C3 1.595(4), C3–C4 1.596(4), C4–B5 1.702(5), B5–B6 1.780(5), C2–B6 1.684(5), B6–C2–C3 111.1(3), C2–C3–C4 109.7(2), C3–C4–B5 110.8(2), C4–B5–B6 103.8(3), B5–B6–C2 104.5(2). Molecule 2: Co1–C2 2.054(3), Co1–C3 2.035(3), Co1–C4 2.048(3), Co1–B5 2.096(4), Co1–B6 2.096(3), C2–C3 1.595(4), C3–C4 1.599(5), C4–B5 1.701(5), B5–B6 1.771(5), C2–B6 1.695(5), B6–C2–C3 110.9(3), C2–C3–C4 109.4(3), C3–C4–B5 111.2(2), C4–B5–B6 103.8(3), B5–B6–C2 104.7(3).

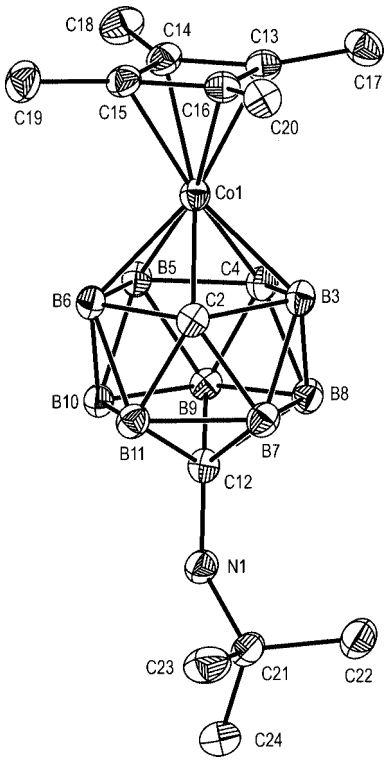


Figure 2. The molecular structure of 1-Cb*-12-*t*BuNH-1,2,4,12-$CoC_3B_8H_{10}$ (**7b**). Ellipsoids are shown at the 50% level. Selected bond lengths [Å] and angles [°]: Co1–C2 2.033(3), Co1–B3 2.028(3), Co1–C4 2.041(2), Co1–B5 2.058(3), Co1–B6 2.050(3), C2–B3 1.724(4), B3–C4 1.705(4), C4–B5 1.714(4), B5–B6 1.792(4), C2–B6 1.708(4), C12–B11 1.733(4), C12–B10 1.724(4), C12–B9 1.723(4), C12–B8 1.720(4), C12–B7 1.719(4), C12–N1 1.437(3); B5–B6–C2 104.86(19), B6–C2–B3 112.94(19), C2–B3–C4 103.19(19), B3–C4–B5 112.83(19), C4–B5–B6 105.5(2).

**1a**,**c**. However, according to electrochemical data, **1a**,**c** are stronger donors than tricarbollides.[18] Apparently, the Co···Cb* distance also depends on other effects.

### DFT Calculations

Despite wide application of DFT calculations for transition-metal complexes,[19] their use in the case of metallacarboranes is rather limited.[20–24] Recently, we have shown that the calculations of ferratricarbollides $CpFeC_3B_8H_{11}$ provide reliable geometry, energy, and spectroscopic data.[8] In order to estimate the thermodynamic stability and $^{11}B$ NMR spectra of cobaltatricarbollides **4a**, **5**, and **6a**, we carried out DFT calculations (at the B3LYP/6-31G* level) for their nonmethylated analogs $(C_4H_4)CoC_3B_8H_{11}$ (**4a′**, **5′**, and **6a′**).[25]

The carbon-adjacent complex **4a′** was found to be the least thermodynamically stable, presumably because of the Coulomb repulsion of the negatively charged CH vertexes. The isomeric compounds **5′** and **6a′** are more stable than **4a′** for 17.2 and 26.2 kcal/mol, respectively. Thus, the observed rearrangement sequence **4a** → **5** → **6a** correlates with the stepwise increase of the thermodynamic stability of the isomers. Interestingly, the corresponding values for the CpFe analogs of **5′** and **6a′** are 17.0 and 25.5 kcal/mol, respectively, indicating that relative stability of isomers is mainly determined by the arrangement of the carbon atoms and is practically independent of the metal vertex.

The calculated $^{11}B$ NMR chemical shifts for **4a′**, **5′**, and **6a′** (Table 1) are in good agreement with the experimental values for **4a**, **5**, and **6a** (av. deviation 1.1 ppm), thus providing additional confirmation of their structures. The only significant deviation (about 3–5 ppm) is observed for the signal of the B12 atom, apparently because of approximation of the Cb* ligand with $C_4H_4$. Indeed, the calculation for the methylated complex **4a** decreases the deviation to 0.8 ppm. Such strong influence of the antipodal vertex on the $^{11}B$ NMR shift has been observed previously for various heteroboranes.[26]

Table 1. Calculated and experimental $^{11}B$ NMR chemical shifts of the $(C_4R_4)CoC_3B_8H_{11}$ isomers.

| Compound | $^{11}B$ NMR shifts | | | | |
|---|---|---|---|---|---|
| | B5,6 | B10 | B9,11 | B12 | B7,8 |
| **4a** exp.[a] | –9.6 | –12.6 | –17.1 | –19.5 | –26.1 |
| **4a′** calcd. | –9.7 | –9.7 | –16.5 | –14.3 | –27.6 |
| **4a** calcd. | –9.9 | –11.0 | –17.1 | –18.7 | –27.7 |
| | B12 | B9,10 | B7 | B4,6 | B8,11 |
| **5** exp.[a] | –16.6 | –16.6 | –16.6 | –19.0 | –24.6 |
| **5′** calcd. | –14.7 | –15.5 | –20.1 | –17.0 | –23.7 |
| | B3 | B5,6 | B9,11 | B12 | B7,8 |
| **6a** exp.[a] | –10.2 | –11.1 | –17.9 | –19.0 | –23.0 |
| **6a′** calcd. | –10.4 | –12.0 | –18.5 | –17.0 | –22.9 |

[a] In $CDCl_3$.

 © 2006 Wiley-VCH Verlag GmbH & Co. KGaA, Weinheim 

## Conclusion

The methods previously used for the preparation of Cb*Co($C_4R_4E$) compounds proved to be effective for the synthesis of Cb*Co complexes with monoanionic tricarbollide ligands. Similar to iron and ruthenium analogs, these complexes undergo cluster rearrangements in relatively mild conditions. Identical isomerization sequences observed for Cb*Co, CpFe, and Cp*Ru tricarbollides suggest that relative stability of isomers is mainly determined by the arrangement of the carbon atoms and is practically independent of the metal vertex. This conclusion is also confirmed by DFT calculations for ($C_4H_4$)Co and CpFe tricarbollide isomers.

## Experimental Section

**General:** All reactions were carried out under argon in anhydrous solvents that were purified and dried using standard procedures. The isolation of products was conducted in air. Starting materials were prepared as described in the literature: Cb*Co$(CO)_2$I,[3,13] [Cb*Co$(C_6H_6)$]$PF_6$,[3,13] [Cb*Co$(MeCN)_3$]$PF_6$,[3,13] [$Me_4$N][**2a**],[5c] Tl[**2b**],[15] and [$Ph_4$P][**3**].[5c] Irradiation was conducted in a Schlenk tube using a high-pressure mercury vapor lamp with a phosphor-coated bulb (400 W). Both the tube and the lamp were placed in a vessel of an appropriate volume covered inside with aluminum foil; cooling was accomplished by running water. Column chromatography was performed on silica gel L 100/400 (0.5 × 10 cm) using $CH_2Cl_2$/petroleum ether (1:5) as an eluent. The $^1$H and $^{11}$B NMR spectra were recorded with a Bruker AMX 400 spectrometer operating at 400.13 and 128.38 MHz, respectively.

**Preparation of 1-Cb*-12-*t*BuNH-1,2,4,12-$CoC_3B_8H_{10}$ (7b). Method A [Starting from Cb*Co$(CO)_2$I]:** A mixture of Cb*Co$(CO)_2$I (100 mg, 0.29 mmol) and Tl[**2b**] (143 mg, 0.35 mmol) in THF (20 mL) was stirred under reflux for 13 h. The solvent was removed in vacuo and the residue was extracted with $CH_2Cl_2$/petroleum ether (1:1). Filtration and evaporation left a crude product, which was purified by column chromatography followed by washing with pentane (about 1 mL). Yield 90 mg (84%) of a yellow solid. $^1$H NMR ($CDCl_3$): $\delta$ = 2.28 (s, 1 H, NH), 1.52 (s, 12 H, Cb*), 1.50 (s, 2 H, CH), 1.25 (s, 9 H, *t*Bu) ppm. $^{11}$B NMR: $\delta$ = –10.4 [d (148), 2B, B5,6], –15.1 [d (170), 1B, B3], –15.5 [d (160), 2B, B9,11], –17.9 [d (156), 1B, B10], –22.3 [d (173), 2B, B7,8] ppm. $C_{15}H_{32}B_8CoN$ (371.83): calcd. C 48.45, H 8.68, B 23.26, N 3.77; found C 48.63, H 8.74, B 23.30, N 3.59.

**Method B {Starting from [Cb*Co$(C_6H_6)$]$PF_6$}:** A mixture of [Cb*Co$(C_6H_6)$]$PF_6$ (50 mg, 0.13 mmol) and Tl[**2b**] (57 mg, 0.14 mmol) in $CH_2Cl_2$/THF (15:3 mL) was irradiated with stirring for 6 h. The solvent was removed in vacuo and the residue was extracted with $CH_2Cl_2$/petroleum ether (1:1). Filtration and evaporation left a crude product, which was purified by column chromatography followed by washing with pentane (about 0.5 mL). Yield 30 mg (62%).

**Method C {Starting from [Cb*Co$(MeCN)_3$]$PF_6$}:** Tl[**2b**] (102 mg, 0.25 mmol) was added to a frozen (–196 °C) solution of [Cb*Co$(MeCN)_3$]$PF_6$ (100 mg, 0.23 mmol) in THF (5 mL). The temperature was allowed to rise to ambient and the mixture was stirred overnight. The solvent was removed in vacuo and the residue was extracted with $CH_2Cl_2$/petroleum ether (1:1). Filtration and evaporation left a crude product, which was purified by column chromatography followed by washing with pentane (about 0.5 mL). Yield 68 mg (79%).

**Preparation of 1-Cb*-1,2,3,4-$CoC_3B_8H_{11}$ (4a):** Complex **4a** was obtained in a similar manner to **7b**, using [$Me_4$N][**2a**]. Yield 41% (method B) and 35% (method C) of a yellow solid. $^1$H NMR ([$D_6$]-acetone): $\delta$ = 4.53 (s, 1 H, CH), 2.77 (s, 2 H, CH), 1.68 (s, 12 H, Cb*) ppm. $^{11}$B NMR: $\delta$ = –9.56 [d (148), 2B, B5,6], –12.72 [d (144), 1B, B10], –17.10 [d (158), 2B, B9,11], –19.03 [d (146), 1B, B12], –26.12 [d (170), 2B, B7,8] ppm. $C_{11}H_{23}B_8Co$ (300.70): calcd. C 43.93, H 7.71; found C 43.96, H 7.70.

**Preparation of 1-Cb*-1,2,3,5-$CoC_3B_8H_{11}$ (5):** Complex **5** was obtained in a similar manner to **7b**, using [$Ph_4$P][**3**]. Yield 61% (method C) of a yellow solid. $^1$H NMR ($CDCl_3$): $\delta$ = 2.50 (s, 2 H, CH), 1.91 (s, 1 H, CH), 1.60 (s, 12 H, Cb*) ppm. $^{11}$B NMR: $\delta$ = –16.59 [d (159), 4B, B7,9,10,12], –18.99 [d (161), 2B, B4,6], –24.55 [d (159), 2B, B8,11] ppm. $C_{11}H_{23}B_8Co$ (300.70): calcd. C 43.93, H 7.71; found C 44.03, H 7.84.

**Preparation of 1-Cb*-10-*t*BuNH-1,2,4,10-$CoC_3B_8H_{10}$ (6b):** A solution of **7b** (50 mg, 0.13 mmol) in diglyme (3 mL) was refluxed for 6 h. The solvent was removed in vacuo, and the residue was dissolved in petroleum ether and filtered through a short layer of silica gel (about 2 cm). Evaporation left a yellow oil which crystallized at –10 °C. Yield 33 mg (66%) of a yellow solid. $^1$H NMR ($CDCl_3$): $\delta$ = 1.70 (s, 1 H, NH), 1.60 (s, 12 H, Cb*), 1.55 (s, 2 H, CH), 1.13 (s, 9 H, *t*Bu) ppm. $^{11}$B NMR: $\delta$ = –8.4 [d (134), 2B, B5,6], –15.2 [d (156), 1B, B3], –16.0 [d (168), 2B, B9,11], –16.8 [d (190), 1B, B12], –24.7 [d (159), 2B, B7,8] ppm. $C_{15}H_{32}B_8CoN$ (371.83): calcd. C 48.45, H 8.68, B 23.26, N 3.77; found C 49.08, H 8.71, B 23.25, N 3.72.

**Preparation of 1-Cb*-1,2,4,10-$CoC_3B_8H_{11}$ (6a):** Complex **6a** was obtained in a similar manner to **6b** by refluxing a solution of **4a** or **5** (50 mg, 0.17 mmol) in diglyme (3 mL) for 13 h. Yield 35–38 mg (70–75%) of a yellow solid. $^1$H NMR ([$D_6$]acetone): $\delta$ = 2.33 (s, 1 H, CH), 1.76 (s, 2 H, CH), 1.65 (s, 12 H, Cb*) ppm. $^{11}$B NMR: $\delta$ = –10.15 [d (151), 1B, B3], –11.08 [d (155), 2B, B5,6], –17.90 [d (167), 2B, B9,11], –18.95 [d (161), 1B, B12], –23.03 [d (158), 2B, B7,8] ppm. $C_{11}H_{23}B_8Co$ (300.70): calcd. C 43.93, H 7.71, found C 44.05, H 7.82.

**Computational Details:** All calculations were performed using Gaussian 98 (revision A.7) software[27] at the B3LYP/6-31G* level. In the case of geometry optimization of **4a**, the methyl groups of the Cb* ring were fixed with ModRedundant option and treated with 3-21G* basis. The structures of the **4a**′, **5**′, and **6a**′ isomers were optimized using tightened SCF convergence criteria (SCF = Tight option). The frequency calculations were performed to confirm the global minimum and include ZPE corrections to the energy. The $^{11}$B NMR shifts were calculated using the GIAO method by subtraction of calculated isotropic shielding values from those of $B_2H_6$ (93.50 at B3LYP/6-31G*). The experimental chemical shift of $B_2H_6$ was assigned 16.6 ppm.[28]

**X-ray Crystallography:** Crystals of **4a** and **7b** suitable for X-ray diffraction were grown by slow evaporation of toluene solution under argon (**4a**) or by evaporation of petroleum ether solution in air (**7b**). The structures were solved by direct method and refined by the full-matrix least-squares against $F^2$ in anisotropic approximation for non-hydrogen atoms. All polyhedron hydrogen atoms were located from the Fourier density synthesis and refined in isotropic approximation. Crystal data and structure-refinement parameters for **4a** and **7b** are given in Table 2. All calculations were performed using the SHELXTL software.[29]

CCDC-279628 (for **4a**) and -279627 (for **7b**) contain the supplementary crystallographic data for this paper. These data can be

 © 2006 Wiley-VCH Verlag GmbH & Co. KGaA, Weinheim 

Table 2. Crystallographic data and structure-refinement parameters for **4a** and **7b**.

| | **4a** | **7b** |
|---|---|---|
| Empirical formula | $C_{11}H_{23}B_8Co$ | $C_{15}H_{32}B_8CoN$ |
| Formula mass | 300.70 | 371.83 |
| Crystal color, habit | yellow prism | yellow prism |
| Crystal size [mm] | 0.20 × 0.20 × 0.35 | 0.16 × 0.20 × 0.30 |
| Diffractometer | Smart CCD | Smart CCD |
| Scan type | $\omega$ | $\omega$ |
| Temperature [K] | 120 | 120 |
| Crystal system | monoclinic | monoclinic |
| Space group | $P2_1/c$ | $P2_1/c$ |
| $a$ [Å] | 12.366(2) | 8.746(1) |
| $b$ [Å] | 13.166(2) | 18.540(3) |
| $c$ [Å] | 19.030(2) | 12.750(2) |
| $\beta$ [°] | 92.730(3) | 104.844(5) |
| $V$ [Å$^3$] | 3094.9(7) | 1998.3(4) |
| $Z$ [$Z'$] | 8 (2) | 4(1) |
| $D_{calcd.}$ [g/cm$^3$] | 1.291 | 1.236 |
| $F$ (000) | 1248 | 784 |
| $\mu$(Mo-$K_\alpha$) [mm$^{-3}$] | 10.87 | 8.56 |
| $\theta$ range [°] | 1.88–28.50 | 1.98–28.01 |
| Collected reflections | 18596 | 13672 |
| Independent reflections ($R_{int}$) | 7571 (0.0674) | 4660 (0.0394) |
| Observed reflections [$I > 2\sigma(I)$] | 4328 | 3388 |
| Parameters | 457 | 354 |
| $R_1$ (on $F$ for obsd. refls.)[a] | 0.0477 | 0.0472 |
| $wR_2$ (on $F^2$ for all refls.)[b] | 0.1026 | 0.1099 |
| Gof | 0.945 | 1.068 |
| Largest diff. peak and hole [e/Å$^3$] | 0.647/–0.351 | 0.456/–0.418 |

[a] $R_1 = \Sigma||F_o| - |F_c||/\Sigma(F_o)$ for observed reflections. [b] $wR_2 = \{\Sigma[w(F_o^2 - F_c^2)^2]/\Sigma[w(F_o^2)^2]\}^{0.5}$ for all reflections.

obtained free of charge from The Cambridge Crystallographic Data Centre via www.ccdc.cam.ac.uk/data_request/cif.

**Supporting Information** (see footnote on the first page of this article): Contains details of DFT calculations for compounds **4a**, **4a′**, **5′**, and **6a′** (atomic coordinates for optimized geometry, energy data, summary of natural population analysis, and GIAO NMR shielding parameters).

## Acknowledgments

This work was supported by the Division of Chemistry and Material Sciences of Russian Academy of Sciences (Grant No. 01). B. Š. acknowledges the Grant Agency (Project No. 203/05/2646) and Ministry of Education (Project No. LC523) of the Czech Republic.

[1] V. I. Meshcheryakov, P. S. Kitaev, K. A. Lyssenko, Z. A. Starikova, P. V. Petrovskii, Z. Janoušek, M. Corsini, F. Laschi, P. Zanello, A. R. Kudinov, *J. Organomet. Chem.* **2005**, *690*, 4745–4754.

[2] A. R. Kudinov, E. V. Mutseneck, D. A. Loginov, *Coord. Chem. Rev.* **2004**, *248*, 571–585.

[3] E. V. Mutseneck, D. A. Loginov, D. S. Perekalin, Z. A. Starikova, D. G. Golovanov, P. V. Petrovskii, P. Zanello, M. Corsini, F. Laschi, A. R. Kudinov, *Organometallics* **2004**, *23*, 5944–5957.

[4] A. R. Kudinov, V. I. Meshcheryakov, P. V. Petrovskii, M. I. Rybinskaya, *Izv. Akad. Nauk, Ser. Khim.* **1999**, 177–179 [*Russ. Chem. Bull.* **1999**, *48*, 176–178 (Engl. Transl.)].

[5] a) B. Štíbr, J. Holub, F. Teixidor, C. Viñas, *J. Chem. Soc., Chem. Commun.* **1995**, 795–796; b) B. Štíbr, J. Holub, J. Plešek, T. Jelínek, B. Grüner, F. Teixidor, C. Viñas, *J. Organomet. Chem.* **1999**, *582*, 282–285; c) J. Holub, B. Štíbr, D. Hnyk, J. Fusek, I. Císařová, F. Teixidor, C. Viñas, Z. Plzák, P. v. R. Schleyer, *J. Am. Chem. Soc.* **1997**, *119*, 7750–7759; d) B. Štíbr, J. Holub, I. Císařová, F. Teixidor, C. Viñas, *Inorg. Chim. Acta* **1996**, *245*, 129–131.

[6] D. S. Perekalin, K. A. Lyssenko, P. V. Petrovskii, J. Holub, B. Štíbr, A. R. Kudinov, *J. Organomet. Chem.* **2005**, *690*, 2775–2779.

[7] J. Holub, B. Grüner, D. S. Perekalin, D. G. Golovanov, K. A. Lyssenko, P. V. Petrovskii, A. R. Kudinov, B. Štíbr, *Inorg. Chem.* **2005**, *44*, 1655–1659.

[8] D. S. Perekalin, J. Holub, D. G. Golovanov, K. A. Lyssenko, P. V. Petrovskii, B. Štíbr, A. R. Kudinov, *Organometallics* **2005**, *24*, 4387–4392.

[9] For review see: B. Štíbr, *J. Organomet. Chem.* **2005**, *690*, 2694–2700.

[10] B. Grüner, F. Teixidor, C. Viñas, R. Sillanpää, R. Kivekäs, J. Holub, A. Lehtonen, B. Štíbr, *Inorg. Chem. Commun.* **1999**, *2*, 411–413.

[11] We use a numbering system in which the metal vertex bears number 1.

[12] The use of this method is possible due to low nucleophilicity of anion **2a**: a) see ref.[5a,5b]; b) A. M. Shedlow, L. G. Sneddon, *Collect. Czech. Chem. Commun.* **1999**, *64*, 865–882. In the case of $Cp^-$ this method is inapplicable owing to nucleophilic addition to the benzene ring.

[13] M. V. Butovskii, U. Englert, A. A. Fil'chikov, G. E. Herberich, U. Koelle, A. R. Kudinov, *Eur. J. Inorg. Chem.* **2002**, 2656–2663.

[14] W. N. Lipscomb, *Science* **1966**, *153*, 373–378.

[15] J. Holub, B. Grüner, I. Císařová, J. Fusek, Z. Plzák, F. Teixidor, C. Viñas, B. Štíbr, *Inorg. Chem.* **1999**, *38*, 2775–2780.

[16] B. Grüner, A. Lehtonen, R. Kivekäs, R. Sillanpää, J. Holub, F. Teixidor, C. Viñas, B. Štíbr, *Inorg. Chem.* **2000**, *39*, 2577–2580.

[17] DFT calculations for the related iron complex 1-Cp-2-*t*BuNH-1,2,3,4-$FeC_3B_8H_{10}$ revealed the nonbonding character of the C2–C3 connectivity in accordance with the strong electron donation from the nitrogen lone pair: D. S. Perekalin, I. V.

 © 2006 Wiley-VCH Verlag GmbH & Co. KGaA, Weinheim 

Glukhov, B. Štibr, A. R. Kudinov, *Inorg. Chim. Acta*, manuscript submitted.

[18] E. V. Mutseneck, D. S. Perekalin, J. Holub, Z. A. Starikova, P. V. Petrovskii, P. Zanello, M. Corsini, B. Štíbr, A. R. Kudinov, *Organometallics* **2006**, in press.

[19] E. R. Davidson, *Chem. Rev.* **2000**, *100*, 351–352, and other papers in the same issue.

[20] M. F. Hawthorne, J. I. Zink, J. M. Skelton, M. J. Bayer, C. Liu, E. Livshits, R. Baer, D. Neuhauser, *Science* **2004**, *303*, 1849–1851.

[21] M. J. Fischer, P. A. Jelliss, L. M. Phifer, N. P. Rath, *Inorg. Chim. Acta* **2005**, *358*, 1531–1544.

[22] D. S. Perekalin, A. R. Kudinov, *Izv. Akad. Nauk, Ser. Khim.* **2005**, 1557–1559.

[23] F. A. Kiani, M. Hofmann, *Organometallics* **2006**, *25*, 485–490.

[24] M. Bühl, D. Hnyk, J. Macháček, *Chem. Eur. J.* **2005**, *11*, 4109–4120.

[25] The primed compound numbers correspond to derivatives with an unsubstituted cyclobutadiene ring.

[26] S. Heřmánek, *Inorg. Chim. Acta* **1999**, *289*, 20–44.

[27] M. J. Frisch, G. W. Trucks, H. B. Schlegel, G. E. Scuseria, M. A. Robb, J. R. Cheeseman, V. G. Zakrzewski, J. A. Montgomery Jr, R. E. Stratmann, J. C. Burant, S. Dapprich, J. M. Millam, A. D. Daniels, K. N. Kudin, M. C. Strain, O. Farkas, J. Tomasi, V. Barone, M. Cossi, R. Cammi, B. Mennucci, C. Pomelli, C. Adamo, S. Clifford, J. Ochterski, G. A. Petersson, P. Y. Ayala, Q. Cui, K. Morokuma, D. K. Malick, A. D. Rabuck, K. Raghavachari, J. B. Foresman, J. Cioslowski, J. V. Ortiz, A. G. Baboul, B. B. Stefanov, G. Liu, A. Liashenko, P. Piskorz, I. Komaromi, R. Gomperts, R. L. Martin, D. J. Fox, T. Keith, M. A. Al-Laham, C. Y. Peng, A. Nanayakkara, C. Gonzalez, M. Challacombe, P. M. W. Gill, B. G. Johnson, W. Chen, M. W. Wong, J. L. Andres, M. Head-Gordon, E. S. Replogle, J. A. Pople, *GAUSSIAN98*, *Revision A.7*, Gaussian, Inc., Pittsburgh, PA, **1998**.

[28] U. Dörfler, D. L. Ormsby, R. Greatrex, J. D. Kennedy, *Inorg. Chim. Acta* **2000**, *304*, 268–273.

[29] G. M. Sheldrick, *SHELXTL V5.10*, Bruker AXS Inc., Madison, WI, **1997**.

Received: January 17, 2006
Published Online: March 9, 2006

 © 2006 Wiley-VCH Verlag GmbH & Co. KGaA, Weinheim 

DOI: 10.1002/ejic.200501004

# Electronic Characterisation and Significant Second-Order NLO Response of 10,20-Diphenylporphyrins and Their $Zn^{II}$ Complexes Substituted in the *meso* Position with π-Delocalised Linkers Carrying Push or Pull Groups

**Tamara Morotti,[a] Maddalena Pizzotti,*[b] Renato Ugo,[b] Silvio Quici,[c] Maurizio Bruschi,[d] Patrizia Mussini,[e] and Stefania Righetto[b]**

**Keywords:** Nonlinear optics / Porphyrins / Cyclic voltammetry / UV/Vis spectroscopy

This work describes the synthesis and the electronic characterisation by electronic absorption spectroscopy, cyclic voltammetry and dipole moments of diphenyl porphyrins and their $Zn^{II}$ complexes substituted at the *meso* position by a pseudo-linear π-delocalised substituent carrying an electron-donor or an electron-withdrawing group. The second-order NLO response was investigated by the EFISH technique working with a nonresonant incident wavelength of 1.907 μm. This work confirms the ambivalent role of the polarisable porphyrin ring, which, already in the ground state, acts as a donor or acceptor depending on the nature (acceptor or donor) of the substituent in the *meso* position, as was pointed out in our previous work on tetraphenyl porphyrins substituted at the β-pyrrolic position.

The second-order NLO response has been discussed by comparing the nature of the substituent (electron donor or acceptor) and the kind of substitution (β pyrrolic or *meso*). This comparison evidenced a significant increase of the electron-donor properties of $NBu_2$ or $NMe_2$ when they are connected to the *meso* position or to the β-pyrrolic position, probably because of an auxiliary donor effect of the electron-rich porphyrin ring. When the substituent is the electron-withdrawing $NO_2$ group, the substituent position (*meso* or β pyrrolic) is influential, with the existance of a significant increase in the second order NLO response when substitution occurs at the *meso* position.
(© Wiley-VCH Verlag GmbH & Co. KGaA, 69451 Weinheim, Germany, 2006)

## Introduction

Over the last two decades molecular materials for nonlinear optics (NLO) have been investigated for their promising applications in optoelectronics and photonics.[1] Although most studies deal with pseudo-linear 1D organic[2] or organometallic[3] push-pull chromophores with second-order nonlinear optical response, more recent investigations have been devoted to two-dimensional push-pull chromophores based on highly π-delocalised macrocycles such as porphyrins[4–6] and phthalocyanines.[7] Porphyrins and their metal complexes appear to be advantageous, given their acceptable solubility, good thermal and chemical stability, and potential processability as layers.[8]

In addition, the architectural flexibility of porphyrins is well exemplified by the large number of structures reported in the literature, as well as by a large variety of substituents that can be attached at the *meso* or β-pyrrolic positions[5,6] of the porphyrin ring or to the axial position of a metal complex.[9]

Starting from studies carried out by Suslick and coworkers at the beginning of the 90s[4a,4b] and later by Therien and coworkers,[5a,5b] and following the theoretical approach of Marks, Ratner et al.,[10] who suggested that the presence of a π spacer between an electron-donor or acceptor group and the porphyrin ring together with the right ring substitution (β pyrrolic or *meso*) could produce chromophores with a large second-order NLO response, we recently investigated the second-order NLO response of push-pull porphyrinic chromophores with electron-donor or withdrawing groups linked, through a π spacer, to the β-pyrrolic position of the 5,10,15,20-tetraphenylporphyrin or its $Zn^{II}$ complex.[6]

Our experimental results, in agreement with the suggestion of Marks, Ratner et al.,[10] have shown that the second-order NLO response is enhanced when an electron-donor substituent is attached at the electron-rich β-pyrrolic position of the porphyrin ring. We also evidenced an ambivalent

[a] Dipartimento di Chimica Organica e Industriale, Via Golgi 19, 20133 Milan, Italy
[b] Dipartimento di Chimica Inorganica Metallorganica e Analitica dell'Università di Milano, Unità di Ricerca dell'INSTM, Centro di Eccellenza CIMAINA dell'Università di Milano e Istituto di Scienze e Tecnologie Molecolari del CNR (ISTM), Via Venezian 21, 20133 Milan, Italy
Fax: +39-2-50314405
E-mail: maddalena.pizzotti@unimi.it
[c] Istituto di Scienze e Tecnologie Molecolari del CNR (ISTM), via Golgi 19, 20133 Milan, Italy
[d] Dipartimento di Biotecnologie e Bioscienze, Università di Milano Bicocca, Piazza della Scienza 2, 20126 Milan, Italy
[e] Dipartimento di Chimica Fisica ed Elettrochimica dell'Università di Milano, Via Golgi 19, 20133 Milan, Italy

 © 2006 Wiley-VCH Verlag GmbH & Co. KGaA, Weinheim 

role of the porphyrin ring (in the ground state but also in charge transfer processes), behaving as an electron donor or as an electron-rich enhancer of the donor properties of an amino group, according to the nature of the substituent in the β-pyrrolic position.

Very few studies have been devoted to the experimental investigation of the second-order NLO response of push-pull porphyrinic chromophores according to the nature of the substituents and their position on the porphyrin ring. Thus, in an effort to produce additional evidence of the ambivalent role of the porphyrin ring, we extended our investigation to the electronic characterisation and second-order NLO response of a series of 10,20-diphenylporphyrins ($H_2$DPP) and their $Zn^{II}$ complexes substituted, at the *meso* position, by electron-donor or electron-withdrawing groups connected through a π spacer.

In order to avoid resonance effects or interference resulting from fluorescent emissions, the second-order NLO response was measured by the EFISH technique working with a nonresonant 1.907 μm incident wavelength.[5a] Calculations based on density functional theory (DFT)[11] were also performed to evaluate the dipole moment of the optimised structures of the investigated porphyrinic macrocycles, using the BP86[12] functional and an all-electron valence triple-ξ basis set with polarisation functions on all atoms.[13]

## Results and Discussion

### Synthesis of Porphyrins and Their $Zn^{II}$ Complexes

The asymmetrical 10,20-diphenylporphyrins and their $Zn^{II}$ complexes investigated in this work are reported in Figure 1; the $Zn^{II}$ complexes **2** and **4** have already been synthesised by Anderson et al.[14]

The porphyrin **1** was synthesised with a modification of the synthetic route described by Anderson et al.,[14] involving a Wittig condensation of 5-formyl-10,20-diphenylporphyrin with 4-nitrobenzyltriphenylphosphonium bromide in refluxing 1,2-dichloroethane, using solid NaOH 20–40 mesh beads as the base. This reaction afforded **1** in 49%

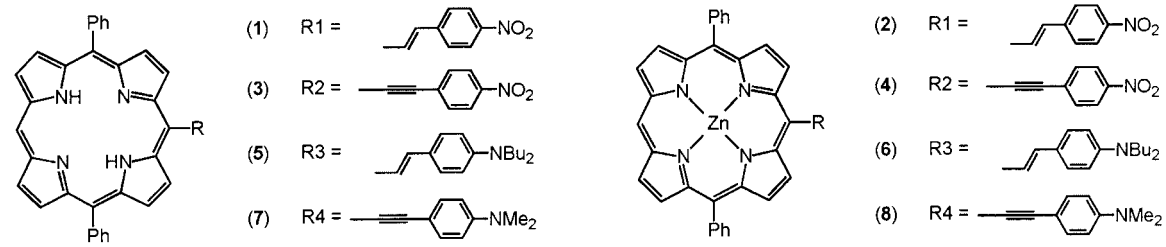


Figure 1. Asymmetrical 10,20-diphenylporphyrins and their $Zn^{II}$ complexes substituted at the *meso* position with electron-withdrawing or electron-donor groups.

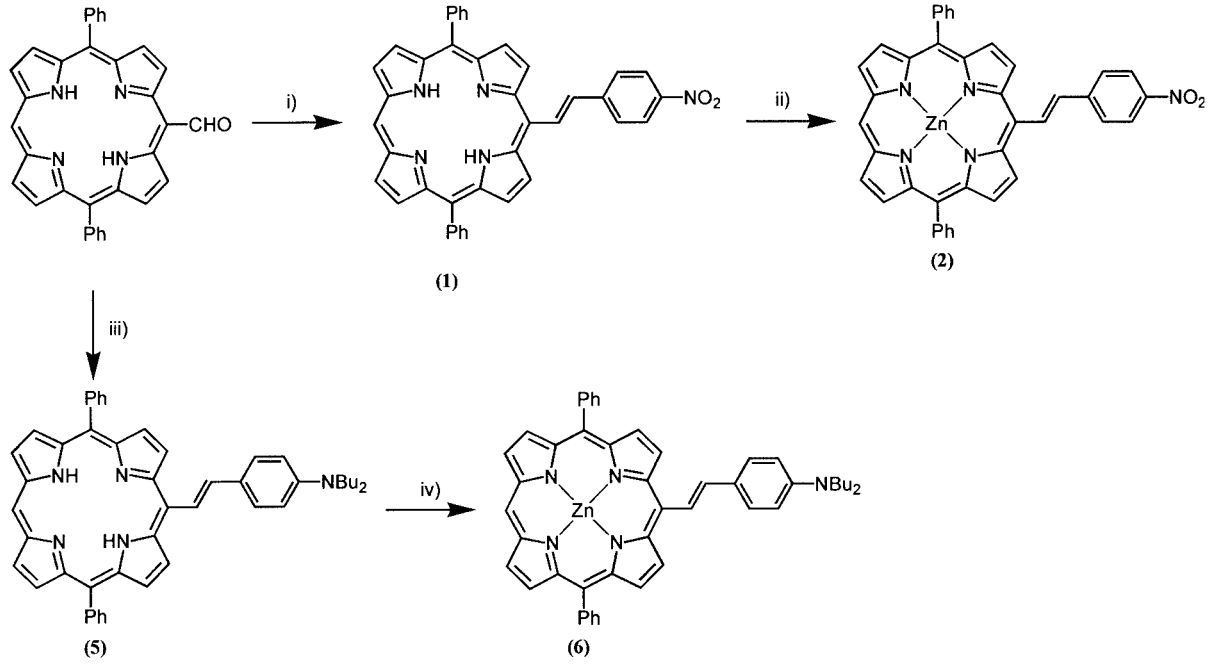


Scheme 1. i) 4-Nitrobenzyltriphenylphosphonium bromide, NaOH, $CH_2Cl_2$, reflux, 4 h; ii) $Zn(OAc)_2{\cdot}2H_2O$, $CHCl_3$/MeOH, reflux, 1 h; iii) 4-(Dibutylamino)benzyltriphenylphosphonium chloride, NaOH, $CH_2Cl_2$, room temp., 4 h; iv) $Zn(OAc)_2{\cdot}2H_2O$, $CHCl_3$/MeOH, reflux, 1 h.

 © 2006 Wiley-VCH Verlag GmbH & Co. KGaA, Weinheim 

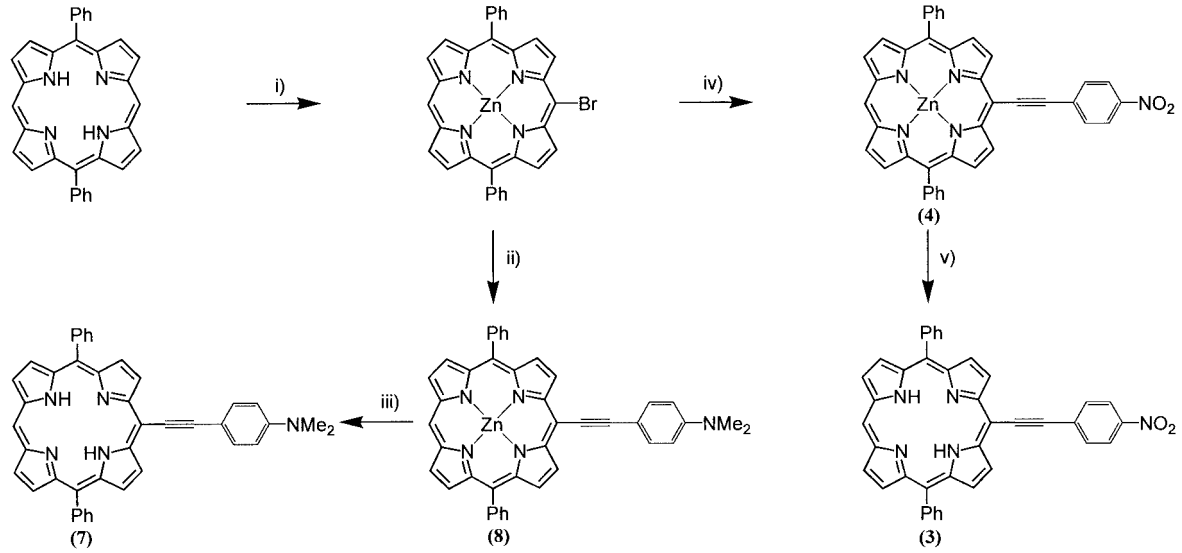


Scheme 2. i) NBS, $CHCl_3$, room temp., 30 min.; $Zn(OAc)_2{\cdot}2H_2O$, $CHCl_3$/MeOH, reflux, 1 h; ii) catalyst (see Exp. Sect.), [4-(dimethylamino)phenyl]acetylene, pyridine, toluene, 80 °C, 1.5 h; iii) TFA, $CH_2Cl_2$, 18 h; iv) catalyst (see Exp. Sect.), (4-nitrophenyl)acetylene, pyridine, toluene, 80 °C, 1 h; v) TFA, $CH_2Cl_2$, 18 h.

yield after purification by column chromatography and crystallisation from $CH_2Cl_2$/MeOH.

Analogously, Wittig condensation of 5-formyl-10,20-diphenylporphyrin with 4-(dibutylamino)benzyltriphenylphosphonium chloride afforded **5** in 59% yield after purification by column chromatography.

The corresponding $Zn^{II}$ complexes **2** and **6** were obtained in quantitative yield after refluxing **1** and **5** with $Zn^{II}$ acetate in $CH_2Cl_2$/MeOH for 1 h[15] (Scheme 1).

5-Formyl-10,20-diphenylporphyrin was prepared in 80% yield by the Vilsmaier formylation of the $Cu^{II}$ complex of 10,20-diphenylporphyrin, obtained in 83% yield by reaction of 10,20-diphenylporphyrin with $Cu^{II}$ acetate in refluxing $CHCl_3$/MeOH, followed by quantitative demetallation of the $Cu^{II}$ complex with a mixture of trifluoroacetic acid/concentrated sulfuric acid (9:1), as reported by Susumu et al.[15]

$Zn^{II}$ complexes **4** and **8** (85% and 59% yields, respectively) were synthesised, as described by Anderson et al.,[14] by the coupling reaction of the $Zn^{II}$ complex of 5-bromo-10,20-diphenylporphyrin with 4-nitrophenylacetylene and [4-(dimethylamino)phenyl]acetylene, respectively. The reaction was carried out in anhydrous toluene and pyridine at 80 °C in the presence of a $Pd^0$ catalyst, prepared in situ by the reaction, at 70 °C, of $[Pd_2(dba)_3]$ and $PPh_3$ in freshly distilled $Et_3N$ in the presence of CuI.

The free base porphyrins **3** and **7** were obtained in quantitative yields by controlled demetallation, at room temperature, of the $Zn^{II}$ complexes **4** and **8** with trifluoroacetic acid working in $CH_2Cl_2$ (Scheme 2).

### Electronic Absorption and Emission Spectra

Anderson et al.[14] have already investigated the electronic absorption and emission spectra of the $Zn^{II}$ complexes **2** and **4**, which evidence significant changes in comparison with those of the complex [Zn(DPP)]·THF of 10,20-diphenylporphyrin ($H_2$DPP). The significant red shift of both the Soret B band and the $Q_\alpha$ band at lower energy, with an increase in the intensity of this latter band suggests an electronic conjugation between the porphyrin ring and the π linker. The spectra, obtained in $CH_2Cl_2$ solution in the presence of 1% pyridine, refer to pentacoordinate species with a pyridine in the axial position.

Here we report (Table 1) and discuss the absorption and emission spectra of the $Zn^{II}$ complexes **2** and **4** in $CHCl_3$ solution, with and without pyridine addition, together with those of the corresponding porphyrins **1** and **3**.

A comparison of the absorption spectra of the porphyrins **1** and **3** with those of **2** and **4** indicates a decrease in the number of Q bands, from four to two, with the complete disappearance of the $Q_\alpha$ band at low energy (around 655–660 nm) as expected for an increase of the microsymmetry upon coordination.[6] Compounds **2** and **4**, but also **1** and **3**, still show a significant red shift of the Soret B band and of the $Q_\alpha$ band at lower energy, which increases its intensity, in comparison with that of [Zn(DPP)]·THF and $H_2$DPP (Table 1). The red shift of the Soret B band is more significant for **4** than for **2**, in agreement with the suggested[14] better π conjugation of the triple bond with the π core of the porphyrin ring.

Differently from 5,10,15,20-tetraphenylporphyrin and its $Zn^{II}$ complex substituted in the β-pyrrolic position by a similar series of π-delocalised substituents,[6] the Soret B band of porphyrins **1** and **3** and of their $Zn^{II}$ complexes **2** and **4** is quite symmetric, but with an increase of the bandwidth of the Soret B bands, which is further evidence of electronic conjugation[6] (Table 1).

Both **2** and **4** show, in the presence of pyridine, an additional small red shift of the Soret B band, and a more significant red shift of the $Q_\alpha$ band at lower energy, which is expected for the axial coordination of pyridine[9] (Table 1). The $Zn^{II}$ complex **4** is quite insoluble, suggesting

 © 2006 Wiley-VCH Verlag GmbH & Co. KGaA, Weinheim 

Table 1. Absorption ($\lambda_{max}$) and emission ($\lambda_e$) spectra in $CHCl_3$ (Soret B band in **bold**).

| Compound | Soret B Half bandwidth $\Delta\nu_{1/2}$ [$cm^{-1}$][b] | $\lambda_{max}$ [nm] (log$\varepsilon$) | $\lambda_e$ [nm][c] |
|---|---|---|---|
| $H_2$DPP[a] | 874 | **409** (5.49), 502 (4.27), 536 (3.74), 575 (3.78), 630 (3.18) | 638, 695 |
| [ZnDPP]·THF | 718 | **407** (5.65), 536 (4.19), 571 (2.84) | 579, 627<br>594, 646[d][h] |
| (1*E*)-5-[2-(4′-Nitrophenyl)ethenyl]-10,20-$H_2$DPP (**1**) | 2606 | **422** (5.27), 518 (4.07), 564 (4.11), 594 (3.89), 655 (3.65) | 673.5, 760 (sh) |
| (1*E*)-5-[2-(4′-Nitrophenyl)ethenyl]10,20 ZnDPP (**2**) | 2629 | **422** (5.23), 552 (4.19), 599 (4.04)<br>**428** (5.05), 566 (3.72), 626 (3.89)[d] | 647(sh), 692<br>671[d] |
| 5-[2-(4′-Nitrophenyl)ethynyl]-10,20-$H_2$DPP (**3**) | 1521 | **436** (5.15), 529 (3.91), 573 (4.32), 602 (3.79), 661 (3.94) | 665, 765 (sh) |
| 5-[2-(4′-Nitrophenyl)ethynyl]-10,20-ZnDPP (**4**) | n.d.[e] | **439** (5.16), 560 (3.68), 608 (4.07)<br>**449** (5.17), 575 (3.92), 634 (4.47)[d] | 617, 667 (sh)<br>700[d] |
| (1*E*)-5-[2-(4′-Dibutylaminophenyl)ethenyl]-10,20-$H_2$DPP (**5**) | 2550 | **410** (5.06), 521 (4.00), 579 (4.15), 665 (3.76), 747 (3.52) | 660 (sh), 702 |
| (1*E*)-5-[2-(4′-Dibutylaminophenyl)ethenyl]-10,20-ZnDPP (**6**) | n.d.[f] | **408** (5.26), 554 (4.27), 606 (4.32)<br>**428** (5.20), 563 (4.06), 613 (4.09)[d] | 696<br>695[d] |
| 5-[2-(4′-Dimethylaminophenyl)ethynyl]-10,20-$H_2$DPP (**7**) | 2514 | **425** (5.02), **441** (sh), 523 (3.93), 587 (4.32), 673 (3.94) | 697, 746 (sh) |
| 5-[2-(4′-Dimethylaminophenyl)ethynyl]-10,20-ZnDPP (**8**) | n.d.[g] | **428** (4.97), **448** (4.98), 565 (4.02), 615 (4.24)<br>**451** (5.14), 579 (3.87), 632 (4.30)[d] | 640, 688<br>654, 702[d] |

[a] $H_2$DPP = 10,20-diphenylporphyrin. [b] Values were obtained according to equation $\Delta\nu_{1/2} = f/(4.33\times10^{-9}\times\varepsilon)$ (F. L. Pilar, *Elementary Quantum Chem.*, McGraw-Hill Book Comp., **1968**) where $f$ is the oscillator strength and $\varepsilon$ is the extinction coefficient of the maximum. [c] Values obtained by irradiation at the Soret wavelength. [d] With addition of pyridine. [e] Not soluble enough for a reliable determination. [f] Highly asymmetric band. [g] Two Soret bands of relative intensities depending on the concentration. [h] In $CH_2Cl_2$ solution from ref.[14]

strong association in the solid state.[16] In accordance it becomes soluble with the addition of pyridine.

When an *E*-ethylenic linker connects a basic dibutylamino electron-donor group with the porphyrin ring as in porphyrin **5** and its $Zn^{II}$ complex **6** (Table 1), all the Q bands are notably red shifted, (notably for **5** the $Q_\alpha$ band at lower energy shifts from 630 to 747 nm), while the Soret B band is not red shifted when compared with $H_2$DPP and [ZnDPP]·THF. Both compounds **5** and **6** show a significantly asymmetric Soret B band, with the asymmetry centred at lower energy (Figure 2). Interestingly the compound with the same substituent bound to the β-pyrrolic position of the 5,10,15,20-tetraphenylporphyrin or its $Zn^{II}$ complex, shows a symmetric Soret B band.[6]

The $Zn^{II}$ complex **8** with a dimethylamino electron-donor group connected through a π-acetylenic linker to the porphyrin ring shows, in $CHCl_3$ solution even at concentrations about $10^{-6}$ M, two well-separated Soret B bands, with a relative intensity changing with the concentration (Table 1 and Figure 3, a), which is evidence of aggregation.[16]

The position of the two bands suggests that aggregation occurs via the interaction of the donor dimethylamino group of the π-delocalised substituent with the axial position of another molecule, since the Soret B band at 448 nm is typical of pentacoordination, while that at 428 nm may be because of some unassociated species. Intermolecular aggregation is also supported by the addition of traces of pyridine, which produces only one symmetric Soret B band at 451 nm (Figure 3, b) that does not shift on dilution as would be expected for an unaggregated pentacoordinate species.[9]

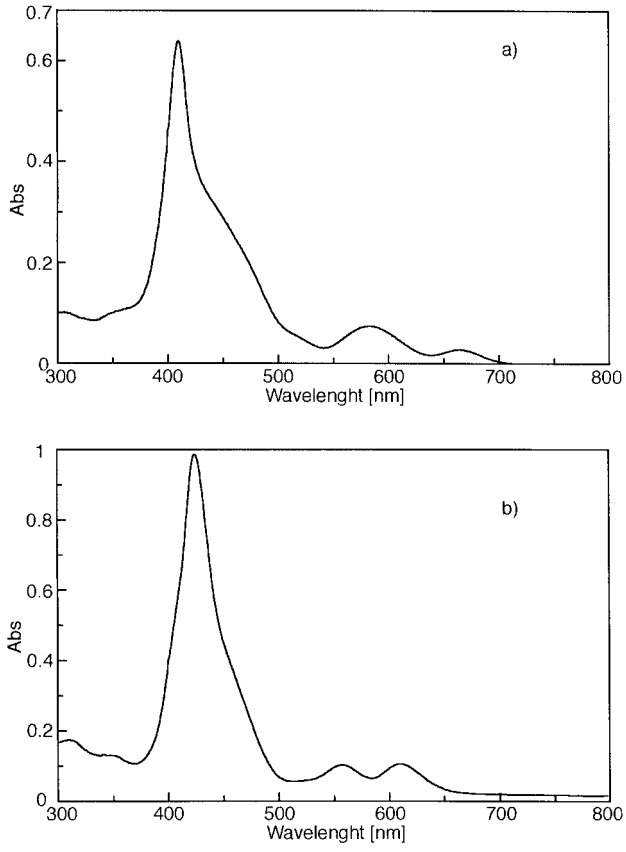


Figure 2. (a) Electronic absorption spectrum of **5** in $CHCl_3$, (b) Electronic absorption spectrum of **6** in $CHCl_3$.

 © 2006 Wiley-VCH Verlag GmbH & Co. KGaA, Weinheim 

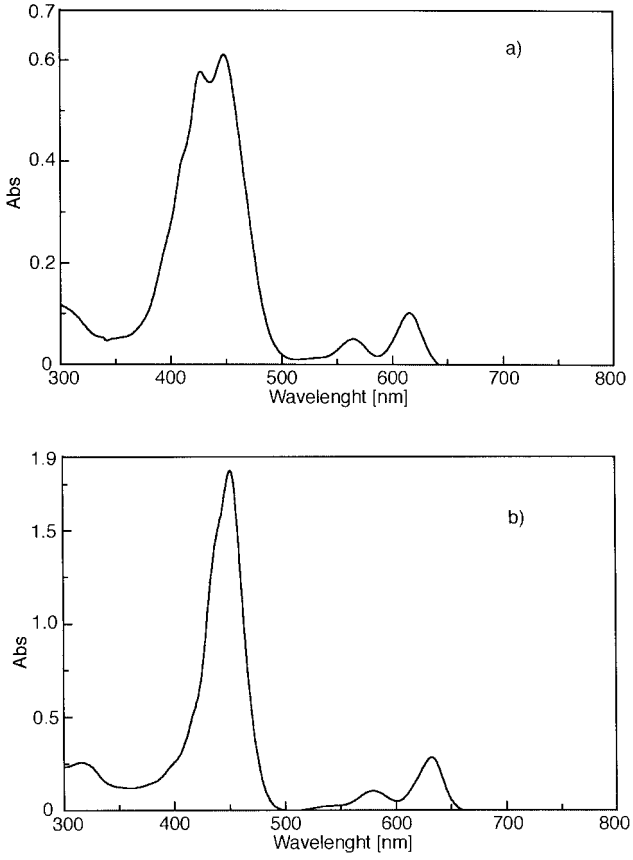


Figure 3. (a) Electronic absorption spectrum of **8** in $CHCl_3$, (b) Electronic absorption spectrum of **8** in $CHCl_3$ with the addition of pyridine.

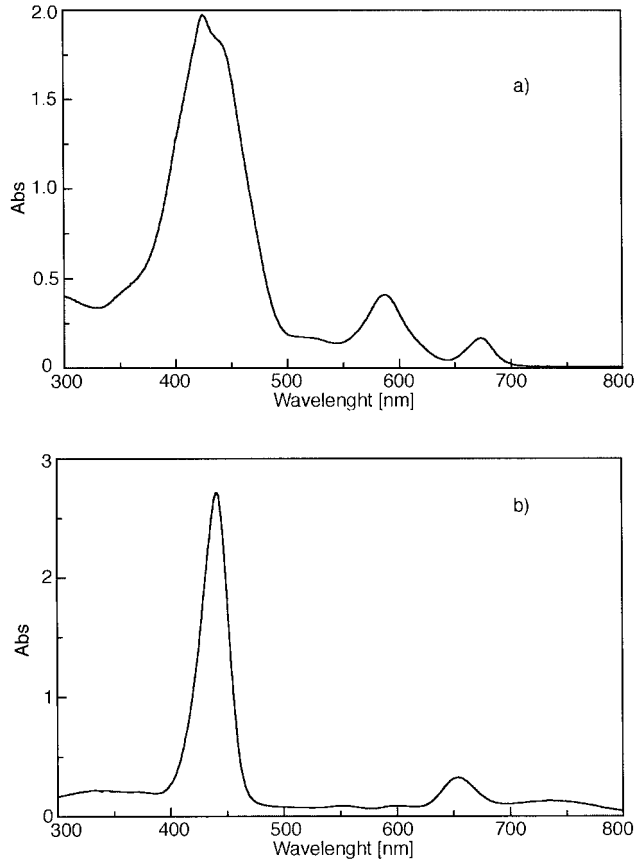


Figure 4. (a) Electronic absorption spectrum of **7** in $CHCl_3$, (b) Electronic absorption spectrum of **7** in $CHCl_3$ with the addition of trifluoroacetic acid.

Also the $Zn^{II}$ complex **6** shows a Soret B band with some asymmetry (Figure 2, b), which disappears on addition of pyridine suggesting a similar kind of aggregation. A slow aggregation process of **6** is confirmed by an $^1H$ NMR spectroscopic investigation, but working at higher concentrations (about $10^{-3}$ M). In fact, the $^1H$ NMR spectrum of **6** in $CDCl_3$ is initially the one expected for a monomeric species, but after one hour significant changes take place.

A weaker intermolecular aggregation, probably by hydrogen bonding between the NH and $NMe_2$ groups of two molecules, seems to occur for porphyrin **7**, where two poorly resolved Soret B bands are seen (Figure 4, a). On dilution two isosbestic points were evidenced, as expected for the dissociation of a dimeric species, resulting in a monomeric species only at about $10^{-6}$ M concentration.

The addition of traces of trifluoroacetic acid to a $10^{-5}$ M solution of **7** in $CHCl_3$ produced only one Soret B band (Figure 4, b) as expected for the protonation of the dimethylamino group with disruption of the hydrogen bond and therefore of the intermolecular aggregation involving the dimethylamino group of the substituent.

Interestingly compounds **1**–**3**, with a π-delocalised substituent carrying an electron-withdrawing nitro group, did not show such spectroscopic evidence for significant aggregation, for instance by π stacking,[16] at concentrations of about $10^{-4}$–$10^{-6}$ M in $CHCl_3$.

Both $H_2DPP$ and [ZnDPP]·THF, when irradiated at the Soret B band wavelength in a $CHCl_3$ solution, show two well-separated emission bands, the one at lower energy being slightly more intense. On the contrary the porphyrins **1**, **3**, **5** and **7** show only one major emission with shoulders at lower (**1**, **3**, **7**) or at higher energies (**5**). Also the $Zn^{II}$ complexes **2** and **4** in $CHCl_3$ solution show one major emission, with much weaker emission bands at lower (**4**) or higher energies (**2**). Only the $Zn^{II}$ complexes **6** and **8** show one significant emission band and two well-separated emission bands of comparable intensity (Table 1). The shift at lower energy of the emission bands of **1**–**8** compared to those of $H_2DPP$ and [ZnDPP]·THF (Table 1) is further evidence of conjugation of the π core of the porphyrin ring by the π-delocalised linker.

The $Zn^{II}$ complexes **2** and **4** in $CHCl_3$ solution show, after the addition of traces of pyridine, only one emission band shifted at lower energy, while complex **6** shows the same unshifted emission band. Only the $Zn^{II}$ complex **8** shows two well-separated emission bands as for [ZnTPP]·THF, but at much lower energy (Table 1).

In summary, we have added further evidence to the proposal of Anderson et al.[14] for a conjugation of the π core of the porphyrin ring, particularly when the π-delocalised linker carries a nitro electron-withdrawing group. In addition, when the linker carries a donor dibutyl or dimeth-

 © 2006 Wiley-VCH Verlag GmbH & Co. KGaA, Weinheim 

ylamino group, we found evidence of significant aggregation by intermolecular processes involving donor amino groups or hydrogen bonds.

### Voltammetric Investigation

The electronic properties of the porphyrins **1**, **3** and **5** and of their $Zn^{II}$ complexes **2**, **4** and **6** were investigated by cyclic voltammetry in $CH_2Cl_2$ solution. The relevant oxidation and reduction peak potentials are reported in Table 2. The investigation was not extended to **7** and **8**, because of the previously discussed significant aggregation in $CHCl_3$ solution, in the concentration range used for the voltammetric investigation ($10^{-3}$ to $10^{-4}$ M).

#### *Oxidation Processes*

The anodic oxidation of the porphyrins **1** and **3** and their $Zn^{II}$ complexes **2** and **4** does not take place by two monoelectronic, chemically reversible steps as such oxidation does for compounds carrying the same π-delocalised substituents in the β-pyrrolic position of 5,10,15,20-tetraphenylporphyrin or its $Zn^{II}$ complex.[6] Porphyrins **1** and **3** show a partial return peak of the first oxidation step that can clearly be perceived only by reversing the potential scan immediately after the peak and increasing the potential scan rate. This behaviour, typical of the parent compound $H_2$DPP, suggests a short-lived radical cation formed in the first oxidation step. Continuing the potential scan beyond the first oxidation peak, porphyrins **1** and **3** give a complex, ill-defined anodic pattern, with multiple maxima without a neat second oxidation step, which on the contrary was easily detected not only for 5,10,15,20-tetraphenylporphyrins carrying the same substituents in the β-pyrrolic position,[6] but also, although to a lesser extent, for the parent compound $H_2$DPP (Table 2).

The $Zn^{II}$ complex **2** shows the more usual pattern, with two subsequent neat oxidation peaks (but with the corresponding return peaks less distinguishable), while we have been unable to finely characterise the voltammetric behaviour of the $Zn^{II}$ complex **4** because of its poor solubility.

The first oxidation peak potentials of the porphyrins **1** and **3** and of the $Zn^{II}$ complex **2** are similar to those of the parent compounds $H_2$DPP and [ZnDPP]·THF or of the analogues carrying the same substituents in the β-pyrrolic position of 5,10,15,20-tetraphenylporphyrin.[6] The oxidisability sequence is the same, since in both series the *E*-double bond of the π linker seems to negligibly transmit the electron attractor effect of the nitro group, resulting in slightly higher oxidisability when compared with the case of the triple bond. This observation is an additional support to the suggested easier π conjugation of the triple bond with the π core of the porphyrin ring.[14] The complexation of **1** and **3** to $Zn^{II}$ results in the expected strong enhancement of oxidisability since the charge density on the porphyrin ring increases (negative shift of the first oxidation peak of 0.20 V for **2** compared with **1** and 0.17 V for **4** com-

Table 2. Oxidation and reduction peak potentials $E_p$/V(SCE) for porphyrins **1**, **3**, **5** and their $Zn^{II}$ complexes **2**, **4**, **6**, and four reference compounds ($CH_2Cl_2$ + 0.1 M TBAP, glassy carbon electrode, potential scan rate: 0.2 V·s$^{-1}$).

| Compound[a] | Reduction peaks[b] | Oxidation Peaks[b] |
|---|---|---|
| (1*E*)-5[2-(4'-Nitrophenyl)ethenyl-10,20-$H_2$DPP (**1**) | **–0.996** (*n* = 2; –0.961 V(SCE)$^{i}$; 0.043 V$^{ii}$; 0.071 V$^{iii}$), –1.65(*n* = 4) | **1.02** (*n* = 1), *1.23, 1.37, 1.58* |
| (1*E*)-5-[2-(4'-Nitrophenyl)ethenyl]-10,20 ZnDPP (**2**) | –1.71, –1.56, –1.24, –1.06 | **0.823** (*n* = 1; 0.789 V(SCE)$^{i}$; 0.059 V$^{ii}$; 0.068 V$^{iii}$), **1.09** (*n* = 1), *1.34, 1.55* |
| 5-[2-(4'-Nitrophenyl)ethynyl]-10,20-$H_2$DPP (**3**) | –1.00 (*n* = 2), –1.65 | **1.09** (*n* = 1), *1.25, 1.58* |
| 5-[2-(4'-Nitrophenyl)ethynyl]-10,20-ZnDPP (**4**)[c] | –1.59(*n* = 4), –0.96 (*n* = 2) | **0.92** (*n* = 1) |
| (1*E*)-5-[2-(4'-Dibutylaminophenyl)ethenyl]-10,20-$H_2$DPP (**5**) | **–1.239** (*n* = 1; 1.202 V(SCE)$^{i}$; 0.060 V$^{ii}$; 0.075 V$^{iii}$), **–1.557** (*n* = 1; 1.519 V(SCE)$^{i}$; 0.059 V$^{ii}$; 0.077 V$^{iii}$) | **0.657** (*n* = 1; 0.628 V(SCE)$^{i}$; 0.058 V$^{ii}$; 0.063 V$^{iii}$), **0.774** (*n* = 1; 0743 V(SCE)$^{i}$; 0.062 V$^{iii}$), 1.54 |
| (1*E*)-5-[2-(4'-Dibutylaminophenyl)ethenyl]-10,20-ZnDPP (**6**) | **–1.369** (*n* = 1; 1.339 V(SCE)$^{i}$; 0.053 V$^{ii}$; 0.061 V$^{iii}$), **–1.721** (*n* = 1; 1.679 V(SCE)$^{i}$; 0.066 V$^{ii}$; 0.084 V$^{iii}$) | **0.588** (*n* = 2; –0.557 V(SCE)$^{i}$; 0.047 V$^{ii}$; 0.062 V$^{iii}$), 1.41 |
| $H_2$DPP | **–1.238** (*n* = 1; 1.207 V(SCE)$^{i}$; 0.056 V$^{ii}$; 0.062 V$^{iii}$), **–1.595** (*n* = 1; 1.565 V(SCE)$^{i}$; 0.055 V$^{ii}$; 0.060 V$^{iii}$) | **1.084** (*n* = 1; 1.057 V(SCE)$^{i}$; 0.057 V$^{ii}$; 0.054 V$^{iii}$), **1.41** (*n* = 1) |
| [ZnDPP]·THF | **–1.404** (*n* = 1; 1.374 V(SCE)$^{i}$; 0.054 V$^{ii}$; 0.061 V$^{iii}$), **–1.807** (*n* = 1; 1.761 V(SCE)$^{i}$; 0.059 V$^{ii}$; 0.092 V$^{iii}$) | **0.826** (*n* = 1; 0.798 V(SCE)$^{i}$; 0.053 V$^{ii}$; 0.056 V$^{iii}$), **1.159** (*n* = 1; 1.133 V(SCE)$^{i}$; 0.046 V$^{ii}$; 0.053 V$^{iii}$) |
| 4'-(*p*-Nitrophenyl)-2,2':6',2"-terpyridine | **–1.037** (*n* = 1; 1.006 V(SCE)$^{i}$; 0.057 V$^{ii}$; 0.063 V$^{iii}$), –1.42 (*n* = 3) | no peaks |
| Ferrocene | | **0.513** (*n* =1; 0.484 V(SCE)$^{i}$; 0.056V$^{ii}$; 0.059 V$^{iii}$) |

[a] $H_2$DPP = 10,20-diphenylporphyrin. [b] Chemically reversible peaks (i.e. featuring a return peak) are underlined (in particular, a dotted line indicates partial return peaks, which are more evident at higher scan rates). The number of exchanged electrons, when assignable, is reported in parenthesis. Bold characters denote electrochemically reversible or quasi-reversible peaks; the corresponding half-wave potentials, $E_{1/2}$, half-peak widths, ($E_p - E_{p/2}$), and distances between anodic and cathodic peak ($E_{p,a} - E_{p,c}$), are reported with $^{i}$, $^{ii}$, and $^{iii}$ superscripts, respectively. Italic characters denote shoulders or ill-defined peaks. [c] The voltammetric characterisation is poor because of the low solubility.

 © 2006 Wiley-VCH Verlag GmbH & Co. KGaA, Weinheim 

pared with **3**). This effect is only slightly lower than that found for the parent compounds $H_2$DPP and [ZnDPP]·THF and for the analogues carrying the same substituents in the β-pyrrolic position of the 5,10,15,20-tetraphenylporphyrin.[6] For porphyrins **1** and **3**, the poor chemical reversibility of the first step and the ill-defined anodic pattern beyond the first oxidation peak seems to suggest instability, introduced by the substitution at the *meso* position, of the radical cation produced by the first oxidation step. This instability after the first electron loss is not evident when porphyrin **1** is complexed to $Zn^{II}$ with increased negative charge on the porphyrin ring, since complex **2** produces a more stable radical cation (possibly because it is generated at a far less positive potential), which can evolve to the dication upon loss of a second electron.

Porphyrin **5** and its $Zn^{II}$ complex **6**, carrying a dibutylamino electron-donor group bound through an *E*-ethylene linker at the *meso* position, show a first chemically and electrochemically reversible oxidation peak at nearly the same potential as their analogues with the same substituent in the β-pyrrolic position of 5,10,15,20-tetraphenylporphyrin.[6] In this last case, the first oxidation step was assumed to be centred out of the HOMO energies of the porphyrin π core, probably at the amino functionality.[6] This assumption was justified by several experimental observations, which still hold for **5** and **6**. For instance their $\Delta E_{(ox–red)}$ parameters are 1.83 V and 1.89 V, respectively [considering half-wave potentials, defined as $(E_{p,a} + E_{p,c})/2$], which deviate significantly from the expected Kadish relationship [$\Delta E_{(ox–red)} = 2.25 \pm 0.15$ V typical of the π porphyrin core].[17] In addition, complexation is not so effective since the first oxidation peak of the $Zn^{II}$ complex **6** occurs at a potential that is only 0.070 V less positive than that of the parent porphyrin **5**.

If we assume for **5** and **6** that only the second oxidation peak is centred on the porphyrin π core, as suggested by the acceptable agreement of their potentials with the Kadish relationship (see later), and as proposed for the analogues with the same substitution in the β-pyrrolic position,[6] it seems more appropriate to discuss the oxidisability of their porphyrin core by comparing the first oxidation peak potentials of unsubstituted reference compounds $H_2$DPP (1.07 V) and [ZnDPP]·THF (0.84 V) with their second oxidation peak potentials, i.e. 0.77 V for **5** and 0.59 V for **6** (in which case the huge shift in the negative direction of the second peak results in a bielectronic peak accounting for both the first and the second oxidation steps). For the analogues substituted in the β-pyrrolic position, the second oxidation peak potentials are 1.01 V and 0.79 V, respectively.[6]

Since the second oxidation of **5** and **6** occurs at a significantly less positive potential (0.25–0.30 V) than the first oxidation of the unsubstituted reference compounds, and also those (0.20–0.24 V) of the analogues with the same substitution in the β-pyrrolic position, we can conclude that the increased oxidisability suggests a significant donor effect of the dibutylamino group together with a significant role of the position on the porphyrin ring (β pyrrolic or *meso*). Shifting the substituent from the β-pyrrolic to the *meso* position appears to enhance this donor effect.

In conclusion, if the oxidation peaks (the first for **1**, **2**, **3** and **4** and the second for **5** and **6**) can be taken as a first indication of the HOMO energy, we may conclude that its perturbation by substitution in the β-pyrrolic position or the *meso* is not so relevant when the π-delocalised substituent carries an electron-withdrawing nitro group; instead such perturbation will be quite significant, leading to destabilisation, if the substituent carries an electron-donor dibutylamino group, particularly when substitution occurs in the *meso* position.

### *Reduction Processes*

Turning to the cathodic section of the voltammetric pattern (Table 2), the porphyrins **1** and **3** appear significantly more reducible than their analogues with the same kind of substitution in the β-pyrrolic position.[6] Complexes **2** and **4**, although characterised by a lower and broader pattern of the voltammetric cathodic portion, show a first reduction peak at nearly the same potential as the corresponding porphyrins **1** and **3** (Table 2) and appear to be slightly more reducible than their analogues with the same substituent in the β-pyrrolic position.[6]

It must be noted that we cannot reliably compare the potentials of the first reduction peak of **1**–**4** with those of the reference, unsubstituted compounds $H_2$DPP and [ZnDPP]·THF. In fact the cathodic portion of the voltammetric pattern of **1**–**4** is strongly influenced by the presence of the nitro group, which, when bound to a π-delocalised aromatic system, is more reducible than an unsubstituted porphyrin core {see Table 2 with potentials at –1.26 V and –1.03 V for reference compounds $H_2$DPP and [4′-(*p*-nitrophenyl)-2,2′:6′,2′′-terpyridine], respectively}. Therefore, when we have a nitro group interacting very closely with a reducible π-delocalised system, as in our case, it is particularly hard to discriminate whether the first electron enters at the nitro group or the porphyrin core. The effect of the nitro group on the reduction of the conjugated molecule is clearly perceived since the difference $\Delta E_{(ox–red)}$ between the first oxidation and the first reduction process, which, for a strictly porphyrin ring-based redox process, should always be within $2.25 \pm 0.15$ V (Kadish relationship),[17] for porphyrins **1** and **3** is 1.96 V and 2.03 V, respectively. Interestingly, the above values of $\Delta E_{(ox–red)}$ are significantly smaller than 2.18 V and 2.10 V, in quite good agreement with the Kadish relationship, found for the analogues with the same substituents in the β-pyrrolic position of 5,10,15,20-tetraphenylporphyrin.[6] Therefore it appears that in compounds **1**–**4**, differently from their analogues with the same substituents in the β-pyrrolic position, the nitro group strongly influences the energy of the conjugated system so that we have a significant shift to less negative potentials of the first reduction peak with respect to Kadish's rule, an indication of a reduction process that does not involve just the π porphyrin core. The complexity of the first reduction step is, for instance, reflected by the observation that the first reduction peak of porphyrin **1** is bielectronic, unlike

 © 2006 Wiley-VCH Verlag GmbH & Co. KGaA, Weinheim 

the classical monoelectronic first reduction peak of a nitro group bound to a π-delocalised aromatic system [see Table 2 for the properties of the first reduction peak of the reference aromatic compound 4′-(*p*-nitrophenyl)-2,2′:6′,2′′-terpyridine].

If the first reduction peak is an indication of the tendency of the whole molecule to be reduced, and therefore of the LUMO energy, we can suggest that while the shift from the β-pyrrolic to the *meso* position of π-delocalised substituents carrying a nitro group has little effect on the HOMO energy, it has a marked effect on the LUMO energy.

When the substituent carries an electron-donor dibutylamino group as in **5** and **6** or in their analogues substituted in the β-pyrrolic position,[6] the cathodic section of the voltammetric pattern is quite similar and closely resembles that of their unsubstituted reference compounds $H_2$DPP and [ZnDPP]·THF, with two neat monoelectronic reduction steps, chemically and electrochemically reversible. Considering the reduction potentials (Table 2 and ref.[6]) it appears that the displacement of the substituent carrying a dibutylamino group from the β-pyrrolic position to the *meso* one produces a less reducible system and thus has a marked effect on the LUMO energy, in agreement with the previously proposed enhancement of the electron donor effect of the dibutylamino group. The same conclusion can be applied to the reduction peaks of the $Zn^{II}$ complex **6**, which are also characterised by the expected shift to the negative direction.

The increased role of the donor amino group on the π system of the conjugated molecule is reflected, in the case of substitution at the *meso* position, by the significant deviation from Kadish's rule; for instance let us consider the second oxidation peak discussed above: $\Delta E_{(ox–red)}$ is 1.90 V for **5** and 2.05 V for its analogue with the substituent in the β-pyrrolic position, compared with the regular value of 2.34 V for the reference unsubstituted compound $H_2$DPP. For the $Zn^{II}$ complex **6** the value of $\Delta E_{(ox–red)}$ is 1.90 V, compared with 2.07 V for its analogue with the substituent in the β-pyrrolic position and 2.23 V for the unsubstituted ZnDPP.

**Dipole Moments**

Differently from 5,10,15,20-tetraphenylporphyrins and their $Zn^{II}$ complexes substituted in the β-pyrrolic position,[6] the experimental determination by the Guggenheim method[18] of the dipole moment of 10,20-diphenyl porphyrins and their $Zn^{II}$ complexes with the same substituents in the *meso* position, was not always reproducible because of insolubility or aggregation processes, the exceptions being the porphyrins **1** and **3** (Table 3). Therefore best geometries first, and then dipole moments, were theoretically calculated by an ab initio approach based on density functional theory (DFT),[11,12] using an extended basis set[13] (see Exp. Sect.).

As already suggested by the X-ray crystal structural determinations or by molecular mechanics modelling using the MM2 force field[14] our DFT calculations confirm that the aromatic ring of porphyrin $Zn^{II}$ complexes with an *E*-ethylenic linker, such as **2** or **6**, is significantly twisted. (Table 4).

Our calculated angle of twisting for **2** (53.1°) is slightly higher than that obtained in the solid state by the X-ray crystal structure determination of the analogous compound, but without the nitro group in the *para* position (44.7°).[14] In general our calculations have produced an angle of twisting of 10,20-diphenylporphyrin $Zn^{II}$ complexes with an *E*-ethylenic linker (about 52–54°) or an acetylenic linker (about 10–14.5°) (Table 4) that is higher than that calculated by the less sophisticated molecular mechanism modelling approach using the MM2 force field (about 38° for the *E*-ethylenic linker and about <0.1° for the acetylenic linker[14]).

The twisting of the porphyrin and aromatic rings calculated by our DFT approach is much less significant when the same *para*-substituted aromatic rings are bound, by the same linkers, to the β-pyrrolic position of 5,10,15,20-tetraphenylporphyrin or its $Zn^{II}$ complex, since the optimised geometries show a twisting angle of about 20–30° for an *E*-ethylenic linker (Table 4) or a much lower value for an acetylenic one.

In conclusion, we have produced additional structural evidence that the triple bond, because of the lower twisting

Table 3. Theoretical and experimental dipole moments ($\mu$) in $CHCl_3$ and EFISH quadratic hyperpolarisability ($\beta_{1.907}$) measured in $CHCl_3$ working with an incident wavelength of 1.907 μm.

| Compound[a] | $\mu_{theor}$[b] ($\mu_{exp}$) [D] | $\beta_{1.907}$ [$10^{-30}$ esu][c] |
|---|---|---|
| (1*E*)-5[2-(4′-Nitrophenyl)ethenyl]-10,20-$H_2$DPP (**1**) | 7.70[d] (6.45) | 67 |
| (1*E*)-5-[2-(4′-Nitrophenyl)ethenyl]10,20 ZnDPP (**2**) | 7.73 | –94 |
| 5-[2-(4′-Nitrophenyl)ethynyl]-10,20-$H_2$DPP (**3**) | 8.54[d] (7.26) | 64 |
| 5-[2-(4′-Nitrophenyl)ethynyl]-10,20-ZnDPP (**4**) | 8.48 | n.d.[e] |
| (1*E*)-5-[2-(4′-Dibutylaminophenyl)ethenyl]-10,20-$H_2$DPP (**5**) | 6.07[d] | 64 |
| (1*E*)-5-[2-(4′-Dibutylaminophenyl)ethenyl]-10,20-ZnDPP (**6**) | 5.89 | 87.5 |
| 5-[2-(4′-Dimethylaminophenyl)ethynyl]-10,20-$H_2$DPP (**7**) | 5.77[d] | 99 |
| 5-[2-(4′-Dimethylaminophenyl)ethynyl]-10,20-ZnDPP (**8**) | 5.65 | 112 |

[a] $H_2$DPP = 10,20-diphenylporphyrin. [b] ab initio DFT calculations (see Experimental Section). [c] Mean values of measurements done at concencentrations $10^{-3}$ to $5\times10^{-4}$ M. [d] Mean values of the two isomers with different locations of the NH bonds. [e] not soluble enough.

 © 2006 Wiley-VCH Verlag GmbH & Co. KGaA, Weinheim 

Table 4. Dihedral angle between the plane of the porphyrin ring and the plane of the aromatic ring (*meso* substituted porphyrinic molecules).

| Compound[a] | $\theta$ [°] |
|---|---|
| (1*E*)-5[2-(4′-Nitrophenyl)ethenyl]-10,20-$H_2$DPP (**1**) | 54.8 |
| (1*E*)-5-[2-(4′-Nitrophenyl)ethenyl]10,20 ZnDPP (**2**) | 53.1 |
| 5-[2-(4′-Nitrophenyl)ethynyl]-10,20-$H_2$DPP (**3**) | 10.1 |
| 5-[2-(4′-Nitrophenyl)ethynyl]-10,20-ZnDPP (**4**) | 10.0 |
| (1*E*)-5-[2-(4′-Dibutylaminophenyl)ethenyl]-10,20-$H_2$DPP (**5**) | 52.7 |
| (1*E*)-5-[2-(4′-Dibutylaminophenyl)ethenyl]-10,20-ZnDPP (**6**) | 51.8 |
| 5-[2-(4′-Dimethylaminophenyl)ethynyl]-10,20-$H_2$DPP (**7**) | 14.3 |
| 5-[2-(4′-Dimethylaminophenyl)ethynyl]-10,20-ZnDPP (**8**) | 14.6 |
| Dihedral angle between the plane of the porphyrin ring and the plane of the aromatic ring (porphyrinic molecules substituted in β-pyrrolic position)[6] | |
| Compound[b] | $\theta$ [°] |
| (1*E*)-2-(4-Nitrophenyl)ethenyl-$H_2$TPP | 29.2 |
| (1*E*)-2-(4-Nitrophenyl)ethenyl-ZnTPP | 17.6 |
| (1*E*,3*E*)-2-(4-Nitrophenyl)buta-1,3-dienyl-$H_2$TPP | 18.5 |
| (1*E*,3*E*)-2-(4-Nitrophenyl)buta-1,3-dienyl-ZnTPP | 19.3 |
| (1*E*)-2-(4-Dibutylaminophenyl)ethenyl-$H_2$TPP | 20.3 |
| (1*E*)-2-(4-Dibutylaminophenyl)ethenyl-ZnTPP | 27.9 |

[a] $H_2$DPP = 10,20-diphenylporphyrin. [b] $H_2$TPP = 5,10,15,20-tetraphenylporphyrin.

of the aromatic ring should, in all cases, favour a more facile electronic communication between the aromatic ring (and therefore the electron-withdrawing or electron-donor groups) and the porphyrin ring.

The porphyrins **1** and **3**, with a substituent carrying an electron-withdrawing nitro group, and their $Zn^{II}$ complexes **2** and **4** show dipole moments that are higher, and completely opposite in polarity, than those of porphyrins **5** and **7** and their $Zn^{II}$ complexes **6** and **8**, with a substituent carrying an amino electron-donor group (Table 3), as reported for porphyrins and their $Zn^{II}$ complexes with the same series of substituents in the β-pyrrolic position of 5,10,15,20-tetraphenylporphyrin or its $Zn^{II}$ complex.[6]

When there is excellent π conjugation between the porphyrin ring and the π linker, as when the linker is acetylenic, the calculated dipole moments of the compounds with a substituent carrying a nitro group are quite independent (about 8.5–8.8 D) of the position of substitution on the porphyrin ring (*meso* or β pyrrolic).[6] However, when the nitro or the dibutylamino groups are connected to the porphyrin ring by an *E*-ethylenic linker, the calculated dipole moments are slightly higher when substitution occurs in the β-pyrrolic position (8.5–8.8 D compared with 7.70–7.73 D for a substituent carrying a nitro group and 6.07–5.89 D compared with 5.33–5.16 D for a substituent carrying a dibutylamino group). The validity of our DFT calculated dipole moments is supported by the fairly good agreement between calculated values of porphyrins **1** and **3** and those measured experimentally (Table 3).

In conclusion the DFT calculations also provide evidence that for compounds **1**–**8** the π core of the porphyrin ring, already in the ground state, acts as an electron donor if the π-delocalised substituent in the *meso* position carries a nitro group, while it acts as an electron acceptor if it carries a dimethylamino or dibutylamino group. Such a trend was already observed when the same substituents were bound to the β-pyrrolic position of 5,10,15,20-tetraphenylporphyrin or its $Zn^{II}$ complex.[6]

### Determination of the Quadratic Hyperpolarisability by the EFISH Technique

The determination of the second-order NLO response was carried out by the EFISH technique[19], which allows the evaluation of the molecular quadratic hyperpolarisability, $\beta_\lambda$, from Equation (1) (see Exp. Sect.). In order to avoid resonance enhancement, we worked with an off resonance incident wavelength, $\lambda$, of 1.907 μm. When applying Equation (1) to highly π-conjugated two-dimensional molecules, such as porphyrins and phthalocyanines, the usual approach that ignores the third-order electronic contribution to $\gamma_{EFISH}$, could not be considered to be completely reliable.[4c,20] However, for asymmetrically substituted phthalocyanines, structurally related to the porphyrinic chromophores investigated in this work, and carrying an aryl ethenyl or an aryl butadienyl spacer connecting the phthalocyanine ring to a nitro group in the *para* position, the third-order electronic contribution to $\gamma_{EFISH}$ was evaluated as being much smaller than the dipolar orientational one and therefore negligible.[20] In accordance we reliably neglected the third-order electronic contribution in the determination of the quadratic hyperpolarisability $\beta_{1.907}$ from $\gamma_{EFISH}$ by Equation (1).

According to our DFT calculations, the push-pull porphyrinic chromophores investigated in this work are characterised by a dipole moment axis, parallel to the π linker axis, as in 1D pseudo-linear organometallic push-pull chromophores.[21] In this approximation $\beta_{vec}$, which is the vectorial part of the quadratic hyperpolarisability tensor, and EFISH $\beta_{1.907}$, which is the projection of $\beta_{vec}$ along the dipole moment axis, should coincide.

 © 2006 Wiley-VCH Verlag GmbH & Co. KGaA, Weinheim 

Since our investigation of the electronic absorption spectra provided evidence, particularly for compounds carrying a donor amino group, of aggregation processes even at low concentrations in nondonor solvents of low polarity such as $CHCl_3$, we carried out a series of EFISH measurements in $CHCl_3$ solutions of different concentrations of compound **2**, which could aggregate at relatively high concentration only by π-π stacking[16] and of compounds **5**–**8**, which could aggregate by intermolecular hydrogen bonding, or by intermolecular interaction of the amino donor group of the π-delocalised substituent with $Zn^{II}$ via the axial position of another molecule. For the $Zn^{II}$ complexes **2**, **4**, **6** and **8** the EFISH measurements were also carried out in the presence of an excess of pyridine, while for porphyrins **5** and **7** in the presence of traces of trifluoroacetic acid in order to suppress any intermolecular aggregation (Table 5).

In the presence of pyridine or trifluoroacetic acid, the product $\mu\beta_{1.907}$, obtained from $\gamma_{EFISH}$ using Equation (1), was shown not to be dependent on dilution (within the experimental error of EFISH measurements on diluted solutions) while, without these additions, a significant increase by dilution was observed as expected for an increased dissociation (Table 5). Such an effect is less relevant for the $Zn^{II}$ complex **2** confirming, as already suggested by the investigation on electronic absorption spectra, that strong aggregation occurs mainly when the π-delocalised substituent carries a donor amino group. Measurements on the $Zn^{II}$ complex **4** were done only in the presence of pyridine because of the low solubility of the complex. Interestingly the order of magnitude and the sign of the product $\mu\beta_{1.907}$ do not change upon addition of pyridine or trifluoroacetic acid (Table 5).

Since the $\mu\beta_{1.907}$ values of the porphyrins **5** and **7** and of the $Zn^{II}$ complexes **2**, **6** and **8** are dependent on dilution, it is expected that monomeric species prevail at higher dilutions (concentrations lower than $10^{-4}$ M). However, at these dilutions EFISH measurements are affected by a larger experimental error. Therefore, the values of EFISH $\beta_{1.907}$ reported in Table 3 are the mean values of many measurements carried out at concentrations about $10^{-4}$ M, thus discussions mainly concern their order of magnitude, rather than their absolute value.

The EFISH $\beta_{1.907}$ values (Table 3) of the porphyrins **1** and **3** are positive and higher than those of porphyrins carrying the same substituents in the β-pyrrolic position of 5,10,15,20-tetraphenylporphyrin[6] (about $65\times10^{-30}$ esu for **1** and **3** against $30–40\times10^{-30}$ esu, respectively).

Unexpectedly, EFISH $\beta_{1.907}$ of the $Zn^{II}$ complex **2** is negative and with a significant absolute value, while the value of EFISH $\beta_{1.907}$ of the analogous $Zn^{II}$ complex with the same substituent in the β-pyrrolic position of 5,10,15,20-tetraphenylporphyrin is positive and with a lower absolute value[6] (about $-94\times10^{-30}$ esu for **2** compared with $30\times10^{-30}$ esu for the analogous $Zn^{II}$ complex ).

Both porphyrins **5** and **7** and their $Zn^{II}$ complexes **6** and **8** show, at concentrations about $10^{-4}$ M, a positive and fairly high value of EFISH $\beta_{1.907}$ (Table 3). As suggested by the significant increase of $\mu\beta_{1.907}$ by dilution (Table 5), the value of EFISH $\beta_{1.907}$ of the monomeric species of **6**–**8** should be higher. For **5** and **6**, the value of EFISH $\beta_{1.907}$ is quite similar to that of the corresponding chromophores with the same π-delocalised substituent in the β-pyrrolic position ($64\times10^{-30}$ esu for **5** and $87.5\times10^{-30}$ esu for **6** compared with $75.7\times10^{-30}$ esu and $127.5\times10^{-30}$ esu).

In summary, with the exception of the anomaly of the sign of EFISH $\beta_{1.907}$ of **2** and **4**, the major differences between the two classes of porphyrinic chromophores carrying the same π-delocalised substituents in the β-pyrrolic[6] or *meso* positions is given by the higher absolute values of EFISH $\beta_{1.907}$ when the substituent carrying a nitro electron-withdrawing group is bound to the *meso* position. This latter result is in accordance with the proposal of Ratner, Marks et al.,[10] who suggested that second-order NLO responses should increase when π-delocalised substituents

Table 5. $\mu\beta_{1.907}$ values at different concentrations in $CHCl_3$ and in $CHCl_3$ with addition of pyridine or trifluoroacetic acid.

| Compound[a] | Concentration | $\mu\beta_{1.907}$ [$10^{-48}$ esu][b] | $\mu\beta_{1.907}$ [$10^{-48}$ esu] |
|---|---|---|---|
| (1*E*)-5-[2-(4′-Nitrophenyl)ethenyl]-10,20-ZnDPP (**2**) | $10^{-3}$ | –630 | –815[c] |
| | $5\times10^{-4}$ | –816 | –1015[c] |
| | $10^{-4}$ | –960 | –1210[c] |
| 5-[2-(4′-Nitrophenyl)ethynyl]-10,20-ZnDPP (**4**) | $10^{-3}$ | n.d.[d] | –645[c] |
| | $5\times10^{-4}$ | | –795[c] |
| (1*E*)-5-[2-(4′-Dibutylaminophenyl)ethenyl]-10,20-$H_2$DPP (**5**) | $10^{-3}$ | 350 | 525[e] |
| | $5\times10^{-4}$ | 427 | 615[e] |
| | $10^{-4}$ | 690 | 660[e] |
| (1*E*)-5-[2-(4′-Dibutylaminophenyl)ethenyl]-10,20-ZnDPP (**6**) | $10^{-3}$ | 407 | 815[c] |
| | $5\times10^{-4}$ | 611 | 930[c] |
| | $10^{-4}$ | 1450 | 950[c] |
| 5-[2-(4′-Dimethylaminophenyl)ethynyl]-10,20-$H_2$DPP (**7**) | $10^{-3}$ | 514 | 750[e] |
| | $5\times10^{-4}$ | 629 | 860[e] |
| | $10^{-4}$ | 1260 | 940[e] |
| 5-[2-(4′-Dimethylaminophenyl)ethynyl]-10,20-ZnDPP (**8**) | $10^{-3}$ | 473 | 625[c] |
| | $2\times10^{-4}$ | 789 | 755[c] |
| | $10^{-4}$ | 1630 | 830[c] |

[a] $H_2$DPP = 10,20-diphenylporphyrin. [b] In $CHCl_3$. [c] In $CHCl_3$ with the addition of pyridine. [d] Too insoluble for acceptable measurements. [e] In $CHCl_3$ with traces of trifluoroacetic acid.

 © 2006 Wiley-VCH Verlag GmbH & Co. KGaA, Weinheim 

with electron-acceptor groups are appended to *meso* electron-deficient centres instead of β-pyrrolic electron-rich centres.

We previously suggested[6] that in porphyrinic chromophores with a π-delocalised substituent carrying a nitro group the second-order NLO response can originate mainly from a charge transfer from the occupied π orbitals of the porphyrin ring to the π*-antibonding orbitals of the π linker in accordance with a significant π conjugation between the π core of the porphyrin ring and the π linker. In this hypothesis the porphyrin ring acts as donor to the acceptor aromatic ring carrying the nitro group in the *para* position and the charge transfer takes place in the same direction as the dipole moment, in agreement with the positive value of the quadratic hyperpolarisability EFISH $\beta_{1.907}$.

For compounds **1**–**4**, our analysis of the absorption electronic spectra failed to produce clear direct evidence of such a charge transfer process. However, the voltammetric investigation not only has shown a significant effect on the LUMO energy of the porphyrin ring when conjugated with a π linker, but also revealed a more relevant effect when substitution occurs in the *meso* position, supporting a shift of the above proposed charge transfer process at lower energy, in agreement with the observed increased absolute value of EFISH $\beta_{1.907}$.

However, the anomalous negative sign of EFISH $\beta_{1.907}$ found for the $Zn^{II}$ complexes **2** and **4** cannot be explained by such a charge transfer process, given that EFISH $\beta_{1.907}$ remains positive for analogous $Zn^{II}$ complexes carrying the same π-delocalised substituents in the β-pyrrolic position.[6] At the moment only a detailed theoretical investigation, which is underway, may produce an explanation for the negative EFISH $\beta_{1.907}$ found for the $Zn^{II}$ complexes **2** and **4**, since the involvement of aggregation by π-π stacking,[16] which occurs certainly more easily in derivatives of 10,20-diphenylporphyrin than in those of 5,10,15,20-tetraphenylporphyrin, can be discarded because the second-order NLO response of **2** and **4** remains negative also in the presence of pyridine (Table 5), which prevents this kind of aggregation.

The lack of a significant decrease of EFISH $\beta_{1.907}$ when the π-delocalised substituent, carrying a strong electron-donor group, is moved from the electron-rich β-pyrrolic position to the electron deficient *meso* position does not completely fit with the proposal of Ratner, Marks et al.[10].

As for the analogues of **5** and **6** with the same π-delocalised substituent in the β-pyrrolic position,[6] we can tentatively propose that the high and positive EFISH $\beta_{1.907}$ values of chromophores **5**–**8** originate from an enhancement of the donor properties of the dibutylamino or dimethylamino group, induced by the very electron-rich π system of the porphyrin, which produces a significant depletion of the electron density on the donor group and thereby a reduction of the ground state polarisation.[22] In this view there is no involvement of the π core of the porphyrin ring in the excitation process controlling the second-order NLO response.

In agreement with this proposal, our voltammetric investigation has shown, in both classes of porphyrinic chromophores investigated by us up to now,[6] an enhanced donor effect of the dibutylamino or dimethylamino group.

## Conclusions

This and our previous investigation[6] on push-pull chromophores with electron-withdrawing groups connected to the porphyrinic ring, either in the β-pyrrolic or *meso* position by an arylethenyl or arylethynyl linker, provide clear evidence for the significant π conjugation between the porphyrin π core and the π-delocalised substituent, as a possible origin of the second-order NLO responses by a charge transfer process. Such conjugation seems to be more facile, according to the voltammetric investigation, if the π-delocalised substituent is bound to the *meso* position instead of the β-pyrrolic one. Therefore if the substitution occurs in the *meso* position, the second-order NLO response is favoured due to a more facile charge transfer and to the increased push properties of the porphyrin ring if we assume a rather simplified description of these new push-pull chromophores as pseudo 1D push-pull systems.

Accordingly, the experimental values of EFISH $\beta_{1.907}$ of chromophores **1** and **3** are comparable with those of structurally related organic push pull chromophores having, as the push group, a *para*-dimethylamino phenyl moiety, and are more significant than that having, as the push group, a ferrocenyl or of a 5,10,15,20-tetraphenylporphyrin moiety substituted in the β-pyrrolic position (Table 6).

Table 6. Quadratic hyperpolarisability $\beta_{1.907}$ of some organic and organometallic push-pull systems measured in $CHCl_3$ by the EFISH technique at an incident wavelength of 1.907 μm.

| Compound[a] | $\beta_{1.907}$ $10^{-30}$ (esu) |
|---|---|
| 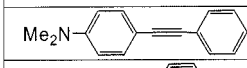 | 46[b] |
| 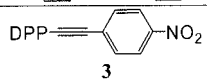 **3** | 64 |
| 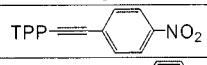 | 30.1[c] |
| 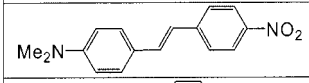 | 73[b] |
| 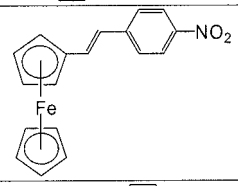 | 31[d] |
| 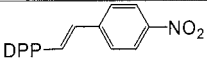 **1** | 67 |
| 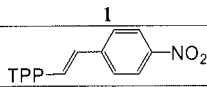 | 39.3[c] |

[a] DPP = 10,20-diphenylporphyrin substituted in the *meso* position; TPP = 5,10,15,20-tetraphenylporphyrin substituted in the β-pyrrolic position. [b] Ref.[23] [c] Ref.[6] [d] Ref.[24]

 © 2006 Wiley-VCH Verlag GmbH & Co. KGaA, Weinheim 

We also propose, when the substituent bound to the *meso* or β-pyrrolic position carries an electron-donor group, that the electron-rich and highly polarisable character of the porphyrin ring may be the origin of an electron screening of the ground-state polarisation, so that the electron-rich ring system weakly withdraws excessive electron density from the donor substituent through inductive effects, thereby increasing its donor properties.[22] Thus this process produces an enhancement of the second-order NLO response controlled by the $n \rightarrow \pi^*$ transition.

In accordance with this hypothesis the value of EFISH $\beta_{1.907}$ of chromophores **5**, **6** and **7**, **8** increases by complexation to $Zn^{II}$ (e.g. **6** > **5** and **8** > **7** see Table 3), which produces a higher and more polarisable electron density on the porphyrin ring as supported by the voltammetric investigation.

Since the π-electron core of the porphyrin ring is not directly involved in the excitation process controlling the second-order NLO response, it becomes irrelevant if the π-delocalised substituent is appended to an electron-rich (β-pyrrolic) or electron-deficient (*meso*) position of the porphyrin ring, as experimentally observed.

Despite the above reported agreement with a series of experimental observations, our interpretation of the electronic origin of the second-order NLO response in the series of compounds investigated in this and in our previous work,[6] does not explain the negative sign of EFISH $\beta_{1.907}$ of the $Zn^{II}$ complexes **2** and **4**.

Probably, the two-dimensional highly polarisable π system of the porphyrin core is far too complex for such a relatively simple approach based just on considerations typical of traditional 1D organic or organometallic push-pull chromophores. As already mentioned, ab initio time-dependent DFT investigations are underway in our laboratory in an effort to achieve a more profound understanding of the electronic origin of the significant second-order NLO response of these new push-pull chromophores based on the porphyrin ring.

In conclusion this and our previous work[6] have experimentally confirmed an interesting role of the porphyrin ring in push-pull chromophores, already theoretically suggested by Ratner, Marks et al.[10]

## Experimental Section

All solvents and chemicals were of reagent-grade quality, purchased commercially and used without further purification unless otherwise stated. 10,20-diphenylporphyrin[25a] was prepared according to literature methods from dipyrrylmethane.[25b] 4-Nitrobenzyltriphenylphosphonium bromide and 4-(dibutylamino)benzyltriphenylphosphonium chloride were prepared following the new procedure described in our previous work.[6] 5-Bromo-10,20-diphenylporphyrin was synthesised using the method described by Yeung et al.[5c] 4-Nitrophenyl acetylene was prepared according to Takahashi el al.[26] $^1$H NMR spectra were recorded with a Bruker AC-300 spectrometer in $CDCl_3$ as solvent; electronic absorption spectra were obtained in $CHCl_3$ with a Jasco V-530 spectrometer; emission spectra were obtained in $CHCl_3$ with a Jasco FP-777 spectrofluorimeter. Elemental analyses were carried out in the Analytical Laboratories of the Department of Inorganic, Metallorganic and Analytical Chemistry of Milan University. Dipole moments were determined in $CHCl_3$ solution, according to the Guggenheim method,[18] using a WTW-DM01 dipolemeter (dielectric constant) coupled with a Pulfrich Zeiss PR2 refractometer (refractive index).

### Cyclic Voltammetry

The cyclovoltammetric (CV) investigation was carried out using an Autolab PGSTAT 12 potentiostat/galvanostat (EcoChemie, The Netherlands) run by a PC with GPES software, correcting the ohmic drop by the positive feedback technique,[27] with a glassy carbon GC (Amel, radius 1.5 mm) as the working electrode, a platinum counter-electrode, and an aqueous saturated calomel electrode (SCE) as the operating reference electrode (the half-wave potential of the ferrocinium|ferrocene redox couple, recommended by IUPAC for inter-solvent comparison of potential scales,[28] being 0.484 V when measured in $CH_2Cl_2$, added with 0.1 M TBAP against our aqueous SCE). The working solutions were made up in dichloromethane $CH_2Cl_2$ (Merck, HPLC grade), added with 0.1 M tetrabutylammonium perchlorate TBAP (FLUKA) as the supporting electrolyte, working in a cell thermostatted at 298 K. The solutions, carefully deaerated by nitrogen bubbling, had concentrations ranging from $5 \times 10^{-4}$ to $7 \times 10^{-4}$ M (with the exception of the less soluble porphyrin complex **4**, which reaches saturation at concentrations below $3 \times 10^{-4}$ M). The optimised polishing procedure for the working GC electrode consisted of surface treatment with diamond powder (Aldrich diameter 1 μm) on a wet cloth (DP-Nap, Struers).

The electrochemical reversibility and electron number of each well-defined CV peak were checked by classical tests[29] including analysis of (a) the $I_p$ vs. $v^{1/2}$ characteristics; (b) the $E_p$ vs. $\log v$ characteristics; (c) the $(E_p - E_{p/2})$ vs. $\log v$ characteristics, and (d) the "stationary", step-like waves obtained by convolutive analysis of the original CV characteristics.

For comparison purposes, the CV characteristics of the reference compounds $H_2$DPP, [ZnDPP]·THF and 4′-(*p*-nitrophenyl)-2,2′:6′,2′′-terpyridine, recorded under the same experimental conditions, are reported in Table 2. The 4′-(*p*-nitrophenyl)-2,2′:6′,2′′-terpyridine has been included as a model for the nitro group reactivity.

### EFISH Measurements

EFISH measurements were performed in $CHCl_3$ solutions, as a function of concentration, working at 1.907 μm incident wavelengths using a Q-switched Nd:YAG laser with 60 and 20 ns pulse durations, manufactured by Atalaser. The 1.907 μm fundamental wavelength was obtained by Raman shifting of the 1.064 μm emission of the Q-switched Nd:YAG laser in a high pressure hydrogen cell (60 bar). A liquid cell with thick windows in the wedge configuration was used to obtain the Maker fringe pattern (harmonic intensity variation as a function of liquid cell translation).[19] In the EFISH experiments the incident beam was synchronised with a DC field applied to the solution containing the molecular species in order to break the centrosymmetry of the solution. The apparatus for the EFISH measurements was a prototype made by SOPRA (France).

From the concentration dependence ($10^{-3}$–$10^{-4}$ M) of the harmonic signal with respect to that of the pure solvent, the NLO response

 © 2006 Wiley-VCH Verlag GmbH & Co. KGaA, Weinheim 

$\beta_\lambda$ was determined (assumed to be real as the imaginary was neglected) from the experimental value $\gamma_{EFISH}$, using Equation (1).

$$\gamma_{EFISH} = \frac{\mu\beta_\lambda(-2\omega;\omega,\omega)}{5kT} + \gamma(-2\omega;\omega,\omega,0) \quad (1)$$

where $\gamma_{EFISH}$ is the sum of a cubic electronic contribution $\gamma(-2\omega; \omega, \omega, 0)$ and of a quadratic orientational contribution $\mu\beta_\lambda$ $(-2\omega; \omega, \omega)/5kT$; $\mu$ is the ground state dipole moment and $\beta_\lambda$ is the projection along the dipole moment direction of the vectorial component $\beta_{vec}$ of the tensorial quadratic hyperpolarisability working with the incident wavelength, $\lambda$.

**Computational Methods**

Geometry optimisation and population analysis of the compounds **1**–**8** were carried out in the framework of the density functional theory (DFT) by using the BP86 functional[12] and an all-electron valence triple-ζ basis set with polarisation functions on all atoms (TZVP).[13] Values of the dipole moments moduli and components were computed using the Turbomole suite of programs[30] in connection with the resolution of identity (RI) approximation.[31]

**Synthesis of Porphyrins**

For the numering of atoms see below.

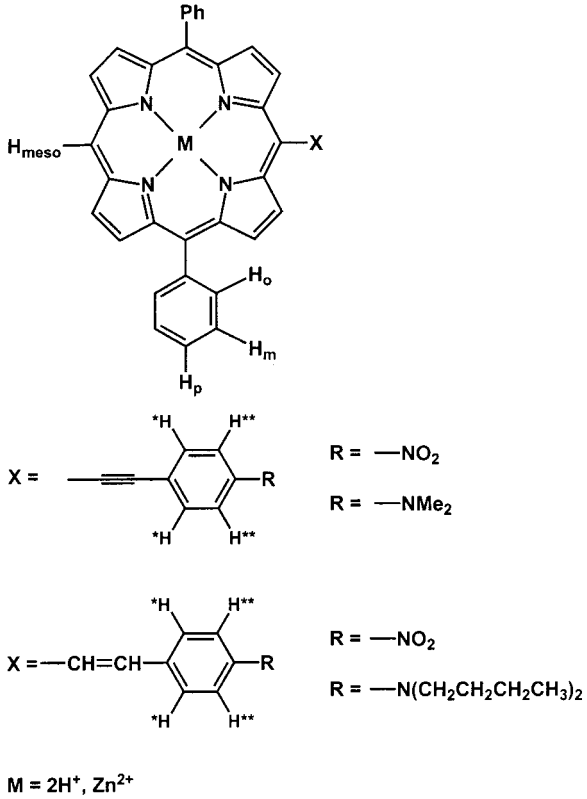


**5-Formyl-10,20-diphenylporphyrin:** This porphyrin was prepared by the following three steps:[15]

**(a) 10,20-Diphenylporphyrinatocopper(II):** A slightly warm solution of $Cu(OAc)_2 \cdot H_2O$ (125 mg, 0.627 mmol) in MeOH (15 mL) was slowly added to a refluxing solution of 10,20-diphenylporphyrin (264 mg, 0.570 mmol) in $CHCl_3$ (60 mL). After two hours the red reaction mixture was cooled and the solvents evaporated to dryness in vacuo. The red residue was collected with MeOH, filtered and washed with MeOH to afford 248 mg (83%) of a red powder. UV/Vis ($CHCl_3$): $\lambda_{max}$ ($\log\varepsilon$) = 405 (5.63), 527 (4.23), 561 (3.65) nm. $C_{32}H_{20}CuN_4$ (523.5): calcd. C 73.35, H 3.82, N 10.70; found C 72.94, H 3.78, N 10.89.

**(b) 5-Formyl-10,20-diphenylporphyrinatocopper(II):** A solution of dimethylformamide (1.1 mL, 14.2 mmol) and phosphoryl chloride (1.1 mL, 12.0 mmol) was left at room temperature and under magnetic stirring for 30 min. After this time, a solution of 10,20-diphenylporphyrinatocopper(II) (114 mg, 0.218 mmol) in 1,2-dichloroethane (50 mL) was added and the reaction mixture was stirred at 60 °C for 2 h. The dark green solution was then diluted with a saturated aqueous solution of $CH_3COONa$ (150 mL) and maintained at 60 °C whilst stirring for a further 2 h. The organic phase was separated, washed with $H_2O$ (2 × 100 mL), dried with $Na_2SO_4$ and evaporated in vacuo. Purification of the residue by column chromatography (silica gel, $CH_2Cl_2$/*n*-hexane, 7:3) afforded 96 mg (80%) of pure product. UV/Vis ($CHCl_3$): $\lambda_{max}$ ($\log\varepsilon$) = 417 (5.42), 547 (3.97), 591 (4.15) nm. $C_{33}H_{20}CuN_4O$ (551.5): calcd. C 71.80, H 3.63, N 10.15; found C 72.30, H 3.76, N 10.30.

**(c) 5-Formyl-10,20-diphenylporphyrin:** A solution of 5-formyl-10,20-diphenylporphyrinatocopper(II) (251 mg, 0.455 mmol) in a mixture of $H_2SO_4$/TFA (1:10 v/v, 15 mL) was stirred for 10 min at room temperature, and then quenched by adding an excess of ice. The product was extracted with $CH_2Cl_2$ (2 × 50 mL), the organic phase was washed with aqueous NaOH (20%, 50 mL) and with $H_2O$ (2 × 50 mL), the solvent was evaporated to dryness and the residue was washed with pentane to afford 220 mg (quantitative yield) of a violet powder. $^1$H NMR (300 MHz, $CDCl_3$): $\delta$ = 12.62 (s, 1 H, CHO), 10.28 (s, 1 H, $H_{meso}$), 10.10 (d, $J$ = 4.98 Hz, 2 H, $H_{pyrrolic}$), 9.30 (d, $J$ = 4.44 Hz, 2 H, $H_{pyrrolic}$), 9.08 (d, $J$ = 4.98 Hz, 2 H, $H_{pyrrolic}$), 8.91 (d, $J$ = 4.44 Hz, 2 H, $H_{pyrrolic}$), 8.22 (m, 4 H, $H_o$), 7.85 (m, 6 H, $H_{m,p}$), –2.41 (s, 2 H, NH) ppm. UV/Vis ($CHCl_3$): $\lambda_{max}$ ($\log\varepsilon$) = 420 (5.35), 520 (4.01), 559 (3.95), 593 (3.77), 648 (3.81) nm. $C_{33}H_{22}N_4O$ (490): calcd. C 80.82, H 4.49, N 11.43; found C 80.65, H 4.36, N 11.60.

**(1*E*)-5-[2-(4′-Nitrophenyl)ethenyl]-10,20-diphenylporphyrin (1):** A suspension of 5-formyl-10,20-diphenylporphyrin (238 mg, 0.484 mmol), 4-nitrobenzyltriphenylphosphonium bromide (670 mg, 1.407 mmol) and solid NaOH 20–40 mesh beads (400 mg, 10 mmol) in anhydrous 1,2-dichloroethane (25 mL) was refluxed, with magnetic stirring and under a nitrogen atmosphere for 4 h. After this time the solvent was evaporated to dryness, the residue was purified by column chromatography (silica gel $CH_2Cl_2$/*n*-hexane, 7:3). The product obtained from the column chromatography was first washed with MeOH and then crystallised from $CH_2Cl_2$/MeOH to give 145 mg (49%) of pure **1**. $^1$H NMR (300 MHz, $CDCl_3$): $\delta$ = 10.17 (s, 1 H, $H_{meso}$), 9.89 (d, $J$ = 15.87 Hz, 1 H, =CH), 9.50 (d, $J$ = 4.83 Hz, 2 H, $H_{pyrrolic}$), 9.30 (d, $J$ = 4.65 Hz, 2 H, $H_{pyrrolic}$), 8.97 (d, $J$ = 4.77 Hz, 4 H, $H_{pyrrolic}$), 8.43 (d, $J$ = 8.76 Hz, 2 H, H**), 8.24 (m, 4 H, $H_o$), 8.05 (d, $J$ = 8.76 Hz, 2 H, H*), 7.80 (m, 6 H, $H_{m,p}$), 7.42 (d, $J$ = 15.93 Hz, 1 H, CH=), –2.78 (s, 2 H, NH) ppm. UV/Vis ($CHCl_3$): $\lambda_{max}$ ($\log\varepsilon$) = 422 (5.27), 518 (4.07), 564 (4.11), 594 (3.89), 655 (3.65) nm. $C_{40}H_{27}N_5O_2$ (609): calcd. C 78.82, H 4.43, N 11.49; found C 78.65, H 4.30, N 11.48.

**5-[2-(4′-Nitrophenyl)ethynyl]-10,20-diphenylporphyrin (3):** Trifluoroacetic acid (2 mL) was added in four portions to a suspension of 5-[2-(4′-nitrophenyl)ethynyl]-10,20-diphenylporphyrinatozinc(II) (**4**) (100 mg, 0.149 mmol) in $CH_2Cl_2$ (50 mL) and the reaction mixture was stirred at room temperature for 18 h. After this time, water (30 mL) was added and the mixture was carefully neutralised with a saturated aqueous solution of $NaHCO_3$. The organic phase was separated, dried with $MgSO_4$ and the solvent evaporated in vacuo

 © 2006 Wiley-VCH Verlag GmbH & Co. KGaA, Weinheim 

to afford 90 mg (quantitative yield) of porphyrin **3**. $^1$H NMR (300 MHz, $CDCl_3$): $\delta$ = 10.21(s, 1 H, $H_{meso}$), 9.76 (d, $J$ = 4.83 Hz, 2 H, $H_{pyrrolic}$), 9.30 (d, $J$ = 4.62 Hz, 2 H, $H_{pyrrolic}$), 9.01 (d, $J$ = 4.80 Hz, 2 H, $H_{pyrrolic}$), 8.95 (d, $J$ = 4.62 Hz, 2 H, $H_{pyrrolic}$), 8.41(d, $J$ = 8.76 Hz, 2 H, H**), 8.23 (m, 4 H, $H_o$), 8.13 (d, $J$ = 8.73 Hz, 2 H, H*), 7.81 (m, 6 H, $H_{m,p}$), –2.54 (s, 2 H, NH) ppm. UV/Vis ($CHCl_3$): $\lambda_{max}$ ($\log\varepsilon$) = 436 (5.15), 529 (3.91), 573 (4.32), 602 (3.79), 661 (3.94) nm. $C_{40}H_{25}N_5O_2$ (607): calcd. C 79.08, H 4,12, N 11.53; found C 78.96, H 4.16, N 11.53.

**(1*E*)-5-[2-(4′-Dibutylaminophenyl)ethenyl]-10,20-diphenylporphyrin (5):** A suspension of 5-formyl-10,20-diphenylporphyrin (103 mg, 0.211 mmol), 4-(dibutylamino)benzyltriphenylphosphonium chloride (185 mg, 0.358 mmol) and solid NaOH 20–40 mesh beads (337 mg, 8.436 mmol) in anhydrous $CH_2Cl_2$ (20 mL) was stirred at room temperature, under a nitrogen atmosphere, for 4 h. After this time the solvent was evaporated and the residue was purified by column chromatography (silica gel, $CH_2Cl_2$/*n*-hexane, 7:3) to afford 87 mg (59%) of **5** as a violet powder. $^1$H NMR (300 MHz, $CDCl_3$): $\delta$ = 10.08 (s, 1 H, $H_{meso}$), 9.56 (m, 3 H, CH, $H_{pyrrolic}$), 9.27 (d, $J$ = 4.53 Hz, 2 H, $H_{pyrrolic}$), 8.96 (d, $J$ = 4.53 Hz, 2 H, $H_{pyrrolic}$), 8.91 (d, $J$ = 4.68 Hz, 2 H, $H_{pyrrolic}$), 8.26(m, 4 H, $H_o$), 7.82, (m, 8 H, H*, $H_{m,p}$), 7.27 (d, $J$ = 16.0 Hz, 1 H, =CH), 6.86 (d, $J$ = 8.58 Hz, 2 H, H**), 3.43 (t, $J$ = 7.45 Hz, 2 H, $CH_{2Butyl}$), 1.72 (m, 2 H, $CH_{2Butyl}$), 1.46 (m, 2 H, $CH_{2Butyl}$), 1.05 (t, $J$ = 7.23 Hz, 3 H, $CH_{3Butyl}$), –2.62 (s, 2 H, NH) ppm. UV/Vis ($CHCl_3$): $\lambda_{max}$ ($\log\varepsilon$) = 353 (4.34), 410 (5.06), 521 (4.00), 579 (4.15), 665 (3.76), 747 (3.52) nm. $C_{48}H_{45}N_5$ (691): calcd. C 83.36, H 6.51, N 10.13; found C 82.95, H 6.57, N 9.97.

**5-[2-(4′-Dimethylaminophenyl)ethynyl]-10,20-diphenylporphyrin (7):** Trifluoroacetic acid (2 mL) was added in four portions to a suspension of 5-[2-(4′-dimethylaminophenyl)ethynyl]-10,20-diphenylporphyrinatozinc(II) (**8**) (100 mg, 0.150 mmol) in $CH_2Cl_2$ (50 mL) and the reaction mixture was stirred at room temperature for 18 h. After this time, water (30 mL) was added and the mixture was carefully neutralised with a saturated aqueous solution of $NaHCO_3$. The organic phase was separated, dried with $MgSO_4$ and the solvent evaporated in vacuo to afford 90 mg (quantitative yield) of porphyrin **7**. $^1$H NMR (300 MHz, $CDCl_3$): $\delta$ = 10.09 (s, 1 H, $H_{meso}$), 9.81 (d, $J$ = 4.74 Hz, 2 H, $H_{pyrrolic}$), 9.24 (d, $J$ = 4.65 Hz, 2 H, $H_{pyrrolic}$), 8.93 (d, $J$ = 4.35 Hz, 2 H, $H_{pyrrolic}$), 8.92 (d, $J$ = 4.20 Hz, 2 H, $H_{pyrrolic}$), 8.23 (m, 4 H, $H_o$), 7.91 (d, $J$ = 8.76 Hz, 2 H, H*), 7.79 (m, 6 H, $H_{m,p}$), 6.87 (d, $J$ = 8.82 Hz, 2 H, H**), 3.11 (s, 6 H, $NCH_3$), –2.47 (s, 2 H, NH) ppm. UV/Vis ($CHCl_3$): $\lambda_{max}$ ($\log\varepsilon$) = 425 (5.02), 441, 523 (3.93), 587 (4.32), 673 (3.94) nm. $C_{42}H_{31}N_5$ (605): calcd. C 83.31, H 5.12, N 11.57; found C 82.98, H 5.17, N 11.46.

### Synthesis of $Zn^{II}$ Complexes

$Zn^{II}$ complexes **2** and **6** were synthesised following the general procedure described in the literature.[32] In a typical preparation the free porphyrin (100 mg) was dissolved in slightly warmed $CHCl_3$ (20 mL) and a solution of $Zn(OAc)_2{\cdot}2H_2O$ (free porphyrin/metal salt = 1:1.1) in MeOH (10 mL) was then added. The mixture was refluxed for 1 h, was then evaporated to dryness and the residue was collected with MeOH, filtered and washed with MeOH.

**(1*E*)-5-[2-(4′-Nitrophenyl)ethenyl]-10,20-diphenylporphyrinatozinc(II) (2):** This compound was obtained in quantitative yield as a violet powder. $^1$H NMR (300 MHz, $CDCl_3$): $\delta$ = 10.10 (s, 1 H, $H_{meso}$), 9.89 (d, $J$ = 16.32 Hz, 1 H, =CH), 9.56 (d, $J$ = 4.41 Hz, 2 H, $H_{pyrrolic}$), 9.35 (d, $J$ = 4.29 Hz, 2 H, $H_{pyrrolic}$), 9.04 (d, $J$ = 3.99 Hz, 4 H, $H_{pyrrolic}$), 8.43 (d, $J$ = 7.59 Hz, 2 H, H**), 8.22 (m, 4 H, $H_o$), 8.05 (d, $J$ = 7.74 Hz, 2 H, H*), 7.79 (m, 6 H, $H_{m,p}$), 7.41 (d, $J$ = 16.24 Hz, 1 H, CH=) ppm. UV/Vis ($CHCl_3$): $\lambda_{max}$ ($\log\varepsilon$) 422 (5.23), 552 (4.19), 599 (4.04) nm; ($CHCl_3$ with addition of pyridine): $\lambda_{max}$ ($\log\varepsilon$) = 428 (5.05), 566 (3.72), 626 (3.89) nm. $C_{40}H_{25}N_5O_2Zn$ (672.4): calcd. C 71.39, H 3.72, N 10.41; found C 71.50, H 3.61, N 10.30.

**(1*E*)-5-[2-(4′-Dibutylaminophenyl)ethenyl]-10,20-diphenylporphyrinatozinc(II) (6):** This compound was obtained in quantitative yield as a violet powder. $^1$H NMR (300 MHz, $CDCl_3$): $\delta$ = 10.06 (s, 1 H, $H_{meso}$), 9.61 (d, $J$ = 4.65 Hz, 2 H, $H_{pyrrolic}$), 9.48 (d, $J$ = 15.75 Hz, 1 H, CH=), 9.28 (d, $J$ = 4.53 Hz, 2 H, $H_{pyrrolic}$), 8.99 (d, $J$ = 4.53 Hz, 4 H, $H_{pyrrolic}$), 8.96 (d, $J$ = 4.65 Hz, 2 H, $H_{pyrrolic}$), 8.21 (m, 4 H, $H_o$), 7.77 (m, 8 H, H*, $H_{m,p}$), 7.25 (d, $J$ = 15.75 Hz, 1 H, =CH), 6.82 (d, $J$ = 8.55 Hz, 2 H, H**), 3.40 (t, $J$ = 7.52 Hz, 2 H, $CH_{2Butyl}$), 1.67 (m, 2 H, $CH_{2Butyl}$), 1.43 (m, 2 H, $CH_{2Butyl}$), 1.02 (t, $J$ = 7.28 Hz, 3 H, $CH_{3Butyl}$) ppm. UV/Vis ($CHCl_3$): $\lambda_{max}$ ($\log\varepsilon$) = 349 (4.35), 408 (5.26), 554 (4.27), 606 (4.32) nm; ($CHCl_3$ with addition of pyridine): $\lambda_{max}$ ($\log\varepsilon$) = 428 (5.20), 563 (4.06), 613 (4.09) nm. $C_{48}H_{43}N_5Zn$ (754.4): calcd. C 76.35, H 5.70, N 9.28; found C 75.99, H 5.68, N 9.41.

**5-[2-(4′-Nitrophenyl)ethynyl]-10,20-diphenylporphyrinatozinc(II) (4):** The catalytic solution was prepared by heating $Pd_2(dba)_3$ (9.5 mg, $9.9{\cdot}10^{-3}$ mmol), $PPh_3$ (21.8 mg, $8.3{\cdot}10^{-2}$ mmol) and CuI (7.8 mg, $4.1\times10^{-2}$ mmol) in freshly distilled $Et_3N$ (25 mL) at 70 °C for 30 min under a nitrogen atmosphere. This solution was transferred into a solution of 5-bromo-10,20-diphenylporphyrinatozinc(II) (100 mg, 0.165 mmol) and (4-nitrophenyl)acetylene (74 mg, 0.50 mmol) in anhydrous toluene (25 mL) and pyridine (0.6 mL) under a nitrogen atmosphere, and the mixture was heated at 80 °C and stirred for 1 h. After this time the solution was cooled and filtered through silica eluting with toluene and the solvent was evaporated to dryness. The residue was washed several times with small amounts of MeOH and $CHCl_3$ alternately to afford 93 mg (85%) of pure **4**. $^1$H NMR (300 MHz, $CDCl_3$ + Pyridine $d_5$): $\delta$ = 10.12 (s, 1 H, $H_{meso}$), 9.74 (d, $J$ = 4.59 Hz, 2 H, $H_{pyrrolic}$), 9.26 (d, $J$ = 4.47 Hz, 2 H, $H_{pyrrolic}$), 8.99 (d, $J$ = 4.59 Hz, 2 H, $H_{pyrrolic}$), 8.92 (d, $J$ = 4.44 Hz, 2 H, $H_{pyrrolic}$), 8.36 (d, $J$ = 7.47 Hz, 2 H, H**), 8.20 (m, 4 H, $H_o$), 8.08 (d, $J$ = 7.47 Hz, 2 H, H*), 7.75 (m, 6 H, $H_{m,p}$) ppm. UV/Vis ($CHCl_3$): $\lambda_{max}$ ($\log\varepsilon$) = 439 (5.16), 560 (3.68), 608 (4.07) nm; ($CHCl_3$ with addition of pyridine): $\lambda_{max}$ ($\log\varepsilon$) = 449 (5.17), 575 (3.92), 634 (4.47) nm. $C_{40}H_{23}N_5O_2Zn$ (670.4): calcd. C 71.60, H 3.43, N 10.44; found C 71.51, H 3.48, N 10.32.

**5-[2-(4′-Dimethylaminophenyl)ethynyl]-10,20-diphenylporphyrinatozinc(II) (8):** The catalytic solution was prepared by heating a solution of $Pd_2(dba)_3$ (9.5 mg, $9.9{\cdot}10^{-3}$ mmol), $PPh_3$ (21.8 mg, $8.3{\cdot}10^{-2}$ mmol) and CuI (7.8 mg, $4.1{\cdot}10^{-2}$ mmol) in freshly distilled $Et_3N$ (25 mL) at 70 °C for 30 min under a nitrogen atmosphere. This solution was transferred into a solution of 5-bromo-10,20-diphenylporphyrinatozinc(II) (100 mg, 0.165 mmol) and [4-(dimethylamino)phenyl]acetylene (73 mg, 0.50 mmol) in anhydrous toluene (25 mL) and pyridine (0.6 mL) under a nitrogen atmosphere, and the mixture was heated at 80 °C and stirred for 1.5 h. After this time the solution was cooled, filtered through silica gel, eluted with toluene, and the solvent was evaporated to dryness. The residue was washed several times with small amounts of MeOH and $CHCl_3$ alternately to afford 65 mg (59%) of pure **8**. $^1$H NMR (300 MHz, $CDCl_3$ with addition of Pyridine $d_5$): $\delta$ = 10.05 (s, 1 H, $H_{meso}$), 9.83 (d, $J$ = 4.56 Hz, 2 H, $H_{pyrrolic}$), 9.25 (d, $J$ = 4.47 Hz, 2 H, $H_{pyrrolic}$), 8.95 (d, $J$ = 4.92 Hz, 2 H, $H_{pyrrolic}$), 8.94 (d, $J$ = 4.98 Hz, 2 H, $H_{pyrrolic}$), 8.23 (m, 4 H, $H_o$), 7.92 (d, $J$ = 8.82 Hz, 2 H, H*), 7.77 (m, 6 H, $H_{m,p}$), 6.89 (d, $J$ = 8.88 Hz, 2 H, H**), 3.11 (s, 6 H, $NCH_3$) ppm. UV/Vis ($CHCl_3$): $\lambda_{max}$ ($\log\varepsilon$) = 428 (4.97), 448 (4.98), 565 (4.02), 615 (4.24) nm; ($CHCl_3$ with addition of pyridine):

 © 2006 Wiley-VCH Verlag GmbH & Co. KGaA, Weinheim 

$\lambda_{max}$ (log $\varepsilon$) = 451 (5.14), 579 (3.87), 632 (4.30) nm. $C_{42}H_{29}N_5Zn$ (668.4): calcd. C 75.40, H 4.34, N 10.47; found C 75.47, H 4.30, N 10.33.

## Acknowledgments

This work was supported by the Ministero dell'Istruzione, dell'Università e della Ricerca [PRIN 1999 – Research Title: *Molecole per Materiali Funzionali Nanostrutturati: Composti organometallici con proprietà ottiche non lineari (NLO) per materiali nanostrutturati*; FIRB 2001 – Research Title: *Nano-organisation of hybrid organic-inorganic molecules with magnetic and non linear optical properties*] and by the Consiglio Nazionale delle Ricerche. We thank Mr. Pasquale Illiano for the NMR spectroscopy measurements.

[1] a) J. Zyss, *Molecular Non Linear Optics: Materials, Physics and Devices*, Ed Academic Press, Boston **1993**; b) B. E. A. Saleh, M. C. Telch, *Fundamentals of Photonics*, Wiley: New York **1991**.

[2] a) D. R. Kanis, M. A. Ratner, T. J. Marks, *Chem. Rev.* **1994**, *94*, 195–242; b) P. M. Burland, R. D. Miller, C. A. Walash, *Chem. Rev.* **1994**, *94*, 31–75; c) T. J. Marks, M. A. Ratner, *Angew. Chem. Int. Ed. Engl.* **1995**, *34*, 155–173.

[3] a) I. R. Whittal, A. M. McDonagh, M. G. Humphrey, *Adv. Organomet. Chem.* **1998**, *42*, 291–362; b) S. Di Bella, *Chem. Soc. Rev.* **2001**, *30*, 355–366; c) N. J. Long, *Angew. Chem. Int. Ed. Engl.* **1995**, *34*, 21–38; d) B. J. Coe, *Comprehensive Coordination Chemistry II* (Eds.: J. A. Meyer, T. J. McCleverty); Elsevier Pergamon: Oxford, U. K., **2004**; vol. 9, pp. 621–687.

[4] a) K. S. Suslick, C. T. Chen, G. R. Meredith, L. T. Cheng, *J. Am. Chem. Soc.* **1992**, *114*, 6928–6930; b) H. Chou, C.-T. Chen, K. F. Stork, P. W. Bohn, K. S. Suslick, *J. Phys. Chem.* **1994**, *98*, 383–385; c) M. Pizzotti, R. Ugo, E. Annoni, S. Quici, I. Ledoux-Rak, G. Zerbi, M. Del Zoppo, P. Fantucci, I. Invernizzi, *Inorg. Chim. Acta* **2002**, *340*, 70–80.

[5] a) S. M. Le Cours, H. W. Guan, S. G. Di Magno, C. H. Wang, M. J. Therien, *J. Am. Chem. Soc.* **1996**, *118*, 1497–1503; b) L. Karki, F. W. Vance, J. H. Hupp, S. M. Le Cours, M. J. Therien, *J. Am. Chem. Soc.* **1998**, *120*, 2606–2611; c) M. Yeung, A. C. H. Ng, M. G. D. Drew, E. Vorpagel, E. M. Breitung, R. J. McMahon, D. K. P. Ng, *J. Org. Chem.* **1998**, *63*, 7143–7150; d) M. Pizzotti, E. Annoni, R. Ugo, S. Bruni, S. Quici, P. Fantucci, M. Bruschi, G. Zerbi, M. Del Zoppo, *J. Porphyrins Phthalocyanines* **2004**, *8*, 1311–1324.

[6] E. Annoni, M. Pizzotti, R. Ugo, S. Quici, T. Morotti, M. Bruschi, P. Mussini, *Eur. J. Inorg. Chem.* **2005**, 3857–3874.

[7] a) G. de La Torre, P. Vàsquez, F. Agullò-Lòpez, T. Torres, *J. Mater. Chem.* **1998**, *8*, 1671–1683 and references cited therein; b) G. de La Torre, T. Torres, F. Agullò-Lòpez, *Adv. Mater.* **1997**, *9*, 265–269 and references cited therein; c) G. de la Torre, P. Vazquez, F. Agullò-Lòpez, T. Torres, *Chem. Rev.* **2004**, *104*, 3723–3750.

[8] D. A. Offord, S. B. Sachs, M. S. Ennis, T. A. Eberspacher, J. H. Griffin, C. E. D. Chidsey, J. P. Collman, *J. Am. Chem. Soc.* **1998**, *120*, 4478–4487.

[9] a) M. Nappa, J. S. Valentine, *J. Am. Chem. Soc.* **1978**, *100*, 5075–5080; b) A. Antipas, J. W. Buchler, M. Gouterman, P. D. Smith, *J. Am. Chem. Soc.* **1978**, *100*, 3015–3024.

[10] I. D. L. Albert, T. J. Marks, M. A. Ratner, *Chem. Mater.* **1998**, *10*, 753–762.

[11] a) A. D. Becke, *J. Chem. Phys.* **1993**, *98*, 5648–5652; b) C. Lee, W. Yang, R. G. Parr, *Phys. Rev. B* **1988**, *37*, 785–789.

[12] a) A. D. Becke, *Phys. Rev. A* **1988**, *38*, 3098–3100; b) J. P. Perdew, *Phys. Rev. B* **1986**, *33*, 8822–8824.

[13] A. Schafer, C. Huber, R. Ahlrichs, *J. Chem. Phys.* **1994**, *100*, 5829–5835.

[14] T. E. O. Screen, I. M. Blake, L. H. Rees, W. Clegg, S. J. Borwick, H. L. Anderson, *J. Chem. Soc., Perkin Trans. 1* **2002**, 320–329.

[15] K. Susumu, T. Shimidzu, K. Tanaka, H. Segawa, *Tetrahedron Lett.* **1996**, *37*, 8399–8402.

[16] W. I. White, *The Porphyrins*, vol. V, pp. 303–335 (Ed.: D. Dolphin), Acad. Press, New York, **1978**.

[17] J. H. Furhop, K. M. Kadish, D. G. Davis, *J. Am. Chem. Soc.* **1973**, *95*, 5140–5147.

[18] E. A. Guggenheim, *Trans. Faraday Soc.* **1949**, *45*, 203.

[19] a) I. Ledoux, J. Zyss, *Chem. Phys.* **1982**, *73*, 203–213; b) D. J. Williams, *Angew. Chem. Int. Ed. Engl.* **1984**, *23*, 690–703 and references cited therein.

[20] G. Rojo, G. de la Torre, J. Garcia-Ruiz, I. Ledoux, T. Torres, J. Zyss, F. Agullo-Lopez, *Chem. Phys.* **1999**, *245*, 27–34 and references cited therein.

[21] a) D. Roberto, R. Ugo, S. Bruni, E. Cariati, F. Cariati, P. Fantucci, S. Quici, I. Ledoux, J. Zyss, *Organometallics* **2000**, *19*, 1775–1788; b) E. Lucenti, E. Cariati, C. Dragonetti, L. Manassero, F. Tessore, *Organometallics* **2004**, *23*, 687–692.

[22] I. D. L. Albert, T. J. Marks, M. A. Ratner, *J. Am. Chem. Soc.* **1997**, *119*, 6575–6582.

[23] L. T. Cheng, W. Tam, S. H. Stevenson, G. R. Meredith, G. Rikken, S. R. Marder, *J. Phys. Chem.* **1991**, *95*, 10631–10643.

[24] D. R. Kanis, M. A. Ratner, T. J. Marks, *J. Am. Chem. Soc.* **1992**, *114*, 10338–10357.

[25] a) S. G. Di Magno, V. S. Y. Lin, M. J. Therien, *J. Org. Chem.* **1993**, *58*, 5983–5993; b) M. J. Plater, S. Aiken, G. Bourhill, *Tetrahedron* **2002**, *58*, 2405–2413.

[26] S. Takahashi, Y. Kuroyama, K. Sorogashira, N. Hagihara, *Synthesis* **1980**, 627–629.

[27] D. Britz, *Electroanal. Chem.* **1978**, *88*, 309–352.

[28] G. Gritzner, J. Kuta, *Pure Appl. Chem.* **1984**, *56*, 461–466.

[29] A. J. Bard, L. R. Faulkner, *Electrochemical Methods. Fundamentals and Applications*, Wiley, New York, **2002**.

[30] R. Ahlrichs, M. Bar, M. Haser, C. Horn, C. Kolmel, *Chem. Phys. Lett.* **1989**, *162*, 165–169.

[31] a) K. Eichkorn, O. Treutler, H. Öhm, M. Haser, R. Ahlrichs, *Chem. Phys. Lett.* **1995**, *240*, 283–289; b) K. Eichkorn, F. Weigend, O. Treutler, R. Ahlrichs, *Theor. Chem. Acc.* **1997**, *97*, 119–124.

[32] A. D. Adler, F. R. Longo, F. Kampas, J. Kim, *J. Inorg. Nucl. Chem.* **1970**, *32*, 2443–2445.

Received: November 10, 2005
Published Online: March 6, 2006

 © 2006 Wiley-VCH Verlag GmbH & Co. KGaA, Weinheim 

DOI: 10.1002/ejic.200501013

# A New and Fast Synthesis of Nanosized $LiFePO_4$ Electrode Materials

**Alvaro Caballero,[a] Manuel Cruz-Yusta,[a] Julián Morales,[a] Jesús Santos-Peña,*[a] and Enrique Rodríguez-Castellón[b]**

**Keywords:** Copper / Lithium ion batteries / Materials science / Nanostructures / Phosphates

$LiFePO_4$ has been prepared as highly crystalline nanoparticles (approx. 80 nm in diameter) of well-defined shape by heating a mixture containing lithium acetylacetonate, iron oxalate, ammonium hydrogen phosphate and oxalic acid under argon at 550 °C for 2 h. The resulting solid contains about 6 % magnetite ($Fe_3O_4$) as an impurity. Despite its small particle size, this nanomaterial exhibits relatively poor electrochemical performance in lithium cells owing to its lack of electronic conductivity. Its electrochemical response contrasts with previously reported data for nano-$LiFePO_4$ materials prepared at such low temperatures. In order to overcome its lack of conductivity, the compound was treated with a copper precursor. The copper phosphate nanocomposite thus obtained exhibits improved electrochemical performance in terms of capacity and cycling life in lithium cells. Thus Cu-$LiFePO_4$-based cells deliver capacity values close to 80 mAh g$^{-1}$ over at least 50 cycles under a C/10 regime. These values testify to the usefulness of the proposed synthetic method for preparing nanoparticulated lithium phosphate-based electrodes.
(© Wiley-VCH Verlag GmbH & Co. KGaA, 69451 Weinheim, Germany, 2006)

## Introduction

Recently, a new class of cathode materials based on polyanionic compounds has aroused much interest among researchers, particularly $LiFePO_4$, which is a compound with an olivine-type structure that yields a flat voltage plateau at 3.5 V during charging and a theoretical capacity of 170 mAh g$^{-1}$.[1] There have been many attempts to overcome the electronic and lithium-diffusion limitations of this electrode, which impair its electrochemical performance under high-current regimes. Some authors have obtained acceptable cycling properties by coating the particles with carbon, usually by pyrolysing organic compounds during the synthesis[2–5] or by decomposing a gaseous carbon precursor onto the phosphate at 700 °C,[6,7] whereas other authors have dispersed a metal (copper or silver[8]) in the phosphate or added a conductive organic compound such as polypyrrole.[9] The intrinsic electronic conductivity can also be increased by doping the structure with ions such as $Mg^{+2}$, $Al^{+3}$, $Ti^{+4}$ or $Nb^{+5}$, among others.[10,11]

The most common method for obtaining $LiFePO_4$ is a solid-state reaction involving the decomposition of various oxy salts. The reaction takes place at moderate temperatures, where the size of the as-formed phosphate particles is in the micron range.[12] Because lithium diffusion in the olivine structure is very slow ($10^{-18}$ cm$^2$ s$^{-1}$),[3,13] some authors have noted the importance of controlling particle size.[4,12,14,15] Thus, Prosini et al.[14] have reported that chemical lithiation of nanosized anhydrous $FePO_4$ by lithium iodide and subsequent heating under an $Ar/H_2$ atmosphere at 550 °C produces nanoparticulated $LiFePO_4$ with very good electrochemical activity; however, this procedure requires a pristine nanomaterial. Huang et al.[4] have succeeded in limiting the size of $LiFePO_4$ by introducing oxidized carbon particles as nucleating agent. The particles obtained at 700 °C were 100–200 nm in size. Recently, Hsu et al.[15] have used a method involving the calcination of a mixture of citric acid, iron oxalate, diammonium hydrogen phosphate and lithium carbonate to obtain nanometric phosphates over the temperature range 400–900 °C. Interestingly, it was necessary to decompose the oxalates and citrate at around 700 °C in order to obtain an electroactive powder; below this temperature the organic compounds are seemingly incompletely decomposed, so the carbon coating required to ensure electronic conductivity in the phosphate is not formed. Singhal et al.[7] have precipitated a precursor by using lithium oxalate, iron hydroxide and $NH_4H_2PO_4$. Heating at 350 °C and annealing between 550 and 800 °C provided $LiFePO_4$ in particles sizes over the range 5–50 nm.

In this work, we use a method that produces nanoparticulated spinels with excellent performance in lithium ion batteries. The method involves the mechanical grinding of lithium, nickel and manganese salts in the presence of a large excess of hydrated oxalic acid[16] to obtain $LiNi_xMn_{2-x}O_4$ phases. The slurry thus obtained provides a nanomaterial upon calcination at low and moderate temperatures. We

[a] Departamento de Química Inorgánica e Ingeniería Química, Edificio Marie Curie,
Campus de Rabanales, Universidad de Córdoba, 14071 Córdoba, Spain
E-mail: iq2sanpe@uco.es
[b] Departamento de Química Inorgánica,
Universidad de Málaga, Spain

 © 2006 Wiley-VCH Verlag GmbH & Co. KGaA, Weinheim 

have adapted this procedure to the phosphate phases and obtained electroactive nanosized $LiFePO_4$ at 550 °C. The material was characterised by X-ray diffraction (XRD), X-ray photoelectron spectroscopy (XPS) and transmission electron microscopy (TEM), and its electrochemical properties in lithium cells determined. The performance of the material, which was initially poorer than that of carbon-coated materials, was successfully improved by adding copper in a very low weight ratio.

## Results and Discussion

### Nanostructured Lithium Iron Phosphate

Lithium iron phosphate is typically prepared by heating a mixture of precursors above 500 °C. Iron(II) is usually protected from oxidation under an inert atmosphere during the thermal treatment. The introduction of carbon (or a carbon precursor such as glucose) into the system can produce iron or iron phosphides[11] during the thermal treatment by carbothermal reduction. The main difference of our method from other solid-state methods using related precursors is that it includes previous grinding and the use of a large excess of hydrated oxalic acid, two factors that seemingly have a significant effect on the results. Thus, they facilitate the formation of a highly homogeneous nanometric mixed oxalate precursor.[17] Also, the oxalic acid released during heating isolates the nanoparticles from one another, thereby hindering particle growth or agglomeration. In addition, water of hydration facilitates nucleation and growth of the reaction products. We checked the purity

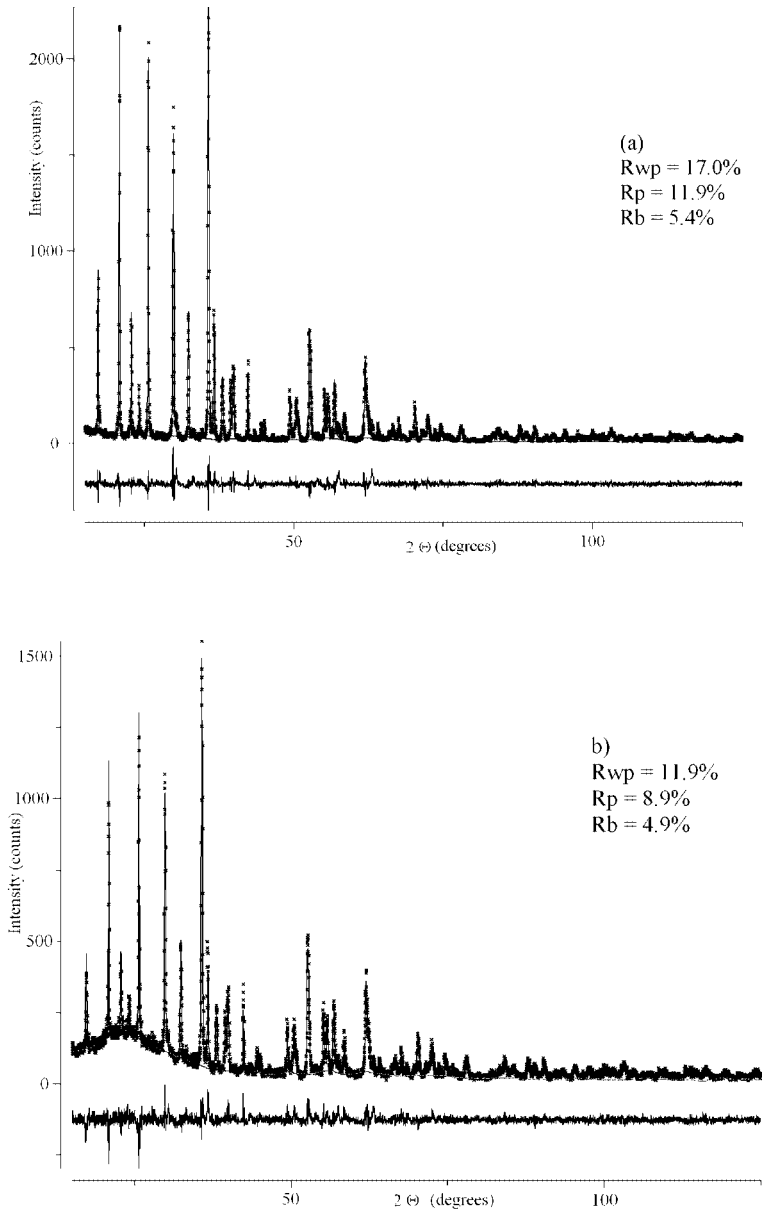


Figure 1. XRD patterns for (a) nanosized $LiFePO_4$ and (b) Cu-$LiFePO_4$ system. Experimental (dotted), calculated (line) and the difference (bottom).

 © 2006 Wiley-VCH Verlag GmbH & Co. KGaA, Weinheim 

of the obtained phases by XRD (Figure 1, a). The peaks associated with the compound matched those of the orthorhombic phase (space group *Pnmb*). Rietveld refinements, performed using the GSAS software suite,[18] yielded the following cell parameter values: $a$ = 10.298, $b$ = 5.995 and $c$ = 4.695 Å; $\alpha = \beta = \gamma = 90°$. The fitted parameters are included in Figure 1. There were also a few peaks at 30.35, 43.39 and 57.56° ($2\theta$) that could not be indexed in the olivine-type structure; such peaks could be indexed in a cubic structure with a lattice constant of 8.34 Å and are consistent with either maghemite ($\gamma$-$Fe_2O_3$) or magnetite ($Fe_3O_4$). The presence of one of these phases made the sample magnetic (as checked with a magnet stick). Based on the heating temperature used, only the magnetite phase should be stable; its content as calculated from the Rietveld refinement was found to be about 6%. The magnetite may have been formed from traces of oxygen contained in the argon flow or occluded in particle pores.[12] Other authors[6] have found that $LiFePO_4$ can yield $Fe_2O_3$ and $Li_3Fe_2(PO_4)_3$ directly during oxidation in the air at 400 °C. Interestingly, $Fe_2O_3$ has been found as an impurity in a related solid-state reaction.[15] This phase seemingly appears when no citric acid − the carbon precursor used in their preparation − is present. This phenomenon was also observed by Dokko et al.,[19] who added ascorbic acid to the reaction mixture in order to remove an amorphous layer of iron oxide that appeared at 400 °C. Based on these findings, our precursors can be deemed ineffective for obtaining carbon-rich materials, as confirmed by elemental analyses.

The TEM images provided direct evidence of crystallinity in the material. The sample consists of nanoparticles (Figure 2, a) with reasonably well-defined edges and sizes below 80 nm. Figure 2 (b) shows an HRTEM image of a crystallite exhibiting structural uniformity and a lattice spacing of 0.25 nm, which corresponds to the (311) lattice planes. Note that our particles are better defined than those formed by Chimie Douce methods[14] or a related solid-state reaction at 550 °C.[15]

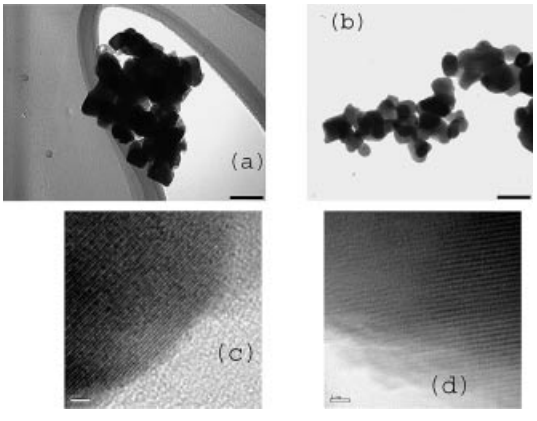


Figure 2. TEM images of (a) and (c) $LiFePO_4$; (b) and (d) Cu-$LiFePO_4$ composite. The black bar corresponds to 100 nm for the upper images and the white bar to 2 nm for the lower ones.

The oxidation states of iron and phosphorus, and the Fe/P atomic ratio, were checked by XPS. The corresponding data are shown in Table 1. The Fe/P ratio thus obtained (1.02) is consistent with the compound stoichiometry. The low intensity/background ratio of the Li 1s emission peak, which results from its low scattering coefficient towards X-rays, precluded accurate determination of its binding energy and estimation of the element content. Figure 3 (a) shows the spectrum for Fe. The shape and binding energies of the Fe 2p emission peaks are consistent with those obtained by other authors for phospholivines[20] and hinder the identification of iron oxides. Furthermore, the P 2p binding energy corresponds to the $PO_4^{3-}$ group and rules out the presence of iron phosphide,[11] a product formed when carbothermal reduction occurs during the preparation of a phospholivine. Thus, no carbothermal reaction takes place during the calcining process.

Table 1. XPS binding energies for various atoms in the $LiFePO_4$ and Cu-$LiFePO_4$ samples.

| Sample | Atom | Emission peak | Binding energy (eV) | Assignation |
|---|---|---|---|---|
| $LiFePO_4$ | Fe | $2p_{3/2}$ | 711.4 | $Fe^{2+}$ |
| | | $2p_{1/2}$ | 724.6 | |
| | P | $2p$ | 133.7 | $[PO_4]^{3-}$ |
| | O | $1s$ | 531.4 | $O^{=}$ |
| Cu-$LiFePO_4$ | Fe | $2p_{3/2}$ | 711.2 | $Fe^{2+}$ |
| | | $2p_{1/2}$ | 724.4 | |
| | P | $2p$ | 133.7 | $[PO_4]^{3-}$ |
| | O | $1s$ | 531.3 | $O^{=}$ |
| | Cu | $2p_{3/2}$ | 930.0 | $Cu^0$ |
| | | $2p_{3/2}$ | 932.9 | $Cu^{I}$–O |
| | | $2p_{3/2}$ | 934.6 | $Cu^{II}$–O |
| | | $2p_{1/2}$ | 949.8 | $Cu^0$ |
| | | $2p_{1/2}$ | 952.8 | $Cu^{I}$–O |
| | | $2p_{1/2}$ | 954.5 | $Cu^{II}$–O |

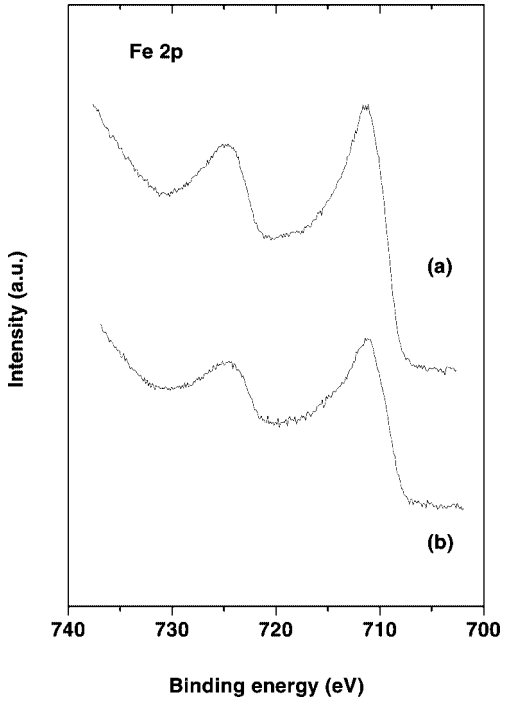


Figure 3. XPS spectrum for iron in (a) $LiFePO_4$ and (b) Cu-$LiFePO_4$.

 © 2006 Wiley-VCH Verlag GmbH & Co. KGaA, Weinheim 

Figure 4 (a) shows selected potentiostatic charge/discharge curves for a cell made from nanosized $LiFePO_4$. A broad peak centred at 3.55 V was obtained in the first cycle. This oxidation peak corresponds to the extraction of lithium from the structure according to Equation (1).

$$LiFe^{II}PO_4 \rightarrow Li^+ + e^- + Fe^{III}PO_4 \quad (1)$$

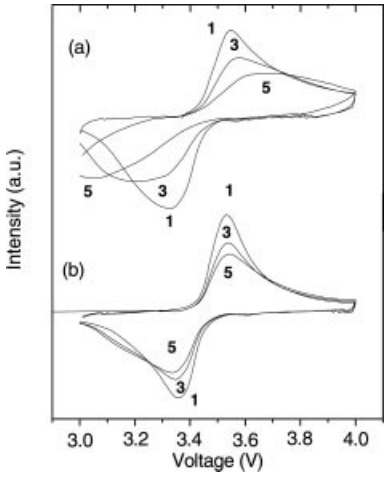


Figure 4. Voltammetric cycling of Li/$LiPF_6$(EC,DMC)/lithium iron phosphate electrodes over the 3.0–4.0 V voltage range. (a) Nanosized $LiFePO_4$, (b) Cu-$LiFePO_4$. Scan rate 5 mV/min.

The reverse reaction − the insertion of lithium into the heterosite structure − provides a broad peak at 3.33 V. The difference between both potentials, $\Delta E_p$, is 220 mV and testifies to the kinetic limitation of these electrodes due to their high resistivity.[5,8,21] The intensity of the peaks decreased in the third cycle, which suggests that the oxidation and reduction processes are much more strongly hindered; $\Delta E_p$ rose to 360 mV. In the fifth cycle, the peaks were clearly shifted from their original positions and much broader, consistent with the decreased electrochemical activity. Figure 5 (a) shows selected galvanostatic charge/discharge cycles for the nanosized $LiFePO_4$ cell. A typical flat voltage plateau close to 3.5 V was obtained during the first charge and discharge. The first capacity was 120 mAh g$^{-1}$, which, however, is 50 mAh g$^{-1}$ less than the theoretical capacity associated with the total delithiation of the phosphate. These values depart markedly from those obtained by Hsu et al.[15] for nanoparticles prepared at the same temperature, which were electrochemically inactive. Furthermore, our capacity values are higher than those found for an hydrothermally synthesised $LiFePO_4$ containing amorphous iron oxides[19] and for a nanostructured phosphate prepared by Sighal et al.[7] Note that, in the latter case, the authors used 20 wt.-% rather than 12% wt.-% carbon black to prepare the electrode mixture.

Consistent with the potentiostatic results, the capacity value was barely retained upon cycling (Figure 6) and, after five cycles, faded by 42%. This behaviour is typical of a phosphate-electrode system and illustrates the inadequate

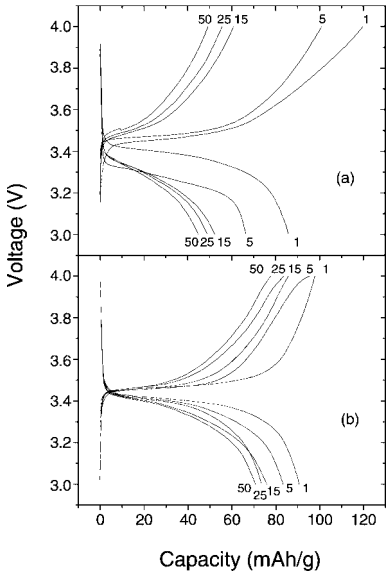


Figure 5. Galvanostatic cycles under a C/10 regime for cells with cathode based on (a) nanosized $LiFePO_4$ and (b) Cu-$LiFePO_4$.

electronic conductivity of nanoparticles. Moreover, as suggested by Yamada et al.,[12] the presence of iron oxide impurities may detract from cell performance.

### Copper-Treated Lithium Iron Phosphate

As noted earlier, the nanoparticles obtained in this work, while somewhat more electroactive than other $LiFePO_4$ nanoparticles provided by more complex methods, exhibit an electrochemical response rather different from theoretical calculations and quite poor cell performance. This is widely ascribed to the lack of a carbon or phosphide network that ensures electron conduction between particles. Based on the results of Hsu et al.,[15] the electroactivity of the nanosized phosphates is determined not only by the presence of the conductive network, but also by the particle shape, which was well defined in our case. In order to improve the electrical conductivity of the electrode, we added a metal to our original material. Like Croce et al.,[8] we chose copper for this purpose on the grounds of its low toxicity and cost; however, we used a different approach that involves formation of $Cu^0$ in situ by chemical reduction of $Cu^ICl$. The reaction of this salt with $NaBH_4$ has been confirmed to yield nanoparticulated copper[22] and proceeds according to Equation (2).

$$2\,Cu^ICl + 2\,NaBH_4 \rightarrow 2\,NaCl + B_2H_6 + 2\,Cu + H_2 \quad (2)$$

Formally, the copper thus obtained should be more effectively dispersed than submicrosized commercial copper[8] and hence increase the conductivity of the Cu-$LiFePO_4$ composite.

Rietveld refinements on the XRD patterns for the new material (Figure 1, b) confirmed that the olivine-type structure was maintained during the reaction and that the cell

 © 2006 Wiley-VCH Verlag GmbH & Co. KGaA, Weinheim 

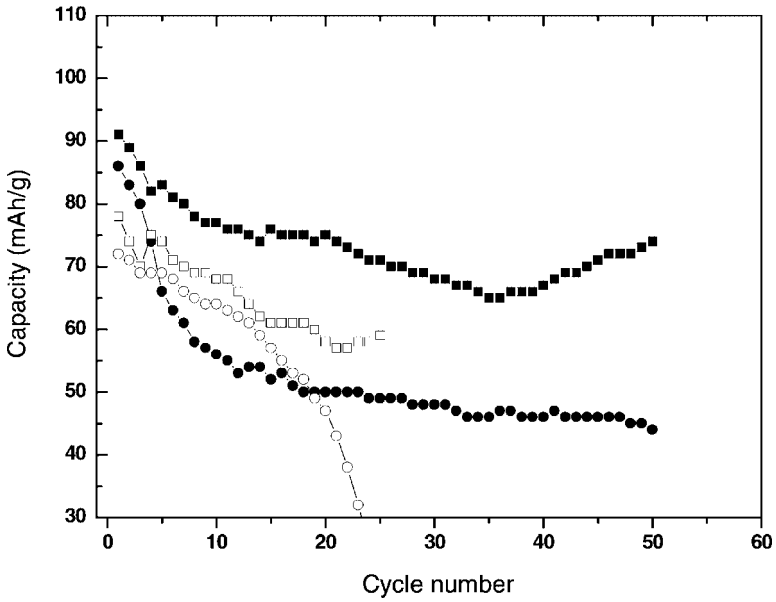


Figure 6. Variation of cell capacity as a function of the number of cycles. (●) $LiFePO_4$ under C/10, (■) Cu-$LiFePO_4$ under C/10, (○) $LiFePO_4$ under C/5 and (□) Cu-$LiFePO_4$ under C/5.

parameters were only slightly different ($a$ = 10.302, $b$ = 5.998, $c$ = 4.695, $\alpha = \beta = \gamma = 90°$). No copper was detected in the XRD pattern, although iron oxide peaks were again observed. TEM images (Figure 2, b) revealed that stirring resulted in rounder particle edges and hindered the observation of well-defined particles. The crystallographic orientation of the particles was seemingly unaffected (Figure 2, d), and the d-spacing, as calculated from the fringes, was again consistent with the value for the (311) planes. No copper could be identified from TEM images. So far, all attempts at detecting isolated or agglomerated copper particles by combining microdiffraction and energy-dispersive microanalysis have failed. The diffuse diffraction peak in Cu/Li-$FePO_4$ nanocomposites should be due to a particle microstructure degradation under the stirring conditions rather than to the diffusion of Cu atoms into the phosphate framework.

The presence of copper was confirmed from XPS measurements, which also ruled out the formation of metallic iron (by reduction of $Fe^{II}$ from the phosphate) or residual chloride. The binding-energy values obtained are listed in Table 1. The fact that the P and Fe peaks retain their positions (Figure 2, b) provides direct evidence of the stability of $LiFePO_4$ upon contact with $NaBH_4$. One unexpected finding was a complex Cu 2p profile (Figure 7) that can be resolved into the contributions of three different oxidation states ($Cu^{II}$, $Cu^{I}$ and $Cu^0$). The presence of divalent copper is also supported by the typical shake-up observed at 940 and 943 eV. These data suggest a pronounced reactivity of Cu towards oxygen as the likely result of the nanometric size of the particles. Despite the precautions exercised to minimize contact of the composite material with the air, the element was partially oxidized, at least at a surface level. The $Cu^{II}$:$Cu^{I}$:$Cu^0$ atomic ratio was found to be 2:1:1. Therefore, only 1.25% by weight of the Cu-$LiFePO_4$ mixture consists of metallic copper and the improvement in conductivity should be less than expected for total conversion (5 wt.-%). This accounts for the inability to detect copper nanoparticles by XRD or from the HRTEM images.

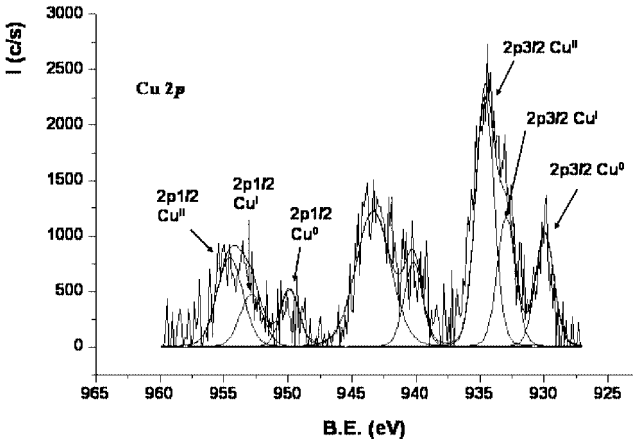


Figure 7. Cu 2p spectrum for the Cu-$LiFePO_4$ composite. Peak deconvolution is also shown.

Notwithstanding the low copper content, the favourable effect of the element on the electrochemical performance of the cell is clearly apparent. Figure 4 (b) shows the potentiostatic cycles for the cell based on the Cu-$LiFePO_4$ mixture. Now, the oxidation and reduction peaks are shaper than those for untreated $LiFePO_4$ (Figure 4, a), with this effect being stronger for the reduction peak. On further cycling, the positions of the peaks remain unchanged, even though their area decreases gradually. This suggests that electron charge-transfer is facilitated by a lower resistivity in the nanocomposite. Copper oxidation was not detected in our samples, probably because it is masked by the main reaction (the Cu potentials are 3.36–3.51 V for $Cu^{2+}$/Cu

 © 2006 Wiley-VCH Verlag GmbH & Co. KGaA, Weinheim 

and $Cu^+/Cu$ vs. $Li^+/Li$, respectively). If copper is oxidised, the as-formed $Cu^I$ or $Cu^{II}$ species might dissolve into the EC/DMC solvent and poison the negative electrode. Nevertheless, this plausible inconvenience seems to be negligible as the cell performance is maintained even for bigger amounts of Cu, as reported by Croce et al.[8]

Galvanostatic cycling (Figure 5, b) also provided direct evidence of the favourable effect of copper on the electrochemical properties of the electrode. In the first charge, the compound provided a flat voltage profile and a capacity of 100 mAh g$^{-1}$; however, 10 mAh g$^{-1}$ was lost after discharge. The voltage plateau remained remarkably stable on cycling, but the plateau length decreased with cycling. The composite retained part of the capacity and voltage profiles over several cycles (Figure 6, b); thus, 70% of the original capacity was retained in the 50th cycle. In order to further check the performance of our composites we tested the electrodes under a faster regime, i.e. C/5. As shown in Figure 6, the faster cycling lowered the capacity for the first cycle. However, and once again, the copper composite showed a higher capacity retention (75% in capacity in the 25th cycle vs. 50% for the copper-free material). This means that the addition of Cu is insufficient to obtain high capacities under higher charge/discharge rates. The presence of iron oxides may be an important factor that hinders approach to the theoretical capacity values. We expect to be able to avoid the formation of this phase either by using alternative precursors or by modifying the thermal treatment.

## Conclusion

Well-crystallised nanometric $LiFePO_4$ of uniform particle size (ca. 80 nm) was synthesised at 550 °C by using a simple method involving a homogeneous mixture of iron oxalate, diammonium hydrogen phosphate, lithium acetylacetonate and excess oxalic acid plus grinding. In contrast to the typically inactive or poorly active nanomaterials provided by alternative solid-state reactions at the same temperature, our nanomaterial is electroactive in lithium batteries. The initial charge capacity of the cell, 120 mAh·g$^{-1}$, was not completely recovered during the first discharge owing to the poor electronic properties of the material – no chemical treatment such as the addition of a conductor (e.g. carbon) was performed. In order to improve the cycling efficiency, we introduced copper (hypothetically in nanosized form) thoroughly mixed with the phosphate via a chemical reaction. Although copper was partially oxidized, a small fraction (less than 1.5% by weight) sufficed to increase the reversibility of the lithium extraction/insertion process by a factor close to 2 relative to the copper-free material. The capacities delivered by the Cu-$LiFePO_4$ composite in the 50$^{th}$ cycle were close to 80 mAh·g$^{-1}$. These electrochemical properties are acceptable for a nanophosphate prepared in a fast one-step method using a moderate temperature. The electroactivity of our sample appears to be determined by two main factors, namely: the nanometric size of the particles and their well-defined shape. We are currently analysing carefully the influence of both factors on the electrochemical properties of the phosphate. The proposed method can also be used to prepare other phospholivines such as $LiMnPO_4$ and $LiCoPO_4$, the electrochemical properties of which will be reported in a future paper.

## Experimental Section

Lithium iron phosphate was obtained as follows: $FeC_2O_4{\cdot}2H_2O$ (1.80 g; Fluka), $(NH_4)_2HPO_4$ (1.32 g; Fluka), $LiC_5H_7O_2$ (1.60 g; Strem Chemicals), and $H_2C_2O_4{\cdot}2H_2O$ (8 g; Fluka) were ball-milled in a Retsch mill at 50 rpm for 30 min. The resulting slurry was supplied with 2 mL of ethanol and air-dried. The powder collected was subsequently calcined at 550 °C under argon for 2 h. We chose this moderate temperature in order to ensure adequate crystallinity in the compound and avoid sintering, which increases particle size. After cooling to room temperature, a brown solid, nanometric $LiFePO_4$, was obtained. For copper coating, the nanomaterial was immersed in a solution containing freshly prepared CuCl in methanol.[22] The Cu/$LiFePO_4$ weight ratio used was 5:95. Because this compound is readily oxidized, the process was carried out inside a glove box (Mbraun 150). After addition of several milligrams of $NaBH_4$ under continuous stirring the brown solid darkened. The solid was collected by filtration after 2 h of stirring and thoroughly washed with methanol. dried in an inert atmosphere and stored in tightly sealed glass containers under argon for transportation.

Transmission electron microscopy (TEM) images were obtained on a Jeol 2010 microscope operating at 200 keV. Samples were prepared in an ultrasonic bath, using hexane as dispersing agent and a grid covered with a carbon perforated film. X-ray diffraction patterns were recorded with a Siemens D5000 X-ray diffractometer, using Cu-$K_\alpha$ radiation and a graphite monochromator. The scan conditions for structural refinement included a 15–125° ($2\theta$) recording range, a 0.02° step size and 8 s per step. X-ray photoelectron spectra were obtained on a Physical Electronics PHI 5700 spectrometer, using non–monochromatic Mg-$K_\alpha$ radiation (300 W, 15 kV, 1253.6 eV) and a multi-channel detector. Spectra were recorded in the constant pass energy mode at 29.35 eV, using a 720 μm diameter analysis area. Binding energy (BE) values were referred to the C 1s peak (284.8 eV) from the adventitious contamination layer during data processing of the XPS spectra. Recorded spectra were always fitted using Gauss–Lorentz curves in order to more accurately determine the binding energy of the different element core levels. The error in BE was estimated to be ca. ±0.1 eV. The spectra for the C 1s and Cu 2p regions were initially recorded for 10 min. Such a short acquisition time was intended to avoid the previously reported reduction of $Cu^{2+}$ species to $Cu^+$ by the action of the X-ray excitation source as much as possible.[23] For recording of XPS spectra, the containers were opened in the air and the pellets, rapidly transferred to the preparation chamber of the XPS spectrometer. In this way, the exposure time of the sample to air was minimised.

Electrochemical measurements were carried out in CR2032 coin cells, using an electrode mixture consisting of active material, carbon black and Teflon in a weight ratio 85:12:3. The working electrode consisted of a stainless steel grid onto which approximately 3 mg of the mixture was pressed. The electrolyte used was 1 M $LiPF_6$ in 2:1 EC/DMC as solvent. Both the reference electrode and the counter-electrode consisted of a lithium disk. Potentiostatic cycles were carried out in a MacPile II (BioLogic) potentiostat under a regime of 10 mV/2 min. Galvanostatic discharges were performed

 © 2006 Wiley-VCH Verlag GmbH & Co. KGaA, Weinheim 

on a Arbin system under a regime of C/10 (i.e. one lithium mol was transferred in 10 h) or C/5 (i.e. one lithium mol was transferred in 5 h).

## Acknowledgments

The authors acknowledge financial support of the Spanish's Ministerio de Educación y Ciencia (Project MAT2002-04477-C02-02). J. S. P. is indebted to the Junta de Andalucia by the Researcher's Return Program.

[1] A. K. Padhi, K. S. Nanjundaswany, C. Masquelier, S. Okada, J. B. Goodenough, *J. Electrochem. Soc.* **1997**, *144*, 1609–1613.
[2] S. Franger, F. Le Cras, C. Bourbon, H. Rouault, *J. Power Sources* **2003**, *119–121*, 252–257.
[3] S. Franger, F. Le Cras, C. Bourbon, H. Rouault, *Electrochem. Solid-State Lett.* **2002**, *5*, A231–A233.
[4] H. Huang, S.-C. Yin, L. F. Nazar, *Electrochem. Solid-State Lett.* **2001**, *4*, A170–A172.
[5] N. Ravet, Y. Chuvinard, J. F. Magnan, S. Berver, M. Gauthier, M. Armand, *J. Power Sources* **2001**, *97–98*, 503–507.
[6] I. Belharouak, C. Johnson, K. Amine, *Electrochem. Commun.* **2005**, *7*, 983–988.
[7] A. Singhal, G. Skandan, G. Amatucci, F. Badway, N. Ye, A. Manthiram, H. Ye, J. J. Xu, *J. Power Sources* **2004**, *129*, 38–44.
[8] F. Croce, A. D'Epifanio, J. Hassoun, A. Deptula, T. Olczac, B. Scrosati, *Electrochem. Solid-State Lett.* **2002**, *5*, A47–A50.
[9] G. X. Wang, L. Yang, Y. Chen, J. Z. Wang, S. Bewlay, H. K. Liu, *Electrochim. Acta* **2005**, *50*, 4649–4654.
[10] S. Y. Chung, J. T. Bloking, Y. M. Chiang, *Nat. Mater.* **2002**, *1*, 123–128.
[11] P. Subramanya Herle, B. Ellis, N. Coombs, L. F. Nazar, *Nat. Mater.* **2004**, *3*, 147–152.
[12] A. Yamada, S. C. Chung, K. Hinokuma, *J. Electrochem. Soc.* **2001**, *148*, 224–229.
[13] V. Srinivasan, J. Newman, *J. Electrochem. Soc.* **2004**, *151*, 1517–1529.
[14] P. P. Prosini, M. Carewska, S. Scaccia, P. Wisniewski, M. Pasquali, *Electrochim. Acta* **2003**, *48*, 4205–41211.
[15] K.-F. Hsu, S.-Y. Tsay, B.-J. Hwang, *J. Mater. Chem.* **2004**, *14*, 2690–2695.
[16] A. Caballero, M. Cruz, L. Hernán, M. Melero, J. Morales, E. Rodríguez Castellón, *J. Electrochem. Soc.* **2005**, *152*, A552.
[17] X. R. Ye, D. Z. Jia, J. Q. Yu, X. Q. Xin, Z. Xue, *Adv. Mater.* **1999**, *11*, 941.
[18] A. C. Larson, R. B. Von Dreele, *Los Alamos National Lab. Rep.* No. LA-UR-86, **1994**, p. 748.
[19] K. Dokko, K. Shiraishi, K. Kanamura, *J. Electrochem. Soc.* **2005**, *152*, 2199–2202.
[20] J. Lu, Z. Tang, Z. Zhang, W. Shen, *Mater. Res. Bull.* **2005**, *40*, 2039–2046.
[21] C. R. Sides, F. Croce, V. Y. Young, C. R. Martin, B. Scrosati, *Electrochem. Solid-State Lett.* **2005**, *8*, 484–487.
[22] J. A. Haber, N. V. Gunda, W. E. Buhro, *J. Aerosol Sci.* **1998**, *29*, 637–645.
[23] E. Cano, C. L. Torres, J. M. Bastidas, *Mater. Corros.* **2001**, *52*, 667–676.

Received: November 15, 2005
Published Online: March 9, 2006

 © 2006 Wiley-VCH Verlag GmbH & Co. KGaA, Weinheim 

DOI: 10.1002/ejic.200501086

# Highly Symmetrical Tetranuclear Cluster Complexes Supported by *p-tert*-Butylsulfonylcalix[4]arene as a Cluster-Forming Ligand

**Takashi Kajiwara,*[a] Takanori Kobashi,[b] Reiko Shinagawa,[b] Tasuku Ito,[b] Shinya Takaishi,[a] Masahiro Yamashita,[a] and Nobuhiko Iki*[c]**

**Keywords:** Cluster compounds / Calixarenes / Magnetic properties / Ligand exchange

Square-planar tetranuclear clusters $[M_4(\mathbf{L})(AcO)_4(\mu_4\text{-}OH)]^-$ (M = $Mn^{II}$, $Co^{II}$, and $Ni^{II}$) are synthesized using tetra-anionic *p-tert*-butylsulfonylcalix[4]arene ($\mathbf{L}^{4-}$) as a cluster-forming ligand. Three complexes are crystallographically isostructural, being crystallized in the triclinic crystal system with space group $P\bar{1}$. The calix[4]arene acts as a tetrakis *fac*-tridentate ligand through four phenoxo and four sulfonyl oxygen atoms to form square arrangement of four metal ions, which are further bridged by four chelating acetate ions and one hydroxo ion in a $\mu_4$ manner to complete the hexacoordination of each metal center. Although the whole molecule of each complex is crystallographically independent, the molecule is highly symmetrical with a pseudo-four-fold axis lying on the $\mu_4$-$OH^-$ group. The tetranuclear clusters are stable enough to maintain the core structures even in highly dilute solution (≈10 μM), which was confirmed by mass spectroscopic study, however, bridging acetates were easily exchanged by other carboxylate chelates to form derivatives such as $[M_4(\mathbf{L})(BzO)_4(OH)]^-$. Metal–metal interactions were investigated by means of magnetic susceptibility, and it was revealed that both ferro- and antiferromagnetic interactions occur in the $Ni^{II}$ complex depending on the bridging angles of Ni–O–Ni.
(© Wiley-VCH Verlag GmbH & Co. KGaA, 69451 Weinheim, Germany, 2006)

## Introduction

Multinuclear transition-metal complexes and metal clusters have attracted much attention owing to the interesting properties and the functionalities that originate from direct and/or indirect metal–metal interactions. Recent developments of synthetic methods for metal-based assemblies have enabled construction of a variety of well-organized architectures such as helicates,[1] cages,[2] and grids,[3] and the resulting assemblies are also interesting in their possibility to be novel materials incorporating magnetic, electronic, or optical features. For example, some square-shaped [2 × 2] dot systems having reversible redox properties are considered to be candidates for quantum-dot cellular automated devices.[3d,4] Synthetic strategies to produce such metal assemblies often employ well-designed multinucleating ligand systems.[5,6] As we have demonstrated, the thiacalix[*n*]arene[6a,6b,6c,6d] and its oxidized derivatives sulfonyl- and sulfinylcalix[*n*]arenes[6e,6f,6g,6h] can act as novel metal-assembling and cluster-forming ligands. We reported in previous papers that the thiacalix[6]arene gives tetranuclear and pentanuclear cluster complexes[6c,6d] when treated with first-row transition-metal acetate involving coordination bonds with 6 phenoxo oxygen and 6 sulfur atoms. In the case of pentanuclear clusters, hexa-anionic thiacalix[6]arene in the pinched-cone conformation formed a pocket-like cavity surrounded by 12 donor atoms. The cavity had an appropriate size to include a metal-cluster core, and five metal ions with compositions of $Ni_4M$ (M = Co, Mn, or Cu) and $Co_5$ were included to form the pyramidally shaped cluster cores. Sulfonylcalix[4]arene (part a in Figure 1, $H_4\mathbf{L}$) led to octalanthanide cluster complexes ("lanthanide wheels") when it was treated with $Ln(AcO)_3 \cdot nH_2O$, in which each $\mathbf{L}^{4-}$ coordinated to one lanthanide ion as a tetradentate ligand through four phenoxo oxygen atoms,[6e] as the lanthanide ions with large ionic radii were in agreement with the cyclic donor system of $\mathbf{L}^{4-}$ to be included. However, for smaller ions such as first-row transition metals, $\mathbf{L}^{4-}$ and $H_2\mathbf{L}^{2-}$ act as a *fac*-tridentate ligand through three adjoining donor atoms, that is, two phenoxo and one sulfonyl oxygen atoms.[6f,6g] In a conic $H_{4-n}\mathbf{L}^{n-}$, eight donor atoms (four phenoxo and four axial sulfonyl oxygen atoms shown in Figure 1, b) are arranged in a flat manner where four *fac*-tridentate sites (**A**–**D**) are formed, each consisting of three donor oxygens. In the zinc(II) complex, $[Zn(H_2\mathbf{L})(tacn)]$ (tacn denotes 1,4,7-triazacyclononane), the zinc(II) ion

[a] Department of Chemistry, Graduate School of Science, Tohoku University and CREST, Japan Science and Technology Agency (JST),
Aoba-ku, Sendai 980-8578, Japan
Fax: +81-22-795-6547
E-mail: kajiwara@agnus.chem.tohoku.ac.jp
[b] Department of Chemistry, Graduate School of Science, Tohoku University,
Aoba-ku, Sendai 980-8578, Japan
[c] Department of Biomolecular Engineering, Graduate School of Engineering, Tohoku University,
Aoba-ku, Sendai 980-8579, Japan
E-mail: iki@orgsynth.che.tohoku.ac.jp
Supporting information for this article is available on the WWW under http://www.eurjic.org or from the author.

 © 2006 Wiley-VCH Verlag GmbH & Co. KGaA, Weinheim 

smoothly slides on this oxo-surface from one tridentate site to the adjoining site,[6f] and this result indicates that the four tridentate sites **A**–**D** in $\mathbf{L}^{4-}$ are equivalent and each site can bind a metal ion in a similar manner. As a result, $\mathbf{L}^{4-}$ can act as a tetranucleating ligand to give highly symmetrical square-planar clusters. Herein we report syntheses and properties of tetranuclear cluster complexes $(Me_4N)[M_4(\mathbf{L})(AcO)_4(\mu_4\text{-}OH)]$ {$M^{II}$ = $Mn^{II}$ ($Me_4N$[**1**]), $Co^{II}$ ($Me_4N$[**2**]), and $Ni^{II}$ ($Me_4N$[**3**])}, which are constructed on the basis of the cluster-forming ability of $\mathbf{L}^{4-}$.

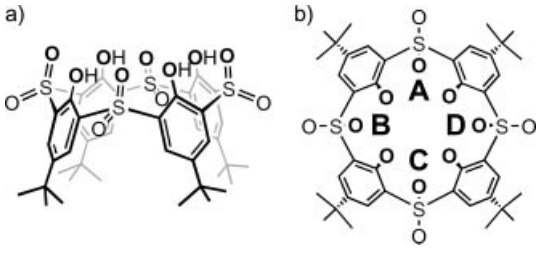


Figure 1. (a) Structure of *p*-(*tert*-butylsulfonyl)calix[4]arene ($H_4\mathbf{L}$). (b) Four equivalent coordination sites (**A**–**D**) of $\mathbf{L}^{4-}$.

## Results and Discussion

### Syntheses and Crystal Structures of Complexes

The reaction of $H_4\mathbf{L}$ and $Mn(AcO)_2{\cdot}4H_2O$ in a 1:5 ratio in $CHCl_3$/MeOH followed by crystallization from an EtOH/dimethylformamide (DMF) solution including $Me_4NCl$ gave colorless crystals of $Me_4N$[**1**] in 36% yield. With a similar procedure, using $Co(AcO)_2{\cdot}4H_2O$ and $Ni(AcO)_2{\cdot}4H_2O$, $Me_4N$[**2**] and $Me_4N$[**3**] were also obtained in yields of 25 and 30%. In the formation of tetranuclear clusters, the acetate ions acted as a base to remove protons from $H_4\mathbf{L}$ to give $\mathbf{L}^{4-}$ and also from $H_2O$ to give $OH^-$. To achieve the best yield, we found that the reaction ratio of the ligand and metal acetate must be 1:5 or larger.

Figure 2 shows the crystal structure of $[Mn_4(\mathbf{L})(AcO)_4(\mu_4\text{-}OH)]^-$ ($[\mathbf{1}]^-$). The complex crystallized in the triclinic crystal system and the four metal coordination sites are crystallographically independent of each other; however, the cluster is highly symmetrical and a pseudo-four-fold axis lies on the central $\mu_4$-$OH^-$ group (O13), and each metal ion is in a similar coordination environment. The conic $\mathbf{L}^{4-}$ supports the formation of the square $Mn_4$ cluster core. Four phenoxo (O3, O6, O9, and O12 in Figure 3) and four axial sulfonyl (O1, O4, O7, and O10) oxygen atoms form an almost flat surface with deviations from the ideal plane ranging from –0.132(3) to 0.220(3) Å, and $\mathbf{L}^{4-}$ acts as a tetrakis tridentate ligand through these eight oxygen atoms. Each $Mn^{II}$ ion is ligated by one sulfonyl and two phenoxo oxygens in a *fac* manner similar to that found in $[Zn(H_2\mathbf{L})(tacn)]$, with distances of $Mn\text{–}O_{phenoxo}$ = 2.1550(18)–2.248(2) Å and $Mn\text{–}O_{sulfonyl}$ = 2.150(2)–2.1832(18) Å. Four $AcO^-$ ions bridge adjoining $Mn^{II}$ ion pairs [$Mn\text{–}O_{acetate}$ = 2.097(2)–2.132(2) Å], four $Mn^{II}$ ions are further bridged by $OH^-$ in an $\mu_4$ manner [Mn–O13 = 2.2309(19)–2.3262(19) Å], and each $Mn^{II}$ ion in $[\mathbf{1}]^-$ is in an octahedral coordination. Bridging hydroxide in an $\mu_4$ manner is rather rare, and few complexes involving first-row transition-metal ions are reported in the Cambridge Crystallographic Data Base.[7] The most remarkable compounds in such a system are square-planar tetranuclear complexes constructed in the aperture of huge macrocyclic Schiff-base ligands reported by Edwards, Kruger, and McKee.[8] In our previous papers,[6d] we have demonstrated the formation of pyramidally arranged pentanuclear cluster complexes using thiacalix[6]arene, in which the basal four metal ions were also connected by $OH^-$ in the same manner. In these complexes, the valence electrons from central oxygen are insufficient to make four M–O coordination bonds, which reflects the long bond lengths found not only in $[\mathbf{1}]^-$ but also in $[\mathbf{2}]^-$ and $[\mathbf{3}]^-$ mentioned below. Hence one can conclude that the $\mu_4$-$OH^-$ system is stable only in a cluster core with the support of huge macrocyclic ligands as a template. One crystal water molecule is bound to the $\mu_4$-$OH^-$ group through hydrogen bonding [O13···O22 = 2.747(6) Å], one DMF molecule is included in the cavity of conic $\mathbf{L}^{4-}$, and one tetramethylammonium ion is included in the lattice as a countercation. $Me_4N$[**2**] and $Me_4N$[**3**] are crystallographically isostructural to $Me_4N$[**1**], showing slight differences in

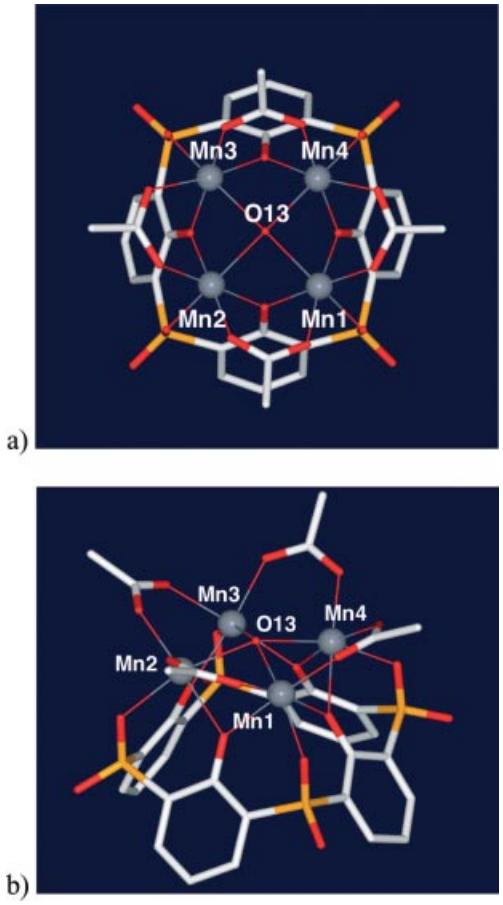


Figure 2. Crystal structure of $[\mathbf{1}]^-$. (a) Top view and (b) side view. *tert*-Butyl groups and hydrogen atoms are omitted. Each atom is depicted as follows: $Mn^{II}$ gray, S orange, O red, and C white.

 © 2006 Wiley-VCH Verlag GmbH & Co. KGaA, Weinheim 

coordination distances. For $[\mathbf{2}]^-$, Co–$O_{phenoxo}$ distances were found in the range of 2.042(4)–2.117(4) Å, Co–$O_{sulfonyl}$ distances in 2.102(5)–2.121(4) Å, 2.013(5)–2.042(4) Å for Co–$O_{acetate}$, and Co–O13 was found to be 2.147(5)–2.290(5) Å. Coordination angles were found to fall in the range of 84.45(17)–92.32(17)°, and the $Co^{II}$ ions are in a nearly ideal octahedral except for the slightly long bonding with the $\mu_4$-$OH^-$ group. For $[\mathbf{3}]^-$, nickel(II) ions are in a slightly elongated octahedral coordination with phenoxo and acetate oxygen atoms occupying equatorial positions [Ni–$O_{phenoxo}$ = 2.016(2)–2.072(2) and Ni–$O_{acetate}$ = 1.986(3)–2.005(3) Å] and sulfonyl and hydroxo oxygen atoms being at axial positions [Ni–$O_{sulfonyl}$ = 2.058(3)–2.079(2) and Ni–O13 = 2.142(3)–2.258(2) Å]. In $[\mathbf{3}]^-$, a residual electron peak with considerable density was found between the $\mu_4$-$OH^-$ group and a neighboring water molecule. This peak was assigned to a carbon atom and the reflection data were analyzed as a superposition of two molecules of $[Ni_4(\mathbf{L})(AcO)_4(\mu_4\text{-}OH)]^-$ ($[\mathbf{3}]^-$) and $[Ni_4(\mathbf{L})(AcO)_4(\mu_4\text{-}OMe)]^-$ ($[\mathbf{3b}]^-$) with 67% and 33% probabilities. The formation of $\mu_4$-OMe bridged complex $[\mathbf{3b}]^-$ might be due to the higher acidity of $Ni^{II}$ ion compared with $Mn^{II}$ and $Co^{II}$. The presence of $\mu_4$-OMe bridged species was also confirmed by mass spectroscopic studies (vide infra).

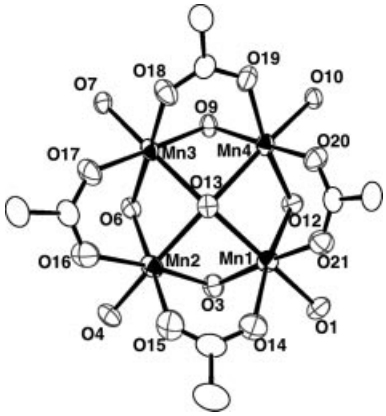


Figure 3. ORTEP diagram of tetranuclear manganese(II) core with thermal ellipsoids at 40% probability.

## Ligand Exchange Reactions

The complexes maintain the tetranuclear cluster cores in a dilute MeCN solution, which was confirmed by ESI-mass spectroscopy. For $Me_4N[\mathbf{1}]$, intense parent peaks were observed at around *m*/*z* = 1317.0, which is related to $[Mn_4(\mathbf{L})(AcO)_4(OH)]^-$ (= $[\mathbf{1}]^-$) (Figure 4, a). Similar spectra were obtained for $[\mathbf{2}]^-$, with the main peaks positioned at around *m*/*z* = 1333.0 being related to $[Co_4(\mathbf{L})(AcO)_4(OH)]^-$ (= $[\mathbf{2}]^-$) (see Figure 1Sa in the Supporting Information), and for $[\mathbf{1}]^-$ and $[\mathbf{2}]^-$ minor species were observed at around *m*/*z* = 1292.9 and *m*/*z* = 1308.9 related to $[Mn_4(\mathbf{L})(AcO)_3(\mu_4\text{-}O)(H_2O)_2]^-$ (= $[\mathbf{1}]^-$ – AcOH + $2H_2O$) and $[Co_4(\mathbf{L})(AcO)_3(\mu_4\text{-}O)(H_2O)_2]^-$ (= $[\mathbf{2}]^-$ – AcOH + $2H_2O$), respectively. For $[\mathbf{3}]^-$, the main peaks at around *m*/*z* = 1306.9 and 1331.0 related to $[Ni_4(\mathbf{L})(AcO)_3(\mu_4\text{-}O)(H_2O)_2]^-$ (= $[\mathbf{3}]^-$ – AcOH + $2H_2O$) and $[Ni_4(\mathbf{L})(AcO)_4(\mu_4\text{-}OH)]^-$ (= $[\mathbf{3}]^-$), respectively, and a minor species involving $\mu_4$-OMe $[Ni_4(\mathbf{L})(AcO)_4(\mu_4\text{-}OMe)]^-$ (= $[\mathbf{3b}]^-$) at around *m*/*z* = 1345.0 were observed (Figure 2Sa, Supporting Information). We assumed that the ligand exchange gave minor species such as $[M_4(\mathbf{L})(AcO)_3(\mu_4\text{-}O)(H_2O)_2]^-$, that is, $\mu_4$-oxo-diaqua complexes. There are other possible formulas for these species including $[M_4(\mathbf{L})(AcO)_3(\mu_4\text{-}OH)(H_2O)(OH)]^-$, $\mu_4$-hydroxo-aqua-hydroxo complexes, and this possibility was rejected by an absence of MS signals for corresponding $[Ni_4(\mathbf{L})(AcO)_3(\mu_4\text{-}OMe)(H_2O)(OH)]^-$ for $[\mathbf{3b}]^-$. The above results reveal that the tetranuclear cores in $[\mathbf{1}]^-$–$[\mathbf{3}]^-$ are stable enough to maintain their core structures even in a highly dilute coordinating solvent (≈10 μM), and moreover, formation of $[M_4(\mathbf{L})(AcO)_3(O)(H_2O)_2]^-$ species indicate that bridging acetate ions can be removed to realize a ligand exchange reaction to give some derivative complexes even in a mild condition. To confirm this, an exchange reaction of bridging acetate by benzoate was performed for all complexes. When $[\mathbf{1}]^-$ was treated with an excess of benzoic acid (1:5 molar ratio) in acetonitrile at ambient temperature, ligand exchange soon occurred to give a mixture of $[Mn_4(\mathbf{L})(AcO)_{4-n}(BzO)_n(OH)]^-$ ($n$ = 2–4) and $[Mn_4(\mathbf{L})(AcO)_{3-m}(BzO)_m(O)(H_2O)_2]^-$ ($m$ = 2–3), which was confirmed by FT-MS (Figure 4, b), and also by X-ray crystallography for $[Mn_4(\mathbf{L})(BzO)_4(OH)]^-$ (Figure 3S). Specific peaks were observed in Figure 4, b where $[Mn_4(\mathbf{L})(BzO)_4(OH)]^-$ was found to be a major component. To complete the exchange reaction, the mixed solution was evaporated once to dryness to remove AcOH, and the residue was again dissolved to the same solvent (Figure 4, c). The mass spectrum for this solution shows two main signals at around *m*/*z* = 1479.0 and 1565.0, being related to $[Mn_4(\mathbf{L})(BzO)_3(O)(H_2O)_2]^-$ and $[Mn_4(\mathbf{L})(BzO)_4(OH)]^-$, respectively, indicating that the acetate bridges were exchanged by benzoate almost quantitatively. The resulting $[Mn_4(\mathbf{L})(BzO)_4(OH)]^-$ was isolated as single crystals with the yield higher than 70%. Similar reactions for $[\mathbf{2}]^-$ and $[\mathbf{3}]^-$ also give the same result. For $[\mathbf{2}]^-$, the main signals at around *m*/*z* = 1495.0 and 1581.0 were observed for the reaction solution, which are related to $[Co_4(\mathbf{L})(BzO)_3(O)(H_2O)_2]^-$ and $[Co_4(\mathbf{L})(BzO)_4(OH)]^-$, respectively, and for $[\mathbf{3}]^-$ the main peaks at around *m*/*z* = 1493.0 and 1579.0 related to $[Ni_4(\mathbf{L})(BzO)_3(O)(H_2O)_2]^-$ and $[Ni_4(\mathbf{L})(BzO)_4(OH)]^-$ were found, indicating that $[Co_4(\mathbf{L})(BzO)_4(OH)]^-$ and $[Ni_4(\mathbf{L})(BzO)_4(OH)]^-$ should be the main products for both cases (Figure 1Sc and Figure 2Sc, respectively). For the case of $[\mathbf{3}]^-$, minor species involving $\mu_4$-OMe formulated as $[Ni_4(\mathbf{L})(BzO)_4(OMe)]^-$ at around *m*/*z* = 1593.0 were observed in Figure 3Sc. The observed ratio between $\mu_4$-OH species ($[Ni_4(\mathbf{L})(AcO)_3(O)(H_2O)_2]^-$ and $[Ni_4(\mathbf{L})(AcO)_4(OH)]^-$ for acetate-bridged complexes, and $[Ni_4(\mathbf{L})(BzO)_3(O)(H_2O)_2]^-$ and $[Ni_4(\mathbf{L})(BzO)_4(OH)]^-$ for benzoate-bridged complexes) and $\mu_4$-OMe species ($[Ni_4(\mathbf{L})(AcO)_4(OMe)]^-$ and $[Ni_4(\mathbf{L})(BzO)_4(OMe)]^-$, respectively) were estimated to be similar for acetate-bridged species (64.6:35.4) and for benzoate-bridged species (64.9:35.1), indicating that the exchange of the central $\mu_4$-OH group does not occur during

 © 2006 Wiley-VCH Verlag GmbH & Co. KGaA, Weinheim 

the exchange reaction of bridging carboxylates. This result suggests that core fragmentation does not occur during this reaction.

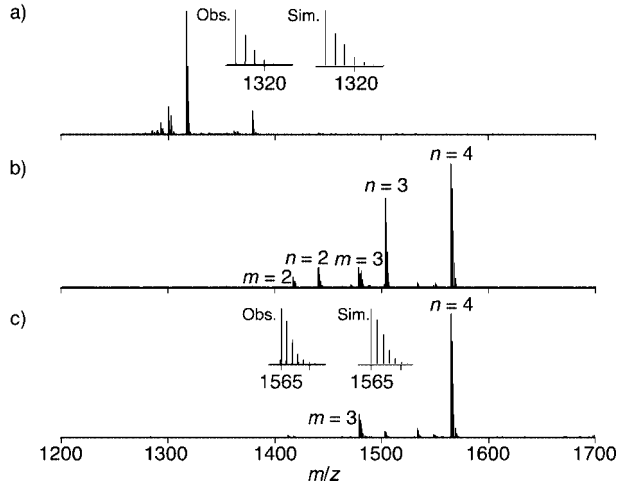


Figure 4. ESI-mass spectra of (a) complex $Me_4N$[**1**] in acetonitrile, (b) mixtures of benzoic acid and $Me_4N$[**1**] in a 5:1 ratio in acetonitrile, and (c) reaction products which were obtained by drying up the reaction solution of benzoic acid and $Me_4N$[**1**]. *n* and *m* denote the numbers of bridging benzoic groups in the species of $[M_4(\mathbf{L})(AcO)_{4-n}(BzO)_n(OH)]^-$ and $[M_4(\mathbf{L})(AcO)_{3-m}(BzO)_m(O)(H_2O)_2]^-$, respectively.

As the complexes maintain their cluster cores in the solution, electrochemical behaviors of these clusters in the same solution were preliminarily investigated by the cyclic voltammetry method at room temperature. No significant peak was observed in the range of –1.0 to +1.0 V versus $Ag/Ag^+$ for all three complexes (Figure 4S), indicating that the divalent tetranuclear complexes are rather stable under the experimental conditions.

### Magnetic Behavior

To investigate the metal–metal interactions in square-shaped clusters, dc-magnetic susceptibilities were measured in the temperature range of 2–300 K. The $\chi_M T$ versus $T$ plots for these complexes show continuous decreases of $\chi_M T$ values as the temperature is lowered (Figure 5, a). The $\chi_M T$ value at room temperature for $Me_4N$[**2**] is larger than the expected spin-only value for four isolated $S = 3/2$ spins, being due to the spin-orbit interactions, which is frequently observed for the $Co^{II}$ ion in a slightly distorted octahedron,[9] and the magnitude of the interaction was hard to analyze. For $Me_4N$[**1**] and $Me_4N$[**3**], temperature dependences of the $\chi_M T$ values were analyzed on the basis of the Hamiltonian,[9]

$$\boldsymbol{H} = -2J_1\Sigma(\boldsymbol{S}_1\cdot\boldsymbol{S}_2 + \boldsymbol{S}_2\cdot\boldsymbol{S}_3 + \boldsymbol{S}_3\cdot\boldsymbol{S}_4 + \boldsymbol{S}_4\cdot\boldsymbol{S}_1) - 2J_2\Sigma(\boldsymbol{S}_1\cdot\boldsymbol{S}_3 + \boldsymbol{S}_2\cdot\boldsymbol{S}_4)$$

where $J_1$ denotes the interaction between adjoining metal ions and $J_2$ is for the diagonal metal ions (Figure 5, b). The best-fit parameters were obtained as $J_1 = -3.0\ cm^{-1}$ and $J_2 = -4.4\ cm^{-1}$ for $Me_4N$[**1**] and $J_1 = 24.9\ cm^{-1}$ and $J_2 = -43.9\ cm^{-1}$ for $Me_4N$[**3**]. For $Ni^{II}$ ions, it is widely thought that the character of magnetic interactions clearly depends

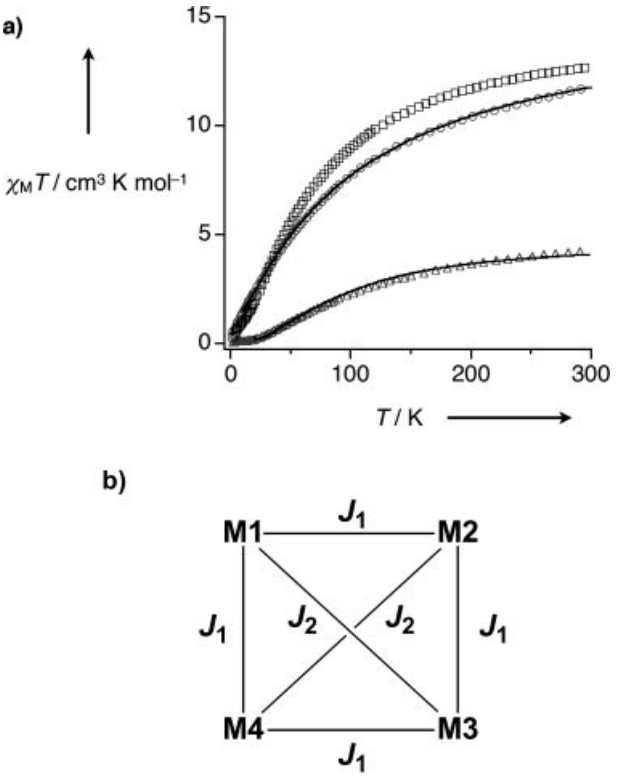


Figure 5. (a) Plots of $\chi_M T$ vs. $T$ for $Me_4N$[**1**] (circle), $Me_4N$[**2**] (square), and $Me_4N$[**3**] (triangle). The solid lines correspond to the theoretical curves for which parameters are given in the text. (b) A schematic drawing of $J_1$ and $J_2$.

on the bridging angle.[10] As two spins are located on the $e_g$ orbitals with dσ characters for $Ni^{II}$, a strict orbital orthogonality occurs and ferromagnetic interaction operates when the bridging angle is smaller than 100°, and a strong antiferromagnetic interaction occurs when the bridging angle reaches linearity. In $Me_4N$[**3**], because each adjoining $Ni^{II}$ ion is bridged by two oxygen atoms involving one phenoxo and one $\mu_4$-hydroxo oxygen atom with angles of 84.13(9)–93.18(10)°, a ferromagnetic interaction operates between two neighboring $Ni^{II}$ ions with relatively strong magnitude. However, the diagonal $Ni^{II}$ ions (two sets of Ni1/Ni3 and Ni2/Ni4) are bridged by the $\mu_4$-$OH^-$ group with angles of 144.88(12)° and 146.87(12)°, so an antiferromagnetic interaction occurs between nickel(II) ions in these two sets. In $Me_4N$[**1**], as the $Mn^{II}$ ion has dσ and dπ spins, orbital overlap through bridging oxygen atoms occurs both in adjoining $Mn^{II}$ sets and in diagonal $Mn^{II}$ sets, and this causes antiferromagnetic interactions in both pathways.

## Conclusion

In conclusion, a tetra-anionic sulfonylcalix[4]arene was used to construct three tetranuclear clusters having a highly symmetrical structure. The complexes are stable enough to maintain their structures in solution and moderate metal–metal interactions were estimated by magnetic susceptibility measurements. It is expected that $\mathbf{L}^{4-}$ generally acts as a tetranucleating ligand for other transition-metal ions, and

 © 2006 Wiley-VCH Verlag GmbH & Co. KGaA, Weinheim 

further studies for the development of a square-shaped tetranuclear system with reversible redox features are now in progress.

## Experimental Section

Solvents and chemicals except for acetonitrile were purchased as reagent grade and used without further purification. Acetonitrile was distilled from calcium hydride immediately prior to use in the cyclic voltammetry measurements. ESI-MS experiments were performed using a Fourier Transform Ion Cyclotron Resonance (FTICR) mass spectrometer APEX III (Bruker). The reaction solution was diluted with acetonitrile, methanol, or acetonitrile/dichloromethane (1:1 v/v) to allow the mass spectroscopic measurement, which gave the same result. Variable-temperature magnetic susceptibility measurements were made using a SQUID magnetometer MPMS 5S (Quantum Design) at 1 T for $Me_4N$[**2**], and 0.25 T and 0.5 T field for $Me_4N$[**1**] and $Me_4N$[**3**], respectively. Diamagnetic correction for each sample was determined from Pascal's constants.

**Synthesis of $Me_4N$[1] (Table 1):** $Mn(AcO)_2{\cdot}4H_2O$ (12.3 mg, 0.05 mmol) and $H_4$**L** (8.5 mg, 0.01 mmol) were mixed and refluxed in MeOH/$CHCl_3$ (1:1, v/v, 10 mL) for an hour, and the solvents evaporated to dryness. The pale brown residue was dissolved into DMF (0.5 mL), added to $Me_4NCl$ (2.2 mg, 0.02 mmol) in ethanol (2 mL), and then evaporated slowly. Colorless crystals of $Me_4N$[**1**]·3.5DMF·$H_2O$ were formed in two weeks. Crystals were filtered and dried in vacuo. Yield, 5.2 mg, 36%. $C_{53.5}H_{74.5}Mn_4N_{1.5}O_{22.5}S_4$ ($Me_4N$[**1**]·0.5DMF·$H_2O$; 1446.69): calcd. C 44.42, H 5.19, N 1.45; found C 44.25, H 5.32, N 1.46.

Table 1. Selected bond lengths [Å] and angles [°] for $Me_4N$[**1**].

| | | | |
|---|---|---|---|
| Mn1–O1 | 2.179(2) | Mn3–O6 | 2.1550(18) |
| Mn1–O3 | 2.213(2) | Mn3–O7 | 2.1832(18) |
| Mn1–O12 | 2.227(2) | Mn3–O9 | 2.233(2) |
| Mn1–O13 | 2.289(2) | Mn3–O13 | 2.3262(19) |
| Mn1–O14 | 2.115(2) | Mn3–O17 | 2.132(2) |
| Mn1–O21 | 2.100(2) | Mn3–O18 | 2.097(2) |
| Mn2–O3 | 2.240(2) | Mn4–O9 | 2.248(2) |
| Mn2–O4 | 2.150(2) | Mn4–O10 | 2.173(2) |
| Mn2–O6 | 2.2284(19) | Mn4–O12 | 2.2335(19) |
| Mn2–O13 | 2.2449(18) | Mn4–O13 | 2.2309(19) |
| Mn2–O15 | 2.122(2) | Mn4–O19 | 2.1108(19) |
| Mn2–O16 | 2.122(2) | Mn4–O20 | 2.111(2) |
| Mn1–O3–Mn2 | 89.17(6) | Mn2–O6–Mn3 | 90.24(8) |
| Mn1–O13–Mn2 | 87.16(6) | Mn2–O13–Mn3 | 85.60(7) |
| Mn1–O13–Mn3 | 150.37(7) | Mn2–O13–Mn4 | 153.41(7) |
| Mn1–O12–Mn4 | 88.62(7) | Mn3–O9–Mn4 | 88.49(6) |
| Mn1–O13–Mn4 | 87.16(7) | Mn3–O13–Mn4 | 86.61(7) |

**Synthesis of $Me_4N$[2] (Table 2):** $Co(AcO)_2{\cdot}4H_2O$ (12.5 mg, 0.05 mmol) and $H_4$**L** (8.5 mg, 0.01 mmol) were mixed and refluxed in MeOH/$CHCl_3$ (1:1, v/v, 10 mL) for an hour, and the solvents evaporated to dryness. The pink residue was dissolved into DMF (0.5 mL), added to $Me_4NCl$ (2.2 mg, 0.02 mmol) in ethanol (2 mL), and then evaporated slowly. Pink crystals of $Me_4N$[**2**]·2DMF·2$H_2O$·EtOH were formed in two weeks. Crystals were filtered and dried in vacuo. Yield, 4.3 mg, 30%. $C_{52}H_{71}Co_4NO_{22}S_4$ ($Me_4N$[**2**]·$H_2O$; 1426.13): calcd. C 43.80, H 5.02, N 0.98; found C 43.49, H 5.15, N 1.24.

Table 2. Selected bond lengths [Å] and angles [°] for $Me_4N$[**2**].

| | | | |
|---|---|---|---|
| Co1–O1 | 2.117(5) | Co3–O6 | 2.042(4) |
| Co1–O3 | 2.100(4) | Co3–O7 | 2.121(4) |
| Co1–O12 | 2.096(5) | Co3–O9 | 2.100(4) |
| Co1–O13 | 2.228(5) | Co3–O13 | 2.290(5) |
| Co1–O14 | 2.014(5) | Co3–O17 | 2.029(5) |
| Co1–O21 | 2.020(5) | Co3–O18 | 2.013(5) |
| Co2–O3 | 2.106(5) | Co4–O9 | 2.117(4) |
| Co2–O4 | 2.102(5) | Co4–O10 | 2.120(5) |
| Co2–O6 | 2.110(4) | Co4–O12 | 2.108(5) |
| Co2–O13 | 2.165(5) | Co4–O13 | 2.147(5) |
| Co2–O15 | 2.042(4) | Co4–O19 | 2.028(5) |
| Co2–O16 | 2.034(5) | Co4–O20 | 2.024(5) |
| Co1–O3–Co2 | 90.88(17) | Co2–O6–Co3 | 92.32(17) |
| Co1–O13–Co2 | 86.04(18) | Co2–O13–Co3 | 84.45(17) |
| Co1–O13–Co3 | 146.9(2) | Co2–O13–Co4 | 149.3(3) |
| Co1–O12–Co4 | 91.26(19) | Co3–O9–Co4 | 91.21(16) |
| Co1–O13–Co4 | 86.75(19) | Co3–O13–Co4 | 85.48(17) |

**Synthesis of $Me_4N$[3] (Table 3):** $Ni(AcO)_2{\cdot}4H_2O$ (12.4 mg, 0.05 mmol) and $H_4$**L** (8.5 mg, 0.01 mmol) were mixed and refluxed in MeOH/$CHCl_3$ (1:1, v/v, 10 mL) for an hour, and the solvents evaporated to dryness. The pale green residue was dissolved into DMF (0.5 mL), added to $Me_4NCl$ (2.2 mg, 0.02 mmol) in ethanol (2 mL), and then evaporated slowly. Pale green crystals of $Me_4N$·0.67[**3**]·0.33[**3b**]·3.5DMF·0.67$H_2O$ were formed in two weeks. Crystals were filtered and dried in vacuo. Yield 3.6 mg, 25%. $C_{52.33}H_{71}NNi_4O_{21.67}S_4$ ($Me_4N$·0.67[**3**]·0.33[**3b**]·0.67$H_2O$; 1423.85): calcd. C 44.14, H 5.03, N 0.98; found C 43.75, H 5.26, N 1.33.

Table 3. Selected bond lengths [Å] and angles [°] for $Me_4N$[**3**].

| | | | |
|---|---|---|---|
| Ni1–O1 | 2.077(3) | Ni3–O6 | 2.016(2) |
| Ni1–O3 | 2.051(2) | Ni3–O7 | 2.079(2) |
| Ni1–O12 | 2.056(3) | Ni3–O9 | 2.066(2) |
| Ni1–O13 | 2.216(3) | Ni3–O13 | 2.258(2) |
| Ni1–O14 | 1.986(3) | Ni3–O17 | 2.003(3) |
| Ni1–O21 | 2.004(3) | Ni3–O18 | 1.986(3) |
| Ni2–O3 | 2.061(2) | Ni4–O9 | 2.072(2) |
| Ni2–O4 | 2.058(3) | Ni4–O10 | 2.071(3) |
| Ni2–O6 | 2.064(2) | Ni4–O12 | 2.068(3) |
| Ni2–O13 | 2.165(3) | Ni4–O13 | 2.142(3) |
| Ni2–O15 | 2.001(3) | Ni4–O19 | 1.999(3) |
| Ni2–O16 | 2.004(3) | Ni4–O20 | 2.005(3) |
| Ni1–O3–Ni2 | 92.29(10) | Ni2–O6–Ni3 | 93.18(10) |
| Ni1–O13–Ni2 | 85.20(9) | Ni2–O13–Ni3 | 84.13(9) |
| Ni1–O13–Ni3 | 144.88(12) | Ni2–O13–Ni4 | 146.87(12) |
| Ni1–O12–Ni4 | 91.97(10) | Ni3–O9–Ni4 | 92.08(10) |
| Ni1–O13–Ni4 | 85.77(9) | Ni3–O13–Ni4 | 85.17(9) |

**X-ray Crystallography:** Data for all of the compounds were collected by a Bruker SMART APEX diffractometer employing graphite-monochromated Mo-$K_\alpha$ radiation ($\lambda$ = 0.71073 Å) at low temperature (200–233 K). The data integration and reduction were undertaken with SAINT and XPREP.[11] An empirical correction determined with SADABS[12] was applied to all data. The structures were solved by the direct method using SHELXS-97[13] and refined using least-squares methods on $F^2$ with SHELXL-97.[13] Non-hydrogen atoms were modeled with anisotropic displacement parameters, and hydrogen atoms were placed by the differential Fourier syntheses and refined isotropically (Table 4).

CCDC-249858 to -249860 contain the supplementary crystallographic data for this paper. These data can be obtained free of charge from The Cambridge Crystallographic Data Centre via www.ccdc.cam.ac.uk/data_request/cif.

 © 2006 Wiley-VCH Verlag GmbH & Co. KGaA, Weinheim 

Table 4.Crystallographic data and structural refinement for $Me_4N$[**1**]–$Me_4N$[**3**].

| | $Me_4N$[**1**]·3.5DMF·$H_2O$ | $Me_4N$[**2**]·2DMF·$2H_2O$·EtOH | $Me_4N$·0.67[**3**]·0.33[**3b**]·3.5DMF·$0.67H_2O$ |
|---|---|---|---|
| Empirical formula | $C_{62.5}H_{90}Mn_4N_{4.5}O_{25.5}S_4$ | $C_{60}H_{93}Co_4N_3O_{26}S_4$ | $C_{62.83}H_{95.5}N_{4.5}Ni_4O_{25.17}S_4$ |
| Formula mass | 1660.39 | 1636.33 | 1680.50 |
| Crystal system | triclinic | triclinic | triclinic |
| Space group | $P\bar{1}$ | $P\bar{1}$ | $P\bar{1}$ |
| $a$ [Å] | 14.158(11) | 14.093(2) | 14.0698(14) |
| $b$ [Å] | 14.469(12) | 14.278(2) | 14.2101(14) |
| $c$ [Å] | 18.983(15) | 18.796(3) | 18.8762(19) |
| $\alpha$ [°] | 87.463(17) | 87.765(5) | 87.151(2) |
| $\beta$ [°] | 89.952(16) | 89.435(5) | 89.546(2) |
| $\gamma$ [°] | 86.414(16) | 86.276(5) | 86.462(2) |
| $V$ [Å$^3$] | 3877(5) | 3771.3(11) | 3762.1(6) |
| $Z$ | 2 | 2 | 2 |
| $F$ (000) | 1729 | 1708 | 1764 |
| $T$ [K] | 200(2) | 183(2) | 200(2) |
| $\rho_{calcd.}$ [g cm$^{-3}$] | 1.422 | 1.441 | 1.484 |
| Reflections collected | 28627 | 30747 | 30925 |
| Independent reflections | 13600 [$R_{int}$ = 0.0841] | 13239 [$R_{int}$ = 0.0924] | 13231 [$R_{int}$ = 0.0555] |
| $\mu$ [mm$^{-1}$] | 0.820 | 1.051 | 1.175 |
| $R_1$, $wR_2$ [$I > 2\sigma(I)$] | 0.0628, 0.01361 | 0.0707, 0.1323 | 0.0417, 0.0904 |
| $R_1$, $wR_2$ (all data) | 0.1259, 0.1588 | 0.1601, 0.1544 | 0.0760, 0.0974 |
| Gof (for $F^2$) | 0.932 | 0.897 | 0.861 |

**Supporting Information** (for details see the footnote on the first page of this article): ESI-mass spectra of complexes $Me_4N$[**2**] and $Me_4N$[**3**], crystal structure of $[Mn(\mathbf{L})(BzO)_4(OH)]^-$, and cyclic voltammograms of $Me_4N$[**1**] to $Me_4N$[**3**] (Figures 1S–4S).

## Acknowledgments

This work was supported by a Grant-in Aid for Scientific Research from the Ministry of Education, Culture, Sports, Science, and Technology, Japan.

[1] For example: C. Piguet, G. Bernardinelli, G. Hopfgartner, *Chem. Rev.* **1997**, *97*, 2005–2062.

[2] a) P. N. W. Baxter, J.-M. Lehn, G. Baum, D. Fenske, *Chem. Eur. J.* **1999**, *5*, 102–112; b) P. N. W. Baxter, J.-M. Lehn, B. O. Kneisel, G. Baum, D. Fenske, *Chem. Eur. J.* **1999**, *5*, 113–120; c) J. S. Fleming, K. L. V. Mann, C.-A. Carraz, E. Psillakis, J. C. Jeffery, J. A. McCleverty, M. D. Ward, *Angew. Chem. Int. Ed.* **1998**, *37*, 1279–1281; d) A. Kamiyama, T. Kajiwara, T. Ito, *Chem. Lett.* **2002**, 980–981.

[3] a) G. S. Hanan, D. Volkmer, U. S. Schubert, J.-M. Lehn, G. Baum, D. Fenske, *Angew. Chem. Int. Ed. Engl.* **1997**, *36*, 1842–1844; b) D. M. Bassani, J.-M. Lehn, K. Fromm, D. Fenske, *Angew. Chem. Int. Ed.* **1998**, *37*, 2364–2367; c) L. Zhao, Z. Xu, L. K. Thompson, S. L. Heath, D. O. Miller, M. Ohba, *Angew. Chem. Int. Ed.* **2000**, *39*, 3114–3117; d) L. H. Uppadine, J.-M. Lehn, *Angew. Chem. Int. Ed.* **2004**, *43*, 240–243.

[4] C. S. Lent, B. Isaksen, M. Lieberman, *J. Am. Chem. Soc.* **2003**, *125*, 1056–1063.

[5] For example: a) S. S. Tandon, L. K. Thompson, J. N. Bridson, C. Benelli, *Inorg. Chem.* **1995**, *34*, 5507–5515; b) B. F. Hoskins, R. Robson, P. Smith, *J. Chem. Soc., Chem. Commun.* **1990**, 488–489; c) H. C. Aspinall, J. Black, I. Dodd, M. M. Harding, S. J. Winkley, *J. Chem. Soc., Dalton Trans.* **1993**, 709–714; d) S. Brooker, V. McKee, W. B. Shepard, L. K. Pannell, *J. Chem. Soc., Dalton Trans.* **1987**, 2555–2562; e) S. Cromie, F. Launay, V. McKee, *Chem. Commun.* **2001**, 1918–1919; f) M. Yonemura, H. Okawa, M. Ohba, D. E. Fenton, L. K. Thompson, *Chem. Commun.* **2000**, 817–818.

[6] a) H. Akdas, E. Graf, M. W. Hosseini, A. De Cian, A. Bilyk, B. W. Skelton, G. A. Koutsantonis, I. Murray, J. M. Harrowfield, A. H. White, *Chem. Commun.* **2002**, 1042–1043; b) A. Bilyk, A. K. Hall, J. M. Harrowfield, M. W. Hosseini, B. W. Skelton, A. H. White, *Inorg. Chem.* **2001**, *40*, 672–686; c) T. Kajiwara, N. Kon, S. Yokozawa, T. Ito, N. Iki, S. Miyano, *J. Am. Chem. Soc.* **2002**, *124*, 11274–11275; d) T. Kajiwara, R. Shinagawa, T. Ito, N. Kon, N. Iki, S. Miyano, *Bull. Chem. Soc. Jpn.* **2003**, *76*, 2267–2275; e) T. Kajiwara, H. Wu, T. Ito, N. Iki, S. Miyano, *Angew. Chem. Int. Ed.* **2004**, *43*, 1832–1835; f) T. Kajiwara, S. Yokozawa, T. Ito, N. Iki, N. Morohashi, S. Miyano, *Angew. Chem. Int. Ed.* **2002**, *41*, 2076–2078; g) T. Kajiwara, S. Yokozawa, T. Ito, N. Iki, N. Morohashi, S. Miyano, *Chem. Lett.* **2001**, 6–7; h) N. Morohashi, N. Iki, S. Miyano, T. Kajiwara, T. Ito, *Chem. Lett.* **2001**, 66–67.

[7] Conquest, Software for searching the Cambridge Structural Database and visualizing crystal structures: I. J. Bruno, J. C. Cole, P. R. Edgington, M. Kessler, C. F. Macrae, P. McCabe, J. Pearson, R. Taylor, *Acta Crystallogr., Sect. B* **2002**, *58*, 389–397.

[8] a) A. J. Edwards, B. F. Hoskins, E. H. Kachab, A. Markiewicz, K. S. Murray, R. Robson, *Inorg. Chem.* **1992**, *31*, 3585–3591; b) P. E. Kruger, V. McKee, *Chem. Commun.* **1997**, 1341–1342; c) J. McKee, V. McKee, T. Metcalfe, S. S. Tandon, J. Wikaira, *Inorg. Chim. Acta* **2000**, *297*, 220–230.

[9] O. Kahn, *Molecular Magnetism*, VCH, Weinheim, **1993**.

[10] M. A. Halcrow, J.-S. Sun, J. C. Huffman, G. Christou, *Inorg. Chem.* **1995**, *34*, 4167–4177.

[11] SMART, SAINT and XPREP, Area detector control and data integration and reduction software, Bruker Analytical X-ray Instruments Inc., Madison, WI, **1995**.

[12] G. M. Sheldrick, SADABS, Empirical absorption correction program for area detector data, University of Göttingen, Germany, **1996**.

[13] G. M. Sheldrick, SHELX97, Programs for Crystal Structure Analysis, University of Göttingen, Germany, **1998**.

Received: December 5, 2005
Published Online: March 6, 2006

 © 2006 Wiley-VCH Verlag GmbH & Co. KGaA, Weinheim 

DOI: 10.1002/ejic.200501099

# Alteration in the Binding Property of a Laterally Nonsymmetric Aza Cryptand toward $Cu^{II}$, $Ag^{I}$, and $Tl^{I}$ Ions upon Derivatization with a Cyanomethyl Group

**Debdas Ray[a] and Parimal K. Bharadwaj*[a]**

**Keywords:** Cryptands / Coordination chemistry / Metal cryptate / Silver / Copper / Thallium

The laterally nonsymmetric aza cryptand $\mathbf{L_o}$ readily forms mononuclear inclusion complexes with metal ions like $Cu^{II}$, $Ni^{II}$, $Ag^{I}$, $Tl^{I}$, and so forth. However, when the secondary amines present in the three bridges are substituted by a cyanomethyl group to yield a new cryptand **L**, its metal-binding properties are drastically altered. Thus, while $\mathbf{L_o}$ binds $Ag^{I}$ at the tren end, showing $AgN_4$ coordination, in **L**, the bridgehead nitrogen atoms are pulled inside to form a two-coordinate complex of $Ag^{I}$ and none of the O or N atoms present in the three bridges are involved in coordination. This is probably the first example where the two bridgehead atoms are pulled inside to the maximum to bind the metal ion. Likewise, the $Tl^{I}$ ion shows $TlN_4$ coordination with $\mathbf{L_o}$, while in **L** it is loosely bound at the tren end, showing $TlN_3$ coordination. Upon treatment with a $Ag^{I}$ salt, the $Tl^{I}$ can be replaced almost instantaneously. On the other hand, with copper(II) tetrafluoroborate salt in moist DMF, two of the cyanide groups in **L** are converted to carboxylic acid groups and bind the metal ion from outside. The $Cu^{II}$ ion in this complex shows distorted octahedral coordination where the two O atoms from the two carboxylic acid groups and the two corresponding N atoms in the two bridges are bound equatorially. The two axial sites are occupied by the nearby bridgehead N atom and the O atom of a DMF molecule. All five complexes and the free ligands are characterized by spectroscopic and X-ray crystallographic studies.
(© Wiley-VCH Verlag GmbH & Co. KGaA, 69451 Weinheim, Germany, 2006)

## Introduction

Macrobicyclic cryptands[1] possess several desirable properties, such as the topology of the donor atoms, binding-site rigidity, layer effects, and so forth, that determine stability, selectivity, and properties of their complexes with metal ions. One of the important factors in the formation of metal cryptates is the cryptand conformation equilibria. For cryptands with N bridgeheads, the principal conformers arise from different orientations of the lone pairs of the electrons on the bridgehead atoms.[2] Each lone pair may be oriented into the cavity (*endo*) or away from the cavity (*exo*). Therefore, it is easy to envision a minimum of three possible conformations for the nitrogen atoms as *exo-exo*, *exo-endo*, and *endo-endo*. The cryptand $\mathbf{L_o}$ (Figure 1) has a large cavity in which two distinct binding sites are separated by a hydrophobic spacer. The tren end ($N_4$ moiety) represents[1c,3] a suitable binding site for transition as well as main-group metal ions such as $Ni^{II}$, $Cu^{II}$, $Zn^{II}$, $Pb^{II}$, $Ag^{I}$, and so forth. The $NO_3$ moiety can be expected to be effective in binding harder cations. We were interested in observing any possible alteration in the coordinating ability of the cryptand when the donor ability of the nitrogen atoms was suppressed by attaching electron-withdrawing cyanomethyl groups to them (Figure 1). Tuning the stereoelectronic factors associated with the binding site has the ultimate aim of enforcing unusual coordination mode(s) on the metal ion besides potential applications associated with metal bind-

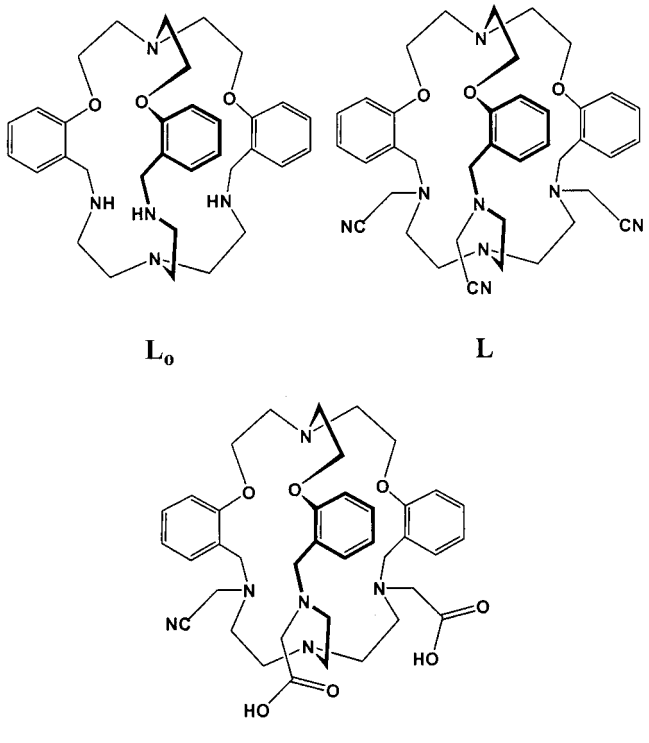


Figure 1. Schematic diagrams of cryptands $\mathbf{L_o}$, **L**, and **L**′.

[a] Department of Chemistry, Indian Institute of Technology, Kanpur 208016, India
E-mail: pkb@iitk.ac.in

 © 2006 Wiley-VCH Verlag GmbH & Co. KGaA, Weinheim 

ing.[4–6] In the present study, $Cu^{II}$, $Ag^{I}$, and $Tl^{I}$ ions are used to probe the complexing ability of the cryptands.

## Results and Discussion

The structure of $\mathbf{L_o}$ has an *endo-exo* conformation in which the distance between the bridgehead N atoms is 6.272(12) Å (Figure 2). A pseudo threefold axis passes through the bridgehead N atoms.

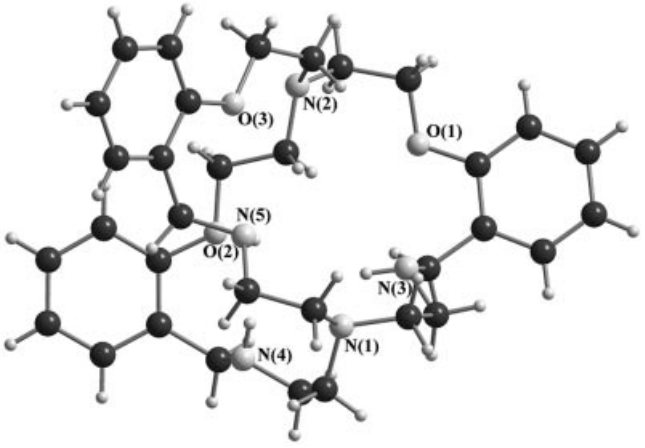


Figure 2. Perspective view of the cryptand $\mathbf{L_o}$.

For comparison, in the room-temperature structure of this cryptand,[7] the distance between the two bridgehead nitrogen atoms is 6.249(14) Å. The O···O and N···N nonbonding distances are also comparable between the two structures [$\mathbf{L_o}$ (LT) and $\mathbf{L_o}$ (RT)[7]]. Thus, temperature variation has little effect on cryptand conformation.

The asymmetric unit of **L** consists of a single strand of the cryptand and a water molecule. The nonbonding distances between two ethereal O atoms [4.72(1) Å] or two amino N atoms [4.29(1) Å] are the same because of crystallographically imposed symmetry. Therefore, in the solid state, the molecule has a threefold symmetry axis passing through the two bridgehead atoms. This cryptand has an *endo-endo* conformation in which the distance between the two bridgehead N atoms is 5.939(2) Å (Figure 3a). The shrinkage of the cryptand cavity relative to that of $\mathbf{L_o}$ may be due to a combination of delocalization of the electron density from the N atoms in the three bridges onto the cyanomethyl groups and the steric effects of these groups. The bond lengths and bond angles in the cryptand are within normal statistical errors. The $^1$H NMR spectroscopic data of **L** also indicate threefold symmetry in the molecule in $CDCl_3$. An interesting feature of this structure is the presence of a triangular planar trimeric water cluster, which shows positional disorder and can be described as two sets of triangular planar water clusters. Six cryptand molecules surround the water cluster (Figure 3b) where each water molecule shows a weak C–H···O hydrogen-bonding interaction [$d$(H···O) = 2.340(16) Å] with the nearest benzene group. The existence of aromatic C–H···O hydrogen bonds has been inferred from several theoretical[8] as well as experimental[9] studies in different organic crystal lattices.[10]

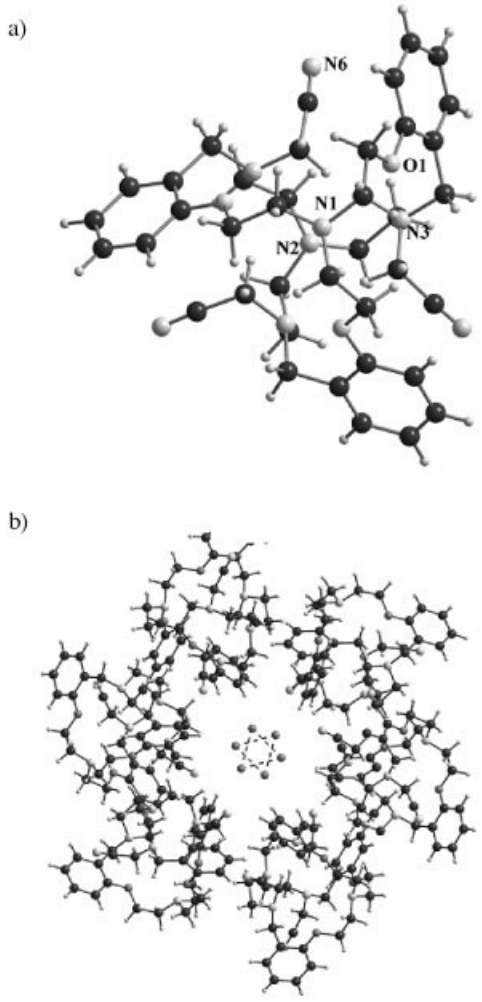


Figure 3. (a) Cryptand **L** viewed approximately along the threefold axis. (b) Packing of six **L** molecules around a cyclic water trimer. Two trimers are shown illustrating positional disorder.

The structure of complex **1** consists of an $[AgL]^+$cation and a nitrate anion. One molecule of methanol is also present in the lattice. The $Ag^{I}$ ion is bonded to four nitrogen atoms at the tren end of the cryptand and is positioned 0.71 Å above the plane described by three amino N atoms in the direction away from the bridgehead N atom (Figure 4). Thus, the coordination geometry is very distorted; all four nitrogen atoms are on one side of the metal ion. Such distorted geometry for an $Ag^{I}$ cryptate was reported[11] earlier. The bond lengths and angles involving the metal ion are similar to those found[11–13] in other Ag cryptates. The metal ion is more than 2.9(1) Å away from the ethereal oxygen atoms and so is considered to be nonbonded. The separation between the two bridgehead N atoms is found to be 5.983(7) Å, which is slightly less than the distance found in $\mathbf{L_o}$ (Table 1). The other N···N and O···O nonbonding distances do not vary appreciably upon metal binding, which means that the cryptand is mostly preorganized.

 © 2006 Wiley-VCH Verlag GmbH & Co. KGaA, Weinheim 

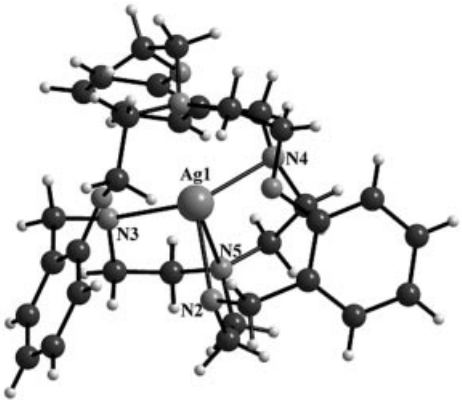


Figure 4. View of the $Ag^{I}$ ion bound at the tren end of the cavity in $\mathbf{L_o}$.

The structure of **2** shows that the $Ag^{I}$ ion is bonded inside the cavity of **L** in an unprecedented fashion (Figure 5). Here, either the electron-withdrawing groups attached to the amino groups make the lone pair unavailable for metal binding or the methylene group of the $-CH_2CN$ moiety near the aromatic group might prevent closer interaction between the amino nitrogen atom and a metal ion. However, the $Ag^{I}$ ion shows dicoordination, binding the two bridgehead N atoms at Ag–N distances of 2.325(8) and 2.388(8) Å and at an N–Ag–N angle of 167.7(10)°. Few two-coordinate $Ag^{I}$ complexes are known[14] in the literature with similar bond lengths and angles. The distance between the metal ion and any other N atoms in the three bridges is 2.82(6) Å or more, while the distance between the metal ion and an ethereal O atom is at least 2.63(5) Å; the metal ion may be considered to be semibonded to the oxygen atom. The bond lengths and bond angles of the cryptand moiety are within normal statistical errors. The two bridgehead N atoms are significantly pulled inside by the $Ag^{I}$ ion; the distance between them is 4.687(15) Å. A water dimer is also present in the lattice, which is hydrogen-bonded to the nitrate anion [O···Ow1 3.019(12) Å].

The unsubstituted cryptand $\mathbf{L_o}$ forms an inclusion complex with $Tl^{I}$ (complex **3**) in which the metal ion occupies a site at the tren end. The $Tl^{I}$ ion is in a "4+3" coordination environment with four normal[15] Tl–N bonds [2.788(8)–2.869(9) Å] and three long interactions [3.07(9)–3.14(9) Å]; the ethereal O atoms are in the cryptand side arms (Figure 6). However, the Tl–N bond lengths are at the long end of the range for Tl–N distances, and therefore are ionic in character,[15a,15b] although Tl–O bond lengths are comparable to literature values.[15f] In complex **4**, on the other hand, $Tl^{I}$ exhibits "3+5" coordination (Figure 7), which comprises three normal Tl–N bonds and five long interactions with the remaining donor atoms (Table 1). The Tl–N bond lengths are significantly increased relative to the values obtained for **3**. Hence, even though the $Tl^{I}$ ion is positioned at the tren end and bonds to the N atoms attached to the cyanomethyl groups, the bonding is weak and ionic in character. In either **3** or **4**, the metal ion is symmetrically bonded to N and O donors and the lone pair on $Tl^{I}$ does

Table 1. Selected bond lengths [Å], angles [°], and nonbonded distances [Å].

| $\mathbf{L_o}$ | | **L** | |
|---|---|---|---|
| N(3)···N(4) | 4.067 | N(3)···N(3′) | 4.298 |
| N(3)···N(5) | 4.417 | N(1)···N(2) | 5.936 |
| N(4)···N(5) | 3.547 | O(1)···O(1′) | 4.731 |
| N(1)···N(2) | 6.272 | | |
| O(1)···O(2) | 4.855 | | |
| O(1)···O(3) | 5.380 | | |
| O(2)···O(3) | 3.967 | | |
| **1** | | **2** | |
| Ag–N(3) | 2.425(5) | Ag–N(2) | 2.326(8) |
| Ag–N(4) | 2.402(5) | Ag–N(1) | 2.388(8) |
| Ag–N(5) | 2.569(5) | | |
| Ag–N(2) | 2.465(5) | | |
| N(3)–Ag–N(4) | 117.63(17) | N(2)–Ag–N(1) | 167.71(10) |
| N(3)–Ag–N(5) | 73.51(17) | | |
| N(4)–Ag–N(5) | 73.82 (15) | | |
| N(3)–Ag–N(2) | 100.54(15) | | |
| N(4)–Ag–N(2) | 117.93(15) | | |
| N(5)–Ag–N(2) | 72.75(14) | | |
| N(3)···N(4) | 4.130 | N(3)···N(4) | 5.058 |
| N(3)···N(5) | 2.990 | N(3)···N(5) | 5.684 |
| N(4)···N(5) | 2.988 | N(4)···N(5) | 4.387 |
| N(1)···N(2) | 4.903 | N(1)···N(2) | 4.687 |
| O(1)···O(2) | 3.999 | O(1)···O(2) | 4.662 |
| O(1)···O(3) | 4.357 | O(1)···O(3) | 4.878 |
| O(2)···O(3) | 4.210 | O(2)···O(3) | 4.667 |
| | **3** | | **4** |
| Tl–N(2) | 2.869(9) | Tl–N(2) | 2.902(9) |
| Tl–N(3) | 2.788(5) | Tl–N(3) | 3.013(5) |
| Tl–N(4) | 2.865(8) | Tl–N(4) | 2.907(5) |
| Tl–N(5) | 2.848(9) | Tl–N(5) | 2.834(7) |
| Tl–O(1) | 3.077(9) | Tl–O(1) | 3.099(5) |
| Tl–O(2) | 3.084(5) | Tl–O(2) | 3.182(5) |
| Tl–O(3) | 3.144(9) | Tl–O(3) | 3.010(8) |
| N(3)–Tl–(N4) | 95.59(15) | N(3)–Tl–N(4) | 107.65(7) |
| N(3)–Tl–N(5) | 116.11(15) | N(3)–Tl–N(5) | 99.86(8) |
| N(4)–Tl–N(5) | 95.42(15) | N(4)–Tl–N(5) | 101.06(8) |
| N(3)–Tl–N(2) | 65.42(15) | N(3)–Tl–N(2) | 62.98(7) |
| N(4)–Tl–N(2) | 62.96(14) | N(4)–Tl–N(2) | 65.40(8) |
| N(5)–Tl–N(2) | 64.93(14) | N(5)–Tl–N(2) | 65.44(8) |
| N(3)···N(4) | 4.187 | N(3)–N(4) | 4.779 |
| N(3)···N(5) | 4.782 | N(3)···N(5) | 4.476 |
| N(4)···N(5) | 4.226 | N(4)···N(5) | 4.432 |
| N(1)···N(2) | 6.073 | N(1)···N(2) | 6.007 |
| O(1)···O(2) | 4.907 | O(1)···O(2) | 4.733 |
| O(1)···O(3) | 4.284 | O(1)···O(3) | 4.522 |
| O(2)···O(3) | 4.395 | O(2)···O(3) | 4.544 |
| **5** | | | |
| Cu–O(8) | 1.980 | | |
| Cu–O(4) | 1.985 | | |
| Cu–N(2) | 2.056 | | |
| Cu–N(4) | 2.059 | | |
| Cu–O(6) | 2.330 | | |
| Cu–N(3) | 2.349 | | |
| O(8)–Cu–O(4) | 95.24(2) | | |
| O(8)–Cu–N(2) | 170.71(2) | | |
| O(4)–Cu–N(2) | 91.47(2) | | |
| O(8)–Cu–N(4) | 87.66(2) | | |
| O(4)–Cu–N(4) | 164.75(3) | | |
| N(2)–Cu–N(4) | 87.54(2) | | |
| O(8)–Cu–O(6) | 90.11(1) | | |
| O(4)–Cu–O(6) | 89.26(2) | | |
| N(2)–Cu–O(6) | 96.39(2) | | |
| N(4)–Cu–O(6) | 75.74(1) | | |
| O(8)–Cu–N(3) | 90.14(1) | | |
| O(4)–Cu–N(3) | 80.12(1) | | |
| N(2)–Cu–N(3) | 84.69(2) | | |
| N(4)–Cu–N(3) | 114.90(2) | | |
| O(6)–Cu–N(3) | 169.36(2) | | |
| N(3)···N(4) | 3.719 | | |
| N(3)···N(5) | 5.693 | | |
| N(4)···N(5) | 5.515 | | |
| N(1)···N(2) | 4.653 | | |
| O(1)···O(2) | 4.505 | | |
| O(1)···O(3) | 5.482 | | |
| O(2)···O(3) | 5.794 | | |

 © 2006 Wiley-VCH Verlag GmbH & Co. KGaA, Weinheim 

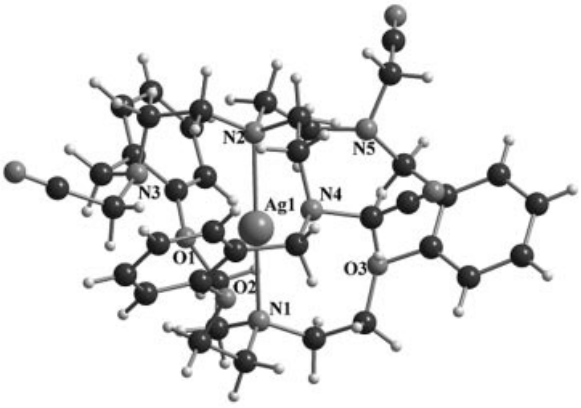


Figure 5. View of the $Ag^{I}$ ion bound to the two bridgehead N atoms in **L**. H atoms are omitted for clarity.

not seem to be stereochemically active.[16] When an equivalent amount of $AgNO_3$ is added to an acetonitrile solution of either **2** or **3**, the $Tl^{I}$ ion is quantitatively replaced by $Ag^{I}$-forming crystals of **1** or **2** overnight.

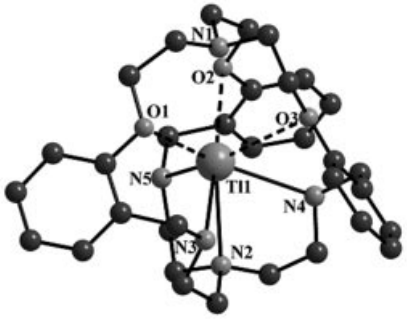


Figure 6. Perspective view of **3** showing the $Tl^{I}$ ion bound at the tren end of $\mathbf{L_o}$.

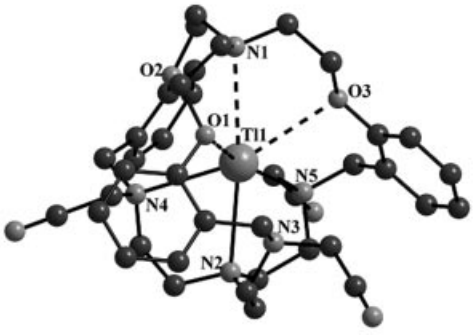


Figure 7. View of **4** showing the $Tl^{I}$ ion bound to three N atoms at the tren end of **L**.

The structure of **5** consists of discrete $[Cu(\mathbf{L}')(DMF)]^{2+}$ cations (Figure 8) and $BF_4^-$ anions. One DMF molecule is also present in the lattice. This structure reveals that two out of three cyano groups are hydrolyzed to carboxylic acid groups and bind a $Cu^{II}$ ion from outside at the tren end of the cavity. The H atoms bonded to the carboxylic acid groups could be easily found in the difference map. We speculate that $Cu^{II}$ initially binds the cryptand outside the cavity and activates the cyano group, which is then attacked by $H_2O$. Only two cyano groups are activated, as the third one is far away from the metal ion. However, the UV/Vis data for the hydrolysis of the cyano group taken at different intervals were not informative. Many metal-mediated processes of cyano group hydrolysis are known in the literature.[17] As a result of hydrolysis of the two cyano groups to carboxylic acid groups, the corresponding N atoms in the two bridges are no longer electron-deficient and bind the $Cu^{II}$ ion along with the two O atoms from the two carboxylic acid groups equatorially. The two axial sites are occupied by the nearby bridgehead N atom and the O atom of a DMF molecule, forming a distorted octahedral coordination geometry (Table 1) around the metal ion. The three N donors from the cryptand are inverted, their lone pairs being directed toward the metal ion, and the cryptand adopts an *exo-endo* conformation. The bond lengths and angles in the cryptand moiety are within normal statistical error, while those involving the metal ion (Table 1) are similar[18] to other $Cu^{II}$ cryptates.

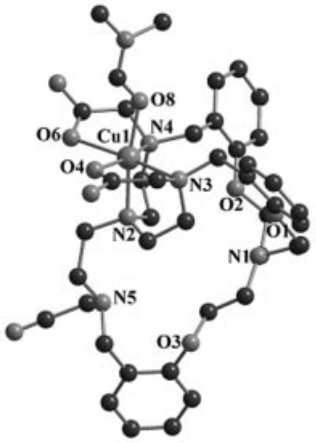


Figure 8. A view of the $Cu^{II}$ ion bound outside the cryptand cavity. Lattice DMF and H atoms bonded to C are omitted for clarity.

In the UV/Vis spectral studies, **5** shows a broad ligand-field band at 685 nm and a charge-transfer band at 325 nm, with molar extinction coefficients of 35 and 600 $cm^2 \cdot mol^{-1}$, respectively. The effective magnetic moment value ($\mu_{eff}/\mu_B$) for **3** after diamagnetic correction is found to be 2.02 at 293 K, which is consistent[19] with the discrete, mononuclear formulation of the complex. EPR spectral studies were carried out in the solid state and in DMF solution at 295 and 77 K. In the solid state at 295 K, a broad signal with $g_{av}$ = 2.09 is observed. The signal sharpens at 80 K without revealing any fine structure. In DMF solution at 80 K, an axial spectrum is obtained with $g_{\|}$ = 2.21, $g_{\perp}$ = 2.08, and $A_{\|} = 148 \times 10^{-4}$ $cm^{-1}$.

## Conclusion

We show here that, although the unsubstituted cryptand binds an $Ag^{I}$ ion inside the cavity without significant change of the cryptand conformation, it behaves very dif-

 © 2006 Wiley-VCH Verlag GmbH & Co. KGaA, Weinheim 

ferently when electron-withdrawing groups are attached to the amino nitrogen atoms in the three bridges. The amino nitrogen atoms lose their ability to bind $Ag^{I}$. Instead, the metal ion binds the two bridgehead N atoms, which is unprecedented. On the other hand, the $Tl^{I}$ ion forms an inclusion complex with $\mathbf{L_o}$, in which the metal ion occupies the tren end of the cavity and is ligated by all four N atoms. With **L**, $Tl^{I}$ still occupies the same end of the cavity but is loosely bound to three N atoms and can be readily replaced by $Ag^{I}$. In the case of $Cu^{II}$, two of the cyano groups are hydrolyzed to carboxylic acid groups at room temperature. This change restores the donor ability of the amino N atoms and the cryptand binds a $Cu^{II}$ ion outside the cavity in a distorted octahedral fashion. We are presently probing whether it is possible to have mixed-metal complexes with this and other related cryptands.

## Experimental Section

**Materials:** All reagent-grade chemicals were used without purification unless otherwise specified. The metal salts, bromoacetonitrile, and tris(2-aminoethyl)amine were obtained from Aldrich. Triethanolamine, salicylaldehyde, sodium borohydride, sodium hydroxide, anhydrous sodium sulfate, potassium carbonate, thionyl chloride, and solvents were received from S. D. Fine Chemicals (India). Thionyl chloride and all the solvents were freshly distilled prior to use, and all the reactions were carried out under $N_2$.

**Physical Measurements:** Spectroscopic data were collected as follows: IR (KBr disk, 400–4000 $cm^{-1}$) Perkin–Elmer Model 1320; $^1H$ NMR ([$D_6$]DMSO, TMS) JEOL JNM-LA400 FT, 400 MHz. FAB MS (positive ion, argon as the FAB gas, 6 kV, 10 mA, 10 kV accelerating voltage) JEOL SX 102/DA-6000. Magnetic susceptibility measurements were made by using a Cahn Faraday Balance with [$CoHg(SCN)_4$] as the standard and applying diamagnetic corrections as described earlier.[18] The EPR spectrum for complex **3** was recorded at X-band frequency with a BRUKER 300E automatic spectrometer at 298 and 80 K. Melting points were determined with an electrical melting point apparatus by PERFIT, India, and were uncorrected. Elemental analyses were obtained from CDRI, Lucknow.

### Synthesis

**Cryptand $\mathbf{L_o}$:** It was synthesized as reported[7] earlier. Single crystals suitable for X-ray crystallography were grown by slow concentration of an acetonitrile solution at room temperature.

**Cryptand L:** Cryptand $\mathbf{L_o}$ (1 g, 1.78 mmol) was added to a suspension of anhydrous potassium carbonate (0.86 g, 6.25 mmol) in dry acetonitrile (100 mL). The solution was stirred at 30 °C. After 30 min, bromoacetonitrile (0.42 mL, 6.25 mmol) was added to the stirred solution. The mixture was stirred at 30 °C for 24 h, and the solvent was removed completely in a rotary evaporator. The black solid that remained was shaken with water and then extracted with chloroform (3 × 50 mL). The chloroform layer, after being decolorized with activated charcoal and dried with anhydrous sodium sulfate, was concentrated completely to yield a yellowish white solid as the desired product. It was purified further by crystallization from dichloromethane to obtain colorless crystals in the form of rectangular parallelepipeds. Yield ca. 85% (1.02 g). M.p. 160 °C. $^1H$ NMR (400 MHz, $CDCl_3$, 25 °C, TMS): aliphatic: δ = 2.65 (dd, $J$ = 22.12, 5.4 Hz, 12 H), 3.18 (t, $J$ = 5.32 Hz, 6 H), 3.46 (s, 6 H), 3.52 (s, 6 H), 4.06 (t, $J$ = 5.12 Hz, 6 H); aromatic: δ = 6.78 (d, $J$ = 8.04 Hz, 3 H), 6.93 (t, $J$ = 7.32 Hz, 3 H), 7.14–7.26 (m, 6 H) ppm. FAB-MS: $m/z$ (%) = 677 $[\mathbf{L}]^+$ (100). $C_{39}H_{48}N_8O_3$ (678): calcd. C 69.21, H 7.15, N 16.56; found C 69.28, H 7.21, N 16.67.

**$[Ag(L_o)]\cdot(NO_3)\cdot CH_3OH$ (1):** Cryptand $\mathbf{L_o}$ (0.56 g, 1 mmol) in dry methanol (5 mL) was added at once to an acetonitrile solution (5 mL) of $AgNO_3$ (0.17 g, 1 mmol) at room temperature in the dark. The light brown solution formed was filtered and the filtrate stored in the dark for crystallization. Colorless X-ray quality crystals in the form of rectangular parallelepipeds appeared in about 2 d. Yield ca. 35% (0.67 g). $C_{34}H_{49}AgN_6O_7$ (761.66): calcd. C 53.61, H 6.48, N 11.034; found C 53.43, H 6.52, N 10.98.

**$[Ag(L)]\cdot(NO_3)\cdot 2H_2O$ (2):** Cryptand **L** (0.68 g, 1 mmol) in dry acetonitrile (5 mL) was added to an acetonitrile solution (5 mL) of $AgNO_3$ (0.17 g; 1 mmol) at room temperature in the dark. The light brown solution was filtered and the filtrate kept for crystallization. Colorless, X-ray-quality, square crystals appeared in 3 d. Yield ca. 55% (0.47 g). $C_{39}H_{52}AgN_9O_8$ (882.75): calcd. C 53.06, H 5.93, N 14.28; found C 52.92, H 5.90, N 14.13.

**$[Tl(L_o)](CH_3OH)(ClO_4)$ (3):** The cryptand $\mathbf{L_o}$ (0.56 g, 1 mmol) dissolved in dry methanol (5 mL) was added all at once to a $CH_3CN$ solution (3 mL) of $Tl(ClO_4)\cdot xH_2O$ (0.36 g, 1.2 mmol) at room temperature in the dark. A brown solution was obtained that was filtered, and the filtrate was stored at room temperature while the solvent evaporated. White X-ray-quality rectangular crystals of **4** appeared in about 2 d. Yield ca. 50% (0.45 g). $C_{34}H_{49}Cl_1N_5O_8Tl$ (895.62): calcd. C 45.60, H 5.51, N 7.82; found C 45.78, H 5.38, N 7.40.

**$[Tl(L)](H_2O)(ClO_4)$ (4):** Cryptand **L** (0.68 g; 1 mmol) in dry acetonitrile (5 mL) was added to an acetonitrile solution (5 mL) of $Tl(ClO_4)\cdot xH_2O$ (0.36 g, 1.2 mmol) at room temperature in the dark. The light brown solution was filtered and the filtrate kept for crystallization. Colorless, X-ray-quality, square crystals appeared in 3 d. Yield ca. 55% (0.55 g). $C_{39}H_{50}Cl_1N_8O_8Tl$ (998.70): calcd. C 46.90, H 5.05, N 11.22; found C 49.75, H 5.11, N 11.09.

**$[Cu(L')(DMF)]\cdot(BF_4)_2\cdot DMF$ (5):** Cryptand **L** (0.68 g, 1 mmol), dissolved in dry DMF (3 mL) was added all at once to a DMF solution (3 mL) of $Cu(BF_4)_2\cdot xH_2O$ (0.23 g, 1.2 mmol) at room temperature. A blue-green solution was obtained that was filtered and the filtrate was stored at room temperature while the solvent evaporated. Blue-green, X-ray-quality, rectangular crystals of **5** appeared in about 7 d. Yield ca. 50% (0.55 g). $C_{45}H_{64}CuN_8O_9(BF_4)_2$ (1098.2): calcd. C 49.21, H 5.87, N 10.20; found C 49.44, H 5.99, N 10.38.

**X-ray Structural Studies:** Single-crystal X-ray data were collected at 100 K with a Bruker SMART APEX CCD diffractometer using graphite-monochromated Mo-$K_\alpha$ radiation ($\lambda$ = 0.71073 Å). The linear absorption coefficients, scattering factors for the atoms, and the anomalous dispersion corrections were taken from the International Tables for X-ray Crystallography. Data integration and reduction were processed with the SAINT[20] software. The structure was solved by direct methods using SHELXTL and was refined on $F^2$ by full-matrix least-squares techniques using the SHELXL-97 program[21] package. All non-hydrogen atoms were refined anisotropically except C(33) of compound **1**, which was refined isotropically. All hydrogen atoms were located in successive difference Fourier maps and they were treated as riding atoms by using SHELXL default parameters. The crystal data for the structures are collected in Tables 1 and 2. CCDC-290844 to -290850 contain the supplementary crystallographic data for this paper. These data can be obtained free of charge from The Cambridge Crystallographic Data Centre via www.ccdc.ac.uk/data_request/cif.

 © 2006 Wiley-VCH Verlag GmbH & Co. KGaA, Weinheim 

Table 2. Crystal data and structure refinement for $\mathbf{L_o}$, **L**, **1**–**5**.

| | $\mathbf{L_o}$ | **L** | **1** | **2** | **3** | **4** | **5** |
|---|---|---|---|---|---|---|---|
| Empirical formula | $C_{33}H_{45}NO_3$ | $C_{13}H_{14}NO_2$ | $C_{34}H_{48}AgN_6O_7$ | $C_{39}H_{48}AgN_9O_8$ | $C_{34}H_{49}ClN_5O_7Tl$ | $C_{39}H_{50}ClN_5O_8Tl$ | $C_{45}H_{64}B_2CuF_9N_8O_{10}$ |
| Formula mass | 559.74 | 258.28 | 760.65 | 878.73 | 879.59 | 998.31 | 1133.20 |
| $T$ [K] | 100 | 100 | 100 | 100 | 100 | 100 | 100 |
| Radiation | Mo-$K_\alpha$ | Mo-$K_\alpha$ | Mo-$K_\alpha$ | Mo-$K_\alpha$ | Mo-$K_\alpha$ | Mo-$K_\alpha$ | Mo-$K_\alpha$ |
| Wavelength [Å] | 0.71073 | 0.71073 | 0.71073 | 0.71073 | 0.71073 | 0.71073 | 0.71073 |
| Crystal system | triclinic | cubic | triclinic | monoclinic | triclinic | monoclinic | triclinic |
| Space group | $P\bar{1}$ | $Pa$-3 | $P\bar{1}$ | $P2_1/n$ | $P\bar{1}$ | $P2_1/n$ | $P\bar{1}$ |
| $a$ [Å] | 10.114(5) | 19.4675(6) | 9.6638(8) | 11.135(5) | 9.869(5) | 11.865(5) | 13.896(5) |
| $b$ [Å] | 11.823(5) | 19.4675(6) | 12.6337(10) | 19.080(5) | 13.036(5) | 19.239(5) | 16.210(5) |
| $c$ [Å] | 13.297(5) | 19.4675(6) | 13.8277(11) | 19.250(5) | 14.200(5) | 18.268(5) | 16.396(5) |
| $\alpha$ [°] | 106.953(5) | 90 | 86.2680(10) | 90 | 90.118(5) | 90 | 107.285(5) |
| $\beta$ [°] | 91.408(5) | 90 | 88.076(2) | 105.182(5) | 101.290(5) | 103.036(5) | 101.442(5) |
| $\gamma$ [°] | 91.032(5) | 90 | 86.9580(10) | 90 | 99.934(5) | 90 | 112.632(5) |
| $V$ [Å$^3$] | 1519.9(11) | 7377.9(4) | 1681.5(2) | 3947(2) | 1763.4(14) | 4063(2) | 3043.1(17) |
| $Z$ | 2 | 24 | 2 | 4 | 2 | 4 | 2 |
| $\rho_{calcd.}$ [mg·m$^{-3}$] | 1.223 | 1.248 | 1.502 | 1.479 | 1.687 | 1.633 | 1.199 |
| $\mu$ [mm$^{-1}$] | 0.079 | 0.083 | 0.657 | 0.575 | 4.713 | 4.103 | 0.435 |
| $F$ (000)[a] | 604 | 2960 | 794 | 1824 | 900 | 2008 | 1146 |
| Reflections collected | 9804 | 47225 | 11217 | 26186 | 11670 | 26621 | 20385 |
| Independent reflections | 7158 | 3065 | 7983 | 9756 | 8354 | 9905 | 14479 |
| Goof | 1.029 | 1.118 | 1.067 | 0.849 | 1.017 | 1.033 | 1.043 |
| Final $R$[b] indices | | | | | | | |
| $R_1$ | 0.0652 | 0.0759 | 0.0597 | 0.0577 | 0.0497 | 0.0331 | 0.0718 |
| $wR_2$ | 0.1482 | 0.1727 | 0.1428 | 0.1413 | 0.1296 | 0.0793 | 0.2219 |
| $R$ indices | | | | | | | |
| $R_1$ | 0.1280 | 0.0962 | 0.0689 | 0.0750 | 0.0542 | 0.0439 | 0.0927 |
| (all) $wR_2$ | 0.1746 | 0.1837 | 0.1486 | 0.1542 | 0.1327 | 0.0838 | 0.2072 |

[a] Refinement method: full-matrix least squares on $F^2$. [b] $R = \Sigma||F_o| - |F_c||/|F_o|$; $wR_2 = \Sigma[w(F_o^2 - F_c^2)^2]/\Sigma[w(F_o^2)^2]^{1/2}$.

## Acknowledgments

Financial support from the Department of Science and Technology, New Delhi, India (grant no. SR/S5/NM-38/2003 to P. K. B.) and an SRF (CSIR, New Delhi) to D. R. are gratefully acknowledged.

[1] a) J.-M. Lehn, *Supramolecular Chemistry – Concepts and Perspectives*, VCH Publishers, Weinheim, Germany, **1995**; b) J. Nelson, J. V. McKee, G. Morgan, *Prog. Inorg. Chem.* **1998**, *47*, 167–316; c) B. Sarkar, P. Mukhopadhyay, P. K. Bharadwaj, *Coord. Chem. Rev.* **2003**, *236*, 1–13.
[2] R. Geue, S. H. Jacobson, R. Pizer, *J. Am. Chem. Soc.* **1986**, *108*, 1150–1155.
[3] P. K. Bharadwaj, *Prog. Inorg. Chem.* **2003**, *51*, 251–331.
[4] P. Mukhopadhyay, B. Sarkar, P. K. Bharadwaj, K. Nättinen, K. Rissanen, *Inorg. Chem.* **2003**, *42*, 4955–4960.
[5] a) P. Ghosh, P. K. Bharadwaj, J. Roy, S. Ghosh, *J. Am. Chem. Soc.* **1997**, *119*, 11903–11909; b) P. Mukhopadhyay, P. K. Bharadwaj, G. Savitha, A. Krishnan, P. K. Das, *Chem. Commun.* **2000**, 1815–1816.
[6] B. P. Bag, P. K. Bharadwaj, *Inorg. Chem.* **2004**, *43*, 4626–4630.
[7] D. K. Chand, K. Ragunathan, P. K. Bharadwaj, *J. Org. Chem.* **1996**, *61*, 1169–1171.
[8] S. Scheiner, *Hydrogen Bonding: A Theoretical Perspective*, Oxford University Press, New York, **1997**.
[9] H. Matsuura, H. Yoshida, M. Hieda, S. Yamanaka, T. Harada, K. Shin-ya, K. Ohno, *J. Am. Chem. Soc.* **2003**, *125*, 13910–13911.
[10] R. Thaimattam, F. Xue, J. A. R. P. Sarma, T. C. W. Mak, G. R. Desiraju, *J. Am. Chem. Soc.* **2001**, *123*, 4432–4445.
[11] O. W. Howarth, G. G. Morgan, V. McKee, J. Nelson, *J. Chem. Soc., Dalton Trans.* **1999**, 2097–2102.
[12] J. de Mendoza, E. Mesa, J.-C. Rodriguez-Ubis, P. Vàzquez, F. Vögtle, P.-M. Windscheif, K. Rissanen, J.-M. Lehn, D. Lilienbaum, R. Ziessel, *Angew. Chem. Int. Ed. Engl.* **1991**, *30*, 1331–1333.
[13] T. Sato, A. Suziki, K. Sakai, T. Tsubomura, *Bull. Chem. Soc. Jpn.* **1996**, *69*, 379–388.
[14] a) P. I. Richards, A. Steiner, *Inorg. Chem.* **2004**, *43*, 2810–2817; b) N. Schultheiss, D. R. Powell, E. Bosch, *Inorg. Chem.* **2003**, *42*, 8886–8890; c) R. R. Fenton, P. C. Junk, R. Gauci, L. F. Lindoy, R. C. Luckay, G. V. Meehan, J. R. Price, P. Turner, G. Wei, *J. Chem. Soc., Dalton Trans.* **2002**, 2185–2193.
[15] a) H. V. R. Dias, S. Singh, T. R. Cundari, *Angew. Chem. Int. Ed.* **2005**, *44*, 4907–4910; b) O. W. Howarth, J. Nelson, V. Mckee, *Chem. Commun.* **2000**, 21–22; c) B. H. Hamilton, C. J. Ziegler, *Inorg. Chem.* **2004**, *43*, 4272–4277; d) E. Craven, E. Mutlu, D. Lundberg, S. Temizdemir, S. Dechert, H. Brombacher, C. Janiak, *Polyhedron* **2002**, *21*, 553–562; e) A. J. Amoroso, J. C. Jeffery, P. J. Jones, J. A. McCleverty, E. Psillakis, M. D. Ward, *J. Chem. Soc., Chem. Commun.* **1995**, 1175–1176; f) P. L. Jones, K. L. V. Mann, J. C. Jeffery, J. A. McCleverty, M. D. Ward, *Polyhedron* **1997**, *16*, 2435–2440.
[16] A.-V. Mudring, F. Rieger, *Inorg. Chem.* **2005**, *44*, 6240–6243.
[17] V. Yu. Kukushkin, A. J. L. Pombeiro, *Chem. Rev.* **2002**, *102*, 1771–1802.
[18] D. K. Chand, P. K. Bharadwaj, *Inorg. Chem.* **1996**, *35*, 3380–3387.
[19] F. A. Cotton, G. Wilkinson, *Advanced Inorganic Chemistry*, 5th ed., Wiley, New York, **1988**.
[20] SAINT+, 6.02ed., Bruker AXS, Madison, WI, **1999**.
[21] G. M. Sheldrick, *SHELXTL™ Reference Manual*, version 5.1, Bruker AXS, Madison, WI, **1997**.

Received: December 7, 2005
Published Online: March 1, 2006

 © 2006 Wiley-VCH Verlag GmbH & Co. KGaA, Weinheim 

DOI: 10.1002/ejic.200501126

# Phosphanylborohydrides: First Assessment of the Relative Lewis Basicities of $[BH_3PPh_2]^-$, $CH_3PPh_2$, and $HPPh_2$

**Franz Dornhaus,[a] Michael Bolte,[a] Hans-Wolfram Lerner,[a] and Matthias Wagner*[a]**

**Keywords:** P Ligands / Phosphanylborohydride / Ligand design / Donor–acceptor systems / Isoelectronic analogues

The compounds $K[PPh_2]$, $HPPh_2$, $CH_3PPh_2$, $BH_3(H)PPh_2$, $BBr_3(H)PPh_2$, $BH_3(CH_3)PPh_2$, $BBr_3(CH_3)PPh_2$, $[H_2PPh_2]I$, $[CH_3(H)PPh_2]I$, $[(CH_3)_2PPh_2]I$, and $K[(BH_3)_2PPh_2]$ have been investigated by NMR spectroscopy. In addition, X-ray crystal structures have been determined for K(18-crown-6)$[PPh_2]$, $BBr_3(H)PPh_2$, $BBr_3(CH_3)PPh_2$, $[H_2PPh_2]I$, $[CH_3(H)PPh_2]I$, $[(CH_3)_2PPh_2]I$, and K(18-crown-6)$[(BH_3)_2PPh_2]$. An evaluation of coupling constants (e.g. $^1J_{PC_i}$; $C_i$ = *ipso* carbon atom of a phenyl ring) augmented by an inspection of key structural parameters (e.g. the angles $C_i$–P–$C_i'$) leads to the conclusion that dative bonds originating from ligand $[BH_3PPh_2]^-$ possess a significantly higher p character than dative bonds involving the ligands $HPPh_2$ and $CH_3PPh_2$. The $^1J_{PB}$ values obtained for $BH_3(H)PPh_2$, $BH_3(CH_3)PPh_2$, and $[(BH_3)_2PPh_2]^-$ suggest $[BH_3PPh_2]^-$ to form the strongest $[BH_3]$ adduct of all three compounds which is in agreement with the results of displacement reactions employing the couples $CH_3PPh_2$/$[(BH_3)_2PPh_2]^-$ and $[BH_3PPh_2]^-$/$BH_3(CH_3)PPh_2$.
(© Wiley-VCH Verlag GmbH & Co. KGaA, 69451 Weinheim, Germany, 2006)

## Introduction

Organophosphanes have been extensively studied as ligands to both main group Lewis acids and transition metals in order to unveil the factors governing the stability and reactivity of coordination complexes.[1] In the course of these studies it soon became apparent that phosphanes may not generally be viewed as simple σ donors because often an intricate interplay exists between the P → M σ interaction and an M → ligand π back-donation. The π acceptor strength of $PF_3$, for example, is comparable to that of CO, commonly regarded as the archetypical π acceptor ligand. If, on the other hand, electropositive substituents are attached to the phosphorus atom, one would expect an increase in Lewis basicity likely together with a decrease in π acidity of the respective phosphane molecule. One way to test this assumption is through replacement of alkyl groups on phosphorus by borane moieties. Using parent $[BH_3]$, we thereby arrive at a class of anionic species $[BH_3PRR']^-$ which are the heavier homologues of the better-known aminoborohydrides $[BH_3NRR']^-$.[2] Until today, phosphanylborohydrides $[BH_3PRR']^-$ have mainly been generated in situ and used as building blocks for the preparation of chiral organophosphanes.[3–6] Moreover, aiming at the synthesis of polymeric materials involving group 13 and group 15 elements, Manners and co-workers have recently employed the compound $Li[BH_3PPh_2]$ in the preparation of linear hybrid aminoborane/phosphanylborane chains.[7] The same group has also reported on the synthesis of the platinum phosphanylborohydride complexes *trans*-$[PtH(BH_3PPhR)(PEt_3)_2]$ (R = H, Ph) by the regioselective insertion of the $Pt(PEt_3)_2$ fragment into the P–H bond of $BH_3(H)_2PPh$ or $BH_3(H)PPh_2$.[8] Other examples of structurally characterised phosphanylborohydride complexes include the compounds $[(dppp)Pd(C_6F_5)(BH_3PPh_2)]$[9] and $[(C_5Me_5)Fe(CO)_2(BH_3PPh_2)]$.[10] Finally, Müller et al. have explored the complexation potential of $[BH_3P(CH_3)_2]^-$ and $[BH_3P(Ph)tBu]^-$ toward lithium and aluminium.[11]

In a 1996 paper, Fu et al. described diphenylphosphidoboratabenzene, $[(BC_5H_5)PPh_2]^-$, as anionic analogue of the ubiquitous triphenylphosphane ligand and explored its coordination chemistry.[12] Stimulated by their investigations, our group embarked on a systematic study of the ligand properties of anionic phosphanylborohydrides $[BH_3PRR']^-$ in comparison to their neutral isoelectronic and isostructural methyl analogues $CH_3PRR'$. For a start, we are focusing on compounds in which the phosphorus atom is exclusively engaged in σ bonds. Effects of π bonding will be considered at a later stage. All compounds under investigation here are based on the $PPh_2$ fragment (Figure 1). The series of derivatives starts with the $[PPh_2]^-$ ion ($K[PPh_2]$, **1**) and continues with the phosphanes $HPPh_2$ (**2**) and $H_3CPPh_2$ (**3**), followed by their complexes with the main group Lewis acids $[BH_3]$, $H^+$, and $[CH_3]^+$ (cf. **4H**, **5H**, and **6**–**8**). As we were not able to grow X-ray quality crystals of the $[BH_3]$ adducts **4H** and **5H**, the corresponding $BBr_3$ ad-

[a] Institut für Anorganische Chemie, Johann Wolfgang Goethe-Universität Frankfurt am Main,
Marie-Curie-Straße 11, 60439 Frankfurt, Germany
Fax: +49-69-798-29260
E-mail: Matthias.Wagner@chemie.uni-frankfurt.de
Supporting information for this article is available on the WWW under http://www.eurjic.org or from the author.

 © 2006 Wiley-VCH Verlag GmbH & Co. KGaA, Weinheim 

ducts **4Br** and **5Br** were structurally characterised instead. The series closes with the anionic species $K[(BH_3)_2PPh_2]$ (**9**).

| | | | |
|---|---|---|---|
| $K[PPh_2]$ | $HPPh_2$ | $CH_3PPh_2$ | $BH_3(H)PPh_2$ |
| **1** | **2** | **3** | **4H** |
| $BBr_3(H)PPh_2$ | $BH_3(CH_3)PPh_2$ | $BBr_3(CH_3)PPh_2$ | |
| **4Br** | **5H** | **5Br** | |
| $[H_2PPh_2]I$ | $[CH_3(H)PPh_2]I$ | $[(CH_3)_2PPh_2]I$ | $K[(BH_3)_2PPh_2]$ |
| **6** | **7** | **8** | **9** |

Figure 1. The potassium phosphide **1**, the phosphanes **2**, **3**, and the phosphane adducts **4**–**9**.

With this selection of molecules it is possible to study systematic trends in NMR- and structural parameters (i) upon increasing the coordination number of phosphorus from two to three and four (e.g. $[PPh_2]^-$ vs. $HPPh_2$ vs. $[H_2PPh_2]^+$) and (ii) by comparing isoelectronic and isostructural species of different charge (e.g. $[(BH_3)_2PPh_2]^-$ vs. $[(CH_3)_2PPh_2]^+$). It is to be mentioned that some of the compounds under investigation here are already known in the literature (see below). However, crystal structure analyses were missing and even though selected NMR spectroscopic data have been reported, measurement conditions vary to such an extent that a re-investigation using the same solvent and (in the case of **6**–**8**) counterion was inevitable, because these can greatly influence the chemical shift values.[13]

## Results and Discussion

**Syntheses:** $K[PPh_2]$ (**1**) was prepared through deprotonation of $HPPh_2$ (**2**) with potassium metal in THF. $BH_3(H)PPh_2$ (**4H**) is accessible from $HPPh_2$ (**2**) and $B_2H_6$.[14] However, we preferred to use a calibrated solution of $BH_3$·THF in THF which is more convenient to handle. $BBr_3(H)PPh_2$ (**4Br**) was synthesised from $HPPh_2$ (**2**) and $BBr_3$ following a published procedure.[14] $BH_3(CH_3)PPh_2$ (**5H**) is formed similar to $BH_3(H)PPh_2$ (**4H**) upon treatment of $CH_3PPh_2$ (**3**) with $BH_3$·THF in THF (Manners et al. have used $BH_3$·$SMe_2$ instead[7]). An alternative route to **5H** employs $ClPPh_2$ as starting material which is first methylated with MeMgI and subsequently borylated with $NaBH_4/I_2$.[15] $BBr_3(CH_3)PPh_2$ (**5Br**) was synthesised from $CH_3PPh_2$ (**3**) and $BBr_3$ following a published procedure.[16] The phosphonium iodide salts $[H_2PPh_2]I$ (**6**) and $[CH_3(H)PPh_2]I$ (**7**) were prepared by treatment of $HPPh_2$ (**2**) and $CH_3PPh_2$ (**3**) with excess HI in toluene; for the syntheses of $[CH_3(H)PPh_2]Br$ and $[(CH_3)_2PPh_2]I$ (**8**) see refs.[17,18] The synthesis of $K[(BH_3)_2PPh_2]$ was accomplished by deprotonation of $BH_3(H)PPh_2$ (**4H**) with KH and subsequent addition of $BH_3$·THF in THF.

In the following, all compounds under investigation will be viewed as adducts between the Lewis bases $HPPh_2$ (**2**), $CH_3PPh_2$ (**3**), and $[BH_3PPh_2]^-$ with the Lewis acids $H^+$, $[BH_3]$, $BBr_3$, and $[CH_3]^+$.

**X-ray Crystallography:** Single crystals of the potassium salts **1** and **9** were obtained only after potassium complexation with 18-crown-6. The compounds K(18-crown-6)$[PPh_2]$ and K(18-crown-6)$[(BH_3)_2PPh_2]$ will be referred to as **1c** and **9c**, respectively. Selected bond lengths and angles of compounds **1c**, **4Br**, **5Br**, **6**, **7**, **8**, and **9c** are compiled in Table 1.

The potassium diphenylphosphide K(18-crown-6)$[PPh_2]$ (**1c**) crystallises from THF in the monoclinic space group $P2_1/n$ (Figure 2).

The asymmetric unit of **1c** contains two formula units and features diphenylphosphide anions in distinctly different chemical environments: The first $[PPh_2]^-$ fragment coordinates to two potassium counterions with bond lengths P(1)–K(1) and P(1)–K(1A) of 3.347(1) Å and 3.267(1) Å, respectively (sum of the ionic radius of $K^+$ and the van-der-Waals radius of phosphorus: 3.55 Å[19]). Each potassium centre is encapsulated by one crown ether ligand; in addition, a relatively short intermolecular contact is established between K(1A) and one phenyl ring [K(1A)···C(25A) = 3.518(2) Å]. The bond angles around the phosphorus atom P(1) cover the wide range from 84.0(1)° for C(21)–P(1)–K(1A) to 150.1(1)° for K(1)–P(1)–K(1A). However, the angle defined by the two phenyl *ipso*-carbon atoms and the phosphorus atom is close to the ideal tetrahedral angle of 109.5° [C(21)–P(1)–C(31) = 107.1(1)°]. A largely two-coordinate phosphorus atom is found in the second $[PPh_2]^-$ ion [shortest P(1A)···K contact: 5.918 Å]. Nevertheless, both the P–$C_i$ bond lengths ($C_i$ = *ipso* carbon atom of a phenyl ring) and the $C_i$–P–$C_i'$ bond angles of the two different $PPh_2$ fragments are almost identical within experimental error [C(21A)–P(1A)–C(31A) = 108.3(1)°; Table 1]. Two other adducts of $K[PPh_2]$ have previously been characterised, the *N*,*N*,*N*′,*N*′′,*N*′′-pentamethyldiethylenetriamine complex $\{K(pmdta)[PPh_2]\}_n$[20] and the 1,4-dioxane complex $\{K(dioxane)_2[PPh_2]\}_n$.[21] Most notably, Eaborn, Smith

Table 1. Key structural parameters of compounds **1c**, **4Br**, **5Br**, **6**, **7**, **8**, and **9c**.

| | | P–B | P–$C_i$ | P–$CH_3$ | $C_i$–P–$C_i'$ |
|---|---|---|---|---|---|
| **1c** | K(18-c-6)$[PPh_2]$ | – | 1.811(2)/1.815(2)[a] | – | 107.1(1)[a] |
| | | – | 1.807(2)/1.817(2)[b] | – | 108.3(1)[b] |
| **4Br** | $BBr_3(H)PPh_2$ | 1.965(4) | 1.803(4)/1.805(4) | – | 110.8(2) |
| **5Br** | $BBr_3(CH_3)PPh_2$ | 1.976(9) | 1.801(11)/1.810(10) | 1.814(11) | 106.5(5) |
| **6** | $[H_2PPh_2]I$ | – | 1.794(2)/1.798(2) | – | 109.6(1) |
| **7** | $[CH_3(H)PPh_2]I$ | – | 1.796(3)/1.797(3) | 1.798(3) | 110.8(1) |
| **8**[18] | $[(CH_3)_2PPh_2]I$ | – | 1.794(3) | 1.782(3) | 107.6(2) |
| **9c** | K(18-c-6)$[(BH_3)_2PPh_2]$ | 1.930(2)/1.940(2) | 1.829(2)/1.831(2) | – | 100.2(1) |

[a] Coordinated $[PPh_2]$ unit. [b] Non-coordinated $[PPh_2]$ unit.

 © 2006 Wiley-VCH Verlag GmbH & Co. KGaA, Weinheim 

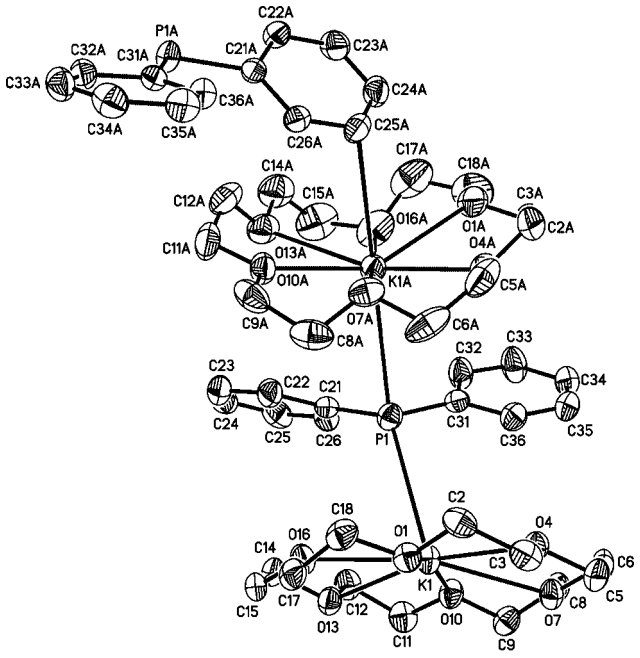


Figure 2. Molecular structure and numbering scheme of compound **1**[c]; thermal ellipsoids shown at the 50% probability level; hydrogen atoms omitted for clarity. Selected bond lengths [Å] and bond angles [°]: P(1)–C(21) = 1.815(2), P(1)–C(31) = 1.811(2), P(1A)–C(21A) = 1.817(2), P(1A)–C(31A) = 1.807(2), P(1)–K(1) = 3.347(1), P(1)–K(1A) = 3.267(1), K(1A)···C(25A) = 3.518(2); C(21)–P(1)–K(1A) = 84.0(1), K(1)–P(1)–K(1A) = 150.1(1), C(21)–P(1)–C(31) = 107.1(1), C(21A)–P(1A)–C(31A) = 108.3(1).

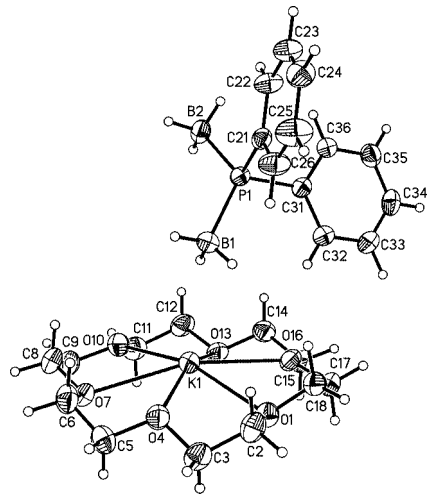


Figure 3. Molecular structure and numbering scheme of compound **9**[c]; thermal ellipsoids shown at the 50% probability level. Selected bond lengths [Å] and bond angles [°]: P(1)–B(1) = 1.930(2), P(1)–B(2) = 1.940(2), P(1)–C(21) = 1.829(2), P(1)–C(31) = 1.831(2), C(34)–K(1)$^{\#}$ = 3.372(2), K(1)–H(1A) = 2.683, K(1)···H(1B) = 3.452, K(1)–H(1C) = 3.003, B(1)···K(1) = 3.205; B(1)–P(1)–B(2) = 116.3(1), C(21)–P(1)–C(31) = 100.2(1). Symmetry transformation used to generate equivalent atoms: $x$, $-y + 1/2$, $z - 1/2$ ($^{\#}$).

et al.[22] have determined the crystal structure of solvent-free $\{K[PPh_2]\}_n$ which contains seven molecules in the asymmetric unit.

ORTEP drawings of the molecular structures of the boron–phosphorus adducts $(BBr_3)HPPh_2$ (**4Br**) and $BBr_3(CH_3)PPh_2$ (**5Br**) as well as of the phosphonium salts $[H_2PPh_2]I$ (**6**), $[CH_3(H)PPh_2]I$ (**7**), and $[(CH_3)_2PPh_2]I$ (**8**)[18,23] can be found in the Supporting Information. In all these compounds, the phosphorus atom is surrounded by four substituents. Important bond lengths and angles for comparison are listed in Table 1. In the case of **6** and **7**, the iodide ions are part of a complex network of P–H···I and Ph–H···I hydrogen bridges.

The phosphanylborohydride adduct K(18-crown-6)-$[(BH_3)_2PPh_2]$ (**9**[c]) crystallises in the monoclinic space group $P2_1/c$ (Figure 3).

Each $K^+$ ion is complexed by six oxygen atoms of a crown ether molecule and establishes two short and one significantly longer contact to the hydrogen atoms of one $[BH_3]$ fragment [K(1)–H(1A) = 2.683 Å, K(1)–H(1C) = 3.003 Å, K(1)···H(1B) = 3.452 Å]. Using Edelstein's correlation[24] of metal–boron distances as a measure of the denticity of borohydride groups, values of 1.6 ± 0.1 Å and 1.36 ± 0.06 Å are estimated for the ionic radii of bidentate and tridentate borohydride ligands, respectively. Thus, B···K distances of about 3.25 Å and 3.01 Å are to be expected for K-$\mu_2$-$BH_3R$ and K-$\mu_3$-$BH_3R$ coordination modes (ionic radius of octacoordinated $K^+$ = 1.65 Å[25]). Since the B(1)···K(1) distance in **9**[c] amounts to 3.205 Å, it may be concluded that $[(BH_3)_2PPh_2]^-$ acts as bidentate ligand toward the potassium cation which is the most common binding mode in metal borohydrides.[24] Further short contacts between the phenyl carbon atom C(34) and the neighbouring potassium ion K(1)$^{\#}$ [C(34)–K(1)$^{\#}$ = 3.372(2) Å] stabilize the molecular packing as zig-zag chains in the crystal lattice (Figure 4).

Looking at the series of compounds **1**[c], **4Br**, **5Br**, **6**, **7**, **8**, and **9**[c], it is our goal to find out whether differences in the electron-density distribution at phosphorus can be correlated to systematic trends in the key structural parameters of these molecules (cf. Table 1). To this end we are considering the P–$C_i$ bond lengths and the $C_i$–P–$C_i'$ bond angles of the $PPh_2$ fragments first. According to Bent's rule,[26] a tetracoordinate atom A directs hybrids of greater p character toward more electronegative substituents S and S′ which in turn leads to smaller S–A–S′ bond angles. In this context, lone pairs on atoms not involved in multiple bonds are in a first approximation viewed as residing in tetrahedral hybrid orbitals. Deviations from perfect $sp^3$ hybridisation that occur are in a direction that concentrates s character in the lone-pair orbitals. This effect normally becomes more pronounced as the number of unshared electron pairs about the heavy atom increases.[26]

The $K^+$-coordinated $[PPh_2]^-$ ion of **1**[c] shows a more acute $C_i$–P–$C_i'$ angle [107.1(1)°] than the free $[PPh_2]^-$ ion [108.3(1)°], however, the actual difference of 1.2(1)° is very small. One reason for this seeming violation of Bent's rule could be that the interaction of P(1) with the two potassium ions is merely electrostatic in nature and thus has no pronounced effect on the orbital composition of the phosphorus atom. In the case of the two $BBr_3$ adducts **4Br** and **5Br**,

 © 2006 Wiley-VCH Verlag GmbH & Co. KGaA, Weinheim 

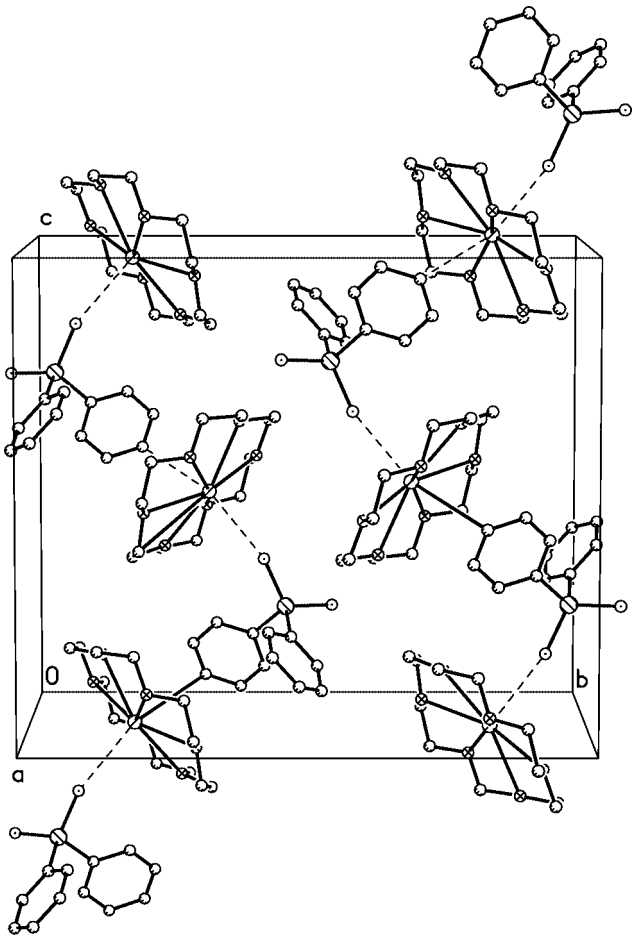


Figure 4. Crystal packing diagram of compound **9c**.

we find a significantly smaller $C_i$–P–$C_i'$ angle for the methyl derivative [**4Br**: 110.8(2)°, **5Br**: 106.5(5)°]. Given the well-known positive inductive effect of the $CH_3$ substituent, this indicates a higher p character in the P–Ph bonds of **5Br** than in those of **4Br**. Within the series **6** → **7** → **8**, only small differences between the individual $C_i$–P–$C_i'$ angles are observed, which, moreover, do not follow a systematic trend since the respective angle in the mixed compound **7** does not interpolate that of the doubly protonated molecule **6** and the doubly methylated compound **8**. By far the most pronounced deviation of $C_i$–P–$C_i'$ from the ideal tetrahedral angle is observed in the adduct K(18-crown-6)-$[(BH_3)_2PPh_2]$ (**9c**). In line with Bent's rule, the value of 100.2(1)°, as compared to 107.6(2)° in $[(CH_3)_2PPh_2]I$ (**8**), points towards a high degree of p character in the P–$C_i$ bond orbitals of **9c**. This interpretation is supported by the fact that the corresponding P–$C_i$ bond lengths are significantly elongated [cf. **9c**: 1.829(2) Å/1.831(2) Å; **8**: 1.794(3) Å]. In contrast to a priori expectations, they are even longer and the $C_i$–P–$C_i'$ angle is more acute than in the potassium phosphide **1** [1.807(2) Å to 1.817(2) Å; average value for $C_i$–P–$C_i'$: 107.7°].

**NMR Spectroscopy:** The most characteristic NMR parameters of the compounds **1**–**9** are compiled in Table 2.

For comparability and solubility reasons, all NMR spectra were run at ambient temperature (300 K). However, as $[H_2PPh_2]I$ (**6**) appeared to be largely dissociated in $CDCl_3$ solution under these conditions, the compounds **6** and **7** have also been investigated at low temperature (233 K) in order to shift the dissociation–association equilibrium to the adduct side (low-temperature data included in Table 2). In order to assess the relative degree of s and p character in the P–E bonding orbitals (E = H, C, B), we will mainly rely on the corresponding $^1J_{PE}$ coupling constants. Common wisdom has it that NMR coupling constants via a certain bond are governed by the Fermi contact term, which increases with increasing s character of the respective bond. We are aware of the fact that $^1J_{PE}$ values may change their sign upon going from one compound to another. In such cases, a correlation of $^1J_{PE}$ with the s character of the P–E bond is not possible until the signs of the coupling constants are known. We have not determined any relative sign data, however, it is firmly established in the literature that $^1J_{PB}$ coupling constants in phosphane–boranes[27] as well as $^1J_{PH}$ coupling constants[28] are generally positive. $^1J_{PC}$ coupling constants tend to be negative in three-coordinate phosphanes (cf. $PPh_3$: $^1J_{PC}$ = –12.5 Hz) and positive in compounds containing four-coordinate phosphorus centres (cf. $[PPh_4]^+$: $^1J_{PC}$ = +88.4 Hz).[28] For a detailed description

Table 2. Selected NMR parameters of compounds **1**–**9**; solvents: THF (**1**–**5Br**, **9**), $CDCl_3$ (**6**–**8**); upfield shifts are denoted by a minus sign and downfield shifts by a plus sign.

| | | Chemical shift values [ppm] ($^1J_{PX}$ [Hz]) | | | | |
|---|---|---|---|---|---|---|
| | Nucleus | $^{31}P$ | $^{11}B$ ($^1J_{PB}$) | P–$^1H$ ($^1J_{PH}$) | P–$^{13}C_i$ ($^1J_{PC}$) | P–$^{13}CH_3$ ($^1J_{PC}$) |
| **1** | $K[PPh_2]$ | –9.8 | – | – | 157.1 (56.0) | – |
| **2** | $HPPh_2$ | –39.5 | – | 5.11 (215.7) | 135.4 (10.7) | – |
| **3** | $CH_3PPh_2$ | –26.1 | – | – | 140.8 (10.0) | 12.9 (12.0) |
| **4H** | $BH_3(H)PPh_2$ | 1.7 | –40.0 (42) | 6.16 (380.8) | 127.6 (56.2) | – |
| **4Br** | $BBr_3(H)PPh_2$ | –13.6 | –17.1 (142) | 6.97 (444.4) | 121.3 (65.7) | – |
| **5H** | $BH_3(CH_3)PPh_2$ | 11.5 | –37.9 (55) | – | 131.9 (54.8) | 11.4 (40.0) |
| **5Br** | $BBr_3(CH_3)PPh_2$ | –9.2 | –14.6 (150) | – | 124.2 (68.2) | 7.1 (48.7) |
| **6** | $[H_2PPh_2]I$ | –31.0[a] | – | 9.91 (530.6)[a] | 128.0 (83.0)[a] | – |
| **7** | $[CH_3(H)PPh_2]I$ | –5.2[a] | – | 9.87 (521.7)[a] | 115.9 (85.4)[a] | 7.1 (53.8)[a] |
| **8** | $[(CH_3)_2PPh_2]I$ | 21.9 | – | – | 120.5 (87.6) | 11.4 (56.4) |
| **9** | $K[(BH_3)_2PPh_2]$ | –11.1 | –34.6 (64) | – | 140.2 (38.5) | – |

[a] Recorded at 233 K.

 © 2006 Wiley-VCH Verlag GmbH & Co. KGaA, Weinheim 

of the effect of electron lone pairs on nuclear spin–spin coupling constants, the reader is referred to the work of Gil and Philipsborn.[29]

At first, we are considering systematic changes in the NMR parameters of the three Lewis bases $HPPh_2$ (**2**), $CH_3PPh_2$ (**3**), and $[BH_3PPh_2]^-$ upon variation of the coordinated acid. Drake et al. have determined the P–H proton chemical shifts for five series of $BX_3$–P(H)RR′ adducts (R/R′ = H/H, $CD_3$/H, $CD_3$/$CD_3$, Ph/H, Ph/Ph; X = F, Cl, Br, I).[14] As a general trend within any of the five groups, the shielding of the proton on phosphorus was found to decrease in a manner parallel to the accepted order of Lewis acidity ($BF_3 < BCl_3 < BBr_3 < BI_3$). Consistently, we observe a downfield shift of the P–*H* resonance along the series $P(H)Ph_2$ (**2**; $\delta$ = 5.11) → $BH_3$–P(H)$Ph_2$ (**4H**; $\delta$ = 6.16) → $BBr_3$–P(H)$Ph_2$ (**4Br**; $\delta$ = 6.97) → $[CH_3$–P(H)$Ph_2]^+$ (**7**; $\delta$ = 9.87) → $[H$–P(H)$Ph_2]^+$ (**6**; $\delta$ = 9.91). Parallel to that, $^1J_{PH}$ becomes larger, thereby indicating an increasing degree of s character in the P–H bond. Moreover, the absolute value of the coupling constant $^1J_{PCi}$ between phosphorus and the *ipso* carbon atoms of the attached phenyl rings also increases in the same order: **2** (10.7 Hz) < **4H** (56.2 Hz) < **4Br** (65.7 Hz) < **7** (85.4 Hz) ≈ **6** (83.0 Hz). A similar trend in the $^1J_{PC}$ values of the P–$CH_3$ and the P–Ph fragments is evident within the series of methylphosphane adducts: **3** < **5H** < **5Br** < **7** < **8** (Table 2). Thus, there is obviously an increase in s character in the P–H and P–C bonding orbitals of **2** and **3** upon adduct formation. Concomitantly, an increase in the p character of the phosphorus lone pair has to be postulated as it becomes involved in dative bonding. In line with the isovalent hybridisation hypothesis,[26] the p character of the donor-acceptor bond is more pronounced when more Lewis acidic electrophiles are coordinated. Of special interest is an evaluation of the characteristic NMR parameters of the isoelectronic donors $P(CH_3)Ph_2$ (**3**) and $[P(BH_3)Ph_2]^-$ after coordination of $[BH_3]$, $H^+$, and $[CH_3]^+$, respectively. As far as the $^{31}P$–$^{13}C_i$ coupling constants are concerned, we obtain qualitatively similar results for both ligands with $^1J_{PCi}$ being consistently smaller in the $[BH_3]$ adducts as compared to the protonated or methylated derivatives {cf. $K[BH_3$–P(B$H_3$)$Ph_2]$ (**9**), H–P(B$H_3$)$Ph_2$ (**4H**), $CH_3$–P(B$H_3$)$Ph_2$ (**5H**): $^1J_{PCi}$ = 38.5 Hz, 56.2 Hz, 54.8 Hz; $BH_3$–P(C$H_3$)$Ph_2$ (**5H**), $[H$–P(C$H_3$)$Ph_2]$I (**7**), $[CH_3$–P(C$H_3$)$Ph_2]$I (**8**): $^1J_{PCi}$ = 54.8 Hz, 85.4 Hz, 87.6 Hz}.

The $^{31}P$ NMR resonances within the series $P(H)Ph_2$ (**2**), $BH_3$–P(H)$Ph_2$ (**4H**), $BBr_3$–P(H)$Ph_2$ (**4Br**), and $[CH_3$–P(H)$Ph_2]$I (**7**) possess chemical shift values of $\delta$ = –39.5 ppm, 1.7 ppm, –13.6 ppm, and –5.2 ppm, respectively (Table 2). This observation is in agreement with the known fact that in most cases quaternisation of phosphanes leads to a downfield shift of the $^{31}P$ NMR signal as the shielding effect of the lone pair is removed.[13] Deshielding is most pronounced after coordination of the isoelectronic and isosteric Lewis acids $[BH_3]$ and $[CH_3]^+$. Adduct formation of $P(H)Ph_2$ with $BBr_3$ leads to a smaller downfield shift. Within the series of $P(CH_3)Ph_2$ adducts, the following $^{31}P$ NMR shifts are observed (Table 2): **3** ($\delta$ = –26.1), **5H** ($\delta$ = 11.5), **5Br** ($\delta$ = –9.2), **8** ($\delta$ = 21.9). Thus, substitution of P–*CH*$_3$ for P–*H* results in a general deshielding of the respective $^{31}P$ nucleus. The isosteric couples **4H/7**, **5H/8**, and **8/9** deserve special attention. The $^{31}P$ NMR resonance of H–P(B$H_3$)$Ph_2$ (**4H**) is shifted by 6.9 ppm to lower field as compared to the resonance of $[H$–P(C$H_3$)$Ph_2]$I (**7**). However, this order is reversed and the absolute difference increases ($\Delta\delta$ = –10.4) in the case of $CH_3$–P(B$H_3$)$Ph_2$ (**5H**; $\delta$ = 11.5) vs. $[CH_3$–P(C$H_3$)$Ph_2]$I (**8**; $\delta$ = 21.9). Finally, the largest shift difference ($\Delta\delta$ = –33.0) is found between $K[BH_3$–P(B$H_3$)-$Ph_2]$ (**9**; $\delta$ = –11.1) and $[CH_3$–P(C$H_3$)$Ph_2]$I (**8**; $\delta$ = 21.9).

$^{11}B$ NMR spectroscopy reveals a slight downfield shift of the boron nucleus upon going from **4H** ($\delta$ = –40.0) to **5H** ($\delta$ = –37.9) and **9** ($\delta$ = –34.6). A qualitatively similar effect is observed for the couple **4Br/5Br** (Table 2).

In the second stage, we will now consider three groups of aggregates of the ligands $P(H)Ph_2$ (**2**), $P(CH_3)Ph_2$ (**3**), and $[P(BH_3)Ph_2]^-$ in which the Lewis acid is kept constant (Figure 5). Special emphasis is placed on the $^1J_{DA}$ coupling constants (D and A = donor and acceptor nuclei, respectively) because they are a property of the donor–acceptor bond in question and thus likely to provide insight into the relative base strengths of the three phosphorus donors. The proton adducts (series a, Figure 5) show similar $^1J_{PH}$ values for the $P(H)Ph_2$ and $P(CH_3)Ph_2$ ligand and a much smaller value in H–P(B$H_3$)$Ph_2$. The same is true for $^1J_{PC}$ in the $[CH_3]^+$ adducts of series b (Figure 5).

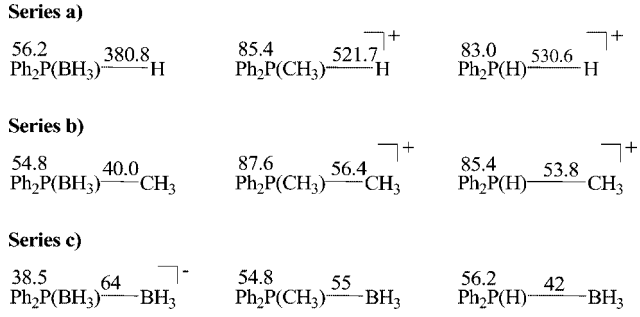


Figure 5. Systematic trends in the $^1J_{DA}$ and $^1J_{PCi}$ coupling constants along three series of $[P(BH_3)Ph_2]^-$, $P(CH_3)Ph_2$, and $P(H)Ph_2$ adducts.

Thus, compared to the neutral phosphane ligands, $[P(BH_3)Ph_2]^-$ is able to provide an electron pair of higher p character such that the charge density is more strongly polarized in the direction of the acceptor orbital. This interpretation most likely holds also for the $[BH_3]$ adducts of series c (Figure 5) even though $^{31}P$–$^{11}B$ coupling via the dative bond is now *larger* in $K[BH_3$–P(B$H_3$)$Ph_2]$ (**9**) and *smaller* in $BH_3$–P(H)$Ph_2$ (**4H**), and $BH_3$–P(C$H_3$)$Ph_2$ (**5H**). Here, the decisive factor is the rehybridisation of $[BH_3]$ as it moves from a planar $sp^2$ configuration to a tetrahedral $sp^3$ arrangement. As a consequence, we are facing two opposing trends:[14] When phosphane forms an adduct, the phosphorus orbital involved in bond formation decreases in s character. On the other hand, the stronger the donor-acceptor interaction, the more pyramidalized the coordinated borane which in turn results in more B(2s) character being diverted into the P–B bond. Despite of the fact that

 © 2006 Wiley-VCH Verlag GmbH & Co. KGaA, Weinheim 

a quantitative assessment of these two competing factors is obviously difficult, an empirical correlation between the magnitude of $^1J_{PB}$ and dative bond strength became evident from several studies on [$BH_3$] adducts of selected series employing smoothly varying phosphane ligands.[14,30–32] Based on the development of $^1J_{PB}$ coupling constants along the sequence **4H** (42 Hz), **5H** (55 Hz), and **9** (64 Hz) we therefore confidently assign the highest Lewis basicity to the phosphanylborohydride ligand $[P(BH_3)Ph_2]^-$ (note that for $Li[(BH_3)_2P(CH_3)_2]$ a coupling constant $^1J_{PB}$ = 107 Hz has been published,[33] which is even larger than $^1J_{PB}$ of **9**).

To test this hypothesis, two displacement experiments have been carried out and monitored by $^{31}P$ NMR spectroscopy. First, we investigated an equimolar mixture of $K[(BH_3)_2PPh_2]$ (**9**) and $CH_3PPh_2$ (**3**) in THF. Even after prolonged storage of the NMR vessel at ambient temperature, no transfer of [$BH_3$] with formation of $K[BH_3PPh_2]$ and $BH_3(CH_3)PPh_2$ (**5H**) was observable. The result remained the same at higher temperatures. In contrast, between $BH_3(CH_3)PPh_2$ (**5H**) and $K[BH_3PPh_2]$ a reaction to $CH_3PPh_2$ (**3**) and $K[(BH_3)_2PPh_2]$ (**9**) takes place already at ambient temperature (ca. 10% conversion after 2 d). Heating of the sample to a temperature of 50 °C for 2 h leads to ca. 50% conversion.

## Conclusion

Based on NMR spectroscopy ($^1J_{PB}$ values) and displacement experiments we come to the conclusion that the phosphanylborohydride ligand $[BH_3PPh_2]^-$ possesses a higher Lewis basicity towards [$BH_3$] than its neutral isoelectronic and isostructural congener $P(CH_3)Ph_2$. Moreover, NMR spectroscopy ($^1J_{PB}$, $^1J_{PH}$, and $^1J_{PCi}$ values) and X-ray crystallography ($C_i$–P–$C_i'$ angles; $C_i$ = *ipso* carbon atom of the phenyl ring) on selected adducts of the ligands $HPPh_2$, $CH_3PPh_2$, and $[BH_3PPh_2]^-$ indicate $[BH_3PPh_2]^-$ to form dative bonds of the highest p character within this series. Consequently, $[BH_3PPh_2]^-$ is best suited to direct the charge density of its electron lone pair in the direction of the acceptor orbital of a coordinated Lewis acid.

## Experimental Section

**General Considerations:** All reactions and manipulations of air-sensitive compounds were carried out under dry nitrogen using standard Schlenk techniques. Solvents were freshly distilled under argon from sodium/benzophenone (THF, diethyl ether, toluene) or sodium-lead alloy (pentane, hexane) prior to use. NMR spectra were recorded with Bruker AMX 250 or AMX 400 spectrometers. Approximately 0.1 mL of $C_6D_6$ was added to all samples recorded in undeuterated THF (0.6 mL) to provide a lock signal. $^1H$- and $^{13}C$ NMR shifts are reported relative to tetramethylsilane and were referenced against residual solvent peaks ($C_6D_5H$: $\delta$ = 7.16, $C_6D_6$: $\delta$ = 128.06; $CHCl_3$: $\delta$ = 7.26, $CDCl_3$: $\delta$ = 77.16 ppm).[34] $^{11}B$ NMR spectra were referenced against external $BF_3{\cdot}OEt_2$. $^{31}P$ NMR spectra are reported relative to external $H_3PO_4$ (85%). Abbreviations: s = singlet, d = doublet, tr = triplet, vtr = virtual triplet, q = quartet, dq = doublet of quartets, m = multiplet, br. = broad, n.o. = signal not observed, *i* = *ipso*, *o* = *ortho*, *m* = *meta*, *p* = *para*. Elemental analyses were performed by the microanalytical laboratory of the J. W. Goethe University, Frankfurt/Main, Germany.

**Materials:** Lithium and potassium metal, $PPh_3$, $CH_3PPh_2$ (**3**), $BH_3{\cdot}THF$ solution (1 mol/ L in THF) and 18-crown-6 were purchased from Aldrich or Fluka and used as received. $HPPh_2$ (**2**) was obtained through reductive cleavage of triphenylphosphane with lithium powder in THF and subsequent hydrolysis and distillation as described by Bianco and Doronzo.[35]

**Synthesis of K[$PPh_2$] (1):** The compound was obtained through deprotonation of $HPPh_2$ (**2**; 320 mg, 1.72 mmol) with potassium metal (120 mg, 3.07 mmol) in THF (5 mL). The resulting orange solution was decanted from excess potassium and directly used for the NMR measurements. X-ray quality crystals of **1**·18-crown-6 (**1c**) were grown by gas-phase diffusion of diethyl ether into a THF solution containing K[$PPh_2$] and an equimolar amount of 18-crown-6. $^1H$ NMR (THF, 250.13 MHz): $\delta$ = 6.42 (tr, $^3J_{HH}$ = 7.2 Hz, 2 H, H-*p*), 6.73 (vtr, $^3J_{HH}$ = 7.5 Hz, 4 H, H-*m*) 7.40–7.49 (m, 4 H, H-*o*) ppm. $^{13}C\{^1H\}$ NMR (THF, 62.90 MHz): $\delta$ = 118.6 (br., C-*p*), 127.5 (d, $^3J_{PC}$ = 5.5 Hz, C-*m*), 129.2 (d, $^2J_{PC}$ = 18.6 Hz, C-*o*), 157.1 (br. d, $^1J_{PC}$ = 56.0 Hz, C-*i*) ppm. $^{31}P$ NMR (THF, 161.98 MHz): $\delta$ = –9.8 (s) ppm.

**Synthesis of $BH_3(H)PPh_2$ (4H):** To a solution of $HPPh_2$ (2.53 g, 13.5 mmol) in THF (10 mL) was added a calibrated solution (1 mol/ L) of $BH_3{\cdot}THF$ in THF (13.5 mL, 13.5 mmol) at –78 °C with stirring. After the mixture had been warmed to ambient temperature overnight, all volatiles were removed in vacuo. The resulting oily residue was purified by column-chromatography (50 g silica-gel; eluent: hexane/toluene, 1:1). After evaporation of the eluate, the resulting oil of **4H** was triturated with pentane whereupon it solidified to give a colourless waxy material. Yield: 2.29 g (85%). $^1H$ NMR (THF, 400.13 MHz): $\delta$ = 1.15 (q, $^1J_{BH}$ = 100 Hz, 3 H, $BH_3$), 6.16 (dq, $^1J_{PH}$ = 380.8 Hz, $^3J_{HH}$ = 7.1 Hz, 1 H, PH), 7.19–7.30 (m, 6 H, H-*m*,*p*), 7.51–7.65 (m, 4 H, H-*o*) ppm. $^{11}B$ NMR (THF, 128.38 MHz): $\delta$ = –40.0 (dq, $^1J_{PB}$ = 42 Hz, $^1J_{BH}$ = 100 Hz) ppm. $^{13}C\{^1H\}$ NMR (THF, 62.90 MHz): $\delta$ = 127.6 (d, $^1J_{PC}$ = 56.2 Hz, C-*i*), 129.3 (d, $^3J_{PC}$ = 10.1 Hz, C-*m*), 131.8 (d, $^4J_{PC}$ = 2.5 Hz, C-*p*) 133.3 (d, $^2J_{PC}$ = 9.3 Hz, C-*o*) ppm. $^{31}P\{^1H\}$ NMR (THF, 161.98 MHz): $\delta$ = 1.7 (m) ppm.

**Synthesis of $BBr_3(H)PPh_2$ (4Br):** The compound was synthesised from $BBr_3$ (320 mg, 1.28 mmol) and $HPPh_2$ (230 mg, 1.24 mmol) in hexane (5 mL) as described in the literature.[14] Yield: 489 mg (92%). X-ray-quality crystals were grown by gas-phase diffusion of pentane into a solution of **4Br** in toluene. Since the compound is not stable in THF for extended periods of time, NMR measurements have to be carried out immediately after sample preparation. $C_{12}H_{11}BBr_3P$ (436.72): calcd. C 33.00, H 2.54; found: C 33.15, H 2.50. $^1H$ NMR (THF, 400.13 MHz): $\delta$ = 6.97 (d, $^1J_{PH}$ = 444.4 Hz, 1 H, PH), 7.31–7.39 (m, 4 H, H-*m*), 7.43–7.48 (m, 2 H, H-*p*), 7.76–7.84 (m, 4 H, H-*o*) ppm. $^{11}B$ NMR (THF, 128.38 MHz): $\delta$ = –17.1 (d, $^1J_{PB}$ = 142 Hz) ppm. $^{13}C\{^1H\}$ NMR (THF, 100.62 MHz): $\delta$ = 121.3 (d, $^1J_{PC}$ = 65.7 Hz, C-*i*), 129.7 (d, $^3J_{PC}$ = 11.7 Hz, C-*m*), 133.4 (d, $^4J_{PC}$ = 2.8 Hz, C-*p*), 134.6 (d, $^2J_{PC}$ = 8.2 Hz, C-*o*) ppm. $^{31}P\{^1H\}$ NMR (THF, 161.98 MHz): $\delta$ = –13.6 (q, $^1J_{PB}$ = 142 Hz) ppm.

**Synthesis of $BH_3(CH_3)PPh_2$ (5H):** To a solution of $CH_3PPh_2$ (270 mg, 1.35 mmol) in THF (2 mL) was added a calibrated solution (1 mol/ L) of $BH_3{\cdot}THF$ in THF (1.3 mL, 1.3 mmol) at –78 °C with stirring. After the mixture had been warmed to ambient temperature overnight, all volatiles were removed in vacuo. **5H** was obtained in essentially quantitative yield as a colourless oil. $^1H$ NMR (THF, 250.13 MHz): $\delta$ = 1.03 (q, 3 H, $BH_3$), 1.66 (d, $^2J_{PH}$

 © 2006 Wiley-VCH Verlag GmbH & Co. KGaA, Weinheim 

= 10.0 Hz, 3 H, $CH_3$), 7.18–7.31 (m, 6 H, H-*m*,*p*), 7.51–7.63 (m, 4 H, H-*o*) ppm. $^{11}B$ NMR (THF, 128.38 MHz): $\delta$ = –37.9 (dq, $^1J_{PB}$ = 55 Hz, $^1J_{BH}$ = 99 Hz) ppm. $^{13}C\{^1H\}$ NMR (THF, 62.90 MHz): $\delta$ = 11.4 (d, $^1J_{PC}$ = 40.0 Hz, $CH_3$), 129.0 (d, $^3J_{PC}$ = 9.8 Hz, C-*m*), 131.2 (d, $^4J_{PC}$ = 2.4 Hz, C-*p*), 131.9 (d, $^1J_{PC}$ = 54.8 Hz, C-*i*), 132.2 (d, $^2J_{PC}$ = 9.6 Hz, C-*o*) ppm. $^{31}P\{^1H\}$ NMR (THF, 161.98 MHz): $\delta$ = 11.5 (m) ppm.

**Synthesis of $BBr_3(CH_3)PPh_2$ (5Br):** The compound was synthesised from $CH_3PPh_2$ (235 mg, 1.17 mmol) and $BBr_3$ (302 mg, 1.21 mmol) in hexane (5 mL) following a published procedure.[16] Yield: 487 mg (90%). X-ray quality crystals were grown by gas-phase diffusion of pentane into a solution of **5Br** in toluene. $C_{13}H_{13}BBr_3P$ (450.74): calcd. C 34.64, H 2.91; found: C 34.41, H 2.79. $^1H$ NMR (THF, 400.13 MHz): $\delta$ = 2.11 (d, $^2J_{PH}$ = 11.9 Hz, 3 H, $CH_3$), 7.28–7.34 (m, 4 H, H-*m*), 7.39–7.44, (m, 2 H, H-*p*), 7.74–7.80 (m, 4 H, H-*o*) ppm. $^{11}B$ NMR (THF, 128.38 MHz): $\delta$ = –14.6 (d, $^1J_{PB}$ = 150 Hz) ppm. $^{13}C\{^1H\}$ NMR (THF, 100.62 MHz): $\delta$ = 7.1 (d, $^1J_{PC}$ = 48.7 Hz, $CH_3$), 124.2 (d, $^1J_{PC}$ = 68.2 Hz, C-*i*), 129.2 (d, $^3J_{PC}$ = 10.9 Hz, C-*m*), 132.9 (d, $^4J_{PC}$ = 2.7 Hz, C-*p*), 134.3 (d, $^2J_{PC}$ = 8.1 Hz, C-*o*) ppm. $^{31}P\{^1H\}$ NMR (THF, 161.98 MHz): $\delta$ = –9.2 (q, $^1J_{PB}$ = 150 Hz) ppm.

Table 3. Crystallographic data for compounds **1**[c], **4Br**, **5Br**, **6**, **7**, and **9**[c].

| | **1**[c] | **4Br** | **5Br** |
|---|---|---|---|
| Formula | $C_{24}H_{34}KO_6P$ | $C_{12}H_{11}BBr_3P$ | $C_{13}H_{13}BBr_3P$ |
| *Fw* | 488.58 | 436.72 | 450.74 |
| Colour, shape | orange, block | colourless, plate | colourless, block |
| Temperature [K] | 173(2) | 173(2) | 173(2) |
| Crystal system | monoclinic | orthorhombic | monoclinic |
| Space group | $P2_1/n$ | *Pbca* | *C*2/*c* |
| *a* [Å] | 10.5151(7) | 10.2401(3) | 32.935(5) |
| *b* [Å] | 14.8018(7) | 8.7189(3) | 7.074(1) |
| *c* [Å] | 32.593(2) | 32.686(2) | 13.842(2) |
| $\alpha$ [°] | 90 | 90 | 90 |
| $\beta$ [°] | 96.286(5) | 90 | 100.25(1) |
| $\gamma$ [°] | 90 | 90 | 90 |
| *V* [Å$^3$] | 5042.4(5) | 2918.3(2) | 3173.4(8) |
| *Z* | 8 | 8 | 8 |
| $D_{calcd.}$ [g cm$^{-3}$] | 1.287 | 1.988 | 1.887 |
| *F*(000) | 2080 | 1664 | 1728 |
| $\mu$ [mm$^{-1}$] | 0.310 | 8.378 | 7.708 |
| Crystal size [mm] | 0.49 × 0.46 × 0.42 | 0.28 × 0.26 × 0.13 | 0.28 × 0.26 × 0.24 |
| Reflections collected | 20677 | 46394 | 8766 |
| Independent reflections ($R_{int}$) | 9044 (0.0392) | 3151 (0.0887) | 2800 (0.1247) |
| Data/restraints/parameters | 9044/0/577 | 3151/0/159 | 2800/0/163 |
| GOOF on $F^2$ | 0.981 | 1.077 | 1.102 |
| $R_1$, $wR_2$ [$I > 2\sigma(I)$] | 0.0423, 0.1043 | 0.0391, 0.1046 | 0.0839, 0.2000 |
| $R_1$, $wR_2$ (all data) | 0.0599, 0.1122 | 0.0419, 0.1073 | 0.0981, 0.2116 |
| Largest diff. peak and hole [e·Å$^{-3}$] | 0.688 and –0.404 | 0.951 and –0.643 | 1.345 and –2.047 |
| | **6** | **7** | **9**[c] |
| Formula | $C_{12}H_{12}IP$ | $C_{13}H_{14}IP$ | $C_{24}H_{40}B_2KO_6P$ |
| *Fw* | 314.09 | 328.11 | 516.25 |
| Colour, shape | colourless, block | colourless, block | colourless, block |
| Temperature [K] | 173(2) | 173(2) | 173(2) |
| Crystal system | monoclinic | orthorhombic | monoclinic |
| Space group | $P2_1/c$ | *Pbca* | $P2_1/c$ |
| *a* [Å] | 8.8460(5) | 16.2294(7) | 8.4076(10) |
| *b* [Å] | 14.3281(9) | 9.6942(3) | 19.714(2) |
| *c* [Å] | 9.8352(6) | 17.1034(6) | 16.867(2) |
| $\alpha$ [°] | 90 | 90 | 90 |
| $\beta$ [°] | 99.437(5) | 90 | 96.674(10) |
| $\gamma$ [°] | 90 | 90 | 90 |
| *V* [Å$^3$] | 1229.7(1) | 2690.9(2) | 2776.7(6) |
| *Z* | 4 | 8 | 4 |
| $D_{calcd.}$ [g cm$^{-3}$] | 1.697 | 1.620 | 1.235 |
| *F*(000) | 608 | 1280 | 1104 |
| $\mu$ [mm$^{-1}$] | 2.695 | 2.467 | 0.284 |
| Crystal size [mm] | 0.37 × 0.33 × 0.25 | 0.27 × 0.25 × 0.24 | 0.48 × 0.46 × 0.43 |
| Reflections collected | 19524 | 57301 | 11881 |
| Independent reflections ($R_{int}$) | 2229 (0.0363) | 3902 (0.0384) | 5347 (0.0739) |
| Data/restraints/parameters | 2229/0/136 | 3902/0/141 | 5347/0/309 |
| GOOF on $F^2$ | 1.087 | 1.298 | 0.871 |
| $R_1$, $wR_2$ [$I > 2\sigma(I)$] | 0.0161, 0.0389 | 0.0297, 0.0706 | 0.0404, 0.0950 |
| $R_1$, $wR_2$ (all data) | 0.0175, 0.0395 | 0.0312, 0.0724 | 0.0549, 0.0982 |
| Largest diff. peak and hole [e·Å$^{-3}$] | 0.289 and –0.439 | 0.493 and –0.560 | 0.611 and –0.460 |

 © 2006 Wiley-VCH Verlag GmbH & Co. KGaA, Weinheim 

**Synthesis of $[H_2PPh_2]I$ (6):** For the synthesis of **6**, $HPPh_2$ (322 mg, 1.73 mmol) was treated with excess HI in toluene (3 mL) at –78 °C. Yield: 429 mg (80%). Crystals suitable for X-ray crystallography formed when a concentrated $CHCl_3$ solution of **6** was slowly cooled to –30 °C. $C_{12}H_{12}IP$ (314.09): calcd. C 45.89, H 3.85; found: C 46.16, H 3.83. $^1H$ NMR ($CDCl_3$, 250.13 MHz, 300 K): $\delta$ = 5.8 (very br., 2 H, $PH_2$), 7.41–7.56 (m, 6 H, H-*m*,*p*), 7.73–7.84 (m, 4 H, H-*o*) ppm. $^1H$ NMR ($CDCl_3$, 250.13 MHz, 233 K): $\delta$ = 7.45–7.85 (m, 6 H, H-*m*,*p*), 7.94–8.15 (m, 4 H, H-*o*), 9.91 (br. d, 2 H, $PH_2$) ppm. $^{13}C\{^1H\}$ NMR ($CDCl_3$, 62.90 MHz, 300 K): broad, poorly resolved signals. $^{13}C\{^1H\}$ NMR ($CDCl_3$, 62.90 MHz, 233 K): 128.0 (d, $^1J_{PC}$ = 83.0 Hz, C-*i*), 129.2 (d, $^3J_{PC}$ = 13.2 Hz, C-*m*), 131.1 (d, $^2J_{PC}$ = 11.8 Hz, C-*o*), 133.4 (d, $^4J_{PC}$ = 1.6 Hz C-*p*) ppm. $^{31}P\{^1H\}$ NMR ($CDCl_3$, 161.98 MHz, 300 K): $\delta$ = –34.2 (br. s) ppm. $^{31}P\{^1H\}$ NMR ($CDCl_3$, 161.98 MHz, 233 K): $\delta$ = –31.0 (tr, $^1J_{PH}$ = 530.6 Hz) ppm.

**Synthesis of $[CH_3(H)PPh_2]I$ (7):** Following a published procedure,[17] $CH_3PPh_2$ (336 mg, 1.68 mmol) was treated with excess HI in toluene (3 mL) at –78 °C. Yield: 385 mg (70%). Crystals suitable for X-ray crystallography formed when a concentrated $CHCl_3$ solution of **7** was slowly cooled to –30 °C. $C_{13}H_{14}IP$ (328.11): calcd. C 47.59, H 4.30; found: C 47.82, H 4.53. $^1H$ NMR ($CDCl_3$, 250.13 MHz, 300 K): $\delta$ = 2.58 (d, $^2J_{PH}$ = 14.7 Hz, 3 H, $CH_3$), 7.51–7.61 (m, 4 H, H-*m*), 7.64–7.73 (m, 2 H, H-*p*), 7.91–8.03 (m, 4 H, H-*o*), 10.1 (d, $^1J_{PH}$ = 521.7 Hz, 1 H, PH) ppm. $^1H$ NMR ($CDCl_3$, 250.13 MHz, 233 K): $\delta$ = 2.57 (dd, $^2J_{PH}$ = 14.6 Hz, $^3J_{HH}$ = 5.7 Hz, 3 H, $CH_3$), 7.47–8.01 (m, 10 H, H-*o*/*m*/*p*), 9.87 (d, $^1J_{PH}$ = 521.7 Hz, 1 H, PH) ppm. $^{13}C\{^1H\}$ NMR ($CDCl_3$, 62.90 MHz, 300 K): $\delta$ = 7.7 (d, $^1J_{PC}$ = 54.1 Hz, $CH_3$), 116.8 (d, $^1J_{PC}$ = 84.9 Hz, C-*i*), 130.3 (d, $^3J_{PC}$ = 13.2 Hz, C-*m*), 133.3 (d, $^2J_{PC}$ = 10.9 Hz, C-*o*), 135.1 (d, $^4J_{PC}$ = 3.1 Hz, C-*p*) ppm. $^{13}C\{^1H\}$ NMR ($CDCl_3$, 62.90 MHz, 233 K): $\delta$ = 7.1 (d, $^1J_{PC}$ = 53.8 Hz, $CH_3$), 115.9 (d, $^1J_{PC}$ = 85.4 Hz, C-*i*), 130.2 (d, $^3J_{PC}$ = 13.1 Hz, C-*m*), 133.0 (d, $^2J_{PC}$ = 10.8 Hz, C-*o*), 135.1 (br., C-*p*) ppm. $^{31}P\{^1H\}$ NMR ($CDCl_3$, 161.98 MHz, 300 K): $\delta$ = –4.7 (s) ppm. $^{31}P\{^1H\}$ NMR ($CDCl_3$, 161.98 MHz, 233 K): $\delta$ = –5.2 (s) ppm.

**Synthesis of $[(CH_3)_2PPh_2]I$ (8):** The compound was synthesised following a published procedure[36] via the reaction of $HPPh_2$ (204 mg, 1.10 mmol) with $ICH_3$ (217 mg, 1.53 mmol) in THF (4 mL). Yield: 353 mg (94%). Crystals suitable for X-ray crystallography formed when a concentrated $CHCl_3$ solution of **8** was slowly cooled to –30 °C. $C_{14}H_{16}IP$ (342.15): calcd. C 49.15, H 4.71; found: C 48.92, H 4.58. $^1H$ NMR ($CDCl_3$, 250.13 MHz): $\delta$ = 2.88 (d, $^2J_{PH}$ = 13.9 Hz, 3 H, $CH_3$), 7.60–7.79 (m, 6 H, H-*m*,*p*), 7.83–7.95 (m, 4 H, H-*o*) ppm. $^{13}C\{^1H\}$ NMR ($CDCl_3$, 62.90 MHz): $\delta$ = 11.4 (d, $^1J_{PC}$ = 56.4 Hz, $CH_3$), 120.5 (d, $^1J_{PC}$ = 87.6 Hz, C-*i*), 130.3 (d, $^3J_{PC}$ = 12.8 Hz, C-*m*), 132.3 (d, $^2J_{PC}$ = 10.7 Hz, C-*o*), 135.0 (d, $^4J_{PC}$ = 3.0 Hz, C-*p*) ppm. $^{31}P\{^1H\}$ NMR ($CDCl_3$, 161.98 MHz): $\delta$ = 21.9 (s) ppm.

**Synthesis of $K[(BH_3)_2PPh_2]$ (9):** To a solution of 435 mg $K[BH_3PPh_2]$ (1.82 mmol) in THF (5 mL) was added a calibrated solution (1 mol/ L) of $BH_3$·THF (1.8 mL, 1.8 mol) at –78 °C with stirring. After 30 min, the cooling bath was removed and the reaction mixture warmed to ambient temperature with subsequent stirring for another 60 min. All volatiles were removed in vacuo and the resulting colourless solid was washed twice with pentane (2 mL). Yield: 423 mg (92%). X-ray quality crystals were grown by gas-phase diffusion of diethyl ether onto a solution containing $K[(BH_3)_2PPh_2]$ and an equimolar amount of 18-crown-6. $C_{24}H_{40}B_2KO_6P$ (516.25): calcd. C 55.84, H 7.81; found C 55.38, H 7.63. $^1H$ NMR (THF, 250.13 MHz): $\delta$ = 1.0 (q, $^1J_{BH}$ = 89 Hz, 6 H, $BH_3$), 7.00–7.10 (m, 6 H, H-*m*,*p*), 7.74–7.85 (m, 4 H, H-*o*) ppm. $^{11}B\{^1H\}$ NMR (THF, 128.38 MHz): $\delta$ = –34.6 (d, $^1J_{PB}$ = 64 Hz, $BH_3$) ppm. $^{13}C\{^1H\}$ NMR (THF, 62.90 MHz): 127.4 (d, $^3J_{PC}$ = 8.2 Hz, C-*m*), 127.9 (d, $^4J_{PC}$ = 2.0 Hz, C-*p*), 133.4 (d, $^2J_{PC}$ = 7.7 Hz, C-*o*), 140.2 (d, $^1J_{PC}$ = 38.5 Hz, C-*i*) ppm. $^{31}P$ NMR (THF, 161.98 MHz): $\delta$ = –11.1 (m) ppm.

**X-ray Structural Characterisation:** Data collections were performed on a Stoe IPDS-II two-circle diffractometer with graphite-monochromated Mo-$K_\alpha$ radiation. Empirical absorption corrections with the MULABS option[37] in the program PLATON[38] were performed. Equivalent reflections were averaged. The structures were solved by direct methods[39] and refined with full-matrix least-squares on $F^2$ using the program SHELXL-97.[40] Hydrogen atoms bonded to carbon and boron were placed on ideal positions and refined with fixed isotropic displacement parameters using a riding model. H atoms bonded to phosphorus were refined isotropically. Details of the X-ray crystal structure analyses of **1**[c], **4Br**, **5Br**, **6**, **7**, and **9**[c] are summarised in Table 3.

CCDC-290838 (for **1**[c]), -290839 (for **4Br**), -290840 (for **5Br**), -290841 (for **6**), -290842 (for **7**), and -290843 (for **9**[c]) contain the supplementary crystallographic data for this paper. These data can be obtained free of charge from The Cambridge Crystallographic Data Centre via www.ccdc.cam.ac.uk/data_request/cif.

**Supporting Information** (for details see the footnote on the first page of this article): ORTEP drawings of **4Br**, **5Br**, **6**, **7**, and **8**.

## Acknowledgments

The authors are grateful to the Deutsche Forschungsgemeinschaft (DFG) and the Fonds der Chemischen Industrie (FCI) for financial support.

[1] L. H. Gade, *Koordinationschemie*, Wiley-VCH, Weinheim, **1998**.
[2] C. T. Goralski, B. Singaram, C. J. Collins, J. R. Cuzens, M. Lanz, in: *ACS Symposium Series*, vol. 783 (Eds.: P. V. Ramachandran, H. C. Brown), American Chemical Society, Washington, DC, **2001**, pp. 18–32.
[3] J.-M. Camus, J. Andrieu, P. Richard, R. Poli, C. Darcel, S. Jugé, *Tetrahedron: Asymmetry* **2004**, *15*, 2061–2065.
[4] B. Wolfe, T. Livinghouse, *J. Org. Chem.* **2001**, *66*, 1514–1516.
[5] T. Miura, H. Yamada, S. Kikuchi, T. Imamoto, *J. Org. Chem.* **2000**, *65*, 1877–1880.
[6] B. Wolfe, T. Livinghouse, *J. Am. Chem. Soc.* **1998**, *120*, 5116–5117.
[7] C. A. Jaska, A. J. Lough, I. Manners, *Inorg. Chem.* **2004**, *43*, 1090–1099.
[8] H. Dorn, C. A. Jaska, R. A. Singh, A. J. Lough, I. Manners, *Chem. Commun.* **2000**, 1041–1042.
[9] A.-C. Gaumont, M. B. Hursthouse, S. J. Coles, J. M. Brown, *Chem. Commun.* **1999**, 63–64.
[10] W. Angerer, W. S. Sheldrick, W. Malisch, *Chem. Ber.* **1985**, *118*, 1261–1266.
[11] G. Müller, J. Brand, *Organometallics* **2003**, *22*, 1463–1467.
[12] D. A. Hoic, W. M. Davis, G. C. Fu, *J. Am. Chem. Soc.* **1996**, *118*, 8176–8177.
[13] L. D. Quin, *A Guide to Organophosphorus Chemistry*, John Wiley & Sons, Inc., New York, **2000**.
[14] B. Rapp, J. E. Drake, *Inorg. Chem.* **1973**, *12*, 2868–2873.
[15] M. A. Mathur, W. H. Myers, H. H. Sisler, G. E. Ryschkewitsch, *Inorg. Synth.* **1974**, *15*, 128–133.
[16] M. L. Denniston, D. R. Martin, *J. Inorg. Nucl. Chem.* **1974**, *36*, 1461–1464.
[17] S. O. Grim, W. McFarlan, *Can. J. Chem.* **1968**, *46*, 2071–2074.
[18] F. Dornhaus, H.-W. Lerner, M. Bolte, *Acta Crystallogr., Sect. E* **2005**, *61*, o1657–o1658.

 © 2006 Wiley-VCH Verlag GmbH & Co. KGaA, Weinheim 

[19] A. F. Holleman, N. Wiberg, *Lehrbuch der Anorganischen Chemie*, 101 ed., de Gruyter, Berlin, New York, **1995**.
[20] K. Izod, W. McFarlane, B. V. Tyson, W. Clegg, R. W. Harrington, S. T. Liddle, *Organometallics* **2003**, *22*, 3684–3690.
[21] O. Kühl, J. Sieler, E. Hey-Hawkins, *Z. Kristallogr.* **1999**, *214*, 496–499.
[22] A. G. Avent, D. Bonafoux, C. Eaborn, M. S. Hill, P. B. Hitchcock, J. D. Smith, *J. Chem. Soc. Dalton Trans.* **2000**, 2183–2190.
[23] R. J. Staples, T. Carlson, S. Wang, J. P. Fackler Jr, *Acta Crystallogr., Sect. C* **1995**, *51*, 498–500.
[24] N. Edelstein, *Inorg. Chem.* **1981**, *20*, 297–299.
[25] R. D. Shannon, *Acta Crystallogr., Sect. A* **1976**, *32*, 751–767.
[26] H. A. Bent, *Chem. Rev.* **1961**, *61*, 275–311.
[27] H. Nöth, B. Wrackmeyer, in: *NMR Basic Principles and Progress.* (Eds.: P. Diehl, E. Fluck, R. Kosfeld), vol. 14: *Nuclear Magnetic Resonance Spectroscopy of Boron Compounds*, Springer, Berlin, **1978**.
[28] S. Berger, S. Braun, H.-O. Kalinowski, *NMR-Spektroskopie von Nichtmetallen; Band 3; $^{31}$P-NMR-Spektroskopie*, Thieme, Stuttgart, **1993**.
[29] V. M. S. Gil, W. von Philipsborn, *Magn. Res. Chem.* **1989**, *27*, 409–430.
[30] A. H. Cowley, M. C. Damasco, *J. Am. Chem. Soc.* **1971**, *93*, 6815–6821.
[31] R. W. Rudolph, C. W. Schultz, *J. Am. Chem. Soc.* **1971**, *93*, 6821–6822.
[32] R. Foester, K. Cohn, *Inorg. Chem.* **1972**, *11*, 2590–2593.
[33] L. D. Schwartz, P. C. Keller, *Inorg. Chem.* **1971**, *10*, 645–647.
[34] H. E. Gottlieb, V. Kotlyar, A. Nudelman, *J. Org. Chem.* **1997**, *62*, 7512–7515.
[35] V. D. Bianco, S. Doronzo, *Inorg. Synth.* **1976**, *16*, 161–163.
[36] H. J. Cristau, Y. Ribeill, *Synthesis* **1988**, *11*, 911–912.
[37] R. H. Blessing, *Acta Crystallogr., Sect. A* **1995**, *51*, 33–38.
[38] A. L. Spek, *Acta Crystallogr., Sect. A* **1990**, *46*, C34.
[39] G. M. Sheldrick, *Acta Crystallogr., Sect. A* **1990**, *46*, 467–473.
[40] G. M. Sheldrick, *SHELXL-97. A Program for the Refinement of Crystal Structures*, University of Göttingen, **1997**.

Received: December 20, 2005
Published Online: March 22, 2006

 © 2006 Wiley-VCH Verlag GmbH & Co. KGaA, Weinheim 

DOI: 10.1002/ejic.200501136

# Synthesis, Structure, Electrochemistry, and Metal-Atom Dynamics of Cyclopentadienyl Ferracarboranes

**Rolfe H. Herber,*[a] Alexander R. Kudinov,[b] Piero Zanello,[c] Israel Nowik,[a] Dmitry S. Perekalin,[b] Vladimir I. Meshcheryakov,[b] Konstantin A. Lyssenko,[b] Maddalena Corsini,[c] and Serena Fedi[c]**

**Keywords:** Cyclopentadienyl ferracarboranes / Electrochemistry / X-ray diffraction / Mössbauer spectroscopy

A series of metallacarboranes, incorporating the CpFe fragment, were studied by electrochemical techniques, temperature-dependent Mössbauer effect (ME) spectroscopy, and X-ray diffraction. The compounds studied include the parent dicarbollide complex $CpFeC_2B_9H_{11}$ (**1**) and its reduced form [**1**]$^-$, the charge-compensated ferradicarbollides 1-Cp-4-L-1,2,3-$FeC_2B_9H_{10}$ [L = $SMe_2$ (**2a**), $NMe_3$ (**2b**), py (**2c**)] and their methylated analogs 1-Cp-2,3-$Me_2$-4-$SMe_2$-1,2,3-$FeC_2B_9H_8$ (**2d**) and 1-Cp*-4-$SMe_2$-1,2,3-$FeC_2B_9H_{10}$ (**2e**), the isomeric ferratricarbollides $CpFeC_3B_8H_{11}$ (**3a–c**), and the amino-substituted derivative 1-Cp-12-*t*BuNH-1,2,4,12-$FeC_3B_8H_{10}$ (**3d**). The ferradicarbollides **2a–e** were synthesized by reactions of the charge-compensated dicarbollide anions [9-L-7,8-$R_2$-7,8-$C_2B_9H_8$]$^-$ (R = H, Me) with [($C_5R_5$)-$Fe(MeCN)_3$]$^+$ cations. The structures of **1**, [$NMe_3Ph$][**1**], and **2b** were investigated by X-ray diffraction. The ME spectroscopic study elucidated the relationship between the nature of the five-membered carborane face coordinated to the metal center and the hyperfine interaction parameters of the Fe atom. Temperature-dependent recoil-free fraction studies yielded the root-mean-square-amplitude-of-vibration (rmsav) of the metal atom over a wide temperature range, which proved to be in good agreement with crystallographic $U_{i,j}$ data for **1** and **3a**,**b**. Electrochemistry shows that the isomeric ferratricarbollides **3a–c** undergo reversible oxidation to the corresponding $Fe^{III}$ derivatives at potential values higher, on average, by about 0.4 V than those of the charge-compensated complexes **2a–c** and by about 0.8 V than that of the parent ferradicarbollide [**1**]$^-$. This result indicates the strong electron-withdrawing ability of the extra carbon atom relative to that of the replaced boron atom. As a consequence of the shift of the HOMO–LUMO frontier orbitals to the high energy levels, the $Fe^{II}/Fe^{I}$ reduction becomes accessible.

(© Wiley-VCH Verlag GmbH & Co. KGaA, 69451 Weinheim, Germany, 2006)

## Introduction

Similar to ferrocene, the ferracarborane anion $[CpFeC_2B_9H_{11}]^-$ ([**1**]$^-$)[1] can be easily oxidized to give the neutral compound $CpFeC_2B_9H_{11}$ (**1**) which contains $Fe^{III}$. However, different charges of the $[C_2B_9H_{11}]^{2-}$ and $Cp^-$ ligands lead to significant differences in the properties of [**1**]$^-$ and $FeCp_2$. Usage of monoanionic carborane ligands of two types, [9-L-7,8-$C_2B_9H_{10}$]$^-$ and $[C_3B_8H_{11}]^-$, allows one to obtain closer analogs of ferrocene such as charge-compensated ferradicarbollides **2a–e** and ferratricarbollides **3a–d** (Scheme 1). Herein we describe the synthesis and structural, electrochemical, and Mössbauer studies of these compounds, along with a reinvestigation of key metallacarboranes **1** and [**1**]$^-$.

[a] Racah Institute of Physics, The Hebrew University, 91904 Jerusalem, Israel
E-mail: herber@vms.huji.ac.il
[b] A. N. Nesmeyanov Institute of Organoelement Compounds, Russian Academy of Sciences, 119991 Moscow, Russian Federation
E-mail: arkudinov@ineos.ac.ru
[c] Department of Chemistry, University of Siena, 53100 Siena, Italy
E-mail: zanello@unisi.it

Supporting information for this article is available on the WWW under http://www.eurjic.org or from the author.

## Results and Discussion

### Synthesis

The charge-compensated ferradicarbollides **2a–c** were prepared by reactions of anions [9-L-7,8-$C_2B_9H_{10}$]$^-$ with the acetonitrile complex $[CpFe(MeCN)_3]^+$ (Scheme 2).[2] The starting iron complex is stable only below –40 °C,[3] and therefore its in situ generation by irradiation of $[CpFe(C_6H_6)]^+$ in a mixture of MeCN/THF and further complexation were carried out at low temperature. The analogous reaction of [9-$SMe_2$-7,8-$Me_2$-7,8-$C_2B_9H_8$]$^-$ gave the cage-methylated derivative **2d**. The ring-methylated complex **2e** was prepared by reaction of [9-$SMe_2$-7,8-$C_2B_9H_{10}$]$^-$ with $[Cp^*Fe(MeCN)_3]^+$.[4]

Ferratricarbollides **3a**[5] and **3d**[6] were recently obtained by room-temperature photochemical reaction of the tricarbollide anions [7-R-7,8,9-$C_3B_9H_{10}$]$^-$ (R = H, *t*BuNH) with $[CpFe(C_6H_6)]^+$, while compounds **3b** and **3c** were prepared by stepwise thermal rearrangement of **3a**.[5]

 © 2006 Wiley-VCH Verlag GmbH & Co. KGaA, Weinheim 

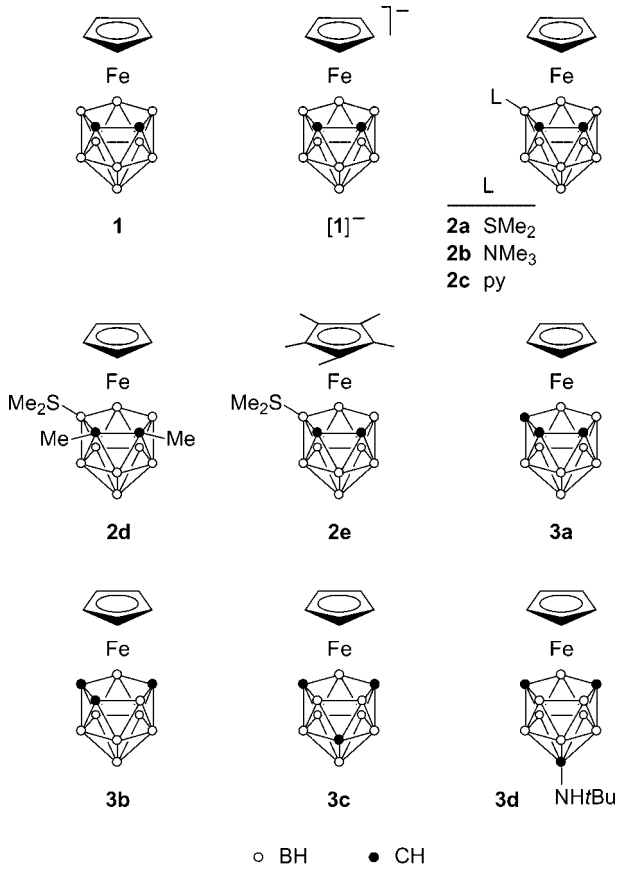


Scheme 1.

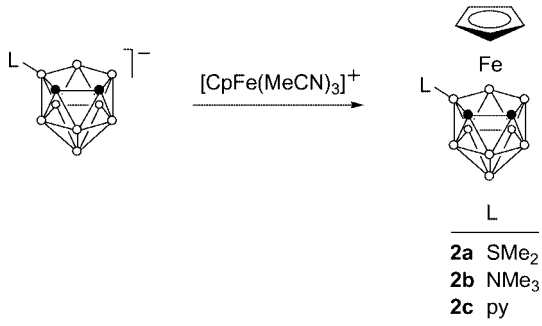


Scheme 2.

## Structures

The structure of ferradicarbollide **1** was studied by X-ray diffraction in 1965, but the instrumental limitations of that time resulted in approximate data only, with significant uncertainty (ca. 0.05 Å) caused by large thermal motion.[7] Low-temperature experiments allowed us to obtain highly accurate structures of **1** and its reduced form $[\mathbf{1}]^-$ (as a $[NMe_3Ph]^+$ salt) with only minor librations of the Cp rings (Figure 1 and Figure 2).[8]

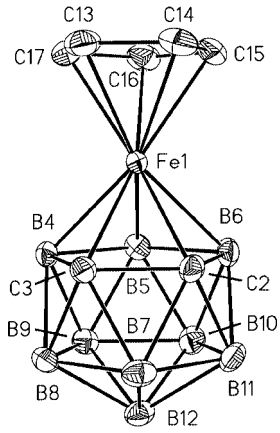


Figure 1. The molecular structure of anion $[\mathbf{1}]^-$ (thermal ellipsoids at 50% probability). Hydrogen atoms are omitted for clarity. Selected interatomic distances [Å]: Fe1–C2 2.0101(7), Fe1–C3 2.0108(7), Fe1–B4 2.0709(7), Fe1–B5 2.1090(7), Fe1–B6 2.0749(8), Fe1–C13 2.0721(7), Fe1–C14 2.0649(7), Fe1–C15 2.0514(7), Fe1–C16 2.0441(7), Fe1–C17 2.0606(7), C3–C2 1.6324(10).

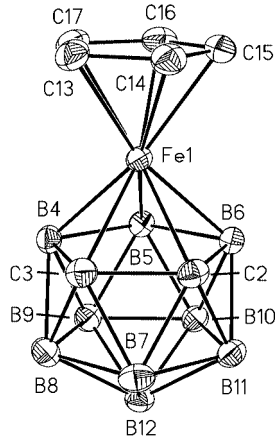


Figure 2. The molecular structure of **1** (thermal ellipsoids at 50% probability). Hydrogen atoms are omitted for clarity. Selected interatomic distances [Å]: Fe1–C16 2.0651(11), Fe1–C2 2.0716(9), Fe1–C3 2.0773(9), Fe1–C17 2.0893(11), Fe1–B6 2.0952(11), Fe1–C15 2.0961(10), Fe1–B4 2.1017(10), Fe1–B5 2.1079(11), Fe1–C13 2.1356(11), Fe1–C14 2.1399(11), C2–C3 1.6002(13).

The structure of the 18-electron anion $[\mathbf{1}]^-$ possesses a classical sandwich geometry with the Fe···$C_2B_3$ and Fe···$C_5$ distances equal to 1.437 and 1.663 Å, respectively. It is noteworthy that the latter value is very close to that in ferrocene[9] (1.660 Å), confirming a similarity of their electronic structures. The $C_2B_3$ and $C_5$ rings are nearly eclipsed (torsion angle 14°) and almost parallel (1.6°) to each other. The $C_2B_3$ face is notably nonplanar with the central B5 atom deviating from the B6–C2–C3–B4 plane by 0.061 Å away from the iron atom. Similar distortion was previously observed in structures of **3a**,**b**.[5]

The structure of the 17-electron neutral compound **1** is significantly different from anion $[\mathbf{1}]^-$. Both the Fe···$C_2B_3$ (1.487 Å) and Fe···$C_5$ (1.723 Å) distances in **1** are ca. 0.05 Å longer than those in $[\mathbf{1}]^-$. The latter distance is also longer than that in the similar 17-electron $[FeCp_2]^+$ cation (1.706 Å).[10] The $C_5$ ring is almost perfectly eclipsed with

 © 2006 Wiley-VCH Verlag GmbH & Co. KGaA, Weinheim 

$C_2B_3$ (torsion angle 4.5°) and inclined by 4.6° away from the cage carbon atoms. The $C_{Carb}$–$C_{Carb}$ and average $C_{Cp}$–$C_{Cp}$ distances in **1** (1.594 and 1.401 Å, respectively) are considerably shorter than those in [**1**]$^-$ (1.640 and 1.430 Å, respectively).

In order to arrive at a MO explanation for the difference between the structures of **1** and [**1**]$^-$, we carried out DFT calculations (at B3LYP/6-31G* level) of the anion [**1**]$^-$. It was found that the HOMO (Figure 3) is similar to the $e_{2g}$/$d_{x^2-y^2}$ orbital of ferrocene, with bonding for Fe···$C_2B_3$ and Fe···Cp interactions and antibonding for $C_{Cp}$–$C_{Cp}$ and $C_{Carb}$–$C_{Carb}$ interactions.[11] Accordingly, removal of one electron from this orbital leads to the lengthening of Fe···$C_2B_3$ and Fe···Cp distances and shortening of $C_{Cp}$–$C_{Cp}$ and $C_{Carb}$–$C_{Carb}$ distances.

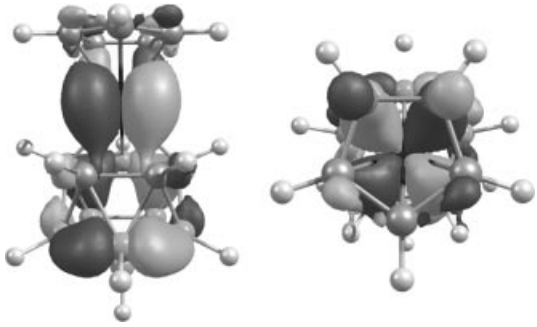

Figure 3. The plot of the HOMO of [**1**]$^-$.

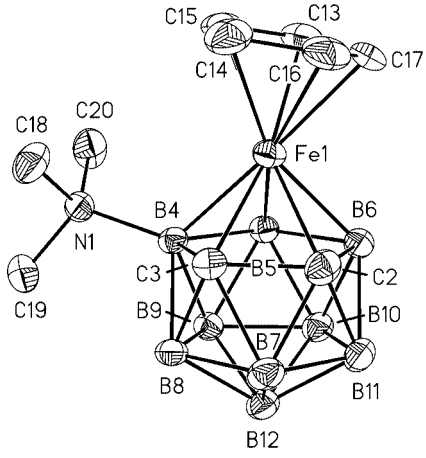


Figure 4. The molecular structure of **2b** (thermal ellipsoids at 30% probability). The second conformation of the disordered Cp ring and hydrogen atoms are omitted for clarity. Selected interatomic distances [Å]: Fe1–C2 1.995(3), Fe1–C3 2.018(3), Fe1–B4 2.108(4), Fe1–B5 2.113(3), Fe1–B6 2.072(3), Fe1–C17 2.054(9), Fe1–C16 2.079(6), Fe1–C13 2.082(7), Fe1–C14 2.091(6), Fe1–C15 2.093(5), C2–C3 1.632(5), N1–B4 1.611(4).

The structure of the charge-compensated ferradicarbollide **2b** was also confirmed by X-ray diffraction (Figure 4). In contrast to [**1**]$^-$ and **1**, the Cp ligand is disordered over two positions. The presence of the bulky $NMe_3$ substituent leads to the significantly bent sandwich geometry with a 9.7° angle between $C_5$ and $C_2B_3$ planes. The Fe···Cp and Fe···$C_2B_3$ distances (1.690 and 1.451 Å, respectively) are ca. 0.03 Å longer than those in [**1**]$^-$, probably also a result of the steric repulsion.

## Mössbauer Study

Similar to other neutral, diamagnetic ferrocenoid compounds, all of the cyclopentadienyl ferracarboranes examined in the present study, namely **1**, [$NMe_3Ph$][**1**], **2a**,**c**, and **3a**–**d**, display a ME resonance which consists of a single, well-separated doublet spectrum characterized by its isomer shift (IS), quadrupole splitting (QS), and area under the resonance curve ($A$). A representative spectrum of **3c** at 92 K is shown in Figure 5. The IS and QS values at 90 K, as well as the parameters derived from the temperature-dependent data for all of the compounds are summarized in Table 1. In the following discussion, the trends in the ME hyperfine parameters are discussed in some detail.

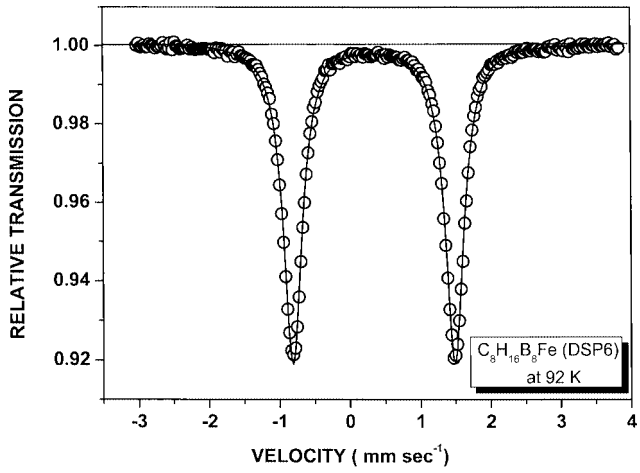


Figure 5. $^{57}$Fe Mössbauer spectrum of **3c** ("DSP-6") at 92 K. The velocity scale is with reference to the centroid of a room-temperature α-Fe spectrum which was also used for spectrometer calibration.

Table 1. $^{57}$Fe Mössbauer parameters for the compounds discussed in the text.

| | **1** | [$NMe_3Ph$][**1**] | **2a** | **2c** | **3a** | **3b** | **3c** | **3d** | Units |
|---|---|---|---|---|---|---|---|---|---|
| IS(90) | 0.337(3) | 0.357(3) | 0.383(5) | 0.380(4) | 0.430(3) | 0.439(4) | 0.344(4) | 0.344(3) | $mm\,s^{-1}$ |
| QS(90) | 0.525(3) | 2.431(3) | 2.490(5) | 2.480(4) | 2.501(3) | 2.471(5) | 2.302(4) | 2.360(3) | $mm\,s^{-1}$ |
| –d(IS)/d($T$) | 5.3(3) | 5.5(4) | 5.1(5) | 6.8(1) | 5.1(1) | 4.0(1) | 4.8(4) | 4.8(1) | $10^{-4}\,mm\,s^{-1}$ |
| –d(ln $A$)/d($T$) | 7.9(1) | 15.9(2) | 6.3(5) | 5.4(2) | 4.4(3) | 5.9(3) | 6.7(2) | 11.3(11) | $10^{-3}\,K^{-1}$ |
| $M_{eff}$ | 78(4) | 76(5) | 82(3) | n.a. | 100(1) | 103(3) | 86(3) | 86(1) | Da |
| $\Theta_M$ | 113 | 80 | 123 | – | 131 | – | 116 | 89 | K |

 © 2006 Wiley-VCH Verlag GmbH & Co. KGaA, Weinheim 

### *Isomer Shift*

The IS parameters show a distinct partition into two groups: those which pertain to the ferracarboranes in which two carbon atoms of the five-membered carborane face interact with the metal atom (e.g., **3c** and **3d**), and those in which there are three carbon atoms in the pentagonal ring (e.g., **3a** and **3b**). As is evident from the electronegativity of carbon and boron and also in accordance with the results of previous DFT calculations,[5] the C atoms of the framework are more negatively charged than the B atoms. This greater electron density, which is reflected in greater shielding of the nearby iron nucleus, results in a larger IS, since it is well established that $\delta R/R$ for the 14.4 keV level of $^{57}Fe$ is negative.[12] The average difference in the IS parameter between the $B_2C_3$ and $B_3C_2$ compounds is almost 0.1 mm s$^{-1}$, a value some 30 times greater than the experimental errors in the individual measurements. An argument which further bolsters this explanation is based on the observation that other iron carboranes, in which the carborane ligand contains three carbon atoms (of which only two are located in the pentagonal ring facing the metal atom) (e.g., **3c** and **3d**), show an IS which is close to those reported for the $C_2B_3$ complexes noted earlier.

The temperature dependence of the IS, –d(IS)/d($T$), is negative for all of the compounds examined, in consonance with similar observations reported earlier for ferrocene-related complexes. For **3a**–**c**, this temperature dependence is linear within experimental error over the accessible range of temperatures, and the corresponding values are included in the data listed in Table 1. A representative data set is shown in Figure 6. For [$NMe_3Ph$][**1**], **2a**, and **3d**, the data are better approximated by two linear segments, with a minor break at $T \approx 230$ K. Again, a representative data set is included in Figure 6. For **2c**, the temperature dependence of the IS parameter shows continuous curvature, and no effort was made to separate two regions of the $T$ range in this case. As indicated in the literature,[13] the value of the –d(IS)/d($T$) parameter (in the high-temperature limit) can be used to extract an effective vibrating mass, $M_{eff}$, for the ME active atom, and the corresponding values for the cyclopentadienyl iron carboranes of the present study fall into the range of 82 ± 4 Da for the five $B_3C_2$ compounds and 102 ± 4 Da for the two $B_2C_3$ compounds. The difference between these values and the "bare atom" iron mass of 57 Da reflects the covalence of the metal–ligand interaction, and is consistent with a larger electron density of the ring in the latter than in the former compounds, as mentioned earlier.

### *Quadrupole Splitting*

The QS parameters at 90 K are included in the data summarized in Table 1. With the exception of the value for **1**, the data again fall into two groups: those with the $B_2C_3$ ring structure and those with the $B_3C_2$ configuration. At 90 K, the former have a QS ≈ 2.49 mm s$^{-1}$, while the latter have a QS ≈ 2.36 mm s$^{-1}$. However, it should be noted that the QS parameters are temperature-dependent, and (with some minor variations) show the normal decrease with increasing temperature because of the effects on the field gradient arising from thermal expansion. A typical data set showing this temperature dependence is shown in Figure 7. An exception to the earlier generalization is the data for the QS of **1**, which is smaller by about a factor of 4.6 than the values for the remainder of the carboranes reported here. This difference is readily understood in terms of the formal +3 oxidation state of the iron atom in **1** compared with the divalent state in the remainder. As has been previously noted[14] for ferrocene-related compounds, the removal of one electron from the metal atom on oxidation incurs an almost complete collapse of the QS, as has been discussed in detail in a classic paper by Collins[14] and elsewhere.[15] Typically, the change in the QS parameter on oxidation of the neutral parent compound is from 2.57 to 0.15 mm s$^{-1}$ for octamethylferrocene and the corresponding cation as $BF_4^-$ and $PF_6^-$ salts,[16] from 2.42 to 0.21 mm s$^{-1}$ for a bis-(isodicyclopentadienyl)iron complex and the cation as a $PF_6^-$ salt,[17] and from 2.41 to 0.15 mm s$^{-1}$ for ethynyloctamethylferrocene and the cation as a $PF_6^-$ salt.[18] In the case of **1**, the QS parameter at 90 K is 0.525 ± 0.003 mm s$^{-1}$, presumably due to the presence of both B and C atoms in the

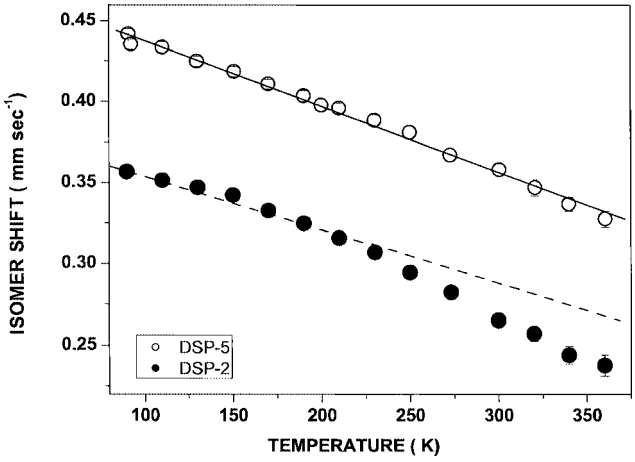


Figure 6. Temperature dependence of the isomer shift for [$NMe_3Ph$][**1**] ("DSP-2", filled circles) and **3b** ("DSP-5", open circles).

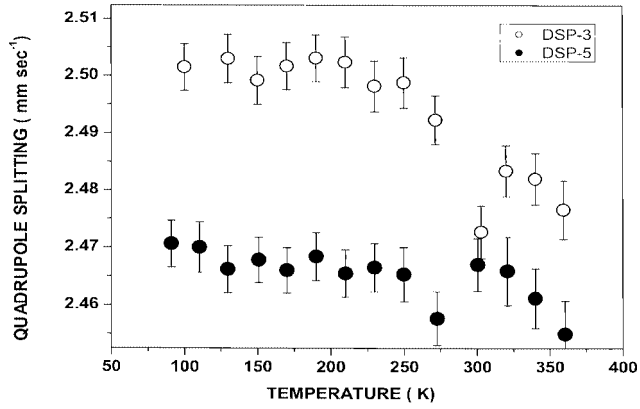


Figure 7. Temperature dependence of the quadrupole splitting for **3a** ("DSP-3") and **3b** ("DSP-5") showing the "normal" decrease with increasing temperature.

 © 2006 Wiley-VCH Verlag GmbH & Co. KGaA, Weinheim 

five-membered ring facing the metal atom. This larger value permits the resolution of the two components of the ME spectrum and the detailed temperature dependence of the QS parameter. The relevant data are summarized in Figure 8 which shows that in the low-temperature region (90 to ≈250 K) the QS parameter *increases* with increasing temperature, and then decreases normally in the higher temperature range. This relatively unusual behavior is not observed for the remainder of the $Fe^{II}$ complexes as mentioned earlier.

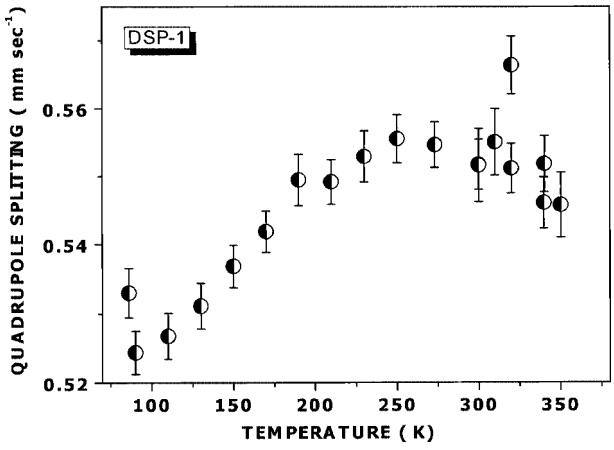


Figure 8. Temperature dependence of the quadrupole splitting for **1** ("DSP-1").

### *Recoil-Free Fraction and Vibrational Amplitude*

For an optically "thin" absorber, the area under the resonance curve scales directly with the recoil-free fraction, $f$, of the 14.4 keV gamma ray of $^{57}Fe$. Since $f = -\exp(k^2\langle x^2\rangle)$, where $k$ is the wave vector of the gamma ray and $\langle x^2\rangle$ is the mean-square-amplitude-of-vibration (msav) of the metal atom, detailed information on the temperature dependence of the area under the resonance curve can provide information on the dynamics of the iron atom in a variety of environments. To this end, the temperature dependence of the logarithm under the resonance curve, $-\mathrm{d}\ln[A(T)/A(90)]/\mathrm{d}T$, has been determined for the ferracarboranes of the present study. A representative data set is summarized graphically in Figure 9 for [$NMe_3Ph$][**1**] and **3b**. Two qualitatively different types of behavior are reflected in the data listed in Table 1. In the case of **2c** and **3b**, the data are well-represented by a linear regression over the whole temperature range. More frequently, however, as in the case of the other compounds studied, the data are better represented by two different linear functions: one at low temperatures and one at high temperatures. In the case of **3d**, the data show continuous curvature over the accessible temperature range and have not been subjected to further analysis. As has been shown previously, using the slope of $\mathrm{d}\ln[A(T)/A(90)]/\mathrm{d}T$ it is possible to calculate $\langle x_{ave}{}^2\rangle$ from the ME data and compare this to the corresponding (average) value extracted from the $U_{i,j}$ data acquired in single-crystal X-ray diffraction studies. This comparison has been performed for three of the carboranes examined in this work, and these will now be discussed in some detail.

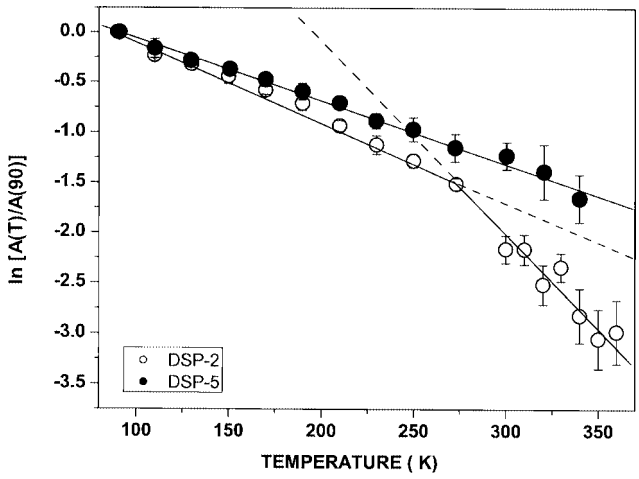


Figure 9. Temperature dependence of the logarithm of the area under the resonance curve for [$NMe_3Ph$][**1**] ("DSP-2") and **3b** ("DSP-5") showing the two types of dependencies discussed in the text.

For **1**, the ME $f$ slope is $(8.00 \pm 0.09)\cdot 10^3\ K^{-1}$ with a correlation coefficient ($R$) of 0.992 for 11 data points. From this slope, $\langle x^2_{ave}\rangle = 0.021\ Å^2$ at 120 K, while the X-ray data yield a value of 0.0229 $Å^2$ at this temperature. In addition, the early X-ray data of Zalkin et al.[7] reflected a value of 0.053 $Å^2$ at room temperature, while the present ME data at 300 K yields $\langle x^2_{ave}\rangle = 0.045\ Å^2$ which is in reasonable agreement. A similar comparison for **3a** yields a value of $\langle x^2_{ave}\rangle = 0.0192\ Å^2$ at 120 K from the X-ray data of Kudinov et al.,[5] while the present ME data show $\langle x^2_{ave}\rangle = 0.0176\ Å^2$ at the same temperature. Finally, for **3b**, $\langle x^2_{ave}\rangle$ calculated from the X-ray data at 120 K is 0.0210 $Å^2$, while that extracted from the ME data is 0.0134 $Å^2$ which is only in modest agreement. Nonetheless, it is clear from this data, that the temperature dependence of $f$ can provide a reasonable estimate of the msav of the metal atom in these compounds, and it can be used to compare the rmsav of the iron atom in different bonding environments.

The rmsav data for **3a** and **3b** at several different temperatures are summarized in Table 2, along with the corresponding data for ferrocene. This parameter is identical (within experimental error) for **3a** and ferrocene for all temperatures in the indicated range. In this context, the following correlation between the X-ray and ME data for **3a** and **3b** is significant. The corresponding rmsav data are displayed in Figure 10, which shows that this parameter is larger for **3a** than for **3b** over the whole temperature range, suggesting that the vibrational amplitude of the Fe atom in **3b** is smaller than it is for **3a**. This conclusion is in good agreement with the X-ray data at 120 K, which show that the average Fe–B bond lengths are 2.055 Å in **3b** and 2.085 Å in **3a**. Moreover, these results are also consistent with the DFT calculations which show that **3b** is 16.95 kcal $mol^{-1}$ more stable than **3a**.[5]

 © 2006 Wiley-VCH Verlag GmbH & Co. KGaA, Weinheim 

Table 2. The rmsav [Å] for ferrocene, **3a**, and **3b**.

| **3b** | **3a** | $FeCp_2$ | *T* [K] |
|---|---|---|---|
| 0.11 | 0.13 | 0.13 | 100 |
| 0.13 | 0.15 | 0.15 | 150 |
| 0.15 | 0.18 | 0.18 | 200 |
| 0.17 | 0.20 | 0.20 | 250 |
| 0.18 | 0.22 | 0.22 | 300 |

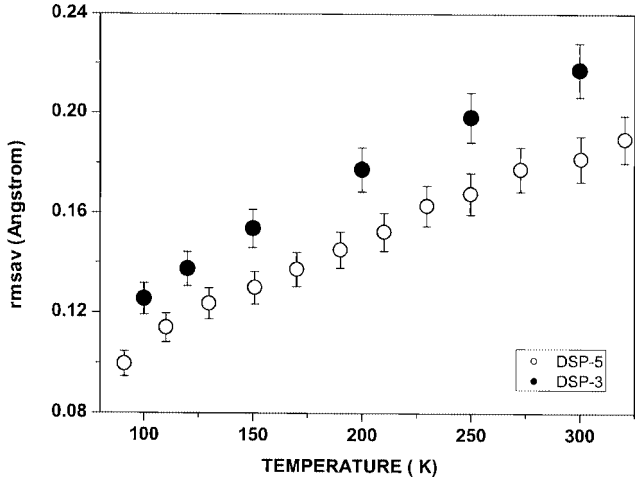


Figure 10. Temperature dependence of the rmsav of the iron atom in **3a** ("DSP-3") and **3b** ("DSP-5"). The larger vibrational amplitude is associated with the longer Fe–B bond lengths in the former than the latter compound as extracted from the 120 K X-ray data.

## Electrochemistry

The redox activity of the $Fe^{II}$ complexes shown in Scheme 1 was studied by electrochemical techniques. Before illustrating the redox aptitude of the ferratricarbollides, let us compare the classical (cyclopentadienyl)ferradicarbollide $[\mathbf{1}]^-$ with the charge-compensated analogs **2a**–**e** and bis(carboranyl) complex Fe(η-9-$SMe_2$-7,8-$C_2B_9H_{10})_2$ (**4**).

Since the $Fe^{III}$ complex **1**, in MeCN solution, undergoes reversible reduction to the corresponding $Fe^{II}$ monoanion,[20] it is not unexpected that $[\mathbf{1}]^-$, in $CH_2Cl_2$ solution, affords the complementary reversible $Fe^{II}/Fe^{III}$ oxidation. In fact, exhaustive one-electron oxidation makes the original golden-yellow solution turn wine-red, and in confirmation of the chemical reversibility of the $[\mathbf{1}]^-/\mathbf{1}$ couple also in the long timescale of macroelectrolysis, cyclic voltammetric tests show a profile quite complementary to the original profile.

Similar behavior is displayed by complexes **2a**–**e**, except that the $Fe^{II}/Fe^{III}$ oxidation occurs at markedly higher potential values, as illustrated in Table 3.

The charge compensation of the carborane ligand in 1-Cp-4-L-1,2,3,4-$Fe^{II}C_2B_9H_{10}$ makes the oxidation notably difficult with respect to the unsubstituted dicarbollyl ligand in $[\mathbf{1}]^-$, which is not only because of Coulombic effects, but in part also from the intrinsic electronic effect of the half-unit 9-L-7,8-$C_2B_9H_{10}$, as testified by the positive shift of the bis(carboranyl) derivative **4** relative to **2a**.[21] On the other hand, the methyl substitution at the carbon atoms of the carboranyl ligand in **2d** does not substantially have any effect with respect to **2a**, whereas the permethylation of the cyclopentadienyl ring in **2e** makes the oxidation significantly easier.

In order to evaluate the electronic effects played by the introduction of a third carbon atom in the framework of the classical dicarbollide dianion $[C_2B_9H_{11}]^{2-}$, Figure 11 compares the cyclic voltammetric behavior of complex **3c** with that of $[\mathbf{1}]^-$ in $CH_2Cl_2$ solution.

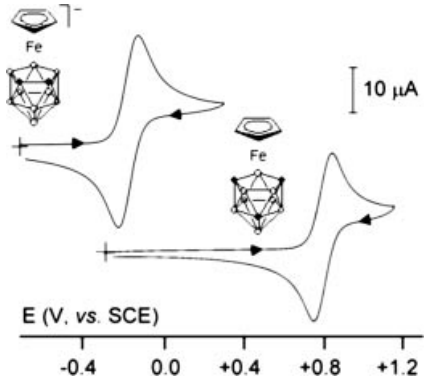


Figure 11. Cyclic voltammetric responses recorded at a platinum electrode in $CH_2Cl_2$ solutions of $[\mathbf{1}]^-$ ($1.3\cdot10^{-3}$ mol dm$^{-3}$) and **3c** ($1.2\cdot10^{-3}$ mol dm$^{-3}$); $[NBu_4][PF_6]$ (0.2 mol dm$^{-3}$) as supporting electrolyte; scan rate 0.2 V s$^{-1}$.

Similar to $[\mathbf{1}]^-$ and its charge-compensated derivatives, **3c** undergoes the reversible $Fe^{II}/Fe^{III}$ step, but the oxidation is further shifted towards positive potential values. In fact, analysis of the cyclic voltammograms with scan rates varying from 0.02 to 2.00 V s$^{-1}$ shows that (i) the current function $i_{pa}\cdot v^{-1/2}$ decreases by about 10% for each 10-fold in-

Table 3. Formal electrode potentials [V vs. SCE], peak-to-peak separations [mV], and color changes [$\lambda_{max}$ in nm] accompanying the $Fe^{II}/Fe^{III}$ oxidation of the dicarbollide complex $[\mathbf{1}]^-$ and the related charge-compensated complexes **2a**–**e** and **4** in $CH_2Cl_2$ solution.

| Complex | $E°'$ | $\Delta E_p$[a] | Original color [$\lambda_{max}$] | Color of the oxidized solution [$\lambda_{max}$] |
|---|---|---|---|---|
| $[\mathbf{1}]^-$ | –0.18 | 84 | yellow | red-wine (570) |
| **2a** | +0.47 | 72 | orange (475) | gray (594) |
| **2b** | +0.40 | 72 | orange (470) | pink-brown (580) |
| **2c** | +0.40 | 62 | red (415) | gray-green (593) |
| **2d** | +0.49 | 65 | pink-orange (470) | green (615) |
| **2e** | +0.21 | 66 | pale-orange (478) | olive-green (636; 710) |
| **4**[a] | +0.55 | 80 | pink | pink-orange |
| $FeCp_2$ | +0.39 | 80 | yellow | green (618) |

[a] Cf. with ref.[20]

 © 2006 Wiley-VCH Verlag GmbH & Co. KGaA, Weinheim 

crease of the scan rate, (ii) the current ratio $i_{pc}/i_{pa}$ remains constantly equal to 1, and (iii) the peak-to-peak separation progressively increases from 84 to 154 mV. These parameters are diagnostic for a one-electron, chemically reversible, and electrochemically quasireversible process, in the short times of cyclic voltammetry.[22] Controlled-potential exhaustive oxidation ($E_w$ = +1.0 V) consumes one electron *per* molecule. The original yellow solution turns pale green, and also in this case, the cyclic voltammetric test shows a profile quite complementary to the original profile.

Figure 12 compares the spectral changes accompanying the progressive passage from $[\mathbf{1}]^-$ to **1** (top) with those from **3c** to $[\mathbf{3c}]^+$ (bottom).

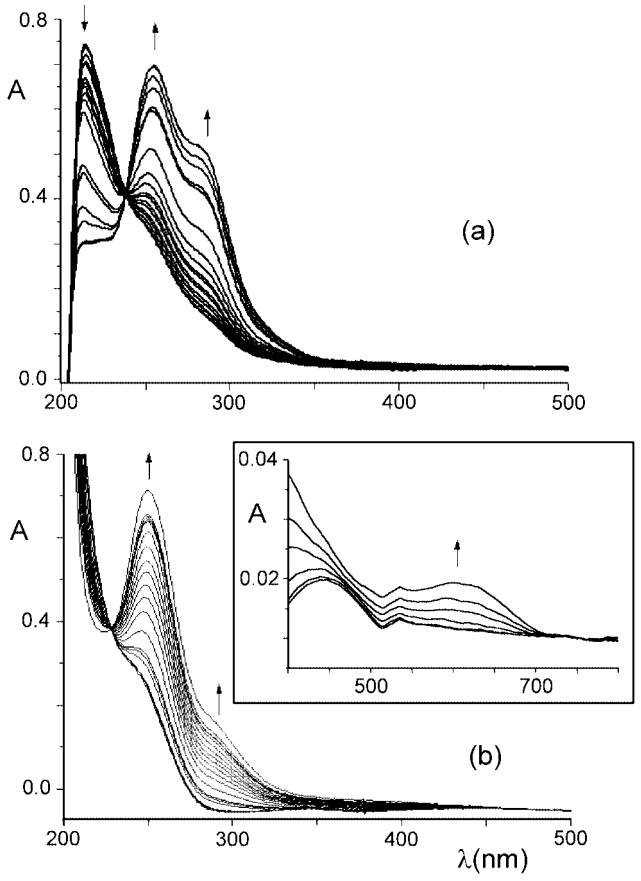


Figure 12. Spectral changes recorded in an OTTLE cell upon progressive oxidation of (a) $[\mathbf{1}]^-$ and (b) **3c**; $CH_2Cl_2$ solution with $[NBu_4][PF_6]$ (0.2 mol dm$^{-3}$) as supporting electrolyte.

In both cases, the appearance of the isosbestic point ($[\mathbf{1}]^-/\mathbf{1}$: $\lambda$ = 238 nm; $\mathbf{3c}/[\mathbf{3c}]^+$: $\lambda$ = 228 nm) further supports the chemical reversibility of the pertinent oxidation processes. The bands arising in the UV region are conceivably assigned to LMCT transitions. In agreement with the final pale-green color of the solution of $[\mathbf{3c}]^+$, a weak band also appears at $\lambda_{max}$ = 620 nm (inset of Figure 12).

A similar redox activity holds in THF solution, except that, because of the larger cathodic window of this solvent, a reduction process can also be detected, which possesses features of chemical reversibility in the cyclic voltammetric timescale (see Figure 13).

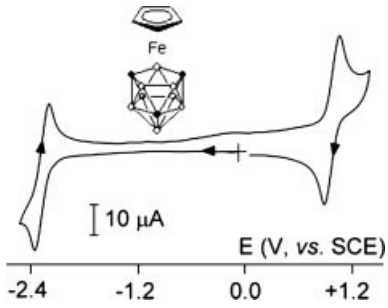


Figure 13. Cyclic voltammetric response recorded at a gold electrode in THF solution of **3c** ($1.0\cdot10^{-3}$ mol dm$^{-3}$); $[NBu_4][PF_6]$ (0.2 mol dm$^{-3}$) as supporting electrolyte; scan rate 0.2 V s$^{-1}$.

The extremely negative potential value of the process prevented the experimental measurement by controlled-potential coulometry of the number of electrons involved, but the similarity of the peak height with that of the anodic process suggests it is a one-electron process. In the first instance, we therefore assign it to the $Fe^{II}/Fe^{I}$ passage; a redox change not too unusual in organometallic chemistry,[23] but quite new in ferracarborane chemistry. The separation between the one-electron oxidation and the one-electron reduction (3.2 eV) can be roughly considered as an experimental measurement of the HOMO–LUMO separation.

Complexes **3b** and **3d** also display a chemically reversible one-electron oxidation. However, in contrast to **3c**, no reduction process is detected in THF for complex **3d**, whereas complex **3b** gives rise to an irreversible reduction. Upon exhaustive oxidation, the original orange solution of complex **3b** turns brown, and the spectroelectrochemical trend in the UV region is very similar to that illustrated for **3c**. A similar spectroelectrochemical pattern was recorded in the UV region during the golden-yellow/maroon transition from **3d** to $[\mathbf{3d}]^+$, except for a new band at 350 nm (see Supporting Information).

Finally, the one-electron oxidation of complex **3a** in $CH_2Cl_2$ solution is accompanied by chemical complica-

Table 4. Formal electrode potentials [V vs. SCE], peak-to-peak separations [mV], and current ratios for the redox activity of the ferratricarbollides **3a**–**d**.

| | Oxidation | | | Reduction | | | Solvent |
|---|---|---|---|---|---|---|---|
| | $E°'$ | $\Delta E_p$[a] | $i_{pc}/i_{pa}$[a] | $E°'$ | $\Delta E_p$[a] | $i_{pa}/i_{pc}$[a] | |
| $[\mathbf{1}]^-$ | –0.18 | 84 | 1.0 | – | – | – | $CH_2Cl_2$ |
| | –0.04 | 89 | 1.0 | – | – | – | THF |
| **3a** | +0.74 | 72 | 0.8[b] | – | – | – | $CH_2Cl_2$ |
| | +0.91 | 103 | 0.5 | –1.56 | 74 | 0.5 | THF |
| **3b** | +0.82 | 73 | 1.0 | – | – | – | $CH_2Cl_2$ |
| | +0.94 | 72 | | –2.05[c] | – | 1.0 | THF |
| **3c** | +0.80 | 82 | 1.0 | – | – | – | $CH_2Cl_2$ |
| | +0.96 | 96 | 1.0 | –2.29 | 127 | 0.8[d] | THF |
| **3d** | +0.60 | 73 | 1.0 | – | – | – | $CH_2Cl_2$ |
| | +0.77 | 78 | 1.0 | – | – | – | THF |
| $FeCp_2$ | +0.39 | 80 | 1.0 | – | – | – | $CH_2Cl_2$ |
| | +0.53 | 82 | 1.0 | – | – | – | THF |

[a] Measured at 0.1 V s$^{-1}$. [b] Accompanied by chemical complications (see text). [c] Peak-potential value for irreversible processes. [d] Because of the close solvent discharge, the present value is of limited accuracy as far as the extent of chemical reversibility is concerned.

 © 2006 Wiley-VCH Verlag GmbH & Co. KGaA, Weinheim 

tions. The current ratio $i_{pc}/i_{pa}$ is lower than unity at low scan rate and progressively tends to increase with an increase of the scan rate. In fact, exhaustive one-electron oxidation leads to a presently unknown species, which reduces at $E°' = +0.34$ V. The $Fe^{II}/Fe^{I}$ reduction in THF (in such solvent the complex is stable only for short times) is also partially chemically reversible and occurs at potential values less negative than that of **3c**. In fact, a HOMO–LUMO separation of 2.5 eV can be calculated. The formal electrode potentials of the mentioned electrode processes are compiled in Table 4.

## Conclusions

The X-ray diffraction study revealed that the Fe···$C_2B_3$ and Fe···Cp distances in 17-electron ferracarborane **1** are significantly longer than those in its 18-electron congener $[\mathbf{1}]^-$, in accordance with one-electron removal from the bonding HOMO. The electrochemical investigation revealed that the $Fe^{II}$-tricarbollide complexes are more difficult to oxidize than the charge-compensated dicarbollide analogs, which in turn are more difficult to oxidize than the parent ferracarborane $[\mathbf{1}]^-$. The location of the $Fe^{II}/Fe^{III}$ couple for **3a**–**c** at highly positive potential values makes the $Fe^{II}/Fe^{I}$ reduction accessible. The fact that the redox changes of the different isomers occur at different potential values constitutes a further supporting technique in their selective recognition. Temperature-dependent $^{57}Fe$ Mössbauer effect spectroscopy (TDMES) was used to elucidate the hyperfine interaction parameters of the neutral carbollide complexes, as well as the dynamical aspects of the iron atom motion as a function of temperature. For a number of ferracarboranes studied in detail, modestly good agreement, within experimental error, was obtained for the msav extracted from single-crystal X-ray diffraction studies and TDMES.

## Experimental Section

**General Remarks:** All reactions were carried out under argon in anhydrous solvents which were purified and dried using standard procedures. The isolation of products was conducted in air. Ferracarboranes **1**, $[NMe_3Ph][\mathbf{1}]$,[20] and **3a**–**d**[5,6] were prepared as described in the literature. The solutions of sodium salts Na[9-L-7,8-$R_2$-7,8-$C_2B_9H_8$] were obtained by reaction of the corresponding carborane with NaH in THF.[24] Irradiation was conducted in a Schlenk tube using a high-pressure mercury-vapor lamp with a phosphor-coated bulb (400 W). The $^1H$- and $^{11}B$ NMR spectra were measured with a Bruker AMX-400 instrument at room temp. in [$D_6$]acetone unless otherwise stated. Materials and apparatus for electrochemistry and spectroelectrochemistry have been described elsewhere.[25] All the potential values are referred to the saturated calomel electrode (SCE).

**1-Cp-4-$SMe_2$-1,2,3-$FeC_2B_9H_{10}$ (2a):** To a solution of [$CpFe(C_6H_6)$]-$PF_6$ (344 mg, 1 mmol) in a mixture of THF (16 mL) and MeCN (4 mL) which was chilled to –78 °C, was added a solution of Na[9-$SMe_2$-7,8-$C_2B_9H_{10}$] in THF (4 mL, 1 mmol). The resulting mixture was irradiated with stirring at –60 to –40 °C within 1 h, and the solvents evaporated in vacuo. The residue was washed several times with MeOH giving red solid **2a** which was 95% pure according to $^1H$- and $^{11}B$ NMR spectroscopy. The analytically pure sample was obtained by reprecipitation using heptane from $CH_2Cl_2$. Yield 255 mg (80%). $^1H$ NMR: $\delta = 4.54$ (s, 5 H, Cp), 4.08 (br. s, 1 H, cage CH), 3.52 (br. s, 1 H, cage CH), 2.73 (s, 3 H, $SMe_2$), 2.73 (s, 3 H, $SMe_2$) ppm. $^{11}B$ NMR (*J*, Hz): $\delta = -6.04$ (d, 136, 1B), –6.04 (s, 1B, $BSMe_2$), –10.20 (d, 142, 1B), –11.30 (d, 142, 1B), –13.24 (d, 142, 1B), –17.87 (d, 138, 1B), –24.55 (d, 152, 1B), –27.11 (d, 165, 1B), –28.71 (d, 202, 1B) ppm. $C_9H_{21}B_9FeS$ (314.46): calcd. C 34.38, H 6.73, B 30.94, Fe 17.76; found C 34.32, H 6.48, B 30.80, Fe 17.44.

**1-Cp-4-$NMe_3$-1,2,3-$FeC_2B_9H_{10}$ (2b):** Compound **2b** was synthesized in a similar manner to **2a**. However, when the irradiation was finished, the reaction tube was placed into a Dewar vessel with an acetone/dry ice mixture, and the reaction mixture was additionally stirred for 24 h with gradual rising of temp. to 20 °C. Yield 32%. $^1H$ NMR: $\delta = 4.63$ (s, 5 H, Cp), 4.56 (br. s, 1 H, cage CH), 3.58 (br. s, 1 H, cage CH), 3.19 (s, 9 H, $NMe_3$) ppm. $^{11}B$ NMR (*J*, Hz): $\delta = 5.27$ (s, 1B, $BNMe_3$), –5.45 (d, 129, 1B), –10.13 (d, 130, 1B), –10.84 (d, 109, 1B), –13.31 (d, 156, 1B), –14.94 (d, 151, 1B), –24.85 (d, 152, 1B), –26.08 (d, 157, 1B), –28.30 (d, 167, 1B) ppm. $C_{10}H_{24}B_9FeN$ (311.44): calcd. C 38.57, H 7.77, N 4.50; found C 38.59, H 7.91, N 4.54.

**1-Cp-4-py-1,2,3-$FeC_2B_9H_{10}$ (2c):** To a solution of [$CpFe(C_6H_6)$]$PF_6$ (172 mg, 0.5 mmol) in a mixture of THF (3 mL) and MeCN (3 mL) which was chilled to –78 °C, was added a solution of Na[9-py-7,8-$C_2B_9H_{10}$] in THF (10 mL, 0.5 mmol). The resulting mixture was irradiated with stirring at –60 to –40 °C within 3 h, treated with MeOH (1 mL), and filtered. The filtrate was evaporated in vacuo, and the residue was eluted on a silica gel column (7 cm) with a $CH_2Cl_2$/petroleum ether (1:1) mixture. The bright-red band was collected, evaporated in vacuo, and washed several times with ether to give dark-red crystals of **2c**. Yield 60 mg (48%). $^1H$ NMR: $\delta =$ 9.00 (d, 5.6, 2 H, $C_5H_5N$), 8.46 (t, 7.6, 1 H, $C_5H_5N$), 8.00 (t, 7.2, 2 H, $C_5H_5N$), 4.72 (br. s, 1 H, cage CH), 4.15 (s, 5 H, Cp), 3.53 (br. s, 1 H, cage CH) ppm. $^{11}B$ NMR (*J*, Hz): $\delta = 2.56$ (s, 1B, Bpy), –5.68 (d, 129, 1B), –9.83 (d, 147, 1B), –11.03 (d, 158, 1B), –12.64 (d, 141, 1B), –13.72 (d, 139, 1B), –23.03 (d, 153, 1B), –25.92 (d, 151, 1B), –28.05 (d, 167, 1B) ppm. $C_{12}H_{20}B_9FeN$ (331.43): calcd. C 43.49, H 6.08, B 29.35; found C 43.49, H 6.02, B 29.08.

**1-Cp-2,3-$Me_2$-4-$SMe_2$-1,2,3-$FeC_2B_9H_8$ (2d):** Compound **2d** was prepared in a similar manner to **2a**. Yield 220 mg (64%). $^1H$ NMR: $\delta = 4.48$ (s, 5 H, Cp), 2.86 (s, 3 H, $SMe_2$), 2.60 (s, 3 H, $SMe_2$), 2.44 (s, 3 H, CMe), 2.22 (s, 3 H, CMe) ppm. $^{11}B$ NMR (*J*, Hz; $CD_2Cl_2$): $\delta = -1.65$ (s, 1B, BPy), –4.86 (d, 157, 1B), –6.20 (d, 155, 1B), –9.35 (d, 142, 1B), –12.66 (d, 138, 1B), –17.68 (d, 130, 2B), –18.55 (d, 140, 1B), –20.64 (d, 150, 1B) ppm. $C_{11}H_{26}B_9FeS$ (343.52): calcd. C 38.46, H 7.63; found C 38.39, H 7.21.

**1-Cp*-4-$SMe_2$-1,2,3-$FeC_2B_9H_{10}$ (2e):** A solution of Na[9-$SMe_2$-7,8-$C_2B_9H_{10}$] in THF (2 mL, 0.5 mmol) was added to a solution of [$Cp^*Fe(MeCN)_3$]$BF_4$ (200 mg, 0.5 mmol) in THF (10 mL) at 0 °C. The resulting mixture was stirred at this temp. for 1 h, and compound **2e** was isolated in a similar manner to **2a**. Yield 155 mg (80%). $^1H$ NMR: $\delta = 5.32$ (br. s, 1 H, cage CH), 3.58 (br. s, 1 H, cage CH), 2.59 (s, 6 H, $SMe_2$), 2.39 (s, 6 H, $SMe_2$), 2.35 (br. s, 1 H, cage CH), 1.79 (s, 15 H, Cp*) ppm. $^{11}B$ NMR (*J*, Hz): $\delta =$ –4.90 (d, 195, 1B), –6.02 (s, 1B, $BSMe_2$), –9.19 (d, 144, 1B), –12.90 (d, 130, 1B), –13.80 (d, 130, 1B), –18.18 (d, 138, 1B), –25.28 (d, 159, 1B), –27.27 (d, 176, 1B), –29.13 (d, 227, 1B) ppm.

**Mössbauer Spectroscopy:** The solid compounds were transferred to plastic sample holders and examined by standard transmission

 © 2006 Wiley-VCH Verlag GmbH & Co. KGaA, Weinheim 

Table 5. Crystal data and structure-refinement parameters for **1**, [$NMe_3Ph$][**1**], and **2b**.

| Compound | **1** | [$NMe_3Ph$][**1**] | **2b** |
|---|---|---|---|
| Empirical formula | $C_7H_{16}B_9Fe$ | $C_{16}H_{30}B_9FeN$ | $C_{10}H_{23}B_9FeN$ |
| Formula weight | 253.34 | 389.55 | 310.43 |
| Crystal color, habit | violet plate | red plate | red prism |
| Crystal size [mm] | 0.30×0.10×0.10 | 0.40×0.10×0.10 | 0.30×0.20×0.20 |
| Temperature [K] | 120(2) | 120(2) | 120(2) |
| Crystal system | monoclinic | monoclinic | orthorhombic |
| Space group | $P2_1/c$ | $P2_1/n$ | $Pna2_1$ |
| $a$ [Å] | 11.4669(1) | 8.2460(2) | 14.846(2) |
| $b$ [Å] | 6.4619(1) | 16.9626(5) | 8.788(1) |
| $c$ [Å] | 16.6791(2) | 14.3504(4) | 11.827(2) |
| $\beta$ [°] | 100.650(1) | 96.8406(16) | 90 |
| $V$ [Å$^3$] | 1214.60(3) | 1992.95(9) | 1543.1(4) |
| $Z(Z')$ | 4(1) | 4(1) | 4(1) |
| $F(000)$ | 516 | 816 | 644 |
| $D_{calcd.}$ [g cm$^{-1}$] | 1.385 | 1.298 | 1.336 |
| Linear absorption, $\mu$ [cm$^{-1}$] | 11.99 | 7.57 | 9.59 |
| $T_{min}/T_{max}$ | 0.7150/0.8895 | 0.7516/0.9281 | 0.7619/0.8314 |
| Scan type | $\omega$ | $\omega$ | $\omega$ |
| $\theta$ range [°] | 1.81–45.00 | 1.87–50.34 | 2.69–30.01 |
| Completeness of dataset [%] | 98.4 | 98.1 | 99.9 |
| Reflections measured | 36197 | 71800 | 11745 |
| Independent reflections | 9862 [$R_{int}$ = 0.0456] | 20808 [0.0396] | 4327 [0.0276] |
| Observed reflections [$I > 2\sigma(I)$] | 7912 | 15599 | 3148 |
| Parameters | 218 | 364 | 247 |
| Final $R(F_{hkl})$:$R_1$ ratio | 0.0435 | 0.0431 | 0.0475 |
| w$R_2$ | 0.0981 | 0.0894 | 0.1169 |
| GOF | 1.014 | 0.993 | 0.945 |
| $\Delta\rho_{max}$, $\Delta\rho_{min}$ [e Å$^{-3}$] | 0.628, –0.636 | 0.669, –0.544 | 0.969, –0.760 |

Mössbauer effect spectroscopy (MES) using a 50 mCi $^{57}$Co/Rh source as described previously.[26] Spectrometer calibration was performed using a 10 mg cm$^{-2}$ α-Fe foil at room temp., and all isomer shifts are referred to the centroid of such a spectrum. ME data acquisition times varied from 7 to 30 h (depending on the temp.), and since one of the objectives of this research was to elucidate the temperature-dependent parameters extracted from the ME data, the thermal variation with time was continuously monitored using the Daswin program of Glaberson and Brettschneider.[27] The temp. uncertainties are estimated as ±0.1 K over the data acquisition intervals.

**Calculation Details:** All calculations were performed using Gaussian 98 package.[28] The structure of [**1**]$^-$ was optimized at B3LYP/6-31G* level in $C_s$ symmetry. The molecular orbital visualization was performed by ChemCraft software, version 1.5 (www.chemcraftprog.org).

**X-ray Crystallography:** Crystals of **1** and [$NMe_3Ph$][**1**] suitable for X-ray diffraction were grown by slow evaporation of $CH_2Cl_2$ solutions. Crystals of **2b** were grown by slow diffusion in a two-layer system, solution of the complex in [$D_6$]acetone/petroleum ether, placed in an NMR tube. X-ray diffraction experiments were carried out with a Bruker SMART 1000 CCD area detector, using graphite-monochromated Mo-$K_\alpha$ radiation at 110 K. Low temp. of the crystals was maintained with a Cryostream (Oxford Cryosystems) open-flow nitrogen gas cryostat. Reflection intensities were integrated using SAINT software,[29] and absorption correction was applied semi-empirically using SADABS program. The structures were solved by direct method and refined by the full-matrix least-squares against $F^2$ in anisotropic approximation for non-hydrogen atoms. All polyhedron hydrogen atoms were located from the Fourier density synthesis and refined in isotropic approximation. Crystal data and structure-refinement parameters for **1**, [$NMe_3Ph$][**1**], and **2b** are given in Table 5. All calculations were performed using the SHELXTL software.[30]

CCDC-291166 (for [$NMe_3Ph$][**1**]), -291167 (for **1**), and -291168 (for **2b**) contain the supplementary crystallographic data for this paper. These data can be obtained free of charge from The Cambridge Crystallographic Data Centre via www.ccdc.cam.ac.uk/data_request/cif.

**Supporting Information** (for details see the footnote on the first page of this article): Spectroelectrochemical data for transition from **3d** to [**3d**]$^+$ and the optimized coordinates from DFT calculations of [**1**]$^-$.

## Acknowledgments

We thank Prof. W. Glaberson and Dr. M. Brettschneider for the use of their Daswin program prior to publication. Financial support from the Racah Institute and the Division of General Chemistry and Material Sciences of Russian Academy of Sciences, as well as the University of Siena (PAR 2005) is also gratefully acknowledged. D. S. P. thanks INTAS for a Young Scientist Fellowship (Grant No. 04-83-3848).

[1] M. F. Hawthorne, R. L. Pilling, *J. Am. Chem. Soc.* **1965**, *87*, 3987–3988.
[2] Synthesis of **2a** and **2e** was described in a short communication: A. R. Kudinov, V. I. Meshcheryakov, P. V. Petrovskii, M. I. Rybinskaya, *Izv. Akad. Nauk, Ser. Khim.* **1999**, 177–179; *Russ. Chem. Bull.* **1999**, *48*, 176–177 *(Engl. Transl.)*.
[3] T. P. Gill, K. R. Mann, *Inorg. Chem.* **1983**, *22*, 1986–1991.
[4] Complex **2e** was prepared earlier in 30% yield by reaction of the corresponding anion with [Cp*FeCl]$_2$: Y.-K. Yan, D. M. P. Mingos, T. E. Müller, D. J. Williams, M. Kurmoo, *J. Chem. Soc., Dalton Trans.* **1995**, 2509–2514.

 © 2006 Wiley-VCH Verlag GmbH & Co. KGaA, Weinheim 

[5] D. S. Perekalin, J. Holub, D. G. Golovanov, K. A. Lyssenko, P. V. Petrovskii, B. Štibr, A. R. Kudinov, *Organometallics* **2005**, *24*, 4387–4392.
[6] J. Holub, B. Grüner, D. S. Perekalin, D. G. Golovanov, K. A. Lyssenko, P. V. Petrovskii, A. R. Kudinov, B. Štibr, *Inorg. Chem.* **2005**, *44*, 1655–1659.
[7] A. Zalkin, D. H. Templeton, T. E. Hopkins, *J. Am. Chem. Soc.* **1965**, *87*, 3988–3990.
[8] The numbering system where the metal vertex bears number 1 is used for metallacarboranes.
[9] A. Haaland, J. E. Nilsson, *Acta Chem. Scand.* **1968**, *23*, 2653–2670.
[10] B. M. Yamin, H. K. Fun, K. Sivakumar, B. C. Yip, O. B. Shawkataly, *Acta Crystallogr. Sect. C* **1996**, *52*, 600–602, and references therein.
[11] The $^2$E ground state of **1** is in accordance with low-temperature EPR data: A. H. Maki, T. E. Berry, *J. Am. Chem. Soc.* **1965**, *87*, 4437–4441.
[12] a) V. I. Goldansakii, E. F. Makarov in *Chemical Applications of Mössbauer Spectroscopy* (Eds.: V. I. Goldanskii, R. H. Herber), Academic Press, New York, **1968**, pp. 47–55; b) B. D. Dunlap, G. M. Kalvius in *Mössbauer Isomer Shifts* (Eds.: G. K. Shenoy, F. E. Wagner), North Holland Publishing, Amsterdam, **1978**, pp. 15–48.
[13] R. H. Herber in *Chemical Mössbauer Spectroscopy* (Ed.: R. H. Herber), Plenum Press, New York, **1984**, pp. 199–216.
[14] I. Nowik, R. H. Herber, *Inorg. Chim. Acta* **2000**, *310*, 191–195; I. Nowik, R. H. Herber, *Hyperfine Interact.* **2005**, in press.
[15] R. L. Collins, *J. Chem. Phys.* **1965**, *42*, 1072–1080.
[16] See the discussion in: N. N. Greenwood, T. C. Gibb, *Mössbauer Spectroscopy*, Chapman and Hall, London, **1971**, pp. 233–236.
[17] H. Schottenberger, K. Wurst, U. J. Griesser, R. K. R. Jetti, G. Laus, R. H. Herber, I. Nowik, *J. Am. Chem. Soc.* **2005**, *127*, 6795–6801.
[18] R. H. Herber, I. Gattinger, F. H. Köhler, *Inorg. Chem.* **2000**, *39*, 851–853.
[19] H. Schottenberger, K. Wurst, R. H. Herber, *J. Organomet. Chem.* **2001**, *625*, 200–207.
[20] M. F. Hawthorne, D. C. Young, T. D. Andrews, D. V. Howe, R. L. Pilling, A. D. Pitts, M. Reintjes, L. F. Warren Jr., P. A. Wegner, *J. Am. Chem. Soc.* **1968**, *90*, 879–896.
[21] Y.-K. Yan, D. M. P. Mingos, T. E. Müller, D. J. Williams, M. Kurmoo, *J. Chem. Soc., Dalton Trans.* **1994**, 1735–1741.
[22] P. Zanello, *Inorganic Electrochemistry: Theory, Practice, and Application*, RSC, United Kingdom, **2003**.
[23] a) M. C. Rakowski, D. H. Bush, *J. Am. Chem. Soc.* **1975**, *97*, 2570–2571; b) A. Croisy, D. Lexa, M. Momenteau, J. M. Saveant, *Organometallics* **1985**, *4*, 1574–1579; c) M. H. Desbois, D. Astruc, J. Guillin, J. P. Mariot, F. Varret, *J. Am. Chem. Soc.* **1985**, *107*, 5280–5282; d) K. R. Rodgers, R. A. Reed, Y. O. Su, T. G. Spiro, *Inorg. Chem.* **1992**, *31*, 2688–2700; e) C. Bianchini, F. Laschi, D. Masi, F. M. Ottaviani, A. Pastor, M. Peruzzini, P. Zanello, F. Zanobini, *J. Am. Chem. Soc.* **1993**, *115*, 2723–2730; f) D. Mimica, J. H. Zagal, F. Bedioui, *J. Electroanal. Chem.* **2001**, *497*, 106–143; g) S. Rigaut, M.-H. Delville, J. Losada, D. Astruc, *Inorg. Chim. Acta* **2002**, *334*, 225–242.
[24] V. I. Meshcheryakov, P. S. Kitaev, K. A. Lyssenko, Z. A. Starikova, P. V. Petrovskii, Z. Janoušek, M. Corsini, F. Laschi, P. Zanello, A. R. Kudinov, *J. Organomet. Chem.* **2005**, *690*, 4745–4754.
[25] F. Fabrizi de Biani, M. Corsini, P. Zanello, H. Yao, M. E. Bluhm, R. N. Grimes, *J. Am. Chem. Soc.* **2004**, *126*, 11360–11369.
[26] R. H. Herber, I. Nowik, D. A. Loginov, Z. A. Starikova, A. R. Kudinov, *Eur. J. Inorg. Chem.* **2004**, 3476–3483, and references therein.
[27] W. Glaberson, M. Brettschneider; see: www.PHYS.HUJI.AC.IL/~glabersn.
[28] M. J. Frisch, G. W. Trucks, H. B. Schlegel, G. E. Scuseria, M. A. Robb, J. R. Cheeseman, V. G. Zakrzewski, J. A. Montgomery Jr., R. E. Stratmann, J. C. Burant, S. Dapprich, J. M. Millam, A. D. Daniels, K. N. Kudin, M. C. Strain, O. Farkas, J. Tomasi, V. Barone, M. Cossi, R. Cammi, B. Mennucci, C. Pomelli, C. Adamo, S. Clifford, J. Ochterski, G. A. Petersson, P. Y. Ayala, Q. Cui, K. Morokuma, D. K. Malick, A. D. Rabuck, K. Raghavachari, J. B. Foresman, J. Cioslowski, J. V. Ortiz, B. B. Stefanov, G. Liu, A. Liashenko, P. Piskorz, I. Komaromi, R. Gomperts, R. L. Martin, D. J. Fox, T. Keith, M. A. Al-Laham, C. Y. Peng, A. Nanayakkara, C. Gonzalez, M. Challacombe, P. M. W. Gill, B. G. Johnson, W. Chen, M. W. Wong, J. L. Andres, M. Head-Gordon, E. S. Replogle, J. A. Pople, *Gaussian 98*, revision A.7, Gaussian, Inc., Pittsburgh, PA, **1998**.
[29] SMART V5.051 and SAINT V5.00, Area detector control and integration software, Bruker AXS Inc., Madison,WI-53719, USA, **1998**.
[30] G. M. Sheldrick, SHELXTL-97, V5.10, Bruker AXS Inc., Madison, WI-53719, USA, **1997**.

Received: December 22, 2005
Published Online: March 22, 2006

 © 2006 Wiley-VCH Verlag GmbH & Co. KGaA, Weinheim 

DOI: 10.1002/ejic.200600005

# Catalytic Activity of Copper Oxide/Zinc Oxide Composites Prepared by Thermolysis of Crystallographically Defined Bimetallic Coordination Compounds

**Rainer Weiss,[a] Yanzhi Guo,[a] Sascha Vukojević,[b] Lamma Khodeir,[c] Roland Boese,[a] Ferdi Schüth,[b] Martin Muhler,[c] and Matthias Epple*[a]**

**Keywords:** Heterogeneous catalysis / Copper / Zinc / Thermochemistry / Structural chemistry

The suitability of bimetallic coordination compounds in the systems Cu/Zn/CN and Cu/Zn/CN/ethylenediamine as precursors for CuO/ZnO was explored. The kinetic and thermodynamic equilibria in these systems are discussed. The introduction of ethylenediamine led to crystalline precursor compounds, and the bimetallic coordination compounds $[Zn(en)]_2[Cu_2(CN)_6]$ and $[Zn(en)_3]_6[Cu_2(CN)_7]_2[Cu(CN)_3]\cdot 8.4H_2O$ were structurally characterised. The oxide mixtures of CuO/ZnO, prepared by mild thermolysis of the precursor compounds, were tested for their catalytic activity in the formation of methanol from synthesis gas, i.e. $CO/CO_2/H_2$. While the oxide mixtures from $Zn[Cu(CN)_3]$ were not catalytically active, the oxide mixtures derived from the crystalline compounds with ethylenediamine as the ligand had about 20–30 % of the activity of an industrial methanol catalyst. This underscores the importance of the origin of the catalyst, i.e. the dependence of its activity from the structure of its precursor.
(© Wiley-VCH Verlag GmbH & Co. KGaA, 69451 Weinheim, Germany, 2006)

## Introduction

Cu/ZnO is a widely used system in heterogeneous catalysis for methanol synthesis and steam reforming.[1–3] Although $Cu/ZnO/Al_2O_3$ is a more efficient catalyst, Cu/ZnO is often examined as an easier model to understand the catalytic process (note that even ZnO alone is an active catalyst in methanol synthesis[4]). Conventionally, such catalysts are prepared by thermolysis of coprecipitated carbonates or oxalates.[5] Here we report on the preparation, structural characterisation, thermolysis and catalytic activity of two bimetallic coordination compounds that contain copper and zinc within the same crystal. We showed earlier that it is possible to prepare $Zn[Cu(CN)_3]$ with two metals in the same crystal.[6] It is reasonable to assume that the oxides prepared by oxidative thermolysis occur in an intimately dispersed state, thereby enhancing the catalytic activity. Two well-defined bimetallic coordination compounds can be decomposed to intimate mixtures of CuO and ZnO. The catalytic activity of the oxides derived from these precursor compounds containing Cu–Zn–CN and Cu–Zn–CN–ethylenediamine in methanol synthesis was investigated. Therefore, a comprehensive picture ranging from the single crystal structure, through to thermolysis and on to the catalytic performance is presented here.

[a] Inorganic Chemistry, University of Duisburg-Essen, Universitätsstrasse 5–7, 45117 Essen, Germany
Fax: +49-201-183-2621
E-mail: matthias.epple@uni-due.de
[b] Max-Planck-Institut für Kohlenforschung, Kaiser-Wilhelm-Platz 1, 45470 Mülheim an der Ruhr, Germany
[c] Industrial Chemistry, Ruhr University of Bochum, Universitätsstrasse 150, 44801 Bochum, Germany

## Results and Discussion

### Some General Remarks about the Thermodynamic and Kinetic Equilibria in the Cu/Zn/CN Precursor System

All syntheses were typically performed by mixing aqueous solutions of the first metal with aqueous solutions of a cyanide complex of the second metal. It turned out that a number of different species are present in solution, e.g. $[Cu^{II}(H_2O)_6]^{2+}$, $[Zn^{II}(H_2O)_6]^{2+}$, $[Zn^{II}(CN)_4]^{2-}$, "$[Cu^{II}(CN)_4]^{2-}$", $[Cu^{I}(CN)_4]^{3-}$ and $[Cu^{I}(CN)_3]^{2-}$.[7] Note that "$[Cu(CN)_4]^{2-}$" is just a formal description because $Cu^{II}$ cyanide complexes are subject to an internal redox reaction resulting in $Cu^{I}$ and $(CN)_2$. In the case of the reaction of $Cu^{2+}$ with $[Zn^{II}(CN)_4]^{2-}$, the kinetic lability of the cyanocomplexes of copper and zinc had a strong influence on the products that formed. Starting with solutions of $[Zn^{II}(CN)_4]^{2-}$ and $Cu^{2+}$, the main product was $Zn^{II}[Cu^{I}(CN)_3]$, whereas $Cu^{II}[Zn^{II}(CN)_4]$ and $Zn^{II}[Zn^{II}(CN)_4]$ were only found as side products.[6]

Furthermore, in the system Cu/CN there are not only different species in solution, but also many different types of structural elements consisting of $Cu^{I}$ coordinated by $CN^-$ exist in the solid state. For instance, the unit "$[Cu(CN)_3]^{2-}$" can be either a mononuclear trigonal-planar complex, or a dinuclear complex $[Cu_2(CN)_6]^{4-}$, as in

 © 2006 Wiley-VCH Verlag GmbH & Co. KGaA, Weinheim 

$[Cu^{II}(en)_2]_4[Cu^{I}(CN)_3]_2[Cu^{I}_2(CN)_6]\cdot 2H_2O$ (ref.[8]) or a part of an infinite three-dimensional network as in $[Zn(en)]_2[Cu_2(CN)_6]$ (**1**; see the structure below). It is essential to have the crystal structures of the precursors in this system because the crystal structure of the precursor determines the structure and morphology of the reaction products if the thermolysis is carried out at moderate temperature, i.e. not under thermodynamic equilibrium conditions.[1,9] This is of particular interest in heterogeneous catalysis where surface effects are often more important than the composition.[10,11]

The different kinetic stabilities of cyanometallate complexes are important for the preparation: In a bimetallic system which contains a kinetically stable complex, e.g. $[Fe(CN)_6]^{3-}$, and a counterion which does not form a cyanide complex itself, e.g. $Gd^{3+}$, the preparation of a bimetallic coordination compound like $Gd[Fe(CN)_6]$ is straightforward and easy.

In the pair $Cu^{I/II}$ and $Zn^{II}$, two metals are present which form kinetically unstable cyanocomplexes with comparable stability constants. The stability constant of $[Zn^{II}(CN)_4]^{2-}$ is $4\times10^{19}$ M$^{-4}$ (ref.[12]) and much smaller than that of $[Cu^{II}(CN)_4]^{2-}$ with $1\times10^{27}$ M$^{-4}$ (ref.[13]), therefore the latter compound is preferred in equilibrium. However, $Cu^{II}$ is reduced by $CN^-$ to $Cu^{I}$ upon mixing $[Zn^{II}(CN)_4]^{2-}$ and $Cu^{II}$, and the anion $[Cu^{I}(CN)_3]^{2-}$ is formed as the main copper species in solution.[6] This may serve as an example as to how the constitution of the complexes found in the solid state often cannot be predicted from the formulae of the dissolved precursor molecules, making a rational synthesis difficult.

### Bimetallic Cyanides as Precursors for CuO/ZnO for Methanol Catalysis

Mixtures of CuO and ZnO were prepared from $Zn[Cu(CN)_3]$ by oxidative thermolysis under different conditions (temperature from 200 to 500 °C). In addition, the grain size of $Zn[Cu(CN)_3]$ was adjusted by variation of the precipitation conditions as reported earlier (continuous overflow method).[6] Although the oxide mixtures (CuO and ZnO) were analytically pure (no residual cyanide compound was left after thermolysis, which was checked by IR spectroscopy and elemental analysis), the catalytic activities for methanol synthesis were practically zero in all cases. The reason for this behaviour is not known, but it is possible that the decomposition temperature was too high to preserve a sufficiently high specific surface (the BET surface area was around 5 to 10 $m^2 g^{-1}$ for these samples) and possibly some sintering had occurred.[14] On the other hand, the surface of the active copper and zinc oxide particles may have been poisoned by small amounts of cyanide that were still adsorbed under these conditions, but no longer detectable by bulk-phase techniques.

### The Precursor System Cu/Zn/CN/Ethylenediamine (en)

A better control over the precursor is possible if its crystal structure is known, yielding the coordination environment of both metals and also the unequivocal evidence that both metals are present within the same crystal. To obtain such single crystalline precursors, the solubility of the coordination compounds in the system Cu/Zn/CN had to be increased. The chelating ligand ethylenediamine, $H_2N–CH_2–CH_2–NH_2$, can substitute cyanide as a ligand.[15] It also prevents the formation of metal–cyanide–metal bonds, which lead to rapid precipitation of polymeric compounds, like the well-known Prussian Blue that contains a three-dimensional network of Fe–CN–Fe bridges or like $Zn(CN)_2$ that contains an adamantane-like network.

In the system Cu/Zn/CN/en, the formation of compounds does not only depend on the composition of the solutions. It also depends on the pH and the content of $K^+$. This was found by experiments with solutions of the formal composition "$[Cu^{II}(en)_2][Zn^{II}(CN)_4]$". From this solution, two different bimetallic compounds were obtained, just by simple modification of the conditions:

(1) From KCN and in the presence of $(NH_4)_2SO_4$ buffer (pH about 8), the compound $[Zn^{II}(en)]_2[Cu^{I}_2(CN)_6]$ (**1**) (pale green crystals) was obtained.

(2) From NaCN (not buffered; pH about 10), the compound $[Zn^{II}(en)_3]_6[Cu^{I}_2(CN)_7]_2[Cu^{I}(CN)_3]\cdot 8.4H_2O$ (**2**) (bluish or colourless crystals) was obtained.

These structures indicate that in these systems $Zn^{2+}$ has a close affinity to ethylenediamine and that $Cu^+$ has a close affinity to cyanide. The coordination geometry around zinc and copper depends on the synthesis conditions. Chi and Fedkiw reported that $[Cu(CN)_3]^{2-}$ is the main species in the system $Cu^+/CN^-$, even if cyanide is present in excess.[16] The formation of the dinuclear anion $[Cu_2(CN)_7]^{5-}$ can be derived from joining a $[Cu(CN)_3]^{2-}$ unit with a $[Cu(CN)_4]^{3-}$ unit. The fact that both compounds are slightly coloured suggests that small amounts of $Cu^{2+}$ are also present in the crystal, possibly as substitution for $Zn^{2+}$ ($Cu^{I}$ and $Zn^{II}$ are both colourless).

Here, the structure of $[Zn^{II}(en)]_2[Cu^{I}_2(CN)_6]$ (**1**) was determined for the first time (see Figure 1, Table 1 and Table 2). Crystalline $[Zn^{II}(en)]_2[Cu^{I}_2(CN)_6]$ contains units of $[Cu^{I}_2(CN)_6]^{4-}$ and $[Zn^{II}(en)]^{2+}$, which together form a three-dimensional network. Each zinc atom is connected to three $[Cu_2(CN)_6]^{4-}$ units by one cyanide ligand. This leads to an unusual square-pyramidal coordination of zinc where two nitrogen atoms from ethylenediamine and two nitrogen atoms from cyanide form the base of the pyramid. Copper and zinc atoms are in close vicinity in the crystal structure. The structure of $[Zn^{II}(en)_3]_6[Cu^{I}_2(CN)_7]_2[Cu^{I}(CN)_3]\cdot 8.4H_2O$ (**2**) was reported earlier by Kappenstein et al.[17,18] and confirmed here by single-crystal structure analysis.

The infrared spectra (Figure 2) show strong similarities between the two compounds. Especially the N–H bands ($[Zn^{II}(en)]_2[Cu^{I}_2(CN)_6]$ (**1**): 3367/3352/3292 $cm^{-1}$; $[Zn^{II}(en)_3]_6[Cu^{I}_2(CN)_7]_2[Cu^{I}(CN)_3]\cdot 8.4H_2O$ (**2**): 3342/3293 $cm^{-1}$) and the C–H bands ($[Zn^{II}(en)]_2[Cu^{I}_2(CN)_6]$ (**1**): 2962/2924/2899 $cm^{-1}$; $[Zn^{II}(en)_3]_6[Cu^{I}_2(CN)_7]_2[Cu^{I}(CN)_3]\cdot 8.4H_2O$ (**2**): 2962/2934/2883 $cm^{-1}$) are almost identical whereas the C–N bands ($[Zn^{II}(en)]_2[Cu^{I}_2(CN)_6]$ (**1**): 2116 $cm^{-1}$;

 © 2006 Wiley-VCH Verlag GmbH & Co. KGaA, Weinheim 

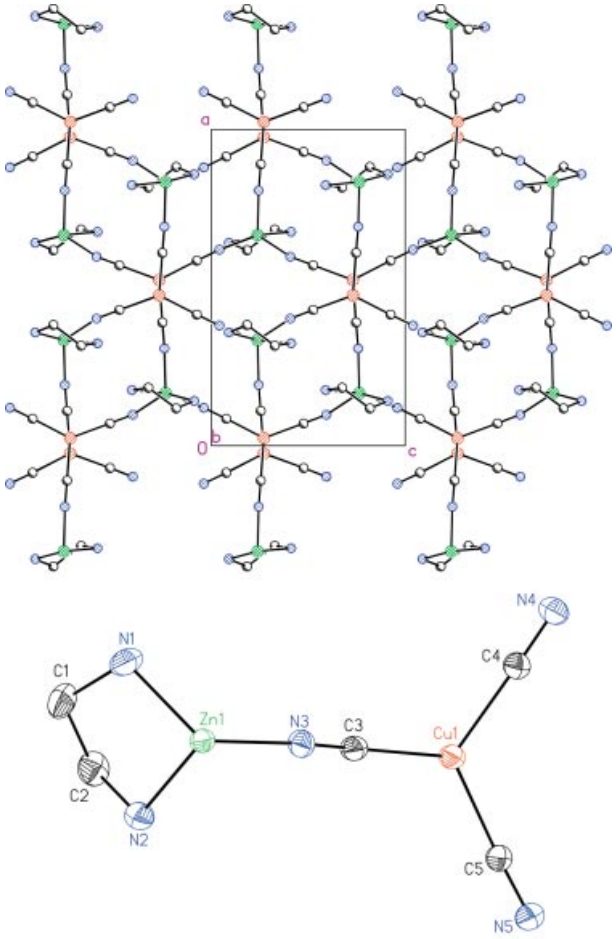


Figure 1. Structure of $[Zn^{II}(en)]_2[Cu^{I}_2(CN)_6]$ (**1**): Top: Packing of $[Zn^{II}(en)]_2[Cu^{I}_2(CN)_6]$ in the crystal; bottom: Asymmetric unit of $[Zn^{II}(en)]_2[Cu^{I}_2(CN)_6]$. Hydrogen atoms from ethylenediamine were omitted for clarity.

Table 1. Crystallographic data of $[Zn^{II}(en)]_2[Cu^{I}_2(CN)_6]$ (**1**).

| | |
|---|---|
| Empirical formula | $C_5H_8CuN_5Zn$ |
| $\rho_{calcd.}$ [g cm$^{-3}$] | 2.000 |
| Wavelength [Å] | 0.71073 |
| Space group | $P2_12_12$ (orthorhombic) |
| $F(000)$ | 528 |
| Temperature [K] | 203(2) |
| Crystal size [mm$^3$] | 0.14 × 0.11 × 0.03 |
| Crystal colour | cyan |
| Crystal description | plate |
| $a$ [Å] | 13.7514(4) |
| $b$ [Å] | 7.6762(3) |
| $c$ [Å] | 8.4007(3) |
| $\alpha$ [°] | 90.000(2) |
| $\beta$ [°] | 90.000(2) |
| $\gamma$ [°] | 90.000(2) |
| Volume [Å$^3$] | 886.77(5) |
| $Z$ | 4 |
| Reflections collected | 82644 |
| Independent reflections | 5459 [$R$(int) = 0.0619] |
| Final $R$ indices [$I > 2\sigma(I)$] | $R_1$ = 0.0320, $wR_2$ = 0.0693 |
| $R$ indices (all data) | $R_1$ = 0.0477, $wR_2$ = 0.0755 |
| Diffractometer | Siemens SMART three axis goniometer with an APEX II area detector system |
| Computing structure solution | Bruker AXS SHELXTL 6.12 |

Table 2. Atomic coordinates (× 10$^4$) and equivalent isotropic displacement parameters (Å$^2$ × 10$^3$) for $[Zn^{II}(en)]_2[Cu^{I}_2(CN)_6]$. $U$(eq) is defined as one third of the trace of the orthogonalised $U_{ij}$ tensor.

| | $x$ | $y$ | $z$ | $U$(eq) |
|---|---|---|---|---|
| Zn(1) | –3338(1) | 5234(1) | 12376(1) | 20(1) |
| Cu(1) | 243(1) | 6874(1) | 12703(1) | 25(1) |
| C(1) | –3817(2) | 1502(3) | 11828(3) | 35(1) |
| C(2) | –3166(2) | 1440(3) | 13263(3) | 33(1) |
| C(3) | –1100(1) | 6111(2) | 12540(2) | 24(1) |
| C(4) | 854(1) | 7735(3) | 10761(2) | 24(1) |
| C(5) | 706(1) | 7709(3) | 14757(2) | 25(1) |
| N(1) | –3583(2) | 3089(3) | 10899(2) | 32(1) |
| N(2) | –3239(2) | 3125(3) | 14110(2) | 31(1) |
| N(3) | –1928(1) | 5896(2) | 12430(2) | 24(1) |
| N(4) | 1198(1) | 8227(3) | 9595(2) | 29(1) |
| N(5) | 980(1) | 8297(3) | 15935(2) | 28(1) |

$[Zn^{II}(en)_3]_6[Cu^{I}_2(CN)_7]_2[Cu^{I}(CN)_3]\cdot 8.4\ H_2O$ (**2**): 2081 cm$^{-1}$) can clearly be distinguished and may be used to distinguish both compounds.

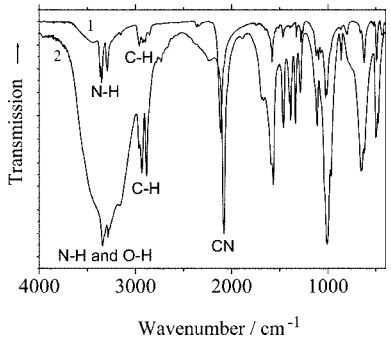


Figure 2. Infrared spectra of $[Zn^{II}(en)]_2[Cu^{I}_2(CN)_6]$ (**1**) and $[Zn^{II}(en)_3]_6[Cu^{I}_2(CN)_7]_2[Cu^{I}(CN)_3]\cdot 8.4H_2O$ (**2**).

### Thermolysis of 1 and 2

The thermolysis of $[Zn^{II}(en)]_2[Cu^{I}_2(CN)_6]$ (**1**) and $[Zn^{II}(en)_3]_6[Cu^{I}_2(CN)_7]_2[Cu^{I}(CN)_3]\cdot 8.4H_2O$ (**2**) under oxygen to CuO/ZnO was followed in situ by thermogravimetry combined with infrared spectroscopic gas analysis (Figure 3 and Figure 4).

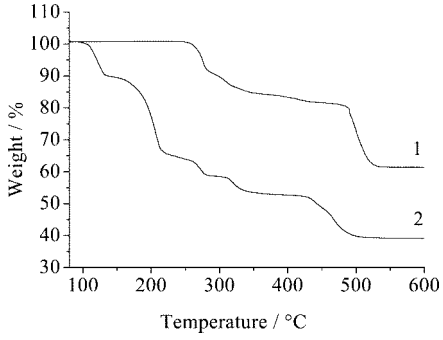


Figure 3.Thermogravimetry of **1** and $[Zn^{II}(en)_3]_6[Cu^{I}_2(CN)_7]_2[Cu^{I}(CN)_3]\cdot 8.4H_2O$ (**2**) to CuO/ZnO under a dynamic oxygen atmosphere.

The thermolysis of $[Zn^{II}(en)]_2[Cu^{I}_2(CN)_6]$ (**1**) can be divided into three parts. In a first step from 250 °C to about

 © 2006 Wiley-VCH Verlag GmbH & Co. KGaA, Weinheim 

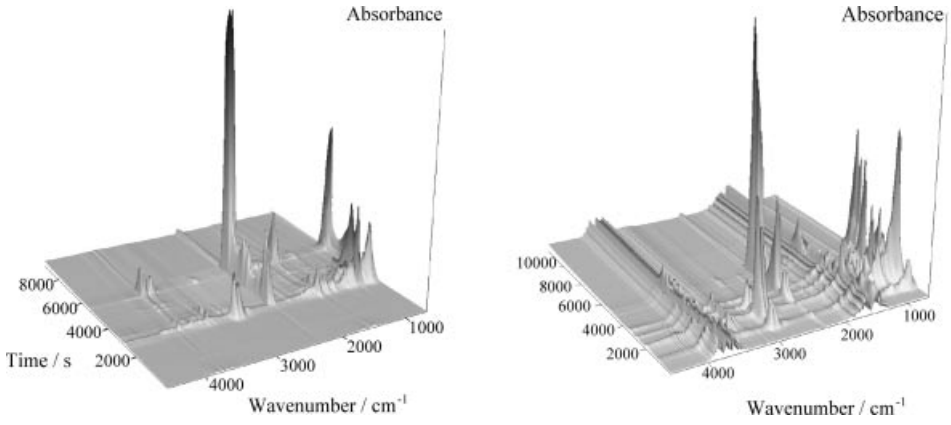


Figure 4. Time-resolved IR spectra of gases evolved from $[Zn^{II}(en)]_2[Cu^{I}_2(CN)_6]$ (**1**) (left) and $[Zn^{II}(en)_3]_6[Cu^{I}_2(CN)_7]_2[Cu^{I}(CN)_3]\cdot 8.4H_2O$ (**2**) (right) during thermolysis to CuO/ZnO.

295 °C, ethylenediamine is released without oxidation, as is visible from the C–H bands in the infrared spectrum at around 3000 cm$^{-1}$. From 295 to 490 °C the remainder of the ethylenediamine and a part of the cyanide undergo combustion as indicated by the evolution of $CO_2$ (four bands from 3740 to 3590 cm$^{-1}$ and several bands from 2560 to 2310 cm$^{-1}$) and $H_2O$. Finally, the combustion of cyanide to carbon dioxide and nitrous oxide (NO) occurs above 490 °C. The residual mass of 61.43 wt.-% corresponds well to the theoretical value of 60.25 wt.-% for a 1:1 mixture of ZnO and CuO.

The thermolysis of $[Zn^{II}(en)_3]_6[Cu^{I}_2(CN)_7]_2[Cu^{I}(CN)_3]\cdot 8.4H_2O$ occurs in five well-separated steps. In the first step, from 90 to 145 °C first water and then also ethylenediamine are released. Up to 240 °C, about 10 of the 18 molecules of ethylenediamine and all the crystal waters are lost. Starting around 240 °C, the reaction turns to oxidative combustion with the release of $CO_2$, first of ethylenediamine and then of cyanide. The final mass of 38.9 wt.-% corresponds well to the calculated value of 37.1 wt.-% for a 6:5 mixture of ZnO and CuO.

The morphology of the oxide mixtures, prepared by mild thermolysis of $[Zn^{II}(en)]_2[Cu^{I}_2(CN)_6]$ (**1**) and $[Zn^{II}(en)_3]_6[Cu^{I}_2(CN)_7]_2[Cu^{I}(CN)_3]\cdot 8.4H_2O$ (**2**) in air at 300 °C for 48 h was investigated by scanning electron microscopy (Figure 5). The crystallites have a size of a few 100 nm up to a micrometer, comparable to those obtained earlier by thermolysis of $Zn[Cu(CN)_3]$.[6] High-resolution X-ray powder diffraction (synchrotron) confirmed the absence of precursors or other crystalline impurities.

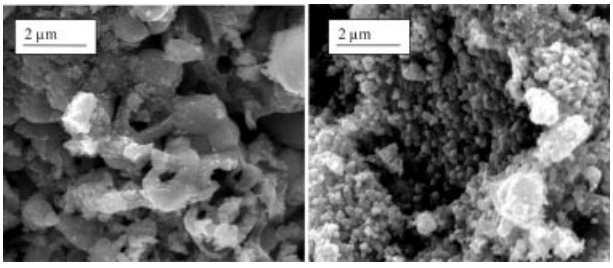


Figure 5. Scanning electron micrographs of the resulting CuO/ZnO mixtures from $[Zn^{II}(en)]_2[Cu^{I}_2(CN)_6]$ (**1**) (left) and $[Zn^{II}(en)_3]_6[Cu^{I}_2(CN)_7]_2[Cu^{I}(CN)_3]\cdot 8.4H_2O$ (**2**) (right) after annealing for 48 h at 300 °C.

### Catalytic Activity of Cu/ZnO from the Precursor System Cu/Zn/CN/Ethylenediamine (en)

The oxide samples were tested for their catalytic activity in the formation reaction of methanol from $CO/CO_2/H_2$ by two different methods. First, a 49-channel parallel flow multitubular reactor was used for rapid scanning of many samples (Table 3).[19] Note that CuO/ZnO was always reduced prior to the catalytic test in order to obtain the active catalyst Cu/ZnO. This was done in situ in the catalytic reactor. Because the absolute catalytic performance strongly depends on the specific conditions, all activities were related to an industrial benchmark catalyst (ICI Katalco 51–8) whose activity was set to 100%. This multitubular reactor permitted highly efficient parallel testing of numerous samples, including control experiments with the same sample. The oxides derived from $[Zn^{II}(en)]_2[Cu^{I}_2(CN)_6]$ (**1**) and $[Zn^{II}(en)_3]_6[Cu^{I}_2(CN)_7]_2[Cu^{I}(CN)_3]\cdot 8.4H_2O$ (**2**) showed similar activities that were much higher than the activities of the oxide mixtures from $Zn[Cu(CN)_3]$, which contained only cyanide as a ligand (see above; almost no activity). In a second experiment, both precursors were mixed with finely dispersed $Al_2O_3$ (for chromatography) as a support before the thermal decomposition to increase the specific surface. However, with this support, the catalytic activity (related to the content of CuO/ZnO in the catalyst) decreased considerably, i.e. the active surface of the catalyst could not be increased by this method.

In a single-tube reactor, the oxide mixture derived from $[Zn^{II}(en)]_2[Cu^{I}_2(CN)_6]$ (**1**) was studied more closely with regard to its reduction to Cu/ZnO, the specific copper surface area and the catalytic activity. Again, it was compared to the industrial benchmark catalyst (ICI) and also to another oxide sample derived by the conventional coprecipitation method of carbonates.[20] The content of CuO was approxi-

 © 2006 Wiley-VCH Verlag GmbH & Co. KGaA, Weinheim 

Table 3. Catalytic activity of CuO/ZnO samples after in situ reduction to Cu/ZnO in the multitubular reactor.

| Sample | Activity |
|---|---|
| Cu/ZnO from $Zn[Cu(CN)_3]$ | ≈ 0% |
| Cu/ZnO from $[Zn^{II}(en)]_2[Cu^{I}{}_2(CN)_6]$ (**1**) | 30% |
| 5 Cu/6 ZnO from $[Zn^{II}(en)_3]_6[Cu^{I}{}_2(CN)_7]_2[Cu^{I}(CN)_3]\cdot 8.4\ H_2O$ (**2**) | 29% |
| Cu/ZnO from $[Zn^{II}(en)]_2[Cu^{I}{}_2(CN)_6]$ (**1**) + $Al_2O_3$ | 13% |
| 5 Cu/6 ZnO from $[Zn^{II}(en)_3]_6[Cu^{I}{}_2(CN)_7]_2[Cu^{I}(CN)_3]\cdot 8.4\ H_2O$ (**2**) + $Al_2O_3$ | 9% |
| Industrial reference catalyst (ICI) | 100% |

mately 50 mol-% for these three samples. The content of CuO in the oxide derived from $[Zn^{II}(en)]_2[Cu^{I}{}_2(CN)_6]$ (**1**) was confirmed by the quantitative reduction (Figure 6). After reduction, the sample had a copper surface area of 2.42 $m^2 g^{-1}$ (Figure 7). Compared with the catalyst based on coprecipitated carbonate and the industrial catalyst, the sample had a smaller copper surface area, but the activity related to the copper surface area was surprisingly high (see Table 4). Note that an adsorption of nonvolatile fragments of the organic ligands on the copper surface that leads to a decrease in activity is unlikely but cannot be excluded with this compound. It was shown earlier that the Cu surface generally decreases during the catalytic process because of sintering of the Cu particles.[14]

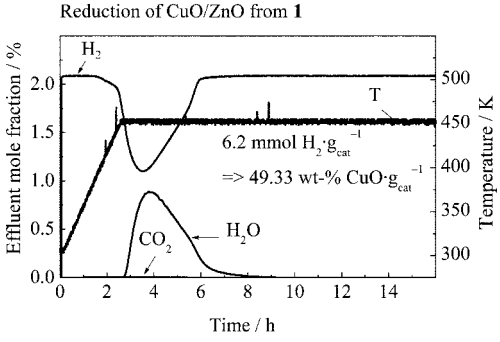


Figure 6. Reduction of CuO/ZnO from thermolysis of $[Zn^{II}(en)]_2[Cu^{I}{}_2(CN)_6]$ (**1**) to Cu/ZnO in the single-tube reactor.

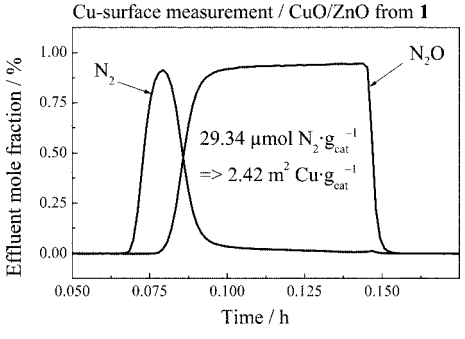


Figure 7. Measurement of the specific copper surface of Cu/ZnO prepared from the oxide derived from $[Zn^{II}(en)]_2[Cu^{I}{}_2(CN)_6]$ (**1**) by reaction with $N_2O$ in the single-tube reactor.

Note that the catalytic activity results obtained with the multitubular reactor cannot be directly compared with data from the single channel flow system. This is a result of the different set-ups as well as differences in the reduction process, different pressures (4.5 MPa for the parallel set-up vs. atmospheric pressure in the single-tube reactor) and slightly different feed compositions. Thus the catalytic activity of Cu/ZnO prepared from $[Zn^{II}(en)]_2[Cu^{I}{}_2(CN)_6]$ (**1**) measured in the single-tube reactor corresponds to 23% of the activity of the commercial ICI catalyst, which is in satisfactory agreement to the data obtained from the parallel set-up (30% of ICI). In general, the efficiency of the Cu/ZnO mixture derived from the cyanide/ethylenediamine coordination compounds is between 20 and 30% of the industrial reference catalyst.

Table 4. Catalytic activity of CuO/ZnO prepared from $[Zn^{II}(en)]_2[Cu^{I}{}_2(CN)_6]$ (**1**) in the single-tube reactor (reduced to Cu/ZnO) and of two reference catalysts.

| Sample | Cu surface [$m^2 g^{-1}$] | Production rate [$\mu mol\, g^{-1}{}_{cat}\, h^{-1}$] |
|---|---|---|
| Cu/ZnO from **1** | 2.42 | 92 |
| Cu/ZnO from coprecipitated carbonate | 17.0 | 115 |
| Industrial $Cu/ZnO/Al_2O_3$ catalyst (ICI) | 23.4 | 410 |

Kurtz et al. gave a linear relationship between the specific copper surface and the catalytic activity.[14] For our CuO/ZnO catalyst from $[Zn^{II}(en)]_2[Cu^{I}{}_2(CN)_6]$ (**1**), only 40% of the actually observed activity would have been expected, i.e. about 40 $\mu mol\, g^{-1}{}_{cat}\, h^{-1}$. An optimised thermolysis of $[Zn^{II}(en)]_2[Cu^{I}{}_2(CN)_6]$ (**1**) with regard to a high surface area of copper oxide may lead to an even higher catalytic activity. Unfortunately, the "easy route" to increase the specific surface area by adding $Al_2O_3$, as further support, was not successful (see Table 3).

## Conclusions

By the preparation and thermolysis of bimetallic coordination compounds, which contain copper and zinc in the same crystal, it is possible to prepare active Cu/ZnO catalysts for methanol synthesis. However, if only cyanide is present as the ligand, the activity of the resulting oxide mixture is almost zero, possibly because of poisoning of the surface. The introduction of ethylenediamine as an additional ligand leads to Cu/ZnO with a catalytic activity of 20 to 30% of the industrial reference catalyst. It is important to note that the morphology (by scanning electron microscopy) and the chemical composition (CuO and ZnO) of the thermolysis products from both kinds of precursors are practically indistinguishable. This underscores the strong influence of the precursor structure on the catalytic activity of the resulting oxide,[1,2] which, despite sophisticated in situ studies,[21,22] is not yet fully understood.

 © 2006 Wiley-VCH Verlag GmbH & Co. KGaA, Weinheim 

## Experimental Section

For all preparations, deionised water was used.

**Preparation of $[Zn^{II}(en)]_2[Cu^{I}_2(CN)_6]$ (1):** KCN (2.6 g, 40 mmol) and $(NH_4)_2SO_4$ (2.64 g, 20 mmol) were dissolved in water (50 mL). $ZnSO_4{\cdot}7H_2O$ (2.91 g, 10 mmol) was added to this solution whilst stirring until complete dissolution occurred. A second solution of $CuSO_4{\cdot}5H_2O$ (2.53 g, 10 mmol) and ethylenediamine (1.1 mL, 20 mmol) was prepared in water (25 mL). The solutions were poured together whilst stirring and a slightly blue precipitate was obtained. Water was added to a volume of 100 mL, and the unfiltered mixture of precipitate and solution was stored in a closed flask for three days. Pale green crystals were obtained, filtered, washed with water and dried for several days at room temperature in air. Yield: 43%. $C_{10}H_{16}Cu_2N_{10}Zn_2$ (534.16) (average of four independent preparations with standard deviations): calcd. C 22.49, H 3.02, Cu 23.79, N 26.22, Zn 24.48; found C 22.16 ± 0.64, H 2.76 ± 0.34, Cu 25.06 ± 1.38, N 25.64 ± 0.86, Zn 23.70 ± 1.47. The powder diffraction pattern of $[Zn^{II}(en)]_2[Cu^{I}_2(CN)_6]$ (**1**) was simulated using the single-crystal structure data. It showed an excellent agreement with the experimental powder diffraction pattern, therefore the bulk phase has the same structure as the single crystal.

**Preparation of $[Zn^{II}(en)_3]_6[Cu^{I}_2(CN)_7]_2[Cu^{I}(CN)_3]{\cdot}8.4H_2O$ (2):** NaCN (1.96 g, 40 mmol) was dissolved in water (40 mL). CuCl (0.99 g, 10 mmol) was added to this solution whilst stirring until complete dissolution occurred. A second solution of $Zn(OAc)_2{\cdot}2H_2O$ (3.29 g, 15 mmol) and ethylenediamine (3 mL, 45 mmol) was prepared in water (35 mL). The solutions were mixed and then stored in a sealed flask for a week. Slightly bluish crystals were obtained. After addition of a small amount of ethanol, more crystals were obtained from the mother liquor. Yield: 51%. $C_{53}H_{160.8}Cu_5N_5Zn_6$ (2385.41) (average of four independent preparations with standard deviations): calcd. C 26.69, H 6.79, Cu 13.32, N 31.12, Zn 16.44; found C 26.50 ± 0.54, H 6.83 ± 0.15, Cu 12.71 ± 0.46, N 30.60 ± 0.39, Zn 16.37 ± 0.39; traces of Na were also detected (0.58 ± 0.28 from three preparations). The powder diffraction pattern of **2** was simulated using the single-crystal structure data. It showed an excellent agreement with the experimental powder diffraction pattern, therefore the bulk phase has the same structure as the single crystal.

**Preparation of CuO/ZnO from $[Zn^{II}(en)]_2[Cu^{I}_2(CN)_6]$ (1) and $[Zn^{II}(en)_3]_6[Cu^{I}_2(CN)_7]_2[Cu^{I}(CN)_3]{\cdot}8.4H_2O$ (2):** The compounds were heated in an open crucible in air at 300 °C for 24 h. The product was then ground and heated again for 24 h at 300 °C. For the carrier experiment the precursor (100 mg) was intimately ground with $Al_2O_3$ (400 mg). The thermolysis was carried out as before.

**Catalytic Measurements:** (a) High-throughput screening in the multitubular reactor: Measurements were performed with a high-throughput 49-parallel channel reactor.[19] The catalyst (100 mg diluted by 200 mg quartz per well) was placed in a sample holder consisting of a stainless-steel cartridge closed at the bottom by a stainless-steel sinter metal frit. Prior to the catalytic measurements, the catalysts were reduced with $H_2$ at 518 K following the procedure for the commercial benchmark catalyst ICI Katalco 51–8. Before measuring the catalytic activity, all samples were equilibrated for 3 h (reaction pressure 4.5 MPa, reaction temperature 518 K, analytic flow 20 mL min$^{-1}$). The reaction gas consisted of 70% $H_2$, 24% CO and 6% $CO_2$. A double GC system (HP GC 6890) equipped with a methaniser FID was used for online gas analysis. Oxo-product separation ($H_3COH$, $HCOOCH_3$, $H_3CCOOCH_3$, $H_3CCH_2OH$) was carried out on a SuppelcoWAX 0.53 mm column and CO, $CO_2$ and $CH_4$ were separated on a Carboxen 1006 column. Methanol productivities for all measured samples were compared to the productivity of the industrial benchmark catalyst ICI Katalco 51–8 [$P_{ICI}$ = 40 mmol MeOH/($g^{-1}_{cat}\,h^{-1}$) at 518 K and 4.5 MPa].

(b) Single-tube reactor: 100 mg of the sample (sieves fraction 250–355 μm) were placed in a fixed-bed glass-lined U-tube reactor. The reduction was performed under flowing diluted $H_2$ (2% $H_2$ in He) by increasing the temperature up to 448 K by 1 K min$^{-1}$ and maintaining it there for 14 h. To ensure complete reduction, the temperature was then increased to 513 K and the sample was treated with pure $H_2$. The active surface area of Cu was determined by $N_2O$ reactive frontal chromatography at 300 K as described earlier.[23] The methanol formation activity was measured at 493 K under atmospheric pressure. The feed gas consisted of 72% $H_2$, 10% CO, 4% $CO_2$ and 14% He. Gases of the highest available purity (>99.9995%) were used. The online analysis of the products was performed by a previously calibrated quadrupole mass spectrometer (Balzers GAM 422).

**Analytical Techniques:** Combined thermogravimetry-infrared spectroscopy (TG-IR) was carried out with a Netzsch STA 209 TG-DTA/DSC instrument connected to a Bruker Vertex 70 infrared system with a TGA-IR measurement cell for gas analysis. Samples were heated from 30 °C to 800 °C at a rate of 5 K min$^{-1}$ under a dynamic $O_2$ atmosphere at a flow rate of 50 mL min$^{-1}$. Infrared spectroscopy was carried out with a Bruker Vertex 70 (KBr pellets), scanning electron microscopy with an ESEM Quanta 400 instrument (FEI) on nonsputtered samples. High-resolution X-ray powder diffractometry was carried out in transmission geometry at beamline B2 at HASYLAB/DESY, Hamburg, Germany.[24]

## Acknowledgments

This work was supported by the Deutsche Forschungsgemeinschaft within the scope of the Collaborative Research Center SFB 558: Metal–substrate interactions in heterogeneous catalysis. We thank HASYLAB at DESY, Hamburg, for the generous allocation of X-ray diffraction beam time.

[1] B. Bems, M. Schur, A. Dassenoy, H. Junkes, D. Herein, R. Schlögl, *Chem. Eur. J.* **2003**, *9*, 2039.
[2] M. Schur, B. Bems, A. Dassenoy, I. Kassatkine, J. Urban, H. Wilmes, O. Hinrichsen, M. Muhler, R. Schlögl, *Angew. Chem.* **2003**, *115*, 3945; *Angew. Chem. Int. Ed. Engl.* **2003**, *42*, 3815–3817.
[3] B. L. Kniep, T. Ressler, A. Rabis, F. Girgsdies, M. Baenitz, F. Steglich, R. Schlögl, *Angew. Chem.* **2004**, *116*, 114; *Angew. Chem. Int. Ed. Engl.* **2004**, *43*, 112–115.
[4] H. Wilmer, M. Kurtz, K. Klementiev, O. Tkachenko, W. Grünert, O. Hinrichsen, A. Birkner, S. Rabe, K. Merz, M. Driess, C. Wöll, M. Muhler, *Phys. Chem. Chem. Phys.* **2003**, *5*, 4736.
[5] G. J. Hutchings, J. C. Vedrine, in *Basic principles in applied catalysis*, vol. 75 (Ed.: M. Baerns), Springer, New York, **2004**, pp. 217.
[6] Y. Guo, R. Weiss, M. Epple, *Eur. J. Inorg. Chem.* **2005**, 3072.
[7] B. M. Chadwick, A. G. Sharpe, *Adv. Inorg. Chem. Radiochem.* **1966**, *8*, 83.
[8] R. Weiss, G. Jansen, R. Boese, M. Epple, *Dalton Trans.* **2006**, in press.
[9] R. Schlögl, *Angew. Chem. Int. Ed. Engl.* **1993**, *32*, 381.
[10] C. R. A. Catlow, S. A. French, A. A. Sokol, M. Alfredsson, S. T. Bromley, *Faraday Discuss.* **2003**, *124*, 185.
[11] S. A. French, A. A. Sokol, S. T. Bromley, C. R. A. Catlow, P. Sherwood, *Top. Catal.* **2003**, *24*, 161.

 © 2006 Wiley-VCH Verlag GmbH & Co. KGaA, Weinheim 

[12] R. M. Izatt, J. J. Christensen, J. W. Hansen, G. D. Watt, *Inorg. Chem.* **1965**, *4*, 718.
[13] R. Paterson, J. Bjerrum, *Acta Chim. Scand.* **1965**, *19*, 729.
[14] M. Kurtz, H. Wilmer, T. Genger, O. Hinrichsen, M. Muhler, *Catal. Lett.* **2003**, *86*, 77.
[15] Y. Guo, R. Weiss, R. Boese, M. Epple, *Thermochim. Acta* **2006**, in press.
[16] D. Chi, P. S. Fedkiw, *J. Electroanalyt. Chem.* **1993**, *345*, 107.
[17] C. Kappenstein, J. Cernak, R. Brahmi, D. Duprez, *Thermochim. Acta* **1996**, *279*, 65.
[18] J. Cernak, J. Chomic, C. Kappenstein, R. Brahmi, D. Duprez, *Thermochim. Acta* **1996**, *276*, 209.
[19] C. Kiener, M. Kurtz, H. Wilmer, C. Hoffmann, H. W. Schmidt, J. D. Grunwaldt, M. Muhler, F. Schüth, *J. Catal.* **2003**, *216*, 110.
[20] M. M. Günter, T. Ressler, B. Bems, C. Büscher, T. Genger, O. Hinrichsen, M. Muhler, R. Schlögl, *Catal. Lett.* **2001**, *71*, 37.
[21] J. D. Grunwaldt, A. M. Molenbroek, N. Y. Topsoe, H. Topsoe, B. S. Clausen, *J. Catal.* **2000**, *194*, 452.
[22] P. L. Hansen, J. B. Wagner, S. Helveg, J. R. Rostrup-Nielsen, B. S. Clausen, H. Topsoe, *Science* **2002**, *295*, 2053.
[23] O. Hinrichsen, T. Genger, M. Muhler, *Chem. Engl. Technol.* **2000**, *11*, 956.
[24] M. Knapp, C. Baehtz, H. Ehrenberg, H. Fuess, *J. Synchr. Rad.* **2004**, *11*, 328.

Received: January 4, 2006
Published Online: March 9, 2006

 © 2006 Wiley-VCH Verlag GmbH & Co. KGaA, Weinheim 

DOI: 10.1002/ejic.200600065

# Coordination Chemistry and Diphenylacetylene Hydrogenation Catalysis of Planar Chiral Ferrocenylphosphane-Thioether Ligands with Cyclooctadieneiridium(I)

**Raluca Malacea,[a] Eric Manoury,*[a] Lucie Routaboul,[a] Jean-Claude Daran,[a] Rinaldo Poli,[a] John P. Dunne,[b] Adrian C. Withwood,[b] Cyril Godard,[b] and Simon B. Duckett[b]**

**Keywords:** Ferrocenylphosphane ligands / Hemilability / Hydrogenation / Iridium / Planar chirality / Thioether ligands

The reaction of the P,S ligands CpFe{1,2-$C_5H_3(PPh_2)(CH_2SR)$}, (**1-R**; R = Et, Ph, *t*Bu), with 0.5 equivalents of $[Ir(COD)Cl]_2$ (metal/ligand = 1:1) furnishes the stable mononuclear adducts [Ir(COD)Cl(**1-R**)], **2-R**, in high yields. The molecular structures of the three complexes **2-R** have been determined by single-crystal X-ray diffraction. Compounds **2-Et** and **2-Ph** have similar five-coordinate molecular structures, with an intermediate coordination geometry between a distorted trigonal-bipyramid and a distorted square-pyramid. In the solid state, the sulfur atom chirality (R group *exo*, lone pair *endo* and parallel to the Cp-Fe axis) as well as the iridium chirality (Cl atom *exo* relative to the ferrocene group) is controlled by the ligand planar chirality. In solution, only one diastereoisomer is observed in both cases, indicating that the geometries observed in the solid state are maintained in solution, or that the different species are in rapid exchange on the NMR time scale. Complex **2-*t*Bu**, on the other hand, shows a four-coordinate square-planar molecular structure with a dangling thioether moiety, probably for steric reasons. For metal/ligand ratios greater than 1, the compounds [Ir(COD){$\kappa^2$-*P:S*-(**1-R**)}]$^+$[$Ir(COD)Cl_2]^-$ (**3-R**) are obtained, resulting from the chloride abstraction by the excess iridium metal on complex **2-R**. The structure of **3-Ph** was confirmed by single-crystal X-ray diffraction. A rapid equilibration between **2-R** and **3-R** gives rise to only one set of NMR signals for each metal/ligand ratio. For the ligand **1-*t*Bu**, a similar equilibration between **2-*t*Bu** and **3-*t*Bu** is again observed, in addition to a slower equilibration with a third product, [Ir(COD)Cl](μ-**1-R**)[Ir(COD)Cl] (**4-*t*Bu**), which is proposed to contain a bridging P,S ligand spanning two Ir centres. Complex **2-Ph** reacts with $[Rh(COD)Cl]_2$ to give only the heterometallic ionic pair [Ir(COD){$\kappa^2$-*P:S*-(**1-Ph**)}][$Rh(COD)Cl_2$] without transfer of ligand **1-Ph** from Ir to Rh. Furthermore, the rhodium complex RhCl(COD)(**1-Ph**) reacts quantitatively with $[Ir(COD)Cl]_2$ at room temp. to yield **2-Ph** and $[Rh(COD)Cl]_2$, thereby illustrating the much stronger affinity of ligands **1-Ph** for iridium compared to rhodium. Finally, the complexes **2-*t*Bu** and **2-Ph** were found to be efficient catalysts for the diphenylacetylene hydrogenation, affording a mixture of monohydrogenation [both (*E*)- and (*Z*)-stilbene] and dihydrogenation (1,2-diphenylethane) products.

(© Wiley-VCH Verlag GmbH & Co. KGaA, 69451 Weinheim, Germany, 2006)

## Introduction

The coordination chemistry of iridium has been widely studied during the last few decades, in part because of numerous applications that have been found in various catalytic systems[1] since the pioneering work of Crabtree et al.[2] In particular, iridium has been successfully applied to asymmetric catalyses, such as olefin hydrogenation,[3–12] C=N hydrogenation,[13–21] transfer hydrogenation[22–28] and allylic substitution.[29–40] Furthermore, the largest scale industrial enantioselective catalytic process involves an iridium-based hydrogenation step in the synthesis of chiral herbicide (1*S*)-Metolachlor.[41,42] Although many catalytic systems are generated in situ by the ligand addition to the readily available chloro(cycloocta-1,5-diene)iridium dimer, a good number of ligand adducts have been isolated and crystallographically characterized. When the supporting ligand (L-L′) is bidentate, several species can be envisaged depending on the ability of the ligand to act in a monodentate or bidentate fashion, and on the competition between the donor atoms and the chloride ion for the metal center. These species correspond to five-coordinate [Ir($\kappa^2$-L-L′)(COD)Cl], four-coordinate neutral [Ir($\kappa^1$-L-L′)(COD)Cl] with a dangling L or L′ donor atom, and four-coordinate ionic [Ir($\kappa^2$-L-L′)(COD)]$^+Cl^-$. Whereas several solid-state structures are available for five-coordinate complexes[43–47] and an exam-

[a] Laboratoire de Chimie de Coordination, UPR-CNRS 8241, 205 Route de Narbonne, 31077 Toulouse Cedex, France
Fax: +33-5-61553131
E-mail: manoury@lcc-toulouse.fr
[b] Department of Chemistry, University of York, YO10 5DD, United Kingdom
E-mail: sbd3@york.ac.uk

Supporting information for this article is available on the WWW under http://www.eurjic.org or from the author.

 © 2006 Wiley-VCH Verlag GmbH & Co. KGaA, Weinheim 

ple is also reported for neutral four-coordinate structure with a dangling phosphanyl ester ligand,[48] no examples are known, to the best of our knowledge, of four-coordinate ionic $[Ir(\kappa^2\text{-L-L}')(COD)]^+$ complexes with chloride as counterion (though they are known for rhodium).[49–51] Whether, for a given metal/ligand combination, the solid-state structure is maintained in solution and whether it is solvent dependent, or whether equilibria between different structures are established, has not been the subject of detailed studies to the best of our knowledge. In addition, how the ligand stereoelectronic properties may influence this structural choice is also an obscure point.

The coordination chemistry of sulfur-containing ligands,[52,53] as well as their potential in homogeneous catalysis[54,55] have recently attracted much interest, amongst other things because the sulfur atom could become asymmetric upon coordination to a metal. We have recently reported the synthesis of a family of planar-chiral P,S ligands, namely (*R*/*S*)-2-diphenylphosphanyl-[R-thiomethyl)ferrocenes (**1-R**), for instance with R = Et, *t*Bu, Ph, which proved to be very efficient in palladium-based asymmetric allylic alkylation.[56] As a first step toward the development of iridium-based catalytic systems, we wished to explore the iridium coordination chemistry of such ligands, with a particular focus on the stoichiometry, stereochemistry, potential (hemi)lability, etc. In this paper, we describe the synthesis and structure of a family of iridium complexes produced upon reaction of the racemic **1-R** (R = Et, *t*Bu, Ph) ligands with the cyclooctadieneiridium(I) moiety. We place particular emphasis on probing the relationship between the solution behaviour, the solid-state structure, and the nature of the R substituent on the ferrocenyl thioether function. New structural features and an unsuspected complex solution behaviour have been found through these investigations. Preliminary results on the catalytic diphenylacetylene hydrogenation reaction are also reported. Although the COD ligand is replaced by other ligands or substrates under most catalytic conditions (e.g. it is hydrogenated to cyclooctane under hydrogenation conditions) the structural and dynamic features observed for the pre-catalyst (i.e., the coordination stereoselectivity, the hemilability) are potentially relevant to the behaviour that one may expect under catalytic conditions.

## Results

### (a) Syntheses

Addition of the 2 equivalents of the bidentate ligands $[CpFe\{1,2\text{-}C_5H_3(PPh_2)(CH_2SR)\}]$ (**1-R**, R = Et, *t*Bu, Ph), which will be abbreviated as (P,SR), to complex $[Ir(COD)Cl]_2$ [i.e. 1 equiv. of (P,SR) to Ir] causes the splitting of the chloride-bridged dinuclear structure of the iridium precursor and formation of mononuclear products, according to the stoichiometry of Equation (1).

$$[(COD)Ir(\mu\text{-}Cl)_2Ir(COD)] + 2\ (P,SR) \longrightarrow 2\ IrCl(COD)(P,SR) \quad (1)$$

**1-R** **2-R**

The products **2-R** have been characterized by analytical and spectroscopic ($^1H$, $^{31}P$, $^{13}C$ NMR) methods. The NMR properties are shown in Table 1. These are spectra recorded on solutions obtained upon redissolving the isolated crystals, but correspond to complex equilibria between different species, as will be discussed in detail after the description of the structures. The three compounds show grossly similar physical (color, solubility) and spectroscopic properties in solution, but have different structures in the solid state. Whereas **2-Et** and **2-Ph** proved to be five-coordinate with a $\kappa^2$-*P*,*S* coordination mode for the bidentate ligand, their **2-*t*Bu** analogue is only four-coordinate, with a $\kappa^1$-*P* coordination mode and a dangling thioether functionality (see X-ray structures below).

Another remarkable feature has been observed during the crystallization of the crude product obtained from the reaction of **1-Ph** and $[Ir(COD)Cl]_2$ (2:1 ratio). Whereas crystals of **2-Ph** were obtained from dichloromethane/hexane, when the same procedure was followed for a toluene/hexane, crystals of a different compound, namely [Ir(COD)(P,SPh)][$Ir(COD)Cl_2$] (**3-Ph**) were produced. In fact, a $CDCl_3$ solution of **3-Ph** gave a $^{31}P$ resonance at 9.1 ppm, quite different from the value observed for **2-Ph** (–3.1 ppm). As will be shown later, this resonance results from an equilibrium mixture of **2-Ph** and **3-Ph**. When the synthesis was repeated for a 1:1 ratio of **1-Ph** and $[Ir(COD)Cl]_2$ (**1-Ph**/Ir = 2), the resulting orange solid displayed solution-state NMR properties in close correspondence with those of the isolated crystals of **3-Ph**. However, this solid also yielded crystals of **2-Ph** when recrystallized from dichloromethane/hexane. It seems therefore that the choice of crystallization solvent dictates the nature of the isolated product, indicating a possible equilibrium between **2-Ph** and **3-Ph** [Equation (2)]. A more detailed study of this equilibrium will be described below.

$$IrCl(COD)(P,SR) + \tfrac{1}{2}\,[Ir(COD)Cl]_2 \rightleftharpoons [Ir(COD)(P,SR)][Ir(COD)Cl_2] \quad (2)$$

**2-R** **3-R**

### (b) X-ray Structures

Views of the molecular geometries of compounds **2-Et**, **2-*t*Bu** and **2-Ph** are presented in Figure 1. It is immediately evident that the Et and Ph derivatives are five-coordinate because the S atoms are within reasonable bonding distances from the Ir centers [2.3928(17) Å and 2.3835(12) Å, respectively], whereas the *t*Bu derivative is only four-coordinate (the S···Ir distance is 5.13 Å). A comparable Ir–S bonding distances [2.3594(15) Å] has been reported for a $[(COD)Ir(P,S\textit{t}Bu)]^+$ complex containing a chiral phosphin-

 © 2006 Wiley-VCH Verlag GmbH & Co. KGaA, Weinheim 

Table 1. NMR properties of compounds **2-R** (R = Et, *t*Bu, Ph) in $CDCl_3$ solution.[a]

| | **2-Et** | **2-*t*Bu** | **2-Ph** |
|---|---|---|---|
| $^1H$ | | | |
| $PPh_2$ | 8.25 (m, 2 H) | 8.02 (m, 2 H) | 8.01 [d, 2 H (7)] |
| | 7.58 (m, 3 H) | 7.50–7.46 (m, 5 H) | 7.66–7.61 (m, 4 H)[e] |
| | 7.24 (s, 3 H) | 7.37–7.35 (m, 3 H) | 7.46–7.41 (m, 3 H)[e] |
| | 7.05 (m, 2 H) | | 7.27 (m, 4 H)[e] |
| | | | 7.12–7.09 (m, 2 H)[e] |
| $SCH_2$ | 4.69 [d, 1 H (12)] | 4.09 [d, 1 H (13)] | 5.55 [d, 1 H (12)] |
| | 3.97 [d, 1 H (12)] | 3.87 [d, 1 H (13)] | 4.09 (br. s, 2 H)[f] |
| $C_3H_5$ | 4.49 (s, 1 H) | 4.64 [d, 1 H (2)] | 4.44 (br. s, 1 H) |
| | 4.22 (s, 1 H) | 4.39 [t, 1 H (2.5)] | 4.25 [t, 1 H (2.5)] |
| | 4.00 (s, 1 H) | 4.28 (br. s, 1 H) | 4.09 (br. s, 2 H)[f] |
| Cp | 3.83 | 4.11 | 3.82 |
| COD(C*H*) | 3.48–3.53 (m, 4 H)[b] | 3.7 (broad, 4 H) | 3.32 {t, 2 H (7)} |
| | 2.96 (m, 1 H) | | 3.09 (m, 2 H) |
| | 2.86 (m, 1 H) | | |
| COD($CH_2$) | 2.62 (m, 2 H) | 2.33–2.28 (m, 2 H) | 2.61–2.55 (m, 2 H) |
| | 2.04 (m, 4 H) | 2.13–2.11(m, 2 H) | 2.01–1.93 (m, 4 H) |
| | 1.40 (m, 5 H)[c] | 1.80–1.77 (m, 2 H) | 1.35–1.32 (m, 2 H) |
| | | 1.60–1.57 (m, 2 H) | |
| S*R* | 3.48–3.53 (m, 4 H)[b] | 1.42 (s, 9 H) | [e] |
| | 1.40 (m, 5 H)[c] | | |
| $^{13}C$ | | | |
| Ph-*ipso* | 135.1 [d (30)] | 133.8 [d (52)] | 134.8 [d (46)] |
| | 133.3 [d (51)] | 132.6 [d (50)] | 134.0 [d (51)] |
| Ph-*o*,*m*,*p* | 135.4 [d, 2 C (13)] | 135.2 [d, 2 C (11)] | 132.3 [d, 2 C (9)] |
| | 132.0 [d, 2 C (9)] | 134.2 [d, 2 C (10)] | 130.7 [d, 2 C (2)] |
| | 130.6 [d, 1 C (2)] | 130.1 [d, 1 C (2)] | 128.9 [d, 2 C (2)] |
| | 129.0 (1 C) | 129.7 [d, 1 C (2)] | 127.9 [d, 2 C (10)] |
| | 127.8 [d, 2 C (10)] | 127.6 [d, 2 C (10)] | 127.0 [d, 2 C (9)] |
| | 127.2 [d, 2 C (9)] | 127.4 [d, 2 C (10)] | |
| Cp | 70.6 | 71.0 | 70.7 |
| $C_5H_3$ | 88.0 [d, 1 C (18)] | 90.0 [d, 1 C (14)] | 88.7 [d, 1 C (18)] |
| | 72.6 [d, 1 C (7)] | 74.9 [d, 1 C (8)] | 72.3 (s, 1 C) |
| | 72.5 (s, 1 C) | 74.4 [d, 1 C (50)] | 72.0 [d, 1 C (7)] |
| | 70.3 [d, 1 C (38)] | 71.3 [d, 1 C (17)] | 71.0 [d, 1 C (43)] |
| | 68.7 [d, 1 C (5)] | 69.7 [d, 1 C (7)] | 69.0 [d, 1 C (5)] |
| $SCH_2$ | 30.9 | 28.7 | 37.3 |
| S*R* | 66.8 ($CH_2$) | 43.6 [*C* ($CH_3$)] | 135.9 [d, *i*C (11)] |
| | 13.5 ($CH_3$) | 30.9 [C($CH_3$)] | 132.1 (s, 2 C) |
| | | | 129.8 (s, 1 C) |
| | | | 129.0 (s, 2 C) |
| COD(*C*H) | 64.5 [d, 2 C (13)] | [d] | 67.4 (s, 2 C) |
| | 29.8 [d, 2 C(5)] | | 65.1 [d, 2 C (15)] |
| COD($CH_2$) | 35.8 (s, 2 C) | 32.6 (s, 2 C) | 35.5 (s, 2 C) |
| | 28.6 (s, 2 C) | 30.6 (s, 2 C) | 28.7 (s, 2 C) |
| $^{31}P$ | | | |
| | –3.1 | 15.7 | –4.2 |

[a] Chemical shifts are reported as measured, for solutions containing ca. $10^{-2}$ mol/L of the isolated crystals. [b] Overlap between COD(C*H*) and SEt ($CH_2$) resonances. [c] Overlap between COD($CH_2$) and SEt ($CH_3$) resonances. [d] Not visible (see text). [e] Overlap between the $PPh_2$ and SPh resonances. [f] Overlap between one $SCH_2$ and one $C_5H_3$ resonance.

ite–thioether donor.[57] Other significant bonding parameters are shown in Table 2 for the five-coordinate compounds and in Table 3 for the four-coordinate one. When considering the coordination sites as corresponding to the midpoints of the COD C–C double bonds, the geometry of **2-*t*Bu** corresponds quite closely to an ideal square plane, the Ir atom being only 0.0206(2) Å away from the least-squares coordination plane. The coordination geometries of compounds **2-Et** and **2-Ph**, on the other hand, may be best viewed as intermediate between a distorted trigonal-bipyramid and a distorted square-pyramid. In the distorted trigonal-bipyramidal view, the center of one C=C donor function of the COD ligand (CO2) and the S1 donor atom define the axial positions [angles of 168.1(4) and 166.703(18)°, respectively]. However, the equatorial angles deviate severely from the ideal 120° value, for instance the CT01–Ir(1)–P(1) angle in the two compounds is 153.2(4) and 156.06(2)°, respectively, whereas the P(1)–Ir(1)–Cl(1) angle is 91.33(7) and 90.03(3). In the alternative distorted square-pyramidal view, the axial ligand would be the Cl(1) ligand,

 © 2006 Wiley-VCH Verlag GmbH & Co. KGaA, Weinheim 

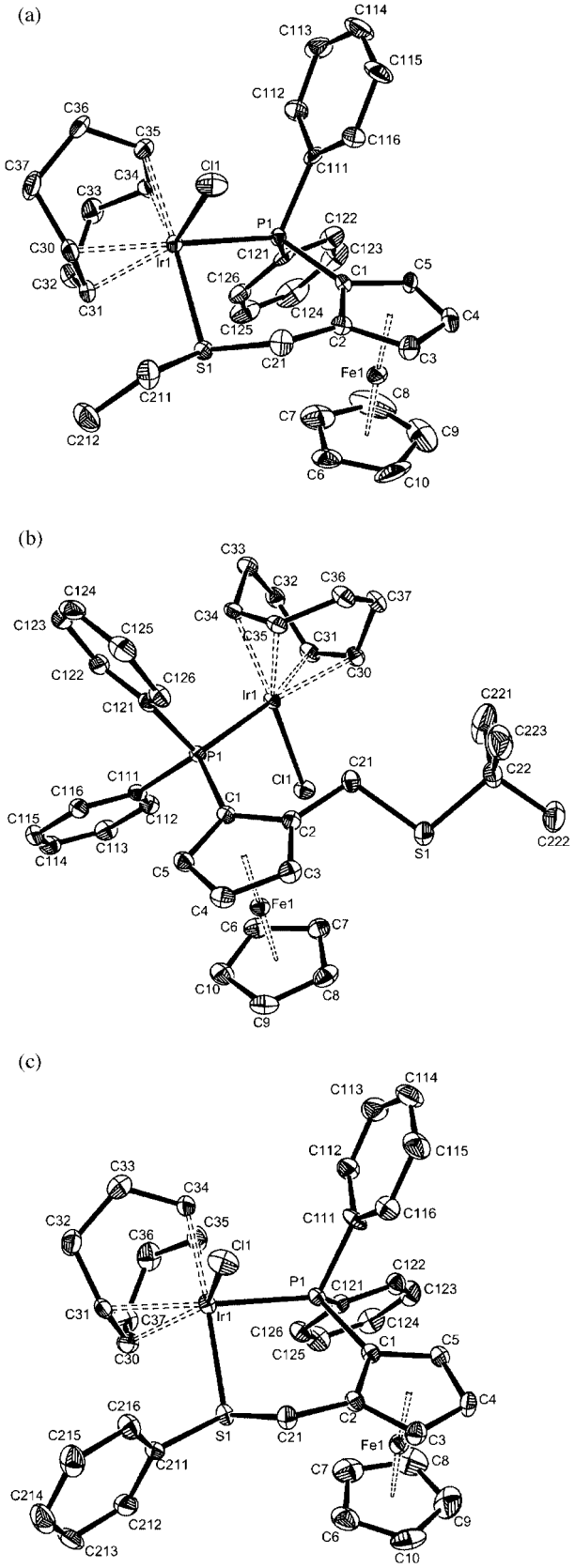


Figure 1. ORTEP views of the molecular structures of compounds **2-Et** (a); **2-*t*Bu** (b) and **2-Ph** (c). Ellipsoids are drawn at the 50% probability level and hydrogen atoms are omitted for clarity.

although a few of the Cl(1)–Ir–X angles [X = P(1), S(1), CO1 and CO2] are relatively close to 90°. It is interesting to note that in both **2-Et** and **2-Ph**, the Ir is located off the basal square plane by 0.363(8) Å and 0.3506(3) Å respectively, moreover the Ir is displaced toward the Cl atom. The distance from Cl to the square plane is 2.875(6) Å and 2.850(2) Å respectively. In fact, it would seem possible to view the structure as derived from that of the corresponding square planar $[Ir(COD)(P,SR)]^+$ by addition of $Cl^-$, resulting in a minimal perturbation of the square-planar geometry. Structures of five-coordinate $[IrX(COD)L_2]$ (X = any halogen) are not uncommon. They comprise examples with $L_2$ = diphosphanes[43,44] including a ferrocenyl-functionalized diphosphane,[45] diimines,[46,47] and also with L = monodentate phosphane.[58] The compounds reported here are the first such examples containing a bidentate P,S-type framework. More importantly, they illustrate the delicate

Table 2. Selected bond lengths [Å] and angled [°] for the pentacoordinate compounds **2-R** (R = Et, Ph).

| | **2-Et** | **2-Ph** |
|---|---|---|
| Ir(1)–CT01 | 2.026(8) | 2.0216(9) |
| Ir(1)–CT02 | 2.030(7) | 2.0433(8) |
| C(30)–C(31) | 1.441(10) | 1.445(4) |
| C(34)–C(35) | 1.407(11) | 1.395(4) |
| Ir(1)–P(1) | 2.3322(15) | 2.3289(13) |
| Ir(1)–S(1) | 2.3928(17) | 2.3835(12) |
| Ir(1)–Cl(1) | 2.5739(19) | 2.5576(12) |
| P(1)–C(1) | 1.796(7) | 1.807(3) |
| P(1)–C(111) | 1.843(7) | 1.835(3) |
| P(1)–C(121) | 1.819(7) | 1.837(3) |
| S(1)–C(21) | 1.809(8) | 1.826(3) |
| S(1)–C(211) | 1.842(7) | 1.790(3) |
| C(2)–C(21) | 1.496(9) | 1.488(4) |
| CT01–Ir(1)–CT02 | 85.118(19) | 85.298(8) |
| CT01–Ir(1)–P(1) | 153.2(4) | 156.06(2) |
| CT02–Ir(1)–P(1) | 90.69(6) | 91.583(19) |
| CT01–Ir(1)–S(1) | 90.3(3) | 90.020(18) |
| CT02–Ir(1)–S(1) | 168.1(4) | 166.703(18) |
| P(1)–Ir(1)–S(1) | 88.48(7) | 87.66(2) |
| CT01–Ir(1)–Cl(1) | 115.4(3) | 113.814(19) |
| CT02–Ir(1)–Cl(1) | 103.0(4) | 102.980(19) |
| P(1)–Ir(1)–Cl(1) | 91.33(7) | 90.03(3) |
| S(1)–Ir(1)–Cl(1) | 88.84(8) | 90.30(2) |
| C(1)–P(1)–C(111) | 99.6(4) | 100.46(13) |
| C(1)–P(1)–C(121) | 103.4(3) | 103.36(12) |
| C(111)–P(1)–C(121) | 104.0(3) | 101.25(12) |
| C(1)–P(1)–Ir(1) | 118.06(19) | 117.07(9) |
| C(111)–P(1)–Ir(1) | 113.2(2) | 114.85(10) |
| C(121)–P(1)–Ir(1) | 116.4(3) | 117.31(9) |
| C(21)–S(1)–C(211) | 94.5(3) | 98.62(13) |
| C(211)–S(1)–Ir(1) | 110.7(3) | 112.14(9) |
| C(21)–S(1)–Ir(1) | 108.8(3) | 108.09(10) |
| C(2)–C(1)–P(1) | 126.8(4) | 127.2(2) |
| C(5)–C(1)–P(1) | 126.5(5) | 126.0(2) |
| C(3)–C(2)–C(21) | 123.2(6) | 123.1(2) |
| C(1)–C(2)–C(21) | 128.8(6) | 128.7(2) |
| C(2)–C(21)–S(1) | 114.8(5) | 111.23(18) |
| C(116)–C(111)–P(1) | 118.9(6) | 121.6(2) |
| C(112)–C(111)–P(1) | 121.8(6) | 120.1(2) |
| C(126)–C(121)–P(1) | 119.9(6) | 118.9(2) |
| C(122)–C(121)–P(1) | 122.4(6) | 122.1(2) |
| C(216)–C(211)–S(1) | | 122.7(2) |
| C(212)–C(211)–S(1) | | 116.9(2) |

 © 2006 Wiley-VCH Verlag GmbH & Co. KGaA, Weinheim 

Table 3. Selected bond lengths [Å] and angles [°] for the square planar compound **2-*t*Bu**.

| | | | |
|---|---|---|---|
| Ir(1)–CT01 | 2.0859(6) | Ir(1)–CT02 | 1.9988(5) |
| Ir(1)–C(30) | 2.204(2) | Ir(1)–C(34) | 2.131(3) |
| Ir(1)–C(31) | 2.194(2) | Ir(1)–C(35) | 2.110(3) |
| Ir(1)–P(1) | 2.3312(9) | Ir(1)–Cl(1) | 2.3625(8) |
| P(1)–C(1) | 1.811(3) | S(1)–C(21) | 1.818(3) |
| P(1)–C(111) | 1.831(3) | P(1)–C(121) | 1.835(3) |
| S(1)–C(22) | 1.828(3) | C(30)–C(31) | 1.392(4) |
| | | C(34)–C(35) | 1.418(4) |
| CT02–Ir(1)–CT01 | 86.434(11) | P(1)–Ir(1)–Cl(1) | 92.49(2) |
| CT01–Ir(1)–P(1) | 177.594(17) | CT02–Ir(1)–P(1) | 93.369(19) |
| CT01–Ir(1)–Cl(1) | 87.904(18) | CT02–Ir(1)–Cl(1) | 172.601(17) |
| C(1)–P(1)–C(111) | 105.28(11) | C(1)–P(1)–C(121) | 100.70(12) |
| C(111)–P(1)–C(121) | 101.02(12) | C(111)–P(1)–Ir(1) | 116.53(8) |
| C(1)–P(1)–Ir(1) | 116.81(9) | C(121)–P(1)–Ir(1) | 114.22(8) |
| C(21)–S(1)–C(22) | 103.56(13) | C(221)–C(22)–S(1) | 111.1(2) |
| C(5)–C(1)–P(1) | 124.1(2) | C(223)–C(22)–S(1) | 110.5(2) |
| C(2)–C(1)–P(1) | 127.77(18) | C(222)–C(22)–S(1) | 104.3(2) |
| C(3)–C(2)–C(21) | 124.5(2) | C(1)–C(2)–C(21) | 128.0(2) |
| C(2)–C(21)–S(1) | 109.91(18) | | |
| C(116)–C(111)–P(1) | 120.86(19) | C(126)–C(121)–P(1) | 120.8(2) |
| C(112)–C(111)–P(1) | 120.18(19) | C(122)–C(121)–P(1) | 120.8(2) |

control exerted by the ligand structure on the coordination geometry. This control is unlikely to have an electronic origin, as the Et and *t*Bu substituents impart analogous electronic effects, and different from those of the Ph substituent. A steric effect appears more likely, because the *t*Bu group is more encumbering than either the Et or the Ph group and thus prevents the compound to attain the five-coordinate geometry (Figure 1).

The S coordination step is interesting from the stereochemical point of view. Coordination renders the S atom and the Ir atom asymmetric. In combination with the planar chirality of the substituted ferrocene moiety, eight possible stereoisomers, namely four diastereomeric pairs of enantiomers, can be obtained. There is, however, no indication from the NMR spectrum for the formation of more than one compound. Either the diastereoisomers have significantly different energies such that only one is present at equilibrium, or the isomerization proceeds through a low energy barrier (for instance by decoordination and recoordination through a four-coordinate square planar intermediate), or finally there may be a combination of both effects. Other observations, shown below, indicate that these compounds undergo dynamic rearrangements very rapidly. In the solid state, the compounds **2-Et** and **2-Ph** show the S atom with the same configuration relative to the ferrocene unit (R group *exo*, lone pair *endo* and parallel to the Cp–Fe axis), and the Cl ligand is located on the same side (*exo*) relative to the ferrocene group. The Ir–Cl distances of 2.5739(19) and 2.5576(12) Å compare with those in other five-coordinate [IrCl(COD)$L_2$] derivatives with chelating ligands, for instance 2.549 Å in [IrCl(COD)$L_2$] [$L_2$ = (2*R*,3*R*)-2,3-*O*-isopropylidene-1,4-bis(5*H*-dibenzophosphol-5-yl)-2,3-butanediol],[43] and 2.585(3) Å in [IrCl(COD)(dppp)].[44] However, these distances are longer relative to neutral four-coordinate complexes [e.g. 2.363(1) Å in Ir(COD)[= C($NCH_2$-*p*-Tol)$_2C_2H_2$]Cl,[59] and 2.3625(8) Å in complex **2-*t*Bu**]. A lengthening of ca. 0.2 Å accompanies this coordination number increase. This observation gives credence to the hypothesis that the Ir–Cl bond in the five-coordinate complexes is highly polarized, especially when comparing it with the insignificant change of the Ir–P distance [2.3322(15) Å and 2.3289(13) Å in five-coordinate **2-Et** and **2-Ph**, respectively; 2.3312(9) Å in four-coordinate **2-*t*Bu**] and Ir–CT distances [CT = center of the COD C=C bond; averages are 2.028(8) Å for **2-Et**, 2.032(10) Å for **2-Ph** and 2.04(4) Å for **2-*t*Bu**].

The structure of compound **3-Ph** contains discrete square-planar [Ir(COD)($\kappa^2$-P,SPh)]$^+$ and [Ir(COD)$Cl_2$]$^-$ anions. An interstitial toluene molecule completes the crystal packing. One H atom of a $CH_2$ group of the COD ligand in the cation is located at a relatively short intermolecular contact (2.759 Å) above the Ir atom in the anion, see Figure 2, a location which places it in an approximately ideal axial position. Indentification of such an interaction in solution by NMR spectroscopy was precluded by the complex redistribution equilibria (see below). However, the Ir atom in each ion sits very close to the ideal square place defined by the middle of the C=C bonds and the P,S or Cl donors, respectively [0.0158(5) Å in the cation, 0.0066(5) Å in the anion]. Structures of four-coordinate cationic complexes of type [Ir(COD)$L_2$]$^+$ are quite common in the literature with various types of bidentate $L_2$ and monodentate L ligands, including two precedents with a chelating P,S-type ligand, $Ph_2$PO(1,2-*cyclo*-$C_6H_{10}$)S*t*Bu and $Ph_2PCH_2$P(*t*Bu)$_2$S.[57,60] All these previously reported salts contain $BF_4^-$, $PF_6^-$, $SbF_6^-$, $CF_3SO_3^-$, or tetraarylborates as counterions. None contains the [Ir(COD)$Cl_2$]$^-$ anion. In fact, this quite simple anion does not appear to have previously been crystallographically characterized. This situation differs considerably from that of the rhodium congeners, for which several structure of salts of type [Rh(COD)$L_2$][Rh(COD)$Cl_2$] have been reported.[61–65]

Selected bonding parameters for compounds **3-Ph** are shown in Table 4. Both ions exhibit a relatively undistorted

 © 2006 Wiley-VCH Verlag GmbH & Co. KGaA, Weinheim 

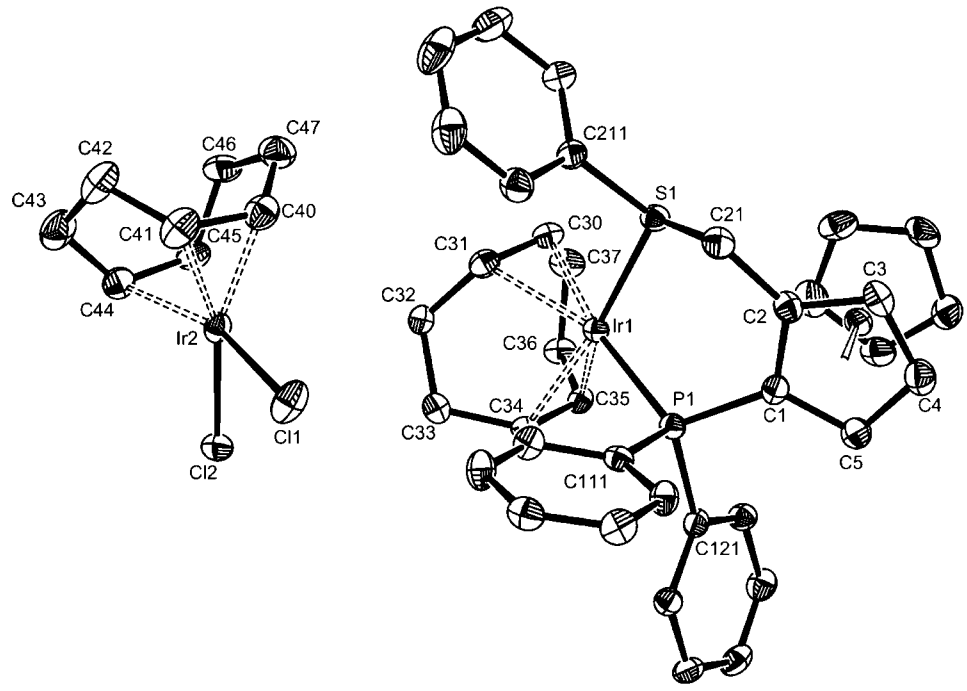


Figure 2. ORTEP view of the molecular structures of compounds **3-Ph**. Ellipsoids are drawn at the 50% probability level and hydrogen atoms are omitted for clarity.

square-planar geometry when considering the center of the COD C=C bonds (CT) as defining the coordination positions. The Ir–CT distances are significantly shorter in the anion [average 1.976(5) Å] than in the cation [average 2.09(4) Å], and the latter are marginally longer than in the 4- and five-coordinate neutral complexes **2-R** discussed above, attesting to the importance of back-bonding for the Ir–COD interaction. The Ir–P and Ir–S bond lengths in the cation are shorter than those in the neutral complexes, irrespective of their coordination number. This effect can be attributed to the metal ion contraction on going from the neutral to the charged system, because of an increase of

Table 4. Selected bond lengths [Å] and angles [°] for compounds **3-Ph**.

| | | | |
|---|---|---|---|
| Ir(1)–CT01 | 2.1242(2) | Ir(2)–CT03 | 1.9807(2) |
| Ir(1)–CT02 | 2.0518(2) | Ir(2)–CT04 | 1.9708(2) |
| Ir(1)–C(30) | 2.239(5) | Ir(2)–C(40) | 2.094(6) |
| Ir(1)–C(31) | 2.228(5) | Ir(2)–C(41) | 2.113(6) |
| Ir(1)–C(34) | 2.171(5) | Ir(2)–C(43) | 2.086(5) |
| Ir(1)–C(35) | 2.164(5) | Ir(2)–C(44) | 2.101(5) |
| Ir(1)–P(1) | 2.2820(13) | Ir(2)–Cl(1) | 2.3644(13) |
| Ir(1)–S(1) | 2.3280(12) | Ir(2)–Cl(2) | 2.3706(13) |
| C(30)–C(31) | 1.381(7) | C(40)–C(41) | 1.415(8) |
| C(34)–C(35) | 1.397(7) | C(43)–C(44) | 1.414(8) |
| P(1)–C(1) | 1.806(5) | | |
| P(1)–C(111) | 1.828(5) | P(1)–C(121) | 1.824(5) |
| C(21)–S(1) | 1.823(5) | S(1)–C(211) | 1.786(5) |
| CT02–Ir(1)–CT01 | 85.612(7) | CT04–Ir(2)–CT03 | 88.285(9) |
| CT01–Ir(1)–P(1) | 173.43(3) | CT03–Ir(2)–Cl(1) | 90.96(4) |
| CT01–Ir(1)–S(1) | 89.93(3) | CT04–Ir(2)–Cl(1) | 177.05(4) |
| CT02–Ir(1)–P(1) | 92.99(3) | CT03–Ir(2)–Cl(2) | 177.63(3) |
| CT02–Ir(1)–S(1) | 170.56(3) | CT04–Ir(2)–Cl(2) | 90.72(3) |
| P(1)–Ir(1)–S(1) | 92.35(4) | Cl(1)–Ir(2)–Cl(2) | 90.14(5) |
| C(1)–P(1)–C(111) | 102.6(2) | C(1)–P(1)–C(121) | 103.6(2) |
| C(121)–P(1)–C(111) | 105.2(2) | C(121)–P(1)–Ir(1) | 118.79(17) |
| C(1)–P(1)–Ir(1) | 114.86(16) | C(111)–P(1)–Ir(1) | 110.19(16) |
| C(2)–C(1)–P(1) | 122.4(4) | C(5)–C(1)–P(1) | 129.0(4) |
| C(1)–C(2)–C(21) | 126.4(4) | C(2)–C(21)–S(1) | 111.9(3) |
| C(112)–C(111)–P(1) | 121.5(4) | C(122)–C(121)– P(1) | 117.9(4) |
| C(116)–C(111)–P(1) | 119.1(4) | C(126)–C(121)–P(1) | 123.2(4) |
| C(211)–S(1)–C(21) | 100.5(2) | C(216)–C(211)–S(1) | 117.7(4) |
| C(211)–S(1)–Ir(1) | 108.55(17) | C(21)–S(1)–Ir(1) | 115.67(17) |
| C(212)–C(211)–S(1) | 121.5(4) | | |

 © 2006 Wiley-VCH Verlag GmbH & Co. KGaA, Weinheim 

effective nuclear charge, and agrees with a predominant σ-bonding component for the Ir–P and Ir–S interactions.

### (c) NMR Spectroscopy of Compounds 2-R

Given the subtle structural difference observed for compounds **2** in the solid state depending on R, one might wonder whether the same structural dichotomy is maintained in solution. A detailed analysis of the NMR properties seems to suggest that this is the case. The $^{31}P$ resonance chemical shift is essentially identical for compounds **2-Et** and **2-Ph**, whereas it is significantly shifted downfield for **2-*t*Bu** (see Table 1), in apparent agreement with donation from the phosphorus atom to a less electron-rich metal in the latter case. This observation is the strongest indication in favor of a similar structure in the solid state and in chloroform solution for compounds **2**. Given the planar chirality of the functionalized Cp ring of the ferrocene moiety, all COD proton and carbon nuclei are magnetically inequivalent in both types of structure, although a higher degree of inequivalence could be expected for the five-coordinate structures where there is coordination-induced chirality at both the S and Ir atoms. The NMR spectra are, however, deceptively simple as only two sets of $^{13}C$ resonances are observed for both the *C*H and the *C*$H_2$ nuclei for all three compounds. For compound **2-*t*Bu**, the *C*H resonances could not be identified, even by an $^{1}H$–$^{13}C$ HMQC experiment at temperatures down to 213 K. On the other hand, these peaks were visible when the spectrum was recorded in [$D_8$]toluene solution (see Exp. Sect.). The pairs of C atoms with distinct chemical shifts are probably associated to the different coordination positions (i.e. *trans* to P and *trans* to S/Cl), whereas the asymmetry above and below the square coordination plane has a negligible effect on the chemical shift. Only for the $^{1}H$ C*H* (COD) resonances in compound **2-Et** was a slight asymmetry detected in the corresponding NMR spectra due to this asymmetry. This observation alone is not sufficient to confirm the difference in coordination geometry within the three compounds. However, the chemical shifts of the CH(COD) $^{1}H$ and $^{13}C$ resonances change significantly on going from **2-Et** and **2-Ph**. In particular, the C*H* resonances in the $^{1}H$ NMR spectrum proved to be more spread apart in **2-*t*Bu**, while one of the two *C*H resonances in the corresponding $^{13}C$ NMR spectrum is upfield shifted by ca. 15 ppm relative to the same resonance in the other two compounds. The chemical shift of the single $^{1}H$ resonance of the unsubstituted Cp ligand is also significantly different for **2-*t*Bu** relative to the other two compounds, and a slight difference is even observable for the $^{13}C$ resonance of the same group. The $^{1}H$ and $^{13}C$ resonances of the $CH_2$ group linking the S donor to the ferrocene unit, on the other hand, seem sensitive to the electronic nature of the SR group, because they are similar for the Et and *t*Bu derivatives and different for the Ph derivative. In conclusion, the overall NMR behaviour suggests that the solution structures of compounds **2** may be identical to those observed in the solid state.

### (d) Study of Solution Equilibria

Solutions obtained by mixing the complexes $[Ir(COD)Cl]_2$ and the free ligand **1-Ph** in various ratios were investigated by $^{1}H$ and $^{31}P$ NMR spectroscopy. Only one set of resonances was observed for all ratios up to **1-Ph**/Ir = 1:1, but several individual resonances of this set (notably the $^{31}P$ resonance and the $^{1}H$ resonances of the ferrocene unsubstituted Cp, of one of the substituted Cp protons, and of the two $CH_2$ protons) exhibited a continuous variation of the chemical shift as a function of the **1-Ph**/Ir ratio (see Figure 3). The COD resonances were too broad to allow their accurate monitoring. For **1-Ph**/Ir ratios greater than 1, the resonances of the free ligand **1-Ph** (mostly evident from the $^{31}P$ NMR spectrum) also appeared.

The behaviour illustrated in Figure 3 can be rationalized on the basis of Scheme 1, where rapid site exchange between the species participating in the equilibrium is required. A similar equilibrium has previously been proposed for an analogous system with the hemilabile N,O ligand 3-dimethylamino-1-(2′-pyridyl)-2-propen-1-one.[64] The resonances did not decoalesce into those of the individual species upon cooling to 213 K for a solution containing a **1-Ph**/Ir ratio of 0.6. The first ligand–metal equilibrium leading to **3-Ph** must be essentially quantitative, because the NMR signals of free **1-Ph** appear immediately after consumption of one equivalent of the ligand per Ir dimer, whereas they are not visible before this ratio is attained.

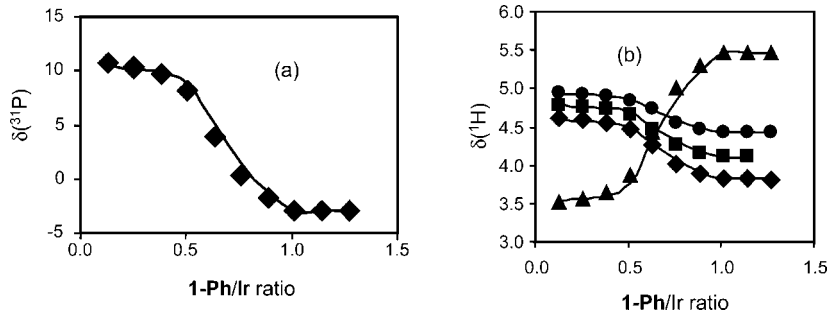


Figure 3. Dependence of the chemical shift of a few resonance for the $[Ir(COD)Cl]_2$/**1-Ph** system on the **1-Ph**/Ir ratio. (a) $^{31}P$ resonance; (b) $^{1}H$ resonances: unsubstituted Cp (5 H, diamonds); substituted Cp (1 H, circles); $CH_2$ (1 H, squares; 1 H, triangles). The solid lines are obtained by fitting the data according to Scheme 1 (see text).

 © 2006 Wiley-VCH Verlag GmbH & Co. KGaA, Weinheim 

$$[Ir(COD)Cl]_2 + P,SPh \longrightarrow [Ir(COD)(\kappa^2\text{-}P,SPh)]^+ [Ir(COD)Cl_2]^-$$

**1-Ph** **3-Ph**

$$[Ir(COD)(\kappa^2\text{-}P,SPh)]^+ [Ir(COD)Cl_2]^- \rightleftharpoons \tfrac{1}{2}[Ir(COD)Cl]_2 + IrCl(COD)(\kappa^2\text{-}P,SPh)$$

**3-Ph** **2-Ph**

Scheme 1.

Under the assumption of a first quantitative addition of **1-Ph** to $[Ir(COD)Cl]_2$, the individual concentrations of **2-Ph** and **3-Ph** for each measured solution were obtained from the equilibrium expression denoted in Equation (3), R = Ph, using *K* as an adjustable parameter. These concentrations were then used to calculate, for each resonance, the chemical shifts according to Equation (4) (R = Ph). Fitting to the experimental data yielded a reasonable agreement, using the same value of the equilibrium constant (0.008) for all resonances, as shown in Figure 3. The full fitting procedure and the values of $\delta$2–Ph and $\delta$3–Ph for each resonance, as obtained from the fittings, are given in the Supporting Information (for details see the footnote on the first page of this article).

$$K = \frac{[\mathbf{2\text{-}R}][Ir_2Cl_2(COD)_2]^{1/2}}{[\mathbf{3\text{-}R}]} \quad (3)$$

$$\delta_{calc} = \delta_{\mathbf{2\text{-}R}}[\mathbf{2\text{-}R}]/([\mathbf{2\text{-}R}]+[\mathbf{3\text{-}R}]) + \delta_{\mathbf{3\text{-}R}}[\mathbf{3\text{-}R}]/([\mathbf{2\text{-}R}]+[\mathbf{3\text{-}R}]) \quad (4)$$

When a sample of **1-Et** was added to $[Ir(COD)Cl]_2$ in a 1:1 molar ratio in $CDCl_3$ (i.e. a **1-Et**/Ir ratio of 0.5), a single $^{31}P$ NMR resonance was observed at $\delta$ = 10.9 ppm. The isolated complex **2-Et** (having a **1-Et**/Ir ratio of 1), on the other hand, yielded a $^{31}P$ resonance at $\delta$ –4.2 under the same conditions (see Table 1), whereas the resonance of the free ligand **1-Et** is at –20. Addition of an excess of ligand **1-Et** shifted this resonance further to $\delta$ = –4.6 ppm. We therefore presume that the solution behaviour of "Ir(COD)-Cl" in the presence of **1-Et** is the same as with the **1-Ph** ligand. A more detailed equilibrium study was not carried out in this case. In contrast, treatment of complex $[Ir(COD)Cl]_2$ with various amounts of **1-*t*Bu** in $CDCl_3$ led to the observation of two new $^{31}P$ NMR resonances. Whereas one of these (at $\delta$ = 17.5 ppm) exhibited the same chemical shift at all **1-*t*Bu**/Ir ratios, the other one shifted continuously from ca. $\delta$ = 14.6 at **1-*t*Bu**/Ir = 0.2 to ca. 15.7 at **1-*t*Bu**/Ir = 1, see Figure 4 (a). In addition, the relative intensity of these two resonances changed in favor of the second one upon increasing the **1-*t*Bu**/Ir ratio, until the first one completely disappeared at the point when **1-*t*Bu**/Ir = ca. 1, see Figure 4 (b). Further additions of the free ligand no longer moved the $\delta$ = 15.7 resonance, although, a new resonance due to the excess of free **1-*t*Bu** started to appear at $\delta$ = –20.0 ppm. This observed behaviour suggests the presence of at least three P-containing Ir complexes: two that are in rapid exchange on the NMR time scale, generating the resonance that is shifting in the $\delta$ = 14.6–15.7 ppm range, and a third one giving the $\delta$ = 17.5 ppm resonance. The latter species exchanges slowly on the NMR timescale, or not at all, with the other two. In addition, the appearance of the free **1-*t*Bu** resonance immediately after attaining the **1-*t*Bu**/Ir ratio of 1, suggested an essentially quantitative first addition of **1-*t*Bu** to $[Ir(COD)Cl]_2$ to generate **3-*t*Bu**, like for the case of the **1-Ph** addition.

It seems logical to assume, on the basis of the results shown above for the **1-Ph**/Ir system, that the shifting resonance is due to the rapidly equilibrating mixture of compounds **2-*t*Bu** and the salt $[Ir(COD)(\kappa^2\text{-}P,S\textit{t}Bu)]^+[Ir(COD)Cl_2]^-$, **3-*t*Bu** [equilibrium of Equation (2)]. The chemical shift observed at low **1-*t*Bu**/Ir ratio [Figure 4 (a), ca. $\delta$ = 14.5 ppm] is close to that observed at low **1-Ph**/Ir ratio (Figure 3, ca. $\delta$ = 11 ppm) and attributed to compound **3-Ph**. For the **1-Ph**/Ir system, addition of the free ligand leads to an upfield shift toward the resonance of five-coordinate **2-Ph** (ca. $\delta$ = –3 ppm), whereas for the **1-*t*Bu**/Ir system, addition of the free ligand leads to a downfield shift toward the resonance of four-coordinate **2-*t*Bu** (ca. $\delta$ = 15.5 ppm). This proposition is in agreement with the observed behaviour of the same system in $C_6D_6$: the lower polarity of this solvent is expected to disfavor formation of the ionic system and, indeed, the resonance does not shift significantly by

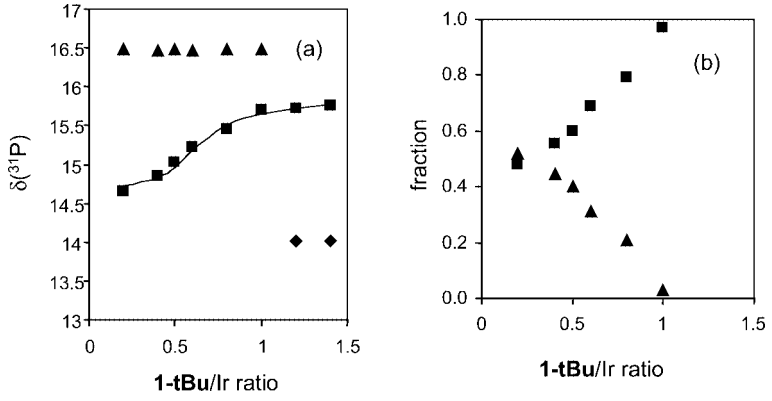


Figure 4. Chemical shift (a) and relative ratio (b) of the $^{31}P$ NMR resonances for the $[Ir(COD)Cl]_2$/1-*t*Bu system as a function of the 1-*t*Bu/Ir ratio. Squares: rapidly equilibrating mixture of 2-*t*Bu and 3-*t*Bu; triangles: 4-*t*Bu; diamonds: 1-*t*Bu. The solid line in (a) is the data fit to the model of Scheme 2 (see text).

 © 2006 Wiley-VCH Verlag GmbH & Co. KGaA, Weinheim 

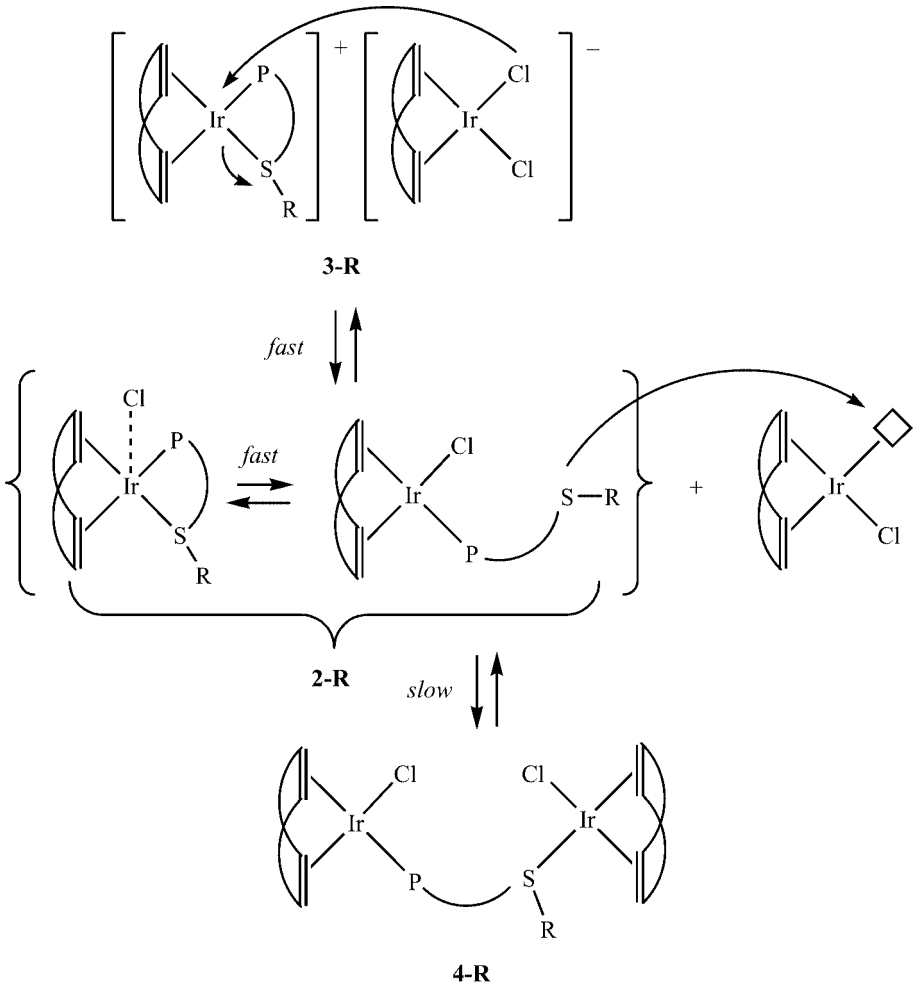


Scheme 2.

varying the **1-*t*Bu**/Ir ratio in the 0 to > 1 range ($\delta$ always in the 15.68–15.71 range).

We now need to assign the $\delta$ = 17.5 ppm resonance and to rationalize the fact that it is observed only for the **1-*t*Bu**/Ir system. The most reasonable proposal that we are able to advance involves a neutral dinuclear complex with a bridging P,S*t*Bu ligand (**4-*t*Bu**), see Scheme 2. Precedents for this type of structural arrangement exist for P,N ligands.[66,67] As the equilibrium between the five-coordinate and the four-coordinate isomers of **2-R** lies strongly in favor of the latter when R = *t*Bu, the pendant S*t*Bu arm is available to coordinate the Ir center in the unsaturated [Ir(COD)Cl] complex, which is in equilibrium with the dichloro-bridged dimer. It is rather remarkable, however, that this process is slower than the addition of the chloride anion to the same position. We presume that this is so for steric reasons. The reversible association/dissociation process of the pendant S*t*Bu arm leading from **2-*t*Bu** to **3-*t*Bu** is fast because it is intramolecular. The reason why analogous compounds **4-Ph** and **4-Et** are not observed would then be related to the preferred sulfur coordination to the same Ir center, in the five-coordinate geometry of **2-Ph** and **2-Et**.

According to this proposal, compound **4** has an identical stoichiometry to compound **3**. Therefore, the **3-*t*Bu**/**4-*t*Bu** ratio should be independent on the **1-*t*Bu**/Ir ratio. This ratio can be estimated from the extrapolated relative intensities of the $\delta$ = 14.6 and 17.5 ppmpeaks as **1-*t*Bu**/Ir → 0 (ca. 42.3:57.7), from Figure 4 (b). This number can in turn be used to estimate the individual concentrations of **2-*t*Bu** and **3-*t*Bu** at each **1-*t*Bu**/Ir ratio. At this point, the concentration of each iridium-containing species can be calculated solving the equilibrium relationship [Equation (3), R = *t*Bu], using *K* as an adjustable parameter. These concentrations were then used to calculate the $^{31}$P chemical shift according to Equation (4) (R = *t*Bu). Fitting of the simulated and experimental data yielded a reasonable agreement for an equilibrium constant of 0.036, as shown in Figure 4 (a). Thus, *K* is greater for R = *t*Bu (0.036) than for R = Ph (0.008). The release of steric pressure upon transforming the chelating P,S*t*Bu ligand into a dangling one (whereas the P,SPh ligand remains chelating in compound **2-Ph**) may provide an explanation of this difference.

### (e) Comparison with Rh Coordination Chemistry and Mixed Rh–Ir Studies

When samples of **1-R** (R = Ph, Et, *t*Bu) were treated with [Rh(COD)Cl]$_2$ in a 2:1 molar ratio, a single $^{31}$P resonance,

 © 2006 Wiley-VCH Verlag GmbH & Co. KGaA, Weinheim 

Table 5. $^{31}P$ resonances assigned to the products of 1:1 and 2:1 ligand **1-R** addition to $[M(COD)Cl]_2$ (solvent = $CDCl_3$).

| Complex | **1-R**/M ratio | $\delta = {}^{31}P$ ($J_{PRh}$) M = Rh | M = Ir[a] |
|---|---|---|---|
| M(COD)Cl(P,SEt) | 1:1 | **5-Et:** 25.2 (142 Hz) | **2-Et:** –4.6 |
| M(COD)Cl(P,S*t*Bu) | 1:1 | **5-*t*Bu:** 24.5 (147 Hz) | **2-*t*Bu:** 15.6 |
| M(COD)Cl(P,SPh) | 1:1 | **5-Ph:** 22.2 (143 Hz) | **2-Ph:** –2.9 |
| [M(COD)(P,SPh)][M(COD)$Cl_2$] | 1:2 | **6-Ph**: 24.0 (143 Hz) | **3-Ph**: 11.0 |

[a] Following the chemical shift analysis as a function of **1-R**/M ratio, as outlined in the text and described in detail in the Supporting Information.

split into a doublet by a rhodium coupling, was observed in each case in the NMR spectrum. This resonance is therefore assigned to a product with the stoichiometry RhCl(COD)(P,SR) (**5-R**) see Table 5. The very similar values of the chemical shifts and coupling constants, in contrast to the behaviour observed for the Ir complexes, strongly indicates the same coordination mode for the three ligands with respect to $Rh^I$.

When a sample of **1-Ph** in $CDCl_3$ was treated with $[Rh(COD)Cl]_2$ in a 1:1 molar ratio, a doublet resonance was observed at $\delta$ = 24 ppm (143 Hz) in the $^{31}P$ NMR spectrum. Both the chemical shift and the coupling constant of this resonance are very close, but not identical, to those obtained using a 2:1 ratio. Therefore, we presume that the compound formed under these conditions (**6-Ph**) has the same structure as the iridium analogue **3-Ph**, namely $[Rh(COD)(P,SPh)][Rh(COD)Cl_2]$. As for compounds **5-R**, there are two possibilities: an ionic structure $[Rh(COD)(P,SR)]^+Cl^-$, and a neutral structure with a dangling thioether function, [RhCl(COD)($\kappa^1$-P,SR)], as seen for the iridium analogue **2-*t*Bu**. In both cases, the rhodium complexes are consistently four-coordinate, in agreement with the lower propensity of $Rh^I$, relative to $Ir^I$, to give five-coordinate geometries with the involvement of the $d_z2$ orbital. A few examples of four-coordinate $[Rh(COD)L_2]^+$ complexes having $Cl^-$ as the counterion have been characterized by X-ray crystallography, namely $[Rh(COD)(bipy)_2]^+$,[49] $[Rh(COD)L_2]^+$ (L = 1,3-dimethylimidazolin-2-ylidene),[50] and a chelated version of the latter {$L_2$ = $[MeNC_3H_2N\text{-}(CH_2)_3\text{-}NC_3H_2NMe]$}.[51] However, addition of the **1-R** ligands to $[Rh(COD)Cl]_2$ in $C_6D_6$ generated soluble products whose $^{31}P$ NMR resonances [**5-Et**: 21.8 (147 Hz); **5-*t*Bu**: 23.6 (148 Hz); **5-Ph**: 21.6 (148 Hz)] turned out to be essentially identical to those recorded in $CDCl_3$. This result strongly suggests that the adducts are neutral. In conclusion, the $Ir^I$ center has a greater tendency to coordinate both the thioether function and the $Cl^-$ ion. The latter, however, is rather weakly coordinated as shown by the long Ir–Cl distances in the X-ray structures (vide supra).

Subsequent mixing experiments were carried out in order to probe the relative stability of $Rh^I$ and $Ir^I$ complexes with the coordinated P,SR ligands. The addition of $[Ir(COD)Cl]_2$ to a sample of **5-Ph** in a 1:2 molar ratio made the $^{31}P$ NMR resonance of the starting Rh complex and the P–Rh coupling disappear, yielding a new resonance (singlet) at $\delta$ = –0.25 ppm. From the observed chemical shift (cf. Table 5) and the absence of Rh coupling, we propose that the reaction leads to complex **2-Ph**, according to Equation (5). The same $^{31}P$ NMR resonance ($\delta$ = –0.21 ppm) was obtained by adding 1/2 mol of $[Ir(COD)Cl]_2$ and 1/2 mol of $[Rh(COD)Cl]_2$ simultaneously to one mol of **1-Ph**. However, complex **2-Ph** cannot be the only species in solution, because its resonance is shifted relative to that assigned to pure **2-Ph**. From the observed NMR behaviour of complex **2-Ph** in the presence of variable amounts of $[Ir(COD)Cl]_2$ (see Figure 3 and related discussion above), we can presume that the reaction mixture also contains equilibrium amounts of complex $[Ir(COD)(\kappa^2\text{-P,SPh})][Rh(COD)Cl_2]$, **3′**, obtained by transfer of the chloride ligand to the dinuclear rhodium complex as shown in Equation (6).

$$\underset{\textbf{5-Ph}}{RhCl(COD)(P,SPh)} + \tfrac{1}{2}[Ir(COD)Cl]_2 \longrightarrow \underset{\textbf{2-Ph}}{[Ir(COD)(\kappa^2\text{-P,SPh})Cl]} + \tfrac{1}{2}[Rh(COD)Cl]_2 \quad (5)$$

$$\underset{\textbf{2-Ph}}{[Ir(COD)(\kappa^2\text{-P,SPh})Cl]} + \tfrac{1}{2}[Rh(COD)Cl]_2 \rightleftharpoons \underset{\textbf{3'}}{[Ir(COD)(\kappa^2\text{-P,SPh})][Rh(COD)Cl_2]} \quad (6)$$

It is interesting to remark that the resonance observed for this mixture (ca. –0.2 ppm), which contains a P,SPh:(Rh+Ir) ratio of 0.5, is much closer to the resonance of **2-Ph** than that of a solution with the same P,SPh to metal ratio, but containing only Ir (ca. 8 ppm, see Figure 3). This observation shows that $[Ir(COD)Cl]_2$ is a stronger chloride scavenger than its rhodium analogue. Another obvious conclusion of this study is that the iridium ion forms stronger bonds with the phosphorus and sulfur atoms of the P,SPh ligand than does the rhodium ion.

### (f) Catalytic Studies

Complexes **2** were tested as catalyst for the hydrogenation of diphenylacetylene. The results are presented in Table 6. Under 30 bar of dihydrogen pressure at room temperature with 1 mol-% of precatalyst, compound **2-*t*Bu** gave a quantitative conversion after 6 h, whereas complex **2-Ph** was less active, yielding only a 59% conversion. In both cases, significant amounts of 1,2-diphenylethane were de-

 © 2006 Wiley-VCH Verlag GmbH & Co. KGaA, Weinheim 

Table 6. Diphenylacetylene hydrogenation in presence of complexes **2-Ph** and **2-*t*Bu**.

| Entry | Complex | Reaction time | Conversion[a,b] | Yield of *cis*-stilbene[b] | Yield of *trans*-stilbene[b] | Yield of 1,2-diphenylethane[b] |
|---|---|---|---|---|---|---|
| 1 | **2-Ph** | 6 h | 59% | 79% | 8% | 13% |
| 2 | **2-*t*Bu** | 6 h | 100% | 64% | 14% | 22% |

[a] Reaction run with 1 mmol of diphenylacetylene, 0.01 mmol of complex **2** (1 mol-%) in 2 mL $CH_2Cl_2$ at room temperature under 30 bars of dihydrogen. [b] Determined by GC.

tected by GC (alkenes/alkane ratio is 92:8 for **2-Ph** and 78:22 for **2-*t*Bu**). Compared to other hydrogenation systems for the selective transformation of alkynes into alkenes, these systems perform rather poorly.[68–75]

Furthermore, the stereoselectivity of the reaction, especially with compound **2-*t*Bu**, is also quite poor (*cis*-stilbene/*trans*-stilbene ratio is 91:9 for **2-Ph** and 82:18 for **2-*t*Bu**). The presence of (*E*)-alkenes after hydrogenation of alkynes is commonly explained by the isomerisation of (*Z*)-alkenes, which are the primary products arising from the *syn*-addition of $H_2$ to the C–C triple bonds.[76–78] In order to determine whether similar reasons are involved in our system, we carried out the reaction of *cis*-stilbene with dihydrogen in presence of complexes **2-Ph** or **2-*t*Bu** under the same conditions described in Table 6 for diphenylacetylene. Isomerisation to *trans*-stilbene as well as hydrogenation to 1,2-diphenylethane did occur, although the rate of this transformation was slower than the direct formation of these two products from diphenylacetylene. This result suggests that the isomerization and further hydrogenation processes probably occur mostly from the vinyl intermediate, before the primary *cis*-stilbene product is formed by reductive elimination. However, recoordination of the *cis*-stilbene followed by both isomerization and further hydrogenation are also possible.

## Conclusion

The use of the ferrocenyl phosphane–thioether ligands **1-R** (R = Et, Ph, *t*Bu) has allowed to reveal that the coordination geometry of chlorocyclooctadieneiridium(I) ligand adducts, both in the solid state and in solution, is delicately controlled by the nature of the R substituent, yielding five-coordinate complexes **2-R** for R = Et, Ph and a four-coordinate one for R = *t*Bu, the latter featuring a dangling thioether group. The ligand chirality controls the geometry at the sulfur and iridium atoms, producing single diastereomers.

The solid state geometries appear to be maintained in solution. However, complex equilibria between various structures are established. The chloride ligand is loosely bound to iridium in the five-coordinate complexes **2-R**, leading to its scavenging by excess metal complex and to a rapid equilibration between the complexes **2-R** and ionic $[Ir(COD)(\kappa^2\text{-P,SR})]^+[Ir(COD)Cl_2]^-$ (**3-R**). Salt-like compounds of type $[Ir(COD)(k^2\text{-L-L}')][Ir(COD)X_2]^-$ have not been structurally characterized previously for any L-L′ or X, though they are quite common for the Rh congener. Furthermore, competitive coordination reactions between rhodium and iridium for ligand **1-Ph** lead only to iridium coordination, probing the greater affinity of P,SR ligands for the heavier metal. The same solution is obtained whether the P,SR ligand is initially bonded to Rh or Ir, indicating a high lability for such systems.

Complexes **2-R** catalyse the hydrogenation of diphenylacetylene at room temperature, paving the way to the application of such complexes to other hydrogenation reactions. Our particular attention is devoted to asymmetric hydrogenation, taking advantage of the availability of the chiral ligands **1-R** in optically pure form. Further studies in this direction are currently in progress in our laboratories.

## Experimental Section

**General:** All reactions were carried out under an argon using standard Schlenk techniques. Solvents were carefully dried by conventional methods and distilled under argon before use. The (*R*/*S*)-2-diphenylphosphanyl-(R-thiomethyl)ferrocene ligands (**1-R**, R = Et, *t*Bu, Ph) were prepared according to a published procedure[56] from racemic 2-(diphenylthiophosphanylferrocenyl)methanol.[79] NMR spectra were recorded with Bruker AC200 and Bruker Avance 500 FT-NMR spectrometers. The resonances were calibrated relative to the residual solvent peaks and are reported with positive values downfield from TMS. The NMR spectra of the new compounds **2-R** (R = Et, *t*Bu, Ph) are collected in Table 1.

**Synthesis of [IrCl(COD)(P,SEt)] (2-Et):** In a Schlenk tube, under argon, ligand **1-Et** (69 mg, 0.155 mmol) was dissolved in dichloromethane (3 mL) and $[Ir(COD)Cl]_2$ (52 mg, 0.077 mmol) was added. After 1 h of stirring, the addition of pentane (10 mL) yielded a yellow precipitate, which was filtered off to give [IrCl(COD)(P,SEt)] (104 g, 86% yield). $C_{33}H_{37}ClFeIrPS$ (780.21): calcd. C 50.80, H 4.78; found C 50.64, H 5.05.

**Synthesis of IrCl(COD)(P,S*t*Bu) (2-*t*Bu):** In a Schlenk tube, under nitrogen, ligand **1-*t*Bu** (272 mg, 0.576 mmol) was dissolved in dichloromethane (3 mL) and $[Ir(COD)Cl]_2$ (193 mg, 0.288 mmol) was added. The solution was stirred for 2 h at room temperature and 10 mL of hexane was the added to form a yellow precipitate. The precipitate was filtered off under nitrogen and washed with hexane, to give [IrCl(COD)(P,S*t*Bu)] (416 mg, 89% yield). $C_{35}H_{41}ClFeIrPS{\cdot}CH_2Cl_2$ (893.13): calcd. C 48.41, H 4.85; found C 48.62, H 4.70. The presence of dichloromethane was evident from the NMR spectrum recorded on a solution of the single crystals. $^1$H NMR (500 MHz, [D$_8$]toluene: $\delta$ = 8.33 (dd, $J_{HH}$ = 10 Hz, $J_{HP}$ = 12 Hz, 2 H, Ph), 7.38 (dd, $J_{HH}$ = 10 Hz, $J_{HP}$ = 12 Hz, 2 H, Ph), 7.19 (m, 2 H, Ph), 7.17 (m, 1 H, Ph), 6.97 (m, 2 H, Ph), 6.95 (m, 1 H, Ph), 4.67 (s, sCp), 4.58 (d, $J_{HH}$ = 13 Hz, 1 H, $CH_2$), 4.24 (d, $J_{HH}$ = 13 Hz, 1 H, $CH_2$), 4.18 (s, sCp), 4.16 (s, 5 H, Cp), 4.13 (t, $J_{HH}$ = 2 Hz, sCp), 3.88 (br., COD), 2.30 (m, COD), 2.08 (m, COD), 1.65 (m, COD), 1.49 (m, COD), 1.44 (s, 9 H, *t*Bu) ppm. $^{13}$C NMR (500 MHz, [D$_8$]toluene): $\delta$ = 136.05 (d, $J_{CP}$ = 12 Hz, 2 C, Ph), 135.0 (d, $J_{CP}$ = 50 Hz, quat. Ph), 133.70 (d, $J_{CP}$ = 12 Hz, 2 C, Ph), 133.4 (d, $J_{CP}$ = 50 Hz, quat. Ph), 130.00 (d, $J_{CP}$ = 3 Hz, 1 C, Ph), 129.05 (d, Ph, $J_{CP}$ = 2 Hz, 1 C), 127.40 (d, $J_{CP}$ = 6 Hz, 2 C, Ph),

 © 2006 Wiley-VCH Verlag GmbH & Co. KGaA, Weinheim 

Table 7. Crystal data and structure refinement for all compounds.

| Identification code | **2-Et** | **2-Ph** | **2-*t*Bu** | **3-Ph** |
|---|---|---|---|---|
| Empirical formula | $C_{33}H_{37}ClFeIrPS{\cdot}CH_2Cl_2$ | $C_{37}H_{37}ClFeIrPS{\cdot}CH_2Cl_2$ | $C_{35}H_{41}ClFeIrPS{\cdot}CH_2Cl_2$ | $C_{45}H_{49}Cl_2FeIr_2PS{\cdot}(C_7H_8)_{0.5}$ |
| Formula weight | 865.08 | 913.12 | 893.13 | 1210.09 |
| Temperature [K] | 180(2) | 180(2) | 115(2) | 105(2) |
| Wavelength [Å] | 0.71073 | 0.71073 | 0.71073 | 0.71073 |
| Crystal system | monoclinic | triclinic | orthorhombic | triclinic |
| Space group | $P2_1$ | $P\bar{1}$ | *Pbca* | $P\bar{1}$ |
| *a* [Å] | 11.6753(13) | 10.177(5) | 14.778(5) | 10.1650(8) |
| *b* [Å] | 10.9974(9) | 12.983(5) | 19.216(6) | 13.4775(11) |
| *c* [Å] | 12.7284(13) | 13.676(5) | 24.110(8). | 16.7698(13) |
| *α* [°] | 90.0 | 102.045(5) | 90.0 | 81.296(2) |
| *β* [°] | 100.717(13) | 93.653(5) | 90.0 | 72.575(2) |
| *γ* [°] | 90.0 | 102.670(5) | 90.0 | 78.406(2) |
| Volume [Å]$^3$ | 1605.8(3) | 1712.8(12) | 6847(4) | 2137.1(3) |
| *Z* | 2 | 2 | 8 | 2 |
| Density (calcd) [Mg/m$^3$] | 1.789 | 1.771 | 1.733 | 1.881 |
| Absorption coefficient [mm$^{-1}$] | 4.980 | 4.674 | 4.675 | 6.792 |
| *F*(000) | 856 | 904 | 3552 | 1178 |
| Crystal size [mm$^3$] | 0.22 × 0.17 × 0.01 | 0.20 × 0.12 × 0.055 | 0.35 × 0.12 × 0.03 | 0.22 × 0.19 × 0.07 |
| Theta range [°] | 2.17 to 26.14 | 3.30 to 32.05 | 1.93 to 28.40°. | 2.10 to 28.32 |
| Reflections collected | 12676 | 18279 | 66063 | 22207 |
| Independent reflections [*R*(int)] | 6263 (0.0500) | 10876 (0.0311) | 8540 (0.0483) | 10541 (0.0312) |
| Completeness [%] | 98.5 | 90.3 | 99.2 | 98.8 |
| Absorption correction | multi-scan | analytical | SADABS | SADABS |
| Max., min. transmission | 0.6451 and 0.5709 | 0.64910 and 0.24012 | 1.000 and 0.724635 | 1.0 and 0.812 |
| Refinement method | $F^2$ | $F^2$ | $F^2$ | $F^2$ |
| Data:restraints:parameters | 6263/395/372 | 10876/0/406 | 8540/0/391 | 10541/55/498 |
| Goodness-of-fit on $F^2$ | 0.967 | 0.914 | 1.031 | 1.041 |
| Final *R* indices [$I > 2\sigma(I)$] | $R_1$ = 0.0326, $wR_2$ = 0.0682 | $R_1$ = 0.0304, $wR_2$ = 0.0494 | $R_1$ = 0.0241, $wR_2$ = 0.0534 | $R_1$ = 0.0358, $wR_2$ = 0.0815 |
| *R* indices (all data) | $R_1$ = 0.0437, $wR_2$ = 0.0714 | $R_1$ = 0.0415, $wR_2$ = 0.0516 | $R_1$ = 0.0335 $wR_2$ = 0.0569 | $R_1$ = 0.0456, $wR_2$ = 0.0855 |
| Absolute structure parameter | 0.571(7) | | | |
| Largest diff. peak and hole [e·Å$^{-3}$] | 1.141 and –0.817 | 2.188 and –1.362 | 1.831 and –0.749 | 4.945 and –1.048 |

126.95 (d, $J_{CP}$ = 10 Hz, 2 C, Ph), 91.02 (d, $J_{CP}$ = 16 Hz, quat. Cp), 74.8 (d, $J_{CP}$ = 50 Hz, quat. Cp), 74.42 (d, $J_{CP}$ = 6 Hz, 1 C, sCp), 71.37 (s, Cp), 71.24 (d, $J_{CP}$ = 7.4 Hz, 1 C, sCp), 69.7 (d, $J_{CP}$ = 6.5 Hz, 1 C, sCp), 52 (COD), 43.05 [s, S-*C* ($CH_3$)]. 30.75 (COD), 32.72 (COD), 30.7 [s, S-C(*C*$H_3$)], 29.1 (s, $CH_2$) ppm. $^{31}$P NMR (500 MHz, [$D_8$]toluene): $\delta$ = 11.8 ppm.

**Synthesis of IrCl(COD)(P,SPh) (2-Ph):** In a Schlenk tube, under nitrogen, ligand **1-Ph** (240 mg, 0.488 mmol) was dissolved in dichloromethane (4 mL) and solid $[Ir(COD)Cl]_2$ (163 mg, 0.244 mmol) was subsequently added. After 10 min of stirring, a yellow precipitate was formed. Hexane (10 mL) was added to complete the precipitation and the yellow solid was filtered off to yield [IrCl(COD)(P,SPh)] (347 g, 86% yield). $C_{37}H_{37}ClFeIrPS{\cdot}CH_2Cl_2$ (913.12): calcd. C 53.66, H 4.50; found C 53.83, H 4.53.

**X-ray Crystallography:** Yellow single crystals of complexes **2-R** (R = Et, *t*Bu, Ph) were obtained by slow diffusion of light hydrocarbon vapors (pentane for Et, hexane for *t*Bu and Ph) into a $CH_2Cl_2$ solution. Diffusion of hexane vapors into a toluene solution of **2-Ph** gave yellow crystals of compound **3-Ph**. A single crystal of each compound was mounted under inert perfluoropolyether on the tip of glass fibre and cooled in the cryostream of either an Oxford-Diffraction XCALIBUR CCD diffractometer for **2-Ph**, a Stoe IPDS diffractometer for **2Et** or a Bruker SMART CCD diffractometer for **2-*t*Bu** and **3**. Data were collected using the monochromatic Mo$K_\alpha$ radiation ($\lambda$ = 0.71073). The structures were solved by direct methods (SIR97)[80] and refined by least-squares procedures on $F^2$ using SHELXL-97.[81] All H atoms attached to carbon were introduced in calculation in idealised positions and treated as riding models. As indicated by the refinement of the Flack's parameter,[82] compound **2-Et** is twinned by inversion ("racemic twin"). In compound **3** a toluene solvent molecule is statistically disordered around an inversion center. The drawing of the molecules was realised with the help of ORTEP32.[83] Crystal data and refinement parameters are shown in Table 7.

CCDC-283190 to -283193 contain the supplementary crystallographic data for this paper. These data can be obtained free of charge from The Cambridge Crystallographic Data Centre via www.ccdc.cam.ac.uk/data_request/cif.

**Supporting Information** (see also the footnote on the first page of this article): Procedures for fitting the equilibrium constant of Equation (1) to the experimental NMR spectroscopic data (Ir/**1-Ph** and Ir/**1-*t*Bu** systems).

## Acknowledgments

We are grateful to the EPSRC, the CNRS, and the European Union for funding under the Hydrochem network (contract HPRN-CT-2002-00176).

[1] L. J. Yellowlees, K. G. Mcnamara, in *Comprehensive Coordination Chemistry II, vol. 6* (Eds.: J. A. McCleverty, T. J. Meyer), Elsevier, Oxford, **2004**, pp. 147–246.
[2] R. H. Crabtree, *Acc. Chem. Res.* **1979**, *12*, 331–337.
[3] J. M. Brown, in *Comprehensive Asymmetric Catalysis, vol. 1* (Eds.: E. N. Jacobsen, A. Pfaltz, H. Yamamoto), Springer-Verlag, Berlin, **1999**, pp. 121–182.

 © 2006 Wiley-VCH Verlag GmbH & Co. KGaA, Weinheim 

[4] W. Tang, X. Zhang, *Chem. Rev.* **2003**, *103*, 3029–3069.
[5] A. Lightfoot, P. Schnider, A. Pfaltz, *Angew. Chem. Int. Ed. Engl.* **1998**, *37*, 2897–2899.
[6] A. Pfaltz, J. Blankenstein, R. Hilgraf, E. Hormann, S. Mcintyre, F. Menges, M. Schonleber, S. P. Smidt, B. Wustenberg, N. Zimmermann, *Adv. Synth. Catal.* **2003**, *345*, 33–44.
[7] W. J. Drury III, N. Zimmermann, M. Keenan, M. Hayashi, S. Kaiser, R. Goddard, A. Pfaltz, *Angew. Chem. Int. Ed.* **2004**, *43*, 70–74.
[8] T. Bunlaksananusorn, K. Polborn, P. Knochel, *Angew. Chem. Int. Ed.* **2003**, *42*, 3941–3943.
[9] P. Maire, S. Deblon, F. Breher, J. Geier, C. Boehler, H. Rueegger, H. Schoenberg, H. Gruetzmacher, *Chem. Eur. J.* **2004**, *10*, 4198–4205.
[10] K. Kaellstroem, C. Hedberg, P. Brandt, A. Bayer, P. G. Andersson, *J. Am. Chem. Soc.* **2004**, *126*, 14308–14309.
[11] D. Liu, Q. Dai, X. Zhang, *Tetrahedron* **2005**, *61*, 6460–6471.
[12] E. Guimet, M. Dieguez, A. Ruiz, C. Claver, *Dalton Trans.* **2005**, 2557–2562.
[13] F. Spindler, B. Pugin, H. U. Blaser, *Angew. Chem. Int. Ed. Engl.* **1990**, *29*, 558–559.
[14] Y. Ng Cheong Chan, J. A. Osborn, *J. Am. Chem. Soc.* **1990**, *112*, 9400–9401.
[15] S. Kainz, A. Brinkmann, W. Leitner, A. Pfaltz, *J. Am. Chem. Soc.* **1999**, *121*, 6421–6429.
[16] D. Xiao, X. Zhang, *Angew. Chem. Int. Ed.* **2001**, *40*, 3425–3428.
[17] C. Blanc, F. Agbossou-Niedercorn, G. Nowogrocki, *Tetrahedron: Asymmetry* **2004**, *15*, 2159–2163.
[18] E. Guiu, C. Claver, J. Benet-Buchholz, S. Castillon, *Tetrahedron: Asymmetry* **2004**, *15*, 3365–3373.
[19] A. Trifonova, J. S. Diesen, C. J. Chapman, P. G. Andersson, *Org. Lett.* **2004**, *6*, 3825–3827.
[20] S. Vargas, M. Rubio, A. Suarez, A. Pizzano, *Tetrahedron Lett.* **2005**, *46*, 2049–2052.
[21] S.-M. Lu, X.-W. Han, Y.-G. Zhou, *Adv. Synth. Catal.* **2004**, *346*, 909–912.
[22] G. Zassinovich, G. Mestroni, S. Gladiali, *Chem. Rev.* **1992**, *92*, 1051–1069.
[23] M. J. Palmer, M. Wills, *Tetrahedron: Asymmetry* **1999**, *10*, 2045–2061.
[24] D. Mueller, G. Umbricht, B. Weber, A. Pfaltz, *Helv. Chim. Acta* **1991**, *74*, 232–240.
[25] R. Ter Halle, A. Breheret, E. Schulz, C. Pinel, M. Lemaire, *Tetrahedron: Asymmetry* **1997**, *8*, 2101–2108.
[26] D. G. I. Petra, P. C. J. Kamer, A. L. Spek, H. E. Schoemaker, P. W. N. M. Van Leeuwen, *J. Org. Chem.* **2000**, *65*, 3010–3017.
[27] J.-S. Chen, Y.-Y. Li, Z.-R. Dong, B.-Z. Li, J.-X. Gao, *Tetrahedron Lett.* **2004**, *45*, 8415–8418.
[28] Z.-R. Dong, Y.-Y. Li, J.-S. Chen, B.-Z. Li, Y. Xing, J.-X. Gao, *Org. Lett.* **2005**, *7*, 1043–1045.
[29] B. M. Trost, D. L. Van Vranken, *Chem. Rev.* **1996**, *96*, 395–422.
[30] A. Pfalz, H. Yamamoto, J. M. Brown, in *Comprehensive Asymmetric Catalysis, vol. II* (Eds.: E. N. Jacobsen, A. Pfaltz, H. Yamamoto), Springer-Verlag, Berlin, **1999**, pp. 834–884.
[31] R. Takeuchi, *Synlett* **2002**, 1954–1965.
[32] R. Takeuchi, M. Kashio, *Angew. Chem. Int. Ed. Engl.* **1997**, *36*, 263–265.
[33] B. Bartels, G. Helmchen, *Chem. Commun.* **1999**, 741–742.
[34] C. Garcia-Yebra, J. P. Janssen, F. Rominger, G. Helmchen, *Organometallics* **2004**, *23*, 5459–5470.
[35] G. Lipowsky, N. Miller, G. Helmchen, *Angew. Chem. Int. Ed.* **2004**, *43*, 4595–4597.
[36] T. Ohmura, J. F. Hartwig, *J. Am. Chem. Soc.* **2002**, *124*, 15164–15165.
[37] A. Leitner, C. Shu, J. F. Hartwig, *Org. Lett.* **2005**, *7*, 1093–1096.
[38] N. Kinoshita, K. H. Marx, K. Tanaka, K. Tsubaki, T. Kawabata, N. Yoshikai, E. Nakamura, K. Fuji, *J. Org. Chem.* **2004**, *69*, 7960–7964.
[39] K. Tissot-Croset, D. Polet, A. Alexakis, *Angew. Chem. Int. Ed.* **2004**, *43*, 2426–2428.
[40] D. Polet, A. Alexakis, *Org. Lett.* **2005**, *7*, 1621–1624.
[41] H.-U. Blaser, *Adv. Synth. Catal.* **2002**, *344*, 17–31.
[42] H.-U. Blaser, W. Brieden, B. Pugin, F. Spindler, M. Studer, A. Togni, *Top. Catal.* **2002**, *19*, 3–16.
[43] T. Hayashi, M. Tanaka, I. Ogata, T. Kodama, T. Takahashi, Y. Uchida, T. Uchida, *Bull. Chem. Soc. Jpn.* **1983**, *56*, 1780–1785.
[44] T. Shibata, K. Yamashita, H. Ishida, K. Takagi, *Org. Lett.* **2001**, *3*, 1217–1219.
[45] R. Dorta, D. Broggini, R. Stoop, H. Ruegger, F. Spindler, A. Togni, *Chem. Eur. J.* **2004**, *10*, 267–278.
[46] G. Zassinovich, R. Bettella, G. Mestroni, N. Bresciani-Pahor, S. Geremia, L. Randaccio, *J. Organomet. Chem.* **1989**, *370*, 187–202.
[47] M. Shivakumar, J. Gangopadhyay, A. Chakravorty, *Polyhedron* **2001**, *20*, 2089–2093.
[48] C. M. Thomas, R. Mafua, B. Therrien, E. Rusanov, H. Stoeckli-Evans, G. Suss-Fink, *Chem. Eur. J.* **2002**, *8*, 3343–3352.
[49] J. J. Robertson, A. Kadziola, R. A. Krause, S. Larsen, *Inorg. Chem.* **1989**, *28*, 2097–2102.
[50] W. A. Herrmann, M. Elison, J. Fischer, C. Koecher, G. R. J. Artus, *Chem. Eur. J.* **1996**, *2*, 772–780.
[51] J. A. Mata, A. R. Chianese, J. R. Miecznikowski, M. Poyatos, E. Peris, J. W. Faller, R. H. Crabtree, *Organometallics* **2004**, *23*, 1253–1263.
[52] S. G. Murray, F. R. Hartley, *Chem. Rev.* **1981**, *81*, 365–414.
[53] J. R. Dilworth, N. Wheatley, *Coord. Chem. Rev.* **2000**, *199*, 89–158.
[54] J. C. Bayon, C. Claver, A. M. Masdeu-Bulto, *Coord. Chem. Rev.* **1999**, *193–195*, 73–145.
[55] A. M. Masdeu-Bulto, M. Dieguez, E. Martin, M. Gomez, *Coord. Chem. Rev.* **2003**, *242*, 159–201.
[56] L. Routaboul, S. Vincendeau, J.-C. Daran, E. Manoury, *Tetrahedron: Asymmetry* **2005**, *16*, 2685–2690.
[57] D. A. Evans, F. E. Michael, J. S. Tedrow, K. R. Campos, *J. Am. Chem. Soc.* **2003**, *125*, 3534–3543.
[58] M. Brym, C. Jones, *Transition Met. Chem.* **2003**, *28*, 595–599.
[59] A. R. Chianese, X. W. Li, M. C. Janzen, J. W. Faller, R. H. Crabtree, *Organometallics* **2003**, *22*, 1663–1667.
[60] J. Browning, G. W. Bushnell, K. R. Dixon, R. W. Hilts, *J. Organomet. Chem.* **1993**, *452*, 205–218.
[61] G. Vasapollo, A. Sacco, C. F. Nobile, M. A. Pellinghelli, M. Lanfranchi, *J. Organomet. Chem.* **1986**, *312*, 249–262.
[62] E. Anzuela, M. A. Garralda, R. Hernandez, L. Ibarlucca, E. Pinilla, M. Angeles Monge, *Inorg. Chim. Acta* **1991**, *185*, 211–219.
[63] M. A. Garralda, R. Hernandez, L. Ibarlucea, M. I. Arriortua, M. K. Urtiaga, *Inorg. Chim. Acta* **1995**, *232*, 9–17.
[64] A. P. Martinez, M. P. Garcia, F. J. Lahoz, L. A. Oro, *Inorg. Chim. Acta* **2003**, *347*, 86–98.
[65] P. Imhoff, C. J. Elsevier, *J. Organomet. Chem.* **1989**, *361*, C61–C65.
[66] S. Lo Schiavo, M. Grassi, G. De Munno, F. Nicolo, G. Tresoldi, *Inorg. Chim. Acta* **1994**, *216*, 209–216.
[67] C. Tejel, R. Bravi, M. A. Ciriano, L. A. Oro, M. Bordonaba, C. Graiff, A. Tiripicchio, A. Burini, *Organometallics* **2000**, *19*, 3115–3119.
[68] A. Molnar, A. Sarkany, M. Varga, *J. Mol. Catal. A* **2001**, *173*, 185–221.
[69] R. R. Schrock, J. A. Osborn, *J. Am. Chem. Soc.* **1976**, *98*, 2143–2147.
[70] F. Morandini, B. Longato, S. Bresadola, *J. Organomet. Chem.* **1982**, *239*, 377–384.
[71] M. Sodeoka, M. Shibasaki, *J. Org. Chem.* **1985**, *50*, 1147–1149.
[72] B. S. Nkosi, N. J. Coville, M. O. Albers, C. Gordon, M. M. Viney, E. Singleton, *J. Organomet. Chem.* **1990**, *386*, 111–119.
[73] M. W. Van Laren, C. J. Elsevier, *Angew. Chem. Int. Ed.* **1999**, *38*, 3715–3717.


 © 2006 Wiley-VCH Verlag GmbH & Co. KGaA, Weinheim 

[74] M. W. Van Laren, M. A. Duin, C. Klerk, M. Naglia, D. Rogolino, P. Pelagatti, A. Bacchi, C. Pelizzi, C. J. Elsevier, *Organometallics* **2002**, *21*, 1546–1553.
[75] J. W. Sprengers, J. Wassenaar, N. D. Clement, K. J. Cavell, C. J. Elsevier, *Angew. Chem. Int. Ed.* **2005**, *44*, 2026–2029.
[76] A. C. Cooper, K. G. Caulton, *Inorg. Chim. Acta* **1996**, *251*, 41–51.
[77] P. J. Albietz Jr, B. P. Cleary, W. Paw, R. Eisenberg, *J. Am. Chem. Soc.* **2001**, *123*, 12091–12092.
[78] J. Kovacs, T. D. Todd, J. H. Reibenspies, F. Joo, D. J. Darensbourg, *Organometallics* **2000**, *19*, 3963–3969.
[79] T. Hayashi, T. Mise, M. Fukushima, M. Kagotani, N. Nagashima, Y. Hamada, A. Matsumoto, S. Kawakami, M. Konishi, K. Yamamoto, M. Kumada, *Bull. Chem. Soc. Jpn.* **1980**, *53*, 1138–1151.
[80] A. Altomare, M. Burla, M. Camalli, G. Cascarano, C. Giacovazzo, A. Guagliardi, A. Moliterni, G. Polidori, R. Spagna, *J. Appl. Crystallogr.* **1999**, *32*, 115–119.
[81] G. M. Sheldrick, *SHELXL97, Program for Crystal Structure refinement*, University of Göttingen, Göttingen, Germany, **1997**.
[82] H. D. Flack, *Acta Crystallogr., Sect. A* **1983**, *39*, 876–881.
[83] L. J. Farrugia, *J. Appl. Crystallogr.* **1997**, *30*, 565.

Received: September 19, 2005
Published Online: March 15, 2006

 © 2006 Wiley-VCH Verlag GmbH & Co. KGaA, Weinheim 

DOI: 10.1002/ejic.200600069

# Investigations into the Reactivity of Organoelement Gallium Subhalides – Syntheses of Bifunctional Digallium Carboxylate Iodides Possessing Bridged Ga–Ga Bonds and Terminal Iodine Atoms

**Werner Uhl,*[a] Abdelhakim El-Hamdan,[a] and Klaus Peter Schindler[a]**

*Dedicated to Prof. Dr. H. Schnöckel on the occasion of his 65th birthday*

**Keywords:** Gallium / Subvalent compounds / Subhalides / Metal–metal bonds / Carboxylato ligands

The organoelement subhalide $R_2Ga_2I_2$ (**1**) [R = $C(SiMe_3)_3$] reacted with one equivalent of different lithium carboxylates $LiO_2CR$ [R = -$C_6H_5$, -4-$Me_3C$–$C_6H_4$, -4-$BrC_6H_4$, -3,5-$Me_2C_6H_3$, -$CMe_3$] by the selective replacement of only one iodine atom. Bifunctional digallium compounds were formed, in which one chelating carboxylato group bridges the Ga–Ga bonds. Thus, both gallium atoms are coordinated to one carbon atom of the tris(trimethylsilyl)methyl groups and one oxygen atom of the chelating ligand, while only one is further attached to a terminal iodine atom. This asymmetric substitution pattern results in different coordination numbers of three and four for the gallium atoms.
(© Wiley-VCH Verlag GmbH & Co. KGaA, 69451 Weinheim, Germany, 2006)

## Introduction

The tetrahedral cluster compounds $E_4[C(SiMe_3)_3]_4$ (E = Ga, In) are easily available by the reduction of the corresponding alkyltrichlorogallate with magnesium[1] or by the treatment of indium(I) bromide with $LiC(SiMe_3)_3$.[2] These compounds possess the gallium or indium atoms in an unusual low oxidation state of +1. Careful oxidation reactions employing the halogens or appropriate halogen donors open the facile access to organoelement subhalides, which proved to be very effective starting compounds for the generation of secondary products still containing the elements in low oxidation states. Different kinds of subhalides were obtained depending on the halogen source or the stoichiometric ratio of the starting compounds. Transfer of one bromine molecule to the tetraindium cluster gave the remarkable compound $Br_2In_4[C(SiMe_3)_3]_4$, in which the overall tetrahedral arrangement of the indium atoms is retained with some distortion.[3] The bromine atoms occupy one face of the tetrahedron and one edge of that particular face. The average oxidation state of the metal atoms is +1.5. Such a derivative could not be isolated with gallium atoms, which may be caused by the ready dissociation of the tetrahedral tetragallium cluster owing to the relatively strong steric interaction between the bulky substituents.[1] An oxidation state of +2 occurs in the compounds R(X)E–E(X)R (X = Cl, Br, I), which have E–E single bonds. They are monomeric for gallium with coordinatively unsaturated central atoms,[4,5] while $In_4X_4$ cages with all of the halogen atoms in a bridging position are formed with the larger indium atoms.[3] A further structural motif of these subhalides was observed for the compounds $I_2E_3[C(SiMe_3)_3]_3$, which contain chains of three gallium or indium atoms and iodine bridges between both terminal metal atoms.[5,6] A halogen adduct of the triindium compound with all indium atoms possessing a coordination number of four was obtained as a by-product of the cluster synthesis.[7] Organoelement subhalides that are not derived from clusters are also known in the literature.[8,9]

The organoelement subhalides of the type $X_2E_2R_2$ have been employed in several secondary reactions, which impressively showed their importance for the generation of new compounds. Treatment with two equivalents of lithium or silver acetylacetonates yielded the corresponding diacetylacetonato derivatives by the replacement of both halogen atoms and retainment of the E–E bonds.[10] The chelating ligands occupy terminal positions at each gallium or indium atom. In contrast, the bridging of the E–E bonds was observed for dicarboxylato compounds.[11] A very short E–E distance resulted in particular for the indium derivative owing to the small bite of the carboxylato group. Lithium diphenylphosphanide and the subhalide $I_2Ga_2R_2$ (**1**) gave an interesting reaction course with the formation of a gallium phosphanide possessing a $Ga_2P_2$ heterocycle.[12] Oxidation of the gallium atoms occurred and Ga–H bonds were probably formed by the reaction of radical intermediates with

[a] Institut für Anorganische und Analytische Chemie der Universität Münster,
Corrensstraße 30, 48149 Münster, Germany
Fax: +49-251-8336660

 © 2006 Wiley-VCH Verlag GmbH & Co. KGaA, Weinheim 

the solvent. The reduction of some subhalides substituted by aryl groups afforded products containing E–E multiple bonds.[9] Several transition metal gallium or indium compounds could be synthesized by treatment of these subhalides with transition metal carbonylate anions.[13] In general, the introduction of monodentate ligands such as alkyl or alkoxy groups proved to be rather difficult, and in most cases secondary reactions were induced with the cleavage of the E–E bonds. This instability is probably caused by the coordinative unsaturation of the central gallium or indium atoms, which favors intramolecular substituent exchange processes as the starting step for disproportionation reactions. This behavior is similar to that of the solvent-free subhalides of these elements, $E_2X_4$, which do not possess E–E bonds, but are mixed valent with the formulae $E^I[E^{III}X_4]$.[14] Therefore, we tried to synthesize digallium compounds bearing a protecting chelating group at one gallium atom, while the second one still bears its halogen atom. These bifunctional compounds are valuable starting compounds for the generation of a broad variety of secondary products.

## Results and Discussion

### Reactions of $I_2Ga_2R_2$ (1) [R = $C(SiMe_3)_3$] with Lithium Benzoates

The replacement of both iodine atoms of the subhalide $I_2Ga_2R_2$ (**1**) [R = $C(SiMe_3)_3$] by carboxylato groups resulted in reasonable yields and reaction times only when silver benzoate was employed as a starting compound,[11] while lithium benzoate gave complicated mixtures of products. However, it seems that only the exchange of the second iodine atom is relatively slow and unselective. Therefore, we did not employ the silver salts of the carboxylic acids, but treated **1** with one equivalent of the more easily available lithium carboxylates. The most selective reactions were observed when the components were mixed at a very low temperature (–90 °C). Slow warming to room temperature and stirring for a further 24–48 h gave almost quantitative formation of the pure monosubstitution products **2**–**6**, see Equation (1). Despite the high selectivity of all the reactions only compound **2** could be isolated by recrystallization in good yield (82%). In all other cases the high solubility in the noncoordinating solvents prevented the effective recrystallization and yields only between 20 and 60% were achieved. In one case (**5**), all attempts of crystallization failed and the characterization was done with the solid raw product of the reaction.

The NMR spectroscopic characterization is in complete agreement with the molecular structures of these compounds, which are schematically shown in Equation (1). The integration ratios of the resonances of the $^1$H NMR spectra clearly verify that one iodine atom of the starting compound **1** is replaced by a carboxylato ligand. Interestingly, only one resonance is observed for the trimethylsilyl groups although the molecule is unsymmetrical in the solid state with coordination numbers of three and four for the

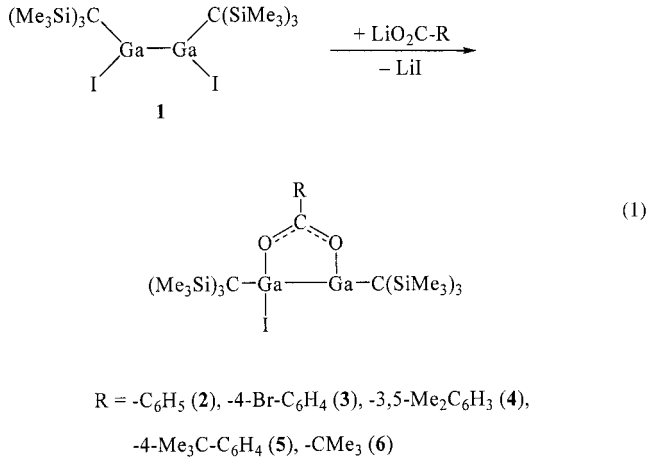


(1)

R = -$C_6H_5$ (**2**), -4-Br-$C_6H_4$ (**3**), -3,5-$Me_2C_6H_3$ (**4**), -4-$Me_3C$-$C_6H_4$ (**5**), -$CMe_3$ (**6**)

gallium atoms. A splitting of these signals could not be detected even on cooling the solutions of **2** and **6** in toluene to –100 °C. Obviously a very fast exchange process occurs, probably including the migration of the iodine atoms. We suppose that this process is a key step in disproportionation reactions, which were discussed above in the Introduction chapter and have been observed often for similar digallium or diindium compounds bearing monodentate ligands.[15] In the case of compounds **2**–**6** the opening of the Ga–Ga bond is prevented by the chelating ligands, which bridge the Ga–Ga bond, since they act as a clamp and stabilize that particular arrangement. The $^{13}$C NMR shift of the inner carbon atoms of the tris(trimethylsilyl)methyl group is worth mentioning. Owing to the fast exchange processes only one resonance is detected for each compound showing a chemical shift of about $\delta$ = 30 ppm. This is in the characteristic range of carbon atoms attached to tricoordinate gallium. A coordination number of four causes significant high field shifts to about $\delta$ = 5 ppm.[16] Thus, although one half of the gallium atoms are coordinatively saturated, the expected average value is not detected here, instead a low coordination number is suggested by the NMR spectroscopic data.

Two compounds (**2** and **4**) were characterized by crystal structure determinations. The molecular structures are depicted in Figure 1 (a and b) and Figure 2, respectively. Both compounds contain an intact Ga–Ga bond bridged by the chelating carboxylato ligand. One gallium atom is further attached to an iodine atom, so that different coordination numbers of three (Ga2) and four (Ga1) result for the metal atoms of one molecule. Ga2 has an almost ideal planar surrounding (sum of the angles 358.5 and 357.2° for **2** and **4**, respectively), while Ga1 has a strongly distorted tetrahedral coordination sphere. The Ga–Ga bond lengths (239.9 and 240.7 pm) are quite similar to that of the starting compound **1** (240.1 pm)[4] and to the corresponding dicarboxylato derivative, in which two chelating ligands bridge the Ga–Ga bond.[11,17] However, they are shorter than the unsupported Ga–Ga bonds of tetraalkyl or tetraaryl digallium compounds (>260 pm,[18] for a review see ref.[5]). Despite the different coordination numbers the Ga–C distances differ only slightly by about 1.5 pm, the slightly longer ones belong to the coordinatively saturated gallium atoms (CN

 © 2006 Wiley-VCH Verlag GmbH & Co. KGaA, Weinheim 

= 4). Also, the Ga–O distances are in a narrow range between 198.3 and 199.6 pm. In compound **2** the Ga–O bond length to the tetracoordinate gallium atom is the slightly shorter one. The Ga–I bonds are relatively long (267.8 and 263.2 pm) compared to those of the starting compound **1** (258.7 pm)[4] or other compounds bearing terminal iodine atoms.[10,19] The Ga–Ga–C groups approach linearity at the tricoordinate gallium atoms (165.2 and 162.5°) as often observed before for dicarboxylato digallium compounds.[11,17] Smaller angles were detected at the tetracoordinate atoms (147.0 and 142.7°). The Ga–O bonds are almost ideally perpendicular to the Ga–Ga bonds (angle Ga–Ga–O about 88° on average), independent of the coordination numbers of the metal atoms. The same holds for the Ga–Ga–I moieties where a relatively small angle of 81.8° was observed for compound **2**. The five-membered heterocycles obtained by the bridging of the Ga–Ga bonds are almost ideally planar, the strongest deviation was observed in both cases for the atom O2 with a value of 8.1 and 2.1 pm, respectively, for compounds **2** and **4**. The Ga–I bonds are nearly perpendicular to these planes, and the angles between their normals and the Ga–I bonds are 11.9 and 7.7°. The distances of the iodine atoms to the second gallium atoms are long (**2**: 333.1 pm; **4**: 350.1 pm) and do not indicate a significant bonding interaction. Interestingly, a disorder occurred with compound **2**, in which the iodine atom, with an occupation factor of 16%, approaches an ideal bridging position between both gallium atoms [Ga–I 278.8(9) and 306.4(12) pm, Ga–Ga 234.3(7) pm, Figure 1, b]. This arrangement reflects excellently the transition state postulated for the fast exchange process observed in solutions of these monocarboxylato compounds (**2**–**6**). Furthermore, all inner carbon atoms of the $C(SiMe_3)_3$ groups are located in the nodal planes of the gallium p orbitals, which are oriented perpendicularly to the $Ga_2C_2O_2$ plane. This particular situation may cause the shift of the $^{13}C$ NMR resonances to a relatively low field position at about $\delta$ = 30 ppm. As discussed before these shifts are normally very characteristic of compounds possessing tricoordinate, coordinatively unsaturated gallium atoms.

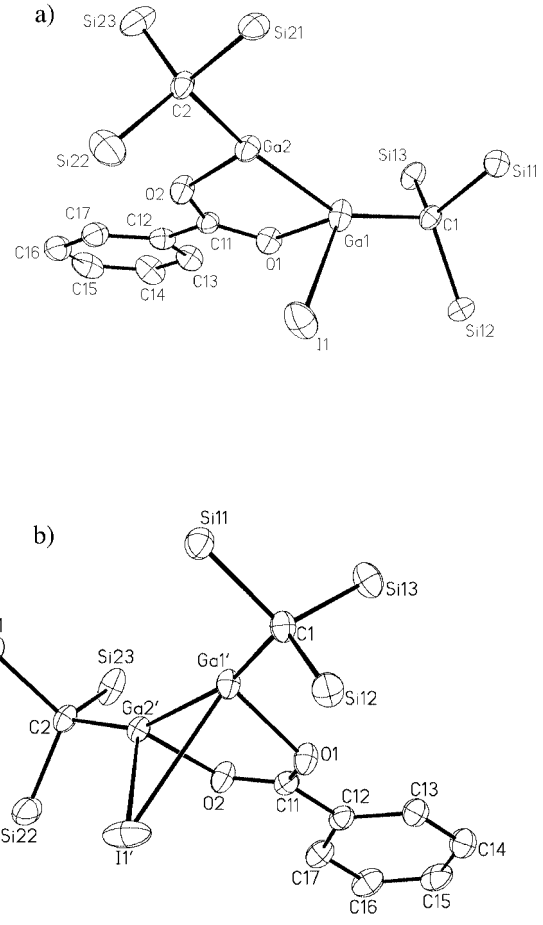


Figure 1. (a). Molecular structure and numbering scheme of compound **2**; the thermal ellipsoids are drawn at the 40% probability level; methyl groups of $SiMe_3$ substituents and hydrogen atoms are omitted; of the disordered gallium and iodine atoms only those with the highest occupancy factors (0.84) were considered. Selected bond lengths [pm] and angles [°]: Ga1–Ga2 239.9(1), Ga1–C1 198.7(3), Ga2–C2 197.3(3), Ga1–O1 199.2(2), Ga2–O2 199.4(2), Ga1–I1 267.8(2), Ga1–Ga2–C2 165.2(1), Ga2–Ga1–C1 147.0(1), O1–Ga1–Ga2 87.69(7), O2–Ga2–Ga1 87.44(7), I1–Ga1–Ga2 81.81(9), I1–Ga1–O1 96.91(9). (b) Molecular structure and numbering scheme of the second individual of the disordered compound **2** possessing the lower occupation factors of the gallium and iodine atoms (16%); the thermal ellipsoids are drawn at the 40% probability level; methyl groups of $SiMe_3$ substituents and hydrogen atoms are omitted. Selected bond lengths [pm] and angles [°]: Ga1′–Ga2′ 234.3(7), Ga1′–I1′ 306(1), Ga2′–I1′ 278.8(8), Ga1′–C1 196.7(5), Ga2′–C2 198.5(7), Ga1′–Ga2′–I1′ 72.8(4), Ga2′–Ga1′–I1′ 60.3(4), Ga1′–I1′–Ga2′ 46.9(2).

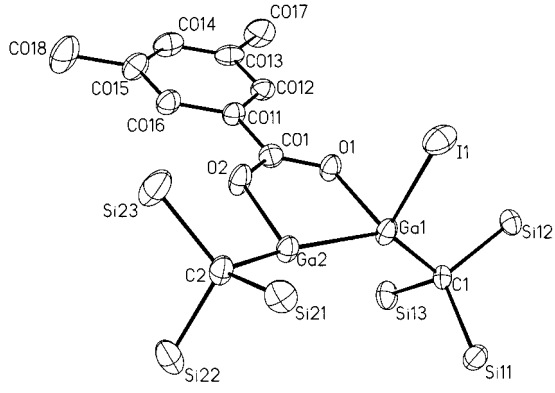


Figure 2. Molecular structure and numbering scheme of compound **4**; the thermal ellipsoids are drawn at the 40% probability level; methyl groups of $SiMe_3$ substituents and hydrogen atoms are omitted. Selected bond lengths [pm] and angles [°]:Ga1–Ga2 240.67(7), Ga1–C1 198.2(4), Ga2–C2 196.7(4), Ga1–O1 199.6(3), Ga2–O2 198.3(3), Ga1–I1 263.23(7), Ga1–Ga2–C2 162.5(1), Ga2–Ga1–C1 142.7(1), O1–Ga1–Ga2 87.43(9), O2–Ga2–Ga1 87.92(9), I1–Ga1–Ga2 87.90(2), I1–Ga1–O1 97.2(1).

### Reaction of $I_2Ga_2R_2$ (1) [R = $C(SiMe_3)_3$] with Lithium Dibenzoylmethanide

Two equivalents of silver or lithium acetylacetonate reacted readily with the digallium(II) (**1**) or diindium(II) subhalides by the formation of the corresponding bis(acetyl-

 © 2006 Wiley-VCH Verlag GmbH & Co. KGaA, Weinheim 

acetonato)dielement compounds.[10,15,20] In contrast to the bridging carboxylato ligands, the acetylacetonato groups occupy terminal positions at the E–E bonds. These compounds are thermally quite stable and decompose or melt only above 170 °C. We hoped to synthesize products analogous to **2**–**6** bearing one chelating acetylacetonato ligand along with one halogen atom by procedures similar to Equation (1).

However, the treatment of the subhalide **1** with one equivalent of lithium dibenzoylmethanide afforded a mixture of products. The three main components occur in an almost equimolar ratio and have chemical shifts in the $^1$H NMR spectrum at $\delta$ = 0.55, 0.51, and 0.23 ppm. One product could be isolated by recrystallization as a bright yellow, crystalline solid. It possesses the $C(SiMe_3)_3$ group ($\delta$ = 0.55 ppm) and the chelating ligand in a 1:1 ratio, which clearly excludes the formation of the desired mixed halogeno acetylacetonato digallium species, see Equation (2). Instead, crystal structure determination revealed a gallium(III) compound (**7**) with a $C(SiMe_3)_3$ group, an iodine atom, and a chelating ligand bonded to the central gallium atom. Thus in this case disproportionation occurred, and the saturation of the coordination sphere by a terminal chelating ligand may not be sufficient to stabilize the gallium(II) compound. Elemental gallium is not formed. The chemical shift of one resonance in the $^1$H NMR spectrum of the raw product at $\delta$ = 0.51 ppm is identical to that of the corresponding tetraalkyltetragallium(I) cluster, which has gallium atoms in an oxidation state of +1. Thus, we suppose that this cluster may be the second product of the disproportionation, however, we were unable to isolate the characteristic red crystals of that compound. Also the third main component of the reaction mixture could not be isolated in a pure form. Its constitution remains unknown. Cleavage of the Ga–Ga bond with the formation of an alkylgallium(III) iodide bearing a chelating ligand was also observed for the reaction of **1** with lithium diphenyltriazenide.[10]

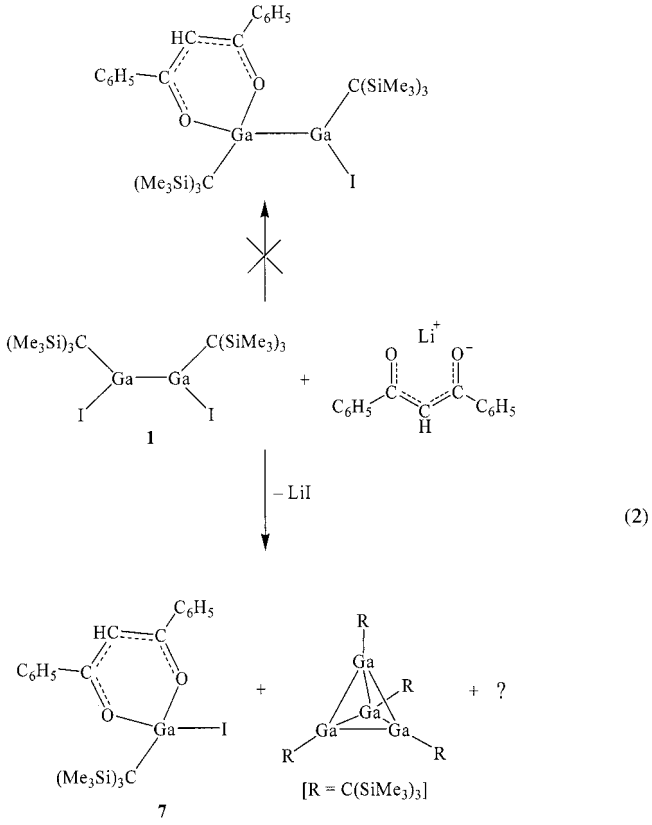


The structural parameters of the molecule of **7** in the solid state (Figure 3) are as expected and do not require a detailed discussion. The gallium atom has a distorted tetrahedral coordination sphere. The Ga–I distance (254.1 pm) is shorter than that for **2** and **4** and is in the normal range for terminal Ga–I bonds.[10,19]

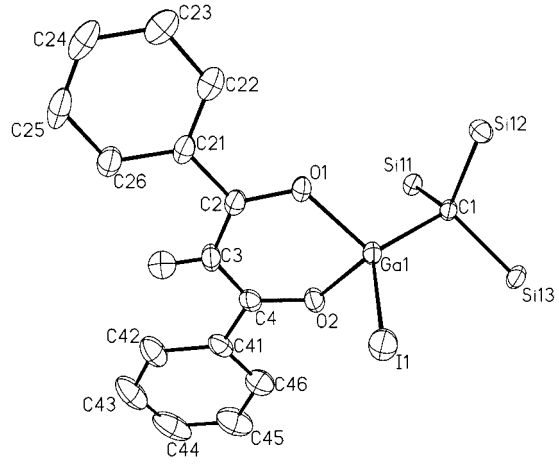


Figure 3. Molecular structure and numbering scheme of compound **7**; the thermal ellipsoids are drawn at the 40% probability level; methyl groups of $SiMe_3$ substituents and hydrogen atoms are omitted. Selected bond lengths [pm] and angles [°]: Ga1–I1 254.11(4), Ga1–C1 195.9(2), Ga1–O1 189.5(2), Ga1–O2 189.3(2), O1–Ga1–O2 95.22(8), C1–Ga1–O1 114.80(9), C1–Ga1–O2 112.64(9), C1–Ga1–I1 125.53(7), O1–Ga1–I1 101.95(6), O2–Ga1–I1 101.86(6).

## Experimental Section

**General:** All procedures were carried out under purified argon in dried solvents (toluene over Na/benzophenone; *n*-hexane and cyclopentane over $LiAlH_4$). The compound $R_2Ga_2I_2$ (**1**) was synthesized according to a literature procedure.[4] The commercially available carboxylic acids were sublimed in vacuo prior to use.

**Synthesis of $Ga_2I(\mu\text{-}O_2C\text{–}C_6H_5)R_2$ (2) [R = $C(SiMe_3)_3$]:** Freshly sublimed benzoic acid (17 mg, 0.141 mmol) was dissolved in toluene (20 mL) and treated with an equimolar quantity of a solution of *n*-butyllithium (0.145 M) in *n*-hexane (0.97 mL, 0.141 mmol) at room temperature. The mixture was heated to its boiling point for a minute. A suspension of lithium benzoate was obtained, which was cooled to –90 °C and treated with a solution of the subhalide **1** (121 mg, 0.141 mmol) in toluene (10 mL). The light yellow mixture was warmed slowly to room temperature und stirred for 48 h. After filtration all volatile components were removed in vacuo. The yellowish residue was dissolved in *n*-hexane and cooled to –70 °C. After a week an amorphous powder of the colorless product **2** was isolated. Yield: 97 mg (82%), m.p. (argon, sealed capillary) = 160 °C. $^1$H NMR ($C_6D_6$, 400 MHz, 298 K): $\delta$ = 0.46 (s, 54 H, $SiMe_3$), 7.04 (m, 3 H, *m*- and *p*-H of phenyl), 8.31 (2 H, *pseudo*-d,

 © 2006 Wiley-VCH Verlag GmbH & Co. KGaA, Weinheim 

*o*-H of phenyl) ppm. $^{13}$C NMR ($C_6D_6$, 100.6 MHz, 298 K): $\delta$ = 5.5 ($SiMe_3$), 30.2 (Ga–C), 128.9 (*p*-C of phenyl), 130.8 (*m*-C of phenyl), 131.0 (*i*-C of phenyl), 134.4 (*o*-C of phenyl), 178.3 ($CO_2$) ppm. IR (CsBr, paraffin): $\tilde{\nu}$ = 1600 (w, phenyl), 1503 [m, $\nu(CO_2)$], 1461 (vs, paraffin), 1409 [m, $\delta$(CH)], 1377 (s, paraffin), 1320 (w), 1263 (m), 1251 [m, $\delta(CH_3)$], 1177 (vw), 976 (vw), 920 (vw), 857 (vs), 788 {sh, $\rho[CH_3(Si)]$}, 719 (w, paraffin), 681 (m), 662 [m, $\nu_{as}$(SiC)], 633 (vw), 617 [vw, $\nu_s$(SiC)], 488 (w), 474 [sh, $\nu$(GaC), $\nu$(GaO)] cm$^{-1}$. $C_{27}H_{59}Ga_2IO_2Si_6$ (850.6): calcd. C 38.1, H 7.0; found C 38.5, H 7.1.

**Synthesis of $Ga_2I(\mu\text{-}O_2C\text{–}4\text{-}Br\text{–}C_6H_4)R_2$ (3) [R = $C(SiMe_3)_3$]:** 4-Bromo-benzoic acid (41 mg, 0.207 mmol) was suspended in 50 mL of *n*-hexane and treated with 1.4 mL of a 0.145 M solution of *n*-butyllithium (0.207 mmol) in *n*-hexane. The mixture was stirred at room temperature for 2 h and cooled to –90 °C. A solution of the subhalide **1** (177 mg, 0.207 mmol) in 20 mL of *n*-hexane was added. The mixture was warmed to room temperature and stirred for 4 d. LiI was separated by filtration, and the solvent was removed in vacuo. The residue was dissolved in cyclopentane and cooled to –80 °C for 4 d. The product precipitated as a colorless solid. Yield: 35 mg (18%); m.p. (argon, sealed capillary) = 135 °C. $^1$H NMR ($C_6D_6$, 300 MHz, 298 K): $\delta$ = 0.45 (s, 54 H, $SiMe_3$), 6.99 (d, 2 H, $^3J_{HH}$ = 8 Hz, *m*-H of phenyl), 7.89 (d, 2 H, $^3J_{HH}$ = 8 Hz, *o*-H of phenyl) ppm. $^{13}$C NMR ($C_6D_6$, 50 MHz, 298 K): $\delta$ = 5.4 ($SiMe_3$), 30.2 (Ga–C), 129.1 and 129.9 (*i*-C and *p*-C of phenyl), 132.1 and 132.3 (*o*-C and *p*-C of phenyl), 177.5 ($CO_2$) ppm. IR (CsBr, paraffin): $\tilde{\nu}$ = 1589 (m, phenyl) 1532 (m), 1505 [m, $\nu(CO_2)$], 1463 (vs, paraffin), 1407 [s, $\delta$(CH)], 1377 (s, paraffin), 1320 (w), 1263 (m), 1252 [m, $\delta(CH_3)$], 1174 (w), 1155 (vw), 1074 (w), 1012 (w), 857 (vs), 824 (w), 770 {w, $\rho[CH_3(Si)]$}, 721 (w, paraffin), 676 (w), 663 [w, $\nu_{as}$(SiC)], 634 (vw), 620 [vw, $\nu_s$(SiC)], 529 (w), 471 [vw, $\nu$(GaC), $\nu$(GaO)] cm$^{-1}$.

**Synthesis of $Ga_2I(\mu\text{-}O_2C\text{–}3,5\text{-}Me_2C_6H_3)R_2$ (4) [R = $C(SiMe_3)_3$]:** 3,5-Dimethylbenzoic acid (47 mg, 0.313 mmol) was suspended in 50 mL of toluene and treated with 2.0 mL of a 0.145 M solution of *n*-butyllithium (0.207 mmol) in *n*-hexane. The mixture was stirred at room temperature for 15 min and cooled to –90 °C. A solution of the subhalide **1** (255 mg, 0.298 mmol) in 25 mL of toluene was added. The mixture was warmed to room temperature and stirred for 24 h. All volatiles were removed in vacuo. The residue was treated with *n*-hexane and filtered. The colorless product was obtained upon cooling the filtrate to –80 °C. Yield: 147 mg (54%); colorless crystals; m.p. (argon, sealed capillary) = 187 °C. $^1$H NMR ($C_6D_6$, 300 MHz, 298 K): $\delta$ = 0.49 (s, 54 H, $SiMe_3$), 2.08 (s, 6 H, Me attached to phenyl), 6.79 (s, 1 H, *p*-H of phenyl), 8.02 (s, 2 H, *o*-H of phenyl) ppm. $^{13}$C NMR ($C_6D_6$, 50 MHz, 298 K): $\delta$ = 5.5 ($SiMe_3$), 21.1 (Me attached to phenyl), 31.9 (Ga–C), 128.3, 130.6, 136.2 and 138.6 (all phenyl), 178.7 ($CO_2$) ppm. IR (CsBr, paraffin): $\tilde{\nu}$ = 1652 (br, w, phenyl), 1494 [m, $\nu(CO)_2$] 1461 (vs, paraffin), 1392 [m, $\delta$(CH)], 1376 (s, paraffin), 1320 (w), 1264 (m), 1251 [m, $\delta(CH_3)$, 1152 (vw), 1077 (vw), 1040 (br, w), 856 (vs), 785 (w), 768 {w, $\rho[CH_3(Si)]$}, 722 (w, paraffin), 675 (m), 661 [m, $\nu_{as}$(SiC)], 634 (vw), 618 [vw, $\nu_s$(SiC)], 548 (w), 488 [w, $\nu$(GaC), $\nu$(GaO)] cm$^{-1}$. UV/Vis (*n*-hexane): $\lambda_{max}$ (log $\varepsilon$) = 254 (3.54), 331 (2.84) nm. $C_{29}H_{63}Ga_2IO_2Si_6$ (878.7): calcd. C 39.6, H 7.2; found C 38.5, H 7.4.

**Synthesis of $Ga_2I(\mu\text{-}O_2C\text{–}4\text{-}Me_3C\text{–}C_6H_4)R_2$ (5) [R = $C(SiMe_3)_3$]:** The procedure is similar to that for the synthesis of **4** (4-*tert*-butylbenzoic acid: 48 mg, 0.269 mmol; subhalide **1**: 230 mg, 0.269 mmol). We did not succeed in recrystallizing compound **5** from different solvents. However, the compound was formed directly in high purity, and the characterization was done with the raw product of the reaction. Owing to the unsuccessful purification by recrystallization no elemental analysis was conducted. Yield: 188 mg (77%); pale yellow amorphous solid; m.p. (argon, sealed capillary) = 97 °C. $^1$H NMR ($C_6D_6$, 200 MHz, 298 K): $\delta$ = 0.51 (s, 54 H, $SiMe_3$), 1.09 (s, 9 H, $CMe_3$), 7.16 (d, 2 H, $^3J_{HH}$ = 8 Hz, *m*-H of phenyl), 8.31 (d, 2 H, $^3J_{HH}$ = 8 Hz, *o*-H of phenyl). $^{13}$C NMR ($C_6D_6$, 50 MHz, 298 K): $\delta$ = 5.6 ($SiMe_3$), 30.1 (Ga–C), 30.9 (Me of *tert*-butyl), 35.1 ($CMe_3$), 126.2, 128.3, 131.2, and 158.2 (all phenyl), 178.3 ($CO_2$) ppm. IR (CsBr, paraffin): $\tilde{\nu}$ = 1606 (m), 1579 (m, phenyl), 1515 (m), 1491 [s, $\nu(CO_2)$], 1460 (vs, paraffin), 1407 [vs, $\delta$(CH)], 1377 (s, paraffin), 1263 (m), 1252 [m, $\delta(CH_3)$], 1193 (m), 1150 (w), 1107 (w), 1016 (m, br), 855 (vs), 800 (m), 786 (m), 749 {vw, $\rho[CH_3(Si)]$}, 728 (w, paraffin), 675 (m), 661 [m, $\nu_{as}$(SiC)], 637 (vw), 621 [vw, $\nu_s$(SiC)], 599 (w), 584 (vw), 541 (vw), 490 [w, $\nu$(GaC), $\nu$(GaO), $\delta(C_3C)$] cm$^{-1}$. UV/Vis (*n*-hexane): $\lambda_{max}$ (log $\varepsilon$) = 240 (3.53), 330 (2.87) nm.

**Synthesis of $Ga_2I(\mu\text{-}O_2C\text{–}CMe_3)R_2$ (6) [R = $C(SiMe_3)_3$]:** The procedure is similar to that for the synthesis of **4** (pivalic acid: 19 mg, 0.187 mmol, after addition of butyllithium stirred for 2 h at room temperature; subhalide **1**: 160 mg, 0.187 mmol). The colorless product was obtained upon cooling the filtrate to –80 °C. Yield: 77 mg (50%); colorless solid; m.p. (argon, sealed capillary) = 127 °C. $^1$H NMR ($C_6D_6$, 200 MHz, 298 K): $\delta$ = 0.42 (s, 54 H, $SiMe_3$), 1.15 (s, 9 H, $CMe_3$). $^{13}$C NMR ($C_6D_6$, 50 MHz, 298 K): $\delta$ = 5.4 ($SiMe_3$), 27.0 (Me of *tert*-butyl), 30.2 (Ga–C), 39.6 ($CMe_3$), 192.0 ($CO_2$) ppm. IR (CsBr, paraffin): $\tilde{\nu}$ = 1600 (m), 1502 (s), 1484 [s, $\nu(CO_2)$], 1461 (vs, paraffin), 1421 [s, $\delta$(CH)], 1378 (s, paraffin), 1364 (sh), 1293 (w), 1263 (s), 1252 [s, $\delta(CH_3)$], 1222 (m), 1169 (w), 1000 (m, br), 855 (vs), 789 (m), 752 {vw, $\rho[CH_3(Si)]$}, 721 (m, paraffin), 675 (s), 661 [s, $\nu_{as}$(SiC)], 632 (w), 618 [m, $\nu_s$(SiC), 529 (vw), 443 [w, $\nu$(GaC), $\nu$(GaO), $\delta(C_3C)$] cm$^{-1}$. UV/Vis (*n*-hexane): $\lambda_{max}$ (log $\varepsilon$) = 254 (3.60) nm. $Ga_2IO_2Si_6C_{25}H_{63}$ (830.6): calcd. Ga 16.8; found Ga 16.1.

**Reaction of $R_2Ga_2I_2$ 1 with Dibenzoylmethyllithium. Synthesis of 7:** The procedure is similar to that for the synthesis of compound **4** (dibenzoylmethane: 76 mg, 0.341 mmol, after addition of butyllithium stirred for 2 h; subhalide **1**: 292 mg, 0.341 mmol). The intensively yellow reaction mixture was filtered, toluene was removed in vacuo, and the residue was recrystallized from cyclopentane (20/–45 °C). Product **7** was precipitated as an amorphous solid. Yield: 51 mg (23%), yellow solid; m.p. (argon, sealed capillary) = 213 °C. $^1$H NMR ($C_6D_6$, 200 MHz, 298 K): $\delta$ = 0.55 (s, 27 H, $SiMe_3$), 6.80 (s, 1 H, inner H atom of the acac ligand), 7.02 (m, 6 H, *m*-H and *p*-H of phenyl), 7.84 (4 H, pseudo-d, *o*-H of phenyl) ppm. $^{13}$C NMR ($C_6D_6$, 50 MHz, 298 K): $\delta$ = 5.1 ($SiMe_3$), 31.9 (Ga–C), 96.0 (inner C of the acac ligand), 128.9, 132.5, 133.3, and 137.0 (phenyl), 186.0 (CO) ppm. IR (CsBr, paraffin): $\tilde{\nu}$ = 1590 (m, phenyl), 1523 (vs), 1478 [s, $\nu(CO_2)$], 1460 (vs, paraffin), 1377 (m, paraffin), 1364 (m), 1347 (s), 1326 (m), 1303 (m), 1263 (s), 1253 [s $\delta(CH_3)$, 1229 (m), 1173 (w), 1153 (w), 1122 (w), 1096 (w), 1064 (w), 1024 (w), 997 (w), 949 (w), 852 (vs), 772 (w) 758 {w, $\rho[CH_3(Si)]$}, 719 (m, paraffin), 677 (m, $\nu_{as}$(SiC), 643 (vw), 622 [v, $\nu_s$(SiC)], 592 (w), 544 (w), 462 [vw, $\nu$(GaC), $\nu$(GaO)] cm$^{-1}$. UV/Vis (*n*-hexane): $\lambda_{max}$ (log $\varepsilon$) = 226 (3.98), 266 (3.81), 372 (3.85) nm. $GaIO_2Si_3C_{25}H_{38}$ (651.5): calcd. C 46.1, H 5.9; found C 47.1, H 6.6.

**Crystal Structure Determinations:** Single crystals of the compounds **2**, **4**, and **7** were obtained by cooling the solutions in *n*-hexane (20/–30 °C, **2**), cyclopentane (20/–45 °C, **4**), and again cyclopentane (20/+5 °C, **7**). Crystal data and structure refinement parameters are given in Table 1.[23] The crystals of **2** enclose one molecule of *n*-hexane per formula unit of **2**. Owing to their relatively large isotropic displacement parameters the solvent carbon atoms were not

 © 2006 Wiley-VCH Verlag GmbH & Co. KGaA, Weinheim 

Table 1. Crystal data and structure refinement for the compounds **2**, **4**, and **7**.[a]

| | **2** | **4** | **7** |
|---|---|---|---|
| Formula | $C_{33}H_{73}Ga_2IO_2Si_6$ | $C_{34}H_{73}Ga_2IO_2Si_6$ | $C_{30}H_{48}GaIO_2Si_3$ |
| Crystal system | monoclinic | monoclinic | triclinic |
| Space group[21] | $P2_1/c$ (no. 14) | $P2_1/n$ (no. 14) | $P\bar{1}$ (no. 2) |
| $Z$ | 4 | 4 | 2 |
| $T$ [K] | 153(2) | 153(2) | 153(2) |
| $d_{calcd.}$ [g·cm$^{-3}$] | 1.317 | 1.335 | 1.404 |
| $a$ [pm] | 1914.45(8) | 1950.9(1) | 886.64(7) |
| $b$ [pm] | 910.19(2) | 928.04(5) | 1341.6(1) |
| $c$ [pm] | 2837.9(1) | 2676.2(1) | 1609.4(1) |
| $\alpha$ [°] | 90 | 90 | 65.516(1) |
| $\beta$ [°] | 107.119(3) | 103.106(1) | 84.529(2) |
| $\gamma$ [°] | 90 | 90 | 78.393(2) |
| $V$ [10$^{-30}$ m$^3$] | 4726.0(3) | 4719.0(4) | 1706.5(2) |
| $\mu$ [mm$^{-1}$] | 1.970 | 1.974 | 1.840 |
| Crystal size [mm] | 0.32×0.18×0.10 | 0.12×0.06×0.06 | 0.26×0.24×0.16 |
| Diffractometer | STOE IPDS | Bruker Smart Apex | Bruker Smart Apex |
| Radiation | Mo-$K_\alpha$; graphite monochromator | | |
| $\theta$ range [°] | $1.58 \le \theta \le 27.05$ | $1.17 \le \theta \le 30.07$ | $1.39 \le \theta \le 31.23$ |
| Index ranges | $-24 \le h \le 24$ | $-27 \le h \le 27$ | $-12 \le h \le 12$ |
| | $-11 \le k \le 10$ | $-13 \le k \le 13$ | $-19 \le k \le 18$ |
| | $-36 \le l \le 36$ | $-37 \le l \le 35$ | $-22 \le l \le 22$ |
| Independent reflections | 10185 [$R_{int}$ = 0.0359] | 13701 [$R_{int}$ = 0.0887] | 10067 [$R_{int}$ = 0.0321] |
| Reflections $I > 2\sigma(I)$ | 8827 | 6575 | 7393 |
| Parameters | 388 | 507 | 343 |
| $R = \Sigma\|\|F_o\| - \|F_c\|\| / \Sigma\|F_o\|$ [$I > 2\sigma(I)$] | 0.0346 | 0.0546 | 0.0421 |
| $wR_2 = \{\Sigma w(\|F_o\|^2 - \|F_c\|^2)^2 / \Sigma\|F_o\|^2\}^{1/2}$ (all data) | 0.1036 | 0.1271 | 0.0860 |
| Max./min. residual [10$^{30}$ e·m$^{-3}$] | 1.053/–0.630 | 1.385/–0.821 | 1.109/–0.848 |

[a] Program SHELXL-97;[22] solutions by direct methods, full-matrix refinement with all independent structure factors.

refined anisotropically. The central Ga–Ga–I group showed a disorder over two positions, see the Results and Discussion chapter for details. These atoms were refined with occupancy factors of 0.84 and 0.16. The refinement of the substituents was not affected by this disorder. The tris(trimethylsilyl)methyl group at C2 of compound **4** was disordered. Its atoms were refined with site occupation factors of 0.84 and 0.16. One molecule of cyclopentane was enclosed per formula unit of **4**. Its carbon atoms were refined only with isotropic displacement factors. Also the crystals of **7** contained one cyclopentane molecule.

## Acknowledgments

We are grateful to the Deutsche Forschungsgemeinschaft and the Fonds der Chemischen Industrie for generous financial support.

[1] a) W. Uhl, A. Jantschak, *J. Organomet. Chem.* **1998**, *555*, 263; b) W. Uhl, W. Hiller, M. Layh, W. Schwarz, *Angew. Chem.* **1992**, *104*, 1378; *Angew. Chem. Int. Ed. Engl.* **1992**, *31*, 1364.
[2] a) W. Uhl, R. Graupner, M. Layh, U. Schütz, *J. Organomet. Chem.* **1995**, *493*, C1; b) W. Uhl, A. Jantschak, W. Saak, M. Kaupp, R. Wartchow, *Organometallics* **1998**, *17*, 5009.
[3] W. Uhl, S. Melle, *Chem. Eur. J.* **2001**, *7*, 4216.
[4] W. Uhl, A. El-Hamdan, M. Prött, P. Spuhler, G. Frenking, *Dalton Trans.* **2003**, 1360.
[5] a) W. Uhl, A. El-Hamdan, G. Geiseler, K. Harms, *Z. Anorg. Allg. Chem.* **2004**, *630*, 821; for a review see: b) W. Uhl, *Adv. Organomet. Chem.* **2004**, *51*, 53.
[6] W. Uhl, S. Melle, G. Geiseler, K. Harms, *Organometallics* **2001**, *20*, 3355.
[7] W. Uhl, F. Schmock, G. Geiseler, *Z. Anorg. Allg. Chem.* **2002**, *628*, 1963.
[8] a) M. Kehrwald, W. Köstler, A. Rodig, G. Linti, T. Blank, N. Wiberg, *Organometallics* **2001**, *20*, 860; b) C. Klemp, C. Üffing, E. Baum, H. Schnöckel, *Z. Anorg. Allg. Chem.* **2000**, *626*, 1787; c) G. Linti, W. Köstler, *Angew. Chem.* **1996**, *108*, 593; *Angew. Chem. Int. Ed. Engl.* **1996**, *35*, 550; d) A. H. Cowley, A. Decken, C. A. Olazabal, *J. Organomet. Chem.* **1996**, *534*, 271; e) N. Wiberg, T. Blank, M. Westerhausen, S. Schneiderbauer, H. Schnöckel, I. Krossing, A. Schnepf, *Eur. J. Inorg. Chem.* **2002**, 351; f) V. Lomeli, B. G. McBurnett, A. H. Cowley, *J. Organomet. Chem.* **1998**, *562*, 123.
[9] a) N. J. Hardman, R. J. Wright, A. D. Phillips, P. P. Power, *Angew. Chem.* **2002**, *114*, 2966; *Angew. Chem. Int. Ed.* **2002**, *41*, 2842; b) N. J. Hardman, R. J. Wright, A. D. Phillips, P. P. Power, *J. Am. Chem. Soc.* **2003**, *125*, 2667.
[10] W. Uhl, A. El-Hamdan, A. Lawerenz, *Eur. J. Inorg. Chem.* **2005**, 1056.
[11] W. Uhl, A. El-Hamdan, *Eur. J. Inorg. Chem.* **2004**, 969.
[12] W. Uhl, A. El-Hamdan, *Z. Anorg. Allg. Chem.*, in press.
[13] a) W. Uhl, F. Schmock, W. Petz, *Z. Naturforsch., Teil B* **2003**, *58*, 385; b) W. Uhl, A. El-Hamdan, W. Petz, G. Geiseler, K. Harms, *Z. Naturforsch., Teil B* **2004**, *59*, 789; c) G. Linti, W. Köstler, *Chem. Eur. J.* **1998**, *4*, 942; d) G. Linti, G. Li, H. Pritzkow, *J. Organomet. Chem.* **2001**, *626*, 82.
[14] See for instance: a) H. Schmidbaur, R. Nowak, W. Bublak, P. Burkert, B. Huber, G. Müller, *Z. Naturforsch., Teil B* **1987**, *42*, 553; b) W. Hönle, A. Simon, G. Gerlach, *Naturforsch., Teil B* **1987**, *42*, 546; c) M. A. Khan, D. G. Tuck, *Inorg. Chim. Acta* **1985**, *97*, 73; d) H. P. Beck, *Z. Naturforsch., Teil B* **1987**, *42*, 251.
[15] W. Uhl, R. Graupner, I. Hahn, T. Spies, W. Frank, *Eur. J. Inorg. Chem.* **1998**, 355.
[16] W. Uhl, M. Benter, W. Saak, P. G. Jones, *Z. Anorg. Allg. Chem.* **1998**, *624*, 1622; cited references.
[17] a) W. Uhl, I. Hahn, H. Reuter, *Chem. Ber.* **1996**, *129*, 1425; b) W. Uhl, T. Spies, W. Saak, *Eur. J. Inorg. Chem.* **1998**, 1661; c) W. Uhl, T. Spies, R. Koch, *J. Chem. Soc., Dalton Trans.* **1999**, 2385.
[18] a) W. Uhl, M. Layh, T. Hildenbrand, *J. Organomet. Chem.* **1989**, *364*, 289; b) R. J. Wehmschulte, K. Ruhlandt-Senge,

 © 2006 Wiley-VCH Verlag GmbH & Co. KGaA, Weinheim 

M. M. Olmstead, H. Hope, B. E. Sturgeon, P. P. Power, *Inorg. Chem.* **1993**, *32*, 2983; c) X. He, R. A. Bartlett, M. M. Olmstead, K. Ruhlandt-Senge, B. E. Sturgeon, P. P. Power, *Angew. Chem.* **1993**, *105*, 761; *Angew. Chem. Int. Ed. Engl.* **1993**, *32*, 717; d) R. D. Schluter, A. H. Cowley, D. A. Atwood, R. A. Jones, M. R. Bond, C. J. Carrano, *J. Am. Chem. Soc.* **1993**, *115*, 2070.

[19] a) R. C. Crittendon, B. C. Beck, J. Su, X.-W. Li, G. H. Robinson, *Organometallics* **1999**, *18*, 156; b) P. Jutzi, B. Neumann, G. Reumann, H. G. Stammler, *Organometallics* **1998**, *17*, 1305; c) A. Schnepf, C. Doriat, E. Möllhausen, H. Schnöckel, *Chem. Commun.* **1997**, 2111.

[20] W. Uhl, L. Cuypers, K. Schüler, T. Spies, C. Strohmann, K. Lehmen, *Z. Anorg. Allg. Chem.* **2000**, *626*, 1526.

[21] T. Hahn (Ed.), *International Tables for Crystallography, Space-Group Symmetry*, vol. A, Kluwer Academic Publishers, Dordrecht, Boston, London, **1989**.

[22] *SHELXTL-Plus, REL. 4.2*; for Siemens R3 Crystallographic Research Systems, Siemens Analytical X-ray Instruments Inc., Madison, USA, **1990**; G. M. Sheldrick, *SHELXL-97*, *Program for the Refinement of Structures*, University of Göttingen **1997**.

[23] CCDC-295626 (for **2**), -2956127 (for **4**), and -295628 (for **7**) contain the supplementary crystallographic data for this paper. These data can be obtained free of charge from The Cambridge Crystallographic Data Centre via www.ccdc.cam.ac.uk/data_request/cif.

Received: January 23, 2005
Published Online: March 9, 2006

 © 2006 Wiley-VCH Verlag GmbH & Co. KGaA, Weinheim 

DOI: 10.1002/ejic.200500753

# Binuclear Mixed Valence Oxovanadium(IV/V) Complexes Containing a $[OV^{IV}(\mu\text{-}O_{oxo})(\mu\text{-}O_{phen})V^{V}O]^{2+}$ Core: Synthesis, EPR Spectra, Molecular and Electronic Structure

**Amrita Mondal,[a] Sucharita Basak,[a] Sumana Sarkar,[a] Deepak Chopra,[b] Ranjan Das,[c] and Kajal Krishna Rajak*[a]**

**Keywords:** Vanadium / Oxovanadium complexes / Mixed valence

Binuclear mixed valence oxovanadium(IV/V) complexes of general formula $[V_2O_3L]$ containing a $[OV^{IV}(\mu\text{-}O_{oxo})(\mu\text{-}O_{phen})V^{V}O]^{2+}$ core have been synthesised using conformationally labile $N_4O_3$-coordinating heptadentate ligands ($H_3L$). The X-ray structure of one complex has been examined. Solution EPR spectra revealed that the unpaired electron of the complexes is delocalised between the two vanadium centres. The simulated EPR spectrum of one complex confirms this experimental observation. DFT studies have been performed using crystallographic coordinates in order to obtain further insight into the electronic structure of this type of molecule.
(© Wiley-VCH Verlag GmbH & Co. KGaA, 69451 Weinheim, Germany, 2006)

## Introduction

The chemistry of mixed valence vanadium complexes has been of considerable interest. The main interest arises from the complete or partial delocalisation of the single 3d electron of the vanadium(IV) over both vanadium centres or its complete localisation on one vanadium centre. A sizeable number of oxo-bridged binuclear mixed valence oxovanadium(IV/V) complexes have been cited in the literature[1–14] and depending on the geometry of $[V_2O_3]^{3+}$ core, the structurally characterised mixed valence binuclear complexes have been classified into several categories. For the $[V_2O_3]^{3+}$ core, containing a linear V–O–V bridge[1a,2,5,10,12,13] with the terminal oxo groups in mutual *trans* position, delocalisation is anticipated because of significant metal $d_{xy}$ orbital overlap with the $p_x$ orbital of the oxo bridge. Schulz et al.[7] reported that for the nearly *trans* V=O groups with a bent V–O–V moiety, the delocalisation of the odd electron between the two vanadium centres depends on the pi-donating ability of the equatorial ligands. Localised electronic structures have also been documented[6] for angular V–O–V moieties with *syn* or *twist* V=O groups, which probably occur due to insufficient overlap between the metal $d_{xy}$ orbitals.

Recently we have found[15] complete delocalisation of the unpaired electron between the two vanadium atoms in a mixed bridged mixed valence species containing the $[OV^{IV}(\mu\text{-}O_x)(\mu\text{-}O_{phen})V^{V}O]^{2+}$ moiety, which has an angular V–O–V group and nearly *syn* V=O groups. However the reason for the delocalisation of the odd electron is not clear. Thus, further studies of this type of system are required to allow for a better understanding of the behaviour of the unpaired electron.

In connection with our previous work,[15] herein we describe the synthesis of a series of mixed bridged mixed valence binuclear oxovanadium(IV/V) complexes incorporating $N_4O_3$-coordinating heptadentate ligands. The crystal structure of one representative case is reported. A simulated EPR spectrum is found to be similar to the EPR spectra of the complexes observed in solution at room temperature. In addition, DFT calculations have enabled us to understand qualitatively the nature of the delocalisation of the unpaired electron.

## Results and Discussion

In this paper four heptadentate ligands $H_3L^7$–$H_3L^{10}$ (general abbreviation, $H_3L$) have been used (Scheme 1).

Treatment of a solution of $VO(acac)_2$ in acetone under air with the heptadentate ligands in a 2:1 ratio afforded green coloured complexes with the general formula $[V^{IV}V^{V}O_2L]$ in good yields. The oxygen in the air is believed to act as the oxidant in this synthesis. The data for the characterisation of these binuclear mixed valence species are listed in the experimental section. All the compounds display a strong V=O stretch near 950 $cm^{-1}$in their IR spectra, and the V–O–V vibration occurs near 752 $cm^{-1}$. The green solution of the complexes absorb at ca. 1030 and ca. 660 nm

[a] Inorganic Chemistry Section, Department of Chemistry, Jadavpur University,
Kolkata 700032, India
E-mail: kajalrajak@hotmail.com
[b] Solid State and Structural Chemistry Unit, Indian Institute of Science,
Bangalore 560012, India
[c] Department of Chemical Sciences, Tata Institute of Fundamental Research,
Mumbai, India

 © 2006 Wiley-VCH Verlag GmbH & Co. KGaA, Weinheim 

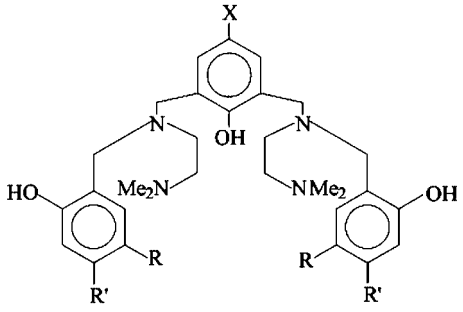


| | | |
|---|---|---|
| X = $CH_3$, R = H, R' = H: | $H_3L^1$ | $[V_2O_3L^1]$ |
| X = Cl, R = H, R' = H: | $H_3L^7$ | $[V_2O_3L^7]$ |
| X = Cl, R = Me, R' = H: | $H_3L^8$ | $[V_2O_3L^8]$ |
| X = Cl, R = Cl, R' = H: | $H_3L^9$ | $[V_2O_3L^9]$ |
| X = Cl, R = Cl, R' = Me: | $H_3L^{10}$ | $[V_2O_3L^{10}]$ |

Scheme 1.

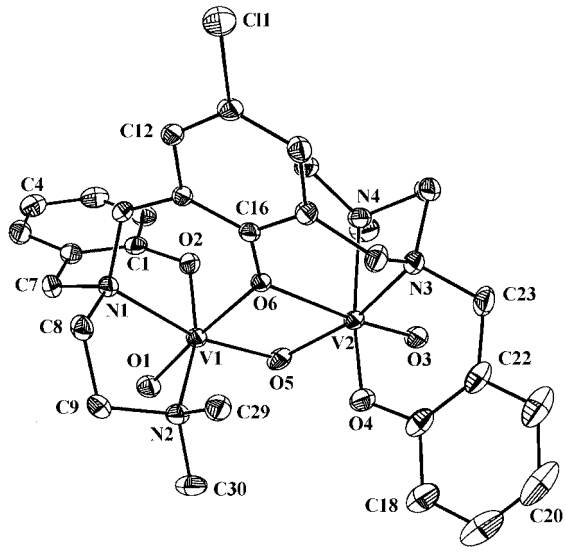


Figure 1. Perspective view and atom labeling scheme for $[V_2O_3L^7]$ $CH_2Cl_2$. The solvent molecule is excluded. All non-hydrogen atoms are represented by 30% thermal probability ellipsoids.

respectively. The band near 1030 nm in their UV/Vis spectra is assigned to the inter valence charge transfer transition,[15] and the absorption at 660 nm is due to ligand field excitation. The complexes exhibit an irreversible anodic response near 0.45 V vs. SCE. The stabilisation of the mixed valence oxovanadium(IV/V) binuclear species by the trianionic heptadentate ligand is reflected in the irreversible $[OV^V(\mu\text{-}O_{oxo})(\mu\text{-}O_{phen})V^VO]^{3+}$ – $[OV^{IV}(\mu\text{-}O_x)(\mu\text{-}O_{phen})\text{-}V^VO]^{2+}$ anodic response. All the compounds are paramagnetic, and the magnetic moment value is, $\mu \approx 1.75$ BM per molecule.

## Crystal Structure

The X-ray structure of **1** has been determined, and the molecular structure is shown in Figure 1. Selected inter atomic distances and bond angles relevant to the coordination sphere are given in Table 1.

In **1** the vanadium centres are linked asymmetrically by a bridging oxygen atom, O5, and the central phenolato oxygen, O6. The V1–O5–V2 and V1–O6–V2 angles are 116.11(10)° and 91.79(7)° respectively. The geometry of each vanadium atom appears to be distorted octahedral. In the $VO_4N_2$ environment, the V=O, V–O and V–N bond lengths are as expected[15] and are in the ranges of 1.605–1.615 Å, 1.798–2.212 Å and 2.188–2.251 Å respectively. In the octahedral coordination environment, the tripodal nitrogen atom (N1 for V1 and N3 for V2) is *trans* to the O5 atom, while the terminal nitrogen atoms (N2 and N4) occupy positions *trans* to the terminal phenoxide groups (O2 and O4). The V2–O4 [1.871 (2) Å], V2–O5 [1.885 (2) Å] and V2–O6 [2.212 (2) Å] bond lengths are slightly longer than the respective V1–O2 [1.838 (2) Å], V1–O5 [1.798 (2) Å] and V1–O6 [2.140 (2) Å] bonds. The V1–N bond lengths are slightly longer than the V2–N distances, and this can be ascribed to the short V1–O2 and V1–O5 bonds.

Table 1. Selected bond lengths [Å] and angles (°) for $[V_2O_3L^7]$ $CH_2Cl_2$.

| Distances | | | |
|---|---|---|---|
| V1–O1 | 1.605(2) | V2–O3 | 1.615(2) |
| V1–O2 | 1.838(2) | V2–O4 | 1.871(2) |
| V1–O5 | 1.798(2) | V2–O5 | 1.885(2) |
| V1–O6 | 2.140(2) | V2–O6 | 2.212(2) |
| V1–N1 | 2.238(2) | V2–N3 | 2.188(3) |
| V1–N2 | 2.251(3) | V2–N4 | 2.231(3) |
| V1···V2 | 3.125(5) | | |
| **Angles** | | | |
| O1–V1–O2 | 98.53(10) | O3–V2–O4 | 97.08(11) |
| O1–V1–O5 | 104.65(10) | O3–V2–O5 | 104.54(11) |
| O1–V1–O6 | 169.44(10) | O3–V2–O6 | 171.63(10) |
| O1–V1–N1 | 94.36(10) | O3–V2–N3 | 98.39(11) |
| O1–V1–N2 | 85.41(10) | O3–V2–N4 | 85.16(10) |
| O2–V1–O5 | 95.12(10) | O4–V2–O5 | 89.69(10) |
| O2–V1–O6 | 91.42(8) | O4–V2–O6 | 91.22(9) |
| O2–V1–N1 | 82.85(9) | O4–V2–N3 | 86.46(10) |
| O2–V1–N2 | 159.60(9) | O4–V2–N4 | 165.27(11) |
| O5 –V1–O6 | 77.80(8) | O5–V2–O6 | 74.28(8) |
| O5–V1–N1 | 160.96(9) | O5–V2–N3 | 157.05(9) |
| O5–V1–N2 | 103.28(10) | O5–V2–N4 | 103.89(10) |
| O6–V1–N1 | 83.31(8) | O6–V2–N3 | 83.18(8) |
| O6–V1–N2 | 84.04(8) | O6–V2–N4 | 87.10(8) |
| N1–V1–N2 | 76.87(9) | N3–V2–N4 | 78.81(10) |
| V1–O5–V2 | 116.11(10) | V1–O6–V2 | 91.79(7) |

## EPR Spectra

EPR spectra of the complexes were recorded at 300 K and 77 K. Resonance parameters are shown in Table 2.

The complexes exhibit 15 nearly equally spaced lines, with isotropic structure, in dichloromethane solution (Figure 2, a). The 15 line spectrum arises from the hyperfine interaction of the unpaired electron with the two vanadium

 © 2006 Wiley-VCH Verlag GmbH & Co. KGaA, Weinheim 

Table 2. EPR spectral data.

| Complex | Matrix | $g_{iso}$ | $A_{iso}\times10^4$ [cm$^{-1}$] | $g_{\parallel}$ | $g_{\perp}$ | $g_{av}$[a] | $A_{\parallel}\times10^4$ [cm$^{-1}$] | $A_{\perp}\times10^4$ [cm$^{-1}$] | $A_{av}$[b]$\times10^4$ [cm$^{-1}$] |
|---|---|---|---|---|---|---|---|---|---|
| | $CH_2Cl_2$, 300 K | 1.974 | 49.3 | | | | | | |
| $[V_2O_3L^7]$ | $CH_2Cl_2$/toluene, 77 K | | | | | | | | |
| | solid, 77 K | 1.984 | | 1.984 | 1.966 | 1.972 | 168.8 | 66.5 | 100.2 |
| | $CH_2Cl_2$, 300 K | | | | | | | | |
| $[V_2O_3L^8]$ | $CH_2Cl_2$/toluene, 77 K | 1.984 | 51 | | | | | | |
| | solid, 77 K | | | 1.972 | 1.986 | 1.981 | 169.2 | 69.9 | 103 |
| | | 1.989 | | | | | | | |
| | $CH_2Cl_2$, 300 K | | | | | | | | |
| $[V_2O_3L^9]$ | $CH_2Cl_2$/toluene, 77 K | 1.972 | 48.1 | | | | | | |
| | solid, 77 K | | | 1.973 | 1.982 | 1.979 | 166.9 | 62.35 | 97.2 |
| | | 1.986 | | | | | | | |
| | $CH_2Cl_2$, 300 K | | | | | | | | |
| $[V_2O_3L^{10}]$ | $CH_2Cl_2$/toluene, 77 K | 1.977 | 50.2 | | | | | | |
| | solid, 77 K | | | 1.946 | 1.997 | 1.980 | 164 | 68.75 | 100.5 |
| | | 1.985 | | | | | | | |

[a] $g_{av} = {}^1/_3[2\,g_{\perp} + g_{\parallel}]$. [b] $A_{av} = {}^1/_3[2A_{\perp} + A_{\parallel}]$.

nuclei (nuclear spin $I = 7/2$), which appear to be equivalent on the EPR timescale. The difference in the separation of the hyperfine lines at the lowest and highest fields is less than 2 gauss, suggesting that the second order shift[16] in the line position is small. We neglected this small shift, and determined the isotropic hyperfine coupling constant due to vanadium to be $49.3 \pm 0.2$ G. In the same way, neglecting the second order shift, the centre of the EPR spectrum was assumed to be the centre of the middle hyperfine line, and the $g$ value for the complex was determined to be $1.9741 \pm 0.0005$. The isotropic coupling constant and the g value are typical for binuclear complexes,[15] and the value of the isotropic hyperfine coupling constant is about half of the value observed in oxovanadium(IV) complexes.[17] This indicates that in solution at 300 K, the single unpaired electron is shared by the two vanadium nuclei. The observed line width in not same for all the hyperfine lines. The dependence of the line width on the hyperfine lines of the EPR spectrum in solution has been modelled theoretically, using a model that incorporates incomplete motional narrowing, the anisotropic $g$-tensor, and hyperfine tensor interactions.[18,19] Using the Kivelson's model[18] the line width, $\Delta H$, of a hyperfine line associated with the nuclear spin component $M_I$ is given as equation (2) in ref.[20]

Where the parameters $\alpha$, $\beta$, $\gamma$ and $\delta$ are functions of the principal values of the g-tensor, hyperfine coupling tensor, and rotational correlation time. The line width expression given in [Equation (1)] has been highly successful in explaining the variation in the widths of the EPR lines in the spectrum of vanadyl acetylacetonate in toluene,[20] and has been used to obtain the anisotropic EPR parameters from solution spectra of copper complexes.[21,22] We have assumed that Equation 1 is approximately applicable to our binuclear complex, and have simulated the EPR spectrum based on this line width expression with $M_I = -7, -6, \ldots, +6, +7$, corresponding to the two equivalent vanadium nuclei. The simulated spectrum is shown in Figure 2 (b). Here we simply note that the simulated spectrum reproduces the

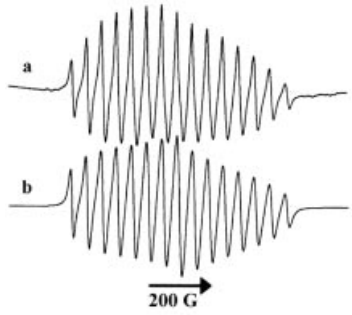


Figure 2. EPR spectra for $[V_2O_3L^7]$ (a) in DCM at 300 K. Instrument settings: microwave frequency, 9.45385 GHz; microwave power, 2.0 mW; modulation frequency, 100 kHz; modulation amplitude, ca. 1 G. (b) Simulated EPR spectrum using isotropic hyperfine coupling constant = $49.3 \pm 0.2$ G, and Kivelson's parameters $\alpha$ = 21.21 G, $\beta$ = 0.2943 G, $\gamma$ = –0.1538 and $\delta$ = 0.0007 G.

essential features of the experimental EPR spectrum of the binuclear complex at room temperature.

$$\Delta H = \alpha + \beta M_I + \gamma M_I^2 + \delta M_I^3 \quad (1)$$

The complexes display axial spectra at 77 K (Figure 3). The hyperfine structure can be attributed to the coupling of the unpaired electron to a single $^{51}$V centre ($I = 7/2$), at least on the EPR timescale.[6,8]

In frozen solution (77 K) and fluid solution (300 K) the spectral parameters are related by the following equations:[23]

$g_{av} \approx g_{iso}$

$A_{av} \approx 2A_{iso}$

From the above relationships it may be deduced that the unpaired electron is equally delocalised between the two vanadium atoms, at least on the X-band EPR timescale, and the complexes behave as class III type[5,24,25] mixed valance species at room temperature.

 © 2006 Wiley-VCH Verlag GmbH & Co. KGaA, Weinheim 

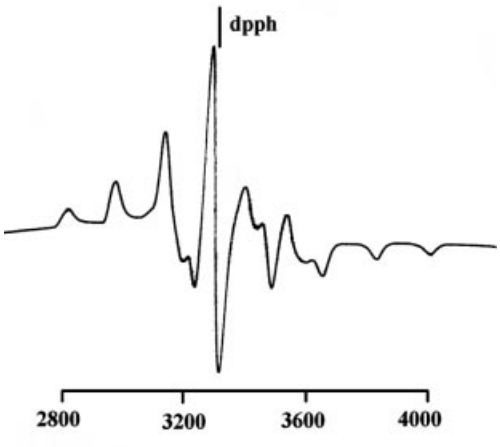


Figure 3. EPR spectra for $[V_2O_3L^7]$ in DCM/toluene at 77 K. Instrument settings: microwave frequency, 9.1 GHz; microwave power, 30 dB; modulation frequency, 100 kHz; modulation amplitude, 12.5 G; sweep centre, 3200 G.

## DFT Study

DFT calculation have been performed on the full molecular structure using the crystallographic coordinates for $[V_2O_3L^7]$ and the previously reported $[V_2O_3L^1]$ complex[15] (ligand $H_3L^1$ is shown in Scheme 1) in order to get a better insight into the electronic structure of μ-oxo μ-phenoxo bridged binuclear oxovanadium(IV/V) complexes. The spin density, singly occupied molecular orbital (SOMO), and the lowest unoccupied molecular orbital (LUMO) plots for the complexes are shown in Figure 4, Figure 5 and Figure 6 respectively.

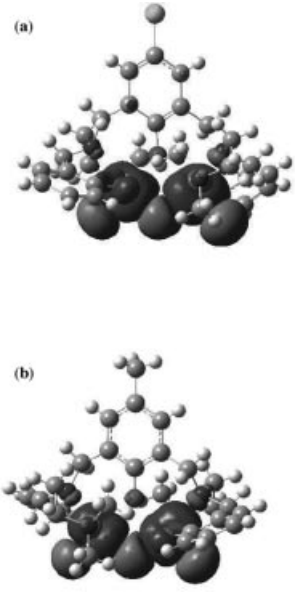


Figure 4. Spin density plots (a). $[V_2O_3L^7]$ (b). $[V_2O_3L^1]$.

The spin density population of the electron between the two vanadium atoms is 0.5700 and 0.4300 for $[V_2O_3L^7]$, and 0.5664 and 0.4336 for $[V_2O_3L^1]$. It is clear from the spin density plots (Figure 4) that the unpaired electron is delocalised between the two vanadium centres.

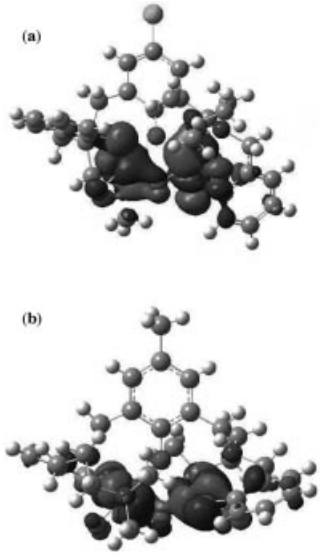


Figure 5. SOMO plots (a). $[V_2O_3L^7]$ (b). $[V_2O_3L^1]$.

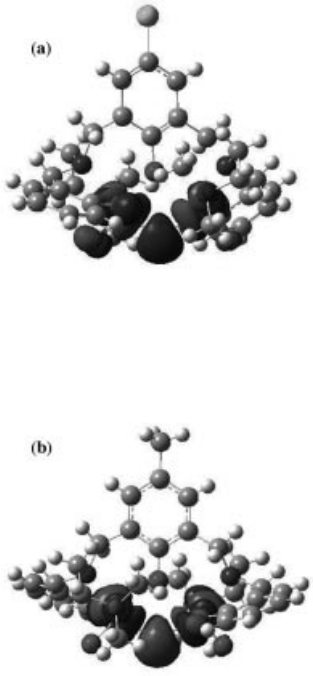


Figure 6. LUMO plots (a). $[V_2O_3L^7]$ (b). $[V_2O_3L^1]$.

It is interesting to note that the bridging oxo oxygen atom takes part in the construction of the SOMO, while the contribution of the bridging phenoxy oxygen to the SOMO is zero (Figure 5). The $p_z$ orbital of the bridging oxo oxygen atom interacts with the $d_{xz}$ orbital of the vanadium atoms asymmetrically in the $[V_2O_3L^7]$ complex, and symmetrically in the $[V_2O_3L^1]$ complex. These results are consistent with the $V–O_{oxo}–V$ bond lengths observed in these complexes. It is found from the LUMO plots that the bridging oxo oxygen (Figure 6) and the bridging phenoxy group do not in-

 © 2006 Wiley-VCH Verlag GmbH & Co. KGaA, Weinheim 

teract with the metal orbital. The above results suggest that the delocalisation of the electron between the two vanadium centres takes place via a $d_{xz}$–$p_z$–$d_{xz}$ super exchange pathway in the ground state.

In summary, DFT studies reveal that in case of binuclear mixed valence oxovanadium(IV/V) complexes containing a $[OV^{IV}(\mu\text{-}O_{oxo})(\mu\text{-}O_{phen})V^{V}O]^{2+}$core with a bent V–O–V moiety, only the bridging oxo group is responsible for the unpaired electron delocalisation, and as such the delocalisation occurs via a $d_{xz}$–$p_z$–$d_{xz}$ super exchange pathway.

## Conclusion

Binuclear mixed valence oxovanadium(IV/V) complexes containing the $[OV^{IV}(\mu\text{-}O_{oxo})(\mu\text{-}O_{phen})V^{V}O]^{2+}$ moiety have been synthesised using $N_4O_3$-coordinating heptadentate ligands. In $[V_2O_3L^7]$, the V1–O5–V2 moiety is angular, and the V1–O5 and V2–O5 bond lengths are slight different [V1–O5 = 1.798(2) and V2–O5 = 1.885(2) Å]. Solution EPR spectra reveal that the unpaired electron is delocalised between the two vanadium atoms, which is attested by the simulated EPR spectrum. We have also found some important trends in the electronic structure, and hence in the behaviour of the unpaired electron, from the DFT studies. DFT calculations show that the bridging phenoxo group has no role to play in the electron delocalisation. Although the V–O–V group is angular, the delocalisation in such systems is anticipated to occur via an $d_{xz}$–$p_z$–$d_{xz}$ exchange pathway involving the oxo oxygen atom.

## Experimental Section

**Materials:** Bis(acetylacetonato)oxovanadium(IV)[26] and the ligands[27] were prepared as reported in the literature. All the starting chemicals were analytically pure and used without further purification, and the solvents were purified by standard procedures.[28]

**Physical Measurements:** UV/Vis spectra were recorded on a Perkin–Elmer LAMBDA 25 spectrophotometer, and IR spectra were measured with a Perkin–Elmer L-0100 spectrometer. Electrochemical measurements were performed (acetonitrile solution) on a CH 620A electrochemical analyzer using a platinum electrode. Tetraethylammonium perchlorate (TEAP)[29] was used as the supporting electrolyte, and the potentials are referenced to the standard calomel electrode (SCE) without junction correction. Magnetic susceptibilities were measured on a PAR-155 vibrating-sample magnetometer.

The room temperature solution EPR spectra were recorded for **1** in the following manner: the complex (ca. 10 mM in dichloromethane) was placed in a glass tube, and degassed by repeated freeze-pump-thaw cycles with a vacuum line working at a pressure of about $10^{-4}$ Torr., and then sealed off. This sealed sample was used for recording the CW-EPR spectrum at room temperature, using a home-built EPR spectrometer,[30] which was further modified.[31] Low microwave power (ca. 2 mW) and 100 kHz magnetic field modulation (ca. 1 gauss) were used to avoid distortion of the EPR lines. A proton NMR magnetometer was used to calibrate the scan range of the magnetic field. An Agilent frequency counter, model 53181A, equipped with a highly stable oven-controlled time base, was used to measure the microwave and NMR frequencies. For determining the $g$ value of the complex, a very small amount of DPPH powder ($g = 2.0037 \pm 0.0002$)[32] was attached to the outside wall of the sealed sample, and the EPR spectrum of the complex with DPPH was recorded.

The room temperature solution EPR spectra of the other complexes, and the low temperature spectra for all the complexes, were recorded on a Varian E-109C X-band spectrometer. Elemental analyses (C, H, N) were performed on a Perkin–Elmer 2400 Series II elemental analyzer.

**DFT Calculation:** DFT calculations were performed using the Gaussian-03 program.[33] The complexes were described in the unrestricted formalism using the B3LYP hybrid density function in combination with a standard 3-21 G basis set.

**Crystallographic Studies:** Single crystals of suitable quality for single-crystal X-ray diffraction studies were grown by the slow diffusion of hexane into a dichloromethane solution containing $[V_2O_3L^7]\,CH_2Cl_2$. The X-ray intensity data were measured at 293 K on a Bruker AXS SMART APEX CCD diffractometer (Mo-$K_\alpha$, $\lambda$ = 0.71073 Å). The detector was placed at a distance of 6.03 cm from the crystal. A total of 606 frames were collected over a scan width of 0.3° at different settings of $\varphi$. The data were reduced with SAINTPLUS[34] and an empirical absorption correction was applied using the SADABS package.[24] Vanadium atoms were located by Direct Methods, and the rest of the non-hydrogen atoms emerged from successive Fourier syntheses. SHELXL-97[35] was used for structure solution, and for full-matrix least-squares structure refinement on $F^2$. All non-hydrogen atoms were refined anisotropically. All the hydrogen atoms were included at calculated positions. The dichloromethane solvent molecule is disordered over two positions. The disorder was modelled using the PART instruction in SHELXTL, with an initial occupancy of 0.5, which after refinement gave a final value of 0.583(5). Molecular structure plots were drawn using ORTEP.[36] Relevant crystal data are given in Table 3.

Table 3. Crystal data and structure refinement parameters for $[V_2O_3L^7]\cdot CH_2Cl_2$.

| $[V_2O_3L^7]\cdot CH_2Cl_2$ | |
|---|---|
| Formula | $C_{31}H_{40}Cl_3N_4O_6V_2$ |
| Formula weight | 772.90 |
| Crystal system | monoclinic |
| Space group | $P2_1/c$ |
| $a$ [Å] | 16.181(3) |
| $B$ [Å] | 13.986(3) |
| $c$ [Å] | 15.024(3) |
| $\beta$ [°] | 97.16(3) |
| $V$ [Å$^3$] | 3373.6(12) |
| $T$ [K] | 293(2) |
| $Z$ | 4 |
| $D_{calcd.}$ (mg·m$^{-3}$) | 1.522 |
| $\mu$ [mm$^{-1}$] | 0.841 |
| $R_1$,[a] $wR_2$[b] [$I > 2\sigma(I)$] | 0.0490, 0.1121 |
| $R_1$,[a] $wR_2$[b] [all] | 0.0616, 0.1196 |
| $R_{int}$, $R_{sigma}$ | 2.65, 2.47 |
| G.O.F on $F^2$ | 1.058 |

[a] $R_1 = \Sigma||F_o| - |F_c||/\Sigma|F_o|$. [b] $wR_2 = [\Sigma w(F_o^2 - F_c^2)^2/\Sigma w(F_o^2)^2]^{1/2}$.

CCDC-281762 contains the supplementary crystallographic data for this paper. These data can be obtained free of charge from The Cambridge Crystallographic Data Centre via www.ccdc.cam.ac.uk/data_request/cif.

**Synthesis of Complexes:** The complexes were prepared by the same general method. Details are given here for a representative case.

 © 2006 Wiley-VCH Verlag GmbH & Co. KGaA, Weinheim 

**$[V_2O_3L^7]$:** To a stirred solution of $[VO(acac)_2]$ (0.10 g, 0.37 mmol) in 20 mL acetone was added the $H_3L^7$ ligand (0.098 g, 0.19 mmol). The reaction mixture was then stirred for 2 h at ambient temperature in air, and a green precipitate separated from the solution. The solution was filtered, washed with acetone, and then dried in vacuo over fused calcium chloride. Yield: 0.116 g (90%). $C_{30}H_{38}ClN_4O_6V_2$ (687.5): calcd. C 52.36, H 5.53, N 8.15; found: C 52.61, H 5.70, N 8.31. UV/Vis ($CH_2Cl_2$): $\lambda_{max}$ ($\varepsilon$) = 1031 nm (255 $M^{-1}$ $cm^{-1}$); 640 (700). IR (KBr): $\nu$(V=O) 950, $\nu$(V–O–V) 752 $cm^{-1}$. $E_{pa}$ ($[OV^V(\mu\text{-}O_{oxo})(\mu\text{-}O_{phen})V^VO]^{3+}/[OV^{IV}(\mu\text{-}O_x)(\mu\text{-}O_{phen})V^VO]^{2+}$): +0.56 V (irr). $\mu_{eff}$ = 1.76 BM.

**$[V_2O_3L^8]$:** Yield: 0.117 g (87%). $C_{32}H_{42}ClN_4O_6V_2$ (701.5): calcd. C 53.66, H 5.87, N 7.82; found: C 53.75, H 5.99, N 7.95. UV/Vis ($CH_2Cl_2$): $\lambda_{max}$ ($\varepsilon$) = 1036 nm (590 $M^{-1}$ $cm^{-1}$), 650 (785). IR (KBr): $\nu$(V=O) 947, $\nu$(V–O–V) 755 $cm^{-1}$. $E_{pa}$ ($[OV^V(\mu\text{-}O_{oxo})(\mu\text{-}O_{phen})V^VO]^{3+}/[OV^{IV}(\mu\text{-}O_{oxo})(\mu\text{-}O_{phen})V^VO]^{2+}$): +0.55 V (irr); $\mu_{eff}$ = 1.79 BM.

**$[V_2O_3L^9]$:** Yield: 0.121 g (85%). $C_{30}H_{36}Cl_3N_4O_6V_2$ (757.5): calcd. C 47.5, H 4.88, N 7.39; found: C 47.64, H 4.96, N 7.54. UV/Vis ($CH_2Cl_2$): $\lambda_{max}$ ($\varepsilon$) = 1032 nm (458 $M^{-1}$ $cm^{-1}$), 665 (1217). IR (KBr): $\nu$(V=O) 955, $\nu$(V–O–V) 745 $cm^{-1}$. $E_{pa}$ ($[OV^V(\mu\text{-}O_{oxo})(\mu\text{-}O_{phen})V^VO]^{3+}/[OV^{IV}(\mu\text{-}O_{oxo})(\mu\text{-}O_{phen})V^VO]^{2+}$): +0.49 V (irr); $\mu_{eff}$ = 1.75 BM.

**$[V_2O_3L^{10}]$:** Yield: 0.130 g (88%). $C_{32}H_{40}Cl_3N_4O_6V_2$ (784.5): calcd. C 48.94, H 5.09, N 7.14; found: C 49.12, H 5.21, N 7.25. UV/Vis ($CH_2Cl_2$): $\lambda_{max}$ ($\varepsilon$) = 1036 nm (590 $M^{-1}$ $cm^{-1}$), 650 (785). IR (KBr): $\nu$(V=O) 958, $\nu$(V–O–V) 748 $cm^{-1}$. $E_{pa}$ ($[OV^V(\mu\text{-}O_{oxo})(\mu\text{-}O_{phen})V^VO]^{3+}/[OV^{IV}(\mu\text{-}O_{oxo})(\mu\text{-}O_{phen})V^VO]^{2+}$): +0.56 V (irr); $\mu_{eff}$ = 1.72 BM.

## Acknowledgments

Financial support from the Council of Scientific and Industrial Research [Project Number: 01(2015)/05/EMR-II], New Delhi, India is gratefully acknowledged. We are also thankful to DST for the data collection on the CCD facility setup (Indian Institute of Science, Bangalore, India) under IRHPA-DST program. Authors are also thankful to Dr. Swapan K. Pati, Jawaharlal Nehru Centre for Advanced Scientific Research, Bangalore, India, for his help regarding the DFT study.

[1] a) M. Mahroof-Tahir, A. D. Keramidas, R. B. Goldfrab, O. P. Anderson, M. M. Miller, D. C. Crans, *Inorg. Chem.* **1997**, *36*, 1657; b) E. P. Copeland, I. A. Kahwa, J. T. Mague, G. L. McPherson, *J. Chem. Soc. Dalton Trans.* **1997**, 2849.
[2] J. C. Pessoa, M. J. Calhorda, I. Cavaco, I. Correia, M. T. Duarte, V. Felix, R. T. Henriques, M. F. Piedade, I. Tomaz, *J. Chem. Soc. Dalton Trans.* **2002**, 4407.
[3] S. Ghosh, K. K. Nanda, A. W. Addison, R. J. Butcher, *Inorg. Chem.* **2002**, *41*, 2243.
[4] S. K. Dutta, S. Samanta, S. B. Kumar, O. H. Han, P. Burckel, A. A. Pinkerton, M. Chaudhury, *Inorg. Chem.* **1999**, *38*, 1982.
[5] R. A. Holwerda, B. R. Whittlesey, *Inorg. Chem.* **1998**, *37*, 64.
[6] S. Mondal, P. Ghosh, A. Chakravorty, *Inorg. Chem.* **1997**, *36*, 59.
[7] D. Schulz, T. Weyhermüller, K. Wieghardt, B. Nuber, *Inorg. Chim. Acta* **1995**, *240*, 217.
[8] J. Chakravarty, S. Dutta, A. Chakravorty, *J. Chem. Soc. Dalton Trans.* **1993**, 2857.
[9] J. C. Silva, J. A. L. Pessoa, A. L. Vieira, L. Vilas-Boas, P. Ó. Brien, *J. Chem. Soc. Dalton Trans.* **1992**, 1745.
[10] J.-P. Launay, Y. Jeannin, M. Daoudi, *Inorg. Chem.* **1985**, *24*, 1052.
[11] A. Kojima, K. Okazaki, S. Ooi, K. Saito, *Inorg. Chem.* **1983**, *22*, 1168.
[12] F. Babonneau, C. Sanchez, J. Livage, J. P. Launay, M. Daoudi, Y. Jeannin, *Nouv. J. Chim.* **1982**, *6*, 353.
[13] M. Nishizawa, K. Hirotsu, S. Ooi, K. Saito, *J. Chem. Soc. Chem. Commun.* **1979**, 707.
[14] T. L. Riechel, D. T. Sawyer, *Inorg. Chem.* **1975**, *14*, 1869.
[15] A. Mondal, S. Sarkar, D. Chopra, T. N. Guru Row, K. Pramanik, K. K. Rajak, *Inorg. Chem.* **2005**, *44*, 703.
[16] R. W. Fessenden, *J. Chem. Phys.* **1962**, *37*, 747.
[17] A. Togni, G. Rist, G. Rihs, A. Schweiger, *J. Am. Chem. Soc.* **1993**, *115*, 1908.
[18] D. Kivelson, *J. Chem. Phys.* **1960**, *33*, 1094.
[19] J. H. Freed, G. K. Fraenkel, *J. Chem. Phys.* **1963**, *39*, 326.
[20] R. Wilson, D. Kivelson, *J. Chem. Phys.* **1966**, *44*, 154.
[21] B. S. Prabhananda, *Molecules Molec. Phys.* **1979**, *38*, 209.
[22] R. Das, B. S. Prabhananda, *J. Magn. Reson.* **1983**, *54*, 89.
[23] a) J. E. Wertz, J. R. Bolton, *Electron Spin Resonance*, McGraw Hill, New York, **1972**, p. 208–210; b) J. R. Pilbrow, *Transition Ion Electron Paramagnetic Resonance*, Clarendon Press, Oxford, **1990**, p. 339.
[24] M. B. Robin, P. Day, *Adv. Inorg. Chem. Radiochem.* **1967**, *10*, 247.
[25] K. Y. Wong, P. N. Schatz, *Prog. Inorg. Chem.* **1981**, *28*, 369.
[26] R. A. Rowe, M. M. Jones, *Inorg. Synth.* **1957**, *5*, 113.
[27] R. Kannappan, R. Mahalakshmy, T. M. Rajendiram, R. Venkatesan, P. Sambasiva Rao, *Proc. Indian Acad. Sci. (Chem. Sci.)* **2003**, *115*, 1.
[28] B. S. Furniss, A. J. P. W. G. Hannaford, Smith, A. R. Tatchell, in *Vogel's Textbook of Practical Organic Chemistry*, Pearson Education, Singapore, **2004**, p. 395–412.
[29] G. K. Lahiri, S. Bhattacharya, B. K. Ghosh, A. Chakravorty, *Inorg. Chem.* **1987**, *26*, 4324.
[30] R. Das, B. Venkataraman, V. R. Bhagat, A. S. Ghangrekar, T. Kuruvilla, B. K. Chaturvedi, G. S. Isola, B. M. Marwaha, P. G. Nair, R. S. Parolia, B. K. Sarkar, *Pramana – J. Phys.* **1986**, *27*, 661.
[31] R. Das, B. Venkataraman, *Res. Chem. Intermed.* **2005**, *31*, 167.
[32] J. E. Wertz, J. R. Bolton, in: *Electron Spin Resonance – Elementary Theory and Practical Applications*, McGraw-Hill Book Company, New York, **1972**, p. 465.
[33] M. J. Frisch, G. W. Trucks, H. B. Schlegel, G. E. Scuseria, M. A. Robb, J. R. Cheeseman, J. A. Montgomery Jr, T. Vreven, K. N. Kudin, J. C. Burant, J. M. Millam, S. S. Iyengar, J. Tomasi, V. Barone, B. Mennucci, M. Cossi, G. Scalmani, N. Rega, G. A. Petersson, H. Nakatsuji, M. Hada, M. Ehara, K. Toyota, R. Fukuda, J. Hasegawa, M. Ishida, T. Nakajima, Y. Honda, O. Kitao, H. Nakai, M. Klene, X. Li, J. E. Knox, H. P. Hratchian, J. B. Cross, C. Adamo, J. Jaramillo, R. Gomperts, R. E. Stratmann, O. Yazyev, A. J. Austin, R. Cammi, C. Pomelli, J. W. Ochterski, P. Y. Ayala, K. Morokuma, G. A. Voth, P. Salvador, J. J. Dannenberg, V. G. Zakrzewski, S. Dapprich, A. D. Daniels, M. C. Strain, O. Farkas, D. K. Malick, A. D. Rabuck, K. Raghavachari, J. B. Foresman, J. V. Ortiz, Q. Cui, A. G. Baboul, S. Clifford, J. Cioslowski, B. B. Stefanov, G. Liu, A. Liashenko, P. Piskorz, I. Komaromi, R. L. Martin, D. J. Fox, T. Keith, M. A. Al-Laham, C. Y. Peng, A. Nanayakkara, M. Challacombe, P. M. W. Gill, B. Johnson, W. Chen, M. W. Wong, C. Gonzalez, J. A. Pople, *Gaussian 03, Revision B.05*, Gaussian, Inc., Pittsburgh PA, **2003**.
[34] Bruker software: *SMART, SAINT, SADABS, XPREP, SHELXTL*, Bruker AXS Inc., Madison, Wisconsin, USA, **2004**.
[35] G. M. Sheldrick, SHELXL97, *Program for Crystal Structure Refinement*, University of Göttingen, Germany, **1997**.
[36] C. K. Johnson, ORTEP. Report ORNL-5138; *Oak Ridge National Laboratory*: Oak Ridge, TN, **1976**.

Received: August 26, 2005
Published Online: March 16, 2006

 © 2006 Wiley-VCH Verlag GmbH & Co. KGaA, Weinheim 

DOI: 10.1002/ejic.200500788

# Metal Phosphonates Based on {[(Benzimidazol-2-ylmethyl)imino]bis-(methylene)}bis(phosphonic Acid): Syntheses, Structures and Magnetic Properties of the Chain Compounds $[M\{(C_7H_5N_2)CH_2N(CH_2PO_3H)_2\}]$ (M = Mn, Fe, Co, Cu, Cd)

**Deng-Ke Cao,[a] Jing Xiao,[a] Yi-Zhi Li,[a] Juan Modesto Clemente-Juan,[b] Eugenio Coronado,[b] and Li-Min Zheng*[a]**

**Keywords:** Chain structures / Magnetic properties / N,O ligands / Organic–inorganic hybrid composites / Transition metals

Five compounds based on {[(benzimidazol-2-ylmethyl)imino-]bis(methylene)}bis(phosphonic acid) $[(C_7H_5N_2)CH_2N(CH_2PO_3H_2)_2]$, namely $[M\{(C_7H_5N_2)CH_2N(CH_2PO_3H)_2\}]$ [M = Mn (**1**), Fe (**2**), Co (**3**), Cu (**4**), Cd (**5**)] have been synthesized under hydrothermal conditions. These compounds are isostructural, crystallizing in the orthorhombic space group *Pbca*, with $a$ = 15.331(2), $b$ = 10.7150(16), and $c$ = 16.715(2) Å for **1**; $a$ = 15.320(3), $b$ = 10.477(2), and $c$ = 16.764(3) Å for **2**; $a$ = 15.207(2), $b$ = 10.4626(16), and $c$ = 16.794(3) Å for **3**; $a$ = 15.101(3), $b$ = 10.3517(17), and $c$ = 16.997(3) Å for **4**; and $a$ = 15.4679(19), $b$ = 10.8923(13), and $c$ = 16.6175(19) for **5**. Each compound shows a one-dimensional chain structure where $\{MO_3N_2\}$ trigonal bipyramids are connected by $\{CPO_3\}$ tetrahedra through corner-sharing. The chains are further connected to each other through aromatic stacking of the benzimidazole rings and extensive hydrogen bonds, forming a supramolecular 3D structure. Magnetic susceptibility studies of **1**–**4** reveal that weak antiferromagnetic interactions occur between the metal centers.

(© Wiley-VCH Verlag GmbH & Co. KGaA, 69451 Weinheim, Germany, 2006)

## Introduction

Increasing attention has been paid in recent years to metal phosphonate materials due to their potential applications in catalysis, nonlinear optics, magnetism, and biotechnology etc.[1] Meanwhile, the rapid development in the rational design and synthesis of coordination polymers, by using different organic ligands, has provided a variety of compounds with interesting architectures and possible functionalities.[2] The integration of the inorganic phosphonate ($CPO_3$) group and numerous rigid or flexible organic functional groups within the same composite would, therefore, be expected to result in new inorganic–organic hybrid materials with interesting structures and properties. Efforts along this line have been made where the organic moieties of the phosphonate ligand contain amino,[3] carboxylate,[4] pyridyl,[5] macrocyclic,[6] and ferrocene[7] groups etc. In this article, we report a new route to the synthesis of {[(benzimidazol-2-ylmethyl)imino]bis(methylene)}bis-(phosphonic acid) $[(C_7H_5N_2)CH_2N(CH_2PO_3H_2)_2$, bibmp$H_4$], where a benzimidazole group is incorporated into the diphosphonic acid. Five isostructural compounds based on this ligand, namely $[M\{(C_7H_5N_2)CH_2N(CH_2PO_3H)_2\}]$ [M = Mn (**1**), Fe (**2**), Co (**3**), Cu (**4**), Cd (**5**)] are obtained by hydrothermal reactions; all exhibit one-dimensional chain structures. The magnetic properties of **1**–**4** were also investigated.

[a] State Key Laboratory of Coordination Chemistry, Coordination Chemistry Institute, Nanjing University, Nanjing 210093, P. R. China
Fax: +86-25-8331-4502
E-mail: lmzheng@nju.edu.cn
[b] Institut de Ciència Molecular, Universitat de València, Dr. Moliner 50, 46100 Burjassot, Spain

Supporting information for this article is available on the WWW under http://www.eurjic.org or from the author.

## Results and Discussion

### Syntheses and Preliminary Characterization

The synthesis of bibmp$H_4$ was previously reported from 2-(2-aminomethyl)benzimidazole, phosphorus, and formaldehyde by a Mannich reaction.[8] In this paper we describe a new synthetic route to the same acid from the reaction between *N*,*N*-bis(phosphonomethyl)aminoacetic acid and 1,2-diaminobenzene (Scheme 1). The final product can be easily isolated with a much higher yield (82%) than that reported in the patent (17%).[8]

The hydrothermal reaction of bibmp$H_4$ and the appropriate metal sulfate at 140 °C for one day resulted in compounds **1**–**5**, which have identical structures even though the experimental conditions for the formation of these compounds are slightly different. A series of experiments was conducted by changing the molar ratio of the starting materials and the pH of the reaction mixture. It was found that

 © 2006 Wiley-VCH Verlag GmbH & Co. KGaA, Weinheim 

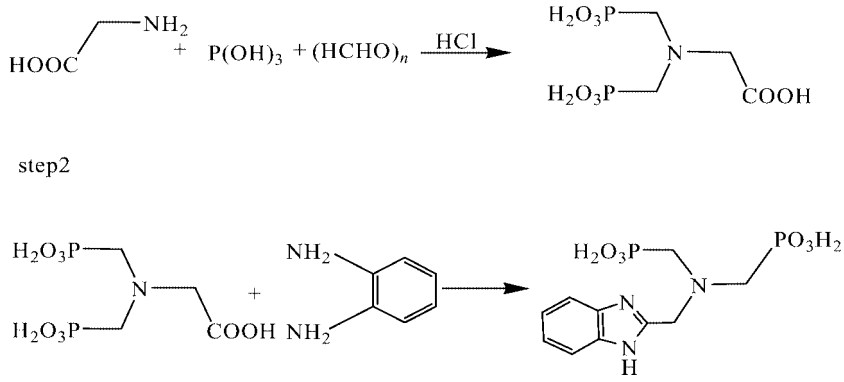


Scheme 1.

pure phases of compounds **1**, **3**, and **5** can be obtained with good yields when the molar ratio of M/ligand and the pH are 1:1 and 2.5–3.5 for **1**, 1:1 and 3.0–4.0 for **3**, and 1:1 and 2.0–4.0 for **5**, respectively. For compounds **2** and **4**, the crystallization of the products is always accompanied by the formation of brown powdery impurities when the molar ratio of M/ligand and the pH are 1:0.75–1 and 2.9–7.0 for **2** and 1:0.75–1 and 3.0–5.9 for **4**, respectively. Crystals with the best quality are formed when the pH is 7.03 for **2** and 4.90 for **4**. In preparing compound **2**, $Me_4NOH$ was used instead of NaOH to adjust the pH of the reaction mixture in order to improve the crystal quality. The same product can also be obtained with NaOH.

The IR spectra of compounds **1**–**5** are almost identical. The broad bands appearing around 3000 $cm^{-1}$ can be assigned to NH and OH stretching vibrations with the presence of extensive hydrogen bonds.[9] The sharp bands at around 1622, 1598, and 1522 $cm^{-1}$ are characteristic of the phenyl ring, and the bands near 1467 and 1455 $cm^{-1}$ are typical for ν(C=N) of the imidazole ring.[10] A series of bands between 1236 and 915 $cm^{-1}$ correspond to the the $CPO_3$ groups.[11]

### Crystal Structures of Compounds 1–5

Compounds **1**–**5** are isostructural and crystallize in the orthorhombic space group *Pbca*. Crystallographic and re-

Table 1. Selected bond lengths [Å] and angles [°] for **1**–**5**.[a]

| | **1** | **2** | **3** | **4** | **5** |
|---|---|---|---|---|---|
| M1–O1 | 2.032(3) | 1.980(3) | 1.978(3) | 2.000(2) | 2.148(3) |
| M1–O4 | 2.090(3) | 2.029(3) | 2.004(3) | 2.142(2) | 2.198(3) |
| M1–N1 | 2.486(4) | 2.364(3) | 2.345(4) | 2.137(3) | 2.551(3) |
| M1–N2 | 2.127(4) | 2.067(3) | 2.024(4) | 1.981(3) | 2.213(4) |
| M1–O5A | 2.033(3) | 2.035(3) | 2.005(3) | 1.926(2) | 2.152(3) |
| P1–O1 | 1.496(4) | 1.501(3) | 1.504(3) | 1.509(2) | 1.492(3) |
| P1–O2 | 1.517(4) | 1.494(3) | 1.495(4) | 1.513(2) | 1.494(3) |
| P1–O3 | 1.580(4) | 1.569(3) | 1.573(3) | 1.564(2) | 1.604(3) |
| P2–O4 | 1.507(4) | 1.524(3) | 1.524(3) | 1.501(2) | 1.525(3) |
| P2–O5 | 1.506(4) | 1.494(3) | 1.493(3) | 1.513(2) | 1.487(3) |
| P2–O6 | 1.552(3) | 1.558(3) | 1.563(3) | 1.554(2) | 1.573(3) |
| O1–M1–O4 | 115.95(15) | 122.72(12) | 118.82(14) | 113.52(9) | 111.24(10) |
| O1–M1–N1 | 79.21(13) | 82.30(11) | 82.49(13) | 87.18(9) | 78.53(10) |
| O1–M1–N2 | 114.37(17) | 113.09(13) | 115.30(15) | 125.68(11) | 117.01(12) |
| O1–M1–O5A | 105.68(14) | 101.24(12) | 100.05(13) | 96.31(9) | 110.01(12) |
| O4–M1–N1 | 79.16(13) | 81.87(11) | 82.12(12) | 84.55(9) | 77.49(10) |
| O4–M1–N2 | 115.67(15) | 115.80(13) | 118.10(14) | 117.56(10) | 114.86(12) |
| O4–M1–O5A | 98.01(13) | 94.78(12) | 95.24(12) | 91.09(9) | 95.16(11) |
| N1–M1–N2 | 73.63(15) | 76.41(12) | 77.25(14) | 80.52(10) | 72.34(12) |
| O5A–M1–N1 | 175.09(14) | 176.11(12) | 177.02(13) | 175.25(10) | 170.52(11) |
| O5A–M1–N2 | 104.32(16) | 103.45(13) | 102.92(14) | 99.92(10) | 106.06(13) |
| M1–N1–C1 | 106.4(3) | 105.7(2) | 106.5(3) | 107.95(17) | 105.1(2) |
| M1–N1–C2 | 106.2(3) | 107.9(2) | 107.5(3) | 109.77(19) | 105.7(2) |
| M1–N1–C3 | 108.1(3) | 107.8(2) | 107.2(3) | 107.02(19) | 105.5(2) |
| M1–N2–C4 | 119.8(5) | 118.0(3) | 118.5(3) | 114.9(2) | 119.4(3) |
| M1–N2–C5 | 135.3(4) | 136.5(3) | 136.1(3) | 139.9(2) | 134.8(3) |
| M1–O1–P1 | 124.9(2) | 122.96(17) | 122.6(2) | 117.48(12) | 122.86(15) |
| M1–O4–P2 | 123.58(19) | 122.01(16) | 122.37(17) | 116.85(14) | 121.94(16) |
| M1B–O5–P2 | 135.5(2) | 138.15(19) | 137.95(19) | 136.27(15) | 128.28(19) |

[a] Symmetry codes: A: $-x$, $y + 1/2$, $-z + 1/2$; B: $-x$, $y - 1/2$, $-z + 1/2$.

 © 2006 Wiley-VCH Verlag GmbH & Co. KGaA, Weinheim 

finement details of **1**–**5** are listed in the Experimental Section, and selected bond lengths and angles are given in Table 1. Figure 1 displays the building unit of **1** with the atomic labeling scheme. The asymmetric unit of compound

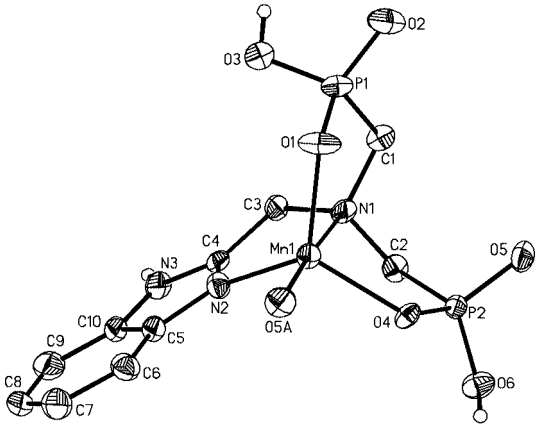


Figure 1. Asymmetric building unit of compound **1** with atomic labeling scheme (50% probability). All H atoms except H3A, H3B and H6A are omitted for clarity.

**1** contains one $Mn^{II}$ ion and one $bibmpH_2^{2-}$ ligand. The Mn1 atom has a distorted trigonal bipyramidal geometry, with the basal plane defined by the atoms O1, O4, and N2 from the same $bibmpH_2^{2-}$ ligand. The Mn1–O1, Mn1–O4, and Mn1–N2 bond lengths are 2.032(3), 2.090(3), and 2.127(4) Å, respectively, while the O1–Mn1–O4, O1–Mn1–N2, and O4–Mn1–N2 bond angles are 116.0(2)°, 114.4(2)°, and 115.7(2)°, respectively. The axial positions are occupied by the atom N1 from the same $bibmpH_2^{2-}$ ligand and O5A from the other equivalent $bibmpH_2^{2-}$ ligand. The N1–Mn1–O5A bond angle is 175.1(1)°, and the Mn1–N1 and Mn1–O5A bond lengths are 2.486(4) and 2.033(3) Å, respectively.

Each $bibmpH_2^{2-}$ behaves as a pentadentate ligand, binding through three phosphonate oxygen atoms (O1, O4, O5), one imino nitrogen atom (N1), and one benzimidazole nitrogen atom (N2). Two phosphonate oxygen atoms (O3, O6), each from a $\{CPO_3\}$ terminus, are protonated [P1–O3 = 1.580(4), P2–O6 = 1.552(3) Å]. The remaining phosphonate oxygen (O2) is pendant [P1–O2 = 1.517(4) Å]. The equivalent Mn atoms are bridged by phosphonate oxygen atoms O4 and O5 to form a zigzag chain along the *b*-axis

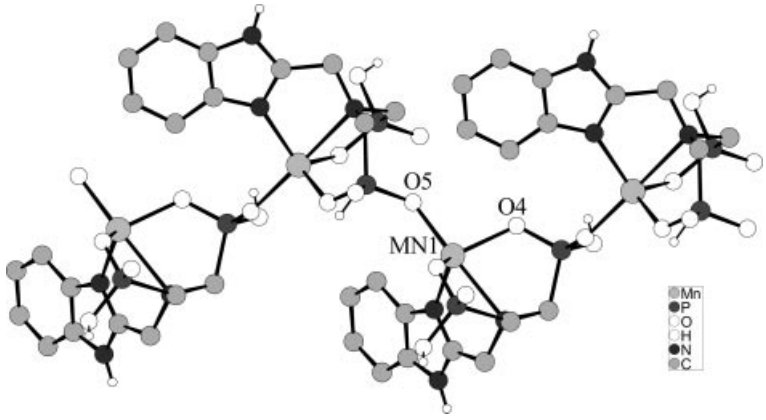


Figure 2. A fragment of chain in structure **1**. All H atoms except H3A, H3B and H6A are omitted for clarity.

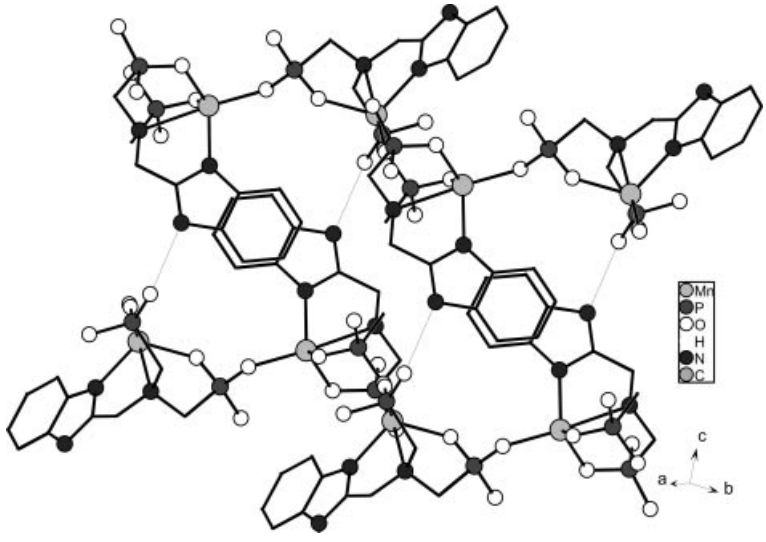


Figure 3. The inter-chain π-π stacking and N···O hydrogen bond interactions in structure **1**. All H atoms are omitted for clarity.

 © 2006 Wiley-VCH Verlag GmbH & Co. KGaA, Weinheim 

(Figure 2). The Mn1···Mn1A distance over the O4–P2–O5 bridge is 5.849 Å. The benzimidazole rings are arranged tilted on two sides of the chain.

Between the chains, the benzimidazole rings are approximately parallel and are π–π stacked (the average centroid–centroid distance between the two phenyl rings of the benzimidazole groups is 3.547 Å for **1**; Figure 3).[12] Hydrogen-bond interactions are found between the imidazole nitrogen atom (N3) and the phosphonate oxygen atom (O2) approximately along the *c*-axis, and among phosphonate oxygen atoms along the *a*-axis (Figures 3 and 4). The N3···O2$^{i}$, O3···O4$^{ii}$, and O6···O2$^{iii}$ distances are 2.753(6), 2.723(5), and 2.536(5) Å, respectively (symmetry codes: i: $x$, $-y + 3/2$, $z - 1/2$; ii: $x + 1/2$, $y$, $-z + 1/2$; iii: $x - 1/2$, $y$, $-z + 1/2$). Therefore, a three-dimensional network structure is built up. Figure 5 shows the packing diagram of compound **1** viewed down the *b*-axis.

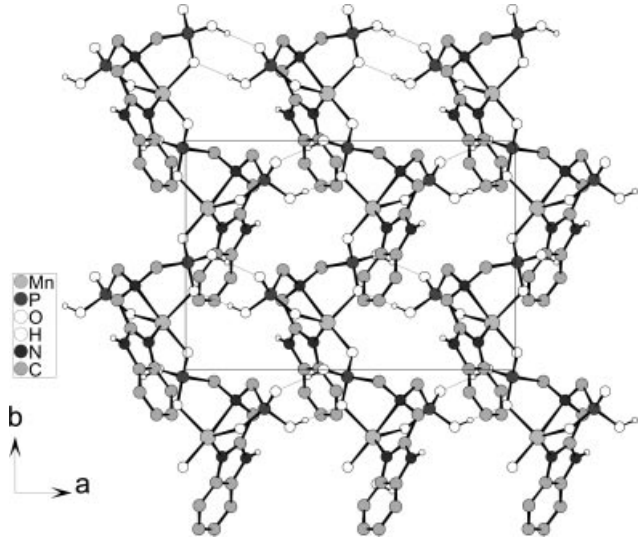


Figure 4. The inter-chain hydrogen bond interactions among the phosphonate oxygen atoms in structure **1**. All H atoms except H3A, H3B and H6A are omitted for clarity.

The structures of compounds **2**–**4** are analogous to **1** except that the $Mn^{II}$ ion in **1** is replaced by $Fe^{II}$ in **2**, $Co^{II}$ in **3**, $Cu^{II}$ in **4**, and $Cd^{II}$ in **5**. The cell volume decreases in the sequence **5** > **1** > **2** > **3** > **4**, in accordance with the decreasing sequence of the ionic radii of the corresponding metal ions.[13] Therefore, the metal atoms in **2**–**5** also have distorted trigonal bipyramidal geometries. The M–N1 distance [2.364(3) Å in **2**, 2.345(4) Å in **3**, 2.137(3) Å in **4**, and 2.551(3) Å in **5**] is significantly longer than the other M–O(N) bond lengths, although the Cu1–N1 bond length in **4** [2.137(3) Å] is much shorter. The metal atoms are bridged by O–P–O units to form infinite chains. The M···M distances across the O–P–O unit within the chain are 5.813 Å for **2**, 5.794 Å for **3**, 5.767 Å for **4**, and 5.941 Å for **5**. These chains are connected by hydrogen-bond interactions as well as π–π stacking interactions. The average centroid–centroid distances between the two phenyl rings of the benzimidazole groups are 3.482 Å for **2**, 3.470 Å for **3**, 3.490 Å for **4**, and 3.620 Å for **5**. The N3···O2$^{i}$, O3···O4$^{ii}$, and O6···O2$^{iii}$ distances are 2.757(4), 2.690(4), and 2.583(4) Å for **2**, 2.739(5), 2.699(4), and 2.570(4) Å for **3**, 2.715(3), 2.632(3), and 2.550(3) Å for **4**, and 2.805(5), 2.702(4), and 2.529(4) Å for **5**, respectively.

It could be of interest to compare the coordination capabilities of the bibmp$^{4-}$ ligand with that of *N*,*N*-bis(phosphonomethyl)aminoacetate (bpmaa$^{5-}$; Scheme 2) as both can offer up to six phosphonate oxygen atoms for coordination with the metal ions. For the bpmaa$^{5-}$ ligand, the carboxylate group has additional two oxygen donors. Thus, several transition metal/bpmada$^{5-}$ compounds have been prepared that show two- and three-dimensional structures.[14] For the bibmp$^{4-}$ ligand, only one nitrogen atom of each benzimidazole group can be used for the coordination when the reaction pH is not high enough. Besides, the benzimidazole group present in this ligand also provides a topologi-

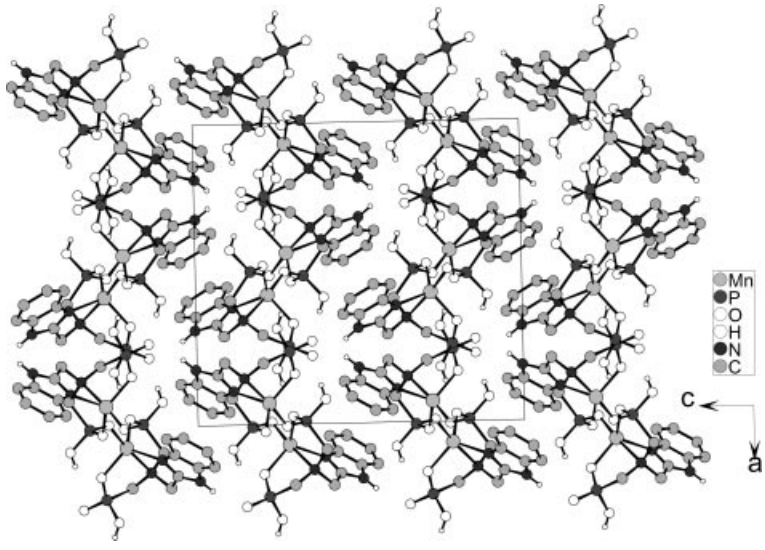


Figure 5. Packing diagram of structure **1** projected along *b*-axis. All H atoms are omitted for clarity.

 © 2006 Wiley-VCH Verlag GmbH & Co. KGaA, Weinheim 

cal hydrophobic environment, possible π–π stacking interactions between the phenyl rings, and steric hindrance as well. Hence, it is not unexpected that different structures will be constructed when metal sources react with $bibmpH_4$ and $bpmaaH_5$ acids. This paper shows that metal/$bibmpH_2^{2-}$ compounds with zigzag chain structures can be obtained through hydrothermal reactions of metal sulfates and the acid $bibmpH_4$.

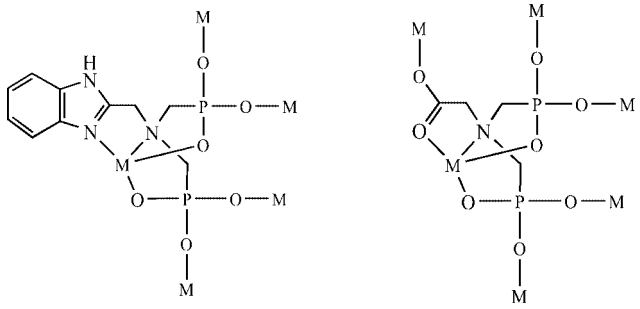

$bibmp^{4-}$ $bpmaa^{5-}$

Scheme 2.

## Magnetic Properties

The temperature-dependent magnetic behaviors of compounds **1**–**4** were investigated in the temperature range 1.8–300 K. The room-temperature effective magnetic moments are 6.24 $\mu_B$/Mn for **1** (expected 5.92 $\mu_B$ for $S = 5/2$), 5.12 $\mu_B$/Fe for **2** (expected 4.90 $\mu_B$ for $S = 2$), 4.57 $\mu_B$/Co for **3** (expected 3.87 $\mu_B$ for $S = 3/2$), and 1.82 $\mu_B$/Cu for **4** (expected 1.73 $\mu_B$ for $S = 1/2$). Figure 6 shows the $\chi_M$ and $\chi_M T$ vs. $T$ plots for compound **1**. The continuous decrease of $\chi_M T$ upon cooling suggests a dominant antiferromagnetic exchange coupling between the $Mn^{II}$ centers. Since structure **1** is one-dimensional and the $Mn^{II}$ ions are linked purely through O–P–O units, the susceptibility data can be analyzed by Fisher's expression for a uniform chain based on the Heisenberg Hamiltonian $H = -J\sum S_{Ai} \cdot S_{Ai+1}$, with the classical spins scaled to a real quantum spin $S = 5/2$ [Equation (1)],[15]

$$\chi_M = \frac{Ng^2\beta^2 S(S+1)}{3kT}\frac{1+u}{1-u} + N_\alpha$$

$$u = \coth\left[\frac{JS(S+1)}{kT}\right] - \left[\frac{kT}{JS(S+1)}\right] \quad (1)$$

where $J$ is the coupling constant, $N$, $g$, $\beta$ and $k$ have their usual meanings, and $N_\alpha$ accounts for both the diamagnetic and TIP contributions. A good fit, shown as the solid line in Figure 6, gives the parameters $g = 2.09$, $J = -0.075$ cm$^{-1}$, and $N_\alpha = 4.0 \times 10^{-4}$ cm$^3$ mol$^{-1}$. The value of $g$ is higher than that expected for a high-spin $Mn^{II}$ ion ($g = 2$). A higher $g$ value has also been reported for the compounds $[Mn(N_3)_2(bte)]$ [bte = 1,2-bis(1,2,4-triazol-1-ylethane)] ($g = 2.06$),[16] $[\{Mn(oda)(H_2O)\}\cdot H_2O]_n$ [oda = $O(CH_2COO)_2^{2-}$] ($g = 2.07$),[17] and $[Mn(OAc)(terpy)(\mu_{1,5}\text{-dca})]_n$ [dca = $N(CN)_2^-$, OAc = acetate, terpy = 2,2′:6′,2′′-terpyridine] ($g = 2.15$).[18]

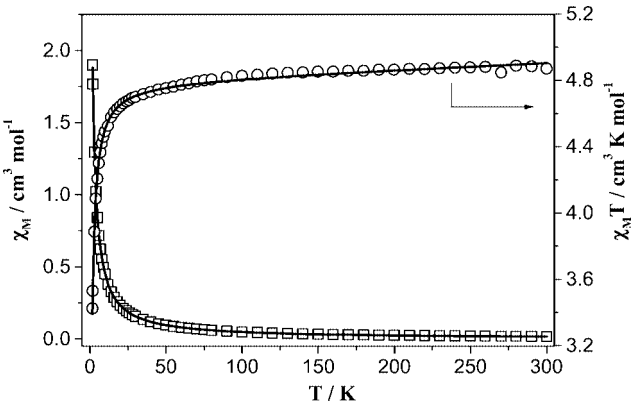


Figure 6. The $\chi_M T$ and $\chi_M$ vs. $T$ plots for **1**.

Dominant antiferromagnetic interactions are also observed in compounds **2** and **3** (Figures 7 and 8, respectively). As is well known, both $Fe^{II}$ and $Co^{II}$ ions in octahedral environments show significant single-ion anisotropies or spin-orbital couplings. When the symmetry of the molecule is lowered, the orbital contribution can be partially removed. In the present case each metal atom has a distorted trigonal-bipyramidal geometry, therefore the orbital contributions of both $Fe^{II}$ and $Co^{II}$ would be reduced. The susceptibility data were initially fitted by the Fisher formula [Equation (1)], with $S = 2$ for **2** and $S = 3/2$ for **3**, which leads to the parameters $g = 2.07$, $J = -0.33$ cm$^{-1}$, and $N_\alpha = 2.0 \times 10^{-4}$ cm$^3$ mol$^{-1}$ for **2** and $g = 2.15$, $J = -0.35$ cm$^{-1}$, and $N_\alpha = 1.7 \times 10^{-3}$ cm$^3$ mol$^{-1}$ for **3**. The $J$ value of compound **2** is comparable to that for $[NH_3(CH_2)_2NH_3][Fe\{HO_3PC(CH_3)(OH)(PO_3H)\}_2]\cdot 2H_2O$, in which the $Fe^{II}$ ions are doubly bridged by O–P–O units ($J = -0.46$ cm$^{-1}$) and the same equation was employed for the data fitting.[19] The Fisher formula, however, is a simplified model that assumes Heisenberg exchange couplings between all spins and does not take into account the single-ion anisotropy or spin-orbit coupling of either $Fe^{II}$ or $Co^{II}$ ions. A theoretical analysis considering both zero-field splitting (ZFS) and a small antiferromagnetic interaction would be a more logical approach. In order to fit the $\chi_M T$ vs. $T$ plots of compounds **2** and **3**, we calculated the magnetic susceptibility of six-membered closed rings. Due to the high-spin value we can suppose that the magnetic behavior of these closed rings is very similar to that of an infinite chain.[20] The Hamiltonian can therefore be used in its simplified axial form with an axial ZFS parameter ($D$), the antiferromagnetic exchange interaction ($J$), an axial $g$ vector, and a temperature-independent paramagnetism (TIP). The analysis of the data was performed with the full-matrix diagonalization program MAGPACK.[21] After a least-squares fitting the following parameters were found: $J = -0.1$ cm$^{-1}$, $D = 0.51$ cm$^{-1}$, $g = 2.09$, and TIP $= 3.3 \times 10^{-4}$ for the $Fe^{II}$ complex **2** and $J = -0.15$ cm$^{-1}$, $D = 7.6$ cm$^{-1}$, $g_z = 2.33$, $g_{xy} = 2.08$, and TIP $= 1.1 \times 10^{-3}$ for the $Co^{II}$ complex **3**, shown as solid lines in

 © 2006 Wiley-VCH Verlag GmbH & Co. KGaA, Weinheim 

Figures 7 and 8, respectively. The $J$ values obtained for compounds **2** and **3** are comparable to that of compound **1**.

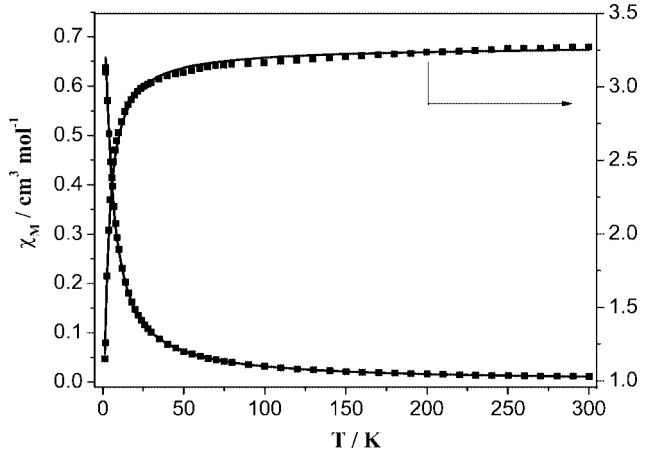


Figure 7. The $\chi_M T$ and $\chi_M$ vs. $T$ plots for **2**.

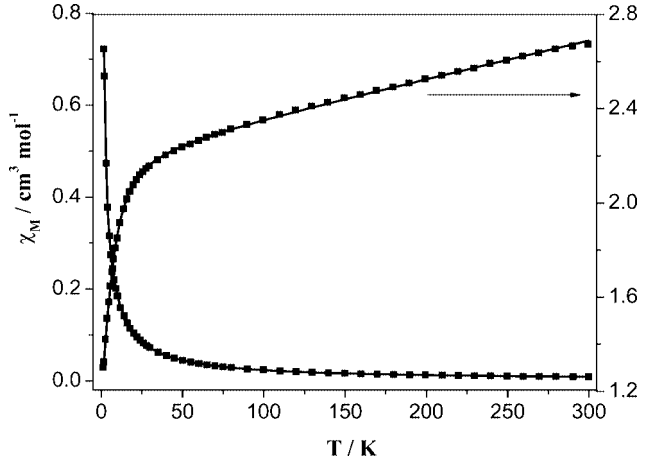


Figure 8. The $\chi_M T$ and $\chi_M$ vs. $T$ plots for **3**.

For compound **4** there is a maximum at around 3 K in the $\chi_M$ vs. $T$ plot (Figure 7), which is consistent with the antiferromagnetic nature of the magnetic interactions. Considering that compound **4** also has a chain structure with equally spaced $Cu^{II}$ ions ($S$ = 1/2), the susceptibility data can be fitted by the following equation based on the Heisenberg Hamiltonian $H = -J\sum S_{Ai} \cdot S_{Ai+1}$ [Equation (2)],[15]

$$\chi_M = \frac{Ng^2\beta^2}{kT}\frac{0.25 + 0.074975x + 0.075235x^2}{1 + 0.9931x + 0.172135x^2 + 0.757825x^3} + N_\alpha \quad (2)$$

where $x = |J|/kT$. A good fit, shown as the solid line in Figure 9, results in the parameters $g$ = 2.18, $J$ = –2.96 $cm^{-1}$, and $N_\alpha = -2.9 \times 10^{-5}$ $cm^3 mol^{-1}$. The $J$ value is smaller than those found for compounds $[\{Cu_3(di\text{-}2\text{-}pyridylamine)_3(\mu\text{-}HPO_4)(\mu\text{-}PO_4)(H_2O)\}(PF_6)(H_2O)_3]_n$ (–4.98 $cm^{-1}$)[22] and $[\{(bipy)Cu(H_2O)\}_2(\mu\text{-}P_2O_7)\cdot 7H_2O]$ ($J$ = –20 $cm^{-1}$),[23] where the $Cu^{II}$ ions are also linked by O–P–O units.

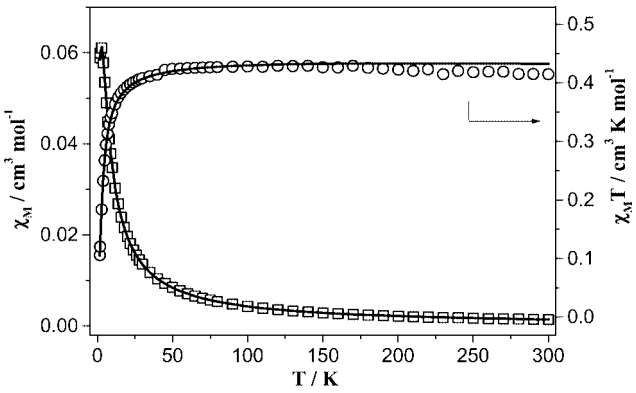


Figure 9. The $\chi_M T$ and $\chi_M$ vs. $T$ plots for **4**.

## Conclusion

Hydrothermal reactions of metal sulfates and (benzimidazol-2-ylmethyl)imino bis(methylenephosphonic acid) have resulted in five isostructural compounds with the formula $[M\{(C_7H_5N_2)CH_2N(CH_2PO_3H)_2\}]$ [M = Mn (**1**), Fe (**2**), Co (**3**), Cu (**4**), and Cd (**5**)]. Each compound shows a one-dimensional chain structure where $\{MO_3N_2\}$ trigonal bipyramids are connected by $\{CPO_3\}$ tetrahedra through corner-sharing. The benzimidazole rings are involved in both aromatic stacking and hydrogen bonds. Further work is in progress to explore new materials with other topologies based on the same phosphonate ligand.

## Experimental Section

**Materials and Methods:** *N*,*N*-Bis(phosphonomethyl)aminoacetic acid was synthesized according to the literature procedure.[14a] All other reagents were purchased as reagent-grade chemicals and used without further purification. Elemental analyses were performed with a Perkin–Elmer 240C elemental analyzer. The IR spectra were obtained as KBr disks on a VECTOR 22 spectrometer. Variable-temperature magnetic susceptibility data were obtained for microcrystalline samples using a Quantum Design MPMS-XL7 SQUID magnetometer.

**Synthesis of {[(Benzimidazol-2-ylmethyl)imino]bis(methylene)}bis(phosphonic Acid) $[(C_7H_5N_2)CH_2N(CH_2PO_3H)_2$, bibmpH$_4$]:** Bis(phosphonomethyl)imino acetic acid (5.26 g, 20 mmol) and 1,2-diaminobenzene (2.06 g, 20 mmol) were fully mixed by grinding. The mixture was transferred to an open, single-necked flask and then heated at 190 °C until no steam was produced. After cooling, 6 M hydrochloric acid (8 mL) was added to the flask. The resulting solution was refluxed at 120 °C for 2 h, and then concentrated to dryness. The blue solid was taken up in water (20 mL) and KOH was added until the solid had dissolved (pH about 5–6). After refluxing with decoloring charcoal for 30 min, the solution was filtered off. The filtrate was acidified with 6 M HCl until pH ≤ 1.0.The white precipitate was collected, washed with methanol, and dried in vacuo. Yield: 5.5 g (82%). IR (KBr): $\tilde{\nu}$ = 3153–2346 (br) $cm^{-1}$, 1625 (m), 1573 (w), 1524 (w), 1491 (w), 1460 (m), 1438 (w), 1418 (w), 1400 (m), 1383 (w), 1367 (w), 1344 (m), 1308 (m), 1285 (m), 1252 (s), 1219 (s), 1159 (s), 1134 (s), 1059 (s), 1019 (s), 992 (s), 958 (s), 926 (s), 899 (m), 887 (m), 851 (m), 828 (m), 752 (s), 727 (w), 620 (w), 572 (w), 544 (w), 496 (s), 468 (m), 456 (m), 434 (w),

 © 2006 Wiley-VCH Verlag GmbH & Co. KGaA, Weinheim 

411 (w). $C_{10}H_{15}N_3O_6P_2$: calcd. C 35.85, H 4.51, N 12.54; found C 35.72, H 4.82, N 12.55.

**Synthesis of [Mn{(C$_7$H$_5$N$_2$)CH$_2$N(CH$_2$PO$_3$H)$_2$}] (1):** A mixture of bibmpH$_4$ (0.15 mmol, 0.0495 g) and $MnSO_4 \cdot H_2O$ (0.15 mmol, 0.0253 g) in 8 mL of $H_2O$, adjusted to pH 2.5–3.5 with 1 M NaOH, was kept in a Teflon-lined autoclave at 140 °C for 24 h. After slow cooling to room temperature, gray-blue, block-shaped crystals were obtained as a monophasic material (according to the powder X-ray diffraction pattern). Yield: 23 mg (40%). $C_{10}H_{13}MnN_3O_6P_2$: calcd. C 30.92, H 3.35, N 10.82; found C 30.93, H 3.21, N 10.80. IR (KBr): $\tilde{\nu}$ = 3104 (m, br) cm$^{-1}$, 2939 (w), 2874 (w), 1622 (w), 1598 (w), 1522 (w), 1467 (m), 1455 (m), 1432 (m), 1387 (w), 1377 (w), 1343 (w), 1324 (w), 1309 (w), 1282 (w), 1266 (w), 1236 (m), 1181 (s), 1133 (s), 1100 (m), 1073 (s), 1035 (m), 958 (w), 941 (w), 915 (s), 852 (w), 832 (w), 754 (m), 686 (w), 651 (w), 576 (s), 505 (w), 499 (w), 472 (w), 448 (w), 408 (w).

**Synthesis of [Fe{(C$_7$H$_5$N$_2$)CH$_2$N(CH$_2$PO$_3$H)$_2$}] (2):** A mixture of bibmpH$_4$ (0.10 mmol, 0.0330 g) and $FeSO_4 \cdot 7H_2O$ (0.20 mmol, 0.0556 g) in 8 mL of $H_2O$, adjusted to pH 7.03 by adding 0.2 mmol of $Me_4NOH$, was kept in a Teflon-lined autoclave at 140 °C for 24 h. After slow cooling to room temperature, gray-green, block-shaped crystals were obtained together with a brown powder. The crystals were selected manually and were used for single-crystal structural determination and physical measurements. Yield: 16 mg (41% based on bibmpH$_4$). $C_{10}H_{13}FeN_3O_6P_2$: calcd. C 30.85, H 3.34, N 10.80; found C 30.35, H 3.56, N 10.46. IR (KBr): $\tilde{\nu}$ = 3104–2886 (m, br) cm$^{-1}$, 1623 (w), 1598 (w), 1524 (w), 1467 (m), 1456 (m), 1434 (m), 1420 (m), 1387 (w), 1377 (w), 1342 (m), 1323 (w), 1309 (w), 1281 (w), 1264 (w), 1236 (m), 1185 (s), 1140 (s), 1091 (m), 1065 (s), 1036 (s), 1021 (s), 981 (m), 968 (m), 955 (m), 941 (m), 918 (s), 898 (m), 833 (m), 778 (m), 756 (m), 704 (w), 653 (w), 577 (s), 560 (m), 509 (w), 496 (w), 470 (w), 447 (w), 420 (w).

**Synthesis of [Co{(C$_7$H$_5$N$_2$)CH$_2$N(CH$_2$PO$_3$H)$_2$}] (3):** A mixture of bibmpH$_4$ (0.15 mmol, 0.0495 g) and $CoSO_4 \cdot 7H_2O$ (0.15 mmol, 0.0422 g) in 8 mL of $H_2O$, adjusted to pH 3.0–4.0 with 1 M NaOH, was kept in a Teflon-lined autoclave at 140 °C for 24 h. After slow cooling to room temperature, magenta, block-shaped crystals were obtained as a monophasic material (according to the powder X-ray diffraction pattern). Yield: 46 mg (78%). Anal. found (calcd.) for $C_{10}H_{13}N_3O_6P_2Co$: calcd. C 30.60, H 3.32, N 10.71; found C 30.66, H 3.30, N 10.53. IR (KBr): $\tilde{\nu}$ = 3100–2887 (m, br) cm$^{-1}$, 1625 (w), 1598 (w), 1529 (w), 1469 (m), 1457 (m), 1433 (m), 1420 (w), 1388 (w), 1342 (w), 1323 (w), 1311 (w), 1282 (w), 1184 (s), 1132 (s), 1093 (m), 1067 (s), 1040 (m), 1021 (w), 982 (w), 969 (w), 918 (s), 834 (w), 781 (w), 756 (m), 714 (w), 653 (w), 578 (s), 513 (w), 499 (w), 472 (w), 448 (w), 423 (w), 408 (w).

**Synthesis of [Cu{(C$_7$H$_5$N$_2$)CH$_2$N(CH$_2$PO$_3$H)$_2$}] (4):** A mixture of bibmpH$_4$ (0.10 mmol, 0.0330 g) and $CuSO_4$ (0.13 mmol, 0.0208 g) in 8 mL of $H_2O$, adjusted to pH 4.90 with 1 M NaOH, was kept in a Teflon-lined autoclave at 140 °C for 24 h. After slow cooling to room temperature, green, block-shaped crystals were obtained together with a brown powder. The crystals were selected manually and were used for single-crystal structural determination and physical measurements. Yield: 22 mg (55% based on bibmpH$_4$). $C_{10}H_{13}CuN_3O_6P_2$: calcd. C 30.25, H 3.28, N 10.59; found C 30.34, H 3.43, N 10.62. IR (KBr): $\tilde{\nu}$ = 3121–2900 (m, br) cm$^{-1}$, 1622 (w), 1597 (w), 1529 (w), 1494 (w), 1473 (m), 1456 (m), 1434 (m), 1419 (m), 1378 (w), 1341 (w), 1320 (w), 1281 (w), 1256 (m), 1238 (s), 1193 (s), 1128 (s), 1095 (m), 1059 (m), 1035 (m), 988 (w), 961 (w), 944 (w), 918 (s), 834 (w), 784 (w), 767 (m), 757 (m), 721 (w), 653 (w), 584 (s), 560 (m), 512 (w), 499 (w), 474 (w), 447 (w), 414 (w).

**Synthesis of [Cd{(C$_7$H$_5$N$_2$)CH$_2$N(CH$_2$PO$_3$H)$_2$}] (5):** A mixture of bibmpH$_4$ (0.15 mmol, 0.0495 g) and $CdSO_4 \cdot 2.7H_2O$ (0.15 mmol, 0.0380 g) in 8 mL of $H_2O$, adjusted to pH 3.0–4.0 with 1 M NaOH, was kept in a Teflon-lined autoclave at 140 °C for 24 h. After slow cooling to room temperature, gray-blue block-shaped crystals were obtained as a monophasic material (according to the powder X-ray diffraction pattern). Yield: 37 mg (55%). Anal. found (calcd.) for $C_{10}H_{13}CdN_3O_6P_2$: calcd. C 26.93, H 2.92, N 9.43; found C 26.82, H 2.85, N 9.28. IR (KBr): $\tilde{\nu}$ = 3102 (m) cm$^{-1}$, 2939 (w), 2868 (w), 1619 (w), 1598 (w), 1521 (w), 1490 (w), 1469 (m), 1456 (m), 1432 (m), 1386 (w), 1377 (w), 1344 (w), 1325 (w), 1311 (w), 1286 (w), 1266 (w), 1238 (m), 1206 (m), 1176 (s), 1129 (s), 1097 (m), 1072 (s), 1038 (m), 979 (w), 967 (w), 955 (w), 942 (w), 913 (s), 853 (w), 830 (w), 765 (w), 754 (m), 684 (w), 649 (w), 576 (s), 502 (w), 487 (w), 460 (w), 442 (w), 410 (w).

**X-ray Crystallographic Studies:** Single crystals of dimensions $0.1 \times 0.04 \times 0.04$ mm$^3$ for **1**, $0.1 \times 0.05 \times 0.05$ mm$^3$ for **2**, $0.15 \times 0.15 \times 0.15$ mm$^3$ for **3**, $0.04 \times 0.02 \times 0.02$ mm$^3$ for **4**, and $0.1 \times 0.05 \times 0.05$ mm$^3$ for **5** were used for structural determinations on a Bruker SMART APEX CCD diffractometer using graphite-monochromatized Mo-$K_\alpha$ radiation ($\lambda$ = 0.71073 Å) at room temperature. Further details can be found in Table 2. A hemisphere of

Table 2. Crystallographic data and refinement parameters for **1**–**5**.

| Compound | **1** | **2** | **3** | **4** | **5** |
|---|---|---|---|---|---|
| Empirical formula | $C_{10}H_{13}MnN_3O_6P_2$ | $C_{10}H_{13}FeN_3O_6P_2$ | $C_{10}H_{13}CoN_3O_6P_2$ | $C_{10}H_{13}CuN_3O_6P_2$ | $C_{10}H_{13}CdN_3O_6P_2$ |
| *Fw* | 388.11 | 389.02 | 392.10 | 396.71 | 445.57 |
| Crystal system | orthorhombic | orthorhombic | orthorhombic | orthorhombic | orthorhombic |
| Space group | *Pbca* | *Pbca* | *Pbca* | *Pbca* | *Pbca* |
| *a* [Å] | 15.331(2) | 15.320(3) | 15.207(2) | 15.101(3) | 15.4679(19) |
| *b* [Å] | 10.7150(16) | 10.477(2) | 10.4626(16) | 10.3517(17) | 10.8923(13) |
| *c* [Å] | 16.715(2) | 16.764(3) | 16.794(3) | 16.997(3) | 16.6175(19) |
| *V* [Å$^3$] | 2745.8(6) | 2690.7(9) | 2672.0(7) | 2656.9(7) | 2799.7(6) |
| *Z* | 8 | 8 | 8 | 8 | 8 |
| $\rho_{calcd.}$ [g cm$^{-3}$] | 1.878 | 1.921 | 1.949 | 1.984 | 2.114 |
| *F*(000) | 1576 | 1584 | 1592 | 1608 | 1760 |
| $R_{int}$ | 0.0835 | 0.0585 | 0.073 | 0.0517 | 0.056 |
| Goodness of fit on $F^2$ | 1.042 | 1.042 | 1.090 | 1.136 | 1.141 |
| $R_1$, $wR_2$ [$I > 2\sigma(I)$] | 0.0641, 0.1169 | 0.0484, 0.1105 | 0.0564, 0.0998 | 0.0426, 0.0901 | 0.0429, 0.0599 |
| $R_1$, $wR_2$[a] (all data) | 0.1107, 0.1281 | 0.0715, 0.1205 | 0.0876, 0.1110 | 0.0557, 0.0926 | 0.0707, 0.0636 |
| $(\Delta\rho)_{max}$, $(\Delta\rho)_{min}$ [e Å$^{-3}$] | 0.407, –0.438 | 0.979, –1.231 | 0.550, –0.458 | 0.397, –0.433 | 0.870, –0.952 |

[a] $R_1 = \sum ||F_o| - |F_c||/\sum|F_o|$; $wR_2 = [\sum w(F_o^2 - F_c^2)^2/\sum w(F_o^2)^2]^{1/2}$.

 © 2006 Wiley-VCH Verlag GmbH & Co. KGaA, Weinheim 

data were collected in the $\theta$ range 2.62–26.00° for **1**, 2.43–26.00° for **2**, 2.43–25.99° for **3**, 2.40–25.99° for **4**, and 2.45–26.00° for **5** using a narrow-frame method with scan widths of 0.30° in $\omega$ and an exposure time of 5 s per frame. Numbers of observed and unique [$I > 2\sigma(I)$] reflections are 13496 and 2700 ($R_{int}$ = 0.0835) for **1**, 13174 and 2634 ($R_{int}$ = 0.0585) for **2**, 13176 and 2618 ($R_{int}$ = 0.073) for **3**, 12675 and 2605 ($R_{int}$ = 0.0517) for **4**, and 14077 and 2754 ($R_{int}$ = 0.056) for **5**, respectively. The data were integrated using the Siemens SAINT program,[24] with the intensities corrected for Lorentz factors, polarization, air absorption, and absorption due to variation in the path length through the detector faceplate. Multi-scan absorption corrections were applied. The structures were solved by direct methods and refined on $F^2$ by full-matrix least-squares using SHELXTL.[25] All the non-hydrogen atoms were located from the Fourier maps, and were refined anisotropically. All H atoms were refined isotropically, with the isotropic vibration parameters related to the non-H atom to which they are bonded.

CCDC-283019 to -283023 (for **1**–**5**, respectively) contain the supplementary crystallographic data for this paper. These data can be obtained free of charge from The Cambridge Crystallographic Data Center via www.ccdc.cam.ac.uk/data_request/cif.

## Acknowledgments

We thank the NNSF of China (No. 20325103), the Ministry of Education of China and the NSF of Jiangsu province (No. BK2002078) for financial supports, Mr. Yong-Jiang Liu for crystal data collections, Dr. You Song and Mr. Tian-Wei Wang for magnetic measurements.

[1] a) C. Maillet, P. Janvier, M. Pipelier, T. Praveen, Y. Andres, B. Bujoli, *Chem. Mater.* **2001**, *13*, 2879; b) A. Hu, H. L. Ngo, W. Lin, *Angew. Chem. Int. Ed.* **2003**, *42*, 6000; c) P. Ayyappan, O. R. Evans, Y. Cui, K. A. Wheeler, W. Lin, *Inorg. Chem.* **2002**, *41*, 4978; d) E. M. Bauer, C. Bellitto, M. Colapietro, G. Portalone, G. Righini, *Inorg. Chem.* **2003**, *42*, 6345; e) D. Kong, Y. Li, J. H. Ross Jr, A. Clearfield, *Chem. Commun.* **2003**, 1720; f) P. Yin, S. Gao, Z.-M. Wang, C.-H. Yan, L.-M. Zheng, X.-Q. Xin, *Inorg. Chem.* **2005**, *44*, 2761; g) S. Maheswaran, G. Chastanet, S. J. Teat, T. Mallah, R. Sessoli, W. Wernsdorfer, R. E. P. Winpenny, *Angew. Chem. Int. Ed.* **2005**, *44*, 5044; h) S. Langley, M. Helliwell, J. Raftery, E. L. Tolis, R. E. P. Winpenny, *Chem. Commun.* **2004**, 142; i) G. Nonglaton, I. O. Benitez, I. Guisle, M. Pipelier, J. Leger, D. Dubreuil, C. Tellier, D. R. Talham, B. Bujoli, *J. Am. Chem. Soc.* **2004**, *126*, 1497.

[2] a) B. Moulton, M. J. Zaworotko, *Chem. Rev.* **2001**, *101*, 1629; b) M. Eddaoudi, D. B. Moler, H. Li, B. Chen, T. M. Reineke, M. O'Keeffe, O. M. Yaghi, *Acc. Chem. Res.* **2001**, *34*, 319.

[3] a) S. Drumel, P. Janvier, D. Deniaud, B. Bujoli, *J. Chem. Soc., Chem. Commun.* **1995**, 1051; b) F. Fredoueil, D. Massiot, P. Janvier, F. Gingl, M. Bujoli-Doeuff, M. Evain, A. Clearfield, B. Bujoli, *Inorg. Chem.* **1999**, *38*, 1831; c) S. Drumel, P. Janvier, M. Bujoli-Doeuff, B. Bujoli, *Inorg. Chem.* **1996**, *35*, 5786; d) N. Zakowsky, P. S. Wheatley, I. Bull, M. P. Attfield, R. E. Morris, *J. Chem. Soc., Dalton Trans.* **2001**, 2899.

[4] For example: a) J. Zhu, X. Bu, P. Feng, G. D. Stucky, *J. Am. Chem. Soc.* **2000**, *122*, 11563; b) M. Riou-Cavellec, M. Sanselme, N. Guillou, G. Ferey, *Inorg. Chem.* **2001**, *40*, 723; c) G. B. Hix, D. S. Wragg, P. A. Wright, R. E. Morris, *J. Chem. Soc., Dalton Trans.* **1998**, 3359; d) F. Fredoueil, D. Massiot, D. Poojary, M. Bujoli-Doeuff, A. Clearfield, B. Bujoli, *Chem. Commun.* **1998**, 175; e) E. Burkholder, V. Golub, C. J. O'Connor, J. Zubieta, *Inorg. Chem.* **2003**, *42*, 6729; f) B. A. Adair, S. Neeraj, A. K. Cheetham, *Chem. Mater.* **2003**, *15*, 1518; g) C. Serre, N. Stock, T. Bein, G. Ferey, *Inorg. Chem.* **2004**, *43*, 3159; h) B.-P. Yang, J.-G. Mao, Y.-Q. Sun, H.-H. Zhao, A. Clearfield, *Eur. J. Inorg. Chem.* **2003**, 4211; i) X. Shi, G.-S. Zhu, S.-L. Qiu, K.-L. Huang, J.-H. Yu, R.-R. Xu, *Angew. Chem. Int. Ed.* **2004**, *43*, 6482.

[5] a) P. Ayyappan, O. R. Evans, B. M. Foxman, K. A. Wheeler, T. H. Warren, W. Lin, *Inorg. Chem.* **2001**, *40*, 5954; b) X.-Y. Yi, L.-M. Zheng, W. Xu, S. Feng, *Dalton Trans.* **2003**, 953; c) J. Ochocki, K. Kostka, B. Zurowska, J. Mrozinski, E. Galdecka, Z. Galdecki, J. Reedijk, *J. Chem. Soc., Dalton Trans.* **1992**, 2955; d) L. A. Vermeulen, R. Z. Fateen, P. D. Robinson, *Inorg. Chem.* **2002**, *41*, 2310; e) J. L. Song, J.-G. Mao, Y. Q. Sun, A. Clearfield, *Eur. J. Inorg. Chem.* **2003**, 4218; f) D.-K. Cao, Y.-J. Liu, Y. Song, L.-M. Zheng, *New J. Chem.* **2005**, *29*, 721; g) D.-K. Cao, Y.-Z. Li, L.-M. Zheng, *Inorg. Chem.* **2005**, *44*, 2984; h) D.-K. Cao, Y.-Z. Li, Y. Song, L.-M. Zheng, *Inorg. Chem.* **2005**, *44*, 3599.

[6] a) A. Clearfield, D. Poojary, B. Zhang, B. Zhao, A. Derecskei-Kovacs, *Chem. Mater.* **2000**, *12*, 2745; b) H. L. Ngo, W. Lin, *J. Am. Chem. Soc.* **2002**, *124*, 14298; c) D. Kong, D. G. Medvedev, A. Clearfield, *Inorg. Chem.* **2004**, *43*, 7308; d) G. Giambastiani, W. Oberhauser, C. Bianchini, F. Laschi, L. Sorace, P. Brueggeller, R. Gutmann, A. Orlandini, F. Vizza, *Eur. J. Inorg. Chem.* **2005**, 2027.

[7] O. Oms, J. Le Bideau, F. Leroux, A. van der Lee, D. Leclercq, A. Vioux, *J. Am. Chem. Soc.* **2004**, *126*, 12090.

[8] K. Yoshikawa, Heterocyclic Iminobismethylenebisphosphonic Acid Derivatives. *U. S. Patent* 5, **1995**, *441*, 945.

[9] K. Nakamoto, *Infrared and Raman Spectra of Inorganic and Coordination Compounds*, 3rd ed., John Wiley & Sons, **1978**.

[10] X.-L. Liu, R. Zhao, X.-H. Liu, J.-J. Yue, Y.-X. Yin, Y. Sun, X. Zhang, *Chinese J. Chem.* **2003**, *21*, 1047.

[11] N. Stock, T. Bein, *J. Solid State Chem.* **2002**, *167*, 330.

[12] C. Janiak, *J. Chem. Soc., Dalton Trans.* **2000**, 3885.

[13] R. D. Shannon, *Acta Crystallogr. Sect. A* **1976**, *32*, 751.

[14] a) J.-G. Mao, Z. Wang, A. Clearfield, *New J. Chem.* **2002**, *26*, 1010; b) J.-L. Song, J.-G. Mao, Y.-Q. Sun, H.-Y. Zeng, R. K. Kremer, A. Clearfield, *J. Solid State Chem.* **2004**, *177*, 633.

[15] O. Kahn, *Molecular Magnetism*, VCH Publishers, New York, **1993**.

[16] X.-Y. Wang, B.-L. Li, X. Zhu, S. Gao, *Eur. J. Inorg. Chem.* **2005**, 3277.

[17] A. Grirrane, A. Pastor, E. Alvarez, C. Mealli, A. Ienco, P. Rosa, F. Montilla, A. Galindo, *Eur. J. Inorg. Chem.* **2004**, 707.

[18] A. Escuer, F. A. Mautner, N. Sanz, R. Vicente, *Inorg. Chim. Acta* **2002**, *340*, 163.

[19] H.-H. Song, L.-M. Zheng, G. Zhu, Z. Shi, S. Feng, S. Gao, Z. Hu, X.-Q. Xin, *J. Solid State Chem.* **2002**, *164*, 367–373.

[20] E. Coronado, M. Drillon, R. Georges, in *Reseach Frontiers in Magentochemistry* (Ed.: C. O'Connor), Word Scientific Publishing, Singapore, **1993**, pp. 27–66.

[21] a) J. J. Borrás-Almenar, J. M. Clemente-Juan, E. Coronado, B. S. Tsukerblat, *Inorg. Chem.* **1999**, *38*, 6081; b) J. J. Borrás-Almenar, J. M. Clemente-Juan, E. Coronado, B. S. Tsukerblat, *J. Comput. Chem.* **2001**, *22*, 985.

[22] S. Youngme, P. Phuengphai, C. Pakawatchai, G. A. van Albada, J. Reedijk, *Inorg. Chim. Acta* **2005**, *358*, 2125.

[23] P. E. Kruger, R. P. Doyle, M. Julve, F. Lloret, M. Nieuwenhuyzen, *Inorg. Chem.* **2001**, *40*, 1726.

[24] SAINT, Program for Data Extraction and Reduction, Siemens Analytical X-ray Instruments, Madison, WI, **1994**–1996.

[25] SHELXTL (version 5.0), Reference Manual, Siemens Industrial Automation, Analytical Instruments, Madison, WI, **1997**.

Received: September 7, 2005
Published Online: March 13, 2006

 © 2006 Wiley-VCH Verlag GmbH & Co. KGaA, Weinheim 

DOI: 10.1002/ejic.200500829

# Binding of an Oxo-Bridged Dinuclear Iron(III) Complex $\{[Fe(phen)(H_2O)_3]_2O\}(SO_4)_2$ to DNA and Its Recognition of Single- and Double-Stranded DNA As Determined by Electrochemical Studies

**Qing Xiang Wang,[a] Kui Jiao,*[a] Wei Sun,[a] Fang Fang Jian,[b] and Xuan Hu[a]**

**Keywords:** Oxo-bridged diiron(III) complex / Crystallography / DNA recognition / Voltammetry

An oxo-bridged dinuclear iron(III) complex, $\{[Fe(phen)(H_2O)_3]_2O\}(SO_4)_2$, was synthesized and the molecular structure was determined by X-ray crystallography. Cyclic voltammetry shows that the complex has a cathodic peak at +0.325 V and a pair of redox peaks at +1.011 V and +0.811 V, respectively, which can be explained by an EC–C–EC mechanism. The binding property of the complex to fish-sperm DNA was investigated by electronic absorption spectrophotometry and electrochemical methods. The change in the electrochemical behavior of the complex after treatment with DNA shows that the oxo-bridged diiron(III) complex interacts with DNA mainly through electrostatic binding, while the electrochemical and chemical (EC–C) process product interacts mainly by intercalation. This result is further supported by experiments examining the influence of ionic strength. The difference in the binding modes of $\{[Fe(phen)(H_2O)_3]_2O\}(SO_4)_2$ and its EC–C product, namely a mononuclear phen-ligated ferrous complex, to DNA implies that this strategy can be used to distinguish single-stranded (ss-) and double-stranded (ds-) DNA.
(© Wiley-VCH Verlag GmbH & Co. KGaA, 69451 Weinheim, Germany, 2006)

## Introduction

Studies on the interaction between DNA and small molecules are central to probing the accurate local structures of DNA,[1–5] and to understanding the natural DNA-mediated biological mechanisms.[6] The fields of applied pharmacology, novel drug design[7–8] and chemotherapy[9] also emphasize the interactions of small molecules with DNA. Among DNA-binding molecules, iron complexes with the ligands 1,10-phenanthroline (phen) or modified phen are particularly attractive because these metal complexes can effectively bind to DNA through different modes[10–13] and the iron ions and the ligands of these complexes can easily be controlled to facilitate the clear study of the DNA-binding mechanism.[14–15]

A number of studies have addressed the synthesis of a series of mononuclear iron-phen complexes and their interaction with DNA.[16–20] However, compared with the mononuclear iron complexes, the synthesis and interaction with DNA of dinuclear iron complexes have received much less attention.[21–24] Que Jr. et al.[22] have reported a dinuclear ferric complex, $Fe_2(HPTB)(OH)(NO_3)_4$ [HPTB = *N*,*N*,*N*′,*N*′′-tetrakis(2-benzimidazolylmethyl)-2-hydroxy-1,3-diaminopropane], and found that, in the presence of hydrogen peroxide or $O_2$ and a reductant, this diiron complex can promote the cleavage of plasmid DNA in a "hydrolytic fashion". This is similar to the DNA cleavage mediated by the Fe–bleomycin complex and its mimetic compounds.[23] Additionally, Xu et al.[24] have investigated the interaction of DNA with a diiron complex $Fe_2(DTPB)(\mu\text{-}O)(\mu\text{-}Ac)Cl(BF_4)_2$ [DTPB = 1,1,4,7,7-penta(2′-benzimidazol-2-ylmethyl)triazaheptane, Ac = acetate] by spectroscopic methods. In addition, the hydrolytic cleavage of the supercoiled and linear DNA by the diiron complex was supported by evidence from anaerobic reactions, free-radical quenching, high-performance liquid chromatography experiments, enzymatic manipulation, footprinting analysis, and so forth.

On the other hand, nonheme oxo-bridged dinuclear iron(III) complexes have been extensively studied because of their distinctive magnetic and spectroscopic properties.[25–26] Furthermore, the significant biological activity of these kinds of dinuclear complexes has also attracted considerable attention from researchers, as they can provide structural models for diiron sites in nonheme proteins, such as ribonucleotide reductase, which converts ribonucleotides into deoxyribonucleotides in the first step in the biosynthesis of DNA.[27–29] However, only a few crystal structures of dinuclear iron(III) complexes with phenanthroline as a terminal ligand have been reported to date.[30] Knowledge of the exact molecular structure, and electrochemical and DNA-binding properties of nonheme oxo-bridged dinuclear

[a] College of Chemistry and Molecular Engineering, Qingdao University of Science and Technology,
Qingdao, 266042 P. R. China
Fax: +86-532-84855916
E-mail: kjiao@qust.edu.cn
[b] The Laboratory of New Materials and Functional Compounds, Qingdao University of Science and Technology,
Qingdao, 266042 P. R. China.

 InterScience © 2006 Wiley-VCH Verlag GmbH & Co. KGaA, Weinheim 

iron(III) complexes will be helpful for us to understand the reaction mechanisms of these active models in cells and the body.

Herein we report the synthesis, crystal structure, and electrochemical property of a new oxo-bridged dinuclear iron(III) complex with the ligand phen, $\{[Fe(phen)(H_2O)_3]_2O\}(SO_4)_2$. Additionally, we paid particular attention to the binding properties of this dinuclear iron(III) complex to DNA by using absorption spectroscopic and voltammetric methods. The notable phenomenon is that the dinuclear iron complex, and its EC–C mononuclear product (EC and C mean electrochemical process and chemical dissociation process, respectively), bind to DNA through different modes under the same conditions. This suggests that, on the basis of its electrochemical behavior, the complex could be an effective recognition probe for dsDNA and ssDNA. We also hope that this investigation is of value for the understanding of the biological mechanism in nonheme protein–DNA interactions and of the structure–activity relationship of nonheme oxo-bridged dinuclear iron(III) complexes in biological processes.

## Results and Discussion

### Crystal Structure of the Title Oxo-Bridged Diiron(III) Compound

The crystal structure of the title compound consists of discrete molecules in which all the atoms lie on general positions. The molecular structure of the complex is illustrated in Figure 1. The cationic complex of $\{[Fe(phen)(H_2O)_3]_2O\}^{4+}$ has a $C_2$ symmetry axis through the bridging O(6) atom. The two sulfate anions are present in the lattice to balance the charge. The iron atoms are surrounded by two nitrogen and four oxygen atoms to form a distorted octahedral geometry. The two parts of the dinuclear iron(III) cation complex are bridged by the O(6) atom. Three water molecues coordinate to the $Fe^{III}$ ion, with Fe–O distances of 2.004(4) Å, 2.019(4) Å, and 2.153(4) Å for Fe(1)–O(5), Fe(1)–O(7), and Fe(1)–O(8), respectively. The Fe–O–Fe linkage is nonlinear, exhibiting an angle of 163.9(4)° for Fe(1)–O(6)–Fe(1A). The Fe–μ-O(6) distance [1.7877(12) Å] is in accordance with those previously reported for $(FeL)_2O$ (1.76–1.82 Å).[31] The combination of the nonlinear bridge and the strong Fe–μ-O bonding produces an intermetallic spacing of 3.5417 Å. The bond lengths of C–N and C–C in the phenanthroline all fall within the range of the literature values,[32] and the two aromatic ring systems in each phen are coplanar within the experimental error.

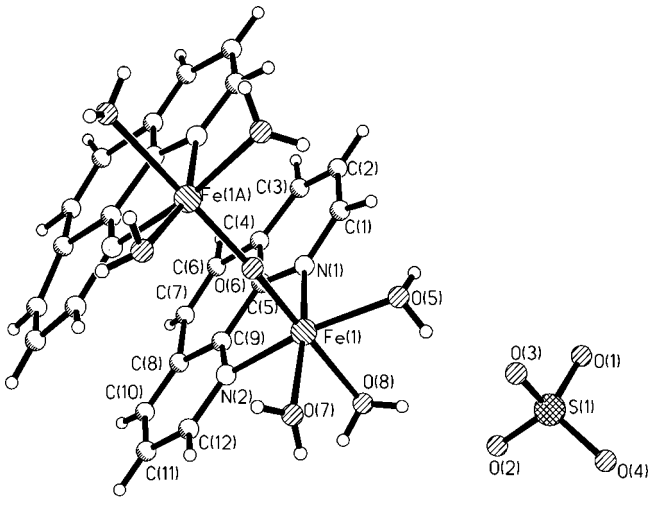


Figure 1. Perspective view of $\{[Fe(phen)(H_2O)_3]_2O\}(SO_4)_2$ showing the atom labeling scheme.

### Studies on the Electrochemical Behavior of $\{[Fe(phen)(H_2O)_3]_2O\}^{4+}$

The cyclic voltammetry (CV) of $\{[Fe(phen)(H_2O)_3]_2O\}^{4+}$ in a 0.01 M NaOAc/HOAc solution at a gold electrode was investigated, and the results are shown in Figure 2. It is found that the complex has a cathodic peak ($p_1$) at +0.325 V and a pair of redox peaks ($p_2$ and $p_2'$) at +1.011 V and +0.811 V, respectively. From Figure 2b, the formal potential ($E^{0\prime}$) of the redox peaks ($p_2$ and $p_2'$) was calculated to be +0.911 V, with the formula $E^{0\prime} = (E_{p_2}+E_{p_2'})/2$. This potential is consistent with that reported for the conversion of ferrous complexes to ferric complexes,[33] and suggests that this pair of redox peaks may be attributed to the electro-oxidation and electro-reduction of the mononuclear iron complex. The ratio of the peak height of $p_2'$ to that of $p_2$ is much smaller than that for the complex $Fe^{III/II}$-(*tris*-phen); this may result from the lack of phen coordinating to the iron atom.[34] The electron transfer number ($n$) of the irreversible reduction peak $p_1$ was calculated to be 2 according to the formula $|E_p–E_{p/2}| = 47.7/n\alpha$ (mV, 25 °C) when $\alpha$ is assumed to be 0.5,[35] ($E_p$ and $E_{p/2}$ are the peak potential and the half-peak potential, respectively, $\alpha$ the electron transfer coefficient). This indicates that the two trivalent iron atoms in the title complex have been reduced to a diferrous analog. The peak potential of $p_1$ (+0.325 V) is almost the same as the reduction potential reported for similar diiron(III) complexes.[36] According to these results, we speculate that the electrode reaction of the title diiron(III) complex may involve an EC–C–EC process, which is described in Scheme 1.

There are similar mechanisms in the literature. Walczak et al. have studied the electrochemical behavior of the oxo-bridged diiron-phen complex $[Fe_2^{III,III}O(phen)_4(H_2O)]^{4+}$ and reached the conclusion that the complex undergoes a 2e reduction to an oxo-bridged diferrous-phen complex $[Fe_2^{II,II}O(phen)_4(H_2O)_2]^{2+}$, which is unstable and quickly decomposes by a fast chemical reaction to form its mononuclear ferrous complex.[36] The electro-redox processes of the $Fe^{II/III}$ complex result in a pair of redox peaks. Chen[37] and other authors[38–39] have also studied the electrochemical behavior of oxo-bridged diiron complexes under different conditions and have obtained similar results. Namely, the electrochemical processes of these species appear as an irreversible reduction peak, corresponding to the re-

 © 2006 Wiley-VCH Verlag GmbH & Co. KGaA, Weinheim 

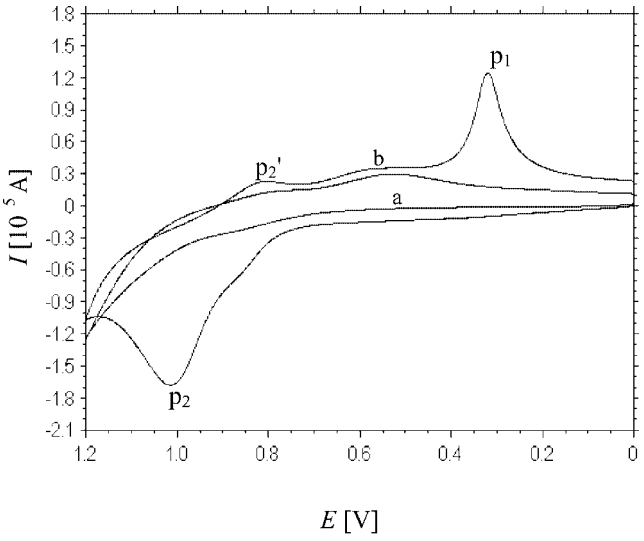


Figure 2. Cyclic voltammograms of 0.01 M NaOAc/HOAc solution, pH 6.8, without (a) and with $4.00\times10^{-4}$ M $\{[Fe(phen)(H_2O)_3]_2O\}^{4+}$ (b). Rest time: 2 s. Scan rate: 100 mV/s.

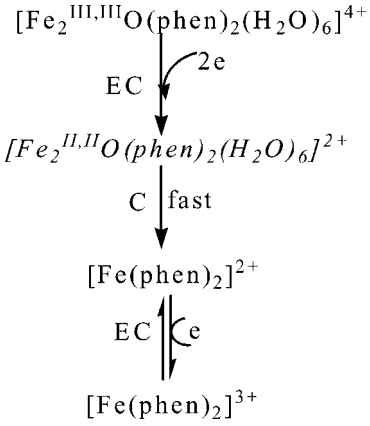


Scheme 1. Electrochemical mechanism of the complex $\{[Fe(phen)(H_2O)_3]_2O\}^{4+}$. The italic font of $[Fe_2^{II,II}O(phen)_2(H_2O)_6]^{2+}$ implies that this intermediate product is unstable.

duction of diiron(III) complex, and a pair of redox peaks with the formal potential ($E^{0\prime}$) at approximately +0.911 V, which is ascribed to the redox of the mononuclear iron(II)/(III) complex. Thus, the electrochemical behavior of the title complex reported here is very similar to those described in the conclusions in the literature.

The influence of the initial potential ($E_i$) on the cyclic voltammetric behavior of the title complex was studied to further prove the above theory involving the EC–C–EC mechanism of the diiron(III) complex. The results are shown in Figure 3. When the cyclic voltammogram was recorded in the potential range 0.400–1.200 V with an $E_i$ of 0.400 V, there were no longer any electro-redox peaks (Figure 3a), suggesting that no mononuclear iron complex was present in the solution. If $E_i$ was set to +1.000 V, and the potential was scanned in the negative direction towards 0 V and then back to +1.200 V, the reduction peak ($p_2'$) for the mononuclear ferric complex still does not appear; while at +0.325 V, there is an obvious reduction peak ($p_1$) that corresponds to the reduction of the title diiron(III) complex. There is a well-defined oxidation peak corresponding to the oxidation of the mononuclear divalent iron complex to the trivalent form (Figure 3b). If $E_i$ was set to 0 V, which is more negative than the reduction potential of the title complex, and the cyclic voltammogram ranging from 0 V to +1.200 V was recorded, all the peaks appear (Figure 3c). This experiment demonstrates that the prerequisite for the formation of the mononuclear ferrous complex is the electro-reduction of the title oxo-bridged diiron(III) complex, which is consistent with the proposed EC–C–EC mechanism.

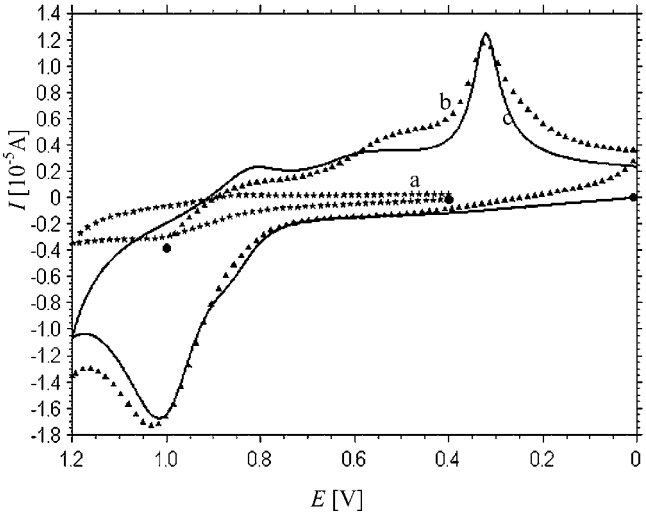


Figure 3. Dependence of the cyclic voltammograms of $4.00\times10^{-4}$ M $\{[Fe(phen)(H_2O)_3]_2O\}^{4+}$ in 0.01 MNaOAc/HOAc solution (pH 6.8) on the initial scan potential ($E_i$, represented by ●). (a) $E_i$ = 0.400 V, a cyclic scan in the potential range from 0.400 to 1.200 V; (b) $E_i$ = 1.000 V, the scan from 1.000 to 0 V, followed by a positive scan from 0 to +1.200 V; (c) $E_i$ = 0 V, the scan from 0 to +1.200 V, and then scanned reversibly to 0 V. Scan rate: 100 mV/s.

In the following electrochemical studies, only the cathodic peak $p_1$ and the anodic peak $p_2$ are considered, as they represent the different species involved in the electrochemical processes and are more sensitive than the cathodic peak $p_2'$.

## Studies on the Interaction of the Iron-Phen Complex with DNA

### *UVIVis Spectroscopy*

As shown in Figure 4a, the complex has a broad absorption band and a sharp peak in the spectral region 200–320 nm, and a weak absorption band in the range 380–520 nm, which is magnified in the inset of Figure 4. From comparison with the spectral data from the paper by Que Jr. et al.[40] and with those from previously studied oxo-diiron(III) complexes,[41] it is known that the lower energy band is assigned to a phenolate-to-$Fe^{III}$ charge-transfer transition, and the higher energy band has been attributed to both phenolate- and oxo-to-$Fe^{III}$ charge-transfer transitions. While, the 300–400 nm region is featureless in Figure 4, the broad and weak absorption peak around 500 nm

 © 2006 Wiley-VCH Verlag GmbH & Co. KGaA, Weinheim 

is probably related to a small amount of phen-ligated ferrous complex, as the dinuclear unit is somewhat oxidative under the present conditions. After the addition of dsDNA to the diiron(III) complex solution, it is clearly observed that the absorption peaks in the 200–300 nm region undergo a significant decrease in molecular absorption (the hypochromism effect) and no detectable shift in wavelength (Figure 4b–c).

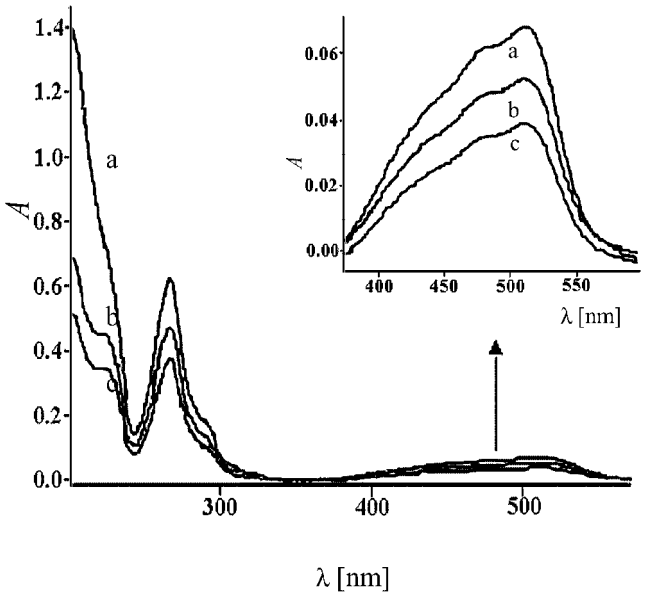


Figure 4. UV/Vis spectra of $4.00\times10^{-4}$ M $\{[Fe(phen)(H_2O)_3]_2O\}^{4+}$ in the absence (a) and the presence of $3.69\times10^{-6}$ M (b) and $7.37\times10^{-6}$ M (c) DNA.

Similarly, the broad absorption band around 500 nm, ascribed to the charge transfer transition of the ferrous complex, decreases gradually and is accompanied by a weak red shift (≈2 nm) from 507.7 nm to 509.6 nm, as shown in the inset in Figure 4. In the case of 1,10-phenanthroline metal complexes, some authors have pointed out that these species interact with dsDNA mainly by the outside-binding mode,[42] while other authors suggest that the binding mode is through intercalation, which involves a stacking interaction of the aromatic chromophores with the base-pairs of the dsDNA duplex.[43] In this paper, according to the rule that when small molecules interact with dsDNA differences in binding mode are reflected by spectral changes,[44] we can speculate that the original diiron(III) complex interacts with dsDNA mainly through external electrostatic binding, while a small amount of the ferrous complex probably binds through intercalation. This rationale is plausible because the size of the ferrous complex is much smaller than that of the diiron(III) complex. This difference in binding mode will be tested by the following electrochemical experiments.

### *Electrochemical Recognition of dsDNA and ssDNA*

Figure 5 shows the cyclic voltammetric behavior of $\{[Fe(phen)(H_2O)_3]_2O\}^{4+}$ after reacting with dsDNA and ssDNA. From Figure 5b, it is observed that the currents of both $p_1$ and $p_2$ decrease significantly in the presence of dsDNA, which proves that both the original oxo-bridged diiron complex and its EC–C product can interact with dsDNA. Nonetheless, it is interesting that the potentials of $p_1$ and $p_2$ shift in different directions after reacting with dsDNA. Bard et al. have pointed out that the shift direction of the electrochemical potential of a small molecule, after reacting with DNA, is related to its binding mode with DNA. A positive shift of the peak potential indicates an intercalative interaction between the small molecule and DNA, and a negative shift is characteristic of an electrostatic interaction.[45] Therefore, according to this rule, we can conclude that $\{[Fe(phen)(H_2O)_3]_2O\}^{4+}$ may interact with dsDNA through an electrostatic interaction, while its EC–C product interacts by intercalation. It is noticeable that when varying the pH values of the NaOAc/HOAc solution, the current difference of $p_2$ ($\Delta I_{p_2}$) and $p_1$ ($\Delta I_{p_1}$) reach maximum values at pH 6.8 and pH 5.5, respectively, after reacting with dsDNA (data not shown). Since pH 6.8 is closer to natural biological conditions, and hence can avoid the denaturing of dsDNA, which occurs at high or low acidity, a NaOAc/HOAc solution at pH 6.8 was chosen as the supporting electrolyte.

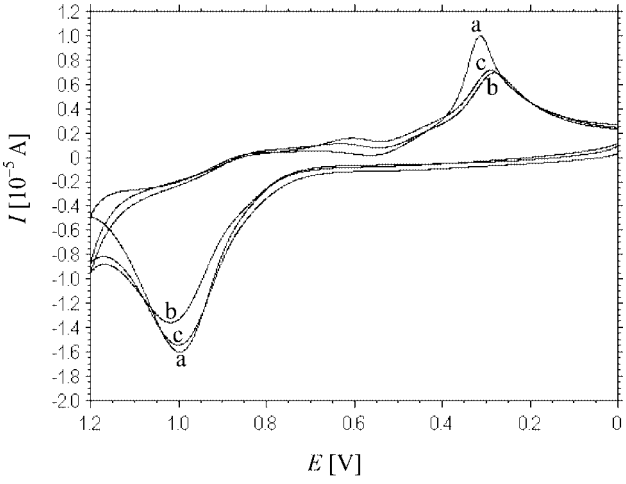


Figure 5. Cyclic voltammograms of $2.00\times10^{-4}$ M $\{[Fe(phen)(H_2O)_3]_2O\}^{4+}$ in 0.01 M NaOAc/HOAc solution at pH 6.8 (a), and after the addition of $2.68\times10^{-7}$ M dsDNA (b) and $2.68\times10^{-7}$ M ssDNA (c). Rest time: 2 s, scan rate: 100 mV/s.

The change in the cyclic voltammetric behavior of $\{[Fe(phen)(H_2O)_3]_2O\}^{4+}$ after reacting with ssDNA confirms the above conclusions. As shown in Figure 5c, both the peak current and the peak potential of $p_1$ change relative to those in Figure 5b, illustrating that the electrostatic binding between the diiron(III) complex and ssDNA still exists. However, the inconspicuous changes in both the peak current and the peak potential of $p_2$, relative to those in Figure 5a, indicate the disappearance or weakness of the intercalation of the mononuclear ferrous complex into ssDNA. This can be ascribed to the uncoiling of the double helix structure because of the denaturing of the native DNA. According to the above experiments, we can conclude that the oxo-bridged diiron complex and the mononuclear ferrous complex bind to DNA through different modes. In other words, the diiron(III) complex can recognize

 © 2006 Wiley-VCH Verlag GmbH & Co. KGaA, Weinheim 

dsDNA and ssDNA on the basis of the two steps of the electrochemical process on a gold electrode. To further confirm the above conclusions on the binding modes of $\{[Fe(phen)(H_2O)_3]_2O\}^{4+}$ and its mononuclear product to DNA, the influence of ionic strength on their interactions was investigated, and the results are reported in the following section.

Figure 6 shows the effect of the ionic strength ($\mu$) on the peak potential of $p_2$. The change in the ionic strength was controlled by the addition of different concentrations of KCl. In the absence of dsDNA, the shift in the anodic peak potential ($\Delta E_{p_{2,a}}$) induced by the addition of KCl is obtained by the relation $\Delta E_{p_{2,a}} = E_{p_{2,a}} - E_{p_{2,a,\mu=20}}$, where $E_{p_{2,a}}$ and $E_{p_{2,a,\mu=20}}$ represent the peak potentials of $p_2$ in the presence and absence of KCl in solution, respectively.

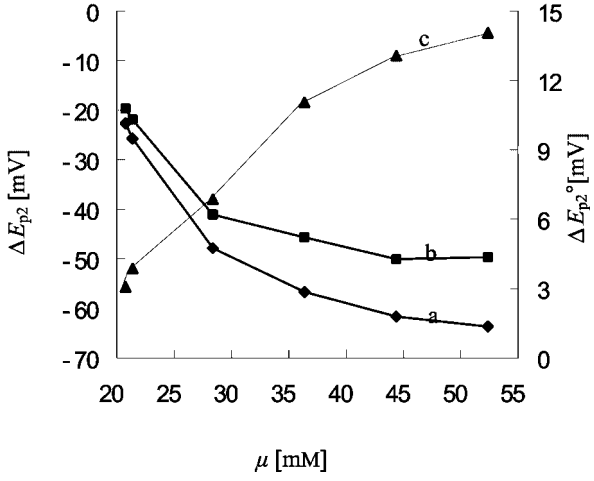


Figure 6. Effect of ionic strength ($\mu$) on the shift in the anodic peak potential ($\Delta E_{p_2}$) of the EC–C product of $4.00\times10^{-4}$ M $\{[Fe(phen)(H_2O)_3]_2O\}^{4+}$, in the absence (a) and the presence of $7.40\times10^{-6}$ M dsDNA (b). Curve (c) is the plot of $\Delta E_{p_2}°$ versus $\mu$, where $\Delta E_{p_2}° = \Delta E_{p_{2,b}} - \Delta E_{p_{2,a}}$.

The subscript "a" and "$\mu = 20$" in the formula indicate that DNA is absent from the solution and that the original ionic strength calculated for the 0.01 M NaOAc/HOAc electrolyte is 20 mM, respectively. Analogously, when DNA is present in solution, the shift in $E_{p_2}$ caused by the ionic strength is denoted as $\Delta E_{p_{2,b}}$, and its value is obtained by the formula $\Delta E_{p_{2,b}} = E_{p_{2,b}} - E_{p_{2,b,\mu=20}}$. Curve a and b in Figure 6 are the plots of $\Delta E_{p_{2,a}}$ versus $\mu$ and $\Delta E_{p_{2,b}}$ versus $\mu$, respectively. From the two curves, it is found that both $\Delta E_{p_{2,a}}$ and $\Delta E_{p_{2,b}}$ are negative on the time scale of CV measurements. Furthermore, the values of $\Delta E_{p_{2,a}}$ and $\Delta E_{p_{2,b}}$ decrease gradually with an increase in $\mu$, which suggests that, whether DNA exists in solution or not, the oxidation potential of the phen-ligated ferrous complex shifts to more negative values after the addition of KCl. Nonetheless, the values of $\Delta E_{p_2}°$ reveal the real effect of the ionic strength on the binding of $Fe(phen)_2^{2+}$ to dsDNA, and are positive on the time scale of the CV measurements and increase with an increase in $\mu$, as shown in Figure 6c. According to the literature,[46] the positive shift in $\Delta E_{p_2}°$ induced by the increase in the ionic strength demonstrates the intercalative binding mode of the mononuclear iron complex to dsDNA. This result is also consistent with the hypothesis drawn from Figure 5 with regard to the binding mode of the EC–C product to dsDNA.

However, the change in the reduction peak potential of $\{[Fe(phen)(H_2O)_3]_2O\}^{4+}$ ($E_{p_1}$) with an increase in the ionic strength is much more complicated. As shown in Figure 7a, the difference ($\Delta E_{p_{1,a}}$) between $E_{p_1}$ at $\mu > 20$ and that at $\mu = 20$ in the absence of dsDNA is negative and decreases with an increase in the ionic strength. This indicates that the reduction peak potential of $\{[Fe(phen)(H_2O)_3]_2O\}^{4+}$ also shifts negatively with an increase in the ionic strength in the absence of dsDNA. After binding to dsDNA, the plot of $\Delta E_{p_{1,b}}$ versus $\mu$ has a turning point at $\mu = 24$ mM with an increase of the ionic strength, as shown in Figure 7b. For $\mu < 24$ mM, $\Delta E_{p_{1,b}}$ decreases with an increase in $\mu$ and then increases for $\mu > 24$ mM. The plot of $\Delta E_{p_1}°$ ($\Delta E_{p_1}° = \Delta E_{p_{1,b}} - \Delta E_{p_{1,a}}$) versus $\mu$ shows the real effect of $\mu$ on the binding of $\{[Fe(phen)(H_2O)_3]_2O\}^{4+}$ to dsDNA and is presented in Figure 7c. The dashed line divides the plot into two regions corresponding to $\Delta E_{p_1}° < 0$ and $\Delta E_{p_1}° > 0$. This also demonstrates the change in the nature of the interaction between dsDNA and $\{[Fe(phen)(H_2O)_3]_2O\}^{4+}$ from electrostatic to an intercalative mode with an increase in the ionic strength. At $\Delta E_{p_1}° = 0$, the electrostatic interaction is equal to the intercalative interaction in strength, and the corresponding value for the ionic strength ($\mu = 29$ mM) is called the critical-ionic strength (CIS).[46]

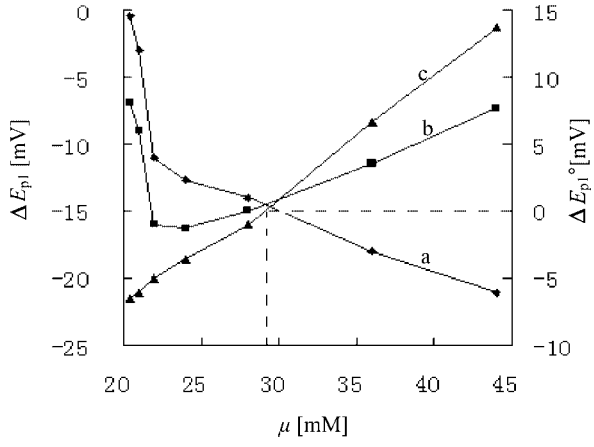


Figure 7. Effect of the ionic strength ($\mu$) on the shift in the reduction peak potential of $\{[Fe(phen)(H_2O)_3]_2O\}^{4+}$. The conditions are the same as those in Figure 6.

From electrostatic considerations, $\Delta E_{p_1}°$ should vary linearly with $\mu^{1/2}$ according to Debye–Hückel theory.[47] Figure 8 illustrates the dependence of $\Delta E_{p_1}°$ on $\mu^{1/2}$. It is observed that the plot is linear for $\mu$ up to 28 mM, with an intercept of –38 mV and a slope of 7 mV/mmol$^{1/2}$, which suggests that electrostatic interactions play a dominant role in this ionic strength range. For values of the ionic strength above 28 mM, $\Delta E_{p_1}°$ deviates from a straight line. These observations also prove the results mentioned above with regard to the change in binding mode of {[Fe(phen)-

 © 2006 Wiley-VCH Verlag GmbH & Co. KGaA, Weinheim 

$(H_2O)_3]_2O\}^{4+}$ to dsDNA, that is, from electrostatic binding to intercalative binding with an increase in the ionic strength. In addition, from the value of the intercept of –38 mV, a limiting ratio ($K_O'/K_R'$) from the binding constants for the oxidized ($K_O'$) and reduced ($K_R'$) forms ($\{[Fe(phen)(H_2O)_3]_2O\}^{4+}$ and $\{[Fe(phen)(H_2O)_3]_2O\}^{2+}$, respectively) can be estimated. A value of 19 is found for the ratio with the equations $\Delta E^{0\prime} = \Delta E_1^{0\prime} + B\mu^{1/2}$ (for $C_{KCl} << 1$ M)[46] and $\Delta E_1^{0\prime} = (-RT/nF)\ln(K_O'/K_R')$,[45–48] where $\Delta E_1^{0\prime}$ is the limiting difference in the formal potential at $\mu = 0$; $B$ is a constant which depends on the valences of the ions, the dielectric characteristics of the environment surrounding the ions , temperature, and the density of the solvent. This result suggests that the electrostatic interaction between the diiron(III) complex and DNA is significantly more dominant than the intercalative interaction.[45–46]

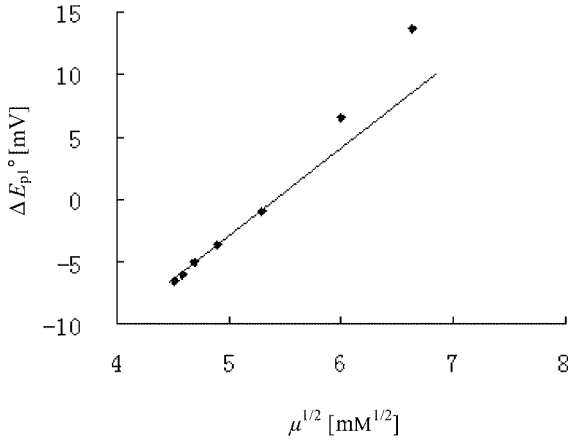


Figure 8. Dependence of $\Delta E_{p_1}$° on $\mu^{1/2}$. The conditions are the same as those in Figure 6.

The effect of the ionic strength on the difference in peak currents before and after the addition of dsDNA was also investigated. It was found that both the cathodic and anodic peak current difference ($\Delta I_{p_1}$ and $\Delta I_{p_2}$) decrease with an increase in the ionic strength, as shown in Figure 9a and Figure 9b, respectively. This suggests that the extent of the binding of both the diiron(III) complex and its EC–C product to dsDNA becomes weaker at high ionic strength.

This can be explained by the fact that the excess positively charged $K^+$ ion binds to negatively charged dsDNA phosphatediester backbone, which results in an inhibition in the binding of the cationic complex to dsDNA.[49]

The dependenc of the cyclic voltammetric behavior of the dinuclear iron(III) complex in the absence and presence of dsDNA on the scan rate ($v$) are shown in Figure 10(A) and Figure 10(B), respectively. It is found that both $I_{p_1}$ and $I_{p_2}$ vary linearly with the square root of the scan rate ($v^{1/2}$) both in the absence and presence of dsDNA, as shown in the insets of Figure 10(A) and Figure 10(B). This is as expected for a diffusion-controlled process.[50]

Furthermore, the slopes of both plots ($I_{p_1}$ versus $v^{1/2}$ and $I_{p_2}$ versus $v^{1/2}$) decrease after the addition of dsDNA, which indicates a reduction in the apparent diffusion coefficient of the complex in the presence of dsDNA.We can therefore

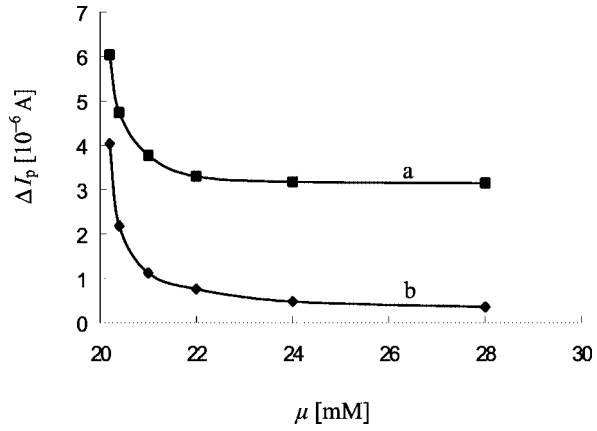


Figure 9. Influence of ionic strength ($\mu$) on $\Delta I_{p_1}$ (a) and $\Delta I_{p_2}$ (b). The conditions are the same as those in Figure 6.

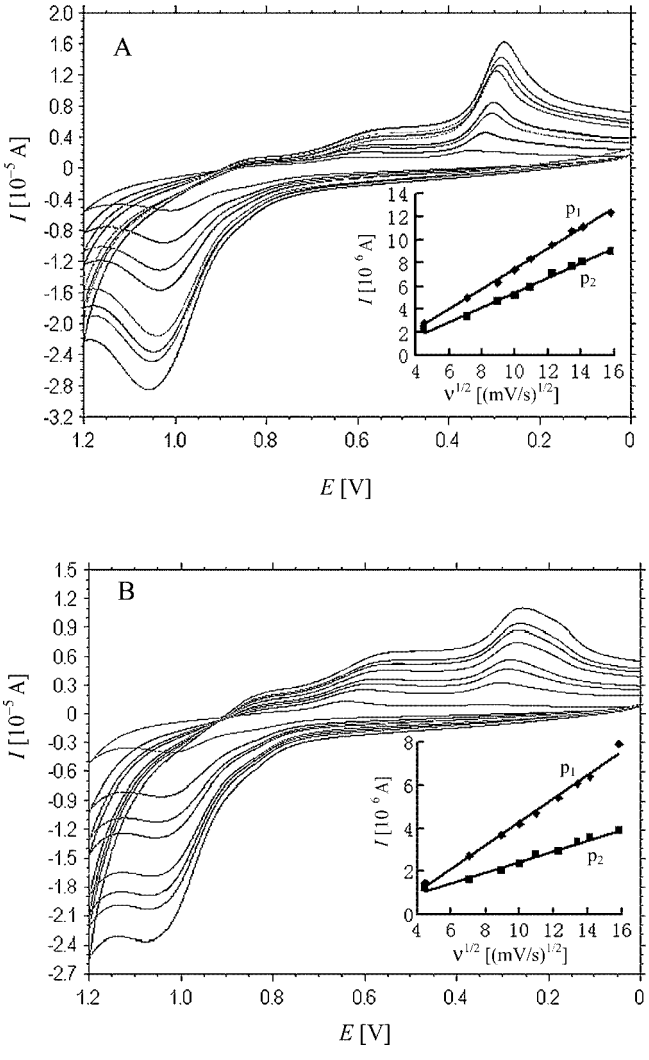


Figure 10. Dependenc of cyclic voltammetric behavior of $4.00\times10^{-4}$ M $\{[Fe(phen)(H_2O)_3]_2O\}^{4+}$ on the scan rate ($v$), in the absence (A) and the presence (B) of $7.37\times10^{-6}$ M dsDNA. Inset: plots of the peak current of $p_1$ and $p_2$ versus the square root of the scan rate ($v^{1/2}$).

 © 2006 Wiley-VCH Verlag GmbH & Co. KGaA, Weinheim 

interpret the change in current upon dsDNA addition in terms of the diffusion of an equilibrium mixture of free and dsDNA-bound complex to the electrode surface.[46]

The relationship of both $\Delta I_{p_1}$ and $\Delta I_{p_2}$ to the concentration of dsDNA ($C_{DNA}$) was also studied. From Figure 11a, it can be seen that the relationship between $\Delta I_{p_1}$ and $C_{DNA}$ is linear in two $C_{DNA}$ ranges corresponding to $9.36\times10^{-7}$–$9.36\times10^{-6}$ M and $9.36\times10^{-6}$–$7.49\times10^{-5}$ M, with correlation coefficients of 0.985 and 0.998, respectively. $\Delta I_{p_2}$ becomes constant when the $C_{DNA}$ is larger than $1.87\times10^{-5}$ M (Figure 11b), which demonstrates that the intercalation between the ferrous complex and dsDNA is saturated when the concentration of dsDNA is over $1.87\times10^{-5}$ M.

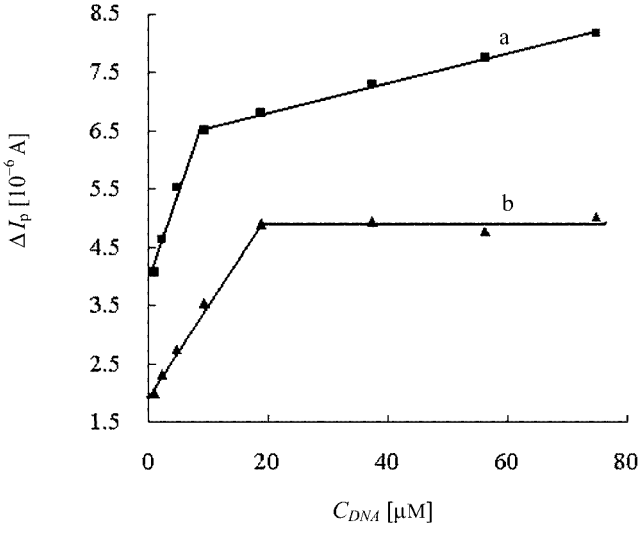


Figure 11. Plots of $\Delta I_{p_1}$ (a) and $\Delta I_{p_2}$ (b) versus the concentration of dsDNA ($C_{DNA}$).

## Conclusions

In summary, a new dinuclear iron(III) complex $\{[Fe(phen)(H_2O)_3]_2O\}(SO_4)_2$ was synthesized and characterized by X-ray crystallography. The electrochemical behavior of the diiron(III) complex indicated an EC–C–EC mechanism at the gold electrode, and the binding mode of the diiron(III) complex and its final mononuclear product to dsDNA was studied in detail. The results indicate that $\{[Fe(phen)(H_2O)_3]_2O\}(SO_4)_2$ interacts with dsDNA mainly through electrostatic binding, while the mononuclear EC–C product interacts mainly by intercalation. On the basis of its electrochemical behavior, the complex may be an effective recognition probe for dsDNA and ssDNA.

## Experimental Section

**Chemicals and Measurements:** Native double-stranded fish sperm DNA (dsDNA) from Beijing Baitai Biochemistry Technology Company (China) was used as received. The ratio of the absorbance at 260 and 280 nm ($A_{260}/A_{280}$) was checked to be 1.89, which indicates that the DNA was sufficiently free from protein.[51] The concentration of dsDNA (per nucleotide phosphate) was determined spectrophotometrically using the known molar-extinction coefficient value of 6600 $M^{-1}cm^{-1}$.[52] Denatured single-stranded DNA (ssDNA) was produced by heating a dsDNA solution in a water bath at 100 °C for 5–6 min, followed by rapid cooling in an ice bath.[46] The other chemical reagents used in the synthesis of the title complex were all of analytical reagent grade, purchased commercially, and used without further purification. The electrochemical and spectroscopic assays were all carried out in 0.01 M NaOAc/HOAc medium. Double-distilled water was used for preparing all the solutions. Elemental analyses were measured with a Perkin–Elmer 1400C analyzer. Voltammetry was performed with a CHI 832 electrochemical analysis system (CHI Instrument, China). A three-electrode system was used which consisted of a gold electrode ($\Phi$ = 3 mm) as the working electrode, a saturated calomel electrode (SCE) as the reference electrode, and a platinum wire as the auxiliary electrode. All the electrochemical measurements were carried out in a 10 mL electrolytic cell. UV/Vis absorption spectra were recorded on a Cary 50 probe spectrophotometer (Varian, Australia).

**Preparation and Crystallographic Study of $\{[Fe(phen)(H_2O)_3]_2O\}(SO_4)_2$:** 1,10-phenanthroline (0.35 g, 2.0 mmol) was dissolved in ethanol (15 mL), and a 10 mL solution of iron(III) chloride hexahydrate (0.28 g, 1.0 mmol) was then added while stirring. The mixture was adjusted to a pH of 1.0 with a dilute sulfuric acid solution and sealed in a 50 mL stainless-steel reactor with Teflon liner. The reactor was heated at 100 °C for 72 h, which resulted in the formation of red crystals. C, H and N contents were determined by elemental analysis. $C_{24}H_{28}Fe_2N_4O_{15}S_2$ (788.32): calcd. C 36.53, H 3.55, N 7.10; found C 36.16, H 3.30, N 6.82.

The X-ray diffraction data for the crystal-structure determination was collected using graphite-monochromated Mo-$K_\alpha$ radiation ($\lambda$ = 0.71073 Å) and $\omega$-scans with $\theta$ limits $2.04° < \theta < 27.52°$. An empirical absorption correction was carried out with the SADABS program.[53] The structure of $\{[Fe(phen)(H_2O)_3]_2O\}(SO_4)_2$ was

Table 1. Crystal data and structure refinement for $\{[Fe(phen)(H_2O)_3]_2O\}(SO_4)_2$.

| | |
|---|---|
| Empirical formula | $C_{24}H_{28}Fe_2N_4O_{15}S_2$ |
| Formula weight | 788.32 |
| Temperature [K] | 293(2) |
| Wavelength [Å] | 0.71073 |
| Crystal system, space group | Orthorhombic, $P2_12_12$ |
| Unit cell dimensions | |
| $a$ [Å] | 17.650(4) |
| $b$ [Å] | 8.5133(17) |
| $c$ [Å] | 9.971(2) |
| Volume [Å$^3$] | 1498.2(5) |
| $Z$, Calculated density [Mg/m$^3$] | 4, 1.748 |
| Absorption coefficient [mm$^{-1}$] | 1.189 |
| $F$(000) | 808 |
| Crystal size [mm] | $0.20\times0.20\times0.30$ |
| $\theta$ range for data collection [°] | 2.04–27.52 |
| Limiting indices | $-22 \le h \le 22$ |
| | $-11 \le k \le 11$ |
| | $0 \le l \le 12$ |
| Reflections collected/unique | 5376/3101[$R_{(int)}$ = 0.0618] |
| Completeness to $\theta$ = 27.53 [%] | 93.7 |
| Refinement method | Full-matrix least-squares on $F^2$ |
| Data/restraints/parameters | 3101/0/214 |
| Goodness-of-fit on $F^2$ | 1.010 |
| Final $R$ indices[ $I > 2\sigma(I)$] | $R_1$ = 0.0558, $wR_2$ = 0.1338 |
| $R$ indices (all data) | $R_1$ = 0.0762, $wR_2$ = 0.1417 |
| Extinction coefficient | 0.0081(18) |
| Largest diff. peak and hole [e Å$^{-3}$] | 0.551 and –0.448 |

 © 2006 Wiley-VCH Verlag GmbH & Co. KGaA, Weinheim 

solved by direct methods and refined by least-squares on $F_{obsd.}^2$ by using the SHELXTL software package.[54] All non-H atoms were anisotropically refined. The hydrogen atoms were located by difference synthesis and refined isotropically. The final conventional $R$ indices were $R(F) = 0.0601$ and $wR(F^2) = 0.1496$ for 2391 reflections $I > 2\sigma(I)$ with weighting scheme, $w = 1/[\sigma^2(F_o^2) + (0.0905P)^2]$, where $P = (F_o^2 + 2F_c^2)/3$. The molecular graphics were plotted using SHELXTL. Atomic scattering factors and anomalous dispersion corrections were taken from the *International Tables for X-ray Crystallography*.[55] A summary of the key crystallographic information is given in Table 1. CCDC-227065 contains the supplementary crystallographic data for this paper. These data can be obtained free of charge from The Cambridge Crystallographic Data Centre via www.ccdc.cam.ac.uk/data_request/cif.

## Acknowledgments

This work is supported by the National Natural Science Foundation of China (Grant No. 20375020, No. 20405008) and Natural Science Foundation of Qingdao City (Grant No. 04-2-JZP-8, No. 04-2-JZ-114).

[1] R. T. Espejo, J. Lebowitz, *Anal. Biochem.* **1976**, *72*, 95–103.
[2] M. Mariappan, B. G. Maiya, *Eur. J. Inorg. Chem.* **2005**, 2164–2173.
[3] J. K. Barton, A. L. Raphael, *Proc. Natl. Acad. Sci. USA* **1985**, *82*, 6460–6464.
[4] M. Kobayashi, T. Kusakawa, M. Saito, K. Sakiko, M. Oomura, S. Iwabuchi, Y. Morita, Q. Hasan, T. Eiichi, *Electrochem. Commun.* **2004**, *6*, 337–343.
[5] H. J. Karlsson, P. Lincoln, G. Westman, *Bioorg. Med. Chem.* **2003**, *11*, 1035–1040.
[6] J. P. Zheng, Z. Li, A. G. Wu, H. L. Zhou, H. Y. Bai, Y. H. Song, *Biochem. Biophys. Res. Commun.* **2002**, *299*, 910–915.
[7] G. V. Kalayda, S. Komeda, K. Ikeda, T. Sato, M. Chikuma, J. Reedijk, *Eur. J. Inorg. Chem.* **2003**, 4347–4355.
[8] J. Y. Douillard, D. Cunningham, A. D. Roth, J. R. Germa, R. D. James, P. Karasek, P. Jandik, J. Iveson, J. Carmichael, *Proc. Am. Soc., Clin. Oncol.* **1999**, *18*, 899–905.
[9] F. P. Intini, A. B. V. C. Francia, C. P. M. F. Sivo, G. Natile, D. G. P. D. Rinaldis, M. Coluccia, *J. Biol. Inorg. Chem.* **2004**, *9*, 768–780.
[10] P. G. Sammes, G. Yohioglu, *Chem. Soc. Rev.* **1994**, *23*, 327–334.
[11] E. J. C. Olson, D. Hu, A. Hormann, A. M. Jonkman, M. R. Arkin, E. D. A. Stemp, J. K. Barton, B. F. Barbara, *J. Am. Chem. Soc.* **1997**, *119*, 11458–11467.
[12] C. S. Chow, F. M. Bogdan, *Chem. Rev.* **1997**, *97*, 1489–1514.
[13] K. Gisselfalt, P. Lincoln, B. Norden, M. Jonsson, *J. Phys. Chem. B* **2000**, *104*, 3651–3659.
[14] S. Arounaguiri, B. G. Maiya, *Inorg. Chem.* **1996**, *35*, 4267–4267.
[15] M. N. Yoshioka, H. Inoue, *J. Inorg. Biochem.* **1999**, *77*, 239–247.
[16] T. Hard, B. Norden, *Biopolymers* **1986**, *25*, 1209–1228.
[17] T. Kobayashi, S. Nishino, H. Masud, H. Einag, Y. Nishid, *Inorg. Chem. Commun.* **2000**, *3*, 608–610.
[18] A. Silvestri, G. Barone, G. Ruisi, M. T. L. Giudice, S. Tumminello, *J. Inorg. Biochem.* **2004**, *98*, 589–594.
[19] A. Trotta, A. B. Paulsen, A. Silvestri, G. Ruisi, M. A. Girasolo, R. Barbieri, *J. Inorg. Biochem.* **2002**, *88*, 14–18.
[20] A. Silvestri, G. Ruisi, M. A. Girasolo, *J. Inorg. Biochem.* **2002**, *92*, 171–176.
[21] C. L. Liu, M. Wang, T. L. Zhang, H. Z. Sun, *Coordin. Chem. Rev.* **2004**, *248*, 147–168.
[22] L. M. T. Schnaith, R. S. Hanson, L. Que Jr, *Proc. Natl. Acad. Sci. USA* **1994**, *91*, 569–573.
[23] G. Roelfes, M. E. Branum, L. Wang, L. Que Jr, B. L. Feringa, *J. Am. Chem. Soc.* **2000**, *122*, 11517–11518.
[24] C. Liu, S. Yu, D. Li, Z. Liao, X. Sun, H. Xu, *Inorg. Chem.* **2002**, *41*, 913–922.
[25] J. K. Sessler, J. W. Sibert, A. K. Burrell, V. Lynch, J. T. Markert, C. L. Wooten, *Inorg. Chem.* **1993**, *32*, 4277–4283.
[26] P. G. Romero, G. C. DeFotis, G. B. Jameson, *J. Am. Chem. Soc.* **1986**, *108*, 851–853.
[27] S. Menage, J. B. Galey, G. Hussler, M. Seite, M. Fontecave, *Angew. Chem. Int. Ed. Engl.* **1996**, *35*, 2353–2355.
[28] L. Que Jr, A. E. True, *Prog. Inorg. Chem.* **1990**, *38*, 97–103.
[29] A. L. Feig, S. J. Lippard, *Chem. Rev.* **1994**, *94*, 759–805.
[30] D. F. Xiang, X. S. Tan, S. W. Zhang, Y. Han, K. B. Yu, W. X. Tang, *Polyhedron* **1998**, *17*, 2095–2100.
[31] K. S. Murrays, *Coord. Chem. Rev.* **1974**, *12*, 1–35.
[32] Y. P. Tian, C. Y. Duan, X. X. Xu, X. Z. You, *Acta Crystallogr., Sect. C* **1995**, *51*, 2309–2312.
[33] K. Ogura, H. Urable, T. Yosino, *Electrochim. Acta* **1977**, *22*, 285–287.
[34] Y. L. Zhang, H. X. Shen, C. X. Zhang, A. Ottova, H. T. Tien, *Electrochim. Acta* **2001**, *46*, 1251 –1257.
[35] Z. Galus, *Fundamentals of Electrochemical Analysis*, Chichester, Ellis Horwood. **1976**, p. 237.
[36] M. M. Walczak, N. T. Flynn, *J. Electroanal. Chem.* **1998**, *441*, 43–49.
[37] S. M. Chen, *Inorg. Chim. Acta* **1996**, *249*, 143–150.
[38] M. C. Dunand-Sauthier, A. Deronzier, C. D. Toia, M. Fontecave, K. Gorgy, J. Lepretre, S. Menage, *J. Electroanal. Chem.* **1999**, *469*, 53–62.
[39] M. D. Luque de Castro, M. Valcarcel, F. N. Albahadily, H. A. Mottola, *J. Electroanal. Chem.* **1987**, *219*, 139–151.
[40] S. Ménage, L. Que Jr, *New J. Chem.* **1991**, *15*, 431–438.
[41] E. W. Ainscough, A. M. Brodie, J. E. Plowman, K. L. Brown, A. W. Addison, A. R. Gainsford, *Inorg. Chem.* **1980**, *19*, 3655–3663.
[42] S. Satyanarayana, J. C. Dabrowiak, J. B. Chaires, *Biochemistry* **1993**, *32*, 2573–2584.
[43] A. M. Pyle, J. P. Rehman, R. Meshoyrer, C. V. Kumar, N. J. Turro, J. K. Barton, *J. Am. Chem. Soc.* **1989**, *111*, 3051–3058.
[44] J. K. Barton, A. L. Raphael, *J. Am. Chem. Soc.* **1984**, *106*, 2172–2176.
[45] M. T. Carter, M. Rodriguez, A. J. Bard, *J. Am. Chem. Soc.* **1989**, *111*, 8901–8911.
[46] D. W. Pang, H. D. Abruna, *Anal. Chem.* **1998**, *70*, 3162–3169.
[47] H. S. Harned, B. B. Owen, *The Physical Chemistry of Electrolytic Solution*, Reinhold, New York, **1950**, p. 32.
[48] Y. L. Zhang, H. X. Shen, C. X. Zhang, A. Ottova, H. T. Tien, *Electrochim. Acta* **2001**, *46*, 1251–1257.
[49] P. O. Vardevanyan, A. P. Antonyan, G. A. Manukyan, A. T. Karapetyan, *Exp. Mol. Med.* **2001**, *33*, 205–208.
[50] A. J. Bard, L. R. Faulkner, *Electrochemical Methods: Fundamentals and Applications*, Wiley, New York **1980**.
[51] M. E. Reichman, S. A. Rice, C. A. Thomas, P. Doty, *J. Am. Chem. Soc.* **1954**, *76*, 3047–3053.
[52] C. V. Kumar, E. H. Asuncion, *J. Am. Chem. Soc.* **1993**, *115*, 8547–8553.
[53] G. M. Sheldrick, *SADABS*, University of Göttingen, Germany, **1996**.
[54] G. M Sheldrick, *SHELXTL97, Program for Crystal Structure Refinement*, University of Göttingen, Germany, **1993**.
[55] A. J. Wilson, *International Tables for X-ray Crystallography*, V. C, Kluwer Academic Publishers, Dordrecht, Tables 6.1.1.4 and 4.2.6.8, **1992**, p. 500 and p. 219, respectively.

Received: September 16, 2005
Published Online: March 16, 2006

 © 2006 Wiley-VCH Verlag GmbH & Co. KGaA, Weinheim 

DOI: 10.1002/ejic.200500999

# One Dimensional 3d–4f Heterometallic Compounds: Synthesis, Structure and Magnetic Properties

**Albert Figuerola,[a] Joan Ribas,[a] Xavier Solans,[b] Merce Font-Bardía,[b] Miguel Maestro,[c] and Carmen Diaz*[a]**

**Keywords:** Lanthanides / Chromium / Cyanide / Magnetic properties

The reaction of $Ln(NO_3)_3$·aq with $K_3[Fe(CN)_6]$ or $K_3[Co(CN)_6]$ and 2,2′:6′,2′′-terpyridine in water/methanol solution led to three one-dimensional complexes: *trans*-$[Ln(H_2O)_4(terpy)(\mu\text{-}CN)_2M(CN)_4]_n$ (Ln = $La^{3+}$ or $Sm^{3+}$; M = $Fe^{3+}$ or $Co^{3+}$). The structures of $[SmFe]_n$ (**1**), $[SmCo]_n$ (**2**) and $[LaFe]_n$ (**3**) have been solved; the complexes **1** and **2** crystallize in the monoclinic space $P2_1/c$ and are isomorphous, complex **3** crystallizes in the triclinic space $P\bar{1}$. No significant magnetic interaction was found between the samarium(III) and the iron(III) ions.
(© Wiley-VCH Verlag GmbH & Co. KGaA, 69451 Weinheim, Germany, 2006)

## Introduction

The design of supramolecular architectures with novel spin-carrier topologies is of current interest in the field of molecular magnetism. A successful strategy leading to heteropolymetallic systems with extended structures consists in self-assembly processes involving anionic building blocks, which contain a paramagnetic ion, and assembling complex cations with potentially free coordination sites. Cyano-bridged bimetallic systems with interesting magnetic and photomagnetic properties have been characterized.[1] Most of these systems contain two different transition-metal ions. In contrast, the lanthanide cations have not been used as much as nodes for the construction of cyano-bridged heteropolymetallic coordination networks.[2] Thus, although the research on cyano-bridged complexes has mainly focused on transition-metal ions with polycyanometallates and 4f ions, several compounds with different dimensionality have been reported.[3–19] In most cases the magnetic properties of these complexes do not seem exciting, as the coupling between the lanthanide and transition metals is very weak because of the effective shielding of the 4f electrons by the outer-shell electrons.

Important magnetic properties were found in only a few cyano-bridged rare earth transition-metal complexes. Most of the 3d–4f complexes that show long-range magnetic ordering involved the $Sm^{3+}$ ion.[3b,4b,5,13a,20] We are exploring a strategy to control the structure in the solid state that combines elements of design towards crystal engineering and the study of magnetic properties. We successfully applied this strategy in the preparation of new species starting from the mononuclear species $[M(CN)_6]^{3-}$ (M = $Fe^{3+}$, $Cr^{3+}$ and $Co^{3+}$) as building blocks, $Ln(NO_3)_3$·$xH_2O$ and different blocking ligands; a) with M = $Fe^{3+}$ or $Co^{3+}$ and dimethylformamide (DMF) as blocking ligand, working with the same conditions, we reported a family of 25 dinuclear complexes of the formula $[Ln(DMF)_4(H_2O)_3(\mu\text{-}CN)M(CN)_5]$·$nH_2O$ (with Ln = all lanthanide(III) ions except Pm and Lu) (Scheme 1, a).[4a] Structural studies of these families show that they are isomorphous; b) changes in the anionic building block modifies the structural types: using $[Cr(CN)_6]^{3-}$, $Gd(NO_3)_3$·$6H_2O$, DMF and the same conditions of reaction, a one-dimensional *cis*-$[Cr(CN)_4(\mu\text{-}CN)_2Gd(H_2O)(DMF)_4]_n$·$nH_2O$ was previously reported by the authors (Scheme 1, c).[4c] c) Changes in the terminal blocking ligand introduce new changes in the structural types: reactions involving $Ln^{3+}$ and $[Co(CN)_6]^{3-}$, $[Fe(CN)_6]^{3-}$ or $[Cr(CN)_6]^{3-}$ ions using bpy as terminal ligand instead of DMF lead to one-dimensional complexes of formula *trans*-$[M(CN)_4(\mu\text{-}CN)_2Ln(H_2O)(bpy)]_n$·$XnH_2O$ (bpy = 2,2′-bipyridine) form the late lanthanide ions (Scheme 1, b)[4e] and trinuclear complexes of the formula *trans*-$[M(CN)_4(\mu\text{-}CN)_2\text{-}\{Ln(H_2O)_4(bpy)_2\}_2][M(CN)_6]$·$8H_2O$ from the early ones (Scheme 1, d); for the one-dimensional complexes, hydrogen bonds and π–π interactions give three-dimensional networks. This work is focused on the synthesis, structures, and magnetic properties of the new one-dimensional compounds with 2,2′:6′,2′′-terpyridine (terpy) (Scheme 1, e)

[a] Departament de Química Inorgànica, Universitat de Barcelona, Martí i Franquès 1–11, 08028 Barcelona, Spain
E-mail: carme.diaz@qi.ub.es
[b] Departament de Cristallografia Mineralogia i Dipòsits Minerals, Universitat de Barcelona,
Martí I Franquès s/n, 08028 Barcelona, Spain
[c] Departamento de Química Fundamental, Universidade da Coruña
15071 A Coruña, Spain
Supporting information for this article is available on the WWW under http://www.eurjic.org or from the author.

 © 2006 Wiley-VCH Verlag GmbH & Co. KGaA, Weinheim 

acting as blocking ligand: *trans*-[$Sm(H_2O)_4$(terpy)(μ-$CN)_2$-$Fe(CN)_4]_n$ (**1**), *trans*-[$Sm(H_2O)_4$(terpy)(μ-$CN)_2Co(CN)_4]_n$ (**2**) and *trans*-[$La(H_2O)_4$(terpy)(μ-$CN)_2$ $Fe(CN)_4]_n$ (**3**).

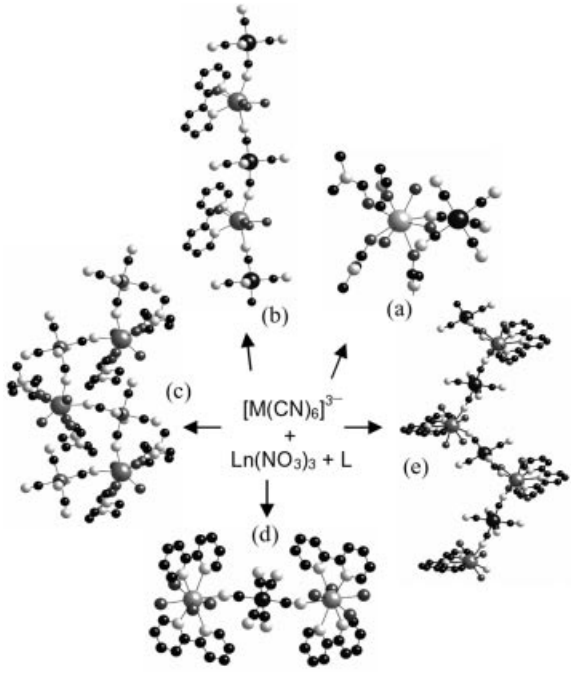


Scheme 1.

## Results and Discussion

### Description of the Structure of Complexes 1–3

Their crystallographic analysis revealed that complex **1** and **2** are isomorphous. Complexes **1** and **2** crystallize in the monoclinic system and complex **3** in the triclinic system. The structure of the three complexes consists of one-dimensional (1-D) chain polymer. An ORTEP view of $[SmCo]_n$ (**2**) and $[LaFe]_n$ (**3**) complexes with the atom-labeling scheme is given in Figure 1 and Figure 2, respectively. Selected bond lengths and angles for **1**–**3** are listed in Table 1. The coordination sphere around the $Ln^{3+}$ ion comprises three nitrogen atoms of the 2,2′:6′,2′′-terpyridine ligand, four oxygen atoms of four water molecules, and two nitrogen atoms of the cyanide bridges, their coordination number is nine. Six cyanide ligands surround the $M^{3+}$ (Fe, Co) ion in a distorted octahedral environment. In complex **3** the La–O and La–N distances are longer than the Sm–O and Sm–N of complexes **1** and **2** in accordance with the variation of the radius of the two-lanthanide ions. The lowest M–C distances correspond as expected to the $[Co(CN)_6]^{3-}$. In the three complexes, the chains show an alternation of $[Ln(H_2O)_4(terpy)]$ and $[M(CN)_6]$ ($M^{3+}$ = Fe, Co) fragments linked by cyanide bridges in the *trans* geometry, a schematic view of the chain of $[SmFe]_n$ (**1**) and $[LaFe]_n$ (**2**) are shown in Figure 3. In the complexes **1** and **2** the distances M–Sm ($M^{3+}$ = Co, Fe) are the same along the chain, but in complex **3** there are two different distances Fe1–La of 5.412 and Fe2–Ln of 5.446 Å. For complexes **1** and **2**, the angles Sm–M–Sm and M–Sm–M are different (176.48 and 102.32° for **1**, and 175.73 and 102.97° for **2**). For complex **3**, the angles values Fe1–La–Fe2, La–Fe1–La and La–Fe2–La are 103.69°, 179.97° and 179.98°, respectively. The chains are not in a linear configuration, the [LnMLn] trinuclear entities run along the chain in a zigzag path. An interesting feature of the conformation of the ligands around the $Sm^{3+}$ and $La^{3+}$ (complex **3**) ions is that they are chiral. As each $Sm^{3+}$ (complexes **1** and **2**) is related to the neighboring one by a glide plane, there are two enantiomeric coordination spheres in an achiral chain. In complex **3**, each $La^{3+}$ ion is related to the neighboring one by the inversion center at the $Fe^{3+}$ ion that is bridging them, there are two enantiomeric coordination spheres in the achiral trinuclear unit. For complexes **1**–**3**, the supramolecular structures are created by hydrogen bonding. Shortest inter-contacts for complexes **1** and **2** (the hydrogen atoms of coordinated water molecules were not located) are listed in the Supporting Information, Table S1 (for details see the footnote on the first page of

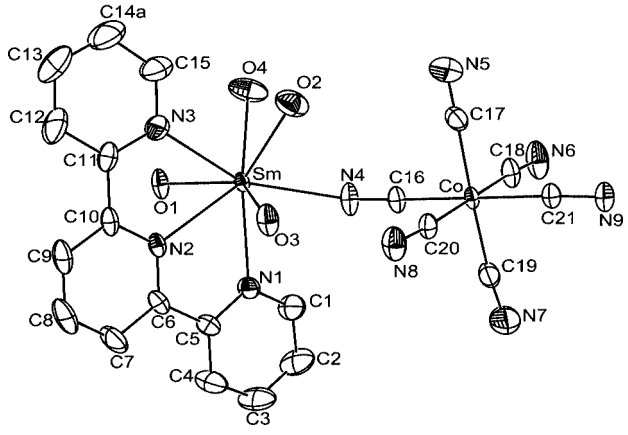


Figure 1. ORTEP view of complex *trans*-$[SmCo]_n$ (**2**) with atom labeling Scheme (ellipsoids draw at 50% probability level).

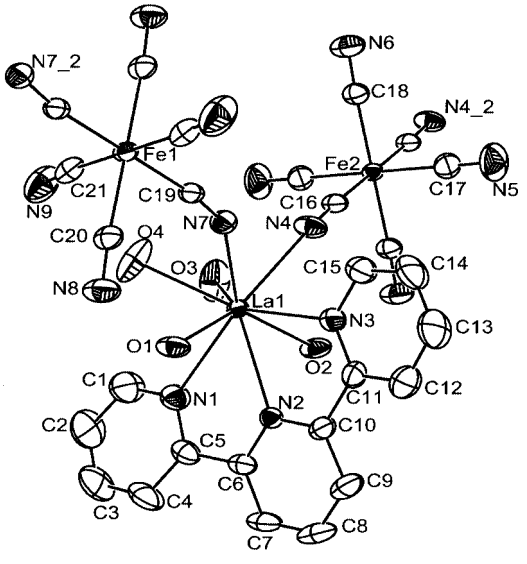


Figure 2. ORTEP view of complex *trans*-$[LaFe]_n$ (**3**) with atom labeling scheme (ellipsoids draw at 50% probability level).

 © 2006 Wiley-VCH Verlag GmbH & Co. KGaA, Weinheim 

Table 1. Selected bond lengths [Å] and angles [°] for **1**–**3**.

| | [SmFe]$_n$ (**1**) | [SmCo]$_n$ (**2**) | | [LaFe]$_n$ (**3**) |
|---|---|---|---|---|
| Sm–O(1) | 2.460(3) | 2.4660(16) | La(1)–O(1) | 2.533(2) |
| Sm–O(2) | 2.572(4) | 2.558(2) | La(1)–O(2) | 2.562(2) |
| Sm–O(3) | 2.475(3) | 2.4723(17) | La(1)–O(3) | 2.623(2) |
| Sm–O(4) | 2.503(4) | 2.489(2) | La(1)–O(4) | 2.561(3) |
| Sm–N(1) | 2.592(3) | 2.576(2) | La(1)–N(1) | 2.666(3) |
| Sm–N(2) | 2.654(4) | 2.5667(18) | La(1)–N(2) | 2.660(2) |
| Sm–N(3) | 2.579(5) | 2.582(2) | La(1)–N(3) | 2.656(2) |
| Sm–N(4) | 2.514(4) | 2.497(2) | La(1)–N(4) | 2.601(2) |
| Sm–N(9) | 2.538(4) | 2.5428(19) | La(1)–N(7) | 2.609(2) |
| M–C(16) | 1.909(5) | 1.873(2) | Fe(1)–C(19) | 1.926(3) |
| M–C(17) | 1.941(5) | 1.889(3) | Fe(1)–C(20) | 1.947(3) |
| M–C(18) | 1.954(5) | 1.896(2) | Fe(1)–C(21) | 1.937(3) |
| M–C(19) | 1.943(6) | 1.890(3) | Fe(2)–C(16) | 1.926(3) |
| M–C(20) | 1.953(5) | 1.900(2) | Fe(2)–C(17) | 1.930(3) |
| M–C(21) | 1.940(5) | 1.8837(19) | Fe(2)–C(18) | 1.945(3) |
| N(4)–C(16) | 1.142(6) | 1.151(3) | N(7)–C(19) | 1.144(4) |
| Sm–N(4)–C(16) | 154.4(4) | 154.4(2) | La(1)–N(4)–C(16) | 152.2(2) |
| M–C(16)–N(4) | 173.0(4) | 172.5(2) | La(1)–N(7)–C(19) | 150.4(2) |
| | | | Fe(2)–C(16)–N(4) | 173.3(3) |
| | | | Fe(1)–C(19)–N(7) | 171.4(3) |

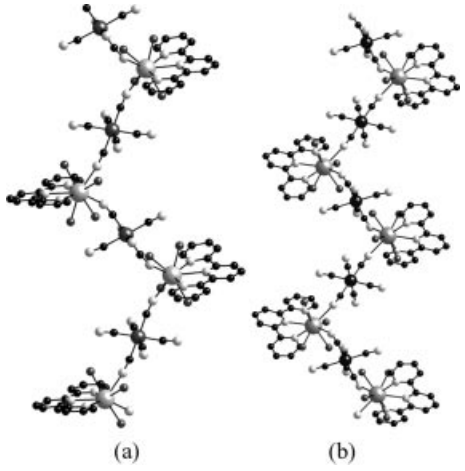


Figure 3. Schematic representation of the chains of [SmFe]$_n$ (a) and [LaFe]$_n$ (b).

this article); for complex **3**, the distances and angles corresponding to the hydrogen bonds are listed in the Supporting Information, Table S2. Complexes **1** and **2** show the same pathway of hydrogen bonds, but different than complex **3**. In complexes **1** and **2** the chains are self-assembled through hydrogen bonds in two different pathways. The O1 and O4 atoms of two coordinated water molecules to the samarium(III) ion and the two nitrogen atoms, N5 and N8 of the [M(CN)$_6$] entity, give an extensive 3D network. In Figure 4 the different ways and the atoms involved in the self-assembled structure for complex [SmFe]$_n$ (**1**), as example, are shown. In complex **3**, the O1, O2 and O3 oxygen atoms of the coordinated water molecules to the lanthanum(III) ion and three nitrogen atoms, N5, N6 and N8 of the [Fe(CN)$_6$] entity, give an extensive 3D network. In Figure 5 the different ways and the atoms involved in the self-assembled structure for complex [LaFe]$_n$ (**3**) are shown. The π–π interactions between the terpy ligands of neighboring chains are

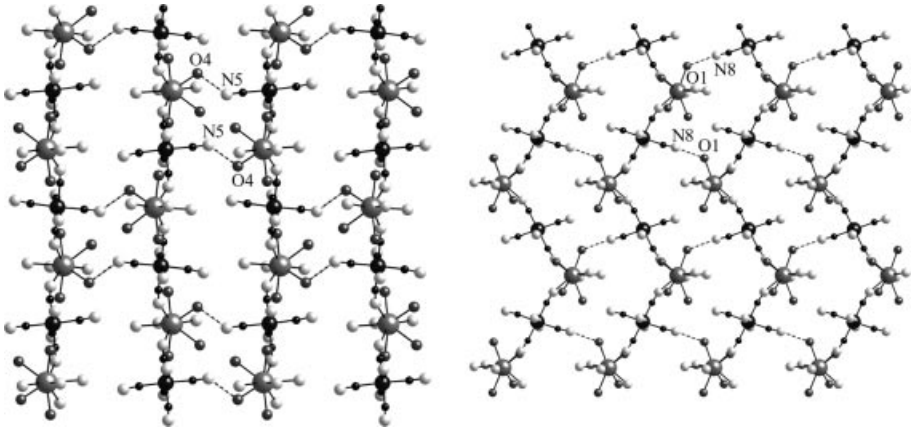


Figure 4. Schematic representation, for complex [SmFe]$_n$ (**1**), of different pathways in which the chains are self-assembled through hydrogen bonds. Complex **2** show similar self-assembly.

 © 2006 Wiley-VCH Verlag GmbH & Co. KGaA, Weinheim 

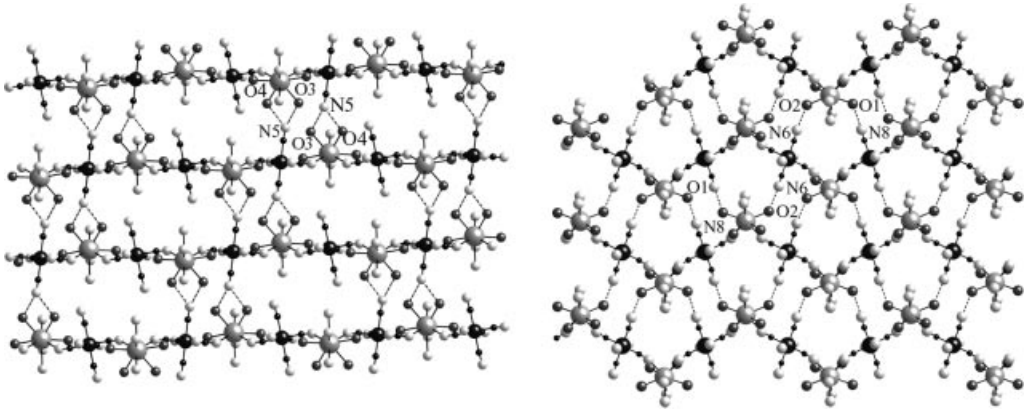


Figure 5. Schematic representation, for complex $[LaFe]_n$ (**3**), of different pathways in which the chains are self-assembled through hydrogen bonds.

very weak. Intermolecular stacking distances between centroids of the terpy rings are shown for complexes **1**–**3** in the Supporting Information, Table S3.

**Magnetic Properties:** Magnetic measurements were performed for the $[SmFe]_n$ (**1**), $[SmCo]_n$ (**2**) and $[LaFe]_n$ (**3**) complexes. The $Sm^{3+}$ and the $Fe^{3+}$ ions possess a first-order angular momentum, which prevents the use of a spin-only Hamiltonian for isotropic exchange. Not much is known about the nature of the exchange interaction of rare earth ions between themselves and with other magnetic groups, because the large orbital contribution of these ions makes a quantitative interpretation of the magnetic data of their complexes very complicated. The difficulty in having quantitative information on both these contributions has so far reduced the analysis of the magnetic properties of the anisotropic lanthanides mainly at a qualitative level, especially in molecular complexes. The most diffuse experimental approach to separate the different contributions of crystal field and exchange coupling to the magnetic properties in either heterometallic or lanthanide radical complexes involves the determination of magnetic properties of a corresponding complex where the second spin carrier is substituted by a diamagnetic analog, which gives rise to comparable ligand-field effects on the lanthanides.[21,4a,4b,4d,4e] Together with the $[SmFe]_n$ complex, we attempted to synthesize and characterize the homologous $[SmCo]_n$ and $[LaFe]_n$ complexes to use the typical empirical approach, mentioned above, to obtain insights into the nature of the $[SmFe]_n$ coupling. The approach consists of comparing its magnetic susceptibility data with the corresponding isostructural $[SmCo]_n$ compounds together with the magnetic properties of the $[LaFe]_n$ complex to take the anisotropy of the $Fe^{3+}$ ion into account. The $Co^{3+}$ and the $La^{3+}$ ions are obviously diamagnetic, and the deviation of the magnetic susceptibility of the $[SmCo]_n$ and the $[LaFe]_n$ compounds with respect to the Curie law is due entirely to the thermal population of the $Sm^{3+}$ Stark components and the anisotropy of $Fe^{3+}$, respectively. The comparison of the experimental magnetization at low temperature of the exchange-coupled system with that of the corresponding uncorrelated spin systems constitutes a further way to discriminate the sign of the coupling. Indeed if the $M$ vs. $H$ curve of the coupled system is running below the curve of the non-correlated system; an antiferromagnetic interaction within the molecular spin system is revealed, while the reverse would be true for a ferromagnetic situation.[22]

For most of the rare-earth compounds, the $\chi_M T$ value at room temperature is close to what is predicted in the free-ion approximation for the cases where only one level, $^{2S+1}L_j$, is thermally populated and second-order contributions are ignored.[23] For the complexes containing the $Sm^{3+}$ ion, the magnetic susceptibility is affected by the thermally populated excited states because of the spin-orbit coupling. The $[LaFe]_n$ complex is not isostructural with the $[SmFe]_n$ and $[SmCo]_n$ ones, but taking into account that the structural features round the $[Fe(CN)_6]$ entity are very similar in the three complexes, we can consider that the crystal field parameters around the $Fe^{3+}$ ion are analogous. So we apply the approach in order to evaluate the presence or not of magnetic interaction between the $Sm^{3+}$ and $Fe^{3+}$ ions.

***trans*-$[Sm(H_2O)_4(terpy)(\mu\text{-}CN)_2Fe(CN)_4]_n$, *trans*-$[Sm(H_2O)_4(terpy)(\mu\text{-}CN)_2Co(CN)_4]_n$ and *trans*-$[La(H_2O)_4(terpy)(\mu\text{-}CN)_2Fe(CN)_4]_n$:** The temperature dependence of the $\chi_M T$ for the three complexes is shown in Figure 6 (top). For the $[SmCo]_n$ complex, the $\chi_M T$ value at 300 K is approximately equal to 0.37 $cm^3 mol^{-1} K$. At room temperature, allowing for $\chi_M T$ = 0.05 $cm^3 mol^{-1} K$ of $Co^{3+}$ (l.s), from the TIP value for the $Co^{3+}$ ion,[24] the $\chi_M T$ value corresponding to the $Sm^{3+}$ is 0.32 $cm^3 mol^{-1} K$. At room temperature, the experimental $\chi_M T$ values found in the literature are around 0.32 $cm^3 mol^{-1} K$. These observed values are inconsistent with the theoretical value of 0.09 $cm^3 mol^{-1} K$ expected for one $Sm^{3+}$ ($^6H_{5/2}$) ion. This disagreement is ascribed to the presence of thermal populated excited states, as is well known for $Sm^{3+}$ complexes. On lowering the temperature, the $\chi_M T$ value decreases monotonically to 0.05 $cm^3 mol^{-1} K$. For the $[LaFe]_n$ complex, the $\chi_M T$ value at 300 K is approximately equal to 0.80 $cm^3 mol^{-1} K$, while it decreases with temperature to 0.53 $cm^3 mol^{-1} K$. For the $[SmFe]_n$ complex, the $\chi_M T$ value at 300 K is approximately equal to 1.14 $cm^3 mol^{-1} K$, while it decreases with temperature to 0.63 $cm^3 mol^{-1} K$. The $\chi_M T$

 © 2006 Wiley-VCH Verlag GmbH & Co. KGaA, Weinheim 

value at room temperature fits nicely to the sum (1.12 $cm^3 mol^{-1} K$) of the measured values for the $Sm^{3+}$ ion (0.32 $cm^3 mol^{-1} K$) in the $[SmCo]_n$ complex and for the $Fe^{3+}$ ion (0.80 $cm^3 mol^{-1} K$) in the $[LaFe]_n$ complex. The $\Delta\chi_M T$ vs. $T$ curve is practically superimposable with the $\chi_M T$ vs. $T$ curve of the $[LaFe]_n$ complex along the whole range of temperatures indicating that no noticeable interaction is active. The experimental magnetization of $[SmFe]_n$ at 2 K (Figure 6, bottom) is superimposable with that of the uncorrelated spin system, corroborating that no exchange interaction is active.

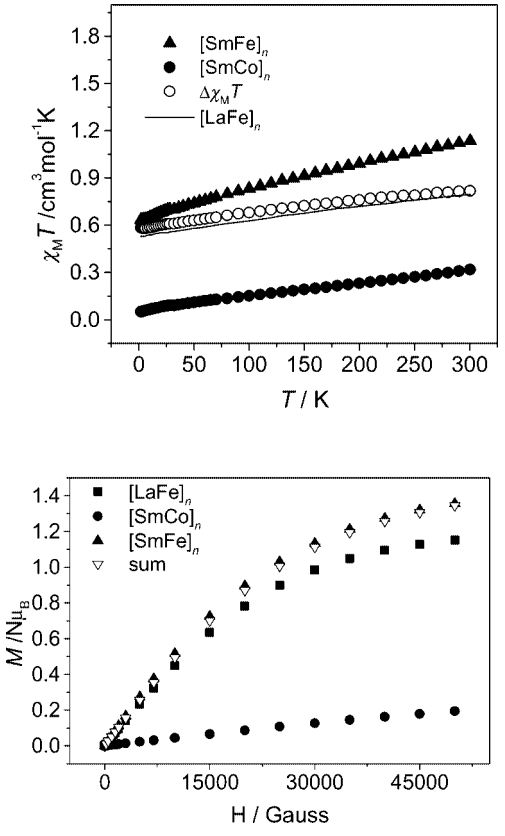


Figure 6. Top: thermal dependence at 0.1 T of $\chi_M^{[SmFe]_n}T$, $\chi_M^{[SmCo]_n}T$, $\chi_M^{[LaFe]_n}T$ and $\Delta\chi_M T = \chi_M^{[SmFe]_n}T - \chi_M^{[SmCo]_n}T$, the TIP value of the $Co^{3+}$ ion has been considered (see text). Bottom: magnetization vs. $H$ (2 K) of $M^{[SmFe]_n}$, $M^{[SmCo]_n}$, $M^{[LaFe]_n}$ and sum $M^{[LaFe]_n} + M^{[SmCo]_n}$.

## Conclusions

Three one-dimensional $[SmFe]_n$, $[SmCo]_n$ and $[LaFe]_n$ complexes, have been structurally characterized and magnetically studied. Most of the 3d–4f complexes that show long-range magnetic ordering involved the $Sm^{3+}$ ion. The replacement of $Sm^{3+}$ ion by another lanthanide ion usually gives rise to isostructural compounds that lose all three-dimensional magnetic properties. Unfortunately the magnetic interaction between the $Sm^{3+}$ and the $Fe^{3+}$ ions in the $[SmFe]_n$ complex is negligible. Trying to make magneto-structural correlations has proved impossible until now due to the complexity of the 3d–4f magnetic interactions and to the few complexes reported in the literature with similar Ln–CN–Fe core.

## Experimental Section

**Materials:** All starting materials were purchased from Aldrich and were used without further purification.

**Physical Measurements:** Magnetic measurements were carried out in the "Servei de Magnetoquímica (Universitat de Barcelona)" on polycrystalline samples (20 mg) with a Quantum Design SQUID MPMS-XL magnetometer working in the 2–300 K range. The magnetic field was 0.1 T. The field-dependent magnetization was measured in the applied magnetic field range 0–5 T. The diamagnetic corrections were evaluated from Pascal's constants.

**Synthesis of *trans*-$[Sm(H_2O)_4(terpy)(\mu\text{-}CN)_2Fe(CN)_4]_n$(1), and *trans*-$[La(H_2O)_4(terpy)(\mu\text{-}CN)_2Fe(CN)_4]_n$ (3):** The two $[Ln–Fe]_n$ complexes were obtained by adding a solution of $Ln(NO_3)_3{\cdot}nH_2O$ (0.2 mmol) in water (50 mL) to an equimolar solution of $K_3[Fe(CN)_6]$ in water (50 mL). To this mixture an ethanolic solution (20 mL) of 2,2′:6′,2′′-terpyridine (0.3 mmol) was added. The solution was left undisturbed, and well-formed crystals (orange for both complexes) were obtained after several days.

**Synthesis of *trans*-$[Sm(H_2O)_4(terpy)(\mu\text{-}CN)_2Co(CN)_4]_n$ (2):** The complex was obtained by the same procedure using $K_3[Co(CN)_6]$ instead of $K_3[Fe(CN)_6]$. Well-formed colourless crystals were obtained after several days.

**Complex 1:** Yield: 100 mg (75%). $C_{21}H_{19}FeN_9O_4Sm$ (667.65): calcd. C 40.70, N 16.84, H 4.19; found C 40.9, N 17.0, H 4.0.

**Complex 2:** Yield: 107 mg (80%). $C_{21}H_{19}CoN_9O_4Sm$ (670.73): calcd. C 41.44, N 17.15, H 4.04; found C 41.5, N 17.2, H 4.0.

**Complex 3:** Yields: 96 mg (73%). $C_{21}H_{18}FeLaN_9O_4$ (656.19): calcd. C 41.20, N 17.05, H 4.01; found C 41.1, N17.2, H 3.9.

**Crystallographic Studies:** Crystal data and refinement are summarized in Table 2. Prismatic crystals, (0.1 × 0.1 × 0.2 mm), (0.1 × 0.2 × 0.2 mm) and (0.1 × 0.3 × 0.3 mm) of complexes **1**, **2** and **3** were selected and mounted on a Enraf–Nonius CAD4 four-circle diffractometer for **1**, on a MAR 345 diffractometer with an image plate detector for **2**, and on a Bruker SMART-CCD area diffractometer for **3**. Unit-cell parameters were determined from automatic centering of 25 reflections ($12 < \theta < 21°$) for **1**, from 24410 reflections ($3 < \theta < 21°$) for **2**, and from 1271 frames of intensity data covering 0.3° in $\omega$ over a hemisphere of the reciprocal space by combination of three exposure sets, and refined by least-square method for **3**. Intensities were collected with graphite-monochromatized Mo-$K_\alpha$ radiation ($\lambda$ = 0.71073 Å), using $\omega/2\theta$ for **1** and **3**, and $\varphi$ scan-technique for **2**; 7269 reflections for **1**, 26881 for **2** and 8230 for **3** were measured in the range $2.43 \leq \theta \leq 29$, $2.45 \leq \theta \leq 31.55$, and $2.12 \leq \theta \leq 28.31$, respectively. For complex **2**, 7477 of which were non-equivalent by symmetry [$R_{int}(I)$ = 0.017]; 4330 reflections of **1**, 7126 reflections of **2**, and 5231 of **3** were assumed as observed applying the condition $I > 2\sigma(I)$. Lorentz polarization and absorption corrections were made.

The structures were solved by Patterson synthesis for **1** and by direct methods for **2** and **3**, using SHELXS computer program[25] and refined by full-matrix least-squares method with SHELX97 computer program,[25] using 7269 reflections for **1**, 7477 reflections for **2**, and 5231 for **3**. The function minimized was $\Sigma w||F_o|^2 - |F_c|^2|^2$, where $w = [\sigma^2(I) + (0.0345P)^2]^{-1}$ for **1**, $w = [\sigma^2(I) + (0.0274P)^2 + 1.8065P]^{-1}$ for **2**, and $w = [\sigma^2(I) + (0.0297P)^2 + 0.8875P]^{-1}$ for **3**,

 © 2006 Wiley-VCH Verlag GmbH & Co. KGaA, Weinheim 

Table 2. Crystal parameters for **1**, **2** and **3**.

| | $[SmFe]_n$ (**1**) | $[SmCo]_n$ (**2**) | $[LaFe]_n$ (**3**) |
|---|---|---|---|
| Empirical formula | $C_{21}H_{19}FeN_9O_4Sm$ | $C_{21}H_{19}CoN_9O_4Sm$ | $C_{21}H_{19}FeLaN_9O_4$ |
| Formula mass | 667.65 | 670.73 | 656.21 |
| Crystal system | monoclinic | monoclinic | triclinic |
| Space group | $P2_1/c$ | $P2_1/c$ | $P\bar{1}$ |
| $Z$ | 4 | 4 | 2 |
| $a$ [Å] | 9.710(2) | 9.625(1) | 9.0673(7) |
| $b$ [Å] | 16.745(5) | 16.656(1) | 9.7385(7) |
| $c$ [Å] | 15.709(9) | 15.706(1) | 14.8550(11) |
| $\alpha$ [°] | 90 | 90 | 84.9580(1) |
| $\beta$ [°] | 98.98(3) | 99.28(1) | 87.5980(10) |
| $\gamma$ [°] | 90 | 90 | 82.5540(10) |
| $V$ [Å$^3$] | 2522.9(17) | 2484.9(3) | 1295.01(17) |
| Radiation (Mo-$K_\alpha$) [Å] | 0.71069 | 0.71073 | 0.71073 |
| $\rho_{calcd.}$ [g/cm$^3$] | 1.758 | 1.793 | 1.683 |
| $\mu_{calcd.}$ [mm$^{-1}$] | 2.925 | 3.054 | 2.232 |
| $T$ [K] | 293(2) | 293(2) | 298(2) |
| $F$[000] | 1312 | 1316 | 643 |
| $\Theta$ range for data | 2.43–29.97° | 2.45–31.55° | 2.12–28.31° |
| Total reflections | 7269 | 26881 | 8230 |
| Independent reflections ($R_{int}$) | 7269 (0.0367) | 7477 (0.0177) | 5231 (0.0169) |
| $\Theta_{max}$ [%] | 95.9 | 90.1 | 91.0 |
| Parameters refined, restraints | 313.0 | 353.0 | 328.8 |
| Final $R$ indices[a] [$I > 2\sigma(I)$] | $R_1 = 0.0341$ | $R_1 = 0.0238$ | $R_1 = 0.0256$ |
| Final $wR_2$ indices[a] | $wR_2 = 0.0706$ | $wR_2 = 0.0692$ | $wR_2 = 0.0608$ |
| Final $R$ (for all data)[a] | $R_1 = 0.0896$ | $R_1 = 0.0256$ | $R_1 = 0.0312$ |
| Final $wR_2$ (for all data)[a] | $wR_2 = 0.0830$ | $wR_2 = 0.0701$ | $wR_2 = 0.0632$ |
| Goodness-of-fit on $F^2$ | 0.897 | 1.307 | 1.012 |

[a] $R_1 = \Sigma||F_o| - |F_c||$ and $wR_2 = \{\Sigma[w(F_o^2 - F_c^2)]/\Sigma[w(F_o^2)^2]\}^{1/2}$.

and $P = (|F_o|^2 + 2|F_c|^2)/3$, $f$, $f'$ and $f''$ were taken from International Tables of X-ray Crystallography.[26] For **1** all non-water hydrogen atoms were computed and refined, using a riding model. For complex **2**, 7 hydrogen atoms were located from a difference synthesis and 4 hydrogen atoms were computed and refined using a riding model. For complex **3**, 4 hydrogen atoms were located from a difference synthesis and refined using a riding model. For all complexes, the isotropic temperature factor for H atoms was equal to 1.2 times the equivalent temperature factor of the atom, which is linked. For complex **1**, the final $R$ (on $F$) factor was 0.034, $wR$ (on $|F|^2$) = 0.070 and goodness of fit = 0.897 for all observed reflections; for complex **2**, the final $R$ (on $F$) factor was 0.0238, $wR$ (on $|F|^2$) = 0.0692 and goodness of fit = 1.307 for all observed reflections; and for complex **3**, the final $R$ (on $F$) factor was 0.0256, $wR$ (on $|F|^2$) = 0.0608 and goodness of fit = 1.012 for all observed reflections. For complex **1**, the number of refined parameters was 313. Max. shift/esd. = 0.00, Mean shift/esd. = 0.00. Max. and min. peaks in final difference synthesis was 0.802 and –0.811 e·Å$^{-3}$, respectively. For complex **2**, the number of refined parameters was 353. Max. shift/esd. = 0.00, Mean shift/esd. = 0.00. Max. and min. peaks in final difference synthesis was 0.583 and –0.518 e·Å$^{-3}$, respectively. For complex **3**, the number of refined parameters was 328, 8 restrictions were applied. Max. shift/esd. = 0.01, Mean shift/esd. = 0.00. Max. and min. peaks in final difference synthesis was 0.590 and –0.79 e·Å$^{-3}$, respectively.

CCDC-289051 (for **1**), -289050 (for **2**) and -289049 (for **3**) contain the supplementary crystallographic data for this paper. These data can be obtained free of charge from Cambridge Crystallographic Data Center via www.ccdc.cam.ac.uk/data_request/cif.

**Supporting Information** (see also the footnote on the first page of this article): Additional Tables with hydrogen bonds and π–π interactions.

## Acknowledgments

This work was financially supported by the Spanish Government (Grant BQU2003–00539).

[1] a) V. Marvaud, C. Decroix, A. Scuiller, C. Guyard-Duhayon, J. Vaissermann, F. Gonnet, M. Verdaguer, *Chem. Eur. J.* **2003**, *9*, 1677 an references therein; b) M. Ohba, H. Ōkawa, *Coord. Chem. Rev.* **2000**, *198*, 313; c) M. Verdaguer, A. Bleuzen, V. Marvaud, J. Vaissermann, M. Seuleiman, C. Desplanches, A. Scuiller, C. Train, R. Garde, G. Gelly, C. Lomenech, I. Rosenman, P. Veillet, C. Cartier, F. Villain, *Coord. Chem. Rev.* **1999**, *190–192*, 1023.

[2] a) C. Benelli, D. Gatteschi, *Chem. Rev.* **2002**, *102*, 2369; b) G.-F. de Sá, O. P. Malta, C. de Mello Donegá, A. M. Simas, R. L. Longo, P. A. Santacruz, E. F. da Silva Jr, *Coord. Chem. Rev.* **2000**, *196*, 165.

[3] a) F. Hulliger, M. Landolt, H. Vetsch, *J. Solid State Chem.* **1976**, *18*, 307; b) F. Hulliger, M. Landolt, H. Vetsch, *J. Solid State Chem.* **1976**, *18*, 283.

[4] a) A. Figuerola, C. Diaz, J. Ribas, V. Tangoulis, J. Granell, F. Lloret, J. Mahía, M. Maestro, *Inorg. Chem.* **2003**, *42*, 641; b) A. Figuerola, C. Diaz, J. Ribas, V. Tangoulis, C. Sangregorio, D. Gatteschi, M. Maestro, J. Mahía, *Inorg. Chem.* **2003**, *42*, 5274; c) A. Figuerola, C. Diaz, M. S. El Fallah, J. Ribas, M. Maestro, J. Mahía, *Chem. Commun.* **2001**, 1204; d) A. Figuerola, J. Ribas, M. Llunell, D. Casanova, M. Maestro, S. Alvarez, C. Diaz, *Inorg. Chem.* **2005**, *44*, 6939; e) A. Figuerola, J. Ribas, D. Casanovas, M. Maestro, S. Alvarez, C. Diaz, *Inorg. Chem.* **2005**, *44*, 6949.

[5] H. Z. Kou, S. Gao, X. Jin, *Inorg. Chem.* **2001**, *40*, 6295.

[6] a) B. Q. Ma, S. Gao, G. Su, G. X. Xu, *Angew. Chem. Int. Ed.* **2001**, *40*, 434; b) R. Gheorghe, M. Andruh, J. P. Costes, B. Donnadieu, *Chem. Commun.* **2003**, 2778.

 © 2006 Wiley-VCH Verlag GmbH & Co. KGaA, Weinheim 

[7] D. W. Knoeppel, J. Liu, E. A. Meyers, S. G. Shore, *Inorg. Chem.* **1998**, *37*, 4828.
[8] B. Du, E. Ding, E. A. Meyers, S. G. Shore, *Inorg. Chem.* **2001**, *40*, 3637.
[9] B. Yan, H. D. Wang, Z. D. Chen, *Polyhedron* **2001**, *20*, 591.
[10] B. Yan, Z. Chen, S. Wang, S. Gao, *Chem. Lett.* **2001**, 350.
[11] S. Tanase, M. Andruh, A. Müller, M. Schmidtmann, C. Mathonière, G. Rombaut, *Chem. Commun.* **2001**, 1084.
[12] H. Z. Kou, S. Gao, C. H. Li, D. Z. Liao, B. C. Zhou, R. J. Wang, Y. Li, *Inorg. Chem.* **2002**, *41*, 4756.
[13] a) B. Yan, Z. Chen, *Helvetica Chim. Acta* **2001**, 817; b) B. Yan, Z. Chen, *Trans. Met., Chem.* **2001**, *26*, 287.
[14] S. Liu, E. A. Meyers, S. G. Shore, *Angw. Chem. Int. Ed.* **2002**, *41*, 3609.
[15] J. A. Kautz, D. F. Mullica, B. P. Cunningham, R. A. Combs, J. M. Farmer, *J. Mol. Struct.* **2000**, *523*, 175.
[16] H. Z. Kou, G. M. Yang, D. Z. Liao, P. Cheng, Z. H. Jiang, S. P. Yan, X. Y. Huang, G. L. Wang, *J. Chem. Crystallogr.* **1998**, *28*, 303.
[17] D. F. Mullica, J. M. Farmer, B. P. Cunningham, J. A. Kautz, *J. Coord. Chem.* **2000**, *49*, 239.
[18] a) B. Yan, Z. Chen, *Chem. Lett.* **2000**, *11*, 1244; b) Q. Yue, J. Yang, G. H. Li, W. Xu, J. S. Chen, S. N. Wang, *Inorg. Chem.* **2005**, *44*, 5241.
[19] a) T. Yi, S. Gao, X. W. Chen, C. H. Yan, B. G. Li, *Acta Crystallogr., Sect. C* **1998**, *54*, 41; b) H. Z. Kou, S. Gao, B. W. Sun, *J. Chem. Mater.* **2001**, *13*, 1431.
[20] H. L. Sun, H. Shi, F. Zhao, L. Qi, S. Gao, *Chem. Commun.* **2005**, 4339.
[21] a) J. P. Costes, F. Dahan, A. Dupuis, J. P. Laurent, *Chem. Eur. J.* **1998**, *4*, 1616; b) A. Caneschi, A. Dei, D. Gatteschi, S. Poussereau, L. Sorace, *Dalton Trans.* **2004**, 1048 and references there in.
[22] J. P. Sutter, M. L. Khan, O. Khan, *Adv. Mater.* **1999**, *11*, 863.
[23] O. Kahn, *Molecular Magnetism*, VCH: Weinheim, **1993**.
[24] a) B. N. Figgis, J. Lewis, *Prog. Inorg. Chem.* **1964**, *6*, 72; b) B.N. Figgis, *Compreh. Coord. Chem.* (Eds.: G. Wilkinson, R. D. Gillard, J. A. McClaverty), vol. 1, Theory and Background, Pergamon, Oxford **1987**, 273.
[25] G. M. Sheldrick, **1997**, *A computer program for determination of crystal structure*, University of Göttingen, Germany.
[26] International Tables of X-ray Crystallography, **1974**, Kynoch Press, vol. IV, pp. 99–100 and 149.

Received: November 9, 2005
Published Online: March 9, 2006

 © 2006 Wiley-VCH Verlag GmbH & Co. KGaA, Weinheim 

DOI: 10.1002/ejic.200501021

# A New $Bi_4Mn_{1/3}W_{2/3}O_8Cl$ Sillén–Aurivillius Intergrowth: Synthesis and Structural Characterisation by Quantitative Transmission Electron Microscopy

**David Ávila-Brande,*[a] L. Carlos Otero-Díaz,[a,b] Ángel R. Landa-Cánovas,[c] Sara Bals,[d] and Gustaaf Van Tendeloo[d]**

**Keywords:** Sillén–Aurivillius intergrowths / Layered oxyhalide / Electron microscopy / Exit-wave reconstruction / Bismuth

The synthesis and structural characterisation of a new phase with nominal composition $Bi_4Mn_{1/3}W_{2/3}O_8Cl$ is presented. Conventional and analytical transmission electron microscopy are used to determine the composition, unit-cell symmetry and space group of the compound, whereas a structural model is deducted by exit-wave reconstruction in the transmission electron microscope. This technique allows the microscope information limit of 1.1 Å to be reached and the (light) oxygen atoms in the presence of heavier atoms (Bi, W, Mn) to be imaged. The average structure is refined from X-ray powder diffraction data using the Rietveld method yielding an orthorhombic unit cell with lattice parameters $a$ = 5.467(4) Å, $b$ = 5.466(7) Å and $c$ = 14.159(3) Å and space group $Cm2m$, which could be described as a Sillén–Aurivillius intergrowth.

(© Wiley-VCH Verlag GmbH & Co. KGaA, 69451 Weinheim, Germany, 2006)

## Introduction

Bismuth-based systems have been extensively studied because of their ability to form new complex intergrowth structures with variable properties. For example, the high Tc superconducting bismuth phases[1,2] can be described as an alternation of $n$ slabs of perovskite-like layers with a double $[BiO]^+$ layer. Related to those structures, the Aurivillius phases with general composition $[Bi_2O_2][A_{n-1}B_nO_{3n+1}]$ are built up as a regular intergrowth of perovskite slabs $[A_{n-1}B_nO_{3n+1}]^{2-}$ and $[Bi_2O_2]^{2+}$ fluorite layers.[3,4] Despite the structural similarities, superconducting properties have not yet been found for the Aurivillius phases, whereas ferroelectric properties with large spontaneous polarisations[5] and high Curie temperatures[6] have been reported.

The complex oxyhalides described by Sillén[7] form another structural variant of layered compounds containing the $[Bi_2O_2]^{2+}$ structural block. These compounds are built up from single, double or triple halide ion sheets separated by $[Bi_2O_2]^{2+}$ layers.

The presence of the $[Bi_2O_2]^{2+}$ layer in the Aurivillius phases as well as in the Sillén complex oxyhalides suggests that intergrowth in these structures might yield a number of new phases. In fact, Aurivillius reported a number of intergrowths with the general sequence $[Bi_2O_2][A_{n-1}B_nO_{3n+1}]$-$[Bi_2O_2][X_m]$ in which A is a large cation (A: $Bi^{3+}$, $Pb^{2+}$, $Sr^{2+}$), B a small transition metal (B: $Nb^{5+}$, $Ta^{5+}$, $W^{6+}$, $Ti^{4+}$, $Al^{3+}$) and X a halide (Cl, Br).[8] In the above sequence, $n$ denotes the thickness of the perovskite layers in terms of $\{BO_6\}$ octahedra and $m$ the number of halide slabs.

The general formula for the simplest member ($n$ = 1 and $m$ = 1) of the Sillén–Aurivillius intergrowth can be written as $Bi_4BO_8X$ and hence B must be a pentavalent cation. However, if another lone pair cation like $Pb^{2+}$ with a lower oxidation state substituting for $Bi^{3+}$ is introduced, the B cation must be replaced by a hexavalent one like $W^{6+}$.

Aurivillius[8] was the first to synthesise the $Bi_4NbO_8Cl$ and $PbBi_3WO_8Cl$ phases. His characterisation indicated a phase mixture ($c_1$ = 14.5 Å and $c_2$ = 29.0 Å) for $Bi_4NbO_8Cl$ and a single phase for $PbBi_3WO_8Cl$ ($a \approx b$ = 5.51 Å; $c$ = 14.35 Å; space group $Cm2m$). Ackerman[9] revised these structures and assigned the orthorhombic space group $P2_1cn$ to the niobium oxychloride $Bi_4NbO_8Cl$ ($a \approx b$ = 5.49 Å and $c$ = 28.75 Å) and the tetragonal space group $P_4$ ($a = b$ = 3.84 Å; $c$ = 14.35 Å) to $PbBi_3WO_8Cl$. Recently, Kusainova et al.[10] reanalysed the structure of $Bi_4NbO_8Cl$ by using neutron diffraction powder data in the same $P2_1cn$ space group ($a$ = 5.44 Å, $b$ = 5.49 Å and $c$ = 28.81 Å). A study of the ferroelectric properties yields a $T_c$ of 765 K.

By inserting adequate transition metals in the Aurivillius block, phases with interesting electric and magnetic properties can be obtained. Manganese, for example, has attracted great attention because of the colossal magnetoresistance (CMR) observed in manganese perovskites.[11,12] In this work, we present the synthesis as well as the structural char-

[a] Dpto. Química Inorgánica, Fac. CC. Químicas, Universidad Complutense,
28040 Madrid, Spain
E-mail: david@brunilda.sme.ucm.es
[b] Centro de Microscopía, Universidad Complutense,
28040 Madrid, Spain
[c] Inst. Ciencia de Materiales de Madrid, CSIC,
28049 Madrid, Spain
[d] Electron Microscopy for Materials Science (EMAT), University of Antwerp,
Groenenborgerlaan 171, 2020 Antwerpen, Belgium

 © 2006 Wiley-VCH Verlag GmbH & Co. KGaA, Weinheim 

acterisation of a new phase with nominal composition $Bi_4Mn_{1/3}W_{2/3}O_8Cl$.

## Results and Discussion

### Composition Analysis and Mn Oxidation State Determination

X-ray energy dispersive spectroscopy (XEDS) analyses performed on several microcrystallites yield an average composition $Bi_{3.99(2)}Mn_{0.33(1)}W_{0.70(7)}Cl_{0.62(9)}$. The measured chlorine content is lower than the nominal value, which is due to severe overlapping between the Bi–$M_\alpha$ and the Cl–$K_\alpha$ peak, making it impossible to assert the presence of chlorine using XEDS. The chlorine edge is more distinctly present in the electron energy loss spectrum (EELS) presented in Figure 1, which shows the chlorine-$L_{2,3}$ absorption edge at 200 eV and the oxygen-$K$ edge at 532 eV. The carbon-$K$ edge at 284 eV is due to the carbon coating grid of the transmission electron microscopy (TEM) specimen-supporting grid.

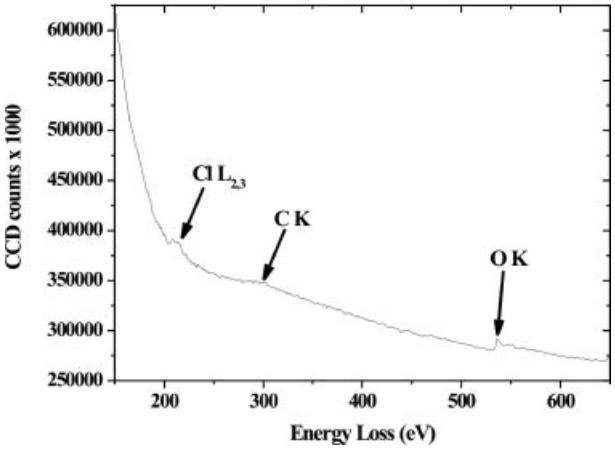


Figure 1. EEL spectrum showing the presence of the different lighter elements (Cl, O).

Figure 2 shows the magnetic susceptibility curve, with the $\chi^{-1}$ curve shown as an inset. This curve obeys the Curie–Weiss law between 50 and 300 K and $\mu_{eff}$ equals $5.20\mu_B$.

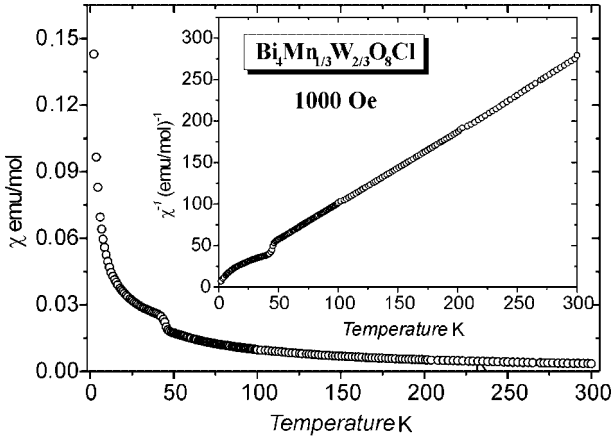


Figure 2. Curve of the magnetic susceptibility vs. temperature. The inset shows the $\chi^{-1}$ curve for the sample.

This value is slightly higher than the theoretical one ($4.90\mu_B$)[13] corresponding to a high-spin $Mn^{3+}$.

### Unit Cell and Symmetry Determination

Selected area electron diffraction (SAED) patterns of several crystals show a homogeneous sample with an either tetragonal primitive cell ($a_o = b_o = 3.8$ Å and $c_o = 14.1$ Å) or a pseudotetragonal centred one ($a \approx b = 2a_o = 5.4$ Å and $c = 14.1$ Å). In order to distinguish between the two, microdiffraction is performed following the method proposed by Morniroli and Steeds.[14] It is important to note that in Mornirolli's work, the lattice parameters for the orthorhombic system were chosen such that $c < a < b$, whereas we have chosen the setting *bca* taking into account the variation in the zone axes notation, for example, [001] changes to [010] after the application of the *bca* setting.

In the first step the crystal system is determined. The experimental [010] pattern, which displays the highest "net" symmetry, has (2mm) symmetry for the zero-order Laue zone (ZOLZ) and 2mm for the whole pattern [ZOLZ + first-order Laue zone (FOLZ)] (Figure 3, a). According to Table 7 in ref.[14] the crystal system is therefore orthorhombic. In order to determine the Bravais lattice as well as the presence of glide planes, a comparison between experimental and simulated [001] and [010] microdiffraction patterns is made (Figure 3, parts a and b). The [001] zone axis contains a "net" mirror m1 in the ZOLZ and the FOLZ reflections; the [010] pattern on the other hand exhibits two perpendicular "net" mirrors m1 and m2 in both the ZOLZ and FOLZ, but the shift between the ZOLZ and the FOLZ reflections parallel to the m2 allows identification of a C centring. According to ref.[15] this gives the extinction symbols:

C.-. for [010]

C..- for [001]

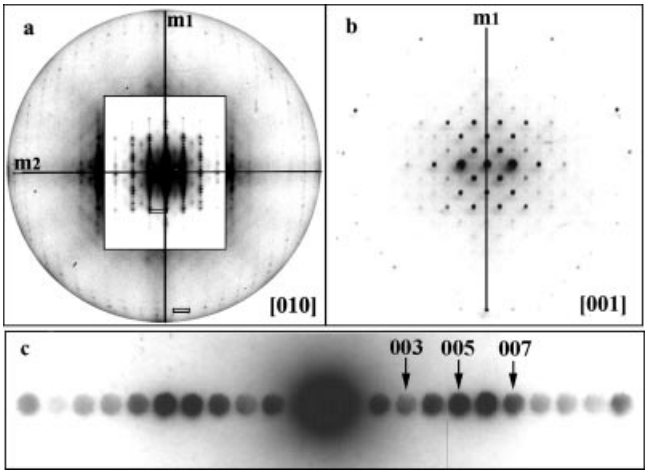


Figure 3. Microdiffraction patterns along (a) [010] and (b) [001]. (c) Enlarged systematic row from [010] showing the 00*l* reflections.

Combining these results, we find a partial extinction symbol C.-- (Table 1), which is in agreement with two pos-

 © 2006 Wiley-VCH Verlag GmbH & Co. KGaA, Weinheim 

sible space groups: *Cm*2*m* and *Cc*2*m*.[15] When looking at the magnified central row of the [010] zone (Figure 3, c) it is easy to note the presence of 00*l* reflections with $l = 2n + 1$. The absence of Gjønnes–Moodie lines in those reflections indicates that they are kinematically allowed. The distinction between both can be made by analysing the reflections listed in Table 2. In *Cc*2*m* the 00*l* reflections with $l = 2n + 1$ are forbidden, whereas they are allowed in *Cm*2*m*. Figure 4 shows that 00*l* reflections with $l = 2n + 1$ are observed along the [010] and [1–10] zone axes. *Cm*2*m* is therefore identified as the correct space group for $Bi_4Mn_{1/3}W_{2/3}O_8Cl$, which is isostructural with $Bi_4Ti_{1/2}W_{1/2}O_8Cl$[16] and lattice parameters $a \approx b = 5.4$ Å and $c = 14.1$ Å.

Table 1. "Net" and "ideal" symmetries as well as the extinction symbols.

| $Bi_4Mn_{1/3}W_{2/3}O_8Cl$ | Symmetries (N = "net"; I = "ideal") | | | |
|---|---|---|---|---|
| | *b* = [010] | | *c* = [001] | |
| | N | I | N | I |
| ZOLZ | (2mm) | (2mm) | (m) | (m) |
| FOLZ | 2mm | 2mm | m | m |
| Extinction symbol | C.-. | | C..- | |

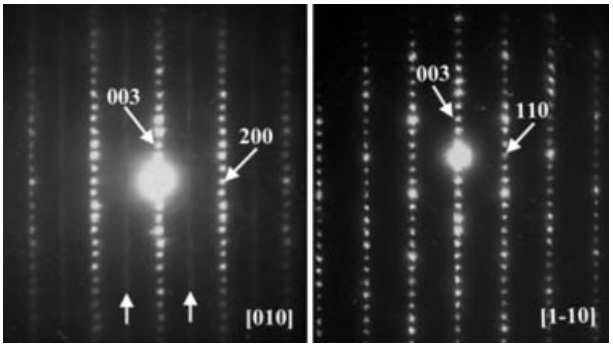


Figure 4. SAED patterns of $Bi_4Mn_{1/3}W_{2/3}O_8Cl$ along the [010] and [1–10] zone axes.

SAED patterns along the main zone axes reveal a well-ordered phase. Only the presence of a weak streaking along [10*l*] in the [010] zone axis (Figure 4, indicated by arrows) indicates some defects or extra ordering.

## Structure Model Determination by Exit-Wave Reconstruction

Although high-resolution electron microscopy (HREM) is considered as a standard technique to image the atomic structure of materials, interpretation is not always straightforward because of aberrations of the electromagnetic lens system. The information that can be obtained by qualitative HREM is therefore limited by the Scherzer point-resolution, but for a coherent electron source (field emission gun) the information limit of the microscope reaches beyond this point-resolution. The information limit can be reached by correcting the phase changes due to the spherical aberration ($C_s$) of the objective lens. Exit-wave reconstruction uses a set of images taken from the same area but for different defocus values of the objective lens. The idea is to invert the image formation process so that lens aberrations can be eliminated and a better resolution can be obtained. A great advantage of this inversion is that the amplitude as well as the phase of the exit wave (i.e., the electron wave leaving the specimen) is reconstructed. As the light atom columns are revealed in the phase of the exit wave,[17] we are able to image the light oxygen atoms in the presence of heavy Bi, W and Mn atoms. In this manner, we directly obtain the projected coordinates, which allow us to build a structural model, assuming the *Cm*2*m* space group.

A focal series of 20 images with an equidistant focal decrease is recorded along the [1–10] zone axis using a slow-scan CCD camera. After reconstruction, using the TrueImage software, and correction for the aberrations, the complex exit wave is retrieved and split into amplitude and phase.

Figure 5 shows the phase of the reconstructed exit wave with the atom positions corresponding to the bright dots; the projected unit cell is outlined. The projected coordinates are directly determined from the phase image and the results are listed together with the ideal positions deduced for the *Cm*2*m* space group in Table 3.

The phase image clearly shows the projected octahedra $\{WO_6\}/\{MnO_6\}$ and it should be noted that also the oxygen atoms are revealed; they are indicated in Figure 5. We have fixed the W/Mn position in the origin (0,0,0) corresponding to the Wyckoff site *2a*. If we assume a model based on a Sillén–Aurivillius intergrowth, the octahedral layer from the Aurivillius block presents eight oxygens in two nonequivalent positions: four in the apex [called O(1)] and four in the equatorial plane [called O(2)]. From the reconstructed phase we can easily determine the projected positions for both, which correspond to 4c and 4d positions respectively in an ideal model.

Two types of bismuth, that is, Bi(1) and Bi(2), are present. Next to Bi(2) we can still observe smaller dots corresponding to the O(3) oxygen. Around Bi(1) we can also observe an extension of the blobs corresponding to the O(3)

Table 2. Reflection conditions for the two possible space groups.

| Space group | Reflection conditions | | | | | | |
|---|---|---|---|---|---|---|---|
| | *hkl* | **0*kl*** | *h*0*l* | *hk*0 | *h*00 | 0*k*0 | **00*l*** |
| *Cm*2*m* | $h + k = 2n$ | $\mathbf{k = 2n}$ | $h = 2n$ | $h + k = 2n$ | $h = 2n$ | $k = 2n$ | – |
| *Cc*2*m* | $h + k = 2n$ | $\mathbf{k,l = 2n}$ | $h = 2n$ | $h + k = 2n$ | $h = 2n$ | $k = 2n$ | $\mathbf{l = 2n}$ |

 © 2006 Wiley-VCH Verlag GmbH & Co. KGaA, Weinheim 

Table 3. Measured and determined coordinates from the ESW-phase image along [1–10].

| Atom | Coordinates measured in the phase image | | Site | Coordinates determined in the space group *Cm*2*m* | | |
|---|---|---|---|---|---|---|
| | $\sqrt{(x^2 + y^2)}$ | *z* | | *x* | *y* | *z* |
| Bi(1) | 0 | 0.35 | *4c* | 0 | 0 | 0.35 |
| Bi(2) | 0.5 | 0.18 | *4c* | 0 | 0.5 | 0.18 |
| W | 0 | 0 | *2a* | 0 | 0 | 0 |
| Mn | 0 | 0 | *2a* | 0 | 0 | 0 |
| Cl | 0.5 | 0.5 | *2b* | 0 | 0.5 | 0.5 |
| O(1) | 0 | 0.12 | *4c* | 0 | 0 | 0.12 |
| O(2) | 0.31 | 0 | *4d* | 0.22 | 0.22 | 0 |
| O(3) | 0.31 | 0.31 | *8f* | 0.22 | 0.22 | 0.31 |

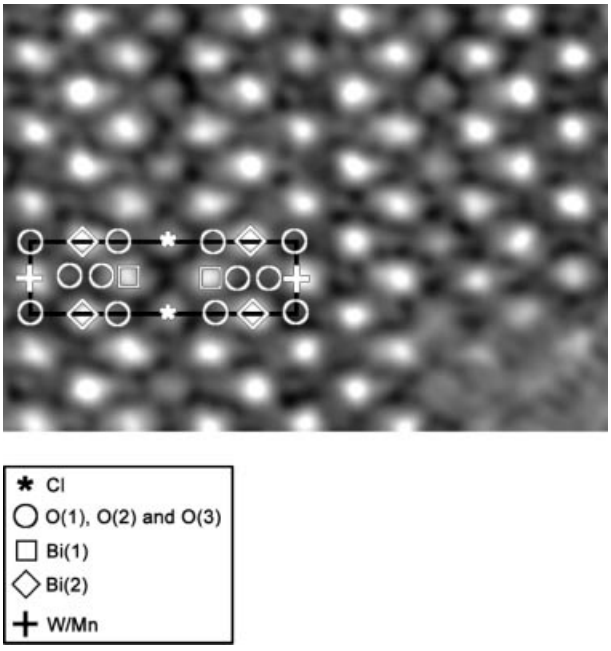


Figure 5. Phase of the reconstructed exit wave along [1–10]. The bright dots correspond to the projected position of the different atoms.

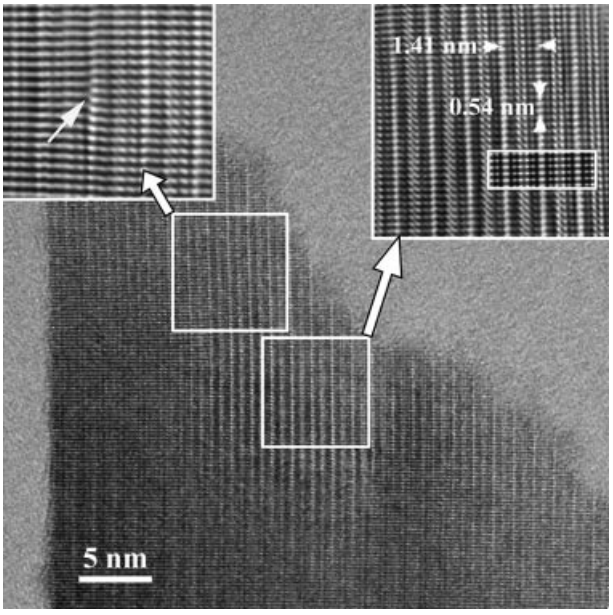


Figure 6. Experimental [010] HREM image. The upper-right enlarged area is a filtered image and shows a good match between the experimental and the simulated image ($\Delta f$ = –300 Å; $t$ = 30 Å). The filtered image on the left shows the presence of a dislocation marked by an arrow.

atoms. As the projected distance Bi(1)–O(3) is equal to 0.97 Å, which is below the information limit, it is not possible to observe Bi(1) and O(3) separately.

The measured coordinate for O(3) is only in agreement with the site symmetry *8f* for the *Cm*2*m* space group. Finally, the chlorine atom was located in a *2b* site according to the coordinates determined in the image. A more accurate fit of the projected positions of the atomic columns is being performed using statistical parameter estimation.[18]

Figure 6 displays an HREM image recorded along the [010] zone, with an enlarged (filtered) area presented as an inset on the right. This inset also shows a simulated part, which was calculated starting from the structural model obtained by exit-wave reconstruction (defocus value $\Delta f$ = –300 Å, sample thickness was 30 Å). Obviously, a good fit between the experimental image and the simulated one is found. Here, the cation positions correspond to the dark dots. The only defects observed in the HREM images are dislocations; one of them is marked with an arrow in the filtered image shown as an inset on the left.

## Average Structure: Powder X-ray Diffraction Refinement

Once the unit cell, the space group and the structural model are determined from electron microscopy data, the refinement of the average structure is carried out by X-ray powder diffraction.

The Rietveld refinement of $Bi_4Mn_{1/3}W_{2/3}O_8Cl$ (Figure 7) is performed using the structural data obtained from the phase of the reconstructed exit wave (see Table 3). Because of the stronger X-ray scattering of $Bi^{3+}$, $Mn^{3+}$ and $W^{6+}$, the isotropic atomic displacement parameters (ADPs) of chlorine and oxygen atoms are all fixed at a reasonable value of 0.8 Å$^2$. Table 4 summarises the refined structural parameters; the $R$ factors of weighted pattern ($R_{wp}$), pattern ($R_p$) and Bragg ($R_B$) converge to 16.1%, 12.9% and 5.87% respectively. These values agree with those obtained in other Aurivillius[19,20] and Sillén–Aurivillius[8] phases. It is worth mentioning that the high B value obtained for Bi(2) in the refinement agrees with our previous work on the isostructural $Bi_4Ti_{1/2}W_{1/2}O_8Cl$ compound.[16] This high value

 © 2006 Wiley-VCH Verlag GmbH & Co. KGaA, Weinheim 

Table 4. Refined structural parameters and main interatomic distances for $Bi_4Mn_{1/3}W_{2/3}O_8Cl$ phase.

| Atom | Site | *x* | *y* | *z* | *B* [Å$^2$] | *n* | Distances [Å] | | |
|---|---|---|---|---|---|---|---|---|---|
| Bi(1) | *4c* | 0 | 0.004(8) | 0.364(5) | 0.33(6) | 0.5 | Bi(1)–O(3) | 2.14(7) | x2 |
| Bi(2) | *4c* | 0 | 0.528(8) | 0.181(2) | 1.6(1) | 0.5 | Bi(1)–O(3) | 2.17(7) | x2 |
| W | *2a* | 0 | 0.013(1) | 0 | 0.3(1) | 0.1666 | Bi(1)–Cl | 3.26(6) | x1 |
| Mn | *2a* | 0 | 0.013(1) | 0 | 0.3(1) | 0.0833 | Bi(1)–Cl | 3.34(1) | x2 |
| Cl | *2b* | 0 | 0.521(7) | 0.5 | 0.8 | 0.25 | Bi(1)–Cl | 3.41(3) | x1 |
| O(1) | *4c* | 0 | –0.083(7) | 0.117(1) | 0.8 | 0.5 | Bi(2)–O(3) | 2.51(6) | x2 |
| O(2) | *4d* | 0.188(1) | 0.289(4) | 0 | 0.8 | 0.5 | Bi(2)–O(3) | 2.54(6) | x2 |
| O(3) | *8f* | 0.233(1) | 0.266(6) | 0.296(1) | 0.8 | 1 | Bi(2)–O(1) | 2.31(6) | x1 |
| | | | | | | | WMn–O(1) | 1.74(3) | x2 |
| | | | Space group *Cm*2*m* | | | | WMn–O(2) | 1.82(7) | x2 |
| | | | $a$ = 5.467(4) Å, $b$ = 5.466(7) Å, $c$ = 14.159(3) Å | | | | WMn–O(2) | 2.09(9) | x2 |
| | | | $R_p$ = 12.9%, $R_{wp}$ = 16.1%, $R_B$ = 5.87% | | | | | | |

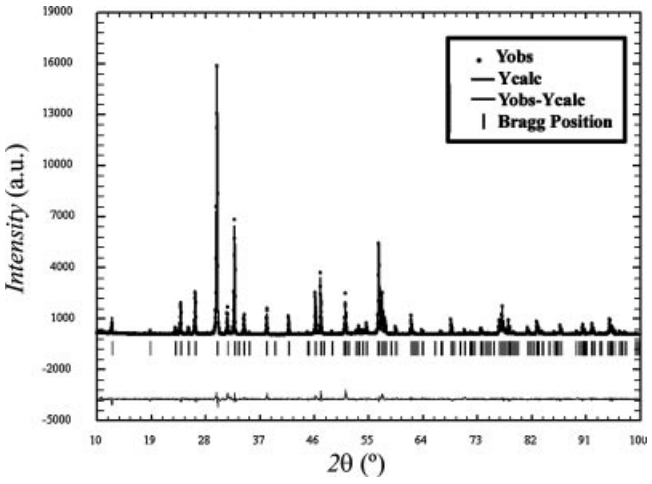


Figure 7. Experimental (circles), calculated and difference (solid lines) powder X-ray diffraction patterns of the $Bi_4Mn_{1/3}W_{2/3}O_8Cl$ phase. Vertical bars indicate the calculated Bragg angle positions.

is due to an asymmetric surrounding around the $Bi_2O_2$ layer; Bi(1) is close to the Cl sheet whereas Bi(2) is much closer to the $\{BO_6\}$ octahedral layer and can establish short contacts to the apex oxygen atoms O(1) (see Table 4), changing its coordination from 4 to 5, as can be seen in the structural model built for the new Sillén–Aurivillius intergrowth (Figure 8, a).

Within the distorted octahedra $(W/Mn)O_6$, the W/Mn–O(1) bonds are shorter than the W/Mn–O(2) bonds. This observation can be understood in terms of the Jahn–Teller effect originated by the $Mn^{3+}$ cation replacing the $W^{6+}$. It is known that while the $W^{6+}$ cation is spherical and symmetric, the $Mn^{3+}$ cation causes a Jahn–Teller effect (compression or elongation). In this case, the presence of $Mn^{3+}$ determined by the previous magnetic susceptibility measurements confirms the Jahn–Teller effect, giving rise to an average compression of the $MnO_6$ octahedra involving a decrease of the apical bonds. This phenomenon is described in more detail in ref.[18]

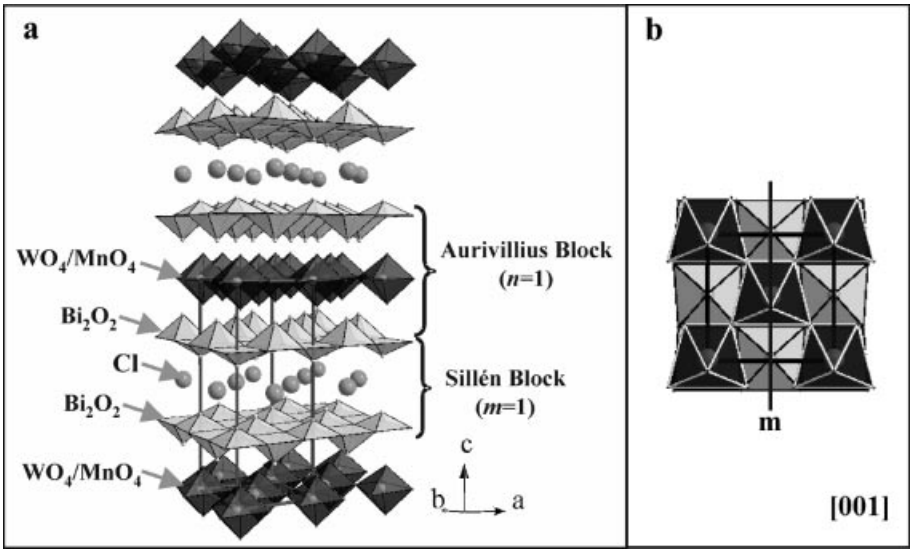


Figure 8. (a) Structure model of the Sillén–Aurivillius intergrowth $[Bi_2O_2][A_{n-1}B_nO_{3n+1}][Bi_2O_2][X_m]$ for $n$ = 1 and $m$ = 1. The stacking along $c$ shows the Aurivillius block with the octahedral sheet ($WO_4/MnO_4$) sandwiched between the square pyramidal layers ($Bi_2O_2$) and the Sillén one with a chlorine (Cl) monolayer. The unit cell is marked by a continuous line. (b) Structural projection along [001] showing in dark grey the distorted octahedra of the perovskite layer.

 © 2006 Wiley-VCH Verlag GmbH & Co. KGaA, Weinheim 

These distorted polyhedra are shown in Figure 8 (b), where the structure of this new phase $Bi_4Mn_{1/3}W_{2/3}O_8Cl$ is projected along [001], presenting the lower space group *Cm*2*m* (instead of *P*4/*mmm*) demonstrated previously by microdiffraction observations.

## Conclusions

A new phase with nominal composition $Bi_4Mn_{1/3}W_{2/3}O_8Cl$ is synthesised. The composition and homogeneity of the sample is determined by XEDS and EELS, whereas the oxidation state of $Mn^{3+}$ is confirmed by magnetic susceptibility measurements.

The unit-cell symmetry and the space group are determined from microdiffraction and SAED experiments yielding an orthorhombic unit cell ($a \approx b$ = 5.4 Å and $c$ = 14.1 Å) with space group *Cm*2*m*. A direct structural model is retrieved from a focal series of HREM images along the [1–10] zone axis. From the phase of the reconstructed exit-wave the projected coordinates can be directly determined. This model is used as input for a Rietveld refinement of the powder X-ray diffraction data.

## Experimental Section

**Preparation of the Samples:** A polycrystalline sample with nominal composition $Bi_4Mn_{1/3}W_{2/3}O_8Cl$ was prepared by heating stoichiometric amounts of the oxides $Bi_2O_3$ (4N), $WO_3$ (4N), $Mn_2O_3$ (4N) and BiOCl (4N) at 993 K for a week in an evacuated ($P$ = $10^{-4}$ Torr) sealed silica tube. The sample was then slowly cooled to room temperature for 24 h.

**Characterisation Techniques:** Samples for transmission electron microscopy (TEM) were prepared by ultrasonic dispersion of the crystals in *n*-butanol. Drops of this dispersion were deposited on a holey carbon-coated copper grid. A JEOL 2000FX equipped with a LINK ISIS 300 analyser was used for XEDS analysis, microdiffraction and SAED. The EEL spectra were acquired using a Philips CM200 FEG TEM equipped with a Gatan Image Filter (GIF) 200. High-resolution electron microscopy (HREM) was performed using a JEOL 3000F TEM and a Philips CM30 FEG TEM, yielding an information limit of 1.1 Å. The exit wave was reconstructed from the focal series using TrueImage software.[21] HREM image simulations were performed with NCEMSS software.[22]

X-ray powder diffraction patterns were recorded with a Siemens D-501 (Cu-$K_{\alpha 1}$ radiation $\lambda$ = 1.5406 Å) over the angular range 10–100°, with a step scan of 0.04°. Rietveld full-profile refinement was done with the FULLPROF program.[23] A pseudo-Voigt function was chosen to generate the line shape of the diffraction peaks. In the final runs, the following parameters were refined: scale factor, background point to point, unit-cell parameters, asymmetry parameters, positional coordinates and isotropic thermal parameters. Further details of the crystal-structure investigation may be obtained from the Fachinformationszentrum Karlsruhe, 76344 Eggenstein-Leopoldshafen, Germany, on quoting the depository number CSD-416293.

Magnetic susceptibility measurements were performed on polycrystalline samples between 2 and 300 K, using a Quantum Design SQUID MPMS-X.

## Acknowledgments

This work was supported by the CYCIT project MAT-2000-0753-C02-01. D. Á.-B. is grateful to MECD for a predoctoral grant and S. B. is grateful to the Fund for Scientific Research – Flanders.

[1] K. A. Yee, T. A. Albright, D. Jung, M. H. Whangbo, *Angew. Chem. Int. Ed. Engl.* **1989**, *28*, 750–751.
[2] R. L. Withers, J. G. Thompson, L. R. Wallenberg, J. D. Fitzgerald, J. S. Anderson, B. G. Hyde, *J. Phys. C: Solid State Phys.* **1988**, *21*, 6067–6083.
[3] A. F. Wells, *Structural Inorganic Chemistry*, 5th ed., Clarendon Press, Oxford, UK, **1984**.
[4] B. Aurivillius, *Arkiv. Kemi* **1949**, *1*, 463–480.
[5] J. F. Scott, *Ferroelectrics Rev.* **1998**, *1*, 1–130.
[6] J. F. Scott, *Phys. World* **1995**, *8*, 46.
[7] A. J. C. Wilson, *Structure Reports*, Oosthoek, Utrecht, **1947**, vol. 11.
[8] B. Aurivillius, *Chem. Scr.* **1984**, *23*, 143–156.
[9] J. F. Ackerman, *J. Solid State Chem.* **1986**, *62*, 92–104.
[10] A. M. Kusainova, S. Y. Stefanovich, V. A. Dolgikh, A. V. Mosunov, C. H. Hervoches, P. Lightfoot, *J. Mater. Chem.* **2001**, *11*, 1141–1145.
[11] C. N. Rao, B. Raveau, *Colossal Magnetoresistance, Charge Ordering and Related Properties of Manganese Oxides*, World Scientific, Singapore, **1998**.
[12] A. P. Ramirez, *J. Phys.: Condens. Matter* **1997**, *9*, 8171–8199.
[13] L. Smart, E. Moore, *Solid State Chemistry: An Introduction*, Chapman & Hall, London, **1992**, p. 240.
[14] J. P. Morniroli, J. W. Steeds, *Ultramicroscopy* **1992**, *45*, 219–239.
[15] T. Hahn, *International Tables for Crystallography*, vol. A, D. Reidel, Dordrecht, Holland, **1983**.
[16] D. Ávila-Brande, A. Gómez-Herrero, A. R. Landa-Cánovas, L. C. Otero-Díaz, *Solid State Sci.* **2005**, *7*, 486–496.
[17] D. Van Dyck, H. Lichte, K. D. Van der Mast, *Ultramicroscopy* **1996**, *64*, 1–15.
[18] S. Bals, S. Van Aert, G. Van Tendeloo, D. Ávila-Brande, *Phys. Rev. Lett.* **2006**, in press.
[19] W. J. Yu, Y. I. Kim, D. H. Ha, J. H. Lee, Y. K. Park, S. Seong, N. H. Hur, *Solid State Commun.* **1999**, *111*, 705–709.
[20] L. Y. Yang, L. Qiu, W. T. A. Harrison, R. Christoffersen, A. J. Jacobson, *J. Mater. Chem.* **1997**, *7*, 243–248.
[21] *TrueImage: Focal-series reconstruction package*,Version 1.0.2, FEI company, **2003**..
[22] *NCEMSS*, X-Window Version 1.8, R. Kilaar, December **2000**.
[23] Fullprof.2k, Version 1.9c, LLB, J. Rodriguez Carvajal, May **2001**.

Received: November 16, 2005
Published Online: March 13, 2006

 © 2006 Wiley-VCH Verlag GmbH & Co. KGaA, Weinheim 

DOI: 10.1002/ejic.200501023

# Ten-Coordinate Neodymium(III) Complexes with Triethylenetetraaminehexaacetic Acid

**Anna Mondry*[a] and Przemysław Starynowicz[a]**

*Dedicated to our teacher and friend Professor Krystyna Bukietyńska*

**Keywords:** Chelates / Lanthanides / N ligands / Neodymium / UV/Vis spectroscopy

The crystal structures and spectroscopic (IR, Raman, UV/Vis) data for the complexes $[C(NH_2)_3]_2[Nd(HTTHA)]\cdot 3H_2O$ (**I**) and $[C(NH_2)_3]_3[Nd(TTHA)]\cdot 6H_2O$ (**II**) are presented. Crystals of **I** are triclinic, $P\bar{1}$, $a$ = 9.998(2), $b$ = 10.730(2), $c$ = 15.557(3) Å, $\alpha$ = 106.89(3)°, $\beta$ = 90.27(3)°, $\gamma$ = 93.24(3)°, $V$ = 1594.0(5) Å$^3$, $Z$ = 2, while the chiral crystals of **II** are monoclinic, $P2_1$, $a$ = 10.157(2), $b$ = 15.958(3), $c$ = 12.788(3) Å, $\beta$ = 112.68(3)°, $V$ = 1912.5(7) Å$^3$, $Z$ = 2. Both structures consist of the complex monomeric anions, guanidinium cations and water of hydration. The $Nd^{III}$ ions are ten-coordinate. The TTHA ligand coordinates to the $Nd^{III}$ ions with six of its carboxyl oxygen atoms and four nitrogen atoms. Although the coordination environments of both $Nd^{III}$ cations are essentially the same, the spectral results of both crystals reveal the influence of the degree of protonation of the ligand on the $Nd^{III}$ ion. The IR and Raman spectra allowed us to assign some important frequencies. A comparison of the electronic absorption spectra of $Nd^{III}$–TTHA complexes in solution and in single crystals of **I** and **II** allows the detection of a small elongation of the Nd–O and Nd–N bonds in these complexes as compared to the $[Nd(TTHA)]^{3-}$ moiety in the previously reported complex $Na_3[Nd(TTHA)]\cdot 2.5NaClO_4\cdot 7.617H_2O$ and indicates that the coordination geometry of the ten-coordinate neodymium complex in solution is the same as in the chiral crystal **II**. The intensities of the f–f transitions in $Nd^{III}$–TTHA solutions and of crystals **I** and **II** were analysed on the basis of the Judd–Ofelt theory.

(© Wiley-VCH Verlag GmbH & Co. KGaA, 69451 Weinheim, Germany, 2006)

## Introduction

The wide variety of biomedical applications of lanthanide complexes with polyamino polycarboxylic acids, including their use as contrast agents in MRI[1] and X-ray[2] diagnosis, NMR hyperfine shift-reagents[3] and bioanalytical assays,[4] is the reason for their being extensively investigated both in solution and in the solid state. The principal aim of these studies is to understand the physicochemical properties of these compounds in solution. In the case of lanthanide systems, one of the methods of choice is electron spectroscopy. Effective analysis of the spectroscopic data is, however, not a trivial task since the properties of these systems are dominated by the intraconfigurational f–f transitions, which are slightly influenced by the ligand field. Therefore, the results obtained by spectroscopic and electrochemical methods concerning the structure of complexes in aqueous solution are difficult to interpret. The situation is even more complicated in the case of lanthanide complexes with ligands characterised by a great number of functional groups, and tautomeric species of variously protonated donor groups of the ligand may be a reason that differently coordinated lanthanide species of diverse labilities coexist in solution. The lanthanide complexes with triethylenetetraaminehexaacetic acid ($H_6TTHA$), a ligand which has a sufficient number of donor atoms (six oxygen atoms and four nitrogen ones) to completely fill the first coordination sphere of the $Ln^{III}$ ion, well exemplify the problems related to lanthanide species in solution. The absence of inner-sphere water molecules for $Ln^{III}$–TTHA solutions at pH above 3 has been proved by emission spectroscopy[5,6] as well as NMR studies,[7] and was also confirmed in the crystal structures.[8–16] Previously, the coexistence of two distinct complexes of $Eu^{III}$–TTHA in solution over the entire pH range has been reported.[5,17] This is different to the $La^{III}$–TTHA system, where the $^1H$ and $^{13}C$ NMR spectra revealed the existence of only one coordination arrangement around the metal cation in solution.[5] Our results based on the optical properties of $Nd^{III}$,[8,16] $Eu^{III}$[17,18] and $Ho^{III}$[13] complexes with TTHA revealed that species differing in the number of coordinated nitrogen and oxygen atoms, namely $[Ln(N_4O_6)]^{3-}$/$[Ln(N_3O_6)]^{3-}$ and $[Ln(N_4O_5)]^{3-}$/$[Ln(N_3O_6)]^{3-}$, are present in the solution for the light and heavy lanthanide ions, respectively. Each of these species may form various stereoisomers, some of which may be op-

[a] Faculty of Chemistry, University of Wrocław,
Joliot-Curie 14, 50383 Wrocław, Poland
E-mail: anm@wchuwr.chem.uni.wroc.pl

 © 2006 Wiley-VCH Verlag GmbH & Co. KGaA, Weinheim 

tically active. Circularly polarized luminescence (CPL) spectroscopy following photoselective excitation has demonstrated the presence of the optically active enantiomers in a racemic mixture for the $Eu^{III}$–TTHA system.[19]

Although many structural relationships among $Ln^{III}$–TTHA complexes in solution are still unresolved, the spectroscopic results obtained for single crystals of these complexes are very helpful in understanding the background of the various processes that may occur in solution. Since the spectral properties of lanthanide complexes with TTHA in crystals, particularly those of $Nd^{III}$–TTHA crystals,[8,16] play an important role in determining the structure of $[Nd(TTHA)]^{3-}$ solution species, it seems advisable to examine the influence of the protonation degree and the countercation on the spectral properties of these complexes. In this paper we therefore report the crystal structures and UV/Vis spectroscopic data of crystalline guanidinium salts of the monoprotonated and deprotonated $Nd^{III}$–TTHA complexes in order to compare their spectral properties with the sodium salt of the $Nd^{III}$–TTHA complex in the crystal[8] and in aqueous solution at various pH values.

## Results and Discussion

### Crystal Structures

The crystal structures of $[C(NH_2)_3]_2[Nd(HTTHA)]\cdot 3H_2O$ (crystal **I**) and $[C(NH_2)_3]_3[Nd(TTHA)]\cdot 6H_2O$ (crystal **II**) were determined and it was found that **I** is isomorphic with $[C(NH_3)_2][La(HTTHA)]\cdot 3H_2O$.[9] The crystals of both compounds are composed of complex $Nd^{III}$–TTHA anions, guanidinium cations and water of crystallisation. As the TTHA anion is hexa-negative, a proton must be present in **I** to compensate the deficiency of the positive charge caused by the $Nd^{III}$ ion and two guanidinium cations. The complex anions in both crystals are similar (Figure 1) and are composed of the TTHA residue wrapped around the neodymium cations. The metal ions are ten-coordinate, forming bonds with six carboxylic oxygen atoms and four nitrogen ones in each complex. The Nd–O and Nd–N bond lengths for **I** and **II** (Table 1) are typical and are similar to those found for the complex $Na_3[Nd(TTHA)]\cdot 2.5NaClO_4\cdot 7.617H_2O$,[8] denoted here as **Na1**. The differences between the positions of the atoms in both anions are most pronounced for the outer-sphere carboxylate oxygen atoms, which is most probably caused by different networks of hydrogen bonds. For example, the O(10) atom in **I** is involved in a short (2.67 Å) H-bond with a water molecule and a moderate bond with a guanidinium cation (O···N = 2.91 Å), whereas in **II** the O(10) atom forms three H-bonds of moderate lengths (2.87–3.08 Å) with two water molecules and a guanidinium cation. The proton that is necessary for the electric charge compensation in **I** is probably attached to O(12) as the C(17)–O(12) distance of 1.306(4) Å is about 0.05 Å longer than the other C–O bond lengths.

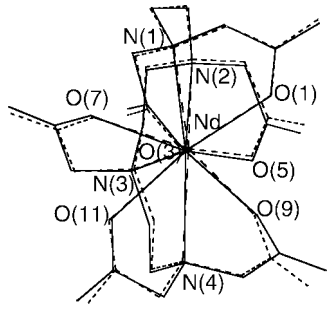


Figure 1. A view of the superimposed complex anions of **I** and **II**. The dashed lines represent **I** and the solid ones **II**. The atoms labels are given for the neodymium coordination sphere only, for the sake of clarity.

### Spectral Results

#### *IR and Raman Spectra of Crystals*

A comparison of the IR and Raman spectra of **I** and **II** with the spectra of **Na1** and $H_6TTHA$ allowed us to assign some important frequencies. These are given in Table 2. The IR bands of the three crystals **I**, **II** and **Na1**, in which the coordination environment ($N_4O_6$) around the $Nd^{III}$ ion is the same, are displayed in Figure 2 (A). The vibrations of the OH and $CH_2$ groups, as well as of the $NH_2$ group in the case of the guanidinium crystals, occur in the broad and intense IR band located in the range 2750–3750 $cm^{-1}$. Since

Table 1. Selected bond lengths [Å] for $Nd^{III}$–TTHA crystals.

| | $[C(NH_3)_2]_2[Nd(HTTHA)]\cdot 3H_2O$ **I** | $[C(NH_3)_2]_3[Nd(TTHA)]\cdot 6H_2O$ **II** | $Na_3[Nd(TTHA)]\cdot 2.5NaClO_4\cdot 7.617H_2O$[8] **Na1** |
|---|---|---|---|
| Nd–O(1) | 2.448(3) | 2.521(5) | 2.537(3) |
| Nd–O(3) | 2.492(3) | 2.515(4) | 2.491(4) |
| Nd–O(5) | 2.418(3) | 2.472(4) | 2.434(4) |
| Nd–O(7) | 2.435(2) | 2.474(5) | 2.430(3) |
| Nd–O(9) | 2.439(3) | 2.498(5) | 2.521(3) |
| Nd–O(11) | 2.801(3) | 2.595(5) | 2.524(4) |
| $Nd–O_{av}$ | 2.505 | 2.513 | 2.490 |
| Nd–N(1) | 2.774(3) | 2.814(5) | 2.742(4) |
| Nd–N(2) | 2.764(3) | 2.789(6) | 2.763(4) |
| Nd–N(3) | 2.720(2) | 2.745(6) | 2.724(4) |
| Nd–N(4) | 2.853(3) | 2.830(6) | 2.823(4) |
| $Nd–N_{av}$ | 2.778 | 2.795 | 2.763 |
| Nd–Nd | 9.183(3) | 10.157(3) | 9.515(4) |

 © 2006 Wiley-VCH Verlag GmbH & Co. KGaA, Weinheim 

combinations and/or overtones transitions may also appear in this spectral region, only the ν(OH) frequency of crystal water molecules can be unequivocally assigned. The positions of the ν(OH) peaks found in the three crystals may indicate that the overall strength of the hydrogen bond between water molecules and the polyatomic anion is the weakest in the case of **Na1** (Table 2). Broad bands of the $\nu(NH_2)$ mode were found in the Raman spectra of **I** and **II**. These vibrations, which are due to the guanidinium cation, appear in the range 3200–3400 $cm^{-1}$, where a combination band of the $\delta(NH_2)$ and $\nu_{as}(COO)$ overtones also appears. The positions of the $\nu(CH_2)$ oscillations in the IR spectra agree well with those very intense found in the Raman spectra. For both guanidinium crystals a strong band of the $\delta(NH_2)$ vibration was found in the region of 1650–1700 $cm^{-1}$. The $\nu_{as}(COO)$ frequencies of the studied crystals are very similar, with the highest frequency being found for **Na1**. The presence of a protonated carboxylate group in **I**, as the long $Nd^{III}$–O(11) distance attests (Table 1), is the reason for a much broader and split band of the $\nu_s(COO)$ vibration in **I** as compared with the bands of **II** and **Na1**.

The difference, $\Delta$, between the antisymmetric and symmetric frequencies of the carboxylate groups has been suggested to be an indicator of the share of the M–O(COO) bond covalency,[20] the latter being higher when $\Delta$ increases. Accordingly, the $\Delta$ differences determined from the spectra of the three crystals were compared. Two values of $\Delta$ were found for the protonated crystal **I**. One of these differences was the highest one of all (200 $cm^{-1}$), while the second (187 $cm^{-1}$) is close to the $\Delta$ value of **Na1** (188 $cm^{-1}$). The smallest $\Delta$ was found for **II** (181 $cm^{-1}$). Comparing these $\Delta$ values with the structural data given in Table 1 one can see that they have no connection with the M–O bond lengths. A similar problem was encountered in the case of the $Nd^{III}$–N bond lengths, which may be reflected by the ν[C–$N(CH_2)$] modes. The smallest ν[C–$N(CH_2)$] frequency was found in the case of **I** (1116 $cm^{-1}$), whereas the ν(C–N) vibrations of **II** (1120 $cm^{-1}$) and **Na1** (1121 $cm^{-1}$) are similar to that of the ligand (1125 $cm^{-1}$). For both guanidinium crystals the most intense Raman bands of 1007 $cm^{-1}$ were assigned to the ν[C–$N(NH_2)$] vibrations of the guanidinium cation. All ν(C–C) frequencies of the three crystals are blue-shifted relative to the frequency of the $H_6$TTHA ligand.

Although some similarity between the IR spectra of the crystals can be seen (Figure 2, **A**), one cannot say the same about their NIR spectra. These spectra, recorded at room temperature and 4 K, are shown in Figure 2 (**B**). Apart from the oscillation bands, the electronic $^4I_{9/2} \rightarrow {}^4I_{15/2}$ transition can also be observed in this region. Recently, we have shown that the f–f transitions in this spectral region are seriously affected by coincident combination and/or overtone bands.[21,22] The present data also reveal that these

Table 2. Wavenumbers [$cm^{-1}$] and relative intensities[a] of the bands observed in the IR and Raman spectra of $H_6$TTHA and crystals of **I**, **II** and **Na1**.

| Tentative assignment | $H_6$TTHA IR | R | **I** IR | R | **II** IR | R | **Na1** IR |
|---|---|---|---|---|---|---|---|
| ν(OH) | | | 3392 (s) | | 3411 (vs) | | 3438 (vs) |
| $\nu(NH_2)$[b] | | | | 3386 (m) | | 3369 (m) | |
| | | | | 3249 (m) | | 3242 (m) | |
| $\nu(CH_2)$ | 3026 (m) | 3025 (m) | | | | | |
| | 3019 (m) | 3017 (m) | 2986 (w) | | 2986 (w) | | |
| | 3006 (m) | 3010 (m) | 2970 (w) | 2973 (vs) | | 2967 (s) | 2955 (m) |
| | 2995 (m) | 2982 (s) | | 2946 (s) | | 2944 (s) | 2923 (m) |
| | 2966 (s) | 2966 (vs) | 2917 (w) | 2901 (vs) | 2890 (w) | 2885 (s) | |
| | | 2934 (s) | 2853 (w) | 2851 (s) | 2848 (w) | 2849 (s) | 2855 (m) |
| | | 2896 (m) | 2833 (w) | | | | |
| ν(COOH) | 1739 (vs) | 1739 (vw) | | | | | |
| | | 1702 (m) | | | | | |
| | 1689 (sh) | 1680 (w) | | | | | |
| | 1644 (sh) | 1640 (vw) | | | | | |
| $\delta(NH_2)$[b] | | | 1709 (sh) | 1707 (vw) | | 1681 (vw) | |
| | | | 1675 (sh) | 1677 (vw) | 1675 (vs) | | |
| | | | 1659 (s) | 1659 (vw) | | 1666 (vw) | |
| $\nu_{as}(COO)$ | | | 1595 (vs) | 1601 (vw) | 1593 (vs) | 1592 (vw) | 1597 (vs) |
| | | | | 1585 (vw) | | | |
| $\delta(CH_2)$ | 1465 (s) | 1467 (sh) | 1473 (m) | 1475 (s) | | 1466 (sh) | |
| | | 1456 (sh) | | 1460 (s) | | 1458 (sh) | |
| | | 1447 (s) | 1437 (s) | 1447 (s) | 1437 (s) | 1439 (s) | 1440 (s) |
| | | 1433 (vs) | | | | | |
| $\nu_s(COO)$ | 1415 (vs) | 1414 (s) | 1408 (s) | 1417 (s) | 1412 (s) | 1414 (s) | 1409 (s) |
| | | | 1395 (s) | 1405 (s) | | | |
| | | | | 1397 (s) | | | |
| ν[C–$N(CH_2)$] | 1125 (w) | 1128 (s) | 1116 (w) | 1118 (m) | 1120 (w) | 1123 (m) | 1121 (m) |
| ν[C–$N(NH_2)$][b] | | | 1007 (vw) | 1007 (vs) | 1006 (vw) | 1007 (vs) | |
| ν(C–C) | 899 (w) | 902 (vs) | 928 (m) | 933 (vs) | 932 (m) | 933 (vs) | 932 (m) |

[a] vs: very strong; s: strong; m: medium; w: weak; vw: very weak; sh: shoulder. [b] Bands derived from the guanidinium cation.

 © 2006 Wiley-VCH Verlag GmbH & Co. KGaA, Weinheim 

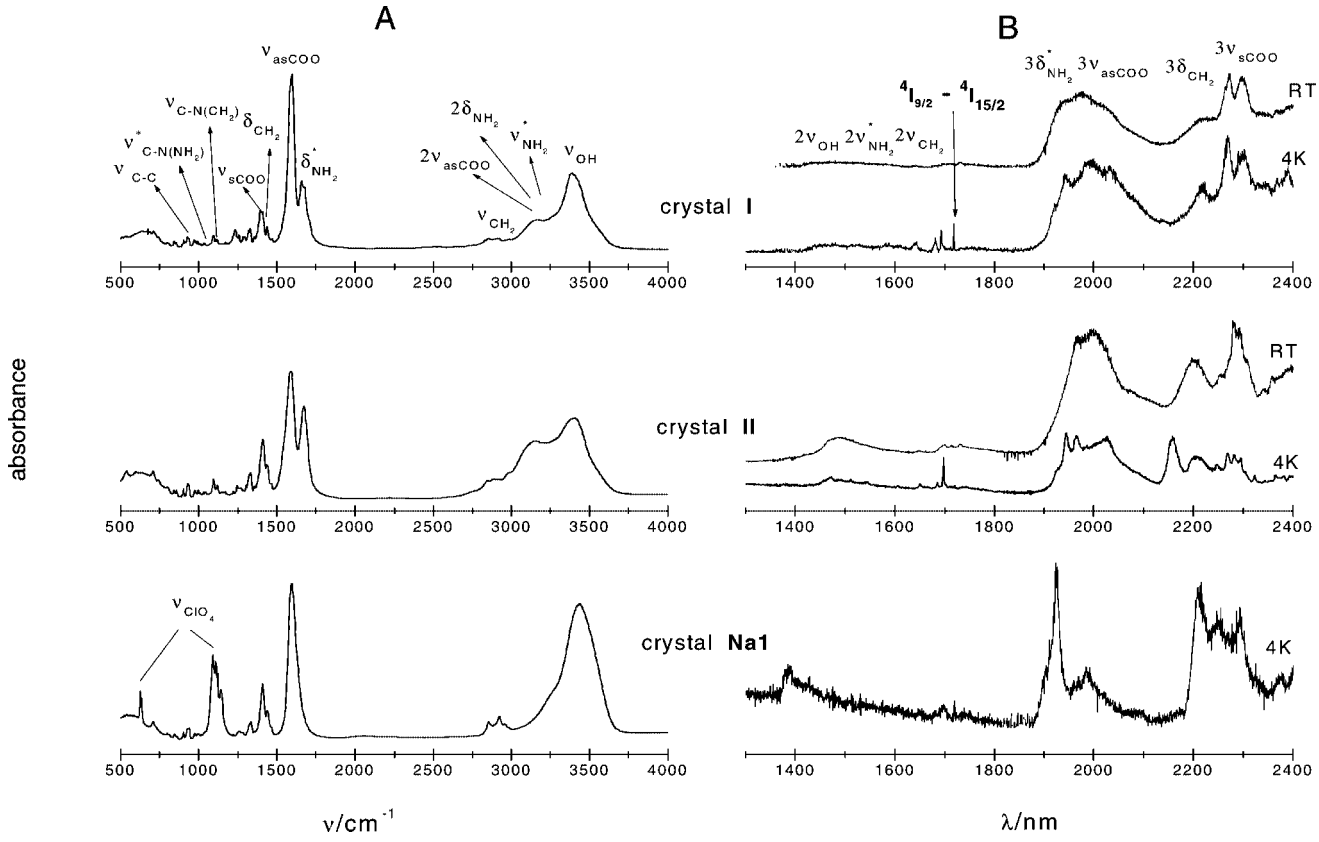


Figure 2. **A** – IR (powder crystals with KBr) and **B** – NIR (single crystals) spectra of $Nd^{III}$–TTHA complexes in **I**, **II** and **Na1**. Some identified bands are labelled, asterisks respond to bands of the guanidinium cation.

bands strongly dominate the f–f transitions of the $Nd^{III}$ ion in the NIR region and this domination is different for the three non-isomorphic crystals studied.

### *UV/Vis Spectra of the $Nd^{III}$–TTHA Complex in Solutions and in Single Crystals*

Two transitions in the $Nd^{III}$ absorption spectrum, namely $^4I_{9/2} \rightarrow {}^2P_{1/2}$ and $^4I_{9/2} \rightarrow {}^4G_{5/2}/{}^2G_{7/2}$, are particularly suitable to perform studies of equilibria changes between different species of the $Nd^{III}$–TTHA complex in solution. The peak positions in the first transition indicate splitting of the ground level in the ligand field of the $Nd^{III}$ environment, whereas the intensity of the hypersensitive $^4I_{9/2} \rightarrow {}^4G_{5/2}/{}^2G_{7/2}$ transition is influenced the most among all the f–f transitions by changes in the immediate surrounding of the $Nd^{III}$ ion.

#### *Analysis of the $^4I_{9/2} \rightarrow {}^2P_{1/2}$ Transition*

As can be seen from the equilibria variations between different species for sodium salts of $Nd^{III}$–TTHA solutions, exemplified by the $^4I_{9/2} \rightarrow {}^2P_{1/2}$ transition in Figure 3, the shape and intensity of these bands do not change further when the pH of the solution exceeds 4. This observation is true for all f–f transitions in spectra of $Nd^{III}$–TTHA solutions for which the pH was adjusted with either NaOH or $[C(NH_2)_3]_2CO_3$. It can easily be seen from Figure 3 that the number of Stark components in the $^4I_{9/2} \rightarrow {}^2P_{1/2}$ spectra of all studied solutions exceeds five, the number of optical lines predicted by group theory for a single environment of the $Nd^{III}$ ion. This means that for $Nd^{III}$–TTHA solutions at least two complexes with a different coordination arrangement around the metal ion exist over the entire pH range. At low pH, the peak maximum of the $^4I_{9/2} \rightarrow {}^2P_{1/2}$ transition is at 23248 $cm^{-1}$, whereas for solutions at pH above 3 it appears at 23310 $cm^{-1}$. The positions of these peaks correspond to the two different coordination cores of the lanthanide ion found in the previously studied single crystals of the $Nd^{III}$–TTHA complexes.[8,16] The neodymium entities in those crystals, which were obtained as sodium salts from the same mother liquor at pH 4.5, are $[Nd_2(N_3O_6)_2]^{6-}$ (peak maximum at 23231 $cm^{-1}$)[16] and $[Nd(N_4O_6)]^{3-}$ (peak maximum at 23302 $cm^{-1}$).[8] From the comparative studies of UV/Vis spectra of single crystals and the solution at pH 7.65 it was proved that the $[Nd(N_3O_6)]^{3-}$ and $[Nd(N_4O_6)]^{3-}$ species are present in this solution in the molar ratio of 1:4.[16] As can be seen from Figure 3, the highest concentration of the first species appears in the solution at a pH below 3, whereas the second species dominates in solution at a pH above 3.5. Hence, one could expect that crystals obtained from solutions in which one of these species prevails will contain this species. Since attempts to obtain crystals from solutions containing sodium cations at very low pH failed, the guanidinium salt solutions were used. The $^4I_{9/2} \rightarrow {}^2P_{1/2}$ spectra of crystals **I** and **II** and solutions from which they were obtained are presented in Fig-

 © 2006 Wiley-VCH Verlag GmbH & Co. KGaA, Weinheim 

ure 4. Comparing the sodium (Figure 3) and guanidinium (Figure 4) spectra of $Nd^{III}$–TTHA solutions one can see that a nine-coordinate species with a peak maximum at 23248 $cm^{-1}$ for the sodium solution and 23254 $cm^{-1}$ for the guanidinium solution prevails at a pH below 3. However, the ten-coordinate form is more favoured upon crystallisation in the presence of guanidinium cations. Although the coordination environment of the lanthanide cation is essentially the same in crystals of **I** and **II**, small differences between the bond lengths and angles bring about changes in the position of the $^2P_{1/2}$ state. It is worthwhile noting that the first two peaks in the spectrum of the chiral crystal **II** exactly match the first two peaks of the $Nd^{III}$–TTHA solution at a pH above 4.

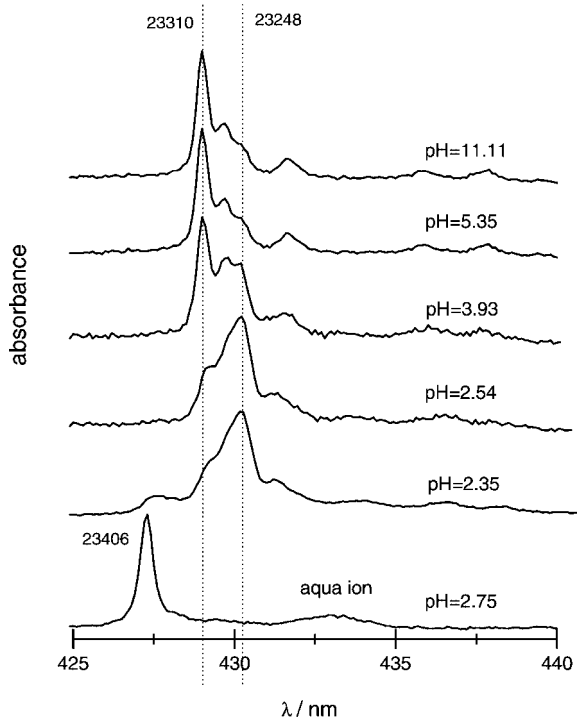


Figure 3. Absorption spectra of the $^4I_{9/2} \rightarrow {}^2P_{1/2}$ transition of the $Nd^{III}$–TTHA complex in solutions at different pH values adjusted by NaOH ($c_{Nd}$ = 2.219·10$^{-2}$ M, $d$ = 2 cm).

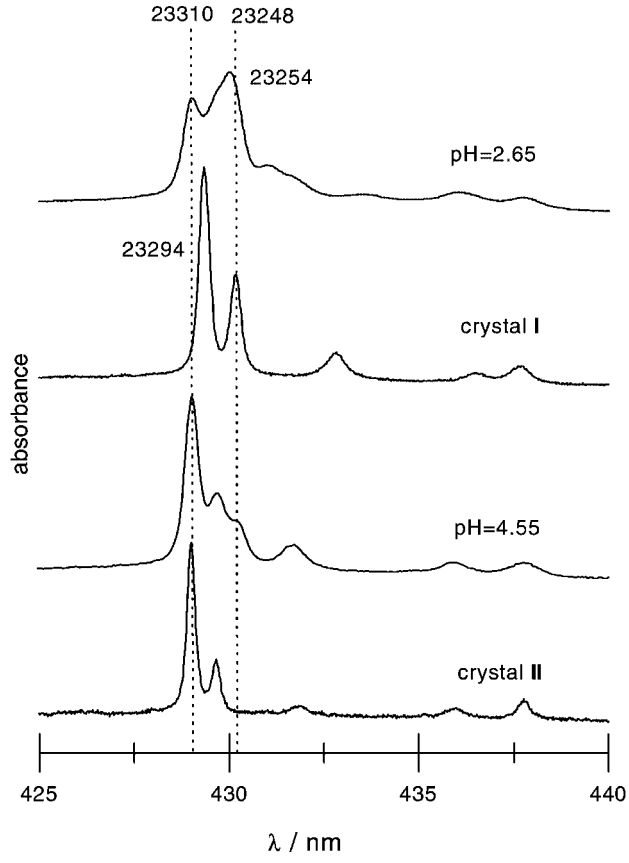


Figure 4. Absorption spectra of the $^4I_{9/2} \rightarrow {}^2P_{1/2}$ transition of guanidinium salts of the $Nd^{III}$–TTHA complex in solutions and in crystals obtained from these solutions (in solutions: $c_{Nd}$ = 5·10$^{-2}$ M, $d$ = 2 cm; in crystals: $c_{Nd}$ = 2.270 M, $d$ = 0.031 cm for **I** and $c_{Nd}$ = 1.898 M, $d$ = 0.059 cm for **II**).

The positions of the $^4I_{9/2} \rightarrow {}^2P_{1/2}$ peaks and the splittings of the neodymium $^4I_{9/2}$ ground state by the ligand field in the $Nd^{III}$–TTHA solutions at pH above 4 and in crystals of **Na1**,[8] **Na2**[16] (where **Na2** are crystals of $Na_{0.5}H_{5.5}[Nd_2(TTHA)_2]\cdot 7.5NaClO_4\cdot 16.83H_2O$ with the $[Nd_2(N_3O_6)_2]^{6-}$ core) as well of **I** and **II** are given in Table 3.

As it can be seen from Table 3 and Figure 4, the second intense peak in the $^4I_{9/2} \rightarrow {}^2P_{1/2}$ spectrum of **I** has the same position as the peak that belongs to the $[Nd(N_3O_6)]^{3-}$ species. Therefore, to be sure that the peak at 23248 $cm^{-1}$ in

Table 3. Positions of the $^4I_{9/2} \rightarrow {}^2P_{1/2}$ peaks and the splittings of the neodymium $^4I_{9/2}$ ground state by the ligand field in $Nd^{III}$–TTHA solutions at pH above 4 and in crystals of **Na1**, **Na2**, **I** and **II**.

| Position [$cm^{-1}$] Solution | Splitting | Position [$cm^{-1}$] **Na1** | Splitting | Position [$cm^{-1}$] **Na2** | Splitting | Position [$cm^{-1}$] **I** | Splitting | Position [$cm^{-1}$] **II** | Splitting |
|---|---|---|---|---|---|---|---|---|---|
| 23310 | 0 | 23302 | 0 | | | 23294 | 0 | 23310 | 0 |
| 23273 | 37 | 23264 | 38 | | | | | 23273 | 37 |
| 23248 | 62 | | | 23231 | 0 | 23248 | 46 | | |
| 23165 | 145 | 23162 | 140 | 23164 | 67 | 23106 | 188 | 23157 | 153 |
| 22942 | 368 | 22946 | 356 | 23060 | 171 | 22913 | 381 | 22937 | 373 |
| 22845 | 465 | 22834 | 468 | 22899 | 332 | 22852 | 442 | 22844 | 466 |
| | | | | 22824 | 407 | | | | |

 © 2006 Wiley-VCH Verlag GmbH & Co. KGaA, Weinheim 

solution belongs to the nine-coordinate species, the solution at pH 7.8 (NaOH) was frozen. It was shown previously that only monomeric species exist in solution at this pH value.[6,23] The $^4I_{9/2} \rightarrow {}^2P_{1/2}$ spectrum of this solution, as well as of both sodium and guanidinium crystals recorded at 4 K, are displayed in Figure 5. The spectrum of the frozen solution shows a very intense peak at 23310 $cm^{-1}$ and a very weak shoulder at 23248 $cm^{-1}$, which confirms the domination of the $[Nd(N_4O_6)]^{3-}$ species over the $[Nd(N_3O_6)]^{3-}$ one and that the peak at 23248 $cm^{-1}$ in the solution indeed represents the nine-coordinate form.

The peak maxima of the deprotonated sodium (**Na1**) as well as guanidinium (**II**) crystals do not shift on cooling the samples down to 4 K, whereas the peak at 23294 $cm^{-1}$ in the spectrum of **I** at room temperature splits into two with energies of 23302 and 23293 $cm^{-1}$ at 4 K. Since in all the spectra of **I** at 4 K there are more lines than would be expected from the relevant multiplicities ($J$ + 1/2), one can assume that a phase transition occurs in **I** below room temperature. This phase transition may also be reflected in the value of the oscillator strength ($P$) determined at 4 K. The smaller decrease of $P$ in the spectra of crystal **I** than those of crystal **II** at 4 K in comparison with the respective $P$ values determined at room temperature can readily be seen from the $P_{exp}$ results given in Table 4.

It should be pointed out that for crystals of **Na1** and **II**, for which no phase transition is observed, all f–f transitions in the spectra of **Na1** at 4 K are similarly, as can be seen for the $^4I_{9/2} \rightarrow {}^2P_{1/2}$ spectrum, broadened and red-shifted in relation to the spectra of crystal **II**. This may result from vibrational lattice and/or internal ligand modes coupled with the excited levels. This coupling is apparently much weaker for the chiral crystal.

The non-degeneracy of the $^2P_{1/2}$ level means that its shift can be used to study the nephelauxetic effect in neodymium

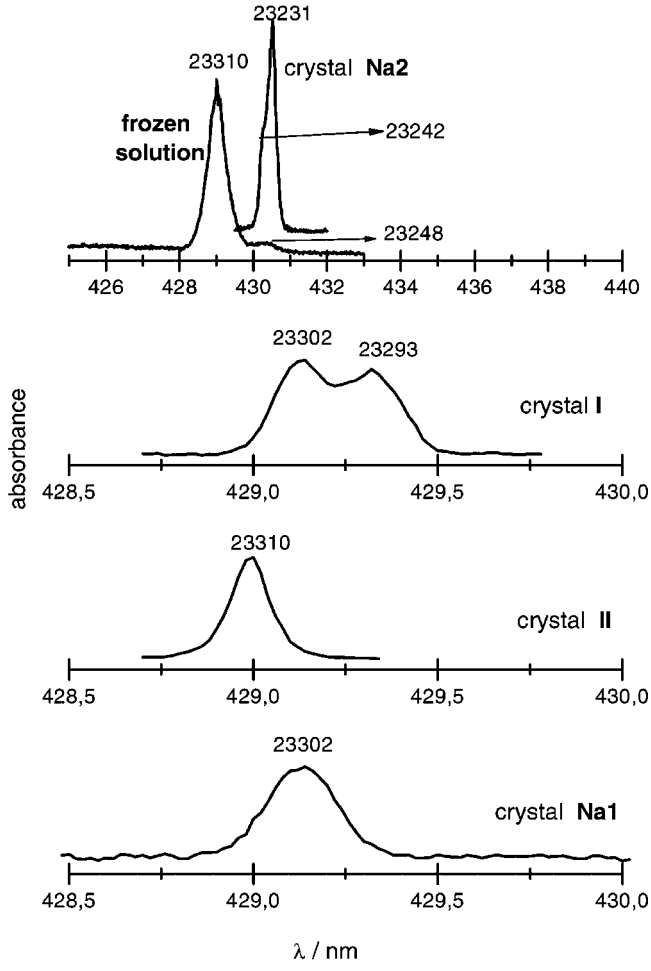


Figure 5. Absorption spectra of the $^4I_{9/2} \rightarrow {}^2P_{1/2}$ transition of the frozen $Nd^{III}$–TTHA solution with pH 7.8 and crystals of **I**, **II**, **Na1**[8] and **Na2**[16] at 4 K.

Table 4. Oscillator strength values ($P_{exp}$) and $\Omega_\lambda$ parameters for $Nd^{III}$–TTHA complexes in solution at different pH values (adjusted by NaOH) and single crystals of **I** and **II**.

| | Solution $Nd^{III}$/TTHA = 1:1.1 $c_{Nd}$ = 2.219 × $10^{-2}$ M | | | $[C(NH_2)_3]_2[Nd(HTTHA)]\cdot 3H_2O$ Crystal **I** $c_{Nd}$ = 2.270 M | | $[C(NH_2)_3]_3[Nd(TTHA)]\cdot 6H_2O$ Crystal **II** $c_{Nd}$ = 1.898 M | |
|---|---|---|---|---|---|---|---|
| | pH = 2.45 | pH = 5.35 | pH = 10.58 | 293 K | $d$ = 0.031 cm 4 K | 293 K | $d$ = 0.059 cm 4 K |
| Transition(s) $^4I_{9/2} \rightarrow$ | $10^8P_{exp}$ | $10^8P_{exp}$ | $10^8P_{exp}$ | $10^8P_{exp}$ | $10^8P_{exp}$ | $10^8P_{exp}$ | $10^8P_{exp}$ |
| $^4F_{3/2}$ | 235.55 | 188.07 | 233.40 | 269.20 | 221.90 | 207.61 | 92.01 |
| $^4F_{5/2}$, $^2H_{9/2}$ | 1079.71 | 934.61 | 936.76 | 886.50 | 744.21 | 861.22 | 459.57 |
| $^4F_{7/2}$, $^4S_{3/2}$ | 1156.00 | 1020.77 | 1030.57 | 883.18 | 651.98 | 913.49 | 571.49 |
| $^4F_{9/2}$ | 80.36 | 79.68 | 82.92 | 70.65 | 44.41 | 76.27 | 26.57 |
| $^2H_{11/2}$ | 20.73 | 20.31 | 20.40 | 15.48 | 15.59 | 17.67 | 10.83 |
| $^4G_{5/2}$, $^2G_{7/2}$ | 1688.05 | 1901.53 | 1935.43 | 1292.23 | 860.40 | 1066.66 | 588.19 |
| $^2K_{13/2}$, $^4G_{7/2}$, $^4G_{9/2}$ | 873.72 | 805.78 | 809.34 | 712.30 | 554.93 | 695.79 | 433.97 |
| $^2K_{15/2}$, $^2G_{9/2}$, ($^2D$, $^2F)_{3/2}$, $^4G_{11/2}$ | 224.32 | 207.22 | 197.55 | 193.30 | 234.82 | 198.87 | 206.56 |
| $^2P_{1/2}$ | 36.87 | 32.2 | 33.87 | 39.27 | 37.92 | 39.57 | 16.18 |
| $^2D_{5/2}$ | 6.10 | 8.31 | 9.14 | 15.39 | 11.44 | 13.49 | 12.05 |
| $^4D_{3/2}$, $^4D_{5/2}$, $^2I_{11/2}$, $^4D_{1/2}$, $^2L_{15/2}$ | 1118.69 | 983.68 | 985.24 | 1081.66 | 1011.79 | 912.33 | – |
| $10^{20}\Omega_2$ [$cm^2$] | 4.06 ± 0.46 | 5.53 ± 0.47 | 5.66 ± 0.40 | 2.10 ± 0.32 | | 1.65 ± 0.36 | |
| $10^{20}\Omega_4$ [$cm^2$] | 5.11 ± 0.43 | 4.46 ± 0.44 | 4.48 ± 0.37 | 4.56 ± 0.30 | | 3.75 ± 0.33 | |
| $10^{20}\Omega_6$ [$cm^2$] | 10.26 ± 0.59 | 8.91 ± 0.60 | 9.04 ± 0.52 | 6.95 ± 0.41 | | 7.22 ± 0.46 | |
| rms·$10^7$ | 8.24 | 8.39 | 7.24 | 6.38 | | 7.25 | |

 © 2006 Wiley-VCH Verlag GmbH & Co. KGaA, Weinheim 

systems. This effect is interpreted as a covalent contribution to the bonding between the metal ion and the ligands and is connected with metal–ligand distances and coordination numbers.[24] However, a comparison of the structural data given in Table 1 with the spectroscopic data of the $^4I_{9/2} \rightarrow {}^2P_{1/2}$ transition of $[Nd(N_4O_6)]^{3-}$ crystals contradicts this interpretation: of the three $[Nd(N_4O_6)]^{3-}$ crystals, the smallest $Nd^{III}$–O and $Nd^{III}$–N distances are found in the sodium crystal, but the spectral results of this crystal do not reflect this in a decrease of the $^2P_{1/2}$ energy level. The $^2P_{1/2}$ energy level shifts, however, agree well with the $\Delta$ differences between the $\nu_{as}$ and $\nu_s$ frequencies of the carboxylate groups. Therefore, our results seem to indicate that the nephelauxetic effect is caused by the change of local polarizability within the inner sphere of the metal ion.

*Analysis of the Hypersensitive Transition and f–f Intensities*

A comparison of the f–f transitions of all $Nd^{III}$–TTHA crystals as well as of the solution at pH 5.35, for which there is no difference in the spectra when the pH is adjusted with either NaOH or $[C(NH_2)_3]_2CO_3$, is shown in Figure 6. From the presented spectra, one can see a very good correspondence between the spectra of the monomeric sodium crystal **Na1** of the $[Nd(N_4O_6)]^{3-}$ complex and the solution, in spite of the fact that the presence of 20% of the $[Nd(N_3O_6)]^{3-}$ species was evidenced in the solution.[16] The remarkable similarity of the band shape and the intensities of the most intense f–f transitions between the spectra of the solution and the crystal of **Na1** is not preserved in the case of the protonated crystal **I** or in the deprotonated crystal **II**. For the latter crystal, although the shape of the f–f bands corresponds, to a considerable degree, to that of the solution, the intensity of the $^4I_{9/2} \rightarrow {}^4G_{5/2}/{}^2G_{7/2}$ transition is significantly lower. It is worthwhile stressing that the discussed crystals show low optical anisotropy, as measured by the difference of the intensities of various f–f transitions with different light polarisations and crystal orientations. The intensity results for solutions at different pH values adjusted by NaOH, as well as of crystals of **I** and **II**, are collected in Table 4. An inspection of the oscillator strengths given in this table shows that the largest differences between experimentally determined $P$ values of solutions and crystals occur for the hypersensitive transition. The oscillator strengths of the $^4I_{9/2} \rightarrow {}^4G_{5/2}/{}^2G_{7/2}$ transition of both guanidinium crystals are about two times smaller than those calculated for the solution in which the $[Nd(N_4O_6)]^{3-}$ species dominates. One might suppose that the discrepancies between the $P$ values of the solution and crystals may result from a more symmetrical arrangement of the first coordination sphere in the single crystal. However, this is not the case. In the case of the sodium crystal **Na1**, the $^4I_{9/2} \rightarrow {}^4G_{5/2}/{}^2G_{7/2}$ intensity ($P = 2076.51 \times 10^{-8}$)[8] is higher than that of the solution. Recalculation of the oscillator strengths of the most intense transitions, namely $^4I_{9/2} \rightarrow {}^4G_{5/2}/{}^2G_{7/2}$ (560–600 nm), $^4I_{9/2} \rightarrow {}^4S_{3/2}/{}^4F_{7/2}$ (720–770 nm) and $^4I_{9/2} \rightarrow {}^2H_{9/2}/{}^4F_{5/2}$ (770–830 nm), of the solution at a pH above 4.5 with the $P$ values determined for both **Na1**[8] and **Na2**[16] crystals and the percentage shares of both species reproduces well the oscillator strengths determined experimentally for the solution. This experimental fact is noteworthy, since it can be a helpful indicator of the hypersensitivity mechanism. The small decrease of metal–ligand bond lengths of the crystal **Na1** as compared with

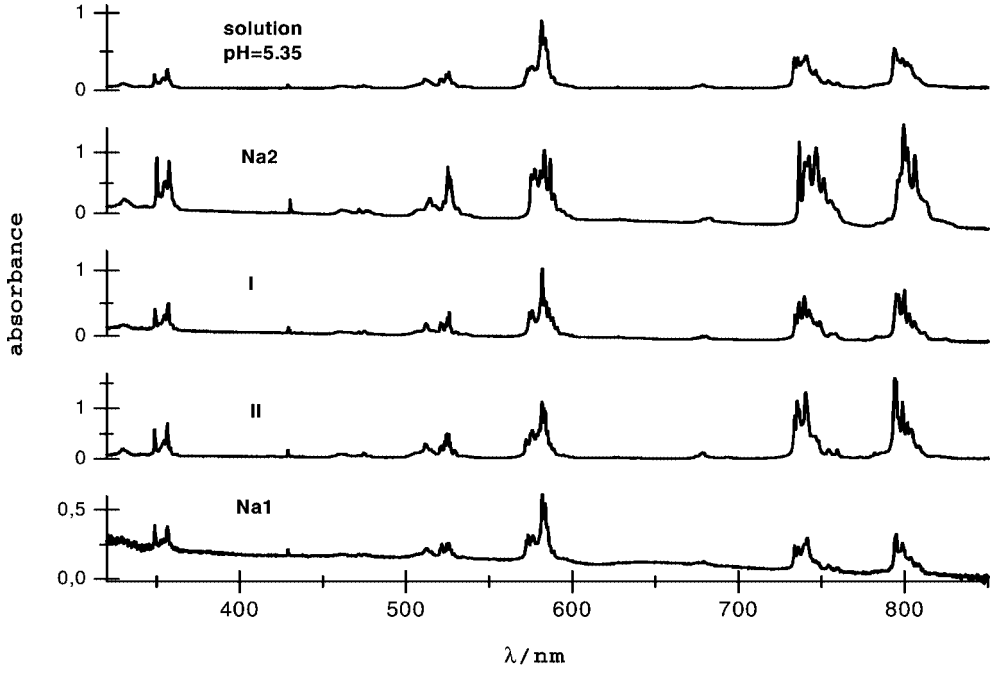


Figure 6. Absorption spectra of f–f transitions of the $Nd^{III}$–TTHA complex in solution at pH 5.35 ($c_{Nd}$ = 2.219·10$^{-2}$ M, $d$ = 2 cm) and in crystals **Na2** ($c_{Nd}$ = 1.631 M, $d$ = 0.147 cm), **I** ($c_{Nd}$ = 2.270 M, $d$ = 0.031 cm), **II** ($c_{Nd}$ = 1.898 M, $d$ = 0.059 cm) and **Na1** ($c_{Nd}$ = 1.671 M, $d$ = 0.0145 cm).

 © 2006 Wiley-VCH Verlag GmbH & Co. KGaA, Weinheim 

guanidinium crystals (Table 1) is probably a reason for the intensity enhancement in **Na1**. We also note that somewhat different factors affect the intensities of the hypersensitive transition and the position of the dominant peak in the $^4I_{9/2} \rightarrow {}^2P_{1/2}$ transition discussed above.

## Conclusions

Continuing our previous investigations of the structures and spectroscopic properties of complexes of TTHA with lanthanides, we have obtained crystals of two new complexes, namely $[C(NH_2)_3]_2[Nd(HTTHA)]\cdot 3H_2O$ and $[C(NH_2)_3]_3[Nd(TTHA)]\cdot 6H_2O$. The use of different countercations (guanidinium in the present compounds and sodium in our previous reports) has enabled us to observe their role in crystal formation as well as their influence on the spectroscopic properties of the investigated crystals. The complex anions $[Nd(TTHA)]^{3-}$ are monomeric and the neodymium cations are ten-coordinate in both crystals described. Although the coordination environment in both the present complexes is similar to that found in a previously published sodium salt,[8] the oscillator strengths of the hypersensitive transition differ remarkably. This may be attributed to the small differences of the Nd–O and Nd–N bond lengths, which may in turn be induced by networks of H-bonds, strong in the case of guanidinium crystals and competing with the Na–O electrostatic interactions in the case of the sodium crystal.

## Experimental Section

**Material and Sample Preparation:** A stock solution of neodymium perchlorate was prepared from $Nd_2O_3$ (99.9% Merck). The $Nd^{III}$ concentration was determined complexometrically using xylenol orange as indicator. The stock solution of $H_6TTHA$ (98% Aldrich) was prepared by half-neutralisation with NaOH. The NaOH solution was also used to adjust the pH of the investigated solutions. All measured solutions were prepared with the same ionic strength (0.5 M $NaClO_4$). Crystals of neodymium with the TTHA ligand were prepared by a slightly different method to that described by Ruloff et al.[9] The molar ratio of the applied parent substances of $Nd_2O_3$, $H_6TTHA$ and $[C(NH_2)_3]_2CO_3$ was 1:2:2. The mixture of substrates was dissolved in water and the pH of the resulting solution was 2.65. This solution was divided into two portions, one of which was basified with guanidinium carbonate to a final pH of 4.55. These solutions of pH 2.65 and 4.55 were left to crystallise and large, well-formed violet crystals of the formula $[C(NH_2)_3]_2[Nd(HTTHA)]\cdot 3H_2O$ and $[C(NH_2)_3]_3[Nd(TTHA)]\cdot 6H_2O$, denoted as **I** (pH 2.65) and **II** (pH 4.55), were obtained. The $Nd^{III}$ concentration in these crystals, determined by ICP, was 2.270 M for **I** and 1.898 M for **II**. **I**: calcd. C 29.71, H 5.20, N 17.33, Nd 17.85; found C 29.23, H 5.45, N 16.87, Nd 19.26. **II**: calcd. C 27.36, H 5.86, N 19.76, Nd 15.66; found C 27.77, H 5.75, N 19.96, Nd 17.11. The density of **I** and **II** was measured by the flotation method in $CH_3Cl$ and $CH_3Br$ and was found to be 1.70 and 1.60 g cm$^{-3}$, respectively. The refractive index, $n$, of the crystals was assumed to be 1.50 and that of the measured solutions 1.33.

**Crystal Structure Determinations of Complexes I and II:** Data for **I** and **II** were collected on a Kuma KM4 diffractometer equipped with a CCD counter. The structures were solved by Patterson methods with SHELXS-97[25] and then refined with SHELXL-97.[26] The C- and N-bonded hydrogen atoms were placed in geometrically calculated positions. All non-H atoms were refined anisotropically. The temperature factors for H-atoms were set as 1.2-times the factors of the C or N atoms to which they are bonded. For **II** the enantiomorph with the better Flack parameter [–0.019(15)] was chosen.

**Crystal Data for I:** $[C(NH_2)_3]_2[Nd(HTTHA)]\cdot 3H_2O$, $C_{20}H_{43}N_{10}NdO_{15}$, $M$ = 807.88, triclinic, $P\bar{1}$, $a$ = 9.998(2), $b$ = 10.730(2), $c$ = 15.557(3) Å, $\alpha$ = 106.89(3)°, $\beta$ = 90.27(3)°, $\gamma$ = 93.24(3)°, $V$ = 1594.0(5) Å$^3$, $Z$ = 2, $T$ = 293(2) K, $\mu$ = 1.711 mm$^{-1}$, number of reflections measured 11381, number of reflections observed [$I \geq 2\sigma(I)$] 6691, $R(F)$ = 0.0374, $R_w(F^2)$ = 0.0835.

**Crystal Data for II:** $[C(NH_2)_3]_3[Nd(TTHA)]\cdot 6H_2O$, $C_{21}H_{54}N_{13}NdO_{18}$, $M$ = 921.01, monoclinic, $P2_1$, $a$ = 10.157(2), $b$ = 15.958(3), $c$ = 12.788(3) Å, $\beta$ = 112.68(3)°, $V$ = 1912.5(7) Å$^3$, $Z$ = 2, $T$ = 293(2) K, $\mu$ = 1.445 mm$^{-1}$, number of reflections measured 5688, number of reflections observed [$I \geq 2\sigma(I)$] 4837, $R(F)$ = 0.0273, $R_w(F^2)$ = 0.0731.

CCDC-282725 (for **I**) and -282726 (for **II**) contain the supplementary crystallographic data for this paper. These data can be obtained free of charge from The Cambridge Crystallographic Data Centre via www.ccdc.cam.ac.uk/data_request/cif.

**Spectroscopic Measurements and Calculations:** IR spectra of crystals and $H_6TTHA$ were recorded from KBr pellets on a Bruker FTIR IFS66 spectrometer, while FT-Raman spectra of powder samples were measured on a Bruker RFS 100/S spectrometer with a spectral resolution of 2 cm$^{-1}$. All electronic absorption spectra were recorded with a Cary 500 UV/Vis/near-IR spectrophotometer which was equipped with an Oxford CF 1204 continuous flow helium cryostat for single crystal measurements at 293 and 4 K.

The intensities of the 4f–4f transitions ($P$) and values of the $\Omega_\lambda$ parameters were calculated from the Judd–Ofelt[27,28] relation [Equation (1)]:

$$P = \chi \frac{8\pi^2 mc\sigma}{3h(2J+1)} \sum_{\lambda=2,4,6} \Omega_\lambda (f^n \psi J \| U^{(\lambda)} \| f^n \psi' J')^2 \quad (1)$$

where $P$ denotes the oscillator strength, $\chi = (n^2 + 2)^2/9n$ ($n$ is the refractive index), $J$ is the total quantum number of the ground state, $(f^n \psi J \| U^{(\lambda)} \| f^n \psi' J')$ is the reduced matrix element of the respective unit tensor operator $U^{(\lambda)}$, tabulated by Carnall et al.,[29] and $\Omega_\lambda$ is the empirical least-squares-fitted parameter.

## Acknowledgments

The authors would like to thank Dr. B. Łydżba-Kopczyńska and Dr. L. Macalik for recording the Raman spectra.

[1] P. Caravan, J. J. Ellison, T. J. McMurry, R. B. Lauffer, *Chem. Rev.* **1999**, *99*, 2293–2352.
[2] S.-B. Yu, A. D. Watson, *Chem. Rev.* **1999**, *99*, 2353–2378.
[3] R. M. Sink, D. C. Buster, A. D. Sherry, *Inorg. Chem.* **1990**, *29*, 3645–3649.
[4] E. F. Gudgin Dickson, A. Pollak, E. P. Diamandis, *J. Photochem. Photobiol. B: Biol.* **1995**, *27*, 3–19.
[5] R. C. Holz, W. DeWitt Horrocks Jr, *Inorg. Chim. Acta* **1990**, *171*, 193–198.

 © 2006 Wiley-VCH Verlag GmbH & Co. KGaA, Weinheim 

[6] C. A. Chang, H. G. Brittain, J. Telser, M. F. Tweedle, *Inorg. Chem.* **1990**, *29*, 4468–4473.
[7] M. C. Alpoim, A. M. Urbano, C. F. G. C. Geraldes, J. A. Peters, *J. Chem. Soc., Dalton Trans.* **1992**, 463–467.
[8] A. Mondry, P. Starynowicz, *Inorg. Chem.* **1997**, *36*, 1176–1180.
[9] R. Ruloff, P. Prokop, J. Sieler, E. Hoyer, L. Beyer, *Z. Naturforsch., Teil B* **1996**, *51*, 963–968.
[10] R.-Y. Wang, J.-R. Li, T.-Z. Jin, G.-X. Xu, Z.-Y. Zhou, X.-G. Zhou, *Polyhedron* **1997**, *16*, 1361–1364.
[11] R.-Y. Wang, J.-R. Li, T.-Z. Jin, G.-X. Xu, Z.-Y. Zhou, X.-G. Zhou, *Polyhedron* **1997**, *16*, 2037–2040.
[12] R. Ruloff, T. Gelbrich, J. Sieler, E. Hoyer, L. Beyer, *Z. Naturforsch., Teil B* **1997**, *52*, 805–809.
[13] A. Mondry, P. Starynowicz, *New J. Chem.* **2000**, *24*, 603–607.
[14] J. Wang, Z.-R. Liu, X.-D. Zhang, W.-G. Jia, H.-F. Li, *J. Mol. Struct.* **2003**, *644*, 29–36.
[15] D.-F. Chen, W.-C. Yang, R.-Y. Wang, T.-Z. Jin, *Acta Chim. Sin. (Engl. Ed.)* **1997**, *55*, 672–677.
[16] A. Mondry, P. Starynowicz, *J. Chem. Soc., Dalton Trans.* **1998**, 859–863.
[17] A. Mondry, J. P. Riehl, *Acta Phys. Polon. A* **1993**, *84*, 969–974.
[18] C. L. Maupin, A. Mondry, L. Leifer, J. P. Riehl, *J. Phys. Chem. A* **2001**, *105*, 3071–3076.
[19] A. Mondry, S. C. J. Meskers, J. P. Riehl, *J. Lumin.* **1994**, *62*, 17–23.
[20] D. Chapman, D. R. Lloyd, R. H. Prince, *J. Chem. Soc.* **1963**, *85*, 3645–3658.
[21] A. Mondry, K. Bukietyńska, *Molec. Phys.* **2003**, *101*, 923–934.
[22] A. Mondry, K. Bukietyńska, *J. Alloys Compd.* **2004**, *374*, 27–31.
[23] H. G. Brittain, *J. Coord. Chem.* **1990**, *21*, 295–299.
[24] R. D. Peacock, *Struct. Bond.* **1975**, *22*, 83–122.
[25] G. M. Sheldrick, *SHELXS-97, Program for solution of crystal structures*, University of Göttingen, Germany, **1997**.
[26] G. M.Sheldrick, *SHELXL-97*, *Program for refinement of crystal structures*, University of Göttingen, Germany, **1997**.
[27] B. R. Judd, *Phys. Rev.* **1962**, *127*, 750–761.
[28] G. S. Ofelt, *J. Chem. Phys.* **1962**, *37*, 511–520.
[29] W. T. Carnall, P. R. Fields, K. Rajnak, *J. Phys. Chem.* **1968**, *49*, 4424–4442.

Received: November 16, 2005
Published Online: March 16, 2006

 © 2006 Wiley-VCH Verlag GmbH & Co. KGaA, Weinheim 

DOI: 10.1002/ejic.200501024

# Synthesis of Polyamines from Ethylenediamine and Their Platinum(II) Complexes, Potential Antitumor Agents

**Mara Rubia Costa Couri,[a] Mauro Vieira de Almeida,[a] Ana Paula Soares Fontes,*[a] Joana D'Arc Souza Chaves,[a] Eloi Teixeira Cesar,[b] Ricardo José Alves,[c] Elene Cristina Pereira-Maia,[d] and Arlette Garnier-Suillerot[e]**

**Keywords:** Amines / Platinum / Antitumor agents

This work describes the synthesis and characterization of five new amine ligands and also the preparation and characterization of their respective platinum(II) complexes by reaction with $K_2PtCl_4$ in water. These ligands were obtained by treatment of different halides or epoxides with ethylenediamine. Cytotoxic activity and cellular accumulation of three complexes were investigated in a human small-cell lung carcinoma cell line and its cisplatin resistant subline. The introduction of a spacer (cycle) between the two platinum atoms leads to a significant decrease in cytotoxic activity. At equitoxic doses, the intracellular platinum concentrations found for compounds **12** and **15** were significantly higher than those found for the reference compounds, cisplatin, carboplatin, or compound **9**. This fact suggests that the formation of adducts between compounds **12** and **15** and the putative pharmacological target, DNA, is less favored. If these compounds bind more slowly to DNA, interaction with other intracellular ligands such as sulfur-containing molecules will become relevant and it may be the reason for the elevated intracellular platinum concentrations.
(© Wiley-VCH Verlag GmbH & Co. KGaA, 69451 Weinheim, Germany, 2006)

## Introduction

The polyamines spermidine (1,8-diamino-4-azaoctane) and spermine (1,12-diamino-4,9-diazadodecane), as well as the precursor molecule putrescine (1,4-diaminobutane), are polycation compounds that are found in significant amounts in nearly every prokaryotic and eukaryotic cell type.[1]

Many of these bases and their derivatives play key roles in a number of biological processes and possess a variety of pharmacological properties.[2] Polyamines may act as carcinogenesis promoting factors.[2,3] The connection between polyamines and cancer growth has been established by biological and molecular techniques.[4] Polyamines have been shown to accumulate in cancer tissues, and the concentration of polyamines and their derivatives increases in cancer patient fluids.[5–9] These compounds also represent an important target for chemotherapeutic intervention, since depletion of polyamines results in the disruption of a variety of functions and may, in specific cases, result in cytotoxicity.[10] Inhibitors of the polyamine pathway, therefore, have traditionally been developed as potential antitumor agents.[11]

Polyamines have multiple cellular functions that can interfere with cell growth and cell death. Therefore, their analogs can play an important role in controlling cancer. Compounds of this class can directly bind to DNA and modulate DNA–protein interactions. The production of hydrogen peroxide from polyamine catabolism might also be responsible for cell death or apoptosis.[12]

In addition to these facts, neutral ligands derived from amines have been utilized to prepare platinum(II) complexes since the discovery of the anticancer activity of cisplatin by Rosenberg et al.[13] *cis*-Diaminedichloroplatinum(II) (cisplatin, CDDP)[14] is one of the most widely used and effective oncological agents against cancers of the testicles, ovaries, bladder, head, and neck.[14–16] It is also an important adjunct for cancers of the lung, cervix, and breast.[16] However, its clinical usefulness has frequently been limited by severe side effects,[17–19] such as nephrotoxicity, ototoxicity, and neurotoxicity, and by the emergence of cancer cells resistant to cisplatin.

Tumor cells having the resistance phenotype exhibit a reduced sensitivity to cytotoxic drugs relative to sensitive cells. The molecular basis for resistance has been the subject of intensive research. Three main events are frequently observed: (i) decreased accumulation of the drug; the intracel-

[a] Departamento de Química, Universidade Federal de Juiz de Fora,
36036-900, Juiz de Fora-MG, Brazil
E-mail: ana.fontes@ufjf.edu.br
[b] Colégio de Aplicação João XXIII,
Juiz de Fora-MG, Brazil
[c] Faculdade de Farmácia, Universidade Federal de Minas Gerais,
Belo Horizonte-MG, Brazil
[d] Departamento de Química, Universidade Federal de Minas Gerais,
Belo Horizonte-MG, Brazil
[e] Laboratoire de Physicochimie Biomoléculaire et cellulaire (ESA 7033), Université Paris Nord,
Bobigny, France

 © 2006 Wiley-VCH Verlag GmbH & Co. KGaA, Weinheim 

lular drug concentration falls below the threshold necessary for cytotoxic activity; (ii) increased levels of sulfur-containing molecules, such as glutathione or metallothionein; these molecules could play a role in metal detoxification; and (iii) enhanced repair of DNA damage caused by cisplatin–DNA adducts.[20–22]

The need to overcome these problems, as well as to increase the antitumor activity of the platinum complexes, led to the development of structurally different compounds, which might act in different ways against the tumor cells.[23] The family of dinuclear complexes containing two monofunctional platinum spheres linked by a variable diamine chain has been extensively studied.[24] The first cytotoxic dinuclear platinum compounds described in the literature received special attention because they have shown a degree of cytotoxicity comparable to that of cisplatin in sensitive cell lines, but a significantly higher activity in acquired cisplatin-resistant cell lines.[25,26]

Since some substituted ethylenediamine platinum complexes have shown antitumor activity against a variety of cell tumors,[27,28] we sought to synthesize platinum(II) mono- and dinuclear complexes containing ethylenediamine derivatives as ligands. The novel compounds that were prepared may show a different reactivity towards DNA with the possibility of the formation of new adducts; they therefore may be active in cisplatin-resistant cell lines. In addition, compound **12** could possibly intercalate between the DNA base pairs because of its aromatic ring. Furthermore, we intended to prepare potentially active antitumor compounds in an attempt to combine the activity of the ligand to that of the metal.

## Results and Discussion

The intermediate **3** was obtained in 92% yield by the reaction of diol **2** with iodine, imidazole, and triphenylphosphane in toluene at reflux (Scheme 1). The diepoxide **8** (not isolated) was prepared by treatment of ditosylate **7** with sodium methoxide in methanol according to the procedure previously described in the literature.[29] The ligand **a** and complex **9** were prepared as described in ref.[26] The ligands **b**–**g** were prepared in satisfactory yields by treating ethylenediamine with the corresponding intermediate (halide or epoxide) in ethanol at room temperature for 24 h. In the preparation of the ligand *N*,*N*′-bis(2-aminoethyl)-2-xylylenediamine (**e**), we have also isolated the ligand *N*-(2-aminoethyl)-isoindoline (**f**). In the IR spectra, absorptions corresponding to $\nu_{N-H}$ at 3300–3100 $cm^{-1}$ can be observed for these ligands. In the $^1H$ and $^{13}C$ NMR spectra signals for the ethylenediamine moiety are observed.

The platinum(II) complexes **10**–**15** were obtained by the reaction of the corresponding ligands with potassium tetrachloroplatinate(II) in water at room temperature for 24 h, and were isolated by simple filtration (Scheme 2). Even though we have used 2 mmol of $K_2PtCl_4$ we have observed that under these reaction conditions, ligand **c** was transformed into the mononuclear platinum(II) complex **11**. For these compounds, one may observe IR spectra absorptions corresponding to $\nu_{Pt-N}$ and $\nu_{Pt-Cl}$ at 550 and 325 $cm^{-1}$, respectively, in addition to the absorptions observed for the ligand. In the $^1H$ NMR spectra there is a downfield shift for the signals corresponding to NH and $NH_2$ relative to the free ligands. The $^{195}Pt$ NMR spectra for the complexes show only one signal, and the chemical shift values are expected to be close to those of similar compounds in which the platinum is coordinated to two chlorides and two nitrogens.[30]

### Cell Growth Inhibition

The $IC_{50}$ values obtained for complexes **9**, **12**, and **15** in sensitive and resistant cells, together with the resistant factor (RF) and the intracellular platinum concentration, Ci, are shown in Table 1. For the sake of comparison, cisplatin and carboplatin data are also shown. The GLC4/CDDP subline is 6.3-fold resistant to cisplatin and 1.4- to carboplatin.

The cytotoxic activity of the compounds decreases in the order **9** > **12** > **15**. The sensitivity of the GLC4 cell line to compound **9** is comparable to that of carboplatin, and the GLC4/CDDP subline is not cross-resistant to compound **9**. The cytotoxic activity of compounds **12** and **15** is very low relative to that of the reference compounds. For **12** the RF obtained is 2.9, and for **15** the RF is 1.2 (Figure 1). In other words, the GLC4/CDDP cells are 3- and 1.2 times less sensitive than the GLC4 cells to **12** and **15**, respectively.

### Platinum Accumulation

Resistance to cisplatin has been intensively studied in tumor cells repeatedly exposed to the drug in vitro. Among the numerous mechanisms of acquired resistance to cisplatin that have been reported, decreased accumulation is frequently present in resistant cells as a result of reduced drug uptake. In a previous study, we have determined the uptake rate of cisplatin, carboplatin, and aqua-substituted cisplatin in both GLC4 and GLC4/CDDP cell lines.[31] The sensitive cell line accumulates approximately twice as much cisplatin as the resistant subline, mainly by an energy-dependent mechanism. We have postulated that the uptake of cisplatin is composed of passive diffusion of the $[Pt(NH_3)_2Cl_2]$ species, which is neutral, and of an active uptake of an aqua-substituted species, probably the $[Pt(NH_3)_2(H_2O)OH]^+$ or $[Pt(NH_3)_2(H_2O)Cl]^+$ species. For carboplatin, the rate constant for the first aquation reaction is 100-fold lower than that for cisplatin. Therefore, the concentration of aquated species will be 100 times lower. The uptake rate of carboplatin is similar in both GLC4 and GLC4/CDDP cell lines because the active uptake becomes negligible. Therefore, carboplatin enters the cells mainly by passive diffusion, which is in accordance with the low RF observed for carboplatin (Table 1).

The cytotoxic activities of compounds **12** and **15** were much lower than those exhibited by cisplatin and by com-

 © 2006 Wiley-VCH Verlag GmbH & Co. KGaA, Weinheim 

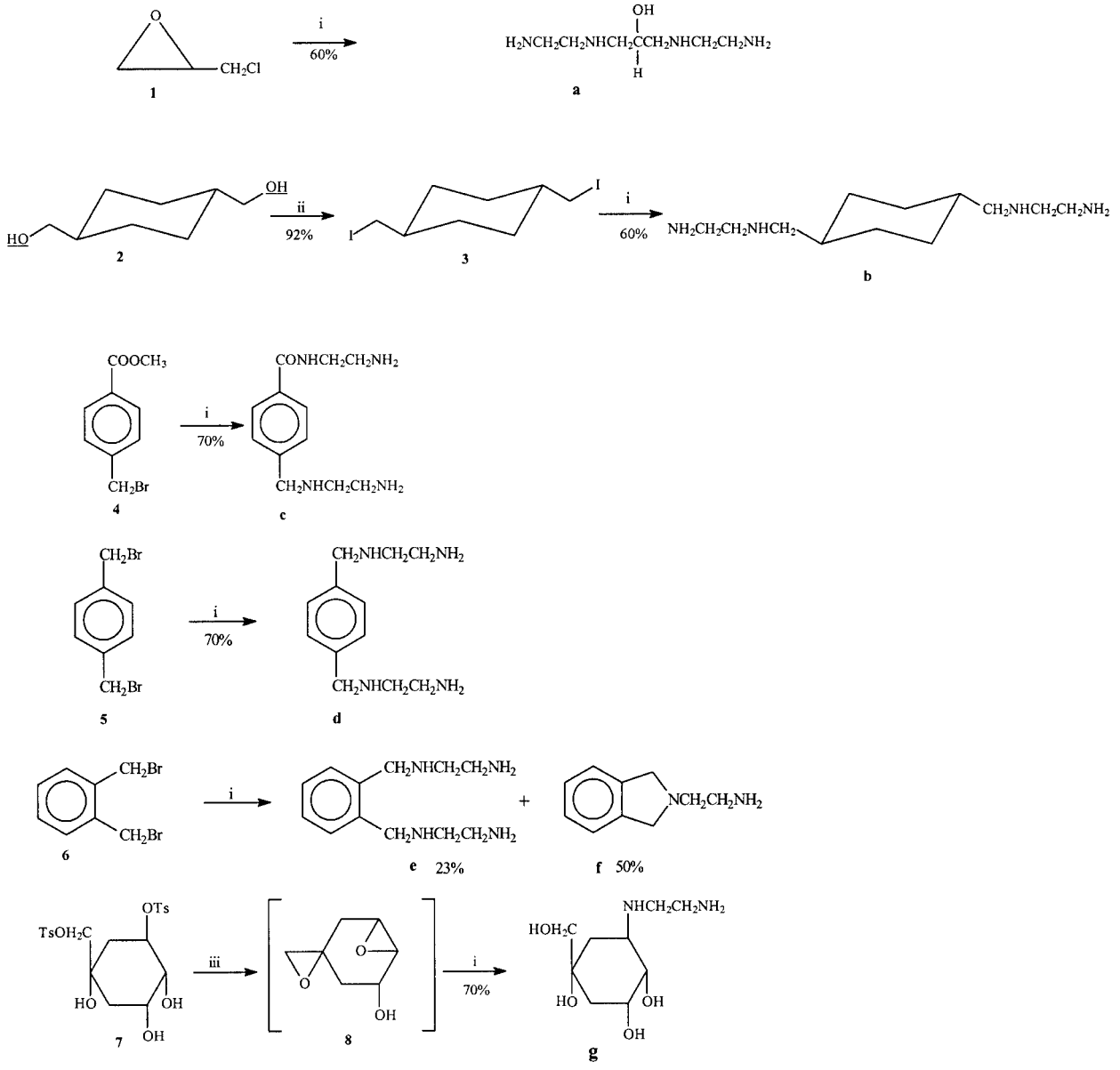


Scheme 1. Reagents and conditions: (i) $NH_2CH_2CH_2NH_2$/EtOH, reflux; (ii) $Ph_3P/I_2$/imidazole, toluene, reflux, 24 h; (iii) $MeO^-Na^+$/MeOH, room temp., 30 min.

pound **9**. These results can be explained by two possibilities: (i) the uptake of compounds **12** and **15** is very slow, thus a much higher concentration is needed to force their transport into cells (similar to the case of carboplatin when compared to cisplatin) or (ii) the interaction of the compounds with the pharmacological target, i.e. DNA, is deficient. In order to investigate whether the reason for this low activity is related to a deficient uptake, we have determined the intracellular platinum concentration after 72 h of incubation.

Let us first discuss the results obtained with the sensitive cell line. In a previous study, we found that cytotoxic activity correlates well with the intracellular drug concentration for cisplatin and carboplatin, and at $IC_{50}$, the intracellular platinum concentration was about $10 \times 10^{-17}$ mol/cell.[31] Furthermore, by studying the effect of some dinuclear platinum compounds, we also found that equitoxic platinum concentrations lead to similar intracellular platinum concentrations.[26]

Compound **9** exhibits the same behavior, for example, by incubating cells with the $IC_{50}$ dose, the intracellular concentration is approximately $10 \times 10^{-17}$ mol/cell. The ratio between the $IC_{50}$ of carboplatin and that of cisplatin is approximately 25, i.e. more carboplatin is needed to produce a cytotoxic effect because the former enters cells more slowly. Our results showed that the reason for the low cytotoxic activities of **12** and **15** was not an insufficient intracellular platinum concentration. On the contrary, the intracellular platinum concentrations found for compounds **12** and **15** were significantly higher than those found for the reference compounds, cisplatin and carboplatin, and compound **9**. For the sensitive cell line, at $IC_{50}$ values, the intracellular platinum concentrations were 14.9- and 9.3-fold higher for

 © 2006 Wiley-VCH Verlag GmbH & Co. KGaA, Weinheim 

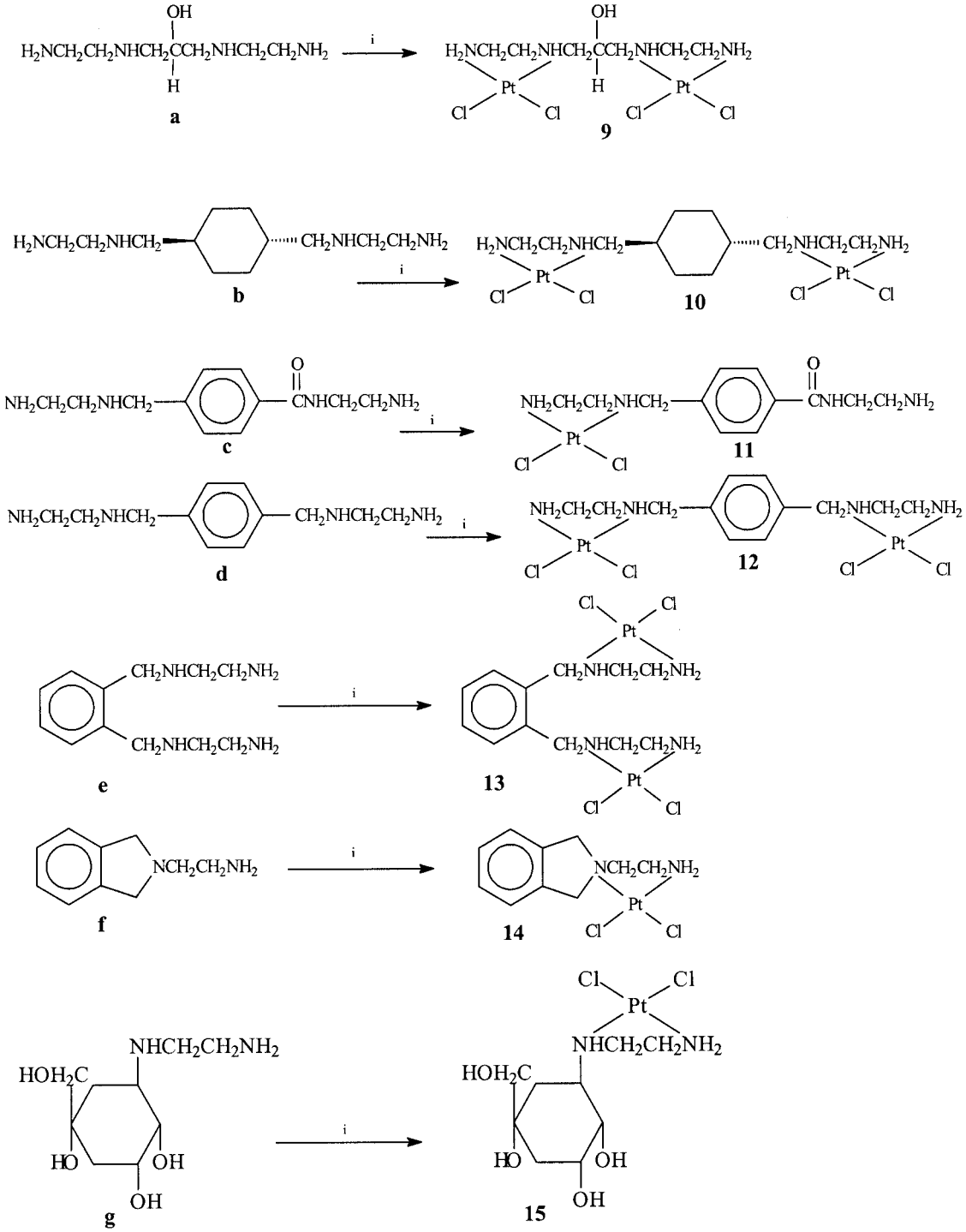


Scheme 2. Reagents and conditions: (i) $K_2PtCl_4$, $H_2O$, room temp.

compounds **12** and **15**, respectively, than that attained with cisplatin. This fact suggests that the formation of adducts between compounds **12** and **15** and the putative pharmacological target DNA is less favored. Knox et al.[32] postulated that the difference in the kinetics of the interaction with DNA is responsible for the different sensitivity of the same cell line to cisplatin and carboplatin. According to these authors, 20- to 40-fold larger doses of carboplatin were required to produce equal binding to DNA and equal cytotoxicity. In a review of structure–activity relationships of some dinuclear platinum compounds, Farrell et al.[33] reported that the cytotoxic activity of a dinuclear compound containing cyclohexane-1,4-diamine as a linker between two platinum atoms was very disappointing, probably because sterically hindered compounds bind more slowly to DNA. Assuming that equal binding to DNA would result in an equal cytotoxic effect, the fact that the intracellular concentrations found for compounds **12** and **15** are much

 © 2006 Wiley-VCH Verlag GmbH & Co. KGaA, Weinheim 

Table 1. $IC_{50}$, RF, and intracellular platinum concentration[a] for complexes **9**, **12**, and **15**.

| Compound | Cell Line | $IC_{50}$ [μM] | RF | $Ci \times 10^{16}$ [mol/cell] |
|---|---|---|---|---|
| DDP[b] | GLC4 | 0.40 ± 0.05 | | 0.98 ± 0.09 |
| CDDP[b] | GLC4/CDDP | 2.5 ± 0.2 | 6.3 | 1.07 ± 0.11 |
| CBDCA[b] | GLC4 | 9.9 ± 1.1 | | 0.79 ± 0.08 |
| CBDCA[b] | GLC4/CDDP | 13.5 ± 1.3 | 1.4 | 1.02 ± 0.11 |
| **9** | GLC4 | 9.9 ± 0.9 | | 0.96 ± 0.10 |
| **9** | GLC4/CDDP | 8.9 ± 0.9 | 0.9 | 1.05 ± 0.10 |
| **12** | GLC4 | 28.10 ± 2.80 | | 14.92 ± 1.50 |
| **12** | GLC4/CDDP | 81.0 ± 8.1 | 2.88 | 65.90 ± 6.70 |
| **15** | GLC4 | 84.0 ± 8.3 | | 9.28 ± 0.90 |
| **15** | GLC4/CDDP | 102.5 ± 10.3 | 1.22 | 24.10 ± 2.50 |

[a] $IC_{50}$ is the complex concentration required to inhibit 50% of cell growth. [b] ref.[31] RF value was calculated as resistant cell $IC_{50}$/sensitive cell $IC_{50}$. The values represent the mean ± SD of triplicate determinations;·Ci is the mol number of platinum per cell at $IC_{50}$ doses after 3 d.

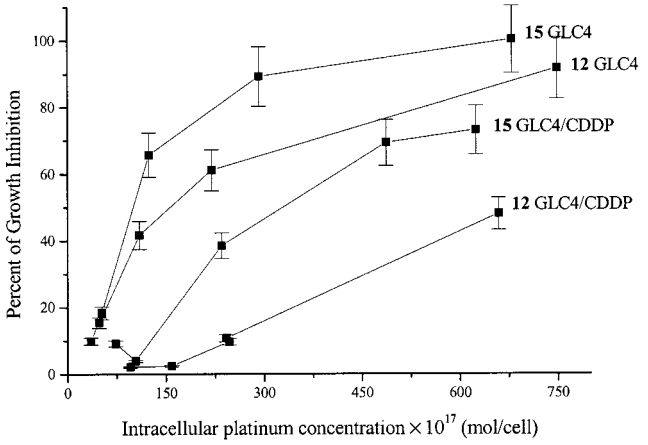


Figure 1. Growth inhibition of GLC4 and GLC4/CDDP cells as a function of the intracellular platinum concentration after 3 d of incubation with equitoxic doses of complexes **12** and **15**. The values are the mean values of two independent experiments. The platinum content was assessed by flameless atomic absorption spectroscopy.

higher than those of the reference compounds indicates that **12** and **15** bind to DNA more slowly or with a lower affinity, probably because of steric hindrance.

If these compounds bind more slowly to DNA, interaction with other intracellular ligands such as sulfur-containing molecules will become relevant and this may be the reason for the elevated intracellular platinum concentrations.

Considering **9** and **12**, these dinuclear platinum compounds are expected to form interstrand cross-links with DNA. The structural difference between them lies in the diamine linker. One can speculate that the insertion of a spacer (cycle) between the two platinum atoms engenders a steric hindrance to form DNA adducts. It is also possible that **12** only forms monoadducts with DNA.

An intriguing point to be considered is that a substantially higher intracellular platinum concentration is required to achieve a comparable cytotoxic effect in resistant cells by compounds **12** and **15** than in sensitive cells. Increased levels of sulfur-containing molecules have been found in various resistant cell lines. Hospers et al.[34] found that the GLC4/CDDP cell line possesses a significantly higher amount of sulfur-containing molecules than the GLC4 cell line, especially glutathione. Increased levels of sulfhydryl compounds are pointed as a possible mechanism for resistance. These thiols could bind to platinum and prevent it from attaining its target, DNA. If resistant cells possess higher levels of sulfur-containing compounds, one could expect to find a higher platinum concentration within resistant cells, because these compounds could bind to platinum in a detoxification mechanism. This is the case for compounds **12** and **15**. A possible explanation is that the interactions of these compounds with DNA are very slow, thus interactions of other intracellular ligands such as glutathione become determinant. They are able to accumulate in cells but are not very effective in binding to DNA and inhibiting cell growth.

In the cases of cisplatin, carboplatin, and compound **9** we have observed that the equal intracellular platinum amounts are responsible for equal cytotoxicity. Thus, the larger doses required in the case of resistant cells are necessary to force the uptake, and, once inside cells, equal platinum amounts can produce equal binding to DNA and equal cytotoxic effects. Sadowitz et al.[35] have shown that at low concentrations of cisplatin, endogenous thiols intercept cellular platinum, but this mechanism is not relevant at CDDP concentrations within the therapeutic range.

## Conclusion

This work describes the synthesis and characterization of different amine-ligand derivatives of 1,2-ethylenediamine, and also the preparation and characterization of their respective platinum(II) complexes.

Concerning the dinuclear platinum complexes, the introduction of a spacer (cycle) between the two platinum atoms leads to a significant decrease in cytotoxic activity. This finding is very important in guiding further design of dinuclear platinum compounds aimed at treating cancer.

## Experimental Section

**Reagents:** All chemicals were of reagent grade and were used without further purification.

### Starting Materials

**Compound 3:** Imidazole (2.82 g, 41.6 mmol), triphenylphosphane (10.92 g, 41.6 mmol), and iodine (10.6 g, 41.6 mmol) were added to a solution of *trans*-1,4-bis(hydroxymethyl)cyclohexane (**2**) (2.0 g, 14 mmol) in toluene (50 mL). The reaction mixture was stirred at 60 °C in an oil bath for 2 h. The solution was cooled, treated with an aqueous solution of sodium bisulfite and extracted with toluene (3 × 50 mL). The organic phases were combined and concentrated.

 © 2006 Wiley-VCH Verlag GmbH & Co. KGaA, Weinheim 

The crude product was purified on silica gel using *n*-hexane as the eluent to give **3** in 92% yield (4.65 g, 12.77 mmol).

**Compound 8:**[29] Methanolic sodium methoxide (25 mmol of sodium in 10 mL of methanol) was slowly added to a solution of ditosylate **7** (5 g, 10.35 mmol) in methanol (15 mL). The reaction was stirred for 30 min at room temperature, concentrated under reduced pressure and added to chloroform (10 mL). The resulting precipitate was collected and washed, and the filtrate was concentrated under reduced pressure to give **8** in quantitative yield.

### Synthesis of Ligands

**Ligand a:** This ligand was prepared by following the procedure described in ref.[26]

General procedure for the preparation of ligands **b**–**g** is shown in Scheme 1.

The corresponding halide or epoxide (10 mmol) was slowly added to a solution of ethylenediamine (6.7 mL, 100 mmol) in ethanol (20 mL) over 5 h. The reaction mixture was stirred for 12–24 h under reflux, evaporated under reduced pressure, and the residue purified on silica gel using dichloromethane/methanol as the eluent. Yields: (**b**) 1.37 g (60%), (**c**) 1.18 g (50%), (**d**) 1.56 g (70%), (**e**) 1.20 g (54%), (**f**) 0.18 g (11%), and (**g**) 1.54 g (70%)

**(b):** IR (KBr): $\tilde{\nu}_{max}$ = 2925, 2853, 1634, 1401, 1350, 1037, 772 $cm^{-1}$. $^1H$ NMR (200 MHz, $CD_3OD$): $\delta$ = 3.25 (m, 8 H, $CH_2N$), 1.38 (m, 6 H, CH, $CH_2$ cyclohexyl) ppm. $^{13}C$ NMR (50 MHz, $CD_3OD$): $\delta$ = 54.0 ($CH_2NHCH_2CH_2NH_2$), 44.7 ($NHCH_2$), 36.5 ($CH_2NH_2$), 35.4, 28.6 (cyclohexyl) ppm.

**(c):** IR (KBr): $\tilde{\nu}_{max}$ = 2933, 1646, 1543, 1506, 1313, 1160, 1108, 1019, 859, 757 $cm^{-1}$. $^1H$ NMR (200 MHz, $CD_3OD$): $\delta$ = 7.79 (d, 2 H, H-2, H-6, $J$ = 8.0 Hz), 7.55 (d, 2 H, H-3, H-5, $J$ = 8.0 Hz) ppm. $^{13}C$ NMR (50 MHz, $CD_3OD$): $\delta$ = 170.6 (C=O), 134.6, 134.0, 130.1, 128.1 (Ph), 51.0 ($CH_2Ph$), 44.0, 39.3 ($CH_2NH$), 37.4, 35.7 ($CH_2NH_2$) ppm.

**(d):** IR (KBr): $\tilde{\nu}_{max}$ = 2948, 2821, 1594, 1384, 1352, 1247, 1055, 774, 669 $cm^{-1}$. $^1H$ NMR (200 MHz, $CD_3OD$): $\delta$ = 7.32 (s, 4 H, CH), 3.74 (s, 4 H, CH), 3.74 (s, 4 H, $CH_2Ph$), 2.71 (t, 8 H, $NHCH_2$, $CH_2NH_2$) ppm. $^{13}C$ NMR (50 MHz, $CD_3OD$): $\delta$ = 139.7, 129.6 (Ph), 54.1 ($CH_2Ph$), 51.8 ($NHCH_2$), 41.7 ($CH_2NH_2$) ppm.

**(e):** IR (KBr): $\tilde{\nu}_{max}$ = 2950, 2820, 1592, 1386, 1352, 1248, 1055, 772, 669 $cm^{-1}$. $^1H$ NMR (200 MHz, $CD_3OD$): $\delta$ = 7.44 (m, 4 H, Ph), 4.17 (s, 4 H, $CH_2Ph$), 3.11 (m, 8 H, $NHCH_2$, $CH_2NH_2$) ppm. $^{13}C$ NMR (50 MHz, $CD_3OD$): $\delta$ = 136.6, 132.9, 130.4 (Ph), 52.2 ($CH_2Ph$), 46.6 ($CH_2NH$), 39.5 ($CH_2NH_2$) ppm.

**(f):** IR (KBr): $\tilde{\nu}_{max}$ = 2948, 1594, 1383, 1352, 1058, 775, 667 $cm^{-1}$. $^1H$ NMR (200 MHz, $CD_3OD$): $\delta$ = 7.21 (m, 4 H, Ph), 4.04 (s, 4 H, $CH_2Ph$), 3.09 (m, 4 H, $NHCH_2$, $CH_2NH_2$) ppm. $^{13}C$ NMR (50 MHz, $CD_3OD$): $\delta$ = 140.4, 130.0, 124.6 (Ph), 59.9 ($CH_2Ph$), 53.5 ($CH_2NH$), 39.1 ($CH_2NH_2$) ppm.

**(g):** IR (KBr): $\tilde{\nu}_{max}$ = 3403, 2936, 2862, 1648, 1573, 1460, 1343, 1301, 1151, 1052, 958 $cm^{-1}$. $^1H$ NMR (200 MHz, $CD_3OD$): $\delta$ = 3.92 (m, 1 H, H-3), 3.70 (t, 1 H, H-4), 3.13 (t, 1 H, H-5), 2.64 (m, 4 H, $CH_2NH$, $CH_2NH_2$), 1.80 (m, 4 H, H-2, H-2′, H-6, H-6′) ppm. $^{13}C$ NMR (50 MHz, $CD_3OD$): $\delta$ = 76.7, 71.1, 68.5, 65.6 (C-1, C-3, C-4, C-7), 63.8, 59.8, 44.0 (C-5, $CH_2N$), 38.7, 36.7 (C-2, C-6) ppm.

### Synthesis of Complexes 9–15

**Complex 9:** Prepared following the procedure described in ref.[26]

**Complexes 10–15 (Scheme 2):** The appropriate ligand (1 mmol), dissolved in water (5 mL), was slowly added to a solution of $K_2PtCl_4$ (0.830 g, 2 mmol) in water (10 mL). After stirring for 24 h in the dark at room temperature, the solid that formed was filtered off, washed with water, and dried. In the case of complexes **14** and **15** only 1 mmol of $K_2PtCl_4$ was used. Yields: (**10**) 0.47 g (62%), (**11**) 0.25 g (50%), (**12**) 0.69 g (92%), (**13**) 0.32 g (42%), (**14**) 0.17 g (40%), (**15**) 0.364 g (75%).

**(10):** IR (KBr): $\tilde{\nu}_{max}$ = 3270, 2910, 2846, 1628, 1313, 1045, 827, 549, 326 $cm^{-1}$. $^{195}Pt$ NMR (86 MHz, [D$_6$]DMSO) (DMSO = dimethyl sulfoxide): $\delta$ = –2380 ppm. $C_{12}H_{28}N_4Pt_2Cl_4$ (760.18): calcd. C 18.95, H 3.68, N 7.37; found C 19.15, H 3.86, N 7.35.

**(11):** IR (KBr): $\tilde{\nu}_{max}$ = 3207, 3114, 2923, 2847, 1639, 1541, 1462, 1306, 1188, 1060, 1014, 861, 759, 569, 317 $cm^{-1}$. $^1H$ NMR (400 MHz, [D$_6$]DMSO): $\delta$ = 2.83, 3.59 (m, 4 H, $CH_2NH$, $CH_2NH_2$), 4.25 (m, 4 H, $CH_2Ph$), 5.08, 6.29 (s, 3 H, NH, $NH_2$), 7.95 (m, 4 H, Ar) ppm. $^{13}C$ NMR (100 MHz, [D$_6$]DMSO): $\delta$ = 54.3–45.6 ($CH_2NH$, $CH_2NH_2$), 61.1 ($CH_2Ph$); 128.0–130.4 (Ar) ppm. $^{195}Pt$ NMR (86 MHz, [D$_6$]DMSO): $\delta$ = –2018 ppm. $C_{12}H_{20}N_4PtCl_2$ (486.21): calcd. C 28.69, H 3.98, N 11.15; found C 29.03, H 3.86, N 11.45.

**(12):** IR (KBr): $\tilde{\nu}_{max}$ = 3130, 3056, 2984, 2952, 2883, 1643, 1451, 1287, 1189, 1064, 1018, 954, 853, 759, 576, 501, 324 $cm^{-1}$. $^1H$ NMR (400 MHz, [D$_6$]DMSO): $\delta$ = 2.53 (m, 8 H, $CH_2NH$, $CH_2NH_2$), 3.98 (s, 4 H, $CH_2Ph$), 5.30, 6.25 (s, 4 H, $NH_2$), 6.38 (s, 2 H, NH), 7.56 (m, 4 H, Ph) ppm. $^{13}C$ NMR (100 MHz, [D$_6$]DMSO): $\delta$ = 43.8, 44.7 ($CH_2NH_2$), 45.6, 46.9 ($CH_2NH$), 54.3, 54.9 ($CH_2Ph$), 130.4–136.7 (Ar) ppm. $C_{12}H_{22}N_4Pt_2Cl_4$ (754,14): calcd. C 19.10, H 2.92, N 7.43; found C 19.45, H 2.86, N 7.75.

**(13):** IR (KBr): $\tilde{\nu}_{max}$ = 3259, 3192, 3109, 2954, 2885, 2858, 1586, 1441, 1191, 1164, 1064, 762, 531, 314 $cm^{-1}$. $^1H$ NMR (400 MHz, [D$_6$]DMSO): $\delta$ = 3.40 (m, 4 H, $CH_2NH_2$); 3.80 (m, 4 H, $CH_2NH$); 4.30 (s, 4 H, $CH_2Ph$); 5.52 (s, 4 H, $NH_2$); 5.80, 6.30 (s, 2 H, NH); 7.50 (m, 4 H, Ar) ppm.

**(14):** IR (KBr): $\tilde{\nu}_{max}$ = 3200, 3116, 2949, 1622, 1313, 1158, 1049, 978, 926, 894, 823, 749, 609, 409 $cm^{-1}$. $^1H$ NMR (400 MHz, [D$_6$]-DMSO): $\delta$ = 2.51, 2.84 (2m, 4 H, $CH_2NH_2$); 4.25, 4.45 (2d, 2 H, $CH_2N$); 4.25, 4.45, 4.87, 4.97 (4d, 4 H, $CH_2Ph$), 5.52 (s, 1 H, $NH_2$), 6.31 (s, 1 H, $NH_2$), 7.28 (m, 4 H, Ph) ppm. $^{13}C$ NMR (100 MHz, [D$_6$]DMSO): $\delta$ = 44.7 ($CH_2NH_2$), 46.2 ($NCH_2$), 64.4, 65.4 ($CH_2Ph$), 122.9–136.7 (Ar). $C_{10}H_{14}N_2PtCl_2$ (428.13): calcd. C 28.04, H 3.27, N 6.54; found C 28.40, H 2.96, N 6.75.

**(15):** IR (KBr): $\tilde{\nu}_{max}$ = 3415, 3269, 3197, 2958, 2928, 1140, 1034, 1018, 716, 549, 326 $cm^{-1}$. $C_9H_{20}N_2O_4PtCl_2$ (486.17): calcd. C 22.20, H 4.12, N 5.76; found C 22.15, H 3.86, N 5.75.

### Cell Lines and Cultures

The GLC4 cell line was derived from pleural effusion of a patient with small-cell lung carcinoma in the laboratory of Prof. E. G. E. de Vries (Department of Internal Medicine, University Hospital, Groningen, The Netherlands). The GLC4/CDDP was obtained in the same laboratory by continuous exposure to CDDP. No amplification of the MDR gene or expression of P-glycoprotein was found in the GLC4/CDDP subline.

The cell lines were cultured in an RPMI 1640 (Sigma Chemical Co.) medium supplemented with 10% fetal calf serum (Biomedia Co.) at 37 °C in a humidified 5% $CO_2$ atmosphere. Cultures grow exponentially from $10^5$ cells/mL to about $10^6$ cells/mL in 3 d. Cell viability was checked by Trypan blue exclusion. The cell number was determined by Coulter counter analysis. For the cytotoxicity assessment, $1 \times 10^5$ cells/mL were cultured for 72 h in the absence and the presence of various concentrations of each platinum-based compound. The sensitivity to the drug was evaluated by the drug concentration that inhibits cell growth by 50%, $IC_{50}$. A resistance

 © 2006 Wiley-VCH Verlag GmbH & Co. KGaA, Weinheim 

factor (RF) was obtained by dividing the $IC_{50}$ of resistant cells by the $IC_{50}$ of sensitive cells. The RF to cisplatin is 6.3.

Stock solutions of compounds **9**, **12**, and **15** were prepared in a mixture of water/DMSO (90:10). In the cytotoxic assays, the final concentration of DMSO was below 1.5%.

**Cellular Accumulation**

Cells were incubated with different complex concentrations for 3 d. After incubation, an aliquot was removed, washed twice with ice-cold PBS (phosphate-buffered saline), and the pellet mineralized in 65% $HNO_3$. The platinum concentration was determined by atomic absorption spectroscopy with a Varian model Zeeman 220 spectrophotometer equipped with a graphite tube atomizer and an autosampler. The heating program consisted of sequential drying (85 °C for 5 s, 95 °C for 40 s, and 95 °C for 20 s), an ashing stage (500 °C for 5.0 s followed by 15 s at 1100 °C), and atomizing at 2500 °C for 5 s.

## Acknowledgments

We acknowledge CNPq, CAPES, and FAPEMIG for the financial support and fellowships.

[1] A. E. Pegg, *Cancer Res.* **1988**, *48*, 759–774.
[2] M. L. Edwards, N. J. Prakash, D. M. Stemerick, S. P. Sunkara, A. J. Bitonti, G. F. Davis, J. A. Dumont, P. Bey, *J. Med. Chem.* **1990**, *33*, 1369–1375.
[3] M. L. Edwards, D. M. Stemerick, R. D. Snyder, *J. Med. Chem.* **1991**, *34*, 2414–2420.
[4] P. S. Sunkara, S. B. Baylin, G. D. Luk in *Inhibitors of polyamine biosynthesis: cellular and in vivo effects on tumor proliferation. Inhibition of Polyamine Metabolism: Biological Significance and Basis for New Therapies* (Eds.: P. P. MacCann, A. E. Pegg, A. Sjoerdsma), Academic Press, New York, **1987**, 121.
[5] D. H. Russel, *Nature* **1971**, *233*, 144–145.
[6] B. Cipolla, J. P. Moulinoux, V. Quemener, R. Havouis, L. A. Martin, F. Guille, B. Lobel, *J. Urol.* **1990**, *144*, 1164–1166.
[7] T. Matsumoto, O. Suzuki, in *The Physiology of Polyamines* (Eds.: U. Bacharach, Y. M. Heimer), CRC Press, Boca Raton, **1989**, vol. 2, 219–234.
[8] U. Bacharach, in: *The Physiology of Polyamines* (Eds.: U. Bacharach, Y. M. Heimer), CRC Press, Boca Raton, **1989**, vol. 2, 235–250.
[9] C. W. Porter, J. R. Sufrin, *Anticancer Res.* **1986**, *6*, 525–542.
[10] I. D. Algranati, S. H. Goldemberg, *Contrib. Gynecol. Obstet. TIBS* **1977**, *2*, 272–274.
[11] R. A. Casero, A. E. Pegg, *FASEB J.* **1993**, *7*, 653–661.
[12] T. Thomas, T. J. Thomas, *Cell. Mol. Life Sci.* **2001**, *58*, 244–258.
[13] B. Rosenberg, L. Van Camp, J. E. Trosco, V. H. Mansour, *Nature* **1969**, *222*, 385–386.
[14] Bristol-Myers Squibb & Johnson Matthey, *Drugs of the Future* **1990**, *15*, 739.
[15] W. B. Pratt, R. W. Ruddon, W. D. Ensminger, J. Maybaum, in: *The Anticancer Drugs*, Oxford University Press, New York, 2nd Ed., **1994**, 133–139.
[16] T. W. Hambley, *Coord. Chem. Rev.* **1997**, *166*, 181–223.
[17] A. G. Sykes, *Platinum Met. Rev.* **1988**, *32*, 170–178.
[18] A. Pasini, F. Zunino, *Angew. Chem. Int. Ed. Engl.* **1987**, *26*, 615–624.
[19] N. Farrell, Y. Qu, M. P. Hacker, *J. Med. Chem.* **1990**, *33*, 2179–2184.
[20] F. M. Muggia, G. Los, *Stem Cells* **1993**, *11*, 182–193.
[21] Z. H. Siddik, *Oncogene* **2003**, *22*, 7265–7279.
[22] R. P. Wernyj, P. J. Morin, *Drug Resist Updat.* **2004**, *7*, 227–232.
[23] N. Farrell, S. G. de Almeida, K. A. Skov, *J. Am. Chem. Soc.* **1988**, *110*, 5018–5019.
[24] N. Farrell, T. G. Appleton, Y. Qu, J. D. Roberts, A. P. S. Fontes, K. A. Skov, P. Wu, Y. Zou, *Biochemistry* **1995**, *34*, 15480–15486, and references therein.
[25] J. D. Roberts, B. V. Houten, Y. Qu, N. Farrell, *Nucleic Acids Res.* **1989**, *17*, 9719–9733.
[26] E. T. Cesar, M. V. de Almeida, A. P. S. Fontes, E. C. P. Maia, A. Garnier-Suillerot, M. R. C. Couri, E. C. A. Felício, *J. Inorg. Biochem.* **2003**, *95*, 297–305.
[27] E. Wong, G. M. Giandomenico, *Chem. Rev.* **1999**, *99*, 2451–2466.
[28] K. P. Beaumont, C. A. Mcauliffe, M. J. Cleare, *Chem. Biol. Interact.* **1976**, *14*, 179–193.
[29] D. Mercier, J. Leboul, J. Cleophax, S. D. Gero, *Carbohydr. Res.* **1971**, *20*, 299–304.
[30] M. V. de Almeida, E. T. Cesar, E. C. A. Felício, A. P. S. Fontes, *J. Braz. Chem. Soc.* **2000**, *11*, 154–158.
[31] E. Pereira-Maia, A. Garnier-Suillerot, *J. Biol. Inorg. Chem.* **2003**, *8*, 626–634.
[32] R. J. Knox, F. Friedlos, D. A. Lydall, J. J. Roberts, *Cancer Res.* **1986**, *46*, 1972–1979.
[33] N. Farrell, Y. Qu, U. Bierbach, M. Valsecchi, E. Menta, in: *Cisplatin: Chemistry and Biochemistry of a Leading Anticancer Drug* (Ed.: B. Lippert), VHCA and Wiley-VCH, Zurich, **1999**, 479–496.
[34] G. A. P. Hospers, N. H. Mulder, B. de Jong, L. de Ley, D. R. A. Uges, A. M. J. Fichtinger-Schepman, R. J. Scheper, E. G. E. de Vries, *Cancer Res.* **1988**, *48*, 6803–6807.
[35] P. D. Sadowitz, B. A. Hubbard, J. C. Dabrowiak, J. Goodisman, K. A. Tacka, M. K. Aktas, M. J. Cunningham, R. L. Dubowy, A. Souid, *Drug Metabolism and Disposition* **2002**, *30*, 183–190.

Received: November 16, 2005
Published Online: March 16, 2006

 © 2006 Wiley-VCH Verlag GmbH & Co. KGaA, Weinheim 

DOI: 10.1002/ejic.200501107

# Reactions of $^{13}CO$ with Ethoxycarbonylcarbene-Bridged Dicobalt Carbonyl Complexes: [$\mu_2$-{Ethoxycarbonyl(methylene)}-$\mu_2$-(carbonyl)-bis(tricarbonylcobalt)(*Co–Co*)] and [Di-$\mu_2$-{ethoxycarbonyl(methylene)}-bis(tricarbonylcobalt)(*Co–Co*)]

**Eszter Fördős,[a] Neszta Ungvári,[a] Tamás Kégl,[b] and Ferenc Ungváry*[a,b]**

**Keywords:** Isotopic labeling / C–C coupling / Carbene and carbonyl ligands / Cobalt / Fluxionality

In a $CH_2Cl_2$ solution, under an atmospheric pressure of $^{13}CO$, the bridging and terminal CO ligands of the cobalt complex [$\mu_2$-{ethoxycarbonyl(methylene)}-$\mu_2$-(carbonyl)bis(tricarbonylcobalt)(*Co–Co*)] (**1**) exchange with external $^{13}CO$ at the same rate. The overall rate of CO exchange is $k_{obs}$ (10 °C) = $9.4 \times 10^{-3}$ s$^{-1}$ and $k_{obs}$ (25 °C) = $(20.1 \pm 1.2) \times 10^{-3}$ s$^{-1}$. In the presence of excess ethanol diethyl malonate (DEM), $EtO_2{}^{13}CCH_2CO_2Et$ is formed from **1** at a much smaller rate [$k_{DEM}$ (10 °C) = $0.40 \times 10^{-5}$ s$^{-1}$ and $k_{DEM}$ (25 °C) = $(1.2 \pm 0.1) \times 10^{-5}$ s$^{-1}$]. On the other hand, the complex [di-$\mu_2$-{ethoxycarbonyl(methylene)}bis(tricarbonylcobalt)(*Co–Co*)] (**2**) does not exchange its CO ligands for $^{13}CO$ at all at 10 or 25 °C. In the presence of excess ethanol, diethyl malonate with natural isotopic distribution, and $^{13}CO$, ligands containing complex **1** are formed simultaneously and at the same rate, which is $k_{obs}$ (10 °C) = $(15.2 \pm 1.1) \times 10^{-5}$ s$^{-1}$ and $k_{obs}$ (25 °C) = $(33.5 \pm 1.8) \times 10^{-5}$ s$^{-1}$. Variable temperature $^{13}C$ NMR spectra of **1** and **2** reveal fluxional behavior for both complexes.

(© Wiley-VCH Verlag GmbH & Co. KGaA, 69451 Weinheim, Germany, 2006)

## Introduction

In the course of the past decades several dicobalt carbonyl complexes having no more than one or two carbene ligands have been prepared and the crystal structures of some representative examples determined.[1] In most of these complexes the substituted methylene- and vinylidene-type carbenes are in a bridging position between the two cobalt atoms,[2–18] while in a few recent examples *N*-heterocyclic carbene(s) are in terminal positions.[19,20]

Diverse methods of preparation have been applied to obtain dicobalt carbonyl carbene complexes. In the case of **1** and **2** (see Scheme 1) the two $\mu_2$-CO ligands in $Co_2(CO)_8$ were replaced effectively one by one by ethoxycarbonylcarbene[18] using the carbene transfer reaction[21] between ethyl diazoacetate and $Co_2(CO)_8$.

The complexes [$\mu_2$-{ethoxycarbonyl(methylene)}-$\mu_2$-(carbonyl)bis(tricarbonylcobalt)(*Co–Co*)] (**1**) and [di-$\mu_2$-{ethoxycarbonyl(methylene)}bis(tricarbonylcobalt)(*Co–Co*)] (**2**) were found to be intermediates in the octacarbonyldicobalt-catalyzed carbonylation of ethyl diazoacetate to ethyl malonic acid derivatives.[18] The key step in these carbonylation reactions is the facile coupling of carbon monoxide

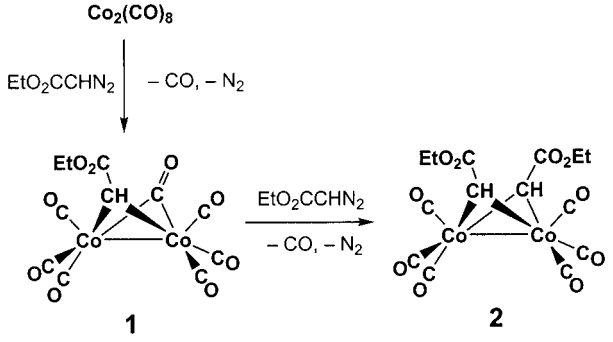


Scheme 1.

with the bridging carbene ligand to form the highly reactive ethoxycarbonyl ketene,[22] which rapidly converts in the presence of a suitable scavenger to the corresponding malonic acid monoethyl ester derivative. For example, using ethanol as the scavenger results in the formation of diethyl malonate [Equations (1) and (2)].

$$\mathbf{2} + 2CO + EtOH \xrightarrow[1\ bar]{25\ °C} \mathbf{1} + EtO_2CCH_2CO_2Et \quad (1)$$

$$\mathbf{1} + 2CO + EtOH \xrightarrow[1\ bar]{25\ °C} Co_2(CO)_8 + EtO_2CCH_2CO_2Et \quad (2)$$

[a] Department of Organic Chemistry, University of Veszprém, 8201 Veszprém, Hungary
E-mail: ungvary@almos.vein.hu (F. Ungváry)
[b] Research Group for Petrochemistry of the Hungarian Academy of Sciences, 8201 Veszprém, Hungary

 © 2006 Wiley-VCH Verlag GmbH & Co. KGaA, Weinheim 

Applying $^{13}CO$ in the gas phase, as in Equations (1) and (2), a clear decision could be made as to whether $^{13}CO$ from the gas phase or the CO from the complexes is incorporated into the diethyl malonate product.

## Results and Discussion

The infrared spectrum of a solution of **1** in dichloromethane under an atmosphere of $^{13}CO$ changes rapidly with time. Next to the original terminal carbonyl absorptions at 2112, 2075, 2048 $cm^{-1}$, and next to the bridging carbonyl absorption at 1853 $cm^{-1}$, several new initially rapidly growing bands in the terminal ν(C≡O) range and one in the bridging ν(C=O) range appeared immediately after exposing the solution to $^{13}CO$. The well separated bridging $\nu(^{12}C{=}O)$ and $\nu(^{13}C{=}O)$ bands at 1853 and 1810 $cm^{-1}$, respectively, were suitable for quantitative analysis and to calculate the rate of $^{13}CO$ exchange. The strongly overlapping various terminal ν(C≡O) bands prevented the calculation of the concentrations of the different $^{13}CO$ containing species. However, the relative intensity values of the different totally symmetric bands of the complexes containing one, two, three, four, and five $^{13}CO$ ligands at 2112, 2107, 2101, 2096, and 2090 $cm^{-1}$, respectively, could be established. From the beginning of the reaction a parallelity of the growing amounts of complexes having $^{13}C$ in the bridging CO and the shift of the relative intensity values of the total symmetric bands is observed (see Table 1). Therefore the extent of $^{13}CO$ incorporation as calculated from the intensity of the $\nu(^{13}C{=}O)$ band reflects the overall level of $^{13}CO$ incorporation in complex **1**. Because there is no perceptible difference in the $^{13}CO$ exchange rate of the bridging and the terminal CO ligands it can be concluded that the intramolecular exchange of the different CO groups in complex **1** is much faster than the rate of $^{13}CO$ incorporation. This is in agreement with the fluxional behavior deduced from the results of the variable temperature $^{13}C$ NMR experiments of **1** in $CD_2Cl_2$ solutions. At ambient temperature we observed only one coordinated carbonyl resonance at $\delta$ = 201.85 ppm, which splits at 185 K into resonances at 195.65, 196.95, 198.16 ppm (three different terminal CO ligands), and 227.26 ppm (bridging CO) showing virtually 2:2:2:1 integral ratios.

From the data in Table 1 the overall rate of $^{13}CO$ exchange of complex **1** was calculated as $k_{obs}$ (10 °C) = $9.4 \times 10^{-3}$ $s^{-1}$. This rate is about 50% higher than that for $Co_2(CO)_8$ extrapolated at 10 °C from literature values[23] or as measured by us in order to check our technique applied in the present work. The CO-exchange reaction of $Co_2(CO)_8$ with external CO and the fluxional behavior of $Co_2(CO)_8$ have been intensively investigated in the past On the basis of X-ray structure determination it is known that $Co_2(CO)_8$ in the solid state exists exclusively in the form of a bridged isomer with two $\mu_2$-CO and six terminal CO ligands.[24] In solution this bridged isomer is in fast equilibrium with two nonbridged isomers.[25] The fast inter-conversion of the bridged and nonbridged structures makes it understandable that in the slower exchange reaction with external CO all eight CO ligands exchange at the same rate.[23] Because the rate of CO exchange was found not to depend on the CO concentrations it was concluded that the CO exchange happens by a dissociative mechanism with the involvement of a $Co_2(CO)_7$ intermediate.[23] A similar mechanism might be operating in the case of complex **1**, which involves the rate-determining formation of a coordinative unsaturated $Co_2(CO)_6(CHCO_2Et)$ intermediate that takes up CO in a fast reaction. A very fast intramolecular exchange of the bridging and terminal CO ligands distributes labeled car-

Table 1. The amount of $^{13}CO$ found in the $\mu_2$-position of $Co_2(CO)_6(\mu_2\text{-}CO)(\mu_2\text{-}CHCO_2Et)$ (**1**) (0.0224 mmol) in a $CH_2Cl_2$ solution (7.0 $cm^3$), and the observed relative intensity values of the total symmetric ν(C≡O) bands in the reaction with $CH_2Cl_2$-saturated $^{13}CO$ (99% $^{13}C$) (0.30 mmol) at 10 °C and 740 Torr total pressure at various reaction times.

| Reaction time [s] | $^{13}CO$ found in the $\mu_2$-position[a] [mmol] | Relative intensity values of the observed total symmetric ν(C≡O) bands at: 2112 | 2107 | 2101 | 2096 | 2090 | (2087)[b] | 2080 [$cm^{-1}$] |
|---|---|---|---|---|---|---|---|---|
| 97 | 0.0035 | 10.0 | 7.4 | 2.2 | 0.5 | | | |
| 150 | 0.0051 | 6.1 | 10.0 | 7.7 | 2.7 | 0.4 | | |
| 195 | 0.0066 | 5.1 | 10.0 | 9.1 | 4.6 | 1.0 | | |
| 240 | 0.0076 | 3.1 | 8.7 | 10.0 | 6.0 | 1.6 | | |
| 296 | 0.0087 | 2.0 | 7.3 | 10.0 | 7.6 | 2.7 | | |
| 341 | 0.0095 | 1.2 | 6.0 | 10.0 | 8.9 | 3.9 | | |
| 389 | 0.0099 | 0.8 | 5.0 | 10.0 | 9.5 | 5.1 | | |
| 428 | 0.0105 | 0.6 | 4.4 | 9.5 | 10.0 | 6.0 | | |
| 465 | 0.0110 | 0.5 | 3.8 | 8.8 | 10.0 | 6.4 | | |
| 508 | 0.0116 | | 2.1 | 8.0 | 10.0 | 6.8 | | |
| 548 | 0.0120 | | 2.1 | 7.8 | 10.0 | 7.5 | | |
| 596 | 0.0123 | | 2.0 | 7.5 | 10.0 | 7.6 | | |
| 635 | 0.0128 | | 2.0 | 7.3 | 10.0 | 8.0 | | |
| 686 | 0.0130 | | | 7.1 | 10.0 | 8.2 | | |
| 731 | 0.0132 | | | 6.6 | 10.0 | 8.5 | | |
| 2028 | 0.0146 | | | 4.5 | 9.4 | 10.0 | | 1.7 |

[a] Calculated from the intensity value of the observed $\nu(^{13}C{=}O)$ band at 1810 $cm^{-1}$ using $\varepsilon_M$ = 916 $cm^2$/mmol. [b] Shoulder. Its relative intensity value could not be established.

 © 2006 Wiley-VCH Verlag GmbH & Co. KGaA, Weinheim 

bon monoxide statistically in the bridging and terminal positions.

In the presence of ethanol, the reaction of carbon monoxide with complex **1** results in the formation of $Co_2(CO)_8$ and diethyl malonate [Equation (2)]. The data in Table 2 show that complex **1** reacts three orders of magnitude slower to form diethyl malonate and $Co_2(CO)_8$ than in the $^{13}CO$-exchange reaction. Under an atmosphere of $^{13}CO$, owing to the preceding fast $^{13}CO$-exchange and the subsequent slow diethyl malonate formation, we could not decide whether complex-bound $^{13}CO$ or external $^{13}CO$ is incorporated in the $EtO_2{}^{13}CCH_2CO_2Et$ product. Performing the reaction of **1** with ethanol under an atmosphere of argon leads to reaction products of $Co_4(CO)_{12}$ and diethyl malonate [Equation (3)], as seen from the growing intensities of bands in the infrared spectra of the reaction solution with elapsing reaction time at 2065 and 2055 $cm^{-1}$ [most intensive $\nu(C{\equiv}O)$ bands of $Co_4(CO)_{12}$ in $CH_2Cl_2$] and at 1749 and 1732 $cm^{-1}$ [$\nu(C{=}O)$ bands of $EtO_2CCH_2CO_2Et$]. This result strongly suggests that the source of CO is one of the coordinated carbonyls in complex **1**.

$$\mathbf{1} + EtOH \xrightarrow[Argon]{25\ ^\circ C} \mathbf{1/2\ Co_4(CO)_{12}} + EtO_2CCH_2CO_2Et \quad (3)$$

The reaction of complex **2** with ethanol under an atmosphere of argon gave **1** and diethyl malonate [Equation (4)]. The amount of complex **1** formed in the reaction [Equation (4)] was found to be only about 70% of that expected according to the stoichiometry. A reason for this might be that the missing amount served, by decomposition, as a CO source for complex **1**.

$$\mathbf{2} + EtOH \xrightarrow[Argon]{10\ ^\circ C} \mathbf{1} + EtO_2CCH_2CO_2Et \quad (4)$$

In the absence of ethanol complex **2** and CO convert to complex **1** and the ethoxycarbonyl ketene dimer [one characteristic $\nu(C{=}O)$ band is at 1733 $cm^{-1}$] according to Equation (5).

$$\mathbf{2} + 2CO \xrightarrow[1\ bar]{10\ ^\circ C} \mathbf{1} + 1/2(EtO_2CCH{=}C{=}O)_2 \quad (5)$$

Performing the reaction in Equation (1) under an atmosphere of $^{13}CO$ results in the formation of the $^{13}C$-labeled complex **1** and diethyl malonate with a natural abundance of $^{13}C$; these compounds were simultaneously observed in the infrared spectrum of the reaction solution. Thus, the several new $\nu(^{13}C{\equiv}O)$ absorptions in the 2107–1959 $cm^{-1}$ range and the one new $\nu(^{13}C{=}O)$ absorption at 1810 $cm^{-1}$ could be assigned to complex **1**, and the new $\nu(C{=}O)$ absorptions at 1749 and 1732 $cm^{-1}$ are characteristic of $EtO_2CCH_2CO_2Et$. The observed rate of formation of complex **1** and that of diethyl malonate in Equation (1) was found to be practically the same (see Table 3). The GC-MS analysis of the reaction product confirmed the presence of diethyl malonate showing an identical mass spectrum to that of an authentic sample and the published mass spec-

Table 2. Initial rate of the overall $^{13}CO$ incorporation ($r_{in}$) and the observed rate constant ($k_{obs} = r_{in}/[\mathbf{1}]$) in the reaction of complex **1** with $^{13}CO$ at 740 Torr total pressure in $CH_2Cl_2$ solution, and the initial rate of diethyl malonate formation ($r_{DEM}$) and the observed rate constant ($k_{DEM} = r_{DEM}/[\mathbf{1}]$) in the presence of ethanol.

| Temperature [°C] | [**1**] [mol/dm$^3$] | [EtOH] [mol/dm$^3$] | $r_{in} \times 10^5$ [mol/dm$^3$ s] | $k_{obs} \times 10^3$ [1/s] | $r_{DEM} \times 10^7$ [mol/dm$^3$ s] | $k_{DEM} \times 10^5$ [1/s] |
|---|---|---|---|---|---|---|
| 10 | 0.0032 | 0.000 | 3.0 | 9.4 | – | – |
| 10 | 0.0166 | 0.070 | – | – | 0.66[a] | 0.40[a] |
| 25 | 0.0030 | 0.000 | 5.9 | 19.7 | – | – |
| 25 | 0.0030[b] | 0.070 | – | – | 0.39 | 1.30 |
| 25 | 0.0061 | 0.070 | 11.7 | 19.2 | 0.71 | 1.16 |
| 25 | 0.0142 | 0.070 | 30.3 | 21.3 | 1.67 | 1.18 |
| 25 | 0.0142 | 0.070 | | | 4.40[c] | 3.10[c] |

[a] Reaction was started under an atmosphere of CO instead of $^{13}CO$. [b] Using $Co_2(^{13}CO)_7(CHCO_2Et)$ with 63% $^{13}C$ enrichment of the coordinated carbonyl ligands. [c] Reaction was started under argon.

Table 3. The initial rate of diethyl malonate formation ($r_{DEM}$), the observed rate constant ($k_{DEM} = r_{DEM}/[\mathbf{2}]$), the initial rate of complex **1** formation ($r_{\mathbf{2}\rightarrow\mathbf{1}}$), and the observed rate constant ($k_{\mathbf{2}\rightarrow\mathbf{1}} = r_{\mathbf{2}\rightarrow\mathbf{1}}/[\mathbf{2}]$) in the reaction of complex **2** with $^{13}CO$ at 745 Torr total pressure in $CH_2Cl_2$ solution.

| Temperature [°C] | [**2**] [mol/dm$^3$] | [EtOH] [mol/dm$^3$] | $r_{DEM} \times 10^7$ [mol/dm$^3$ s] | $k_{DEM} \times 10^5$ [1/s] | $r_{\mathbf{2}\rightarrow\mathbf{1}} \times 10^7$ [mol/dm$^3$ s] | $k_{\mathbf{2}\rightarrow\mathbf{1}} \times 10^5$ [1/s] |
|---|---|---|---|---|---|---|
| 10 | 0.0166 | 0.070 | 27.0 | 16.3 | 26.4 | 15.9 |
| 10 | 0.0063 | 0.070 | 9.5 | 15.1 | 8.9 | 14.2 |
| 10 | 0.0166 | 0.070 | 9.13[a] | 5.5[a] | 3.3[a] | 2.0[a] |
| 10 | 0.0063 | 0.000 | | | 3.2 | 5.1 |
| 25 | 0.0063 | 0.070 | 21.7[b] | 34.4[b] | 20.5[b] | 32.6[b] |

[a] Reaction was started under argon. [b] Reaction was started under CO.

 © 2006 Wiley-VCH Verlag GmbH & Co. KGaA, Weinheim 

trum.[26] As the reaction progressed the $\nu$(C≡O) range in the infrared spectrum became very complex with the appearance of various $^{13}$CO-containing **1** products in the reaction solution. However, the $\nu$(C≡O) bands of the starting complex **2** at 2112 and 2080 cm$^{-1}$ are well recognized until the conversion according to Equation (1) is complete. This means that in contrast to complex **1** no $^{13}$CO incorporation takes place in complex **2** during the contact with external $^{13}$CO. Hence, the source of CO involved in the formation of diethyl malonate is one of the coordinated carbon monoxide ligands of complex **2**.

Complex **2** in solution shows fluxional behavior. In $CDCl_3$ at ambient temperature only one coordinated carbonyl resonance at $\delta$ = 196.63 ppm can be seen in the $^{13}$C NMR spectrum. However, in $CD_2Cl_2$ solution at 200 K this resonance splits into resonances at 195.91 and 197.84 ppm with an integral ratio of 1:2. GIAO NMR shielding calculations gave the same qualitative results (see Table 4).

Table 4. GIAO and experimental $^{13}$C chemical shifts $\delta$ [ppm] and intensity ratios (in parenthesis) of the coordinated carbonyl ligands of $Co_2(CO)_8$, $Co_2(CO)_7(CHCO_2Et)$ (**1**), and $Co_2(CO)_6(CHCO_2Et)_2$ (**2**).

| Complex | Calculated $^{13}$C chemical shifts at the B3LYP/6-31G* level of theory | Experimentally found $^{13}$C chemical shifts |
|---|---|---|
| $Co_2(CO)_8$ | 193.3, 201.3, 237.8 (1:2:1) | 182, 234 (approximately 4:1)[a] |
| **1** | 195.9, 199,7, 205.2, 234.8 (2:2:2:1) | 195.65, 196.95, 198.16, 227.26 (2:2:2:1)[b] |
| **2** | 200.5, 201.5 (1:2) | 195.91, 197.84 (1:2)[b] |

[a] See ref.[32] [b] This work.

## Conclusions

The results of experiments with complex **1** and **2** in the presence and in the absence of the reagents $^{13}$CO, CO, and ethanol suggest that the origin of the new organic carbonyl group, formed through the coupling of CO and a $\mu_2$-ethoxycarbonylcarbene ligand of the complexes, is one of the complex-bound carbonyl ligands and not an external CO.

## Experimental Section

**General Comments:** Handling of $Co_2(CO)_8$ and other carbonyl cobalt complexes was carried out in an atmosphere of dry ($P_4O_{10}$) and deoxygenated (BTS contact, room temp.) argon or carbon monoxide utilizing standard Schlenk techniques.[27] Solvents were dried and distilled under an atmosphere of argon according to standard procedures.[28] IR spectra were recorded with a Thermo Nicolet Avatar 330 FTIR spectrometer using 0.00265, 0.00765, 0.02095, or 0.05097 cm $CaF_2$ solution cells, calibrated by the interference method.[29] $^{13}$C NMR spectra were recorded with a Bruker 400 MHz spectrometer at 100 MHz using $CD_2Cl_2$ as the solvent. Chemical shifts $\delta$ are reported in ppm relative to $CH_2Cl_2$ ($\delta$ = 53.10 ppm). The GC-MS analyses were performed with an HP 5890 instrument equipped with a mass-selective detector working at 70 eV. Octacarbonyldicobalt[30] and the $\mu_2$-ethoxycarbonylcarbene complexes **1**[18] and **2**[18] were prepared by literature procedures. $^{13}$CO was obtained from Sigma–Aldrich.

**$^{13}$CO Exchange Experiment with $Co_2(CO)_8$:** The $^{13}$CO exchange reactions were performed in a magnetically stirred thermostatted glass reactor (18, 35, or 61 cm$^3$ total volume), equipped with a gas inlet and with a silicon disk port. The gas inlet was connected through a two-way stopcock to a vacuum pump and a $^{13}$CO-filled gas burette. A stainless-steel cannula connected to a 3-port T-valve was immersed close to the bottom of the reactor through the silicon disk. A Hamilton TLL syringe (2.5 cm$^3$ volume) and the IR cell (through a PTFE tube) were connected to the two other ports of the valve. Samples from the reaction mixture for IR analyses were withdrawn through the stainless steel cannula, and pumped into the IR cell continuously by using the Hamilton TLL syringe, allowing the liquid sample to return from the IR cell to the reactor through a second PTFE tube. The solvent and the solution of the reactant were added to the $^{13}$CO-filled reactor through the silicon disk using Hamilton TLL syringes. IR spectra were recorded at every minutes or less. The initial rates of $^{13}$CO exchange were calculated from the intensity values of the $\nu$($^{13}$C=O) band using the first 3 to 8 points. The $\varepsilon_M$ of the $\nu$($^{13}$C=O) band was calculated from the known $\varepsilon_M$ value of the $\nu$($^{12}$C=O) band[18,31] by multiplying it with the mass correction value $(12/13)^{-0.5}$ = 0.96077. In a typical experiment using the reactor with a 35-cm$^3$ total volume, the reactor and its connected parts were first evacuated then filled with $^{13}$CO, and $CH_2Cl_2$ (4.5 cm$^3$) was added. After stirring at 10 °C for 10 min the reaction was started by injection of $Co_2(CO)_8$ (0.064 mmol) in a precooled $CH_2Cl_2$ solution (2.5 cm$^3$). Infrared spectra were recorded from four scans after 38, 75, 114, 164, 207, 253, 297, 345 s, and so on, until $^{13}$CO enrichment of 65% had been reached. The rate constant of the overall $^{13}$CO exchange $(6.0 \pm 1.2) \times 10^{-3}$ s$^{-1}$ was calculated from the initial changes of the $Co_2(CO)_8$ concentration as obtained from the intensity values measured at 1847 cm$^{-1}$ ($\varepsilon_M$ = 938 cm$^2$/mmol), or that of $Co_2(^{13}CO)_x(CO)_{8-x}$ from the intensity values measured at 1807 cm$^{-1}$ ($\varepsilon_M$ = 902 cm$^2$/mmol) by dividing the observed initial rate by the initial $Co_2(CO)_8$ concentration.

**$^{13}$CO Exchange Experiments with Complex 1:** In a typical experiment using the reactor with an 18-cm$^3$ total volume, the reactor and its connected parts were first evacuated and then filled with $^{13}$CO (740 Torr total pressure), and then $CH_2Cl_2$ (4.5 cm$^3$) was added. After stirring at 10 °C for 10 min the reaction was started by injection of a precooled solution of complex **1** (0.0224 mmol) in $CH_2Cl_2$ (2.5 cm$^3$). Infrared spectra were recorded from four scans after 97, 150, 195, 240, 296, 341 s, and so on (see Table 1), until a $^{13}$CO enrichment of 63% had been reached in ca. 34 min. The rate constant of the overall $^{13}$CO incorporation ($9.4 \times 10^{-3}$ s$^{-1}$) was calculated from the initial changes of the concentration of complex **1**, as obtained from the intensity values measured at 1853 cm$^{-1}$ ($\varepsilon_M$ = 953 cm$^2$/mmol), or that of $Co_2(^{13}CO)_x(CO)_{7-x}(CHCO_2Et)$ from the intensity values measured at 1810 cm$^{-1}$ ($\varepsilon_M$ = 916 cm$^2$/mmol), by dividing the observed initial rate by the initial concentration of complex **1**.

At higher initial concentrations of complex **1** and at 25 °C the reactor with a volume of 35 or 61 cm$^3$ was used in order to achieve at least 50% $^{13}$CO enrichment at the end of the reaction.

**Diethyl Malonate Formation from Complex 1 and Ethanol under $^{13}$CO:** Absolute ethanol (0.029 cm$^3$, 0.496 mmol) was added to a solution of complex **1** in $CH_2Cl_2$ (7.0 cm$^3$, 0.003 mol/dm$^3$) with 62.6% $^{13}$C-enrichment, obtained in a reactor with a 61-cm$^3$ volume at 25 °C under a $^{13}$CO atmosphere in 10 min. The initial rate of diethyl malonate formation ($r_{DEM}$) was calculated from the inten-

 © 2006 Wiley-VCH Verlag GmbH & Co. KGaA, Weinheim 

sity values measured at 1749 $cm^{-1}$ ($\varepsilon_M$ = 579 $cm^2$/mmol, unlabeled diethyl malonate), at 1731 $cm^{-1}$ ($\varepsilon_M$ = 597 $cm^2$/mmol, 62.6% $^{13}C$-labeled and 37.4% unlabeled diethyl malonate), and at 1713 $cm^{-1}$ ($\varepsilon_M$ = 640 $cm^2$/mmol, $^{13}C$-labeled diethyl malonate) The observed rate constant ($k_{DEM}$) was obtained from the initial rate of diethyl malonate formation by dividing it with the initial concentration of complex **1**. The GC-MS analyses of the diethyl malonate product show an $M^{+\cdot}$ peak at *m*/*z* = 161, and the characteristic fragment peaks: M – 27, M – 45, and M – 72 at *m*/*z* = 134, 116, and 89, respectively.

**Diethyl Malonate Formation from Complex 1 and Ethanol under Ar:** Absolute ethanol (0.031 $cm^3$, 0.531 mmol) was added to a solution of complex **1** (0.1075 mmol) in $CH_2Cl_2$ (7.5 $cm^3$) under an atmosphere of argon at 25 °C, and the initial rate of diethyl malonate formation ($r_{DEM}$) and the observed rate constant ($k_{DEM}$) were determined as described above but using the intensity values measured at 1749 and 1732 $cm^{-1}$.

**Attempted $^{13}CO$ Exchange Experiments with Complex 2:** In a typical experiment using the reactor with a 35-$cm^3$ total volume, the reactor and its connected parts were first evacuated and then filled with $^{13}CO$ (745 Torr total pressure), and finally $CH_2Cl_2$ (4.3 $cm^3$) was added. After stirring at 10 °C for 10 min the reaction was started by injection of a precooled solution of complex **2** (0.0475 mmol) in $CH_2Cl_2$ (3.2 $cm^3$). Infrared spectra were recorded from 16 scans after 2, 10, 15, 20 min, and so on, until almost all of complex **2** was converted to complex **1** (8 h), afterwhich conversion could be followed by the gradual decrease of intensity of the characteristic bands of complex **2** at 2112 $cm^{-1}$ ($\varepsilon_M$ = 1100 $cm^2$/mmol) and 2080 $cm^{-1}$ ($\varepsilon_M$ = 3768 $cm^2$/mmol) and the increase of intensity of the characteristic $\nu$(C=O) bands of the labeled and unlabeled complex **1** at 1810 $cm^{-1}$ ($\varepsilon_M$ = 916 $cm^2$/mmol) and 1853 $cm^{-1}$ ($\varepsilon_M$ = 953 $cm^2$/mmol), respectively. At the end of the reaction 57% $^{13}CO$ enrichment of complex **1** was found based on the intensity values measured at 1853 and 1810 $cm^{-1}$. From the initial rate of the formation of complex **1** ($r_{\mathbf{2}\rightarrow\mathbf{1}} = 3.2\times10^{-7}$ mol/$dm^3$ s) the observed rate constant ($k_{\mathbf{2}\rightarrow\mathbf{1}} = 5.1\times10^{-5}\ s^{-1}$) was calculated by dividing the observed initial rate by the initial concentration of complex **2**.

**Diethyl Malonate Formation from Complex 2 and Ethanol under $^{13}CO$:** In a typical experiment the reactor (35-$cm^3$ total volume) and its connected parts were first evacuated and then filled with $^{13}CO$ until a barometric pressure of 740 Torr. $CH_2Cl_2$ (1.0 $cm^3$) and absolute ethanol (0.033 $cm^3$, 0.565 mmol) were added. After stirring at 10 °C for 10 min the reaction was started by injection of complex **2** (0.133 mmol) into a precooled $CH_2Cl_2$ solution (7.0 $cm^3$) maintaining the pressure in the reactor at 740 Torr by means of the connected gas burette. Infrared spectra were recorded from four scans after 61, 107, 164, 221, 300, 427, 530, 645, 750, 865 s, and so on, until the infrared spectrum showed no more changes in the 2200–1600 $cm^{-1}$ range (3.5 h). The rate constant for the formation of $EtO_2CCH_2CO_2Et$ was calculated from the initial changes of its concentration as obtained from the intensity values measured at 1749 $cm^{-1}$ ($\varepsilon_M$ = 579 $cm^2$/mmol) and at 1732 $cm^{-1}$ ($\varepsilon_M$ = 666 $cm^2$/mmol) by dividing the observed initial rate by the initial concentration of complex **2**. The GC-MS analyses of the diethyl malonate product show an $M^{+\cdot}$ peak at *m*/*z* = 160, and the characteristic fragment peaks: M – 27, M – 45, and M – 72 at *m*/*z* = 133, 115, and 88, respectively.

**Diethyl Malonate Formation from Complex 2 and Ethanol under Ar:** Absolute ethanol (0.033 $cm^3$, 0.565 mmol) was added to a solution of complex **2** (0.133 mmol) in $CH_2Cl_2$ (8.0 $cm^3$) under an atmosphere of argon at 10 °C, and the initial rate of diethyl malonate formation ($r_{DEM}$) and the observed rate constant ($k_{DEM}$) were determined as described above using the intensity values of diethyl malonate measured at 1749 and 1732 $cm^{-1}$.

**Variable-Temperature $^{13}C$ NMR Spectra of Complex 1 and 2:** From freshly chromatographed dichloromethane solutions of complex **1** and **2**, or from $^{13}CO$ enriched samples of complex **1** (see above), 0.25 mol/$dm^3$ solutions in $CD_2Cl_2$ were prepared by removing the dichloromethane solvent at –5 °C in vacuo (17 Torr) and dissolving the oily residue in $CD_2Cl_2$ under an atmosphere of argon. The $^{13}C$ NMR spectra were recorded at 273, 233, 200, and 185 K.

## Acknowledgments

The authors thank the Hungarian Academy of Sciences and the Hungarian Scientific Research Fund for financial support under Grant No OTKA T037817 and F046959.

[1] a) R. D. W. Kemmitt, D. R. Russel, in: *Comprehensive Organometallic Chemistry* (Eds.: G. Wilkinson, F. G. A. Stone, E. W. Abel), Pergamon Press, Oxford, UK, **1982**, vol. 5, 1–276; b) R. L. Sweany, in: *Comprehensive Organometallic Chemistry II* (Eds.: E. W. Abel, F. G. A. Stone, G. Wilkinson), Elsevier Science, Oxford, UK, **1995**, vol. 8, 1–114.
[2] H. W. Sternberg, J. G. Shukys, C. D. Donne, R. Markby, R. A. Friedel, I. Wender, *J. Am. Chem. Soc.* **1959**, *81*, 2339–2342.
[3] O. S. Mills, G. Robinson, *Inorg. Chim. Acta* **1967**, *1*, 61–64.
[4] B. L. Booth, R. N. Haszeldine, P. R. Mitchell, J. J. Cox, *Chem. Commun. (London)* **1967**, 529–530.
[5] B. L. Booth, R. N. Haszeldine, P. R. Mitchell, J. J. Cox, *J. Chem. Soc. A* **1969**, 691–698.
[6] J. Cooke, W. R. Cullen, M. Green, F. G. A. Stone, *Chem. Commun. (London)* **1968**, 170–171.
[7] J. Cooke, W. R. Cullen, M. Green, F. G. A. Stone, *J. Chem. Soc. A* **1969**, 1872–1874.
[8] F. Seel, G. V. Röschenthaler, *Angew. Chem.* **1970**, *82*, 182.
[9] F. Seel, G. V. Röschenthaler, *Z. Anorg. Allg. Chem.* **1971**, *386*, 297–315.
[10] G. Schenker, Dissertation, Saarbrücken, **1972**.
[11] R. D. Adams, D. F. Chodosh, N. M. Golembeski, *J. Organomet. Chem.* **1977**, *139*, C39–C43.
[12] F. Seel, R. D. Flaccus, *J. Fluorine Chem.* **1978**, *12*, 81–100.
[13] I. T. Horváth, G. Pályi, L. Markó, G. Andreetti, *J. Chem. Soc. Chem. Commun.* **1979**, 1054–1055.
[14] I. T. Horváth, G. Pályi, L. Markó, G. Andreetti, *Inorg. Chem.* **1983**, *22*, 1049–1053.
[15] W. Schulze, H. Hartl, K. Seppelt, *Angew. Chem.* **1986**, *98*, 189–190.
[16] A. Sisak, A. Sironi, M. Moret, C. Zucchi, F. Ghelfi, G. Pályi, *J. Chem. Soc. Chem. Commun.* **1991**, 176–178.
[17] C. Zucchi, E. Soós, V. Galamb, G. Váradi, L. Párkányi, G. Pályi, *Eur. J. Inorg. Chem.* **2001**, 2207–2209.
[18] R. Tuba, F. Ungváry, *J. Mol. Catal. A* **2003**, *203*, 59–67.
[19] S. E. Gibson, C. Johnstone, J. A. Loch, J. W. Steed, A. Stevenazzi, *Organometallics* **2003**, *22*, 5374–5377.
[20] H. van Rensburg, R. P. Tooze, D. F. Foster, A. M. Z. Slawin, *Inorg. Chem.* **2004**, *43*, 2468–2470.
[21] a) H. Zollinger, *Diazo Chemistry II. Aliphatic, Inorganic, and Organometallic Compounds*, VCH, Weinheim, **1995**, pp. 314–318; b) M. P. Doyle, M. A. McKervey, T. Ye, *Modern Catalytic Methods for Organic Synthesis with Diazo Compounds*, Wiley, New York, **1998**, pp. 61–111; c) F. Zaragoza-Dörwald, *Metal Carbenes in Organic Synthesis*, Wiley-VCH, Weinheim, **1999**, pp. 90–93.
[22] T. T. Tidwell, *Ketenes*, Wiley, New York, **1995**, 227–254.
[23] a) D. F. Keeley, R. E. Johnson, *J. Inorg. Nucl. Chem.* **1959**, *11*, 33–41; b) F. Basolo, A. Wojcicki, *J. Am. Chem. Soc.* **1961**, *83*, 520–528; c) S. Bereitschaft, F. Basolo, *J. Am. Chem. Soc.* **1966**,

 © 2006 Wiley-VCH Verlag GmbH & Co. KGaA, Weinheim 

*88*, 2702–2706; d) M. Absi-Halabi, J. D. Atwood, N. P. Forbus, T. L. Brown, *J. Am. Chem. Soc.* **1980**, *102*, 6248–6254; e) D. C. Roe, *Organometallics* **1987**, *6*, 942–946.
[24] a) G. G. Sumner, H. P. Klug, L. E. Alexander, *Acta Crystallogr.* **1964**, *17*, 732–742; b) P. C. Leung, P. Coppens, *Acta Crystallogr. Sect. B* **1983**, *39*, 535–542; c) D. Braga, F. Grepioni, P. Sabatino, A. Gavezzotti, *J. Chem. Soc. Dalton Trans.* **1992**, 1185–1191.
[25] a) J. P. Kenny, R. B. King, H. F. Schaefer III, *Inorg. Chem.* **2001**, *40*, 900–911; b) G. Aullón, S. Alvarez, *Eur. J. Inorg. Chem.* **2001**, 3031–3038, and references therein.
[26] J. H. Bowie, D. H. Williams, S.-O. Lawesson, G. Schroll, *J. Org. Chem.* **1966**, *31*, 1792–1797.
[27] D. F. Shriver, *The Manipulation of Air-Sensitive Compounds*, Krieger, Malabar, FL, **1982**.
[28] W. L. F. Armarego, D. D. Perrin, *Purification of Laboratory Chemicals*, 4th ed., Butterworth-Heinemann, Oxford, **1996**.
[29] H. H. Willard, L. L. Merritt Jr, J. A. Dean, F. A. Settle Jr, *Instrumental Methods of Analysis*, 6th ed, Wadsworth, Belmont, CA, **1981**. p. 206.
[30] P. Szabó, L. Markó, G. Bor, *Chem. Technol. (Leipzig)* **1961**, *13*, 549–550; *Chem. Abstr.* **1962**, *56*, 43933.
[31] R. Tuba, E. Fördős, F. Ungváry, *J. Mol. Catal. A* **2005**, *236*, 113–118.
[32] B. E. Hanson, M. J. Sullivan, R. J. Davis, *J. Am. Chem. Soc.* **1984**, *106*, 251–253.

Received: December 9, 2005
Published Online: March 1, 2006

 © 2006 Wiley-VCH Verlag GmbH & Co. KGaA, Weinheim 

DOI: 10.1002/ejic.200501110

# Synthesis, Crystal Structures, Magnetic Properties and Photoconductivity of $C_{60}$ and $C_{70}$ Complexes with Metal Dialkyldithiocarbamates $M(R_2dtc)_x$, where M = $Cu^{II}$, $Cu^{I}$, $Ag^{I}$, $Zn^{II}$, $Cd^{II}$, $Hg^{II}$, $Mn^{II}$, $Ni^{II}$, and $Pt^{II}$; R = Me, Et, and *n*Pr

**Dmitri V. Konarev,*[a] Andrey Y. Kovalevsky,[b] Salavat S. Khasanov,[c] Gunzi Saito,[d] Dmitri V. Lopatin,[e] Alexey V. Umrikhin,[e] Akihiro Otsuka,[f] and Rimma N. Lyubovskaya[a]**

**Keywords:** Crystal engineering / Fullerenes / Metal dialkyldithiocarbamates / Magnetic properties / Photoconductivity

New complexes of fullerenes $C_{60}$ and $C_{70}$ with metal dialkyldithiocarbamates, $[M(R_2dtc)_x]\cdot[C_{60(70)}]\cdot$[Solvent], R = Et [M = $Cu^{II}$ ($C_{60}$, **1**; $C_{70}$, **2**), $Cu^{I}$ ($C_{60}$, **3**; $C_{70}$, **4**), $Ag^{I}$ ($C_{60}$, **5**), $Zn^{II}$ ($C_{60}$, **6**), $Cd^{II}$ ($C_{60}$, **7**; $C_{70}$, **8**), $Hg^{II}$ ($C_{60}$, **9**), $Mn^{II}$ ($C_{70}$, **10**)], R = Et and Me [M = $Cu^{II}$ ($C_{60}$, **11**), and $Zn^{II}$ ($C_{60}$, **12**)], and R = *n*Pr [M = $Cu^{II}$ ($C_{60}$, **13**), $Ni^{II}$ ($C_{60}$, **14**), and $Pt^{II}$ ($C_{60}$, **15**)] were obtained. $M(R_2dtc)_x$ efficiently cocrystallized with fullerene molecules as tetrahedral monomers (**6**, **12**), dimers (**1**, **7**, **11**), and tetramers (**3**, **4**). Fullerene molecules form closely packed hexagonal and square layers in **1**, **7**, and **11**, hexagonal and tetragonal 3D structures in **6** and **12**, and island motifs in **3** and **4**. Complexes **1**–**15** have a neutral ground state. However, the formation of the complexes with fullerenes changes the environment of paramagnetic $Cu^{II}$ and $Mn^{II}$. The EPR spectra of **1**, **2**, **11**, and **13** are essentially modified relative to those of pristine $Cu(R_2dtc)_2$ because of a weak coordination of $Cu^{II}$ to fullerene and a flattening of the central $(NCS_2)_2Cu$ fragments. Complex **10** shows a spectrum exhibiting features from 50 to 600 mT and manifests strong antiferromagnetic coupling of spins with a Weiss temperature of –96 K and the maximum of magnetic susceptibility at 46 K. Such magnetic behavior can be explained by the formation of $[Mn(Et_2dtc)_2]_2$ dimers in **10**. The illumination of the crystals of **1**, **2**, and **7** by white light results in up to a $10^3$ increase in photocurrent. The photoconductivity spectra have maxima at 470, 450–650, and 660 nm for **1**, **2**, and **7**, respectively. Photogeneration of free charge carriers is realized by photoexcitation of $Cu(Et_2dtc)_2$ in **1** and **2**, and by charge transfer from $Cd(Et_2dtc)_2$ to $C_{60}$ molecules in **7**. The decrease of photocurrent in **1** and **7** in a weak magnetic field with $B_0 < 0.5$ T was found.
(© Wiley-VCH Verlag GmbH & Co. KGaA, 69451 Weinheim, Germany, 2006)

## Introduction

Fullerenes form a wide variety of donor-acceptor complexes ranging from molecular to ionic ones[1–3] with different classes of organic and organometallic donors: aromatic hydrocarbons,[4] amines,[5–7] tetrathiafulvalenes,[6,8] porphyrins and metalloporphyrins,[9–11] porphyrazines,[12] metallocenes,[13–17] and others.[6] Great interest in fullerene complexes was evoked by their intriguing properties. Ionic compounds show ferromagnetism[5] and reversibly form σ-bonded structures.[15–17] Neutral complexes were also used as templates for the preparation of fullerene polymers.[18] They can manifest photoconductivity[19] and excited ionic states upon photoexcitation by white light.[20] The variation of a donor component allows one to affect the packing of fullerene molecules in a crystal, the charged state of fullerenes and, consequently, the properties of the resulting complexes. The search for new classes of donor molecules for the preparation of fullerene complexes can result in the design of new promising compounds. Recently, we have found that dimeric copper(II) diethyldithiocarbamate, $Cu(Et_2dtc)_2$, co-crystallizes with fullerenes to form a molecular complex, $[Cu(Et_2dtc)_2]_2\cdot C_{60}$, with a layered structure.[21] This work was extended to metal(II) dithiocarbamates with bulkier benzyl substituents (abbreviation: Bnz), namely, $Cu(Bnz_2dtc)_2$, $Ni(Bnz_2dtc)_2$, $Pd(Bnz_2dtc)_2$, and $Pt(Bnz_2dtc)_2$. They co-crystallize with $C_{60}$ to form $M(Bnz_2dtc)_2\cdot C_{60}\cdot(C_6H_5Cl)_{0.5}$ complexes.[22] In contrast to dimeric $Cu(dedtc)_2$, $M(Bnz_2dtc)_2$ are monomers with planar conformation of the central $(NCS_2)_2M$ fragment, which is charac-

[a] Institute of Problems of Chemical Physics RAS, Chernogolovka, Moscow region 142432, Russia
Fax: +7-96-515-5420
E-mail: konarev@icp.ac.ru
[b] State University of New York at Buffalo, Buffalo, New York, 14260 USA
E-mail: bioayk@langate.gsu.edu
[c] Institute of Solid State Physics RAS, Chernogolovka, Moscow region, 142432, Russia
E-mail: khasanov@issp.ac.ru
[d] Division of Chemistry, Graduate School of Science, Kyoto University, Sakyo-ku, Kyoto 606-8502, Japan
Fax: +81-75-753-4035
E-mail: saito@kuchem.kyoto-u.ac.jp
[e] Department of Physics, Tambov State University, Tambov, 392622 Russia
E-mail: lopatin@tsu.tmb.ru
[f] Research Center for Low Temperature and Materials Sciences, Kyoto University, Sakyo-ku, Kyoto, 606-8502, Japan
E-mail: otsuka@kuchem.kyoto-u.ac.jp
Supporting information for this article is available on the WWW under http://www.eurjic.org or from the author.

 © 2006 Wiley-VCH Verlag GmbH & Co. KGaA, Weinheim 

teristic of $Ni^{II}$, $Pd^{II}$, and $Pt^{II}$ dithiocarbamates.[23–27] Moreover, $Pd(Bnz_2dtc)_2$ forms a multi-component ionic complex containing $C_{60}$ and bis(benzene)chromium ion-radicals: $[Cr^{I}(C_6H_6)_2^{\cdot+}]\cdot(C_{60}^{\cdot-})\cdot[Pd(Bnz_2dtc)_2]_{0.5}$. The complex demonstrates unusual low-temperature dimerization of $C_{60}^{\cdot-}$ with a relatively large hysteresis and the decrease of the dimerization temperature at a fast cooling rate.[22] Thus, metal dialkyldithiocarbamates, $M(R_2dtc)_x$, can successfully be used in the design of molecular and ionic complexes with fullerenes. It should be noted that although we have known about $M(R_2dtc)_x$ for a long time, their donor-acceptor complexes with π-acceptors are rare. To our knowledge, only some complexes of molybdenum and tungsten dialkyldithiocarbamates with tetracyanoquinodimethane were described.[28,29]

$M(R_2dtc)_x$ can easily be modified. It is possible to vary molecular structures of $M(R_2dtc)_x$ by changing "M" or the length of alkyl substituents (R). Donor properties of $M(R_2dtc)_x$ can also be varied from weak donors to strong ones[30] potentially able to ionize fullerenes. Some of $M(R_2dtc)_x$ have broad absorption in the visible range or outstanding magnetic properties [for example, $Fe^{III}(Et_2dtc)_2Cl$ is the first single-component ferromagnet with $T_c$ = 2.46 K][31] and, therefore, they can be used as light harvesting or magnetic components for the complexes.

In the present work we studied the effect of $M(R_2dtc)_x$ (depending on M and R) on composition, structure, electronic, and physical properties of their complexes with fullerenes. We used monomeric, dimeric, and tetrameric $M(R_2dtc)_x$ and varied the length of alkyl (R) substituents (Me, Et, and *n*Pr). $M(R_2dtc)_x$ were both weak and strong donors. The interaction of $C_{60}$ with the strongest donors ($Cu^{I}$, $Mn^{II}$, $Co^{II}$, and $V^{II}$ diethyldithiocarbamates) was studied in benzonitrile solution. Fifteen complexes of $C_{60}$ and $C_{70}$ with $Cu^{II}$, $Cu^{I}$, $Ag^{I}$, $Zn^{II}$, $Cd^{II}$, $Hg^{II}$, $Mn^{II}$, $Ni^{II}$, and $Pt^{II}$ dialkyldithiocarbamates were obtained and characterized in the solid state. The composition of the complexes was determined from elemental analysis and X-ray diffraction on single crystals. Crystal structures of seven complexes were solved. FTIR- and UV/Visible-NIR spectra of the complexes were studied. Magnetic properties of the complexes with $M(R_2dtc)_x$ (M = $Cu^{I}$, $Cu^{II}$, and $Mn^{II}$) were investigated by SQUID and EPR techniques. Photoconductivity of single crystals of four $C_{60}$ and $C_{70}$ complexes with $Cu(Et_2dtc)_2$ and $Cd(Et_2dtc)_2$ was studied upon illumination with white light. The comparison of the photoconductivity and the absorption spectra allows one to suggest the mechanisms of free charge carrier generation. The effect of magnetic field with $B_0 < 0.5$ T on photoconductivity was determined.

## Results and Discussion

### 1. Interaction of Fullerenes with Metal(II) Diethyldithiocarbamates in Solution

The interaction of the strongest $M(Et_2dtc)_2$ donors (M = $Cu^{I}$, $Mn^{II}$, $Co^{II}$, and $V^{II}$) with $C_{60}$ was studied in solution. $C_{60}$ and a fivefold molar excess of the corresponding $M(Et_2dtc)_x$ were dissolved in benzonitrile at 60 °C over 2 h, the solutions were cooled down, filtered off, and the spectra of the resulting solutions were measured in anaerobic conditions in the 600–1600 nm range. $Cu^{I}$, $Co^{II}$, and $V^{II}$ diethyldithiocarbamates reduce $C_{60}$ to a radical anion, and an absorption band characteristic of $C_{60}^{-}$ is manifested at 1070 nm. On the contrary, $Mn(Et_2dtc)_2$ cannot reduce $C_{60}$. These observations are in agreement with redox potentials of metal(II) dithiocarbamates. Related octahedral $M^{III}(dtc)_3^{1-/0}$ ($M^{3+}/M^{2+}$ transition) are reduced at –0.77 V for $V^{3+/2+}$, and –0.92 V for $Co^{3+/2+}$, whereas the reduction potential for $Mn^{3+/2+}$ (–0.08 V) is shifted to positive values (all vs. Ag/AgCl).[30] $C_{60}$ has the first $E^{0/-}$ potential at –0.485 V(vs. Ag/AgCl).[32]

### 2. Synthesis of Solid Complexes

The complexes obtained and the data from the elemental analysis are listed in Table 1. The ability of $M(R_2dtc)_x$ to co-crystallize with $C_{60}$ and $C_{70}$ as well as the composition of the complexes depend on the metal (M) and the length of the alkyl substituents (R). Pristine $M(R_2dtc)_2$ (R = Et, *n*Pr) have different conformations of the central $(NCS_2)_2M$ fragment. $Ni(R_2dtc)_2$ and $Pt(R_2dtc)_2$ have square planar conformation.[23–27] $Zn(R_2dtc)_2$,[33–35] $Cd(R_2dtc)_2$,[36,37] and $Fe(Et_2dtc)_2$[38] are dimers with a tetrahedral environment of $M^{II}$. $Mn(Et_2dtc)_2$ is a polymer with an octahedral environment of $Mn^{II}$.[39] $Hg(R_2dtc)_2$[40–42] and $Cu(R_2dtc)_2$[43] have both square planar or square pyramidal dimeric conformations.

$M(Et_2dtc)_2$ (M = $Cd^{II}$, $Hg^{II}$, and $Mn^{II}$) co-crystallize with fullerenes in dimeric conformation to form 1:2 [$C_{60}$/$M(R_2dtc)_2$] complexes. As this takes place, $Cd(Et_2dtc)_2$, and $Mn(Et_2dtc)_2$ precipitate $C_{60}$ and $C_{70}$ complexes from $C_6H_6$, $C_6H_5Cl$, and $C_6H_4Cl_2$ solutions in nearly a quantitative yield [a similar ability was found for $Fe(Et_2dtc)_2$]. On the contrary, square planar $Ni(Et_2dtc)_2$, and $Pt(Et_2dtc)_2$ or $Co(Et_2dtc)_2$ and $V(Et_2dtc)_2$, which reduce $C_{60}$ in solution, do not form crystals of the complexes with fullerenes.

Elongation of alkyl substituents in $M(nPr_2dtc)_2$ drastically changes their complex formation with fullerenes. $Ni(nPr_2dtc)_2$ and $Pt(nPr_2dtc)_2$ with square planar conformation form 2:1 [$C_{60}$/$M(nPr_2dtc)_2$] complexes with $C_{60}$. Similarly, among different metal(II) dibenzyldithiocarbamates only $Ni(Bnz_2dtc)_2$, $Pd(Bnz_2dtc)_2$, and $Pt(Bnz_2dtc)_2$ with the same conformation co-crystallize with $C_{60}$.[22] It is interesting to note that $Cu(R_2dtc)_2$ form 1:2, 2:1, and 1:1 [$C_{60}$:$Cu(R_2dtc)_2$] complexes independently of the R (MeEt, Et, *n*Pr, and Bnz) length. It seems possible that $Cu(R_2dtc)_2$ in the complexes with fullerenes can adopt both square planar[43,44] and square pyramidal dimeric conformations.[43]

The crystals of the complexes were obtained by the evaporation of solutions containing fullerenes and corresponding donors. We used the diffusion method to prepare the complexes with air-sensitive $M(R_2dtc)_x$ and $Cd(Et_2dtc)_2$.

 © 2006 Wiley-VCH Verlag GmbH & Co. KGaA, Weinheim 

Table 1. Data of elemental analysis for **1**–**15**.

| | | Elemental analysis found/calcd. | | | | | | Color and shape |
|---|---|---|---|---|---|---|---|---|
| | | C [%] | H [%] | N [%] | Cl [%] | S [%] | M [%] | |
| $[Cu(Et_2dtc)_2]_2{\cdot}C_{60}$[a] [21] | **1** | 66.46 | 3.08 | 4.10 | 0 | | | black hexagonal |
| | | 66.70 | 2.77 | 3.88 | 0 | 17.77 | 8.88 | plates |
| $[Cu(Et_2dtc)_2]{\cdot}(C_{70})_2{\cdot}(C_6H_5Cl)_{0.5}$ | **2** | 83.54 | 2.24 | 1.75 | 0.91 | | | black prisms |
| | | 83.51 | 1.42 | 1.77 | 1.12 | 8.12 | 4.06 | |
| $\{[Cu^I(Et_2dtc)]_4\}_5{\cdot}(C_{60})_3{\cdot}(C_6H_4Cl_2)_4$[a] | **3** | 51.71 | 3.11 | 3.75 | 5.58 | | | black prisms |
| | | 50.75 | 3.19 | 4.14 | 4.21 | 18.93 | 18.78 | |
| $\{[Cu^I(Et_2dtc)]_4\}_5{\cdot}(C_{70})_3{\cdot}(C_6H_4Cl_2)_4$[a] | **4** | 53.68 | 2.97 | 3.50 | 4.64 | | | black prisms |
| | | 53.26 | 3.03 | 3.93 | 3.93 | 17.97 | 17.83 | |
| $Ag^I(Et_2dtc){\cdot}C_{60}{\cdot}C_6H_6$ | **5** | 82.14 | 1.48 | 1.33 | – | | | black prisms |
| | | 80.85 | 1.52 | 1.32 | – | 6.07 | 10.24 | |
| $Zn(Et_2dtc)_2{\cdot}C_{60}{\cdot}(C_6H_5Cl)_{0.5}{\cdot}(C_6H_6)_{0.5}$[a] | **6** | According to X-ray diffraction data | | | | | | brown prisms |
| $\{Cd(Et_2dtc)_2\}_2{\cdot}C_{60}$[a] | **7** | 61.02 | 3.04 | 3.79 | – | | | red-brown rhombus |
| | | 61.50 | 2.67 | 3.73 | – | 17.09 | 15.01 | |
| $\{Cd(Et_2dtc)_2\}_2{\cdot}C_{70}$ | **8** | 64.41 | 3.32 | 3.38 | <0.7 | | | red-brown rhombus |
| | | 65.20 | 2.41 | 3.33 | 0 | 15.45 | 13.57 | |
| $\{Hg(Et_2dtc)_2\}_2{\cdot}C_{60}$ | **9** | 56.00 | 2.35 | 3.37 | – | | | black hexagonal |
| | | 55.02 | 2.39 | 3.34 | – | 15.29 | 23.96 | plates |
| $\{Mn(Et_2dtc)_2\}_2{\cdot}C_{70}$ | **10** | 68.88[b] | 2.59 | 3.69 | 0 | | | black elongated parallelepipeds |
| | | 70.05 | 2.98 | 3.63 | 0 | 16.60 | 7.13 | |
| $[Cu(EtMedtc)_2]_2{\cdot}C_{60}$[a] | **11** | 66.13 | 2.21 | 4.01 | – | | | black rhombus |
| | | 65.92 | 2.31 | 4.04 | – | 18.49 | 9.24 | |
| $[Zn(EtMedtc)_2]_3{\cdot}(C_{60})_2$[a] | **12** | According to X-ray diffraction data | | | | | | black rhombus |
| $[Cu(nPr_2dtc)_2]{\cdot}(C_{60})_2$ | **13** | 86.74 | 1.48 | 1.44 | 0 | | | thin needles |
| | | 86.67 | 1.51 | 1.51 | 0 | 6.89 | 3.42 | |
| $[Ni(nPr_2dtc)_2]{\cdot}(C_{60})_2$ | **14** | 87.01 | 1.50 | 1.47 | 0 | | | thin needles |
| | | 86.91 | 1.50 | 1.50 | 0 | 6.88 | 3.21 | |
| $[Pt(nPr_2dtc)_2]{\cdot}(C_{60})_2$ | **15** | 80.81 | 2.30 | 1.70 | 0 | | | thin needles |
| | | 80.93 | 1.41 | 1.41 | 0 | 6.44 | 9.81 | |

[a] The composition of the complex was proved by X-ray diffraction on single crystals. [b] A smaller content of carbon relative to the calculated values may have been caused by the addition of oxygen during elemental analysis because of the high air-sensitivity of $Mn(Et_2dtc)_2$.

## 3. Crystal Structures

Main geometric parameters of $M(R_2dtc)_x$ and van der Waals (vdW) contacts in the complexes with fullerenes are listed in Table 2. Molecular structures of $M(R_2dtc)_x$ are shown in Figure 1.

The crystal structure of $[Cu(Et_2dtc)_2]_2{\cdot}C_{60}$ (**1**) has been described previously.[21]

$[Cd(Et_2dtc)_2]_2{\cdot}C_{60}$ (**7**) has a crystal structure similar to that of **1**. $Cd(Et_2dtc)_2$ and $C_{60}$ molecules are ordered at 120 K. Complex **7** has a layered structure (Figure 2, parts a and b), in which layers of closely packed $C_{60}$ molecules alternate with those composed of $Cd(Et_2dtc)_2$ dimers. Each $C_{60}$ molecule has four neighbors in the layer with the shortest interfullerene center-to-center distance of 9.99 Å along the diagonal to the *bc*-plane (Figure 2, b). This distance is close to that in pure $C_{60}$ crystals at 153 K (9.94 Å).[45] The vdW C···C contacts are 3.33–3.77 Å. Two other neighboring fullerenes are arranged in the *c*-direction with a center-to-center distance of 10.54 Å (longer than the vdW diameter of $C_{60}$ molecules of 10.18 Å). Therefore, $C_{60}$ molecules have a square arrangement in the layers.

The projection of the $Cd(Et_2dtc)_2$ layer on the $C_{60}$ one is shown in part b of Figure 2. The central $CdS_4$ fragments are arranged strictly above the $C_{60}$ spheres, whereas flexible ethyl substituents occupy available cavities in the $C_{60}$ layers. The effective packing of $Cd(Et_2dtc)_2$ and $C_{60}$ molecules in a crystal is attained due to a butterfly shape of $Cd(Et_2dtc)_2$ dimers (Figure 1), which allows them to encapsulate $C_{60}$ molecules (Figure 2, c).

The packing of $Cd(Et_2dtc)_2$ dimers in the layer has a parquet-like motif (Figure 2, b). The shortest Cd···C($C_{60}$) contacts of 3.587 and 3.592 Å are formed with two carbon atoms of the 6–6 bond of $C_{60}$. These contacts are noticeably longer than the Cu···C($C_{60}$) contacts in **1** (3.334 and 3.379 Å).[21] Co-crystallization of $Cd(Et_2dtc)_2$ with $C_{60}$ does not affect its geometry. The pristine donor has a dimeric structure with a nearly tetrahedral environment of $Cd^{II}$ with three short equatorial bonds and one short axial bond (an average length is 2.575 Å). One equatorial bond is noticeably longer than the other ones (2.812 Å).[36] The dimeric structure of $Cd(Et_2dtc)_2$ is retained in **7**. Averaged lengths of three short equatorial bonds and one short axial bond are nearly the same (2.577 Å), but the long equatorial bond is elongated to 2.877 Å. Two of four ethyl groups of $Cd(Et_2dtc)_2$ are directed towards the fullerene layer in **7** (Figure 2, c), whereas in **1** three of four ethyl groups of $Cu(Et_2dtc)_2$ are directed towards the fullerene layer.[21]

 © 2006 Wiley-VCH Verlag GmbH & Co. KGaA, Weinheim 

Table 2. Geometric parameters for metal dialkyldithiocarbamates in the complexes with fullerenes.

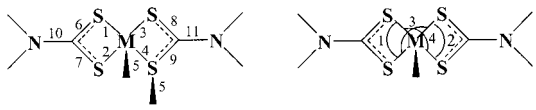

| Complex<br>Geometry | **1**<br>Dimer | **11**<br>Dimer | **7**<br>Dimer | **3**<br>Tetramer[a] | **4**<br>Tetramer[a] | **6**<br>Tetrahedral monomer | **12**<br>Tetrahedral monomer[b] |
|---|---|---|---|---|---|---|---|
| Bond lengths [Å] | | | | | | | |
| **1** | 2.3354(8) | 2.3057(15) | 2.8771(10) | 2.245(3)–<br>2.281(3) | 2.247(3)–<br>2.278(3) | 2.3449(9) | 2.340(3) |
| **2** | 2.2978(8) | 2.3361(12) | 2.544(9) | | | 2.3390(9) | 2.343(3) |
| **3** | 2.2994(9) | 2.3389(12) | 2.5333(10) | | | 2.3425(10) | 2.394(3) |
| **4** | 2.3218(8) | 2.3177(14) | 2.6330(10) | | | 2.3350(9) | 2.357(3) |
| **5** | 3.030(1) | 2.7869(12) | 2.5988(12) | | | – | – |
| **6** | 1.725 (3) | 1.718(5) | 1.758(4) | | | 1.705(4) | 1.695(13) |
| **7** | 1.722(3) | 1.707(5) | 1.714(3) | 1.700(10)–<br>1.764(10) | 1.698(11)–<br>1.777(10) | 1.735(3) | 1.712(14) |
| **8** | 1.720(3) | 1.717(6) | 1.737(3) | | | 1.733(3) | 1.743(12) |
| **9** | 1.724(3) | 1.724(5) | 1.717(4) | | | 1.733(6) | 1.1.754(11) |
| **10** | 1.321(4) | 1.328(7) | 1.337(4) | 1.324(4)–<br>1.335(4) | 1.317(14)–<br>1.342(15) | 1.340(5) | 1.281(14) |
| **11** | 1.320(4) | 1.335(7) | 1.331(5) | | | 1.326(4) | 1.355(16) |
| M···S (**1**–**4**) aver. | 2.3135 | 2.3246 | 2.6468 | 2.2567 | 2.2618 | 2.3403 | 2.358 |
| Bond angles [°] | | | | | | | |
| **1** | 76.90(3) | 76.73(5) | 66.67(3) | 122.6(1)–<br>123.18(11) | 121.83(11)–<br>123.65(10) | 77.89(3) | 78.17(12) |
| **2** | 77.06(3) | 76.44(5) | 70.29(3) | | | 78.29(3) | 78.15(13) |
| **3** | 164.84(3) | 162.67(6) | 143.80(3) | | | 127.18(4) | 129.21(13) |
| **4** | 173.00(3) | 169.49(5) | 157.64(4) | | | 128.19(4) | 130.28(12) |
| M···M distances [Å] | 3.529(1) | 3.561(2) | 3.802(2) | tetrahedron<br>2.5855(17)–<br>2.6239(17) | tetrahedron<br>2.5698(18)–<br>2.6306(18) | – | – |
| Donor–Fullerene interactions, shortest vdW contacts | | | | | | | |
| M···C(Ful.) [Å] | 3.269, 3.307 | 3.334, 3.379 | 3.587, 3.592 | 4.800, 4.838 | 4.437,4.476 | 3.659, 3.822 | 3.66–3.94 |
| S···C(Ful.) [Å] | 3.52–3.89 | 3.52–3.95 | 3.51–3.80 | 3.59–3.99 | 3.66–3.84 | 3.35–3.76 | 3.43–3.63 |
| N···C(Ful.) [Å] | 3.68–3.81 | 3.72–3.77 | 3.52–3.77 | 3.89–3.95 | 3.66–3.95 | 3.37–3.52 | 3.65–3.75 |
| H···C(Ful.) [Å] | 2.84–2.94 | 2.97–3.00 | 2.86–3.13 | 2.92–3.26 | 2.78–3.08 | 2.95–3.13 | 3.06–3.28 |
| Fullerene–Fullerene interaction | | | | | | | |
| Packing of fullerenes | hexagonal layers, 6 neighbors | hexagonal layers, 6 neighbors | square layers, 4 neighbors | isolated | isolated | hexagonal, 3D, 6 neighbors | tetragonal, 3D, 4 neighbors |
| Interfullerene center-to-center distances [Å] | 10.02 (×4), 10.25 (×2) | 9.89 (×4), 10.02 (×2) | 9.99 (×4) | shortest 13.5 | shortest 13.5 | 10.38 (×2), 10.13, 9.93, 9.81, 9.74 | 9.83, 9.86, 9.88, 10.09 |
| Interfullerene C···C contacts [Å] | 3.329–3.466, – | 3.276–3.410, 3.392–3.470 | 3.328–3.770, – | – | – | 3.250–3.360 | 3.269–3.410 |

[a] The ranges for the bond lengths and angles are given for **3** and **4**. [b] The bond lengths and angles for $Zn(EtMedtc)_2$ are given for one of three crystallographically independent molecules.

$[Cu(EtMedtc)_2]_2{\cdot}C_{60}$ (**11**) is isostructural to **1**. The substitution of two of four ethyl groups by methyl ones results in the decrease of the unit cell parameters of **11** relative to those of **1** (see Table 4). $C_{60}$ and $Cu(EtMedtc)_2$ molecules are ordered. Complex **11** also has a layered structure (Figure 3, a and b) with six neighbors to each $C_{60}$ molecule. The shortest interfullerene center-to-center distances are 9.89 (four neighbors along the diagonal to the *bc*-plane) and 10.02 Å (two neighbors in the *c*-direction; Figure 3, b). For both cases the vdW C···C contacts between adjacent fullerenes of 3.28–3.41 and 3.39–3.47 Å are shorter than 3.42 Å and center-to-center distances are close to the distance in pure $C_{60}$[45] justifying the formation of closely packed hexagonal layers.

The projection of the $Cu(EtMedtc)_2$ layer on the $C_{60}$ layer is shown in Figure 3, b. The central $CuS_4$ fragments arranged above $C_{60}$ spheres allow two flexible ethyl groups to occupy cavities in the $C_{60}$ layers. $C_{60}$ forms shortened Cu···C($C_{60}$) contacts of 3.334 and 3.379 Å by two carbon atoms of one 6–6 bond (Figure 3, b). VdW S, N and H···C($C_{60}$) contacts are close to those in **1** and **7** (Table 2).

$Cu(EtMedtc)_2$ has a dimeric structure in **11** with a square pyramidal environment of $Cu^{II}$ atoms (Figure 1) with four

 © 2006 Wiley-VCH Verlag GmbH & Co. KGaA, Weinheim 

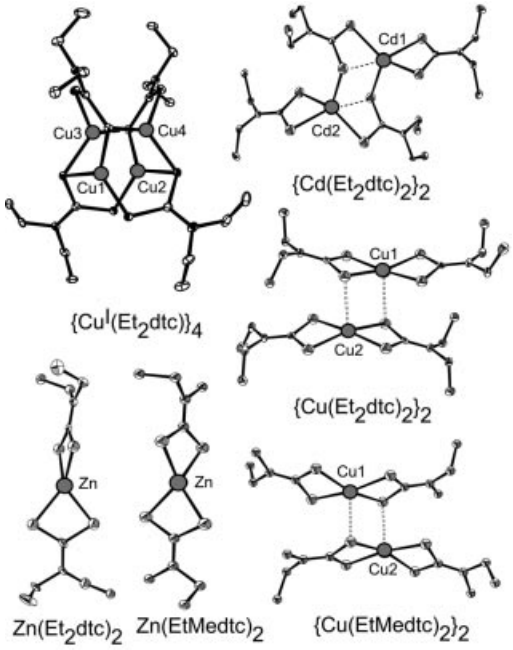


Figure 1. Molecular structures of $M(R_2dtc)_x$ in the complexes with fullerenes: $\{Cd(Et_2dtc)_2\}_2$, $\{Cu(Et_2dtc)_2\}_2$ and $\{Cu(EtMedtc)_2\}_2$ dimers; tetrahedral $Zn(Et_2dtc)_2$ and $Zn(EtMedtc)_2$ monomers and $[Cu^I(Et_2dtc)]_4$ tetramers.

short equatorial bonds (the average length is 2.325 Å) and one relatively long axial bond (2.787 Å). Both ethyl groups of $Cu(EtMedtc)_2$ are directed towards the fullerene layer.

Thus, **1**, **7**, and **11** have similar crystal structures. However, the differences in the molecular structures of $M(R_2dtc)_2$ and the length of the alkyl substituents provide their noticeable modifications. The packing motif of the fullerene layer changes from closely packed hexagonal layers in **11**, to intermediate layers in **1** (four and two neighbors with 10.02 and 10.25 Å center-to-center interfullerene distances)[21] and finally to square layers in **7**. The character of $M(R_2dtc)_2$-fullerene interactions also changes. Weakly bound $Cu(R_2dtc)_2$ dimers with relatively long axial bonds have a more planar shape of the $(NCS_2)_2M$ fragments than those in strongly bound $Cd(Et_2dtc)_2$ dimers with a short axial bond. The dihedral angles between the $NCS_2M$ planes are 160.9 and 158.6° in **1** and **11**, and only 143.8° in **7** providing shorter Cu···C($C_{60}$) distances (by about 0.3 Å) in **11** and **1** than the Cd···C($C_{60}$) distances in **7**. However, the more concave surface of the $Cd(Et_2dtc)_2$ fragments results in better conditions for the π-π interaction between the $NCS_2Cd$ planes and two adjacent $C_{60}$ hexagons (Figure 2, c) since the dihedral angle of 143.8° is close to that between adjacent $C_{60}$ hexagons (138.5°). As a result, the $NCS_2Cd$ planes and the $C_{60}$ hexagons arrange parallel to each other with the dihedral angles between them equal only to 0.8 and 8.2°. High steric complementarity is probably a reason for the ability of $Cd(Et_2dtc)_2$ to quantitatively precipitate $C_{60}$ and $C_{70}$ complexes from solutions. More planar $Cu(R_2dtc)_2$ provides worse conditions for the π-π interactions in **1** and **11** with corresponding dihedral angles of 9.8, 13.6° and 9.5, 12.6°, respectively.

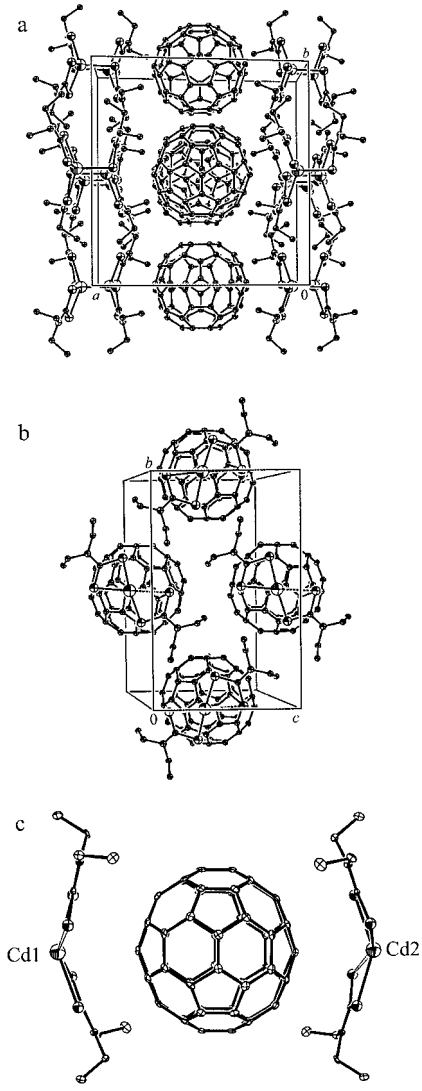


Figure 2. Crystal structure of **7**: the view of the unit cell on the *ab*-(a) and *bc*-planes (b); a mutual arrangement of concave $Cd(Et_2dtc)_2$ fragments and a spherical $C_{60}$ molecule (c).

$Zn(Et_2dtc)_2 \cdot C_{60} \cdot (C_6H_5Cl)_{0.5} \cdot (C_6H_6)_{0.5}$ (**6**) crystallizes in a triclinic lattice. $C_{60}$ and $Zn(Et_2dtc)_2$ molecules are ordered, whereas $C_6H_5Cl$ and $C_6H_6$ molecules share one position with equal occupancies and are disordered. Complex **6** has a unique cage structure with large channels along the *a*-axis accommodating $Zn(Et_2dtc)_2$ and solvent molecules. The channels are completely surrounded by the fullerene molecules, which form a hexagonal 3D framework (Figure 4). Each $C_{60}$ molecule has six neighbors. The center-to-center distances for three of them (9.74, 9.81, and 9.93 Å) are close to that distance in pure $C_{60}$,[45] whereas the other ones are larger (10.38 Å ×2 and 10.13 Å). Shortened vdW C···C contacts between the closest fullerenes are 3.250–3.360 Å.

$Zn(Et_2dtc)_2$ forms a complex with $C_{60}$ in a monomeric state with nonplanar *pseudo*-tetrahedral configuration of $Zn^{II}$ (the dihedral angle between two $NCS_2Zn$ planes being

 © 2006 Wiley-VCH Verlag GmbH & Co. KGaA, Weinheim 

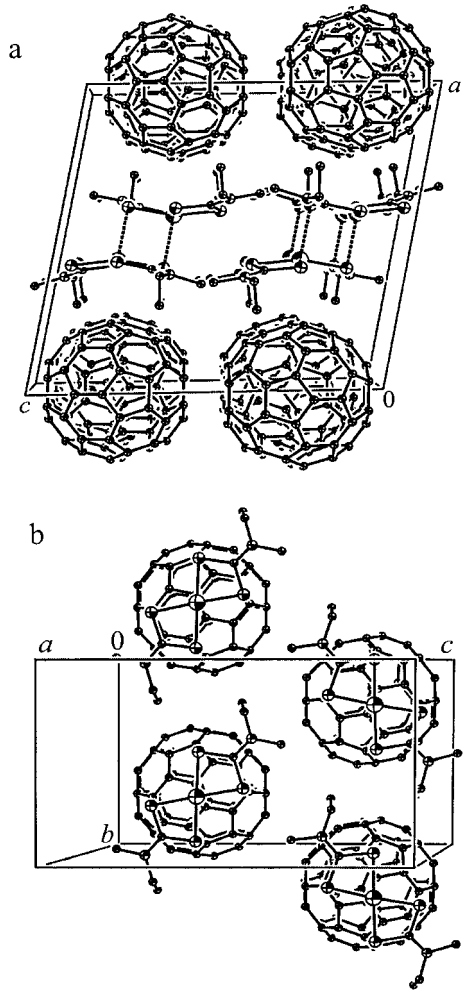


Figure 3. Crystal structure of **11**: the view of the unit cell of **11** on the *ac*- (a) and *bc*-planes (b).

91.5°) (Figure 1). This conformation is for the first time observed for $Zn(Et_2dtc)_2$. Similar geometry of the $(NCS_2)_2Zn$ fragment was reported for $Zn(Bnz_2dtc)_2$ with bulky benzyl substituents,[46] whereas pristine $Zn(R_2dtc)_2$ with R = Et, *n*Pr, *i*Pr substituents have dimeric structures.[33–35]

Because of the tetrahedral geometry, only half of each $Zn(Et_2dtc)_2$ molecule forms vdW contacts with $C_{60}$ (Table 2). The closest Zn···C($C_{60}$) distances are 3.659 and 3.822 Å. The other half of the $Zn(Et_2dtc)_2$ molecule locates above the adjacent $Zn(Et_2dtc)_2$.

The substitution of two ethyl groups by methyl ones changes the packing motif in $[Zn(EtMedtc)_2]_3 \cdot (C_{60})_2$ (**12**). In contrast to previously described complexes, both $C_{60}$ molecules are disordered at 90 K between two orientations with 66/34 and 58/42% occupancies. These orientations are linked by the rotation of the $C_{60}$ molecule by 180° about the axis passing through the centers of two oppositely located 5–6 bonds. There is also certain disorder in the positions of ethyl and methyl groups in $Zn(EtMedtc)_2$. The complex has 3D packing of fullerenes, in which each $C_{60}$ molecule has four neighbors and is located in the center of a distorted tetrahedron. This 3D packing can be split in strongly puckered $C_{60}$ layers parallel to the *ac*-plane (Figure 5). Three neighbors are seen in this plane, whereas the fourth neighbor is located in the adjacent layers. The center-to-center distances are in the 9.83–10.09 Å range (the vdW radius of $C_{60}$ is 10.18 Å) and the shortest C···C contacts lie in the 3.27–3.41 Å range. The cavities in the 3D framework are occupied by $Zn(EtMedtc)_2$ molecules. One $Zn(EtMedtc)_2$ molecule arranges parallel to the *ac*-plane and two other ones are perpendicular to this plane (Figure 5). Because of the strong puckering of fullerene layers, each $Zn(EtMedtc)_2$ molecule forms vdW contacts with four fullerene ones. The Zn···C($C_{60}$) distances of 3.66–3.94 Å are similar to those in **6**.

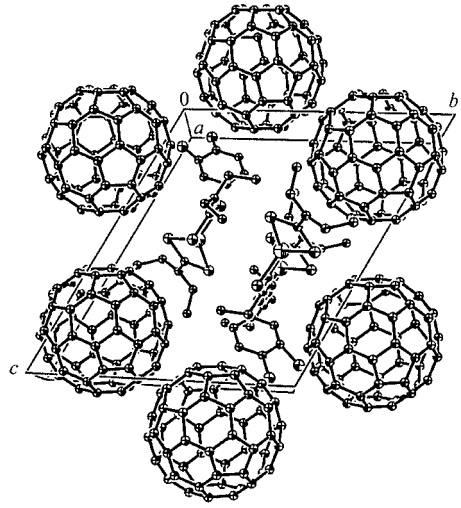


Figure 4. The view of the unit cell of **6** along the *a*-axis.

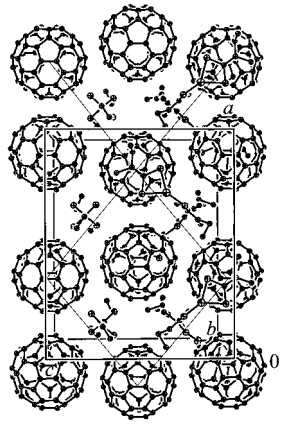


Figure 5. The view of the crystal structure of **12** on the *ac*-plane. $C_{60}$ molecules occupy two levels. Molecules belonging to one level are connected by thin lines.

$\{[Cu^I(Et_2dtc)]_4\}_5 \cdot (C_{60})_3 \cdot (C_6H_4Cl_2)_4$ (**3**) and $\{[Cu^I(Et_2dtc)]_4\}_5 \cdot (C_{70})_3 \cdot (C_6H_4Cl_2)_4$ (**4**) are isostructural and have high-symmetry cubic unit cells with parameters of

 © 2006 Wiley-VCH Verlag GmbH & Co. KGaA, Weinheim 

43.7822(4) (**3**) and 44.2911(3) (**4**) Å and unusually great volumes of 83925.3(13) (**3**) and 86885.9(10) Å (**4**). Two symmetrically independent $C_{60}$ molecules are disordered. One of them is located on a twofold axis and the other molecule is on a fourfold axis. Because of the disorder, $C_{60}$ molecules have two and four orientations, respectively. $[Cu^{I}(Et_2dtc)]_4$ and solvent $C_6H_4Cl_2$ molecules are located in general positions and are ordered.

The complexes have an island motif of fullerene packing with the shortest interfullerene center-to-center distances of 13.5 Å. Loose layers can be outlined in the *bc*-plane. The main structural motif of these layers is shown in Figure 6. There are large (right in Figure 6) and small (left in Figure 6) squares consisting of five and four fullerene molecules. Each small square is surrounded by four large squares and vice versa. As this takes place, both squares have one common $C_{60}$ molecule. Small squares accommodate five $[Cu^{I}(Et_2dtc)]_4$ molecules, whereas large squares accommodate eight $[Cu^{I}(Et_2dtc)]_4$ and eight $C_6H_4Cl_2$ molecules. It is interesting that all eight $C_6H_4Cl_2$ molecules surround one $C_{60}$ molecule (Figure 6). The adjacent fullerene layers in 3D packing are arranged in such a way that large fullerene squares are located above and below small fullerene squares.

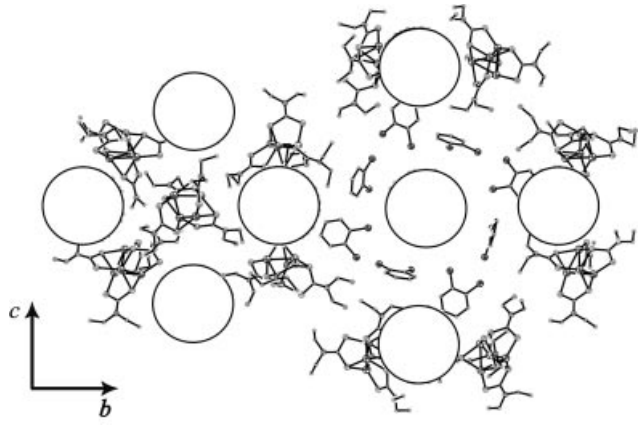


Figure 6. The view of the crystal structure of **3** on the *bc*-plane.

$[Cu^{I}(Et_2dtc)]_4$ is a tetramer containing four $Cu^{I}(Et_2dtc)$ units (Figure 1). $Cu^{I}$ atoms form a slightly distorted tetrahedron with the Cu···Cu distance of 2.5698(18)–2.6306(18) Å. Each $Cu^{I}$ atom forms three Cu–S coordination bonds of 2.245(3)–2.281(3) Å length. Therefore, the coordination number of $Cu^{I}$ is 3. Pristine $Cu^{I}(Et_2dtc)$ and $Au^{I}(Et_2dtc)$ form dimers,[47,48] and for $Ag^{I}(Et_2dtc)$ hexamers and polymers are also known.[49,50] According to the best of our knowledge, a tetrameric structure is for the first time observed for $Cu^{I}(Et_2dtc)$. Probably, the formation of complexes with $C_{60}$ and $C_{70}$ stabilizes the tetrameric structure. The Cu···C($C_{60}$) and Cu···C($C_{70}$) distances (4.80 and 4.44 Å), as well as the vdW N and S···C(fullerene) contacts (Table 2) are large enough to show low efficiency of the π-π interaction in **3** and **4**.

## 4. Magnetic Properties of the Complexes

EPR spectroscopy is a sensitive tool used to study changes in a local environment of $Cu^{II}$ atoms at the formation of fullerene complexes with $Cu(R_2dtc)_2$. Pristine $Cu(R_2dtc)_2$ with R = Et, *n*Pr possess dimeric structures with square pyramidal geometry of $Cu^{II}$ (the coordination number is 5).[43] Such geometry is characterized by the EPR spectrum shown in part a of Figure 7. $Cu(EtMedtc)_2$ has an asymmetric structure and as a result shows a more asymmetric EPR signal (Supporting Information).

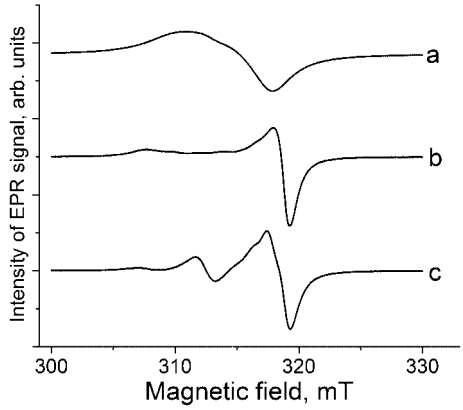


Figure 7. The EPR spectra of polycrystalline pristine $Cu(Et_2dtc)_2$ (a); **1** (b), and **2** (c) at 290 K.

The EPR signal of **1** (Figure 7, b) is noticeably different from that of pristine $Cu(Et_2dtc)_2$. According to X-ray diffraction data, $Cu(Et_2dtc)_2$ has a dimeric structure in **1** as well.[21] However, noticeable changes are observed in the environment of $Cu^{II}$. Weak axial coordination of $Cu^{II}$ to $C_{60}$ with a rather short Cu···C($C_{60}$) distance of 3.27 Å enhances the asymmetry of the environment of $Cu^{II}$. This coordination directs oppositely to the axial Cu–S bond and results in noticeable elongation of this bond from 2.844(1) in the pristine donor to 3.030(2) Å in **1**. Consequently, the central $(NCS_2)_2Cu$ fragments become more planar in **1** than in the pristine donor. Coordination of $Cu^{II}$ to $C_{60}$ is more favorable for planar conformation of $M(Et_2dtc)_2$, and most probably namely this coordination evokes the flattening of the central $(NCS_2)_2Cu$ fragments. The M···C($C_{60}$) distances (3.587, 3.334, and 3.269 Å) decrease together with the flattening of $M(Et_2dtc)_2$ fragments in the following order: **7**, **11**, and **1** (the length of axial M–S bonds are 2.599, 2.787, and 3.030 Å, respectively).

The EPR spectra of $[Cu(Et_2dtc)_2]\cdot(C_{70})_2\cdot(C_6H_5Cl)_{0.5}$ (**2**, Figure 7, c), $[Cu(EtMedtc)_2]_2\cdot C_{60}$ (**11**), and $[Cu(nPr_2dtc)_2]\cdot(C_{60})_2$ (**13**) (for spectra of **11** and **13** see supporting information) are also noticeably changed relative to those of pristine $Cu(R_2dtc)_2$. These changes are similar to those observed in the spectrum of **1** suggesting that weak coordination of $Cu^{II}$ to fullerenes and a flattening of the central $(NCS_2)_2Cu$ fragments can be realized in these complexes as well.

 © 2006 Wiley-VCH Verlag GmbH & Co. KGaA, Weinheim 

Magnetic susceptibilities of **1** and **2** were measured from 300 down to 1.9 K and were shown to follow the Curie–Weiss law with the small negative Weiss constants of –2.5 K (**1**) and –2.0 K (**2**), which indicate only a weak antiferromagnetic interaction between $Cu^{II}$ centers. Axial Cu–S bonds transfer the magnetic interaction in the $\{Cu(Et_2dtc)_2\}_2$ dimers and their elongation at the formation of complexes with fullerenes can weaken the antiferromagnetic interaction between $Cu^{II}$ centers.

The spectrum of $C_{60}$ and an excess of $Cu^{I}(Et_2dtc)$ in benzonitrile shows that CT is realized from donor to fullerene molecules in solution. To study CT in the solid state we measured the EPR spectra (4–290 K) and magnetic susceptibilities of $\{[Cu^{I}(Et_2dtc)]_4\}_5\cdot(C_{60})_3\cdot(C_6H_4Cl_2)_4$ (**3**) and $\{[Cu^{I}(Et_2dtc)]_4\}_5\cdot(C_{70})_3\cdot(C_6H_4Cl_2)_4$ (**4**) in the 2–300 K range. Pristine $Cu^{I}(Et_2dtc)$ is diamagnetic and EPR silent. **3** and **4** are also diamagnetic with temperature-independent diamagnetic contributions of –0.00522 and –0.00666 emu/mol$^{-1}$. Paramagnetic contributions of the Curie impurities are only 0.23 and 1.3% for **3** and **4**. According to EPR at 290 K (two narrow lines with $g_1$ = 2.0009 and $g_2$ = 2.0025 for **3** and one narrow line with $g$ = 2.0019 for **4**) these impurities originate mainly from defects.[51] Thus, in spite of the observation of CT in solution, both complexes are molecular ones in the solid state. Most probably, this is associated with the formation of $[Cu^{I}(Et_2dtc)]_4$ tetramers, whose shape is unfavorable for effective CT to fullerene molecules.

It is known that pristine $Mn^{II}(Et_2dtc)_2$ has a polymeric structure with a distorted octahedral environment of $Mn^{II}$.[39] In EPR it shows a single Lorentzian line with $g$ = 2.0115 and $\Delta H$ = 61.8 mT (Figure 8, a), which is characteristic of this environment of $Mn^{II}$.[52] The formation of $\{Mn(Et_2dtc)_2\}_2\cdot C_{70}$ (**10**) results in considerable changes in the EPR spectrum indicating noticeable modification of the local environment of $Mn^{II}$. The EPR spectrum exhibits features extending from 50 to about 500 mT (Figure 8, b). Such a spectrum is typical for dinuclear $Mn^{II}$ species[53] and previously a very similar EPR spectrum has been observed, for example, in a dinuclear $Mn^{II}$ complex bridged by chlorine atoms.[54] Magnetic susceptibility data provides evidence of a strong exchange interaction between $Mn^{II}$ centers. The magnetic moment of **10** is equal to 7.78 $\mu_B$ per formula unit at 300 K, which is close to the calculated value of 7.75 $\mu_B$ if two 5/2 spins contribute to magnetic susceptibility. $Mn^{II}$ spins interact antiferromagnetically in the 150–300 K range with a large negative Weiss constant of –96 K and magnetic susceptibility decreases below 46 K (Figure 9). Such exchange interactions between $Mn^{II}$ can be realized if $Mn(Et_2dtc)_2$ forms dimers in **10** [similar to $\{Cd(Et_2dtc)_2\}_2$ dimers in **7**]. EPR data support this conclusion. The EPR signal from $Mn(Et_2dtc)_2$ in **10** remains unchanged qualitatively down to 4 K. No EPR signals attributed to $C_{70}^{\cdot-}$ [55] were found indicating the absence of CT to fullerene molecules. Thus, $Mn(Et_2dtc)_2$ cannot ionize $C_{70}$ in the solid state. Similarly, $Mn^{II}$TPP (tetraphenylporphyrinate) ($E^{+/0}_{1/2}$ = –0.23 V vs. SCE)[56] forms only molecular complexes with fullerenes $C_{60}$ and $C_{70}$.[57]

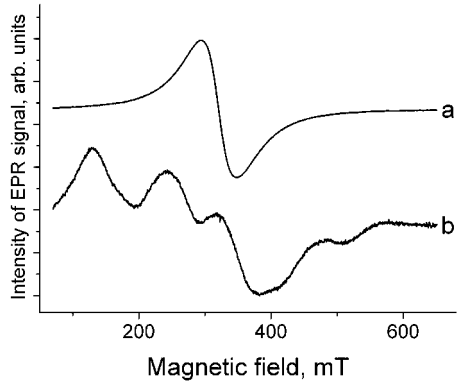


Figure 8. The EPR spectra of polycrystalline pristine $Mn(Et_2dtc)_2$ (a) and polycrystalline **10** (b) at 290 K.

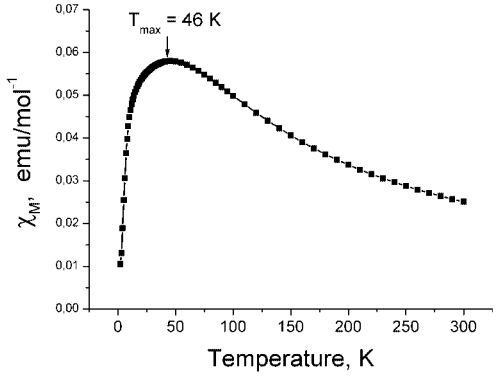


Figure 9. Molar magnetic susceptibility of polycrystalline **10** in the 1.9–300 K range.

## 5. IR- and UV/Visible-NIR Spectra of the Complexes

The IR spectra of **1**–**15** (see Supporting Information) are a superposition of those of pristine metal dithiocarbamates, fullerenes, and solvent molecules. The positions of peaks in the UV/Visible-NIR spectra of **1**–**15** and pristine donors are listed in Table 3. The absence of absorption in the NIR spectra of **1**–**15** at 1070 nm indicates neutral ground states of the complexes. Pristine $Cu(Et_2dtc)_2$ has broad absorption in the visible range with the maximum at 442 nm and a shoulder at 660 nm (Figure 10, part 1, c). This absorption retains in the spectra of the complexes with the maximum at 437 nm (**1**, Figure 10, part 1, b) and 455 nm (**2**, Figure 10, part 1, a). The bands at 341 and 263 nm (**1**) and 230 nm (**2**) were ascribed to intramolecular transitions in fullerenes.[58] The spectra of **6** (Figure 10, part 2, b) and **7** (Figure 10, part 2, a) also contain $C_{60}$ absorption bands at 263 and 340 nm and a relatively weak band at 470 nm. The latter band ascribed to intermolecular CT between neighboring $C_{60}$ molecules was also found in the spectra of fullerene films.[59] A condition necessary for the observation of this band in the solid-state spectra of the complexes is close packing of fullerene molecules in the crystal.[7,60] Since $C_{60}$ molecules are closely packed in **1**, **7**, and **6**, this band can manifest itself in their spectra. However, in the spectrum

 © 2006 Wiley-VCH Verlag GmbH & Co. KGaA, Weinheim 

Table 3. UV/Vis-NIR spectra of the starting compounds and **1**–**15**.

| Compounds | The bands of fullerenes [nm] | $M[d(alkyl)dtc]_x$ [nm] | CT bands [nm] **A** (Full.) | **C** (D.-Full.) |
|---|---|---|---|---|
| $C_{60}$ | 262 s, 341 s | | 470 m | |
| $C_{70}$ | –, 420 s, 540 m | | | |
| $Cu(EtMedtc)_2$ | | 267 s, 438 s, ca. 660 w | | |
| $Cu(Et_2dtc)_2$ | | 271 s, 442s, ca. 660 w | | |
| $Cu(nPr_2dtc)_2$ | | 277 s, 449s, ca. 650 w | | |
| $Ni(nPr_2dtc)_2$ | | 322 s, 389 s, 606 w | | |
| **1** | 263 s[a], 341 s | 263 s[a], 434 m[a], ca. 650 w | | – |
| **2** | 383 s, 455 m[a] | 455 m[a] | | |
| **3** | 262 s, 340 m | | | |
| **4** | 383 s, 480 m | | | |
| **5** | 263 s, 334 s | | | |
| **6** | 261 s, 337 s | | | |
| **7** | 263 s, 340 s | | 470 w | 610 w |
| **8** | 379 s, 462 m | | | |
| **9** | 255 s, 332 s | | | |
| **10** | 388 s, 484 m | | | |
| **11** | 265 s[a], 337 s | 265 s[a], 443 m[a], ca. 650 w | | – |
| **12** | 261 s, 338 m | | | |
| **13** | 262 s[a], 341 s | 262 s[a], 434 m,[a] ca. 615 w | 434 m[a] | 900 w |
| **14** | 266 s, 340 s, | ca. 605 w[a] | 450 w | ca. 770 w[a] |
| **15** | 266 s, 340 s | | 450 w | 650 w |

[a] The bands overlap.

of **1** it is closed by absorption of $Cu(Et_2dtc)_2$. A similar interfullerene CT band was reported for pristine $C_{70}$ at 550 nm,[59] and it can also contribute to broad absorption of **2** at 500–600 nm (Figure 10, part 1, a).

The spectrum of **7** additionally contains a broad weak band at 610 nm (Figure 10, part 2, a). Because $C_{60}$ and $Cd(Et_2dtc)_2$ do not absorb noticeably in this range, it can be attributed to intermolecular CT from $Cd(Et_2dtc)_2$ to $C_{60}$. The observation of this band is possible due to favorable π-π interaction between $Cd(Et_2dtc)_2$ and $C_{60}$ molecules (Figure 2, c). CT bands are absent in the spectra of **6** (Figure 10, part 2, b) and **1**–**5**, **8**–**12** (Supporting Information) indicating worse conditions for the π-π interaction between nonplanar $M^{II}(R_2dtc)_x$ and fullerenes. Absorption at 600–700 nm in the spectra of **1**, **2**, and **11** was attributed mainly to $Cu(R_2dtc)_2$ (a shoulder at 660 nm).

Several processes can occur at photoexcitation of **1**, **2**, and **7** in the visible range. In **1** and **2** mainly photoexcitation of $Cu^{II}(Et_2dtc)_2$ (437 and 660 nm) is realized together with a minor contribution of intermolecular CT between neighboring $C_{60}$ and $C_{70}$ molecules (470 and 550 nm, respectively), whereas in **7** intermolecular CT from $Cd(Et_2dtc)_2$ to $C_{60}$ molecules (610 nm) and between $C_{60}$ molecules (470 nm) is mainly realized.

The absorption spectra of **13** and pristine $Cu(nPr_2dtc)_2$ are shown in part 3 of Figure 10. Additionally to absorption of $Cu(nPr_2dtc)_2$ in the visible range (Figure 10, part 3, a, and Table 3), the intense band with the maximum at 900 nm (Figure 10, part 3, a) was attributed to CT from the $Cu(nPr_2dtc)_2$ to the $C_{60}$ molecules. Similar bands are observed in the spectra of **14** and **15**. Therefore, planar $M(nPr_2dtc)_2$ have better conditions for the π-π interaction with fullerenes than nonplanar $M[(Et, Me)_2dtc]_2$.

### 6. Photoconductivity in $C_{60}$ and $C_{70}$ Complexes with $Cu(Et_2dtc)_2$ and $Cd(Et_2dtc)_2$ (1, 2, 7, and 8)

According to the IR- and EPR data, **1**, **2**, **7**, and **8** are molecular complexes without CT in the ground state. The crystals of **1**, **2**, and **7** have low "dark" conductivity $\sigma \approx 10^{-10}$ to $10^{-11}$ S·cm$^{-1}$. The photoexcitation of single crystals of the complexes by white light from a 150 W halogen tube with $10^{12}$ to $10^{14}$ photons/cm$^2$·s intensity results in a 20–50-fold increase in the photocurrent in **1**, two orders of magnitude in **2**, and three orders of magnitude in **7**. These values remain unchanged under the illumination of the crystals for $10^4$ s and are completely reproducible. The crystals of **8** do not show a noticeable increase in photocurrent at photoexcitation.

Photoconductivity spectra of the complexes are shown in Figure 11. Photoconductivity has maxima at 470 nm for **1**, 450–650 nm for **2**, and about 660 nm for **7**. The comparison of the photoconductivity spectra of **1**, **2**, and **7** with their absorption spectra allows one to suppose the mechanisms of free charge carrier generation. In **1** and **2** the main contribution is given by the photoexcitation of $Cu(Et_2dtc)_2$ (440 and 660 nm) as well as interfullerene CT between neighboring $C_{60}$ or $C_{70}$ molecules (470 nm for **1** and 550 nm for **2**, Figure 11, a and b). The major contribution is given in **7** by CT from the $Cd(Et_2dtc)_2$ to the $C_{60}$ molecule (610 nm) with a small contribution of interfullerene CT between neighboring $C_{60}$ molecules (470 nm) (Figure 11, c). In spite of similar crystal structures, the mechanisms of free charge carrier generation are different in **1** and **7**. In **1** $Cu(Et_2dtc)_2$ has intense absorption in the visible range, whereas $Cd(Et_2dtc)_2$ is transparent in **7** in this range. However, steric compatibility of the $Cd(Et_2dtc)_2$ and $C_{60}$ molecules (Figure 2, c) provides better

 © 2006 Wiley-VCH Verlag GmbH & Co. KGaA, Weinheim 

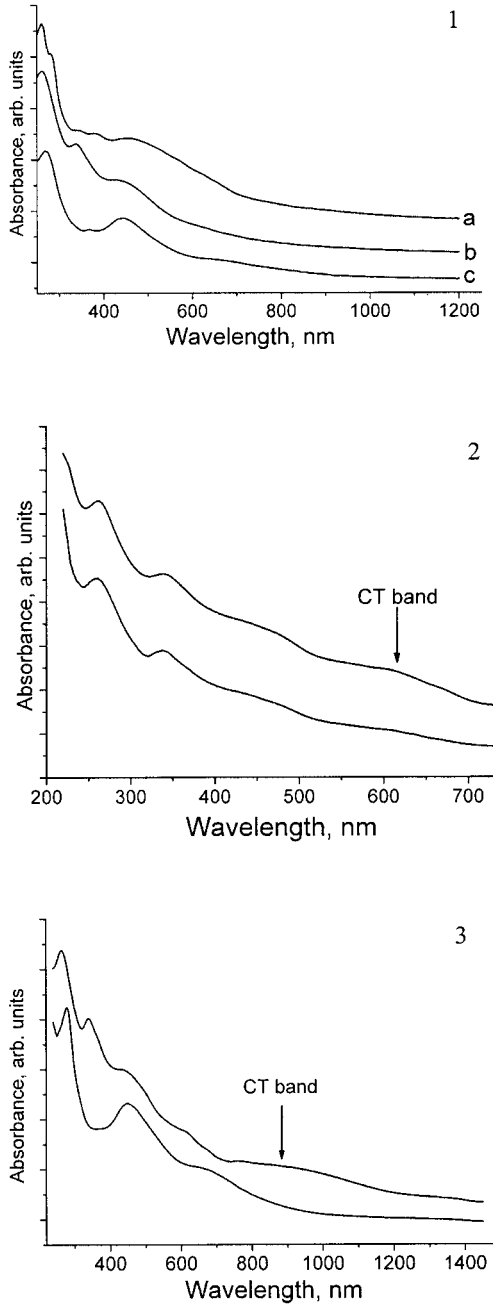


Figure 10. The UV/Visible-NIR spectra of: (1) **2** (a); **1** (b); and pristine $Cu(Et_2dtc)_2$ (c). (2) **7** (a); and **6** (b). (3) **13** (a); and pristine $Cu(nPr_2dtc)_2$ (b) in KBr pellets.

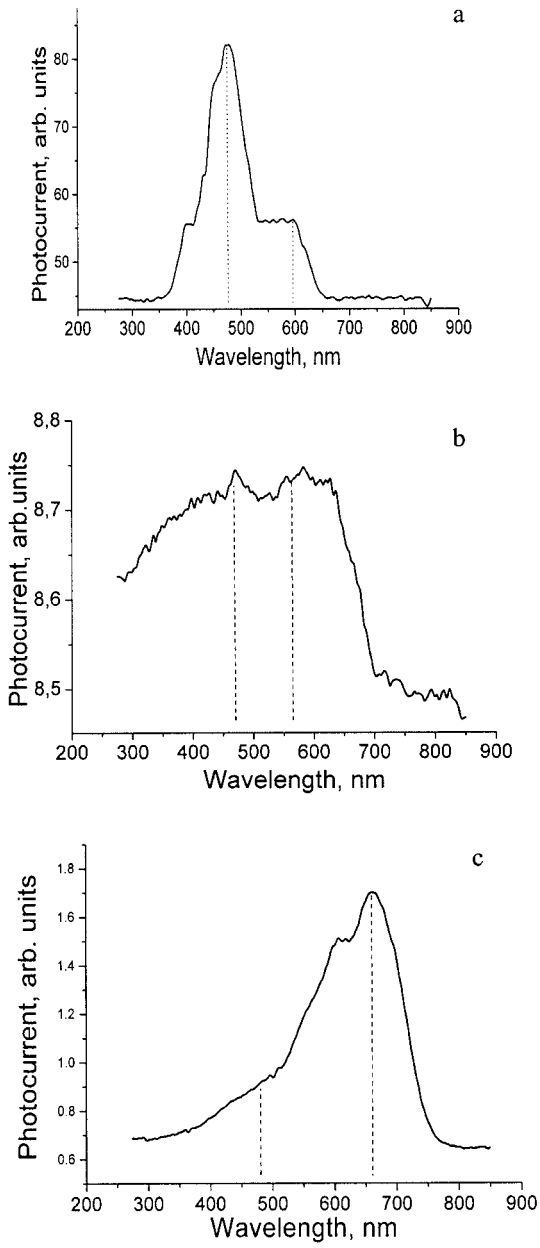


Figure 11. Photoconductivity spectra of the crystals of **1** (a), **2** (b), and **7** (c). The positions of the main peaks in the spectra are shown by dashed lines.

conditions for the π-π interaction and correspondingly for intermolecular CT in **7** than in **1**. Complex **8** has no CT band in the visible range and as a result photoconductivity was not found in this complex.

Photoconductivity of **1** and **7** is sensitive to weak magnetic field (MF) with $B_0 < 0.5$ T (Figure 12). A negative MF effect on photoconductivity is because of the reaction involving triplet CT excitons and paramagnetic centers. This interaction releases charges from deep-seated traps and increases photocurrent. A collision of triplet CT-excitons with doublet paramagnetic species may lead either to spin-independent triplet scattering or quenching. During quenching a transition from the initial spin state, which is a mixture of a doublet and a quartet, to a purely doublet final state takes place:

$$^3T + {}^2R \underset{k_{-1}}{\overset{k_1}{\rightleftarrows}} {}^{2,4}({}^3T\ldots{}^2R) \xrightarrow{k_L} {}^1S + {}^2R$$

The rate constant $k_L$ of the transition from each of the six $L$-th initial spin states of an intermediate complex to a final one depends on the amplitude of the doublet compo-

 © 2006 Wiley-VCH Verlag GmbH & Co. KGaA, Weinheim 

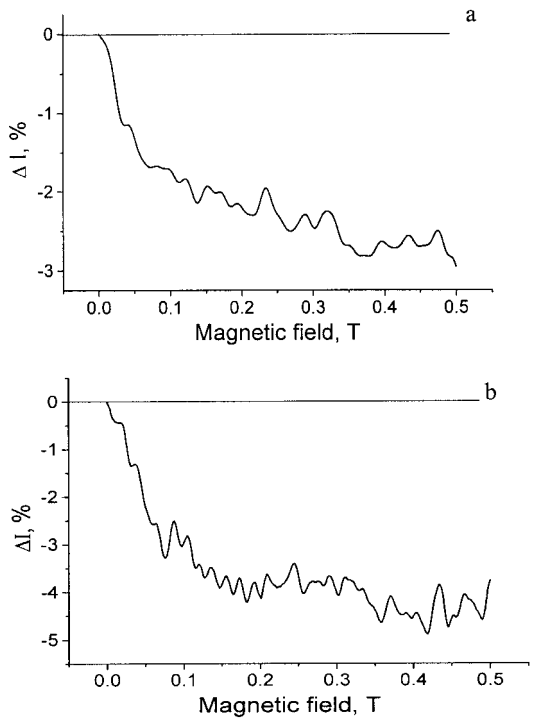


Figure 12. Magnetic field ($B_0$, $T$) dependence of photocurrent (I, %) in **1** (a) and **7** (b).

nent therein. The total rate of exciton quenching by paramagnetic impurity is:

$$Q = \frac{1}{6} k_1 \sum_{L=1}^{6} \frac{k_L}{k_{-1} - k_L},$$

where $k_1$ and $k_{-1}$ are rate constants of collision and back scattering, respectively. The value of $Q$ has a maximum, when a doublet component is uniformly distributed over all six substates, the minimum of $Q$ is attained at the complete separation of a doublet and a quartet. The quenching rate is maximal in ZMF. With the application of an external MF, the doublet component concentrates on four states and the value of $Q$ decreases together with the rate of dissociation of CT excitons and, consequently, a number of free charge carriers. A similar negative MF dependence was found in anthracene.[61]

## Conclusions

We studied the formation of the complexes between metal dialkyldithiocarbamates, $M(R_2dtc)_x$ with R = EtMe ($Cu^{II}$, $Zn^{II}$); Et ($Cu^{II}$, $Cu^{I}$, $Ag^{I}$, $Zn^{II}$, $Cd^{II}$, $Hg^{II}$, $Mn^{II}$, $Fe^{II}$, $Co^{II}$, $V^{II}$, $Ni^{II}$, and $Pt^{II}$); *n*Pr ($Cu^{II}$, $Cu^{I}$, $Zn^{II}$, $Cd^{II}$, $Ni^{II}$, and $Pt^{II}$) and fullerenes $C_{60}$ and $C_{70}$. It was shown that $M(R_2dtc)_x$ co-crystallize with fullerenes $C_{60}$ and $C_{70}$ to form complexes of different structures and compositions (**1**–**15**). Pristine $M(R_2dtc)_x$ (R = Et, *n*Pr) have a large variety of molecular structures in fullerene complexes, which can be square planar or tetrahedral monomers, strongly and weakly bound dimers and tetramers. Tetrahedral monomeric conformations for $Zn(EtMedtc)_2$ and $Zn(Et_2dtc)_2$ and tetrameric $\{Cu^{I}(Et_2dtc)\}_4$ were for the first time found for these metal dithiocarbamates.

Butterfly-shaped $[M\{(Me, Et)_2dtc\}_2]_2$ dimers (M = Cu and Cd) form layered structures in **1**, **7**, and **11**, where the packing of $C_{60}$ layers varies from a square to hexagonal one. The dimeric structure of dithiocarbamates provides a characteristic 1:2 composition of the complexes {Fullerene/$M[(Et, Me)dtc]_2$}. Complexes **8**–**10** have the same composition, and $M(R_2dtc)_2$ can have similar dimeric structures in these complexes. This supposition was justified for **10** by magnetic data. $Cd(Et_2dtc)_2$ has geometry conforming well to the spherical shape of fullerene molecules and shows high ability to nearly quantitatively precipitate $C_{60}$ and $C_{70}$ complexes from solutions. A similar ability was found for $Mn(Et_2dtc)_2$ and $Fe(Et_2dtc)_2$. Monomeric $Ni(nPr_2dtc)_2$ and $Pt(nPr_2dtc)_2$ with square planar conformation of the central $(NCS_2)_2M$ fragment form **12** and **13** with a 2:1 composition [Fullerene/$M(nPr_2dtc)_2$]. Complexes **2** and **13** have the same composition and the formation of $Cu(Et_2dtc)_2$ and $Cu(nPr_2dtc)_2$ monomers can be supposed for these complexes as well especially because pristine $Cu(R_2dtc)_2$ can adopt a square planar conformation.[43,44] However, X-ray diffraction data are needed to prove this supposition. Nonplanar tetrahedral $Zn(EtMedtc)_2$ and $Zn(Et_2dtc)_2$ provide 3D packing of fullerenes with their tetrahedral and hexahedral arrangements. Bulky $[Cu^{I}(Et_2dtc)]_4$ promotes an island motif in fullerene packing.

Using $M(Et_2dtc)_x$ with different donor ability (the strongest donors contain M = $Cu^{I}$, $Co^{II}$, $V^{II}$, and $Mn^{II}$) we found that $Cu^{I}(R_2dtc)$, $Co(R_2dtc)_2$, and $V(R_2dtc)_2$ reduce $C_{60}$ in benzonitrile. However, among these strong donors only fullerene complexes with $Mn(Et_2dtc)_2$ and $Cu^{I}(Et_2dtc)$ were obtained as crystals and no CT to fullerene molecules was found in them. The EPR spectra of paramagnetic $Cu(R_2dtc)_2$ and $Mn(Et_2dtc)_2$ noticeably change at the complex formation with fullerenes most probably due to changes in the environment of $M^{II}$. The EPR spectra of **1**, **2**, **11**, and **13** are noticeably modified relative to those of pristine $Cu(R_2dtc)_2$. Such changes can be a result of additional weak coordination of $Cu^{II}$ to $C_{60}$ and the flattening of the central $(NCS_2)_2Cu$ fragment. The changes in the EPR spectrum of $Mn(Et_2dtc)_2$ at the formation of **10** are most probably evoked by the transition from a polymeric structure of pristine $Mn(Et_2dtc)_2$ with an octahedral environment of $Mn^{II}$ to the formation in **10** of $\{Mn(Et_2dtc)_2\}_2$ dimers, in which strong antiferromagnetic exchange interaction between $Mn^{II}$ centers is possible.

The spectra of the complexes in the visible and NIR ranges indicate their neutral ground state. $Cu(R_2dtc)_2$ (**1**, **2**, **11**, and **13**) and $Ni(nPr_2dtc)_2$ (**14**) absorb in the visible range, whereas other $M(R_2dtc)_2$ are nearly transparent in this range. In addition to the bands associated with intramolecular transitions in fullerenes and $M(R_2dtc)_x$, the bands associated with intermolecular CT between neighboring fullerene molecules (at 470 nm for $C_{60}$ and at 550 nm for $C_{70}$)[59] and CT from $M(R_2dtc)_2$ to fullerene molecules are observed. The latter CT bands are observed only in the

 © 2006 Wiley-VCH Verlag GmbH & Co. KGaA, Weinheim 

spectra of **7** and the complexes with planar $M(nPr_2dtc)_2$ (**13**–**15**). The other complexes demonstrate either weak or no CT bands indicating worse conditions for the π-π interaction between fullerenes and nonplanar $M(R_2dtc)_x$. In accordance with the neutral ground state, the crystals of **1**, **2**, and **7** show low dark conductivity of $10^{-10}$ to $10^{-11}$ S·cm$^{-1}$. The illumination of the crystals by white light with $10^{12}$ to $10^{14}$ photons/cm$^2$·s intensity results in up to a $10^3$ increase in photocurrent. The photoconductivity spectra exhibit maxima at 470, 450–650, and 660 nm for **1**, **2**, and **7**, respectively. Three processes generate free charge carriers in the complexes. Photoexcitation of $Cu(Et_2dtc)_2$ contributes to photoconductivity of **1** and **2** since this donor has intense absorption in the visible range. A similar mechanism was observed in $Bz_4BTPE{\cdot}C_{60}$ {$Bz_4BTPE$: tetrabenzo[1,2-bis(4*H*-thiopyran-4-ylidene)ethane]},[62] and conjugated polymer-fullerene composites.[63] CT from donor to fullerene molecules contributes to photoconductivity of the complexes with relatively intense CT bands in the visible-NIR range: **7** and $TBPDA{\cdot}(C_{60})_2$ (*N*,*N*,*N*′,*N*′-tetrabenzyl-*p*-phenylenediamine).[19] Interfullerene CT between neighboring fullerene molecules also contributes to photoconductivity in **1** and **7** as well as in pure fullerene crystals[64] and films.[59] Common peculiarity of the $C_{60}$ complexes showing photoconductivity is a layered arrangement of fullerene and donor molecules in a crystal, which allow the movement of photogenerated carriers through the crystal. Weak MF with $B_0 < 0.5$ T differently affects photoconductivity of fullerene complexes. We found negative (**1** and **7**) and positive ($Bz_4BTPE{\cdot}C_{60}$)[64] MF dependences as well as the field dependence with sign inversion at 0.3 T [$TBPDA{\cdot}(C_{60})_2$].[19] A variety of dependences indicates that the interaction of MF with photogenerated excitons can be different in fullerene complexes depending on the donor used. The mechanisms of the effects of MF on photoconductivity involve triplet CT excitons and paramagnetic centers[61] or the population of a triplet state from a singlet one in MF.[65] Thus, fullerene complexes with $M\{Et_2dtc\}_2$ and other $M\{R_2dtc\}_x$ may be a new wide family of photoactive compounds. A study of the photophysical properties of these complexes is now in progress.

## Experimental Section

**Materials:** Sodium diethyldithiocarbamate trihydrate, [$Na(Et_2dtc){\cdot}3H_2O$], was purchased from Aldrich and recrystallized from an acetonitrile/benzene mixture. Sodium ethylmethyldithiocarbamate, Na(EtMedtc), and sodium di(*n*-propyl)dithiocarbamate, $Na(nPr_2dtc)$, were obtained by the reported procedure.[43] Carbon disulfide (3.1 mL, 0.052 mol) and sodium hydroxide (50% aqueous solution, 4 mL) were added to a stirred solution of $R_2NH$ (0.05 mol) ($R_2NH$=EtMeNH, Aldrich, and $nPr_2NH$, Wako) in ethanol (5 mL) at $T < 4$ °C (ice bath). After stirring for 4–6 h at $T <$ 4 °C Na(EtMedtc) precipitated as white crystals. $Na(nPr_2dtc)$ was obtained by the evaporation of an ethanol/water solution without heating. Pure $Na(R_2dtc)$ were obtained by recrystallization from acetonitrile/benzene mixtures (50–80% yields). Air-sensitive $M(R_2dtc)_x$ compounds (R = Et, M = Cu$^{I}$, Co$^{II}$, V$^{II}$, Fe$^{II}$, and Mn$^{II}$; R = *n*Pr, M = Cu$^{I}$) were obtained by stirring anhydrous CuCl (100 mg), $CoBr_2$ (150 mg), $VCl_2$ (100 mg), $FeBr_2$ (150 mg), and $MnI_2$ (150 mg) and $x$ [$x$ = 1 (Cu$^{I}$) or 2 (other metals)] molar equivalents of $Na(Et_2dtc)$ in 10 mL of degassed acetonitrile over 4 h in a glove box. $M(R_2dtc)_x$ were precipitated from acetonitrile as light yellow (Cu$^{I}$ and Mn$^{II}$), light pink (Fe$^{II}$), dark green-brown (Co$^{II}$), and light brown (V$^{II}$) powders together with NaCl(Br, I). The precipitates were washed with acetonitrile (3 mL) and dried. NaCl(Br, I) as well as possible admixtures of unreacted $MCl(Br, I)_x$ and $Na(Et_2dtc)$ were separated from $M(R_2dtc)_x$ at a stage of complex formation with fullerene because of their insolubility in *o*-dichlorobenzene ($C_6H_4Cl_2$). Air-stable $M(R_2dtc)_2$ (R = EtMe, M = Cu$^{II}$, and Zn$^{II}$; R = Et, M = Cu$^{II}$, Zn$^{II}$, Cd$^{II}$, Hg$^{II}$, Ag$^{I}$, Ni$^{II}$, and Pt$^{II}$; R = *n*Pr, M = Cu$^{II}$, Zn$^{II}$, Cd$^{II}$, Ni$^{II}$, and Pt$^{II}$) were obtained in aqueous solution from $CuBr_2$, $ZnCl_2$, $CdBr_2{\cdot}4H_2O$, $Hg(NO_3)_2{\cdot}H_2O$, $AgNO_3$, $NiCl_2$, $PtCl_2$, and $Na(R_2dtc)$.[43] $M(R_2dtc)_2$ were dissolved in hot chlorobenzene ($C_6H_5Cl$), filtered off from NaCl, NaBr, or $NaNO_3$ and the solvent was removed to dryness on a rotary evaporator to yield pure $M(R_2dtc)_2$ with satisfactory elemental analyses (50–80% yield). $C_{60}$ of 99.98% purity and $C_{70}$ of 99.0% purity were used from MTR Ltd. Solvents were purified under argon. $C_6H_4Cl_2$ and $C_6H_5Cl$ were distilled over $CaH_2$. Hexane and benzonitrile ($C_6H_5CN$) were distilled over Na/benzophenone. For the synthesis of air-sensitive $M(R_2dtc)_x$ (R = Et, M = Cu$^{I}$, Co$^{II}$, V$^{II}$, Fe$^{II}$, and Mn$^{II}$; R = *n*Pr, M = Cu$^{I}$) and the preparation of the fullerene complexes, solvents were degassed and stored in a MBraun 150B-G glove box with a controlled atmosphere with contents of $H_2O$ and $O_2$ of less than 1 ppm. The crystals of **3**, **4**, and **10** were stored in a glove box and were sealed in 2-mm quartz tubes for EPR and SQUID measurements under $10^{-5}$ Torr. KBr pellets for IR- and UV/Visible-NIR measurements were prepared in a glove box.

**Synthesis:** The composition of **1**–**5**, **7**–**11**, and **13**–**15** was determined from the elemental analysis (Table 1) and was justified for **1**, **3**, **4**, **6**, **7**, **11**, and **12** by X-ray diffraction on a single crystal.

The crystals of **1**, **2**, **5**, **6**, **9**, and **11**–**15** were obtained by a slow evaporation of chlorobenzene solution (15 mL) containing $C_{60}$ (25 mg, 0.0347 mmol) and two molar equivalents of $M(R_2dtc)_x$ (0.06940 mmol) over 1 week. The crystals precipitated were washed with an excess of acetone (50–80% yield). The shapes of the crystals are presented in Table 1.

The crystals of **3** and **4** were obtained under anaerobic conditions by a slow diffusion of hexane (20 mL) in $C_6H_4Cl_2$ solution (20 mL) containing $C_{60}$ (25 mg, 0.0347 mmol) (**3**) or $C_{70}$ (20 mg, 0.0238 mmol) (**4**) and a fourfold molar excess of $Cu^{I}(Et_2dtc)$ in a glass tube of 45 mL volume with a ground glass plug. After 1 month large black prisms of **3** and **4** were precipitated on the wall of the tube (up to $0.5 \times 0.5 \times 0.8$ mm$^3$ size). The solvent was decanted and the crystals were washed with hexane (50–60% yield).

$Cd(Et_2dtc)_2$, $Mn(Et_2dtc)_2$, and $Fe(Et_2dtc)_2$ nearly quantitatively precipitate $C_{60}$ and $C_{70}$ from different solvents ($C_6H_6$, $C_6H_5Cl$, and $C_6H_4Cl_2$). Because of this, the crystals of **7** and **8** were obtained by the diffusion of a benzene solution (20 mL) of $C_{60}$ (20 mg, 0.02775 mmol) (**7**) or $C_{70}$ (20 mg, 0.0238 mmol) (**8**) in $CHCl_3$ solution (20 mL) containing a twofold molar excess of $Cd(Et_2dtc)_2$. The crystals precipitated on the wall of the tube after 1 month. They were washed with acetone (70–90% yield).

The crystals of **10** were obtained similarly under anaerobic conditions by the diffusion of benzene solution (20 mL) of $C_{70}$ (20 mg, 0.0238 mmol) (**8**) into $C_6H_4Cl_2$ containing a twofold molar excess of $Mn(Et_2dtc)_2$. The crystals precipitated on the wall of the tube after 1 month. They were washed with hexane (70% yield).

 © 2006 Wiley-VCH Verlag GmbH & Co. KGaA, Weinheim 

Table 4. X-ray diffraction data for **1**, **3**, **4**, **6**, **7**, **11**, and **12**.

| | **1**[21] | **3** | **4** | |
|---|---|---|---|---|
| Structural formula | $[Cu(Et_2dtc)_2]_2{\cdot}C_{60}$ | $\{[Cu^I(Et_2dtc)]_4\}_5{\cdot}(C_{60})_3{\cdot}(C_6H_4Cl_2)_4$ | $\{[Cu^I(Et_2dtc)]_4\}_5{\cdot}(C_{70})_3{\cdot}(C_6H_4Cl_2)_4$ | |
| Empirical formula | $C_{80}H_{40}Cu_2N_4S_8$ | $C_{76}H_{54}Cl_2Cu_5N_5S_{10}$ | $C_{83.50}H_{54}Cl_2Cu_5N_5S_{10}$ | |
| $M_r$ [g·mol$^{-1}$] | 1440.72 | 1746.41 | 1836.52 | |
| Crystal shape and color | black hexagonal prisms | black cubes | black cubes | |
| Size [mm×mm×mm] | 0.40×0.30×0.25 | 0.50×0.40×0.40 | 0.40×0.30×0.30 | |
| Crystal system | monoclinic | cubic | cubic | |
| Space group | $P2_1/c$ | $Pn\bar{3}n$ | $Pn\bar{3}n$ | |
| $a$ [Å] | 16.1948(8) | 43.7822(4) | 44.2911(3) | |
| $b$ [Å] | 10.2552(5) | 43.7822(4) | 44.2911(3) | |
| $c$ [Å] | 17.2192(9) | 43.7822(4) | 44.2911(3) | |
| $\alpha$ [°] | 90 | 90 | 90 | |
| $\beta$ [°] | 102.504(2) | 90 | 90 | |
| $\gamma$ [°] | 90 | 90 | 90 | |
| $V$ [Å$^3$] | 2791.9(2) | 83925.3(13) | 86885.9(10) | |
| $Z$ | 2 | 48 | 48 | |
| $\rho_{calc}$ [g/cm$^3$] | 1.714 | 1.655 | 1.685 | |
| $\mu$ [mm$^{-1}$] | 1.12 | 1.921 | 1.860 | |
| $F$(000) | 1468 | 42240 | 44592 | |
| Absorption correction | no correction | no correction | SADABS[66] | |
| Max./min. transmission | 0.77/0.66 | 0.51/0.45 | 0.60/0.52 | |
| $T$ [K] | 90(2) | 90(2) | 90(1) | |
| Max. 2$\theta$ [°] | 54.12 | 50.04 | 50.04 | |
| Reflections measured | 25977 | 524031 | 690665 | |
| Unique reflections | 5683 | 12379 | 12798 | |
| $R_{int}$ | 0.036 | 0.0429 | 0.0637 | |
| Parameters, restraints | 425, 0 | 450, 0 | 458, 0 | |
| Reflections [$F_o > 2\sigma(F_o)$] | 4983 | 9398 | 8774 | |
| $R_1$ [$F_o > 2\sigma(F_o)$] | 0.0404 | 0.0984 | 0.0935 | |
| $wR_2$ (all data)[a] | 0.1064 | 0.2904 | 0.3181 | |
| $a$ | 0.0341 | 0.1060 | 0.1330 | |
| $b$ | 8.2311 | 2219.48 | 2964.08 | |
| *G.O.F.* | 1.082 | 1.132 | 1.054 | |
| Restr. *G.O.F.* | 1.082 | 1.132 | 1.054 | |
| CCDC number | 260289 | 286142 | 286143 | |

| | **6** | **7** | **11** | **12** |
|---|---|---|---|---|
| Structural formula | $Zn(Et_2dtc)_2{\cdot}C_{60}{\cdot}(C_6H_5Cl)_{0.5}{\cdot}(C_6H_6)_{0.5}$ | $[Cd(Et_2dtc)_2]_2{\cdot}C_{60}$ | $[Cu(EtMedtc)_2]_2{\cdot}C_{60}$ | $[Zn(EtMedtc)_2]_3{\cdot}(C_{60})_2$ |
| Empirical formula | $C_{76}H_{25.5}Cl_{0.5}N_2S_4Zn$ | $C_{80}H_{40}Cd_2N_4S_8$ | $C_{76}H_{32}Cu_2N_4S_8$ | $C_{144}H_{54}N_6S_{12}Zn_3$ |
| $M_r$ [g·mol$^{-1}$] | 1177.82 | 1538.44 | 1384.62 | 2442.71 |
| Crystal shape and color | black parallelepipeds | brown rhombus | black rhombus | black rhombus |
| Size [mm×mm×mm] | 0.33×0.20×0.20 | 0.40×0.30×0.10 | 0.42×0.38×0.10 | 0.40×0.30×0.20 |
| Crystal system | triclinic | monoclinic | monoclinic | orthorhombic |
| Space group | $P\bar{1}$ | $P2_1/c$ | $P2_1$ | $Pn2_1a$ |
| $a$ [Å] | 10.3762(5) | 16.1712(13) | 16.0626(4) | 20.815(5) |
| $b$ [Å] | 15.1717(7) | 16.9680(12) | 10.0196(3) | 26.072(6) |
| $c$ [Å] | 17.0002(8) | 10.5355(8) | 17.0653(5) | 17.128(4) |
| $\alpha$ [°] | 115.893(1) | 90 | 90 | 90 |
| $\beta$ [°] | 91.555(1) | 99.857(2) | 100.9490(13) | 90 |
| $\gamma$ [°] | 102.938(1) | 90 | 90 | 90 |
| $V$ [Å$^3$] | 2322.53(19) | 2848.2(4) | 2696.51(13) | 9298.88(12) |
| $Z$ | 2 | 2 | 2 | 4 |
| $\rho_{calc}$ [g/cm$^3$] | 1.684 | 1.794 | 1.705 | 1.746 |
| $\mu$ [mm$^{-1}$] | 0.797 | 1.098 | 1.156 | 1.109 |
| $F$(000) | 1196 | 1544 | 1404 | 4944 |
| Absorption correction | SADABS[66] | SADABS[66] | no correction | no correction |
| Max./min. transmission | 0.86/0.78 | 0.90/0.72 | 0.89/0.64 | 0.81/0.66 |
| $T$ [K] | 90(1) | 123(2) | 100(2) | 100(2) |
| Max. 2$\theta$ [°] | 58.0 | 51.88 | 54.96 | 51.48 |
| Reflections measured | 25011 | 13023 | 20222 | 42780 |
| Unique reflections | 7276 | 3602 | 11660 | 17592 |
| $R_{int}$ | 0.03 | 0.0333 | | |
| Parameters, restraints | 724, 10 | 424, 423 | 812, 0 | 2393, 11252 |
| Reflections [$F_o > 2\sigma(F_o)$] | 6312 | 3100 | 10282 | 8450 |
| $R_1$ [$F_o > 2\sigma(F_o)$] | 0.042 | 0.0358 | 0.0381 | 0.1038 |
| $wR_2$ (all data)[a] | 0.1177 | 0.085 | 0.0902 | 0.3023 |
| $a$ | 0.0582 | 0.040 | 0.0294 | 0.1956 |
| $b$ | 5.0135 | 5.096 | 3.4011 | 0.0000 |
| *G.O.F.* | 1.042 | 1.055 | 1.033 | 0.954 |
| Restr. *G.O.F.* | 1.056 | 1.006 | 1.033 | 0.758 |
| CCDC number | 286144 | 288291 | 288292 | 288293 |

[a] (a) $w = 1/[\sigma^2(F_o^2) + (aP)^2 + bP]$, $P = [\max(F_o^2,0) + 2F_c^2]/3$.

 © 2006 Wiley-VCH Verlag GmbH & Co. KGaA, Weinheim 

The $C_{60}$ complexes with $Mn(Et_2dtc)_2$ and $Fe(Et_2dtc)_2$ were also obtained as powders by mixing $C_{60}$ (25 mg, 0.0347 mmol) and a twofold molar excess of $M(Et_2dtc)_2$ in $C_6H_4Cl_2$ (20 mL) on heating (60 °C, 2 h). The hot solution was filtered, cooled down to room temperature, and stood overnight. The solution became colorless, and a light brown polycrystalline precipitate was formed. However, in contrast to crystals of **10**, powdered samples did not show reasonable elemental analyses probably because of the high air-sensitivity of the complexes. Indeed, $Mn(Et_2dtc)_2$ and $Fe(Et_2dtc)_2$ are extremely air-sensitive and oxidize in a few seconds in air.

We tried to crystallize the $C_{60}$ complexes with $Co(Et_2dtc)_2$ and $V(Et_2dtc)_2$. $C_{60}$ (25 mg, 0.0347 mmol) and a twofold molar excess of $M(Et_2dtc)_2$ were dissolved in $C_6H_4Cl_2$ (20 mL) on stirring at 60 °C for 4 h. The hot solution was filtered, cooled down to room temperature, and filtered in a glass tube of 45 mL volume with a ground glass plug. Slow diffusion of hexane (20 mL) was carried out under anaerobic conditions. However, only black powder without crystals formed after 2 months.

**General:** UV/Visible-NIR spectra were measured with a Shimadzu-3100 spectrometer in the 240–2600 nm range. FT-IR spectra were measured in KBr pellets with a Perkin–Elmer 1000 Series spectrometer (400–7800 $cm^{-1}$). A Quantum Design MPMS-XL SQUID magnetometer was used to measure static magnetic susceptibilities of **1**–**4** and **10** from 1.9 up to 300 K. A sample holder contribution and core temperature independent diamagnetic susceptibility ($\chi_0$) were subtracted from the experimental values. The values of $\Theta$, $\chi_0$ were calculated using the appropriate formula: $\chi_M = C/(T - \Theta) + \chi_0$. EPR spectra were recorded for **1**, **2**, **11**, and **13** at room temp. and for **3**, **4**, and **10** from RT down to 4 K with a JEOL JES-TE 200 X-band ESR spectrometer equipped with a JEOL ES-CT470 cryostat. Photoconductivity of **1**, **2**, **7**, and **8** was excited using a white light halogen tube with $10^{12}$–$10^{14}$ photons/$cm^2$s intensity. To record the spectra of photoconductivity the light beam of a xenon lamp was transmitted through a high-aperture monochromator. A static magnetic field with the induction up to 1 T was generated by an electromagnet of a Radiopan SE/X 2547 ESR spectrometer.

**X-ray Crystal Structure Determination:** X-ray diffraction data for **1**, **3**, **4**, **6**, **7**, **11**, and **12** were collected with a Bruker SMART1000 CCD diffractometer installed at a rotating anode source (Mo-$K_\alpha$ radiation, $\lambda$ = 0.71073 Å), and equipped with an Oxford Cryosystems nitrogen gas-flow apparatus. The data were collected by the rotation method with 0.3° frame-width (ω scan) and 10 s exposure time per frame. Four sets of data (600 frames in each set) were collected, nominally covering half of the reciprocal space. The data were integrated, scaled, sorted and averaged using the SMART software package.[66] The structures were solved by the direct methods using SHELXTL NT Version 5.10.[67] The structure was refined by full-matrix least-squares against $F^2$. The details of the X-ray crystal structure analysis for **1**, **3**, **4**, **6**, **7**, **11**, and **12** including CCDC numbers for the structures are given in Table 4. Non-hydrogen atoms were refined in the anisotropic approximation. Positions of hydrogen atoms were calculated geometrically. Subsequently, the positions of H-atoms were refined by the "riding" model with $U_{iso} = 1.2U_{eq}$ of the connected non-hydrogen atom or as ideal $CH_3$ groups with $U_{iso} = 1.5U_{eq}$. The supplementary crystallographic data for this paper can be obtained free of charge from The Cambridge Crystallographic Data Centre via www.ccdc.cam.ac.uk/data_request/cif.

**Supporting Information** (for details see the footnote on the first page of this article): IR-data, UV/Vis-NIR spectra of pristine donors and complexes **1**–**15**, and EPR spectra of pristine Cu(EtMedtc)$_2$ and Cu($n$Pr$_2$dtc)$_2$ and complexes **11** and **13** (Tables S1 and S2, Figures S1–S7).

## Acknowledgments

The work was supported by the RFBR grants N 03-03-32699-a and 03-03-20003 BNTS-a, the Russian Science Support Foundation, Rosnauka grant 2006-RI-19.0/001/058, and partly by Grant-in-Aid Scientific Research from the Ministry of Education, Culture, Sports, Science and Technology, Japan (152005019, 21st Century COE, and Elements Science 12CE2005). We thank Dr. E.I. Yudanova for help with the EPR investigations.

[1] A. L. Balch, M. M. Olmstead, *Chem. Rev.* **1998**, *98*, 2123–2165.
[2] D. V. Konarev, R. N. Lyubovskaya, *Russ. Chem. Rev.* **1999**, *68*, 19–38.
[3] C. A. Reed, R. D. Bolskar, *Chem. Rev.* **2000**, *100*, 1075–1120.
[4] A. L. Litvinov, D. V. Konarev, A. Y. Kovalevsky, I. S. Neretin, Y. L. Slovokhotov, P. Coppens, R. N. Lyubovskaya, *CrystEngComm* **2002**, *4*, 618–622.
[5] P.-M. Allemand, K. C. Khemani, A. Koch, F. Wudl, K. Holczer, S. Donovan, G. Grüner, J. D. Thompson, *Science* **1991**, *253*, 301–303.
[6] D. V. Konarev, R. N. Lyubovskaya, N. V. Drichko, E. I. Yudanova, Y. M. Shul'ga, A. L. Litvinov, V. N. Semkin, B. P. Tarasov, *J. Mater. Chem.* **2000**, *10*, 803–818.
[7] D. V. Konarev, A. Y. Kovalevsky, A. L. Litvinov, N. V. Drichko, B. P. Tarasov, P. Coppens, R. N. Lyubovskaya, *J. Solid State Chem.* **2002**, *168*, 474–485.
[8] G. Saito, T. Teramoto, A. Otsuka, Y. Sugita, T. Ban, M. Kusunoki, K. Sakaguchi, *Synth. Met.* **1994**, *64*, 359–368.
[9] M. M. Olmstead, D. A. Costa, K. Maitra, B. C. Noll, S. L. Phillips, P. M. Van Calcar, A. L. Balch, *J. Am. Chem. Soc.* **1999**, *121*, 7090–7097.
[10] P. D. W. Boyd, M. C. Hodgson, C. E. F. Rickard, A. G. Oliver, L. Chaker, P. J. Brothers, R. D. Bolskar, F. S. Tham, C. A. Reed, *J. Am. Chem. Soc.* **1999**, *121*, 10487–10495.
[11] D. V. Konarev, I. S. Neretin, Y. L. Slovokhotov, E. I. Yudanova, N. V. Drichko, Y. M. Shul'ga, B. P. Tarasov, L. L. Gumanov, A. S. Batsanov, J. A. K. Howard, R. N. Lyubovskaya, *Chem. Eur. J.* **2001**, *7*, 2605–2616.
[12] D. H. Hochmuth, S. L. J. Michel, A. J. P. White, D. J. Williams, A. G. M. Barrett, B. M. Hoffman, *Eur. J. Inorg. Chem.* **2000**, 593–596.
[13] J. D. Crane, P. B. Hitchcock, H. W. Kroto, R. Taylor, D. R. M. Walton, *J. Chem. Soc. Chem. Commun.* **1992**, 1764–1765.
[14] W. C. Wan, X. Liu, G. M. Sweeney, W. E. Broderick, *J. Am. Chem. Soc.* **1995**, *117*, 9580–9581.
[15] A. Hönnerscheid, L. van Wüllen, M. Jansen, J. Rahmer, M. Mehring, *J. Chem. Phys.* **2001**, *115*, 7161–7165.
[16] D. V. Konarev, S. S. Khasanov, A. Otsuka, G. Saito, *J. Am. Chem. Soc.* **2002**, *124*, 8520–8521.
[17] D. V. Konarev, S. S. Khasanov, G. Saito, A. Otsuka, Y. Yoshida, R. N. Lyubovskaya, *J. Am. Chem. Soc.* **2003**, *125*, 10074–10083.
[18] D. Y. Sun, C. A. Reed, *Chem. Commun.* **2000**, 2391–2392.
[19] D. V. Lopatin, V. V. Rodaev, A. V. Umrikhin, D. V. Konarev, A. L. Litvinov, R. N. Lyubovskaya, *J. Mater. Chem.* **2005**, *15*, 657–660.
[20] D. V. Konarev, G. Zerza, M. C. Scharber, N. S. Sariciftci, R. N. Lyubovskaya, *Mol. Crys. Liq. Crys.* **2005**, *427*, 315–333.
[21] D. V. Konarev, A. Y. Kovalevsky, D. V. Lopatin, V. V. Rodaev, A. V. Umrikhin, E. I. Yudanova, P. Coppens, R. N. Lyubovskaya, G. Saito, *Dalton Trans.* **2005**, 1821–1825.
[22] D. V. Konarev, A. Y. Kovalevsky, A. Otsuka, G. Saito, R. N. Lyubovskaya, *Inorg. Chem.* **2005**, *44*, 9547–9556.
[23] A. Bonamiko, G. Dessy, C. Mariani, A. Vaciago, L. Zambonelli, *Acta Crystallogr.* **1965**, *19*, 619–626.

 © 2006 Wiley-VCH Verlag GmbH & Co. KGaA, Weinheim 

[24] A. Z. Amanov, G. A. Kukina, M. A. Porai-Koshits, *Dokl. Akad. Nauk Az. SSR* **1977**, *33*, 23–26.
[25] J. Lokaj, V. Vrabel, E. Kello, *Chem. Zvesti* **1984**, *38*, 313–317.
[26] M.-L. Riekkola, T. Pakkanen, L. Niinisto, *Acta Chem. Scand. Ser. A* **1983**, *37*, 807–812.
[27] P. W. G. Newnan, A. H. White, *J. Chem. Soc. Dalton Trans.* **1972**, 2239–2243.
[28] M. Decoster, F. Conan, J. E. Guerchais, Y. Le Mest, J. Sala Pala, J. C. Jeffery, E. Faulques, A. Leblanc, P. Molinié, *Polyhedron* **1995**, *14*, 1741–1750.
[29] F. Conan, J. Sala Pala, M.-T. Garland, R. Baggio, *Inorg. Chim. Acta* **1998**, *278*, 108–112.
[30] H. L. M. Van Gaal, J. G. M. Van der Linden, *Coord. Chem. Rev.* **1982**, *47*, 41–54.
[31] H. H. Wickman, A. M. Trozzolo, H. J. Williams, G. W. Hull, F. R. Merritt, *Phys. Rev.* **1967**, *155*, 563–566.
[32] D. Dubois, K. M. Kadish, S. Flanagan, R. E. Haufler, L. P. F. Chibante, L. J. Wilson, *J. Am. Chem. Soc.* **1991**, *113*, 4364–4366.
[33] M. Bonamico, G. Mazzone, A. Vaciago, L. Zambonelli, *Acta Crystallogr.* **1965**, *19*, 898–909.
[34] N. Sreehari, B. Varghese, P. T. Manoharan, *Inorg. Chem.* **1990**, *29*, 4011–4015.
[35] H. Miyamae, M. Ito, H. Iwasaki, *Acta Crystallogr. Sect. B* **1979**, *35*, 1480–1482.
[36] A. Domenicano, L. Torelli, A. Vaciago, L. Zambonelli, *J. Chem. Soc. A* **1968**, 1351–1361.
[37] F. Jian, Z. Wang, Z. Bai, X. You, H.-K. Fun, K. Chinnakali, *J. Chem. Crystallogr.* **1999**, *29*, 227–231.
[38] D. A. Ileperuma, R. D. Feltham, *Inorg. Chem.* **1975**, *14*, 3042–3045.
[39] M. Ciampolini, C. Mengozzi, P. Orioli, *J. Chem. Soc. Dalton Trans.* **1975**, 2051–2054.
[40] P. C. Healy, A. H. White, *J. Chem. Soc. Dalton Trans.* **1973**, 284–287.
[41] H. Iwasaki, *Acta Crystallogr. Sect. B* **1973**, *29*, 2115–2124.
[42] C. S. Lai, E. R. T. Tiekink, *Z. Kristallogr. New Crystal Structures* **2002**, *217*, 593–597.
[43] F. Jian, Z. Wang, Z. Bai, X. You, H.-K. Fun, K. Chinnakali, I. A. Razak, *Polyhedron* **1999**, *18*, 3401–3406.
[44] S. C. Ngo, K. K. Banger, M. J. DelaRosa, P. J. Toscano, J. T. Welch, *Polyhedron* **2003**, *22*, 1575–1583.
[45] H.-B. Bürgi, E. Blanc, D. Schwarzenbach, S. Liu, Y. Lu, M. M. Kappes, J. A. Ibers, *Angew. Chem. Int. Ed. Engl.* **1992**, *31*, 640–643.
[46] A. Decken, R. A. Gossage, M. Y. Chan, C. S. Lai, E. R. T. Tiekink, *Appl. Organomet. Chem.* **2004**, *18*, 101–102.
[47] R. Hesse, *Ark. Kemi* **1963**, *20*, 481–484.
[48] D. D. Heinrich, J.-C. Wang, J. P. Fackler Junior, *Acta Crystallogr. Sect. C* **1990**, *46*, 1444–1447.
[49] H. Yamaguchi, A. Kido, T. Uechi, K. Yasukouchi, *Bull. Chem. Soc. Jpn*. **1976**, *49*, 1271–1276.
[50] R. Hesse, L. Nilson, *Acta Chem. Scand.* **1969**, *23*, 825–828.
[51] M. D. Pace, T. C. Christidis, J. J. Yin, J. Milliken, *J. Phys. Chem.* **1992**, *96*, 6855–6858.
[52] R. D. Dowsing, B. Nieuwenhuijse, J. Reedijk, *Inorg. Chim. Acta* **1971**, *5*, 301–308.
[53] S. V. Khangulov, A. J. Dessiki, V. V. Barynin, D. E. Ass, G. C. Dismukes, *Biochemistry* **1995**, *34*, 2015–2025.
[54] I. Romero, M.-N. Collomb, A. Deronyier, A. Llobet, E. Perret, J. Pèkaut, L. Le Pare, J.-M. Latour, *Eur. J. Inorg. Chem.* **2001**, 69–72.
[55] A. Pénicaud, A. P. Pérez-Benítez, R. Escudero, C. Coulon, *Solid State Commun.* **1995**, *96*, 147–150.
[56] K. Nagai, T. Iyoda, K. Hashimoto, A. Fujishima, *Perspectives in Organic-Inorganic Hybrid Solids*, Abstr. Int. Conf., Nagoya, Japan, **1996**, p. 118.
[57] E. I. Yudanova, D. V. Konarev, L. L. Gumanov, R. N. Lyubovskaya, *Russ. Chem. Bull.* **1999**, *48*, 718–721.
[58] M. S. Dresselhaus, G. Dresselhaus, P. C. Eklund, *Science of Fullerenes and Carbon Nanotubes*, Academic Press, San Diego, **1996**.
[59] S. Kazaoui, N. Minami, Y. Tanabe, H. J. Byrne, A. Eilmes, P. Petelenz, *Phys. Rev. B* **1998**, *58*, 7689–7700.
[60] D. V. Konarev, N. V. Drichko, R. N. Lyubovskaya, Y. M. Shul'ga, A. L. Litvinov, V. N. Semkin, Y. A. Dubitsky, A. Zaopo, *J. Mol. Struct.* **2000**, *526*, 25–29.
[61] V. Ern, R. E. Merrifield, *Phys. Rev. Lett.* **1968**, *21*, 609–611.
[62] D. V. Konarev, S. S. Khasanov, G. Saito, D. V. Lopatin, V. V. Rodaev, A. V. Umrikhin, A. L. Litvinov, R. N. Lyubovskaya, *J. Phys. Chem. Solids* **2005**, *66*, 711–715.
[63] N. S. Sariciftci, A. J. Heeger in *Handbook of Organic Conductive Molecules and Polymers* (Ed.: H. S. Nalwa), Wiley & Sons Ltd., **1997**, vol. 1, p. 414.
[64] Y. A. Ossipyan, Y. I. Golovin, D. V. Lopatin, R. B. Morgunov, R. K. Nikolaev, S. Z. Shmurak, *Phys. Stat. Sol. B* **2001**, *223*, R14–R15.
[65] A. L. Buchachenko, E. L. Frankevich, *Chemical Generation and Reception of Radio- and Microwaves*, Wiley, New York, **1994**, p. 180.
[66] *SMART and SAINT*, Area detector control and integration software, Ver. 6.01. Bruker Analytical X-ray Systems, Madison, Wisconsin, U. S.A, **1999**.
[67] G. W. Sheldrick, *SHELXTL*, An Integrated System for Solving, Refining and Displaying Crystal Structures from Diffraction Data, Version 5.10, Bruker Analytical Systems, Madison, **1997**.

Received: December 12, 2005
Published Online: March 15, 2006

 © 2006 Wiley-VCH Verlag GmbH & Co. KGaA, Weinheim 

EurJIC
European Journal of Inorganic Chemistry

Issue 10/2006

Pages 1901–2100

*Papers available ahead of print in Early View at www.interscience.wiley.com*

*Earliest available Table of Contents:*
*Automatically, free of charge by e-mail through*
*www.interscience.wiley.com/alerts*

## COVER PICTURE

**The cover picture shows** a mixed metal $Mn_6Ni_{12}$ compound that results when manganese(II) and nickel(II) percursor building blocks are allowed to self-assemble. The resulting structure contains a trigonal-prismatic central framework portion made up by linking six manganese(II) coordination compound precursors with meridionally arranged labile water ligands, which are replaced here by linking carboxylate units. This framework is decorated with three self-assembled nickel(II) acetate/methoxide cubane units. The overall structure is similar to a wind turbine having a hexanuclear manganese spindle with the nickel cubanes as blades. The synthetic strategy is a promising means for obtaining high-nuclearity heterometallic assemblies with interesting magnetic properties. Details of this work are described in the Short Communication by A. K. Powell et al. on p. 1927 ff.

## MICROREVIEW

**Contents**

**1913** **R. Hille***

Structure and Function of Xanthine Oxidoreductase

**Keywords:** Bioinorganic chemistry / Enzymes / Molybdenum / Xanthine / Oxidoreductase

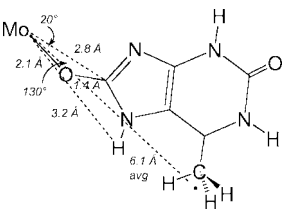


 © 2006 Wiley-VCH Verlag GmbH & Co. KGaA, Weinheim 

# SHORT COMMUNICATIONS


**1927** **G. Wu, R. Clérac, W. Wernsdorfer, S. Qiu,* C. E. Anson, I. J. Hewitt, A. K. Powell***

The "Building-Block" Assembly of a $[Ni_{12}Mn_6]$ Aggregate

**Keywords:** Cluster compounds / Carboxylate ligands / Cooperative effects / Nickel / Manganese


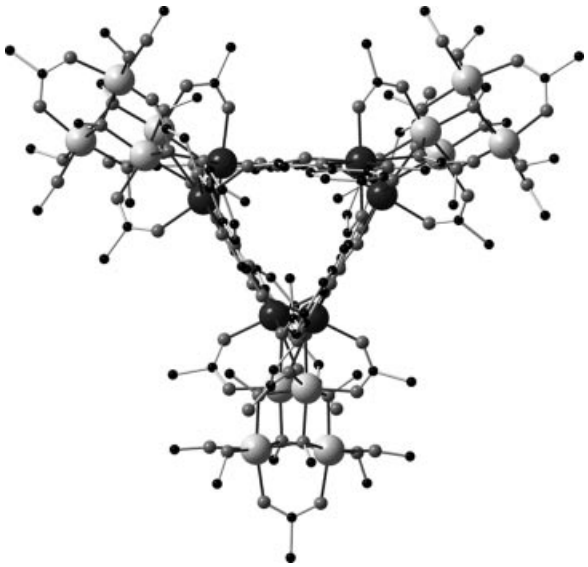


**1931** **C.-J. Li, S. Hu, W. Li, C.-K. Lam, Y.-Z. Zheng, M.-L. Tong***

Rational Design and Control of the Dimensions of Channels in Three-Dimensional, Porous Metal-Organic Frameworks Constructed with Predesigned Hexagonal Layers and Pillars

**Keywords:** Cobalt / Microporous / MOFs / Imidazole-4,5-dicarboxylate / Pillar / Magnetism


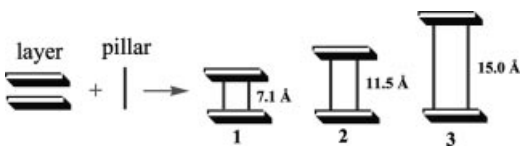



**1936** **X. Shi, J. Yang, Q. Yang***

Mesoporous Aluminium Organophosphonates Functionalized with Chiral L-Proline Groups in the Pore

**Keywords:** Chiral / Mesoporous compounds / Aluminium organophosphonates


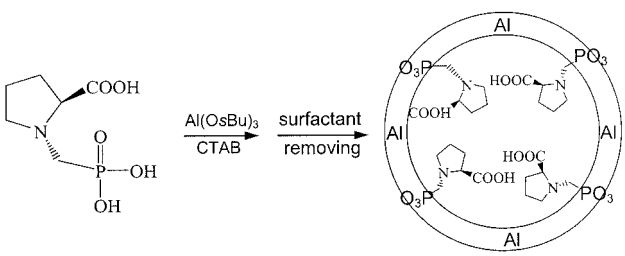



**1940** **G. Aromí,* P. Gamez, C. Boldron, H. Kooijman, A. L. Spek, J. Reedijk**

A Zig-Zag $[Mn^{II}_4]$ Cluster from a Novel Bis(β-diketonate) Ligand

**Keywords:** Ligand design / O ligands / NMR spectroscopy / Magnetism / Mn


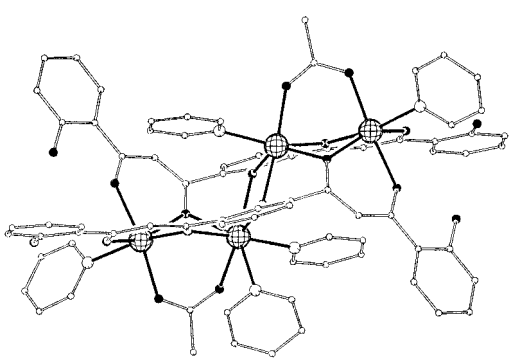

**1945** **A. Mateescu, C. P. Raptopoulou, A. Terzis, V. Tangoulis, A. Salifoglou***

pH-Specific Synthesis and Structural and Spectroscopic Characterization of a Complex between $Co^{II}$ and *N*,*N*-Bis(phosphonomethyl)-glycine: Cobalt−Phosphonate Interactions in the Solid State and in Solution

**Keywords:** Cobalt / Magnetic properties / Materials science / Phosphonates / Structural speciation

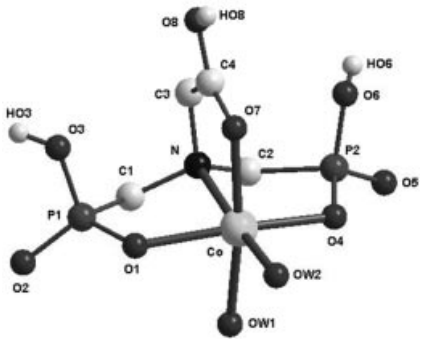


**1957** **M. Menelaou, C. P. Raptopoulou, A. Terzis, V. Tangoulis, A. Salifoglou***

In Search of Binary Hybrid Systems in Manganese Chemistry: The Synthesis, Spectroscopic and Structural Characterization, and Magnetic Properties of a New Species in the Aqueous $Mn^{II}$-Quinic System

**Keywords:** Manganese / Structural speciation / $Mn^{II}$−quinate interactions / Magnetic properties / Hybrid materials

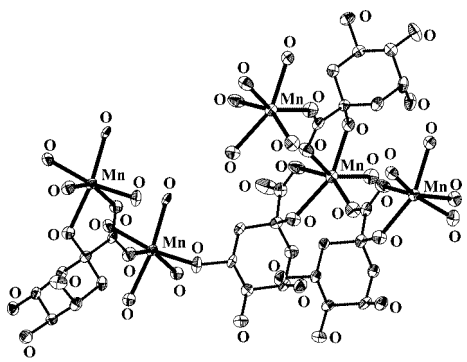


**1968** **J. J. Eisch,* J. N. Gitua, D. C. Doetschman**

Direct Epimetallation of π-Bonded Organic Substrates with Titanium(II) Isopropoxide: Intermediacy of Biradical, Oligomeric Titanium(II) Reagents

**Keywords:** Titanium(II) / EPR determination of biradicals / Titanium(II) isopropoxide trimer / Epititanation / Nonstereochemical $Ti^{II}$ additions

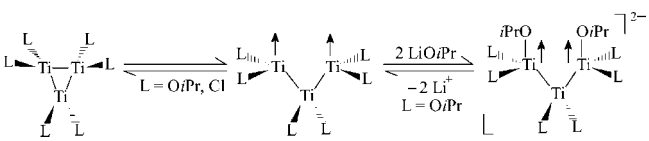


**1976** **J. Kotek,* F. K. Kálmán, P. Hermann, E. Brücher, K. Binnemans, I. Lukeš**

Study of Thermodynamic and Kinetic Stability of Transition Metal and Lanthanide Complexes of DTPA Analogues with a Phosphorus Acid Pendant Arm

**Keywords:** Phosphonate complexes / Phosphinate complexes / MRI contrast agents / Kinetics / Thermodynamics

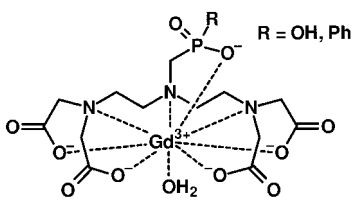


 © 2006 Wiley-VCH Verlag GmbH & Co. KGaA, Weinheim 

**1987** **K. V. Zaitsev, S. S. Karlov,* A. A. Selina, Y. F. Oprunenko, A. V. Churakov, B. Neumüller, J. A. K. Howard, G. S. Zaitseva**

Titanium Complexes of Dialkanolamine Ligands: Synthesis and Structure

**Keywords:** Titanium / Alkoxides / Pentacoordination / Hexacoordination / Dialkanolamine complexes

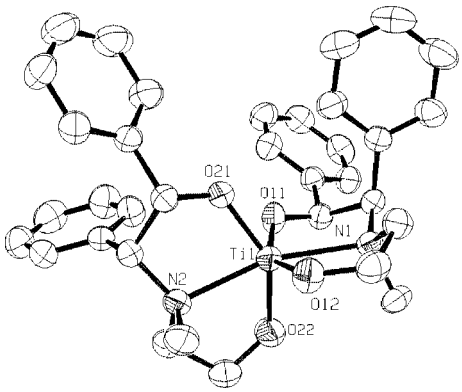


**2000** **K. Müller-Buschbaum,* Y. Mokaddem**

Rare Earth Benzotriazolates: Coordination Polymers Incorporating Decomposition Products from Ammonia to 1,2-Diaminobenzene in $^{1}_{\infty}[Ln(Btz)_3(BtzH)]$ (Ln = Ce, Pr), $^{1}_{\infty}[Ln(Btz)_3\{Ph(NH_2)_2\}]$ (Ln = Nd, Tb, Yb), and $^{1}_{\infty}[Ho_2(Btz)_6(BtzH)(NH_3)]$

**Keywords:** Solvent-free synthesis / Lanthanides / Benzotriazolate / Crystal structure / X-ray diffraction

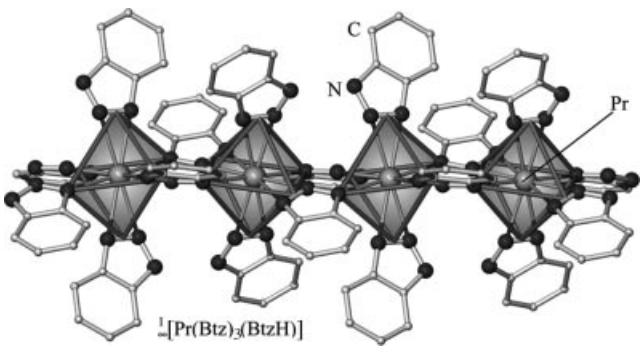


**2011** **S.-F. Tang, J.-L. Song, J.-G. Mao***

Syntheses, Crystal Structures, and Characterizations of a Series of New Layered Lanthanide Carboxylate-Phosphonates

**Keywords:** Lanthanides / Phosphonate / Luminescence

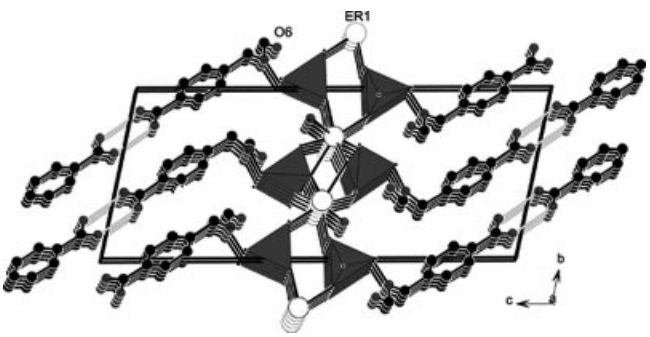


**2020** **F. O. N. Silva, S. X. B. Araújo, A. K. M. Holanda, E. Meyer, F. A. M. Sales, I. C. N. Diógenes, I. M. M. Carvalho, Í. S. Moreira,* L. G. F. Lopes***

Synthesis, Characterization, and NO Release Study of the *cis*- and *trans*-$[Ru(Bpy)_2(SO_3)(NO)]^{+}$ Complexes

**Keywords:** Ruthenium / Nitrogen oxides / Bioinorganic chemistry / Drug design

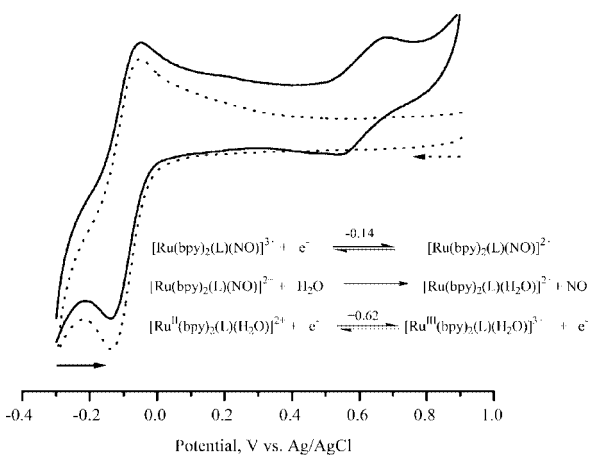


 © 2006 Wiley-VCH Verlag GmbH & Co. KGaA, Weinheim 

**2027** **F. D. Sokolov, D. A. Safin,* N. G. Zabirov, V. V. Brusko, B. I. Khairutdinov, D. B. Krivolapov, I. A. Litvinov**

Coordination Mode of the Zinc(II) and Cadmium(II) Cations with *N*-(Diisopropoxyphosphoryl)thiobenzamide

**Keywords:** Chelates / Coordination modes / Crystal structures / (Thioacylamido)phosphates / Zinc(II) / Cadmium(II) complexes

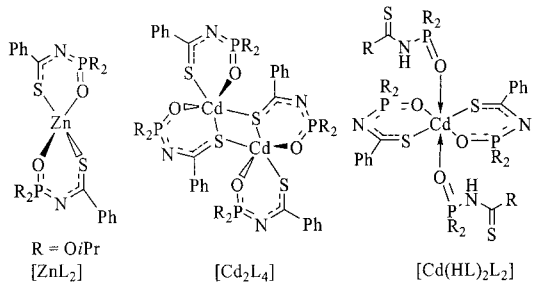


**2035** **M. Doux, P. Le Floch, Y. Jean***

Diamagnetic versus Paramagnetic Structure of SPS-Type Pincer-Based $Co^{I}$, $Rh^{I}$, and $Ir^{I}$ Complexes

**Keywords:** Group 9 / Density functional calculations / P ligands / S ligands / QM/MM

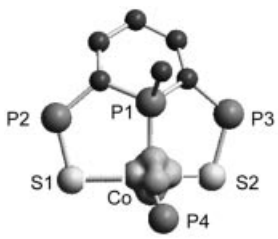


**2040** **K. Heinze,* K. Hempel, M. Beckmann**

Multielectron Storage and Photo-Induced Electron Transfer in Oligonuclear Complexes Containing Ruthenium(II) Terpyridine and Ferrocene Building Blocks

**Keywords:** Electron transfer / Heterometallic complexes / Luminescence / Metallocenes / Ruthenium

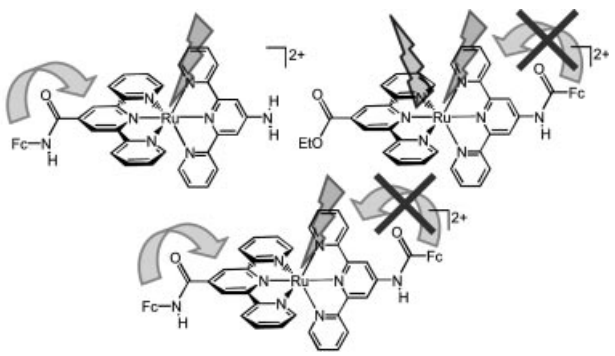

**2051** **N. Götz, S. Herler, P. Mayer, A. Schulz,* A. Villinger, J. J. Weigand**

On the Staudinger Reaction of $SP(N_3)_3$ with $PPh_3$ and $(Me_3Si)_2N-(Me_3Si)N-PPh_2$

**Keywords:** Azides / PN rings / Phosphazenes / Staudinger reaction

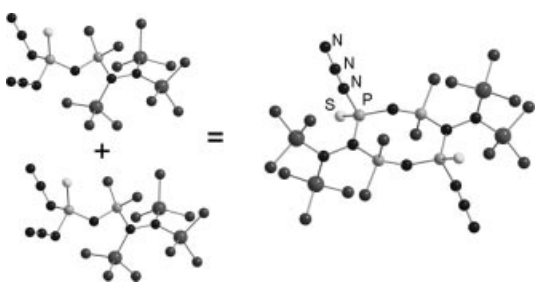

**2058** **N. K. Kiriakidou Kazemifar, M. J. Stchedroff, M. Abdul Mottalib, S. Selva, M. Monari, E. Nordlander***

Syntheses and Fluxional Processes of Diphenyl-(2-thienyl)phosphane Derivatives of Triosmium Clusters

**Keywords:** Cluster / Thienylphosphane / Fluxionality / Hydrodesulfurisation

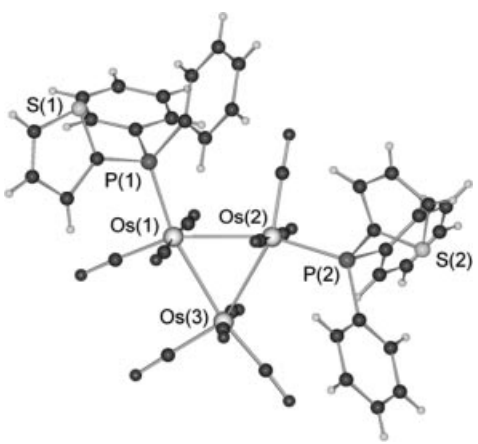


 © 2006 Wiley-VCH Verlag GmbH & Co. KGaA, Weinheim 

**2069** **J. Wang, S. Hu, M.-L. Tong***

Rational Synthesis and Characterization of Two Three-Dimensional Metal-Organic Frameworks Incorporating Silver Chains and 1,2,3,4,5,6-Cyclohexanehexacarboxylate

**Keywords:** Silver / MOFs / Cyclohexanehexacarboxylate / Water tape / Ag···Ag interactions / Supramolecular chemistry

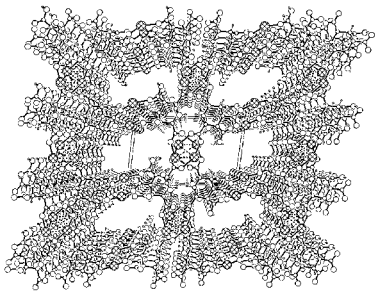

**2078** **J. Ipaktschi,* F. Munz**

Single-Electron Oxidation of Tungsten Acetylide Complexes $[(\eta^5\text{-}C_5H_5)(CO)(NO)W{-}C{\equiv}C{-}R]Li$

**Keywords:** Tungsten / Alkyne ligands / Oxidation / Bridging ligands / Metal−metal interactions

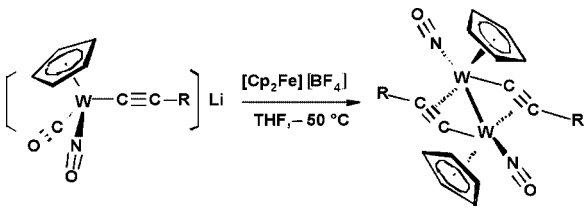


**2083** **P. A. Papanikolaou, P. C. Christidis, A. T. Chaviara, C. A. Bolos,* A. C. Tsipis***

An Experimental and Density Functional Study of the Interaction of $Cu^{II}$ Complexes of Diethylenetriamine (Dien) with Pyridine, Nicotinic Acid, and Nicotinamide: The Crystal Structure of [Cu(dien)(nicotinamide)$(NO_3)_2$]

**Keywords:** Copper / Density functional calculations / N ligands / Thermal analysis

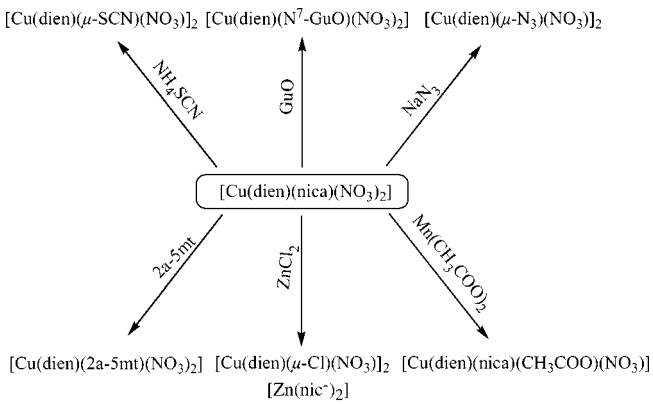

DOI: 10.1002/ejic.200600087

# Structure and Function of Xanthine Oxidoreductase

**Russ Hille***[a]

**Keywords:** Bioinorganic chemistry / Enzymes / Molybdenum / Xanthine / Oxidoreductase

An overview of the current state of our understanding of the reaction mechanism of the molybdenum-containing enzyme xanthine oxidoreductase is presented, with an emphasis on work done in the past five years. Recent studies of the biosynthesis of the pterin cofactor bound to the metal in the active site are also reviewed, as is crystallographic work that has clarified the coordination geometry of the molybdenum center. This structural work provides the context in which to understand recent mechanistic studies of the enzyme, in particular those aimed at elucidating the role of specific amino acid residues in the active site of the enzyme.

(© Wiley-VCH Verlag GmbH & Co. KGaA, 69451 Weinheim, Germany, 2006)

## Introduction

Xanthine oxidoreductase (until recently also referred to as xanthine oxidase) was first isolated from cow's milk by Dixon and Thurlow some 80 years ago,[1] and was shown to be identical to the so-called Schardinger enzyme responsible for catalyzing the oxidation of aldehydes (reducing redox-active dyes in the process) that had been described even earlier. In 1966, using an elegant $^{95}$Mo substitution protocol (and with protein from a very large eukaryote), R. C. Bray showed that the enzyme from cow's milk possessed molybdenum in its active site, and that the metal was reduced to the paramagnetic $Mo^{V}$ state in the course of reduction of substrate.[2] This work provided the first demonstration of a specific biological role for molybdenum. In the intervening years, xanthine oxidoreductase has been the subject of a great many mechanistic, structural and biophysical studies, and has come to represent the paradigm for the molybdenum-containing hydroxylases. Unlike other biological systems that hydroxylate carbon centers (including those that possess flavin, heme, non-heme iron or copper in their active sites), members of this large and phylogenetically diverse family of enzymes utilize water rather than $O_2$ as the source of the oxygen atom incorporated into product, and generate rather than consume reducing equivalents. These enzymes thus utilize a fundamentally different reaction stoichiometry than the monooxygenases. It is the catalysis of familiar chemistry in an unfamiliar way that has been the principal reason for the continued interest in the reaction mechanism of xanthine oxidoreductase and related enzymes.

The molybdenum hydroxylases constitute by far the largest of the three categories of molybdenum-containing enzymes, with more than 30 discrete members known from sources ranging from hyperthermophilic archaea to higher vertebrates.[3] Most of these enzymes catalyze the hydroxylation of (relatively activated) carbon centers of aromatic heterocycles, but some (like aldehyde oxidase and CO dehydrogenase) catalyze other types of reactions. The human genome encodes four molybdenum hydroxylases: xanthine oxidoreductase proper (expressed under normal circum-

[a] Department of Molecular and Cellular Biochemistry, The Ohio State University,
333 Hamilton Hall, 1645 Neil Avenue, Columbus, OH 43210-1218, USA
E-mail: Hille.1@osu.edu

*Russ Hille received a B.S. in Chemistry from Texas Tech University in 1974 and a Ph.D. in Biochemistry from Rice University in 1979. He did post-doctoral work at the University of Michigan in the laboratory of Vincent Massey, in affiliation with the Department of Biological Chemistry and the Michigan Society of Fellows. Afterwards, he took a faculty position in the Department of Molecular and Cellular Biochemistry at The Ohio State University, where he is now Professor. His principal research interests concern the mechanism of action of molybdenum- and flavin-containing enzymes, and biological electron transfer.*

**MICROREVIEWS:** This feature introduces the readers to the authors' research through a concise overview of the selected topic. Reference to important work from others in the field is included.

 © 2006 Wiley-VCH Verlag GmbH & Co. KGaA, Weinheim 

stances as a $NAD^+$-reducing dehydrogenase form), and three different aldehyde oxidases [which, like the oxidase form of xanthine oxidoreductase generated under a variety of (patho)physiological conditions, reduce $O_2$ to either $O_2^{\cdot-}$ or $H_2O_2$].[4] The aldehyde oxidases appear to represent tissue-specific isozymes that are under different regulation of gene expression. This is certainly the case in higher plants, where one aldehyde oxidase isozyme oxidizes indoleacetaldehyde to the hormone indoleacetic acid, and a second the oxidation of abscissaldehyde to abscissic acid, a second plant hormone.[5] The physiological circumstances under which these two hormones are synthesized are quite distinct and genetic expression of the enzymes involved in the two biosynthetic pathways is under completely separate regulatory control. Thus, while the isolated enzymes may well exhibit considerable overlapping substrate specificity (most members of this family of enzymes exhibit rather broad substrate specificity),[6] under physiological conditions each has a specific physiological reaction for which it is responsible.

What follows is a review of our present understanding of the structure and function of xanthine oxidoreductase. Recent crystallographic studies of the enzyme have refined our understanding of the structure of the active site, particularly with regard to the coordination geometry of the molybdenum center, and this provides the structural context in which the reaction mechanism can be understood – both in the sense of the nature of the chemistry catalyzed and the roles of specific active site amino acid residues in accelerating reaction rate. Before considering these, however, we first review the current status of our understanding of the biosynthesis of the novel pterin cofactor found coordinated to the metal in the enzyme active site. Related subjects, particularly dealing with inorganic systems related to the enzymes of interest here, have been dealt with in recent reviews by other authors.[7–11]

## The Pterin Cofactor

With the exception of the extraordinary $MoFe_7$ active site of nitrogenase, molybdenum-containing enzymes all possess an organic pterin cofactor that is coordinated to the metal through an enedithiolate side chain of a third pyran ring, as shown in Figure 1.[12,13] The cofactor is in fact frequently referred to in the literature as molybdopterin, although this is somewhat confusing since: (i) the term refers to the organic component only, not to the metal complexed center; and (ii) the identical cofactor is found in tungsten-containing enzymes – the first crystal structure of an enzyme possessing this cofactor was in fact the tungsten-containing aldehyde oxidoreductase from *Pyrococcus furiosus*.[14] We will use the term pyranopterin here to avoid any possible confusion, but will occasionally use the trivial abbreviation "MPT" (for "*molybdopterin*" or "*metal-binding pterin*"[15]) when convenient. In eukaryotes the cofactor has only the phosphorylated side chain shown, but in many bacterial systems it is elaborated as the dinucleotide of guanosine, cytosine, adenosine or even inosine. As shown in Figure 2, the biosynthetic pathway for the pyranopterin cofactor can be divided into steps leading from GTP to an intermediate initially termed Precursor Z,[16,17] but more recently renamed cyclic pyranopterin monophosphate, cPMP,[18] and then on to the mature cofactor with molybdenum incorporated and (where appropriate in prokaryotes) elaborated to the dinucleotide form. The gene products required for most of the discrete steps are known; many have been crystallographically characterized and their functions are increasingly well understood, as discussed below.

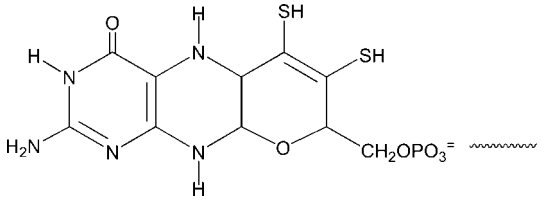


Figure 1. The structure of the pyranopterin cofactor found in molybdenum-containing enzymes. The cofactor consists of a pterin system fused to a pyran ring with a phosphorylated side-chain; molybdenum is coordinated by the dithiolene moiety of the pyran ring. As indicated in the text, the cofactor shown is that seen in eukaryotes. In prokaryotes, it is most often extended as a dinucleotide.

The intermediate cPMP is synthesized from GTP in a reaction that expands the imidazole subnucleus of the guanine moiety to a six-membered pyrazine ring using a carbon from the ribose ring of the nucleotide; the remainder of the ribose ring and α-phosphate group become incorporated into the phosphorylated four-carbon side chain destined to become the pyran ring of the mature cofactor.[19,20] The system responsible for catalyzing this reaction (in *E. coli* consisting of the MoaA and MoaC gene products) is distinct from those involved in biopterin, folate and flavin biosynthesis, and the crystal structures of MoaA[21] and MoaC[22] are each known (Table 1). MoaA is a homodimer, with a [4Fe-4S] cluster in the N-terminal domain that has only three external cysteine ligands to the irons. The missing fourth cysteine position constitutes the binding site for S-adenosylmethionine, with its α-amino and carboxyl groups coordinated to the unique iron site of the cluster in a bidentate fashion. As with other [4Fe-4S]/SAM-containing systems, it is likely that the overall reaction involves reductive cleavage of SAM by the iron-sulfur cluster to initiate a radical-based mechanism for formation of the pterin ring, and specific mechanisms have been proposed.[20,23] A second [4Fe-4S] cluster of unknown function is present in the C-terminal portion of MoaA, and like the N-terminal cluster it lacks one of the external cysteine ligands; the C-terminal [4Fe-4S] cluster lies opposite the active site from the N-terminal [4Fe-4S] cluster and may be involved in binding of GTP, or alternatively in quenching the radical-initiated reaction. The role of MoaC is at present unknown, although it is believed to form a complex with MoaA and may play a role in modulating its activity.[22]

 © 2006 Wiley-VCH Verlag GmbH & Co. KGaA, Weinheim 

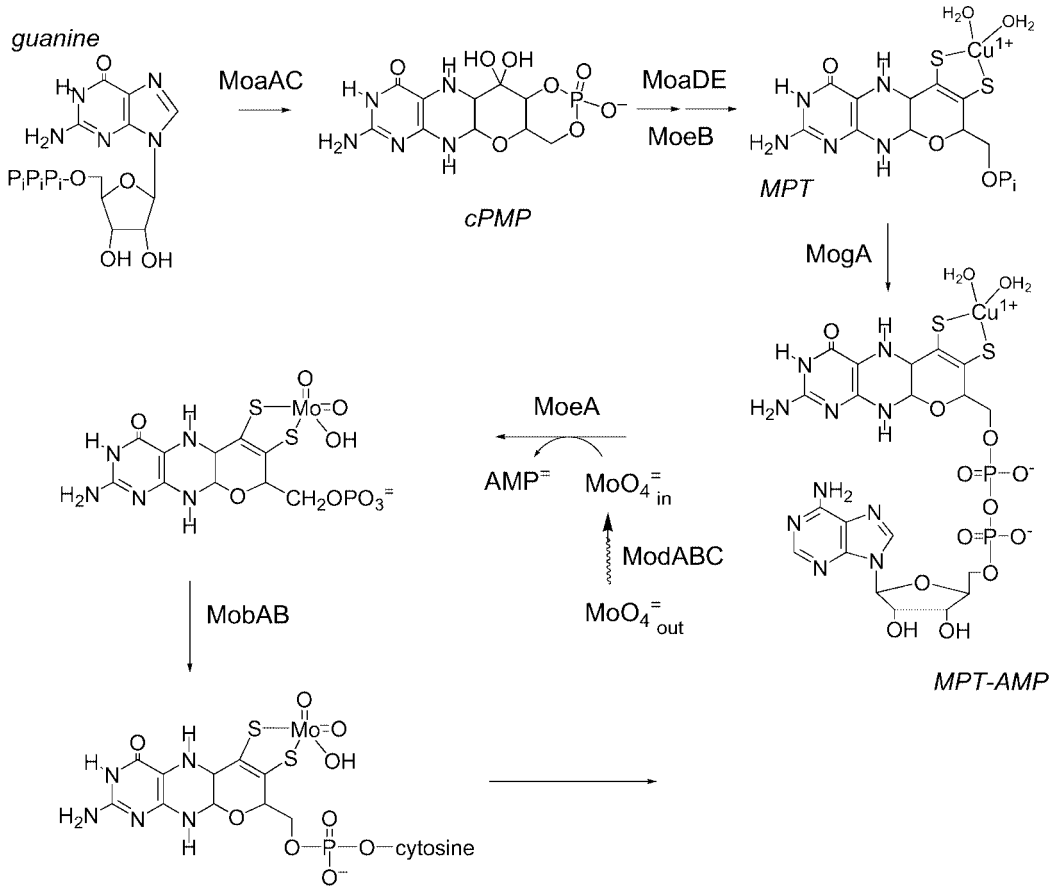


| | | | |
|---|---|---|---|
| MoaA | cPMP synthesis (2x[4Fe-4S] | ModA | periplasmic $MoO_4^=$ binding protein |
| MoaB | carrier/insertion protein | ModB | transmembrane channel protein |
| MoaC | cPMP synthesis | ModC | ATPase |
| MoaD | MPT synthase α | ModD | chaperone protein |
| MoaE | MPT synthase β | ModE | $MoO_4^=$-sensitive transcription regulator |
| MoeA | molybdate insertion into cofactor | MogA | MPT-AMP synthase |
| MoeB | sulfur charging of MPT synthase | Aba3 | sulfido group formation |
| MobA | pterin dinucleotide synthase α | | |
| MobB | pterin dinucleotide synthase β | | |

Figure 2. The biosynthetic pathway for the pyranopterin cofactor. Starting from GTP, the key intermediates are: cyclic pyranopterin monophosphate (cPMP), the pyranopterin itself (MPT), and its adenylylated form generated in the course of molybdenum insertion (MPT-AMP).

The structure of cPMP, the product of the MoaAC reaction, was originally thought to be a dihydropterin with a keto (or enol) group at C1′ of the side chain.[19,20] More recently, however, a detailed NMR and mass spectrometric analysis has shown that the pterin ring is fully reduced in cPMP, that C1′ has a geminal diol and that the pyran ring has closed, as shown in Figure 2.[24]

Once formed by MoaAC, cPMP is next doubly sulfurated, a reaction catalyzed by MPT synthase. In *E. coli*, MPT synthase is an $\alpha_2\beta_2$ tetramer consisting of two subunits each of the MoaD (small subunit) and MoaE (large subunit) gene products. Each αβ dimer appears to be functionally independent, with the C-terminal tail of the smaller MoaD subunit inserted into an active site on its partner

 © 2006 Wiley-VCH Verlag GmbH & Co. KGaA, Weinheim 

Table 1. Orthologues among proteins involved in pyranopterin biosynthesis from various organisms.

| *E. coli* | *A. thaliana* | *H. sapiens* | *Function* |
|---|---|---|---|
| **MPT synthesis** | | | |
| MoaA | Cnx2 | MOCS1A | Synthesis of cPMP (2x[4Fe-4S]; SAM) |
| MoaB | | | Carrier/insertion protein |
| MoaC | Cnx3 | MOCS1B | Synthesis of cPMP |
| MoaD | Cnx6 | MOCS2B | MPT synthase a (large subunit) |
| MoaE | Cnx7 | MOCS2A | MPT synthase ß (small subunit) |
| **Dinucleotide synthesis** | | | |
| MobA | – | – | MPT dinucleotide synthase a |
| MobB | – | – | MPT dinucleotide synthase ß |
| **Molybdate transport** | | | |
| ModA | | | Periplasmic molybdate-binding protein |
| ModB | | | Transmembrane channel protein |
| ModC | | | ATPase |
| ModD | | | Chaperone protein |
| ModE | | | Molybdate-sensitive transcription regulator |
| **Molybdate insertion, sulfuration** | | | |
| MoeA | Cnx1(E) | | Molybdate insertion into cofactor |
| MoeB | Cnx5 | MOCS3 | Sulfur charging of MPT synthase |
| MogA | Cnx1(G) | | MPT-AMP synthase |
| ? | ABA3 | | Mo=S insertion (into hydroxylases) |

MoaE subunit within the tetramer.[25] Interestingly, MoaD has strong structural similarity to ubiquitin, including a C-terminal gly–gly pair, suggesting similar modes of action. Indeed, the overall reaction of MPT synthase involves the formation of an acyl-adenylate at the C-terminus of MoaD (using ATP as the source, by analogy to the mechanism of ubiquitin), with the subsequent formation of a thiocarboxylate. The sulfur atom used to form this thiocarboxylate is delivered by the MoeB gene product, which functions as a biotin-dependent MPT synthase sulfurase and is itself homologous to the E1 family of enzymes involved in adenylylation of ubiquitin.[26] The crystal structure of a $(MoeB)_2$-$(MoaD)_2$ heterotetramer has been reported in several forms, including one in which the C-terminus of MoaD has become adenylylated.[27] For the bacterial system, no evidence has been found for the occurrence of a transiently sulfurated form of *E. coli* MoeB in the course of thiocarboxylate formation, but eukaryotic homologues of MoeB (including the human MOCS3) possess a C-terminal extension with distant homology to rhodanese, and recently it has been shown that Cys 412 of MOCS3 is converted to a persulfide upon incubation with thiosulfate (analogous to the reaction of rhodanese).[28] This persulfide presumably represents the proximal donor of sulfur to the adenylylated MoaD C-terminus, at least in eukaryotic systems. Once charged with sulfur, the synthase first makes a mono-sulfurated form of the pterin (at either C1′ or C2′ of the pterin side chain), at which point it must be recharged with a second sulfur by MoeB prior to completing formation of the dithiolene side chain of the mature pyranopterin cofactor.[29,30]

At least some organisms encode proteins that appear to serve a storage or transport function for the now mature pyranopterin cofactor. Fernandez and co-workers have characterized a protein from *Chlamydomonas rheinhardtii*, for example, that binds pyranopterin and prevents its oxidation.[31–33] The protein is a 64 kDa homotetramer which on the basis of its amino acid sequence is likely to possess a typical nucleotide-binding Rossman fold. Similar proteins exist in both bacteria and higher plants,[33] and may well prove to be widely distributed in nature.

Once the dithiolene moiety is incorporated into the pyranopterin cofactor, molybdenum must be inserted. In *E. coli*, molybdenum is taken up as molybdate by a specific ABC-type transporter system encoded by the *modABCD* operon.[34] The first component of this system is ModA,[35] which has the classic two-domain structure of a periplasmic binding protein.[36] Molybdenum is subsequently transfer-

 © 2006 Wiley-VCH Verlag GmbH & Co. KGaA, Weinheim 

red to ModB, a peripheral membrane protein in the inner membrane, then internalized to the cytoplasm in an ATP-dependent reaction catalyzed by the membrane-integral ModC gene product.[34] The fourth component of this transport system, the ModD gene product, has an as-yet unidentified function. Recent crystallographic work[37–39] has demonstrated that the process by which molybdate, once in the cell cytoplasm, becomes bound to the pyranopterin cofactor is considerably more complicated than might have been suspected. In particular, solving crystal structures of two forms of the N-terminal Cnx1G domain of the Cnx1 gene product from *A. thaliana* (equivalent to MogA from *E. coli*) in complex with the mature cofactor,[39] it has been shown that the cofactor is first adenylylated to MPT-AMP by Cnx1G, and at this point is coordinated to a copper ion. The cuprated MPT-AMP is then thought to be transferred to the C-terminal Cnx1E domain of Cnx1 (equivalent to MoeA of *E. coli*), which hydrolyzes the dinucleotide in the course of replacing the copper with molybdate. The manner in which this reaction occurs is not yet understood, although the process is known to require magnesium.[39] It is interesting that Cnx1 exhibits significant homology to the mammalian protein gephyrin,[38] a cellular structural element involved in, among other things, neuroreceptor aggregation in certain cell signaling processes.

With molybdate incorporated, the cofactor is in the form seen utilized in two different types of eukaryotic molybdenum enzyme, sulfite oxidase and the assimilatory nitrate reductase, and may now be directly incorporated into the apoproteins. The structure of the center is as indicated in Figure 2, with the molybdenum having a (presumably square-pyramidal) $LMo^{VI}O_2(OH)$, with L representing the bidentate pyranopterin cofactor coordinated to the metal by its enedithiolate side chain. Insertion into apoprotein, which involves replacement of the Mo–OH ligand by a cysteine residue in the active site of the protein, likely involves additional gene products. For example, for some prokaryotic molybdenum enzymes (notably the dissimilatory nitrate reductases and the xanthine dehydrogenase from bacteria such as *R. capsulatus*), cofactor incorporation appears to involve an enzyme-specific "chaperone" protein. The *nar* operon of *E. coli* encodes a NarJ protein that is not a component of the mature protein, but whose deletion prevents proper maturation of the molybdenum center.[40] The XdhC gene product of *R. capsulatus* appears to play a similar role in the maturation of the xanthine dehydrogenase of that organism.[41]

As mentioned above, most prokaryotic enzymes utilize a dinucleotide form of the cofactor, most frequently of guanosine but occasionally of adenosine, cytosine or inosine, which must be generated prior to insertion into the apoprotein. In *E. coli*, MGD ("*M*PT *g*uanosine *d*inucleotide") is synthesized by MGD synthase, which consists of the MobA and MobB gene products.[42] The active site is found in MobA, whose crystal structure has been determined.[43] MobB appears not to be essential for the in vitro synthesis of MGD, although it seems to increase the efficiency of the process in vivo.[44] The dinucleotide form of the cofactor is now ready to be incorporated into appropriate prokaryotic apoprotein. For those enzymes that require two equivalents of the pyranopterin, however, it is not known at present whether incorporation of the second equivalent occurs before or after insertion of the first (with molybdenum attached) into the apoprotein. There is suggestive evidence that the MoeA gene product may play a specific, if as yet unidentified, role in the maturation of *bis*MPT-containing active sites (as discussed by Schwarz[18]).

Once incorporated into the polypeptide, the molybdenum center is in its functional form for those molybdenum enzymes that catalyze oxygen atom transfer reactions (e.g., sulfite oxidase, the nitrate reductases and DMSO reductase). For the molybdenum hydroxylases from both prokaryotic and eukaryotic sources, however, there is a final aspect of maturation: the replacement of one of the two Mo=O groups of the cofactor by a sulfido (Mo=S) group. This sulfuration is strictly required for activity of these enzymes – the so-called desulfo form of enzymes such as xanthine oxidoreductase have been well-characterized and are devoid of catalytic activity.[45,46] In *A. thaliana*, the sulfuration reaction is catalyzed by the ABA3 gene product,[47,48] a pyridoxal phosphate-utilizing enzyme that uses cysteine as the ultimate source of the sulfur atom incorporated into the molybdenum coordination sphere. ABA3 is a homodimer whose subunits fold into distinct N- and C-terminal domains. Pyridoxal phosphate binds to the N-terminal domain, which exhibits considerable homology to the NifS family of gene products, cysteine desulfurases that are involved in the maturation of, for example, iron-sulfur clusters.[49] The ABA3 reaction proceeds with the transient formation of a cysteine persulfide at Cys 430 of ABA3, which then transfers its terminal sulfur to the molybdenum center,[50] and there is evidence to suggest that the sulfur is transferred transiently to the C-terminal domain of ABA3. This appears not to be an essential step, however: deletion of the C-terminal domain of ABA3 compromises the effectiveness of sulfur incorporation, but does not eliminate it altogether. Interestingly, ABA3 is also able to utilize selenocysteine as substrate,[51] raising the possibility of preparing selenido forms of the hydroxylases which may have interesting catalytic properties.

## The Structure of the Active Site of Xanthine Oxidoreductase

The molybdenum hydroxylases are fairly complicated systems as enzymes go, since in addition to the molybdenum center, all members of this family possess additional redox-active centers. The typical constitution is a pair of [2Fe-2S] clusters of the spinach ferredoxin variety and, usually, FAD as well (see Figure 3 for the structure of the bovine xanthine oxidoreductase). In most enzymes, all these prosthetic groups are to be found in discrete domains within a single subunit of an $\alpha_2$ dimer, although in the *R. capsulatus* xanthine dehydrogenase the iron-sulfur centers and FAD are found in one subunit and the molybdenum

 © 2006 Wiley-VCH Verlag GmbH & Co. KGaA, Weinheim 

center in a second within an $\alpha_2\beta_2$ tetramer.[51] In the CO dehydrogenase from *O. carboxydovorans* [52] and the quinoline-2-oxidoreductase from *Pseudomonas putida*,[53] the two iron–sulfur centers, the FAD and the molybdenum center are found in separate subunits within an $\alpha_2\beta_2\gamma_2$ hexamer. It is evident from an inspection of the genes encoding these proteins from a variety of organisms that they were built up in gene duplication/fusion events over the course of evolution: not only do the protein domains fold into autonomous structural elements, but they are encoded by contiguous stretches of the gene.

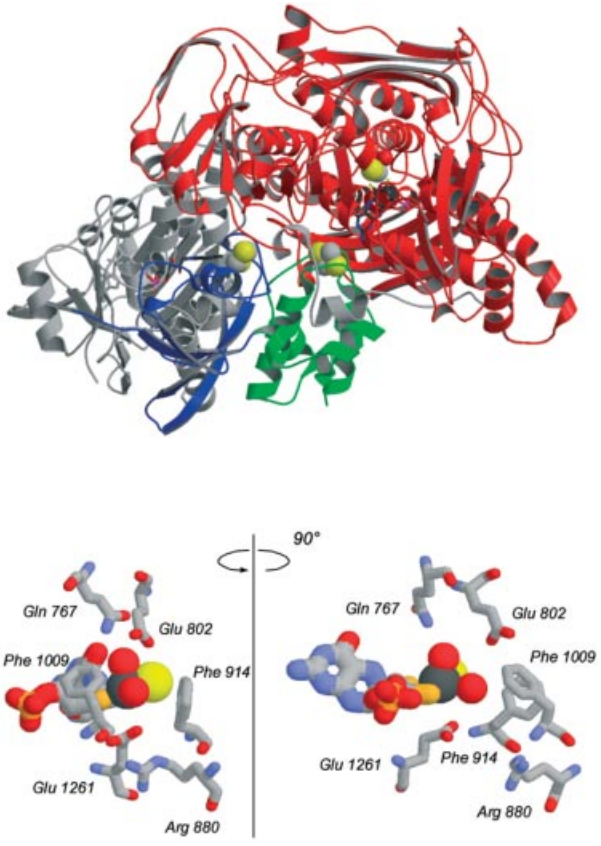


Figure 3. The structure of bovine xanthine oxidoreductase. Top, the overall domain fold of the enzyme, with (from the N-terminus): the two [2Fe–2S] domains in blue and green; the FAD domain in gray (the FAD is shown edge-on, immediately to the left of the first iron-sulfur cluster); and the molybdenum-binding portion of the protein in red. The illustration was prepared with the application MOLSCRIPT, using the structure reported by Enroth et al.[99] Bottom, two representations of the active site with specific amino acid residues discussed in the text indicated.

The first molybdenum hydroxylase to be crystallographically characterized was the aldehyde oxidoreductase from *Desulfovibrio gigas*.[54,55] Several important structural features of the enzyme were established in this work, including: the overall domain architecture of the protein (with the two [2Fe–2S] clusters of the enzyme in separate N-terminal domains and the molybdenum center at the interface of two much larger C-terminal domains); the orientation of the molybdenum center with respect to the remaining redox-active centers of the enzyme (including the hydrogen-bonding interaction between the distal amino group of the pyranopterin cofactor to one of the cysteine ligands of the nearer [2Fe–2S] cluster); the identity of specific amino acid residues in the active site likely to be involved in catalysis (including, most importantly, a highly conserved glutamate residue that was suggested to function as an active-site base[55] – see Figure 3, *bottom* for the active site of the bovine xanthine oxidoreductase); the overall square-pyramidal coordination geometry of the molybdenum coordination sphere, with an $LMoO_2(OH_{(2)})$ coordination geometry and a hydroxy/water ligand that points toward the substrate binding site; and the long channel that provides solvent access to the deeply buried active site. Unfortunately, the *D. gigas* aldehyde oxidoreductase is an example of the molybdenum hydroxylases that does not possess FAD, and the structure provided no information regarding the flavin site found in most other molybdenum hydroxylases. More importantly, the enzyme used in this initial crystallographic study was predominantly in the inactive desulfo form and lacked the catalytically essential Mo=S group. It was not possible to say which of the two Mo=O groups present in the molybdenum coordination sphere of the desulfo form (one in the apical position and the other in an equatorial position) was the one that was replaced by a sulfido group in the functional enzyme. A subsequent study of (partially) activated enzyme, obtained by treating crystals with a resulfurating agent, suggested on the basis of electron density analysis that is was the apical Mo=O that was replaced by sulfur to become Mo=S.[55] This assignment is surprising from the standpoint of the known coordination chemistry of model molybdenum complexes – inevitably, a single Mo=O group is located in the apical position within a square-pyramidal coordination sphere, opposite the vacant ligand position, owing to its strong *trans* effect. This being the case, one would have expected the equatorial position to be substituted by sulfur, not the apical one. Indeed, the magnetic circular dichroism electron of a catalytically relevant $Mo^V$ form of xanthine oxidoreductase, that giving rise to the "very rapid" EPR signal (see below), is virtually identical to that exhibited by simple model complexes known to have an apical Mo=O, indicating that the enzyme has an electronic (and presumably also physical) structure fundamentally the same as the crystallographically defined model complexes.[56]

More recently, three other enzyme crystal structures have become available that strongly indicate it is indeed the equatorial position that becomes sulfurated upon activation in the molybdenum hydroxylases. The first of these is that of the molybdenum-containing CO dehydrogenase from the aerobic *Oligotropha carboxydovorans* (as opposed to the Ni-containing enzyme from anaerobes such as *Methanosarcina thermophila* or *Rhodospirillum rubrum*[57,58]). This enzyme is an interesting variation on the theme of the molybdenum hydroxylases, with a binuclear Mo/Cu active site.[59,60] In the crystal structure,[59] the copper ion occupies a position in the equatorial plane of the molybdenum coordination sphere, connected to the molybdenum itself by a bridging

 © 2006 Wiley-VCH Verlag GmbH & Co. KGaA, Weinheim 

acid-labile sulfur that is analogous to the catalytically essential sulfur of other members of this enzyme family. Although unique among the molybdenum hydroxylases characterized to date in possessing a binuclear center, the active-site structure of CO dehydrogenase is clearly related to those of other members of this class of enzyme, and the position of the copper site suggests an equatorial Mo=S in the other enzymes. The second structure is that of the *P. putida* quinoline-2-oxidoreductase, where a careful analysis of the structure of the molybdenum center in the oxidized enzyme indicated an apical Mo=O at 1.69 Å and an equatorial Mo=S at 2.13 Å.[53] The third structure is that of a high-specific activity preparation of the (reduced) bovine oxidoreductase in complex with a potent mechanism-based inhibitor termed FYX-051.[61] This inhibitor is actually a substrate for the enzyme, but once hydroxylated becomes very tightly bound to the reduced enzyme in a classic mechanism-based mode of enzyme inhibition. In the crystal structure of this complex, it is abundantly clear that it is the equatorial position, adjacent to the bound inhibitor (which is coordinated to the molybdenum center through the newly introduced hydroxy group of the product), that has the added electron density of sulfur and not the apical position. On the basis of the present evidence, it thus seems clear that the apical position of the molybdenum centers in the molybdenum hydroxylases is an Mo=O, with an equatorial Mo=S in the oxidized from of the enzyme (or Mo–SH in the reduced form, see below).

## The Reaction Mechanism of Xanthine Oxidoreductase

The structure of the molybdenum center of xanthine oxidoreductase (Figure 3, *bottom*) provides the structural context in which to understand the reaction mechanism of the enzyme. It had been known for many years that the active site began in a $Mo^{VI}OS$ oxidation state and at the completion of the reaction was reduced by two equivalents and protonated at the Mo=S group to give a $Mo^{IV}O(SH)$.[62,63] Rather more recently it was also shown that a proximal site on the enzyme was the source the oxygen atom incorporated into product;[64] this site was regenerated with oxygen from solvent (i.e., already reduced to the level of water) at the completion of each catalytic cycle.[65] It has subsequently been demonstrated that $^{17}O$ from water exchanges into the molybdenum center rapidly under turnover conditions, and that the site labeled is strongly and anisotropically coupled to the molybdenum when in the $Mo^{V}$ valence state.[66] From a comparison with model compounds of known structure,[67] the labeled site corresponds to the equatorial Mo–OH rather than the equatorial Mo=O site. A similar conclusion has been drawn from the inability to observe a second, more weakly $^{17}O$ coupling in the "very rapid" EPR signal underneath the stronger coupling of the Mo–O-product oxygen under conditions when the molybdenum should have become labeled catalytically.[68] It is noteworthy that although initially assigned as a bound water molecule on the basis of the crystallographically determined Mo–O distance in the *D. gigas* aldehyde oxidoreductase structure, a more precise determination of this distance using X-ray absorption spectroscopy with the bovine xanthine oxidoreductase indicates that at 2.1 Å it is in fact a hydroxide ligand.[69] This is actually a fairly important mechanistic point, because a Mo–OH group deprotonated to $Mo–O^-$ is expected to be a considerably better nucleophile in initiating catalysis than would be a $Mo–OH_2$ group deprotonated to Mo–OH (see below). The protonation of the Mo=S group upon reduction of the molybdenum center in going from an $LMo^{VI}OS(OH)$ to an $LMo^{IV}O(SH)(OH)$ center is consistent with the concept of electroneutrality – that the protein environments of metal centers are designed to accommodate a specific net charge, and that changes in charge associated with reduction tend to be compensated by uptake of protons at or near the metal center. The uptake of protons by ligands to molybdenum upon reduction of the metal is in fact a property of even the simplest molybdate complexes.[70,71]

Other clues as to the chemical course of the reaction of xanthine oxidoreductases come from studies of the reaction of enzyme with the (poor) substrate 2-hydroxy-6-methylpurine. Although turnover with this substrate is some $10^3$-fold slower than with xanthine, the reaction (at least at high pH) proceeds with sequentially smaller rate constants associated with each of several steps in the catalytic sequence.[72] The result is that two reaction intermediates accumulate to an appreciable degree. The first of these has an absorption maximum (relative to oxidized enzyme) at 470 nm in the visible region, and upon *oxidation* by one equivalent is converted to a second species with an absorption maximum at 540 nm.[72] Formation of this latter species is coincident with the accumulation of the EPR-active $Mo^{V}$ state giving rise to the "very rapid" signal referred to above. This signal, so named on the basis of the kinetics of its formation and decay in the course of the reaction of enzyme with xanthine,[73,74] has long been recognized to be a fully competent catalytic intermediate. The implication of the work with the hydroxymethylpurine substrate is that the 470 nm-absorbing species must be the $Mo^{IV}$ species from which the $Mo^{V}$ species arises, and that the initial step of the reaction involves the two-electron reduction of the molybdenum center. Further, since earlier work had demonstrated that weak coupling to $^{13}C$ ($I$ = 1/2) is observed in the "very rapid" EPR signal when the sample is prepared using 8–$^{13}C$-labeled substrate,[75] the purine nucleus must be present in the EPR-active species (and hence also in its mechanistic precursor). The final mechanistically relevant observation is that the Mo–O bond of product has formed at the point of formation of the $Mo^{IV}$ species: acid quenching of the reaction mix at the point of maximum accumulation of this species followed by work-up affords the hydroxylated product of the reaction and not substrate.[72]

Under the conditions used, with 2-hydroxy-6-methylpurine as substrate and at pH 10, the entirety of the catalytic throughput passes through the "very rapid" EPR-active

 © 2006 Wiley-VCH Verlag GmbH & Co. KGaA, Weinheim 

state, and the integrated EPR intensity at maximum accumulation of the species (approximately 85% of the functional enzyme) agrees well with that expected given the observed rate constants for formation and decay of the species (1.0 and 0.1 $s^{-1}$, respectively, at 25 °C). With other substrates, and at other reaction conditions, however, the observed accumulation of this EPR-active state is significantly smaller than expected on the basis of the observed rate constants for formation and decay of the "very rapid" species.[76,77] The most likely explanation is that the reaction mechanism is bifurcated at the point of the Mo(VI)*P intermediate that precedes the "very rapid" species; oxidation by one electron yields the EPR-active species, but alternatively product may dissociate prior to oxidation of the $Mo^{IV}$ with the result that the "very rapid" species does not form. On the basis of the amount of "very rapid" signal accumulating under a variety of conditions with a wide range of substrate, it is evident that the fraction of total catalytic flux that passes through the EPR-active "very rapid" species is in fact usually quite small.

While the "very rapid" species may arise in only a relatively small fraction of turnover events, it nevertheless provides an important opportunity to understand the structure of the $Mo^{IV}$ state that precedes it, and this $Mo^{IV}$ species appears to be an obligatory catalytic intermediate. The "very rapid" EPR signal is devoid of proton superhyperfine splitting and has strong, anisotropic coupling to $^{33}S$ when enzyme is appropriately labeled, consistent with the existence of an $Mo^{V}$=S unit.[78] Strong but isotropic coupling is also observed when the sample is prepared in $^{17}O$-labeled water,[79] interpreted as evidence for a Mo–O product species. Overall, EPR work had thus early on provided strong evidence that the "very rapid" species possessed a MoOS(O-product) structure.

As indicated above, when the "very rapid" species is generated using substrate that has been labeled at $C_8$, weak superhyperfine coupling is seen in the EPR signal due to the I = 1/2 spin of the $^{13}C$ nucleus. This permits a distance from the carbon to the molybdenum to be obtained from the anisotropy of the coupling as ascertained by ENDOR spectroscopy. An initial study arrived at a short Mo–C distance – ca. 2.4 Å or shorter – which was interpreted as evidence in favor of a direct metal–carbon bond.[68] Subsequent work, however, has demonstrated convincingly that the distance is no shorter than 2.8 Å, indicating that the carbon is in the second coordination shell of the molybdenum rather than the first.[80] Further, although no proton superhyperfine is evident in the "very rapid" EPR signal, weak coupling to two sets of protons is seen using electron spin echo spectroscopy and as in the case with ENDOR distances can be estimated from the molybdenum: the results of the analysis indicate a single proton at ca. 2.4 Å and a set of two or more at ca. 6.1 Å (from the methyl group of the 2-hydroxy-6-methylpurine substrate that was used in the study).[81] With the Mo–C distance obtained from the ENDOR experiments above, it is possible to triangulate and obtain the orientation of the purine nucleus relative to the molybdenum atom. The data are consistent with binding of the (now hydroxylated) purine nucleus directly to molybdenum in an end-on fashion by the catalytically introduced hydroxy oxygen (Figure 4).

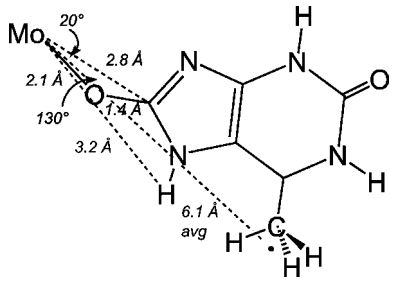


Figure 4. The structure of bound product to the molybdenum in the active site of xanthine oxidoreductase. The structure shown is for the product of the enzyme reaction with the slow substrate 2-hydroxy-6-methylpurine, which was used in the work. The Mo–C distance was obtained by ENDOR spectroscopy with 8-$^{13}C$-labeled substrate as substrate,[80] and the Mo–H distances by ESEEM spectroscopy,[81] as discussed in the text.

The above work using MCD, EPR and related methods to probe the $Mo^{V}$ state of the molybdenum center has been used to infer the structure of the preceding $Mo^{IV}$ intermediate in the catalytic sequence. Happily, with certain substrates of the enzyme this intermediate can be prepared in a stable form simply by addition of the hydroxylated product to enzyme that has been non-catalytically reduced by a reagent such as sodium dithionite. The best characterized case is that of violapterin, the product of enzyme action on the pteridine substrate lumazine (2,6-dihydroxypteridine). Addition of violapterin to reduced enzyme results in formation of a $Mo^{IV}$-containing reduced enzyme–product complex ($E_{red}$·P) that exhibits a relatively strong and broad charge-transfer transition centered at 640 nm.[82–84] This characteristic long-wavelength absorbance has been used in kinetic experiments to demonstrate that the charge-transfer complex is indeed an authentic catalytic intermediate.[83] The inhibitor FYX-051 used in the crystallographic work described above is another substrate that forms such a charge-transfer complex, and it is the $E_{red}$·P complex formed with this substrate whose structure has recently been reported.[61] In addition to establishing that the sulfido sulfur of the active form of the enzyme is in the equatorial rather than apical position, this work unambiguously shows product coordinated end-on to the molybdenum atom by the catalytically introduced hydroxy oxygen in a manner comparable to that shown in Figure 4. The position in the molybdenum coordination sphere is that occupied by the Mo–OH group of oxidized enzyme, lending further support to the conclusion that the Mo–OH represents the catalytically labile oxygen in the active site. Wedd and co-workers had in fact previously suggested that the catalytically labile oxygen could be a molybdenum-bound hydroxide.[67] The simple end-on binding of product (which formally is in the enolate tautomer at $C^7$, the site that has become hydroxylated) contrasts with other proposals where product, in the keto tautomer, binds side-on (a so-called $\eta_2$ interaction with

 © 2006 Wiley-VCH Verlag GmbH & Co. KGaA, Weinheim 

the molybdenum) with partial formation of a Mo–C bond.[68] It is evident from the crystal structure that such a binding mode is sterically impossible in the active site.

The evidence thus summarized above indicates that the $Mo^{IV}$ species is formed in the first step of the catalytic sequence: the molybdenum has been reduced from $Mo^{VI}$ to $Mo^{IV}$, the O–C bond of product formed and the Mo=S of oxidized enzyme protonated to Mo–SH, all simultaneously. An important clue as to the chemical mechanism by which the $E_{red}$·P intermediate is generated comes from the pH dependence of its formation, as reflected in the kinetic parameter $k_{cat}/k_m$ from steady-state experiments (or equivalently, since the rate-limiting step for turnover is known to be in the reductive half-reaction, $k_{red}/K_d$ from rapid reaction studies following the rate of reduction of enzyme by excess xanthine as a function of substrate concentration). The pH profile for both kinetic parameters track the reaction of free enzyme with free substrate through to the formation of the $E_{red}$·P complex; it is bell-shaped with a p$K_a$ for the acid limb of 6.6 and for the alkaline limb of 7.4.[85] The latter value agrees very well with the p$K_a$ for the first ionization of substrate, indicating that enzyme acts on the neutral rather than monoanionic form of substrate. This is expected if the reaction is initiated by nucleophilic attack, since a negative charge on substrate would compromise this first step of catalysis. The former p$K_a$ has been assigned to Glu 1261 in the active site of the enzyme, the same highly conserved glutamate first seen in the crystal structure of the *D. gigas* aldehyde oxidoreductase and proposed to be the active-site base.[55] The implication is that the glutamate must be unprotonated prior to the onset of catalysis, as should be the case if its role is to abstract a proton from substrate to initiate the catalytic sequence.

The chemical mechanism for formation of the initial $E_{red}$·P complex that emerges from all of the above is one in which the reaction is initiated by base-catalyzed abstraction of a proton from the Mo–OH group by Glu 1261, followed by nucleophilic attack of the oxyanion thus generated on the $C^8$ of substrate. Concomitant hydride transfer to the Mo=S group in the equatorial plane of the molybdenum coordination sphere generates $E_{red}$·P as shown in Figure 5. Direct hydride transfer to the Mo=S in the course of the reaction is consistent with the observation of Bray and Knowles that the $C^8$–H proton of substrate is initially transferred to the molybdenum center, and only subsequently exchanges with solvent.[86] Since both pairs of electrons in the Mo=S bond belong to the sulfur in a formal valence count, conversion of Mo=S to Mo–SH with this hydride transfer brings about the formal two-electron reduction of $Mo^{VI}$ to $Mo^{IV}$. The reaction is completed by electron transfer from the molybdenum to the other redox-active centers of the enzyme and deprotonation of the $Mo^{IV}$–SH group. Displacement of bound product by hydroxide from solvent may occur prior to transfer of the first electron out of the molybdenum center or after (in which case the "very rapid" species is generated).

A reaction predicated on nucleophilic attack on the heterocycle nucleus had in fact been suggested previously be Lee and Skibo,[87] who showed that for enzyme acting on a homologous series of substituted quinazoline substrates, a linear correlation existed between $\log(k_{cat}/K_m)$ and the p$K_a$ of the quinazoline (at least for substrates having a p$K_a$ > 9). The implication was that, as with xanthine, the substrate was required to be in the neutral rather than monoanionic form for the reaction to proceed. In addition, a variety of computational studies of the reaction mechanism are fully consistent with a mechanism involving concomitant nucleophilic attack and hydride transfer.[88–91] In the earliest of these studies, Voityuk and co-workers[88] showed that the Mo–OH form of a model for the molybdenum center was considerably more stable than a Mo–$OH_2$ form, an important observation because deprotonating the latter species (to Mo–OH) is unlikely to generate a sufficiently effective base as to function catalytically, as discussed above. Subsequent work by this same group[89] examined the reaction of the model (surprisingly, starting from a Mo–$OH_2$ species rather than the more stable Mo–OH shown in their previous study) with formaldehyde, a known inhibitor of xanthine oxidoreductase. The work implicated a reaction mechanism involving hydride transfer from the substrate to the $Mo^{VI}$=S, yielding $Mo^{IV}$–SH, in the course of the nucleophilic attack on substrate. Working with a similar model for the enzyme molybdenum center, but importantly starting with a Mo–OH rather than Mo–$OH_2$ species, Ilich et al.[90] established the same two points (i.e., nucleophilic attack on substrate with concomitant hydride transfer to the Mo=S) for the reaction of the model with the bona fide enzyme substrate formamide (which is hydroxylated to carbamate). Most significantly from this study, the transition state was well-defined, permitting the unambiguous demonstration of partial negative charge on the hydrogen being transferred and indicating hydride-like character.[90] Subsequent work with the same system provided a rationale as to why substitution of a second Mo=O group for the Mo=S of functional enzyme resulted in loss of activity: the transition state for the reaction of the $MoO_2$ model was found to lie considerably earlier along the reaction coordinate than with the MoOS model and at approximately 13 kcal/mol higher in energy (corresponding to a reduction in rate of over nine orders of magnitude as compared with the sulfido form).[91] Interestingly, although calculations with a putative selenated form of the model (MoOSe) did not converge, those with a tellurated form (MoOTe) were successful and suggested that such a form of the enzyme should exhibit even greater reactivity than the naturally occurring MoOS form.[91]

Finally, it has been suggested that the initial $E_{red}$·P complex forms through a radical mechanism rather than the two-electron chemistry implicit in a mechanism involving nucleophilic attack, with rate-limiting formation of a (presumably extremely unstable) $Mo^{V}$···xanthine$^{\cdot+}$ diradical species upon direct one-electron transfer from substrate to molybdenum in the $Mo^{VI}$···xanthine Michaelis complex.[92] Were this the case, however, a linear relationship should exist between the substrate/substrate$^{\cdot+}$ one-electron reduction potential and reaction rate. Examining a homologous series

 © 2006 Wiley-VCH Verlag GmbH & Co. KGaA, Weinheim 

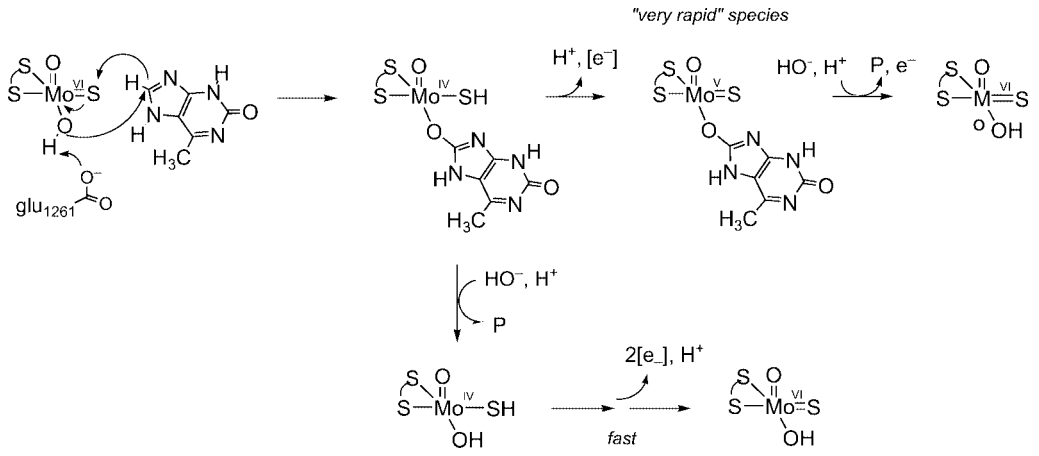


Figure 5. The reaction mechanism of xanthine oxidoreductase. The reaction involves base-assisted nucleophilic attack on the $C^8$ position of substrate, with concomitant hydride transfer to the Mo=S group of the oxidized enzyme and reduction of the molybdenum itself by two equivalents. From the initial $E_{red}$·P intermediate, the molybdenum may become oxidized (by electron transfer to the other redox-active centers of the enzyme) and deprotonated to form the species giving rise to the "very rapid" EPR signal as discussed in the text, or alternatively hydroxide may displace product from the molybdenum coordination sphere, followed by subsequent reoxidation of the molybdenum.

of purine substrates for xanthine oxidoreductase, Stockert et al. failed to observe such a relationship[93] arguing strongly against a radical-based mechanism and leaving the two-electron chemistry shown in the proposed reaction predicated on nucleophilic attack as the most likely mechanistic alternative. It is worth noting that for the molybdenum-containing aldehyde oxidases a reaction mechanism involving nucleophilic attack on the aldehyde carbonyl moiety had long been the preferred reaction mechanism for oxidation of aldehydes to carboxylic acids. It thus appears that the two principal subclasses of the molybdenum hydroxylases (those that act on aromatic heterocycles and those that act on aldehyde substrates) utilize fundamentally the same mechanism to accelerate reaction rate. This goes a long way in explaining the extremely broad and overlapping substrate specificities of the mammalian xanthine oxidoreductases and aldehyde oxidases.

## The Roles of Specific Amino Acid Residues in Catalysis

On the basis of the above, there is broad experimental support for a reaction mechanism initiated by nucleophilic attack, and in the past five years such a mechanism (Figure 5) has received general acceptance in the field. It is significant that computational studies, involving minimal structures for both the molybdenum center and substrate and not including the protein structure at all, have successfully defined the trajectory of the system across the potential energy surface that defines the reaction. This indicates that the course of the reaction is dictated by the electronic structure of the metal center itself; that is, the reactivity of the enzyme is an intrinsic property of the metal center. Having said this, it is evident that (as in all enzymes) the polypeptide (and specific amino acid residues in the active site of the enzyme in particular) is crucially involved in lowering the energies of the transition states encountered along this trajectory, in some cases enormously so. The structure of the active site of bovine xanthine oxidoreductase is shown in Figure 3, with several specific amino acid residues that are likely to play a role in catalysis indicated. Glu 1261 (in the bovine enzyme sequence) has already been referred to as the candidate active-site base that initiates nucleophilic attack on substrate. This residue is universally conserved in the molybdenum hydroxylases, both in those enzymes hydroxylating aromatic heterocycles and in the aldehyde oxidases. In addition, a second glutamate (802 in the bovine enzyme) is conserved in the heterocycle-hydroxylating enzymes, but not in those that have aldehydes as substrates. Other residues that are conserved in the heterocycle-hydroxylating enzymes, (but not always in those that act on aldehydes) include the two phenylalanine residues between which the aromatic substrate is sandwiched on binding in the active site (914 and 1009 in the bovine enzyme), Gln 767 which is within hydrogen-bonding distance of the apical Mo=O, and Arg 880, which appears to interact with the distal end of substrate opposite the $C^8$ position that becomes hydroxylated. We consider now the results of recent studies of the roles of these active-site residues in two recombinant systems that have been developed for site-directed mutagenesis studies: the bacterial xanthine dehydrogenase from *Rhodobacter capsulatus* (as expressed in *E. coli*)[94] and the rat xanthine oxidoreductase, as expressed in insect cells using the baculovirus vector.[95]

The residues that have been examined to date are the two glutamates in the active site. Leimkühler et al.[96] have mutated both Glu232 and Glu730 in the xanthine dehydrogenase from *R. capsulatus* to alanine (these residues correspond to Glu 802 and Glu1261, respectively, in the bovine enzyme). The E232A mutant exhibits considerably reduced activity, with the limiting rate of reduction of enzyme by

 © 2006 Wiley-VCH Verlag GmbH & Co. KGaA, Weinheim 

xanthine in rapid kinetic experiments decreased from 67 $s^{-1}$ for the wild-type enzyme to 5.5 $s^{-1}$ for the mutant. The $K_d$ is correspondingly affected, increasing from 34 μM to 410 μM. It is evident that the free energy associated with the interaction of this residue with substrate, ca. 3 kcal/mol, is used approximately equally to bind substrate on the one hand, and lower the activation barrier for the reaction on the other. The result is that $k_{red}/K_d$ (the effective second-order rate constant of free enzyme with free substrate in the lower [S] regime) is compromised by over two orders of magnitude in the mutant enzyme. The E730A mutant is profoundly compromised in reactivity toward substrate – no reduction of enzyme was detected in an overnight incubation with excess xanthine under anaerobic conditions (with wild-type enzyme, the reaction is complete in less than 200 ms under the conditions). Control experiments established that the mutant enzyme had only about 30% functional active sites (based on molybdenum and sulfur content), but still the absorbance change associated with reduction of the active enzyme should have been easily detected. Further, other mutants (notably E730Q and E730R) had more molybdenum and sulfur incorporated, but were similarly inactive. Conservatively, the E730A mutant has a lower limiting rate of reduction by substrate of at least $10^7$ compared to wild-type enzyme, indicating that this residue contributes at least 10 kcal/mol toward transition state stabilization in the reduction of enzyme by substrate. Clearly, this residue is essential for catalysis, consistent with its proposed role as an active base initiating the reaction. Unfortunately, it was not possible to carry out a "chemical rescue" of the E730A mutant by addition of acetate (which conceivably might have bound in the empty pocket otherwise occupied by the glutamate side chain, possibly restoring at least some activity) and an E730G mutant is not stable (S. Leimkühler, unpublished). It thus remains to be established that Glu 730 functions specifically as an active-site base in the course of the reaction.

## Resonance Roman Studies of the Molybdenum Center of Xanthine Oxidoreductase

The above site-directed mutagenesis studies illustrate how interactions between substrate and enzyme can be mapped out in the active site, and rapid reaction kinetic studies used to quantitate the extent to which the free energy associated with these interactions is used to either bind substrate (i.e. influence $K_d$) or accelerate reaction time (i.e. influence $k_{red}$). It is also possible to probe enzyme-substrate interactions using resonance Raman spectroscopy, which provides detailed information about the vibrational frequencies (and hence bond strengths) of bonds in chromophores. The method is particularly useful when applied to metalloproteins, where by virtue of resonance enhancement it is frequently possible to focus on just those bonds in the active site, ignoring those of the polypeptide in general. In the case of xanthine oxidoreductase, Kitagawa, Nishino and co-workers have examined the as-isolated, oxidized enzyme by resonance Raman spectroscopy and identified specific vibrational modes attributable to ligands to the metal, in particular the Mo=O and Mo=S stretching frequencies at 899 and 474 $cm^{-1}$, respectively.[97] Interestingly, while substitution of the Mo=S with $^{34}S$ was facile, the Mo=O group could not be exchanged with solvent $H_2{}^{18}O$ even under rather extreme reaction conditions, indicating that the apical oxo group is stable and does not readily exchange with solvent. Other vibrational modes due to the [2Fe–2S] clusters and FAD of the enzyme were assigned, but no modes attributable to the enedithiolate ligand to molybdenum could be identified.

Advantage can also be taken of the long-wavelength absorption of the $E_{red}$·P complex seen with violapterin that was discussed earlier to use resonance Raman as an active-site probe. As illustrated in Figure 6 (bottom) the (ordinary) Raman spectrum of violapterin is significantly perturbed on binding to the reduced enzyme (top).[98] Apart from the differences in band intensity, which have largely to do with the fact that only certain modes seen in the $E_{red}$·P complex are resonance-enhanced (while those of the violapterin in free solution are not), it is evident that almost every mode seen in the spectrum of violapterin is shifted in the enzyme complex to at least a small extent. The principal reason for this is that while both the free and enzyme complexed forms are monoanionic under the experimental conditions, the free violapterin has the negative charge accumulated in the $N_3$ region of the pyrimidine subnucleus, while in the enzyme complexed formal negative charge accumulates to a much greater extent at the $C^7$–O, which coordinates to the molybdenum [by analogy to the crystal structure of the $E_{red}$·(FYX-051) complex]. Two of the most prominent vibrational modes in the free violapterin monoanion, at 704 and 1286 $cm^{-1}$, are shifted modestly (to 699 and 1294 $cm^{-1}$, respectively), and the third, at 1379 $cm^{-1}$, is greatly diminished in intensity. The shifts are on the order expected for increased negative charge accumulation at the $C^7$–O upon binding the enzyme. A normal mode analysis of the $E_{red}$·P complex indicates that the bands seen at 699, 852, 1294 and 146 $cm^{-1}$ vibrations have motions that include significant ring deformation.[98] In addition, the set of modes in the 1550–1700 $cm^{-1}$ region can be assigned to a second group of vibrations that have major contributions by $C^2$=O and $C^4$=O stretching motions. It is interesting that when the sample is prepared in such a way as to label the bridging oxygen between $C^7$ of the pterin nucleus and the molybdenum that the two most isotope-sensitive modes are those seen at 1467 and 1563 $cm^{-1}$, shifting 12 and 15 $cm^{-1}$, respectively, to lower energy with the heavier isotope.[98] That both these modes lie to considerably lower energy than expected for a typical carbonyl group is consistent with the $C^7$–O bond having significant single-bond character in the enzyme-bound product.

With the mode assignments for specific experimentally observed vibrational bands that have been made to date,[98] it is possible to begin to map out the regions on the heterocycle that interact with specific amino acid residues in the

 © 2006 Wiley-VCH Verlag GmbH & Co. KGaA, Weinheim 

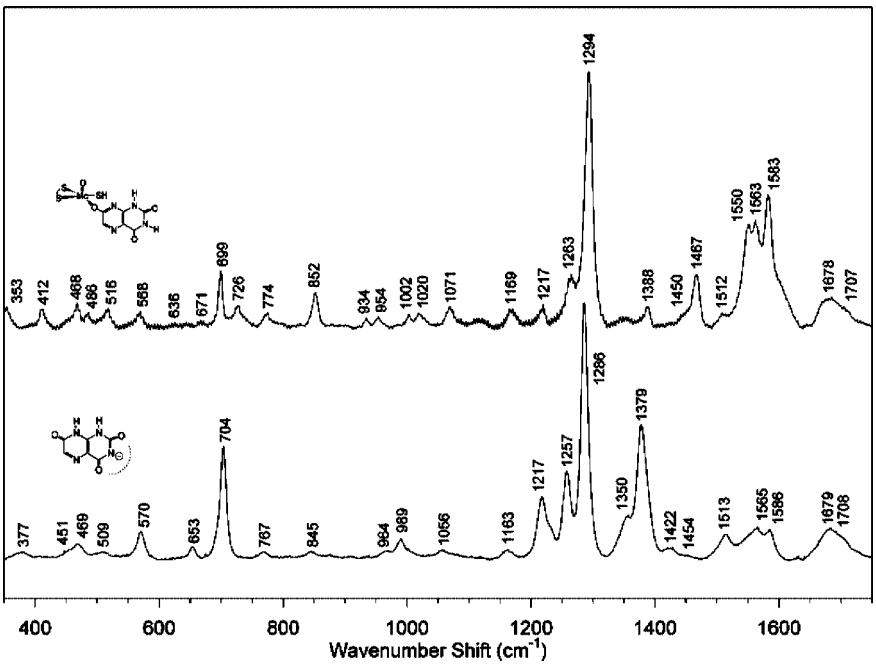


Figure 6. Resonance Raman spectra of the monoanion of violapterin (bottom) and the complex of reduced enzyme with violapterin (top). The spectra were obtained using 647-nm excitation.

active site and, importantly, quantify the amount of free energy associated with each interaction using site-directed mutagenesis. It is to be expected that work along these lines in the immediate future will provide a quantitative map of enzyme-substrate interactions, which can be correlated with changes in reactivity among the set of enzyme mutants.

## Prospectus

The crystal structures of an increasing number of members of the molybdenum hydroxylase family of enzymes have become known, and both the common and unique structural elements of these enzymes identified. There is an emerging consensus regarding the fundamental nature of carbon center hydroxylation as catalyzed by enzymes such as xanthine oxidoreductase, and the specific roles of active site amino acid residues in accelerating reaction rate at each of the several steps of this mechanism are increasingly well understood. The continued application of site-directed mutagenesis will very likely further our understanding of the catalytic process in the near future, and computational approaches in conjunction with spectroscopic methods such as resonance Raman can be expected to advance our understanding of the electronic as well as physical structures of intermediates and transition states. Finally, it can be hoped that new enzymes similar to CO dehydrogenase will be identified whose active-site structures and reaction mechanisms represent interesting variations on the theme for these enzymes that reflect the diversity of chemistry available to molybdenum in a biological context.


[1] M. Dixon, S. Thurlow, *Biochem. J.* **1924**, *18*, 976.
[2] R. C. Bray, L. Meriwether, *Nature* **1966**, *212*, 467.
[3] R. Hille, *Chem. Rev.* **1996**, *96*, 2757.
[4] R. Hille, T. Nishino, *FASEB J.* **1995**, *9*, 995.
[5] M. Seo, A. J. Peeters, H. Kiowai, T. Oritani, A. Marion-Poll, *Proc. Natl. Acad. Sci. USA* **2000**, *97*, 12908.
[6] V. Massey, in *Iron-Sulfur Proteins*, vol. 1 (Ed.: A. Ehrenberg), Academic Press, New York, **1973**, pp. 301–360.
[7] J. M. Tunney, J. McMaster, C. D. Garner, in *Comparative Coordination Chemistry II* (Eds.: J. A. McCleverty, T. J. Meyer), vol. 8, p. 459, Elsevier SA, Amsterdam, **2004**.
[8] C. G. Young, in *Encyclopedia of Inorganic Chemistry 2*, vol. 5, Wiley, **2005**, p. 3321.
[9] *Metals in Biology*, vol. 39. *Molybdenum and Tungsten: Their Roles in Biological Systems* (Eds.: H. Segel, I. Segel), **2002**, Marcel Dekker, New York.
[10] K. D. Karlin, E. I. Stiefel (Eds.), *Progress in Inorganic Chemistry*, *Dithiolene Chemistry, Synthesis Properties and Applications*, vol. 52, Wiley, **2004**.
[11] J. H. Enemark, *Chem. Rev.* **2004**, *104*, 1175.
[12] J. L. Johnson, K. V. Rajagopalan, *Proc. Natl. Acad. Sci. USA* **1982**, *79*, 5414.
[13] S. P. Kramer, J. L. Johnson, A. A. Rebeiro, D. S. Millington, K. V. Rajagopalan, *J. Biol. Chem.* **1987**, *262*, 16357.
[14] M. K. Chan, S. Mukund, A. Kletzin, M. W. W. Adams, D. C. Rees, *Science* **1995**, *267*, 1463.
[15] B. Fischer, J. H. Enemark, P. Basu, *J. Inorg. Biochem.* **1998**, *72*, 13.
[16] J. L. Johnson, M. M. Wuebbens, K. V. Rajagopalan, *J. Biol. Chem.* **1987**, *264*, 13440.
[17] M. M. Wuebbens, K. V. Rajagopalan, *J. Biol. Chem.* **1993**, *268*, 13493.
[18] G. Schwarz, *Cell. Mol. Life Sci.* **2005**, *62*, 2792.
[19] M. M. Wuebbens, K. V. Rajagopalan, *J. Biol. Chem.* **1993**, *268*, 13493.


 © 2006 Wiley-VCH Verlag GmbH & Co. KGaA, Weinheim 

[20] M. M. Wuebbens, K. V. Rajagopalan, *J. Biol. Chem.* **1995**, *270*, 1082.
[21] P. Hänzelmann, H. Schindelin, *Proc. Natl. Acad. Sci. USA* **2004**, *101*, 12870.
[22] M. M. Wuebbens, M. T. W. Liu, K. V. Rajagopalan, H. Schindelin, *Structure* **2000**, *8*, 709.
[23] C. Rieder, W. Eisenreich, J. O'Brien, G. Richter, E. Götze, P. Boyle, S. Blanchard, A. Bacher, H. Simon, *Eur. J. Biochem.* **1998**, *255*, 24.
[24] J. A. Santamaria-Araujo, B. Fischer, T. Otte, M. Nimtz, R. R. Mendel, V. Wray, G. Schwarz, *J. Biol. Chem.* **2004**, *279*, 15994.
[25] M. J. Rudolph, M. M. Wuebbens, K. V. Rajagopalan, H. Schindelin, *Nat. Struct. Biol.* **2001**, *8*, 42.
[26] A. Matthies, K. V. Rajagopalan, R. R. Mendel, S. Leimkühler, *Proc. Natl. Acad. Sci. USA* **2004**, *101*, 5946.
[27] M. W. Lake, M. M. Wuebbens, K. V. Rajagopalan, H. Schindelin, *Nature* **2001**, *414*, 325.
[28] A. Matthies, M. Nimtz, S. Leimkühler, *Biochemistry* **2005**, *44*, 7912.
[29] G. Gutzke, B. Fischer, R. R. Mendel, G. Schwarz, *J. Biol. Chem.* **2001**, *276*, 36268.
[30] M. M. Wuebbens, K. V. Rajagopalan, *J. Biol. Chem.* **2003**, *278*, 14523.
[31] M. Aguilar, J. Cardenas, E. Fernandez, *Biochim. Biophys. Acta* **1992**, *1160*, 269.
[32] C. P. Witte, M. I. Igeno, R. Mendel, G. Schwarz, E. Fernandez, *FEBS Lett.* **1998**, *4321*, 205.
[33] F. S. Ataya, C. P. Witte, A. Galvan, M. I. Igeno, E. Fernandez, *J. Biol. Chem.* **2003**, *278*, 10885.
[34] J. A. Maupin-Furlow, J. K. Rosentel, J. H. Lee, U. Deppenmeier, R. P. Gunsalus, K. T. Shanmugan, *J. Bacteriol.* **1995**, *177*, 4851.
[35] S. Rech, C. Wolin, R. P. Gunsalus, *J. Biol. Chem.* **1996**, *271*, 2557.
[36] Y. Hu, S. Rech, R. P. Gunsalus, D. C. Rees, *Nat. Struct. Biol.* **1997**, *4*, 703.
[37] M. T. W. Liu, M. M. Wuebbens, K. V. Rajagopalan, H. Schindelin, *J. Biol. Chem.* **2000**, *275*, 1814.
[38] G. Schwarz, N. Schrader, R. R. Mendel, H.-J. Hecht, H. Schindelin, *J. Mol. Biol.* **2001**, *312*, 405.
[39] J. Kuper, A. Llamas, H.-J. Hecht, R. R. Mendel, G. Schwarz, *Nature* **2004**, *430*, 803.
[40] F. Blasco, J. Pommier, V. Augier, M. Chippaux, G. Giordano, *Mol. Microbiol.* **1992**, *6*, 221.
[41] S. Leimkühler, W. Klipp, *J. Bacteriol.* **1999**, *181*, 2745.
[42] M. J. Rudolph, M. M. Wuebbens, O. Turque, K. V. Rajagopalan, *J. Biol. Chem.* **2003**, *278*, 14514.
[43] M. W. Lake, C. A. Temple, K. V. Rajagopalan, H. Schindelin, *J. Biol. Chem.* **2000**, *275*, 40211.
[44] T. Palmer, C.-L. Santini, C. Lobbi-Nivol, D. J. Eaves, D. H. Boxer, *Mol. Microbiol.* **1996**, *20*, 875.
[45] V. Massey, D. E. Edmondson, *J. Biol. Chem.* **1970**, *245*, 6595.
[46] T. Nishino, C. Usami, K. Tsushima, *Proc. Natl. Acad. Sci. USA* **1983**, *80*, 1826.
[47] L. Xiong, M. Ishitani, H. Lee, J.-K. Zhu, *Plant Cell* **2001**, *13*, 2063.
[48] F. Bittner, M. Oreb, R. R. Mendel, *J. Biol. Chem.* **2001**, *276*, 40381.
[49] L. Zheng, R. H. White, V. L. Cash, R. F. Jack, D. R. Dean, *Proc. Natl. Acad. Sci. USA* **1993**, *90*, 2754.
[50] T. Heidenreich, S. Wollers, R. R. Mendel, F. Bittner, *J. Biol. Chem.* **2005**, *280*, 4213.
[51] J. J. Truglio, K. Theis, S. Leimkühler, R. Rappa, K. V. Rajagopalan, C. Kisker, *Structure* **2002**, *10*, 115.
[52] H. Dobbek, L. Gremer, O. Meyer, R. Huber, *Proc. Natl. Acad. Sci. USA* **1999**, *96*, 8884.
[53] I. Bonin, B. M. Martins, V. Pruvanov, S. Fetzner, R. Huber, H. Dobbek, *Structure* **2004**, *12*, 1425.
[54] M. J. Romão, M. Archer, I. Moura, J. J. G. Moura, J. LeGall, R. Engh, M. Schneider, P. Hof, R. Huber, *Science* **1995**, *270*, 1170.
[55] R. Huber, P. Hof, R. O. Duarto, J. J. G. Moura, I. Moura, M.-Y. Liu, J. LeGall, R. Hille, M. Archer, M. J. Romão, *Proc. Natl. Acad. Sci. USA* **1996**, *93*, 8846.
[56] R. M. Jones, F. E. Inscore, R. Hille, M. L. Kirk, *Inorg. Chem.* **1999**, *38*, 4963.
[57] S. W. Ragsdale, *Crit. Rev. Biochem. Mol. Biol.* **2004**, *39*, 165.
[58] R. K. Watt, P. W. Ludden, *Cell. Mol. Life Sci.* **1999**, *56*, 604.
[59] H. Dobbek, L. Gremer, R. Kiefersauer, R. Huber, O. Meyer, *Proc. Natl. Acad. Sci. USA* **2002**, *99*, 15971.
[60] M. Gnida, R. Ferner, L. Gremer, O. Meyer, W. Meyer-Klaucke, *J. Biochem.* **2003**, *42*, 222.
[61] K. Okamoto, K. Matsumoto, R. Hille, B. T. Eger, E. F. Pai, T. Nishino, *Proc. Natl. Acad. Sci. USA* **2004**, *101*, 7931.
[62] T. D. Tullius, D. M. Kurtz, S. D. Conradson, K. O. Hodgson, *J. Am. Chem. Soc.* **1979**, *101*, 2776.
[63] J. Bordas, R. C. Bray, C. D. Garner, S. Gutteridge, S. Hasnain, *Biochem. J.* **1983**, *191*, 499.
[64] R. Hille, H. Sprecher, *J. Biol. Chem.* **1987**, *262*, 10914.
[65] K. N. Murray, J. G. Watson, S. Chaykin, *J. Biol. Chem.* **1966**, *241*, 4798.
[66] M. Xia, R. Dempski, R. Hille, *J. Biol. Chem.* **1999**, *274*, 3323.
[67] R. J. Greenwood, G. L. Wilson, J. R. Pilbrow, A. G. Wedd, *J. Am. Chem. Soc.* **1993**, *115*, 5385.
[68] B. D. Howes, R. C. Bray, R. L. Richards, N. A. Turner, B. Bennett, D. J. Lowe, *Biochemistry* **1996**, *35*, 1432.
[69] C. J. Doonan, A. L. Stockert, R. Hille, G. N. George, *J. Am. Chem. Soc.* **2005**, *127*, 4518.
[70] E. I. Stiefel, *Proc. Natl. Acad. Sci.* **1977**, *70*, 988.
[71] E. I. Stiefel, *Prog. Inorg. Chem.* **1977**, *22*, 1.
[72] R. B. McWhirter, R. Hille, *J. Biol. Chem.* **1991**, *266*, 23724.
[73] R. C. Bray, G. Palmer, H. Beinert, *J. Biol. Chem.* **1964**, *239*, 2667.
[74] R. C. Bray, T. Vånngärd, *Biochem. J.* **1969**, *114*, 725.
[75] S. J. Tanner, R. C. Bray, F. Bergmann, *BioChem. Soc. Trans.* **1978**, *6*, 1328.
[76] D. Edmondson, D. Ballou, A. van Heuvelen, G. Palmer, V. Massey, *J. Biol. Chem.* **1973**, *248*, 6135.
[77] R. C. Bray, G. N. George, *BioChem. Soc. Trans.* **1985**, *13*, 560.
[78] J. P. G. Malthouse, G. N. George, D. J. Lowe, R. C. Bray, *Biochem. J.* **1981**, *199*, 629.
[79] S. Gutteridge, R. C. Bray, *Biochem. J.* **1980**, *189*, 615.
[80] P. Manikandan, E.-Y. Choi, R. Hille, B. M. Hoffman, *J. Am. Chem. Soc.* **2001**, *123*, 2658.
[81] G. A. Lorigan, R. D. Britt, J. H. Kim, R. Hille, *Biochim. Biophys. Acta* **1994**, *1185*, 284.
[82] M. D. Davis, J. S. Olson, G. Palmer, *J. Biol. Chem.* **1982**, *257*, 14730.
[83] M. D. Davis, J. S. Olson, G. Palmer, *J. Biol. Chem.* **1984**, *259*, 3526.
[84] R. Hille, G. N. George, M. K. Eidsness, S. P. Cramer, *Inorg. Chem.* **1989**, *28*, 4018.
[85] J. H. Kim, M. G. Ryan, H. Knaut, R. Hille, *J. Biol. Chem.* **1996**, *271*, 6771.
[86] R. C. Bray, P. F. Knowles, *Proc. R. Soc. London, Ser. A* **1968**, *302*, 351.
[87] C.-H. Lee, E. B. Skibo, *Biochemistry* **1987**, *26*, 7355.
[88] A. A. Voityuk, K. Albert, S. Kostlmeier, V. A. Nasluzov, K. M. Neyman, P. Hof, R. Huber, M. J. Romão, N. Rösch, *J. Am. Chem. Soc.* **1997**, *119*, 3159.
[89] A. A. Voityuk, K. Albert, M. J. Romão, R. Huber, N. Rösch, *Inorg. Chem.* **1998**, *37*, 176.
[90] P. Ilich, R. Hille, *J. Phys. Chem. B* **1999**, *103*, 5406.
[91] P. Ilich, R. Hille, *J. Am. Chem. Soc.* **2002**, *124*, 6796.
[92] C. C. Page, C. C. Moser, X. Chen, P. L. Dutton, *Nature* **1999**, *402*, 47.
[93] A. L. Stockert, S. Shinde, R. F. Anderson, R. Hille, *J. Am. Chem. Soc.* **2002**, *124*, 14555.

 © 2006 Wiley-VCH Verlag GmbH & Co. KGaA, Weinheim 

[94] S. Leimkühler, R. Hodson, G. N. George, K. V. Rajagopalan, *J. Biol. Chem.* **2003**, *278*, 20802.
[95] T. Nishino, Y. Amaya, S. Kawamoto, Y. Kashima, K. Okamoto, T. Nishino, *J. Biol. Chem.* **2002**, *132*, 597.
[96] S. Leimkühler, A. L. Stockert, K. Igarashi, T. Nishino, R. Hille, *J. Biol. Chem.* **2004**, *279*, 40437.
[97] N. C. Maiti, T. Tomita, T. Kitagawa, K. Okamoto, T. Nishino, *J. Biol. Inorg. Chem.* **2003**, *8*, 327.
[98] C. Hemann, P. Ilich, A. L. Stockert, E.-Y. Choi, R. Hille, *J. Phys. Chem. B* **2005**, *109*, 3023.
[99] C. Enroth, B. T. Eger, K. Okamoto, T. Nishino, T. Nishino, E. F. Pai, *Proc. Natl. Acad. Sci. USA* **2000**, *97*, 10723.

Received: January 27, 2006
Published Online: April 25, 2006

 © 2006 Wiley-VCH Verlag GmbH & Co. KGaA, Weinheim 

DOI: 10.1002/ejic.200600144

# The "Building-Block" Assembly of a $[Ni_{12}Mn_6]$ Aggregate

**Gang Wu,[a,d] Rodolphe Clérac,[b] Wolfgang Wernsdorfer,[c] Shilun Qiu,*[d] Christopher E. Anson,[a] Ian J. Hewitt,[a] and Annie K. Powell*[a]**

**Keywords:** Cluster compounds / Carboxylate ligands / Cooperative effects / Nickel / Manganese

Reaction of $Mn^{II}(bdoa)(H_2O)_3$ with $Ni(CH_3COO)_2{\cdot}3H_2O$ in methanol gives a heterometallic cluster, $[Ni_{12}Mn_6(bdoa)_6(O_2CMe)_{12}(\mu_3\text{-}OMe)_{12}(MeOH)_{12}]{\cdot}21MeOH$, which was structurally characterised by single-crystal X-ray diffraction and possesses three self-assembled tetranuclear nickel cubes connected by a $Mn^{II}_6(bdoa)_6(CH_3COO)_3$ subunit. The magnetic properties were studied in detail and indicate that the compound possesses a high density of spin states with small energy gaps between them.

(© Wiley-VCH Verlag GmbH & Co. KGaA, 69451 Weinheim, Germany, 2006)

One of the principal synthetic challenges in the area of polynuclear metal complexes is control of molecular topology. In recent years, this has become of particular importance in the field of Single-Molecule Magnets, in which a combination of high-spin ground states and uniaxial anisotropy leads to an energy barrier to the reversal of the magnetization.[1] Heterometallic aggregates are also of particular interest in the understanding of magnetic interactions between different spin carriers.[2] For the construction of such aggregates, the "metal complex as ligand" approach has often proved to be fruitful in the designed synthesis of compounds,[3] amongst the most successful examples of which are the pre-designed metal-cyanide complexes. By careful selection of such building blocks, the fine control of target compounds with desirable architectures and magnetic properties therefore becomes a reality.[3c,3d,3f] Such a strategy has also been successfully employed in the synthesis of framework compounds constructed from secondary building units (SBUs) in which coordination-compound units are connected through rigid ligands such as 1,3,5-benzenetricarcoxylate or 4,4′-bipyridyl.[4] Using such ideas we thought it should be possible to construct a discrete molecule by choosing the correct combination of SBUs or SBU precursors. For example, a suitable metal-complex building block is one that possesses coordinated functional groups, such as carboxylate groups, which can form magnetically active bridges to other paramagnetic metal ions, and/or has exchangeable terminal ligands (e.g. $H_2O$, MeOH) that can be replaced by bridging units from other metal complexes. On the other hand, synthetic conditions can be chosen to favour known self-assembly motifs such as metal-cubane structures. Ideally, the components should be soluble in common solvents, and the desired structural motifs should be conserved during the reaction leading to a predictable final structure. Here we present the realisation of such a strategy with the synthesis, structure and magnetic properties of the large heterometallic aggregate $[Ni_{12}Mn_6(bdoa)_6(O_2CMe)_{12}(\mu_3\text{-}OMe)_{12}(MeOH)_{12}]{\cdot}21MeOH$ (**2**·21MeOH) ($bdoa^{2-}$ = benzene-1,2-dioxyacetate), which can be described in terms of a trigonal prismatic framework that corresponds to a central $\{Mn^{II}_6(bdoa)_6(\mu\text{-}O_2CMe)_3\}$ core decorated by three self-assembled $\{Ni_4(\mu_3\text{-}OMe)_4\}$ cubane units.

The complex $[Mn^{II}(bdoa)(H_2O)_3]$ (**1**) was selected as the mononuclear, metal-complex building block since, as the X-ray crystal structure[5] shows, the compound is monomeric and has a seven-coordinate metal centre, the tetradentate ligand and three aqua ligands forming a pentagonal-bipyramidal geometry (Figure 1 top). In this way, the two non-coordinated oxygen atoms of the carboxylate groups can be used to form bridges to other metal centres and the three *mer*-distributed aqua ligands can either be replaced by other bridging units, as we indeed observe in the final product, or be deprotonated to form single- or double-hydroxo bridges to other metal centres.

Reaction of complex **1** with $Ni(O_2CMe)_2{\cdot}3H_2O$ in methanol in a 1:2 molar ratio gave pale-green plate-like crystals of **2**·21MeOH in good yield after one week. The structure of **2**, viewed down the molecular threefold axis, is shown in Figure 1. The structure can be described as being built up

[a] Institute für Anorganische Chemie, Universität Karlsruhe, Engesserstr. Geb 30,45, 76128 Karlsruhe, Germany
Fax: +49-721-608-8142
E-mail: powell@chemie.uni-karlsruhe.de
[b] Centre de Recherche Paul Pascal, CNRS UPR-8641, 115 Av. Albert Schweitzer, 33600 Pessac, France
[c] Laboratoire Louis Néel, CNRS, B. P. 166, 25 Av. des Martyrs, 38042 Grenoble, France
[d] State Key Laboratory of Inorganic Synthesis & Preparative Chemistry, Jilin University, 2699 Qianjin Street, Changchun 130012, P. R. China
Fax: +86-431-5166279
E-mail: sqiu@mail.jlu.edu.cn

Supporting information for this article is available on the WWW under http://www.eurjic.org or from the author.

 © 2006 Wiley-VCH Verlag GmbH & Co. KGaA, Weinheim 

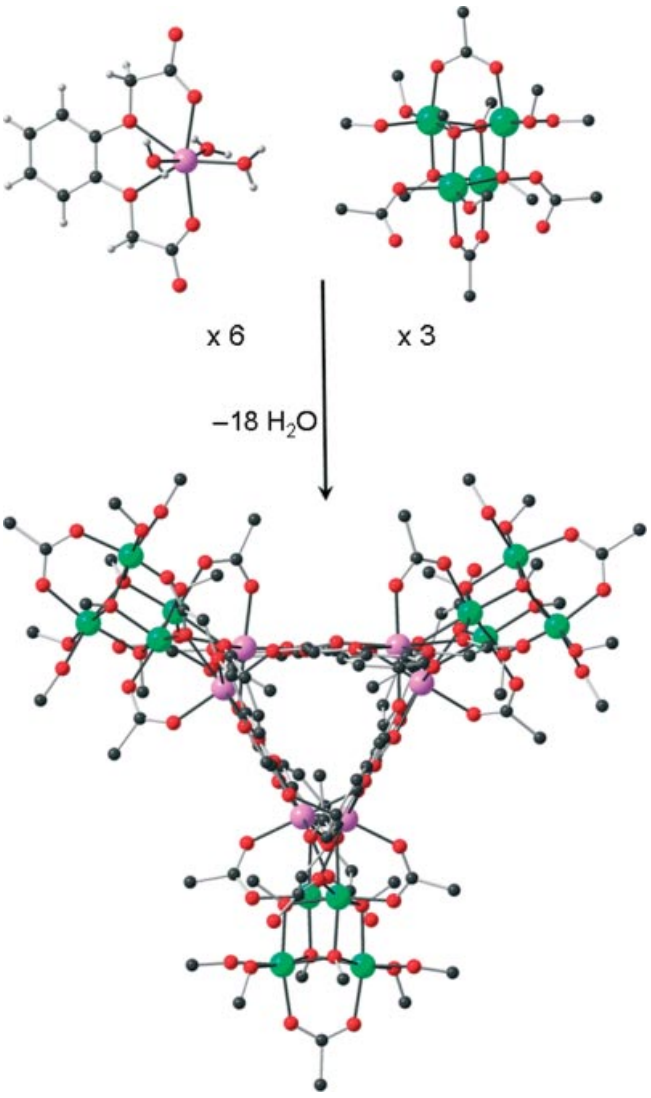


Figure 1. The self-assembly of six $Mn^{II}(bdoa)(H_2O)_3$ building blocks and three $[Ni_4(O_2CMe)_4(OMe)_4(MeOH)_4]$ cubanes to form the $[Ni_{12}Mn_6]$ cluster. The bottom picture shows the structure of **2**, viewed down the molecular threefold axis.

round a central, slightly twisted, trigonal-prismatic $\{Mn_6(bdoa)_6(\mu\text{-}O_2CMe)_3\}$ core, and the triangular faces correspond to two trinuclear units in which each Mn(bdoa) centre is bridged, through an outer, non-chelating $bdoa^{2-}$ carboxylate oxygen atom, to the next manganese atom in a cyclic fashion. The resulting $\{Mn_3(bdoa)_3\}$ triangles are linked by three *anti-anti*-bridging acetate ligands to form the prism, which has an idealised $D_3$ (32) molecular symmetry. The pentagonal-bipyramidal coordination geometry of the $Mn^{II}$ centres in precursor **1** (Figure 1, top) has been preserved during the self-assembly process. As hoped, the three *mer* terminal water ligands have been substituted and replaced by oxygen atoms from two acetate ligands and one carboxylate oxygen atom from another precursor unit. In the structure of **2**, each of the three acetate ligands that link the triangles together is incorporated into and is thus also structurally part of each of the $[Ni_4(O_2CMe)_4(OMe)_4(MeOH)_4]$ cubane structures. They are oriented such that their methyl groups point towards the centre of the core and bridge the two $Ni^{II}$ centres of one face of the cubane in a *syn*,*syn* coordination mode. Another acetate ligand bridges across the opposite face of the cubane in the same fashion and the remaining two acetates provide further links between the cubane and the Mn core. The $\mu_3$-methoxy ligands bridge three Ni centres rather unsymmetrically, and for each ligand, the three Ni–O–Ni angles fall in the ranges 89.3–91.5°, 96.3–97.5° and 99.6–101.8°; the smallest angle refers to an acetate-bridged Ni···Ni edge. All Ni centres are six coordinate, and the coordination spheres of the outer Ni centres are completed by two further methanol ligands on each centre. Conceptually, compound **2** is the combination of three neutral $Ni^{II}$ cubanes and six neutral $Mn^{II}$ precursors, which results in a neutral molecular framework.

Figure 2 shows the attachment of the cubanes onto the $Mn_6$ core in detail. As well as the links involving ligand oxygen atoms mentioned above, in which each Mn···Ni linkage involves a pair of oxygen bridges with Mn–O–Ni angles in the range 96.5–99.0°, further stabilisation of the overall structure is provided by rather strong hydrogen bonds between the methanol ligands on the cubanes and the carboxylate oxygen atom of the $Mn_6$ core unit. Complex **2** can be likened to a wind-turbine and the three $Ni_4(OMe)_4$ cubanes correspond to the blades attached to the $Mn_6(bdoa)_6(\mu\text{-}O_2CMe)_3$ core that acts as the spindle (Figure 1 bottom).

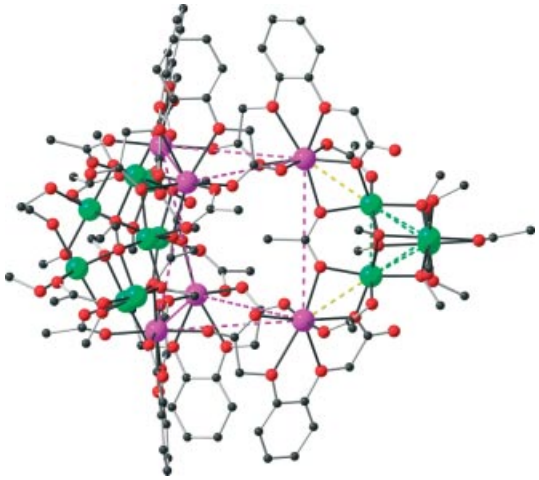

Figure 2. The linkage of the $Ni_4Mn_2$ units to the $\{Mn_6(bdoa)_6(O_2CMe)_3\}$ core in **2**; the magnetic interaction pathways are highlighted by dashed lines and the triangular prismatic framework in pink.

Metal-cubane complexes, which have four metal ions and four $\mu_3$-bridging atoms alternately aligned at the vertices of the cube, often have high-spin ground states because of the orthogonality of the magnetic orbitals. The Ni–O–Ni angles and Ni–Ni distances of the $Ni_4(OMe)_4$ portions in complex **2** are very similar to those in previous examples in which all the $Ni^{II}$ couple ferromagnetically to give an $S_T = 4$ spin ground state.[6] To the best of our knowledge, **2** is the first cluster compound that contains more than one such tetranuclear Ni cubane complex in which the cubane units are

 © 2006 Wiley-VCH Verlag GmbH & Co. KGaA, Weinheim 

well-separated but linked through a magnetically active structure. The magnetic properties of **2** were therefore investigated.

The temperature dependence of the magnetic susceptibility of **2**·21$CH_3OH$ was measured between 1.8 and 300 K at H = 1000 Oe (Figure 3). The $\chi T$ value at room temperature is 42.3 $cm^3 K mol^{-1}$, which is in very good agreement with the spin-only value of twelve $S = 1$ $Ni^{II}$ and six $S = 5/2$ $Mn^{II}$ metal ions (42.25 $cm^3 K mol^{-1}$ with $g = 2$). Upon decreasing the temperature, the slight increase followed by a decrease in the $\chi T$ product reveals the presence of competing magnetic interactions. The maximum value of 44.6 $cm^3$ K $mol^{-1}$ for $\chi T$, reached at ca. 12 K, suggests, at a first glance, that **2** has a large-spin ground state. Below 12 K, the $\chi T$ product significantly decreases rapidly, probably as a result of zero-field splitting of the ground state or antiferromagnetic intra-/intercluster interactions.

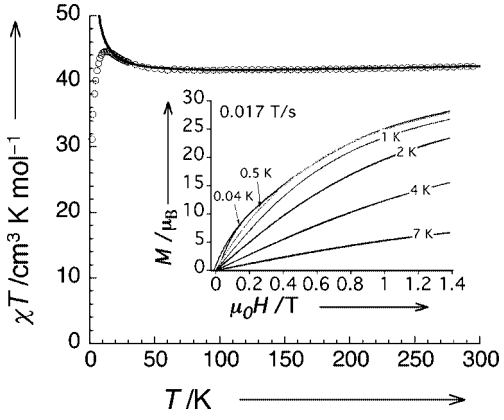


Figure 3. Plot of $\chi T$ vs. $T$ for **2** measured at 1000 Oe. The solid line is the best fit using the model described in the text. Inset: $M$ vs. $H$ data for **2** between 0.04 and 7 K at a sweep field rate of 0.017 T/s.

Unfortunately, the large number of magnetic centres and the presence of multiple magnetic exchange pathways preclude a determination of the individual exchange parameters in **2**. Nevertheless, by considering previously reported magneto–structural analyses of different bridging modes in the literature, two qualitative approaches can be carried out in order to analyse the magnetic properties. The strongest magnetic couplings are most likely located in a $Ni_4Mn_2$ unit (Figure 2) that contains two types of magnetic interactions: $Ni^{II}$–$Ni^{II}$ ($J_{Ni–Ni}$) and $Ni^{II}$–$Mn^{II}$ ($J_{Ni–Mn}$). Since all of the previously reported $Ni_4O_4$ cubane complexes were found to possess an $S_T = 4$ spin ground state with intracubane ferromagnetic Ni–Ni interactions,[6] we can predict that in the $Ni_4Mn_2$ units, $J_{Ni–Ni}$ couplings are also likely to be ferromagnetic. We are not aware of any previous case of $J_{Ni–Mn}$ mediated by a double alkoxo- and a *syn-syn* carboxylate bridge, although there are two reports on weakly ferromagnetic $Ni^{II}$–$Mn^{III}$ interactions through two alkoxo bridges.[7] In **2**, three such $Ni_4Mn_2$ units are linked in a triangular arrangement through *anti-anti* carboxylate bridges between $Mn^{II}$ ions ($J_{Mn–Mn}$) that are known to be very weakly antiferromagnetic.[8]

On the basis of this analysis, two possibilities can be considered, depending on the magnitude of these interactions. Firstly, these interactions could be strong enough to stabilise a well-defined ground state at 12 K, which corresponds to a $\chi T$ value of 44.6 $cm^3 K mol^{-1}$. In this case, the resulting overall ground state ($S_T$) of **2** is obtained by considering an antiferromagnetically coupled triangle of $Ni_4Mn_2$ units. In other words, $S_T$ corresponds to the spin ground state of one $Ni_4Mn_2$ unit. In order to reproduce the experimental $\chi T$ value at low temperature, the only possibility is to have ferromagnetic $J_{Ni–Mn}$ couplings, which leads to an $S_T = 9$ $Ni_4Mn_2$ unit and thus $S_T = 9$ for the cluster **2** as a whole, giving a theoretical $\chi T$ value of 45 $cm^3 K mol^{-1}$ (with $g = 2$). Nevertheless, a second hypothesis can be proposed. From the increase in the $\chi T$ product, it is clear that the ferromagnetic interactions are dominant, but the other exchanges could be very weak and only experimentally observable below 12 K with the decrease in the $\chi T$ product. In this case, the magnetic behaviour of **2** should be described at a first approximation by the magnetism of three isolated $Ni_4$ cubanes in addition to the Curie contributions from the six Mn metal ions. By using an isotropic Heisenberg model and the same $J_{Ni–Ni}$ value between the Ni spins,[9] the magnetic susceptibility was perfectly reproduced down to 15 K[10] and leads to $J_{Ni–Ni}/k_B = +0.99(1)$ K and $g = 2.19(1)$ (solid line Figure 3). Hence, both hypotheses might be relevant even if the usually weak antiferromagnetic $J_{Mn–Mn}$ interactions are in favour of the second one. $M$ vs. $H$ measurements were performed on powdered crystalline samples in fields of up to 7 T at 1.8 K. Even at 7 T, the magnetization is not completely saturated, and reaches 42 $\mu_B$. This value is much larger than expected for a well-defined $S_T = 9$ spin ground state. On the other hand, this result is not surprising as a high-nuclearity complex such as **2**, particularly one in which many of the magnetic interactions are likely to be weak, as would be the case for our second hypothesis, vide supra, is likely to possess a high density of spin states with small energy gaps. So low-lying excited states, including those of greater $S$ value (for example, an $S = 27$ spin state where the spins of the three $Ni_4Mn_2$ units are aligned parallel), can be populated under an applied field.[11]

Since some $Ni_4$ cubane complexes have either been found to be or suspected to be SMMs,[6c,6d] magnetization measurements were made on **2** at low temperatures by using a microSQUID. Measurements performed at different angles of the applied field with respect to the molecule showed no significant differences. A typical measurement at several temperatures is presented in the inset of Figure 3. Only very small hysteresis effects were observed below 0.3 K in the rather featureless magnetization curves. However, for a cluster with $S_T = 9$ as the ground state, a sharp step in the magnetization at $H = 0$ should be observed at very low temperature (0.04 K). The absence of such a step thus confirms the second hypothesis given above and suggests that, at 0.04 K, **2** possesses a small spin ground state. Moreover, the absence of significant anisotropy in the $M$ vs. $H$ data is indicative of rather low anisotropy within the cluster.

In summary, a new building block, $Mn^{II}(bdoa)(H_2O)_3$, has been successfully incorporated into the framework of a new heterometallic cluster, [$Ni_{12}Mn_6(bdoa)_6(O_2CMe)_{12}(\mu_3$-

 © 2006 Wiley-VCH Verlag GmbH & Co. KGaA, Weinheim 

$OMe)_{12}(MeOH)_{12}]\cdot 21MeOH$, which suggests that $Mn^{II}(bdoa)(H_2O)_3$ is a useful precursor for the construction of heterometallic assembles in a rational manner and thus is a potential candidate for the synthesis of new SMMs. A further attractive feature of this strategy is that it should be possible to decorate the $M_6(bdoa)_6(O_2CMe)_3$ frame with different metal cube units, allowing us to probe the effect on magnetic interactions between metal cubes with high-spin ground states and different transition-metal ions. Attempts to synthesize new heterometallic compounds with this precursor are underway.

## Experimental Section

Reaction of **1** (prepared following a reported method[5a]) (0.2 mmol) and $Ni(OAc)_2\cdot 3H_2O$ (0.4 mmol) in wet methanol (15 mL) gave a light-green solution, which was filtered and layered with diethyl ether (10 mL). Green plates of **2** were collected in high yield (100 mg, 70%) by filtration after 1 week. $C_{128}H_{248}Mn_6Ni_{12}O_{104}$ (4486.44): calcd. C 34.25, H 5.53; found: C 33.89, H 5.21.

**Crystal Structural Data for 2:** $C_{129}H_{252}Mn_6Ni_{12}O_{105}$, $F_W$ = 4517.47 g mol$^{-1}$; monoclinic, $P2_1/c$, $a$ = 20.4004(11), $b$ = 20.0722(9), $c$ = 48.307(3) Å, $\beta$ = 94.067(5)°, $U$ = 19730.9(18) Å$^3$, $Z$ = 4, $T$ = 150 K, $\rho_{calcd.}$ = 1.521 Mg m$^{-3}$, $\rho$(Mo-$K_\alpha$) = 1.582 mm$^{-1}$, $F$(000) = 9408; pale-green plate 0.21 × 0.17 × 0.03 mm, Stoe IPDS-II area detector diffractometer with graphite-monochromated Mo-$K_\alpha$ radiation; 98171 data measured and corrected for absorption, 33821 unique. $R_{int}$ = 0.1378, $2\theta_{max}$ = 50°, $wR_2$ = 0.2248, $S$ = 0.966 (all data), $R_1$ = 0.0942 [13949 reflections with $I \geq 2\sigma(I)$], 2166 parameters, residual electron density +0.72/–0.61 e Å$^{-3}$; structure solution (direct methods) and full-matrix least-squares refinement with SHELXTL;[12] anisotropic refinement for all non-H atoms in the cluster and one lattice methanol, C and O of remaining methanol groups isotropic, hydrogen atoms in calculated position except for OH of coordinated methanol groups. Most of the lattice methanol groups were disordered; solvent-accessible voids remained in the structure, and the data were corrected using the *squeeze* option in PLATON,[13] which indicated the presence of an additional lattice methanol per cluster.

CCDC-295080 contains the supplementary crystallographic data for this paper. These data can be obtained free of charge from The Cambridge Crystallographic Data Centre via www.ccdc.cam.ac.uk/data_request/cif.

**Supporting Information** (see footnote on the first page of this article): MicroSQUID data is available.

## Acknowledgments

G. W. wishes to thank DAAD for providing a scholarship (Oct. 2004–Oct. 2006, Section 423). This work was supported by the D.F.G. (SPP 1137 and the Center for Functional Nanostructures), QuEMolNa (MRTN-CT2003-504880), CNRS, the University of Bordeaux 1, the Conseil Régional d'Aquitaine and MAGMANet (NMP3-CT-2005-515767), and the National Science Foundation of China (Grants 20571030 and 20531030).

[1] a) G. Christou, D. Gatteschi, D. N. Hendrickson, R. Sessoli, *MRS Bull.* **2000**, *25*, 66–71; b) D. Gatteschi, R. Sessoli, *Angew. Chem. Int. Ed.* **2003**, *42*, 268–297.

[2] a) J. J. Sokol, A. G. Hee, J. R. Long, *J. Am. Chem. Soc.* **2002**, *124*, 7656–7657; b) C. M. Zaleski, E. C. Depperman, J. W. Kampf, M. L. Kirk, V. L. Pecoraro, *Angew. Chem. Int. Ed.* **2004**, *43*, 3912–3914; c) A. Mishra, W. Wernsdorfer, K. A. Abboud, G. Christou, *J. Am. Chem. Soc.* **2004**, *126*, 15648–15649; d) H. Oshio, M. Nihei, S. Koizumi, T. Shiga, H. Nojiri, M. Nakano, N. Shirakawa, M. Akatsu, *J. Am. Chem. Soc.* **2005**, *127*, 4568–4569; e) H. Miyasaka, T. Nezu, K. Sugimoto, K. Sugiura, M. Yamashita, R. Clérac, *Chem. Eur. J.* **2005**, *11*, 1592–1602.

[3] a) Y. Pei, O. Kahn, J. Sletten, *J. Am. Chem. Soc.* **1986**, *108*, 3142–3145; b) K. R. Dunbar, R. A. Heintz, *Prog. Inorg. Chem.* **1997**, *45*, 283–391; c) M. Verdaguer, A. Bleuzen, V. Marvaud, J. Vaissermann, M. Seuleiman, C. Desplanches, A. Scuiller, C. Train, R. Garde, G. Gelly, C. Lomenech, I. Rosenman, P. Veillet, C. Cartier dit Moulin, F. Villain, *Coord. Chem. Rev.* **1999**, *190*, 1023–1047; d) V. Marvaud, C. Decroix, A. Scuiller, C. Guyard-Duhayon, J. Vaissermann, F. Gonnet, M. Verdaguer, *Chem. Eur. J.* **2003**, *9*, 1677–1691; V. Marvaud, C. Decroix, A. Scuiller, C. Guyard-Duhayon, J. Vaissermann, F. Gonnet, M. Verdaguer, *Chem. Eur. J.* **2003**, *9*, 1692–1705; e) S. Noro, H. Miyasaka, S. Kitagawa, T. Wada, T. Okubo, M. Yamashita, T. Mitani, *Inorg. Chem.* **2005**, *44*, 133–146; f) L. M. C. Beltran, J. R. Long, *Acc. Chem. Res.* **2005**, *38*, 325–334; g) T. E. Vos, J. S. Miller, *Angew. Chem. Int. Ed.* **2005**, *44*, 2416–2419.

[4] a) O. M. Yaghi, H. Li, C. Davis, D. Richardson, T. L. Groy, *Acc. Chem. Res.* **1998**, *31*, 474–484; b) M. Eddaoudi, D. Moler, H. Li, T. M. Reineke, M. O'Keeffe, O. M. Yaghi, *Acc. Chem. Res.* **2001**, *34*, 319–330; c) M. Eddaoudi, J. Kim, J. B. Wachter, H. K. Chae, M. O'Keeffe, O. M. Yaghi, *J. Am. Chem. Soc.* **2001**, *123*, 4368–4369; d) H. K. Chae, J. Kim, O. Delgado Friedrichs, M. O'Keeffe, O. M. Yaghi, *Angew. Chem. Int. Ed.* **2003**, *42*, 3907–3909; e) N. Rosi, J. Kim, B. Chen, M. Eddaoudi, M. O'Keeffe, O. M. Yaghi, *J. Am. Chem. Soc.* **2005**, *127*, 1504–1518.

[5] a) M. McCann, R. M. T. Casey, M. Devereux, M. Curran, C. Cardin, A. Todd, *Polyhedron* **1996**, *15*, 2117–2120; b) G. Smith, E. J. O'Reilly, C. H. L. Kennard, *Polyhedron* **1987**, *6*, 871–879.

[6] a) J. A. Barnes, A. P. Ginsberg, R. I. Kaplan, C. E. Kirkwood, R. L. Martin, R. C. Sherwood, *Inorg. Chem.* **1971**, *10*, 240–246; b) M. A. Halcrow, J. Sun, J. C. Huffman, G. Christou, *Inorg. Chem.* **1995**, *34*, 4167–4177; c) E.-C. Yang, W. Wernsdorfer, S. Hill, R. S. Edwards, M. Nakano, S. Maccagnano, L. N. Zakharov, A. L. Rheingold, G. Christou, D. N. Hendrickson, *Polyhedron* **2003**, *22*, 1727–1733; d) G. Chaboussant, R. Basler, H.-U. Güdel, S. Ochsenbein, A. Parkin, S. Parsons, G. Rajaraman, A. Sieber, A. A. Smith, G. A. Timco, R. E. P. Winpenny, *Dalton Trans.* **2004**, 2758–2766.

[7] a) C. J. O'Connor, D. P. Freyberg, E. Sinn, *Inorg. Chem.* **1979**, *18*, 1077–1088; b) I. M. Mbomekalle, B. Keita, M. Nierlich, U. Kortz, P. Berthet, L. Nadjo, *Inorg. Chem.* **2003**, *42*, 5143–5152.

[8] M. J. Baldwin, J. F. Kramf, M. L. Kirk, V. L. Pecoraro, *Inorg. Chem.* **1995**, *34*, 5252–5260.

[9] J. A. Bertrand, A. P. Ginsberg, R. I. Kaplan, C. E. Kirkwood, R. L. Martin, R. C. Sherwood, *Inorg. Chem.* **1971**, *10*, 240.

[10] With the following spin Hamiltonian for the $Ni_4$ unit: $H = 2J\{S_1\cdot S_2 + S_3\cdot S_4 + S_1\cdot S_3 + S_1\cdot S_4 + S_2\cdot S_3 + S_2\cdot S_4\}$.

[11] a) C. Boskovic, W. Wernsdorfer, K. Folting, J. C. Huffman, D. N. Hendrickson, G. Christou, *Inorg. Chem.* **2002**, *41*, 5107–5118; b) M. Soler, W. Wernsdorfer, K. Folting, M. Pink, G. Christou, *J. Am. Chem. Soc.* **2004**, *126*, 2156–2165.

[12] G. M. Sheldrick, *SHELXTL 5.1*, Bruker AXS Inc., 6300 Enterpise Lane, Madison WI 53719–1173, USA, **1997**.

[13] A. L. Spek, *PLATON – A Multipurpose Crystallographic Tool*, Utrecht University, Utrecht, The Netherlands, **2002**.

Received: January 19, 2006
Published Online: April 4, 2006

 © 2006 Wiley-VCH Verlag GmbH & Co. KGaA, Weinheim 

DOI: 10.1002/ejic.200501121

# Rational Design and Control of the Dimensions of Channels in Three-Dimensional, Porous Metal-Organic Frameworks Constructed with Predesigned Hexagonal Layers and Pillars

**Cui-Jin Li,[a] Sheng Hu,[a] Wei Li,[b] Chi-Keung Lam,[a] Yan-Zhen Zheng,[a] and Ming-Liang Tong*[a]**

**Keywords:** Cobalt / Microporous / MOFs / Imidazole-4,5-dicarboxylate / Pillar / Magnetism

New three-dimensional, microporous metal-organic frameworks exhibiting reversible water adsorption, constructed from hexagonal $[Co_3(imda)_2]$ layers and *N*,*N*′-pillars, in which the dimensions of the channels are rationally adjustable by varying the lengths of pillars, have been designed, hydrothermally synthesized, and characterized.
(© Wiley-VCH Verlag GmbH & Co. KGaA, 69451 Weinheim, Germany, 2006)

## Introduction

Pillared metal-organic framework (MOF) structures, analogous to natural clays and zeolites, are potentially important for applications in adsorption, separation and catalysis.[1,2] Although many attempts have been made to prepare functionalized pillared materials through cross-linking metal-phosphate, metal-phosphonate, or metal-sulfonate layers,[1a] these structures are built upon closed-window layers and pillars.[1,2] Contrasting the metal-phosphate, -phosphonate or -sulfonate systems, we have, with the aid of crystal engineering, been recently investigating rational synthetic strategies towards designed assembly of microporous MOFs constructed from the cationic layers with "open windows" and anionic linear dicarboxylates as pillars.[3] The advantage of this synthetic method promises not only to produce a wide variety of porous MOF materials with controlled channel sizes but also to mediate their chemical behavior by the decoration of diverse functional groups as part of the pillars. Recently, imidazole-4,5-dicarboxylic acid ($imdaH_3$) has been used as a versatile ligand to construct some intriguing porous MOFs, such as the molecular square[4a] and cube[4b,4c] in $Na_2[Co_4(imda)_4(2,2'\text{-bpy})]$ and $[Ni_8(imdaH)_{12}]^{8-}$, respectively. Among the coordination modes of the $imda^{3-}$ ligand in the reported complexes, the most remarkable one is the triangular arrangement of the three metal ions around $imda^{3-}$ (Scheme 1), which implies that it can be employed as a module in the construction of hexagonal layers by sharing the corners of the trigonal subunit $[M_3(imda)_2]$. In this communication, we report a strategy for pillaring the hexagonal $[M_3(imda)_2]$ layers into three 3D, porous MOF solids with controlled channel sizes (Scheme 2): $[Co_3(imda)_2(pyz)_3]\cdot 8H_2O$ (**1**), $[Co_3(imda)_2(4,4'\text{-bpy})_3]\cdot 4,4'\text{-bpy}\cdot 8H_2O$ (**2**), and $[Co_3(imda)_2(2,5\text{-bptz})_3]\cdot 2,5\text{-bptz}\cdot 9H_2O$ (**3**) [pyz = pyrazine, 4,4′-bpy = 4,4′-bipyridine, 2,5-bptz = 2,5-bis(pyrid-4-yl)-1,3,4-thiadiazole].

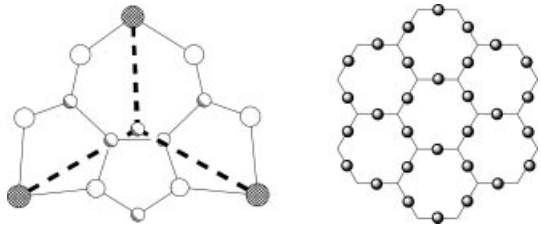

Scheme 1. Predesigned hexagonal layer constructed from the 3-connected 4,5-imda ligand.

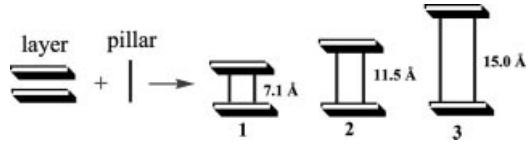


Scheme 2. A strategy for design and control of the channels in **1**–**3**.

## Results and Discussion

Hydrothermal reactions of $CoCl_2\cdot 6H_2O$, $imdaH_3$, NaOH, and different *N*,*N*′-pillars (pyz, 4,4′-bpy, or 2,5-bptz) in a mol ratio of 1.5:1:3:1.5 generate crystals of **1**–**3**.

[a] State Key Laboratory of Optoelectronic Materials and Technologies, Institute of Optoelectronic and Functional Composite Materials & School of Chemistry and Chemical Engineering, Sun Yat-Sen University,
Guangzhou 510275, China
Fax: +86-20-8411-2245
E-mail: tongml@mail.sysu.edu.cn
[b] Department of Chemistry, Hanshan Teacher's College, Chaozhou, Guangdong 521041, China
Supporting information for this article is available on the WWW under http://www.eurjic.org or from the author.

 © 2006 Wiley-VCH Verlag GmbH & Co. KGaA, Weinheim 

Single-crystal X-ray analysis has revealed that **1** crystallizes in the hexagonal space group *P6/mmm*. The $Co^{II}$ ions occupy Wyckoff position 3(*f*) with site symmetry *mmm*. Notably, the ideal molecular symmetries of the pyz ligand ($D_{2h}$) and the imda trianion ($C_{2v}$) are retained in the crystal structure, but the imda trianion exhibits a threefold disorder about the $\bar{6}$-axis (Figure S1). The $Co^{II}$ ions are located in two different distorted octahedral coordination environments, $[CoO_2N_4]$ or $[CoO_4N_2]$ (Figure 1a). The coordination sphere is formed by four N atoms (two from pyz and two from imidazolate) and two carboxylato O atoms, or by two pyridyl N atoms and four carboxylato O atoms [Co–$N_{imda}$ = 1.955(13), Co–$N_{bpy}$ = 2.162(12), Co–O = 2.193(15) Å]. Each imda ligand bridges three Co atoms [Co···Co separations of 6.091(4) Å] to generate neutral and essentially planar $[Co_3(imda)_2]$ layers with (6,3) topology (Figure 2a). For simplicity, one of three possible orientations of $imda^{3-}$ is considered. Each 2D layer consists of two types of hexagonal 24-membered rings: $Co_6$(imidazolato)$_6$ and $Co_6$(carboxylato)$_6$. Interestingly, each $Co_6$(imidazolato)$_6$ ring is surrounded by six $Co_6$(carboxylato)$_6$ rings, while each $Co_6$(carboxylato)$_6$ ring is alternately surrounded by three $Co_6$(imidazolato)$_6$ rings and three $Co_6$(carboxylato)$_6$ rings. A sixfold axis lies across each cavity of the hexagonal layer. It is noteworthy that the hexagonal $[Co_3(imda)_2]$ layers are ideally stacked in an AAA fashion along the *c*-axis and are further pillared by pyz spacers into a non-interpenetrated 3D microporous MOF structure with the effective channel size of 4.7 × 4.7 Å estimated from the van der Waals radii for carbon (1.70 Å), hydrogen (1.20 Å),

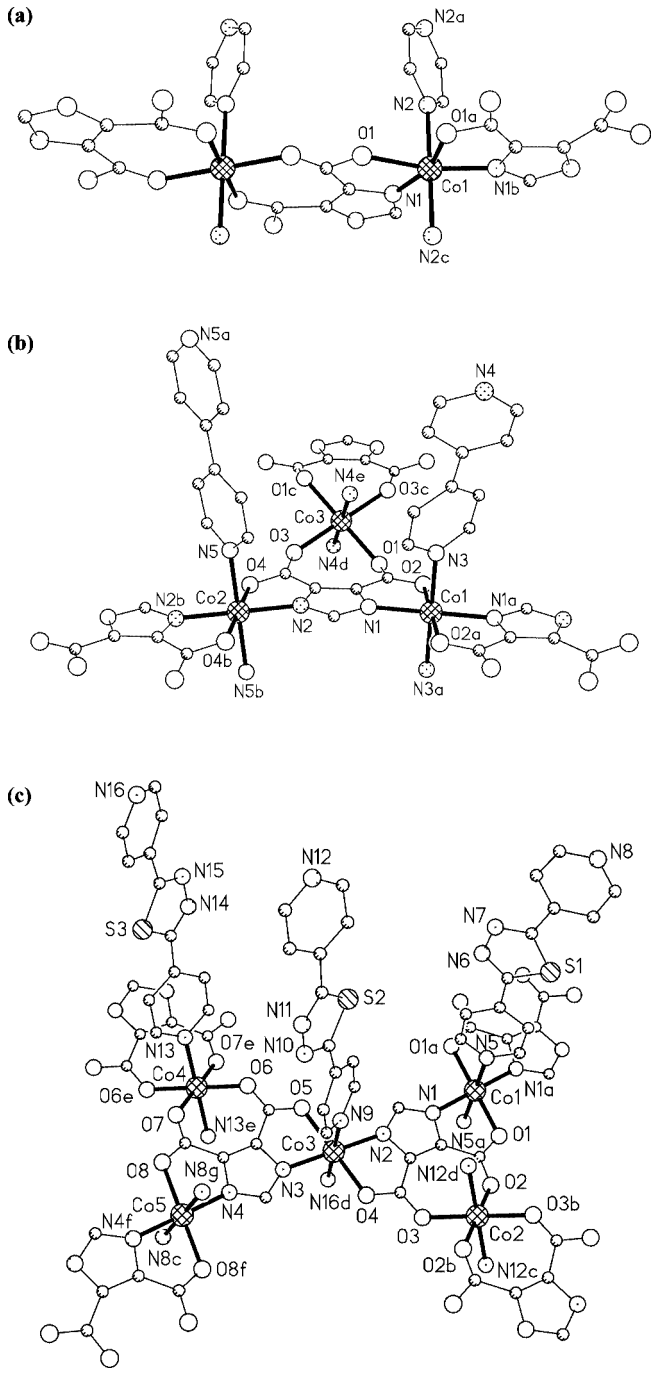


Figure 1. Coordination geometries of the $Co^{2+}$ ions in **1** (a), **2** (b), and **3** (c).

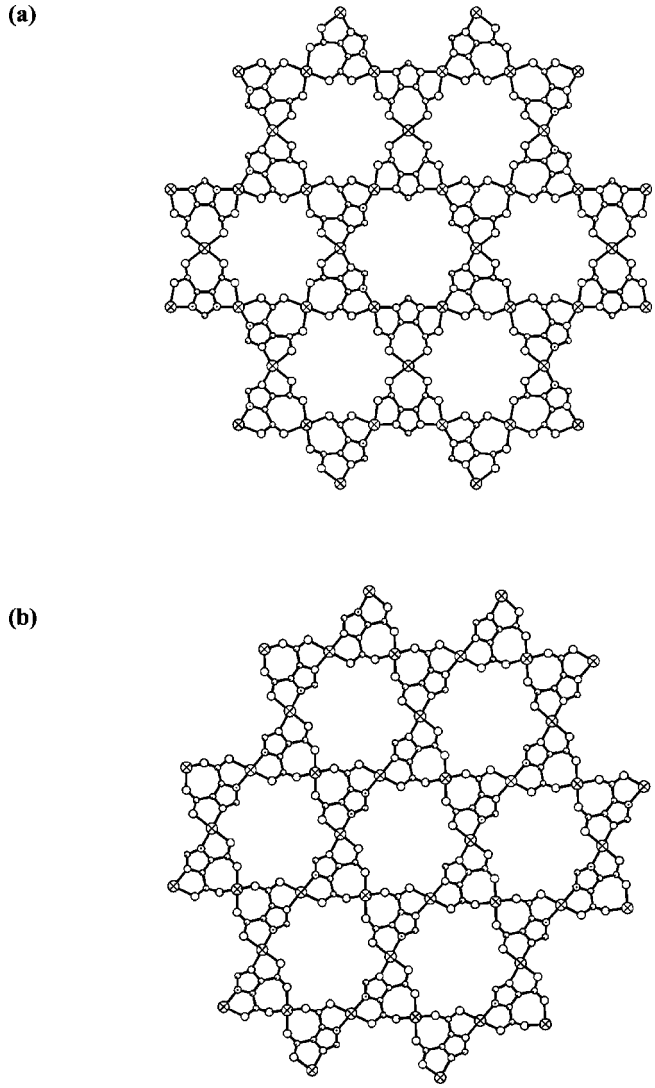


Figure 2. 2D hexagonal layers in **1** (a), and **2** or **3** (b).

 © 2006 Wiley-VCH Verlag GmbH & Co. KGaA, Weinheim 

nitrogen (1.55 Å), and oxygen (1.40 Å) (Figure S2 and Figure 3a). The disordered guest water molecules are located within these channels. An analysis with PLATON[5] suggested that the channels occupy 39.1% of the crystal volume. The network topology can be simplified by considering just the cobalt atoms (represented by a square-planar node) and the tri-connected imda ligands (represented by a triangular node); the bidentate pyz ligands can be represented simply as links between the cobalt nodes. The resulting net, shown in Figure 3b, is a rare 3D (3,4)-connected net with triangular and square-planar nodes in the ratio 2:3. A topological analysis of this net was performed with OLEX.[6] The long topological (O'Keeffe) vertex symbol is $6_2.6_2.6_2.6_2.12_2$ for the Co node and $6_2.6_2.6_2$ for the imda node, giving the short vertex symbol $(6^3)_2(6^4.8.10)_3$. The net is different to other previously identified (3,4)-connected networks.[7]

The porous MOF structures of **2** and **3** are similar to that of **1**. Both of them are built of neutral hexagonal $[Co_3(imda)_2]$ layers and longer 4,4′-bpy or 2,5-bptz pillars. The asymmetric unit of **2** contains one and a half 4,4′-bpy ligand, one $imda^{3-}$ ion, and three independent $Co^{II}$ ions lying at inversion centers (Figure 1b). Both Co1 and Co2 atoms are similarly in a distorted octahedral $[CoO_2N_4]$ environment, in which the coordination sphere for Co1 or Co2 is formed by two pyridyl N atoms, two imidazolate N atoms, and two carboxylate O atoms [Co–$N_{imda}$ = 2.046(3)–2.048(4), Co–$N_{bpy}$ = 2.172(4)–2.206(3), Co–O = 2.106(3)–2.119(3) Å], while the coordination sphere for Co3 is formed by two pyridyl N atoms and four carboxylato O atoms [Co–N = 2.157(3), Co–O = 2.063(3)–2.066(3) Å]. Each imda ligand bridges three Co atoms with Co···Co separations of 5.7704(5)–6.2939(4) Å. For **3**, the asymmetric unit of the host MOF contains five unique $Co^{II}$ atoms, four (Co1, Co2, Co4, and Co5) of which lie across inversion centers and the other one (Co3) on a general position, two imda ligands which lie on general positions, and three unique 2,5-bptz ligands (Figure 1c). The adjacent intralayer Co···Co distances separated by the imda ligands are 5.8168(9)–6.3064(9) Å.

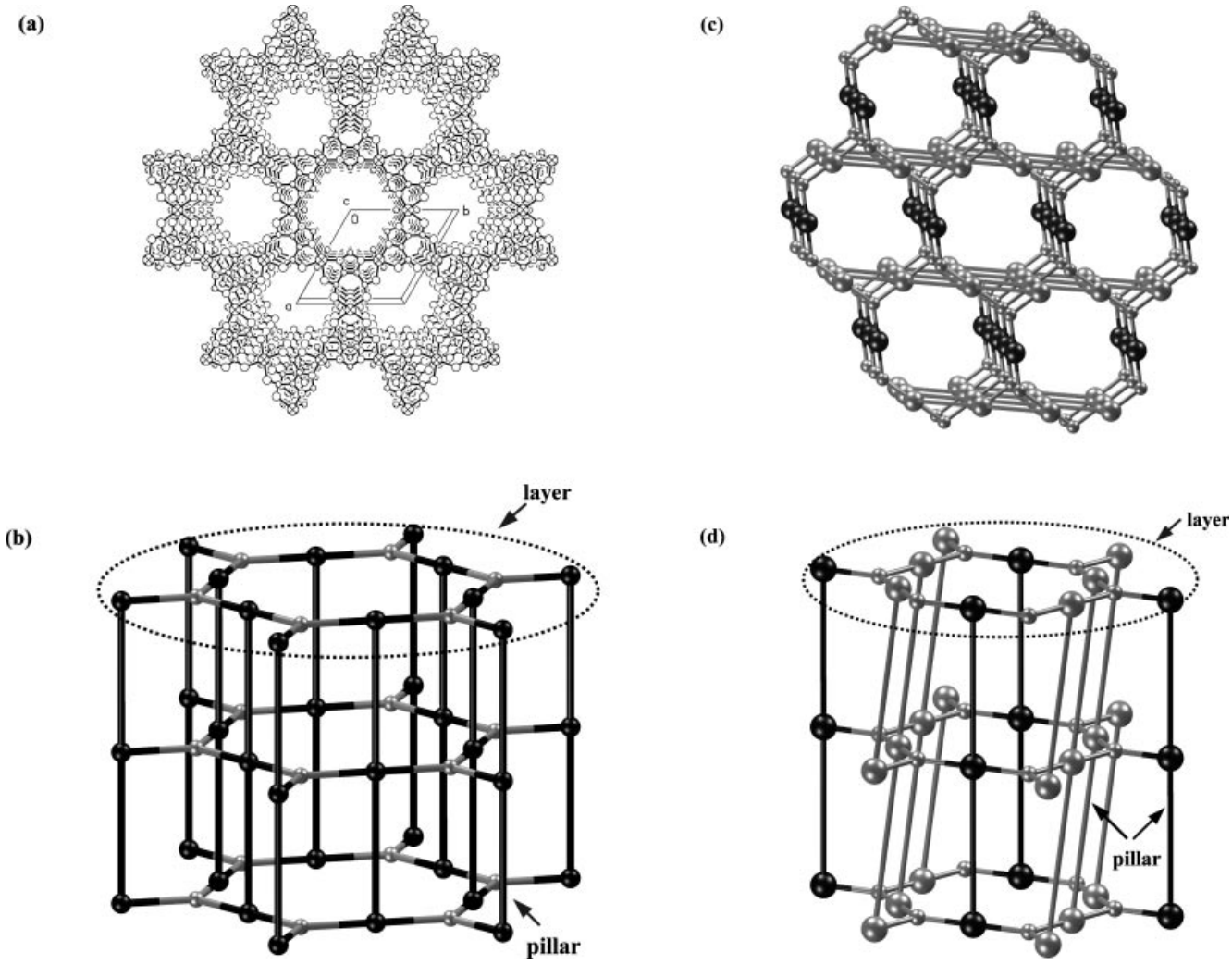


Figure 3. (a) The pillared 3D MOF in **1**. (b) Topological connectivity in **1**. (c) Topological net of the pillared 3D MOF in **2** or **3**. (d) Topological connectivity in **2** or **3**. The big dark grey or black spheres represent cobalt atoms, while the small grey spheres represent the centers of mass of imda ligands. The *N*,*N*′-pillar ligands are represented by interlayer bold lines.

 © 2006 Wiley-VCH Verlag GmbH & Co. KGaA, Weinheim 

In contrast to that in **1**, each 2D hexagonal layer in **2** or **3** consists of only hexagonal $Co_6$(imidazolato)$_2$(carboxylato)$_4$ 24-membered rings (Figure 2b). Adjacent hexagonal layers are stacked in a ABAB fashion and are further pillared by 4,4′-bpy or 2,5-bptz spacers into a non-interpenetrated 3D microporous MOF structure with the effective channel sizes of 4.2×6.2 Å and 4.7×6.5 Å for **2** and **3**, respectively. It should be noted that the network topology of **2** and **3** are identical, but different from that of **1** though the three 3D MOF structures are 3D (3,4)-connected nets with triangular and square-planar nodes in the ratio 2:3. In **1**, all the Co nodes are the same. But in **2** and **3**, only two-thirds of the Co nodes are equivalent (for **2**: Co1 and Co3; for **3**: Co1, Co2, Co4 and Co5). The difference between the two types of nodes can be seen in Figure 3c, d. The long topological (O'Keeffe) vertex symbol is $6_2.6_2.6.6.12_2.12_2$ and $6.6.6.6.10_2$ for the two kinds of Co nodes, and $6.6.6_2$ for the imda node, giving the short vertex symbol $(6^3)_2(6^4.8^2)_2$-$(6^4.10^2)$. An analysis with PLATON[5] suggested that the channels occupy 38.8% and 44.6% of the crystal volume for **2** and **3**, respectively. The guest 4,4′-bpy/2,5-bptz and water molecules are located within these channels. The calculated crystal densities (in the absence of guests) of 1.172 g cm$^{-3}$ and 1.09 g cm$^{-3}$ are comparable to those found for some porous MOF materials with low density.[8]

To examine the thermal stability of these porous networks, thermal gravimetric (TG) analyses and powder X-ray diffraction (XRD) measurements were carried out. The thermal decomposition behaviors of **1**, **2**, and **3** are much alike. For **1**, the first weight loss of 15.7% from 20 to 180 °C is in accordance with the loss of eight lattice water molecules per $Co_3$ (calculated: 16.6%), while the release of the pyz and imda components occurs at ca. 250 °C and 360 °C in two separate steps (Figure S4) to yield the residue $Co_3O_4$ at ca. 410 °C (found: 28.6%; calculated: 27.8%). The TG curve of **2** indicate the release of all lattice water molecules before 106 °C (found: 11.3%; calc: 11.5%). At 265 °C, the solvated 4,4′-bpy and coordinated ligands start to be released (Figure 4). No chemical decomposition was observed between 106 and 265 °C. The TG curves of the dehydrated and rehydrated samples of **2** show that it exhibits reversible water adsorption. Powder XRD patterns of **2** and dehydrated samples of **2** are nearly identical, indicating that the initial framework is retained after the lattice water molecules are removed by heating at 180 °C under vacuum for 8 h. For **3**, the first weight loss of 9.9% from 20 to 120 °C is in accordance with the loss of nine lattice water molecules per Co3 (calculated: 10.1%). No chemical decomposition was observed between 120 and 350 °C (Figure S6). Similar reversible dehydration and rehydration are also found for **1** and **3** (Figures S4–6).

The temperature-dependent magnetic susceptibility, $\chi_M$, of **1**, **2**, and **3** were measured in a 5.0-kOe field (Figure S7). At room temperature, $\chi_M T$ is 8.30, 8.29, and 7.20 cm$^3$ mol$^{-1}$ K per $Co_3$ unit for **1**, **2**, and **3**, respectively, which is significantly higher than the spin-only value (5.63 cm$^3$ mol$^{-1}$ K) expected for three uncoupled $Co^{II}$ ions ($S$ = 3/2), indicating that the orbital contribution is incompletely quenched. Upon cooling, the $\chi_M T$ gradually decreases owing to the contribution of single-ion behavior of high-spin $Co^{II}$ ions and also to antiferromagnetic exchange between the Co centers. The $\chi_M(T)$ in the high-temperature region (30–280 K) can be fit into the Curie–Weiss equation with $C$ = 9.77 cm$^3$ mol$^{-1}$ K and $\theta$ = –53.99 K for **1**, $C$ = 9.69 cm$^3$ mol$^{-1}$ K, and $\theta$ = –46.24 K for **2** and $C$ = 8.48 cm$^3$ mol$^{-1}$ K and $\theta$ = –58.94 K for **3**; these values agree well with those expected for high-spin $Co^{II}$ ions in octahedral sites.[9a] The negative sign of $\theta$ and the decrease of $\chi T$ point to the existence of antiferromagnetic exchange interactions. Spin-orbit coupling most certainly also contributes to this decay.[9a–9c] Detailed magnetic studies and other functions of this porous family are under way.

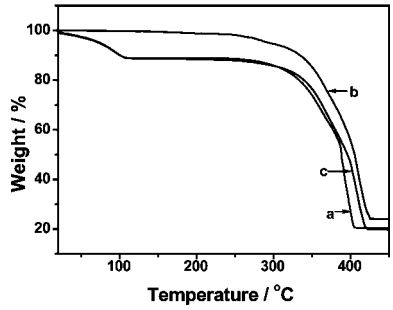


Figure 4. TG data for **2**: (a) as-synthesized sample, (b) dehydrated sample at 180 °C, (c) re-hydrated sample.

In conclusion, we present a new strategy for the generation of novel 3D porous metal-organic framework solids that exhibit reversible water adsorption with predesigned hexagonal [$Co_3$(imda)$_2$] layers and length-controllable $N,N'$-spacers as pillars. They may be good candidates for porous materials owing to their high thermal stability and reversible guest exchange.

## Experimental Section

**X-ray Crystallographic Study:** Diffraction intensities of **1**, **2**, and **3** were collected with a Bruker Apex CCD area-detector diffractometer (Mo-$K_\alpha$, $\lambda$ = 0.71073 Å). Absorption corrections were applied by using the multiscan program SADABS.[10] The structures were solved with direct methods and refined with a full-matrix least-squares technique with the SHELXTL program package.[11]

Crystal and structure-refinement parameters. Compound **1**: $C_{22}H_{30}Co_3N_{10}O_{16}$, $M$ = 867.35, hexagonal, space group *P6/mmm* (No. 191), $a$ = 12.183(1), $c$ = 7.092(1) Å, $V$ = 911.6(2) Å$^3$, $Z$ = 1, $T$ = 123(2) K, $F$(000) = 441, $D_c$ = 1.580 g cm$^{-3}$, $\mu$(Mo-$K_\alpha$) = 1.427 mm$^{-1}$; $R_1$ = 0.0847, $wR_2$ = 0.1687 and GOF = 1.159 for 61 parameters, 307 reflections with $|F_o| \geq 4\sigma(F_o)$. Compound **2**: $C_{50}H_{50}Co_3N_{12}O_{16}$, $M$ = 1251.81, triclinic, space group $P\bar{1}$ (No. 2), $a$ = 11.448(1), $b$ = 11.541(1), $c$ = 11.766(1) Å, $\alpha$ = 65.370(1), $\beta$ = 80.540(1) $\gamma$ = 72.759(1)°, $V$ = 1348.2(2) Å$^3$, $Z$ = 1, $T$ = 123(2) K, $F$(000) = 663, $D_c$ = 1.542 g cm$^{-3}$, $\mu$(Mo-$K_\alpha$) = 0.993 mm$^{-1}$; $R_1$ = 0.0580, $wR_2$ = 0.1552 and GOF = 1.036 for 412 parameters, 4147 reflections with $|F_o| \geq 4\sigma(F_o)$. Compound **3**: $C_{58}H_{52}Co_3N_{20}O_{17}S_4$, $M$ = 1606.23, triclinic, space group $P\bar{1}$ (No. 2), $a$ = 11.791(1), $b$ = 17.050(2), $c$ = 20.795(2) Å, $\alpha$ = 104.726(2), $\beta$ = 106.360(2), $\gamma$ = 103.481(2)°, $V$ = 3664.6(7) Å$^3$, $Z$ = 2, $T$ = 123(2) K, $F$(000) = 1642,

 © 2006 Wiley-VCH Verlag GmbH & Co. KGaA, Weinheim 

$D_c$ = 1.456 g cm$^{-3}$, $\mu$(Mo-$K_\alpha$) = 0.862 mm$^{-1}$; $R_1$ = 0.0834, $wR_2$ = 0.2467 and GOF = 1.029 for 955 parameters, 7210 reflections with $|F_o| \geq 4\sigma(F_o)$. The PLATON SQUEEZE procedure[12] was also used to treat regions of disordered solvent in **2** which could not be sensibly modeled in terms of atomic sites. Their contribution to the diffraction pattern was removed and modified $F_o^2$ written to a new HKL file. The number of electrons thus located, 160.1 per unit cell, is included in the formula, formula weight, calculated density, $\mu$, and $F$(000). This residual electron density was assigned to eight water molecules and a 4,4′-bpy [8 × 10 ($H_2O$) + 1 × 82 (4,4′-bpy) = 162e]. However, the disordered solvents in **1** and **3** could not be subtracted from the corresponding diffraction patterns by the squeeze/bypass procedure because of their disordered host MOF structures.

CCDC-289570 (**1**), CCDC-284833 (**2**) and CCDC-284834 (**3**) contain the supplementary crystallographic data for this paper. These data can be obtained free of charge from The Cambridge Crystallographic Data Centre via www.ccdc.cam.ac.uk/data_request/cif.

**Supporting Information** (see footnote on the first page of this article): X-ray crystallographic files of **1**–**3** (CIF), synthesis, packing plots, TG curves, simulated and experimental powder XRD data, temperature- and field-dependent magnetic susceptibility of **1**–**3**.

## Acknowledgments

We thank Dr. S. R. Batten for his helpful discussions about the topology. This work was supported by the National Science Funds for Distinguished Young Scholars of China (No. 20525102), the NSFC (20471069), the FANEDD of China (200122), and the Scientific and Technological Project of Guangdong Province (04205405).

[1] a) A. Clearfield, Z. Wang, *J. Chem. Soc., Dalton Trans.* **2002**, 2937; b) S. Kitagawa, R. Kitaura, S.-i. Noro, *Angew. Chem. Int. Ed.* **2004**, *43*, 2334; c) B. F. Hoskins, R. Robson, *J. Am. Chem. Soc.* **1990**, *112*, 1546; d) M. Eddaoudi, D. B. Moler, H. Li, B. Chen, T. M. Reineke, M. O'Keeffe, O. M. Yaghi, *Acc. Chem. Res.* **2001**, *34*, 319; e) P. J. Hagrman, D. Hagrman, J. Zubieta, *Angew. Chem. Int. Ed.* **1999**, *38*, 2638; f) C. Janiak, *Dalton Trans.* **2003**, 2781.

[2] a) *Pillared Layered Structures: Current Trends and Applications* (Ed.: I. V. Mitchell), Elsevier, London, **1990**; b) L. Pan, B. S. Finkel, X. Huang, J. Li, *Chem. Commun.* **2001**, 105.

[3] a) S.-L. Zheng, M.-L. Tong, R.-W. Fu, X.-M. Chen, S. W. Ng, *Inorg. Chem.* **2001**, *40*, 3562; b) S.-L. Zheng, M.-L. Tong, X.-M. Chen, *Coord. Chem. Rev.* **2003**, *246*, 185.

[4] a) C.-F. Wang, E.-Q. Gao, Z. He, C.-H. Yan, *Chem. Commun.* **2004**, 720; b) Y. Liu, V. Kravtsov, R. D. Walsh, P. Poddar, H. Srikanth, M. Eddaoudi, *Chem. Commun.* **2004**, 2806; c) R.-Q. Zou, L. Jiang, H. Senoh, N. Takeichia, Q. Xu, *Chem. Commun.* **2005**, 3526; d) T. K. Maji, G. Mostafa, H.-C. Chang, S. Kitagawa, *Chem. Commun.* **2005**, 2436; e) Y.-L. Wang, D.-Q. Yuan, W.-H. Bi, X. Li, X.-J. Li, F. Li, R. Cao, *Cryst. Growth Des.* **2005**; *5*, 1849; f) Y.-Q. Sun, J. Zhang, Y.-M. Chen, G.-Y. Yang, *Angew. Chem. Int. Ed.* **2005**, *44*, 5814; g) W.-G. Lu, C.-Y. Su, T.-B. Lu, L. Jiang, J.-M. Chen, *J. Am. Chem. Soc.* **2006**, *128*, 34; h) W.-G. Lu, L. Jiang, X.-L. Feng, T.-B. Lu, *Cryst. Growth Des.* **2006**, *6*, 564.

[5] A. L. Spek, *PLATON, A Multipurpose Crystallographic Tool*, Utrecht University, Utrecht, The Netherlands, **2003**.

[6] O. V. Dolomanov, A. J. Blake, N. R. Champness, M. Schröder, *J. Appl. Crystallogr.* **2003**, *36*, 1283.

[7] a) B. F. Abrahams, S. R. Batten, H. Hamit, B. F. Hoskins, R. Robson, *Angew. Chem. Int. Ed. Engl.* **1996**, *35*, 1690; b) V. A. Blatov, L. Carlucci, G. Ciani, D. M. Proserpio, *CrystEngComm* **2004**, *6*, 377.

[8] a) O. M. Yaghi, M. O'Keeffe, N. W. Ockwig, H. K. Chae, M. Eddaoudi, J. Kim, *Nature* **2003**, *423*, 705; b) S. Hu, J.-C. Chen, M.-L. Tong, B. Wang, Y.-X. Yan, S. R. Batten, *Angew. Chem. Int. Ed.* **2005**, *44*, 5471.

[9] a) R. L. Carlin, *Magnetochemistry*, Springer, Berlin, **1986**; b) F. E. Mabbs, D. J. Machin, *Magnetism and Transition Metal Complexes*, Chapman and Hall, London, **1973**; c) E. Coronado, M. Drillon, P. R. Nugteren, L. J. De Jongh, D. Beltran, *J. Am. Chem. Soc.* **1988**, *110*, 3907.

[10] G. M. Sheldrick, *SADABS 2.05*, University Göttingen.

[11] *SHELXTL 6.10*, Bruker Analytical Instrumentation, Madison, Wisconsin, USA, **2000**.

[12] a) P. van der Sluis, A. L. Spek, *Acta Crystallogr., Sect. A* **1990**, *46*, 194; b) A. L. Spek, *Acta Crystallogr., Sect. A* **1990**, *46*, C34.

Received: December 19, 2005
Published Online: April 10, 2006

 © 2006 Wiley-VCH Verlag GmbH & Co. KGaA, Weinheim 

DOI: 10.1002/ejic.200501084

# Mesoporous Aluminium Organophosphonates Functionalized with Chiral L-Proline Groups in the Pore

Xin Shi,[a] Jie Yang,[a] and Qihua Yang*[a]

**Keywords:** Chiral / Mesoporous compounds / Aluminium organophosphonates

Mesoporous aluminium organophosphonates with chiral L-proline groups in the pore were synthesized for the first time through surfactant-assisted one-pot co-condensation of $Al(OsBu)_3$ with a mixture of 1-phosphonomethylproline (*S*)-$H_2PO_3CH_2NC_4H_7COOH$ ($H_3PMP$) and phosphoric acid ($H_3PO_4$) [$H_3PMP/(H_3PMP + H_3PO_4)$ = 50, 75, 100 mol-%] under basic conditions in the presence of cetyltrimethylammonium bromide.
(© Wiley-VCH Verlag GmbH & Co. KGaA, 69451 Weinheim, Germany, 2006)

## Introduction

Recently, the interest in the design and fabrication of organic-inorganic materials with high surface area and hierarchically ordered porous structure is growing because of their potential applications in the fields of optics, electronics, membranes, catalysis, biology and etc.[1,2] The periodic mesoporous organosilicas (PMOs) with organic bridging groups in the framework were regarded as one of the recent breakthroughs in the fields of hybrid organic-inorganic mesoporous materials.[3,4] Compared with the silica-based materials, metal organophosphonates are more promising in respect of their unique properties, such as proton conductivity, nonlinear optical effects, electron transfer, topochemical reactivity, and photochromism.[5–7] Inspired by the success of PMOs, a pure mesostructured aluminium organophosphonate (AOPs) containing internal methylene groups was first reported by Kimura in 2003.[8] To the best of our knowledge, only limited types of organic groups (alkyl, alkylene and phenyl) were incorporated in the mesoporous metal organophosphonates,[8–12] however, mesoporous AOPs functionalized with chiral organic groups have not been reported so far.

Amino acids are the principal building blocks of proteins and enzymes. Among them, L-proline is one of the cyclic aliphatic amino acids that is a major component of the protein collagen. Also, L-proline is an efficient catalyst for the asymmetric catalysis and chiral selector for the chiral separation.[13,14] The combination of the mesoporous AOPs with L-proline will be interesting in view of the enzyme adsorption, chiral synthesis etc. Here, we report for the first time the synthesis of mesoporous AOPs containing chiral L-proline groups in the pore by a one-pot synthetic method.

## Results and Discussion

Mesoporous AOPs with different amounts of L-proline were synthesized through the "atrane route" previously reported for the synthesis of aluminium phosphonates and diphosphonates with slight modification.[11] During the synthesis, the pre-hydrolysis of aluminium species is essential for the formation of pure mesoporous AOPs, otherwise pure mesoporous AOPs cannot be obtained. The mesoporous AOPs with different amounts of L-proline in the pore are designated as MAOP-*n*, while *n* (= 50, 75, 100) is the mol-% value of $H_3PMP/(H_3PMP + H_3PO_4)$ in the initial mixture.

The powder XRD patterns of all as-synthesized MAOPs-*n* display a single broad diffraction peak at low diffraction angle, suggesting that these hybrid materials have a "worm-like" mesoporous structure (Figure 1). The TEM images of as-synthesized MAOPs-*n* clearly show the "worm-like" pore arrangement throughout the materials, which is consistent with the XRD results (Figure 2). It is noteworthy to mention that the mesoporous structure could be formed even for MAOP-100, synthesized from 100 mol-% of $H_3PMP$. With the amounts of organophosphonic acid, $H_3PMP$, in the initial mixture increasing, the intensity of the diffraction peak decreased. The XRD patterns of MAOPs-*n* remain almost the same before and after the surfactant extraction, showing that the mesoporous structure of MAOPs-*n* is stable enough to survive during the surfactant removal process. Additionally, the diffraction peaks shift toward lower 2θ angles after removal of the surfactant, which is in agreement with the results of previous reports on mesoporous ALPOs.[11,15,16] All surfactant-extracted MAOP-*n* solids present typical type IV isotherms with H2

[a] State Key Laboratory of Catalysis, Dalian Institute of Chemical Physics, Chinese Academy of Sciences,
Dalian 116023, China
Fax: + 86-411-84694447,
E-mail: yangqh@dicp.ac.cn
Supporting information for this article is available on the WWW under http://www.eurjic.org or from the author.

 © 2006 Wiley-VCH Verlag GmbH & Co. KGaA, Weinheim 

hysteresis loop according to IUPAC classification, characteristic of the mesoporous material with "ink-bottle" pores (see Supporting Information). The BET surface area, the pore volume, and the pore diameter of MAOP-100 are lower than those of MAOP-50 and MAOP-75. The results of XRD and $N_2$ sorption isotherms imply that the mesoporous structure of MAOPs-*n* are disturbed by the incorporation of L-proline groups in the materials. This can be explained by the fact that it is difficult for the monophosphonic acid to construct the mesoporous framework[11] and the steric hindrance resulting from the large L-proline group.

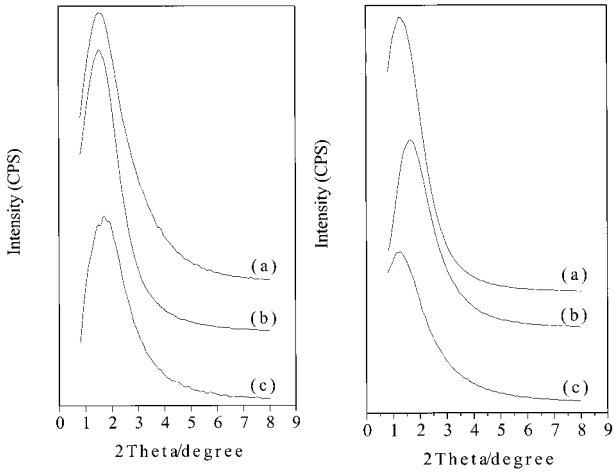


Figure 1. Powder X-ray diffraction patterns of (left) as-synthesized and (right) surfactant-extracted MAOPs-*n*: (a) MAOP-50; (b) MAOP-75; (c) MAOP-100.

The ratio of Al/P for the mesoporous aluminium phosphates varies in the range of 1.0 to 5.5 depending on the synthetic conditions.[17] The ratio of Al/P for MAOPs-*n* is about 3, which is higher than the ideal stoichiometric value of 1 (Table 1). This fact shows that the extra aluminium species participate in the formation of the mesoporous framework. During the synthesis, the reaction rate between the aluminium species and $H_3PMP$ is retarded because of the steric restriction derived from the L-proline group. Also, before the addition of $H_3PMP/H_3PO_4$, the aluminium precursor was allowed to pre-hydrolyze. As a result, the interaction of the hydrolyzed aluminium species with $H_3PMP$ and the condensation between the hydrolyzed aluminium species occurred simultaneously. The excess aluminium species that could be incorporated in the mesoporous framework of MAOPs-*n* in a controllable way can act as a stabilizer in the pore wall to stabilize the mesoporous framework of MAOPs-*n*.

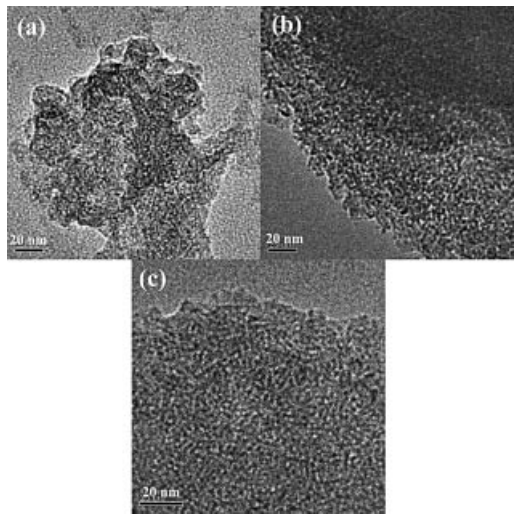


Figure 2. TEM images of as-synthesized MAOPs-*n*: (a) MAOP-50; (b) MAOP-75; (c) MAOP-100.

$^{31}P$ MAS NMR spectra of the surfactant-extracted MAOPs-*n* show that the organophosphonate groups are actually incorporated in the materials (Figure 3). MAOP-100 displays a broad peak centered at δ = 2 ppm with a shoulder at δ = 6 ppm, which could be assigned to P atoms of $RPO_3^{2-}$ and $RPO_3H^-$, respectively. The presence of $RPO_3H^-$ in MAOP-100 is also supported by the FT-IR. The stretching vibration of the P–OH band was clearly observed at 950 $cm^{-1}$ (see Supporting Information). A broad signal centered at δ = –12 ppm was observed in $^{31}P$ MAS NMR spectra of MAOP-50 and MAOP-75. After deconvolution by computer simulation, the broad peak was divided into two singals. The signal at δ = –12 ppm is attributed to the inorganic phosphorus species according to ref.[18], while the singal at δ = 2 ppm is derived from the organic phosphorus species, $RPO_3^{2-}$. From the ratio of $P_{inorg}/P_{org}$ (calculated from the peak area, Table 1), we could see that only 10 and 22 mol-% of $H_3PMP$ could be incorporated in MAOP-50 and MAOP-75, respectively. This is probably due to the severe steric hindrance of $H_3PMP$.

$^{13}C$ MAS NMR spectrum of MAOP-100 also confirms that L-proline groups have been incorporated in the material (Figure 4). The signals at δ = 174 and 179 ppm are associated with the C atoms of $CO_2H$ and $CO^{2-}$, respectively. The resonance at $\delta$ = 72 ppm can be assigned to the C atom of

Table 1. Physicochemical data for surfactant-extracted MAOPs-*n*.[a]

| Sample | $H_3PMP$ in the solution [mol%] | $H_3PMP$ in the solid[b] [mol%] | *d*(100) [nm] | Al/P[c] | $S_{BET}$ [$m^2g^{-1}$] | Pore volume [$cm^3g^{-1}$] | BJH pore diameter[d] [nm] |
|---|---|---|---|---|---|---|---|
| MAOP-50 | 50 | 10 | 6.7 (5.8) | 3.22 | 373 | 0.43 | 3.5 |
| MAOP-75 | 75 | 22 | 5.3 (5.1) | 3.41 | 422 | 0.54 | 3.7 |
| MAOP-100 | 100 | 100 | 6.9 (5.5) | 2.78 | 215 | 0.13 | 2.9 |

[a] Data in parentheses are for the as-synthesized materials. [b] Based on $^{31}P$ MAS NMR spectroscopy. [c] Calculated from ICP analysis. [d] Calculated by using the BJH model on the adsorption branch of the isotherm.

 © 2006 Wiley-VCH Verlag GmbH & Co. KGaA, Weinheim 

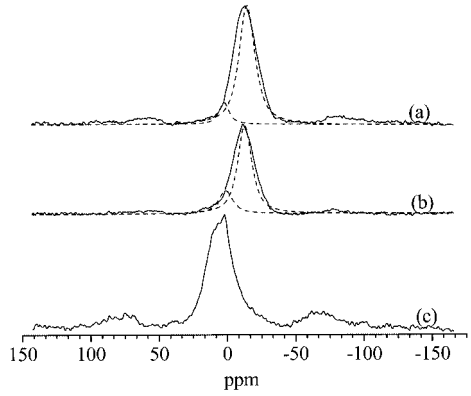


Figure 3. $^{31}$P MAS NMR spectra of surfactant-extracted MAOPs-*n*: (a) MAOP-50; (b) MAOP-75; (c) MAOP-100.

the CH group connected with the carboxy group, while the signal at $\delta$ = 56 ppm is attributed to the C atom of $CH_2$ group connected with the phosphonic group. The signals related to the $CH_2$ group of the pyrrolidine ring are observed at $\delta$ = 23, 29 and 59 ppm. The $^{13}$C MAS NMR spectrum shows that organophosphonic acid, $H_3PMP$, retains its integrity in the mesoporous solid. In addition, the peak at $\delta \approx 15$ ppm, associated with the C atom of the terminal $CH_3$ group of the surfactant CTAB, cannot be observed in the spectrum, which illuminates that the surfactant is almost completely removed using the extraction method.

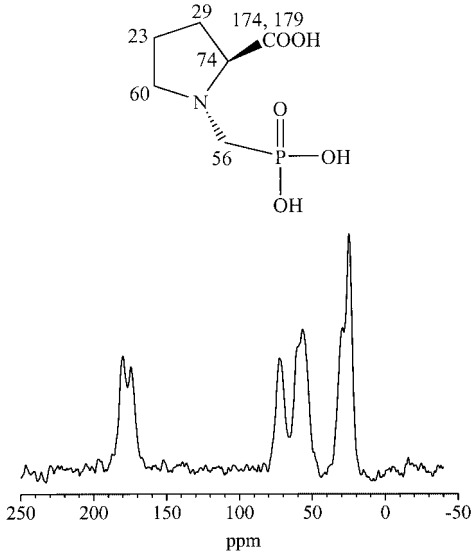


Figure 4. $^{13}$C MAS NMR spectra of surfactant-extracted MAOP-100.

The $^{27}$Al MAS NMR spectra of surfactant-extracted MAOPs-*n* give information of the aluminium coordination environment (see Supporting Information). Two signals at $\delta$ = 0 and 50 ppm are observed in the spectra of MAOP-50 and MAOP-75, which could be assigned to octahedral and tetrahedral Al centers, respectively. The peak at $\delta$ = 0 ppm is dominant, showing that almost all aluminium species are six-coordinate. Only a six-coordinate Al species is observed for MAOP-100. This may be due to the large influence of the charge balance of MAOPs-*n* on the coordination environment of the Al species. The different charges between $H_3PO_4$ and $H_3PMP$ may be the main reason for the different aluminium coordination environments in MAOPs-*n*.

The chirality of L-proline in the solid product was analyzed by CD spectroscopy (see Supporting Information). A positive Cotton effect was observed for MAOP-100, which is consistent with that of $H_3PMP$. From the CD results, we can draw the conclusion that L-proline groups retain their chirality during the synthesis and subsequent surfactant-removing process.

## Conclusion

In summary, mesoporous AOPs with different amounts of chiral L-proline groups in the pore were synthesized for the first time through the surfactant-templated method. The existence of extra aluminium species in the mesoporous framework (formed through "pre-hydrolysis" of the aluminium precursor) plays an important role in stabilizing the mesoporous structure of the materials. The integrity and chirality of L-proline were retained in the mesoporous AOPs. The successful synthesis of mesoporous AOPs containing chiral molecules may provide a new method for the design and synthesis of chiral solid materials.

## Experimental Section

**MAOP-*n* Materials:** In a typical synthesis, Al(O*s*Bu)$_3$ (0.985 g, 4 mmol) was added dropwise to a solution of triethanolamine (2.389 g, 16 mmol) at 160 °C. After cooling to 120 °C, cetyltrimethylammonium bromide (0.364 g, 1 mmol) was added to the above mixture. The solution was further cooled to 70 °C and distilled water (20 mL) was added. The mixture was stirred for a few minutes to "pre-hydrolyze" the aluminium precursor (this "pre-hydrolysis" process for the aluminium precursor is essential, otherwise pure mesoporous AOPs cannot be obtained). An aqueous solution (20 mL) containing a mixture (6 mmol) of phosphoric acid and 1-phosphonomethylproline [(*S*)-$H_2PO_3CH_2NC_4H_7COOH$, $H_3PMP$] was added to above mixture under vigorous stirring. The mixture was kept at 70 °C for 30 min. After filtration, the resulting white powder was dried under vacuum at 60 °C. The surfactant was extracted using an acetic acid/ethanol solution (1 g of powder in 130 mL of ethanol containing 16 mL of acetic acid) at room temperature.

**Supporting Information** (see footnote on the first page of this article): $N_2$ sorption isotherms, FT-IR spectra, and $^{27}$Al MAS NMR specra of MAOPs-*n*; CD spectrum of MAOP-100.

## Acknowledgments

Financial support of this work was provided by the National Natural Science Foundation of China (20321303, 20503028), National Basic Research Program of China (2003CB615803), China Postdoctoral Science Foundation and Talent Science Program of the Chinese Academy of Sciences.

[1] D. A. Loy, K. J. Shea, *Chem. Rev.* **1995**, *95*, 1431–1442; R. J. P. Corriu, *Angew. Chem. Int. Ed.* **2000**, *39*, 1376–1378; B. M. Novak, *Adv. Mater.* **1993**, *5*, 422–433.

 © 2006 Wiley-VCH Verlag GmbH & Co. KGaA, Weinheim 

[2] C. Sanchez, B. Lebeau, F. Chaput and J.-P. Boilot, *Adv. Mater.* **2003**, *15*, 1969–1994; *Functional Hybrid Materials* (Ed.: P. Gomez-Romero), Wiley VCH, Weinheim, **2004**.
[3] S. Inagaki, S. Guan, Y. Fukushima, T. Ohsuna, O. Terasaki, *J. Am. Chem. Soc.* **1999**, *121*, 9611–9614; B. J. Melde, B. T. Holland, C. F. Blanford, A. Stein, *Chem. Mater.* **1999**, *11*, 3302–3308; T. Asefa, M. J. MacLachlan, N. Coombs, G. A. Ozin, *Nature* **1999**, *402*, 867–871.
[4] Z. Zhou, X. Bao, X. Zhao, *Chem. Commun* **2004**, 1376–1377; X. Bao, X. Zhao, X. Li, P. Chia, J. Li, *J. Phys. Chem. B* **2004**, *108*, 4684–4689.
[5] H. E. Katz, G. Scheller, T. M. Putvinski, M. L. Schilling, W. L. Wilson, C. E. D. Chidsey, *Science* **1991**, *254*, 1485–1487; L. A. Vermeulen, M. E. Thompson, *Nature* **1992**, *358*, 656–658.
[6] G. Cao, H. Hong, T. E. Mallouk, *Acc. Chem. Res.* **1992**, *25*, 420–427.
[7] P. Dutta, *Nature* **1992**, *358*, 621–621.
[8] T. Kimura, *Chem. Mater.* **2003**, *15*, 3742–3744.
[9] A. Bhaumik, S. Inagaki, *J. Am. Chem. Soc.* **2001**, *123*, 691–696.
[10] N. Ren, Y. Tang, Y. Wang, S. Hu, A. Dong, W. Hua, Y. Yue, J. Shen, *Chem. Lett.* **2002**, 1036–1037.
[11] J. EI Haskouri, C. Guillem, J. Latorre, A. Beltrán, D. Beltrán, P. Amorós, *Eur. J. Inorg. Chem.* **2004**, 1804–1807; J. EI Haskouri, C. Guillem, J. Latorre, A. Beltrán, D. Beltrán, P. Amorós, *Chem. Mater.* **2004**, *16*, 4359–4372.
[12] T. Kimura, *Chem. Mater.* **2005**, *17*, 337–344; T. Kimura, *Chem. Mater.* **2005**, *17*, 5521–5528.
[13] R. O. Duthaler, *Angew. Chem. Int. Ed.* **2003**, *42*, 975–978; P. Dalko, L. Moisan, *Angew. Chem. Int. Ed.* **2004**, *43*, 5138–5175; A. Bøgevig, K. Juhl, N. Kumaragurubaran, W. Zhuang, K. A. Jørgensen, *Angew. Chem. Int. Ed.* **2002**, *41*, 1790–1793.
[14] J. Z. Min, T. Toyo'oka, M. Kato, T. Fukushima, *Biomed. Chromatogr.* **2005**, *19*, 43–50; Z. Chai, S. Xu, X. Hou, *Chromatographia* **2004**, *60*, 25–31.
[15] T. Kimura, Y. Sugahara, K. Kuroda, *Microporous Mesoporous Mater.* **1998**, *22*, 115–126; Z. Luan, D. Zhao, H. He, J. Klinowski, L. Kevan, *J. Phys. Chem. B* **1998**, *102*, 1250–1259.
[16] Y. Z. Khimyak, J. Klinowski, *J. Mater. Chem.* **2002**, *12*, 1079–1085.
[17] B. T. Holland, P. K. Isbester, C. F. Blanford, E. J. Munson, A. Stein, *J. Am. Chem. Soc.* **1997**, *119*, 6796–6803; M. Tiemann, M. Fröba, *Chem. Mater.* **2001**, *13*, 3211–3217.
[18] A. Sayari, I. Moudrakovski, J. S. Reddy, C. I. Ratcliffe, J. A. Ripmeester, K. F. Preston, *Chem. Mater.* **1996**, *8*, 2080–2088; M. Tiemann, M. Schulz, C. Jäger, M. Fröba, *Chem. Mater.* **2001**, *13*, 2885–2891.

Received: December 5, 2005
Published Online: April 11, 2006

 © 2006 Wiley-VCH Verlag GmbH & Co. KGaA, Weinheim 

DOI: 10.1002/ejic.200600105

# A Zig-Zag [$Mn^{II}_4$] Cluster from a Novel Bis(β-diketonate) Ligand

**Guillem Aromí,*[a] Patrick Gamez,[b] Christophe Boldron,[b] Huub Kooijman,[c] Anthony L. Spek,[c] and Jan Reedijk[b]**

**Keywords:** Ligand design / O ligands / NMR spectroscopy / Magnetism / Mn

A new ligand, $H_5L3$, has been synthesized featuring seven linearly arranged oxygen donors in form of two 1,3-diketone and three phenol groups. The X-ray structure of $H_5L3$ unveils a rare case where one of the diketones is in the enolic form and the other one in the bis(carbonyl) form. This structure is shown by $^1H$ NMR to persist in solution. Reaction of $H_5L3$ with $Mn(AcO)_2$ in pyridine leads to the novel tetranuclear cluster $[Mn_4(H_2L3)_2(OAc)_2(py)_5]$ (**1**), which displays an unusual core in form of a zig-zag chain. Bulk magnetic measurements revealed the existence of weak antiferromagnetic coupling within the molecule. Numerical fits to a model described by the Hamiltonian $H = -2J_1(S_1S_2 + S_3S_4) - 2J_2(S_2S_3)$ yield coupling constants of $J_1 = -2.23\ cm^{-1}$, $J_2 = -0.85\ cm^{-1}$ and $g = 2.08$.
(© Wiley-VCH Verlag GmbH & Co. KGaA, 69451 Weinheim, Germany, 2006)

The preparation of molecular cluster complexes of interacting transition-metal ions is useful to areas as important and diverse as molecular magnetism,[1,2] homogeneous catalysis[3] or bioinorganic chemistry.[4,5] A very successful approach for accessing such species has been the assembly of metal ions by means of small bridging ligands, such as carboxylates, where growth into infinite arrays is often prevented by additional terminal ligands.[6,7] Such a method has been sometimes termed "serendipitous approach" since it does not allow prediction of the structure of the final species.[8] An alternative strategy has been the design and preparation of complicated multidentate ligands favoring the assembly of metal ions into aggregates with topologies that may be anticipated from the structure of these ligands. This second course of action has led to the production of a large amount of polynuclear edifices displaying sophisticated shapes and architectures, such as helicates,[9] grids,[10] cylinders,[11] catenates,[12] and many more. Of these molecular species, only a minority have the metal ions disposed in close proximity so as to show cooperative effects resulting from strong magnetic-exchange interactions[13] or metal–metal bonding.[14] We have been interested in preparing new ligands incorporating various β-diketone units and other donor groups in a linear fashion ($H_3L1$ and $H_4L2$ in Scheme 1),[15,16] aimed at forming molecular strings of metal ions in close proximity. Maximum occupancy of their coordination pockets would result in tetranuclear clusters in form of $[M_4]$ chains[17] for $H_3L1$ and aligned $[M_2]_2$ dimers of dimers for $H_4L2$. Reactions of the latter with $M(OAc)_2$ salts have resulted invariably in the formation of complexes of the type $[M_2(H_2L2)_2(S)_n]$ ($n$ = 2 or 4; S = solvent; M = Mn, Ni, Co, Cu).[16] Similar dinuclear compounds have been obtained with $H_3L1$.[18] However, in the absence of a coordinating solvent, molecules exhibiting higher occupancy, $[Co_3(HL1)_3]$ and $[Mn_3(HL1)_3]$, were characterized, which represented a new asymmetric topology within the context of coordination helicates.[19] Inspired by these early results, we have now designed and synthesized a new ligand displaying as many as six adjacent coordination pockets ($H_5L3$, Scheme 1). Reaction of $H_5L3$ with $Mn^{II}$ produces a very rare magnetically exchanged tetranuclear complex featuring an $[Mn_4O_6]$ core in form of a zig-zag chain.

The new ligand $H_5L3$ {2-hydroxy-1,3-bis[3-(2-hydroxyphenyl)-3-oxopropionyl]benzene} was prepared from the methoxide derivative $H_4L4$ (Scheme 1).[20] The latter is also a new molecule not described in the literature and constitutes a bis(β-diketone) with potentially interesting coordination chemistry. The NMR spectra ($^1H$ and $^{13}C$) of $H_5L3$ (Figure 1) do not reflect the symmetry presumed for this molecule in Scheme 1. The crystal structure of the compound (Figure 1),[21] obtained following its recrystallization from MeOH, threw light into the solution structure responsible of its $^1H$ NMR pattern, allowing its assignment, with help of a COSY spectrum (see Supporting Information). In fact, the molecule of $H_5L3$ crystallizes with one of its 1,3-diketone groups in its enolic form and the other one in the bis(carbonyl) form, constituting a very rare example where

[a] Departament de Química Inorgànica, Universitat de Barcelona, Diagonal 647, 08028 Barcelona, Spain
Fax: +34-93-490-7725
E-mail: guillem.aromi@qi.ub.es
[b] Leiden Institute of Chemistry, Gorlaeus Laboratories, Leiden University,
P. O. Box 9502, 2300 RA Leiden, The Netherlands
[c] Bijvoet Center for Biomolecular Research, Crystal and Structural Chemistry, Utrecht University,
Padualaan 8, 3584 CH Utrecht, The Netherlands
Supporting information for this article is available on the WWW under http://www.eurjic.org or from the author.

 InterScience © 2006 Wiley-VCH Verlag GmbH & Co. KGaA, Weinheim 

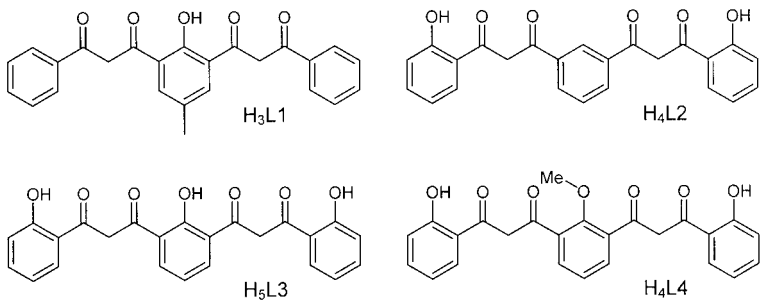


Scheme 1.

both forms are present simultaneously in one molecule. The only such previous example featured by the Cambridge data base is a cyclic polyketide lactone where the strain of the macrocycle is forcing the formation of the mixed tautomer.[22] In $H_5L3$, the simultaneous occurrence of both forms may be favored by the formation of five intramolecular [O–H···O] hydrogen bonds, which are all part of π-delocalized systems. The structural parameters within these delocalized systems follow indeed the criteria of resonance-assisted hydrogen bonding (RAHB).[23] According to this theory, intramolecular hydrogen bonds within β-diketone enols are reinforced by the existence of π-delocalization within the heterodienic O=C–C–C=O–H chain, translating into abnormally short O···O distances. The same phenomenon occurs, although less pronounced, within 2-hydroxybenzoketones, such as these present in $H_5L3$, and this trend is clearly observed on the crystal structure of the molecule. RAHB predicts a good correlation between *d*(O···O) and the $^1$H NMR chemical shift of the proton concerned by the H-bond, and this criterion was used to assign this class of protons in $H_5L3$ (Figure 1).

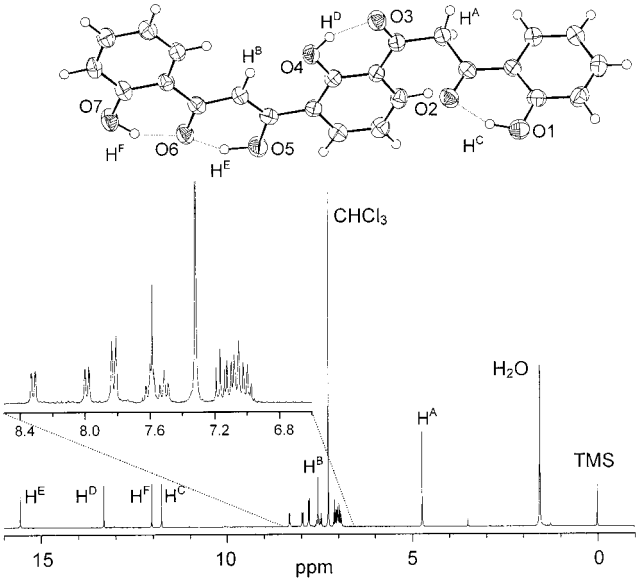


Figure 1. Top: ORTEP representation at the 50% probability level of the ligand $H_5L3$. Only the oxygen atoms are labeled. Intramolecular hydrogen bonds are shown as dashed lines. H-bond [O–H···O] distances [Å]: 2.578(2) (O1,O2), 2.533(2) (O3,O4), 2.488(2) (O5,O6), 2.536(2) (O6,O7). Bottom: 300 MHz $^1$H NMR spectrum of $H_5L3$ in $CDCl_3$ reflecting the symmetry of the solid state. The assignment of the non-aromatic protons is shown (see text for details). Full assignments are given in the Supporting Information.

The reaction of $H_5L3$ with 2 equiv. of $Mn(OAc)_2{\cdot}H_2O$ in pyridine affords a dark orange solution that produces orange crystals upon layering with $Et_2O$. This product was identified by single-crystal X-ray diffraction to be $[Mn_4(H_2L3)_2(OAc)_2(py)_5]$ (**1**).[24] The structure of **1** (Figures 2 and 3)[21] reveals a linear tetranuclear array of $Mn^{II}$, assembled by the action of two triply deprotonated $\mu_4$-$(H_2L3)^{3-}$ ligands located face-to-face, through four adjacent chelating units per side constituted by the five central oxygen donors of each ligand. All chelating units form six-membered rings. The peripheral ones, formed by the 1,3-diketonate units, deviate significantly from planarity [Cremer and Pople puckering amplitude in the range 0.0756(13)–0.2321(15) Å],[25] although not as much as the central ones, involving the phenoxide moiety [puckering amplitudes in the range 0.3804(15)–0.8351(16) Å]. The latter can be described as in a distorted boat, twist-boat or screw-boat conformation. The ionizable protons remaining on each $(H_2L3)^{3-}$ moiety are those of the peripheral neutral phenol groups and are involved in internal hydrogen bonds, as seen with the free ligand. Interestingly, each chelating pocket binds a metal ion disposed in *cis* configuration with respect to its counterpart from the other ligand. This is presumably because the ionic radius of $Mn^{II}$ is too large to accommodate the four metal ions in a linear array with the chelating units disposed equatorially (i.e. *trans*). The result is an $[Mn(\mu\text{-}O)_2Mn(\mu\text{-}O)_2Mn(\mu\text{-}O)_2Mn]$ chain with a very unusual "zig-zag" shape. In complex **1**, each peripheral pair of metal ions is further bridged by one μ-$OAc^-$ ligand, while pyridine ligands complete the six- (Mn1, Mn2 and Mn4) or seven-donor (Mn3) coordination spheres present in this system. Thus, the external $Mn_2$ pairs are bridged by one *syn*,*syn*-OAc and two alkoxide-type μ-O donors, while the central $Mn_2$ is linked by just two phenoxide-type bridges. The bond lengths around the metal ions range from 2.066(1) to 2.488(2) Å, within the limits expected for $Mn^{II}$ ions (ranges for each type of bond are listed in the caption of Figure 2). The average nearest and second-nearest neighbor Mn···Mn separations are 3.378 and 5.826 Å, respectively.

 © 2006 Wiley-VCH Verlag GmbH & Co. KGaA, Weinheim 

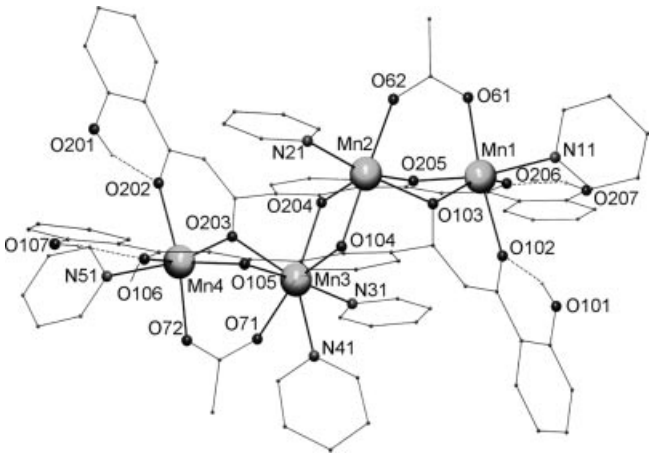


Figure 2. Labeled Pov-ray representation of $[Mn_4(H_2L3)_2(AcO)_2(py)_5]$ (**1**). Only hydroxy H-atoms are shown. Intramolecular hydrogen bonds are shown as dashed lines. Ranges of selected interatomic distances [Å] and angles [°]: Mn–O 2.0661(14) to 2.4031(14), Mn–N 2.2660(18) to 2.488(2), Mn1···Mn2 3.2876(6), Mn2···Mn3 3.4950(7), Mn3···Mn4 3.3502(6), Mn2···Mn4 5.7526(9), Mn3···Mn1 5.8984(9), Mn1···Mn4 8.8046, Mn1–Mn2–Mn3 120.80(2), Mn2–Mn3–Mn4 114.35(2), O107–H···O106 2.513(2), O207–H···O206 2.500(2), O101–H···O102 2.501(2), O201–H···O202 2.495(2).

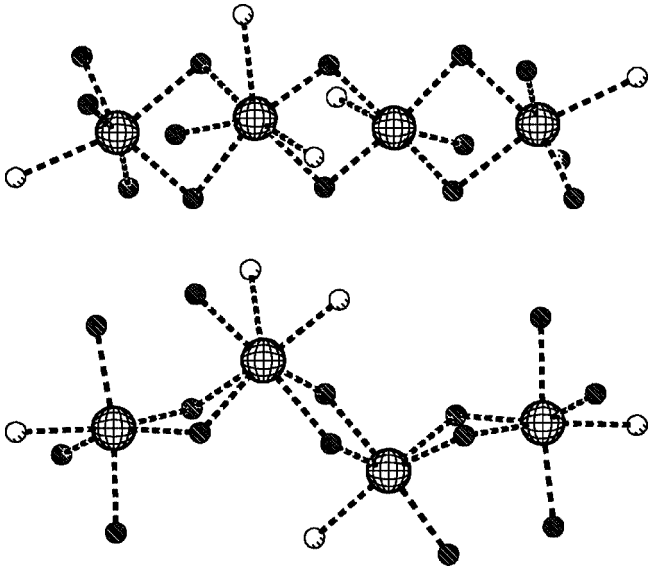

Figure 3. Platon representation of the core of $[Mn_4(H_2L3)_2(AcO)_2(py)_5]$ (**1**) emphasizing two different views. Code for atoms: large, Mn; small hatched, O; shaded, N.

Tetranuclear manganese clusters are interesting from the magnetic point of view,[26] or as synthetic models of the dioxygen-evolving complex of photosystem II.[27] Of the dozens of examples existing in the literature only three types consist of linear arrays of fused $[Mn_2(\mu\text{-}O)_2]$ moieties as in **1**; the $[Mn_4^{IV}O_6(bpy)_6]^{4+}$ cation,[28,29] the $[Mn_2^{III}Mn_2^{II}(Me\text{-}hmp)_6Cl_4]$ cluster [Me-hmpH = 2-(hydroxymethyl)-6-methylpyridine],[30] and the cations $[Mn_4^{II}L_6]^{2+}$ [HL = a (2-hydroxyphenyl)bipyridine or -phenanthroline ligand].[31,32] All of these display a *cis* conformation with respect to the central $[Mn_2O_2]$ unit (Scheme 2), while complex **1** is the first example of the *trans* form as forced presumably by the structure of the $(H_2L3)^{3-}$ ligand.

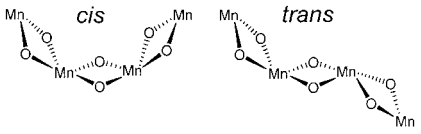


Scheme 2.

The magnetic exchange within complex **1** was examined by means of variable-temperature (2–300 K) bulk-magnetization measurements under a constant magnetic field of 0.3 T. The results are given in Figure 4 in form of a $\chi_M T$ vs. $T$ plot. The product $\chi_M T$ at 300 K is 18.43 $cm^3 \cdot K \cdot mol^{-1}$ (quite near to the value of 17.5 $cm^3 \cdot K \cdot mol^{-1}$ for four independent high-spin $Mn^{II}$ centers with $g = 2$), and it decreases slowly and then more rapidly near 70 K to reach a value of 1.22 $cm^3 \cdot K \cdot mol^{-1}$ at 2 K. This indicates the presence of dominant antiferromagnetic interactions within the cluster. A fit of the experimental data was obtained through a matrix diagonalization procedure using the program CLUMAG,[33] by considering the Heisenberg spin Hamiltonian $H = -2J_1(S_1S_2 + S_3S_4) - 2J_2(S_2S_3)$, where $S_i$ is the spin angular momentum operator of $Mn_i$ ($S_i = 5/2$) and the interaction between the metal ions of both external $Mn_2$ pairs was assumed to be equal (see inset in Figure 4). Good fits were obtained for two sets of solutions. One was reached for values $J_1 = -1.37$ $cm^{-1}$, $J_2 = +0.77$ $cm^{-1}$ and $g = 2.06$, which leads to a total spin ground state of $S_T = 0$. Since $J_1 > J_2$, a very similar behavior is expected if $J_2$ were instead negative but with comparable absolute value. This turns out to be the case if the fit is performed by restricting both coupling constants to be antiferromagnetic, yielding the parameters $J_1 = -2.23$ $cm^{-1}$, $J_2 = -0.85$ $cm^{-1}$ and $g = 2.08$. The latter fit is preferred since it yields a smaller error factor $R$ ($R = \Sigma[\chi_M T_{exp} - \chi_M T_{calc}]^2/\Sigma[\chi_M T_{exp}]^2$) than the first fit ($R = 7.73 \cdot 10^{-5}$ vs. $1.62 \cdot 10^{-4}$). The value of $g$ is similar in both cases; however, it must be taken with caution, since this parameter is the most affected by errors in the molecular weight used for treatment of the magnetic data. The bridging arrangement found within the $Mn_{1-2}$ and $Mn_{3-4}$ pairs (see above) is very uncommon for $Mn^{II}$ ions; however, the few reports showing preliminary magnetic studies on systems containing this moiety suggest weak antiferromagnetic coupling as found in **1**.[34,35] The central $[Mn_2O_2]$ unit on the other hand, is bridged by two phenoxide-type ligands. Such a type of link between divalent Mn centers has been reported to lead to both, ferro-[31,36–39] and antiferromagnetic interactions.[40–43] The actual magnetic behaviour depends strongly on the efficiency of the overlap between $d_{x^2-y^2}$ orbitals of the metal ions through the phenoxide O-donors, which is considered the main pathway to antiferromagnetism. In **1**, the latter is expected to be much reduced, given the weakening of antiferromagnetic pathways that might be caused by the severe distortion in the coordination geometry shown by the metal ions. The coupling appears thus antiferromagnetic and very weak in any case, as for all previous analogous cases.

 © 2006 Wiley-VCH Verlag GmbH & Co. KGaA, Weinheim 

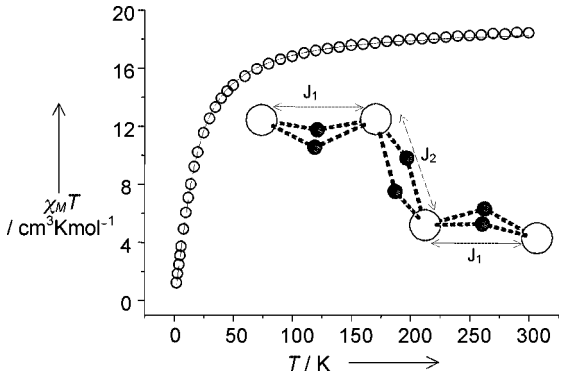


Figure 4. Plot of $\chi_M T$ vs. $T$ per mol of $[Mn_4(H_2L3)_2(AcO)_2(py)_5]$ (**1**). The solid line is a fit to the experimental data (see text for details). The inset shows the model and spin coupling scheme used for the fitting procedure.

The preparation of $H_5L3$ and its association with $Mn^{II}$ ions have demonstrated that rigid ligands with linearly disposed O-donors do provide access to metallic coordination chains with interesting magnetic properties, difficult to obtain otherwise. The preparation of **1** offers a very promising prospect in this direction. We are currently exploring the coordination chemistry of this new ligand with other metals and in the presence of other small co-ligands.

**Supporting Information** (see footnote on the first page of this article): This material includes the description of the preparation of ligands $H_5L3$ and $H_4L4$, full $^1H$ NMR characterization of the ligands and the COSY diagram of $H_5L3$.

## Acknowledgments

This work was supported by grants from the Spanish Ministerio de Ciencia y Tecnología, the Agència de Gestió d'Ajuts Univesitaris i de Recerca (Generalitat de Catalunya), the Dutch WFMO (Werkgroep Fundamenteel-Materialen Onderzoek) and the CW-NWO (Council for Chemical Sciences of the Netherlands Organization for Scientific Research).

[1] J. S. Miller, M. Drillon, in: *Magnetism: Molecules to Materials V* (Eds.: J. S. Miller, M. Drillon), Wiley-VCH, Weinheim, **2005**.
[2] G. Aromí, E. K. Brechin, *Struct. Bonding*, DOI: 10.1007/430_022.
[3] R. D. Adams, F. A. Cotton, in *Catalysis by Di- and Polynuclear Metal Cluster Complexes* (Eds.: R. D. Adams, F. A. Cotton), Wiley-VCH, New York, **1999**.
[4] H. A. O. Hill, P. J. Sadler, A. J. Thompson, in *Metal Sites in Proteins and Models* (Eds.: H. A. O. Hill, P. J. Sadler, A. J. Thompson), Springer, Berlin, **1999**, vol. 1–3.
[5] P. V. Rao, R. H. Holm, *Chem. Rev.* **2004**, *104*, 527.
[6] R. E. P. Winpenny, *Adv. Inorg. Chem.* **2001**, *52*, 1.
[7] G. Aromí, S. M. J. Aubin, M. A. Bolcar, G. Christou, H. J. Eppley, K. Folting, D. N. Hendrickson, J. C. Huffman, R. C. Squire, H. L. Tsai, S. Wang, M. W. Wemple, *Polyhedron* **1998**, *17*, 3005.
[8] R. E. P. Winpenny, *J. Chem. Soc., Dalton Trans.* **2002**, 1.
[9] C. Piguet, G. Bernardinelli, G. Hopfgartner, *Chem. Rev.* **1997**, *97*, 2005.
[10] G. S. Hanan, D. Volkmer, J. M. Lehn, *Can. J. Chem. – Rev. Can. Chim.* **2004**, *82*, 1428.
[11] D. W. Johnson, J. D. Xu, R. W. Saalfrank, K. N. Raymond, *Angew. Chem. Int. Ed.* **1999**, *38*, 2882.
[12] D. J. Cardenas, J. P. Collin, P. Gavina, J. P. Sauvage, A. De Cian, J. Fischer, N. Armaroli, L. Flamigni, V. Vicinelli, V. Balzani, *J. Am. Chem. Soc.* **1999**, *121*, 5481.
[13] L. Thompson, *Can. J. Chem. – Rev. Can. Chim.* **2005**, *83*, 77.
[14] Y. H. Chen, C. C. Lee, C. C. Wang, G. H. Lee, S. Y. Lai, F. Y. Li, C. Y. Mou, S. M. Peng, *Chem. Commun.* **1999**, 1667.
[15] G. Aromí, P. Gamez, P. C. Berzal, W. L. Driessen, J. Reedijk, *Synth. Commun.* **2003**, *33*, 11.
[16] G. Aromí, C. Boldron, P. Gamez, O. Roubeau, H. Kooijman, A. L. Spek, H. Stoeckli-Evans, J. Ribas, J. Reedijk, *Dalton Trans.* **2004**, 3586.
[17] G. Aromí, J. Ribas, P. Gamez, O. Roubeau, H. Kooijman, A. L. Spek, S. Teat, E. MacLean, H. Stoeckli-Evans, J. Reedijk, *Chem. Eur. J.* **2004**, *10*, 6476.
[18] G. Aromí, P. Gamez, O. Roubeau, P. Carrero-Berzal, H. Kooijman, A. L. Spek, W. L. Driessen, J. Reedijk, *Eur. J. Inorg. Chem.* **2002**, 1046.
[19] G. Aromí, P. C. Berzal, P. Gamez, O. Roubeau, H. Kooijman, A. L. Spek, W. L. Driessen, J. Reedijk, *Angew. Chem. Int. Ed.* **2001**, *40*, 3444.
[20] See Supporting Information for experimental details on organic synthesis and characterization of $H_5L3$ and $H_4L4$.
[21] Crystals of $H_5L3$ and **1** were measured with a Nonius KappaCCD diffractometer on a rotating anode ($\theta_{max}$ = 25.3°, $T$ = 150 K, Mo-$K_\alpha$ radiation, $\lambda$ = 0.71073 Å, no absorption correction). The structures were solved with direct methods and refined on $F^2$ (SHELXL-97). Pertinent data for $H_5L3$: $C_{24}H_{18}O_7$, yellow block-shaped crystal (0.10×0.25×0.35 mm), orthorhombic, space group *Pbcn* (no. 60) with $a$ = 13.9229(15), $b$ = 8.5263(12), $c$ = 32.190(5) Å, $V$ = 3821.3(9) Å$^3$, $Z$ = 8, 18194 reflections measured, 3410 independent, $R_{int}$ = 0.1106, $R_\sigma$ = 0.0664. The structure was solved with SHELXS-86. All hydrogen atoms could be located on a difference Fourier map and their coordinates were refined. Refinement of 334 parameters converged at a final $wR_2$ value of 0.1254, $R_1$ = 0.0468 [for 2302 reflections with $I > 2\sigma(I)$], $S$ = 1.044, $-0.22 < \Delta\rho < 0.20$ e·Å$^{-3}$. Pertinent data for **1**: $C_{77}H_{61}Mn_4N_5O_{18}$+solvent (vide infra), pale orange blockshaped crystal (0.05×0.18×0.35 mm), triclinic, space group $P\bar{1}$ (no. 2) with $a$ = 10.8441(10), $b$ = 18.591(2), $c$ = 20.904(3) Å, $\alpha$ = 85.172(15), $\beta$ = 77.893(15), $\gamma$ = 87.872(15)°, $V$ = 4105.1(9) Å$^3$, $Z$ = 2, 83947 reflections measured, 14832 independent, $R_{int}$ = 0.0443, $R_\sigma$ = 0.0330. The structure was solved with SHELXL-97. Electron density in a cavity with a volume of 896 Å$^3$, filled with a disordered mixture of $Et_2O$ and pyridine, was taken into account in the refinement with PLATON/SQUEEZE. A total number of 321 electrons per unit cell were found. Where relevant, data cited above are given without disordered solvent contribution. The coordinated pyridine molecule containing N11 is disordered and is described with a two-site disorder model. The hydroxy hydrogen atoms could be located on a difference Fourier map and their coordinates were refined. All other hydrogen atoms were included with calculated positions and riding on their carrier atoms. Refinement of 967 parameters converged at a final $wR_2$ value of 0.1203, $R_1$ = 0.0407 [for 11825 reflections with $I > 2\sigma(I)$], $S$ = 1.074, $-0.44 < \Delta\rho < 0.59$ e·Å$^{-3}$. CCDC-293439 and -293440 contain the supplementary crystallographic data for this paper. These data can be obtained free of charge from The Cambridge Crystallographic Data Centre via www.ccdc.cam.ac.uk/data_request/cif.
[22] K. Tatsuta, M. Chino, N. Kojima, S. Shinojima, M. Nakata, M. Morooka, S. Ohba, *Tetrahedron Lett.* **1993**, *34*, 4957.
[23] V. Bertolasi, P. Gilli, V. Ferretti, G. Gilli, *J. Chem. Soc., Perkin Trans. 2* **1997**, 945.
[24] Elemental analysis reveals partial substitution of pyridine by water upon exposure to air. Calcd. (found) for **1** (– 1.5py + 1·5$H_2O$): C 56.69 (56.86), H 3.87 (3.68), N 3.33 (3.09).
[25] D. Cremer, J. A. Pople, *J. Am. Chem. Soc.* **1975**, *97*, 1354.
[26] H. Andres, R. Basler, H. U. Güdel, G. Aromí, G. Christou, H. Buttner, B. Ruffle, *J. Am. Chem. Soc.* **2000**, *122*, 12469.

 © 2006 Wiley-VCH Verlag GmbH & Co. KGaA, Weinheim 

[27] H. Chen, M.-N. Collomb, C. Duboc, G. Blondin, E. Rivière, J. W. Faller, R. H. Crabtree, G. W. Brudvig, *Inorg. Chem.* **2005**, *44*, 9567.
[28] B. C. Dave, R. S. Czernuszewicz, *New J. Chem.* **1994**, *18*, 149.
[29] C. Philouze, G. Blondin, J. J. Girerd, J. Guilhem, C. Pascard, D. Lexa, *J. Am. Chem. Soc.* **1994**, *116*, 8557.
[30] J. Yoo, A. Yamaguchi, M. Nakano, J. Krzystek, W. E. Streib, L. C. Brunel, H. Ishimoto, G. Christou, D. N. Hendrickson, *Inorg. Chem.* **2001**, *40*, 4604.
[31] J. C. Jeffery, P. Thornton, M. D. Ward, *Inorg. Chem.* **1994**, *33*, 3612.
[32] D. A. Bardwell, J. C. Jeffery, M. D. Ward, *J. Chem. Soc., Dalton Trans.* **1995**, 3071.
[33] D. Gatteschi, L. Pardi, *Gazz. Chim. Ital.* **1993**, *123*, 231.
[34] S. Brooker, V. McKee, T. Metcalfe, *Inorg. Chim. Acta* **1996**, *246*, 171.
[35] Z. J. Zhong, X. Z. You, *Polyhedron* **1994**, *13*, 2157.
[36] E. O. Gao, S. Q. Bai, Z. He, C. H. Yan, *Inorg. Chem.* **2005**, *44*, 2566.
[37] M. Mikuriya, K. Nakadera, T. Tokii, *Inorg. Chim. Acta* **1992**, *194*, 129.
[38] H. R. Chang, S. K. Larsen, P. D. W. Boyd, C. G. Pierpont, D. N. Hendrickson, *J. Am. Chem. Soc.* **1988**, *110*, 4565.
[39] D. Luneau, J. M. Savariault, P. Cassoux, J. P. Tuchagues, *J. Chem. Soc., Dalton Trans.* **1988**, 1225.
[40] I. A. Koval, M. Huisman, A. F. Stassen, P. Gamez, M. Lutz, A. L. Spek, D. Pursche, B. Krebs, J. Reedijk, *Inorg. Chim. Acta* **2004**, *357*, 294.
[41] C. Hureau, E. Anxolabehere-Mallart, M. Nierlich, F. Gonnet, E. Rivière, G. Blondin, *Eur. J. Inorg. Chem.* **2002**, 2710.
[42] M. Qian, S. H. Gou, S. Chantrapromma, S. S. S. Raj, H. K. Fun, Q. D. Zeng, Z. Yu, X. Z. You, *Inorg. Chim. Acta* **2000**, *305*, 83.
[43] T. C. Higgs, K. Spartalian, C. J. O'Connor, B. F. Matzanke, C. J. Carrano, *Inorg. Chem.* **1998**, *37*, 2263.

Received: February 6, 2006
Published Online: April 3, 2006

 © 2006 Wiley-VCH Verlag GmbH & Co. KGaA, Weinheim 

DOI: 10.1002/ejic.200500835

# pH-Specific Synthesis and Structural and Spectroscopic Characterization of a Complex between $Co^{II}$ and *N*,*N*-Bis(phosphonomethyl)glycine: Cobalt–Phosphonate Interactions in the Solid State and in Solution

**Anca Mateescu,[a] Catherine P. Raptopoulou,[b] Aris Terzis,[b] Vassilis Tangoulis,[c] and Athanasios Salifoglou*[d]**

**Keywords:** Cobalt / Magnetic properties / Materials science / Phosphonates / Structural speciation

The presence of cobalt in biological systems has been associated with a variety of regulatory roles as an inorganic cofactor. Its involvement in (bio)chemical processes, where it contributes to the integrity of the physiology of humans, underscores its ability to promote (bio)chemistry with molecular targets of variable mass and biological properties. Given the fact that organic phosphonates are widespread substrates/ligands in biological fluids, we sought to investigate the relevant chemistry with $Co^{II}$. With the organophosphonate ligand *N*,*N*-bis(phosphonomethyl)glycine ($H_5$NTA2P) as the main metal ion binder, aqueous reactions with $Co^{II}$ were examined, ultimately leading to the isolation of the complex $[Co(C_4H_9O_8NP_2)(H_2O)_2]\cdot 2H_2O$ (**1**) at pH 1.5. This complex was characterized analytically, spectroscopically (FT-IR, UV/Vis, EPR), magnetically, and by cyclic voltammetry. X-ray crystallography shows that **1** is a compound with a molecular type of lattice. The complex consists of a mononuclear, octahedral $Co^{II}$ center coordinated by oxygen atoms belonging to the terminal phosphonate and carboxylate groups of $H_3NTA2P^{2-}$, the ligand nitrogen, and two bound water molecules. It should be emphasized that similar structural features have been observed in other metal organophosphonate lattices of materials with potential catalytic and chemical reactivity. The magnetic and EPR data for **1** suggest the presence of a high-spin octahedral $Co^{II}$, with a ground state of an effective spin $S = 1/2$. The solution UV/Vis and EPR spectra suggest retention of the integrity of **1**, which is consistent with the magnetization measurements in the solid state. Collectively, the data suggest a soluble $Co^{II}$–organodiphosphonate species, not unlike those expected in bio-fluids containing the specific ligand or ligands structurally akin to $H_3NTA2P^{2-}$.The biological relevance of **1** to species in biofluids and the structural association with $Co^{II}$–organophosphonate materials is discussed.
(© Wiley-VCH Verlag GmbH & Co. KGaA, 69451 Weinheim, Germany, 2006)

## Introduction

Cobalt has been known to be present in biological systems for a long time. Its involvement in biomolecular activity is intimately linked to its entry in molecular targets like $B_{12}$ coenzyme and vitamin $B_{12}$ and its potential as an inorganic cofactor to influence biological processes.[1–4] To this end, cobalt has been found in metallohydrolases like methionine aminopeptidase,[5] nitrile hydratases,[6] ribonucleotide reductase, glutamate mutase, and others.[7] Beyond that, an absence or excess of cobalt has been linked to pathological aberrations in human physiology. In particular, vitamin B12 deficiency has been linked to pernicious anemia,[8] while overexposure to the metal has been associated with toxic effects linked to heart disease and excessive formation of red corpuscles.[9,10]

Understanding the role of cobalt in those biological systems entails a deep understanding of its (bio)chemical interactions with low as well as high molecular mass biomolecules in the requisite fluids.[2,3,6,7] These interactions reflect the potential binding of cobalt to organic substrates/ligands of variable structure and function in physiological or aberrant processes thereof. The binary and ternary species of cobalt thus formed participate in complex equilibria, the delineation of which is essential in defining soluble bioavailable species that actively participate in bioprocesses. At the low mass end of the spectrum of molecular targets are molecules like organic acids, amino acids, small peptides, and other molecules that possess variable structural features, prominent among which are the carboxylate and phosphonate groups.[11] Phosphonate groups are known to participate in key phosphorylation events that influence the (bio)chemical activity, signal transduction, enzyme inhibition, neuroactivity, plant-growth regulation, antibiotic, and herbicidal activity of both small and large molecules.[11,12]

[a] Department of Chemistry, University of Crete, Heraklion 71409, Greece
[b] Institute of Materials Science, NCSR "Demokritos", Aghia Paraskevi 15310, Attiki, Greece
[c] Department of Materials Science, University of Patras, Patras 26500, Greece
[d] Laboratory of Inorganic Chemistry, Department of Chemical Engineering, Aristotle University of Thessaloniki, Thessaloniki 54124 and Chemical Process Engineering Research Institute, Thermi, Thessaloniki 57001, Greece
Fax: +30-2310-996-196
E-mail: salif@auth.gr

 © 2006 Wiley-VCH Verlag GmbH & Co. KGaA, Weinheim 

Organophosphonates are a particularly interesting family of organic targets in the biochemistry of metal ions and the chemistry of materials.[13] Such materials have been known for some time for their versatility in coordination and variability in nuclearity.[14] Both these properties are intimately associated with variable dimensionality[15] materials and layered metal organophosphonates[16] and also with a diverse reactivity that is linked to catalysis, intercalation chemistry, optical properties of novel materials, and others.[17,18]

The significance of metal organophosphonate chemistry in the fields of research mentioned above necessitates the extensive perusal of the relevant chemistry with $Co^{II}$, many aspects of which[19] have yet to be discovered. Bearing in mind that the structural features of potential metal ion binders, like organophosphonates, dictate the chemistry of interactions with the metal ion under investigation and most likely influence any arising physical and/or biological properties, we have launched research efforts targeting the reactivity of one such class of diphosphonic ligands toward $Co^{II}$. Herein, we report on the synthesis, isolation, spectroscopic and structural characterization, and cyclic voltammetric, magnetic, and EPR studies of a new species between $Co^{II}$ and the carboxydiphosphonate ligand *N*,*N*-bis(phosphonomethyl)glycine ($H_5NTA2P$).

## Results and Discussion

### Synthesis

The synthesis of complex **1** was carried out in aqueous solutions containing $Co^{II}$ and *N*,*N*-bis(phosphonomethyl)-glycine. The overall reaction leading to compound **1** is depicted schematically below.

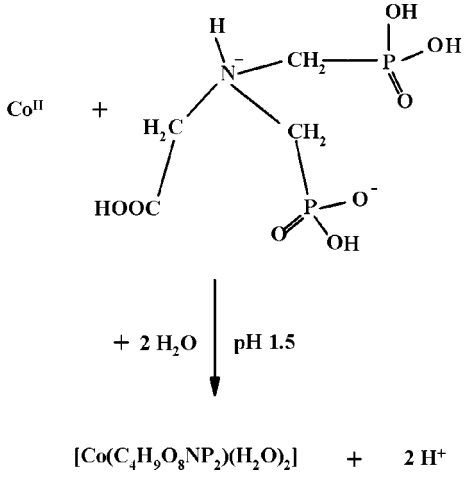


The metal-to-ligand stoichiometry employed was 1:1, with a pH of 1.5. Slow diffusion of ethanol into the reaction mixture led to the precipitation of well-formed pink prismatic crystals. Elemental analysis of the crystalline material was consistent with the formulation $[Co(C_4H_9O_8NP_2)(H_2O)_2]\cdot 2H_2O$ for complex **1**. The yield of the reaction was approximately 60%.

The isolated crystalline material **1** appears to be stable in the solid state for long periods of time, with no discernible deterioration. Complex **1** is soluble in water and insoluble in alcohols ($CH_3OH$, *i*PrOH), acetonitrile, and DMSO.

### X-ray Crystal Structure of $[Co(C_4H_9O_8NP_2)(H_2O)_2]\cdot 2H_2O$ (1)

The X-ray crystal structure of **1** reveals the presence of a molecular lattice. The compound crystallizes in the monoclinic system $P2_1$. Crystallographic details are given in the Experimental Section. The ORTEP diagram of **1** is shown in Figure 1, and selected interatomic distances and bond angles for **1** are listed in Table 1. The structure consists of a mononuclear core unit containing an octahedral $Co^{II}$ ion. The coordination sphere of $Co^{II}$ is formulated by an oxygen–nitrogen donor atom environment created by the two main participant ligands, namely bis(phosphonomethyl)glycinate [$(^{-}HO_3PCH_2)_2NCH_2COOH$ = $H_3NTA2P^{2-}$] and water. More specifically, each $H_3NTA2P^{2-}$ ligand, employing both phosphonate groups as well as the carboxylic terminal oxygen, coordinates to the metal ion through its singly deprotonated phosphonates, with the carboxylic acid anchor staying in its protonated form. In addition, two water molecules are coordinated to the $Co^{II}$ ion. Both they as well as the $H_3NTA2P^{2-}$ ligand fulfill the coordination requirements of the octahedral sphere around $Co^{II}$. A closer look at the octahedron shows that one of the water molecules along with the two phosphonate oxygens and the terminal carboxylate of the $H_3NTA2P^{2-}$ ligand form the equatorial plane of the octahedral metal ion. The second bound water molecule along with the nitrogen of the $H_3NTA2P^{2-}$ ligand bound to $Co^{II}$ occupy the axial positions in the octahedron. In view of the above description and the available structural data, the mononuclear $Co^{II}$ ion resides in a distorted octahedron.

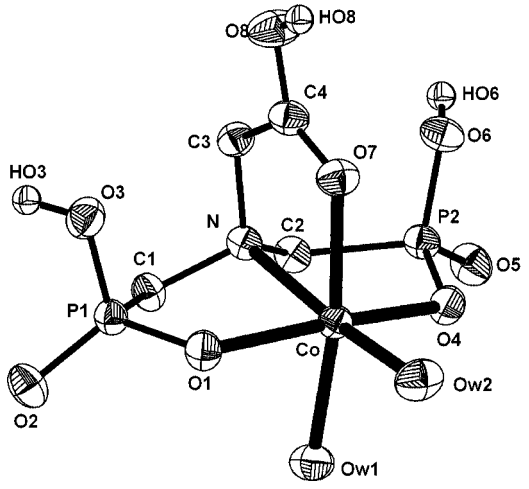


Figure 1. The molecular structure of the $Co(C_4H_9O_8NP_2)(H_2O)_2$ unit, with the atom labeling scheme in **1**. Thermal ellipsoids represent 50% probability surfaces.

The Co–O distances in **1** are similar to those observed in other mononuclear octahedral $Co^{II}$ sites, among which are

 © 2006 Wiley-VCH Verlag GmbH & Co. KGaA, Weinheim 

Table 1. Bond lengths [Å] and angles [°] for $[Co(C_4H_9O_8NP_2)(H_2O)_2]\cdot 2H_2O$ (**1**).

| | | | |
|---|---|---|---|
| Co–Ow2 | 2.012(2) | Co–Ow1 | 2.127(2) |
| Co–O(1) | 2.100(2) | Co–O(7) | 2.141(2) |
| Co–O(4) | 2.101(2) | Co–N | 2.229(2) |
| Ow2–Co–O(1) | 95.99(8) | O(4)–Co–O(7) | 97.58(8) |
| Ow2–Co–O(4) | 95.41(9) | Ow1–Co–O(7) | 172.24(8) |
| O(1)–Co–O(4) | 164.81(7) | Ow2–Co–N | 173.94(9) |
| Ow2–Co–Ow1 | 90.06(9) | O(1)–Co–N | 84.22(7) |
| O(1)–Co–Ow1 | 82.68(8) | O(4)–Co–N | 85.51(7) |
| O(4)–Co–Ow1 | 87.30(8) | Ow1–Co–N | 95.97(8) |
| Ow2–Co–O(7) | 95.46(9) | O(7)–Co–N | 78.47(7) |
| O(1)–Co–O(7) | 91.30(8) | | |

those in $[Co(C_2H_8O_6NP_2)_2(H_2O)_2]$ [2.067(2)–2.132(2) Å] (**2**),[20] $(NH_4)_4[Co(C_6H_5O_7)_2]$ [2.051(2)–2.157(2) Å] (**3**),[21] $[Co\{COOCH_2CH(OH)COO\}]\cdot 3H_2O$ [2.067(3)–2.136(3) Å] (**4**),[22] the phosphonate derivatives $[Co(NH_3CH_2PO_3)_2(H_2O)_2]_n\cdot nH_2O$ [2.104(4)–2.121(4) Å] (**5**),[23] $[Co\{HO_3PC(CH_3)(OH)PO_3H\}_2(H_2O)_2][NH_2(C_2H_5)_2]_2$ [2.064(2)–2.179(2) Å] (**6**),[24] and $[Co(OPMe_3)_3(H_2O)_2]I_2\cdot[Co(OPMe_3)_3(H_2O)_3]I_2$ [1.87(6)–2.18(4) Å for the octahedral site].[25]

The Co–O distances in the equatorial plane of the octahedron are of similar length [2.100(2)–2.141(2) Å], despite the variable nature of the anchor terminals in the two different ligand components in the coordination sphere of $Co^{II}$ and the fact that they all utilize their oxygens as terminal anchors to the metal ion. In contrast to the equatorial distances, the corresponding axial Co–L bonds reflect more radically varying lengths, with the Co–N distance being about 0.1 Å longer than the equatorial ones, while the Co–$O_w$ distance is about 0.1 Å shorter than the equatorial ones. It is not unlikely that such bond-length variations might be due to Jahn–Teller distortions, which are usually encountered in high-spin $Co^{II}$ octahedral species.

The angles within the equatorial plane defined by O(1), O(4), $O_w(1)$, and O(7) are in the range 82.68(8)–97.58(8)°, with the average being very close to the ideal octahedral angle of 90°. A similar yet wider angle variation is observed between the axial donor atoms N and $O_w(2)$ and those in the equatorial plane [range: 78.47(7)–95.99(8)°]. The aforementioned sets of angles are similar to those observed in **2**–**6** and in the complexes $[Cu\{HO_3PC(CH_3)(OH)PO_3H\}_2(H_2O)_2]^{2-}$ [84.7(2)–95.3(2)° and 87.8(2)–92.2(2)°, respectively][24] and $[Zn\{HO_3PC(CH_3)(OH)PO_3H\}_2(H_2O)_2]^{2-}$ [84.98(6)–95.02(6)° and 88.65(6)–91.37(6)°, respectively].[26]

The $H_3NTA2P^{2-}$ ligand in **1** binds to the central metal ion through all of its available anchors each in a unidentate coordination mode. This is in contrast to the bidentate mode of coordination that the $H_3IDA2P^-$ ligand employs in its binding to the same metal ion in $[Co(C_2H_8O_6NP_2)_2(H_2O)_2]$. The latter observation is exemplified through the binding of the two phosphonate anchors to two different $Co^{II}$ ions. Moreover, the four $H_3IDA2P^-$ molecules surrounding the central metal ion are also coordinated to four other $Co^{II}$ ions as a consequence of the presence of the second phosphonate group in each molecule. In this sense, occupancy of the coordination sites in contiguous octahedral $Co^{II}$ ions extends to infinity, thus affording the molecular lattice in **2**.

Another interesting attribute of the $H_3NTA2P^{2-}$ ligand's participation in the coordination sphere of $Co^{II}$ is the presence of a nonprotonated central imino moiety in the ligand.

Table 2. Hydrogen bonds in $[Co(C_4H_9O_8NP_2)(H_2O)_2]\cdot 2H_2O$ (**1**).

| Interaction | D···A [Å] | H···A [Å] | D–H···A [°] | Symmetry operation |
|---|---|---|---|---|
| O3–HO3···O5 | 2.547 | 1.704 | 174.9 | 1 – *x*, –0.5 + *y*, 1 – *z* |
| O6–HO6···O1 | 2.559 | 1.812 | 174.2 | 1 + *x*, *y*, *z* |
| O8–HO8···O4 | 2.593 | 1.850 | 158.7 | 1 – *x*, –0.5 + *y*, –*z* |
| Ow1–Hw1A···Ow3 | 2.720 | 1.841 | 166.4 | *x*, *y*, *z* |
| Ow1–Hw1B···O5 | 2.922 | 2.111 | 166.7 | –1 + *x*, *y*, *z* |
| Ow2–Hw2A···Ow4 | 2.672 | 1.906 | 162.6 | –*x*, 0.5 + *y*,–*z* |
| Ow2–Hw2B···O2 | 2.691 | 1.845 | 167.8 | *x*, *y*, –1 + *z* |
| Ow3–Hw3A···O2 | 2.785 | 1.970 | 166.8 | –*x*, 0.5 + *y*, 1 – *z* |
| Ow3–Hw3B···O6 | 2.934 | 2.187 | 157.8 | 1 – *x*, 0.5 + *y*, –*z* |
| Ow4–Hw4A···O3 | 2.983 | 2.203 | 171.8 | *x*, *y*, *z* |

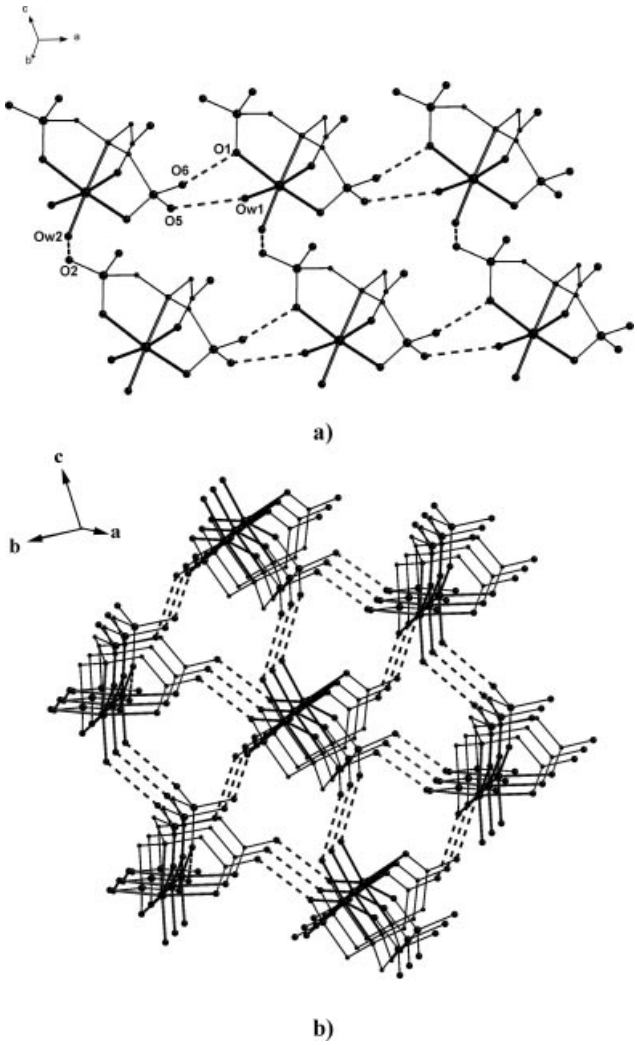


Figure 2. a) The polymeric chains of **1** along the *a* axis and their connection along the *c* axis due to hydrogen-bonding interactions (dashed lines). b) The 3D network of **1** formed by H bonds as shown looking down the *a* axis.

 © 2006 Wiley-VCH Verlag GmbH & Co. KGaA, Weinheim 

As a result, the overall charge of the $H_3NTA2P^{2-}$ ligand coordinated to $Co^{II}$ is 2–, which means that the overall charge for complex **1** is zero. Again, this behavior contrasts with that which has been previously observed for $H_3IDA2P^-$ bound to $Co^{II}$ in complex **2**. There, the central imino moiety of the bound ligand is protonated, thus yielding an overall charge of 1– for the ligand and a zero charge for the complex.

Hydrogen-bonding interactions are present in the crystal structure of **1** (Table 2). These interactions involve the coordinated water molecules, the phosphonate oxygen and hydroxy moieties on the $H_3NTA2P^{2-}$ ligand, and the solvent water molecules. These hydrogen-bonding interactions (Figures 2, parts a and b) generate an extensive network, which very likely contributes to the overall stability of the crystal lattice in **1** (see Discussion).

### Electronic Spectroscopy

The UV/Vis spectrum of **1** was recorded in water at the autogenous pH (Figure 3). The spectrum shows a shoulder-like band at around $\lambda_{max}$ = 550 nm ($\varepsilon \approx 6.8$), ultimately reaching a well-formed major peak at $\lambda_{max}$ = 517 nm (10), with ensuing, subtly discernible, shoulders at around 473 (4) and 462 nm (7.6). A distant band rising into the UV region appears at 222 nm (122.7). The absorption features are likely due to d–d transitions, which are typical for a $Co^{II}$ $d^7$ octahedral species.[27] The multiply structured band around 517 nm can be tentatively attributed to the $^4T_{1g} \rightarrow {}^4T_{1g}(P)$ transition. The observed multiple structure is in line with literature reports that invoke an admixture of spin-forbidden transitions to doublet states derived from $^2G$ and $^2H$, spin-orbit coupling, and vibrational or low-symmetry components to account for the complexity of the spectrum.[28] No further assignments can be made in the absence of detailed specific studies. The spectrum of **1** in water is different from that of $Co^{II}_{aq}$,[29] thus indicating that the coordination sphere of $Co^{II}$ in **1** is likely to be retained in solution.

### FT-IR Spectroscopy

The FT-IR spectrum of complex **1** in KBr shows strong absorptions for the various vibrationally active groups. Antisymmetric as well as symmetric vibrations for the carboxylate group of the coordinated $H_3NTA2P^{2-}$ ligand dominate the spectrum. Specifically, the antisymmetric stretching vibrations, $\nu_{as}(COO^-)$, are present for the carboxylate carbonyls at around 1664 $cm^{-1}$, with the symmetric vibrations, $\nu_s(COO^-)$, for the same group appearing in the range 1461–1408 $cm^{-1}$. The frequencies of the observed carbonyl vibrations are shifted to lower values in comparison to the corresponding vibrations in the free $H_5NTA2P$ acid. The difference between the symmetric and antisymmetric stretches, $\Delta[\nu_{as}(COO^-) - \nu_s(COO^-)]$, is greater than 200 $cm^{-1}$, which indicates that the carboxylate group of the $H_3NTA2P^{2-}$ ligand is either free or coordinated to the metal ion in a monodentate fashion.[30] This was further confirmed by the X-ray crystal structure of **1**.

Vibrations for the $PO_3$ groups were observed for the antisymmetric stretching vibrations, $\nu_{as}(PO_3)$, between 1060 and 986 $cm^{-1}$. Symmetric stretching vibrations, $\nu_s(PO_3)$, were observed in the range 967–906 $cm^{-1}$. The frequencies for the aforementioned stretches appear to be shifted to lower values compared to those of free $H_5NTA2P$ acid, thereby indicating changes in the vibrational status of the ligand upon binding to the $Co^{II}$ ion.[31,32] The aforementioned tentative assignments are also in line with previous data reported for iminophosphonate-containing complexes of various metals.[33]

### Cyclic Voltammetry

The cyclic voltammetric behavior of complex **1** was studied in aqueous solution at the autogenous pH, in the presence of $KNO_3$ as a supporting electrolyte. The cyclic voltammogram shows an irreversible oxidation wave at $E_{1/2}$ = 1.18 V vs. Ag/AgCl, corresponding to the $Co^{II}/Co^{III}$ redox couple and a quasi-reversible wave ($\Delta E$ = 105 mV,

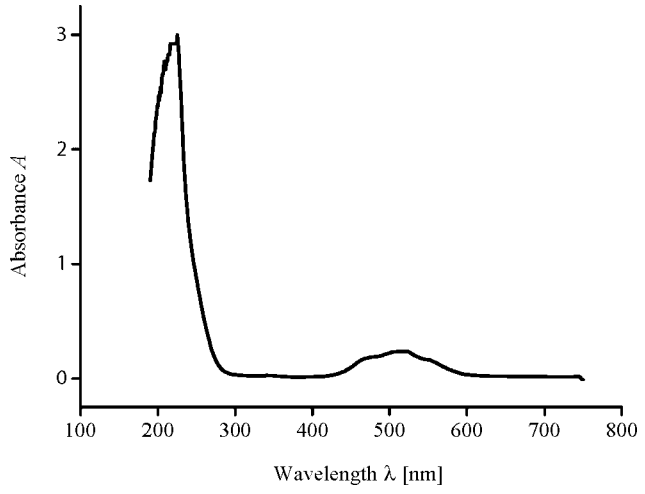


Figure 3. UV/Visible spectrum of **1** in water.

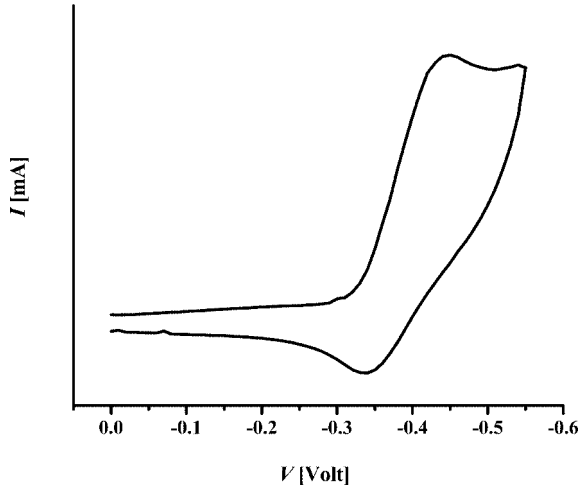


Figure 4. Cyclic voltammogram of **1** in water.

 © 2006 Wiley-VCH Verlag GmbH & Co. KGaA, Weinheim 

$0 < i_{pa}/i_{pc} < 1$, $i_{pc}/\{(v)^{1/2}C\}$ variable) at $E_{1/2}$ = –0.40 V vs. Ag/AgCl corresponding to the $Co^{II}/Co^{I}$ redox couple (Figure 4). The observed $E_{1/2}$ value for the reduction wave is comparable to, albeit lower than, the one reported for other $Co^{II}$–organophosphonate species. Attempts to pursue the isolation of the one-electron-reduced product of the title complex **1** are currently ongoing.

## Magnetic-Susceptibility Studies

### *Magnetic Susceptibility*

Magnetic-susceptibility measurements were carried out at different magnetic fields and in the temperature range 2.3–300 K. Figure 5 shows the $\chi_M T$ vs. $T$ susceptibility data at 0.1 T, where the solid line represents the fit according to the following general Hamiltonian [Equation (1)]

$$H = D\left[S_z^2 - \frac{1}{3}S(S+1)\right] + E(S_x^2 - S_y^2) + g\mu_B H \cdot S \quad (1)$$

where all the parameters have their usual definitions, and $S$ = 3/2.

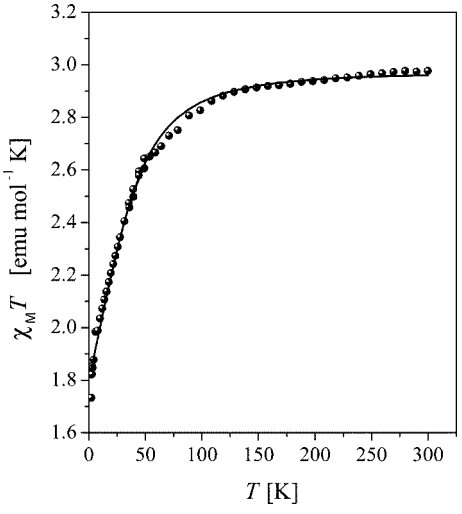


Figure 5. Temperature dependence of the magnetic susceptibility of **1**, in the form of $\chi_M T$ [emu mol$^{-1}$ K] vs. $T$ [K], in the temperature range 2.3–300 K using an external magnetic field of 0.1 T. The solid line represents the fitting results (see text).

The $\chi_M T$ values decrease smoothly from 2.98 emu mol$^{-1}$ K at 300 K to 2.82 emu mol$^{-1}$ K at 98 K and then more steeply to a value of 1.73 emu mol$^{-1}$ K at 2.3 K. The high-temperature value of $\chi_M T$ is higher than 1.875 emu mol$^{-1}$ K, the value that would be expected for a $Co^{II}$ system with $S$ = 3/2. This behavior is consistent with the presence of a significant orbital contribution to the anisotropic nature of the $Co^{II}$ system investigated. The fitting model employed for the susceptibility data is shown in Equation (1). The model takes into account both the axial and rhombic parts of the distortion of the crystal field ($D$, $E$), and an isotropic $g$ value, with the fitting results yielding the following parameters: $D$ = 41.1 cm$^{-1}$ and $g$ = 2.53. The theoretical curve is shown as a solid line in the same figure. It must be pointed out that the signs of $D$ and $E$ cannot be resolved from the magnetic measurements, while introduction of an axial symmetry to $g$ ($g_\perp$, $g_\parallel$) leads to no improvement of the fit. The large value of $D$ is in accordance with an octahedral $Co^{II}$, where the ground-state doublet is well-isolated from the excited ones.[34]

## Magnetization Studies

The magnetization data for **1** in the form of an $M/N\mu_B$ vs. $H$ plot are shown in Figure 6 for two different temperatures and in the field range 0–6 T. The dotted lines represent the theoretical magnetization curves for a system having a ground state with an effective spin, $S$, of 1/2 and an effective $g$ value equal to 4.697. The ground state of the free high-spin $Co^{II}$ ion in an octahedral environment is $^4F$, but the orbital degeneracy is removed in an octahedral crystal field, yielding one $^4A$ and two $^4T$ levels, with the lowest-lying state being a $^4T_{1g}$. The degeneracy of the $^4T_{1g}$ level is removed through the action of axial and rhombic distortions of the crystal field as well as through spin-orbit coupling. The overall effect of low-symmetry crystal-field components and spin-orbit coupling produces six Kramers doublets and results in a doublet ground state. Since the same doublet energy level remains lowest in energy for all values of the applied field strength, and the energy difference between the two lowest lying doublets is relatively large with respect to the thermal energy present at low temperatures (<30 K), the $Co^{II}$ system may be described as having a ground state with an effective spin of $S$ = 1/2.

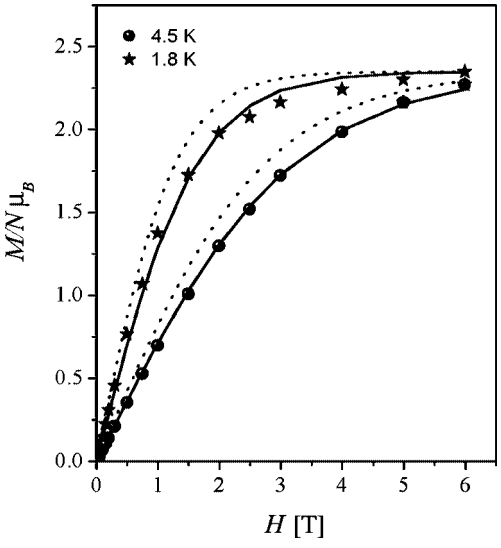


Figure 6. Magnetization of **1**, in the form of $M/N\mu_B$ vs. $H$ [T], at different temperatures and in the field range 0-6 T. The dotted lines represent the theoretical Brillouin functions for an isolated $S$ = 1/2 system with a $g_{eff}$ = 4.697, while the solid lines represent a mean field correction ($zJ$ = –1.5 cm$^{-1}$) taking into account the complex intermolecular interactions.

 © 2006 Wiley-VCH Verlag GmbH & Co. KGaA, Weinheim 

The discrepancy between the theoretical and the experimental curves is mainly due to the fact that a complex hydrogen-bonding network exists, which introduces intermolecular interactions that are important in the low-temperature regime.

A different magnetic model was used to fit the magnetization data according to the following modified Hamiltonian:

$$H = g\mu_B H \cdot S_z - zJ\langle S_z\rangle S_z \quad (2)$$

where the magnetic field is assumed to be along the $z$ direction and the $g$-tensor is taken to be isotropic. $\langle S_z\rangle$ is given by the Boltzmann distribution law

$$\langle S_z\rangle = \frac{\sum_{M_s=-S}^{S} M_s \exp[-E(S,M_s)/kT]}{\sum_{M_s=-S}^{S} \exp[-E(S,M_s)/kT]} = \frac{\sum_{M_s=-S}^{S} M_s \exp\left[1 - M_s\left(g\mu_n H - zJ\langle S_z\rangle\right)/kT\right]}{\sum_{M_s=-S}^{S} \exp\left[1 - M_s\left(g\mu_n H - zJ\langle S_z\rangle\right)/kT\right]} \quad (3)$$

According to Equations (2) and (3) the magnetization formula becomes [Equation (4)]

$$M = -Ng\mu_B\langle S_z\rangle \quad (4)$$

with the negative sign originating from the negative charge of the electron.

An excellent agreement between the experimental modified and theoretical curves (solid lines) was obtained for the following fitting parameters: $zJ = -1.5$ cm$^{-1}$, $g_{eff} = 4.7$.

## EPR Spectroscopy

X-Band EPR measurements were carried out in powder samples as well as in frozen solutions of **1** in water and are shown in Figures 7 and 8, respectively. As a consequence of the fast spin-lattice relaxation time of high-spin $Co^{II}$, signals were observed only below 70 K. For the powder spectra, a strong signal appears at low fields and a small broad one at $g = 2.30$ at temperatures below 23 K. In an attempt to comprehend the observed behavior, a simulation[34] was carried out in order to derive the effective $g$ values riding on a Hamiltonian formalism [Equation (5)]

$$H = g_z\mu_B H_z S_z + g_x\mu_B H_x S_x + g_y\mu_B H_y S_y \quad (5)$$

with an effective spin of 1/2 and an anisotropic $g$-tensor. The results are shown in Figure 9. An isotropic magnetic-field domain line-width was used in both cases (lw = 35 G for the powder and 75 G for the frozen solution), with the broadness of the spectra revealing $g$-strain effects. Gaussian distributions of the $g$-principal values were used and the results were $\sigma g_x = \sigma g_z = 0.78$, $\sigma g_y = 0.23$ for the powder, and $\sigma g_x = \sigma g_y = \sigma g_z = 0.78$ for the frozen solution. The principal $g$ values for the powder spectrum are $g_x = 4.92(1)$, $g_y = 2.28(1)$, $g_z = 6.33(1)$ ($g_{eff} = 4.51$) and for the frozen solution $g_x = 4.20(1)$, $g_y = 2.35(1)$, $g_z = 5.33(1)$ ($g_{eff} = 3.96$).

The dominant broadening effect emerges when the $g$-strain is converted into $B$-strain through the equation $\Delta B = -(h\nu/\mu_B)\cdot(\Delta g/g^2)$, where the parameters have their usual meaning. Thus, the largest and smallest $g$ values of the powder and solution spectra have field widths that differ by an order of magnitude, thereby rationalizing the broad high-field features of the spectrum.

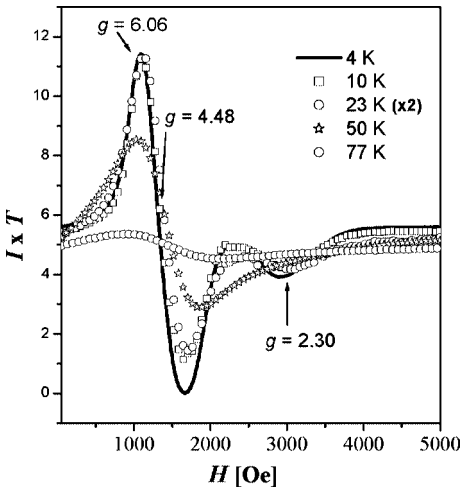


Figure 7. Temperature dependence of the powder X-Band EPR spectrum (the intensity is multiplied by the temperature) of **1** in the field range 0–5000 Oe.

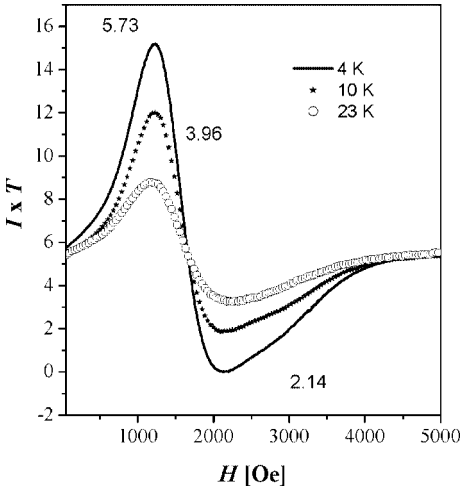


Figure 8. Temperature dependence of the water solution X-Band EPR spectrum (the intensity is multiplied by the temperature) in the field range 0–5000 Oe.

A very important feature of the $Co^{II}$ ion is the value of the effective $g$ parameter, $g_{eff}$, extracted from the EPR measurements, as a result of which interesting comments can be made. To this end, one important issue, not sufficiently discussed in the literature, pertains to an octahedron in a high-spin $Co^{II}$ system with a small tetragonal or trigonal distortion, whereby additional terms are added in the ground-state doublet. Provided that these terms are small compared with the spin-orbit coupling of the ground-state doublet, they may be written in the form [Equation (6)]

 © 2006 Wiley-VCH Verlag GmbH & Co. KGaA, Weinheim 

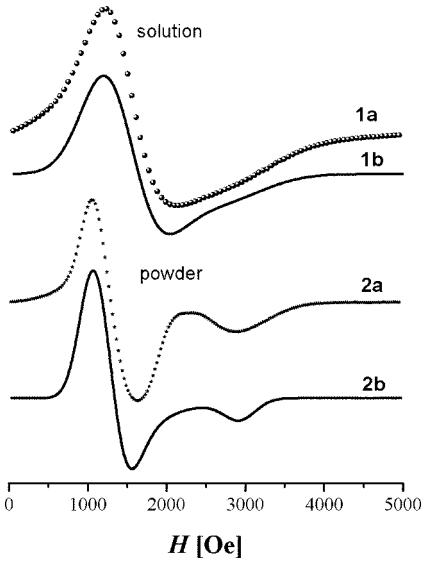


Figure 9. Simulations of the solution (1a) and powder (2a) EPR spectrum are shown as solid lines (1b) and (2b), respectively. The derived g values and the distribution widths of the g principal values in each case are given in the text.

$$\left|J=\frac{1}{2},J_z=\pm\frac{1}{2}\right\rangle+a\left|\frac{3}{2},\pm\frac{1}{2}\right\rangle+b\left|\frac{5}{2},\pm\frac{1}{2}\right\rangle \quad (6)$$

where $a$, and even more so $b$, are small compared to unity. According to Abragam and Bleaney,[35] and by neglecting terms of order $a^2$ and $b^2$, the expressions for the $g$ parameters of the $Co^{II}$ system are [Equations (7)]

$$g_{\parallel}=\frac{5}{3}g_s-\frac{2}{3}g_l+\left(\frac{4\sqrt{5}a}{3}\right)(2g_s-g_l)$$
$$g_{\perp}=\frac{5}{3}g_s-\frac{2}{3}g_l-\left(\frac{2\sqrt{5}a}{3}\right)(2g_s-g_l) \quad (7)$$

where $g_s = 2.0$ and $g_l = -3/2$.

The dependence of the $g$ parameters on the $a$ parameter of Equation (6) is shown in Figure 10. From Equations (7) and Figure 10, it is clear that the value of $g_{eff} = (g_{\parallel} + 2g_{\perp})/3 \approx (5g_s - 2g_l)/3 \approx 4.33$. Therefore, an isotropic $g$ value of $g_{\parallel} = g_{\perp} = 4.33$ corresponds to $a = 0$ (the energy difference between the ground-state doublet and the excited one is very large), whereas for an admixture of other terms the value of $g_{eff}$ increases accordingly (Figure 10).

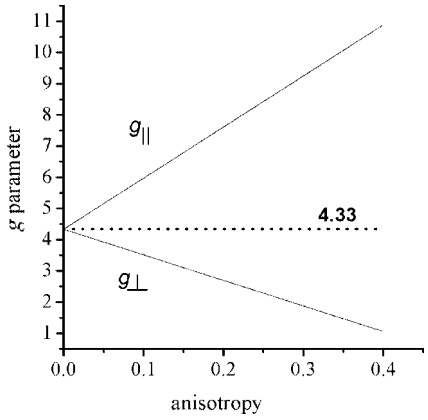


Figure 10. Anisotropy dependence of the $g$ parameters ($g_{\parallel}$ and $g_{\perp}$) of a high-spin $Co^{II}$ octahedron resulting from a small tetragonal or trigonal distortion.

Another issue emerges from the fact that weak intermolecular interactions (hydrogen bonding) between $Co^{II}$ ions can influence the value of $g_{eff}$, and this can be resolved only if EPR measurements are carried out in both powder and solution samples.

The magnetic and EPR parameters of different high-spin $Co^{II}$ complexes are shown in Table 3.[36] Based on the collective data and the aforementioned comments, several interesting conclusions can be drawn. First of all, it seems that for values of $g_{eff}$ above 4.33 (in the EPR spectra of powder samples), the intermolecular interactions contribute significantly to the magnetic behavior of the system. In the case of $[Co(C_4H_8NO_3)_2(H_2O)_2]$,[36a] a weak exchange interaction transmitted through hydrogen bonds is proposed between neighboring $Co^{II}$ centers in the exchange limit $0.25 < |J| < 1.2\ cm^{-1}$. To this end, the Brillouin function of an isolated $S = 1/2$ system could reproduce the magnetization curves, leading to the conclusion that its contribution is small. For all the other cases ($g_{eff} < 4.33$) no significant

Table 3. Magnetic and EPR properties of various $Co^{II}$ carboxylate and mixed carboxylate-phosphonate compounds.

| Compounds | $g_{eff}$[a] (EPR) | $g_{eff}$ [b] (Magnetization) | Model $S = 3/2$[c] |
|---|---|---|---|
| This work | 4.51(1) (p)<br>3.96(1) (s) | 4.70(1)<br>$zJ = -1.5\ cm^{-1}$ | $g = 2.53(1)$, $D = 41(1)\ cm^{-1}$ |
| $[Co(C_4H_8NO_3)_2(H_2O)_2]$[36a] | 4.45(1) (p) | 4.50(1) | $g = 2.60(1)$, $D = 114(4)\ cm^{-1}$ |
| $[Co(C_2H_8O_6NP_2)_2(H_2O)_2]$[20] | 4.10(1) (p)<br>4.10(1) (s) | 4.20(1) | $g = 2.33$, $D = 40(1)\ cm^{-1}$<br>($g_{\parallel} = 1.7$, $g_{\perp} = 2.53$), $D = 52(1)\ cm^{-1}$<br>$\lambda = 0.33$ |
| $(NH_4)_4[Co(C_6H_5O_7)]_2$[21] | 4.00(1) (p) | 4.50(1)[d] | $g = 2.42$, $D = 0.83\ cm^{-1}$ |
| $K_2[Co_2(C_6H_5O_7)_2(H_2O)_4]\cdot 6\ H_2O$[e][36b] | 3.75(1) (s) | 3.87(1) | – |

[a] $g_{eff}$ $[(g_x + g_y + g_z)/3]$ is derived from the EPR measurements performed in powder (p) or solution (s) samples. [b] $g_{eff}$ is derived by simulation of the magnetization data at different temperatures using the Brillouin function for an isolated $S = 1/2$ system, or Equation (4) in the case of intermolecular interactions. [c] Fitting parameters ($D$, $E$, $g$) obtained from Equation (1) for the fit of the susceptibility data. [d] The simulation was carried out using the magnetization data from ref.[21]. [e] This complex is a dimer in the solid state. We only used the solution spectrum of the complex, since it dissociates into monomers in solution.[36b]

 © 2006 Wiley-VCH Verlag GmbH & Co. KGaA, Weinheim 

intermolecular interactions are observed. The significance of the aforementioned point is also exemplified in the small $g_{eff}$ value of the frozen-solution spectrum, where the hydrogen-bonding system breaks apart and no longer exists. Secondly, the $g_{eff}$ value derived from the magnetization data is not equal to the value obtained from EPR measurements due to the fact that, in the magnetization data, there is also some contribution from intermolecular interactions, a fact amply emphasized and alluded to in the magnetization study of this work.

### Linking the Aqueous Chemistry of the Binary $Co^{II}$–$H_5NTA2P$ System to the Organophosphonate Structural Features

In a simple and pH-specific manner, the employment of the binary system $Co^{II}$-($H_5NTA2P$) led to the isolation of a clean product **1** in crystalline form. The idea was to initially explore the reactivity of the aforementioned system at low pH. The $H_5NTA2P$ ligand projects important features that emerge due to its structure containing both carboxylic and phosphonic moieties (see below). Under such conditions, addition of ethanol contributed to the isolation of $[Co(C_4H_9O_8NP_2)(H_2O)_2]\cdot 2H_2O$ (**1**) at pH 1.5. The nature of **1** is that of a molecular type of lattice comprised of mononuclear units linked together through water molecules of crystallization and an extensive network of hydrogen bonds.

The carboxydiphosphonate ligand anchored onto the octahedral $Co^{II}$ site reveals a coordination mode that reflects employment of all potential anchor sites in $H_5NTA2P$. Variable modes of phosphonate coordination have previously been observed in a plethora of metal organophosphonate complexes containing the phosphonate ligand termini in varying deprotonation states.[37] In the present case, the coordinated $H_5NTA2P$ ligand loses two of its protons from the two terminal phosphonate groups, rendering each one of them singly deprotonated. As a result, the remaining carboxylic acid moiety remains protonated and, as such, it is anchored to the metal site. The double deprotonation of the $H_5NTA2P$ ligand yields an overall charge of zero for the assembled mononuclear complex, affording the previously mentioned molecular type of lattice in **1**.

The nitrogen center plays a prominent role in the coordination of the $H_5NTA2P$ ligand around $Co^{II}$. A strong interaction with the metal center brings it to a distance of 2.229(2) Å from $Co^{II}$. Thus, the tetradentate ligand imparts significant stability upon the resulting species. Due to the fact that the ligand itself employs four potential anchoring sites to bind the metal ion, the octahedral coordination environment is left with two unoccupied sites, which are occupied by water molecules from the reaction medium.

As a consequence of the molecular chemistry between the $H_5NTA2P$ and $Co^{II}$, discrete moieties evolve as mixed carboxylate-phosphonate species in aqueous media. This is in contrast to the intermolecular chemistry previously observed between another diphosphonate ligand, namely iminodiphosphonic acid (IDA2P), and $Co^{II}$.[36b] There, the ligand promotes an intermolecular linkage of nearby $Co^{II}$ centers, affording a molecular lattice with distinct structural features, at low pH.

The magnetic susceptibility and magnetization measurements on complex **1** support the presence of a high-spin octahedral $Co^{II}$ species having a ground state with an effective spin of 1/2. EPR measurements in the solid state and in aqueous solution corroborate the magnetization data, suggesting the existence of a high-spin $Co^{II}$ complex in solution. Such a complex would very likely include the ligand octahedral environment provided by $H_3NTA2P^{2-}$ and the two water molecules.[37] To this end, both UV/Vis and EPR data suggest a species with a formulation not unlike that of the title complex $[Co(C_4H_9O_8NP_2)(H_2O)_2]^0$. A similar behavior has previously been observed for $[Co(C_2H_8O_6NP_2)_2(H_2O)_2]$.[20]

To the extent that the title complex is an aqueous species of $Co^{II}$, it appears that the aqueous distribution of species arising from the binary system $Co^{II}$–$H_5NTA2P$ encompasses such components emerging at low pH. That, in turn, hints at the existence of other species that might participate in the requisite speciation at higher pH values. This contention is potentially exemplified by the nature of the $H_5NTA2P$ ligand, with its mixed composition eliciting variable chemical coordination events around $Co^{II}$ with equally variable protonation states. Furthermore, $H_5NTA2P$ is a ligand that can be viewed as a derivative of the nitrilotriacetic acid ligand $(HOOCCH_2)_3N$ ($H_3NTA$), with the two terminal carboxylates replaced by phosphonates. Solution as well as synthetic studies have been carried out for dicarboxylic acids,[38,39] aminoalkylphosphonates, and IDA-derived phosphonate ligands, like *N*-(phosphonomethyl)glycine,[40] in the presence of various metal ions.[41,42] These studies suggest that these ligands bind metal ions like $Co^{II}$ efficiently to form soluble complexes.[12a] Despite the fact that analogous studies with $(H_2O_3PCH_2)_2NCH_2COOH$ and $Co^{II}$ have not been carried out, it would not be unreasonable to suggest that a similar chemistry may be unfolding in this system too. In this sense, solution investigations would be helpful in revealing the nature of the interaction as well as the properties of the arising species as a function of pH and molecular stoichiometry. Such studies are under way in our laboratory.

Given that solubility is a prerequisite for bioavailability of species eliciting interactions at the cellular level, the structural and molecular composition of complex **1** suggest that significant features of $Co^{II}$ might be associated with interactions with biological targets. The distinct nature of $H_5NTA2P$ allows both phosphorylated and carboxylic sidechains of abutting biomolecular sites to interact concurrently with $Co^{II}$, thus giving rise to soluble species. Even though studies of soluble bioavailable $Co^{II}$–carboxyphosphonate species have yet to be performed, they could provide significant insight into the nature and properties of binary or ternary $Co^{II}$–ligand species of potential biological value to variable activity pathways in human physiology. Along these lines, the value of $E_{1/2}$ (–0.40 V) observed in the cyclic voltammogram of **1** for $Co^{II}/Co^{I}$ is an indicator

 © 2006 Wiley-VCH Verlag GmbH & Co. KGaA, Weinheim 

of the physicochemical properties bestowed on $Co^{II}$ upon coordination by $H_5NTA2P$ and tuned into in the biologically relevant redox potential range.

### Potential Formation of Organophosphonate-Containing Materials

The nature and properties of organophosphonate substrates have drawn keen interest in the search for new materials containing a variety of metals. Numerous approaches and synthetic methodologies have been employed in the quest for metal-organophosphonate materials with varying structures. The search for new materials has targeted diverse applications, extending from electronics to catalysis. To that end, organophosphonic acid substrates like $H_2O_3PCH_2CH_2$-COOH, or diphosphonic acids[43] like $H_2O_3PRPO_3H_2$, have been employed with different R groups [$C_6H_4$, $(CH_2)_n$],[44] joining the phosphonate moieties, that influence the structural features of the derived material significantly (compare [$Co(C_4H_9O_8NP_2)(H_2O)_2$]·$2H_2O$ (**1**) with [$Zn_2\{O_2CCH_2NH$-$(CH_2PO_3)_2\}$]).[45,46] Such features include lattice parameters, shape, size, and dimensionality, all of which affect the applied chemistry in selective and specific low molecular mass (alcohol, amine, etc.) transformation processes.

One such key factor that influences the nature of the lattice formed in a solid-state material is hydrogen bonding. This dominates the lattice structure of **1** and involves the coordinated and solvent water molecules as well as the protonated phosphonate and carboxylate moieties. The extensive network of hydrogen bonds can be simplified if one attempts to assemble it step by step. Specifically, the mononuclear species of **1** are hydrogen bonded through O6–HO6···O1 (1 + *x*, *y*, *z*) and Ow1–Hw1B···O5 (–1 + *x*, *y*, *z*) interactions to form polymeric chains that extend in a direction parallel to the crystallographic *a* axis. These chains are further hydrogen bonded through an Ow2–Hw2B···O2 (*x*, *y*, –1 + *z*) interaction to form a two-dimensional network lying parallel to the crystallographic *ac* plane. As shown in Figure 2 (a), the layered structure thus formed contains vacancies between the mononuclear species. Furthermore, the involvement of the remaining protonated phosphonate and carboxylate moieties in hydrogen-bonding interactions [O3–HO3···O5 (1 – *x*, –0.5 + *y*, 1 – *z*) and O8–HO8···O4 (1 – *x*, –0.5 + *y*, –*z*)] leads to the extended 3D lattice structure of **1**. As shown in Figure 2 (b), tubular channels are formed down the crystallographic *a* axis, where the lattice water molecules are encapsulated. Ostensibly, hydrogen-bonding interactions between the encapsulated lattice water molecules and the protonated phosphonate and carboxylate groups of the ligand, as well as the coordinated water molecules, are responsible for the stabilization of the encapsulated solvent molecules.

The nature of the metal ion is another key factor in metal organophosphonate materials. To this end, phosphonate-containing pillared layered structures have been synthesized from vanadium, such as the material [(VO)$(H_2O)$-$\{O_3PCH_2NH(C_2H_4)_2NHCH_2PO_3\}$],[46,47a] while manganese- and cobalt-containing materials such as [$M\{O_3PCH_2NH(C_2H_4)_2NHCH_2PO_3\}$]·$H_2O$ (M = $Mn^{II}$, $Co^{II}$) have also been isolated.[47b] Numerous such materials have emerged in the past few years, with key representatives including the compounds [$Co\{(CH_3COO)_2NCH_2PO_3\}$-$(H_2O)_5$]·$H_2O$,[48] [$Co(C_2H_8O_6NP_2)_2(H_2O)_2$],[20] [$Co_2(O_3$-$PC_6H_4PO_3)(H_2O)_2$],[49] and [$Co_2(O_3PC_6H_4OC_6H_4PO_3)$]·$2H_2O$,[50] amongst others. Collectively, the physical and chemical properties of $Co^{II}$–organophosphonate materials signify the decisive role of features upon which rests the design of future compounds with specific attributes for potential selective applications. To this end, examination of the herein described binary $Co^{II}$-$H_5NTA2P$ system under conditions far removed from a room-temperature environment (e.g. hydrothermal conditions) could, in principle, result in a material with distinct physical and chemical characteristics not necessarily similar to those observed in the title species **1**. This approach could prove to be effective in affording diverse species that could potentially participate in the aqueous binary speciation scheme and possess physicochemical characteristics associated with applications alluded to above in other cobalt-containing materials.

## Conclusions

The mixed carboxydiphosphonate complex of $Co^{II}$, reflected in the structural formulation of [$Co(C_4H_9O_8NP_2)$-$(H_2O)_2$]$^0$ (**1**), contains basic structural features of species that might arise as a result of the interaction of $Co^{II}$ with adjacent carboxy and phosphorylated sites on low molecular mass biotargets in biological fluids. Complex **1**, in fact, constitutes proof of a species arising from speciation of binary systems containing $Co^{II}$ and simple phosphonate ligands.[40] In the absence of solution speciation studies on the specific $Co^{II}$-$H_5NTA2P$ system, the synthetic efforts of this work prove the existence of discrete species with characteristic structural and chemical properties both in the solid state as well as in solution. Spectroscopic studies combined with cyclic voltammetric, magnetic, and EPR data in the solid state and in solution support the experimental observations and formulate the speciation signature of the investigated binary system, and hint at the existence of other, as yet elusive, species arising in a pH-dependent fashion across the pH physiological range under both room temperature and hydrothermal conditions. Albeit low, the pH at which the assembly of the investigated species was pursued gives clues to the physicochemical properties of soluble species that might become bioavailable in the presence of suitable molecular targets at the cellular level. The investigation of such interactions and in-depth research of related materials and their potential applications are currently being pursued in our laboratory.

## Experimental Section

**Materials and Methods:** All experiments were carried out in the open air at room temperature. Nanopure-quality water was used

 © 2006 Wiley-VCH Verlag GmbH & Co. KGaA, Weinheim 

for all reactions. $Co(NO_3)_2 \cdot 6H_2O$ and *N*,*N*-bis(phosphonomethyl)-glycine ($H_5NTA2P$) were purchased from Aldrich.

**Physical Measurements:** FT-IR measurements were taken with a Perkin–Elmer 1760X FT-infrared spectrometer. UV/Vis spectra were recorded with a Hitachi U-2001 spectrophotometer in the range 200–1000 nm. The EPR spectra of complex **1** in the solid state and in aqueous solution were recorded with a Bruker ER 200D-SRC X-band spectrometer, equipped with an Oxford ESR 9 cryostat. The powder spectra were recorded at 9.4261 GHz in the temperature range 4–77 K. The solution spectra were recorded at 9.3979 GHz in the temperature range 4–23 K. Magnetic susceptibility data were collected on powdered samples of **1** with a Quantum Design SQUID susceptometer in the temperature range 2.3–300 K, under various applied magnetic fields. Magnetization measurements were carried out at three different temperatures in the field range 0–6 T. Fitting procedures for the acquired experimental data were applied through the use of Fortran programming routines relating to the Hamiltonians employed and the basic parameters *D*, *E*, and *g*.[20,21,36b] Elemental analyses were performed by Quantitative Technologies, Inc. Electrochemical measurements were carried out with a Uniscan Instruments Ltd. model PG580 potensiostat-galvanostat. The entire system was under computer control and supported by the appropriate computer software (Ui Chem. Version 1.08RD) running on Windows. The electrochemical cell used had platinum (disk) working and auxiliary (wire) electrodes; an Ag/AgCl electrode was used as reference electrode. The water used in the electrochemical measurements was of nanopure quality. $KNO_3$ was used as supporting electrolyte. Normal concentrations used were 1–6 mM in electroanalyte and 0.1 M in supporting electrolyte. Purified argon was used to purge the solutions prior to the electrochemical measurements.

**Preparation of $[Co(C_4H_9O_8NP_2)(H_2O)_2]\cdot 2H_2O$ (1):** $Co(NO_3)_2 \cdot 6H_2O$ (0.17 g, 0.58 mmol) and *N*,*N*-bis(phosphonomethyl)glycine ($H_5NTA2P$; 0.16 g, 0.59 mmol) were dissolved in nanopure water. The pH of the resulting solution was 1.5. This reaction mixture was stirred at room temperature for 10–15 min. Subsequently, the reaction flask was cooled to 4 °C in the presence of ethanol. A couple of weeks later pink prismatic crystals grew out of the solution. The crystalline material was collected by filtration, and was dried under vacuum. Yield: 0.14 g (≈ 61%). $C_4H_{17}CoNO_{12}P_2$ (392.06): calcd. C 12.24, H 4.34, N 3.57; found C 12.53, H 4.45, N 3.54.

**X-ray Crystal Structure Determination of 1:** X-ray quality crystals of compound **1** were grown from aqueous solution. A single crystal with dimensions $0.12 \times 0.40 \times 0.60$ mm$^3$ was mounted on a Crystal Logic dual-goniometer diffractometer equipped with a graphite-monochromated Mo-$K_\alpha$ radiation source. Unit-cell dimensions for **1** were determined and refined by using the angular settings of 25 automatically centered reflections in the range $11 < 2\theta < 23°$. Intensity data were measured by the $\theta$–$2\theta$ scans technique. Throughout data collection, three standard reflections were monitored every 97 reflections, and showed less than 2% variation and no decay. Lorentz, polarization, and psi-scan absorption corrections were applied by using Crystal Logic software. Further experimental crystallographic details for **1**: $2\theta_{max} = 50°$; scan speed: 4.0° min$^{-1}$; scan range: $2.25 + \alpha_1\alpha_2$ separation; number of reflections collected/unique/used: 2670/2474 ($R_{int}$ = 0.0198)/2474; 249 parameters refined; $F(000)$ = 402; $(\Delta/\sigma)_{max}$ = 0.015; $(\Delta\rho)_{max}/(\Delta\rho)_{min}$ = 0.341/–0.227 e Å$^{-3}$; GOF = 1.049; $R/R_w$ (for all data), 0.0226/0.0611.

The structure of complex **1** (Table 4) was solved by direct methods using SHELXS-86,[51] and refined by full-matrix least-squares techniques on $F^2$ with SHELXL-97.[52] All non-H atoms in the structure of **1** were refined anisotropically. All H atoms in the structure of **1** were located by difference maps and were refined isotropically.

Table 4. Summary of crystal, intensity collection, and refinement data for $[Co(C_4H_9O_8NP_2)(H_2O)_2]\cdot 2H_2O$ (**1**).

| | |
|---|---|
| Formula | $C_4H_{17}CoNO_{12}P_2$ |
| Formula weight | 392.06 |
| Temperature [K] | 298 |
| Wavelength [Å] | 0.71073, Mo-$K_\alpha$ |
| Space group | $P2_1$ |
| $a$ [Å] | 7.566(3) |
| $b$ [Å] | 12.721(5) |
| $c$ [Å] | 7.361(3) |
| $\beta$ [°] | 96.271(13) |
| $V$ [Å$^3$] | 704.2(5) |
| $Z$ | 2 |
| $D_{calcd.}/D_{measd}$ (Mg m$^{-3}$) | 1.849/1.83 |
| Abs. coeff. ($\mu$) [mm$^{-1}$] | 1.504 |
| Range of $h,k,l$ | –8→8, –15→15, 0→8 |
| Goodness-of-fit on $F^2$ | 1.049 |
| $w$* | $a$ = 0.0337 $b$ = 0.1093 |
| $R$[a] | $R$ = 0.0226[b] |
| $R_w$[a] | $R_w$ = 0.0610[b] |

[a] $R$ Values are based on $F$ values, $R_w$ values are based on $F^2$ $R = \frac{\sum \| F_o | - | F_c \|}{\sum (| F_o |)}$, $R_w = \sqrt{\sum [w(F_o^2 - F_c^2)^2] / \sum [w(F_o^2)^2]}$. [b] For 2468 reflections with $I > 2\sigma(I)$; $w^* = 1/[\sigma^2(F_o^2) + (aP)^2 + bP]$ where $P = [\mathrm{Max}(F_o^2,0) + 2F_c^2]/3$.

CCDC-283144 (for **1**) contains the supplementary crystallographic data for this paper. These data can be obtained free of charge from the Cambridge Crystallographic Data Center via www.ccdc.cam.ac.uk/data_request/cif.

## Acknowledgments

This work was supported by a "Pythagoras" grant from the National Ministry of Education and Religious Affairs and by a "PENED" grant from the General Secretariat of Research and Technology, Greece. V.T. would like to thank Dr. I. Sanakis of the N.C.S.R "Demokritos", Athens, Greece, for the EPR measurements and Dr. C. Sangregorio of the Department of Chemistry, Florence, Italy, for magnetic data collection.

[1] T. D. M. Taylor, D. R. Williams, *Trace Element Medicine and Chelation Therapy*, Royal Society of Chemistry, Cambridge, **1995**.
[2] S. Balachandran, R. A. Vishwakarma, S. M. Monaghan, A. Prelle, N. P. J. Stamford, F. J. Leeper, A. R. Battersby, *J. Chem. Soc., Perkin Trans. 1* **1994**, 487–491.
[3] A. R. Battersby, *Acc. Chem. Res.* **1993**, *26*, 15–21.
[4] L. Debussche, M. Couder, D. Thibaut, B. Cameron, J. Crouzet, F. Blanche, *J. Bacteriol.* **1992**, *22*, 7445–7451.
[5] a) S. L. Roderick, B. W. Matthews, *Biochemistry* **1993**, *32*, 3907–3912; b) A. Ben-Bassat, K. Bauer, S.-Y. Chang, K. Myambo, A. Boosman, S. Chang, *J. Bacteriol.* **1987**, *169*, 751–757.
[6] M. S. Payne, S. Wu, R. D. Fallon, G. Tudor, B. Stieglitz, I. M. Turner Jr, M. J. Nelson, *Biochemistry* **1997**, *36*, 5447–5454.
[7] S. J. Lippard, J. M. Berg, *Principles of Bioinorganic Chemistry*, University Science Books, Mill Valley, CA (USA), **1994**, chapter 11, p. 336–347.
[8] E. M. N. Hamilton, S. A. S. Gropper, *The Biochemistry of Human Nutrition*, West Publishing Company, New York, **1987**, p. 298–301.

 © 2006 Wiley-VCH Verlag GmbH & Co. KGaA, Weinheim 

[9] H. M. Helis, P. de Meester, D. J. Hodgson, *J. Am. Chem. Soc.* **1976**, *99*, 3309–3312.

[10] G. L. Waldbott, *Health Effects of Environmental Pollutants*, C. V. Mosby, Co.: St. Louis, MO, USA, **1973**.

[11] a) T. Kiss, *Bioinorganic Chemistry* (Ed.: K. Burger), Ellis Horwood, Chichester, **1990**, p. 56; b) R. B. Martin, *J. Inorg. Biochem.* **1986**, *28*, 181–187; c) P. M. May, P. W. Linder, D. R. Williams, *J. Chem. Soc., Dalton Trans.* **1977**, 588–595; d) D. D. Perrin, *Nature* **1965**, *206*, 170.

[12] a) D. Sanna, I. Bodi, S. Bouhsina, G. Micera, T. Kiss, *J. Chem. Soc., Dalton Trans.* **1999**, 3275–3282; b) T. Kiss, *Bioinorganic Chemistry* (Ed.: K. Burger), Ellis Horwood, Chichester, **1990**, p. 56.

[13] a) J. Zubieta, *Comments Inorg. Chem.* **1994**, *16*, 153–183; b) C. Bhardwaj, H. Hu, A. Clearfield, *Inorg. Chem.* **1993**, *32*, 4294–4299; c) A. Clearfield, *Comments Inorg. Chem.* **1990**, *10*, 89–128.

[14] a) Q. Chen, J. Salta, J. Zubieta, *Inorg. Chem.* **1993**, *32*, 4485–4486; b) E. T. Clarke, P. R. Rudolph, A. E. Martell, A. Clearfield, *Inorg. Chim. Acta* **1989**, *164*, 59–63; c) P. R. Rudolph, E. T. Clarke, A. E. Martell, A. Clearfield, *J. Coord. Chem.* **1985**, *14*, 139–149.

[15] B. Bujoli, P. Palvadeau, J. Rouxel, *Chem. Mater.* **1990**, *2*, 582–589.

[16] a) Y. Zhang, A. Clearfield, *Inorg. Chem.* **1992**, *31*, 2821–2826; b) G. H. Huan, A. J. Jacobson, J. W. Johnson, E. W. Corcoran Jr, *Chem. Mater.* **1990**, *2*, 91–93; c) G. Cao, H. Lee, V. Lynch, T. E. Mallouk, *Inorg. Chem.* **1988**, *27*, 2781–2785.

[17] a) D. A. Burwell, K. G. Valentine, J. H. Timmermans, M. E. Thompson, *J. Am. Chem. Soc.* **1992**, *114*, 4144–4150; b) G. L. Rosenthal, J. Caruso, *Inorg. Chem.* **1992**, *31*, 3104–3106; c) M. B. Dines, P. C. Griffith, *Inorg. Chem.* **1983**, *22*, 567–569; d) M. B. Dines, P. M. DiGiacomo, *Inorg. Chem.* **1981**, *20*, 92–97.

[18] a) H. Byrd, J. K. Pike, D. R. Talham, *J. Am. Chem. Soc.* **1994**, *116*, 7903–7904; b) H. E. Katz, W. L. Wilson, G. Scheller, *J. Am. Chem. Soc.* **1994**, *116*, 6636–6640; c) S. B. Ungashe, W. L. Wilson, H. E. Katz, G. R. Scheller, T. M. Putrinski, *J. Am. Chem. Soc.* **1992**, *114*, 8717–8719; d) R.-C. Wang, Y. Zhang, H. Hu, R. R. Frausto, A. Clearfield, *Chem. Mater.* **1992**, *4*, 864–871; e) G. L. Rosenthal, J. Caruso, *Inorg. Chem.* **1992**, *31*, 144–145.

[19] a) G. Cao, T. E. Mallouk, *Inorg. Chem.* **1991**, *30*, 1434–1438; b) K. J. Frink, R.-C. Wang, J. L. Colon, A. Clearfield, *Inorg. Chem.* **1991**, *30*, 1438–1441.

[20] H. Jankovics, M. Daskalakis, C. P. Raptopoulou, A. Terzis, V. Tangoulis, J. Giapintzakis, T. Kiss, A. Salifoglou, *Inorg. Chem.* **2002**, *41*, 3366–3374.

[21] M. Matzapetakis, M. Dakanali, C. P. Raptopoulou, V. Tangoulis, A. Terzis, N. Moon, J. Giapintzakis, A. Salifoglou, *J. Biol. Inorg. Chem.* **2000**, *5*, 469–474.

[22] L. Kryger, S. E. Rasmussen, *Acta Chem. Scand.* **1972**, *26*, 2349–2359.

[23] T. Glowiak, W. Sawka-Dobrowolska, B. Jezowska-Trzebiatowska, *Inorg. Chim. Acta* **1980**, *45*, L105–L106.

[24] V. S. Sergienko, G. G. Aleksandrov, E. G. Afonin, *Zh. Neorg. Khim.* **1997**, *42*, 1291–1296.

[25] S. M. Godfrey, D. G. Kelly, C. A. McAuliffe, R. G. Pritchard, *J. Chem. Soc., Dalton Trans.* **1995**, 1095–1101.

[26] V. S. Sergienko, E. G. Afonin, G. G. Aleksandrov, *Zh. Neorg. Khim.* **1998**, *43*, 1002–1007.

[27] R. S. Drago, *Physical Methods in Chemistry*, W. B. Saunders Company, Philadelphia, **1977**, p. 359–410.

[28] A. B. P. Lever, *Inorganic Electronic Spectroscopy*, 2nd Edition, Elsevier, Amsterdam, **1984**, p. 480–490.

[29] a) B. N. Figgis, *Introduction to Ligand Fields*, Interscience Publishers, New York, **1966**; b) C. K. Jorgensen, *Adv. Chem. Phys.* **1963**, *5*, 33–146; c) C. J. Ballhausen, *Introduction to Ligand Field Theory*, McGraw-Hill Book Co.: New York, **1962**.

[30] a) C. Djordjevic, M. Lee, E. Sinn, *Inorg. Chem.* **1989**, *28*, 719–723; b) G. B. Deacon, R. Philips, *J. Coord. Chem. Rev.* **1980**, *33*, 227–250.

[31] a) D. E. C. Corbridge, *J. Appl. Chem.* **1956**, *6*, 456–465; b) R. C. Gore, *Discuss. Faraday Soc.* **1950**, *9*, 138–143; c) J. V. Bell, J. Heisler, H. Tannenbaum, J. Goldenson, *J. Am. Chem. Soc.* **1954**, *76*, 5185–5189; d) L. C. Thomas, R. A. Chittenden, *Spectrochim. Acta* **1964**, *20*, 467–487.

[32] a) R. A. McIvor, C. E. Hubley, *Can. J. Chem.* **1959**, *37*, 869–876; b) L. C. Thomas, R. A. Chittenden, *Chem. Ind. (London)* **1961**, 1913.

[33] a) D. S. Sagatys, C. Dahlgren, G. Smith, R. C. Bott, A. C. Willis, *Aust. J. Chem.* **2000**, *53*, 77–81; b) S. Shoval, S. Yariv, *Agrochimica* **1981**, *25*, 377–386; c) V. Subramanian, P. E. Hoggard, *J. Agric. Food Chem.* **1988**, *36*, 1326–1329.

[34] R. Boca, *Coord. Chem. Rev.* **2004**, *248*, 757–815.

[35] A. Abragam, B. Bleaney, *Electron Paramagnetic Resonance of Transition Ions*, Clarendon Press, Oxford, **1970**.

[36] a) A. C. Rizzi, C. D. Brondino, R. Calvo, R. Baggio, M. T. Garland, R. E. Rapp, *Inorg. Chem.* **2003**, *42*, 4409–4416; b) N. Kotsakis, C. P. Raptopoulou, V. Tangoulis, A. Terzis, J. Giapintzakis, T. Jakusch, T. Kiss, A. Salifoglou, *Inorg. Chem.* **2003**, *42*, 22–31.

[37] a) V. S. Sergienko, G. G. Aleksandrov, E. G. Afonin, *Kristallografiya* **2000**, *45*, 262–265; b) P. H. Smith, K. N. Raymomd, *Inorg. Chem.* **1988**, *27*, 1056–1061; c) T. Glowiak, W. Sawka-Dobrowolska, B. Jezowska-Trzebiatowska, A. Antonow, *J. Cryst. Mol. Struct.* **1980**, *10*, 1–10; d) P. Fenot, J. Darriet, C. Garrigou-Lagrange, *J. Mol. Struct.* **1978**, *43*, 49–60.

[38] a) S. P. Petrosyants, M. A. Malyarik, A. B. Ilyukhin, *Zh. Neorg. Khim.* **1995**, *40*, 769–775; b) B. B. Smith, D. T. Sawyer, *Inorg. Chem.* **1968**, *7*, 922–928.

[39] a) D. Mootz, H. Wunderlich, *Acta Crystallogr., Sect. B* **1980**, *36*, 445–447; b) N. J. Mammano, D. H. Templeton, A. Zalkin, *Acta Crystallogr., Sect. B* **1977**, *33*, 1251–1254; c) A. B. Corradi, C. G. Palmieri, M. Nardelli, M. A. Pellinghelli, M. E. V. Tani, *J. Chem. Soc., Dalton Trans.* **1973**, 655–658.

[40] a) R. J. Motekaitis, A. E. Martell, *J. Coord. Chem.* **1985**, *14*, 139–149; b) H. E. Lundager Madsen, H. H. Christensen, C. Gottlieb-Petersen, *Acta Chem. Scand. A* **1978**, *32*, 79–83.

[41] a) M. Wozniak, G. Nowogrocki, *Talanta* **1979**, *26*, 1135–1141; b) M. Wozniak, G. Nowogrocki, *Talanta* **1979**, *26*, 381–388; c) T. Kiss, G. Balla, G. Nagy, H. Kozlowski, J. Kowalik, *Inorg. Chim. Acta* **1987**, *138*, 25–30; d) B. Radomska, E. Matczak-Jon, W. Woiciechowski, *Inorg. Chim. Acta* **1986**, *124*, 83–85; e) T. I. Ignat'eva, A. N. Bovin, A. V. Yarkov, A. N. Chekhlov, E. N. Tsvetkov, O. A. Raevskii, *Koord. Khim.* **1989**, *15*, 1179–1185.

[42] a) T. Appleton, J. R. Hall, I. J. McMahon, *Inorg. Chem.* **1986**, *25*, 726–734; b) R. J. Motekaitis, I. Murase, A. E. Martell, *Inorg. Chem.* **1976**, *15*, 2303–2306.

[43] a) S. Drumel, P. Janvier, P. Barboux, M. Bujoli-Doeuff, B. Bujoli, *Inorg. Chem.* **1995**, *34*, 148–156; b) S. Drumel, P. Janvier, P. Barboux, M. Bujoli-Doeuff, B. Bujoli, *New J. Chem.* **1995**, *19*, 239–242.

[44] A. Choudhury, S. Natarajan, *Solid State Sci.* **2000**, *2*, 365–372.

[45] a) G. Cao, V. M. Lynch, J. S. Swinnea, T. E. Mallouk, *Inorg. Chem.* **1990**, *29*, 2112–2117; b) G. B. Hix, V. J. Carter, D. S. Wragg, R. E. Morris, P. A. Wright, *J. Mater. Chem.* **1999**, *9*, 179–185.

[46] a) J.-G. Mao, Z. Wang, A. Clearfield, *N. J. Chem.* **2002**, *26*, 1010–1014; b) V. Soghomonian, Q. Chen, R. C. Haushalter, J. Zubieta, *Angew. Chem. Int. Ed. Engl.* **1995**, *34*, 223–226.

[47] a) V. Soghomonian, R. Diaz, R. C. Haushalter, C. J. O'Connor, J. Zubieta, *Inorg. Chem.* **1995**, *34*, 4460–4466; b) R. LaDuca, D. Rose, J. R. D. DeBord, R. C. Haushalter, C. J. O'Connor, J. Zubieta, *J. Solid State Chem.* **1996**, *123*, 408–412.

[48] J.-G. Mao, A. Clearfield, *Inorg. Chem.* **2002**, *41*, 2319–2324.

[49] D.-K. Cao, S. Gao, L.-M. Zheng, *J. Solid State Chem.* **2004**, *177*, 2311–2315.


 © 2006 Wiley-VCH Verlag GmbH & Co. KGaA, Weinheim 

[50] M. M. Gomez-Alcantara, A. Cabeza, M. Martinez-Lara, M. A. G. Aranda, R. Suau, N. Bhuvanesh, A. Clearfield, *Inorg. Chem.* **2004**, *43*, 5283–5293.
[51] G. M. Sheldrick, *SHELXS-86: Structure Solving Program*, University of Göttingen, Germany, **1986**.
[52] G. M. Sheldrick, *SHELXL-97: Structure Refinement Program*, University of Göttingen, Germany, **1997**.
Received: September 19, 2005
Published Online: March 30, 2006

 © 2006 Wiley-VCH Verlag GmbH & Co. KGaA, Weinheim 

DOI: 10.1002/ejic.200501093

# In Search of Binary Hybrid Systems in Manganese Chemistry: The Synthesis, Spectroscopic and Structural Characterization, and Magnetic Properties of a New Species in the Aqueous $Mn^{II}$-Quinic System

**Melita Menelaou,[a] Catherine P. Raptopoulou,[b] Aris Terzis,[b] Vassilis Tangoulis,[c] and Athanasios Salifoglou*[a]**

**Keywords:** Manganese / Structural speciation / $Mn^{II}$–quinate interactions / Magnetic properties / Hybrid materials

Manganese is a metal with diverse (bio)chemical reactivity in aqueous media in the presence of biologically relevant ligands. Key to that reactivity is the existence of soluble and bioavailable forms of $Mn^{II}$ across the physiological range of pH. To probe the interactions arising between $Mn^{II}$ and the low-molecular-mass ligand D-(–)-quinic acid, research efforts were targeted at the synthetic aqueous chemistry in the requisite binary system. The pH-specific synthetic reaction of $Mn^{II}$ with D-(–)-quinic acid led to the isolation of the new species $[Mn_2(C_7H_{11}O_6)_4]_n \cdot nH_2O$ (**1**). Complex **1** was characterized by elemental analysis, spectroscopic techniques (EPR, FTIR), thermal and magnetic studies, and X-ray crystallography. The molecular lattice of **1** reveals the presence of dimeric units of $Mn^{II}$ centers, with the quinate ligands coordinated to the metal ions through variable binding modes, indicating the diversity of chemical reactivity in the system. The octahedral $Mn^{II}$ centers in the molecular assembly of **1** serve as chemical prototypes of the forms of interactions that most likely develop in biologically relevant fluids, similar to those encountered in plant exudates and plant cellular structures. Concurrently, the physicochemical features of **1** (from the 3D hydrogen-bonding network to the magnetic susceptibility properties and EPR spectral results) exemplify the key features that constitute the rudiments of $Mn^{II}$-organic hybrid lattices of specific functions and (bio)chemical reactivity patterns. The collective properties of **1** are discussed in the context of their occurrence in natural binary $Mn^{II}$-influenced systems and advanced metal-hybrid materials of potential applications.

(© Wiley-VCH Verlag GmbH & Co. KGaA, 69451 Weinheim, Germany, 2006)

## Introduction

Manganese is an element of considerable occurrence in the earth's lithosphere. It is found in minerals as well as biological systems. In the biotic systems, manganese is an essential element[1] and is involved in the active sites of metalloenzymes, key to the integrity of cellular processes.[2] Among those are catalases,[3] the mitochondrial superoxide dismutase (SOD) and pyruvate carboxylase, the glial-specific enzyme glutamine synthetase, and others.[4] Albeit controversial, the role of manganese in cellular processes in the brain has been the subject of considerable research, given that the specific metal in its ionic forms can cross the blood brain barrier and behave as a neurotoxin.[5] As a result, manganese ions and their chemical reactivity have been associated with physiological aberrations in humans, including manganism and a number of other neurological impairments such as Parkinson's disease. Outstanding, on the other hand, is the participation of manganese in the oxygen-evolving complex of photosystem II (PSII), with the manganese playing an important role as an inorganic cofactor of catalytic importance.[6]

Metal ions in biological systems are mobilized efficiently through interactions with organic substrates, that is, ligands capable of coordinating them and solubilizing them in biological fluids. These ligands include both low- and high-molecular-mass cellular targets. Manganese, as $Mn^{II}$ and/or $Mn^{III}$, aptly coordinates to such ligands and enters further ternary interactions with biological molecules. One such low-molecular-mass molecule is D-(–)-quinic acid, 1α,3α,4α,5β-tetrahydroxy-1-cyclohexane carboxylic acid. It is a molecule that is found widely in plants where it is a precursor to shikimic acid.[7] The latter molecule is involved in the synthesis of essential amino acids. Hence, the presence of quinic acid appears to be vital to cellular physiology,[7a,8] with the organic acid capable of binding metal ions in biological fluids. Among the metal-ion nutrients targeted by such ligands are $Fe^{II,III}$, $Mn^{II}$, $Zn^{II}$, $Cu^{II}$, and others. In exemplifying its chemical reactivity towards $Mn^{II}$, quinic acid contains three very important features that render it

[a] Department of Chemical Engineering, Aristotle University of Thessaloniki, Thessaloniki 54124 and Chemical Process Engineering Research Institute,
Thermi, Thessaloniki 57001, Greece
Fax: +30-2310-996-196
E-mail: salif@auth.gr
[b] Institute of Materials Science, NCSR "Demokritos", Aghia Paraskevi 15310, Attiki, Greece
[c] Department of Materials Science, University of Patras, Patras 26500, Greece

 © 2006 Wiley-VCH Verlag GmbH & Co. KGaA, Weinheim 

an efficient metal-ion binder. It contains (a) a carboxylate moiety known to promote binding, (b) alcohol moieties, one of which is in an α position to the carboxylate group, and (c) three alcohol groups relevant to polyol functionalities. In all cases, coordination to a metal ion like $Mn^{II}$ promotes solubilization and contributes to $Mn^{II}$ bioavailability, leading to metallo(bio)chemical interactions characterizing the role of the specific metal ion in cellular environments like those of a plant.

On the basis of these views, the exploration of the aqueous chemistry of $Mn^{II}$ with α-hydroxycarboxylate binders, like D-(–)-quinic acid, is expected to (a) shed light on the structural speciation of that aqueous binary system and (b) provide chemical clues on the interaction of that metal ion with a biologically important substrate, the reactivity of which plays an important role in cellular biosynthetic pathways. The paucity of related $Mn^{II}$-quinic acid derivative species prompted us to look into the pH-specific synthetic chemistry of that binary system. To this end, we herein report on (a) the synthesis and spectroscopic properties of a new $Mn^{II}$-quinate species $[Mn_2(C_7H_{11}O_6)_4]_n{\cdot}nH_2O$ (**1**) and (b) the relevance of the physicochemical properties of **1** in the development of interactions of $Mn^{II}$ with biologically relevant targets and the assembly of lattices illustrating the solid-state features of multimodal quinate-containing $Mn^{II}$ materials.

## Results and Discussion

### Synthesis

A simple procedure was employed for the synthesis of **1**. A facile reaction between $Mn^{II}$ and quinic acid in aqueous media occurred at pH 3. The pH was adjusted to 3 by addition of aqueous ammonia. The stoichiometric reaction that led to the formation of compound **1** is shown by Reaction 1.

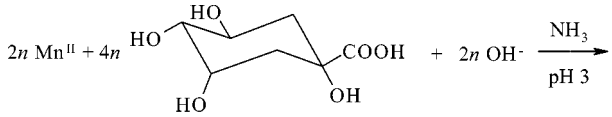


D-(-)-quinic acid

$$[Mn_2(C_7H_{11}O_6)_4]_n \cdot n\,H_2O \quad + \quad 2n\,H_2O \qquad \text{(Reaction1)}$$

The derived hybrid $Mn^{II}$-quinate material was easily retrieved in pure crystalline form upon standing of the reaction mixture at room temperature and allowing for slow evaporation over a period of 24 to 36 hours. Elemental analysis of the isolated colorless crystalline product indicated the molecular formulation $[Mn_2(C_7H_{11}O_6)_4]{\cdot}H_2O$. Further evaluation of the crystalline product by FTIR spectroscopy confirmed the presence of quinate bound to $Mn^{II}$, consistent with the proposed formulation. Finally, X-ray crystallography confirmed the analytical and spectroscopic results by rendering the molecular formulation of the crystalline product as $[Mn_2(C_7H_{11}O_6)_4]_n{\cdot}nH_2O$ (**1**). In a synthetic effort making use of various bases, the same reaction mixture of $Mn^{II}$ and quinic acid reacted in the presence of NaOH and KOH to a final pH value of 3, finally affording a crystalline solid. That solid proved to be complex **1** by virtue of its identical FTIR spectrum with that of the title compound beyond the elemental analysis results. Attempts to synthesize a congener $Mn^{III}$-quinate species in aqueous solutions under identical conditions to Reaction 1 [using $M^{III}(acetate)_3$ and quinic acid with a molecular ratio 1:2 in the presence of ammonia] consistently led to the isolation of a $Mn^{II}$ species, which was shown to be **1** by spectroscopic and crystallographic methods. Other reaction conditions leading to $Mn^{III}$ species of quinate are currently being investigated.

Compound **1** is insoluble in water. It is also insoluble in organic solvents like methanol, acetonitrile, chlorinated solvents ($CHCl_3$, $CH_2Cl_2$), toluene, and DMF. Complex **1** is stable in the crystalline form in the air at room temperature for long periods of time.

### Description of the Crystal Structure

Compound **1** emerges from a molecular type of crystal lattice. The ORTEP diagram for complex **1** is shown in Figure 1. Selected bond lengths and angles for **1** are given in Table 1. Complex **1** crystallizes in the monoclinic space group $P2_1$ with two molecules per unit cell. In complex **1**, there are two distinct types of $Mn^{II}$ ions, with each residing in a variable-nature coordination environment. In the first type of $Mn^{II}$ ions, reflected in the $Mn1^{II}$ assembly, one quinate ligand coordinates to the metal ion through the carboxylate and alcohol oxygens O1 and O3, respectively. These two moieties bind to $Mn^{II}$ through the formation of a five-membered metallacyclic ring, rendering the arising species quite stable. The second carboxylate oxygen atom, O2, of that quinate ligand coordinates to a neighboring Mn1′ ion [(′): 1 + *x*, *y*, *z*] leading to the *syn-anti* bridging mode of the carboxylate moiety depicted as mode I in Scheme 1. The interatomic distance between the so bridged $Mn^{II}$ ions (Mn1 and Mn1′) is evidently equal to the length of the *a* crystallographic axis [5.813(3) Å]. This type of bridging is responsible for the formation of chains of Mn1 assemblies along the *a* axis (Figure 2). A second quinate ligand entering the coordination sphere of the Mn1 ion employs a similar coordination mode by using one of the carboxylate and the alcohol oxygen atoms to anchor to Mn1 (O11 and O13, respectively). The second terminal oxygen, O12, of the carboxylate group, however, does not participate in the coordination of an adjacent manganese ion as was the case with the first quinate ligand. Thus, the carboxylate group of the second quinate ligand adopts the monodentate coordination mode depicted as mode II in Scheme 1. The remaining two coordination sites around Mn1 are taken up by the oxygen terminals O21′′ [(′′): 2 – *x*, –0.5 + *y*, 1 – *z*] and O2′′′ [(′′′): –1 + *x*, *y*, *z*] of the quinate ligands belonging to two abutting $Mn^{II}$ ions in the lattice

 © 2006 Wiley-VCH Verlag GmbH & Co. KGaA, Weinheim 

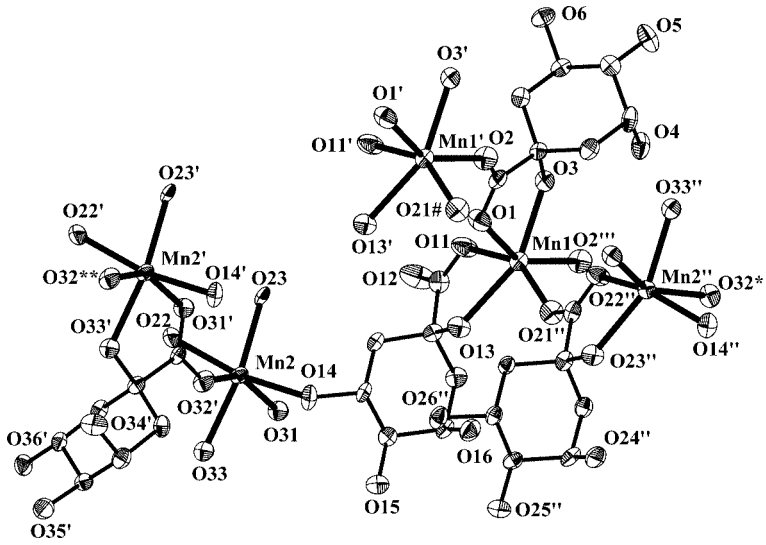


Figure 1. The molecular structure of $[Mn_2(C_7H_{11}O_6)_4]_n \cdot nH_2O$ (**1**) with the atom labeling scheme (50% thermal probability ellipsoids). Symmetry operations shown: (′): 1 + *x*, *y*, *z*; (′′): 2 – *x*, –0.5 + *y*, 1 – *z*; (′′′): –1 + *x*, *y*, *z*; (*): 1 – *x*, –0.5 + *y*, 1 – *z*; (**): 2 + *x*, *y*, *z*; (#): 3 – *x*, –0.5 + *y*, 1 – *z*.

{Mn2′′ [(′′): 2 – *x*, –0.5 + *y*, 1 – *z*] and Mn1′′′ [(′′′): –1 + *x*, *y*, *z*], respectively}. Collectively, the assembly of the aforementioned quinate ligands render the Mn1 ion six-coordinate with distorted octahedral geometry. In this octahedron, the terminal oxygens O1, O11, O21′′, and O2′′′ define the equatorial plane, while the two remaining oxygens O3 and O13 occupy the axial positions.

A different type of coordination sphere is formulated around a second distinct manganese ion in the lattice. In particular, four coordination sites are taken up by two quinate ligands, both of which bind the manganese ion Mn2 through the carboxylate and alcohol oxygen terminals.

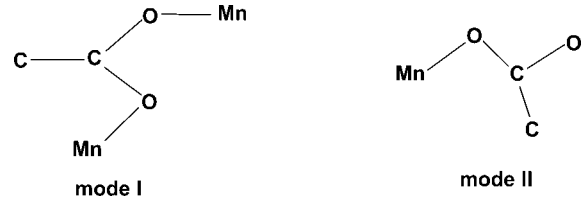


Scheme 1.

These oxygen anchors are O31, O33 and O22, O23 for the corresponding carboxylate and alcohol oxygen terminals. One coordination site is occupied by the oxygen terminal

Table 1. Bond lengths [Å] and angles [°] in **1**.[a]

| Lengths | | | |
|---|---|---|---|
| Mn1–O21′′ | 2.067(4) | Mn2–O32′ | 2.104(4) |
| Mn1–O2′′′ | 2.132(4) | Mn2–O31 | 2.132(4) |
| Mn1–O11 | 2.134(5) | Mn2–O22 | 2.142(4) |
| Mn1–O1 | 2.178(4) | Mn2–O33 | 2.202(4) |
| Mn1–O3 | 2.199(4) | Mn2–O23 | 2.216(5) |
| Mn1–O13 | 2.324(4) | Mn2–O14 | 2.314(4) |
| **Angles** | | | |
| O21′′–Mn1–O2′′′ | 96.75(17) | O32′–Mn2–O31 | 149.62(15) |
| O21′′–Mn1–O11 | 148.53(17) | O32′–Mn2–O22 | 88.94(17) |
| O2′′′–Mn1–O11 | 90.58(19) | O31–Mn2–O22 | 108.90(17) |
| O21′′–Mn1–O1 | 92.25(18) | O32′–Mn2–O33 | 81.82(15) |
| O2′′′–Mn1–O1 | 146.94(16) | O31–Mn2–O33 | 73.55(13) |
| O11–Mn1–O1 | 98.1(2) | O22–Mn2–O33 | 91.54(15) |
| O21′′–Mn1–O3 | 119.46(16) | O32′–Mn2–O23 | 113.60(17) |
| O2′′′–Mn1–O3 | 76.52(15) | O31–Mn2–O23 | 95.41(15) |
| O11–Mn1–O3 | 92.00(16) | O22–Mn2–O23 | 73.02(15) |
| O1–Mn1–O3 | 71.38(14) | O33–Mn2–O23 | 157.31(16) |
| O21′′–Mn1–O13 | 80.11(16) | O32′–Mn2–O14 | 79.49(15) |
| O2′′′–Mn1–O13 | 118.34(16) | O31–Mn2–O14 | 87.53(16) |
| O11–Mn1–O13 | 69.56(15) | O22–Mn2–O14 | 162.08(17) |
| O1–Mn1–O13 | 94.52(15) | O33–Mn2–O14 | 100.20(15) |
| O3–Mn1–O13 | 155.38(16) | O23–Mn2–O14 | 99.03(16) |

[a] Symmetry transformations used to generate equivalent atoms: (′): 1 + *x*, *y*, *z*; (′′): 2 – *x*, –0.5 + *y*, 1 – *z*; (′′′): –1 + *x*, *y*, *z*.

 © 2006 Wiley-VCH Verlag GmbH & Co. KGaA, Weinheim 

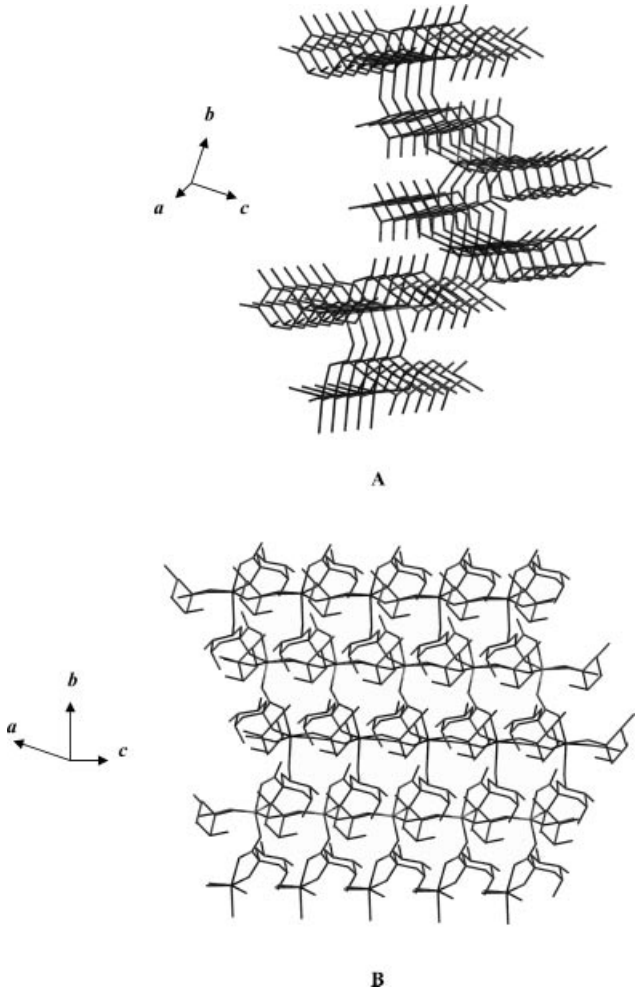


Figure 2. **A**: Packing diagram showing the chains of the Mn1 and Mn2 assemblies in **1** along the *a* axis. **B**: Layer diagram showing the bridging between Mn1 and Mn2 assemblies of **1** along the *a* axis forming the 2D polymeric structure.

O32′ [(′): 1 + *x*, *y*, *z*] of the carboxylate group of an abutting quinate ligand attached to a nearby manganese ion Mn2′ [(′): 1 + *x*, *y*, *z*], leading to a Mn2···Mn2′ separation equal to 5.813(3) Å, which is the length of the *a* axis. As a result, polymeric chains of the Mn2 assemblies are formed which are parallel to the crystallographic *a* axis. The last coordination site is occupied by the oxygen atom of one of the three alcohol moieties borne by the quinate ligand, namely O14, which is anchored to the first discrete Mn1 site discussed earlier. Overall, the coordination number of the Mn2 site is six, and the arising environment is distorted octahedral. The oxygen terminals O22, O32′, O31, and O14 formulate the equatorial composition of the octahedron, whereas the alcohol oxygen atoms O23 and O33 fulfil the axial requirements of the Mn2 environment.

The four crystallographically independent quinate ligands are divided into two groups according to their coordination mode around the two $Mn^{II}$ ions. The first group contains three members which anchor to $Mn^{II}$ through the carboxylate and alcohol oxygen atoms (O1, O3, O22, O23, O31, O33). In particular, the first member of the group binds to Mn1, while the two remaining members bind to Mn2 assemblies. The second carboxylate oxygen atom in all three quinate ligands is attached to a neighboring $Mn^{II}$ ion in a *syn*,*anti* binding mode. More specifically, O1, O2 and O31, O32 bridge $Mn^{II}$ ions belonging to Mn1 and Mn2 assemblies, respectively, and are responsible for the formation of the Mn1 and Mn2 polymeric chains along the *a* axis, while O21, O22 bridge Mn1 and Mn2′′ [Mn1···Mn2′′ 5.758(3) Å] and are responsible for the linkage of the chains. The second group contains one quinate ligand, which is anchored to Mn1 through O11 and O13, in the same way as the quinate ligands of the first group. In this case, however, the carboxylate moiety is coordinated to the metal ion in an $\eta^1$ fashion, and the alcohol oxygen O14 is used as a bridge to Mn2. Thus, that particular quinate ligand is used as an extended bridge between the chains of the two $Mn^{II}$ assemblies yielding an 8.065(11) Å separation between Mn1 and Mn2. In conclusion, the multifunctional nature of the crystallographically distinct quinate ligands and the way they extend into the coordination sphere of $Mn^{II}$ ions, promoting various coordination modes, are responsible for the formation of the 2D polymeric structure of compound **1** (Figure 2). This structure becomes even more complicated when hydrogen-bonding interactions are taken into consideration for the assembly of the requisite network.

Variable coordination modes of carboxylate-bearing organic ligands were previously observed in the coordination sphere of other divalent metal ions like $Cd^{II}$ and $Pb^{II}$. Representative examples of such complexes include $Cu^{I}(OOCCH_3)$,[9] and the physiological ligand citrate-containing complexes $[Cd(C_6H_6O_7)(H_2O)]_n$ (**2**),[10] $[Cd_3(C_6H_5O_7)_2(H_2O)_5]\cdot H_2O$ (**3**) and $(NH_4)[Cd(C_6H_5O_7)(H_2O)]\cdot H_2O$ (**4**), and $[Pb(C_6H_6O_7)]_n\cdot nH_2O$ (**5**).[11]

The Mn–O bond lengths for **1** are in the range from 2.067(4) to 2.324(4) Å, very similar to corresponding distances in complexes $(NH_4)_4[Mn^{II}(C_6H_5O_7)_2]$ (**6**),[12] $Mn^{II}(C_4H_4O_5)\cdot 3H_2O$ [2.111(2)–2.220(2) Å],[13] $Mn^{II}(C_7H_3NO_5)(H_2O)_2$ [2.124(3)–2.262(1) Å],[14] $Mn^{II}(C_2H_3O_3)_2\cdot 2H_2O$ [2.124(3)–2.225(3) Å],[15] $[Mn^{II}(XDK)(NO_3)(CH_3OH)_4(H_2O)_2](NO_3)$ [2.116(2)–2.345(2) Å][16] [$H_2XDK$ = *m*-xylenediamine bis(Kemp's triacid imide)] and $[Mn^{II}(bpca)_2\{Mn^{II}(hfac)_2\}_2]$ [2.113(3)–2.190(2) Å],[17] [Hbpca = bis(2-pyridylcarbonyl)amine; Hhfac = hexafluoroacetylacetone], where oxygen-containing octahedral coordination is the predominant feature of the structure around the $Mn^{II}$ ion. Also worth noting is the case of the polymeric material $[Mn^{II}(H_2O)_6][Mn^{II}(C_6H_5O_7)(H_2O)]_2\cdot 2H_2O$.[18] In this compound, the observed Mn–O distances between the tridentate citrate and $Mn^{II}$ range from 2.123(2) to 2.224(2) Å and compare favorably with those seen in **1**. The octahedral $Mn^{II}$ ion in **1** corresponds to other octahedral divalent metal ions like $Zn^{II}$,[19] $Cu^{II}$,[20] and $Ni^{II}$[21] in analogous octahedral species bearing citrates. The M–O distances observed in those complexes are in agreement with those seen in **1** and range from 2.052(2) to 2.164(2) Å ($Zn^{II}$) and 2.021(3) to 2.072(3) Å ($Ni^{II}$), while a wider range due to Jahn–Teller distortions is observed in the copper analog [1.969(3)–2.341(3) Å]. Equally comparable are the M–O distances oc-

 © 2006 Wiley-VCH Verlag GmbH & Co. KGaA, Weinheim 

curring in the congener quinate complexes $[Zn(C_7H_{11}O_6)_2]$,[22] $[Cd(C_7H_{11}O_6)_2]\cdot H_2O$, $[Cu(C_7H_{10}O_6)(H_2O)]_2(H_2O)_2$,[23] $\{[Cu(NO_3)(C_7H_{11}O_6)(H_2O)]\cdot 2H_2O\}_n$, $\{[CuCl(C_7H_{11}O_6)(H_2O)]\cdot H_2O\}_n$,[24] $[Pt(C_6H_{14}N_2)(C_7H_{10}O_6)]$,[25] and the trinuclear $(NH_4)_2\{[V(O)_2]_2[V(O)](\mu\text{-}C_7H_{10}O_6)_2\}\cdot H_2O$.[26]

Overall, the quinate ligand plays the role of an efficient metal-ion chelator, employing all possible types of anchors available in its structure and effectively formulating the coordination environment around $Mn^{II}$.

Hydrogen-bonding interactions are a dominant feature of the crystal structure of **1**. Specifically in **1**, the alcohol and carboxylate moieties of the quinate ligands along with the lattice water molecules participate in an extensive network of intra- and intermolecular hydrogen bonds (Table 2), which very likely contributes to the stability of the crystal lattice.

Table 2. Hydrogen bonds in **1**.

| Interaction | D···A [Å] | H···A [Å] | D–H···A [°] | Symmetry operation |
|---|---|---|---|---|
| O3–HO3···O4 | 2.663 | 1.891 | 155.3 | *x*, *y*, *z* |
| O4–HO4···O36 | 2.793 | 1.980 | 166.1 | 1 – *x*, –0.5 + *y*, 1 – *z* |
| O5–HO5···O26 | 2.955 | 2.115 | 157.2 | 2 – *x*, –0.5 + *y*, –*z* |
| O6–HO6···O15 | 2.769 | 1.786 | 151.1 | 1 + *x*, *y*, –1 + *z* |
| O13–HO13···O16 | 2.704 | 1.963 | 142.9 | *x*, *y*, *z* |
| O14–HO14···O6 | 2.725 | 1.820 | 169.8 | *x*, *y*, 1 + *z* |
| O15–HO15···O5 | 2.831 | 2.001 | 145.2 | *x*, *y*, 1 + *z* |
| O16–HO16···O26 | 2.872 | 2.098 | 177.9 | 1 – *x*, –0.5 + *y*, 1 – *z* |
| O23–HO23···O24 | 2.667 | 2.017 | 148.5 | *x*, *y*, *z* |
| O24–HO24···O12 | 2.768 | 1.917 | 123.3 | 1 + *x*, *y*, *z* |
| O25–HO25···O35 | 2.740 | 1.904 | 169.4 | *x*, *y*, –1 + *z* |
| O26–HO26···O36 | 2.919 | 2.162 | 159.9 | *x*, *y*, –1 + *z* |
| O33–HO33···O34 | 2.648 | 1.962 | 146.5 | *x*, *y*, *z* |
| O34–HO34···OW1 | 2.719 | 1.719 | 166.5 | 1 + *x*, *y*, 1 + *z* |
| O35–HO35···O12 | 2.683 | 1.800 | 162.2 | *x*, *y*, 1 + *z* |
| O36–HO36···O25 | 2.781 | 1.831 | 164.1 | –1 + *x*, *y*, 1 + *z* |
| OW1–HW1A···O12 | 2.960 | 2.282 | 143.7 | *x*, *y*, *z* |
| OW1–HW1B···O11 | 2.908 | 1.959 | 167.4 | –1 + *x*, *y*, *z* |

## FTIR Spectroscopy

The FTIR spectrum of **1** exhibits strong absorptions for the carbonyl groups of the carboxylate groups in both the antisymmetric and symmetric vibration regions. The antisymmetric stretching vibrations $\nu_{as}(COO^-)$ appear in the range 1639–1607 $cm^{-1}$, whereas the symmetric stretches $\nu_s(COO^-)$ appear in the range 1451–1380 $cm^{-1}$. The frequencies for the carbonyl stretches in **1** are shifted to lower values relative to those of the free quinic acid. Hence, they indicate a change in the vibrational status of the quinate anion upon coordination to the metal ion. The difference between the symmetric and antisymmetric stretches, $\Delta[\nu_{as}(COO^-) - \nu_s(COO^-)]$, is greater than 200 $cm^{-1}$, indicating that the carboxylate groups of the quinate ligand are either free or coordinated to the metal ion in a monodentate fashion.[9b,27] The latter contention is further confirmed by the X-ray crystal structure of **1**. Similar trends in the frequencies for the carboxylate carbonyl groups have also been observed in the FTIR spectra of other metal-quinate complexes as well as α-hydroxycarboxylate complexes with metal ions.[28]

## Thermal Studies

The thermal decomposition of the title complex was studied by TGA-DSC under an atmosphere of oxygen. $[Mn_2(C_7H_{11}O_6)_4]_n\cdot nH_2O$ (**1**) is thermally stable up to 190 °C. From that point on, an initial process emerges that involves dehydration of **1**, with the release of water between 190 and 210 °C signifying an endothermic process. A fairly clear plateau is reached at 210 °C, suggesting that the arising anhydrous species is thermally stable. The observed weight loss, attributed to the release of the water content, amounts to 4.8%, a value very close to the calculated value of 5.1% based on the molecular formula of the title complex **1**.

Two additional steps are observed in the thermal decomposition of complex **1**. No clear plateaus are reached in these stages, suggesting that the derived products are unstable and decompose further. The total weight loss of 83%, due to the decomposition of the title complex, is reached at 450 °C with no further loss up to 1000 °C. This value is in agreement with the calculated weight loss of 83%, derived upon the proposition that the final product at 1000 °C is $Mn_3O_4$. The DSC profile of the complex exhibits clear features that correspond to the TGA diagram. Collectively, the rather small number of observed TGA and DSC peaks likely reflects simple mechanisms of decomposition pathways for the title complex.

## Magnetic Susceptibility

The temperature dependence of $\chi_M$ and $\chi_M T$ ($\chi_M$ being the magnetic susceptibility for two $Mn^{II}$ ions) for complex **1** is shown in Figure 3. The $\chi_M T$ value is 8.5 emu $mol^{-1}$ K at 300 K (close to the value expected for two isolated $Mn^{II}$ ions). From 300 K down to 50 K there is a smooth decrease of the $\chi_M T$ value (Figure 3, A), while from 50 K down to 2 K there is a more pronounced decline of the $\chi_M T$ ultimately reaching the value of 1.5 emu $mol^{-1}$ K. In the inset of Figure 3 (A), the maximum of the $\chi_M$ data is shown at 3.5 K. The shape of these curves is characteristic of the occurrence of weak antiferromagnetic interactions between the $Mn^{II}$ centers. Taking into account the 2D character of **1**, the susceptibility data were fitted through the following approaches:

(a) The first one was based on the expansion series[29] of Lines for a $S = 5/2$ antiferromagnetic quadratic layer, riding on the exchange Hamiltonian $\boldsymbol{H} = \sum_{nn} \boldsymbol{J}\boldsymbol{S}_i\cdot\boldsymbol{S}_j$, where $\sum_{nn}$ runs over all pairs of nearest-neighbor spins $i$ and $j$ [Equation (1)], in which $\theta = kT/|J|S(S+1)$ $C_1 = 4$, $C_2 = 1.448$, $C_3 = 0.228$, $C_4 = 0.262$, $C_5 = 0.119$, $C_6 = 0.017$, and $N$, $g$, and $\beta$ have their usual meanings.

$$\frac{Ng^2\beta^2}{\chi|J|} = 3\theta + \left(\sum \frac{C_n}{\theta^{n-1}}\right) \quad (1)$$

 © 2006 Wiley-VCH Verlag GmbH & Co. KGaA, Weinheim 

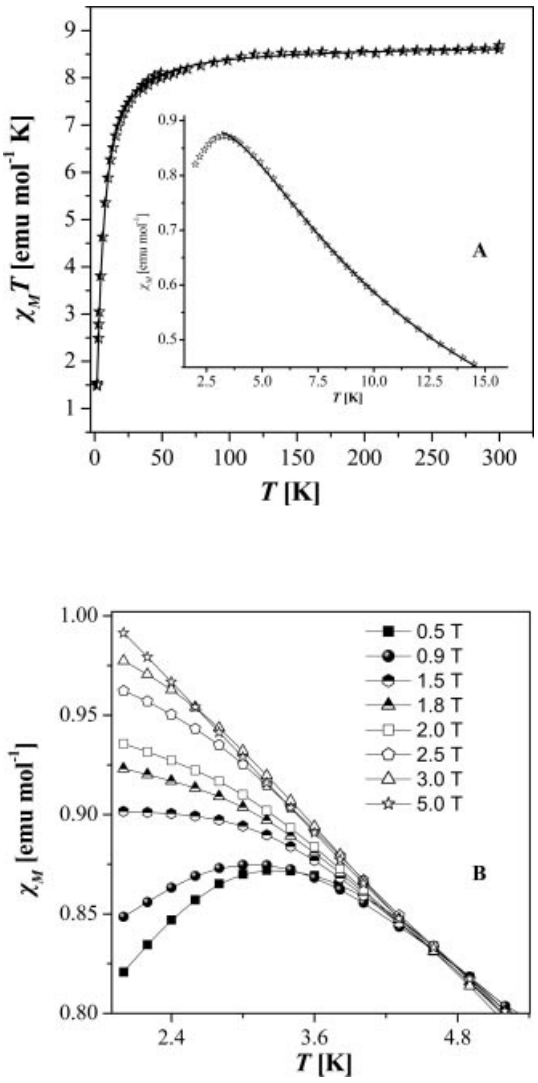


Figure 3. **A**: Temperature dependence of the susceptibility data at 0.6 T, in the form of $\chi_M T$ vs. $T$ (solid stars). In the inset, the temperature dependence of the susceptibility data is shown at 0.6 T, in the form of $\chi_M$ vs. $T$ near the maximum. The solid line represents the best fit according to the model discussed in the magnetic susceptibility section. **B**: Temperature dependence of the susceptibility data at different external fields in the range 0.5–5 T. The solid line represents the best fit according to the model discussed in the text.

The best fit is given by the superexchange parameters $J$ = –0.28 cm$^{-1}$ and $g$ = 1.98. In this hypothesis, a quadratic character of the layer has been assumed, that is, only one $J$ value. In fact, in complex **1** there are two $J$ values because there are two chemically distinct pathways: The first coupling pathway involves pairs of abutting Mn$^{II}$ ions, with the intervening linker emanating from a specific Mn$^{II}$ ion and traversing through the α-hydroxycarboxylate moiety, the quinate cyclic backbone, and the terminal alcohol anchor, ultimately binding the abutting Mn$^{II}$ ion. The second coupling pathway involves adjacent Mn$^{II}$ ions with the shorter spacer linker being the α-hydroxycarboxylate moiety. The two distinct pathways in the *ab* plane are explicitly portrayed in Figure 4, with the appropriate schematic and the associated $J$ ($J_1$ and $J_2$) coupling constants. As indicated earlier, both cases give a weak antiferromagnetic coupling, which we can assume to be similar for the fit.

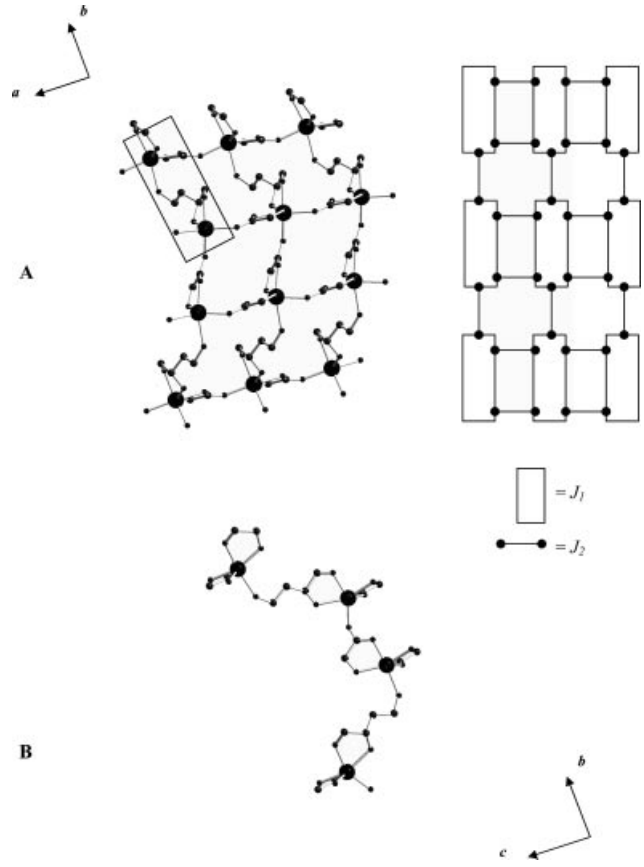


Figure 4. Different views (**A** and **B**) of the magnetic pathways of the system in **1**.

(b) The second one involved the analytical expression, derived by Curely, for an infinite 2D square lattice composed of classical spins ($S$ = 5/2) isotropically coupled and based on the exchange Hamiltonian $\boldsymbol{H} = \sum_{nn} \boldsymbol{J S_i \cdot S_j}$, where $\sum_{nn}$ runs over all pairs of nearest-neighbor spins $i$ and $j$ (Heisenberg couplings), see Equation (2).[30]

$$\chi = \frac{\left[Ng^2\beta^2 S(S+1)(1+u)^2\right]}{\left[3kT(1-u)^2\right]} \quad (2)$$

Here, $N$ is Avogadro's number, $\beta$ is Bohr's magneton, $k$ is Boltzmann's constant, and $u$ is the well-known Langevin function, see Equation (3).

$$u = L\left(\frac{JS(S+1)}{kT}\right) = \coth\left(\frac{JS(S+1)}{kT}\right) - \frac{kT}{JS(S+1)} \quad (3)$$

The best fit leads to $J$ = –0.2 cm$^{-1}$ and $g$ = 1.98 (Figure 3, part A, solid line). The $J$ values obtained through the Lines

 © 2006 Wiley-VCH Verlag GmbH & Co. KGaA, Weinheim 

or Curely expressions are very similar: –0.28 and –0.2 $cm^{-1}$, respectively. Taking into consideration the fact that the Curely formula is more accurate and is valid down to 0 K (the Lines formula is only valid up to the maximum of $\chi_M$, approximately), the value of –0.2 $cm^{-1}$ seems to be the most accurate estimate for complex **1**.

(c) Another possible magnetic model could also be considered. Such a model takes into account the fact that the only significant and maybe measurable interaction is the one through the α-hydroxycarboxylate ligand, thus reflecting a potential 1D character for **1**. For that reason, the susceptibility data were fitted to the following Equation (4),

$$\chi_M = \frac{Ng^2\beta^2}{kT}\frac{\left(A+Bx^2\right)}{\left(1+Cx+Dx^3\right)} \quad (4)$$

which is based on Weng's numerical approach,[31] and the coefficients have been generated by Hatfield et al.[32] for a $S = 5/2$ antiferromagnetic linear chain, where $x = |J|/kT$, $A = 2.9167$, $B = 208.04$, $C = 15.543$, $D = 2707.2$, and $N$, $g$, and $\beta$ have their usual meanings. The best fit is given by the parameters $J = -0.2\ cm^{-1}$ and $g = 2.0$, and it is equally good, indicating that the couplings are weak. The distinction between a 2D and 1D magnetic model is quite difficult to address solely through the fitting of the susceptibility data. In order to investigate and confirm the 2D magnetic character of the system, a different experimental approach was employed and it is explained later.

The comparison of $\chi_M$ (note that here the quantity actually measured is the ratio between the magnetization and the applied magnetic field) versus $T$ curves at different magnetic fields from 0.5 to 5.0 T applied fields (Figure 3, B) provides additional information. At the lower field, a clear sign of a transition to an antiferromagnetic state is observed with a maximum at 3.5 K. The critical temperature, taken as the maximum of the $T\mathrm{d}\chi/\mathrm{d}T$ versus $T$ curve, was estimated to occur at 2.0 K.[33] On the other hand, no maximum is observed at 5 T, thus indicating that the transition is suppressed at this field. Interestingly, ZFC/FC curves measured at 50 G (not shown) did not reveal any divergence, thus indicating that no hysteretic phenomenon is active below the ordering temperature.

Isothermal magnetization curves at $T = 2$–5 K in the applied field 0–5 T are shown in Figure 5 (A). The curves for the increasing and decreasing fields are identical. The magnetization at 5 T reaches 8.4 and 6.8 $\mu_B$ at $T = 2$ and 5 K, respectively, values which are smaller than the expected saturation value of 10 $\mu_B$ (two isolated $Mn^{II}$ ions) for the molecule of **1**. The sigmoidal shape of the $M(H)$ dependence is shown in Figure 5 (B), where a pronounced peak appears in the $\mathrm{d}M(H)/\mathrm{d}H$ curve that disappears at temperatures higher than 5 K.[34] This shape reveals the metamagnetic-like behavioral characteristic for systems in which the magnetocrystalline anisotropy is superimposed on the exchange couplings. Similar features have been recently observed for $Cu^{II}$–$W^{V}$ coordination polymers with 2D structures.[35] The shape of the $T = 2$ K curve suggests that the effective anisotropy field ($H_A$) is less than the exchange field ($H_E$), in contrast to the case of metamagnets, where $H_A \geq H_E$ and an immediate *spin-flip* transition to the saturated ferromagnetic state occurs. When the anisotropy field is of moderate intensity, the magnetization process proceeds through the *spin-flop* transition connected with reorientation of the antiferromagnetically coupled spins to the configuration perpendicular to the field. The threshold field for the spin-flop transition in the polycrystalline sample is 0.3 T, whereas the inflection point of the $\mathrm{d}M(H)/\mathrm{d}H$ curve (Figure 5, B) occurs at $H_{SF} = 2.1$ T. At $T = 5$ K, the $M(H)$ curve hardly shows any transition, most probably because of the change of the $H_A/H_E$ ratio.[36]

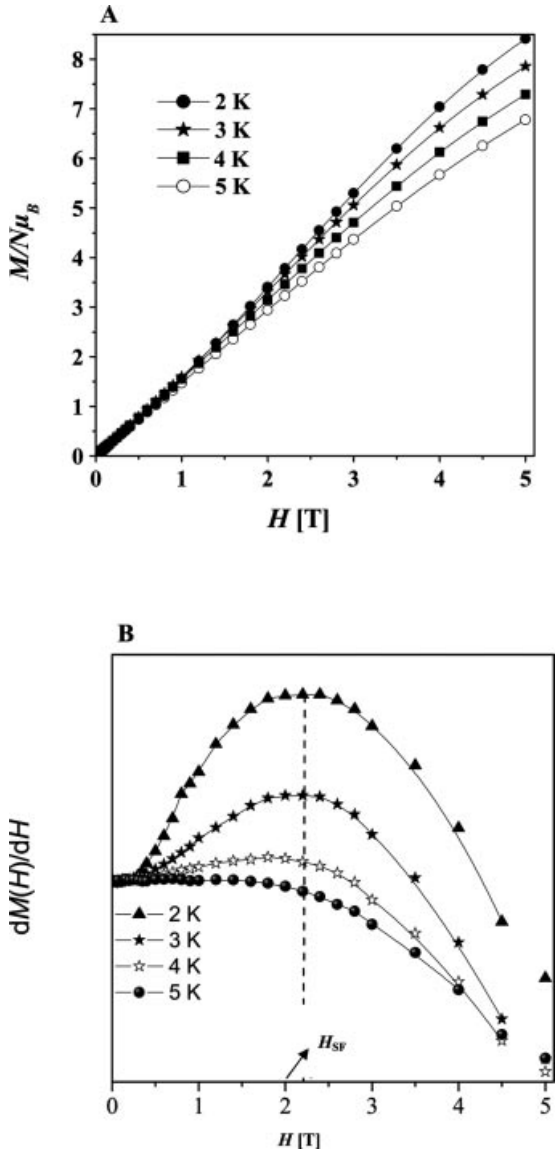


Figure 5. **A**: Magnetization curves at different temperatures in the field range 0–5 T. **B**: Field dependence of the magnetization derivatives in order to reveal their sigmoidal character (see text for details).

 © 2006 Wiley-VCH Verlag GmbH & Co. KGaA, Weinheim 

### EPR Spectroscopy

The EPR spectrum of complex **1** measured on a polycrystalline powder at room temperature shows an isotropic signal centered at $g = 2.00$, with a line width of 380 G. The spectra measured at variable temperatures are practically identical, but the line width of the signal increases upon lowering of the temperature (at 4 K it is 650 G). Since the EPR signal does not vanish at low temperatures, proof for antiferromagnetic ordering below the temperature of the transition, the possible magnetic ordering, needs further measurements at a lower temperature (about 2 K, see earlier).

### The Binary $Mn^{II}$-Quinate System in Aqueous Media

The synthesis of $[Mn_2(C_7H_{11}O_6)_4]_n{\cdot}nH_2O$ (**1**) through a facile reaction of $MnCl_2$ with quinic acid at pH 3, demonstrates the strong affinity of D-(–)-quinic acid for the divalent metal ion $Mn^{II}$. Albeit low, the pH of the reaction solution was sufficient to promote the reaction to completion and to afford the crystalline product in a pure form in a few hours. The physicochemical characterization of the derived material reflected the physical and chemical properties of **1** and revealed a considerable number of structural details linked to the reactivity of the binary system investigated. Specifically, the points worth noting are the following:

(a) *the retention of the protonation of the α-hydroxy group in the quinate ligand*. It appears that in the presence of $Mn^{II}$, the alcohol group adjacent to the carboxylic acid moiety retains its proton, following binding of the quinate group to the metal ion. Protonation of the alcohol group in the α position to the carboxylate group has also been observed in the case of the congener α-hydroxycarboxylic acid, citric acid, upon binding of the latter to $Mn^{II}$.[12]

(b) *employment of the terminal alcohol moieties in the coordination of the quinate ligand to an adjacently located $Mn^{II}$ ion*. In that respect, the organic moiety extends its coordination to two distinct manganese ions by (1) employing different anchors to bind them, (2) satisfying the coordination requirements of both $Mn^{II}$ ions, (3) preserving the protonation state of the alcohol group(s) upon binding to the metal ions, and (4) retaining the overall (de)protonation state of the carboxylate ligand bound to the manganese ion(s) to –1.

(c) *the variable mode of binding of the quinate carboxylate group to the $Mn^{II}$ ions*. Here, there exist two coordination modes, one of which is the conventional mode and is often observed in the case of other metal ions bound to carboxylate-containing substrates. The second one is a characteristic coordination-binding motif (Scheme 1). In this sense, the two $Mn^{II}$ ions to which the carboxylate group spans lie in the *syn-anti* conformation. This distinct mode of coordination has been observed for other metal ions bound to carboxylate-bearing molecules.[37] The two manganese ions lie in the same plane with carboxylate oxygen atoms and the abutting carbon atoms (the atoms, C1, C2, O1, O2, of the quinate backbone, Mn1, and Mn1′ are coplanar with the largest standard deviation 0.18 Å for O2).

The aforementioned structural features define the physical formulation of complex **1** and reflect the chemical reactivity, due to which the title species arose out of the reaction mixture and crystallized out of solution. The distinct modes of binding of the quinate ligand to the $Mn^{II}$ ions led inevitably to the formulation of a dimeric assembly $Mn_2(C_7H_{11}O_6)_4$ in **1**. The latter moiety is the repeat unit of the polymeric compound **1**. To this end, species **1** is a polymer similar to the one in the previously reported polymeric manganese complex $[Mn^{II}(H_2O)_6][Mn^{II}(C_6H_5O_7)(H_2O)]_2{\cdot}2H_2O$. Despite the obvious differences between the fundamental ligands bound to the $Mn^{II}$ in the two different complexes, (a) the underlying variability in the coordination mode of the two ligands to $Mn^{II}$ and (b) the resulting geometric features with the associated total variable charges, signify the diversity of the chemical reactivity of the $Mn^{II}$ ions towards α-hydroxycarboxylate ligands differing in their structure. In this case, the structural differences in the organic ligands reflect commensurate structural differences in the metal complexes in the two polymeric species. Such profoundly different chemical reactivity and structural variability may reflect analogously variable chemical reactivity at the biological level, where the two organic ligands constitute key molecular targets of essential biosynthetic pathways linked to cellular integrity and survival in bacteria and plants.

Further structural characteristics inherent to the lattice of **1** include the involvement of water molecules in the assembly. To that end, solvent water molecules of crystallization participate in the establishment of extensive hydrogen-bonding interactions throughout the lattice of **1**.

### $Mn^{II}$ Aqueous Speciation in Plants and Plant Fluids

Manganese is widely found in various structures and compartments in plants (e.g., older leaves, the plant stem, etc.),[38,39] contributing to their physiology.[40] Given that any influence of cellular biochemical processes entail bioavailable and thus soluble forms of manganese ions, $Mn^{II}$ bound to quinic acid presents a distinct form of an essential ion promoting binary and ternary interactions in biological fluids. Akin to this notion is the fact that solubility of $Mn^{II}$ increases at low pH, that is, under conditions employed in this work.[41] It is through such interactions that (bio)chemical reactivity arises, similar to the one linked to enzymes in the shikimate pathway in plants.[42] Of the variety of species that might form in solution, compound **1**, albeit insoluble itself, illustrates multimodal interactions of quinic acid with $Mn^{II}$ at low pH. In this sense, the dinuclear core species in **1**, is only one of the various forms potentially arising in the aqueous milieu. Undoubtedly, a solution speciation study would help delineate the nature and properties of species forming as a function of pH and metal-ligand stoichiometry.

Furthermore, the chemical reactivity of the binary system studied here exemplifies one more aspect of the chemis-

 © 2006 Wiley-VCH Verlag GmbH & Co. KGaA, Weinheim 

try unfolding at the biological level, that is, the ability of the cell to seek and identify micronutrients influencing its physiology. In that respect, aqueous $Mn^{II}$-quinate species at low pH provide a first glimpse of the chemistry promoted by bacterial organisms to (a) internalize, and/or (b) metabolize organic substrates in the presence of $Mn^{II}$, and/or (c) bind substrates in the presence of toxic metal ions (e.g., $Cd^{II}$), thus inhibiting their metabolic processing.[43,44] Such chemistries could arise from the needs of a plant under variable environmental adversities (e.g., nutritional deficiencies, extreme changes in soil pH, accumulation of toxic metals and substrates, etc.).[45]

### $Mn^{II}$-Containing Lattices in $Mn^{II}$-Organic Hybrid Materials

The lattice in **1** indicates the diversity of structural motifs generated by a single polydentate ligand: D-(–)-quinic acid gives rise to distinct $Mn^{II}$ sites, binding to it through the hydroxy carboxylate groups on one hand and the triol moieties on the other. The 1D wires strewn along the *a* axis formulate a 2D lattice with gaps in between the $Mn^{II}$-quinate strings that potentially allow for variable chemical reactivity in the intervening space (Figure 2). In those strings, the octahedrality of $Mn^{II}$ sites is a feature previously observed in $[Zn(C_7H_{11}O_6)_2]$, but not in $[Cd(C_7H_{11}O_6)_2]\cdot H_2O$, where a monocapped trigonal prismatic arrangement of quinates around $Cd^{II}$ dictates a different lattice. Equally interesting is $[Cu(C_7H_{10}O_6)(H_2O)]_2(H_2O)_2$, where the lattice is dictated by the square pyramidal geometry around $Cu^{II}$. Even more complex appears to be the 3D $Mn^{II}$–citrate lattices of various species, like $[NaMn(C_6H_5O_7)]$ and $[Ca_2Mn(C_6H_5O_7)_2(H_2O)_4]_n$.[46] This plethora of lattice types involving variable structure ligands bearing similarity to quinic acid, project an equally diverse type of hybrid materials still eluding isolation and characterization under speciation conditions in binary and even ternary systems.

## Conclusions

Collectively, the work on the binary $Mn^{II}$-quinic system of **1** (a) projects a clear view of the complexity of the speciation in aqueous media and the diversity of interactions developing in plant fluids, (b) sheds light on specific structural features of the related solid-state lattices that could be useful in designing new $Mn^{II}$-organic hybrid materials, and (c) defines the challenges of the future in the bioinorganic chemistry of quinic acid.

## Experimental Section

**Materials and Methods:** All manipulations were carried out in the open air. $MnCl_2\cdot 4H_2O$ was purchased from Merck and D-(–)-quinic acid from Fluka. Nanopure-quality water was used for all reactions.

**Physical Measurements:** FTIR measurements were recorded with a 1760X FT-Infra Red spectrometer from Perkin–Elmer, using KBr pellets. A ThermoFinnigan Flash EA 1112 CHNS elemental analyzer was used for the simultaneous determination of carbon, hydrogen, and nitrogen (%). The analyzer was based on the dynamic flash combustion of the sample (at 1800 °C) followed by reduction, trapping, complete GC separation and detection of the products. The instrument was fully automated and controlled by PC using the Eager 300 dedicated software and was capable of handling solid, liquid or gaseous substances.

A TA Instruments thermal analyzer, model Q 600, system was used to run the simultaneous TGA-DSC experiments. The employed heating rate was 10 °C min$^{-1}$. The instrument mass precision was 0.1 μg. Sample (about 20 mg) was placed in an open alumina sample pan for each experiment. High purity helium and air (80:20 in $N_2/O_2$) were used at a constant flow rate of 100 mL min$^{-1}$, depending on the conditions required for running the experiment(s). During the experiments, the sample weight loss and rate of weight loss were recorded continuously under dynamic conditions, as a function of time or temp., in the range 30–1000 °C. Prior to activating the heating routine program, the entire system was purged with the appropriate gas for 10 min, at a rate 400 mL min$^{-1}$, to ensure that the desired environment was established.

The EPR spectra of complex **1** in the solid state and in aqueous solutions were recorded with a Bruker ER 200D-SRC X-band spectrometer, equipped with an Oxford ESR 9 cryostat at 9.174 GHz, 10 dB, and at 4 K. Magnetic susceptibility data were collected using powdered samples of **1** with a Quantum Design SQUID susceptometer in the 2–300 K temp. range, under various applied magnetic fields. Magnetization measurements were carried out at three different temp. in the field range 0.5–5 T.

**Synthesis of $[Mn_2(C_7H_{11}O_6)_4]_n\cdot nH_2O$ (1):** $MnCl_2\cdot 4H_2O$ (0.50 g, 2.5 mmol) and D-(–)-quinic acid (0.97 g, 5.0 mmol) were placed in a round-bottomed flask (25 mL) and dissolved in water (5 mL). The reaction mixture was then stirred at room temp. until both reactants were completely dissolved. Subsequently, the pH of the clear solution was adjusted to 3 with aqueous ammonia. The resulting reaction mixture was allowed to stand at room temp. for slow evaporation. A few hours later, colorless crystalline material appeared on the bottom of the flask. The crystalline product was isolated by filtration and dried in vacuo. Yield 0.56 g (50%). **1**, $[Mn_2(C_7H_{11}O_6)_4]_n\cdot nH_2O$, $C_{28}H_{46}Mn_2O_{25}$ (892.52): calcd. C 37.64, H 5.15; found C 37.39, H 5.09.

**X-ray Crystal Structure Determination:** X-ray quality crystals of compound **1** (Table 3) were grown from reaction mixtures upon slow evaporation. A single crystal with dimensions $0.50\times0.30\times0.20$ mm (**1**) was mounted on a $P2_1$ Nicolet diffractometer using graphite monochromated Cu-$K_\alpha$ radiation. Unit cell dimensions for **1** were determined and refined by using the angular settings of 25 automatically centered reflections in the range $22 < 2\theta < 54°$. Relevant crystallographic data appear in Table 3. Intensity data were measured by using a $\theta$-$2\theta$ scan. Three standard reflections were monitored every 97 reflections, over the course of data collection. They showed less than 3% variation and no decay. Lorentz, polarization, and psi-scan absorption corrections were applied using Crystal Logic software. Further crystallographic details for **1**: $2\theta_{max} = 118°$; scan speed 3.0° min$^{-1}$; scan range $2.45 + \alpha_1\alpha_2$ separation; reflections collected/unique/used, 4667/4467[$R_{int}$ = 0.0372]/4467; 620 parameters refined; $[\Delta/\sigma]_{max}$ = 0.018; Flack parameter = 0.023(5); $[\Delta\rho]_{max}/[\Delta\rho]_{min}$ = 0.312/–0.639 e Å$^{-3}$; $R/R_w$ (for all data) = 0.0506/0.1140. The structure of compound **1** was solved by direct methods using SHELXS-86[47] and refined by full-matrix least-squares techniques on $F^2$ by using SHELXL-97.[48] All the non-hydrogen atoms were refined aniso-

 © 2006 Wiley-VCH Verlag GmbH & Co. KGaA, Weinheim 

tropically. The methylene hydrogen atoms of the quinate ligand were introduced at calculated positions as riding on bonded atoms. The remainder of the hydrogen atoms were located by difference Fourier maps and were refined isotropically.

Table 3. Summary of crystal, intensity collection, and refinement data for $[Mn_2(C_7H_{11}O_6)_4]_n{\cdot}nH_2O$ (**1**).

| | |
|---|---|
| Formula | $C_{28}H_{46}Mn_2O_{25}$ |
| Formula weight | 892.52 |
| $T$ [K] | 298 |
| Wavelength | Cu-$K_\alpha$ 1.5480 |
| Space group | $P2_1$ |
| $a$ [Å] | 5.813(3) |
| $b$ [Å] | 21.72(1) |
| $c$ [Å] | 13.334(8) |
| $\beta$ [°] | 93.17(2) |
| $V$ [Å$^3$] | 1681.0(15) |
| $Z$ | 2 |
| $D_{calcd.}/D_{measd.}$ [Mg m$^{-3}$] | 1.763/1.77 |
| Absorption coeff. ($\mu$) [mm$^{-1}$] | 7.061 |
| Range of $h$, $k$, $l$ | –6 to 6, –24 to 23, –14 to 0 |
| Goodness-of-fit on $F^2$ | 1.031 |
| $R$ indices[a] | $R$ = 0.0440, $R_w$ = 0.1085[b] |

[a] $R$ values are based on $F$ values, $R_w$ values are based on $F^2$. $R = \frac{\sum||F_o|-|F_c||}{\sum(|F_o|)}$, $R_w = \sqrt{\sum[w(F_o^2-F_c^2)^2]/\sum[w(F_o^2)^2]}$. [b] For 4058 reflections with $I > 2\sigma(I)$.

CCDC-290297 (for **1**) contains the supplementary crystallographic data for this paper. These data can be obtained free of charge from The Cambridge Crystallographic Data Centre via www.ccdc.cam.ac.uk/data_request/cif.

## Acknowledgments

This work was supported with funds provided by the Department of Chemical Engineering, Aristotle University of Thessaloniki. A.S. would like to acknowledge the financial support to this project by a "Pythagoras" grant from the National Ministry of Education and Religious Affairs and by a "PENED" grant from the General Secretariat of Research and Technology, Greece.

[1] P. Chappuis, J. Poupon, J. Arnaud, in *Trace Elements and Free Radicals in Oxidative Diseases* (Eds.: A. E. Favier, J. Neve, P. Faure), AOCS Press, Champaign, Illinois, **1994**, p. 46.
[2] a) C. D. Davis, J. L. Greger, *Am. J. Clin. Nutr.* **1992**, *55*, 747–752; b) L. L. Ji, F. W. Stratman, H. A. Lardy, *J. Am. Coll. Nutr.* **1992**, *11*, 79–86.
[3] a) J. E. Penner-Hahn, in *Manganese Redox Enzymes* (Ed.: V. L. Pecoraro), Verlag Chemie, New York, **1992**, p. 29; b) Y. Kono, I. Fridovich, *J. Biol. Chem.* **1983**, *258*, 13646–13648; c) Y. Kono, I. Fridovich, *J. Biol. Chem.* **1983**, *258*, 6015–6019; d) G. S. Allgood, J. J. Perry, *J. Bacteriol.* **1986**, *168*, 563–567; e) V. V. Barynin, A. Grebenko, *Dokl. Akad. Nauk U. S. S. R.* **1986**, *286*, 461.
[4] a) M. Aschner, in *Metals and Oxidative Damage in Neurological Disorders* (Ed.: J. R. Connor), Plenum Press, New York, **1997**, chapter 5, pp. 77–130; b) J. R. Prohaska, *Physiol. Rev.* **1987**, *67*, 858–901; c) F. C. Wedler, in *Progress in Medicinal Chemistry* (Eds.: G. P. Ellis, D. K. Luskombe), Elsevier Science, Amsterdam, **1993**, *30*, pp. 89–133.
[5] a) D. B. Calne, N. S. Chu, C. C. Huang, C. S. Lu, W. Olanow, *Neurology* **1994**, *44*, 1583–1586; b) S. E. Chia, S. C. Foo, S. L. Gan, J. Jeratnam, C. S. Tian, *Scand. J. Work Environ. Health* **1993**, *19*, 264–270; c) M. Florence, in *Proceeding on the Workshop on the Bioavailability and Oral Toxicity of Manganese* (Ed.: S. Velasquez), EPA Liaison, US EPA, **1995**, pp. 83–94.
[6] a) V. L. Pecoraro, in *Manganese Redox Enzymes* (Ed.: V. L. Pecoraro), Verlag Chemie, New York, **1992**; b) V. L. Pecoraro, M. J. Baldwin, A. Gelasco, *Chem. Rev.* **1994**, *94*, 807; c) G. C. Dismukes, *Chem. Rev.* **1996**, *96*, 2909; d) V. K. Yachandra, K. Sauer, M. P. Klein, *Chem. Rev.* **1996**, *96*, 2927.
[7] a) E. Haslam, *Shikimic Acid: Metabolism and Metabolites*, John Wiley & Sons, New York, **1993**; b) A. J. Pittard, in *Escherichia coli and Salmonella: Cellular and Molecular Biology* (Ed.: F. C. Neidhardt), ASM Press, Washington, DC, **1996**, chapter 28.
[8] R. Bentley, *Crit. Rev. Biochem. Mol. Biol.* **1990**, *25*, 307–384.
[9] a) R. D. Mounts, T. Ogura, Q. Fernando, *Inorg. Chem.* **1974**, *13*, 802–805; b) G. B. Deacon, R. Philips, *J. Coord. Chem. Rev.* **1980**, *33*, 227–250.
[10] M. Dakanali, E. T. Kefalas, C. P. Raptopoulou, A. Terzis, T. Mavromoustakos, A. Salifoglou, *Inorg. Chem.* **2003**, *42*, 2531–2537.
[11] M. Kourgiantakis, M. Matzapetakis, C. P. Raptopoulou, A. Terzis, A. Salifoglou, *Inorg. Chim. Acta* **2000**, *297*, 134–138.
[12] M. Matzapetakis, N. Karligiano, A. Bino, M. Dakanali, C. P. Raptopoulou, V. Tangoulis, A. Terzis, J. Giapintzakis, A. Salifoglou, *Inorg. Chem.* **2000**, *39*, 4044–4051.
[13] W. Van Havere, A. T. H. Lenstra, H. J. Geise, *Acta Crystallogr., Sect. B* **1980**, *36*, 3117–3120.
[14] L. C. Nathan, C. A. Doyle, A. M. Mooring, D. C. Zapien, S. K. Larsen, C. G. Pierpont, *Inorg. Chem.* **1985**, *24*, 2763–2766.
[15] T. Lis, *Acta Crystallogr., Sect. B* **1980**, *36*, 701–703.
[16] T. Tanase, S. J. Lippard, *Inorg. Chem.* **1995**, *34*, 4682–4690.
[17] T. Kajiwara, I. J. Tasuku, *J. Chem. Soc., Dalton Trans.* **1998**, 3351–3352.
[18] H. L. Carrell, H. P. Glusker, *Acta Crystallogr., Sect. B* **1973**, *29*, 638–640.
[19] R. Swanson, W. H. Ilsley, A. G. Stanislowski, *J. Inorg. Biochem.* **1983**, *18*, 187–194.
[20] R. C. Bott, D. S. Sagatys, D. E. Lynch, G. Smith, C. H. L. Kennard, T. C. W. Mak, *Aust. J. Chem.* **1991**, *44*, 1495–1498.
[21] Z.-H. Zhou, Y.-J. Lin, H.-B. Zhang, G.-D. Lin, K.-R. Tsai, *J. Coord. Chem.* **1997**, *42*, 131–141.
[22] Y. Inomata, T. Haneda, F. S. Howell, *J. Inorg. Biochem.* **1999**, *76*, 13–17.
[23] N. Barba-Behrens, F. Salazar-Garcia, A. M. Bello-Ramirez, E. Garcia-Baez, M. J. Rosales-Hoz, R. Contreras, A. Flores-Parra, *Trans. Met. Chem.* **1994**, *19*, 575.
[24] I. Bkouche-Walksman, *Acta Crystallogr., Sect. C* **1994**, *50*, 62.
[25] G. Hata, Y. Kitano, T. Kaneko, H. Kawai, M. Mutoh, *Chem. Pharm. Bull.* **1992**, *40*, 1604.
[26] R. Codd, T. W. Hambley, P. A. Lay, *Inorg. Chem.* **1995**, *34*, 877.
[27] C. Djordjevic, M. Lee, E. Sinn, *Inorg. Chem.* **1989**, *28*, 719–723.
[28] a) M. Matzapetakis, C. P. Raptopoulou, A. Tsohos, B. Papaefthymiou, N. Moon, A. Salifoglou, *J. Am. Chem. Soc.* **1998**, *120*, 13266–13267; b) M. Matzapetakis, C. P. Raptopoulou, A. Terzis, A. Lakatos, T. Kiss, A. Salifoglou, *Inorg. Chem.* **1999**, *38*, 618–619.
[29] a) M. E. Lines, *J. Phys. Chem. Solids* **1970**, *31*, 101; b) A. Escuer, R. Vicente, M. A. S. Goher, F. A. Mautner, *J. Chem. Soc., Dalton Trans.* **1997**, 4431 and references cited therein.
[30] a) J. Curely, *Europhys. Lett.* **1995**, *32*, 529; b) J. Curely, *Physica B* **1998**, *245*, 263; c) J. Curely, *Physica B* **1998**, *254*, 277; d) J. Curely, J. Rouch, *Physica B* **1998**, *254*, 298.
[31] C. H. Weng, Ph. D. Dissertation, Carnegie-Mellon University, Pittsburgh, PA, **1968**.
[32] W. Hiller, J. Strahle, A. Datz, M. Hanack, W. E. Hatfield, L. W. ter Haar, P. Gutlich, *J. Am. Chem. Soc.* **1984**, *106*, 329.
[33] M. E. Fisher, *Proc. R. Soc. (London) A* **1960**, *254*, 66.

 © 2006 Wiley-VCH Verlag GmbH & Co. KGaA, Weinheim 

[34] P. Przychodzen, K. Lewinski, M. Bałanda, R. Pełka, M. Rams, T. Wasiutynski, C. Guyard-Duhayon, B. Sieklucka, *Inorg. Chem.* **2004**, *43*, 2967.
[35] a) D.-F. Li, L. M. Zheng, X. Y. Wang, J. Huang, S. Gao, W. X. Tang, *Chem. Mater.* **2003**, *15*, 2094; b) S.-I. Ohkoshi, Y. Arimoto, T. Hozumi, H. Seino, Y. Mizobe, K. Hashimoto, *Chem. Commun.* **2003**, 2772.
[36] L. J. deJongh, A. R. Miedema, *Adv. Phys.* **1974**, *23*, 220.
[37] B.-H. Ye, X.-Y. Li, I. D. Williams, X.-M. Chen, *Inorg. Chem.* **2002**, *41*, 6426–6431.
[38] W. Hofner, *Physiol. Plant.* **1970**, *23*, 673.
[39] J. Vlamis, D. E. Williams, *Plant Sci.* **1973**, *39*, 245.
[40] F. Adams, J. I. Wear, *Soil Sci. Soc. Am. Proc.* **1957**, *21*, 305.
[41] G. H. Godo, H. M. Reisennauer, *Soil Sci. Soc. Am. J.* **1980**, *44*, 993.
[42] R. Entus, M. Poling, K. M. Herrmann, *Plant Physiology* **2002**, *129*, 1866–1871.
[43] A. J. Francis, C. J. Dodge, J. B. Gillow, *Nature* **1992**, *356*, 140–142.
[44] a) G. Joshi-Toppe, A. J. Francis, *J. Bacteriol.* **1995**, *177*, 1989–1993; b) L. Brynhildsen, T. Rosswall, *Appl. Env. Microbiol.* **1989**, *55*, 1375–1379.
[45] E. Hiltbrunner, W. Flückiger, *Tree Physiol.* **1996**, *16*, 963–975.
[46] W. Wang, X. Zhang, F. Chen, C. Ma, C. Chen, Q. Liu, D. Liao, L. Li, *Polyhedron* **2005**, in press.
[47] G. M. Sheldrick, *SHELXS-86: Structure Solving Program*, University of Göttingen, Germany, **1986**.
[48] G. M. Sheldrick, *SHELXL-97: Structure Refinement Program*, University of Göttingen, Germany, **1997**.

Received: December 6, 2005
Published Online: March 30, 2006

 © 2006 Wiley-VCH Verlag GmbH & Co. KGaA, Weinheim 

DOI: 10.1002/ejic.200501074

# Direct Epimetallation of π-Bonded Organic Substrates with Titanium(II) Isopropoxide: Intermediacy of Biradical, Oligomeric Titanium(II) Reagents[‡]

John J. Eisch,*[a] John N. Gitua,[a] and David C. Doetschman[a][b]

**Keywords:** Titanium(II) / EPR determination of biradicals / Titanium(II) isopropoxide trimer / Epititanation / Nonstereochemical $Ti^{II}$ additions

Extensive EPR experiments show that a titanium-containing molecular triplet state is formed in solution by the reaction of two equivalents of butyllithium with one equivalent of titanium(IV) isopropoxide. At higher concentrations this product, titanium(II) isopropoxide, admixed with two equivalents of lithium isopropoxide, is accompanied by the formation of a variety of nontitanium-containing side products. The powder EPR spectrum of the molecular triplet state in frozen solution is consistent with an asymmetric molecular chain of three Ti centers on which the unpaired electron centers are three metal atoms apart. Dilution experiments show that at lower concentrations, where the nontitanium-containing side products have dissipated, the intensity of the molecular triplet spectrum varies approximately linearly with concentration. Thus there is no evidence that the observed triplet molecule is one component in a series of concentration-dependent oligomerization steps. The bulky isopropoxy substituents and the coordination of the isopropoxide anions from the LiO*i*Pr present appear to prevent closure of the $Ti_3$ centers into an equilateral triangular diamagnetic structure. This steric hindrance, operative at the terminal diisopropoxytitanium centers and preventing closure to a ring, seems not to be observed with $TiCl_2$·2THF, which is diamagnetic and may thus be expected to exist as an equilateral triangular cluster of three units of $TiCl_2$·2THF, a structural model currently under further investigation. The smaller steric demand of the chloro and THF units would seem to permit octahedral coordination about each Ti center in such an equilateral trigonal array of $Ti_3$ atoms. Chemical reactions carried out individually with diphenylacetylene, *cis*-stilbene or *cis*-stilbene oxide and titanium(II) diisopropoxide provide stoichiometric and stereochemical evidence that the attacking titanium(II) reagent is in fact the trimeric biradical. The role of the lithium isopropoxide byproduct in fostering the course of the previously reported SET reactions of titanium(II) isopropoxide and in determining the detailed structure of the open-chain Ti trimer biradical has been explicated.

(© Wiley-VCH Verlag GmbH & Co. KGaA, 69451 Weinheim, Germany, 2006)

## Introduction

The complexation of subvalent transition-metal reagents ($L_mM_t^n$, **1**) with various C=C, C≡C, C=O, or C=N linkages (as in **2**) has led to adducts **3** that may be considered as π complexes **3a**, where the metal has undergone little change in oxidation number ($M_t^n$). On the other hand, the metal center can have released significant electron density to the π*-orbital of the organic substrate with the formation of three-membered metallocycles **3b**, and the metal may thereby have a higher oxidation number ($M_t^{n+2}$) [Equation (1)]. To determine which of the resonance structures **3a** and **3b** is the better single structure of adduct **3**, it is necessary to perform individual evaluations of the structural parameters of adduct **3**, if isolated, or of its observed chemical reactions.[2–4]

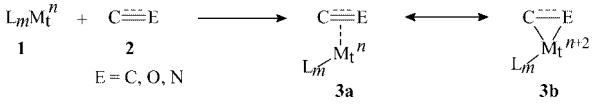


(1)

The process involved in the formation of adduct **3** has been termed epimetallation, because the metal reagent **1** is added with the rupture of a π-bond.[2] If reagent **1** is generated in a separate step and then added to **2**, this process may be termed direct epimetallation (Scheme 1, path a). More recently, however, we have found that a precursor dialkyl derivative of higher oxidation number, $R_2M_t^{n+2}L_m$ (**4**), can itself transfer the $L_mM_t^n$ unit to the unsaturated substrate **2** with concomitant loss of the R groups (Scheme 1, path b). This latter process has accordingly been termed transfer-epimetallation.[5a, 6]

[‡] Organic Chemistry of Subvalent Transition-Metal Complexes, 38. Part 37: Ref.[1]

[a] State University of New York at Binghamton, Department of Chemistry,
P. O. Box 6000, Binghamton, NY 13902-6000, U.S.A.
Fax: +1-607-777-4865
E-mail: jjeisch@binghamton.edu
[b] Professor of Chemistry & Director, Regional Center for Pulsed EPR & Photochemical Studies, State University of New York at Binghamton, Department of Chemistry,
P. O. Box 6000, Binghamton, NY 13902-6000, U.S.A.

 InterScience © 2006 Wiley-VCH Verlag GmbH & Co. KGaA, Weinheim 

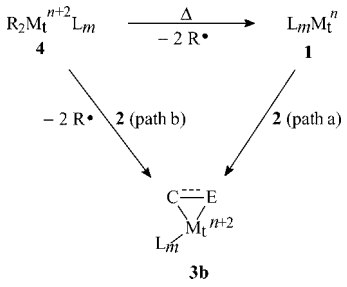


Scheme 1.

It is noteworthy to observe that the epititanation of ethylene by titanium(II) diisopropoxide (**7**) is widely thought to lead to 1,1-diisopropoxy-1-titanacyclopropane, postulated as the key intermediate in the Kulinkovich cyclopropanol synthesis.[5]

A most unusual and unexpected observation made in comparing such epimetallations with titanium reagents is that the direct epititanations with preformed $TiL_2$ (L = Cl, O*i*Pr)$_2$ are much slower than transfer-epititanations with $Bu_2TiL_2$.[2,5] For example, preformed $TiCl_2$ (**5**) in THF can achieve no epititanation of diphenylacetylene (**6**) whatsoever at 25 °C; similarly, Ti(O*i*Pr)$_2$ (**7**) in THF reacts with **6** over 24 h to provide only 31% of the epititanation product **9**, presumed to stem from adduct **8**, which was detected through $D_2O$ cleavage as **9** [Equation (2)]. In considering this low reactivity of $TiCl_2$ or Ti(O*i*Pr)$_2$ in direct epititanations, it is still noteworthy that some moderate activity is shown by Ti(O*i*Pr)$_2$ at 25 °C, while $TiCl_2$ is completely unreactive. As will be observed later in this study, this distinct difference in the chemical reactivity of Ti(O*i*Pr)$_2$ vs. $TiCl_2$ is also reflected in their respective EPR activity.

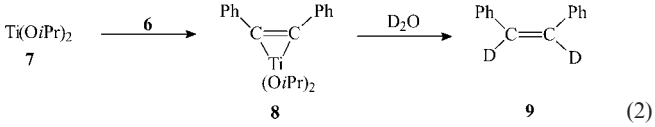


(2)

In sharp contrast, however, when either $Bu_2TiCl_2$ (**10**) or $Bu_2Ti(OiPr)_2$ (**11**) was generated in THF at –78 °C and 0.9 equiv. of diphenylacetylene (**6**) was then added, subsequent warming to 25 °C and treatment with $D_2O$ gave a 91–99% yield of *cis*-[$D_{1,2}$]stilbene (**9**). This outcome clearly demonstrates that **10** or **11** achieves a rapid epititanation of **6** at or below 25 °C. The facility of such transfer-epititanation has been rationalized by the formation of an octahedral transition state **12** with **6**, in which the new, incipient C–Ti bonds of the epititanated product are formed as the butyl–titanium bonds are thereby predisposed to homolytic cleavage [Equation (3)].

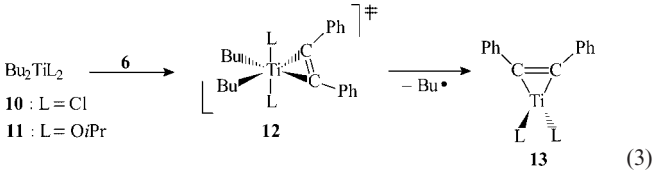


(3)

A most likely reason for the greater epititanation activity of $Bu_2TiL_2$ (**10** or **11**) over that of $TiL_2$ (**5** or **7**) may well be the more associated character of $TiL_2$. In the solid state, it should be noted that the $TiCl_2$ crystal lattice consists of layers of an infinite plane of Ti atoms flanked on both sides by infinite planes of chlorine atoms. It is understandable that considerable activation energy would be required to generate monomeric $TiL_2$ units, even from a far less associated form of these titanium(II) salts. As produced from 2 equiv. of butyllithium with 1 equiv. of $TiCl_4$ or Ti(O*i*Pr)$_4$, the resulting $TiL_2$ remains admixed with 2 equiv. of either LiCl or Li(O*i*Pr)$_2$. The separation of pure $TiCl_2$ or Ti(O*i*Pr)$_2$, free of Li salts, for analytical or molecular weight measurements, is a difficult task. We have been able to isolate and analyze successfully $TiCl_2$·2THF, free of LiCl, but we have been uniformly unsuccessful in separating Ti(O*i*Pr)$_2$ from LiO*i*Pr, since both components are freely soluble in pure THF or in hexane.

Hindered from determining the degree of association of pure Ti(O*i*Pr)$_2$ (**7**) in solution, we have availed ourselves of another interesting physical property of **7**. In contrast with the diamagnetic character of $TiCl_2$ (**5**) in THF over a range of temperatures below 25 °C, we have found that Ti(O*i*Pr)$_2$ with its byproduct LiO*i*Pr in heptane/toluene solution is pronouncedly paramagnetic and displays an EPR triplet signal characteristic of a biradical. The detailed study of such an EPR spectrum now permits us to estimate the degree of association of such Ti(O*i*Pr)$_2$ units.[7] Extrapolating from data on alkali metal complexes of $TiCl_2$, such as $Na_2Ti_3Cl_8$, we now suggest a possible similarity in the association of $TiCl_2$ units in THF.

## Results and Discussion

### The EPR Investigation of the 1:2 Mixture of Titanium(II) Diisopropoxide (7) and Lithium Isopropoxide in 1:1 Solutions of Heptane/Toluene

The initial CW EPR investigation of diluted samples of such mixtures, where the concentration of **7**, formally considered as the monomer, was successively 20.0, 7.0, 2.0, and 0.7 mM, revealed a broad, strong line at $g$ = 1.944, a sharp line at $g$ = 1.964, and a complex set of lines around $g$ = 1.98. Subsequent examination of this flash-frozen sample at 80 K gave a spectrum with a central set of features between 3100 and 3800 Gauss (microwave frequency, $\nu$ = 9.36947 GHz) and a weak feature at 1690 Gauss (microwave frequency, $\nu$ = 9.36583 GHz). The experiment was repeated with the spin-echo technique at 25 K, which confirmed the CW EPR results. In both cases, the central region appeared to comprise weak wing features at 3150 and 3750 Gauss, shoulders at 3125 and 3575 Gauss, and a peak at 3460 Gauss, relative to $\nu$ = 9.4181 GHz. After refinements in sample preparation had been made, the 3150 and 3575-Gauss features were eliminated. Please note the $g$-value representation of the central region of the spectrum as presented in Figure 1, as the derivative of EPR absorption with respect to the field. An integral (absorption vs.

 © 2006 Wiley-VCH Verlag GmbH & Co. KGaA, Weinheim 

field) of the EPR spectrum in this region is shown in Figure 2. The low-field part of the EPR spectrum is shown in Figure 3.

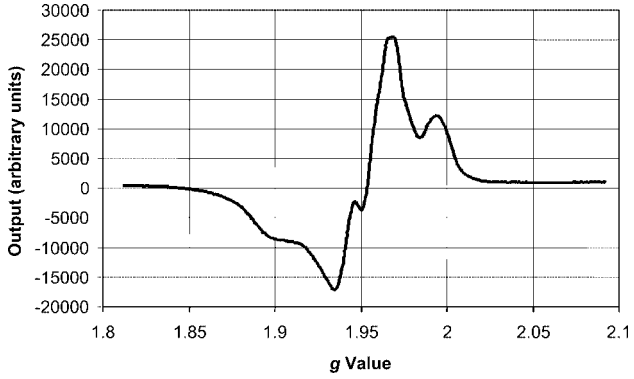


Figure 1. CW EPR derivative spectrum of a 0.7 mM frozen 1:1 hexane/toluene solution of titanium isopropoxide at 50 K as a function of $g$ value in the $g$ = 2 region.

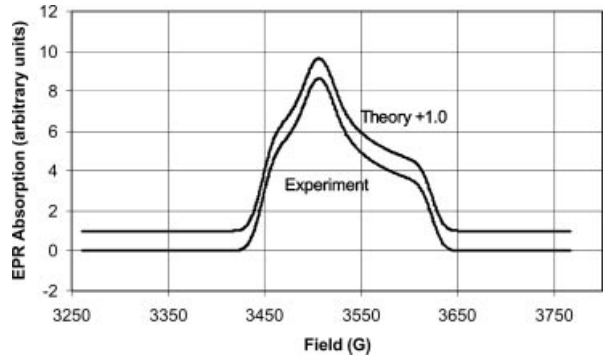


Figure 2. CW EPR absorption spectrum of a 0.7 mM frozen 1:1 hexane/toluene solution of titanium isopropoxide at 50 K, experiment and theory at microwave frequency 9.54971 GHz. (The normal derivative output of the EPR spectrometer has been numerically integrated.).

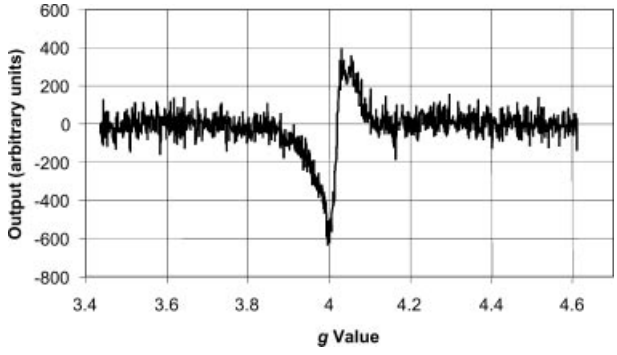


Figure 3. CW EPR derivative spectrum of a 0.7 mM frozen 1:1 hexane/toluene solution of titanium isopropoxide at 50 K as a function of $g$ value in the $g$ = 4 region.

Dilution experiments were done in order to try to understand the relationships between the several features observed in the CW EPR solution spectrum (not shown) and to consider the possibility that various oligomers of titanium(II) isopropoxide were being observed. Four sets of dilution experiments at nominal monomeric titanium(II) isopropoxide concentrations of 20.0, 7.0, 2.0, and 0.7 mM were done with successively greater refinements in the procedures. The sharp line at $g$ = 1.964 observed at 20.0 and 7.0 mM was largely eliminated with this improved procedure. The complex set of weak lines around $g$ = 1.98 initially observed at all concentrations except 0.7 mM was eliminated by means of the improved technique at all concentrations except 20.0 mM. The intensity of the triplet signal varies approximately in a linear dependence with the concentration, once the complex at $g$ = 1.98 disappears upon dilution.

## Analysis of the Observed EPR Spectra of Titanium Diisopropoxide (7)

The central part of the frozen solution spectrum, shown in integral form in Figure 2, is characteristic of a powder pattern of a molecular triplet state. The so-called half-field feature shown in the frozen solution spectrum of Figure 3 is located at a field consistent with a weakly allowed $\Delta m_s = \pm 2$ transition between the levels of a triplet state under the influence of the dipole–dipole interaction of the unpaired triplet-state electrons.[8] The parameters determined with the following triplet-state spin Hamiltonian [Equation ()] are given in Table 1.

$$\mathbf{H} = H\cdot g\cdot S + DS_z^2 + E(S_x^2 - S_y^2) \quad (4)$$

Table 1. Spin Hamiltonian parameters obtained from a least-squares fit of the parameters in Equation (4) to the titanium diisopropoxide frozen solution in Figure 2. (The standard deviations $\sigma$ in the parameters are also presented. The absolute signs of $D$ and $E$ are unknown but their relative signs are opposite.).

| | Value | $\sigma$ |
|---|---|---|
| $D$ ($10^{-4}$ cm$^{-1}$ $hc$) | ±81.7 | 1.8 |
| $E$ ($10^{-4}$ cm$^{-1}$ $hc$) | ∓23.1 | 0.2 |
| $g_{xx}$ | 1.9293 | 0.0002 |
| $g_{yy}$ | 1.9449 | 0.0002 |
| $g_{zz}$ | 1.9304 | 0.0002 |
| $\Delta H$ (Gauss) | 18.7 | 0.5 |

The $g$ value (1.944) of the broad strong line in the solution spectrum (not shown) is the same as that of the triplet molecule. Thus the solution spectrum is believed to be the motionally averaged spectrum of the powder pattern of the triplet molecule observed at lower temperatures (See Figure 2). The relatively smaller $g$-shift of the complexes giving the variable set of lines at $g$ = 1.98 suggests that these are radicals free of a Ti center. In the most highly refined dilution spectra it appears that the only highly concentration-dependent spectrum is that of the non-Ti-containing complex. It would appear that the triplet spectrum associated with Ti at $g$ = 1.944 is present at all concentrations and its spectrum does not change appreciably with concentration. Its intensity scales approximately with concentration, once the complex at $g$ = 1.98 disappears upon dilution.

Ignoring the $E$ value for the moment, the $D$ value alone corresponds to the dipolar interaction of two point-electron spins on titanium atoms at a distance of 0.668 nm.[9] Since

 © 2006 Wiley-VCH Verlag GmbH & Co. KGaA, Weinheim 

this Ti–Ti separation is more than twice the titanium atom separation in the $[Ti_3]$ cluster found in $Na_2Ti_3Cl_8$, the unpaired electrons are clearly not on the same Ti center or unlikely even on adjacent Ti centers. The nonzero $E$ value rules out a symmetric trigonal (equilateral) array, such as the $[Ti_3]$ cluster[10] for which $E = 0$ by symmetry.

Quantitative estimates of the triplet component(s) present in samples with 0.7, 2.0, 7.0, and 20.0 mM Ti content gave an average of $0.28 \pm 0.14$ triplet spins per Ti atom. Although within one standard deviation such a value is not consistent with triplet spins on the same Ti atom (1.0) or on adjacent Ti atoms (0.50). However, this value is in agreement with three Ti atoms per triplet molecule (0.33). Of course, this value is also consistent with four (0.25), five (0.20), six (0.17), or seven (0.14) Ti atoms per triplet molecule. This outcome supports the conclusion that a determination of the number of Ti atoms per triple molecule, measured with a precision typical of such experiments, cannot by itself be expected to determine the specific number of Ti atoms per Ti cluster.

### Comparison of the EPR Data for Titanium(II) Diisopropoxide (7) with Various Structural Models

A continuum of titanium(II) isopropoxide oligomers come under consideration (**7a**–**7d**, arrow = relative orientation of electron spin). From the $D$ and $E$ values, monomer **7a** and diamagnetic trimer **7d** can be excluded from further consideration. From the $D$ values alone the Ti–Ti distance in **7b** (0.2996 nm) is too short, and even a linear trimer of **7c** ($\theta = 180°$) falls short (0.599 nm) of the calculated experimental value of 0.668 nm (see Figure 4). The linear tetramer of **7** would lead to a $D$ value of 0.8988; however, the substantial value of $E$ is not predicted by a range of models reproducing the value of $D$, including one with parallel $p$-type orbitals simulated by point spins on terminal Ti atoms, a model with a twist angle between the terminal Ti $p$-type orbitals, and a model with in-plane $p$-type point spins and a Ti–Ti–Ti bond angle $\theta = 105°$. This failure in prediction suggests that there may also be one-center dipole–dipole contributions from different orbitals for different spin contributions or spin-orbit contributions to the zero-field parameters of Equation (4). The $D$ value and the nonzero $E$ value suggest a structure differing fundamentally in two respects from that of the $[Ti_3]^{6+}$ cluster found by Hinz et al. in $Na_2Ti_3Cl_8$ at low temperatures.[10] The $D$ value suggests a greater average triplet electron separation than the ≤0.2996 nm value in the $[Ti_3]^{6+}$ cluster. The nonzero $E$ value rules out a symmetric trigonal structure, such as was found for the $[Ti_3]^{6+}$ cluster, for which $E = 0$ by symmetry. Thus, with all factors considered, the structural model most in accord with the EPR data would appear to be **7c**, where $\theta$ approaches 180°, and the individual Ti–Ti bonds are lengthened to greater than 0.2996 nm by the steric repulsion of the isopropoxy groups attached to adjacent titanium centers (**7e**, L = O*i*Pr) (See Figure 4). The same steric bulk of the isopropoxy groups would weaken any coordination of THF units to Ti centers, as well as hindering spin-pairing and closure to the symmetrical $[Ti_3]$ cluster **7f** [Equation (5)].

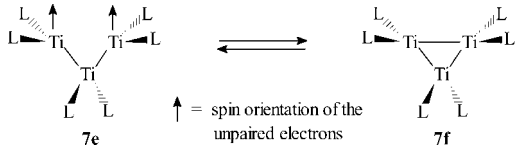


**7e** **7f** (5)

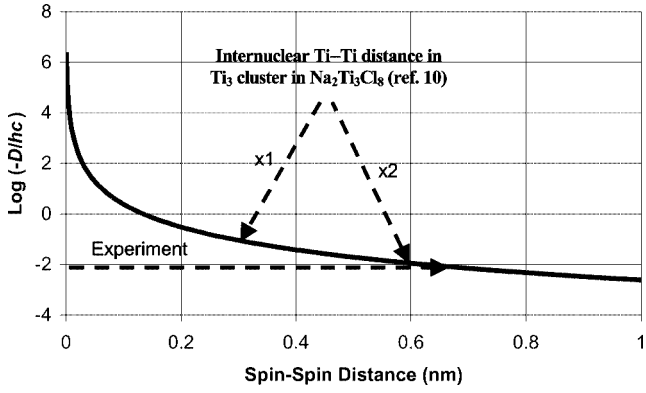


Figure 4. Logarithmic plot of the $D$ values as a function of point-spin–point-spin distance, according to a simple dipole-dipole model placing the spins on terminal Ti atoms. On this plot, the experimentally measured value of $D$ is indicated in relation to multiples of the Ti–Ti internuclear distance in the $Ti_3$ cluster reported by Hinz and co-workers.[10]

The tendency of divalent titanium centers to form trimeric Ti clusters, as in the solid state of $Na_2Ti_3Cl_8$[10] and as here in solutions of $Ti(OiPr)_2$ (**7**), encourages us to suggest that diamagnetic $TiCl_2$·2THF (**5**·2THF) may exist in solution as the cyclic symmetrical structure **7f**, (L = Cl), in which each Ti center, because of the smaller, electronegative chlorine ligand, could further accommodate two THF ligands and thereby attain octahedral coordination. The possible existence of cyclic and open-chain trimeric clusters of **7e** and **7f** (L = Cl) will be probed by EPR measurements of $TiCl_2$·2THF conducted at higher temperatures.[11]

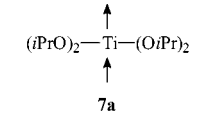

**7a**

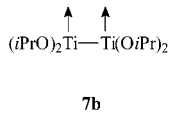

**7b**

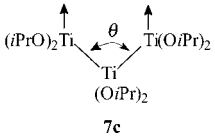

**7c**

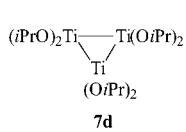

**7d**

### Structure of Titanium(II) Diisopropoxide (7) Implied by Its Chemical Reactions

In both $[Ti(OiPr)_2]_3$ and $[TiCl_2$·2THF$]_3$, it is readily apparent that the monomeric $TiL_2$ unit, necessary for the epi-

 © 2006 Wiley-VCH Verlag GmbH & Co. KGaA, Weinheim 

titanation of unsaturated organic ligands [Equation (1)], would require considerable activation energy to be liberated from its trimer, and thus such direct epititanations [Equation (1)] would understandably be slower than transfer-epititanations [Equation (3)].

Moreover, certain reactions of $Ti(OiPr)_2$ (**7**) with organic substrates, as reported in this study, follow pathways consistent with the participation mainly of the trimeric biradical **7c**. For example, with 1 equiv. of diphenylacetylene (**6**) and 2 equiv. of **7**, the addition reaction leading to *cis*-stilbene (**15**) upon hydrolysis proceeded to the extent of 30% at 25 °C. When a similar reaction mixture was heated at reflux, the reaction went only to an extent of 74%, despite the presence of an excess of **7**. Now, if the 2 equiv. of **7** is actually present as trimer **7c**, then the 0.67 equiv. of **7c** could react with only 0.67 equiv. of **6**, close to the observed 0.74 equiv. of **6** consumed. Thus, we conclude that the addition reaction to **6** should be described as involving mostly attack by **7c** [Equation (6)] to form **14**. Hydrolysis would then yield **15** or with $D_2O$, 1,2-dideuterio-*cis*-stilbene (**9**), as is observed.

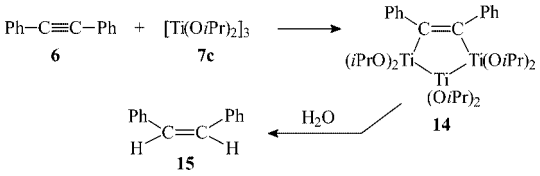


(6)

Two other reactions giving evidence for the participation of biradical **7c** directly are those involving *cis*-stilbene (**15**) itself and *cis*-stilbene oxide (**20**). Regardless of how long and at what temperature the reaction proceeded and whether **7** contained LiO*i*Pr or not, the main reaction of a 1:2 equiv. ratio of **15** and **7**, as revealed by hydrolysis, was isomerization to *trans*-stilbene (**17**), rather than addition to form **18** (detected as deuteriolysis product **19**). Workup with $D_2O$ produced 1,2-dideuteriobibenzyl (**19**), consistent with its formation from organotitanium precursor **18**. Again, we suggest that the 0.67 equiv. of trimer **7c** is operative, as shown in Scheme 2. The *trans*-stilbene could be formed directly from **16** by reeliminating **7c** or from **18** by stepwise Ti–C bond homolysis. In the conversion of **16** into **17**, the greater thermodynamic stability of **17** over **15** (about 91:9) should favor the formation of the *trans* isomer.

In a similar manner, the deoxygenation of *cis*-stilbene oxide (**20**) by **7** to give the thermodynamic mixture of *trans*- and *cis*-stilbenes (**17** and **15**) in a 91:9 ratio is consistent with the stepwise attack of biradical **7c** on **20** to form an acyclic biradical intermediate **21**. Biradical **21** could exist sufficiently long to permit rotation about the C–C bond before the second Ti–C bond undergoes induced homolysis and thereby produces the thermodynamic mixture of **15** and **17** (Scheme 3).

The first indication that the isopropoxy ligand exerts an activating effect on titanium(II), over that observed with the chloro ligand, was the faster direct epimetallating action of the $Ti(OiPr)_2/2LiOiPr$ system on diphenylacetylene (**6**) over

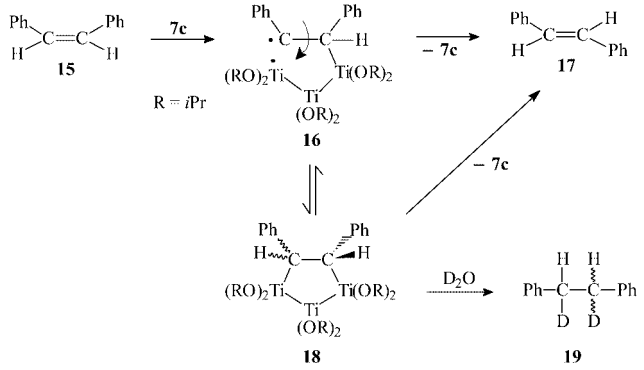


Scheme 2.

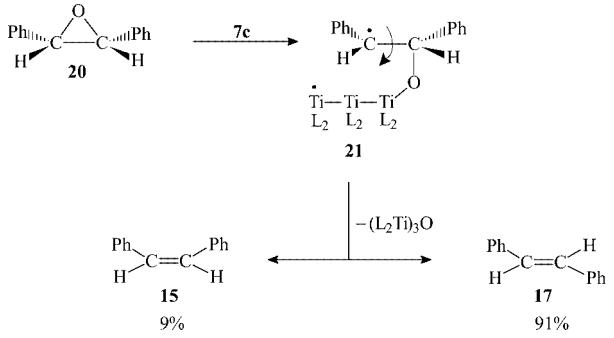


Scheme 3.

that of the similar $TiCl_2/2LiCl$ reagent (**5**) on **6** [Equation (2) and related text]. The greater reactivity of **7** over **5** has been ascribed to the electron-withdrawal effect of the isopropoxy groups already bonded in **7**, as well as any isopropoxy anions (from the LiO*i*Pr) that may also coordinate with the $Ti(OiPr)_2$ with the formation of complex titanium(II) anions, such as $[Ti(OiPr)_4]^{2-}$.[12]

A final previously studied reaction of **7** that clearly involves the participation of radical intermediates in SET (Single Electron Transfer) processes and implicates the byproduct LiO*i*Pr as an essential coreactant, is the reaction of **7** with aromatic nitriles (**22**) or geminal dichlorides (**23**), as shown in Scheme 4. The hydrolysis products, **24** and **25** respectively, had individually resulted from a reductive isopropylation. Since $Ti(OiPr)_2$ containing *no LiOiPr byproduct* (only LiCl) was *unable* to bring about such a reaction, the necessary SET reagent was proposed to be **26**, a complex of LiO*i*Pr with the supposed monomer $Ti(OiPr)_2$.[12]

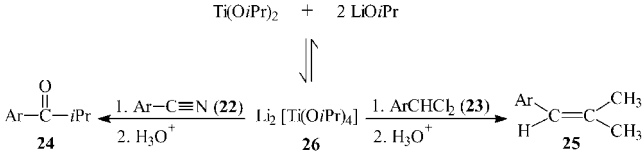


Scheme 4.

With the new structural insight into the nature of **7** offered by the present study, we would now propose that trimeric **7c** or **7d** undergoes coordination with one or more equivalents of LiO*i*Pr to form anionic coordination com-

 © 2006 Wiley-VCH Verlag GmbH & Co. KGaA, Weinheim 

plex(es), such as **27** [Equation (7)]. The coordination of the LiO*i*Pr with adjacent Ti atoms in **7d** or terminal Ti atoms in **7c** would tend to force the Ti trimer into the open-chain dianionic biradical **27**. Therefore, we can deduce from this chemical evidence that a mixture of **7** and LiO*i*Pr most likely exists in solution as one or more coordination complexes of the type depicted in **27**.

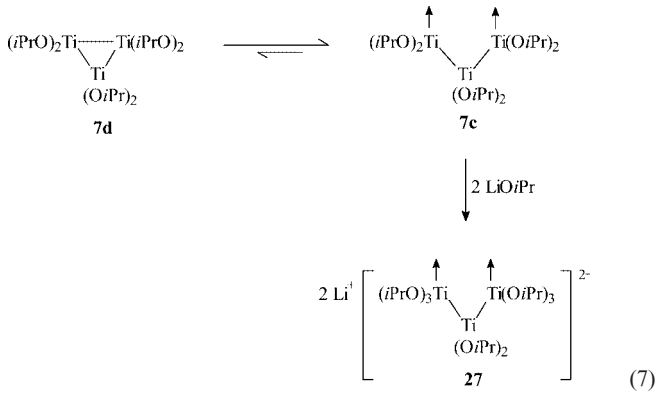

(7)

A corollary deduction of these considerations is that highly pure titanium(II) diisopropoxide, absolutely free of coordinating anions, such as from LiO*i*Pr or LiCl, and perhaps even free of coordinating solvents such as THF, might well exist at lower temperatures as the diamagnetic trimer **7d**. This possibility is currently under investigation.[11]

## Conclusions

In summary, the EPR experiments show that a Ti-containing molecular triplet state is formed in solution from the reaction of 2 equiv. of butyllithium with 1 equiv. of titanium(IV) isopropoxide. At high concentrations this product, titanium(II) isopropoxide, admixed with 2 equiv. of lithium isopropoxide, is accompanied by the formation of a variety of non-Ti-containing side products. The powder EPR spectrum of the molecular triplet state in frozen solution is consistent with an asymmetric molecule or chain of three Ti centers on which the unpaired electron centers are most probably three centers apart. Dilution experiments show that at lower concentrations, where the non-Ti-containing side products have dissipated, the molecular triplet spectrum intensity varies approximately linearly with concentration. Thus there is no evidence that the observed triplet molecule is one component in a series of concentration-dependent oligomerization steps. Coordination of this open-chain, three-titanium cluster with the lithium isopropoxide byproduct would, for steric reasons, tend to keep such anions in their open-chain biradical form. This steric hindrance for the terminal diisopropoxytitanium centers closing to a ring seems not to be observed with $TiCl_2$·2THF, which is diamagnetic and may thus exist as an equilateral triangular cluster of three units of $TiCl_2$·2THF. The smaller steric demand of the chloro and THF units may permit octahedral coordination about each Ti center in such a trigonal array of $Ti_3$ atoms.

Finally, chemical reactions carried out individually with diphenylacetylene, *cis*-stilbene, or *cis*-stilbene oxide and titanium(II) isopropoxide provide stoichiometric and stereochemical evidence that the attacking titanium(II) reagent is in fact the trimeric biradical **7c**, rather than some monomeric form of titanium(II) isopropoxide. The previously reported SET reductive isopropylation of aromatic nitriles and geminal dichlorides is reinterpreted in light of this new evidence on the structure of titanium(II) isopropoxide, and the essential role of lithium isopropoxide in shaping the detailed structure of the trimeric titanium biradical is explicated.

## Experimental Section

### Starting Materials, Reaction Conditions, and Instrumentation

The starting $TiCl_4$ and Ti(O*i*Pr)$_4$ employed were of 98% or greater purity as commercially available, and the *n*-butyllithium used was as a 1.60-M solution in hexane. All reactions, transfers, and separations were carried out under a positive pressure of anhydrous, oxygen-free argon. All solvents, mainly tetrahydrofuran, heptane, and toluene, employed with these air- and moisture-sensitive reagents were dried and distilled from a mixture of sodium metal and benzophenone ketyl prior to use.[13] The $^1$H- and $^{13}$C NMR spectra were recorded with a Bruker spectrometer, model EM-360, with tetramethylsilane ($Me_4Si$) as the internal standard. The chemical shifts reported are expressed on the $\delta$-scale in parts per million (ppm) from the $Me_4Si$ reference signal.

The electron paramagnetic spectra (EPR) measurements were performed with a Bruker EPR spectrometer, model ESP580 X-band, equipped with a split-ring ER4AA9 resonator and were detected with 100-kHz field modulation and phase-sensitive detection. Temperatures below room temperature were achieved with an Oxford Instruments CF935 cryostat and an ITC502 temperature controller. Two types of EPR experiments were performed on solutions of the divalent titanium derivatives in THF, heptane, or 1:1 (v/v) heptane/toluene mixtures: (1) CW EPR scans of various widths (200–1000 Gauss) were performed at room temperature (20–25 °C), mainly about fields corresponding to $g = 2$, and similar CW EPR experiments were performed with solutions flash-frozen at 50 K or 80 K; and then (2) a Hahn-echo detected, pulsed EPR spectrum was acquired at 20 K. Quantitative estimates of the concentrations of paramagnetic components present in the samples were obtained by comparison with the spectrum of a freshly prepared 1.032-mM standard solution of 1,1-diphenyl-2-picrylhydrazyl.

**Preparation of Titanium(II) Isopropoxide (7, containing LiO*i*Pr):** In a typical procedure on a 10-mmol scale, a solution of titanium(IV) isopropoxide (1.28 g, 10 mmol) in THF (40 mL) and cooled to –78 °C was slowly treated with *n*-butyllithium (12.5 mL, 1.6 M) in hexane (20 mmol) in an argon atmosphere. Stirring the light-brown mixture for 2 h at this temperature and then warming to 25 °C over 10 h gave a black, completely soluble mixture of titanium(II) diisopropoxide (**7**) containing lithium isopropoxide (2 equiv.). This THF solution measured directly gave a strong EPR signal (cf. Results) and was employed for reactions with diphenylacetylene (**6**), with *cis*-stilbene (**15**) and with *cis*-stilbene oxide (**20**).[12]

Upon removal of all volatiles from THF solutions of **7** and redissolving the residue in heptane or 1:1 mixtures of heptane and toluene (v/v), black complete solutions of the 1:2 mixtures of **7** and LiO*i*Pr resulted. For EPR studies, solutions of **7** in a 1:1 heptane/

 © 2006 Wiley-VCH Verlag GmbH & Co. KGaA, Weinheim 

toluene mixture were prepared individually at concentrations of 20.0, 7.0, 2.0, and 0.7 mM. That the THF had been completely removed was indicated by $^1$H NMR spectra of these hydrocarbon solutions of **7**, which showed no $^1$H triplets of THF at $\delta$ = 3.72 and 1.84 ppm. Instead, only broad $^1$H signals of the isopropoxy group were evident at around 4.0 and 1.2 ppm. These hydrocarbon solutions also displayed strong EPR signals.

**Preparation of Titanium(II) Diisopropoxide (7, free of LiO*i*Pr):** To a stirred solution of titanium(IV) chloride (1.89 g, 10 mmol) in THF (40 mL), prepared and maintained under an argon atmosphere at –78 °C, in order to avoid cleavage of the THF ring by the $TiCl_4$, was added slowly with stirring *n*BuLi (2 equiv.) in hexane (12.5 mL, 1.6 M, 20 mmol), and the resulting mixture was stirred for 30 min. The di-*n*-butyltitanium(IV) dichloride thereby formed was then treated with isopropyl alcohol (2 equiv., 1.20 g, 20 mmol), also at –78 °C. The resulting mixture was warmed to 25 °C over 10 h, and the dark brown suspension of the proposed titanium(IV) dichloride diisopropoxide was cooled again to –78 °C. Finally, a further aliquot of *n*BuLi (2 equiv.) was added. A subsequent warming of this last reaction product gave a black solution of titanium(II) diisopropoxide from which the white LiCl slowly precipitated. Concentration and cooling of the solution permitted about 1.6 g (94%) of the LiCl to be removed. Thus the yield of titanium(II) seems to have been almost quantitative.[12]

The careful examination of such titanium(II) diisopropoxide solutions, which contain little LiO*i*Pr or LiCl, will have to await further refinements in mixing the reactants and filtering the solutions to remove suspected paramagnetic particles in suspension. It will be of great interest to learn whether solutions of absolutely pure titanium(II) diisopropoxide show any EPR activity. Such information will be valuable in determining what the role of LiO*i*Pr in influencing the triplet character of trimeric clusters of $[Ti(OiPr)_2]_3$, commingled with LiO*i*Pr.

**Preparation of Titanium(II) Chloride (5):** In a procedure analogous to the foregoing, a stirred solution of titanium(IV) chloride (1.89 g, 10 mmol) in THF (40 mL) was treated at –78 °C under argon with *n*-butyllithium (20 mmol) in hexane. Further stirring at –78 °C and warming to 25 °C yielded a gray-black suspension of titanium(II) chloride (**5**) and lithium chloride as a 1:2 mixture. The resulting black solution of **5** with suspended LiCl showed no EPR signal, either at 25 °C or at lower temperatures.

As already has been published,[14] titanium(II) chloride (**5**) can be isolated free of LiCl from the suspension in THF by removing the THF and all volatiles under reduced pressure in argon. The residue is then slurried with toluene, and the suspension is filtered to remove all the LiCl. The filtrate is concentrated and chilled, in order to deposit black crystals, whose analysis corresponds to a 1:2 ratio of Ti/Cl and a Ti analysis agreeing with the empirical formula of $TiCl_2$·THF (**5**). Solutions of **5** in toluene again showed no EPR signal either at room temperature or at 80 K.

**Reactions of Titanium(II) Isopropoxide with *cis*-Stilbene (15)**

(1) The reaction of **15** (5.0 mmol, 0.89 mL) with **7** (10 mmol, containing LiO*i*Pr) in THF (30 mL) for 24 h gave a product (880 mg) after hydrolytic workup with aqueous HCl (6 N) and extraction of the organic products into ethyl ether, drying of the ether with $Na_2SO_4$, and removal of volatiles by rotary evaporation. Analysis of the product by $^1$H NMR spectroscopy showed the presence of 35% of *trans*-stilbene (**17**), 25% of bibenzyl, and 40% of the starting **15**.

(2) A reaction identical to that given above, except that **7** did not contain any LiO*i*Pr, produced a somewhat greater amount of isomerization of *cis*-stilbene: 50% of *trans*-stilbene (**17**), 15% of bibenzyl, and 35% of the starting **15**.

(3) A reaction identical to run (1), except that a 3-h reflux period was included, yielded 64% of *trans*-stilbene (**17**), 27% of bibenzyl, and 9% of the starting **15**.

(4) One-half of the reaction mixture in run (3) was worked up with $D_2O$ (min. 98%). The *cis*- and *trans*-stilbenes were found to contain no deuterium, but the bibenzyl was found to be 1,2-dideuteriated (PhCHD-CHDPh, **19**).

**Diphenylacetylene (6)**

(1) A solution of **6** (5.0 mmol, 890 mg) and **7** (10 mmol, containing LiO*i*Pr) in THF (40 mL) was heated at reflux for 12 h and then subjected to the usual hydrolytic workup. Flash column chromatography of the product by using a 60:1 (v/v) hexane/THF mixture showed the presence of 74% of *cis*-stilbene (**15**), 5% of bibenzyl, 1% of hexaphenylbenzene, and 20% of the starting **6**.

(2) A reaction mixture identical with the foregoing was stirred for 24 h at 25 °C. Hydrolysis and a similar $^1$H NMR analysis revealed the presence of only 30% of *cis*-stilbene (**15**) and 5% of bibenzyl, the rest being unreacted **6**. A deuteriolytic workup produced exclusively *cis*-1,2-dideuterio-*cis*-stilbene (**9**, with deuterons at the vinyl carbons).

(3) A reaction mixture treated as in run (2), except that **7** did not contain any LiO*i*Pr, gave again 31% of **15** and 4% of bibenzyl, essentially in the same product ratio as in section (2).

***cis*-Stilbene Oxide (20):** A mixture of **20** (5.0 mmol) and **7** (10 mmol) in THF (30 mL) was allowed to react for 12 h at 25 °C. Hydrolytic workup and $^1$H NMR analysis of the flash-chromatography eluate obtained with a 60:1 (v/v) mixture of hexane/THF showed the presence of 91% of *trans*-stilbene (**17**) and 9% of its *cis* isomer (**15**).

## Acknowledgments

The authors are grateful to the Boulder Scientific Company, Mead, Colorado, for the general support of their research with transition-metal alkyls and to the Alexander von Humboldt Foundation for a Senior Scientist Award to the first-cited author, renewed in 2005 for studies in the laboratory of Professor W. A. Herrmann, Institute of Inorganic Chemistry, Technische Universität München, Munich, Germany.
Furthermore, they thank the Regional Facility for Pulsed EPR and Photochemistry at Binghamton University, established with National Science Foundation support (CHE9512274), for its services in performing the EPR experiments.

[1] J. J. Eisch, S.Dutta, J. N. Gitua, *Organometallics* **2005**, *24*, 6291–6294.
[2] J. J. Eisch, X. Ma, K. I. Han, J. N. Gitua, C. Krüger, *Eur. J. Inorg. Chem.* **2001**, 77–88.
[3] J. J. Eisch, *J. Organomet. Chem.* **2001**, *617–618*, 148–157.
[4] J. J. Eisch, J. N. Gitua, P. O. Otieno, X. Shi, *J. Organomet. Chem.* **2001**, *624*, 229–238.
[5] a) J. J. Eisch, J. N. Gitua, *Organometallics* **2003**, *22*, 24–26; b) J. J. Eisch, A. A. Adeosun, J. N. Gitua, *Eur. J. Org. Chem.* **2003**, 4721–4727.
[6] J. J. Eisch, J. N. Gitua, *Organometallics* **2003**, *22*, 4172–4174.
[7] A. Carrington, A. D. McLachlan, *Introduction to Magnetic Resonance*, Wiley, New York, **1979**.
[8] J. H. Van der Waals, M. S. DeGroot, *J. Chim. Phys.* **1964**, 1643–1654.

 © 2006 Wiley-VCH Verlag GmbH & Co. KGaA, Weinheim 

[9] S. P. McGlynn, T. Azumi, M. Hinoshite, *Molecular Spectroscopy of the Triplet State*, Prentice-Hall, Englewood.
[10] D. J. Hinz, G. Meyer, T. Dedecke, W. Urland, *Angew. Chem. Int. Ed. Engl.* **1995**, *34*, 71–73.
[11] J. J. Eisch, D. C. Doetschman, unpublished studies in progress.
[12] J. J. Eisch, J. N. Gitua, *Eur. J. Inorg. Chem.* **2002**, 3091–3096.
[13] J. J. Eisch, *Organometallic Synthesis*, vol. 2, Academic Press, New York, N. Y., **1981**, ch. 1.
[14] J. J. Eisch, X. Shi, J. Lasota, *Z. Naturforsch., Teil B* **1995**, *50*, 342–350.

Received: December 1, 2005
Published Online: March 20, 2006

 © 2006 Wiley-VCH Verlag GmbH & Co. KGaA, Weinheim 

DOI: 10.1002/ejic.200501114

# Study of Thermodynamic and Kinetic Stability of Transition Metal and Lanthanide Complexes of DTPA Analogues with a Phosphorus Acid Pendant Arm

**Jan Kotek,*[a,c] Ferenc K. Kálmán,[b] Petr Hermann,[a] Ernő Brücher,[b] Koen Binnemans,[c] and Ivan Lukeš[a]**

**Keywords:** Phosphonate complexes / Phosphinate complexes / MRI contrast agents / Kinetics / Thermodynamics

The thermodynamic and kinetic stabilities of the complexes of phosphonate and phenylphosphinate analogues of $H_5$dtpa with selected transition- and lanthanide-metal ions are presented. Both phosphorus-containing ligands form thermodynamically very stable complexes, with stability constants comparable with or even higher than those reported for the parent $H_5$dtpa. However, the kinetic inertness of their gadolinium(III) complexes against acid- and metal-assisted decomplexations is surprisingly much lower. The half-life times of gadolinium(III) complexes of the new ligands in the presence of excess of concurrent metal ions [copper(II) or europium(III)] are about 2–3 orders of magnitude shorter compared to $H_5$dtpa and its amide derivatives. The behaviour can probably be attributed to steric strain in the new complexes, to the high affinity of phosphonate ligand for proton, and/or to easy formation of binuclear complexes, which act as intermediates in the complex dissociation.

(© Wiley-VCH Verlag GmbH & Co. KGaA, 69451 Weinheim, Germany, 2006)

## Introduction

Multidentate ligands and their complexes are frequently used in medicine. Gadolinium(III) complexes of octadentate ligands having the ninth coordination site occupied with a water molecule are utilized as contrast agents (CA) in magnetic resonance imaging (MRI).[1–3] As such toxic-metal-containing contrast agents have to be administered in relatively high doses, the gadolinium(III) ion must be encapsulated in stable complexes. These must survive with no decomplexation in body fluids containing many concurrent ligands (amino acids, phosphate anion, peptides etc.) and metal ions (e.g. $Ca^{2+}$, $Zn^{2+}$, $Cu^{2+}$). Ligands whose complexes fulfil such stability requirements are mostly derivatives of two prototype ligands (Scheme 1) – macrocyclic 1,4,7,10-tetraazacyclododecane-1,4,7,10-tetraacetic acid ($H_4$dota) and acyclic diethylenetriaminepentaacetic acid ($H_5$dtpa, 1,4,7-triazaheptane-1,1,4,7,7-pentaacetic acid). In vivo stability of the complexes may be estimated from thermodynamic and kinetic properties. The thermodynamic stability of metal complexes of $H_5$dtpa and $H_4$dota (expressed as stability constants) is very high. Ligands derived from the linear ligand $H_5$dtpa are in general much cheaper and more easily available than derivatives of the macrocyclic $H_4$dota. However, the resistance of complexes of macrocyclic ligands against decomplexation in body fluids (measured e.g. as acid- or metal-assisted dissociations) is usually much higher.[4,5]

According to theory, the water molecule which saturates the coordination sphere of the central $Gd^{3+}$ ion should be bound in the complex for an optimal residence time before exchange with bulk water. The residence time should lay in the range of 20–30 ns for MRI contrast agents used at magnetic fields applied in commercial tomographs, and in addition, the molecular tumbling of the CA should be as slow as possible.[1–3,6] However, the complexes of $H_4$dota and $H_5$dtpa themselves are far from such optimum.[7] In the search for better MRI contrast agents, sterically crowded ligands were developed as the enhanced steric strain around metal-binding site increases the exchange rate of coordinated water molecule. The steric strain was usually reached by introduction of one extra methylene group into the backbone (propylene group instead of ethylene bridge) or in one of the pendant arms (i.e. with propionate pendant instead of acetate),[8–11] or by substitution of ligand backbone by alkyl/aryl group.[12,13] The complexes formed with these new ligands are thermodynamically usually slightly less stable than those of $H_4$dota and $H_5$dtpa.[9,10,14,15] Unfortunately, no detailed kinetic studies are available in the literature for these complexes.

[a] Department of Inorganic Chemistry, Charles University, Hlavova 2030, 128 40 Prague 2, Czech Republic
[b] Department of Inorganic and Analytical Chemistry, University of Debrecen, 4010 Debrecen, Hungary
[c] Department of Chemistry, Katholieke Universiteit Leuven, Celestijnenlaan 200F, 3001 Leuven, Belgium
E-mail: modrej@natur.cuni.cz
Supporting information for this article is available on the WWW under http://www.eurjic.org or from the author.

 InterScience © 2006 Wiley-VCH Verlag GmbH & Co. KGaA, Weinheim 

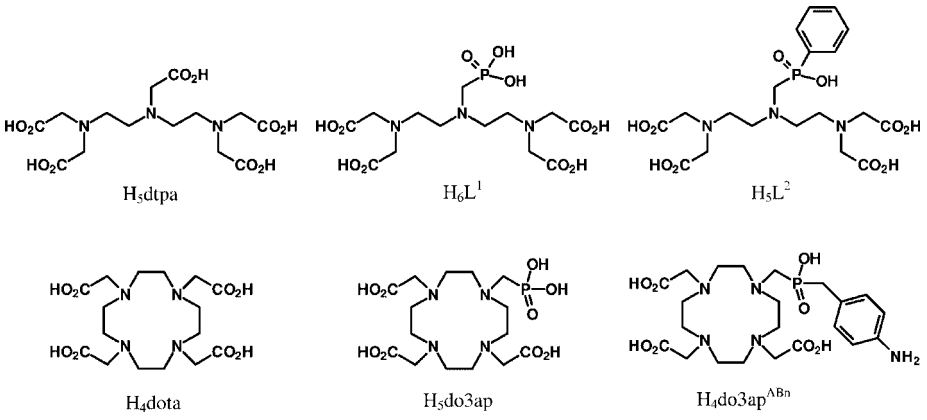


Scheme 1. Structural formulas of the ligands mentioned in the text.

To contribute to this field, we prepared several analogues of $H_4$dota and $H_5$dtpa having a bulkier phosphorus acid pendant moiety instead of the carboxylate group. The corresponding lanthanide(III) complexes of the linear ligands $H_6L^1$ and $H_5L^2$ (Scheme 1) have been studied by NMR and relaxometry.[16] It was shown, that the water-exchange rate is much higher for the complexes with phosphorus-containing ligands than what was reported for the complexes of $H_5$dtpa and its amides. Noticeable acceleration of water exchange was observed also for macrocyclic ligands with one phosphorus-based pendant arm (e.g. $H_5$do3ap or $H_4$do3ap$^{ABn}$, Scheme 1) comparing to $H_4$dota.[17,18] Furthermore, the relatively easy substitution on the phosphorus atom offers the possibility to attach the complex to a macromolecular carrier,[19–21] or to bind it non-covalently to plasma proteins (e.g. by hydrophobic interactions).[16] Here we report on the thermodynamic and kinetic stability studies of the complexes of two linear ligands – phosphonate and phenylphosphinate derivatives $H_6L^1$ and $H_5L^2$, respectively (Scheme 1) – with selected divalent transition and trivalent lanthanide metal ions.

## Results and Discussion

### Crystal Structure of $H_6L^1 \cdot HCl \cdot 1.5H_2O$

In the crystal structure, a molecule of the ligand is present in the charged sevenfold-protonated form $(H_7L^1)^+$ (Figure 1). All the nitrogen atoms of the backbone are protonated together with one oxygen atom of the phosphonate moiety (O1) and three carboxylate oxygen atoms (O111, O211 and O311). The geometry around the phosphorus atom is tetrahedral, with noticeably longer P–O bond to the protonated oxygen O1 comparing to others (Table 1). One chloride anion serves as counterion. Additionally, two water molecules were found in the structure, but one of them (O2W) is best refined with a half-occupancy. Molecules of the ligand are connected by short hydrogen bonds (2.45–

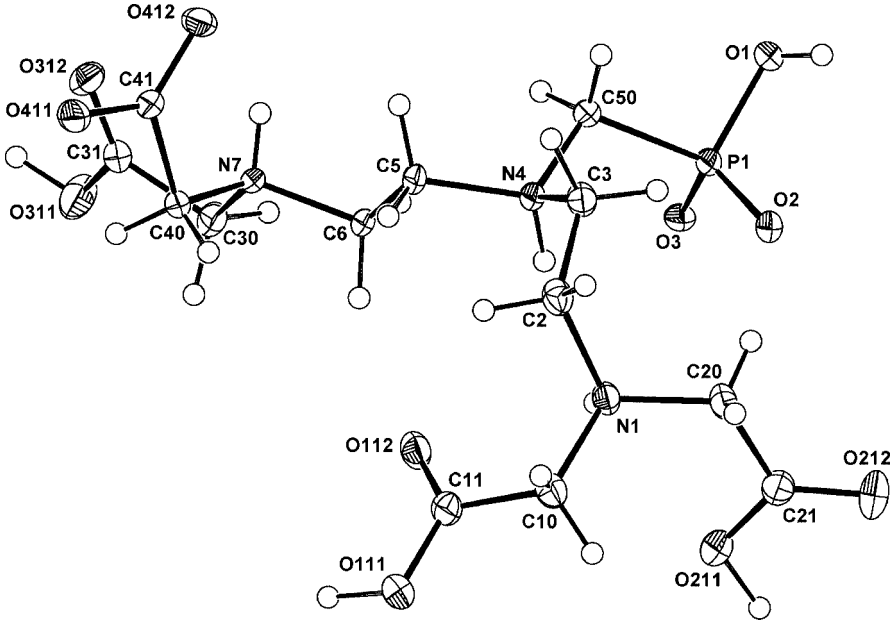


Figure 1. Molecular structure of $(H_7L^1)^+$ with atom numbering scheme.

 © 2006 Wiley-VCH Verlag GmbH & Co. KGaA, Weinheim 

2.65 Å) between protonated and unprotonated oxygen atoms of acetate and phosphonate moieties. Furthermore, the protonated amino groups are also involved in rather strong (2.64–2.77 Å) hydrogen binding to oxygen atoms of neighbouring ligand molecules. Additionally, the solvate water molecules and chloride anion bind each other (3.04–3.20 Å), and also the water molecule O1W has a short contact to protonated carboxylate oxygen atom O311 (Table S1).

Table 1. Geometry of the phosphonate group in the structure of $H_6L^1 \cdot HCl \cdot 1.5H_2O$.

| Distances [Å] | | Angles [°] | |
|---|---|---|---|
| P1–O1 | 1.5740(13) | O1–P1–O2 | 110.00(8) |
| P1–O2 | 1.5038(13) | O1–P1–O3 | 110.87(7) |
| P1–O3 | 1.4977(13) | O2–P1–O3 | 115.71(7) |
| P1–C50 | 1.827(2) | C50–P1–O1 | 101.94(8) |
| | | C50–P1–O2 | 109.53(8) |
| | | C50–P1–O3 | 107.85(9) |

## Equilibrium Studies

The protonation and complexation equilibrium were studied by conventional potentiometry. Table 2 lists the protonation constants of concerned ligands together with those of $H_5$dtpa. Distribution diagrams of $H_6L^1$ and $H_5L^2$ are shown in Figure S1 (supporting information; for supp. inf. see also the footnote on the first page of this article. As polydentate aminocarboxylic acids can form relatively strong complexes with alkali metal ions, the potentiometric studies were performed using tetramethylammonium chloride (TMAC) as a background electrolyte. Indeed, the determined values of the highest protonation constants are systematically higher than those reported previously,[16] which were obtained by NMR and are lower as a consequence of sodium(I)-induced deprotonation (Table 2). A similar trend was observed also for $H_5$dtpa, where constant $\log\beta_1$ determined with NaCl as the supporting electrolyte is about one order of magnitude lower (9.45[22]) than that measured in TMAC (10.41,[22] Table 2). Accordingly to NMR-assigned sites of protonations[16] and well-known protonation Scheme of $H_5$dtpa itself,[23] the first and second protonations take place on the nitrogen atoms of the ligand backbone. In the case of the phosphonate ligand $H_6L^1$, the third protonation ($pK_A$ = 7.57) corresponds to the protonation of the phosphonate moiety. Other protonations have $pK_A$'s values close to each other and correspond to the carboxylate pendants. Deprotonation of the singly protonated phosphonate ligand $(HL^1)^{5-}$ occurs at very high pH ($pK_A$ = 11.82) comparing to the phosphinate derivative and $H_5$dtpa ($pK_A$'s 10.28 and 10.41, respectively), as a result of spreading of high electron density of fully deprotonated phosphonate (charge 2–) to the neighbouring nitrogen atom. This trend is usually observed for analogous aminocarboxylic/phosphorus acid derivatives.[24] The potentiometric data of the ligand/metal mixtures were best fitted according to a model employing the formation of 1:1 and 1:2 ligand-to-metal complexes in various protonation states. The resulting stability constants of the complexes are compiled in Tables 3, 4, 5 and 6. In the case of 1:1 complexes with the transition-metal ions $Cu^{2+}$ and $Zn^{2+}$, all nitrogen atoms of the ligands are probably coordinated to the metal ion, and no free metal ions are present in the mixtures above pH ≈ 2.7. As usual, the coordination number of transition metal ions is 6, and the hapticity of the ligands studied is higher (8), the coordination sphere of the central metal ion is closed by two or three oxygen atoms of the pendant arms and some pendants remain uncoordinated (and can bind another metal ion in binuclear complexes, see below). The protonation of the $[M(L^1)]^{4-}$ species takes place on the phosphonate pendant moiety, which is probably coordinated (corresponding $pK_A$ slightly dropped comparing to the free ligand, 6.86 and 7.24 vs. 7.57, respectively). Other protonations takes place on oxygen atoms of the uncoordinated carboxylates ($pK_A$'s in range 1.37–3.97). Contrary, protonation of calcium(II) complexes takes place on the nitrogen atoms, as the corresponding $pK_A$'s are noticeably higher than that of acetates in the free ligands. In a twofold excess of the metal ion, complexes of $M_2L$ stoichiometry are formed. They loose additional two protons with increasing pH, forming bis(hydroxo) species. Because the corresponding dissociation constants are similar for both stepwise deprotonations [9.39 and 7.74 for copper(II) and 8.81 and 8.86 for zinc(II) complexes, respectively], these deprotonations occur almost simultaneously. The stability constant of the dinuclear species is lower, but still comparable to that of iminodiacetic acid, so the coordination of each

Table 2. Protonation constants $\log\beta_h$[a] of $H_6L^1$, $H_5L^2$ and $H_5$dtpa and corresponding dissociation constants $pK_{A,h}$[a] ($I$ = 0.1 M $NMe_4Cl$, 25 °C, unless stated otherwise).

| Constant | $H_6L^1$ present work | | ref.[16][b] | | $H_5L^2$ present work | | ref.[16][b] | | $H_5$dtpa ref.[22] | |
|---|---|---|---|---|---|---|---|---|---|---|
| | $\log\beta_h$ | $pK_{A,h}$ | $\log\beta_h$ | $pK_{A,h}$ | $\log\beta_h$ | $pK_{A,h}$ | $\log\beta_h$ | $pK_{A,h}$ | $\log\beta_h$ | $pK_{A,h}$ |
| $\log\beta_1$ | 11.82(8) | 11.82 | 10.75 | 10.75 | 10.28(1) | 10.28 | 9.60 | 9.60 | 10.41 | 10.41 |
| $\log\beta_2$ | 20.12(5) | 8.30 | 18.63 | 7.88 | 19.29(1) | 9.01 | 18.7 | 9.10 | 18.78 | 8.37 |
| $\log\beta_3$ | 27.69(3) | 7.57 | 25.55 | 6.92 | 22.46(2) | 3.17 | 21.33 | 2.63 | 22.87 | 4.09 |
| $\log\beta_4$ | 30.78(7) | 3.09 | 28.25 | 2.70 | 24.82(2) | 2.36 | 23.48 | 2.15 | 25.38 | 2.51 |
| $\log\beta_5$ | 33.33(5) | 2.55 | 30.42 | 2.17 | 26.97(2) | 2.15 | – | – | 27.42 | 2.04 |
| $\log\beta_6$ | 35.23(8) | 1.90 | – | – | – | – | – | – | – | – |
| $\log\beta_7$ | 36.44(9) | 1.21 | – | – | – | – | – | – | – | – |

[a] $\beta_h = [H_hL]/([H]^h[L])$; $K_{A,h} = ([H][H_{h-1}L])/[H_hL]$. [b] NMR titration, no control of ionic strength, NaOH/HCl/$D_2O$ for pH adjustment.

 © 2006 Wiley-VCH Verlag GmbH & Co. KGaA, Weinheim 

Table 3. Stability constants $\log\beta_{hlm}$[a] of complexes of $H_6L^1$, $H_5L^2$ and $H_5$dtpa with divalent metal ions and corresponding dissociation constants $pK_{A,hlm}$[a] ($I$ = 0.1 M $NMe_4Cl$, 25 °C, unless stated otherwise). Metal-coordinated water molecules are omitted for clarity.

| Equilibrium | | $Cu^{2+}$ | | | $Zn^{2+}$ | | | $Ca^{2+}$ | | |
|---|---|---|---|---|---|---|---|---|---|---|
| | | $H_6L^1$ | $H_5L^2$ | $H_5$dtpa[b] | $H_6L^1$ | $H_5L^2$ | $H_5$dtpa[b] | $H_6L^1$ | $H_5L^2$ | $H_5$dtpa[b] |
| | | $\log\beta_{hlm}$ | | | | | | | | |
| $M^{2+} + L^{n-} \rightleftharpoons [M(L)]^{(n-2)-}$ | $\log\beta_{011}$ | 21.43(6) | 19.47(4) | 21.2 | 19.67(6) | 18.18(3) | 18.2 | 10.70(4) | 9.38(2) | 10.75 |
| $M^{2+} + L^{n-} + H^+ \rightleftharpoons [M(HL)]^{(n-3)-}$ | $\log\beta_{111}$ | 28.29(5) | 23.30(3) | 26.00 | 26.92(5) | 22.15(2) | 23.80 | 18.27(2) | 15.48(5) | 16.86 |
| $M^{2+} + L^{n-} + 2H^+ \rightleftharpoons [M(H_2L)]^{(n-4)-}$ | $\log\beta_{211}$ | 31.95(3) | 25.90(3) | 28.96 | 30.65(2) | 24.32(1) | – | 23.83(8) | 21.03(4) | – |
| $M^{2+} + L^{n-} + 3H^+ \rightleftharpoons [M(H_3L)]^{(n-5)-}$ | $\log\beta_{311}$ | 34.41(4) | – | – | 32.82(3) | 25.69(8) | – | – | 24.06(4) | – |
| $2M^{2+} + L^{n-} + 2H_2O \rightleftharpoons [M_2(OH)_2(L)]^{(n-2)-} + 2H^+$ | $\log\beta_{-212}$ | 11.02(7) | 8.25(5) | – | 7.43(9) | 5.10(4) | – | – | – | – |
| $2M^{2+} + L^{n-} + H_2O \rightleftharpoons [M_2(OH)(L)]^{(n-3)-} + H^+$ | $\log\beta_{-112}$ | 20.41(7) | 16.46(7) | – | 16.2(1) | – | – | – | – | – |
| $2M^{2+} + L^{n-} \rightleftharpoons [M_2(L)]^{(n-4)-}$ | $\log\beta_{012}$ | 28.15(7) | 24.10(4) | – | 25.10(9) | 20.81(8) | – | 13.23(8) | 11.62(8) | – |
| $2M^{2+} + L^{n-} + H^+ \rightleftharpoons [M_2(HL)]^{(n-5)-}$ | $\log\beta_{112}$ | 32.60(4) | – | – | – | – | – | – | – | – |
| | | $pK_{A,hlm}$ | | | | | | | | |
| $[M(HL)]^{(n-3)-} \rightleftharpoons [M(L)]^{(n-2)-} + H^+$ | | 6.86 | 3.83 | 4.80 | 7.24 | 3.97 | 5.60 | 7.57 | 6.10 | 6.11 |
| $[M(H_2L)]^{(n-4)-} \rightleftharpoons [M(HL)]^{(n-3)-} + H^+$ | | 3.66 | 2.60 | 2.96 | 3.74 | 2.17 | – | 5.56 | 5.55 | – |
| $[M(H_3L)]^{(n-5)-} \rightleftharpoons [M(H_2L)]^{(n-4)-} + H^+$ | | 2.46 | – | – | 2.16 | 1.37 | – | – | 3.03 | – |
| $[M_2(OH)(L)]^{(n-3)-} + H_2O \rightleftharpoons [M_2(OH)_2(L)]^{(n-2)-} + H^+$ | | 9.39 | 8.21 | – | 8.81 | *7.86*[c] | – | – | – | – |
| $[M_2(L)]^{(n-4)-} + H_2O \rightleftharpoons [M_2(OH)(L)]^{(n-3)-} + H^+$ | | 7.74 | 7.64 | – | 8.86 | *7.86*[c] | – | – | – | – |
| $[M_2(HL)]^{(n-5)-} \rightleftharpoons [M_2(L)]^{(n-4)-} + H^+$ | | 4.45 | – | – | – | – | – | – | – | – |

[a] $\beta_{hlm} = [H_hL_lM_m]/([H]^h[L]^l[M]^m)$; $K_{A,hlm} = ([H][H_{h-1}L_lM_m])/[H_hL_lM_m]$. [b] Ref.[25], 0.1 M $K^+$ salts as background electrolytes. [c] Simultaneous dissociation of two protons.

Table 4. Stability constants $\log\beta_{hlm}$[a] of complexes of $H_6L^1$, $H_5L^2$ and $H_5$dtpa with trivalent metal ions $La^{3+}$, $Eu^{3+}$ and $Gd^{3+}$ and corresponding dissociation constants $pK_{A,hlm}$[a] ($I$ = 0.1 M $NMe_4Cl$, 25 °C, unless stated otherwise). Metal-coordinated water molecules are omitted for clarity.

| Equilibrium | | $La^{3+}$ | | | $Eu^{3+}$ | | | $Gd^{3+}$ | | |
|---|---|---|---|---|---|---|---|---|---|---|
| | | $H_6L^1$ | $H_5L^2$ | $H_5$dtpa[b] | $H_6L^1$ | $H_5L^2$ | $H_5$dtpa[b] | $H_6L^1$ | $H_5L^2$ | $H_5$dtpa[b] |
| | | $\log\beta_{hlm}$ | | | | | | | | |
| $M^{3+} + L^{n-} \rightleftharpoons [M(L)]^{(n-3)-}$ | $\log\beta_{011}$ | 20.54(8) | 17.54(2) | 19.5 | 22.36(3) | 19.82(1) | 22.4 | 22.34(2) | 19.47(2) | 22.2[c] |
| $M^{3+} + L^{n-} + H^+ \rightleftharpoons [M(HL)]^{(n-4)-}$ | $\log\beta_{111}$ | 26.25(5) | 20.44(5) | 21.1 | 28.75(1) | 22.23(1) | 24.6 | 28.82(1) | 22.01(2) | 24.6 |
| $M^{3+} + L^{n-} + 2H^+ \rightleftharpoons [M(H_2L)]^{(n-5)-}$ | $\log\beta_{211}$ | 29.43(3) | 22.86(7) | – | 31.07(1) | 23.52(8) | – | 31.17(1) | 23.4(1) | |
| $M^{3+} + L^{n-} + 3H^+ \rightleftharpoons [M(H_3L)]^{(n-6)-}$ | $\log\beta_{311}$ | – | 25.26(6) | – | – | – | – | – | – | |
| $2M^{3+} + L^{n-} + 2H_2O \rightleftharpoons [M_2(OH)_2(L)]^{(n-4)-} + 2H^+$ | $\log\beta_{-212}$ | 7.3(2) | 3.45(4) | – | 10.94(6) | 7.39(6) | – | 11.53(7) | 7.29(6) | |
| $2M^{3+} + L^{n-} + H_2O \rightleftharpoons [M_2(OH)(L)]^{(n-5)-} + H^+$ | $\log\beta_{-112}$ | 17.2(2) | – | – | 20.04(6) | – | – | 20.46(8) | – | |
| $2M^{3+} + L^{n-} \rightleftharpoons [M_2(L)]^{(n-6)-}$ | $\log\beta_{012}$ | 25.2(2) | – | – | 27.53(5) | – | – | 27.92(5) | 22.10(9) | |
| $2M^{3+} + L^{n-} + H^+ \rightleftharpoons [M_2(HL)]^{(n-7)-}$ | $\log\beta_{112}$ | – | – | – | – | – | – | 31.05(8) | – | |
| | | $pK_{A,hlm}$ | | | | | | | | |
| $[M(HL)]^{(n-4)-} \rightleftharpoons [M(L)]^{(n-3)-} + H^+$ | | 5.70 | 2.99 | 2.6 | 6.39 | 2.41 | 2.2 | 6.48 | 2.54 | 2.4 |
| $[M(H_2L)]^{(n-5)-} \rightleftharpoons [M(HL)]^{(n-4)-} + H^+$ | | 3.18 | 2.42 | – | 2.32 | 1.29 | – | 2.34 | 1.41 | |
| $[M(H_3L)]^{(n-6)-} \rightleftharpoons [M(H_2L)]^{(n-5)-} + H^+$ | | – | 2.40 | – | – | – | – | – | – | – |
| $[M_2(OH)(L)]^{(n-5)-} + H_2O \rightleftharpoons [M_2(OH)_2(L)]^{(n-4)-} + H^+$ | | 9.9 | – | – | 9.10 | – | – | 8.92 | *7.41*[d] | – |
| $[M_2(L)]^{(n-6)-} + H_2O \rightleftharpoons [M_2(OH)(L)]^{(n-5)-} + H^+$ | | 8.1 | – | – | 7.49 | – | – | 7.46 | *7.41*[d] | – |
| $[M_2(HL)]^{(n-7)-} \rightleftharpoons [M_2(L)]^{(n-6)-} + H^+$ | | – | – | – | – | – | – | 3.14 | – | – |

[a] $\beta_{hlm} = [H_hL_lM_m]/([H]^h[L]^l[M]^m)$; $K_{A,hlm} = ([H][H_{h-1}L_lM_m])/[H_hL_lM_m]$. [b] Ref.[25], 0.1 M $K^+$ salts as background electrolytes. [c] Ref.[22] [d] Simultaneous dissociation of two protons.

metal ion to these ligands is probably analogous. Therefore, one can suggest that both metal ions in the dinuclear complexes are coordinated separately by the opposite $H_2$ida-like sides of ligands and behave almost independently. The stabilities of these dinuclear complexes with transition-metal ions are comparable in the cases of $H_6L^1$ and $H_5$dtpa, but corresponding complexes of the phosphinate ligand are much less stable. However, stability of calcium(II) dinuclear complexes is comparable in all the cases (Table 6). Representative distribution diagrams of copper(II)/ligand systems are shown in Figures S2 and S3 (see Supporting Information).

Lanthanide(III) ions are usually fully encapsulated in eight coordinating atoms of $H_5$dtpa-like ligands. This coordination mode was also proved in the case of these phosphorus-containing ligands.[16] Therefore, protonations of their complexes occurs on non-coordinated oxygen atoms of the coordinated pendant moieties. In the case of the phosphonic ligand, first $pK_A$'s are in range 5.70–6.48, which corresponds to the deprotonation of the coordinated

 © 2006 Wiley-VCH Verlag GmbH & Co. KGaA, Weinheim 

Table 5. Stability constants $\log\beta_{hlm}$[a] of complexes of $H_6L^1$, $H_5L^2$ and $H_5$dtpa with the trivalent metal ions $Lu^{3+}$ and $Y^{3+}$and corresponding dissociation constants $pK_{A,hlm}$[a] ($I$ = 0.1 M $NMe_4Cl$, 25 °C, unless stated otherwise). Metal-coordinated water molecules are omitted for clarity.

| Equilibrium | | $Lu^{3+}$ $H_6L^1$ | $H_5L^2$ | $H_5$dtpa[b] | $Y^{3+}$ $H_6L^1$ | $H_5L^2$ | $H_5$dtpa[b] |
|---|---|---|---|---|---|---|---|
| | | $\log\beta_{hlm}$ | | | | | |
| $M^{3+} + L^{n-} \leftrightharpoons [M(L)]^{(n-3)-}$ | $\log\beta_{011}$ | 21.82(4) | 19.35(3) | 22.5 | 21.16(2) | 18.80(3) | 22.5[c] |
| $M^{3+} + L^{n-} + H^+ \leftrightharpoons [M(HL)]^{(n-4)-}$ | $\log\beta_{111}$ | 27.85(2) | 21.81(3) | 24.7 | 27.52(1) | 21.30(4) | 24.4 |
| $M^{3+} + L^{n-} + 2H^+ \leftrightharpoons [M(H_2L)]^{(n-5)-}$ | $\log\beta_{211}$ | 30.27(3) | 23.79(5) | – | 30.18(1) | 23.34(7) | |
| $M^{3+} + L^{n-} + 3H^+ \leftrightharpoons [M(H_3L)]^{(n-6)-}$ | $\log\beta_{311}$ | 32.11(5) | – | – | – | – | – |
| $2M^{3+} + L^{n-} + 2H_2O \leftrightharpoons [M_2(OH)_2(L)]^{(n-4)-} + 2H^+$ | $\log\beta_{-212}$ | 11.99(8) | 8.28(6) | – | – | 6.7(1) | – |
| $2M^{3+} + L^{n-} + H_2O \leftrightharpoons [M_2(OH)(L)]^{(n-5)-} + H^+$ | $\log\beta_{-112}$ | 20.05(8) | – | – | 16.48(4) | – | – |
| $2M^{3+} + L^{n-} \leftrightharpoons [M_2(L)]^{(n-6)-}$ | $\log\beta_{012}$ | 26.74(7) | – | – | – | – | – |
| $2M^{3+} + L^{n-} + H^+ \leftrightharpoons [M_2(HL)]^{(n-7)-}$ | $\log\beta_{112}$ | 30.42(6) | – | – | – | – | – |
| | | $pK_{A,hlm}$ | | | | | |
| $[M(HL)]^{(n-4)-} \leftrightharpoons [M(L)]^{(n-3)-} + H^+$ | | 6.04 | 2.46 | 2.2 | 6.36 | 2.50 | 1.9 |
| $[M(H_2L)]^{(n-5)-} \leftrightharpoons [M(HL)]^{(n-4)-} + H^+$ | | 2.41 | 1.98 | – | 2.66 | 2.04 | – |
| $[M(H_3L)]^{(n-6)-} \leftrightharpoons [M(H_2L)]^{(n-5)-} + H^+$ | | 1.84 | – | – | – | – | – |
| $[M_2(OH)(L)]^{(n-5)-} + H_2O \leftrightharpoons [M_2(OH)_2(L)]^{(n-4)-} + H^+$ | | 8.05 | – | – | – | – | – |
| $[M_2(L)]^{(n-6)-} + H_2O \leftrightharpoons [M_2(OH)(L)]^{(n-5)-} + H^+$ | | 6.69 | – | – | – | – | – |
| $[M_2(HL)]^{(n-7)-} \leftrightharpoons [M_2(L)]^{(n-6)-} + H^+$ | | 3.68 | – | – | – | – | – |

[a] $\beta_{hlm} = [H_hL_lM_m]/([H]^h[L]^l[M]^m)$; $K_{A,hlm} = ([H][H_{h-1}L_lM_m])/[H_hL_lM_m]$. [b] Ref.[25], 0.1 M $K^+$ salts as background electrolytes. [c] Ref.[22]

Table 6. Stability constants of dinuclear complexes $[M_2L]$ of $H_6L^1$, $H_5L^2$ and $H_5$dtpa and the complex [ML] of $H_2$ida with selected metal ions ($I$ = 0.1 M $NMe_4Cl$, 25 °C, unless stated otherwise).

| Ligand | $\log K$[a] $Cu^{2+}$ | $Zn^{2+}$ | $Ca^{2+}$ | $La^{3+}$ | $Eu^{3+}$ | $Gd^{3+}$ | $Lu^{3+}$ |
|---|---|---|---|---|---|---|---|
| $H_6L^1$ | 6.72 | 5.43 | 2.53 | 4.7 | 5.17 | 5.58 | 4.92 |
| $H_5L^2$ | 4.63 | 2.63 | 2.24 | – | – | 2.63 | – |
| $H_5$dtpa[b] | 6.79 | 4.48 | 1.6 | – | 3.2 | – | – |
| $H_2$ida[b,c] | 10.56 | 7.15 | 2.60 | 5.88 | 6.73 | 6.68 | 7.61 |

[a] $K = [M_2L]/([M][ML])$ for $H_6L^1$, $H_5L^2$ and $H_5$dtpa and $K = [ML]/([M][L])$ for $H_2$ida. [b] Ref.[25], 0.1 M $K^+$ salts as background electrolytes. [c] $H_2$ida = iminodiacetic acid.

phosphonate arm. Second protonations occur with $pK_A$'s in the range 2.3–3.2, comparable to that reported for complexes of $H_5$dtpa (1.9–2.6) and take place on carboxylate moieties. The phosphonate ligand forms relatively stable dinuclear complexes, which is probably a consequence of the high charge of the deprotonated phosphonate and its ability to bridge coordination polyhedrons (Table 6). Contrary, dinuclear complexes of the phenylphosphinate ligand and $H_5$dtpa itself are much less stable and were detected only in few cases due to a precipitation of metal hydroxides, which occurred in the other systems.

Representative distribution diagrams of gadolinium(III)/ligand systems are shown in Figure 2 and Figure 3. In the 1:1 mixtures, the $Gd^{3+}$ ion is fully encapsulated to the complexes above pH 3. Comparing the distributions simulated for twofold excess of the metal ion, the phosphonate ligand binds second $Gd^{3+}$ ion much better than the phosphinate, as a result of the higher negative charge of the ligand and the better possibility of the phosphonate to serve as a bridging group in the binuclear complexes (see parts B in Figures 2 and 3). Relatively high concentration of the free $Gd^{3+}$ ion in Figure 3 (B) at high pH values is not reasonable, and it is a result of the conditions used for the simulation. In

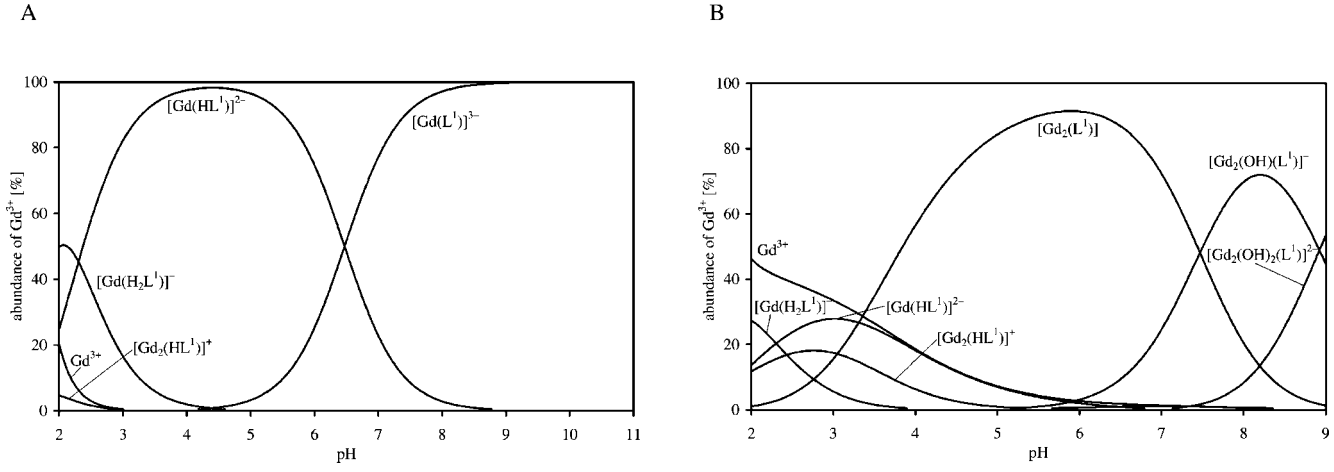


Figure 2. Distribution diagrams of $H_6L^1/Gd^{3+}$ systems in (A) 1:1 and (B) 1:2 ratios [$c(H_6L^1)$ = 0.004 M].

 © 2006 Wiley-VCH Verlag GmbH & Co. KGaA, Weinheim 

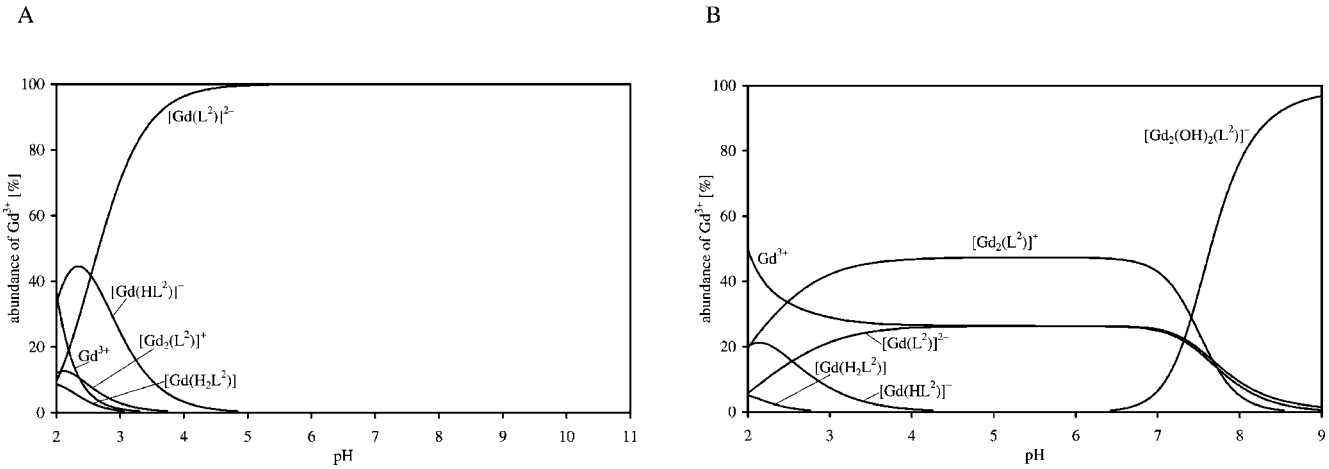


Figure 3. Distribution diagrams of $H_5L^2/Gd^{3+}$ systems in (A) 1:1 and (B) 1:2 ratios [$c(H_5L^2)$ = 0.004 M].

the real titration of $H_5L^2/Ln^{3+}$ systems, only 1.5-fold excess of hydrolyzable $Ln^{3+}$ ions was used and, therefore, the concentration of the free metal ions was suppressed.

Comparison of the determined stability constants of phosphorus acid derivatives with those found for $H_5$dtpa and $H_2$ida shows differences. The stability constants in $H_2$ida series follow the expected trend and increase from lanthanum(III) to lutetium(III). For $H_5$dtpa, the values increase from $La^{III}$ to $Eu^{III}$ and then are similar to the end of lanthanide series. For the phosphorus acid derivatives, the highest values were found for $Eu^{III}$ and $Gd^{III}$, and then decrease to $Lu^{III}$ and $Y^{III}$. These results indicate that size of the coordination cavity of $H_5$dtpa and its phosphorus acid derivatives is optimal for ions in the middle of lanthanide series. In contrast to the $H_5$dtpa, in the new ligands the phosphorus groups are too large and the ligands form bigger cavity which do not fit to the heavy lanthanides(III) or yttrium(III).

## Dissociation Kinetics

In preliminary experiments, the gadolinium(III) complexes with the new ligands were found to be much less stable against proton- and metal-assisted dissociations, comparing to the gadolinium(III) complex of $H_5$dtpa[26] and its mono- and bis-amides.[27,28] Therefore, the kinetic data had to be acquired by a stopped-flow technique. Dissociation reactions were performed in high excess (10–70×) of the concurrent metal ion ($Cu^{2+}$ or $Eu^{3+}$), ensuring pseudo-first-order reaction conditions, and in buffered solutions (pH in range 3.5–5.7). The dependences of the observed pseudo-first-order rate constants on the acidity of the solutions are shown in Figure 4, together with the best fits of the experimental data (for discussion of fittings see below).

For decomplexation of the gadolinium(III) complexes of $H_5$dtpa-like ligands, the general reaction Scheme is usually accepted,[26] where proton and metal-assisted pathways are taking place as shown in Scheme 2.

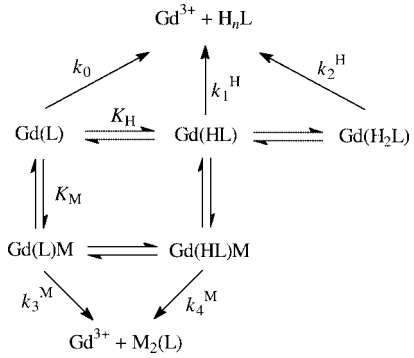


Scheme 2. Reaction mechanism of the dissociation of gadolinium(III) complexes of $H_5$dtpa-like ligands (charges are omitted for clarity).

Rearrangement of the corresponding rate law gives dependence of pseudo-first order constant $k_{obsd.}$ on proton and concurrent metal ion concentrations as given in Equation (1), similarly as it was evaluated for the fitting of dissociation kinetics of the $[Gd(dtpa)]^{2-}$ complex.[26] Here, the constants $K_H$ and $K_M$ are the protonation constant of the gadolinium(III) complex [Gd(HL)] and the stability constant for the mixed dinuclear gadolinium(III)-attacking metal-ion complex [Gd(L)M], respectively. The protonation and stability constants of $[Gd(H_2L)]$ and [Gd(HL)M] can be omitted from the denominator as the concentration of these complexes is negligible (the values of the corresponding constants are low).

$$k_{obsd.} = \frac{k_0 + k_1^H[H^+] + k_2^H[H^+]^2 + k_3^M[M^{n+}] + k_4^M[H^+][M^{n+}]}{1 + K_H[H^+] + K_M[M^{n+}]} \quad (1)$$

As $k_1^H$ and $k_2^H$ are independent of the nature of concurrent metal ion, the dissociation kinetics for copper(II) and europium(III) systems with the same starting gadolinium(III) complex were fitted simultaneously keeping these parameters identical in both cases. The results of these fittings are

 © 2006 Wiley-VCH Verlag GmbH & Co. KGaA, Weinheim 

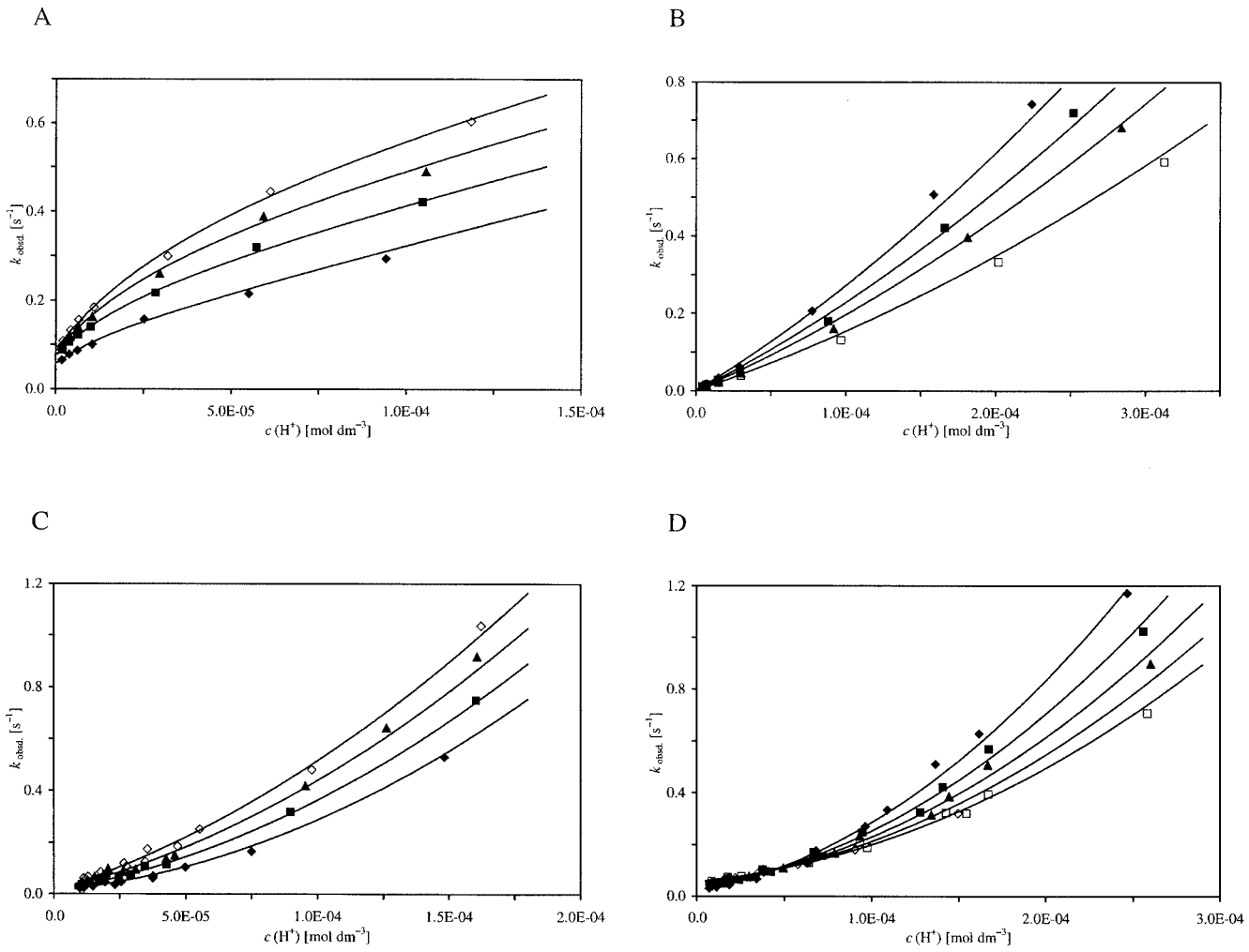


Figure 4. Dependence of pseudo-first-order rate constant $k_{obsd.}$ on proton and metal ion concentrations. Excess of the concurrent metal ion: 10×: full diamond; 20×: full square; 30×: full triangle; 40×: open diamond; 50×: open square; (A) $[Gd(L^1)]^{3-}/Cu^{2+}$ system, (B) $[Gd(L^1)]^{3-}/Eu^{3+}$ system, (C) $[Gd(L^2)]^{2-}/Cu^{2+}$ system, (D) $[Gd(L^2)]^{2-}/Eu^{3+}$ system.

compiled in Table 7 and the representative fits of the pH-dependence of the first-order rate constants $k_{obsd.}$ are shown in Figure 4.

As the pH region where dissociations were studied is much lower (3.5–5.7) than the p$K_A$ of the $[Gd(HL^1)]^{2-}$ complex (6.5, Table 4), one can suggest that the singly protonated complex species $[Gd(HL^1)]^{2-}$ is the major species in the reacting solution (Figure 2). Therefore, the calculated constant $K_H$ corresponds to the second protonation of the complex species. This hypothesis can be supported by the relatively low value of this constant (the corresponding p$K_A$ is 3.7, Table 7).

In the case of the copper(II)-assisted dissociation of the $[Gd(L^1)]^{3-}$ complex (Figure 4, A), the most complicated rate

Table 7. Rate and equilibrium constants characterizing the dissociation reactions between the complexes $[Gd(L^1)]^{3-}$, $[Gd(L^2)]^{2-}$ and $[Gd(dtpa)]^{2-}$, and $Cu^{2+}$ and $Eu^{3+}$ ions (25 °C, 1.0 M KCl).

| Constant | Complex $[Gd(L^1)]^{3-}$ | $[Gd(L^2)]^{2-}$ | $[Gd(dtpa)]^{2-}$ [a] |
|---|---|---|---|
| $k_1^H$ [M$^{-1}$ s$^{-1}$] | $(3.38 \pm 0.22) \times 10^3$ | $(1.57 \pm 0.18) \times 10^3$ | 0.58 |
| $k_2^H$ [M$^{-2}$ s$^{-1}$] | $(1.02 \pm 0.20) \times 10^7$ | $(1.51 \pm 0.11) \times 10^7$ | $9.7 \cdot 10^4$ |
| $k_3^{Cu}$ [M$^{-1}$ s$^{-1}$] | $33 \pm 3$ | – | 0.93 |
| $k_4^{Cu}$ [M$^{-2}$ s$^{-1}$] | $(9.4 \pm 1.3) \times 10^5$ | $(5.4 \pm 0.3) \times 10^5$ | – |
| $K_{Cu}$ [M$^{-1}$] | – | – | 13 |
| $k_3^{Eu}$ [M$^{-1}$ s$^{-1}$] | – | $2.2 \pm 0.5$ | $4.9 \cdot 10^{-4}$ |
| $k_4^{Eu}$ [M$^{-2}$ s$^{-1}$] | – | – | 40 |
| $K_{Eu}$ [M$^{-1}$] | $50 \pm 7$ | $20.0 \pm 2.3$ | 20 |
| $K_H$ [M$^{-1}$] | $(5.7 \pm 0.8) \times 10^3$ | – | 100 |

[a] Ref.[26]

 © 2006 Wiley-VCH Verlag GmbH & Co. KGaA, Weinheim 

law was found. The best fits were obtained according to Equation (2) which is formally derived from Equation (1) when the term $K_M[Cu^{2+}]$ in the denominator is neglected, as can be because the $K_M$ value is low, comparing to the value of the protonation constant $K_H$. The reaction rate increases with both proton and copper(II) concentrations, and a saturation-like shape of $k_{obsd.}$ dependences (Figure 4, A) reveals a formation of the protonated complex, which slightly slow down the dissociation reaction as the $Cu^{2+}$ ion cannot easily attack the less negatively charged protonated complex $[Gd(H_2L^1)]^-$ in comparison with $[Gd(HL^1)]^{2-}$.

$$k_{obsd.} = \frac{k_1^H[H^+] + k_2^H[H^+]^2 + k_3^{Cu}[Cu^{2+}] + k_4^{Cu}[H^+][Cu^{2+}]}{1 + K_H[H^+]} \quad (2)$$

However, in the europium(III)-promoted dissociation of $[Gd(L^1)]^{3-}$ complex, only proton-assisted pathways were found, as the observed rate constant $k_{obsd.}$ can be extrapolated to zero at zero proton concentration. Furthermore, the increase in the $Eu^{3+}$ concentration dropped the value of $k_{obsd.}$ (Figure 4, B), which is an evidence for the formation of a dinuclear complex. This complex is kinetically relatively stable, and its structure should be analogous to the dinuclear $[Gd_2(L^1)]$ species (Figure 2, B). The presence of the highly charged metal ions bound on opposite sides of the complex prevents the attack by an additional proton. Therefore, the data were best fitted according to Equation (3).

$$k_{obsd.} = \frac{k_1^H[H^+] + k_2^H[H^+]^2}{1 + K_{Eu}[Eu^{3+}]} \quad (3)$$

The copper(II)-assisted dissociation of the $[Gd(L^2)]^{2-}$ complex can be best fitted by Equation (4), which can be derived from Equation (1) by neglecting of the stabilization of the gadolinium(III) complex by the protonated and dinuclear species formation [i.e. $1 >> K_H[H^+] + K_M[Cu^{2+}]$ in the denominator of Equation (1)], as the stability of the dinuclear complex with $Cu^{2+}$ is even lower for the phosphinate derivative $H_5L^2$ comparing to phosphonate ligand $H_6L^1$ and also because of the lower protonation constants of the $[Gd(L^2)]^{2-}$ complex the term $K_H[H^+]$ is of a low importance. The representative data are given together with the best fits in Figure 4 (C).

$$k_{obsd.} = k_1^H[H^+] + k_2^H[H^+]^2 + k_4^{Cu}[H^+][Cu^{2+}] \quad (4)$$

In the case of the europium(III)-assisted dissociation of the $[Gd(L^2)]^{2-}$ complex, the crossing region in $k_{obsd.}$ dependences on the proton concentration was found at $[H^+]$ of about $5 \cdot 10^{-5}$ M (pH ≈ 4.3, Figure 4, D). At higher proton concentrations, the increase in $Eu^{3+}$ concentration slows down the reaction rate, contrary, at low proton concentrations, the reaction accelerates with increasing $Eu^{3+}$ concentration. Similar behaviour was reported for the $Eu^{3+}$-promoted dissociation of the $[Gd(dtpa)]^{2-}$ complex.[26] The non-zero reaction rate at the zero proton concentration is an evidence for the proton-independent term in the rate law. Therefore, the best fits were obtained using Equation (5).

$$k_{obsd.} = \frac{k_1^H[H^+] + k_2^H[H^+]^2 + k_3^{Eu}[Eu^{3+}]}{1 + K_{Eu}[Eu^{3+}]} \quad (5)$$

Spontaneous dissociation of diprotonated complex $[Gd(H_2L^1)]^-$ and the monoprotonated complexes $[Gd(HL^2)]^-$ is about three orders in magnitude faster than in the case of $[Gd(Hdtpa)]^-$ complex (Table 7). Further protonation causes noticeable increase in the reaction rate of about four orders in all the cases.

To compare the kinetic inertness of the complex species with the new ligands and that with $H_5$dtpa, we calculated half-life times of all the complex species under various conditions (Table 8).

Table 8. Comparison of half-life times of the complexes $[Gd(L^1)]^{3-}$, $[Gd(L^2)]^{2-}$ and $[Gd(dtpa)]^{2-}$ in various reaction media (25 °C, $I$ = 1.0 M KCl).

| Conditions | Half-life times [s] $[Gd(L^1)]^{3-}$ | $[Gd(L^2)]^{2-}$ | $[Gd(dtpa)]^{2-}$ |
|---|---|---|---|
| | pH = 4.0 | | |
| without metal ions | 2.5 | 2.2 | 680 |
| 0.001 M $Cu^{2+}$ | 1.9 | 1.9 | 360 |
| 0.001 M $Eu^{3+}$ | 2.6 | 2.3 | 690 |
| 0.01 M $Cu^{2+}$ | 0.6 | 0.8 | 77 |
| 0.01 M $Eu^{3+}$ | 3.3 | 2.5 | 780 |
| | pH = 5.0 | | |
| without metal ions | 21 | 40 | $4.5 \cdot 10^4$ |
| 0.001 M $Cu^{2+}$ | 9.5 | 31 | 740 |
| 0.001 M $Eu^{3+}$ | 22 | 37 | $4.3 \cdot 10^4$ |
| 0.01 M $Cu^{2+}$ | 1.6 | 9.7 | 84 |
| 0.01 M $Eu^{3+}$ | 31 | 21 | $3.4 \cdot 10^4$ |
| | pH = 6.0 | | |
| without metal ions | 210 | 440 | $1.0 \cdot 10^6$ |
| 0.001 M $Cu^{2+}$ | 19 | 330 | 750 |
| 0.001 M $Eu^{3+}$ | 220 | 190 | $5.8 \cdot 10^5$ |
| 0.01 M $Cu^{2+}$ | 2.0 | 99 | 84 |
| 0.01 M $Eu^{3+}$ | 310 | 35 | $1.4 \cdot 10^5$ |

In general, the stability of the complexes of new phosphorus-containing ligands is much lower comparing to that of $[Gd(dtpa)]^{2-}$. Increase in copper(II) concentration speed-up the dissociation reaction in all the cases, bud especially, for $[Gd(dtpa)]^{2-}$ complex in neutral solutions, where is the half-life time comparable to that calculated for $[Gd(L^2)]^{2-}$. It is a consequence of a spontaneous dissociation of dinuclear [Gd(dtpa)Cu] complex. In the case of $[Gd(L^2)]^{2-}$, the lower basicity of the donor groups results in lower ability of binuclear complex formation (see also the values of stability constants of dinuclear species, Table 6) and therefore, to worse formation of such reactive intermediate. For europium(III)-promoted dissociations, the stabilization of [Gd(L)] complexes with increasing $Eu^{3+}$ concentration was found in all the cases at low pH. It is the result of formation of [Gd(L)Eu] complexes, which cannot be easily attacked by

 © 2006 Wiley-VCH Verlag GmbH & Co. KGaA, Weinheim 

proton and their own dissociation is slower comparing to proton-assisted pathway. Increasing the pH, half-life times slightly drop with increasing $Eu^{3+}$ concentration for $[Gd(dtpa)]^{2-}$ and $[Gd(L^2)]^{2-}$ complexes, as result of their spontaneous dissociation. However, in the case of $[Gd(L^1)Eu]$, there was no evidence for such process and therefore, half-life times still increase.

For the $H_5$dtpa and its various amide derivatives, all the gadolinium(III) complexes have similar kinetic stability comparing to each other.[26–28] Surprisingly, we found that the gadolinium(III) complexes with $H_5$dtpa-analogues derived on the central nitrogen atom by the phosphorus acid pendant arm are much less kinetically stable with the half-life times about two to three orders of magnitude shorter. This can probably be attributed to a steric strain in the new complexes, which coordination sphere is not so compact and which can be attacked by a proton or by an additional metal ion. Furthermore, the complex of phosphonate ligand can easily be protonated due to the high basicity of the pendant arm. Also, it can easily form dinuclear complexes, which are the intermediates in the dissociation mechanism. Anyway, the rate constants for complexes of both ligands with phosphorus pendant arm are comparable, so the stereochemistry of both the complexes and the intermediates is probably similar. It should be noticed that assistance of proton or the metal ions in the decomplexation is much more pronounced for $H_5$dtpa complex itself. The results obtained here correspond very well with *trans*-chelation experiments between the gadolinium(III) complexes and $Zn^{2+}$ followed by $^1H$ relaxation measurements ($Gd^{3+}$ complex/$Zn^{2+}$ = 1:1, pH 7, phosphate buffer, 37 °C).[16] The experiments gave the same relative kinetic inertness of the complexes $[Gd(dtpa)]^{2-} >> [Gd(L^1)]^{3-} \approx [Gd(L^2)]^{2-}$. On the other hand, a difference in kinetic inertness (pH 2, 25 °C) of the gadolinium(III) complexes of $H_4$dota and its monophosphonate analog $H_5$do3ap are much smaller; the $[Gd(do3ap)]^{2-}$ complex decomposes about one order of magnitude faster ($\tau_{1/2}$ = 7.9 h) than the $[Gd(dota)]^-$ complex ($\tau_{1/2}$ = 95.5 h).[29]

## Conclusions

The study of thermodynamic and kinetic stabilities of the complexes of phosphonate and phenylphosphinate analogues of $H_5$dtpa (derived by phosphorus functionality on the central nitrogen atom) with selected transition and lanthanide metal ions is presented. Both phosphorus-containing ligands form thermodynamically very stable complexes, with stability constants comparable or even higher than those reported for parent $H_5$dtpa. However, the kinetic stability of their gadolinium(III) complexes against acid- and metal-assisted decomplexations is surprisingly much lower. The half-life times of the gadolinium(III) complexes of the new ligands in the presence of an excess of the concurrent metal ions [copper(II) or europium(III)] are shorter by about 2–3 orders of magnitude comparing to those of $H_5$dtpa and its amidic derivatives. This can probably be attributed to the steric strain in the new complexes, to a high affinity of the phosphonate ligand for protons and/or to the easy formation of binuclear complexes, which acts as the intermediates in the dissociation mechanism. The data presented here show that lanthanide(III) complexes of this class of ligands are less suitable for medicinal use due to the rather low kinetic inertness.

## Experimental Section

**Materials:** The ligands used in this work were prepared according to reported procedures.[16] Metal salts were of analytical grade and were used as obtained from commercial sources or after recrystallization from water. The deionized water (Milli-Q, Millipore, 20 kΩ) was used for physico-chemical experiments. Materials (analytical grade) for preparation of the buffer solutions were obtained from commercial sources.

### Equilibrium Studies

The stock solution of hydrochloric acid (ca. 0.03 mol·dm$^{-3}$) was prepared from 35% aqueous solution (quality "puriss.", Fluka). Commercial $NMe_4Cl$ (99%, Fluka) was recrystallized from boiling *i*PrOH and the solid salt was dried with $P_2O_5$ in vacuo to constant weight (this dried form of the salt is extremely hygroscopic).[29] Carbonate-free $NMe_4OH$ solution (ca. 0.2 mol·dm$^{-3}$) was prepared from $NMe_4Cl$ using ion exchanger Dowex 1 in the $OH^-$ form (elution with carbonate-free water, under argon). The hydroxide solution was standardized against potassium hydrogen phthalate and the HCl solution against the ca. 0.2 mol·dm$^{-3}$ $NMe_4OH$ solution.

The ligand stock solutions ($c \approx 0.02$ mol·dm$^{-3}$) were prepared by dissolution of a weighted amount of the solid hydrochloride salts of ligands ($H_6L^1$·HCl·2$H_2O$ and $H_5L^2$·2HCl·$H_2O$, respectively) in an appropriate amount of deionized water. The exact content of hydrochloric acid was determined gravimetrically as AgCl. Concentrations of the ligands were calculated from potentiometrical data during the determination of the protonation constants using the OPIUM program package.[30] The exact concentrations of metal chlorides stock solutions were determined by titrations with standardized solution of $Na_2H_2$edta.

Titrations were carried out in a vessel thermostatted at 25 ± 0.1 °C, at an ionic strength $I(NMe_4Cl)$ = 0.1 mol·dm$^{-3}$ and in the presence of extra HCl in the $-\log[H^+]$ range 1.5–12.0 (except of titrations in presence of excess of hydrolyzing metal ions, which were finished at $-\log[H^+]$ of about 9.5) using a PHM 240 pH meter, 2-mL ABU 900 automatic piston burette and a GK 2401B combined electrode (Radiometer). The initial volume of the measured solution was about 5 cm$^3$ and concentrations of ligands were about 0.004 mol·dm$^{-3}$. For determination of the stability constants of metal complexes, the mixtures with one or 1.5–2 equivalents of metal ions were used. Titration of each system in each M:L ratio was carried out at least three times and each titration consisted of about 40 data points. An inert atmosphere was ensured by constant flow of dinitrogen saturated with the water vapour by passing through 0.1 mol·dm$^{-3}$ solution of $NMe_4Cl$. The concentration protonation constants $\beta_h$ are defined by the equation

$$\beta_h = [H_hL]/([H]^h[L])$$

As dissociation constant $K_{A,h}$ is commonly defined by

$$K_{A,h} = ([H][H_{h-1}L])/[H_hL],$$

it is evident, that $pK_{A,h} = \log\beta_h - \log\beta_{h-1}$.

 © 2006 Wiley-VCH Verlag GmbH & Co. KGaA, Weinheim 

The concentration stability constants $\beta_{hlm}$ are defined by the equation

$\beta_{hlm} = [H_hL_lM_m]/([H]^h[L]^l[M]^m)$,

and dissociation constant $K_{A,hlm}$ can be defined similarly to the case of free ligand as

$K_{A,hlm} = ([H][H_{h-1}L_lM_m])/[H_hL_lM_m]$.

Analogously, $pK_{A,hlm} = \log\beta_{hlm} - \log\beta_{h-1lm}$.

The constants (and their standard deviations) were calculated with the OPIUM program package.[30] This program minimizes the criterion of the generalized least-squares method using the calibration function

$E = E_0 + S\times\log[H^+] + j_1\times[H^+] + j_2\times K_w/[H^+]$

where the additive term $E_0$ contains the standard potentials of the electrodes used and contributions of inert ions to the liquid-junction potential, $S$ corresponds to the Nernstian slope, the value of which should be close to the theoretical value of $RT/zF\{\log(e)\}$ = 59.159 mV. It was reported in the literature that for a glass electrode this value can oscillate at about 99.7% of the theoretical value.[31] The terms $j_1\times[H^+]$ and $j_2\times K_w/[H^+] = j_2\times[OH^-]$ are contributions of $H^+$ and $OH^-$ ions to the liquid-junction potential. By simple view on the calibration function, it is clear, that they cause a deviation from a linear dependence of $E$ on $[H^+]$ and are significant only in strong acidic and strong alkaline solutions. The calibration parameters were determined from titration of standard HCl with standard $NMe_4OH$ before and immediately after the titration of ligand or ligand-metal system. Thus, two sets of calibration parameters for each titration were used for the calculations of the constants. The water ion product $pK_w$ = 13.81 and the stability constants of hydroxo metal complexes were taken from the literature.[25,32]

**Kinetic Studies**

The stock solutions of ligands of the concentration of about 0.05 mol·dm$^{-3}$ were prepared by dissolution of a weighted amount of solid hydrochloride salts ($H_6L^1$·HCl·2$H_2O$ and $H_5L^2$·2HCl·$H_2O$, respectively) in appropriate amounts of double-distilled water. Exact content of ligands was determined by addition of a defined excess of $EuCl_3$ and re-titration with a standardized solution of $Na_2H_2$edta (xylenol orange indicator, pH 5.8–6.0, urotropine buffer). The concentrations of lanthanide(III) chlorides stock solutions were determined by titrations with standardized solution of $Na_2H_2$edta. From the solutions, the gadolinium(III) complexes [$c$ = 0.2 mmol·dm$^{-3}$ for copper(II)-exchange reaction and 2 mmol·dm$^{-3}$ for europium(III)-exchange reaction, respectively] of each ligand were prepared. Constant ionic strength of potassium chloride (1 mol·dm$^{-3}$) and buffers [0.02 mol·dm$^{-3}$ boric acid in 0.08 mol·dm$^{-3}$ mannitol for the copper(II)-exchange reaction and 0.02 mol·dm$^{-3}$ *N*-methylpiperazine for the europium(III)-exchange reaction] were used to adjust the pH in the range 3.5–5.7. Large excesses of copper(II) (10–50×) and europium(III) (10–70×) chlorides were employed to assure pseudo-first order conditions of the exchange reactions. All metal-assisted dissociation kinetics experiments were followed spectrophotometrically on a stopped-flow apparatus (Applied Photophisics DX-17MV) at 25 °C at 300 nm [copper(II)-promoted decomplexations], 250 nm [europium(III)-exchange on Gd–$H_6L^1$ system] and 290 nm [europium(III)-exchange on Gd–$H_5L^2$ system]. The rate constants $k_{obsd.}$ were determined by fitting of the time-dependence of the absorbance with $A_t = (A_\infty - A_0)e^{-kt} + A_0$ and were reproducible within ±5% in the independent runs. The values of the rate constants used for the fittings were the averages from at least two independent runs using a firmware.

**X-ray Measurement**

A single crystal of $H_6L^1$·HCl·1.5$H_2O$ suitable for a diffraction experiment was prepared by slow evaporation of a saturated aqueous solution at room temperature. The colourless block-like crystal was mounted on a glass fibre by silicone fat. Diffraction data were collected using graphite-monochromated Mo-$K_\alpha$ radiation with an Enraf–Nonius KappaCCD diffractometer at 150(1) K [Cryostream Cooler (Oxford Cryosystem)] and analyzed using the HKL DENZO program package (ref.[33]). Cell parameters were determined from all data by the same program package.[33] The structure was solved by direct methods (SIR 97[34]) and refined by full-matrix least-squares techniques (SHELXL97[35]). The used scattering factors for neutral atoms were included in the SHELXL97 program. All non-hydrogen atoms were refined anisotropically. The hydrogen atoms were localized in the difference map of electronic density and refined isotropically. The pertinent crystallographic data are presented in Table 9. CCDC-287906 contains the supplementary crystallographic data for this paper. These data can be obtained free of charge from The Cambridge Crystallographic Data Centre via www.ccdc.cam.ac.uk/data_request/cif.

Table 9. Experimental data for determination of the crystal structure of $H_6L^1$·HCl·1.5$H_2O$.

| | |
|---|---|
| Formula | $C_{13}H_{28}ClN_3O_{12.50}P$ |
| $M$ | 492.80 |
| $T$ [K] | 150 |
| Crystal dimension, mm | 0.25×0.28×0.55 |
| Colour and shape | colourless block |
| Crystal system | triclinic |
| Space group | $P\bar{1}$ (No. 2) |
| $a$ [Å] | 8.6219(2) |
| $b$ [Å] | 11.8231(2) |
| $c$ [Å] | 12.0663(3) |
| $\alpha$ [°] | 114.9404(12) |
| $\beta$ [°] | 96.9488(12) |
| $\gamma$ [°] | 105.7311(14) |
| $V$ [Å$^3$] | 1033.78(4) |
| $Z$ | 2 |
| $D_c$ [g cm$^{-3}$] | 1.583 |
| $\lambda$ [Å] | 0.71073 |
| $\mu$ [mm$^{-1}$] | 0.333 |
| $F(000)$ | 518 |
| $\theta$ range of data collection [°] | 2.63–27.50 |
| Index ranges | $-11 < h < 11$<br>$-15 < k < 15$<br>$-15 < l < 15$ |
| Data, restraints, parameters | 4735, 0, 390 |
| GOF on $F^2$ | 1.025 |
| $wR$ (all data), $wR'$ [$I > 2\sigma(I)$][a] | 0.1097, 0.0984 |
| $R$ (all data), $R'$ [$I > 2\sigma(I)$][b] | 0.0604, 0.0391 |
| Largest diff. peak and hole [e·Å$^{-3}$] | 0.386, –0.493 |

[a] $wR = [\Sigma w(F_o^2 - F_c^2)^2/\Sigma w(F_o^2)^2]^{1/2}$, $w = 1/[\sigma^2(F_o^2) + (A\times P)^2 + B\times P]$; where $P = (F_o^2 + 2F_c^2)/3$. [b] $R = \Sigma|F_o - F_c|/\Sigma|F_c|$.

**Supporting Information** (see footnote on the first page of this article): Table of hydrogen bonds found in the structure of $H_6L^1$·HCl·1.5$H_2O$; and distribution diagrams of free $H_6L^1$, free $H_5L^2$, and 1:1 and 2:1 copper(II)/ligands ($H_6L^1$ and $H_5L^2$) mixtures on pH.

## Acknowledgments

We thank Dr. I. Císařová for X-ray data collection and Ms. M. Malíková for help with titration experiments. This work was supported by the Grant Agency of the Czech Republic (No. 203/03/

 © 2006 Wiley-VCH Verlag GmbH & Co. KGaA, Weinheim 

0168), the FP6-projects EMIL (LSHC-2004-503569) and DiMI (LSHB-CT-2005-512146) and COST D18 are acknowledged. JK thanks the Flemish government for a postdoctoral fellowship (bilateral project between Flanders and the Czech Republic BIL/03/10).

[1] *The Chemistry of Contrast Agents in Medical Magnetic Resonance Imaging* (Eds.: A. E. Merbach, É. Tóth), Wiley, Chichester, U.K., **2001**.
[2] *Topics in Current Chemistry*, vol. 221, Springer, Frankfurt/Main, Germany, **2002**.
[3] P. Caravan, J. J. Ellison, T. J. McMurry, R. B. Lauffer, *Chem. Rev.* **1999**, *99*, 2293–2352.
[4] E. Brücher, *Top. Curr. Chem.* **2002**, *221*, 103–122.
[5] S. Laurent, L. Vander Elst, F. Copoix, R. N. Muller, *Invest. Radiol.* **2001**, *36*, 115–122.
[6] S. Aime, M. Botta, M. Fasano, E. Terreno, *Chem. Soc. Rev.* **1998**, *27*, 19–29.
[7] D. H. Powell, O. M. N. Dhubhghaill, D. Pubanz, L. Helm, Y. S. Lebedev, W. Schlaepfer, A. E. Merbach, *J. Am. Chem. Soc.* **1996**, *118*, 9333–9346.
[8] R. Ruloff, É. Tóth, R. Scopelliti, R. Tripier, H. Handel, A. E. Merbach, *Chem. Commun.* **2002**, 2630–2631.
[9] S. Laus, R. Ruloff, É. Tóth, A. E. Merbach, *Chem. Eur. J.* **2003**, *9*, 3555–3566.
[10] Z. Jászberényi, A. Sour, É. Tóth, M. Benmelouka, A. E. Merbach, *Dalton Trans.* **2005**, 2713–2719.
[11] S. Laus, A. Sour, R. Ruloff, É. Tóth, A. E. Merbach, *Chem. Eur. J.* **2005**, *11*, 3064–3076.
[12] S. Laurent, F. Botteman, L. Vander Elst, R. N. Muller, *Eur. J. Inorg. Chem.* **2004**, 463–468.
[13] L. Burai, É. Tóth, A. Sour, A. E. Merbach, *Inorg. Chem.* **2005**, *44*, 3561–3568.
[14] D. J. Sawyer, J. E. Powell, *Polyhedron* **1989**, *8*, 1425–1430.
[15] Y.-M. Wang, C. H. Lee, G.-C. Liu, R.-S. Sheu, *J. Chem. Soc. Dalton Trans.* **1998**, 4113–4118.
[16] J. Kotek, P. Lebdušková, P. Hermann, L. Vander Elst, R. N. Muller, C. F. G. C. Geraldes, T. Maschmeyer, I. Lukeš, J. A. Peters, *Chem. Eur. J.* **2003**, *9*, 5899–5915.
[17] J. Rudovský, J. Kotek, P. Hermann, I. Lukeš, V. Mainero, S. Aime, *Org. Biomol. Chem.* **2005**, *3*, 112–117.
[18] J. Rudovský, P. Cígler, J. Kotek, P. Hermann, P. Vojtíšek, I. Lukeš, J. A. Peters, L. Vander Elst, R. N. Muller, *Chem. Eur. J.* **2005**, *11*, 2373–2384.
[19] P. Lebdušková, J. Kotek, P. Hermann, L. Vander Elst, R. N. Muller, I. Lukeš, J. A. Peters, *Bioconjugate Chem.* **2004**, *15*, 881–889.
[20] J. Rudovský, P. Hermann, M. Botta, S. Aime, I. Lukeš, *Chem. Commun.* **2005**, 2390–2391.
[21] P. Lebdušková, A. Sour, L. Helm, É. Tóth, J. Kotek, I. Lukeš, A. E. Merbach, *Dalton Trans.*, in press.
[22] K. Kumar, C. A. Chang, L. C. Francesconi, D. D. Dischino, M. F. Malley, J. Z. Gougoutas, M. F. Tweedle, *Inorg. Chem.* **1994**, *33*, 3567–3575.
[23] C. F. G. C. Geraldes, A. M. Urbano, M. C. Alpoim, A. D. Sherry, K.-T. Kuan, R. Rajagopalan, F. Maton, R. N. Muller, *Magn. Reson. Imaging* **1995**, *13*, 401–420.
[24] I. Lukeš, J. Kotek, P. Vojtíšek, P. Hermann, *Coord. Chem. Rev.* **2001**, *216–217*, 287–312.
[25] *NIST Standard Reference Database 46 (Critically Selected Stability Constants of Metal Complexes)*, Version 7.0, **2003**.
[26] L. Sarka, L. Burai, E. Brücher, *Chem. Eur. J.* **2000**, *6*, 719–724.
[27] L. Sarka, L. Burai, R. Király, L. Zékány, E. Brücher, *J. Inorg. Biochem.* **2002**, *91*, 320–326.
[28] Z. Jászberényi, É. Tóth, T. Kálai, R. Király, E. Brücher, A. E. Merbach, K. Hideg, *Dalton Trans.* **2005**, 694–701.
[29] P. Táborský, P. Lubal, J. Havel, J. Kotek, P. Hermann, I. Lukeš, *Collect. Czech. Chem. Commun.* **2005**, *70*, 1909–1942.
[30] M. Kývala, I. Lukeš, CHEMOMETRICS '95, Pardubice, Czech Republic, **1995**, Book of Abstracts, p. 63; M. Kývala, P. Lubal, I. Lukeš, SIMEC '98, Girona, Spain, **1998**, Book of Abstracts, p. 94; available free of charge at: http://www.natur.cuni.cz/~kyvala/opium.html.
[31] D. C. Harris, in: *Quantitative Chemical Analysis*, 3rd ed., W. H. Freeman, New York, **1991**, p. 365.
[32] C. F. Baes Jr, R. E. Mesmer, *The Hydrolysis of Cations*, Wiley, New York, **1976**.
[33] Z. Otwinowski, W. Minor, *HKL Denzo and Scalepack Program Package*, Nonius BV, Delft, **1997**; Z. Otwinowski, W. Minor, *Methods Enzymol.* **1997**, *276*, 307–326.
[34] A. Altomare, M. C. Burla, M. Camalli, G. L. Cascarano, C. Giacovazzo, A. Guagliardi, A. G. G. Moliterni, G. Polidori, R. Spagna, *J. Appl. Crystallogr.* **1999**, *32*, 115–119.
[35] G. M. Sheldrick, *SHELXL97. Program for Crystal Structure Refinement from Diffraction Data*, University of Göttingen. Göttingen, **1997**.

Received: December 14, 2005
Published Online: March 22, 2006

 © 2006 Wiley-VCH Verlag GmbH & Co. KGaA, Weinheim 

DOI: 10.1002/ejic.200501154

# Titanium Complexes of Dialkanolamine Ligands: Synthesis and Structure

**Kirill V. Zaitsev,[a] Sergey S. Karlov,*[a] Anastasia A. Selina,[a] Yu. F. Oprunenko,[a] Andrei V. Churakov,[b] Bernhard Neumüller,[c] Judith A. K. Howard,[d] and Galina S. Zaitseva[a]**

**Keywords:** Titanium / Alkoxides / Pentacoordination / Hexacoordination / Dialkanolamine complexes

Synthesis of the title compounds, viz. $[RN(CH_2CH_2O)(CHR^1CR^2R^3O)]Ti(OiPr)_2$ (**13**–**15**) and $[RN(CH_2CH_2O)(CHR^1CR^2R^3O)]_2Ti$ (**18**–**28**), by the reaction of one or two equivalents of the corresponding dialkanolamines $RN(CH_2CH_2OH)(CHR^1CR^2R^3OH)$ (**1**–**12**) with $Ti(OiPr)_4$ is reported. Other routes to $[RN(CH_2CH_2O)(CHR^1CR^2R^3O)]_2Ti$, such as the reaction of $Ti(CH_2Ph)_4$ with dialkanolamine and the reaction of $TiCl_4(THF)_2$ with dialkanolamine/$Et_3N$ were also tested. Dimeric titanocane **16**, $[PhCH_2N(CH_2CH_2O)_2Ti(OMe)_2]_2$, was obtained from the reaction of one equivalent of dialkanolamine **3** with $CpTi(OMe)_3$. $PhCH_2N(CH_2CH_2O)_2Ti(OMenth)_2$ (**17**) was prepared from the transalkoxylation reaction of **15** with two equivalents of menthol. The composition and structures of all novel compounds were established by $^1H$ and $^{13}C$ NMR spectroscopy as well as elemental analysis data. The possible solution structure features of **13**–**28** are discussed. The single-crystal X-ray diffraction study of titanocane **16** clearly indicates a dimeric structure for this compound in the solid state. According to X-ray data, compounds $[PhCH_2N(CH_2CH_2O)_2]_2Ti$ (**19**), $[MeN(CH_2CH_2O)(CH_2CHPhO)]_2Ti$ (**20**), $[MeN(CH_2CH_2O)(CH_2CPh_2O)]_2Ti$ (**23**), *erythro*-$[MeN(CH_2CH_2O)(CHPhCHPhO)]_2Ti$ (**24**), *threo*-$[MeN(CH_2CH_2O)(CHPhCHPhO)]_2Ti$ (**25**), and $\{MeN(CH_2CH_2O)[CH(CH_2)_4CHO]\}_2Ti$ (**27**) possess a monomeric structure with a hexacoordinate titanium atom in the solid state. Among them complexes **19**, **20**, **23**, **25**, and **27** are characterized by a *cis* disposition of the nitrogen atoms in the coordination environment of the Ti atom, while nitrogen atoms in **24** occupy *trans* positions.

(© Wiley-VCH Verlag GmbH & Co. KGaA, 69451 Weinheim, Germany, 2006)

## Introduction

Alkoxy- or aroxytitanium derivatives have attracted the attention of researchers during the last five decades because of their possible application as catalysts in various organic reactions,[1–8] as well as precursors for titanium sol-gel chemistry[9] and metal-organic chemical vapor deposition (MOCVD) processes.[10] Among these species, the compounds with different trialkanolamines, titanatranes, $N(CR^1R^4CR^2R^3O)_3TiX$, with different substituents at the carbon atoms of the atrane skeleton, have been investigated to a considerable extent because of their rich structural features and catalytic activities including polymerization reactions of alkenes (see key references and references cited therein).[11–19] At the same time the closely related derivatives of dialkanolamines, titanocanes, $RN(CR^1R^4CR^2R^3O)_2Ti(X)X'$, are less studied.[20–26] However, this class of compounds could be more promising for investigations because of their greater chemical and structural flexibility. In addition, some cyclic titanium alkoxides with transannular interactions were recently found to be good catalysts in olefin polymerization reactions.[27–33]

As a part of our program to investigate the structure and chemical behavior of metal complexes containing di- and trialkanolamine ligands,[34–43] we present the study of reactions of dialkanolamines **1**–**12** with $Ti(OiPr)_4$. In the case of the reaction of $RN(CH_2CH_2OH)_2$ with $Ti(OiPr)_4$ (1:1 ratio) novel titanocanes **13**–**15** formed (R = Ph, Me, $PhCH_2$). The dimer $[PhCH_2N(CH_2CH_2O)_2Ti(OMe)_2]_2$ (**16**), was obtained from the reaction of dialkanolamine **3** with $CpTi(OMe)_3$. The reaction of **15** with two equivalents of menthol led to $PhCH_2N(CH_2CH_2O)_2Ti(OMenth)_2$ (**17**). 1,1′-Spirobititanocanes **18**–**28** of type $[RN(CH_2CH_2O)(CHR^1CR^2R^3O)]_2Ti$ were prepared from the reaction of two equivalents of the corresponding dialkanolamines with $Ti(OiPr)_4$. The solid state and solution structures of prepared compounds are discussed on the basis of X-ray diffraction and NMR spectroscopic data. Once this work had been finished the report of Carpentier and coworkers was published where the synthesis and structural investigations of several closely related titanocanes and 1,1′-spirobititanocanes were reported.[44]

[a] Chemistry Department Moscow State University, B-234 Leninskie Gory, 119899 Moscow, Russia
Fax: +007-095-932-8846
E-mail: sergej@org.chem.msu.su
[b] Institute of General and Inorganic Chemistry, RAS, Leninskii pr., 31, 119991 Moscow, Russia
[c] Fachbereich Chemie, Philipps-Universität Marburg, Hans-Meerwein-Strasse, 35032 Marburg/Lahn, Germany
[d] Department of Chemistry, University of Durham, South Road, DH1 3LE Durham, United Kingdom

 © 2006 Wiley-VCH Verlag GmbH & Co. KGaA, Weinheim 

## Results and Discussion

Dialkanolamines **1**–**12** were involved in this study. The compounds **8**–**12** were obtained from the reaction of the corresponding alkene oxides with *N*-methylethanolamine in high yields (Scheme 1). The reaction with indene oxide was previously reported, but the structure of product **12** was not discussed.[45] Compound **7** was previously prepared by another method.[46] Compounds **8**–**11** are novel.

The reactions proceeded regiospecifically, only one expected product formed in the reactions with but-1-ene oxide, 1,1-diphenylethylene oxide, and indene oxide. Only one diastereomer formed in the reactions with *cis*- and *trans*-stilbene oxides, as well as cyclopentene and cyclohexene oxides.

**Titanocanes:** According to the literature, the most suitable approach to the dialkoxy complexes of titanium with chelate ligands is the transalkoxylation reaction of $Ti(OAlk)_4$ with the free ligand containing two OH groups. This method was used in the case of the closely related ligands $RN(CH_2\text{-}o\text{-}ArOH)_2$, where *o*-Ar is a benzene ring with different alkyl (methyl or *tert*-butyl) substituents and R is $CH_2CH_2NMe_2$.[27] When R is *n*Pr, the presence of an alkyl group in the other *ortho* position to the OH group of such ligands is required for the formation of bis(isopropoxide) complexes, otherwise the formation of bishomoleptic substances $[RN(CH_2\text{-}o\text{-}ArO)_2]_2Ti$ has been found.[27] Analogous results were found for other structurally close bis(phenols). The treatment of $Ti(OAlk)_4$ (Alk = *i*Pr, Me) with one equivalent of the bis(phenol), $CH_2[(3\text{-}t\text{Bu-}5\text{-}MeC_6H_2)\text{-}2\text{-}OH]_2$, gave monomeric complexes with a tetracoordinate Ti atom (NMR spectroscopic data), $CH_2[(3\text{-}t\text{Bu-}5\text{-}MeC_6H_2)\text{-}2\text{-}O]_2Ti(OAlk)_2$.[30] Reacting the thio-bis(phenol), $S[(3\text{-}t\text{Bu-}5\text{-}MeC_6H_2)\text{-}2\text{-}OH]_2$, with $Ti(OiPr)_4$ resulted in the dimeric $[S[(3\text{-}t\text{Bu-}5\text{-}MeC_6H_2)\text{-}2\text{-}O]_2Ti(OiPr)_2]_2$ (X-ray data) where dimerization ensues from the interaction of the oxygen atom of the isopropoxy group of one monomeric unit with the Ti atom of the other.[31] The diisopropoxy titanium complexes based on diamino-dialkoxide ligands, $[\text{-}CH_2N(Me)CH_2C(CF_3)_2OH]_2$ and $CH_2[CH_2N(Me)CH_2C(CF_3)_2OH]_2$, were also recently prepared by Carpentier and coworkers by the transalkoxylation reaction of $Ti(OiPr)_4$.[32]

To the best of our knowledge, the reactions of dialkanolamines with $Ti(OiPr)_4$ have only been published in a series of works by Kemmitt et al. and very recently in the report of Lavanant et al.[20–23,44] Kemmitt et al. noted that the reaction of two equivalents of dialkanolamine **2** with $Ti(OiPr)_4$ gave the bishomoleptic complex $[MeN(CH_2\text{-}CH_2O)_2]_2Ti$ (**29**). This transformation was supposed to proceed through a very reactive and unstable $MeN(CH_2\text{-}CH_2O)_2Ti(OiPr)_2$ but this suggestion was not confirmed by any analytical methods.[20] Increasing the amount of $Ti(OiPr)_4$ in the reaction mixture led to the unexpected $[Ti_2\{\mu_2\text{-}(OCH_2CH_2)_2NMe\}(\mu_2\text{-}OiPr)(OiPr)_5]$.[21] The analogous species, $Ti_2(OCH_2CH_2NMe)_2(OtBu)_6$, was prepared by the reaction of $Ti(OtBu)_4$ with **2**.[22] The treatment of $Ti(OiPr)_4$ with one equivalent of **2** in the presence of one equivalent of different diols led to dimeric titanium aminoalkoxydiolates, $[MeN(CH_2CH_2O)_2Ti(O\text{-}A\text{-}O)]_2$ (O-A-O = $OCMe_2CMe_2O$, $OCEt_2CEt_2O$, $OCMe_2CH_2CMe_2O$, $OCMe_2CH_2CHMeO$). Dimerization in latter complexes is realized by the interaction of the oxygen atom of one dialkanolamine "arm" of one monomeric unit with the Ti atom of the other.[23] Lavanant et al. have found that the reaction of one equivalent of $PhCH_2N(CH_2CMe_2OH)_2$ with $Ti(OiPr)_4$ gave the complex $PhCH_2N(CH_2CMe_2O)_2Ti(OiPr)_2$, which is monomeric in the solid state and in solution ($[D_8]$toluene).[44]

We have found that dialkanolamines **1**–**3** reacted readily with an equimolar amount of $Ti(OiPr)_4$ at room temperature in chloroform or toluene solution to give the corresponding titanocanes **13**–**15** in high yields (Scheme 2). We also tested two other reactions that may lead to the titanocanes, where X = X′. However, both reactions did not result in the desired products (Scheme 2). $CpSn\text{-}nBu_3$, one of the possible by-products in the reaction of $Cp_2TiCl_2$ with $MeN(CH_2CH_2OSn\text{-}nBu_3)_2$, was detected by NMR spectroscopy.

Our efforts to prepare titanocane with different substituents X and X′ by the transalkoxylation reaction of dialkanolamine **3** with $(MeO)_3TiCp$ failed. Only the dimer **16** was obtained. In contrast, Kim et al. synthesized $RN(CH_2CH_2O)_2Ti(Cl)Cp^*$ by the reaction of $Cl_3TiCp^*$ (where $Cp^*$ = pentamethylcyclopentadienyl) with $RN(CH_2CH_2OH)_2$ (R = Me, *n*Bu).[25] We believe that the difference in the behavior of $(MeO)_3TiCp$ and $Cl_3TiCp^*$ (the rupture of Ti–Cp bond and the stability of Ti–$Cp^*$ bond in the course of the reaction) is because of the different properties of these bonds.

The possibility of alkoxy groups exchanging at the titanium atom was confirmed by the formation of complex **17** in the reaction of diisopropoxy derivative **15** with L-(–)-menthol (Scheme 2).

**6–12**

| | $R^1$ | $R^2$ | $R^3$ | |
|---|---|---|---|---|
| **6** | H | Et | H | |
| **7** | H | Ph | Ph | |
| **8** | Ph | Ph | H | *erythro* |
| **9** | Ph | Ph | H | *threo* |

| | $R^1$ | $R^2$ | $R^3$ |
|---|---|---|---|
| **10** | $(CH_2)_3$ | | H |
| **11** | $(CH_2)_4$ | | H |
| **12** | $C_6H_4CH_2$ | | H |

Scheme 1.

 © 2006 Wiley-VCH Verlag GmbH & Co. KGaA, Weinheim 

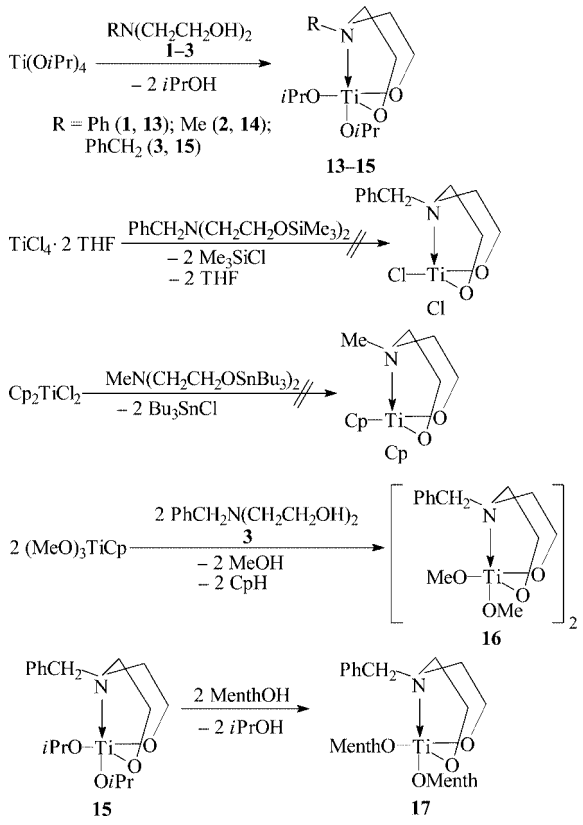


Scheme 2.

One of the most important questions in the chemistry of titanium is the coordination state of the Ti atom both in the solid state and in solutions. In our opinion the type of coordination environment around the titanium atoms is very important because of the potential ability of these compounds to catalyze different organic reactions where the stereochemistry of the catalytic center is significant.[3–8] Titanocanes prepared by us may possess monomeric structures with pentacoordinate titanium atoms or dimeric structures with hexacoordinate titanium atoms. There are two possibilities for dimerization: through the dialkanolamine moiety or through the alkoxy groups. According to the literature, most of the titanocanes prepared to date, $[MeN(CH_2CH_2O)_2Ti(O\text{-}A\text{-}O)]_2$ (O-A-O = $OCMe_2CMe_2O$, $OCEt_2CEt_2O$, $OCMe_2CH_2CMe_2O$, $OCMe_2CH_2CH$-MeO),[23] are dimeric in the solid state. The dimerization is realized by the additional contact of the oxygen atom of one diethanolamine "arm". In $CDCl_3$ solutions two compounds are also dimeric at room temperature (O-A-O = $OCMe_2CMe_2O$, $OCEt_2CEt_2O$) while two others are monomeric (O-A-O = $OCMe_2CH_2CMe_2O$, $OCMe_2CH_2CH$-MeO).[23] $PhCH_2N(CH_2CMe_2O)_2Ti(OiPr)_2$ is monomeric in the solid state and in solution (toluene-$d_8$).[44] As cited above, the closely related derivatives, $n$PrN{$CH_2$[3,5-bis($t$Bu)-$C_6H_2$]-2-O}$_2$Ti(O$i$Pr)$_2$ and $n$PrN{$CH_2$[3,5-bis(Me)-$C_6H_2$]-2-O}$_2$Ti(O$i$Pr)$_2$, are monomeric both in the solid state and in solution ($C_6D_6$).[27]

Among five dialkoxytitanocanes prepared by us only one compound **16**, the titanocane with two methoxy groups at the titanium atom, gave crystals suitable for an X-ray diffraction study. The molecular structure of **16** is shown in Figure 1. Table 1 lists selected geometrical parameters for **16**. The molecule of **16** represents a centrosymmetric complex with a $Ti_2O_2$ lozenge. The dimer results from $\mu_2$-bridging by one methoxy group of one monomeric unit. The diethanolamine ligands in each dimer are bound meridionally to each titanium atom. Of interest, all previously studied alkoxytitanocanes except $PhCH_2N(CH_2CMe_2O)_2Ti(OiPr)_2$ are also dimeric, but the dimerization results from $\mu_2$-bridging by one alkoxy "arm" of the diethanolamine ligand.[23,44] The coordination polyhedron of the Ti atoms in compound **16** represents a distorted octahedral geometry with the N(1) atom and O(4) atom (nonbridging methoxy group) in a *trans* orientation. The Ti(1)–N(1) distance in **16** [2.355(2) Å] is close to that previously found for $[MeN(CH_2CH_2O)_2$-Ti(O-A-O)]$_2$ [2.351(4)–2.431(4) Å].[23] The longest Ti–O distances in **16** [Ti(1)–O(3A) 2.024(1); Ti(1)–O(3) 2.066(1) Å] correspond to the bonds of titanium with both bridging methoxy groups, as expected. All five-membered rings of the ocane skeletons in **16** adopt an envelope-like conformation, all carbon atoms in the α positions to the N atom occupy "flap" sites, while the C-β atoms form the base of these envelope planes.

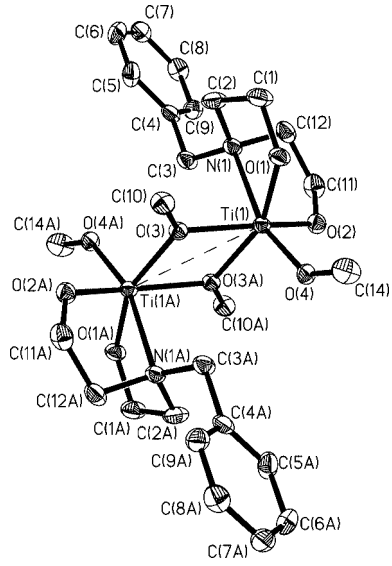


Figure 1. Molecular structure of **16**. Hydrogen atoms and solvate dichloromethane molecules are omitted for clarity.

Table 1. Selected bond lengths [Å] and angles [°] for **16**.

| | | | |
|---|---|---|---|
| Ti(1)–O(4) | 1.808(1) | O(4)–Ti(1)–N(1) | 162.26(6) |
| Ti(1)–O(1) | 1.868(1) | O(1)–Ti(1)–N(1) | 75.59(6) |
| Ti(1)–O(2) | 1.873(1) | O(2)–Ti(1)–N(1) | 76.79(6) |
| Ti(1)–O(3A) | 2.024(1) | O(3A)–Ti(1)–N(1) | 94.03(5) |
| Ti(1)–O(3) | 2.066(1) | O(3)–Ti(1)–N(1) | 92.07(5) |
| Ti(1)–N(1) | 2.355(2) | | |

$^1$H and $^{13}$C NMR spectroscopic data ($CDCl_3$ solution, room temperature) of **16** are in agreement with the centrosymmetric dimeric solid-state structure. In the $^1$H NMR spectrum of **16** there are two singlets of methoxy groups.

 © 2006 Wiley-VCH Verlag GmbH & Co. KGaA, Weinheim 

The signals of the methylene protons of one ocane skeleton appear as a set of multiplets resulting from the nonequivalence of all protons. Separate $^{13}C$ NMR signals were found for each carbon of the diethanolamine ligand in **16**. On the contrary, two other titanocanes with the benzyl group at the nitrogen atom (**15** and **17**) are monomeric in $CDCl_3$ solution at room temperature. This conclusion is based on the presence of one signal of the $OCH_2$ group and one signal of the $NCH_2$ group for the C atoms of the ocane skeleton of these compounds. Thus, these species (**15** and **17**) possess monomeric structures with trigonal-bipyramidal coordination environments of the titanium atom. These compounds may undergo exchange processes in solution (the exchange between equatorial and axial alkoxy groups).[44] Thus, the drastic difference in $^1H$ NMR spectra of **15** (OCH protons of the isoproxy group represent one broad singlet) and **17** (OCH protons of two menthoxy groups represent two spaced multiplets), to our opinion, resulted from the different dynamic behavior of these compounds in solution. While isopropoxy groups in **15** undergo fast position exchange around the Ti atom, more bulky menthoxy groups in **17** resulted in the rigid structure of the molecule. It should be noted that previously prepared $PhCH_2N(CH_2CMe_2O)_2Ti(OiPr)_2$ demonstrated the same trends in the NMR spectra as compound **15**.[44] The authors concluded that a monomeric structure of $PhCH_2N(CH_2CMe_2O)_2Ti(OiPr)_2$ occurs. This conclusion was also supported by variable temperature NMR spectroscopy.[44] The structure of diisopropoxytitanocane **14** is close to that of **15** according to the NMR spectroscopic data. In the $^{13}C$ spectrum of **13** the broadening of each signal is observed, probably because of possible monomer-dimer interconversion in this compound. Thus we can conclude that the steric bulkiness of alkoxy ligands in titanocanes is the determining factor that governs the coordination number in titanocanes.

**Spirobititanocanes:** Only two spirobititanocanes were reported by the beginning of our investigation, one of them is $[MeN(CH_2CH_2O)_2]_2Ti$ (**29**).[20] Very recently the synthesis of $[PhCH_2N(CH_2CMe_2O)_2]_2Ti$ from the reaction of $Ti(OiPr)_4$ with two equivalents of corresponding dialkanolamine was reported.[44] For synthesis of **29** the treatment of two equivalents of dialkanolamine **2** with $Ti(OiPr)_4$ or freshly prepared α-titanic acid was used. The structure of **29** was confirmed by X-ray diffraction, this species is monomeric in the solid state. The coordination polyhedron of the Ti atom represents a distorted octahedral geometry with two nitrogen atoms in a *cis* orientation (Scheme 3).[20] We have very recently found an analogous situation in spirobigermocanes. Both $[PhN(CH_2CH_2O)_2]_2Ge$ and $[MeN(CH_2CH_2O)(CH_2CHPhO)]_2Ge$ possess the structure of the *cis* isomer.[34] The bishomoleptic titanium derivative, $\{S[(3\text{-}tBu\text{-}5\text{-}MeC_6H_2)\text{-}2\text{-}O]_2\}_2Ti$, has an analogous structure.[47] Lavanant et al. supposed that the monomeric structure is present in solution for $[PhCH_2N(CH_2CMe_2O)_2]_2Ti$.[44]

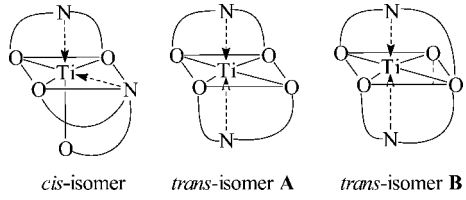


Scheme 3.

The closely related spiro-bishomoleptic or spiro-bisheteroleptic complexes of titanium were prepared by Tshuva et al. by the reaction of $nPrN(CH_2\text{-}o\text{-}ArOH)_2$ or $RN(CH_2\text{-}o\text{-}Ar'OH)_2$ (R = *n*Pr or $CH_2CH_2NMe_2$) with $Ti(OiPr)_4$ lead-

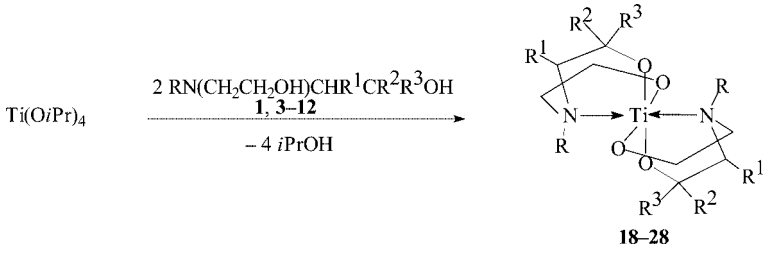


| | R | $R^1$ | $R^2$ | $R^3$ |
|---|---|---|---|---|
| **18** | Ph | H | H | H |
| **19** | $PhCH_2$ | H | H | H |
| **20** | Me | H | Ph | H |
| **21** | Me | H | Me | H |
| **22** | Me | H | Et | H |
| **23** | Me | H | Ph | Ph |

| | R | $R^1$ | $R^2$ | $R^3$ | |
|---|---|---|---|---|---|
| **24** | Me | Ph | Ph | H | *erythro* |
| **25** | Me | Ph | Ph | H | *threo* |
| **26** | Me | $(CH_2)_3$ | | H | |
| **27** | Me | $(CH_2)_4$ | | H | |
| **28** | Me | $C_6H_4CH_2$ | | H | |

$TiCl_4 \cdot 2\ THF$ —(2 $PhCH_2N(CH_2CH_2OH)_2$ (**3**) / 4 $Et_3N$; – 4 $Et_3N \cdot HCl$, – 2 THF)→ **19**

$Ti(CH_2Ph)_4$ —(2 $RN(CH_2CH_2OH)CHR^1CR^2R^3OH$, **3, 7**; – 4 $PhCH_3$)→ **19** or **23**

Scheme 4.

 © 2006 Wiley-VCH Verlag GmbH & Co. KGaA, Weinheim 

ing to [*n*PrN(CH$_2$-*o*-ArO)$_2$]$_2$Ti or [*n*PrN(CH$_2$-*o*-ArO)$_2$]Ti[(O-*o*-Ar′-CH$_2$)$_2$NR], respectively.[27] Three complexes were studied by X-ray diffraction and showed the structure of *trans*-isomer **A** (Scheme 3). The authors noted that the bulky substituents in the Ar groups prevent the formation of spiro-bishomoleptic species and the reaction stops at the titanocanes.[27] An analogous result in Zr chemistry has been found by Mountford and coworkers.[33] A very interesting result was found by Lavanant et al. for Zr derivatives of two dialkanolamines: [PhCH$_2$N(CH$_2$CMe$_2$O)$_2$]$_2$Zr and [PhCH$_2$N(CH$_2$C-*p*-Tol$_2$O)$_2$]$_2$Zr.[44] According to the NMR spectroscopic data both spirobizirconocanes are monomeric in solution while the X-ray diffraction study of [PhCH$_2$N(CH$_2$CMe$_2$O)$_2$]$_2$Zr showed the dimeric structure of this compound in the solid state resulting from the rupture of three of the four Zr–N bonds into two monomeric units.[44] Thus, one can conclude that the structure of the ligand is the main factor governing the coordination environment around the metal atom in spirobiocanes.

In order to clarify the structure of the ligand influence we explored the synthesis and structures of the number of novel spirobititanocanes. The compounds **18**–**28** were obtained in high yields from the reaction of Ti(O*i*Pr)$_4$ with two equivalents of corresponding dialkanolamines **1**, **3**–**12** at reflux in toluene (Scheme 4). Compound **19** was also prepared in 33% yield from the treatment of TiCl$_4$·(THF)$_2$ with **3** in the presence of Et$_3$N or in quantitative yield from the reaction of Ti(CH$_2$Ph)$_4$ with two equivalents of **3** (Scheme 4). The latter approach was also used for the synthesis of **23**.

We also tried to prepare spiro-bisheteroleptic ocanes (Scheme 5), but in all of the studied cases equimolar mixtures of spiro-bishomoleptic ocanes were obtained (NMR spectroscopic data). This result contradicts that previously found for bis(aminophenol)-type ligands, where the bisheteroleptic species are stable.[27] We suppose that, on the one hand, the symmetric bis(ocanes) are more thermodynamically stable in the case of dialkanolamine type ligands. On the other hand, the unsymmetric bis(ocanes) are probably formed in the course of the reactions, but because of their higher flexibility in comparison with that for phenolic species[27] a mixture of symmetric compounds forms through a metathetical process.

One dialkanolamine ligand in spirobititanocane **18** can easily be exchanged by the treatment with equimolar amounts of Ti(O*i*Pr)$_4$ (Scheme 6). The reaction of **19** with one equivalent of TiCl$_4$ resulted in a mixture of unidentified products (Scheme 6).

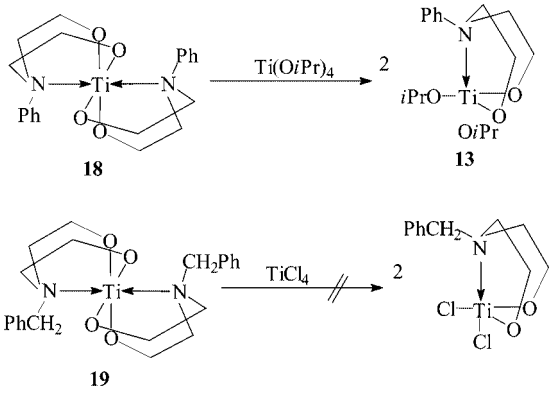


Scheme 6.

According to the NMR spectroscopic data, spirobititanocane **19** possesses a monomeric structure in solution ($CDCl_3$) and exists as one isomer (Scheme 3). It should be noted that in the *trans* and *cis* isomers of **19** the two dialkanolamine groups are equivalent. Thus, in theory it is impossible to define what kind of isomer exists in $CDCl_3$ solution, but we can conclude that only one isomer is present under these conditions. We believe that spirobititanocane **18** is also monomeric in solution, but the broadening of

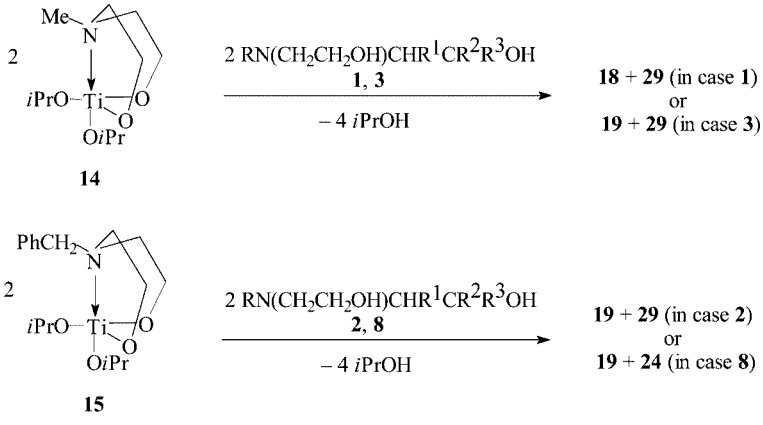


| | R | $R^1$ | $R^2$ | $R^3$ | |
|---|---|---|---|---|---|
| **18** | Ph | H | H | H | |
| **19** | $PhCH_2$ | H | H | H | |
| **24** | Me | Ph | Ph | H | *erythro* |
| **29** | Me | H | H | H | |

Scheme 5.

 © 2006 Wiley-VCH Verlag GmbH & Co. KGaA, Weinheim 

signals was found for its NMR spectra (like in closely related titanocane **13**). This indicates the presence of dynamic processes in solution of **18**, such as Berry pseudorotation, *cis-trans* isomerization and/or N–Ti bond dissociation. Although different sets of signals should be present in the $^{13}C$ NMR spectra of the *trans* and *cis* isomers for compound **20**–**28**, it is very difficult to determine unambiguously the type of isomer in this case because of the presence of several diastereomers of these compounds in solution resulting from the asymmetric carbon atoms. However, the importance of the synthesis of compounds with asymmetric car-

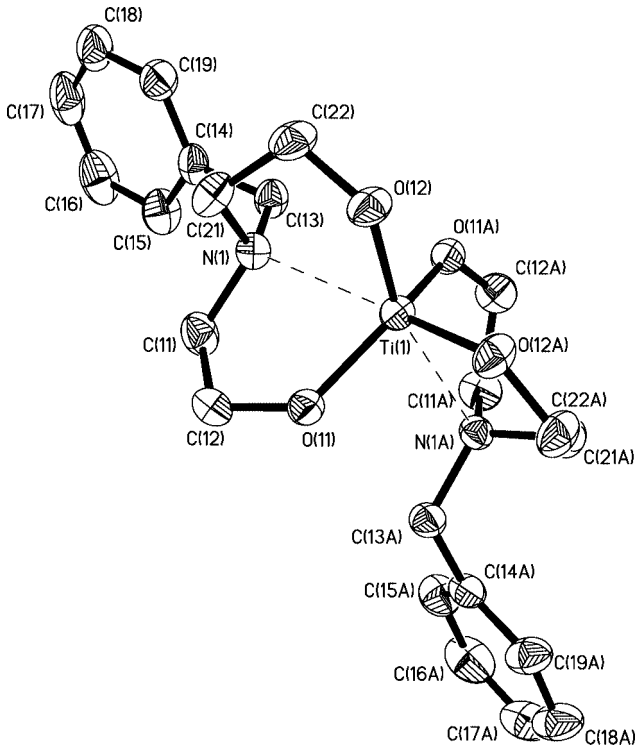


Figure 2. Molecular structure of **19** (one independent molecule). Hydrogen atoms are omitted for clarity.

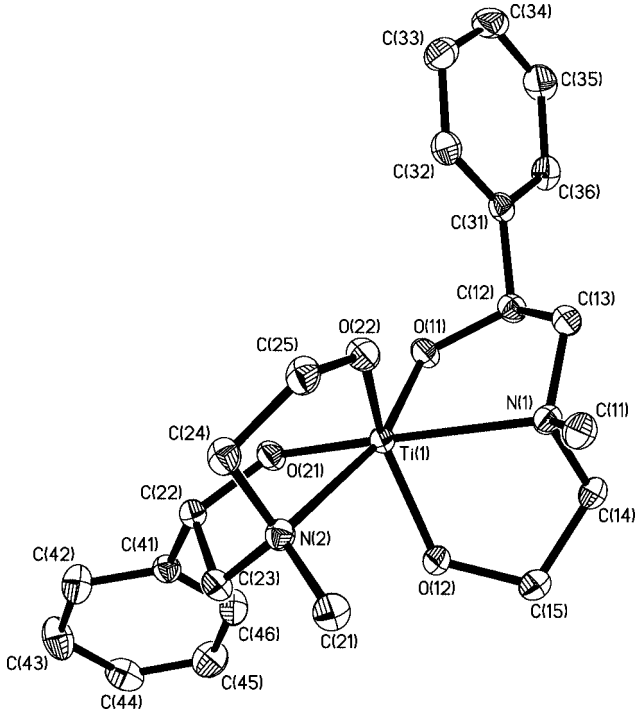


Figure 3. Molecular structure of **20**. Hydrogen atoms and solvate toluene molecules are omitted for clarity.

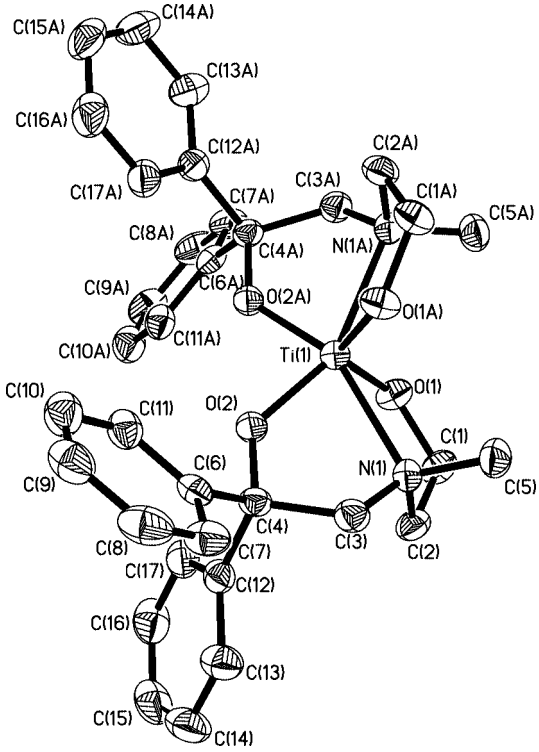


Figure 4. Molecular structure of **23**. Hydrogen atoms and solvate dichloromethane molecules are omitted for clarity.

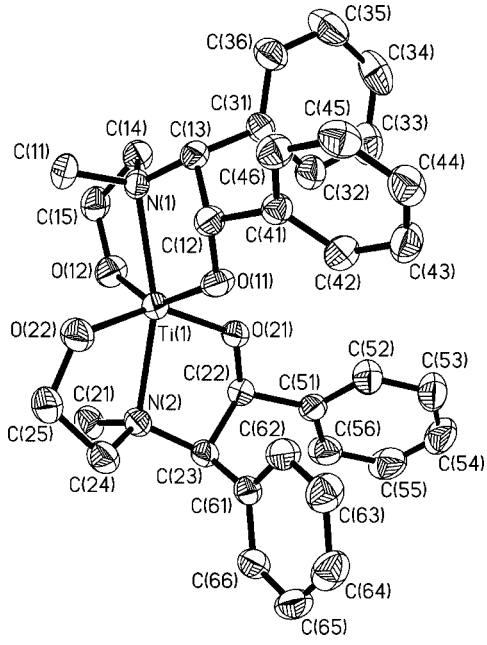


Figure 5. Molecular structure of **24**. Hydrogen atoms and solvate toluene molecules are omitted for clarity.

 © 2006 Wiley-VCH Verlag GmbH & Co. KGaA, Weinheim 

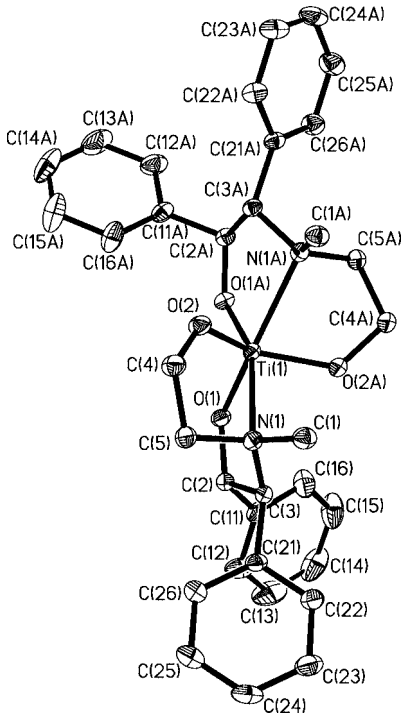


Figure 6. Molecular structure of **25**. Hydrogen atoms and solvate dichloromethane molecules are omitted for clarity.

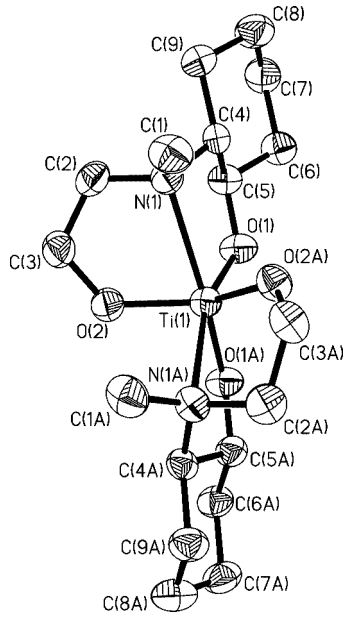


Figure 7. Molecular structure of **27**. Hydrogen atoms are omitted for clarity.

bon atoms is connected with the usefulness of these derivatives in catalytic processes.

The structures of six spirobititanocanes **19**, **20**, **23**, **24**, **25**, **27** were studied by X-ray diffraction. The monomeric nature of all the studied species with a hexacoordinate titanium center was confirmed. The coordination polyhedron of the titanium atom in these compounds represents a distorted octahedron. The molecular structures of **19** (one independent molecule), **20**, **23**, **24**, **25**, and **27** are shown in Figure 2, Figure 3, Figure 4, Figure 5, Figure 6, and Figure 7, respectively. Table 2 and Table 3 list selected geometrical parameters for these compounds.

Table 3. Selected bond lengths [Å] and angles [°] for **24**.

| | | | |
|---|---|---|---|
| Ti(1)–N(1) | 2.339(2) | O(12)–Ti(1)–O(21) | 95.6(1) |
| Ti(1)–N(2) | 2.310(2) | O(22)–Ti(1)–O(21) | 146.1(1) |
| Ti(1)–O(11) | 1.878(2) | O(11)–Ti(1)–O(21) | 86.41(9) |
| Ti(1)–O(12) | 1.864(2) | O(12)–Ti(1)–N(1) | 74.34(9) |
| Ti(1)–O(21) | 1.883(2) | O(22)–Ti(1)–N(1) | 93.17(9) |
| Ti(1)–O(22) | 1.873(2) | O(11)–Ti(1)–N(1) | 74.39(8) |
| O(12)–Ti(1)–O(22) | 102.1(1) | O(21)–Ti(1)–N(1) | 119.57(8) |
| O(12)–Ti(1)–O(11) | 145.0(1) | N(2)–Ti(1)–N(1) | 162.91(8) |
| O(22)–Ti(1)–O(11) | 95.0(1) | | |

The compounds **19**, **20**, **23**, **25**, and **27** exhibit a *cis* disposition of the two nitrogen atoms at the Ti atom. An analogous structure was previously found in **29**.[20] On the contrary, the nitrogen atoms in **24** occupy the *trans* positions in an octahedral environment of the Ti atom. This type of

Table 2. Selected bond lengths [Å] and angles [°] for **19**, **20**, **23**, **25**, **27**.

| | **19** | | **20** | **23** | **25** | **27** |
|---|---|---|---|---|---|---|
| Ti–N | 2.451(2) | 2.467(2) | 2.352(2)<br>2.367(2) | 2.357(2) | 2.363(2) | 2.471(3) |
| Ti–$O_{trans\ to\ N}$ | 1.839(2) | 1.830(2) | 1.855(2)<br>1.862(2) | 1.865(1) | 1.872(2) | 1.849(2) |
| Ti–$O_{trans\ to\ O}$ | 1.852(2) | 1.844(2) | 1.875(2)<br>1.885(2) | 1.859(1) | 1.867(2) | 1.845(3) |
| N(1)–Ti–O | 73.40(7)<br>75.87(7)<br>83.15(7)<br>163.61(7) | 74.55(9)<br>75.52(8)<br>81.94(8)<br>164.91(8) | 75.66(7)<br>75.88(7)<br>82.31(7)<br>163.95(7) | 73.68(5)<br>75.46(6)<br>82.34(6)<br>154.98(5) | 74.55(6)<br>75.12(7)<br>82.15(7)<br>158.18(7) | 74.1(1)<br>75.2(1)<br>81.7(1)<br>161.9(1) |
| N–Ti–N | 118.1(1) | 117.8(1) | 117.58(7) | 129.69(8) | 125.37(9) | 120.5(1) |
| O–Ti–O | 91.9(1)<br>101.50(8)<br>110.35(8)<br>133.7(1) | 92.4(1)<br>101.9(1)<br>109.8(1)<br>133.7(1) | 92.38(7)<br>98.95(7)<br>99.17(7)<br>110.72(7)<br>111.40(7)<br>136.17(8) | 85.33(8)<br>102.89(6)<br>116.23(6)<br>126.24(9) | 87.68(9)<br>101.81(7)<br>114.44(7)<br>129.2(1) | 91.2(2)<br>101.4(1)<br>113.3(1)<br>130.0(2) |

 © 2006 Wiley-VCH Verlag GmbH & Co. KGaA, Weinheim 

structure is considered to be *trans*-isomer **B** (Scheme 3). To the best of our knowledge, compound **24** is the first example of such a structure; however, a similar *trans* disposition of the nitrogen atoms in $TiO_4N_2$ was previously found.[48]

The Ti–N distances in **19**, **20**, **23**, **24**, **25**, and **27** vary over the range 2.310(2)–2.471(3) Å, the shortest distance being found in compound **24** (*trans* disposition of N atoms). These values are close to that previously found for **29** [2.422(2) Å].[20] The substitution of hydrogen atoms (**19**, **29**) of the ocane skeleton for phenyl groups (**20**, **23**, **24**, **25**) shortens the Ti–N bond, while the substitution with alkyl groups (**27**) slightly elongates this distance. In general, the Ti–N distances in phenolic compounds [*n*PrN($CH_2$-*o*-ArO)$_2$]-Ti[(O-*o*-Ar′$CH_2$)$_2$NR] [2.248(2)–2.308(4) Å][27] are shorter than those in **19**, **20**, **23**, **24**, **25**, **27**, and **29** based on dialkanolamine-type ligands. This difference is probably explained by the higher polarity of the Ti–O bonds in phenolic species, which leads to depletion of electron density at the titanium center. A similar tendency was found for Ti–O bonds in hexacoordinate compounds discussed above. In general, the shorter Ti–N bonds in the molecules correspond to longer Ti–O bonds. This tendency is also supported by the fact that Ti–O bonds in the only X-ray studied monomeric tetraalkoxy titanium derivative with a tetracoordinate Ti atom [1.752(2)–1.825(2) Å][49] are considerably shorter than those in the hexacoordinate compounds.

All five-membered unsubstituted rings of the ocane skeletons in **19**, **20**, **23**, **24**, **25**, and **27** adopt an "envelope"-like conformation, all carbon atoms in the α positions to the N atom occupy "flap" sites. In the case of substituted rings their conformation may be treated as an "envelope" with α-C atoms in "flap" sites (**20**, **23**, and **25**) or a "twist" (**24** and **27**).

## Conclusion

We have found that tetraisopropoxytitanium or cyclopentadienyltrimethoxytitanium react with one equivalent of dialkanolamines **1**–**3** leading to the formation of the corresponding dialkoxytitanocanes **13**–**16**. The substitution reaction of diisopropoxy derivative **15** with L-(–)-menthol easily occurs to give dimenthoxytitanocane **17**. The nature of the alkoxy substituent at the Ti atom strongly affects the structure and dynamic behavior of **13**–**17** in solution. The reaction of Ti(O*i*Pr)$_4$ with two equivalents of dialkanolamines **1**, **3**–**12** led to the corresponding spirobititanocanes **18**–**28** with a hexacoordinate Ti atom. The structure of latter compounds is governed by the nature of the ligands: depending on the substituents in the ocane skeleton the nitrogen atoms occupy *cis* or *trans* positions around the Ti atom. Spirobititanocane **18** is easily converted into the corresponding titanocane **13** by its reaction with one equivalent of Ti(O*i*Pr)$_4$. The reaction of titanocanes **14** and **15** with the different dialkanolamines (**1**, **3** and **2**, **8**, respectively) did not give the expected bisheteroleptic compounds but resulted in a mixture of bishomoleptic titanocanes **18** and **29**, **19** and **29** and **19** and **29**, **19** and **24**, respectively.

## Experimental Section

**General Remarks:** All manipulations were performed under a dry, oxygen-free argon atmosphere using standard Schlenk techniques. Solvents were dried by standard methods and distilled prior to use. PhN($CH_2CH_2OH$)$_2$ (**1**), MeNH$CH_2CH_2OH$ (Aldrich) and (1*R*,2*S*,5*R*)-menthol (Acros) were used as supplied. HN($SiMe_3$)$_2$ (Aldrich), Ti(O*i*Pr)$_4$ (Aldrich), and $TiCl_4$ (Aldrich) were distilled before use. CpTi(OMe)$_3$,[50] $TiCl_4$(THF)$_2$,[51] Ti($CH_2Ph$)$_4$,[52] MeN($CH_2CH_2OH$)$_2$ (**2**),[53] PhC$H_2$N($CH_2CH_2OH$)$_2$ (**3**),[54] MeN($CH_2CH_2OH$)$CH_2$CH(Ph)OH (**4a**) and MeN($CH_2CH_2OH$)-CH(Ph)$CH_2OH$ (**4b**) as a mixture 9:1,[34] MeN($CH_2CH_2OH$)-$CH_2$CH(Me)OH (**5**),[55] and MeN($CH_2CH_2OH$)$CH_2$CH(Et)OH (**6**)[55] were prepared according to the literature. $^{13}C\{^1H\}$ NMR spectrum for **5**: $\delta$ = 20.17 (Me), 42.42 (MeN), 59.21, 59.73 (2 $NCH_2$ groups), 63.65, 65.52 ($OCH_2$ and OCH groups) ppm. $^{13}C\{^1H\}$ NMR spectrum for **6**: $\delta$ = 9.86 ($CH_2CH_3$), 27.71 ($CH_2CH_3$), 42.48 ($NCH_3$), 59.30, 59.75 ($NCH_2$), 63.77, 68.91 (OCH and $OCH_2$) ppm. PhC$H_2$N($CH_2CH_2OSiMe_3$)$_2$[43] and MeN($CH_2$-$CH_2$OSn-*n*Bu$_3$)$_2$[38] were prepared according to the method reported previously. PhC$H_2$N($CH_2CH_2OSiMe_3$)$_2$: B.p. = 126–129 °C (0.7 Torr). NMR spectra: $^1H$ NMR: $\delta$ = 0.07 (s, 18 H, $SiMe_3$), 2.67 (t, 4 H, $NCH_2$), 3.61 (t, 4 H, $OCH_2$), 3.69 (s, 4 H, PhC$H_2$N), 7.18–7.32 (m, 5 H, $C_6H_5$) ppm. $^{13}C\{^1H\}$ NMR: $\delta$ = –0.54 ($SiMe_3$), 56.66 ($NCH_2$), 60.07 ($OCH_2$), 61.17 (PhC$H_2$), 126.83, 128.13, 128.78, 139.83 (aromatic carbons) ppm. MeN($CH_2CH_2OSn$-*n*Bu$_3$)$_2$: NMR spectra: $^1H$ NMR: $\delta$ = 0.95–0.82 (m, 18 H, $CH_2CH_3$), 1.14–0.98 (m, 12 H, $CH_2CH_3$), 1.33–1.26 (m, 12 H, $SnCH_2CH_2$), 1.57–1.49 (m, 12 H, $SnCH_2$), 2.24 (s, 3 H, $NCH_3$), 2.47 (t, 4 H, $NCH_2$), 3.74 (t, 4 H, $OCH_2$) ppm. $^{13}C\{^1H\}$ NMR: $\delta$ = 13.61 ($CH_2CH_3$), 14.55 ($CH_2CH_3$), 27.16 ($SnCH_2CH_2$), 27.95 ($SnCH_2$), 43.83 ($NCH_3$), 62.65 ($NCH_2$), 64.04 ($OCH_2$) ppm.

A solution of *n*-butyllithium in hexane was obtained and analyzed by the Gilman double-titration method.[56] $CDCl_3$ was obtained from Deutero GmbH and dried with $P_4O_{10}$. $^1H$ NMR (300 MHz) and $^{13}C$ NMR (75 MHz) spectra were recorded with a Bruker–Evance spectrometer (in $CDCl_3$ at 295 K unless otherwise stated). Chemical shifts in the $^1H$ and $^{13}C$ NMR spectra are given in ppm relative to internal $Me_4Si$. Elemental analyses were carried out by the Microanalytical Laboratory of the Chemistry Department of the Moscow State University.

**MeN($CH_2CH_2OH$)$CH_2$C(Ph)$_2$OH (7):** A mixture of *N*-methylethanolamine (1.15 g, 15 mmol) and 2,2-diphenyloxyrane (3.00 g, 15 mmol) was heated at 90 °C for 35 h. The resulting dense yellow oil was crystallized from the mixture diethyl ether/hexane (1:1) at –20 °C to give **7** as a white crystalline solid [3.14 g, 77%; 109–110 °C (110–111 °C[46])]. NMR spectra: $^1H$ NMR: $\delta$ = 2.12 (s, 3 H, $NCH_3$), 2.61 (t, 2 H, $NCH_2$), 3.36 (s, 2 H, $NCH_2$), 3.56 (t, 2 H, $OCH_2$), 7.16–7.20, 7.26–7.31, 7.46–7.49 (3 m, 10 H, 2 $C_6H_5$) ppm, the signal from the OH groups was not observed. $^{13}C\{^1H\}$ NMR: $\delta$ = 44.15 ($NCH_3$), 59.86, 61.27, 67.76 (2 $NCH_2$ and $OCH_2$ groups), 75.60 [C($C_6H_5$)$_2$], 125.79, 126.73, 128.15, 146.55 ($C_6H_5$) ppm.

***erythro*-MeN($CH_2CH_2OH$)CH(Ph)CH(Ph)OH (8):** A mixture of *N*-methylethanolamine (2.0 mL, 25 mmol) and *trans*-stilbene oxide (4.91 g, 25 mmol) was heated at 130 °C for 22 h. The resulting dense orange oil was crystallized from the mixture of diethyl ether/hexane (1:1) at –20 °C to give **8** as a light yellow crystalline solid (6.20 g, 91%; 90–91 °C). NMR spectra: $^1H$ NMR: $\delta$ = 1.98 (br. s, 2 H, 2 OH), 2.13 (s, 3 H, $NCH_3$), 2.38–2.51 (m, 2 H, $NCH_2$), 3.30–3.40 (m, 2 H, $OCH_2$), 3.71 (d, 1 H, NCH), 5.22 (d, 1 H, OCH), 7.23–7.37 (m, 10 H, 2 $C_6H_5$) ppm. $^{13}C\{^1H\}$ NMR: $\delta$ = 37.36 ($NCH_3$), 56.78 ($NCH_2$), 57.97 ($OCH_2$), 72.98 (NCH), 74.63 (OCH), 126.58, 127.89, 127.92, 128.30, 129.51, 134.85, 142.19 ($C_6H_5$).

 © 2006 Wiley-VCH Verlag GmbH & Co. KGaA, Weinheim 

$C_{17}H_{21}NO_2$ (271.35): calcd. C 75.25, H 7.80, N 5.16; found C 75.33, H 7.82, N 5.32 ppm.

***threo*-MeN(CH$_2$CH$_2$OH)CH(Ph)CH(Ph)OH (9):** Analogously to **8**, dialkanolamine **9** was obtained from *N*-methylethanolamine (0.82 mL, 10 mmol) and *cis*-stilbene oxide (1.96 g, 10 mmol) as a light yellow crystalline solid (2.26 g, 83%; 88–89 °C). NMR spectra: $^1$H NMR: $\delta$ = 2.27 (s, 3 H, $NCH_3$), 2.42–2.49 (m, 1 H), 2.69–2.76 (m, 1 H) ($NCH_2$), 3.65–3.78 (m, 2 H, $OCH_2$), 3.69 (d, 1 H, NCH), 5.05 (d, 1 H, OCH), 7.05–7.15, 7.18–7.23 (2 m, 10 H, 2 $C_6H_5$) ppm, the signal of OH groups was not observed. $^{13}$C{$^1$H} NMR: $\delta$ = 37.37 ($NCH_3$), 55.39 ($NCH_2$), 59.51 ($OCH_2$), 71.49 (NCH), 75.24 (OCH), 127.33, 127.39, 127.68, 127.89, 127.92, 129.77, 133.36, 141.10 ($C_6H_5$) ppm. $C_{17}H_{21}NO_2$ (271.35): calcd. C 75.25, H 7.80, N 5.16; found C 75.39, H 7.86, N 5.25.

**MeN(CH$_2$CH$_2$OH)CH(C$_3$H$_6$)CHOH (10):** A mixture of *N*-methylethanolamine (2.95 g, 40 mmol) and cyclopentene oxide (3.36 g, 40 mmol) was stirred at 85 °C for 20 h. The distillation of the reaction mixture gave **10** as a viscous light-yellow liquid [5.29 g, 91%; 105–106 °C (0.2 Torr)]. NMR spectra: $^1$H NMR: $\delta$ = 1.93–1.35 (m, 6 H, cyclopentane 3$CH_2$), 2.25 (s, 3 H, $NCH_3$), 2.59 (m, 2 H, $NCH_2$), 2.74–2.81 (m, 1 H, NCH), 3.52–3.65 (m, 2 H, $OCH_2$), 3.76 (br. s, 2 H, OH), 3.99–4.06 (m, 1 H, OCH) ppm. $^{13}$C{$^1$H} NMR: $\delta$ = 20.72, 24.39, 33.15 (cyclopentane carbons $CH_2$), 38.64 ($NCH_3$), 56.20 ($NCH_2$), 58.57 ($OCH_2$), 73.34 (NCH), 74.41 (OCH) ppm. $C_8H_{17}NO_2$ (159.23): calcd. C 60.35, H 10.76, N 8.80; found C 59.98, H 10.63, N 9.20.

**MeN(CH$_2$CH$_2$OH)CH(C$_4$H$_8$)CHOH (11):** A mixture of *N*-methylethanolamine (13.2 mL, 0.165 mol) and cyclohexene oxide (15.2 mL, 0.15 mol) was heated at 100 °C for 48 h. The distillation of the reaction mixture gave **11** as a viscous colorless liquid [22.89 g, 88%; 105–107 °C (0.2 Torr)]. NMR spectra: $^1$H NMR: $\delta$ = 0.99–1.24, 1.59–1.69, 1.96–2.03 (3 m, 8 H, cyclohexane, 4 $CH_2$), 2.19 (s, 3 H, $NCH_3$), 2.14–2.22, 2.36–2.44, 2.58–2.67, 3.27–3.35, 3.48–3.59 (5 m, 6 H, $NCH_2$, $OCH_2$, NCH, OCH), 3.75 (br. s, 2 H, 2 OH) ppm. $^{13}$C{$^1$H} NMR: $\delta$ = 21.82, 24.12, 25.20, 33.38 (cyclohexane carbons $CH_2$), 36.68 ($NCH_3$), 54.98 ($NCH_2$), 59.42 ($OCH_2$), 69.25, 69.42 (NCH, OCH) ppm. $C_9H_{19}NO_2$ (173.25): calcd. C 62.39, H 11.05, N 8.08; found C 61.99, H 11.07, N 8.42.

**MeN(CH$_2$CH$_2$OH)CH(C$_6$H$_4$CH$_2$)CHOH (12):** Analogously to **8** (except only diethyl ether was used for recrystallization), dialkanolamine **12** was obtained from *N*-methylethanolamine (2.30 g, 30 mmol) and indene oxide (3.96 g, 30 mmol) as a light-yellow crystalline solid (5.82 g, 94%; 75–76 °C). NMR spectra: $^1$H NMR: $\delta$ = 2.44 (s, 3 H, $NCH_3$), 2.82–2.95, 3.26–3.34 [2 m, 2 H, C$H_2$C(OH) H], 2.88–2.95 (m, 2 H, $NCH_2$), 3.19 (br. s, 2 H, 2 OH), 3.66–3.79 (m, 2 H, $OCH_2$), 4.29 (d, 1 H, NCH), 4.66 (q, 1 H, OCH), 7.23–7.35 (m, 4 H, aromatic protons) ppm. $^{13}$C{$^1$H} NMR: $\delta$ = 37.34 ($CHCH_2$), 39.68 ($NCH_3$), 55.87 ($NCH_2$), 58.44 (NCH), 73.75 ($OCH_2$), 113.46 (OCH), 125.06, 125.08, 126.79, 127.94, 140.00, 140.10 (aromatic carbons) ppm.

**PhN(CH$_2$CH$_2$O)$_2$Ti(O*i*Pr)$_2$ (13):** A mixture of alkanolamine **1** (2.00 g, 11.0 mmol), Ti(O*i*Pr)$_4$ (3.14 g, 11.0 mmol), and chloroform (20 mL) was refluxed for 8 h, and all volatiles were removed under reduced pressure. Hexane (20 mL) was added to a yellow, waxy solid. The solution was filtered and the solvent removed under reduced pressure to give **13** as a yellow solid (3.05 g, 80%). NMR spectra: $^1$H NMR: $\delta$ = 1.19 (br. s, 12 H, $CH_3$), 3.47 (br. s, 4 H, $NCH_2$), 4.30–4.90 (br. m, 6 H, $OCH_2$, OCH), 6.53–6.70, 7.07–7.19 (2 m, 5 H, $C_6H_5$) ppm. $^{13}$C{$^1$H} NMR (323 K): $\delta$ = 26.24 ($CH_3$), 55.21 (broad, $NCH_2$), 73.22 (broad, $OCH_2$), 77.44 (OCH), 113.38, 116.58, 130.05, 149.41 (broad, $C_6H_5$) ppm. Satisfactory results for the elemental analyses were unobtainable because of the presence of traces of **18**.

**MeN(CH$_2$CH$_2$O)$_2$Ti(O*i*Pr)$_2$ (14):** A mixture of alkanolamine **2** (2.14 g, 18.0 mmol), Ti(O*i*Pr)$_4$ (5.11 g, 18.0 mmol), and chloroform (20 mL) was refluxed for 7 h, all volatiles were removed under reduced pressure. The residue was dissolved in hexane (20 mL), the solution was filtered and stored at –30 °C for 18 h to give an oil under a supernatant solution. The solvent was removed through a cannula and **14** was obtained as a colorless oil (4.53 g, 89%). NMR spectra: $^1$H NMR: $\delta$ = 1.07 (d, 12 H, CHC$H_3$), 2.48 (s, 3 H, $NCH_3$), 2.80 (br. s, 4 H, $NCH_2$), 4.20 (br. s, 4 H, $OCH_2$), 4.48 (br. s, 2 H, OCH) ppm. $^{13}$C{$^1$H} NMR: $\delta$ = 25.70 (CHC$H_3$), 44.38 ($NCH_3$), 59.50 ($NCH_2$), 69.20 ($OCH_2$), 76.30 (OCH) ppm. Satisfactory results for the elemental analyses were unobtainable because of the presence of traces of **29**.

**PhCH$_2$N(CH$_2$CH$_2$O)$_2$Ti(O*i*Pr)$_2$ (15):** The procedure was the same as for **14** except that Ti(O*i*Pr)$_4$ (3.70 g, 13.0 mmol) was treated with alkanolamine **3** (2.50 g, 13.0 mmol) in toluene. The compound **15** was obtained as a white oil (4.30 g, 92%). NMR spectra: $^1$H NMR: $\delta$ = 1.26 (d, 12 H, CH$CH_3$), 2.93 (br. s, 4 H, $NCH_2$), 4.19 (s, 2 H, $PhCH_2$), 4.39 (br. s, 4 H, $OCH_2$), 4.66 (br. s, 2 H, OCH), 7.23–7.34 (m, 5 H, $C_6H_5$) ppm. $^{13}$C{$^1$H} NMR: $\delta$ = 26.11 (CH$CH_3$), 54.21 ($NCH_2$), 58.01 ($PhCH_2$), 69.43 ($OCH_2$), 76.53 (OCH), 128.01, 128.30, 131.01, 133.74 ($C_6H_5$) ppm. $C_{17}H_{29}NO_4Ti$ (359.28): calcd. C 56.51, H 7.98, N 3.72; found C 56.83, H 8.14, N, 3.90.

**Reaction of PhCH$_2$N(CH$_2$CH$_2$OSiMe$_3$)$_2$ with TiCl$_4$(THF)$_2$:** $PhCH_2N(CH_2CH_2OSiMe_3)_2$ (0.95 g, 2.8 mmol) was added dropwise to a suspension of $TiCl_4(THF)_2$ (0.94 g, 2.8 mmol) in toluene (15 mL). The reaction mixture was refluxed for 14 h, and then filtered off to give a yellow solid, which was insoluble in the usual organic solvents. According to NMR spectroscopic data in $(CD_3)_2$-SO, a mixture of unidentified compounds formed.

**Reaction of MeN(CH$_2$CH$_2$OSn-*n*Bu$_3$)$_2$ with Cp$_2$TiCl$_2$:** $MeN(CH_2CH_2OSn\text{-}nBu_3)_2$ (2.35 g, 3.4 mmol) was added dropwise to a solution of $Cp_2TiCl_2$ (0.60 g, 2.4 mmol) in $CHCl_3$ (65 mL). The reaction mixture was stirred for 10 h, then all volatiles were removed under reduced pressure. According to NMR spectroscopic data of the residue a mixture of CpSn-*n*Bu$_3$ with unidentified compounds formed.

**[PhCH$_2$N(CH$_2$CH$_2$O)$_2$Ti(OMe)$_2$]$_2$ (16):** A solution of alkanolamine **3** (0.71 g, 3.6 mmol) in THF (10 mL) was added dropwise at –50 °C to a solution of $CpTi(OMe)_3$ (0.75 g, 3.6 mmol) in THF (20 mL). The mixture was warmed to room temperature and stirred overnight. The solid that formed was filtered off and recrystallized from the mixture of dichloromethane/heptane (1:1) to give **16** as white microcrystals (0.84 g, 77%). NMR spectra: $^1$H NMR: $\delta$ = 2.85–2.90, 3.05–3.10 (2 br. m, 4 H, $NCH_2$), 4.17, 4.22 (2 s, 6 H, $OCH_3$), 4.43 (br. s, 2 H, $PhCH_2$), 4.28–4.36, 4.57–4.63 (2 br. m, 4 H, $OCH_2$), 7.25–7.36 (m, 5 H, $C_6H_5$) ppm. $^{13}$C{$^1$H} NMR: $\delta$ = 54.22 ($NCH_2$), 55.70 ($PhCH_2$), 60.46, 64.74 ($OCH_3$), 68.82 ($OCH_2$), 127.88, 128.22, 131.47, 134.01 ($C_6H_5$) ppm. Satisfactory results for the elemental analyses were unobtainable because of the presence of traces of **19**.

**PhCH$_2$N(CH$_2$CH$_2$O)$_2$Ti(OMenth)$_2$ (17):** L-(–)-Menthol (1.56 g, 10 mmol) was added to a stirred solution of the compound **15** (1.80 g, 5.0 mmol) in chloroform (30 mL) at room temperature. The reaction mixture was refluxed for 6 h, all volatiles were removed under reduced pressure. Hexane (20 mL) was added to the white oil. The mixture was stored at –30 °C for several days. The solid that formed was filtered off to give **17** as a white powder (2.64 g, 96%). NMR spectra: $^1$H NMR: $\delta$ = 0.76 (d, 3 H, $CH_3$), 0.82 (br.

 © 2006 Wiley-VCH Verlag GmbH & Co. KGaA, Weinheim 

d, 6 H, $CH_3$), 0.85–0.95 (m, 13 H, $CH_3$, $CH_2$), 1.01–1.18 (m, 4 H, $CH_2$), 1.38 (br. s, 2 H, CH), 1.50–1.62 (br. m, 4 H, $CH_2$), 2.07–2.12, 2.17–2.22 (2 br. m, 2 H, CH), 2.33–2.48 (br. m, 2 H, CH), 2.84, 3.00 (2 br. s, 4 H, $NCH_2$), 3.83–3.90, 4.05–4.14 (2 m, 2 H, OCH), 4.16 (br. s, 2 H, $PhCH_2$), 4.33, 4.46 (2 br. s, 4 H, $OCH_2$), 7.26–7.37 (m, 5 H, $C_6H_5$) ppm. $^{13}C\{^1H\}$ NMR: $\delta$ = 15.78, 21.20, 22.25 ($CH_3$), 22.70 ($CH_2$), 25.45, 31.65 (CH), 34.63, 46.51 ($CH_2$), 50.98 (CH), 54.22 (broad, $NCH_2$), 57.84 ($PhCH_2$), 69.37 ($OCH_2$), 84.14, 85.01 (OCH), 128.05, 128.36, 131.10, 133.89 ($C_6H_5$) ppm. Satisfactory results for the elemental analyses were unobtainable because of the presence of traces of **19**.

**[PhN(CH$_2$CH$_2$O)$_2$]$_2$Ti (18):** A mixture of alkanolamine **1** (0.83 g, 4.6 mmol), Ti(O*i*Pr)$_4$ (0.65 g, 2.3 mmol), and toluene (15 mL) was refluxed for 13 h, and all volatiles were removed under reduced pressure. The residue was recrystallized from toluene to give **18** as a yellow solid (0.77 g, 82%). NMR spectra: $^1H$ NMR: $\delta$ = 3.41 (br. s, 8 H, $NCH_2$), 4.17 (br. s, 8 H, $OCH_2$), 6.58–6.70, 7.13–7.26 (m, 10 H, $C_6H_5$) ppm $^{13}C\{^1H\}$ NMR: $\delta$ = 56.71 (broad, $NCH_2$), 73.52 (broad, $OCH_2$), 112.01, 116.02, 130.46, 148.16 ($C_6H_5$) ppm. $C_{20}H_{26}N_2O_4Ti$ (406.30): calcd. C 59.12, H 6.45, Ti 11.79; found C 59.46, H 6.44, Ti 11.51.

**[PhCH$_2$N(CH$_2$CH$_2$O)$_2$]$_2$Ti (19). Method 1:** The procedure was the same as that for **18** except that Ti(O*i*Pr)$_4$ (0.94 g, 3.3 mmol) was treated with alkanolamine **3** (1.29 g, 6.6 mmol). The compound was obtained as white microcrystals (1.22 g, 85%). NMR spectra: $^1H$ NMR: $\delta$ = 3.00 (t, 8 H, $NCH_2$), 4.11 (s, 4 H, $PhCH_2$), 4.49 (t, 8 H, $OCH_2$), 7.27–7.38 (m, 10 H, $C_6H_5$) ppm. $^{13}C\{^1H\}$ NMR: $\delta$ = 53.48 (broad, $NCH_2$), 56.73 ($PhCH_2$), 70.22 ($OCH_2$), 127.92, 128.29, 130.99, 133.90 ($C_6H_5$) ppm. $C_{22}H_{30}N_2O_4Ti$ (434.38): calcd. C 60.83, H 6.96, N 6.45; found C 61.01, H 7.10, N 6.59.

**Method 2:** A solution of alkanolamine **3** (1.10 g, 5.6 mmol) and triethylamine (1.15 g, 11.4 mmol) in THF (30 mL) was added dropwise at –50 °C to a suspension of $TiCl_4(THF)_2$ (0.94 g, 2.8 mmol) in THF (20 mL). The mixture was stirred for 1 h at the same temperature, and was then warmed to room temperature overnight. All volatiles were evaporated under reduced pressure. A white solid was extracted with hot benzene (3 × 20 mL). The solvent was removed under reduced pressure, and the residue was recrystallized from toluene to give **19** as white microcrystals (0.4 g, 33%).

**Method 3:** A solution of alkanolamine **3** (0.70 g, 3.6 mmol) in toluene (5 mL) was added dropwise to a solution of Ti($CH_2Ph$)$_4$ (0.75 g, 1.8 mmol) in toluene (40 mL) at (–40 °C). The reaction mixture was slowly warmed to room temperature and then refluxed for 1 h. The resulting solution was concentrated under vacuum, to give **20** as a white solid (0.78 g, 100%).

**[MeN(CH$_2$CH$_2$O)(CH$_2$CHPhO)]$_2$Ti (20):** The procedure was the same as that for **18** except that Ti(O*i*Pr)$_4$ (0.77 g, 2.7 mmol) was treated with a mixture of (**4a** and **4b**) (9:1) (1.05 g, 5.4 mmol). The compound **20** was obtained as colorless microcrystals, a mixture of diastereomers. NMR spectra: $^1H$ NMR: $\delta$ = 2.61, 2.64, 2.66 (3 s, 6 H, $NCH_3$), 2.72–2.85, 2.98–3.25, 3.37–3.54 (3 m, 8 H, $NCH_2$), 4.26–4.31, 4.57–4.66 (2 m, 4 H, $OCH_2$), 5.63–5.70, 5.75–5.81 (2 m, 2 H, OCH), 7.13–7.47 (m, 10 H, $C_6H_5$) ppm. $^{13}C\{^1H\}$ NMR: $\delta$ = 42.15, 42.72, 44.18 ($NCH_3$), 56.23, 59.49 ($NCH_2$), 69.43 (broad, $OCH_2$), 80.67, 80.78 (OCH), 124.33, 124.86, 125.55, 126.18, 126.35, 126.93, 127.32, 128.04, 128.24, 143.73, 143.85, 144.18 ($C_6H_5$) ppm, the signals of several carbons were not found, the signals of solvated toluene are not described. $C_{22}H_{30}N_2O_4Ti$*$PhCH_3$ (526.51): calcd. C 66.16, H 7.27, N 5.32; found C 66.06, H 7.01, N 4.89.

**[MeN(CH$_2$CH$_2$O)(CH$_2$CHMeO)]$_2$Ti (21):** The procedure was the same as for **18** except that the mixture of alkanolamine **5** (2.40 g, 18.0 mmol) and Ti(O*i*Pr)$_4$ (2.56 g, 9.0 mmol) was refluxed for 15 h in toluene (15 mL). The compound **21** was obtained as a colorless oil (2.67 g, 96%), a mixture of diastereomers. NMR spectra: $^1H$ NMR: $\delta$ = 1.00, 1.02, 1.11 (3 d, 6 H, CH*C*H$_3$), 2.41, 2.43, 2.45 (3 s, 6 H, $NCH_3$), 2.48–2.53, 2.60–2.81, 3.00–3.24 (3 br. m, 8 H, $NCH_2$), 4.00–4.09, 4.46–4.51 (2 m, 4 H, $OCH_2$), 4.70 (br. s, 2 H, OCH) ppm. $^{13}C\{^1H\}$ NMR (323 K): $\delta$ = 20.90, 21.05, 21.22 (CH*C*H$_3$), 43.42, 44.27, 44.51 ($NCH_3$), 58.92, 59.70, 59.91 ($NCH_2$), 69.57, 69.51 ($OCH_2$), 74.89, 75.04 (OCH) ppm, the signals of several carbons were not found. $C_{12}H_{26}N_2O_4Ti$ (310.21): calcd. C 46.46, H 8.45, N 9.03; found C 46.20, H 8.56, N 8.94.

**[MeN(CH$_2$CH$_2$O)(CH$_2$CHEtO)]$_2$Ti (22):** The procedure was the same as for **18** except that alkanolamine **6** (2.97 g, 20 mmol) was treated with Ti(O*i*Pr)$_4$ (2.87 g, 10 mmol) in toluene (15 mL). Compound **22** was obtained as a colorless oil (3.18 g, 94%), a mixture of diastereomers. NMR spectra: $^1H$, $\delta$ = 0.78–0.81 (m, 6 H, $CH_2CH_3$), 1.30 (br. s, 4 H, $CH_2CH_3$), 2.42 (br. s, 6 H, $NCH_3$), 2.45–2.55, 2.76–2.85, 3.15–3.39 (3 br. m, 8 H, $NCH_2$), 4.07, 4.48 (2 br. s, 6 H, $OCH_2$, OCH); $^{13}C\{^1H\}$, $\delta$ = 9.08 (broad, $CH_2CH_3$), 27.67 (broad, $CH_2CH_3$), 41.93, 43.71 ($NCH_3$), 59.22, 60.35 ($NCH_2$), 68.25 (broad, $OCH_2$), 79.64 (broad, OCH), the signals of several carbons were not found. $C_{14}H_{30}N_2O_4Ti$ (338.27): calcd. C 49.71, H 8.94, N 8.28; found C 49.29, H 8.73, N 8.09.

**[MeN(CH$_2$CH$_2$O)(CH$_2$CPh$_2$O)]$_2$Ti (23). Method 1:** The procedure was the same as for **18** except that alkanolamine **7** (0.97 g, 3.6 mmol) was treated with Ti(O*i*Pr)$_4$ (0.51 g, 1.8 mmol) in chloroform (10 mL). Compound **23** was obtained as white microcrystals (0.70 g, 90%). NMR spectra: $^1H$ NMR: $\delta$ = 2.42 (br. s, 6 H, $NCH_3$), 2.84, 2.97 (2 br. s, 4 H, N*C*H$_2$), 3.85, 3.98 (2 d, 4 H, N*C*H$_2$CPh$_2$), 4.35 (br. s, 4 H, $OCH_2$), 7.10–7.30, 7.50–7.56 (2 m, 20 H, $C_6H_5$) ppm. $^{13}C\{^1H\}$ NMR: $\delta$ = 44.79 ($NCH_3$), 61.45 ($NCH_2$), 70.41 ($OCH_2$), 88.75 (O*C*Ph$_2$), 125.46, 125.51, 126.08, 126.14, 127.98, 128.01, 149.68 ($C_6H_5$) ppm, the signals of several carbons were not found. $C_{34}H_{38}N_2O_4Ti$ (586.54): calcd. C 69.62, H 6.53, Ti 8.16; found C 69.86, H 6.64, Ti 8.17.

**Method 2:** Alkanolamine **7** (1.14 g,4.2 mmol) was added to a solution of titanium tetrabenzyl (0.87 g, 2.1 mmol) in toluene (50 mL) at (–40 °C). The reaction mixture was slowly warmed to room temperature and then refluxed for 1 h. The resulting colorless solution was concentrated under vacuum, to give **23** as a white solid (1.23 g, 100%). Crystals, suitable for X-ray analysis, were obtained by recrystallization from the mixture of dichloromethane/*n*-hexane.

***erythro*-[MeN(CH$_2$CH$_2$O)(CHPhCHPhO)]$_2$Ti (24):** The procedure was the same as that for **13** except that alkanolamine **8** (2.17 g, 8.0 mmol) was treated with Ti(O*i*Pr)$_4$ (1.14 g, 4.0 mmol) in chloroform (20 mL). Compound **24** was obtained as colorless microcrystals (1.97 g, 84%), a mixture of diastereomers. NMR spectra: $^1H$ NMR: $\delta$ = 2.57 (br. s, 6 H, $NCH_3$), 2.96–3.38 (br. m, 4 H, $NCH_2$), 4.15–4.32 (br. m, 4 H, $OCH_2$), 4.50–4.59 (br. m, 2 H, NCH), 6.10–6.15, 6.26–6.45 (br. m, 2 H, OCH), 7.05–7.34 (m, 20 H, $C_6H_5$) ppm. $^{13}C\{^1H\}$ NMR: $\delta$ = 42.29, 42.36, 45.82 ($NCH_3$), 60.63 (broad, $NCH_2$), 69.72, 70.46 71.48, 71.52 ($OCH_2$, NCHPh), 86.51 (broad, OCHPh), 125.90, 126.22, 126.43, 126.90, 127.11, 127.27, 127.45, 127.68, 127.84, 131.21, 142.11, 142.77 ($C_6H_5$) ppm, the signals of several carbons were not found. $C_{34}H_{38}N_2O_4Ti$ (586.54): calcd. C 69.62, H 6.53, Ti 8.16; found C 70.55, H 6.83, N 4.55.

***threo*-[MeN(CH$_2$CH$_2$O)(CHPhCHPhO)]$_2$Ti (25):** The procedure was the same as that for **13** except that the mixture of alkanolamine **9** (2.00 g, 7.4 mmol),Ti(O*i*Pr)$_4$ (1.05 g, 3.7 mmol) and chloroform (20 mL) was refluxed for 16 h. The compound **25** was recrystallized from the mixture of dichloromethane/heptane (4:1) and isolated as colorless microcrystals (1.52 g, 96%), a mixture of diastereomers.

 © 2006 Wiley-VCH Verlag GmbH & Co. KGaA, Weinheim 

NMR spectra: $^1$H NMR: $\delta$ = 2.42, 2.47, 2.55 (s, 6 H, $NCH_3$), 2.68–2.79, 3.35–3.48, 3.93–4.05 (m, 4 H, $NCH_2$), 4.26–4.32, 4.41–4.48 (m, 2 H, NCH), 4.50–4.58, 4.92–4.97 (m, 4 H, $OCH_2$), 5.94–6.02 (m, 2 H, OCH), 7.00–7.42 (m, 20 H, $C_6H_5$) ppm. $^{13}C\{^1H\}$ NMR: $\delta$ = 38.40, 39.87, 40.20 ($NCH_3$), 54.10, 56.84 ($NCH_2$), 69.80, 70.00, 73.09 (NCHPh), 78.84, 79.36 ($OCH_2$), 84.93, 86.01 (OCH), 126.86, 127.08, 127.37, 127.54, 127.84, 128.14, 128.38, 130.15, 131.01, 131.75, 133.36, 143.45 ($C_6H_5$) ppm, the signals of several carbons were not found, the signals of solvated dichloromethane are not described. $C_{34}H_{38}N_2O_4Ti{\cdot}CH_2Cl_2$ (671.49): calcd. C 62.60, H 6.00, N 4.17; found C 62.08, H 5.84, N 3.85.

**{MeN(CH$_2$CH$_2$O)[CH(CH$_2$)$_3$CHO]}$_2$Ti (26):** The procedure was the same as that for **18** except that the mixture of alkanolamine **10** (1.08 g, 6.8 mmol), Ti(O*i*Pr)$_4$ (0.97 g, 3.4 mmol) and toluene (7 mL) was refluxed for 15 h. The compound **26** was obtained as a yellow solid (1.10 g, 89%), a mixture of diastereomers. NMR spectra: $^1$H NMR: $\delta$ = 1.21–1.36, 1.55–1.79 (br. m, 12 H, cyclopentane 6 $CH_2$), 2.46, 2.49, 2.50 (c, 6 H, $NCH_3$), 2.41–2.46, 3.01–3.15 (br. s, 6 H, $NCH_2$, NCH), 4.04–4.08, 4.65–4.72 (m, 4 H, $OCH_2$), 4.73–4.81 (m, 2 H, OCH) ppm $^{13}C\{^1H\}$ NMR: $\delta$ = 16.20, 18.56, 27.34 (broad, $CH_2$ groups of cyclopentane rings), 40.61, 41.20, 41.53 ($NCH_3$), 53.59, 53.88 ($NCH_2$), 71.02, 71.17, 71.38 ($OCH_2$), 73.50 (broad, NCH), 84.28 (broad, OCH) ppm, the signals of several carbons were not found. $C_{16}H_{30}N_2O_4Ti$ (362.29): calcd. C 53.04, H 8.35, N 7.73; found C 52.12, H 8.11, N 7.53.

**{MeN(CH$_2$CH$_2$O)[CH(CH$_2$)$_4$CHO]}$_2$Ti (27):** The procedure was the same as that for **18** except that alkanolamine **11** (1.49 g, 8.6 mmol) was treated with Ti(O*i*Pr)$_4$ (1.22 g, 4.3 mmol) in toluene (15 mL). Compound **27** was obtained as colorless microcrystals (1.54 g, 92%), a mixture of diastereomers. NMR spectra: $^1$H, $\delta$ = 1.07–1.15, 1.61–1.68, 1.85–1.91 (br. m, 16 H, cyclopentane 8 $CH_2$), 2.41 (br. s, 6 H, $NCH_3$), 2.25–2.37, 2.60–2.90, 3.10–3.14, 3.29–3.36 (br. m, 6 H, NCH, $NCH_2$), 3.91–4.13, 4.29–4.37 (br. m, 4 H, $OCH_2$), 4.41–4.63 (br. m, 2 H, OCH); $^{13}C\{^1H\}$, $\delta$ = 23.14, 24.57, 24.88, 34.95 (broad, $CH_2$ groups of cyclohexane ring), 39.61 ($NCH_3$), 52.38 ($NCH_2$), 70.34, 73.00 (NCH, $OCH_2$), 82.90 (broad, OCH), the signals of several carbons were not found. $C_{18}H_{34}N_2O_4Ti$ (390.37): calcd. C 55.39, H 8.78, N 7.19; found C 55.65, H 8.76, N 7.21.

**{MeN(CH$_2$CH$_2$O)[CH(C$_6$H$_4$CH$_2$)CHO]}$_2$Ti (28):** The procedure was the same as that for **18** except that alkanolamine **12** (1.00 g, 4.8 mmol) was treated with Ti(O*i*Pr)$_4$ (0.69 g, 2.4 mmol) in toluene (15 mL). The compound **28** was recrystallized from the mixture of toluene/heptane (2:1) and isolated as a yellow solid (0.91 g, 83%), a mixture of diastereomers. NMR spectra: $^1$H (323 K), $\delta$ = 2.71 (br. s, 6 H, $NCH_3$), 2.60–2.66, 2.92–3.04 (m, $CH_2$), 3.15, 3.28 (br. s, 4 H, $NCH_2$), 4.25–4.34 (m, 4 H, $OCH_2$), 4.64 (br. s, 2 H, NCH), 5.13 (br. s, 2 H, OCH), 7.09–7.28 (m, 8 H, $C_6H_4$); $^{13}C\{^1H\}$ (323 K), $\delta$ = 37.85 (broad, $NCH_3$, $CH_2$), 57.88 (broad, $NCH_2$), 69.09 (broad, $OCH_2$), 76.31 (broad, NCH), 83.62 (broad, OCH) 123.82, 125.44, 126.22, 127.20, 139.37, 140.39 ($C_6H_4$). $C_{24}H_{30}N_2O_4Ti$ (458.37): calcd. C 62.89, H 6.60, N 6.11; found C 62.43, H 6.32, N 5.94.

**Reaction of 14 with Alkanolamine 1:** Alkanolamine **1** (0.83 g, 4.6 mmol) was added to a solution of **14** (1.30 g, 4.6 mmol) in toluene (10 mL). The mixture was refluxed for 2 h, and all volatiles were removed under reduced pressure. According to NMR spectroscopic data a mixture of **18** and **29**[20] was formed.

**Reaction of 14 with Alkanolamine 3:** Alkanolamine **3** (0.90 g, 4.6 mmol) was added to a solution of **14** (1.30 g, 4.6 mmol) in tolu-

Table 4. Crystal data, data collection, structure solution, and refinement parameters for **16**, **19**, **20**, **23**, **24**, **25**, and **27**.

| | **16** | **19** | **20** | **23** | **24** | **25** | **27** |
|---|---|---|---|---|---|---|---|
| Formula | $C_{26}H_{38}N_2O_8Ti_2{\cdot}2CH_2Cl_2$ | $C_{22}H_{30}N_2O_4Ti$ | $C_{22}H_{30}N_2O_4Ti{\cdot}C_7H_8$ | $C_{34}H_{38}N_2O_4Ti{\cdot}2CH_2Cl_2$ | $C_{34}H_{38}N_2O_4Ti{\cdot}0.5C_7H_8$ | $C_{34}H_{38}N_2O_4Ti{\cdot}CH_2Cl_2$ | $C_{18}H_{34}N_2O_4Ti$ |
| $M_r$ [g·mol$^{-1}$] | 772.24 | 434.38 | 526.51 | 756.42 | 632.63 | 671.49 | 390.37 |
| Crystal system | orthorhombic | monoclinic | monoclinic | monoclinic | monoclinic | orthorhombic | monoclinic |
| Space group | *Pbcn* | *P*2/*n* | *P*2$_1$/*c* | *C*2/*c* | *P*2$_1$/*c* | *Pbcn* | *C*2/*c* |
| *a* [Å] | 15.9481(9) | 9.443(4) | 12.8626(12) | 21.447(3) | 13.401(1) | 6.9964(4) | 21.545(5) |
| *b* [Å] | 9.8954(5) | 12.749(3) | 16.5027(16) | 8.223(1) | 12.780(2) | 20.5113(11) | 8.943(4) |
| *c* [Å] | 22.2450(12) | 18.207(3) | 12.5842(13) | 21.056(3) | 19.660(3) | 23.6918(14) | 10.435(6) |
| $\beta$ [°] | | 93.17(2) | 90.558(2) | 98.54(1) | 91.28(1) | | 93.79(4) |
| *V* [Å$^3$] | 3510.5(3) | 2188.6(11) | 2671.1(5) | 3672.2(9) | 3366.2(8) | 3399.9(3) | 2006.2(15) |
| *Z* | 4 | 4 | 4 | 4 | 4 | 4 | 4 |
| $d_{calcd}$ [g·cm$^{-3}$] | 1.461 | 1.318 | 1.309 | 1.368 | 1.248 | 1.312 | 1.292 |
| Abs. coeff. [mm$^{-1}$] | 0.807 | 0.421 | 1.357 | 0.564 | 0.295 | 0.449 | 0.450 |
| *F*(000) | 1600 | 920 | 1120 | 1576 | 1340 | 1408 | 840 |
| Diffractometer | Bruker SMART | Nonius CAD4 | Bruker SMART | Stoe IPDS II | Nonius CAD4 | Bruker SMART | Nonius CAD4 |
| Temperature [K] | 120 | 293 | 120 | 173 | 293 | 120 | 293 |
| $\theta$ range [°] | 3.04–28.00 | 2.24–25.48 | 1.23–28.00 | 1.92–25.98 | 2.07–25.47 | 1.72–28.00 | 2.47–25.97 |
| Index ranges | $-15 \le h \le 21$<br>$-13 \le k \le 8$<br>$-29 \le l \le 29$ | $-11 \le h \le 11$<br>$-3 \le k \le 15$<br>$-4 \le l \le 22$ | $-14 \le h \le 16$<br>$-21 \le k \le 21$<br>$-15 \le l \le 16$ | $-26 \le h \le 26$<br>$-10 \le k \le 9$<br>$-25 \le l \le 25$ | $-16 \le h \le 16$<br>$-2 \le k \le 15$<br>$-3 \le l \le 23$ | $-9 \le h \le 9$<br>$-27 \le k \le 15$<br>$-31 \le l \le 29$ | $-26 \le h \le 26$<br>$-4 \le k \le 11$<br>$-4 \le l \le 12$ |
| Reflections collected | 16611 | 6766 | 17996 | 24987 | 9029 | 21508 | 4419 |
| Independent reflections | 4205 | 4071 | 6400 | 3570 | 6247 | 4120 | 1969 |
| $R_{int}$ | 0.03332 | 0.0283 | 0.0401 | 0.0746 | 0.0306 | 0.0394 | 0.1158 |
| Data/param. | 4205/283 | 4071/281 | 6400/478 | 3570/215 | 6247/390 | 4120/281 | 1969/115 |
| GOF on $F^2$ | 1.051 | 1.008 | 1.027 | 0.787 | 1.007 | 1.090 | 0.991 |
| $R_1$ [$I > 2\sigma(I)$] | 0.0399 | 0.0372 | 0.0507 | 0.0323 | 0.0446 | 0.0536 | 0.0637 |
| $wR_2$ (all data) | 0.1088 | 0.1094 | 0.1352 | 0.0619 | 0.1498 | 0.1315 | 0.1788 |
| Largest diff. peak/hole [e·Å$^{-3}$] | 0.875/–0.312 | 0.226/–0.238 | 0.403/–0.476 | 0.265/–0.379 | 0.691/–0.399 | 1.318/–1.085 | 1.059/–0.589 |

 © 2006 Wiley-VCH Verlag GmbH & Co. KGaA, Weinheim 

ene (10 mL). The mixture was refluxed for 2 h, and all volatiles were removed under reduced pressure. According to NMR spectroscopic data, a mixture of **19** and **29**[20] was formed.

**Reaction of 15 with Alkanolamine 2:** Alkanolamine **2** (0.46 g, 2.5 mmol) was added to a solution of **15** (0.91 g, 2.5 mmol) in chloroform (15 mL). The mixture was refluxed for 3 h, and all volatiles were removed under reduced pressure. According to NMR spectroscopic data, a mixture of **19** and **29**[20] was formed.

**Reaction of 15 with Alkanolamine 8:** Alkanolamine **8** (1.32 g, 4.9 mmol) was added to a solution of compound **15** (1.75 g, 4.9 mmol) in toluene (10 mL). The mixture was refluxed for 2 h, and all volatiles were removed under reduced pressure. Ether (20 mL) was added to the residue, the precipitate was filtered off to give **19** as a white powder (1.02 g). According to NMR spectroscopic data, the mother liquor contained a mixture of **19** and **24**.

**Reaction of 18 with Ti(O*i*Pr)$_4$:** Ti(O*i*Pr)$_4$ (0.52 g, 1.8 mmol) was added dropwise to a solution of compound **18** (0.74 g, 1.8 mmol) in chloroform (20 mL), and the reaction mixture was refluxed for 5 h. After cooling to room temperature, all volatiles were removed under reduced pressure. Hexane (10 mL) was added to the yellow oil. The solution was filtered, and the solvent was removed under reduced pressure to give **13** as a yellow solid (1.22 g, 97%).

**Reaction of 19 with TiCl$_4$:** TiCl$_4$ (0.44 g, 2.3 mmol) was added at –78 °C to a suspension of **19** (1.00 g, 2.3 mmol) in toluene (15 mL) and the mixture was stirred for 2 h at the same temperature. A yellow solid formed. The reaction mixture was warmed to room temperature, and all volatiles were removed under reduced pressure. The formed yellow solid was insoluble in the usual organic solvents. According to NMR spectroscopic data in $(CD_3)_2SO$, a mixture of unidentified compounds formed.

**X-ray Crystallographic Study:** Crystal data, data collection, structure solution, and refinement parameters for compounds **16**, **19**, **20**, **23**, **24**, **25**, and **27** are given in Table 4. Experimental data were collected using Mo-$K_\alpha$ radiation ($\lambda$ = 0.71073 Å). The structures were solved by direct methods[57] and refined by full-matrix least-squares based on $F^2$ with anisotropic thermal parameters for all non-hydrogen atoms.[58] In the structures **16**, **20**, and **25**, all hydrogen atoms were found from diff. Fourier syntheses and refined isotropically. As for **19**, **23**, **24**, and **27** all hydrogen atoms were placed in calculated positions and refined using a riding model. The structure **25** contains disordered $CH_2Cl_2$ molecules lying on a crystallographic twofold axis; **24** contains disordered toluene molecules lying on a crystallographic inversion center. In **19**, one of the two independent molecules possesses disordered -$CH_2CH_2$- skeleton fragments with an occupancy ratio of 0.71/0.29.

CCDC-292591 to -292597 contain the supplementary crystallographic data for this paper. These data can be obtained free of charge from The Cambridge Crystallographic Data Centre via www.ccdc.cam.ac.uk/data_request/cif.

## Acknowledgments

A. V. C. is grateful to the Russian Science Support Foundation. This work was supported by the Philipps-University Marburg, Chemistry Department, with a grant for K. V. Z., as well as RFBR under grant 06-03-33032-a.

[1] L. Lu, R. A. Johnson, M. G. Finn, K. B. Sharpless, *J. Org. Chem.* **1984**, *49*, 728–732.
[2] S. F. Pedersen, J. C. Dewan, R. R. Eckman, K. B. Sharpless, *J. Am. Chem. Soc.* **1987**, *109*, 1279–1282.
[3] B. P. Santora, A. O. Larsen, M. R. Gagne, *Organometallics* **1998**, *17*, 3138–3140.
[4] J. Balsells, T. J. Davis, P. Carroll, P. J. Walsh, *J. Am. Chem. Soc.* **2002**, *124*, 10336–10348.
[5] K. Mikami, M. Terada, T. Nakai, *J. Am. Chem. Soc.* **1990**, *112*, 3949–3954.
[6] S. Piana, I. Devillers, A. Togni, U. Rothlisberger, *Angew. Chem. Int. Ed.* **2002**, *41*, 979–982.
[7] T. Kotsuki, K. B. Sharpless, *J. Am. Chem. Soc.* **1980**, *102*, 5974–5976.
[8] B. Stowasser, K. H. Budt, L. Jian-Qi, A. Peynan, D. Ruppert, *Tetrahedron Lett.* **1992**, *33*, 6625–6628.
[9] Y. Takahashi, Y. Matsuoka, *J. Mater. Sci.* **1988**, *23*, 2259–2271.
[10] A. C. Jones, T. J. Leedham, P. J. Wright, M. J. Crosbie, K. A. Fleeting, D. J. Otway, P. O'Brien, M. E. Pemble, *J. Mater. Chem.* **1998**, *8*, 1773–1777.
[11] M. Bonchio, G. Licini, G. Modena, O. Bortolini, S. Moro, W. A. Nugent, *J. Am. Chem. Soc.* **1999**, *121*, 6258–6268.
[12] W. A. Nugent, R. L. Harlow, *J. Am. Chem. Soc.* **1994**, *116*, 6142–6148.
[13] T. Kemmitt, N. I. Al-Salim, G. J. Gainsford, *Inorg. Chem.* **2000**, *39*, 6067–6071.
[14] Y. Kim, G. K. Jnaneshwara, J. G. Verkade, *Inorg. Chem.* **2003**, *42*, 1437–1447.
[15] P. Sudhakar, C. V. Amburose, G. Sundararajan, M. Nethaji, *Organometallics* **2004**, *23*, 4462–4467.
[16] R. Taube, P. Knoth, *Z. Anorg. Allg. Chem.* **1990**, *581*, 89–98.
[17] Y. Kim, Y. Han, J.-W. Hwang, M. W. Kim, Y. Do, *Organometallics* **2002**, *21*, 1127–1135.
[18] A. A. Naiini, S. L. Ringrose, Y. Su, R. A. Jacobson, J. G. Verkade, *Inorg. Chem.* **1993**, *32*, 1290–1296.
[19] G. Boche, K. Mobus, K. Harms, M. Marsch, *J. Am. Chem. Soc.* **1996**, *118*, 2770–2771.
[20] T. Kemmitt, N. I. Al-Salim, G. J. Gainsford, W. Henderson, *Aust. J. Chem.* **1999**, *52*, 915–919.
[21] T. Kemmitt, N. I. Al-Salim, G. J. Gainsford, *Aust. J. Chem.* **2002**, *55*, 513–517.
[22] T. Kemmitt, G. J. Gainsford, N. I. Al-Salim, *Acta Crystallogr., Sect. C* **2004**, *60*, m42–m43.
[23] T. Kemmitt, G. J. Gainsford, N. I. Al-Salim, H. Robson-Marsden, D. V. Sevast'yanov, *Aust. J. Chem.* **2003**, *56*, 1147–1152.
[24] T. Kemmitt, N. I. Al-Salim, G. J. Gainsford, *Eur. J. Inorg. Chem.* **1999**, 1847–1849.
[25] Y. Kim, H. Han, Y. Do, *J. Organomet. Chem.* **2001**, *634*, 19–24.
[26] R. Manivannan, G. Sundararajan, *Macromolecules* **2002**, *35*, 7883–7890.
[27] E. Y. Tshuva, I. Goldberg, M. Kol, Z. Goldschmidt, *Inorg. Chem.* **2001**, *40*, 4263–4270.
[28] S. Groysman, I. Goldberg, M. Kol, E. Genizi, Z. Goldschmidt, *Organometallics* **2003**, *22*, 3013–3015.
[29] E. Y. Tshuva, I. Goldberg, M. Kol, Z. Goldschmidt, *Organometallics* **2001**, *20*, 3017–3028.
[30] J. Okuda, S. Fokken, H.-C. Kang, W. Massa, *Chem. Ber.* **1995**, *128*, 221–227.
[31] S. Fokken, T. Spaniol, H.-C. Kang, W. Massa, J. Okuda, *Organometallics* **1996**, *15*, 5069–5072.
[32] L. Lavant, T.-I. Chou, Y. Chi, C. W. Lehmann, L. Toupet, J.-F. Carpentier, *Organometallics* **2004**, *23*, 5450–5458.
[33] T. Toupance, S. R. Dubberley, N. H. Rees, B. R. Tyrrell, P. Mountford, *Organometallics* **2002**, *21*, 1367–1382.
[34] S. S. Karlov, E. Kh. Lermontova, M. V. Zabalov, A. A. Selina, A. V. Churakov, J. A. K. Howard, M. Yu. Antipin, G. S. Zaitseva, *Inorg. Chem.* **2005**, *44*, 4879–4886.
[35] S. S. Karlov, D. A. Tyurin, M. V. Zabalov, A. V. Churakov, G. S. Zaitseva, *J. Mol. Struct.: THEOCHEM* **2005**, *724*, 31–37.

 © 2006 Wiley-VCH Verlag GmbH & Co. KGaA, Weinheim 

[36] S. S. Karlov, A. A. Selina, E. S. Chernyshova, M. V. Zabalov, A. V. Churakov, J. A. K. Howard, V. A. Tafeenko, G. S. Zaitseva, *J. Mol. Struct.* **2005**, *740*, 1–8.
[37] I. F. Shishkov, L. V. Khristenko, F. M. Rudakov, A. B. Golubinskii, L. V. Vilkov, S. S. Karlov, G. S. Zaitseva, S. Samdal, *Struct. Chem.* **2004**, *15*, 11–16.
[38] S. S. Karlov, E. Kh. Yakubova, E. V. Gauchenova, A. A. Selina, A. V. Churakov, J. A. K. Howard, D. A. Tyurin, J. Lorberth, G. S. Zaitseva, *Z. Naturforsch. Teil B* **2003**, *58*, 1165–1170.
[39] A. A. Selina, S. S. Karlov, K. Harms, D. A. Tyurin, Yu. F. Oprunenko, J. Lorberth, G. S. Zaitseva, *Z. Naturforsch.* **2003**, *58b*, 613–619.
[40] E. V. Gauchenova, S. S. Karlov, A. A. Selina, E. S. Chernyshova, A. V. Churakov, J. A. K. Howard, N. A. Troitsky, S. N. Tandura, J. Lorberth, G. S. Zaitseva, *J. Organomet. Chem.* **2003**, *676*, 8–21.
[41] I. F. Shishkov, L. V. Khristenko, F. M. Rudakov, L. V. Vilkov, S. S. Karlov, G. S. Zaitseva, S. Samdal, *J. Mol. Struct.* **2002**, *641*, 199–205.
[42] S. S. Karlov, P. L. Shutov, N. G. Akhmedov, M. A. Seip, J. Lorberth, G. S. Zaitseva, *J. Organomet. Chem.* **2000**, *598*, 387–394.
[43] G. S. Zaitseva, L. I. Livantsova, M. Nasim, S. S. Karlov, A. V. Churakov, J. A. K. Howard, E. V. Avtomonov, J. Lorberth, *Chem. Ber./Recueil* **1997**, *130*, 739–746.
[44] L. Lavanant, L. Toupet, C. W. Lehmann, J.-F. Carpentier, *Organometallics* **2005**, *24*, 5620–5633.
[45] K. P. Iordanova, D. K. Danchev, V. I. Shvedov, *Khim.-Pharm Zhurn.* **1982**, *16*, 552–556.
[46] H. Gilman, C. C. Wanser, *J. Am. Chem. Soc.* **1951**, *73*, 4030–4031.
[47] A. van der Linden, C. J. Schaverien, A. G. Orpen, *J. Am. Chem. Soc.* **1995**, *117*, 3008–3021.
[48] A. Caneschi, A. Dei, D. Gatteschi, *J. Chem. Soc., Chem. Commun.* **1992**, 630–631.
[49] S. M. Damo, K.-C. Lam, A. Rheingold, M. A. Walters, *Inorg. Chem.* **2000**, *39*, 1635–1638.
[50] A. N. Nesmeyanov, O. V. Nogina, N. A. Lazareva, V. A. Dubovitskii, *Izv. Akad. Nauk SSSR, Ser. Khim.* **1967**, 808–814.
[51] L. E. Manzer, *Inorg. Synth.* **1982**, *21*, 135–136.
[52] U. Zucchini, E. Albizzati, U. Giannini, *J. Organomet. Chem.* **1971**, *26*, 357.
[53] W. E. Hanby, H. N. Rydon, *J. Chem. Soc.* **1947**, 513–519.
[54] A. Sonoda, N. Takagi, K. Ooi, T. Hirotsu, *Bull. Chem. Soc. Jpn.* **1998**, *71*, 161–166.
[55] G. Perrault, *Can. J. Chem.* **1967**, *45*, 1063–1067.
[56] H. Gilman, A. H. Haubein, *J. Am. Chem. Soc.* **1944**, *66*, 1515–1516.
[57] G. M. Sheldrick, *Acta Crystallogr., Sect. A* **1990**, *46*, 467–473.
[58] G. M. Sheldrick, *SHELXL-97. Program for the Refinement of Crystal Structures*; University of Göttingen: Göttingen, Germany, **1997**.

Received: December 29, 2005
Published Online: March 23, 2006

 © 2006 Wiley-VCH Verlag GmbH & Co. KGaA, Weinheim 

DOI: 10.1002/ejic.200600010

# Rare Earth Benzotriazolates: Coordination Polymers Incorporating Decomposition Products from Ammonia to 1,2-Diaminobenzene in $^1_\infty[Ln(Btz)_3(BtzH)]$ (Ln = Ce, Pr), $^1_\infty[Ln(Btz)_3\{Ph(NH_2)_2\}]$ (Ln = Nd, Tb, Yb), and $^1_\infty[Ho_2(Btz)_6(BtzH)(NH_3)]$[‡]

**Klaus Müller-Buschbaum,*[a] and Yassin Mokaddem[a]**

**Keywords:** Solvent-free synthesis / Lanthanides / Benzotriazolate / Crystal structure / X-ray diffraction

The solvent-free melt reactions of benzotriazole (BtzH, $C_6H_4N_2NH$) with rare earth metals result in three different types of benzotriazolate coordination polymers. Early 4f metals yield $^1_\infty[Ln(Btz)_3(BtzH)]$ [Ln = Ce (**1**), Pr (**2**)], from neodymium to ytterbium the type $^1_\infty[Ln(Btz)_3\{Ph(NH_2)_2\}]$ is observed [Ln = Nd (**3**), Tb (**4**), Yb (**5**)], whereas the late 4f metal Ho gives $^1_\infty[Ho_2(Btz)_6(BtzH)(NH_3)]$ (**6**). Depending on the reaction conditions and the respective rare earth element, ligand fragments originating from decomposition products are incorporated in the coordination polymers. Compounds **1**–**3** and **6** were obtained as single crystals and their crystal structures determined by single-crystal X-ray analysis, whilst **4** and **5** were obtained as powders. X-ray powder diffraction shows the isotypic character of polymers **3**, **4**, and **5**. The benzotriazolates contain trivalent lanthanide ions with complete nitrogen coordination. Decomposition of the ligand accompanies the formation of the coordination polymers. X-ray analysis was combined with thermal analysis and mass spectrometry to investigate the influence of reaction temperatures on ligand decomposition. Ln-benzotriazolates exhibit aspects of materials science such as luminescence {$^5D_4 \rightarrow {}^7F_J$, $J$ = 4–6 for $^1_\infty[Tb(Btz)_3\{Ph(NH_2)_2\}]$ (**4**)} without quenching by concentration.

(© Wiley-VCH Verlag GmbH & Co. KGaA, 69451 Weinheim, Germany, 2006)

## Introduction

Nearly all syntheses in coordination chemistry, including rare earth chemistry, are carried out in solution, mostly in classical solvents such as THF, toluene, DME etc.[1–7] These syntheses are used to form a range of complexes, from the first cyclopentadienyl complexes[8] and metallocenes[9] to the oxo and amido complexes of today.[1–7] In contrast solvent-free syntheses by high-temperature reactions have been successfully utilized to obtain organic amides of the rare earth elements over the past seven years.[10–20] It has been shown that novel coordination chemistry is possible without classical solvent procedures. The products obtained from the extreme conditions of melt reactions are unique and exhibit interesting features such as the formation of homoleptic compounds[10–16] and coordination polymers,[10,16,17,19,20] whereas for syntheses in solvents, ligand criteria such as multi-chelating[21–27] are necessary to obtain homoleptic complexes. The reactivity of rare earth metals has proven to be high enough so that they can directly react with amine melts without the need for multi-chelation or high steric congestion. We have systematically developed this kind of solvent-free synthesis including the crystallization of products under the reaction conditions.[9,12–17,19,20] Independent from the synthesis, a systematic approach that involves the amine ligand leads from ammonia to unsubstituted and substituted 1-N heterocycles such as pyrrole[28–32] and carbazole,[16,20] to 2-N ligands such as imidazole[33] and pyrazole,[11,12,17,19] and to ring systems that contain three or more nitrogen atoms per ring. The tendency to release $N_2$ upon heating N-heterocycles increases as the number of N atoms they contain increases. It becomes exothermic for triazoles, whereas tetrazoles tend to become explosive.[34] Accordingly, high-temperature chemistry with these ligands is a synthetic challenge. 1*H*-Benzotriazole (BtzH) marks the first step in our approach as it is thermally more stable than one-ring 3-N ligands. Nonetheless, our results (**1**–**6**) already illustrate the influence of thermal decomposition on this chemistry. To the best of our knowledge no benzotriazolates of the rare earth elements have been previously known.

## Results and Discussion

The solvent-free ampoule reactions of cerium, praseodymium, neodymium, terbium, holmium, and ytterbium with 1*H*-benzotriazole were carried out in the amine melt. The reactions with cerium and praseodymium yield single crystals of $^1_\infty[Ln(Btz)_3(BtzH)]$ (**1**, **2**) [Equation (1)], whereas

[‡] $Btz^-$: benzotriazolate anion, $C_6H_4N_3^-$; BtzH: benzotriazole, $C_6H_4N_2NH$

[a] Institut für Anorganische Chemie, Universität zu Köln, Greinstrasse 6, 50939 Köln, Germany
E-mail: Klaus.Mueller-Buschbaum@Uni-Koeln.DE

 InterScience © 2006 Wiley-VCH Verlag GmbH & Co. KGaA, Weinheim 

reactions with neodymium, terbium, holmium, and ytterbium metal result in compounds that contain additional ligands, 1,2-diaminobenzene and ammonia. Two different types are observed depending on the metal, $^1_\infty$[Ln(Btz)$_3${Ph(NH$_2$)$_2$}] for Ln = Nd (**3**), Tb (**4**), and Yb (**5**) [Equation (2)], and $^1_\infty$[Ln$_2$(Btz)$_6$(BtzH)(NH$_3$)] for Ln = Ho (**6**) [Equation (3)].

$$\text{Ln} + 4\ \text{H–Btz} \xrightarrow{\Delta T} {}^1_\infty[\text{Ln(Btz)}_3\text{(BtzH)}] + \text{H}_2 \quad (1)$$

$$\text{Ln} + 4\ \text{H–Btz} \xrightarrow{\Delta T} {}^1_\infty[\text{Ln(Btz)}_3\{\text{Ph(NH}_2)_2\}] + \tfrac{1}{2}\ \text{N}_2 \quad (2)$$

$$2\ \text{Ln} + 8\ \text{H–Btz} \xrightarrow{\Delta T} {}^1_\infty[\text{Ln}_2\text{(Btz)}_6\text{(BtzH)(NH}_3)] + \text{N}_2 + \text{H}_2 + \text{C}_6\text{H}_6 \quad (3)$$

Of the decomposition products of 1*H*-benzotriazole, both 1,2-diaminobenzene and ammonia are incorporated into the products and in the coordination spheres of the metal atoms, whilst the neutral molecules $N_2$, $H_2$, and benzene are not. Consequently, **6** was formed at the highest reaction temperatures used as Ho is the metal with the highest melting point in **1**–**6**. In order to illuminate this decomposition influence, we investigated the thermal behavior of 1*H*-benzotriazole and of the products of the syntheses.[35,36] It can be concluded that rare earth metals promote and induce the decomposition of BtzH by a redox reaction. With compound **5** a red phase is reproducibly formed in a ratio of 4:1, which probably contains $Yb^{II}$ though this has not yet been confirmed as we have not succeeded in crystallizing it. In order to crystallize the products from Equation (2), solvothermal reaction and crystallization from pyrrole were carried out for **3**, whereas the melt synthesis results in powders to microcrystalline products as for **4** and **5**.

The thermal decomposition of each type of lanthanide benzotriazolates was investigated by simultaneous DTA/TG[37] on the bulk as well as on single crystalline materials of **1**, **3**, and **6**. This analysis provides additional information with regard to the completeness of the reactions, the possible phase impurities, and the decomposition path of the product of the melt reactions and the ligand used. We have already shown the value of this method for the comprehension of comparable melt reactions with 2,2-(pyridyl)benzimidazole, 2,2′-dipyridylamine, as well as with pyrazole.[10,14,38,39]

The DTA/TG versus temperature diagrams of the rare earth benzotriazolates presented here show an ensemble of endothermic as well as exothermic signals in the heat flow and are accompanied by several steps of mass losses, which end in the decomposition of the coordination polymers. Investigations of the bulk materials show additional signals that can be identified with excess ligand (BtzH: m.p. 98 °C, b.p. 204 °C, measured 95 °C, 205 °C). The diagram of the single crystalline material is free of these signals and exhibits the thermal processes of the products only (see Figure 1).

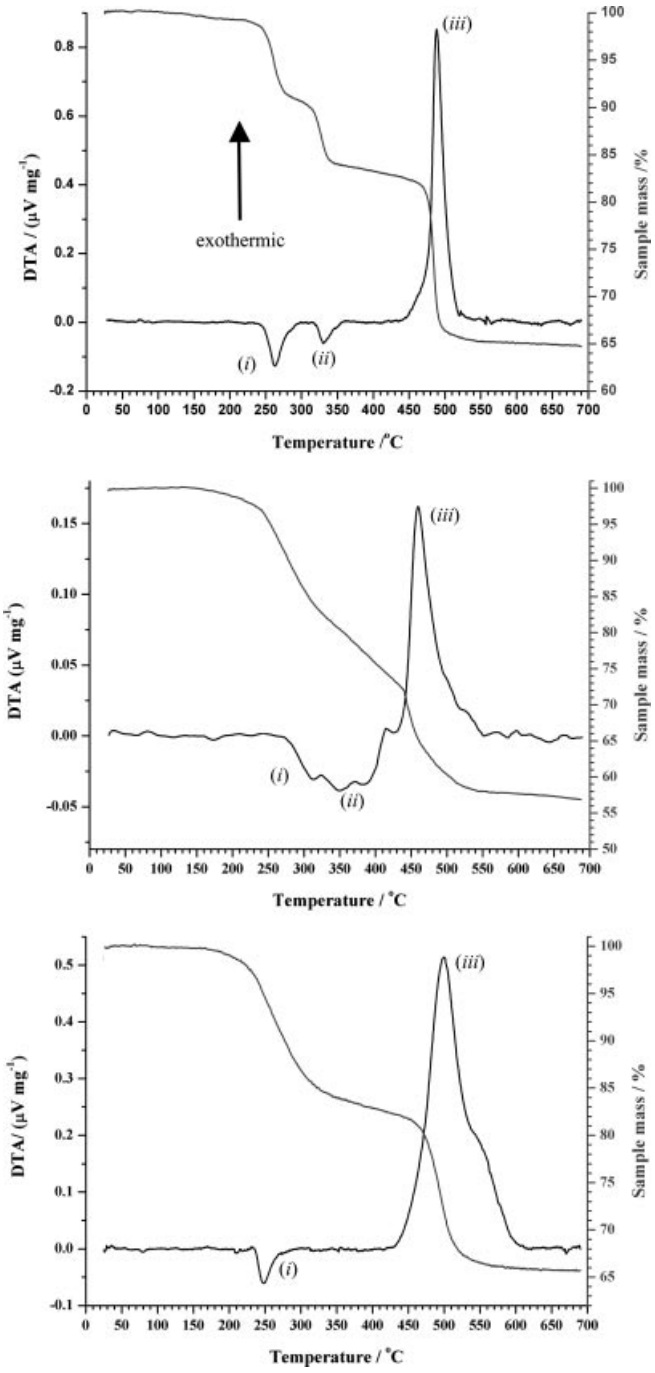


Figure 1. The thermal decompositions of $^1_\infty$[Ce(Btz)$_3$(BtzH)] (**1**, top), $^1_\infty$[Nd(Btz)$_3$(BtzH)] (**3**, middle) and $^1_\infty$[Ho$_2$(Btz)$_6$(BtzH)(NH$_3$)] (**6**, bottom), which were purified by sublimation. The compounds were investigated by simultaneous DTA/TG in the temperature range 20–700 °C. The release of amine ligands is observed first and is endothermic, whereas the decomposition of the amido backbone of the polymers is exothermic releasing $N_2$.

$^1_\infty$[Ce(Btz)$_3$(BtzH)] (**1**) releases coordinating benzotriazole in two endothermic steps at 250 °C and 320 °C [signals (*i*) and (*ii*)], which adds up to the mass loss of one equivalent of BtzH per formula (calculated 19%, observed 18%) and thus all coordinating BtzH. A strong exothermic peak [signal (*iii*)] follows at 470 °C, indicating decomposition of the

 © 2006 Wiley-VCH Verlag GmbH & Co. KGaA, Weinheim 

homoleptic polymer [Ce(Btz)$_3$] with the release of $N_2$. Furthermore, Ph(NH$_2$)$_2$, its decomposition products, and $NH_3$ can be observed in the mass spectrum.

Because of the different chemical formulas of $^1_\infty$[Nd(Btz)$_3${Ph(NH$_2$)$_2$}] (**3**) and **1**, differences in their simultaneous DTA/TG/MS **1** can be seen. Compound **3** shows a multistep decomposition with endothermic and exothermic signals but also three mass loss steps. At 270 °C [signal (*i*)], the release of coordinated Ph(NH$_2$)$_2$ begins [Ph(NH$_2$)$_2$: calculated 17.8%, observed 18%] before the polymer [Nd(Btz)$_3$] decomposes without a stable temperature plateau [310 °C: at least two steps, endothermic signal group (*ii*); 440 °C: exothermic step (*iii*)]. Prior to the exothermic release of $N_2$, Ph(NH$_2$)$_2$ as well as $NH_3$ are formed again from the coordinating Btz$^-$ anions.

$^1_\infty$[Ho$_2$(Btz)$_6$(BtzH)(NH$_3$)] (**6**) exhibits only two thermal decomposition steps. The first step at 240 °C [signal (*i*)] is, again, endothermic and can be identified with the release of the coordinated equivalent of BtzH and $NH_3$ (calculated 13.8%, observed 15.5%). Signal (*ii*) at 450 °C represents decomposition of [Ho(Btz)$_3$] accompanied by the release of the same products as for **1** and **3** (observed 17%).

It can thus be deduced that none of the coordination polymers melts congruently, that additional coordinating amine ligands in **1**–**6** are released prior to amide anions, and that the release of amide groups results in overall decomposition of the polymers. A general formula for a homoleptic decomposition intermediate is assumed to be [Ln(Btz)$_3$], though investigation of **3** shows that it is questionable to isolate these polymers for all lanthanide ions. Thermal stabilities of these coordination polymers are high, up to 450 °C for **5**. The exothermic release of $N_2$ is delayed to higher temperatures for **1**–**6** than for the free ligand.

Each of the far-infrared as well as Raman spectra of **1**–**6** show bands that cannot be identified with the ligand and thus represent the ν(Ln–N) and δ(N–Ln–N) stretching modes {$^1_\infty$[Ce(Btz)$_3$(BtzH)] (**1**) FarIR: 244, 200, 183, 169, Raman 123 cm$^{-1}$; $^1_\infty$[Pr(Btz)$_3$(BtzH)] (**2**) FarIR: 250, 195, 179, 171, Raman: 120 cm$^{-1}$; $^1_\infty$[Nd(Btz)$_3$(Ph(NH$_2$)$_2$)] (**3**) FarIR: 249, 195, 178, 147, Raman 150, 124 cm$^{-1}$; $^1_\infty$[Tb(Btz)$_3$(Ph(NH$_2$)$_2$)] (**4**) FarIR: 247, 193, 175, 146, Raman: 150 sh, 125 cm$^{-1}$; $^1_\infty$[Yb$_2$(Btz)$_6$(BtzH)(NH$_3$)] (**5**) FarIR: 254, 214, 173, 144 cm$^{-1}$; $^1_\infty$[Ho$_2$(Btz)$_6$(BtzH)(NH$_3$)] (**6**) FarIR: 249, 230, 210, 191, 176, 158, 146, Raman 122 cm$^{-1}$}. These bands match well with other Ln–N containing compounds like rare earth porphyrin complexes,[40] dipyridyl amides,[10,15,38] pyridylbenzimidazolates,[10,13,14] and carbazolates[10,16,20] with regard to the coordination spheres, valences, and ionic radii. Ligand lattice stretching modes are reflected by rather broad bands (FarIR: 423, 286 cm$^{-1}$). The MIR and Raman spectra additionally present vibrational bands of the benzotriazolate, diaminobenzene, and ammonia ligands, which are shifted by about ten wavenumbers relative to those of the free ligand, or show band splitting as a result of coordination to the metal centers and thus weakening of the C–N and C–C bonds. The ν(N–H) vibrational bands[41] of the amine ligands are also observed [**1**, **2**: BtzH: 3430 and 3422 cm$^{-1}$, respectively; **3**, **4**, **5**: Ph(NH$_2$)$_2$: 3360 and 3339, 3362 and 3333, 3363 and 3342 cm$^{-1}$, respectively; **6**: BtzH and $NH_3$: 3390 and 3367 cm$^{-1}$, respectively] and are confirmed by the MIR spectrum of the free ligands.[34] Furthermore, **3** shows a strong and broad band at 1975 cm$^{-1}$ in the Raman spectrum according to the luminescence $^4I_{11/2}\rightarrow{}^4I_{9/2}$ for Nd$^{III}$[42] resulting from the frequency of the Nd-YAG laser of the IR-/Raman spectrometer.

The crystal structures of **1**–**6** consist of structurally related one-dimensional coordination polymers. Benzotriazolate ligands connect the metal centers and are thus vital for the formation of the strands. The coordination spheres of the 4f ions contain N atoms only of both amido and amino character. No π coordination is observed. As the

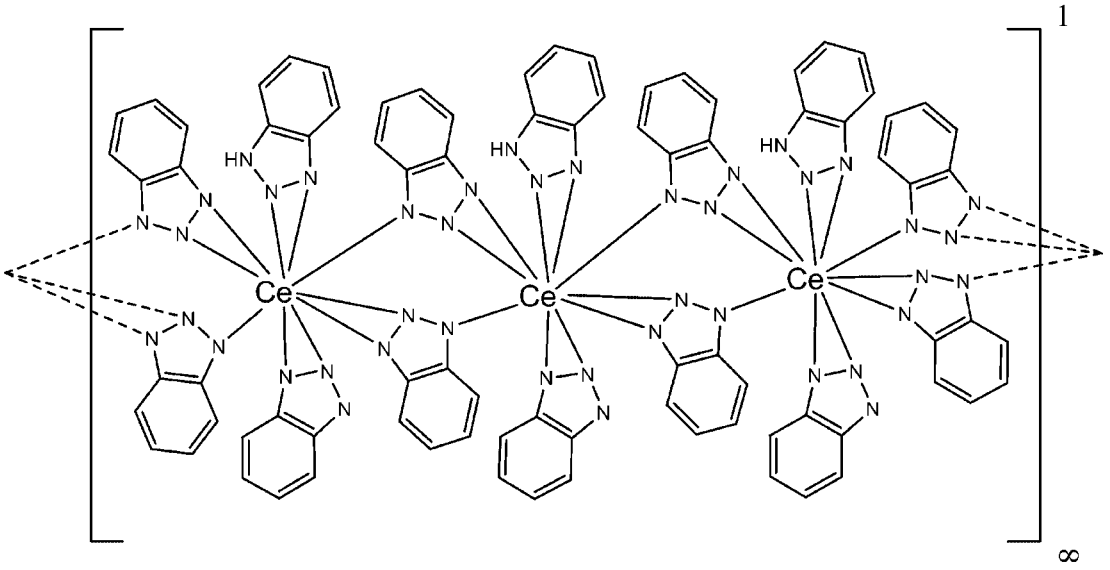


Scheme 1. μ-η$^2$;η$^1$- and η$^2$ coordination of the benzotriazolate and 1*H*-benzotriazole ligands in the coordination polymer $^1_\infty$[Ce(Btz)$_3$(BtzH)] (**1**). Pr$^{III}$ exhibits an identical coordination in **2**.

 © 2006 Wiley-VCH Verlag GmbH & Co. KGaA, Weinheim 

structure analyses of **1** and **2** show, four $Btz^-$ anions link a cerium or praseodymium center with two adjacent metal cations in a $\mu$-$\eta^2$;$\eta^1$ manner such that two nitrogen atoms of one ligand coordinate to one metal ion and the third to the next metal center (see Scheme 1). Another $Btz^-$ anion and the coordinated BtzH molecule do not participate in the polymer backbone and are coordinated to a single cerium atom in an $\eta^2$ fashion; a hydrogen bond between the two noncoordinating N atoms is present. The $\eta^2$ coordination shows a slight asymmetry of 5–10 pm in the corresponding Ln–N distances of **1** and **2**. Despite an octahedral arrangement of ligands the C.N. is ten for each Ce/Pr. Figure 2 depicts a part of the polymeric structure of $^1_\infty$[Ln(Btz)$_3$(BtzH)] [Ln = Ce (**1**) and Pr (**2**)] and Figure 3 the unit cell of the crystal structure.

The backbone of polymer **3** is identical to that of **1**, the difference stems from coordinated 1,2-diaminobenzene ligands that replace the benzotriazole molecules (see Scheme 2). The diaminobenzene ligands coordinate in a $\eta^1$;$\eta^1$ manner, with no hydrogen bond to the noncoordinating N atom of the third benzotriazolate equivalent. Replacement of the BtzH ligand in **1** and **2** with a Ph(NH$_2$)$_2$ ligand neither changes the C.N. nor the coordination polyhedron for **3**–**5**. Figure 4 displays part of the polymeric structure of $^1_\infty$[Nd(Btz)$_3${Ph(NH$_2$)$_2$}] (**3**) and Figure 5 the unit cell of the crystal structure.

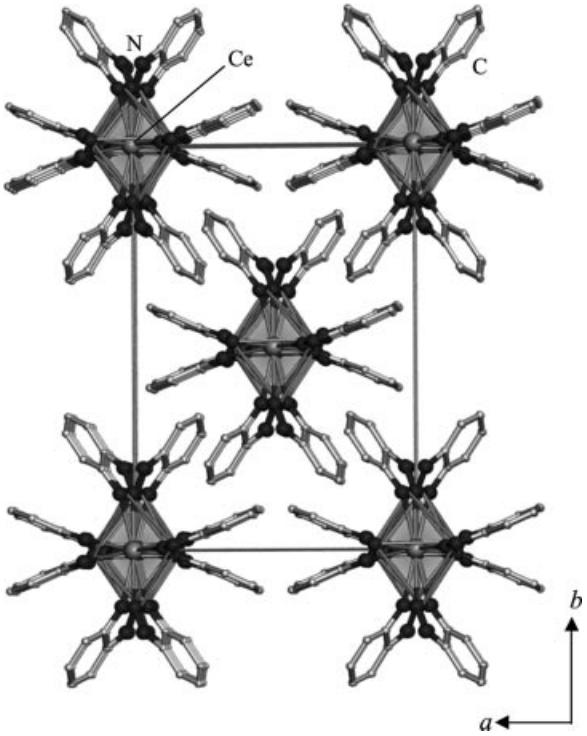


Figure 3. The crystal structure of $^1_\infty$[Ce(Btz)$_3$(BtzH)] (**1**) with a view along the chain direction [001]. N–N connection lines mark only the coordination polyhedra and not bonds.

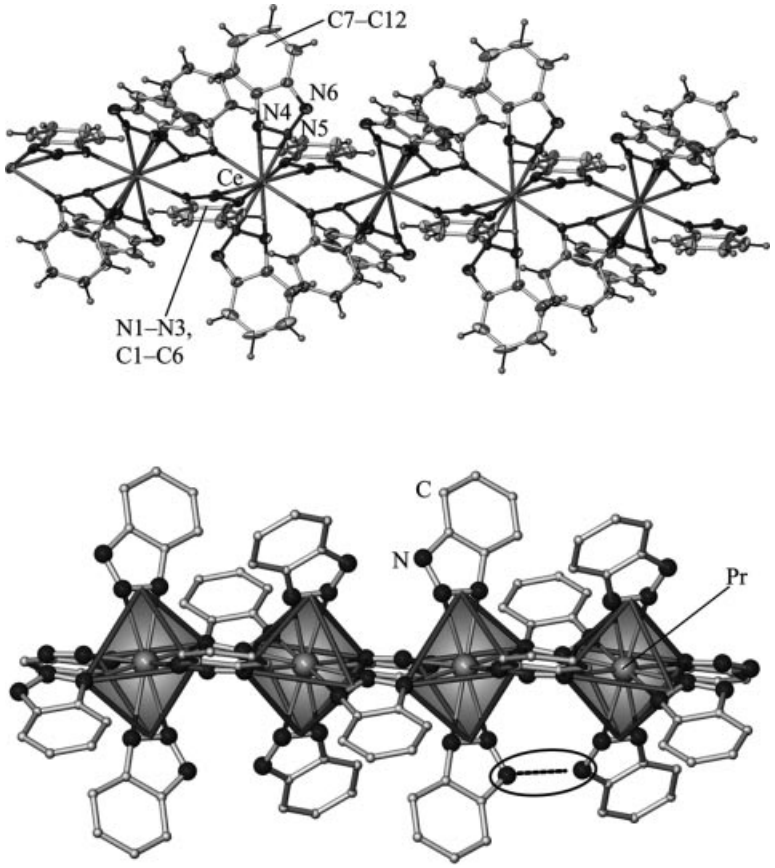


Figure 2. Section of the polymeric structure of $^1_\infty$[Ln(Btz)$_3$(BtzH)], Ln = Ce (**1**, top) and Pr (**2**, bottom). The hydrogen bond between the terminal $Btz^-$ and BtzH ligands is represented by a dotted line. In this, and the following Figures, the thermal ellipsoids are scaled to a probability density level of the atoms of 50%. N–N connection lines mark only the coordination polyhedra and do not represent bonds. Metal atoms are depicted by large mid grey balls, nitrogen atoms by dark grey balls, and carbon atoms by small light grey balls.

 © 2006 Wiley-VCH Verlag GmbH & Co. KGaA, Weinheim 

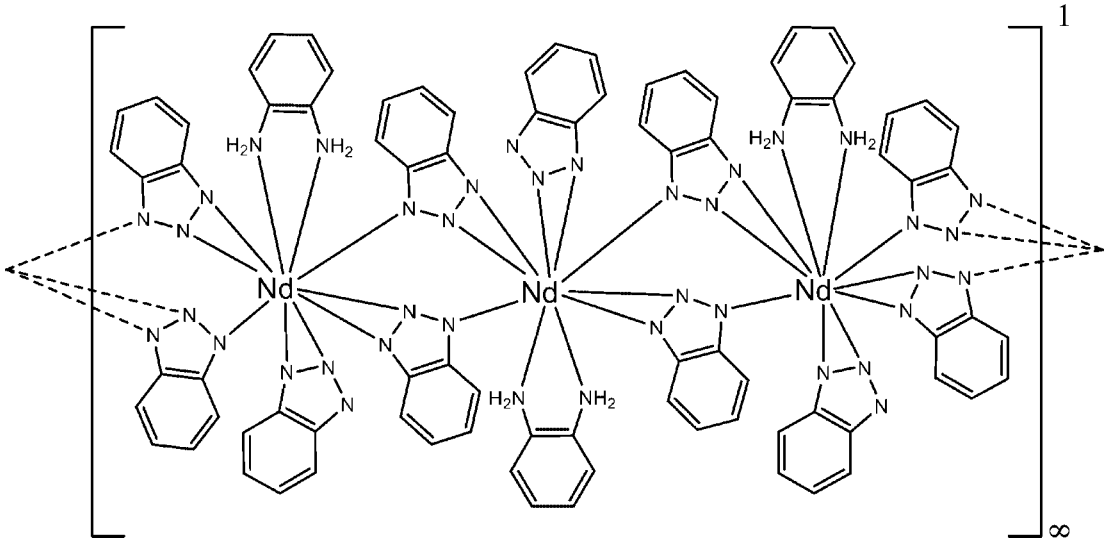


Scheme 2. μ-$\eta^2$;$\eta^1$- and $\eta^1$;$\eta^1$ coordination of the benzotriazolate and 1,2-diaminobenzene ligands in the coordination polymer $^1_\infty$[Nd(Btz)$_3${Ph(NH$_2$)$_2$}] (**3**). $Tb^{III}$ and $Yb^{III}$ exhibit identical polymers in **4** and **5**.

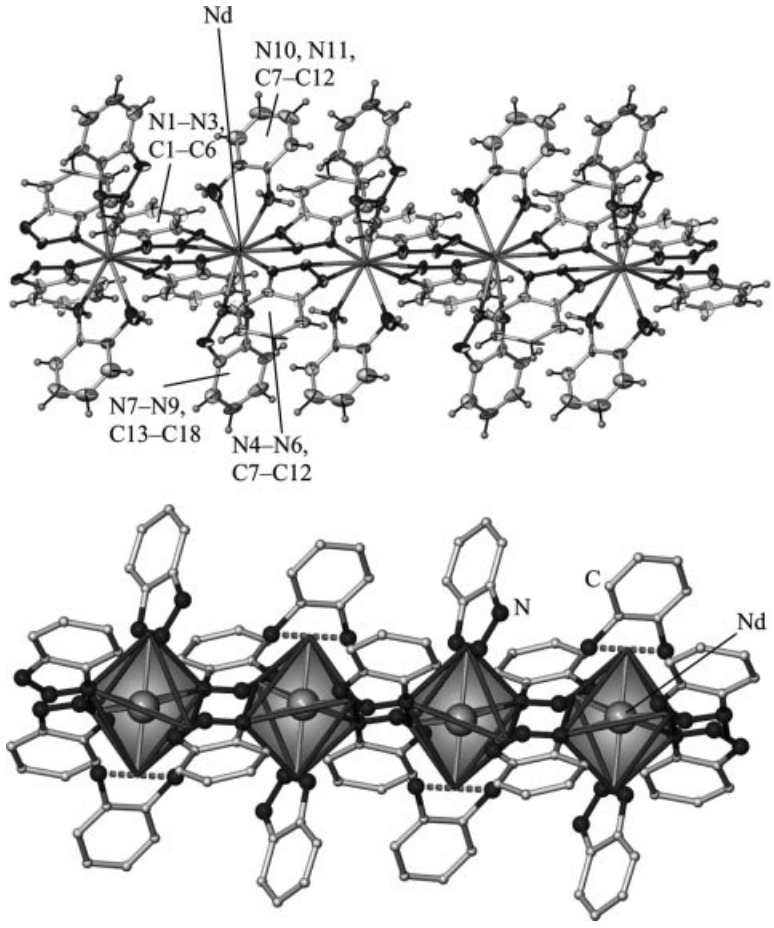


Figure 4. Section of the polymeric structure of $^1_\infty$[Nd(Btz)$_3${Ph(NH$_2$)$_2$}] (**3**) displaying thermal ellipsoids (top) and coordination polyhedra (bottom).

Polymer **6** differs from **1** and **3** in its backbone and additional ligands. The holmium ions are arranged in a triangular fashion that resembles a ladder-like structure (see Figure 6). No Ho–Ho bonds are observed in the triangles as benzotriazolate ligands again link the metal centers to build up a polymeric strand (see Scheme 3). Benzotriazole and ammonia molecules complete the coordination spheres of Ho. In contrast to **1**–**5**, the holmium polymer **6** exhibits

 © 2006 Wiley-VCH Verlag GmbH & Co. KGaA, Weinheim 

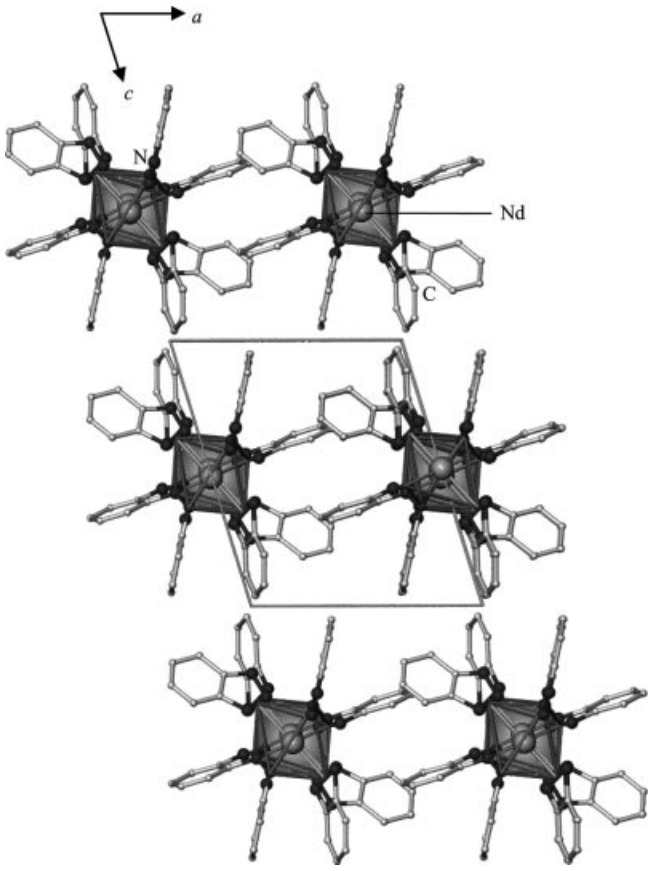


Figure 5. The crystal structure of $^{1}_{\infty}$[Nd(Btz)$_3${Ph(NH$_2$)$_2$}] (**3**) with a view along the chain direction [010]. The relation between the structures of the types $^{1}_{\infty}$[Ln(Btz)$_3${Ph(NH$_2$)$_2$}], Ln = Nd (**3**), Tb (**4**), Yb (**5**), and $^{1}_{\infty}$[Ln(Btz)$_3$(BtzH)], Ln = Ce (**1**), Pr (**2**), is evident.

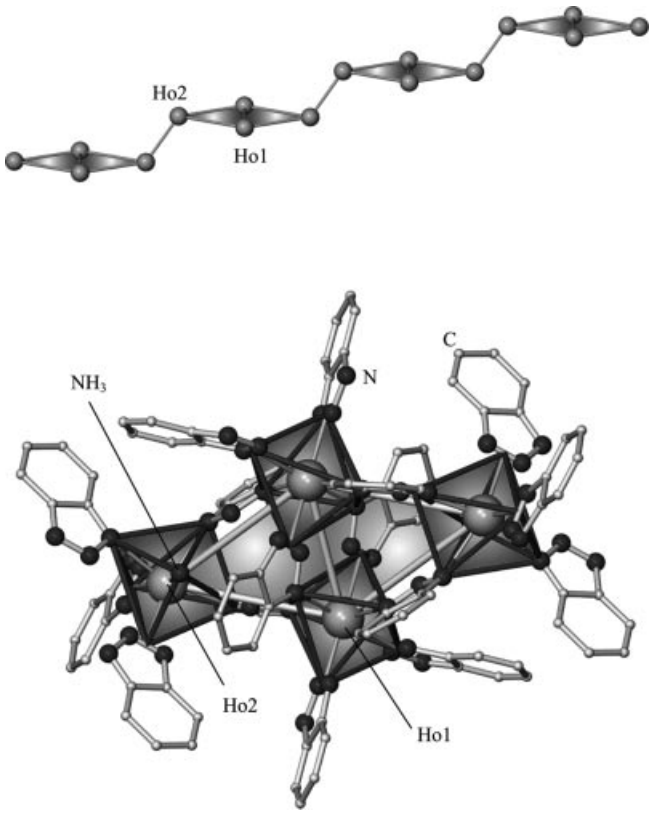


Figure 6. The arrangement of Ho atoms in **6** (top). Triangular units are combined to di-triangles with a common edge and form a ladder-like arrangement with no Ln–Ln bonds. The depiction at the bottom displays the ligands linking the metals to form double triangles. No triangular arrangement is observed for **1**–**5**.

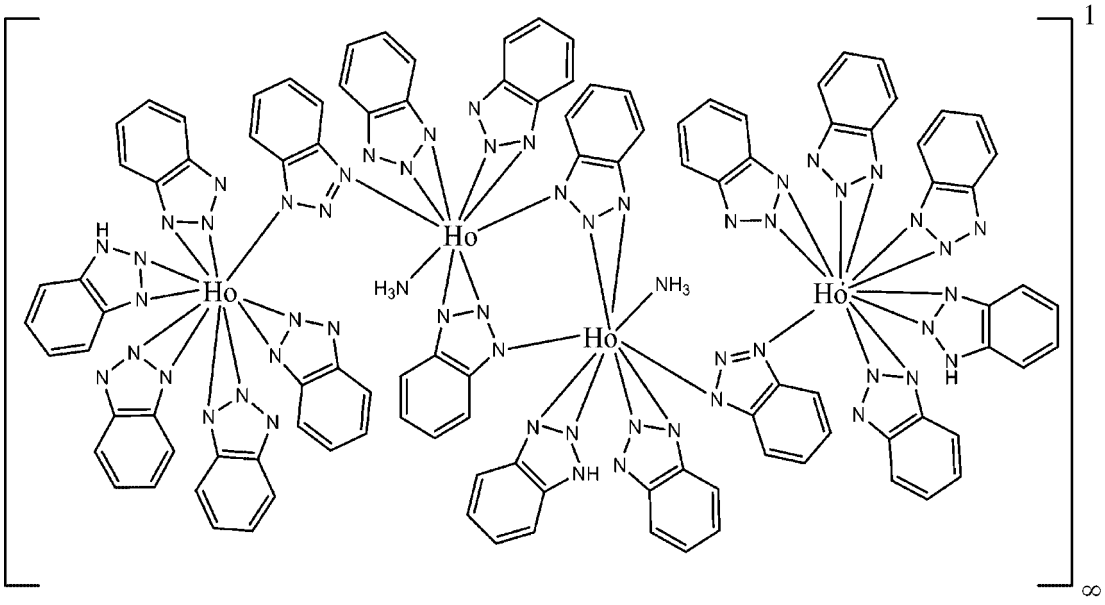


Scheme 3. μ-$\eta^2$:$\eta^1$-, $\eta^2$- and $\eta^1$:$\eta^1$ coordination of the benzotriazolate and 1*H*-benzotriazole ligands as well as the $\eta^1$ coordination of ammonia in polymeric $^{1}_{\infty}$[Ho$_2$(Btz)$_6$(BtzH)(NH$_3$)] (**6**).

 © 2006 Wiley-VCH Verlag GmbH & Co. KGaA, Weinheim 

a C.N. of 9 with two different holmium ions. Ho1 is surrounded by four μ-$\eta^2$;$\eta^1$ $Btz^-$ ligands, one $\eta^1$;$\eta^1$ coordinated BtzH molecule, and one μ-($\eta^1$;$\eta^1$) $Btz^-$ anion that is linked to Ho2. Ho2 is also coordinated by four μ-$\eta^2$;$\eta^1$ $Btz^-$ ligands, one μ-($\eta^1$;$\eta^1$) $Btz^-$ anion that is linked to Ho1, and one $\eta^1$-coordinated $NH_3$ molecule. Thus, one of the benzotriazolate ligands does not coordinate with its center nitrogen atom to any Ho atom. Two of the $\eta^2$-coordinated $Btz^-$ anions show a strong asymmetry of >25 pm in their Ho–N distances, so that this coordination mode can also be referred to as μ-$\eta^1$;$\eta^1$;$\eta^1$. Figure 7 displays part of the polymeric structure of $^1_\infty[Ho_2(Btz)_6(BtzH)(NH_3)]$ (**6**) and Figure 8 the unit cell of the crystal structure.

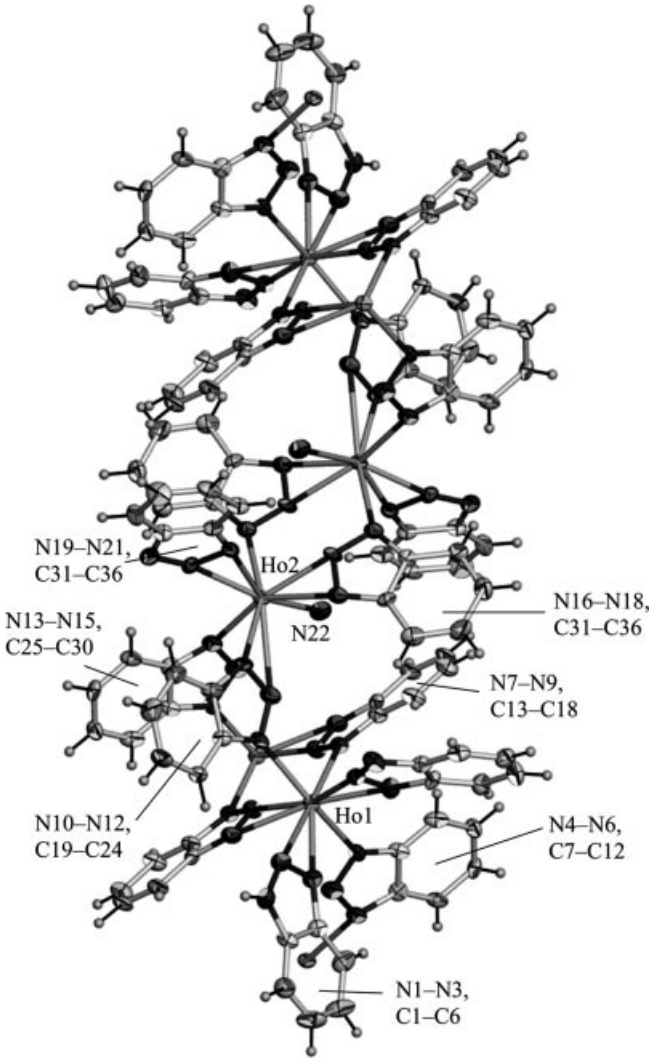


Figure 7. Part of the polymeric structure of $^1_\infty[Ho_2(Btz)_6(BtzH)(NH_3)]$ (**6**) displaying thermal ellipsoids (top) and coordination polyhedra (bottom).

The contraction of the radii of the lanthanide ions[43] influences both the C.N. as well as the Ln–N distances and is observed throughout the course of the products. In general, the C.N.s are high also for lanthanides, which mainly derives from the $\eta^1$;$\eta^1$ mode of the coordinated neighboring N atoms of the ligands. All rare earth ions are trivalent in

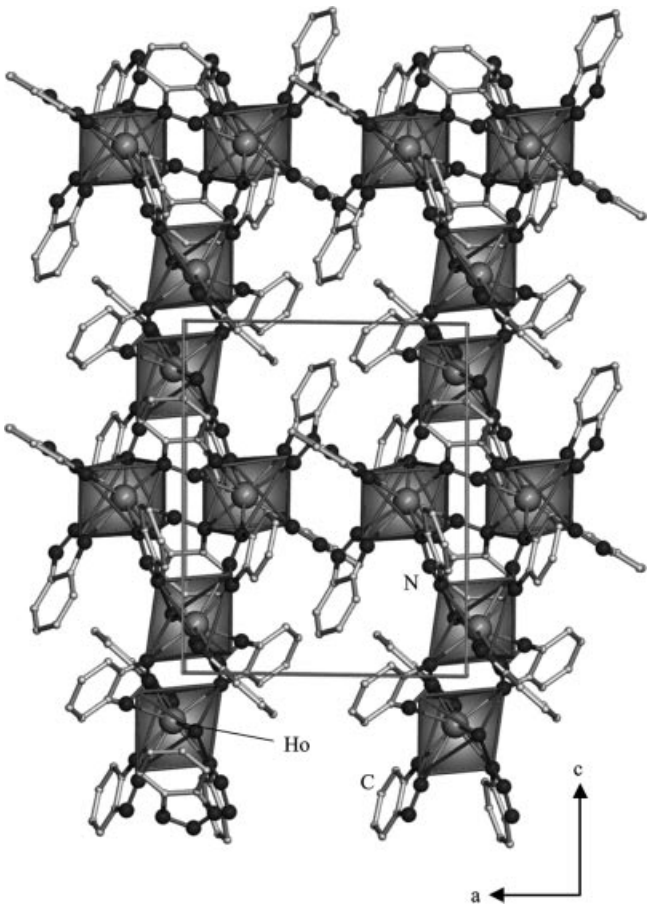


Figure 8. The crystal structure of $^1_\infty[Ho_2(Btz)_6(BtzH)(NH_3)]$ (**6**) with a view on the chains along [010].

**1**–**6**. The Ln–N distances range from 232.6(9)–253(1) pm for Ho–N amide and amine distances, to 248(2)–264(2) pm for Nd, through to 251.6(9)–265.0(9) pm for Ce. These distances match well with those of other trivalent lanthanide amido and amino complexes in which the metal ions are linked such as dipyridylamides $[Ln_2(Dpa)_6]$, $Dpa^-$ = $(C_5H_4N)_2N^-$, with 236–255 pm for $Ho^{III}$, 244–268 pm for $Nd^{III}$, and 247–273 pm for $Ce^{III}$.[38] For a detailed selection of interatomic distances and angles see Table 1. Deviations of the coordination polyhedron from a regular octahedron are less than five degrees for all metal ions.

Powder diffraction of $^1_\infty[Tb(Btz)_3\{Ph(NH_2)_2\}]$ (**4**) and $^1_\infty[Yb(Btz)_3\{Ph(NH_2)_2\}]$ (**5**) shows that the compounds crystallize in a manner isotypic to that of $^1_\infty[Nd(Btz)_3\{Ph(NH_2)_2\}]$ (**3**). Thus, the description of the crystal structure in the space group $P\bar{1}$ is analogous to that of **3**. According to the larger ionic radius of $Nd^{III}$ than those of $Tb^{III}$ and $Yb^{III}$,[43] the unit cells of **4** and **5** are smaller than that of **3** {**3**: 1314.2(2), **4**: 1258.2(3), **5**: 1232(1) [$\times 10^6$ pm$^3$]}.

$^1_\infty[Tb(Btz)_3\{Ph(NH_2)_2\}]$ (**4**) exhibits a strong green emission when exposed to UV light. The luminescence can be identified with the emission processes of the $Tb^{3+}$ ions $^5D_4 \rightarrow {}^7F_4$ at 590 nm, $^5D_4 \rightarrow {}^7F_5$ at 545 nm, and $^5D_4 \rightarrow {}^7F_6$ at 490 nm.[44,45] Though **4** contains 100% Tb and is not a doped compound, no quenching of the luminescence by

 © 2006 Wiley-VCH Verlag GmbH & Co. KGaA, Weinheim 

Table 1. Selected distances and angles for $^1_\infty$[Ce(Btz)$_3$(BtzH)] (**1**), $^1_\infty$[Pr(Btz)$_3$(BtzH)] (**2**), $^1_\infty$[Nd(Btz)$_3${Ph(NH$_2$)$_2$}] (**3**), and $^1_\infty$[Ho$_2$(Btz)$_6$(BtzH)(NH$_3$)] (**6**). Deviations are given in brackets.

| $^1_\infty$[Ce(Btz)$_3$(BtzH)] (**1**) | | $^1_\infty$[Pr(Btz)$_3$(BtzH)] (**2**) | |
|---|---|---|---|
| Atoms | Distance [pm] | Atoms | Distance [pm] |
| Ce–N1 | 259(1) | Pr–N1 | 256.2(6) |
| Ce–N2 | 252.1(9) | Pr–N2 | 251.7(5) |
| Ce–N3[a] | 265.3(9) | Pr–N3[a] | 265.6(5) |
| Ce–N4 | 259.1(8) | Pr–N4 | 258.1(8) |
| Ce–N5 | 264.1(7) | Pr–N5 | 262.5(7) |
| Ce–Ce[a] | 535.8(1) | Pr–Pr[a] | 534.9(1) |
| N–C(range) | 136(2)–138(2) | N–C(range) | 135.3(9)–137.1(9) |
| N–N(range) | 132(1)–135(1) | N–N(range) | 132.8(8)–133.6(8) |
| Atoms | Angles [°] | Atoms | Angles [°] |
| N1–Ce–N2 | 30.2(3) | N1–Pr–N2 | 30.5(2) |
| N1–Ce–N3 | 102.1(3) | N1–Pr–N3 | 102.0(2) |
| N2–Ce–N4 | 86.5(4) | N2–Pr–N4 | 86.6(3) |
| N2–Ce–N5 | 102.4(3) | N2–Pr–N5 | 103.6(3) |
| N3–Ce–N2 | 74.0(3) | N3–Pr–N2 | 73.7(2) |
| N3–Ce–N5 | 97.4(3) | N3–Pr–N5 | 98.0(3) |
| N4–Ce–N5 | 29.1(3) | N4–Pr–N5 | 29.5(2) |

| $^1_\infty$[Nd(Btz)$_3${Ph(NH$_2$)$_2$}] (**3**) | | $^1_\infty$[Ho$_2$(Btz)$_6$(BtzH)(NH$_3$)] (**6**) | |
|---|---|---|---|
| Atoms | Distance [pm] | Atoms | Distance [pm] |
| Nd–N1 | 262(2) | Ho1–N1 | 244(1) |
| Nd–N2 | 250(2) | Ho1–N2 | 279.5(8) |
| Nd–N3[b] | 259(2) | Ho1–N4 | 245(1) |
| Nd–N4 | 258(2) | Ho1–N5 | 236.5(9) |
| Nd–N5[c] | 250(2) | Ho1–N7 | 244.5(9) |
| Nd–N6[c] | 257(2) | Ho1–N13 | 244.3(9) |
| Nd–N8 | 248(2) | Ho1–N14[d] | 236.5(9) |
| Nd–N9 | 255(2) | Ho1–N15[d] | 253(1) |
| Nd–N10 | 261(2) | Ho1–N18[d] | 244.8(9) |
| Nd–N11 | 264(2) | Ho2–N8 | 283(1) |
| N–C(range) | 136(2)–145(3) | Ho2–N9 | 234.4(9) |
| N–N(range) | 132(2)–136(2) | Ho2–N10 | 232.6(9) |
| Nd–Nd[b] | 521.6(1) | Ho2–N11 | 242.4(9) |
| Nd–Nd[c] | 514.8(1) | Ho2–N16 | 241(1) |
| | | Ho2–N19 | 249(1) |
| | | Ho2–N20 | 241.2(9) |
| | | Ho2–N21[e] | 247.4(9) |
| | | Ho2–N22 | 245.6(9) |
| | | Ho1–Ho2 | 591.5(1) |
| | | Ho1–Ho1[d] | 493.6(1) |
| | | Ho2–Ho2[e] | 478.5(1) |
| | | N–C(range) | 134(2)–138(2) |
| | | N–N(range) | 132(1)–136(2) |
| Atoms | Angles [°] | Atoms | Angles [°] |
| N1–Nd–N2 | 30.1(4) | N1–Ho1–N4 | 86.7(4) |
| N1–Nd–N3 | 107.2(5) | N2–Ho1–N7 | 88.2(3) |
| N2–Nd–N4 | 101.6(5) | N5–Ho1–N13 | 99.8(3) |
| N5–Nd–N6 | 30.1(5) | N9–Ho2–N10 | 88.0(4) |
| N4–Nd–N5 | 78.5(6) | N11–Ho2–N16 | 89.6(3) |
| N8–Nd–N9 | 30.2(4) | N8–Ho2–N9 | 27.7(3) |
| N10–Nd–N11 | 63.3(5) | N19–Ho2–N22 | 78.8(4) |

[a] $-x$, $y$, $-z + 1/2$. [b] $-x + 1$, $-y$, $-z + 1$. [c] $-x + 2$, $-y$, $-z + 1$. [d] $-x + 2$, $-y + 1$, $-z + 1$. [e] $-x + 2$, $-y + 1$, $-z$.

concentration is observed. The emission spectrum of **4**, and the absorption spectra of **4** (room temperature and 120 K) and 1*H*-benzotriazole (room temperature) can be seen in Figure 9. A comparison of the absorption spectra of the free ligand with that of polymer **4** shows excitation of the ligand into the Soret band in the UV region. Benzotriazole and its derivatives are commercially used as UV absorbers.[46,47] We assume an energy transfer from the ligand to the metal ions as the luminescence is present independent of whether the excited states of Tb or the ligand are populated; additionally both absorption maxima of $^1_\infty$[Tb(Btz)$_3${Ph(NH$_2$)$_2$}] (**4**) at 310 and 205 nm cannot be identified with $Tb^{III}$ absorptions. We chose 310 nm as the excitation wavelength for the emission spectrum of **4**. Furthermore, an energy back-transfer from the metal centers to the ligand is possible, which would lead to quenching. Presently, we cannot explain why no quenching by concentration is observed. High resolution excitation spectra of **4** as well as of BtzH, emission efficiency, and decay time measurements are planned to further investigate the luminescence properties of $^1_\infty$[Tb(Btz)$_3${Ph(NH$_2$)$_2$}].

## Conclusions

The formation of **1**–**6** shows that triazolates can also be utilized for high-temperature oxidations of rare earth metals with amines. Though the release of $N_2$ from BtzH is exothermic, coordination polymers of the 4f elements can be obtained below the decomposition temperature. Depending on the temperature and lanthanide, three chemically different polymers can be obtained. With the largest lanthanide ions and the lowest melt temperatures, $^1_\infty$[Ln(Btz)$_3$(BtzH)] is formed up to praseodymium. $^1_\infty$[Ln(Btz)$_3${Ph(NH$_2$)$_2$}] is formed from neodymium to ytterbium. $^1_\infty$[Ln$_2$(Btz)$_6$(BtzH)(NH$_3$)] has so far been isolated for holmium only, and at the highest reaction temperatures investigated. Compounds **1**–**6** are the first triazolates of the lanthanides. Partial decomposition of the benzotriazole ligands accompanies the syntheses and yields 1,2-diaminobenzene as well as ammonia, which are both incorporated in the coordination polymers of the heavier 4f elements. Thermal analyses of **1**, **3**, and **6** lead to the assumption that homoleptic polymers [Ln(Btz)$_3$] are formed upon release of the coordinated amine ligands, though these polymers could not be isolated as single crystalline material so far. The coordination polymers also exhibit aspects of materials science such as a green luminescence {$^5D_4 \rightarrow {}^7F_J$, $J$ = 4–6 for $^1_\infty$[Tb(Btz)$_3${Ph(NH$_2$)$_2$}] (**4**)} without quenching by concentration, and an energy transfer from the ligand to the $Tb^{3+}$ ions.

## Experimental Section

All reactions were carried out under argon using a dry box and standard Schlenk and ampoule techniques because of the air- and moisture-sensitivity of **1**–**6**. The lanthanide metals (ChemPur, STREM, 99.9%) and 1*H*-benzotriazole (ACROS, 99%) were used

 © 2006 Wiley-VCH Verlag GmbH & Co. KGaA, Weinheim 

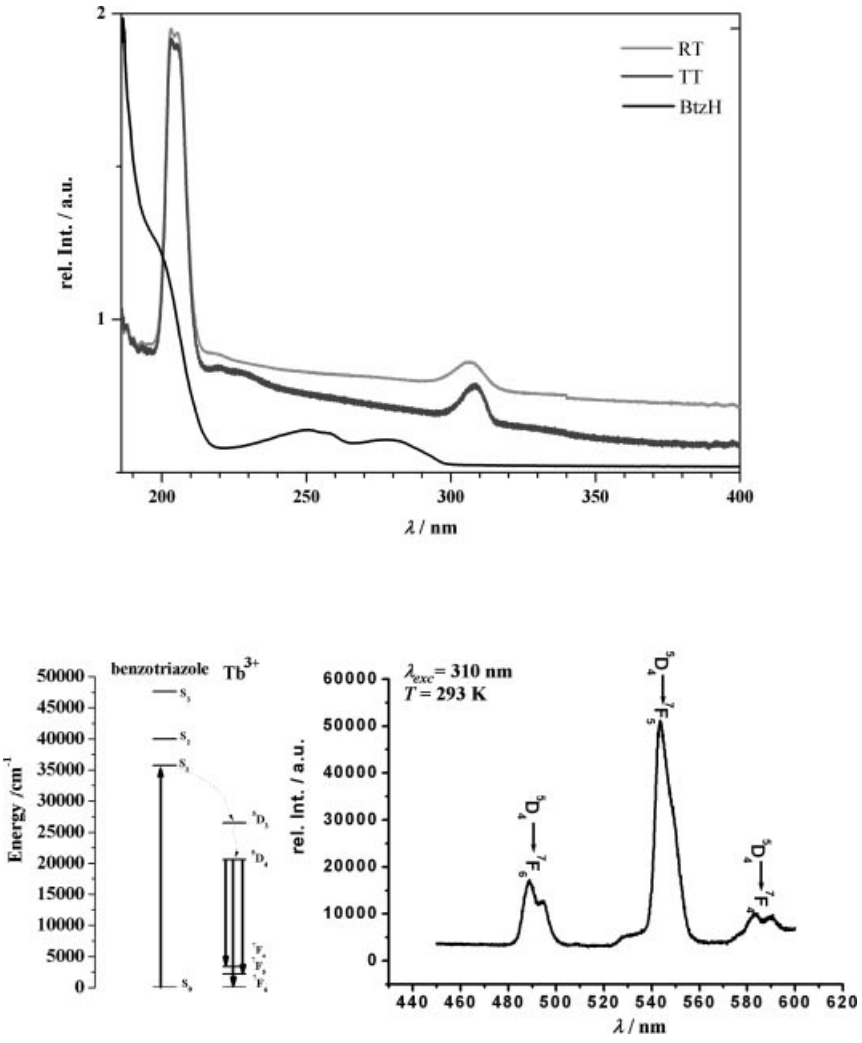


Figure 9. The absorption spectra of $^{1}_{\infty}$[Tb(Btz)$_3${Ph(NH$_2$)$_2$}] (**4**) at 293 and 120 K and that of 1*H*-benzotriazole at 293 K (top), and the emission spectrum of **4** with an excitation wavelength of $\lambda$ = 310 nm (bottom).

as purchased. Mercury (Fluka, 99.9%) was used for activation of the metals. The IR spectra were recorded with a BRUKER FTIR-IS66V-S spectrometer, the Raman spectra with a BRUKER FRA 106-S spectrometer. For MIR investigations KBr pellets and for FIR measurements PE pellets were used under vacuum. The absorption spectroscopy was carried out at 293 and 120 K with a VARIAN Carey 05E (BRUKER) spectrometer on samples sealed under argon between $CaF_2$ windows. Emission spectroscopy was carried out with a SPEX-Flurolog DM3000F fluorescence spectrometer (JOBIN YVON GmbH) on samples sealed under vacuum in quartz tubes. The thermal decompositions of **1**, **3**, and **6** were studied using simultaneous DTA/TG (NETZSCH STA-409) on samples that were previously purified of excess BtzH and pyrrole by evaporation (16.1 mg of the Ce product **1**, 18.5 mg of the Nd product **3**, and 12.0 mg of the Ho product **6**). The samples were heated from 20–700 °C at a heating rate of 10 °C/min in a constant Ar flow of 60 mL/ min.

**$^{1}_{\infty}$[Ce(Btz)$_3$(BtzH)] (1):** Cerium metal (70 mg, $0.5\times10^{-3}$ mol), the amine 1*H*-benzotriazole (BtzH, $C_6H_4N_2NH$; 179 mg, $1.5\times10^{-3}$ mol), and Hg (20 mg) were sealed in an evacuated DURAN glass ampoule. The reaction mixture was heated over 5 h to 100 °C and over another 80 h to 140 °C. The temperature was held constant for 48 h. The melt was cooled down to 90 °C over 150 h and then to room temperature over 14 h. Except for a slight excess of Ce metal and BtzH, the reaction reached completion to give highly reflective colorless crystals of **1** (0.2–0.3 mm in size). Yield: 275 mg (91%). MIR: 3430 (m), 3343 (m), 3260 (m), 3076 (m), 1577 (m), 1502 (m), 1483 (m), 1444 (m), 1388 (w), 1280 (s), 1259 (m), 1208 (m), 1188 (s), 1143 (s), 1084 (m), 991 (m), 937 (m), 914 (s), 781 (vs), 753 (vssh), 744 (vs), 694 (m), 633 (s) cm$^{-1}$. FarIR: 551 (s), 438 (m), 420 (w), 286 (w), 244 (m), 200 (s), 183 (m), 169 (s), 101 (w) cm$^{-1}$. Raman: 3307 (w), 3247 (s), 3078 (w), 1575 (w), 1387 (m), 1283 (w), 1128 (w), 1020 (m), 782 (m), 631 (s), 123 (s), 100 (msh) cm$^{-1}$. $CeC_{24}H_{17}N_{12}$ (613.36): calcd. C 47.28, H 2.79, N 27.55; found C 47.8, H 3.0, N 27.6.

**$^{1}_{\infty}$[Pr(Btz)$_3$(BtzH)] (2):** Praseodymium metal (71 mg, $0.5\times10^{-3}$ mol), the amine 1*H*-benzotriazole (BtzH, $C_6H_4N_2NH$; 179 mg, $1.5\times10^{-3}$ mol), and Hg (20 mg) were sealed in an evacuated DURAN glass ampoule. The reaction mixture was heated over 18 h to 135 °C. The temperature was held constant for 672 h. The melt was cooled down to room temperature over 18 h. Except for a slight excess of Pr metal and BtzH, the reaction reached completion to give highly reflective greenish yellow crystals of **2** (0.05–0.15 mm in size). Yield: 260 mg (84%). MIR: 3422 (m), 3341 (m), 3135 (s), 1577 (w), 1502 (w), 1484 (w), 1442 (m), 1401 (vs), 1281 (m), 1259 (w), 1208 (w), 1175 (s), 1151 (m), 1085 (w), 1008 (w), 988 (w), 962

 © 2006 Wiley-VCH Verlag GmbH & Co. KGaA, Weinheim 

(w), 914 (m), 781 (s), 744 (vs), 694 (w), 633 (m) $cm^{-1}$. FarIR: 550 (m), 433 (w), 422 (w), 290 (w), 242 (w), 195 (m), 179 (m), 171 (m), 101 (w) $cm^{-1}$. Raman: 3216 (w), 3066 (m), 1574 (m), 1485 (w), 1442 (w), 1386 (s), 1283 (m), 1127 (m), 1020 (s), 783 (s), 633 (m), 551 (w), 120 (vssh), 110 (vs) $cm^{-1}$. $C_{24}H_{17}N_{12}Pr$ (614.24): calcd. C 46.91, H 2.77, N 27.34; found C 47.0, H 2.9, N 27.3.

**$^1_\infty$[Nd(Btz)$_3${Ph(NH$_2$)$_2$}] (3):** Neodymium metal (72 mg, $5\times10^{-4}$ mol), pyrrole (503 mg, $7.5\times10^{-3}$ mol), the amine 1*H*-benzotriazole (BtzH, $C_6H_4N_2NH$; 179 mg, $1.5\times10^{-3}$ mol) together with Hg (20 mg) were frozen with liquid nitrogen, degassed, and sealed in an evacuated DURAN glass ampoule. The reaction mixture was heated over 4 h to 100 °C and over another 100 h to 150 °C. The temperature was held constant for 48 h. The reaction was cooled to 90 °C over 200 h and down to room temperature over 13 h. Except for the liquid pyrrole, the reaction reached completion to give reflective violet crystals of **3** (0.15–0.2 mm in size). Yield: 285 mg (94%). MIR: 3360 (m), 3338 (m), 3138 (s), 1593 (w), 1576 (m), 1484 (m), 1443 (m), 1400 (s), 1283 (m), 1259 (m), 1181 (s), 1150 (s), 1082 (m), 1010 (w), 989 (w), 942 (w), 914 (m), 848 (w), 781 (vs), 747 (vs), 696 (m), 633 (m) $cm^{-1}$. FarIR: 550 (m), 433 (w), 277 (w), 249 (w), 195 (m), 178 (m), 147 (w) $cm^{-1}$. Raman: 3067 (m), 1975 (vs), 1568 (w), 1386 (m), 1282 (w), 1127 (m), 1020 (m), 782 (m), 631 (w), 551 (w), 150 (vssh), 124 (vs) $cm^{-1}$. $C_{24}H_{20}N_{11}Nd$ (606.48): calcd. C 47.47, H 3.30, N 25.38; found C 48.0, H 3.3, N 25.5.

**$^1_\infty$[Tb(Btz)$_3${Ph(NH$_2$)$_2$}] (4):** Terbium metal (80 mg, $5\times10^{-4}$ mol), the amine 1*H*-benzotriazole (BtzH, $C_6H_4N_2NH$; 179 mg, $1.5\times10^{-3}$ mol) together with Hg (20 mg) were sealed in an evacuated DURAN glass ampoule. The reaction mixture was heated over 4 h to 100 °C and over another 120 h to 160 °C. The temperature was held constant for 240 h. The melt was cooled to 90 °C over 140 h and down to room temperature over 13 h. Except for a slight excess of the reactants, the reaction reached completion to give a reflective colorless microcrystalline material of **4**. Yield: 265 mg (85%). MIR: 3333 (w), 3146 (m), 3069 (m), 1593 (w), 1577 (m), 1487 (m), 1443 (m), 1400 (m), 1284 (m), 1259 (m), 1183 (s), 1167 (s), 1141 (m), 1008 (w), 990 (m), 942 (w), 915 (m), 781 (vs), 742 (vs), 694 (m), 634 (m) $cm^{-1}$. FarIR: 550 (s), 432 (m), 279 (w), 247 (w), 193 (m), 175 (m), 146 (w) $cm^{-1}$. Raman: 3066 (s), 1567 (m), 1442 (m), 1387 (s), 1285 (m), 1172 (w), 1127 (m), 1022 (s), 784 (s), 631 (m), 432 (w), 150 (mssh), 125 (vssh), 110 (vs) $cm^{-1}$. $C_{24}H_{20}N_{11}Tb$ (621.16): calcd. C 46.38, H 3.22, N 24.78; found C 46.0, H 2.8, N 25.1.

**$^1_\infty$[Yb(Btz)$_3${Ph(NH$_2$)$_2$}] (5):** Ytterbium metal (87 mg, $5\times10^{-4}$ mol), the amine 1*H*-benzotriazole (BtzH, $C_6H_4N_2NH$; 179 mg, $1.5\times10^{-3}$ mol), and Hg (20 mg) were sealed in an evacuated DURAN glass ampoule. The reaction mixture was heated over 4 h to 100 °C and over another 168 h to 150 °C. The temperature was held constant for 48 h. The melt was cooled to 90 °C over 200 h and down to room temperature over 13 h. Except for a slight excess of the reactants, the reaction gave reflective colorless microcrystalline material of **5** as well as an unknown, poorly crystalline, red material in a ratio of 4:1. Yield: 178 mg (60%). MIR: 3393 (w), 3342 (w), 3141 (m), 3065 (m), 1613 (w), 1570 (m), 1501 (w), 1487 (m), 1443 (m), 1390 (m), 1285 (s), 1258 (m), 1205 (s), 1175 (s), 1140 (m), 1129 (w), 1076 (w), 990 (m), 914 (m), 782 (vs), 742 (vs), 694 (m), 633 (s) $cm^{-1}$. FarIR: 552 (m), 431 (m), 279 (w), 254 (m), 214 (msh), 173 (msh), 148 (m) $cm^{-1}$. $C_{24}H_{20}N_{11}Yb$ (635.28): calcd. C 45.35, H 3.15, N 24.23; found C 44.9, H 3.1, N 24.1.

**$^1_\infty$[Ho$_2$(Btz)$_6$(BtzH)(NH$_3$)] (6):** Holmium metal (83 mg, $5\times10^{-4}$ mol), the amine 1*H*-benzotriazole (BtzH, $C_6H_4N_2NH$; 179 mg, $1.5\times10^{-3}$ mol), and Hg (20 mg) were sealed in an evacuated DURAN glass ampoule. The reaction mixture was heated over 8 h to 100 °C and over another 200 h to 180 °C. The melt was cooled without a temperature plateau to 90 °C over 100 h and down to room temperature over 24 h. Except for a slight excess of the reactants, the reaction reached completion to give pink crystals of **6** (0.15–0.2 mm in size). Yield: 280 mg (95%). MIR: 3367 (w), 3150 (m), 3073 (m), 1593 (w), 1502 (w), 1485 (m), 1444 (m), 1387 (w), 1285 (m), 1261 (m), 1207 (s), 1184 (s), 1149 (m), 1129 (w), 1009 (w), 989 (m), 915 (m), 782 (vs), 744 (vs), 695 (m), 634 (m) $cm^{-1}$. FarIR: 551 (m), 430 (m), 422 (m), 409 (w), 286 (w), 249 (w), 230 (w), 210 (ssh), 191 (s), 176 (s), 158 (m), 146 (w) $cm^{-1}$. Raman: 3071 (s), 1570 (m), 1443 (w), 1386 (s), 1284 (m), 1172 (w), 1127 (m), 1040 (w), 1022 (s), 1000 (w), 784 (s), 633 (m), 123 (vs), 107 (vs) $cm^{-1}$. $C_{42}H_{32}Ho_2N_{22}$ (1174.58): calcd. C 42.94, H 2.75, N 26.23; found C 43.1, H 2.9, N 26.1.

**X-ray Crystal Structure Determination:** The data collections for single-crystal X-ray determinations of **1**, **2**, **3**, and **6** were carried out with an IPDS-II diffractometer (STOE). Structure solutions: SHELXS-86;[48] structure refinements: SHELXL-97.[49] Integrity of symmetry and geometry: PLATON.[50] All non-hydrogen atoms were refined anisotropically. The hydrogen atoms were placed in calculated positions and assigned to an isotropic displacement parameter of 1.2× the size of the isotropic displacement parameter of the referring carbon atom. The crystal of **3** used for data collection shows another small crystalline individual that grows on the surface (RECIPE).[51] The two individuals were separated (TWIN)[52] and refined individually.

The powder samples of compounds **4** and **5** were investigated in sealed capillaries with a Huber Image Foil Guniner Camera 670 diffractometer with a focused single crystal germanium monochromator (Mo-$K_{\alpha1}$ radiation, $\lambda$ = 0.709300 Å for **4** and Cu-$K_{\alpha1}$ radiation, $\lambda$ = 1.540598 Å for **5**). Because **4** and **5** decline in their grade of crystallinity upon grinding, samples of both compounds could be made only roughly homogeneous and were investigated in 0.3 mm capillaries, though this led to a higher background due to absorption phenomena of the rare earth atoms. The diffraction patterns of the terbium (**4**) and the ytterbium (**5**) compounds were compared with simulated diffractograms of **1**, **2**, **3**, and **6** and reveal that **3**, **4**, and **5** crystallize isotypically, whereas the powder patterns of **1**, **2**, and **6** are completely different. The cell constants of **4** were refined on 23 reflections, and the best possible resolution leads to a triclinic unit cell without unindexed lines and an average $\delta(2\theta)$ of 0.020° [$T$ = 293(2) K, $a$ = 1019.0(14) pm, $b$ = 1061.3(21), $c$ = 1248.1(21) pm, $\alpha$ = 72.27(13), $\beta$ = 84.12(14), $\gamma$ = 78.43(13)°, $V$ = 1258.3(24)$\times10^6$ pm$^3$]. The cell constants of **5** were refined on 20 reflections with the best possible resolution without unindexed lines and an average $\delta(2\theta)$ of 0.044° [$T$ = 293(2) K, $a$ = 1008.7(9) pm, $b$ = 1068.7(10), $c$ = 1214.6(11) pm, $V$ = 1232.2(12) $10^6$ pm$^3$].[53]

**Crystallographic Data for $CeC_{24}H_{17}N_{12}$ (1):** monoclinic, $C2/c$, $Z$ = 4, $T$ = 170(1) K, $a$ = 1385.2(3), $b$ = 1789.7(4), $c$ = 1071.5(3) pm, $\beta$ = 115.90(3)°, $V$ = 2389.7(5)·$10^6$ pm$^3$, $\mu$ = 19.5 $cm^{-1}$, Mo-$K_\alpha$, 4.56 ≤ 2 $\theta$ ≤ 59.30°, –6 ≤ $h$ ≤ 18, –24 ≤ $k$ ≤ 24, –12 ≤ $l$ ≤ 13, $F$(000) = 1212, $R_1$ = 0.0827 for 1523 reflections [$I > 2\sigma(I)$], $R_1$ = 0.1313 and $wR_2$ = 0.1670 for all 2333 unique reflections, GOOF on $F_2$ = 1.008.

**Crystallographic Data for $C_{24}H_{17}N_{12}Pr$ (2):** monoclinic, $C2/c$, $Z$ = 4, $T$ = 170(1) K, $a$ = 1382.1(3), $b$ = 1792.8(4), $c$ = 1069.8(3) pm, $\beta$ = 115.85(3)°, $V$ = 2385.5(5)·$10^6$ pm$^3$, $\mu$ = 20.1 $cm^{-1}$, Mo-$K_\alpha$, 3.98 ≤ 2 $\theta$ ≤ 59.26°, –19 ≤ $h$ ≤ 19, –24 ≤ $k$ ≤ 24, –14 ≤ $l$ ≤ 14, $F$(000) = 1216, $R_1$ = 0.0526 for 1781 reflections [$I > 2\sigma(I)$], $R_1$ = 0.1295 and $wR_2$ = 0.1121 for all 3309 unique reflections, GOOF on $F_2$ = 0.994.

**Crystallographic Data for $C_{24}H_{20}N_{11}Nd$ (3):** triclinic, $P\bar{1}$, $Z$ = 2, $T$ = 170(1) K, $a$ = 1034.0(2), $b$ = 1075.0(2), $c$ = 1270.2(2) pm, $\alpha$ =

 © 2006 Wiley-VCH Verlag GmbH & Co. KGaA, Weinheim 

72.51(3), $\beta$ = 84.96(3), $\gamma$ = 78.93(3)°, $V$ = 1320.9(4)·10$^6$ pm$^3$, $\mu$ = 20.4 cm$^{-1}$, Mo-$K_\alpha$, 3.76 ≤ 2 $\theta$ ≤ 50.0°, –12 ≤ $h$ ≤ 12, –12 ≤ $k$ ≤ 12, –15 ≤ $l$ ≤ 15, $F$(000) = 864, $R_1$ = 0.0779 for 1718 reflections [$I > 2\sigma(I)$], $R_1$ = 0.2006 and $wR_2$ = 0.1839 for all 4631 unique reflections, GOOF on $F_2$ = 0.956.

**Crystallographic Data for $C_{42}H_{32}Ho_2N_{22}$ (6):** triclinic, $P\bar{1}$, $Z$ = 2, $T$ = 170(1) K, $a$ = 1239.1(3), $b$ = 1294.4(4), $c$ = 1443.0(3) pm, $\alpha$ = 85.43(2), $\beta$ = 87.81(2), $\gamma$ = 68.99(2)°, $V$ = 2153.5(4)·10$^6$ pm$^3$, $\mu$ = 37.1 cm$^{-1}$, Mo-$K_\alpha$, 2.82 ≤ 2 $\theta$ ≤ 54.60°, –15 ≤ $h$ ≤ 15, –16 ≤ $k$ ≤ 16, –18 ≤ $l$ ≤ 18, $F$(000) = 1144, $R_1$ = 0.0593 for 5192 reflections [$I > 2\sigma(I)$], $R_1$ = 0.1262 and $wR_2$ = 0.1305 for all 9449 unique reflections, GOOF on $F_2$ = 0.896.

CCDC-294357 (**1**), -294360 (**2**), -294359 (**3**) and -294358 (**6**) contains the supplementary crystallographic data for this paper. These data can be obtained free of charge from The Cambridge Crystallographic Data Centre via www.ccdc.cam.ac.uk/data_request/cif.

## Acknowledgments

We gratefully acknowledge the Deutsche Forschungsgemeinschaft for supporting this work through the two SPP 1166 projects "Hoch- und Tieftemperatursynthesen von Selten-Erd-Elementen mit Aminen" and "Synthese von Selten-Erd-N-Komplexen unter extremen Bedingungen bezüglich Temperatur und Druck", and Prof. Dr. G. Meyer for his generous support.

[1] H. Schumann, *Angew. Chem. Int. Ed. Engl.* **1984**, *23*, 474–492; *Angew. Chem.* **1984**, *96*, 475–493.
[2] H. Schumann, J. A. Meese-Marktscheffel, L. Esser, *Chem. Rev.* **1995**, *95*, 865–986.
[3] W. J. Evans, *Coord. Chem. Rev.* **2000**, *206–207*, 263–283.
[4] R. Kempe, *Angew. Chem. Int. Ed.* **2000**, *39*, 468–494; *Angew. Chem.* **2000**, *112*, 478–504.
[5] W. J. Evans, B. L. Davis, *Chem. Rev.* **2002**, *102*, 2119–2136.
[6] S. Arndt, J. Okuda, *Chem. Rev.* **2002**, *102*, 1953–1976.
[7] K. Dehnicke, A. Greiner, *Angew. Chem.* **2003**, *115*, 1378–1392; *Angew. Chem. Int. Ed.* **2003**, *42*, 1340–1354.
[8] G. Wilkinson, J. M. Birmingham, *J. Am. Chem. Soc.* **1954**, *76*, 6210.
[9] R. G. Hayes, J. L. Thomas, *J. Am. Chem. Soc.* **1969**, *91*, 6876.
[10] K. Müller-Buschbaum, *Z. Anorg. Allg. Chem.* **2005**, *631*, 811–828.
[11] G. B. Deacon, A. Gitlits, B. W. Skelton, A. H. White, *Chem. Commun.* **1999**, 1213–1214.
[12] G. B. Deacon, A. Gitlits, P. W. Roesky, M. R. Bürgstein, K. C. Lim, B. W. Skelton, A. H. White, *Chem. Eur. J.* **2001**, *7*, 127–138.
[13] K. Müller-Buschbaum, *Z. Anorg. Allg. Chem.* **2002**, *628*, 2731–2737.
[14] K. Müller-Buschbaum, C. C. Quitmann, *Inorg. Chem.* **2003**, *42*, 2742–2750.
[15] K. Müller-Buschbaum, *Z. Anorg. Allg. Chem.* **2003**, *629*, 2127–3132.
[16] K. Müller-Buschbaum, C. C. Quitmann, *Eur. J. Inorg. Chem.* **2004**, 4330–4337.
[17] C. C. Quitmann, K. Müller-Buschbaum, *Z. Naturforsch.* **2004**, *59b*, 562–566.
[18] G. B. Deacon, C. M. Forsyth, A. Gitlits, B. W. Skelton, A. H. White, *Dalton Trans.* **2004**, 1239–1247.
[19] C. C. Quitmann, K. Müller-Buschbaum, *Z. Anorg. Allg. Chem.* **2005**, *631*, 1191–1198.
[20] K. Müller-Buschbaum, C. C. Quitmann, *Z. Anorg. Allg. Chem.* **2003**, *629*, 1610–1616.
[21] A. de Cian, M. Moussavi, J. Fischer, R. Weiss, *Inorg. Chem.* **1985**, *24*, 3162.
[22] A. A. Trifonov, M. N. Bochkarev, H. Schumann, J. Loebel, *Angew. Chem. Int. Ed. Engl.* **1991**, *30*, 1149–1151; *Angew. Chem.* **1991**, *103*, 1170–1172.
[23] J. Magull, A. Simon, *Z. Anorg. Allg. Chem.* **1992**, *618*, 81–86.
[24] C. Piguet, A. F. Williams, G. Bernardinelli, J.-C. G. Bünzli, *Inorg. Chem.* **1993**, *32*, 4139–4149.
[25] S. Petoud, J.-C. G. Bünzli, F. Renaud, C. Piguet, K. J. Schenk, G. Hopfgartner, *Inorg. Chem.* **1997**, *36*, 5750–5760.
[26] P. B. Iveson, C. Riviere, D. Guillaneux, M. Nierlich, P. Thuery, M. Ephritikhine, C. Madic, *Chem. Commun.* **2001**, 1512–1513.
[27] L. Natrajan, J. Pecaut, M. Mazzanti, C. LeBrun, *Inorg. Chem.* **2005**, *44*, 4756–4765.
[28] M. Ganesan, C. D. Berube, S. Gambarotta, G. P. A. Yap, *Organometallics* **2002**, *21*, 1707–1713.
[29] T. Dube, D. M. M. Freckmann, S. Conoci, S. Gambarotta, G. P. A. Yap, *Organometallics* **2000**, *19*, 209–211.
[30] T. Dube, S. Conoci, S. Gambarotta, G. P. A. Yap, G. Vasapollo, *Angew. Chem. Int. Ed.* **1999**, *40*, 3657–3659; *Angew. Chem.* **1999**, *111*, 3890–3892.
[31] C. C. Quitmann, K. Müller-Buschbaum, *Z. Anorg. Allg. Chem.* **2004**, *630*, 2422–2430.
[32] C. C. Quitmann, K. Müller-Buschbaum, *Z. Anorg. Allg. Chem.* **2005**, *631*, 564–568.
[33] W. J. Evans, G. W. Rabe, J. W. Ziller, *Inorg. Chem.* **1994**, *33*, 3072–3078.
[34] E. Schaumann in *Hetarene III, Part 4 (Houben-Weyl)*, Georg Thieme Verlag, Stuttgart and New York, **1994**, Vol. E8d.
[35] A. Escande, J. Lapasset, R. Faure, E.-J. Vincent, J. Elguero, *Tetrahedron* **1974**, *30*, 2903–2909.
[36] A. Escande, J. L. Galigne, J. Lapasset, *Acta Crystallogr., Sect. B* **1974**, *30*, 1490–1495.
[37] W. F. Hemminger, H. K. Cammenga, *Methoden der Thermischen Analyse*, Springer Verlag, Berlin Heidelberg New York, **1989**.
[38] K. Müller-Buschbaum, C. C. Quitmann, *Inorg. Chem.* **2006**, in press.
[39] C. C. Quitmann, V. Bezugly, F. R. Wagner, K. Müller-Buschbaum, *Z. Anorg. Allg. Chem*. **2006**, in press.
[40] G. Ostendorp, H. W. Rotter, H. Homborg, *Z. Anorg. Allg. Chem.* **1996**, *622*, 235–244.
[41] J. Weidlein, U. Müller, K. Dehnicke, *Schwingungsfrequenzen II, Nebengruppenelemente*, Georg Thieme Verlag, Stuttgart and New York, **1986**.
[42] S. Hüfner, *Optical Spectra of Transparent Rare Earth Compounds*, Academic Press, New York, **1978**.
[43] R. D. Shannon, *Acta Crystallogr. Sect. A* **1976**, *32*, 751–767.
[44] G. Blasse, B. C. Grabmeier, *Luminscent Materials*, Springer Verlag, Berlin Heidelberg New York, **1994**.
[45] J. Sokolnicki, R. Wiglusz, S. Radzki, A. Graczyk, J. Legendziewicz, *Optical Mater.* **2004**, *26*, 199–206.
[46] BASF Technical Information, *Uvinul Lichtschutzmittel*, EVP 004605 d, **2005**.
[47] UMID, UmweltMedizinischerDienst, *Abschlussbericht zur multizentrischen MCS-Studie*, Bundesamt für Strahlenschutz, Umwelt Bundesamt, **2005**.
[48] G. M. Sheldrick, *SHELXS-97*, Program for the Resolution of Crystal Structures, University of Göttingen, **1997**.
[49] G. M. Sheldrick, *SHELXL-97*, Program for the Refinement of Crystal Structures, University of Göttingen, **1997**.
[50] A. L. Spek, *PLATON-2000*, A Multipurpose Crystallographic Tool, University of Utrecht, **2000**.
[51] *STOE Software Package v.1.16*, *RECIPE*, Program for the Identification of Crystalline Individuals, Wiesbaden, **2001**.
[52] *STOE Software Package v.1.16*, *TWIN*, Program for the Separation of Crystalline Individuals, Wiesbaden, **2001**.
[53] *STOE WINXPOW v.1.04*, Program Package for the Operation of Powder Diffractometers and Analysis of Powder Diffractograms, STOE, Darmstadt, **1999**.

Received: January 6, 2005
Published Online: April 10, 2006

 © 2006 Wiley-VCH Verlag GmbH & Co. KGaA, Weinheim 

DOI: 10.1002/ejic.200600039

# Syntheses, Crystal Structures, and Characterizations of a Series of New Layered Lanthanide Carboxylate-Phosphonates

Si-Fu Tang,[a] Jun-Ling Song,[a] and Jiang-Gao Mao*[a]

**Keywords:** Lanthanides / Phosphonate / Luminescence

Hydrothermal reactions of different lanthanide(III) salts with $(H_2O_3PCH_2)_2NCH_2COOH$ ($H_5L^1$) led to two new layered lanthanide(III) carboxylate-diphosphonates, namely La($H_2L^1$)($H_2O$)$_2$·$H_2O$ (**1**) and La($H_2L^1$)($H_2O$) (**2**). The structure of compound **1** features a layered architecture in which the nine-coordinate $La^{3+}$ ions are bridged by phosphonate groups of the ligands. The carboxylate group of the phosphonate ligand remains protonated and is involved in the interlayer hydrogen bonding. Compound **2** features a double layer structure in which the $La^{3+}$ ion is eight-coordinated and the carboxylate group of the ligand is chelated to a $La^{3+}$ ion in a bidentate fashion. Hydrothermal reactions of lanthanide(III) salts with 4-HOOC–$C_6H_4$–$CH_2N(CH_2PO_3H_2)_2$ ($H_5L^2$) afforded three new compounds, namely, La($H_4L^2$)($H_3L^2$)-($H_2O$)·2$H_2O$ (**3**), Er($H_3L^2$)($H_4L^2$) (**4**), and Er($HL^3$)($H_2L^3$)($H_2O$) (**5**) [$H_2L^3$ = $H_2O_3PCH_2N(CHO)(CH_2–C_6H_4–COOH)$]. $H_2L^3$ was formed by the in situ oxidation of one P–C bond of the $H_5L^2$ ligand. Compound **3** features a (002) lanthanum(III) phosphonate layer in which the seven-coordinate $La^{3+}$ ions are bridged by diphosphonate moieties of the ligands. The carboxylate group remains protonated and is involved in the interlayer hydrogen bonding. The structure of compound **4** contains a 1D chain along the *a* axis in which each pair of $ErO_6$ octahedra is bridged by a pair of phosphonate groups. These 1D chains are further interconnected by hydrogen bonds between noncoordinated phosphonate oxygen atoms into a (002) layer with the phenyl carboxylate groups hanging on the interlayer space. The structure of compound **5** is also layered. The interconnection of $Er^{3+}$ ions by bidentate and tetradentate bridging phosphonate groups resulted in a (002) inorganic layer with the organic groups orientated to the interlayer space. Luminescence properties of compounds **4** and **5** have also been studied.

(© Wiley-VCH Verlag GmbH & Co. KGaA, 69451 Weinheim, Germany, 2006)

## Introduction

During the past two decades, a lot of research attention has been devoted to the chemistry of metal phosphonates for their potential applications in the areas of catalysis, ion exchange, proton conductivity, intercalation chemistry, photochemistry, and materials chemistry.[1] Most metal phosphonates exhibit a variety of open framework architectures such as layered and microporous structures. The use of bifunctional or multifunctional anionic units, such as diphosphonates, aminophosphonates, or phosphonocarboxylates, has been found to be an effective method to prepare new materials with microporous or open framework structures.[2–5] Results from ours and other groups indicate that amino-carboxylic-phosphonic acids are good ligands for building inorganic–organic hybrid open frameworks.[6] Reports on lanthanide phosphonates are rather limited and a number of them are based on X-ray powder diffraction.[7–11,13–16] Low solubility and poor crystallinity are two big obstacles for the structural studies for these lanthanide(III) compounds. The elucidation of the structures of lanthanide phosphonates is very important, as these compounds may exhibit useful luminescent properties in both visible and near IR regions.[12] A series of lanthanide diphosphonates with a 3D pillared-layer structure were isolated by the Ferey group.[13] Several lanthanide phosphonates with a crown ether or calixarene moiety have been reported by Clearfield, Bligh, Lukes, and Lin et al.[8a,14] Their structures normally feature a chelating mononuclear unit or a layer architecture. A series of one-dimensional lanthanide diphosphonates containing a hydroxy group were also reported.[15] Results from our group indicate that introducing a second ligand such as 5-sulfoisophthalic acid ($H_3BTS$) or oxalate acid, whose lanthanide compounds have good solubility and very good crystallinity, into the lanthanide–phosphonate system can lead to novel luminescent lanthanide phosphonate hybrids.[16] Another useful alternative method is the use of a phosphonic acid to which the carboxylate group or amino acid moiety is directly attached. So far, research on this aspect is scarce. Only a few 2D or 3D lanthanide phosphonates with additional carboxylate group or amino acid moiety have been prepared.[17] We have initiated a research project to systematically study the influence of counteranion, pH value, the ionic size of the lanthanide(III)

[a] State Key Laboratory of Structural Chemistry, Fujian Institute of Research on the Structure of Matter, Chinese Academy of Sciences,
Fuzhou 350002, P. R. China
E-mail: mjg@ms.fjirsm.ac.cn

Supporting information for this article is available on the WWW under http://www.eurjic.org or from the author.

 © 2006 Wiley-VCH Verlag GmbH & Co. KGaA, Weinheim 

ion and the substituent on the structures, and luminescence properties of lanthanide amino-carboxylate-phosphonates formed. Two carboxylate-phosphonic acids, $H_5L^1$ [$H_5L^1$ = $(H_2O_3PCH_2)_2NCH_2COOH$] and $H_5L^2$ [$H_5L^2$ = 4-HOOC–$C_6H_4$–$CH_2N(CH_2PO_3H_2)_2$], in which the carboxylate group is well separated from the diphosphonate moiety were selected. Hydrothermal reactions of the lanthanide(III) salts with the above two phosphonic acids afforded five new compounds, namely, $La(H_2L^1)(H_2O)_2{\cdot}H_2O$ (**1**), $La(H_2L^1)(H_2O)$ (**2**), $La(H_4L^2)(H_3L^2)(H_2O){\cdot}2H_2O$ (**3**), $Er(H_3L^2)(H_4L^2)$ (**4**), and $Er(HL^3)(H_2L^3)(H_2O)$ (**5**) [$H_3L^3$ = $H_2O_3PCH_2N(CHO)(CH_2–C_6H_4–COOH)$]. $H_3L^3$ resulted from the in situ oxidation of one P–C bond of the $H_5L^2$ ligand during the reaction (Scheme 1). Herein we report their syntheses, crystal structures, and luminescent properties.

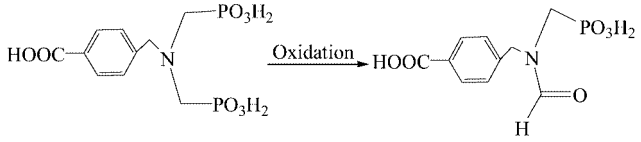


$H_5L^2$ $H_3L^3$

Scheme 1. The formation of $H_3L^3$ by the in situ oxidation of $H_5L^2$.

## Results and Discussion

Hydrothermal reactions of different lanthanide(III) salts with $(H_2O_3PCH_2)_2NCH_2COOH$ ($H_5L^1$) at two different temperatures lead to two new layered lanthanide(III) carboxylate-diphosphonates, namely $La(H_2L^1)(H_2O)_2{\cdot}H_2O$ (**1**) and $La(H_2L^1)(H_2O)$ (**2**). The higher temperature used for the synthesis resulted in compound **2** with fewer water molecules. Hydrothermal reactions of lanthanide(III) salts with 4-HOOC–$C_6H_4$–$CH_2N(CH_2PO_3H_2)_2$ ($H_5L^2$) afforded three new compounds, namely, $La(H_4L^2)(H_3L^2)(H_2O){\cdot}2H_2O$ (**3**), $Er(H_3L^2)(H_4L^2)$ (**4**), and $Er(HL^3)(H_2L^3)(H_2O)$ (**5**) [$H_2L^3$ = $H_2O_3PCH_2N(CHO)(CH_2–C_6H_4–COOH)$]. The higher number of water molecules present in the lanthanum(III) compound are probably due to the higher coordination number for the $La^{3+}$ ion than that for the $Er^{3+}$ ion. $H_2L^3$ was formed by the in situ oxidation of one P–C bond of the $H_5L^2$ ligand by oxidizing nitrate anion. Hence the counteranion, the temperature, and the ionic size of the lanthanide(III) ion have a strong effect on lanthanide phosphonates formed.

Compound **1** features a layered structure. The $La^{III}$ ion is nine-coordinate by seven phosphonate oxygen atoms from five $\{H_2L^1\}^{3-}$ anions and two aqua ligands (Figure 1). The La–O distances are in the range 2.4453(19)–2.888(2) Å, which is comparable to those reported for other $La^{III}$ phosphonates.[16] The $H_2L^1$ anion is septadentate; it chelates bidentately with one $La^{3+}$ ion by using a phosphonate group and another $La^{III}$ ion by using two oxygen atoms from two phosphonate groups, and also bridges with three other $La^{III}$ ions. Two phosphonate oxygen atoms [O(11) and O(12)] are bidentate metal linkers. The carboxylate group of the ligand remains protonated and noncoordinated; so does its amine group. The protonation of the amine group in a phosphonate ligand is well known, as amino-phosphonic acid usually exists as a zwitterion in which a proton of the phosphonate group is transferred to the basic amine group.[1,5]

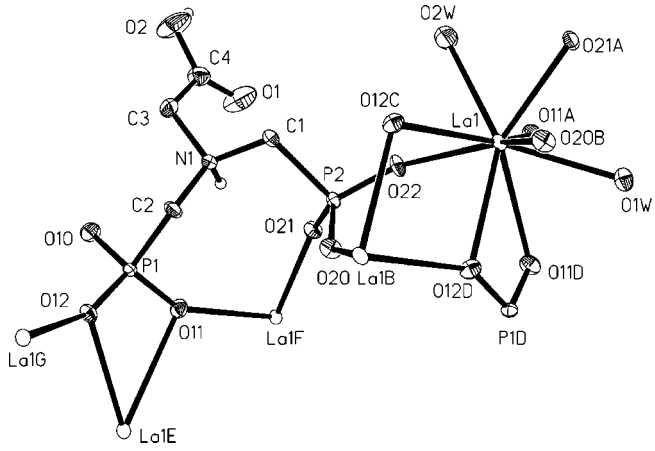


Figure 1. ORTEP representation of the selected unit of compound **1**. The thermal ellipsoids are drawn at 50% probability. The lattice water molecules have been omitted for clarity. Symmetry codes for generated atoms: A) $x$, $-y + 1/2$, $-z - 1/2$; B) $-x + 2$, $-y + 1$, $-z + 1$; C) $x$, $-y + 3/2$, $-z - 1/2$; D) $-x + 2$, $-y - 1/2$, $-z + 3/2$; E) $-x + 2$, $y + 1/2$, $-z + 3/2$; F) $x$, $-y + 1/2$, $z + 1/2$; G) $x$, $-y + 3/2$, $z + 1/2$.

The interconnection of the $La^{3+}$ ions by bridging phosphonate ligands resulted in (100) inorganic layers with the carboxylate moieties orientating toward the interlayer space (Figure 2). The interlayer distance is about 12.0 Å. Neighboring layers are held together by hydrogen bonds among carboxylate oxygens, noncoordinated phosphonate oxygen [O(10)], aqua ligand O(2w), and lattice water [O(3w)] (Table 1).

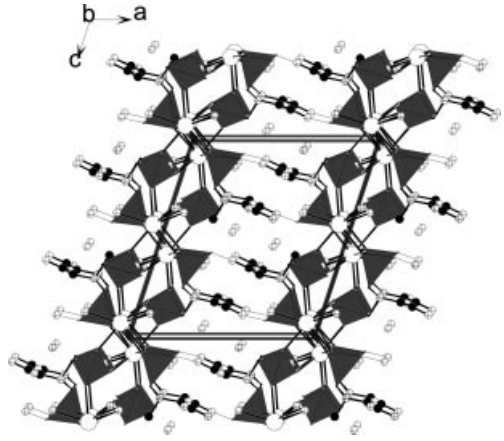


Figure 2. View of the structure of compound **1** down the *b* axis. The phosphonate tetrahedra are shaded in medium gray. La, C, N, and O atoms are drawn as open, black, octand, and crossed circles, respectively.

 © 2006 Wiley-VCH Verlag GmbH & Co. KGaA, Weinheim 

Compound **2** has a different layered structure. The asymmetric unit of **2** consists of one unique $La^{3+}$ ion, one $\{H_2L^1\}^{3-}$ anion, and an aqua ligand (Figure 3). The $La^{3+}$ ion is eight-coordinate by five phosphonate oxygen atoms from five phosphonate groups of four $\{H_2L^1\}^{3-}$ anions, two carboxylate oxygens of another phosphonate ligand, and an aqua ligand. The La–O distances are in the range 2.360(9)–2.728(8) Å, which is comparable to those in compound **1** and other lanthanum(III) phosphonates.[16] The coordinating mode of the phosphonate anion is different from that in compound **1**. The singly protonated phosphonate group (P1) is bidentate and connects with two $La^{3+}$ ions. The fully deprotonated phosphonate group (P2) is tridentate and is bridged to three $La^{3+}$ ions. Unlike that in compound **1**, the carboxylate group of the phosphonate ligand in compound **2** is deprotonated and forms a four-member chelating ring [La(1)–O(2)–C(4)–O(1)] (Figure 3). The amine group is protonated as in compound **1**.

Table 1. Selected bond lengths [Å] for compounds **1**–**5**.[a]

| | | | |
|---|---|---|---|
| Compound **1** | | | |
| La(1)–O(21)#1 | 2.445(2) | P(1)–O(12) | 1.524(2) |
| La(1)–O(20)#2 | 2.485(2) | P(1)–O(10) | 1.534(2) |
| La(1)–O(11)#1 | 2.509(2) | P(2)–O(22) | 1.520(2) |
| La(1)–O(22) | 2.517(2) | P(2)–O(20) | 1.523(2) |
| La(1)–O(1w) | 2.564(2) | P(2)–O(21) | 1.524(2) |
| La(1)–O(12)#3 | 2.587(2) | C(4)–O(1) | 1.225(4) |
| La(1)–O(2w) | 2.589(3) | C(4)–O(2) | 1.276(4) |
| La(1)–O(12)#4 | 2.694(2) | O(2)···O(10)#5 | 2.478(3) |
| La(1)–O(11)#4 | 2.888(2) | O(2)···O(2w)#6 | 2.835(4) |
| O(1)···O(2 W)#7 | 2.800(4) | O(10)···O(3 W) | 2.822(4) |
| Compound **2** | | | |
| La(1)–O(11)#1 | 2.360(9) | La(1)–O(2) | 2.728(8) |
| La(1)–O(22)#2 | 2.407(9) | P(1)–O(11) | 1.499(9) |
| La(1)–O(21)#3 | 2.456(8) | P(1)–O(12) | 1.504(8) |
| La(1)–O(12)#3 | 2.469(9) | P(1)–O(13) | 1.562(8) |
| La(1)–O(23)#4 | 2.509(9) | P(2)–O(21) | 1.489(9) |
| La(1)–O(1w) | 2.630(9) | P(2)–O(22) | 1.508(9) |
| La(1)–O(1) | 2.693(8) | P(2)–O(23) | 1.515(9) |
| N(1)···O(13) | 3.24(1) | N(1)···O(1w)#5 | 3.32(1) |
| Compound **3** | | | |
| La(1)–O(43)#1 | 2.409(5) | P(3)–O(32) | 1.574(4) |
| La(1)–O(13)#2 | 2.430(5) | P(4)–O(43) | 1.511(4) |
| La(1)–O(42) | 2.441(5) | P(4)–O(42) | 1.515(4) |
| La(1)–O(33)#1 | 2.466(5) | P(4)–O(41) | 1.520(4) |
| La(1)–O(22) | 2.495(5) | C(10)–O(1) | 1.196(8) |
| La(1)–O(31)#3 | 2.575(6) | C(10)–O(2) | 1.302(8) |
| La(1)–O(1w) | 2.632(7) | O(1)···O(2w)#4 | 2.732(7) |
| P(1)–O(13) | 1.490(4) | O(2)···O(23)#5 | 2.700(8) |
| P(1)–O(11) | 1.528(4) | O(4)···O(41)#6 | 2.505(7) |
| P(1)–O(12) | 1.533(5) | O(11)···O(11)#7 | 2.474(8) |
| P(2)–O(22) | 1.504(4) | O(12)···O(23)#8 | 2.493(7) |
| P(2)–O(23) | 1.517(4) | O(21)···O(21)#2 | 2.606(8) |
| P(2)–O(21) | 1.542(4) | O(32)···O(41)#8 | 2.539(7) |
| P(3)–O(33) | 1.496(5) | N(2)···O(2w) | 2.782(8) |
| P(3)–O(31) | 1.504(4) | N(1)···O(3w) | 2.757(8) |
| Compound **4** | | | |
| Er(1)–O(12) | 2.206(4) | Er(1)–O(23)#1 | 2.208(4) |
| Er(1)–O(13)#2 | 2.230(4) | Er(1)–O(33)#3 | 2.237(4) |
| Er(1)–O(42) | 2.244(4) | Er(1)–O(43)#1 | 2.258(4) |
| P(1)–O(11) | 1.512(5) | P(1)–O(13) | 1.513(5) |
| P(1)–O(12) | 1.516(5) | P(2)–O(23) | 1.495(5) |
| P(2)–O(22) | 1.499(4) | P(2)–O(21) | 1.568(4) |
| P(3)–O(32) | 1.494(5) | P(3)–O(33) | 1.504(4) |
| P(3)–O(31) | 1.564(5) | P(4)–O(42) | 1.501(4) |
| P(4)–O(43) | 1.507(4) | P(4)–O(41) | 1.556(5) |
| C(10)–O(1) | 1.192(12) | C(10)–O(2) | 1.309(11) |
| C(20)–O(4) | 1.203(11) | C(20)–O(3) | 1.323(11) |
| N(1)···O(32)#1 | 2.680(7) | N(2)···O(22)#1 | 2.772(7) |
| O(3)···O(11)#4 | 2.624(8) | O(11)···O(41) | 2.535(7) |
| O(21)···O(22)#5 | 2.558(6) | O(31)···O(32)#6 | 2.681(6) |
| Compound **5** | | | |
| Er(1)–O(13)#1 | 2.213(6) | P(2)–O(23) | 1.523(6) |
| Er(1)–O(23)#2 | 2.239(7) | P(2)–O(21) | 1.549(6) |
| Er(1)–O(12) | 2.253(7) | N(1)–C(4) | 1.314(13) |
| Er(1)–O(21)#3 | 2.290(6) | N(2)–C(21) | 1.285(14) |
| Er(1)–O(1w) | 2.356(7) | O(5)–C(4) | 1.167(14) |
| Er(1)–O(21) | 2.403(6) | O(6)–C(21) | 1.186(14) |
| Er(1)–O(22) | 2.437(6) | C(6)–O(1) | 1.266(16) |
| P(1)–O(12) | 1.497(6) | C(6)–O(2) | 1.290(14) |
| P(1)–O(13) | 1.502(6) | C(27)–O(4) | 1.228(16) |
| P(1)–O(11) | 1.586(8) | C(27)–O(3) | 1.270(17) |
| P(2)–O(22) | 1.517(7) | O(1)···O(4)#4 | 2.614(13) |
| O(2)···O(3)#4 | 2.585(13) | | |

[a] Symmetry transformations used to generate equivalent atoms: For **1**: #1 *x*, –*y* + 1/2, –*z* + 1/2; #2 –*x* + 2, –*y* + 1, –*z* + 1; #3 *x*, –*y* + 3/2, –*z* – 1/2; #4 –*x* + 2, *y* – 1/2, –*z* + 3/2; #5 –*x* + 1, –*y* – 1/2, –*z* + 3/2; #6 –*x* + 1, –*y* + 1, –*z* + 1; #7 *x*, 1/2 – *y*, 1/2 + *z*. For **2**: #1 –*x* – 1/2, *y*, *z* – 1/2; #2 *x* + 1/2, –*y*, *z*; #3 *x* + 1, *y*, *z*; #4 –*x* – 1/2, *y*, *z* + 1/2; #5 –1/2 + *x*, –*y*, *z*. For **3**: #1 –*x* + 2, –*y* + 1, –*z* + 1; #2 –*x* + 2, –*y* + 2, –*z* + 1; #3 –*x* + 1, –*y* + 1, –*z* + 1; #4 *x*, *y*, *z* + 1; #5 –*x* + 2, –*y* + 2, –*z* + 2; #6 –*x* + 2, –*y* + 1, –*z*; #7 –*x* + 1, –*y* + 2, –*z* + 1; #8 *x* – 1, *y*, *z*. For **4**: #1 –*x* + 1, –*y* + 2, –*z* + 1; #2 –*x* + 2, –*y* + 2, –*z* + 1; #3 *x* + 1, *y*, *z*; #4 –*x* + 1, –*y* + 1, –*z*; #5 –*x* + 1, –*y* + 3, –*z* + 1; #6 –*x*, –*y* + 1, –*z* + 1. For **5**: #1 –*x*, –*y* + 2, –*z* + 1; #2 –*x* – 1, –*y* + 1, –*z* + 1; #3 –*x*, –*y* + 1, –*z* + 1; #4 *x* + 1, *y* + 1, –1 + *z*.

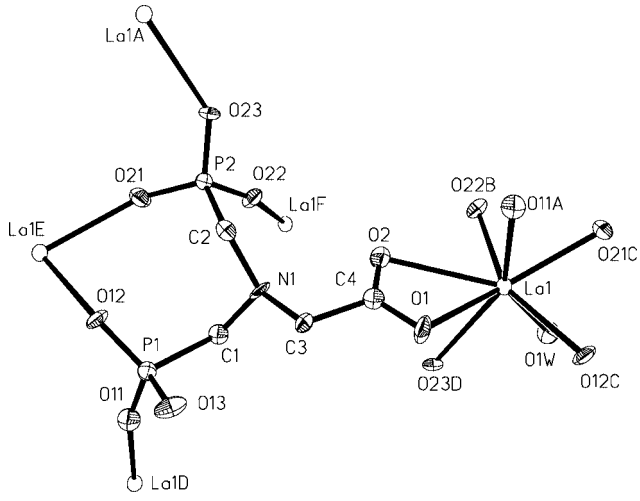


Figure 3. ORTEP representation of the selected unit of compound **2**. The thermal ellipsoids are drawn at 50% probability. Symmetry codes for the generated atoms: A) –*x* – 1/2, *y*, –*z* – 1/2; B) *x* + 1/2, –*y*, *z*; C) *x* + 1, *y*, *z*; D) –*x* – 1/2, *y*, *z* + 1/2; E) *x* – 1, *y*, *z*; F) *x* – 1/2, –*y*, *z*.

The interconnection of $La^{3+}$ ions by phosphonate ligands led to a (010) double layer (Figure 4). The thicknes of the double layer is about 9.0 Å. Neighboring 2D layers

 © 2006 Wiley-VCH Verlag GmbH & Co. KGaA, Weinheim 

are held together by weak hydrogen bonds among the amine group, aqua ligand, and noncoordination phosphonate oxygen, as well as a weak van der Waals force (Table 1, Figure 4).

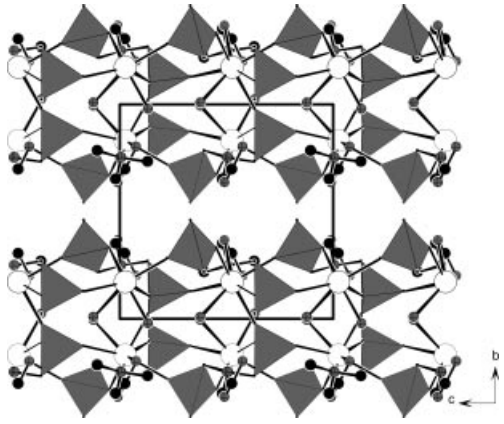


Figure 4. View of the structure of compound **2** down the *a* axis. The phosphonate tetrahedra are shaded in medium gray. La, C, N, and O atoms are drawn as open, black, octand, and crossed circles, respectively.

Compound **3** also features a layered structure. The asymmetric unit of **3** consists of one $La^{3+}$ ion, one $\{H_4L^2\}^-$ anion, one $\{H_3L^2\}^{2-}$ dianion, an aqua ligand, and two lattice water molecules (Figure 5). The $La^{3+}$ ion is seven-coordinate by six phosphonate oxygen atoms from five phosphonate ligands and an aqua ligand. The La–O distances are in the range 2.409(5)–2.632(7) Å, which is comparable to those in compounds **1** and **2**. The $\{H_4L^2\}^-$ anion composed of P(1) and P(2) is bidentate and bridges with two $La^{3+}$ ions; each phosphonate group is singly protonated, as are the amine group and the carboxylate group. The $\{H_3L^2\}^{2-}$ anion composed of P(3) and P(4) is tetradentate; it forms an eight-member chelating ring with a $La^{3+}$ ion, and also bridges with two other $La^{3+}$ ions. Only one phosphonate group is singly protonated; the amine group and the carboxylate group are also protonated.

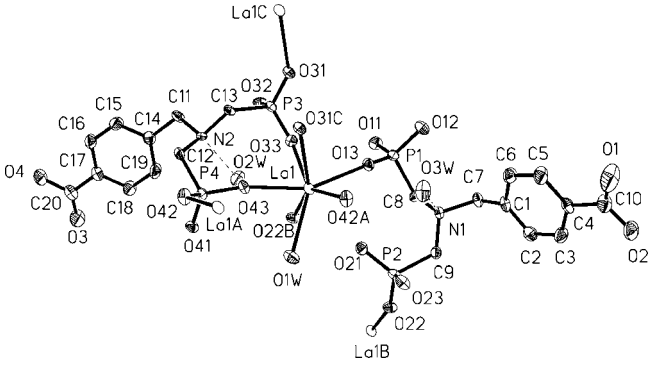


Figure 5. ORTEP representation of the selected unit of compound **3**. The thermal ellipsoids are drawn at 50% probability. Hydrogen bonds are drawn as dashed lines. Symmetry codes for the generated atoms: A: $-x + 2, -y + 1, -z + 1$; B) $-x + 2, -y + 2, -z + 1$; C) $-x + 1, -y + 1, -z + 1$.

Adjacent $La^{3+}$ ions are bridged by the above two types of phosphonate anions into a (002) lanthanide phosphonate layer with $-C_6H_4-$COOH moieties hanging on both sides of the layer (Figure 6). Extensive intralayer and interlayer hydrogen bonds further crosslink these layers into a 3D supramolecular network (Figure 6, Table 1). The lattice water molecules are located at the voids of the structure and are involved in hydrogen bonding (Figure 6, Table 1). The interlayer distance of about 16.8 Å is significantly larger than that in compound **1**, which is due to the introduction of the additional phenyl group into the phosphonate ligand.

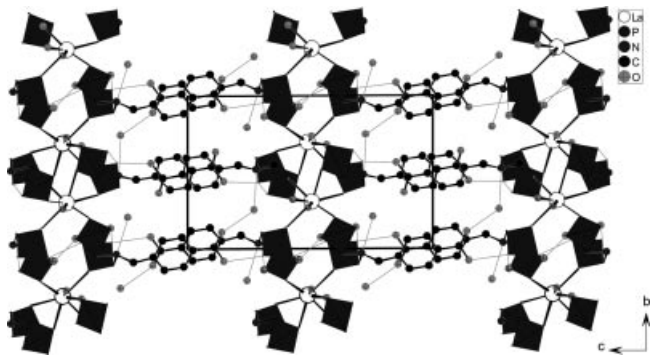


Figure 6. View of the structure of compound **3** down the *a* axis. The phosphonate tetrahedra are shaded in grey. La, N, C, and O atoms are represented by open, dark grey, black, and light grey circles, respectively. Hydrogen bonds are drawn as dashed lines.

The structure of $Er(H_3L^2)(H_4L^2)$ (**4**) features a 3D supramolecular network based on 1D erbium(III) phosphonate chains. The asymmetric unit of **4** is composed of one $Er^{3+}$ ion, one $(H_3L^2)^{2-}$ dianion, and one $(H_4L^2)^-$ anion. The $Er^{3+}$ ion is octahedrally coordinated by six phosphonate oxygens from six different phosphonate ligands (Figure 7). The Er–O distances [2.280(2)–2.331(2) Å] are comparable to those found in the other erbium(III) phosphonate.[16] The coordination modes for the $(H_3L^2)^{2-}$ dianion and $(H_4L^2)^-$ anion are similar. One phosphonate group is monodentate whereas the other is bidentate. The amine group and the carboxylate group for both types of anion are singly protonated. The main difference between the two phosphonate anions are that both phosphonate groups are singly protonated for the $(H_4L^2)^-$ anion [O(31) and O(41)] whereas only one phosphonate group is singly protonated for the $(H_3L^2)^{2-}$ dianion [O(21)].

Each pair of $Er^{3+}$ ions is bridged by a pair of phosphonate groups to form a 1D chain along the *a* axis. Such chains are further interconnected by strong hydrogen bonds between noncoordinated phosphonate oxygens into a (002) layer. These hydrogen bonds are O(21)···O(22) 2.558(6) Å (symmetry code: $1 - x, 3 - y, 1 - z$) and O(31)···O(32) 2.681(6) Å (symmetry code: $-x, 1 - y, 1 - z$). The $-CH_2-C_6H_4-$COOH groups of the phosphonate ligands are hanging on the interlayer space (Figure 8). Intrachain hydrogen bonds are also formed between the amine group and noncoordinated phosphonate oxygens, and between two noncoordinated phosphonate oxygens (Table 1). The interlayer distance is about 14.3 Å, which is shorter than that of compound **3**. These 2D layers are further interlinked by hydro-

 © 2006 Wiley-VCH Verlag GmbH & Co. KGaA, Weinheim 

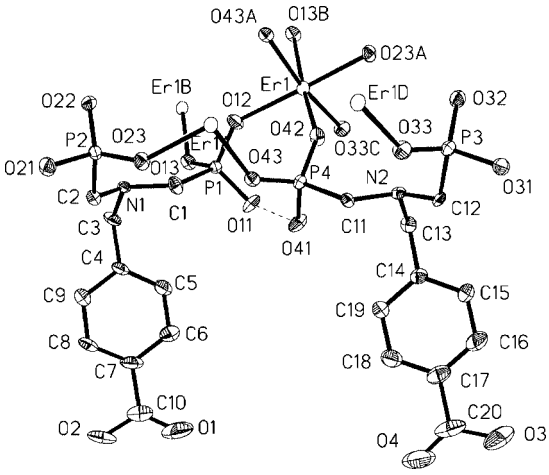


Figure 7. ORTEP representation of the selected unit of compound **4**. The thermal ellipsoids are drawn at 50% probability. Hydrogen bonds are drawn as dashed lines. Symmetry codes for the generated atoms: A) 1 + *x*, *y*, *z*; B) 2 – *x*, 1 – *y*, 1 – *z*; C) 2 – *x*, 2 – *y*, 1 – *z*; D) –1 + *x*, *y*, *z*.

gen bonds between carboxylate oxygen and noncoordinated phosphonate oxygen [O(3)···O(11) 2.624(8) Å, symmetry code: 1 – *x*, 1 – *y*, –*z*].

When erbium(III) nitrate was used instead of erbium(III) chloride, compound **5** was isolated. $H_5L^2$ was also oxidized by the nitrate anion to a new ligand, $H_3L^3$ (Scheme 1). Such in situ oxidation of the P–C bond has also been observed during the hydrothermal reactions of cobalt(II) nitrate with $H_5L$.[2,18] The asymmetric unit of **5** consists of one erbium(III) ion, a $\{H_2L^3\}^-$ anion, a $\{HL^3\}^{2-}$ dianion, and an aqua ligand (Figure 9). The erbium(III) ion is seven-coordinate by six phosphonate oxygens from five phosphonate ligands and an aqua ligand. The Er–O distances range from 2.214(6) to 2.438(6) Å, which is comparable to those in compound **4**. The $\{HL^3\}^{2-}$ dianion is tetradentate; it forms a chelating ring with an erbium(III) ion [Er(1)–O(21)–P(2)–O(22)] and also bridges with two other erbium(III) ions [Er(1b) and Er(1c)]. The phosphonate group is fully deprotonated whereas the amine group remains protonated. The $\{H_2L^3\}^-$ anion is bidentate and bridges with two erbium(III)

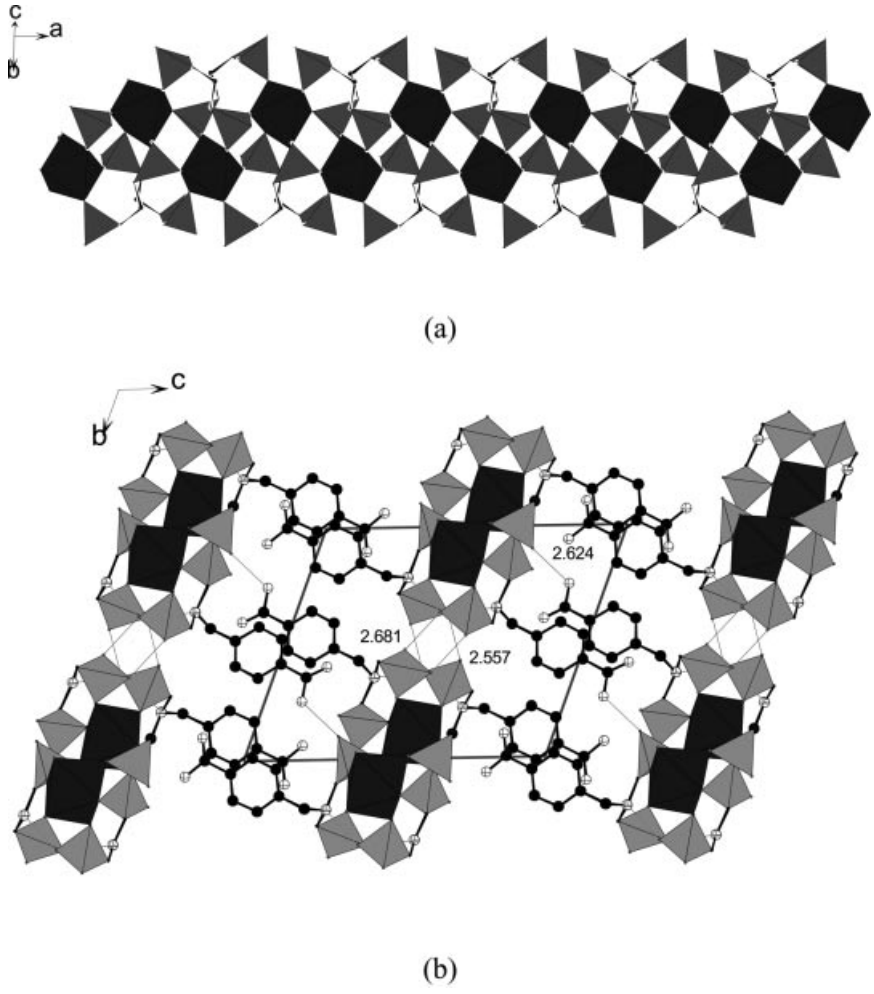


Figure 8. An erbium(III) phosphonate inorganic chain along the *a* axis (a) and view of the structure of compound **4** down the *a* axis (b). The $ErO_6$ octahedra and phosphonate tetrahedra are shaded in dark gray and medium gray, respectively. N, C, and O atoms are represented by octand, black, and crossed circles, respectively.

 © 2006 Wiley-VCH Verlag GmbH & Co. KGaA, Weinheim 

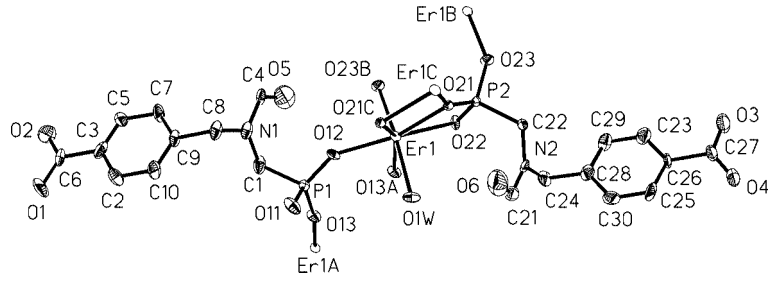


Figure 9. ORTEP representation of the selected unit of compound **5**. The thermal ellipsoids are drawn at 50% probability. Symmetry codes for the generated atoms: A) $-x, -y + 2, -z + 1$; B) $-x - 1, -y + 1, -z + 1$; C) $-x, -y + 1, -z + 1$.

ions using two oxygen atoms [O(12) and O(13)]. The third phosphonate oxygen and the amine group are protonated and noncoordinated. The carboxylate groups in both types of anions are noncoordinated.

The $Er^{3+}$ ions in compound **5** are bridged by phosphonate groups of ligands into a (002) inorganic layer (Figure 10). Within the layer, $Er_2O_2$ rings and $Er(-O-P-O-)_2Er$ rings can be found. Neighboring 2D layers are further interlinked by hydrogen bonds between carboxylate groups. These hydrogen bonds are O(1)···O(4) 2.614(13) Å and O(2)···O(3) 2.585(13) Å (symmetry codes are the same for both bonds: $1 + x$, $1 + y$, $-1 + z$). The interlayer distance of about 21.6 Å is the largest among five compounds, because the carboxylate groups in other compounds are directly hydrogen bonded to a neighboring inorganic layer, whereas the interlayer hydrogen bonding in compound **5** is between two hanging organic groups (head to head).

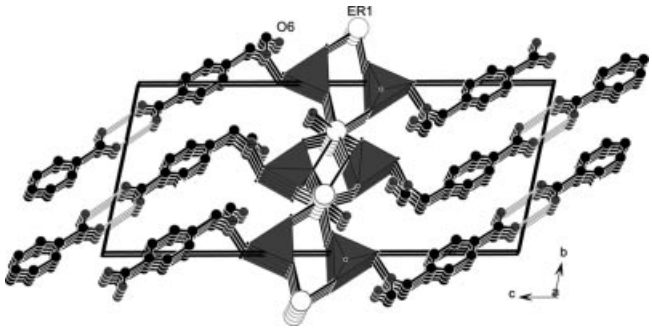


Figure 10. View of the structure of compound **5** down the *a* axis. The phosphonate tetrahedra are shaded in medium gray. Er, C, N, and O atoms are drawn as open, black, octand, and crossed circles, respectively. Hydrogen bonds are shown as dashed lines.

Based on X-ray powder diffraction studies, compounds **2**–**5** are prepared as single phases. The measured patterns are in good agreement with those simulated from single-crystal structures (see Supporting Information).

The solid-state luminescent properties of compounds **4** and **5** were investigated at room temperature. The emission spectrum of compound **4** shows three strong near IR emission bands at 1477, 1541, and 1561 nm under 520 nm excitation (Figure 11a), all of which can be attributed to the $^4I_{13/2} \rightarrow {}^4I_{15/2}$ transition for the $Er^{3+}$ ion.[16] The splitting of the $^4I_{13/2} \rightarrow {}^4I_{15/2}$ transition into several sub-bands is due to the low symmetry of the coordination geometry around the $Er^{3+}$ ion ($C_1$). The luminescence properties of compound **5** are very interesting. Under emission of 330 nm, the excitation spectrum of compound **5** displays one weak

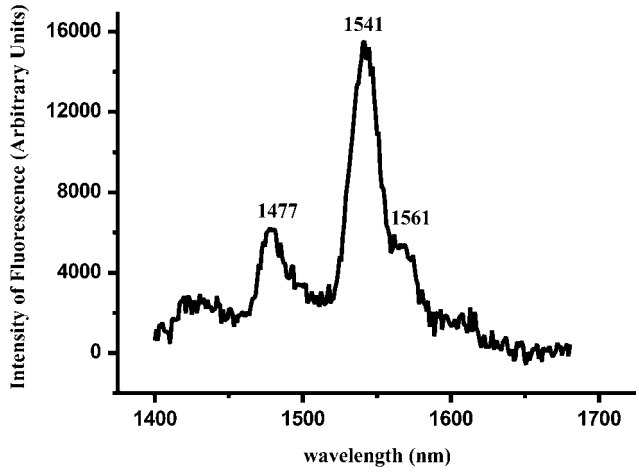


(a)

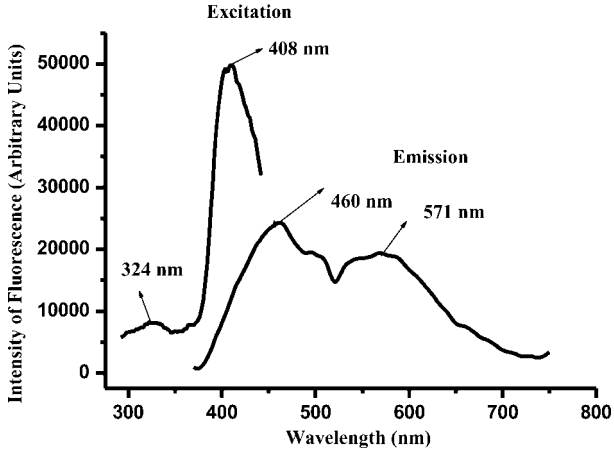


(b)

Figure 11. Luminescence spectra for compounds **4** (a) and **5** (b) at room temperature.

 © 2006 Wiley-VCH Verlag GmbH & Co. KGaA, Weinheim 

absorption peak at 324 nm and a very strong absorption peak at 408 nm. Surprisingly, compound **5** shows no near IR emission band under our experimental conditions. Under excitation of 408 nm, the emission spectrum of compound **5** exhibits a very broad band with two maximum intensity peaks at 460 and 571 nm (Figure 11b), which may be assigned to the intraligand π–π* fluorescence. The absence of near IR emission is probably due to the quenching effect of the luminescent state by high-frequency vibrating water molecules.[16a]

TGA curves for compounds **2**–**5** are shown in Figure 12. TGA curves of compound **2** indicate one main step of weight loss. The weight loss between 260 and 620 °C corresponds to the release of water molecules and the combustion of the phosphonate ligand. The weight loss is about 20.5%. There is small weight loss starting from 800 °C, which can be attributed to the further decomposition of the compound. The total weight loss at 1000 °C is 24.4%. The residue was not characterized. Compound **3** shows no obvious weight loss before 135 °C. The weight loss in the temperature range of 135–270 °C corresponds to the release of two lattice water molecules and an aqua ligand. The observed weight loss of 6.8% is close to the calculated value (6.2%). Then the compound decomposes continuously up to 1000 °C, which corresponds to the combustion of organic groups. The total weight loss at 1000 °C is 48.6% and the residue was not characterized. Compound **4** is stable up to 355 °C. Then it exhibits a sharp weight loss between 355 and 575 °C with a weight loss of 23.8%. The total weight at 1000 °C is 34.3% and the final residue was not characterized. TGA curves for compound **5** display two main steps of weight losses. There is no obvious weight loss before 280 °C. The weight loss in the range of 280–340 °C corresponds to the release of an aqua ligand and the decomposition of the two carboxylate groups of two phosphonate ligands. The observed weight loss of 13.4% is slightly smaller than the calculated one (14.5%). The second weight loss covers a temperature range from 340 to 650 °C, which corresponds to further combustion of the phosphonate ligands. The total weight loss at 1000 °C is 34.3% and the final residue was not characterized.

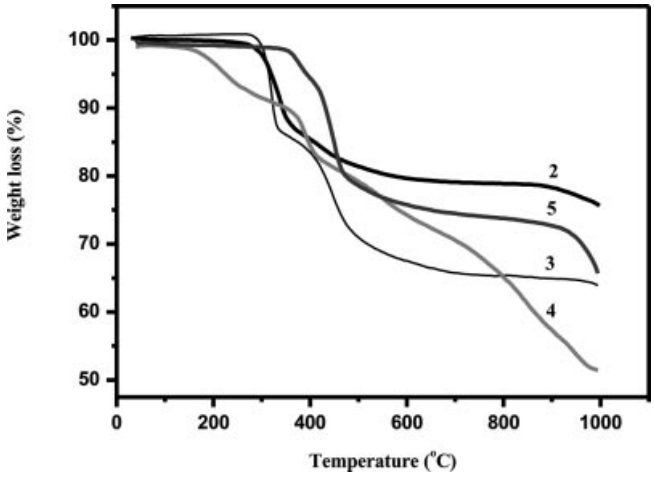


Figure 12. TGA curves for **2** (thick line, black), **3** (thin line, black), **4** (light grey line), and **5** (medium grey line).

## Conclusion

In summary, the hydrothermal syntheses, crystal structures, and luminescent properties of five new lanthanide(III) phosphonates with layered structures have been described. Results from this and previous work indicate that we can greatly improve the solubility and crystallinity of lanthanide phosphonates by attaching amino acid moiety to the phosphonic acid or introducing a second ligand such as oxalate or carboxylate-sulfonate. The counteranion used plays an important role. It affects the acidity of the solution and the extent of deprotonation of phosphonate ligands, as well as the coordination mode a phosphonate ligand adopts. Oxidizing anions such as nitrate groups may also trigger the in situ oxidation of P–C bonds. Furthermore, the so-called "lanthanide contraction" is also important. Heavy lanthanide ions usually have smaller coordination numbers than the light ones, which may result in different coordination modes for the phosphonate ligands. However, more systematic studies are still needed to further understand the chemistry of lanthanide phosphonates.

## Experimental Section

**Materials and Methods:** $(H_2O_3PCH_2)_2NCH_2CO_2H$ ($H_5L^1$) and 4-$HO_2C$–$C_6H_4$–$CH_2N(CH_2PO_3H_2)_2$ ($H_5L^2$) were prepared by a Mannich-type reaction according to the procedures described previously.[6] All other chemicals were obtained from commercial sources and used without further purification. Elemental analyses were performed on a Vario EL III elemental analyzer. Thermogravimetric analyses were carried out on a NETZSCH STA 449C unit at a heating rate of 15 °C/min under nitrogen. IR spectra were recorded with a Magna 750 FTIR spectrometer photometer as KBr pellets in the range 4000–400 $cm^{-1}$. Photoluminescence analyses were performed on an Edinburgh FLS920 fluorescence spectrometer. X-ray powder diffraction patterns (Cu-$K_\alpha$) were collected in a sealed glass capillary on a XPERT-MPD $\theta$–$2\theta$ diffractometer.

**Preparation of $La(H_2L^1)(H_2O)_2{\cdot}H_2O$ (1):** A mixture of $LaCl_3{\cdot}6H_2O$ (176.7 mg, 0.5 mmol), $H_5L^1$ (131.6 mg, 0.5 mmol), and 2-hydroxypyridine (95.1 mg, 1.0 mmol) in 10 mL of distilled water was sealed into an autoclave equipped with a Teflon liner (25 mL) and then heated at 120 °C for 4 days. The initial pH value of the resultant solution was 3.0. Colorless plate-shaped crystals of **1** were collected. Yield: 11.3 mg (5%, based on La). Based on the X-ray powder diffraction study, the majority of impurity was powder of compound **2**. Efforts to prepare a single-phase product of compound **1** were unsuccessful.

**Preparation of $La(H_2L^1)(H_2O)$ (2):** A mixture of $La(OH)_3$ (189.9 mg, 1.0 mmol) and $H_5L^1$ (263.1 mg, 1.0 mmol) in 10 mL of distilled water was sealed into a bomb equipped with a Teflon liner (25 mL) and then heated at 150 °C for 4 days. The initial and final pH values of the resultant solution were 3.5 and 2.5, respectively. Colorless plate-shaped crystals of **2** were collected. Yield: 250 mg (60%, based on La). IR (KBr): $\tilde{\nu}$ = 3359 m, 3139 m, 1607 m, 1448 w, 1407 s, 1371 m, 1305 w, 1214 m, 1164 m, 1083 vs, 1008 m, 974 w, 949 w, 844 w, 768 w, 720 m, 587 w, 496 w, 468 w, 447 w $cm^{-1}$.

 © 2006 Wiley-VCH Verlag GmbH & Co. KGaA, Weinheim 

$C_4H_{10}LaNO_9P_2$ (416.98): calcd. C 11.52, H 2.42, N 3.36; found C 11.60, H 2.54, N 3.28.

**Preparation of $La(H_4L^2)(H_3L^2)(H_2O)\cdot 2H_2O$ (3):** A mixture of $La(OH)_3$ (56.98 mg, 0.3 mmol) and $H_5L^2$ (169.6 mg, 0.5 mmol) in 10 mL of distilled water was sealed into a bomb equipped with a Teflon liner (25 mL) and then heated at 145 °C for 4 days. The initial and final pH values of the resultant solution were 4.5 and 2.5, respectively. Colorless plate-shaped crystals of **3** were collected. Yield: 121.6 mg (56%, based on $H_5L^2$). IR (KBr): $\tilde{\nu}$ = 3480 m, 3387 m, 3219 m, 3020 w, 3010 w, 2614 w, 1697 s, 1642 m, 1460 w, 1403 m, 1321 w, 1274 w, 1163 m, 1115 vs, 991 m, 931 m, 825 w, 761 m, 644 w, 560 m, 535 m, 484 w, 451 w $cm^{-1}$. $C_{20}H_{33}LaN_2O_{19}P_4$ (868.27): calcd. C 27.65, H 3.83, N 3.23; found C 27.70, H 3.92, N 3.18.

**Preparation of $Er(H_3L^2)(H_4L^2)$ (4):** A mixture of $ErCl_3\cdot 6H_2O$ (95.4 mg, 0.25 mmol) and $H_5L^2$ (84.8 mg, 0.25 mmol) in 10 mL of distilled water was sealed into an autoclave equipped with a Teflon liner (25 mL) and heated at 145 °C for 5 days. The initial and final pH values of the resultant solution were 3.5 and 2.0, respectively. Pink brick-shaped crystals of **4** were collected. Yield: 147 mg (70%, based on Er). IR (KBr): $\tilde{\nu}$ = 3494 m, 3114 m, 2674 w, 2557 w, 1705 s, 1401 m, 1318 m, 1206 m, 1113 vs, 1020 m, 994 m, 951 m, 908 w, 879 w, 820 w, 808 w, 763 m, 719 m, 681 w, 637 w, 582 m, 515 w, 493 w, 465 w, 413 w $cm^{-1}$. $C_{20}H_{26}ErN_2O_{16}P_4$ (841.57): calcd. C 28.54, H 3.11, N 3.33; found C 28.50, H 3.17, N 3.39.

**Synthesis of $Er(HL^3)(H_2L^3)(H_2O)$ (5):** A mixture of $Er(NO_3)_3\cdot 6H_2O$ (230.70 mg, 0.5 mmol), $H_5L^2$ (169.6 mg, 0.5 mmol), and 2-hydroxypyridine (95.10 mg, 1.0 mmol) in 10 mL of distilled water was sealed into a bomb equipped with a Teflon liner (25 mL) and then heated at 120 °C for 4 days. The initial and final pH values of the resultant solution were 3.0 and 2.5, respectively. Light yellow brick-shaped crystals of **5** were collected. Yield: 91 mg (25%, based on Er). IR (KBr): $\tilde{\nu}$ = 3494 m, 3116 m, 2674 w, 2557 w, 1686 s, 1611 m, 1579 w, 1511 w, 1453 m, 1430 m, 1324 m, 1296 m, 1239 m, 1175 w, 1104 vs, 1025 m, 994 m, 951 m, 908 w, 879 w, 820 w, 791 w, 763 m, 719 w, 681 w, 641 w, 575 m, 506 w, 493 w, 465 w, 414 w $cm^{-1}$. $C_{20}H_{23}ErN_2O_{13}P_2$ (728.60): calcd. C 29.59, H 3.18, N 7.51; found C 30.08, H 3.26, N 7.46.

**Single-Crystal Structure Determination:** Data collections for compounds **1**–**5** were performed with a Rigaku Mercury CCD diffractometer equipped with graphite-monochromated Mo-$K_\alpha$ radiation ($\lambda$ = 0.71073 Å). Intensity data were collected by the narrow frame method at 293 K. The data sets were corrected for Lorentz and polarization factors as well as for absorption by the multiscan technique.[18] All five structures were solved by the direct methods and refined by full-matrix least-squares fitting on $F^2$ by SHELX-97.[19] All non-hydrogen atoms were refined with anisotropic thermal parameters, except for C(1), C(4), and O(11) in compound **2**, and C(21) in compound **5**, which were refined isotropically. The lattice water molecule in compound **1** was disordered over two orientations [O(3w) and O(3w′)], with an interatomic distance of 0.932 Å. Each orientation was refined with 50% occupancy. Hydrogen atoms attached to carbon atoms, amine groups, and phosphonate groups were located at geometrically calculated positions and refined with isotropic thermal parameters. The protonation for the amine groups as well as phosphonate groups was based on P–O distances and charge balance. Hydrogen atoms for water molecules were not included in refinements.

**Crystal Data for 1:** $C_4H_{14}LaNO_{11}P_2$ (453.01), monoclinic, space group $P2_1/c$, $T$ = 293(2) K, $a$ = 12.675, $b$ = 7.300, $c$ = 14.212 Å, $\beta$ = 108.125(2)°, $V$ = 1249.6 $Å^3$, $Z$ = 4, $d_{calcd}$ = 2.408 $Mg/m^3$, $F(000)$ = 880, $\mu$(Mo-$K_\alpha$) = 3.730 $mm^{-1}$, 9815 reflections collected, 3093 unique ($R_{int}$ = 0.0307). $R_1$ = 0.0236, $wR_2$ = 0.0612 [$I > 2\sigma(I)$], $R_1$ = 0.0263 and $wR_2$ = 0.0627 (all data) and final Gof = 1.056.

**Crystal Data for 2:** $C_4H_{10}LaNO_9P_2$ (416.98), orthorhombic, space group $Pca2_1$, $T$ = 293(2) K, $a$ = 9.9649(13), $b$ = 10.5833(15), $c$ = 10.5288(15) Å, $V$ = 1110.4(3) $Å^3$, $Z$ = 4, $d_{calcd}$ = 2.494 $Mg/m^3$, $F(000)$ = 800, $\mu$(Mo-$K_\alpha$) = 4.173 $mm^{-1}$, 8258 reflections collected, 2418 unique ($R_{int}$ = 0.0891). $R_1$ = 0.0644, $wR_2$ = 0.1039 [$I > 2\sigma(I)$], $R_1$ = 0.0793 and $wR_2$ = 0.1113 (all data) and final Gof = 1.142.

**Crystal Data for 3:** $C_{20}H_{33}LaN_2O_{19}P_4$ (868.27), triclinic, space group $P\bar{1}$, $T$ = 293(2) K, $a$ = 8.246(17), $b$ = 10.58(2), $c$ = 16.79(3) Å, $\alpha$ = 90.34(3), $\beta$ = 90.21(4), $\gamma$ = 93.52(3)°, $V$ = 1461(5) $Å^3$, $Z$ = 2, $d_{calcd}$ = 1.973 $Mg/m^3$, $F(000)$ = 872, $\mu$(Mo-$K_\alpha$) = 1.772 $mm^{-1}$, 11453 reflections collected, 6609 unique ($R_{int}$ = 0.0456). $R_1$ = 0.0542, $wR_2$ = 0.1036 [$I > 2\sigma(I)$], $R_1$ = 0.0722 and $wR_2$ = 0.1143 (all data) and final Gof = 1.088.

**Crystal Data for 4:** $C_{20}H_{26}ErN_2O_{16}P_4$ (841.57), triclinic, space group $P\bar{1}$, $T$ = 293(2) K, $a$ = 7.9178(7), $b$ = 12.5608(5), $c$ = 15.3008(7) Å, $\alpha$ = 110.453(7), $\beta$ = 90.296(12), $\gamma$ = 90.586(13)°, $V$ = 1425.66(15) $Å^3$, $Z$ = 2, $d_{calcd}$ = 1.960 $Mg/m^3$, $F(000)$ = 832, $\mu$(Mo-$K_\alpha$) = 3.247 $mm^{-1}$, 11127 reflections collected, 6439 unique ($R_{int}$ = 0.0456). $R_1$ = 0.0528, $wR_2$ = 0.0984 [$I > 2\sigma(I)$], $R_1$ = 0.0684 and $wR_2$ = 0.1072 (all data) and final Gof = 1.107.

**Crystal Data for 5:** $C_{20}H_{23}ErN_2O_{13}P_2$ (728.60), triclinic, space group $P\bar{1}$, $T$ = 293(2) K, $a$ = 5.752(4), $b$ = 9.382(5), $c$ = 22.050(15) Å, $\alpha$ = 101.507(16), $\beta$ = 92.62(2), $\gamma$ = 98.155(19)°, $V$ = 1151.0(12) $Å^3$, $Z$ = 2, $d_{calcd}$ = 1.715 $Mg/m^3$, $F(000)$ = 718, $\mu$(Mo-$K_\alpha$) = 3.839 $mm^{-1}$, 3176 reflections collected, 2217 unique ($R_{int}$ = 0.0277). $R_1$ = 0.0440, $wR_2$ = 0.1207 [$I > 2\sigma(I)$], $R_1$ = 0.0469 and $wR_2$ = 0.1239 (all data) and final Gof = 1.033.

CCDC-295013 to -295017 (for **1**–**5**) contain the supplementary crystallographic data for this paper. These data can be obtained free of charge from The Cambridge Crystallographic Data Centre via www.ccdc.cam.ac.uk/data_request/cif.

**Supporting Information** (see footnote on the first page of this article): X-ray powder diffraction patterns for compounds **2**–**5**.

## Acknowledgments

This work was supported by the National Natural Science Foundation of China (20371047, 20521101) and NSF of Fujian Province (E0420003).

[1] a) E. W. Stein Sr, A. Clearfield, M. A. Subramanian, *Solid State Ionics* **1996**, *83*, 113; b) G. Alberti, U. Costantino in *Comprehensive Supramolecular Chemistry* (Ed.: J. M. Lehn), Pergamon-Elsevier Science Ltd., London, **1996**, p. 1; c) A. Clearfield, *Curr. Opin. Solid State Mater. Sci.* **1996**, *1*, 268; d) A. Clearfield, "Metal phosphonate chemistry", in *Progress in Inorganic Chemistry* (Ed.: K. D. Karlin), John Wiley & Sons, New York, **1998**, vol. 47, p. 371 (and references therein).

[2] a) N. L. Rosi, M. Eddaoudi, J. Kim, M. O'Keeffe, O. M. Yaghi, *Angew. Chem. Int. Ed.* **2002**, *41*, 284; b) M. Eddaoudi, J. Kim, M. O'Keeffe, O. M. Yaghi, *J. Am. Chem. Soc.* **2002**, *124*, 376–377; c) M. E. Braun, C. D. Steffek, J. Kim, P. G. Rasmussen, O. M. Yaghi, *Chem. Commun.* **2001**, 2532.

[3] a) A. Distler, L. Lohse, S. C. Sevov, *J. Chem. Soc., Dalton Trans.* **1999**, 1805; b) V. Soghomonian, Q. Chen, R. C. Haushalter, J. Zubieta, *Angew. Chem. Int. Ed. Engl.* **1995**, *34*, 223.

[4] a) S. Drumel, P. Janvier, D. Deniaud, B. Bujoli, *J. Chem. Soc., Chem. Commun.* **1995**, 1051; b) U. Costantino, M. Nocchetti, R. Vivani, *J. Am. Chem. Soc.* **2002**, *124*, 8428; c) S. O. H. Gutschke, D. J. Price, A. K. Powell, P. T. Wood, *Angew. Chem.*

 © 2006 Wiley-VCH Verlag GmbH & Co. KGaA, Weinheim 

*Int. Ed.* **1999**, *38*, 1088; d) E. Galdecka, Z. Galdecki, P. Gawryszewska, J. Legendziewicz, *New J. Chem.* **2000**, *24*, 387; e) L.-M. Zheng, P. Yin, X.-Q. Xin, *Inorg. Chem.* **2002**, *41*, 4084.
[5] a) N. Stock, S. A. Frey, G. D. Stucky, A. K. Cheetham, *J. Chem. Soc., Dalton Trans.* **2000**, 4292; b) S. Ayyappan, G. D. Delgado, A. K. Cheetham, G. Ferey, C. N. R. Rao, *J. Chem. Soc., Dalton Trans.* **1999**, 2905; c) S. Drumel, M. Bujolidoeuff, P. Janvier, B. Bujoli, *New J. Chem.* **1995**, *19*, 239.
[6] a) C. Lei, J.-G. Mao, Y.-Q. Sun, H.-Y. Zeng, A. Clearfield, *Inorg. Chem.* **2003**, *42*, 6157; b) J.-L. Song, J.-G. Mao, Y.-Q. Sun, A. Clearfield, *Eur. J. Inorg. Chem.* **2003**, 4218; c) S.-M. Ying, J.-G. Mao, *Eur. J. Inorg. Chem.* **2004**, 1270; d) J.-L. Song, C. Lei, Y.-Q. Sun, J.-G. Mao, *J. Solid State Chem.* **2004**, *177*, 2557.
[7] F. Serpaggi, G. Ferey, *J. Mater. Chem.* **1998**, *8*, 2749.
[8] a) H. L. Ngo, W.-B. Lin, *J. Am. Chem. Soc.* **2002**, *124*, 14298; b) J. Plutnar, J. Rohovec, J. Kotek, Z. Zak, I. Lukes, *Inorg. Chim. Acta* **2002**, *335*, 27.
[9] a) K. L. Nash, R. D. Rogers, J. Ferraro, J. Zhang, *Inorg. Chim. Acta* **1998**, *269*, 211; b) L. V. Meervelt, P. Martello, J. P. Silvestre, R. Rochdaoui, M. R. Lee, N. Q. Dao, C. G. Walrand, *Z. Kristallogr.* **2002**, *217*, 27; c) L. M. Shkolnikova, A. A. Masyuk, G. V. Polyanchuk, E. G. Afonin, A. L. Poznyak, V. E. Zavodnik, *Koord. Khim.* **1989**, *15*, 1424.
[10] C. Serre, N. Stock, T. Bein, G. Ferey, *Inorg. Chem.* **2004**, *43*, 3159.
[11] a) R. C. Wang, Y. P. Zhang, H. L. Hu, R. R. Frausto, A. Clearfield, *Chem. Mater.* **1992**, *4*, 864; b) T. Glowiak, E. Huskowska, J. Legendziewicz, *Polyhedron* **1991**, *10*, 175.
[12] a) F. S. Richardson, *Chem. Rev.* **1982**, *82*, 541; b) W. D. Horrocks, D. R. Sudnik, *J. Am. Chem. Soc.* **1979**, *101*, 334; c) *Biochemistry of the Elements* vol. 8 (*Biochemistry of the Lanthanides*) (C. H. Evans), Plenum, New York, **1990**; d) J. Legendziewicz, *J. Appl. Spectrosc.* **1995**, *62*, 189.
[13] F. Serpaggi, G. Ferey, *Inorg. Chem.* **1999**, *38*, 4741.
[14] a) A. Clearfield, C. V. K. Sharma, B.-L. Zhang, *Chem. Mater.* **2001**, *13*, 3099; b) S. W. A. Bligh, N. Choi, C. F. G. C. Geraldes, S. Knoke, M. McPartlin, M. J. Sanganee, T. M. Woodroffe, *J. Chem. Soc., Dalton Trans.* **1997**, 4119; c) P. Vojtisek, P. Ciger, J. Kotek, J. Rudovsky, P. Hermann, I. Lukes, *Inorg. Chem.* **2005**, *44*, 5591.
[15] J. P. Silvestre, N. Q. Dao, M. R. Lee, *Phosphorus, Sulfur Silicon Relat. Elem.* **2001**, *176*, 173.
[16] a) J.-L. Song, C. Lei, J.-G. Mao, *Inorg. Chem.* **2004**, *43*, 5630; b) J.-L. Song, J.-G. Mao, *Chem. Eur. J.* **2005**, *11*, 1417.
[17] a) E. Galdecka, Z. Galdecki, P. Gawryszewska, J. Legendziewicz, *New J. Chem.* **2000**, *24*, 387; b) J. Legendziewicz, P. Gawryszewska, E. Gałdecka, Z. Gałdecki, *J. Alloys Compd.* **1998**, *275*, 356.
[18] S. Bauer, T. Bein, N. Stock, *Inorg. Chem.* **2005**, *44*, 5882.
[19] a) CrystalClear ver. 1.3.5., Rigaku Corp., Woodlands, TX, **1999**; b) G. M. Sheldrick, *SHELXTL*, *Crystallographic Software Package*, SHELXTL, Version 5.1, Bruker-AXS, Madison, WI, **1998**.

Received: January 14, 2006
Published Online: March 27, 2006

 © 2006 Wiley-VCH Verlag GmbH & Co. KGaA, Weinheim 

DOI: 10.1002/ejic.200500871

# Synthesis, Characterization, and NO Release Study of the *cis*- and *trans*-$[Ru(Bpy)_2(SO_3)(NO)]^+$ Complexes

**Francisco O. N. Silva,[a] Sérgio X. B. Araújo,[a] Alda K. M. Holanda,[a] Emerson Meyer,[a] Francisco A. M. Sales,[a] Izaura C. N. Diógenes,[a] Idalina M. M. Carvalho,[a] Ícaro S. Moreira,*[a] and Luiz G. F. Lopes*[a]**

**Keywords:** Ruthenium / Nitrogen oxides / Bioinorganic chemistry / Drug design

Aiming at the development of novel NO donors, the synthesis and reactivity of the *trans*-$[Ru(bpy)_2(SO_3)(NO)](PF_6)$ and *cis*-$[Ru(bpy)_2(L)(NO)](PF_6)_n$ complexes (L = imidazole, isonicotinamide, or sulfite ions) were investigated. The complexes were characterized and the NO release capabilities were evaluated. The rate constant for NO dissociation for the *cis*-$[Ru(bpy)_2(SO_3)(NO)]^+$ complex is $k = 2.0 \cdot 10^{-3}$ s$^{-1}$. The *cis* and *trans*- $[Ru(bpy)_2(SO_3)(NO)]^+$ complexes showed promising physical-chemical properties towards nitric oxide generation, and great stability towards hydroxide attack in the 2.0–9.0 pH range. The reduction potential of the $\{RuNO\}^{6/7}$ process of the *cis* and *trans*-$[Ru(bpy)_2(SO_3)NO]^+$ complexes ($E_{1/2}$ = –0.14 and –0.34 V vs. Ag/AgCl) is appropriated for reduction in vivo by biological reducing agents, with consequent NO release.

(© Wiley-VCH Verlag GmbH & Co. KGaA, 69451 Weinheim, Germany, 2006)

## Introduction

Nitric oxide (NO) has a critical role in physiological and pathophysiological processes in the cardiovascular system.[1–3] NO insufficiency limits NO-mediated signal transduction of normal or protective physiological processes. Dysfunction of the normally protective endothelium is found in several cardiovascular diseases, including hypertension, coronary heart disease, and arterial thrombotic disorders.[4] The endothelial dysfunction leads to nitric oxide (NO) deficiency, which has been implicated in the underlying pathobiology of many of these disorders.[5] Exogenously administered NO donors have provided the basis for a broad field of pharmacotherapeutics in cardiovascular medicine. Pharmacological compounds that release NO have been useful tools for evaluating the pivotal role of NO in cardiovascular physiology and therapeutics. NO donors are pharmacologically active substances that spontaneously release or are metabolized to NO or its redox partners. For example in cases of emergency hypertension or heart attacks, NO needs to be administered due to its vasodilator effect. Sodium nitroprusside, $Na_2[Fe(CN)_5NO]\cdot 2H_2O$, is part of a class of compounds that release NO spontaneously and is the unique NO metal complex used clinically.[6] Problems associated with the use of $Na_2[Fe(CN)_5NO]\cdot 2H_2O$ include susceptibility to photolysis and oxidative breakdown through the action of the immune system, both of which lead to the release of cyanide.[7] There are also Ru-edta complexes that can control the levels of circulating NO such as K[Ru(Hedta)Cl] that exists in equilibrium with its aqua species.[8] This aqua species has been shown to be useful in some conditions such as septic shock (also for diabetes, arthritis, inflammation, and epilepsy) where excessive production of NO can be a problem. This can lead to arteries responding poorly to vasoconstrictor drugs during treatment.[9]

Many drugs have direct vasoactive effects and have been used to treat ischemic heart disease, heart failure, and hypertension for many years. Nevertheless, undesirable effects such as the short therapeutic half-life, adverse hemodynamic effects, and drug tolerance limit the use of most of them.[5] To overcome these limitations, the development of novel NO donors are of great interest. The literature[10–12] has pointed out that it is possible to modulate the NO reduction potential by coordination to transition metals and by the π character of the spectator ligands. Hence, the correct establishment of the NO reduction potential in a specific compound is an important requirement for its use as a metallodrug.[10] With this purpose in mind, we have investigated the synthesis and reactivity of the *trans*-$[Ru(bpy)_2(SO_3)(NO)](PF_6)$ and *cis*-$[Ru(bpy)_2(L)(NO)](PF_6)_n$ complexes, where L = imidazole (imN), isonicotinamide (isn), or sulfite ions ($SO_3^{2-}$), and bpy = 2,2′-bipyridine. The complexes were characterized in order to infer the correct composition and coordination modes of the ligands, and to evaluate their NO release capabilities.

[a] Departamento de Química Orgânica e Inorgânica, Universidade Federal do Ceará, Campus do Pici s/n,
cx. Postal 12200, 60455-900 Fortaleza-Ceará, Brazil
E-mail: icarosm@dqoi.ufc.br,
lopeslu@dqoi.ufc.br


InterScience
© 2006 Wiley-VCH Verlag GmbH & Co. KGaA, Weinheim

## Results and Discussion

The electronic spectra of the *cis*-$[Ru(bpy)_2L(NO_2)]^{+/-}$ nitro complexes (L = imN, isn, $SO_3^{2-}$) are dominated by intense (bpy)π*←dπ(Ru) MLCT bands (around 410 nm) and by the bpy intraligand bands, which are characteristic of the $Ru^{II}$-bipyridine complexes.[13,14] The bands observed in the 320–326 nm range for the *cis*-$[Ru(bpy)_2L(NO)]^{n+}$ and *trans*-$[Ru(bpy)_2(SO_3)(NO)]^+$ nitrosyl complexes (Table 1) are attributed to the (bpy)π*←dπ(Ru) MLCT transition. These bands are shifted to a higher energy range when compared with the spectra of the corresponding nitro complexes. This effect can be explained by the strong $(NO^+)$π*←dπ(Ru) backbonding interaction, which causes a large stabilization of the molecular orbitals that have a high contribution of the metal dπ levels. Unfortunately, the $(NO^+)$π*←dπ(Ru) transitions were not detected in the spectra probably because of superposition with those of (bpy)π*←dπ(Ru) transitions. These bands are expected to appear in the higher energy region of the spectra because of the stabilization of the dπ levels by the (bpy)π*←dπ(Ru) backbonding interaction. In fact, the $(NO^+)$π*←dπ(Ru) transition is observed in the range of 420–480 nm for $[Ru(NH_3)_4(NO)X]^{n+}$ complexes (X = $OH^-$, $Cl^-$, $Br^-$, and $I^-$), with a very weak intensity ($\varepsilon < 50$ $mol^{-1}\cdot cm^{-1}\cdot L$).[15,16] The intense bands observed at about 290 nm are assigned to the π*←π (bpy) transition, which commonly appears in the spectra of bis(2,2′-bipyridine)ruthenium(II) complexes.[17]

Table 1. Electronic spectra data for the nitro and nitrosyl-bis(2,2′-bipyridine)ruthenium(II) complexes, in 0.10 M $CF_3CO_2Na$ aqueous solution.

| Complexes | (bpy)π*←dπ(Ru) MLCT, $\lambda$ [nm] ($\varepsilon$, $mol^{-1}$ L·$cm^{-1}$) |
|---|---|
| *cis*-$[Ru(bpy)_2(imN)(NO_2)]^+$ | 412 ($7.30\cdot10^3$) |
| *cis*-$[Ru(bpy)_2(isn)(NO_2)]^+$ | 408 ($9.04\cdot10^3$) |
| *cis*-$[Ru(bpy)_2(SO_3)(NO_2)]^-$ | 405 ($1.02\cdot10^3$) |
| *cis*-$[Ru(bpy)_2(imN)(NO)]^{3+}$ | 325 sh ($8.92 \times 10^3$) |
| *cis*-$[Ru(bpy)_2(isn)(NO)]^{3+}$ | 321 sh ($1.11\cdot10^4$) |
| *cis*-$[Ru(bpy)_2(SO_3)(NO)]^+$ | 326 ($8.27\cdot10^3$) |
| *trans*-$[Ru(bpy)_2(SO_3)(NO)]^+$ | 320 sh ($3.08\cdot10^4$) |

The electronic spectra of the nitrosyl complexes were observed to be pH dependent. As the pH of the solutions containing these complexes is increased, new intense bands with a maximum in the 400–450 nm range are observed. These bands can be assigned to the (bpy)π*←dπ(Ru) MLCT transition of the nitro species formed according to the chemical equilibrium displayed in Reaction (1).[18–20] Similar behavior was observed in the spectra of the *trans*-$[Ru(NH_3)_4(L)(NO)]^{3+}$ complexes.[21]

The pH vs. absorbance plots for all nitrosyl complexes showed only one inflection (Figure 1), indicating a unique equilibrium assigned to the $[NO]^+ \rightleftharpoons [NO_2]^-$ interconversion, with both species present in equal concentrations at pH = 1.45 for L = isn, pH = 5.54 for L = imN, and pH = 10.32 for L = $SO_3^{2-}$. The calculated $K_{eq}$ equilibrium constants are displayed in Table 2 together with $\nu(NO^+)$ and $E_{1/2}\{RuNO\}^{6/7}$ values for correlation purposes. The electrophilic character of coordinated nitrosyl has been associated with the ν(NO) frequency.[22] The ν(NO) values reflect the electron density at the nitrogen atom of the nitrosyl group, which is the target for the nucleophilic attack. The literature has established that complexes with ν(NO) greater than 1860 $cm^{-1}$ are reactive $OH^-$.[16] It has also been observed that the equilibrium constant [Reaction (1)] is greater as the ν(NO) frequency is more positive. Therefore, the $K_{eq}$ values might also reflect the electrophilic character of the nitrosyl complex involved in the chemical equilibrium.

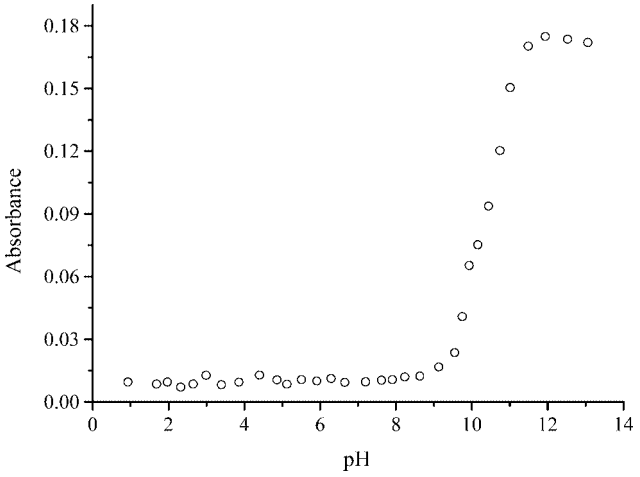


Figure 1. Spectrophotometric titration of $[Ru(bpy)_2(SO_3)(NO)]^+$ complex, $\lambda_{max}$ = 410 nm; $\mu$ = 1.0 M $CF_3CO_2Na$ aqueous solution.

Table 2. Values of $K_{eq}$ for the equilibrium (*1*), $\nu(NO^+)$, and $E_{1/2}\{RuNO\}^{6/7}$ for the $[Ru(bpy)_2(L)(NO)]^{n+}$ complexes, pH = 2.0; *pH = 1.0.

| Complexes | $K_{eq}$ | $\nu(NO^+)$ [$cm^{-1}$] | $E_{1/2}$, $\{RuNO\}^{6/7}$ [V] |
|---|---|---|---|
| *cis*-$[Ru(bpy)_2(isn)(NO)](PF_6)_3$ | $1.80\cdot10^{25}$ | 1948 | +0.34* |
| *cis*-$[Ru(bpy)_2(imN)(NO)](PF_6)_3$ | $1.42\cdot10^{16}$ | 1944 | +0.20 |
| *cis*-$[Ru(bpy)_2(SO_3)(NO)](PF_6)$ | $1.74\cdot10^{7}$ | 1911 | –0.14 |
| *trans*-$[Ru(bpy)_2(SO_3)(NO)](PF_6)$ | $6.42\cdot10^{3}$ | 1881 | –0.34 |

From the data presented in Table 2, the proportionality between the $K_{eq}$, $\nu(NO^+)$, and $E_{1/2}$ parameters is clearly observed. Compounds in which the $NO^+$ character is favored [larger $\nu(NO^+)$] present large $K_{eq}$ values in the whole series. In fact, the greater the electron deficiency of the NO moiety resulting from the π-acid character of the $[Ru(bpy)_2L]^{2+}$ group, the larger will be the driving force for reaction of

$$[Ru(bpy)_2(L)(NO)]^n_{(aq)} + 2\ OH^-_{(aq)} \overset{K_{eq}}{\rightleftharpoons} [Ru(bpy)_2(L)(NO_2)]^{(n-2)}_{(aq)} + H_2O_{(aq)} \quad (1)$$

 © 2006 Wiley-VCH Verlag GmbH & Co. KGaA, Weinheim 

the coordinated $NO^+$ with $OH^-$ in Reaction (1). The $E_{1/2}$ values are in accordance with the $\nu(NO^+)$ and $K_{eq}$ data, and reflect well the influence of electronic effects on the reactivity of the nitrosyl metal complexes. In addition, a good linear correlation between $E_{1/2}$ $\{RuNO\}^{6/7}$ and $\nu(NO^+)$ is observed for the series of nitrosyl complexes. From Figure 2, it is observed that the lower redox potential of the $\{RuNO\}^{6/7}$ redox couple gives also a lower $\nu(NO^+)$, which is in agreement with the decrease seen in the electronic density of the $NO^+$ group because of the higher π-acceptor character of the L ligand.

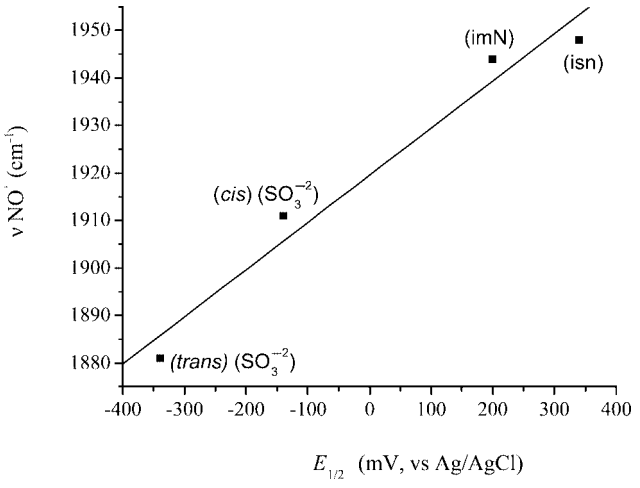


Figure 2. $\nu(NO^+)$ vs. $E_{1/2}$ $\{RuNO\}^{6/7}$ plot for the $[Ru(bpy)_2(L)NO]^{n+}$ complexes.

Generally, when a good σ-donor ligand is coordinated to nitrosyl-metal complexes in the *trans* position in relation to the $NO^+$ moiety, an increase of the $NO^+\leftarrow M$ backbonding interaction occurs and the $\nu(NO^+)$ stretching shifts to a lower frequency in the infrared (IR) spectrum. Conversely, the electron-withdrawing capability of π-acid ligands reduces the $NO^+\leftarrow M$ backbonding interaction causing an opposite effect on the $\nu(NO^+)$.[23] It should be noted that the $\nu(NO^+)$ peak of free NO is located at 1876 $cm^{-1}$, but in the metal complexes it is very sensitive to the binding properties and oxidation states of the metal ion. The literature reports that the $\nu(NO^+)$ frequencies for *cis*-$[Ru^{II}(bpy)_2(NO)L]$ complexes (L = $N_3^-$, $Cl^-$, $NO_2^-$, $NH_3$, py, $CH_3CN$) have been observed in the 1923–1970 $cm^{-1}$ range.[17] For $[Ru^{II}(NH_3)_5(NO)]^{3+}$[24] and *trans*-$[Ru^{II}(NH_3)_4(NO)L]$[25] complexes [L = imidazole, L-histidine, py, isonicotinamide, pyrazine, $P(OEt)_3$], $\nu(NO^+)$ values lie in the 1909–1941 $cm^{-1}$ range, whereas for L = $SO_3^{2-}$, the ν(NO) value is 1871 $cm^{-1}$. In the case of *trans*-$[Ru^{II}(py)_4(NO)L]$[26] complexes, for L = $Cl^-$ and $Br^-$, $\nu(NO^+)$ = 1910 and 1901 $cm^{-1}$, respectively, but for L = $OH^-$, $\nu(NO^+)$ = 1860 $cm^{-1}$. Also, $\nu(NO^+)$ = 1860 $cm^{-1}$ is observed for the *trans*-$[RuCl([15]aneN_4)NO]^{2+}$ complex.[27] In such examples, the ruthenium center has been considered as mainly $Ru^{II}$, thus giving a predominantly $NO^+$ character to the nitrosyl ligand.

On the basis of these discussions, the very intense peaks observed in the IR spectra of the nitrosyl complexes at 1948, 1944, 1911, and 1882 $cm^{-1}$ for the *cis*-$[Ru(bpy)_2(isn)(NO)](PF_6)_3$, *cis*-$[Ru(bpy)_2(imN)(NO)](PF_6)_3$, *cis*-$[Ru(bpy)_2(SO_3)(NO)](PF_6)$, and *trans*-$[Ru(bpy)_2(SO_3)(NO)](PF_6)$ complexes, respectively, are assigned to $\nu(NO^+)$. The most relevant features in the IR spectra of the nitro complexes are the strong absorptions at 1340 and 1280 $cm^{-1}$ attributed respectively to the symmetric and asymmetric $\nu(NO_2)$ stretching modes of the coordinated nitro ligand.[28] It is important to point out that the infrared spectrum for the product isolated from Reaction (1) for L = $SO_3^{2-}$ at pH 12.0 does not show the ν(NO) frequency value, characteristic of the $NO^+$ form. Instead of the band at 1911 $cm^{-1}$, this spectrum presented bands at 1321 and 1271 $cm^{-1}$, which are associated with the asymmetric and symmetric stretching mode of the nitro ligand ($NO_2$). This result supports the proposed equilibrium suggested by Reaction (1), in agreement with that reported in the literature.[21,23]

To better characterize the nitrosyl complexes, their $^1H$ NMR, 2D COSY, and HMQC spectra were acquired. Figure 3 illustrates the HMQC spectrum for the *cis*-$[Ru(bpy)_2(imN)(NO)]^{3+}$ complex. The presence of all signals of the N-heterocyclic ring suggests that the imN and isn ligands are coordinated to the metal center through the nitrogen atom.[10] The appearance of 16 signals for the hydrogen atoms of the two bipyridine molecules suggests that all hydrogen atoms are nondiamagnetically equivalent,[29,30] strongly indicating the *cis* configuration for the $[Ru(bpy)_2(isn)(NO)]^{3+}$, $[Ru(bpy)_2(imN)(NO)]^{3+}$, and $[Ru(bpy)_2(SO_3)(NO)]^+$ complexes. On the other hand, the $^1H$ NMR spectrum of the *trans*-$[Ru(bpy)_2(SO_3)(NO)]^+$ complex shows only four signals at $\delta$ = 8.85 ppm (d; $H_6$, $H_{11}$), $\delta$ = 8.57 ppm (d; $H_3$, $H_8$), $\delta$ = 8.40 ppm (t; $H_5$, $H_{10}$), and $\delta$ = 7.87 ppm (t; $H_4$, $H_9$), which is characteristic of the *trans* configuration of the bipyridine ligands.[31]

The cyclic voltammograms (Figure 4) of the nitro complexes show only one reversible redox process. The data are summarized in Table 3.

Because of the π-acceptor character of the imidazole, isonicotinamide, and nitro moieties, all values of $E_{1/2}$ for the $Ru^{III/II}$ redox couple are more positive than that for the $[Ru(bpy)_2Cl_2]$ complex in aqueous solution.[32]

The electrochemical studies of the nitrosyl complexes were performed by using cyclic voltammetry and square wave voltammetry techniques. Figure 5 presents the cyclic voltammogram of the *cis*-$[Ru(bpy)_2(SO_3)(NO)]^+$ complex in an aqueous medium, at pH = 7.0. The electrochemical data for all complexes are illustrated in Table 2.

By applying a negative scan potential to the working electrode, starting from +0.90 V, only one reversible electrochemical process characteristic of the $\{RuNO\}^{6/7}$ redox couple was observed (Figure 5, dotted line). With a positive scan potential, a second electrochemical process is observed at 0.72, 0.70, and 0.62 V for L = isn, imN, and $SO_3^{2-}$, respectively. This process is strongly dependent on the $NO^{+/0}$ redox couple, as can be observed in Figure 5 (solid line), and is assigned to the $Ru^{III/II}$ redox process of the $[Ru(bpy)_2(L)(H_2O)]^{2+}$ complexes, which are generated by NO dissociation from the $[Ru(bpy)_2(L)(NO)]^{n+}$ nitrosyl compounds. These results suggest the existence of a chemi-

 © 2006 Wiley-VCH Verlag GmbH & Co. KGaA, Weinheim 

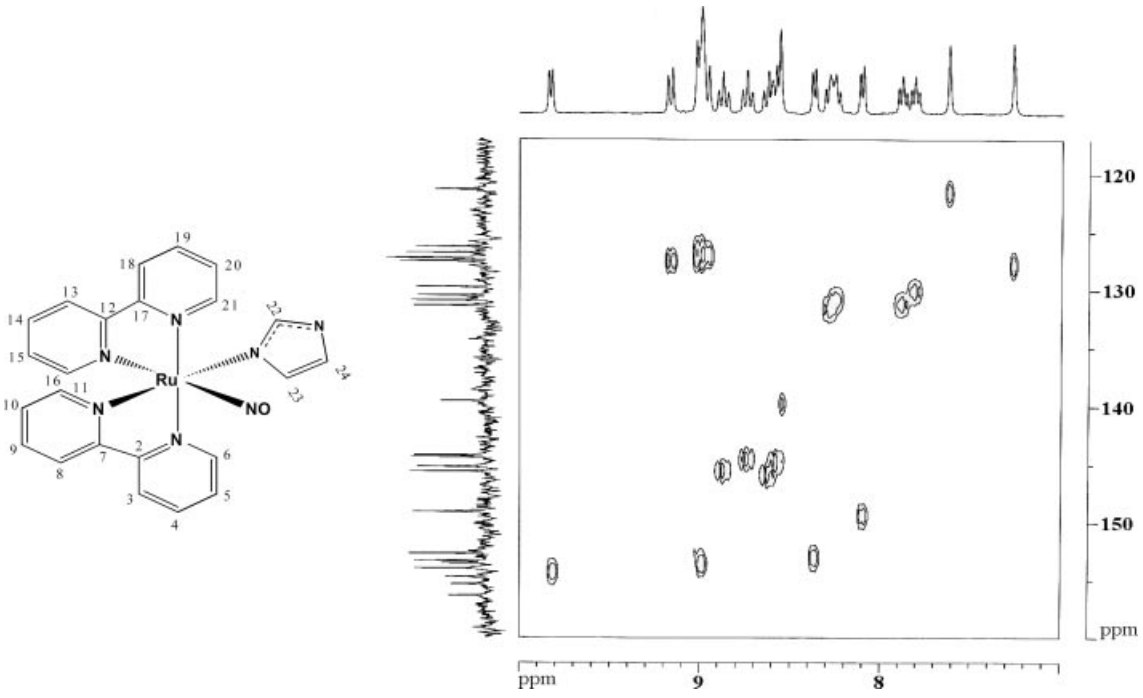


Figure 3. HMQC spectrum of *cis*-$[Ru(bpy)_2(imN)(NO)]^{3+}$ in $CD_3COCD_3$.

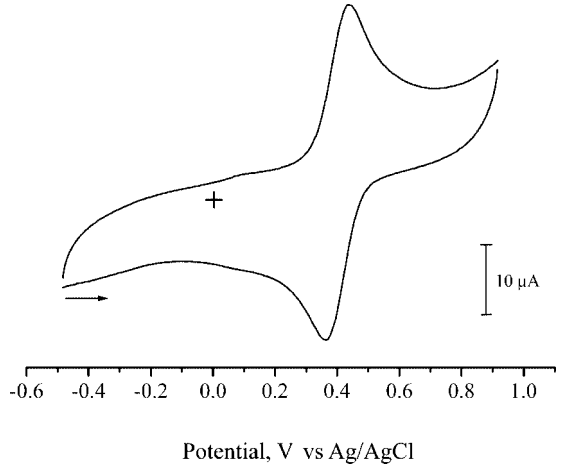


Figure 4. Cyclic voltammograms at 0.10 $Vs^{-1}$ of the *cis*-$[Ru(bpy)_2(SO_3)(NO_2)]^-$ complex in 0.10 M $CF_3CO_2Na$ aqueous solution, pH 7.0.

Table 3. $E_{1/2}$ values for the $Ru^{III/II}$ redox couple in $[Ru(bpy)_2L^1L^2]^{+/2+}$ complex ions.

| $L^1$, $L^2$ | $E_{1/2}$ [V] |
|---|---|
| isn, $NO_2^-$ | +0.97 |
| imN, $NO_2^-$ | +0.75 |
| $SO_3^{2-}$, $NO_2^-$ | +0.45 |
| $SO_3^{2-}$, $H_2O$ | +0.38 |

cal reaction that precedes the oxidation of the metal center in the aqua complexes. A reasonable interpretation of the electrochemical results is proposed in Reactions (2), (3), and (4).

$$[Ru^{II}(bpy)_2(L)(NO^+)]^{3+} + e^- \underset{}{\overset{-0.14}{\rightleftharpoons}} [Ru^{II}(bpy)_2(L)(NO^0)]^{2+} \quad (2)$$

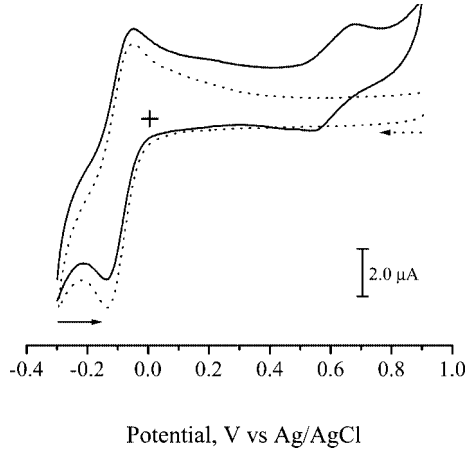


Figure 5. Cyclic voltammograms at 0.10 $Vs^{-1}$ of the *cis*-$[Ru(bpy)_2(SO_3)(NO)]^+$ complex in 0.10 M $CF_3CO_2Na$ aqueous solution, pH 7.0, scan starting at –0.3 V (solid line) and at 0.9 V (dotted line). + → $i$ = 0.0 μA and $E$ = 0.0 V.

$$[Ru(bpy)_2(L)(NO^0)]^{2+} + H_2O \xrightarrow{k_{NO}} [Ru(bpy)_2(L)(H_2O)]^{2+} + NO^0 \quad (3)$$

$$[Ru^{II}(bpy)_2(L)(H_2O)]^{2+} \underset{}{\overset{+0.62}{\rightleftharpoons}} [Ru^{III}(bpy)_2(L)(H_2O)]^{3+} + e^- \quad (4)$$

The chemical scheme of the reaction proposed in Reaction (3) is corroborated by the redox process observed in the 0.72–0.62 V range, which is characteristic of the aqua complex, illustrated in Figure 5 (solid line).

Aiming to reinforce this assignment, the square wave voltammograms for the *cis*-$[Ru(bpy)_2(L)(NO)]^{n+}$ complexes were acquired by a change in the time polarization of the

 © 2006 Wiley-VCH Verlag GmbH & Co. KGaA, Weinheim 

working electrode, at –0.30 V. For all nitrosyl complex series, it was observed that the peak current related to the $Ru^{III/II}$ redox process increases with an increase in time polarization. Figure 6 illustrates the electrochemical behavior of the *cis*-$[Ru(bpy)_2(SO_3)(NO)]^+$ complex.

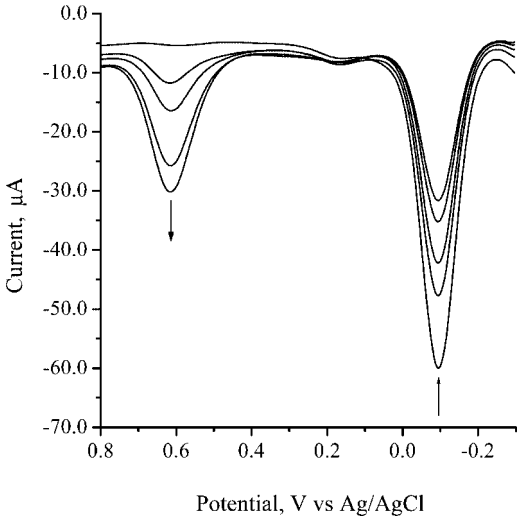


Figure 6. Square wave voltammogram at 0.10 $Vs^{-1}$ of the *cis*-$[Ru(bpy)_2(SO_3)(NO)]^+$ complex in 0.10 M $CF_3CO_2Na$ aqueous solution, pH 7.0, scans starting at –0.30 V.

The proposed scheme for the reaction is also supported by the electronic and FTIR spectra obtained for the $[Ru(bpy)_2(L)(NO)]^{3+}$ complexes acquired after the electrolysis experiments in which the potential was controlled at –0.30 V. Upon reduction, the electronic spectrum showed the two MLCT bands characteristic of the $[Ru(bpy)_2(L)(H_2O)]^{2+}$ complexes.[32] Furthermore, the IR spectra of all the reduced species, in the solid state, do not present the characteristic $\nu(NO^+)$ band. The rate constant of the NO dissociation, determined by the chronoamperometric method, was $k_{NO} = 2.0 \cdot 10^{-3} \cdot s^{-1}$ for $L = SO_3^{2-}$.

Preliminary photochemical studies of the nitrosyl complexes presented here were performed by irradiation at 355 nm wavelength. The electronic spectra changes observed during the photolysis of the *cis*-$[Ru(bpy)_2(SO_3)(NO)]^+$ complex in aqueous solution are presented in Figure 7.

From Figure 6, the appearance of the LMCT band at 450 nm is clearly observed, typical of the *cis*-$[Ru(bpy)_2(SO_3)(OH)]$ generated after the release of NO, in accordance with Scheme 1.[33]

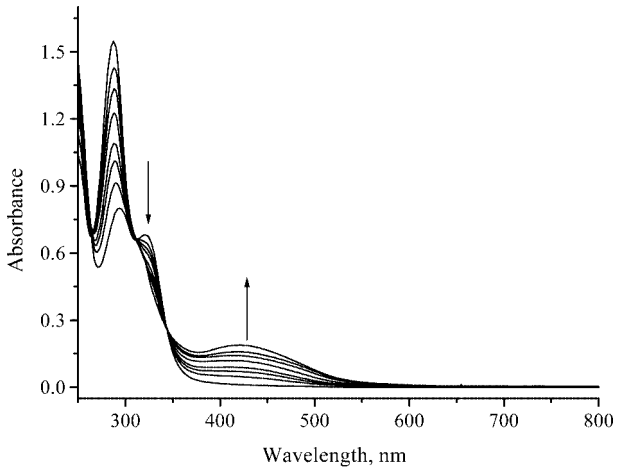


Figure 7. Spectral changes observed during the photolysis of the *cis*-$[Ru(bpy)_2(SO_3)(NO)]^+$ complex in $CF_3CO_2Na$ aqueous solution, pH 7.0 at 355 nm.

The calculated quantum yield for photochemical NO release from the *cis*-$[Ru(bpy)_2(SO_3)(NO)]^+$ complex was $0.10 \pm 0.01$. A similar photochemical behavior is found for the other complexes as reported in the literature.[34,35]

In addition, the photolysis of the *cis*-$[Ru(bpy)_2(SO_3)(NO)](PF_6)$ complex dispersed in solid KBr was performed and monitored by IR spectroscopy. The successively acquired IR spectra show the decrease in the intensity of the $\nu(NO^+)$ peak at 1915 $cm^{-1}$, which corroborates the proposed photochemical reaction (Scheme 1). The same behav-

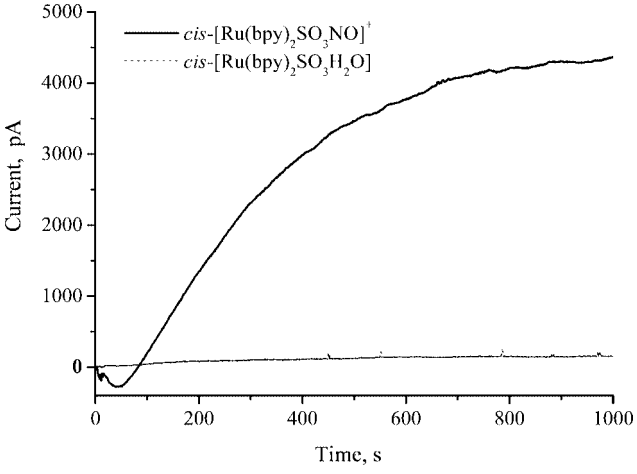


Figure 8. Chronoamperogram of NO release by reaction of $1.0 \cdot 10^{-4}$ M of $[Ru(bpy)_2(SO_3)(NO)]^+$ aqueous solution with cysteine, in a pH 7.4 phosphate buffer solution.

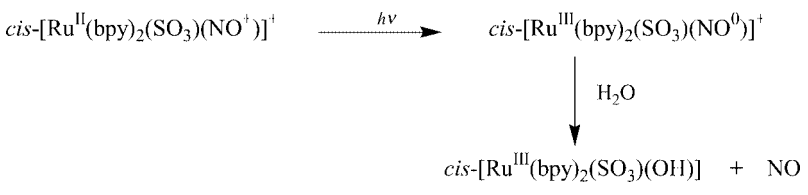


Scheme 1. Photochemical reaction of NO release by the *cis*-$[Ru(bpy)_2(SO_3)(NO)]^+$ complex.

 © 2006 Wiley-VCH Verlag GmbH & Co. KGaA, Weinheim 

ior has been observed for several nitrosyl ruthenium complexes.[25,27,35]

The *cis*- and *trans*-$[Ru(bpy)_2(SO_3)(NO)]^+$ nitrosyl complexes are also reduced by biological reducing agents, such as cysteine, with subsequent NO release. The signal recorded by the NO sensor was observed when a reaction with cysteine was initiated (Figure 8), which indicated the presence of free NO. These results, along with other biological experiments, are currently under investigation and will be reported in a further publication.

## Conclusion

The properties of the *cis* and *trans*- $[Ru(bpy)_2(SO_3)(NO)]^+$ species reported here suggest the considerable advantages provided by these complexes because of their nitric oxide generation, when compared with other NO donors reported in the literature.[36–38] For instance, the *trans*-$[Ru(NH_3)_4P(OEt)_3(NO)]^{3+}$ complex is considered a promising compound that enhances neuronal firing in mice hippocampal slices.[39] Unfortunately, this complex is chemically modified by hydroxide attack on the $NO^+$ moiety, resulting in dissociation of nitrite ions in physiological conditions.[39] Since the *cis* and *trans*- $[Ru(bpy)_2(SO_3)(NO)]^+$ complexes are inert to hydroxide attack in the 2.0–9.0 pH range, and the reduction potential of the $\{RuNO\}^{6/7}$ redox process for the *cis*-$[Ru(bpy)_2(SO_3)(NO)]^+$ species ($E_{1/2}$ = –0.14 V vs. Ag/AgCl) is close to that of the *trans*-$[Ru(NH_3)_4P(OEt)_3(NO)]^{3+}$ complex,[38] the sulfite complex is potentially a better NO donor in vivo.

## Experimental Section

**Chemicals and Reagents:** Ultrahigh purity water from a Millipore system was used throughout the experiments. $RuCl_3{\cdot}xH_2O$, imidazole, isonicotinamide, cysteine, and sodium sulfite were purchased from Aldrich and used without further purification. $[Ru(bpy)_2Cl_2]$ and *trans*-$[Ru(NH_3)_4(SO_2)Cl]Cl$ were prepared according to the literature procedures.[13,14,40]

**Synthesis of the Complexes:** The $[Ru(bpy)_2(SO_3)(H_2O)]$ complex was prepared by dissolving *trans*-$[Ru(NH_3)_4(SO_2)Cl]Cl$ (0.080 g, 0.26 mmol) in water (5.0 mL) under argon. 2,2′-Bipyridine (0.082 g, 0.52 mmol) was then added, and the mixture was stirred for 2 h. The solution volume was reduced under vacuum to approximately 2 mL. Addition of ethanol (10 mL) resulted in the precipitation of the product as a black solid. The precipitation of the product was induced by the addition of ethanol (10 mL). Yield (0.107 g) >80%. $C_{20}H_{16}N_4O_4RuS$ (511.38): calcd. C 46.92, H 3.52, S 6.25; found C 46.83, H 3.50, N 6.21.

The $[Ru(bpy)_2(L)(NO_2)](PF_6)_n$ complexes were prepared by following a standard procedure in all series. In a typical procedure, the reactions were performed by mixing a sample of $[Ru(bpy)_2Cl_2]$ (0.200 g, 0.41 mmol) and L (0.49 mmol; L = imidazole, isonicotinamide, sodium sulfide) in a 1:1 ethanol/water solution (20 mL). The mixtures were kept under reflux for 1 h. To these solutions, $NaNO_2$ (0.034 g, 0.49 mmol) was added and the mixtures were then allowed to react for 2 h, under reflux. The resulting solutions were concentrated by rotary evaporation until reduction of the volume to approximately 10 mL has been achieved. The solids were precipitated by the addition of saturated aqueous $NH_4PF_6$ solution (2 mL). Yields (0.209 g, 0.126 g, and 0.195 g for L = imidazole, isonicotinamide and sulfite, respectively) >75%. $C_{23}H_{19}F_6N_7O_2PRu$ (672.36): calcd. C 41.05, H 2.82, N 14.58; found C 41.23, H 2.79, N 14.38. $C_{26}H_{22}F_6N_7O_3PRu$ (726.46): calcd. C 42.94, H 3.02, N 13.49; found C 42.65, H 2.98, N 13.32. $C_{20}H_{16}N_5NaO_5Ru$ (562.38): calcd. C 42.67, H 2.85, N 12.45; found C 42.37, H 2.78, N 12.19.

The $[Ru(bpy)_2L(NO)](PF_6)_n$ complexes (L = imidazole, isonicotinamide, sulfite) were prepared by dissolving the $[Ru(bpy)_2L(NO_2)](PF_6)_n$ complexes (0.2 mmol) in methanol (15 mL) under an argon atmosphere. To this mixture, concentrated trifluoroacetic acid solution (2 mL) was added to promote the conversion of $NO_2$ to $NO^+$.[28] The reaction was monitored by HPLC by following the decrease of the peak at *Rt* = 6.78 min of the nitro complex at the expense of the increase of the peak at *Rt* = 3.93 min of the nitrosyl complex. After 2 h, no changes in the heights of the peaks were observed, indicating that the reaction is close to the saturation kinetics point. The solvent was then concentrated in a rotary evaporator to near 8 mL, and the solid was precipitated by the addition of ammonium hexafluorophosphate (1.0 g), collected by filtration and stored under vacuum. Yields (0.151 g, 0.160 g, and 0.107 g for L = imidazole, isonicotinamide, and sulfite, respectively) >80%. $C_{23}H_{23}F_{18}N_7O_3P_3Ru$ (982.36): calcd. C 28.15, H 2.36, N 9.99; found C 28.23, H 2.29, N 9.68. $C_{26}H_{22}F_{18}N_7O_2P_3Ru$ (1000.42): calcd. C 31.18, H 2.19, N 9.80; found C 31.09, H 2.12, N 9.75. $C_{20}H_{16}F_6N_5OPRuS$ (619.98): calcd. C 35.90, H 2.39, N 10.47; found C 35.81, H 2.31, N 10.32.

**Determination of the Equilibrium Constant:** The literature reports of the study of some similar chemical systems that exhibit the $NO_2^- \rightleftharpoons NO^+$ equilibrium.[23,41] The determination of the equilibrium constant $K_{eq}$ for Reaction (1) was carried out using the spectrophotometric method (absorbance measurements were performed at 410 nm). The total ionic strength was kept at 1.0 M with $CF_3CO_2Na$, according to similar studies reported for the $Fe^{II}$ [42] and $Ru^{II}$ [28] systems.

**Determination of the Rate Constant for the NO Dissociation:** The rate constant for the NO dissociation in the $[Ru(bpy)_2(SO_3)(NO)](PF_6)$ complex was determined by the chronoamperometric method, according to the procedure reported in the literature.[43]

**Quantum Yield:** Quantum yield was determined from initial spectral changes and was plotted vs. reaction percentage and extrapolated back to 0% reaction to minimize inner filter effects. The reported quantum yield is the average of, at least, three independent experiments.

**Apparatus:** Electrochemical experiments were performed with an electrochemical analyzer BAS 100W from Bioanalytical Systems at 25.0 ± 0.2 °C. These were generally performed on millimolar solutions of the complexes in 0.10 M $CF_3CO_2Na$ (pH = 7.0) aqueous solution by using a conventional three-electrode glass cell with a glassy carbon (ca. 0.13 $cm^2$ of geometrical area) and Pt foil as the working and auxiliary electrodes, respectively. The electrochemical experiments were performed at room temperature. The reversibility of the electrochemical processes was checked by the linearity of the peak height for the reduction process as a function of the square root of the scan rate, and the separation between the anodic (Ea) and cathodic potential peaks in the range of 50–80 mV at 25 °C.[44] NO release was measured with an ISONOP NO meter from World Precision Instruments that directly detects NO concentration by an amperometric technique.

The chromatographic analyses were performed with a Shimadzu liquid chromatograph equipped with a model LC-10AD pump and

 © 2006 Wiley-VCH Verlag GmbH & Co. KGaA, Weinheim 

an SPD-M10A UV/Visible photodiode-array detector with a CBM-10AD interface. An ODS column (250 mm × 4.6 mm id., 5 μm particles; from Altech) was used with an isocratic elution with 20:80 acetonitrile/water containing 0.1% $CF_3CO_2H$, pH = 3.7. The chromatograms were taken at a constant flow rate of 1.0 mL·min$^{-1}$. Samples for analyses were dissolved in the mobile phase and 5 μL of volumes were injected.

Elemental analyses were performed with a Perkin–Elmer CHN 2400 analyzer. Electronic spectra were acquired with a HP-8453 diode-array spectrophotometer. NMR spectra were obtained with a Bruker AVANCE DPX 500 spectrometer in $D_2O$ and $CD_3COCD_3$. IR spectra were obtained in KBr pellets with a Shimadzu IR Prestige-21 spectrophotometer.

Monochromatic irradiation at 355 nm was carried out using an Oriel 200-Watt universal arc lamp source in model 68805. The irradiation wavelength was selected with an Oriel interference filter for photolysis at the appropriate wavelength. The interference filter had an average band pass of 10 nm and the collimated beam intensities ranged from $4{\cdot}10^{-8}$ to $1{\cdot}10^{-9}$ einstein$^{-1}$·cm$^{-2}$ as determined by ferrioxalate actinometry. The progress of the photoreactions was monitored spectrophotometrically with an HP-8453 diode-array spectrophotometer.

## Acknowledgments

The authors acknowledge CNPq and CAPES, the Brazilian financial agencies. I. S. M. (CNPq, 477610/2003-0); F. O. N. S., A. K. M. H., S. X. B. A., F. A. M. S and E. M. are supported by the National Council for Scientific and Technological Development of Brazil. We are also grateful to CENAUREMN and Prof. D. W. Franco (IQSC) for use of the NMR and NO meter equipment, respectively.

[1] G. Kojda, K. Kottenberg, *Cardiovasc. Res.* **1999**, *41*, 514–523.
[2] R. P. Patel, J. McAndrew, H. Sellak, C. R. White, H. Jo, B. A. Freeman, V. M. Darley-Usmar, *Biochim. Biophys. Acta* **1999**, *1416–1455*, 385–400.
[3] B. D. Prendergast, V. F. Sagach, A. M. Shah, *Circulation* **1997**, *96*, 1320–1329.
[4] G. Kojda, D. Harrison, *Cardiovasc Res.* **1999**, 562–571.
[5] C. Napoli, L. J. Ignarro, *Nitric Oxide - Biology and Chemistry* **2001**, *5*, 88–97.
[6] Z. Guo, P. J. Sadler, *Adv. Inorg. Chem.* **2000**, 183–305.
[7] J. N. Bates, M. T. Baker, R. Guerra Jr, D. G. Harrison, *Biochem. Pharmacol.* **1991**, 157–165.
[8] S. P. Fricker, *Platinum Metals Rev.* **1995**, 150–159.
[9] Z. Guo, P. J. Sadler, *Angew. Chem. Int. Ed.* **1999**, *38*, 1513–1530.
[10] L. G. F. Lopes, A. Wieraszko, Y. El-Sherif, M. J. Clarke, *Inorg. Chim. Acta* **2001**, *312*, 15–22.
[11] E. S. Dodsworth, A. A. Vleck, A. B. P. Lever, *Inorg. Chem.* **1994**, *33*, 1045–1049.
[12] P. G. Wang, M. Xian, X. Tang, X. Wu, Z. Wen, T. Cai, A. J. Janczuk, *Chem. Rev.* **2002**, *102*, 1091–1134.
[13] B. P. Sullivan, D. J. Salmon, T. J. Meyer, *Inorg. Chem.* **1978**, *17*, 3334–3341.
[14] B. Durham, J. L. Walsh, C. L. Carter, T. J. Meyer, *Inorg. Chem.* **1980**, *19*, 860–865.
[15] A. A. Chevalier, L. A. Gentil, J. A. Olabe, *J. Chem. Soc., Dalton Trans.* **1991**, 1959.
[16] F. Roncaroli, M. E. Ruggiero, D. W. Franco, G. Estiu, J. A. Olabe, *Inorg. Chem.* **2002**, *41*, 5760–5769.
[17] R. W. Callahan, T. J. Meyer, *Inorg. Chem.* **1977**, *16*, 574–581.
[18] B. L. Heymore, J. A. Ibers, *Inorg. Chem.* **1975**, *14*, 3060–3070.
[19] R. S. Sundberg, R. F. Bryan, F. Taylor Jr, H. Taube, *J. Am. Chem. Soc.* **1974**, *96* 381–392.
[20] M. S. Thompson, T. J. Meyer, *J. Am. Chem. Soc.* **1981**, *103*, 5577–5579.
[21] S. S. S. Borges, C. U. Davanzo, E. E. Castellano, J. Zukerman-Schpector, S. C. Silva, D. W. Franco, *Inorg. Chem.* **1998**, *37*, 2670–2677.
[22] F. Bottomley, *Acc. Chem. Res.* **1978**, *11*, 158–165.
[23] E. Tfouni, M. Krieger, B. R. McGarvey, D. W. Franco, *Coord. Chem. Rev.* **2003**, 57–69.
[24] M. B. Fairey, R. J. Irving, *Spectrochim. Acta* **1966**, *22*, 359–365.
[25] M. G. Gomes, C. U. Davanzo, S. C. Silva, L. G. F. Lopes, P. S. Santos, D. W. Franco, *J. Chem. Soc., Dalton Trans.* **1998**, 601–607.
[26] F. Bottomley, M. Mukaida, *J. Chem. Soc., Dalton Trans.* **1982**, 1933–1937.
[27] F. S. Oliveira, V. Togniolo, T. T. Pupo, A. C. Tedesco, R. S. Da Silva, *Inorg. Chem. Com.* **2004**, 160–164.
[28] B. J. Godwin, T. J. Meyer, *Inorg. Chem.* **1971**, *10*, 471–474.
[29] R. Llanguri, J. J. Morris, W. C. Stanley, E. T. Bell-Loncella, M. Turner, W. J. Boyko, C. A. Bessel, *Inorg. Chim. Acta* **2001**, *315*, 53–65.
[30] M. Brissard, O. Convert, M. Gruselle, C. Guyard-Duhayon, R. Thouvenot, *Inorg. Chem.* **2003**, *42*, 1378–1385.
[31] H. Nagao, H. Nishimura, H. Funato, Y. Ichikawa, F. S. Howell, M. Mukaida, H. Kakihana, *Inorg. Chem.* **1989**, *28*, 3955–3959.
[32] J. L. Walsh, B. Durham, *Inorg. Chem.* **1982**, *21*, 329–332.
[33] V. Togniolo, R. S. Da Silva, A. C. Tadesco, *Inorg. Chim. Acta* **2001**, *316*, 7–12.
[34] R. G. Lima, M. G. Sauaia, D. Bonaventura, A. C. Tedesco, R. F. V. Lopez, L. M. Bendhack, R. S. Silva, *Inorg. Chim. Acta* **2005**, *358*, 2643–2650.
[35] R. M. Carlos, A. A. Ferro, H. A. S. Silva, M. G. Gomes, S. S. S. Borges, P. C. Ford, E. Tfouni, D. W. Franco, *Inorg. Chim. Acta* **2004**, *357*, 1381–1388.
[36] B. F. De Barros, J. C. Toledo, D. W. Franco, E. Tfouni, M. H. Krieger, *Nitric Oxide – Biology and Chemistry* **2002**, *6*, 50–56.
[37] D. Bonaventura, F. S. Oliveira, V. Togniolo, A. C. Tedesco, R. S. Da Silva, L. M. Bendhack, *Nitric Oxide* **2004**, *8*, 83–91.
[38] L. G. F. Lopes, E. E. Castellano, A. G. Ferreira, C. U. Davanzo, M. J. Clarke, D. W. Franco, *Inorg. Chim. Acta* **2005**, *358*, 2883–2890.
[39] A. Wieraszko, M. J. Clarke, D. K. Lang, L. G. F. Lopes, D. W. Franco, *Life Sci.* **2001**, *68*, 1535–1544.
[40] L. H. Vogt, J. L. Katz, S. E. Wiberley, *Inorg. Chem.* **1965**, *4*, 1157–1163.
[41] A. K. M. Holanda, D. L. Pontes, I. C. N. Diógenes, I. S. Moreira, L. G. F. Lopes, *Transition Met. Chem.* **2004**, *29*, 430–436.
[42] J. H. Swinehart, P. A. Rock, *Inorg. Chem.* **1966**, *5*, 573–576.
[43] W. M. Scwarz, I. Shain, *J. Phys. Chem.* **1965**, *69*, 30–40.
[44] I. Taniguchi in *Redox Chemistry and Interfacial Behaviour of Biological Molecules* (Eds.: D. Glenn, N. Katsumi), Plenum Press, New York, **1988**, 113.

Received: September 27, 2005
Published Online: March 27, 2006

 © 2006 Wiley-VCH Verlag GmbH & Co. KGaA, Weinheim 

DOI: 10.1002/ejic.200501005

# Coordination Mode of the Zinc(II) and Cadmium(II) Cations with *N*-(Diisopropoxyphosphoryl)thiobenzamide

**Felix D. Sokolov,[a] Damir A. Safin,*[a] Nail G. Zabirov,[a] Vasiliy V. Brusko,[a] Bulat I. Khairutdinov,[a] Dmitry B. Krivolapov,[b] and Igor A. Litvinov[b]**

**Keywords:** Chelates / Coordination modes / Crystal structures / (Thioacylamido)phosphates / Zinc(II) / Cadmium(II) complexes

Reaction of the potassium salt of *N*-(diisopropoxyphosphoryl)thiobenzamide ($i$PrO)$_2$P(O)NHC(S)C$_6$H$_5$ (**HL**) with Zn$^{II}$ and Cd$^{II}$ cations in aqueous EtOH leads to three different complexes: [Zn(L-*O*,*S*)$_2$] (**1**), [Cd$_2$(L-*O*,*S*)$_4$] (**2**) and [Cd(HL-*O*)$_2$(L-*O*,*S*)$_2$] (**3**). The structures of these compounds were investigated by single-crystal X-ray diffraction analysis, EI-MS and ES-MS, IR, $^1$H, $^{13}$C and $^{31}$P NMR spectroscopy and microanalysis. The zinc(II) atom in complex **1** is in a distorted tetrahedral ZnO$_2$S$_2$ environment formed by the C=S sulfur atoms and the P=O oxygen atoms of two deprotonated ligands. The cadmium(II) complex **2** is centrosymmetric and consists of dimeric species. Two [Cd(L-*O*,*S*)$_2$] moieties are connected by two bridging [S–Cd–S] units through the sulfur atoms of the ligand C=S groups. Complex **2** has a distorted trigonal-bipyramidal Cd(O$^{ax}$)$_2$(S$^{eq}$)$_3$ core. Complex **3** has a tetragonal-bipyramidal environment, Cd(O$^{ax}$)$_2$(O$^{eq}$)$_2$(S$^{eq}$)$_2$, and two neutral ligand molecules are coordinated in the axial positions through the oxygen atoms of the P=O groups. The base of the bipyramid is formed by two anionic ligands in a typical 1,5-O,S coordination mode. The ligands are in a *trans* configuration.

(© Wiley-VCH Verlag GmbH & Co. KGaA, 69451 Weinheim, Germany, 2006)

## Introduction

Amidophosphates of the type RC(X)NHP(Y)R′$_2$ (X, Y = O or S; R = Alk, Ar, ArNH, AlkNH, Alk$_2$N; R′ = OAlk, OAr, Ar) are attractive because of their ability to form stable chelates with d- and f-metal cations. These complexes possess antivirus[1] and anticancer activity,[2] and show nonlinear optical properties.[3] They can be used as components of ion-selective electrodes,[4–7] or as extragents and masking reagents in analytical chemistry.[8,9]

An application as structural blocks for the synthesis of supramolecular coordination compounds has excited a new wave of interest in the coordination chemistry of amidophosphates[10,11] and their nearest analogues such as 1,3-dichalcogenimidodiphosphinates R$_2$P(X)NHP(Y)R′$_2$[12] or carbamoylphosphane oxide R$_2$P(O)CH$_2$C(X)R′.[13] Polynuclear complexes of the type M$_n$L$_n$ (M = Co$^{II}$, Ni$^{II}$, Pd$^{II}$, Ag$^{I}$, Zn$^{II}$, Cd$^{II}$, Hg$^{II}$) of bis(bipodal) amidothiophosphates with the general formula [($i$PrO)$_2$P(S)NHC(S)NH]$_2$Z [Z = (CH$_2$)$_2$O(CH$_2$)$_2$, (CH$_2$)$_2$O(CH$_2$)$_2$O(CH$_2$)$_2$, (CH$_2$)$_2$, (CH$_2$)$_7$] have been investigated.[14,15] It was established that the cadmium(II) complex with bipodal amidophosphate, where Z = (CH$_2$)$_2$,[15] represents a macrocyclic dimer ($n$ = 2) containing two Cd$^{II}$ cations in a distorted tetrahedral CdS$_4$ environment.

The structure of Zn$^{II}$ and Cd$^{II}$ complexes with the general formula M[L-*S*,*S*′]$_2$ {L = [H$_2$NC(S)NP(S)(C$_6$H$_5$)$_2$]$^-$, M = Zn$^{II}$;[16] L = [C$_6$H$_5$NHC(S)NP(S)(O$i$Pr)$_2$]$^-$, M = Zn$^{II}$ or Cd$^{II}$;[17] L = [C$_6$H$_5$C(S)NP(S)(O$i$Pr)$_2$]$^-$, M = Zn$^{II}$[17] and Cd$^{II}$[18]} has been investigated by IR and NMR spectroscopy[16–18] and X-ray analysis.[16] It was established that, in all cases, there is chelate formation in which the metal cation has a distorted tetrahedral MS$_4$ environment.

In contrast to dithio derivatives, the Zn$^{II}$ and Cd$^{II}$ complexes with *N*-acylamidophosphates RC(X)NHP(Y)R′$_2$, containing both donor atoms of sulfur and oxygen (X ≠ Y), were not studied earlier. The substitution of two sulfur atoms in the central ion coordination sphere by oxygen atoms lowers the degree of stabilisation of π interactions. This leads to an increase in the coordination numbers of the Zn$^{II}$ and Cd$^{II}$ cation from 4 to 5 and 6, respectively. For example, it is known that Cd$^{II}$ complexes with R$_2$P(X)-NHP(Y)R′$_2$ (X = S, Y = O or X = Y = O) exhibit dinuclear structures in which the imidodiphosphinate anions act simultaneously as didentate ligands and as bridging units through the oxygen atoms of the P=O groups.[12]

The present work was carried out with the aim of appraising the influence of the cation (M$^{II}$ = Zn$^{II}$ and Cd$^{II}$) on the formation of either mono- or dinuclear complexes with the amidophosphate ligand ($i$PrO)$_2$P(O)NHC(S)C$_6$H$_5$ (**HL**).

[a] Department of Chemistry, Kazan State University, Kremlevskaya St. 18, 420008 Kazan, Russia
Fax: +7-843-254-3734
E-mail: damir.safin@ksu.ru
[b] A. E. Arbuzov Institute of Organic and Physical Chemistry, Arbuzov St. 8, 420088 Kazan, Russia

 © 2006 Wiley-VCH Verlag GmbH & Co. KGaA, Weinheim 

## Results and Discussion

### Synthesis

The ligand **HL** was prepared by reaction of thiobenzamide $C_6H_5C(S)NH_2$ with diisopropyl chlorophosphate $(iPrO)_2P(O)Cl$.

Complexes of **HL** with $Zn^{II}$ and $Cd^{II}$ cations (**1**–**3**) were prepared by the following procedure: the ligand was converted into the potassium salt **KL**, followed by reaction with salts of the corresponding metals. The compounds obtained are crystalline solids that are soluble in most polar solvents. Reaction of the salt **KL** with $ZnCl_2$ in aqueous EtOH leads only to the formation of the complex $[ZnL_2]$ (**1**). Reaction with $Cd(CH_3COO)_2$ leads to the formation of two complexes: $[Cd_2L_4]$ (**2**) and $[Cd(HL)_2L_2]$ (**3**) (Scheme 1). Complex **3** was separated from the mixture by extraction with *n*-hexane.

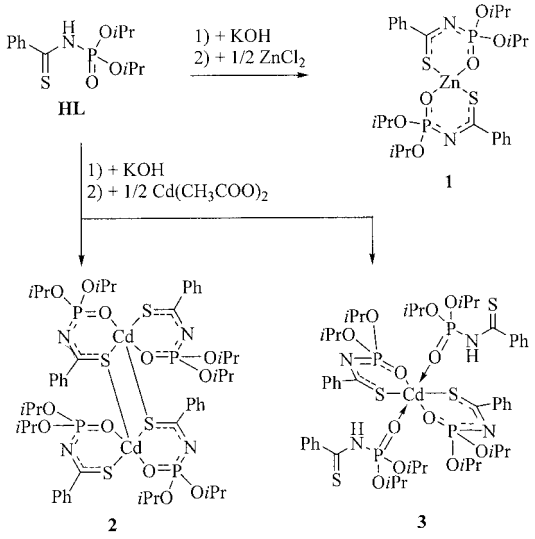


Scheme 1.

It has been shown that in the crystal form all listed complexes have various coordination environments at the metal atoms. The IR and NMR spectroscopic data confirm that in $CDCl_3$ and $CCl_4$ solutions and in all three cases the dominating forms are $[ML_2]$ chelates with a tetrahedral $MO_2S_2$ core.

### IR and NMR Spectroscopy

The IR spectrum of **1** in Nujol is similar to the spectrum of **2**. The absorption bands of the P=O group of the anionic forms **L** in complexes **1** and **2** are shifted by approximately 70 $cm^{-1}$ to low frequencies relative to the band of the parent ligand **HL**. This confirms their participation in chelate formation. The signal for the NH proton is absent in the IR spectra of complexes **1** and **2**.

The main difference involves the absorption bands of the SCN group.[19,20] In the spectrum of a suspension of **1** in Nujol there is an intense absorption band at 1528 $cm^{-1}$, whereas in **2** the participation of sulfur atoms in dimer formation results in the occurrence of three intense absorption bands in the given area: 1536, 1576 and 1584 $cm^{-1}$. In a $CCl_4$ solution of complex **2** the bands merge into one with a maximum of 1536 $cm^{-1}$, which suggests the dissociation of the dimeric molecules.

The IR spectrum of **3** contains two bands for different phosphorus groups. Along with the above band corresponding to the **L** form, a strong P=O band is observed at 1240 $cm^{-1}$ because of the bound neutral molecules of **HL**. Its frequency also decreases relative to that of the band of the free ligand; however, the shift is 12 $cm^{-1}$. The absorption band for the NH group at 3176 $cm^{-1}$ also indicates the presence of **HL** molecules in complex **3**.

The $^{31}P\{^1H\}$ NMR signals of complexes **1** and **2** appear at $\delta$ = 5.7 and 3.0 ppm, respectively, and a down-field shift, relative to that of the free ligand **HL** ($\delta$ = –5.6 ppm), is observed. Full width at half peak maximum is in the range 1.0–5.0 Hz.

The $^1H$ NMR spectra contain a single set of signals for the $(iPrO)_2P(O)$ and $C_6H_5$ protons. The *o*-phenyl proton signals in complexes **1** and **2** are shifted down-field. The signal for the NHP(O) group proton is absent in $^1H$ NMR spectra. This confirms the presence of the **HL** anionic form in the structures of complexes **1** and **2**.

The formation of dimeric structures in solution would lead to doubling or to exchange broadening of the signals in the NMR spectra. Distinction between the trailer and bridging ligand forms should be shown in the NMR spectra for $^{13}C$ and $^{31}P$ nuclei. Experimental evidence has shown that in both complexes **1** and **2** the $^{13}C$ and $^{31}P$ NMR spectra indicate that there is no doubling or exchange broadening of the signals for carbon and phosphorus atoms. Thus, the NMR spectroscopic data confirm that in $CDCl_3$ solution complexes **1** and **2** are exclusively in the monomeric form.

There are two singlet signals at $\delta$ = –6.0 and 3.7 ppm, which have identical integrated intensities, in the $^{31}P\{^1H\}$ NMR spectrum of complex **3**. The signal at $\delta$ = –6.0 ppm is in the region that is characteristic for neutral *N*-phosphorylated thioamides and thioureas, whereas the second signal corresponds to the amidophosphate environment in complexes of *N*-acylamidophosphate anions.

The $^1H$ NMR spectrum contains a double set of equal-intensity signals for the $(iPrO)_2P(O)$ and $C_6H_5$ protons. The spectrum of complex **3** basically represents the sum of the spectra of ligand **HL** and complex **2** (Figure 1). The assignment of the $^1H$ NMR spectrum of compound **3** is executed by comparing the spectrum of **3** with those of **HL** and complex **2**. For a more exact reference of OCH proton signals of complex **3**, the spectrum of a mixture of **3** and **HL** was run at a molar ratio of 3:1. The increase in intensities of the low-field OCH group signal and the signal for the high-field *o*-$C_6H_5$ protons, concerning the neutral **HL** form, confirms the reference made by comparison of the spectra.

 © 2006 Wiley-VCH Verlag GmbH & Co. KGaA, Weinheim 

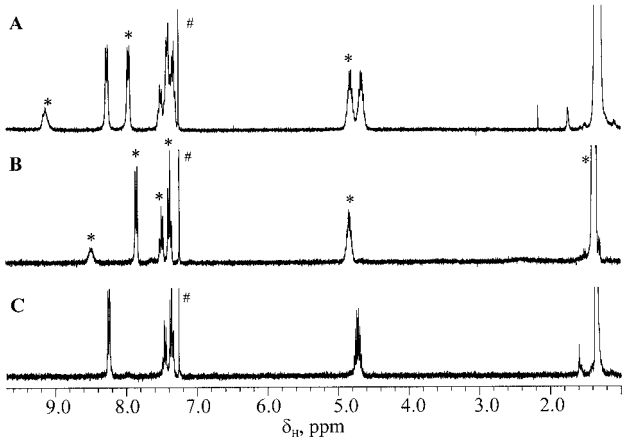


Figure 1. $^1H$ NMR spectra of complexes **3** (A), **2** (C) and **HL** (B). Signals of **HL** (free and in the structure of **3**) are marked * and a signal for the solvent #.

## EI and ES Mass Spectrometry

The electron impact mass spectrum (EI-MS) of **1** contains the $[ZnL_2]^+$ structure molecular ion peak. The molecular ions of **2** $[Cd_2L_4]^+$ and **3** $[Cd(HL)_2L_2]^+$ are unstable under the measurement conditions, and the heaviest molecular ion observed in the spectra of **2** and **3** corresponds to the neutral $[CdL_2]^+$ complex core.

ES-MS experiments (electrospray method) on complexes **1** and **2** show peaks for the molecular ions $[ML_2 + Na]^+$ and $[ML_2 + K]^+$. The cations $[ML_2 + H]^+$, on the contrary, are unstable. This is, apparently, connected to the separating of the **HL** molecule.

The ES-MS data of **2** (Figure 2) shows propensity to dimer formation. The intensity of the $[Cd_2L_3]^+$ peak in the electrospray spectrum of complex **2** is 38% and is maximal in a number of the investigated compounds. The $[Cd_2L_4 + Na]^+$ peak has an intensity of 0.8%.

The molecular ion peak of **3** is absent. Its electrospray spectrum contains all ions characteristic of the $[CdL_2]$ complex core: $[CdL_2 + H]^+$ (low intensity), $[CdL_2 + Na]^+$, $[CdL_2 + K]^+$, $[Cd_2L_3]^+$.

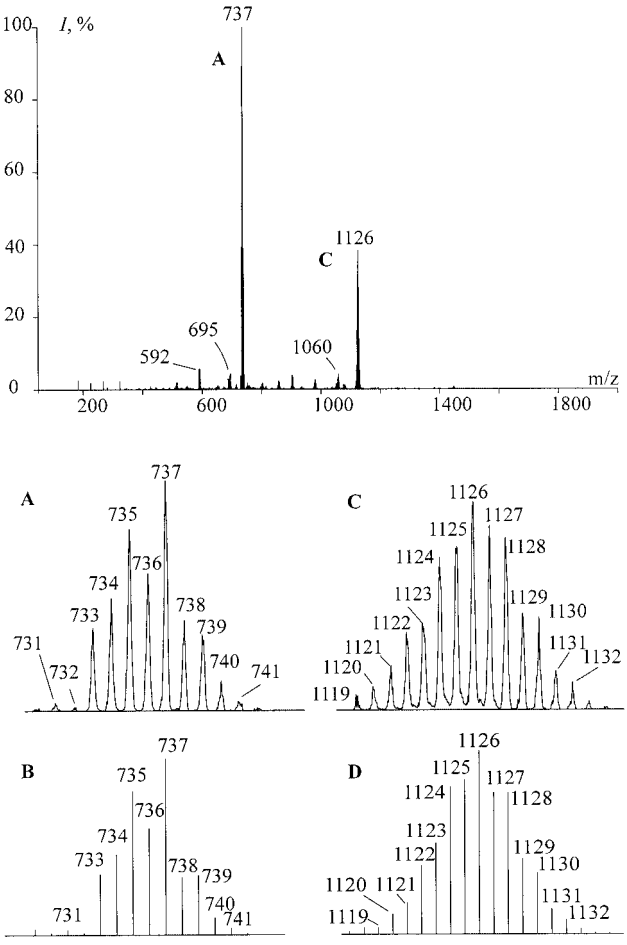


Figure 2. ES-MS spectra of complex **2**. Peak **A** is observed for the $[CdL_2 + Na]^+$ cation, pattern **B** is calculated for $C_{26}H_{38}CdN_2NaO_6P_2S_2$, peak **C** is observed for the $[Cd_2L_3]^+$ cation and pattern **D** is calculated for $C_{39}H_{57}Cd_2N_3O_9P_3S_3$.

## Crystal Structure of 1

According to the X-ray data, complex **1** is a spirocyclic chelate with a distorted tetrahedral $ZnO_2S_2$ core (Figure 3).

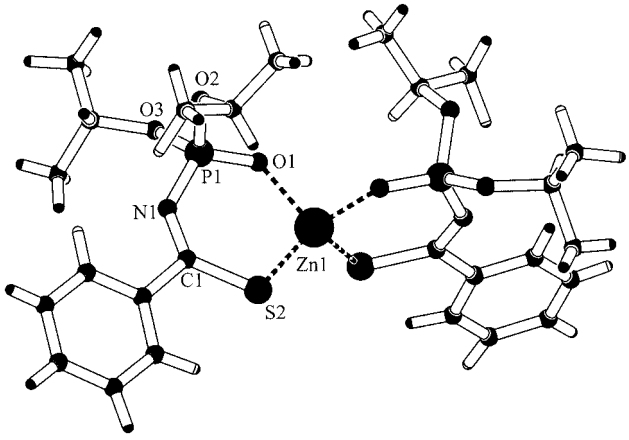


Figure 3. Molecular structure of complex **1**.

Table 1. Selected bond lengths [Å], and bond and torsion angles [°] for complex **1**.[a]

| | | | |
|---|---|---|---|
| Bond lengths | | | |
| Zn1–S2 | 2.288(1) | P1–O1 | 1.492(2) |
| Zn1–O1 | 1.962(2) | P1–N1 | 1.614(2) |
| S2–C1 | 1.735(3) | N1–C1 | 1.285(3) |
| Bond angles | | | |
| S2–Zn1–O1 | 102.83(8) | O1–P1–N1 | 118.9(1) |
| S2–Zn1–S2_a | 118.82(8) | Zn1–O1–P1 | 125.1(1) |
| S2–Zn1–O1_a | 104.52(14) | P1–N1–C1 | 133.4(1) |
| O1–Zn1–O1_a | 113.64(80) | S2–C1–N1 | 129.1(2) |
| Zn1–S2–C1 | 107.7(1) | S2–C1–C2 | 114.7(2) |
| Torsion angles | | | |
| O1–Zn1–S2–C1 | 1.4(1) | N1–P1–O1–Zn1 | –21.2(2) |
| S2–Zn1–O1–P1 | 11.4(2) | O1–P1–N1–C1 | –108.6(3) |
| Zn1–S2–C1–N1 | –4.9(3) | P1–N1–C1–S2 | –4.6(4) |

[a] Symmetry transformations used to generate equivalent atoms: _a (–*x*, *y*, –*z* + 1/2).

 © 2006 Wiley-VCH Verlag GmbH & Co. KGaA, Weinheim 

Similarly to those of the [$Co^{II}L_2$] complex with the same ligand, investigated by us earlier,[21] the six-membered chelate rings are practically flat. The phosphorus atoms usually have a tetrahedral configuration in such compounds. Selected values of bond lengths, bond and torsion angles are given in Table 1.

### Crystal Structure of 2

The X-ray data show that in a crystal form complex **2** is a centrosymmetric dimer. In contrast to the imidodiphosphinate complexes, the bond does not occur through the oxygen atoms of the P=O[12] groups, but through the sulfur atoms of the C=S groups of the deprotonated ligand **HL**. Complex **2** contains two types of ligand anions – tridentate bridging and didentate terminal (Figure 4).

The $Cd^{II}$ cations are in a distorted trigonal-bipyramidal environment ($CdO_2S_3$). The axial positions are occupied by the oxygen atoms of the P=O groups, and the sulfur atoms lie in its base. The $Cd_2S_4$ moiety is flat in the molecule of **2** (Table 2). Predictably, coordination bonds with the sulfur atoms of terminal ligands Cd01–S2A are, essentially, more than 0.16 Å shorter than with the bridging sulfur atoms Cd01–S2B. The lengths of the Cd–O bonds in the $Cd^{II}$ cation's coordination sphere are practically equivalent, but the bond with the oxygen atom of the bridging ligand, Cd01–O1B, deviates from the normal to the $Cd_2S_4$ plane (O1A–Cd01–O1B 155°), while the Cd01–O1A bond is practically perpendicular to the $Cd_2S_4$ plane. The S2B–Cd01–S2B_a angle in the $Cd_2S_4$ plane is more than 50° sharper than S2A–Cd01–S2B.

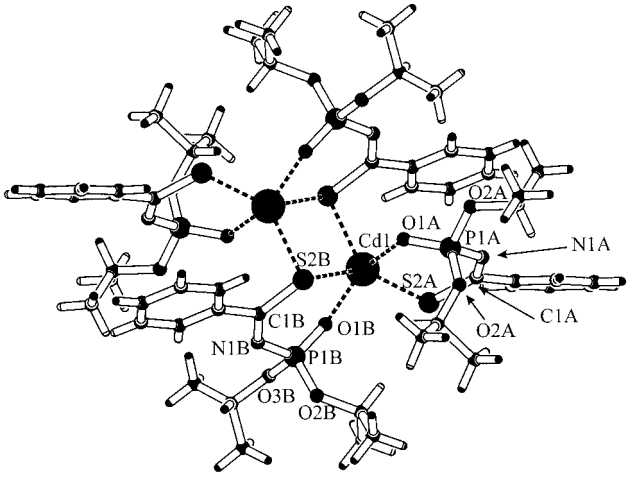


Figure 4. Molecular structure of complex **2**.

The lengths of the bonds in the S–C–*N*–P–O backbone confirm the distinction in negative charge delocalisation mechanisms in bridging and terminal ligands. It is known that three tautomeric forms, A, B and C, contribute to the distribution of electronic density in six-membered chelates of (thioacylamido)phosphates (Scheme 2).

Table 2. Selected bond lengths [Å], and bond and torsion angles [°] for complex **2**.[a]

| Bond lengths | | | |
|---|---|---|---|
| Cd01–S2A | 2.5015(2) | P1A–O1A | 1.444(2) |
| Cd01–S2B | 2.6620(1) | P1A–N1A | 1.616(5) |
| Cd01–O1A | 2.313(3) | P1B–O1B | 1.468(4) |
| Cd01–O1B | 2.300(3) | P1B–N1B | 1.625(5) |
| Cd01–S2B_a | 2.5957(1) | N1A–C1A | 1.283(7) |
| S2A–C1A | 1.744(5) | N1B–C1B | 1.278(7) |
| S2B–C1B | 1.761(5) | | |
| **Bond angles** | | | |
| S2A–Cd01–S2B | 143.94(5) | Cd01–S2B–C1B | 114.2(2) |
| S2A–Cd01–S2B_a | 123.91(5) | Cd01–S2B–Cd01_a | 87.86(4) |
| S2B–Cd01–S2B_a | 92.14(4) | C1B–S2B–Cd01_a | 96.4(2) |
| O1B–Cd01–S2B_a | 105.9(1) | O1A–P1A–N1A | 119.7(2) |
| S2A–Cd01–O1A | 91.3(1) | O1B–P1B–N1B | 120.6(2) |
| S2A–Cd01–O1B | 85.0(1) | Cd01–O1A–P1A | 125.2(2) |
| S2B–Cd01–O1A | 83.46(9) | Cd01–O1B–P1B | 128.8(2) |
| S2B–Cd01–O1B | 85.33(9) | P1A–N1A–C1A | 132.8(4) |
| O1A–Cd01–O1B | 155.3(1) | P1B–N1B–C1B | 130.4(4) |
| O1A–Cd01–S2B_a | 96.4(1) | S2A–C1A–N1A | 128.6(4) |
| Cd01–S2A–C1A | 110.6(2) | S2B–C1B–N1B | 127.6(4) |
| **Torsion angles** | | | |
| C1A–S2A–Cd01–O1A | –18.2(2) | C1B–S2B–Cd01–O1B | –167.73(19) |
| P1A–O1A–Cd01–S2A | –6.8(2) | P1B–O1B–Cd01–S2B | –19.3(3) |
| Cd01–O1A–P1A–N1A | –34.5(6) | Cd01–O1B–P1B–N1B | 43.7(4) |
| C1A–N1A–P1A–O1A | –34.5(6) | C1B–N1B–P1B–O1B | –35.5(6) |
| N1A–C1A–S2A–Cd01 | 25.8(5) | N1B–C1B–S2B–Cd01 | 20.5(5) |
| S2A–C1A–N1A–P1A | –0.1(8) | S2B–C1B–N1B–P1B | –0.3(7) |

[a] Symmetry transformations used to generate equivalent atoms: _a (1–*x*, 1 –*y*, 1 –*z*).

 © 2006 Wiley-VCH Verlag GmbH & Co. KGaA, Weinheim 

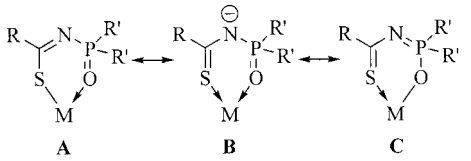

Scheme 2.

Displacement of electronic density on the sulfur atom in bridging ligands leads to the shortening of the C–N and P=O bonds and also to the lengthening of the P–N and C=S bonds because of the prevalence of the tautomeric form A. The P=O bond in these ligands is even shorter than in the free ligand molecule.[19] In the cases with terminal ligands, the contribution of forms B and C which leads to average bonds lengths in the cycle, is shown to a greater degree.

The dimer formation leads to a significant lengthening of the Cd–S bonds in six-membered chelate cycles of the bridging ligands. Therefore, these bonds are the longest in a number of compounds investigated by us, their lengths exceeding even those of the bridging Cd–S bonds connecting [$CdL_2$] moieties in the structure of the dimer.

## Crystal Structure of 3

According to the Cambridge Crystallographic Database, there are no structural analogues of complex **3** that involve *N*-acylamidophosphates or related chelators such as imidodiphosphinates and β-dicarbonyl compounds and Group IIB cations. The nearest analogue of complex **3** is described for $iBu_2NC(S)NHC(O)C_6H_5$ (**HQ**). The complex has the structure [Cd(HQ-*S*)(Q-*O*,*S*)$_2$] (**4**).[22] As in complex **2**, the $Cd^{II}$ cation in complex **4** is in a distorted trigonal-bipyramidal $Cd(O^{ax})_2(S^{eq})_3$ environment.

The molecule of complex **3** in a crystal is located in a special position at the symmetry centre. The coordination geometry of the $Cd^{II}$ atom is tetragonal bipyramidal ($D_{2h}$) (Figure 5). Isostructural complexes of $Co^{II}$ and $Ni^{II}$ with **HL** exist and have been synthesised by us previously.[21]

The equatorial positions of the bipyramid are occupied by two *N*-phosphorylthiobenzamide anions, bonded through sulfur atoms and oxygen atoms of the phosphoryl groups. The six-membered Cd–O–P–*N*–C–S cycle has a half-chair conformation; the O–P–*N*–C–S backbone is flat (Table 3). The ligands are in a *trans* configuration. A negative charge delocalisation in the S–C–*N*–P–O moiety also takes place in this case. This leads to the contraction of the C–N and P–N bonds and also to the lengthening of the C=S bonds, but the P=O bond lengths decrease by 0.013 Å relative to that of the free ligand **HL**. As in complex **2**, this observation results from a significant preference of the form A (Scheme 2).

Neutral ligand molecules are coordinated in the axial positions through the oxygen atoms of the phosphoryl groups. The conformation of the neutral molecules and the lengths of C–N and P–N bonds in a crystal are practically identical to those of free *N*-phosphorylthiobenzamide **HL**. Some lengthening of the P=O and C=S bonds is observed, which results from the displacement of electronic density in the S–C–*N*–P–O moiety on the oxygen atom of the phosphoryl group.

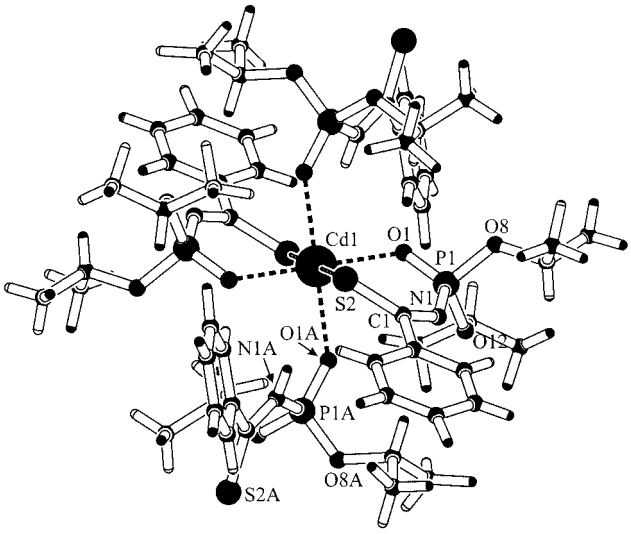


Figure 5. Molecular structure of complex **3**.

Table 3. Selected bond lengths [Å], and bond and torsion angles [°] for complex **3**.[a]

| Bond lengths | | | |
|---|---|---|---|
| Cd1–S2 | 2.546(2) | P1–N1 | 1.611(3) |
| Cd1–O1 | 2.273(2) | P1A–O1A | 1.467(2) |
| Cd1–O1A | 2.372(2) | P1A–N1A | 1.677(3) |
| S2–C1 | 1.687(3) | N1–C1 | 1.289(3) |
| S2A–C1A | 1.637(3) | N1A–C1A | 1.363(4) |
| P1–O1 | 1.444(2) | N1A–H1A | 0.81(3) |
| **Bond angles** | | | |
| S2–Cd1–O1 | 89.74(8) | O1A–P1A–N1A | 106.4(1) |
| S2–Cd1–O1A | 88.76(7) | Cd1–O1–P1 | 120.6(1) |
| S2–Cd1–S2_a | 180.00 | Cd1–O1A–P1A | 137.0(1) |
| O1–Cd1–O1A | 89.25(8) | P1–N1–C1 | 134.6(2) |
| O1–Cd1–O1_a | 180.00 | P1A–N1A–C1A | 131.1(2) |
| O1A–Cd1–O1A_a | 180.00 | N1–C1–C2 | 116.7(2) |
| Cd1–S2–C1 | 105.1(1) | S2–C1–N1 | 128.6(2) |
| O1–P1–N1 | 122.3(1) | S2–C1–C2 | 114.6(2) |
| N1A–C1A–C2A | 114.9(2) | S2A–C1A–N1A | 123.4(2) |
| S2A–C1A–C2A | 121.8(2) | | |
| **Torsion angles** | | | |
| O1–Cd1–S2–C1 | –39.8(1) | O1–P1–N1–C1 | –15.6(3) |
| O1A–Cd1–S2–C1 | 49.5(1) | O1A–P1A–N1A–C1A | 177.2(2) |
| S2–Cd1–O1–P1 | 39.2(1) | N1A–P1A–O1A–Cd1 | –30.1(2) |
| O1A–Cd1–O1–P1 | –49.5(1) | P1–N1–C1–C2 | –174.5(2) |
| S2–Cd1–O1A–P1A | 68.8(2) | P1–N1–C1–S2 | 5.9(4) |
| Cd1–S2–C1–N1 | 27.8(3) | P1A–N1A–C1A–S2A | 0.1(4) |
| N1–P1–O1–Cd1 | –18.9(2) | P1A–N1A–C1A–C2A | 179.1(2) |

[a] Symmetry transformations used to generate equivalent atoms: _a (2 – *x*, –*y*, 2 – *z*).

 © 2006 Wiley-VCH Verlag GmbH & Co. KGaA, Weinheim 

There are two intramolecular NH···S bonds between the neutral and anionic ligands in the crystal of complex **3**. The hydrogen bond parameters are as follows: N(1A)–H(1A)···S(2) (*–x*, *–y*, *–z*), *d*(N–H) 0.81(3) Å, *d*(H···S) 2.72(3) Å, *d*(N···S) 3.499(3) Å, ∠(N–H···S) 164(2)°.

## Conclusion

Comparison of the data of complex compounds of cadmium(II), known from the literature, with acylureas and imidodiphosphinates shows that the cadmium(II) cation in the structure of the complex $CdO_2S_2$ core exhibits properties of a "universal" Lewis acid. Its coordination environment can be expanded because of interaction with both "soft" and "hard" bases. Differences in modes of interaction are apparently related to the distribution of electronic density in the ligand molecules.

These features of complexes with a $CdO_2S_2$ core can be used in the future for the creation of new types of building blocks for polynuclear metal-containing macrocyclic compounds. We have recently reported the synthesis of close structural analogues of the ligand **HL** that contain crown ether moieties and their complexes with $Ni^{II}$ and $Cu^{I}$.[11,23–25] The cavities of the macrocycles in the given structures remain free and are capable of participating in secondary coordination. We suppose that the combination of the $CdO_2S_2$ core and crown ether in the molecule will allow one to synthesise compounds that are able to bind cations, by the crown ether moiety, and anions and neutral molecules, by the electrophilic $CdO_2S_2$ core. Such kinds of compounds are of interest as agents for molecular recognition and membrane transport.

## Experimental Section

**Physical Measurements:** Infrared spectra (Nujol) were recorded with a Specord M-80 spectrometer in the range 400–3600 $cm^{-1}$. NMR spectra were obtained on a Varian Unity-300 NMR spectrometer at 25 °C. $^1H$, $^{31}P\{^1H\}$ and $^{13}C\{^1H\}$ NMR spectra were recorded at 299.948, 121.420 and 75.429 MHz, respectively. Chemical shifts are reported with reference to $SiMe_4$ ($^1H$ and $^{13}C\{^1H\}$) and $H_3PO_4$ ($^{31}P\{^1H\}$). Electron ionisation mass spectra were measured on a TRACE MS Finnigan MAT instrument. The ionisation energy was 70 eV. The substance was injected directly into the ion source at 150 °C. Heating was carried out in a programmed mode from 35–200 °C at a rate of 35 °C/min. Electrospray ionisation mass spectra were measured with a Thermo Finnigan LCQ mass spectrometer on a $10^{-6}$ M solution in a $CHCl_3/CH_3OH$ mixture (1:1 v/v). The speed of a sample submission was 3 μL/min. The ionisation energy was 4.1 kV. The capillary temperature was 210 °C. Elemental analyses were performed on a Perkin–Elmer 2400 CHN microanalyser.

**Synthesis of $(i\mathrm{PrO})_2\mathrm{P(O)NHC(S)C_6H_5}$ (HL):** *N*-Diisopropoxyphosphorylthiobenzamide was prepared according to previously described methods.[26] M.p. 134 °C. $^1H$ NMR ($CDCl_3$): $\delta$ = 1.34 (d, $^3J_{H,H}$ = 5.9 Hz, 6 H, $CH_3$), 1.38 (d, $^3J_{H,H}$ = 6.2 Hz, 6 H, $CH_3$), 4.83 (d. sept, $^3J_{POCH}$ = $^3J_{H,H}$ = 6.1 Hz, 2 H, OCH), 8.49 [s, 1 H, NHP(O)], 7.37–7.42 (m, 2 H, *m*-H, $C_6H_5$), 7.49–7.54 (m, 1 H, *p*-H, $C_6H_5$), 7.85–7.88 (m, 2 H, *o*-H, $C_6H_5$), 8.49 (s, 1 H, NH) ppm. $^{31}P\{^1H\}$ NMR ($CDCl_3$): $\delta$ = –5.6 ppm. IR: $\tilde{\nu}$ = 3104 (NH), 1500 (S=C–N), 1012 (POC), 1252 (P=O) $cm^{-1}$.

**Synthesis of $[ZnL_2]$ (1):** A suspension of **HL** (1.505 g, 5 mmol) in aqueous ethanol (20 mL) was mixed with an ethanol solution of potassium hydroxide (0.28 g, 5 mmol). An aqueous (20 mL) solution of $ZnCl_2$ (0.381 g, 2.8 mmol) was added dropwise under vigorous stirring to the resulting potassium salt. The mixture was stirred at room temperature for a further 3 h and left overnight. The resulting complex was extracted with dichloromethane, washed with water and dried with anhydrous $MgSO_4$. The solvent was then removed in vacuo. A colourless precipitate was isolated from dichloromethane by *n*-hexane. Yield (based on the metal salt): 0.865 g (52%). M.p. 92 °C. $^1H$ NMR ($CDCl_3$): $\delta$ = 1.34 (d, $^3J_{H,H}$ = 5.9 Hz, 12 H, $CH_3$), 1.35 (d, $^3J_{H,H}$ = 5.8 Hz, 12 H, $CH_3$), 4.72 (d. sept, $^3J_{POCH}$ = 7.6 Hz, $^3J_{H,H}$ = 6.2 Hz, 4 H, OCH), 7.35–7.40 (m, 4 H, *m*-H, $C_6H_5$), 7.45–7.50 (m, 2 H, *p*-H, $C_6H_5$), 8.26–8.29 (m, 4 H, *o*-H, $C_6H_5$) ppm. $^{13}C\{^1H\}$ NMR ($CDCl_3$): 24.5 ($CH_3$), 73.5 (OCH), 128.4 (*o*-C, $C_6H_5$), 129.3 (*m*-C, $C_6H_5$), 132.6 (*p*-C, $C_6H_5$), 143.8 (*ipso*-C, $C_6H_5$), 195.2 (C=S) ppm. $^{31}P\{^1H\}$ NMR ($CDCl_3$): 5.7 ppm. IR: $\tilde{\nu}$ = 1528 (SCN), 996 (POC), 1152 (P=O) $cm^{-1}$. EI-MS: *m*/*z* (%) = 664 (8) $[M]^+$, 301 (8) $[HL]^+$. ES-MS (positive ion): *m*/*z* (%) = 687 (100) $[M + Na]^+$, 703 (10) $[M + K]^+$, 1032 (1) $[M_2L_3]^+$, 1353 $[M_2L_4 + Na]^+$. $C_{26}H_{38}N_2O_6P_2S_2Zn$ (666.05): calcd. C 46.87, H 5.77, N 4.18; found C 46.88, H 5.75, N 4.19.

**Synthesis of $[Cd_2L_4]$ (2) and $[Cd(HL)_2L_2]$ (3):** A suspension of **HL** (1.806 g, 6 mmol) in aqueous ethanol (20 mL) was mixed with an ethanol solution of potassium hydroxide (0.336 g, 6 mmol). An aqueous (20 mL) solution of $Cd(CH_3COO)_2{\cdot}2H_2O$ (0.798 g, 3 mmol) was added dropwise to the resulting potassium salt under vigorous stirring. The mixture was stirred at room temperature for a further 3 h and left overnight. The resulting complex was extracted with dichloromethane, washed with water and dried with anhydrous $MgSO_4$. The solvent was then removed in vacuo. The residue was extracted by *n*-hexane. A hexane insoluble deposit was recrystallised from a dichloromethane/*n*-hexane mixture, and complex **2** was isolated. Complex **2** was obtained as colourless crystals. Yield (based on the metal salt): 0.918 g (43%). M.p. 102 °C. $^1H$ NMR ($CDCl_3$): 1.40 (d, $^3J_{H,H}$ = 6.4 Hz, 24 H, $CH_3$), 4.82 (d. sept, $^3J_{POCH}$ = 7.5 Hz, $^3J_{H,H}$ = 6.4 Hz, 4 H, OCH), 7.34–7.39 (m, 4 H, *m*-H, $C_6H_5$), 7.44–7.49 (m, 2 H, *p*-H, $C_6H_5$), 8.23–8.26 (m, 4 H, *o*-H, $C_6H_5$) ppm. $^{13}C\{^1H\}$ NMR ($CDCl_3$): 24.5 ($CH_3$), 73.2 (OCH), 128.4 (*o*-C, $C_6H_5$), 129.5 (*m*-C, $C_6H_5$), 132.4 (*p*-C, $C_6H_5$), 144.3 (*ipso*-C, $C_6H_5$), 193.9 (C=S) ppm. $^{31}P\{^1H\}$ NMR ($CDCl_3$): 3.0 ppm. IR: $\tilde{\nu}$ = 1536, 1576, 1584 (SCN), 1015 (POC), 1184 (P=O) $cm^{-1}$. EI-MS: *m*/*z* (%) = 714 (34) $[ML_2]^+$, 301 (15) $[HL]^+$. ES-MS (positive ion): *m*/*z* (%) = 715 (2) $[ML_2 + H]^+$, 737 (100) $[ML_2 + Na]^+$, 753 (2) $[ML_2 + K]^+$, 1126 (38) $[M_2L_3]^+$, 1449 (0.8) $[M_2L_4 + Na]^+$. $C_{52}H_{76}Cd_2N_4O_{12}P_4S_4$ (1424.12): calcd. C 43.80, H 5.34, N 3.97; found C 43.81, H 5.33, N 3.98.

At the solvent-removal stage (hexane soluble), product **3** was isolated. Complex **3** was obtained as yellow crystals. Yield (based on the metal salt): 0.355 g (18%). M.p. 94 °C. $^1H$ NMR ($CDCl_3$): 1.29 (d, $^3J_{H,H}$ = 6.1 Hz, 36 H, $CH_3$, L + HL), 1.35 (d, $^3J_{H,H}$ = 6.1 Hz, 12 H, $CH_3$, L), 4.67 (d. sept, $^3J_{POCH}$ = $^3J_{H,H}$ = 6.2 Hz, 4 H, OCH, L), 4.82 (d. sept, $^3J_{POCH}$ = $^3J_{H,H}$ = 6.4 Hz, 4 H, OCH, HL), 7.47–7.74 (m, 12 H, *m*-H + *p*-H, $C_6H_5$, L + HL), 7.95–7.98 (m, 4 H, *o*-H, $C_6H_5$, HL), 8.26–8.28 (m, 4 H, *o*-H, $C_6H_5$, L), 9.15 [s, 2 H, NHP(O)] ppm. $^{31}P\{^1H\}$ NMR ($CDCl_3$): –6.0 (HL), 3.7 (L) ppm. IR: $\tilde{\nu}$ = 1536 (SCN), 1013 (POC), 1168 (L, P=O), 1240 (HL, P=O) $cm^{-1}$. EI-MS: *m*/*z* (%) = 714 (29) $[M – 2HL]^+$, 301 (73) $[HL]^+$. ES-MS (positive ion): *m*/*z* (%) = 715 (2) $[ML_2 + H]^+$, 737 (100) $[ML_2 +$

 © 2006 Wiley-VCH Verlag GmbH & Co. KGaA, Weinheim 

Table 4. Crystal data, data collection and refinement details for complexes **1**–**3**.

| | **1** | **2** | **3** |
|---|---|---|---|
| Empirical formula | $C_{26}H_{38}N_2O_6P_2S_2Zn$ | $C_{52}H_{78}Cd_2N_6O_{10}P_4S_4$ | $C_{52}H_{78}CdN_4O_{12}P_4S_4$ |
| Formula mass | 666.05 | 1424.12 | 1315.70 |
| Space group | *C*2/*c* (molecule in special position on the axis 2) | $P\bar{1}$ (molecule in special position) | $P2_1/n$ (molecule in special position) |
| *a* [Å] | 18.324(9) | 10.569(3) | 13.375(9) |
| *b* [Å] | 9.730(9) | 10.941(2) | 12.858(7) |
| *c* [Å] | 18.24(2) | 15.560(4) | 18.594(7) |
| *α* [°] | 90 | 74.11(2) | 90 |
| *β* [°] | 93.35(7) | 72.92(3) | 90.71(6) |
| *γ* [°] | 90 | 79.93(3) | 90 |
| *V* [Å$^3$] | 3247(5) | 1645.5(8) | 3197(3) |
| *Z* | 4 | 1 | 2 |
| $D_{calcd.}$ (mg/m$^3$) | 1.36 | 1.44 | 1.37 |
| *F*(000) | 1392 | 732 | 1372 |
| Crystal colour | colourless | colourless | colourless |
| Crystal form | prismatic | prismatic | prismatic |
| Crystal size [mm] | 0.3 × 0.3 × 0.3 | 0.4 × 0.3 × 0.2 | 0.2 × 0.3 × 0.2 |
| Radiation [Å] | | 1.54184 | 0.71073 |
| Temperature [K] | 293 | 293 | 293 |
| Scan mode | *ω* | *ω* | *ω* |
| Recording range $\theta_{max}$ [°] | 70.07 | 57.19 | 6.29 |
| Absorption correction | *ψ*-scan | *ψ*-scan | *ψ*-scan |
| *μ* [cm$^{-1}$] | 35.14 | 77.46 | 28.11 |
| Scan speed (°/min) | variable, 1–16.4 | variable, 1–16.4 | variable, 1–16.4 |
| No. of recorded reflections | 3373 | 3726 | 7205 |
| No. of independent reflections with $I \geq 3\sigma(I)$ | 3016 | 3695 | 5022 |
| No. of independent reflections with $F^2 \geq 2\sigma(F^2)$ | 2999 | 3239 | 6606 |
| *R* (%) | 0.0449 | 0.0557 | 0.033 |
| $R_w$ (%) | 0.1236 | 0.1362 | 0.083 |
| *S* | 1.061 | 1.047 | 1.011 |

Na]$^+$, 753 (2) [$ML_2$ + K]$^+$, 1126 (7) [$M_2L_3$]$^+$. $C_{52}H_{78}CdN_4O_{12}P_4S_4$ (1315.70): calcd. C 47.44, H 6.01, N 4.29; found C 47.42, H 6.03, N 4.28.

**Crystal Structure Determination and Refinement:** The X-ray diffraction data for the crystals of **1**–**3** were collected on a CAD4 Enraf–Nonius automatic diffractometer using graphite-monochromated Mo-$K_\alpha$ (0.71073 Å) and Cu-$K_\alpha$ (1.54184 Å) radiation. The crystal data, data collection and the refinement are given in Table 4. The stability of the crystals and the experimental conditions were checked every 2 h using three control reflections, while the orientation was monitored every 200 reflections by centring two standards. No significant decay was observed. An empirical absorption correction based on *ψ*-scans was applied. The structure was solved by direct methods using the SIR[27] program and refined by the full-matrix least-squares using the SHELXS-97[28] program. All non-hydrogen atoms were refined anisotropically. Hydrogen atoms for compounds **1** and **3** were located from a subsequent difference map and refined isotropically in the final cycles. The hydrogen atoms for compound **2** were included in calculated positions with thermal parameters 30% larger than the atom to which they were attached. All calculations were performed on a PC using the WinGX[29] program. Cell parameters, data collection and data reduction were performed on an Alpha Station 200 computer using the MolEN[30] program. All figures were made using the program PLATON.[31]

CCDC-286427, CCDC-286426 and CCDC-286425 contain the supplementary crystallographic data for this paper. These data can be obtained free of charge from The Cambridge Crystallographic Data Centre via www.ccdc.cam.ac.uk/data_request/cif.

## Acknowledgments

This work was supported by the Russian Foundation for Basic Research (grant nos. 03-03-32372-a, 03-03-96225-r2003tatarstan_a), the joint program of CRDF and the Russian Ministry of Education (BHRE 2004 Y2-C-07-02, grants REC-007). D.A.S. thanks the Faculty of Chemistry of the University of Wroclaw for a scholarship.

[1] N. G. Zabirov, O. K. Pozdeev, F. M. Shamsevaleev, R. A. Cherkasov, G. H. Gilmanova, *Pharm. Chem. J.* **1989**, *23*, 423–425.
[2] a) V. Amirkhanov, C. Janczak, L. Macalik, J. Hanuza, J. Legendziewicz, *J. Appl. Spectrosc.* **1995**, *62*, 5–17; b) V. Amirkhanov, V. Ovchinnikov, J. Legendziewicz, A. Graczyk, J. Hanuza, L. Macalik, *Acta Phys. Polon., A* **1996**, *90*, 455–460.
[3] a) M. Borzechowska, V. Trush, I. Turowska-Tyrk, W. Amirkhanov, J. Legendziewicz, *J. Alloys Compd.* **2002**, *341*, 98–106; b) Correlation between spectroscopic characteristics and structure of lanthanide phosphoro-azo derivatives of β-diketones: J. Legendziewicz, G. Oczko, R. Wiglusz, V. Amirkhanov, *J. Alloys Compd.* **2001**, *323–324*, 792–799; c) J. Sokolnicki, J. Legendziewicz, W. Amirkhanov, V. Ovchinnikov, L. Macalik, J. Hanuza, *Spectrochim. Acta, Part A* **1999**, *55*, 349–367.
[4] L. G. Shaidarova, A. V. Gedmina, V. V. Brusko, N. G. Zabirov, N. A. Ulakhovich, H. K. Budnikov, *Anal. Sci.* **2001**, *17*, 957–958.
[5] M. P. Kutyreva, N. G. Zabirov, V. V. Brusko, N. A. Ulakhovich, *Anal. Sci.* **2001**, *17*, 1049–1051.
[6] L. G. Shaidarova, A. V. Gedmina, V. V. Brusko, N. G. Zabirov, N. A. Ulakhovich, H. K. Budnikov, *Russ. J. Appl. Chem.* **2002**, *75*, 919–925.

 © 2006 Wiley-VCH Verlag GmbH & Co. KGaA, Weinheim 

[7] L. G. Shaidarova, A. V. Gedmina, N. A. Ulahovich, G. K. Budnikov, N. G. Zabirov, *Zh. Obshch. Khim.* **2002**, *72*. 1662–1668; *Russ. J. Gen. Chem.* **2002**, *72*, 1565–1570.

[8] O. Navratil, E. Herrmann, N. T. T. Chau, Ch. Tea, J. Smola, *Collect. Czech. Chem. Commun.* **1993**, *58*, 798–805.

[9] M. G. Zimin, G. A. Lazareva, N. I. Savelieva, R. G. Islamov, N. G. Zabirov, V. F. Toropova, A. N. Pudovik, *Zh. Obshch. Khim.* [*J. Gen. Chem. USSR*] **1982**, *52*, 1573–1581.

[10] a) V. V. Skopenko, V. M. Amirkhanov, T. Yu. Sliva, I. S. Vasilchenko, E. L. Anpilova, A. D. Garnovskii, *Uspekhi Khimii* **2004**, *73*, 797–813; *Russ. Chem. Rev.* **2004**, *73*, 737–752; b) E. A. Trush, V. M. Amirkhanov, V. A. Ovchynnikov, J. Swiatek-Kozlowska, K. A. Lanikina, K. V. Domasevitch, *Polyhedron* **2003**, *22*, 1221–1229; c) K. E. Gubina, V. A. Ovchynnikov, J. Swiatek-Kozlowska, V. M. Amirkhanov, T. Yu. Sliva, K. V. Domasevitch, *Polyhedron* **2002**, *21*, 963–967.

[11] F. D. Sokolov, V. V. Brusko, N. G. Zabirov, R. A. Cherkasov, *Curr. Org. Chem.* **2006**, *10*, 27–42.

[12] C. Silvestru, J. E. Drake, *Coord. Chem. Rev.* **2001**, *223*, 117–216.

[13] C. Boehme, G. Wipff, *Inorg. Chem.* **2002**, *41*, 727–737.

[14] N. G. Zabirov, V. V. Brusko, S. V. Kashevarov, F. D. Sokolov, V. A. Sherbakova, A. Yu. Verat, R. A. Cherkasov, *Zh. Obshch. Khim.* **2000**, *70*, 1294–1302; *Russ. J. Gen. Chem.* **2000**, *70*, 1214–1222.

[15] N. G. Zabirov, V. V. Brusko, A. Yu. Verat, D. B. Krivolapov, I. A. Litvinov, R. A. Cherkasov, *Polyhedron* **2004**, *23*, 2243–2252.

[16] D. J. Birdsall, J. Green, T. Q. Ly, J. Novosad, M. Necas, A. M. Z. Slawin, J. D. Woollins, Z. Zak, *Eur. J. Inorg. Chem.* **1999**, *9*, 1445–1452.

[17] V. V. Brusko, A. I. Rakhmatullin, N. G. Zabirov, *Zh. Obshch. Khim.* **2000**, *70*, 1705–1711; *Russ. J. Gen. Chem.* **2000**, *70*, 1603–1609.

[18] Z. P. Vetrova, N. G. Zabirov, N. N. Shuvalova, L. S. Smerkovich, L. A. Ivanova, A. K. Golberg, N. T. Karabanov, *Zh. Obshch. Khim.* **1992**, *62*, 1079–1083; *Russ. J. Gen. Chem.* **1992**, *62*, 883–886.

[19] N. G. Zabirov, V. N. Soloviev, F. M. Shamsevaleev, R. A. Cherkasov, A. N. Chechlov, A. G. Tsyfarkin, I. V. Martynov, *Zh. Obshch. Khim.* **1991**, *61*, 657–666; *J. Gen. Chem. USSR* **1991**, *61*, 597–604.

[20] E. G. Yarkova, N. R. Safiullina, I. G. Chistyakova, N. G. Zabirov, F. M. Shamsevaleev, R. A. Cherkasov, *Zh. Obshch. Khim.* **1990**, *60*, 1790–1796.

[21] F. D. Sokolov, D. A. Safin, N. G. Zabirov, L. N. Yamalieva, D. B. Krivolapov, I. A. Litvinov, *Mendeleev Commun.* **2004**, *14*, 51–52.

[22] M. Reinel, R. Richter, R. Kirmse, *Z. Anorg. Allg. Chem.* **2002**, *628*, 41–44.

[23] N. G. Zabirov, F. D. Sokolov, V. V. Brusko, A. K. Tashmukhamedova, N. I. Saifullina, R. A. Cherkasov, *Mendeleev Commun.* **2002**, *12*, 154–155.

[24] a) N. G. Zabirov, A. Yu. Verat, F. D. Sokolov, M. G. Babashkina, D. B. Krivolapov, V. V. Brusko, *Mendeleev Commun.* **2003**, *13*, 163–164; b) A. Y. Verat, F. D. Sokolov, N. G. Zabirov, M. G. Babashkina, D. B. Krivolapov, V. V. Brusko, I. A. Litvinov, *Inorg. Chim. Acta* **2006**, *359*, 475–483.

[25] F. D. Sokolov, N. G. Zabirov, V. V. Brusko, D. B. Krivolapov, I. A. Litvinov, *Mendeleev Commun.* **2003**, *13*, 72–73.

[26] M. G. Zimin, N. G. Zabirov, R. M. Kamalov, A. N. Pudovik, *Zh. Obshch. Khim.* **1986**, *56*, 2352–2357.

[27] A. Altomare, G. Cascarano, C. Giacovazzo, D. Viterbo, *Acta Crystallogr., Sect. A: Found Crystallogr.* **1991**, *47*, 744–748.

[28] G. M. Sheldrick, *SHELXS-97, Program for the Solution of Crystal Structures*, Unuversity of Göttingen, Göttingen, Germany, **1997**.

[29] L. J. Farrugia, WinGX 1.64.05: an integrated system of Windows programs for the solution, refinement and analysis of single crystal X-ray diffraction data, *J. Appl. Crystallogr.* **1999**, *32*, 837–838.

[30] L. H. Straver, A. J. Schierbeek, *MOLEN. Structure Determination System*. Nonius B. V., Delft, Netherlands, **1994**, *1, 2*.

[31] A. L. Spek, *Acta Crystallogr., Sect. A: Found Crystallogr.* **1990**, *46*, C-34.

Received: November 11, 2005
Published Online: March 23, 2006

 © 2006 Wiley-VCH Verlag GmbH & Co. KGaA, Weinheim 

DOI: 10.1002/ejic.200501075

# Diamagnetic versus Paramagnetic Structure of SPS-Type Pincer-Based $Co^{I}$, $Rh^{I}$, and $Ir^{I}$ Complexes

**Marjolaine Doux,[a] Pascal Le Floch,[a] and Yves Jean*[a]**

**Keywords:** Group 9 / Density functional calculations / P ligands / S ligands / QM/MM

The lowest singlet and triplet states of SPS-type pincer-based [M(SPS)($PPh_3$)] complexes (M = Co, Rh, and Ir) were studied by means of DFT/B3PW91 calculations on the model complexes in which the nine phenyl substituents were replaced by H atoms. Although the Rh and Ir compounds were found to be diamagnetic with a square-planar geometry, the yet unknown Co complex was predicted to be paramagnetic ($\Delta E_{S/T}$ = –22.4 kcal·mol$^{-1}$) with two unpaired electrons localized on the metal center. Three minima were actually located on the triplet potential energy surface that differ by the arrangement of the ligands (nearly tetrahedral or butterfly geometries), two of them being close in energy ($\Delta E$ = 2.5 kcal·mol$^{-1}$). Finally, the paramagnetism of the Co complex was confirmed by calculations on the real complex at the B3PW91//ONIOM(B3PW91:UFF) level of theory ($\Delta E_{S/T}$ = –29.6 kcal·mol$^{-1}$).
(© Wiley-VCH Verlag GmbH & Co. KGaA, 69451 Weinheim, Germany, 2006)

## Introduction

Since the pioneering work of Shaw in 1976,[1] the development of pincer-based ligands has been flourishing and many of these polydentate systems have found numerous applications in coordination chemistry, homogeneous and heterogeneous catalysis.[2–4] Whereas the first studies focussed on PCP-based systems, it rapidly appeared that the introduction of heteroatoms (N, O, P, S) either as central or ancillary ligands could be used to finely tune the electronic properties of the corresponding complexes.[5–7] However, the use of oxygen and sulfur as ancillary ligands remains limited compared to their nitrogen (amine, amide, imine), phosphorus (phosphane, phosphite, phosphaalkene), or carbon (NHC) counterparts. Sulfur-based systems are of great interest as they can be used to modelize enzyme active sites.[8] Sulfur ligands can be found either as thioethers,[9–12] thiolates,[13,14] sulfoxides,[15] or phosphanyl sulfides.[16–19]

Recently, we described the synthesis and the coordination chemistry of the anionic SPS-based pincer ligand **I**, which features two ancillary P=S ligands and a phosphorus atom as the central binding site (Scheme 1).[20] In a series of papers we showed that these ligands can accommodate various metal fragments in different oxidation states ($Re^{I}$, $Mn^{I}$, $Rh^{I}$, $Rh^{II}$, $Rh^{III}$, $Ir^{I}$, $Ir^{III}$, $Ni^{II}$, $Pd^{II}$, $Pt^{II}$, $Au^{I}$, $Cu^{I}$).[21–24] Some of these complexes have found applications in catalysis,[25] photochemistry[21] and activation of small molecules.[26–28] Among these complexes, the 16 VE square-planar $Rh^{I}$ complex [Rh(SPS)($PPh_3$)] (**II**) proved to be particularly reactive towards small molecules such as CO, $SO_2$, $O_2$, $CS_2$, and $H_2$ and the corresponding $Rh^{III}$ complexes, [Rh($\eta^2$-$O_2$)(SPS)($PPh_3$)], [Rh($\eta^2$-$CS_2$)(SPS)($PPh_3$)], and [Rh$(H)_2$(SPS)($PPh_3$)], or $Rh^{I}$ complexes, [Rh($\eta^1$-CO)(SPS)($PPh_3$)] and [Rh($\eta^1$-$SO_2$)(SPS)($PPh_3$)], were isolated and structurally characterized in most cases

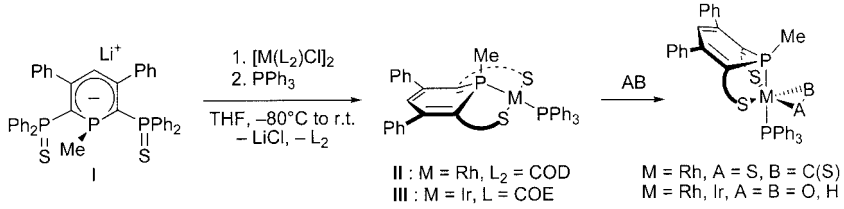


Scheme 1.

(Scheme 1).[23,28] Later it was found that the iridium counterpart of **II**, the [Ir(SPS)($PPh_3$)] complex **III**, could also activate $O_2$ and $H_2$.[27,28] Moreover, the attack of the small molecule proved to be stereospecific and only led to a single isomer (the attack occurring *syn* to the P–Me moiety). This

[a] Laboratoire "Hétéroéléments et Coordination", UMR CNRS 7653 (DCPH), Ecole Polytechnique,
91128 Palaiseau Cédex, France
Fax: +33-1-69-33-39-90
E-mail: yves.jean@polytechnique.fr
Supporting information for this article is available on the WWW under http://www.eurjic.org or from the author.

 © 2006 Wiley-VCH Verlag GmbH & Co. KGaA, Weinheim 

planar discrimination has been studied in the case of $O_2$,[27] CO,[26] and $H_2$.[28]

We now wish to report on a theoretical study of the cobalt complex [Co(SPS)($PPh_3$)], analog of **II** and **III**. In order to shed some light on the electronic structure of these SPS-based complexes, examination of the singlet and triplet states of this yet unknown cobalt complex is presented herein and a comparison is drawn with its Rh and Ir analogs.

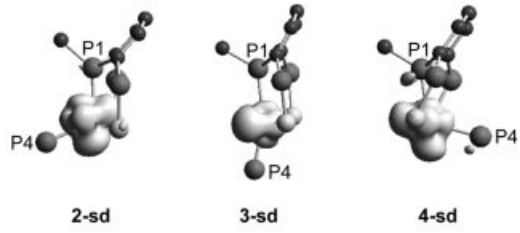


Figure 2. Total spin density (**sd**) surfaces computed for the triplet state of the cobalt complexes **2**, **3**, and **4**. Hydrogen atoms are omitted for clarity.

## Results and Discussion

The geometry of the [Co(SPS)($PH_3$)] model complex was first optimized in the singlet state without any symmetry constraint. The optimized structure (**1**, Figure 1) came out to be nearly of $C_s$ symmetry with an almost perfect square-planar (SP) arrangement around the metal center (S1–Co–S2 = 178.4° and P1–Co–P4 = 177.8°), a geometry usual for a diamagnetic complex of the $d^8$-[$ML_4$] type.

The optimization of the triplet state led to three minima of $C_s$ symmetry (**2**, **3**, and **4**, Figure 1), which differ by the arrangement of the ligands around the metal center. A pseudotetrahedral (*Td*) geometry was found for **2** ($^3A'$) with S1–Co–S2 and P1–Co–P4 angles of 128.3 and 113.1°, respectively. The two other minima can be described as butterfly structures: in **3** ($^3A''$) there is a large P1–Co–P4 angle (164.2°) and a smaller S1–Co–S2 angle (124.2°), while the reverse is true for **4** ($^3A'$) (111.5 and 169.3°, respectively). Such a change in the geometry in going from the singlet to the triplet state is consistent with qualitative molecular orbital arguments: moving away from the square-planar geometry towards tetrahedral or butterfly structures reduces the energy gap between the frontier MOs of $d^8$-[$ML_4$] complexes,[29] a trend which is favorable for the triplet state. The total spin density (**sd**) surface is pictured in Figure 2 and, for each complex, it was found to be mainly developed on the metal center with a Mulliken spin density of 1.970, 1.993, and 1.857 for **2**, **3**, and **4**, respectively.

From an energetic point of view, complex **2** was found to be more stable than **3** and **4** by 2.5 and 12.9 kcal·mol$^{-1}$, respectively. Interestingly, all these triplet-state structures are lower in energy than the singlet-state **1**, as $\Delta E_{S/T}$ = –22.4 kcal·mol$^{-1}$ between **1** (singlet state) and **2** (lowest triplet state) (Figure 1). Note that **2** and **3**, which differ by their symmetry ($^3A'$ and $^3A''$) and their geometry [nearly tetrahedral (**2**) and butterfly-type with a wide P1–Co–P4 angle (**3**)], are predicted to be competitive in energy ($\Delta E$ = 2.5 kcal·mol$^{-1}$). It is remarkable that large changes in the metal–ligand bond angles induce rather small energy changes on the triplet potential energy surface. Note, however, that relative energies and even orderings can depend critically on the amount of HF exchange included in the functional. The energy separation of the four structures was therefore tested by single-point ab initio calculations at the MP2 level. The same energy ordering is found: **2** (0.0) < **3** (+4.1) < **4** (+14.1) < **1** (+34.5) (in kcal·mol$^{-1}$), the main change being an increase of the singlet–triplet energy separation (34.5 instead of 22.4 kcal·mol$^{-1}$ at the B3PW91 level). These values are large enough to conclude unambiguously that the model complex [Co(SPS)($PH_3$)] is paramagnetic. The energy ordering of the three triplet-state structures can be qualitatively traced to two factors: (i) the energy required to distort the complex in its singlet state from the equilibrium square-planar geometry to the actual geometry in the triplet-state structure. This distortion energy (in kcal·mol$^{-1}$) increases in the order **3** (14.0) < **2** (19.8) < **4** (23.7) (restricted B3PW91 calculations); (ii) the energy gap

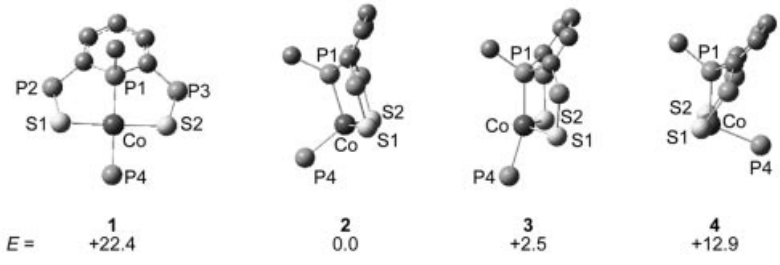


Figure 1. Optimized geometries for the [Co(SPS)($PH_3$)] complex in its singlet (**1**) and triplet (**2**, **3**, and **4**) states. Hydrogen atoms are omitted for clarity. *E*: relative energies (at the B3PW91 level) are given in kcal·mol$^{-1}$. Selected geometrical parameters (bond lengths in Å and bond angles in °): **1**: Co–S 2.292, Co–P1 2.175, Co–P4 2.203; S1–Co–S2 178.4, P1–Co–P4 177.8. **2**: Co–S 2.455, Co–P1 2.324, Co–P4 2.288; S1–Co–S2 128.3, P1–Co–P4 113.1. **3**: Co–S 2.513, Co–P1 2.317, Co–P4 2.308; S1–Co–S2 124.2, P1–Co–P4 164.2. **4**: Co–S 2.568, Co–P1 2.286, Co–P4 2.340; S1–Co–S2 169.3, P1–Co–P4 111.5.

 © 2006 Wiley-VCH Verlag GmbH & Co. KGaA, Weinheim 

between the two singly occupied MOs in the triplet state (a small value favoring a low-lying triplet state), which increases in the order **2** (10.7) < **3** (23.8) < **4** (29.5). Therefore structure **4** appears to be the least favorable, while the two factors work in opposite direction for structures **2** and **3**, which were actually found to be close in energy.

For the sake of comparison, similar calculations were performed on the rhodium and iridium analogs, the energetic results and the main geometrical parameters being reported in Table 1. A nearly square-planar geometry was found for the singlet state[26,27] and three minima were located for the triplet state. Their geometries are close to that pictured in Figure 1 for the cobalt complex and two of them (**2** and **3**) are still found to be close in energy. However, the singlet state is now located well below the lowest triplet state, by 19.0 and 26.2 kcal·mol$^{-1}$ for M = Rh and Ir, respectively (Table 1). The electronic ground state of the Rh and Ir complexes is thus found to be diamagnetic, in agreement with NMR spectroscopic data.[23,27] Therefore, the trend for the first-row transition metals to form high-spin complexes is large enough to induce a change of the magnetic properties in this family of SPS-based complexes.

Table 1. Relative energies (given in kcal·mol$^{-1}$) at the B3PW91 level of the lowest square-planar (SP) singlet state (**1**) and triplet states [**2** (pseudo-*Td*), **3** (butterfly-1), and **4** (butterfly-2)] of the [M(SPS)(PH$_3$)] model complexes (M = Co, Rh, and Ir).[a]

| | **1** (SP) $^1$A′ | **2** (pseudo-*Td*) $^3$A′ | **3** (butterfly-1) $^3$A′′ | **4** (butterfly-2) $^3$A′ |
|---|---|---|---|---|
| Co | +22.4 | 0.0 | +2.5 | +12.9 |
| Rh | 0.0 | +19.0 | +19.9 | +27.8 |
| Ir | 0.0 | +26.7 | +26.2 | +39.7 |

[a] Selected geometrical parameters (bond lengths in Å and bond angles in °) for Rh and Ir complexes: **Rh(1)**: Rh–S 2.401, Rh–P1 2.259, Rh–P4 2.303; S1–Rh–S2 173.9, P1–Rh–P4 174.3. **Rh(2)**: Rh–S 2.551 (av.), Rh–P1 2.335, Rh–P4 2.304; S1–Rh–S2 138.1, P1–Rh–P4 106.6. **Rh(3)**: Rh–S 2.568, Rh–P1 2.358, Rh–P4 2.369; S1–Rh–S2 111.3, P1–Rh–P4 170.4. **Rh(4)**: Rh–S 2.642, Rh–P1 2.309, Rh–P4 2.332; S1–Rh–S2 168.3, P1–Rh–P4 103.2. **Ir(1)**: Ir–S 2.380, Ir–P1 2.274, Ir–P4 2.272; S1–Ir–S2 172.7, P1–Ir–P4 171.4. **Ir(2)**: Ir–S 2.461, Ir–P1 2.275, Ir–P4 2.240; S1–Ir–S2 128.6, P1–Ir–P4 106.5. **Ir(3)**: Ir–S 2.509, Ir–P1 2.304, Ir–P4 2.300; S1–Ir–S2 106.0, P1–Ir–P4 166.5. **Ir(4)**: Ir–S 2.453, Ir–P1 2.266, Ir–P4 2.284; S1–Ir–S2 163.1, P1–Ir–P4 107.6.

Finally, optimizations of both the singlet and triplet states were performed at the ONIOM(B3PW91:UFF) level of calculation on the real complex (**rc**) [Co(SPS)(PPh$_3$)] bearing nine phenyl substituents. The square-planar singlet state (**1-rc**) and the two lowest structures optimized for the triplet state (**2-rc** and **3-rc**) are pictured in Figure 3.[30] Complex **2-rc** is a slightly distorted tetrahedral complex with S1–Co–S2 and P1–Co–P4 angles of 119.8 and 112.2°, respectively, and **3-rc** adopts a butterfly-type structure with S1–Co–S2 and P1–Co–P4 angles of 103.2 and 150.9°, respectively. From an energetic point of view, complex **2-rc** was found to be more stable than **3-rc** by 6.2 kcal·mol$^{-1}$, the two triplet-state structures being lower in energy than the singlet-state **1-rc** ($\Delta E_{S/T}$ = –20.3 kcal·mol$^{-1}$ between **2-rc** and **1-rc**). Finally, the influence of a QM treatment of the phenyl ligands was tested by single-point calculations at the B3PW91//ONIOM(B3PW91:UFF) level (Figure 3). A triplet ground state was still found, with **2-rc** and **3-rc** very close in energy (only 0.4 kcal·mol$^{-1}$ in favor of **3-rc**) and significantly more stable than the square-planar singlet-state **1-rc** ($\Delta E_{S/T}$ = –29.6 kcal·mol$^{-1}$ between **3-rc** and **1-rc**). Both from the geometrical and energetic points of view, the results of these calculations on the real complex are similar to those from the study of the model complex (Figure 1).

## Conclusion

According to DFT calculations, there is a change in the nature of the electronic ground state when Rh or Ir is replaced by Co in the family of SPS-based pincer-based [M(SPS)(PH$_3$)] model complexes. While Rh and Ir compounds are found to be diamagnetic, a triplet ground state is predicted for the yet unknown cobalt complex, a conclusion confirmed by calculations on the real complex [Co(SPS)(PPh$_3$)] with nine phenyl substituents. This change in the electronic ground state in going from (Rh, Ir) to Co is likely to result in a different chemical behavior of the Co complex compared to its rhodium or iridium analogs. This

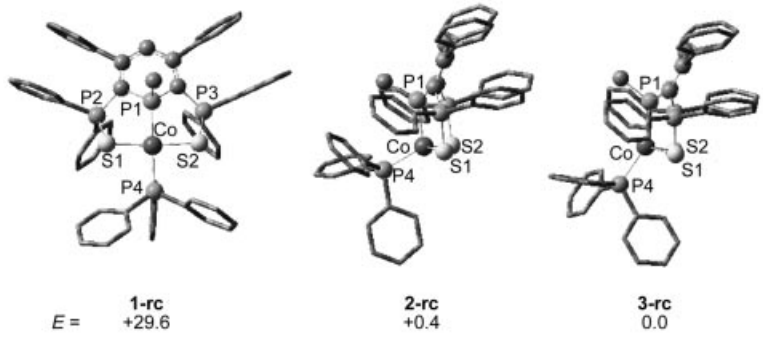


Figure 3. Optimized geometries for the real complex [Co(SPS)(PPh$_3$)] in its singlet (**1-rc**) and triplet (**2-rc** and **3-rc**) states. Hydrogen atoms are omitted for clarity. *E*: relative energies [at the B3PW91//ONIOM(B3PW91:UFF) level] are given in kcal·mol$^{-1}$. Selected geometrical parameters (bond lengths in Å and bond angles in °): **1-rc**: Co–S1 2.290, Co–S2 2.283, Co–P1 2.176, Co–P4 2.244; S1–Co–S2 172.5, P1–Co–P4 173.2. **2-rc**: Co–S1 2.405, Co–S2 2.367, Co–P1 2.285, Co–P4 2.278; S1–Co–S2 119.8, P1–Co–P4 112.2. **3-rc**: Co–S1 2.428, Co–S2 2.420, Co–P1 2.277, Co–P4 2.299; S1–Co–S2 103.2, P1–Co–P4 150.9.

 © 2006 Wiley-VCH Verlag GmbH & Co. KGaA, Weinheim 

result has prompted us to synthesize this interesting Co derivative and to study its reactivity towards small molecules.

## Computational Details

Calculations on the model complexes (quoted as [M(SPS)($PH_3$)] with M = Co, Rh, and Ir), in which the phenyl groups were replaced by H atoms, were performed with the GAUSSIAN 03 series of programs.[31] Density functional theory (DFT)[32,33] was applied with the B3PW91 functional.[34] A quasirelativistic effective core potential operator was used to represent the 10 innermost electrons of the cobalt atom, the 28 innermost electrons of the rhodium atom, and the 60 innermost electrons of the iridium atom.[35] The basis set for the metal atom was that associated with the pseudopotential, with a standard double-ζ LANL2DZ contraction[35] completed by a set of polarization *f* functions.[36] Geometry optimizations were performed with the 6-31+G* basis for phosphorus and sulfur atoms, 6-31G* for the carbon atoms, and 6-31G for hydrogen atoms[37–40] (basis set A) and the minimum energy structures were characterized by vibration frequency calculations. Finally, the energies were recomputed by single-point calculations on the optimized structures using the same basis set for the metal center and the 6-31+G* basis set for all the other atoms (basis set B). Note that the changes in relative energies were found to be lower than 0.7 kcal·$mol^{-1}$ in going from basis set A to basis set B. The restricted singlet-state wave function was reoptimized in the Co complex **1**, as an RHF → UHF instability was detected (single-point calculation on the geometry optimized at the restricted level). The geometry of the real complex (**rc**) [Co(SPS)($PPh_3$)] with nine phenyl substituents was optimized and characterized by vibration frequency calculations by means of QM/MM calculations at the ONIOM(B3PW91:UFF) level with the phenyl substituents in the MM part.[41] The QM part was treated at the DFT/B3PW91 level with the basis set A (see above) and the UFF force field was used for the MM part.[42] Finally, DFT-B3PW91 single-point calculations were performed on the optimized structures [B3PW91//ONIOM(B3PW91:UFF) calculations] using the 6-31G basis set for the phenyl substituents and the basis set A for the other atoms.

**Supporting Information** (see footnote on the first page of this article): Optimized geometry and frequencies of **1**–**4**, **1-rc**, **2-rc**, **3-rc**, **Rh(1)**, **Rh(2)**, **Rh(3)**, **Rh(4)**, **Ir(1)**, **Ir(2)**, **Ir(3)**, and **Ir(4)**.

## Acknowledgments

The authors thank the CNRS and the Ecole Polytechnique for supporting this work and IDRIS (Project no. 061616, Orsay, Paris XI) for the allowance of computer time. We are grateful to L. Ricard and O. Piechaczyk for computational assistance.

[1] C. J. Moulton, B. L. Shaw, *J. Chem. Soc., Dalton Trans.* **1976**, 1020–1024.
[2] M. E. van der Boom, D. Milstein, *Chem. Rev.* **2003**, *103*, 1759–1792.
[3] J. T. Singleton, *Tetrahedron Lett.* **2003**, *59*, 1837–1857.
[4] M. Albrecht, G. Van Koten, *Angew. Chem. Int. Ed.* **2001**, *40*, 3750–3781.
[5] S. Grundemann, M. Albrecht, J. A. Loch, J. W. Faller, R. H. Crabtree, *Organometallics* **2001**, *20*, 5485–5488.
[6] A. S. Ionkin, W. J. Marshall, *Heteroatom Chem.* **2002**, *13*, 662–666.
[7] P. Kapoor, A. Pathak, R. Kapoor, P. Venugopalan, M. Corbella, M. Rodriguez, J. Robles, A. Llobet, *Inorg. Chem.* **2002**, *41*, 6153–6160.
[8] J. D. Niemoth-Anderson, K. A. Clark, T. A. George, C. R. Ross, *J. Am. Chem. Soc.* **2000**, *122*, 3977–3978.
[9] D. R. Evans, M. Huang, W. M. Seganish, E. W. Chege, Y. F. Lam, J. C. Fettinger, T. L. Williams, *Inorg. Chem.* **2002**, *41*, 2633–2641.
[10] D. A. Evans, K. R. Campos, J. S. Tedrow, F. E. Michael, M. R. Gagne, *J. Am. Chem. Soc.* **2000**, *122*, 7905–7920.
[11] M. Tschoerner, G. Trabesinger, A. Albinati, P. S. Pregosin, *Organometallics* **1997**, *16*, 3447–3453.
[12] X. Verdaguer, M. A. Pericàs, A. Riera, M. A. Maestro, J. Mahia, *Organometallics* **2003**, *22*, 1868–1877.
[13] K. Ortner, L. Hilditch, Y. F. Zheng, J. R. Dilworth, U. Abram, *Inorg. Chem.* **2000**, *39*, 2801–2806.
[14] N. Brugat, A. Polo, A. Alvarez-Larena, J. F. Piniella, J. Real, *Inorg. Chem.* **1999**, *38*, 4829–4837.
[15] D. R. Evans, M. S. Huang, W. M. Seganish, J. C. Fettinger, T. L. Williams, *Organometallics* **2002**, *21*, 893–900.
[16] H. Brunner, H. J. Lautenschlager, W. A. König, R. Krebber, *Chem. Ber.* **1990**, *123*, 847–853.
[17] S. M. Aucott, A. M. Z. Slawin, J. D. Woolins, *Eur. J. Inorg. Chem.* **2002**, 2408–2418.
[18] P. J. Heard, A. E. Aliev, *Polyhedron* **1998**, *17*, 3981–3987.
[19] T. Kanbara, T. Yamamoto, *J. Organomet. Chem.* **2003**, *688*, 15–19.
[20] M. Doux, N. Mézailles, L. Ricard, P. Le Floch, *Eur. J. Inorg. Chem.* **2003**, 3878–3894.
[21] M. Doux, N. Mézailles, L. Ricard, P. Le Floch, P. D. Vaz, M. J. Calhorda, T. Mahabiersing, F. Hartl, *Inorg. Chem.* **2005**, *44*, 9213–9224.
[22] M. Doux, N. Mézailles, L. Ricard, P. Le Floch, P. Adkine, T. Berclaz, M. Geoffroy, *Inorg. Chem.* **2005**, *44*, 1147–1152.
[23] M. Doux, N. Mézailles, L. Ricard, P. Le Floch, *Organometallics* **2003**, *22*, 4624–4626.
[24] M. Doux, L. Ricard, P. Le Floch, N. Mézailles, *Dalton Trans.* **2004**, *16*, 2593–2600.
[25] M. Doux, N. Mézailles, M. Melaimi, L. Ricard, P. Le Floch, *Chem. Commun.* **2002**, 1566–1567.
[26] M. Doux, P. Le Floch, Y. Jean, *J. Mol. Struct. (THEOCHEM)* **2005**, *724*, 73–79.
[27] M. Doux, L. Ricard, P. Le Floch, Y. Jean, *Organometallics* **2005**, *24*, 1608–1613.
[28] M. Doux, L. Ricard, P. Le Floch, Y. Jean, *Organometallics* **2006**, *25*, 1101–1111.
[29] Y. Jean, *Molecular Orbitals of Transition Metal Complexes*, Oxford University Press, London, **2005**.
[30] Note that attempts to optimize the other butterfly geometry (**4**) led to the tetrahedron geometry (**2-rc**).
[31] M. J. Frisch, G. W. Trucks, H. B. Schlegel, G. E. Scuseria, M. A. Robb, J. R. Cheeseman, J. J. A. Montgomery, T. Vreven, K. N. Kudin, J. C. Burant, J. M. Millam, S. S. Iyengar, J. Tomasi, V. Barone, B. Mennucci, M. Cossi, G. Scalmani, N. Rega, G. A. Petersson, H. Nakatsuji, M. Hada, M. Ehara, K. Toyota, R. Fukuda, J. Hasegawa, M. Ishida, T. Nakajima, Y. Honda, O. Kitao, H. Nakai, M. Klene, X. Li, J. E. Knox, H. P. Hratchian, J. B. Cross, C. Adamo, J. Jaramillo, R. Gomperts, R. E. Stratmann, O. Yazyev, A. J. Austin, R. Cammi, C. Pomelli, J. W. Ochterski, P. Y. Ayala, K. Morokuma, G. A. Voth, P. Salvador, J. J. Dannenberg, V. G. Zakrzewski, S. Dapprich, A. D. Daniels, M. C. Strain, O. Farkas, D. K. Malick, A. D. Rabuck, K. Raghavachari, J. B. Foresman, J. V. Ortiz, Q. Cui, A. G. Baboul, S. Clifford, J. Cioslowski, B. B. Stefanov, G. Liu, A. Liashenko, P. Piskorz, I. Komaromi, R. L. Martin, D. J. Fox, T. Keith, M. A. Al-Laham, C. Y. Peng, A. Nanayakkara, M. Challacombe, P. M. W. Gill, B. Johnson, W. Chen, M. W. Wong, C. Gonzalez, J. A. Pople, *Gaussian 03, Revision B.04*, Pittsburgh, PA, USA, **2003**.
[32] R. G. Parr, W. Yang, *DFT*, Oxford University Press, Oxford, UK, **1989**.
[33] T. Ziegler, *Chem. Rev.* **1991**, *91*, 651.
[34] A. D. Becke, *J. Chem. Phys.* **1993**, *98*, 5648–5652.

 © 2006 Wiley-VCH Verlag GmbH & Co. KGaA, Weinheim 

[35] P. J. Hay, W. R. Wadt, *J. Chem. Phys.* **1985**, *82*, 299.
[36] A. Ehlers, M. Böhme, S. Dapprich, A. Gobbi, A. Höllwarth, V. Jonas, K. F. Köhler, R. Stegmann, A. Veldkamp, G. Frenking, *Chem. Phys. Lett.* **1993**, *208*, 111–114.
[37] W. J. Hehre, R. Ditchfield, J. A. Pople, *J. Chem. Phys.* **1972**, *56*, 2257–2272.
[38] M. M. Francl, W. J. Petro, W. J. Hehre, J. S. Binkley, M. S. Gordon, D. J. DeFrees, J. A. Pople, *J. Chem. Phys.* **1982**, *77*, 3654–3665.
[39] T. Clark, J. Chandrasekhar, G. W. Spitznagel, P. von Ragué Schleyer, *J. Comput. Chem.* **1983**, *4*, 294–301.
[40] P. C. Hariharan, J. A. Pople, *Theor. Chim. Acta* **1973**, *28*, 213–222.
[41] M. Svensson, S. Humbel, R. D. J. Froese, T. Matsubara, S. Sieber, K. J. Morokuma, *J. Phys. Chem.* **1996**, *100*, 19357–19363.
[42] A. K. Rappé, C. J. Casewitt, K. S. Colwell, W. A. Goddard, W. M. Skiff, *J. Am. Chem. Soc.* **1992**, *114*, 10024–10035.

Received: December 1, 2005
Published Online: March 22, 2006

 © 2006 Wiley-VCH Verlag GmbH & Co. KGaA, Weinheim 

DOI: 10.1002/ejic.200501078

# Multielectron Storage and Photo-Induced Electron Transfer in Oligonuclear Complexes Containing Ruthenium(II) Terpyridine and Ferrocene Building Blocks

**Katja Heinze,*[a] Klaus Hempel,[a] and Manuela Beckmann[a]**

**Keywords:** Electron transfer / Heterometallic complexes / Luminescence / Metallocenes / Ruthenium

The heteroleptic complex $[(HOOC\text{-}tpy)Ru(tpy\text{-}NH_2)](PF_6)_2$ (tpy = 2,2′;6′,2′′-terpyridine) has been incorporated into a multicomponent system with ferrocene moieties attached on either the N-terminal end or the C-terminal end and on both ends of the ruthenium complex. Electrochemical studies reveal almost noninteracting subunits in the oligonuclear systems, whereas ground-state and excited-state optical properties are shown to strongly depend on the site of ferrocene attachment. Interpretation of the experimental results is supported by DFT calculations.
(© Wiley-VCH Verlag GmbH & Co. KGaA, 69451 Weinheim, Germany, 2006)

## Introduction

Design and synthesis of multicomponent systems such as polynuclear metal complexes incorporating electroactive and/or photoactive moieties, especially ruthenium polypyridine complexes,[1–11] is of great current interest for fundamental studies of energy and electron transfer and photoinduced charge separation modelling natural photosynthesis[12] as well as in terms of potential applications in molecular wires and devices, photocatalysis, energy conversion and information storage.[13–17] Most of these topics rely fundamentally on vectorial energy or electron transfer that requires asymmetric multicomponent systems. This requirement has been elegantly met by the design of metallostars and metallodendrimers.[18,19]

Natural proteins represent an archetype for directional multicomponent systems with a well-defined sequence of building blocks. Biological peptides and proteins already provide interesting functions such as molecular recognition and catalysis,[20,21] while artificial amino acid building blocks expand the diversity of peptides and proteins. Combining metal-containing electroactive and photoactive units in peptide-like structures should merge the advantages of both worlds: the amide linkage provides directionality and the introduction of metal complexes provides functionality.[22–31]

In this contribution the synthesis of a bis(terpyridine) ruthenium complex with amino and carboxylato substituents and its conjugates with ferrocene units attached on the N or C terminus as well as on both ends is reported. The influence of the site of ferrocene attachment on ground- and excited-state properties of the multicomponent systems is investigated.

[a] Anorganisch-Chemisches Institut der Universität Heidelberg, Im Neuenheimer Feld 270, 69120 Heidelberg, Germany
Fax: +49-6221-545707
E-mail: katja.heinze@urz.uni-heidelberg.de
Supporting information for this article is available on the WWW under http://www.eurjic.org or from the author.

## Results and Discussion

### Design and Synthetic Strategy

The assembly of ruthenium and ferrocene building blocks is based on a modular approach using peptide chemistry.[22–24,32] The key building block is the heteroleptic complex $\mathbf{2}(PF_6)_2$ with a bis(terpyridine) ruthenium(II) core. This asymmetrical complex can be functionalised on either the C-terminal or the N-terminal end giving access to asymmetric multinuclear complexes with a well-defined sequence of building blocks.

Two synthetic challenges have to be met for the success of the synthetic strategy: (i) the selective formation of the heteroleptic complex $\mathbf{2}(PF_6)_2$ and (ii) the activation of the unreactive amino group of the positively charged complex for amide formation. The synthetic approach to $\mathbf{2}(PF_6)_2$ is outlined in Scheme 1.

The terpyridine ligands tpy-COOEt and tpy-$NH_2$ were prepared using Stille coupling reactions according to literature procedures.[33–35] To selectively obtain the heteroleptic complex $\mathbf{1}(PF_6)_2$ the ester-substituted terpyridine ligand is coordinated to ruthenium trichloride[34] before the amino-substituted terpyridine is attached using microwave irradiation (Scheme 1). This optimised procedure results in a negligible amount of homoleptic complexes and $\mathbf{1}(PF_6)_2$ was isolated in 85% yield. In the $^1H$ NMR spectrum of $\mathbf{1}(PF_6)_2$ characteristic singlet signals for the protons $H^2$ and $H^{2'}$ are observed at $\delta$ = 9.15 and $\delta$ = 7.96, respectively, while the

 © 2006 Wiley-VCH Verlag GmbH & Co. KGaA, Weinheim 

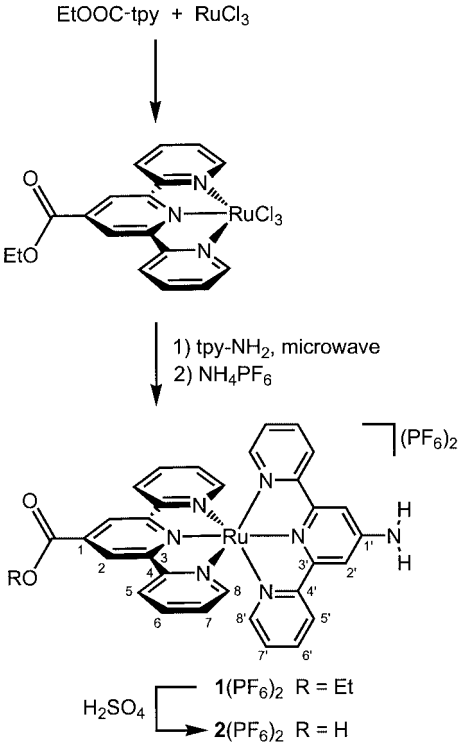


Scheme 1.

amine protons resonate at $\delta$ = 6.00 and the aliphatic protons of the ethyl group at $\delta$ = 4.64 and $\delta$ = 1.57 with expected intensity ratios (for full assignment see Table 1). The assignment of $^{13}$C NMR signals is summarised in the Exp. Sect. (Table 5). The FAB mass spectra establish the composition of $\mathbf{1}^{2+}$ showing signals for $[\mathbf{1} + H,PF_6]^+$ and $[\mathbf{1}]^+$ at $m/z$ = 801 and $m/z$ = 655, respectively. In the IR spectrum of $\mathbf{1}(PF_6)_2$ characteristic absorption bands are observed for the substituents and the hexafluorophosphate counterions (Table 2; Supporting Information, see footnote on the first page of this article).

Table 2. Characteristic IR spectroscopic data [$\tilde{\nu}$/cm$^{-1}$] of complexes $\mathbf{1}(PF_6)_2$–$\mathbf{5}(PF_6)_2$.

| | $\mathbf{1}(PF_6)_2$ | $\mathbf{2}(PF_6)_2$ | $\mathbf{3}(PF_6)_2$ | $\mathbf{4}(PF_6)_2$ | $\mathbf{5}(PF_6)_2$ |
|---|---|---|---|---|---|
| CO (ester/acid) | 1723 | 1719 | – | – | 1721 |
| Amide I | – | – | 1622 | 1668, 1619 | 1674 |
| Amide II | – | – | 1551 | 1574, 1560 | 1577 |
| $NH_2$ (def.) | 1636 | 1634 | 1634 | – | – |
| PF | 838 | 838 | 841 | 839 | 841 |

Hydrolysis of the ester moiety of $\mathbf{1}(PF_6)_2$ to the corresponding acid was unsuccessful with a catalytic amount of hydrochloric acid at room temperature and under microwave heating, while under more forcing conditions (20% sulfuric acid, reflux) the acid $\mathbf{2}(PF_6)_2$ was isolated in 74% yield (Scheme 1). The successful synthesis of $\mathbf{2}(PF_6)_2$ was confirmed by NMR and IR spectroscopy (Tables 1, 2 and 5) as well as mass spectrometry (see Exp. Sect.).

Single crystals have been obtained from an aqueous acidic solution of $\mathbf{2}(PF_6)_2$. The mixed salt $\mathbf{2}(PF_6)(F)$ crystallises in the triclinic space group $P\bar{1}$ with two independent cationic molecules in the asymmetric unit (Figure 1). The cations and anions are embedded in strands of solvent water (about 4–5 per ruthenium centre) held together by

Table 1. $^1$H NMR spectroscopic data of complexes $\mathbf{1}(PF_6)_2$–$\mathbf{5}(PF_6)_2$ in $CD_3CN$ (atom numbering according to Scheme 1).

| | $\mathbf{1}(PF_6)_2$ | $\mathbf{2}(PF_6)_2$[a] | $\mathbf{3}(PF_6)_2$ | $\mathbf{4}(PF_6)_2$ | $\mathbf{5}(PF_6)_2$ |
|---|---|---|---|---|---|
| $H^2$ | 9.15 (s, 2 H) | 9.18 (s, 2 H) | 9.16 (s, 2 H) | 9.16 (s, 2 H) | 9.20 (s, 2 H) |
| $H^5$ | 8.63 (d, 2 H, $^3J_{HH}$ = 8.0 Hz) | 8.63 (d, 2 H, $^3J_{HH}$ = 8.1 Hz) | 8.64 (d, 2 H, $^3J_{HH}$ = 7.5 Hz) | 8.65 (d, 2 H, $^3J_{HH}$ = 8.0 Hz) | 8.67 (d, 2 H, $^3J_{HH}$ = 8.0 Hz) |
| $H^6$ | 7.89 (m, 2 H) | 7.93 (m, 2 H) | 7.96 (m, 2 H) | 7.97 (m, 2 H) | 7.97 (m, 2 H) |
| $H^7$ | 7.26 (dd, 2 H, $^3J_{HH}$ = 5.4; $^4J_{HH}$ = 1.2 Hz) | 7.28 (dd, 2 H, $^3J_{HH}$ = 5.4; $^4J_{HH}$ = 1.2 Hz) | 7.26 (pt, 2 H) | 7.31 (pt, 2 H) | 7.26 (m, 2 H) |
| $H^8$ | 7.56 (d, 2 H, $^3J_{HH}$ = 5.0 Hz) | 7.55 (d, 2 H, $^3J_{HH}$ = 5.4 Hz) | 7.56 (d, 2 H, $^3J_{HH}$ = 5.4 Hz) | 7.52 (d, 2 H, $^3J_{HH}$ = 5.2 Hz) | 7.52 (d, 2 H, $^3J_{HH}$ = 5.0 Hz) |
| $H^{2'}$ | 7.96 (s, 2 H) | 7.98 (s, 2 H) | 7.97 (s, 2 H) | 9.24 (s, 2 H) | 9.28 (s, 2 H) |
| $H^{5'}$ | 8.26 (d, 2 H, $^3J_{HH}$ = 8.0 Hz) | 8.27 (d, 2 H, $^3J_{HH}$ = 8.1 Hz) | 8.27 (d, 2 H, $^3J_{HH}$ = 8.0 Hz) | 8.43 (d, 2 H, $^3J_{HH}$ = 8.0 Hz) | 8.45 (d, 2 H, $^3J_{HH}$ = 8.0 Hz) |
| $H^{6'}$ | 7.84 (m, 2 H) | 7.83 (m, 2 H) | 7.84 (m, 2 H) | 7.93 (m, 2 H) | 7.93 (m, 2 H) |
| $H^{7'}$ | 7.03 (dd, 2 H, $^3J_{HH}$ = 5.2; $^4J_{HH}$ = 1.2 Hz) | 7.03 (dd, 2 H, $^3J_{HH}$ = 5.2; $^4J_{HH}$ = 1.2 Hz) | 7.05 (pt, 2 H) | 7.14 (pt, 2 H) | 7.13 (pt, 2 H) |
| $H^{8'}$ | 7.16 (d, 2 H, $^3J_{HH}$ = 5.2 Hz) | 7.18 (d, 2 H, $^3J_{HH}$ = 5.2 Hz) | 7.22 (d, 2 H, $^3J_{HH}$ = 5.2 Hz) | 7.23 (d, 2 H, $^3J_{HH}$ = 5.4 Hz) | 7.28 (d, 2 H, $^3J_{HH}$ = 5.2 Hz) |
| $CH_2$ | 4.64 (q, 2 H, $^3J_{HH}$ = 7.1 Hz) | – | – | – | 4.67 (q, 2 H, $^3J_{HH}$ = 7.1 Hz) |
| $CH_3$ | 1.56 (t, 3 H, $^3J_{HH}$ = 7.1 Hz) | – | – | – | 1.59 (t, 3 H, $^3J_{HH}$ = 7.0 Hz) |
| $NH_2$ | 6.00 (br. s, 2 H) | 6.03 (br. s, 2 H) | 6.00 (br. s, 2 H) | – | – |
| NH | – | – | 9.21 (s, 1 H) | 9.08 (s, 1 H)[b] | – |
| NH′ | – | – | – | 9.31 (s, 1 H)[b] | 9.43 (s, 1 H) |
| Cp-H | | | 4.99 (s, 2 H), 4.29 (s, 5 H), 4.18 (s, 2 H) | 4.98 (s, 2 H), 4.31 (s, 5 H), 4.19 (s, 2 H) | |
| Cp′-H | – | – | | 5.14 (s, 2 H), 4.66 (s, 2 H), 4.41 (s, 5 H) | 5.17 (s, 2 H), 4.68 (s, 2 H), 4.42 (s, 5 H) |

[a] At pH 2. [b] Assignment according to NOE crosspeak NH′–Cp–H.

 © 2006 Wiley-VCH Verlag GmbH & Co. KGaA, Weinheim 

hydrogen bonds and involving both the acid and amine groups of the cations. Selected bond lengths and angles of the independent complex molecules (Table 3) show that both cations exhibit similar primary coordination geometries. However, the two cations display different secondary coordination spheres. The amine group of one cation is hydrogen-bonded to a hexafluorophosphate counterion while the amine group of the other cation is hydrogen-bonded to solvent water (Figure 1).

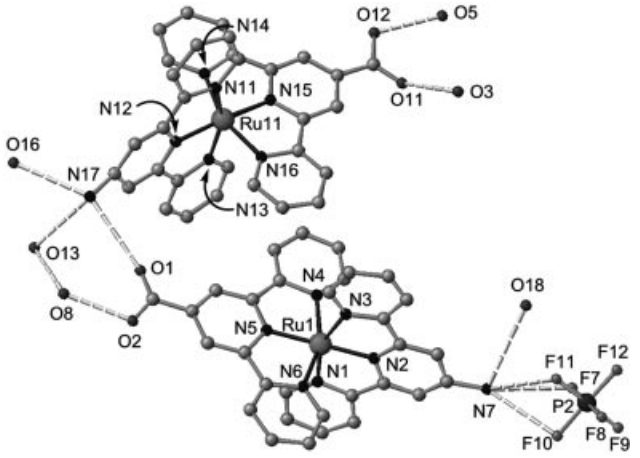


Figure 1. Two independent complex cations of $\mathbf{2}(PF_6)(F)$ and their partial secondary coordination sphere (O3, O5, O8, O13, O16 and O18 denote solvent water).

The acid group of $\mathbf{2}(PF_6)_2$ is activated by 1-hydroxybenzotriazole (HOBt) in the presence of 1,3-dicyclohexylcarbodiimide (DCC). Subsequent reaction with aminoferrocene[22] gives the C-terminal-substituted ferrocene conjugate $\mathbf{3}(PF_6)_2$ (Scheme 2). Under these conditions the less reactive aromatic amino group of $\mathbf{2}(PF_6)_2$ remains intact, thus the use of protective groups can be avoided.

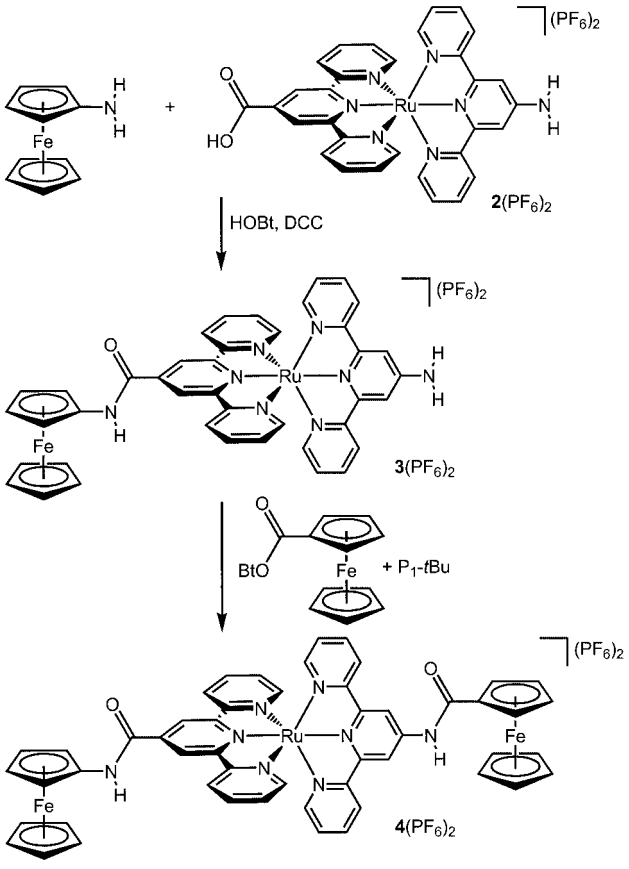


Scheme 2.

Under more forcing conditions employing the organic-soluble, nonionic Schwesinger phosphazene base $P_1$-*t*Bu[36–38] the amino groups of $\mathbf{1}(PF_6)_2$ and $\mathbf{3}(PF_6)_2$ form peptide bonds with ferrocenoyl benzotriazol ester Fc-CO-OBt[39] to give the N-terminal-substituted ferrocene conjugate $\mathbf{5}(PF_6)_2$ and the bis-ferrocene bisamide $\mathbf{4}(PF_6)_2$, respec-

Table 3. Experimental and DFT calculated selected bond lengths [Å] and angles [°] of $\mathbf{2}(PF_6)(F)$.

| | Ru1 | Ru11 | DFT | | Ru1 | Ru11 | DFT |
|---|---|---|---|---|---|---|---|
| Ru1–N1 | 2.082(9) | 2.063(9) | 2.111 | N1–Ru1–N2 | 78.3(4) | 79.2(4) | 78.4 |
| Ru1–N2 | 1.988(10) | 1.975(11) | 2.023 | N1–Ru1–N3 | 156.4(4) | 156.9(4) | 156.7 |
| Ru1–N3 | 2.077(8) | 2.101(8) | 2.111 | N1–Ru1–N4 | 94.7(4) | 89.7(4) | 92.1 |
| Ru1–N4 | 2.090(10) | 2.066(10) | 2.110 | N1–Ru1–N5 | 101.5(4) | 103.5(4) | 101.7 |
| Ru1–N5 | 1.969(9) | 1.974(10) | 1.998 | N1–Ru1–N6 | 89.3(4) | 94.7(4) | 92.1 |
| Ru1–N6 | 2.049(9) | 2.084(10) | 2.110 | N2–Ru1–N3 | 78.2(3) | 77.8(4) | 78.4 |
| C31–O1 | 1.211(16) | 1.231(16) | 1.230 | N2–Ru1–N4 | 101.7(4) | 104.2(4) | 100.9 |
| C31–O2 | 1.284(18) | 1.295(15) | 1.375 | N2–Ru1–N5 | 179.1(4) | 176.9(4) | 179.4 |
| N7···F7 | 3.0 | | – | N2–Ru1–N6 | 99.8(4) | 99.1(4) | 101.0 |
| N7···F10 | 3.3 | | – | N3–Ru1–N4 | 91.5(4) | 94.3(4) | 92.1 |
| N7···F11 | 3.2 | | – | N3–Ru1–N5 | 102.0(3) | 99.6(3) | 101.2 |
| N7···O18 | 3.5 | | – | N3–Ru1–N6 | 93.2(4) | 90.6(4) | 92.2 |
| N17···O1 | | 3.4 | – | N4–Ru1–N5 | 79.2(4) | 77.6(4) | 79.1 |
| N17···O13 | | 3.2 | – | N4–Ru1–N6 | 158.5(4) | 156.7(4) | 158.1 |
| N17···O16 | | 3.1 | – | N5–Ru1–N6 | 79.4(4) | 79.1(4) | 79.0 |
| O2···O8 | 2.6 | | – | O1–C31–O2 | 123(1) | 122(1) | 124.3 |
| O8···O13 | 2.8 | | – | | | | |
| O11···O3 | | 2.8 | – | | | | |
| O12···O5 | | 2.6 | – | | | | |

 © 2006 Wiley-VCH Verlag GmbH & Co. KGaA, Weinheim 

tively (Scheme 2 and Scheme 3). All ferrocene conjugates, **3**$(PF_6)_2$, **4**$(PF_6)_2$ and **5**$(PF_6)_2$, were fully characterised by NMR and IR spectroscopy (see Tables 1, 2, 5 and Supporting Information) as well as mass spectrometry and elemental analyses (see Exp. Sect.).

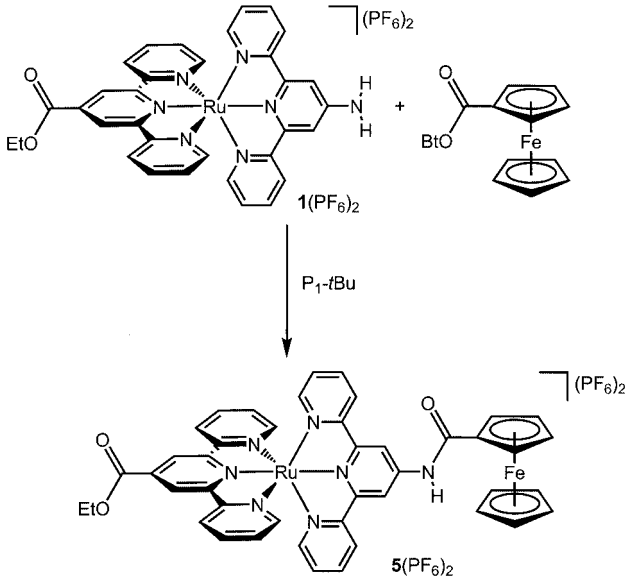


Scheme 3.

The amide protons of **3**$(PF_6)_2$, **4**$(PF_6)_2$ and **5**$(PF_6)_2$ resonate at low field around $\delta$ = 9.0–9.4 ppm. The signals of the cyclopentadienyl protons are found between $\delta$ = 4.2 and 5.2 ppm with typical chemical shifts of N- and C-substituted ferrocenes.[22,24,39] Amide formation at the N terminus of the terpyridine complex results in a downfield shift of the terpyridine proton signal $H^{2'}$ by 1.3 ppm, confirming the activation of the amino group.

## Acid/Base Equilibria of 2$(PF_6)_2$

Solubility and reactivity of **2**$(PF_6)_2$ strongly depends on the pH of the solution. Thus **2**$(PF_6)_2$ was investigated in aqueous solution at different pH values. The corresponding UV/Vis spectra are shown in Figure 2 and Figure 3. As can be deduced from the spectra, three different species exist in aqueous solution, which are assigned different protonated forms of $\mathbf{2}^{2+}$ namely $[\mathbf{2} - H]^+$, $[\mathbf{2}]^{2+}$ and $[\mathbf{2} + H]^{3+}$ (Scheme 4) with absorption maxima of the MLCT transitions at 494, 498 and 486 nm, respectively. Isosbestic points are observed in the spectra of $[\mathbf{2} - H]^+$ and $[\mathbf{2}]^{2+}$ at 494 and 531 nm (Figure 2) and in the spectra of $[\mathbf{2}]^{2+}$ and $[\mathbf{2} + H]^{3+}$ at 491 and 533 nm (Figure 3). The monocationic deprotonated carboxylate complex $[\mathbf{2} - H]^+$ exists at pH > 4 (up to pH ≈ 12 in aqueous solution) and the ammonium trication $[\mathbf{2} + H]^{3+}$ at pH < 0 (concentrated sulfuric acid), while the dication $[\mathbf{2}]^{2+}$ dominates in the intermediate pH range. The p$K_a$ values for the two protonation steps are p$K_{a1}$ = 2.69(8) and p$K_{a2}$ < 0, showing that $[\mathbf{2}]^{2+}$ is a stronger acid than benzoic acid and a weaker base than aniline.

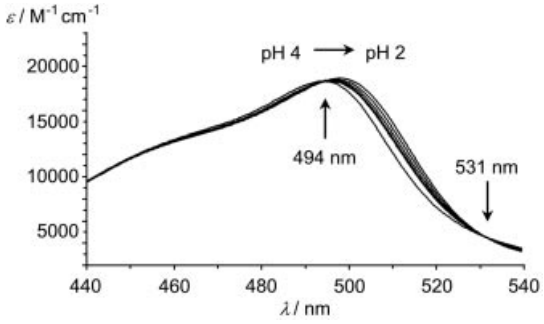


Figure 2. Absorption spectra of **2**$(PF_6)_2$ measured between pH 4 and pH 2.

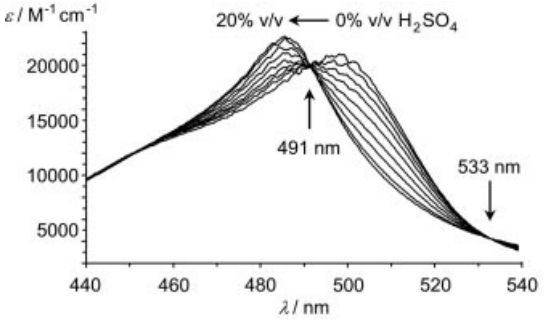


Figure 3. Absorption spectra of **2**$(PF_6)_2$ during titration with conc. sulfuric acid.

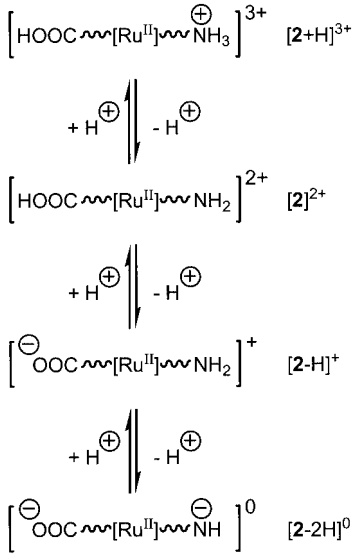


Scheme 4.

The strong base $P_1$-*t*Bu activates the amino groups in the ruthenium complexes **1**$(PF_6)_2$ and **3**$(PF_6)_2$ (see above). This can also be monitored in the UV/Vis spectra of **2**$(PF_6)_2$ during titration with $P_1$-*t*Bu in $CH_3CN$ (Figure 4). The acid group of $[\mathbf{2}]^{2+}$ is deprotonated first to give $[\mathbf{2} - H]^+$ (Figure 4 top, $\lambda_{max}$ = 491 nm; isosbestic points at 351, 474, 489 and 523 nm) and upon further addition of $P_1$-*t*Bu the amino group is deprotonated to give the neutral complex $[\mathbf{2} - 2H]^0$ with an absorption maximum at $\lambda_{max}$ = 493 nm (Figure 4 bottom, isosbestic points at 342, 423 and 515 nm).

 © 2006 Wiley-VCH Verlag GmbH & Co. KGaA, Weinheim 

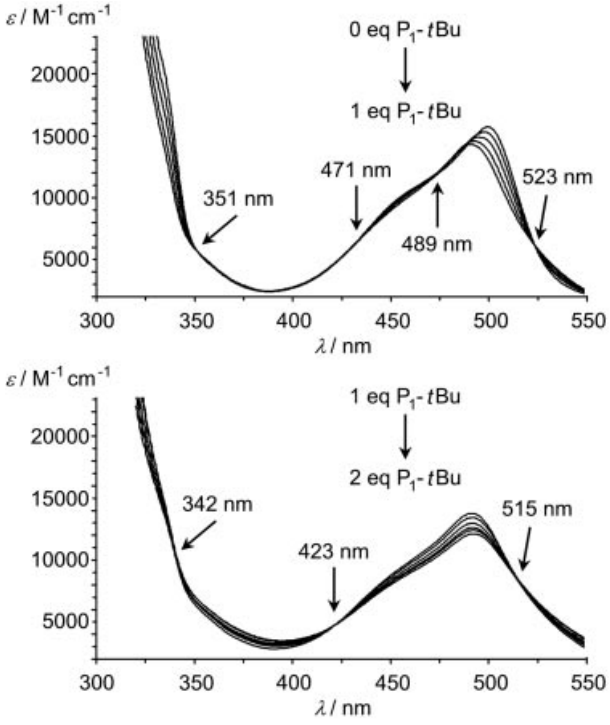


Figure 4. Absorption spectra of $\mathbf{2}(PF_6)_2$ during titration with $P_1$-*t*Bu in $CH_3CN$ from $[\mathbf{2}]^{2+}$ to $[\mathbf{2} - H]^+$ (top) and from $[\mathbf{2} - H]^+$ to $[\mathbf{2} - 2H]^0$ (bottom).

For both $[\mathbf{2} + H]^{3+}$ and $[\mathbf{2} - H]^+$ the low-energy $^1$MLCT absorption (involving the tpy-COOH and the tpy-$COO^-$ ligands, respectively; see below) is shifted to higher energy as compared to $[\mathbf{2}]^{2+}$. Protonation of the amino group renders the tpy-$NH_3^+$ ligand a weaker σ donor, thus decreasing the electron density at the metal centre and lowering the occupied metal-based orbitals.[12,40] Deprotonation of the COOH group of $[\mathbf{2}]^{2+}$ shifts the unoccupied orbitals of the tpy-$COO^-$ ligand to higher energies. Further deprotonation (of the $NH_2$ group) renders the tpy-$NH^-$ ligand a better donor, increasing the energy of the occupied ruthenium orbitals and thus shifting the $^1$MLCT absorption to lower energy. These simple molecular orbital arguments explain the experimentally observed relative positions of the absorption maxima of $[\mathbf{2} + H]^{3+}$, $[\mathbf{2}]^{2+}$, $[\mathbf{2} - H]^+$ and $[\mathbf{2} - 2H]^0$.

The proton NMR spectrum of $[\mathbf{2}]^{2+}$ (precipitated from solutions of pH 2) shows a singlet at $\delta = 6.03$ for the amine substituent with an intensity corresponding to two protons (Figure 5). At lower pH the amino group of $[\mathbf{2}]^{2+}$ is protonated to give $[\mathbf{2} + H]^{3+}$, which does not display any signal for the nitrogen-bonded hydrogen nuclei because of fast proton exchange. Raising the pH to 7 (presence of $[\mathbf{2} - H]^+$) results in downfield shifts of the $^1$H NMR signals of the amino group and the protons $H^2$ and $H^{2'}$ (Figure 5). Thus the NMR spectra confirm that the amine group is protonated only at pH < 2. On the other hand the IR spectrum of $[\mathbf{2}]^{2+}$ in dilute solution shows a signal at 1732 $cm^{-1}$, characteristic for a COOH group (see Supporting Information).

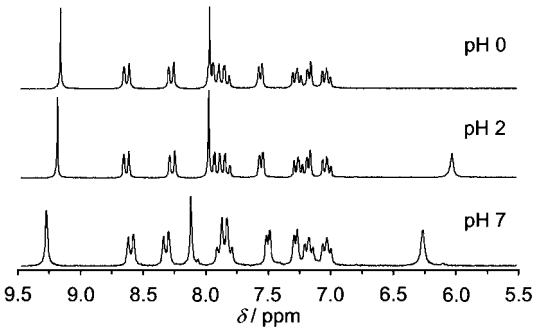


Figure 5. NMR spectra of $\mathbf{2}(PF_6)_2$ at pH 0, 2 and 7.

Thus the NMR and IR spectra provide evidence that $[\mathbf{2}]^{2+}$ does not form a zwitterion in solution in contrast to aliphatic amino acids with basic amino groups. This finding is easily explained by the very low basicity of the aromatic amino group of $[\mathbf{2}]^{2+}$.

### Electrochemistry, Absorption and Emission Spectra

Optical and electrochemical data of $\mathbf{1}(PF_6)_2$–$\mathbf{5}(PF_6)_2$ are collected in Table 4. For all complexes a ruthenium-centred oxidation is observed around 1.1 V versus SCE and two ligand-centred reductions are found around –1.2 V and –1.5 V (irr.). The ferrocene conjugates $\mathbf{3}(PF_6)_2$ and $\mathbf{5}(PF_6)_2$ undergo additional oxidations at 0.37 and 0.64 V, respectively, while $\mathbf{4}(PF_6)_2$ shows two further oxidation waves at 0.37 and 0.66 V corresponding to the two differently substituted ferrocene moieties in the oligonuclear species (Figure 6).

All compounds display two intense $^1$MLCT bands centred around 460–500 nm with a tail on the low-energy side extending as far as 650 nm and corresponding to spin-forbidden $^3$MLCT transitions around 550–600 nm, which become partially allowed because of spin-orbit coupling (Table 4, Figure 7). The $^1$MLCT bands undergo a slight bathochromic shift with increasing solvent polarity from acetonitrile to DMSO (Table 4).

For $\mathbf{3}(PF_6)_2$–$\mathbf{5}(PF_6)_2$, distinct transitions that could be assigned to ferrocene → terpyridine transitions have not been observed on the low-energy side of the absorption bands as found in, for example, $[Ru(tpy\text{-}Fc)_2](PF_6)_2$[42] or [(Fc-tpy)Ru(tpy-FcFc-tpy)Ru(tpy-Fc)]$(PF_6)_4$.[43] However, the extinction coefficients of the MLCT bands of $\mathbf{4}(PF_6)_2$ and $\mathbf{5}(PF_6)_2$ are significantly higher than those of $\mathbf{1}(PF_6)_2$–$\mathbf{3}(PF_6)_2$. The difference spectra "$\mathbf{4}(PF_6)_2 - \mathbf{3}(PF_6)_2$" and "$\mathbf{5}(PF_6)_2 - \mathbf{1}(PF_6)_2$" (Supporting Information) reveal an additional band around $\lambda_{max} \approx 493$ nm with $\varepsilon \approx 7000$ $M^{-1}cm^{-1}$, which could be assigned to a d(Fe) → π*(tpy-NHR′) transition originating from the C-substituted (the N-terminal) ferrocene to the electron-deficient aromatic tpy system.[22,42,43] Thus the $^1$MLCT region contains contributions arising from electron injection from the ruthenium centre and from the ferrocene [in the case of $\mathbf{4}(PF_6)_2$ and $\mathbf{5}(PF_6)_2$] into the differently substituted terpyridine ligands (see below).

 © 2006 Wiley-VCH Verlag GmbH & Co. KGaA, Weinheim 

Table 4. Cyclic voltammetric (vs. SCE), absorption and emission data of complexes $\mathbf{1}(PF_6)_2$–$\mathbf{5}(PF_6)_2$.

| | $\mathbf{1}(PF_6)_2$ | $\mathbf{2}(PF_6)_2$[a] | $\mathbf{3}(PF_6)_2$ | $\mathbf{4}(PF_6)_2$ | $\mathbf{5}(PF_6)_2$ |
|---|---|---|---|---|---|
| **CV**[b] | | | | | |
| $E_{1/2}$ [V] ($\Delta E$ [V]) $Ru^{II}/Ru^{III}$ | 1.08 (0.09) | 1.06 (0.08) | 1.30 (qrev.)[c] | 1.30 (0.19)[c] | 1.05 (0.15)[c] |
| $E_{1/2}$ [V] ($\Delta E$ [V]) $Fc/Fc^+$ | – | – | 0.37 (0.06) | 0.37 (0.11) | – |
| $E_{1/2}$ [V] ($\Delta E$ [V]) $Fc'/Fc'^+$ | – | – | – | 0.66 (0.12) | 0.64 (0.07) |
| $E_{1/2}$ [V] ($\Delta E$ [V]) $tpy/tpy^-$ | –1.14 (0.08), –1.59 (0.12) | –1.20 (irr.), –1.39 (irr.) | –1.21 (0.10), –1.6 (irr.) | –1.18 (0.12), –1.50 (irr.) | –1.10 (0.09), –1.55 (irr.) |
| **Absorption**[41] | | | | | |
| $\lambda_{max}$ [nm] ($\varepsilon$ [$M^{-1}cm^{-1}$])[b][f] | 557 (3690), 502 (19080), 467 (13790) | 570 (1900), 501 (20740), 467 (14370) | 601 (1830), 502 (19260), 479 (15630) | 597 (2380), 496 (25310), 477 (20030) | 583 (2350), 496 (26190), 476 (18270) |
| $\lambda_{max}$ [nm] ($\varepsilon$ [$M^{-1}cm^{-1}$])[d][f] | 560 (3700), 503 (19250), 472 (13550) | 569 (1700), 502 (20970), 469 (14600) | 612 (1610), 502 (18320), 478 (14910) | 601 (2290), 496 (25200), 478 (20090) | 546 (6570), 498 (25730), 478 (19080) |
| $\lambda_{max}$ [nm] ($\varepsilon$ [$M^{-1}cm^{-1}$])[e][f] | 562 (4170), 509 (19640), 475 (13810) | 571 (2230), 507 (20550), 474 (14390) | 626 (1260), 508 (19570), 482 (15820) | 547 (10950), 505 (26440), 485 (21470) | 552 (8940), 506 (26940), 477 (18240) |
| **Emission**[d] | | | | | |
| $\lambda_{max}$ [nm][g] | 799 | 739 | 739 | 704 | 704 |
| $\Phi$[h] | $3.4\times10^{-4}$ | $1.1\times10^{-4}$ | $<0.1\times10^{-4}$ | $<0.1\times10^{-4}$ | $1.1\times10^{-4}$ |
| $E_{0'-0}$ [eV][i] | 1.88 | 1.82 | n.d. | n.d. | 1.89 |

[a] Species obtained by precipitating from solutions of pH 2. [b] In acetonitrile. [c] These waves are no more reversible as oxidation to a highly charged species (+4, +5) results in precipitation of the complexes on the electrode. [d] In acetone. [e] In DMSO. [f] The extinction coefficients $\varepsilon$ are the experimentally observed values at the fitted band maxima. [g] Excitation at low-energy $^1$MLCT absorption maximum. [h] Luminescence quantum yield (±15%), using fluorescein in ethanol as standard. [i] Determined by fitting the emission data to Meyers equation.[44]

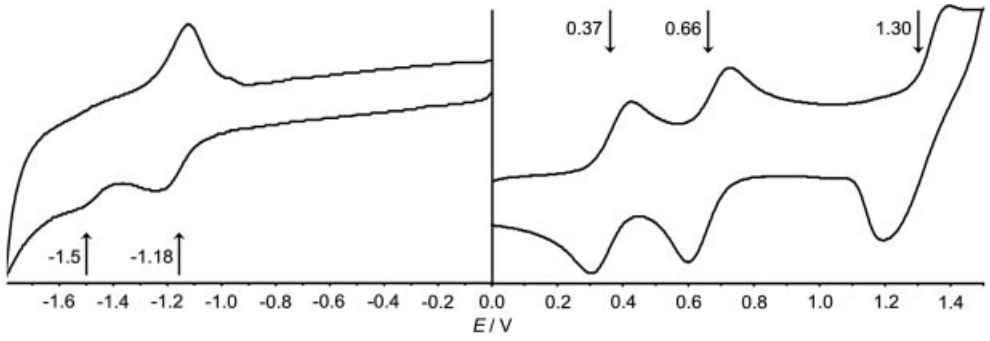


Figure 6. Cyclic voltammogram of $\mathbf{4}(PF_6)_2$ in $CH_3CN/nBu_4NPF_6$.

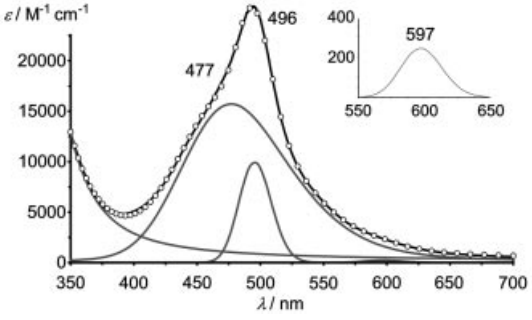


Figure 7. Absorption spectrum of $\mathbf{4}(PF_6)_2$ in $CH_3CN$ and calculated band profiles (the open circles represent the sum of the calculated profiles[41]). The inset shows an expansion of the $^3$MLCT region (fitted band profile).

All complexes are luminescent in argon-saturated acetone at room temperature ($\lambda_{max} \approx$ 700–800 nm; Table 4), although intensity is very weak for $\mathbf{3}(PF_6)_2$ and $\mathbf{4}(PF_6)_2$ ($\Phi < 0.1\times10^{-4}$). Deactivation of the emitting state ($^3$MLCT) in the parent complex $[Ru(tpy)_2]^{2+}$ occurs through a $^3$MC(Ru) state.[1,12] In complexes $\mathbf{1}(PF_6)_2$–$\mathbf{5}(PF_6)_2$ the $^3$MC(Ru) state is shifted to higher energy because of the stronger averaged ligand field raising the energy of the $e_g$ (Ru) orbitals and increasing the $^3$MLCT–$^3$MC(Ru) energy gap.[1,12]

The emission spectra of $\mathbf{1}(PF_6)_2$, $\mathbf{2}(PF_6)_2$ and $\mathbf{5}(PF_6)_2$ could be fitted to the Meyers equation[44] with $E_{0'-0}$ around 1.9 eV (Figure 8). The emission properties of $\mathbf{2}(PF_6)_2$ strongly depend on the pH with higher luminescence quantum yield ($\Phi = 2.1\times10^{-4}$ in water) between pH > 4 and pH < 10 (corresponding to the presence of $[\mathbf{2} - H]^+$, see above) and weak emission at either lower or higher pH ($\Phi = 0.6\times10^{-4}$ in water; see Supporting Information).

For $\mathbf{1}(PF_6)_2$ and $\mathbf{2}(PF_6)_2$ emission gains intensity with increasing excitation wavelength ($\lambda_{exc}$ = 500–650 nm), while for $\mathbf{5}(PF_6)_2$ the reverse is observed (see Supporting Infor-

 © 2006 Wiley-VCH Verlag GmbH & Co. KGaA, Weinheim 

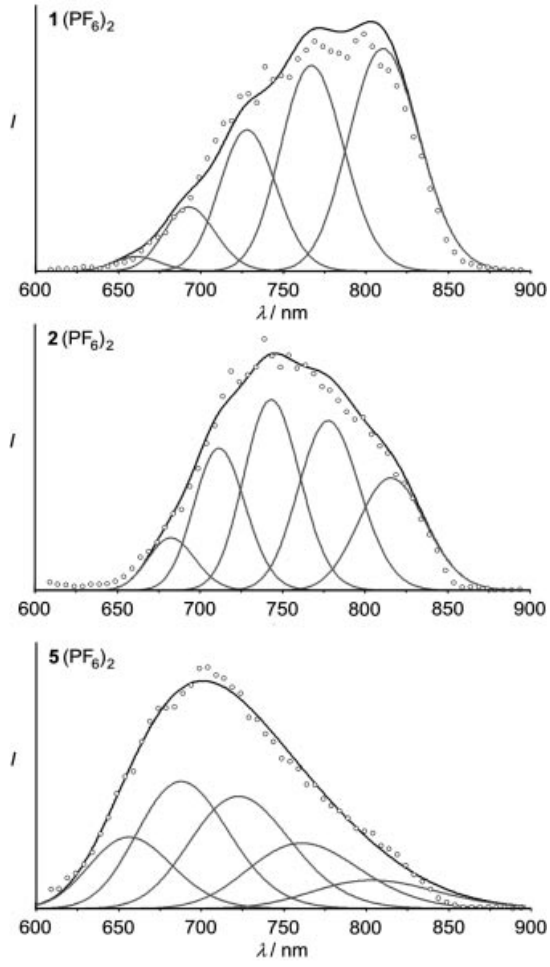


Figure 8. Emission spectra of **1**$(PF_6)_2$, **2**$(PF_6)_2$ and **5**$(PF_6)_2$ (○) in acetone at room temperature and spectral fitting according to Meyers equation.[44]

mation). The C-terminal ferrocene conjugates **3**$(PF_6)_2$ and **4**$(PF_6)_2$ show a much weaker luminescence than their ester analogues **1**$(PF_6)_2$ and **5**$(PF_6)_2$, respectively (Table 4).[45]

### DFT Calculations

All complex cations $\mathbf{1}^{2+}$–$\mathbf{5}^{2+}$ were studied using the B3LYP/LanL2DZ functional. The energy-minimised structure of $\mathbf{5}^{2+}$ shown in Figure 9 as an example shows the expected pseudo-octahedral geometry around the ruthenium centre. The geometric results of the calculation for $\mathbf{2}^{2+}$ reproduce the experimental data of **2**$(PF_6)$(F) sufficiently well (Table 3).

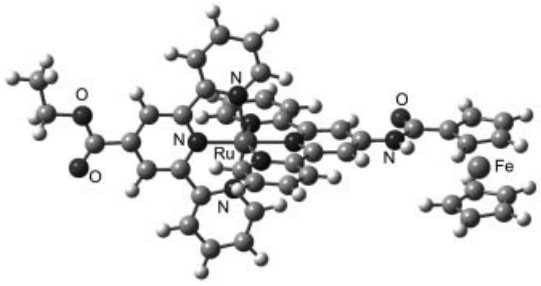


Figure 9. Energy-minimised structure of $\mathbf{5}^{2+}$.

The frontier orbital region of the complex cations consists of closely spaced molecular orbitals (Figure 10). The lowest unoccupied molecular orbitals are π* orbitals of the terpyridine ligands with the LUMO level lying 0.2–0.3 eV below the next highest virtual orbital. Throughout the series the LUMO is localised on the C-terminal terpyridine (tpy-COR). The "$t_{2g}$" manifold of the ruthenium centre provides the high-lying occupied orbitals. For the ferrocene conjugates $\mathbf{3}^{2+}$–$\mathbf{5}^{2+}$ molecular orbitals composed of iron and cyclopentadienyl moieties are inserted in between (Figure 10). The C-terminal ferrocene orbitals d(Fe) + π*(Cp-NHR′′) are found at higher energies than the N-terminal ferrocene orbitals d(Fe) + π*(Cp-COR′′′), as expected from the respective oxidation potentials (Table 4).

The $^1$MLCT transitions arise from $t_{2g}$ (Ru) → π*(tpy) excitations. The low-energy transition (≈500 nm) can be assigned to involve the C-terminal terpyridine tpy-COR, while the next highest transitions (≈480 nm) can be assigned to involve mixtures of both terpyridine ligands tpy-NHR′ and tpy-COR. Low-energy d(Fe) → π*(tpy-NHR′) transitions were observed experimentally for **4**$(PF_6)_2$ and **5**$(PF_6)_2$ around 493 nm with significant intensity (Supporting Information).

A schematic energy level diagram (Figure 11) shows the typical ruthenium $^1$MLCT and $^3$MLCT states. The numerical values are estimates using experimental data obtained under different conditions, thus some caution in their interpretation is advisable. The UV/Vis spectroscopic data

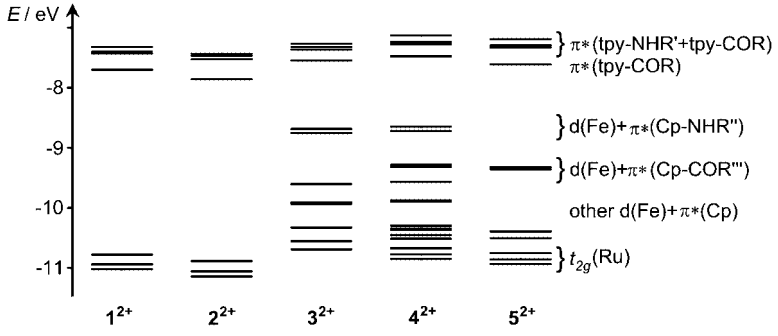


Figure 10. Partial molecular orbital diagrams for $\mathbf{1}^{2+}$–$\mathbf{5}^{2+}$.

 © 2006 Wiley-VCH Verlag GmbH & Co. KGaA, Weinheim 

provide estimates for the energies of the Franck–Condon excited $^1$MLCT states around 2.5 eV. The emission data indicate that the energy level of the emitting $^3$MLCT state has an energy around 1.9 eV,[44] which fits to the Franck-Condon excited $^3$MLCT state (not shown in Figure 11), estimated to be around 2.1–2.2 eV (Table 4).

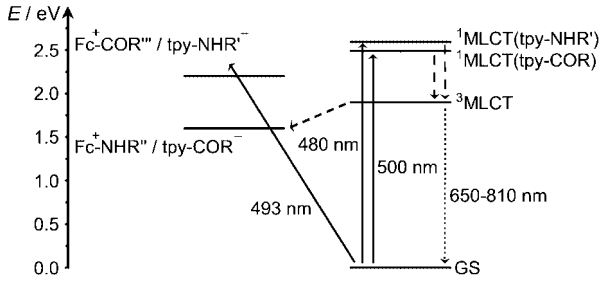


Figure 11. Schematic Jablonski-type energy level diagram (solid lines: excitation; dashed lines: intersystem crossing and electron transfer; dotted line: emission).

Excitation of **1**$(PF_6)_2$ or **2**$(PF_6)_2$ with $\lambda_{exc}$ = 480–500 nm will populate the $^1$MLCT states that undergo intersystem crossing to the emitting $^3$MLCT state while excitation of **1**$(PF_6)_2$ or **2**$(PF_6)_2$ with $\lambda_{exc} > 500$ nm will also directly populate the $^3$MLCT state leading to the experimentally observed increase of the emission intensity (see above; Supporting Information).

For **3**$(PF_6)_2$–**5**$(PF_6)_2$ states arising from the presence of the ferrocene moieties are depicted on the left side of Figure 11. The Franck–Condon excited state d(Fe) → π*(tpy-NHR′) could be observed for **4**$(PF_6)_2$ and **5**$(PF_6)_2$ in the UV/Vis difference spectra around 493 nm (see above and Supporting Information). The ferrocene oxidation potentials and ligand reduction potentials of **3**$(PF_6)_2$–**5**$(PF_6)_2$ (Table 4) allow approximation of the energies of the charge separated states [$Fc^+$-COR′′′/tpy-NHR′$^-$] and [$Fc^+$-NHR′′/tpy-$COR^-$] by 2.2 and 1.6 eV. The former level lies above and the latter below the emitting $^3$MLCT state of the ruthenium core. For **3**$(PF_6)_2$ and **4**$(PF_6)_2$ with a C-terminal ferrocene photoinduced electron transfer is exergonic by 0.3 eV while for **5**$(PF_6)_2$ containing an N-terminal ferrocene photoinduced electron transfer would be endergonic by 0.3 eV. Thus reductive electron transfer from ferrocene to ruthenium is conceivable for **3**$(PF_6)_2$ and **4**$(PF_6)_2$ but not for **5**$(PF_6)_2$, accounting for the experimentally observed luminescence quenching (Table 4).

In contrast to **1**$(PF_6)_2$ and **2**$(PF_6)_2$, direct population of the $^3$MLCT state of **5**$(PF_6)_2$ is hampered because of the population of the d(Fe) → π*(tpy-NHR′) state leading to the experimentally observed decrease in emission intensity at $\lambda_{exc} > 500$ nm (see above and Supporting Information).

The low-lying ferrocene triplet state (not shown in the diagram) has been estimated at an energy between 1.1 and 1.8 eV,[1] that is, in the same energy range as the $^3$MLCT and charge-separated states. Thus energy transfer might also be an additional channel for radiationless excited-state decay.[46–50] Further photophysical investigations including low-temperature emission spectroscopy, lifetime measurements and transient absorption spectroscopy as well as DFT calculations on excited states are currently underway.

## Conclusion

The amino-substituted acid **2**$(PF_6)_2$ and its ester **1**$(PF_6)_2$ have been synthesised and characterised. Complex $\mathbf{2}^{2+}$ undergoes several protonation and deprotonation steps, which have been observed by UV/Vis and emission spectroscopy as well as NMR spectroscopy. Amide formation of **1**$(PF_6)_2$ or **2**$(PF_6)_2$ with ferrocene derivatives was successful in spite of the low reactivity of the aromatic amino group. Ferrocenes have been attached on either side or on both sides of the bis(terpyridine) ruthenium(II) core [**3**$(PF_6)_2$–**5**$(PF_6)_2$].

The ground-state electronic situation of these multinuclear species has been investigated by electronic spectroscopy and cyclic voltammetry, while preliminary emission studies gave insight into the excited-state properties. The ground-state properties of the bis(terpyridine) ruthenium(II) moiety are only slightly modified by the presence of the ferrocenes. The exception is an additional charge-transfer band observed in the absorption spectra of **4**$(PF_6)_2$ and **5**$(PF_6)_2$ but not in the spectra of **3**$(PF_6)_2$. This transition is associated with N-terminal bound ferrocenes and has been assigned d(Fe) → π*(tpy-NHR′) charge transfer character.

The excited-state behaviour of the ferrocene conjugates is strongly dependent on the site of ferrocene attachment: **5**$(PF_6)_2$ with an N-terminal bound ferrocene is luminescent with an inverse correlation to the excitation wavelength as compared to the ferrocene-free **1**$(PF_6)_2$. This behaviour arises from the presence of d(Fe) → π*(tpy-NHR′) charge-transfer bands. Complexes **3**$(PF_6)_2$ and **4**$(PF_6)_2$ with C-terminal bound ferrocenes are much less luminescent. This finding is explained on the assumption that electron transfer from the ferrocene to the ruthenium centre efficiently quenches the $^3$MLCT state of ruthenium.

Thus the optical ground-state properties of the bis(ferrocene) conjugate **4**$(PF_6)_2$ resemble those of the N-terminal conjugate **5**$(PF_6)_2$, while its excited-state properties are analogous to those of the C-terminal conjugate **3**$(PF_6)_2$.

To expand the scope of this design strategy we currently build larger arrays from ruthenium and ferrocene amino acids as well as chiral α-amino acids[22–24] using peptide chemistry for application in electron storage devices, molecular wires, photosensitisers and molecular sensors.

## Experimental Section

**General Methods:** Unless otherwise noted, starting materials were obtained from commercial suppliers and used without further purification. The terpyridine ligands tpy-COOEt[33] and tpy-$NH_2$[34,35] as well as the ferrocene derivatives[22,39] were synthesised according to literature procedures.

NMR spectra were recorded with a Bruker Avance DPX 200 at 200.15 MHz ($^1$H) and 50.323 MHz ($^{13}$C); chemical shifts ($\delta$) in ppm with respect to residual solvent peaks as internal standards:

 © 2006 Wiley-VCH Verlag GmbH & Co. KGaA, Weinheim 

$CD_3CN$ ($^1H$: $\delta$ = 1.93; $^{13}C$: $\delta$ = 1.3 ppm). IR spectra were recorded with a BioRad Excalibur FTS 3000 spectrometer using $CaF_2$ cells or CsI disks. UV/Vis/NIR spectra were recorded with a Perkin–Elmer Lambda 19, 0.2-cm cells (Hellma, suprasil). Cyclic voltammetry was performed using a glassy carbon electrode, a platinum electrode and a SCE electrode, $10^{-3}$ M in 0.1 M $n$Bu$_4$NPF$_6$/$CH_3CN$; potentials are given relative to that of SCE. Mass spectra were recorded with a Finnigan MAT 8400 spectrometer. Emission spectra were recorded with a Varian Cary Eclipse Fluorescence Spectrometer, slit widths 5 nm, in argon-saturated solution. Quantum yields were determined by comparing the areas under the emission spectra recorded for optically matched solutions of the samples and the fluorescein reference ($\Phi$ = 0.79 in ethanol). Elemental analyses were performed by the microanalytical laboratory of the Organic Chemistry Department, University of Heidelberg. Microwave-assisted reactions were performed in a domestic microwave oven operating at a frequency of 2450 MHz and maximum power of 700 W in 20-mL test tubes (Rotilabo).

**Computational Method:** Density functional calculations were carried out with the Gaussian03/DFT[51] series of programs. The B3LYP formulation of density functional theory was used employing the LanL2DZ basis set.[51] All structures were characterised as minima by frequency analysis ($N_{imag}$ = 0) except **3**$^{2+}$, which shows one imaginary frequency for Cp rotation (–10.4 cm$^{-1}$).

**X-ray Crystallography:** Data were collected with an Enraf–Nonius Kappa CCD diffractometer using graphite-monochromated Mo-$K_\alpha$ radiation. The data were processed using the standard Nonius software.[52] All calculations were performed using the SHELXT PLUS software package. Structures were solved using direct or Patterson methods with the SHELXS-97 program and refined with the SHELXL-97 program.[53] Graphical handling of the structural data during refinement was performed using XMPA[54] and WinRay.[55] Atomic coordinates and anisotropic thermal parameters were refined by full-matrix least-squares calculations on $F^2$.

Crystal dimensions 0.1 × 0.02 × 0.02 mm; triclinic crystal system; space group $P\bar{1}$; $a$ = 8.6940(17), $b$ = 21.412(4), $c$ = 21.588(4) Å; $\alpha$ = 94.86(3); $\beta$ = 96.52(3); $\gamma$ = 101.01(3)°; $V$ = 3895.9(13) Å$^3$; $\rho_{calcd.}$ = 1.474 g cm$^{-3}$; $2\theta_{max}$ = 50.1°; $\omega$-scans; $T$ = 200 K; measured reflections 21949; independent reflections 13619; observed reflections 6146 [$I > 2\sigma(I)$]; Lorentz and polarisation correction; $\mu$ = 0.530 mm$^{-1}$; $R_1$ = 0.102 [$I > 2\sigma(I)$]; $wR_2$ = 0.271 [$I > 2\sigma(I)$]; residual electron density 0.915 e Å$^{-3}$.

Because of the large amount of solvent water present in the crystal of **2**(PF$_6$)(F) causing diffuse reflection data and the rather poor data/parameter ratio, carbon atoms, solvent water, some counterions and hydrogen atoms have been refined isotropically.

CCDC-280162 contains the supplementary crystallographic data for this paper. These data can be obtained free of charge from The Cambridge Crystallographic Data Centre via www.ccdc.cam.ac.uk/data_request/cif.

**Synthesis of 1(PF$_6$)$_2$:** (EtOOC-tpy)RuCl$_3$[33–35] (200 mg, 0.39 mmol) and tpy-NH$_2$ (97 mg, 0.39 mmol) were finely suspended in dry ethanol (15 mL) with the aid of an ultrasonic bath. The test tube was closed and heated in the microwave oven for 5 × 1 min at the lowest operating power (80 W). The solution was filtered through a small pad of Celite, washed with water, and $NH_4PF_6$ (191 mg, 1.17 mmol) dissolved in 1 mL water was added. After cooling for 12 h to 4 °C the red product was collected by filtration, washed with water and dried in vacuo. Yield 85% (312 mg, 0.33 mmol). MS (FAB): $m/z$ (%) = 801 (11) [M + H,PF$_6$]$^+$, 655 (55) [M$^+$]. $C_{33}H_{27}F_{12}N_7O_2P_2Ru$ (944.6): calcd. C 41.96, H 2.88, N 10.38; found C 42.09, H 3.15, N 10.22. $^{13}C$ NMR data see Table 5.

**Synthesis of 2(PF$_6$)$_2$:** **1**(PF$_6$)$_2$ (250 mg, 0.27 mmol) was dissolved in 20% sulfuric acid (50 mL) and heated under reflux for 2 h. After cooling to room temperature and adjusting the pH to 2 with $NaOH_{aq}$, $NH_4PF_6$ (132 mg, 0.81 mmol) dissolved in 1 mL water was added and the product precipitated. The red product was collected by filtration, washed with water and dried. Yield 74% (185 mg, 0.20 mmol). MS (FAB): $m/z$ (%) = 772 (60) [M, PF$_6$]$^+$, 626 (100) [M$^+$ – H]. $C_{31}H_{23}F_{12}N_7O_2P_2Ru$ (916.6): calcd. C 40.62, H 2.53, N 10.70; found C 40.63, H 3.20, N 10.65. $^{13}C$ NMR data see Table 5.

**Synthesis of 3(PF$_6$)$_2$:** **2**(PF$_6$)$_2$ (150 mg, 0.16 mmol) was activated with HOBt (34 mg, 0.25 mmol) and DCC (52 mg, 0.25 mmol) in acetonitrile (25 mL) for 2.5 h. A solution of aminoferrocene (51 mg, 0.25 mmol) and *N*-ethylmorpholine (0.1 mL) in acetonitrile (5 mL) was added and the reaction mixture was stirred at room temperature for 2.5 h. The solvent was removed in vacuo, the residue was dissolved in dichloromethane and the product was

Table 5. $^{13}C$ NMR spectroscopic data of complexes **1**(PF$_6$)$_2$–**5**(PF$_6$)$_2$ in $CD_3CN$ (atom numbering according to Scheme 1).

| | **1**(PF$_6$)$_2$ | **2**(PF$_6$)$_2$[a] | **3**(PF$_6$)$_2$ | **4**(PF$_6$)$_2$ | **5**(PF$_6$)$_2$ |
|---|---|---|---|---|---|
| C$^1$ | 135.6 | 135.3 | 159.5 | 156.6 | 136.6 |
| C$^2$ | 125.0 | 125.0 | 121.6 | 121.7 | 123.1 |
| C$^{3,3',4,4'}$ | 158.7, 158.4, 157.5, 156.5 | 158.7, 158.4, 157.5, 156.5 | 158.8, 158.6, 157.1, 156.4 | 158.6, 158.5, 158.3, 158.1 | 158.4, 158.2, 157.0, 155.2 |
| C$^5$ | 124.2 | 124.2 | 124.8 | 125.0 | 124.8 |
| C$^6$ | 138.2 | 138.2 | 138.2 | 138.5 | 138.5 |
| C$^7$ | 128.3 | 128.3 | 128.2 | 128.2 | 128.3 |
| C$^8$ | 152.5 | 152.5 | 152.6 | 152.9 | 152.7 |
| C$^{1'}$ | 154.4 | 154.4 | 154.5 | 155.3 | 148.0 |
| C$^{2'}$ | 109.1 | 109.1 | 109.1 | 114.0 | 114.0 |
| C$^{5'}$ | 122.9 | 123.3 | 124.2 | 124.7 | 125.2 |
| C$^{6'}$ | 138.6 | 138.6 | 138.5 | 138.8 | 138.8 |
| C$^{7'}$ | 127.4 | 127.4 | 127.4 | 127.9 | 127.8 |
| C$^{8'}$ | 153.2 | 153.1 | 153.1 | 153.1 | 153.2 |
| $CH_2$ | 63.2 | – | – | – | 63.3 |
| $CH_3$ | 14.1 | – | – | – | 14.1 |
| C=O | n.o.[b] | 165.1 | 162.6 | n.o.[b] | 164.5 |
| C′=O | – | – | – | n.o.[b] | 171.2 |
| Cp–C | – | – | 69.7 ($C_5H_5$), 65.4, 62.4[c] | 69.8 ($C_5H_5$), 65.4, 62.4[c] | – |
| Cp′–C | – | – | – | 70.6 ($C_5H_5$), 72.5, 69.5[c] | 70.6 ($C_5H_5$), 72.5, 69.5[c] |

[a] At pH 2. [b] n.o., not observed. [c] $C_{ipso}$ of the cyclopentadienyl rings not observed.

 © 2006 Wiley-VCH Verlag GmbH & Co. KGaA, Weinheim 

precipitated by adding diethyl ether. Recrystallisation from hot ethanol and precipitating with $NH_4PF_6$ (78 mg, 0.48 mmol) dissolved in 1 mL water gave the pure product. Yield 88% (150 mg, 0.14 mmol). MS (FAB): *m*/*z* (%) = 810 (40) [$M^+$ – H]. $C_{41}H_{32}F_{12}FeN_8OP_2Ru{\cdot}2H_2O$ (1099.6·$2H_2O$): calcd. C 43.36, H 3.20, N 9.87; found C 43.44, H 3.61, N 10.07. $^{13}C$ NMR data see Table 5.

**Synthesis of 4(PF$_6$)$_2$:** **3**$(PF_6)_2$ (100 mg, 0.09 mmol), ferrocenoyl benzotriazol ester Fc-COOBt (38 mg, 0.11 mmol) and phosphazene base $P_1$-*t*Bu (43 mg, 0.18 mmol) were dissolved in acetonitrile (15 mL) and stirred at room temperature for 16 h. The solvent was removed in vacuo, the residue was dissolved in dichloromethane and the product was precipitated by adding diethyl ether. Recrystallisation from hot ethanol and precipitating with $NH_4PF_6$ (44 mg, 0.27 mmol) dissolved in 1 mL water gave the pure product. Yield 89% (110 mg, 0.08 mmol). MS (FAB): *m*/*z* (%) = 1167 (92) [M, $PF_6$]$^+$, 1021 (100) [$M^+$ – H]. $C_{52}H_{40}F_{12}Fe_2N_8O_2P_2Ru{\cdot}5H_2O$ (1311.6·$5H_2O$): calcd. C 44.56, H 3.60, N 7.99; found C 44.40, H 3.60, N 8.11. $^{13}C$ NMR data see Table 5.

**Synthesis of 5(PF$_6$)$_2$:** **2**$(PF_6)_2$ (100 mg, 0.11 mmol), ferrocenoyl benzotriazol ester Fc-COOBt (37 mg, 0.11 mmol) and phosphazene base $P_1$-*t*Bu (53 mg, 0.22 mmol) were dissolved in acetonitrile (15 mL) and stirred at room temperature for 16 h. The solvent was removed in vacuo, the residue was dissolved in dichloromethane and the product was precipitated by adding diethyl ether. Recrystallisation from hot ethanol and precipitating with $NH_4PF_6$ (54 mg, 0.33 mmol) dissolved in 1 mL water gave the pure product. Yield 91% (115 mg, 0.10 mmol). MS (FAB): *m*/*z* (%) = 1113 (50) [M + H, $PF_6$]$^+$, 866 (100) [$M^+$ – H]. $C_{44}H_{35}F_{12}FeN_7O_3P_2Ru{\cdot}H_2O$ (1156.6·$H_2O$): calcd. C 44.99, H 3.17, N 8.35; found C 44.96, H 3.52, N 8.68. $^{13}C$ NMR data see Table 5.

**Supporting Information Available** (for details see the footnote on the first page of this article): Absorption spectra of **1**$(PF_6)_2$–**5**$(PF_6)_2$ in $CH_3CN$, difference spectrum "**3**$(PF_6)_2$ – **1**$(PF_6)_2$", difference spectrum "**4**$(PF_6)_2$ – **3**$(PF_6)_2$", difference spectrum "**5**$(PF_6)_2$ – **1**$(PF_6)_2$", IR spectra of **1**$(PF_6)_2$, **2**$(PF_6)_2$ and **5**$(PF_6)_2$ in $CH_3CN$, emission spectra of **3**$(PF_6)_2$ and **4**$(PF_6)_2$ with excitation at $\lambda_{max}$ in acetone at room temperature, emission spectra of **2**$(PF_6)_2$ at different pH in water (excitation wavelength 497 nm) at room temperature, pH profile of the emission of **2**$(PF_6)_2$ (excitation wavelength 497 nm, monitored at $\lambda$ = 719 nm), emission spectra of **1**$(PF_6)_2$, **2**$(PF_6)_2$ and **5**$(PF_6)_2$ with different excitation wavelengths in acetone at room temperature, excitation profiles of **1**$(PF_6)_2$, **2**$(PF_6)_2$ and **5**$(PF_6)_2$ in acetone at room temperature, Cartesian coordinates of DFT calculated geometries of **1**$^{2+}$–**5**$^{2+}$, molecular orbital energies (eV) of selected orbitals of **1**$^{2+}$–**5**$^{2+}$, absorption spectrum of **2**$(PF_6)_2$ in $CH_3CN$ in the range 250–800 nm.

## Acknowledgments

This work was supported by the Deutsche Forschungsgemeinschaft, the Fonds der Chemischen Industrie and the Dr. Otto Röhm Gedächtnisstiftung. The permanent, generous support from Prof. Dr. G. Huttner is gratefully acknowledged. We thank Simone Leingang and Jens Nägele for preparative assistance.

[1] J.-P. Sauvage, J.-P. Collin, J.-C. Chambron, S. Guillerez, C. Coudret, V. Balzani, F. Barigelletti, L. De Cola, L. Flamigni, *Chem. Rev.* **1994**, *94*, 993–1019.
[2] V. Balzani, A. Juri, M. Venturi, S. Campagna, S. Serroni, *Chem. Rev.* **1996**, *96*, 759–833.
[3] C. E. Housecroft in *Comprehensive Coordination Chemistry II* (Eds.: J. A. McCleverty, T. J. Meyer), Elsevier, Oxford, **2004**, vol. 5, pp. 555–731.
[4] A.-M. Stadler, F. Puntoriero, S. Campagna, N. Kyritsakas, F. Welter, J.-M. Lehn, *Chem. Eur. J.* **2005**, *11*, 3997–4009.
[5] J. Hjelm, R. W. Handel, A. Hagfeld, E. C. Constable, C. E. Housecroft, R. J. Foster, *Inorg. Chem.* **2005**, *44*, 1073–1081.
[6] R. Ziessel, P. Bäuerle, M. Ammann, A. Barbieri, F. Barigelletti, *Chem. Commun.* **2005**, 802–804.
[7] R. Ziessel, V. Grosshenny, M. Hissler, C. Stroh, *Inorg. Chem.* **2004**, *43*, 4262–4271.
[8] A. Barbieri, B. Ventura, F. Barigelletti, A. De Nicola, M. Quesada, R. Ziessel, *Inorg. Chem.* **2004**, *43*, 7359–7368.
[9] A. Harriman, A. Mayeux, C. Stroh, R. Ziessel, *Dalton Trans.* **2005**, 2925–2932.
[10] C. Patoux, J.-P. Launay, M. Beley, S. Chodorowski-Kimmes, J.-P. Collin, S. James, J.-P. Sauvage, *J. Am. Chem. Soc.* **1998**, *120*, 3717–3725.
[11] J. R. Soonover, D. M. Dattelbaum, A. Malko, V. I. Klimov, T. J. Meyer, D. J. Styers-Barnett, E. Z. Gannon, J. C. Granger, W. S. Aldridge, J. M. Papanikolas, *J. Phys. Chem. A* **2005**, *109*, 2472–2475.
[12] W. R. Browne, N. M. O'Boyle, J. J. McGarvey, J. G. Vos, *Chem. Soc. Rev.* **2005**, *34*, 641–663.
[13] Md. K. Nazeeruddin, M. Grätzel in *Comprehensive Coordination Chemistry II* (Eds.: J. A. McCleverty, T. J. Meyer), Elsevier, Oxford, **2004**, vol. 9, pp. 719–758.
[14] A. Hagfeldt, M. Grätzel, *Acc. Chem. Res.* **2000**, *33*, 269–277.
[15] T. J. Meyer, *Acc. Chem. Res.* **1989**, *22*, 163–170.
[16] E. Baranoff, J.-P. Collin, L. Flamigni, J.-P. Sauvage, *Chem. Soc. Rev.* **2004**, *33*, 147–155.
[17] M. Grätzel, *Inorg. Chem.* **2005**, *44*, 6841–6851.
[18] E. C. Constable in *Comprehensive Coordination Chemistry II* (Eds.: J. A. McCleverty, T. J. Meyer), Elsevier, Oxford, **2004**, vol. 7, pp. 263–302.
[19] M.-C. Daniel, J. Ruiz Aranzaes, D. Astruc, *Chem. Commun.* **2005**, 1569–1571.
[20] N. Sewald, H.-D. Jakubke, *Peptides: Chemistry and Biology*, Wiley-VCH, Weinheim (Germany), **2003**.
[21] T. Schrader, A. D. Hamilton, *Functional Synthetic Receptors*, Wiley-VCH, Weinheim (Germany), **2005**.
[22] K. Heinze, M. Schlenker, *Eur. J. Inorg. Chem.* **2004**, 2974–2988.
[23] K. Heinze, M. Schlenker, *Eur. J. Inorg. Chem.* **2005**, 66–71.
[24] K. Heinze, M. Beckmann, *Eur. J. Inorg. Chem.* **2005**, 3450–3457.
[25] T. Okamura, T. Iwamura, S. Seno, H. Yamamoto, N. Ueyama, *J. Am. Chem. Soc.* **2004**, *126*, 15972–15973.
[26] D. R. van Staveren, N. Metzler-Nolte, *Chem. Rev.* **2004**, *104*, 5931–5985.
[27] A. Maurer, H.-B. Kraatz, N. Metzler-Nolte, *Eur. J. Inorg. Chem.* **2005**, 3207–3210.
[28] F. Noor, A. Wüstholz, R. Kinscherf, N. Metzler-Nolte, *Angew. Chem.* **2005**, *117*, 2481–2485; *Angew. Chem. Int. Ed.* **2005**, *44*, 2429–2432.
[29] Y.-T. Long, E. Abu-Irhayem, H.-B. Kraatz, *Chem. Eur. J.* **2005**, *11*, 5186–5194.
[30] G. A. Orlowski, S. Chowhury, Y.-T. Long, T. C. Sutherland, H.-B. Kraatz, *Chem. Commun.* **2005**, 1330–1332.
[31] X.-J. Yang, F. Drepper, B. Wu, W.-H. Sun, W. Haehnel, C. Janiak, *Dalton Trans.* **2005**, 256–267.
[32] *Fmoc Solid Phase Peptide Synthesis* (Eds.: W. C. Chan, P. D. White), Oxford University Press, Oxford, **2000**.
[33] R.-A. Fallahpour, *Synthesis* **2000**, *8*, 1138–1142.
[34] R.-A. Fallahpour, *Eur. J. Inorg. Chem.* **1998**, 1205–1207.
[35] R.-A. Fallahpour, M. Neuburger, M. Zehnder, *New J. Chem.* **1999**, *23*, 53–61.
[36] R. Schwesinger, C. Hasenfratz, H. Schlemper, L. Walz, E. M. Peters, K. Peters, H. G. von Schnering, *Angew. Chem.* **1993**, *105*, 1420–1422; *Angew. Chem. Int. Ed. Engl.* **1993**, *32*, 1361–1363.

 © 2006 Wiley-VCH Verlag GmbH & Co. KGaA, Weinheim 

[37] R. Schwesinger, *Nachr. Chem. Tech. Lab.* **1990**, *38*, 1214–1226.
[38] C. Palomo, A. L. Palomo, F. Palomo, A. Mielgo, *Org. Lett.* **2002**, *4*, 4005–4008.
[39] H.-B. Kraatz, J. Lusztyk, G. D. Enright, *Inorg. Chem.* **1997**, *36*, 2400–2405.
[40] M. Duati, S. Tasca, F. C. Lynch, H. Bohlen, J. G. Vos, S. Stagni, M. D. Ward, *Inorg. Chem.* **2003**, *42*, 8377–8384.
[41] Band profiles were fitted using pseudo-Voigt functions (weighted Lorentz/Gauss band profiles) given by the equation: $y = y_0 + A[\mu(2/\pi)\{\omega/[4(x - x_c)^2 + \omega^2]\} + (1 - \mu)\{\sqrt{[4\ln(2)]}/[\sqrt{(\pi)}\omega]\}\exp\{-[4\ln(2)/\omega^2](x - x_c)^2\}]$ using Origin® V 7.0303.
[42] K. Hutchison, J. C. Morris, T. A. Nile, J. L. Walsh, D. W. Thompson, J. D. Peterson, J. R. Schoonover, *Inorg. Chem.* **1999**, *38*, 2516–2523.
[43] T.-Y. Dong, M.-C. Lin, M. Y.-N. Chiang, J.-Y. Wu, *Organometallics* **2004**, *23*, 3921–3930.
[44] Z. Murtaza, D. K. Graff, A. P. Zipp, L. A. Worl, W. E. Jones, W. D. Bates, T. J. Meyer, *J. Phys. Chem.* **1994**, *98*, 10504–10513.
[45] Recently a luminescent complex $[Ru(tpy)(tpy\text{-}COOEt)](PF_6)_2$ with $\Phi = 2.7 \times 10^{-4}$ has been incorporated in a light-emitting electrochemical cell: H. J. Bolink, L. Cappelli, E. Coronado, P. Gaviña, *Inorg. Chem.* **2005**, *44*, 5966–5968.
[46] J.-C. Chambron, C. Coudret, J.-P. Sauvage, *New J. Chem.* **1992**, *16*, 361–367.
[47] E. J. Lee, M. S. Wrighton, *J. Am. Chem. Soc.* **1991**, *113*, 8562–8564.
[48] M. Furue, M. Ishibashi, A. Satoh, T. Oguni, K. Mauyama, K. Sumi, M. Kamachi, *Coord. Chem. Rev.* **2000**, *208*, 103–113.
[49] E. C. Constable, R. W. Handel, C. E. Housecroft, A. F. Morales, B. Ventura, L. Flamigni, F. Barigelletti, *Chem. Eur. J.* **2005**, *11*, 4024–4034.
[50] M. W. Cooke, G. S. Hanan, F. Loiseau, S. Campagna, M. Watanabe, Y. Tanaka, *Angew. Chem.* **2005**, *117*, 4959–4962; *Angew. Chem. Int. Ed.* **2005**, *44*, 4881–4884.
[51] M. J. Frisch, G. W. Trucks, H. B. Schlegel, G. E. Scuseria, M. A. Robb, J. R. Cheeseman, J. A. Montgomery Jr, T. Vreven, K. N. Kudin, J. C. Burant, J. M. Millam, S. S. Iyengar, J. Tomasi, V. Barone, B. Mennucci, M. Cossi, G. Scalmani, N. Rega, G. A. Petersson, H. Nakatsuji, M. Hada, M. Ehara, K. Toyota, R. Fukuda, J. Hasegawa, M. Ishida, T. Nakajima, Y. Honda, O. Kitao, H. Nakai, M. Klene, X. Li, J. E. Knox, H. P. Hratchian, J. B. Cross, C. Adamo, J. Jaramillo, R. Gomperts, R. E. Stratmann, O. Yazyev, A. J. Austin, R. Cammi, C. Pomelli, J. W. Ochterski, P. Y. Ayala, K. Morokuma, G. A. Voth, P. Salvador, J. J. Dannenberg, V. G. Zakrzewski, S. Dapprich, A. D. Daniels, M. C. Strain, O. Farkas, D. K. Malick, A. D. Rabuck, K. Raghavachari, J. B. Foresman, J. V. Ortiz, Q. Cui, A. G. Baboul, S. Clifford, J. Cioslowski, B. B. Stefanov, G. Liu, A. Liashenko, P. Piskorz, I. Komaromi, R. L. Martin, D. J. Fox, T. Keith, M. A. Al-Laham, C. Y. Peng, A. Nanayakkara, M. Challacombe, P. M. W. Gill, B. Johnson, W. Chen, M. W. Wong, C. Gonzalez, J. A. Pople, *Gaussian 03*, Revision B.03, Gaussian, Inc., Pittsburgh, PA, **2003**.
[52] R. Hooft, Collect, Data Collection Software, Nonius, The Netherlands, **1998**; http://www.nonius.com.
[53] G. M. Sheldrick, *SHELXS-97, Program for Crystal Structure Solution*, University of Göttingen, Germany, **1997**; G. M. Sheldrick, *SHELXL-97, Program for Crystal Structure Refinement*, University of Göttingen, Germany, **1997**; http://www.shelx.uni-ac.gwdg.de/shelx/index.html; *International Tables for X-ray Crystallography*, Kynoch Press, Birmingham, UK, **1974**, vol. 4.
[54] L. Zsolnai, G. Huttner, *XPMA*, University of Heidelberg, Germany, **1998**; http://www.rzuser.uni-heidelberg.de/~il1/laszlo/xpm.html.
[55] R. Soltek, G. Huttner, *WinRay*, University of Heidelberg, Germany, **1999**; http://www.uni-heidelberg.de/institute/fak12/AC/huttner/frame/frame_soft.html.

Received: December 2, 2005
Published Online: March 22, 2006

 © 2006 Wiley-VCH Verlag GmbH & Co. KGaA, Weinheim 

DOI: 10.1002/ejic.200501131

# On the Staudinger Reaction of $SP(N_3)_3$ with $PPh_3$ and $(Me_3Si)_2N–(Me_3Si)N–PPh_2$

**Nadine Götz,[a] Sebastian Herler,[a] Peter Mayer,[a] Axel Schulz,*[a] Alexander Villinger,[a] and Jan J. Weigand[a][‡]**

**Keywords:** Azides / PN rings / Phosphazenes / Staudinger reaction

The Staudinger reactions of $SP(N_3)_3$ (**1**) with 1, 2 and 3 equiv. of triphenylphosphane $PPh_3$ and $(TMS)_2N–(TMS)N–PPh_2$ (**2**) have been investigated (TMS = $Me_3Si$). Reaction with $PPh_3$ yields the single and double Staudinger products $SP(N_3)_2NPPh_3$ (**3**) and $SP(N_3)(NPPh_3)_2$ (**4**), but not the triple, while the reaction with **2** results only in the formation of the single Staudinger product $SP(N_3)_2NPPh_2[N(TMS)N(TMS)]_2$ (**5**). Compound **5** is air- and moisture-sensitive but stable under argon over a long period in the solid state and in common organic solvents. Although there are covalently bound azide groups in **3**, **4** and **5**, these Staudinger products are neither shock- nor heat-sensitive in contrast to **1**. Furthermore **3**, **4** and **5** are easily prepared in bulk (yield > 95 %), and unlimitedly stable when cooled and stored in the dark. Compound **5** is thermally stable up to over 150 °C while **3** and **4** are stable only up to 96 °C. However, when a solution of **5** is heated, a new surprising eight-membered ring (**6**) is formed in an intermolecular $TMS–N_3$ elimination reaction. The structure and bonding is discussed on the basis of experimental X-ray data and theoretical B3LYP calculations (thermodynamics, energy landscape and charge distribution).

(© Wiley-VCH Verlag GmbH & Co. KGaA, 69451 Weinheim, Germany, 2006)

## Introduction

As early as 1919, Staudinger and Meyer investigated the reaction of triphenylphosphane and phenylazide in diethyl ether.[1] Ever since, this reaction has been known as the Staudinger reaction and describes an oxidation of phosphorus(III) to phosphorus(V) compounds, which is accompanied by a linkage of a P (phosphane) and a N (azide) atom of two different molecules upon $N_2$ release. With respect to the azide and phosphorus(III) compounds, the Staudinger reaction is very flexible. Hence, a great diversity of iminophosphanes and their applications are well known.[2–6] Phosphorus(V) nitrogen species represent a well-established group of compounds that is still growing. Of special interest are PN compounds that can be used as interesting reagents in organic synthesis.[7]

Recently, we reported on the reaction of 2,4,6-triazido-1,3,5-triazine with triphenylphosphane resulting in the formation of different triphenylphosphanimino-azido- or tetrazolo[1,3,5]triazines, depending on the stoichiometry of the azide and phosphane component (1:1, 1:2, 1:3).[8] Because the azido group in 2,4,6-triazido-1,3,5-triazine is attached to a C atom adjacent to an annular nitrogen, it can spontaneously cyclise to give a tetrazole.

Lately, the chemistry of hydrazinophosphanes of the type $(TMS)_2N–(TMS)N–PR_2$ (R = Ph, Cl; TMS = $Me_3Si$) has attracted considerable interest.[9] Experimentally and theoretically the intramolecular $GaCl_3$-assisted TMS–Cl elimination in $(TMS)_2N–N(TMS)–PCl_2$ has been studied, resulting in the first binary triazadiphosphole.[10]

We found it of interest to investigate the Staudinger reaction of hydrazinophosphanes with phosphorus azides. Table 1 displays a compilation of neutral phosphorus azides. However, only a few neutral singly, doubly or multiply substituted phosphorus azides are known that have been structurally characterised (Table 1). More structural data of phosphorus azides are needed to gain further insight into the relationship between bonding and stability.

In this study we demonstrate that the final products of the reaction of highly explosive $SP(N_3)_3$ (**1**) with $PPh_3$ and *N*,*N*′,*N*′-[tris(trimethyl)silyl]hydrazinodiphenylphosphane $[(TMS)_2N–(TMS)N–PPh_2]$ (**2**), as well as their distribution, strongly depend on the reaction conditions, stoichiometry and temperature (Figure 1). Depending on the temperature, different products are formed, which can be isolated and characterised.

[a] Department Chemie und Biochemie, Ludwig-Maximilians-Universität München,
Butenandtstr. 5–13 (Haus D), 81377 München, Germany
Fax: +49-89-218077492
E-mail: Axel.Schulz@cup.uni-muenchen.de
[‡] Current address: Department of Chemistry, Dalhousie University,
Halifax, Nova Scotia B3H 1J3, Canada
Supporting information for this article is available on the WWW under http://www.eurjic.org or from the author.

 © 2006 Wiley-VCH Verlag GmbH & Co. KGaA, Weinheim 

Table 1. Hitherto known neutral phosphorus azides.

| Species | Reference |
|---|---|
| $P(N_3)_3$ | [29,30,31] |
| $P(N_3)_5$ | [29] |
| $PCl_{5-n}(N_3)_nL$ ($n$ = 0–4) L = pyridine | [32] |
| $OP(N_3)_3$ | [29,30] |
| $SP(N_3)_3$ | [30] |
| $SPX_n(N_3)_{3-n}$ (X = Cl, Br; $n$ = 1,2) | [30] |
| $SPX_n(N_3)_{3-n}$ (X = Cl, Br; $n$ = 1,2) | [30] |
| $RP(N_3)_2$, R = Mes* [a] | [24,33] |
| $R_2P(N_3)$, R = *e.g.* N*i*Pr$_2$,[a] $CF_3$, F | [24,24g,34,35,36][a] |
| $OPR_2(N_3)$, R = H, $NMe_2$, NH*i*Pr, *O*-bis[4-(phenylazo)phenyl] ester, $OCH_2CF_3$, | [37,38,39] |
| $SPR_2(N_3)$, R = Me[a] | [24a,40] |
| 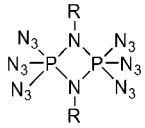 | R = $C_6H_5$,[a] $C_6F_5$[a] [41,42] |
| 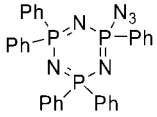 | [43] |
| 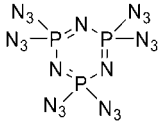 | [44] |
| 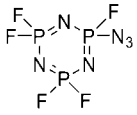 | [45a,b] |
| 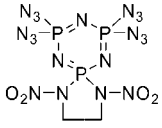 | [46] |
| 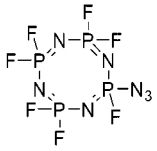 | [44b] |
| 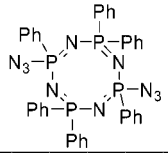 | [47] |

[a] Characterised by X-ray analysis.

## Results and Discussion

### Reaction of $SP(N_3)_3$ with $PPh_3$

By addition of 1 equiv. of triphenylphosphane to a solution of **1** in ether at ambient temperature, initially a yellow-green intermediate is formed, thought to be due to the formation of R–NNN–$P(C_6H_5)_3$ [R = $SP(N_3)_2$]. This adduct has only a fleeting existence and decomposes by giving off $N_2$, resulting in the formation of a monophosphaniminodiazide species, $SP(N_3)_2(NPPh_3)$ (**3**) (Figure 1), as illustrated by $^{31}$P NMR experiments; two duplets with the same intensity are detected at $\delta$ = 50.3 ppm [S*P*$(N_3)_2$NP$Ph_3$] and 16.8 ppm [SP$(N_3)_2$N*P*$Ph_3$] ($^2J_{PP}$ = 22.6 Hz). By addition of a second equiv. of triphenylphosphane, again $N_2$ release was observed. $^{31}$P NMR spectroscopic data suggest the exclusive formation of only one species (Table 2): a triplet at $\delta$ = 42.4 ppm [t, S*P*$(N_3)$$(NPPh_3)_2$] and a duplet at 7.5 ppm [d, SP$(N_3)$(N*P*$Ph_3)_2$] are observed as expected for the double Staudinger product, $SP(N_3)(NPPh_3)_2$ (**4**) ($^2J_{PP}$ = 7.6 Hz). Addition of a third equiv. of $PPh_3$ results in no further reaction, as shown by $^{31}$P NMR experiments. Also heating under reflux condition of this reaction mixture does not support the release of a third molecule $N_2$ and finally the formation of the triple Staudinger product [$SP(NPPh_3)_3$, Figure 1].

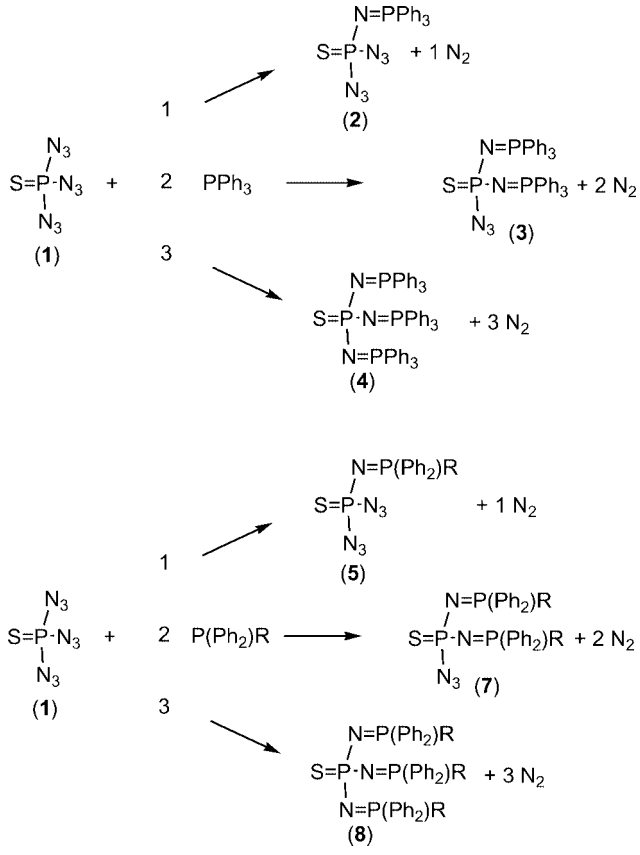


Figure 1. Top: Staudinger reaction of thiophosphoryl azide, $SP(N_3)_3$, with triphenylphosphane; bottom: Staudinger reaction of thiophosphoryl azide and *N*,*N*′,*N*′-[tris(trimethyl)silyl]hydrazinodiphenylphosphane, $(TMS)_2N$–(TMS)N–$PPh_2$ (**2**) [R = N(TMS)–$N(TMS)_2$].

Table 2. $^{31}$P NMR spectroscopic data of different Staudinger products and the starting materials.

| Compound | $\delta$ [ppm] | $^2J_{PP}$ [Hz] |
|---|---|---|
| $SP(N_3)_3$ (**1**) | 65.0 (s), ref.[29] | – |
| $(Me_3Si)_2N$–$(Me_3Si)$N–$PPh_2$ (**2**) | 61.4 (s), ref.[9] | – |
| $SP(N_3)_2NPPh_3$ (**3**) | 50.3 (d); 16.8 (d) | 22.6 |
| $SP(N_3)(NPPh_3)_2$ (**4**) | 42.4 (t); 7.5 (d) | 7.6 |
| $SP(N_3)_2NPPh_2N(TMS)N(TMS)_2$ (**5**) | 46.6 (d); 26.5 (d)[a] | 34.3 |

[a] $^{31}$P MAS: 30.7 and 51.0 ppm.

 © 2006 Wiley-VCH Verlag GmbH & Co. KGaA, Weinheim 

### Reaction of $SP(N_3)_3$ with $Ph_2P–N(TMS)N(TMS)_2$ (TMS = $Me_3Si$)

Similar to the reaction with $PPh_3$, 1 equiv. of $Ph_2P–N(TMS)N(TMS)_2$ reacts spontaneously with $SP(N_3)_3$ in an ether/acetonitrile mixture at ambient temperature to give the single Staudinger product $SP(N_3)_2NPPh_2[N(TMS)-N(TMS)]_2$ (**5**). As expected, two duplets, at $\delta$ = 46.6 ppm $\{SP(N_3)_2N–PPh_2[N(TMS)N(TMS)_2]\}$ and 26.5 ppm $\{SP(N_3)_2NPPh_2[N(TMS)N(TMS)_2]\}$ ($^2J_{PP}$ = 34.3 Hz), are observed in the $^{31}P$ NMR experiment ($^{31}P$ MAS: 30.7 and 51.0 ppm). The presence of two remaining azide groups in the single Staudinger product (Figure 1) was also deduced from Raman and IR spectroscopy. Bands at 2153 and 2129 $cm^{-1}$ assigned to the characteristic asymmetric stretching vibration of the azide group in combination with the molecular peak (mass spectrometry) supported this assumption. Crystals (colourless plates) of sufficient quality for X-ray structure determination were obtained from a colourless ether/$CH_3CN$ solution of **5** after stepwise removal of solvent at –10 °C.

In contrast to the Staudinger reaction with $PPh_3$, addition of another equivalent of **2** to **5** leads to no further substitution in solution, even upon long heating.[11] However, when this reaction mixture was slowly cooled, two different types of crystals were obtained within two weeks: colourless plates and needles. X-ray investigations of crystals of both types revealed a surprising eight-membered ring, **6**, for the colourless needles and again the single Staudinger product **5** for the plates.

The exothermic formation ($\Delta_{calc}E$ = –8.8 kcal/mol, see computational details) of an eight-membered $P_4N_4$ ring starting from **5** seems to be quite interesting, as two intermolecular TMS–$N_3$ elimination steps (corresponding to two condensation steps) are required (Figure 2).

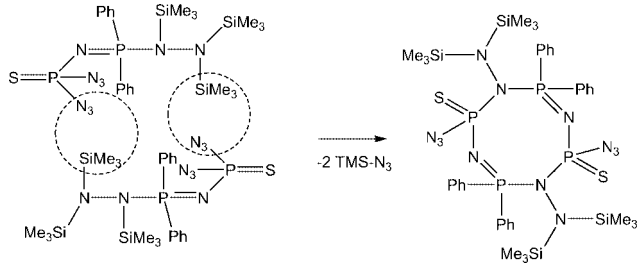


Figure 2. Formation of **6** by two intermolecular TMS–$N_3$ elimination steps (TMS = $Me_3Si$).

The single Staudinger product **5** is air- and moisture-sensitive but stable under argon over a long period in the solid state and in common organic solvents (e.g. benzene, $CH_2Cl_2$, diethyl ether etc.). Although there are two azide groups, **5** is neither shock- nor heat-sensitive, is easily prepared in bulk (yield > 95%) and infinitely stable when stored in a sealed tube and kept cool at 5 °C in the dark. Compound **5** is thermally stable up to over 150 °C while **3** and **4** are stable only up to 96 °C. At these temperatures decomposition starts, accompanied by a slow release of nitrogen (MS experiments).

### X-ray Structure Elucidation of 5 and Bonding

Compound **5** crystallises in the monoclinic space group $P2_1/c$ with four molecules in the unit cell. The perspective view of **5** is depicted in Figure 3 and selected bond lengths and angles are given in Table 3.

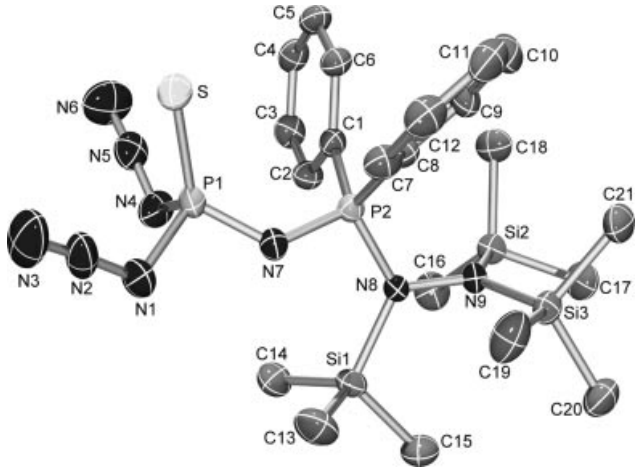


Figure 3. ORTEP drawing of the molecular structure of **5** in the crystal. Thermal ellipsoids with 50% probability at 200 K (hydrogen atoms omitted for clarity).

Table 3. X-ray analysis of **5**: selected bond lengths [Å] and angles [°].

| | | | |
|---|---|---|---|
| S–P1 | 1.9305(8) | Si1–N8 | 1.803(2) |
| P1–N1 | 1.713(3) | Si2–N9 | 1.767(2) |
| P1–N4 | 1.713(3) | Si3–N9 | 1.776(2) |
| P1–N7 | 1.583(2) | N1–N2 | 1.235(4) |
| P2–N7 | 1.586(2) | N2–N3 | 1.135(4) |
| P2–N8 | 1.662(2) | N4–N5 | 1.225(3) |
| P2–C1 | 1.801(2) | N5–N6 | 1.124(4) |
| P2–C7 | 1.795(2) | N8–N9 | 1.475(3) |
| S–P1–N1 | 113.00(9) | P1–N1–N2 | 116.3(2) |
| S–P1–N4 | 111.91(8) | N1–N2–N3 | 175.2(3) |
| S–P1–N7 | 123.55(8) | P1–N4–N5 | 118.5(2) |
| N1–P1–N4 | 99.3(1) | N4–N5–N6 | 174.0(3) |
| N1–P1–N7 | 99.9(1) | P1–N7–P2 | 129.1(1) |
| N4–P1–N7 | 105.9(1) | P2–C1–C2 | 117.5(2) |
| N7–P2–N8 | 103.2(1) | P2–C1–C6 | 123.2(2) |

Both $P^V$ atoms in **5** sit in a slightly distorted tetrahedral environment (angles around the P atoms between 99 and 112°) with the two azide groups at P1 in a *cis* position to the sulfur atom. Interestingly, two further isomers are possible with respect to the two azide groups: (i) only one azide group in a *trans* position, and (ii) both azide groups in a *trans* position to the sulfur atom. In agreement with the experiment, the close inspection of the conformational space of **5** revealed the experimentally observed *cis*/*cis* isomer to be the global minimum. The potential energy surface (PES) with respect to the rotation about all P–N bonds is very flat (see Supporting Information). The energy difference between the rotamers is smaller than 8 kcal/mol. The largest energy gap was found for the *cis*/*trans* isomers, whereas a *trans*/*trans* arrangement of both azide groups does not represent a minimum on the PES of **5**.

 © 2006 Wiley-VCH Verlag GmbH & Co. KGaA, Weinheim 

As shown on numerous occasions,[12] both covalently bound azide groups display a *trans*-bent configuration (regarding the P atom) with a N–N–N bond angle of 175.2(3) (N1–N2–N3) and 174.0(3)° (N4–N5–N6). The P1–N7–P2 angle is rather large at 129.1(1)° compared to the N9–N8–P2 angle at 117.4°(1). Another interesting feature of this structure is the almost planar environment of both hydrazine nitrogen atoms (<Si3–N9–Si2–N8 = 173.1, <N9–N8–Si1–P2 = 177.1°; all N–N–X angles are between 117 and 121°, X = P, Si; Table 3), however both planes are almost perpendicular to each other. Hence, as displayed by NBO analysis,[13] the lone pair on both nitrogen atoms is localised in a pure p-type atomic orbital. Both lone pairs are also perpendicular to each other.[9]

Three different types of P–N bond lengths are found: (i) the longest between P1 and the N atoms of the azide groups with 1.713(3) Å, (ii) 1.662(1) Å for the P2–N8 bond (N atom of the hydrazine group) and (iii) the smallest with 1.583(2) and 1.586(2) Å for the two P–N bonds of the dicoordinated imino N atom connecting the two P atoms. These P–N distances are substantially shorter than the sum of the covalent radii [$d_{cov}$(N–P) = 1.8, $d_{cov}$(N=P) = 1.6 Å],[14,15] which indicates partial double bond character, especially for the P1–N7 and P2–N7 bonds. A typical P–N bond with π character is found in R–P=N–R′ species with P–N distances between 1.495(4) Å (R = Cl, R′ = aryl)[16] and 1.619(2) Å [R = $t$Bu$_2$P, R′ = N(SiMe$_3$)$_2$].[17] According to NBO analysis, all P–N bonds are highly polarised (25–27% P, 73–75% N) and almost ideally covalent between the adjacent N–N and P–S bonds (P: 48%, S: 52%).

Figure 4 shows the energetically preferred Lewis representation (from NBO analysis) along with the calculated partial charges of **5**, indicating a highly ionic molecular system.[18] Both four-coordinate P atoms formally obey the octet rule by forming only four single bonds. A positive formal charge is found on both P atoms and a negative on the dicoordinated N atom and the S atom. The experimentally found short P–N (between P1–N7 and P2–N7, Table 3) and P–S bonds possess double bond character, which can be explained by intramolecular donor–acceptor interactions (hyperconjugation, noncovalent effects) along the P1(S)–N7–P2 moiety (Figure 3). As shown by NBO analysis (see below), these interactions describe a highly delocalised π system including the lone pairs of the dicoordinated N atom (N7) and the S atom but *not* the tricoordinated N atom (N8).[19]

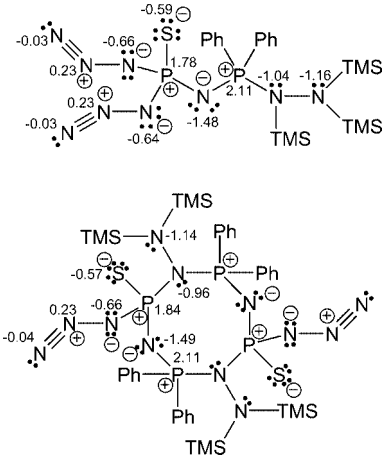


Figure 4. Lewis representations of **5** (top) and **6** (bottom) along with NPA partial charges (TMS = Me$_3$Si).

### X-ray Structure Elucidation of 6 and Bonding

SP(N$_3$)[NP(Ph)$_2$NN(TMS)$_2$]$_2$ (**6**) crystallises in the monoclinic space group $P2_1/n$ with four molecules in the unit cell (Figure 5, Table 4). The eight-membered $P_4N_4$ ring adopts a chair conformation with all four N atoms being in one plane as well as all four P atoms. An inversion centre is found right in the middle of the $P_4N_4$ ring. Interestingly, all N and P ring atoms of each of the monomeric fragments lie within a plane (e.g. N1–P1–N2–P2 = 3.6°). These two N–P–N–P planes are distorted by about 104°, forming the eight-membered $P_4N_4$ chair. As two tri- and dicoordinated nitrogen atoms form the $P_4N_4$ ring, **6** cannot be regarded to be a phosphazene, but a tetrazatetraphosphocine with two formal double and two single P–N bonds. Traditional bonding descriptions for cyclic PN rings have involved N(2p)–P(3d) overlap,[20] both in and perpendicular to the plane of the PN ring. However, this model is not consistent with the fact that phosphorus makes little or no use of its 3d orbitals (see above).[18,21] In accord with this, NBO analysis localises only single bonds (Figure 4) within the ring, again obeying the octet rule for all involved elements. However, according to the X-ray analysis, two smaller P–N bond lengths [π PN: $d$(N1–P2) = 1.573(3), $d$(N1–P2) = 1.586(3) Å] and two longer P–N distances [σ PN: $d$(N2–P1) = 1.703(2), $d$(N2–P2) = 1.707(2) Å] are experimentally observed. Both types of P–N bond lengths are a little bit shorter than the sum of the covalent radii for a single [$d_{cov}$(N–P) = 1.8 Å] and a double bond [$d_{cov}$(N=P) = 1.6 Å],[22,23] indicating a certain degree of multiple bond

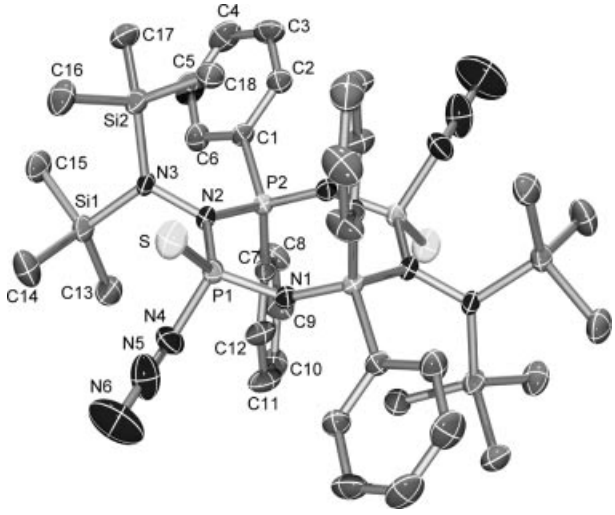


Figure 5. ORTEP drawing of the molecular structure of **6** in the crystal. Thermal ellipsoids with 50% probability at 200 K (hydrogen atoms omitted for clarity).

 © 2006 Wiley-VCH Verlag GmbH & Co. KGaA, Weinheim 

character due to intramolecular donor–acceptor interactions. For comparison, the P–NNN distance with 1.738(3) Å represents a typical single bond.

Table 4. X-ray analysis of **6**: selected bond lengths [Å] and angles [°].

| | | | |
|---|---|---|---|
| S–P1 | 1.932(1) | P2–C1 | 1.805(3) |
| P1–N1 | 1.586(3) | P2–C7 | 1.810(3) |
| P1–N2 | 1.703(2) | N2–N3 | 1.462(3) |
| P1–N4 | 1.738(3) | N2–P2 | 1.707(2) |
| P2–N1 | 1.573(3) | N4–N5 | 1.113(5) |
| P2–N2 | 1.707(2) | N5–N6 | 1.193(7) |
| N1–P1–N2 | 104.9(1) | N1–P2–N2 | 108.9(1) |
| N1–P1–N4 | 103.1(1) | N1–P2–C1 | 108.5(1) |
| N2–P1–N4 | 99.6(1) | N2–P2–C1 | 108.4(1) |
| N1–P1–S | 122.1(1) | N1–P2–C7 | 114.8(1) |
| N2–P1–S | 115.35(9) | N2–P2–C7 | 110.3(1) |
| N4–P1–S | 108.9(1) | C1–P2–C7 | 105.6(1) |

NBO analysis of **6** gives an almost identical picture compared to **5** (Figure 4) with respect to the type and magnitude of intramolecular donor–acceptor interactions, charge distribution and bond properties. Upon ring closure the partial charges of all atoms hardly change. The same holds for polarisation effects (similar PN and SP bond polarisation, see above) and the intramolecular donor–acceptor interactions describing the π system along the P–N moieties.[19,20] Only a close inspection of these interactions utilising the NBO partitioning scheme clearly indicates a highly delocalised π system along the P1(S)–N1–P2 moiety, which includes the lone pairs of both the S and the dicoordinated N atoms but not the azide group and the tricoordinated N atoms. These noncovalent effects represent typical $n(X) \rightarrow \sigma^*(Y–Z)$ hyperconjugative interactions ($n$ = sp$^{\lambda}$- or p-type lone pair; X = S, N1; Y = P1, P2; Z = C1, C7, S, N1, N2, N4) and explain the partial double bond character of the P1–S, P1–N1 and N1–P2 bonds (Figure 4 and Figure 5).[19,20]

To summarise, the molecular and electronic structure of **6** strongly resembles the molecular structure of **5**: (i) a staggered conformation with two perpendicular planes was also found for the hydrazine groups (dihedral angle: <P2–N2–N3–Si2 = –90.1°), (ii) both nitrogen atoms of the hydrazine group are in an almost planar environment [Σ<(N2) = 359.98°, Σ<(N3) = 358.9°][9] and (iii) the azide groups are slightly *trans*-bent with an N–N–N angle of 171.7(5)°, which is in accordance with the structures of other covalent phosphorus azides.[24] Because of inversion symmetry, both azide groups adopt a *trans* position to each other. It is interesting to note that the longest chain composed of only pnictogen atoms in **6** consists of eleven pnictogens (eight N and three P atoms) compared to eight in compound **5** (six N and two P atoms). Moreover, **6** represents a rare example of a structurally characterised phosphorus azide involving a binary PN ring (Table 1).

## Summary and Conclusions

Two different Staudinger reactions of thiophosphoryl triazide have been investigated: (i) with triphenylphosphane, $PPh_3$, and, (ii) with *N*,*N*′,*N*′-[tris(trimethyl)silyl]hydrazinediphenylphosphane, $(Me_3Si)_2N–(Me_3Si)N–PPh_2$ (**2**). While the reactions with $PPh_3$ utilising 1:1, 1:2 and 1:3 stoichiometries yield the single and double but not the triple Staudinger product, only the single Staudinger product was observed when $(Me_3Si)_2N–(Me_3Si)N–PPh_2$ was reacted. Even upon heating no further reaction of the remaining two azide groups with an excess of $(Me_3Si)_2N–(Me_3Si)N–PPh_2$ was detected. However, heating results in a partial intermolecular trimethylsilylazide elimination, which is combined with two condensation steps, yielding an eight-membered $P_4N_4$ ring (**6**). All four isolated Staudinger products represent new substituted phosphorus azides, are neither heat- nor shock-sensitive and, except for **6**, all can be prepared in large quantities (with yields >95%). Moreover, only a few neutral singly, doubly or multiply substituted phosphorus azides are known that have been structurally characterised (Table 1). Hence, the X-ray data of compound **5** and **6** may fill this gap.

## Experimental Section

***Caution:*** Although compounds **2**–**5** are kinetically stable compounds, they are nonetheless energetic materials and appropriate safety precautions should be taken, especially when these compounds are prepared on a larger scale. In the case of $SP(N_3)_3$ (**1**), special care has to be taken because of the extreme risk of explosion. Never handle this compound neat.

**General Remarks:** Solvents were freshly distilled, dried and stored under nitrogen. NMR: JEOL Eclipse 400 and 270 ($^1$H, $^{13}$C chemical shifts refer to $\delta_{TMS}$ = 0.00; $^{31}$P to $\delta_{H_3PO_4(85\%)}$ = 0.00). IR: Nicolet 520 FTIR (as KBr pellets or in Nujol mulls between KBr windows). Raman: Perkin–Elmer Spectrum 2000R NIR FT equipped with a Nd:YAG laser (1064 nm). CHN analyses: Analysator Elementar Vario EL. MS: Jeol MStation JMS 700. Melting points are uncorrected (Büchi B540). Thiophosphoryl triazide[30] and *N*,*N*′,*N*′-[tris(trimethyl)silyl]hydrazinediphenylphosphane[9] were prepared according to the procedures given in the literature.

**Synthesis of 5:** A solution of freshly prepared $SP(N_3)_3$ (0.242 g, 1.28 mmol) in acetonitrile (25 mL) was added to a solution of $Ph_2PN(TMS)N(TMS)_2$ (0.55 g, 1.28 mmol) in diethyl ether (50 mL) over a period of 1 h at ambient temperature. An immediate release of gas was observed. After the $N_2$ release stopped (about 2 h) the solvent was removed in vacuo and a white solid (**5**) was obtained. Complex **5** was purified by recrystallisation from an ether/acetonitrile mixture. $SP(N_3)_2[NP(Ph)_2N(TMS)N(TMS)_2]$ (**5**) (593.86) yield: 714 mg (94%) colourless crystals, m.p. 153 °C (decomposition). IR (KBr): $\tilde{\nu}$ = 3051 w, 2960 w, 2109 vs, 1588 w, 1482 w, 1436 s, 1260 vs, 1219 vs, 1177 s, 1111 vs, 1026 m, 996 m, 803 m, 777 m, 745 m, 718 s, 690 s, 675 m, 586 w, 529 s, 505 w cm$^{-1}$. Raman (200 mW, 25 °C, 100 scans): 3178 (4), 3146 (5), 3066 (100), 3052 (56), 2993 (18), 2958 (23), 2907 (84), 2255(2), 2153 (10), 2129 (7), 1591 (58), 1576 (21), 1442 (5), 1411 (6), 1316 (3), 1288 (17), 1267 (4), 1256 (4), 1184 (13), 1168 (9), 1107 (25), 1031 (40), 1002 (82), 935 (2), 858 (5), 762 (5), 728 (6), 692 (18), 650 (39), 619 (19), 598 (3), 569 (10), 542 (39), 523 (6), 506 (18), 381 (14), 345 (13), 314 (14), 296 (13), 270 (40), 239 (29), 191 (21), 168 (21), 139 (22) cm$^{-1}$. $^1$H NMR (109 MHz, $C_6D_6$, 25 °C): $\delta$ = 0.01 (s, 18 H, $N[Si(CH_3)_3]$-$N[Si(CH_3)_3]_2$), 0.37 (s, 9 H, $N[Si(CH_3)_3]N[Si(CH_3)_3]_2$), 7.5–8.0 (m, 10 H, $C_6H_5$) ppm. $^{13}$C NMR (68 MHz, $CDCl_3$, 25 °C): $\delta$ = 3.90 (s,

 © 2006 Wiley-VCH Verlag GmbH & Co. KGaA, Weinheim 

N[Si($CH_3$)$_3$]$_2$), 4.54 (s, PN[Si($CH_3$)$_3$]), 128.2 (d, $^1J_{CP}$ = 113.9 Hz, $C_{phenyl}$), 128.3 (d, $^3J_{CP}$ = 12.5 Hz, $C_{phenyl}$), 133.1 (d, $^4J_{CP}$ = 3.1 Hz, $C_{phenyl}$), 134.7 (d, $^1J_{CP}$ = 10.4 Hz, $C_{phenyl}$) ppm. $^{14}$N NMR (28.9 MHz, $C_6D_6$, 25 °C): $\delta$ = –142 ($N_\beta$, $\Delta\nu_{1/2}$ 57 Hz), –163 ($N_\gamma$, $\Delta\nu_{1/2}$ 245 Hz), –285 ($N_\alpha$, $\Delta\nu_{1/2}$ 580 Hz) ppm. $^{29}$Si{$^1$H} NMR (270 MHz, $C_6D_6$, 25 °C): $\delta$ = 12.92 (s, N[*Si*($CH_3$)$_3$]$_2$), 18.15 (d, $^2J_{SiP}$ = 19.0 Hz, N[*Si*($CH_3$)$_3$]) ppm. $^{31}$P NMR (109 MHz, $CH_3CN/Et_2O$, 25 °C): $\delta$ = 46.6 (d, $^2J_{PP}$ = 34.3 Hz, S*P*($N_3$)[NP($Ph_2$)N(TMS)-N(TMS)$_2$]), 26.5 (d, $^2J_{PP}$ = 34.3 Hz, SP($N_3$)[N*P*($Ph_2$)N(TMS)-N(TMS)$_2$]) ppm. $^{31}$P MAS NMR (25 kHz, 25°°C): 30.7 (SP($N_3$)[N*P*($Ph_2$)N(TMS)N(TMS)$_2$]), 51.0 (S*P*($N_3$)[NP($Ph_2$)N-(TMS)N(TMS)$_2$]). MS (EI = 70 eV, >5%): *m*/*z* (%) = 593 (11) [$M^+$], 578 (40) [$M^+$ – $CH_3$], 493 (9), 492 (23) {NPNP$h_2$PN[Si-($CH_3$)$_3$]N[Si($CH_3$)$_3$]$_2^+$}, 404 (7), 377 (8) [$N_2$(S)PNP$h_2$PNSi-($CH_3$)$_3^+$], 334 (6), 290 (9), 275 (6) [($Ph_2$)$PN_2$Si($CH_3$)$_3$ + 2H$^+$], 272 (20) [($Ph_2$)$PN_2$Si($CH_3$)$_3$ – H$^+$], 247 (10) {[Si($CH_3$)$_3$]$_2$N – N[Si-($CH_3$)$_3$]$^+$}, 217 (11), 200 (5) [($Ph_2$)PN – H$^+$], 199 (5), 185 (7) [($Ph_2$)P – H$^+$], 183 (8), 175 (5) [($CH_3$)$_3$SiNNSi($CH_3$)$_3$ – H$^+$], 174 (28) [($CH_3$)$_3$SiNNSi($CH_3$)$_3$ – 2H$^+$], 146 (12) [Si($CH_3$)$_3$ – Si-($CH_3$)$_3^+$], 135 (13) [SP$N_3$P$^+$], 122 (8), 77 (30) [Ph$^+$], 74 (12) [HSi($CH_3$)$_3^+$], 73 (100) [Si($CH_3$)$_3^+$]. $C_{21}H_{37}N_9P_2S_1Si_3$ (593.86): calcd. C 42.47, H 6.28, N 21.23, S 5.40; found C 42.60, H 6.30, N 21.42, S 5.95.

**Supporting Information** (see footnote on the first page of this article): Experimental details for the synthesis of **3**, **4** and **6**, and computational details.

**X-ray Analyses of 5 and 6:** Crystals of sufficient quality for X-ray structure determination were mounted on a glass fibre and the X-ray crystallographic data collected on a Nonius Kappa CCD diffractometer with graphite-monochromated Mo-$K_\alpha$ radiation ($\lambda$ = 0.71073 Å). Selected bond lengths and angles are available in Table 3 and Table 4. All structures were solved by direct methods (structure solution program: SIR97[25] for **5** and **6**) and refined by full-matrix least-squares methods with SHELXL-97.[26] Hydrogen atoms were included at geometrically idealised positions and were not refined; the non-hydrogen atoms were refined anisotropically.

**Crystallographic Data for 5:** $C_{21}H_{37}N_9P_2SSi_3$, *fw* = 593.87, monoclinic, $P2_1/c$, $a$ = 9.0514(1), $b$ = 18.2759(3), $c$ = 18.7805(3) Å, $\alpha$ = 90.0, $\beta$ = 96.4276(8), $\gamma$ = 90.0°, $V$ = 3087.19(8) Å$^3$, $Z$ = 4, $\rho_{calcd.}$ = 1.278 g/cm$^3$, $\mu$ = 0.353 mm$^{-1}$, $\lambda$(Mo-$K_\alpha$) = 0.71073 Å, $T$ = 200 K, 36065 reflections collected, 6983 independent reflections, $R_{int}$ = 0.092, 5381 observed reflections, $R_1$ = 0.0469, $wR_2$ = 0.1308.

**Crystallographic Data for 6:** $C_{36}H_{56}N_{12}P_4S_2Si_4$, *fw* = 957.29, monoclinic, $P2_1/n$, $a$ = 11.6491(3), $b$ = 13.8277(4), $c$ = 15.1723(5) Å, $\alpha$ = 90.0, $\beta$ = 95.776(1), $\gamma$ = 90.0°, $V$ = 2431.5(1) Å$^3$, $Z$ = 2, $\rho_{calcd.}$ = 1.308 g/cm$^3$, $\mu$ = 0.381 mm$^{-1}$, $\lambda$(Mo-$K_\alpha$) = 0.71073 Å, $T$ = 200 K, 5520 reflections collected, 28073 independent reflections, $R_{int}$ = 0.080, 3880 observed reflections, $R_1$ = 0.0558, $wR_2$ = 0.1364.

CCDC-283470 (for **5**) and -283471 (for **6**) contain the supplementary crystallographic data for this paper. These data can be obtained free of charge from The Cambridge Crystallographic Data Centre via www.ccdc.cam.ac.uk/data_request/cif.

**Computational Details:** The structural data of all considered species were calculated using the hybrid density functional theory (B3LYP) with the program package Gaussian 98.[27] For all elements a standard 6-31G(d,p) basis set was used. Comparison with experimental data shows differences in bond lengths no larger than 0.01–0.02 Å.[12a] As frequency analyses were not possible because of the large size of all species at the B3LYP level, PM3 optimised structures (stationary points) were characterised by a frequency analysis displaying only positive frequencies. NBO analyses[13a,28] were carried out to investigate the bonding in all molecules at the SCF level utilising the optimised B3LYP/6-31G(d,p) geometry and RHF orbitals. Also, NBO population analysis for **5** and **6** was carried out with the structure fixed at the position determined from X-ray analysis of **5** and **6** to investigate the bonding and hybridisation in this experimentally observed species. The computed geometrical parameters for all molecules, relative energies, details of the NBO analyses and absolute energies are given as Supporting Information. The computed frequencies can be obtained from the authors. It should be emphasised that the computation was carried out for a single, isolated (gas-phase) molecule. There may well be significant differences among gas-phase, solution and solid-state data.

## Acknowledgments

A.S. thanks Prof. Dr. T. M. Klapötke (LMU München) for his generous support and advice. We also wish to thank the Leibniz Rechenzentrum for the generous allocation of CPU time. This research was supported by the DFG SCHU 1170/4-1.

[1] H. Staudinger, J. Meyer, *Helv. Chim. Acta* **1919**, *2*, 635–646.
[2] a) K. Sasse, in *Methoden der Organischen Chemie*, *vol. 12, part 1: Organische Phosphorverbindungen (Houben-Weyl)*, Georg Thieme Verlag, Stuttgart, **1963**, p. 73; b) R. F. Hudson, *Structure and Mechanism in Organophosphorus Chemistry*, Academic Press, London and New York, **1965**, p. 198; c) A. W. Johnson, *Ylid Chemistry*, Academic Press, London and New York, **1966**, p. 219; d) H. J. Bestmann, J. Zimmermann, in: *Organic Phosphorus Compounds* (Eds.: G. M. Kosalapoff, L. Maier), Wiley Interscience, New York, London, Sydney, Toronto, **1972**, vol. 3, p. 11; e) M. Regitz (Ed.), in: *Methoden der Organischen Chemie, vol. E II: Phosphorverbindungen (Houben-Weyl)*, Georg Thieme Verlag, Stuttgart, **1982**, p. 96.
[3] A. W. Johnson, *Ylides and Imines of Phosphorus*, Wiley, New York, **1993**.
[4] K. Dehnicke, F. Weller, *Coord. Chem. Rev.* **1997**, *158*, 103–169.
[5] K. Dehnicke, M. Krieger, W. Massa, *Coord. Chem. Rev.* **1999**, *182*, 19–65.
[6] M. Köhn, R. Breinbauer, *Angew. Chem. Int. Ed.* **2004**, *43*, 3106–3116.
[7] a) K. P. C Vollhardt, N. E. Schore, *Organische Chemie*, 3rd ed., Wiley-VCH, Weinheim, **2000**; b) O. I. Kolodiazhnyi, *Phosphorus Ylides*, Wiley-VCH, Weinheim, **1999**.
[8] E. Kessenich, K. Polborn, A. Schulz, *Inorg. Chem.* **2001**, *40*, 1102–1109.
[9] G. Fischer, S. Herler, P. Mayer, A. Schulz, A. Villinger, J. J. Weigand, *Inorg. Chem.* **2005**, *44*, 1740–1751.
[10] S. Herler, A. Villinger, P. Mayer, A. Schulz, J. J. Weigand, *Angew. Chem.* **2005**, *117*, 7968–7971; *Angew. Chem. Int. Ed.* **2005**, *44*, 7790–7793.
[11] Mass spectrometric studies revelead traces of the double Staudinger product.
[12] a) "Ab initio methods", in: *Main Group Chemistry* (Eds.: T. M. Klapötke, A. Schulz, with an invited chapter by R. D. Harcourt about VB theory), John Wiley & Sons, New York, **1998**; b) A. Schulz, I. C. Tornieporth-Oetting, T. M. Klapötke, *Inorg. Chem.* **1995**, *34*, 4343 and references cited therein.
[13] a) E. D. Glendening, A. E. Reed, J. E. Carpenter, F. Weinhold, NBO Version 3.1; b) A. E. Reed, L. A. Curtiss, F. Weinhold, *Chem. Rev.* **1988**, *88*, 899–926.
[14] Sum of covalent radii: $r$(P) = 1.1 and $r$(N) = 0.7; A. F. Holleman, E. Wiberg (Eds.), *Lehrbuch der Anorganischen Chemie*, 101st ed., Walter de Gruyter, **1995**, Anhang V.
[15] E. Niecke, O. Altmeyer, M. Nieger, *J. Chem. Soc., Chem. Commun.* **1988**, 945–946.

 © 2006 Wiley-VCH Verlag GmbH & Co. KGaA, Weinheim 

[16] E. Niecke, M. Nieger, F. Reichert, *Angew. Chem.* **1988**, *100*, 1781–1784; *Angew. Chem. Int. Ed. Engl.* **1988**, *27*, 1715–1718.
[17] O. Altmeyer, E. Niecke, M. Nieger, T. Busch, W. W. Schoeller, D. Stalke, *Heteroat. Chem.* **1990**, *1*, 191–194.
[18] V. Luana, A. Pendas, A. Costales, G. A. Carriedo, F. J. Garcia-Alonso, *J. Phys. Chem. A* **2001**, *105*, 5280–5291.
[19] Estimated donor-accepted energies are between 10 and 20 kcal/mol.
[20] a) D. P. Craig, N. L. Paddock, *Nature* **1958**, *181*, 1052; b) M. J. S. Dewar, E. A. C. Lucken, M. A. Whitehead, *J. Chem. Soc.* **1960**, 2423.
[21] a) NBO natural atomic population B3LYP/6-31G(d,p): 3d (P) $< 0.02$; e.g. **5**: natural electron configuration for P: [core] 3s (0.89), 3p (1.91), 3d (0.07). Because phosphorus AOs (n.4, 5 etc.) make only very minor contributions to bonding in the ground states of phosphorus-containing molecules, further consideration will not be given herein to the high-energy expanded valence-shell structures; b) E. Kessenich, A. Schulz, K. Polborn, *Acta Crystallogr., Sect. E* **2002**, *58*, i15–i16.
[22] Sum of covalent radii: $r(P) = 1.1$ and $r(N) = 0.7$; A. F. Holleman, E. Wiberg (Eds.), *Lehrbuch der Anorganischen Chemie*, 101st ed., Walter de Gruyter, **1995**, Anhang V.
[23] E. Niecke, O. Altmeyer, M. Nieger, *J. Chem. Soc., Chem. Commun.* **1988**, 945–946.
[24] a) U. Müller, *Chem. Ber.* **1977**, *110*, 788–791; b) H. W. Roesky, M. Noltemeyer, G. M. Sheldrick, *Z. Naturforsch., Teil B* **1986**, *41*, 803–807; c) D. Schomburg, U. Wermuth, R. Schmutzler, *Chem. Ber.* **1987**, *120*, 1713–1718; d) A. H. Cowley, F. Gabbai, R. Schluter, D. Atwood, *J. Am. Chem. Soc.* **1992**, *114*, 3142–3144; e) U. Englert, P. Paetzold, E. Eversheim, *Z. Kristallogr.* **1993**, *208*, 307–309; f) A. H. Cowley, F. P. Gabbai, G. Bertrand, C. J. Carrano, M. R. Bond, *J. Organomet. Chem.* **1995**, *493*, 95–99; g) M. Larbig, M. Nieger, V. v. d. Gönna, A. V. Ruban, E. Niecke, *Angew. Chem. Int. Ed. Engl.* **1995**, *34*, 460–462.
[25] A. Altomare, M. Burla, M. Camalli, G. L. Cascarano, C. Giacorazzo, *J. Appl. Crystallogr.* **1999**, *32*, 115–119.
[26] G. M. Sheldrick, *SHELXL-97*, *Program for Solution of Crystal Structures*, University of Göttingen, Göttingen, Germany, **1997**.
[27] M. J. Frisch, G. W. Trucks, H. B. Schlegel, G. E. Scuseria, M. A. Robb, J. R. Cheeseman, V. G. Zakrzewski, J. A. Montgomery Jr, R. E. Stratmann, J. C. Burant, S. Dapprich, J. M. Millam, A. D. Daniels, K. N. Kudin, M. C. Strain, O. Farkas, J. Tomasi, V. Barone, M. Cossi, R. Cammi, B. Mennucci, C. Pomelli, C. Adamo, S. Clifford, J. Ochterski, G. A. Petersson, P. Y. Ayala, Q. Cui, K. Morokuma, D. K. Malick, A. D. Rabuck, K. Raghavachari, J. B. Foresman, J. Cioslowski, J. V. Ortiz, B. B. Stefanov, G. Liu, A. Liashenko, P. Piskorz, I. Komaromi, R. Gomperts, R. L. Martin, D. J. Fox, T. Keith, M. A. Al-Laham, C. Y. Peng, A. Nanayakkara, C. Gonzalez, M. Challacombe, P. M. W. Gill, B. Johnson, W. Chen, M. W. Wong, J. L. Andres, C. Gonzalez, M. Head-Gordon, E. S. Replogle, J. A. Pople, *Gaussian 98*, Revision A.6, Gaussian, Inc., Pittsburgh, PA, **1998**.
[28] a) J. E. Carpenter, F. Weinhold, *J. Mol. Struct.: THEOCHEM* **1988**, *169*, 41–62 and references cited therein; b) F. Weinhold, J. E. Carpenter, J. E. *The Structure of Small Molecules and Ions*, Plenum Press, New York, **1988**, p. 227.
[29] W. Buder, A. Schmidt, *Z. Anorg. Allg. Chem.* **1975**, *415*, 263–267.
[30] K. B. Dillon, A. W. G. Platt, T. C. Waddington, *Inorg. Nucl. Chem. Lett.* **1978**, *14*, 511–513.
[31] a) A. Schmidt, *Chem. Ber.* **1970**, *103*, 3923–3927; b) A. Schmidt, *Chem. Ber.* **1968**, *101*, 4015–4021.
[32] K. B. Dillon, A. W. G. Platt, T. C. Waddington, *J. Chem. Soc., Dalton Trans.* **1981**, *12*, 2292–2295.
[33] A. H. Cowly, F. Gabbai, R. Schluter, D. Atwood, *J. Am. Chem. Soc.* **1992**, *114*, 3142–3144.
[34] A. Maquestiau, L. Z. Chen, R. Flammang, J. P. Majoral, G. Bertrand, *Inorg. Chem.* **1990**, *29*, 3097–3102.
[35] G. Tesi, C. M. Douglas, Ch. P. Haber, *US 3087937*, **1963**.
[36] E. L. Lines, L. F. Centofanti, *Inorg. Chem.* **1972**, *11*, 2269–2270.
[37] G. S. Hartley, D. W. Pound, *US 2649464*, **1953**.
[38] G. Magro, B. Donnadieu, A.-M. Caminade, J.-P. Majoral, *Chem. Eur. J.* **2003**, *9*, 2151–2159.
[39] Ch. M. Timperley, S. N. Marriott, M. J. Waters, *J. Fluorine Chem.* **2002**, *113*, 111–122.
[40] H. F. Schröder, J. Müller, *Z. Anorg. Allg. Chem.* **1975**, *418*, 247–258.
[41] C. Aubauer, T. M. Klapötke, H. Nöth, A. Schulz, M. Suter, J. Weigand, *Chem. Commun.* **2000**, 2491–2492.
[42] C. Aubauer, K. Karaghiosoff, T. M. Klapötke, G. Kramer, A. Schulz, J. Weigand, *Z. Anorg. Allg. Chem.* **2001**, *627*, 2547–2552.
[43] C. M. Sharts, US patent, *US 3347876*, **1967**.
[44] a) C. Grundmann, R. Rätz, *Z. Naturforsch., Teil B: Chem. Sci.* **1955**, *10*, 116; b) R. A. Shaw, B. W. Fitzsimmons, B. C. Smith, *Chem. Rev.* **1962**, *62*, 247; c) M. S. Chang, A. J. Matuszko, *J. Am. Chem. Soc.* **1960**, *82*, 5756; d) I. C. Tornieporth-Oetting, T. M. Klapötke, *Angew. Chem. Int. Ed. Engl.* **1995**, *34*, 511–520.
[45] a) H. W. Roesky, M. Banek, *Chem.-Ztg.* **1978**, *102*, 155–156; b) H. W. Roesky, M. Banek, *Z. Naturforsch., Teil B: Chem. Sci.* **1979**, *34*, 752–754.
[46] P. R. Dave, F. Forohar, T. Axenrod, C. D. Bedford, M. Chaykovsky, M.-K. Rho, R. Gilardi, C. George, *Phosphorus, Sulfur Silicon Relat. Elem.* **1994**, *90*, 175–184.
[47] C. M. Sharts, A. J. Bilbo, D. R. Gewntry, *Inorg. Chem.* **1966**, *5*, 2140–2145.

Received: December 21, 2005
Published Online: March 22, 2006

 © 2006 Wiley-VCH Verlag GmbH & Co. KGaA, Weinheim 

DOI: 10.1002/ejic.200501141

# Syntheses and Fluxional Processes of Diphenyl(2-thienyl)phosphane Derivatives of Triosmium Clusters

Nitsa K. Kiriakidou Kazemifar,[a] Marc J. Stchedroff,[a] M. Abdul Mottalib,[a][‡] Simona Selva,[b] Magda Monari,[b] and Ebbe Nordlander*[a]

**Keywords:** Cluster / Thienylphosphane / Fluxionality / Hydrodesulfurisation

Thermal treatment of $[Os_3(CO)_{12}]$ with diphenyl(2-thienyl)-phosphane, $Ph_2P(C_4H_3S)$, results in the formation of $[Os_3(CO)_{12-x}\{Ph_2P(C_4H_3S)\}_x]$ (x = 1–3, **1**–**3**), but no C–H bond activation was observed. Reaction of $[H_2Os_3(CO)_{10}]$ with diphenyl(2-thienyl)phosphane at ambient temperature affords $[HOs_3(\mu\text{-}H)(CO)_{10}\{Ph_2P(C_4H_3S)\}]$ (**4**), but when the same reaction is repeated at elevated temperatures, the cyclometallated species $[(\mu\text{-}H)Os_3(CO)_9\{\mu_3\text{-}Ph_2P(C_4H_2S)\}]$ (**5**) and $[(\mu\text{-}H)Os_3(CO)_8\{\mu_3\text{-}Ph_2P(C_4H_2S)\}\{Ph_2P(C_4H_3S)\}]$ (**6**) are formed. In addition, two more products, tentatively assigned as $[(\mu\text{-}H)Os_3(CO)_6\{\mu_3\text{-}Ph_2P(C_4H_2S)\}\{\mu\text{-}Ph_2P(C_4H_3S)\}\{Ph_2P(C_4H_3S)\}]$ (**7**) and $[(\mu\text{-}H)Os_3(CO)_7\{\mu\text{-}Ph_2P(C_4H_2S)\}\{\mu\text{-}Ph_2P(C_4H_3S)\}\{Ph_2P(C_4H_3S)\}]$ (**8**) are obtained. The dynamic behaviours of **2**, **5** and **6** have been studied by variable-temperature (VT) $^1H$ and $^{31}P\{^1H\}$ NMR spectroscopy. The VT $^{31}P\{^1H\}$ NMR spectra of $[Os_3(CO)_{10}\{Ph_2P(C_4H_3S)\}_2]$ (**2**) demonstrate that a mixture of two isomers, which are in rapid exchange at room temperature, is present and that the less common *cis-trans* isomer, whose structure has been determined by X-ray crystallography, is favoured for this cluster. The VT $^1H$ NMR spectra of **5** indicate the presence of two isomers which are proposed to arise from an oscillation of the $\sigma,\eta^2$-vinyl group of the thienyl moiety between two metal atoms. A similar fluxional process is proposed to occur in **6** and the assignment of the room-temperature structure(s) of this cluster was confirmed by $^1H$-$^{187}Os$ 2D HMQC spectroscopy. In addition to **2**, the solid-state structures of **3**, **5** and **6** have been determined by X-ray crystallography.
(© Wiley-VCH Verlag GmbH & Co. KGaA, 69451 Weinheim, Germany, 2006)

## Introduction

More strict laws concerning sulfur-containing emissions have intensified the interest in hydrodesulfurisation (HDS) processes. As a consequence, studies of adsorption and activation of organosulfur compounds onto metal surfaces is a rapidly developing area. The objectives of this research are the understanding of the nature of the active HDS catalysts, the binding modes and the activation of sulfur-containing molecules – in particular thiophenes – at the active catalyst sites, and the improvement of the efficiency of the catalysts.[1–6] Organometallic complexes,[3–5] including transition-metal clusters,[7] have been used as models for HDS catalysts because mechanistic information easily can be extracted by spectroscopic and analytical studies of discrete molecular complexes.

One of the very first reports of the interaction of thiophene with organometallic compounds described the desulfurisation of the heterocycle by a metal cluster, $[Fe_3(CO)_{12}]$.[8,9] Rauchfuss and co-workers[10] demonstrated shortly after, that thiaferroles are easily converted into the corresponding ferroles on heating and thereby established that insertion of an iron atom into a C–S bond clearly activates the heterocycle towards desulfurisation [Scheme 1(a)]. Similarly, the reaction of $[Ru_3(CO)_{12}]$ with thiophene proceeds through C–S bond cleavage, producing the sulfur-free ferrole-type compound $[Ru_2(\mu\text{-}C_4H_4)(CO)_6]$ and the tetranuclear cluster $[Ru_4(\mu_3\text{-}S)(\mu\text{-}C_4H_4)(CO)_{11}]$;[11] this is the first reported example of desulfurisation of a thiophene in which both the extruded sulfur and the hydrocarbon residue remain coordinated within the same complex [Scheme 1(b)]. More recently, Angelici and co-workers[12] have demonstrated $[Re_2(CO)_{10}]$-promoted C–S bond cleavage in benzothiophenes.

Despite the above-mentioned examples of C–S bond activation, C–H bond activation predominates over other types of oxidative addition in reactions of thiophenes with $[M_3(CO)_{12}]$ (M = Ru, Os) and their derivatives.[7] Thus, the carbonyltriosmium clusters $[Os_3(CO)_{12}]$ and $[Os_3(CO)_{10}(MeCN)_2]$ react with thiophene and thiophene derivatives through C–H bond cleavage in preference to C–S bond cleavage to afford the *endo*- and *exo*-thienyl isomers of

[a] Inorganic Chemistry, Center for Chemistry and Chemical Engineering, Lund University,
Box 124, 22100 Lund, Sweden
Fax: + 46-46222-4439
E-mail: Ebbe.Nordlander@inorg.lu.se
[b] Dipartimento di Chimica "G. Ciamician", Università degli Studi di Bologna,
via Selmi 2, 40126 Bologna, Italy
[‡] On leave from: Bangladesh College of Leather Technology, Hazaribagh, Dhaka 1209, Bangladesh
Supporting information for this article is available on the WWW under http://www.eurjic.org or from the author.

 © 2006 Wiley-VCH Verlag GmbH & Co. KGaA, Weinheim 

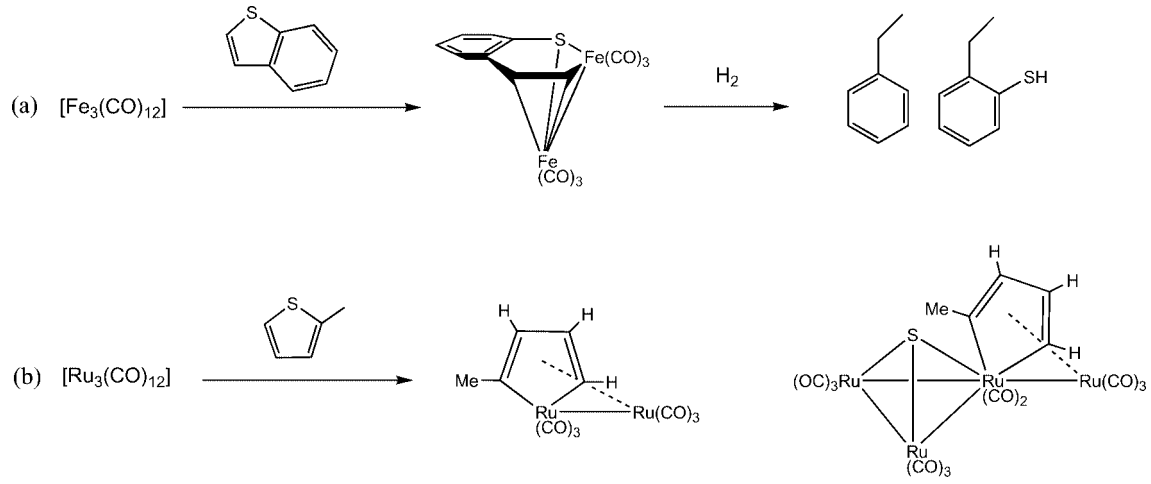


Scheme 1. Examples of desulfurisation of benzothiophene and 2-methylthiophene by carbonyl transition-metal clusters (see text and references cited therein).

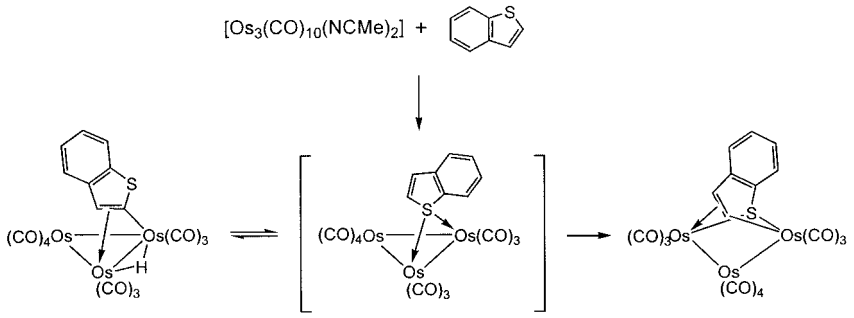


Scheme 2. Room-temperature C–S bond cleavage effected by a carbonyltriosmium cluster (cf. ref.[17]).

$[Os_3(\mu\text{-}H)(CO)_9(\mu\text{-}C_4H_2S)]$, which are in rapid equilibrium at room temperature.[13–15] Similar results have been observed for 2-methylthiophene, 2,2′-bithiophene and 2,2′:5′,2′′-terthiophene.[16] The first room-temperature C–S bond cleavage of a (benzo)thiophene coordinated to a metallic cluster was reported by Arce et al.[17] In chloroform at room temperature the cluster $[Os_3(\mu\text{-}H)(CO)_{10}(\mu\text{-}C_8H_5S)]$, which contains a $\mu\text{-}\eta^2$-benzothienyl ligand, undergoes C(vinyl)–S bond cleavage to yield the cluster $[Os_3(CO)_{10}(\mu\text{-}C_8H_6S)]$, which contains an open benzothiophene ligand coordinated to an open $Os_3$ unit through a μ-S atom and a $\mu\text{-}\eta^2$-vinyl group (Scheme 2).

Despite the above-mentioned examples of thiophene coordination and activation, thiophene remains a relatively poor ligand for low-valent metal complexes, and thienylphosphanes [e.g. diphenyl(2-thienyl)phosphane] have therefore been used to bring the heterocycle into the coordination sphere of transition-metal clusters through the phosphane moiety of the ligand.[18–20] Treatment of diphenyl(2-thienyl)phosphane with $[Ru_3(CO)_{12}]$ has led to the incorporation of the thiophene ring into tri- and tetraruthenium clusters by cyclometallation and C–P bond cleavage of the ligand.[20] Here we report the reactions of $[Os_3(CO)_{12}]$ and $[H_2Os_3(CO)_{10}]$ with diphenyl(2-thienyl)phosphane, $Ph_2P(C_4H_3S)$, which have been undertaken in an effort to achieve C–P and C–S bond cleavage of the ligand.

## Results and Discussion

### Thermal Treatment of $[Os_3(CO)_{12}]$ with $Ph_2P(C_4H_3S)$

Reaction of $[Os_3(CO)_{12}]$ with diphenyl(2-thienyl)phosphane, $Ph_2P(C_4H_3S)$, in refluxing toluene yielded, after separation by thin layer chromatography, three yellow, substituted compounds, which were identified as $[Os_3(CO)_{11}\{PPh_2(C_4H_3S)\}]$ (**1**) (23%), $[Os_3(CO)_{10}\{PPh_2(C_4H_3S)\}_2]$ (**2**) (44%), and $[Os_3(CO)_9\{PPh_2(C_4H_3S)\}_3]$ (**3**) (8%) on the basis of their IR spectra. They are analogous with those of known mono-, bis-, and tris(phosphane)-substituted triosmium clusters.[21–24] The FAB mass spectra of all three compounds are also in complete agreement with the proposed formulas.

The $^1H$ NMR spectra of **1**–**3** display only aromatic resonances. No hydrido signals could be detected, indicating that *ortho*-metallation had not taken place. The room-temperature $^{31}P\{^1H\}$ NMR spectra show a singlet at $\delta$ = –16.2 ppm for **1**, a signal at $\delta$ = –17.3 (br.) ppm and doublet at $\delta$ = –32.7 ($J_{P-P}$ = 6.4 Hz) ppm for **2** (vide infra), and a singlet at $\delta$ = –17.2 ppm for **3**. The $^{31}P\{^1H\}$ spectra of both **1** and **3** remain unchanged when the temperature is decreased to –60 °C. This is consistent with the presence of one isomer of both **1** and **3**, in which the phosphane ligand(s) adopt equatorial positions with respect to the clus-

 © 2006 Wiley-VCH Verlag GmbH & Co. KGaA, Weinheim 

ter. However, the low-temperature $^{31}P\{^1H\}$ NMR spectrum of **2** indicates the presence of more than one isomer. The two most reasonable isomers are the *cis-trans* and *trans-trans* isomers (*cis* or *trans* with respect to the Os–Os vector) shown in Figure 1, which have previously been detected for related $[Os_3(CO)_{10}(phosphane)_2]$ clusters.[25,26] The $^{31}P\{^1H\}$ NMR spectrum at –60 °C (Figure 1) reveals that the predominant form is the *cis-trans* isomer with non-equivalent phosphorus nuclei, represented by two singlets at $\delta$ = –18.12 and –21.97 ppm.

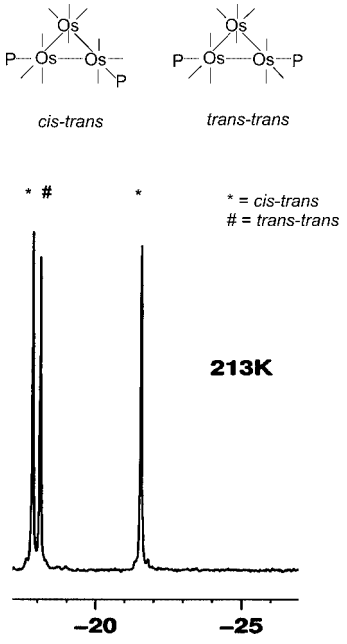


Figure 1. $^{31}P\{^1H\}$ NMR spectrum ($CD_2Cl_2$, 300 MHz) of $[Os_3(CO)_{10}(Ph_2PC_4H_3S)_2]$ (**2**) at –60 °C. The appearance of two equally intense singlets ($\delta$ = –18.12 and –21.97 ppm) is consistent with the *cis-trans* isomer and the third singlet ($\delta$ = –18.26 ppm) is attributed to the *trans-trans* isomer.

Until recently, only the *trans-trans* form of an $[Os_3(CO)_{10}(phosphane)_2]$ cluster had been verified crystallographically. Leong and Liu[27] have reported the first crystallographic confirmation of a *cis-trans* structure, that of *cis-trans*-$[Os_3(CO)_{10}(PPh_3)_2]$, which can be crystallised in both isomeric forms. We were able to grow yellow crystals of compound **2** by slow concentration of a dichloromethane/*n*-hexane solution at 4 °C, and these crystals were somewhat surprisingly found to contain only the *cis-trans* isomer. The molecular structure of **2** is shown in Figure 2; selected bond lengths and angles are listed in Table 1.

The molecule consists of a triangle of osmium atoms with ten carbonyl ligands, four bonded to Os(3) and three to each of Os(1) and Os(2). Two diphenyl(2-thienyl)phosphane ligands occupy equatorial coordination sites on Os(1) and Os(2), respectively. The average Os–Os distance [2.901(1) Å] is slightly longer than that found in the parent cluster, $[Os_3(CO)_{12}]$ [$Os–Os_{ave}$ = 2.877(3) Å].[28] In agreement with previous studies indicating that the presence of a tertiary phosphane ligand tends to lengthen the *cis*-Os–Os bond in $[Os_3(CO)_{11}(phosphane)]$ clusters,[29,30] some

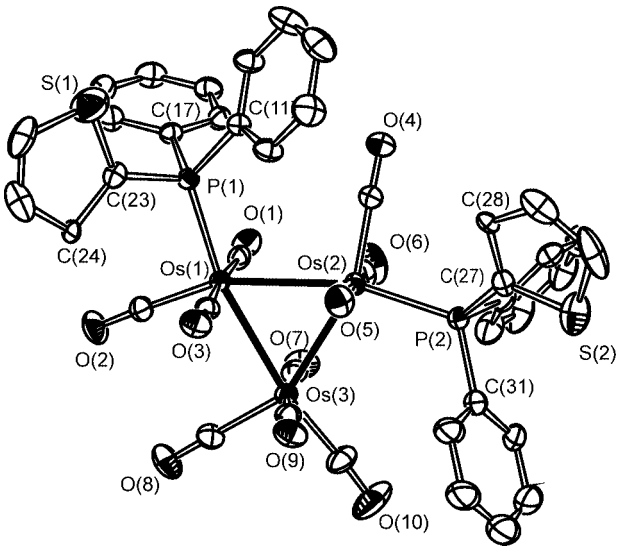


Figure 2. Molecular structure of $[Os_3(CO)_{10}\{Ph_2P(C_4H_3S)\}_2]$ (**2**) (thermal ellipsoids at 30% probability). The carbon atoms of the carbonyl ligands bear the same numbering as the oxygen atoms. Hydrogen atoms have been omitted for clarity.

Table 1. Selected bond lengths [Å] and angles [°] for $[Os_3(CO)_{10}(Ph_2PC_4H_3S)_2]$ (**2**).

| | | | |
|---|---|---|---|
| Os(1)–Os(2) | 2.9104(7) | Os(1)–C(1) | 1.946(7) |
| Os(1)–Os(3) | 2.8860(8) | Os(1)–C(2) | 1.887(6) |
| Os(2)–Os(3) | 2.9072(6) | Os(1)–C(3) | 1.932(6) |
| Os(1)–P(1) | 2.343(2) | Os(2)–C(4) | 1.884(6) |
| Os(2)–P(2) | 2.333(2) | Os(2)–C(5) | 1.948(7) |
| P(1)–C(11) | 1.847(3) | Os(2)–C(6) | 1.918(7) |
| P(1)–C(17) | 1.825(3) | Os(3)–C(7) | 1.947(7) |
| P(1)–C(23) | 1.828(6) | Os(3)–C(8) | 1.920(7) |
| P(2)–C(27) | 1.820(6) | Os(3)–C(9) | 1.951(7) |
| P(2)–C(31) | 1.851(4) | Os(3)–C(10) | 1.885(7) |
| P(2)–C(37) | 1.833(4) | | |
| C(1)–Os(1)–C(3) | 174.9(2) | P(2)–Os(2)–Os(3) | 104.46(4) |
| C(2)–Os(1)–C(3) | 92.6(3) | C(4)–Os(2)–Os(1) | 99.1(2) |
| P(1)–Os(1)–C(2) | 96.0(2) | C(4)–Os(2)–Os(3) | 156.3(2) |
| P(1)–Os(1)–Os(2) | 106.49(4) | C(7)–Os(3)–C(9) | 173.0(3) |
| P(1)–Os(1)–Os(3) | 166.48(4) | C(8)–Os(3)–C(10) | 99.6(3) |
| C(2)–Os(1)–Os(2) | 157.1(2) | C(8)–Os(3)–Os(1) | 90.9(2) |
| C(5)–Os(2)–C(6) | 178.5(3) | C(8)–Os(3)–Os(2) | 151.2(2) |
| P(2)–Os(2)–C(4) | 97.9(2) | C(10)–Os(3)–Os(1) | 169.4(2) |
| P(2)–Os(2)–Os(1) | 162.55(4) | C(10)–Os(3)–Os(2) | 109.2(3) |

lengthening of the Os(1)–Os(2) and Os(2)–Os(3) interactions in *cis* position is observed [2.910(1) and 2.907(1) Å, respectively, vs. Os(1)–Os(3) 2.886(1) Å]. This trend confirms the similar lengthening of the two Os–Os distances in *cis* position in the *cis-trans* form of the cluster $[Os_3(CO)_{10}(PPh_3)_2]$.[27] On the other hand, in *trans-trans* structures of $[Os_3(CO)_{10}(phosphane)_2]$ [phosphane = $PPh_3$, $PPh(OMe)_2$, $P(OMe)_3$] there is no change of Os–Os bond lengths that can be related to the presence of two phosphane ligands.[31] The Os(1)–P(1) (2.343 Å) and Os(2)–P(2) [2.333(2) Å] distances are normal and close to those reported for $[Os_3(CO)_{10}(PPh_3)_2]$.[27] (*cis-trans* and *trans-trans* forms) and the phosphane-substituted compounds mentioned above. The phosphorus atoms are slightly displaced out of the $Os_3$ plane [P(1) +0.102(1) and P(2) +0.292(1) Å]. This structure

 © 2006 Wiley-VCH Verlag GmbH & Co. KGaA, Weinheim 

determination and the above-mentioned low-temperature NMR measurements indicate that the *cis-trans* isomer of **2** is the thermodynamically favoured compound, as has previously been found by Deeming and co-workers for related clusters.[25,26]

Compound **3** crystallises with two independent molecules, which are conformational isomers (vide infra), in the asymmetric unit. The molecular structure of **3** is similar to that of previously characterised trisubstituted complexes of the general formula $[M_3(CO)_9(phosphane)_3]$ [M = Os, Ru and phosphane = $PMe_2(CH_2Ph)$, $PMe_2Ph$, $PPh(OMe)_2$, $P(OEt)_3$, $P(OCH_2CF_3)_3$ and $PPh_3$].[31] The molecular structure of one of the two crystallographically independent molecules of **3** is shown in Figure 3; selected bond lengths and angles are listed in Table 2. The cluster consists of a triangular $Os_3$ core with nine terminal carbonyl ligands. Three diphenyl(2-thienyl) ligands, each one coordinated to an osmium atom, occupy equatorial sites in such a way as to minimize steric interactions. The Os–Os distances average 2.894 Å, which is slightly longer than that found for $[Os_3(CO)_{12}]$ (vide supra), and the Os–P distances are comparable to those observed in compound **2**. It is worth noting that the introduction of the three diphenyl(2-thienyl)-phosphane ligands results in a significant twisting of the $Os(CO)_3(Ph_2PC_4H_3S)$ units with respect to the $Os_3$ plane. This distortion towards $D_3$ symmetry, which presumably occurs to minimize the steric interaction of the large phosphane ligands and may be rationalised in terms of more effective ligand packing, has been observed previously for related mono-, di- and tri-substituted complexes.[29,31,32] The usual arrangement of the phosphane substituents, with one lying below the metal plane and the other two lying above, is found in both of the conformationally distinct molecules that are present in the asymmetric unit. However, these conformational isomers differ in the orientations of the phosphane substituents. In the isomer shown in Figure 3, the two substituents on the same side of the metal plane are one phenyl and one thienyl ring for all three phosphane ligands, and the sulfur atom points towards the inner part of the phosphane cone. In the other isomer, one phosphane ligand is rotated so that its thienyl group occupies the "other" side of the $Os_3$ plane.

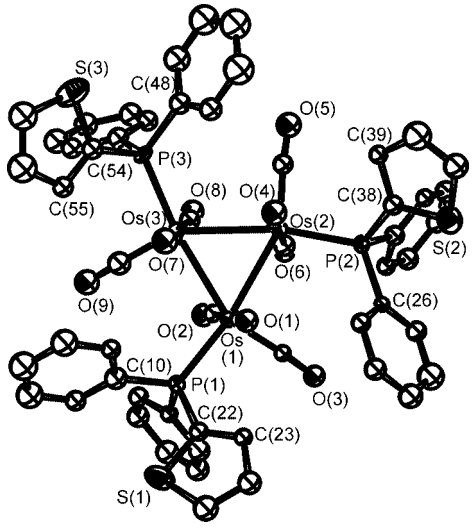


Figure 3. Molecular structure of one of the two crystallographically independent molecules of $[Os_3(CO)_9(Ph_2PC_4H_3S)_3]$ (**3**) (thermal ellipsoids at 30% probability). The carbon atoms of the carbonyl ligands bear the same numbering as the oxygen atoms. Hydrogen atoms have been omitted for clarity.

Table 2. Selected bond lengths [Å] and angles [°] for $[Os_3(CO)_9\{Ph_2P(C_4H_3S)\}_3]$ (**3**).

| | | | |
|---|---|---|---|
| Molecule A | | | |
| Os(1)–Os(2) | 2.902(1) | P(3)–C(42) | 1.81(1) |
| Os(1)–Os(3) | 2.877(2) | P(3)–C(48) | 1.83(1) |
| Os(2)–Os(3) | 2.904(1) | P(3)–C(54) | 1.82(2) |
| Os(1)–P(1) | 2.325(5) | Os(1)–C(1) | 1.94(2) |
| Os(2)–P(2) | 2.333(6) | Os(1)–C(2) | 1.94(2) |
| Os(3)–P(3) | 2.327(6) | Os(1)–C(3) | 1.87(1) |
| P(1)–C(10) | 1.82(1) | Os(2)–C(4) | 1.86(2) |
| P(1)–C(16) | 1.81(1) | Os(2)–C(5) | 1.88(2) |
| P(1)–C(22) | 1.83(2) | Os(2)–C(6) | 1.89(3) |
| P(2)–C(26) | 1.85(1) | Os(3)–C(7) | 1.92(2) |
| P(2)–C(32) | 1.82(1) | Os(3)–C(8) | 1.86(2) |
| P(2)–C(38) | 1.80(2) | Os(3)–C(9) | 1.86(3) |
| C(1)–Os(1)–C(2) | 172.0(9) | P(2)–Os(2)–Os(3) | 165.7(1) |
| P(1)–Os(1)–C(3) | 97.7(6) | C(5)–Os(2)–Os(1) | 150.6(7) |
| P(1)–Os(1)–Os(2) | 167.8(2) | C(5)–Os(2)–Os(3) | 94.4(7) |
| P(1)–Os(1)–Os(3) | 110.0(2) | C(7)–Os(3)–C(8) | 170.1(9) |
| C(3)–Os(1)–Os(2) | 93.0(6) | P(3)–Os(3)–Os(1) | 171.2(2) |
| C(3)–Os(1)–Os(3) | 151.4(6) | P(3)–Os(3)–Os(2) | 111.9(1) |
| C(4)–Os(2)–C(6) | 172.8(9) | C(9)–Os(3)–Os(1) | 91.2(8) |
| P(2)–Os(2)–C(5) | 99.0(7) | C(9)–Os(3)–Os(2) | 149.9(8) |
| P(2)–Os(2)–Os(1) | 108.6(1) | | |
| Molecule B | | | |
| Os(4)–Os(5) | 2.919(1) | P(6)–C(101) | 1.83(1) |
| Os(4)–Os(6) | 2.903(1) | P(6)–C(107) | 1.83(1) |
| Os(5)–Os(6) | 2.912(1) | P(6)–C(113) | 1.78(3) |
| Os(4)–P(4) | 2.347(5) | Os(4)–C(60) | 1.85(3) |
| Os(5)–P(5) | 2.331(6) | Os(4)–C(61) | 1.90(2) |
| Os(6)–P(6) | 2.342(6) | Os(4)–C(62) | 1.90(2) |
| P(4)–C(69) | 1.76(2) | Os(5)–C(63) | 1.90(2) |
| P(4)–C(75) | 1.88(1) | Os(5)–C(64) | 1.90(2) |
| P(4)–C(81) | 1.82(2) | Os(5)–C(65) | 1.90(2) |
| P(5)–C(85) | 1.81(1) | Os(6)–C(66) | 1.87(1) |
| P(5)–C(91) | 1.82(1) | Os(6)–C(67) | 1.89(2) |
| P(5)–C(97) | 1.82(2) | Os(6)–C(68) | 1.89(2) |
| C(61)–Os(4)–C(62) | 175.6(9) | P(5)–Os(5)–Os(6) | 164.4(1) |
| P(4)–Os(4)–C(60) | 96.7(7) | C(64)–Os(5)–Os(4) | 163.8(7) |
| P(4)–Os(4)–Os(5) | 161.7(1) | C(64)–Os(5)–Os(6) | 106.6(7) |
| P(4)–Os(4)–Os(6) | 102.4(1) | P(6)–Os(6)–C(66) | 99.8(7) |
| C(60)–Os(4)–Os(5) | 101.5(7) | P(6)–Os(6)–Os(4) | 154.6(1) |
| C(60)–Os(4)–Os(6) | 159.3(7) | P(6)–Os(6)–Os(5) | 95.3(1) |
| C(63)–Os(5)–C(65) | 172.1(9) | C(66)–Os(6)–Os(4) | 104.8(7) |
| P(5)–Os(5)–C(64) | 89.0(7) | C(66)–Os(6)–Os(5) | 164.9(7) |
| P(5)–Os(5)–Os(4) | 105.1(1) | | |

### Room-Temperature Reaction of $[H_2Os_3(CO)_{10}]$ with $(Ph_2PC_4H_3S)$

A colour change from purple to yellow was observed immediately upon mixing 1 equiv. of diphenyl(2-thienyl)phosphane with $[H_2Os_3(CO)_{10}]$ in dichloromethane at room temperature. Comparison of the IR and NMR spectra of the product to the known $[H_2Os_3(CO)_{10}(L)]$ clusters,[32]

 © 2006 Wiley-VCH Verlag GmbH & Co. KGaA, Weinheim 

indicated that the product is $[HOs_3(\mu\text{-}H)(CO)_{10}\{Ph_2P(C_4H_3S)\}]$ (**4**), which was isolated in 26% yield after TLC purification. The room-temperature $^1H$ NMR spectrum shows a broad hydrido signal ($\delta \approx -15$ ppm) due to rapid exchange of the two hydrido ligands, but at –35 °C the exchange is frozen out and two distinct resonances are observed in the hydrido region – one for the terminal hydrido ligand at $\delta = -10.2$ ppm and one for the bridging hydrido ligand at $\delta = -19.7$ ppm. The $^{31}P\{^1H\}$ NMR spectrum displays one singlet at $\delta = -16.7$ ppm. On the basis of these NMR spectra we propose that the phosphane ligand in **4** is situated *trans* to the Os–Os bond and *cis* to the bridging hydrido ligand, which is reported as the thermodynamically most favourable of the isomers of $[HOs_3(\mu\text{-}H)(CO)_{10}(phosphane)]$ that have been identified.[33,34] Earlier investigations have shown that four more isomers have been detected from the reaction between $[H_2Os_3(CO)_{10}]$ and phosphanes.[35] In contrast to those results, we did not observe any additional isomers, even at –75 °C. This lack of observation of isomers may be related to the relative bulk of the ligand, making the other possible isomers sterically unfavourable. An alternative explanation is that the populations of (transient) isomers were too low to be observed.

### Thermal Treatment of $[H_2Os_3(CO)_{10}]$ with $Ph_2P(C_4H_3S)$

Reaction of an excess of diphenyl(2-thienyl)phosphane with $[H_2Os_3(CO)_{10}]$ in refluxing toluene for 3 h gives a colour change from initial purple colour to yellow, then to dark green and ultimately to brown. Separation by TLC led to the isolation of three products.

The first product was isolated in 21% yield. Although IR spectra of isostructural Os and Ru clusters are not always comparable, the product was identified as the cyclometallated cluster $[(\mu\text{-}H)Os_3(CO)_9\{\mu_3\text{-}Ph_2P(C_4H_2S)\}]$ (**5**) on the basis of the similarity of its IR spectrum to that of the known cluster $[Ru_3(\mu\text{-}H)(CO)_9\{\mu_3\text{-}Ph_2P(C_4H_2S)\}]$.[20] Mass spectrometric and microanalytical data were found to be consistent with the proposed formula. The $^1H$ NMR spectrum displays a doublet at $\delta = -18.0$ ppm confirming the presence of a bridging hydrido ligand, which couples to one phosphorus atom ($J_{P-H} = 13.2$ Hz). In the phenyl region, two *ortho* signals are observed, corresponding to two isomers. This is similar to that previously observed for $[Ru_3(\mu\text{-}H)(CO)_9\{\mu_3\text{-}Ph_2P(C_4H_2S)\}]$.[20] Unlike the ruthenium analogue, where the *ortho*-protons are fluxional at 20 °C and only become static on the NMR timescale at –20 °C, the *ortho*-protons of **5** were not fluxional at ambient temperature. The $^{31}P\{^1H\}$ NMR spectrum of **5** at 27 °C displays a singlet at $\delta = -3.3$ ($^1J_{P-Os} = 147$ Hz) ppm, with a small change of shift to $\delta = -5.3$ ppm at –80 °C. The small $^1J_{P-Os}$ coupling of 147 Hz is in agreement with axial coordination of the phosphorus atom with respect to the plane of the metal triangle. Typical equatorial $^1J_{P-Os}$ couplings are of the order of 185–225 Hz while axial couplings are much smaller as the metal–phosphane bond is no longer aligned with the electron density of the metal triangle.[36–39]

It was possible to grow crystals suitable for X-ray diffraction for cluster **5**, and single-crystal diffraction studies were undertaken in order to confirm the structure. The molecular structure of **5** is shown in Figure 4; selected bond lengths and angles are listed in Table 3. $[Os_3(\mu\text{-}H)(CO)_9\{\mu_3\text{-}Ph_2P(C_4H_2S)\}]$ (**5**) crystallises with two independent slightly different conformers in the asymmetric unit and is isostructural with $[(\mu\text{-}H)Ru_3(CO)_9\{\mu_3\text{-}Ph_2P(C_4H_2S)\}]$.[20] Compound **5** consists of an irregular triangle of osmium atoms, each of which is coordinated by three carbonyl ligands. A triply bridging diphenyl(2-thienyl)phosphane ligand and a bridging hydrido ligand complete the coordination sphere of the cluster. The $\mu_3\text{-}Ph_2P(C_4H_2S)$ ligand, which acts as a five-electron donor, is coordinated through the phosphorus atom in axial position to Os(1) and through the *ortho*-metallated thienyl ring to Os(3) with a C(11)–Os(3) σ-bond [Os(3)–C(11) 2.10(1) and 2.09(1) Å in molecule A and B] and to Os(2) with an $\eta^2(\pi)$-interaction between C(10)–C(11) and Os(2) [Os(2)–C(10) 2.34(1) and 2.36(1) Å, Os(2)–C(11) 2.35(1) and 2.32(1) Å in A and B, respectively]. This $\sigma,\eta^2$-vinyl-type interaction is not unprecedented; it has, for example, been observed in $[(\mu\text{-}H)Ru_3(CO)_9\{\mu_3\text{-}Ph_2P(C_4H_2S)\}]$[20] and $[(\mu\text{-}H)Ru_3(CO)_9\{\mu_3\text{-}Ph_2P(C_8H_4S)\}]$ ($C_8H_4S$ = benzothienyl),[40] $[Os_3(\mu\text{-}H)(CO)_9(\mu\text{-}Ph_2PCH{=}CH)]$,[34] $[Os_3(\mu\text{-}H)(CO)_9\{\mu_3\text{-}PMePh(C_6H_4)\}]$[41] as well as in the closely related $[Os_3(\mu\text{-}H)(MeSC_4H_2S)(CO)_9]$,[42] in which the $Ph_2P$ unit in **5** is substituted by an SMe group. The $C_4H_2S$ ring is tilted with respect to the $Os_3$ plane [dihedral angle between the $Os_3$ and $C_4H_2S$ planes 129.2(3) and 128.5(5)° for A and B, respectively] as has previously been noticed for the triruthenium analogue $[(\mu\text{-}H)Ru_3(CO)_9\{\mu_3\text{-}Ph_2P(C_4H_2S)\}]$[20] and $[Os_3(\mu\text{-}H)(MeSC_4H_2S)(CO)_9]$.[42] This tilt of the thienyl ring, which has been found also for the *ortho*-metallated phenyl ring in $[Os_3(\mu\text{-}H)(CO)_9\{\mu_3\text{-}PMePh(C_6H_4)\}]$,[41] takes place in order

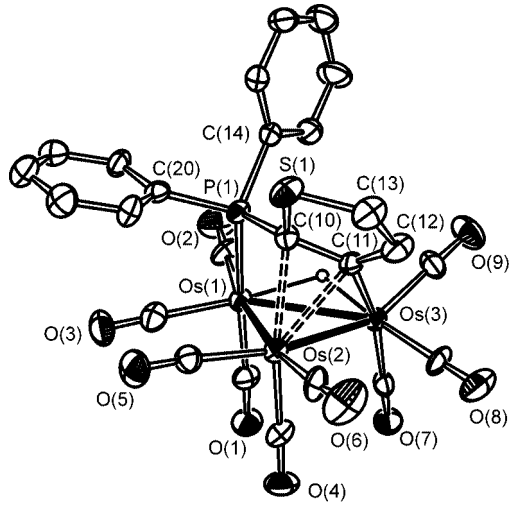


Figure 4. Molecular structure of one of the two crystallographically independent molecules of $[(\mu\text{-}H)Os_3(CO)_9\{\mu_3\text{-}Ph_2P(C_4H_2S)\}]$ (**5**) (thermal ellipsoids at 30% probability). The carbon atoms of the carbonyl ligands bear the same numbering as the oxygen atoms. All hydrogen atoms except the hydrido ligand have been omitted for clarity.

 © 2006 Wiley-VCH Verlag GmbH & Co. KGaA, Weinheim 

Table 3. Selected bond lengths [Å] and angles [°] for [(μ-H)$Os_3$(CO)$_9${$\mu_3$-$Ph_2P(C_4H_2S)$}] (**5**). The values in brackets refer to molecule B.

| | | | |
|---|---|---|---|
| Os(1A)–Os(2A) | 2.857(1) [2.859(1)] | S(1A)–C(13A) | 1.70(1) [1.72(1)] |
| Os(1A)–Os(3A) | 3.004(1) [3.020(1)] | C(12A)–C(13A) | 1.89(1) [1.89(2)] |
| Os(2A)–Os(3A) | 2.755(1) [2.762(1)] | S(1A)–C(13A) | 1.70(1) [1.72(1)] |
| Os(1A)–H(1A) | 1.84(2) [1.83(2)] | C(12A)–C(13A) | 1.34(2) [1.32(2)] |
| Os(3A)–H(1A) | 1.82(2) [1.83(2)] | Os(1A)–C(3A) | 1.90(2) [1.90(1)] |
| Os(1A)–P(1A) | 2.350(3) [2.344(3)] | Os(2A)–C(4A) | 1.88(1) [1.85(1)] |
| Os(2A)–C(11A) | 2.35(1) [2.32(1)] | Os(2A)–C(4A) | 1.88(1) [1.85(1)] |
| Os(3A)–C(11A) | 2.35(1) [2.32(1)] | Os(2A)–C(4A) | 1.88(1) [1.85(1)] |
| P(1A)–C(10A) | 2.10(1) [2.09(1)] | Os(2A)–C(6A) | 1.88(1) [1.90(2)] |
| P(1A)–C(14A) | 1.77(1) [1.78(1)] | Os(3A)–C(7A) | 1.93(1) [1.93(1)] |
| P(1A)–C(20A) | 1.832(7) [1.831(6)] | Os(3A)–C(8A) | 1.89(1) [1.88(1)] |
| C(10A)–C(11A) | 1.801(6) [1.827(7)] | Os(3A)–C(9A) | 1.89(1) [1.88(1)] |
| Os(1A)–C(1A) | 1.45(1) [1.43(1)] | C(10A)–S(1A) | 1.77(1) [1.78(1)] |
| Os(1A)–C(2A) | 1.93(1) [1.93(1)] | C(11A)–C(12A) | 1.46(2) [1.45(2)] |
| C(2A)–Os(1A)–C(3A) | 95.6(6) [95.7(7)] | C(5A)–Os(2A)–Os(3A) | 160.4(4) [160.9(4)] |
| P(1A)–Os(1A)–C(1A) | 170.3(4) [168.5(5)] | C(6A)–Os(2A)–Os(1A) | 170.1(4) [169.4(4)] |
| P(1A)–Os(1A)–Os(2A) | 73.90(7) [74.53(8)] | C(6A)–Os(2A)–Os(3A) | 105.4(4) [105.0(4)] |
| P(1A)–Os(1A)–Os(3A) | 86.17(7) [86.03(7)] | C(11A)–Os(2A)–Os(3A) | 47.7(3) [47.5(3)] |
| C(2A)–Os(1A)–Os(2A) | 167.7(4) [168.5(4)] | C(7A)–Os(3A)–C(11A) | 165.6(5) [166.0(5)] |
| C(2A)–Os(1A)–Os(3A) | 119.1(5) [116.4(4)] | C(8A)–Os(3A)–C(9A) | 95.5(7) [94.0(6)] |
| C(3A)–Os(1A)–Os(2A) | 90.0(4) [92.5(5)] | C(8A)–Os(3A)–Os(2A) | 92.7(5) [95.5(5)] |
| C(3A)–Os(1A)–Os(3A) | 145.4(4) [147.9(5)] | C(8A)–Os(3A)–Os(1A) | 150.3(5) [152.3(5)] |
| C(5A)–Os(2A)–C(6A) | 94.1(5) [93.9(6)] | C(9A)–Os(3A)–Os(2A) | 155.3(4) [151.4(4)] |
| C(5A)–Os(2A)–Os(1A) | 95.8(4) [96.0(4)] | C(9A)–Os(3A)–Os(1A) | 114.1(5) [113.5(4)] |

to favour the $\eta^2$-interaction. The hydrido ligand which, as expected, is bridging the longest edge of the cluster, was located directly in the electron-density map. In both molecules, the hydrido ligand is on the same side of the $Os_3$ plane as the $\mu_3$-$Ph_2P(C_4H_2S)$ ligand [ca. 0.4 Å above the metal plane]. The Os–P bond lengths [Os(3)–P(1) 2.350(3) and 2.344(3) Å in A and B, respectively] are similar to those found in the cyclometallated compounds [$Os_3$(μ-H)(CO)$_9$-{μ-$Ph_2P$(CH=CH)}][34] [2.361(4) Å] and [$Os_3$(μ-H)(CO)$_9$-{$\mu_3$-PMePh($C_6H_4$)}][41] [2.342(6) Å].

The second product, which was isolated in 34% yield, was identified as [(μ-H)$Os_3$(CO)$_8${$\mu_3$-$Ph_2P(C_4H_2S)$}{$Ph_2P$-($C_4H_3S$)}] (**6**). The IR spectrum of **6** is similar to that of [(μ-H)$Ru_3$(CO)$_8${$\mu_3$-$Ph_2P(C_8H_4S)$}{$Ph_2P(C_8H_5S)$}][40] and mass spectrometric and microanalytical data are consistent with the proposed formula. The variable-temperature $^1$H and $^{31}$P{$^1$H} NMR spectra of **6** demonstrate that this complex is highly fluxional. The $^{31}$P{$^1$H} NMR spectrum of **6** at 20 °C shows two doublets at $\delta$ = –0.63 and –1.48 ($J_{P-P}$ = 16.6 Hz) ppm (Figure 5). This is supported by the bridging hydrido signal ($\delta$ = –17.4 ppm), appearing as a doublet of doublets due to the coupling to two non-equivalent phosphorus ligands. At –100 °C, the spectrum freezes out to show two distinct isomers in both the $^{31}$P{$^1$H} and $^1$H NMR spectra, although the $^1$H spectrum had to be acquired at 600 MHz before the shift differences could be clearly discerned (Figure 5). The limiting $^{31}$P{$^1$H} spectrum (–100 °C) shows two pairs of doublets centred at $\delta \approx$ 1.2 ppm, while the signal in the hydrido region of the $^1$H spectrum is shifted upfield and split into two doublets of doublets. It is possible that the two isomers that are observed in solution are related by the relative location of the terminal phosphane ligand with respect to the hydrido ligand. This is supported by the observed differences in the phosphane–hydrido couplings. We believe that this may be explained in terms of an oscillation of the thienyl group identical to that observed for **5** (vide supra) except that, unlike **5**, the isomers of **6** (Figure 6) are observable by NMR due to the presence of the terminally coordinated phosphane ligand, which renders the two hydrido positions non-equivalent.

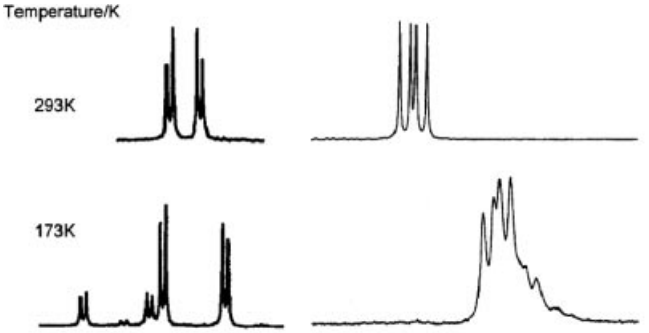


Figure 5. $^{31}$P{$^1$H} and $^1$H NMR spectra of [(μ-H)$Os_3$(CO)$_8${$\mu_3$-$Ph_2P(C_4H_2S)$}{$Ph_2P(C_4H_3S)$}] (**6**) at 293 K and 173 K. The low-temperature $^1$H NMR spectrum ($CD_2Cl_2$, 600 MHz) shows the very small shift differences between the two isomers.

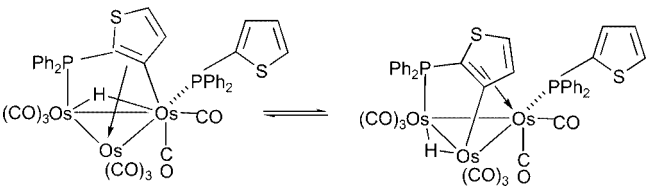


Figure 6. Proposed structures of the two isomers of **6**.

The assignment of the room-temperature structure could be confirmed by the acquisition of a $^{187}$Os NMR spectrum by inverse methods.[38] The presence of a P–P coupling

 © 2006 Wiley-VCH Verlag GmbH & Co. KGaA, Weinheim 

makes it potentially more difficult to extract the $^1J_{Os-P}$ values directly from a $^{31}P\{^1H\}$ spectrum. The $^1H$-$^{187}Os$ 2D HMQC spectrum at –100 °C (Figure 7) shows two shifts ($\delta$ = –13965 and –13230 ppm), corresponding to two osmium centres directly bonded to the bridging hydrido ligands, and it is possible to extract the two $^1J_{Os-P}$ couplings of 147 Hz and 211 Hz from the HMQC spectrum. The first coupling constant corresponds to that observed for **5** (147 Hz) and the coupling constant of 211 Hz is similar to other known $^1J_{Os-P}$ values for terminal phosphane ligands.[39] The fact that the $^1J_{Os-P}$ values for the axial phosphane ligands in **5** and **6** are identical is surprising (and may be coincidental), but it is indicative of the low level of electronic communication between the metal centres in the clusters.

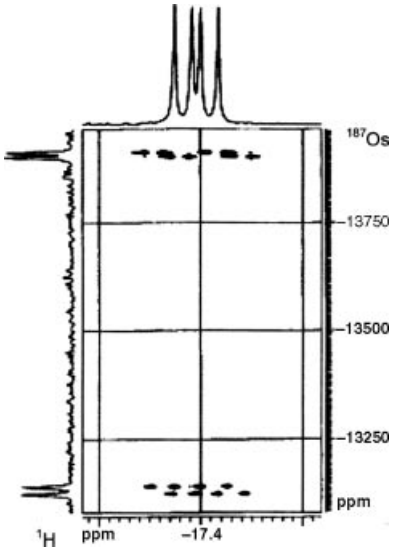


Figure 7. 2D $^1H$-$^{187}Os$ HMQC spectrum of **6** which clearly demonstrates the two different $^{187}Os$-$^{31}P$ couplings for each of the hydrido-bridged osmium centres (cf. Figure 5).

It was possible to grow crystals suitable for X-ray diffraction for cluster **6**, and a single-crystal diffraction study was undertaken in order to confirm its structure and investigate whether isomers could be detected also in the solid state. The structure of $[Os_3(\mu\text{-}H)(CO)_8\{\mu_3\text{-}Ph_2P(C_4H_2S)\}\{Ph_2P(C_4H_3S)\}]$ (**6**) is shown in Figure 8; selected bond lengths and angles are listed in Table 4.

As expected, the structure is similar to that of $[(\mu\text{-}H)Ru_3(CO)_8\{\mu_3\text{-}Ph_2P(C_4H_2S)\}\{Ph_2P(C_4H_3S)\}]$[20] and of $[(\mu\text{-}H)Ru_3(CO)_8\{\mu_3\text{-}Ph_2P(C_8H_4S)\}\{Ph_2P(C_8H_5S)\}]$.[40] It is also closely related to $[Ru_3(\mu\text{-}H)(CO)_8\{\mu_3\text{-}Ph_2P(CH{=}CH)\}\{Ph_2P(CH{=}CH_2)\}]$[43] and differs from **5** only in the substitution of one carbonyl ligand by one terminal thienylphosphane ligand. The cluster consists of a scalene triangle of Os atoms [Os(1)–Os(2) 3.014, Os(1)–Os(3) 2.863 Å, Os(2)–Os(3) 2.780(1) Å] bound to eight terminal carbonyl ligands, a terminal $Ph_2PC_4H_3S$ ligand, a $\mu_3$-$Ph_2PC_4H_2S$ and a $\mu_2$-bridging hydrido ligand. The $\mu_3$-$Ph_2PC_4H_2S$ ligand behaves as a five-electron donor and interacts with all three metal atoms in the same fashion as observed in **5**. The σ- and $\eta^2$-interactions of the *ortho*-metallated thienyl ring [Os(2)–C(22) 2.10(1), Os(3)–C(21) 2.32(1) and Os(3)–C(22) 2.33(1) Å] are very similar to those found in **5** and unaffected by the presence of the terminal phosphane ligand. The C(21)–C(22) distance [1.45(1) Å] in the bridging thienyl ring is identical to the equivalent interaction in **5** and similar to the analogous bonds in $[(\mu\text{-}H)Ru_3(CO)_8\{\mu_3\text{-}Ph_2P(C_4H_2S)\}\{Ph_2P(C_4H_3S)\}]$[20] [1.425(5) Å]. The terminal diphenyl(2-thienyl)phosphane ligand is coordinated in an equatorial position, but the phosphorus atom is displaced out of the metal plane [P(2) +1.034(2) Å] on the same side of the $\mu_3$-$Ph_2PC_4H_2S$ ligand. The two Os–P interactions [Os(1)–P(1)

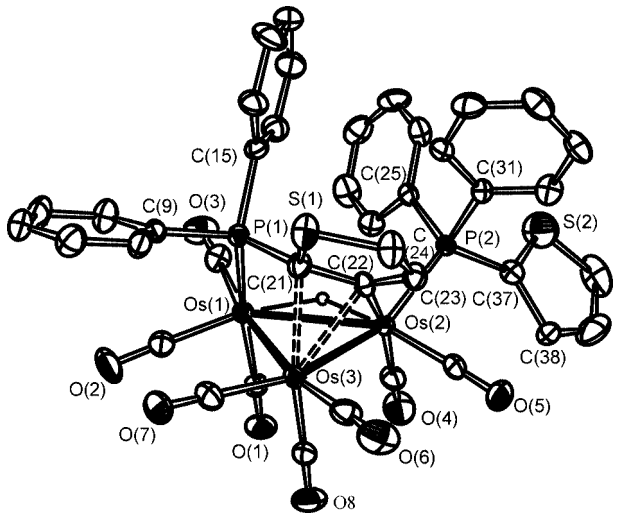


Figure 8. Molecular structure of $[(\mu\text{-}H)Os_3(CO)_8\{\mu_3\text{-}Ph_2P(C_4H_2S)\}\{Ph_2P(C_4H_3S)\}]$ (**6**) (thermal ellipsoids at 30% probability). The carbon atoms of the carbonyl ligands bear the same numbering as the oxygen atoms. All hydrogen atoms except the hydrido ligand have been omitted for clarity.

Table 4. Selected bond lengths [Å] and angles [°] for $[(\mu\text{-}H)Os_3(CO)_8\{\mu_3\text{-}Ph_2P(C_4H_2S)\}\{Ph_2P(C_4H_3S)\}]$ (**6**).

| | | | |
|---|---|---|---|
| Os(1)–Os(2) | 3.0142(6) | P(2)–C(37) | 1.805(9) |
| Os(1)–Os(3) | 2.8626(7) | C(21)–C(22) | 1.45(1) |
| Os(2)–Os(3) | 2.7799(8) | C(21)–S(1) | 1.77(1) |
| Os(1)–H(1) | 1.84(3) | C(23)–C(24) | 1.35(1) |
| Os(2)–H(1) | 1.85(3) | Os(1)–C(1) | 1.93(1) |
| Os(1)–P(1) | 2.360(2) | Os(1)–C(2) | 1.86(1) |
| Os(2)–P(2) | 2.325(3) | Os(1)–C(3) | 1.93(1) |
| Os(2)–C(22) | 2.10(1) | Os(2)–C(4) | 1.92(1) |
| Os(3)–C(21) | 2.32(1) | Os(2)–C(5) | 1.83(1) |
| Os(3)–C(22) | 2.33(1) | Os(3)–C(6) | 1.90(1) |
| P(1)–C(9) | 1.835(5) | Os(3)–C(7) | 1.91(1) |
| P(1)–C(15) | 1.839(6) | Os(3)–C(8) | 1.86(1) |
| P(1)–C(21) | 1.793(9) | C(22)–C(23) | 1.46(1) |
| P(2)–C(25) | 1.833(5) | S(1)–C(24) | 1.69(1) |
| P(2)–C(31) | 1.811(5) | | |
| C(2)–Os(1)–C(3) | 96.4(5) | P(2)–Os(2)–C(22) | 99.9(3) |
| P(1)–Os(1)–C(2) | 92.3(3) | P(2)–Os(2)–Os(1) | 115.53(6) |
| P(1)–Os(1)–C(3) | 98.2(3) | P(2)–Os(2)–Os(3) | 153.52(6) |
| P(1)–Os(1)–Os(2) | 87.37(6) | C(5)–Os(2)–Os(1) | 151.0(3) |
| P(1)–Os(1)–Os(3) | 72.88(6) | C(5)–Os(2)–Os(3) | 93.9(3) |
| C(2)–Os(1)–Os(2) | 145.1(4) | C(6)–Os(3)–C(7) | 93.6(6) |
| C(2)–Os(1)–Os(3) | 90.2(4) | C(7)–Os(3)–C(8) | 99.3(5) |
| C(3)–Os(1)–Os(2) | 118.2(3) | C(6)–Os(3)–Os(1) | 169.2(3) |
| C(3)–Os(1)–Os(3) | 169.1(3) | C(6)–Os(3)–Os(2) | 105.6(4) |
| P(2)–Os(2)–C(4) | 93.2(4) | C(7)–Os(3)–Os(1) | 95.9(4) |
| P(2)–Os(2)–C(5) | 93.3(4) | C(7)–Os(3)–Os(2) | 160.2(4) |

 © 2006 Wiley-VCH Verlag GmbH & Co. KGaA, Weinheim 

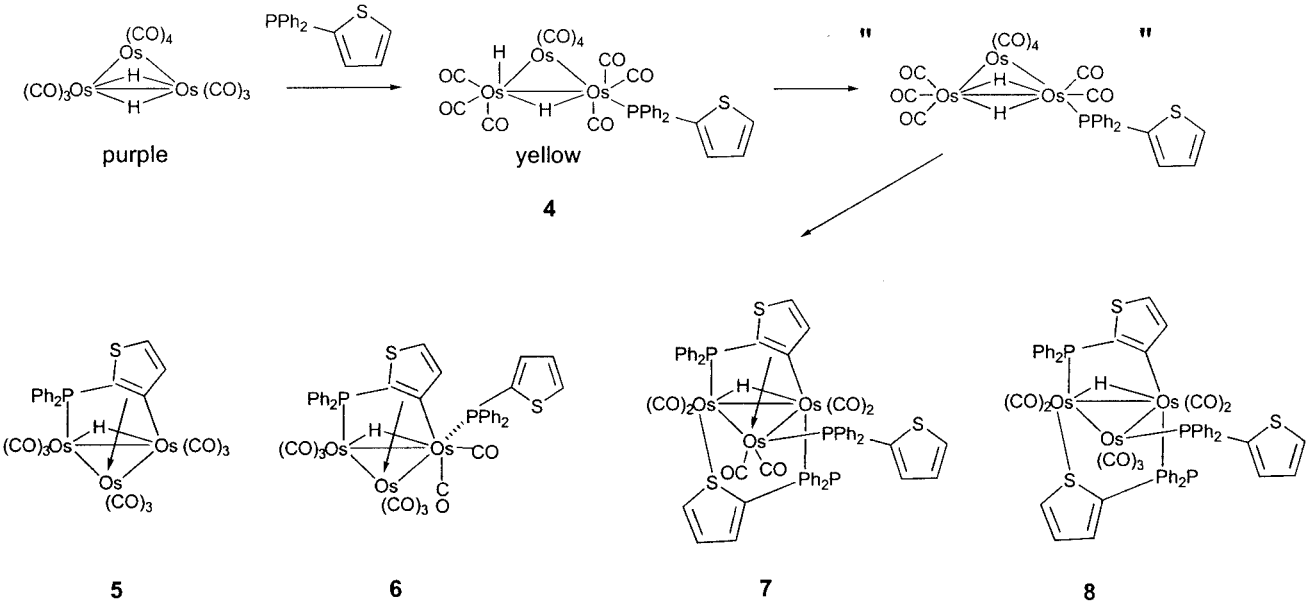


Scheme 3. Possible reaction scheme for the reaction between $[H_2Os_3(CO)_{10}]$ and $Ph_2P(C_4H_3S)$ in toluene.

2.360(2) and Os(2)–P(2) 2.325(3) Å] are not equivalent; the Os–P(axial) distance is longer than the Os–P(equatorial) but very similar to the corresponding distance in **5**. The bridging hydrido ligand has been directly located along the Os(1)–Os(2) edge which is, as usual, the longest Os–Os interaction.

The third product, compound **7**, was isolated in 5% yield. The mass spectrometric analysis suggests the stoichiometric formula $[Os_3(CO)_6\{Ph_2P(C_4H_3S)\}_3]$ for this product, and microanalytical data are consistent with the proposed formula. The $^1H$ NMR spectrum displays a signal in the (bridging) hydrido region ($\delta$ = –16.67 ppm) indicating that an *ortho*-metallation has taken place. The hydrido signal appears as a triplet (overlapping doublet of doublets), indicating coupling to two non-equivalent phosphorus atoms. Three signals are observed in the $^{31}P\{^1H\}$ NMR spectrum, confirming the presence of three non-equivalent phosphorus atoms; a multiplet at $\delta$ = 4.50 ppm, a doublet at $\delta$ = –1.65 ($J_{P-P}$ = 16 Hz) ppm and a multiplet at $\delta$ = –5.98 ppm. On the basis of these data, we propose the molecular formula $[(\mu\text{-H})Os_3(CO)_6\{\mu_3\text{-}Ph_2P(C_4H_2S)\}\{\mu_2\text{-}Ph_2P(C_4H_3S)\}\{Ph_2P(C_4H_3S)\}]$ (cf. Scheme 3) for compound **7**, containing three diphenyl(2-thienyl) ligands coordinated in three different coordination modes; a $\mu_3$-fashion, a $\mu$-(P,S) fashion and a terminal fashion. The $\mu$-(P,S) coordination mode has been detected for a diphenyl(2-benzothienyl)phosphane derivative of $[Os_3(CO)_{12}]$[44] as well as in thienylphosphane derivatives of $[Rh_6(CO)_{16}]$.[45]

The fourth product, compound **8**, was isolated in 3% yield. The mass spectrum of this compound indicates that it has one more carbonyl ligand than compound **7**. The $^1H$ NMR spectrum displays, in addition to signals of aromatic hydrogen atoms, a triplet (overlapping doublet of doublets) at $\delta$ = –17.05 ppm, thus confirming the presence of a single bridging hydrido ligand. In the $^{31}P\{^1H\}$ NMR spectrum, three non-equivalent phosphorus resonances are observed at $\delta$ = –3.19 (m), –5.30 (d) and –9.15 (m) ppm. These data suggest that this complex and compound **7** are structurally similar except for one carbonyl ligand. Therefore, we propose the molecular formula $[(\mu\text{-H})Os_3(CO)_7\{\mu\text{-}Ph_2P(C_4H_2S)\}\{\mu\text{-}Ph_2P(C_4H_3S)\}\{Ph_2P(C_4H_3S)\}]$ for compound **8**, containing the $\mu$-$Ph_2P(C_4H_2S)$ ligand bonded through P and a $\sigma$-interaction to the osmium triangle, but lacking an $\eta^2$-interaction with an osmium atom (cf. Scheme 3).

Several colour changes were observed during the reaction of diphenyl(2-thienyl)phosphane with $[H_2Os_3(CO)_{10}]$, indicating that the reaction proceeds via a number of intermediates. A possible reaction scheme is shown in Scheme 3. Addition of the ligand to the cluster results in an immediate colour change from purple to yellow and formation of $[HOs_3(\mu\text{-H})(CO)_{10}\{Ph_2P(C_4H_3S)\}]$ (**4**) (indicated by IR spectroscopy). Cluster **4** then reacts further, possibly undergoing a loss of one CO ligand and forming an unsaturated intermediate cluster which is likely to be $[H_2Os_3(CO)_9\{Ph_2P(C_4H_3S)\}]$. It has previously been observed, that heating solutions of compounds of the type $[H_2Os_3(CO)_{10}(L)]$ (L = tertiary phosphane), leads to a loss of one carbonyl ligand giving $[H_2Os_3(CO)_9(L)]$.[33,46] $[H_2Os_3(CO)_9\{Ph_2P(C_4H_3S)\}]$ then presumably undergoes further decarbonylation ultimately giving rise to the four products isolated.

## Conclusion

In conclusion, the introduction of diphenyl(2-thienyl)phosphane into the coordination sphere of triosmium clusters by direct thermal substitution of carbonyl ligands or room-temperature reaction with the unsaturated cluster $[H_2Os_3(CO)_{10}]$ is facile. In all cases surveyed in this study, the ligand initially coordinates as a monodentate phos-

 © 2006 Wiley-VCH Verlag GmbH & Co. KGaA, Weinheim 

phane, but further activation/metallation of the ligand is possible at elevated temperatures, although the osmium clusters are considerably less reactive than their ruthenium analogues.[20]

## Experimental Section

**General Remarks:** The clusters $[Os_3(CO)_{12}]$[47] and $[Os_3(\mu\text{-}H)_2(CO)_{10}]$[48–50] and the ligand diphenyl(2-thienyl)phosphane[20] were synthesised by published methods. Solvents were dried by standard methods prior to use. TLC was performed on commercial plates precoated with Merck Kieselgel 60 to 0.5 mm thickness. NMR spectra were acquired with Bruker DRX300 WB, DRX500 and DRX600 spectrometers. Gradient-selected $^{187}$Os 2D HMQC experiments were carried out with a Bruker DMX600 equipped with an XYZ 10A gradient amplifier ($z$-gradient strength 0.05 T m$^{-1}$). Details regarding the experimental setup and acquisition parameters for the $^{187}$Os 2D HMQC experiments are listed in the Supporting Information (see footnote on the first page of this article). IR spectra were acquired with a Nicolet Avatar FT-IR spectrometer and FAB-MS (3-nitrobenzyl alcohol matrix) data with a JEOL SX-102 mass spectrometer.

**Direct Thermal Reaction of $[Os_3(CO)_{12}]$ and Diphenyl(2-thienyl)-phosphane in Toluene:** A solution of $[Os_3(CO)_{12}]$ (300 mg, 0.33 mmol) and diphenyl(2-thienyl)phosphane (98 mg, 0.37 mmol) in toluene (40 mL) was refluxed under nitrogen for 2.5 h. The solvent was removed under reduced pressure. Preparative TLC of the residue, using dichloromethane/*n*-hexane (3:7, v/v) as eluent gave four compounds, in order of decreasing $R_f$: $[Os_3(CO)_{12}]$ (pale yellow, trace), $[Os_3(CO)_{11}\{Ph_2P(C_4H_3S)\}]$ (**1**, intense yellow, 96 mg, 23%), $[Os_3(CO)_{10}\{Ph_2P(C_4H_3S)\}_2]$ (**2**, intense yellow, 203 mg, 44%), $[Os_3(CO)_9\{Ph_2P(C_4H_3S)\}_3]$ (**3**, orange, 42 mg, 8%).

**1:** $C_{27}H_{13}O_{11}Os_3PS$ (1147.12): calcd. C 28.27, H 1.14, P 2.76; found C 28.19, H 1.33, P 2.76. FAB-MS: *m*/*z* = 1148 [M$^+$], [M$^+$ – *n* CO, *n* = 1–11]. IR ($CH_2Cl_2$): $\tilde{\nu}_{co}$ = 2108 s, 2056 s, 2031 sh, 2018 sh, 1988 m, 1958 sh cm$^{-1}$. $^1$H NMR (300 MHz, $CDCl_3$, 30 °C): $\delta$ = 7.9–7.1 (m, 13 H, arom.) ppm. $^{31}$P NMR (300 MHz, $CDCl_3$, 30 °C): $\delta$ = –16.2 (s, 1 P, terminal phosphane) ppm.

**2:** $C_{42}H_{26}O_{10}Os_3P_2S_2$ (1387.42): calcd. C 36.36, H 1.89, P 4.46; found C 36.33, H 1.62, P 4.94. FAB-MS: *m*/*z* = 1388 [M$^+$], [M$^+$ – *n* CO, *n* = 1–10]. IR ($CH_2Cl_2$): $\tilde{\nu}_{co}$ = 2086 w, 2070 s, 2031 s, 1999 s, 1970 w, 1956 w cm$^{-1}$. $^1$H NMR (300 MHz, $CDCl_3$, 20 °C): $\delta$ = 7.82–7.17 (m, 26 H, arom.) ppm. $^{31}$P NMR (300 MHz, $CD_2Cl_2$, –60 °C): $\delta$ = –18.12 (s, 1 P, terminal), –18.26 (s, 2 P, terminal), –21.97 (s, 1 P, terminal) ppm.

**3:** $C_{57}H_{39}O_9Os_3P_3S_3$ (1627.72): calcd. C 42.06, H 2.42, P 5.71: found C 42.48, H 2.85, P 5.23. FAB-MS: *m*/*z* = 1628 [M$^+$], 1600 [M$^+$ – CO]. IR ($CH_2Cl_2$): $\tilde{\nu}_{co}$ = 2068 sh, 2034 sh, 2013 w, 1998 m, 1975 m, 1945 w cm$^{-1}$. $^1$H NMR (500 MHz, $CDCl_3$, 25 °C): $\delta$ = 7.6–7.12 (m, 39 H, arom.) ppm. $^{31}$P NMR (500 MHz, $CDCl_3$, 25 °C): $\delta$ = –17.2 (s, 3 P, terminal) ppm.

**Room-Temperature Reaction of $[H_2Os_3(CO)_{10}]$ with Diphenyl(2-thienyl)phosphane in $CH_2Cl_2$:** Diphenyl(2-thienyl)phosphane (2 equiv., 95 mg, 0.36 mmol) was added to $[H_2Os_3(CO)_{10}]$ (1 equiv., 150 mg, 0.18 mmol) in freshly distilled dichloromethane (30 mL) at room temperature under nitrogen. Within 5 min, the solution turned from purple to yellow and the IR spectrum indicated that no starting material had remained unreacted. The solution was concentrated and absorbed onto TLC plates using dichloromethane/*n*-hexane (3:7, v/v) as eluent. Two bands were recovered, in order of decreasing $R_f$: $[HOs_3(\mu\text{-}H)(CO)_{10}\{Ph_2P(C_4H_3S)\}]$ (**4**, 34 mg, 26%, yellow), uncharacterised product (5 mg, 4%, red).

**4:** $C_{26}H_{15}O_{10}Os_3PS$ (1121.12): calcd. C 27.85, H 1.35, P 2.76; found C 28.86, H 1.38, P 2.72. FAB-MS: *m*/*z* = 1120 [M$^+$], [M$^+$ – *n* CO, *n* = 1–10]. IR ($CH_2Cl_2$): $\tilde{\nu}_{co}$ = 2106 s, 2090 m, 2086 m, 2068 s, 2052 s, 2025 s, 1984 m, 1972 m, 1933 sh cm$^{-1}$. $^1$H NMR (300 MHz, $CDCl_3$, 20 °C): $\delta$ = 7.79–7.27 (m, 13 H, arom.), –10 to –20 (br. s, 2 H, hydrido) ppm. $^1$H NMR (300 MHz, $CDCl_3$, –45 °C): $\delta$ = 7.8–7.3 (m, 13 H, arom.), –10.12 (d, $J_{H,H}$ = 3.3 Hz, 1 H, terminal hydrido), –19.72 (dd, $J_{H,H}$ = 3.3 Hz, $J_{P,H}$ = 11 Hz, 1 H, bridging hydrido) ppm. $^{31}$P NMR (300 MHz, $CDCl_3$, –45 °C): $\delta$ = –16.7 (s, 1 P, terminal phosphane) ppm.

**Thermal Reaction of $[H_2Os_3(CO)_{10}]$ with Diphenyl(2-thienyl)phosphane in Toluene:** A solution of $[H_2Os_3(CO)_{10}]$ (150 mg, 0.18 mmol) and ($Ph_2PC_4H_3S$) (95 mg, 0.36 mmol) in toluene (30 mL) was refluxed under nitrogen for 3 h. During the reaction the colour changed from purple to yellow, to green, and finally to brown. The products were separated by TLC using dichloromethane/*n*-hexane (2:3, v/v) as eluent. Five bands were recovered, in order of decreasing $R_f$: $[H_2Os_3(CO)_{10}]$ (purple, trace), $[(\mu\text{-}H)Os_3(CO)_9\{\mu_3\text{-}Ph_2P(C_4H_2S)\}]$ (**5**, intense yellow, 99 mg, 21%), $[(\mu\text{-}H)Os_3(CO)_8\{\mu_3\text{-}Ph_2P(C_4H_2S)\}\{Ph_2P(C_4H_3S)\}]$ (**6**, intense yellow, 197 mg, 34%), $[(\mu\text{-}H)Os_3(CO)_6\{\mu_3\text{-}Ph_2P(C_4H_2S)\}\{\mu\text{-}Ph_2P(C_4H_3S)\}\{Ph_2P(C_4H_3S)\}]$ (**7**, yellow, 32 mg, 5%), $[(\mu\text{-}H)Os_3(CO)_7\{\mu\text{-}Ph_2P(C_4H_2S)\}\{\mu\text{-}Ph_2P(C_4H_3S)\}\{Ph_2P(C_4H_3S)\}]$ (**8**, intense yellow, 22 mg, 3%).

**5:** $C_{25}H_{13}O_9Os_3PS$ (1091.1). FAB-MS: *m*/*z* = 1092 [M$^+$], [M$^+$ – *n* CO, *n* = 1–9]. IR ($CH_2Cl_2$): $\tilde{\nu}_{co}$ = 2088 s, 2060 s, 2034 s, 2019 s, 1989 s, 1974 w, 1965 m cm$^{-1}$. $^1$H NMR (300 MHz, $CDCl_3$, 20 °C): $\delta$ = 7.93–7.07 (m, 12 H, arom.), –18.0 (d, $J_{H,P}$ = 13.2 Hz, 1 H, bridging hydrido) ppm. $^{31}$P NMR (300 MHz, $CDCl_3$, 20 °C): $\delta$ = –3.27 (s, $J_{Os,P}$ = 147 Hz, 1 P, axial phosphorus) ppm.

**6:** $C_{40}H_{26}O_8Os_3P_2S_2$ (1331.4): calcd. C 36.09, H 1.97, P 4.65; found C 36.09, H 1.97, P 4.56. FAB-MS: *m*/*z* = 1332 [M$^+$], [M$^+$ – *n* CO, *n* = 1–8]. IR ($CH_2Cl_2$): $\tilde{\nu}_{co}$ = 2074 s, 2032 s, 2015 s, 1993 sh, 1981 m, 1967 m, 1957 m, 1945 sh cm$^{-1}$. $^1$H NMR (300 MHz, $CDCl_3$, 20 °C): $\delta$ = 7.86–6.35 (m, 25 H, arom.), –17.4 (dd, $J_{H,P}$ = 15.4 Hz, $J_{H,P}$ = 11 Hz, 1 H, bridging hydrido) ppm. $^{31}$P NMR (300 MHz, $CD_2Cl_2$, 27 °C): $\delta$ = –0.70 (d, $J_{P,P}$ = 16.7 Hz, 1 P), –1.22 (d, $J_{P,P}$ = 16.7 Hz, 1 P) ppm. $^{31}$P NMR (300 MHz, $CD_2Cl_2$, –90 °C): $\delta$ = 1.27 (d, $J_{P,P}$ = 16.8 Hz, 1 P), –0.36 (d, $J_{P,P}$ = 16.8 Hz, 1 P), –0.69 (d, $J_{P,P}$ = 16.5 Hz, 1 P), –2.13 (d, $J_{P,P}$ = 16.4 Hz, 1 P) ppm. $^1$H-$^{187}$Os 2D HMQC NMR (600 MHz, $CD_2Cl_2$, –100 °C): $\delta$ = –13965 ($^1J_{Os,P}$ = 147 Hz), –13230 ($^1J_{Os,P}$ = 211 Hz) ppm.

**7:** $C_{54}H_{39}O_6Os_3P_3S_3$ (1543.69). FAB-MS: *m*/*z* = 1544 [M$^+$], 1516 [M$^+$ – CO], 1488 [M$^+$ – 2 CO], 1460 [M$^+$ – 3 CO]. IR ($CH_2Cl_2$): $\tilde{\nu}_{co}$ = 2068 w, 2058 w, 2025 sh, 2015 m, 1985 s, 1961 sh, 1929 sh cm$^{-1}$. $^1$H NMR (300 MHz, $CDCl_3$, 20 °C): $\delta$ = 7.85–6.65 (m, 38 H, arom.), –16.67 [t, $J_{H,P}$ = 11 Hz, 1 H, bridging hydrido] ppm. $^{31}$P NMR (300 MHz, $CDCl_3$, 20 °C): $\delta$ = 4.50 (m, 1 P), –1.65 (d, $J$ = 16.18 Hz, 1 P), –5.98 (m, 1 P) ppm.

**8:** $C_{55}H_{39}O_7Os_3P_3S_3$ (1571.7). FAB-MS: *m*/*z* = 1572 [M$^+$], 1544 [M$^+$ – CO]. IR ($CH_2Cl_2$): $\tilde{\nu}_{co}$ = 2061 m, 2040 vs, 2002 s, 1988 m, 1968 w, 1944 m cm$^{-1}$. $^1$H NMR (300 MHz, $CDCl_3$, 20 °C): $\delta$ = 7.85–6.20 (m, 38 H, arom.), –17.05 [t (dd), $J_{H,P}$ = 14.7 Hz, $J_{H,P}$ = 13.2 Hz, 1 H, bridging hydrido] ppm. $^1$H NMR (300 MHz, $CD_2Cl_2$, –50 °C, hydrido region): $\delta$ = –17.16 (t, $J$ = 13.5 Hz, 12.9 Hz, 1 H) ppm. $^{31}$P NMR (300 MHz, $CDCl_3$, 20 °C): $\delta$ = –3.19 (m), –5.30 (d, $J$ = 17.1 Hz), –9.15 (m) ppm. $^{31}$P NMR (300 MHz, $CD_2Cl_2$, –35 °C): $\delta$ = –0.58 (d, $J$ = 9.95 Hz, 1 P), –9.5 (2, 1 P), –11.15 (s, 1 P) ppm.

**X-ray Crystallographic Study:** Crystals of **2**, **3**, **5** and **6** were obtained by slow concentration of dichloromethane/*n*-hexane solu-

 © 2006 Wiley-VCH Verlag GmbH & Co. KGaA, Weinheim 

Table 5. Crystal data and experimental details for $[Os_3(CO)_{10}\{Ph_2P(C_4H_3S)\}_2]$ (**2**); $[Os_3(CO)_9\{Ph_2P(C_4H_3S)\}_3]$ (**3**); $[(\mu\text{-H})Os_3(CO)_9\{\mu_3\text{-}Ph_2P(C_4H_2S)\}]$ (**5**); $[(\mu\text{-H})Os_3(CO)_8\{\mu_3\text{-}Ph_2P(C_4H_2S)\}\{Ph_2P(C_4H_3S)\}]$( **6**).

| | **2** | **3** | **5**·0.5$C_6H_{14}$ | **6** |
|---|---|---|---|---|
| Empirical formula | $C_{42}H_{26}O_{10}Os_3P_2S_2$ | $C_{57}H_{42}O_9Os_3P_3S_3$ | $C_{25}H_{13}O_9Os_3PS$·0.5$C_6H_{14}$ | $C_{40}H_{26}O_8Os_3P_2S_2$ |
| Formula mass | 1387.29 | 1630.60 | 1112.53 | 1331.27 |
| $T$ [K] | 293(2) | 293(2) | 293(2) | 293(2) |
| $\lambda$ [Å] | 0.71069 | 0.71069 | 0.71069 | 0.71069 |
| Crystal system | triclinic | triclinic | triclinic | orthorhombic |
| Space group | $P\bar{1}$ (no. 2) | $P\bar{1}$ (no. 2) | $P\bar{1}$ (no. 2) | $P2_12_12_1$ (no. 19) |
| $a$ [Å] | 12.461(2) | 14.067(2) | 13.474(3) | 10.846(4) |
| $b$ [Å] | 12.857(4) | 18.872(5) | 13.669(2) | 14.370(3) |
| $c$ [Å] | 14.180(5) | 25.004(3) | 17.309(5) | 25.455(4) |
| $\alpha$ [°] | 70.69(2) | 70.26(2) | 85.68(2) | 90 |
| $\beta$ [°] | 79.12(2) | 75.08(2) | 77.86(2) | 90 |
| $\gamma$ [°] | 88.55(2) | 86.97(2) | 74.05(1) | 90 |
| $V$ [Å$^3$] | 2103.8(9) | 6033(2) | 2996(1) | 3967(2) |
| $Z$ | 2 | 4 | 4 | 4 |
| $D_{calcd.}$ [Mg·m$^{-3}$] | 2.190 | 1.795 | 2.466 | 2.229 |
| $\mu$(Mo-$K_\alpha$) [mm$^{-1}$] | 9.270 | 6.537 | 12.863 | 9.822 |
| $F$(000) | 1296 | 3108 | 2026 | 2480 |
| Crystal size [mm] | 0.35 × 0.24 × 0.20 | 0.25 × 0.11 × 0.08 | 0.27 × 0.25 × 0.20 | 0.30 × 0.25 × 0.22 |
| $\theta$ limits [°] | 2–27 | 2–25 | 2–27 | 2–27 |
| Reflections collected | 9104 ( ± $h$, ±$k$, +$l$) | 21091 (±$h$, ±$k$, +$l$) | 13008 (±$h$, ±$k$, +$l$) | 4801(+$h$, +$k$, +$l$) |
| Unique observed reflections [$I > 2\sigma(I)$] | 6941 | 8123 | 8000 | 4062 |
| Goodness of fit ($F^2$) | 1.033 | 0.933 | 0.989 | 1.063 |
| $R_1$ ($F$)[a], $wR_2$ ($F^2$)[b] [$I > 2\sigma(I)$] | 0.0268, 0.0683 | 0.0766, 0.1544 | 0.0441, 0.1081 | 0.0249, 0.0601 |
| Absolute structure parameter | – | – | – | –0.02(1) |
| Largest diff. peak/hole [e·Å$^{-3}$] | 1.340/–0.989 | 2.055/–2.330 | 2.204/–2.184 | 0.925/–0.963 |

[a] $R_1 = \Sigma||F_o| - |F_c||/\Sigma|F_o|$. [b] $wR_2 = [\Sigma w(F_o^2 - F_c^2)^2/\Sigma w(F_o^2)^2]^{1/2}$, $w = 1/[\sigma^2(F_o^2) + (aP)^2 + bP]$, $P = (F_o^2 + 2F_c^2)/3$.

tions at 4 °C. Crystal data and other experimental details for all structures are reported in Table 5. The diffraction experiments were carried out with an Enraf–Nonius CAD4 diffractometer at room temperature, using graphite-monochromatized Mo-$K_\alpha$ radiation ($\lambda$ = 0.71073 Å). The unit cells were determined by a least-squares fitting procedure using 25 randomly selected strong reflections. The diffracted intensities were corrected for Lorentz and polarisation effects. An empirical absorption correction was applied using the azimuthal scan method.[51] The positions of the metal atoms were determined by direct methods (SIR-97[52]) and all non-hydrogen atoms were located from Fourier difference syntheses. In compounds **5** and **6**, the bridging hydrido ligands were also located in the Fourier map. The phenyl and thienyl H atoms were added in calculated positions ($d_{C-H}$ 0.93 Å). The final refinement on $F^2$ proceeded by full-matrix least-squares calculations (SHELXL97[53]) using anisotropic thermal parameters for all non-hydrogen atoms in **2**, **5** and **6**, whereas in **3** only the Os, P and S atoms were treated anisotropically. The asymmetric units of **3** and **5** contain two independent molecules, and the latter contains also one-half of a disordered *n*-hexane solvent molecule, which is related to the other half by an inversion centre. The 2-thienyl rings [bound to P(4) and P(5), respectively] of one of the molecules present in the asymmetric unit of **3** showed disorder due to a 180° rotation around the P–C axis, and therefore the sulfur and α-carbon atoms of the rings were refined for the two orientations. The refined occupancy factors of S(4) and S(5) in the second conformer of the molecule (Figure S3, Supporting Information) were 52 and 66%, respectively. The phenyl and thienyl H atoms were assigned isotropic thermal parameters 1.2 times $U_{eq}$ of the carrier carbon atoms. The relatively low quality of the diffraction data for compound **3** was due to the fact that good quality crystals could not be obtained despite repeated crystallisations by different techniques. CCDC-203202 (**2**), -203203 (**3**), -203204 (**5**) and -203205 (**6**) contain the supplementary crystallographic data for this paper. These data can be obtained free of charge from The Cambridge Crystallographic Data Centre via www.ccdc.cam.ac.uk/data_request/cif.

## Acknowledgments

This research was supported by grants to E. N. from the Swedish Research Council (VR) and the European Union (TMR network Metal Clusters in Catalysis and Organic Synthesis, MECATSYN). We would like to thank Dr. Jason D. King for his helpful comments on the variable-temperature NMR spectra, and Prof. Silvio Aime and Dr. Karl-Erik Bergquist for the use of NMR spectrometers. M. M. and S. S. thank the University of Bologna and MIUR (Cofin2003) for financial support.

[1] H. Topsøe, B. S. Claussen, F. E. Massoth, "Hydrotreating Catalysis", in: *Catalysis*: *Science and Technology* (Eds.: J. R. Anderson, M. Boudart), Springer-Verlag, New York, **1996**, vol. 11.
[2] D. G. Churchill, B. M. Bridgewater, G. Parkin, *J. Am. Chem. Soc.* **2000**, *122*, 178.
[3] C. Bianchini, A. Meli, *Acc. Chem. Res.* **1998**, *31*, 109.
[4] R. J. Angelici, *Acc. Chem. Res.* **1988**, *21*, 387.
[5] N. N. Sauer, R. J. Angelici, *J. Catal.* **1989**, *116*, 11.
[6] R. J. Angelici, *Polyhedron* **1997**, *16*, 3073.
[7] M. Brorson, J. D. King, K. Kiriakidou, F. Prestopino, E. Nordlander, *Metal Clusters in Chemistry* (Eds.: P. Braunstein, L. A. Oro, P. R. Raithby), Wiley-VCH, Weinheim, **1999**, vol. 2, chapter 2.6, pp. 741–781.
[8] H. D. Kaesz, R. B. King, T. A. Manuel, L. D. Nichols, F. G. A. Stone, *J. Am. Chem. Soc.* **1960**, *82*, 4749.
[9] R. B. King, P. M. Treichel, F. G. A. Stone, *J. Am. Chem. Soc.* **1961**, *83*, 3600; R. B. King, F. G. A. Stone, *J. Am. Chem. Soc.* **1961**, *82*, 4557.
[10] A. E. Ogilvy, M. Draganjac, T. B. Rauchfuss, S. R. Wilson, *Organometallics* **1988**, *7*, 1171.

 © 2006 Wiley-VCH Verlag GmbH & Co. KGaA, Weinheim 

[11] A. J. Arce, P. Arrojo, A. J. Deeming, Y. De Sanctis, *J. Chem. Soc., Dalton Trans.* **1992**, 2423.
[12] M. A. Reynolds, I. A. Guzei, R. J. Angelici, *Chem. Commun.* **2000**, 513; M. A. Reynolds, I. A. Guzei, R. J. Angelici, *J. Am. Chem. Soc.* **2002**, *124*, 513.
[13] A. J. Arce, J. Manzur, M. Márquez, Y. De Sanctis, A. J. Deeming, *J. Organomet. Chem.* **1991**, *412*, 177.
[14] A. J. Arce, A. J. Deeming, Y. De Sanctis, R. Marchado, J. Manzur, C. Rivas, *J. Chem. Soc., Chem. Commun.* **1990**, 1568.
[15] M. W. Day, K. I. Hardcastle, A. J. Deeming, A. J. Arce, Y. De Sanctis, *Organometallics* **1990**, *9*, 6.
[16] A. J. Arce, P. Arrojo, Y. De Sanctis, M. Márquez, A. J. Deeming, *J. Organomet. Chem.* **1994**, *479*, 159.
[17] A. J. Arce, A. Karam, Y. De Sanctis, M. V. Capparelli, A. J. Deeming, *Inorg. Chim. Acta* **1999**, *285*, 277.
[18] J. D. King, M. Monari, E. Nordlander, *J. Organomet. Chem.* **1999**, *573*, 272.
[19] A. J. Deeming, M. K. Shinhmar, A. J. Arce, Y. De Sanctis, *J. Chem. Soc., Dalton Trans.* **1999**, 1153.
[20] A. J. Deeming, S. N. Jayasuriya, A. J. Arce, Y. De Sanctis, *Organometallics* **1996**, *15*, 786.
[21] M. I. Bruce, B. K. Nicholson, M. L. Williams, *J. Organomet. Chem.* **1983**, *243*, 69.
[22] M. I. Bruce, J. G. Matisons, B. K. Nicholson, *J. Organomet. Chem.* **1983**, *247*, 321.
[23] M. I. Bruce, M. L. Williams, B. K. Nicholson, *J. Organomet. Chem.* **1983**, *258*, 63.
[24] K. Biradha, V. M. Hansen, W. K. Leong, R. K. Pomeroy, M. J. Zaworotko, *J. Cluster Sci.* **2000**, *11*, 285.
[25] R. F. Alex, R. K. Pomeroy, *Organometallics* **1987**, *6*, 2437.
[26] A. J. Deeming, S. Donovan-Mtunzi, S. E. Kabir, P. J. Maning, *J. Chem. Soc., Dalton Trans.* **1985**, 1037.
[27] W. K. Leong, Y. Liu, *J. Organomet. Chem.* **1999**, *584*, 174.
[28] M. R. Churchill, B. G. Deboer, *Inorg. Chem.* **1977**, *16*, 878.
[29] M. I. Bruce, M. J. Liddell, C. A. Hughes, J. M. Patrick, B. W. Skelton, A. H. White, *J. Organomet. Chem.* **1988**, *347*, 157.
[30] V. M. Hansen, A. K. Ma, K. Biradha, R. K. Pomeroy, M. J. Zaworotko, *Organometallics* **1998**, *17*, 5267.
[31] M. I. Bruce, M. J. Liddell, C. A. Hughes, J. M. Patrick, B. W. Skelton, A. H. White, *J. Organomet. Chem.* **1988**, *347*, 181.
[32] M. I. Bruce, M. J. Liddell, O. Shawkataly, C. A. Hughes, B. W. Skelton, A. H. White, *J. Organomet. Chem.* **1988**, *347*, 207.
[33] A. J. Deeming, S. Hasso, *J. Organomet. Chem.* **1975**, *88*, C21.
[34] B. F. G. Johnson, J. Lewis, E. Nordlander, P. R. Raithby, *J. Chem. Soc., Dalton Trans.* **1996**, 3825.
[35] S. Aime, R. Gobetto, E. Valls, *Inorg. Chim. Acta* **1998**, *521*, 275–276.
[36] M. A. Gallop, B. F. G. Johnson, J. Lewis, *J. Chem. Soc., Chem. Commun.* **1987**, 1831.
[37] R. Benn, in: *Transition Metal Nuclear Magnetic Resonance* (Ed.: P. S. Pregosin), Elsevier, Amsterdam, **1991**.
[38] A. E. Aliev, A. J. Deeming, M. J. Stchedroff, J. W. Steed, unpublished results.
[39] M. J. Stchedroff, S. Aime, R. Gobetto, L. Salassa, E. Nordlander, *Magn. Reson. Chem.* **2002**, *40*, 107.
[40] J. D King, J. E. Davies, M. H. Johansson, B. F. G. Johnson, E. Nordlander, unpublished results.
[41] A. J. Deeming, S. E. Kabir, N. J. Powell, P. A. Bates, M. B. Hursthouse, *J. Chem. Soc., Dalton Trans.* **1987**, 1529.
[42] A. J. Arce, A. J. Deeming, Y. De Sanctis, D. M. Speel, A. Di Trapani, *J. Organomet. Chem.* **1999**, *580*, 370.
[43] R. Gobetto, E. Sappa, A. Tiripicchio, M. Tiripicchio Camellini, M. J. Mays, *J. Chem. Soc., Dalton Trans.* **1990**, 807.
[44] N. K. Kiriakidou Kazemifar, M. J. Stchedroff, M. A. Mottalib, M. H. Johansson, M. Monari, S. Selva, E. Nordlander, unpublished results.
[45] S. P. Tunik, I. O. Koshevoy, A. J. Poe, D. H. Farrar, E. Nordlander, T. A. Pakkanen, M. Haukka, *Dalton Trans.* **2003**, 2457.
[46] A. J. Deeming, S. Hasso, *J. Organomet. Chem.* **1976**, *114*, 313.
[47] S. R. Drake, P. Loveday, *Inorg. Synth.* **1990**, *28*, 230.
[48] H. D. Kaesz, S. A. R. Knox, J. W. Koepke, R. B. Saillant, *J. Chem. Soc. D* **1971**, 477.
[49] A. J. Deeming, S. Hasso, M. Underhill, *J. Chem. Soc., Dalton Trans.* **1975**, 1614.
[50] B. F. G. Johnson, J. Lewis, P. Kilty, *J. Chem. Soc. A* **1968**, 2859.
[51] A. C. T. North, D. C. Philips, F. S. Mathews, *Acta Crystallogr., Sect. A* **1968**, *24*, 351.
[52] A. Altomare, M. C. Burla, M. Camalli, G. L. Cascarano, C. Giacovazzo, A. Guagliardi, A. G. G. Moliterni, G. Polidori, R. Spagna, *J. Appl. Crystallogr.* **1999**, *32*, 115.
[53] G. M. Sheldrick, *SHELXL-97, Program for crystal structure refinement*, University of Göttingen, Germany, **1997**.

Received: December 22, 2005
Published Online: March 30, 2006

 © 2006 Wiley-VCH Verlag GmbH & Co. KGaA, Weinheim 

DOI: 10.1002/ejic.200501146

# Rational Synthesis and Characterization of Two Three-Dimensional Metal-Organic Frameworks Incorporating Silver Chains and 1,2,3,4,5,6-Cyclohexanehexacarboxylate

**Jing Wang,[a] Sheng Hu,[a] and Ming-Liang Tong*[a]**

**Keywords:** Silver / MOFs / Cyclohexanehexacarboxylate / Water tape / Ag···Ag interactions / Supramolecular chemistry

Two new silver polycarboxylate coordination polymers, $[Ag_3(H_3L)(H_2O)_2]_n \cdot 2nH_2O$ (**1**) and $[Ag_6L(NH_3)(H_2O)_3]_n \cdot nH_2O$ (**2**), have been obtained from the reaction of $[Ag(NH_3)_2](OH)$ (freshly synthesized from $Ag_2O$ and aqueous ammonia) with *cis*,*cis*,*cis*,*cis*,*cis*,*cis*-1,2,3,4,5,6-cyclohexanehexacarboxylic acid ($H_6L$) by control of the molar ratio of starting materials. The X-ray crystal structure analysis reveals that both of them crystallize in the triclinic space group $P\bar{1}$ with $a$ = 6.375(4), $b$ = 9.505(6), $c$ = 15.097(8) Å, $\alpha$ = 93.249(14), $\beta$ = 100.364(15), $\gamma$ = 96.453(15)°, $V$ = 891.4(9) Å$^3$, $Z$ = 2 for **1**, and $a$ = 8.0380(7), $b$ = 10.1220(9), $c$ = 13.8458(12) Å, $\alpha$ = 76.3450(10), $\beta$ = 80.9370(10), $\gamma$ = 68.7230(10)°, $V$ = 1016.83(15) Å$^3$, $Z$ = 2 for **2**. Complex **1** features a three-dimensional (3D) metal-organic framework (MOF) with one-dimensional (1D) rectangular channels surrounded by carboxylato-supported Ag–Ag dimers, Ag–Ag chains, and half deprotonated $[H_3L]^{3-}$ ligands. Each $[H_3L]^{3-}$ ligand connects eight $Ag^I$ atoms. The weakly coordinated water ligands and lattice water molecules are located at the channels and form interesting 1D hydrogen-bonded T4(2)8(2) water tapes with cyclic $R_8^6(16)$ $(H_2O)_8$ and $R_4^4(8)$ $(H_2O)_4$ units. Complex **2** is also a 3D MOF structure constructed by two types of Ag–Ag chains with Ag8 cluster units and linear Ag4 units, respectively, and fully deprotonated $L^{6-}$ ligands. The silver(I) atoms in **2** exhibit linear, T-shaped, Y-shaped, and tetrahedral coordination geometries. Each $L^{6-}$ ligand connects thirteen $Ag^I$ atoms. The intrachain robust argentophilic interactions play a vital role in the formation of the structure.
(© Wiley-VCH Verlag GmbH & Co. KGaA, 69451 Weinheim, Germany, 2006)

## Introduction

The design and synthesis of metal-organic frameworks (MOFs) are of great interest because of their intriguing structural topologies and novel properties for potential applications.[1–3] In the past few decades, the development of supramolecular assembled chemistry has allowed the possibility to rationally design and prepare supramolecular architectures through noncovalent interactions, in which it is crucial to meet both geometric as well as energetic considerations.[4] Recent advances in this field have led to many periodic MOFs formed through the deliberate selection of functionalized organic ligands and coordination geometries of transition-metal ions.[5] A successful strategy in building such networks is to employ appropriate bridging ligands that can bind metal ions in different modes and provide a possible way to achieve more robust MOF structures.[6] Moreover, the recent development of self-assembled supramolecular chemistry has made it possible to rationally design and synthesize MOFs depending on the ligand geometry and coordination propensity of the metal ion, which has been proved by the reports of a large number of silver MOFs.[7]

Silver(I) ion principally exhibits linear, trigonal, and tetrahedral coordination and has high affinity for hard donor atoms such as nitrogen or oxygen atoms and soft donor atoms such as sulfur atoms, being a favorable and fashionable building block for MOFs.[8] Furthermore, silver ion is apt to form short Ag···Ag contacts as well as ligand unsupported interactions, which have been proved to be two of the most important factors contributing to the formation of such complexes and special properties.[9–11] Previous works[12,13] have proved rigid benzene-multicarboxylic acids, such as 1,4-benzenedicarboxylic acid, 1,3,5-benzenetricarboxylic acid, and 1,2,4,5-benzenetetracarboxylic acid, are a good choice for the construction of MOFs owing to their versatile coordination modes. However, although many benzene multicarboxylate-bridged MOFs have been reported, those on a silver(I) ion are relatively rare, probably because of their low solubility, which makes structural analyses difficult.[14–16] Compared with benzene multicarboxylic acid, cyclohexane multicarboxylic acid not only has advantages over the former such as having rich coordination modes, being the hydrogen-bond donors and acceptors as well as possessing potential high symmetries, but also

[a] State Key Laboratory of Optoelectronic Materials and Technologies, Institute of Optoelectronic and Composite Materials & School of Chemistry and Chemical Engineering, Sun Yat-Sen University,
Guangzhou 510275, China
Fax: +86-20-8411-2245
E-mail: tongml@mail.sysu.edu.cn
Supporting information for this article is available on the WWW under http://www.eurjic.org or from the author.

 © 2006 Wiley-VCH Verlag GmbH & Co. KGaA, Weinheim 

has more conformations and flexibility, which remain largely unexplored for constructing 3D MOFs. Cyclohexanedicarboxylates and cyclohexanetricarboxylates are therefore regarded as excellent candidates for the construction of multidimensional MOFs.[17] Although one could anticipate that 1,2,3,4,5,6-cyclohexanehexacarboxylic acid ($H_6L$) will be applied as a more flexible ligand than cyclohexanedicarboxylates and cyclohexanetricarboxylates in the construction of functional MOFs (Scheme 1), its coordination chemistry has not been explored until now. Herein, we report the creation of two interesting silver(I) complexes with robust argentophilic interactions by the self-assembled reaction of *cis*,*cis*,*cis*,*cis*,*cis*-1,2,3,4,5,6-cyclohexanehexacarboxylic acid ($H_6L$) with freshly synthesized $[Ag(NH_3)_2](OH)$, $[Ag_3(H_3L)(H_2O)_2]_n{\cdot}2nH_2O$ (**1**), and $[Ag_6L(NH_3)(H_2O)_3]_n{\cdot}nH_2O$ (**2**). Complex **1** is a 3D MOF with 1D rectangular channels surrounded by carboxylato-supported Ag–Ag dimers, Ag–Ag chains and half deprotonated $\mu_8$-$[H_3L]^{3-}$ bridges, and water molecules in the channels forming interesting hydrogen-bonded water tapes of eight- and four-membered rings; while **2** is a 3D MOF constructed with two types of Ag–Ag chains with Ag8 cluster units and linear Ag4 units, respectively, and fully deprotonated $\mu_{13}$-$L^{6-}$ bridges.

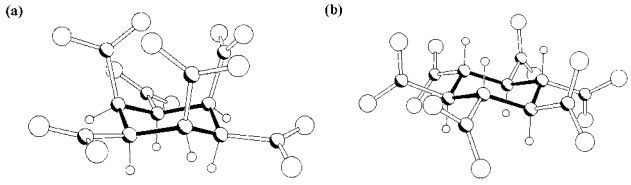


Scheme 1. Schematic presentation of the L ligand in *cis*,*cis*,*cis*,*cis*,*cis* (a) and *trans*,*trans*,*trans*,*trans*,*trans* conformations (b).

## Results and Discussion

### Synthesis and Characterization

As is well known, the reactions of silver(I) ion with multicarboxylates in aqueous solution often result in the formation of insoluble 'silver salts', presumably because of the fast coordination of the carboxylates to silver ion to form polymer structures. Mak and co-workers pioneered the generation of polymeric structures in silver(I)-carboxylate-like complexes by using various zwitterionic betaine ligands.[18] Smith and co-workers[19] obtained a series of Ag–multicarboxylate complexes by using ammoniacal conditions to enhance the solubility of the silver carboxylates. Michaelides and co-workers[14b] reported a novel succinatodisilver(I) complex that was synthesized by gel permeation. Hence, properly tuning the reaction conditions may result in the formation of appropriate crystalline products for X-ray structural analysis. Considering this, we tried reactions of freshly synthesized $[Ag(NH_3)_2](OH)$ and the $H_6L$ ligand in various molar ratios [Equations (1), (2), and (3)].

$$Ag_2O + 4NH_3 + 2H_2O = 2[Ag(NH_3)_2](OH) \quad (1)$$

$$3n[Ag(NH_3)_2](OH) + nH_6L + nH_2O = [Ag_3(H_3L)(H_2O)_2]_n{\cdot}2nH_2O + 6nNH_3 \quad (2)$$

$$6n[Ag(NH_3)_2](OH) + nH_6L = [Ag_6L(NH_3)(H_2O)_3]_n{\cdot}nH_2O + 2nH_2O + 11nNH_3 \quad (3)$$

We first selected the molar ratio of $[Ag(NH_3)_2](OH)/H_6L$ = 3:1, resulting in the formation of complex **1**, which possesses a 3D microporous MOF structure filled with water molecules. As anticipated, only half of the carboxylate groups are deprotonated and the others form intra- or intermolecular hydrogen-bond interactions with the deprotonated ones, which may be attributed to the *cis* conformation of the ligand. The carboxylate groups lie alternately on the axial position and on the equatorial position, which is useful for the formation of intramolecular hydrogen-bonded interactions.

As the self-assembly of the frameworks is greatly influenced by factors such as the solvent system,[3a,20a] the template,[16] the pH value of the solution,[20b,20c] and the steric requirement of the counterion,[21] some changes in the reaction conditions may result in significantly different final reaction products. The successful isolation of **1**, in which not all the carboxylate groups are deprotonated, prompted us to extend our study to change the molar ratio of $[Ag(NH_3)_2](OH)/H_6L$. As expected, when the molar ratio of $[Ag(NH_3)_2](OH)/H_6L$ was increased to 6:1, all the carboxylate groups were deprotonated and then complex **2** was obtained. Furthermore, we attempted to change the silver(I) salts and solvents such as MeOH or EtOH, and raise the pH values in order to prepare different silver MOFs. However, the same product as **2** was obtained, although the yields were somewhat different or precipitates were obtained when treated by other silver(I) salts at higher pH values, suggesting that the proper pH value and molar ratio of the reactants play a vital role in the formation of the products. It should be noted that, in our recently synthesized 3D MOFs $[M_3(trans\text{-}L)(H_2O)_6]_n$ (M = $Co^{2+}$, $Mn^{2+}$, and $Fe^{2+}$; $[trans\text{-}L]^{6-}$ = *trans*,*trans*,*trans*,*trans*,*trans*-1,2,3,4,5,6-cyclohexanehexacarboxylate),[22] the fully deprotonated $L^{6-}$ ligand changed its *cis* conformation to *trans* conformation under hydrothermal conditions, while in **1** and **2**, the half and fully deprotonated L ligands keep their *cis*,*cis*,*cis*,*cis*,*cis* conformation, which may be ascribed to the cooperative effect of the intraligand hydrogen-bonding interaction and the metal coordination.

### Crystal Structure

X-ray crystallography has established that **1** is a 3D MOF structure with 1D rectangular channels along the *a*

 © 2006 Wiley-VCH Verlag GmbH & Co. KGaA, Weinheim 

axis. As illustrated in part (a) of Figure 1, each asymmetric unit in **1** contains three crystallographically unique silver(I) atoms, one $[H_3L]^{3-}$ ligand, two coordinated water molecules, and two lattice water molecules, all of which lie on general positions. The selected bond lengths and angles are listed in Table 1. Noticeably, the three deprotonated carboxylate groups of each $[H_3L]^{3-}$ ligand are located at the equatorial positions and the rest at the axial positions, in agreement with the IR spectrum, where the absorption peak is at around 1720 $cm^{-1}$ for the protonated carboxylic groups. Ag1 is coordinated in a greatly irregular geometry, by three oxygen atoms from three $[H_3L]^{3-}$ ligands [Ag1–O = 2.256(4)–2.584(4) Å, O–Ag1–O = 82.5(2)–162.4(2)°], an aqua ligand [Ag1–O1w = 2.457(5) Å, O–Ag1–O1w = 80.0(2)–116.1(2)°], as well as a Ag···Ag contact [2.916(1) Å]. The Ag1–Ag1*a* distance is significantly shorter than the van der Waals contact distance 3.40 Å,[23a] is comparable to the Ag···Ag separation (2.89 Å) in metallic silver, and twice the covalent radius of silver (1.455 Å for four-coordinate silver),[24] which provides supporting evidence for the significance of argentophilicity.[25] Similar Ag···Ag distances were found in silver benzenesulfonate (2.915 Å)[23b] and in the

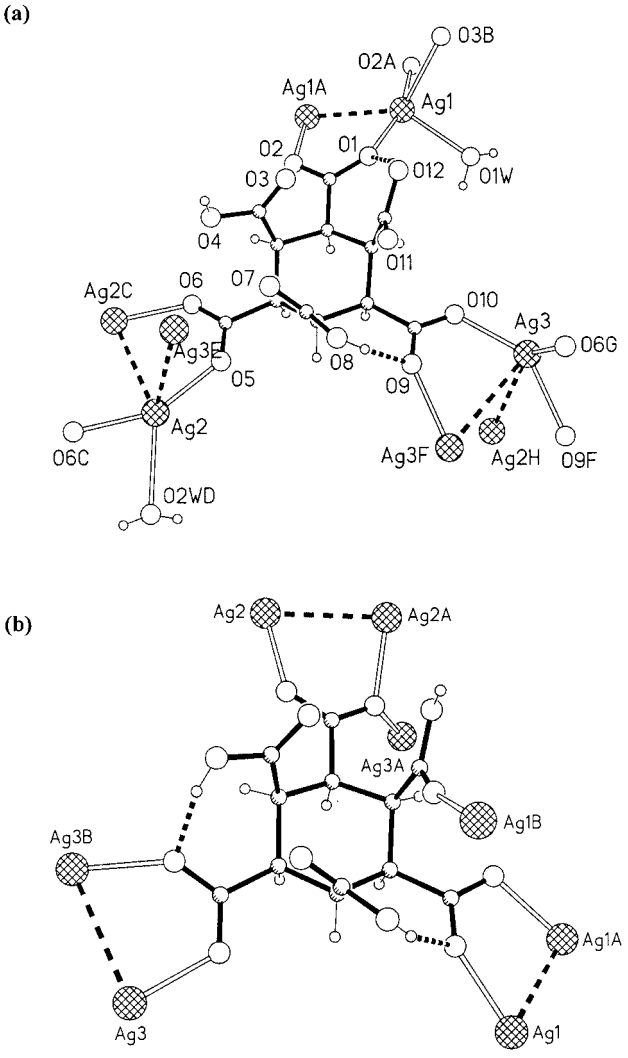


Figure 1. Perspective views showing the coordination environments of silver atoms (a) and the bridging mode of the $[H_3L]^{3-}$ ligand (b) in **1**.

Table 1. Selected bond lengths [Å] and angles [°] for **1** and **2**.[a]

| | | | |
|---|---|---|---|
| Compound **1** | | | |
| Ag(1)–O(2*a*) | 2.256(4) | Ag(3)–O(9*f*) | 2.356(4) |
| Ag(1)–O(1) | 2.267(4) | Ag(3)–O(6*g*) | 2.542(5) |
| Ag(1)–O(1w) | 2.457(5) | Ag(1)···Ag(1*a*) | 2.916(1) |
| Ag(1)–O(3*b*) | 2.584(4) | Ag(2)···Ag(2*c*) | 2.916(1) |
| Ag(2)–O(6*c*) | 2.187(4) | Ag(2)···Ag(3*e*) | 3.162(1) |
| Ag(2)–O(5) | 2.191(4) | Ag(3)···Ag(2*h*) | 3.162(1) |
| Ag(2)–O(2w*d*) | 2.632(6) | Ag(3)···Ag(3*f*) | 3.329(2) |
| Ag(3)–O(10) | 2.235(4) | | |
| O(2*a*)–Ag(1)–O(1) | 162.4(2) | O(5)–Ag(2)–O(2w*d*) | 130.2(2) |
| O(2*a*)–Ag(1)–O(1w) | 116.1(2) | O(10)–Ag(3)–O(9*f*) | 142.3(2) |
| O(1)–Ag(1)–O(1w) | 80.0(2) | O(10)–Ag(3)–O(6*g*) | 115.3(2) |
| O(2*a*)–Ag(1)–O(3*b*) | 82.5(2) | O(9*f*)–Ag(3)–O(6*g*) | 85.0(2) |
| O(1)–Ag(1)–O(3*b*) | 106.5(2) | Ag(2*c*)–O(6)···Ag(3*i*) | 91.2(2) |
| O(1w)–Ag(1)–O(3*b*) | 87.5(2) | Ag(2*c*)···Ag(2)···Ag(3*e*) | 77.56(3) |
| O(6*c*)–Ag(2)–O(5) | 153.8(2) | Ag(2*h*)···Ag(3)···Ag(3*f*) | 62.89(2) |
| O(6*c*)–Ag(2)–O(2w*d*) | 74.5(2) | | |
| Compound **2** | | | |
| Ag(1)–O(1*a*) | 2.213(3) | Ag(5)–O(4*g*) | 2.193(3) |
| Ag(1)–O(1w) | 2.340(4) | Ag(6)–N(1) | 2.125(4) |
| Ag(1)–O(3) | 2.397(3) | Ag(6)–O(11) | 2.135(3) |
| Ag(1)–O(1) | 2.587(3) | Ag(6)–O(10*i*) | 2.528(3) |
| Ag(2)–O(2*c*) | 2.196(3) | Ag(1)···Ag(2*b*) | 3.0938(6) |
| Ag(2)–O(2w) | 2.320(4) | Ag(1)···Ag(1*a*) | 3.3396(8) |
| Ag(2)–O(5) | 2.335(3) | Ag(2)···Ag(2*d*) | 3.336(1) |
| Ag(3)–O(3*e*) | 2.229(3) | Ag(3)···Ag(5*f*) | 2.9040(6) |
| Ag(3)–O(3w) | 2.344(4) | Ag(3)···Ag(4) | 3.1645(6) |
| Ag(3)–O(7) | 2.354(3) | Ag(4)···Ag(6*e*) | 2.9438(5) |
| Ag(3)–O(6) | 2.400(3) | Ag(4)···Ag(5*f*) | 3.1282(6) |
| Ag(4)–O(12*e*) | 2.166(3) | Ag(4)···Ag(5*e*) | 3.3159(6) |
| Ag(4)–O(7*f*) | 2.204(3) | Ag(5)···Ag(5*g*) | 3.1160(8) |
| Ag(4)–O(9) | 2.502(3) | Ag(5)···Ag(6) | 3.1310(6) |
| Ag(5)–O(8) | 2.176(3) | Ag(6)···Ag(6*j*) | 3.2021(8) |
| O(1*a*)–Ag(1)–O(1w) | 132.8(1) | Ag(4*f*)–O(7)–Ag(3) | 125.9(1) |
| O(1*a*)–Ag(1)–O(3) | 134.0(1) | Ag(2*b*)···Ag(1)···Ag(1*a*) | 125.76(2) |
| O(1w)–Ag(1)–O(3) | 93.2(1) | Ag(1*b*)···Ag(2)···Ag(2*d*) | 106.84(2) |
| O(1*a*)–Ag(1)–O(1) | 92.2(1) | Ag(5*f*)···Ag(3)···Ag(4) | 61.88(1) |
| O(1w)–Ag(1)–O(1) | 100.8(1) | Ag(6*e*)···Ag(4)···Ag(5*f*) | 116.21(2) |
| O(3)–Ag(1)–O(1) | 75.6(1) | Ag(6*e*)···Ag(4)···Ag(3) | 160.47(2) |
| O(2*c*)–Ag(2)–O(2w) | 135.3(1) | Ag(5*f*)···Ag(4)···Ag(3) | 54.96(1) |
| O(2*c*)–Ag(2)–O(5) | 136.0(1) | Ag(6*e*)···Ag(4)···Ag(5*e*) | 59.67(1) |
| O(2w)–Ag(2)–O(5) | 87.7(1) | Ag(5*f*)···Ag(4)···Ag(5*e*) | 57.75(2) |
| O(3*e*)–Ag(3)–O(3w) | 126.7(1) | Ag(3)···Ag(4)···Ag(5*e*) | 112.31(1) |
| O(3*e*)–Ag(3)–O(7) | 139.1(1) | Ag(3*f*)···Ag(5)···Ag(5*g*) | 126.77(2) |
| O(3w)–Ag(3)–O(7) | 93.9(1) | Ag(3*f*)···Ag(5)···Ag(4*f*) | 63.15(1) |
| O(3*e*)–Ag(3)–O(6) | 92.9(1) | Ag(5*g*)···Ag(5)···Ag(4*f*) | 64.15(2) |
| O(3w)–Ag(3)–O(6) | 104.6(1) | Ag(3*f*)···Ag(5)···Ag(6) | 121.92(2) |
| O(7)–Ag(3)–O(6) | 79.0(1) | Ag(5*g*)···Ag(5)···Ag(6) | 111.25(2) |
| O(12*e*)–Ag(4)–O(7*f*) | 161.7(1) | Ag(4*f*)···Ag(5)···Ag(6) | 168.66(2) |
| O(12*e*)–Ag(4)–O(9) | 97.7(1) | Ag(3*f*)···Ag(5)···Ag(4*h*) | 171.34(2) |
| O(7*f*)–Ag(4)–O(9) | 100.6(1) | Ag(5*g*)···Ag(5)···Ag(4*h*) | 58.10(1) |
| O(8)–Ag(5)–O(4*g*) | 166.5(1) | Ag(4*f*)···Ag(5)···Ag(4*h*) | 122.25(2) |
| N(1)–Ag(6)–O(11) | 170.1(2) | Ag(6)···Ag(5)···Ag(4*h*) | 54.25(1) |
| N(1)–Ag(6)–O(10*i*) | 93.5(1) | Ag(4*h*)···Ag(6)···Ag(5) | 66.08(1) |
| O(11)–Ag(6)–O(10*i*) | 94.9(1) | Ag(4*h*)···Ag(6)···Ag(6*j*) | 89.51(2) |
| Ag(1*a*)–O(1)–Ag(1) | 87.8(1) | Ag(5)···Ag(6)···Ag(6*j*) | 154.36(2) |
| Ag(3*h*)–O(3)–Ag(1) | 114.0(1) | | |

[a] Symmetry codes for **1**: *a*) $-x + 1, -y + 2, -z$; *b*) $-x, -y + 2, -z$; *c*) $-x, -y + 3, -z - 1$; *d*) $x, y + 1, z$; *e*) $-x, -y + 1, -z$; *f*) $-x - 1, -y + 1, -z - 1$; *g*) $x - 1, y - 1, z$; *h*) $x, y - 1, z$; *i*) $x + 1, y + 1, z$. For **2**: *a*) $-x + 2, -y + 3, -z$; *b*) $-x + 3, -y + 2, -z$; *c*) $x + 1, y - 1, z$; *d*) $-x + 4, -y + 2, -z$; *e*) $x + 1, y, z$; *f*) $-x + 4, -y + 3, -z - 1$; *g*) $-x + 3, -y + 3, -z - 1$; *h*) $x - 1, y, z$; *i*) $-x + 3, -y + 4, -z - 1$; *j*) $-x + 2, -y + 4, -z - 1$; *k*) $x - 1, y + 1, z$.

 © 2006 Wiley-VCH Verlag GmbH & Co. KGaA, Weinheim 

succinatodisilver complex (2.938 and 3.104 Å).[14b] Ag2 adopts a slightly distorted Y-shaped geometry, coordinated by two oxygen atoms from two $[H_3L]^{3-}$ ligands [Ag2–O = 2.187(4) and 2.191(4) Å, O–Ag2–O = 153.8(2)°] and a weakly coordinated aqua ligand [Ag2–O2w = 2.632(6) Å, O–Ag2–O2w = 74.5(2) and 130.2(2)°] as well as two Ag···Ag contacts [2.916(1) and 3.162(1) Å]. Similarly, Ag3 also has a distorted Y-shaped geometry, surrounded by three oxygen atoms from three $[H_3L]^{3-}$ ligands [Ag3–O = 2.235(4)–2.542(5) Å, O–Ag3–O = 85.0(2)–142.3(2)°] as well as by two Ag···Ag contacts [3.162(1) and 3.329(2) Å]. Each $[H_3L]^{3-}$ ligand connects eight $Ag^{I}$ atoms through one protonated carboxylic group and three deprotonated carboxylato groups with $\mu_2$:$\eta^1$:$\eta^1$, $\mu_2$:$\eta^1$:$\eta^1$, and $\mu_3$:$\eta^2$:$\eta^1$ coordination modes, respectively (Figure 1, b). Two of the three protonated carboxylic groups of each $[H_3L]^{3-}$ ligand donate two strong intraligand hydrogen bonds to the deprotonated carboxylato groups, further stabilizing their *cis* conformation [O8···O9 = 2.564(6) Å, O8–H8O···O9 = 164(9)°; O12···O1 = 2.582(6) Å, O12–H12O···O1 = 160(9)°]. Moreover, there are rich intermolecular hydrogen-bond interactions between the protonated or deprotonated carboxylate groups with water molecules (Table 2). Two types of cluster units of Ag···Ag interactions exist: the carboxylato-supported Ag1···Ag1 dimer and the 1D carboxylato-supported Ag2···Ag3···Ag3···Ag2 chain unit (Figure 2, a and b). The distances of Ag2···Ag2*a*, Ag2···Ag3*a*, and Ag3···Ag3*d* are 2.916(1), 3.162(1), and 3.329(2) Å, respectively. Such robust Ag···Ag interactions make the silver(I) atoms form a silver chain running along the *a* axis direction supported by the $\mu_2$- and $\mu_3$-carboxylate bridges. These dimeric motifs and 1D Ag···Ag chains are connected by the $[H_3L]^{3-}$ ligands into an open MOF having a rectangular channel along the *a* axis direction (Figure 2, c). Water molecules are located at these channels and form 1D hydrogen-bonded water tapes[26] (Figure 3, a, b). There are cyclic $R_8^6(16)$ $(H_2O)_8$ and $R_4^4(8)$ $(H_2O)_4$ units with two water molecules shared between the adjacent circles, leading to a T4(2)8(2) water tape. The water tapes further donate hydrogen bonds to the deprotonated carboxylate groups of the host [O···O 2.738(7)–3.161(8) Å] (Table 2). Each water molecule is tetrahedrally surrounded by four hydrogen bonds or three hydrogen bonds and one Ag–$H_2O$ coordination bond (Figure 3, b). Other interesting water chains and tapes have been observed in MOF structures of $[(H_2O)_2\subset\{Ni(Hsglu)(H_2O)_2\}]\cdot H_2O$ [Hsglu = *N*-(2-hydroxybenzyl)-l-glutamic acid],[27a] apdo·$4H_2O$ (apdo = *trans*-4,4′-azopyridine dioxine),[27b] [Co(tartarate)(2,2′-bipy)·$5H_2O$],[27c] [Cu(DPA)$(CO_3)$]·$3H_2O$ (DPA = 2,2′-dipyridylamine),[27d] [Fe(2,2′-bipy)$_2$$(CN)_2$]·

Table 2. Geometrical parameters of hydrogen bonds for **1** and **2**.[a]

| D–H···A | *d*(D–H) | *d*(H···A) | *d*(D···A) | ∠(DHA) |
|---|---|---|---|---|
| Compound **1** | | | | |
| O(4)–H(4O)···O(4w*b*) | 0.85(1) | 1.89(3) | 2.731(6) | 168(13) |
| O(8)–H(8O)···O(9) | 0.85(1) | 1.74(3) | 2.564(6) | 164(9) |
| O(12)–H(12O)···O(1) | 0.85(1) | 1.77(3) | 2.582(6) | 160(9) |
| O(1w)–H(1wa)···O(2w) | 0.85(1) | 2.08(3) | 2.905(9) | 163(8) |
| O(1w)–H(1wb)···O(3w) | 0.85(1) | 1.99(4) | 2.775(7) | 154(9) |
| O(2w)–H(2wa)···O(11*d*) | 0.85(1) | 1.90(3) | 2.738(7) | 168(13) |
| O(2w)–H(2wb)···O(4w*e*) | 0.85(1) | 2.34(3) | 3.161(8) | 162(8) |
| O(3w)–H(3wa)···O(2*c*) | 0.85 | 2.12 | 2.923(6) | 157.9 |
| O(3w)–H(3wb)···O(1w*f*) | 0.85 | 2.02 | 2.790(7) | 151.7 |
| O(4w)–H(4wa)···O(3w) | 0.85 | 2.01 | 2.817 | 159.1 |
| O(4w)–H(4wb)···O(2*a*) | 0.85 | 2.17 | 3.008(6) | 170.7 |
| Compound **2** | | | | |
| O(1w)–H(1wa)···O(4w) | 0.85(1) | 1.94(1) | 2.772(5) | 166(5) |
| O(1w)–H(1wb)···O(5) | 0.85(1) | 1.90(2) | 2.734(5) | 168(7) |
| O(2w)–H(2wa)···O(6*c*) | 0.85(1) | 1.82(2) | 2.644(5) | 162(6) |
| O(2w)–H(2wb)···O(4w) | 0.85(1) | 1.98(2) | 2.811(6) | 165(8) |
| O(3w)–H(3wa)···O(9*d*) | 0.85(1) | 1.84(1) | 2.675(5) | 171(4) |
| O(3w)–H(3wb)···O(10*b*) | 0.85(1) | 1.93(2) | 2.727(5) | 157(5) |
| O(4w)–H(4wa)···O(4*a*) | 0.85(1) | 2.31(4) | 3.039(5) | 144(6) |
| O(4w)–H(4wa)···O(5*a*) | 0.85(1) | 2.33(4) | 2.970(6) | 133(5) |
| O(4w)–H(4wb)···O(10*g*) | 0.85(1) | 1.82(2) | 2.650(5) | 167(6) |
| N(1)–H(1Na)···O(2*f*) | 0.89(1) | 2.24(2) | 3.048(5) | 151(4) |
| N(1)–H(1Nb)···O(3w*e*) | 0.90(1) | 2.26(2) | 3.134(6) | 165(4) |
| N(1)–H(1Nc)···O(6*e*) | 0.89(1) | 2.36(3) | 3.109(6) | 142(4) |

[a] Symmetry codes for **1**: *a*) –*x* + 1, –*y* + 2, –*z*; *b*) –*x*, –*y* + 2, –*z*; *c*) *x*, *y* – 1, *z*; *d*) *x* + 1, *y*, *z*; *e*) –*x* + 1, –*y* + 1, –*z*; *f*) –*x*, –*y* + 1, –*z*. For **2**: *a*) –*x* + 3, –*y* + 2, –*z*; *b*) *x* + 1, *y* – 1, *z*; *c*) –*x* + 4, –*y* + 2, –*z*; *d*) –*x* + 4, –*y* + 3, –*z* – 1; *e*) –*x* + 3, –*y* + 3, –*z* – 1; *f*) –*x* + 2, –*y* + 4, –*z* – 1; *g*) –*x* + 3, –*y* + 3, –*z*.

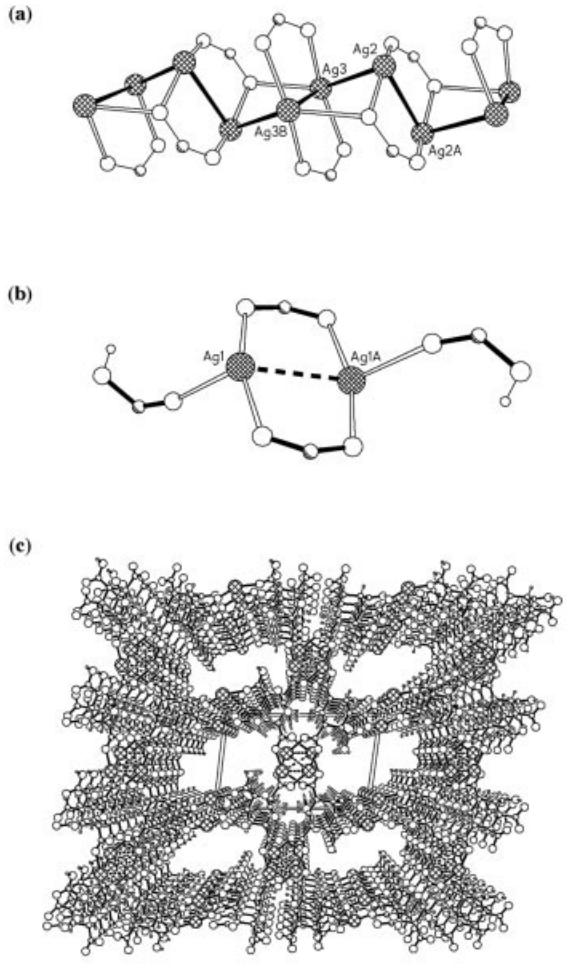


Figure 2. (a) The silver chain along the *a* axis, (b) the binuclear motif of silver atom, and (c) perspective view of the 1D channels along the *a* axis direction in **1**.

 © 2006 Wiley-VCH Verlag GmbH & Co. KGaA, Weinheim 

$2.5H_2O$,[27e] and $[Co_2(ptc)(py)_2(H_2O)_4]\cdot 4H_2O$ (ptc = pyrazine-2,3,5,6-tetracarboxylate).[27f]

Complex **2** is also a 3D MOF structure with more complicated Ag···Ag interactions. As illustrated in Figure 4 (a), each asymmetric unit in **2** contains one formula unit, and therefore there are six crystallographically unique silver(I) atoms, one $L^{6-}$ ligand, one ammonia ligand, three aqua ligands, and one lattice water molecule, all of which lie in general positions. Compared with **1**, all the carboxylate groups are deprotonated, which is in agreement with the IR spectrum with no absorption peak around 1720 $cm^{-1}$. Ag1 and Ag3 have similar greatly distorted tetrahedral coordination geometries. They are coordinated by three carboxylato oxygen atoms from two $L^{6-}$ ligands [Ag1–O = 2.213(3)–2.587(3) Å, O–Ag1–O = 75.6(1)–134.0(1)°; Ag3–O = 2.229(3)–2.400(3) Å, O–Ag3–O = 79.0(1)–139.1(1)°] and an aqua ligand [Ag1–O1w = 2.340(4) Å, O–Ag1–O1w = 93.2(1)–132.8(1)°; Ag3–O3w = 2.340(4) Å, O–Ag3–O3w = 93.9(1)–126.7(1)°] as well as surrounded by two Ag···Ag contacts [3.0938(6) and 3.3396(8) Å for Ag1 and 2.9040(6) and 3.1645(6) Å for Ag3]. Ag2 is coordinated in a Y-shaped coordination geometry by two carboxylato oxygen atoms from different $L^{6-}$ ligands [Ag2–O = 2.196(3) and 2.335(3) Å; O–Ag2–O = 136.0(1)°] and an aqua molecule [Ag2–O2w = 2.320(4), O–Ag2–O2w = 87.7(1) and 135.3(1)°] as well as two relatively weak Ag···Ag contacts

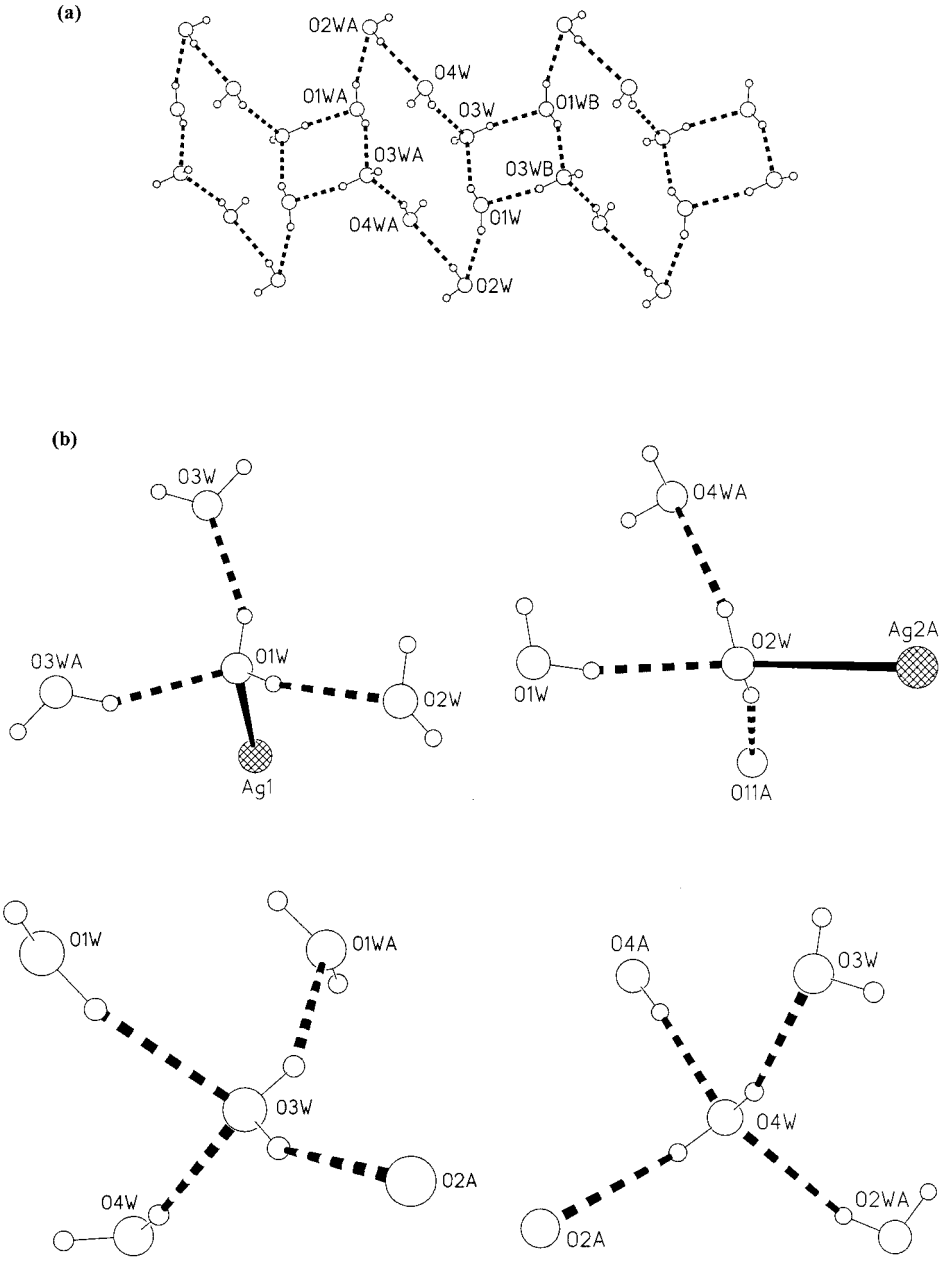


Figure 3. Perspective views showing 1D water tape (a) and the hydrogen-bonding modes of each water molecule (b) in **1**.

 © 2006 Wiley-VCH Verlag GmbH & Co. KGaA, Weinheim 

[Ag2···Ag1*b* = 3.0938(6) Å, Ag2···Ag2*d* = 3.336(1) Å]. Ag4 and Ag6 have similar slightly distorted T-shaped coordination geometries. Ag4 is coordinated by three carboxylato oxygen atoms from three $L^{6-}$ ligands [Ag4–O = 2.166(3), 2.204(3), and 2.502(3) Å, O–Ag4–O = 97.7(1), 100.6(1), and 161.7(1)°], while Ag6 is coordinated by two carboxylato oxygen atoms from two $L^{6-}$ ligands and an ammonia ligand [Ag6–O/N = 2.125(4), 2.135(3), and 2.528(3) Å, O/N–Ag6–O = 93.5(1), 94.9(1), and 170.1(2)°]. Moreover, Ag4 and Ag6 are further surrounded by four and three Ag···Ag contacts, respectively [Ag···Ag = 2.9438(6)–3.3159(6) Å for Ag4 and 2.9438(6)–3.2021(8) Å for Ag6]. Ag5 adopts a nearly linear geometry, coordinated by two oxygen atoms from different $L^{6-}$ ligands [Ag5–O = 2.176(3) and 2.193(3) Å, O–Ag5–O = 166.5(1)°]. Interestingly, Ag5 is surrounded by five strong or weak Ag···Ag contacts [Ag···Ag = 2.9040(6)–3.3159(6) Å]. Most of these Ag···Ag interactions are slightly longer than that found in ternary silver-hexamethylenetetramine-carboxylato compounds (2.8154–2.9144 Å).[9b] Each $L^{6-}$ ligand connects 13 silver atoms (Figure 4, b) to generate a complicated 3D MOF structure.

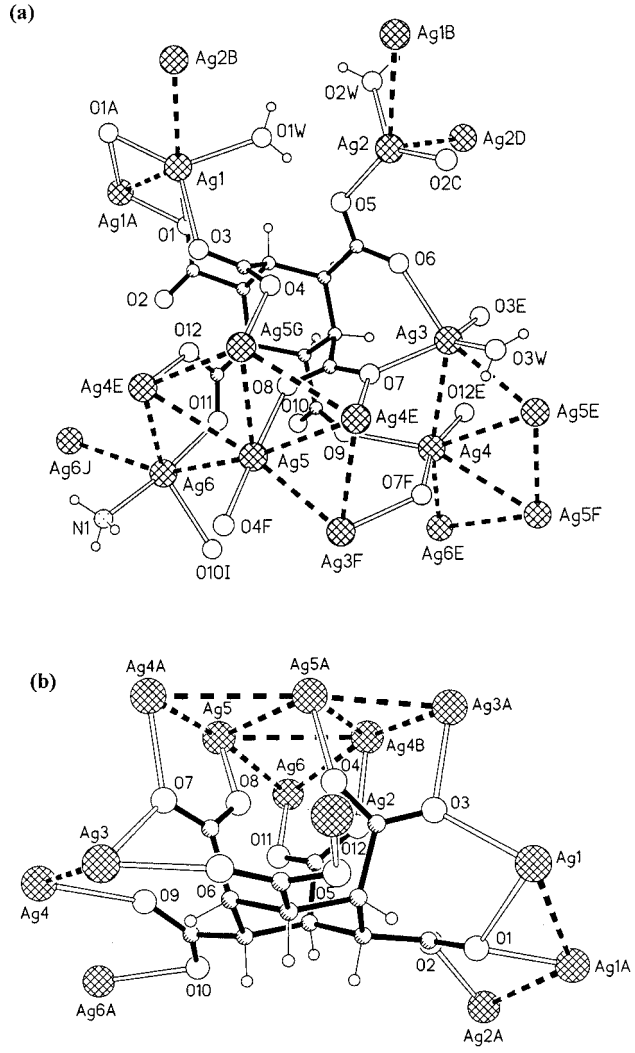


Figure 4. Perspective views showing the coordination environment of silver atoms (a) and the bridging mode of the $L^{6-}$ ligand (b) in **2**.

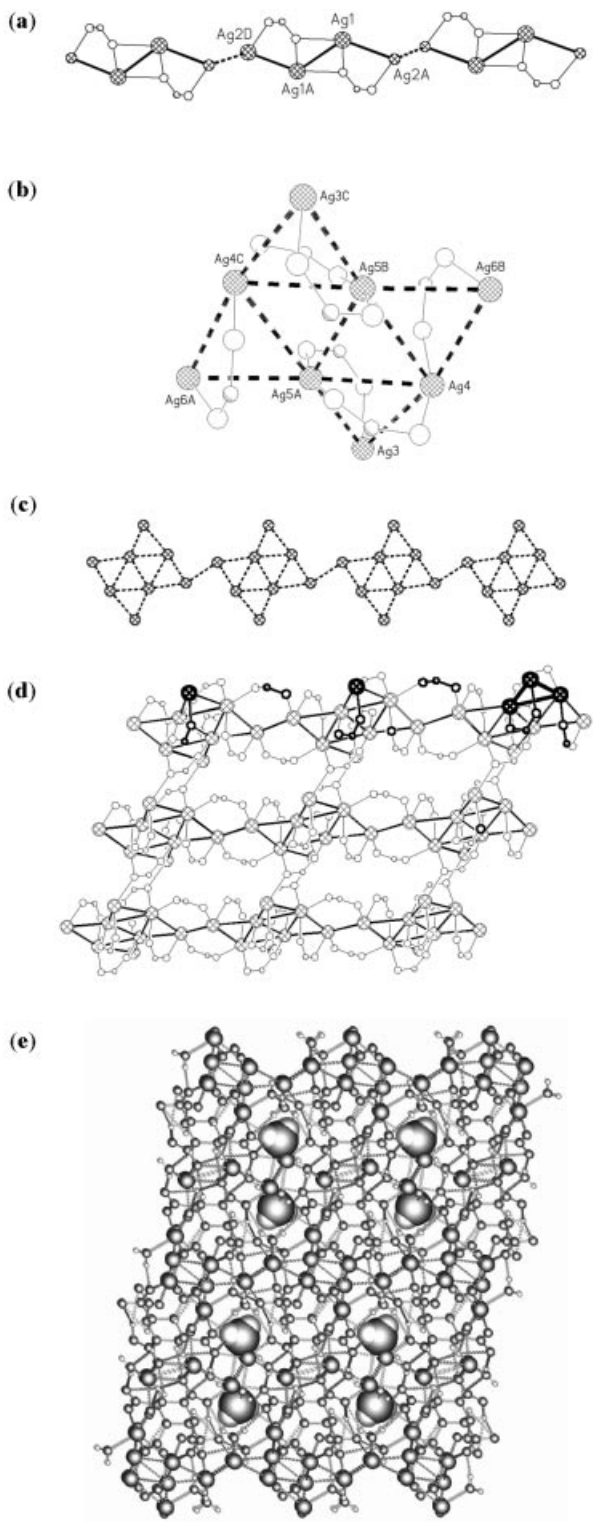


Figure 5. (a) The 1D silver chain constructed from Ag1 and Ag2 atoms by Ag···Ag interactions, (b) the $Ag_8$ cluster aggregated by Ag···Ag interactions, (c) the 1D silver chain constructed by $Ag_8$ clusters, (d) the 2D silver layer formed by the 1D silver chains and carboxylates along the *c* axis, and (e) the 3D MOF along the *b* axis direction in **2**.

 © 2006 Wiley-VCH Verlag GmbH & Co. KGaA, Weinheim 

The Ag···Ag interactions in **2** are much more complicated and interesting than in compound **1**. As shown in Figure 5, the six crystallographically independent silver(I) atoms can be divided into two groups. Ag1 and Ag2 are connected by Ag···Ag interactions to generate 1D $\mu_3$-carboxylato-supported ···Ag1···Ag1···Ag2···Ag2··· silver(I) chains running along the *b* axis (Figure 5, a), while Ag3, Ag4, Ag5, and Ag6 are aggregated by complicated $\mu_2$-carboxylato-supported Ag···Ag interactions into 1D Ag···Ag tapes with a Ag8 cluster unit with six edge-sharing triangles (Figure 5b, c, d). Two of the six triangles constructed by Ag4, Ag4*a*, Ag5, and Ag5*a* are coplanar but others are somewhat out of the plane. The dihedral angles between this plane and the plane made of Ag3, Ag4, and Ag5*a* as well as the plane of Ag5, Ag6, and Ag4*a* by edge-sharing are 7.8 and 13.0°. Interestingly, the 1D Ag···Ag tapes are further connected by carboxylates into 2D layers along the *bc* plane (Figure 5, c), which are further extended by adjacent ···Ag1···Ag1···Ag2···Ag2··· silver(I) chains into a 3D MOF structure (Figure 5e). The lattice water molecules are located at the cavities of **2** and form rich hydrogen-bonding interactions with the MOF host [O4w···O4*a* = 3.039(5) Å, O4w–H4wa···O4*a* = 144(6)°; O4w···O5*a* = 2.970(6) Å, O4w–H4wb···O5*a* = 133(5)°; O4w···O10*g* = 2.650(5) Å, O4w–H4wb···O10*g* = 167(6)°; O1w···O4w = 2.772(5) Å, O1w–H1wa···O4w = 166(5)°; O2w···O4w = 2.811(6) Å, O2w–H2wb···O4w = 165(8)°].

### Thermogravimetric Analysis

In order to examine the thermal stabilities of the porous networks, we carried out thermogravimetric (TG) analyses and measurement of the XPRD patterns to confirm the purity of the two complexes (Figure 6). Samples of the complexes were heated to 600 °C with exposure to air. The TGA curve (Figure 7) of **1** shows that the first weight loss of 5.1% between 20 and 68 °C corresponds to a loss of the included water molecules (calculated: 4.9%), while the second weight loss of 2.4% between 68 and 93 °C is in accordance with the loss of one coordinated water molecule per unit cell (calculated: 2.5%), and the succeeding weight loss of 2.8% corresponds to another coordinated water molecule between 93 and 175 °C (calculated: 2.5%). Complex **1** began to decompose at 190 °C to yield the residue $Ag_2O$ at about 450 °C (found: 43.4%; calculated: 46.9%). The TGA curve of **2** shows that the first weight loss of 4.5% between 50 and 110 °C corresponds to the gradual loss of one included molecule, one coordinated water, and one coordinated ammonia molecule or two coordinated water molecules per unit cell (calculated: 4.8%), while the remaining water molecules were completely removed at 225 °C. Complex **2** began to decompose at 230 °C to yield the residue $Ag_2O$ at about 455 °C (found: 61.3%; calculated: 64.5%). Powder XRD patterns (Figure S2 in the Supporting Information) of the dehydrated samples of **1** and **2** indicate that removal of the guest molecules causes a significant structural change of crystalline to amorphous to the framework of **1** and **2**.

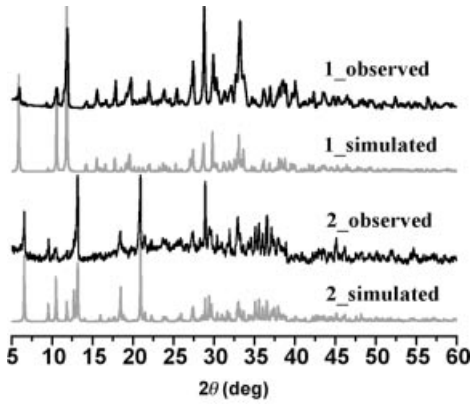


Figure 6. Observed (black) and calculated (gray) powder X-ray diffraction patterns for **1** and **2**.

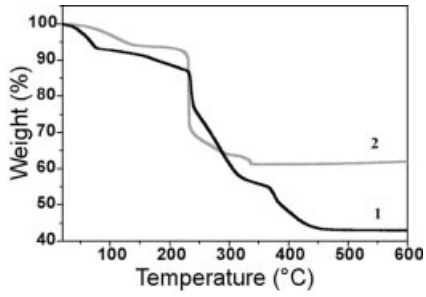


Figure 7. TG analyses for **1** (black) and **2** (gray).

## Conclusion

Two new silver(I) compounds incorporating *cis*,*cis*,*cis*,*cis*,-*cis*,*cis*-1,2,3,4,5,6-cyclohexanehexacarboxylic acid ($H_6L$) have been successfully obtained, by controlling the molar ratio of the self-assembled reactions, and crystallographically characterized. Rich Ag···Ag interactions and versatile coordination modes of the half or fully deprotonated ligands ($[H_3L]^{3-}$ or $L^{6-}$) lead to two interesting microporous MOFs. Our work is the first to reveal that the $H_6L$ ligand is characteristic of multifunctional coordination sites and pH-dependent coordination fashions and has a much more important effect on the structures of MOFs.

## Experimental Section

**General Remarks:** The reagents and solvents employed were commercially available and used as received without further purification. The C, H, and N microanalyses were carried out with an Elementar Vario-EL CHNS elemental analyzer. The IR spectra were recorded from KBr pellets in the range 4000–400 $cm^{-1}$ with a Bio-Rad FTS-7 spectrometer. Powder X-ray diffraction (PXRD) intensities for **1** and **2** were measured at 293 K on a Rigaku D/max-IIIA diffractometer (Cu-$K_\alpha$, $\lambda$ = 1.54056 Å). The crushed single-crystalline powder samples were prepared by crushing the crystals and scanned from 5 to 60° with a step of 0.1°/s.

 © 2006 Wiley-VCH Verlag GmbH & Co. KGaA, Weinheim 

Table 3. Crystal and structure refinement for compounds **1** and **2**.[a]

| Compound | **1** | **2** |
|---|---|---|
| Empirical formula | $C_{12}Ag_3H_{17}O_{16}$ | $C_{12}H_{17}Ag_6NO_{16}$ |
| Formula weight | 740.87 | 1078.49 |
| Temperature [K] | 293(2) | 293(2) |
| Wavelength [Å] | 0.71073 | 0.71073 |
| Crystal system | triclinic (no. 2) | triclinic (no. 2) |
| Space group | $P\bar{1}$ | $P\bar{1}$ |
| $a$ [Å] | 6.375(4) | 8.038(1) |
| $b$ [Å] | 9.505(6) | 10.122(1) |
| $c$ [Å] | 15.097(8) | 13.846(1) |
| $\alpha$ [°] | 96.453(15) | 80.937(1) |
| $\beta$ [°] | 93.249(14) | 76.345(1) |
| $\gamma$ [°] | 100.364(15) | 68.723(1) |
| $V$ [Å$^3$] | 891.4(9) | 1016.8(2) |
| $Z$ | 2 | 2 |
| Calculated density [g/cm$^3$] | 2.768 | 3.522 |
| Absorption coefficient [mm$^{-1}$] | 3.363 | 5.753 |
| $F$(000) | 716 | 1012 |
| Crystal size [mm] | 0.17×0.17×0.14 | 0.18×0.12×0.05 |
| $\theta$ range for data collection [°] | 2.2–27.0 | 2.2–26.0 |
| Limiting indices | $-8 \le h \le 7$, $-11 \le k \le 12$, $-19 \le l \le 16$ | $-9 \le h \le 9$, $-12 \le k \le 12$, $-16 \le l \le 17$ |
| Reflections collected/unique | 6378/3635 | 7866/3894 |
| Completeness | 93.9% ($\theta_{max}$ = 27.0°) | 97.4% ($\theta_{max}$ = 26.0°) |
| Absorption correction | multiscan (SADABS; Bruker, 2002) | multiscan (SADABS; Bruker, 2002) |
| Max. and min. transmission | 0.6521/0.5922 | 0.7619/0.4241 |
| Refinement method | full-matrix least-square on $F^2$ | full-matrix least-square on $F^2$ |
| Data/restraints/parameters | 3635/16/321 | 3894/18/359 |
| Goodness-of-fit on $F^2$ | 1.026 | 1.064 |
| $R$ indexes [$I > 2\sigma(I)$] | $R_1$ = 0.0454, $wR_2$ = 0.1132 | $R_1$ = 0.0270, $wR_2$ = 0.0599 |
| $R$ indices (all data) | $R_1$ = 0.0494, $wR_2$ = 0.1165 | $R_1$ = 0.0315, $wR_2$ = 0.0618 |
| Largest diff. peak and hole [e/Å$^3$] | 2.803/–1.661 | 0.820/–0.751 |

[a] $R_1 = \Sigma||F_o| - |F_c||/\Sigma|F_o|$, $wR_2 = [\Sigma w(F_o^2 - F_c^2)^2/\Sigma w(F_o^2)^2]^{1/2}$.

**Synthesis of 1:** Excess aqueous $NH_3$ solution was dropped slowly into a suspension of $Ag_2O$ (0.087 g, 0.375 mmol) in MeCN/$H_2O$ (30 mL, v/v = 2:1) with magnetic stirring for 15 min. Then the powder of the ligand *cis*,*cis*,*cis*,*cis*,*cis*-1,2,3,4,5,6-cyclohexanehexacarboxylic acid (0.092 g, 0.25 mmol) was slowly added to the former solution and stirred for 30 min after being dissolved. The resultant solution was allowed to slowly diffuse in darkness at room temperature for several weeks to give colorless needle-like crystals. The crystals were isolated by deionized water and dried in air (yield 0.112 g, about 60% based on Ag). $C_{12}H_{17}Ag_3O_{16}$ (740.87): calcd. C 19.45, H 2.31; found C 19.69, H 2.34. IR (KBr) (400–4000 cm$^{-1}$): $\tilde{\nu}$ = 3430 m, 2903 w, 2563 w, 1916 vw, 1717 vs, 1557 vs, 1460 vs, 1385 vs, 1316 s, 1240 s, 1206 s, 1160 m, 1028 m, 994 m, 894 m, 803 m, 760 m 687 m, 618 w, 495 w cm$^{-1}$.

**Synthesis of 2:** Complex **2** was prepared as described for **1** by only changing the molar ratio of $Ag_2O$ to $H_6L$ ligand from 1.5:1 to 3:1. Colorless prism-like crystals were isolated by deionized water and dried in air (yield 0.135 g, about 80% based on Ag). $C_{12}H_{17}Ag_6NO_{16}$ (1078.49): calcd. C 13.36, H 1.59, N 1.30; found C 13.47, H 1.58, N 1.22. IR (KBr) (400–4000 cm$^{-1}$): $\tilde{\nu}$ = 3354 m, 3320 m, 3259 m, 3181 m, 1545 vs, 1386 vs, 1319 s, 1203 m, 1166 m, 1032 w, 994 w, 916 w, 844 m, 767 m, 692 m, 591 m, 523 w cm$^{-1}$.

**X-ray Crystallographic Study:** Single crystals of complexes **1** and **2** with approximate dimensions 0.21×0.20×0.14 mm$^3$ (**1**) and 0.20×0.30×0.26 mm$^3$ (**2**) were used for X-ray diffraction analyses. The crystals were mounted on the end of a thin glass fiber using an inert epoxy gel. Data collection of **1** and **2** was performed with Mo-$K_\alpha$ radiation ($\lambda$ = 0.71073 Å) with a Bruker Apex CCD diffractometer at 123(2) K. The raw data frames were integrated with SAINT$^+$, which also applied corrections for Lorentz and polarization effects. Absorption corrections were applied by using the multiscan program SADABS.[28] The structures were solved by direct methods, and all non-hydrogen atoms were refined anisotropically by least-squares on $F^2$ using the SHELXTL program.[29] Hydrogen atoms on organic ligands were generated by the riding mode (C–H bond length: 0.98 Å); the water, hydroxy, and ammonia hydrogen atoms were located from difference maps, and refined with nominal geometric restraints [O–H 0.85(1), N–H 0.90 Å]. Selected bond lengths and bond angles are listed in Table 1. A summary of the crystal data is given in Table 3.

CCDC-291579 (for **1**) and -291580 (for **2**) contain the supplementary crystallographic data for this paper. These data can be obtained free of charge from The Cambridge Crystallographic Data Centre via www.ccdc.cam.ac.uk/data_request/cif.

**Supporting Information** (for details see the footnote on the first page of this article): The supporting information contains the IR spectra for compounds **1** and **2**, and the powder XRD of the dehydrated samples of **1** and **2**.

## Acknowledgments

This work was supported by the NSFC (20525102 and 20471069), the FANEDD of China (200122), the Scientific and Technological Project of Guangdong Province (04205405), and Sun Yat-Sen University.

[1] a) J. M. Lehn, *Angew. Chem. Int. Ed. Engl.* **1990**, *29*, 1304–1319; b) O. M. Yaghi, G. Li, H. Li, *Nature* **1995**, *378*, 703–706; c) M. J. Zaworotko, *Nature* **1997**, *386*, 220–221.

 © 2006 Wiley-VCH Verlag GmbH & Co. KGaA, Weinheim 

[2] a) M. M. Conn, J. Rebek Jr, *Chem. Rev.* **1997**, *97*, 1647–1668; b) L. J. Prins, J. Huskens, F. Jong, P. Timmerman, D. N. Reinhoudt, *Nature* **1999**, *398*, 498–502; c) G. R. Desiraju, *Nature* **2001**, *412*, 397–400.

[3] a) R. Robson, B. F. Abrahamas, S. R. Batten, R. W. Gable, B. F. Hoskins, J. Liu, *Supramolecular Architecture*, American Chemical Society, Washington, DC, **1992**, p. 256; b) J.-M. Lehn, *Supramolecular Chemistry: Concepts and Perspectives*, VCH, Weinheim, Germany, **1995**, ch. 9; c) A. J. Cheethan, *Science* **1994**, *264*, 794, and refs therein; d) J. M. Thomas, R. Raja, *Chem. Commun.* **2001**, 675–687.

[4] a) V. R. Pedireddi, W. Jones, A. P. Chorlton, R. Docherty, *Chem. Commun.* **1996**, 997–1002; b) Y. B. Dong, M. D. Smith, R. C. Layland, H.-C. zur Loye, *J. Chem. Soc., Dalton Trans.* **2000**, 775–780.

[5] a) X. Xue, X. S. Wang, L. Z. Wang, R. G. Xiong, B. F. Abrahams, X. Z. You, Z. L. Xue, C. M. Che, *Inorg. Chem.* **2002**, *41*, 6544–6546; b) S. Leininger, B. Olenyuk, P. J. Stang, *Chem. Rev.* **2000**, *100*, 853–908; c) Y. Cui, H. L. Ngo, W. Lin, *Inorg. Chem.* **2002**, *41*, 1033–1035; d) L. Carlucci, G. Ciani, D. M. Proserpio, S. Rizzato, *Chem. Eur. J.* **2002**, *8*, 1520–1526.

[6] a) I. M. Müller, R. Robson, *Angew. Chem. Int. Ed.* **2000**, *39*, 4357–4359; b) B. F. Abrahams, P. A. Jackson, R. Robson, *Angew. Chem. Int. Ed.* **1998**, *37*, 2656–2659; c) B. F. Abrahams, J. Coleiro, B. F. Hoskins, R. Robson, *Chem. Commun.* **1996**, 603–604.

[7] a) L. Carlucci, G. Ciani, D. M. Proserpio, A. Sironi, *Angew. Chem. Int. Ed. Engl.* **1995**, *34*, 1895–1898; b) X. H. Bu, K. Biradha, T. Yamaguchi, M. Nishimura, T. Ito, K. Tanaka, M. Shionoya, *Chem. Commun.* **2000**, 1953–1954; c) K. Biradha, M. Fujita, *Chem. Commun.* **2001**, 15–16; d) M.-L. Tong, X.-M. Chen, B.-H. Ye, L.-N. Ji, *Angew. Chem. Int. Ed.* **1999**, *38*, 2237–2240.

[8] a) P. L. Caradoc-Davies, L. R. Hanton, *Chem. Commun.* **2001**, 1098–1099; b) I. Ino, L. P. Wu, M. Munakata, M. Maekawa, Y. Suenaga, T. Kuroda-Sowa, Y. Kitamori, *Inorg. Chem.* **2000**, *39*, 2146–2151; c) K. A. Hirsch, S. R. Wilson, J. S. Moore, *Inorg. Chem.* **1997**, *36*, 2960–2968.

[9] a) M. Maekawa, H. Konaka, Y. Suenaga, T. Kuroda-Sowa, M. Munakata, *J. Chem. Soc., Dalton Trans.* **2000**, 4160–4166; b) M.-L. Tong, S.-L. Zheng, X.-M. Chen, *Chem. Eur. J.* **2000**, *6*, 3729–3738; c) R. Alberto, D. Angst, U. Abram, K. Ortner, T. A. Kaden, A. P. Schubiger, *Chem. Commun.* **1999**, 1513–1514.

[10] a) K. S. Singh, J. R. Long, P. Stavropoulos, *J. Am. Chem. Soc.* **1997**, *119*, 2942–2943; b) L. Pan, E. B. Woodlock, X. T. Wang, K. C. Lam, A. L. Rheingold, *Chem. Commun.* **2001**, 1762–1763; c) O. Kristiansson, *Inorg. Chem.* **2001**, *40*, 5058–5059.

[11] a) M. A. Omary, T. R. Webb, Z. Assefa, G. E. Shankle, H. H. Patterson, *Inorg. Chem.* **1998**, *37*, 1380–1386; b) M.-L. Tong, X.-M. Chen, B.-H. Ye, S. W. Ng, *Inorg. Chem.* **1998**, *37*, 5278–5281; c) A. Erxleben, *Inorg. Chem.* **2001**, *40*, 2928–2931.

[12] a) D. F. Sun, R. Cao, Y. C. Liang, W. P. Su, M. C. Hong, *J. Chem. Soc., Dalton Trans.* **2001**, 2335–2340; b) R. Cao, D. F. Sun, Y. C. Liang, M. C. Hong, K. Tatsumi, Q. Shi, *Inorg. Chem.* **2002**, *41*, 2087–2094; c) D. F. Sun, R. Cao, Y. C. Liang, Q. Shi, M. C. Hong, *J. Chem. Soc., Dalton Trans.* **2002**, 1847–1851.

[13] a) H. J. Choi, M. P. Suh, *Inorg. Chem.* **1999**, *38*, 6309–6312; b) S. M. Lo, S. S. Chui, L. Y. Shek, Z. Y. Lin, X. X. Zhang, G. H. Wen, I. D. William, *J. Am. Chem. Soc.* **2000**, *122*, 6293–6294; c) M. Eddaoudi, H. L. Li, O. M. Yaghi, *J. Am. Chem. Soc.* **2000**, *122*, 1391–1397; d) S. O. Gutschke, D. J. Price, A. K. Powell, P. T. Wood, *Eur. J. Inorg. Chem.* **2001**, 2739–2741.

[14] a) G. Smith, A. N. Reddy, K. A. Byriel, C. H. L. Kennard, *J. Chem. Soc., Dalton Trans.* **1995**, 3565–3570; b) A. Michaelides, V. Kiritsis, S. Skoulika, A. Aubry, *Angew. Chem. Int. Ed. Engl.* **1993**, *32*, 1495–1497.

[15] a) R. L. Griffith, *J. Chem. Phys.* **1943**, *11*, 499; b) D. S. Sagatys, G. Smith, R. C. Bott, D. E. Lynch, C. H. L. Kennard, *Polyhedron* **1993**, *12*, 709–713; c) R. C. Bott, G. Smith, D. S. Sagatys, T. C. W. Mak, D. E. Lynch, C. H. Kennard, *Aust. J. Chem.* **1993**, *46*, 1055–1065; d) P. R. Wei, D. D. Wu, T. C. W. Mak, *Inorg. Chim. Acta* **1996**, *249*, 169–174.

[16] a) F. Jaber, F. Charbonnier, R. Faure, *J. Chem. Crystallogr.* **1997**, *27*, 397; b) F. Jaber, F. Charbonnier, R. Faure, *Polyhedron* **1996**, *15*, 2909–2913; c) X.-M. Chen, T. C. W. Mak, *Aust. J. Chem.* **1991**, *44*, 1783–1787.

[17] a) M. Sanselme, J. M. Grenèche, M. Riou-Cavellec, G. Férey, *Chem. Commun.* **2002**, 2172–2173; b) R. Cao, D. F. Sun, Y. C. Liang, M. C. Hong, K. Tatsumi, Q. Shi, *Inorg. Chem.* **2002**, *41*, 2087–2094; c) N. Snejko, E. Gutierrez-Puebla, J. L. Martinez, M. A. Monge, C. Ruiz-Valero, *Chem. Mater.* **2002**, *14*, 1879–1883; d) Y. Li, N. Hao, Y. Lu, E. Wang, Z. Kang, C. Hu, *Inorg. Chem.* **2003**, *42*, 3119–3124; e) H. Kumagai, M. Akita-Tanaka, K. Inoue, M. Kurmoo, *J. Mater. Chem.* **2001**, *11*, 2146–2151.

[18] a) X. L. Zhao, Q. M. Wang, T. C. W. Mak, *Chem. Eur. J.* **2005**, *11*, 2094–2102; b) X. Zhang, G. C. Guo, F. K. Zheng, G. W. Zhou, J. G. Mao, Z. C. Dong, J. S. Huang, T. C. W. Mak, *J. Chem. Soc., Dalton Trans.* **2002**, 1344–1349; c) D. D. Wu, T. C. W. Mak, *J. Chem. Soc., Dalton Trans.* **1995**, 2671–2678; d) X. M. Chen, T. C. W. Mak, *J. Chem. Soc., Dalton Trans.* **1991**, 3253–3258; e) X. M. Chen, T. C. W. Mak, *J. Chem. Soc., Dalton Trans.* **1991**, 1219–1222.

[19] G. Smith, A. N. Reddy, K. A. Byriel, C. H. L. Kennard, *J. Chem. Soc., Dalton Trans.* **1995**, 3565–3570.

[20] a) C. B. Aakeröy, K. R. Seddon, *Chem. Soc., Rev.* **1993**, 397–407; b) T. L. Hennigar, D. C. MacQuarrie, P. Losier, R. D. Rogers, M. J. Zaworotko, *Angew. Chem.* **1997**, *109*, 1044–1046; *Angew. Chem. Int. Ed. Engl.* **1997**, *36*, 972–973; c) H. Gudbjartson, K. Biradha, K. M. Poirier, M. J. Zaworotko, *J. Am. Chem. Soc.* **1999**, *121*, 2599–2600.

[21] a) L. Carlucci, G. Ciani, D. M. Proserpio, A. Sironi, *Angew. Chem.* **1995**, *107*, 2037–2040; *Angew. Chem. Int. Ed. Engl.* **1995**, *34*, 1895–1898; b) M.-L. Tong, B.-H. Ye, X.-M. Chen, S. W. Ng, *Inorg. Chem.* **1998**, *37*, 2645–2650.

[22] J. Wang, L.-L. Zheng, C.-J. Li, Y.-Z. Zheng, M.-L. Tong, *Cryst. Growth Des.* **2006**, *6*, 357–359.

[23] a) M. Jansen, *Angew. Chem. Int. Ed. Engl.* **1987**, *26*, 1098–1110; b) G. K. H. Shimizu, G. D. Enright, C. I. Ratcliffe, K. F. Preston, J. L. Reid, J. A. Ripmeester, *Chem. Commun.* **1999**, 1485–1486.

[24] a) A. Bayler, A. Schier, G. A. Bowmaker, H. Schmidbaur, *J. Am. Chem. Soc.* **1996**, *118*, 7006–7007; b) U. M. Tripathi, A. Bauer, H. Schmidbaur, *J. Chem. Soc., Dalton Trans.* **1997**, 2865–2868.

[25] a) P. Pyykkö, *Chem. Rev.* **1997**, *97*, 597–636; b) Q.-M. Wang, T. C. W. Mak, *Chem. Commun.* **2001**, 807–808; c) D. Rais, J. Yau, D. M. P. Mingos, R. Vilar, A. J. P. White, D. J. Williams, *Angew. Chem. Int. Ed.* **2001**, *40*, 3464–3467.

[26] a) L. Infantes, S. Motherwell, *CrystEngComm* **2002**, *4*, 454–461; b) L. Infantes, J. Chisholm, S. Motherwell, *CrystEngComm* **2003**, *5*, 480–486.

[27] a) B. Sreenivasulu, J. J. Vittal, *Angew. Chem. Int. Ed.* **2004**, *43*, 5769–5772; b) B.-Q. Ma, H.-L. Sun, S. Gao, *Chem. Commun.* **2004**, 2220–2221; c) J. Lu, J.-H. Yu, X.-Y. Chen, P. Cheng, X. Zhang, J.-Q. Xu, *Inorg. Chem.* **2005**, *44*, 5978–5980; d) J. P. Naskar, M. G. B. Drew, A. Hulme, D. A. Tocher, D. Datta, *CrystEngComm* **2005**, *7*, 67–70; e) B.-Q. Ma, H.-L. Sun, S. Gao, *Eur. J. Inorg. Chem.* **2005**, 3902–3906; f) S. K. Ghosh, P. K. Bharadwaj, *Eur. J. Inorg. Chem.* **2005**, 4880–4885.

[28] G. M. Sheldrick, *SADABS 2.05*, University of Göttingen, Göttingen, Germany.

[29] *SHELXTL 6.10*, Bruker Analytical Instrumentation, Madison, Wisconsin, USA, **2000**.


Received: December 24, 2005
Published Online: March 29, 2006

 © 2006 Wiley-VCH Verlag GmbH & Co. KGaA, Weinheim 

DOI: 10.1002/ejic.200600056

# Single-Electron Oxidation of Tungsten Acetylide Complexes $[(\eta^5\text{-}C_5H_5)(CO)(NO)W\text{–}C{\equiv}C\text{–}R]Li$

**Junes Ipaktschi*[a] and Frank Munz[a]**

**Keywords:** Tungsten / Alkyne ligands / Oxidation / Bridging ligands / Metal–metal interactions

The reaction of a tungsten acetylide complex $[(\eta^5\text{-}C_5H_5)(CO)(NO)W\text{–}C{\equiv}C\text{–}R]Li$ (**1**) [**1a**, R = $C_6H_5$; **1b**, R = $C(CH_3)_3$; **1c**, R = $Si(CH_3)_3$] with one equivalent of ferrocenium tetrafluoroborate $[Cp_2Fe][BF_4]$, acting as a one-electron oxidant in THF at –50 °C, leads to the bimetallic tungsten–alkynyl complexes $[(\eta^5\text{-}C_5H_5)(NO)W\text{–}C{\equiv}C\text{–}R]_2$ (**9**) [**9a**, R = $C_6H_5$; **9b**, R = $C(CH_3)_3$; **9c**, R = $Si(CH_3)_3$] as pale-orange crystals. The crystal structure of complex **9a** is reported.
(© Wiley-VCH Verlag GmbH & Co. KGaA, 69451 Weinheim, Germany, 2006)

## Introduction

The chemistry of transition-metal acetylides M–C≡C–R and $\eta^2$-acetylene complexes has been the subject of much attention in the past years.[1] The nature of the metal–carbon bond in these systems and the possibility of conversion of alkynyl complexes to other organometallic derivatives, such as $\eta^1$-vinylidene complexes, are the subject of many investigations.[2] Furthermore, the fascinating properties of some alkynyl complexes in the field of materials science as possible nonlinear optical or luminescent materials as well as polymeric compounds have attracted much interest in recent years.[3]

As a strong σ-donor, the alkynyl group has a strong tendency to bind terminally to a main-group-metal- or transition-metal center. In the presence of a second metal atom, an alkynyl group can act either as a σ-donor to both metals (structure **A**, Scheme 1), or preferably as a σ-donor to one metal and a π-donor to the other metal center (structures **B** or **C**), depending on the nature of the metal and the ligands.[4,5] In this paper we describe the formation of binuclear σ,π-acetylide bridged complexes of type **D**, a structure analogous to **C** and additionally containing a tungsten–tungsten σ-bond.[6]

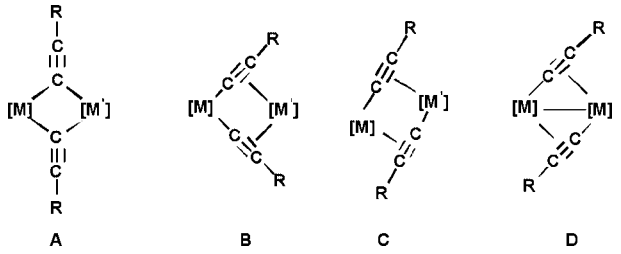


Scheme 1.

In a series of publications we have described the richly faceted chemistry of the σ-acetylide complexes $[(\eta^5\text{-}C_5H_5)(CO)(NO)W\text{–}C{\equiv}C\text{–}R]Li$ (**1**).[7] The preferred reacti-

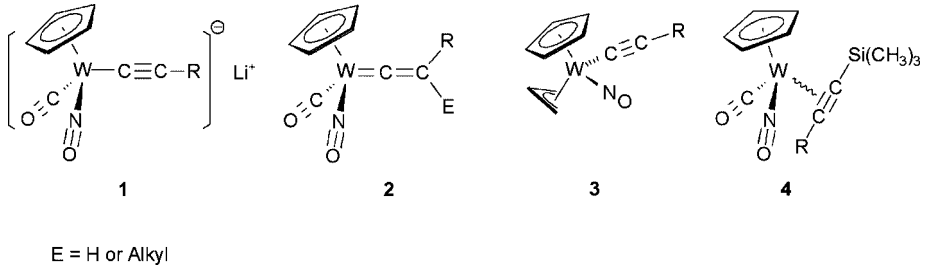


Scheme 2.

vity mode of these $\eta^1$-acetylide complexes is the addition of "hard" electrophiles $E^+$, such as a proton or alkylating reagents e.g. methyl triflate, to the β-carbon atom, which generates the corresponding $\eta^1$-vinylidene complexes **2**.[7g]

[a] Institute of Organic Chemistry, Justus Liebig University Heinrich-Buff-Ring 58, 35392 Giessen, Germany
Fax: +49-641-9934309
E-mail: junes.ipaktschi@org.chemie.uni-giessen.de

 © 2006 Wiley-VCH Verlag GmbH & Co. KGaA, Weinheim 

The addition of "soft" electrophiles, such as allyl iodide, furnishes complex **3**[7f] by allylation of the metal center, and $\eta^2$-acetylene complexes such as **4** are formed by reaction with trimethylsilylchloride (Scheme 2).[7g] The single-electron oxidation of this tungsten σ-acetylide complex by ferrocenium tetrafluoroborate $[Cp_2Fe][BF_4]$ is the subject of the present study.

## Results and Discussion

The reactants $[(\eta^5\text{-}C_5H_5)(CO)(NO)W\text{–}C{\equiv}C\text{–}R]Li$ [**1a**, R = $C_6H_5$; **1b**, R = $C(CH_3)_3$; **1c**, R = $Si(CH_3)_3$] were prepared as described previously,[7] either by the deprotonation of $\eta^1$-vinylidene complexes **5** and **6**, or alternatively by the reaction of lithium $\eta^1$-acetylide **8** with the tungsten–carbonyl complex **7**. Reaction of an emerald-green solution of **1** in THF at –50 °C with 1 equiv. of $[Cp_2Fe][BF_4]$, was monitored by IR spectroscopy. After 2 h the typical $\tilde{\nu}$(CO) band for the acetylide **1** (≈1870 $cm^{-1}$) disappeared while a new band characteristic for the C≡C group, in the range 1820–1852 $cm^{-1}$, appeared. Workup of the dark-red solution resulted, after purification through chromatography, in the formation of binuclear complexes **9a**–**c** as orange crystals in 25–54% yield (Scheme 3). The complexes **9a**–**c** are sparingly soluble in $CHCl_3$ and $CH_2Cl_2$ and can be stored under inert gas at –20 °C.

The unequivocal characterization of complexes **9a**–**c** was achieved by means of elemental analysis and by standard spectroscopic techniques. The structure of the products is further confirmed by the result of the single-crystal structure analysis of complex **9a**. In the IR spectrum, the signal for the $\tilde{\nu}$(C≡C) stretch of **9c** at 1820 $cm^{-1}$ and similar IR bands for complexes **9a** (1847 $cm^{-1}$) and **9b** (1852 $cm^{-1}$) are in accordance with the related absorptions of the zirconocene complexes $[(RCp)_2Zr]_2(\mu\text{-}C{\equiv}C\text{–}R)_2$[5a,5c] (1770–1820 $cm^{-1}$) and the bimetallic tungsten–iron complexes $\{[(\eta^5\text{-}C_5H_5)\text{-}\mu\text{-}(CO)(NO)W][(\eta^5\text{-}C_5H_5)(CO)Fe\text{–}C{\equiv}C\text{–}R]\}$ (1861–1908 $cm^{-1}$).[8] The decrease in the $\tilde{\nu}$(C≡C) stretching frequency of **9c** is a result of the strong electron back-donation $Si{\leftarrow}C_\pi$.[9] Additionally, the IR spectra of complexes **9a**–**c** show for the nitrosyl ligand, as expected, a strong and broad signal in the 1553–1560 $cm^{-1}$ region. At ambient temperature, the $^1H$- and $^{13}C$ NMR spectra of complexes **9b** and **9c** show two singlets for both the Cp ligand and for the methyl groups, in the ratio 6:1 and 5:1 for **9b** and **9c**, respectively, indicating the presence of two isomers. Besides these signals, the most informative absorptions in the $^{13}C$ NMR spectra are the signals for the α-carbon atoms at $\delta$ = 167.7 ppm (**9b**) and 197.9 ppm (**9c**) and for the β-carbon atoms at $\delta$ = 124.4 ppm (**9b**) and 108.1 ppm (**9c**), which are characteristic for the π-bridging acetylide ligand.[8] Because of the β-effect of the $(CH_3)_3Si$ group in complex **9c**, the singlet of the α-carbon atom appears at lower-field. We believe that the minor signals of the Cp ligands and methyl groups present in the NMR spectra can be attributed to a stereoisomer of **9b** and **9c**, with (*Z*)-orientation of the cyclopentadienyl rings.[8]

Contrary to complexes **9b** and **9c**, the $^1H$ NMR spectrum of complex **9a** shows at room temperature, for the cyclopentadienyl ligand, one singlet at $\delta$ = 5.71 ppm, and in the $^{13}C$ NMR spectrum, a broad signal with low intensity at $\delta$ = 98.3 ppm. Signals for the acetylide carbon atoms were not detectable. Low-temperature $^{13}C$ NMR spectroscopy of this

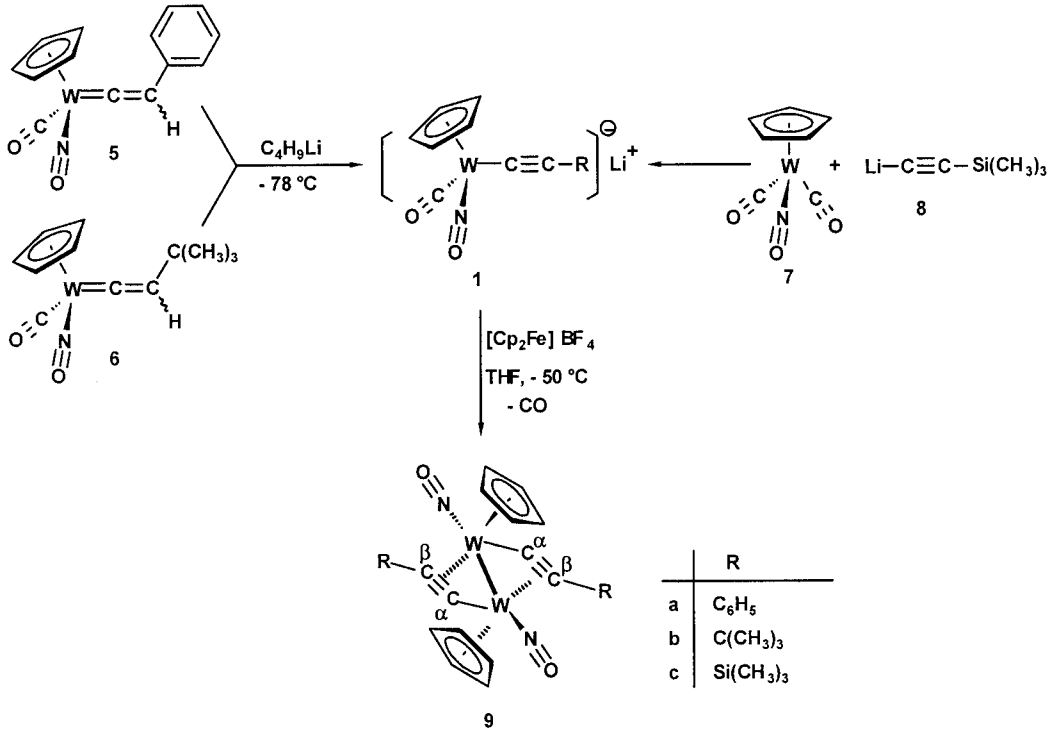


Scheme 3.

 © 2006 Wiley-VCH Verlag GmbH & Co. KGaA, Weinheim 

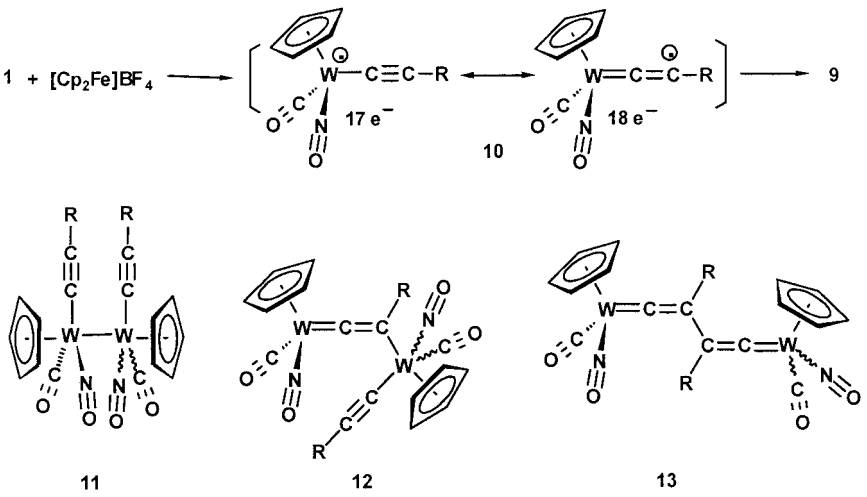


Scheme 4.

complex in $CD_2Cl_2$ at –40 °C revealed sharp singlets for the Cp-carbon atoms ($\delta$ = 98.0 ppm), the α-carbon atom ($\delta$ = 177.3 ppm), and the β-carbon atom ($\delta$ = 112.2 ppm). Additionally, a small signal appeared at $\delta$ = 97.5 ppm, and was attributed to the Cp ligand of a second minor stereoisomer. Increasing the temperature to 90 °C ([$D_2$]-1,1,2,2-tetrachloroethane) also resulted in the sharpening and increased relative intensity of the Cp signal, as well as in the emergence of a signal for the β-carbon atom.[10] The observed dynamic features of complex **9a** are not yet fully understood. One possible explanation would be an (*E*/*Z*) isomerization at the metal center by the reversible opening of the tungsten–tungsten bond.

## Mechanistic Considerations

As expected, the single-electron oxidation of the 18-electron tungsten–alkynyl complex **1** generates the reactive species **10**, which can be represented by resonance structures of a 17-electron metal-centered radical and an 18-electron carbon-centered radical (Scheme 4). As a result of metal-centered reactivity, the 17-electron radical dimerizes to form **11**, which has a metal–metal bond. Subsequent elimination of carbon monoxide leads to the binuclear 18-electron complexes **9a**–**c** with bridged σ,π-acetylide ligands. Products such as **12** and **13**, which could be formed by an alternative path through dimerization of radical **10**, could not be detected.[11,12]

## Molecular Structure of 9a

The structure of **9a** is further supported by single-crystal X-ray diffraction analysis. Single crystals were obtained by slow diffusion of *n*-pentane into a dichloromethane solution of **9a** at –20 °C. The crystal parameters, data collection parameters, and conditions for structure refinement are summarized in Table 1. Selected bond lengths and angles are given in Table 2. The ORTEP drawing with atomic numbering scheme is provided in Figure 1. Complex **9a** crystallizes in a $C_{2h}$-symmetric molecular structure with a planar arrangement of the atoms W(1)–C(6)–W(1$^{\#}$)–C(6$^{\#}$), which have a dihedral angle of 0° and an angle of 163.4° for W(1)–

Table 1. Crystal data and conditions for crystallographic data collection and structure refinement of **9a**.

| | |
|---|---|
| Empirical formula | $C_{26}H_{20}N_2O_2W_2$ |
| Formula mass | 760.14 |
| Color | orange, transparent |
| Crystal system | monoclinic |
| Space group | $P2_1/n$ (No. 14) |
| Cell parameters | $a$ = 9.7353(9) Å |
| | $b$ = 13.0525(13) Å; $\beta$ = 118.073(9)° |
| | $c$ = 9.8758(9) Å |
| $V$ [Å$^3$] | 1107.27(18) |
| Z | 4 |
| $d_{calcd.}$ [g cm$^{-3}$] | 2.280 |
| $\mu$ [cm$^{-1}$] | 104.07 |
| Diffractometer | Image Plate Diffractometer System (STOE) |
| Radiation | Mo-$K_\alpha$ |
| Monochromator | graphite |
| 2$\theta$ [°] | 5.76 ≤ 2$\theta$ ≤ 56.16 |
| $h$, $k$, $l$ range | –12 ≤ $h$ ≤ 12, –17 ≤ $k$ ≤ 17, –13 ≤ $l$ ≤ 12 |
| Reflections measured | 9994 |
| Independent reflections | 2647 |
| $R_{int}$ | 0.0413 |
| Reflections with $F_o > 4\sigma(F_o)$ | 2232 |
| Temperature [K] | 293 |
| Applied corrections | Lorentz and polarization coefficients |
| Structure determination and refinement | W positional parameters from direct methods (SHELXS-97)[a] |
| Refined parameters | 146 |
| $wR2$ | 0.0567 |
| $R1$ | 0.0287 |
| $R1$ [$F_o > 4\sigma(F_o)$] | 0.0212 |
| max, min in $\Delta\sigma$ [e·Å$^{-3}$] | 1.24, –0.80 |

[a] Ref.[18a] Further atoms were found from $\Delta F$ synthesis.[18b] Refinement by anisotropic full-matrix least-squares procedure for all non-hydrogen atoms; hydrogen position refinement by riding model.

 © 2006 Wiley-VCH Verlag GmbH & Co. KGaA, Weinheim 

C(6)–C(7#). The W(1)–C(6) bond length (2.025 Å) is shorter than those reported for the σ-acetylide complexes [(η$^5$-$C_5H_5$)(η$^3$-crotyl)(NO)W–C≡C–Ph] (2.104 Å)[7f] and [(η$^5$-$C_5H_5$)WRe(μ-I)(C≡C–Ph)(CO)$_5$] (2.09 Å).[13] The $C_α$–$C_β$ bond length (1.250 Å) is comparable to those reported for {[(η$^5$-$C_5H_5$)μ-(CO)(NO)W][(η$^5$-$C_5H_5$)(CO)Fe–C≡C–Ph]} (1.25 Å),[8] [{$(H_3CCp)_2Zr$}$_2$(μ-C≡C–Ph)$_2$] (1.261 Å),[5a] and [$Cp_2Zr$(μ-C≡C–$SiMe_3$)(μ-C≡C–Ph)$ZrCp_2$] (1.267 Å),[5b] but elongated compared to non-coordinated C≡C bonds (H–C≡C–H: 1.21 Å; H–C≡C–$CH_3$: 1.207 Å)[14] and σ-acetylide complexes (1.206–1.21 Å).[7f,5a] The tungsten–tungsten distance, with 3.0389 Å, is slightly shorter than the tungsten–tungsten single bond in [{$(OC)_5W$}$_2$C=C=$CPh_2$] (3.15 Å).[15]

Table 2. Selected bond lengths [Å] and angles [°] for **9a**.

| Distances | | Angles | |
|---|---|---|---|
| W(1)–W(1#) | 3.0389(4) | W(1)–C(6)–C(7#) | 163.4(4) |
| W(1)–C(6) | 2.025(4) | C(6#)–C(7)–C(8) | 151.1(4) |
| W(1)–C(6#) | 2.242(4) | C(6)–W(1)–W(1#) | 47.54(11) |
| W(1)–C(7) | 2.298(4) | C(6)–W(1)–C(6#) | 89.32(15) |
| C(6)–C(7#) | 1.250(6) | N(1)–W(1)–C(6) | 96.23(18) |
| C(7)–C(8) | 1.449(6) | N(1)–W(1)–W(1#) | 105.22(13) |

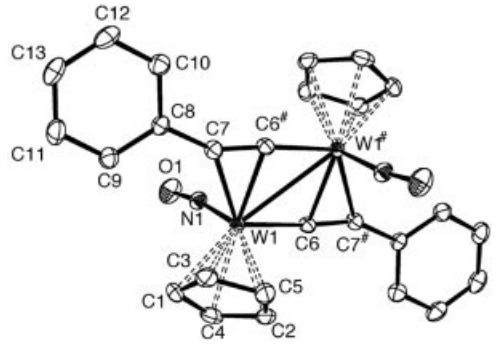


Figure 1. Molecular structure and atom numbering scheme for **9a**. Thermal ellipsoids are shown at the 30% probability level (ORTEP drawing).

## Experimental Section

**General Procedures:** All operations were carried out under argon. All solvents were purified by standard techniques. Literature methods were used to prepare **5**, **6**,[7g] **7**,[16] and [$Cp_2Fe$][$BF_4$].[17] NMR spectra were recorded with a Bruker AM 400 spectrometer. $^1$H NMR spectra were measured at 400 MHz, $^{13}$C NMR spectra were measured at 100 MHz. Proton and carbon-13 chemical shifts are relative to TMS. IR spectra were recorded with a Bruker FT-IR IFS 85. Microanalyses were done with a Carlo–Erba 1104 elemental analyzer.

**Preparation of [(η$^5$-$C_5H_5$)(NO)W–C≡C–$C_6H_5$]$_2$ (9a):** *n*BuLi (1 mmol) in hexane was added to a solution of [(η$^5$-$C_5H_5$)(CO)(NO)W=C=CH($C_6H_5$)] (**5**) (409 mg, 1 mmol) in THF (30 mL) at –78 °C. The resulting emerald-green solution was stirred for 15 min and then warmed up to –50 °C. [$Cp_2Fe$][$BF_4$] (273 mg, 1 mmol) was added in small portions to the solution over 30 min and stirred for 2 h. The color of the solution changed from green to dark red. After removing the solvent under reduced pressure at low temperature (–10 °C), the crude product was extracted several times with pentane to remove ferrocene. Chromatography of the residue on silica gel with pentane/diethyl ether (1:1), followed by crystallization from $CH_2Cl_2$ layered with pentane, gave 130 mg (39%) of complex **9a** as orange crystals [m.p. 252 °C (dec.)]. $C_{26}H_{20}N_2O_2W_2$ (760.16): calcd. C 41.08, H 2.65, N 3.68; found C 41.09, H 2.23, N 3.84. $^1$H NMR (400 MHz, $CDCl_3$, r.t.): δ = 7.90–7.83 (m, 4 H, Ph), 7.53–7.38 (m, 6 H, Ph), 5.71 (s, 10 H, Cp) ppm. $^{13}$C NMR (100 MHz, $CDCl_3$, r.t.): δ = 131.9, 131.4, 128.98, 128.5 (4s, Ph), 111.7 (s, $C_β$), 98.3 (br. s, Cp) ppm. IR (KBr): ṽ = 1847 (C≡C), 1553 (NO) cm$^{-1}$. MS (70 eV): *m*/*z* = 760 [M$^+$, $^{184}$W]. HRMS: calcd. for $C_{26}H_{20}N_2O_2{}^{182}W_2$ [M$^+$] 756.0489; found 756.0474.

**Preparation of [(η$^5$-$C_5H_5$)(NO)W–C≡C–C($CH_3$)$_3$]$_2$ (9b):** The reaction was carried out as described for **9a** by using [(η$^5$-$C_5H_5$)(CO)(NO)W=C=CH{$C(CH_3)_3$}] (**6**) (389 mg, 1 mmol) instead of **5**. Chromatography followed by crystallization yielded 90 mg (25%) of the product as orange crystals [m.p. 245 °C (dec.)]. $C_{22}H_{28}N_2O_2W_2$ (720.18): calcd. C 36.69, H 3.91, N 3.88; found C 36.45, H 3.59, N 3.30. $^1$H NMR (400 MHz, $CDCl_3$, r.t.): δ = 5.69, 5.65 (2 s, 6:1, 10 H, Cp), 1.58 and 1.54 (2 s, 6:1, 18 H, $CH_3$) ppm. $^{13}$C NMR (100 MHz, $CDCl_3$, r.t.): δ = 167.7 (s, $C_α$), 124.5 [t, $^2J$($^{183}$W–$^{13}$C) = 29.6 Hz] and 123.9 (s) (2 $C_β$), 97.0 and 96.1 (2 s, 2 Cp), 37.9 and 37.5 [2 s, *C*($CH_3$)$_3$], 33.2 and 32.7 (2 s, $CH_3$) ppm. IR (KBr): ṽ = 1852 (C≡C), 1560 (NO) cm$^{-1}$. MS (70 eV): *m*/*z* = 720 [M$^+$, $^{184}$W]. HRMS: calcd. for $C_{22}H_{28}N_2O_2{}^{182}W_2$ [M$^+$] 716.1115; found 716.1107.

**Preparation of [(η$^5$-$C_5H_5$)(NO)W–C≡C–Si($CH_3$)$_3$]$_2$ (9c):** *n*BuLi (1.2 mmol) in hexane was added to a solution of ethinyltrimethylsilane (0.167 mL, 1.2 mmol) in THF (15 mL) at –78 °C. The resulting green solution of the tungsten acetylide [(η$^5$-$C_5H_5$)(NO)(CO)W–C≡C–Si($CH_3$)$_3$]Li (**1c**) was transferred dropwise to a precooled (–30 °C) solution of [(η$^5$-$C_5H_5$)(CO)$_2$(NO)W] (**7**) (335 mg, 1 mmol) in THF (15 mL) and stirred for 3 h. The green solution was treated, as above, with [$Cp_2Fe$][$BF_4$] (273 mg, 1 mmol). Removal of the solvent followed by recrystallization yielded 208 mg (54%) of complex **9c** as orange crystals [m.p. 243 °C (dec.)]. $C_{20}H_{28}N_2O_2Si_2W_2$ (752.33): calcd. C 31.93, H 3.75, N 3.72; found C 31.64, H 3.40, N 3.85. $^1$H NMR (400 MHz, $CDCl_3$, r.t.): δ = 5.69 and 5.64 (2 s, 5:1, 10 H, Cp), 0.46 and 0.44 (2 s, 5:1, 18 H, $CH_3$) ppm. $^{13}$C NMR (100 MHz, $CDCl_3$, r.t.): δ = 197.9 (s, $C_α$), 108.1 (s, $C_β$), 97.2 and 96.2 (2 s, Cp), 1.6 and 1.2 (2 s, $CH_3$) ppm. IR (KBr): ṽ = 1820 (C≡C), 1560 (NO) cm$^{-1}$. MS (70 eV): *m*/*z* = 752 [M$^+$, $^{184}$W]. HRMS: calcd. for $C_{20}H_{28}N_2O_2Si_2{}^{182}W_2$ [M$^+$] 748.0653; found 748.0643.

CCDC-602108 contains the supplementary crystallographic data for compound **9a**. These data can be obtained free of charge from The Cambridge Crystallographic Data Centre via www.ccdc.cam.ac.uk/data_request/cif.

## Acknowledgments

This work was supported by the Deutsche Forschungsgemeinschaft (IP 7/5-2; IP 7/5-3).

[1] a) R. Nast, *Coord. Chem. Rev.* **1982**, *47*, 89; b) M. I. Bruce, *Coord. Chem. Rev.* **1997**, *166*, 91; c) R. H. Crabtree, *The Organometallic Chemistry of the Transition Metals*, 3rd ed., Wiley-Interscience, New York, **2001**; d) B. Cornils, W. Herrmann, *Applied Homogeneous Catalysis with Organometallic Compounds* (2 vols.), VCH, Oxford, U. K., **1996**; e) J. P. Collman, L. S. Hegedus, J. R. Norton, R. G. Finke, *Principles and Applications*

 © 2006 Wiley-VCH Verlag GmbH & Co. KGaA, Weinheim 

*of Organotransition Metal Chemestry*, University Science Books, Mill Valley CA, **1987**.
[2] a) E. Peréz-Carreño, P. Paoli, A. Ienco, C. Mealli, *Eur. J. Inorg. Chem.* **1999**, 1315; b) M. I. Bruce, *Chem. Rev.* **1998**, *98*, 2797; c) D. Touchard, P. H. Dixneuf, *Coord. Chem. Rev.* **1998**, *178–180*, 409; d) M. I. Bruce, *Chem. Rev.* **1991**, *91*, 197; e) H. Werner, *Angew. Chem.* **1990**, *102*, 1109; *Angew. Chem. Int. Ed. Engl.* **1990**, *29*, 1077.
[3] a) C. E. Powell, M. G. Humphrey, *Coord. Chem. Rev.* **2004**, *248*, 725; b) N. J. Long, C. K. Williams, *Angew. Chem.* **2003**, *115*, 2690; *Angew. Chem. Int. Ed.* **2003**, *42*, 2586; c) I. R. Whittall, A. M. McDonagh, M. G. Humphrey, M. Samoc, *Adv. Organomet. Chem.* **1999**, *43*, 349.
[4] H. Lang, D. S. A. George, G. Rheinwald, *Coord. Chem. Rev.* **2000**, *206–207*, 101 and references cited therein.
[5] a) G. Erker, W. Frömberg, R. Benn, R. Mynott, K. Angermund, C. Krüger, *Organometallics* **1989**, *8*, 911; b) G. Erker, W. Frömberg, R. Mynott, B. Gabor, C. Krüger, *Angew. Chem.* **1986**, *98*, 456; *Angew. Chem. Int. Ed. Engl.* **1986**, *25*, 463; c) U. Rosenthal, A. Ohff, W. Baumann, R. Kempe, A. Tillack, V. V. Burlakov, *Organometallics* **1994**, *13*, 2903.
[6] J. R. Berenguer, J. Forniés, E. Lalinde, A. Martín, *Angew. Chem.* **1994**, *106*, 2196; *Angew. Chem. Int. Ed. Engl.* **1994**, *33*, 2083.
[7] a) J. Ipaktschi, J. Mohsseni-Ala, A. Dülmer, C. Loschen, G. Frenking, *Organometallics* **2005**, *24*, 977; b) J. Ipaktschi, P. Rooshenas, T. Klotzbach, A. Dülmer, E. Hüseynova, *Organometallics* **2005**, *24*, 1351; c) J. Ipaktschi, F. Munz, *Organometallics* **2002**, *21*, 977; d) J. Ipaktschi, T. Klotzbach, A. Dülmer, *Organometallics* **2000**, *19*, 5281; e) J. Ipaktschi, F. Mirzaei, K. Reimann, J. Beck, M. Serafin, *Organometallics* **1998**, *17*, 5086; f) J. Ipaktschi, F. Mirzaei, G. J. Demuth-Eberle, J. Beck, M. Serafin, *Organometallics* **1997**, *16*, 3965; g) J. Ipaktschi, G. J. Demuth-Eberle, F. Mirzaei, B. G. Müller, J. Beck, M. Serafin, *Organometallics* **1995**, *14*, 3335.
[8] J. Ipaktschi, F. Mirzaei, B. G. Müller, J. Beck, M. Serafin, *J. Organomet. Chem.* **1996**, *526*, 363.
[9] H. Bock, H. Siedl, *J. Chem. Soc. B* **1968**, 1158.
[10] The influence of the relaxation effect on the signal's intensity can be excluded, because the intensity of the signal increases for both a decrease and an increase in the probe temperature.
[11] a) For general reviews see: D. A. Valyaev, O. V. Semeikin, N. A. Ustynyuk, *Coord. Chem. Rev.* **2004**, *248*, 167; b) D. A. Valyaev, O. V. Semeikin, M. G. Peterleitner, Y. A. Borisov, V. N. Khrustalev, A. M. Mazhuga, E. V. Kremer, N. A. Ustynyuk, *J. Organomet. Chem.* **2004**, *689*, 3837.
[12] R. L. Beddoes, C. Bitcon, A. Ricalton, M. W. Whiteley, *J. Organomet. Chem.* **1989**, *367*, C21–C24.
[13] C. W. Pin, J. J. Peng, C. W. Shiu, Y. Chi, S. M. Peng, G. H. Lee, *Organometallics* **1998**, *17*, 438.
[14] a) J. Dale, *Properties of Acetylenic Compounds* in *Chemistry of Acetylenes* (Ed.: H. G. Viehe), Marcel Dekker, New York, **1969**, p. 53; b) L. Pauling, *The Nature of the Chemical Bond*, Cornell University Press, Ithaca NY, **1960**, p. 230.
[15] H. Berke, P. Härter, G. Huttner, L. Zsolnai, *Chem. Ber.* **1982**, *115*, 695.
[16] T. T. Chin, J. K. Hoyano, P. Legzdins, J. T. Malito, *Inorg. Synth.* **1990**, *28*, 196.
[17] H. Schumann, *J. Organomet. Chem.* **1985**, *290*, C34.
[18] a) G. M. Sheldrick, SHELXS-97, *Program for the Solution of Crystal Structures*, University of Göttingen, **1997**; b) G. M. Sheldrick, SHELXL-97, *Program for Crystal Structure Refinement*, University of Göttingen, **1997**.

Received: January 19, 2006
Published Online: March 23, 2006

 © 2006 Wiley-VCH Verlag GmbH & Co. KGaA, Weinheim 

DOI: 10.1002/ejic.200500894

# An Experimental and Density Functional Study of the Interaction of $Cu^{II}$ Complexes of Diethylenetriamine (Dien) with Pyridine, Nicotinic Acid, and Nicotinamide: The Crystal Structure of [Cu(dien)(nicotinamide)$(NO_3)_2$]

**Panagiotis A. Papanikolaou,[a] Panagiotis C. Christidis,[b] Aikaterini Th. Chaviara,[a] Christos A. Bolos,*[a] and Athanassios C. Tsipis*[c]**

**Keywords:** Copper / Density functional calculations / N ligands / Thermal analysis

The reaction of pyridine (py), nicotinamide (nica), nicotinic acid (nic), and its nicotinate anion ($nic^-$) with [Cu(dien)$X_2$] (dien = diethylenetriamine; X = $Br^-$, $NO_3^-$) in a 1:1 molar ratio affords the new compounds [Cu(dien)(py)$(NO_3)_2$], [Cu(dien)(nica)$(NO_3)_2$], [Cu(dien)($nic^-$)$(NO_3)(H_2O)$]·$H_2O$, [Cu(dien)($nic^-$)(Br)$(H_2O)$]·$2H_2O$, and [Cu(dien)$(NO_3)$($nic^-$)(Guo)]·$5H_2O$. These compounds were characterized by elemental analysis, and their molecular structures were determined by spectroscopic methods (infrared and electronic spectra), magnetic susceptibility, and molar conductivity measurements, and further corroborated by geometry optimization using electronic structure calculation methods at the B3LYP/6-31G(d,p) level of theory. The structural, bonding and electronic properties of the complexes are adequately described by B3LYP computational techniques. According to the experimental data, the complexes can be characterized in the solid state as mononuclear, with a distorted octahedral stereochemistry. The distorted octahedral stereochemistry adopted by the complexes was further confirmed by the X-ray structure analysis of [Cu(dien)(nica)$(NO_3)_2$], which consists of a six-coordinate Cu atom in a distorted octahedral environment constructed from four N atoms (three from dien and one from nica) and two O atoms from the loosely associated $NO_3^-$ counteranions, with the former occupying the equatorial square plane of the octahedron and the latter the axial positions, Cu–O bond lengths being rather long (2.373 and 2.858 Å, respectively). Some substitution reactions have also been studied and are discussed in light of the electronic structure of the complexes computed at the B3LYP/6-31G(d,p) level.
(© Wiley-VCH Verlag GmbH & Co. KGaA, 69451 Weinheim, Germany, 2006)

## Introduction

Nicotinamide (nica) and nicotinic acid (nic) are two of most extensively studied pyridine derivatives. The former is a component of the vitamin B complex and of the vital coenzyme NAD (nicotinamide adenine dinucleotide),[1] and is a typical N-donor ligand system in crystal engineering.[2] Furthermore, early administration of nicotinamide has been reported to impair learning and memory in mice.[3] The medicinal chemistry of nicotinamide in the treatment of ischemia and reperfusion has also developed rapidly in the past few years. Nicotinic acid has a wide-ranging ability to reduce lipid levels, but its clinical uses are restricted due to its various side-effects. Nicotinic acid and nicotinamide form niacin, a water-soluble vitamin that reduces VLDL cholesterol and increases HDL cholesterol (the so-called "good" cholesterol).[4] Moreover, coordination compounds of nicotinic acid, nicotinamide, and their derivatives are known to have antiviral or antibacterial activity,[5,6] and they also selectively affect tumor tissues.[7]

Preliminary toxicity and anticancer results of diethylenetriamine (dien)–$Cu^{II}$ mixed-ligand complexes with nicotinic acid (nic) and nicotinamide (nica) ligands encouraged us to thoroughly study such complexes. In effect, what we want to address here is the synthesis and the structural, bonding, electronic, and spectroscopic properties of a number of new compounds resulting from interaction of [Cu(dien)$X_2$] (X = $Br^-$, $NO_3^-$) with pyridine (py), nicotinic acid, and nicotinamide. The electronic structure and bonding of the new complexes was inferred from electronic structure calculation methods at the DFT level.

## Results and Discussion

### Synthesis

The synthetic procedures used to prepare the new complexes can be divided into two categories: the first method is based on the reaction of [Cu(dien)$(NO_3)_2$] with nicotinic acid (nic), nicotinamide (nica), or pyridine (py), while the second one involves the reaction of deprotonated nic ($nic^-$)

[a] Laboratory of Inorganic Chemistry, Department of Chemistry, Aristotle University of Thessaloniki, 54124 Thessaloniki, Greece
[b] Laboratory of Crystallography, Department of Physics, Aristotle University of Thessaloniki, 54124 Thessaloniki, Greece
[c] Section of Inorganic and Analytical Chemistry, Department of Chemistry, University of Ioannina, 451 10 Ioannina, Greece
E-mail: attsipis@cc.uoi.gr

 © 2006 Wiley-VCH Verlag GmbH & Co. KGaA, Weinheim 

with [Cu(dien)$(NO_3)_2$] (**1**) or [Cu(dien)$Br_2$] (**2**). Both syntheses were performed in methanol using a 1:1 molar ratio of the reactants. The new $Cu^{II}$ complexes, formulated as [Cu(dien)(py)$(NO_3)_2$] (**3**), [Cu(dien)(nica)$(NO_3)_2$] (**4**), [Cu(dien)($nic^-$)$(NO_3)(H_2O)$]·$H_2O$ (**5**), [Cu(dien)($nic^-$)(Br)-$(H_2O)$]·$2H_2O$ (**6**), and [Cu(dien)$(NO_3)$($nic^-$)(Guo)]·$5H_2O$ (**7**), are paramagnetic, as expected from the $d^9$ electron configuration of the $Cu^{II}$ central atom, blue in color, and stable in air. They are soluble in water and other coordinating solvents such as DMF and DMSO, slightly soluble in alcohols, but insoluble in common organic solvents.

## Spectroscopy

The salient structural features of the new complexes were determined by spectroscopic methods (infrared and electronic spectra), while details of the structures were obtained by the X-ray structural investigation of a representative complex, namely [Cu(dien)(nica)$(NO_3)_2$] (**4**). In the IR spectra of the precursor complexes [Cu(dien)$(NO_3)_2$] (**1**) and [Cu(dien)$Br_2$] (**2**) the absorption bands at around 3270 and 3233 $cm^{-1}$ are attributed to the antisymmetric and symmetric stretching vibration of the primary and secondary amino group of dien, respectively, thus confirming the tridentate coordination bonding mode of the ligand.[9] In the IR spectrum of [Cu(dien)(py)$(NO_3)_2$] (**3**), the ν(C=N) stretching vibration at 1608 $cm^{-1}$ is shifted towards lower frequencies with respect to that of the free pyridine (1622 $cm^{-1}$), thereby indicating coordination of the pyridine through the endocyclic nitrogen atom. The same also holds true for the rest of the complexes involving the nic and $nic^-$ ligands. In contrast, upon coordination of the nica ligand the absorption band at 1593 $cm^{-1}$ is shifted slightly towards higher frequencies (1603 $cm^{-1}$), in line with previous observations.[10] The new bands at around 520–535 $cm^{-1}$ due to ν(Cu–N) stretching vibrations[11] confirm the N-coordination of py and its derivatives through the endocyclic nitrogen atom. In addition, the experimental ν(C=O) stretching vibration of the free nicotinamide ligand appearing at 1681 $cm^{-1}$ is slightly shifted to higher frequencies (1693 $cm^{-1}$) upon coordination to the metal center in [Cu(dien)(nica)$(NO_3)_2$] (**4**), in line with previous studies.[12–14] In the IR spectrum of nicotinic acid the ν(C=O) stretching vibration absorbing at 1709 $cm^{-1}$[15,16] is shifted to lower frequencies (1661–1668 $cm^{-1}$) upon coordination, regardless of the deprotonation of the ligand. Moreover, the IR spectra of [Cu(dien)-$(NO_3)$($nic^-$)]·$2H_2O$ (**5**) [Cu(dien)(Br)($nic^-$)]·$3H_2O$ (**6**), and [Cu(dien)$(NO_3)$($nic^-$)(Guo)]·$5H_2O$ (**7**) show that the $nic^-$ ligand is not coordinated through the N atom of the pyridine ring. The two IR absorption bands at 1760 and 1745 $cm^{-1}$, combined with a very intense and broad band at around 1380 $cm^{-1}$, are indicative of the unidentate coordination mode of the nitrate anions with copper(II). Finally, the very weak band at 324 $cm^{-1}$ should be attributed to the ν(Cu–Br) stretching vibration of **6**.[11] The presence of water in all hydrated complexes, either as ligands or as lattice water, as well as the large number of hydrogen bonds, was indicated by the appearance of broad bands at 3414 and 3476 $cm^{-1}$, respectively. The former can be attributed to hydrogen bonds and the latter to the existence of water either in the lattice or as a ligand. The presence of water was further corroborated by thermal DTA analysis (vide infra).

The UV/Vis electronic spectra of the complexes in aqueous $10^{-3}$ M solutions show a band in the visible region at 608–623 nm (Figure 1), which can be attributed to crystal-field d–d electronic transitions (probably $3d_{x^2-y^2} \leftarrow 3d_{z^2}$). This band is characteristic for $Cu^{II}$ complexes with a distorted square-pyramidal geometry.

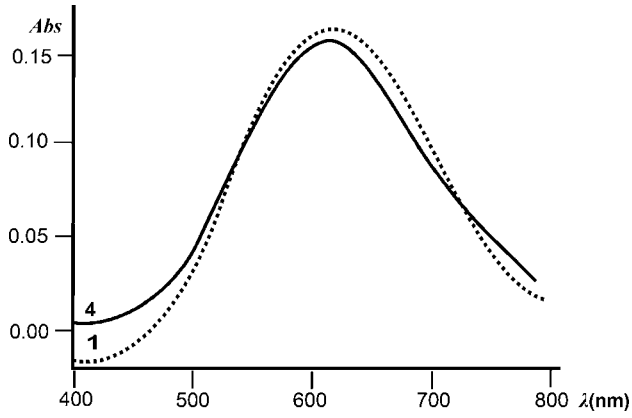


Figure 1. Electronic spectra of [Cu(dien)$(NO_3)_2$] (**1**) and [Cu(dien)-(nica)$(NO_3)_2$] (**4**) in aqueous solution.

In the UV region of the spectra of the "free" py, nic, $nic^-$, and nica ligands the absorption bands and shoulders occur around 240–260 nm ($\log\varepsilon$ = 3.63–3.90), which can be attributed to intraligand π* ← π electronic transitions due to the conjugated C=N, C=C, and C=O groups of the pyridine-ring-containing ligands. These bands are shifted either to lower or higher frequencies, depending on the coordination mode of the ligand. The band at 204–214 nm could be assigned to σ* ← σ type transitions of the free dien molecule, which is not shifted upon coordination.

In the solid state (Nujol mulls), all $Cu^{II}$ complexes show the crystal-field band at around 560–580 nm. Such bands are typical for octahedral $Cu^{II}$ complexes. Therefore, it is obvious that the different structures adopted by the complexes in aqueous and methanol solutions and in the solid state may be due to the dissociation of the compounds in solution.[17]

## Conductivity and Magnetic Measurements

The molar conductivity values, $\Lambda_\mu$, for the complexes, which vary between 159–423 and 77–213 μS $cm^{-1}$ for $10^{-3}$ M aqueous and methanol solutions, respectively, strongly suggest the ionic nature of the complexes. Specifically, in aqueous solutions, the zwitterionic complexes [Cu(dien)($nic^-$)-$(NO_3)(H_2O)$]·$H_2O$ (**5**), [Cu(dien)($nic^-$)(Br)$(H_2O)$]·$2H_2O$ (**6**), and [Cu(dien)$(NO_3)$($nic^-$)(Guo)]·$5H_2O$ (**7**) are 1:1 electrolytes[18] that dissociate according to the following general scheme:

 © 2006 Wiley-VCH Verlag GmbH & Co. KGaA, Weinheim 

$[Cu(dien)(X)(nic^-)(H_2O)] \rightleftharpoons [Cu(dien)(nic^-)]^+ + X^-$ (X = $NO_3^-$, $Br^-$)

$[Cu(dien)(py)(NO_3)_2]$ (**3**) and $[Cu(dien)(nica)(NO_3)_2]$ (**4**) are 2:1 electrolytes in aqueous solutions, with two dissociating nitrate anions. In methanol solution, complexes **3**–**7** are 1:1 electrolytes. Taken together, the above data lead to the conclusion that the complexes dissociate to a lesser degree in methanol solution.

The $\mu_{eff}$ values for the $Cu^{II}$ complexes were found in the range 1.72–1.93 $\mu_B$, consistent with their mononuclear structures.

### Thermal Analysis

The thermal behavior of selected $Cu^{II}$ complexes was studied by TG/DTG/DTA thermal analysis in the temperature range 40–1000 °C. The intermediates were confirmed from the mass-loss calculations. Generally, the thermal decomposition of the complexes proceeds in 4–6 stages, which depend on the nature of the ligands involved. For example, the thermal behavior of **4** (Figure 2) is characterized by four decomposition stages. The first one (200–281 °C) corresponds to the removal of the dien and nica ligands, while during the next two stages, which are non-distinct (281–519 and 519–865 °C), the successive decomposition of two nitrate ions to a nitrite moiety takes place; the calculated and found values for this process are almost identical. During the fourth step (865–973 °C), the elimination of an oxygen molecule, derived from the decomposition of two nitrate ions to the corresponding nitrito moiety, occurs. The elimination of $O_2$ at such a high temperature should be due to its strong binding with Cu as a $CuO_2$ fragment. The last step corresponds to the formation of metallic copper as a residue, as proved by IR spectroscopy and its quantitative analysis.

The thermal analysis of **5** (Figure 3) starts with the dehydration of the molecule, which takes place in a single mass-loss step corresponding to 9.2% (calcd. 9.3%), up to 123 °C, due to the endothermic elimination of lattice and coordinated water molecules. A total weight loss of 58.00% occurs in the temperature range 212–327 °C, presumably due to the loss of $nic^-$ and dien ligands (calcd. 58.22%). The third step (665–964 °C) involves loss of the nitrate anion, while the residue remaining at temperatures higher than 964 °C is metallic copper, as evidenced by the mass loss (calcd. 16.45; found 16.80%) and the IR spectroscopic data.

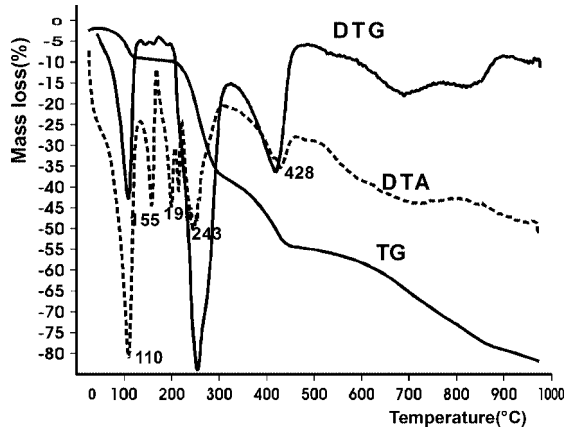


Figure 3. Thermal analysis diagram of $[Cu(dien)(nic^-)(NO_3)(H_2O)]\cdot H_2O$ (**5**).

Complex **6** partly dehydrates up to 110 °C in a single mass-loss process that corresponds to the endothermic elimination of two lattice water molecules, for which the theoretical and experimental mass loss are almost the same (Figure 4). The removal of the nicotinate anion takes place in the temperature range 216–300 °C in a second endothermic mass-loss procedure (28.75% found, 29.36% theoretical), as was proposed by Yeh et al.[19] The Br atom is removed between 300 and 432 °C (18.75% found, 19.37% calcd.), while the liberation of the dien molecule takes place at 432–848 °C (24.38% found, 24.97% calcd.). The elimi-

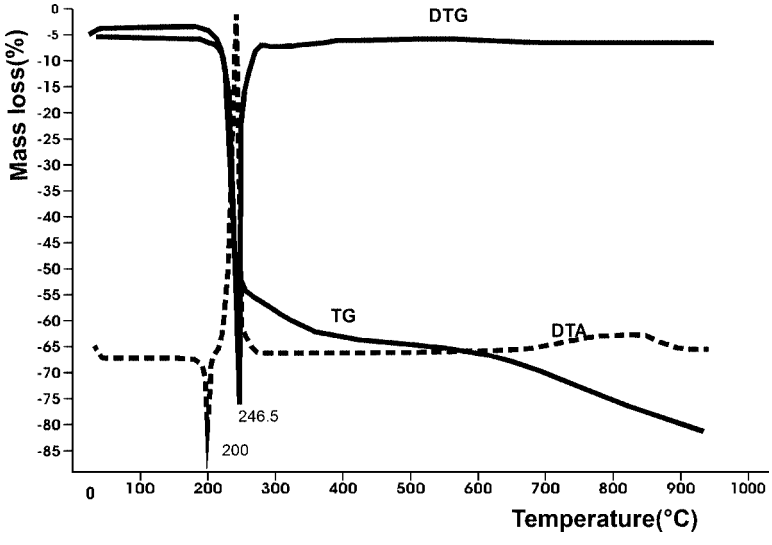


Figure 2. Thermal analysis diagram of $[Cu(dien)(nica)(NO_3)_2]$ (**4**).

 © 2006 Wiley-VCH Verlag GmbH & Co. KGaA, Weinheim 

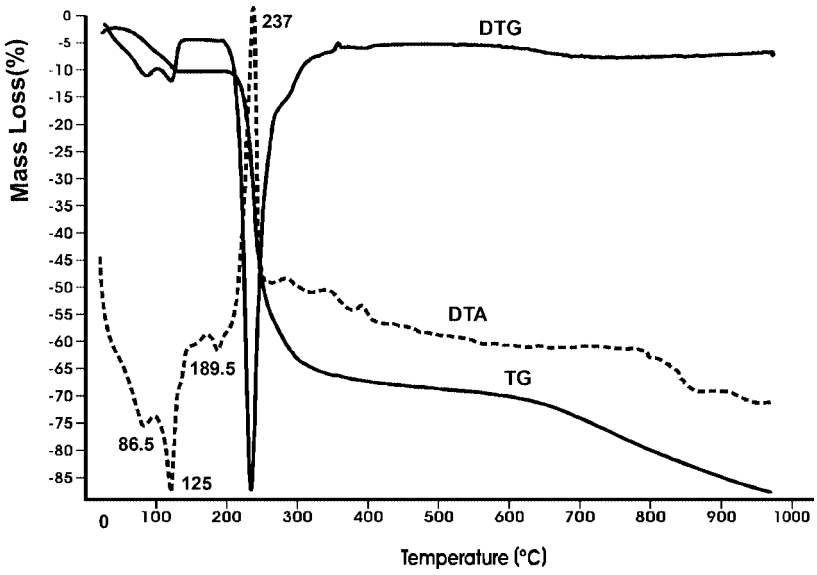


Figure 4. Thermal analysis diagram of [Cu(dien)(nic$^-$)(Br)($H_2O$)]·2$H_2O$ (**6**).

nation of the coordinated water at a higher temperature (848–964 °C) is tentatively proposed. The solid residue of the procedure above 964 °C corresponds to metallic copper.

### Crystal Structure of [Cu(dien)(nica)($NO_3$)$_2$] (4)

The molecular structure of **4** is shown in Figure 5, while bond lengths and angles along with the established hydrogen bonds are given in Table 1. The coordination polyhedron around the $Cu^{II}$ central atom is a distorted octahedron (4 + 1 + 1) with three of the equatorial positions occupied by the three nitrogen atoms of the dien ligand and the fourth position occupied by the nitrogen atom of the pyridine ring. The two axial positions of the coordination polyhedron are occupied by oxygen atoms from each of the two $NO_3^-$ anions at considerably different distances from the copper atom [Cu1–O2 = 2.373(2) and Cu1–O5 = 2.858(3) Å]. The conformation of the dien ligand is as expected.[21–23] The Cu–N distances range from 1.998(3) to 2.015(3) Å, while both the $N^p$–Cu–$N^s$ valence angles ($N^p$ from primary and $N^s$ from secondary amino groups) are smaller than 90° [84.1(1)° and 84.3(1)°]. Moreover, the $N^p$–Cu–$N^p$ angle is much smaller than 180° [163.7(1)°], which indicates a slight strain in the coordinated dien ligand. The reported observation that the Cu–$N^s$ distance is significantly shorter than the Cu–$N^p$ distances[22,24] seems to be generally valid only when referred to the mean Cu–$N^p$ distance [compare, for example, the Cu–N(dien) distances reported previously[8,25]]. The Cu–N(pyridine) distance of 2.036(3) Å deviates only slightly from the mean Cu–N(dien) distance [2.005(5) Å]. The four equatorial nitrogen atoms of the copper coordination polyhedron lie almost on a plane (rms deviation of the fitted atoms of 0.06 Å), forming an angle of 58.9(1)° to the plane of the pyridine ring. The copper atom deviates significantly from the above equatorial plane by 0.150(2) Å towards the axial O(2) atom with the shorter Cu–O bond. The established geometry of the pyridine ring is as expected, with the C–C bond lengths lying in the range 1.375(5)–1.391(5) Å and the C–N bond lengths lying in the range 1.333(4)–1.339(4) Å. The two nitrato groups also have a normal geometry, with the N6–O and N7–O bond lengths ranging from 1.226(4) to 1.258(4) Å and 1.217(4) to 1.246(4) Å, respectively.

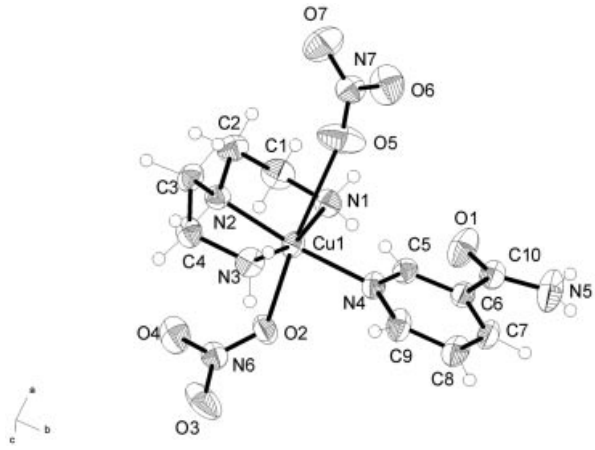


Figure 5. DIAMOND[20] plot of the molecular structure of [Cu(dien)(nica)($NO_3$)$_2$] (**4**), with the labeling scheme of the non-H atoms. Displacement ellipsoids are shown at the 30% probability level.

Hydrogen bonding plays a predominant role in the stabilization of the structure. As can be seen from Table 1, both the $N^p$ atoms of the dien ligand and the N atom of the amide group donate exclusively to oxygen atoms of $NO_3$ groups of neighboring molecules, while the $N^s$ atom of the dien ligand donates to the oxygen atom of the amide group of another molecule.

 © 2006 Wiley-VCH Verlag GmbH & Co. KGaA, Weinheim 

Table 1. Selected bond lengths [Å] and angles [°] for [Cu(dien)(nica)$(NO_3)_2$] (**4**).

| | | | |
|---|---|---|---|
| Cu1–N1 | 2.015(3) | C2–N2 | 1.476(5) |
| Cu1–N2 | 2.002(3) | C3–N2 | 1.479(5) |
| Cu1–N3 | 1.998(3) | C3–C4 | 1.499(6) |
| Cu1–N4 | 2.036(3) | C4–N3 | 1.482(5) |
| Cu1–O2 | 2.373(2) | C6–C10 | 1.515(5) |
| Cu1–O5 | 2.858(3) | C10–N5 | 1.321(5) |
| C1–N1 | 1.479(5) | C10–O1 | 1.211(4) |
| C1–C2 | 1.503(6) | | |
| N1–Cu1–N2 | 84.11(13) | C3–C4–N3 | 109.0(3) |
| N2 –Cu1–N3 | 84.31(13) | Cu1–N4–C5 | 122.5(2) |
| N3–Cu1–N4 | 97.30(13) | Cu1–N4–C9 | 119.4(2) |
| N1–Cu1–N4 | 93.20(13) | C5–N4–C9 | 117.8(3) |
| N1–C1–C2 | 107.9(3) | C6–C10–N5 | 117.6(3) |
| C1–C2–N2 | 107.8(3) | C6–C10–O1 | 119.9(3) |
| C2–N2–C3 | 116.8(3) | N5–C10–O1 | 122.4(4) |
| N2–C3–C4 | 107.6(3) | | |

Hydrogen bonding geometry

| D–H···A | D–H [Å] | H···A [Å] | D···A [Å] | D–H···A [°] |
|---|---|---|---|---|
| N1–H9A···O5[a] | 0.86(4) | 2.50(4) | 3.167(5) | 135(3) |
| N1–H9A···O7[a] | 0.86(4) | 2.54(4) | 3.290(4) | 146(3) |
| N1–H9B···O6 | 0.87(4) | 2.40(4) | 3.216(4) | 157(3) |
| N2–H10···O4 | 0.88(4) | 2.44(4) | 3.161(5) | 140(3) |
| N2–H10···O1[a] | 0.88(4) | 2.42(4) | 3.064(4) | 131(3) |
| N3–H11A···O2[b] | 0.71(4) | 2.57(4) | 3.261(4) | 168(4) |
| N3–H11A···O3[b] | 0.71(4) | 2.45(4) | 2.940(5) | 128(4) |
| N3–H11B···O6[c] | 0.85(5) | 2.34(5) | 3.178(5) | 166(4) |
| N5–H12A···O6[d] | 0.79(5) | 2.19(5) | 2.967(5) | 167(5) |
| N5–H12B···O7[e] | 0.94(5) | 2.16(5) | 3.079(5) | 168(4) |

[a] Symmetry codes: $x$, 1/2 – $y$, 1/2 + $z$. [b] $x$, 1/2 – $y$, –1/2 + $z$. [c] –1 + $x$, $y$, $z$. [d] 1 – $x$, –$y$, –$z$. [e] 1 – $x$, –1/2 + $y$, –1/2 – $z$.

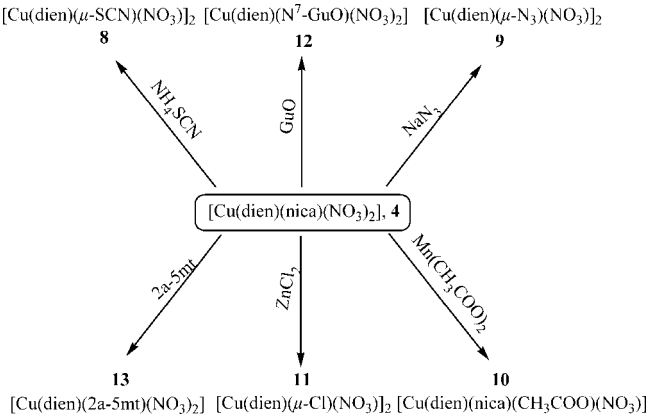


Scheme 1. Reactivity of [Cu(dien)(nica)$(NO_3)_2$] (**4**) towards nucleophiles.

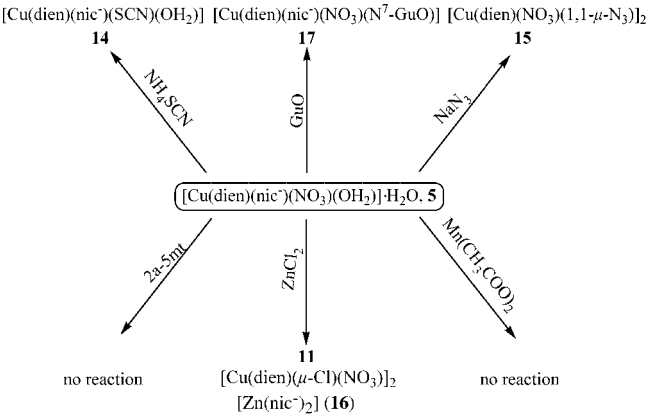


Scheme 2. Reactivity of complex **5** towards nucleophiles.

### Reactivity of [Cu(dien)(nica)$(NO_3)_2$] (4) and [Cu(dien)$(NO_3)$(nic$^-$)$(OH_2)$]·$H_2O$ (5)

We selected [Cu(dien)(nica)$(NO_3)_2$] and the zwitterionic complex [Cu(dien)$(NO_3)$(nic$^-$)$(OH_2)$]·$2H_2O$ to exploit their chemical reactivity towards nucleophiles. In particular, the zwitterionic form is expected to exhibit interesting reactivity due to the different electronic, steric, and nucleophilicity factors of the coordinated dien, $NO_3$, $H_2O$, nic$^-$, and nica ligands. The reactivity studies were performed using the reaction of a water/methanol solution of the precursor complex with various nucleophiles, such as $SCN^-$, $N_3^-$, $Cl^-$, $CH_3COO^-$, guanosine (GuO), and 2-amino-5-methylthiazole (2a-5mt) in a 1:1 molar ratio. All the reactions of complexes **4** and **5** studied are depicted schematically in Schemes 1 and 2, respectively.

The reaction products were identified by elemental analysis, spectroscopic measurements (IR and UV/Vis spectra), and magnetic and molar conductivity measurements, and the results compared with the experimental data available.[26] All reaction products are blue crystalline solids that are very soluble in water and in coordinating solvents, and slightly soluble in alcohols. The compounds are monomers or dimers and their magnetic moments are as expected for the $d^9$ electron configuration of $Cu^{II}$.

The reaction of **4** with $NH_4SCN$ or $NaN_3$ leads to the nucleophilic substitution of the nica and one of the $NO_3^-$ ligands to afford the dinuclear complexes [Cu(dien)(μ-SCN)$(NO_3)_2$] (**8**) and [Cu(dien)(μ-$N_3$)$(NO_3)_2$] (**9**), which are bridged by the ambidentate $SCN^-$ and $N_3^-$ ligands, respectively. In the IR spectra of **8** and **9** the bands related with the nicotinamide ligand disappear, while the new bands absorbing at 2073 and 2049 $cm^{-1}$ are characteristic of the coordinated thiocyanate and azide ligands, respectively. The dinuclear nature of **8** and **9** was further confirmed by their molar conductivity values of 240–250 μS $cm^{-1}$ in water solutions, which are indicative of the 1:2 electrolytic character of the complexes due to the dissociation of the $NO_3^-$ counterion. The UV/Vis spectroscopic data of **8** and **9** in the solid state are characteristic of $Cu^{II}$ complexes with octahedral stereochemistry.[26]

The reaction of **4** with $Mn(CH_3COO)_2·4H_2O$ leads to the substitution of one nitrate ion by an acetato group to yield [Cu(dien)(nica)$(CH_3COO)(NO_3)$] (**10**). This was confirmed by the IR spectrum of **10**, where the nitrato peak at 1749 $cm^{-1}$ has disappeared and a new band at 1604 $cm^{-1}$, characteristic of the acetate ligand, has appeared. The acetate ligand binds in a $\kappa O$ fashion.[27]

The analytical and spectroscopic data of the crystals isolated from the reaction mixture resulting from the reaction of **4** with $ZnCl_2$ correspond to the dinuclear $Cu^{II}$ complex formulated as [Cu(dien)(μ-Cl)]$_2$·[$NO_3$]$_2$ (**11**), which contains

 © 2006 Wiley-VCH Verlag GmbH & Co. KGaA, Weinheim 

bridging chloride ligands.[28] The reaction of **4** with Guo or 2a-5mt leads to the formation of the adducts [Cu(dien)($N^7$-Guo)($NO_3$)$_2$] (**12**) and [Cu(dien)(2a-5mt)($NO_3$)$_2$] (**13**) by replacement of the coordinated nica ligand with the respective nucleophile. The IR spectra of **12** and **13** show the presence of characteristic bands for guanosine and 2-amino-5-methylthiazole, which are indicative of their coordination with copper(II), while the UV/Vis spectra suggest an octahedral geometry of the complexes. The molecular structure of **12** has been determined previously by X-ray crystallography.[29]

The reaction of the zwitterionic complex **5** with $NH_4SCN$ yields blue needles of the mixed-ligand complex [Cu(dien)(NCS)($nic^-$)($H_2O$)] (**14**) by substitution of the nitrate ion by the thiocyanato ligand. The substitution reaction was monitored by the disappearance of the two bands at 1745 and 1380 $cm^{-1}$ due to the stretching vibration of the nitrato ligands, and the appearance of the strong and sharp band at 2072 $cm^{-1}$ due to the isothiocyanato ligand coordinated as a terminal ligand through its hard N-end.[30] The bands due to $nic^-$ remain almost unchanged.

The reaction of **5** with $NaN_3$ leads to the replacement of both the $nic^-$ ligand and the coordinated $H_2O$ molecule by the azido ligand, which bridges the two $Cu^{II}$ centers in an asymmetric end-on fashion to afford the dinuclear complex [Cu(dien)($NO_3$)(1,1-μ-$N_3$)]$_2$ (**15**). The end-on bridging mode of the $N_3^-$ group was proved by the presence of one intense band at 2049 $cm^{-1}$.

The reaction of **5** with $ZnCl_2$ leads to the dissociation of the complex and the formation of two new complexes: one of them, which is blue, corresponds to the dinuclear complex **11**.[28] Specifically, the IR spectrum of **11** is dominated by the absence of peaks for the $nic^-$ ligand, while the bands at 344 and 388 $cm^{-1}$ confirm the bridging mode of the chloro ligand. Moreover, the molar conductivity value (238 μS $cm^{-1}$) in water substantiates the 1:2 electrolytic nature of **11**. The second complex is a white solid that corresponds to Zn(nicotinate)$_2$ (**16**), where the Zn center is coordinated by two bidentate chelating carboxylato groups of the nicotinate anions.

Finally, the reaction of **5** with guanosine leads to the formation of the adduct [Cu(dien)($nic^-$)($NO_3$)($N^7$-Guo)] (**17**) by replacement of the coordinated $H_2O$ ligand. The IR spectrum of **17** shows the presence of both $nic^-$ and Guo bands, which are indicative of their coordination with the copper(II) center, while the UV/Vis spectra suggest an octahedral stereochemistry for the $CuN_5O$ chromophore. The reactions of complexes **4** and **5** with guanosine clearly mirror their ability to react with DNA components in the cell nucleus, which, in turn, could open up a new pathway for their further biological studies. Despite many attempts, the reactions of **5** with Mn($OOCCH_3$)$_2$·4$H_2O$ or 2-amino-5-methylthiazole were unsuccessful.

## Computational Studies Using DFT

### Equilibrium Geometries, Electronic Structure, and Bonding Mechanism of [Cu(dien)(nic)] and [Cu(dien)(nica)] Complexes

In an attempt to understand some marked structural features of the complexes under investigation, we performed electronic-structure calculations based on density functional theory at the B3LYP/6-31G(d,p) level. We started the calculations with the various possible forms of nicotinic acid that exist in aqueous solutions. These species, along with their p$K$ values,[31] are shown in Scheme 3.

The equilibrium geometries of the various forms of nicotinic acid (**A**, **B**, and **C**) and that of a deprotonated form of **A** at the heterocyclic N-atom (**A′**), computed at the B3LYP/6-31G(d,p) level, are given in Figure 6. No significant structural differences can be observed in the pyridine ring of the various forms of nicotinic acid. However, there are some changes in the structural parameters of the carboxylic group. For instance, the C–$COO^-$ bond lengthens and the OCO bond angle decreases upon going from **B** to **C**, following the trend **B** > **A** > **A′** > **C**.

The vibrational frequencies obtained from our calculations are in line with those obtained from a previous theoretical study by Sala et al.[32] The β(COO) in-plane pyridinic ring deformation appears at 629, 631, and 625 $cm^{-1}$ for **A′**, **B**, and **C**, respectively, and the ν(C=O) stretching vibration appears at 1855 and 1796 $cm^{-1}$ for **A′** and **B**, respectively.

The various forms of nicotinic acid are expected to act as ambidentate ligands that coordinate to a metal center either through the carboxylato O- or heterocyclic N-donor atoms. This is clearly illustrated by their frontier molecular orbitals (FMOs; Figure 7).

In both **A** and **A′** the two occupied FMOs (HOMO and HOMO–1), which are involved in the formation of a coor-

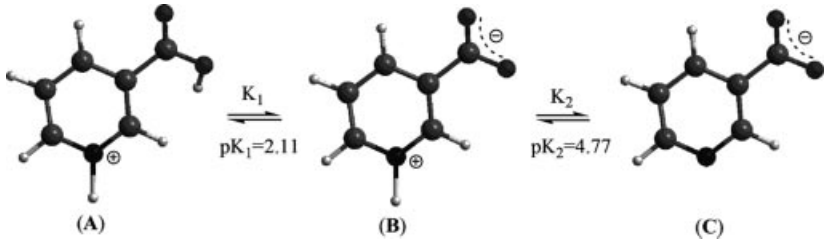


Scheme 3.

 © 2006 Wiley-VCH Verlag GmbH & Co. KGaA, Weinheim 

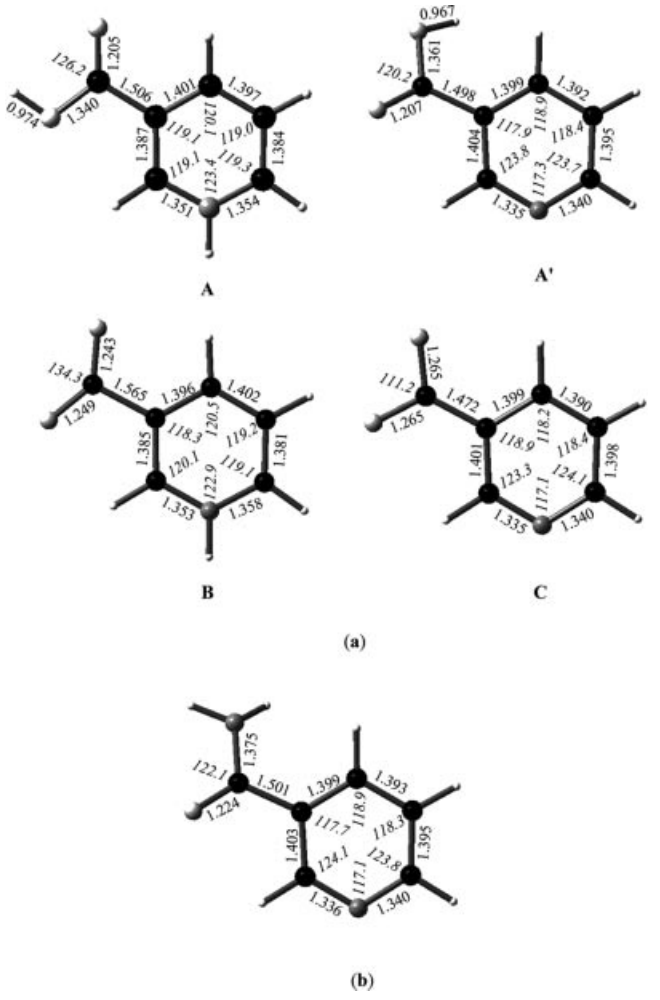


Figure 6. Equilibrium geometries of the various forms of nicotinic acid that exist in aqueous solution (a) and nicotinamide (b) computed at the B3LYP/6-31G(d,p) level of theory.

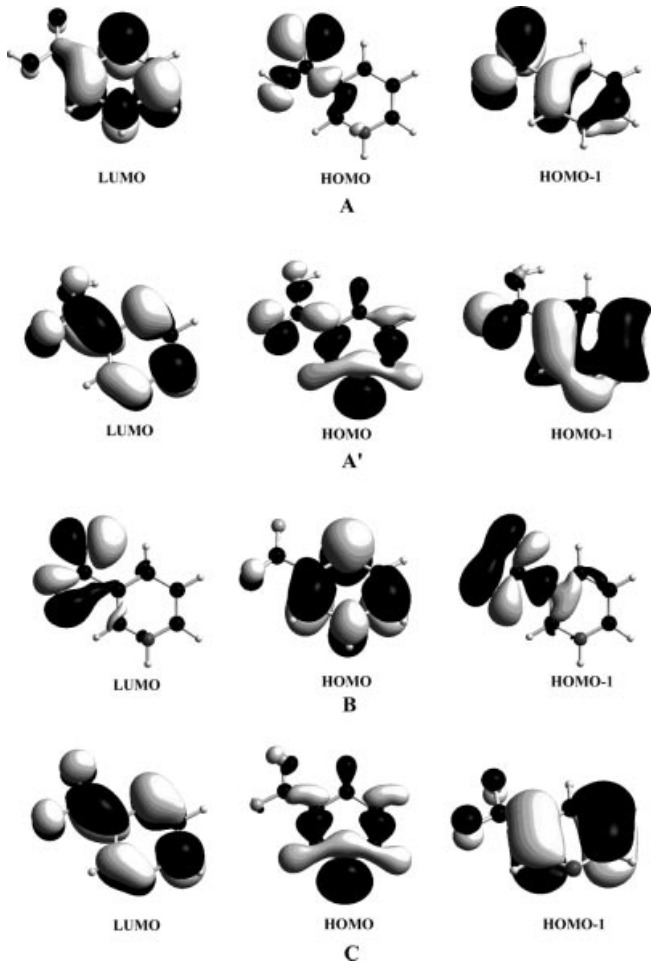


Figure 7. Frontier molecular orbitals (FMOs) of the various forms of nicotinic acid calculated at the B3LYP/6-31G(d,p) level.

dination bond with the Cu$^{II}$ central atom, have significant contributions from p-AOs of the carboxylato O-donor atoms. However, the HOMO–1 has a significant contribution from a p-AO of the heterocyclic N-donor atom only in **A′**. In the latter, the unoccupied FMO (LUMO) has significant contributions from p-AOs located on the carboxylato O- or heterocyclic N-donor atoms, which could be involved in a π-back-bonding interaction with the central

Table 2. Selected energetic and electronic properties along with proton affinities (PA) of the various forms of nicotinic acid and nicotinamide calculated at the B3LYP/6-31G(d,p) level.

| Property | **A** | **A′** | **B** | **C** | nica |
|---|---|---|---|---|---|
| $E$ [hartrees] | –437.118717 | –436.751872 | –436.711249 | –436.100562 | –416.882167 |
| $E_{homo}$ | –0.44047 | –0.26242 | –0.19291 | –0.27399 | –0.25179 |
| $E_{lumo}$ | –0.26295 | –0.06366 | –0.10234 | –0.07168 | –0.05065 |
| $Q$(N)[a] | –0.48 | –0.44 | –0.49 | –0.43 | –0.45 |
| $Q$(O) | –0.54 | –0.6 | –0.7 | –0.34 | –0.6 |
| $Q$(OH) | –0.71 | –0.66 | –0.72 | –0.43 | |
| *nec*(N)[a] | $2s^{1.25}2p^{4.22}$ | $2s^{1.40}2p^{4.02}$ | $2s^{1.25}2p^{4.22}$ | $2s^{1.40}2p^{4.0}$ | $2s^{1.38}2p^{4.05}$ |
| *nec*(O) | $2s^{1.70}2p^{4.81}$ | $2s^{1.73}2p^{4.85}$ | $2s^{1.73}2p^{4.96}$ | $2s^{1.74}2p^{4.67}$ | $2s^{1.70}2p^{4.89}$ |
| *nec*(OH) | $2s^{1.68}2p^{5.02}$ | $2s^{1.64}2p^{5.00}$ | $2s^{1.73}2p^{4.96}$ | $2s^{1.75}2p^{4.59}$ | |
| *bop*(C–COO)[b] | 0.28 | 0.27 | 0.13 | 0.26 | 0.26 |
| *bop*(C=O) | 0.58 | 0.55 | 0.5 | 0.42 | 0.61 |
| *bop*(C–OH)[c] | 0.29 | 0.27 | 0.51 | 0.37 | 0.26 |
| $\eta$ [eV] | 4.83 | 5.41 | 2.46 | 5.5 | 5.47 |
| $\mu_e$ [D] | 6.8 | 5.5 | 13.8 | 3.3 | 4.9 |
| *PA*(N) [kcal mol$^{-1}$] | 230.2 | 230.2 | 383.2 | 383.2 | 225.8 |
| *PA*(O) [kcal mol$^{-1}$] | 255.7 | 255.7 | 408.7 | 408.7 | 213.2 |

[a] Natural charges. [b] Mulliken bond overlap populations [for nica it refers to the C–CO(NH$_2$) bond]. [c] C–NH$_2$ for nica.

 © 2006 Wiley-VCH Verlag GmbH & Co. KGaA, Weinheim 

$Cu^{II}$ atom. The HOMO and LUMO eigenvalues, along with selected electronic properties of the various nicotinic acid forms, are compiled in Table 2.

The proton affinities (PA) of the various forms of nicotinic acid calculated at the B3LYP/6-31G(d,p) level are also given in Table 2. Based upon the PA values, it is expected that the σ-donor ability of **C** and **B** through either the N- or O-donor atoms should be higher than that of **A** or **A′**.

The various forms of nicotinic acid can coordinate to copper(II) either through their endocyclic N-donor atom or through their carboxylato O-donor atoms to form a series of [Cu(dien)(nic)] complexes. The equilibrium geometries of the complexes computed at the B3LYP/6-31G(d,p) level are given in Figure 8 along with selected structural parameters.

All complexes adopt a distorted square-planar geometry. In [Cu(dien)(A′)] (**1A′**) the plane of **A′**, which is coordinated to $Cu^{II}$ through its N-donor atom, is twisted almost 60° out of the coordination plane (Figure 8a). The same also holds true for the complex [Cu(dien)(C)] (**1C**), with **C** coordinated to copper(II) through its N-donor atom (Figure 8c). On the other hand, the torsion angle between the two planes is estimated to be diminished to around 25° in [Cu(dien)(B)] (**1B**) and [Cu(dien)(C′)] (**1C′**; Figures 8b and 8d, respectively), where ligands **B** and **C′** are coordinated to copper(II) through their carboxylato O-donor atoms. The three Cu–N coordination bonds formed between $Cu^{II}$ and the dien ligand are longer in **1B** than in **1A**, **1C**, and **1C′**. The length of the Cu–N coordination bond formed between nicotinic acid and $Cu^{II}$ decreases slightly upon going from

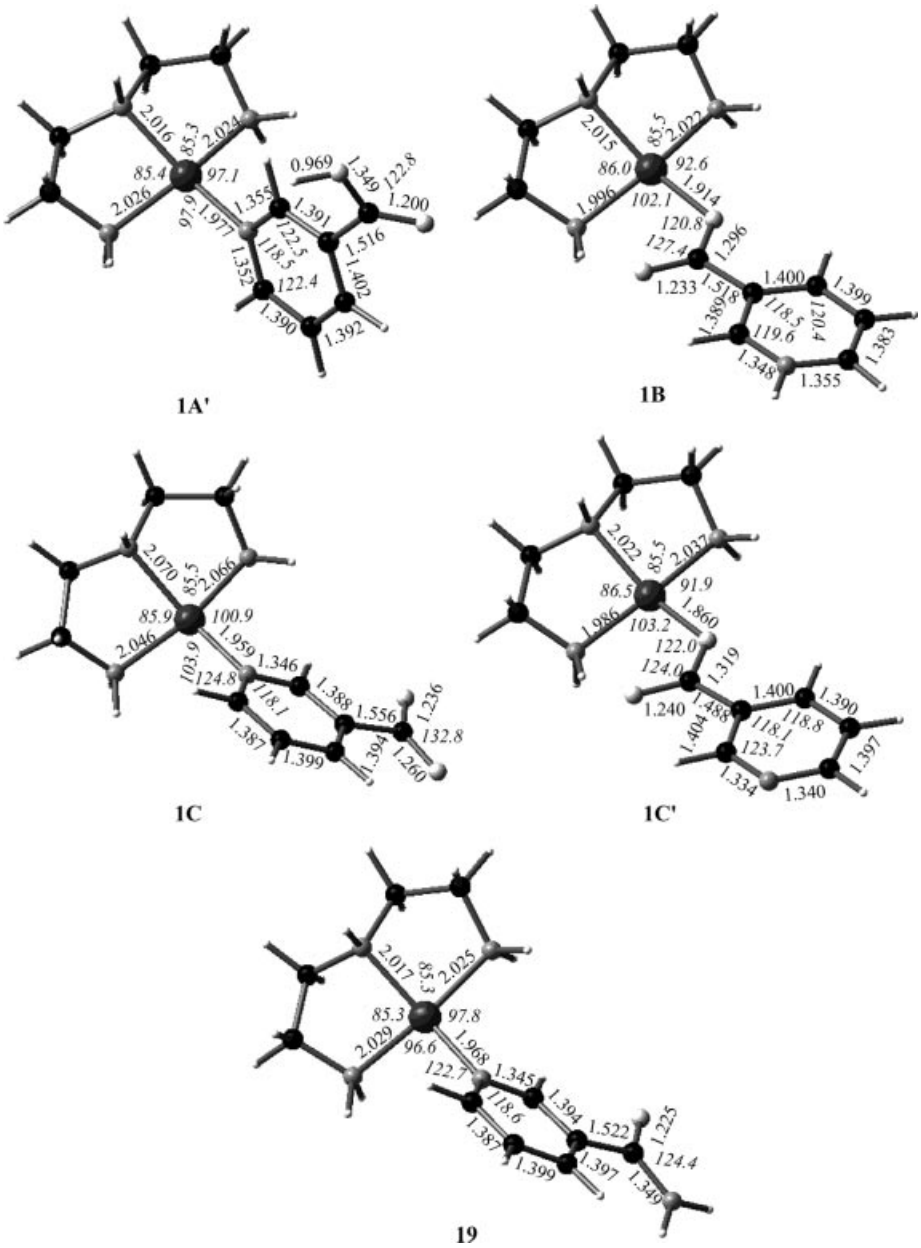


Figure 8. Equilibrium geometries of the [Cu(dien)(nic)] and [Cu(dien)(nica)] complexes computed at the B3LYP/6-31G(d,p) level of theory.

 © 2006 Wiley-VCH Verlag GmbH & Co. KGaA, Weinheim 

**1A** to **1B**. No significant changes in the structural parameters of the various nicotinic acid species could be observed upon coordination to $Cu^{II}$.

Selected energetic and electronic properties of the [Cu(dien)(nic)] and [Cu(dien)(nica)] complexes computed at the B3LYP/6-31G(d,p) level of theory are summarized in Table 3.

According to the natural bond orbital (NBO) analysis the $Cu^{II}$ center acquires a positive natural charge of about 1.20–1.38 |e|. Based upon the natural electron configurations, the electron density is transferred from the N-donor atoms of the dien and nicotinic acid ligands to the 4s- and 3d-AOs of $Cu^{II}$ (Table 2). Note that the natural electron configuration on the $Cu^{II}$ central atom does not vary significantly upon going from **1A′** to **1C**. Interestingly, there is an increase in natural atomic charges of the N-donor atom of the nicotinic acid ligand in **1A′** and **1C** upon coordination to the $Cu^{II}$ center, which could be attributed to a π-backbonding interaction between the 3d lone pair AOs of the $Cu^{II}$ center and the vacant LUMO of **A′** or **C** (Figure 5). On the other hand, the same also holds true for **1B**, where an increase of the natural atomic charge on the O-donor atom of the nicotinic acid ligand is observed upon coordination. In all [Cu(dien)(nic)] complexes the spin density is mainly localized on the $Cu^{II}$ and the N-donor atoms of the dien and nicotinic acid ligands, while in **1C** it is delocalized over the nicotinic acid ring and mainly on one of the carboxylate O donor atoms (Figure 8).

The equilibrium geometry of [Cu(dien)(nica)] (**18**), computed at the B3LYP/6-31G(d,p) level, is also given in Figure 8. The complex adopts a distorted square-planar geometry with the nicotinamide ligand being twisted almost 60° out of the coordination plane. The calculated structural parameters of **18** are in line with those obtained from the X-ray structural analysis for $[Cu(dien)(nica)(NO_3)_2]$ (**4**). No significant structural changes in nicotinamide could be observed upon coordination to $Cu^{II}$.

According to the NBO analysis the $Cu^{II}$ center acquires a positive natural atomic charge of about 1.37 |e|. The natural electron configurations illustrate that the electron density is transferred from the N-donor atoms of the dien and nicotinamide ligands to the 4s- and 3d-AOs of $Cu^{II}$ (Table 3). Also, there is an increase in the natural atomic charge of the N-donor atom upon coordination of the nicotinamide ligand to the $Cu^{II}$ center in **18**, which could be attributed to a π-backbonding interaction between the 3d lone pair AOs of $Cu^{II}$ and the LUMO of the nica ligand (Figure 7). Finally, the bond dissociation energy (BDE) of the nica ligand is predicted to be 67.2 kcal mol$^{-1}$ at the B3LYP/6-31G(d,p) level.

Table 3. Selected energetic and electronic properties of the [Cu(dien)(nic)] and [Cu(dien)(nica)] complexes computed at the B3LYP/6-31G(d,p) level of theory.

| Property | **1A′** | **1B** | **1C** | **1C′** | **18** |
|---|---|---|---|---|---|
| *E* [hartrees][a] | –2400.92235 | –2400.98113 | –2400.60805 | –2400.68319 | –2381.07330 |
| BDE(Cu–X)[b] | 54.2 | 116.6 | 265.7 | 312.8 | 67.2 |
| *Q*(Cu) | 1.38 | 1.39 | 1.20 | 1.35 | 1.37 |
| *Q*(N1)[c] | –0.63 | –0.48 | –0.63 | –0.45 | –0.63 |
| *Q*(O1)[d] | –0.49 | –0.83 | –0.5 | –0.85 | –0.59 |
| *Q*(O2) | –0.68 | –0.66 | –0.66 | –0.68 | |
| *Q*(N2)[e] | –1.00 | –1.01 | –1.00 | –1.01 | –1.00 |
| *Q*(N3)[e] | –1.00 | –1.00 | –1.00 | –0.99 | –1.00 |
| *Q*(N4)[f] | –0.80 | –0.80 | –0.81 | –0.79 | –0.79 |
| *SD*(Cu)[g] | 0.65 | 0.68 | 0.44 | 0.68 | 0.65 |
| *SD*(N1) | 0.08 | 0.00 | 0.06 | 0.00 | 0.07 |
| *SD*(O1) | 0.00 | 0.07 | 0.01 | 0.10 | 0.01 |
| *SD*(O2) | 0.00 | 0.00 | 0.36 | 0.00 | |
| *SD*(N2) | 0.08 | 0.07 | 0.03 | 0.08 | 0.08 |
| *SD*(N3) | 0.09 | 0.08 | 0.04 | 0.07 | 0.09 |
| *SD*(N4) | 0.10 | 0.10 | 0.03 | 0.06 | 0.10 |
| *nec*(Cu)[h] | $4s^{0.42}3d^{9.18}$ | $4s^{0.41}3d^{9.17}$ | $4s^{0.38}3d^{9.36}$ | $4s^{0.41}3d^{9.20}$ | $4s^{0.42}3d^{9.19}$ |
| *nec*(N) | $2s^{1.34}2p^{4.26}$ | $2s^{1.25}2p^{4.21}$ | $2s^{1.35}2p^{4.26}$ | $2s^{1.38}2p^{4.39}$ | $2s^{1.34}2p^{4.26}$ |
| *nec*(O1) | $2s^{1.74}2p^{4.75}$ | $2s^{1.72}2p^{5.10}$ | $2s^{1.72}2p^{4.93}$ | $2s^{1.73}2p^{5.11}$ | $2s^{1.70}2p^{4.87}$ |
| *nec*(O2) | $2s^{1.68}2p^{4.99}$ | $2s^{1.71}2p^{4.93}$ | $2s^{1.74}2p^{4.75}$ | $2s^{1.70}2p^{4.96}$ | |
| *nec*(N2) | $2s^{1.46}2p^{4.52}$ | $2s^{1.45}2p^{4.54}$ | $2s^{1.45}2p^{4.52}$ | $2s^{1.44}2p^{4.55}$ | $2s^{1.46}2p^{4.52}$ |
| *nec*(N3) | $2s^{1.46}2p^{4.52}$ | $2s^{1.45}2p^{4.52}$ | $2s^{1.45}2p^{4.52}$ | $2s^{1.45}2p^{4.52}$ | $2s^{1.46}2p^{4.52}$ |
| *nec*(N4) | $2s^{1.39}2p^{4.39}$ | $2s^{1.38}2p^{4.39}$ | $2s^{1.38}2p^{4.40}$ | $2s^{1.38}2p^{4.39}$ | $2s^{1.39}2p^{4.38}$ |
| *bop*(Cu–X)[i] | 0.18 | 0.19 | 0.21 | 0.21 | 0.19 |
| *bop*(Cu–N2) | 0.16 | 0.16 | 0.14 | 0.16 | 0.16 |
| *bop*(Cu–N3) | 0.16 | 0.16 | 0.14 | 0.15 | 0.16 |
| *bop*(Cu–N4) | 0.16 | 0.15 | 0.14 | 0.14 | 0.16 |

[a] Total electronic energy plus zero point energy. [b] BDE is the bond dissociation energy [kcal mol$^{-1}$] for the Cu–X (X = N or O) bond between $Cu^{II}$ and the X donor atom of nicotinic acid. [c] N1 donor atom of the nicotinic acid or nicotinamide ligands. [d] O1 donor atom of the nicotinic acid ligand. [e] N2 and N3 are the N-donor atoms of the dien ligand *cis* to nicotinic acid or nicotinamide. [f] N4 is the N-donor atom of the dien ligand *trans* to nicotinic acid or nicotinamide. [g] Spin density. [h] Natural electron configuration. [i] Mulliken bond overlap population.

 © 2006 Wiley-VCH Verlag GmbH & Co. KGaA, Weinheim 

### Vibrational and Electronic Spectra of [Cu(dien)(nic)] and [Cu(dien)(nica)] Complexes

The unscaled vibrational frequencies in the vibrational spectra of the [Cu(dien)(nic)] and [Cu(dien)(nica)] complexes, calculated at the B3LYP/6-31G(d,p) level, appear within the range 3450–3530 $cm^{-1}$. The ν(C=O) stretching vibration for **A′**, **B**, and **C** appears at 1855, 1796, and 1591 $cm^{-1}$ respectively. Upon coordination to $Cu^{II}$ this vibration is red-shifted for **1A′**, **1C**, and **1C′**, appearing at 1876, 1688, and 1681 $cm^{-1}$ respectively, while it is blue-shifted for **1B**, appearing at 1731 $cm^{-1}$. The N-coordination of nicotinic acid species is reflected in the calculated unscaled in-plane pyridinic ring deformation, $\delta_{py}$, which is red-shifted in **1A′** and **1C** relative to the corresponding uncoordinated nicotinic acid species **A′** and **C**, appearing at 673 and 668 $cm^{-1}$, respectively. In contrast, it remains almost unaffected in **1B** and **1C′**, appearing at 635 and 633 $cm^{-1}$ respectively. Moreover, the N-coordination of the nicotinamide is also reflected in the calculated in-plane pyridinic

Table 4. Principal electronic transitions, wavelengths (λ), and oscillator strengths (*f*) for [Cu(dien)(nic)] (**1B**) and [Cu(dien)(nica)] (**18**) computed at the B3LYP/6-31G(d,p) level.

| | λ [nm] | *f* | Excitation | Composition of the participating MOs |
|---|---|---|---|---|
| **1B** | | | | |
| | 608 (618)[a] | 0.001 | HOMO–2 → SOMO | $(p_zO_{nic}) \rightarrow (d_\sigma Cu+2pN_{dien}+3pO_{nic})$ |
| | 270 (263) | 0.128 | HOMO–3 → SOMO | $(\pi^*_{nic}) \rightarrow (d_\sigma Cu+2pN_{dien}+3pO_{nic})$ |
| | | | HOMO–10 → SOMO | $(d_\sigma Cu+2pN_{dien}) \rightarrow (d_\sigma Cu+2pN_{dien}+3pO_{nic})$ |
| | 248 (255) | 0.034 | HOMO–5 → SOMO | $(d_\pi Cu+2pN_{dien}+3pO_{nic}) \rightarrow (d_\sigma Cu+2pN_{dien}+3pO_{nic})$ |
| | 208 | 0.065 | HOMO–4 → LUMO+1 | $(d_\pi Cu+2pN_{dien}+3pO_{nic}) \rightarrow (\pi^*_{nic})$ |
| | 185 | 0.018 | HOMO–6 → LUMO+1 | $(d_\pi Cu+2pN_{dien}) \rightarrow (\pi^*_{nic})$ |
| | | | HOMO–7 → LUMO+1 | $(\pi^*_{nic}) \rightarrow (\pi^*_{nic})$ |
| **18** | | | | |
| | 604 (612)[b] | 0.005 | HOMO–1 → SOMO | $(3pO_{nica}) \rightarrow (3pO_{nica})$ |
| | 533 | 0.002 | HOMO–2 → SOMO | $(d_\sigma Cu+2pN_{dien}+\pi^*_{nica}) \rightarrow (3pO_{nica})$ |
| | 344 | 0.004 | SOMO → LUMO | $(3pO_{nica}) \rightarrow (\pi^*_{nica})$ |
| | | | HOMO–1 → LUMO | $(3pO_{nica}) \rightarrow (\pi^*_{nica})$ |
| | 272 (269) | 0.14 | HOMO–5 → SOMO | $(dCu+2pN_{dien}+\pi^*_{nica}) \rightarrow (3pO_{nica})$ |
| | 204 | 0.043 | HOMO–15 → SOMO | $(dCu+2pN_{dien}) \rightarrow (3pO_{nica})$ |
| | 195 | 0.023 | HOMO–16 → SOMO | $(\pi^*_{nica}) \rightarrow (3pO_{nica})$ |

[a] Experimental values for complex **5**. [b] Experimental values for complex **4**.

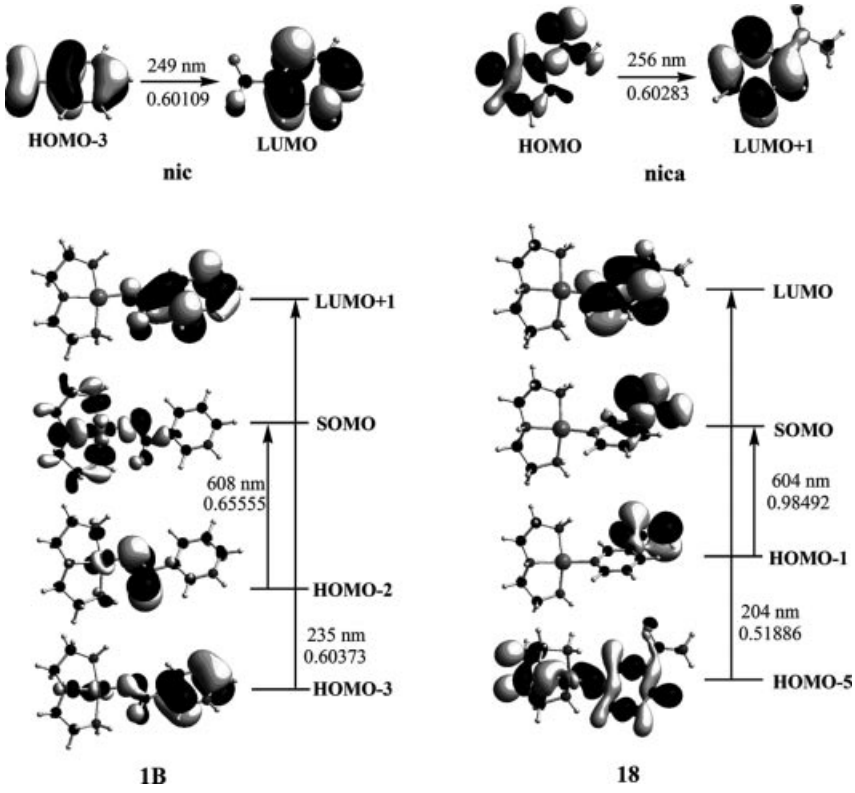


Figure 9. Single-electron transitions with the CI coefficients in the TD-DFT calculations for nic, nica, **1B**, and **18**.

 © 2006 Wiley-VCH Verlag GmbH & Co. KGaA, Weinheim 

ring deformation, $\delta_{py}$, vibrational frequency, which in **18** appears at 801 and 672 $cm^{-1}$, while in uncoordinated nicotinamide it appears at 782 and 642 $cm^{-1}$, respectively.

TD-DFT calculations at the B3LYP/6-31G(d,p) level were performed in order to evaluate the properties of the excited states of [Cu(dien)(nic)] and [Cu(dien)(nica)] complexes. The principal singlet–singlet electronic transitions, excitation energies, and oscillator strengths, along with assignments, for **1B** and **18** are compiled in Table 4.

The computed electronic transitions for **1B** and **18** at 608 and 604 nm, respectively, are in excellent agreement with the experimental values. This broad and very intense band for 1B arises from the HOMO–2 → SOMO electronic transition (Figure 9). However, because of the highly delocalized MOs involved and the high mixing of the excited configurations due to the low symmetry of the complexes, it could not be assigned to one of the well-known LL, MLCT, LMCT, or d → d transitions. On the other hand, for **18** this band arises from a HOMO–1 → SOMO (Figure 9) electronic transition and can be classified as an intraligand (LL) transition.

The calculated electronic transitions at 249 and 256 nm for nic and nica, respectively, are in excellent agreement with the experimental values. These bands arise from π → π* and σ → π* type transitions for nic and nica, respectively (Figure 9). Upon coordination of the latter to $Cu^{II}$ these bands are blue-shifted, appearing at 235 and 204 nm for **1B** and **18**, respectively.

## Conclusions

We have reported the synthesis, structural characterization, and DFT study of the novel mixed-ligand $Cu^{II}$ complexes formed upon reaction of [Cu(dien)$X_2$] (dien = diethylenetriamine; X = $Br^-$, $NO_3^-$) with pyridine (py), nicotinamide (nica), nicotinic acid (nic), and nicotinate anion ($nic^-$) in a 1:1 molar ratio. The salient structural features of the new complexes were determined by spectroscopic measurements (infrared and electronic spectra), while details of the structures were obtained by an X-ray structural investigation of the [Cu(dien)(nica)$(NO_3)_2$] complex. Conductivity measurements revealed the electrolytic nature of the complexes, while magnetic measurements are compatible with the $d^9$ electron configuration of the $Cu^{II}$ centers. Moreover, DFT/B3LYP calculations of the structural, bonding, and electronic properties of the complexes corroborate the experimental evidence for the coordination of nicotinic acid preferably through the pyridine N-donor atom. Finally, the chemical reactivity of the $Cu^{II}$ complexes towards a variety nucleophiles has been studied experimentally and discussed in relation with the electronic structure of the complexes computed at the DFT level.

## Experimental Section

**Materials and Instrumentation:** All chemicals were purchased from Aldrich, EDH Chemicals and Merck, as reagent grade, and were used as received. C, H, and N were analyzed with a Perkin–Elmer 240B elemental analyser. IR spectra were recorded with a Perkin–Elmer Spectrum One spectrophotometer in the 400–4000 $cm^{-1}$ region using KBr pellets and in the 200–400 $cm^{-1}$ region using polyethylene disks. Electronic spectra were recorded with a Hitachi U-2001 spectrophotometer in the 200–1100 nm region, using 10-mm Teflon-stoppered quartz cells. Molar conductivities were measured with a WTW conductivity bridge and a calibrated dip-type cell. Magnetic susceptibilities on powdered samples were measured at room temperature using a Johnson–Matthey balance. Diamagnetic corrections were estimated from Pascal constants. The TG/DTA curves were obtained in a dynamic nitrogen atmosphere with a Setaram SETSYS-1200 thermal analyzer at a heating rate of 5 °C $min^{-1}$ in a platinum crucible, in the temperature range 40–950 °C, with a sample mass of about 10 mg.

**Synthesis of the Complexes:** The starting material [Cu(dien)-$(NO_3)_2$] (**1**) was prepared according to a literature procedure,[9] while [Cu(dien)$Br_2$] (**2**) was prepared by the direct reaction of dien and $CuBr_2$.

**[Cu(dien)(py)$(NO_3)_2$] (3):** Pyridine (0.16 mL) was added dropwise to a suspension of**1** (0.581 g,2 mmol) in of methanol (20 mL). After stirring for 4 h, the solution was filtered to remove any impurities. Diethyl ether (10 mL) was then added to the filtrate, which was left at low temperature (5 °C) overnight. The dark-blue solid formed was isolated by filtration, washed with diethyl ether, and dried in air. Yield: 0.144 g (19%). $C_9H_{18}CuN_6O_6$ (369.82): calcd. C 29.23, H 4.91, N 22.72; found C 29.11, H 4.89, N 22.63. IR (KBr disk): $\nu_a$(N–H) 3266 vs, $\nu_s$(N–H) 3238 vs, $\nu_{sec}$(N–H) 3196 vs, ν(C=N) 1608 s, ν(Cu–N) 523 m, ν(Cu–O) 456 m $cm^{-1}$. UV/Vis ($H_2O$): $\lambda$ (log $\varepsilon$) = 616 nm (1.91), 263 sh, 256 sh, 249 (3.73), 243 sh. $\Lambda\mu$ ($H_2O$) = 247 μS $cm^{-1}$. $\mu_{eff}$ = 1.93 BM. M.p. 247 °C (dec.).

**[Cu(dien)(nica)$(NO_3)_2$] (4):** Complex **1** (1.456 g, 5 mmol) was dissolved in $H_2O$ (2 mL) and further diluted with MeOH (10 mL). Nicotinamide (0.623 g, 5 mmol) in MeOH (15 mL) was added to this solution, with a concomitant darkening of the color. After the addition of diethyl ether (10 mL), the solution was left at low temperature (5 °C). After 14 h at this temperature, the dark-blue crystals formed were isolated by filtration, washed with diethyl ether, and dried at room temperature. Yield: 1.89 g (92%). $C_{10}H_{19}CuN_7O_7$ (412.85): calcd. C 29.09, H 4.64, N 23.75; found C 29.06, H 4.56, N 23.68. IR (KBr disk): $\nu_a$(N–H) 3273 vs, $\nu_s$(N–H) 3244 s, $\nu_{sec}$(N–H) 3156 s-br, ν(C=O) 1693 vs, ν(C=N) 1603 s, ν(Cu–N) 537 m, ν(Cu–O) 461 m $cm^{-1}$. UV/Vis ($H_2O$): $\lambda$ (log $\varepsilon$) = 612 nm (1.87), 269 sh, 254 (3.72). $\Lambda\mu$ ($H_2O$) = 206 μS $cm^{-1}$. $\mu_{eff}$ = 1.82 BM. M.p. 193–195 °C.

**[Cu(dien)($nic^-$)$(NO_3)(H_2O)$]·$H_2O$ (5):** A solution of nicotinic acid (0.62 g,5 mmol) in methanol (10 mL) was added to an aqueous solution of NaOH (0.2 g in 2 mL) with vigorous stirring. This solution of sodium nicotinate was added to a solution of **1** (1.45 g, 5 mmol) in $H_2O$/MeOH (1 mL/10 mL). The final solution was left overnight at room temperature. The blue needles formed were isolated by filtration, washed with diethyl ether, and dried at room temperature. Yield: 0.81 g (42%). $C_{10}H_{21}CuN_5O_7$ (386.85): calcd. C 31.05, H 5.47, N 18.10; found C 31.02, H 5.43, N 18.02. IR (KBr disk): $\nu_a$(N–H) 3270 vs, $\nu_s$(N–H) 3204 vs, $\nu_{sec}$(N–H) 3163 vs, ν(C=O) 1668 s, ν(C=N) 1591 vs, ν(Cu–N) 527 s, ν(Cu–O) 449 m $cm^{-1}$. UV/Vis ($H_2O$): $\lambda$ (log $\varepsilon$) = 618 nm (1.62), 269 sh, 262 sh, 255(3.84). $\Lambda\mu$ ($H_2O$) = 164 μS $cm^{-1}$. $\mu_{eff}$ = 1.76 BM. M.p. 141 °C (dec.).

**[Cu(dien)($nic^-$)(Br)$(H_2O)$]·$2H_2O$ (6):** A solution of nicotinic acid (0.262 g, 2.5 mmol) in methanol (10 mL) was added to an aqueous solution of NaOH (0.2 g in 2 mL) with vigorous stirring. This solu-

 © 2006 Wiley-VCH Verlag GmbH & Co. KGaA, Weinheim 

tion of sodium nicotinate was added to a solution of **2** (0.82 g, 2.5 mmol) in $H_2O$/MeOH (2 mL/10 mL). The final solution was stirred to give a blue solid, which was isolated by filtration, washed with diethyl ether, and dried at room temperature. Yield: 0.44 g (40%). $C_{10}H_{23}BrCuN_4O_5$ (422.76): calcd. C 28.41, H 5.48, N 13.25; found C 28.48, H 5.49, N 13.28. IR (KBr disk): $\nu_a$(N–H) 3271 s, $\nu_s$(N–H) 3203 s, $\nu_{sec}$(N–H) 3163 m, $\nu$(C=O) 1667 m, $\nu$(C=N) 1591 s, $\nu$(Cu–N) 525 m, $\nu$(Cu–O) 448 m $cm^{-1}$. UV/Vis ($H_2O$): $\lambda$ ($\log\varepsilon$) = 608 (1.93), 269 sh, 262 sh, 255 (3.77), 214 sh. $\Lambda\mu$ ($H_2O$) = 173 $\mu S\,cm^{-1}$. $\mu_{eff}$ = 1.80 BM. M.p. 131–133 °C.

**[Cu(dien)($NO_3$)(nic$^-$)($N^7$-Guo)]·5$H_2O$ (7):** A solution of sodium nicotinate (5 mmol) in $H_2O$/EtOH (1 mL/10 mL) was added dropwise to a water/methanol (1 mL/10 mL) solution of **1** (1.453 g, 5 mmol) and the mixture stirred continuously for 5 min. After the addition of guanosine (Guo) (1.516 g, 5 mmol) in small quantities and ethanol (80 mL), the new suspension was further stirred for 12 h so as to allow complete reaction of Guo, after which the blue-purple solid formed was isolated by filtration, washed with diethyl ether, and dried at room temperature. Yield: 3.55 g (98%). $C_{20}H_{40}CuN_{10}O_{15}$ (724.14): calcd. C 33.17, H 5.57, N 19.34; found C 33.52, H 5.66, N 19.71. IR (KBr disk): $\nu_a$(N–H) 3270 vs,br, $\nu_s$(N–H) 3226 vs-br, $\nu_{sec}$(N–H) 3165 vs, $\nu$(C=O) 1680 s, $\nu$(C=N)1591 s, $\nu$(Cu–N) 527 m, $\nu$(Cu–O) 449 w $cm^{-1}$. UV/Vis ($H_2O$): $\lambda$ ($\log\varepsilon$) = 612 (1.86), 269 sh, 253 (4.24). $\Lambda\mu$ ($H_2O$) = 159 $\mu S\,cm^{-1}$. $\mu_{eff}$ = 1.83 BM. M.p. 108–110 °C.

Table 5. Crystal data, data collection and refinement details for [Cu(dien)(nica)($NO_3$)$_2$] (**4**).

| | |
|---|---|
| Empirical formula | $C_{10}H_{19}CuN_7O_7$ |
| Formula mass | 412.86 |
| Crystal size [mm] | 0.45×0.15×0.10 |
| Crystal system | monoclinic |
| Space group | $P2_1/c$ |
| $a$ [Å] | 8.1636(14) |
| $b$ [Å] | 15.7067(18) |
| $c$ [Å] | 12.7266(13) |
| $\beta$ [°] | 98.451(12) |
| Cell volume [Å$^3$] | 1614.1(4) |
| $Z$ | 4 |
| $T$ [K] | 293(2) |
| $D_{calcd.}$ [$Mg\,m^{-3}$] | 1.699 |
| $\mu$ [$mm^{-1}$] | 1.405 |
| $F$(000) | 852 |
| Diffractometer | upgraded Philips PW1100 |
| Radiation | Mo-$K_\alpha$ (0.71073 Å) |
| Monochromator | graphite |
| Data-collection method | $\theta/2\theta$ |
| $2\theta$ range [°] | 4.14–52.04 |
| Index ranges | $-10 \le h \le 9$ |
| | $-19 \le k \le 19$ |
| | $0 \le l \le 15$ |
| Reflections collected | 6710 |
| Independent reflections ($R_{int}$) | 3167 (0.0737) |
| Observed reflections [$I > 2\sigma(I)$] | 1993 |
| Completeness to $\theta$ = 26.02° | 99.9 (%) |
| Max./min. transmission factors | 0.870, 0.498 |
| Refinement method | full-matrix least squares |
| Data/restraints/parameters | 3167/0/283 |
| Final $R$ indices [$I > 2\sigma(I)$][a] | $R_1$ = 0.0403, $wR_2$ = 0.0799 |
| $R$ indices (all data) | $R_1$ = 0.0970, $wR_2$ = 0.0949 |
| GOF | 0.982 |
| Maximum shift/error | 0.007 |
| $\rho_{max}$, $\rho_{min}$ [e Å$^{-3}$] | 0.510, –0.408 |

[a] $R$ indices and GOF defined as: $R_1 = \Sigma||F_o| - |F_c||/\Sigma|F_o|$, $wR_2 = [\Sigma w(F_o^2 - F_c^2)^2/\Sigma w(F_o^2)^2]^{1/2}$, GOF = $\{\Sigma\,[w(F_o^2 - F_c^2)^2]/(n - p)\}^{1/2}$, $n$ = no. of reflections, $p$ = no. of parameters refined.

**Computational Details:** The structural, electronic, and energetic properties of all compounds were computed with Becke's three-parameter hybrid functional[33] combined with the Lee–Yang–Parr correlation functional,[34] abbreviated as B3LYP, using the 6-31G(d,p) basis set. In all computations no constraints were imposed on the geometry. Full geometry optimization was performed for each structure using Schlegel's analytical gradient method[35] and the attainment of the energy minimum was verified by calculating the vibrational frequencies that result in absence of imaginary eigenvalues. All calculations were performed using the GAUSSIAN03 suite of programs.[36]

**X-ray Crystallographic Study:** Crystal data, data collection, and refinement details for [Cu(dien)(nica)($NO_3$)$_2$] are given in Table 5. Cell parameters were calculated by least-squares refinement of the setting angles of 21 reflections and their equivalents ($13.60° < 2\theta < 22.20°$). Intensities were collected using graphite-monochromated Mo-$K_\alpha$ radiation and a scintillation counter.[37] Three standard reflections monitored every 120 min showed no significant deterioration. They were used to scale the intensities, which were further corrected for Lorentz and polarization effects,[38] as well as for absorption (empirical $\psi$-scan method).[39] Most calculations were performed with the WinGX system of programs.[40] The structure was solved by direct methods and subsequent difference Fourier syntheses with the SHELXS-97 program[41] and refined with the SHELXL-97 program.[42] Some of the geometrical calculations were performed with the PLATON program.[43] All the non-hydrogen atoms were refined anisotropically. The hydrogen atoms could be located on the difference Fourier map, and in the final refinement step their positions were varied freely but their displacement parameters were constrained to 1.2 $U_{eq}$ of the corresponding values of the atoms to which they are bonded. CCDC-264390 contains the supplementary crystallographic data for this paper. These data can be obtained free of charge from The Cambridge Crystallographic Data Center via www.ccdc.cam.ac.uk/data_request/cif.

## Acknowledgments

The financial support of this work by the Greek General Secretariat for Research and Technology and the European Commission within the frame of the PENED01 projects is gratefully acknowledged (grant no. 01EΔ367).

[1] Y. Miwa, T. Mizuno, K. Tsuchida, T. Taga, Y. Iwata, *Acta Crystallogr., Sect. B* **1999**, *55*, 78–84.
[2] C. B. Aakeröy, A. M. Beatty, *Chem. Commun.* **1998**, 1067.
[3] J. Yarks, L. He, J. D. Adams Jr, *Pharmacol. Biochem. Behav.* **2004**, *78*, 179–183.
[4] M. M. Mycek, R. A. Harvey, P. C. Champe, *Pharmacology*, 2nd ed., Lippincott-Raven, Philadelphia, **1997**.
[5] P. Zachariadis, S. Hadjikakou, N. Hadjiliadis, A. Michaelides, S. Skoulika, Y. Ming, Y. Xiaolin, *Inorg. Chim. Acta* **2003**, *343*, 361–365.
[6] Z. Chohan, A. Rauf, S. Noreen, A. Scozzafava, C. Supuran, *J. Enzyme Inhib. Med. Chem.* **2002**, *17*, 101–106.
[7] S. Osinsky, I. Levitin, L. Campanella, P. Wadman, *Exp. Oncol.* **2004**, *26*, 140–144.
[8] M. Palicová, P. Segl'a, D. Mikloš, M. Kopcová, M. Melník, B. Dudová, D. Hudecová, T. Glowiak, *Polyhedron* **2000**, *19*, 2689–2695.
[9] R. Allman, M. Krestl, C. Bolos, G. Manoussakis, G. St. Nikolov, *Inorg. Chim. Acta* **1990**, *175*, 255–260.
[10] E. Şahin, S. İde, A. Ataç, Ş. Yurdakul, *J. Mol. Struct.* **2002**, *616*, 253–258.

 © 2006 Wiley-VCH Verlag GmbH & Co. KGaA, Weinheim 

[11] K. Nakamoto, *Infrared and Raman Spectra of Inorganic and Coordination Compounds*, 4th ed., John Wiley & Sons, Inc., New York, **1992**, pp. 256, 324.
[12] S. Bayari, A. Ataç, Ş. Yurdakul, *J. Mol. Struct.* **2003**, *655*, 163–170.
[13] S. Çakir, İ. Bulut, P. Naumov, E. Biçer, O. Çakir, *J. Mol. Struct.* **2001**, *560*, 1–7.
[14] E. A. Velcheva, L. I. Daskalova, *J. Mol. Struct.* **2005**, *741*, 85–92.
[15] P. Koczoń, J. Cz. Dobrowolski, W. Lewandowski, A. P. Mazurek, *J. Mol. Struct.* **2003**, *655*, 89–95.
[16] S. İde, A. Ataç, Ş. Yurdakul, *J. Mol. Struct.* **2002**, *605*, 103–107.
[17] A. B. P. Lever, *Inorganic Electronic Spectroscopy*, 2nd ed., Elsevier, Amsterdam, **1984**.
[18] W. J. Geary, *Coord. Chem. Rev.* **1971**, *7*, 81–122.
[19] C.-W. Yeh, M.-C. Suen, H.-L. Hu, J.-D. Chen, J.-C.- Wang, *Polyhedron* **2004**, *23*, 1947–1952.
[20] G. Bergerhoff, *DIAMOND, Visual Crystal Structure Information System*, Gerhard-Domagk-Str. 1, 53121 Bonn, Germany, **1996**.
[21] C. A. Bolos, P. C. Christidis, S. T. Triantafyllou, *Polyhedron* **1998**, *17*, 2719–2726.
[22] F.-M. Nje, Z.-M. Wang, Y.-M. Li, Y.-F. Zhao, C.-H. Yan, *Acta Crystallogr., Sect. C* **1998**, *54*, 1853–1855.
[23] Y. Zhang, P. Zhang, J. Li, M. Nishiura, *J. Mol. Struct.* **2001**, *570*, 37–42.
[24] M. Sato, S. Nagae, K. Ohmae, J. Nakaya, K. Miki, N. Kasai, *J. Chem. Soc., Dalton Trans.* **1986**, 1949–1953.
[25] Q. Lu, A. Singh, J. R. Deschamps, E. L. Chang, *Inorg. Chim. Acta* **2000**, *309*, 82–90.
[26] G. R. Hall, D. M. Duggan, D. N. Hendrickson, *Inorg. Chem.* **1975**, *14*, 1956–1964.
[27] A. Nielsen, A. D. Bond, C. J. McKenzie, *Acta Crystallogr., Sect. E* **2005**, *61*, m478–m480.
[28] M. K. Urtiaga, M. I. Arriortua, R. Cortes, T. Rojo, *Acta Crystallogr., Sect. C* **1996**, *52*, 3007–3009.
[29] C. A. Bolos, P. C. Christidis, S. T. Triantafyllou, *Polyhedron* **1998**, *17*, 2719–2726.
[30] H.-M. Hu, H. S.-Sun, X.-H. Chen, Q. Zhao, Y. Pan, X.-Y. Huang, X.-Z. You, *Acta Crystallogr., Sect. C* **1997**, *53*, 276–278.
[31] R. W. Green, H. K. Tong, *J. Am. Chem. Soc.* **1956**, *78*, 4896.
[32] O. Sala, N. S. Gonçalves, L. K. Noda, *J. Mol. Struct.* **2001**, *565–566*, 411–416.
[33] a) A. D. Becke, *J. Chem. Phys.* **1992**, *96*, 2155; b) A. D. Becke, *J. Chem. Phys.* **1993**, *98*, 5648.
[34] C. Lee, W. Yang, R. G. Parr, *Phys. Rev. B* **1988**, *37*, 785.
[35] H. B. Schlegel, *J. Comput. Chem.* **1982**, *3*, 214.
[36] M. J. Frisch, G. W. Trucks, H. B. Schlegel, G. E. Scusseria, M. A. Robb, J. R. Cheeseman, V. G. Zakrzewski, J. A. Montgomery, T. Vreven, K. N. Kudin, J. C. Burant, J. M. Millan, S. S. Iyengar, J. Tomasi, V. Barone, B. Mennucci, M. Cossi, G. Scalmani, N. Rega, G. A. Petersson, H. Nakatsuji, M. Hada, M. Ehara, K. Toyota, F. R., J. Hasegawa, M. Ishida, T. Nakajima, Y. Honda, O. Kitao, H. Nakai, M. Klene, X. Li, J. E. Knox, H. P. Hratchian, J. B. Cross, C. Adamo, J. Jaramillo, R. Gomperts, R. E. Stratmann, O. Yazyev, A. J. Austin, R. Cammi, C. Pomelli, J. W. Ochterski, P. Y. Ayala, K. Morokuma, G. A. Voth, P. Salvador, J. J. Dannenberg, V. G. Zakrzewski, S. Dapprich, A. D. Daniels, M. C. Strain, O. Farkas, D. K. Malick, A. D. Rabuck, K. Raghavachari, J. B. Foresman, J. V. Ortiz, Q. Cui, A. G. Baboul, S. Clifford, J. Cioslowski, B. B. Stefanov, G. Liu, A. Liashenko, P. Piskorz, I. Komaromi, R. L. Martin, D. J. Fox, T. Keith, M. A. Al-Laham, C. Y. Peng, A. Nanayakkara, M. Challacombe, P. M. W. Gill, B. Johnson, W. Chen, M. W. Wong, C. Gonzalez, J. A. Pople, *Gaussian 03, Revision B.02*, Gaussian, Inc., Pittsburgh PA, USA, **200**3.
[37] Stoe & Cie, *DIF4 Diffractometer Control Program*, version 6.2, Stoe & Cie, Darmstadt, Germany, **1988**.
[38] Stoe & Cie, *REDU4, Data Reduction Program*, version 6.2, Stoe & Cie, Darmstadt, Germany, **1988**.
[39] Stoe & Cie, *EMPIR, Data Setup for Empirical Absorption Correction*, version 6.2, Stoe & Cie, Darmstadt, Germany, **1988**.
[40] "WinGX, An Integrated System of Windows Programs for the Solution, Refinement and Analysis of Single Crystal Diffraction Data", vers. 1.70.00: L. J. Farrugia, *J. Appl. Crystallogr.* **1999**, *32*, 837.
[41] G. M. Sheldrick, *SHELXS97, Program for Crystal Structure Solution*, University of Göttingen, Germany, **1997**.
[42] G. M. Sheldrick, *SHELXL97, Program for Crystal Structure Refinement*, University of Göttingen, Germany, **1997**.
[43] A. L. Spek, *J. Appl. Crystallogr.* **2003**, *36*, 7–13.

Received: October 7, 2005
Published Online: March 22, 2006

 © 2006 Wiley-VCH Verlag GmbH & Co. KGaA, Weinheim 

EurJIC
European Journal of Inorganic Chemistry

Issue 11/2006

Pages 2101–2320

*Papers available ahead of print in Early View at www.interscience.wiley.com*

*Earliest available Table of Contents:*
*Automatically, free of charge by e-mail through*
*www.interscience.wiley.com/alerts*

## COVER PICTURE

**The cover picture shows** how the treatment of the oxide molecular model [{TiCp*($\mu$-O)}$_3$($\mu_3$-CMe)] (Cp* = $\eta^5$-$C_5Me_5$) with alkaline earth metal amide and alkyl compounds produces the deprotonation of the $\mu_3$-ethylidyne fragment to give $\mu_3$-$CCH_2^-$, $\mu_3$-$CHCH^-$ or $\mu_3$-$CCH^{2-}$ carbanions. Simultaneously, the alkaline earth cation is incorporated through the oxygen atoms to build new cage structures. Details of this chemistry are described by M. Mena et al. on p. 2137ff.

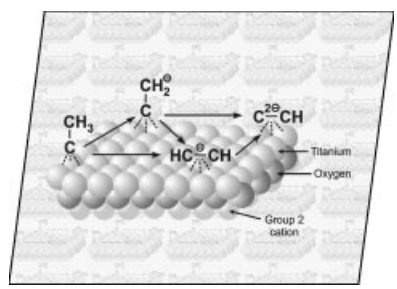


## MICROREVIEW

**Contents**

**2115** **S. Lachaize, S. Sabo-Etienne***

σ-Silane Ruthenium Complexes: The Crucial Role of Secondary Interactions

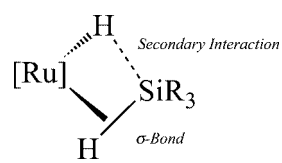


**Keywords:** σ-Complexes / Ruthenium / Silanes / Hydrides / Coordination modes / Intramolecular interactions / Oxidative addition / Hypervalent compounds

 © 2006 Wiley-VCH Verlag GmbH & Co. KGaA, Weinheim 

# SHORT COMMUNICATIONS


**2129** **N. Nakagawa, M. Murata, M. Sugimoto, H. Nishihara***

Dithiolato-Bridged [$MRu_2$] (M = Rh, Ir, Ru) Triangular 50e$^-$ Cluster Complexes Synthesized by Complete Metal Framework Reconstruction

**Keywords:** Metal framework reconstruction / Electron excess / X-ray crystallographic analysis / Three-centers-four-electrons bond


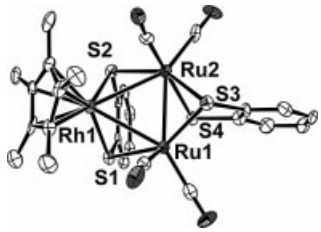



**2132** **T. Wu, M. Chen, D. Li,***

A Coordination Polymer Containing Inorganic Buckybowl Analogues

**Keywords:** Inorganic buckybowl analogues / Tetrazoles / Sharpless' cycloaddition / Copper / Coordination polymers


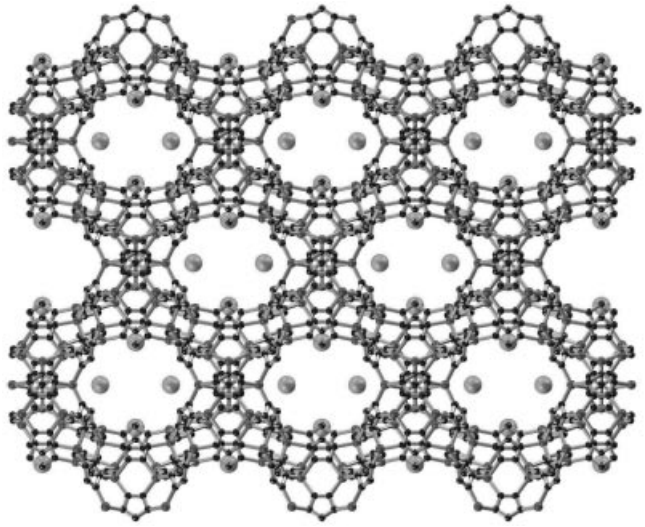

# FULL PAPERS


**2137** **A. Martín, M. Mena,* M. C. Morales-Varela, C. Santamaría**

Titanium−Alkaline Earth Molecular Oxides as Supports for Carbanions Derived from $\mu_3$-Ethylidyne Groups

**Keywords:** Alkaline earth metals / Alkylidyne complexes / Carbanions / O ligands / Titanium


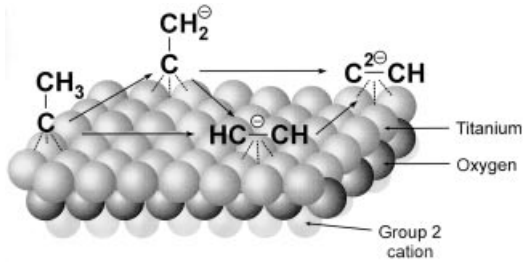



**2146** **M. Enamullah,* A. Sharmin, M. Hasegawa, T. Hoshi, A.-C. Chamayou, C. Janiak***

Syntheses, Spectroscopic Studies, and Crystal Structures of Chiral [Rh(aminocarboxylato)($\eta^4$-cod)] and Chiral [Rh(amino alcohol)($\eta^4$-cod)](acetate) Complexes with an Example of a Spontaneous Resolution of a Racemic Mixture into Homochiral Helix-Enantiomers

**Keywords:** Rhodium(I) / Amino acids / Chirality / Spontaneous resolution / Helix


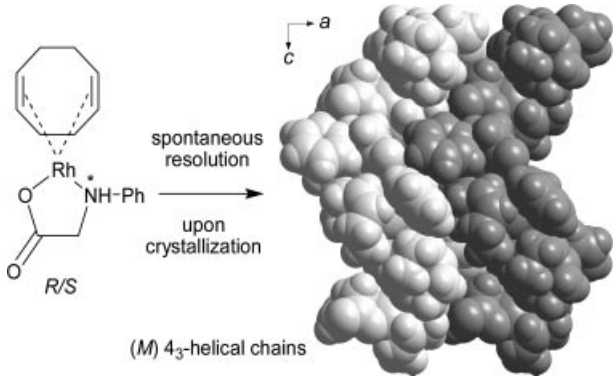

**2155** **L. Flamigni,* A. M. Talarico, B. Ventura, C. Sooambar, N. Solladié***

Photoinduced Processes in a Dendritic Zn Porphyrin Structure with a Free-Base Porphyrin Core

**Keywords:** Dendrimers / Energy transfer / Luminescence / Porphyrinoids / Supramolecular chemistry

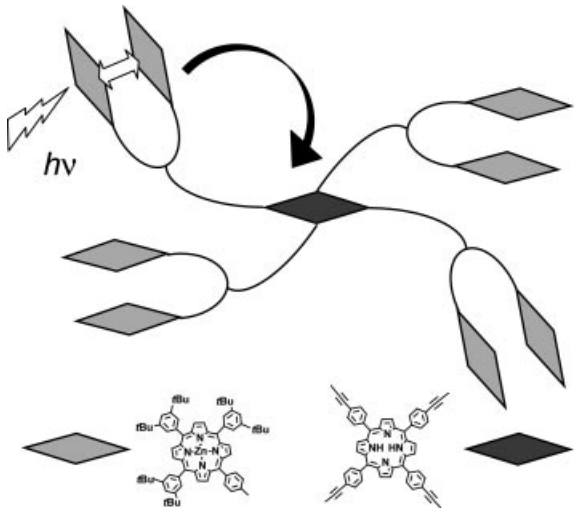


**2166** **M. C. Aragoni, M. Arca, F. A. Devillanova,* P. Grimaldi,* F. Isaia, F. Lelj,* V. Lippolis**

Kinetic and Thermodynamic Aspects of the CT and T-Shaped Adduct Formation Between 1,3-Dimethylimidazoline-2-thione (or -2-selone) and Halogens

**Keywords:** Density functional calculations / Donor−acceptor systems / Hypervalent compounds / Selenium / Sulfur

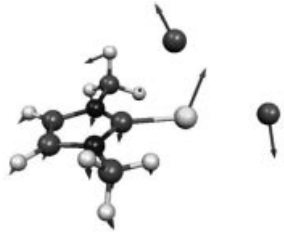

**2175** **M. P. Robalo,* A. P. S. Teixeira, M. H. Garcia, M. F. Minas da Piedade, M. T. Duarte, A. R. Dias, J. Campo, W. Wenseleers,* E. Goovaerts**

Synthesis, Characterisation and Molecular Hyperpolarisabilities of Pseudo-Octahedral Hydrido(nitrile)iron(II) Complexes for Nonlinear Optics: X-ray Structure of $[Fe(H)(dppe)_2(4\text{-}NCC_6H_4NO_2)][PF_6]\cdot CH_2Cl_2$

**Keywords:** Hydride ligands / Iron / Nonlinear optics / Hyperpolarizability / Hyper-Rayleigh scattering

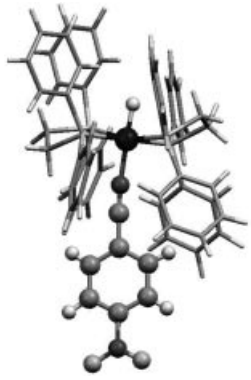

**2186** **X. Liang, X. Wang,* L. Wang, R. Yan, Q. Peng, Y. Li**

Synthesis and Characterization of Ternary $NH_4Ln_2F_7$ (Ln = Y, Ho, Er, Tm, Yb, Lu) Nanocages

**Keywords:** Nanostructures / Lanthanides

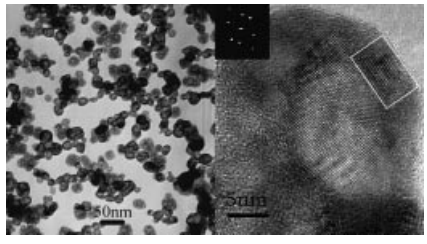


 © 2006 Wiley-VCH Verlag GmbH & Co. KGaA, Weinheim 

**2192** **N. V. Belkova, P. O. Revin, M. Besora, M. Baya, L. M. Epstein, A. Lledós,* R. Poli,* E. S. Shubina,* E. V. Vorontsov**

Hydrogen Bonding and Proton Transfer to the Trihydride Complex [Cp*$MoH_3$(dppe)]: IR, NMR, and Theoretical Investigations

**Keywords:** Dihydrogen bonding / Hydride ligands / Molybdenum / Proton-transfer mechanism / DFT calculations

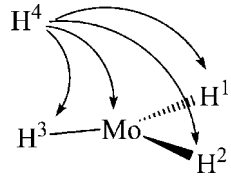


**2210** **A. Hammerl, T. M. Klapötke,* R. Rocha**

Azide−Tetrazole Ring-Chain Isomerism in Polyazido-1,3,5-triazines, Triazido-*s*-heptazine, and Diazidotetrazines

**Keywords:** ab initio calculations / Nitrogen heterocycles / Azides / Nitrogen

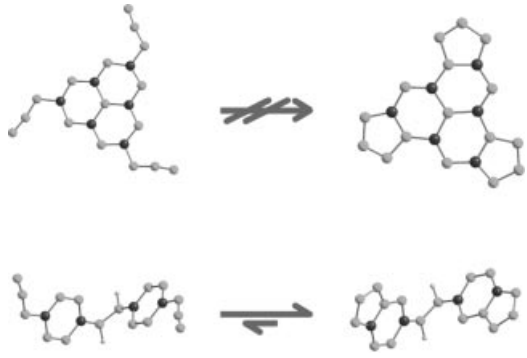

**2229** **X. Yang, H. Konishi, H. F. Xu, M. M. Wu***

Comparative Sol−Hydro(Solvo)thermal Synthesis of $TiO_2$ Nanocrystals

**Keywords:** Crystal growth / Nanostructures / Self-assembly / Solvothermal synthesis / Titanium

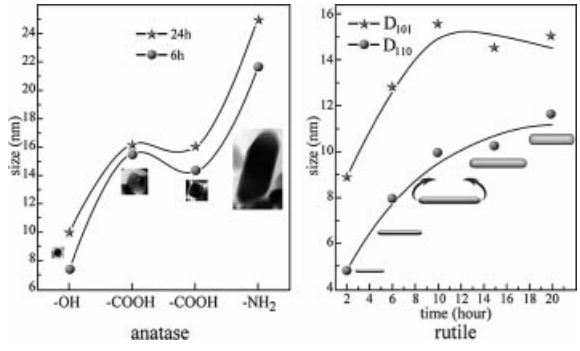


**2236** **C. G. Efthymiou, C. P. Raptopoulou, A. Terzis, R. Boča,* M. Korabic, J. Mrozinski,* S. P. Perlepes,* E. G. Bakalbassis***

A Systematic Exploration of Nickel(II)/Acetate/Di-2-pyridyl Ketone Chemistry: Neutral and Cationic Tetranuclear Clusters, and a Novel Mononuclear Complex

**Keywords:** Acetate ligands / Di-2-pyridyl ketone / Magnetic properties / Nickel(II) cubanes / Nickel(II) defect dicubanes / X-ray diffraction

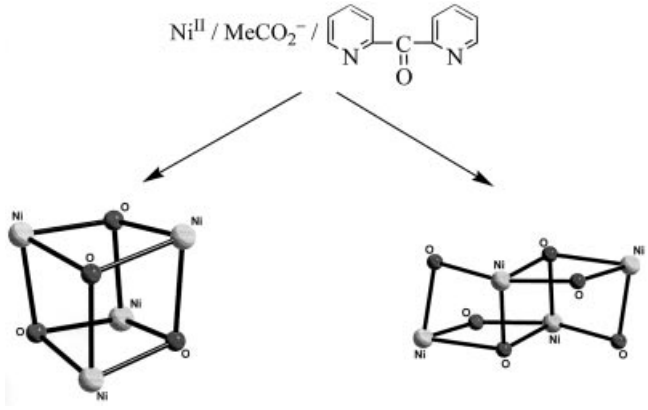


 © 2006 Wiley-VCH Verlag GmbH & Co. KGaA, Weinheim 

**2253** **J. Zhang, Y. Kang, J. Zhang, Z.-J. Li, Y.-Y. Qin, Y.-G. Yao***

Syntheses, Structures and Characterisation of Two $Cu^{II}$ Polymers with 8-Connected Topologies Based on Highly Connected SBUs

**Keywords:** Coordination polymers / Copper / Hydrothermal synthesis / Magnetic properties / N ligands

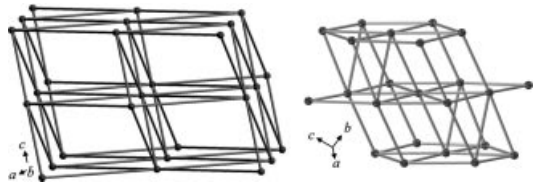

**2259** **Y. Y. Niu, Y. L. Song, N. Zhang, H. W. Hou,* D. Che, Y. T. Fan, Y. Zhu, C. Y. Duan**

Reactivity of Polyiodides Towards 1,3-Bis-(4-pyridyl)propane (bpp): A New CuI Cluster Polycatenane Framework and a Novel 2D AgI Cluster Motif

**Keywords:** Clusters / Copper / Iodine / Lead / Organic#msinorganic hybrid composites / Silver

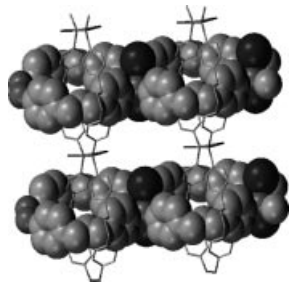

**2268** **A. Lofù, P. Mastrorilli,* C. F. Nobile, G. P. Suranna, P. Frediani, J. Iggo**

(Diphosphane monosulfide)platinum(II) Complexes for Hydroformylation Reactions: Their Catalytic Activity and a High-Pressure NMR Mechanistic Study

**Keywords:** Heteroditopic ligands / Hydroformylation / NMR spectroscopy / P,S ligands / Platinum

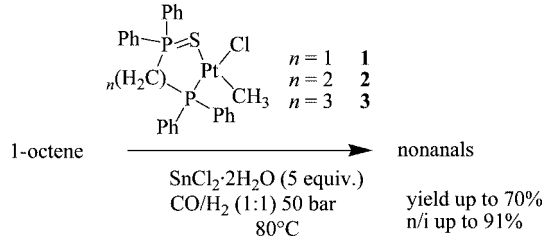


**2277** **D. Zhang, M. Shi, Z. Liu, F. Li,* T. Yi, C. Huang***

Luminescence Modulation of a Terbium Complex with Anions and Its Application as a Reagent

**Keywords:** Luminescence modulations / Fluoride anions / Terbium complexes

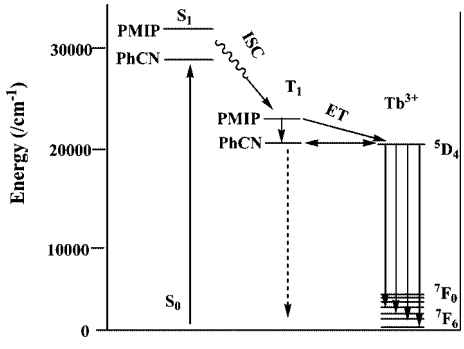


 © 2006 Wiley-VCH Verlag GmbH & Co. KGaA, Weinheim 

**2285** **S. Das, A. Chakravorty***

Oxidorhenium(V) Complexes of a Family of Bipyridine-Like Ligands Including Pyridyltriazines and Pyrazinyltriazine: Oxygen-Atom Transfer, Metal Redox and Correlations

**Keywords:** N ligands / Oxido ligands / Nitrogen heterocycles / Reduction potentials / Rhenium

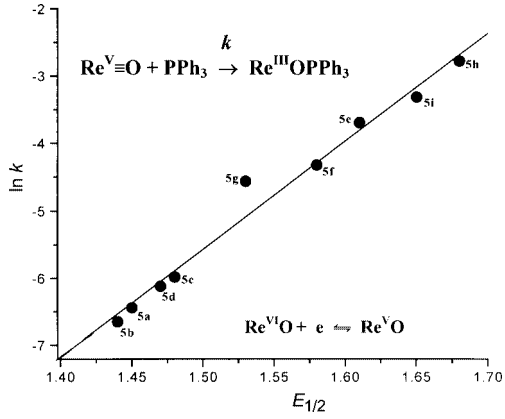


**2292** **Y.-Q. Zhang,* C.-L. Luo**

Relationship Between the Nearest-Neighbor Exchange Coupling Constants and the Number of Exchange Interactions in the Cyano-Bridged $MnMo_6(CN)_{18}$ Cluster: Density Functional Theory Calculations

**Keywords:** Molecular magnetism / Density functional calculations / Broken symmetry / Cyano-bridged clusters / Single-molecule studies

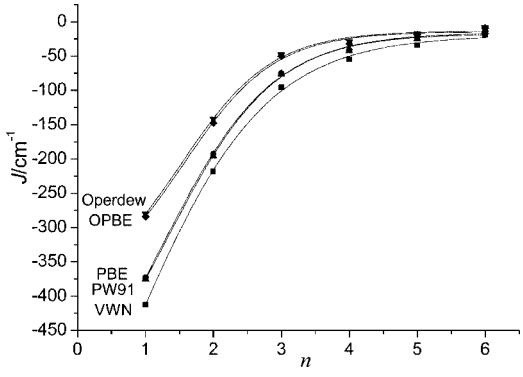


**2299** **L. Weber,* P. Bayer, G. Noveski, H.-G. Stammler, B. Neumann**

Reactivity of the Inversely Polarised Arsaalkenes $R-As=C(NMe_2)_2$ {R = $[(\eta^5\text{-}C_5Me_5)(CO)_2Fe]$, *t*BuC(O)} Towards Vinylidene Complexes $[\eta^5\text{-}(C_5H_5)(CO)(NO)W=C=C(H)R]$ (R = Ph, *t*Bu)

**Keywords:** Arsaalkenes / Heteroallene ligands / Vinylidene complexes / Tungsten

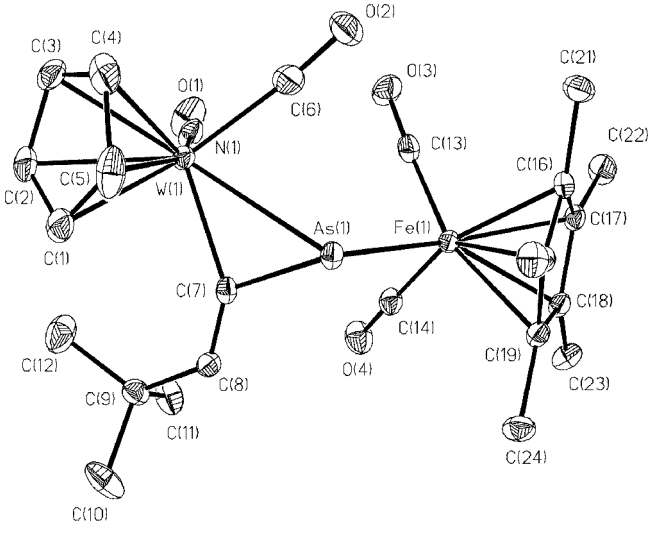


 © 2006 Wiley-VCH Verlag GmbH & Co. KGaA, Weinheim 

**2306** **K.-C. Hsieh, W.-Y. Lee, L.-F. Hsueh, H. M. Lee, J.-H. Huang***

Synthesis and Characterization of Zirconium and Hafnium Aryloxide Compounds and Their Reactivity Towards Lactide and ε-Caprolactone Polymerization

**Keywords:** Hafnium aryloxide / Zirconium aryloxide / Lactide / Caprolactone / Hafnium / Zirconium

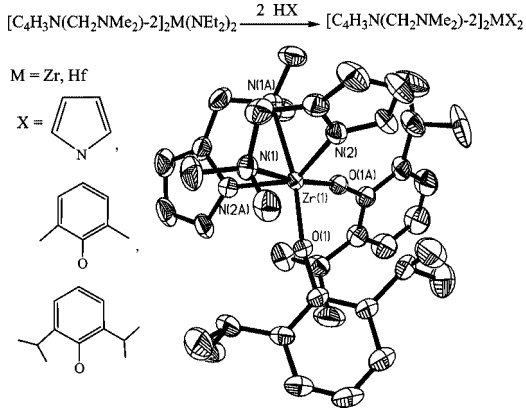


**2313** **G. Wang, B. Tang,* L. Zhuo, J. Ge, M. Xue**

Facile and Selected-Control Synthesis of β-$MnO_2$ Nanorods and Their Magnetic Properties

**Keywords:** β-Manganese dioxide / Nanostructures / Hydrothermal synthesis / Magnetic properties

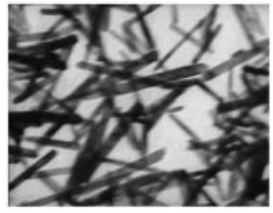

DOI: 10.1002/ejic.200600151

# σ-Silane Ruthenium Complexes: The Crucial Role of Secondary Interactions

**Sébastien Lachaize[a] and Sylviane Sabo-Etienne*[a]**

**Keywords:** σ-Complexes / Ruthenium / Silanes / Hydrides / Coordination modes / Intramolecular interactions / Oxidative addition / Hypervalent compounds

The bonding coordination mode of various silanes to ruthenium complexes is discussed on the basis of a detailed analysis of NMR, IR, X-ray and DFT data. It is now more and more obvious that a continuum exists between the two extreme situations, i.e. formation of a σ-silane complex or Si–H bond breaking leading to oxidative addition. Within this continuum, secondary interactions involving Si and H play a significant role, in particular for the stabilization of unusual structures or as intermediates in exchange processes. Here, we highlight the criteria allowing the best description of the different bonding modes.

(© Wiley-VCH Verlag GmbH & Co. KGaA, 69451 Weinheim, Germany, 2006)

## Introduction

A σ-complex is defined by the coordination of an H–E (E = H, Si, B, C...) bond to a metal center, a three center-two electron bond. "True" σ-complexes display no intramolecular interaction as the one found in the related family of agostic complexes. σ-complexes are now well recognized, and their properties have been reviewed in an excellent monograph by G. Kubas.[1] A parallel is often made with the Chatt–Dewar and Duncanson model, thus involving two components, σ-donation and back-donation (see Figure 1). Among the four main classes of σ-complexes (σ-dihydrogen,[1–3] σ-silane,[1,4–6] σ-borane[1,7] and σ-alcane[1,8,9]) σ-dihydrogen complexes are the most numerous and also the most documented. One of the main reasons is that two identical atoms are involved in the σ-coordination, whereas the situation is much more complex for the other cases. The substituents on the E atom have a tremendous impact, as steric and electronic effects can tune the σ-coordination. We will see in this review that in silane chemistry, the situation is quite complex, in particular as a result of the hyperval-

[a] Laboratoire de Chimie de Coordination du CNRS,
205 route de Narbonne, 31077 Toulouse Cedex 04, France
E-mail: sabo@lcc-toulouse.fr

*Sylviane Sabo-Etienne was born in France in 1956. She received her "Doctorat d'Etat" from the Université Paul Sabatier, Toulouse, in 1984, under the supervision of the late Professor Danièle Gervais, in the field of heterobimetallic complexes. In 1985, she moved to the Université de Bretagne Occidentale in Brest, to work as "Chargée de Recherche" in Prof. Hervé des Abbayes' group in the field of carbonylation. After a year working with Prof. Maurice Brookhart (Chapel Hill, USA) as a NSF-CNRS research associate, on acrylate dimerization, she returned to Toulouse to the Laboratoire de Chimie de Coordination to work in collaboration with Dr. Bruno Chaudret on polyhydride chemistry. She was promoted to the position of "Directrice de Recherche" in 1997. Her research interests deal with various aspects of coordination chemistry, organometallic chemistry and catalysis with some emphasis on the chemistry of σ-complexes. Silane and borane activation, role of secondary interactions, catalytic studies in the field of hydrogenation and C–X bond breaking and formation (X = B, C, Si, S, CN...), hydrogen transfer and C–H activation, assembly of novel functional groups, are present research topics.*

*Sébastien Lachaize was born in France in 1976. After graduating from the Ecole Normale Supérieure, Lyon, in 2001, he moved to Toulouse in the group of Dr. Bruno Chaudret at the Laboratoire de Chimie de Coordination. He received his PhD from the Université Paul Sabatier, Toulouse, in 2004 under the supervision of Dr Sylviane Sabo-Etienne working on σ H–E (E = H, Si and B) bond activation by ruthenium complexes. After one year as a postdoctoral fellow in Rochester, NY, USA, working with Prof. William D. Jones on C–CN bond activation, he came back to Toulouse in September 2005. He is currently a "Attaché Temporaire d'Enseignement et de Recherche" at the Institut National des Sciences Appliquées. His current research interests concern the synthesis of metallic nanoparticles using an organometallic route, with special focus on fundamental aspects of the nucleation-growth mechanism, control of the nanoparticle physical properties, and development of new applications.*

**MICROREVIEWS:** This feature introduces the readers to the authors' research through a concise overview of the selected topic. Reference to important work from others in the field is included.

 © 2006 Wiley-VCH Verlag GmbH & Co. KGaA, Weinheim 

ence properties of silicon.[10] It is first interesting to compare the coordination of a dihydrogen and of a silane ligand to a metal center. The silane ligand imposes a dissymmetry in the coordination mode, due to the difference in size and electronegativity of the two elements. The Si–H bond is more basic than the H–H bond, and thus is a better σ-donor. Moreover, the Si–H bond is also a better π acceptor, as the σ*(Si–H) orbital is lower in energy than the σ*(H–H) orbital (dissociation energy for the Si–H bond in the range 350–430 kJ·mol$^{-1}$ vs. 435 kJ·mol$^{-1}$ for $H_2$). When a competition between σ-dihydrogen or σ-silane coordination exists, σ-silane coordination is thus favoured. By comparison to the dihydrogen complexes, the σ-silanes are generally more advanced in the process of oxidative addition, thanks again to a better back donation. For this reason, it is often difficult to discriminate a σ-silane coordination from a hydrido(silyl) formulation.[11] σ-Silane complexes exist for a wide variety of metals, but this review will focus on ruthenium complexes, a metal of choice to act as catalyst precursor for several processes such as hydrosilylation, dehydrosilylative coupling of alkenes, and dehydrogenative polymerisation.[12,13] Moreover, polyhydride ruthenium complexes offer to analyze a wide range of situations. Indeed, a hydrogen atom can be coordinated to the metal as a classical hydride, involved in a σ-coordination (σ-dihydrogen or σ-silane), or in a secondary interaction with a silicon atom. We will in particular highlight the role of additional interactions in the coordination sphere of a metal, as they play a major role for the stabilization of silane complexes and are involved in most of the exchange processes that are often present in these highly dynamic systems.[14]

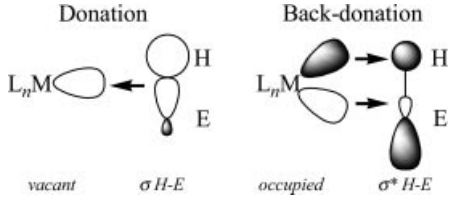


Figure 1. Bonding interactions in a σ-complex.

However, before presenting the different complexes, we would like to give some essential and fairly general features to illustrate the main issues in relation with the degree of activation of the Si–H bond. Between the two extreme situations, formation of a σ-silane complex or Si–H bond breaking and formation of a hydrido(silyl) complex, the Si–H bond activation can be viewed as a continuum (Figure 2). As a consequence, it is extremely difficult to establish the boundaries between the extremes, especially when other hydrogen atoms are present in the coordination sphere of the metal. In such a case, thanks to the tendency of Si to be hypervalent, additional interactions can be established. We have introduced the term *SISHA* to shorten the rather long quotation: *S*econdary *I*nteraction between a *S*ilicon and a *H*ydrogen *A*tom.[14] These interactions play an important role both in the stabilization of unusual geometries and in the exchange processes occurring in polyhydride species. At this point, it is important to remember the preference of ruthenium for oxidation state (II) vs. (IV) and that polyhydride ruthenium chemistry is dominated by σ-ligand coordination.

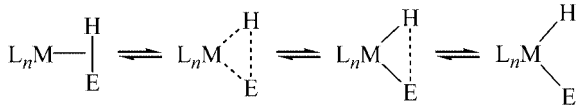


Figure 2. E–H bond activation: a continuum between the σ-complex and the product of oxidative addition.

Multinuclear NMR studies are particularly useful and give key information on the exchange processes and the activation of the Si–H bond. $^1$H chemical shift values are not a very useful parameter, as those for classical hydrides and hydrogen atoms involved in a σ-bond fall in the same range. A similar situation is found for $^{29}$Si chemical shift values of the corresponding silane or silyl complexes. Coupling constant values have been extensively used in particular to discriminate the two extremes, σ-silane complex and oxidative addition product. However, as we will detail below (see *primary silane* section) cautious must be taken in particular for values between 20 and 50 Hz, depending on the substituents on the silicon and in presence of fast exchange processes, which is unfortunately the case for many systems. Activation of the Si–H bond can also be monitored by IR. It is easy to follow the addition of a silane to a transition-metal complex by checking the disappearance of the stretching Si–H bond in the free silane (around 2100–2150 cm$^{-1}$). It is much more difficult to identify the corresponding band in a σ-silane complex (around 1000 cm$^{-1}$) due to extensive mixing of vibrational motions and overlap with some bands of other ligands. However, in many cases, a broad and rather intense band can be observed in the range 1650–1800 cm$^{-1}$, identified as an antisymmetric stretch of the activated Ru–H bond, with H still coordinated to Si. X-ray analysis and DFT calculations are very informative for the identification of σ-bonds and secondary interactions. It is worth noting that X-ray data are now more and more reliable for hydrogen location.[15] Low temperature and high quality measurements are of course required, and comparison with DFT data is very useful. Key parameters, as we will see below, are not only the Si–H distances, but also the Ru–Si distances. The Ru–Si distance within a series of compounds diminishes as the activation of the Si–H bond increases. For Si–H distances of typically 1.7–1.8 Å, σ-bond coordination can be reasonably proposed. The situation becomes more controversial for values around 1.9–2.0 Å. Higher values up to 2.4 Å are typically the range indicating a significant interaction between a hydrogen and a silicon, values still much shorter than the sum of the van der Waals radii, 3.4 Å. The nature of the silicon substituents is highly important. For electron-withdrawing substituents, the tendency of Si to be hypervalent is favored as a result of a σ*(Si–R) orbital lower in energy. The IHI (interligand hypervalent interaction) analysis developed by Nikonov is nothing more than the direct consequence of this well-known hypervalence property applied to hydrido(silyl) complexes.[16]

 © 2006 Wiley-VCH Verlag GmbH & Co. KGaA, Weinheim 

Through some selected examples, we will see the need to combine these various techniques to draw the best view of the bonding nature of a silane. Two main classes of compounds will be examined in details. The first section deals with a series of complexes resulting from the activation of disilane compounds, whereas in a second part we will examine the reactivity of ruthenium complexes with monosilane compounds, either primary or secondary silanes.

### Disilane Coordination

In view of the fascinating chemistry displayed by the bis(dihydrogen) ruthenium complex $RuH_2(H_2)_2(PCy_3)_2$ (**1**),[17] we were interested to isolate an analogous complex but incorporating two other σ-ligands, silane in place of dihydrogen. This was achieved by using disilane compounds. The chelating effect allowed for the stabilization but was not the determinant factor, as we will detail below. The series of general formula $[RuH_2\{(\eta^2\text{-}HSiMe_2)_2X\}(PCy_3)_2]$ [the spacer X between the two Si atoms contains two or three atoms, X = $C_6H_4$, $(CH_2)_n$, $OSiMe_2O$] was isolated and fully characterized (Scheme 1).[18] The most relevant data from multinuclear NMR experiments (see Table 1, compounds **2**–**5**) were the following: (i) one triplet near –8 ppm for the σ-Si–H protons and an AA′XX′ resonance near –12 ppm for the two classical hydrides. Coalescence of the two signals was observed at high temperature and an exchange barrier of roughly 65 kJ·mol$^{-1}$ was determined. Deuterium incorporation was equally observed on the two hydride sites implying a rather easy exchange process between the two types of hydrogen atoms. (ii) The $^{29}Si\{^{31}P\}$ INEPT spectra showed a doublet with $J_{SiH}$ values in the range 65–82 Hz, representing a significant reduction from the values for the free disilane (Δ = 106 to 125 Hz) in agreement with a stretching of the Si–H bond as a result of σ-coordination.

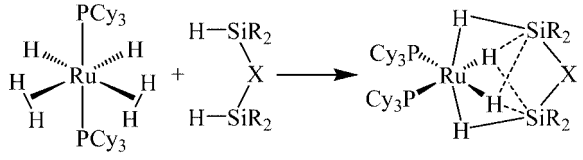


**1**

Scheme 1. Synthesis of the bis(silane) complexes of general formula $[RuH_2\{(\eta^2\text{-}HSiMe_2)_2X\}(PCy_3)_2]$.

The complexes were characterized by X-ray diffraction, and the measurements at low temperature allowed a very good location of the hydrogen atoms, ascertained by DFT calculations (see below and Table 2). They display the same overall structure, a distorted octahedral with two *cis* phosphane groups (P–Ru–P angle close to 108°) and the disilane ligand bonded to the ruthenium through two σ-Si–H bonds in a *trans* position. Activation of the Si–H bond is illustrated by a significant lengthening compared to the free silane. For example for $[RuH_2\{(\eta^2\text{-}HSiMe_2)_2(C_6H_4)\}(PCy_3)_2]$ (**2**) the two σ-Si–H bond lengths are 1.84(2) Å as determined by X-ray diffraction and 1.848 Å by DFT calculations at the B3LYP level, whereas the Ru–Si distances are close to 2.42 Å by X-ray diffraction or DFT calculations (Table 2, Figure 3). After obtaining the first X-ray structure,[19] we were quite surprised by the *cis* position of the bulky phosphane groups. In fact, no matter the nature of the disilane $[HMe_2Si(X)SiMe_2H$ with X = $C_6H_4$, $(CH_2)_2$, $OSiMe_2O]$ or the phosphane ($PCy_3$, $PPh_3$) coordinated, the same overall geometry was obtained (Table 2).[18] We noted that the distances between the classical hydrides and the silicon atoms were close to 2.2 Å, much shorter than the sum of the van der Waals radii (3.4 Å for hydrogen and silicon). Detailed DFT studies by means of two hybrid functionals B3LYP and B3PW91 gave important information on the coordination mode of the disilane ligand to the ruthenium. Three isomers were characterized on the singlet potential energy surface. As an example, we will concentrate on the three isomeric structures of $[RuH_2\{(\eta^2\text{-}HSiH_2)_2(C_6H_4)\}(PH_3)_2]$. The most stable isomer **A** has a geometry closely resembling that found by X-ray diffraction for **2** (Figure 3). The disilane is symmetrically coordinated to the ruthenium with the two σ-hydrogen atoms almost *trans* to each over (the H–Ru–H angle is 172°). The two Si–H distances of 1.848 Å are identical to the values found by X-ray diffraction. More interesting, the classical hydrides are turned toward the silicon atoms, imposing a *cis* position for the phosphane groups. The distances between the silicon atoms and the hydrides are 2.25 Å, indicative of weak attractive interactions again in excellent agreement with X-ray data. It is worth noting that location of hydrogen atoms in the coordination sphere of a metal has been always subject to debate. Very recently, we have published X-ray and neutron data for the bis(dihydrogen) complex $RuH_2(H_2)_2(PCyp_3)_2$ incorporating two tricyclopentylphosphane li-

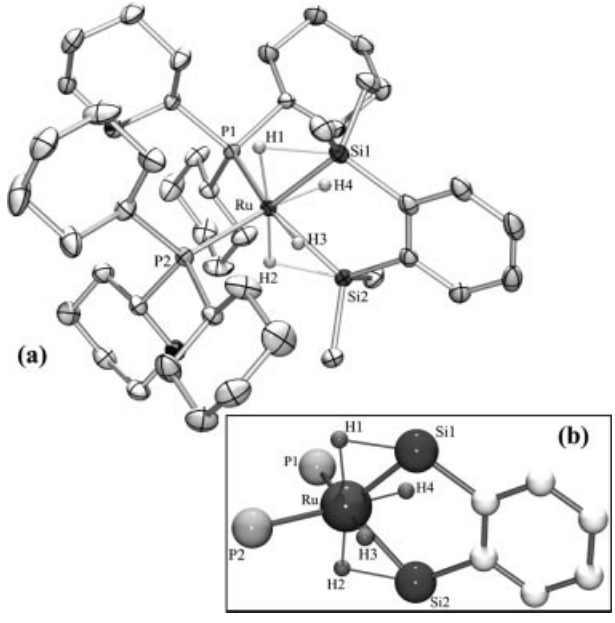


Figure 3. (a) X-ray crystal structure of $[RuH_2\{(\eta^2\text{-}HSiMe_2)_2(C_6H_4)\}(PCy_3)_2]$ (**2**). (b) DFT/B3PW91-optimized geometry of $[RuH_2\{(\eta^2\text{-}HSiH_2)_2(C_6H_4)\}(PH_3)_2]$.

 © 2006 Wiley-VCH Verlag GmbH & Co. KGaA, Weinheim 

Table 1. Selected NMR and IR [$cm^{-1}$] data[a] for various silane and silyl ruthenium complexes.

| | Formula | $\delta$ = $^{1}$H [ppm] | $J_{SiH}$ [Hz] | $\delta$ = $^{29}$Si [ppm] | $\nu_{Ru-H-Si}$ | $\nu_{Ru-H}$ | Ref. |
|---|---|---|---|---|---|---|---|
| **2** | $RuH_2[(\eta^2\text{-}HSiMe_2)_2(C_6H_4)](PCy_3)_2$ | –7.74 (t)<br>–12.03 (m) | 65 | 4.8 | 1778 | 1969<br>1985 | [16,17] |
| **3a** | $RuH_2[(\eta^2\text{-}HSiMe_2)_2(CH_2)_2](PCy_3)_2$ | –8.21 (t)<br>–12.65 (m) | 70 | 12.2 | 1773 | 1981<br>2012 | [16] |
| **3b** | $RuH_2[(\eta^2\text{-}HSiMe_2)_2(CH_2)_2](PCy_3)(PPh_3)$ | –7.68 (t)<br>–11.10 (dd)<br>–11.47 (dd) | 64 | 14.7 | 1768 | <br>1989<br>2008 | [16] |
| **3c** | $RuH_2[(\eta^2\text{-}HSiMe_2)_2(CH_2)_2](PPh_3)_2$ | –7.60 (t)<br>–10.92 (m) | 64 | 16.4 | 1797 | 1961<br>1978 | [16] |
| **4** | $RuH_2[(\eta^2\text{-}HSiMe_2)_2(CH_2)_3](PCy_3)_2$ | –8.49 (t)<br>–12.17 (m) | 75 | –11.1 | 1803 | 1961<br>1994 | [16] |
| **5** | $RuH_2[(\eta^2\text{-}HSiMe_2)_2(OSiMe_2O)](PCy_3)_2$ | –9.14 (t)<br>11.20 (m) | 82 | 4.9 | 1798 | 1955<br>2045 | [16] |
| **6** | $RuH_2[(\eta^2\text{-}HSiMe_2)_2NH](PCy_3)_2$ | –8.36 (br)<br>–8.62 (br)<br>–9.93 (br)<br>–10.76 (br) | – | – | 1712 | <br>1972<br>2040 | [13] |
| **7** | $RuH_2[(\eta^2\text{-}HSiMe_2)_2O](PCy_3)_2$ | –8.1 (br)<br>–8.5 (br)<br>–9.4 (br)<br>–10.2 (br) | 22 (av.)[b] | –5.61 | 1699 | <br>1969<br>2045 | [16,17] |
| **8a** | $RuH_2[(\eta^2\text{-}HSiPh_2)_2O](PCy_3)_2$ (sym) | –7.67 (br)<br>–9.70 (t) | 41 (av.)[b] | 4.80 | 1670 | 1976<br>2019 | [16,12] |
| **8b** | $RuH_2[(\eta^2\text{-}HSiPh_2)_2O](PCy_3)_2$ (non-sym) | –7.08 (br)<br>–8.11 (br)<br>–8.99 (br. t)<br>–9.81 (br. t) | | | | | |
| **9a** | $RuH_2[(\eta^2\text{-}HSiPh_2)\text{-}O\text{-}(SiHPh_2)](PPh_3)_3$ | –8.97 (dt, 1 H)<br>–9.40 (br. t, 2 H) | 35 (av.)[b] | 11.7<br>–21.4 (free) | – | – | [12] |
| **9b** | $RuH_2[(\eta^2\text{-}HSiPh_2)\text{-}O\text{-}(Si(OH)Ph_2)](PPh_3)_3$ | –9.15 (m, 3 H) | – | – | – | – | [12] |
| **10** | $RuH_3(SiCl_2Me)(PPh_3)_3$ | –9.76 (m) | 39.7 (av.)[b] | 36.4 | – | 1961.5 | [19] |
| **11** | $RuH_3(SiPyr_3)(PPh_3)_3$ | –9.80 (m) | 47.4 (av.)[b] | 8.6 | – | 1960<br>1969 | [21] |
| **12a** | $RuH_3(SiMe_3)(PMe_3)_3$ | –10.18 (br. m) | – | –10.8 | – | 1887 (av.) | [25] |
| **12b** | $RuH_3(SiEt_3)(PMe_3)_3$ | –10.53 (br. m) | – | 12.7 | – | 1897 (av.) | [25] |
| **12c** | $RuH_3(SiMe_2CH_2SiMe_3)(PMe_3)_3$ | –10.15 (br. m) | 25 | –9.2<br>–0.9 (free) | – | 1898 (av.) | [20] |
| **13** | $RuH_2(\eta^2\text{-}HSiPh_3)(\eta^2\text{-}H_2)(PCy_3)_2$ | –8.3 (br. s) | 18 (av.)[b] | 5.7 | – | – | [26] |
| **14** | $RuH_2(\eta^2\text{-}HSiMe_2Cl)(\eta^2\text{-}H_2)(PCy_3)_2$ | –8.51 (br. s) | – | 38 | – | – | [27] |
| **15** | $RuH_2\{\eta^4\text{-}HSiMe_2(CH{=}CHMe)\}(PCy_3)_2$ | –8.77 (br.)<br>–9.46 (dt)<br>–12.46 (dt) | 105 | –11.3 | – | 1945<br>2021 | [30] |
| **16** | $RuCl(H)(\text{-}CH_2SiMe_2)(PMe_3)_3$ (fac) | –7.7 (dt) | 75.0 | –19.4 | 1615 | – | [31] |
| | $RuCl(H)(\text{-}CH_2SiMe_2)(PMe_3)_3$ (mer) | –6.0 (dt) | 77.5 | –19.8 | – | – | [31] |
| **17** | $RuH(\eta^2\text{-}HSiEt_3)\{(\eta^3\text{-}C_6H_8)PCy_2\}(PCy_3)$ | –9.54 (br. t)<br>–12.63 (dd) | 36.7<br>24.7 | – | – | – | [36] |
| **18** | $RuH(\eta^2\text{-}HSiMe_2Et)\{(\eta^3\text{-}C_6H_8)PCy_2\}(PCy_3)$ | –9.45 (ps t)<br>–12.46 (dd) | 40.1<br>24.1 | 5.0 | – | – | [35] |
| **19** | $RuH(\eta^2\text{-}HSiMe_2Cl)\{(\eta^3\text{-}C_6H_8)PCy_2\}(PCy_3)$ | –9.06 (ps t)<br>–11.98 (dd) | 37.3<br>24.1 | 46.2 | – | – | [27] |
| **20** | $Cp^*RuCl(\eta^2\text{-}HSiClMe_2)(P\textit{i}Pr_3)$ | –9.65 (t) | 33.5 | – | 1916 | – | [33] |
| **21** | $[CpRuH(SiCl_3)(PMe_3)_2][B(3,5\text{-}(CF_3)_2C_6H_3)_4]$ | –9.87 (t) | 48 | 30.6 | – | – | [37] |
| **22a** | $Ru_2H_4(\mu\text{-}\eta^2\text{:}\eta^2\text{:}\eta^2\text{:}\eta^2\text{-}SiH_4)(PCy_3)_4$ | –6.0 (br.)<br>–8.6 (br.) | 36 (av.)[b] | 290.2 | 1667 | 1911 | [38,39] |
| **23** | $Ru_2H_2[\mu\text{-}\eta^2\text{:}\eta^2\text{-}H_2Si(OMe)_2]_3(PCy_3)_2$ | –9.94 (br.) | 22 (av.)[b] | 85.7 | 1703 | 1899<br>2022 | [39] |
| **24** | $[Cp^*RuH]_2(\eta^2\text{:}\eta^2\text{-}H_2Si\textit{t}Bu_2)$ | –6.15 (s)<br>–16.63 (s) | 75 | 75.5 | 1790 | – | [40] |

 © 2006 Wiley-VCH Verlag GmbH & Co. KGaA, Weinheim 

Table 1. *(continued)*.

| | Formula | $\delta$ = $^{1}$H [ppm] | $J_{SiH}$ [Hz] | $\delta$ = $^{29}$Si [ppm] | $\nu_{Ru-H-Si}$ | $\nu_{Ru-H}$ | Ref. |
|---|---|---|---|---|---|---|---|
| **25a** | $[Cp^*Ru(CO)]_2(\eta^2:\eta^2\text{-}H_2SitBu_2)$ | –13.60 (s) | 22.4 | 186.2 | – | – | [40] |
| **25b** | $[Cp^*Ru(CO)]_2(\eta^2:\eta^2\text{-}HSitBu_2)H$ | –11.79 (s)<br>–14.40 (s) | 31.6 | 168.2 | – | – | [40] |
| **26a** | $[Cp^*Ru]_2(\mu\text{-}\eta^2\text{-}HSitBu_2)(\mu\text{-}\eta^2\text{-}HSiPhH)(\mu\text{-}H)H$ | –11.64 (s)<br>–12.84 (s)<br>–14.00 (s)<br>–16.46 (s) | 26<br><br>49<br> | – | 1813<br>1613 | 2054 | [40] |
| **26b** | $[Cp^*Ru]_2(\mu\text{-}\eta^2\text{-}HSitBu_2)(\mu\text{-}\eta^2\text{-}HSiEtH)(\mu\text{-}H)H$ | –12.32 (s)<br>–13.26 (s)<br>–14.29 (s)<br>–16.67 (s) | –<br><br><br> | – | 1835<br>1659 | 2062 | [40] |

[a] NMR/IR data were obtained under the following conditions: **2**–**5**,**12**,**17**,**23**, $C_6D_6$, room temp./Nujol mull; **6**,**8**,**9a**,**22**, $C_7D_8$, 193 K/Nujol mull; **7**, $C_7D_8$, 178 K/Nujol mull; **9b**,**11**,**13**–**15**,**18**–**19**, $C_7D_8$, room temp./Nujol mull; **10**, $CD_2Cl_2$, room temp./KBr; **16**, $C_7D_8$, 301 K/Fluorolube; **20**, $C_7D_8$, 233 K/Nujol mull; **21**, $CD_2Cl_2$, 298 K; **24**–**26**, $C_7D_8$, 298 K/KBr. [b] $J_{SiH}$ values were determined at room temperature. Average values involving all the hydrides and dihydrogen ligand in the case of **13**.

Table 2. Selected interatomic distances [Å] for various silane and silyl ruthenium complexes.

| | Formula | Ru–Si<br>X-ray data | <br>DFT[a] | Si–H<br>X-ray data | <br>DFT[a] | Si···H<br>X-ray data | <br>DFT[a] | Ref. |
|---|---|---|---|---|---|---|---|---|
| **2** | $RuH_2[(\eta^2\text{-}HSiMe_2)_2(C_6H_4)](PCy_3)_2$ | 2.425(1) | 2.425 | 1.84(2) | 1.848 | 2.22(2)<br>2.18(2) | 2.253<br>2.253 | [16,17] |
| | | 2.429(2) | 2.425 | 1.84(2) | 1.848 | 2.12(2)<br>2.21(2) | 2.253<br>2.253 | |
| **3a** | $RuH_2[(\eta^2\text{-}HSiMe_2)_2(CH_2)_2](PCy_3)_2$ | 2.428(1) | 2.441 | 1.73(3) | 1.853 | 2.27(3)<br>2.13(3) | 2.22<br>2.329 | [16] |
| | | 2.411(1) | 2.441 | 1.78(3) | 1.853 | 2.12(3)<br>2.31(3) | 2.329<br>2.22 | |
| **5** | $RuH_2[(\eta^2\text{-}HSiMe_2)_2(OSiMe_2O)](PCy_3)_2$ | 2.484(1) | 2.451 | 1.77(4) | 1.826 | 2.25(3)<br>2.43(3) | 2.170<br>2.484 | [16] |
| | | 2.434(1) | 2.447 | 1.81(3) | 1.839 | 2.32(3)<br>2.04(3) | 2.426<br>2.168 | |
| **6** | $RuH_2[(\eta^2\text{-}HSiMe_2)_2NH](PCy_3)_2$ | 2.395(2) | 2.416 | 1.93(5) | 1.922 | 2.35(6)<br>2.25(6) | 2.510<br>2.191 | [13] |
| | | 2.434(2) | 2.490 | 1.91(5) | 1.775 | 2.39(5)<br>2.09(6) | 2.500<br>2.367 | |
| **9b** | $RuH_2[(\eta^2\text{-}HSiPh_2)\text{-}O\text{-}(Si(OH)Ph_2)](PPh_3)_3$ | 2.356(2) | – | 1.97(5) | – | 2.03(5)<br>2.07(5) | – | [12] |
| **10** | $RuH_3(SiCl_2Me)(PPh_3)_3$ | 2.2760(4) | – | – | – | 1.86(2)<br>1.94(2)<br>1.94(3) | – | [19] |
| **12a** | $RuH_3(SiMe_3)(PMe_3)_3$ | 2.376(1) | – | – | – | 2.13(5)<br>2.18(5)<br>2.23(5) | – | [25] |
| **12c** | $RuH_3(SiMe_2CH_2SiMe_3)(PMe_3)_3$ | 2.3774(8) | – | – | – | 2.00(4)<br>2.09(4)<br>2.05(5) | – | [20] |
| **12d** | $RuH_2(SiMe_2CH_2CH_2SiMe_2)(PMe_3)_3$ | 2.4682(9)<br>2.4514(9) | – | 1.81(4) | – | – | – | [20] |
| **13** | $RuH_2(\eta^2\text{-}HSiPh_3)(\eta^2\text{-}H_2)(PCy_3)_2$ | 2.385(2) | 2.394 | 1.72(3) | 1.946 | 1.83(3)<br>2.40(4) | 2.071<br>2.116 | [23] |
| **15** | $RuH_2\{\eta^4\text{-}HSiMe_2(CH{=}CHMe)\}(PCy_3)_2$ | 2.498(2) | 2.499 | 1.59(8) | 1.658 | – | – | [31] |
| **16** | $RuCl(H)(\text{-}CH_2SiMe_2)(PMe_3)_3$ (*fac*) | 2.526(2) | – | 1.664 | – | – | – | [25] |
| **16** | $RuCl(H)(\text{-}CH_2SiMe_2)(PMe_3)_3$ (*mer*) | 2.468(2) | – | 1.557 | – | – | – | [25] |
| **18** | $RuH(\eta^2\text{-}HSiMe_2Et)\{(\eta^3\text{-}C_6H_8)PCy_2\}(PCy_3)$ | 2.418(1) | 2.468 | – | 1.847 | – | 2.164 | [35] |
| **19**[b] | $RuH(\eta^2\text{-}HSiMe_2Cl)\{(\eta^3\text{-}C_6H_8)PCy_2\}(PCy_3)$ | 2.353(2) | 2.398 | 1.91 (2) | 1.891 | 1.99(2) | 2.076 | [27] |
| **20** | $Cp^*RuCl(\eta^2\text{-}HSiClMe_2)(PiPr_3)$ | 2.398(1) | 2.427 | 2.05 | 2.072 | – | – | [33] |
| **21** | $[CpRuH(SiCl_3)(PMe_3)_2]^+$ | 2.329(1) | – | 1.77(5) | – | – | – | [37] |
| **22b** | $Ru_2H_4(\mu\text{-}\eta^2\text{:}\eta^2\text{:}\eta^2\text{-}SiH_4)(PiPr_3)_4$ | 2.1875(4) | 2.229 | 1.69(3)<br>1.73(3) | 1.685<br>1.685 | – | – | [39] |

 © 2006 Wiley-VCH Verlag GmbH & Co. KGaA, Weinheim 

Table 2. *(continued)*.

| | Formula | Ru–Si X-ray data | Ru–Si DFT[a] | Si–H X-ray data | Si–H DFT[a] | Si···H X-ray data | Si···H DFT[a] | Ref. |
|---|---|---|---|---|---|---|---|---|
| **23** | $Ru_2H_2[\mu\text{-}\eta^2\text{:}\eta^2\text{-}H_2Si(OMe)_2]_3(PCy_3)_2$ | 2.456(3)<br>2.364(3)<br>2.408(3)<br>2.419(3)<br>2.355(3)<br>2.408(3) | 2.486<br>2.398<br>2.551<br>2.551<br>2.400<br>2.487 | – | in the range 1.654–1.760 | – | – | [39] |

[a] All the calculations were carried out at the B3LYP level of theory, except for compounds **2**, **6** (B3PW91) and **20** (BP86), by using the following model compounds: **2** $RuH_2[(\eta^2\text{-}HSiH_2)_2(C_6H_4)](PH_3)_2$, **3a** $RuH_2[(\eta^2\text{-}HSiH_2)_2(CH_2)_2](PH_3)_2$, **5** $RuH_2[(\eta^2\text{-}HSiH_2)_2(OSiH_2O)](PH_3)_2$, **6** $RuH_2[(\eta^2\text{-}HSiMe_2)_2NH](PCy_3)_2$, **13** $RuH_2(\eta^2\text{-}HSiH_3)(\eta^2\text{-}H_2)(PH_3)_2$, **15** $RuH_2\{\eta^4\text{-}HSiH_2(CH{=}CHMe)\}(PH_3)_2$, **18** $RuH(\eta^2\text{-}HSiMe_3)\{(\eta^3\text{-}C_6H_8)PH_2\}(PH_3)$, **19** $RuH(\eta^2\text{-}HSiMe_2Cl)\{(\eta^3\text{-}C_6H_8)PH_2\}(PH_3)$, **20** $Cp^*RuCl(\eta^2\text{-}HSiClMe_2)(P\mathit{i}Pr_3)$, **22** $Ru_2H_4(\mu\text{-}SiH_4)(PH_3)_4$, **23** $Ru_2H_2(\mu\text{-}H_2Si(OMe)_2)]_3(PH_3)_2$. [b] Data for one isomer.

gands.[15] Additional comparison with DFT values shows that X-ray data are more and more reliable for hydride location, when of course, high quality measurements can be obtained at low temperature. Isomer **B** was optimized as a minimum lying 32 kJ·mol$^{-1}$ above **A**. Isomer **B** has no symmetry whatsoever, and the two Si–H bonds are now very different: one is *trans* to a phosphane whereas the second one is *trans* to a hydride. One more striking difference with isomer **A** is that all the distances between the hydrides and the silicon atoms exceed the sum of the van der Waals radii (3.52 and 3.58 Å). A similar situation is found in isomer **C** with distances between the hydrides and the silicon atoms of 3.42 Å. Isomer **C** is characterized by a *trans* position of the phosphane groups, with the two Si–H bonds being *trans* to a hydride. Thus, **C** displaying an analogous geometry to the bis(dihydrogen) complex **1**, with in particular *trans* phosphane groups and two σ-ligands *trans* to the hydrides, is not the most stable isomer and is in fact 45 kJ·mol$^{-1}$ above **A**. Similar observations were found when using various disilanes with at least two atoms bridging the two Si. Thus, these close H···Si contacts are a stabilizing feature of the overall structure: we call them *SISHA* interactions (*S*econdary *I*nteraction between a *S*ilicon and a *H*ydrogen *A*tom). These SISHA interactions energetically compensate not only the hindered *cis* position of the bulky phosphane groups, but also the disfavored *trans* position of the σ-bonds (back-donation competition).

In the specific case of only one atom between the two Si, as for example in the case of disiloxane or disilazane, the situation is different as a result of a steric constraint upon coordination of the disilane ligand. Indeed, we have recently characterized both by X-ray diffraction and DFT calculations the disilazane complex $[RuH_2\{(\eta^2\text{-}HSiMe_2)_2NH\}(PCy_3)_2]$ (**6**).[20] For the first time the choice of the functional for DFT calculations in silane ruthenium chemistry turned to be crucial. Major differences were observed with the use of B3LYP by comparison to the X-ray data, whereas a very good match was obtained with B3PW91 (Figure 4). The two phosphane groups in **6** are still in a *cis* disposition but the disilazane ligand has now the two Si–H bonds also in a *cis* disposition, similarly to the case of isomer **B** described above. In **2** by X-ray diffraction or **A** by DFT calculations, the four Si···H distances between the hydrides and the silicon atoms were close to 2.2 Å, whereas in **6** they lie between 2.1 and 3.7 Å by X-ray diffraction and 2.2 to 3.9 Å by DFT calculations. It is now interesting to compare the NMR properties of the two complexes. At room temperature, as already pointed out, the $^1$H NMR spectrum of **2** displays two signals for the two types of hydrogen atoms. Coalescence is observed at much higher temperature. In contrast, in the case of **6**, only one signal is observed at room temperature, whereas decoalescence is achieved at low temperature. The exchange process is thus easier in the case of **6**. In-depth NMR and theoretical studies of the mechanism of the exchange process were undertaken on $[RuH_2\{(\eta^2\text{-}HSiMe_2)_2(C_2H_4)\}(PCy_3)_2]$ (**3a**), a complex very similar to **2** as shown by X-ray, NMR and DFT data.[14] The free energy of activation for exchange is 72 kJ·mol$^{-1}$ at 376 K, and the entropy of activation is close to zero, indicative of an intramolecular process. A complete

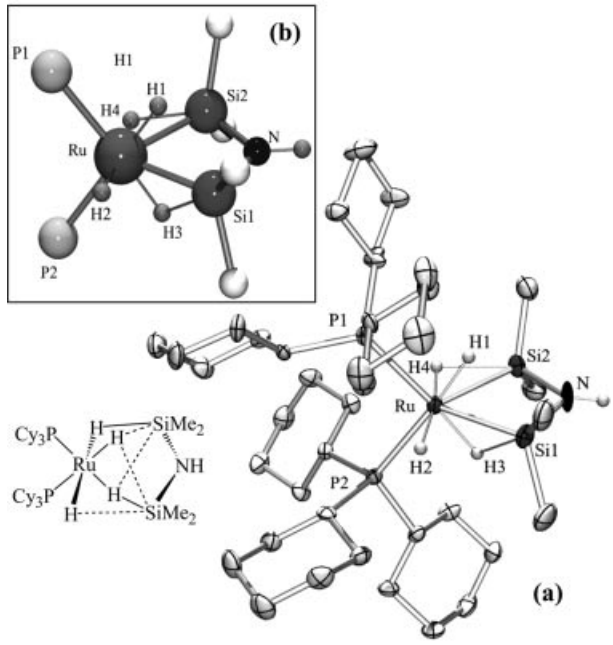


Figure 4. (a) X-ray crystal structure of $[RuH_2\{(\eta^2\text{-}HSiMe_2)_2NH\}(PCy_3)_2]$ (**6**). (b) DFT/B3PW91-optimized geometry of $[RuH_2\{(\eta^2\text{-}HSiMe_2)_2NH\}(PCy_3)_2]$.

 © 2006 Wiley-VCH Verlag GmbH & Co. KGaA, Weinheim 

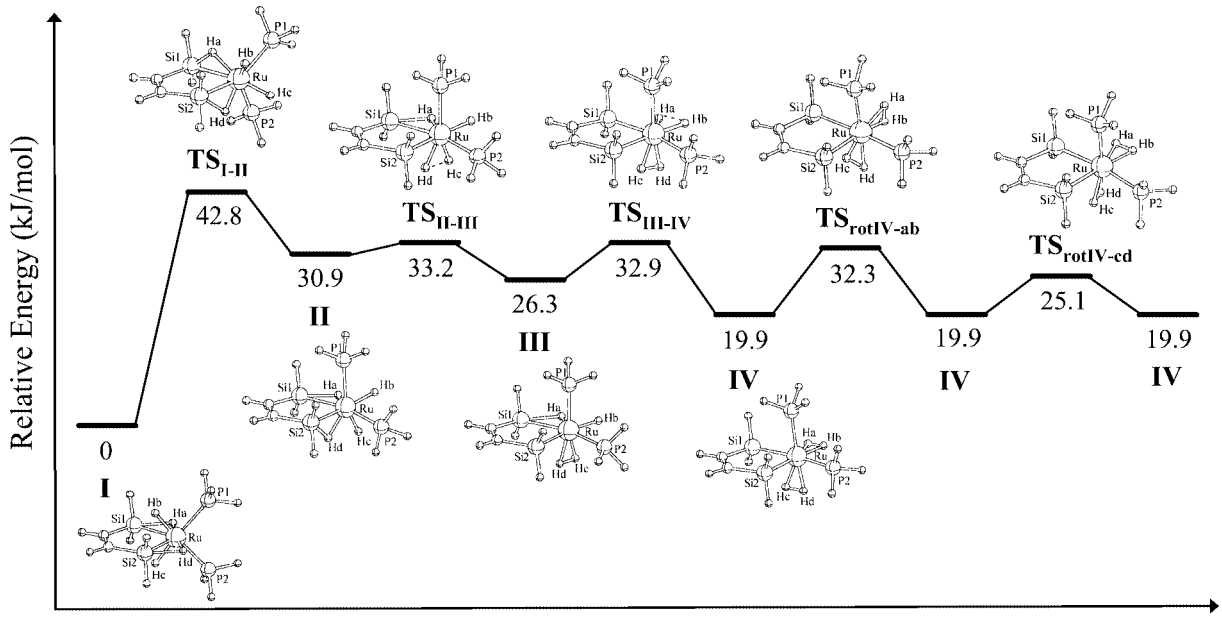


Figure 5. A picture of the intermediates and the transition states involved in the exchange process between the hydrides and the Si–H hydrogen atoms within the model complex $[RuH_2\{(\eta^2\text{-}HSiH_2)_2(C_2H_2)\}(PH_3)_2]$ at the DFT/B3LYP level.

picture of the exchange process deriving from DFT calculations is drawn in Figure 5. Isomer **I** $[RuH_2\{(\eta^2\text{-}HSiH_2)_2(C_2H_2)\}(PH_3)_2]$ was also used as a model complex for **3a**. Exchange of all the different hydrogen atoms can be achieved through the intermediacy of new σ-dihydrogen complexes. Indeed conversion of isomer **I** to the asymmetric isomer **II** in which the SISHA interactions have been broken is the first step. It is then easy to break a Si–H bond. Two hydrogen atoms are now close enough to form a new σ-ligand as in isomer **III**. A similar process with the second Si–H bond leads to isomer **IV** with two dihydrogen ligands. Exchange can now occur via rotation of the dihydrogen ligands and reversal of the isomerisation process. All the transition states connecting the different isomers have been calculated. $\mathbf{TS_{I-II}}$ is the most energetically demanding step. The overall barrier is 42.8 kJ·mol$^{-1}$. In summary, breaking of the SISHA interactions is responsible for the most energetically demanding step in the exchange process.

## Monosilane Coordination

### *Primary Silanes*

A wide variety of monosilanes of the type $HSiR_3$ (R = alkyl, aryl, alkoxy or halogen) reacts with dihydride ruthenium complexes to form the corresponding silane complexes stabilized by various interactions between the hydrides and the silicon atom (see Figure 6).[21–25] Depending on the activation degree of the Si–H bond, they can be interpreted as σ-silane or silyl hydride complexes, namely $RuH_2(\sigma\text{-}HSiR_3)L_2L'$ or $RuH_3(SiR_3)L_2L'$, respectively (L, L′ = $PR_3$, CO, σ-$H_2$). The NMR spectroscopic data are very similar for most of the complexes, as can be seen from Table 1. In the case of $RuH_3(SiCl_2Me)(PPh_3)_3$ (**10**) for example,[21] the $^1$H NMR spectrum exhibits only one hydride resonance at –9.76 ppm with the characteristic AA′A′′XX′X′′ coupling pattern of $MH_3(SiX_3)(PR_3)_3$ complexes arising from the sum of three phosphorus–hydrogen coupling constants, $|^2J_{HPtrans} + 2\ ^2J_{HPcis}|$. The $^1H\{^{31}P\}$ NMR spectrum gives a singlet with $^{29}$Si satellites ($J_{SiH}$ = 39.7 Hz) in agreement with a possible σ-silane bonding mode and/or Si···H interactions. The $^{31}P\{^1H\}$ NMR spectrum shows only a singlet at $\delta$ = 38.31 ppm, suggesting that the three phosphorus are equivalent on the NMR time scale. This is confirmed by the $^{29}Si\{^1H\}$ DEPT NMR spectrum that exhibits a quadruplet centered at $\delta$ = 36.4 ppm ($^2J_{SiP}$ = 12.8 Hz). No decoalescence of the hydride or phosphorus signals was observed even at low temperature, indicative of a fast exchange process in this unsymmetrical compound.

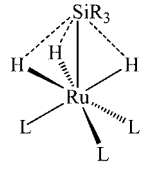


L = phosphane, CO, σ-$H_2$
R = alkyl, aryl, alkoxy, amino or halogen

Figure 6. Schematic representation of a series of complexes of general formula $RuH_3(SiR_3)L_2L'$.

In the case of symmetrical complexes ($C_3$ axis), the equivalency of the hydrides prevents any further interpretation regarding the bonding mode. This situation leads to some disagreement on whether or not the $SiPyr_3$ group is rotating in $RuH_3(SiPyr_3)(PPh_3)_3$ (**11**) for example (Pyr = pyrrolyl). Hübler et al. proposed a bonding scheme that allows a facile rotation when considering the contribution represented in Figure 7 (b) to be preponderant.[23] On the

 © 2006 Wiley-VCH Verlag GmbH & Co. KGaA, Weinheim 

contrary, Nikonov pleads an electron-density transfer from the σ(M–H) bonding orbitals into the σ*(Si–N) antibonding orbitals to be the main contribution, thus leading to a rigid structure (Figure 6 and Figure 7, a).[26] However, Nikonov uses a DFT study reported by Hübler et al. to support his argumentation, but this was actually a MP2 study of an osmium analogue, which is certainly not transposable to the ruthenium case. It is thus difficult to make conclusions on the basis of these experimental and computational data. In the case of the $SiMe_3$ group, Berry et al. observed no dynamic process in $RuH_3(SiMe_3)(PMe_3)_3$ (**12a**) on the NMR time scale (only a slight broadening of the Ru–H resonances at 190 K).[27] In these symmetrical compounds, the presence of a Ru-$\eta^2$-H–Si bond (or one strong Si···H interaction) could have led to decoalescence of the hydride signal. However, due to the limited range in temperatures, one cannot conclude on whether the activation energy for the formation/breaking of such interactions would be very low or very high.

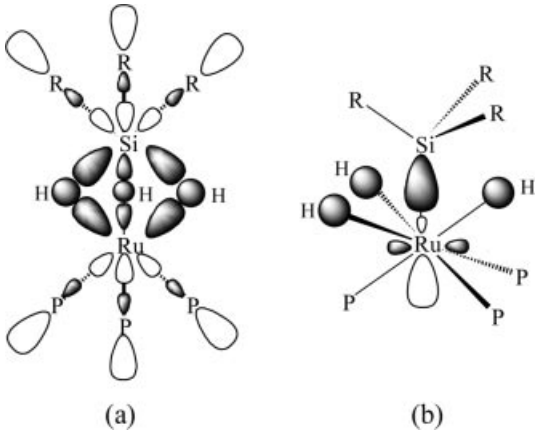


Figure 7. Orbital representation of Ru–H···Si bonding adapted from ref.[19,21]

The fluxionality observed at the NMR time scale for $RuH_3(SiMeCl_2)(PPh_3)_3$,[21] (**10**) but also for $RuH_2(\eta^2\text{-}HSiPh_3)(\eta^2\text{-}H_2)(PCy_3)_2$ (**13**),[28] $RuH_2(\eta^2\text{-}HSiMe_2Cl)(\eta^2\text{-}H_2)(PCy_3)_2$ (**14**),[29] and $RuH_3(SiMe_2CH_2SiMe_3)(PMe_3)_3$ (**12c**),[22] is consistent with exchange processes characterized by low activation energy barriers. In **10** and **12c**, the silane ligand is bearing different substituents (a situation not depicted in Figure 7, a). The presence of different R substituents should affect more or less the balance between the three Si···H interactions in the contribution shown in Figure 7 (a). In **13** and **14**, one phosphane is now replaced by a dihydrogen ligand. It is thus expected a reinforcement of hydride inequivalency. Again, one cannot conclude when no decoalescence of the hydride resonance is observed. NMR spectroscopy can still provide $J_{SiH}$ coupling constants but they are mean values. The interpretation of the raw values has to be done cautiously since the typical ranges for which the Si–H bonds were considered to be either fully activated ($< 20$ Hz) or just partially elongated (20–70 Hz) have been recently reconsidered.[22,30] The free silane $^1J_{SiH}$ substituent-dependency clearly illustrates the problem. Values vary from 190 Hz in $HSiMe_3$ to 370.6 Hz in $HSiCl_3$ due in part to an increase in the s character in the Si–H bond (Bent's rule). This naturally applies to the $J_{SiH}$ coupling in a complex, more precisely to its two contributions of opposite signs, $^1J_{SiH}$ and $^2J_{SiH}$. The measured $J_{SiH}$ value corresponds to the sum $|^1J_{SiH} + {}^2J_{SiH}|$. In the series of $CpRu(SiR_3)(PR'_3)_2$ complexes, Lemke et al. have shown that an increase in the electron-withdrawing character of the $SiR_3$ group leads to stronger Ru–Si bonds as monitored by the increase of the $|^2J_{SiP}|$ values.[31] For hydrido(silyl) or σ-silane species with different $SiR_3$ groups, but considering a similar activation of the Si–H bond, the $|^1J_{SiH}|$ values should increase as a function of the R substituent, with the highest value for the more electronegative group. As an example, coordination of $HSiR_3$ to a metal center leading to 80% activation of the Si–H bond would result to a $|^1J_{SiH}|$ value of 74 Hz for R = Cl and 38 Hz for R = Me. Assuming that the $|^2J_{SiH}|$ values will follow the same trend as the $|^2J_{SiP}|$ values in silyl complexes, the magnitude of the apparent $J_{SiH}$ coupling may not necessarily reflect the silane bonding and its modifications. For example, the apparent $J_{SiH}$ values of 39.7 Hz in $RuH_3(SiMeCl_2)(PPh_3)_3$ (**10**) and 47.4 Hz in $RuH_3(SiPyr_3)(PPh_3)_3$ (**11**) do not necessarily indicate the presence of a σ-silane bond. However, in order to define a trend for the $J_{SiH}$ coupling constants in silane ruthenium complexes, one can start with the coupling constant of 105 Hz measured in the allylsilane complex $RuH_2[\eta^4\text{-}HSiMe_2(CH{=}CHMe)](PCy_3)_2$ (**15**) to give an idea of the upper limit corresponding to an agostic Si–H interaction.[32] We can then consider the *fac* and *mer* isomers of $RuCl(CH_2SiHMe_2)(PMe_3)_3$ described by Berry et al. that reflect a further point on the oxidative addition process (still close to the agostic interaction type).[33] They respectively exhibit $J_{SiH}$ values of 75 and 77.5 Hz associated to Si–H distances of 1.664 Å in the *fac* isomer and 1.557 Å in the *mer* one, in agreement with only slightly elongated Si–H bonds. The next step can be represented by the bis(σ-silane) complexes described in the previous section with coupling constants around 70 Hz. Below that value, it is recommended to interpret the $J_{SiH}$ values with caution, especially when the silicon atom has electron-withdrawing substituents. More information could be now gained thanks to recent improvements in DFT calculations, which allow calculations of $J_{SiH}$ values.[34] Generally, a negative value is the sign of a direct Si–H interaction as $^1J_{SiH}$ are negative due to the negative magnetogyric value of silicon.[35]

Decoalescence of the hydride signal in a polyhydride system is rarely observed. The $^1H$ NMR spectrum of $RuH_2\{(\eta^2\text{-}HSiPh_2)O(SiHPh_2)\}(PPh_3)_3$ (**9a**) at 203 K, a complex with a dangling Si–H ligand, shows two broad multiplets at –8.97 ppm and –9.40 ppm ($^2J_{HP\,trans}$ = 50 Hz and $^2J_{HP\,cis}$ = 25 Hz) in a 2:1 ratio.[14] At this temperature, the $^{31}P\{^1H\}$ NMR spectrum displays a triplet at $\delta$ = 42.62 and a doublet at $\delta$ = 38.49 with $J_{PP}$ of 23 Hz. The $^{29}Si$-$^1H$ COSY spectrum acquired at 203 K shows a signal corresponding to the dangling Si–H bond ($\delta$ –21.4) and another one ($\delta$ = 11.7 ppm) correlated to the hydride high-field resonance at $\delta$ –8.97 ppm attributed to an ($\eta^2$-Si–H) hydrogen.

 © 2006 Wiley-VCH Verlag GmbH & Co. KGaA, Weinheim 

The fast exchange at room temperature is associated to a $J_{SiH}$ mean value of 35 Hz. Due to line broadening, no $J_{SiH}$ value could be measured at low temperature. According to the above discussion about coupling constants, a definitive assignment between the two formulations, dihydride σ-silane or trihydride silyl with one strong Si···H interaction, is difficult. An X-ray structure of $RuH_2\{(\eta^2\text{-}HSiPh_2)\text{-}O(Si(OH)Ph_2)\}(PPh_3)_3$ (**9b**), resulting from hydrolysis of the dangling Si–H bond of **9a** was obtained. The structure is similar to those described for other $RuH_3(SiR_3)L_3$. The ruthenium is surrounded by the three phosphane groups in a tripodal position with P–Ru–P angles of 103° (av.) and Si–Ru–P angles of 115° (av.). However, one Si–Ru–P angle is 119°, indicating a dissymmetric geometry. The hydrogen atoms were located in the vicinity of the ruthenium at 1.6 Å (av.). The distances between the silicon and the three hydrides are 1.97(5), 2.03(5) and 2.07(5) Å. They are in agreement with an elongated σ-Si–H bond and two SISHA interactions (unfortunately, we have no DFT data for comparison). The Ru–Si distance is 2.356(2) Å, thus at the lower limit of the Ru–Si distances observed in other silane ruthenium complexes. We note that steric hindrance between the phosphane groups and the $OSi(OH)Ph_2$ group may have influenced the bonding. As a matter of fact, there is no decoalescence of the hydride resonance for $RuH_3(SiMe_2CH_2SiMe_3)(PMe_3)_3$ (**12c**) in which the phosphane groups are rather small.[22] In this series of complexes, X-ray data show that the Ru–Si bond lengths range from 2.2760(4) Å in $RuH_3(SiCl_2Me)(PPh_3)_3$ to 2.385(2) Å in $RuH_2(\eta^2\text{-}HSiPh_3)(\eta^2\text{-}H_2)(PCy_3)_2$ (see Table 2). They overlap the distances reported for silyl and σ-silane species and they are mainly in the lower limit region (taking into account the nature of the silicon substituents). In fact, the process of Si–H bond activation can be described similarly to the one proposed for C–H bond activation. Once the proton/metal interaction is established, the Si–M distance decreases while the M–H and Si–H distances stay almost unchanged (until a certain point).[6,36] The main difference comes from the silicon hypervalence that may favor Si···H interactions, keeping the atoms close together in a *cis* position. Lin has discussed this point in a previous review on the structural and bonding characteristics in transition metal–silane complexes.[5] Consequently, a long Ru–Si distance is consistent with an early stage in the activation, i.e. a σ-silane bonding mode, while it remains difficult to conclude for a short one, which appears to be the case in this series. When comparing the Ru–Si distances obtained for this family to the ones measured in the bis(σ-silane) complexes, we deduce that the latter represents an earlier stage in the Si–H bond activation process. This is confirmed by the shorter σ-Si–H bond lengths and the weaker SISHA interactions (longer Si···H distances). For the complexes we are considering here, the SISHA interactions are dedicated to only one silicon atom. This certainly results in a better stabilization of the activated silane and consequently highlights a tight relationship between the Si–H bond activation level and the SISHA interaction strength. The Si–H bond oxidative addition process is better seen as a continuum in energy. SISHA interactions help to equilibrate the electronic density transfers between the ruthenium, the hydrides and the silicon.

The X-ray structure analysis of $RuH_2(\eta^2\text{-}HSiPh_3)(\eta^2\text{-}H_2)(PCy_3)_2$ (**13**) done at 160 K exhibits an elongated σ-Si–H bond [1.72(3) Å] and one strong SISHA interaction [1.843(3) Å]. The remaining hydride is at 2.40(4) Å. This can be related to the nature of the *trans* ligands ($PCy_3$ and $\sigma\text{-}H_2$) and the steric hindrance as much as the electronic effects can be invoked. The Ru–Si distance [2.385(2) Å] is the longest reported for that series, consistent with a rather early stage in the Si–H bond activation process and one main SISHA interaction. A $J_{SiH}$ value of 18 Hz was recently determined. Considering that five hydrogen atoms are in fast exchange, this observed value is in agreement with the presence of a σ-silane. However the overall geometry was not predictable by NMR spectroscopy, but was confirmed by DFT/B3LYP calculations on the model $RuH_2(\eta^2\text{-}HSiH_3)(\eta^2\text{-}H_2)(PH_3)_2$.[25] The ground state structure shows two SISHA interactions (2.071 and 2.116 Å) and an elongated σ-Si–H (1.946 Å) that is less than 0.2 Å shorter. This short difference is in agreement with the high fluxionality observed by NMR spectroscopy. An analogous study performed on the model $RuH_2(\eta^2\text{-}HSiMe_2Cl)(\eta^2\text{-}H_2)(PH_3)_2$ gives the same results. The location of Cl with respect to the hydrides influences the positioning of the σ-Si–H bond but does not change the energy that much ($\Delta E$ = 4.8 kJ/mol between isomers A and B) (see Figure 8 and Table 3). The closest Si···H contact is not in a position *trans* to Cl, as would be predicted for a hydrido(silyl) formulation by using the Nikonov model of interaction, IHI. All the observations are consistent with a σ-bonding mode of the silane.

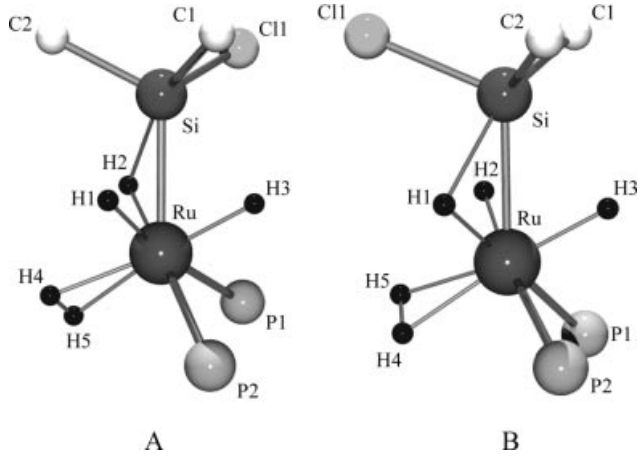


Figure 8. The two DFT/B3LYP-optimized isomeric structures of $RuH_2(\eta^2\text{-}HSiMe_2Cl)(\eta^2\text{-}H_2)(PH_3)_2$.

We undertook a detailed investigation on the complexes $RuH(\eta^2\text{-}HSiR_3)\{(\eta^3\text{-}C_6H_8)PCy_2\}(PCy_3)$ ($SiR_3$ = $SiEt_3$, $SiMe_2Et$ and $SiMe_2Cl$). In this series, the situation is different because there is no hydride exchange at room temperature, as the result of the presence of two different phosphane groups.[29,37,38] In $RuH(\eta^2\text{-}HSiMe_2Cl)\{(\eta^3\text{-}C_6H_8)PCy_2\}(PCy_3)$ (**19**) for example, the two hydrides resonate at –9.06 ppm (br. t) and –11.98 ppm (dd) and an AB pattern

 © 2006 Wiley-VCH Verlag GmbH & Co. KGaA, Weinheim 

Table 3. Selected distances [Å] and angles [°] for $RuH_2(\eta^2\text{-}HSiMe_2Cl)(\eta^2\text{-}H_2)(PH_3)_2$ rotamers optimized at the DFT/B3LYP level.

| | Rotamer **A** | Rotamer **B** |
|---|---|---|
| Ru–P1 | 2.373 | 2.371 |
| Ru–P2 | 2.372 | 2.375 |
| Ru–Si | 2.382 | 2.387 |
| Si–Cl | 2.158 | 2.145 |
| Si–C | 1.892 (C1) | 1.893 (C1) |
| | 1.890 (C2) | 1.893 (C2) |
| Ru–H1 | 1.644 | 1.637 |
| Ru–H2 | 1.636 | 1.633 |
| Ru–H3 | 1.619 | 1.627 |
| Ru–H4 | 1.788 | 1.808 |
| Ru–H5 | 1.807 | 1.786 |
| H4–H5 | 0.849 | 0.847 |
| Si–H1 | 2.091 | 1.924 |
| Si–H2 | 1.919 | 2.076 |
| Si–H3 | 2.159 | 2.166 |
| P1–Ru–P2 | 98.1 | 97.8 |
| P1–Ru–H1 | 171.0 | 178.4 |
| P2–Ru–H2 | 178.5 | 173.5 |
| P1–Ru–H3 | 82.0 | 84.3 |
| P2–Ru–H3 | 83.0 | 83.4 |
| Si–H1–Ru | 78.2 | 83.7 |
| Si–H2–Ru | 83.7 | 79.1 |
| Si–H3–Ru | 76.7 | 76.5 |
| Cl1–Si–H1 | 153.4 | 89.0 |
| Cl1–Si–H3 | 91.3 | 154.2 |
| C1–Si–H1 | 90.3 | 158.0 |
| C1–Si–H2 | 158.1 | 86.4 |
| C2–Si–H3 | 158.3 | 94.7 |
| H4–Ru–H5 | 27.3 | 27.3 |
| Cent(H4,H5)–Ru–H3 | 176.8 | 176.6 |
| $\Delta E$ [kJ/mol] | 0.0 | +4.8 |

(83.9 and 68.8 ppm, $J_{PP}$ = 18.6 Hz) is observed in the $^{31}P\{^1H\}$ spectrum. A 1D HMQC $^{29}Si\text{-}^1H\{^{31}P\}$ experiment shows two doublets in the high-field region with $J_{SiH}$ values of 37.3 and 24.1 Hz (see Figure 9). The coupling of H1 and H2 with silicon are different by more than 10 Hz, but are surprisingly almost the same in the two analogous complexes **17** and **18** with $HSiEt_3$ and $HSiMe_2Et$, respectively (see Table 1). A rather significant change on the Si–H bond activation was expected at least between $HSiMe_2Cl$ and $HSiMe_2Et$ because of the chloride substituent. This point comforts the idea that a direct interpretation of the $J_{SiH}$ value is not appropriate to the description of the bonding mode of the silane. The X-ray structures of the latter two species have been obtained. A partial disorder on the Si substituents could not be solved and the hydrides could only be detected for **19** (see Figure 10). The Si–H distances of 1.91(2) Å (1.891 by DFT calculations) and 1.99(2) Å (2.076 by DFT calculations) can be assigned to an $\eta^2$-Si–H and a SISHA interaction, respectively. Even if the values overlap when taking into account the standard deviations, they seem to be in agreement with the corresponding coupling constants. The Ru–Si bond lengths in **18** [2.418(1) Å] and **19** [2.353(2) Å] are clearly different, in agreement with the higher electronegativity of the more tightly bound $SiMe_2Cl$ group. The Ru–Si distances mirror the stability of the silane bonding. As a matter of fact, **19** is stable under an atmospheric pressure of ethylene in toluene, whereas **18** leads to C–Si coupling product and formation of $RuH(\eta^2\text{-}C_2H_4)\{(\eta^3\text{-}C_6H_8)PCy_2\}(PCy_3)$.[37] Compound reactivity is certainly an interesting criterion to differentiate the bonding in this series of silanes. However, what does this shorter Ru–Si bond really mean? The Ru–Si interaction can be strong both in a silyl and in a σ-silane species and increased by the hypervalence tendency of Si. The Ru–Si bond can be shorter thanks to an additional contribution: a bonding overlap between an occupied d(Ru) orbital and empty σ*(Si–R) orbitals. Such a bonding contribution, favored by chloro substituents, has already been used by Lemke et al. to describe a large series of silyl ruthenium complexes.[31] When no d(Ru) orbital is "available", one can consider that the σ(Ru–H) orbital can play the same role. As we have already explained, SISHA interactions help back-donation of electronic density from Ru to Si via the hydrides. This has also been extensively studied by Nikonov et al. but mainly in the particular case of Cl substituents.[16] In summary, the interpretation of the similarities and differences

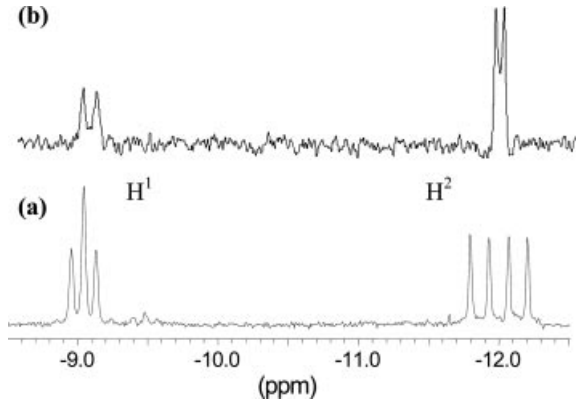


Figure 9. (a) $^1H$ NMR spectrum ($C_6D_6$, 400 MHz) and (b) 1D HMQC $^{29}Si\text{-}^1H\text{-}\{^{31}P\}$ in the hydride region of $RuH(\eta^2\text{-}HSiMe_2Cl)\{(\eta^3\text{-}C_6H_8)PCy_2\}(PCy_3)$ (**19**).

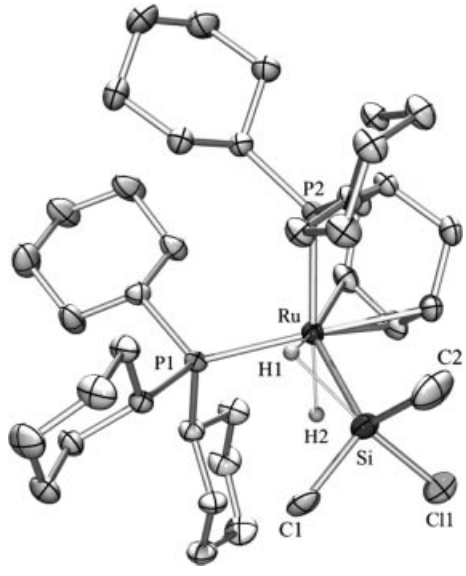


Figure 10. X-ray crystal structure of $RuH(\eta^2\text{-}HSiMe_2Cl)\{(\eta^3\text{-}C_6H_8)PCy_2\}(PCy_3)$ (**19**).

 © 2006 Wiley-VCH Verlag GmbH & Co. KGaA, Weinheim 

between **18** and **19** is tricky and requires more information. We will publish in due course a full experimental and theoretical study on that series, focusing particularly on the bonding nature of the silane as a function of the chloride number.

It is worth to note that SISHA interactions are not limited to chloride-containing silanes as they clearly appear in most of the examples presented above. But Cl seems to favor secondary interactions as illustrated by the work of Nikonov et al. Cp*RuCl($\eta^2$-HSiMe$_2$Cl)(P*i*Pr$_3$) (**20**) is defined as a σ-silane complex on the basis of experimental and theoretical data (see Figure 11 and Table 1, Table 2).[35] Its X-ray structure exhibits an unusual interaction between the Cl ligand and the silicon atom [$d_{Cl\cdots Si}$ = 3.014(1) Å and the sum of the van der Waals radii is 3.81 Å]. This is well reproduced by DFT calculations on the model CpRuCl($\eta^2$-HSiMe$_2$Cl)(PMe$_3$). The ground state corresponds to the X-ray structure, i.e. the chloride substituent on the silicon is almost "*trans*" to the chloride [Cl–Si···Cl = 165.61(3)°]. The rotamer with a methyl group in "*trans*" is 10.5 kJ/mol less stable and the Si···Cl distance is elongated by about 0.2 Å. This confirms the stabilizing role played by the chloride as it is more electron-withdrawing than the methyl group. A small elongation of the Si–R bond "*trans*" to the secondary interaction is always reported, in agreement with the implication of the σ*(Si–R). In this example, the Si–H bond is absolutely not in the same plane as the Cl substituent which is the case in several silyl hydrido complexes with IHI described by Nikonov et al. Here, the compound is a "real" σ-silane complex. In the absence of any other hydride, further stabilization can only be gained by the formation of a secondary interaction between Si and Ru–Cl. Such an interaction is maximized for a Ru–Cl not orientated *trans* to Si–H. As discussed above, a similar situation has been observed when considering the RuH$_2$($\eta^2$-HSiMe$_2$Cl)($\eta^2$-H$_2$)(PH$_3$)$_2$ rotamers.

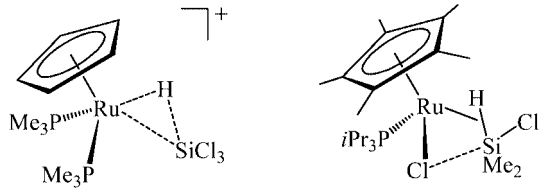


**21** **20**

Figure 11. Schematic view of Cp*RuCl($\eta^2$-HSiMe$_2$Cl)(P*i*Pr$_3$) (**20**) and [CpRu($\eta^2$-HSiCl$_3$)(PMe$_3$)$_2$]$^+$ (**21**).

Lemke et al. reported the full characterization of the cationic complex [CpRu($\eta^2$-HSiCl$_3$)(PMe$_3$)$_2$]$^+$ (**21**) formed by protonation of the silyl complex CpRu(SiCl$_3$)(PMe$_3$)$_2$.[39] Compound **21** was formulated as a σ-silane species on the basis of X-ray diffraction and NMR spectroscopic data (see Figure 11). The silane ligand was characterized by a Si–H bond length of 1.77(5) Å in the typical range for σ-silane ligands. The $J_{SiH}$ value of 48 Hz is also in the range expected for a σ-coordination. However, comparison with the corresponding value for the free silane HSiCl$_3$ (370 Hz) denotes a very strong reduction in the Si–H interaction. NMR spectroscopic data also indicate some fluxionality of the silane with respect to its orientation with the two phosphane ligands. The authors associate their data to a σ-silane arrested in its oxidative addition to the ruthenium center indicative of a latter stage of such a process. The geometry can be described as a "three- or four-legged piano stool" depending on how the HSiCl$_3$ ligand is considered. This appears to be in agreement with the measured Si–H distance, only if we analyze this strong interaction to be the consequence of the silicon hypervalence enhanced by the chloro substituents. This is a perfect example to highlight the crucial role of silicon hypervalency on silane bonding.

### *Secondary Silane*

The next step in our silane studies was to examine the reactivity of the bis(dihydrogen) complex **1** with dihydrogenosilanes. We mentioned in the introduction the complexity of silane activation toward σ-coordination as compared to dihydrogen activation. Steric and electronic effects of the Si substituents can tune the σ-coordination as well as the hypervalence properties of the silicon. But one can also face redistribution reactions. Indeed, by adding dihydrogenosilanes to **1**, several silanes were generated in situ. For example, when starting with H$_2$SiMePh, HSiMe$_2$Ph and HSiMePh$_2$ were formed and remained in solution whereas formation of SiH$_4$ and HSiPh$_3$ resulted in their coordination to a metal fragment to produce the corresponding complexes [Ru$_2$H$_4$(μ-$\eta^2$:$\eta^2$:$\eta^2$-SiH$_4$)(PCy$_3$)$_4$] (**22**) and [RuH$_2$($\eta^2$-H$_2$)($\eta^2$-HSiPh$_3$)(PCy$_3$)$_2$] (**13**) (Scheme 2).[40,41] Compound **22** is a unique example of a SiH$_4$ ligand in a bridging position. It is coordinated to two Ru through four σ-Si–H bonds. Each σ-bond [$d_{Si-H}$ = 1.69(3) Å and 1.73(3) Å by X-ray diffraction and 1.685 Å by DFT calculations] is the result of a σ-donation to an empty d orbital of one ruthenium and backbonding from the occupied d orbital of *the other* ruthenium into the σ*(Si–H) antibonding orbital. Interestingly, **22** is characterized by a fast exchange process as the eight hydrogen atoms (four hydrides and four involved in the σ-Si–H bonds) gave a nonet in the $^{29}$Si INEPT spectrum with an average $J_{SiH}$ value of 36 Hz. The $^1$H NMR spectrum displayed one signal in the hydride region at room temperature, but decoalescence into two signals of equal intensity was obtained at 203 K characterized by a low barrier of 36 kJ·mol$^{-1}$. Another redistribution process was observed by adding an excess of HSi(OMe)$_3$ to **22** (Scheme 2). Formation of Si(OMe)$_4$ and of a new dinuclear complex [Ru$_2$H$_2$(μ–$\eta^2$:$\eta^2$-H$_2$Si(OMe)$_2$)$_3$(PCy$_3$)$_2$] (**23**) was obtained. Compound **23** represents a very interesting case, illustrating the difficulty in assigning a defined structure in such highly delocalized species. Again eight hydrogen atoms in fast exchange are detected by multinuclear NMR studies with an average $J_{SiH}$ value of 22 Hz. Location of the hydrides was not possible by X-ray diffraction and the proposed formulation was deduced in particular from DFT studies (see Figure 12) and correlated to NMR spectroscopic data. In the model complex [Ru$_2$H$_2$(μ-H$_2$Si(OMe)$_2$)$_3$(PH$_3$)$_2$], one bridging H$_2$Si(OMe)$_2$ ligand is symmetrically coordinated to the two Ru with rather long Ru–

 © 2006 Wiley-VCH Verlag GmbH & Co. KGaA, Weinheim 

Si distances (2.551 Å) and short Si–H distances (1.653 Å) whereas the two other ligands are dissymetrically bonded to the ruthenium but with shorter Ru–Si distances (2.40 and 2.49 Å) and longer Si–H distances (1.74 and 1.76 Å). The Wiberg bond indices obtained from a natural bond orbital analysis are also in agreement with a different level of activation within the three ligands.

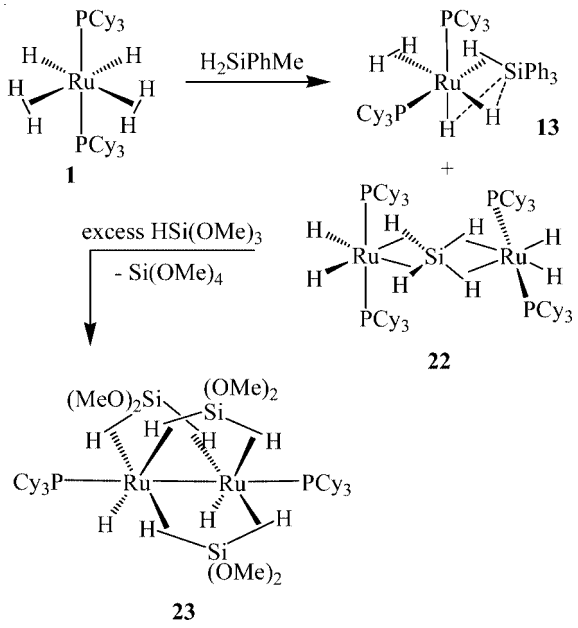


Scheme 2. Redistribution at silicon.

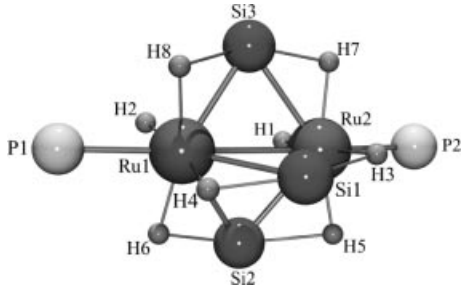


Figure 12. DFT/B3LYP-optimized structure of $[Ru_2H_2(\mu\text{-}H_2Si(OMe)_2)_3(PH_3)_2]$.

An elegant study concerning the synthesis of dinuclear silane ruthenium complexes was reported by Suzuki et al.[42] The mono(silane) complex $[Cp^*Ru(\mu\text{-}H)]_2(\mu\text{-}\eta^2\text{:}\eta^2\text{-}H_2Si\textit{t}Bu_2)$ (**24**) was obtained by reacting $H_2Si\textit{t}Bu_2$ with the ruthenium tetrahydride complex $Cp^*Ru(\mu\text{-}H)_4Cp^*Ru$ (see Scheme 3). The fluxionality observed by NMR at room temperature for the two types of hydrogen was blocked at 153 K resulting in the formation of two signals. The signal at –6.15 ppm displaying a coupling constant of 75 Hz was thus assigned to the σ-ligands, whereas the signal at –16.63 ppm was assigned to the bridging hydrides. The broad adsorption in the IR spectrum at 1790 $cm^{-1}$ (confirmed by deuterium labeling) was also in agreement with σ-silane coordination. Reaction of (**24**) with CO yields a mixture of two new σ-complexes $[Cp^*Ru(CO)]_2(\mu\text{-}\eta^2\text{:}\eta^2\text{-}H_2Si\textit{t}Bu_2)$ (**25a**) and $[Cp^*Ru(CO)]_2(\mu\text{-}\eta^2\text{-}HSi\textit{t}Bu_2)H$ (**25b**). The X-ray structure of **25a** shows long Ru–Si bonds [2.447(1) Å and 2.457(1) Å] and two Si–H bond lengths of 1.77(3) Å and 1.75(3) Å in agreement with two σ-Si–H bonds. (**25a**) is in equilibrium in solution with **25b**. When compound **24** was treated with $H_3SiPh$ or $H_2SiEt_2$ the corresponding mixed-bridge complexes were obtained, $[Cp^*Ru]_2(\mu\text{-}\eta^2\text{-}HSi\textit{t}Bu_2)(\mu\text{-}\eta^2\text{-}HSiPhH)(\mu\text{-}H)H$ (**26a**) and $[Cp^*Ru]_2(\mu\text{-}\eta^2\text{-}HSi\textit{t}Bu_2)(\mu\text{-}\eta^2\text{-}HSiEtH)(\mu\text{-}H)H$ (**26b**), respectively. Again the σ-Si–H bonds are characterized by long Ru–Si bond lengths.

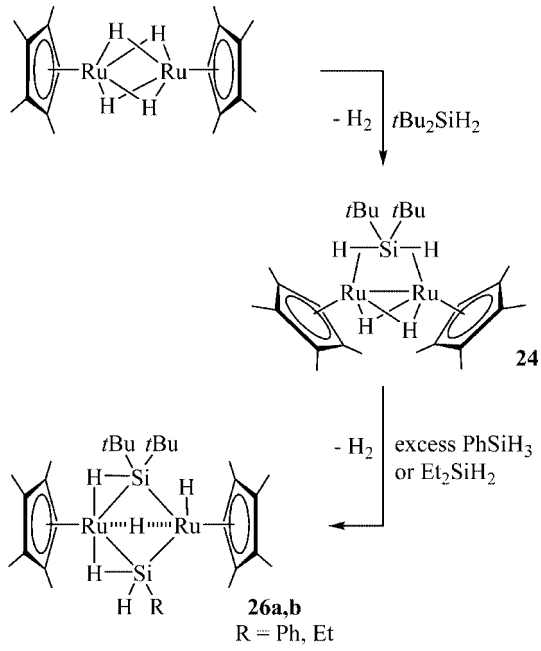


Scheme 3. Synthesis of diruthenium complexes containing μ-silane ligands.

## Conclusions

Much work has been published in the area of catalytic silane activation by metal complexes as a wide variety of valuable substrates can be produced. No matter the catalytic process in consideration, one of the main important goal remains selectivity control. This can be achieved by a knowledge of the different key steps occurring in a catalytic cycle. Silane activation by the metal complex is one of these key steps. Throughout all the examples we have considered, it is clear that it is difficult to control this activation process. A continuum exists between the two extremes leading either to σ-silane coordination or oxidative addition. There is no doubt that the tendency of silicon to be hypervalent favors such a continuum, by creating secondary interactions as described above (SISHA interactions).

None of the useful criteria i.e. $J_{SiH}$, IR bands, $d_{Si-H}$ and $d_{Ru-Si}$ by X-ray diffraction or DFT calculations, can be used *alone* to evaluate the degree of silane activation. In particular, it appears that the interpretation of $J_{SiH}$ values can be difficult, especially for systems including electron-withdrawing substituents and showing fluxional behavior.

 © 2006 Wiley-VCH Verlag GmbH & Co. KGaA, Weinheim 

The lower limit of 20 Hz used by several authors (including us) should now be set up to 65 Hz for a secure criterion of a σ-Si–H bond. Observation of a broad and intense IR band in the range 1650–1800 $cm^{-1}$ remains a good indication of σ-coordination. When X-ray data involving hydrogen atoms can be supported by DFT calculations, one can considered that a $d_{Si–H}$ value around 1.7–1.8 Å will support the formation of a σ-silane complex. Moreover, silicon-hydrogen distances around 1.9–2.4 Å should alert the researchers of the presence of secondary interactions. The Ru–Si bond strength depends significantly on the silicon-attached substituents, but a short bond length will be consistent with an advanced oxidative addition process.

We have shown that σ-Si–H bonds and SISHA interactions play a major role in alkyl and chloro silane catalytic activation.[29,32,38,43] Moreover, in 2002 we proposed a σ-bond metathesis mechanism which offers alternatives that are distinct from the standard σ-bond metathesis mechanisms and the oxidative addition pathways.[14,44] Successive formation of σ-bonds and secondary interactions (see Scheme 4) allow operating at constant oxidation state whereas oxidative addition/reductive elimination mechanisms change oxidation states by two units. More work is needed both at the stoichiometric and catalytic level to examine the relevance of these types of bonding (σ-Si–H bonds and SISHA interactions) in various catalytic systems with the main goal to achieve better selectivity.

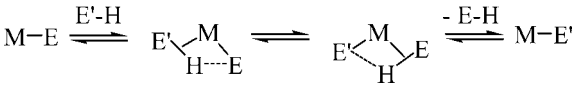


Scheme 4. Functionalization assisted by σ-ligand substitutions and secondary interactions.

## Acknowledgments

The CNRS is gratefully acknowledged for financial support of this work. S. S.-E. warmly thanks all her co-workers and colleagues for their contribution to the work presented in this review.

[1] G. J. Kubas, *Metal Dihydrogen and σ-Bond Complexes*, Kluwer Academic/Plenum Publishers, New York, **2001**.
[2] M. A. Esteruelas, L. A. Oro, *Chem. Rev.* **1998**, *98*, 577–588.
[3] G. S. McGrady, G. Guilera, *Chem. Soc. Rev.* **2003**, *32*, 383–392.
[4] J. Y. Corey, J. Braddock-Wilking, *Chem. Rev.* **1999**, *99*, 175–292.
[5] Z. Lin, *Chem. Soc. Rev.* **2002**, *31*, 239–245.
[6] U. Schubert, *Adv. Organomet. Chem.* **1990**, *30*, 151–187.
[7] S. Lachaize, K. Essalah, V. Montiel-Palma, L. Vendier, B. Chaudret, J.-C. Barthelat, S. Sabo-Etienne, *Organometallics* **2005**, *24*, 2935–2943.
[8] C. Hall, R. N. Perutz, *Chem. Rev.* **1996**, *96*, 3125–3146.
[9] D. J. Lawes, S. Geftakis, G. E. Ball, *J. Am. Chem. Soc.* **2005**, *127*, 4134–4135.
[10] R. J. P. Corriu, *J. Organomet. Chem.* **1990**, *400*, 81–106.
[11] R. F. W. Bader, C. F. Matta, F. Cortés-Guzmán, *Organometallics* **2004**, *23*, 6253–6263.
[12] B. Marciniec, *Coord. Chem. Rev.* **2005**, *249*, 2374–2390.
[13] G. J. Kubas, *Catal. Lett.* **2005**, *104*, 79–101.
[14] I. Atheaux, F. Delpech, B. Donnadieu, S. Sabo-Etienne, B. Chaudret, K. Hussein, J. C. Barthelat, T. Braun, S. B. Duckett, R. N. Perutz, *Organometallics* **2002**, *21*, 5347–5357.
[15] M. Grellier, L. Vendier, B. Chaudret, A. Albinati, S. Rizzato, S. Mason, S. Sabo-Etienne, *J. Am. Chem. Soc.* **2005**, *127*, 17592–17593.
[16] G. I. Nikonov, *J. Organomet. Chem.* **2001**, *635*, 24–36.
[17] S. Sabo-Etienne, B. Chaudret, *Coord. Chem. Rev.* **1998**, *178–180*, 381–407.
[18] F. Delpech, S. Sabo-Etienne, J. C. Daran, B. Chaudret, K. Hussein, C. J. Marsden, J. C. Barthelat, *J. Am. Chem. Soc.* **1999**, *121*, 6668–6682.
[19] F. Delpech, S. Sabo-Etienne, B. Chaudret, J.-C. Daran, *J. Am. Chem. Soc.* **1997**, *119*, 3167–3168.
[20] T. Ayed, J.-C. Barthelat, B. Tangour, C. Pradère, B. Donnadieu, M. Grellier, S. Sabo-Etienne, *Organometallics* **2005**, *24*, 3824–3826.
[21] N. M. Yardy, F. R. Lemke, L. Brammer, *Organometallics* **2001**, *20*, 5670–5674.
[22] V. K. Dioumaev, B. R. Yoo, L. J. Procopio, P. J. Carroll, D. H. Berry, *J. Am. Chem. Soc.* **2003**, *125*, 8936–8948.
[23] K. Hübler, U. Hübler, W. R. Roper, P. Schwerdtfeger, L. J. Wright, *Chem. Eur. J.* **1997**, *3*, 1608–1616.
[24] M. Mohlen, C. E. F. Rickard, W. R. Roper, D. M. Salter, L. J. Wright, *J. Organomet. Chem.* **2000**, *593–594*, 458–464.
[25] K. Hussein, C. J. Marsden, J. C. Barthelat, V. Rodriguez, S. Conejero, S. Sabo-Etienne, B. Donnadieu, B. Chaudret, *Chem. Commun.* **1999**, 1315–1316.
[26] G. I. Nikonov, *Angew. Chem. Int. Ed.* **2001**, *40*, 3353–3355.
[27] V. K. Dioumaev, L. J. Procopio, P. J. Carroll, D. H. Berry, *J. Am. Chem. Soc.* **2003**, *125*, 8043–8058.
[28] S. Sabo-Etienne, M. Hernandez, G. Chung, B. Chaudret, *New J. Chem.* **1994**, *18*, 175–177.
[29] S. Lachaize, S. Sabo-Etienne, B. Donnadieu, B. Chaudret, *Chem. Commun.* **2003**, 214–215.
[30] S. R. Dubberley, S. K. Ignatov, N. H. Rees, A. G. Razuvaev, P. Mountford, G. I. Nikonov, *J. Am. Chem. Soc.* **2003**, *125*, 642–643.
[31] S. T. N. Freeman, J. L. Petersen, F. R. Lemke, *Organometallics* **2004**, *23*, 1153–1156.
[32] F. Delpech, S. Sabo-Etienne, B. Donnadieu, B. Chaudret, *Organometallics* **1998**, *17*, 4926 –4928.
[33] V. K. Dioumaev, P. J. Carroll, D. H. Berry, *Angew. Chem. Int. Ed.* **2003**, *42*, 3947–3949.
[34] D. L. Lichtenberger, *Organometallics* **2003**, *22*, 1599–1602.
[35] A. L. Osipov, S. F. Vyboishchikov, K. Y. Dorogov, L. G. Kuzmina, J. A. K. Howard, D. A. Lemenovskii, G. I. Nikonov, *Chem. Commun.* **2005**, 3349–3351.
[36] R. H. Crabtree, *Angew. Chem. Int. Ed. Engl.* **1993**, *32*, 789–805.
[37] S. Lachaize, Ph. D. Thesis, Université Toulouse III – Paul Sabatier (France), **2004**.
[38] M. L. Christ, S. Sabo-Etienne, B. Chaudret, *Organometallics* **1995**, *14*, 1082–1084.
[39] S. T. N. Freeman, F. R. Lemke, L. Brammer, *Organometallics* **2002**, *21*, 2030–2032.
[40] I. Atheaux, B. Donnadieu, V. Rodriguez, S. Sabo-Etienne, B. Chaudret, K. Hussein, J. C. Barthelat, *J. Am. Chem. Soc.* **2000**, *122*, 5664–5665.
[41] R. Ben Said, K. Hussein, J.-C. Barthelat, I. Atheaux, S. Sabo-Etienne, M. Grellier, B. Donnadieu, B. Chaudret, *Dalton Trans.* **2003**, 4139–4146.
[42] T. Takao, S. Yoshida, H. Suzuki, M. Tanaka, *Organometallics* **1995**, *14*, 3855–3868.
[43] F. Delpech, J. Mansas, H. Leuser, S. Sabo-Etienne, B. Chaudret, *Organometallics* **2000**, *19*, 5750–5757.
[44] R. N. Perutz, S. Sabo-Etienne, *Angew. Chem. Int. Ed.*, paper to be submitted.

Received: February 21, 2006
Published Online: April 21, 2006

 © 2006 Wiley-VCH Verlag GmbH & Co. KGaA, Weinheim 

DOI: 10.1002/ejic.200600255

# Dithiolato-Bridged [$MRu_2$] (M = Rh, Ir, Ru) Triangular 50e$^-$ Cluster Complexes Synthesized by Complete Metal Framework Reconstruction

**Norikiyo Nakagawa,[a] Masaki Murata,[a] Manabu Sugimoto,[b] and Hiroshi Nishihara*[a]**

**Keywords:** Metal framework reconstruction / Electron excess / X-ray crystallographic analysis / Three-centers-four-electrons bond

A method for synthesizing triangular dithiolene-bridged trinuclear cluster complexes [{LM($S_2C_6H_4$)}$Ru_2$(CO)$_4$($S_2C_6H_4$)] [M = Rh, L = ($\eta^5$-$C_5Me_5$); M = Ir, L = ($\eta^5$-$C_5Me_5$); M = Ru, L = ($\eta^6$-$C_6Me_6$)] by complete reconstruction of the metal framework was developed. The complexes thus obtained have 50 electrons around the metal atoms, indicating 3c4e$^-$ bonds; their molecular structures were determined by X-ray diffraction analyses and theoretical calculations.
(© Wiley-VCH Verlag GmbH & Co. KGaA, 69451 Weinheim, Germany, 2006)

There have been various reports about syntheses of transition-metal cluster complexes and their unique properties, and the finding of a new metal–metal bond formation reaction and a new metal–metal bond character can lead to the creation of valuable metal cluster materials with novel chemical functions (including catalytic reactivity) and with novel optical, magnetic, and electronic properties.[1] We have recently reported the synthesis of a triangular trinuclear heterometal cluster complex [{($\eta^6$-$C_6Me_6$)Ru($S_2C_6H_4$)}$Co_2$(CO)$_5$] (**3**), a rare example containing a planar metalladithiolene ring.[2] The number of the electrons around the trimetal framework in **3** is 48, adjusted to make three metal–metal single bonds in a triangle. We report here the unique reactivity of **3** and [{($\eta^6$-*p*-cymene)Ru($S_2C_6H_4$)}$Co_2$(CO)$_5$] (**4**) [*p*-cymene = *p*-($Me_2CH$)-$C_6H_4$Me], with mononuclear complexes [($\eta^5$-$C_5Me_5$)Rh($S_2C_6H_4$)] (**1**) and [($\eta^5$-$C_5Me_5$)Ir($S_2C_6H_4$)] (**2**) to give new triangular cluster complexes composed of other metals. These reactions show the first complete reconstruction of the trimetal framework caused by successive metal–metal bond scission and formation reactions. The obtained complexes [{($\eta^5$-$C_5Me_5$)Rh($S_2C_6H_4$)}$Ru_2$(CO)$_4$($S_2C_6H_4$)] (**5**), [{($\eta^5$-$C_5Me_5$)Ir($S_2C_6H_4$)}$Ru_2$(CO)$_4$($S_2C_6H_4$)] (**6**), and [{($\eta^6$-$C_6Me_6$)Ru($S_2C_6H_4$)}$Ru_2$(CO)$_4$($S_2C_6H_4$)] (**7**) have triangular metal frameworks with 50 electrons around the trimetal framework, indicating that they belong to electron-rich compounds. Their unusual metal–metal bond properties were clarified by X-ray crystallography and molecular orbital calculations.

The reactions of the cluster complexes **3** and **4** with the mononuclear complexes **1** and **2** are summarized in Scheme 1 and Table 1. Scheme 1 shows the formation of the cluster complexes by transmetallation; products **5**–**7** were synthesized from another cluster complex consisting of completely different transition metals. There have been reports on syntheses of cluster complexes by transmetallation,[1d] but the syntheses of cluster complexes by complete metal framework reconstruction is new. A mixture of **1** and **3** in a 1:1 molar ratio was refluxed in 1,4-dioxane to afford a red compound **5** in 41% yield based on the Ru cluster **3** (Entry 1). Product **5** seems to be generated from 1 equiv. of **1** and 2 equiv. of **3**; when the same reaction of **1** and **3** was performed in a 1:2 molar ratio, the same product **5** formed, however in a lower yield (24%). Similarly, the reaction of **2** with **3** gave the red compound **6** in 10% yield as a major product and a trace amount of **7** (Entry 2). The same cluster complexes **5** and **6** were obtained when **4** was used instead of **3**, but in relatively low yields (Entries 3 and 4). The trinuclear complexes **5**–**7** did not appear to be air- or moisture-sensitive either in the crystalline state or in solution, irrespective of their unusual electronic configuration (vide infra). In these reactions, a black powder precipitated which contained Co, but unfortunately it could not be characterized because of the insolubility in common solvents.

The molecular structures of **5**, **6**, and **7** were determined by single-crystal X-ray diffraction analysis, and an ORTEP drawing of **5** is shown in Figure 1.[3] The metal frameworks of **5**–**7** are those of isosceles triangles, and the bond lengths and angles of **5**–**7** are similar to each other (Figure 1; Figures S1 and S2, Supporting Information). There are two benzenedithiolato ligands in **5**; one of them bridges two Ru atoms, and the other one bridges Rh and Ru atoms. The dihedral angle of the SRuS plane vs. the SCCS plane in the

[a] Department of Chemistry, School of Science, The University of Tokyo,
7-3-1 Hongo, Bunkyo ku, Tokyo 113-0033, Japan
Fax: +81-3-5841-8063
E-mail: nisihara@chem.s.u-tokyo.ac.jp
[b] Department of Applied Chemistry, Biochemistry, Graduate School of Science and Technology, Kumamoto University, Kumamoto 860-8555, Japan
Supporting information for this article is available on the WWW under http://www.eurjic.org or from the author.

 © 2006 Wiley-VCH Verlag GmbH & Co. KGaA, Weinheim 

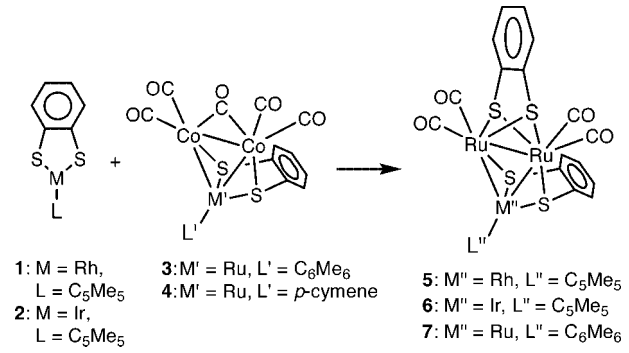


Scheme 1. Reactions of the mononuclear complexes **1** and **2** with the trinuclear cluster complexes **3** and **4**.

Table 1. Reactions of **1** and **2** with **3** and **4**.

| Entry | Starting compounds | Products | Yield |
|---|---|---|---|
| 1 | **1** + **3** | **5** | 41% |
| 2 | **2** + **4** | **6** (major) and **7** (minor) | 10% (for **6**) |
| 3 | **1** + **3** | **5** | 28% |
| 4 | **2** + **4** | **6** | 4% |

ruthenadithiolene in **5**, which bridges two Ru atoms, is 48.5°, indicating that the planarity of the metalladithiolene is lost; in contrast, the dihedral angle in the rhodiadithiolene, which bridges Rh and Ru atoms, is 15.5°, indicating that the planarity and thus the quasi-aromaticity of the metalladithiolene ring are not totally lost after coordination of S to Ru. The maintenance of the planarity of the metalladithiolene ring with the coordination of S to other metal atoms is rare but is found in some cases like **3**, [{($\eta^5$-$C_5Me_5$)Rh($S_2C_6H_4$)}$Co_2(CO)_5$] (**8**), and [{($\eta^5$-$C_5Me_5$)Ir($S_2C_6H_4$)}$Co_2(CO)_5$] (**9**), the structures of which are similar to each other.[2] As mentioned above, an intriguing difference in the electronic structure of the trinuclear complexes between the starting materials **3** or **4** and the products **5**–**7** is the number of electrons around the three metal atoms; in **3** or **4** this number is 48, satisfying the 18-electron rule at each metal atom for three metal–metal single bonds in a triangle, which is common in transition-metal cluster complexes containing three metals in a triangular arrangement,[4,5] whereas in **5**–**7** this number is 50. We have previously reported that the molecular structure of **3** as determined by X-ray crystallography is actually consistent with the existence of three metal–metal single bonds (Figure 2, closed form **A**).[2] In contrast, the existence of two excess electrons around the trimetal framework in **5**–**7** suggests that some of the metal–metal bonds should be weaker than a single bond. Most trinuclear 50e⁻ complexes are known to have linear or bent metal frameworks with two direct metal–metal single bonds (Figure 2, open form **B**),[6] while some triangular cluster complexes exist that have more than 48 electrons around their metal frameworks and longer metal–metal bonds than the usual single metal bonds (Figure 2, closed form **C**).[7] Compounds **5**–**7** are new examples of 50e⁻ closed triangle complexes for which the Ru–Ru distance is 2.7648(4) Å, which is nearly equal to a single Ru–Ru bond in other complexes.[8] The average Rh–Ru distance is 3.019 Å, which is apparently longer than a single bond.

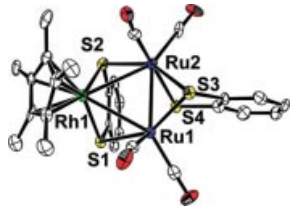


Figure 1. ORTEP drawing of **5** with 50% probability; hydrogen atoms are omitted for clarity. Selected bond lengths [Å] and angles [°]: Rh1–Ru1 3.0062(4), Rh1–Ru2 3.0308(4), Ru1–Ru2 2.7648(4), Rh1–S1 2.2910(8), Rh1–S2 2.2968(8), Ru1–S1 2.3838(8), Ru1–S3 2.3862(9), Ru1–S4 2.4531(9), Ru2–S2 2.3832(9), Ru2–S3 2.3693(9), Ru2–S4 2.4555(9); Ru1–Rh1–Ru2 54.511(9), Rh1–Ru1–Ru2 63.198(9), Rh1–Ru2–Ru1 62.29(1).

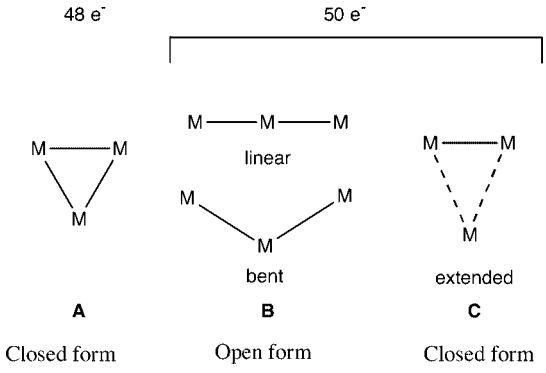


Figure 2. The metal frameworks of a trinuclear 48e⁻ cluster complex and trinuclear 50e⁻ cluster complexes.

To clarify the metal–metal bond characters in these 50e⁻ triangle complexes, theoretical calculations were carried out for **5** using the DFT(B3LYP) method based on the molecular structures determined by X-ray crystallography. The HOMO of **5**, is drawn in Figure 3, together with the frontier orbitals of the molecular fragments, ($\eta^5$-$C_5Me_5$)-Rh($S_2C_6H_4$) and $Ru_2(S_2C_6H_4)(CO)_4$. The result shows that the HOMO of the Rh fragment is primarily the Rh $d_{z^2}$ orbital directing the midpoint of the Ru–Ru bond, and the LUMO of the $Ru_2$ fragment is the Ru–Ru π-bonding orbital primarily made up of $d_{z^2}$ orbitals of two Ru atoms. The HOMO of **5** is a bonding orbital among three metal atoms that includes π-electron donation from the HOMO of the $Ru_2$ fragment to the LUMO of the Rh fragment. Therefore, the trimetal framework is composed of one Ru–Ru single bond and one coordination bond from $Ru_2$ to Rh, and thus the trimetal bonding character in **5** is a three-centers-four-electrons (3c4e⁻) bond. This finding is consistent with the longer Ru–Rh distances than that observed for a regular Ru–Rh single bond. Compounds **6** and **7** can be elucidated to have similar 3c4e⁻ characteristics according to their similarity in structure and in the bond length distribution to **5**.

 © 2006 Wiley-VCH Verlag GmbH & Co. KGaA, Weinheim 

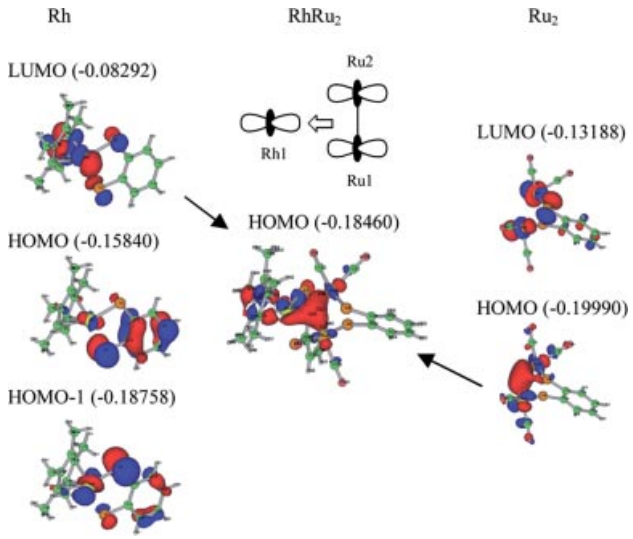


Figure 3. HOMO of **5** and frontier orbitals of the $Ru_2$ fragment and the Rh fragment calculated by the DFT(B3LYP) method. The core electrons of Ru and Rh have been replaced with the effective core potential, and their valence orbitals are described with the LANL2DZ basis set. To the other atoms, the all-electron 6-31G basis set was applied. Energy values of the orbitals in eV are given in the parentheses. The HOMO of **5** was composed of the interaction of an Ru–Ru π-bonding orbital (HOMO of the $Ru_2$ fragment) and an Rh orbital (LUMO of the Rh fragment).

UV/Vis/NIR spectra of **5** and **6** show no absorption peak around 900 nm, whereas **3**, **8**, and **9** have peaks attributable to the excitation from the HOMO to the LUMO.[2] This result indicates that the energy gaps between the HOMO and the LUMO in 50e⁻ trinuclear cluster complexes **5**–**7** are larger than those in 48e⁻ trinuclear cluster complexes **3**, **4**, **8**, and **9** because the metal–metal bonds in **5**–**7** are weaker than those in **3**, **4**, **8**, and **9**. Cyclic voltammetry of **5**–**7** in $Bu_4NClO_4$ in $CH_2Cl_2$ showed an irreversible reduction peak at –1.79 V vs. ferrocenium/ferrocene, while metalladithiolene cluster complexes **3**, **4**, **8**, and **9** underwent reversible 1e⁻ reduction.[2] This result indicates that the metal frameworks of **5**–**7** would be corrupted when electrons are added to the LUMO, the antibonding orbital of metal atoms.

Contrary to the reactions of **1** (Rh) or **2** (Ir) with **3** ($RuCo_2$) or **4** ($RuCo_2$), a mixture of **1** (Rh) and **9** ($IrCo_2$) in a 1:1 molar ratio was refluxed in 1,4-dioxane to give a 1:1 mixture of **8** ($RhCo_2$) and **9** ($IrCo_2$). The same result was obtained by the reaction of **2** (Ir) with **8** ($RhCo_2$). The differences in reactivity of the cluster complexes were thought to be due to the leaving ability of the ligands; neutral $\eta^6$ ligands, $C_6Me_6$ and *p*-cymene, on Ru cluster complexes **3** and **4**, have a higher leaving ability than $C_5Me_5$, an anionic $\eta^5$ ligand on Rh cluster complex **8** and Ir cluster complex **9**.

In summary, we have found a novel synthetic method for cluster complexes involving complete reconstruction of the trimetal framework. The cluster complexes obtained have 50 electrons around the trimetal framework, which is explained by a 3c4e⁻ bond character supported by bond lengths and theoretical calculation of molecular orbitals.

**Supporting Information** (see the footnote on the first page of this article): Synthesis, characterization of **8**, **9**, and **10**, $^1H$ and $^{13}C$ NMR spectra and UV/Vis/NIR spectra of **8** and **9**, X-ray crystallography of **9** and **10**, DFT calculation results for **8**, and a cyclic voltammogram of **8**.

## Acknowledgments

This work was supported by Grants-in-Aid for Scientific Research [Nos. 16047204 (area 434) and 17205007], by a grant from The 21st Century COE Program for Frontiers in Fundamental Chemistry from MEXT, and by CREST, JST, Japan.

[1] a) J. F. Berry, *Multiple Bonds between Metal Atoms*, 3rd ed., Springer Science and Business Media, Inc., New York, **2005**, p. 669; b) P. J. Dyson, *Coord. Chem. Rev.* **2004**, *248*, 2443–2458; c) P. Macchi, A. Sironi, *Coord. Chem. Rev.* **2003**, *238–239*, 383–412; d) R. D. Adams, *Comprehensive Organometallic Chemistry II*, Pergamon, Oxford, **1995**, vol. 10, p. 1.
[2] N. Nakagawa, T. Yamada, M. Murata, M. Sugimoto, H. Nishihara, *Inorg. Chem.* **2006**, *45*, 14–16.
[3] Details for crystal data and refinement parameters of **5**, **6**, and **7** are summarized in Table S1 (Supporting Information).
[4] J. W. Lauher, *J. Am. Chem. Soc.* **1978**, *100*, 5306–5315.
[5] See, for example: a) M. N. Sokolov, A. L. Gushchin, D. Y. Naumov, O. A. Gerasko, V. P. Fedin, *Inorg. Chem.* **2005**, *44*, 2431–2436; b) J. A. Cabeza, I. Río, V. Riera, M. Suárez, S. García-Granda, *Organometallics* **2004**, *23*, 1107–1115; c) C. Allasia, M. Castiglioni, G. Predieri, E. Sappa, *J. Mol. Catal. A* **2003**, *204–205*, 351–359; d) M. Feriz, R. Llusar, S. Uriel, C. Vicent, M. G. Humphrey, N. T. Lucas, M. Samoc, B. Luther-Davies, *Inorg. Chim. Acta* **2003**, *349*, 69–77; e) W. A. Herrmann, C. E. Barnes, T. Zahn, M. L. Ziegler, *Organometallics* **1985**, *4*, 172–180.
[6] a) M. Nihei, T. Nankawa, M. Kurihara, H. Nishihara, *Angew. Chem. Int. Ed.* **1999**, *38*, 1098–1100; b) M. Murata, S. Habe, S. Araki, K. Namiki, T. Yamada, N. Nakagawa, T. Nankawa, M. Nihei, J. Mizutani, M. Kurihara, H. Nishihara, *Inorg. Chem.* **2006**, *45*, 1108–1116; c) M. Freytag, F. T. Edelmann, L. Ernst, P. G. Jones, R. Schmutzler, *Z. Anorg. Allg. Chem.* **2004**, *630*, 377–383; d) C. H. Hsuan, L. F. Dahl, *Inorg. Chem.* **1965**, *4*, 493–499.
[7] a) H.-C. Böttcher, M. Graf, K. Merzweiler, C. Bruhn, *Polyhedron* **1997**, *16*, 3253–3260; b) T. E. North, J. B. Thoden, B. Spencer, L. F. Dahl, *Organometallics* **1993**, *12*, 1299–1313; c) T. E. North, J. B. Thoden, B. Spencer, A. Bjarnason, L. F. Dahl, *Organometallics* **1992**, *11*, 4326–4337; d) C. R. Pullian, J. B. Thoden, A. M. Stacy, B. Spencer, M. H. Englert, L. F. Darl, *J. Am. Chem. Soc.* **1991**, *113*, 7398–7410.
[8] a) A. L. Eckermann, D. Fenske, B. Rauchfuss, *Inorg. Chem.* **2001**, *40*, 1459–1465; b) M. I. Bruce, B. W. Skelton, A. L. White, N. N. Zaitseva, *J. Cluster Sci.* **2002**, *13*, 235–247.

Received: January 19, 2006
Published Online: April 21, 2006

 © 2006 Wiley-VCH Verlag GmbH & Co. KGaA, Weinheim 

DOI: 10.1002/ejic.200501105

# A Coordination Polymer Containing Inorganic Buckybowl Analogues

Tao Wu,[a] Miao Chen,[a] and Dan Li*[a]

**Keywords:** Inorganic buckybowl analogues / Tetrazoles / Sharpless' cycloaddition / Copper / Coordination polymers

Two photoluminescent coordination polymers, $\{[Cu_{10}(\mu_3\text{-Mtta})_3(\mu_4\text{-Mtta})_7]\cdot 2H_2O\}_n$ (**1**), containing 2-D wavy motifs with inorganic buckybowl analogues, and $[Cu_5(\mu_3\text{-Mtta})_2(\mu_4\text{-Mtta})_3(NH_3)_2]_n$ (**2**, Mtta = 5-methyl tetrazolate), were obtained by the control of solvents and auxiliary complexing agent. The ligand Mtta is a likely candidate for the construction of metal-organic, fullerene-like molecules. The luminescent properties of **1** and **2** are discussed.
(© Wiley-VCH Verlag GmbH & Co. KGaA, 69451 Weinheim, Germany, 2006)

## Introduction

As a bridge between the fullerene family and flat aromatic compounds, buckybowls, curved-surface fragments of fullerenes, were found a few years ago, and only a few examples are available to date.[1] Great attention has been paid to the coordination chemistry of transition-metal buckybowl complexes because of their intriguing curvatures and reactivity.[2] On the other hand, substantial effort has recently been directed towards studies of metal-containing, inorganic, fullerene-like molecules that comprise five- and six-membered rings mapping onto the surface of the $C_{60}$ analogue.[3] The design and construction of inorganic, fullerene-like molecules, even of their fragments, are still a great challenge for inorganic chemists because of the difficulty to control the formation of the curvature. The five-membered ring tetrazole is possibly a potential candidate for constructing fullerene-like fragments. In our continuing research of designing novel coordination networks,[4] herein we report the synthesis and the structural characterization of a supramolecular network containing inorganic buckybowl analogs, and of another 2D polymeric network for comparison, by using Sharpless' cycloaddition reactions of nitriles and azides.[5]

## Results and Discussion

Reactions of $Cu(NO_3)_2$, $NaN_3$, and $CH_3CN$ with 2, 2′-bipyridine/$H_2O$ or toluene/$NH_3\cdot H_2O$ (v/v, 2:1) gave two complexes $\{[Cu_{10}(\mu_3\text{-Mtta})_3(\mu_4\text{-Mtta})_7]\cdot 2H_2O\}_n$ (**1**) or $[Cu_5(\mu_3\text{-Mtta})_2(\mu_4\text{-Mtta})_3(NH_3)_2]_n$ (**2**), respectively, (Mtta = 5-methyltetrazolate). Interestingly, 2, 2′-bipiridine does not appear in **1**. The influence of bipyridine on the self-assembly of the complex is obvious because **1** cannot be synthesized in the absence of bipyridine.

X-ray single-crystal analyses of **1** and **2** confirm the formation of 5-methyl tetrazolate. Complex **1** is composed of guest water molecules and a 3D neutral microporous framework based on copper(I) and the ligand Mtta, with a space group of *C*2/*m* (Figure 1a, and Figures S1 and S2 in the Supporting Information). The elliptic cavities along the *c* axis in the 3D framework of **1** are constructed by stacking two different kinds of 2D layers (Part A and Part B, Figure 1b and Figure 1c, respectively) in the alternative mode ABAB. Approximately 18.3% of the crystal volume can be occupied by free water molecules, with a volume of ca. 958.6 Å$^3$ in each cell unit.[6]

In Part A (Figure 1b), each $Cu^I$ center adopts a distorted tetrahedral geometry. The copper atoms bound to the tetradentate Mtta ligands show significant out-of-plane displacements with respect to the "best plane" of the heterocycle (in the range +0.1328 to +1.6078 Å). Markedly, the out-of-plane displacements result in the formation of a buckybowl analogue that possesses 26 inorganic core atoms of $Cu_6(Mtta)_4$ with four five-membered rings and five six-membered rings (Figure 2a). In the buckybowl analogue, each $N_4C$ ring of Mtta is surrounded by six-membered $N_4Cu_2$ rings. Adjacent buckybowl analogues facing the opposite direction in an alternating convex and concave fashion are linked by Cu–N coordination bonds to form a wavy ribbon along the *b* direction (Figure 2b). Adjacent ribbons are fused by the Cu–N bonds into a 2D wavy layer (Figure 1b, Figure S3). The ligand Mtta possesses a $\mu_4$-$\eta^1{:}\eta^1{:}\eta^1{:}\eta^1$ coordination mode which is rare in tetrazolate derivatives.[7] Because of the tetrahedral coordination sphere of the $Cu^I$ ions, the nonplanar, six-membered rings formed are folded along the Cu···Cu axis by about 131–170°. The existence of carbon atoms that cannot be coordi-

[a] Department of Chemistry, Shantou University,
Shantou, Guangdong, 515063, P. R. China
Fax: +86-754-2902767
E-mail: dli@stu.edu.cn
Supporting information for this article is available on the WWW under http://www.eurjic.org or from the author.

 © 2006 Wiley-VCH Verlag GmbH & Co. KGaA, Weinheim 

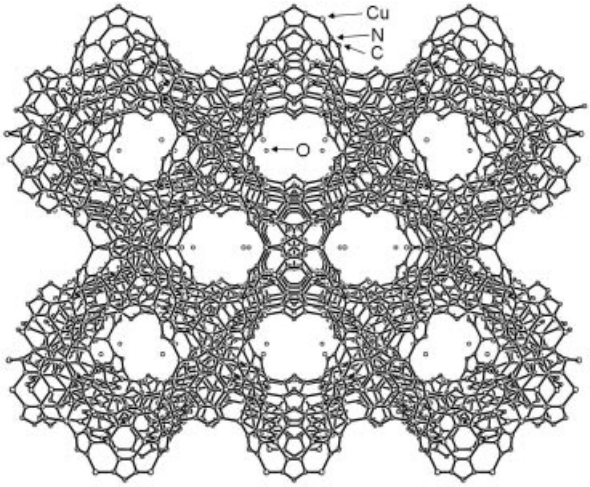


(a)

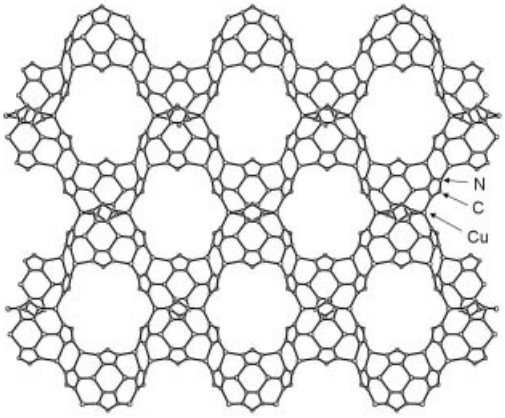


(b)

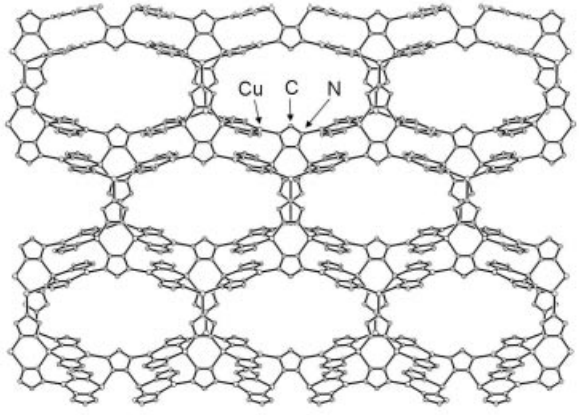


(c)

Figure 1. Structure of **1**: (a) Three dimensional packing diagram along the *ab* plane; (b) 2D layer of Part A; (c) 2D layer of Part B.

nated and the steric hindrance of methyl groups most likely prevents the assembly from developing a larger fullerene-like fragment.

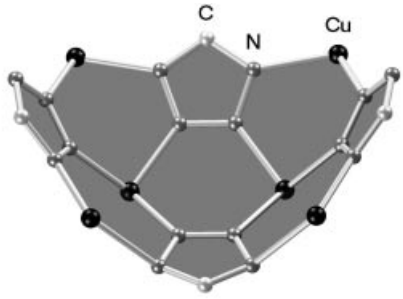


(a)

(b)

Figure 2. View of the buckybowl composed of $Cu_6(Mtta)_4$ with four five-membered rings and five six-membered rings. (b) 1D wavy ribbon constructed by alternating convex and concave buckybowls.

In Part B, the copper(I) centers adopt two types of coordination geometries: the trigonal planar copper(I) center that binds three nitrogen atoms from three different ligands, and the distorted tetrahedral copper(I) center that binds four nitrogen atoms from four different ligands. The Mtta ligand bridges the copper atom through $\mu_3$ and $\mu_4$ bridging modes (in the ratio 1:1) to form a 2D double-layer plane with an approximately rectangular cavity (Figure 1c). All Mtta ligands located above and below the double-layer plane occupy the fourth coordination site of the copper atoms of Part A and form Cu–N bonds to construct the final 3D framework (Figure S2).

In **2**, there are four crystallographically unique copper atoms, which adopt trigonal and tetrahedral geometries (Figures S4 and S5). The Mtta ligand bridges the copper atom through $\mu_3$ and $\mu_4$ bridging modes (in the ratio 2:3) to form a 2D double-layer plane with rectangular cavities as shown in Figure 3. The coordination geometry around the rectangular cavities is identical to that of our previously reported 3D network $[Cu(\mu_4\text{-Mtta})]_n$[4c] shown in Figure S6 (top). The $NH_3$ molecules most likely act as a "molecular scissor" to cut the 3D network of $[Cu(\mu_4\text{-Mtta})]_n$ along the *b* axis to form the 2D layer and to occupy the vacancy of the $Cu^I$ center.

The tetrazolate group in Part B of **1** and **2**, which bears a $\mu_3$ bridging mode, does not allow for the formation of a buckybowl. It seems that the $\mu_4$-$\eta^1$:$\eta^1$:$\eta^1$:$\eta^1$ coordination mode is crucial for the construction of an arched surface.

Both **1** and **2** in the solid state show strong photoluminescence at room temperature with emission maxima at 469 nm and 497 nm, respectively (Figure 4). In comparison

 © 2006 Wiley-VCH Verlag GmbH & Co. KGaA, Weinheim 

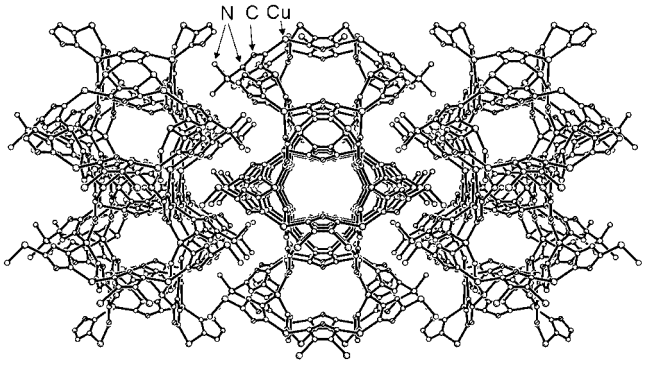


Figure 3. 2D double-layer plane with rectangular cavitivies in complex **2**.

with the photoluminescence of $Cu^I$ azolate,[8] the possibility of an MLCT [Cu→Mtta] excited state in the two complexes may be suggested. The similar emission spectra of these two complexes imply that the properties of the excited state are related only to the local coordination geometry. This explains the red shift of the bands in the spectrum of complex **2** relative to that of complex **1**, since the d* energy level in trigonal planar $Cu^I$ is higher than that in tetrahedral $Cu^I$.

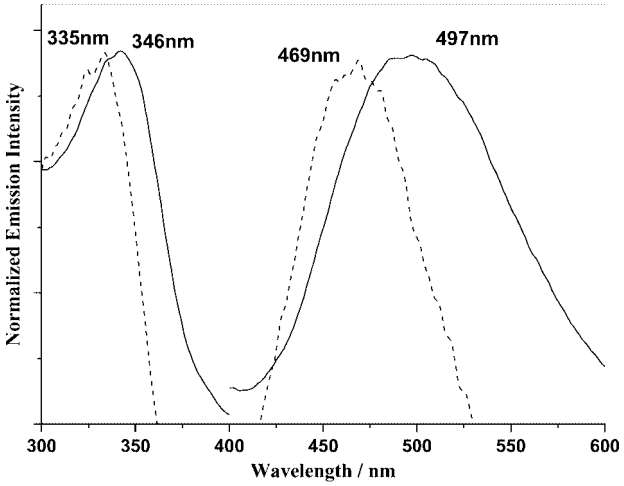


Figure 4. Solid-state excitation (left) and emission (right) spectra of complex **1** (dashed line) and **2** (solid line) at room temperature.

The TG curve of **1** shows a weight loss of 2.28% (calcd. 2.39%) from 45–230 °C that corresponds to the release of lattice water (Figure S7). After a stable platform, complex **1** begins to decompose at 298 °C and finally sublime at 415 °C. The observed weight loss that corresponds to $NH_3$ (5.15%) in complex **2** is in good agreement with the calculated value from 202–229 °C. A very stable platform from 229–276 °C is observed, which increases the possibility of the solid transformation from **2** to $[Cu(\mu_4\text{-Mtta})]_n$, and this is followed by an abrupt decline (approximately 100%). Unfortunately, the XPRD pattern of the solid prepared by heating complex **2** at 250 °C under argon for 0.5 h is different from the simulated pattern of $[Cu(\mu_4\text{-Mtta})]_n$ (Figure S8), which implies that the solid transformation from **2** to $[Cu(\mu_4\text{-Mtta})]_n$ was unsuccessful.

## Conclusions

In summary, we obtained a 3D coordination network containing inorganic buckybowl analogues. The ligand Mtta with a $\mu_4$-$\eta^1$:$\eta^1$:$\eta^1$:$\eta^1$ coordination mode is most likely a good candidate for the construction of inorganic, fullerene-like molecules. Furthermore, the $N_5$ ring may be an optimal component, demonstrating the great potential for the synthesis of other half shells, nano-sized molecules, and full-shell structural motifs. This work provides a new avenue for designing and constructing an inorganic, fullerene-like molecule.

## Experimental Section

**Preparation of Complex 1:** A mixture of $Cu(NO_3)_2{\cdot}3H_2O$ (0.241 g, 1.0 mmol), $NaN_3$ (0.065 g, 1.0 mmol), 2, 2′-bipyridine (0.156 g, 1.0 mmol), and acetonitrile (5.0 mL) was stirred for 10 min in air, and then transferred and sealed in a 15-mL Teflon-lined reactor. The reactor was heated in an oven to 140 °C for 72 h and then cooled to room temperature at a rate of 5 °C $h^{-1}$. The pale-yellow block crystal was attained in a reasonable yield (35.5%, 0.053 g) based on $Cu(NO_3)_2{\cdot}3H_2O$. $C_{20}H_{34}Cu_{10}N_{40}O_2$ (1502.27): calcd. H 2.28, C 15.99, N 37.29; found H 2.31, C15.90, N 37.34. IR data (KBr): 2921 (m), 1634 (m), 1499 (s), 1384 (s), 1135 (m), 1045 (m), 698 (w) $cm^{-1}$.

**Preparation of Complex 2:** A mixture of $Cu(NO_3)_2{\cdot}3H_2O$ (0.241 g, 1.0 mmol), $NaN_3$ (0.065 g, 1.0 mmol), acetonitrile (5.0 mL), and aqueous ammonia (25%, 5.0 mL) was stirred for 10 min in air, and then transferred and sealed in a 15-mL Teflon-lined reactor. The reactor was heated in an oven to 140 °C for 50 h and then cooled to room temperature at a rate of 5 °C $h^{-1}$. The colorless, bar crystal was attained in a reasonable yield (46.3%, 0.036 g) based on $Cu(NO_3)_2{\cdot}3H_2O$. $C_{10}H_{21}Cu_5N_{22}$ (767.19): calcd. H 2.76, C 15.66, N 40.17; found H 2.72, C15.71, N 40.60. IR data (KBr): 3419 (s), 2921 (m), 1646 (m), 1482 (s), 1372 (s), 1123 (s), 1083 (m), 702 (w) $cm^{-1}$.

**X-ray Crystallographic Study:** Data collections of **1** and **2** were performed on a Bruker Smart Apex CCD diffractometer with Mo-$K_\alpha$ radiation ($\lambda$ = 0.71073 Å), using frames of 0.3° oscillation ($2\theta \leq 56°$). The structures were solved with direct methods and refined with the full-matrix least-squares technique with the SHELXTL programs. Anisotropic thermal parameters were applied to all non-hydrogen atoms. The hydrogen atoms were generated geometrically (C–H = 0.960 Å). The crystallographic calculations were conducted with the SHELXL-97 programs.[9] Crystal data for **1**: $C_{20}H_{34}Cu_{10}N_{40}O_2$, monoclinic, space group *C*2/*m* (no. 12), *Mr* = 1502.27, *a* = 21.5327(12) Å, *b* = 16.4443(9) Å, *c* = 14.8195(8) Å, $\beta$ = 92.5190(10)°, *V* = 5242.4(5) $Å^3$, *Z* = 4, $D_c$ = 1.903 g $cm^{-3}$, $\mu$ = 4.036 $mm^{-1}$, *F*(000) = 2960, *T* = 298(2) K, 16576 reflections measured, 6175 unique ($R_{int}$ = 0.0268), final $R_1$ = 0.0553, $wR_2$ = 0.1483, *S* = 1.083 for all data. Crystal data for **2**: $C_{10}H_{21}Cu_5N_{22}$, monoclinic, space group *C*2/*m* (no. 12), *Mr* = 767.19, *a* = 11.5328(6) Å, *b* = 30.1639(17) Å, *c* = 8.8471(5) Å, $\beta$ = 130.2320(10)°, *V* = 2349.6(2) $Å^3$, *Z* = 4, $D_c$ = 2.169 g $cm^{-3}$, $\mu$ = 4.504 $mm^{-1}$, *F*(000) = 1520, *T* = 298(2) K, 7343 reflections measured, 2762 unique ($R_{int}$ = 0.0185), final $R_1$ = 0.0294, $wR_2$ = 0.0791, *S* = 1.108 for all data. CCDC-279776 and CCDC-279777 contain the supplementary crystallographic data for this paper. These data can be obtained free of charge from the Cambridge Crystallographic Data Centre via www.ccdc.cam.ac.uk/data_request/cif.

 © 2006 Wiley-VCH Verlag GmbH & Co. KGaA, Weinheim 

**Supporting Information** (see footnote on the first page of this article): Additional figures for structural illustration (Figures S1–S6), TG analysis of complexes **1** and **2** (Figure S7), and XPRD pattern of the solid prepared by heating complex **2** (Figure S8) are available.

## Acknowledgments

This work was supported by the National Natural Science Foundation of China (No. 20571050 & 20271031) and the Natural Science Foundation of Guangdong Province of China (No. 021240).

[1] Recent reviews: a) M. A. Petrukhina, L. T. Scott, *Dalton Trans.* **2005**, 2969–2975; b) L. T. Scott, *Angew. Chem. Int. Ed.* **2004**, *43*, 4994–5009.

[2] See examples: a) M. A. Petrukhina, K. W. Andreini, L. Peng, L. T. Scott, *Angew. Chem. Int. Ed.* **2004**, *43*, 5477–5481; b) P. A. Vecchi, C. M. Alvarez, A. Ellern, R. J. Angelici, A. Sygula, R. Sygula, P. W. Rabideau, *Angew. Chem. Int. Ed.* **2004**, *43*, 4497–4499; c) M. A. Petrukhina, K. W. Andreini, J. Mack, L. T. Scott, *Angew. Chem. Int. Ed.* **2003**, *42*, 3375–3379; d) R. M. Shaltout, R. Sygula, A. Sygula, F. R. Fronczek, G. G. Stanley, P. W. Rabideau, *J. Am. Chem. Soc.* **1998**, *120*, 835–836; e) T. J. Seiders, K. K. Baldridge, J. M. O'Connor, J. S. Siegel, *J. Am. Chem. Soc.* **1997**, *119*, 4781–4782; f) C. M. Alvarez, R. J. Angelici, A. Sygula, R. Sygula, P. W. Rabideau, *Organometallics* **2003**, *22*, 624–626; g) P. C. Andrews, J. L. Atwood, L. J. Barbour, P. J. Nichols, C. L. Raston, *Chem. Eur. J.* **1998**, *4*, 1384–1387; h) P. C. Andrews, J. L. Atwood, L. J. Barbour, P. D. Croucher, P. J. Nichols, N. O. Smith, B. W. Skelton, A. H. White, C. L. Raston, *J. Chem. Soc., Dalton Trans.* **1999**, 2927–2932.

[3] a) J.-F. Bai, A. V. Virovets, M. Scheer, *Science* **2003**, *300*, 781–783; b) A. Müller, E. Krickemeyer, H. Bögge, M. Schmidtmann, S. Roy, A. Berkle, *Angew. Chem. Int. Ed.* **2002**, *41*, 3604–3609; c) A. Müller, E. Krickemeyer, H. Bögge, M. Schmidtmann, F. Peters, *Angew. Chem. Int. Ed. Engl.* **1998**, *37*, 3360–3363; d) S. C. Sevov, J. D. Corbett, *Science* **1993**, *262*, 880–883.

[4] a) D. Li, T. Wu, X.-P. Zhou, R. Zhou, X.-C. Huang, *Angew. Chem. Int. Ed.* **2005**, *44*, 4175–4179; b) D. Li, T. Wu, *Inorg. Chem.* **2005**, *44*, 1175–1177; c) T. Wu, B.-H. Yi, D. Li, *Inorg. Chem.* **2005**, *44*, 4130–4132; d) T. Wu, D. Li, S. W. Seik, *CrystEngComm* **2005**, *7*, 514–518.

[5] a) Z. P. Demko, K. B. Sharpless, *Angew. Chem. Int. Ed.* **2002**, *41*, 2110–2113; b) Z. P. Demko, K. B. Sharpless, *Angew. Chem. Int. Ed.* **2002**, *41*, 2113–2116; c) R.-G. Xiong, X. Xue, H. Zhao, X.-Z. You, B. F. Abrahams, Z.-L. Xue, *Angew. Chem. Int. Ed.* **2002**, *41*, 3800–3803; and references cited therein.

[6] A. L. Spek, *PLATON*, Utrecht University, Utrecht, The Netherlands, **2003**.

[7] L. Carlucci, G. Ciani, D. M. Proserpio, *Angew. Chem. Int. Ed.* **1999**, *38*, 3488–3492.

[8] a) V. W.-W. Yam, K. K.-W. Lo, *Chem. Soc. Rev.* **1999**, *28*, 323–334; b) J.-P. Zhang, Y.-Y. Lin, X.-C. Huang, X.-M. Chen, *J. Am. Chem. Soc.* **2005**, *127*, 5495–5506.

[9] *SHELXTL 6.10*, Bruker Analytical Instrumentation, Madison, Wisconsin, USA, **2000**.

Received: December 9, 2005
Published Online: March 30, 2006

 © 2006 Wiley-VCH Verlag GmbH & Co. KGaA, Weinheim 

DOI: 10.1002/ejic.200600082

# Titanium–Alkaline Earth Molecular Oxides as Supports for Carbanions Derived from $\mu_3$-Ethylidyne Groups

**Avelino Martín,[a] Miguel Mena,*[a] María del Carmen Morales-Varela,[a] and Cristina Santamaría[a]**

*Dedicated to Professor Victor Riera on the occasion of his 70th birthday*

**Keywords:** Alkaline earth metals / Alkylidyne complexes / Carbanions / O ligands / Titanium

Treatment of the $\mu_3$-ethylidyne complex [{TiCp*($\mu$-O)}$_3$($\mu_3$-CMe)] (**1**) (Cp* = $\eta^5$-$C_5Me_5$) with the alkaline earth amides [M{N(SiMe$_3$)$_2$}$_2$(thf)$_2$] (M = Mg, Ca, Sr) promotes the deprotonation of the alkylidyne moiety $\mu_3$-CMe and leads to the oxoheterometallocubane derivatives [{(thf)$_x$(Me$_3$Si)$_2$NM}-($\mu_3$-O)$_3${Ti$_3$Cp*$_3$($\mu_3$-CCH$_2$)}] [M = Mg, *x* = 0 (**2a**); Ca, *x* = 1 (**3**); Sr, *x* = 1 (**4**)]. In the case of the magnesium amide, complex **2a** is obtained together with the isomer [{(Me$_3$Si)$_2$NMg}-($\mu_3$-O)$_3${Ti$_3$Cp*$_3$($\mu_3$-$\eta^2$-CHCH)}] (**2b**). The addition of pentamethylcyclopentadiene ($C_5Me_5H$) or triphenylmethanol ($Ph_3COH$) to these compounds causes the displacement of the amide fragment to give the heterometallocubanes [RM($\mu_3$-O)$_3${Ti$_3$Cp*$_3$($\mu_3$-$C_2H_2$)}] [R = $C_5Me_5$, M = Ca (**5**), Sr (**6**); R = $Ph_3CO$, M = Mg (**7a**,**b**), Ca (**8**), Sr (**9**)]. This substitution can also be performed on **3** and **4** by treatment with the starting complex **1**, which gives the corner-shared double cubanes [M{($\mu_3$-O)$_3$(Ti$_3$Cp*$_3$)($\mu_3$-CCH$_2$)}$_2$] [M = Ca (**11**), Sr (**12**)]. Complexes **2a**,**b** do not react with **1**, and heating of this mixture affords the edge-linked double cubane [Mg($\mu_4$-O)-($\mu_3$-O)$_2${Ti$_3$Cp*$_3$($\mu_3$-CCH)}]$_2$ (**10**). The combination of the barium reagents [Ba(CH$_2$Ph)$_2$] or [Ba{N(SiMe$_3$)$_2$}$_2$] with **1** leads to the corner-shared double cubane [Ba{($\mu_3$-O)$_3$(Ti$_3$Cp*$_3$)($\mu_3$-CCH$_2$)}$_2$] (**13**). The molecular structures of **3** and **10** have been established by single-crystal X-ray analysis.
(© Wiley-VCH Verlag GmbH & Co. KGaA, 69451 Weinheim, Germany, 2006)

## Introduction

The alkylidyne groups of the complexes [{TiCp*($\mu$-O)}$_3$-($\mu_3$-CR)] (Cp* = $\eta^5$-$C_5Me_5$; R = H, Me)[1] have revealed a surprising and unprecedented reactivity[2] that allows us to form an understanding between molecular and surface chemistry.[3] Both discrete systems may provide relevant information about the mechanisms and the presence of intermediate species on catalytic surfaces even though the reaction conditions are different.

Ethylidyne, in particular, is a well-known hydrocarbon fragment in the dehydrogenation of ethylene on metallic surfaces and its transformation has been actively investigated.[4] However, at present, detailed studies concerning the titanium surface reactivity are scarce and evidence for the formation of ethylidyne has only recently appeared during the decomposition of ethylene on carbon–modified titanium surfaces.[5] Nevertheless, complete dissociation to produce carbon and hydrogen takes place when a clean titanium surface interacts with ethylene.[5] However, the pathways for ethylidyne dehydrogenation to $C_2H_2$, $C_2H$ or carbonaceous species and possible hydrogen exchange have not been well established.

In our molecular approach to the interaction of hydrocarbons with a surface, we have shown that $\mu_3$-ethylidyne groups supported on a $Ti_3O_3$ core can be sequentially hydrogenated (ethylidene, ethyl, and ethane) upon reaction with amines (see Scheme 1).[2d] The dehydrogenation of the $\mu_3$-ethylidyne ligand has also been observed during the incorporation of ketones into the complex [{TiCp*($\mu$-O)}$_3$-($\mu_3$-CMe)] (**1**) by an insertion of the carbonyl groups into a Ti–H bond of the hydridovinylidene intermediate [{TiCp*($\mu$-O)}$_3$($\mu$-CCH$_2$)(H)] formed in situ.[2b] Recently, we have also shown how the incorporation of alkali metal cations into the organometallic titanium oxide **1** takes place with proton abstraction from the alkylidyne and formation of the species [M($\mu_3$-O)$_3${Ti$_3$Cp*$_3$($\mu_3$-CCH$_2$)}] (M = Li, Na, K, Rb, Cs).[6]

Herein we discuss the evolution of the ethylidyne fragment when the molecular model [{TiCp*($\mu$-O)}$_3$($\mu_3$-CMe)] (**1**) tries to incorporate alkaline-earth derivatives.

[a] Departamento de Química Inorgánica, Universidad de Alcalá, Campus Universitario, 28871 Alcalá de Henares, Madrid, Spain
Fax: +34-91-885-4683
E-mail: miguel.mena@uah.es

 © 2006 Wiley-VCH Verlag GmbH & Co. KGaA, Weinheim 

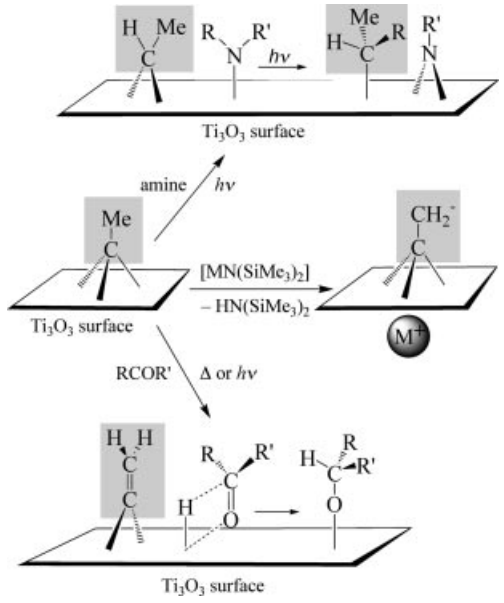


Scheme 1. Chemical reactivity of the $\mu_3$-ethylidyne group on the $Ti_3O_3$ core with amines, alkali metal amides, and ketones.

## Results and Discussion

We began our study with the reaction between the beryllium amide $Be[N(SiMe_3)_2]_2$ and $[\{TiCp^*(\mu\text{-}O)\}_3(\mu_3\text{-}CMe)]$ (**1**), but we did not observe any reaction, even when heating the mixture to over 200 °C. However, the thermal treatment of **1** with $[M\{N(SiMe_3)_2\}_2(thf)_2]$ (M = Ca, Sr) in a 1:1 ratio, in hexane or toluene, leads to the oxoheterometallocubanes $[\{(thf)(Me_3Si)_2NM\}(\mu_3\text{-}O)_3\{Ti_3Cp^*_3(\mu_3\text{-}CCH_2)\}]$ [M = Ca (**3**), Sr (**4**)] in high yields (Scheme 2). The isolated compounds **3** and **4** proved to be stable under argon at room temperature and sufficiently soluble in most common solvents (toluene, hexane, dichloromethane...).

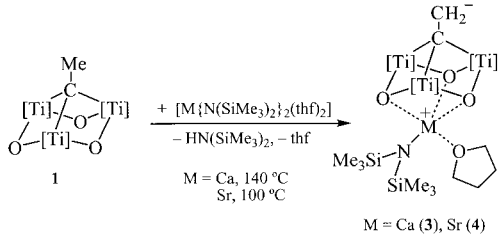


Scheme 2. Reactivity of **1** with calcium and strontium bis(trimethylsilyl)amides. [Ti] = $Ti(\eta^5\text{-}C_5Me_5)$.

The NMR spectra of these species in $[D_6]$benzene show the equivalence of the $\eta^5\text{-}C_5Me_5$ groups, with only one signal in the $^1H$ NMR [$\delta$ = 1.99 (**3**) and 2.00 ppm (**4**)] and two in the $^{13}C\{^1H\}$ NMR spectra [$\delta$ = 11.7 (**3**) and 11.6 ppm (**4**) for $C_5\mathit{Me}_5$ and $\delta$ = 117.9 (**3**) and 117.5 ppm (**4**) for $\mathit{C}_5Me_5$]. The NMR spectra also display resonances due to the $\mu_3\text{-}CCH_2^-$ group, as a singlet at $\delta$ = 2.82 (**3**) and 2.72 ppm (**4**) in the $^1H$ NMR spectra and a triplet at $\delta$ = 82.3 (**3**) and 81.2 ppm (**4**) [$J_{C,H}$ = 149 Hz (av.)], attributed to the $C_\beta$ resonance, in the $^{13}C$ NMR spectra. Furthermore, the apical $\mu_3$-carbon appears as a singlet at $\delta$ = 380.1 (**3**) and 377.3 ppm (**4**), which is shifted to high field with respect to complex **1** [$\delta(\mu_3\text{-}\mathit{C}Me)$ = 401.7 ppm].[1a] These data are in agreement with the rotation of the organometallic ligand around the alkaline-earth metal center, analogously to the situation found in other similar compounds,[7] and with removal of the proton of the starting $\mu_3$-ethylidyne group. The molecular structure of these derivatives was confirmed by an X-ray single crystal structure analysis of **3** (see Figure 1). Selected bond lengths and angles for **3** are included in Table 1.

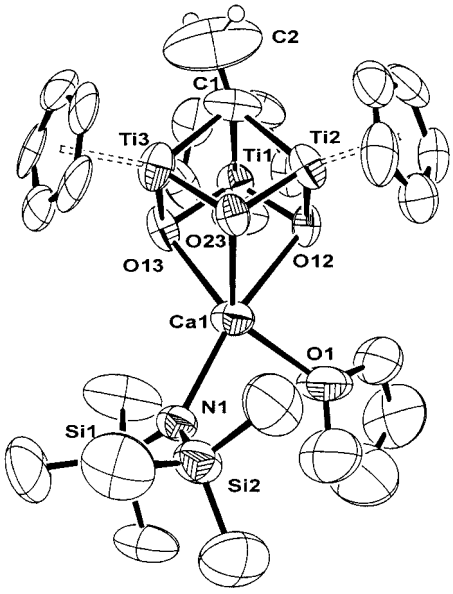


Figure 1. Molecular structure of **3** in the crystal. Hydrogen atoms and the methyl groups of the rings have been omitted for clarity.

Table 1. Selected bond lengths and angles for complex **3**.

| | | | |
|---|---|---|---|
| Ca(1)–N(1) | 2.314(9) | Ca(1)–O(1) | 2.424(11) |
| Ca(1)–O av. | 2.444(8) | Ti···Ca av. | 3.243(3) |
| Ti···Ti av. | 2.832(3) | Ti–C(1) av. | 2.088(15) |
| C(1)–C(2) | 1.23(2) | Ti–O av. | 1.901(8) |
| Si–N(1) av. | 1.685(10) | Si–C av. | 1.872(15) |
| Ca–Si av. | 3.423(5) | Ti–Cp* av. | 2.069 |
| Cp*–Ti–C(1) av. | 129.0 | C(1)–Ti–O av. | 88.9(5) |
| Ti–O–Ti av. | 96.4(3) | O–Ti–O av. | 95.7(3) |
| Ti–O–Ca av. | 95.7(3) | O–Ca–O(1) av. | 113.0(3) |
| O–Ca–O av. | 70.4(2) | | |

The crystal structure of compound **3** reveals a cubic core where the $[CaN(SiMe_3)_2(thf)]$ moiety occupies the free vertex of the incomplete cube-type complex **1**, being linked through the three oxygen atoms. The calcium atom adopts a distorted trigonal bipyramid geometry constituted by the three oxygen atoms of the organometallic oxide, the oxygen of the tetrahydrofuran molecule and the nitrogen atom of the bis(trimethylsilyl)amide ligand, in a similar way to that found for the calcium atom of the previously reported compound $[\{(thf)(Me_3Si)_2NCa\}(\mu_3\text{-}O)_3\{Ti_3Cp^*_3(\mu_3\text{-}C)\}]$.[8] The axial positions of this bipyramid in complex **3** are occupied by the N(1) and O(12) atoms.

The $[CaN(SiMe_3)_2(thf)]$ fragment presents similar bond lengths and angles to other calcium complexes containing

 © 2006 Wiley-VCH Verlag GmbH & Co. KGaA, Weinheim 

this unit.[9] Also, the distances from calcium to the oxygen atoms of the organometallic oxide are in the range 2.421(8)–2.488(8) Å, and the longest is that corresponding to the *trans* position to the bis(trimethylsilyl)amide ligand. Both the amide and the tetrahydrofuran fragments are located in an alternate position with respect to the pentamethylcyclopentadienyl rings to minimize the steric repulsion.

The incorporation of the alkaline earth atom into the organometallic ligand **1** does not produce significant variations in the $[CTi_3O_3]$ core, although it leads to a significant shortening of the C(1)–C(2) length, from 1.514(7) Å[1] in **1** to 1.23(2) Å in **3**. At the same time the C(1)–C(2) bond, which is perpendicular to the plane formed by the three titanium atoms in **1**, now forms an angle of 64.1(1)°.[10] This arrangement contrasts with that found for the complex $[(thf)_2Cs(\mu_3\text{-}O)_3\{Ti_3Cp^*_3(\mu_3\text{-}CCH_2)\}]$, where the spatial disposition of the deprotonated ethylidyne is also perpendicular and the carbon–carbon distance is 1.528(11) Å.[6]

Interestingly, the reaction of **1** with the magnesium amide $[Mg\{N(SiMe_3)_2\}_2(thf)_2]$, in hexane at 180 °C, takes place with deprotonation of the $\mu_3$-ethylidyne group and formation of two compounds, **2a** and **2b**, in approximately a 45:55 ratio (Scheme 3). Both species co-crystallize as red crystals that are soluble in the usual solvents (toluene, hexane...) and are highly air-sensitive. Attempts to separate these compounds were unsuccessful.

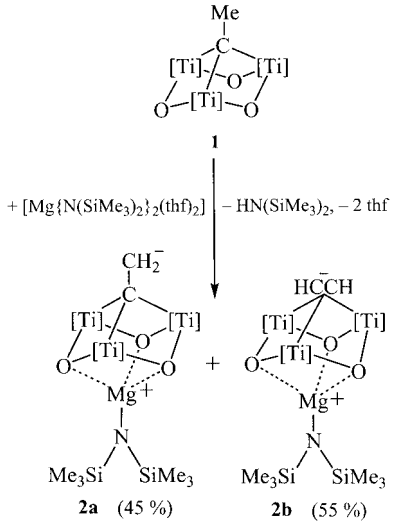


Scheme 3. Reaction of **1** with magnesium bis(trimethylsilyl)amide. [Ti] = Ti($\eta^5$-$C_5Me_5$).

Compounds **2a** and **2b** were characterized by standard analytical and spectroscopic techniques. The most notable features in the $^1H$ and $^{13}C$ NMR spectra of $[\{(Me_3Si)_2NMg\}(\mu_3\text{-}O)_3\{Ti_3Cp^*_3(\mu_3\text{-}CCH_2)\}]$ (**2a**) are the resonances for the $\mu_3$-$CCH_2^-$ group. The $^1H$ NMR spectrum displays a singlet at $\delta$ = 2.95 ppm and the $^{13}C$ NMR spectrum reveals a triplet at $\delta$ = 85.1 ppm ($J_{C,H}$ = 151 Hz), assigned to the β-carbon atom, and the α-carbon atom resonance at $\delta$ = 384.3 ppm, similar to the values found for the calcium (**3**) and strontium (**4**) derivatives. $[\{(Me_3Si)_2NMg\}(\mu_3\text{-}O)_3\{Ti_3Cp^*_3(\mu_3\text{-}\eta^2\text{-}CHCH)\}]$ (**2b**) exhibits a singlet at $\delta$ = 6.55 ppm in the $^1H$ NMR spectrum and a doublet of doublets at $\delta$ = 206.2 ppm ($J_{C,H}$ = 156, $^2J_{C,H}$ = 5.1 Hz) in the $^{13}C$ NMR spectrum for the $\mu_3$-$\eta^2$-$CHCH^-$ group. Furthermore, the presence of single signals at $\delta$ = 1.86 ppm for the methyl group, $\delta$ = 119.9 ppm for the ring carbons, and $\delta$ = 12.5 ppm for the methyl carbons of the Cp* ligands in these spectra suggest a dynamic behavior for compound **2b**. An analogous situation has been reported[11] for the complex $[Rh_3Cp^*_3(\mu_3\text{-}\eta^2\text{-}C_2H_2)(\mu_3\text{-}S)]^{2+}$, where the authors suggest that the cavity constructed by the three Cp* ligands and the metal atoms is big enough to allow the movement of the hydrocarbon ligand $\mu_3$-$\eta^2$-CHCH.

The reaction of **2**–**4** with protic reagents such as pentamethylcyclopentadiene ($C_5Me_5H$) and the alcohol $Ph_3COH$ led to the metathesis of the amide group in a regioselective way, although, surprisingly, the $\mu_3$-ethylidyne group was not regenerated. $C_5Me_5H$ reacts with complexes **3** and **4** at about 90 °C to give the derivatives $[Cp^*M(\mu_3\text{-}O)_3\{Ti_3Cp^*_3(\mu_3\text{-}CCH_2)\}]$ [M = Ca (**5**), Sr (**6**); see Scheme 4]. However, it does not react with the magnesium complexes **2a** and **2b**, probably due to the steric hindrance and low acidity of the pentamethylcyclopentadiene. Compounds **5** and **6** were isolated as brown solids in good yields and characterized by standard analytical and spectroscopic techniques.

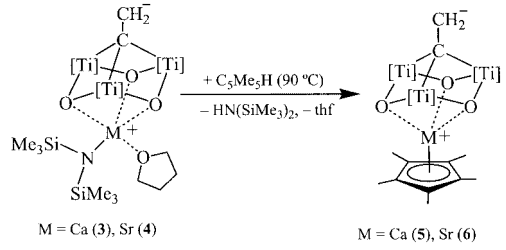


Scheme 4. Reactivity of **3** and **4** with pentamethylcyclopentadiene. [Ti] = Ti($\eta^5$-$C_5Me_5$).

The NMR spectroscopic data are consistent with the structure shown in Scheme 4, thus confirming the existence of the Cp* group at the coordination sphere of the alkaline-earth elements and revealing the presence of the fragment $\mu_3$-$CCH_2^-$ [$\delta(CCH_2)$ = 2.64 (**5**) and 2.55 ppm (**6**) (s); $\delta(CCH_2)$ = 82.5 (**5**) and 81.3 ppm (**6**) (t, $J_{C,H} \approx$ 150 Hz); $\delta(CCH_2)$ = 378.2 (**5**) and 375.6 ppm (**6**)].

The reactions of the alcohol $Ph_3COH$ with complexes **2**–**4** were carried out in NMR tubes in [$D_6$]benzene as solvent at room temperature (see Experimental Section). In all cases the elimination of the amide group as free amine was detected and the complexes $[(Ph_3COMg)(\mu_3\text{-}O)_3\{Ti_3Cp^*_3(\mu_3\text{-}C_2H_2)\}]$ (**7a**,**b**) and $[(Ph_3COM)(\mu_3\text{-}O)_3\{Ti_3Cp^*_3(\mu_3\text{-}CCH_2)\}]$ [M = Ca (**8**) and Sr (**9**)] characterized.

Once the displacement of the amide group by several reagents had been established, we wondered what would happen if compounds **2**–**4** were treated with the starting complex **1** as organometallic tridentate ligand. The oxometallocubanes **2a**,**b** did not react with **1** at room temperature. However, when the solution was heated for several days at

 © 2006 Wiley-VCH Verlag GmbH & Co. KGaA, Weinheim 

about 200 °C and then slowly cooled, an insoluble microcrystalline red solid **10** was isolated in high yield. Curiously, the same result was obtained when complexes **2a**,**b** were heated at that temperature in the absence of **1** (see Scheme 5). Furthermore, compound **10** also resulted from the combination of equimolecular amounts of **1** and the dialkylmagnesiums $[MgR_2(thf)_2]$ (R = $CH_2Ph$, $CMe_3$). Solid **10** proved to be stable under argon at room temperature and insoluble in most common solvents (toluene, hexane, THF...). The new complex was characterized by elemental analysis, IR spectroscopy, and by single-crystal X-ray diffraction.

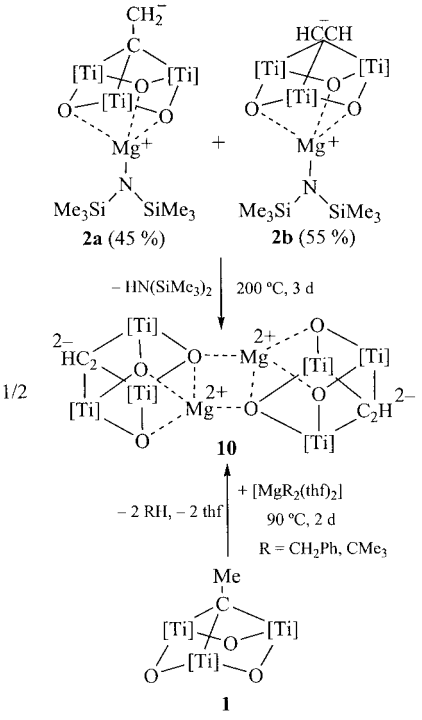


Scheme 5. Thermal treatment of complexes **2a**,**b** and reaction of **1** with dialkylmagnesiums. [Ti] = Ti($\eta^5$-$C_5Me_5$).

The molecular structure of **10** is shown in Figure 2, while selected bond lengths and angles are included in Table 2. The crystallographic study of **10** revealed the presence of two $[MgO_3Ti_3C_2]$ cores directly linked by two Mg–O bonds to form a central planar rhombic $Mg_2O_2$ moiety. The alkaline-earth atoms are located in the vacant vertex of the preorganized organometallic oxide **1** and present a tetracoordinate environment. The pentamethylcyclopentadienyl rings of the cubes adopt an alternate configuration to minimize steric hindrance. The disposition of the core in complex **10** is similar to that reported for $[Li(\mu_4\text{-}O)(\mu_3\text{-}O)_2\{Ti_3Cp^*_3(\mu_3\text{-}C)\}]_2$,[12] and confirms the ability of **1** to encapsulate magnesium atoms.

The magnesium···magnesium distance [2.765(4) Å] is shorter than those found in the literature for other complexes containing $Mg_2O_2$ units,[13] and even shorter than the sum of the Van der Waals radii (3.40 Å).[14] This shortening could be due to the geometry of the molecule itself and the steric hindrance of the ligands around the magnesium

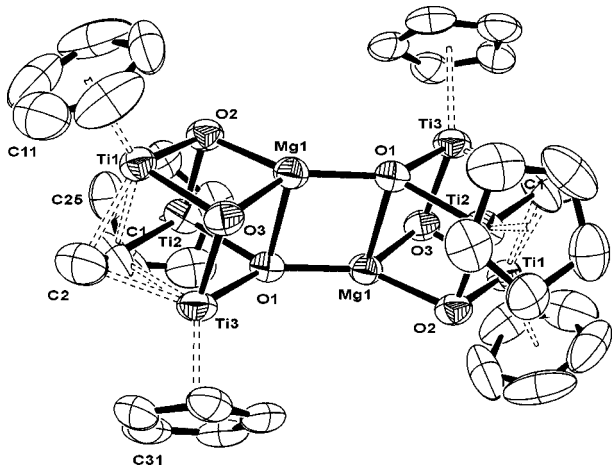


Figure 2. Molecular structure of **10**. The methyl groups of the Cp* rings and hydrogen atoms have been omitted for clarity.

Table 2. Selected bond lengths and angles for complex **10**.

| | | | |
|---|---|---|---|
| C(1)–C(2) | 1.297(12) | C(1)–Ti(1) | 2.147(7) |
| C(1)–Ti(2) | 1.956(7) | C(1)–Ti(3) | 2.068(9) |
| C(2)–Ti(1) | 2.094(9) | C(2)–Ti(3) | 2.239(10) |
| Mg(1)···Mg(1) | 2.765(4) | Mg(1)–O(1) | 2.149(4) |
| Mg(1)–O(2) | 1.986(5) | Mg(1)–O(3) | 1.985(4) |
| Mg(1)–O(1)[a] | 1.929(4) | O(1)–Ti(2) | 2.053(4) |
| O(1)–Ti(3) | 2.115(4) | O(2)–Ti(1) | 2.010(4) |
| O(2)–Ti(2) | 1.909(4) | O(3)–Ti(1) | 1.985(4) |
| O(3)–Ti(3) | 1.930(4) | Ti(1)···Ti(3) | 2.801(2) |
| Ti(1)···Ti(2) | 2.819(2) | Ti(2)···Ti(3) | 2.870(2) |
| C(2)–C(1)–Ti(2) | 155.6(6) | C(2)–C(1)–Ti(3) | 79.8(6) |
| Ti(2)–C(1)–Ti(3) | 90.8(3) | C(2)–C(1)–Ti(1) | 70.0(5) |
| Ti(2)–C(1)–Ti(1) | 86.6(3) | Ti(3)–C(1)–Ti(1) | 83.3(3) |
| C(1)–C(2)–Ti(1) | 74.4(5) | C(1)–C(2)–Ti(3) | 65.4(5) |
| Ti(1)–C(2)–Ti(3) | 80.5(3) | O(1)[a]–Mg(1)–O(3) | 134.3(2) |
| O(1)[a]–Mg(1)–O(2) | 137.1(2) | O(3)–Mg(1)–O(2) | 88.4(2) |
| O(1)[a]–Mg(1)–O(1) | 94.8(2) | O(3)–Mg(1)–O(1) | 83.7(2) |
| O(2)–Mg(1)–O(1) | 84.2(2) | Ti(2)–O(1)–Ti(3) | 86.9(2) |
| Mg(1)–O(1)–Mg(1) | 85.2(2) | Ti(2)–O(1)–Mg(1) | 88.9(2) |
| Ti(3)–O(1)–Mg(1) | 89.8(2) | Ti(2)–O(2)–Mg(1) | 98.1(2) |
| Ti(2)–O(2)–Ti(1) | 91.9(2) | Mg(1)–O(2)–Ti(1) | 90.9(2) |
| Ti(3)–O(3)–Ti(1) | 91.4(2) | Ti(3)–O(3)–Mg(1) | 100.5(2) |
| Ti(1)–O(3)–Mg(1) | 91.6(2) | O(3)–Ti(1)–O(2) | 87.7(2) |
| O(3)–Ti(1)–C(2) | 88.3(3) | O(2)–Ti(1)–C(2) | 121.8(3) |
| O(3)–Ti(1)–C(1) | 90.5(3) | O(2)–Ti(1)–C(1) | 86.4(2) |
| O(2)–Ti(2)–C(1) | 95.0(2) | O(2)–Ti(2)–O(1) | 88.8(2) |
| C(1)–Ti(2)–O(1) | 93.4(3) | O(3)–Ti(3)–C(1) | 94.4(2) |
| O(3)–Ti(3)–O(1) | 85.9(2) | C(1)–Ti(3)–O(1) | 88.5(2) |
| O(3)–Ti(3)–C(2) | 85.7(3) | O(1)–Ti(3)–C(2) | 121.3(3) |

[a] Intercube.

atoms, giving rhombic and not square arrangements. The distance between the magnesium atom and the closer oxygen atom of the other cube Mg(1)–O(1) [1.929(4) Å] is similar to those to O(2) and O(3) of the same cube, while the distance with respect to O(1) of the same cube [2.149(4) Å] is clearly longer and allows us to describe the environment of each magnesium atom as a trigonal pyramid instead of tetrahedral. The sum of the angles in the base of that pyramid is 359.8(2)°.

Complex **10** presents narrower Ti–O–Ti and O–Ti–O angles (10° and 16.5° respectively) and Ti–O distances up to 0.28 Å longer than those found in **1**. However, the Ti···Ti

 © 2006 Wiley-VCH Verlag GmbH & Co. KGaA, Weinheim 

distances stay in the same range [2.819(1) Å in **1** and an average value of 2.830(2) Å in **10**].

The main feature of the solid-state structure of complex **10** is undoubtedly the relative disposition of the hydrocarbyl unit that is formed as a result of the double deprotonation of the $\mu_3$-$CCH_3$ group with respect to the $Ti_3O_3$ surface (see Figure 3). The C(1)–C(2) bond length of 1.297(12) Å is similar to that found in compound **3** but now the Ti–C(1) lengths are quite different, with values ranging from 1.956(7) Å for Ti(2)–C(1) to 2.147(7) Å for Ti(1)–C(1). This means that C(1) is no longer equidistant to the three titanium atoms, being closer to Ti(2). Simultaneously, C(2) shows shorter distances to the titanium atoms [Ti(1)–C(2) = 2.094(9) and Ti(3)–C(2) = 2.239(10) Å] than those found in complex **3**.[15] All this leads to the fact that the C(1)–C(2) line forms an angle of only 20.5° with respect to the plane constituted by the three titanium atoms. The different dispositions of the C(1)–C(2) bond with respect to the $Ti_3$ plane in complexes **1**, **3**, and **10** are represented in Scheme 6.

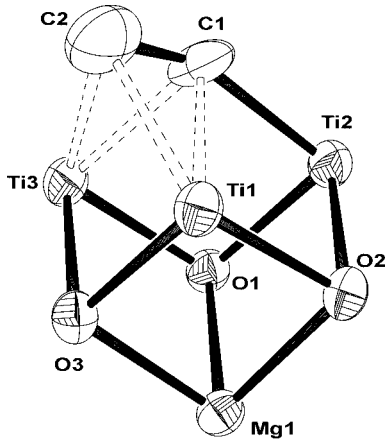


Figure 3. View of the $[MgO_3Ti_3C_2]$ core in complex **10**.

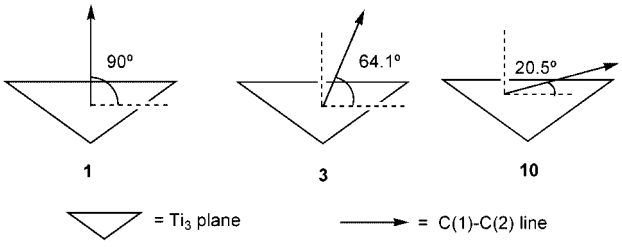


Scheme 6. Disposition of the C(1)–C(2) bond with respect to the $Ti_3$ plane in **1**, **3**, and **10**.

Complexes **1**, **3**, and **10** present an organic ligand supported on an organometallic oxide containing titanium atoms in their higher oxidation state. The electronic deficiency of the titanium centers of **3** and **10** can be alleviated, at least partially, by the donation of electron density from the respective carbanions $\mu_3$-$CCH_2^-$ and $\mu$-$CCH^{2-}$, which bends the C(1)–C(2) bond towards the titanium atoms.

In the case of the calcium and strontium complexes, the addition of **1** to toluene solutions of **3** or **4** and heating to 180 °C for several days afforded the corner-shared double cubane compounds $[M\{(\mu_3\text{-}O)_3Ti_3Cp^*_3(\mu_3\text{-}CCH_2)\}_2]$ [M = Ca (**11**), Sr (**12**)] as dark-red, microcrystalline solids that are insoluble in the usual solvents (toluene, hexane, tetrahydrofuran,...). The IR spectra, elemental analysis, and an X-ray diffraction study of **11** confirmed the structures proposed in Scheme 7.

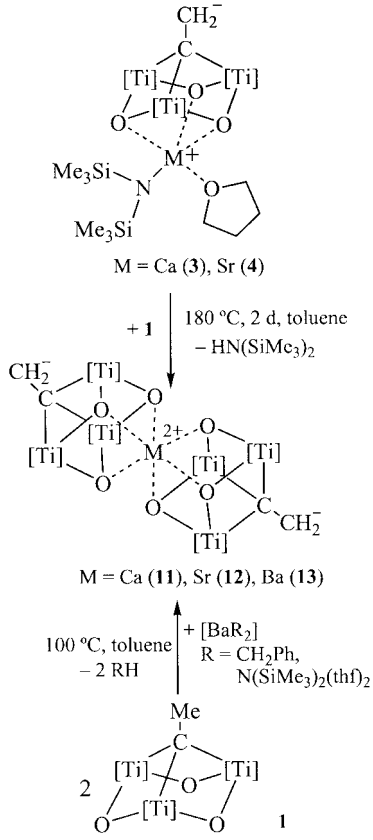


Scheme 7. Formation of calcium, strontium, and barium oxoheterometallodicubanes.

Repeated attempts to obtain crystals of complex **11** failed and only once did we succeed in performing an X-ray diffraction study. The crystals were obtained from a toluene solution at –20 °C, but unfortunately their quality was very poor and the results[16] prevent us from making a detailed discussion of the structure. However, it can be established that **11** shows a double cube $[C_2Ti_6O_6Ca]$ core with the calcium atom located at the shared vertex of a distorted octahedral environment formed by the oxygen atoms of both preorganized ligands (Figure 4) in a similar way to other already reported double cube complexes.[8]

The analogous barium complex $[Ba\{(\mu_3\text{-}O)_3Ti_3Cp^*_3(\mu_3\text{-}CCH_2)\}_2]$ (**13**) can be obtained by treatment of $[BaR_2]$ [R = $N(SiMe_3)_2$, $CH_2Ph$] with the $\mu_3$-ethylidyne complex **1** (see Scheme 7). Both reactions occur with formation of the complex, after heating [R = $N(SiMe_3)_2$, 100 °C, 2 days; R = $CH_2Ph$, 90 °C, one night], to give a red microcrystalline insoluble solid in 77–87% yield. The new complex was characterized by elemental analysis and IR spectroscopy.

 © 2006 Wiley-VCH Verlag GmbH & Co. KGaA, Weinheim 

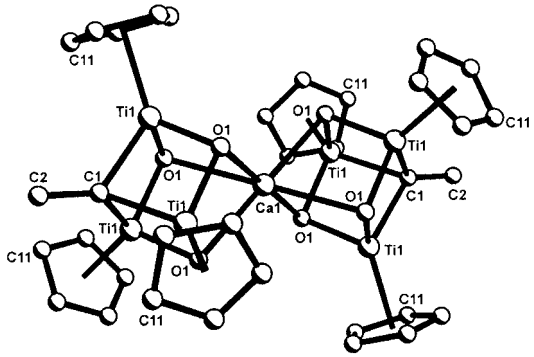


Figure 4. Molecular structure of compound **11**.

## Conclusions

This work is part of an ongoing effort to study the peculiar chemical behavior exhibited by the $\mu_3$-ethylidyne complex [{TiCp*(μ-O)}$_3$($\mu_3$-CMe)] (**1**). Treatment of this molecular model with alkaline-earth metal amides and alkyls produces the deprotonation of the $\mu_3$-ethylidyne fragment to give $\mu_3$-$CCH_2^-$, $\mu_3$-$CHCH^-$, or $\mu_3$-$CCH^{2-}$ carbanions. The interaction of these fragments with the titanium atoms increases with a higher charge of the carbanion. Simultaneously, the alkaline-earth cation is incorporated through the oxygen atoms to build new cage structures.

## Experimental Section

**General Remarks:** All manipulations of the described compounds were carried out with exclusion of air and moisture using Schlenk-line or glovebox techniques. Solvents were carefully dried with the appropriate drying agents and distilled prior to use.

[{TiCp*(μ-O)}$_3$($\mu_3$-CMe)] (**1**) was synthesized according to the published procedure.[1] [$MgR_2(thf)_2$] (R = $CH_2Ph$,[17] $CMe_3$[18]), [$Ba(CH_2Ph)_2$],[19] and [M{$N(SiMe_3)_2$}$_2$(thf)$_2$], (M = Mg,[20] Ca,[21] Sr,[21] Ba[21]) were prepared following the literature methods. Pentamethylcyclopentadiene was purchased from Aldrich and $Ph_3COH$ from Fluka and sublimed before use.

Elemental analyses (C, H, N) were performed with a Heraeus CHN-O-RAPID and/or Perkin–Elmer 2400-Serie II C, H, N, S/O. IR spectra were obtained in KBr pellets with a FT-IR Perkin–Elmer SPECTRUM 2000 spectrophotometer. NMR spectra were recorded on Varian NMR System spectrometers: Gemini-200, Unity-300, or Mercury-VX. Trace amounts of protonated solvents were used as references, and chemical shifts are reported relative to TMS. Thermal reactions were carried out in a Roth autoclave model III (300 mL), with heater model 30S (20–300 °C) and temperature regulator model DR 500.

**Preparation of [{$(Me_3Si)_2NMg$}($\mu_3$-O)$_3${$Ti_3Cp^*_3$($\mu_3$-$C_2H_2$)}] (2a,b):** A 100-mL Carius tube was charged with [{TiCp*(μ-O)}$_3$($\mu_3$-CMe)] (**1**; 0.30 g, 0.48 mmol), [Mg{$N(SiMe_3)_2$}$_2$(thf)$_2$] (0.24 g, 0.48 mmol), and hexane (30 mL) and then sealed under vacuum. This solution was heated in an autoclave at 180 °C for one day. The Carius tube was opened in a glovebox and the solution concentrated and cooled to –40 °C to give a clean mixture of products which contained complexes **2a** and **2b** in approximately a 45:55 ratio (yield: 0.32 g, 82%). IR (KBr): $\tilde{\nu}$ = 2945 $cm^{-1}$ (s), 2911 (vs), 2859 (s), 1492 (w), 1433 (m), 1377 (s), 1242 (s), 1180 (w), 997 (vs), 931 (w), 888 (s), 843 (s), 829 (s), 752 (m), 669 (m), 543 (s), 576 (s), 513 (m), 476 (m), 429 (m). $C_{38}H_{65}MgNO_3Si_2Ti_3$ (807.91): calcd. C 56.48, H 8.11, N 1.73; found C 56.12, H 8.37, N 1.38.

**2a:** $^1$H NMR (300 MHz, [$D_6$]benzene, 20 °C, TMS): $\delta$ = 0.46 [s, 18 H, N(Si$Me_3$)$_2$], 1.91 (s, 45 H, $C_5Me_5$), 2.95 (s, 2 H, $\mu_3$-$CCH_2$) ppm. $^{13}$C{$^1$H} NMR (75 MHz, [$D_6$]benzene, 20 °C, TMS): $\delta$ = 7.4 [N(Si$Me_3$)$_2$], 12.1 ($C_5Me_5$), 85.1 ($\mu_3$-$CCH_2$), 120.0 ($C_5Me_5$), 384.3 ($\mu_3$-$CCH_2$) ppm.

**2b:** $^1$H NMR (300 MHz, [$D_6$]benzene, 20 °C, TMS): $\delta$ = 0.45 [s, 18 H, N(Si$Me_3$)$_2$], 1.86 (s, 45 H, $C_5Me_5$), 6.55 (s, 2 H, $\mu_3$-$\eta^2$-*H*C*C*H) ppm. $^{13}$C{$^1$H} NMR (75 MHz, [$D_6$]benzene, 20 °C, TMS): $\delta$ = 7.2 [N(Si$Me_3$)$_2$], 12.5 ($C_5Me_5$), 119.9 ($C_5Me_5$), 206.2 ($\mu_3$-$\eta^2$-H*C*CH) ppm.

**Preparation of [{(thf)$(Me_3Si)_2NM$}($\mu_3$-O)$_3${$Ti_3Cp^*_3$($\mu_3$-$CCH_2$)}] [M = Ca (3), Sr (4)]:** The preparation of **3** or **4** was performed in a similar fashion to **2**. Complex **1** (0.4 g, 0.64 mmol) was treated with [Ca{$N(SiMe_3)_2$}$_2$(thf)$_2$] (0.32 g, 0.64 mmol) or [Sr{$N(SiMe_3)_2$}$_2$(thf)$_2$] (0.33 g, 0.64 mmol) in hexane (50 mL) at 140 °C for 4 d to afford **3** as red crystals (0.51 g, 88%) or at 100 °C for two days to give **4** as a bright red solid (0.50 g, 83%).

**3:** $^1$H NMR (300 MHz, [$D_6$]benzene, 20 °C, TMS): $\delta$ = 0.37 [s, 18 H, N(Si$Me_3$)$_2$], 1.41 [m, 4 H, O($CH_2CH_2$)$_2$], 1.99 (s, 45 H, $C_5Me_5$), 2.82 (s, 2 H, $\mu_3$-$CCH_2$), 3.87 [m, 4 H, O($CH_2CH_2$)$_2$] ppm. $^{13}$C{$^1$H} NMR (75 MHz, [$D_6$]benzene, 20 °C, TMS): $\delta$ = 6.2 [N(Si$Me_3$)$_2$], 11.7 ($C_5Me_5$), 25.5 [O($CH_2CH_2$)$_2$], 69.6 [O($CH_2CH_2$)$_2$], 82.3 ($\mu_3$-$CCH_2$), 117.9 ($C_5Me_5$), 380.1 ($\mu_3$-$CCH_2$) ppm. IR (KBr): $\tilde{\nu}$ = 2955 $cm^{-1}$ (s), 2908 (vs), 2857 (s), 1493 (w), 1437 (m), 1377 (s), 1254 (s), 1179 (m), 1055 (vs), 1031 (vs), 931 (m) 879 (s), 820 (vs),762 (w), 618 (s), 584 (s), 520 (m), 415 (s). $C_{42}H_{73}CaNO_4Si_2Ti_3$ (895.82): calcd. C 56.31, H 8.21, N 1.56; found C 56.17, H 8.58, N 1.18.

**4:** $^1$H NMR (300 MHz, [$D_6$]benzene, 20 °C, TMS): $\delta$ = 0.35 [s, 18 H, N(Si$Me_3$)$_2$], 1.37 [m, 4 H, O($CH_2CH_2$)$_2$], 2.00 (s, 45 H, $C_5Me_5$), 2.72 (s, 2 H, $\mu_3$-$CCH_2$), 3.62 [m, 4 H, O($CH_2CH_2$)$_2$] ppm. $^{13}$C{$^1$H} NMR (75 MHz, [$D_6$]benzene, 20 °C, TMS): $\delta$ = 5.8 [N(Si$Me_3$)$_2$], 11.6 ($C_5Me_5$), 25.3 [O($CH_2CH_2$)$_2$], 69.4 [O($CH_2CH_2$)$_2$], 81.2 ($\mu_3$-$CCH_2$), 117.5 ($C_5Me_5$), 377.3 ($\mu_3$-$CCH_2$) ppm. IR (KBr): $\tilde{\nu}$ = 2911 $cm^{-1}$ (vs), 2858 (s), 1493 (w), 1435 (s), 1376 (s), 1244 (s), 1178 (w), 1077 (vs), 1033 (s), 932 (m), 879 (s), 819 (vs), 758 (s), 645 (s), 623 (s), 584 (s), 391 (s). $C_{42}H_{73}NO_4Si_2SrTi_3$ (943.34): calcd. C 53.47, H 7.80, N 1.48; found C 53.22, H 7.75, N 1.43.

**Preparation of [Cp*Ca($\mu_3$-O)$_3${$Ti_3Cp^*_3$($\mu_3$-$CCH_2$)}] (5):** Pentamethylcyclopentadiene (53 μL, 0.34 mmol) was added to a solution of **3** (0.30 g, 0.33 mmol) in hexane (40 mL) and the reaction mixture was heated at 90 °C for 6 h to afford a dark-red solution. The solvent was removed in vacuo and the product was isolated in a 75% yield (0.20 g). $^1$H NMR (300 MHz, [$D_6$]benzene, 20 °C, TMS): $\delta$ = 1.90 (s, 45 H, Ti$C_5Me_5$), 2.22 (s, 15 H, Ca$C_5Me_5$) 2.64 (s, 2 H, $\mu_3$-$CCH_2$) ppm. $^{13}$C{$^1$H} NMR (75 MHz, [$D_6$]benzene, 20 °C, TMS): $\delta$ = 11.4 (Ti$C_5Me_5$), 11.4 (Ca$C_5Me_5$), 114.0 (Ca$C_5Me_5$), 118.1 (Ti$C_5Me_5$), 82.5 ($\mu_3$-$CCH_2$), 378.2 ($\mu_3$-$CCH_2$) ppm. IR (KBr): $\tilde{\nu}$ = 2962 $cm^{-1}$ (m), 2910 (s) 2857 (m), 1495 (w), 1438 (m), 1377 (m), 1088 (m), 1022 (m), 791 (vs), 675 (s), 617 (m), 579 (m), 420 (m). $C_{42}H_{62}CaO_3Ti_3$ (798.64): calcd. C 63.16, H 7.82; found C 63.09, H 8.11.

**Preparation of [Cp*Sr($\mu_3$-O)$_3${$Ti_3Cp^*_3$($\mu_3$-$CCH_2$)}] (6):** Complex **4** (0.30 g, 0.32 mmol) was dissolved in toluene (40 mL) in a 100-mL Carius tube fitted with a Young valve and pentamethylcyclopentadiene (50 μL, 0.32 mmol) was added. The reaction mixture was heated at 90 °C for 6 h. After that, the solution was filtered and the solvent was removed to yield **6** (0.20 g, 74% yield). $^1$H NMR (300 MHz, [$D_6$]benzene, 20 °C, TMS): $\delta$ = 1.90 (s, 45 H, Ti$C_5Me_5$),

 © 2006 Wiley-VCH Verlag GmbH & Co. KGaA, Weinheim 

2.20 (s, 15 H, $SrC_5Me_5$) 2.55 (s, 2 H, $\mu_3$-$CCH_2$) ppm. $^{13}C\{^1H\}$ NMR (75 MHz, [D$_6$]benzene, 20 °C, TMS): $\delta$ = 11.0 ($SrC_5Me_5$), 11.3 ($TiC_5Me_5$), 81.3 ($\mu_3$-$CCH_2$), 113.7 ($SrC_5Me_5$), 117.6 ($TiC_5Me_5$), 375.6 ($\mu_3$-$CCH_2$) ppm. IR (KBr): $\tilde{\nu}$ = 2956 cm$^{-1}$ (m), 2908 (s), 2856 (s), 1494 (w), 1437 (m), 1375 (m), 1082 (m), 1024 (m), 791 (vs), 680 (s), 619 (m), 582 (m), 390 (m). $C_{42}H_{62}O_3SrTi_3$ (846.16): calcd. C 59.61, H 7.38; found C 60.26, H 7.70.

**Reaction of [{(Me$_3$Si)$_2$NMg}($\mu_3$-O)$_3${Ti$_3$Cp*$_3$($\mu_3$-C$_2$H$_2$)}] (2a,b) with Ph$_3$COH:** Complexes **2a**,**b** (22 mg, 0.027 mmol) and $Ph_3COH$ (ca. 7 mg, 0.027 mmol) were dissolved in [D$_6$]benzene (1.0 mL). The mixture reaction was transferred to a 5-mm NMR tube and once **2a**,**b** had been consumed at room temperature, the solvent and most of the amine formed, [NH(SiMe$_3$)$_2$], were removed under vacuum. The solid was then dissolved in [D$_6$]benzene and the solution was checked by $^1$H and $^{13}$C NMR spectroscopy allowed us to characterize the products as [($Ph_3COMg$)($\mu_3$-O)$_3${Ti$_3$Cp*$_3$($\mu_3$-C$_2$H$_2$)}] (**7a**,**b**).

**7a:** $^1$H NMR (300 MHz, [D$_6$]benzene, 20 °C, TMS): $\delta$ = 1.87 (s, 45 H, $C_5Me_5$), 2.82 (s, 2 H, $\mu_3$-$CCH_2$), 6.9–7.5 (m, $OCPh_3$) ppm. $^{13}C\{^1H\}$ NMR (75 MHz, [D$_6$]benzene, 20 °C, TMS): $\delta$ = 11.8 ($C_5Me_5$), 83.7 ($\mu_3$-$CCH_2$), 120.0 ($C_5Me_5$), 125.0–155.0 ($OCPh_3$), 379.1 ($\mu_3$-$CCH_2$) ppm.

**7b:** $^1$H NMR (300 MHz, [D$_6$]benzene, 20 °C, TMS): $\delta$ = 1.80 (s, 45 H, $C_5Me_5$), 6.18 (s, 2 H, $\mu_3$-$\eta^2$-$CHCH$), 6.9–7.5 (m, $OCPh_3$) ppm. $^{13}C\{^1H\}$ NMR (75 MHz, [D$_6$]benzene, 20 °C, TMS): $\delta$ = 12.2 ($C_5Me_5$), 120.2 ($C_5Me_5$), 125.0–150.0 ($OCPh_3$), 200.8 ($\mu_3$-$\eta^2$-$CHCH$) ppm.

**Reaction of [{(thf)(Me$_3$Si)$_2$NCa}($\mu_3$-O)$_3${Ti$_3$Cp*$_3$($\mu_3$-CCH$_2$)}] (3) with Ph$_3$COH:** In a similar fashion to **7**, complex **3** (21 mg, 0.023 mmol) and $Ph_3COH$ (ca. 6 mg, 0.023 mmol) were dissolved in [D$_6$]benzene (1.0 mL). After thirty minutes at room temperature, the solvent and most of the amine formed were removed under vacuum and the solid was dissolved in [D$_6$]benzene. The NMR spectra allowed us to characterize the product as [($Ph_3COCa$)($\mu_3$-O)$_3${Ti$_3$Cp*$_3$($\mu_3$-CCH$_2$)}] (**8**). $^1$H NMR (300 MHz, [D$_6$]benzene, 20 °C, TMS): $\delta$ = 1.98 (s, 45 H, $C_5Me_5$), 2.80 (s, 2 H, $\mu_3$-$CCH_2$), 6.9–7.7 (m, $OCPh_3$) ppm. $^{13}C\{^1H\}$ NMR (75 MHz, [D$_6$]benzene, 20 °C, TMS): $\delta$ = 12.0 ($C_5Me_5$), 81.3 ($\mu_3$-$CCH_2$), 117.8 ($C_5Me_5$), 125.0–155.0 ($OCPh_3$), 378.6 ($\mu_3$-$CCH_2$) ppm.

**Reaction of [{(thf)(Me$_3$Si)$_2$NSr}($\mu_3$-O)$_3${Ti$_3$Cp*$_3$($\mu_3$-CCH$_2$)}] (4) with Ph$_3$COH:** The preparation was similar to that for **8**, but with **4** (22 mg, 0.023 mmol) and $Ph_3COH$ (ca. 6 mg, 0.023 mmol) in [D$_6$]benzene (1.0 mL). The NMR spectra of the resulting solution allowed us to characterize the product as [($Ph_3COSr$)($\mu_3$-O)$_3${Ti$_3$Cp*$_3$($\mu_3$-CCH$_2$)}] (**9**). $^1$H NMR (300 MHz, [D$_6$]benzene, 20 °C, TMS): $\delta$ = 2.03 (s, 45 H, $C_5Me_5$), 2.78 (s, 2 H, $\mu_3$-$CCH_2$), 6.9–7.7 (m, $OCPh_3$) ppm. $^{13}C\{^1H\}$ NMR (75 MHz, [D$_6$]benzene, 20 °C, TMS): $\delta$ = 11.6 ($C_5Me_5$), 80.5 ($\mu_3$-$CCH_2$), 82.6 ($OCPh_3$), 117.0 ($C_5Me_5$), 125.0–155.0 ($OCPh_3$), 377.7 ($\mu_3$-$CCH_2$) ppm.

**Preparation of [Mg($\mu_4$-O)($\mu_3$-O)$_2${Ti$_3$Cp*$_3$($\mu_3$-CCH)}]$_2$ (10). Method A:** [{TiCp*($\mu$-O)}$_3$($\mu_3$-CMe)] (**1**; 0.20 g, 0.32 mmol), [Mg{N(SiMe$_3$)$_2$}$_2$(thf)$_2$] (0.16 g, 0.32 mmol), and hexane (30 mL) were placed in a 100-mL Carius tube. The pressure of the argon atmosphere was reduced and the reaction mixture was heated at 200 °C for four days. Slow crystallization of the solution at room temperature afforded **10** as red crystals suitable for an X-ray diffraction analysis. The isolated compound was obtained in 82% (0.17 g) yield.

**Method B:** Complex **1** (0.20 g, 0.32 mmol) and [Mg(CH$_2$Ph)$_2$(thf)$_2$] (0.112 g, 0.32 mmol) or [Mg(CMe$_3$)$_2$(thf)$_2$] (0.091 g, 0.32 mmol) were placed in a 100-mL Carius tube fitted with a Young valve and dissolved in toluene (30 mL). The mixture was heated at 90 °C for two days. The reddish solution was filtered, concentrated until 15 mL, and, finally, cooled to –40 °C to give a dark-red microcrystalline solid with a yield of 77% (0.16 g) from [Mg(CH$_2$Ph)$_2$(thf)$_2$] and 82% (0.17 g) from [Mg(CMe$_3$)$_2$(thf)$_2$]. IR (KBr): $\tilde{\nu}$ = 2906 cm$^{-1}$ (vs), 2855 (s), 1489 (w), 1437 (s), 1373 (s), 1023 (m), 793 (m), 645 (vs), 534 (s), 492 (s), 454 (m), 403 (m). $C_{64}H_{92}Mg_2O_6Ti_6$ (1293.3): calcd. C 59.44, H 7.17; found C 59.29, H 7.52.

**Preparation of [Ca{($\mu_3$-O)$_3$Ti$_3$Cp*$_3$($\mu_3$-CCH$_2$)}$_2$] (11):** Compound **11** was prepared by heating **3** (0.15 g, 0.17 mmol) and **1** (0.104 g, 0.17 mmol) in toluene (20 mL) at 180 °C for two days. The Carius tube was opened in a glovebox and the solution was concentrated and cooled (–20 °C) to yield **11** as a dark-red, microcrystalline solid (0.19 g, 88%). IR (KBr): $\tilde{\nu}$ = 2907 cm$^{-1}$ (vs), 2857 (s), 1492 (w), 1437 (m), 1375 (s), 1023 (m), 793 (m, br), 615 (vs), 518 (m), 472 (w), 418 (s), 387 (s). $C_{64}H_{94}CaO_6Ti_6$ (1286.8): calcd. C 59.74, H 7.36; found C 60.03, H 7.52.

**Preparation of [Sr{($\mu_3$-O)$_3$Ti$_3$Cp*$_3$($\mu_3$-CCH$_2$)}$_2$] (12):** Similarly to the preparation of **11**, **4** (0.15 g, 0.16 mmol) and **1** (99 mg, 0.16 mmol) were heated in toluene (20 mL) at 180 °C for two days to afford **12** as a red, microcrystalline solid (0.16 g, 75%). IR (KBr): $\tilde{\nu}$ = 2908 cm$^{-1}$ (vs), 2857 (s), 1493 (w), 1435 (m), 1375 (s), 1023 (m), 793 (vs), 664 (m), 615 (vs), 528 (m), 416 (m), 389 (m). $C_{64}H_{94}O_6SrTi_6$ (1334.29): calcd. C 57.61, H 7.10; found C 57.70, H 7.20.

**Preparation of [Ba{($\mu_3$-O)$_3$Ti$_3$Cp*$_3$($\mu_3$-CCH$_2$)}$_2$] (13):** The thermal treatment of a mixture of **1** and $BaR_2$ [R = N(SiMe$_3$)$_2$, $CH_2Ph$] led to the formation of compound **13**. Thus, a solution of **1** (0.40 g, 0.64 mmol) and [Ba{N(SiMe$_3$)$_2$}$_2$(thf)$_2$] (0.183 g, 0.32 mmol) in toluene (40 mL), in a 100-mL Carius tube sealed under vacuum by flame, was heated in an autoclave at 100 °C for 2 d. When using [Ba(CH$_2$Ph)$_2$] (0.077 g, 0.24 mmol) and **1** (0.30 g, 0.48 mmol), the solution was heated at 90 °C for one night. After that, the Carius tube was opened in a glovebox and the solution concentrated and cooled to –40 °C to yield a dark-red, microcrystalline solid, which was identified as **13**, in a yield of 86% (0.38 g) for the reaction with [Ba{N(SiMe$_3$)$_2$}$_2$(thf)$_2$] and 78% (0.26 g) with [Ba(CH$_2$Ph)$_2$]. IR (KBr): $\tilde{\nu}$ = 2911 cm$^{-1}$ (vs), 2858 (s), 1493 (w), 1436 (s), 1377 (s), 1103 (m), 1023 (m), 795 (vs), 668 (m), 616 (s), 543 (m), 486 (w), 394 (m). $C_{64}H_{94}BaO_6Ti_6$ (1384.0): calcd. C 55.54, H 6.85; found C 55.02, H 6.97.

**X-ray Structure Determinations of 3 and 10:** Crystals of **3** were grown from a hexane solution at –20 °C. Crystals of **10** were grown as described in the Experimental Section using Method A. Crystals were mounted in a glass capillary in a random orientation and transferred to an Enraf–Nonius CAD4 diffractometer for characterization and data collection at room temperature. Table 3 provides a summary of the crystal data, data collection, and refinement parameters for both complexes.

Intensity measurements were performed by $\omega$–$2\theta$ scans in the range $3° < 2\theta < 46°$ for **3**. Of the 15341 measured reflections, 7387 were independent; $R_1$ = 0.083 and $wR_2$ = 0.219 [for 2706 reflections with $F > 4\sigma(F)$]. The values of $R_1$ and $wR_2$ are defined as: $R_1 = \Sigma||F_o| - |F_c||/[\Sigma|F_o|]$; $wR_2 = \{[\Sigma w(F_o^2 - F_c^2)^2] / [\Sigma w(F_o^2)^2]\}^{1/2}$.

Intensity measurements were performed by $\omega$–$2\theta$ scans in the range $3.6° < 2\theta < 46°$ for **10**. Of the 4721 measured reflections, 4472 were independent; $R_1$ = 0.074 and $wR_2$ = 0.198 [for 3174 reflections with $F > 4\sigma(F)$].

The structures were solved, using the WINGX package,[22] by direct (**3**) and Patterson (**10**) methods (SHELXS-97)[23] and refined by least-squares against $F^2$ (SHELXL-97).[23] Complex **3** crys-

 © 2006 Wiley-VCH Verlag GmbH & Co. KGaA, Weinheim 

Table 3. Crystal data and structure refinement for **3** and **10**.

| | **3** | **10** |
|---|---|---|
| Empirical formula | $C_{42}H_{73}CaNO_4Si_2Ti_3 \cdot 1/2C_6H_{14}$ | $C_{64}H_{92}Mg_2O_6Ti_6$ |
| Formula weight | 939.06 | 1293.40 |
| Temperature [K] | 293(2) | 293(2) |
| Wavelength (Mo-$K_\alpha$) [Å] | 0.71073 | 0.71073 |
| Crystal system | monoclinic | monoclinic |
| Space group | $P2_1/c$ | $P2_1/c$ |
| $a$ [Å] | 11.622(3) | 11.705(5) |
| $b$ [Å] | 21.314(5) | 20.419(6) |
| $c$ [Å] | 24.260(5) | 15.567(7) |
| $\beta$ [°] | 118.0(1) | 119.7(1) |
| $V$ [Å$^3$]; $Z$ | 5307(2); 4 | 3233(2); 2 |
| $\rho_{calcd.}$ [g cm$^{-3}$] | 1.175 | 1.329 |
| $\mu$ [mm$^{-1}$] | 0.619 | 0.772 |
| $F$(000) | 2012 | 1360 |
| Crystal size [mm] | 0.35 × 0.28 × 0.24 | 0.40 × 0.25 × 0.22 |
| Diffractometer | Enraf–Nonius CAD-4 | Enraf–Nonius CAD-4 |
| Scan mode; $\theta$ range | $\omega$–2$\theta$; 1.35 to 23.00° | $\omega$–2$\theta$; 1.81 to 22.96° |
| Index ranges | –12 to 0, –23 to 23, –23 to 26 | –12 to 0, –22 to 0, –14 to 17 |
| Collected reflections | 15341 | 4721 |
| Independent reflections | 7387 [$R_{int}$ = 0.176] | 4472 [$R_{int}$ = 0.103] |
| Goodness-of-fit on $F^2$ | 0.939 | 1.032 |
| Final $R$ indices [$F > 4\sigma(F)$] | $R_1$ = 0.083; $wR_2$ = 0.219 | $R_1$ = 0.074; $wR_2$ = 0.198 |
| $R$ indices (all data) | $R_1$ = 0.251; $wR_2$ = 0.331 | $R_1$ = 0.110; $wR_2$ = 0.225 |
| Largest diff. peak/hole [e Å$^{-3}$] | 0.680 and –0.631 | 0.789 and –0.611 |

tallized with half a molecule of hexane. All non-hydrogen atoms of **3** were refined anisotropically, except those of the solvent, and the hydrogen atoms positioned geometrically and refined by using a riding model in the last cycles of refinement.

Compound **10** showed disorder in the pentamethylcyclopentadienyl linked to Ti(1) and also in C(2). Both disorders were treated conventionally by using the PART command of the SHELXL[23] program and allowing free refinement of the occupancy factors with the FVAR command. The final values were 70% of occupancy for C(2) and 53% for the C(11)–C(20) ring. All non-hydrogen atoms, except those of the disordered pentamethylcyclopentadienyl fragment, were refined anisotropically. All the hydrogen atoms were positioned geometrically and refined by using a riding model in the last cycles of refinement.

CCDC-296004 (for **3**) and -296005 (for **10**) contain the supplementary crystallographic data for this paper. These data can be obtained free of charge from The Cambridge Crystallographic Data Center via www.ccdc.cam.ac.uk/data_request/cif.

## Acknowledgments

The authors wish to acknowledge the financial support of the Spanish Ministerio de Ciencia y Tecnología (BQU2001-1499), the Comunidad de Madrid (07N/0091/2002), and the Universidad de Alcalá.

[1] a) R. Andrés, M. Galakhov, A. Martín, M. Mena, C. Santamaría, *Organometallics* **1994**, *13*, 2159–2163; b) R. Andrés, M. Galakhov, A. Martín, M. Mena, C. Santamaría, *J. Chem. Soc., Chem. Commun.* **1995**, 551–552.

[2] a) R. Andrés, M. V. Galakhov, M. P. Gómez-Sal, A. Martín, M. Mena, C. Santamaría, *Chem. Eur. J.* **1998**, 1206–1213; b) M. V. Galakhov, M. Mena, C. Santamaría, *Chem. Commun.* **1998**, 691–692; c) P. Gómez-Sal, A. Martín, M. Mena, M. C. Morales, C. Santamaría, *Chem. Commun.* **1999**, 1839–1840; d) R. Andrés, M. V. Galakhov, M. P. Gómez-Sal, A. Martín, M. Mena, M. C. Morales-Varela, C. Santamaría, *Chem. Eur. J.* **2002**, 805–811.

[3] a) G. A. Somorjai, *Introduction to Surface Chemistry and Catalysis*, John Wiley and Sons, New York, **1994**, p. 400; b) B. C. Gates, *Catalytic Chemistry*, John Wiley and Sons, New York, **1992**; c) F. Zaera, *Chem. Rev.* **1995**, *95*, 2651–2693; d) B. E. Bent, *Chem. Rev.* **1996**, *26*, 1361–1390; e) H. H. Kung, *Transition Metal Oxides: Surface Chemistry and Catalysis*, Elsevier Science Publishers, Amsterdam, The Netherlands, **1989**; f) M. A. Barteau, *Chem. Rev.* **1996**, *96*, 1413–1430; g) P. M. Maitlis, H. C. R. Long Quyoum, M. L. Turner, Z.-Q. Wang, *Chem. Commun.* **1996**, 1–8; h) F. Zaera, *Catal. Lett.* **2003**, *91*, 1–10; i) H. H. Hwu, J. G. Chen, *Chem. Rev.* **2005**, *105*, 185–212.

[4] a) M. M. Hills, J. E. Parmeter, W. H. Weinberg, *J. Am. Chem. Soc.* **1987**, *109*, 597–599; b) A. J. Slavin, B. E. Bent, C.-T. Kao, G. A. Somorjai, *Surf. Sci.* **1988**, *206*, 124–144; c) C.-H. Hwang, C.-W. Lee, H. Kang, C. M. Kim, *Surf. Sci.* **2001**, *490*, 144–152; d) L. M. Ilharco, A. R. García, R. Brito de Barros, *Surf. Sci.* **2002**, *516*, 85–94; e) H. Kang, C. W. Lee, C. H. Hwang, C. M. Kim, *Appl. Surf. Sci.* **2003**, *203–204*, 842–846; f) M. Sock, A. Eichler, S. Surnev, J. N. Andersen, B. Klötzer, K. Hayek, M. G. Ramsey, F. P. Netzer, *Surf. Sci.* **2003**, *545*, 122–136; g) R. Deng, E. Herceg, M. Trenary, *Surf. Sci.* **2004**, *573*, 310–319.

[5] H. H. Hwu, J. G. Chen, *Surf. Sci.* **2004**, *557*, 144–158.

[6] O. González-del Moral, A. Martín, M. Mena, M. C. Morales-Varela, C. Santamaría, *Chem. Commun.* **2005**, 3682–3684.

[7] A. Abarca, M. V. Galakhov, J. Gracia, A. Martín, M. Mena, J.-M. Poblet, J. P. Sarasa, C. Yélamos, *Chem. Eur. J.* **2003**, *9*, 2337–2346.

[8] A. Martín, M. Mena, M. C. Morales-Varela, C. Santamaría, *Eur. J. Inorg. Chem.* **2004**, 1914–1921.

[9] a) D. J. Burkey, E. K. Alexander, T. P. Hanusa, *Organometallics* **1994**, *13*, 2773–2786; b) M. Westerhausen, M. Hartmann, N. Makropoulos, B. Wieneke, M. Wieneke, W. Schwarz, D. Stalke, *Z. Naturforsch., Teil B* **1998**, *53*, 117–125; c) M. Westerhausen, S. Schneiderbauer, A. N. Kneifel, Y. Soltl, P. Mayer, H. Noth, Z. Zhong, P. J. Dijkstra, J. Feijen, *Eur. J. Inorg. Chem.* **2003**, 3432–3439.

[10] PARST a) M. Nardelli, *Comput. Chem.* **1983**, *7*, 95–97; b) M. Nardelli, *J. Appl. Crystallogr.* **1995**, *28*, 659.

 © 2006 Wiley-VCH Verlag GmbH & Co. KGaA, Weinheim 

[11] T. Nishioka, K. Isobe, I. Kinoshita, Y. Ozawa, A. V. de Miguel, T. Nakai, S. Miyajima, *Organometallics* **1998**, *17*, 1637–1639.
[12] J. Gracia, A. Martín, M. Mena, M. C. Morales-Varela, J.-M. Poblet, C. Santamaría, *Angew. Chem.* **2003**, *115*, 957–960; *Angew. Chem. Int. Ed.* **2003**, *42*, 927–930.
[13] a) J. Calabrese, M. A. Cushing, S. D. Ittel, *Inorg. Chem.* **1988**, *27*, 867–870; b) C.-C. Chang, W.-H. Lee, T.-Y. Her, G.-H. Lee, S.-M. Peng, Y. Wang, *J. Chem. Soc., Dalton Trans.* **1994**, 315–322; c) P. Ghosh, G. Parkin, *Inorg. Chem.* **1996**, *35*, 1429–1430; d) C. A. Zechmann, T. J. Boyle, M. A. Rodriguez, R. A. Kemp, *Inorg. Chim. Acta* **2001**, *319*, 137–146.
[14] A. Bondi, *J. Phys. Chem.* **1964**, *68*, 441–451.
[15] 2.68(2) Å is the shortest distance between the C(2) and titanium atoms in complex **3**.
[16] X-ray data for complex **14**: $C_{64}H_{94}CaO_6Ti_6$, $M$ = 1286.87, trigonal, $R\bar{3}$, $a$ = 19.434(4), $b$ = 19.434(3), $c$ = 14.544(2) Å, $U$ = 4751.6(12) Å$^3$, $Z$ = 3, $\rho_{calc}$ = 1.349 g cm$^{-3}$, $\mu$ = 0.849 mm$^{-1}$, $F$(000) = 2034. 8744 reflections collected at 200 K, 2398 [$R_{int}$ = 0.114] independent, final $R$ indices [$I > 2\sigma(I)$] $R_1$ = 0.165, $wR_2$ = 0.358. Largest diff. peak and hole 0.800 and –0.759 e Å$^{-3}$.
[17] R. R. Schrock, *J. Organomet. Chem.* **1976**, *122*, 209–225.
[18] G. E. Coates, J. A. Heslop, *J. Chem. Soc. A* **1968**, 514–518.
[19] A. Weeber, S. Harder, H. H. Brintzinger, K. Knoll, *Organometallics* **2000**, *19*, 1325–1332.
[20] K. W. Henderson, J. F. Allan, A. R. Kennedy, *Chem. Commun.* **1997**, 1149–1150.
[21] D. C. Bradley, M. B. Hursthouse, A. A. Ibrahim, K. M. A. Malik, M. Motevalli, R. Möseler, H. Powell, J. D. Runnades, A. C. Sullivan, *Polyhedron* **1990**, *9*, 2959–2964.
[22] L. J. Farrugia, *J. Appl. Crystallogr.* **1999**, *32*, 837–838.
[23] *SHELX-97: Programs for Crystal Structure Analysis* (release 97-2), G. M. Sheldrick, University of Göttingen, Germany, **1998**.

Received: January 26, 2006
Published Online: April 18, 2006

 © 2006 Wiley-VCH Verlag GmbH & Co. KGaA, Weinheim 

DOI: 10.1002/ejic.200501033

# Syntheses, Spectroscopic Studies, and Crystal Structures of Chiral [Rh(aminocarboxylato)($\eta^4$-cod)] and Chiral [Rh(amino alcohol)($\eta^4$-cod)]-(acetate) Complexes with an Example of a Spontaneous Resolution of a Racemic Mixture into Homochiral Helix-Enantiomers

**Mohammed Enamullah,*[a] Aisha Sharmin,[a] Miki Hasegawa,[b] Toshihiko Hoshi,[b] Anne-Christine Chamayou,[c] and Christoph Janiak*[c]**

**Keywords:** Rhodium(I) / Amino acids / Chirality / Spontaneous resolution / Helix

The dimeric complex acetato($\eta^4$-cycloocta-1,5-diene)rhodium(I), [Rh($O_2$CMe)($\eta^4$-cod)]$_2$ (cod = cycloocta-1,5-diene), reacts with amino acids [HAA = L-alanine, (*S*)-2-amino-2-phenylacetic acid (L-phenylglycine), *N*-methylglycine, and *N*-phenylglycine] and with the amino alcohol (*S*)-2-amino-2-phenylethanol to afford the aminocarboxylato($\eta^4$-cycloocta-1,5-diene)rhodium(I) complexes [Rh(AA)($\eta^4$-cod)] (AA = deprotonated amino acid = aminocarboxylato ligand) and [(*S*)-2-amino-2-phenylethanol]($\eta^4$-cycloocta-1,5-diene)-rhodium(I) acetate, [Rh{(*S*)-HOCH$_2$–CH(Ph)-NH$_2$}($\eta^4$-cod)]-($O_2$CMe) (**V**). The complexes are characterized by IR, UV/Vis, $^1$H/$^{13}$C NMR and mass spectroscopy. The achiral *N*-phenylglycine ligand gives a chiral *N*-phenylglycinato complex [Rh($O_2$C–CH$_2$–NHPh)($\eta^4$-cod)] (**IV**) with the amine nitrogen atom becoming the stereogenic center upon metal coordination. Complex **IV** crystallizes in the tetragonal, chiral space group $P4_3$ and the crystal structure reveals twofold spontaneous resolution of a racemic mixture into homochiral helix-enantiomers. The investigated crystal contained only one type of helix, namely (left-handed or *M*-) $4_3$-helical chains. This is traced first to an intermolecular N–H···O hydrogen bonding from the stereogenic amino group to a neighboring unligated carboxyl oxygen atom that connects only molecules of the same (*R*)-configuration into (left-handed or *M*-) $4_3$-helical chains. This intrachain homochirality is supplemented, secondly, by the interlocking of adjacent chains with their corrugated van der Waals surface to allow for an interchain transmission of the sense of helicity, building the single crystal from the same homochiral helix-enantiomer. The enantiomeric amino alcohol complex **V** crystallizes in the monoclinic, noncentrosymmetric (Sohncke) space group $P2_1$.
(© Wiley-VCH Verlag GmbH & Co. KGaA, 69451 Weinheim, Germany, 2006)

## Introduction

Syntheses and reactivities of metal complexes with amino acids or peptides are of considerable interest and some of them show potential applications as chiral catalysts.[1] Singh first reported the syntheses of [Rh(AA)($CO)_2$][2a,2b] and [Rh(AA)(CO)($L)_2$] (AA = deprotonated amino acid = aminocarboxylato ligand; L = $PPh_3$ or $AsPh_3$) complexes.[2c,2d] Later, Marko synthesized the [Rh(AA)($CO)_2$] complexes starting from the dimeric [Rh($O_2$CR)($\eta^4$-cod)]$_2$ by synthesis of the intermediate [Rh(AA)($\eta^4$-cod)] complexes (cod = cycloocta-1,5-diene).[3] Accordingly, Beck has reported the syntheses and crystal structures of the [Rh(AA)(CO)(L)] (L = $PPh_3$, $AsPh_3$)[4a] and [Rh(L-aziridin-2-carboxylato)($CO)_2$][4b] complexes and efforts to synthesize the analogous Ru$^{II}$-aminocarboxylato complexes containing the bidentate 2,7-dimethylocta-2,6-dien-1,8-diyl ligand.[4c] Molybdocene and titanocene compounds of the formulae [$Cp_2$Mo$^{IV}$($\kappa N$,$\kappa O$-AA)]$^+$Cl$^-$,[5] [$Cp_2$Mo$^{IV}$($\kappa N$,$\kappa O$-AA)]$^+$-$PF_6^-$,[6] [$Cp_2$Ti$^{IV}$($\kappa O$-AA)$_2$]$^{2+}$,[7,8] and the isoelectronic half-sandwich molybdenum compounds [CpMo$^{II}$($CO)_2$($\kappa N$,$\kappa O$-AA)][9] and [CpMo$^{II}$(NO)(*I*){$\kappa N$,$\kappa O$-L-$H_2$NCH(*t*Bu)-COO}][10] have been prepared and structurally elucidated (Cp = $\eta^5$-$C_5H_5$, $\eta^5$-cyclopentadienyl). However, no detailed studies on the syntheses, spectroscopy, and crystal structures of Rh($\eta^4$-cod) complexes containing chiral amino acid/amino alcohol or *N*-amino acids have been reported so far. It is envisioned that these coligands will exercise strong influences on the stereochemistry as well as the stability and reactivity of the Rh complexes and their uses as catalysts for the enantioselective hydrogenation of olefins, unsaturated carboxylates, amidocinnamic acids, and their ester derivatives.

[a] Department of Chemistry, Jahangirnagar University, Dhaka 1342, Bangladesh
E-mail: menam@juniv.edu
[b] Department of Chemistry, College of Science and Engineering, Aoyama Gakuin University, Sagamihara-shi, Kanagawa 229-8558, Japan
[c] Institut für Anorganische und Analytische Chemie, Universität Freiburg, Albertstr. 21, 79104 Freiburg, Germany
E-mail: janiak@uni-freiburg.de
Supporting information for this article is available on the WWW under http://www.eurjic.org or from the author.

 © 2006 Wiley-VCH Verlag GmbH & Co. KGaA, Weinheim 

Recently, we attempted to synthesize and characterize the Rh($\eta^4$-cod/diphos/triphos) complexes containing chiral amino acids and amino alcohols as coligands[11] and to study their catalytic behaviors in an asymmetric hydrogenation reaction. Here, we report the syntheses and spectroscopic studies of the complexes [Rh(AA)($\eta^4$-cod)] {AA = L-alaninato (**I**), (*S*)-2-amino-2-phenylacetato (**II**), *N*-methylglycinato (**III**), *N*-phenylglycinato (**IV**)} and [Rh{(*S*)-$HOCH_2$–CH(Ph)-$NH_2$}($\eta^4$-cod)]($O_2CMe$) (**V**) as well as the crystal structures of **IV** and **V**.

## Results and Discussion

Reaction of dimeric [Rh($O_2CMe$)($\eta^4$-cod)]$_2$ (cod = 1,5-cyclooctadiene) with amino acids in toluene/MeOH yields the monomeric complexes [Rh(AA)($\eta^4$-cod)] (AA = deprotonated amino acid = aminocarboxylato) (**I**–**IV** in Scheme 1). Reaction of [Rh($O_2CMe$)($\eta^4$-cod)]$_2$ with the amino alcohol (*S*)-2-amino-2-phenylethanol gives the complex [Rh{(*S*)-$HOCH_2$–CH(Ph)-$NH_2$}($\eta^4$-cod)]($O_2CMe$) (**V** in Scheme 1).

UV/Vis absorption spectra of complexes **I**–**IV**, measured in toluene at 25 °C, are identical with each other and different from those of the dimeric [Rh($O_2CMe$)($\eta^4$-cod)]$_2$ and [RhCl($\eta^4$-cod)]$_2$ complexes and different from those of the amino alcohol compound **V** (see Figure S1, Table S1 in the Supporting Information).[12]

In the infrared spectrum the aminocarboxylato complexes **I**–**IV** show a strong carbonyl band ($\nu CO_2$, asymmetric) around 1620 cm$^{-1}$, which is typical for the *N*,*O*-coordination of the aminocarboxylato ligand to $Rh^I$, as is the shifting and splitting of the $\nu NH_{asy}/\nu NH_{sy}$ stretching vibrations.[2–4,11] Absence of the νO–H stretching band (which is usually observed as a strong broad band at about 3450 cm$^{-1}$ for the free carboxylic group of the amino acid) in **I**–**IV** indicates acid deprotonation and bond formation between $Rh^I$ and $^-$O–C(O). The vibrational results strongly suggest that the amino acidato ligand is bound to Rh by its nitrogen and oxygen atoms as a *N*,*O*-chelate, as depicted in Scheme 1.[2–4,11] In contrast to these findings, van Koten synthesized the [Rh(L-alaninato)($\eta^4$-cod)]$_2$ complex starting from [Rh{$C_6H_3(CH_2NMe_2)_2$-*o*,*o*′-C,N}($\eta^4$-cod)] and described it as an *O*,*O*-coordinated carboxylato-bridged dimer.[14]

FAB-MS spectra are dominated by ions containing the species $M_2$, $M_2$ – AA = M + Rh(cod), M + $AAH_2$, M + H, M – $CO_2$, and Rh(cod) (M = molecule, AA = aminocarboxylato) for the aminocarboxylato complexes [Rh(AA)($\eta^4$-cod)] (**I**–**IV**). The appearance of dinuclear species may be due to intermolecular hydrogen bonding as evidenced by the crystal structure of **IV** (see below).

The rhodium-coordinated 1,5-cyclooctadiene ligand shows three proton NMR signals corresponding to the *exo*- and *endo*-methylene proton and to the methine proton.[11,15,16] The $CH_2cod_{exo}$ signal appears as doublet–doublet, while $CH_2cod_{endo}$ and CHcod exhibit a multiplet. In **V** the methylene protons of the chiral amino alcohol ligand are diastereotopic and couple differently to the vicinal

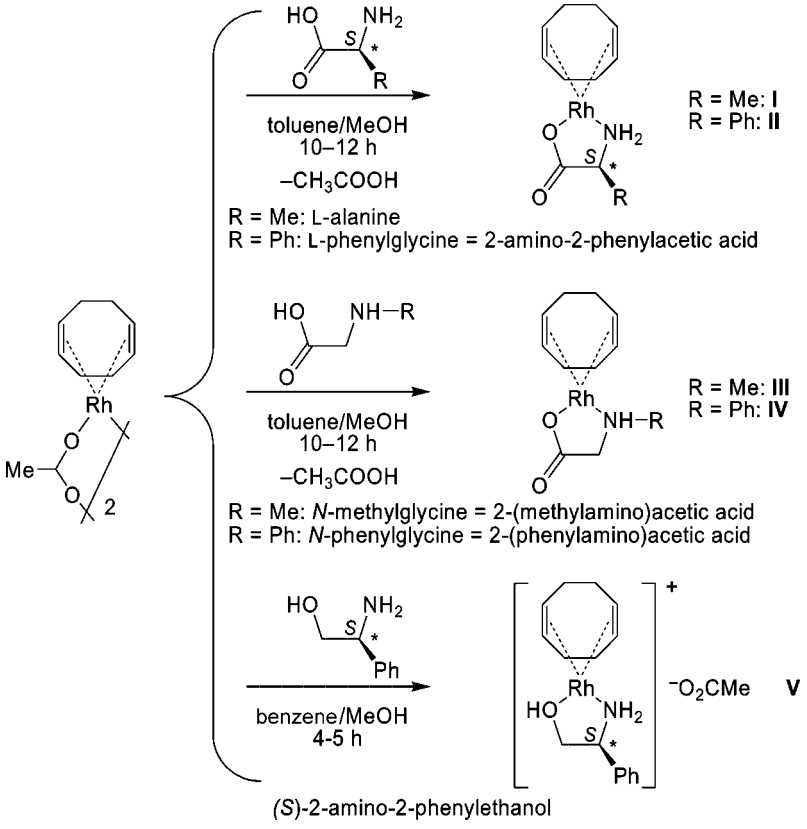


Scheme 1. Synthetic route to and formula of the complexes **I**–**V**.

 © 2006 Wiley-VCH Verlag GmbH & Co. KGaA, Weinheim 

$$[Rh(AA)(\eta^4\text{-cod})] + DCl \xrightarrow{D_2O/CD_3CN} 1/2\,[RhCl(\eta^4\text{-cod})]_2 + DAA$$

**I–IV** AA = deprotonated amino acid = aminocarboxylate

$$[Rh(S\text{-}HOCH_2\text{-}CHPh\text{-}NH_2)(\eta^4\text{-cod})](O_2CMe) + DCl \xrightarrow{D_2O/CD_3CN}$$

**V**

$$1/2\,[RhCl(\eta^4\text{-cod})]_2 + S\text{-}HOCH_2\text{-}CHPh\text{-}NH_2D^+ + {}^-O_2CMe$$

Scheme 2. Hydrolysis of complexes **I**–**V** from NMR studies.

methine proton, thereby showing two sets of doublet of doublets at 3.63 ppm and 3.71 ppm.[13] Similarly in **I** and **II** the amino protons of the chiral amino carboxylate ligands are diastereotopic and appear as two multiplets that are more than 0.7 ppm apart. $^{13}C$ NMR spectra of complexes **I**–**IV** show a singlet at about 30 ppm for *C*$H_2$cod and broad peaks at 72–80 ppm for *C*Hcod in [$D_6$]DMSO.[11,15,16] Complex **V** *shows two peaks* of equal intensity around 30 ppm for *C*$H_2$cod, indicating the nonequivalency of the carbon atoms at either side of the chiral amino alcohol ligand. In contrast to the related chiral complexes **I** and **II**, the nonequivalency of the *C*$H_2$cod carbon atoms may be enhanced in **V** by the acetate anion coordination through N–H···O hydrogen bonding (see structural analysis below).

Upon addition of acid (as 5% DCl/$D_2O$ in $CD_3CN$) the $^1H$ and $^{13}C$ NMR spectra indicate that complexes **I**–**V** are readily hydrolyzed with dissociation of the amino carboxylate or amino alcohol ligand to form the dimeric chloro complex [RhCl($\eta^4$-cod)]$_2$ and the free amino acid or amino alcohol (Scheme 2).[11]

Complexes **IV** and **V** could be crystallized and subjected to single-crystal X-ray diffraction studies. The single-crystal X-ray analysis proved the suggested *N*,*O*-chelate formation of the aminocarboxylato or amino alcohol ligand to the rhodium atom of the Rh($\eta^4$-cod) fragment (Figure 1 and Figure 2). Related Rh($\eta^4$-cod) complexes with a five-membered Rh-*N*,*O*-chelate ligand are structurally elucidated with 8-hydroxyquinolinato,[17] tryptophan benzyl ester,[18] 4-methylpyridinium 2-pyridylcarbonylmethylide,[19] 1-(2′-pyridyl)-3-(dimethylamino)-2-propenone,[20] imidazole-4,5-carboxylato,[21] orotato,[22] and 3-oxo-1-(pyridin-2-yl)-prop-1-en-1-olato.[16a] The five-membered *N*,*O*-chelate ring with rhodium is planar within (largest deviation) ±0.16 Å in **IV** and ±0.28 Å in **V**. Selected distances and angles are compared in Table 1. Both complexes are highly similar in their relevant bonding parameters. The Rh–O distance to the carboxylate oxygen in **IV** and to the alcohol oxygen in **V** is identical.

The achiral (prochiral) *N*-phenylglycine ligand acquires a stereogenic center at the nitrogen atom upon metal coordination. Initially this metal–ligand coordination will give a racemic mixture of (*R*)- and (*S*)-configured complexes. The chiral *N*-phenylglycinato complex [Rh($O_2C$–$CH_2$–NHPh)($\eta^4$-cod)] (**IV**) crystallizes in the tetragonal, chiral space group $P4_3$[23,24] with spontaneous resolution within the single crystal. The homochirality results from the solid-state packing in that N–H···O hydrogen bonding from the stereogenic amino group to a neighboring unligated car-

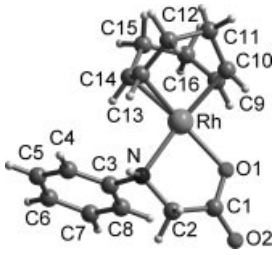


Figure 1. Molecular structure of **IV**.

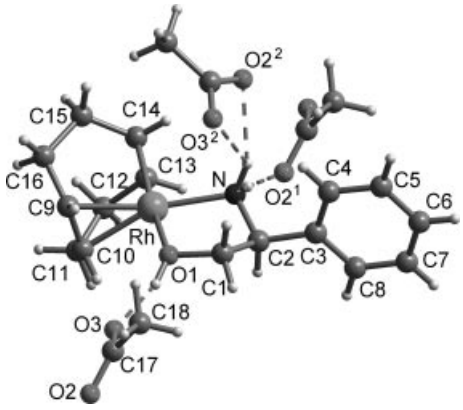


Figure 2. Molecular structure of **V** showing the hydrogen bonding to the surrounding symmetry-related acetate anions. Hydrogen-bonding interactions (dashed lines) as D–H, H···A, D···A, D–H···A [Å (°)]: O1–H1···O3 0.89(5), 1.58(4), 2.429(4), 159(4); N–H2···O2$^2$ 0.99(5), 2.14(5), 3.001(7), 145(4); N–H2···O3$^2$ 0.99(5), 2.51(5), 3.278(7), 134(4); N–H3···O2$^1$ 0.89(4), 2.00(4), 2.885(5), 173(3); symmetry transformations 1 = 1 + *x*, *y*, *z*; 2 = 1 – *x*, *y* + 1/2, 2 – *z*.

Table 1. Selected bond lengths [Å] and angles [°] in **IV** and **V**.

| | **IV** | **V** |
|---|---|---|
| Rh–O1 | 2.059(3) | 2.058(2) |
| Rh–N | 2.145(3) | 2.110(2) |
| Rh–C9 | 2.112(5) | 2.144(6) |
| Rh–C10 | 2.131(4) | 2.113(6) |
| Rh–C13 | 2.108(4) | 2.093(6) |
| Rh–C14 | 2.125(4) | 2.105(6) |
| O1–Rh–N | 80.82(12) | 79.94(8) |
| O1–Rh–C9 | 90.82(16) | 95.8(2) |
| O1–Rh–C10 | 95.39(16) | 93.9(2) |
| O1–Rh–C13 | 160.63(15) | 162.5(2) |
| O1–Rh–C14 | 161.03(17) | 159.0(2) |
| N–Rh–C9 | 158.73(18) | 164.3(2) |
| N–Rh–C10 | 161.51(17) | 156.7(2) |
| N–Rh–C13 | 95.59(16) | 95.97(18) |
| N–Rh–C14 | 99.11(18) | 96.32(17) |

 © 2006 Wiley-VCH Verlag GmbH & Co. KGaA, Weinheim 

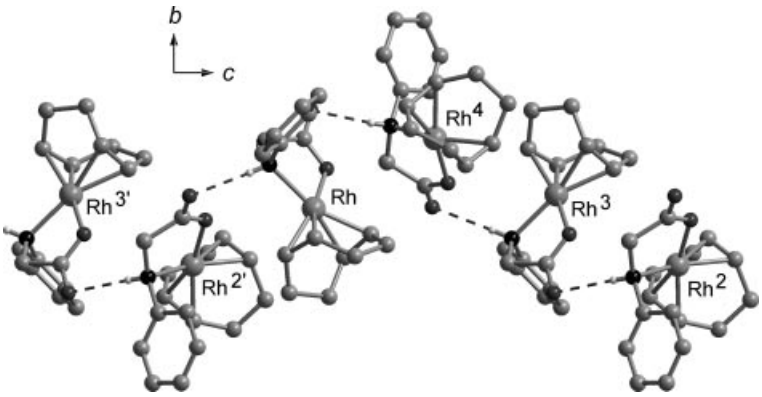


Figure 3. $4_3$-Helical chain in **IV** along *c*. Hydrogen-bonding interaction (dashed line) as D–H, H···A, D···A, D–H···A [Å (°)]: N–H···O2$^{2'}$ 0.73(4), 2.19(4), 2.925(5), 176(5); symmetry transformations: 2 = 2 – *y*, *x*, 0.75 + *z*; 2′ = 2 – *y*, *x*, –0.25 + *z*; 3 = 2 – *x*, 2 – *y*, 0.5 + *z*; 3′ = 2 – *x*, 2 – *y*, –0.5 + *z*; 4 = *y*, 2 – *x*, 0.25 + *z*.

boxyl oxygen atom (Figure 3 and Figure 4) connects and assembles only molecules of the same configuration [here (*R*), see Figure 1 and Figure 3] into a (left-handed or *M*-) $4_3$-helical chain (in the crystal investigated) along *c* (Figure 3 and Figure 4).

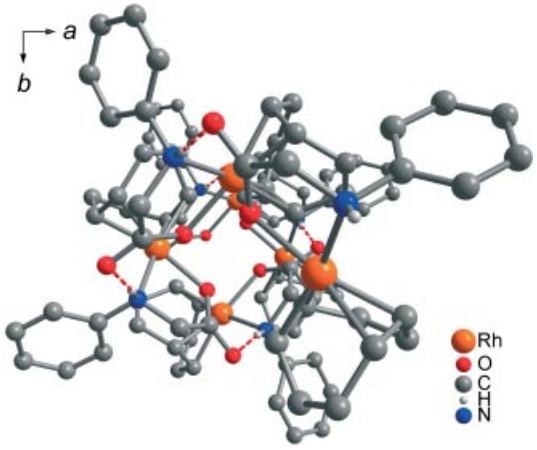


Figure 4. Left-handed $4_3$-helical chain in **IV** viewed along the chain direction.

Yet, most homochiral helices that are formed from achiral ligands and even from racemic mixtures of chiral building blocks almost always lead to racemic mixtures of *P*- and *M*- (right- and left-handed) helices.[25–30] Of interest are structures that spontaneously resolve to contain only one type of helix (within a crystal), that is a single, homochiral helix-enantiomer that requires a sufficient homochiral helicating element in the molecular building block, for example, the ligand. This is typically a stereogenic center of an enantiomerically pure ligand in combination with strong interhelix supramolecular interactions. However, in the structure of **IV** there are no classical hydrogen-bonding interactions between neighboring chains. The exterior of the chains is covered by CH bonds (Figure 4). Also, there are no noteworthy reasonable π–π stacking or C–H···π interactions seen in **IV** (or **V**) [that is, for π–π with centroid–centroid distances <6.0 Å, a dihedral angle between the ring planes <10° and an angle between the centroid vector Cg(I)···Cg(J) and the normal to the plane *I* <60°; for C–H···π, H···Cg < 3.0 Å and an angle between the vector H···Cg(J) and the normal to the plane *J* <30°].[31,32] In **IV** the shortest perpendicular distance of H on a phenyl ring plane is 3.3 Å, about 0.4–0.5 Å longer than seen in typical C–H···π interactions.[33]

The investigated crystal of **IV** contained only one type of helix, namely (left-handed or *M*-) $4_3$-helical chains, thereby representing a case of spontaneous resolution of a racemic mixture into homochiral helix-enantiomers. To account for this fact we invoke an interlocking of adjacent chains with their corrugated van der Waals surface in order to transmit the sense of helicity upon crystallization (Figure 5). The overall ensemble of the crystals in a batch of **IV** can be expected to be racemic, that is, to contain crystals of space groups $P4_3$ and $P4_1$ with left- and right-handed helices based on (*R*)- and (*S*)-configured metal–ligand complexes, respectively, in equal amounts.

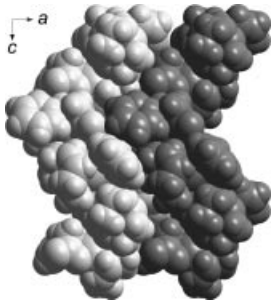


Figure 5. The interlocking of two neighboring left-handed (*M*-) $4_3$-helical chains in **IV** based on the corrugated van der Waals surface without any strong supramolecular interactions; space-filling representation of the chains, which are differentiated by light and dark gray shading.

Spontaneous resolution of achiral or of racemic chiral molecular materials within the single crystal, that is, crystallization in noncentrosymmetric (polar) space groups, can be dictated by supramolecular solid-state packing interactions. This phenomenon has been observed by us in the crystallization of *achiral* hydrotris(pyrazolyl)boratothallium(I) (in $P2_1$),[34,35] dihydrobis(1,2,4-triazolyl)boratothalli-

 © 2006 Wiley-VCH Verlag GmbH & Co. KGaA, Weinheim 

um(I)[35] and -potassium (in $P2_12_12_1$),[36] hydrotris(indazolyl)boratothallium(I) (in $C2$),[35,37] and hydrotris(1,2,4-triazolyl)boratosilver(I) (in polar $Pna2_1$).[38] The spontaneous resolution of a *racemic chiral* material within a noncentrosymmetric space group was seen in the crystallization of $[Ag^+(NH_3)_2](BINOLAT^-)(BINOL)(EtOH)$ (in $P1$).[39] The crystallization of a racemic chiral material within a noncentrosymmetric polar space group was encountered in the crystallization of $[\Lambda/\Delta\text{-}Fe^3(DABP)_3]^{2+}[\Delta/\Lambda\text{-}Fe^2(DABP)_3\subset \Lambda/\Delta\text{-}Fe^1(DABP)_3(nitrophenolate)_6]^{2-}$ (in $P3_1c$).[40] The spontaneous resolution of *rac*-2,3-dihydro-2,3-dipyridylbenzo[*e*]indole with $Cd(ClO_4)_2\cdot 6H_2O$ is a recent example of symmetry breaking through supramolecular interactions and solvent, where in the presence of either 2-butanol or ethanol crystals of the opposite enantiomers were favored (crystallizing in the enantiomorphous space groups $P6_122$ and $P6_522$).[41] Particularly intriguing is the formation of a homochiral (helical) polymer from achiral components through spontaneous enantiomer resolution. A homochiral helix winding together with homochiral crystallization was reported for the adduct of 5-(9-anthracenyl)pyrimidine with $Cd(NO_3)_2\cdot H_2O\cdot EtOH$. The chirality arises from a pyrimidine-$Cd^{2+}$ helical array and is preserved in each crystal by homochiral interstrand water–nitrate hydrogen bonding. All the crystals are of the same chirality as a result of single-colony homochiral crystal growth (homochiral crystallization).[42] The achiral building blocks in $^{\infty}_1\{[Ni(PhCOO)_2(4,4'\text{-bipy})]\cdot 2MeOH\}$ gave rise to a $4_1$- or $4_3$-helical polymer with homochirality in the crystal. Different crystals contain statistically either *P*- or *M*-helices.[43] Homochiral right-handed (*P*-) $6_1$ helices of $Cd\{B(OMe)_4\}$ are found in $^{\infty}_3\{[Cd(tcm)\{B(OMe)_4\}]\cdot x MeOH\}$ with neighboring helices connected by the tricyanomethanide (tcm) ion.[44] Compound $^{\infty}_1\{[Mn(hfac)_2\{ferrocenyl\ bis(nitronyl\ nitroxide)\}]\cdot CH_2Cl_2\}$ spontaneously resolves in enantiomorphous crystals with either Λ- or Δ-configuration at Mn and an additional six sources of chirality within the *P*- or *M*-helices, respectively (hfac = hexafluoroacetylacetonate).[45] Variation of the proton content with $KOH/HCl_{aq}$ allows for a reversible interconversion between the achiral molecular square of $[Cu(HL)(H_2O)_{0.5}]_4(ClO_4)_4$ (high pH) and a spontaneously resolved homochiral double-chain motif of $^{\infty}_1\{[H_3O]_2[Cu_3(L)_2Cl](ClO_4)_2(Cl)\}$ (low pH) {$H_2L$ = 1,5-diazacyclooctane-1,5-bis(3-propionic acid)}.[46]

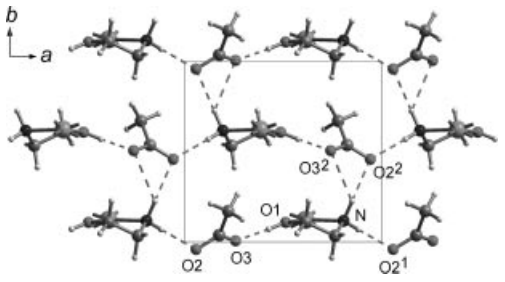


Figure 6. Two-dimensional hydrogen-bonded network in **V**. Phenyl groups and cod ligands are not shown for clarity but only indicated as broken-off bonds. For details of the hydrogen bonds see caption to Figure 2.

The enantiomeric amino alcohol complex **V** crystallizes in the monoclinic, noncentrosymmetric (Sohncke) space group $P2_1$.[23,24] Hydrogen-bonding interactions between the amino and hydroxy donor groups in the metal complex to the acetate anion acceptors link the building blocks into supramolecular two-dimensional nets co-planar to the *ab* plane (Figure 6). Along *c* the nets are separated by the phenyl groups and cod ligands without meaningful π–π-stacking or C–H···π interactions (see above).

## Conclusions

Aminocarboxylato($\eta^4$-cycloocta-1,5-diene)rhodium(I) complexes [Rh(AA)($\eta^4$-cod)] could be easily prepared from dimeric $[Rh(O_2CMe)(\eta^4\text{-cod})]_2$ with amino acids in toluene/MeOH. The compounds [Rh(AA)($\eta^4$-cod)] (AA = deprotonated amino acid = aminocarboxylato) were found to be monomeric. Solid-state structures of $[Rh(O_2C\text{–}CH_2\text{–}NHPh)(\eta^4\text{-cod})]$ (**IV**) and $[Rh\{(S)\text{-}HOCH_2\text{–}CH(Ph)\text{–}NH_2\}(\eta^4\text{-cod})](O_2CMe)$ (**V**) reveal strong intermolecular N–H···O hydrogen-bonding interactions to assemble the molecular units into 1D chains (**IV**) or 2D nets (**V**). In **IV** the achiral (prochiral) *N*-phenylglycine ligand acquires a stereogenic center at nitrogen upon complexation and the racemic compound undergoes spontaneous resolution upon crystallization. Supramolecular N–H···O and van der Waals interactions are responsible for collecting only one enantiomer along fourfold screw axes of the same handedness within a single crystal. This could be called a twofold spontaneous resolution in two homochiral building units, namely the molecular complex and the fourfold helix.

## Experimental Section

All reactions were carried out under dry nitrogen using Schlenk techniques. Solvents used were highly purified and distilled: toluene and benzene over Na metal; petroleum ether (PE) (boiling range 40–60 °C) over $CaH_2$; methanol and ethanol over CaO under nitrogen. The starting complex $[Rh(O_2CMe)(\eta^4\text{-cod})]_2$ was synthesized from $[RhCl(\eta^4\text{-cod})]_2$[47] according to the literature.[3a] UV/Vis spectra were obtained with a Shimadzu UV 3150 spectrophotometer in toluene at 25 °C. IR spectra were recorded as KBr disks with a Bruker IFS 66 FTIR Spectrometer at ambient temperature. NMR spectra were run on a Bruker AC DPX 200 spectrometer operating at 200 MHz ($^1$H) and a JEOL AC 500 at 500 MHz ($^1$H), 125 MHz ($^{13}$C) at 25 °C. NMR grade solvents [$D_6$]DMSO, $CD_3OD$, $CD_3CN$, and $DCl/D_2O$ solution (20% v/v) were used as internal standard and deoxygenated prior to use. $^1$H and $^{13}$C NMR chemical shifts are expressed in ppm relative to $SiMe_4$ ($\delta$ = 0 ppm). FAB-MS (positive mode): Finnigan MAT 8230 with data system SS 300, matrix: *m*-nitrobenzyl alcohol (NBA). EI- and CI-MS: Thermo-Finnigan TSQ 700, with $NH_3$ as ionization gas for CI.

**(L-Alaninato)($\eta^4$-cycloocta-1,5-diene)rhodium(I), {Rh[(*S*)-$O_2C$–CHMe–$NH_2$]($\eta^4$-cod)} (I):** L-Alanine (166 mg, 1.86 mmol) was dissolved in methanol (5 mL) and this solution was poured into a solution of $[Rh(O_2CMe)(\eta^4\text{-cod})]_2$ (503 mg, 0.93 mmol) in toluene (20 mL). Stirring the solution for 10–12 h at room temperature led to the formation of a yellow precipitate. After the solvent was evap-

 © 2006 Wiley-VCH Verlag GmbH & Co. KGaA, Weinheim 

orated in vacuo, toluene/MeOH (4:1, v/v) (10 mL) was added to the dried precipitate and evaporated again. This procedure was repeated three times. Finally, the precipitate was dried in vacuo (0.1–0.2 mbar) at 40 °C to give a yellow powder (yield 417 mg, 75%). $^1$H NMR (200 MHz, $CD_3OD$): $\delta$ = 1.45 (d, $J$ = 7.0 Hz, 3 H, C$H_3$), 1.88 (dd, $J$ = 8.2 Hz, 4 H, C$H_2$cod$_{exo}$), 2.46 (m, 4 H, C$H_2$cod$_{endo}$), 3.43 (q, $J$ = 7.0 Hz, 1 H, C$H$), 4.13 (m, 4 H, C$H$cod) ppm. $^1$H NMR (500 MHz, [D$_6$]DMSO): $\delta$ = 1.20 (d, $J$ = 7.0 Hz, 3 H, C$H_3$), 1.72 (dd, $J$ = 8.0 Hz, 4 H, C$H_2$cod$_{exo}$), 2.32 (m, 4 H, C$H_2$cod$_{endo}$), 3.09 (q, $J$ = 7.0 Hz, H, C$H$), 3.68 (m, 1 H, N$H$), 3.92 (m, 4 H, C$H$cod), 4.31 (m, 1 H, N$H$) ppm. $^1$H NMR (500 MHz, $CD_3CN$ + 5% DCl/$D_2O$): $\delta$ = 1.50 (d, $J$ = 8 Hz, 3 H, C$H_3$), 1.77 (dd, $J$ = 8.5 Hz, 4 H, C$H_2$cod$_{exo}$), 2.36 (m, 4 H, C$H_2$cod$_{endo}$), 4.02 (q, $J$ = 8.5 Hz, 1 H, C$H$), 4.22 (m, 4 H, C$H$cod) ppm. $^{13}$C NMR (125 MHz, [D$_6$]DMSO): $\delta$ = 20.4 (s, $C$H$_3$), 30.1 (s, $C$H$_2$cod), 52.5 (s, $C$H), 72.1, 79.6 (br., $C$Hcod), 183.2 (s, $CO_2$) ppm. $^{13}$C NMR (125 MHz, $CD_3CN$ + 5% DCl/$D_2O$): $\delta$ = 15.1 (s, $C$H$_3$), 30.2 (s, $C$H$_2$cod), 48.5 (s, $C$H), 80.3 (d, $J_{C,Rh}$ = 13 Hz, $C$Hcod), 171.1 (s, $CO_2$) ppm. IR (KBr): $\tilde{\nu}$ = 3258 s, 3190 sh ($\nu$NH$_{asy}$), 3134 s, 3109 s ($\nu$NH$_{sy}$), 2940 s ($\nu$CH), 1620 vs ($\nu$CO$_{2\ asy}$), 1585 sh ($\delta$NH), 1383 s ($\delta$CH$_3$), 1363 s ($\nu$CO$_{2\ sy}$) cm$^{-1}$. MS (FAB): $m/z$ (%) = 601 (20) [M$_2$ + H$^+$ + 2H]$^+$, 510 (58) [M$_2$ – AA$^-$ = M + Rh(cod)$^+$]$^+$, 392 (40) [M + AAH$_2^+$ + 2H]$^+$, 300 (100) [M + H]$^+$, 255 (25) [M$^{+\cdot}$ – CO$_2$]$^+$, 211 (68) [Rh(cod)]$^+$ (AA = aminocarboxylato). MS (EI = 70 eV): 299 (7) [M]$^+$, 297 (13) [M – 2H]$^+$, 255 (40) [M – CO$_2$]$^+$, 210 (50) [Rh(cod) – H]$^+$, 208 (55) [Rh(cod) – 3H]$^+$, 44 (100) [CO$_2$]$^+$. $C_{11}H_{18}NO_2Rh$ (299.18): calcd. C 44.16, H 6.06, N 4.68; found C 44.26, H 6.38, N 4.69.

**[(*S*)-2-Amino-2-phenylacetato](η$^4$-cycloocta-1,5-diene)rhodium(I), (η$^4$-Cycloocta-1,5-diene)(L-phenylglycinato)rhodium(I), {Rh[(*S*)-O$_2$C–CHPh–NH$_2$](η$^4$-cod)} (II):** The compound was prepared following the same procedure as for **I**, using (*S*)-2-amino-2-phenylacetic acid (L-phenylglycine). The complex was obtained as a yellow powder (yield 470 mg, 70%). $^1$H NMR (200 MHz, $CD_3CN$): $\delta$ = 1.84 (dd, $J$ = 8.0 Hz, 4 H, C$H_2$cod$_{exo}$), 2.44 (m, 4 H, C$H_2$cod$_{endo}$), 2.81 (m, 1 H, N$H$), 3.57 (m, 1 H, N$H$), 4.05 (m, 4 H, C$H$cod), 4.36 (m, 1 H, C$H$), 7.42 (m, 3 H, $H_{p/m}$-Ar), 7.76 (d, $J$ = 6.6, 2 H, $H_o$-Ar) ppm. $^1$H NMR (200 MHz, $CD_3OD$): $\delta$ = 1.92 (dd, $J$ = 8.0 Hz, 4 H, C$H_2$cod$_{exo}$), 2.48 (m, 4 H, C$H_2$cod$_{endo}$), 4.16 (m, 4 H, C$H$cod), 4.49 (m, 1 H, C$H$), 7.47 (m, 3 H, $H_{p/m}$-Ar), 7.76 (m, 2 H, $H_o$-Ar) ppm. $^1$H NMR (500 MHz, $CD_3CN$ + 5% DCl/$D_2O$): $\delta$ = 1.76 (dd, $J$ = 8.5 Hz, 4 H, C$H_2$cod$_{exo}$), 2.36 (m, 4 H, C$H_2$cod$_{endo}$), 4.13 (m, 1 H, N$H$), 4.21 (m, 4 H, C$H$cod), 5.07 (m, 1 H, C$H$), 7.46–7.75 (m, 5 H, $H$-Ar) ppm. $^{13}$C NMR (125 MHz, $CD_3CN$ + 5% DCl/$D_2O$): $\delta$ = 30.4 (s, $C$H$_2$cod), 56.1 (s, $C$H), 80.5 (d, $J_{C,Rh}$ = 13 Hz, $C$Hcod), 128.2 (s, $C_m$-Ar), 128.7 (s, $C_p$-Ar), 129.3 (s, $C_o$-Ar), 130.0 (s, $C$-Ar), 170.0 (s, $CO_2$) ppm. IR (KBr): $\tilde{\nu}$ = 3259 m, 3213 m ($\nu$NH$_{asy}$), 3136 sh, 3102 m ($\nu$NH$_{sy}$), 3056 s ($\nu$H-Ar), 2935 s ($\nu$CH), 1621 vs ($\nu$CO$_{2\ asy}$), 1591 s ($\delta$NH), 1363 s ($\nu$CO$_{2\ sy}$) cm$^{-1}$. MS (FAB): $m/z$ (%) = 1017 (20) [(RhAA)$_4$ + 4H + H$^+$]$^+$, 722 (8) [M$_2$]$^+$, 572 (30) [M$_2$ – AA$^-$ = M + Rh(cod)$^+$]$^+$, 362 (100) [M + H]$^+$, 317 (45) [M$^{+\cdot}$ – CO$_2$]$^+$, 211 (60) [Rh(cod)]$^+$ (AA = aminocarboxylato). $C_{16}H_{20}NO_2Rh$ (361.25): calcd. C 53.20, H 5.58, N 3.88; found C 54.04, H 6.57, N 3.98.

**(η$^4$-Cycloocta-1,5-diene)(*N*-methylglycinato)rhodium(I), [Rh(O$_2$C–CH$_2$–NHMe)(η$^4$-cod)] (III):** Two equiv. of *N*-methylglycine [2-(methylamino)acetic acid] (50 mg, 0.56 mmol) were dissolved in MeOH (5 mL) and this solution was poured into a solution of [Rh(O$_2$CMe)(η$^4$-cod)]$_2$ (150.4 mg, 0.28 mmol) in toluene (20 mL). A yellow precipitate was formed after stirring the solution for 10–12 h at room temperature. After the solvent was evaporated in vacuo at 40 °C, the dried precipitate was dissolved in toluene/MeOH (4:1, v/v) (10 mL) and evaporated again. This procedure was repeated three times. Then the dried precipitate was again dissolved in toluene/MeOH (4:1) (10 mL) and the volume reduced to 50% in vacuo at 40 °C. PE (40/60) (10 mL) was added very slowly to this hot solution. The precipitate formed was filtered off, washed with PE (40/60) and dried in vacuo (0.1–0.2 mbar) at 40 °C to give a yellow powder (yield 125 mg, 75%). $^1$H NMR (200 MHz, [D$_6$]-DMSO): $\delta$ = 1.71 (dd, $J$ = 8.0 Hz, 4 H, C$H_2$cod$_{exo}$), 2.14 (s, 2 H, C$H_2$), 2.30 (m, 4 H, C$H_2$cod$_{endo}$), 2.74 (s, 3 H, C$H_3$), 3.51 (m, 4 H, C$H$cod), 3.64 (m, 1 H, N$H$) ppm. $^1$H NMR (500 MHz, $CD_3CN$ + 5% DCl/$D_2O$): $\delta$ = 1.75 (dd, $J$ = 8.0 Hz, 4 H, C$H_2$cod$_{exo}$), 2.35 (m, 4 H, C$H_2$cod$_{endo}$), 2.70 (s, 3 H, C$H_3$), 3.86 (s, 2 H, C$H_2$), 4.19 (m, 4 H, C$H$cod) ppm. $^{13}$C NMR (125 MHz, $CD_3CN$ + 5% DCl/$D_2O$): $\delta$ = 30.6 (s, $C$H$_2$cod), 33.0 (s, $C$H$_3$), 48.7 (s, $C$H$_2$), 80.3 (d, $J_{C,Rh}$ = 13 Hz, $C$Hcod), 167.5 (s, $CO_2$) ppm. IR (KBr): $\tilde{\nu}$ = 3197 m ($\nu$NH$_{asy}$), 3100 sh ($\nu$NH$_{sy}$), 2931 s ($\nu$CH), 1623 vs ($\nu$CO$_{2\ asy}$), 1590 sh ($\delta$NH), 1484 s ($\delta$CH$_2$), 1381 s ($\delta$CH$_3$), 1365 s ($\nu$CO$_{2\ sy}$) cm$^{-1}$. MS (FAB) $m/z$ (%) = 600 (30) [M$_2$ + H$^+$ + H]$^+$, 510 (50) [M$_2$ – AA$^-$ = M + Rh(cod)$^+$]$^+$, 391 (35) [M + AAH$_2^+$ + H]$^+$, 300 (100) [M + H]$^+$, 255 (35) [M – CO$_2$]$^+$, 211 (55) [Rh(cod)]$^+$ (AA = aminocarboxylato). $C_{11}H_{18}NO_2Rh$ (299.18): calcd. C 44.16, H 6.06, N 4.68; found C 43.85, H 5.89, N 4.53.

**(η$^4$-Cycloocta-1,5-diene)(*N*-phenylglycinato)rhodium(I), [Rh(O$_2$C–CH$_2$–NHPh)(η$^4$-cod)] (IV):** Two equiv. of *N*-phenylglycine [2-(phenylamino)acetic acid] (85.9 mg, 0.57 mmol) were dissolved in MeOH (5 mL). This solution was poured into a solution of [Rh(O$_2$CMe)(η$^4$-cod)]$_2$ (150.4 mg, 0.28 mmol) in toluene (20 mL) and stirred for 10–12 h at room temperature. The volume was reduced to 60% in vacuo at 40 °C, PE (40/60) (10 mL) was very slowly added to the hot solution, and the combined solution was left for crystallization. Red-orange needle crystals, suitable for X-ray measurement, were obtained after 3 days. The crystals were filtered off and washed three times with PE (5 mL each). Finally, the red-orange crystals were dried in vacuo (0.1–0.2 mbar) at 40 °C (yield 150 mg, 75%). $^1$H NMR (500 MHz, [D$_6$]DMSO): $\delta$ = 1.64 (dd, $J$ = 8.0 Hz, 4 H, C$H_2$cod$_{exo}$), 2.09 (s, 2 H, C$H_2$), 2.25 (m, 4 H, C$H_2$cod$_{endo}$), 3.60 (m, 4 H, C$H$cod), 3.67 (m, 1 H, N$H$), 7.01 (t, $J$ = 7.0 Hz, 2 H, $H_o$-Ar), 7.27 (t, $J$ = 6.5 Hz, 1 H, $H_p$-Ar), 7.33 (t, $J$ = 7.5 Hz, 2 H, $H_m$-Ar) ppm. $^{13}$C NMR (125 MHz, [D$_6$]DMSO): $\delta$ = 29.7 (s, $C$H$_2$cod), 55.9 (s, $C$H$_2$), 77.9 (br., $C$Hcod), 119.5 (s, $C_o$-Ar), 124.3 (s, $C_p$-Ar), 129.2 (s, $C_m$-Ar), 146.1 (s, N$C$-Ar), 179.2 (s, $CO_2$) ppm. $^1$H NMR (500 MHz, $CD_3CN$ + 5% DCl/$D_2O$): $\delta$ = 1.76 (dd, $J$ = 8.0 Hz, 4 H, C$H_2$cod$_{exo}$), 2.33 (m, 4 H, C$H_2$cod$_{endo}$), 4.19 (m, 3 H, C$H_2$ + N$H$), 4.22 (m, 4 H, C$H$cod), 7.45–7.52 (m, 5 H, $H$-Ar) ppm. $^{13}$C NMR (125 MHz, $CD_3CN$ + 5% DCl/$D_2O$): $\delta$ = 29.9 (s, $C$H$_2$cod), 50.7 (s, $C$H$_2$), 80.5 (d, $J_{CRh}$ = 13 Hz, $C$Hcod), 122.5 (s, $C_o$-Ar), 129.6 (s, $C_p$-Ar), 130.0 (s, $C_m$-Ar), 134.4 (s, N$C$-Ar), 167.3 (s, $CO_2$) ppm. IR (KBr): $\tilde{\nu}$ = 3142 m ($\nu$NH$_{asy}$), 3097 m ($\nu$NH$_{sy}$), 3053 s ($\nu$HAr), 2943 s ($\nu$CH), 1616 vs ($\nu$CO$_{2\ asy}$), 1600 s ($\delta$NH), 1491 s ($\delta$CH$_2$), 1366 s ($\nu$CO$_{2\ sy}$) cm$^{-1}$. MS (FAB) $m/z$ (%) = 723 (5) [M$_2$ + H]$^+$, 573 (100) [M$_2$ + H$^+$ – AA = M + H$^+$ + Rh(cod)]$^+$, 363 (100) [M + H$^+$ + H]$^+$, 315 (100) [M$^{+\cdot}$ – H$_2$ – CO$_2$]$^+$, 211 (100) [Rh(cod)]$^+$ (AA = aminocarboxylato). $C_{16}H_{20}NO_2Rh$ (361.25): calcd. C 53.20, H 5.58, N 3.88; found C 52.90, H 5.46, N 4.00.

**[(*S*)-2-Amino-2-phenylethanol](η$^4$-cycloocta-1,5-diene)rhodium(I) Acetate, [Rh{(*S*)-HOCH$_2$–CH(Ph)-NH$_2$}(η$^4$-cod)](O$_2$CMe) (V):** Two equiv. of (*S*)-2-amino-2-phenylethanol (71 mg, 0.52 mmol) were dissolved in MeOH (5 mL). This solution was poured into a solution of [Rh(O$_2$CMe)(η$^4$-cod)]$_2$ (133.4 mg, 0.25 mmol) in benzene (20 mL) and stirred for 4–5 h at room temperature. The volume was reduced to 60% in vacuo at 40 °C, PE (40/60) (10 mL) was very slowly added to the hot solution, and the combined solution was left for crystallization. Bright-yellow crystals, suitable for

 © 2006 Wiley-VCH Verlag GmbH & Co. KGaA, Weinheim 

X-ray measurement, were obtained after 3 days at room temperature. The crystals were filtered off and washed three times with PE (5 mL each). Finally, the bright-yellow crystals were dried in vacuo (0.1–0.2 mbar) at 40 °C (yield 141 mg, 70%). $^1$H NMR (500 MHz, [D$_6$]DMSO): $\delta$ = 1.65 (dd, $J$ = 8.0 Hz, 4 H, C$H_2$cod$_{exo}$), 1.73 (s, 3 H, C$H_3$), 2.25 (m, 4 H, C$H_2$cod$_{endo}$), 3.55 (t, $J$ = 9.0 Hz, 1 H, C$H$), 3.63 (dd, $^3J$ = 10.5 Hz, $^4J$ = 5.5 Hz, 1 H, C$H_2$), 3.71 (dd, $^3J$ = 8.5 Hz, $^4J$ = 5.5 Hz, 1 H, C$H_2$), 3.87 (m, 4 H, C$H$cod), 7.27 (t, $J$ = 7.5 Hz, 1 H, $H_p$-Ar), 7.34 (t, $J$ = 7.5 Hz, 2 H, $H_o$-Ar), 7.45 (d, $J$ = 7.5 Hz, 2 H, $H_m$-Ar) ppm. $^{13}$C NMR (125 MHz, [D$_6$]DMSO): $\delta$ = 23.6 (s, $C$H$_3$), 30.0, 30.1 (d, $C$H$_2$cod), 60.8 (s, $C$H), 69.1 (s, $C$H$_2$), 75.8 (br., $C$Hcod), 127.2 (s, $C_o$-Ar), 127.3 (s, $C_p$-Ar), 128.1 (s, $C_m$-Ar), 140.3 (s, $C$-Ar), 174.6 (s, $C$O$_2$) ppm. $^1$H NMR (500 MHz, CD$_3$CN + 5% DCl/D$_2$O): $\delta$ = 1.77 (dd, $J$ = 8.0 Hz, 4 H, C$H_2$cod$_{exo}$), 1.93 (s, 3 H, C$H_3$), 2.36 (m, 4 H, C$H_2$cod$_{endo}$), 3.87 (dd, $J$ = 7.0 Hz, 2 H, C$H_2$), 4.21 (m, 4 H, C$H$cod), 4.45 (t, $J$ = 6.0 Hz, 1 H, C$H$), 7.27 (m, 3 H, $H_{p/o}$-Ar), 7.48 (d, $J$ = 2.0 Hz, 2 H, $H_m$-Ar) ppm. $^{13}$C NMR (125 MHz, CD$_3$CN + 5% DCl/D$_2$O): $\delta$ = 20.1 (s, $C$H$_3$), 30.6 (s, $C$H$_2$cod), 57.1 (s, $C$H), 62.7 (s, $C$H$_2$), 80.1 (d, $J_{C,Rh}$ = 13.0 Hz, $C$Hcod), 127.7 (s, $C_o$-Ar), 129.0 (s, $C_m$-Ar), 129.2 (s, $C_p$-Ar), 134.1 (s, $C$-Ar), 173.0 (s, $C$O$_2$) ppm. IR (KBr): $\tilde{\nu}$ = 3410 m ($\nu$OH), 3193 m ($\nu$NH$_{asy}$), 3083 s ($\nu$NH$_{sy}$), 3055 s ($\nu$HAr), 2937 s ($\nu$CH), 1575 s ($\delta$NH), 1558 sh ($\nu$CO$_{2\ asy}$), 1486 s ($\delta$CH$_2$), 1442 s ($\nu$CO$_{2\ sy}$), 1385 s ($\delta$CH$_3$) cm$^{-1}$. MS (EI = 70 eV): 210 (2) [Rh(cod) – H]$^+$, 106 (100) [AA – CH$_2$OH = Ph–CH–NH$_2$]$^+$. MS (CI, NH$_3$): 348 (0.4) [M – acetate = Rh(AA)(cod)]$^+$, 228 (1.5) [Rh(NH$_3$)-(cod)]$^+$, 138 (100) [AA + H]$^+$, 106 (45) [AA – CH$_2$OH = Ph–CH–NH$_2$]$^+$ (AA = amino alcohol). C$_{18}$H$_{26}$NO$_3$Rh (407.31): calcd. C 53.08, H 6.43, N 3.44; found C 53.06, H 6.33, N 3.44.

**X-ray Crystallography:** *Data Collection:* Bruker AXS with CCD area-detector, temperature 203(2) K, Mo-$K_\alpha$ radiation ($\lambda$ = 0.71073 Å), graphite monochromator, $\omega$-scans, data collection and cell refinement with SMART,[48] data reduction with SAINT,[48] experimental absorption correction with SADABS.[49] *Structure Analysis and Refinement:* The structure was solved by direct methods (SHELXS-97);[50] refinement was done by full-matrix least-squares on $F^2$ using the SHELXL-97 program suite.[50] For **IV** structure refinement has also been attempted in the enantiomorphic space group $P4_1$ but this gave a Flack parameter of 1 with the message "absolute structure probably wrong – invert and repeat refinement". All non-hydrogen positions were found and refined with anisotropic temperature factors. Hydrogen atoms on oxygen (–OH) and nitrogen (–NH–Ph, –NH$_2$) were found and refined with $U_{eq}$(H) = 1.2$U_{eq}$(N) in **IV** and freely in **V**. Hydrogen atoms on C (phenyl, CH, CH$_2$, and CH$_3$) were calculated with appropriate riding models (AFIX 43, 13, 23, and 33, respectively) and $U_{eq}$(H) = 1.2$U_{eq}$(C) (CH, CH$_2$) or $U_{eq}$(H) = 1.5$U_{eq}$(C) (CH$_3$). Details of the X-ray structure determinations and refinements are provided in Table 2. Graphics were drawn with DIAMOND (Version 3.0e).[51] Computations on the supramolecular interactions were carried out with PLATON for Windows.[52]

CCDC-297844 (for **IV**) and -297845 (for **V**) contain the supplementary crystallographic data for this paper. These data can be obtained free of charge from The Cambridge Crystallographic Data Centre via www.ccdc.cam.ac.uk/data_request/cif.

**Supporting Information** (for details see the footnote on the first page of this article): UV/Vis spectra and data.

Table 2. Crystal data and structure refinement for **IV** and **V**.

| Compound | **IV** | **V** |
|---|---|---|
| Empirical formula | $C_{16}H_{20}NO_2Rh$ | $C_{18}H_{26}NO_3Rh$ |
| $M$ [g mol$^{-1}$] | 361.24 | 407.31 |
| Crystal size [mm] | 0.42 × 0.10 × 0.09 | 0.40 × 0.27 × 0.16 |
| $\theta$ range [°] | 4.26–58.00 | 3.42–57.56 |
| $h$; $k$; $l$ range | –12, 12; –12, 12; –21, 21 | –12, 12; –10, 10; –16, 17 |
| Crystal system | tetragonal | monoclinic |
| Space group | $P4_3$ | $P2_1$ |
| $a$ [Å] | 9.556(3) | 9.5506(15) |
| $b$ [Å] | 9.556(3) | 7.9810(13) |
| $c$ [Å] | 16.281(6) | 12.773(2) |
| $\alpha$ [°] | 90 | 90 |
| $\beta$ [°] | 90 | 111.524(2) |
| $\gamma$ [°] | 90 | 90 |
| $V$ [Å$^3$] | 1486.8(8) | 905.7(2) |
| $Z$ | 4 | 2 |
| $D_{calcd}$ [g cm$^{-3}$] | 1.614 | 1.493 |
| $F$(000) | 736 | 420 |
| $\mu$ [mm$^{-1}$] | 1.149 | 0.956 |
| Max./min. transmission | 0.9076/0.6440 | 0.8620/0.7010 |
| Reflections collected | 13666 | 8286 |
| Independent reflections | 3671 ($R_{int}$ = 0.0719) | 4189 ($R_{int}$ = 0.0187) |
| Observed reflections [$I > 2\sigma(I)$] | 2700 | 3800 |
| Parameters refined | 184 | 200 |
| Max./min. $\Delta\rho$[a] [e Å$^{-3}$] | 0.566/–0.452 | 0.891/–0.502 |
| $R_1/wR_2$ [$I > 2\sigma(I)$][b] | 0.0372/0.0594 | 0.0265/0.0636 |
| $R_1/wR_2$ (all reflect.) [b] | 0.0581/0.0646 | 0.0295/0.0647 |
| Goodness-of-fit on $F^2$ [c] | 0.897 | 0.976 |
| Weight scheme $w$; $a/b$[d] | 0.0217/0.0000 | 0.0370/0.0000 |
| Absolute structure parameter (Flack value[53]) | 0.01(4) | 0.01(3) |

[a] Largest difference peak and hole. [b] $R_1 = [\Sigma(||F_o| - |F_c||)/\Sigma|F_o|]$; $wR_2 = [\Sigma[w(F_o^2 - F_c^2)^2]/\Sigma[w(F_o^2)^2]]^{1/2}$. [c] Goodness-of-fit = $[\Sigma[w(F_o^2 - F_c^2)^2]/(n - p)]^{1/2}$. [d] $w = 1/[\sigma^2(F_o^2) + (aP)^2 + bP]$ where $P = [\max(F_o^2 \text{ or } 0) + 2F_c^2]/3$.

 © 2006 Wiley-VCH Verlag GmbH & Co. KGaA, Weinheim 

## Acknowledgments

We thank the Alexander von Humboldt Foundation (AvH), Bonn, and the Matsumae International Foundation (MIF), Tokyo, for offering a post-doctoral fellowship to M.E. Our sincere thanks go to Dr. Inayoshi for collecting the mass spectra at the Department of Chemistry, College of Science and Engineering, Aoyama Gekuin University, Tokyo. We acknowledge the financial support under the JU projects, Department of Chemistry, Jahangirnagar University, Bangladesh, by the Deutsche Forschungsgemeinschaft through grant JA-466/14-1, and the Fonds der Chemischen Industrie.

[1] a) H. Brunner, B. Reiter, G. Riepl, *Chem. Ber.* **1984**, *117*, 1330–1354; b) L. Marko, Z. Nagy-Magos, P. Kvintovics, *Abstract*, *IX Intl. Conf. Organomet. Chem.*, Dijon, **1979**; c) P. Kvintovics, B. R. James, B. Heil, *J. Chem. Soc., Chem. Commun.* **1986**, 1810–1811; d) K. Severin, K. Sünkel, W. Beck, *Chem. Ber.* **1994**, *127*, 615–620; e) K. Severin, W. Beck, *Z. Naturforsch., B: Chem. Sci.* **1995**, *50*, 275–279; f) J. Cai, X. Hu, X. Feng, W. Shao, L. Ji, I. Bernal, *Eur. J. Inorg. Chem.* **2000**, 2199–2205; g) R. Dreos, G. Nardin, L. Randaccio, P. Siega, G. Tauzher, *Inorg. Chem.* **2004**, *43*, 3433–3440.

[2] a) D. Dowerah, M. M. Singh, *J. Indian Chem. Soc.* **1980**, *LVII*, 368–371; b) D. Dowerah, M. M. Singh, *Transition Met. Chem.* **1976**, *1*, 294–295; c) D. Dowerah, M. M. Singh, *J. Chem. Res., Synop.* **1979**, 38; d) D. Dowerah, M. M. Singh, *J. Chem. Res. (M)* **1979**, 255–263; e) T. Giraldi, G. Zassinovich, G. Mestroni, *Chem. Biol. Interact.* **1974**, *9*, 389–394; f) T. Giraldi, G. Eava, G. Bertoli, G. Mestroni, G. Zassinovich, *Cancer Res.* **1977**, *37*, 2662–2666.

[3] a) Z. Nagy-Magos, S. Vastag, B. Heil, L. Marko, *J. Organomet. Chem.* **1979**, *171*, 97–102; b) Z. Nagy-Magos, P. Kvintovics, L. Marko, *Transition Met. Chem.* **1980**, *5*, 186–188.

[4] a) K. Severin, S. Mihan, W. Beck, *Chem. Ber.* **1995**, *128*, 1127–1130; b) T. Hauck, K. Sünkel, W. Beck, *Inorg. Chim. Acta* **1995**, *235*, 391–396; c) K. Severin, S. Mihan, W. Beck, *Chem. Ber.* **1995**, *128*, 1117–1125.

[5] G. Vujevic, C. Janiak, *Z. Anorg. Allg. Chem.* **2003**, *629*, 2585–2590.

[6] K. Prout, S. R. Critchley, E. Cannillo, V. Tazzoli, *Acta Crystallogr., Sect. B: Struct. Sci.* **1977**, *33*, 456–462.

[7] I. C. Tornieporth-Oetting, P. S. White, *Organometallics* **1995**, *14*, 1632–1636.

[8] T. M. Klapötke, H. Köpf, I. C. Tornieporth-Oetting, P. S. White, *Organometallics* **1994**, *13*, 3628–3633.

[9] W. Petri, J. Meder, M. Girnth-Weller, K. Bartel, V. Bejenke, G. Huttner, W. Beck, *Chem. Ber.* **1982**, *115*, 846–859.

[10] M. Maurus, B. Aechter, W. Hoffmüller, K. Polborn, W. Beck, *Z. Anorg. Allg. Chem.* **1997**, *623*, 299–303.

[11] a) M. Enamullah, M. Hasegawa, T. Hoshi, *Abstract*, *Bangladesh Chem. Soc. Conf.,* Jahangirnagar University, Dhaka, **2003**; b) M. Enamullah, M. Hasegawa, J. Okubo, T. Hoshi, *Abstract*, *Bangladesh Chem. Soc. Conf.*, Dhaka University, Dhaka, **2004**; c) M. Enamullah, M. Hasegawa, J. Okubo, T. Hoshi, *J. Bangladesh Chem. Soc.*, to be submitted.

[12] See Supporting Information for UV/Vis spectra and data.

[13] E. Pretsch, J. T. Clerc, *Spectra Interpretation of Organic Compounds*, Weinheim, New York, Basel, Cambridge, Tokyo, **1997**, pp. 9, 23.

[14] A. A. H. van der Zeijden, G. van Koten, R. A. Nordemann, B. Kojic-Prodic, A. L. Spek, *Organometallics* **1988**, *7*, 1957–1966.

[15] a) J. Karas, G. Huttner, K. Heinze, P. Rutsh, L. Zsolnai, *Eur. J. Inorg. Chem.* **1999**, 405–420; b) J. Scherer, G. Huttner, M. Buchner, *Chem. Ber.* **1996**, *129*, 697–713.

[16] a) A. P. Martinez, M. P. Garcia, F. J. Lahoz, L. A. Oro, *Inorg. Chem. Commun.* **2002**, *5*, 245–248; b) G. S. Rodman, K. R. Mann, *Inorg. Chem.* **1988**, *27*, 3338–3346.

[17] J. G. Leipoldt, E. C. Grobler, *Inorg. Chim. Acta* **1983**, *72*, 17–20.

[18] J. Rouzaud, M. D. Jones, R. Raja, B. F. G. Johnson, J. M. Thomas, M. J. Duer, *Helv. Chim. Acta* **2003**, *86*, 1753–1759.

[19] G. Matsubayashi, S. Akazawa, *Polyhedron* **1985**, *4*, 419–424.

[20] A. P. Martinez, M. P. Garcia, F. J. Lahoz, L. A. Oro, *Inorg. Chim. Acta* **2003**, *347*, 86–98.

[21] J. C. Bayon, G. Net, P. G. Rasmussen, J. B. Kolowich, *J. Chem. Soc., Dalton Trans.* **1987**, 3003–3007.

[22] S. L. James, D. M. P. Mingos, X. Xu, A. J. P. White, D. J. Williams, *J. Chem. Soc., Dalton Trans.* **1998**, 1335–1340.

[23] H. D. Flack, *Helv. Chim. Acta* **2003**, *86*, 905–921.

[24] A chiral space group needs to have an element from one of the following four pairs of enantiomorphous screw rotations: $\{3_1, 3_2\}$, $\{4_1, 4_3\}$, $\{6_1, 6_5\}$, $\{6_2, 6_4\}$. Only 22 out of the 230 space groups are chiral. A crystal structure in $P2_1$ is chiral but the space group itself is achiral as it does not form one member of an enantiomorphous pair.

[25] C. Janiak, *Dalton Trans.* **2003**, 2781–2804.

[26] H.-P. Wu, C. Janiak, G. Rheinwald, H. Lang, *J. Chem. Soc., Dalton Trans.* **1999**, 183–190.

[27] H.-P. Wu, C. Janiak, L. Uehlin, P. Klüfers, P. Mayer, *Chem. Commun.* **1998**, 2637–2638.

[28] a) M. A. Withersby, A. J. Blake, N. R. Champness, P. Hubberstey, W.-S. Li, M. Schröder, *Angew. Chem. Int. Ed. Engl.* **1997**, *36*, 2327–2329; b) A. J. Blake, N. R. Champness, A. N. Khlobystov, S. Parsons, M. Schröder, *Angew. Chem. Int. Ed.* **2000**, *39*, 2317–2320.

[29] F. Bodar-Houillon, T. Humbert, A. Marsura, J.-B. Regnouf de Vains, O. Dusausoy, N. Bouhmaida, N. E. Ghermani, Y. Dusausoy, *Inorg. Chem.* **1995**, *34*, 5205–5209.

[30] C. Kaes, M. W. Hosseini, C. E. F. Rickard, B. W. Skelton, A. H. White, *Angew. Chem. Int. Ed.* **1998**, *37*, 920–922.

[31] C. Janiak, *J. Chem. Soc., Dalton Trans.* **2000**, 3885–3896.

[32] a) M. Nishio, *CrystEngComm* **2004**, *6*, 130–158; b) M. Nishio, M. Hirota, Y. Umezawa, *The CH/π Interaction: Evidence, Nature and Consequences*, Wiley-VCH, Weinheim, Germany, **1998**; c) Y. Umezawa, S. Tsuboyama, K. Honda, J. Uzawa, M. Nishio, *Bull. Chem. Soc. Jpn.* **1998**, *71*, 1207–1213; d) C. Janiak, S. Temizdemir, S. Dechert, W. Deck, F. Girgsdies, J. Heinze, M. J. Kolm, T. G. Scharmann, O. M. Zipffel, *Eur. J. Inorg. Chem.* **2000**, 1229–1241.

[33] T. Dorn, A.-C. Chamayou, C. Janiak, *New J. Chem.* **2006**, *30*, 156–167; and references cited therein.

[34] C. Janiak, S. Temizdemir, T. G. Scharmann, *Z. Anorg. Allg. Chem.* **1998**, *624*, 755–756.

[35] E. Craven, E. Mutlu, D. Lundberg, S. Temizdemir, S. Dechert, H. Brombacher, C. Janiak, *Polyhedron* **2002**, *21*, 553–561.

[36] C. Janiak, T. G. Scharmann, unpublished results.

[37] C. Janiak, S. Temizdemir, S. Dechert, *Inorg. Chem. Commun.* **2000**, *3*, 271–275.

[38] C. Janiak, T. G. Scharmann, P. Albrecht, F. Marlow, R. Macdonald, *J. Am. Chem. Soc.* **1996**, *118*, 6307–6308.

[39] B. Paul, C. Näther, K. M. Fromm, C. Janiak, *CrystEngComm* **2005**, *7*, 309–319.

[40] X.-J. Yang, B. Wu, C. Janiak, *CrystEngComm* **2004**, *6*, 126–129.

[41] Q. Ye, X.-S. Wang, H. Zhao, R.-G. Xiong, *Tetrahedron: Asymmetry* **2005**, *16*, 1596–1602.

[42] T. Ezuhara, K. Endo, Y. Aoyama, *J. Am. Chem. Soc.* **1999**, *121*, 3279–3283.

[43] K. Biradha, C. Seward, M. J. Zaworotko, *Angew. Chem. Int. Ed.* **1999**, *38*, 492–495.

[44] S. R. Batten, B. F. Hoskins, R. R. Robson, *Angew. Chem. Int. Ed. Engl.* **1997**, *36*, 636–637.

[45] C. Sporer, K. Wurst, D. B. Amabilino, D. Ruiz-Molina, H. Kopacka, P. Jaitner, J. Veciana, *Chem. Commun.* **2002**, 2342–2343.

[46] M. Du, X.-H. Bu, Y.-M. Guo, J. Ribas, C. Diaz, *Chem. Commun.* **2002**, 2550–2551.

[47] a) G. Giordano, R. H. Crabtree, *Inorg. Synth.* **1979**, *19*, 218; b) J. Chatt, L. M. Venanzi, *J. Chem. Soc.* **1957**, 4735–4741.

 © 2006 Wiley-VCH Verlag GmbH & Co. KGaA, Weinheim 

[48] *SMART*, Data Collection Program for the CCD Area-Detector System; *SAINT*, Data Reduction and Frame Integration Program for the CCD Area-Detector System. Bruker Analytical X-ray Systems, Madison, Wisconsin, USA, **1997**.
[49] G. Sheldrick, *Program SADABS: Area-detector absorption correction*, University of Göttingen, Germany, **1996**.
[50] G. M. Sheldrick, *SHELXS-97*, *SHELXL-97*, Programs for Crystal Structure Analysis, University of Göttingen, Germany, **1997**.
[51] *DIAMOND 3.0e for Windows*, Crystal Impact Gbr, Bonn, Germany, http://www.crystalimpact.com/diamond.
[52] a) A. L. Spek, *Acta Crystallogr., Sect. A: Found. Crystallogr.* **1990**, *46*, C34; b) A. L. Spek, *PLATON – A multipurpose crystallographic tool*, Utrecht University, Utrecht, The Netherlands, **2005**. Windows implementation: L. J. Farrugia, University of Glasgow, Scotland, **2005**, version 80205.
[53] H. D. Flack, *Acta Crystallogr., Sect. A: Found. Crystallogr.* **1983**, *39*, 876–881.

Received: November 17, 2005
Published Online: March 30, 2006

 © 2006 Wiley-VCH Verlag GmbH & Co. KGaA, Weinheim 

DOI: 10.1002/ejic.200501042

# Photoinduced Processes in a Dendritic Zn Porphyrin Structure with a Free-Base Porphyrin Core

**Lucia Flamigni,*[a] Anna Maria Talarico,[a] Barbara Ventura,[a] Chloé Sooambar,[b] and Nathalie Solladié*[b]**

**Keywords:** Dendrimers / Energy transfer / Luminescence / Porphyrinoids / Supramolecular chemistry

The photophysical characterization of a nonameric porphyrin assembly made up of a central free-base and eight peripheral zinc porphyrins connected by flexible nucleosidic linkers, and the identification of the photoinduced processes taking place in the array, is reported. Both singlet–singlet and triplet–triplet energy transfer from the peripheral zinc porphyrins to the free-base porphyrin core is detected. The kinetic parameters of singlet–singlet energy transfer are interpreted by assuming the existence of several nonequilibrated conformations in the array due to the flexibility of the linkages. A fast quenching of the donor beyond the time detection limit of the instrument is also hypothesized and assigned to strong interactions between the zinc chromophores in close contact which can give self-quenching phenomena. For the zinc porphyrin triplet excited state, a triplet–triplet annihilation is detected at moderate photon flux as a consequence of multi-excitation of the same array. Drastic reduction of the photon flux allows us to determine the triplet energy transfer rate from zinc porphyrin to free-base porphyrin, which is the final recipient of the energy collected by the array. The decay of the triplet state of the core free-base porphyrin is prolonged with respect to the model, indicating a shielding effect of the peripheral groups. Complexation experiments with monodentate and didentate bases have been performed in order to gain insight into the spatial arrangement of the zinc porphyrin chromophores and the proposed mechanism of self-quenching. Association of didentate bases increases the rigidity of the multi-porphyrin structure and improves the energy collection ability.

(© Wiley-VCH Verlag GmbH & Co. KGaA, 69451 Weinheim, Germany, 2006)

## Introduction

Natural photosynthesis is triggered by the absorption of photons by a light-harvesting antenna system with a large absorption cross-section, followed by a rapid and efficient transfer of excitation energy to the reaction center. To mimic the natural processes, artificial light-harvesting antennae require a great number of chromophore units that are well organized in space and able to transfer the absorbed energy to one specific site with high efficiency. Porphyrins are ideal candidates for the construction of light-harvesting arrays and, in the past decade, many artificial multi-porphyrin systems have been developed, such as linear or linear-branched arrays,[1–5] rings,[6–8] windmills,[9] dendrimers,[10,11] and other assemblies.[12,13] Among these, dendritic frameworks appear to be the most promising arrays as they allow site-specific placement of the dye molecules in a three-dimensional hyperbranched treelike fashion, and a good choice of the chromophoric units permit the conveyance of the collected energy toward the central core.

[a] Istituto per la Sintesi Organica e Fotoreattivita' (ISOF), CNR, Via P. Gobetti 101, 40129 Bologna (Italy)
Fax: +39-051-639-9844
E-mail: flamigni@isof.cnr.it
[b] Groupe de Synthèse de Systèmes Porphyriniques (G2SP), Laboratoire de Chimie de Coordination du CNRS (UPR, 8241), 205 route de Narbonne, 31077 Toulouse Cedex 4 (France)
Fax: +33-5-6155-3003
E-mail: solladie@lcc-toulouse.fr

Many dendritic arrays with a variety of linkers have been developed recently.[10,13] We present here a study of the photoinduced processes in a dendritic nonameric porphyrin assembly (Scheme 1) made up of a central free-base porphyrin and eight peripheral zinc porphyrins connected in pairs to the core by a flexible nucleosidic linker whose synthesis has been reported recently.[14] The structure can be considered a further step in the elaboration of porphyrin-based antennas with respect to a pentaporphyrin previously reported by our groups.[15] The eight peripheral zinc porphyrin chromophores can absorb light extensively over the full visible spectrum and the energy stored can be conveyed to the central free-base porphyrin. The study of convenient model compounds, Zn and FBS (Scheme 1), can help in the elucidation of the fundamental steps occurring upon light absorption in the nonaporphyrin FB-$Zn_8$, whose photophysical behavior could be strongly influenced by the existence of different conformations due to the flexible linkers. Steady-state and time-resolved spectroscopic methods are used to quantify the energy-transfer processes.

## Results and Discussion

### Absorption Spectroscopy

Scheme 1 shows the structures of the nonaporphyrin FB-$Zn_8$ and of the molecules used as models of the periphery

 © 2006 Wiley-VCH Verlag GmbH & Co. KGaA, Weinheim 

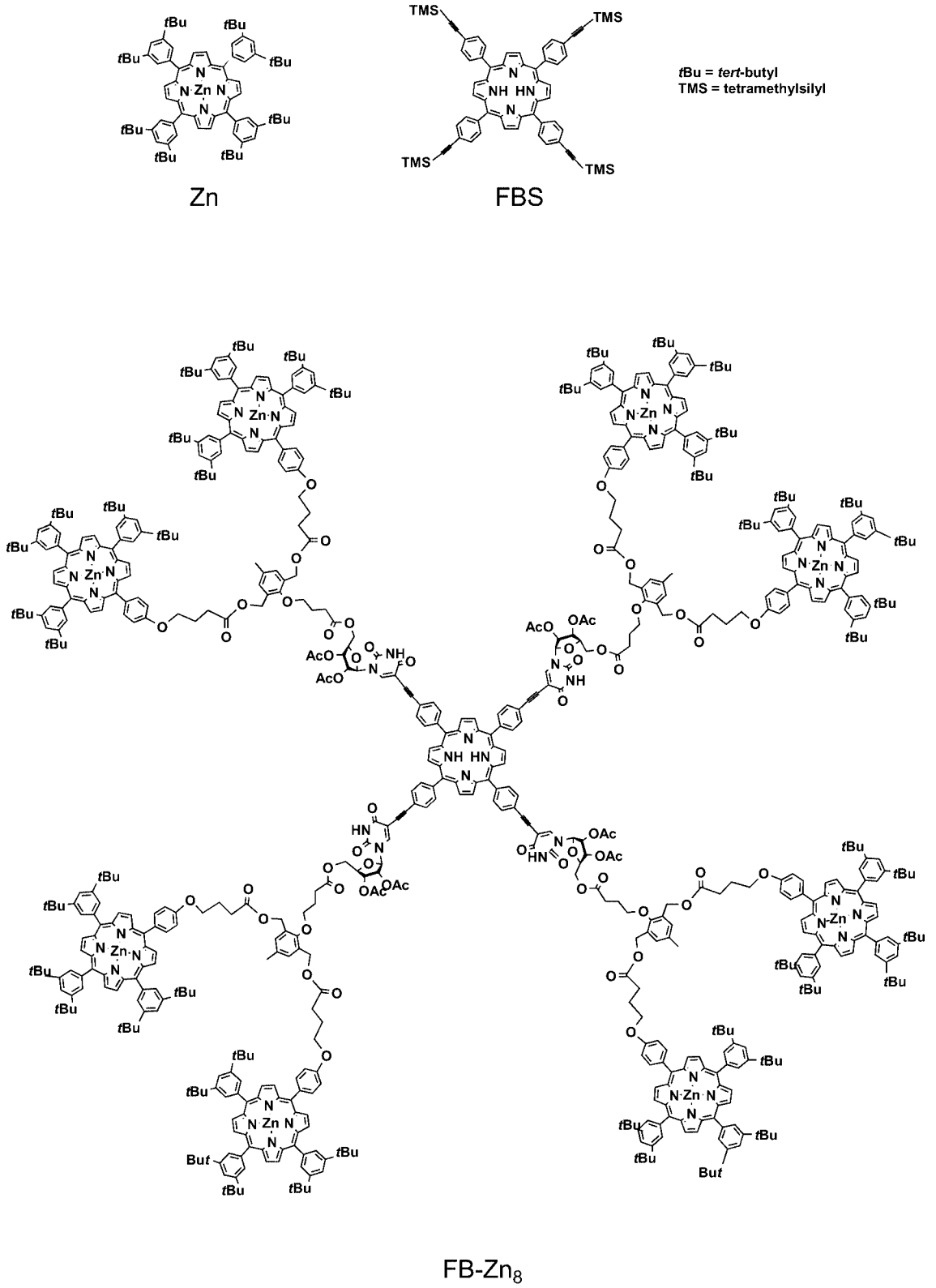


Scheme 1. The component models Zn and FBS and the nonaporphyrin FB-$Zn_8$.

and the core units, Zn and FBS, respectively. The absorption spectrum of FB-$Zn_8$ in toluene is in good agreement with the superposition of the model components, as can be seen in Figure 1, where the absorption spectra of the models are reported with the sum of the nine components and the experimental absorption spectrum of the nonaporphyrin FB-$Zn_8$. In addition to the usual broadening of the Soret band, which is typical of covalently bound porphyrinic ar-

 © 2006 Wiley-VCH Verlag GmbH & Co. KGaA, Weinheim 

rays, a 2–3-nm shift to lower energies can be detected in the maximum wavelength of both the Soret and Q bands with respect to the simple superposition of the components. A long, weak tail extending up to 700 nm can be detected in the array compared to the superposition of components, which can be taken as an indication of some interaction between the porphyrinic chromophores. Nonetheless, this interaction is modest and the single chromophores in the array can be considered to retain essentially their own spectroscopic properties (see below).

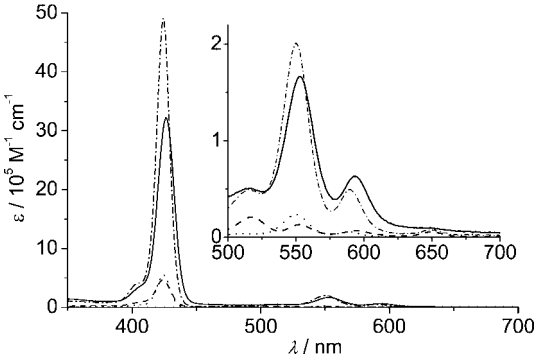


Figure 1. Molar absorption coefficients of the models Zn (dot) and FBS (dash), and of FB-$Zn_8$ (solid) in toluene solution. The sum of the molar absorption coefficients of the nine components is also reported (dash-dot).

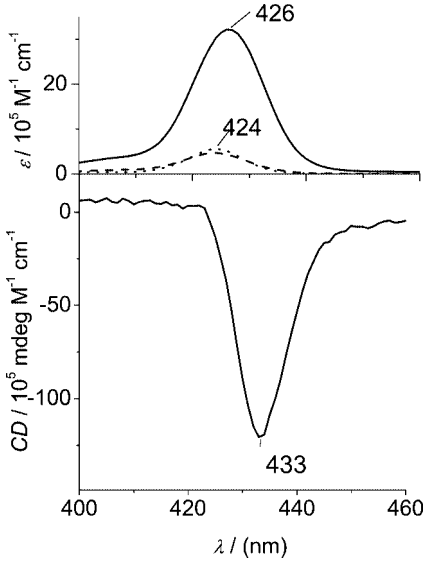


Figure 2. UV (upper panel) and CD (lower panel) spectra of FB-$Zn_8$ (solid) in toluene solutions. In the upper panel the absorption spectra of components Zn (dot) and FBS (dash) are also reported.

FB-$Zn_8$ displays optical activity − the CD spectrum is reported in Figure 2, lower panel, with the absorption spectra of the two models Zn and FBS and the array shown in the upper panel. In the spectrum the positive band is almost absent, whereas a strong, negative band can be detected. Its origin could be assigned to exciton interactions between the porphyrin chromophores, similarly to what was recently reported and discussed in detail for a similar porphyrin pentamer;[15a] however, we cannot exclude a CD effect induced on the porphyrin by the chiral nucleosidic linkers.

## Luminescence

The Zn singlet excited state at 295 K in toluene has a lifetime of 2.2 ns and an emission quantum yield of 0.08,[16] whereas the lifetime of FBS under the same conditions is 9.5 ns and the emission quantum yield is 0.18. The energy levels of the lowest singlet excited state of the models, derived from the maximum of the emission band at 77 K, are 2.08 eV for $^1$Zn and 1.92 eV for $^1$FBS (Table 1), which means that a photoinduced energy transfer from the peripheral Zn to the core FBS would spontaneously occur with a $\Delta G^0$ value of –0.16. Phosphorescence from porphyrin components could be detected in the near-IR region at 77 K in glassy media.[17] From the maximum of the phosphorescence bands, the energy levels of the triplet can be derived for $^3$Zn (1.6 eV) and for $^3$FBS (1.48; Table 1). An energy transfer could also occur spontaneously in this case from the triplet excited state localized on the zinc porphyrin to the free-base central unit with a $\Delta G^0$ of –0.12 eV.

The luminescence spectrum of FB-$Zn_8$ in toluene upon excitation at 550 nm is reported in Figure 3 together with the superposition of the emission spectra of the individual components (Zn and FBS) in toluene, for absorbance corresponding to the same number of photons absorbed by the units in the array. The band positions of the units in the

Table 1. Luminescence properties of the nonaporphyrin and of the models at 295 and 77 K.

| | State | 295 K $\lambda_{max}$ [nm] | $\Phi_{fl}$[a] | $\Phi_{fl}$[b] | $\tau$ [ns][c] (% component) | 77 K $\lambda_{max}$ [nm] | $E$ [eV][d] |
|---|---|---|---|---|---|---|---|
| FBS | $^1$FBS | 652 | 0.18 | | 9.5 | 646 | 1.92 |
| | $^3$FBS[e] | | | | | 840 | 1.48 |
| Zn | $^1$Zn | 594 | | 0.08 | 2.2 | 596 | 2.08 |
| | $^3$Zn[e] | | | | | 776 | 1.60 |
| FB-$Zn_8$ | $^1$FB-$Zn_8$ | 651 | 0.10 | | 9.0 | 648 | 1.91 |
| | FB-$^1Zn_8$ | 600 | | 0.015 | 0.175; 0.990; 2.2 (50%; 30%; 20%) | 605 | 2.05 |
| | $^3$FB-$Zn_8$ | | | | | n.d. | |
| | FB-$^3Zn_8$ | | | | | n.d. | |

[a] FBS Emission quantum yield; selective excitation of the free-base porphyrin unit was at 650 nm. [b] Emission quantum yield, the excitation was at 550 nm; the yield for the array was calculated on the basis of the photons absorbed by the Zn unit. [c] Excitation at 532 nm for lifetimes of less than 1 ns, excitation at 337 nm for lifetimes above 1 ns. [d] Energy levels from the emission maxima at 77 K. [e] Taken from the literature.[16]

 © 2006 Wiley-VCH Verlag GmbH & Co. KGaA, Weinheim 

array are essentially unaltered with respect to the models, thereby confirming that the components retain their own spectroscopic properties. A partial quenching of the zinc porphyrin component ($\lambda_{max}$ = 600 nm) to about 20% can be detected, ($\Phi_{fl}$ = 0.015) but no corresponding sensitization of the free-base component ($\lambda_{max}$ at 651 nm and 720 nm) appears. This observation could be explained by a self-quenching of the zinc porphyrin donors that does not lead to a sensitization of the free-base acceptor and/or to a change in the emissive properties of the free-base core compared to the model FBS. In order to establish whether the present system displays some form of light energy collection and transfer properties, the experiments described below were carried out.

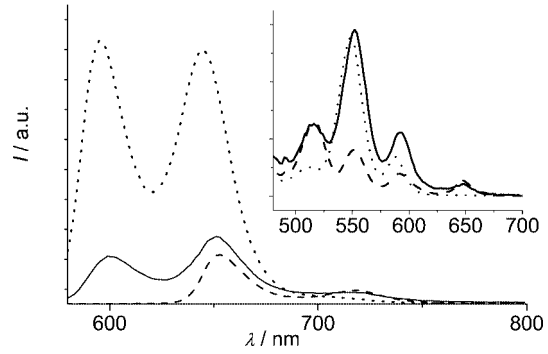


Figure 3. Emission spectra at 295 K of the models Zn (dot), FBS (dash), and of FB-$Zn_8$ (solid) in toluene solution upon excitation at 550 nm. The concentrations are adjusted to provide the same absorbance of the models and of the corresponding unit in FB-$Zn_8$. The inset shows the excitation spectrum registered at $\lambda_{em}$ = 720 nm for the models and the array.

The emission quantum yield of the porphyrin core in the array was determined by selective excitation of the free-base porphyrin unit at 650 nm and turned out to be reduced ($\Phi_{fl} \approx 0.10$[18] with respect to $\Phi_{fl}$ = 0.18 in the model FBS). This perturbation could be the result of interaction of the porphyrin core with some peripheral Zn porphyrin that is in close contact because of the flexibility of the linker. At short distances, low lying charge-transfer states could play a role, leading to a static quenching of the free-base porphyrin. The long absorption tail detected in the nonamer (see above) up to 700 nm could confirm the presence of such an interaction generating low-lying states that are able to quench the free-base porphyrin luminescence. Support in favor of an energy transfer in the array comes from the excitation spectrum detected at $\lambda_{em}$ = 720 nm, where only the free-base porphyrin core emits (inset of Figure 3). From this spectrum, which is displayed with the excitation spectra of the components, the contribution of the zinc porphyrin unit at 550 nm to the emission of the free base at 720 nm is quite evident, and confirms that an energy transfer from the peripheral components to the core is actually taking place. The fact that there is no evidence of this transfer from the steady-state luminescence experiment as a sensitization of the free-base porphyrin unit (Figure 3) could be ascribed to a decreased emission yield of the energy acceptor free-base unit from $\Phi_{fl}$ = 0.18 to 0.10, as reported above.

The spectroscopic data from Table 1 allow us to draw a schematic energy-level diagram for FB-$Zn_8$ (Scheme 2), from which both a singlet-to-singlet (FB-$^1Zn_8 \rightarrow {}^1$FB-$Zn_8$) and a triplet-to-triplet (FB-$^3Zn_8 \rightarrow {}^3$FB-$Zn_8$) energy transfer appear feasible.

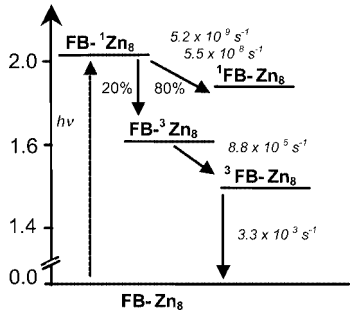


Scheme 2. Schematic energy-level diagram and photoinduced processes in FB-$Zn_8$. The percentage of units following different reaction paths is reported.

## Singlet–Singlet Energy Transfer

The mechanism of singlet–singlet energy transfer between porphyrins is generally of the Förster type,[19] with a mechanism involving a dipole–dipole interaction. For this mechanism it is possible to calculate the rate, $k^F_{en}$, as a function of the donor–acceptor distance, $d_{DA}$, with some accuracy as the emission quantum yield, $\Phi$, and the lifetime, $\tau$, of the donor Zn, the overlap integral, $J^F$, and the refractive index of toluene, $n$, are known; see Equation (1).[19]

$$k^F_{en} = \frac{8.8 \times 10^{-25} \cdot \kappa^2 \cdot \Phi}{n^4 \cdot \tau \cdot {d_{DA}}^6} \cdot J^F \quad (1)$$

$J^F$ is calculated from the experimental emission and absorption spectra to be $5.47 \times 10^{-14}$ cm$^3$ M$^{-1}$ and $\kappa^2$, the orientation factor, is taken as 2/3 since the partners can be assumed to randomly approach each other because of the long, flexible linker. On the basis of these parameters and of the data in Table 1, a critical transfer distance, $R_c$, which is the distance at which the energy transfer rate equals the intrinsic deactivation rate of the donor, of about 28 Å can be calculated. In view of the approximations involved in the present determinations, we can assume that for a fully extended linkage, corresponding to a center-to-center distance of about 34 Å, essentially no quenching of the donor can occur.[20] Due to the flexibility of the linkages, a large number of conformations are expected, characterized by distances varying between a few angstroms, for conformations corresponding to a highly bent linkage, and a maximum distance of 34 Å. The time decay of the luminescence of the zinc porphyrin detected at 600 nm in FB-$Zn_8$ in toluene (Figure 4) is in perfect agreement with this picture as it displays a multi-exponential decay. This is typical of the luminescence decay of Zn porphyrin donors in either flexible or rigid dendritic multiporphyrin arrays for light har-

 © 2006 Wiley-VCH Verlag GmbH & Co. KGaA, Weinheim 

vesting and is due to the existence of several donor–acceptor couples with different distances and orientations.[21] A three exponential fitting of the zinc porphyrin luminescence decay gives satisfactory results, with *average* calculated lifetimes of 0.175, 0.990, and 2.2 ns with relative weights of 50%, 30%, and 20% respectively. Whereas most of the emission is fitted by lifetimes shorter than that of the reference model Zn, indicating an important quenching, a residual 20% (under our experimental conditions) displays the same lifetime (2.2 ns) as the model. This could be due to the fraction of conformers with donor–acceptor distances corresponding to the fully extended array (34 Å), which are not liable to quenching, although the contribution of zinc porphyrin impurities cannot be excluded. The time profile of the luminescence detected at 720 nm, a wavelength typical of the free-base acceptor, is also shown in Figure 4. Although rather weak, it comes, in fact, from one of the nine chromophores − the luminescence-time evolution in FB-$Zn_8$ shows a clear rise in the luminescence at early times on the same time scale as the fast decay of the zinc porphyrin donor at 600 nm. A fitting of the formation and decay signal would be meaningless due to the poor signal-to-noise ratio and the multi-exponential nature of the kinetics. The detected formation at 720 nm can be assigned to sensitization of the free-base porphyrin units by the Zn porphyrin moieties. The subsequent time evolution detected at 720 nm can be considered a superposition of the tail of the zinc porphyrin moiety ($\lambda_{max}$ = 600 nm; lifetime: 2.2 ns) and the decay of the free-base unit emissions ($\lambda_{max}$ = 720 nm; lifetime: 9 ns).

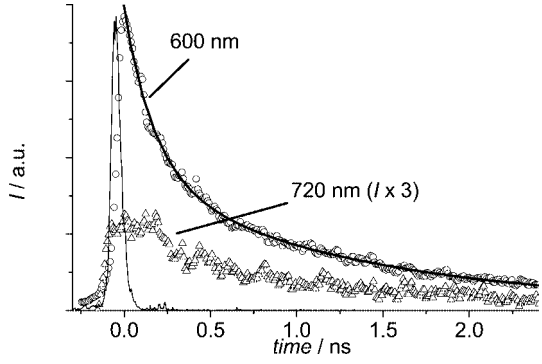


Figure 4. Time-resolved luminescence of FB-$Zn_8$ in toluene solution after excitation at 532 nm. Decay at 600 nm (circle) is shown with the tri-exponential fitting with lifetimes of 175 ps, 990 and 2.2 ns. The time profile of the luminescence at 720 nm is also reported (triangle) with the exciting flash profile.

It is interesting to compare the steady-state luminescence results with the time-resolved data. The emission quantum yield, $\Phi_{fl}$, is related to the lifetime of a species by the equation $\Phi_{fl} = \tau k_r$, where $\tau$ is the lifetime and $k_r$ is the radiative rate constant. In case of more than one lifetimes of the species, as in the present case, where a multi-exponential decay of the luminescence is present, the equation becomes $\Phi_{fl} = \Sigma(f_i\tau_i k_r)$, where $f_i$ is the fraction of component corresponding to the lifetime $\tau_i$. Assuming that $k_r$ of the zinc porphyrin singlet excited state in FB-$Zn_8$ is identical to that of the model Zn ($k_r = \Phi_{fl}/\tau$; $k_r = 3.6\times10^7\ s^{-1}$) the fluorescence quantum yield can be calculated from the following equation: $\Phi_f = k_r\times(f_1\tau_1 + f_2\tau_2 + f_3\tau_3)$, where the index 1, 2, and 3 is relative to the average conformations displaying the three different lifetimes. The result of this calculation is $\Phi_f = 0.03$, which is different from the experimental value ($\Phi_f = 0.015$; Table 1). This discrepancy, which is much higher than the experimental uncertainty, could be accounted for by: (i) the radiative rate constant of the zinc porphyrin moiety in the nonaporphyrin is different than the one of the model, and/or (ii) there is some faster quenching, which escapes the time resolution of the experimental set-up (20 ps) and can therefore be considered a "static quenching". This would be detectable by steady-state techniques, which integrate a signal over time, but *not* by time-resolved methods with time resolution exceeding the timescale of the process. In the latter case, the correct fraction, $f_i$, of each component for the calculation of $\Phi_f$ should be scaled to take into account the component which gives "static" quenching and which is missed by our apparatus.

The luminescence properties at 295 K and 77 K are summarized in Table 1.

### Triplet–Triplet Energy Transfer

Porphyrin triplets exhibit strong and well-characterized triplet absorption spectra and lifetimes in the hundreds of microseconds range in fluid, oxygen-free solutions. They can be conveniently monitored by laser flash photolysis with nanosecond/microsecond resolution. The transient change in the absorption spectra due to the triplet excited states of the models FBS and Zn are reported in Figures 5 and 6, respectively, with one inset (a) showing the lifetime in oxygen-free and the other (b) in air-equilibrated toluene solutions at 295 K. To prevent triplet–triplet second-order competitive reactions, which are a very common phenomenon for long-lived triplet excited states, the lifetime of the species in air-free solutions was measured at extremely low excitation energy (≤0.2 mJ per pulse) in order to provide a low concentration of excited species and a good single exponential decay of the excited triplet [insets (a) of Figures 5 and 6]. The triplets are quenched by oxygen and their lifetime in air-saturated solutions is greatly decreased [see Table 2, insets (b) of Figures 5, and 6]. Since the concentration of $O_2$ in air-equilibrated toluene solutions is $1.8\times10^{-3}$ M,[22] a reaction rate with oxygen in toluene of the order of $1–1.5\times10^9\ M^{-1}s^{-1}$ can be derived for Zn and FBS, in agreement with previous reports.[23]

In FB-$Zn_8$, once the triplet state of the zinc porphyrin unit is formed, a triplet energy transfer to the core free-base porphyrin can be envisaged. Energy transfer between triplet states occurs generally by a Dexter (electron-exchange) mechanism.[24] This type of mechanism involves the synchronized transfer of two electrons, one from the LUMO of the donor to the LUMO of the acceptor and the other from the HOMO of the acceptor to the HOMO of the donor. It requires either a direct physical contact (through

 © 2006 Wiley-VCH Verlag GmbH & Co. KGaA, Weinheim 

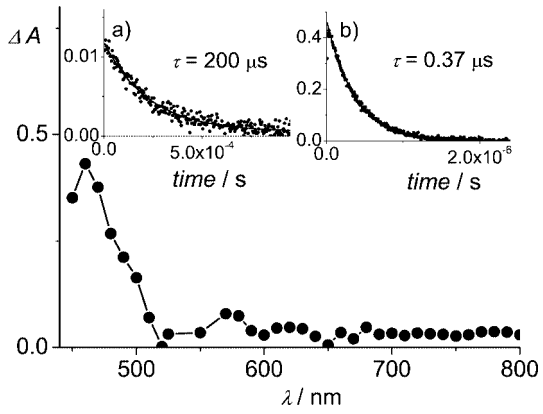


Figure 5. Transient absorbance changes of FBS ($A$ = 0.13) following laser excitation at 532 nm (5 mJ per pulse) in toluene solutions. Inset a) shows the decay in oxygen-free (0.2 mJ per pulse) and inset b) the decay in air-saturated solution (5 mJ per pulse).

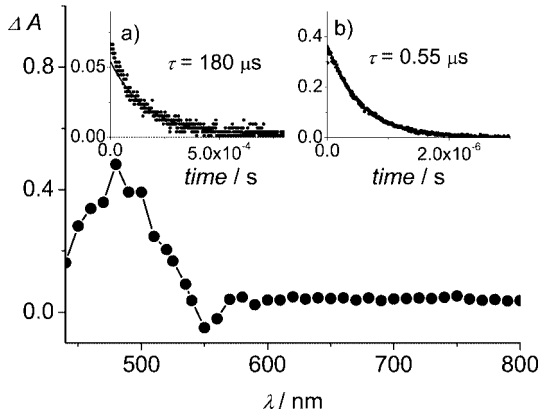


Figure 6. Transient absorbance changes of Zn ($A$ = 0.12) following laser excitation at 532 nm (5 mJ per pulse) in toluene solutions. Inset a) shows the decay in oxygen-free (0.125 mJ per pulse) and inset b) the decay in air-saturated solution (5 mJ per pulse).

Table 2. Transient absorbance data at 295 K in toluene.

| | State | $\tau$ [μs][a] | $\tau$ [μs][b] | $\Phi_T$[c] |
|---|---|---|---|---|
| Zn | $^3$PZn | 250 | 0.50 | 1 |
| FBS | $^3$FBS | 200 | 0.37 | 1 |
| FB-Zn$_8$ | FB-$^3$Zn$_8$ | 1.1 | n.d. | 0.2 |
| | $^3$FB-Zn$_8$ | 300 | n.d. | ca. 1[d] |

[a] Lifetime in air-free toluene, low laser energy (see text). [b] Lifetime in air-saturated toluene. [c] Triplet formation quantum yields, relative to the models and calculated on the basis of the photons absorbed by the unit in the array. [d] Poor signal to noise ratio, the determination is subject to an error of the order of 30%.

space), or the intermediacy of a linkage (through bond), between the reacting partners. Without entering into detail, in the case of through-bond transfer the rate depends on the type of bond and its length. For alkane chains and large distances, as in the present case, the through-bond energy transfer rate is slow and is expected to occur on the microsecond timescale; it is therefore able to compete with the deactivation rate of the Zn porphyrin triplet in air-free solutions.

A nanosecond flash photolysis experiment on the nona FB-Zn$_8$ in air-free solution allowed us to detect an end-of-pulse spectrum mostly ascribable to the zinc porphyrin triplet state (Figure 7). The yield of formation of this state calculated with respect to the model Zn in the wavelength range out of the ground-state absorbance (650–700 nm) is about 20%, which is in good agreement with the fraction of unquenched singlet derived by luminescence time-resolved determinations (see above). This clearly indicates that the triplet states are produced only by the unquenched singlet excited states of the zinc porphyrin donor via an intersystem-crossing step. The end-of-pulse spectrum of FB-Zn$_8$ evolves rapidly, with a slight shift of the maximum from 490 to 480 nm, and after a few microseconds it reaches a value that is stable on the microsecond timescale (Figure 7). The exponential decay rate of the fast decay was found to depend on the laser intensity, as shown in inset (a) of Figure 7. This can be understood by considering that excitation of a $3\times10^{-6}$ M solution with several millijoules at 532 nm is able to produce multiple excitation of porphyrins (mostly of the zinc porphyrin units, which absorb 85% of the incident photons) within the same array.[25] Multiple excitation in an array that has a very high *local* concentration of zinc porphyrins would cause a fast intramolecular triplet–triplet reaction and lead to a rapid self-quenching of the zinc porphyrin triplet. The experimental first-order reaction rate would therefore be due to the contribution of two different processes: the intramolecular triplet–triplet annihilation, which is dependent on the square of the laser energy, and the energy-transfer process, which is independent of it. The rate at different incident laser conditions was measured and a plot of rate versus laser intensity was extrapolated to zero energy [inset (a) of Figure 7] in order to derive the decay rate of FB-$^3$Zn$_8$ in the absence of multi-photonic excitation. Under these conditions, the first-order decay rate of FB-$^3$Zn$_8$ was $8.8\times10^5$ s$^{-1}$ and was assigned to an energy-transfer process from the triplet localized on the zinc porphyrin moiety (FB-$^3$Zn$_8$) to the triplet localized on the free-base central unit ($^3$FB-Zn$_8$).[26] The latter species, which can be identified from the spectrum after 3 μs in Figure 7, decays exponentially with a lifetime of 300 μs [inset (b) of Figure 7]. The lifetime of the triplet porphyrin core in $^3$FB-Zn$_8$ is longer than that determined for the model FBS under the same conditions (ca. 200 μs), very likely because of a sort of shielding effect of the periphery components toward traces of oxygen or quenching contaminants in the solution. A similar protecting effect of the periphery on the triplet excited state of a core chromophore was previously found for a similar pentaporphyrin[15] and has also been reported for a fullerene-based dendrimeric structure.[27]

Scheme 2 shows the rate constants of the intramolecular processes; the decay of the excited state localized on the zinc porphyrin chromophore, FB-$^1$Zn$_8$, is assigned to different processes depending on the type of conformation: the 20% extended conformation decays mainly to the triplet state

 © 2006 Wiley-VCH Verlag GmbH & Co. KGaA, Weinheim 

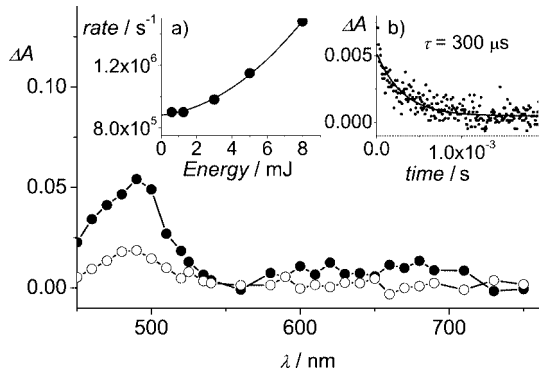


Figure 7. Transient absorbance changes of FB-$Zn_8$ ($A$ = 0.17) following laser excitation at 532 nm (5 mJ per pulse) in toluene solutions; end-of-pulse spectra (filled circle) and 3 μs after the end of the pulse (open circle). Inset a) shows the rate constant dependence of the fast decay (see text) from the laser intensity and inset b) shows the decay of the 3-μs species, assigned to $^3$FB-$Zn_8$, in oxygen-free solutions.

FB-$^3Zn_8$, whereas the other conformations with lower donor–acceptor distances decay by energy transfer to $^1$FB-$Zn_8$ with average rates of $5.2\times10^9$ and $5.5\times10^8$ $s^{-1}$, corresponding respectively to average lifetimes of 175 and 990 ps.

## Complexation

Zinc porphyrins are know to axially bind pyridine or pyridyl residues with association constants of the order of $10^4$ $M^{-1}$. These constants have been found to increase dramatically up to around $10^6$ to $10^8$ $M^{-1}$ when multiple bonds can contribute to the formation of the complex.[28,29]

We have undertaken this type of experiment with both monodentate pyridine (Pyr) and didentate 4,4′-bipyridine (Bipy) in order to gain information about the spatial arrangement and the interactions between the zinc porphyrin chromophores in FB-$Zn_8$. As a reference, the same experiments were performed with Zn. Our aim was to derive the association constants by spectrophotometric and spectrofluorimetric methods and to monitor the effect of FB-$Zn_8$ complexation on CD spectroscopy, in order to gain some insight into the system. The association constants were derived by a nonlinear treatment previously developed for the analysis of absorption and emission signals at a selected wavelength (see Exp. Sect. for details).[29]

The results for the absorption of Zn ($1.7\times10^{-6}$ M) upon titration with increasing amounts of Pyr are reported in Figure 8, together with the emission spectra of the same solutions upon excitation at 428 nm, which is the isosbestic point between the complexed and uncomplexed forms. The insets show the nonlinear fittings to the experimental data, and the derived association constants are summarized in Table 3. The same type of experiment was also performed with Bipy as a titration agent, and the results are illustrated in Figure 9. The plots of the signals at the selected wavelengths (inset) allow us to derive the association constants (Table 3). The behavior with the two different titration agents is essentially the same for Zn: in both cases the absorption of the porphyrin Soret band shifts from 424 to 431 nm (7 nm), with a clear isosbestic at 428 nm typical of the formation of a 1:1 complex.[30] In principle, the didentate Bipy could complex two Zn molecules to form a 2:1 (Zn/Bipy) complex, which should be favored at low concentrations of Bipy. Nonetheless, in the present experimental conditions we were unable to detect the 2:1 complex, which is reported to display a red shift of only about 4 nm with respect to the Zn porphyrin band, i.e. a band maximum at lower wavelengths with respect to the 1:1 complex.[30] The low association constant and the use of a large excess of Bipy are very likely to be unfavorable for the formation of the 2:1 complex.

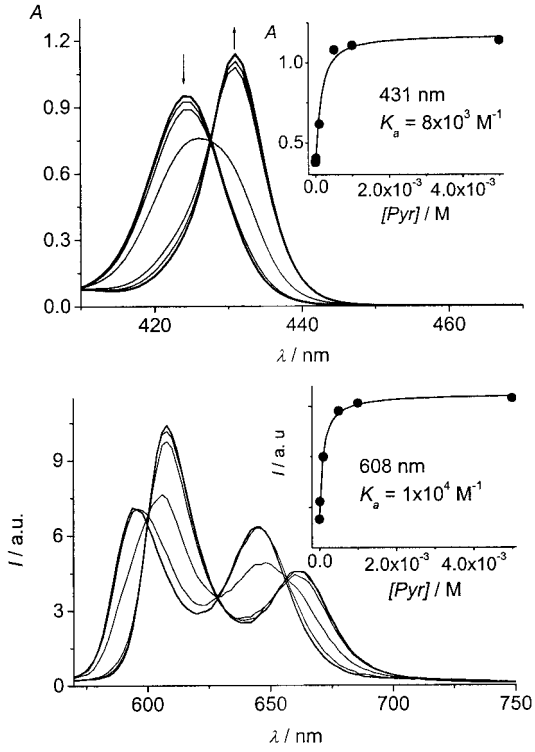


Figure 8. Zn ($1.7\times10^{-6}$ M) in toluene solution upon titration with increasing amounts of Pyr. The upper panel shows the change of absorbance in the Soret band region and the inset shows the data points at 431 nm, fitted according to Equation (2). In the lower panel the change in emission intensity is shown and in the inset the data points at 608 nm, fitted to Equation (2), are reported.

Table 3. Association constants $K_a$ [$M^{-1}$] of the model Zn and of FB-$Zn_8$ with pyridine and bipyridine.

| | Pyr | | | Bipy | | |
|---|---|---|---|---|---|---|
| | Abs | Em | Average | Abs | Em | Average |
| Zn | $8\times10^3$ | $1\times10^4$ | $9\times10^3$ | $9\times10^3$ | $1.4\times10^4$ | $1.2\times10^4$ |
| FB-$Zn_8$ | $6\times10^3$ | $6\times10^3$ | $6\times10^3$ | – | – | – |

In the case of titration of a solution of FB-$Zn_8$ ($2.6\times10^{-7}$ M), the results obtained with Pyr and Bipy are rather different. The effects on the absorption and emission properties upon titration with the monodentate Pyr are shown in Figure 10. The absorption titration data do not differ appreciably from that of the model Zn − the shift in

 © 2006 Wiley-VCH Verlag GmbH & Co. KGaA, Weinheim 

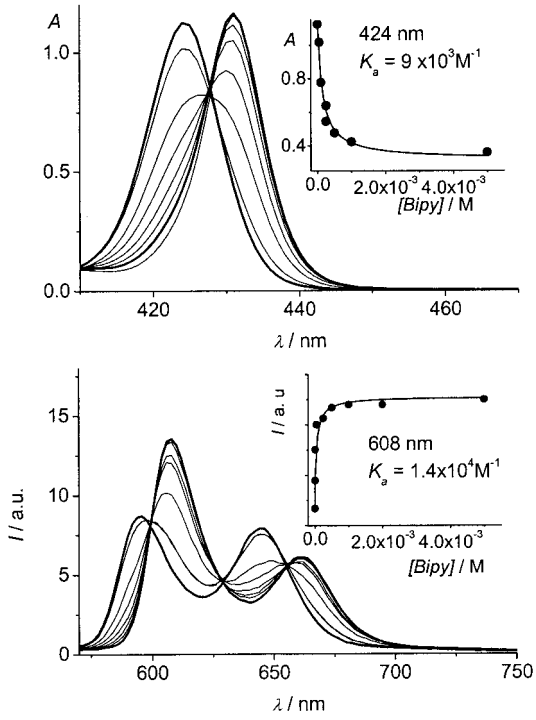


Figure 9. Zn ($1.7\times10^{-6}$ M) in toluene solution upon titration with increasing amounts of Bipy. The upper panel shows the change of absorbance in the Soret band region and the inset shows the data points at 424 nm, fitted according to Equation (2). In the lower panel the change in emission intensity is shown and in the inset the data points at 608 nm, fitted to Equation (2), are reported.

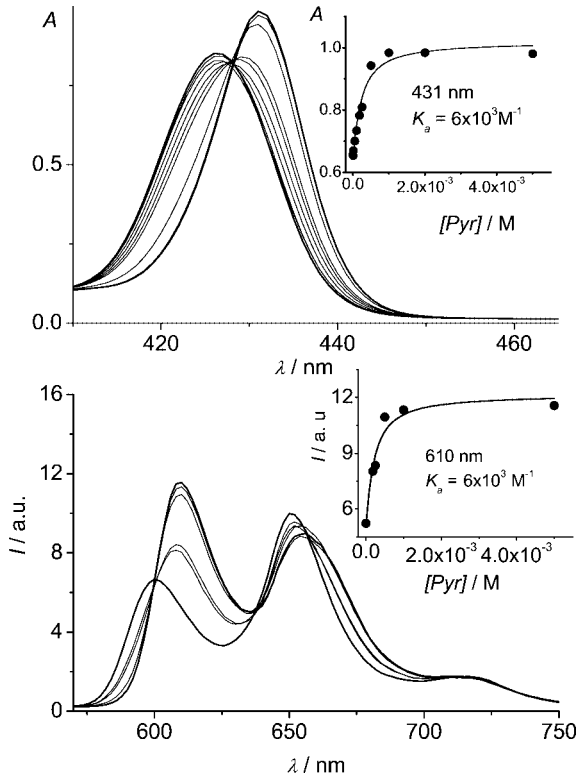


Figure 10. FB-$Zn_8$ ($2.6\times10^{-7}$ M) in toluene solution upon titration with increasing amounts of Pyr. The upper panel shows the change of absorbance in the Soret band region and the inset shows the data points at 431 nm, fitted according to Equation (2). In the lower panel the change in the emission intensity is shown and in the inset the data points at 610 nm, fitted to Equation (2), are reported.

the Soret band of the zinc porphyrin unit upon complexation is from 426 to 431 nm, with a single isosbestic point at 428 nm. The emission data, making allowance for the bands of the free-base unit in FB-$Zn_8$, do not appear different from the titration results of the model Zn in the region 570–640 nm, where only the zinc porphyrin chromophore emits. The derived association constant is slightly lower than that determined for the model Zn, and this is perhaps related to the less accessible Zn porphyrin units in the nona structure compared to simple Zn.

The results of titration of FB-$Zn_8$ with the didentate Bipy are more interesting. Absorption data show that in this case there is no isosbestic point (see Figure 11), but from the initial spectrum of the free nonaporphyrin ($\lambda_{max}$ = 426 nm) a rather complicated evolution can be detected. This shows an initial decrease of the band at 426 nm with a shift to 429 nm in the concentration range from $5\times10^{-7}$ to $5\times10^{-6}$ M, followed by an increase of the band at 429 nm, which reaches a maximum for a Bipy concentration of $10^{-4}$ M, and a final evolution for concentrations above $5\times10^{-3}$ M to the absorption with maximum at 431 nm typical of the 1:1 complex spectrum, in analogy to the model system. An absorption maximum around 429 nm is typical of the 2:1 (Zn/Bipy) complex spectrum, but the exact position of the maximum and the extinction coefficient of the species could change slightly depending on the geometry and conformations of the complex. Similar data have recently been reported by Hunter and Ballester.[31] In one of the cases studied − a calixa-tetraporphyrin titrated by didentate DABCO − they detected a similar behavior in the middle part of the titration by absorption spectroscopy. That behavior was assigned, and confirmed by $^1$H NMR spectroscopy, to the formation of a 2:1 complex (Zn/DABCO) with different conformations and geometries. Whereas in Hunter and Ballester's case the presence of different conformations was mainly ascribed to the possibility of formation of intra- or intermolecular complexes, in the present experiment the possibility of forming different 2:1 complexes depends on the relative positions of the porphyrins involved, i.e. whether they are on the same branch or on different branches. We also expect that, due to the high flexibility of the system, the geometry of the complexes could be extremely variable.

The situation is obviously rather complex, and we can only derive from the present data the information that an intermediate group of slightly different 2:1 complexes is formed prior to the formation of a 1:1 complex, which is favored in conditions of high concentration of Bipy. The determination of one or more association constants for this system is far too complex and beyond the purposes of the present work.

Due to the absence of a clear isosbestic point in the absorption experiment it was not possible to perform a neat luminescence titration experiment, as done in the previous

 © 2006 Wiley-VCH Verlag GmbH & Co. KGaA, Weinheim 

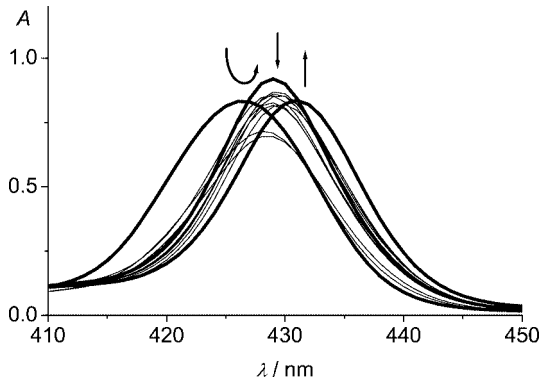


Figure 11. FB-$Zn_8$ ($2.6\times10^{-7}$ M) in toluene solution upon titration with increasing amounts of Bipy (range $5\times10^{-7}$^$5\times10^{-2}$ M).

cases. It was, however, possible to select some concentrations of titrant and to compare the luminescence of the complex to the luminescence of FB-$Zn_8$ alone, upon excitation at the iso-absorbing wavelength for the couple of solutions. The data are reported in Figure 12 and seem to indicate that an increase of the luminescence of the zinc porphyrin at 610 nm *and* of the free-base moiety around 715 nm occurs in FB-$Zn_8$ upon increasing the complexation degree. In fact, comparing the results of Figure 12 with those of Figure 9, which shows data for the model Zn and Bipy, the band at 610 nm, due to the complexed zinc porphyrin component, appears to be higher in the system FB-$Zn_8$ plus Bipy than in the model complex Zn plus Bipy (2.4 vs. 1.6). This finding, which is ascribable to a disruption of the interaction between zinc porphyrin chromophores by Bipy, *could* make available more excitation energy of the zinc porphyrin donor for the energy-transfer process. This type of behavior does not seem to take place for the system FB-$Zn_8$ plus Pyr (see Figure 10); the difference in the two systems could very likely be due to the larger dimensions and to the didentate binding by Bipy.

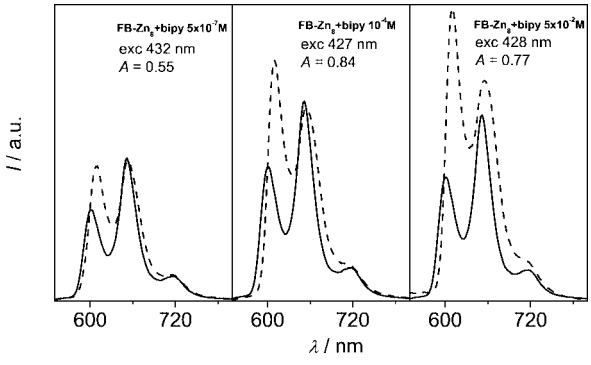


Figure 12. Luminescence spectra of FB-$Zn_8$ ($2.6\times10^{-7}$ M) in toluene solutions upon different Bipy additions compared to the luminescence of FB-$Zn_8$ alone. The excitation wavelength corresponds to the isoabsorbing wavelength for each pair of solutions (see text for details).

What is worth noting is the effect that complexation by both Pyr and Bipy has on the CD signal, as shown in Figure 13. It can be seen that complexation is effective in decreasing the optical activity. The CD signal is, however, not fully cancelled by complexation, as can be seen in the upper panel of Figure 13, where about 40% of the original signal remains at concentrations of Pyr corresponding to complexation of the zinc porphyrin units of 95%.[32] Similar results are obtained for the titration with Bipy (lower panel of Figure 13). These data indicate that a nearly complete association of the array with Pyr and Bipy (the completeness of the complexation reaction in the Bipy case can be derived from the invariance of the absorption spectra upon further addition of Bipy) can decrease most of the CD activity but not completely suppress it. Complexation can certainly interfere with exciton coupling by changing the geometry and/or the distance between interacting porphyrins but can also increase the rigidity and influence the geometry of the structure affecting the CD activity induced by chiral nucleosidic linkers. So this does not help to provide a clear identification of the origin of the observed CD effect.

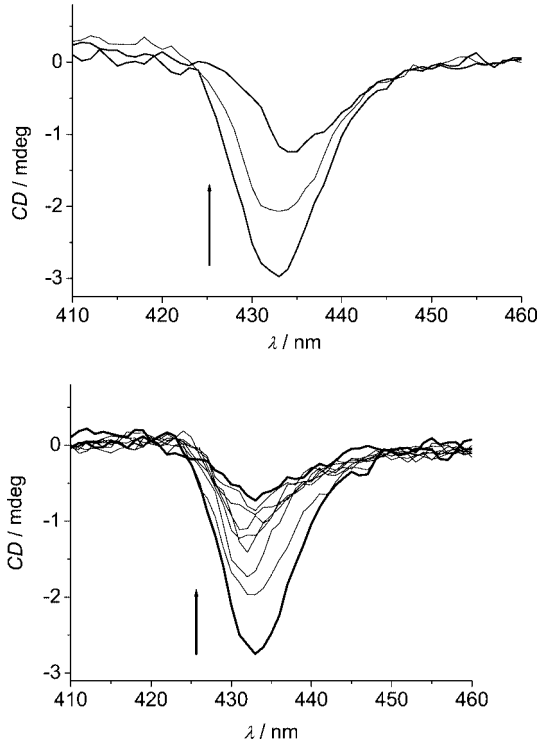


Figure 13. CD spectra of FB-$Zn_8$ in toluene solutions upon Pyr (upper panel; [Pyr] range 0–$10^{-3}$ M) and Bipy complexation (lower panel; [Bipy] range 0–$5\times10^{-2}$ M.

## Conclusions

A full spectroscopic characterization of FB-$Zn_8$ and of the photoinduced processes in this nonaporphyrin have been performed; singlet–singlet and triplet–triplet energy-transfer processes have been detected and their kinetic parameters derived. Complexation experiments withy monodentate Pyr and didentate Bipy have been performed and the association constants have been derived; furthermore, the effect of complexation on the luminescence and on the optical activity have been monitored.

 © 2006 Wiley-VCH Verlag GmbH & Co. KGaA, Weinheim 

Light absorption of this nonaporphyrin structure appears rather promising for possible applications in solar-energy conversion devices; the molar absorption coefficient has, in fact, extremely high values throughout the visible region with a maximum on the Soret band higher than 3000000 $M^{-1}cm^{-1}$. Nonetheless, its performance with respect to the ability to convey the collected light energy to the focal free-base porphyrin seems to be less satisfactory, and transfer to the core free-base porphyrin is not complete in spite of the fact that the quenching of the donor is, for most of the conformations, rather fast. The fact that the absorbed energy is not completely conveyed to the core energy acceptor and/or is not released by the latter as emitted light could be due to interactions between the chromophores, which can come into close contact because of the flexibility of the linkers and bring about self-quenching phenomena. Disruption of the interactions by using some coordinating component to separate the chromophores appears to be a promising strategy to try to overcome/reduce the undesired interactions with a consequent increase of the energy available for the transfer to the core free-base porphyrin acceptor.

## Experimental Section

The synthesis of the nonaporphyrin has been reported elsewhere.[15]

**Spectroscopic and Photophysical Determinations:** The solvent used was spectroscopic grade toluene (C. Erba). Absorption spectra were recorded with a Perkin–Elmer Lambda 9 spectrophotometer and emission spectra, uncorrected if not otherwise specified, were recorded with a Spex Fluorolog II spectrofluorimeter equipped with a Hamamatsu R928 photomultiplier. Relative luminescence intensities were evaluated from the area (on an energy scale) of the luminescence spectra corrected for the photomultiplier response. Luminescence quantum yields, $\Phi$, for the components were obtained with reference to a standard, namely (1,5,10,15-tetra-*tert*-butylphenyl)porphyrinatozinc(II), in toluene with $\Phi = 0.08$.[16] Experiments at 77 K made use of quartz capillary tubes immersed in liquid nitrogen contained in a home-made quartz dewar. Circular dichroism spectra were obtained with a Jasco J-710 dichrograph.

Titration experiments for the determination of the association constants were performed using a constant concentration of porphyrins and variable concentrations of Pyr or Bipy. In titration experiments excitation was performed at the isosbestic point of the complexed and uncomplexed porphyrin spectra. Equation (2) was used to derive the association constant, $K_a$, where $K_a$ is $1/K_d$, *Obs* is any observable (i.e. absorbance or emission intensity), $S_0$ is the constant concentration of FB-$Zn_8$, $X$ is the variable concentration of the complexing agent, $\Delta Obs$ is the maximum variation of the observable under examination and $Obs_0$ is its value at zero concentration of titration agent.[28,29]

$$Obs = Obs_0 + \frac{\Delta Obs}{2S_0}\cdot\{K_d + X + S_0 - [(K_d + X + S_0)^2 - 4XS_0]^{1/2}\} \quad (2)$$

Fluorescence lifetimes in the nanosecond range were detected by an IBH Time-Correlated Single Photon Counting apparatus with excitation at 337 nm. Luminescence lifetimes shorter than one nanosecond were determined by an apparatus based on a Nd:YAG laser (Continuum PY62-10) with a 35-ps pulse duration (532 nm, 1 mJ per pulse) and a Streak Camera (Hamamtsu C1587 equipped with M1952). The luminescence signals from 1000 laser shots were averaged and the time profile was measured from the streak image in a wavelength range of about 20 nm around the selected wavelength. The fitting of the luminescence decays was performed by standard iterative nonlinear programs taking into consideration the instrumental response.[33a] Transient absorbance in the nanosecond range made use of a laser flash photolysis apparatus based on a Nd:YAG laser (JK Lasers) delivering 532-nm pulses of 18 ns. Absorbance of the solutions at the exciting wavelength was about 0.2 and the energy used was 5 mJ per pulse for the determination of the spectra and less than 0.2 mJ per pulse for the triplet lifetime determination, in order to prevent undesired second-order T-T annihilation reactions. Relative triplet yields were calculated with respect to the photons absorbed only by the unit of interest, calculated on the basis of the photon partition in the array, and were determined by comparing the transient absorbance in the region 600–650 nm with that of Zn for FB-$^3Zn_8$ and at 680–700 nm with that of FBS for $^3$FB-$Zn_8$. Experiments on triplets were conducted in homemade, 10-mm optical path cuvettes, bubbled with argon for 5 min, if not otherwise specified. Further details on the experimental setup can be found elsewhere.[33b,33c]

Computation of the integral overlap and of the rate of the energy-transfer processes according to the Förster mechanism was performed with Matlab 5.2.[34]

Estimated errors are 20% for quantum yields, 30% for association constants, and 10% for lifetimes; the working temperature, if not otherwise specified, was 295 ± 2 K. The error in lifetime determinations is increased in case of multi-exponential fitting to 20%.

## Acknowledgments

Funds from the Italian CNR (project PM-P04-ISTM-C1/ISOF-M5: Molecular, supramolecular and macromolecular components with photonic and optoelectronic properties) and from the Ministero dell'Istruzione, dell'Universita' e della Ricerca (FIRB, RBNE019H9K) are acknowledged.

[1] D. Kim, A. Osuka, *J. Phys. Chem. A* **2003**, *107*, 8791–8816.
[2] N. Atratani, A. Osuka, H. S. Cho, D. Kim, *J. Photochem. Photobiol. C: Photochem. Rev.* **2002**, *3*, 25–52.
[3] E. Hindin, R. A. Forties, R. S. Loewe, A. Ambroise, C. Kirmaier, D. F. Bocian, J. S. Lindsey, D. Holten, R. S. Knox, *J. Phys. Chem. B* **2004**, *108*, 12821–12832.
[4] D. Holten, D. F. Bocian, J. S. Lindsey, *Acc. Chem. Res.* **2002**, *35*, 57–69.
[5] D. Furutsu, A. Satake, Y. Kobuke, *Inorg. Chem.* **2005**, *44*, 4460–4462.
[6] Y. Nakamura, I.-W. Hwang, N. Aratani, T. K. Ahn, D. M. Ko, A. Takagi, T. Kawai, T. Matsumoto, D. Kim, A. Osuka, *J. Am. Chem. Soc.* **2005**, *127*, 236–246.
[7] I.-W. Hwang, D. M. Ko, T. K. Ahn, Z. S. Yoon, D. Kim, X. Peng, N. Aratani, A. Osuka, *J. Phys. Chem. B* **2005**, *109*, 8643–8651.
[8] I.-W. Hwang, M. Park, T. K. Ahn, Z. S. Yoon, D. M. Ko, D. Kim, F. Ito, Y. Ishibashi, S. R. Khan, Y. Nagasawa, H. Miyasaka, C. Ikeda, R. Takahashi, K. Ogawa, A. Satake, Y. Kobuke, *Chem. Eur. J.* **2005**, *11*, 3753–3761.
[9] A. Nakano, A. Osuka, T. Yamazaki, Y. Nishimura, S. Akimoto, I. Yamazaki, A. Itaya, M. Murakami, H. Miyasaka, *Chem. Eur. J.* **2001**, *7*, 3134–3151.
[10] Himahori, *J. Phys. Chem. B* **2004**, *108*, 6130–6143 and references cited therein.

 © 2006 Wiley-VCH Verlag GmbH & Co. KGaA, Weinheim 

[11] M.-S. Choi, T. Aida, T. Yamazaki, I. Yamazaki, *Chem. Eur. J.* **2002**, *8*, 2668–2678.
[12] K. Sasaki, K. Sugou, K. Miyamoto, J. Hirai, S. Tsubouchi, H. Miyasaka, A. Itaya, Y. Kuroda, *Org. Biomol. Chem.* **2004**, *2*, 2852–2860.
[13] a) A. Satake, Y. Kobuke, *Tetrahedron* **2005**, *61*, 13–41; b) A. Morandeira, E. Vauthey, A. Schuwey, A. Gossauer, *J. Phys. Chem. A* **2004**, *108*, 5741–5751; c) J. Davila, A. Harriman, L. R. Milgrom, *Chem. Phys. Lett.* **1987**, *136*, 427–430; d) M.-S. Choi, T. Yamazaki, I. Yamazaki, T. Aida, *Angew. Chem. Int. Ed.* **2004**, *43*, 150–158.
[14] N. Solladiè, C. Sooambar, H. Herschbach, J.-M. Strub, E. Leize, A. Van Dorsselaer, A. M. Talarico, B. Ventura, L. Flamigni, *New J. Chem.* **2005**, *29*, 0000–0000.
[15] a) L. Flamigni, A. M. Talarico, B. Ventura, G. Marconi, C. Sooambar, N. Solladie, *Eur. J. Inorg. Chem.* **2004**, 2557–2569; b) N. Solladie, M. Gross, J.-P. Gisselbrecht, C. Sooambar, *Chem. Commun.* **2001**, 2206–2207.
[16] M. Dixon, J. P. Collin, J. P. Sauvage, L. Flamigni, *Inorg. Chem.* **2001**, *40*, 5507–5517.
[17] L. Flamigni, N. Armaroli, F. Barigelletti, V. Balzani, J. P. Collin, J. O. Dalbavie, V. Heitz, J. P. Sauvage, *J. Phys. Chem.* **1997**, *101*, 5936–5943.
[18] The emission quantum yield of FBS may be affected by an error of about 30%. This is caused by the low absorbance value (<0.1) of the unit in the array at the excitation wavelength (650 nm) because of the presence of one FBS unit out of eight Zn porphyrin units.
[19] Th. Förster, *Discuss. Faraday Soc.* **1959**, *27*, 7–17.
[20] Distance calculated with CS Chem. 3D Ultra CambridgeSoft. Com, 2000 Cambridge, MA, USA. The calculated quenching at a distance of 34 Å is about 20%. A lifetime reduction of this order can hardly be detected in our experimental conditions, where a multi-exponential fit of the decay, characterized by a large uncertainty, is involved.
[21] See, for example: A. Nakano, A. Osuka, I. Yamazaki, T. Yamazaki, Y. Nishimura, *Angew. Chem. Int. Ed.* **1998**, *37*, 3023–3027.
[22] S. L. Murov, I. Carmichael and G. L. Hugh, *Handbook of Photochemistry*, Marcel Dekker, New York, **1993**, p. 293.
[23] L. Flamigni, A. M. Talarico, M. J. Gunter, M. R. Johnston, T. P. Jeynes, *New J. Chem.* **2003**, *27*, 551–559.
[24] D. L. Dexter, *J. Chem. Phys.* **1953**, *21*, 836–850.
[25] 5 mJ at 532 nm correspond to $1.3\times10^{16}$ photons, the analyzed volume (0.04 mL) contains $8\times10^{13}$ units of array. The absorbed photons in the analyzed volume are 7.5%, i.e. $1.0\times10^{15}$ and this can clearly lead to multiple excitation of the same array.
[26] In order to derive the decay rate of FB-$^3$Zn$_8$, the following equation was used: $k_{obs} = k_{en} + C{\cdot}I^2$, where $I$ is the laser intensity, $C$ is a constant, $k_{obs}$ is the first-order rate constant observed for the decay of FB-$^3$Zn$_8$ and $k_{en}$ is the energy transfer reaction rate. $k_{en}$ was derived by extrapolation of the observed rate $k_{obs}$ to zero laser intensity.
[27] J. F. Nierengarten, N. Armaroli, G. Accorsi, Y. Rio, J. F. Eckert, *Chem. Eur. J.* **2003**, *9*, 36.
[28] a) L. Flamigni, A. M. Talarico, F. Barigelletti, M. R. Johnston, *Photochem. Photobiol. Sci.* **2002**, *1*, 190–197 and references cited therein; b) E. Iengo, E. Zangrando, E. Alessio, J.-C. Chambron, V. Heitz, L. Flamigni, J.-P. Sauvage, *Chem. Eur. J.* **2003**, *9*, 5879–5887 and references cited therein.
[29] L. Flamigni, A. M. Talarico, B. Ventura, *J. Porphyrins Phthalocyanines* **2003**, *7*, 317–326.
[30] C. C. Mak, N. Bampos, J. K. M. Sanders, *Angew. Chem.* **1998**, *110*, 3169–3172; *Angew. Chem. Int. Ed.* **1998**, *37*, 3020–3023.
[31] a) L. Baldini, P. Ballester, A. Casnati, R. M. Gomila, C. A. Hunter, F. Sansone, R. Ungaro, *J. Am. Chem. Soc.* **2003**, *125*, 14181–14189; b) P. Ballester, A. Costa, A. M. Castilla, P. M. Deyà, A. Frontera, R. M. Gomila, C. H. Hunter, *Chem. Eur. J.* **2005**, *11*, 2196–2206.
[32] The fraction of complexation, $f$, can be determined by the following equation: $f = 1 - [1/(1 + [\mathrm{Pyr}]\,K_a)]$.
[33] a) L. Flamigni, *J. Phys. Chem.* **1993**, *97*, 9566–9572; b) L. Flamigni, *J. Phys. Chem.* **1992**, *96*, 3331–3337; c) L. Flamigni, *J. Chem. Soc., Faraday Trans.* **1994**, *90*, 2331–2336.
[34] *Matlab 5.2*. The MathWorks Inc. Natik Ma 01760, USA.

Received: November 21, 2005
Published Online: March 30, 2006

 © 2006 Wiley-VCH Verlag GmbH & Co. KGaA, Weinheim 

DOI: 10.1002/ejic.200501045

# Kinetic and Thermodynamic Aspects of the CT and T-Shaped Adduct Formation Between 1,3-Dimethylimidazoline-2-thione (or -2-selone) and Halogens

M. Carla Aragoni,[a] Massimiliano Arca,[a] Francesco A. Devillanova,*[a] Patrizio Grimaldi,*[b] Francesco Isaia,[a] Francesco Lelj,*[b] and Vito Lippolis[a]

**Keywords:** Density functional calculations / Donor–acceptor systems / Hypervalent compounds / Selenium / Sulfur

The reactions between L=E donors [L: 1,3-dimethylimidazolyl framework; E: S (**1**), Se (**2**)] and halogens $X_2$ (X: Cl, Br, I) to form either "T-shaped" hypervalent chalcogen (TY) or linear charge-transfer-type adducts (CT) have been studied in the density functional theory (DFT) context by considering both thermodynamic and kinetic aspects. Apart from the case of the adducts between sulfur donors and diiodine, hypervalent compounds are calculated to be always more stable than CT ones in the gas phase, in agreement with the experimental results based on spectroscopic and structural determinations. NBO and FMO analyses suggest explanations for this. Reaction mechanism studies reveal that CT adducts are always the first products of the reactions and no transition states connecting the reactants directly to TY adducts have been found. The present calculations indicate that, at least for **1** and **2**, TY adducts are obtained from CT adducts and not directly from the reactants.

(© Wiley-VCH Verlag GmbH & Co. KGaA, 69451 Weinheim, Germany, 2006)

## Introduction

The reactions between chalcogenone donors (L=E; L: organic framework; E: S, Se) and $X_2$ halogen molecules (X: Cl, Br, I) continue to attract a great deal of interest in the scientific community due to their implication in numerous and different fields of research, which span from synthetic and supramolecular aspects to biological, materials, and industrial chemistry.[1–10] In particular, in the last ten years we have reported[4] the isolation of several classes of compounds from the reactions of thio- and selenoketone donors with halogens. In fact, besides charge transfer (CT) and T-shaped (TY) adducts, which bear linear E–X–X and X–E–X groups, respectively, donor oxidation products with chalcogen–halogen terminal bonds (L–E–X), linear two-coordinate halogen (I) atoms with chalcogen ligands ([LE–X–EL]$^+$), and dications containing a chalcogen–chalcogen single bond ([$(LE)_2$]$^{2+}$) represent some of the most common types of products characterised by X-ray crystallography. In many cases, a very small change in the chemical environment of the donor or the experimental conditions is enough to produce each of the above-mentioned products.[8] Therefore, an important goal in this field is the complete understanding of all possible pathways that allow for the interconversion between the various species in equilibrium.

The first general qualitative criterion that can be used to foresee the formation of CT or TY adducts was based on the electronegativity values of the halogen and the chalcogen: the formation of TY adducts prevails if the electronegativity value of the halogen is higher than that of the chalcogen atom, while CT adducts prevail if the reverse is true.[2] However, a more general attempt to explain the formation of the various types of compounds obtainable by reacting L=E donors with halogens has been made by Husebye and co-workers,[3] who proposed a chemical scheme according to which the [LEX]$^+$ cation plays a central role in determining the different pathways of the reactions and the nature of the final products. This cation might originate from either the CT adduct or from the TY adduct by heterolytic cleavage of the X–X or E–X bond, respectively.

Recently, the central role of the cation [LEX]$^+$ in the formation of the various products has been tested on a series of different L=E donors on the basis of DFT calculations.[4h] In particular, the NBO charge distribution calculated for the hypothetical cationic species allowed the prediction of the preferential formation of CT or TY adducts when X is Br or I. In addition, a criterion was proposed to draw-up an order of ability to form the dicationic species ([L–E–E–L]$^{2+}$) for the considered L=E donors. This criterion suggested imidazoline-2-thione to be the top-ranking sulfur donor in the ability to form these dications, as sub-

[a] Dipartimento di Chimica Inorganica ed Analitica, Università di Cagliari, S.S. 554,
Bivio per Sestu, 09042 Monserrato (CA), Italy
E-mail: devilla@vaxca1.unica.it
[b] LaMI Dipartimento di Chimica and LaSCaMM-INSTM Sezione Basilicata, Università della Basilicata,
Via N. Sauro, 85100 Potenza, Italy
E-mail: grimaldi@unibas.it
lelj@unibas.it

 © 2006 Wiley-VCH Verlag GmbH & Co. KGaA, Weinheim 

sequently observed experimentally.[7] On the basis of these encouraging results, we decided to use DFT calculations in order to achieve further insight into the origin of the relative stability of the various products and to explore the possibility of interconversion among the various species in solution. In fact, this seemed very important in order to clarify the whole reaction mechanism and test the hypothesis of Husebye from a computational point of view. A first problem to clarify was whether it is always necessary to hypothesize the formation of the $[LEX]^+$ cation as an intermediate or whether there are other accessible reaction pathways that lead to formation of the final products.

The most general reactivity scheme of L=E donors with halogens or inter-halogens in forming CT and TY adducts is depicted in Scheme 1.

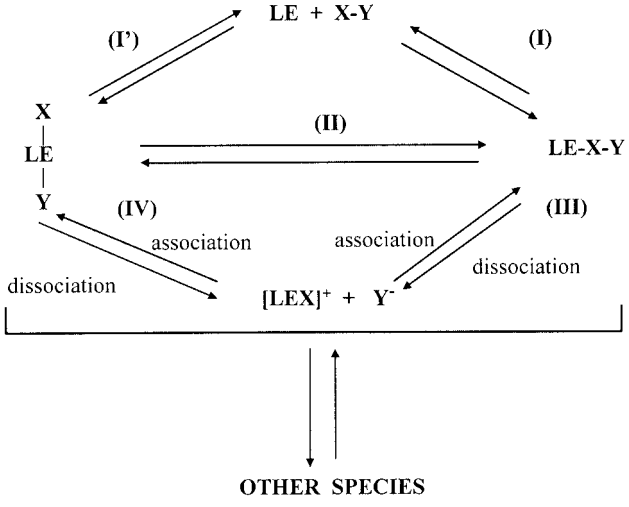


Scheme 1. General scheme for the reactivity of LE donors with halogen (X equal to Y) and interhalogen molecules (X not equal to Y), involving only the CT and TY adducts and the $[LEX^+]$ cation.

In the present study we discuss the mechanistic aspects with respect to non-ionic species also, addressing our attention to the kinetic and thermodynamic aspects of the formation of CT and TY adducts (pathways I′ and I of Figure 1) by direct attack of an $X_2$ molecule (X: Cl, Br or I) on 1,3-dimethylimidazoline-2-thione (**1**) and -2-selone (**2**) (see Scheme 2), and on the possible interconversion between these adducts (pathway II).

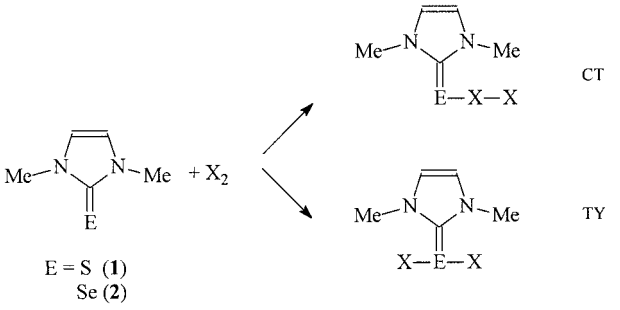


Scheme 2. The two donors and the two possible products (CT and TY adducts) of the interaction between the imidazoline donors and $X_2$.

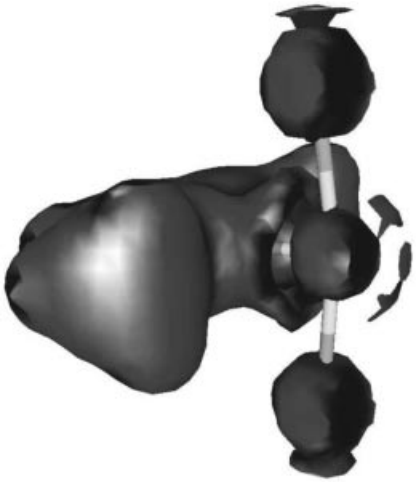

Figure 1. $\nabla^2\rho$ computed for **1**·$Br_2$ using MP2 density showing a charge concentration on the outer side of the chalcogen atom.

## Computational Methods and Search Techniques for Transition States

DFT and MP2[11] calculations were performed on an Alpha workstation using the Gaussian 98 (rev. A7 and A11) program and the implemented version of the NBO (natural bond orbital) analysis program.[12,13] The geometries of the adducts were fully optimised at the DFT level. In our previous DFT calculations on the TY adducts,[4h,4j] we used the hybrid B3LYP functional,[14] the Schafer, Horn and Ahlrichs[15] basis sets for C, H, N, O, S and Se, and the LANL2DZ basis sets together with effective core potentials (ECP)[16] for halogen atoms. The geometries of the CT and TY halogen adducts of 1,3-dimethylimidazoline-2-thione (**1**) and 1,3-dimethylimidazoline-2-selone (**2**) were therefore optimised at the same level of theory. In order to evaluate the influence of the model on the optimisations, CT and TY $Br_2$ adducts of **1** and **2** were also optimised at the MP2 and DFT with an asymptotic corrected hybrid functional[17] level with the Schafer, Huber and Ahlrichs basis sets.[18] $Br_2$ adducts were been chosen because it is possible to use a basis set without pseudo-potentials and because of the intermediate position of Br between Cl and I. In both cases the results showed no significant differences with respect to those obtained with the other model. The transition states of the reactions between **1** and **2** and halogens $X_2$ (X: I, Br, Cl) were localised by the NEPR (negative eigenvalues progressive reduction) technique.[19]

Since it has been observed[20] that the DFT approach can give incorrect indications about the structures and energies of transition states of closed-shell interacting fragments, we have also performed some MP2 calculations on the potential energy surface (PES) of selected reactants (**1** and $Br_2$) towards the CT isomer. The relative stabilities of the CT and TY adducts in the gas phase were analysed according to the NBO method.[13] NBO analysis is based on a method for optimally transforming a given wavefunction into its

 © 2006 Wiley-VCH Verlag GmbH & Co. KGaA, Weinheim 

localised form, corresponding to the one-centre (lone pair) or two-centre (bond) functions. Delocalisation effects appear as weak departures from this idealised localised picture. The energetic importance of these effects can be estimated according to a second-order perturbation theory approach. Since these delocalisation effects lead to loss of occupancy from the localised NBO (σ, π or lone pair) of the idealised Lewis structure into the empty non-Lewis, antibonding (σ* or π*) and Rydberg (R*) orbitals, and thus to departures from the idealised Lewis structure description, they are referred to as "delocalisation" corrections to the zeroth-order Lewis structure. For each donor NBO (*i*) and acceptor NBO (*j*), the stabilisation energy ($\Delta E_{ij}$) associated with delocalisation $i \rightarrow j$ is estimated as $\Delta E_{ij} = q_i \cdot [F(i,j)^2]/(\varepsilon_j - \varepsilon_i)$, where $q_i$ is the donor orbital occupancy, $\varepsilon_j$ and $\varepsilon_i$ are the diagonal elements (orbital energies) and F(*i*,*j*) is the off-diagonal NBO Fock matrix element (see ref.[13] for a detailed discussion).

## Results and Discussion

### Relative Stability of Isomers: Optimisations, NBO and FMO Analysis

Table 1 reports some relevant optimised geometrical parameters together with available experimental data of the CT and TY adducts of **1** and **2**. The agreement is very good and, furthermore, it is worthy to note that for TY adducts the method is able to account for the small deviations of the angle X–E–X from 180°, as observed for **2**·$I_2$ and other related adducts.[4h–4k,8,9] Analysis of $\nabla\rho^2$[22] suggests an explanation for this deviation (see Figure 1). According to the $\nabla\rho^2$ values there is a charge accumulation near the chalcogen on the outer side of the adduct that bends the two halogen atoms towards the molecular ring. DFT calculations indicate that hypervalent compounds for both **1** and **2** are thermodynamically favoured with respect to the CT isomers in all but the case of **1**·$I_2$ (see Table 2). The energy difference between CT and TY adducts decreases as the halogen atomic number increases and the chalcogen one reduces.

Table 2. Calculated stability [kcal mol$^{-1}$] of the CT with respect to the TY isomers (taken as 0.0) for **1** and **2**.

| | **1** | **2** |
|---|---|---|
| $Cl_2$ | 11.5 | 21.3 |
| $Br_2$ | 2.1 | 10.6 |
| $I_2$ | –3.7 | 3.5 |

In the cases of **1**·$Cl_2$, **2**·$Cl_2$, and **2**·$Br_2$ the TY adduct formation is clearly preferred, whereas in the cases of **1**·$Br_2$, **1**·$I_2$ and **2**·$I_2$ the energy differences between the two types of adducts are so small (<4 kcal mol$^{-1}$) that the experimental trend in the stability of the possible isomers can be modified by environmental effects. However, it should be remembered that no CT adducts between thioketonic donors and $Br_2$ or TY adducts with $I_2$ have been characterised so far. This relative order of stability does not change when using different approximations both in basis set and in the level of approximations.

Figure 2 reports the HOMO–1 and HOMO energies of **1** and **2** and the LUMO energies of the $X_2$ molecules. As can be seen, the HOMO energy of **1** is lower than the LUMO energy of $I_2$ only in the case of the couple **1**/$I_2$, and only in this case is the CT adduct thermodynamically favoured with respect to the TY one. It is also interesting to observe that there is a linear relationship between the NBO charges on the chalcogen atom E of the TY adducts and the frontier molecular orbital $(HOMO–1)_{LE}$ – $(LUMO)_{X_2}$ energy difference (see Figure 3).

In fact, Figure 2 shows that $(HOMO–1)_{LE}$ – $(LUMO)_{X_2}$ is lower than the $(HOMO)_{LE}$ – $(LUMO)_{X_2}$ energy difference in all cases, the exception being the case of **1**·$I_2$. Moreover, the HOMO–1 is mainly a p orbital on the chalcogen, whereas the HOMO has a non-negligible delocalisation on the imidazoline ring. This makes the interaction of dihalogen LUMOs with $(HOMO–1)_{LE}$ more relevant than the interaction with $(HOMO)_{LE}$.

Table 1. Relevant geometrical parameters of the optimised geometries of CT and TY adducts of **1** and **2** (X: halogen, E: chalcogen; distances in angstroms and angles in degrees). The structural data available for related compounds are reported in parentheses.

| TY Adducts | **1**·$Cl_2$ | **2**·$Cl_2$ | **1**·$Br_2$ | **1**·$Br_2$[a] | **1**·$Br_2$[4h],[b,c] | **2**·$Br_2$[4k],[d] | **1**·$I_2$ | **2**·$I_2$[8] |
|---|---|---|---|---|---|---|---|---|
| X–E | 2.53 | 2.59 | 2.71 | 2.54 | 2.53 (2.49) | 2.77 (2.66, 2.52) | 2.91 | 2.98 (2.74, 2.89) |
| E–C | 1.78 | 1.90 | 1.78 | 1.73 | 1.73 (1.75) | 1.90 (1.95) | 1.78 | 1.89 (1.89) |
| X–E–X | 170.64 | 170.17 | 171.95 | 168.41 | 170.59 (179.38) | 170.76 (175.7) | 175.70 | 170.24 (178.64) |
| X–E–C–N | 102.30 | 109.15 | 95.06 | 90.01 | 90.09 (76.0) | 102.84 (–101 to 78) | 90.00 | 89.93 (–94.4 to 90.0) |
| **CT Adducts** | **1**·$Cl_2$ | **2**·$Cl_2$ | **1**·$Br_2$ | **1**·$Br_2$[a] | **1**·$Br_2$[b] | **2**·$Br_2$ | **1**·$I_2$[41],[e] | **2**·$I_2$[8],[e] |
| X–X | 2.40 | 2.43 | 2.66 | 2.45 | 2.44 | 2.69 | 3.01 (2.90) | 3.03 (2.99, 2.91) |
| X–E | 2.66 | 2.72 | 2.80 | 2.73 | 2.73 | 2.89 | 2.99 (2.68) | 3.09 (2.72, 2.78) |
| E–C | 1.74 | 1.87 | 1.74 | 1.69 | 1.69 | 1.87 | 1.74 (1.72) | 1.87 (1.88, 1.86) |
| X–X–E | 176.81 | 175.95 | 178.12 | 176.69 | 178.70 | 178.13 | 178.46 (175.7) | 178.37 (176.86, 175.63) |
| X–E–C | 91.94 | 89.88 | 94.45 | 85.83 | 93.56 | 92.34 | 96.64 (96.8) | 93.59 (93.0, 96.9) |
| X–E–C–N | 111.21 | 115.85 | 106.98 | 88.55 | 109.48 | 111.42 | 104.07 (–96.4 to 84.4) | 108.63 (–100.4 to 84.6) |

[a] MP2 calculations. [b] DFT with asymptotic corrected hybrid functional. [c] Structural data refer to *N*,*N*′-dimethylbenzoimidazole-2-ylium dibromosulfanide. [d] Structural data refer to 1,2-bis(3-methyl-4-imidazolin-2-ylium dibromoselenanide)ethane. [e] Structural data refer to 1,1′-bis(3-methyl-4-imidazolin-2-chalcogenone)methane bis(diiodine).

 © 2006 Wiley-VCH Verlag GmbH & Co. KGaA, Weinheim 

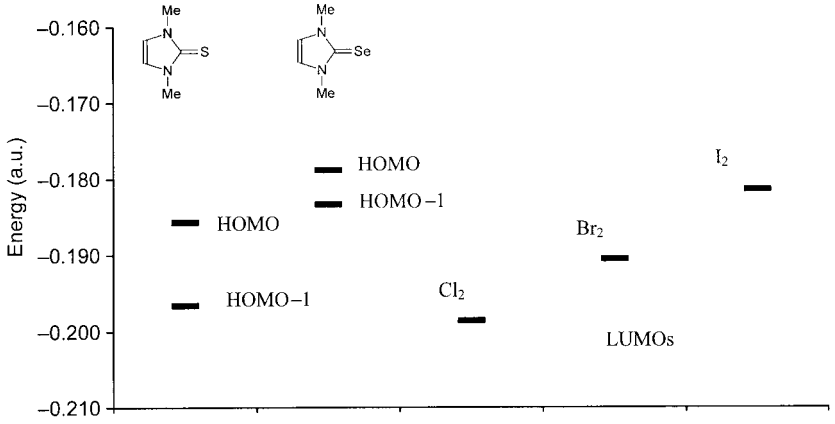


Figure 2. Calculated KS orbital energy of the HOMOs and HOMO–1s of **1** and **2**, and of LUMOs of the halogens $X_2$.

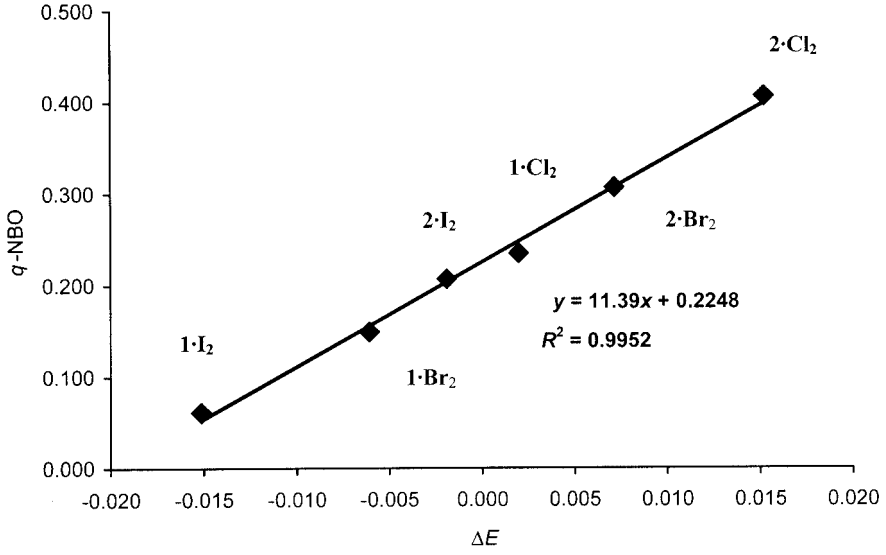


Figure 3. NBO net charges on the chalcogen (E) atoms of the TY adducts between **1** and **2** with the halogen $X_2$ as a function of the energy difference between $(HOMO–1)_{LE}$ and $(LUMO)_{X_2}$.

To gain a deeper insight into the relative stability of TY and CT adducts, an NBO energetic analysis was performed on all the compounds at the B3LYP/(SV-LanL2DZ) level by assigning the electrons in order to obtain two closed-shell fragments: a halide anion, $X^-$, and the remaining $[LEX]^+$ cation. The interaction of $X^-$ either with the chalcogen atom or with the halogen atom of the $[LEX]^+$ cation formally accounts for the formation of the TY and CT adducts, respectively. We must stress, however, that this scheme does not suggest any underlying reaction mechanism but is simply a useful approach that allows us to compare the origin of the stability in the two isomers (CT and TY) with respect to the same reference fragments.

The NBO energetic analysis (see Table 3) and the particular choice of the interacting fragments allow us not only to quantify the energy contribution of the charge transfer from the halide anion to the cation (column e in Table 3) but also to account for the contributions of the polarisation effects within the $[LEX]^+$ fragment. As an example, the NBO orbitals that contribute most to the relative stabilities of the TY adduct **1**·$Br_2$ are depicted in Figure 4.

For all the adducts examined the excitation processes within the $[LEX]^+$ cation involve two-centre localised bond orbitals (σ) and a one-centre valence lone pair (lp) orbital as donors and higher energy empty orbitals (σ*, π* and R*) that can behave as acceptors and, subsequently, as donors. In the interaction between the two fragments, two of the numerous delocalisation contributions are found to be the most relevant ones (see Table 3 and Figure 4). The first of these is due to an intramolecular polarisation effect and involves the reorganisation of the electronic structure of the cation due to the presence of the anion. This reorganisation can be described by two intra-cation charge-transfer processes, one from a carbon–chalcogen bonding orbital to a carbon–nitrogen antibonding orbital, which occurs through two intermediate orbitals: a carbon–chalcogen antibonding and a carbon Rydberg orbital (see columns a–c of Table 3), and the other involving a relatively small back-donation

 © 2006 Wiley-VCH Verlag GmbH & Co. KGaA, Weinheim 

Table 3. NBO energetic analysis results. Columns a–d are relative to the intrafragment polarisation effects. Column e concerns the interfragment charge transfer. All data are in kcal mol$^{-1}$.

| | Intramolecular polarisation effects | | | | Total polarisation effect contributions | Charge transfer |
|---|---|---|---|---|---|---|
| Adducts/Orbitals | *a* $\sigma_{(C-E)} \rightarrow \pi^*_{(C-E)}$ | *b* $\pi^*_{(C-E)} \rightarrow R^*_C$ | *c* $R^*_C \rightarrow \sigma^*_{(C-N)}$ | *d* $\sigma_{(C-N)} \rightarrow \pi^*_{(C-E)}$ | (*a*+*b*+*c*+*d*) $\sigma_{(C-E)} \rightarrow \sigma^*_{(C-N)}$ $\sigma_{(C-N)} \rightarrow \pi^*_{(C-E)}$ | *e* $lp_X \rightarrow \sigma^*_{(E-X)}$ |
| 1·$Cl_2$ (TY) | 1.9 | 45.0 | 45.0 | 5.0 | 96.9 | 48.0 |
| 1·$Cl_2$ (CT) | 5.3 | 14.0 | 0.45 | 3.0 | 22.7 | 110.0 |
| 2·$Cl_2$ (TY) | 3.0 | 20.0 | 50.0 | 12.0 | 85.0 | 45.0 |
| 2·$Cl_2$ (CT) | 6.0 | 11.0 | 0.45 | 5.0 | 22.4 | 90.0 |
| 1·$Br_2$ (TY) | 0.7 | 182.0 | 80.0 | 28.0 | 290.7 | 48.0 |
| 1·$Br_2$ (CT) | 2.0 | 110. | 120. | 13.0 | 245.0 | 92.0 |
| 2·$Br_2$ (TY) | 1.6 | 30.0 | 40.0 | 10.0 | 81.6 | 45.0 |
| 2·$Br_2$ (CT) | 5.0 | 12.0 | 45.0 | 5.0 | 22.5 | 95.0 |
| 1·$I_2$ (TY) | 0.5 | 0.7 | 45 | 37.0 | 83.2 | 48.0 |
| 1·$I_2$ (CT) | 0.6 | 30.0 | 0.5 | 7.0 | 38.1 | 100.0 |
| 2·$I_2$ (TY) | 0.45 | 300.0 | 50.0 | 13.0 | 363.4 | 30.0 |
| 2·$I_2$ (CT) | 40.0 | 250.0 | 0.5 | 1.5 | 292.0 | 97.0 |

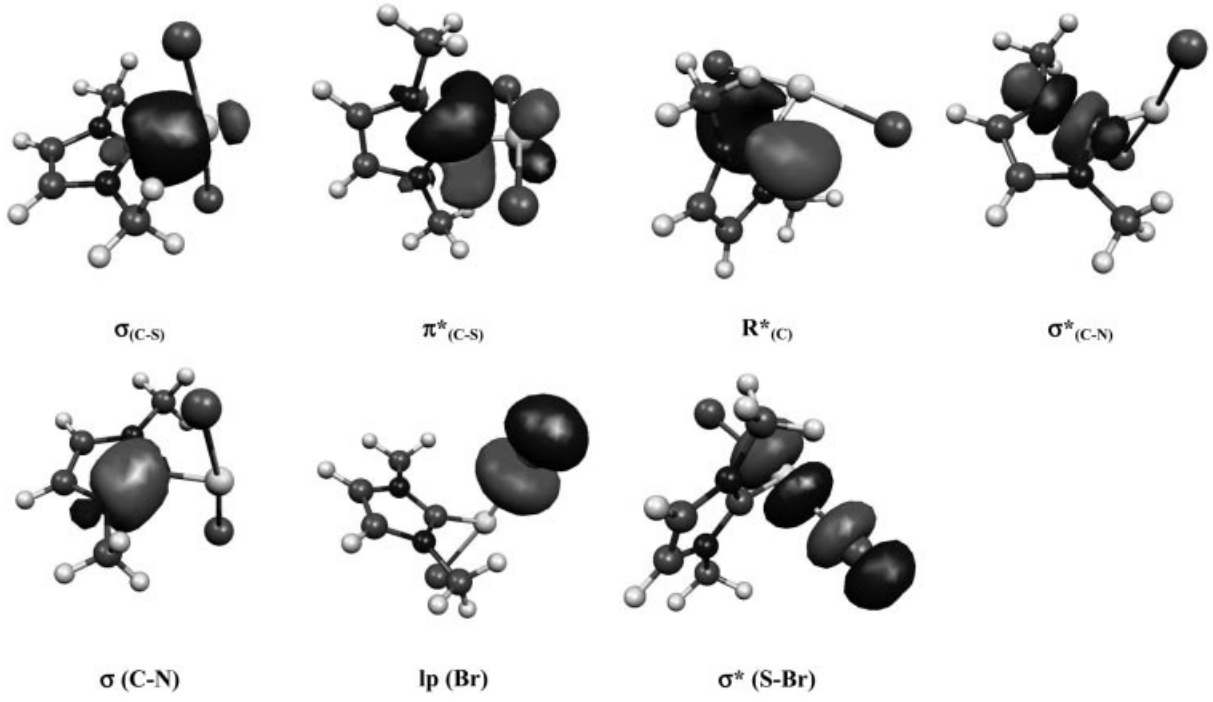


Figure 4. NBO localised orbitals calculated for **1**·$Br_2$ involved in the polarisation effects (see Table 3).

from carbon–nitrogen bonding orbitals to carbon–chalcogen antibonding orbitals (see column d of Table 3). The second is an inter-fragment process that involves the two $[LEX]^+$ and $X^-$ fragments. It is a strong charge-transfer from the halide anion lone pair to the halogen–chalcogen σ* orbital.

The sum of the energy stabilisation contributions (Table 3) gives, approximately, the relative stability for every pair of isomers. As can be deduced from this table, the different weight of each contribution determines the energy differences between the CT and TY compounds (see Table 2). In particular, the total polarisation effect contribution in the cation is bigger for the latter compounds, whereas the interfragment charge-transfer prevails in the former.

This approach also allows us to analyse the different behaviour shown by sulfur and selenium derivatives. The NBO analysis shows that the smaller energy difference between **1**·$Cl_2$ adducts (11.5 kcal mol$^{-1}$) with respect to **2**·$Cl_2$ ones (21.3 kcal mol$^{-1}$) is due to a greater stabilisation energy of the charge transfer in the case of the chlorine anion lone pair towards the antibonding S–Cl NBO orbital of the CT adduct. The growing importance of this charge transfer in the selenium CT adducts is the main factor responsible for the smaller energy difference for bromine and iodine compounds with respect to chlorine ones.

 © 2006 Wiley-VCH Verlag GmbH & Co. KGaA, Weinheim 

## Reaction Mechanism

### *Path I*

Scanning the PES for the motion of $X_2$ toward **1** and **2** allowed the identification of putative transition states, although their refinement did not give definite stationary structures in any case. Therefore a deeper investigation was performed in the case of the motion of $Br_2$ toward **1** using different approximations both in the Hamiltonian and in the basis set. DFT with an asymptotic corrected hybrid functional[17] and a post Hartree–Fock perturbative MP2 approach were used. The MP2 approach was used since long-range dispersive interactions need at least a bi-excited configuration contribution. In all cases the Schafer, Horn and Ahlrichs pVDZ[18] basis sets with polarisation functions on all atoms were used in order to better describe polarisation effects. All the models used showed the same Morse-like shape for the total energy, which can be fitted with the Morse function $y = D^*[1 - e^{-\beta(x-x_0)}]^2$ with the following parameters: $\beta$ = 1.3133, $x_0$ = 2.7180 Å and $D$ = 13.5461 kcal mol$^{-1}$ (see Figure 5), thereby excluding the existence of a transition state between reactants and CT adducts. Indeed, the Morse function, starting from a distance $x = x_0 - \beta\ln 2$, always has a negative value of the second derivative with a stationary point at $x = \infty$. This is the reason why, in our opinion, approximately localised putative transition states did not converge to definite transition states but were taken apart to very large distances during the optimisations.

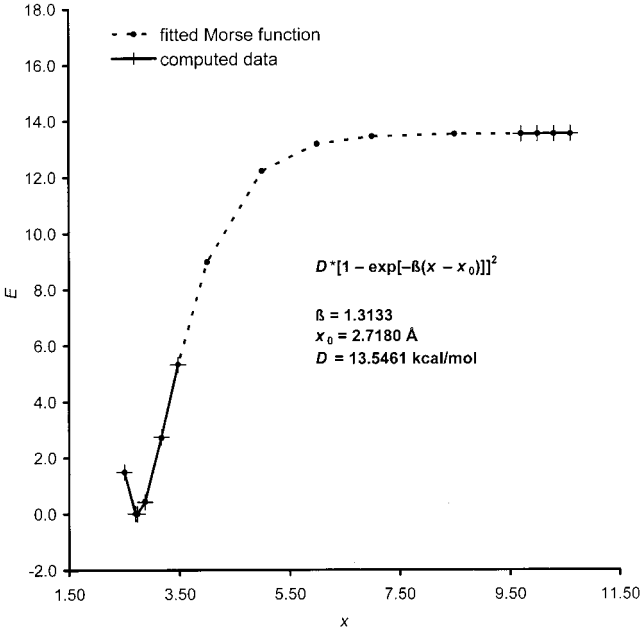


Figure 5. Computed data (in MP2 approximation) and fitted Morse function for the motion of $Br_2$ toward **1**. (energy in kcal mol$^{-1}$ and $x$ in angstroms).

Furthermore, the study of $\nabla^2\rho$[21] allowed us to describe the possible interaction of the two fragments due to electron density. As matter of fact, the $\nabla^2\rho$ (see Figure 6) shows a definite accumulation of the density in an sp shape in front of the chalcogen and a toroidal hole around the π C=E bond in the case of **1**. This can explain the fact that at large distances the interaction is between the "density hole " on the halogen and the charge concentration on the chalcogen, whereas at shorter distances the interaction is on the toroidal hole around the chalcogen and with a spherical charge concentration to even shorter distance in the CT adduct.

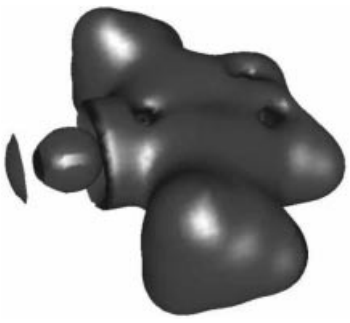

Figure 6. $\nabla^2\rho$ computed for **1** using MP2 density showing a charge concentration in front of the chalcogen atom and a depletion with cylindrical symmetry around the same atom.

### *Path I′ and II*

The six transition states leading to the six TY adducts in the reactions between **1** and **2** with halogens $X_2$ (X: Cl, Br, I) were successfully identified by applying the NEPR technique and confirmed by calculations of the second derivative matrix of the energy with respect to the coordinates. Only one negative eigenvalue was found for each of them, thus confirming the nature of the transition state for the computed structures.

To further confirm the assignment of the transition states to a given reaction path we used the intrinsic reaction coordinate (IRC) approach.[22] This approach allows the connection of each saddle-point to a given reactant/product couple. Indeed, the IRC approach confirmed that the six transition states (of the kind reported in Figure 7) link TY adducts to CT ones but, surprisingly, not to the (LE + $X_2$) reactants. Any further attempt to find a different transition state connecting TY adducts and LE and $X_2$ failed because we always found the same transition state that connected TY and CT adducts. As a consequence of these findings, step I′ of Scheme 1 should be excluded as a possible pathway leading to the TY adduct. Some relevant structural parameters of each optimised transition state are reported in Table 4.

Interestingly, all the six transition states leading to the TY from the CT adducts (see Figure 6) show the halogen molecule occupying the axial and equatorial position of a hypothetical trigonal bipyramid centred on the chalcogen atom. Figure 8 shows the snapshot sequence of the interconversion leading from the CT to the TY adduct through the axial–equatorial transition state. The energy barrier to overcome, with respect to the CT adduct, is in the range 25–40 kcal mol$^{-1}$. In order to evaluate the direct interconversion between the CT and TY adducts (pathway II) of the general Scheme 1 and the paths III and IV

 © 2006 Wiley-VCH Verlag GmbH & Co. KGaA, Weinheim 

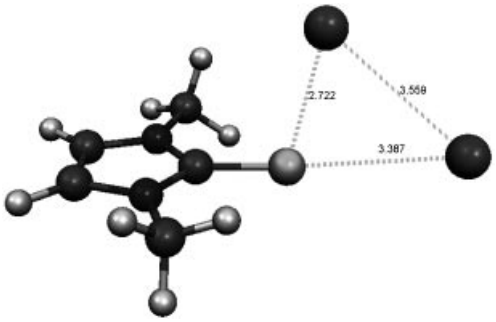


Figure 7. Transition state leading from the CT to the TY adduct in **1**·$I_2$.

Table 4. Relevant geometrical parameters of transition states of TY adducts (distances in angstoms, angles in degreees; X:halogen; E: chalcogen).

| | $E–X_{eq}$ | $E–X_{ax}$ | X–X | X–E–X | $X_{ax}$–E–C–N |
|---|---|---|---|---|---|
| **1**·$Cl_2$ | 2.6 | 2.4 | 3.7 | 97.6 | 81.1 |
| **1**·$Br_2$ | 3.4 | 2.7 | 3.7 | 74.7 | 69.2 |
| **1**·$I_2$ | 3.4 | 2.9 | 4.0 | 76.9 | 71.7 |
| **2**·$Cl_2$ | 3.3 | 2.5 | 4.1 | 89.3 | 111.5 |
| **2**·$Br_2$ | 3.4 | 2.9 | 3.3 | 61.8 | 107.2 |
| **2**·$I_2$ | 3.5 | 3.0 | 3.9 | 72.3 | 64.3 |

through association and dissociation processes, we evaluated the difference between the energy of the transition state leading to the TY from the CT adducts and the energies of the $LEX^+$ and $X^-$ products, which should be lower than the transition state energy of paths III and IV. Our calculation showed that the energies of the $LEX^+$ and $X^-$ ions at infinite distance is of the order of 300 kcal mol$^{-1}$, thus excluding III and IV as possible paths, at least in the gas phase. However, in solvents of high dielectric constant or in the presence of "acid" molecules that can accept the $X^-$ ion (e.g. free $X_2$ molecules), III and IV might compete with the path II. Thus, on the basis of these results it seems very likely that, in the case examined in the present study, the initial product of the interaction between **1** and **2** and $X_2$ is always a linear charge-transfer adduct. In the case of **1** and $I_2$, the CT adduct is the final product of the reaction, otherwise the CT adduct can evolve to the thermodynamically more stable TY adduct. So, although we can't rule out the Husebye hypothesis in polar media, we have shown that a monomolecular process can give rise to the formation of the TY adduct.

## Conclusions

In order to get a deeper insight into the reactions between L=E [L: 1,3-dimethylimidazolyl framework; E: S (**1**), Se (**2**)] and halogens $X_2$ (X: Cl, Br, I), twelve adducts (six of the CT type and six of the TY type) have been theoretically investigated. DFT calculations indicate that, except for the case of **1** and $I_2$, hypervalent adducts (TY) are generally more stable than the linear (CT) ones. Nevertheless, the CT compounds always play an important role in the process as

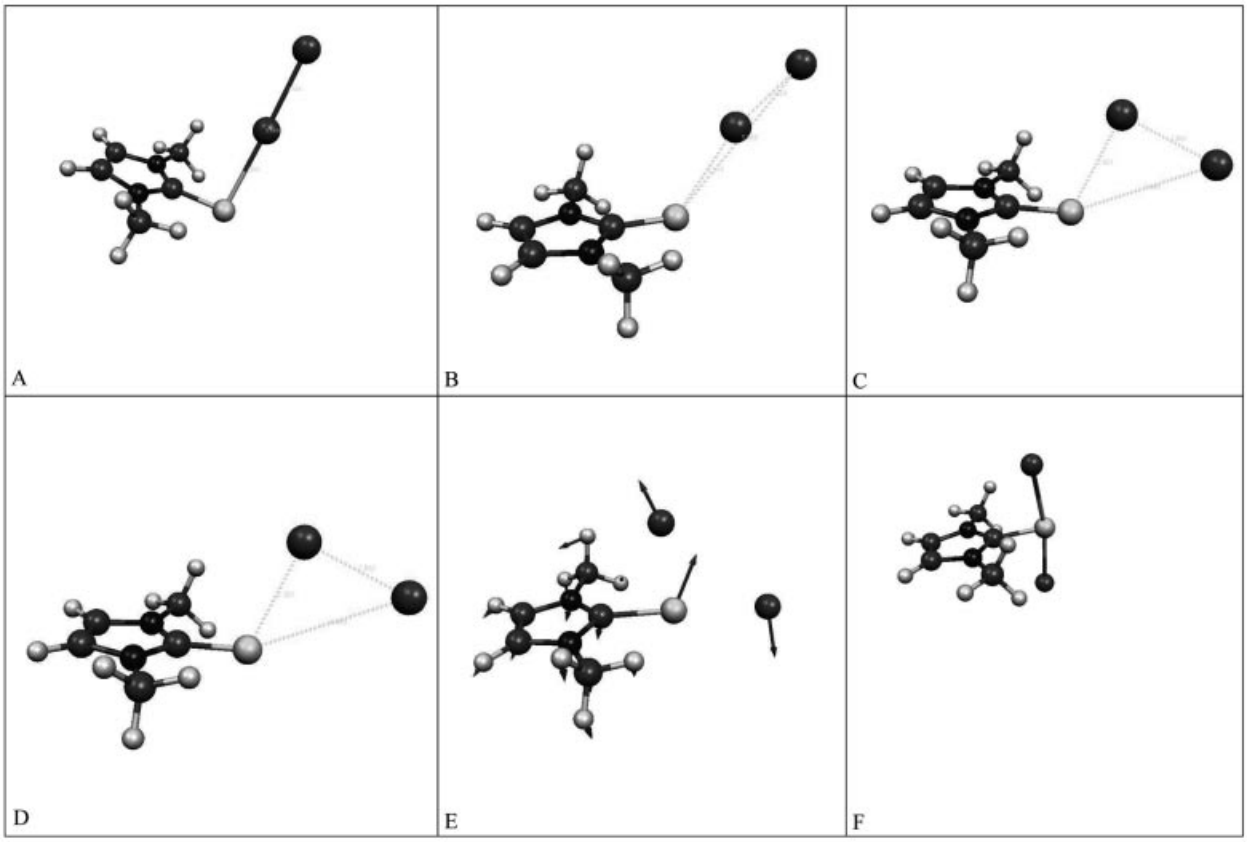


Figure 8. Snapshot sequence from the CT to the TY adduct through an axial–equatorial transition state in **1**·$Br_2$.

 © 2006 Wiley-VCH Verlag GmbH & Co. KGaA, Weinheim 

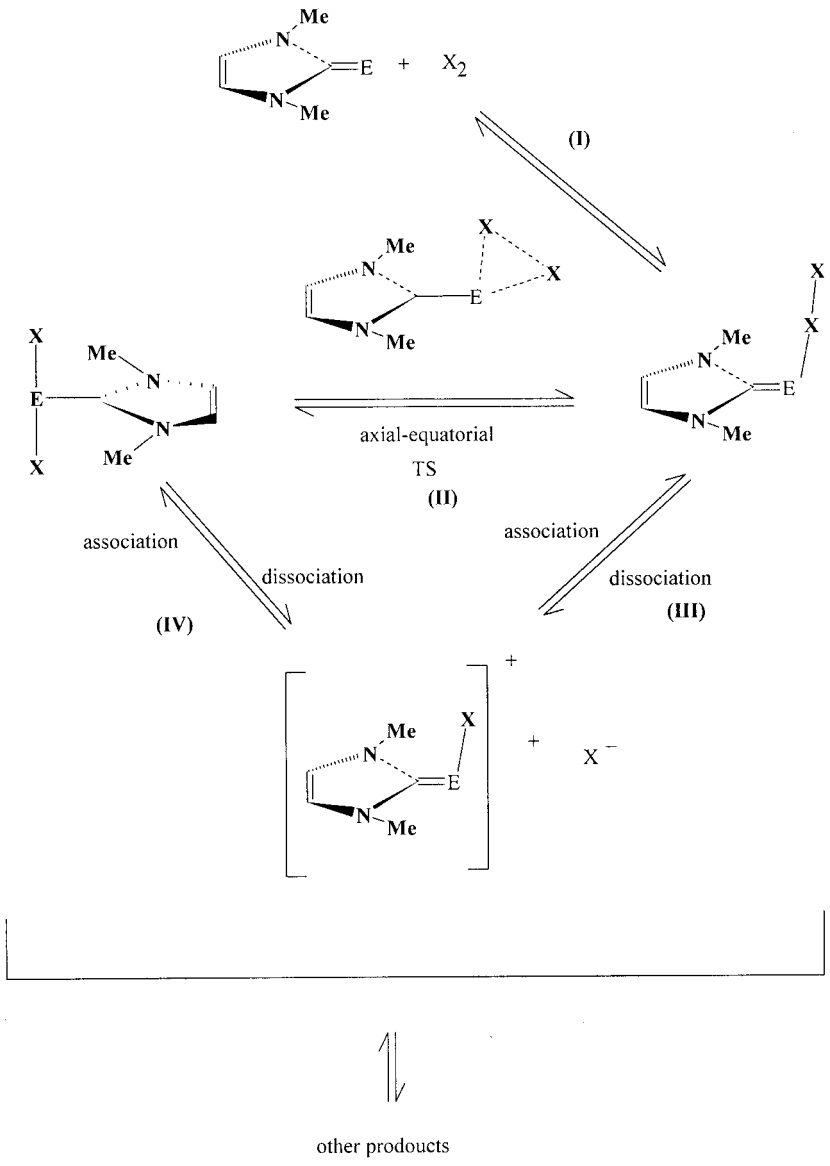


Scheme 3. Reactivity scheme proposed in the present study.

they are always the first product of the reaction from which the TY isomers can be formed through an axial–equatorial transition state.

This study suggests that the supposed formation of the cation $[LEX]^+$ is not always necessary to explain the formation of the TY adducts since the direct interconversion path of the CT to the TY adducts is accessible. In conclusion, on the basis of our calculations we propose the reaction mechanism reported in Scheme 3.

## Acknowledgments

The MIUR Cluster 26 P.O. 8 of legge 488 and MIUR PRIN 2001 and European Union funding through the Regione Basilicata POP 1996-2000 are kindly acknowledged for computational and financial support.

[1] M. C. Baenziger, R. E. Buckles, R. J. Maner, T. D. Simpson, *J. Am. Chem. Soc.* **1969**, *91*, 5749.
[2] W. Nakanishi, S. Hayashi, H. Tukada, H. Iwamura, *J. Phys. Org. Chem.* **1990**, *3*, 358.
[3] M. D. Rudd, S. V. Linderman, S. Husebye, *Acta Chem. Scan.* **1997**, *51*, 689 and references cited therein.
[4] a) M. Arca, F. Demartin, F. A. Devillanova, A. Garau, F. Isaia, V. Lippolis, G. Verani, *J. Chem. Soc., Dalton Trans.* **1999**, 3069; b) F. Demartin, F. A. Devillanova, E. Isaia, V. Lippolis, G. Verani, *Inorg. Chem.* **1993**, *32*, 3694; c) F. Demartin, F. A. Devillanova, A. Garau, F. Isaia, V. Lippolis, G. Verani, *Polyhedron* **1999**, *18*, 3107; d) F. Demartin, F. A. Devillanova, F. Isaia, V. Lippolis, G. Verani, *Inorg. Chim. Acta* **1997**, *255*, 203; e) F. Cristiani, F. A. Devillanova, F. Demartin, F. Isaia, V. Lippolis, G. Verani, *Inorg. Chem.* **1994**, *33*, 6315; f) F. A. Devillanova, P. Deplano, F. Isaia, V. Lippolis, M. L. Mercuri, S. Piludu, G. Verani, F. Demartin, *Polyhedron* **1998**, *7*, 305–312; g) F. Bigoli, E. Demartin, P. Deplano, F. A. Devillanova, F. Isaia, V. Lippolis, M. L. Mercuri, M. A. Pellinghelli, E. E. Trogu, *Inorg.*

 © 2006 Wiley-VCH Verlag GmbH & Co. KGaA, Weinheim 

*Chem.* **1996**, *35*, 3194; h) M. C. Aragoni, M. Arca, F. Demartin, F. A. Devillanova, A. Garau, F. Isaia, F. Lelj, V. Lippolis, G. Verani, *Chem. Eur. J.* **2001**, *7*, 3122 and references cited therein; i) M. Arca, F. A. Devillanova, A. Garau, F. Isaia, V. Lippolis, G. Verani, F. Demartin, *Z. Anorg. Allg. Chem.* **1998**, *624*, 745–749; j) M. C. Aragoni, M. Arca, A. J. Blae, F. A. Devillanova, W.-W. du Mont, A. Garau, F. Isaia, V. Lippolis, G. Verani, C. Wilson, *Angew. Chem. Int. Ed.* **2001**, *40*, 4229; k) F. Bigoli, P. Deplano, F. A. Devillanova, V. Lippolis, M. L. Mercuri, M. A. Pellinghelli, E. F. Trogu, *Eur. J. Inorg. Chem.* **1998**, 137; l) F. Bigoli, P. Deplano, M. L. Mercuri, M. A. Pellinghelli, A. Sabatini, E. F. Trogu, A. Vacca, *J. Chem. Soc., Dalton Trans.* **1996**, 3583.

[5] a) E. Seppala, E. Ruthe, J. Jeske, W.-W. du Mont, P. G. Jones, *Chem. Commun.* **1999**, 1471; b) W.-W. du Mont, *Main Group Chem. News* **1994**, *2*, 18; c) J. Jeske, W.-W. du Mont, P. G. Jones, *Chem. Eur. J.* **1999**, *5*, 385; d) S. Kubiniok, W.-W. du Mont, S. Pohl, W. Saak, *Angew. Chem.* **1988**, *100*, 434; *Angew. Chem. Int. Ed. Engl.* **1988**, *27*, 431; e) W.-W. du Mont, F. Ruthe, *Coord. Chem. Rev.* **1999**, *189*, 101; f) V. Stenzel, J. Jeske, W.-W. du Mont, P. G. Jones, *Inorg. Chem.* **1997**, *36*, 443.

[6] a) P. D. Boyle, W. I. Cross, S. M. Godfrey, C. A. McAuliffe, R. G. Pritchard, S. J. Teat, *J. Chem. Soc., Dalton Trans.* **1999**, 2845; b) S. M. Godfrey, S. L. Jackson, G. A. McAuliffe, R. G. Pritchard, *J. Chem. Soc., Dalton Trans.* **1998**, 4201; c) P. D. Boyle, J. Christie, T. Dyer, S. M. Godfrey, I. R. Howson, C. McArthur, B. Omar, R. G. Pritchard, G. R. Williams, *J. Chem. Soc., Dalton Trans.* **2000**, 3106 and references cited therein.

[7] M. C. Aragoni, M. Arca, F. Demartin, F. A. Devillanova, A. Garau, F. Isaia, V. Lippolis, G. Verani, *J. Am. Chem. Soc.* **2002**, *124*, 4538–4539.

[8] F. Bigoli, A. M. Pellinghelli, P. Deplano, F. A. Devillanova, V. Lippolis, M. L. Mercuri, E. F. Trogu, *Gazz. Chim. It.* **1994**, *124*, 445.

[9] N. Kuhn, T. Kratz, G. Henkel, *Chem. Ber.* **1994**, *127*, 849.

[10] G. L. Abbati, M. C. Aragoni, M. Arca, F. A. Devillanova, A. C. Fabretti, A. Garau, F. Isaia, V. Lippolis, G. Verani, *Dalton Trans.* **2003**, 1515 and references cited therein.

[11] A.Szabo, N. S. Ostlund, in *Modern Quantum Chemistry*, Macmillan Publishing Co. Inc., New York, **1982**.

[12] M. J. Frisch, G. W. Trucks, H. B. Schlegel, G. E. Scuseria, M. A. Robb, J. R. Cheeseman, V. G. Zakrzewski, J. A. Montgomery, R. E. Stratmann, J. C. Burant, S. Dapprich, J. M. Millam, A. D. Daniels, K. N. Kudin, M. C. Strain, O. Farkas, J. Tomasi, V. Barone, M. Cossi, R. Cammi, B. Mennucci, C. Pomelli, C. Adamo, S. Clifford, J. Ochterski, G. A. Petersson, P. Y. Ayala, Q. Cui, K. Morokuma, D. K. Malick, A. D. Rabuck, K. Raghavachari, J. B. Foresman, J. Cioslowski, J. V. Ortiz, B. B. Stefanov, G. Liu, A. Liashenko, P. Piskorz, I. Komaromi, R. Gomperts, R. L. Martin, D. J. Fox, T. Keith, M. A. Al-Laham, C. Y. Peng, A. Nanayakkara, C. Gonzalez, M. Challacombe, P. M. W. Gill, B. G. Johnson, W. Chen, M. W. Wong, J. L. Andres, M. Head-Gordon, E. S. Replogle, J. A. Pople, *Gaussian 98*, Gaussian, Inc. Pittsburgh PA, **1998** (http://www.gaussian.com/).

[13] A. E. Reed, L. A. Curtiss, F. Weinhold, *Chem. Rev.* **1988**, *88*, 899.

[14] a) A. D. Becke, *J. Chem. Phys.* **1993**, *98*, 1372; b) C. Lee, W. Yang, R. G. Parr, *Phys. Rev. B* **1988**, *37*, 785.

[15] A. Schafer, H. Horn, R. Ahlrichs, *J. Chem. Phys.* **1992**, *97*, 2571.

[16] a) P. J. Hay, W. R. Wadt, *J. Chem. Phys.* **1985**, *82*, 270; b) W. R. Wadt, P. J. Hay, *J. Chem. Phys.* **1985**, *82*, 284; c) P. J. Hay, W. R. Wadt, *J. Chem. Phys.* **1985**, *82*, 299.

[17] C. Adamo, V. Barone, *Chem. Phys. Lett.* **1997**, *274*, 242.

[18] A. Schafer, C. Huber, R. Ahlrichs, *J. Chem. Phys.* **1994**, *100*, 5829.

[19] This technique was developed in our laboratory to overcome the problem of the presence of *n*-order saddle points in the research of transition states. In fact, starting from an *n*-order saddle point, the technique allows us to obtain a transition state, i.e. a first-order saddle point, in $n - 1$ optimisation steps.

[20] A. Dreuw, J. L. Weisman, M. Head-Gordon, *J. Chem. Phys.* **2003**, *119*, 2943.

[21] R. F. W. Bader, in *Atoms in Molecules: A Quantum Theory*, Oxford University Press, **1990**.

[22] C. Gonzales, H. B. Schlegel, *J. Chem. Phys.* **1990**, *94*, 5523.

Received: November 23, 2005
Published Online: April 3, 2006

 © 2006 Wiley-VCH Verlag GmbH & Co. KGaA, Weinheim 

DOI: 10.1002/ejic.200501050

# Synthesis, Characterisation and Molecular Hyperpolarisabilities of Pseudo-Octahedral Hydrido(nitrile)iron(II) Complexes for Nonlinear Optics: X-ray Structure of $[Fe(H)(dppe)_2(4\text{-}NCC_6H_4NO_2)][PF_6]\cdot CH_2Cl_2$

**Maria Paula Robalo,*[a,b] António P. S. Teixeira,[b,c] Maria Helena Garcia,[b,d] M. Fátima Minas da Piedade,[b,d] M. Teresa Duarte,[b] Alberto Romão Dias,[b] Jochen Campo,[e] Wim Wenseleers,*[e] and Etienne Goovaerts[e]**

**Keywords:** Hydride ligands / Iron / Nonlinear optics / Hyperpolarizability / Hyper-Rayleigh scattering

A series of ionic pseudo-octahedral *trans*-hydrido(nitrile)-iron(II) complexes with the general formula $[Fe(H)(dppe)_2(4\text{-}NCR)][PF_6]$ [dppe = 1,2-bis(diphenylphosphanyl)ethane; R = acceptor-substituted conjugated ligand] have been synthesised by chloride abstraction from the starting compound *trans*-$[FeHCl(dppe)_2]$ and fully characterised. First hyperpolarisabilities ($\beta$) have been determined by hyper-Rayleigh scattering (HRS) at the fundamental wavelength of 1072 nm and the high near-resonant values obtained (up to $1130\times10^{-30}$ esu) are interpreted in terms of the two-level model (TLM) and are correlated with IR and NMR spectroscopic data. Wavelength-dependent HRS has been performed in the 1072–1580 nm range for two of the compounds, namely $[Fe(H)(dppe)_2\{4\text{-}NC(CH)(CH)C_6H_4NO_2\}][PF_6]$ and $[Fe(H)(dppe)_2\{4\text{-}NCC_6H_4(CH)(CH)C_6H_4NO_2\}][PF_6]$. These results clearly show the two-photon resonance but also the shortcomings of the TLM when it comes to deriving reliable static $\beta$ values. A structural study of the compound $[Fe(H)(dppe)_2(4\text{-}NCC_6H_4NO_2)][PF_6]$ by X-ray diffraction shows that it crystallises in the centrosymmetric monoclinic space group $P2_1/n$, with four molecules in the unit cell and a pairwise antiparallel alignment of the dipoles.
(© Wiley-VCH Verlag GmbH & Co. KGaA, 69451 Weinheim, Germany, 2006)

## Introduction

Organometallic molecules have been extensively studied in the search for new materials with enhanced second-order nonlinear optical (NLO) properties.[1–7] Because of their large first hyperpolarisabilities ($\beta$), fast response times and architectural flexibility, they have many potential applications in photonic devices such as frequency doublers, photonic switches and electro-optic modulators.[8] Many studies have focused on organic and organometallic molecules composed of a highly polarisable π-conjugated backbone with an electron-donor (D) and an -acceptor (A) group attached to opposite ends. In this way a so called asymmetric "push-pull" or D-π-A system is created, which can be used to obtain a macroscopically non-centrosymmetric medium with a large second-order nonlinear susceptibility.[3] In the search for better donor and acceptor groups, it appeared that an organometallic moiety could serve as a very efficient alternative electron-donor group to the traditional, purely organic, push-pull system.[1,2,5–7,9] In these systems, the characteristic charge transfer from metal to ligand (MLCT) could be the origin of a large charge separation over the long conjugated ligand, which can be tuned to optimise the molecular nonlinear optical properties. We have previously reported hyper-Rayleigh scattering (HRS) results for such a systematically varied series of ionic organometallic complexes, consisting of a transition metal centre coordinated by an $\eta^5$-monocyclopentadienyl ring, a bidentate phosphane ligand and a conjugated nitrile ligand.[10–12] By comparing complexes with electron-donor and -acceptor substituted ligands we found that the ruthenium and especially the iron fragments could be used as very efficient electron-donor groups.

In order to further enhance the NLO response new structural changes are now implemented. First of all, the donor fragment is modified by replacing the $\eta^5$-monocyclopentadienyl ring by a second bidentate phosphane ligand [1,2-bis(diphenylphosphanyl)ethane, $Ph_2P(CH_2)_2PPh_2$, dppe] and a hydride, which leads to a pseudo-octahedral coordi-

[a] Departamento de Engenharia Química, Instituto Superior de Engenharia de Lisboa,
Rua Conselheiro Emídio Navarro, 1, 1950-062 Lisboa, Portugal
Fax: +351-21-831-7267
E-mail: mprobalo@deq.isel.ipl.pt
[b] Centro de Química Estrutural, Instituto Superior Técnico, Av. Rovisco Pais, 1049-001 Lisboa, Portugal
[c] Departamento de Química, Universidade de Évora, Colégio Luís A. Verney, Rua Romão Ramalho, 59, 7000-671 Évora, Portugal
[d] Faculdade de Ciências da Universidade de Lisboa, Campo Grande,
Edificio C8, 1749-016 Lisboa, Portugal
[e] Department of Physics, University of Antwerp, Campus Drie Eiken,
Universiteitsplein 1, 2610 Wilrijk-Antwerpen, Belgium
E-mail: wim.wenseleers@ua.ac.be

 © 2006 Wiley-VCH Verlag GmbH & Co. KGaA, Weinheim 

nation at the transition metal. This coordination creates new possibilities for fine-tuning the molecular structure since an extra ligand can be bound to the metal *trans* to the conjugated ligand. Because of the pseudo-octahedral coordination it also becomes possible to use these complexes as a building block for highly branched macromolecules or metallodendrimers,[13,14] which have promising applications in nonlinear optics. A series of pseudo-octahedral ruthenium acetylide compounds[15] exhibits even higher $\beta$ values[16] than the analogous cyclopentadienyl compounds studied before,[17] although they are about equally resonant. Therefore, in this work, the favourable iron centre is combined with the pseudo-octahedral surrounding and with a nitrile linkage in order to obtain very high hyperpolarisabilities together with extensive molecular versatility. Apart from the improvement of the metallic electron donor, we have also looked for a more efficient acceptor by introducing a second nitro group at the conjugated backbone. Finally, the conjugated backbone itself, which connects the electron-acceptor and -donor groups, is also varied in both length and structure to further optimise the hyperpolarisability.

## Results and Discussion

### Preparation of the Pseudo-Octahedral Iron(II) Dppe Derivatives

The complexes of general formula $[Fe(H)(dppe)_2(4\text{-}NCR)][PF_6]$ were prepared following a general procedure that involves chloride abstraction from the starting compound *trans*-$[FeHCl(dppe)_2]$ by $TlPF_6$, in the presence of a slight excess of the corresponding nitrile chromophores (see Scheme 1). The reactions were carried out in $CH_2Cl_2$ or THF by stirring at room temperature for several hours. After work-up, the compounds were obtained in moderate to high yields (37–71%).

### Characterisation of the New Complexes $[Fe(H)(dppe)_2(4\text{-}NCR)][PF_6]$

All of the *trans*-hydrido(nitrile)iron(II) complexes were obtained as deep-red or purple crystals with the exception of $[Fe(H)(dppe)_2\{2,4\text{-}NCC_6H_3(NO_2)_2\}][PF_6]$ (**4**), which is dark green. They are fairly air stable in the solid state towards oxidation, but less stable in solution. They are soluble in polar solvents and insoluble in less polar and apolar organic solvents. The complexes were characterised by a combination of IR and $^1H$, $^{13}C$ and $^{31}P$ NMR spectroscopy, and elemental analysis.

The solid-state IR spectra (KBr pellets) of complexes **1**–**6** present a large number of bands due to the presence of the various co-ligands. They exhibit strong ν(NC) bands in the range 2138–2185 $cm^{-1}$ (see Table 1) at lower wavenumbers than those observed for the corresponding uncoordinated nitriles. Thus, on coordination of the nitrile to the metal fragment, the NC stretching band shifts by 33 to 101 $cm^{-1}$ to lower frequency. This weakening of the NC bond is consistent with a π back-donation interaction $d_\pi(Fe)$–$\pi^*(NC)$, which makes the metal group a more effective donor. This shift is found to be much higher in the present complexes than in the cyclopentadienyl compounds,[10] where shifts of up to 35 $cm^{-1}$ were obtained. The π back-donation is enhanced by the interaction between the electron-donating metal moiety and the electron-accepting nitro group through the conjugated chain, as desired for a large first hyperpolarisability. In agreement with this in-

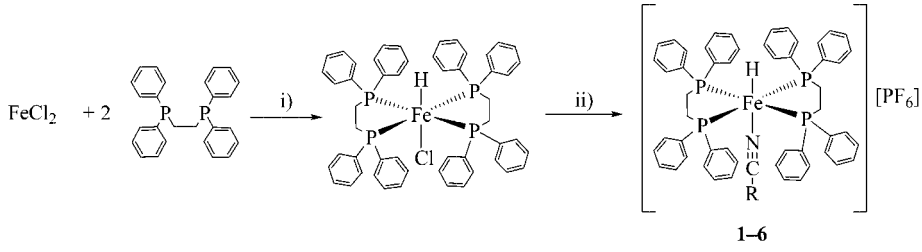


i) $NaBH_4$, $T$ = 60 °C, 2 h, ethanol; ii) exc. NCR, $TlPF_6$, $CH_2Cl_2$ or THF, r.t. 2–18 h

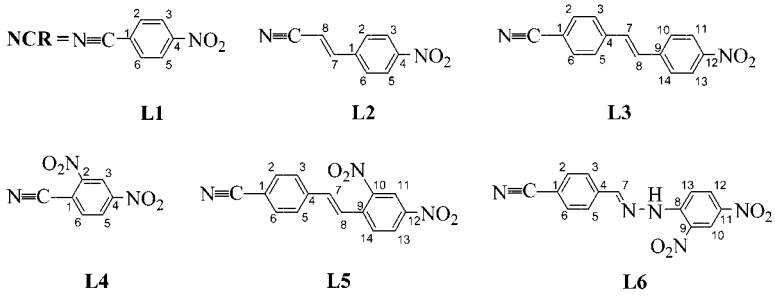


Scheme 1. Synthesis of complexes **1**–**6** (showing the numbering scheme for NMR spectral assignments).

 © 2006 Wiley-VCH Verlag GmbH & Co. KGaA, Weinheim 

Table 1. The experimental hyperpolarisabilities, $\beta_{zzz}$, measured by HRS at $\lambda$ = 1072 nm in chloroform, together with optical and spectroscopic data. $\lambda_{max}$ is the spectral position of the lowest energy transition; $\varepsilon_{max}$ is the corresponding extinction coefficient.

| | Pseudo-octahedral compounds $[Fe(H)(dppe)_2(p\text{-NC-R})]^+ [PF_6]^-$ (for R see Scheme 1) | | | | | | $\eta^5$-Monocyclopentadienyl compounds[12] | |
|---|---|---|---|---|---|---|---|---|
| Complexes | **1** | **2** | **3** | **4** | **5** | **6** | **7** (*p*-NC-R = **L1**) | **8** (*p*-NC-R = **L2**) |
| $\lambda_{max}$ (nm) | 546 | 549 | 485 | 723 | 505 | 503 | 460 | 484 |
| $\varepsilon_{max}$ (L mol$^{-1}$ cm$^{-1}$) | 7700 | 8800 | 8300 | 8300 | 10300 | 10700 | 6000 | 8700 |
| $\beta^{zzz}_{complex}$ ($10^{-30}$ esu) | 700 | 860 | 800 | 435 | 1130 | 1026 | 395[a] | 570[a] |
| $\beta^{zzz}_{ligand}$ ($10^{-30}$esu) | 4.4[a,b] | – | 33 | 5.6 | 41 | 47 | | |
| $\nu$(C≡N)[c] (cm$^{-1}$) | 2177 | 2174 | 2185 | 2138 | 2182 | 2183 | 2205 | 2205 |
| $\Delta\nu$(C≡N)[c] (cm$^{-1}$) | –56 | -43 | –33 | –101 | –40 | –39 | –35 | –15 |
| $\nu$(Fe–H)[c] (cm$^{-1}$) | 1870 | 1853 | 1888 | 1891 | 1891 | 1896 | – | – |
| $\delta(^1H_{hydride})$[d] (ppm) | –17.48 | –18.03 | –18.83 | –14.60 | –18.67 | –18.54 | – | – |
| $\delta(^1H_{ar})$[d]* (ppm) | 6.73 | 5.65 | 6.76 | 5.43 | 6.77 | 6.79 | 6.97[e] | 5.95[e] |
| $\Delta\delta(^1H_{ar})$[d] (ppm) | –1.17 | –0.43 | –0.94 | –2.78 | –0.96 | –1.11 | –1.16[e] | –0.64[e] |
| $\delta(^{31}P_{dppe})$[d] (ppm) | 83.34 | 83.80 | 83.74 | 81.00 | 83.48 | 83.45 | 98.09[f] | 97.64[f] |

[a] At 1064 nm. [b] In methanol.[10] [c] KBr pellets, some bands are very weak. [d] $CD_2Cl_2$, room temperature. [e] $(CD_3)_2CO$, room temperature. [f] $CDCl_3$, room temperature; * H adjacent to NC group.

terpretation, the shifts are dependent on the number of nitro groups present at the nitrile ligand and on the distance between the NC and $NO_2$ groups. Thus, the highest shift is found for **4** due to the presence of two strongly electron-withdrawing nitro groups separated by only a short, well-conjugated link from the donor group. The trend in the values indicates that removal of electron density from the nitrile linkage becomes less marked on chain lengthening. For the dinitro derivatives (compounds **5** and **6**), the position of the ν(NC) absorption seems to be independent of the type of conjugated bridge between the aromatic rings. The ν(Fe–H) bands are very weak, with high frequencies in the range 1853–1896 cm$^{-1}$, consistent with a strongly bound hydride *trans* to an aromatic nitrile.[18,19]

The $^1$H NMR spectra of the compounds were obtained in $CD_2Cl_2$ solutions. The chemical shifts of the dppe protons are within the range of other octahedral iron(II) complexes with coordinated nitriles and are almost constant in all compounds synthesised. The hydride is observed upfield of the TMS signal ($\delta$ = –14.6 to –18.8 ppm) (see Table 1) as a quintuplet due to coupling with the phosphorus atoms of the dppe units, thus showing that all phosphorus atoms are equivalent, in an equatorial position, with a *trans* orientation between the hydride and the nitrile ligands. The position of the hydride signal is affected by the nitrile ligand and it also seems to be dependent on the distance between the NC and $NO_2$ groups, with short distances changing the signal to less-negative chemical shifts. This observation is consistent with a hydride ligand coordinated *trans* to a good π-acceptor like the nitrile ligands, as reported before.[20] Upon coordination of the nitrile ligand, the chemical shifts of the aromatic *ortho* protons (relative to the nitrile group) can be used to assess the electron-donating capabilities of the metal centre (see, for instance, refs.[11,12,21]) and have been shown to be correlated with high molecular hyperpolarisabilities $\beta$. An upfield shift of the *ortho* protons, corresponding to a stronger shielding effect, indeed indicates a back-donation from the metal centre to the nitrile ligand and suggests a more efficient donor and/or a stronger acceptor group. For the present complexes all the *ortho* protons or the $H_\beta$ (in compound **2**) are shielded, with upfield shifts between 0.43 and 2.78 ppm, with the highest shift found for the *ortho* proton of complex **4**. These shifts are much higher than those measured in our previous studies of the cyclopentadienyl compounds (0.05–1.2 ppm),[11,12,21] which makes the high $\beta$ values obtained comprehensible (see Table 1).

The compounds were also characterised by $^{13}$C NMR spectroscopy in [D$_2$]dichloromethane. The deviations in the chemical shifts of the carbon atoms are small and in agreement with the data observed in the $^1$H NMR spectra. The $^{31}P\{^1H\}$ NMR spectra of these compounds show a single sharp signal in the range $\delta$ = 81–84 ppm, attributed to the phosphorus atoms of the dppe ligand, which confirms that all the complexes adopt an exclusively *trans* configuration in solution. These data are also consistent with the expected deshielding effect upon coordination of the phosphane, since free dppe shows a singlet at $\delta$ = –12.1 ppm in the same solvent.

### X-ray Structural Determination of $[Fe(H)(dppe)_2(4\text{-}NCC_6H_4NO_2)][PF_6]$ (1)

Recrystallisation of compound $[Fe(H)(dppe)_2(4\text{-}NCC_6H_4NO_2)][PF_6]$ (**1**) by slow diffusion of diethyl ether into a dichloromethane solution gave crystals suitable for X-ray diffraction studies. The crystals belong to the monoclinic system (space group $P2_1/n$), with four molecules in the unit cell. The structural studies confirm the presence of $\mathbf{1}^+$ cations, hexafluorophosphate anions and a crystallisation solvent molecule of dichloromethane. The molecular structure of the cation is shown in Figure 1 (obtained with ORTEP-3[22]), along with the atom-numbering scheme. Selected bond lengths and angles are given in Table 2.

Complex **1** presents a distorted octahedral coordination geometry with the atoms coordinated to Fe displaying bond angles close to 90° (see Table 2). The X-ray structure confirms the *trans* position of the nitrile and hydride ligands, which define a vertical axis, with the two bidentate phos-

 © 2006 Wiley-VCH Verlag GmbH & Co. KGaA, Weinheim 

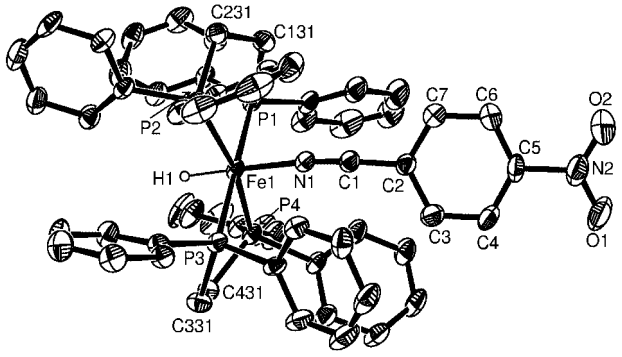


Figure 1. Molecular structure of the cation $[Fe(H)(dppe)_2(4\text{-}NCC_6H_4NO_2)]^+$ with 40% probability thermal ellipsoids, showing the labelling scheme (the hydrogen atoms, except the hydride, have been omitted for clarity).

Table 2. Selected bond lengths [Å], angles [°] and torsion angles [°] for $[Fe(H)(dppe)_2(4\text{-}NCC_6H_4NO_2)][PF_6]$ (**1**).

| Bond lengths [Å] | | Angles [°] | |
|---|---|---|---|
| Fe(1)–H(1) | 1.45(5) | Fe(1)–N(1)–C(1) | 174.2(5) |
| Fe(1)–N(1) | 1.880(5) | N(1)–C(1)–C(2) | 175.4(7) |
| N(1)–C(1) | 1.162(7) | C(1)–C(2)–C(3) | 119.9(6) |
| C(1)–C(2) | 1.429(8) | C(5)–N(2)–O(1) | 118.3(8) |
| N(2)–C(5) | 1.485(9) | C(5)–N(2)–O(2) | 117.8(7) |
| N(2)–O(1) | 1.211(9) | O(1)–N(2)–O(2) | 123.9(7) |
| N(2)–O(2) | 1.225(9) | H(1)–Fe(1)–P(1) | 93(2) |
| C(Ar)–C(Ar) | 1.363–1.388 | P(1)–Fe(1)–N(1) | 87.78(14) |
| Fe(1)–P(1) | 2.274(2) | H(1)–Fe(1)–P(2) | 84(2) |
| Fe(1)–P(2) | 2.256(2) | P(2)–Fe(1)–N(1) | 97.57(15) |
| Fe(1)–P(3) | 2.276(2) | H(1)–Fe(1)–P(3) | 87(2) |
| Fe(1)–P(4) | 2.226(2) | P(3)–Fe(1)–N(1) | 92.37(14) |
| | | H(1)–Fe(1)–P(4) | 81(2) |
| Torsion angles [°] | | | |
| Fe(1)–N(1)–C(1)–C(2) | 29(11) | P(4)–Fe(1)–N(1) | 96.99(15) |
| N(1)–C(1)–C(2)–C(3) | –38(8) | P(1)–Fe(1)–P(2) | 83.15(7) |
| C(2)–C(7)–C(6)–C(5) | –0.2(12) | P(1)–Fe(1)–P(4) | 96.44(7) |
| C(2)–C(3)–C(4)–C(5) | 1.9(11) | P(3)–Fe(1)–P(2) | 97.22(7) |
| C(7)–C(6)–C(5)–N(2) | 177.5(7) | P(3)–Fe(1)–P(4) | 83.14(7) |
| C(6)–C(5)–N(2)–O(1) | 11.4(8) | P(1)–Fe(1)–P(3) | 179.57(8) |
| C(6)–C(5)–N(2)–O(2) | 10.2(11) | P(4)–Fe(1)–P(2) | 165.41(7) |
| C(4)–C(5)–N(2)–O(1) | 10.7(10) | H(1)–Fe(1)–N(1) | 178(2) |
| C(4)–C(5)–N(2)–O(2) | 9.4(8) | | |

phane ligands occupying the equatorial plane. The four phosphorus atoms (P1–P4) are roughly coplanar, with an average atomic displacement of 0.1407(6) Å with the Fe atom lying within the plane.

The investigation of the Fe–N and Fe–H bond lengths is of particular interest as they can often indicate the presence of a d-p π overlap in the Fe–N bond. The hydride could be located and reasonably isotropically refined with an Fe–H bond length of 1.45(5) Å, which is in the lower range of the values observed in similar compounds, as can be seen in Table 3 (hydride structures in refs.[18–20,23,24]). The Fe–N bond length [1.880(5) Å] is slightly shorter than those observed in these compounds, while the N≡C bond length [1.162(7) Å] is relatively longer (see Table 3). These observations, as well as the Fe(1)–N(1)–C(1) and N(1)–C(1)–C(2) bonding angles of 174.2(5)° and 175.4(7)°, respectively, confirm the existence of Fe→N π back-donation. The distances and angles within the benzonitrile group, in particular the absence of any obvious bond-length alternation, are consistent with the retention of aromaticity. The nitro group is slightly twisted relative to the aromatic ring plane, characterised by $C_{ar}$–$C_{ar}$–N–O torsion angles of around 10°.

The dppe chelate ring is not planar but exhibits an envelope conformation, i.e. the atoms Fe, P1, P2 and C(231) are essentially coplanar while atom C(131), the "flap" atom of the envelope, lies more than 0.73 Å away from this plane. The same applies to the other phosphane. The non-planarity of this conformation diminishes the contacts between the chelate phenyl groups and the nitrile ligand.

The compound displays a pseudo-fourfold rotation axis through H–Fe–N, relating the P atoms, which is almost perpendicular to the equatorial plane [87.6(5)°]. This equivalency of the P atoms agrees with the NMR spectroscopic data of the compounds, which show a quintuplet for the H ligand in their $^1H$ NMR spectra and a singlet for the four P atoms in their $^{31}P\{^1H\}$ NMR spectra. These results show that these molecules maintain in the solid state the general structure found in solution.

In the crystal packing, the molecules of compound **1** form pseudo-dimers with an antiparallel alignment due to a $C_{ar}$–H···$O(1)_{nitrile}$ hydrogen-bond interaction [D–A = 2.58(2) Å], thus cancelling their NLO responses in the crystalline state (Figure 2, a). Each constituent of this dimer is part of a chain in which the molecules are aligned due to the other $C_{ar}$–H···$O(2)_{nitrile}$ hydrogen-bond interaction [D–A = 2.58(2) Å] and also through the $PF_6$ anion, with C–H···F interactions [C123–H···F5 = 2.67(2), C7–H···F2 = 2.51(2), C212–H···F2 = 2.30(2), C246–H···F4 = 2.54(2), C226–H···F4 = 2.58(2), C341–H···F1 = 2.50(2) Å], which arrange the molecules in a straight line (along a). Overall, as can be seen in Figure 2 (b), the crystal structure is formed by alternating chains of molecules aligned in opposite directions. It can also be seen that, in each chain, the

Table 3. Structural data for pseudo-octahedral iron derivatives containing hydride and nitrile ligands.

| Compound | Fe–H [Å] | Fe–N [Å] | N≡C [Å] | Reference |
|---|---|---|---|---|
| $[Fe(H)(dppe)_2(NC\text{–}SCH_3)][CF_3SO_3]$ | 1.45(3) | 1.916(2) | 1.153(3) | [23] |
| $[Fe(H)(dppe)_2(NC\text{–}NH_2)][BF_4]$ | 1.59(9) | 1.95(1) | 1.15(2) | [19] |
| $[Fe(H)(depe)_2(NC\text{–}CHCOOEt)]$ | 1.50(6) | 1.945(4) | 1.167(6) | [24] |
| $[Fe(H)(dppe)_2(NC\text{–}CH_3)][BPh_4]$ | 1.50(2) | 1.933(2) | 1.141(3) | [18] |
| $[Fe(H)(dppe)_2(NC\text{–}CH_2CH_2OMe)][BPh_4]$ | 1.44(2) | 1.930(2) | 1.149(2) | [18] |
| $[Fe(H)(dppm)_2(NC\text{–}CH_3)][BF_4]$ | 1.35(6) | 1.927(4) | 1.137(6) | [20] |
| $[Fe(H)(dppe)_2(NC\text{–}C_6H_4NO_2)][PF_6]$ (**1**) | 1.45(5) | 1.880(5) | 1.162(7) | this work |

 © 2006 Wiley-VCH Verlag GmbH & Co. KGaA, Weinheim 

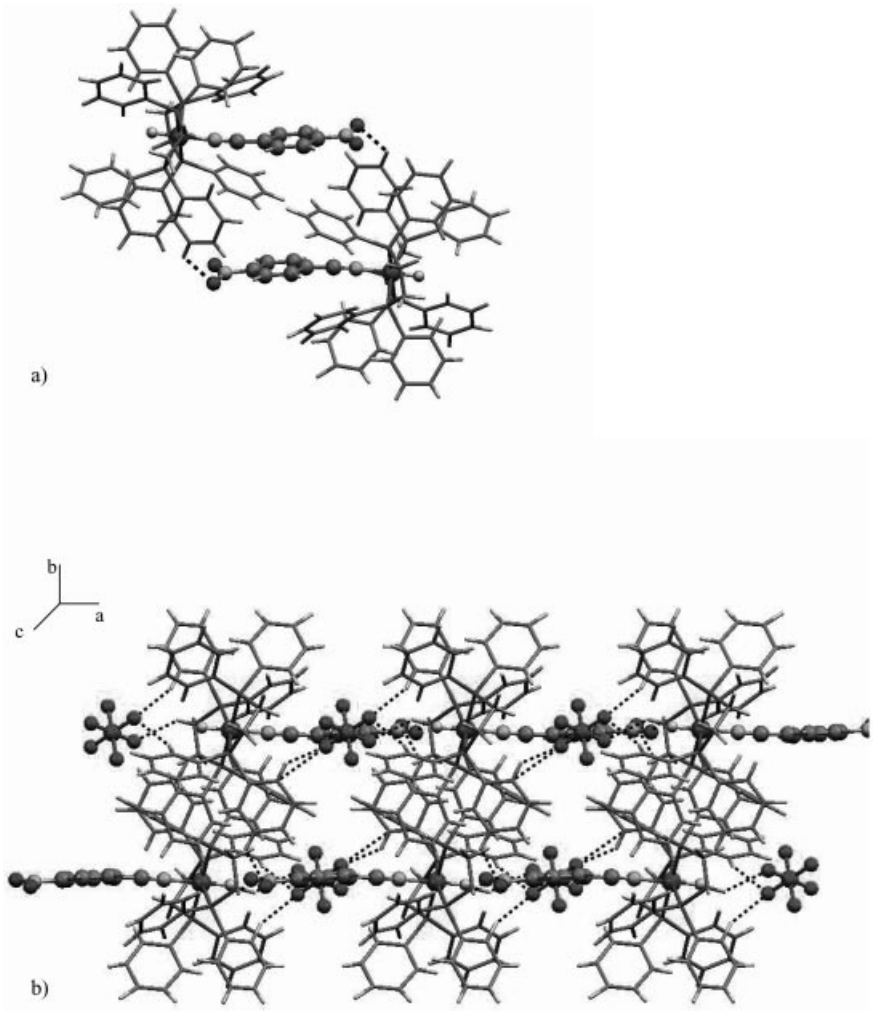


Figure 2. a) View of the antiparallel dimer; b) view of the crystal arrangement showing the alternating chains of cations aligned in opposite directions (solvent molecules have been omitted for clarity).

$PF_6$ anion occupies the "open space" to form an anion channel along *c*.

The second-order NLO response of compound **1** is cancelled in the solid state because of the pairwise antiparallel alignment of the chromophores, which results in a centrosymmetric structure. It has been shown previously that it is possible to overcome this problem of antiparallel alignment of neighbouring dipolar molecules by appropriate design of the molecular shape, in particular by introducing a spacer group between the successive chromophores.[25,26] In this approach, the Coulomb interaction becomes equally favourable for the parallel alignment as for the antiparallel alignment of the chromophores. The actual crystal structure formed is then determined by more subtle factors, such as chirality, hydrogen bonding and steric (van der Waals) interactions. These considerations are the subject of a previous paper,[25] where we have shown that this strategy works for complexes of very similar size and dipole moment. In fact, an ideal crystal structure with perfectly aligned chromophores was obtained for two cyclopentadienylruthenium and -iron complexes with chiral coligands;[25,27] in both cases the analogous complex with an achiral coligand crystallised centrosymmetrically. While the condition of proper spacing along the dipolar axis was met accurately in those Cp complexes,[25] this spacing was hard to control. In view of these design strategies, the new complexes studied here, besides the obvious possibility to replace the dppe co-ligands with chiral phosphanes, have the additional advantage of an available valence *trans* to the nitrile ligand due to their pseudo-octahedral geometry. This should allow a better control of the spacing (adapted to the length of the dipolar chromophore) and thus enable optimisation of the microscopic and macroscopic NLO properties.

## UV/Visible Studies

The electronic spectra of the compounds and of the uncoordinated nitrile ligands were recorded for $10^{-4}$ to $10^{-5}$ M chloroform solutions (Figure 3) in order to identify the M–L charge transfer and π–π* absorption bands expected in

 © 2006 Wiley-VCH Verlag GmbH & Co. KGaA, Weinheim 

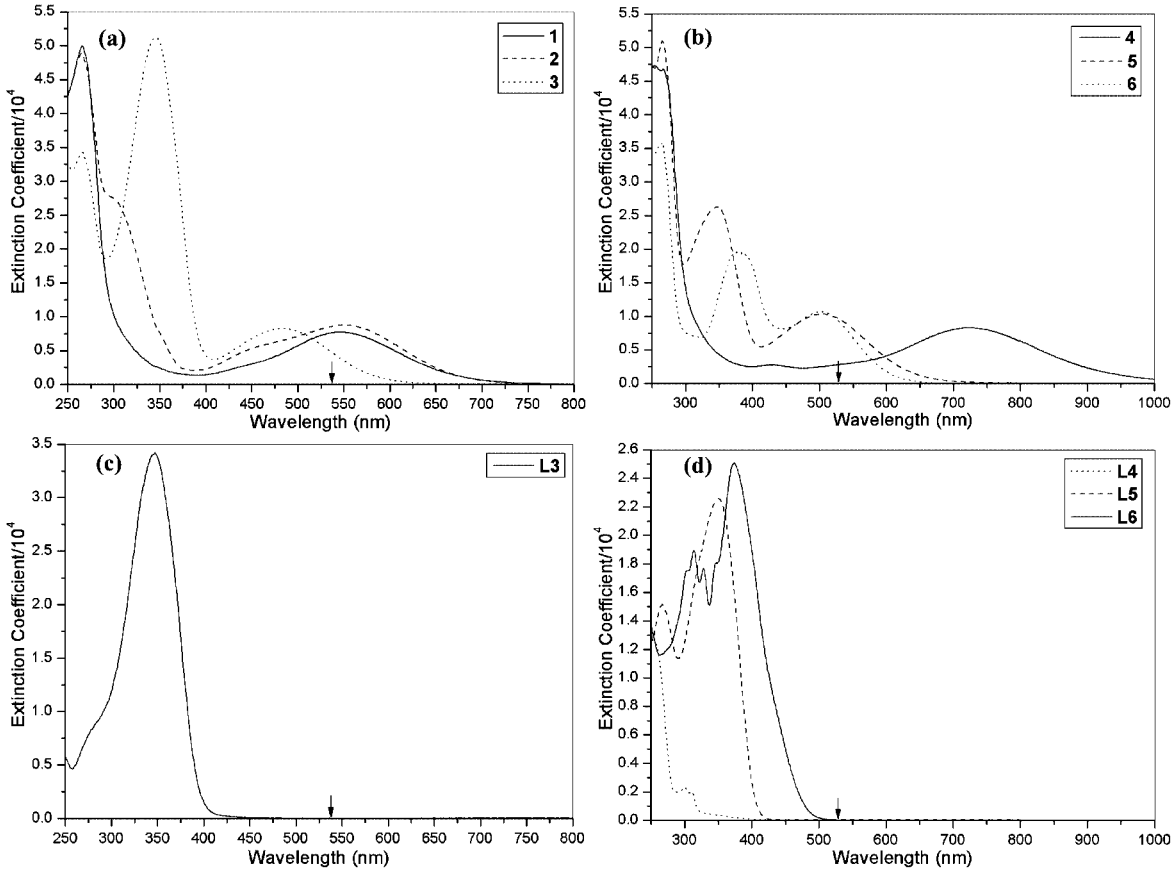


Figure 3. Optical absorption spectra of the compounds of Table 1: The nitro complexes (a) with an associated free ligand (c) and the dinitro complexes (b) with the free ligands (d). The downward arrow indicates the second harmonic wavelength of 536 nm at which most of the HRS measurements were performed.

these complexes. Additionally, a study of one of the compounds in other solvents was carried out to examine the solvatochromic effect.

The absorption bands in the 253–376 nm range are associated with the $\pi \rightarrow \pi^*$ and $n \rightarrow \pi^*$ transitions in the nitrile ligands, since they are also observed in this region for the corresponding free nitriles. Transitions at longer wavelengths (500–725 nm) are due to M–L charge transfer involving the $Fe^{II}$ centre and the nitro-substituted aromatic nitrile and are explained by π back-donation involving $d_\pi(Fe)$–$\pi^*(NC)$ orbitals (see Table 1). Dinitro substitution of the aromatic nitrile, going from **1** to **4**, results in a red-shift of 177 nm for the MLCT band. Chain lengthening leads to different behaviours for the absorption bands in the spectra: while the short wavelength absorption band, associated with the π–π* transition of the conjugated nitrile ligand (250–375 nm range), displays a red-shift with increasing chain length, as would be expected, a reverse effect was observed for the lowest energy band. In fact, going from **1** to **3** (or from **4** to **5**) we can observe a blue-shift and a slight enhancement of the MLCT band. Such a blue-shift has been observed before for CT transitions in organic[28,29] and organometallic[30] strong push-pull systems, for which a lower energy charge-transfer transition is obtained when the donor and acceptor groups are well-coupled through a shorter conjugated path.

Sizable solvent-induced shifts of absorption maxima (solvatochromism) are a measure of the CT character of the transition (large change in dipole moment $\Delta\mu$), and therefore have been used as an indication of appreciable quadratic molecular hyperpolarisabilities $\beta$.[27] It was therefore of interest to assess the solvatochromic response of the MLCT band for the complexes and $[Fe(H)(dppe)_2(4\text{-}NCC_6H_4NO_2)][PF_6]$ (**1**) was studied in solvents of different polarity (chloroform, acetone and DMSO). A positive solvatochromic shift of 21 nm across the range of these solvents was observed, with the lowest energy transition found in the polar solvent DMSO. This identifies this band as a CT transition and shows that the dipole moment increases upon excitation, consistent with a charge transfer from the metallic donor to the acceptor side of the complex.

## Hyper-Rayleigh Scattering Measurements

The experimental resonant hyperpolarisabilities obtained by hyper-Rayleigh scattering (HRS) at 1072 nm for the series of compounds studied in this work and the chemical structures of the acceptor-substituted ligands are summarised in Table 1. In general, high $\beta$ values are obtained for the complexes. HRS measurements were also performed on the free acceptor-substituted nitrile ligands, which exhibit

 © 2006 Wiley-VCH Verlag GmbH & Co. KGaA, Weinheim 

very low hyperpolarisabilities, in contrast to the corresponding push-pull systems.

To interpret the nearly resonant $\beta$ values of the complexes in terms of electronic properties it is useful to consider the two-level model (TLM), which is based on the assumption that only one excited state [i.e. the charge transfer (CT) state] contributes to the $\beta$ value. Assuming that the difference between the dipole moment in the ground and excited state, $\Delta\mu$, and the transition dipole, $\mu_{eg}$, are parallel to each other (along the $z$-axis), the $\beta$ tensor only has a diagonal zzz-component and can be written as[3,31,32]

$$\beta_{zzz}(-2\omega;\omega,\omega) = \frac{3e^2 f_{osc}\Delta\mu}{2\hbar m\omega_{eg}^3}\cdot\frac{\omega_{eg}^4}{(\omega_{eg}^2-\omega^2)(\omega_{eg}^2-4\omega^2)}$$

where $f_{osc}$ is the oscillator strength of the CT transition and $\omega_{eg}$ its frequency. The expression consists of a static value, $\beta_0$, multiplied by a wavelength-dependent resonance factor.

Because this model does not take into account the line broadening of the transition, it cannot be used to describe the dispersion of $\beta$ close to resonance. Hence, because most of the compounds studied in this work have a $\lambda_{max}$ value close to the second harmonic wavelength of 536 nm, the model is not suitable to calculate static $\beta$ values. To study the wavelength dependence of $\beta$ in the NIR, and eventually derive a more reliable estimate of the static value $\beta_0$, two of the compounds (**2** and **3**) were studied in the 1072–1580 nm range. These wavelength-dependent HRS data are presented in Figure 4, where a pronounced resonant enhancement associated with the low-energy charge-transfer transition can be seen in both cases.

The TLM curves based on the most resonant (1072 nm) and the least resonant $\beta$ value (1540 nm, shown for **2** only) are also plotted in Figure 4. For compound **3**, which is not extremely resonant, the TLM curve going through the 1072 nm value appears to give quite a good description of the dispersion of $\beta$, and the obtained static value of $115\times10^{-30}$ esu seems adequate. In fact, this curve is (coincidentally) overlapping with the one based on the 1580 nm

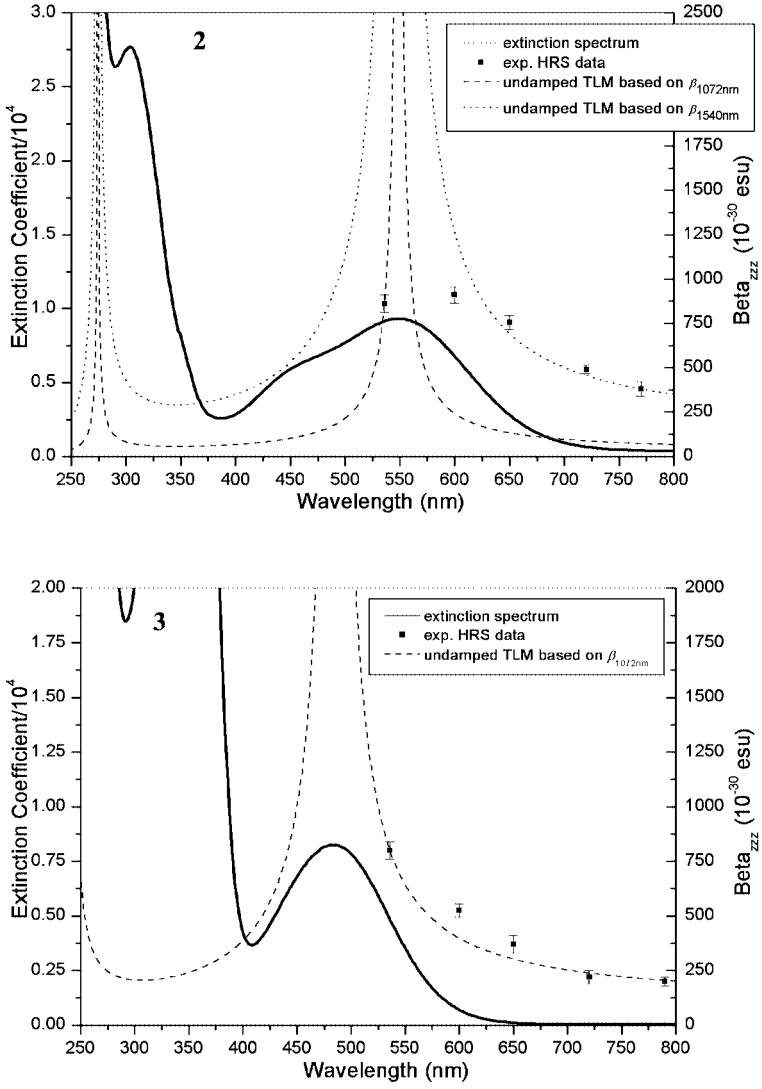


Figure 4. Wavelength-dependent HRS data for complexes **2** (top) and **3** (bottom) together with their extinction spectra. The two-level model (TLM) curves based on the most and least resonant $\beta$ values are also shown (overlapping for **3**). For a clear view of the two-photon resonance, the experimental hyperpolarisabilities and the TLM curves are displayed at the frequency-doubled wavelength.

 © 2006 Wiley-VCH Verlag GmbH & Co. KGaA, Weinheim 

value, which leads to practically the same $\beta_0$ value ($113 \times 10^{-30}$ esu). Compound **2**, on the other hand, is closer to resonance and it is clearly seen that the undamped TLM is totally inadequate to derive the static value from $\beta$ at 1072 nm. The dispersion is very poorly modelled and a far too low $\beta_0$ would be obtained using only this resonant value. However, using only the least resonant $\beta$ (at 1540 nm) shows that the TLM gives a good description of the long wavelength tail of the dispersion curve and yields a more reliable static $\beta_0$ ($163 \times 10^{-30}$ esu). So, this wavelength-dependent HRS study clearly shows that the TLM cannot be used to calculate $\beta_0$ from strongly resonant hyperpolarisabilities and therefore, in the following discussion, we will use the TLM for only qualitative comparisons between the different structural variations. One way to improve on this model is to introduce an ad hoc damping factor, $\Gamma$, into the expression of $\beta$ but, unfortunately, some additional complications arise in this procedure. Firstly, it is not clear whether such a damping factor (i.e. a homogeneous line-broadening) can also be used to properly describe the actual linewidth, which is largely due to inhomogeneous broadening and vibronic coupling, and secondly, there is a possible red-shift between the absorption and the $\beta$ maximum, as reported by Wang et al.[33] Therefore, more extended wavelength-dependent HRS measurements are needed to decide between different possible models.[31,34–37]

The first structural variation which will be discussed is the replacement of the $\eta^5$-monocyclopentadienyl ring at the organometallic donor fragment by a second bidentate phosphane (dppe) ligand to create a pseudo-octahedral surrounding of the iron moiety. Comparing **1** with **7** and **2** with **8** (see Table 1) we can see that in both cases the introduction of the second dppe ligand results in a red-shift of the CT band and an increase of the extinction coefficient, $\varepsilon_{max}$, which results in an increase of the resonant $\beta$ value, in agreement with the two-level model. From IR measurements a significant shift to lower $\nu$(N≡C) values was observed upon coordination ($\Delta\nu_{NC} = -56\ cm^{-1}$ for **1** and $-43\ cm^{-1}$ for **2**; see Table 1). This points to a stronger π back-donation and hence a higher donor efficiency in the pseudo-octahedral cases **1** and **2** as compared to the analogous cyclopentadienyl compounds **7** and **8**, where a shift of only –35 and $-15\ cm^{-1}$ was found, respectively.[12] This is indeed supported by the higher static value of $163 \times 10^{-30}$ esu obtained for the pseudo-octahedral compound **2** than the $\beta_0$ of $112 \times 10^{-30}$ esu for the analogous cyclopentadienyl complex **8**.[12] So, in conclusion, based on the spectroscopic measurements and the increase of the static $\beta$ value it appears that the pseudo-octahedral surrounding yields a more efficient electron donor.

A second strategy we used to optimise the push-pull system was to also increase the strength of the electron-withdrawing moiety by introducing an extra nitro group at the *ortho* position of the last phenyl ring of the conjugated backbone. Comparing compounds **1** and **4** and **3** and **5** we can see that in both cases the introduction of the second nitro group results in a shift of the CT band to higher wavelengths and an increase of the extinction coefficient. It appears that introducing the second nitro group results in a more efficient electron-withdrawing moiety, thereby lowering the energy of the CT transition. The energy shift makes the longer compound **5** more resonant than compound **3**, while for the shorter compound **4**, the shift is much more drastic and results in a CT band in the NIR, beyond resonance. However, compound **4** has a remarkably high $\beta$ value, taking into account that it is farther from resonance, so it probably has a higher static value $\beta_0$ than compound **1**.

The smaller red-shift observed for the longer compounds (**3** and **5**) can be understood by considering that the second nitro group was introduced on the second phenyl ring, farther from the donor metal fragment, leading to a less effective D–A interaction through the π back-donation effect.

The third degree of freedom which can be used to optimise the molecular $\beta$ value is the structure and length of the conjugated backbone connecting the electron donor and acceptor. It is well known that $\beta$ increases sharply with conjugation length, therefore we extended the conjugated backbone of both the nitro (**1**, **2** and **3**) and the dinitro compounds (**4** and **5**). A very surprising result is that, for both forms, the CT band shifts to higher energy for the longer compounds. As we mentioned previously, this can be explained by a better interaction of the donor with the acceptor through the shorter conjugated path, leading to a very low energy CT transition. However, the longer compound **2** yields a larger $\beta$ than the shorter one **1**, which in this case is compatible with the difference in extinction coefficients, $\varepsilon_{max}$. This trend is continued for the even longer compound **3**. Indeed, comparing compounds **2** and **3** we see that although compound **3** is much less resonant and has about the same extinction coefficient, it still has a comparable $\beta$ value to compound **2**. This points to a large static $\beta$ value for compound **3** as a consequence of a large dipole moment difference, according to the two-level model. In the case of the dinitro compounds the difference between the $\beta$ values of the shorter compound **4** and the longer one **5** can be explained in terms of resonant enhancement and difference between extinction coefficients.

Finally, the structural change of introducing one hydrazone spacer (–C=N–NH) between the two phenyl rings forming the backbone on going from compound **5** to **6** seems to have virtually no effect on the $\beta$ values; $\nu$(N≡C), $\delta_{^1H_{hydride}}$ and $\delta_{^{31}P_{dppe}}$ (see Table 1) also remain unchanged, and only $\nu$(Fe–H) is slightly higher. Neither the spectral position of the CT band nor the extinction coefficient is modified significantly so it seems that the D–A interaction is barely changed by this last modification.

In conclusion, a series of hydrido(nitrile)iron(II) complexes have been synthesised that show improved molecular NLO properties, which we ascribe to an improved donor character of the pseudo-octahedral organometallic moiety. The NLO push-pull system was further improved by increasing the conjugation length and by double nitro substitution to form a better electron-accepting moiety. Wavelength-dependent HRS measurements, performed for the first time on organometallic NLO chromophores, show the

 © 2006 Wiley-VCH Verlag GmbH & Co. KGaA, Weinheim 

effect of two-photon resonance enhancement and demonstrate that for highly resonant cases the TLM is inadequate and therefore wavelength-dependent measurements are needed to model the dispersion of $\beta$. The X-ray structure of $[Fe(H)(dppe)_2(4\text{-}NCC_6H_4NO_2)][PF_6]$ (**1**) showed that the NLO response is cancelled at the macroscopic level for this compound by a pairwise antiparallel orientation of the complexes. However, the pseudo-octahedral coordination appears to be very suitable for a more systematic implementation of the previously demonstrated[25,27] design strategies (replacement of dppe by chiral phosphanes and inclusion of appropriate spacing groups along the dipolar axis) to promote a favourable non-centrosymmetric crystal structure.

## Experimental Section

**General Procedures:** All preparations were carried out under vacuum or nitrogen using standard Schlenk techniques. The solvents were dried before use following published methods.[38] The starting material $[FeHCl(dppe)_2]$ was synthesised according to a published method.[39] The aromatic nitrile ligands 4-nitrobenzonitrile and 2,4-dinitrobenzonitrile were purchased from Sigma–Aldrich and used as received. Ligands (*E*)-4-[2-(4-nitrophenyl)ethenyl]benzonitrile,[40] (*E*)-3-(4-nitrophenyl)acrylonitrile,[41] 4-[*N*-(2,4-dinitrophenyl)hydrazonomethyl]benzonitrile[42] and (*E*)-4-[2-(2,4-dinitrophenyl)ethenyl]benzonitrile[43] were prepared following the literature procedures.

IR spectra were recorded for KBr pellets on a Perkin–Elmer Paragon 1000 PC FT-IR or a Bio-Rad Excalibur FTS 3000MX spectrophotometer; only the significant bands are cited. $^1H$, $^{13}C$ and $^{31}P$ NMR spectra were recorded for $[D_2]$dichloromethane solutions with a Varian Unity 300 spectrometer at probe temperature, using $SiMe_4$ as internal reference ($^1H$ and $^{13}C$ NMR chemical shifts) and 85% $H_3PO_4$ as external reference for $^{31}P$ NMR chemical shifts. Spectral assignments follow the numbering scheme given in Scheme 1. The UV/Vis spectra were recorded with a Shimadzu 1603 spectrophotometer for $10^{-4}$ or $10^{-5}$ M solutions in several solvents. Elemental analyses were performed at the Laboratório de Análises of the Instituto Superior Técnico, using a Fisons Instruments EA1108 system, with data acquisition, integration and handling performed with a PC and the software package Eager-200 (Carlo Erba Instruments). Melting points were measured with a Leica Galen III melting point apparatus and are not corrected.

**General Procedure for the Synthesis of the Pseudo-Octahedral Iron(II) Derivatives:** A slight excess of the nitrile chromophore (1.1–1.2 equiv.) and $TlPF_6$ (1.1–1.2 equiv.) were added to a solution of $[Fe(H)(Cl)(dppe)_2]$ (0.68–1.01 mmol) in dichloromethane (THF for compound **1**). The mixture was then stirred at room temperature for 2–4 h (18 h for compounds **1** and **6**). A colour change was observed with simultaneous precipitation of thallium chloride. After filtration, the solvents were evaporated under vacuum to dryness and the residues were washed several times with diethyl ether to remove the excess of nitrile. Recrystallisation from dichloromethane/diethyl ether afforded powder or crystalline samples of the pure compounds.

**$[Fe(H)(dppe)_2(4\text{-}NCC_6H_4NO_2)][PF_6]$ (1):** Yield: 97 mg (37%), purple crystals; m.p. 132.7–134.2 °C. IR (KBr): $\tilde{\nu}_{max}$ = 2177 $cm^{-1}$ (s) (CN), 1870 (w) (Fe–H), 1516 (m) and 1338 (s) ($NO_2$), 838 (s) ($PF_6^-$). $^1H$ NMR (300 MHz, $CD_2Cl_2$): $\delta$ = –17.48 (quint, $^2J_{H,P}$ = 47.6 Hz, 1 H, FeH), 2.13 (s, 4 H, $PCH_2$), 2.59 (s, 4 H, $PCH_2$), 6.73 (d, $J$ = 8.4 Hz, 2 H, H2,H6), 6.77 (s, 8 H, PPh-$H_{ortho}$), 7.07 (t, $J$ = 7.5 Hz, 8 H, PPh-$H_{meta}$), 7.18 (t, $J$ = 7.5 Hz, 8 H, PPh-$H_{meta}$), 7.27–7.36 (m, 8 H, PPh-$H_{para}$), 7.47 (s, 8 H, PPh-$H_{ortho}$), 8.18 (d, $J$ = 8.4 Hz, 2 H, H3,H5) ppm. $^{13}C\{^1H\}$ NMR ($CD_2Cl_2$): $\delta$ = 32.54 (qt, $^1J_{C,P}$ = 11.4 Hz, $PCH_2$), 118.81 (C1), 123.11 (NC), 124.56 (C3,C5), 128.35 and 129.11 (PPh-$C_{meta}$), 130.46 and 130.60 (PPh-$C_{para}$), 132.70 (PPh-$C_{ortho}$), 132.97 (C2,C6), 133.38 (PPh-$C_{ortho}$), 134.64 (m, PPh-$C_{ipso}$), 149.24 (C4) ppm. $^{31}P\{^1H\}$ NMR ($CD_2Cl_2$): $\delta$ = –143.50 (sept, $^1J_{P,F}$ = 709.2 Hz, $PF_6$), 83.34 (s, dppe) ppm. $C_{59}H_{53}F_6FeN_2O_2P_5 \cdot 1/2CH_2Cl_2$ (1190.3) calcd. C 60.09, H 4.58, N 2.36; found C 60.31, H 4.64, N 2.27. UV ($CHCl_3$): $\lambda_{max}$ ($\varepsilon$) = 265 nm (49937 $M^{-1}cm^{-1}$), 546 (7706); [$(CH_3)_2CO$]: 535 (8155); (DMSO): 266 (73979), 556 (11263).

**$[Fe(H)(dppe)_2\{(E)\text{-}4\text{-}NCCH{=}CHC_6H_4NO_2\}][PF_6]$ (2):** Yield, 380 mg (48%), purple solid; m.p. 134.2–135.7 °C. IR (KBr): $\tilde{\nu}_{max}$ = 2174 $cm^{-1}$ (s) (CN), 1853 (w) (Fe–H), 1515 (m) and 1339 (s) ($NO_2$), 839 (s) ($PF_6^-$). $^1H$ NMR (300 MHz, $CD_2Cl_2$): $\delta$ = –18.03 (quint, $^2J_{H,P}$ = 46.8 Hz, 1 H, FeH), 2.12 (s, 4 H, $PCH_2$), 2.61 (s, 4 H, $PCH_2$), 5.65 (d, $J$ = 15.9 Hz, 1 H, H8), 6.22 (d, $J$ = 15.9 Hz, 1 H, H7), 6.76 (s, 8 H, PPh-$H_{ortho}$), 7.17 (t, $J$ = 6.6 Hz, 16 H, PPh-$H_{meta}$), 7.26–7.37 (m, 8 H, PPh-$H_{para}$), 7.49 (s, 10 H, PPh-$H_{ortho}$ and H2,H6), 8.26 (d, $J$ = 7.5 Hz, 2 H, H3,H5) ppm. $^{13}C\{^1H\}$ NMR ($CD_2Cl_2$): $\delta$ = 32.80 (t, $^1J_{C,P}$ = 12.0 Hz, $PCH_2$), 101.10 (C8), 124.58 (NC), 124.69 (C3,C5), 128.12 (C2,C6), 128.23 and 128.90 (PPh-$C_{meta}$), 130.22 and 130.45 (PPh-$C_{para}$), 132.79 and 133.43 (PPh-$C_{ortho}$), 134.07 and 135.07 (m, PPh-$C_{ipso}$), 139.83 (C1), 146.73 (C7), 148.16 (C4) ppm. $^{31}P\{^1H\}$ NMR ($CD_2Cl_2$): $\delta$ = –143.50 (quint, $^1J_{P,F}$ = 710.1 Hz, $PF_6$), 83.80 (s, dppe) ppm. $C_{61}H_{55}F_6FeN_2O_2P_5$ (1172.8) calcd. C 62.47, H 4.73, N 2.39; found. C 62.88, H 4.70, N 2.73. UV ($CHCl_3$): $\lambda_{max}$ ($\varepsilon$) = 265 nm (48916 $M^{-1}cm^{-1}$), 297 (27695), 549 (8762).

**$[Fe(H)(dppe)_2\{(E)\text{-}4\text{-}NCC_6H_4CH{=}CH\text{-}4\text{-}C_6H_4NO_2\}][PF_6]$ (3):** Yield: 900 mg (71%), dark-red solid; m.p. 145.1–145.9 °C. IR (KBr): $\tilde{\nu}_{max}$ = 2185 $cm^{-1}$ (w) (NC), 1888 (w) (Fe–H), 1510 (m) and 1339 (s) ($NO_2$), 830 (s) ($PF_6^-$). $^1H$ NMR (300 MHz, $CD_2Cl_2$): $\delta$ = –18.83 (quint, $^2J_{H,P}$ = 47.0 Hz, 1 H, FeH), 2.12 (s, 4 H, $PCH_2$), 2.55 (s, 4 H, P–$CH_2$), 6.76 (d, $J$ = 8.1 Hz, 2 H, H2,H6), 6.85 (s, 8 H, PPh-$C_{ortho}$), 7.09 (t, $J$ = 7.5 Hz, 8 H, PPh-$C_{meta}$), 7.16 (t, $J$ = 7.5 Hz, 8 H, PPh-$C_{meta}$), 7.25–7.36 (m, 10 H, PPh-$C_{para}$, H7 and H8), 7.45 (s, 8 H, PPh-$C_{ortho}$), 7.57 (d, $J$ = 8.4 Hz, 2 H, H3,H5), 7.74 (d, $J$ = 9.0 Hz, 2 H, H10,H14), 8.27 (d, $J$ = 9.0 Hz, 2 H, H11,H13) ppm; some signals are obscured by the *para* aromatic protons of dppe. $^{13}C\{^1H\}$ NMR ($CD_2Cl_2$): $\delta$ = 32.47 (t, $J$ = 12.2 Hz, $PCH_2$), 111.95 (C1), 124.24 (C11,C13), 126.43 (NC), 127.66 (C10,C14), 127.91 (C3,C5), 128.05 and 128.85 (PPh-$C_{meta}$), 129.98 (C7), 130.12 (PPh-$C_{para}$), 131.35 (C8), 132.34 (C2,C6), 132.65 and 133.20 (PPh-$C_{ortho}$), 133.97 and 134.95 (m, PPh-$C_{ipso}$), 140.79 (C4), 142.97 (C9), 147.45 (C12) ppm. $^{31}P\{^1H\}$ NMR ($CD_2Cl_2$): $\delta$ = –143.47 (sept, $^1J_{P,F}$ = 708.6 Hz, $PF_6$), 84.71 (s, dppe) ppm. $C_{67}H_{59}F_6FeN_2O_2P_5 \cdot CH_2Cl_2$ (1257.7) calcd. C 60.78, H 4.64, N 2.31; found C 60.71, H 4.96, N 1.99. UV ($CHCl_3$): $\lambda_{max}$ ($\varepsilon$) = 266 nm (34316 $M^{-1}cm^{-1}$), 346 (51278), 485 (8255).

**$[Fe(H)(dppe)_2\{2,4\text{-}NCC_6H_3(NO_2)_2\}][PF_6]$ (4):** Yield: 386 mg (48%), dark-green solid; m.p. 144.4 °C (dec.). IR (KBr): $\tilde{\nu}_{max}$ = 2138 $cm^{-1}$ (m) (NC), 1891 (w) (Fe–H), 1527 (m) and 1338 (d) ($NO_2$), 839 (s) ($PF_6^-$). $^1H$ NMR (300 MHz, $CD_2Cl_2$): $\delta$ = –14.60 (quint, $^2J_{H,P}$ = 48.5 Hz, 1 H, FeH), 2.31 (s, 4 H, $PCH_2$), 2.88 (s, 4 H, $PCH_2$), 5.43 (d, $J_{H6,H5}$ = 9.0 Hz, 1 H, H6), 6.72 (s, 8 H, PPh-$C_{ortho}$), 6.99 (t, $J$ = 7.5 Hz, 8 H, PPh-$C_{meta}$), 7.16–7.25 (m, 12 H, PPh-$C_{meta}$ and PPh-$C_{para}$), 7.30 (t, $J$ = 6.9 Hz, 4 H, PPh-$C_{para}$), 7.43 (s, 8 H, PPh-$C_{ortho}$), 7.90 (dd, $J_{H5,H6}$ = 8.4, $^4J_{H5,H3}$ = 2.4 Hz, 1 H, H5), 8.99 (d, $^4J_{H3,H5}$

 © 2006 Wiley-VCH Verlag GmbH & Co. KGaA, Weinheim 

= 2.4 Hz, 1 H, H3) ppm. $^{13}C\{^1H\}$ NMR ($CD_2Cl_2$): $\delta$ = 32.95 (s, $PCH_2$), 113.97 (C1), 118.70 (NC), 121.66 (C3), 127.50 (C5), 128.40 and 129.16 (PPh-$C_{meta}$), 130.66 and 130.85 (PPh-$C_{para}$), 132.76 and 133.44 (PPh-$C_{ortho}$), 134.38 (m, PPh-$C_{ipso}$), 138.07 (C6), 146.78 and 147.24 (C2 and C4) ppm. $^{31}P\{^1H\}$ NMR (300 MHz, $CD_2Cl_2$): $\delta$ = –143.50 (sept, $^1J_{P,F}$ = 708.9 Hz, $PF_6$), 81.00 (s, dppe) ppm. $C_{59}H_{52}F_6FeN_3O_4P_5 \cdot 1/2CH_2Cl_2$ (1237.7) calcd. C 57.90, H 4.33, N 3.40; found C 57.46, H 4.47, N 3.36. UV ($CHCl_3$): $\lambda_{max}$ ($\varepsilon$) = 254 nm (shoulder), 266 (shoulder), 723 (8274 $M^{-1}cm^{-1}$).

**[Fe(H)(dppe)$_2${(*E*)-4-NCC$_6$H$_4$CH=CH-2,4-C$_6$H$_3$(NO$_2$)$_2$}][PF$_6$] (5):** Yield: 444 mg (51%), purple solid; m.p. 161.9–163.6 °C. IR (KBr): $\tilde{\nu}_{max}$ = 2182 $cm^{-1}$ (w) (NC), 1891 (w) (Fe–H), 1528 (m) and 1345 (m) ($NO_2$), 840 (s) ($PF_6^-$). $^1H$ NMR (300 MHz, $CD_2Cl_2$): $\delta$ = –18.67 (quint, $^2J_{H,P}$ = 47.4 Hz, 1 H, FeH), 2.11 (s, 4 H, $PCH_2$), 2.55 (s, 4 H, $PCH_2$), 6.77 (d, $J$ = 7.8 Hz, 2 H, H2,H6), 6.83 (s, 8 H, PPh-$C_{ortho}$), 7.09 (t, $J$ = 7.5 Hz, 8 H, PPh-$C_{meta}$), 7.16 (t, $J$ = 7.2 Hz, 8 H, PPh-$C_{meta}$), 7.28 (t, $J$ = 7.5 Hz, 4 H, PPh-$C_{para}$), 7.35 (t, $J$ = 7.2 Hz, 4 H, PPh-$C_{para}$), 7.46 (s, 8 H, PPh-$C_{ortho}$), 7.60 (d, $J$ = 7.5 Hz, 2 H, H3,H5), 7.73 (d, $J$ = 15.3 Hz, 1 H, H8), 8.08 (d, $J$ = 8.7 Hz, 1 H, H14), 8.52 (dd, $J_{H13,H14}$ = 8.7, $^4J_{H13,H11}$ = 1.8 Hz, 1 H, H13), 8.86 (d, $J_{H11,H13}$ = 2.4 Hz, 1 H, H11) ppm; the signal for H7 is obscured by the *para* aromatic protons of dppe. $^{13}C\{^1H\}$ NMR ($CD_2Cl_2$): $\delta$ = 32.60 (t, $^1J_{C,P}$ = 11.7 Hz, $PCH_2$), 113.07 (C1), 120.97 (C11), 125.42 (C8), 126.28 (NC), 127.98 (C13), 128.28 (PPh-$C_{meta}$), 128.33 (C3,C5), 129.01 (PPh-$C_{meta}$), 130.24 (C14), 130.37 and 130.44 (PPh-$C_{para}$), 132.44 (C2,C6), 132.83 and 133.42 (PPh-$C_{ortho}$), 134.14 and 135.14 (2 m, PPh-$C_{ipso}$), 135.76 (C7), 138.24 (C4), 140.05 (C9), 147.29 and 148.04 (C10 and C12) ppm. $^{31}P\{^1H\}$ NMR ($CD_2Cl_2$): $\delta$ = –143.73 (quint, $^1J_{P,F}$ = 708.0 Hz, $PF_6$), 83.48 (s, dppe) ppm. $C_{67}H_{58}F_6FeN_3O_4P_5$ (1293.9) calcd. C 62.19, H 4.52, N 3.25; found C 61.98, H 4.33, N 3.23. UV ($CHCl_3$): $\lambda_{max}$ ($\varepsilon$) = 265 nm (50967 $M^{-1}cm^{-1}$), 349 (26449), 505 (10348).

**[Fe(H)(dppe)$_2${4-NCC$_6$H$_4$CH=N-NH-2,4-C$_6$H$_3$(NO$_2$)$_2$}][PF$_6$] (6):** Yield: 440 mg (50%), dark-red solid; m.p. 153.5–155.4 °C. IR (KBr): $\tilde{\nu}_{max}$ = 3289 $cm^{-1}$ (w) (N–H), 2183 (w) (NC), 1896 (w) (Fe–H), 1616 (m) (C=N), 1513 (m) and 1333 (m) ($NO_2$), 841 (s) ($PF_6^-$). $^1H$ NMR (300 MHz, $CD_2Cl_2$): $\delta$ = –18.54 (quint, $^2J_{H,P}$ = 47.6 Hz, 1 H, FeH), 2.12 (s, 4 H, $PCH_2$), 2.56 (s, 4 H, $PCH_2$), 6.79 (d, $J$ = 9.3 Hz, 2 H, H2,H6), 6.83 (s, 8 H, PPh-$C_{ortho}$), 7.10 (t, $J$ = 7.8 Hz, 8 H, PPh-$C_{meta}$), 7.17 (t, $J$ = 7.5 Hz, 8 H, PPh-$C_{meta}$), 7.28 (t, $J$ = 7.5 Hz, 4 H, PPh-$C_{para}$), 7.35 (t, $J$ = 7.2 Hz, 4 H, PPh-$C_{para}$), 7.46 (s, 8 H, PPh-$C_{ortho}$), 7.79 (d, $J$ = 8.4 Hz, 2 H, H3,H5), 8.17 (d, $J$ = 8.7 Hz, 1 H, H13), 8.20 (s, 1 H, H7), 8.44 (dd, $J_{H12,H13}$ = 9.6, $^4J_{H12,H10}$ = 2.4 Hz, 1 H, H12), 9.15 (d, $J_{H10,H12}$ = 2.7 Hz, 1 H, H10), 11.44 (s, 1 H, NH) ppm. $^{13}C\{^1H\}$ NMR ($CD_2Cl_2$): $\delta$ = 32.64 (t, $^1J_{C,P}$ = 12.20 Hz, $PCH_2$), 114.08 (C1), 117.31 (C10), 123.65 (C12), 126.03 (NC), 128.18 (C3,C5), 128.31 and 129.05 (PPh-$C_{meta}$), 130.40 and 130.48 (PPh-$C_{para}$), 132.41 (C2,C6), 132.84 and 133.43 (PPh-$C_{ortho}$), 134.14 and 135.12 (2 m, PPh-$C_{ipso}$), 137.15 (C12), 137.55 (C4), 138.02 (C7), 139.32 (C8), 144.93 and 145.74 (C9 and C11) ppm. $^{31}P\{^1H\}$ NMR ($CD_2Cl_2$): $\delta$ = –143.66 (quint, $^1J_{P,F}$ = 707.2 Hz, $PF_6$), 83.45 (s, dppe) ppm. $C_{66}H_{58}F_6FeN_5O_4P_5 \cdot C_4H_{10}O$ (1309.90) calcd. C 58.77, H 4.93, N 5.35; found C 58.91, H 4.59, N 4.90. UV ($CHCl_3$): $\lambda_{max}$ ($\varepsilon$) = 266 nm (35898 $M^{-1}cm^{-1}$), 380 (19559), 503 (10679).

**Crystal Structure of 1:** $C_{59}H_{53}F_6FeN_2O_2P_5 \cdot CH_2Cl_2$, $M$ = 1231.66, $\mu$ = 4.774 $mm^{-1}$, $\rho$ = 1410 $mg\,m^{-3}$, monoclinic, $P2_1/n$, $Z$ = 4, $a$ = 12.48(1), $b$ = 35.599(9), $c$ = 13.243(9) Å, $\beta$ = 99.49(2)°, $V$ = 5803(6) $Å^3$, from 23 reflections (16.7° < 2$\theta$ < 18.9°). Cell dimensions and intensities were measured at 293(2) K with an Enraf–Nonius TURBOCAD4 diffractometer (Cu rotating anode, $\lambda$ = 1.54180 Å). As a general procedure, the intensity of three standard reflections was measured periodically every 5 h. This procedure did not reveal any appreciable decay. Using the CAD4 software, data were corrected for Lorentz and polarisation effects and empirically for absorption (from $\Psi$-scan measurements). Data were collected in the range 3.6° < $\theta$ < 67° (–13 < $h$ < 14, 0 < $k$ < 42, 0 < $l$ < 15); 10579 measured reflections, 10140 of which were considered as observed [$|F_o|^2 > 3\sigma(|F_o|^2)$]; $R_{int}$ = 0.0503 for equivalent reflections. The structure was solved by direct methods using SIR97[44] and refined with SHELXL[45] in the WINGX[46] program package. Full-matrix least-squares refinement based on $F^2$ gave final values $R$ = 0.0729, $wR_2$ = 0.1397 for 923 variables and 10140 contributing reflections. The position of the Fe atom was obtained from a three-dimensional Patterson synthesis, while all the other non-hydrogen atoms were located in subsequent difference Fourier maps. The hydrogen atoms were inserted in calculated positions and refined isotropically as riding on the parent carbon atom. The final difference electron density map showed a maximum of 0.558 and a minimum of –0.695 e $Å^{-3}$.

CCDC-286415 contains the supplementary crystallographic data for this paper. These data can be obtained free of charge from The Cambridge Crystallographic Data Centre via www.ccdc.cam.ac.uk/data_request/cif.

**Hyper-Rayleigh Scattering Measurements:** First hyperpolarisabilities were determined by means of the hyper-Rayleigh scattering (HRS) technique.[47,48] The measurements were performed in a new HRS setup based on an optical parametrical amplifier (OPA) pumped by a Ti:sapphire regenerative amplifier (pulse width: 2 ps, repetition rate: 1.5 kHz, average power: ca. 30 mW). The different fundamental wavelengths used (1072, 1200, 1300, 1440, 1540 and 1580 nm) were obtained by tuning the signal beam of the OPA, and were chosen carefully to avoid vibrational absorption bands of chloroform. To prevent dielectric breakdown and self-focusing, the pulses were focused onto the sample with cylindrical lenses. The scattered second harmonic light was collected at 90° and detected with a combination of a spectrograph and an intensified charge coupled device (ICCD) with red-sensitive photocathode. The ICCD provides nanosecond-gated parallel detection of a small (ca. 23 nm) spectral area around the harmonic wavelength. The outer regions of this range was used to correct the HRS signal for multi-photon fluorescence, as described before.[4,10] A large photoluminescence background was only observed for one of the free ligands (**L3**, see Table 1), for which the luminescence signal, integrated over the central region of 6 nm, was about equal to the actual HRS signal. HRS measurements were performed in a rectangular fused silica cell containing a dilute solution of the compound in chloroform. Concentrations used were of the order of $10^{-6}$–$10^{-4}$ M for the complexes and $10^{-3}$–$10^{-4}$ M for the free ligands. With these concentrations the absorption of the second harmonic wavelength was kept well below 10%, so that an accurate correction for this effect could be carried out. The absorption measurements where performed with a Varian Cary 5 absorption spectrometer. All hyperpolarisabilities were determined by internal reference relative to chloroform,[48] as described before.[4,10] Within the assumption of only one significant diagonal $\beta$ tensor component along the $z$-axis (i.e. the conjugated backbone of the molecule), $\beta_{zzz}$ values can be calculated by measuring the HRS signal for a dilute solution with known concentration of the chromophores and from pure chloroform. The $\beta$ value of $0.49 \times 10^{-30}$ esu for chloroform, determined with the EFISHG technique at 1064 nm,[49] was used as internal reference. The dispersion of the reference value in the explored 1072–1580 nm range was neglected. An upper limit of 5% to this effect was estimated using the TLM expression with the maximum of the longest wavelength absorption band of chloroform (143 nm)[50] taken as $\lambda_{eg}$.

 © 2006 Wiley-VCH Verlag GmbH & Co. KGaA, Weinheim 

## Acknowledgments

Financial support for this work was provided by the TMR network programme "Organometallic dipoles with NLO properties" contract ERBFMRXCT-CT98-0166, by COST D14, and partly by the Fundação para a Ciência e Tecnologia and POCTI (POCTI/QUI/48443/2002). W.W is a Postdoctoral Fellow of the Fund for Scientific Research of Flanders (Belgium) (FWO, Vlaanderen). Financial support from the FWO in the group project G.0041.01 is gratefully acknowledged.

[1] M. L. H. Green, S. R. Marder, M. E. Thompson, J. A. Bandy, D. Bloor, P. V. Kolinsky, R. J. Jones, *Nature* **1987**, *330*, 360–362.
[2] H. S. Nalwa, *Appl. Organomet. Chem.* **1991**, *5*, 349–377 and references cited therein.
[3] P. N. Prasad, D. J. Williams, *Introduction to Nonlinear Optical Effects in Molecules and Polymers*, John Wiley and Sons, Inc., New York, **1991**.
[4] E. Goovaerts, W. Wenseleers, M. H. Garcia, G. H. Cross, *Handbook of Advanced Electronic and Photonic Materials and Devices* (Ed.: H. S. Nalwa), Academic Press, **2001**, vol. 9, p. 127–191 and references cited therein.
[5] I. R. Whittall, A. M. McDonagh, M. G. Humphrey, M. Samoc, *Adv. Organomet. Chem.* **1999**, *43*, 349–405 and references cited therein.
[6] S. Di Bella, *Chem. Soc. Rev.* **2001**, *30*, 355–366 and references cited therein.
[7] C. E. Powell, M. G. Humphrey, *Coord. Chem. Rev.* **2004**, *248*, 725–756 and references cited therein.
[8] J. Zyss, *Molecular Nonlinear Optics: Materials, Physics, and Devices*, Academic Press, San Diego, CA, **1994**.
[9] J. C. Calabrese, L. T. Cheng, J. C. Green, S. R. Marder, W. Tam, *J. Am. Chem. Soc.* **1991**, *113*, 7227–7232.
[10] W. Wenseleers, A. W. Gerbrandij, E. Goovaerts, M. H. Garcia, M. P. Robalo, P. J. Mendes, J. C. Rodrigues, A. R. Dias, *J. Mater. Chem.* **1998**, *8*, 925–930.
[11] M. H. Garcia, M. P. Robalo, A. R. Dias, M. T. Duarte, W. Wenseleers, G. Aerts, E. Goovaerts, M. P. Cifuentes, S. Hurst, M. G. Humphrey, M. Samoc, B. Luther-Davies, *Organometallics* **2002**, *21*, 2107–2118.
[12] M. H. Garcia, M. P. Robalo, A. R. Dias, M. F. M. Piedade, A. Galvão, W. Wenseleers, E. Goovaerts, *J. Organomet. Chem.* **2001**, *619*, 252–264.
[13] A. M. McDonagh, M. G. Humphrey, M. Samoc, B. Luther-Davies, *Organometallics* **1999**, *18*, 5195–5197.
[14] H. Le Bozec, T. Le Bouder, O. Maury, A. Bondon, I. Ledoux, S. Deveau, J. Zyss, *Adv. Mater.* **2001**, *13*, 1677–1681.
[15] A. M. McDonagh, I. R. Whittall, M. G. Humphrey, B. W. Skelton, A. H. White, *J. Organomet. Chem.* **1996**, *519*, 229–235.
[16] R. H. Naulty, A. M. McDonagh, I. R. Whittall, M. P. Cifuentes, M. G. Humphrey, S. Houbrechts, J. Maes, A. Persoons, G. A. Heath, D. C. R. Hockless, *J. Organomet. Chem.* **1998**, *563*, 137–146.
[17] I. R. Whittall, M. P. Cifuentes, M. G. Humphrey, B. Luther-Davies, M. Samoc, S. Houbrechts, A. Persoons, G. A. Heath, D. C. R. Hockless, *J. Organomet. Chem.* **1997**, *549*, 127–137.
[18] J. G. Lee, B. S. Yoo, N. S. Choi, K. I. Park, S. I. Cho, C. M. Lee, S. W. Lee, *J. Organomet. Chem.* **1999**, *589*, 138–149.
[19] L. Martins, J. da Silva, A. J. L. Pombeiro, R. A. Henderson, D. J. Evans, F. Benetollo, G. Bombieri, R. A. Michelin, *Inorg. Chim. Acta* **1999**, *291*, 39–48.
[20] Y. Gao, D. G. Holah, A. N. Hughes, G. J. Spivak, M. D. Havighurst, V. R. Magnuson, *Polyhedron* **1998**, *17*, 3881–3888.
[21] M. H. Garcia, M. P. Robalo, A. P. S. Teixeira, A. R. Dias, M. F. M. Piedade, M. T. Duarte, *J. Organomet. Chem.* **2001**, *632*, 145–156.
[22] L. J. Farrugia, *J. Appl. Crystallogr.* **1997**, *30*, 565.
[23] J. H. Lee, B. S. Yoo, S. W. Lee, *Inorg. Chim. Acta* **2001**, *321*, 75–82.
[24] M. Hirano, S. Kiyota, M. Imoto, S. Komiya, *Chem. Commun.* **2000**, 1679–1680.
[25] W. Wenseleers, E. Goovaerts, P. Hepp, M. H. Garcia, M. P. Robalo, A. R. Dias, M. F. M. Piedade, M. T. Duarte, *Chem. Phys. Lett.* **2003**, *367*, 390–397.
[26] B. J. Coe, C. J. Jones, J. A. McCleverty, D. Bloor, G. Cross, *J. Organomet. Chem.* **1994**, *464*, 225–232.
[27] M. H. Garcia, J. C. Rodrigues, A. R. Dias, M. F. M. Piedade, M. T. Duarte, M. P. Robalo, N. Lopes, *J. Organomet. Chem.* **2001**, *632*, 133–144.
[28] H. Meier, R. Petermann, J. Gerold, *Chem. Commun.* **1999**, 977–978.
[29] J. Luo, J. Hua, J. Qin, J. Chen, Y. Shen, Z. Lu, P. Wang, C. Ye, *Chem. Commun.* **2001**, 171–172.
[30] A. J. Moore, A. Chesney, M. R. Bryce, A. S. Batsanov, J. F. Kelly, J. A. K. Howard, I. F. Perepichka, D. F. Perepichka, G. Meshulam, G. Berkovic, Z. Kotler, R. Mazor, V. Khodorkovsky, *Eur. J. Org. Chem.* **2001**, 2671–2687.
[31] J. L. Oudar, D. S. Chemla, *J. Chem. Phys.* **1977**, *66*, 2664–2668.
[32] A. Willetts, J. E. Rice, D. M. Burland, D. P. Shelton, *J. Chem. Phys.* **1992**, *97*, 7590–7599.
[33] C. H. Wang, Y. C. Lin, O. Y. Tai, A. K. Y. Jen, *J. Chem. Phys.* **2003**, *119*, 6237–6244.
[34] B. J. Orr, J. F. Ward, *Mol. Phys.* **1971**, *20*, 513–526.
[35] A. M. Kelley, *J. Opt. Soc. Am. B: Opt. Phys.* **2002**, *19*, 1890–1900.
[36] G. Berkovic, G. Meshulam, Z. Kotler, *J. Chem. Phys.* **2000**, *112*, 3997–4003.
[37] C. H. Wang, *J. Chem. Phys.* **2000**, *112*, 1917–1924.
[38] D. D. Perrin, W. L. F. Armarego, D. R. Perrin, *Purification of Laboratory Chemicals*, Pergamon Press, New York, **1980**.
[39] P. Giannoccaro, A. Sacco, *Inorganic Synthesis*, McGraw-Hill Book Company, **1977**, vol. XVII.
[40] P. E. Hanna, R. E. Gammans, R. D. Sehon, M. K. Lee, *J. Med. Chem.* **1980**, *23*, 1038–1044.
[41] T. van Es, *J. Chem. Soc.* **1965**, 1564.
[42] L. M. Harwood, C. J. Moody, J. M. Percy, *Experimental Organic Chemistry − Standard and Microscale*, 2nd ed., Blackwell Science Oxford, **1998**.
[43] A. P. S. Teixeira, PhD Thesis, University of Évora, **2004**.
[44] A. Altomare, M. C. Burla, M. Camalli, G. L. Cascarano, C. Giacovazzo, A. Guagliardi, A. G. G. Moliterni, G. Polidori, R. Spagna, *J. Appl. Crystallogr.* **1999**, *32*, 115–119.
[45] G. M. Sheldrick, *SHELXL-97, a program for refining crystal structures* Göttingen, **1997**.
[46] L. J. Farrugia, *J. Appl. Crystallogr.* **1999**, *32*, 837–838.
[47] R. W. Terhune, P. D. Maker, C. M. Savage, *Phys. Rev. Lett.* **1965**, *14*, 681–684.
[48] K. Clays, A. Persoons, *Phys. Rev. Lett.* **1991**, *66*, 2980–2983.
[49] F. Kajzar, I. Ledoux, J. Zyss, *Phys. Rev. A* **1987**, *36*, 2210–2219.
[50] D. P. Seccombe, R. P. Tuckett, H. Baumgartel, H. W. Jochims, *Phys. Chem. Chem. Phys.* **1999**, *1*, 773–782.

Received: November 24, 2005
Published Online: April 11, 2006

 © 2006 Wiley-VCH Verlag GmbH & Co. KGaA, Weinheim 

DOI: 10.1002/ejic.200600076

# Synthesis and Characterization of Ternary $NH_4Ln_2F_7$ (Ln = Y, Ho, Er, Tm, Yb, Lu) Nanocages

Xin Liang,[a] Xun Wang,*[a] Leyu Wang,[a] Ruoxue Yan,[a] Qing Peng,[a] and Yadong Li[a]

**Keywords:** Nanostructures / Lanthanides

In this paper, a new class of $NH_4Ln_2F_7$ (Ln = Y, Ho, Er, Tm, Yb, Lu) inorganic nanocages that has been discovered will be presented. A facile template-free synthetic route was developed for one step, high yield, and large scale synthesis of ternary $NH_4Ln_2F_7$ (Ln = Y, Ho, Er, Tm, Yb, Lu) nanocages. On the basis of our studies, these nanocages are thermodynamically stable forms of this group of $NH_4Ln_2F_7$ compounds. The tendency of $NH_4Ln_2F_7$ (Ln = Y, Ho, Er, Tm, Yb, Lu) to form these new-type nanostructures is believed to have a close relationship with their inherent layered structures, similar to that of inorganic fullerene-like nanoparticles. This new type of nanocage can be easily doped with other lanthanide ions, which may endow these nanocages with novel properties.
(© Wiley-VCH Verlag GmbH & Co. KGaA, 69451 Weinheim, Germany, 2006)

## Introduction

In recent years, novel nano-sized morphologies of inorganic materials have become a new focus of research as they may offer new opportunities for application in various areas of nanotechnology, such as optical, biology, and catalysis, etc. Among these different morphologies, hollow nanostructures, as competitive building blocks for future nanodevices, attract considerable interest due to their high surface area and low-density characteristics as well as their other shape-dependent properties.[1–7] Great effort has been focused on the fabrication of different kinds of hollow nanostructures for this is a crucial step in the research and application of hollow nanostructures. Tenne and co-workers successfully synthesized a series of transition metal sulfide fullerene-like hollow nanostructures, such as $MoS_2$, $WS_2$, and $ReS_2$.[8–11] Many other hollow nanostructures (e.g., $TiO_2$, $SnO_2$, CdTe) have been prepared by using layer-by-layer self-assembly, sonochemical deposition, chemical-bath deposition, and other template-dependent methods.[12–19] On the basis of the colloidal chemical template-free hydrothermal method, binary lanthanide fluoride and hydroxide fullerene-like hollow spheres have been synthesized.[20] However, to the best of our knowledge, there are few reports concerning a colloidal chemistry-based template-free one-step synthesis of hollow nanostructures with small diameters for ternary (quaternary) lanthanide fluoride compounds. As is well known, MF-$LnF_3$ is a big family of compounds including many useful materials, such as $KY_3F_{10}$ and $NaYF_4$, which have great potential as biological labels,[21] in solid lasers, and display panels.[22] The tendency of $NH_4Ln_2F_7$ to form these new types of nanostructures is believed to have a close relationship with their inherent layered structures, similar to inorganic fullerene-like nanoparticles. The synthesis of hollow spheres of such complex compounds has great importance and is worthy of thoughtful research.

Herein we report a facile water/ethanol solvothermal synthetic method for one-step, high-yield preparation of a novel family of ternary $NH_4Ln_2F_7$ (Ln = Y, Ho, Er, Tm, Yb, Lu) nanocages under a temperature of 180 °C. The tendency of $NH_4Ln_2F_7$ to form these new types of nanostructures is believed to have a close relationship with their inherent layered structures, similar to inorganic fullerene-like nanoparticles. Since the structures of such materials have great similarity, especially for the KF-$LnF_3$ and $NH_4F$-$LnF_3$ systems, synthesis of other MF-$LnF_3$ hollow nanostructures should be possible and have great significance.

## Results and Discussion

$NH_4Ln_2F_7$ (Ln = Y, Ho, Er, Tm, Yb, Lu) crystallized in a cubic structure. The XRD pattern of $NH_4Y_2F_7$ shown in part a of Figure 1 can be indexed as arising from the pure cubic phase (JCPDS 43-0842) with lattice constant $a$ = 13.4 Å. Similar XRD patterns of a cubic phase were also observed from $NH_4Ho_2F_7$ (JCPDS 43-0842) to $NH_4Lu_2F_7$ (JCPDS 43-0842). The peak positions and relative intensities in those samples were almost identical to those observed in $NH_4Y_2F_7$, which indicated that this class of compounds shares a similar crystal structure. By careful observation a tiny difference can be found in the $2\theta$ values of

[a] Department of Chemistry, Tsinghua University, Beijing 100084, P. R. China
E-mail: wangxun@mail.tsinghua.edu.cn
Supporting information for this article is available on the WWW under http://www.eurjic.org or from the author.

 © 2006 Wiley-VCH Verlag GmbH & Co. KGaA, Weinheim 

the XRD peaks, which gradually increase on going from $NH_4Ho_2F_7$ to $NH_4Lu_2F_7$, indicating the gradual shrinkage of crystal structures according to the atomic number. The diffraction patterns for $NH_4Ln_2F_7$ (Ln = Y, Ho, Er, Tm, Yb, Lu) group compounds reveal an internal consistency associated with structural isotypes. The work of Krishnan Rajeshwar and Etalo A. Secco et al., showed that the structure of $NH_4Ln_2F_7$ (Ln = Y, Ho, Er, Tm, Yb, Lu) can be visualized as layers of $LnF_6$ octahedron (built up by mutual sharing of corners and edges) with interleaving layers of $NH_4$ groups,[23] which is somewhat similar to that of inorganic fullerene-like nanoparticles.

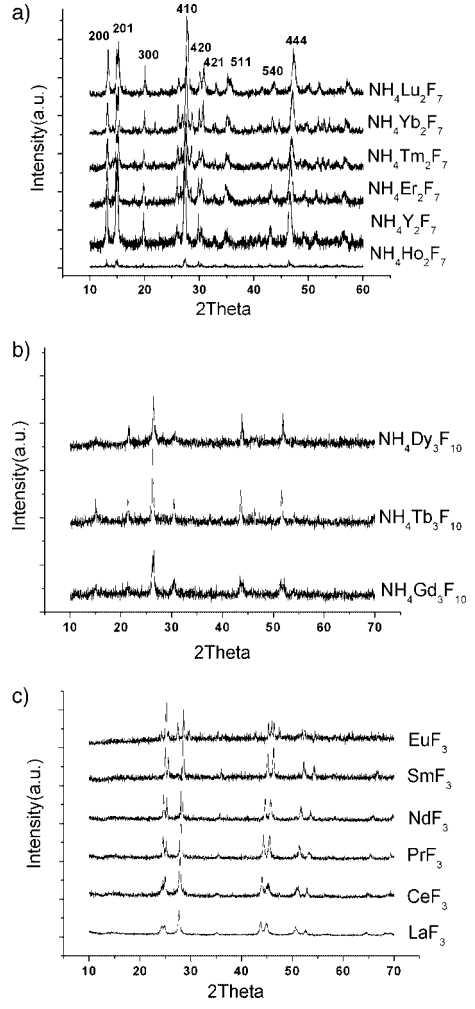


Figure 1. XRD patterns of (a) $NH_4Ln_2F_7$ (Ln = Y, Ho, Er, Tm, Yb, Lu); (b) $NH_4Ln_3F_{10}$ (Ln = Gd, Dy, Tb); (c) $LnF_3$ (Ln = La–Eu).

On the basis of our former work, we realized that for families of lanthanide compounds that share a similar composition, such as $LnF_3$[24] and $LnPO_4$,[25] both the crystal structures and physical properties may vary gradually on ascending the series as a result of the lanthanide contraction. For our system, the ionic radii of lanthanide elements were found to be greatly responsible for the phase formation. For all the lanthanide members, the resulting products derived under the same synthetic conditions were of different structure. The variation in the structure is believed to be caused by the contraction of ionic radii of $Ln^{3+}$ (Table 1). The members from Lu to Ho, ionic radius 0.85–0.89 Å, formed $NH_4Ln_2F_7$ compounds; the members from La to Dy, whose ionic radii range 1.06–0.91 Å, adopt other crystal structures that are different from the layered structures of $NH_4Ln_2F_7$. The XRD patterns of other lanthanide categories from La–Dy can be seen in Figure 1 (parts b, c). For the larger lanthanide ions (Ln = La, Ce, Nd, Pr, Sm, Eu), $LnF_3$ structures were obtained (Ln = La–Sm, the resulting products are pure hexagonal structures; Ln = Eu, a mixture of hexagonal and orthorhombic structures were found). For the intermediate-sized lanthanide ions (Ln = Gd, Tb, Dy) $NH_4Ln_3F_{10}$ was formed.[26]

The morphology and microstructural details can be observed from the TEM, HRTEM observations. The typical low-magnification images of the as-prepared $NH_4Ln_2F_7$ (Ln = Y, Ho, Er, Tm, Yb, Lu) nanocages (here Y, Ho, and Tm have been chosen as examples) are shown in Figure 2. The hollow interior features of $NH_4Ln_2F_7$ nanocages were confirmed by the TEM observations. It can be seen from Figure 2 (a–c) that nearly all the nanoparticles in the images are of hollow interiors and the nanoparticles are uniform with an average size of 20–30 nm. Careful TEM observations were also carried out on both the $LnF_3$ (Ln = La–Eu) and $NH_4Ln_3F_{10}$ (Ln = Gd–Dy) series (TEM images are found in the supporting information). However, only a few hollow-sphere-type structures were found. This morphology difference between $NH_4Ln_2F_7$ (Ln = Y, Ho, Er, Tm, Yb, Lu), $LnF_3$ (Ln = La–Eu), and $NH_4Ln_3F_{10}$ (Ln = Gd–Dy) indicates that the formation of the hollow interior forms is unique to the $NH_4Ln_2F_7$ series and it also excludes the possibility that the nanocages were formed by the Marangoni effect. That is where the concentrated solutes diffuse out into the droplet-vapor interface leaving the pure solvent behind in the center of the nanoparticle. At this point the solvent evaporates leaving the polycrystalline material to deposit on the outer circumference and leaving a hollow core in the center. According to this assumption, nanocages

Table 1. Crystal structure and chemical composition of lanthanide compounds obtained under the identical synthetic condition (h&o is short for hexagonal and orthorhombic).

| $Ln^{3+}$ | La | Ce | Nd | Pr | Sm | Eu | Gd | Tb | Dy | Ho | Y | Er | Tm | Yb | Lu |
|---|---|---|---|---|---|---|---|---|---|---|---|---|---|---|---|
| R($Ln^{3+}$) [Å] | 1.06 | 1.03 | 1.01 | 1.00 | 0.96 | 0.95 | 0.94 | 0.92 | 0.91 | 0.89 | 0.89 | 0.88 | 0.87 | 0.86 | 0.85 |
| Products | $LnF_3$ | | | | | | $NH_4Ln_3F_{10}$ | | | $NH_4Ln_2F_7$ | | | | | |
| Crystal structures | hexagonal | | | | | h&o | cubic | | | cubic | | | | | |

 © 2006 Wiley-VCH Verlag GmbH & Co. KGaA, Weinheim 

would form in other lanthanide categories from La to Dy, because of the similar environments in the growth procedure.

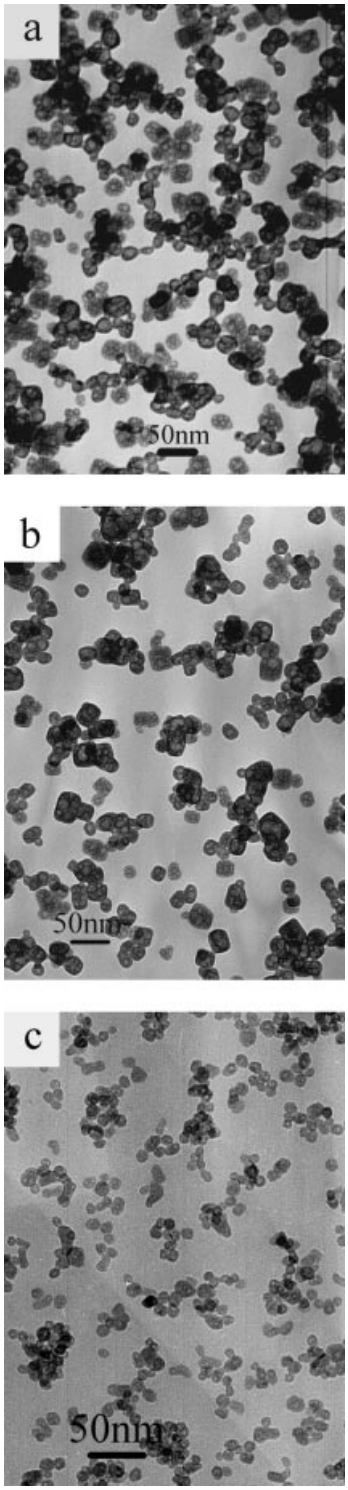


Figure 2. TEM images of (a) $NH_4Y_2F_7$ nanocages; (b) $NH_4Tm_2F_7$ nanocages; (c) the Tem images of $NH_4Ho_2F_7$ nanocages.

HRTEM characterization (Figure 3, a–f) provides us with further insight into the structural details of $NH_4Ln_2F_7$ nanocages. It can be seen from the HRTEM images that most of the nanoparticles usually had a hollow interior, which proved the formation of hollow sphere nanostructures under current experimental conditions. The distance between the inner and outer layers was calculated to be approximately 0.32 nm for $NH_4Y_2F_7$ nanocages, corresponding to the crystal plane of (410), and the other categories show a close value of about 0.32 nm, indicating a similar formation mode under adopted conditions. Though the crystal lattices were somewhat distorted compared with the typical onion-like lattices of fullerene-like nanoparticles, the lattice striations displayed a nearly close-caged configuration with high crystallinity. The electronic diffraction of the selected area (insert in Figure 3, a), where the diffractive dots of single crystal can be clearly seen, further confirmed the single crystal features of the nanocages. It is interesting to note that the inner spaces are usually quite different in shape, including all kinds of irregular polygons, indicating that the growth of these structures might be rather sensitive to fluctuations from the outer environment. Nevertheless, the nanoparticles with hollow interiors can be easily obtained under designed synthetic conditions, and from the TEM images we can see that almost all of the final products are hollow nanostructures. The HRTEM observations confirmed that the formation of the nanocages may have a close relationship with the inherent layered structure of $NH_4Ln_2F_7$.

The thermal gravimetric analysis was carried out to study the thermal stability of these nanocages. $NH_4Ln_2F_7$ (Ln = Y, Ho, Er, Tm, Yb, Lu) decomposes at high temperature. The TGA curves for $NH_4Ln_2F_7$ (Ln = Y, Ho, Tm) powders are shown in Figure 4. From the TGA curves, two weight-loss steps can be observed. The first step is from room temperature to 250 °C, in which, the mild weight loss may be caused by desorption of water and other solvents such as ethanol on the $NH_4Ln_2F_7$ surface. The main weight loss occurs in the temperature range from 250 to 360 °C. In this step, $NH_4Ln_2F_7$ converted to $LnF_3$. The experimental weight loss is about 11.10 wt.-% for $NH_4Y_2F_7$, 7.35 wt.-% for $NH_4Ho_2F_7$, and 6.84 wt.-% for $NH_4Tm_2F_7$, respectively, which agrees well with the theoretical weight loss of the decomposition of $NH_4Ln_2F_7$ to $LnF_3$ (11.25 wt.-% for $NH_4Y_2F_7$, 7.69 wt.-% for $NH_4Ho_2F_7$, and 7.57 wt.-% for $NH_4Tm_2F_7$). The chemical reaction that occurs in the process of this main weight loss can be expressed as follows:

$$NH_4Ln_2F_7 \rightarrow LnF_3 + NH_3 \uparrow + HF \uparrow$$

The decomposition temperature of these three samples is quite similar. It is about 356 °C for $NH_4Y_2F_7$, 352 °C for $NH_4Ho_2F_7$, and 361 °C for $NH_4Tm_2F_7$.

$NH_4Y_2F_7$ samples were annealed at 200 and 400 °C for 3 h to investigate this conversion process. XRD confirmed that the sample annealed at 200 °C remained as $NH_4Y_2F_7$; in contrast the sample annealed at 400 °C converted to $YF_3$ completely. TEM images of the samples derived at different annealing temperatures are shown in Figure 5 from which we can see that most of the $NH_4Y_2F_7$ nanoparticles remain intact with hollow interiors and have no apparent aggregation after being annealed at 200 °C for 3 h, in contrast to the nanoparticles annealed at 400 °C that have aggregated

 © 2006 Wiley-VCH Verlag GmbH & Co. KGaA, Weinheim 

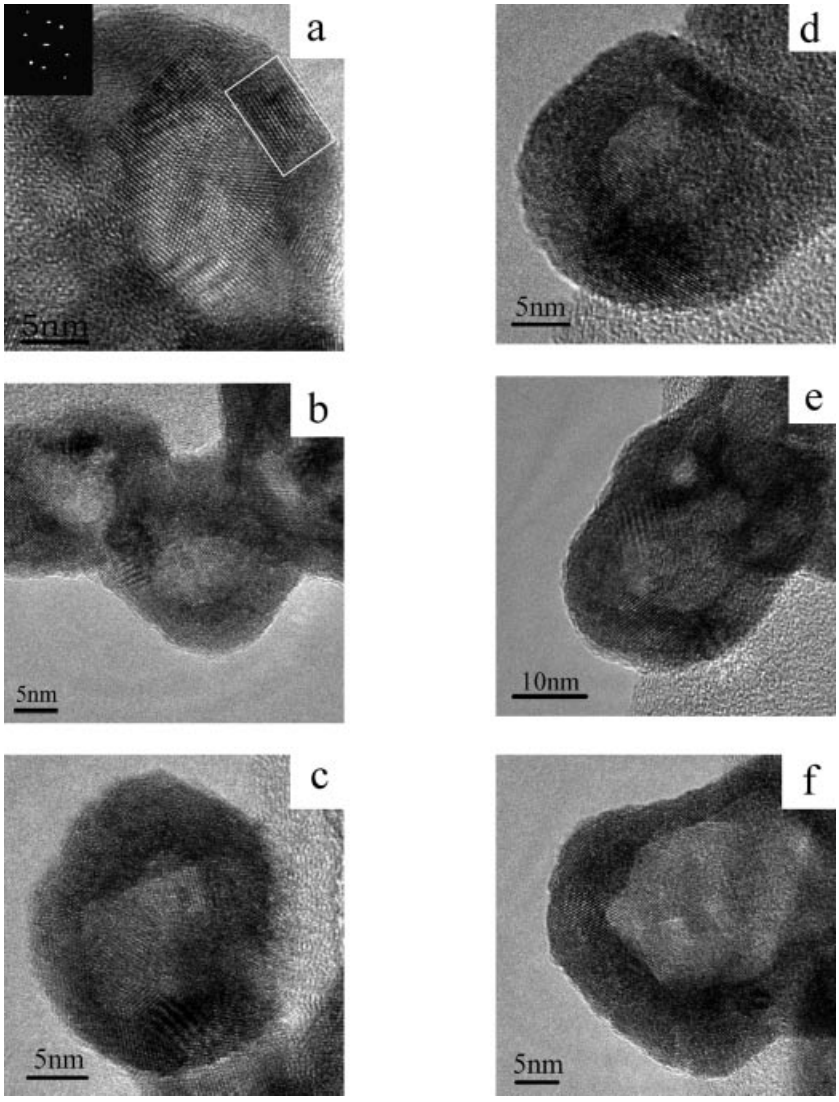


Figure 3. HRTEM image of (a) an individual $NH_4Y_2F_7$ nanocage with diameter about 22 nm, the inset is an EDS analysis of the selected area; (b) three conterminous $NH_4Y_2F_7$ nanocages; (c) an individual $NH_4Y_2F_7$ nanocage with diameter ca. 20 nm; (d) an individual globular $NH_4Tm_2F_7$ nanocage; (e) an individual $NH_4Yb_2F_7$ nanocage; (f) $NH_4Ho_2F_7$ nanocage.

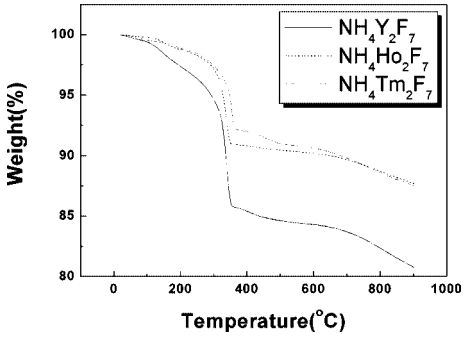


Figure 4. TGA curves of $NH_4Ln_2F_7$ (Ln = Y, Ho, Tm).

to a large extent with no remaining nanocages. These results show that the nanocages can be maintained at the relatively high temperature of 200 °C before the composition of $NH_4Y_2F_7$ and the hollow interior forms collapse as $NH_4Y_2F_7$ converts to $YF_3$ at higher temperature. As the literature has reported, the structure of $NH_4Y_2F_7$ can be visualized as layers of $YF_6$ octahedron with interleaving layers of $NH_4$ groups and the hydrogen bonding effect of $NH_4^+$ is a critical factor responsible for the stability of ammonium fluorometallates.[27–28] The layered structure of $NH_4Y_2F_7$ would collapse if the interleaving layers of $NH_4$ groups were lost. So it is believed that ammonium loss in the process of conversion of $NH_4Y_2F_7$ to $YF_3$ is an important factor in the collapse of the nanocages. These phenomena show that the inner structure of $NH_4Y_2F_7$ is very important for the stability of these hollow interior forms.

$Y^{3+}$, $Ho^{3+}$, $Er^{3+}$, $Tm^{3+}$, $Yb^{3+}$, and $Lu^{3+}$ can crystallize in homogeneous phase $NH_4Ln_2F_7$ and their ionic radii are similar, thus making it convenient to dope $NH_4Ln_2F_7$ nanocages with these lanthanide ions, which may then endow this class of nanocage with novel properties. The most frequently used up-conversion ion $Er^{3+}$ and the sensitizer ion

 © 2006 Wiley-VCH Verlag GmbH & Co. KGaA, Weinheim 

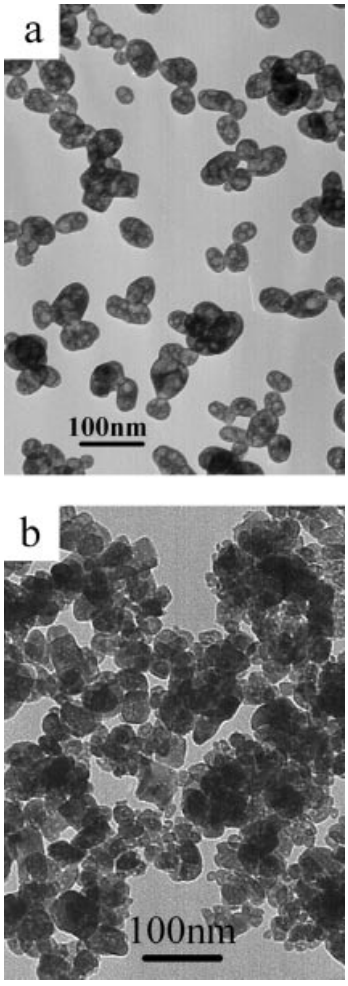


Figure 5. TEM images of samples annealed at (a) 200 °C; (b) 400 °C.

$Yb^{3+}$ were co-doped into $NH_4Y_2F_7$ to denote the feasibility of doping lanthanide ions into $NH_4Ln_2F_7$. Doped samples were prepared by the same synthetic procedure, except for adding 5% (total molar ration) $YbCl_3$ and $ErCl_3$ in $YCl_3$ in the first stage. The up-conversion fluorescence property of the final product was measured by a 980-nm IR laser. The up-conversion emission of doped $NH_4Y_2F_7$ sample is weak due to the quenching effect of ammonium. After being annealed at 500 °C for 3 h, the $NH_4Y_2F_7$ can convert into

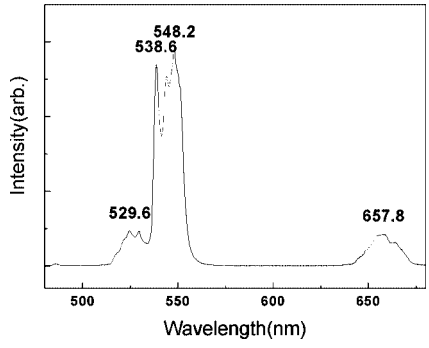


Figure 6. UC emission spectra of $YF_3$ ($Er^{3+}$, $Yb^{3+}$).

$YF_3$ (revealed by the XRD analysis). It can be seen that the up-conversion emission is stronger and can be observed by the naked eye. The UC spectrum exhibits the characteristic peaks of an $Er^{3+}$- and $Yb^{3+}$-doped $YF_3$ system (Figure 6). This consequence proves the successful doping of $Er^{3+}$/$Yb^{3+}$ into $NH_4Y_2F_7$.

## Conclusion

In this work, a novel class of ammonium lanthanide fluoride nanocage was successfully synthesized. The tendency of $NH_4Ln_2F_7$ to form nanocages is believed to have a close relationship with their inner structure. Our study presents the first example of ternary nanocages to the best of our knowledge. We believe that this method could be expanded to the synthesis of other rare-earth hollow nanostructures, especially the MF-$LnF_3$ categories, and thus brings new opportunities to these fast expanding research fields.

## Experimental Section

In a general preparation, EDTA chelated with $Ln^{3+}$ to form a clear solution at pH 2–3 by adding diluted HCl and $NH_3{\cdot}H_2O$ solution. And then $NH_4F$, which was dissolved into water/ethanol mixed solvents, was added. The mixture was transferred to an autoclave and was treated at 180 °C for 20 h under solvothermal conditions. The autoclave was then cooled to room temperature. The precipitate was then filtered, washed with water to remove ions possibly remnant in the final products, and dried at 80 °C in air. Following the above procedures, $NH_4Ln_2F_7$ (Ln = Y, Ho, Er, Tm, Yb, Lu) nanocages with high yield (90%) could be obtained.

$NH_4^+$ and EDTA are found to be responsible for the phase formation of $NH_4Y_2F_7$. To investigate the influence of $NH_4^+$, EDTA was dissolved with NaOH instead of $NH_3{\cdot}H_2O$, and then $NaYF_4$ was prepared and no hollow-sphere structures were found in the samples. This result confirms that it is easy to induce other cations to take the place of ammonium in the products. The concentration of EDTA greatly affects the phase purity of $NH_4Y_2F_7$. Keeping the amount of $Y^{3+}$ (0.2 mmol) unchanged, when the amount of EDTA is less than 0.2 g, the resulting products are mixtures of flakes and hollow-spheres. When the amount of EDTA is more than 1.0 g, the nanocages were elongated to an irregular form. Similar phenomena have been observed on the samples of other $NH_4Ln_2F_7$ (Ln = Ho, Er, Tm, Yb, Lu). When the amount of EDTA is kept at 0.2–1.0 g, regular nanocages can be easily obtained on a large scale.

The obtained sample was characterized by a Bruker D8-Advance X-ray powder diffractometer with Cu-$K_a$ radiation ($\lambda$ = 1.5418 Å). The size and morphology of the IF nanoparticles were determined at 200 kV by a Hitachi H-800 transmission electron microscope (TEM) and a JEOL JEM-2010F high-resolution transmission electron microscope. Fluorescent spectra were recorded with a Hitachi F-4500 Fluorescence Spectrophotometer. Up-conversion fluorescent spectra were obtained with the LS-50B fluorescence spectrophotometer (Perkin–Elmer Corp., Forster City, CA) with an external 0–800 mW adjustable laser (980 nm, Beijing Hi-Tech Optoelectronic Co., China) as the excitation source, instead of the Xenon source in the spectrophotometer, and with an optic fiber accessory. The thermal decomposition behavior of the $NH_4Ln_2F_7$ (Ln = Y, Ho, Tm) samples was studied by thermogravimetric analysis (TGA) with a TGA2050 thermal analysis device (American TA Corpora-

 © 2006 Wiley-VCH Verlag GmbH & Co. KGaA, Weinheim 

tion). TGA determination was carried out in nitrogen at a heating rate of 20 °C/min in a range of room temperature to 900 °C.

**Supporting Information** (for details see the footnote on the first page of this article): XRD patterns of samples that were annealed at 200 °C and 400 °C, respectively, and the TEM images of $CeF_3$, $SmF_3$, and $NH_4Tb_3F_{10}$.

## Acknowledgments

This work was supported by NSFC (20501013, 50372030, 20131030, 90406003), the Foundation for the Author of National Excellent Doctoral Dissertation of P. R. China and the State Key Project of Fundamental Research for Nanomaterials and Nanostructures (2003CB716901).

[1] Y. N. Xia, B. Gates, Y. D. Yin, Y. Lu, *Adv. Mater.* **2000**, *12*, 693–713.
[2] M. Prato, M. Maggini, *Acc. Chem. Res.* **1998**, *31*, 519–526.
[3] A. L. Balch, M. M. Olmstead, *Chem. Rev.* **1998**, *98*, 2123–2165.
[4] F. Caruso, R. A. Caruso, H. Möhwald, *Science* **1998**, *282*, 1111–1114.
[5] C. G. Göltner, *Angew. Chem. Int. Ed.* **1999**, *38*, 3155–3156.
[6] Y. G. Sun, Y. N. Xia, *Science* **2002**, *298*, 2176–2179.
[7] Y. G. Sun, B. Mayers, Y. N. Xia, *Adv. Mater.* **2003**, *15*, 641–646.
[8] R. Tenne, L. Margulis, M. Genut, G. Hodes, *Nature* **1992**, *360*, 444–446.
[9] L. Margulis, G. Salitra, R. Tenne, M. Talianker, *Nature* **1993**, *365*, 113–114.
[10] Y. Feldman, E. Wasserman, D. A. Srolovitz, R. Tenne, *Science* **1995**, *267*, 222–225.
[11] Y. R. Hacohen, E. Grunbaum, R. Tenne, J. Sloan, J. L. Hutchison, *Nature* **1998**, *395*, 336–337.
[12] T. Nakashima, N. Kimizuka, *J. Am. Chem. Soc.* **2003**, *125*, 6386–6387.
[13] N. A. Dhas, K. S. Suslick, *J. Am. Chem. Soc.* **2005**, *127*, 2368–2369.
[14] X. M. Sun, Y. D. Li, *Angew. Chem. Int. Ed.* **2004**, *43*, 3827–3831.
[15] P. Selvakannan, M. Sastry, *Chem. Commun.* **2005**, 1684–1686.
[16] H. Liang, Y. Guo, H. Zhang, J. Hu, L. Wan, C. Bai, *Chem. Commun.* **2004**, 1496–1497.
[17] S. Lei, K. Tang, Q. Yang, H. Zheng, *Eur. J. Inorg. Chem.* **2005**, *20*, 4124–4128.
[18] S. Xu, H. Wang, J. J. Zhu, X. Q. Xin, H. Y. Chen, *Eur. J. Inorg. Chem.* **2004**, *23*, 4653–4659.
[19] G. Zou, Z. P. Liu, D. B. Wang, C. L. Jiang, Y. T. Qian, *Eur. J. Inorg. Chem.* **2004**, *22*, 4521–4524.
[20] X. Wang, Y. D. Li, *Angew. Chem. Int. Ed.* **2003**, *42*, 3497–3500.
[21] L. Y. Wang, R. X. Yan, Z. Y. Huo, L. Wang, J. Z. Hui, J. Bao, X. Wang, Q. Peng, Y. D. Li, *Angew. Chem. Int. Ed.* **2005**, *44*, 6054–6057.
[22] J. H. Zeng, J. Su, Z. H. Li, R. X. Yan, Y. D. Li, *Adv. Mater.* **2005**, *17*, 2119–2123.
[23] K. Rajeshwar, E. A. Secco, *Can. J. Chem.* **1977**, *55*, 2620–2627.
[24] a) X. Wang, Y. D. Li, *Chem. Eur. J.* **2003**, *9*, 5627–5635; b) X. Wang, X. M. Sun, D. P. Yu, B. S. Zhou, Y. D. Li, *Adv. Mater.* **2003**, *15*, 1442–1445.
[25] R. X. Yan, X. M. Sun, X. Wang, Q. Peng, Y. D. Li, *Chem. Eur. J.* **2005**, *11*, 2183–2195.
[26] Z. J. Kang, Y. X. Wang, F. T. You, J. H. Lin, *J. Solid State Chem.* **2001**, *158*, 358–362.
[27] R. E. Thoma, *Inorg. Chem.* **1962**, *1*, 220–226.
[28] A. Tressaud, J. Portier, R. Depage, P. Hagenmuller, *J. Solid State Chem.* **1970**, *2*, 269–275.

Received: January 25, 2006
Published Online: March 31, 2006

 © 2006 Wiley-VCH Verlag GmbH & Co. KGaA, Weinheim 

DOI: 10.1002/ejic.200600093

# Hydrogen Bonding and Proton Transfer to the Trihydride Complex [Cp*$MoH_3$(dppe)]: IR, NMR, and Theoretical Investigations

**Natalia V. Belkova,[a] Pavel O. Revin,[a] Maria Besora,[b] Miguel Baya,[c] Lina M. Epstein,[a] Agustí Lledós,*[b] Rinaldo Poli,*[c] Elena S. Shubina,*[a] and Evgenii V. Vorontsov[a]**

**Keywords:** Dihydrogen bonding / Hydride ligands / Molybdenum / Proton-transfer mechanism / DFT calculations

The interaction between [Cp*$MoH_3$(dppe)] (dppe = $Ph_2PCH_2CH_2PPh_2$) and a variety of proton donors has been investigated by a combination of experiments and DFT calculations. Weak proton donors [2-monofluoroethanol (MFE) and trifluoroethanol (TFE)] allow the determination of basicity factor ($E_j$ = 1.42 ± 0.02) and thermodynamic parameters for the hydrogen bond formation ($\Delta H_{HB}$ = –4.9 ± 0.2 and –6.1 ± 0.3 kcal mol$^{-1}$; $\Delta S_{HB}$ = –15.7 ± 0.7 and –20.4 ± 1 cal mol$^{-1}$ K$^{-1}$ for MFE and TFE, respectively). For TFE, a stable low-temperature proton-transfer equilibrium (220–240 K) with the cationic classical tetrahydrido derivative [Cp*$MoH_4$(dppe)]$^+$ could be investigated independently by UV/Vis ($\Delta H°_{PT}$ = –2.8 ± 0.4 kcal mol$^{-1}$ and $\Delta S°_{PT}$ = –15 ± 2 cal mol$^{-1}$ K$^{-1}$) and $^1$H NMR ($\Delta H°_{PT}$ = –2.7 ± 0.5 kcal mol$^{-1}$ and $\Delta S°_{PT}$ = –11 ± 2 cal mol$^{-1}$ K$^{-1}$) spectroscopy. Upon warming, however, the tetrahydride evolves by dihydrogen loss and formation of a hydride-free diamagnetic product. Stronger proton donors [hexafluoroisopropanol (HFIP), *p*-nitrophenol (PNP), perfluoro-*tert*-butyl alcohol (PFTB), and $HBF_4$·$OEt_2$] lead to more extensive proton transfer at lower donor/Mo ratios. A 1:1 proton-transfer stoichiometry is indicated independently by a titration experiment with UV/Vis monitoring for the [Cp*$MoH_3$(dppe)]–PNP reaction, and by a stopped-flow kinetics investigation for the [Cp*$MoH_3$(dppe)]–HFIP reaction. For all proton-transfer processes investigated, the classical tetrahydrido cation forms directly, without the observation of a nonclassical intermediate. DFT calculations have been carried out on the interaction between TFE and HFIP and the model compound [CpMo$H_3$(dpe)] (dpe = $H_2PCH_2CH_2PH_2$) both in the gas phase and in $CH_2Cl_2$ solvent with the polarizable continuum model and, to a more limited extent, on the full [Cp*$MoH_3$(dppe)] system. A detailed comparison of the observed and calculated frequency shifts for the M–H vibrations is presented. The calculations have explored the relative energy and geometry of various configurations involving either a hydride ligand or the metal as the principal proton-accepting site. They have also probed two principal proton-transfer pathways, leading to the unobserved nonclassical intermediate and to the observed classical product. From these studies, it appears that a nonclassical intermediate may be obtained by a kinetically controlled proton transfer to a hydride site, followed by an intramolecular rearrangement through a very low energy barrier. However, a competitive low-energy pathway for direct proton transfer at the metal site is also revealed by the calculations.
(© Wiley-VCH Verlag GmbH & Co. KGaA, 69451 Weinheim, Germany, 2006)

## Introduction

Proton-transfer processes to and from transition-metal centers and hydride ligand sites continue to attract considerable research interest because of their fundamental importance for catalysis and in biochemistry.[1,2] The kinetic preference for hydride versus metal protonation is now quite firmly established,[3–9] though exceptions have recently been reported from studies carried out in our laboratories.[10,11] The proton transfer occurs via intermediates, for which characteristic spectroscopic signatures have been established, that contain hydrogen bonds between the proton donor and the proton acceptor (the metal center or a hydride ligand) (see Scheme 1).[12,13] The term "nonclassical hydrogen bonding" has been coined to address these interactions, while H-bonding specifically involving a hydride ligand has also been termed "dihydrogen bonding".[14] The relationship between the preferred thermodynamic site of hydrogen bonding (i.e., the relative energy of species **I** and **IV**) and the kinetic site of proton transfer (i.e., the relative energy barrier leading to species **II** and **V**) is of interest to us. We have recently presented combined experimental and theoretical results showing that the preferred hydrogen-

[a] Nesmeyanov Institute of Organoelement Compounds, Russian Academy of Sciences,
Vavilov Street 28, 119991 Moscow, Russia
E-mail: shu@ineos.ac.ru
[b] Departament de Química, Edifici Cn, Universitat Autónoma de Barcelona,
08193 Bellaterra, Spain
E-mail: agusti@klingon.uab.es
[c] Laboratoire de Chimie de Coordination, UPR CNRS 8241, lié par convention à l'Université Paul Sabatier et à l'Institut national Polytechnique de Toulouse,
205 Route de Narbonne, 31077 Toulouse Cedex, France
Fax: +33-561553003
E-mail: poli@lcc-toulouse.fr
Supporting information for this article is available on the WWW under http://www.eurjic.org or from the author.

 © 2006 Wiley-VCH Verlag GmbH & Co. KGaA, Weinheim 

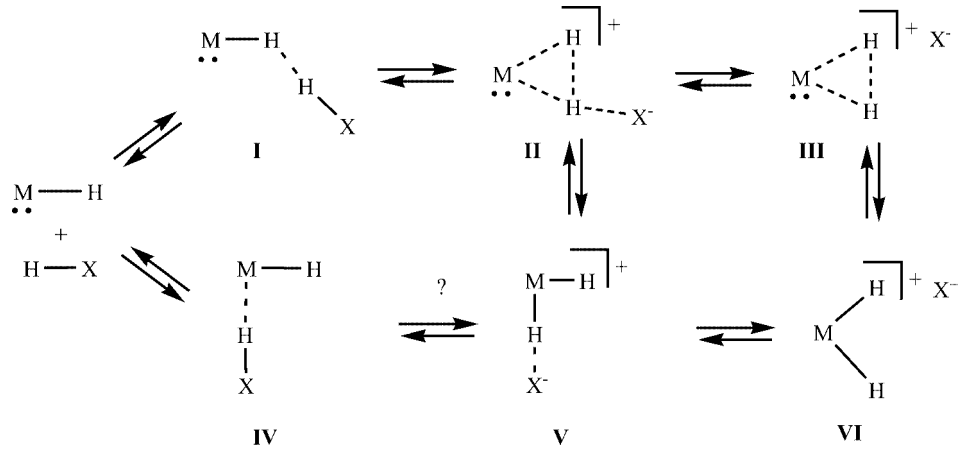


Scheme 1.

bonding site for compound [Cp*Fe(dppe)H], that is, the hydride site, corresponds to the site of preferred proton transfer.[15] In parallel work, some of us have studied the mechanism of the hydride protonation, analyzing the influence of medium polarity and concentration effects, both experimentally and theoretically.[16–18] We have demonstrated the involvement of ion pairs formed by cationic dihydrogen complexes and the anionic conjugate basis of the proton donor. In these studies the stabilizing role of the solvent and the homoconjugate anions [A···H···A]$^-$ in the protonation process has also been recognized.

In order to determine the general relationship between the thermodynamics of hydrogen bonding to various possible sites and the energy barrier leading from each of these sites to proton transfer, a greater number of case studies is necessary, especially for polyhydride complexes where the hydride ligands occupy inequivalent positions so that it is also possible in principle to discriminate between different hydride sites. For this reason, we have selected compound [Cp*Mo(dppe)H$_3$], which was synthesized in one of our laboratories a few years ago.[19] In this system there are four basic potential sites (the metal and the three hydride ligands) able to establish hydrogen bonds with a proton donor. Moreover, several isomers could result from the proton-transfer process. The X-ray structure of the trihydride compound was of sufficient quality to locate the hydride ligands and showed that they occupy two different sites, as shown in Scheme 2.[20] The geometry is best described as an ideal trigonal prism if the Cp* ligand is considered to occupy a single position in correspondence to its ring centroid. However, the compound is highly fluxional and a single hydride resonance, which is split into a binomial triplet by the two equivalent P nuclei, remained sharp down to 183 K.[19]

Protonation studies have previously been carried out only with $HBF_4$, leading to the formal product of metal protonation, the classical tetrahydride complex [Cp*MoH$_4$(dppe)]$^+$.[19] However, this product is unstable and easily loses $H_2$. It could be isolated upon low-temperature protonation in ether, where it precipitates. An X-ray structure was not obtained for the Mo complex, but the

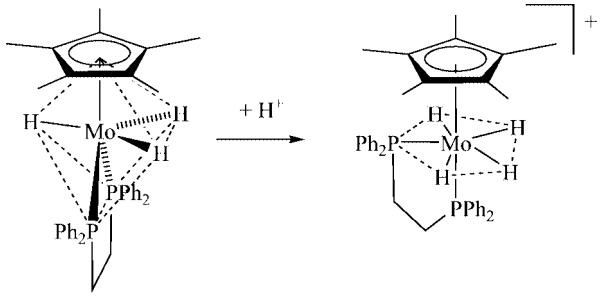


Scheme 2.

analogous W derivative displays a pseudopentagonal bipyramidal structure. As the two metal complexes show analogous NMR properties, the same structure is also assumed to be adopted by the Mo complex and is illustrated in Scheme 2. Both Mo and W cationic tetrahydride complexes are fluxional at room temperature, showing only one hydride resonance and one phosphorus resonance, but the P resonance decoalesces at low temperature, whereas the hydride resonance does not. The protonation of [Cp*Mo(dppe)H$_3$] in MeCN or the dissolution of [Cp*MoH$_4$(dppe)]$^+$ in MeCN gives a variety of products resulting from the substitution of $H_2$ with MeCN. The tungsten compound is stable under these conditions.[19]

Preliminary studies of the hydrogen bonding and proton transfer to the Cp*M(dppe)H$_3$ (M = Mo, W) compounds with weaker proton donors has been recently communicated.[21] We present here a full report of our investigation on the Mo compound, whereas further details concerning the W system, including a comparison of the two metal complexes, will be reported in a forthcoming paper.[22]

## Results

### Experimental Studies

Two solvents – THF or $CH_2Cl_2$ – were used for spectroscopic studies. Their relatively high polarity ($\varepsilon$ = 7.3 for THF and 8.9 for $CH_2Cl_2$) helps maintain the ionic proton-

 © 2006 Wiley-VCH Verlag GmbH & Co. KGaA, Weinheim 

transfer products in solution. However, THF has itself pronounced proton-acceptor properties and competes with the hydride complex for hydrogen bonding to the proton donor. Therefore, much higher proton donor concentrations are needed in order to observe similar spectral changes to those in $CH_2Cl_2$.[23] Unfortunately, compound [Cp*Mo(dppe)$H_3$] slowly decomposes at room temperature in dichloromethane, probably by attack of the solvent C atom by the hydride ligand. The stability of the trihydride complex in $CH_2Cl_2$ is greatly enhanced at low temperatures, with no visible change occurring at 200 K for at least 3 h. Thus IR and UV/Vis studies were carried out either in THF or in $CH_2Cl_2$ at low temperatures, or in $CH_2Cl_2$ at higher temperatures within a short timescale relative to the decomposition reaction. The NMR studies were carried out at low temperatures in $CD_2Cl_2$. In all cases, the extent of decomposition was carefully monitored to insure the significance of the results. The proton donors used in this study were 2-monofluoroethanol (MFE), 2,2,2-trifluoroethanol (TFE), hexafluoroisopropanol (HFIP), perfluoro-*tert*-butyl alcohol (PFTB), and *p*-nitrophenol (PNP).

### *Analysis of the $\nu_{OH}$ Region in the IR Spectra*

The interaction between [Cp*Mo(dppe)$H_3$] and proton donors was first studied by IR in the $\nu_{OH}$ range by using MFE and TFE in $CH_2Cl_2$. The observed decrease of the intensity (A) of the $\nu_{OH(free)}$ band and the appearance of a low-frequency shifted broad $\nu_{OH}$ band for the hydrogen-bonded OH group is unquestionable evidence for the formation of hydrogen bonds between the alcohol OH proton and the transition-metal hydride complex, although it does not establish the nature of the hydrogen-bonding site. The $\Delta\nu_{OH}$ band shift [$\Delta\nu_{OH} = \nu_{OH(free)} - \nu_{OH(bonded)}$] increased with the strength of the proton donors (see Figure 1 and Table 1).

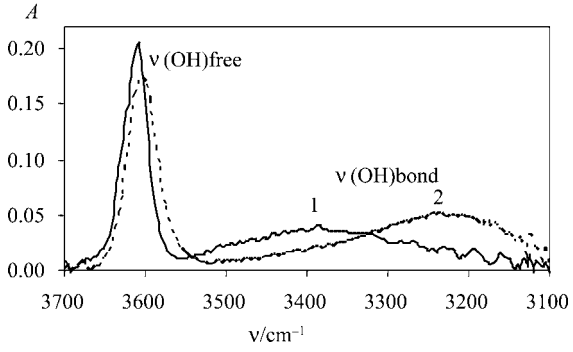


Figure 1. IR spectra in the $\nu(R_FO–H)$ stretching region of MFE (1) or TFE (2) in $CH_2Cl_2$ in the presence of [Cp*Mo(dppe)$H_3$].

The hydrogen bond enthalpies, $\Delta H_{HB}$, were obtained by two independent methods (see Table 1). The first one is based on the empirical correlation outlined in Equation (1), originally established for classical H bonds and later extended to hydrogen bonds to metal centers and to hydride ligands as proton acceptors.[12,13] The van't Hoff method uses the integrated IR intensities for the free alcohol absorption band in the presence or absence of the hydride complex as a function of temperature. It has the advantage of also yielding the reaction entropy. There is quite good agreement between the reaction enthalpies obtained from the two methods. It should be noted that the computed values for the interaction with TFE (see later) are in good agreement with these experimental results.

$$-\Delta H_{HB} = \frac{18\Delta\nu}{\Delta\nu + 720} \quad (1)$$

### *Analysis of the $\nu_{MH}$ Region in the IR Spectra*

The IR analysis in the $\nu_{MH}$ stretching vibration range was carried out with the goal of learning about the nature of the preferred hydrogen-bonding site. Previous studies on monohydride complexes have demonstrated that the interaction with a hydride ligand has the effect of shifting the M–H stretching vibration to lower frequencies, whereas the opposite effect is associated to an interaction with the metal site or other ligands.[12,13] For polyhydride compounds, however, the situation may not be so simple, as each vibrational normal mode results from the combination of more M–H bond stretching vibrations, each of which may be affected by hydrogen bonding in a different way. A previous combined experimental and theoretical study on the dihydride complex $Ru(PP_3)H_2$ [$PP_3 = P(CH_2CH_2PPh_2)_3$][23] was simplified by the fact that the two M–H bonds, being *trans* to ligands that exert a very different *trans* effect, do not mix extensively with each other, thus each of the two bands is composed of an essentially pure stretching vibration of a single M–H bond. The study of hydrogen bonding implicating the $Cp_2NbH_3$ complex,[18] having $C_{2v}$ symmetry and one $\nu_{MH}$ vibrational band resulting from the overlap of $2a_1 + b_1$ vibrations,[24] revealed the formation of dihydrogen-bonded complexes leading to band splitting with a low-frequency shift for the hydrogen-bonded $\nu_{MH}$ band. Although hydrogen bonding for other polyhydride compounds has been investigated,[11] no detailed analysis of the normal modes and how these are affected by hydrogen bonding have been reported. We intend to carry out such

Table 1. Parameters of the dihydrogen bonding between [Cp*Mo(dppe)$H_3$] and MFE or TFE, and basicity factors.

| ROH | $\nu_{OH(free)}$ $cm^{-1}$ | $\nu_{OH(bonded)}$ $cm^{-1}$ | $\Delta\nu$ $cm^{-1}$ | $\Delta H_{HB}$[a] kcal mol$^{-1}$ | $\Delta H_{HB}$[b] kcal mol$^{-1}$ | $\Delta S_{HB}$[b] cal mol$^{-1}$ K$^{-1}$ | $E_j$ |
|---|---|---|---|---|---|---|---|
| MFE | 3612 | 3368 | 244 | –4.9 | –4.9 ± 0.2 | –15.7 ± 0.7 | 1.44 |
| TFE | 3604 | 3248 | 364 | –5.9 | –6.1 ± 0.3 | –20.4 ± 1 | 1.41 |

[a] Calculated by the empirical relationship of Equation (1). [b] From van't Hoff's method.

 © 2006 Wiley-VCH Verlag GmbH & Co. KGaA, Weinheim 

an analysis here for the [Cp*Mo(dppe)H$_3$] complex, by a combination of experimental and computational methods.

The trihydride complex displays wide $\nu_{MH}$ bands of complex shape with the maxima at 1772 cm$^{-1}$ in $CH_2Cl_2$ and at 1785 cm$^{-1}$ in THF. Deconvolution of the spectrum in $CH_2Cl_2$, after subtraction of overtones because of the phenyl groups, yields two overlapping bands at 1821 and 1772 cm$^{-1}$ ($\Delta\nu_{1/2}$ = 57 and 54 cm$^{-1}$, correspondingly) (see Figure 2). A third, much weaker band is found at 1904 cm$^{-1}$ ($\Delta\nu_{1/2}$ = 41 cm$^{-1}$). However, its parameters are less reliable because of the low intensity and superposition with one of the phenyl overtones. Therefore, it will not be used later for the comparison with the theoretical data on $\nu_{MH}$ in hydrogen-bonded complexes. The intensities of the $\nu_{MH}$ bands increase as the temperature is decreased. The extinction coefficient of the strongest band increases from 49.0 to 60.3 L mol$^{-1}$ cm$^{-1}$ upon cooling from 290 to 200 K in THF.

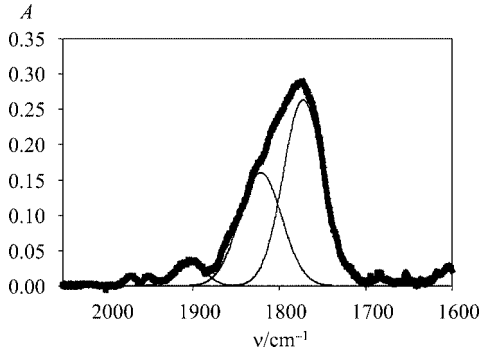


Figure 2. IR spectrum in the ν(Mo–H) stretching region of [Cp*Mo(dppe)H$_3$] (0.030 M) in $CH_2Cl_2$, after subtraction of the phenyl overtones, showing the band decomposition.

Upon interaction between the [Cp*Mo(dppe)H$_3$] complex and MFE at 200 K in $CH_2Cl_2$ the $\nu_{MH}$ band becomes wider and shifts to lower frequencies by about 5 cm$^{-1}$. A band decomposition analysis carried out after the subtraction of both dppe and MFE spectra shows that the two major bands become wider and appear at different positions: 1822 and 1769 cm$^{-1}$ ($\Delta\nu_{1/2}$ = 73 and 60 cm$^{-1}$, $\Delta\nu$ = +1 and –3 cm$^{-1}$, respectively). These changes can be attributed to the effect of hydrogen bonding on the $MoH_3$ moiety. The experiments in THF, as expected, necessitated the use of the stronger proton donors at higher concentrations in order to observe similar changes. For instance, using just a 10-fold excess of TFE, the only observed change was a small low-frequency band shift and intensity decrease upon increasing the temperature, just like in the absence of alcohol, without a shape change. This change is reversible up to 270 K, demonstrating that no proton transfer occurs with this alcohol in THF up to 270 K (cf. proton transfer in $CH_2Cl_2$ later). A deeper analysis of the M–H stretching vibrations in the absence and presence of proton donors will be carried out below in the light of the theoretical data.

### *NMR and IR Studies of Proton Transfer*

As stated in the Introduction, the molybdenum trihydride complex can be protonated by $HBF_4$·$Et_2O$ to give the tetrahydride complex [Cp*Mo(dppe)H$_4$]$^+$.[19] New $^1$H NMR investigations carried out at low temperatures (200–250 K) in $CD_2Cl_2$ using either $HBF_4$·$Et_2O$ or TFE show a direct transformation, without the detection of any intermediate (notably nonclassical species). With the weaker proton donor TFE, an equilibrium between the starting [Cp*Mo(dppe)H$_3$] complex and the protonated product is established and a large excess is needed to achieve a high degree of proton transfer.

Well-established, free, and hydrogen-bonded complexes exchange rapidly on the NMR timescale, yielding only one resonance. Typically, the effect of hydrogen bonding on chemical shifts is small, especially in the case of polyhydrides, where the effect is averaged over the various hydride ligands. The [Cp*Mo(dppe)H$_4$]$^+$ complex on one side, and the rapidly equilibrating mixture of the free trihydride complex and the hydrogen-bonded adduct [Cp*Mo(dppe)H$_3$···HOR$_F$] on the other side, give rise to triplet resonances at about $\delta$ –3.7 ($J_{HP}$ = 37.4 Hz) and –6.0 ($J_{HP}$ = 48.0 Hz) in the $^1$H NMR spectrum at low temperatures (190–210 K). The positions of these peaks change significantly with the temperature, moving to about –3.5 and –5.7 at 300 K. The chemical shift difference between these resonances decreases steadily from 2.32 ppm at 200 K to 2.22 ppm at 300 K. On the other hand, neither chemical shift, at a given temperature, seems highly dependent on the nature of the proton donor (TFE, HFIP, or $HBF_4$) or on its concentration. Furthermore, the $J_{HP}$ values remain practically unchanged over the entire temperature range. Therefore, the chemical shift changes are probably unrelated to variations in hydrogen-bonding equilibria. The relative amounts of the two species are also afforded by a parallel monitoring of the $^{31}$P{$^1$H} NMR spectrum (resonance at –75.0 ppm and –92.8 ppm, respectively). As for the case of the $^1$H NMR resonances, the $^{31}$P{$^1$H} NMR chemical shifts do not depend on the nature and concentration of the proton donor.

The establishment of hydrogen bonding is more clearly evidenced from the change of longitudinal relaxation time ($T_1$) for the trihydride resonance (see Table 2). As expected, this parameter decreases upon addition of proton donors, in proportion to the strength of the donor.[2,13] It is also significant that the temperature corresponding to $T_{1min}$ increases slightly upon protonation from 220 to 230 K. This phenomenon signals a decreased correlation time ($\tau_C$), that is, a slower tumbling motion, for the protonated species, in agreement with its expected larger size. Thus, slightly higher temperatures are needed to again raise $\tau_C$ to the conditions required for the most efficient longitudinal relaxation ($w_0^2\tau_C^2 \approx 1$). The $T_{1min}$ of the tetrahydride product is smaller relative to the parent complex, but not in the range expected for dihydrogen complexes.[25] This decrease is expected, as the dipolar relaxation implicates four hydride ligands instead of three. Note, however, that the tetrahydride resonance $T_1$ value is also sensitive, like that of the parent trihydride, to the nature of the proton donor used. A possible interpretation of this difference is a stronger hydrogen bonding between one or

 © 2006 Wiley-VCH Verlag GmbH & Co. KGaA, Weinheim 

more hydride ligands with the stronger conjugate base $CF_3CH_2O^-$, thereby increasing the average H···H distances.

Table 2. Longitudinal relaxation time $T_{1min}$ (ms) for [Cp*Mo(dppe)$H_3$] in $CD_2Cl_2$ solution under different conditions.[a]

| | $T_{min}$ [K] | [Cp*Mo(dppe)$H_3$] | [Cp*Mo(dppe)$H_4$]$^+$ |
|---|---|---|---|
| Free | 220 | 302 | |
| +$HBF_4$ (1 equiv.) | 230[b] | 274 | 174 |
| +TFE (6 equiv.) | 230[b] | 295 | 191 |

[a] At 400 MHz. [b] The resonances of both complexes have a minimum $T_1$ at the same temperature.

The complex [Cp*Mo(dppe)$H_4$]$^+$ was also characterized by means of IR spectroscopy (see Figure 3). After the addition of 1.1 equiv. of $HBF_4$, new bands appeared in the spectrum at 1818, 1839, and 1920 cm$^{-1}$ (see spectrum b). Formation of bands at higher frequency upon protonation is spectroscopic evidence for the formation of a cationic classical product. Treating [Cp*Mo(dppe)$H_3$] with 7 equiv. of HFIP in THF at 200 K did not lead to significant proton transfer, only a minor decrease of the initial 1785 cm$^{-1}$ band observed after the subtraction of the HFIP spectrum (see spectrum c).

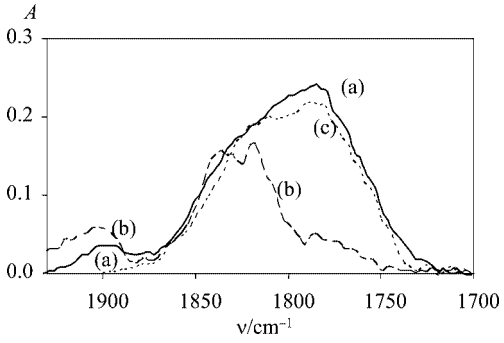


Figure 3. IR spectra in the ν(Mo–H) stretching region of [Cp*Mo(dppe)$H_3$] (0.084 M) in THF at 200 K. (a) Without proton donor. (b) With HBF4 (1.1 equiv.). (c) With HFIP (7 equiv.) after subtraction of the HFIP spectrum.

The protonation process was studied more extensively with a wider range of fluorinated alcohols of different strength in dichloromethane by variable temperature IR. An equilibrium between the hydrogen-bonded system and the tetrahydride complex was observed, which shifts toward the protonation product for stronger alcohols and higher alcohol/Mo ratios. For PFTB, the complete disappearance of the trihydride occurs in the presence of a twofold excess at 200 K. The addition of 2 equiv. of TFE leads to only 20% conversion, while a 10-fold excess is required to consume nearly all the hydride precursor (see Figure 4). For the case of the weakest fluorinated alcohol MFE, a 50-fold excess leads only to a moderate decrease of the MoH band intensity. The proton transfer with TFE at variable temperatures has given kinetic information (see later). Above 250 K, a slow evolution of the spectroscopic properties was observed, indicating instability for the tetrahydride product (see below). A quantitative measurement of the equilibrium position in a wide temperature range was not possible by IR spectroscopy because of the complex shape of the spectra, further complicated by the temperature dependence of the extinction coefficients. The thermodynamic parameters of this equilibrium were obtained from UV and NMR investigations as shown below.

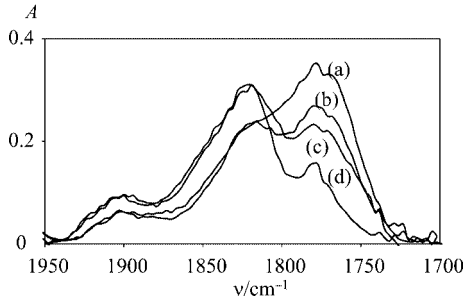


Figure 4. IR spectra in the ν(Mo–H) stretching region of [Cp*Mo(dppe)$H_3$] (0.037 M) in $CH_2Cl_2$ at 200 K. (a) Without TFE. (b) With TFE (2 equiv.). (c) With TFE (5 equiv.). (d) With TFE (10 equiv.).

### *Establishment of the Proton-Transfer Stoichiometry*

The equilibrium resulting from the interaction between [Cp*Mo(dppe)$H_3$] and *p*-nitrophenol (PNP; $P_i$ = 1.27) was investigated by UV/Vis spectroscopy. This was rendered possible by the sensitivity of the proton donor chromophore to hydrogen bonding and proton transfer,[26] making it possible to probe the nature of the species in equilibrium. However, quantitative information on the concentration of each species was not accessible. Spectra were recorded for $CH_2Cl_2$ solutions of PNP (0.001 M) in the presence of [Cp*Mo(dppe)$H_3$] at different ratios from 1:0.1 to 1:2, in the 200–250 K temperature range, where the observed spectral changes were fully reversible. The spectra show wide overlapping bands of both the phenol in its various forms and the hydride complexes (both free and dihydrogen bonded). The absence of free phenolate is signaled by the absence of a band at 430 nm. A deconvolution analysis yields three bands with maxima at 312, 351, and 395 nm. The first two bands are assigned to free PNP and to the dihydrogen-bonded complex [Cp*(dppe)$MoH_3$]···$HOC_6H_4NO_2$. Note that the 351 nm band is red-shifted not only relative to free PNP ($\Delta\lambda$ = 39 nm), but also to the related iron complex [Cp*(dppe)FeH]···$HOC_6H_4NO_2$ (340 nm, $\Delta\lambda$ = 11 nm),[27] signaling a stronger hydrogen bonding. This is consistent with the higher basicity factor of [Cp*Mo(dppe)$H_3$] (Table 1) versus that of [Cp*Fe(dppe)H] (1.35–1.38).[27] The band at 395 nm is attributed to a hydrogen-bonded phenolate ion, [Cp*(dppe)$MoH_4$]$^+$···[OAr]$^-$, because this is blue-shifted from the free phenolate band by 35 nm. Notably, this band is red-shifted in comparison to the corresponding band previously attributed to [Cp*(dppe)Fe($H_2$)]$^+$···[ArOHOAr]$^-$.[15] The assignment of this absorption to the 1:1 hydrogen-bonded ion pair, rather than to a species containing a homoconjugated pair [ArOHOAr]$^-$, was confirmed by the titration experiment (see Figure 5). Therefore, the proton-accepting strength of the Cp*(dppe)-

 © 2006 Wiley-VCH Verlag GmbH & Co. KGaA, Weinheim 

$MoH_3$ complex is sufficiently high to abstract a proton from a single molecule of PNP.

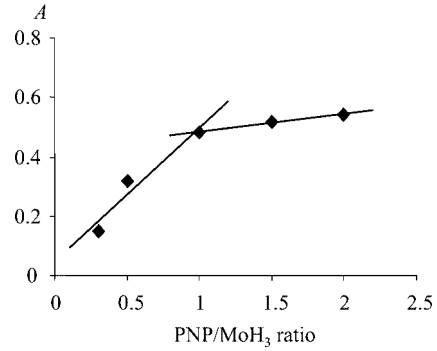


Figure 5. Intensity changes at 390 nm vs. the PNP/Mo ratio.

The stoichiometry was also probed with a weaker proton donor, that is HFIP ($P_i$ = 1.05), by way of a kinetics approach, as HFIP and the species derived from its protonation do not contain chromophores allowing their direct detection. The reaction was studied in toluene at 293 K under pseudo-first-order conditions with HFIP/$MoH_3$ ratios in the 20–80 range, using the stopped-flow technique. The proton-transfer step required a few seconds to reach equilibrium. On a much longer timescale, a slower decomposition reaction occurred, as indicated by NMR monitoring (see below). The time evolution of the spectra could be properly fitted on the basis of a first-order decay, giving an observed rate constant that turned out to be independent of the alcohol concentration (see Figure 6). The average value for $k_{1\,obs}$ is $10.1 \pm 0.2$ s$^{-1}$. This result is consistent with the involvement of a single HFIP molecule in the rate-determining step (Scheme 3), because the hydrogen-bonding pre-equilibrium is heavily shifted to the adduct under these conditions [see Equation (2)]. Therefore, as $K_{HB}$[HA] >> 1, the expression simplifies to $k_{obs} = (k_1 + k_{-1})$. In the previously published kinetics study of the [Cp*Fe(dppe)H] + HFIP system, on the other hand, a first-order dependence on [HFIP] was observed under the same ($K_{HB}$[HA] >> 1) conditions. This difference is again consistent with the higher proton-accepting ability of [Cp*Mo(dppe)$H_3$] versus [Cp*Fe(dppe)H].

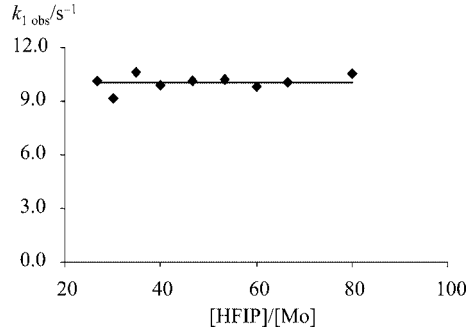


Figure 6. Pseudo-first-order rate constants ($k_{1\,obs}$) for the proton transfer from HFIP to [Cp*Mo(dppe)$H_3$].

$$k_{obs} = \frac{k_1 K_{HB}[HA]}{1+K_{HB}[HA]} + k_{-1} \quad (2)$$

### *Thermodynamics of the Proton-Transfer Equilibrium*

The equilibrium of proton transfer to [Cp*Mo(dppe)$H_3$] was investigated by UV/Vis and $^{31}$P NMR spectroscopy in the 200–240 K temperature range using TFE as proton donors. The results of the UV/Vis study using TFE are shown in Figure 7. The spectra of the initial trihydride (a) and final tetrahydride (b) complexes have very different extinction coefficients at the $\lambda_{max}$ of the trihydride species (400 nm): 2128 and 245, respectively. The UV/Vis properties of the dihydrogen-bonded complexes are essentially indistinguishable from those of the free hydride complex: the UV/Vis spectra of [Cp*Mo(dppe)$H_3$] (0.02 M) in the presence of 15 equiv. MFE do not differ significantly from those of pure trihydride. The same phenomenon was observed earlier for iron hydride.[15] Upon addition of TFE at 200 K, 54% of the complex converts to the tetrahydride, leading to an absorption decrease. The intensity of the band increases upon heating, showing that the equilibrium shifts towards the initial complex. These changes are perfectly reversible in the 200–240 K range.

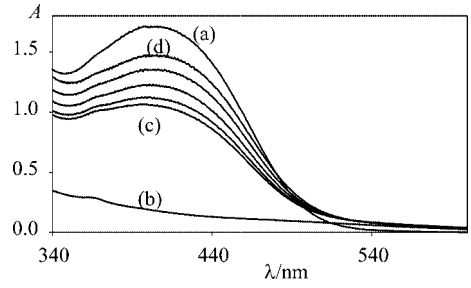


Figure 7. UV/Vis study of the interaction between [Cp*Mo(dppe)$H_3$] and TFE (4 equiv.) in $CH_2Cl_2$. (a) Initial complex $c$ = 0.02 M. (b) Tetrahydride $c$ = 0.02 M. (c) $T$ = 200 K. (d) $T$ = 240 K. The other intermediate spectra were recorded at each 10 K step.

The temperature reversibility enabled the determination of the equilibrium constant for the formation of [Cp*Mo(dppe)$H_4$]$^+$$OCH_2CF_3^-$. It was assumed that the equilibrium involves only one TFE molecule, as experimentally verified for the PNP and HFIP systems (see above, Scheme 3). Taking into account the above-determined hydrogen-bond formation constant $K_{HB}$, the analysis of the data of Figure 7 led to the calculation of the proton-trans-

$$Cp^*Mo(dppe)H_3 + R_FOH \rightleftharpoons Cp^*Mo(dppe)H_3\cdots HOR_F \qquad K_{HB}$$

$$Cp^*Mo(dppe)H_3\cdots HOR_F \rightleftharpoons [Cp^*Mo(dppe)H_4]^+\cdots OR_F^- \qquad K_{PT} = k_1/k_{-1}$$

Scheme 3.

 © 2006 Wiley-VCH Verlag GmbH & Co. KGaA, Weinheim 

fer equilibrium constant $K_{PT}$ at each temperature. A van't Hoff analysis of these $K_{PT}$ constants yields $\Delta H°_{PT} = -2.8 \pm 0.4$ kcal mol$^{-1}$ and $\Delta S°_{PT} = -15 \pm 2$ cal mol$^{-1}$ K$^{-1}$ for the proton-transfer process.

The proton-transfer equilibrium constants were also obtained by $^1$H NMR spectroscopy. Like for the UV/Vis investigation, the NMR technique only provides information on the sum of the concentrations of rapidly equilibrating free trihydride and its hydrogen-bonded adduct. Knowledge of the $K_{HB}$ allowed the calculation of the individual concentrations, from which the $K_{PT}$ constants could be calculated at each temperature. The van't Hoff analysis yields $\Delta H°_{PT} = -2.7 \pm 0.5$ kcal mol$^{-1}$ and $\Delta S°_{PT} = -11 \pm 2$ cal mol$^{-1}$ K$^{-1}$. These values are identical to those established from the low-temperature UV/Vis data within experimental error.

### *Decomposition of the Proton-Transfer Product: Hydrogen Evolution*

NMR monitoring of the [Cp*Mo(dppe)H$_3$]–TFE interaction at high temperatures (>280 K) revealed further irreversible evolution. The hydride resonances of the starting trihydride and the protonated tetrahydride complexes disappeared completely within 2 h at room temperature. No new hydride resonance appeared in the spectrum. On the other hand, the formation of a new diamagnetic product was indicated by the replacement of the Cp* resonances ($\delta$ = 1.69 for the trihydride and 1.83 for the tetrahydride complexes) with a new one at $\delta$ = 1.58 in the $^1$H NMR and by the appearance of a resonance at $\delta$ –69.5 in the $^{31}$P{$^1$H} NMR spectrum. This indicates the selective formation of a single, hydride-free diamagnetic product. This evolution is accompanied by the appearance of a new sharp resonance at $\delta$ = 4.61 in the $^1$H NMR spectrum, which is characteristic of free $H_2$. All this evidence points to reductive elimination of two $H_2$ molecules from the tetrahydride complex [Cp*MoH$_4$(dppe)]$^+$, the product being stabilized by coordination of the trifluoroethoxide anion.

Stable 16-electron compounds of type [(C$_5$R$_5$)MoL$_2$X] (the X ligand has π-donating properties) have previously been reported, for example [CpMo(CO)$_2${As(*t*Bu)$_2$}],[28] [Cp*Mo(PMe$_3$)(PHPh$_2$)(PPh$_2$)],[29] [Cp*Mo(dppe)Cl],[30] and [CpMo(PMe$_3$)$_2$(OH)].[30,31] These precedents suggest that the [Cp*Mo(dppe)(OCH$_2$CF$_3$)] molecule may be stable. Interestingly, compounds [CpMo(PMe$_3$)$_2$(OH)] and [Cp*Mo(dppe)Cl] have two unpaired electrons, whereas our observed $H_2$ elimination product is diamagnetic like compound [Cp*Mo(PMe$_3$)(PHPh$_2$)(PPh$_2$)].[29] It is also possible, however, that one additional TFE molecule adds to the system to afford an 18-electron adduct, which could even be further stabilized by intramolecular hydrogen bonding (see Scheme 4).

The $^1$H NMR spectrum does not remove this ambiguity, because only one $\delta_{CH_2}$ resonance for TFE is observed, at the same position as in free TFE ($\delta \approx 3.9$). It is not split or shifted by the deprotonation process, possibly because of a rapid exchange between the free alcohol and its conjugate anion. The absence of a new resonance for a coordinated TFE molecule represents only negative evidence, because

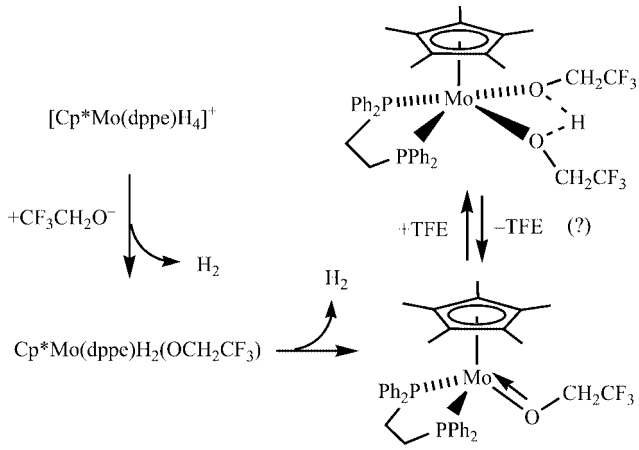


Scheme 4.

fast exchange could also average the resonances of free TFE/$CF_3CH_2O^-$ with that of any coordinated TFE. Neither does the OH resonance give any useful information, as it also remains unsplit under all conditions because of rapid exchange processes. In addition, the position of this resonance is highly temperature- and concentration-dependent, even before any dihydrogen evolution from [Cp*MoH$_4$(dppe)]$^+$ takes place. All our attempts to isolate the final product in the crystalline state have failed. The spin states' dichotomy for complex [Cp*Mo(dppe)(OCH$_2$CF$_3$)], as well as the thermodynamics of further TFE coordination, has been investigated by DFT calculations (vide infra).

## Computational Studies

The interaction of [Cp*Mo(dppe)H$_3$] with fluorinated alcohols has been studied theoretically by using the model complex [CpMo(dpe)H$_3$] (dpe = H$_2$PCH$_2$CH$_2$PH$_2$) and TFE and HFIP as proton donors, both in gas phase and in dichloromethane. Test calculations for the real complex have also been performed. The computational study was carried out with several objectives in mind: (i) explore the thermodynamics of hydrogen bonding at different sites; (ii) investigate the effect of hydrogen bonding at different sites on the vibrational modes of the $MoH_3$ moiety; (iii) investigate the stability of the protonation products and the possible involvement of nonclassical intermediates during the proton-transfer process; (iv) determine the protonation pathway; and (v) rationalize the further evolution of the protonation product.

### *The Free Trihydride Complex*

The optimization of the free [CpMo(dpe)H$_3$] model system gave a geometry that is in close correspondence with that observed experimentally[19,20] for the full [Cp*Mo(dppe)H$_3$] system. For the purpose of the present discussion, the most important parameters are those related to the $MoH_3$ moiety (see Figure 8). Taking the plane that contains the two P atoms and the center of the Cp as a reference, the three H ligands are disposed asymmetrically,

 © 2006 Wiley-VCH Verlag GmbH & Co. KGaA, Weinheim 

two (H1 and H2) on one side and one (H3) on the other side. The unique H3 atom shows the longest distance to the Mo center (1.724 Å). The other two hydrides seem to occupy approximately symmetric positions relative to the Mo–H vector to the unique H ligand (H3–Mo–H1 = 132°, H3–Mo–H2 = 129°), but they in fact show quite different Mo–H distances. One distance (to H2) is similar to that of the unique hydride (1.717 Å), whereas the other one is much shorter (1.682 Å). This asymmetry parallels a slight asymmetry in the Cp*Mo(dppe) moiety (the two CNT–Mo–P angles are different at 131.1 and 143.1°) and its origin is not clear. The three hydride ligands have quite different Mulliken charges: –0.017, –0.003, and –0.053 for H1, H2, and H3, respectively. Thus H3 is clearly the most hydridic site. The distance between H1 and H2 (1.753 Å) indicates that they do not directly interact with each other, because it is longer than the longest separation between hydrogen atoms in what have been described as "stretched dihydrogen ligands" {e.g., 1.49 Å in $[OsH_5(PMe_2Ph)_3]^+$}.[32] In addition, a theoretical analysis of another stretched dihydrogen complex {i.e., $[Os(H\cdots H)(NH_2CH_2CH_2NH_2)_2(HCO_2)]^+$ with a distance of 1.428 Å} indicates no critical point connecting the two atoms.[33]

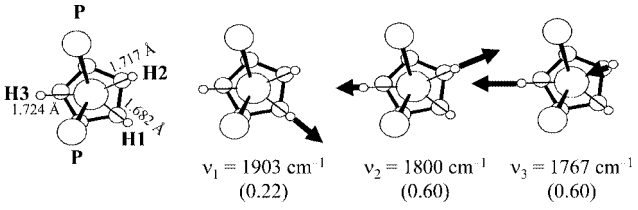


Figure 8. ORTEP view of the DFT optimized [CpMo(dpe)H$_3$] molecule. The Cp- and P-bonded H atoms and ethylene backbone have been omitted for clarity. The M–H normal modes are represented with their respected computed frequency and intensity ($10^4$ L mol$^{-1}$ cm$^{-2}$) in parentheses.

The analysis of the M–H normal modes in the free complex, also represented in Figure 8, will serve as a basis for discussion of the changes induced by hydrogen bonding. A comparison between the experimental spectrum for compound [Cp*Mo(dppe)H$_3$] and the computed one for the [CpMo(dpe)H$_3$] model shows a rather good agreement, both in terms of the frequencies and the relative intensities. As shown in Figure 8, the higher-energy normal mode ($\nu_1$) is essentially a pure stretching vibration of the hydride ligand H1, which shows the shortest (and therefore strongest) bond. The other two vibrations are relatively close to each other in frequency and are a mixture of the other two M–H bond vibrations, the higher-frequency one ($\nu_2$) being an in-phase combination with the major contribution from the shorter bond to H2, and the lower-frequency one ($\nu_3$) being an out-of-phase combination with the major contribution from the longer bond to H3.

### *Hydrogen-Bonded Adducts with TFE: Structures and Vibrational Modes*

[CpMo(dpe)H$_3$] has four potential hydrogen-bonding sites: the three hydrides and the metal (Scheme 5).

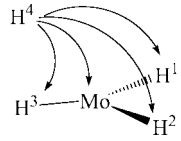


Scheme 5.

To account for all the possible hydrogen-bonded minima we optimized the adduct between TFE and the [CpMo(dpe)H$_3$] starting from the different regions around the metal. In this way five stable hydrogen-bonded structures were obtained, as shown in Figure 9. Table 3 shows the rel-

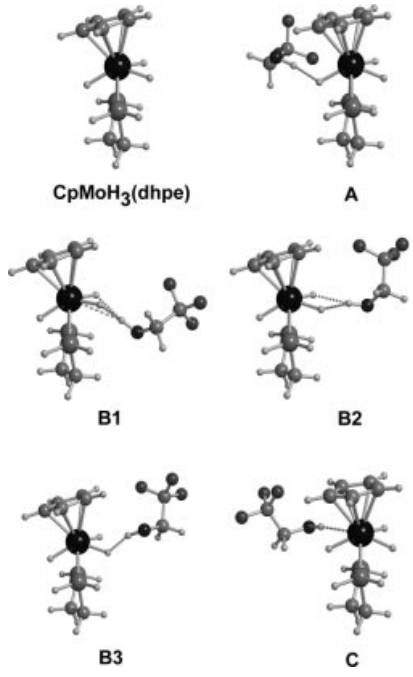


Figure 9. Optimized geometries of [CpMo(dpe)H$_3$] and the [CpMo(dpe)H$_3$···TFE] hydrogen-bonded adducts **A**–**C**.

Table 3. Relevant optimized geometrical parameters (distances in Å; angles in °) for [CpMo(dpe)H$_3$···TFE] (**A**–**C**) adducts.[a]

| | **A** | **B1** | **B2** | **B3** | **C** |
|---|---|---|---|---|---|
| Mo–H1[b] | 1.678 (–0.004) | 1.687 (+0.005) | 1.684 (+0.002) | 1.682 (0.000) | 1.680 (–0.002) |
| Mo–H2[b] | 1.722 (+0.005) | 1.713 (–0.004) | 1.725 (+0.008) | 1.736 (+0.019) | 1.725 (+0.008) |
| Mo–H3[b] | 1.734 (+0.010) | 1.724 (0.000) | 1.720 (–0.004) | 1.717 (–0.007) | 1.731 (+0.007) |
| O–H[c] | 0.977 (+0.012) | 0.980 (+0.015) | 0.977 (+0.012) | 0.979 (+0.014) | 0.979 (+0.014) |
| H···H1 | | 2.057 | 1.944 | 2.942 | |
| H···H2 | | 1.779 | 1.799 | 1.653 | |
| H···H3 | 1.816 | | | | 2.104 |
| H···Mo | 3.068 | 2.927 | 3.034 | 2.987 | 2.864 |
| O–H···H1 | | 152.5 | 148.5 | 147.1 | |
| O–H···H2 | | 150.1 | 150.6 | 160.3 | |
| O–H···H3 | 155.2 | | | | 140.0 |
| O–H···Mo | 152.9 | 160.4 | 177.8 | 170.4 | 172.4 |

[a] For the location of H1, H2, and H3, see Figure 8. [b] Values in parentheses are the changes relative to free [CpMo(dpe)H$_3$]. [c] Values in parentheses are the changes relative to free TFE.

 © 2006 Wiley-VCH Verlag GmbH & Co. KGaA, Weinheim 

evant optimized geometrical parameters. The computed frequencies and the normal modes for the M–H stretching vibrations are depicted in Figure 10.

The adducts can be classified depending on the proton-acceptor site. System **A** is the only one where TFE interacts with the unique hydride ligand H3. In systems **B** (**B1**–**B3**) the interaction occurs at one or both of the other two hydride ligands, H1 and H2, that occupy pseudoequivalent positions. Systems **B2** and **B3** are topologically related, as they exhibit the same Mo–H···H–O moiety. They differ in the relative orientation of the proton donor molecule, which places the C–H bond in front of the second hydride in **B3** and in the opposite direction in **B2**. In system **B1** the alcohol molecule is placed with the same relative orientation as in **B2** but farther from the Cp ring. Both in **B1** and **B2** the proton is closer to H2, but also interacts with H1. Thus, these geometries may be better described as containing a "bifurcated hydrogen bond", similar to that described for the $Cp_2NbH_3{\cdot}HOR_F$ adducts.[18] In addition, the distance of the proton from the metal center in system **B1** is also relatively short. In **B3** the proton interacts only with H2, with H2···H–O and Mo···H–O angles of 160.3° and 170.4°, respectively. Finally, system **C** is the only one where the most important interaction appears to involve the metal center, as indicated by the shortest Mo···H distance and the almost linear Mo···H–O bond. The metal–proton interaction is accompanied by a relatively long H···H3 interaction (2.104 Å). This initial description of the hydrogen-bonded adducts, based on the structural data, will be reinforced by the analysis of the changes in the vibrational frequencies and atomic charges of the $MoH_3$ moiety on going from the free complex to the TFE adduct.

The evolution of the Mulliken charges on the hydride atoms and on the Mo atom upon going from the free complex to the TFE adducts also provides useful information. The relevant charges are collected in Table 4. The O–H bond is lengthened in all complexes, in comparison to free TFE (0.965 Å). The magnitude of this elongation is variable

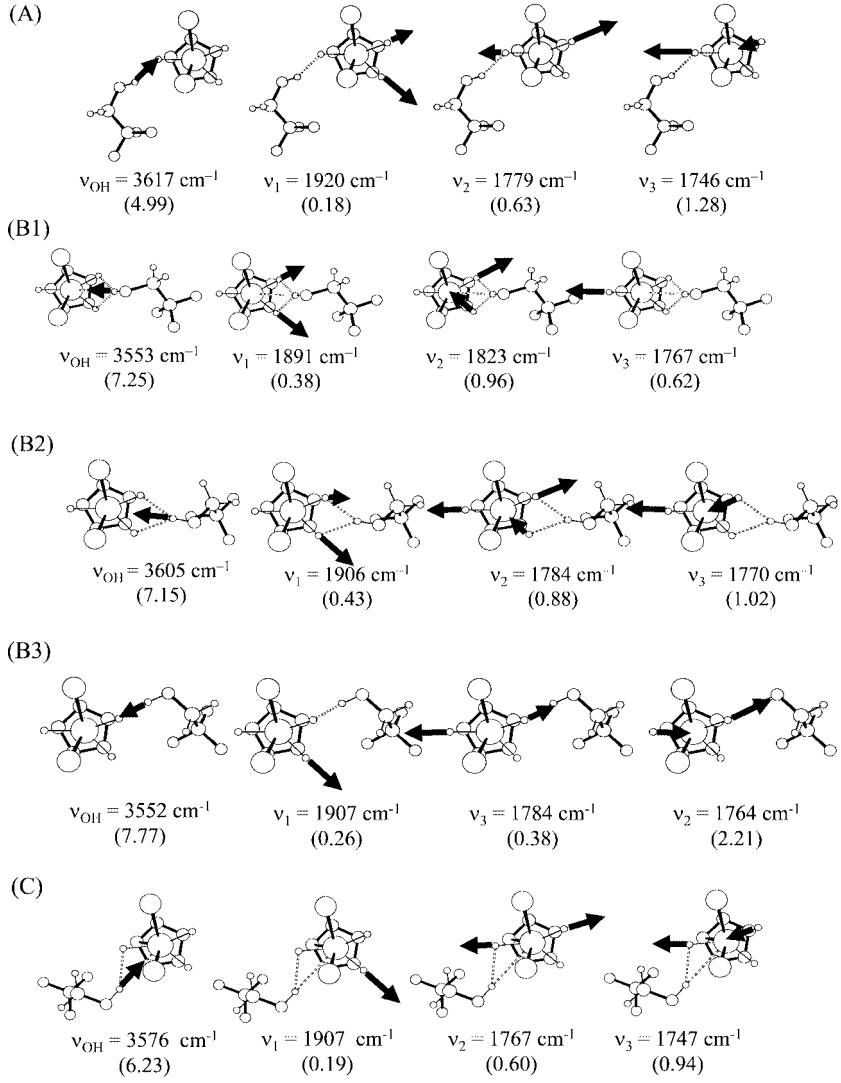


Figure 10. ORTEP view of the DFT optimized [CpMo(dpe)$H_3$···TFE] adducts, showing selected bonding parameters and a representation of the normal modes with the computed frequency and intensity ($A$ = $10^4$ L mol$^{-1}$ cm$^{-2}$) in parentheses. The P-bonded H atoms and ethylene backbone have been omitted for clarity.

 © 2006 Wiley-VCH Verlag GmbH & Co. KGaA, Weinheim 

but is always rather large (0.012–0.015 Å). The positive charge of the proton increases by 0.027–0.047 units. In system **A** TFE interacts only with the unique hydride ligand (H3). The negative charge of H3 increases from –0.053 to –0.128 ($\Delta q$ = –0.075), whereas the charges of H1 and H2 remain essentially unchanged and that of Mo slightly decreases ($\Delta q$ = +0.009). The Mo–H3 bond is significantly elongated ($\Delta r_{M-H}$ = +0.010 Å), whereas the Mo–H1 and Mo–H2 bonds are less affected (slight contraction for the former and slight elongation for the latter). The composition of the three M–H vibrational modes (Figure 10) remains close to that observed in the free trihydride (Figure 8). The $\nu_1$ mode is blue-shifted by +17 cm$^{-1}$, in agreement with the slight contraction of the Mo–H1 bond; the $\nu_2$ mode does not shift significantly (the major contribution is from Mo–H2, which maintains essentially the same distance); and the $\nu_3$ mode is strongly red-shifted ($\Delta\nu_3$ = –21 cm$^{-1}$), correlating with the weakening of the Mo–H3 bond by the hydrogen bond.

Table 4. Computed Mulliken charges for selected atoms in the [CpMo(dpe)H$_3$] complex and its TFE adducts.[a]

| | H(TFE) | Mo | H1 | H2 | H3 |
|---|---|---|---|---|---|
| [CpMo(dpe)H$_3$] | | –0.316 | –0.017 | –0.003 | –0.053 |
| TFE | 0.326 | | | | |
| **A** | 0.353 | –0.307 | –0.015 | –0.001 | –0.128 |
| **B1** | 0.373 | –0.367 | –0.017 | –0.076 | –0.047 |
| **B2** | 0.368 | –0.310 | –0.046 | –0.088 | –0.051 |
| **B3** | 0.364 | –0.296 | –0.020 | –0.123 | –0.049 |
| **C** | 0.373 | –0.422 | –0.010 | 0.002 | –0.072 |

[a] For the location of H1, H2, and H3, see Figure 8.

The H1 and H2 hydrides are involved in the hydrogen bond in systems **B1**–**B3**. For system **B3**, the major observed effects of hydrogen bonding are a significant lengthening of the Mo–H2 bond (+0.019 Å), a slight shortening of Mo–H3 (–0.007 Å), a dramatic increase for the H2 negative charge (–0.120), and a slight decrease for that of Mo (+0.020). Therefore, these charge and bond length changes confirm the description of this adduct as involving a dihydrogen bond to H2. The $\nu_1$ vibration is very weakly influenced by the dihydrogen bonding ($\Delta\nu_1$ = +4 cm$^{-1}$), whereas $\nu_2$ and $\nu_3$ are dramatically affected (Figure 10). In fact, hydrogen bonding with H2 weakens the Mo–H2 bond to such a point that the $\nu_2$ mode (to which the Mo–H2 vibration contributes the most) now appears at a *lower* frequency than $\nu_3$ ($\Delta\nu_2$ = –36 cm$^{-1}$). Conversely, $\nu_3$ is shifted to a higher frequency ($\Delta\nu_3$ = +17 cm$^{-1}$), in agreement with the Mo–H3 bond shortening, and the band intensity is decreased by a factor of two. An additional contribution to the red-shift of $\nu_2$ and to the blue-shift of $\nu_3$ may be associated with the modified mixing: in-phase for $\nu_2$ and out-of-phase for $\nu_3$, that is, the opposite of the situation in the free trihydride.

For system **B2**, the negative charge increases significantly, relative to the free trihydride complex, on both H1 ($\Delta q$ = –0.029) and especially H2 ($\Delta q$ = –0.085), correlating well with the H···H distances (longer for H1, 1.944 Å; shorter for H2, 1.799 Å). The charge slightly decreases on Mo ($\Delta q$ = +0.006). The trends of the H···H distances and hydride charges agree with the evolution of the Mo–H bond lengths: both Mo–H1 and Mo–H2 are lengthened (by +0.002 and +0.008 Å, respectively), whereas Mo–H3 is shortened (–0.004 Å) (Table 3). The O–H vector bisects the H1MoH2 angle, with an essentially coplanar MoH1H2···HO fragment. System **B2**, therefore, appears to be best described as having a bifurcated hydrogen bond with H1 and H2. This situation reflects onto the vibrational modes as follows. The $\nu_1$ mode appears at a slightly higher frequency (+3 cm$^{-1}$), which is unexpected because the Mo–H1 bond is slightly lengthened by the hydrogen bond. The $\nu_2$ mode exhibits a moderate low-frequency shift (–16 cm$^{-1}$; a compromise between the Mo–H2 bond weakening and the Mo–H3 bond strengthening), whereas the $\nu_3$ mode correspondingly shows a moderate high-frequency shift (+3 cm$^{-1}$) for the same reasons.

For system **B1**, on the other hand, the charge on H1 remains unchanged, whereas it increases significantly on H2 (–0.073) *and also on the Mo atom* (–0.051), suggesting that the metal center also participates directly in the hydrogen bonding. The O–H···Mo distance is 0.1 Å shorter in **B1** than in **B2**. A folding of the O–H vector along the H1H2 axis by 141.2° toward the metal, in the opposite direction from the Cp ring, signals an interaction that forces the proton donor to approach the metal center. These changes suggest the description of adduct **B1** as featuring a bifurcated hydrogen bond to H2 and Mo. Note that, whereas the H···H distances would suggest that hydrogen bonding with H2 is stronger in **B1** than in **B2** (1.779 Å vs. 1.799 Å), the Mo–H2 distance shortens (–0.004 Å), rather than lengthens, in **B1**. In addition, the charge on H2 increases to a smaller extent in **B1** than in **B2**. These perturbations may be caused by the Mo···HO interaction and suggest that conclusions about the hydrogen bond nature in a complicated polyatomic system should not be based solely on the H···H distances. The low-frequency shift for $\nu_1$ (–12 cm$^{-1}$) correlates with the lengthening of the Mo–H1 bond and the strong high-frequency shift for $\nu_2$ (+23 cm$^{-1}$) correlates with the Mo–H2 bond compression, whereas there is no clear correlation with the H···H distances. Note that system **B1** exhibits mixing of the Mo–H1 and Mo–H2 vibrations in $\nu_1$ and $\nu_2$, whereas $\nu_3$ is an essentially pure Mo–H3 vibration. The latter experiences no shift relative to the free trihydride compound, consistent with the invariance of the Mo–H3 bond length.

Finally, system **C** shows a dramatic increase of the metal negative charge ($\Delta q$ = –0.106), whereas the charge on H3 increases only slightly ($\Delta q$ = –0.019). Together with the structural features discussed above, these charge variations suggest that the bonding in this adduct is dominated by the metal site, and is unique amongst all the optimized adducts **A**–**C** in this respect. It is interesting to observe that not only is the Mo–H3 bond elongated in this adduct (+0.007), but the Mo–H2 bond is also (+0.008 Å), whereas the Mo–H1 bond is slightly shortened. There is no obvious explanation for this phenomenon. The evolution of the normal modes

 © 2006 Wiley-VCH Verlag GmbH & Co. KGaA, Weinheim 

is again in line with the observed changes of Mo–H bond lengths: $\nu_1$ shows a small high-frequency shift (+4 $cm^{-1}$), whereas $\nu_2$ and $\nu_3$ exhibit large low-frequency shifts (–33 and –20 $cm^{-1}$, respectively).

### *Hydrogen-Bonded Adducts with TFE: Relative Stability*

The relative stability of these systems was estimated in different ways (see Table 5). Comparing the energy changes associated to the hydrogen bond formation, the stronger interactions are those involving the two equivalent hydride ligands. Structures **B** show the most exothermic hydrogen bond. This behavior can be traced back to the establishment of two dihydrogen bonds in **B1** and **B2** or only one strong dihydrogen bond in **B3**.[18] Although the primary interaction is shorter in system **B3**, the relative stability of the three systems is not too different. A fast exchange of the ROH molecule between the three **B** sites can be expected from the structural features and low energy differences found between the three isomers. The interactions at the unique hydride site (**A**) and at the metal site (**C**) have similar energies, around 2 kcal $mol^{-1}$ less exothermic than for the **B** structures. A fast exchange between the **A** and **C** sites can be also expected. The gas-phase complexation energies span a range between 9 and 12 kcal $mol^{-1}$, similar to those calculated for the same kind of interactions in other transition-metal hydride systems,[15,17,18] and notably higher than the experimental enthalpies. Previous results concerning hydrogen bonding in transition-metal systems showed that the Basis Set Superposition Error (BSSE) can be very important in this type of system.[18] BSSE-corrected bonding energies have been calculated, showing that the BSSE accounts for 40–50% of the interaction energy. However, after correction all the adducts are still stable, with interaction energies between 5 and 8 kcal $mol^{-1}$. It is worth mentioning that a negative and significant interaction energy remains at the metal site after the BSSE correction, in contrast with what we have found in a recent study of the hydrogen bonding to the [Cp*Fe(dppe)H].[15] This result demonstrates the basicity of the molybdenum center in this compound and points towards competition between the hydride and the metal sites for the proton.

Table 5. Calculated parameters of the hydrogen bonding between [CpMo(dpe)$H_3$] and TFE.

| | A | B1 | B2 | B3 | C |
|---|---|---|---|---|---|
| $\Delta E$ [kcal $mol^{-1}$] | –9.6 | –11.3 | –11.2 | –11.5 | –10.4 |
| $\Delta E$(BSSE)[a] [kcal $mol^{-1}$] | –5.1 | –7.9 | –7.8 | –5.9 | –5.9 |
| $\Delta H$(BSSE)[b] [kcal $mol^{-1}$] | –3.5 | –6.0 | –6.1 | –5.9 | –4.3 |
| $\nu$(OH) [$cm^{-1}$] | 3617 | 3553 | 3605 | 3552 | 3576 |
| $A$ ($10^{-4}$) [L $mol^{-1}$ $cm^{-2}$] | (4.99) | (7.25) | (7.15) | (7.77) | (6.23) |
| $\Delta H(\Delta\nu)$[c] [kcal $mol^{-1}$] | –4.3 | –5.2 | –4.5 | –5.2 | –4.9 |
| $\Delta H(\Delta A)$[d] [kcal $mol^{-1}$] | –4.7 | –5.8 | –6.0 | –6.3 | –5.5 |
| $\Delta G(CH_2Cl_2)$[e] [kcal $mol^{-1}$] | –1.6 | –3.1 | –3.2 | –3.4 | –2.8 |

[a] Complexation energy corrected by the basis set superposition error. [b] Complexation enthalpy, taking the BSSE-corrected energy. [c] Application of Equation (1),[34] using the computed $\Delta\nu$(OH). [d] Application of Equation (3),[35] using the computed intensities $A$. [e] Complexation free energy in dichloromethane.

The calculated enthalpies, taking the BSSE-corrected energies, are slightly decreased, but the ordering **B** > **C** > **A** is preserved. The interaction enthalpy was also estimated on the basis of Iogansen's empirical relationships [Equation (1)[34] and Equation (3)[35]] using the computed $\nu$(OH) stretching vibration frequencies or $\nu$(OH) band intensities $A$, which are also reported in Table 5. Remarkably, the $\Delta H$ computed in the different ways are very similar. Indeed, the highest values obtained (about 6 kcal $mol^{-1}$) are close to the experimental hydrogen-bond enthalpies. The $\nu$(OH) bands are found at lower frequency {$\Delta\nu$(OH) = 227–292 $cm^{-1}$}, and with a dramatically increased intensity [from $0.38\times10^4$ L $mol^{-1}$ $cm^{-2}$ in free TFE to (4.99–7.77)$\times10^4$ L $mol^{-1}$ $cm^{-2}$ in the H-bonded adducts], in good agreement with the experimental observations. Both correlations work well for medium-strength hydrogen bonds of organic bases and appear to be successfully applicable also to organometallic complexes.[12,13] Note that Equation (3) is considered as universal (valid for different types of H complexes in solution or in the gas phase) and more precise.

$$\Delta H = 2.9\Delta A^{1/2} = 2.9(A^{1/2}_{\text{bonded}} - A^{1/2}_{\text{free}}) \quad (3)$$

PCM calculations give the solvation free energy of a species, and its partition into enthalpic and entropic parts is not possible.[36] From the $\Delta G_{solv}$ of free [CpMo(dpe)$H_3$], free TFE, and their adduct, it is possible to get a rough estimation of the $\Delta G$ of the hydrogen-bond formation in solution, which does not take into account the internal contributions to the entropy. The $\Delta G$ obtained in this way for adducts **A**–**C** in $CH_2Cl_2$ are collected in Table 5. Although the $\Delta G(CH_2Cl_2)$ are less exothermic than the $\Delta H$ in gas phase, for all the adducts $\Delta G(CH_2Cl_2)$ is negative, pointing out the stability of the hydrogen-bonded species in solution. Moreover, the ordering **B** > **C** > **A** is maintained.

### *Protonation Products*

The calculations on the protonation product, the system having the $[CpMo(dpe)H_4]^+$ stoichiometry, reveal the existence of two stable local minima for the classical tetrahydride complex and another two for a dihydrogen–dihydride tautomer, $[CpMo(dpe)(H_2)H_2]^+$. They can be envisaged as the products of the proton transfer to the different proton-acceptor sites revealed by the hydrogen-bonded adducts. The optimized structures are shown in Figure 11. Relevant geometrical parameters are available as Supporting Information.

The most stable isomer is the tetrahydride **TETRA1**. This structure presents a rather symmetrical arrangement, with two hydrides at each side of the plane defined by the two phosphorus atoms and the center of the Cp ring. The tetrahydride nature of this complex is evident from the H···H distances, the shortest one being 1.799 Å. There are two sets of Mo–H distances, longer (1.708 and 1.706 Å) for the two most distant hydrides, and shorter (1.671 and 1.674 Å) for the closest ones. The geometry of **TETRA1** agrees with the experimental structure of $[Cp^*WH_4(dppe)]^+$ and its description as a distorted pseudopentagonal bipyramid (see Scheme 2).[19] The four H ligands are practically in the same

 © 2006 Wiley-VCH Verlag GmbH & Co. KGaA, Weinheim 

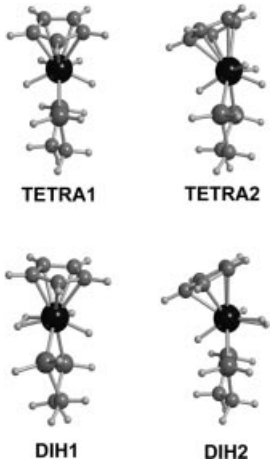


Figure 11. Views of the optimized geometries for isomeric structures having the [CpMo(dpe)H$_4$]$^+$ stoichiometry.

plane (the fourth H is only 0.010 Å away) and one P atom is only 0.035 Å away from the least-squares $H_4$ plane. The five angles between adjacent bonds in the pseudopentagonal plane are relatively similar and close to that expected for the equatorial ligands in a pentagonal bipyramid (72°). **TETRA1** can be considered the product of proton transfer to the metal site, although it may also result from the oxidative addition of a coordinated dihydrogen ligand. Both possibilities will be considered in the next two sections.

The second tetrahydride minimum, **TETRA2**, has three hydrides on one side of the P–Cp$_{centroid}$–P plane and one on the opposite side. The Mo–H distances for the three hydrides on the same side are 1.666, 1.710, and 1.668 Å, the longest one being that to the central hydride. The shortest H···H distance is 1.602 Å (H1···H2), in agreement with the tetrahydride nature of this isomer. The Mo–H distance of the unique hydride H3 is 1.691 Å. **TETRA2** could be regarded as the protonation product at the metal site close to hydrides H1 and H2. **TETRA2** is considerably less stable than **TETRA1**, lying 8.0 kcal mol$^{-1}$ higher.

Two dihydrogen–dihydride structures have been characterized as local minima (**DIH1** and **DIH2**). Their geometries are comparable to that of the parent complex [CpMo(dpe)H$_3$], but with a $\eta^2$-H$_2$ ligand in place of a hydride. **DIH1** is the most stable dihydrogen–dihydride isomer, only 3.7 kcal mol$^{-1}$ above **TETRA1**. The presence of a dihydrogen ligand in the coordination sphere of the metal is apparent from the H–H distance of 0.896 Å between the adjacent H3 and H4 atoms. This structure is reached by protonation of the unique hydride H3 in the initial trihydride. The second dihydrogen–dihydride isomer (**DIH2**) is attained by proton transfer to the H1 or H2 ligands. The H–H distance in the dihydrogen ligand (0.851 Å) is shorter than in **DIH1**, indicating a weaker metal–H$_2$ interaction. In agreement with this, **DIH2** is less stable than **DIH1**, 5.1 kcal mol$^{-1}$ above **TETRA1**.

We have also considered the relative stability of the four [CpMo(dpe)H$_4$]$^+$ isomers in dichloromethane. There is little change on going from the gas phase to the $CH_2Cl_2$ medium. The tetrahydride **TETRA1** remains the most stable species in $CH_2Cl_2$, with **TETRA2**, **DIH1**, and **DIH2** being placed 6.6, 3.3, and 5.0 kcal mol$^{-1}$ above **TETRA1**.

To assess how the chosen model affects the results, we have studied the protonation products in the full system, performing full QM calculations on the actual [Cp*Mo(dppe)H$_4$]$^+$ complex. The four stable structures found for the model [CpMo(dpe)H$_4$]$^+$ system have also been located in the full system, with very similar arrangements of the $MoH_4$ unit to the model systems. A general view of the optimized geometries is shown in the Supporting Information. As can be appreciated in Table S1, the structural changes induced by the modeling of the real ligands are minor.

The relative energies of the different isomers of the full system are comparable to those of the model system. The tetrahydride **TETRA1** is still the most stable species, with **TETRA2**, **DIH1**, and **DIH2** placed 7.0, 4.4, and 6.6 kcal mol$^{-1}$ above **TETRA1**. Thus, the calculations indicate that the classical tetrahydride product **TETRA1** is strongly favored relative to all possible dihydrogen structures. This result agrees with the experiment, as the tetrahydride is the only observed protonation product. The presence of dihydrogen–dihydride species at low relative energies suggests that they may be intermediates along the proton-transfer pathway.

The simplifications introduced in the modeling of the system have very little influence in the relative energies of the protonation products. To further check the differences between the model and the full systems we have computed the gas phase proton affinity (PA), that is the energy change associated to Equation (4)

$$([Mo]\text{-}H_3) + H^+ \rightarrow ([Mo]\text{-}H_4)^+ \quad (4)$$

where [Mo] stands for CpMo(dpe) or Cp*Mo(dppe) and **TETRA1** has been considered the protonation product. The model system presents a slightly lower proton affinity (249.9 kcal mol$^{-1}$) than the full system (271.0 kcal mol$^{-1}$), but the difference amounts to only 8%. As all four protonated structures have very similar relative energies in the full and model systems, we can conclude that all the proton-acceptor sites of the $MoH_3$ unit are a little more basic in the full system than in the model one.

### *Proton-Transfer Reaction Profiles with HFIP*

We have also carried out a study of the [CpMoH$_3$(dpe)·HFIP] adduct, analogous to that illustrated above for the [CpMoH$_3$(dpe)·TFE] adduct. The results are not detailed for the sake of brevity, but the main outcome is that five hydrogen-bonded structures comparable to the **A**–**C** ones reported for TFE (Figure 9) have been located, which will be correspondingly labeled **A′**, **B1′**, **B2′**, **B3′**, and **C′**. They follow the same stability ordering **B′** > **C′** > **A′**, with slightly increased interaction energies, caused by the stronger acidity of HFIP compared with TFE. For instance, the $\Delta H$(BSSE) are –3.9, –6.3, –5.7, –6.8, and –4.4 kcal mol$^{-1}$ for the HFIP adducts **A′**, **B1′**, **B2′**, **B3′**, and **C′**, respectively.

 © 2006 Wiley-VCH Verlag GmbH & Co. KGaA, Weinheim 

When one imagines the reaction trajectory leading to proton transfer, it can be predicted that system **C′** may lead to the classical tetrahydride complex directly, whereas systems **A′**–**B′** could yield dihydrogen intermediates. The most stable protonation product (**TETRA1**) formally arises from proton transfer to **C′**, whereas the most stable dihydrogen complex (**DIH1**) may be viewed as formally arising from proton transfer from **A′** to the H3 hydride site. For this reason we have studied both proton-transfer pathways. In addition, the close vicinity of the protonation sites in the **A′** and **C′** structures will allow a study of the direct competition for the proton between a hydride and the metal sites and a discussion of whether a direct proton transfer to the metal is possible in this case.

Starting from the hydrogen-bonded adducts **C′** and **A′**, the final products of the proton transfer should be the ion pairs made up by the **TETRA1** (metal site protonation) or **DIH1** (hydride site protonation) cations and the $[(CF_3)_2HCO]^-$ (**[X]**$^-$) anion. However, whereas the optimization of the **TETRA1·[X]** ion pair was successful, attempts to optimize the **DIH1·[X]** ion pair failed. Several optimizations starting from different input geometries were tried but led systematically to the same initial hydrogen-bonded adduct. The optimized geometries of hydrogen-bonded complexes and the ion pair are available in the Supporting Information.

As no stable dihydrogen–conjugate base ion pair was found, we have not pursued the proton-transfer pathway at the hydride site. We have further explored the protonation at the metal. Initially the gas-phase reaction profile leading from **C′** to **TETRA1·[X]** has been investigated by using the O–H distance of the HFIP donor as the pivot parameter along the reaction coordinate, all other geometrical parameters being optimized. Then, the maximum of this curve has been used as the starting point to locate the transition state, which practically coincides with this maximum. The profile in the dichloromethane solvent was obtained from single-point calculations on each point of the gas-phase profile with the solvent PCM. The energy of the starting hydrogen-bonded adduct **C′** was taken as the zero of energy. The energetic profiles are depicted in Figure 12.

The gas-phase energy barrier to form the ion pair at the metal site is 24.7 kcal mol$^{-1}$. The $CH_2Cl_2$ solvent slightly favors the kinetics of the proton transfer, decreasing the energy barrier to 22.8 kcal mol$^{-1}$. In the transition state the O–H bond is completely broken (O–H = 1.581 Å) and the Mo–H bond is almost formed (Mo–H = 1.795 Å). The distance between the proton that is being transferred and the contiguous H3 hydride (1.795 Å) is too long to consider the formation of a dihydrogen ligand. Thus, even in this crowded system there is a pathway for protonating the metal, without involvement of the hydride ligands.

There is experimental evidence that the participation of a second molecule of the proton donor might be crucial for the proton transfer to transition-metal hydride by means of the so-called homoconjugate pairing effect.[8,16,27] In our previous theoretical studies, the second proton donor molecule was used to locate the gas-phase minima of the proton-

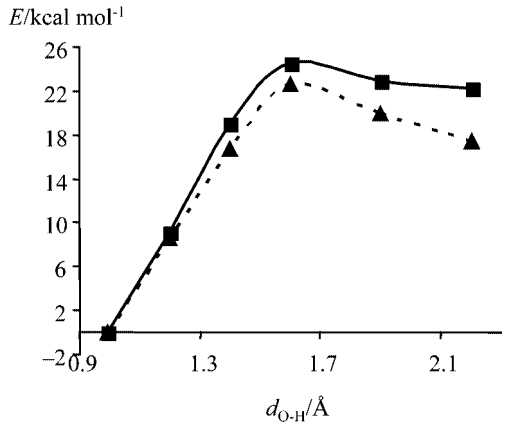


Figure 12. Potential energy curves for the proton transfer from HFIP to the Mo trihydride at the metal site. Plain curve and squares: in the gas phase; dashed line and triangles: in dichloromethane solution. The O–H length of the transferring proton has been taken as the reaction coordinate.

ated species.[15,17,18] Thus, we have also studied the proton transfer to complex $[CpMo(dpe)H_3]$ with two HFIP molecules.[15,27] The final products of the proton transfer are the ion pairs made up by the **TETRA1** or **DIH1** cations and the $[(CF_3)_2HCO\cdots HOCH(CF_3)_2]^-$ (**[XHX]**$^-$) homoconjugate anion. With the inclusion of the second AH molecule, both ion pairs give stable local minima and it is possible to study the proton-transfer process both at the metal and hydride sites. The corresponding starting points are the hydrogen-bonded adducts **C′·HFIP** and **A′·HFIP**, with a second HFIP molecule joined by a O···H hydrogen bond to the first HFIP molecule. The optimized geometries are available in the Supporting Information.

The thermodynamic viability of the proton transfer involving a second alcohol molecule [Equation (5)] is very different from the situation shown above for a single HFIP molecule. Now the reaction is clearly exothermic, by –5.2 kcal mol$^{-1}$ for the **C′**+HFIP/**TETRA1·[XHX]** couple and –3.2 kcal mol$^{-1}$ for the **A′**+HFIP/**DIH1·[XHX]** one. $\Delta G(CH_2Cl_2)$ values, although considerably decreased (–1.6 and –0.7 kcal mol$^{-1}$ for **TETRA1** and **DIH1**, respectively), suggest the thermodynamic feasibility of the reaction in dichloromethane and indicate that the equilibrium is displaced toward the right. The presence of a strong hydrogen bond in the homoconjugated pair has a substantial impact on the overall reaction energy.

$$[CpMoH_3(dpe)\cdots HOCH(CF_3)_2] + (CF_3)_2CHOH \rightarrow [CpMo(dpe)\text{“}H_4\text{”}]^+\cdot[(CF_3)_2CHO\cdots H\cdots O\text{–}CH(CF_3)_2]^- \quad (5)$$

Both reaction profiles, leading from **A′·HFIP** to **DIH1·[XHX]** and from **C′·HFIP** to **TETRA1·[XHX]**, have been investigated, both in the gas phase and in dichloromethane solvent, taking the O–H distance of the transferring proton as the reaction coordinate. The energy of the starting hydrogen-bonded adduct was taken as the zero of energy in each case. The energetic profiles are depicted in Figure 13.

 © 2006 Wiley-VCH Verlag GmbH & Co. KGaA, Weinheim 

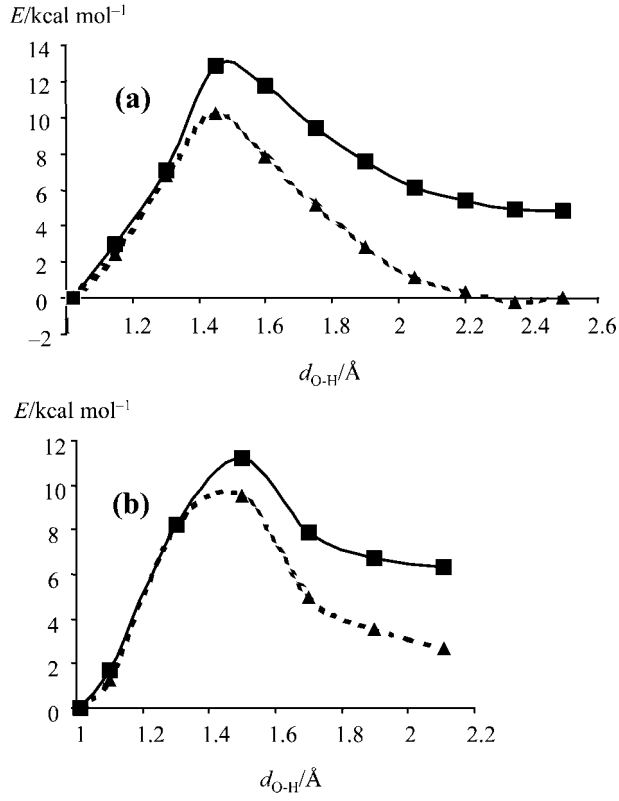


Figure 13. Potential energy curves for the proton transfer from two HFIP molecules to the Mo trihydride: (a) at the metal site; (b) at the hydride site. Plain curves and squares: in the gas phase; dashed lines and triangles: in dichloromethane solution. The O–H length of the transferring proton has been taken as the reaction coordinate.

The gas-phase barriers to form the ion pair at the hydride and the metal site are 11.2 and 12.9 kcal mol$^{-1}$, respectively. As already found with one HFIP molecule, the $CH_2Cl_2$ solvent favors the kinetics of the proton transfer, decreasing the energy barriers to 9.4 and 10.2 kcal mol$^{-1}$, respectively. The ion pairs resulting from the protonation at the hydride ([**DIH1**]$^+$·[**XHX**]$^-$) and metal site ([**TETRA1**]$^+$·[**XHX**]$^-$) are found to be 6.3 and 4.8 kcal mol$^{-1}$, respectively, above the hydrogen-bonded complexes in the gas phase, and 2.7 above and 0.3 kcal mol$^{-1}$ below, in dichloromethane. The solvent also favors the thermodynamics of the proton transfer, stabilizing the charged species to a greater extent than the initial neutral hydrogen-bonded ones. The role played by the homoconjugate pairing in the proton-transfer process can be appreciated following the evolution of the two O–H distances of the HFIP dimer throughout the protonation process. In the hydrogen-bonded initial species **A′·HFIP** and **C′·HFIP** there is a normal hydrogen bond between the oxygen atom of the first HFIP molecule and the proton of the second one. The O···O and O···H distances are 2.718 and 1.761 Å in **A′·HFIP** and 2.703 and 1.745 Å in **C′·HFIP**. The O–H bond of the second HFIP molecule is only slightly lengthened by the hydrogen bond interaction (O–H = 0.980 and 0.981 Å in **A′·HFIP** and **C′·HFIP**, respectively; the O–H distance in free HFIP is 0.968 Å). The presence of a strong [A···H···A]$^-$ hydrogen bond in the anion of the ion pair can be inferred from the shortening of the O···O distance (2.439 and 2.396 Å in [**DIH1**]$^+$·[**XHX**]$^-$ and [**TETRA1**]$^+$·[**XHX**]$^-$, respectively). The O··H distances (1.359 and 1.241 Å) and O–H–O angles (178.5 and 178.1°) also agree with a proton shared by two [**X**]$^-$ units. The acidity of the coordinated dihydrogen makes the homoconjugate anion interact more strongly with the H of the dihydrogen than with that of the tetrahydride (M–H···O distances of 2.467 and 2.493 Å in [**DIH1**]$^+$·[**XHX**]$^-$ and [**TETRA1**]$^+$·[**XHX**]$^-$, respectively). In opposition, the O···H···O interaction in the homoconjugate anion is stronger in [**TETRA1**]$^+$···[**XHX**]$^-$ than in [**DIH1**]$^+$···[**AHA**]$^-$, according to both O···O and O···H distances.

### *Dihydrogen–Dihydride → Tetrahydride Interconversion in the Ion Pair*

To solve the dichotomy between easy protonation at the hydride site and no detection of dihydrogen intermediates, we have studied the interconversion from the [**DIH1**]$^+$···[**XHX**]$^-$ to the [**TETRA1**]$^+$···[**XHX**]$^-$ ion pair. As in previous studies of dihydrogen → dihydride interconversions,[37] we have chosen the H–H distance as a reaction coordinate for the H–H bond breaking. This distance varies from 0.884 Å in the dihydrogen structure to 1.812 Å in the tetrahydride. For each fixed value of the reaction coordinate all the other geometrical parameters, including those of the homoconjugate anion, were optimized. The profiles in dichloromethane solvent were obtained from single-point calculations on each point of the gas-phase profiles with the solvent PCM. The energy of the dihydrogen ion pair was taken as the zero of energy. The energetic profiles in gas phase and $CH_2Cl_2$ are depicted in Figure 14.

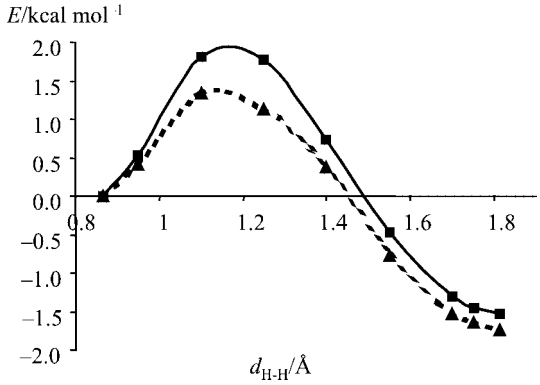


Figure 14. Potential energy curve for the interconversion from the ([**DIH1**]$^+$·[**XHX**]$^-$) to the ([**TETRA1**]$^+$·[**XHX**]$^-$) ion pairs. Plain curves and squares: in the gas phase; dashed lines and triangles: in dichloromethane solution. The H–H length of the coordinated dihydrogen has been taken as the reaction coordinate.

The calculations illustrate that the dihydrogen–dihydride → tetrahydride rearrangement in the ion pairs easily takes place. The energy barrier is only 1.8 kcal mol$^{-1}$ in gas phase and 1.3 kcal mol$^{-1}$ in $CH_2Cl_2$. The homoconjugate anion

 © 2006 Wiley-VCH Verlag GmbH & Co. KGaA, Weinheim 

does not appreciably change its position along the interconversion, as proved by the evolution of the H···O distance (from 1.359 Å in the dihydrogen structure to 1.241 Å in the tetrahydride). The process is exoergic, ending up in a tetrahydride ion pair 1.5 kcal mol$^{-1}$ more stable than the initial dihydrogen in the gas phase (–1.7 kcal mol$^{-1}$ in $CH_2Cl_2$). The solvent influence in this process is very small because it does not involve a charge change.

### *Dihydrogen Evolution*

We have theoretically studied the successive elimination of two $H_2$ molecules in the model [CpMo(dpe)$H_3$]–TFE system. The results are graphically assembled in Figure 15 and discussed only briefly here. More details can be found in the Supporting Information. The significant difference between the results in the gas phase and in $CH_2Cl_2$ can be attributed to the solvation of the free TFE molecules (note that the gap is about twice greater when both molecules have been consumed, relative to the intermediate situations where only one has been consumed). The results show that the first $H_2$ elimination, affording the [CpMo(dpe)-$H_2$($OR_F$)] intermediate (unobserved for the real system), is less favorable than the process leading to loss of two $H_2$ molecules. Note also that the $H_2$ elimination process will further benefit from an entropic drive. Furthermore, the subsequent addition of a second alcohol molecule, to afford the 18-electron adduct, results in a significant stabilization. At least part of this stabilization may be attributed to the intramolecular hydrogen bond. Thus, the calculations point to the identity of the final product as a solvated species. It is also of interest to mention that the 16-electron [CpMo-(dpe)($OR_F$)] intermediate prefers to adopt a singlet ground state (the triplet is higher in energy by 6.5 and 7.3 kcal mol$^{-1}$ in the gas phase and in solution, respectively). On the other hand, a parallel calculation on [CpMo($PMe_3$)$_2$(OH)] shows that the triplet is 2.3 kcal mol$^{-1}$ lower than the singlet, in agreement with the experimental observation or paramagnetism for this molecule.[30,31]

## Discussion

It has been shown in previous spectroscopic[14,38] and theoretical[15,17,39] studies of monohydride compounds that the MH···HX interaction weakens the MH bond (low-frequency shift for the M–H stretching vibration), whereas the HM···HX interaction strengthens it (high-frequency shift). The present contribution reports the first detailed analysis of the effect of hydrogen bonding on the M–H stretching vibrations for a polyhydride compound where the individual M–H stretching components are heavily mixed into the normal modes. The first outcome of this investigation is that the variation of the vibrational frequencies can be predicted, in most cases, by extension of the previously established trends for monohydride complexes:[12,13] normal modes whose main contribution is from M–H vibrations where the hydride is directly implicated in hydrogen bonds as a proton acceptor experience a low-frequency shift. Conversely, normal modes whose main contribution is from M–H vibrations where the hydride is not directly implicated in hydrogen bonds (either the metal center or other hydride ligands act as the proton-acceptor site) experience a low-frequency shift. However, the contribution of various M–H stretching vibrations, some of which may be proton acceptors in hydrogen bonds while others may not, in the normal modes calls for a more detailed and in-depth analysis.

Secondly, the existence, in the present case, of additional interactions with other neighboring proton-accepting sites may be the major cause of the complicated changes found, for example the changes of certain Mo–H bond lengths that are found to be opposite to expectations based on H···H distances (e.g., shortening of Mo–H2 in **B1**, lengthening of Mo–H2 in **C**). An interaction involving exclusively the metal center, without involvement of at least secondary interactions with hydride ligands, does not occur for this compound. It can be easily imagined, by extrapolation, that a direct hydrogen bond with a metal site may be difficult in general, if not impossible, when the system has a relatively

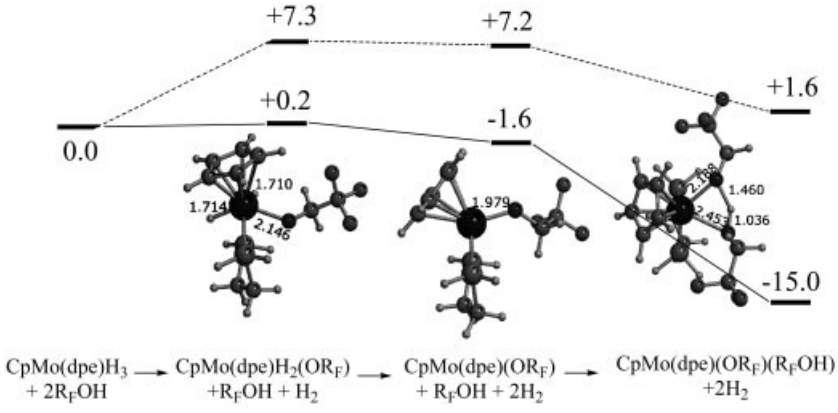


Figure 15. Computed energy profile (solid lines: gas phase; dashed lines: $CH_2Cl_2$ solution) in kcal mol$^{-1}$ for the $H_2$ elimination from complex [CpMo(dpe)$H_3$] ($R_F$OH = TFE). Full details are reported in the Supporting Information.

 © 2006 Wiley-VCH Verlag GmbH & Co. KGaA, Weinheim 

crowded coordination sphere and especially when more than one hydride ligand is present. Also, the same circumstances may favor the establishment of simultaneous interactions with more than one hydride ligand.

The computational study allows rather good reproduction of the experimentally determined hydrogen bond enthalpy for the [Cp*Mo(dppe)$H_3$]·TFE interaction by use of the [CpMo(dpe)$H_3$] model system. The calculations also indicate that the most stable hydrogen-bonded adducts between [CpMo(dpe)$H_3$] and TFE are complexes **B**, where the proton donor approaches the complex from the side of the molecule containing hydrides H1 and H2. Structure **B3**, which yields the lowest energy minimum, is also the model structure that best reproduces the experimentally observed frequency shifts: the $\nu_2$ band experiences a large low-frequency shift and appears 3 $cm^{-1}$ lower than $\nu_3$ mode in free trihydride, whereas the $\nu_3$ band experiences a large high-frequency shift, ending up near the position of the $\nu_2$ mode in free trihydride (compare Figure 8 and Figure 10). The composition of the normal modes is in agreement with this interpretation (the low-frequency band in **B3** has the major component from the Mo–H2 vibration, whereas the low-frequency band in the free trihydride is mostly a Mo–H3 vibration). The other structural models of the hydrogen-bonded adduct (**A**, **B1**, **B2**, and **C**) yield calculated normal mode frequency patterns in greater discrepancy with the experiment. In conclusion, it seems that the proton donor approaches the complex from the side of the molecule containing the hydrides H1 and H2, and establishes a hydrogen bond with the hydride H2.

One interesting issue for proton-transfer reactions to hydride molecules is the number of proton donor molecules that are involved in proton transfer. Although the involvement of only one molecule should be sufficient in principle, it has been shown in several cases that the protonation product contains the homoconjugate anion, therefore implicating two proton donor molecules in the reaction stoichiometry.[8,16,17] It was also shown by kinetics investigations that a second proton donor molecule is necessary to trigger proton transfer from fluorinated alcohols to the hydride complex [Cp*Fe(dppe)H].[15,27] On the other hand, when the stronger acid $CF_3COOH$ was used with the same hydride system, even a single acid molecule was sufficient to transfer the proton. Theoretical calculations have also shown that the involvement of a second proton donor (HX) molecule strengthens hydrogen bonding of the first HA molecule with the proton acceptor in the MH···HX···HX adduct.

The basicity of the hydride ligand of Cp*$MoH_3$(dppe) ($E_j = 1.42 \pm 0.02$) is higher than that of trihydride complexes studied previously [compare with $E_j$ of 0.93 for $Cp_2NbH_3$[18] and 0.94 for Cp*$RuH_3(PCy_3)$][40] and is among the highest reported in the literature.[13] Consequently, it can be protonated by such a weak acid as TFE. Two separate experiments on the proton-transfer process indicate that complex Cp*$MoH_3$(dppe) is able to accept a proton from a *single* molecule of proton donor, at least from donors as weak as HFIP. The UV/Vis study of the Cp*$MoH_3$(dppe)–PNP ($P_i = 1.27$) interaction shows a breakpoint at a 1:1 ratio and a visible band consistent with the formation of the [Cp*(dppe)$MoH_4$]$^+$···[OAr]$^-$ ion pair. On the other hand, the kinetic study of the Cp*$MoH_3$(dppe)–HFIP ($P_i = 1.05$) interaction illustrates the need for only one HFIP molecule to reach the transition state for proton transfer. This situation markedly differs from that previously established for the protonation of the less basic hydride ligand in complex [Cp*Fe(dppe)H] ($E_j = 1.35 \pm 0.02$), where a second molecule is necessary.[27] Interestingly, the formation of hydrogen-bonded ion pairs is not only evident from the UV/Vis study of the Cp*$MoH_3$(dppe)–PNP system, but also from the $^1$H NMR spectroscopic data through the different $T_1$ values obtained for the TFE and $HBF_4$ protonation products (Table 2), although the latter result cannot distinguish between the simple ($X^-$) and the homoconjugate ($XHX^-$) anion.

The low-temperature NMR study does not show any evidence for the formation of a dihydrogen intermediate, whereas the low-temperature IR study suggests that the preferred hydrogen-bonding pathway involves the hydride ligand. Thus, an intermediate dihydrogen complex along the proton-transfer pathway may be expected. The computational investigation suggests that, both in gas phase and in dichloromethane, the tetrahydride ion pair resulting from the protonation at the metal site is more stable than the dihydrogen–dihydride ion pair arising from the hydride protonation, in agreement with the experiment. Both proton-transfer pathways leading to hydride and metal protonation show low barriers, in agreement with the experimental evidence of a very fast process. However, these values are rather similar (9.4 and 10.2 kcal mol$^{-1}$ for proton transfer from the HFIP dimer in $CH_2Cl_2$), indicating that in this molybdenum trihydride there is no clear kinetic preference for the protonation at the hydride site. This theoretical result contrasts with the commonly admitted kinetic preference for the protonation at the hydride site, and with a recent theoretical study of the protonation of CpFe(dpe)H with two HFIP molecules.[15]

If the nonclassical intermediate indeed forms during the proton-transfer process, its activation barrier to the rearrangement leading to the classical tetrahydride product must be very low. Indeed, a very low barrier for the rearrangement of the model compounds ([**DIH1**]$^+$···[**XHX**]$^-$ to [**TETRA1**]$^+$···[**XHX**]$^-$ where HX = HFIP) is shown by the calculations. Note that this rearrangement does not necessitate any ion pair dissociation, as the anion does not appreciably change its position along the interconversion.

To summarize, the tetrahydride product can originate either from the direct protonation at the metal site or from the fast isomerization of the dihydrogen intermediate and the available experimental and theoretical results do not allow us to clearly distinguish these two possibilities. The involvement of a transient dihydrogen species in the formation of trihydride by protonation of a transition-metal dihydride has been reported in a mechanistic study of the protonation of $Cp_2MH_2$ (M = Mo, W) by an excess of anhydrous HCl.[41]

 © 2006 Wiley-VCH Verlag GmbH & Co. KGaA, Weinheim 

## Conclusions

The unambiguous determination of the hydrogen-bonding site for a polyhydride compound by NMR and IR spectroscopic techniques is not an easy task. The high fluxionality of polyhydride complexes on the NMR timescale renders the application of this method less straightforward, while the use of vibrational spectroscopy is complicated by the normal mode structure and weak intensity of the M–H stretching bands. The theoretical analysis of the vibrational modes, which was performed here for the first time for a transition-metal polyhydride compound in the absence and presence of hydrogen bonding, shows a different behavior for each M–H vibrational normal mode. Nevertheless, the evolution of the vibrational frequencies follows in most cases the trends previously established for monohydride complexes: a low-frequency shift for modes that primarily involve the M–H vibrations where the H ligand is implicated in the hydrogen bond and a high-frequency shift for modes that primarily involve M–H vibrations where the H ligand is not implicated in the hydrogen bond (hydrogen bonding to other hydride ligands or to the metal atom). According to the calculations the most stable hydrogen-bonded adducts are those where the proton donor approaches the $Cp^*MoH_3(dppe)$ complex from the side of the molecule containing the hydrides H1 and H2. Of these, the one giving good agreement with the experimental IR observations features a hydrogen bond with H2.

Dihydrogen bond formation precedes the proton transfer to form the cationic tetrahydride $[Cp^*(dppe)MoH_4]^+$ complex, stabilized by hydrogen bonding to the proton donor conjugate base. This is reversible at low temperatures (below 250 K) when using *p*-nitrophenol or TFE. The precursor $Cp^*(dppe)MoH_3$ complex is sufficiently basic to accept the proton from a single molecule of these two proton donors.

The experiments do not show any direct evidence for the formation of a dihydrogen intermediate, whereas the preferred hydrogen-bonding pathway, according to the computational study, appears to involve the hydride ligand. The intermediacy of a dihydrogen complex along the proton-transfer pathway is possible, as suggested by the computations. However, the calculated low barrier for its isomerization into the classical tetrahydride complex would rationalize our inability to observe it experimentally.

## Experimental Section

**General:** All manipulations were carried out under argon by standard Schlenk techniques. The $[Cp^*Mo(dppe)H_3]$ hydride was synthesized according to the literature.[19] All solvents used ($CH_2Cl_2$, THF, toluene) were dried using appropriate agents and freshly distilled prior to use.

**IR and UV/Vis Investigations:** IR measurements were performed on "Specord M82" and Infralum FTIR-81 (Lumex) spectrometers using $CaF_2$ cells (0.12 cm path length). In order to limit the significance of self-association phenomena, a concentration of the proton donor between 0.005 and 0.01 M was used for the ν(OH) measurements. The UV measurements were performed on Specord M-40 and Varian Cary 5 spectrophotometers. Low-temperature IR and UV measurements were carried out by use of a cryostat (Carl Zeiss Jena) in the 200–290 K temperature range. The accuracy of the temperature adjustment was ±0.5 K. The reagents were mixed at low temperature and the cold mixtures were subsequently transferred into the precooled cryostat.

**NMR Investigations:** NMR studies were carried out in standard 5-mm NMR tubes containing solutions of the complexes in $CD_2Cl_2$. $^1H$ and $^{31}P$ NMR spectroscopic data were collected with a Bruker AMX 400 spectrometer operating at 400.13 and 161.98 MHz, respectively. The conventional inversion-recovery-pulse method (180-τ-90) was used to determine the variable-temperature longitudinal relaxation time $T_1$. Low-temperature experiments were carried out in the 180–260 K temperature range using a TV-3000 Bruker temperature control unit. The accuracy and stability of temperature was ±1 K. All mixings between the alcohols and the hydride complexes were performed at low temperature.

**Stopped-Flow Investigations:** The stopped-flow kinetic runs were carried out at 293 K with a Bio-Logic SF20 apparatus coupled to a J&M TIDAS MMS-UV/Vis diode-array UV/Vis spectrophotometer using a cuvette with a 0.15-cm pathlength. The data were collected within the first 10 s, yielding reproducible results. Data analyses were carried out by using the SPECFIT3 global analysis package of programs.[42] At least three runs were averaged to yield the reported results.

**Computational Details:** Calculations were performed with the Gaussian98[43] package at the DFT/B3LYP level.[44–46] Effective core potentials (ECP) were used to represent the innermost electrons of the molybdenum atom as well as the electron core of phosphorus atoms.[47,48] The basis set for the Mo and P atoms was that associated with the pseudopotential,[47,48] with a standard double-ζ LANL2DZ contraction,[43] supplemented in the case of P with a set of d-polarization functions.[49] The carbon and hydrogen atoms of the transition-metal complexes that are not bonded to the metal atom, together with the atoms of proton donor molecules (C, F, H) that are not involved in hydrogen bonds, were described with a 6-31G basis set.[50] The carbon and hydrogen atoms directly bonded to the metal and the proton donor molecules' hydrogen and oxygen atoms involved in hydrogen bonding were described with a 6-31G(d,p) set of basis functions.[51] Geometry optimizations were carried out without symmetry restrictions and the resulting structures were characterized as minima by the real value of all 3N-6 vibrational frequencies. Solvent effects were taken into account by means of polarized continuum model (PCM) calculations,[52,53] using standard options.[43] The solvation free energies were computed in dichloromethane ($\varepsilon = 8.93$) at the gas-phase optimized geometries. The gas-phase complexation energies were corrected from the BSSE according to the counterpoise method of Boys and Bernardi.[54]

**Supporting Information** (for details see the footnote on the first page of this article): Table of optimized geometrical parameters for $[CpMo(dpe)H_3]$ and $[CpMo(dpe)H_4]^+$ complexes, views of optimized $[Cp^*Mo(dppe)H_3]$, $[Cp^*Mo(dppe)H_4]^+$, a variety of dihydrogen-bonded adducts, and a description of computational results on the $H_2$ elimination process from $[CpMo(dpe)H_4]^+$ (7 pages).

## Acknowledgments

We thank the European Commission through the HYDROCHEM program (contract HPRN-CT-2002-00176) for support of this work. Additional bilateral support (PICS, France–Russia) and national support from the CNRS (France), the RFBR

 © 2006 Wiley-VCH Verlag GmbH & Co. KGaA, Weinheim 

(05-03-22001, 05-03-32415), and the Division of Chemistry and Material Sciences of RAS (Russia), and from MEC (project CTQ2005-09000-CO2-01; Spain) is also gratefully acknowledged. A.L. thanks the Generalitat de Catalunya for a Distinció per a la Promocio de la Recerca Universitària. N.B. thanks the Russian Science Support Foundation for an individual grant. M.B. thanks the Spanish Ministerio de Educación y Ciencia for a post-doctoral fellowship.

[1] M. Peruzzini, R. Poli, *Recent Advances in Hydride Chemistry*, Elsevier, Amsterdam, **2001**.
[2] V. I. Bakhmutov, *Eur. J. Inorg. Chem.* **2005**, 245–255.
[3] G. Parkin, J. E. Bercaw, *J. Chem. Soc., Chem. Commun.* **1989**, 255–257.
[4] M. S. Chinn, D. M. Heinekey, *J. Am. Chem. Soc.* **1990**, *112*, 5166–5175.
[5] G. Jia, A. J. Lough, R. H. Morris, *Organometallics* **1992**, *11*, 161–171.
[6] P. Hamon, L. Toupet, J.-R. Hamon, C. Lapinte, *Organometallics* **1992**, *11*, 1429–1431.
[7] J. R. Hamon, P. Hamon, L. Toupet, K. Costuas, J. Y. Saillard, *C. R. Chim.* **2002**, *5*, 89–98.
[8] E. T. Papish, F. C. Rix, N. Spetseris, J. R. Norton, R. D. Williams, *J. Am. Chem. Soc.* **2000**, *122*, 12235–12242.
[9] E. T. Papish, M. P. Magee, J. R. Norton, in *Recent Advances in Hydride Chemistry* (Eds.: M. Peruzzini, R. Poli), Elsevier, Amsterdam, **2001**, pp. 39–74.
[10] E. S. Shubina, A. N. Krylov, N. V. Belkova, L. M. Epstein, A. P. Borisov, V. D. Mahaev, *J. Organomet. Chem.* **1995**, *493*, 275–277.
[11] A. Albinati, V. I. Bakhmutov, N. V. Belkova, C. Bianchini, I. De Los Rios, L. Epstein, E. I. Gutsul, L. Marvelli, M. Peruzzini, R. Rossi, E. S. Shubina, E. V. Vorontsov, F. Zanobini, *Eur. J. Inorg. Chem.* **2002**, 1530–1539.
[12] L. M. Epstein, N. V. Belkova, E. S. Shubina, in *Recent Advances in Hydride Chemistry* (Eds.: M. Peruzzini, R. Poli), Elsevier, Amsterdam, **2001**, pp. 391–418.
[13] L. M. Epstein, E. S. Shubina, *Coord. Chem. Rev.* **2002**, *231*, 165–181.
[14] N. V. Belkova, E. S. Shubina, L. M. Epstein, *Acc. Chem. Res.* **2005**, *38*, 624–631.
[15] N. V. Belkova, E. Collange, P. Dub, L. M. Epstein, D. A. Lemenovskii, A. Lledós, O. Maresca, F. Maseras, R. Poli, P. O. Revin, E. S. Shubina, E. V. Vorontsov, *Chem. Eur. J.* **2005**, *11*, 873–888.
[16] N. V. Belkova, A. V. Ionidis, L. M. Epstein, E. S. Shubina, S. Gruendemann, N. S. Golubev, H. H. Limbach, *Eur. J. Inorg. Chem.* **2001**, 1753–1761.
[17] N. Belkova, M. Besora, L. Epstein, A. Lledós, F. Maseras, E. Shubina, *J. Am. Chem. Soc.* **2003**, *125*, 7715–7725.
[18] E. Bakhmutova, V. Bakhmutov, N. Belkova, M. Besora, L. Epstein, A. Lledós, G. Nikonov, E. Shubina, J. Tomas, E. Vorontsov, *Chem. Eur. J.* **2004**, *10*, 661–671.
[19] B. Pleune, R. Poli, J. C. Fettinger, *Organometallics* **1997**, *16*, 1581–1594.
[20] J. C. Fettinger, B. Pleune, R. Poli, *J. Am. Chem. Soc.* **1996**, *118*, 4906–4907.
[21] J. Andrieu, N. V. Belkova, M. Besora, E. Collange, L. M. Epstein, A. Lledós, R. Poli, P. O. Revin, E. S. Shubina, E. V. Vorontsov, *Russ. Chem. Bull.* **2003**, *52*, 2679–2682.
[22] J. Andrieu, N. V. Belkova, M. Besora, E. Collange, L. M. Epstein, A. Lledós, R. Poli, P. O. Revin, E. S. Shubina, E. V. Vorontsov, paper to be published.
[23] E. Gutsul, N. Belkova, M. Sverdlov, L. Epstein, E. Shubina, V. Bakhmutov, T. Gribanova, R. Minyaev, C. Bianchini, M. Peruzzini, F. Zanobini, *Chem. Eur. J.* **2003**, *9*, 2219–2228.
[24] R. B. Girling, P. Grebenik, R. N. Perutz, *Inorg. Chem.* **1986**, *25*, 31–36.
[25] R. H. Crabtree, D. G. Hamilton, *Adv. Organomet. Chem.* **1988**, *28*, 299–338.
[26] E. I. Gutsul, N. V. Belkova, G. M. Babakhina, L. M. Epstein, E. S. Shubina, C. Bianchini, M. Peruzzini, F. Zanobini, *Russ. Chem. Bull.* **2003**, *52*, 1204–1206.
[27] N. V. Belkova, P. O. Revin, L. M. Epstein, E. V. Vorontsov, V. I. Bakhmutov, E. S. Shubina, E. Collange, R. Poli, *J. Am. Chem. Soc.* **2003**, *125*, 11106–11115.
[28] M. Luksza, S. Kimmer, W. Malisch, *Angew. Chem. Int. Ed. Engl.* **1983**, *22*, 416–417.
[29] R. T. Baker, J. C. Calabrese, R. L. Harlow, I. D. Williams, *Organometallics* **1993**, *12*, 830–841.
[30] R. Poli, E. A. Quadrelli, *New J. Chem.* **1998**, *22*, 435–450.
[31] J. C. Fettinger, H.-B. Kraatz, R. Poli, E. A. Quadrelli, *Chem. Commun.* **1997**, 889–890.
[32] T. J. Johnson, A. Albinati, T. F. Koetzle, J. Ricci, O. Eisenstein, J. C. Huffman, K. G. Caulton, *Inorg. Chem.* **1994**, *33*, 4966–4976.
[33] F. Maseras, A. Lledós, M. Costas, J. M. Poblet, *Organometallics* **1996**, *15*, 2947–2953.
[34] A. V. Iogansen, *Theor. Exp. Chem.* **1971**, *7*, 312–317.
[35] A. V. Iogansen, *Spectrochim. Acta, Part A* **1999**, *55*, 1585–1612.
[36] M. H. Baik, R. A. Friesner, *J. Phys. Chem. A* **2002**, *106*, 7407–7412.
[37] J. Tomàs, A. Lledós, Y. Jean, *Organometallics* **1998**, *17*, 4932–4939.
[38] L. M. Epstein, N. V. Belkova, E. I. Gutsul, E. S. Shubina, *Pol. J. Chem.* **2003**, *77*, 1371–1383.
[39] G. Orlova, S. Scheiner, *J. Phys. Chem. A* **1998**, *102*, 260–269.
[40] N. V. Belkova, L. Epstein, E. S. Shubina, unpublished observations.
[41] R. A. Henderson, K. E. Oglieve, *J. Chem. Soc., Dalton Trans.* **1993**, 3431–3439.
[42] R. A. Binstead, A. D. Zuberbühler, B. Jung, *Specfit/32 v. 3.0.36*, Spectrum Software Associates, Chapel Hill, NC, **2004**.
[43] M. J. Frisch, G. W. Trucks, H. B. Schlegel, G. E. Scuseria, M. A. Robb, J. R. Cheeseman, V. G. Zakrzewski, J. A. Montgomery Jr, R. E. Stratmann, J. C. Burant, S. Dapprich, J. M. Millam, A. D. Daniels, K. N. Kudin, M. C. Strain, O. Farkas, J. Tomasi, V. Barone, M. Cossi, R. Cammi, B. Mennucci, C. Pomelli, C. Adamo, S. Clifford, J. Ochterski, G. A. Petersson, P. Y. Ayala, Q. Cui, K. Morokuma, D. K. Malick, A. D. Rabuck, K. Raghavachari, J. B. Foresman, J. Cioslowski, J. V. Ortiz, A. G. Baboul, B. B. Stefanov, G. Liu, A. Liashenko, P. Piskorz, I. Komaromi, R. Gomperts, R. L. Martin, D. J. Fox, T. Keith, M. A. Al-Laham, C. Y. Peng, A. Nanayakkara, C. Gonzalez, M. Challacombe, P. M. W. Gill, B. Johnson, W. Chen, M. W. Wong, J. L. Andres, C. Gonzalez, M. Head-Gordon, E. S. Replogle, J. A. Pople, *Gaussian 98, Revision A.9*, Gaussian, Inc., Pittsburgh PA, **1998**.
[44] C. T. Lee, W. T. Yang, R. G. Parr, *Phys. Rev. B: Condens. Matter* **1988**, *37*, 785–789.
[45] A. D. Becke, *J. Chem. Phys.* **1993**, *98*, 5648–5652.
[46] P. Stephens, F. Devlin, C. Chabalowski, M. Frisch, *J. Phys. Chem.* **1994**, *98*, 11623–11627.
[47] W. R. Wadt, P. J. Hay, *J. Chem. Phys.* **1985**, *82*, 284–298.
[48] P. J. Hay, W. R. Wadt, *J. Chem. Phys.* **1985**, *82*, 299–310.
[49] A. Höllwarth, M. Bohme, S. Dapprich, A. Ehlers, A. Gobbi, V. Jonas, K. Kohler, R. Stegmann, A. Veldkamp, G. Frenking, *Chem. Phys. Lett.* **1993**, *208*, 237–240.
[50] W. Hehre, R. Ditchfie, J. Pople, *J. Chem. Phys.* **1972**, *56*, 2257–2261.
[51] P. Harihara, J. Pople, *Theor. Chim. Acta* **1973**, *28*, 213–222.
[52] J. Tomasi, M. Persico, *Chem. Rev.* **1994**, *94*, 2027–2094.
[53] C. Amovilli, V. Barone, R. Cammi, E. Cancès, M. Cossi, B. Menucci, C. S. Pomelli, J. Tomasi, *Adv. Quantum Chem.* **1998**, *32*, 227–261.
[54] S. F. Boys, F. Bernardi, *Mol. Phys.* **1970**, *19*, 553–566.

Received: February 2, 2006
Published Online: March 31, 2006

 © 2006 Wiley-VCH Verlag GmbH & Co. KGaA, Weinheim 

DOI: 10.1002/ejic.200600100

# Azide–Tetrazole Ring-Chain Isomerism in Polyazido-1,3,5-triazines, Triazido-*s*-heptazine, and Diazidotetrazines

**Anton Hammerl,[a] Thomas M. Klapötke,*[a] and Reginaldo Rocha[b]**

**Keywords:** ab initio calculations / Nitrogen heterocycles / Azides / Nitrogen

The azide–tetrazole isomerism in several polyazido-1,3,5-triazines, triazido-*sym*-heptazine, and some diazido-1,2,4,5-tetrazines was investigated by ab initio quantum chemical methods in order to determine whether the polyazides are suitable starting materials for the synthesis of the isomeric tetrazoles. The effects of solvation in $CCl_4$, DMSO and water on this isomerism were included using the self consistent reaction field (SCRF) method. The effect of amino- and nitro-substituents on the azide–tetrazole isomerism was also examined. In the gas phase all investigated polyazidoheterocycles do not cyclize to form tetrazoles. An electron-donating amino group favors the ring closure to tetrazoles, whereas an electron-withdrawing nitro group favors the azides. Solvation in polar solvents favors the formation of a tetrazole ring system due to higher charge separation in the tetrazole ring system, but for all polyazido-1,3,5-triazines, including triazido-*s*-heptazine, the effects of solvation are not strong enough to shift the equilibrium to the tetrazole side, which explains why several attempts to detect these compounds have failed. The monotetetrazoles of diazidotetrazine and bis(azido)azo-1,2,4,5-tetrazine and the ditetrazole of bis(azido)hydrazo-1,2,4,5-tetrazine are the minimum energy species in DMSO and water. Thus we predict that the diazidoazo- and hydrazotetrazines will readily cyclize to the tetrazoles in polar solvents.

(© Wiley-VCH Verlag GmbH & Co. KGaA, 69451 Weinheim, Germany, 2006)

## Introduction

In recent years nitrogen-rich azidoheterocycles have been investigated as potential high energy density materials[1] and as precursors for carbon nitrides. Their clean and thermodynamically favorable decomposition, where only $N_2$ is released, makes them good precursors for nitrogen rich carbon nitrides, whose application is not only governed by texture and size of the particles,[2] but also by the relative nitrogen content. Nitrogen-rich carbon nitrides with the bulk formulas $C_3N_4$ and $C_3N_5$ have been prepared from cyanuric azide[3] as well as bis(azido)-1,2,4,5-tetrazine[4] and nitrides with the formulas $C_2N_3$ and $C_3N_5$ have been prepared from tetra(azido)azo-1,3,5-triazine.[5] Unfortunately, all described polyazides are very sensitive toward shock and friction and are classified as primary explosives. This makes the handling of these substances, especially in the amounts needed for commercial purposes, very difficult. The isomeric tetrazoles,[6] which are formed by an 1,5-dipolar cyclization[7] of the polyazides, are potential replacements for the hazardous polyazides. Even though we know of no precise data comparing the sensitivity of an azide to its isomeric tetrazole, the aromatic tetrazoles are, in general, less sensitive toward shock or friction than covalent azides. The nature of $R^1$ and $R^2$ determines whether the azide or the tetrazole isomer is dominant or whether both compounds are in equilibrium.[8] The open-ring azidoimine form is favored by electron-withdrawing groups and the tetrazole form is favored in the presence of electron-donating groups.[9] A wide series of fluoroalkyl-substituted imidoazyl azides is known that do not form a tetrazole.[10]

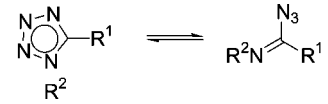

A key prerequisite for this cyclization is a *cis* orientation of the imino lone pair and the azide group. Therefore, electron-rich imidoazyl azides without the required conformation do not cyclize easily to the tetrazoles. Higher temperatures may help to overcome the activation barrier for tetrazole formation,[11] but higher temperatures generally favor the azide form.[12,13]

A decrease of solvent polarity shifts the equilibrium towards the azide form.[14] In the gas phase the reaction from the tetrazoles to the azides is exothermic.[15] Other reports indicate that the ring opening of the tetrazoles in the solid phase is endothermic.[16–18]

[a] Department Chemie, Ludwig-Maximilians Universität München,
Butenandtstr. 5–13 (D), 81377 München, Germany
Fax: +49-89-218077492
E-mail: anton.hammerl@cup.uni-muenchen.de
thomas.m.klapoetke@cup.uni-muenchen.de
[b] Dynamic Experimentation Division DX-2, Materials Dynamics, MS C920, Los Alamos National Laboratories,
Los Alamos, New Mexico 87545
E-mail: rcrocha@lanl.gov

Supporting information for this article is available on the WWW under http://www.eurjic.org or from the author.

 © 2006 Wiley-VCH Verlag GmbH & Co. KGaA, Weinheim 

In this investigation we address several points regarding the azide–tetrazole isomerism of the polyazidoheterocycles shown in Figure 1. Earlier investigations of the azide–tetrazole isomerism of cyanuric azide showed that the azide groups of cyanuric azide do not cyclize to form tetrazoles, but that the reaction of cyanuric acid with $PPh_3$ leads to triphenylphosphanimino compounds where an azide group is in equilibrium with the ring-closed tetrazole in solution and a tetrazole is formed upon precipitation.[19,20] While no tetrazole formed from a polyazido-1,3,5-triazine has yet been detected, the mono- and ditetrazoles of diazido-1,2,4,5-tetrazine were synthesized only very recently.[21] In order to better understand the effects of electron-donating and electron-withdrawing groups on the azide–tetrazole equilibrium of cyanuric azide, we replaced one azide group with an amino and a nitro group, respectively. We also investigated the recently synthesized azo- and hydrazo-bridged dimers[5,22] of bis(azido)-1,3,5-triazine as well as triazido-*s*-heptazine.[23] The same calculations were also performed for several polyazido-1,2,4,5-tetrazines: bis(azido)-tetrazine[4] and the yet unknown azo- and hydrazo- bridged dimers of azidotetrazine.

The differences in electronic energy in the gas phase were used to determine the favored side of the equilibrium in the gas phase. In order to understand the favorization of the azides at higher temperatures, the entropies of the involved species were compared.

The Mulliken charges of the molecules were analyzed to understand the effect of different solvent polarities. Three different continuum environments with the characteristics of $CCl_4$, DMSO, and water were calculated using the polarized continuum model to explore the influence of increasing

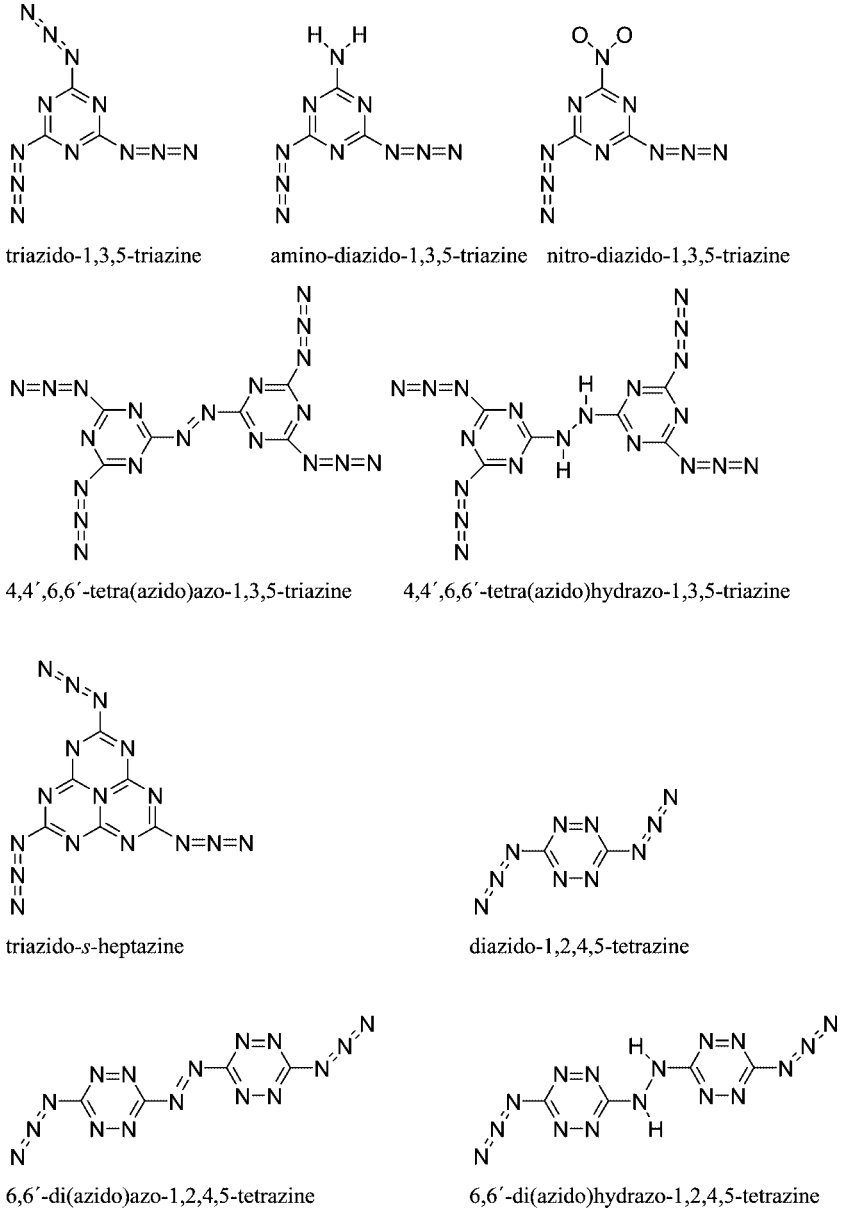


Figure 1. Investigated polyazidoheterocycles.

 © 2006 Wiley-VCH Verlag GmbH & Co. KGaA, Weinheim 

the dielectric permittivity on the potential energy of the investigated compounds.

## Results and Discussion

The azide groups of the discussed compounds can rotate along the C–N σ bond. Scheme 1 shows the energy profile of the rotation of an azide group around the C–N single bond determined by single point energy calculations in 15° intervals. The azide groups prefer a planar configuration with a slight energy difference between the two possible planar configurations. The rotation profiles of the azo-bridged compounds show a slightly higher activation energy for a 180° rotation than for the hydrazo-bridged dimers.

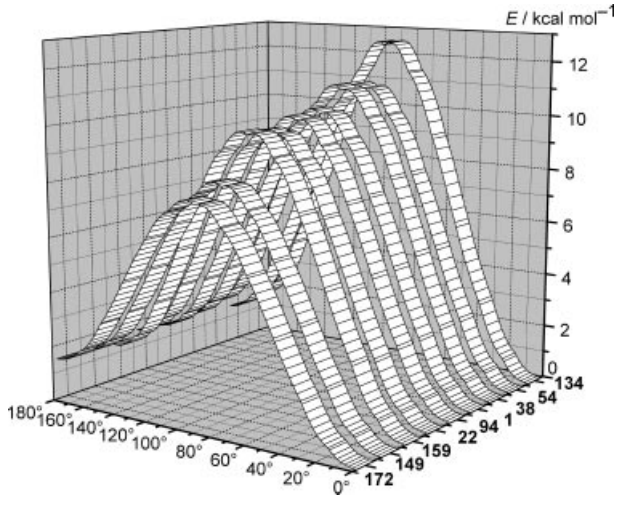


Scheme 1. Energy profile for the rotation of an azide group around the $N_\alpha$–$C_{aryl}$ σ bond at the MP2 level. Single point energy calculations were performed at 15° intervals.

The minimum energy conformations for cyanuric azide and triazido-*s*-heptazine are the $C_{3h}$ isomers **1** and **134**. The global minima **22** and **38** of amino- and nitro-1,3,5-triazine are derived from this structure by replacing one azide group with the respective substituent. The minimum energy structures **54** and **94** of the azo- and hydrazo-bridged dimers of bis(azido)-1,3,5-triazine are dimers of **1**. The global minimum for bis(azido)tetrazine is the $C_{2h}$ conformer **149**. The global minima **159** and **172** of the azo- and hydrazo-bridged dimers of azidotetrazine also have a *trans* alignment of the azido groups.

### Triazido-1,3,5-triazine (Cyanuric Azide)

Structures for all planar isomers and their possible intermediates for all three cyclization steps of cyanuric azide were calculated (Scheme 1). The calculated bonding parameters of **1** (see Supporting Information) are in good agreement with structural data.[19] The $N_\beta$–$N_\gamma$ and bonding distances of the azide unit and the carbon–nitrogen bond of the azide unit are longer than in the X-ray structure.

Two series of rotamers are formed based on the successive cyclization of the isomers **1** and **9**. The minimum energy reaction path (Scheme 2) is formed by cyclization of the $C_{3h}$ isomer **1**, the less symmetric isomer **9** is about 0.5 kcal mol$^{-1}$ higher in energy.

The energy difference calculated at the CCSD(T) level of theory are in good agreement with previously calculated values at the B3LYP level of theory (Table 1).[20] The MP2 energy differences are higher than the CCSD(T) values and increase for isomers with more tetrazole rings. The energy differences between the MP2 and CCSD(T) values are bigger for the transition states than for the ground states. At the CCSD(T) level, isomer **3** with one tetrazole ring system is 11.1 kcal mol$^{-1}$ higher in energy than the triazide **1**, the ditetrazole **6** is 7.9 kcal mol$^{-1}$ higher in energy than **3** and the tritetrazole **8** is 9.7 kcal mol$^{-1}$ higher in energy than the ditetrazole **6**. The formation of the first tetrazole ring system has a CCSD(T) activation energy of 23.8 kcal mol$^{-1}$, the second cyclization requires an activation energy of 21.0 kcal mol$^{-1}$ and the third cyclization requires an activation energy of 22.4 kcal mol$^{-1}$ based on the respective azides. This shows that the formation of the first tetrazole ring system requires the most energy and consecutive ring formations are slightly easier.

The entropies slightly favor the azides over the ring-closed isomers. The entropy decreases with an increasing amount for every ring closure, in agreement with the loss of degrees of freedom upon cyclization. According to the equation $\Delta G = \Delta H - T\Delta S$ a temperature increase would therefore shift the equilibrium from the tetrazole to the azide in the long run. The slight entropy difference allow the use of heat to overcome the activation barrier for the formation of a tetrazole, but at higher temperatures the entropy favors the azides.

The sum of the positive and negative Mulliken charges is higher for the azide than for the tetrazole compounds (see Supporting Information). The individual charges of the atoms are higher in the tetrazoles. The positive charge is spread over more atoms in the azides. In the tetrazoles generally only the carbon atoms retain positive charges while in the azides the azide $N_\beta$ atom is also positively charged. The charge in the tetrazoles is concentrated in the five-membered aromatic ring system, while in the azides the $N_\alpha$ and $N_\beta$ atoms also retain a significant charge. The higher individual charges in the tetrazoles can be stabilized by more polar solvents, thus shifting the azide–tetrazole equilibrium to the tetrazole side. This explains the experimentally observed shift to the azide compounds with a decreasing solvent polarity, which was observed for example for thiazole[3,2-*d*]tetrazole[15] and diazidotetrazine.[21]

The PCM calculations for $CCl_4$, DMSO, and water also indicate that more polar solvents favor the tetrazoles. The ground states are influenced more by solvation than the ground states. Solvation in $CCl_4$ favors the monotetrazole **3** by 3.9 kcal mol$^{-1}$, the ditetrazole **6** by 6.5 kcal mol$^{-1}$ and the tritetrazole **8** by 8.1 kcal mol$^{-1}$. The activation energy for the first cyclization is only slightly favored by 0.6 kcal mol$^{-1}$, the activation energy for the second cyclization is favored by 3.7 kcal mol$^{-1}$ and the activation energy for the third cyclization is favored by 6.0 kcal mol$^{-1}$ over the

 © 2006 Wiley-VCH Verlag GmbH & Co. KGaA, Weinheim 

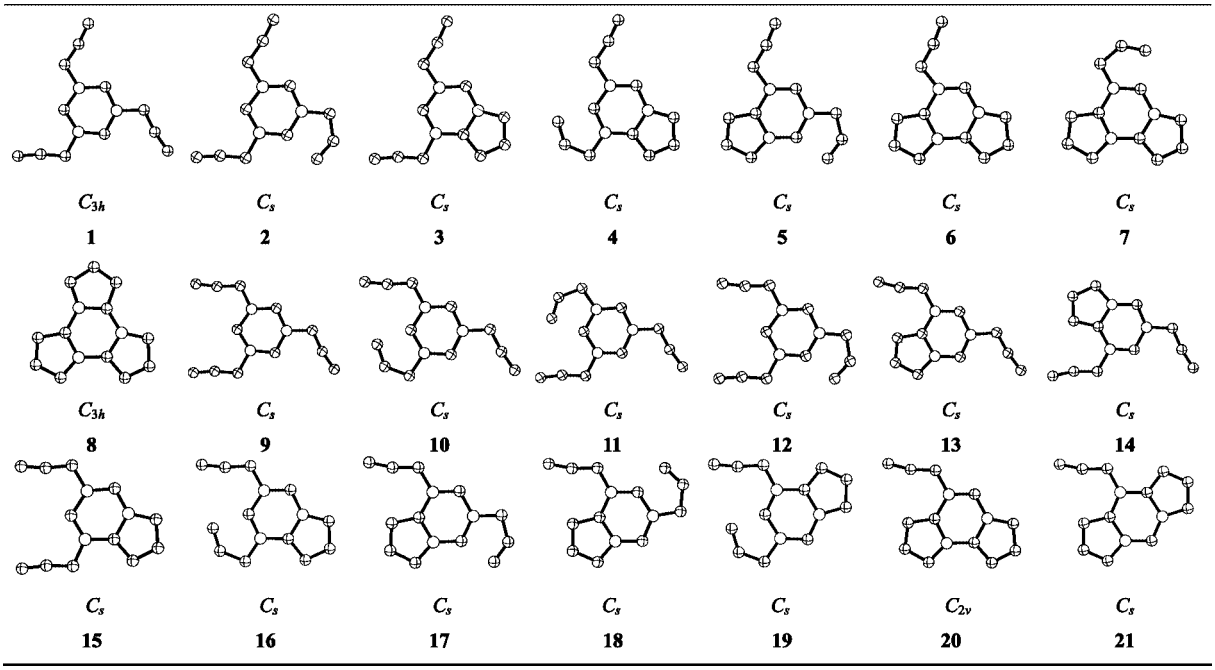


Scheme 2. Calculated triazido-1,3,5-triazine isomers.

Table 1. Calculated energy differences between different triazido-1,3,5-triazine isomers. The gas-phase values include zero point energy corrections. The PCM values represent the differences in free energy of the various species.

| | **1** | **2** | **3** | **4** | **5** | **6** | **7** | **8** | **9** | **10** | **11** |
|---|---|---|---|---|---|---|---|---|---|---|---|
| $E_{rel}$ (B3LYP/6-31G(d)) / kcal mol$^{-1}$ | 0 | 24.0 | 10.6 | 32.5 | 34.1 | 18.5 | 41.8 | 29.3 | 0.5 | – | – |
| $E_{rel}$ (MP2) / kcal mol$^{-1}$ | 0 | 33.4 | 14.5 | 44.3 | 46.3 | 25.4 | 56.5 | 38.2 | 0.3 | 34.4 | 35.2 |
| $E_{rel}$ (CCSD(T)) / kcal mol$^{-1}$ | 0 | 23.8 | 11.1 | 32.1 | 33.7 | 19.0 | 41.4 | 28.7 | 0.5 | 25.0 | 25.7 |
| $S$ / cal mol$^{-1}$ K$^{-1}$ | 108.5 | 105.8 | 105.2 | 100.2 | 100.4 | 99.9 | 95.0 | 92.7 | 110.7 | 105.6 | 105.7 |
| $E_{rel}$ (MP2) / kcal mol$^{-1}$ PCM $H_2O$ | 0 | 32.2 | 7.1 | 37.4 | 39.2 | 13.2 | 45.4 | 22.7 | 0.1 | 32.4 | 32.7 |
| $E_{rel}$ (MP2) / kcal mol$^{-1}$ PCM DMSO | 0 | 32.2 | 7.6 | 37.5 | 40.6 | 13.5 | 45.7 | 23.3 | 0 | 32.3 | 32.7 |
| $E_{rel}$ (MP2) / kcal mol$^{-1}$ PCM $CCl_4$ | 0 | 32.8 | 10.6 | 40.6 | 42.5 | 18.9 | 50.5 | 30.1 | 0.2 | 33.4 | 34.1 |
| | **12** | **13** | **14** | **15** | **16** | **17** | **18** | **19** | **20** | **21** | |
| $E_{rel}$ (B3LYP/6-31G(d)) / kcal mol$^{-1}$ | – | 11.9 | – | 11.9 | – | – | – | – | 22.6 | – | |
| $E_{rel}$ (MP2) / kcal mol$^{-1}$ | 34.5 | 16.5 | 17.5 | 15.8 | 46.2 | 49.1 | 59.3 | 59.7 | 28.5 | 46.1 | |
| $E_{rel}$ (CCSD(T)) / kcal mol$^{-1}$ | 25.0 | 13.8 | 14.7 | 12.6 | 34.3 | 37.1 | 45.4 | 46.0 | 23.1 | 38.9 | |
| $S$ / cal mol$^{-1}$ K$^{-1}$ | 105.9 | 105.2 | 105.2 | 105.3 | 100.2 | 100.7 | 99.8 | 99.8 | 100.4 | 99.1 | |
| $E_{rel}$ (MP2) / kcal mol$^{-1}$ PCM $H_2O$ | 32.7 | 9.6 | 10.1 | 7.7 | 38.0 | 42.0 | 47.5 | 48.9 | 16.3 | 30.4 | |
| $E_{rel}$ (MP2) / kcal mol$^{-1}$ PCM DMSO | 32.6 | 9.7 | 10.3 | 11.7 | 38.2 | 42.2 | 47.8 | 49.2 | 16.6 | 30.8 | |
| $E_{rel}$ (MP2) / kcal mol$^{-1}$ PCM $CCl_4$ | 33.8 | 12.9 | 13.7 | 7.9 | 42.0 | 45.4 | 53.9 | 54.7 | 22.1 | 38.7 | |

gas phase. The solvation in the more polar solvents water and DMSO also favors the tetrazoles. The differences between water and DMSO solvation are less than 0.4 kcal mol$^{-1}$, therefore only water solvatization is discussed here. In water the monotetrazole **3** is favored by 7.4 kcal mol$^{-1}$, the ditetrazole **6** by 12.2 kcal mol$^{-1}$ and the tritetrazole **8** by 15.5 kcal mol$^{-1}$ over the gas phase. The activation energy for the first cyclization is only slightly favored by 1.2 kcal mol$^{-1}$, the activation energy for the second cyclization is favored by 6.6 kcal mol$^{-1}$ and the activation energy for the third cyclization is favored by 11.1 kcal mol$^{-1}$ over the gas phase. While solvation in water favors the tritetrazole **8** to a great extent, it is still 22.7 kcal mol$^{-1}$ higher in energy than **1** and has not yet been detected experimentally.[20,21] Thus cyanuric azide is not a suitable starting material for the synthesis of its tetrazole isomers.

### Amino- and Nitro-diazido-1,3,5-triazine

One azide substituent of cyanuric azide was replaced by the electron-donating amino group and the electron-withdrawing nitro group. As before, all possible planar conformations of the azide groups were considered (see Scheme 2 and Scheme 3).

Both diazides have three planar isomers whose successive cyclization leads to the isomers shown in Scheme 4 and Scheme 5. The minimum energy reaction paths (Scheme 6 and Scheme 7) are formed by cyclization of the isomers **22** and **38**, which are derived from **1**. Isomers **30** and **31** as well as **40** and **41**, which are derived from **9**, have similar energies but their cyclization leads to tetrazoles with higher energies (Tables 2, 3). Interestingly, the amino compound first closes the tetrazole ring next to the amino group whereas

 © 2006 Wiley-VCH Verlag GmbH & Co. KGaA, Weinheim 

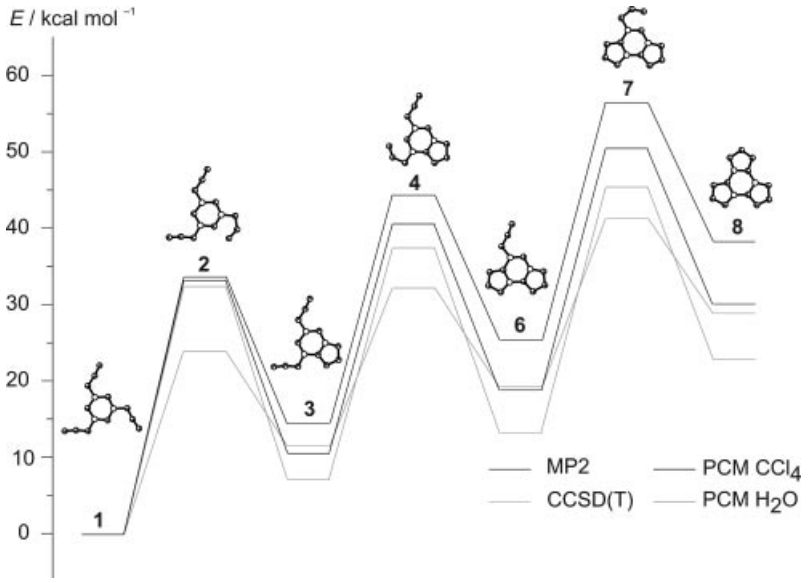


Scheme 3. Reaction profile for the ring closures in triazido-1,3,5-triazine.

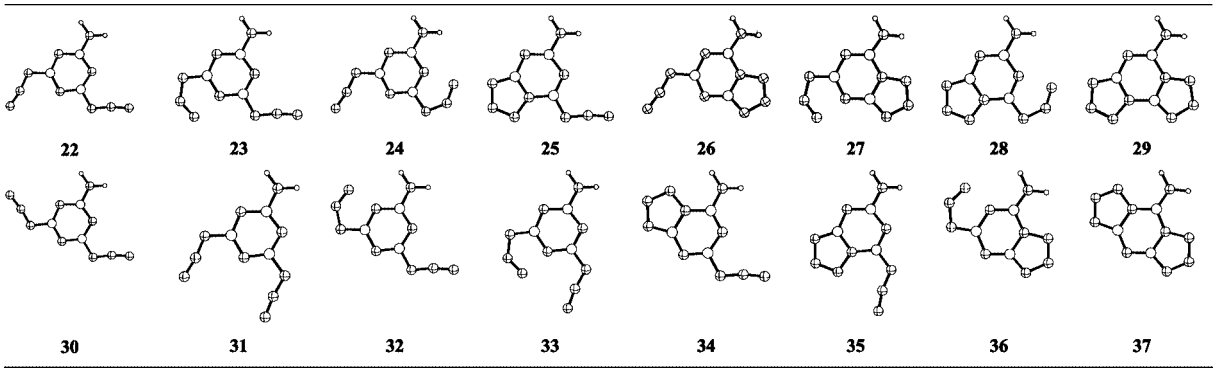


Scheme 4. Calculated amino-diazido-1,3,5-triazine isomers, all isomers have $C_1$ symmetry.

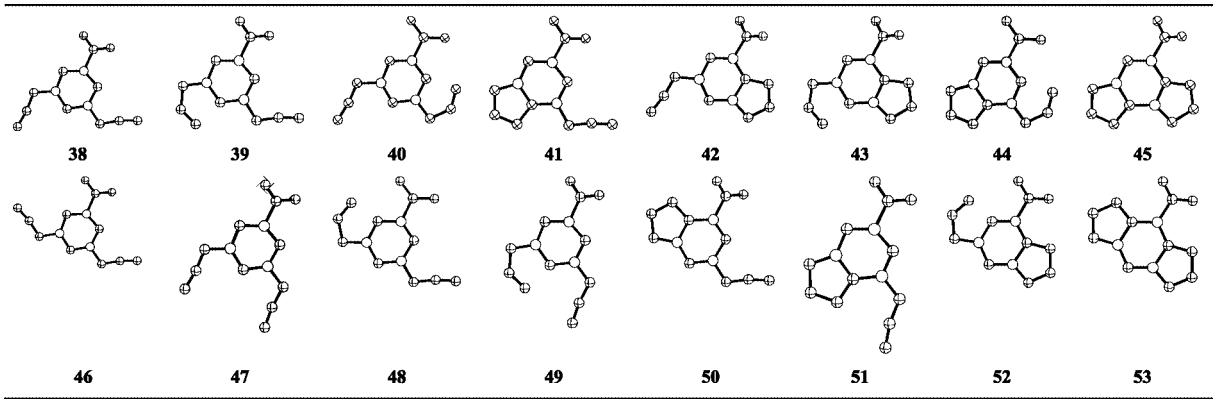


Scheme 5. Calculated diazido-nitro-1,3,5-triazine isomers, isomers have $C_1$ symmetry.

the nitro compound prefers to close the tetrazole ring farther away from the nitro group.

At the CCSD(T) level the amino derivative **26** with one tetrazole ring is 8.1 kcal mol$^{-1}$ higher in energy than the azide **22** and the ditetrazole **29** is 8.5 kcal mol$^{-1}$ higher in energy than the monotetrazole **26**. The activation energy for the cyclization of the amino compound **22** is 23.2 kcal mol$^{-1}$ and the activation energy for the second cyclization is 22.7 kcal mol$^{-1}$. The nitro derivative **41** with one tetrazole group is 11.8 kcal mol$^{-1}$ higher in energy than the azide **38** and the ditetrazole **45** is 13.8 kcal mol$^{-1}$ higher in energy than the monotetrazole **41**. The activation energy for the cyclization of the nitro compound **41** is 24.6 kcal mol$^{-1}$ and the activation energy for the second cyclization is

 © 2006 Wiley-VCH Verlag GmbH & Co. KGaA, Weinheim 

22.6 kcal mol$^{-1}$. As mentioned above for cyanuric azide, the MP2 energy differences for both compounds are larger and increase with the number of tetrazole rings.

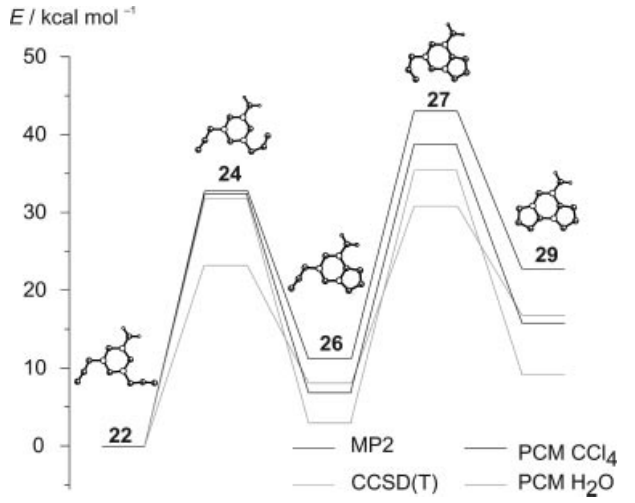


Scheme 6. Reaction profile for the ring closures in 2-amino-4,6-diazido-1,3,5-triazine.

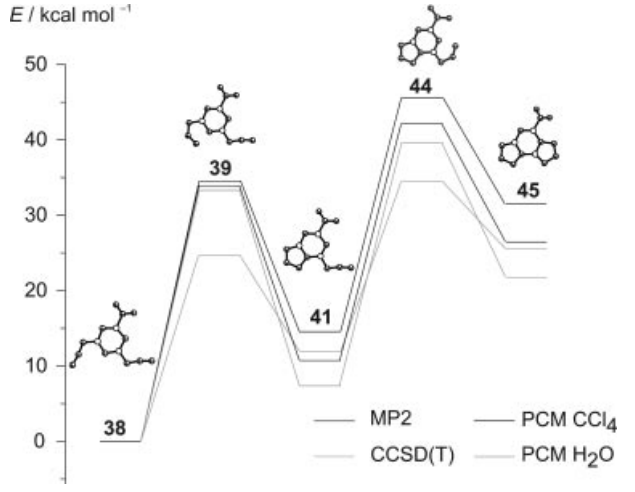


Scheme 7. Reaction profile for the ring closures in 4,6-diazido-2-nitro-1,3,5-triazine.

The formation of a tetrazole system leads to an entropy decrease for both amino- and nitro derivatives.

As observed for cyanuric azide, the sum of the positive and negative Mulliken charges is higher for the azide than for the tetrazole compounds (see Supporting Information) for both the amido and nitro derivatives, but the tetrazoles have higher individual charges. Similar to cyanuric azide, the ground states are influenced more by solvation in $CCl_4$, DMSO and water than the transition states.

Solvation of the amino derivatives in $CCl_4$ favors the monotetrazole **26** by 1.2 kcal mol$^{-1}$ and the ditetrazole **29** by 7.0 kcal mol$^{-1}$ over the gas phase. The activation energy for the first cyclization is only slightly favored by 0.9 kcal mol$^{-1}$ and the activation energy for the second cyclization is favored by 4.2 kcal mol$^{-1}$ over the gas phase. For the nitro derivatives solvation in $CCl_4$ decreases the energy difference to the diazide **1** by 3.6 kcal mol$^{-1}$ for the monotetrazole **39** and by 4.9 kcal mol$^{-1}$ for the ditetrazole **29** over the gas phase. The activation energies are lowered by 0.5 kcal mol$^{-1}$ for the first cyclization and by 3.3 kcal mol$^{-1}$ for the second cyclization compared to the gas phase. As observed for cyanuric azide, the effects of solvation in DMSO and water are similar. The amino-monotetrazole **26** is favored by 8.1 kcal mol$^{-1}$ and the ditetrazole **29** by 13.4 kcal mol$^{-1}$ over the gas phase. The activation energy for the first cyclization is lowered by 1.9 kcal mol$^{-1}$ and the activation energy for the second cyclization by 7.6 kcal mol$^{-1}$ over the gas phase. The nitro derivatives show a similar picture. Here the monotetrazole **41** is favored by 7 kcal mol$^{-1}$ and the ditetrazole 45 by 9.5 kcal mol$^{-1}$ in aqueous solution. The activation energies are lowered by 0.9 kcal mol$^{-1}$ for the first cyclization and by 6.0 kcal mol$^{-1}$ for the second cyclization.

In comparison to cyanuric azide, where the ditetrazole **16** is 19 kcal mol$^{-1}$ higher in energy than the respective diazide **1**, the aminoditetrazole **29** is 16.6 kcal mol$^{-1}$ higher in energy than the diazide **22** and the nitroditetrazole **45** is 25.6 kcal mol$^{-1}$ higher in energy than the diazide **38** [CCDS(T) values]. This shows that substitution with an electron-donating group favors the tetrazole whereas substitution with an electron-withdrawing group favors the azide.

Table 2. Calculated energy differences between different amino-diazido-1,3,5-triazine isomers. The gas phase calculations include zero point energy corrections. The PCM values represent the differences in free energy of the various species.

| | **22** | **23** | **24** | **25** | **26** | **27** | **28** | **29** |
|---|---|---|---|---|---|---|---|---|
| $E_{rel}$ (MP2) / kcal mol$^{-1}$ | 0 | 33.5 | 32.7 | 14.4 | 11.1 | 43.0 | 44.5 | 22.7 |
| $E_{rel}$ (CCSD(T)) / kcal mol$^{-1}$ | 0 | 23.8 | 23.2 | 11.5 | 8.1 | 30.8 | 32.2 | 16.6 |
| $S$ / cal mol$^{-1}$ K$^{-1}$ | 102.7 | 97.4 | 97.9 | 97.1 | 97.6 | 92.9 | 92.1 | 97.8 |
| $E_{rel}$ (MP2) / kcal mol$^{-1}$ PCM $H_2O$ | 0 | 32.1 | 30.8 | 6.7 | 3.0 | 35.4 | 36.3 | 9.3 |
| $E_{rel}$ (MP2) / kcal mol$^{-1}$ PCM DMSO | 0 | 32.1 | 30.9 | 6.9 | 3.2 | 35.6 | 36.6 | 9.7 |
| $E_{rel}$ (MP2) / kcal mol$^{-1}$ PCM $CCl_4$ | 0 | 32.8 | 31.8 | 10.9 | 6.9 | 38.8 | 40.3 | 15.7 |
| | **30** | **31** | **32** | **33** | **34** | **35** | **36** | **37** |
| $E_{rel}$ (MP2) / kcal mol$^{-1}$ | 0.3 | –0.1 | 34.1 | 33.9 | 12.2 | 16.6 | 53.3 | 38.4 |
| $E_{rel}$ (CCSD(T)) / kcal mol$^{-1}$ | 0.5 | –0.1 | 24.4 | 24.3 | 9.2 | 13.4 | 39.6 | 30.6 |
| $S$ / cal mol$^{-1}$ K$^{-1}$ | 102.8 | 102.8 | 98.0 | 98.2 | 97.8 | 97.2 | 93.3 | 91.9 |
| $E_{rel}$ (MP2) / kcal mol$^{-1}$ PCM $H_2O$ | –0.1 | 0.2 | 30.9 | 32.2 | 3.2 | 9.3 | 40.0 | 18.9 |
| $E_{rel}$ (MP2) / kcal mol$^{-1}$ PCM DMSO | –0.1 | 0.1 | 31.1 | 32.1 | 3.5 | 9.4 | 40.6 | 19.6 |
| $E_{rel}$ (MP2) / kcal mol$^{-1}$ PCM $CCl_4$ | 0.2 | –0.1 | 32.6 | 32.9 | 5.3 | 12.7 | 47.3 | 29.3 |

 © 2006 Wiley-VCH Verlag GmbH & Co. KGaA, Weinheim 

Table 3. Calculated energy differences between different diazido-nitro-1,3,5-triazine isomers. The gas phase calculations include zero point energy corrections. The PCM values represent the differences in free energy of the various species.

| | **38** | **39** | **40** | **41** | **42** | **43** | **44** | **45** |
|---|---|---|---|---|---|---|---|---|
| $E_{rel}$ (MP2) / kcal mol$^{-1}$ | 0 | 34.3 | 35.3 | 14.5 | 20.0 | 52.6 | 45.7 | 31.3 |
| $E_{rel}$ (CCSD(T)) / kcal mol$^{-1}$ | 0 | 24.6 | 25.9 | 11.8 | 17.0 | 40.1 | 34.4 | 25.6 |
| $S$ / cal mol$^{-1}$ K$^{-1}$ | 111.9 | 107.0 | 108.4 | 106.3 | 106.1 | 101.5 | 101.9 | 100.6 |
| $E_{rel}$ (MP2) / kcal mol$^{-1}$ PCM $H_2O$ | 0 | 33.4 | 35.1 | 7.5 | 15.0 | 48.4 | 39.7 | 21.8 |
| $E_{rel}$ (MP2) / kcal mol$^{-1}$ PCM DMSO | 0 | 33.4 | 34.5 | 7.7 | 15.1 | 48.5 | 39.8 | 22.1 |
| $E_{rel}$ (MP2) / kcal mol$^{-1}$ PCM $CCl_4$ | 0 | 33.8 | 34.9 | 10.9 | 17.4 | 50.2 | 42.4 | 26.4 |
| | **46** | **47** | **48** | **49** | **50** | **51** | **52** | **53** |
| $E_{rel}$ (MP2) / kcal mol$^{-1}$ | –0.1 | 0.4 | 36.1 | 35.6 | 20.7 | 16.8 | 67.4 | 54.0 |
| $E_{rel}$ (CCSD(T)) / kcal mol$^{-1}$ | 0 | 0.6 | 26.7 | 26.1 | 18.3 | 14.7 | 54.9 | 52.0 |
| $S$ / cal mol$^{-1}$ K$^{-1}$ | 112.1 | 111.9 | 108.0 | 106.9 | 106.3 | 106.2 | 101.3 | 100.7 |
| $E_{rel}$ (MP2) / kcal mol$^{-1}$ PCM $H_2O$ | 0.3 | –0.2 | 35.4 | 33.6 | 16.0 | 9.7 | 60.4 | 44.1 |
| $E_{rel}$ (MP2) / kcal mol$^{-1}$ PCM DMSO | 0.4 | –0.3 | 35.3 | 33.5 | 16.1 | 9.9 | 60.6 | 44.5 |
| $E_{rel}$ (MP2) / kcal mol$^{-1}$ PCM $CCl_4$ | 0.1 | 0.2 | 35.8 | 34.6 | 18.6 | 13.2 | 64.3 | 49.3 |

The activation energies for the first (23.8 kcal mol$^{-1}$ for cyanuric azide, 23.8 kcal mol$^{-1}$ for the amino derivative and 24.6 kcal mol$^{-1}$ for the nitro derivative) and second cyclization (21.0 kcal mol$^{-1}$ for cynuric azide, 22.7 kcal mol$^{-1}$ for the amino derivative and 22.6 kcal mol$^{-1}$ for the nitro derivative) are barely influenced by the substitution.

### 4,4′,6,6′-Tetra(azido)azo-1,3,5-triazine and 4,4′,6,6′-Tetra(azido)hydrazo-1,3,5-triazine

Here the size of the molecules prevented MP2 calculations due to computational cost. The good agreement between the B3LYP and CCSD(T) energy differences for cyanuric azide shows that these compounds could be investigated with density functional theory. Scheme 8, Scheme 9, and Scheme 10 show the rotation profiles around the C–N and N–N single bonds of the hydrazo-bridged **74** and the C–N bond of the azo-bridged dimer **54** with the minimum energy bonding angle set to zero. As expected, the C–N rotation barrier in the azo-bridged dimer is higher due to a partial double bond. The rotation around the N–N single bond in the hydrazo-bridged **94** is sterically hindered.

As there are too many possible routes for cyclization, not all possible isomers for the cyclization were calculated. Instead all possible tetraazides and tetratetrazoles were calculated. Then the isomers on the cyclization route linking the lowest energy tetraazide to the lowest energy tetratetrazole were calculated.

Two conformers of the azo-bridged tetraazide have already been found in the same crystal structure and yet another in a second crystal structure.[22] This confirms that the energy differences between the different tetraazide con-

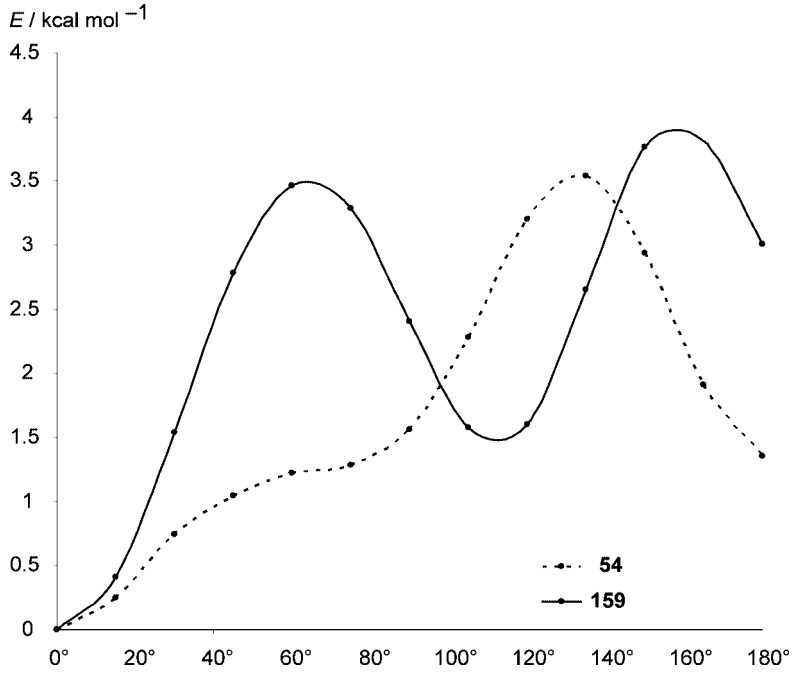


Scheme 8. Energy profile for the rotation of **54** and **159** around the $N_{hydrazo}$–$C_{aryl}$ σ bond with the minimum energy bonding angle set to zero at the MP2 level. Single point energy calculations were performed at 15° intervals.

 © 2006 Wiley-VCH Verlag GmbH & Co. KGaA, Weinheim 

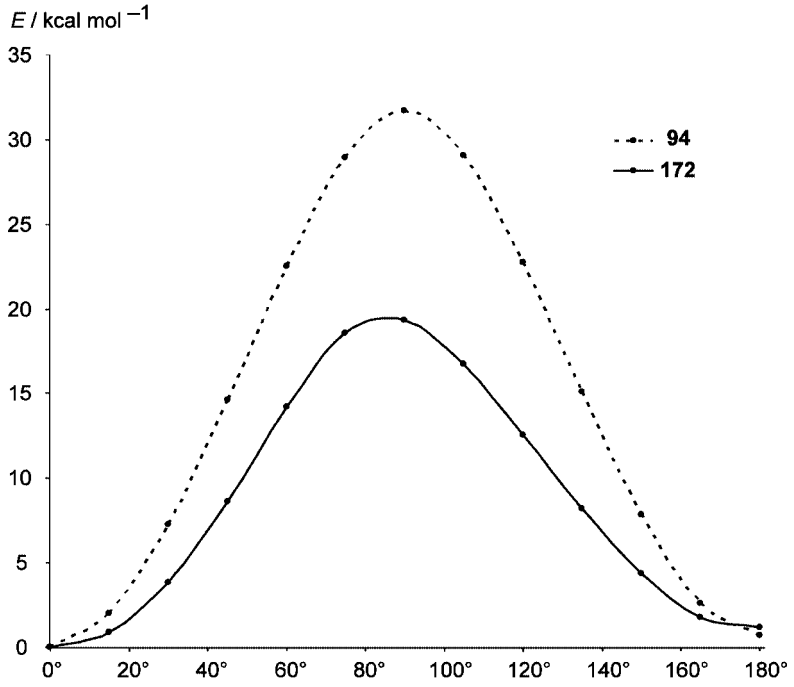


Scheme 9. Energy profile for the rotation of **94** and **172** around the $N_{hydrazo}$–$C_{aryl}$ σ bond with the minimum energy bonding angle set to zero at the MP2 level. Single point energy calculations were performed at 15° intervals.

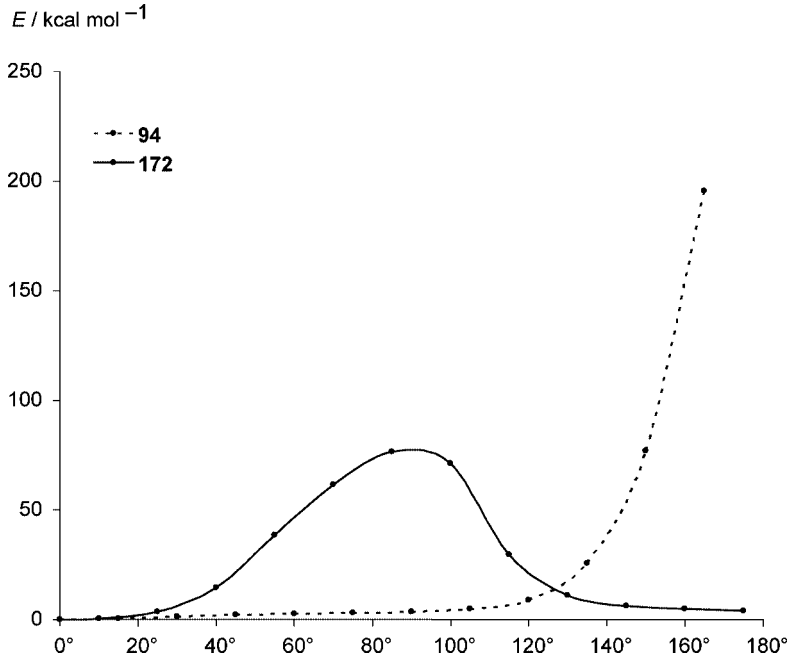


Scheme 10. Energy profile for the rotation of **94** and **159** around the $N_{hydrazo}$–$C_{aryl}$ σ bond with the minimum energy bonding angle set to zero at the MP2 level. Single point energy calculations were performed at 15° intervals.

formers are only slight. For the azo-bridged dimers we find differences of only 1.3 kcal mol$^{-1}$ between isomers **54**–**63**. Interestingly, the highest energy conformer **56** was found in a crystal structure together with conformer **55**. This is probably due to a better space filling in the crystal in the presence of both isomers. While isomer **54** does not have the lowest energy in the gas phase, it is the lowest energy isomer in solution and its cyclization product **88** is the lowest energy tetratetrazole. The tetratetrazoles have higher energy differences of up to 25.7 kcal mol$^{-1}$. Therefore, a cyclization route linking **54** to **88** was calculated. The hydrazo-bridged dimers **94**–**103** are also only separated by 1.5 kcal mol$^{-1}$ in energy. Here the lowest energy tetraazide **94** was also found in the crystal structure[22] and no other conformers have yet been observed. The cyclization route linking **94** to the lowest energy tetratetrazole **128** was calculated. Similar to the

 © 2006 Wiley-VCH Verlag GmbH & Co. KGaA, Weinheim 

azo compounds the tetratetrazole isomers **128**–**133** have energy differences up to 27.0 kcal mol$^{-1}$. The lowest energy azo- and hydrazo-bridged tetraazides **54** and **94** and tetratetrazoles **88** and **128** have the same conformation of the azide groups and are, like the minimum energy amino- and nitro-diazido-1,3,5-triazines, derived from the minimum energy triazido-1,3,5-triazine **1**. The calculated bonding parameters of **55**, **56**, **57**, and **94** are in good agreement with the structural data.[22] The $N_\beta$-$N_\gamma$ bond of the azide units is slightly longer than in the X-ray structures (see Supporting Information).

Scheme 11 and Scheme 12 show that the azo- and hydrazo-bridged dimers first cyclize both azide groups belonging to one triazine ring and then the azide groups of the second triazine unit.

The azo-bridged monotetrazole **67** is 11.2 kcal mol$^{-1}$ higher in energy than the tetraazide **54**, the ditetrazole **74** 20.8 kcal mol$^{-1}$, the tritetrazole **84** 32.5 kcal mol$^{-1}$ and the tetratetrazole **88** 44.3 kcal mol$^{-1}$, which translates to energy differences of 9.6 kcal mol$^{-1}$ between the monotetrazole **67** and the ditetrazole **74**, 11.7 kcal mol$^{-1}$ between the ditetrazole **74** and the tritetrazole **84** and 11.8 kcal mol$^{-1}$ between the tritetrazole **84** and the tetratetrazole **88** (Scheme 13, Table 4). The ditetrazoles **75**–**77** with tetrazole rings at different triazine rings are about 3 kcal mol$^{-1}$ less favored than **74**, where both tetrazole rings are bonded to the same triazine ring. The activation energies for the cyclizations are 23.5 kcal mol$^{-1}$, 21.4 kcal mol$^{-1}$, 23.9 kcal mol$^{-1}$ and 22.5 kcal mol$^{-1}$. The third cyclization transition state **79**, which links ditratrazole **77** with tritetrazole **84**, is 0.6 kcal mol$^{-1}$ lower than **78**, but the ditetrazole **77** is 1.7 kcal mol$^{-1}$ higher in energy than ditetrazole **74**. The cyclization therefore should lead to ditetrazole **77**, which then requires a slightly higher activation energy to cyclize to tritetrazole **84**.

The hydrazo-bridged compounds have slightly lower energy differences than the azo-bridged compound to the tetraazide **94** for the mono- and ditetrazoles, while the tri- and tetratetrazoles have similar energies (Scheme 14, Table 5). The monotetrazole **106** is 10.7 kcal mol$^{-1}$ higher in energy, the ditetrazole **114** 20.5 kcal mol$^{-1}$, the tritetrazole **124** 33.0 kcal mol$^{-1}$ and the tetratetrazole **128** 44.3 kcal mol$^{-1}$. This translates to energy differences of 9.8 kcal mol$^{-1}$ between one and two tetrazole rings, 12.5 kcal mol$^{-1}$ between two and three tetrazole rings and 11.3 kcal mol$^{-1}$ between three and four tetrazole rings. The ditetrazoles **115**–**117**

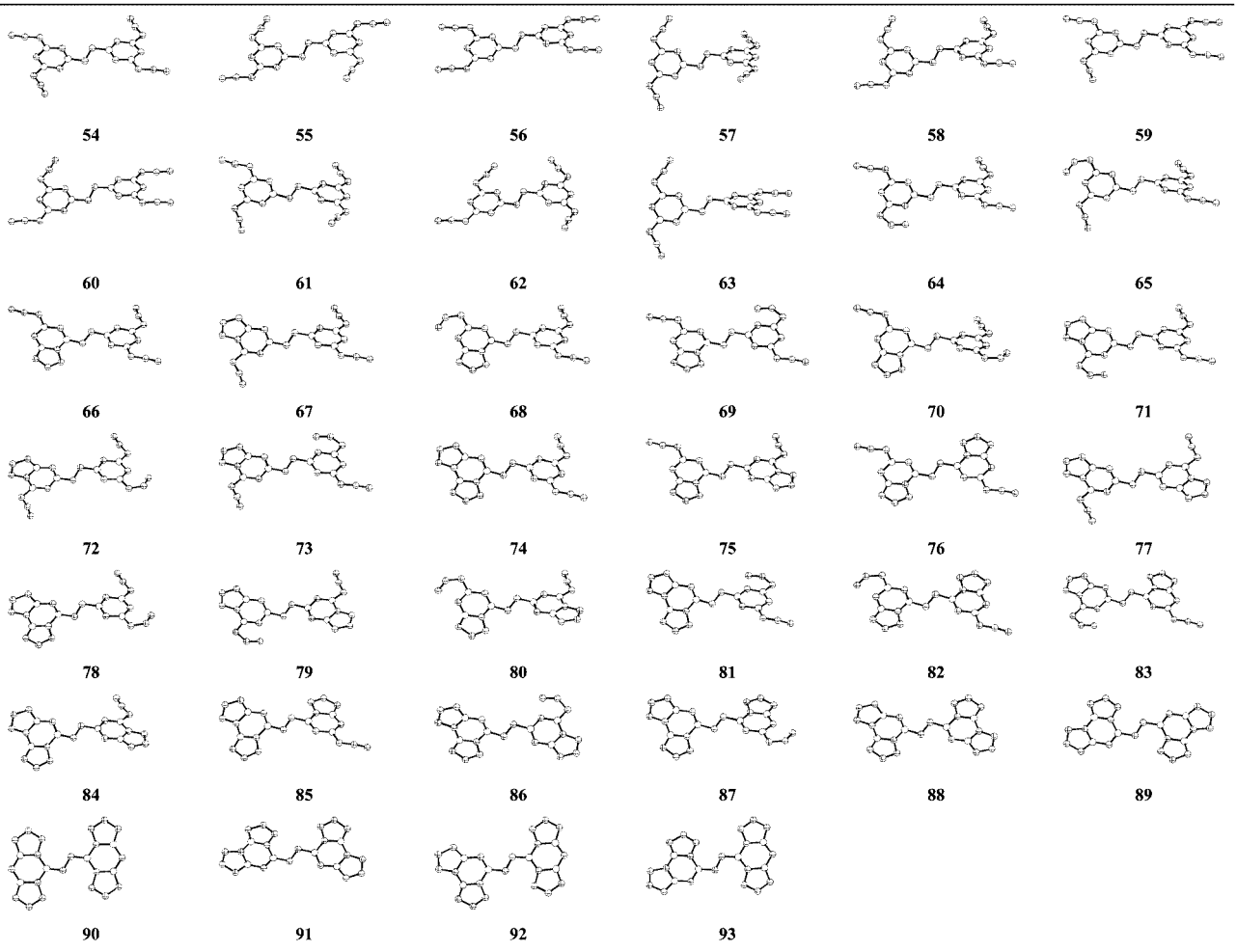


Scheme 11. Calculated isomers of 4,4′,6,6′-tetra(azido)azo-1,3,5-triazine.

 © 2006 Wiley-VCH Verlag GmbH & Co. KGaA, Weinheim 

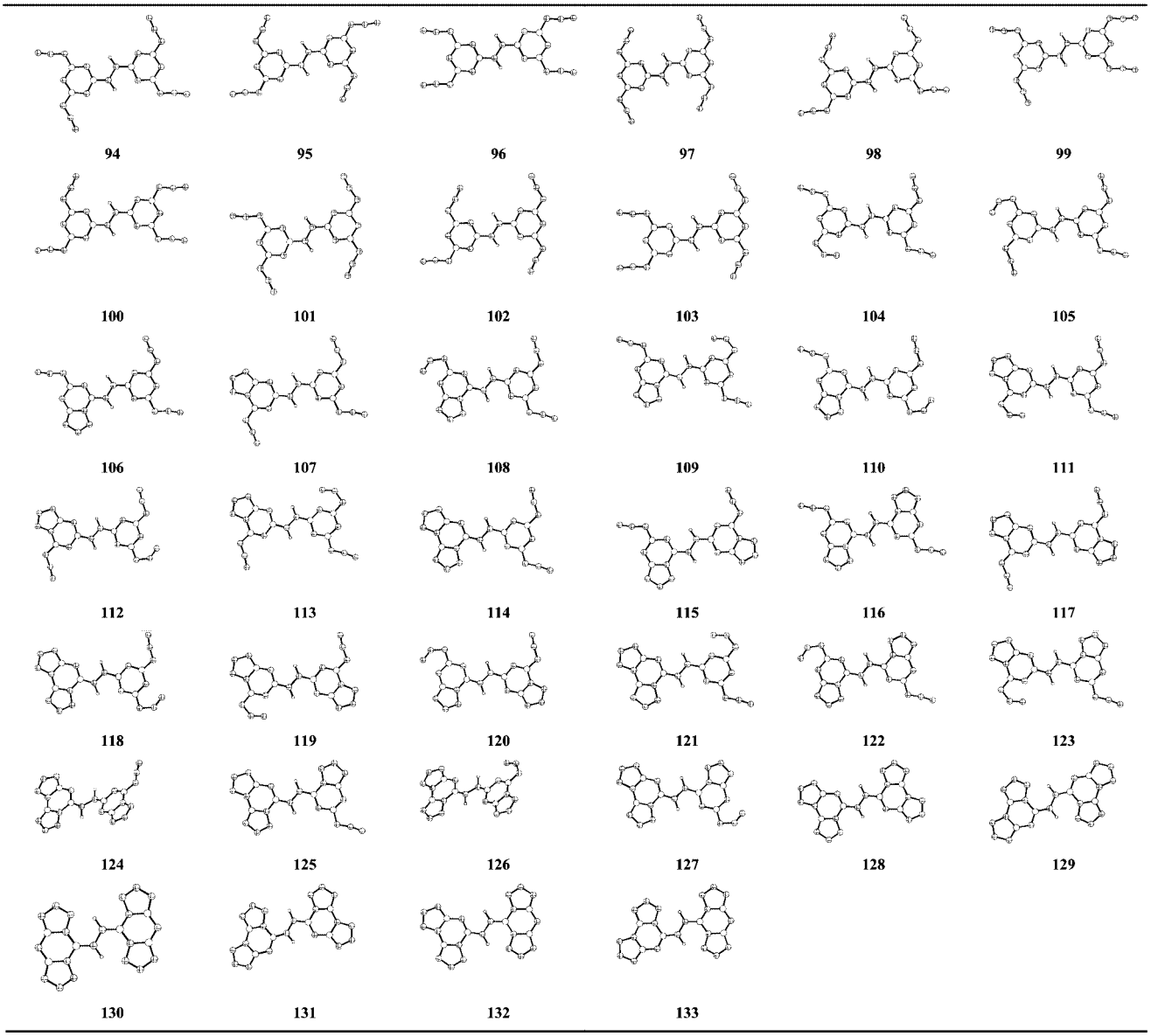


Scheme 12. Calculated isomers of 4,4′,6,6′-tetra(azido)hydrazo-1,3,5-triazine.

with tetrazole rings at both triazine rings are about 2.5 kcal mol$^{-1}$ less favored than **114**, where both tetrazole rings are bonded to the same triazine ring. The activation energies for the cyclizations are 23.4 kcal mol$^{-1}$, 22.3 kcal mol$^{-1}$, 23.0 kcal mol$^{-1}$, and 22.5 kcal mol$^{-1}$. Transition state **105** for the first cyclization, which links the tetraazide **94** with the monotetrazole **107**, is 0.7 kcal mol$^{-1}$ lower than **104**, but the montetrazole **107** is 0.8 kcal mol$^{-1}$ higher in energy than the monotetrazole **106**. The kinetic product **107** also requires a higher activation energy for a second cyclization, therefore the minimum energy cyclization route includes transition state **104** and monotetrazole **106**. As observed for all previous compounds, successive cyclization leads to a successive decrease of the entropy for both azo and hydrazo compounds. The sum of the positive and negative Mulliken charges is higher for the azides than for the tetrazole compounds (see Supporting Information) for both the azo- and hydrazo compounds, but the tetrazoles have higher individual charges.

Solvatization in $CCl_4$, DMSO and water has a higher influence on the ground states than on the transition states. Solvation in $CCl_4$ of the azo compound favors the monotetrazole **67** by 3.5 kcal mol$^{-1}$, the ditetrazole **74** by 5.2 kcal mol$^{-1}$, the tritetrazole **84** by 8.8 kcal mol$^{-1}$ and the tetratetrazole **88** by 10.6 kcal mol$^{-1}$ over the gas phase. The activation energy for the first cyclization is only slightly favored by 0.2 kcal mol$^{-1}$, the second cyclization is favored by 2.8 kcal mol$^{-1}$, the third cyclization by 5.5 kcal mol$^{-1}$ and the final cyclization by 8.1 kcal mol$^{-1}$ over the gas phase. The hydrazo compounds are favored by 3.1 kcal mol$^{-1}$ for the monotetrazole **106**, by 5.8 kcal mol$^{-1}$ for the ditetrazole **114**, by 10.3 kcal mol$^{-1}$ for the tritetrazole **124**, and by

 © 2006 Wiley-VCH Verlag GmbH & Co. KGaA, Weinheim 

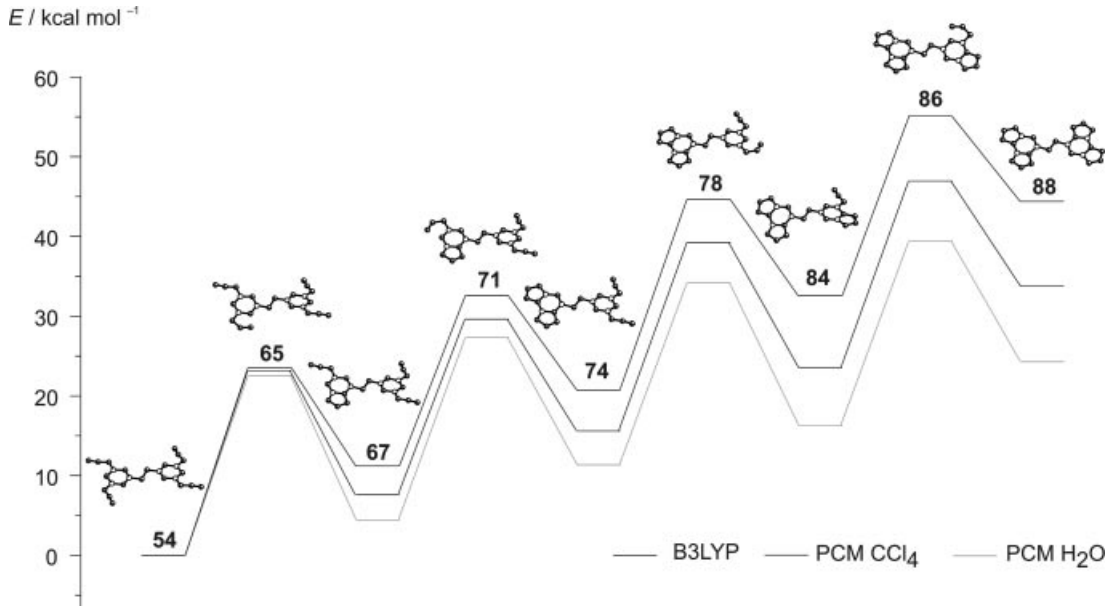


Scheme 13. Reaction profile for the ring closures in 4,4′,6,6′-tetra(azido)azo-1,3,5-triazine.

Table 4. Calculated energy differences between different 4,4′,6,6′-tetra(azido)azo-1,3,5-triazine. The gas phase calculations include zero point energy corrections. The PCM values represent the differences in free energy of the various species.

| | **54** | **55** | **56** | **57** | **58** | **59** | **60** | **61** | **62** | **63** | **64** | **65** | **66** | **67** |
|---|---|---|---|---|---|---|---|---|---|---|---|---|---|---|
| $E_{rel}$ (B3LYP) / kcal mol$^{-1}$ | 0 | –0.2 | 0.9 | –0.1 | –0.1 | 0.5 | 0.3 | –0.1 | –0.2 | 0.4 | 23.8 | 23.5 | 12.1 | 11.2 |
| $S$ / cal mol$^{-1}$ K$^{-1}$ | 160.5 | 160.5 | 160.6 | 160.7 | 160.2 | 160.4 | 160.3 | 160.2 | 160.3 | 160.4 | 155.6 | 155.4 | 154.7 | 154.5 |
| $E_{rel}$ (B3LYP) / kcal mol$^{-1}$ PCM $H_2O$ | 0 | 0.2 | 0.5 | 0.3 | 0.1 | 0.2 | 0.3 | 0.1 | 0.3 | 0.4 | 23.5 | 22.7 | 6.8 | 4.6 |
| $E_{rel}$ (B3LYP) / kcal mol$^{-1}$ PCM DMSO | 0 | 0.5 | 0.3 | 0.7 | 0.2 | 0.1 | 0.4 | 0.3 | 0.6 | 0.5 | 23.5 | 22.7 | 7.0 | 4.9 |
| $E_{rel}$ (B3LYP) / kcal mol$^{-1}$ PCM $CCl_4$ | 0 | 0.2 | 0.8 | 0.4 | 0.1 | 0.3 | 0.4 | 0.1 | 0.3 | 0.5 | 23.8 | 23.3 | 9.2 | 7.7 |
| | **68** | **69** | **70** | **71** | **72** | **73** | **74** | **75** | **76** | **77** | **78** | **79** | **80** | **81** |
| $E_{rel}$ (B3LYP) / kcal mol$^{-1}$ | 35.0 | 36.8 | 35.9 | 32.6 | 34.8 | 35.0 | 20.8 | 23.7 | 25.9 | 22.5 | 44.7 | 44.1 | 46.7 | 45.8 |
| $S$ / cal mol$^{-1}$ K$^{-1}$ | 150.1 | 149.7 | 149.8 | 149.6 | 149.7 | 149.5 | 149.0 | 149.0 | 148.9 | 148.8 | 144.1 | 143.8 | 144.2 | 144.2 |
| $E_{rel}$ (B3LYP) / kcal mol$^{-1}$ PCM $H_2O$ | 30.2 | 30.9 | 29.8 | 27.3 | 27.4 | 28.2 | 11.4 | 11.7 | 14.8 | 9.3 | 34.4 | 32.0 | 35.1 | 35.6 |
| $E_{rel}$ (B3LYP) / kcal mol$^{-1}$ PCM DMSO | 30.5 | 31.2 | 30.1 | 27.4 | 27.6 | 28.4 | 11.7 | 12.1 | 15.2 | 9.6 | 34.8 | 32.4 | 35.5 | 35.9 |
| $E_{rel}$ (B3LYP) / kcal mol$^{-1}$ PCM $CCl_4$ | 32.5 | 33.9 | 32.8 | 29.8 | 31.1 | 31.7 | 15.6 | 17.3 | 20.1 | 15.4 | 39.2 | 37.8 | 40.6 | 40.5 |
| | **82** | **83** | **84** | **85** | **86** | **87** | **88** | **89** | **90** | **91** | **92** | **93** | | |
| $E_{rel}$ (B3LYP) / kcal mol$^{-1}$ | 49.2 | 45.9 | 32.5 | 35.1 | 55.0 | 58.4 | 44.3 | 45.8 | 70.0 | 45.0 | 48.5 | 59.3 | | |
| $S$ / cal mol$^{-1}$ K$^{-1}$ | 144.4 | 144.0 | 143.2 | 143.4 | 138.4 | 138.8 | 137.8 | 137.9 | 138.7 | 137.7 | 137.8 | 137.4 | | |
| $E_{rel}$ (B3LYP) / kcal mol$^{-1}$ PCM $H_2O$ | 38.5 | 16.2 | 16.2 | 19.6 | 39.5 | 43.3 | 24.4 | 26.5 | 49.6 | 25.4 | 38.0 | 39.7 | | |
| $E_{rel}$ (B3LYP) / kcal mol$^{-1}$ PCM DMSO | 38.9 | 16.8 | 16.8 | 20.2 | 40.1 | 44.0 | 25.1 | 27.4 | 50.7 | 27.4 | 39.0 | 40.1 | | |
| $E_{rel}$ (B3LYP) / kcal mol$^{-1}$ PCM $CCl_4$ | 43.7 | 23.7 | 23.7 | 26.7 | 46.9 | 50.6 | 33.7 | 35.6 | 60.6 | 34.6 | 48.5 | 49.5 | | |

11.1 kcal mol$^{-1}$ for the tetratetrazole **128** by solvation in $CCl_4$. The activation energy for the first cyclization is slightly increased by 0.2 kcal mol$^{-1}$ while the activation energy for the second, third and fourth cyclization are favored by 2.9 kcal mol$^{-1}$, 6.0 kcal mol$^{-1}$, and 10.0 kcal mol$^{-1}$.

The difference between solvation in water and DMSO is more pronounced compared to the previous compounds, probably due to different displacement of solvent molecules. Still, the energy differences between DMSO and water solvation are within 1 kcal mol$^{-1}$. The azo-bridged mono- **67**, di- **74**, tri- **84**, and tetratetrazoles 88 are favored by 6.6, 9.4, 16.3, and 19.9 kcal mol$^{-1}$ over the gas phase and the activation energy for the first, second, third, and fourth cyclization by 0.8, 5.3, 10.3, and 15.5 kcal mol$^{-1}$. Solvation of the hydrazo compounds in water leads to an even higher stabilization of the tetrazoles. The hydrazo-bridged mono- **106**, di- **114**, tri- **124**, and tetratetrazoles **128** are stabilized by 6.7, 11.2, 20.4, and 24.6 kcal mol$^{-1}$ over the gas phase. The activation energy for the first, second, third, and fourth cyclizations are favored by 1.4, 6.3, 12.4, and 20.4 kcal mol$^{-1}$ by solvation in water.

As a consequence, both 4,4′,6,6′-tetra(azido)azo-1,3,5-triazine and 4,4′,6,6′-tetra(azido)hydrazo-1,3,5-triazine do not form tetrazoles in gas phase or in solution. Solvation in polar solvents favors the tetrazoles, even more for the

 © 2006 Wiley-VCH Verlag GmbH & Co. KGaA, Weinheim 

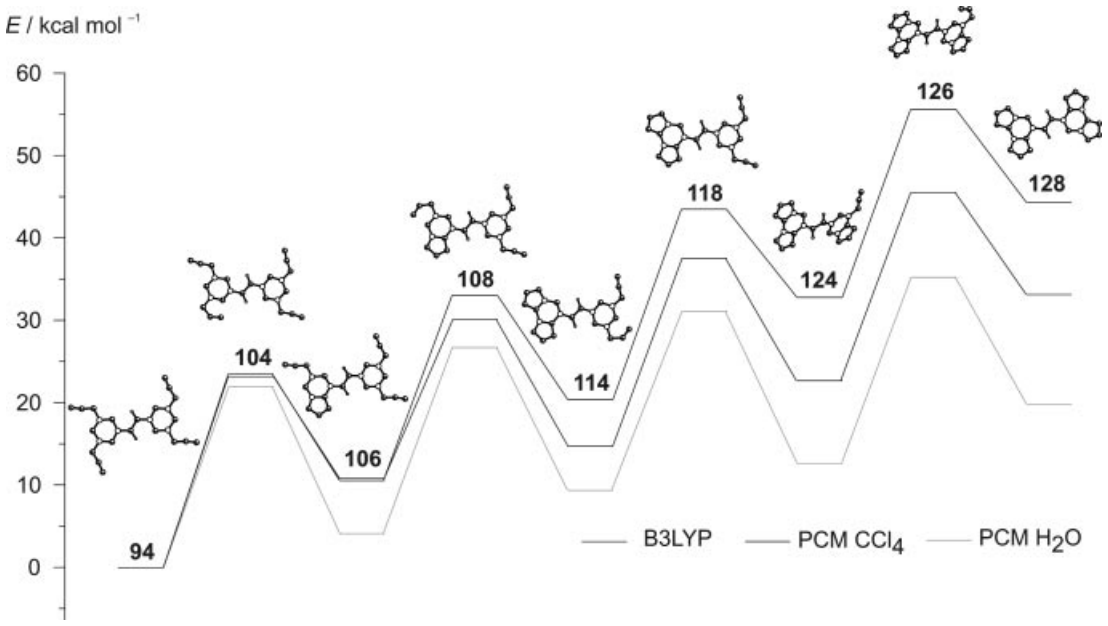


Scheme 14. Reaction profile for the ring closures in 4,4′,6,6′-tetra(azido)hydrazo-1,3,5-triazine.

Table 5. Calculated energy differences between different4,4′,6,6′-Tetra(azido)hydrazo-1,3,5-triazine. The gas phase calculations include zero point energy corrections. The PCM values represent the differences in free energy of the various species.

| | **94** | **95** | **96** | **97** | **98** | **99** | **100** | **101** | **102** | **103** | **104** | **105** | **106** | **107** |
|---|---|---|---|---|---|---|---|---|---|---|---|---|---|---|
| $E_{rel}$ (B3LYP) / kcal mol$^{-1}$ | 0 | 1.0 | 0 | 1.9 | 0.6 | 0.0 | 0.5 | 1.0 | 1.5 | 0.9 | 23.4 | 22.7 | 10.7 | 11.5 |
| $S$ / cal mol$^{-1}$ K$^{-1}$ | 163.6 | 165.0 | 162.9 | 166.4 | 164.2 | 163.6 | 163.4 | 164.3 | 164.6 | 165.9 | 160.9 | 158.6 | 157.1 | 158.9 |
| $E_{rel}$ (B3LYP) / kcal mol$^{-1}$ PCM $H_2O$ | 0 | 2.0 | 0.2 | 2.6 | 1.2 | 0.3 | 1.2 | 1.3 | 2.3 | 1.3 | 22.0 | 21.8 | 4.0 | 4.0 |
| $E_{rel}$ (B3LYP) / kcal mol$^{-1}$ PCM DMSO | 0 | 3.7 | 0 | 4.7 | 2.0 | 0.0 | 1.9 | 2.2 | 4.0 | 2.1 | 23.3 | 21.7 | 5.2 | 4.2 |
| $E_{rel}$ (B3LYP) / kcal mol$^{-1}$ PCM $CCl_4$ | 0 | 2.4 | –0.2 | 3.6 | 1.3 | –0.1 | 1.1 | 1.8 | 2.9 | 1.6 | 23.6 | 22.3 | 7.6 | 7.6 |
| | **108** | **109** | **110** | **111** | **112** | **113** | **114** | **115** | **116** | **117** | **118** | **119** | **120** | **121** |
| $E_{rel}$ (B3LYP) / kcal mol$^{-1}$ | 33.0 | 35.0 | 33.8 | 33.2 | 34.2 | 35.2 | 20.5 | 23.0 | 23.0 | 23.0 | 43.5 | 44.4 | 45.4 | 46.9 |
| $S$ / cal mol$^{-1}$ K$^{-1}$ | 152.6 | 152.8 | 153.8 | 156.3 | 153.0 | 155.5 | 152.7 | 152.3 | 154.1 | 153.4 | 148.7 | 151.3 | 147.5 | 139.9 |
| $E_{rel}$ (B3LYP) / kcal mol$^{-1}$ PCM $H_2O$ | 26.7 | 26.6 | 25.8 | 26.1 | 25.7 | 26.1 | 9.3 | 12.9 | 8.8 | 8.1 | 31.1 | 30.4 | 31.0 | 34.2 |
| $E_{rel}$ (B3LYP) / kcal mol$^{-1}$ PCM DMSO | 27.8 | 29.4 | 27.0 | 27.6 | 25.8 | 37.5 | 10.4 | 9.7 | 12.3 | 8.3 | 32.3 | 30.3 | 23.3 | 37.3 |
| $37E_{rel}$ (B3LYP) / kcal mol$^{-1}$ PCM $CCl_4$ | 30.1 | 32.3 | 30.3 | 30.3 | 29.8 | 31.5 | 14.7 | 16.0 | 17.3 | 15.1 | 37.5 | 38.2 | 23.6 | 42.3 |
| | **122** | **123** | **124** | **125** | **126** | **127** | **128** | **129** | **130** | **131** | **132** | **133** | | |
| $E_{rel}$ (B3LYP) / kcal mol$^{-1}$ | 45.8 | 47.6 | 33.0 | 33.6 | 55.5 | 56.4 | 44.3 | 50.2 | 71.3 | 46.7 | 57.5 | 60.3 | | |
| $S$ / cal mol$^{-1}$ K$^{-1}$ | 148.9 | 140.1 | 144.8 | 151.0 | 140.0 | 149.6 | 146.6 | 139.2 | 137.6 | 141.7 | 140.7 | 138.3 | | |
| $E_{rel}$ (B3LYP) / kcal mol$^{-1}$ PCM $H_2O$ | 31.7 | 33.4 | 12.6 | 14.6 | 35.1 | 37.4 | 19.7 | 29.6 | 46.7 | 23.6 | 33.1 | 37.3 | | |
| $E_{rel}$ (B3LYP) / kcal mol$^{-1}$ PCM DMSO | 35.2 | 37.1 | 13.9 | 17.9 | 36.3 | 40.8 | 23.6 | 30.7 | 47.7 | 25.1 | 35.1 | 38.4 | | |
| $E_{rel}$ (B3LYP) / kcal mol$^{-1}$ PCM $CCl_4$ | 40.2 | 42.6 | 22.7 | 25.2 | 45.5 | 48.1 | 33.2 | 39.2 | 60.1 | 35.0 | 46.1 | 49.0 | | |

hydrazo compounds than the for the azo compounds. The solvation effect is not sufficient so that the detection of the tetrazoles in solution was not observed.[21]

### Triazido-*s*-heptazine

Triazido-*s*-heptazine behaves similarly to triazido-1,3,5-triazine. Two azide rotamers cyclize to different tetrazoles. To save computer time, we only calculated the ground states and the transition states linking the lowest ground states (Scheme 15).

The minimum energy $C_{3h}$ isomer **139** is similar to the minimum energy cyanuric azide isomer **1**. The bonding parameters are in agreement with X-ray structural data,[23] with the same longer azide $N_\beta$–$N_\gamma$ bond found for all previous compounds (Scheme 16, Table 6).

The reaction profile for the cyclization of the triazidoheptazine **139** is similar to the reaction profile of triazidotriazine **1**. The energy differences between the triazide **134** and monotetrazole **136**, the ditetrazole **139** and the tritetrazole **141** are 12.6, 23.8, and 34.9 kcal mol$^{-1}$. The ditetrazole **139** is therefore 11.2 kcal mol$^{-1}$ higher in energy

 © 2006 Wiley-VCH Verlag GmbH & Co. KGaA, Weinheim 

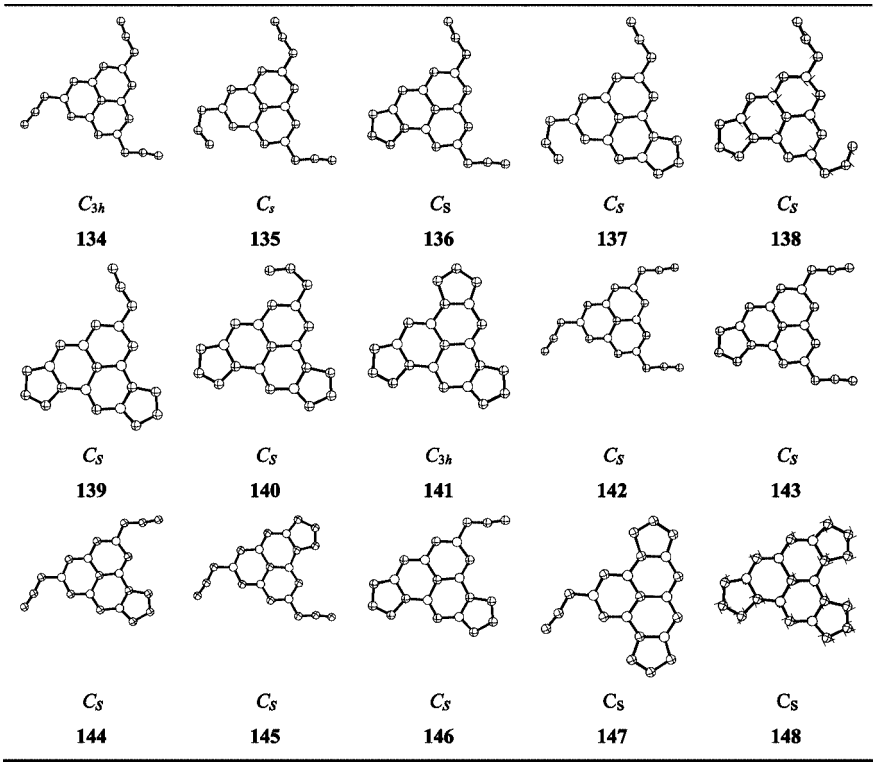


Scheme 15. Calculated isomers of triazido-*s*-heptazine.

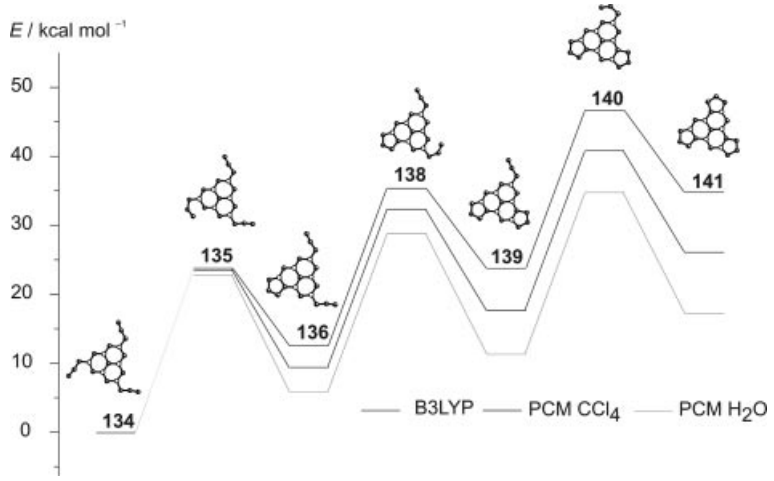


Scheme 16. Reaction profile for the ring closures in triazido-*s*-heptazine.

Table 6. Calculated energy differences between different triazido-*s*-heptazine isomers. The gas phase calculations include zero point energy corrections. The PCM values represent the differences in free energy of the various species.

| | **134** | **135** | **136** | **137** | **138** | **139** | **140** | **141** | **142** | **143** | **144** | **145** | **146** | **147** | **148** |
|---|---|---|---|---|---|---|---|---|---|---|---|---|---|---|---|
| $E_{rel}$ (B3LYP) / kcal mol$^{-1}$ | 0 | 23.5 | 12.6 | 35.4 | 35.4 | 23.8 | 46.5 | 34.9 | 0.1 | 13 | 13.2 | 13.0 | 24.5 | 31.7 | 55.3 |
| $S$ / cal mol$^{-1}$ K$^{-1}$ | 127.8 | 125.4 | 124.9 | 120.5 | 120.4 | 119.8 | 115.3 | 112.5 | 130.0 | 125 | 125.0 | 125.0 | 119.9 | 120.3 | 116.3 |
| $E_{rel}$ (B3LYP) / kcal mol$^{-1}$ PCM $H_2O$ | 0 | 23.1 | 5.9 | 29.0 | 29.0 | 11.4 | 34.7 | 17.1 | 0.0 | 6.0 | 6.4 | 6.4 | 11.9 | 16.6 | 36.3 |
| $E_{rel}$ (B3LYP) / kcal mol$^{-1}$ PCM DMSO | 0 | 23.0 | 6.1 | 29.2 | 29.3 | 11.8 | 35.1 | 17.8 | –[a] | –[a] | 6.7 | 6.6 | 12.4 | 17.2 | 37.0 |
| $E_{rel}$ (B3LYP) / kcal mol$^{-1}$ PCM $CCl_4$ | 0 | 23.5 | 9.3 | 32.4 | 32.4 | 17.6 | 40.8 | 26.1 | –[a] | –[a] | 10.1 | 9.9 | 18.4 | 25.0 | 47.2 |

[a] Calculation did not converge.

 © 2006 Wiley-VCH Verlag GmbH & Co. KGaA, Weinheim 

than the monotetrazole **136** and the tritetrazole **141** 11.1 kcal mol$^{-1}$ higher than the ditetrazole **139**. The activation energies for the first, second and third cyclization are 23.5, 22.8, and 22.7 kcal mol$^{-1}$. The formation of the tetrazole rings is accompanied by a decrease of the entropy and a decrease of the sum of the positive and negative Mulliken charges. The tetrazoles have higher individual positive charges. Similar to cyanuric azide, the ground states are more influenced by solvation in $CCl_4$, DMSO, and water than the ground states.

Solvation in $CCl_4$ favors the monotetrazole **136** by 3.3 kcal mol$^{-1}$ and the ditetrazole **139** by 6.2 kcal mol$^{-1}$ and the tritetrazole **141** by 8.8 kcal mol$^{-1}$ over the gas phase. The activation energy for the first cyclization is only slightly favored by 0.4 kcal mol$^{-1}$ and the activation energy for the second and third cyclization are favored by 3.0 kcal mol$^{-1}$ and 5.7 kcal mol$^{-1}$ over the gas phase. The optimization of the solvation of **142** and **143** in DMSO and $CCl_4$ did not converge. Solvation in water and DMSO is only different by maximally 1 kcal mol$^{-1}$. Solvation lead to a favorization of 6.7 kcal mol$^{-1}$ for the monotetrazole **136**, of 12.4 kcal mol$^{-1}$ for the ditetrazole **139** and of 17.8 kcal mol$^{-1}$ for the tritetrazole **141** over the gas phase. The activation energies for the cyclization are favored by 0.4, 6.4, and 11.8 kcal mol$^{-1}$ for the first, second and third cyclization. Compared to triazido-1,3,5-triazine, triazido-*s*-heptazine is even less likely to form a tetrazole and it is therefore not surprising that the attempt to form a tetrazole isomer from triazido-*s*-heptazine have not been successful.[21]

### Diazidotetrazine

The rotation barriers of the azide unit around the C–N bonds of diazidotetrazine are slightly lower than those of the azido-1,3,5-triazines (see Scheme 1). Cyclization of diazidotetrazine in a *trans* **149** and a *cis* **154** conformation was investigated (Scheme 17). In the crystal structure only *trans* **149** was found.[4] Its bonding parameters are in agreement with the calculation. As observed for the triazines, the azide $N_\beta$–$N_\gamma$ bond is shorter in the X-ray structure (see Supporting Information).

The *trans* and *cis* diazides **149** and **154** as well as the *trans* and *cis* monotetrazoles **151** and **156** are only separated at most 0.5 kcal mol$^{-1}$ at the MP2 level and even less at the CCSD(T) level of theory (Scheme 18). The B3LYP values in Table 7 show the same tendency. Similar to the results for the triazines, the MP2 energy differences between azide and tetrazoles are larger. The *cis* ditetrazole **158** has an energy that is 5.2 kcal mol$^{-1}$ higher than that of the *trans* ditetrazole **153** at the CCSD(T) level of theory. Therefore, the minimum energy cyclization path connects the *trans* diazide **149** with the *trans* ditetrazole **153**. The difference between the ditetrazole **153** and the monotetrazole **151** is with 12.6 kcal mol$^{-1}$ much larger than the difference of 2.9 kcal mol$^{-1}$ between diazide and monotetrazole. The cyclization of an azide group belonging to one of the previously mentioned 1,3,5-triazine derivatives resulted in relatively constant energy differences of 9 to 12 kcal mol$^{-1}$ per tetrazole ring. Therefore the cyclization of an azide group, especially the first cyclization, is favored for the tetrazine ring system compared to the triazine ring system. The activation energies for the first and second cyclization are 23.6 and 28.6 kcal mol$^{-1}$. For comparison, the monotetrazoles of pyridazine diazides and triazides are favoured by about 3 kcal mol$^{-1}$ over the all-azide and all-tetrazole isomers

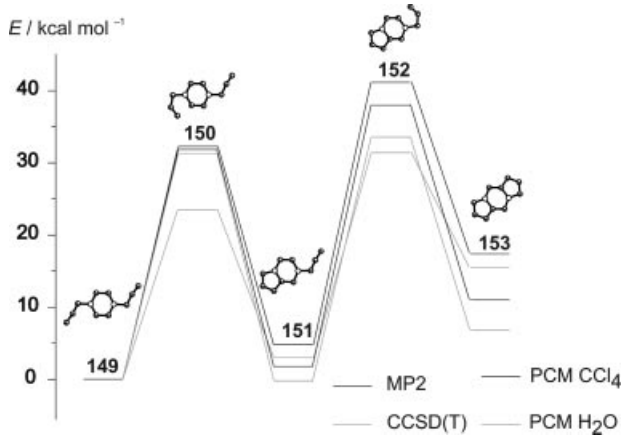


Scheme 18. Reaction profile for the ring closures in diazidotetrazine.

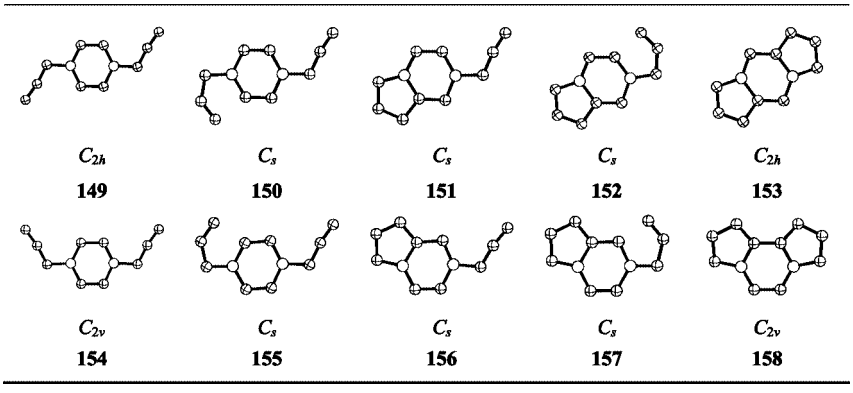


Scheme 17. Calculated diazidotetrazine isomers.

 © 2006 Wiley-VCH Verlag GmbH & Co. KGaA, Weinheim 

Table 7. Calculated energy differences between different diazidotetrazine isomers. The gas phase calculations include zero point energy corrections.

| | 149 | 150 | 151 | 152 | 153 | 154 | 155 | 156 | 157 | 158 |
|---|---|---|---|---|---|---|---|---|---|---|
| $E_{rel}$ (B3LYP/aug-cc-pVTZ) / kcal mol$^{-1}$ | 0 | 24.9 | 5.9 | 34.5 | 19.7 | 0.1 | – | 5.9 | – | 26.9 |
| $E_{rel}$ (MP2) / kcal mol$^{-1}$ | 0 | 31.7 | 4.7 | 41.2 | 17.2 | 0.1 | 31.8 | 5.2 | 42.8 | 24.9 |
| $E_{rel}$ (CCSD(T)) / kcal mol$^{-1}$ | 0 | 23.6 | 2.9 | 31.5 | 15.5 | 0.1 | 23.6 | 3.2 | 31.9 | 20.7 |
| $S$ / cal mol$^{-1}$ K$^{-1}$ | 96.4 | 92.8 | 90.7 | 85.5 | 82.9 | 96.4 | 92.8 | 90.7 | 86.2 | 83.9 |
| $E_{rel}$ (MP2) / kcal mol$^{-1}$ PCM $H_2O$ | 0 | 31.6 | –0.2 | 33.5 | 6.80 | 0.0 | 31.3 | –0.2 | 37.7 | 15.1 |
| $E_{rel}$ (MP2) / kcal mol$^{-1}$ PCM DMSO | 0 | 31.5 | 0.9 | 36.1 | 7.2 | 0.0 | 31.4 | –0.1 | 38.9 | 16.1 |
| $E_{rel}$ (MP2) / kcal mol$^{-1}$ PCM $CCl_4$ | 0 | 31.6 | 2.0 | 37.9 | 10.9 | 0.1 | 31.6 | 2.1 | 40.0 | 19.9 |

with activation energies of about 20 kcal mol$^{-1}$ for one cyclization.[24]

The formation of the tetrazole rings is accompanied by a decrease of the entropy and a decrease of the sum of the positive and negative Mulliken charges. Again the tetrazoles have higher individual positive charges. Solvation has a bigger effect on the ground states than on the transition states. In $CCl_4$ the monotetrazole **151** is favored by 2.7 kcal mol$^{-1}$ and the ditetrazole **153** by 6.3 kcal mol$^{-1}$, while the first and second transition states are favored by 0.1 and 3.3 kcal mol$^{-1}$. As before, the results of DMSO and water are similar. Solvation in water leads to a stabilization of the monotetrazole **151** by 4.9 kcal mol$^{-1}$ and of 10.4 kcal mol$^{-1}$ for the ditetrazole **153**. The activation energies for the first and second cyclization are lowered by 0.1 and 6.7 kcal mol$^{-1}$. After solvation in water, the monotetrazole **151** is 0.2 kcal mol$^{-1}$ lower in energy than the diazide **149**.

Very recently an equilibrium of diazidotetrazine with its monotetrazole in DMSO was observed with NMR spectroscopy.[21] Heating to 80 °C overcame the activation barrier and a ditetrazole was observed. The authors indicate that the ditetrazole **158** was formed. $^{13}C$ NMR spectroscopic data are not sufficient for this prediction. According to the energies caculated for the ditetrazole isomers **153** and **158**, we believe that ditetrazole **153** is formed in this reaction. For better identification of the diazide **149**, the monotetrazole **151** and the ditetrazole **153**, we included the calculated MP2 vibrational spectra in Figure 2 for easier assignment and positive identification of the respective isomers.

### 6,6′-Bis(azido)-azo-1,2,4,5-tetrazine and 6,6′-Bis(azido)-hydrazo-1,2,4,5-tetrazine

For comparison with the polyazidoazo- and hydrazo-1,3,5-triazines we also calculated the yet unknown bis(azido)azo- and bis(azido)hydrazo-1,2,4,5-tetrazines. In order to keep the computational costs low, all calculation were performed at the B3LYP level only. The rotation profiles along the C–N bond of the azo and hydrazo group are given in Scheme 11 and Scheme 12 and the rotation profile around the N–N bond of the hydrazo group in Scheme 13.

Both the azo- and hydrazotetrazines have the same *cis* and *trans* alignments of the azide groups found in bis(azido)-tetrazine. The hydrazo compound also has a third conformation due to the conformation of the hydrazo-hydrogen atoms.

The *trans* orientation of the azide groups is the lowest energy conformation of the azo- and hydrazo compounds, but the energy differences are negligible for the diazides and only very slight for the mono- and ditetrazoles. The azo-bridged monotetrazole **161** is 4.1 kcal mol$^{-1}$ higher than the diazide **159** and the ditetrazole **163** 9.2 kcal mol$^{-1}$ (Scheme 19, Table 8). The activation energies for the first

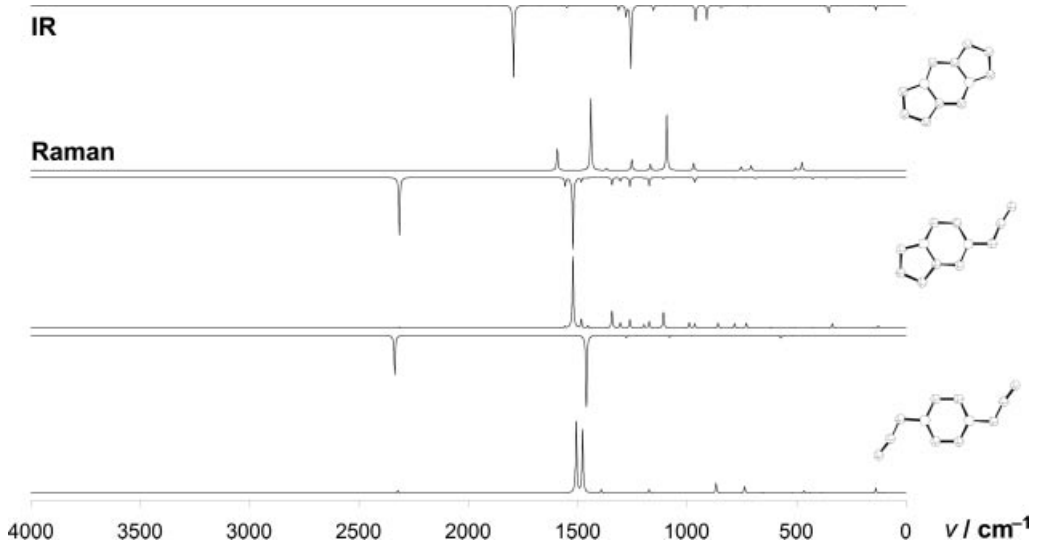


Figure 2. Vibrational spectra of diazidotetrazine isomers.

 © 2006 Wiley-VCH Verlag GmbH & Co. KGaA, Weinheim 

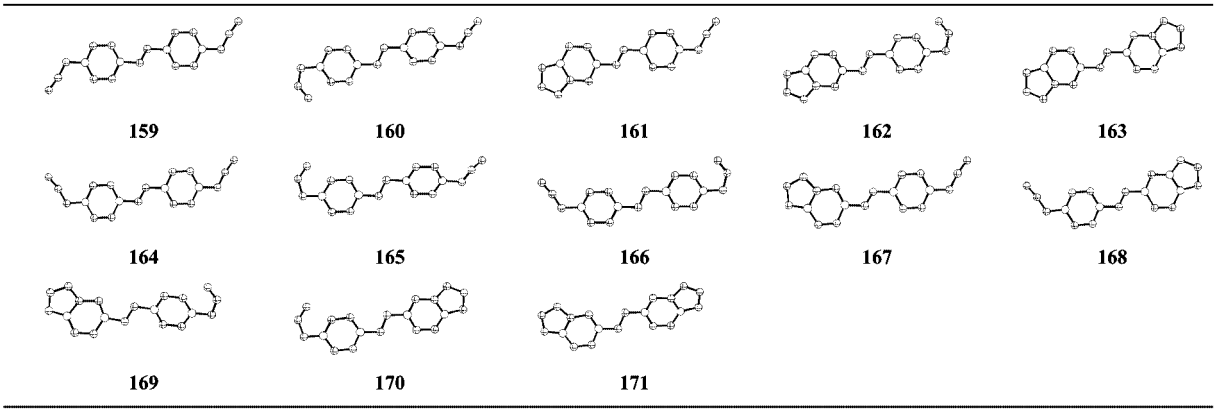


Scheme 19. Calculated isomers of bis(azido)azo-1,2,4,5-tetrazine.

Table 8. Calculated energy differences between different bis(azido)azo-1,2,4,5-tetrazine isomers. The gas phase calculations include zero point energy corrections.

| | **159** | **160** | **161** | **162** | **163** | **164** | **165** | **166** | **167** | **168** | **169** | **170** | **171** |
|---|---|---|---|---|---|---|---|---|---|---|---|---|---|
| $E_{rel}$ (B3LYP) / kcal mol$^{-1}$ | 0 | 20.95 | 4.1 | 25.4 | 9.2 | 0.0 | 21.0 | 21.0 | 4.2 | 4.35 | 26.5 | 25.5 | 9.2 |
| $S$ / cal mol$^{-1}$ K$^{-1}$ | 133.5 | 127.9 | 127.5 | 121.7 | 122.3 | 133.6 | 128.0 | 127.7 | 127.9 | 127.2 | 121.3 | 121.2 | 119.5 |
| $E_{rel}$ (B3LYP) / kcal mol$^{-1}$ PCM $H_2O$ | 0 | 21.63 | –0.3 | 21.6 | 0.1 | 0.0 | 21.7 | 21.8 | –0.2 | 0.1 | 21.8 | 21.8 | 0.7 |
| $E_{rel}$ (B3LYP) / kcal mol$^{-1}$ PCM DMSO | 0 | 21.65 | –0.1 | 21.7 | 0.5 | 0.0 | 21.7 | 21.8 | –0.1 | 0.2 | 21.8 | 22.0 | 6.9 |
| $E_{rel}$ (B3LYP) / kcal mol$^{-1}$ PCM $CCl_4$ | 0 | 21.33 | 1.36 | 23.0 | 3.6 | 0.0 | 21.4 | 21.4 | 1.4 | 1.6 | 21.4 | 23.1 | 3.7 |

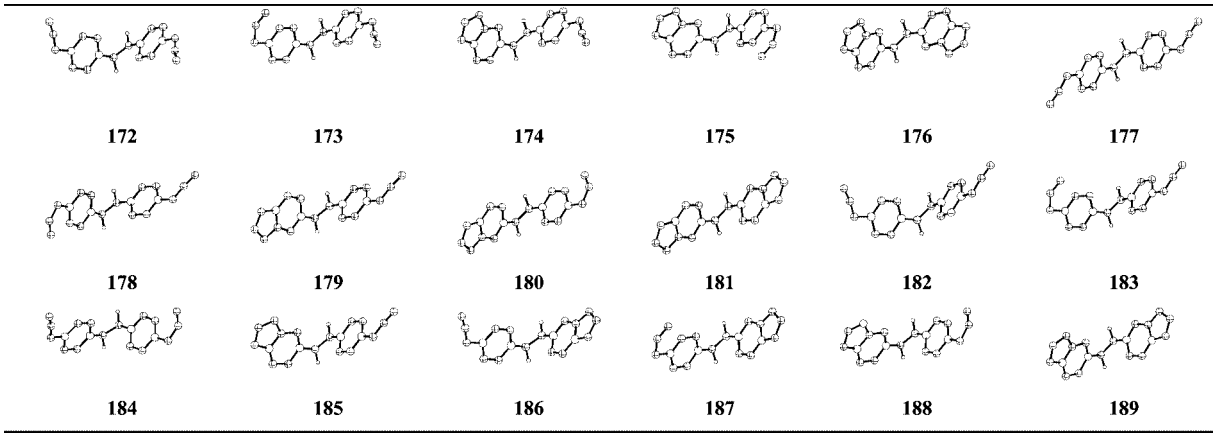


Scheme 20. Calculated isomers of bis(azido)hydrazo-1,2,4,5-tetrazine.

Table 9. Calculated energy differences between different bis(azido)azo-1,2,4,5-tetrazine isomers. The gas phase calculations include zero point energy corrections.

| | **172** | **173** | **174** | **175** | **176** | **177** | **178** | **179** | **180** | **181** |
|---|---|---|---|---|---|---|---|---|---|---|
| $E_{rel}$ (B3LYP) / kcal mol$^{-1}$ | 0 | 22.2 | 1.9 | 24.5 | 4.6 | 0.0 | 22.8 | 3.1 | 26.2 | 6.8 |
| $S$ / cal mol$^{-1}$ K$^{-1}$ | 135.0 | 130.0 | 128.3 | 123.0 | 121.5 | 135.0 | 129.7 | 127.9 | 123.0 | 119.9 |
| $E_{rel}$ (B3LYP) / kcal mol$^{-1}$ PCM $H_2O$ | 0 | 21.6 | –4.2 | 17.6 | –7.9 | 0.0 | 22.1 | –2.7 | 19.9 | –5.25 |
| $E_{rel}$ (B3LYP) / kcal mol$^{-1}$ PCM DMSO | 0 | 21.7 | –3.7 | 18.1 | –7.0 | 0.0 | 22.1 | –2.5 | 19.5 | –4.6 |
| $E_{rel}$ (B3LYP) / kcal mol$^{-1}$ PCM $CCl_4$ | 0 | 22.2 | –1.4 | 20.9 | –2.3 | 0.0 | 22.6 | –0.4 | 22.5 | –0.2 |
| | **182** | **183** | **184** | **185** | **186** | **187** | **188** | **189** | | |
| $E_{rel}$ (B3LYP) / kcal mol$^{-1}$ | 0.0 | 22.2 | 22.8 | 1.9 | 3.1 | 25.4 | 25.6 | 5.6 | | |
| $S$ / cal mol$^{-1}$ K$^{-1}$ | 134.9 | 129.7 | 129.5 | 128.1 | 128.0 | 123.8 | 122.7 | 121.1 | | |
| $E_{rel}$ (B3LYP) / kcal mol$^{-1}$ PCM $H_2O$ | 0 | 21.6 | 22.0 | –4.1 | –2.8 | 18.3 | 18.9 | –6.6 | | |
| $E_{rel}$ (B3LYP) / kcal mol$^{-1}$ PCM DMSO | –0.1 | 21.8 | 22.2 | –3.7 | –2.5 | 18.8 | 19.4 | –5.9 | | |
| $E_{rel}$ (B3LYP) / kcal mol$^{-1}$ PCM $CCl_4$ | 0.0 | 22.2 | 22.6 | –1.5 | –0.4 | 21.7 | 22.1 | –1.3 | | |

 © 2006 Wiley-VCH Verlag GmbH & Co. KGaA, Weinheim 

and second cyclization are 21.0 and 16.2 kcal mol$^{-1}$. The hydrazo-bridged monotetrazole **174** is only 1.9 kcal mol$^{-1}$ higher than the diazide **172** and the ditetrazole **176** 4.6 kcal mol$^{-1}$ (Scheme 20, Table 9). The activation energies for the first and second cyclization of the hydrazo-bridged compound are 22.2 and 19.9 kcal mol$^{-1}$. As observed before, the formation of the tetrazole rings is accompanied by a decrease of the entropy and a decrease of the sum of the positive and negative Mulliken charges with have higher individual charges for the tetrazoles.

Solvation also leads to a stabilization of the tetrazoles. In $CCl_4$ the azo-bridged monotetrazole **160** is favored by 2.4 kcal mol$^{-1}$ and the ditetrazole **163** by 9.1 kcal mol$^{-1}$. The activation energy for the first cyclization is increased by 0.3 kcal mol$^{-1}$ and the activation energy for the second cyclization is decreased by 2.4 kcal mol$^{-1}$. The hydrazo-bridged monotetrazole **174** is favored by 3.3 kcal mol$^{-1}$ and the ditetrazole **174** by 6.9 kcal mol$^{-1}$ in $CCl_4$. The activation energy for the first cyclization of the hydrazoazide is not influenced by $CCl_4$ and the activation energy for the second cyclization is lowered by 3.6 kcal mol$^{-1}$. DMSO and water solvation give similar energy differences. The energy difference to the diazide **159** for the azo-bridged tetrazole is lowered by 4.4 kcal mol$^{-1}$ and for the ditetrazole **163** by 9.1 kcal mol$^{-1}$ (Scheme 21). The activation energies for the first cyclization is increased by 0.6 kcal mol$^{-1}$ and the activation energy for the second cyclization is decreased by 3.8 kcal mol$^{-1}$. The solvation in water has a larger effect on the hydrazo-bridged compounds. Here the monotetrazole **174** is stabilized by 6.1 kcal mol$^{-1}$ and the ditetrazole **176** is stabilized by 12.5 kcal mol$^{-1}$ (Scheme 22). The activation energies for the first and second cyclization are lowered by 0.6 and 6.9 kcal mol$^{-1}$, respectively.

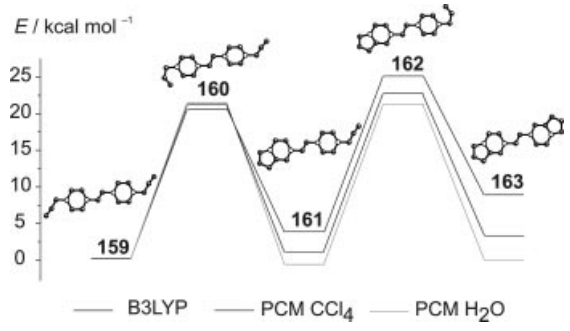


Scheme 21. Reaction profile for the ring closures in bis(azido)azo-1,2,4,5-tetrazine.

In absolute terms, the azo-bridged monotetrazole **161** is favored over the diazide **159** in the investigated solvents and the azo-bridged ditetrazole is only 0.1 kcal mol$^{-1}$ above the diazide in aqueous solution. The hydrazo-bridged mono-**174** and ditetrazoles **176** are even more favored over the diazides in solution. The diazide **176** is the lowest energy diazo-bridged compound in all solvents and is favored by 7.9 kcal mol$^{-1}$ over the diazide in aqueous solution.

For better experimental assignment, the calculated B3LYP vibrational spectra of the azo- and hydrazo-bridged

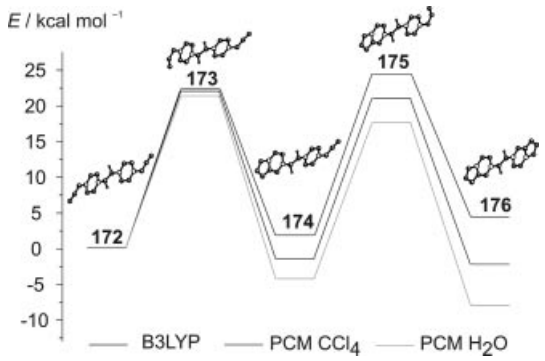


Scheme 22. Reaction profile for the ring closures in bis(azido)-hydrazo-1,2,4,5-tetrazine.

diazides, azidotetrazoles, and ditetrazoles are shown in Figure 3 and Figure 4.

## Conclusions

The formation of a tetrazole ring requires a planar arrangement of the azide group. Both for polyazido-1,3,5-triazines and bis(azido)-1,2,4,5-tetrazines several planar orientations of the azide group are possible. The rotation barrier of the azide group is around 10 kcal mol$^{-1}$ and the energy differences between the different planar conformers of the polyazides are slight. The ring closed polytetrazoles show larger energy differences. The minimum energy conformers derive from the $C_{3h}$ isomer of triazido-1,3,5-triazine and from *trans* bis(azido)tetrazine.

The ring closure of an azide to a tetrazole in the 1,3,5-triazine systems increases the electronic energy by 9–12 kcal mol$^{-1}$ per tetrazole ring, the activation energy for a tetrazole ring formation is around 20 kcal mol$^{-1}$. The electronic energy of the tetrazines increases by 2–5 kcal mol$^{-1}$ for the first tetrazole ring and by another 3–10 kcal mol$^{-1}$ for the second tetrazole ring. It was shown that the electron-donating amino group lowers the energy of a tetrazole ring relative to the azide by about 3 kcal mol$^{-1}$ and the electron-withdrawing nitro group increases the relative energy of a tetrazole ring by about 6 kcal mol$^{-1}$ relative to the azide. The entropy of the investigated compounds decreases slightly with every tetrazole ring closure due to the loss of degrees of freedom. Thus it is possible to overcome the activation barrier for the formation of some tetrazoles, e.g. diazidotetrazine, by heating, but at higher temperatures the azides are generally favored.

Taking into account solvent effects using a continuum of an uniform dielectric, the energy differences between the tetrazoles and the azides are lowered for both the polyazido-1,3,5-triazines and -tetrazines. This is explained by higher charges of individual atoms in the tetrazoles compared to the azides. Polar solvents stabilize these charges compared to the gas phase and lower the energy difference to the azides. The effect is smaller for the apolar $CCl_4$ with about 3 kcal mol$^{-1}$ per tetrazole unit and larger for the more polar solvents DMSO and water with about 6 kcal mol$^{-1}$

 © 2006 Wiley-VCH Verlag GmbH & Co. KGaA, Weinheim 

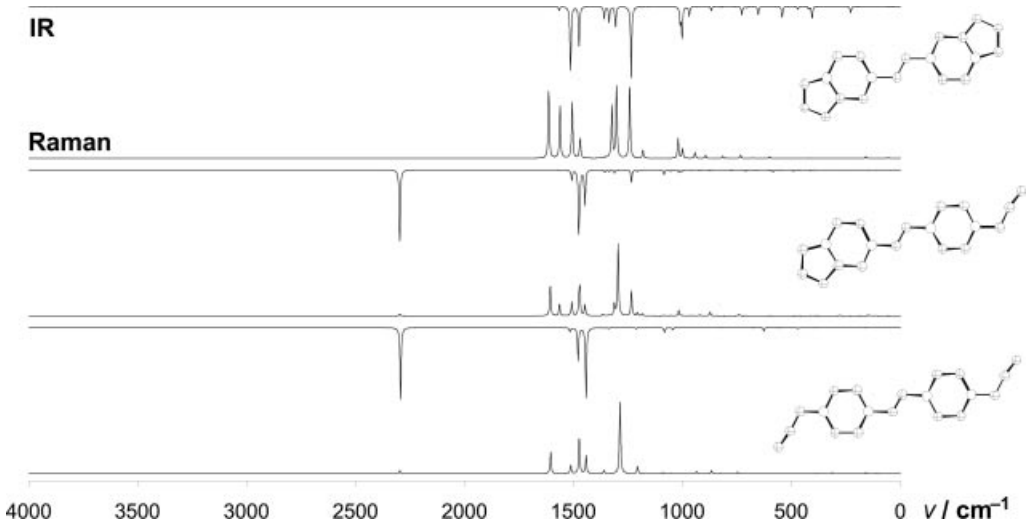


Figure 3. Vibrational spectra of bis(azido)azo-1,2,4,5-tetrazine isomers.

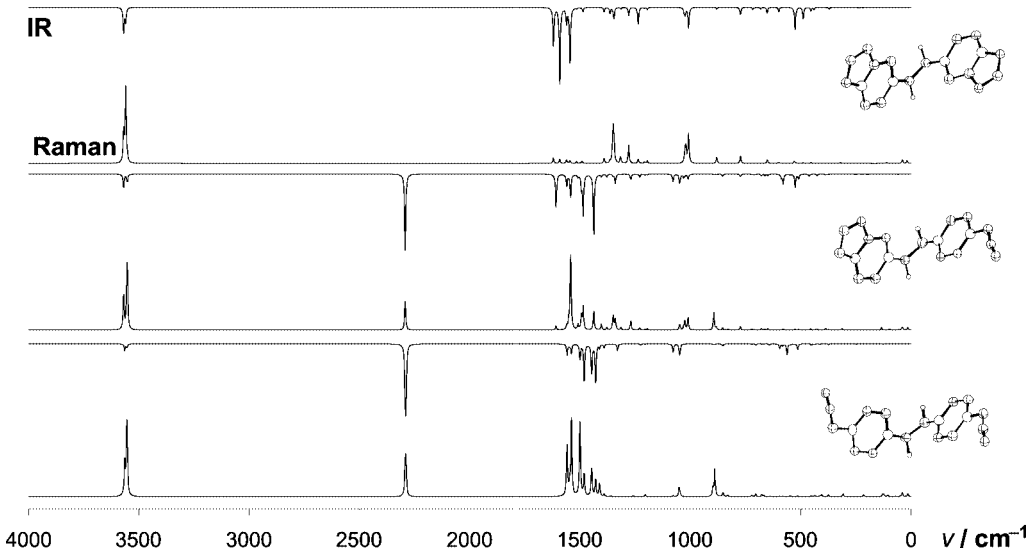


Figure 4. Vibrational spectra of bis(azido)hydrazo-1,2,4,5-tetrazine isomers.

per tetrazole unit. Solvation in DMSO has about the same effect as solvation in water. We conclude that solvation can change the equilibrium for the tetrazines. For the 1,3,5-triazines the energy differences are too large for the effects of the solvation to allow the formation of a tetrazole. For practical consequences two other effects have to be taken into account: hydrogen bonds to solvents like water which are not included in our treatment and the lattice energy of the respective azide and tetrazole species. Depending on lattice energy and therefore solubility, it is possible that both the ditetrazoles and the diazides of tetrazines can be isolated, while the energy differences of the 1,3,5-triazines suggest that the tetrazoles derivatives cannot be prepared from the corresponding azides. Solvation in DMSO and water makes the monotetrazoles **151** and **161** the minimum energy species for the bis(azido)-1,2,4,5-tetrazine and the bis(azido)azo-1,2,4,5-tetrazine system. The ditetrazole **176** is the minimum energy species in the bis(azido)hydrazo-1,2,4,5-tetrazine system.

The calculated data explain the experimental detection of the mono- and ditetrazole derivatives of diazidotetrazine. As the data supplied by the authors do not confirm the conformation of the ditetrazine, we believe that isomer **153**, which is 8.3 kcal mol$^{-1}$ lower in energy, is formed in the reaction in contrast to the reported isomer **158**.

## Computational Methods

The geometries of the triazido-1,3,5-triazine, aminodiazido-1,3,5-triazine, diazidonitro-1,3,5-triazine, and diazidotetrazine compounds were optimized at the MP2 level (full active orbital space) within the symmetry constraints stated in the respective Tables using a cc-pVDZ basis set.[25] Due to computational cost all other compounds were optimized on the B3LYP level of theory with the

 © 2006 Wiley-VCH Verlag GmbH & Co. KGaA, Weinheim 

same basis set. Comparison of the B3LYP energies from reference[20] for cyanuric azide and of values obtained for the diazidotetrazine isomers at the B3LYP/aug-cc-pVTZ level of theory shows good agreement with the energies obtained at the CCSD(T) level. The vibrational frequencies, which were computed at the optimized structures, show true minima on the potential energy surface with no imaginary frequencies for all azides and tetrazoles. The located transition states are of the first order, the Cartesian displacement coordinates of the imaginary frequency mode correspond to the ring opening of a tetrazole to an azide. For further validation single-point CCSD(T) calculations using a cc-pVDZ basis set were performed using the full orbital space for the triazido-1,3,5-triazine, aminodiazido-1,3,5-triazine, diazidonitro-1,3,5-triazine, and diazidotetrazine compounds. A Mulliken analysis was used for the charge discussion. For the discussion of solvent-induced changes, the solvent effects were introduced within the self-consistent reaction field (SCRF) formalism by means of the polarized continuum model (PCM) of Tomasi et al.[26] as implemented in GAUSSIAN 03. This method models the solvent as a continuum of uniform dielectric and therefore does not take into account explicit solvent–solute interactions such as hydrogen bonding. Three different continuum environments with the characteristics of $CCl_4$, DMSO and water were employed to explore the influence of an increasing dielectric permittivity on the potential energy of the investigated compounds. While the isomers of cyanuric azide, triazido-*s*-heptazine and diazidotetrazine were optimized within the PCM model, for all other compounds single point calculations were used due to computational cost. Coupled cluster single point calculations, for which the MP2 geometries were used, were performed with the MOLPRO program package,[27] all other calculations were performed with Gaussian03.[28]

**Supporting Information** (see also the footnote on the first page of this article): Computational details.

## Acknowledgments

Financial support of this work by the University of Munich (LMU), the Fonds der Chemischen Industrie and the European Research Office (ERO) of the U. S. Army Research Laboratory (ARL) under contract no. N 62558-05-C-0027 is gratefully acknowledged. We are indebted to the Leibniz Rechenzentrum for generous allocation of computer time. Thanks are also due to My-Hang V. Huynh and Michael Hiskey for many helpful suggestions and fruitful discussions.

[1] a) A. Hammerl, G. Holl, T. M. Klapötke, H. Nöth, M. Warchhold, *Propellants Explos. Pyrotech.* **2003**, *28*, 165–173; b) A. Hammerl, G. Holl, T. M. Klapötke, P. Mayer, J. J. Weigand, *Propellants Explos. Pyrotech.* **2005**, *30*, 44–52; c) A. Hammerl, T. M. Klapötke, P. Schwerdtfeger, *Chem. Eur. J.* **2003**, *9*, 5511–5519.

[2] I. Widlow, Y. W. Chung, *Braz. J. Phys.* **2000**, *30*, 490–498.

[3] a) E. G. Gillan, *Chem. Mater.* **2000**, *12*, 3906–3912; b) W. Long, Y. Shun, Y. Bing, *Rare Met. Mater. Eng.* **2002**, *31*, 96–100, and references cited therein; c) A. K. Pal, *Curr. Sci.* **2002**, *83*(3), 225–236.

[4] M. H. V. Huynh, M. A. Hiskey, J. G. Archuleta, E. L. Roemer, R. Gilardi, *Angew. Chem.* **2004**, *116*, 5776–5779; *Angew. Chem. Int. Ed.* **2004**, *43*, 5658–5661.

[5] M. H. V. Huynh, M. A. Hiskey, J. G. Archuleta, E. L. Roemer, *Angew. Chem.* **2005**, *117*, 747–749; *Angew. Chem. Int. Ed.* 2005, *44*, 737–739.

[6] A. F. Brigas, *Tetrazoles*, in: *Science of Synthesis* (Eds.: I. Shinkai, R. C. Storr), Thieme Verlag, Stuttgart, **2004**, *13*, 861–915.

[7] R. Huisgen, *Angew. Chem.* **1968**, *80*, 329; *Angew. Chem. Int. Ed. Engl.* **1968**, *7*, 321.

[8] P. Cmoch, *Magn. Reson. Chem.* **2002**, *40*, 507–516.

[9] J. Elguero, R. M. Claramunt, A. J. H. Summers, *Adv. Heterocycl. Chem.* **1978**, *22*, 183–320.

[10] R. N. Butler, *Tetrazoles*, in: *Comprehensive Heterocyclic Chemistry II* (Eds.: A. R. Katritzky, C. W. Ress, E. F. V. Scriven, R. C. Storr), Pargamon, Oxford, **1996**, *4*, 621–678 and 905–1006.

[11] S. Ito, Y. Tanaka, A. Kakehi, *Bull. Chem. Soc. Jpn.* **1984**, *57*, 539–543.

[12] M. T. Nguyen, G. Leroy, M. Sana, J. Elguero, *J. Heterocycl. Chem.* **1982**, *19*, 943–944.

[13] G. L'abbé, *J. Heterocycl. Chem.* **1984**, *21*, 627–638.

[14] P. Cmoch, J. W. Wiench, L. Stefaniak, G. A. Webb, *J. Mol. Struct.* **1999**, *510*, 165–178.

[15] E. Cubero, M. Orozco, F. J. Luque, *J. Am. Chem. Soc.* **1998**, *120*, 4723–4731.

[16] R. Granados, M. Rull, J. Vilarasa, *J. Heterocycl. Chem.* **1976**, *13*, 281.

[17] T. Sasaki, K. Kanematsu, M. Murata, *Tetrahedron* **1971**, *27*, 5121.

[18] C. Temple, M. C. Thorpe, W. C. Coburn, J. A. Montgomery, *J. Org. Chem.* **1966**, *31*, 935–938.

[19] E. Keßenich, T. M. Klapötke, J. Knizek, H. Nöth, A. Schulz, *Eur. J. Inorg. Chem.* **1998**, 2013–2016.

[20] E. Kessenich, K. Polborn, A. Schulz, *Inorg. Chem.* **2001**, *40*, 1102–1109.

[21] M. H. V. Huynh, M. A. Hiskey, D. E. Chavez, D. L. Naud, R. D. Gilardi, *J. Am. Chem. Soc.* **2005**, *127*, 12537–12543.

[22] M. H. V. Huynh, M. A. Hiskey, E. L. Hartline, D. P. Montoya, R. Gilardi, *Angew. Chem. Int. Ed.* **2004**, *43*, 4924–4928.

[23] D. R. Miller, D. C. Swenson, E. G. Gillan, *J. Am. Chem. Soc.* **2004**, *126*, 5372–5373.

[24] R. D. Allan, J. R. Greenwood, T. W. Hambley, J. R. Hanrahan, D. E. Hibbs, S. Itani, H. W. Tran, P. Turner, *Org. Biomol. Chem.* **2004**, *2*, 1782–1788.

[25] D. E. Woon, T. H. Dunning Jr, *J. Chem. Phys.* **1993**, *98*, 1358–1371.

[26] J. Tomasi, B. Mennucci, E. Cancès, *J. Mol. Struct. (Theochem)* **1999**, *464*, 211.

[27] *MOLPRO, a package of ab initio programs*, designed by H.-J. Werner and P. J. Knowles, version 2002.3, R. D. Amos, A. Bernhardsson, A. Berning, P. Celani, D. L. Cooper, M. J. O. Deegan, A. J. Dobbyn, F. Eckert, C. Hampel, G. Hetzer, P. J. Knowles, T. Korona, R. Lindh, A. W. Lloyd, S. J. McNicholas, F. R. Manby, W. Meyer, M. E. Mura, A. Nicklass, P. Palmieri, R. Pitzer, G. Rauhut, M. Schütz, U. Schumann, H. Stoll, A. J. Stone, R. Tarroni, T. Thorsteinsson, H.-J. Werner.

[28] M. J. Frisch, G. W. Trucks, H. B. Schlegel, G. E. Scuseria, M. A. Robb, J. R. Cheeseman, J. A. Montgomery Jr, T. Vreven, K. N. Kudin, J. C. Burant, J. M. Millam, S. S. Iyengar, J. Tomasi, V. Barone, B. Mennucci, M. Cossi, G. Scalmani, N. Rega, G. A. Petersson, H. Nakatsuji, M. Hada, M. Ehara, K. Toyota, R. Fukuda, J. Hasegawa, M. Ishida, T. Nakajima, Y. Honda, O. Kitao, H. Nakai, M. Klene, X. Li, J. E. Knox, H. P. Hratchian, J. B. Cross, C. Adamo, J. Jaramillo, R. Gomperts, R. E. Stratmann, O. Yazyev, A. J. Austin, R. Cammi, C. Pomelli, J. W. Ochterski, P. Y. Ayala, K. Morokuma, G. A. Voth, P. Salvador, J. J. Dannenberg, V. G. Zakrzewski, S. Dapprich, A. D. Daniels, M. C. Strain, O. Farkas, D. K. Malick, A. D. Rabuck, K. Raghavachari, J. B. Foresman, J. V. Ortiz, Q. Cui, A. G. Baboul, S. Clifford, J. Cioslowski, B. B. Stefanov, G. Liu, A. Liashenko, P. Piskorz, I. Komaromi, R. L. Martin, D. J. Fox, T. Keith, M. A. Al-Laham, C. Y. Peng, A. Nanayakkara, M. Challacombe, P. M. W. Gill, B. Johnson, W. Chen, M. W. Wong, C. Gonzalez, J. A. Pople, *Gaussian 03, Revision B.1*, Gaussian, Inc., Pittsburgh PA, **2003**.

Received: February 3, 2006
Published Online: April 20, 2006

 © 2006 Wiley-VCH Verlag GmbH & Co. KGaA, Weinheim 

DOI: 10.1002/ejic.200500855

# Comparative Sol–Hydro(Solvo)thermal Synthesis of $TiO_2$ Nanocrystals

Xianfeng Yang,[a] Hiromi Konishi,[b] Huifang Xu,[c] and Mingmei Wu*[a]

**Keywords:** Crystal growth / Nanostructures / Self-assembly / Solvothermal synthesis / Titanium

Three small inorganic compounds [acetic acid ($CH_3COOH$), nitric acid ($HNO_3$), and hydrochloric acid (HCl)] and five small organic compounds [*n*-butyl alcohol ($CH_3CH_2CH_2CH_2OH$), 1,2-propanediol ($CH_2OHCHOHCH_3$), propane-1,3-dicarboxylic acid ($HOOCCH_2COOH$), butane-1,4-dicarboxylic acid ($HOOCCH_2CH_2COOH$), and ethylenediamine ($H_2NCH_2CH_2NH_2$)] with different donors ($Cl^-$, $NO_3^-$, OH, $COO^-$, and $NH_2$) are used respectively and comparatively in different reaction media for tailoring the sol–hydrothermal synthesis of $TiO_2$ nanocrystals at a specific reaction temperature and/or for different reaction times. Both anatase and rutile with a variety of nanostructures such as nanocubes, nanorods, nanoneedles, and their self-assembled nanospheres are selectively grown. Well-defined and crystalline anatase nanocrystals with a narrow size distribution are prepared in the presence of *n*-butyl alcohol. With the use of HCl, nanoneedles and their assembled nanospheres of phase-pure rutile are obtained under much less drastic conditions, even at 100 °C and for only two hours. The effects of the reaction media, synthesis temperatures, and aging times on the structures and shapes of the products are investigated in detail by powder X-ray diffraction (XRD), scanning electron microscopy (SEM), and transmission electron microscopy (TEM).
(© Wiley-VCH Verlag GmbH & Co. KGaA, 69451 Weinheim, Germany, 2006)

## Introduction

Titanium dioxide has great potential in pigments, sensors, dielectric ceramics, as a catalyst supporter, and in solar cells as it exhibits outstanding ability for deodorization, air purification, and sterilization by strong photocatalysis.[1–10] Its performance depends to a large extent on its physical and chemical nature, which are related to its crystal structure, grain (crystal) size, morphology, and even surface structure.[11] Therefore, there is considerable interest in the controlled preparation of $TiO_2$ with a specific nanostructure.[12–24]

Many chemical routes have been developed to synthesize titania nanoparticles, typically gas condensation and wet chemistry.[25–32] In the former, it is not easy to control grain size and crystal shape; in addition, there are some limitations such as low output, complex equipment, and high cost. In contrast, it is much easier to control and modify the growth by adopting appropriate organic ligands in wet chemical processing such as sol–gel and hydrothermal synthesis.

[a] State Key Laboratory of Optoelectronic Materials and Technologies, School of Chemistry and Chemical Engineering, Sun Yat-Sen (Zhongshan) University,
Guangzhou, 510275, P. R. China,
Fax: +86-20-8403-6766
E-mail: ceswmm@sysu.edu.cn
[b] Department of Earth and Planetary Sciences, Johns Hopkins University,
Baltimore, MD 21218, USA
[c] Department of Geology and Geophysics, University of Wisconsin,
Madison, Wisconsin 53706, USA

The sol–gel approach provides a feasible route to prepare nanosized particles by using organic ligands to confine the growth. However, the high-temperature calcination may lead to aggregation into larger particles, phase transformation, and unavoidable evaporation of organic molecules. More attention has been paid to hydrothermal synthesis because of its much milder and friendly reaction conditions in a tightly closed vessel, and it shows advantages over sol–gel processes in most aspects.[30,31]

Multidispersed nanocrystals are generally produced because of the heterogeneous nature of the reaction and Ostwald ripening during hydrothermal aging. Therefore, the use of an organic solvent as a reaction medium[16,32] and of organic surfactants as ligands to confine the growth has raised great interest.[21,22] It has been reported that rutile nanofibers and poorly crystalline, multidispersed anatase nanoparticles can be prepared using alcohols as solvents.[33] In the first part of this manuscript, we will use *n*-butyl alcohol instead of water as a nonaqueous reaction medium and titanium *n*-butoxide (TNB) as a titanium precursor to prepare monodispersed anatase $TiO_2$ nanocubes.

Besides the use of organic surfactants with long alkyl chains, some smaller organic acids and amines with oxygen and nitrogen as donors have also been employed to modify the growth of titania in aqueous or nonaqueous solvents.[17,34] For example, Sugimoto and co-workers have investigated organic amines for the shape-controlled synthesis of $TiO_2$ nanoparticles by employing titanium isopropoxide as a titanium source[29] while Jiang and co-workers have investigated carboxylic acids for the size-controlled synthesis of $TiO_2$ by employing inorganic metatitanic acid as a

 © 2006 Wiley-VCH Verlag GmbH & Co. KGaA, Weinheim InterScience 

titanium source.[35] The use of diols in an autoclave synthesis of nanosized $TiO_2$ crystals has also been reported in several papers.[36,37] Herein we compare the use of organic diamines, diacids, and diols as additives on the growth of $TiO_2$ nanocrystals in a sol–hydrothermal approach.

As with the use of organic molecules, inorganic acidic aqueous solutions have been extensively used in the past few decades to precipitate $TiO_2$ nanocrystals. Besides our previous work, the influence of some small inorganic acids such as HCl on the growth of products has been investigated in detail.[30,38,39] Recently, the growth process of $TiO_2$ nanocrystals is receiving more and more interests.[40–42] However, to the best of our knowledge there are no reports about the evolution of one-dimensional rutile nanostructures with hydrothermal growth and aging. Such a growth and aging process of pure-phase rutile nanocrystals is investigated here in detail based on our previous work.[30]

## Results and Discussion

### The Use of Pure Water as Solvent

TNB is very reactive towards nucleophilic reagents and its hydrolysis occurs very easily in water. However, its hydrolysis can be modified and the growth of the resultant $TiO_2$ controlled by organic alcohols, acids, and even amines. A comparable experiment was performed without adding any additive or co-solvent to investigate the effect of alcohol, acid, and amine on the crystallization of $TiO_2$. The powder XRD pattern shown in part a of Figure 1 reveals that $TiO_2$ particles from "pure hydrothermal treatment" of TNB crystallize in phase-pure tetragonal anatase (JCPDS card no. 84-1286) in the space group $I4_1/amd$ (no. 141) with unit cell dimensions $a$ = 0.3782 and $c$ = 0.9502 nm. The TEM image in Figure 1 (b) demonstrates that most of the particles range from 10 to 20 nm in size and are finely dispersed. The crystal sizes calculated from the 101 and 200 diffractions using Scherrer's equation are 15.7 and 12.2 nm, respectively. The ratio of $D_{101}/D_{200}$ is about 1.30, which indicates some anisotropic growth. A few aggregates and much larger particles can be clearly observed, which is probably due to the easy hydrolysis of TNB, precipitation of amorphous titania particles, and heterogeneous reactions. In order to obtain more uniform titania nanocrystals, organic solvents such as *n*-butyl alcohol were used as solvents and/or chelating ligands to inhibit hydrolysis and manipulate the growth of $TiO_2$.

### The Use of Organic Compounds

#### *n-Butyl Alcohol as Solvent*

Recently, highly crystalline anatase nanoparticles have been synthesized by the reaction of titanium tetraisopropoxide with common ketones and aldehydes as oxygen-supplying agents under solvothermal conditions.[32] In our present work, highly crystalline and monodispersed anatase nanocrystals are obtained in *n*-butyl alcohol. TNB is dissolved in *n*-butyl alcohol to form a transparent sol. This homogeneous sol can be used in a solvothermal reaction to prepare uniform $TiO_2$ nanocrystals. During the synthesis, the etherification of *n*-butyl alcohol in the system would occur and slowly generate water, which could play a role as an oxygen donor in the hydrolysis of TNB to form titania.[33]

The powder XRD pattern (Figure 2, a2) indicates the product is phase-pure anatase. The calculated crystallite

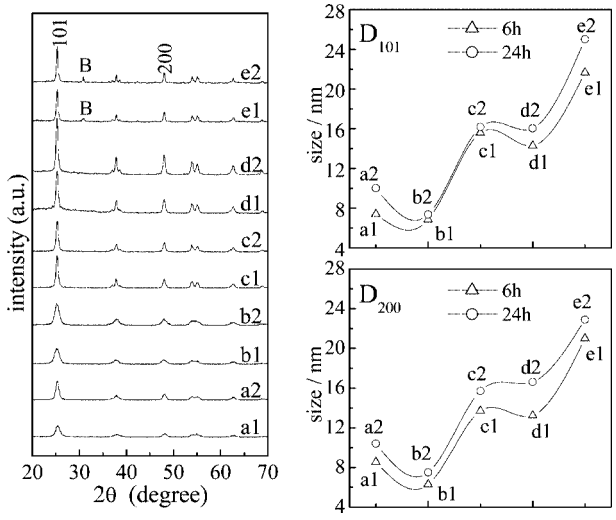


Figure 2. XRD patterns (left panel) of $TiO_2$ powders derived from several different media at 220 °C after 6.0 h (a1–e1) and 24 h (a2–e2), and a comparison of the corresponding calculated particle sizes by fitting the FWHM of (101) (top-right panel) and (200) (bottom-right panel) peaks: (a) *n*-butyl alcohol, (b) 1,2-propanediol, (c) propanedicarboxylic acid, (d) butanedicarboxylic acid, (e) ethylenediamine. B means Brookite.

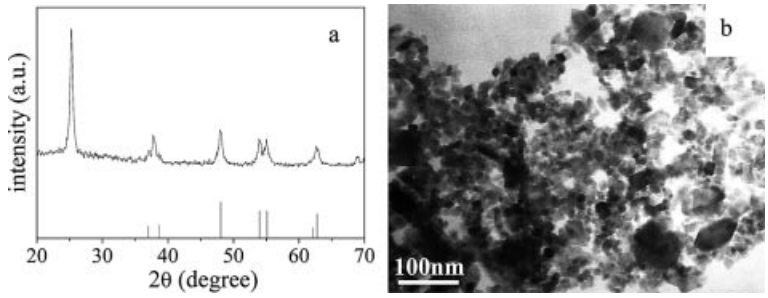


Figure 1. (a) Powder XRD pattern of the nanocrystalline titania product generated in "pure water" at 220 °C for 24 h (top), and pattern with vertical bars (bottom) derived from the JCPDS card (no. 84-1286) of anatase $TiO_2$. (b) TEM image of the product.

 © 2006 Wiley-VCH Verlag GmbH & Co. KGaA, Weinheim 

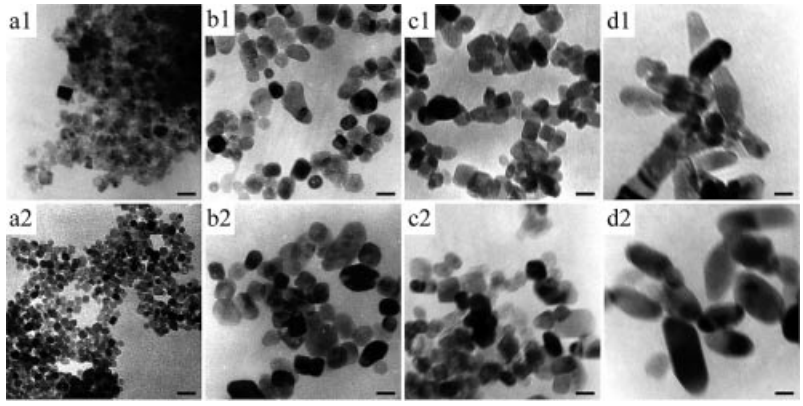


Figure 3. TEM images of nanocrystalline $TiO_2$ samples obtained under various sol–hydrothermal conditions: (a) *n*-butyl alcohol, (b) propanedicarboxylic acid, (c) butanedicarboxylic acid, (d) ethylenediamine. Scale bar: 20 nm.

sizes are 10.0 ($D_{101}$) and 10.4 nm ($D_{200}$), which imply an isotropic growth of $TiO_2$ nanocrystals. Besides the crystal sizes, the particle sizes of $TiO_2$, as displayed in Figure 3 (a2), are smaller than those in Figure 1 (b), further confirming that the use of *n*-butyl alcohol can confine the growth of titanium dioxide. Besides acting as an oxygen donor, *n*-butyl alcohol is also the by-product of the hydrolysis of TNB, therefore the use of *n*-butyl alcohol as a solvent would significantly retard the hydrolysis, polycondensation, and eventual crystallization and growth. More significantly, monodispersed nanocubes of highly crystalline anatase crystals are obtained from such a solvothermal growth in *n*-butyl alcohol.

### *An Organic Diol*

In order to compare the effect of a monoalchol and diol on the growth of $TiO_2$, 1,2-propanediol was used as an additive. A homogeneous sol of the precursor was formed by mixing TNB and 1,2-propanediol with magnetic stirring before performing the reaction. The product was indexed to be anatase, with crystallite sizes of 7.4 ($D_{101}$) and 7.5 nm ($D_{200}$; Figure 2, b2), which also indicate an isotropic growth as compared to that obtained with *n*-butyl alcohol. However, 1,2-propanediol inhibits the growth of $TiO_2$ more, probably due to its stronger chelating ability because of its didentate structure.

### *Organic Diacids*

A carboxyl group could serve as a donor to coordinate titanium atom in aqueous solution,[35] and organic acids can serve as ligands to limit the hydrolysis of TNB. Thus, a homogeneous hydrosol was produced as a hydrothermal reaction precursor for the formation of uniform titania nanoparticles. Herein, propanedicarboxylic acid and butanedicarboxylic acid were chosen as additives in the reaction media to modify the hydrothermal growth of $TiO_2$. The products were identified from their powder XRD patterns to be anatase (parts c2 and d2 in Figure 2). Highly dispersed nanoparticles, as shown in Figure 3 (see b2 and c2), are clearly obtained. Although organic diacids could be used as ligands to complex titanium atoms and might confine the growth of $TiO_2$ crystals, in our present work the calculated crystal sizes ($D_{101}$ = 16.2, $D_{200}$ = 15.7 nm and $D_{101}$ = 16.2, $D_{200}$ = 16.6 nm for propanedicarboxylic acid and butanedicarboxylic acid, respectively) are a little larger than those from a "pure hydrothermal reaction", and are much larger than those from alcohols (Figure 2, right panel). Thus, the ability of these diacids to confine the growth is greatly reduced. This can be attributed to the presence of $H_3O^+$ ions[30,31] and esterification of the acid with *n*-butyl alcohol, which is the by-product of the hydrolysis of TNB. In this way, the chelating ability of the acid is greatly reduced.

### *A Diamine*

The titanium dioxide product from the reaction with the addition of ethylenediamine is anatase with a trace of brookite (Figure 2, e2). The existence of brookite might result from the weakly basic nature of the amine.[43]

The crystal sizes of the product are related to both nucleation and growth: a greater number of nuclei generally result in a smaller crystal size. The isoelectronic point (IEP) of titania is around pH 6. In either basic or acidic medium, the solubility of titania is greater than that in both alcohol and water, which means that the number of nucleation sites in either a basic or acidic medium is less than that in alcohol. Therefore, the sizes of crystals grown in either acidic or basic medium should be larger than those grown in alcohol or water. In addition, it has been well established that both organic amines and acids can catalyze the growth of titania particles.[13,30] The crystal sizes, as shown in Figure 2 (e2), are larger than those from alcohol (parts a2 and b2 in Figure 2).

Figure 3 (d2) reveals that the use of ethylenediamine can significantly promote an anisotropic growth of $TiO_2$ nanocrystals and, consequently, $TiO_2$ nanorods are obtained. The anisotropic growth of anatase is attributed to its stronger adsorption of ethylenediamine onto the crystal faces parallel to the *c*-axis than the others.[29] This organic diamine is a strong ligand for some transition metals such as zinc, copper, and nickel, and is widely used in coordination chemistry.[44] However, the capping ability of nitrogen

 © 2006 Wiley-VCH Verlag GmbH & Co. KGaA, Weinheim 

atoms − the electron donors in amines − with titanium is relatively weaker than the oxygen atoms in carboxyl moieties or hydroxide ions. Therefore, the particle sizes of the final products obtained from the aqueous solution of ethylenediamine are significantly larger than those from the organic media mentioned above (Figure 2).

### Reaction Times

In order to further investigate the growth behavior of $TiO_2$ in various reaction media in the presence of organic alcohol, acid, or amine, the reaction time was shortened to six hours. The powder XRD and TEM images in Figures 2 and 3, respectively, confirm similar growth features to those observed after 24 h, and it can also be observed that the crystal sizes of $TiO_2$ from the amine medium are the largest and those from the alcohol medium are the smallest. However, some titania particles are not well crystallized after a crystallization time of only 6.0 h, as observed in Figure 3 (a1).

Well-crystallized anatase particles can be observed after only a short time either in butanediacarboxylic acid or in propanedicarboxylic acid. Anatase crystals exhibit very similar growth behavior in these two organic acids. The TEM images and calculated crystal sizes indicate a similar isotropic growth behavior of $TiO_2$ nanocrystals in the presence of these organic acids, which have similar structures except for the length of their alkyl chain.

The resultant crystal sizes are dependent on a cooperative effect of hydrolysis, nucleation, growth, and aging. Beside the growth, the other fundamental significance for studying the size and shape control of the nanocrystals lies in the understanding of their nucleation. Facile hydrolysis, such as in "pure water", might yield larger amount of nuclei and reduce crystal sizes, especially without aging, although it could also shorten the time to reach the nucleation and growth step, which might increase the crystal sizes. Therefore, the role of the nucleation and its effect on the crystal sizes is quite complicated and generally poorly understood due to a lack of reliable experimental data.[45] Here, for example, the growth of anatase crystals in alcohol, particularly in the diol, is obviously inhibited, whereas in amine it is considerably accelerated (Figure 2, right panel). In summary, the ability to retard the growth of anatase follows the trend 1,2-propanediol > *n*-butyl alcohol > water > butane(or propane)dicarboxylic acid > ethylenediamine, with the donor sequence OH, $COO^-$, $NH_2$. Based on these experimental results, we are convinced that the growth step generally plays a crucial role during the hydrothermal reaction.[17] Therefore, in order to obtain optimal nanostructured materials, it is quite important to adopt appropriate organic molecule to modify the growth behavior.[45,46]

### The Use of Inorganic Acids: A Typical Growth and Aging of Rutile in Hydrochloric Acid

In our previous work we investigated the effects of inorganic acids on the growth of $TiO_2$ and found that pure-phase anatase, a mixture of anatase and rutile, and pure-phase rutile were obtained in acetic acid, nitric acid, and hydrochloric acid, respectively.[30] It has also been reported that pure rutile can be grown in nitric acid.[47] However, upon changing the TNB and nitric acid concentrations from those in the literature,[30,47] no rutile phase appeared, and phase-pure anatase was formed instead. This suggests that the growth of $TiO_2$ in nitric acid is very complicated. The anatase products formed as nanograins and rutile as nanorods (Figure 4, right panel, parts b and c).

We have previously reported the synthesis of rutile nanocrystals at temperatures above 200 °C by using TNB as a starting material in sol–hydrothermal reactions. A low-temperature preparation of rutile nanorods was also achieved at around 100 °C by using either titanium tetrachloride or trichloride as titanium source.[33,40] However, titanium chlorides release large amounts of heat, which prevents the homogeneous precipitation of $TiO_2$ particles because of the vigorously exothermic reaction, when titanium chloride is dissolved in water.[15,30]

According to the above experimental results with inorganic media (Figure 4), it can be concluded that phase-pure rutile nanorods can be formed in HCl. Therefore, HCl solution was selected as a representative inorganic medium to examine the growth of rutile at a much lower temperature. We used a modified sol–hydrothermal growth to prepare

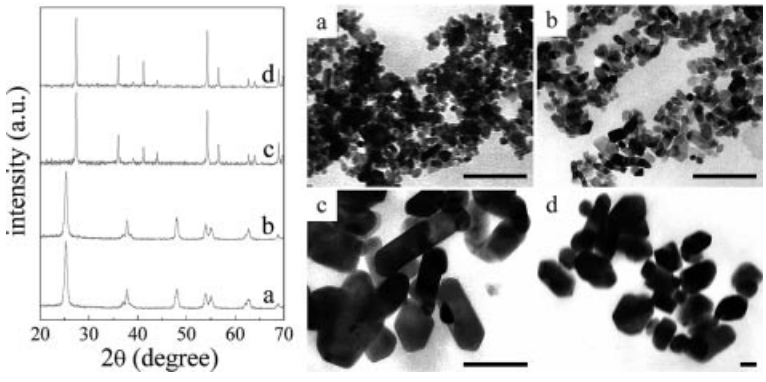


Figure 4. XRD patterns and TEM images of titania samples generated from various solutions at 220 °C: (a) HOAc, (b) $HNO_3$, and (c) HCl for 24 h; (d) HCl for 7 d. Scale bar: 100 nm.

 © 2006 Wiley-VCH Verlag GmbH & Co. KGaA, Weinheim 

rutile nanoneedles with a much higher aspect ratio at 100 and 140 °C, respectively. As indicated in Figure 5 (a1), rutile was obtained as the exclusive product at 100 °C after only two hours. The nanoparticles of rutile prepared at this point are highly aggregated into nanospheres consisting of very thin nanorods (Figure 6, a1 and inset). Their radial assembly in a good geometrical match to create the spherical nanostructure could significantly reduce the total free energy. These spherical structures are present for about 10 h at 100 °C and are then destroyed by further hydrothermal reaction (Figure 6, a4). The calculated crystalline sizes of rutile prepared at 100 °C after two hours are about 2.1 and 5.5 nm for the 110 and 101 diffractions, respectively. With an increase of reaction time, the crystal sizes assigned to $D_{110}$ tend to increase progressively. However, the crystal sizes calculated from the 101 diffraction tend to increase only up to 10 h and decrease a little thereafter (Figure 5, middle).

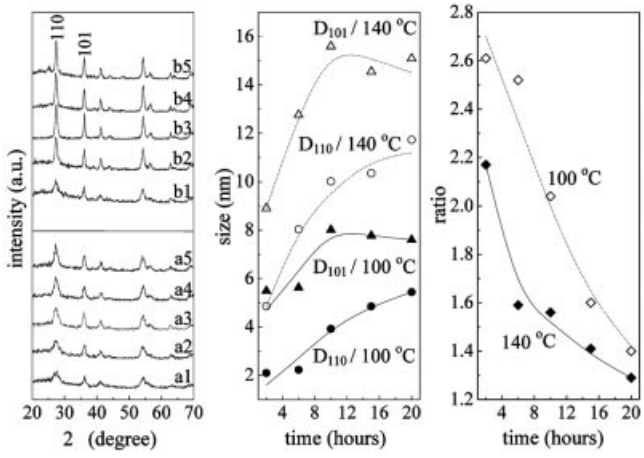


Figure 5. XRD patterns (left panel) of the products formed with HCl at 100 °C (a1–a5) and 140 °C (b1–b5) after 2.0 h (a1, b1), 6.0 h (a2, b2), 10 h (a3, b3), 15 h (a4, b4), and 20 h (a5, b5). Crystallite sizes (middle panel) calculated by fitting the FWHM of the (110) and (101) peaks. $D_{101}/D_{110}$ ratios (right panel).

Phase-pure rutile can also be obtained at 140 °C (Figure 5, b1) and a similar hydrothermal growth behavior to that at 100 °C is observed (Figure 5, middle). These rutile particles synthesized at 140 °C also self-aggregate into microspheres up to 10 h (Figure 6, b1–b3). However, the aggregated microspheres self-disperse after a longer hydrothermal aging such as for 15 h (Figure 6, b4). This might be due to a much higher activation energy for self-aggregation for the formation of larger nanorods. The typical product obtained at 140 °C after 10 h consists of well-defined nanoneedles, as clearly illustrated in Figure 7 (a), in which the sample for TEM observation has been highly and strongly ultrasonically dispersed. The anisotropic growth of rutile nanoneedles into self-assembled sub-microspheres can clearly be observed in the low-magnification TEM image (Figure 7, b). The lattice spacing of 0.32 nm perpendicular to the longitudinal direction in the high-magnification TEM image implies a <001> growth direction (Figure 7, c). The favorable growth along the *c*-axis in the early stages is due to the internal structure, as we described previously.[30] The growth velocity at the initial stage either in the radial or longitudinal direction is much faster than that at 100 °C due to kinetic factors. This type of quick growth feature during the initial stage has been well documented by Peng for semiconductors.[45] With further aging after 10 h, the radial growth tends to be slower and the longitudinal growth also tends to be retarded. The maximum value

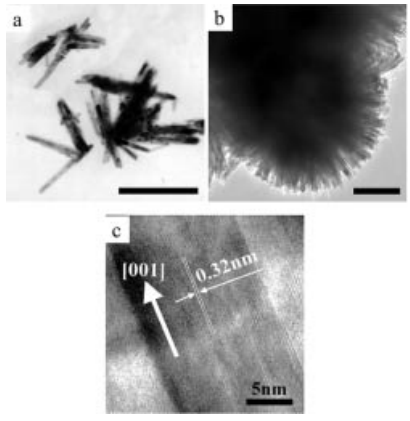


Figure 7. TEM images of ultrasonically dispersed rutile nanoneedles (a), a self-assembled sphere (b), and a high-resolution TEM image of a specific nanoneedle (c). Scale bar: 200 nm.

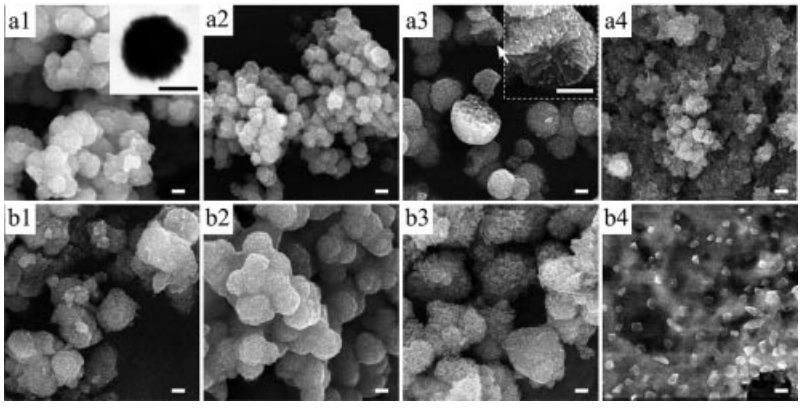


Figure 6. Electron microscopy images of the products obtained with HCl at 100 °C (a1–a4) and 140 °C (b1–b4) after 2.0 h (a1, b1), 6.0 h (a2, b2), 10 h (a3, b3), and 15 h (a4, b4). The inset in a3 is the magnified sphere indicated by the white arrow. Scale bar: 200 nm.

 © 2006 Wiley-VCH Verlag GmbH & Co. KGaA, Weinheim 

of $D_{101}$ at 10 h and the slow decrease of $D_{101}$ after 10 h (Figure 5, middle) reveals an obvious 1D/2D ripening during hydrothermal aging, as described previously for CdSe nanorods.[45]

The ratio of $D_{101}/D_{110}$ indicates that the aspect ratio drops noticeably with hydrothermal reactions longer than two hours in our present work. We did not observe the 1D and 3D growth stage described previously by Peng for the growth of CdSe nanocrystals[45] when our reaction is shorter than two hours (Figure 5, right panel). However, both the short and long axes increase when the reaction time is shorter than 10 h at either 100 °C or 140 °C (Figure 5, middle). Thus, the reaction at times shorter than 10 h can be referred to as a three-dimensional growth stage. After 10 h, the short axis keeps growing while the long axis becomes shorter. There is therefore a noticeable net growth and net dissolution along the short and long axes, respectively, along with a 1D/2D ripening. This produces nanorods with smaller aspect ratios, and granular particles are produced if allowed enough reaction time. A significant experimental result in our present work is that the aspect ratio at 100 °C is greater than that at 140 °C, as shown in Figure 5 (right). This means that the higher reaction temperature accelerates the 1D/2D ripening, especially for longer reaction times. For example, many more and larger granular crystals are noticeable at 220 °C after one day, and even more so after seven days (Figure 4, c, d, right).

## Conclusions

A variety of sol–hydro(solvo)thermal syntheses of anatase and rutile nanocrystals have been comparatively described that use small inorganic and organic compounds as additives at various reaction temperatures for different aging times. Instead of water, alcohol as a solvent in the sol–hydrothermal synthesis can result in a confined growth of well-crystalline and uniform anatase nanocubes. Except for HCl medium, phase-pure anatase can be formed in an organic alcohol, an organic diamine, an organic diacid, and acetic and nitric acids. The use of a diamine promotes the anisotropic growth of anatase nanocrystals, while the use of a diacid cannot do this efficiently because of its stronger capping ability. Rutile nanospheres self-assembled from rutile nanorods are obtained through a facile sol–hydrothermal growth route in HCl medium. More significantly, a 3D growth and 1D/2D ripening mechanism of rutile nanocrystals are revealed. It is proposed that prolonging the reaction time and increasing the reaction temperature will lead to the formation of larger rutile crystals but will reduce the aspect ratios of one-dimensional rutile nanocrystals.

## Experimental Section

**Preparation:** Titanium salts such as titanium chloride ($TiCl_3$ or $TiCl_4$),[40,42] titanium sulfate $Ti(SO_4)_2$,[48,49] and titanium alkoxide $[Ti(OR)_4]$[30,41] in solution are often used as titanium sources to synthesize $TiO_2$ nanoparticles. The hydrolysis of $Ti(OR)_4$ is relatively mild as compared with inorganic salts and is easy to control. Therefore, tetrabutyl titanate was employed here as the titanium source. In the present work, besides $H_2O$ and *n*-butyl alcohol as "pure solvents", the others were used as aqueous 2.0 M solutions of acetic acid, nitric acid, hydrochloric acid, 1,3-propanedicarboxylic acid, 1,4-butanedicarboxylic acid, 1,2-propanediol, and ethylenediamine. Titanium *n*-butoxide $[Ti(OC_4H_9)_4$, TNB] was added dropwise to one of the pure organic solvents or one of the concentrated inorganic acids/amine under magnetic stirring to form a clear sol. Then, distilled water was added dropwise to the sol while stirring to prepare a reagent with a fixed concentration of diol, acid, amine, and titanium (2.0 M). Subsequently, the homogeneous hydrosol was transferred into a Teflon-lined stainless-steel vessel, which was tightly closed instantly for sol–hydrothermal reaction under an autogenous pressure at 220 °C for one day, unless otherwise mentioned. The vessel was then taken out from the oven and cooled to ambient temperature. The white product was filtered, washed with distilled water, and dried in a desiccator at ambient temperature.

**Characterization:** Products were characterized by powder X-ray diffraction using Cu-$K_\alpha$ radiation ($\lambda$ = 0.15045 nm) and a graphite monochromator on a RIGAKUD/MAX 2200 VPC diffractometer operating at 40 kV and 30 mA. Crystallite sizes of $TiO_2$ particles were calculated using Scherrer's equation from the FWHM (full-width at half-maximum) of the anatase (101 and 200) and rutile (110 and 101) diffractions, respectively. Electron microscopy observations were carried out with a JSM-6330F Field Emission scanning electron microscope at 15 kV or JEM-100CX and JEM-2010 transmission electron microscopes at 100 kV and 200 kV, respectively. The samples for TEM examination were prepared by depositing an ultrasonically dispersed suspension of $TiO_2$ powder from a water/alcohol mixture onto a carbon-coated copper grid.

## Acknowledgments

This work was supported financially by the Natural Science Foundation of China, the NSF of Guangdong Province, and the government of Guangzhou City.

[1] B. O'Regan, B. M. Grätzel, *Nature* **1991**, *353*, 737–740.
[2] M. K. Nazeeruddin, A. Kay, L. Rodicio, R. Humphry-Baker, E. Müler, P. Liska, N. Vlachopoulos, M. Grätzel, *J. Am. Chem. Soc.* **1993**, *115*, 6382–6390.
[3] J. Karch, R. Birriger, H. Gleiter, *Nature* **1987**, *330*, 556–558.
[4] R. Wang, K. Hashimoto, A. Fujishima, *Nature* **1997**, *388*, 431–432.
[5] S.-Q. Liu, A.-C. Chen, *Langmuir* **2005**, *21*, 8409–8413.
[6] M. R. Hoffmann, S. T. Martin, W. Choi, D. W. Bahnemann, *Chem. Rev.* **1995**, *95*, 69–96.
[7] L.-X. Cao, Z. Gao, S. L. Suib, T. N. Obee, S. O. Hay, J. D. Freihaut, *J. Catal.* **2000**, *196*, 253–261.
[8] J. Shang, M. Chai, Y.-F. Zhu, *J. Solid State Chem.* **2003**, *174*, 104–110.
[9] U. Diebold, *Surf. Sci. Rep.* **2003**, *48*, 53–229.
[10] C.-F. Lao, Y.-T. Chuai, L. Su, X. Liu, L. Huang, H.-M. Cheng, D.-C. Zou, *Sol. Energ. Mater. Sol. C* **2005**, *85*, 457–465.
[11] R. W. Siegal, S. Ramasamy, H. Hahn, Z.-Q. Li, T. Lu, R. Gronsky, *J. Mater. Res.* **1988**, *3*, 1367.
[12] Z.-R. Tian, J. A. Voigt, J. Liu, B. McKenzie, H.-F. Xu, *J. Am. Chem. Soc.* **2003**, *125*, 12384–12385.
[13] A. Chemseddine, T. Moritz, *Eur. J. Inorg. Chem.* **1999**, *2*, 235–245.
[14] Y. Li, T. J. White, S. H. Lim, *J. Solid State Chem.* **2004**, *177*, 1372.

 © 2006 Wiley-VCH Verlag GmbH & Co. KGaA, Weinheim 

[15] W. Wang, B.-H. Gu, L.-Y. Liang, W. A. Hamilton, D. J. Wesolowski, *J. Phys. Chem. B* **2004**, *108*, 14789–14792.
[16] X.-C. Jiang, T. Herricks, Y.-N. Xia, *Adv. Mater.* **2003**, *15*, 1205–1209.
[17] P. D. Cozzoli, A. Kornowski, H. Weller, *J. Am. Chem. Soc.* **2003**, *125*, 14539–14548.
[18] J. Tang, F. Redl, Y.-M. Zhu, T. Siegrist, L. E. Brus, M. L. Steigerwald, *Nano Lett.* **2005**, *5*, 543–548.
[19] J. Polleux, N. Pinna, M. Antonietti, M. Niederberger, *Adv. Mater.* **2004**, *16*, 436–439.
[20] B.-M. Wen, C.-Y. Liu, Y. Liu, *Chem. Lett.* **2005**, *34*, 396–397.
[21] B.-M. Wen, C.-Y. Liu, Y. Liu, *New J. Chem.* **2005**, *29*, 969–971.
[22] S.-W. Yang, L. Gao, *Chem. Lett.* **2005**, *34*, 964–965.
[23] S.-W. Yang, L. Gao, *Chem. Lett.* **2005**, *34*, 972–973.
[24] J. M. Macák, H. Tsuchiya, P. Schmuki, *Angew. Chem. Int. Ed.* **2005**, *44*, 2100–2102.
[25] V. G. Besserguenev, R. J. F. Pereira, M. C. Mateus, I. V. Khmelinskii, E. Burkel, R. C. Nicula, *Int. J. Photoenergy* **2003**, *5*, 99–105.
[26] S. Seifried, M. Winterer, H. Hahn, *Scr. Mater.* **2001**, *44*, 2165–2168.
[27] E. Beyers, P. Cool, E. F. Vansant, *J. Phys. Chem. B* **2005**, *109*, 10081–10086.
[28] A. K. John, G. D. Surender, *J. Mater. Sci.* **2005**, *40*, 2999–3001.
[29] T. Sugimoto, X.-P. Zhou, A. Muramatsu, *J. Colloid Interface Sci.* **2003**, *259*, 53–61.
[30] M.-M. Wu, G. Lin, D.-H. Chen, G.-G. Wang, D. He, S.-H. Feng, R.-R. Xu, *Chem. Mater.* **2002**, *14*, 1974–1980.
[31] H.-M. Cheng, J.-M. Ma, Z.-G. Zhao, L.-M. Qi, *Chem. Mater.* **1995**, *7*, 663–671.
[32] G. Garnweitner, M. Antonietti, M. Niederberger, *Chem. Commun.* **2005**, *3*, 397–399.
[33] C. Wang, Z.-X. Deng, G.-H. Zhang, S.-H. Fan, Y.-D. Li, *Powder Technol.* **2002**, *125*, 39–44.
[34] M. Ivanda, S. Music, S. Popovic, M. Gotic, *J. Mol. Struct.* **1999**, *481*, 645–649.
[35] B.-P. Jiang, H.-B. Yin, T.-S. Jiang, J. Yan, Z. Fan, C.-S. Li, J. Wu, Y. Wada, *Mater. Chem. Phys.* **2005**, *92*, 595–599.
[36] S. Iwamoto, K. Saito, M. Inoue, *Nano Lett.* **2001**, *1*, 417–421.
[37] W. Payakgula, O. Mekasuwandumrongb, V. Pavarajarna, P. Praserthdama, *Ceram. Int.* **2005**, *31*, 391–397.
[38] C.-C. Wang, J.-Y. Ying, *Chem. Mater.* **1999**, *11*, 3113–3120.
[39] S. T. Aruna, S. Tirosh, A. Zaban, *J. Mater. Chem.* **2000**, *10*, 2388–2391.
[40] X. Bokhimi, A. Morales, F. Pedraza, *J. Solid State Chem.* **2002**, *169*, 176–181.
[41] S. Hyunho, S. J. Hyun, S. H. Kug, L. Jung-Kun, *J. Solid State Chem.* **2005**, *178*, 15–21.
[42] G.-S. Li, L.-P. Li, J. Boerio-Goates, B. F. Woodfield, *J. Am. Chem. Soc.* **2005**, *127*, 8659–8666.
[43] J.-G. Li, C.-C. Tang, D. Li, H. Haneda, T. Ishigaki, *J. Am. Ceram. Soc.* **2004**, *87*, 1358–1361.
[44] E. G. S. Michael, A. C. David, M. Philip, *Chem. Commun.* **2000**, *13*, 1167–1168.
[45] Z.-A. Peng, X.-G. Peng, *J. Am. Chem. Soc.* **2001**, *123*, 1389–1395.
[46] X. Wang, J. Zhuang, Q. Peng, Y.-D. Li, *Nature* **2005**, *437*, 121–124.
[47] Y.-T. Qian, Q.-W. Chen, Z.-Y. Chen, C.-G. Fan, G.-E. Zhou, *J. Mater. Chem.* **1993**, *3*, 203–205.
[48] H. K. Park, Y. T. Moon, D. K. Kim, C. H. Kim, *J. Am. Ceram. Soc.* **1996**, *79*, 2727–2732.
[49] M. Iwasaki, M. Hara, S. Ito, *J. Mater. Sci. Lett.* **1998**, *17*, 1769–1771.

Received: September 26, 2005
Published Online: March 31, 2006

 © 2006 Wiley-VCH Verlag GmbH & Co. KGaA, Weinheim 

DOI: 10.1002/ejic.200500898

# A Systematic Exploration of Nickel(II)/Acetate/Di-2-pyridyl Ketone Chemistry: Neutral and Cationic Tetranuclear Clusters, and a Novel Mononuclear Complex

**Constantinos G. Efthymiou,[a] Catherine P. Raptopoulou,[b] Aris Terzis,[b] Roman Boča,*[c] Maria Korabic,[d] Jerzy Mrozinski,*[d] Spyros P. Perlepes,*[a] and Evangelos G. Bakalbassis*[e]**

**Keywords:** Acetate ligands / Di-2-pyridyl ketone / Magnetic properties / Nickel(II) cubanes / Nickel(II) defect dicubanes / X-ray diffraction

The further use of di-2-pyridyl ketone [$(2\text{-py})_2CO$] in nickel(II) acetate chemistry has been investigated. Various synthetic procedures have led to the synthesis of complexes $[Ni_4(O_2CMe)_2\{(2\text{-py})_2C(OH)O\}_4(H_2O)_2](ClO_4)_2$ (**1**), $[Ni(O_2CMe)\{(2\text{-py})_2C(OH)_2\}\{(2\text{-py})_2CO\}](ClO_4)\cdot H_2O$ (**2**·$H_2O$), $[Ni_4(O_2CMe)_3\{(2\text{-py})_2C(OH)O\}_4](ClO_4)\cdot 2H_2O\cdot 2EtOH$ (**3**·$2H_2O$·2EtOH), $[Ni_4(O_2CMe)_4\{(2\text{-py})_2C(OH)O\}_4]\cdot 2MeCN$ (**4**·2MeCN), and $[Ni_4(O_2CMe)_3\{(2\text{-py})_2C(OH)O\}_4](O_2CMe)\cdot 6H_2O\cdot MeCN$ (**5**·$6H_2O$·MeCN). The $Ni^{II}$-mediated hydrolysis of $(2\text{-py})_2CO$ to give the coordinated molecule $(2\text{-py})_2C(OH)_2$ or the monoanion $(2\text{-py})_2C(OH)O^-$ involves nucleophilic attack by $H_2O$ on the carbonyl group. The $Ni^{II}$ ion in **2**·$H_2O$ is coordinated by one monodentate acetate, one *N*,*N*′,*O*-tridentate chelating $(2\text{-py})_2C(OH)_2$ molecule, and one *N*,*N*′-bidentate chelating $(2\text{-py})_2CO$ ligand. The tetranuclear cluster cation of **1** has a cubane $\{Ni_4(\mu_3\text{-}OR)_4\}^{4+}$ core with $Ni^{II}$ ions and deprotonated oxygen atoms occupying alternate vertices. The $[Ni_4(O_2CMe)_3\{(2\text{-py})_2C(OH)O\}_4]^+$ cations present in the complexes **3**·$2H_2O$·2EtOH and **5**·$6H_2O$·MeCN have almost identical cubane structures that are different from the structure of the cation of **1**. The four metal ions in the centrosymmetric molecules of **4**·2MeCN are located at four vertices of a defect dicubane (with two missing vertices) and are bridged by six oxygen atoms. Characteristic IR bands are discussed in terms of the known structures of **1**–**5**. The magnetic data for the $Ni^{II}$ cubane **1** has been modeled with two *J* values, and shows that the coupling consists of two ferromagnetically coupled pairs that are antiferromagnetically coupled to give a diamagnetic ground state. The magnetic properties of **4** have been modeled with three *J* values, and reveal competing antiferromagnetic and ferromagnetic coupling between the four $Ni^{II}$ ions.
(© Wiley-VCH Verlag GmbH & Co. KGaA, 69451 Weinheim, Germany, 2006)

## Introduction

The last 15 years have witnessed explosive growth in interest in the polynuclear complexes (clusters) of 3d-metals at intermediate oxidation states with primarily oxygen- and/or nitrogen-based ligation.[1] This has been mainly due to their relevance to two fields, bioinorganic chemistry[2] and molecular magnetic materials. For the latter field, the discovery that individual polynuclear molecules can function as nanoscale magnets was a significant development.[3,4] Such molecules have since been named single-molecule magnets (SMMs). Although Mn clusters at various oxidation levels have to date proven to be the most fruitful source of SMMs, complexes displaying SMM behavior are known for several other 3d-metals (e.g., $V^{III}$, $Fe^{II}$, $Fe^{III}$, $Co^{II}$, $Ni^{II}$)[5] with various *S* values, both integer and half-integer. The future health of the field of 3d-metal clusters, and the chances of discovering high-spin molecules (molecules with a large *S*) and/or identifying new SMMs will benefit from the development of new synthetic routes for polynuclear complexes.

With the points mentioned above in mind, and in the context of "serendipitous assembly",[1b] our group[6] and others[7] have been exploring "ligand blend" reactions involving (i) the monoanion, $(2\text{-py})_2C(OH)O^-$, or the dianion, $(2\text{-py})_2CO_2^{2-}$, of the *gem*-diol form (derivative) of di-2-pyridyl ketone, $(2\text{-py})_2CO$, and carboxylates; and (ii) the monoanion, $(2\text{-py})_2C(OR)O^-$, of the hemiacetal form of $(2\text{-py})_2CO$ and carboxylates, with the belief that they might

[a] Department of Chemistry, University of Patras, 26504 Patras, Greece
E-mail: perlepes@patreas.upatras.gr
[b] Institute of Materials Science, NCSR "Demokritos", 15310 Aghia Paraskevi Attikis, Greece
[c] Department of Inorganic Chemistry, Slovak Technical University, 81237 Bratislava, Slovakia
E-mail: roman.boca@stuba.sk
[d] Institute of Chemistry, University of Wroclaw, 14 F. Joliot-Curie, 50383 Wroclaw, Poland
E-mail: jmroz@wchuwr.chem.uni.wrocl.pl
[e] Laboratory of Applied Quantum Chemistry, Department of Chemistry, Aristotle University of Thessaloniki, 54124 Thessaloniki, Greece
E-mail: bakalbas@chem.auth.gr

 © 2006 Wiley-VCH Verlag GmbH & Co. KGaA, Weinheim 

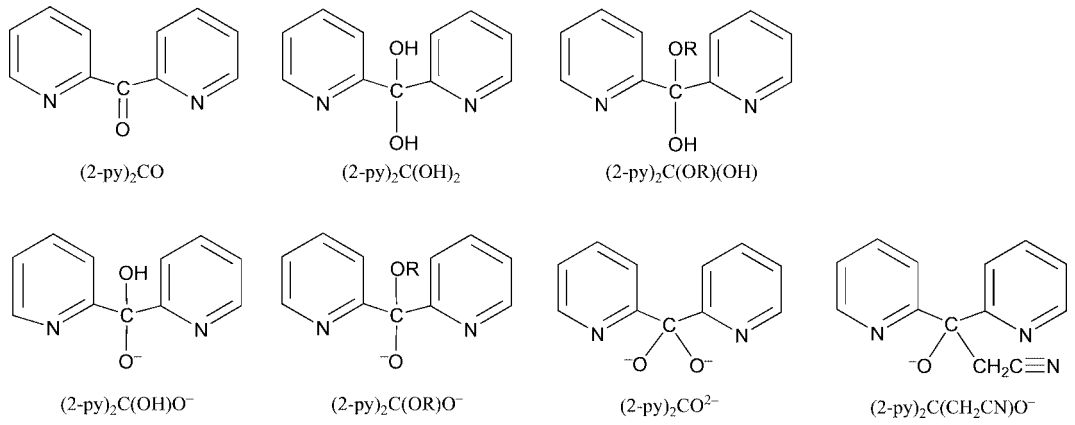


Figure 1. The formulae of the ligands discussed in the text; note that $(2\text{-py})_2C(OH)_2$, $(2\text{-py})_2C(OR)(OH)$, and all four anions do not exist as free species but exist only in their respective metal complexes.

foster the formation of discrete polynuclear metal systems. The formulae of these ligands are shown in Figure 1. The reactions of $(2\text{-py})_2CO$ with 3d-metal ions have been well studied over the years.[6–9] There is a chemical characteristic of $(2\text{-py})_2CO$ that makes this molecule a special ligand, this is its carbonyl group. Water and alcohols (ROH) have been shown to add to the carbonyl group upon coordination of the carbonyl oxygen atom and/or the 2-pyridyl rings forming the ligands $(2\text{-py})_2C(OH)_2$ [the *gem*-diol form of $(2\text{-py})_2CO$] and $(2\text{-py})_2C(OR)(OH)$ [the hemiacetal form of $(2\text{-py})_2CO$], respectively. The neutral ligands $(2\text{-py})_2C(OH)_2$ and $(2\text{-py})_2C(OR)(OH)$ coordinate to the metal centers as *N*,*N*′,*O* chelates, with the M–O bond often being weak; therefore, both neutral ligands do not hold much interest from the viewpoint of cluster formation.[8] Completely different and much more interesting (for cluster chemistry) coordination modes are seen when the ligands $(2\text{-py})_2C(OH)_2$ and $(2\text{-py})_2C(OR)(OH)$ are deprotonated. Upon deprotonation, the latter becomes monoanionic, while the former can function either as mono- or dianionic. The presence of deprotonated hydroxy group(s) leads to a great coordinative flexibility, because of the well-known ability of the negatively charged oxygen atom to bridge two or three metal ions. The monoanionic forms usually bridge two ($\mu_2$) or three ($\mu_3$) metal ions, while the dianionic form can bridge as many as five metal sites ($\mu_5$). The immense structural diversity displayed by the complexes reported stems in part from the ability of $(2\text{-py})_2CO_2^{2-}$, $(2\text{-py})_2C(OH)O^-$, and $(2\text{-py})_2C(OR)O^-$ to exhibit no less than ten distinct coordination modes.[8] Carboxylates ($R'CO_2^-$) are employed for two reasons in the "ligand blends". Firstly, they are able to deprotonate the hydroxy group(s) under mild conditions (the use of external hydroxides often perplexes the reactions). Secondly, they are flexible ligands, a consequence of their ability to adopt a number of different ligation modes, both terminal and bridging as well as both bidentate and tridentate, giving an extraordinary structural versatility in the mixed-ligand systems. Thus, the $(2\text{-py})_2CO_2^{2-}/R'CO_2^-$, $(2\text{-py})_2C(OH)O^-/R'CO_2^-$, and $(2\text{-py})_2C(OR)O^-/R'CO_2^-$ "blends" (R = Me, Et; R′ = Me, $CF_3$, Ph), without (binary "blends") or with (ternary "blends") additional inorganic ligands [$NO_3^-$, $N_3^-$, $SCN^-$, $N(CN)_2^-$] have led to a variety of Mn, Fe, Co, Ni, and Cu clusters with nuclearities ranging from 3 to 14[8] and with interesting magnetic properties, including single-molecule magnetism.[6b]

Restricting further discussion to nickel(II) chemistry, the investigation of the binary $(2\text{-py})_2CO_2^{2-}$, $(2\text{-py})_2C(OH)O^-$, or $(2\text{-py})_2C(OR)O^-/MeCO_2^-$ "blend" has up to now led to clusters $[Ni_9(OH)_2(O_2CMe)_8\{(2\text{-py})_2CO_2\}_4]$,[6f] $[Ni_4(O_2CMe)_3\{(2\text{-py})_2C(OH)O\}_4](ClO_4)$,[7a] and $[Ni_4(O_2CMe)_4\{(2\text{-py})_2C(OH)O\}_4]$.[7b] We suspected that our,[6f] Tong's and Chen's,[7a] and Brown's and Krebs'[7b] groups had merely scratched the surface of this binary reaction system and we, thus, decided to perform a systematic synthetic study of the $Ni^{II}/MeCO_2^-/(2\text{-py})_2CO$ reaction system. Here we discuss the syntheses, structures, and IR spectra of the resulting products; the magnetic properties of two representative clusters will also be described and analyzed. The discovery of single-molecule magnetism in high-spin $Ni^{II}$ cubane clusters[10] revived the interest in such compounds.

## Results and Discussion

### Synthesis

As stated above, we were interested in extending the very small family of $Ni^{II}/MeCO_2^-/(2\text{-py})_2CO$-based ligand complexes[6f,7a,7b] *without* the introduction of additional anionic inorganic ligands (binary "blends"). The chemical and structural identity of the products from the $Ni(O_2CMe)_2\cdot 4H_2O/(2\text{-py})CO$ reaction system depends on the solvent used, the presence/absence of counterions (this synthetic parameter is related to the choice of the solvent), the ligand–to-metal reaction ratio and the $OH^-$ concentration. Our general route for the isolation of heteroleptic $(2\text{-py})_2CO_2^{2-}$, $(2\text{-py})_2C(OH)O^-$, or $(2\text{-py})_2C(OR)O^-/MeCO_2^-$ $Ni^{II}$ clusters was to treat an excess of nickel(II) acetate with $(2\text{-py})_2CO$; we shall describe our efforts in terms of the solvent. Obviously "$(2\text{-py})_2C(OH)_2$" and "$(2\text{-py})_2C(OR)(OH)$" can be fully/partially deprotonated by the basic acetate groups and polynuclear $Ni^{II}/(2\text{-py})_2CO_2^{2-}$, $(2\text{-py})_2C(OH)O^-$, or $(2\text{-py})_2C(OR)O^-/MeCO_2^-$ complexes may result

 © 2006 Wiley-VCH Verlag GmbH & Co. KGaA, Weinheim 

$$4\ Ni(O_2CMe)_2{\cdot}4H_2O + 4\ (2\text{-py})_2CO + 2\ NaClO_4 \xrightarrow{H_2O} \underset{\mathbf{1}}{[Ni_4(O_2CMe)_2\{(2\text{-py})_2C(OH)O\}_4(H_2O)_2](ClO_4)_2} + 2\ NaO_2CMe + 4\ MeCO_2H + 10\ H_2O \quad (1)$$

from the reactions as long as the $MeCO_2^-$-to-$(2\text{-py})_2CO$ ratio is high enough to leave an amount of nonprotonated acetate in the reaction mixture, given the fact that the anionic forms of $(2\text{-py})_2CO$ and the acetate can adopt a variety of terminal and bridging modes.

Complexes **1** and **2** were prepared from aqueous reaction mixtures. The preparation of compound **1** can be achieved by the reaction of $Ni(O_2CMe)_2{\cdot}4H_2O$ with $(2\text{-py})_2CO$ according to the balanced Equation (1). One feature of the chemical Equation (1) deserves a comment.

This is the "wrong" stoichiometry, i.e. $Ni(O_2CMe)_2{\cdot}4H_2O/(2\text{-py})_2CO$ = 1.5:1, employed for the preparation of **1** (see Exp. Sect.) compared with that required by Equation (1) [1:1]. The "incorrect" reaction ratio is because of our desire to avoid the formation of the mononuclear complexes **2** and $[Ni\{(2\text{-py})_2C(OH)O\}\{(2\text{-py})_2C(OH)_2\}]_2[Ni\{(2\text{-py})_2C(OH)O\}_2](ClO_4)_2{\cdot}7H_2O$[11] that contain a 1:2 $Ni^{II}/(2\text{-py})_2CO$-based ligand ratio (vide infra). If we assume that the simplified chemical equilibrium represented by Equation (2) takes place (this is only one of the possible chemical equilibria), then the presence of an excess of nickel(II) acetate shifts the equilibrium to the right.

$$2\ [Ni(O_2CMe)\{(2\text{-py})_2C(OH)_2\}\{(2\text{-py})_2CO\}]^+ + 2\ Ni(O_2CMe)_2 + 4\ H_2O \rightleftharpoons [Ni_4(O_2CMe)_2\{(2\text{-py})_2C(OH)O\}_4(H_2O)_2]^{2+} + 4\ MeCO_2H \quad (2)$$

Having obtained and identified complex **1**, the next question addressed was whether, and in what manner, changes to the $Ni(O_2CMe)_2{\cdot}4H_2O/(2\text{-py})_2CO$ ratio might affect the product identity. In particular, we wondered whether it might be possible to prepare mononuclear complexes containing the ligand $(2\text{-py})_2C(OH)_2$ [the neutral *gem*-diol form of $(2\text{-py})_2CO$, Figure 1] and/or clusters containing the dianion $(2\text{-py})_2CO_2^{2-}$ [Figure 1] that are different from $[Ni_9(OH)_2(O_2CMe)_8\{(2\text{-py})_2CO_2\}_4]$ previously reported.[6f] We were successful with the first goal but unsuccessful with the second.

The 1:2 reaction between $Ni(O_2CMe)_2{\cdot}4H_2O$ and $(2\text{-py})_2CO$ in $H_2O$ in the presence of an excess of $NaClO_4$ gave a mauve solution. Slow solvent evaporation at room temperature yielded crystals that were obviously a mixture of two products. Microscopic examination showed both brown-red prisms and mauve needles to be present in a visual ratio of roughly 3:1. The unit cell dimensions of hand-picked prisms and needles did not correspond to known compounds. Since repeated crystallizations from $H_2O$ or $H_2O/Me_2CO$ could not yield a sample free of the needles for elemental analysis, full data sets were collected for both compounds and the structures solved. The extreme differences in color and in crystal shape were fortuitous and allowed easy manual separation of the two materials. The prisms proved to be $[Ni(O_2CMe)\{(2\text{-py})_2C(OH)_2\}\{(2\text{-py})_2CO\}](ClO_4)$ (**2**) as its mono(water) solvate, while the needles were shown to be $[Ni\{(2\text{-py})_2C(OH)O\}\{(2\text{-py})_2C(OH)_2\}]_2[Ni\{(2\text{-py})_2C(OH)O\}_2](ClO_4)_2{\cdot}7H_2O$ consisting of two chemically similar cations, one neutral complex molecule, two perchlorate anions, and water solvate molecules.[11] The latter compound will not be further discussed because it will be incorporated into a full paper dealing with all the acetate-free complexes that have been isolated from the $Ni(O_2CMe)_2{\cdot}4H_2O/(2\text{-py})_2CO$ and $Ni(O_2CMe)_2{\cdot}4H_2O/(2\text{-py})_2CO/ClO_4^-$ reaction mixtures. The formation of **2** as an individual species can be summarized in the balanced Equation (3). With the identity of **2** established, we subsequently tried to devise a route to pure material. Complex **2** has a $Ni^{II}/ClO_4^-$ ratio of 1:1, whereas the acetate-free complex has a $Ni^{II}/ClO_4^-$ ratio of 3:2, i.e. 1.5:1. Thus, attempts to obtain pure **2** were made by further lowering the $Ni^{II}/ClO_4^-$ ratio.

$$Ni(O_2CMe)_2{\cdot}4H_2O + 2\ (2\text{-py})_2CO + NaClO_4 \xrightarrow{H_2O} \underset{\mathbf{2}}{[Ni(O_2CMe)\{(2\text{-py})_2C(OH)_2\}\{(2\text{-py})_2CO\}](ClO_4)} + NaO_2CMe + 3\ H_2O \quad (3)$$

Somewhat to our disappointment, the use of $Ni^{II}/ClO_4^-$ ratios of 1:2 or even of 1:3 again gave mixtures of **2** and $[Ni\{(2\text{-py})_2C(OH)O\}\{(2\text{-py})_2C(OH)_2\}]_2[Ni\{(2\text{-py})_2C(OH)O\}_2](ClO_4)_2{\cdot}7H_2O$. It is likely that the reaction solution contains a complicated mixture of several mononuclear species in equilibrium, with factors such as relative solubility, lattice energy, crystallization kinetics − amongst others − determining the identity of the isolated products.

The incorporation of a coordinated ligand molecule in its ketone form [$(2\text{-py})_2CO$] (Figure 1) in **2** was unexpected, given the fact that the complex was isolated from $H_2O$.[8] One possible reason for the presence of the $(2\text{-py})_2CO$ ligand is the satisfaction of the requirements of the crystal lattice. Another reason could be the combined tendencies of the acetate ion to coordinate (and not to act as a counterion) in the presence of $ClO_4^-$ ions and of the $Ni^{II}$ ion to adopt the octahedral stereochemistry; the monodentate acetate coordination (vide infra) "forces" the second neutral organic molecule to behave as a bidentate ligand; the bidentate chelating mode is much more common for $(2\text{-py})_2CO$ than for $(2\text{-py})_2C(OH)_2$.

The 3:1:1 or 2 $Ni(O_2CMe)_2{\cdot}4H_2O/(2\text{-py})_2CO/NaClO_4$ reaction mixtures in $H_2O$ were also investigated due to our desire to doubly deprotonate the *gem*-diol form of $(2\text{-py})_2CO$ [as a consequence of the high $MeCO_2^-/(2\text{-py})_2C(OH)_2$ ratio] and to prepare complexes of $(2\text{-py})_2CO_2^{2-}$. However, such efforts were in vain. Complex **1** was again

 © 2006 Wiley-VCH Verlag GmbH & Co. KGaA, Weinheim 

isolated even employing a $Ni(O_2CMe)_2{\cdot}4H_2O/(2\text{-py})_2CO$ ratio of 4:1, emphasizing the fact that $H_2O$ is not the appropriate solvent for the isolation of metal complexes of $(2\text{-py})_2CO_2^{2-}$.[6b,e,f,g,12]

The access to **1** and **2** from $H_2O$ suggested that the reaction system might be capable of extension to other solvents. The 1:1 or 2:1 $Ni(O_2CMe)_2{\cdot}4H_2O/(2\text{-py})_2CO$ reaction mixtures in EtOH gave green crystals upon layering with $Et_2O$. The unit cell dimensions of a hand-picked crystal confirmed this product to be the known complex $[Ni_4(O_2CMe)_4\{(2\text{-py})_2C(OH)O\}_4]{\cdot}4EtOH$,[7b] on the basis of comparison with those of the authentic sample. We were rather surprised to see that this complex could not be easily isolated without the addition of $Et_2O$, e.g. upon slow solvent evaporation at room temperature. We suspected that a cationic species was present in solution and we thus reasoned that adding $ClO_4^-$ ions might give a cationic cluster. Not only did the addition of $ClO_4^-$ confirm our suspicion about the importance of the counterion in determining the reaction product but it also yielded a tetranuclear cluster with a topology (cubane) different from that of the neutral complex $[Ni_4(O_2CMe)_4\{(2\text{-py})_2C(OH)O\}_4]{\cdot}4EtOH$[7b] (defective double cubane). The formation of the tetranuclear cluster $[Ni_4(O_2CMe)_3\{(2\text{-py})_2C(OH)O\}_4](ClO_4)$ (**3**), which was crystallized upon lowering the temperature of the EtOH reaction solution can be summarized in the balanced Equation (4).

$$4\ Ni(O_2CMe)_2{\cdot}4H_2O + 4\ (2\text{-py})_2CO + NaClO_4 \xrightarrow{EtOH}$$

$$[Ni_4(O_2CMe)_3\{(2\text{-py})_2C(OH)O\}_4](ClO_4) + NaO_2CMe + 4\ MeCO_2H + 12\ H_2O \quad (4)$$

**3**

The "wrong" $Ni^{II}/(2\text{-py})_2CO/ClO_4^-$ ratio employed for the preparation of **3** (4:4:2, see Exp. Sect.) compared to that required by Equation (1) [4:4:1] did not prove detrimental to the formation of the complex. With the identity of **3** established, the "correct" stoichiometry was employed and led to the pure compound in high yield. The employment of EtOH as the solvent might imply the presence of the monoanion of the hemiacetal form of di-2-pyridyl ketone, i.e. $(2\text{-py})_2C(OEt)O^-$ (Figure 1) in the complex. However, only $(2\text{-py})_2C(OH)O^-$ ligands are present in complex **3**. It is difficult to rationalize this result; suffice it to say that the moisture present in solution (from the solvent and the starting materials) is responsible for the formation of the $(2\text{-py})_2C(OH)O^-$ ligands and that complex **3** is the thermodynamically stable product from the $Ni(O_2CMe)_2{\cdot}4H_2O/(2\text{-py})_2CO/NaClO_4$ reaction system in nonabsolute EtOH. It should be mentioned at this point that although the incorporation of $(2\text{-py})_2C(OMe)OH/(2\text{-py})_2C(OMe)O^-$ ligands in solid metal complexes isolated from MeOH is common,[8,9d,e,f,g,i,k,l,13] the participation of $(2\text{-py})_2C(OEt)OH/(2\text{-py})_2C(OEt)O^-$ ions in the coordination spheres of metal ions is rare[7b,9k] inspite of the plethora of reactions performed in EtOH.

The last reaction solvent investigated was *MeCN*. Previous synthetic studies on the $Ni(O_2CMe)_2{\cdot}4H_2O/(2\text{-py})_2CO/NaClO_4$ reaction system in $MeCN/H_2O$ ($H_2O$ is necessary to keep the produced $NaO_2CMe$ soluble) had led to the isolation of the cationic cubane cluster $[Ni_4(O_2CMe)_3\{(2\text{-py})_2C(OH)O\}_4](ClO_4)$.[7a] We wondered whether a neutral cluster could be formed in the absence of $ClO_4^-$ ions. The 1:1 reaction between $Ni(O_2CMe)_2{\cdot}4H_2O$ and $(2\text{-py})_2CO$ in MeCN under reflux gave complex $[Ni_4(O_2CMe)_4\{(2\text{-py})_2C(OH)O\}_4]$ (**4**) in high yield according to the balanced Equation (5). We were happy to see (vide infra) that the structural motif in **4** (double defective cubane) is different from that in the cationic cluster isolated from the same solvent (cubane).[7a]

$$4\ Ni(O_2CMe)_2{\cdot}4H_2O + 4\ (2\text{-py})_2CO \xrightarrow[\Delta]{MeCN}$$

$$[Ni_4(O_2CMe)_4\{(2\text{-py})_2C(OH)O\}_4] + 4\ MeCO_2H + 12\ H_2O \quad (5)$$

**4**

The 2:1 and 3:1 reactions of $Ni(O_2CMe)_2{\cdot}4H_2O$ with $(2\text{-py})_2CO$ in MeCN under reflux gave a mixture of green crystals and green powder. The extreme difference in crystallinity was fortuitous and allowed ready manual separation of the two materials. The crystals were shown to be the known complex $[Ni_9(OH)_2(O_2CMe)_8\{(2\text{-py})_2CO_2\}_4]$[6f] by determination of the unit cell dimensions. The double deprotonation of the *gem*-diol form of di-2-pyridyl ketone is a consequence of the high $MeCO_2^-$ (base) to "$(2\text{-py})_2C(OH)_2$" ratio (4:1 or 6:1) used in the reactions. The green powder is certainly $Ni(O_2CMe)_2{\cdot}4H_2O$ (that was not initially dissolved), a conclusion consistent with IR data.

A last synthetic parameter that was studied was the $OH^-$ concentration. Although it is well known that the use of external hydroxides often perplexes the reactions of metal ions with $(2\text{-py})_2CO$, we tried to prepare clusters containing $(2\text{-py})_2CO_2^{2-}$ ligands under conditions that favor formation of neutral or anionic complexes; for the latter purpose we employed bulky noncoordinating countercations, e.g. $NnBu_4^+$, $BPh_4^+$, and $PPh_4^+$. Synthetic studies of hundreds of $Ni(O_2CMe)_2{\cdot}4H_2O/(2\text{-py})_2CO/OH^-$ or $Ni(O_2CMe)_2{\cdot}4H_2O/(2\text{-py})_2CO/OH^-/Z^+$ ($Z^+$ = countercation) reaction systems in various solvents repeatedly led to amorphous or microcrystalline materials with poor analytical results. We were luckier when we employed a solvent mixture comprising EtOH and MeCN, and $LiOH{\cdot}H_2O$ as the base under reflux. Using a rather unusual crystallization process we isolated single crystals of complex $[Ni_4(O_2CMe)_3\{(2\text{-py})_2C(OH)O\}_4](O_2CMe)$ (**5**). However, we were unlucky at the same time because (i) the complex does not contain $(2\text{-py})_2CO_2^{2-}$ and (ii) the molecular structure of the cation is similar to that present in complex **3**. The formation of **5** can be summarized in the balanced Equation (6). The isolation of **5** that contains an acetate counterion was surprising and, needless to say, unexpected. Ethanol is necessary in the solvent mixture to keep $LiOH{\cdot}H_2O$ soluble, while treatment of the obtained residue (obtained after solvent evaporation under reduced pressure) with MeCN allows removal of the produced, insoluble

 © 2006 Wiley-VCH Verlag GmbH & Co. KGaA, Weinheim 

$LiO_2CMe$ and dissolution of the cluster, which is subsequently crystallized pure upon storage of the resulting solution at 5 °C.

$$4\ Ni(O_2CMe)_2{\cdot}4H_2O + 4\ (2\text{-py})_2CO + 4\ LiOH{\cdot}H_2O \xrightarrow{EtOH/MeCN\ (3:1\ v/v)} [Ni_4(O_2CMe)_3\{(2\text{-py})_2C(OH)O\}_4](O_2CMe) + 4\ LiO_2CMe + 20\ H_2O \quad (6)$$

**5**

## Description of Structures

### *[Ni(O$_2$CMe){(2-py)$_2$C(OH)$_2$}{(2-py)$_2$CO}](ClO$_4$)·H$_2$O (2·H$_2$O)*

A partially labeled plot of the mononuclear cation $[Ni(O_2CMe)\{(2\text{-py})_2C(OH)_2\}\{(2\text{-py})_2CO\}]^+$ present in compound **2**·$H_2O$ is shown in Figure 2. Selected bond lengths and angles are listed in Table 1. The structure consists of the above mentioned mononuclear cation, one $ClO_4^-$ anion, and one $H_2O$ solvate molecule.

Table 1. Selected bond lengths [Å] and angles [°] for [Ni(O$_2$CMe)-{(2-py)$_2$C(OH)$_2$}{(2-py)$_2$CO}](ClO$_4$)·H$_2$O (**2**·H$_2$O).

| | | | |
|---|---|---|---|
| Ni–O(1) | 2.157(2) | C(6)–O(1) | 1.417(5) |
| Ni–O(3) | 2.045(3) | C(6)–O(2) | 1.387(4) |
| Ni–N(1) | 2.085(3) | C(26)–O(11) | 1.218(5) |
| Ni–N(2) | 2.094(3) | C(41)–O(3) | 1.248(5) |
| Ni–N(11) | 2.038(3) | C(41)–O(4) | 1.266(5) |
| Ni–N(12) | 2.060(3) | | |
| O(1)–Ni–O(3) | 94.7(1) | O(3)–Ni–N(12) | 89.6(1) |
| O(1)–Ni–N(1) | 76.4(1) | N(1)–Ni–N(2) | 88.0(1) |
| O(1)–Ni–N(2) | 77.0(1) | N(1)–Ni–N(11) | 98.0(1) |
| O(1)–Ni–N(11) | 173.0(1) | N(1)–Ni–N(12) | 94.3(1) |
| O(1)–Ni–N(12) | 95.0(1) | N(2)–Ni–N(11) | 98.7(1) |
| O(3)–Ni–N(1) | 171.1(1) | N(2)–Ni–N(12) | 170.9(1) |
| O(3)–Ni–N(2) | 89.8(1) | N(11)–Ni–N(12) | 89.7(1) |
| O(3)–Ni–N(11) | 90.9(1) | | |

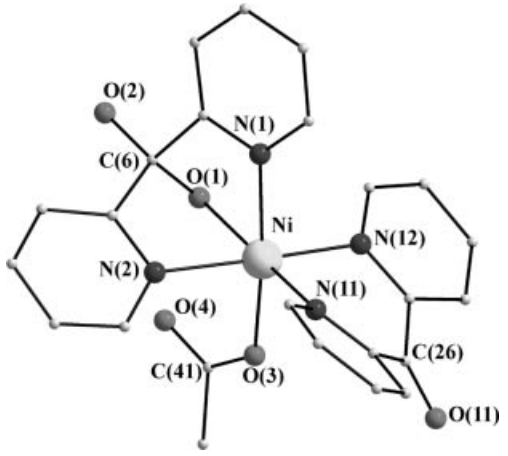


Figure 2. Partially labeled ORTEP plot of the mononuclear cation present in complex **2**·$H_2O$.

The $Ni^{II}$ atom is coordinated by one monodentate acetate, one tridentate chelating $(2\text{-py})_2C(OH)_2$ molecule, and one bidentate chelating $(2\text{-py})_2CO$ ligand. The ligated atoms of the latter are the 2-pyridyl nitrogen atoms (Figure 3), while the *gem*-diol ligand adopts the coordination mode $\eta^1{:}\eta^1{:}\eta^1$, see also Figure 3. The two oxygen atoms [O(1), O(3)] are in *cis* positions. The Ni–N and Ni–O bond lengths agree well with values expected for high-spin $Ni^{II}$ in octahedral environments.[7a,b,10] The distortion from a perfect octahedral geometry is primarily a consequence of the presence of three different ligands in the coordination sphere of $Ni^{II}$. The short length of the C(26)–O(11) bond [1.218(5) Å, compared with the C(6)–O(1, 2) bond lengths of 1.387(4) and 1.417(5) Å] reflects the ketone character of this group. There is one strong intramolecular hydrogen bond with the coordinated hydroxy oxygen of $(2\text{-py})_2C(OH)_2$ as the donor and the uncoordinated acetate oxygen

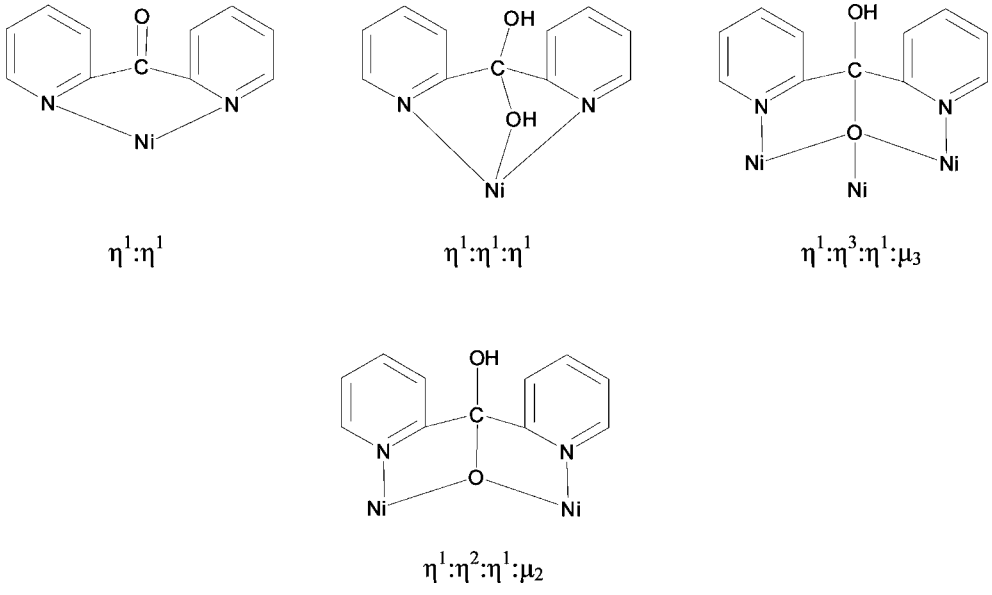


$\eta^1{:}\eta^1$ $\eta^1{:}\eta^1{:}\eta^1$ $\eta^1{:}\eta^3{:}\eta^1{:}\mu_3$

$\eta^1{:}\eta^2{:}\eta^1{:}\mu_2$

Figure 3. The crystallographically established coordination modes of the ligands $(2\text{-py})_2CO$, $(2\text{-py})_2C(OH)_2$, and $(py)_2C(OH)O^-$ present in complexes **1**–**5**.

 © 2006 Wiley-VCH Verlag GmbH & Co. KGaA, Weinheim 

as the acceptor; its dimensions are: O(1)···O(4) 2.525 Å, H(O1)···O(4) 1.688 Å, and O(1)–H(O1)···O(4) 168.7°. The crystal structure is stabilized by a hydrogen bond in which the uncoordinated hydroxy oxygen of the *gem*-diol ligand acts as the donor and one of the perchlorate oxygen atoms as the acceptor; the corresponding dimensions are O(2)···O(7) [$-x$, $y - 1/2$, $-z + 1$] 2.700 Å, H(O2)···O(7) 1.828 Å, and O(2)–H(O2)···O(7) 161.8°.

Compound **2**·$H_2O$ is the first example of a metal complex in which the ketone [$(2\text{-py})_2CO$] and the *gem*-diol [$(2\text{-py})_2C(OH)_2$] forms of di-2-pyridyl ketone co-exist as ligands.

### *[$Ni_4(O_2CMe)_2\{(2\text{-py})_2C(OH)O\}_4(H_2O)_2$](ClO$_4$)$_2$ (1), [$Ni_4(O_2CMe)_3\{(2\text{-py})_2C(OH)O\}_4$](ClO$_4$)·2H$_2$O·2EtOH (3·2H$_2$O·2EtOH), and [$Ni_4(O_2CMe)_3\{(2\text{-py})_2$-$C(OH)O\}_4$]($O_2$CMe)·6H$_2$O·MeCN (5·6H$_2$O·MeCN)*

Partially labeled plots of the tetranuclear cations present in compounds **1**, **3**·2$H_2O$·2EtOH, and **5**·6$H_2O$·MeCN are shown in Figure 4, Figure 5, and Figure 6, respectively. Tables 2, 3, 4, 5, and 6 show selected interatomic distances plus angles and hydrogen bonding data for complexes **1** and **5**·6$H_2O$·MeCN.

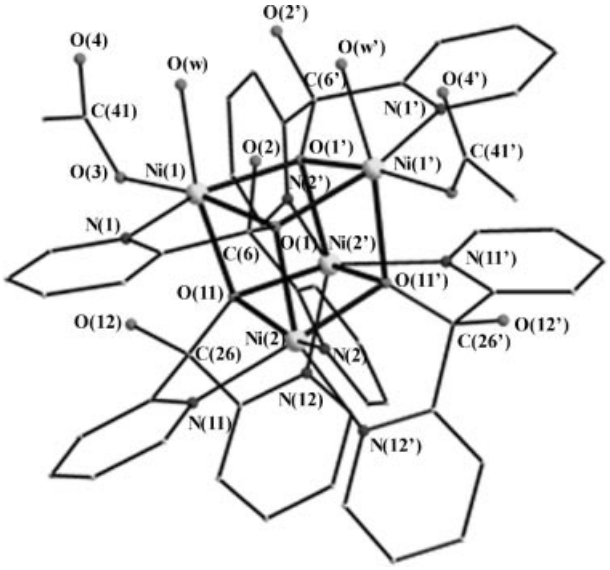


Figure 4. Partially labeled ORTEP plot of the tetranuclear cation present in complex **1**. Primed and unprimed atoms are related by the crystallographic twofold axis.

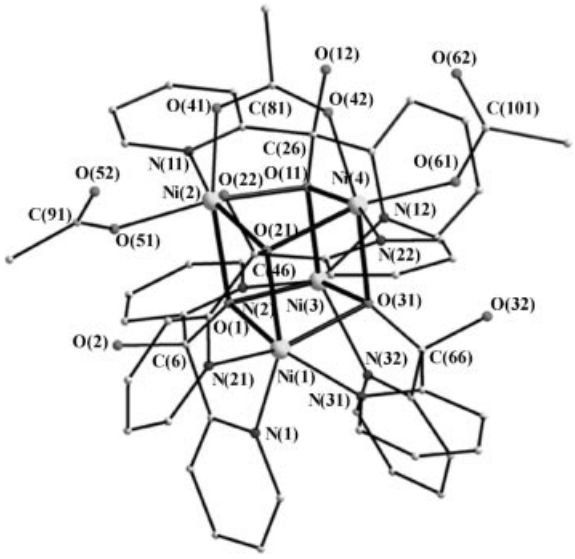


Figure 5. Partially labeled ORTEP plot of the tetranuclear cation present in complex **3**·2$H_2O$·2EtOH. The cubane core is outlined in bold.

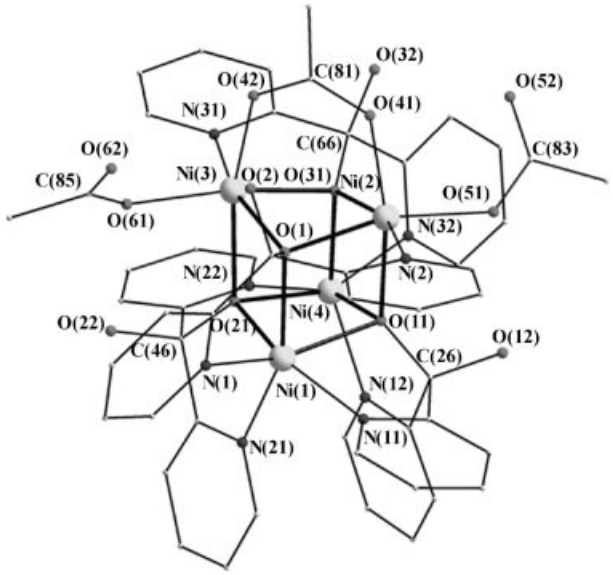


Figure 6. Partially labeled ORTEP plot of the tetranuclear cation present in complex **5**·6$H_2O$·MeCN. The cubane core is outlined in bold.

Complex **1** crystallizes in monoclinic space group *C*2/*c*. Its structure consists of tetranuclear [$Ni_4(O_2CMe)_2\{(2\text{-py})_2$-$C(OH)O\}_4(H_2O)_2$]$^{2+}$ cations and well-separated $ClO_4^-$ counterions; the latter will not be further discussed. The tetranuclear cluster cation of **1** lies on a crystallographic twofold axis and has a cubane $\{Ni_4(\mu_3\text{-}OR)_4\}^{4+}$ core with $Ni^{II}$ and oxygen atoms occupying alternate vertices. In addition to three $\mu_3$-oxygen atoms, each of the metal ions Ni(1) and Ni(1′) is coordinated to one pyridyl N atom, to one aquo ligand, and to one O atom from a monodentate acetate ligand, whereas each of Ni(2) and Ni(2′) is coordinated to three pyridyl N atoms belonging to different $(2\text{-py})_2C(OH)O^-$ ligands. Thus, an octahedral coordination environment is created about each metal center; the chromophores are Ni(1, 1′)$O_5N$ and Ni(2, 2′)$O_3N_3$. One octahedral face of each $Ni^{II}$ atom is occupied by the three alkoxide-type oxygen atoms and the other contains the remaining donor atoms.

One oxygen atom [O(2), O(2′), O(12), O(12′)] of each $(2\text{-py})_2C(OH)O^-$ ligand remains protonated and unbound to the metal ions. The resultant monoanion functions as a $\eta^1{:}\eta^3{:}\eta^1{:}\mu_3$ ligand (Figure 3). This ligation mode is common for $(2\text{-py})_2C(OH)O^-$.[8]

There are two types of Ni–O (alkoxide-type) bonds for each metal ion: one bond is rather short at an average dis-

 © 2006 Wiley-VCH Verlag GmbH & Co. KGaA, Weinheim 

Table 2. Selected interatomic distances [Å] and angles [°] for $[Ni_4(O_2CMe)_2\{(2\text{-py})_2C(OH)O\}_4(H_2O)_2](ClO_4)_2$ (**1**).[a]

| | | | |
|---|---|---|---|
| Ni(1)···Ni(2) | 3.157(1) | Ni(2)–O(1) | 2.122(3) |
| Ni(1)···Ni(2′) | 3.272(1) | Ni(2)–O(11) | 2.111(3) |
| Ni(1)···Ni(1′) | 3.139(1) | Ni(2)–O(11′) | 2.034(3) |
| Ni(2)···Ni(2′) | 3.060(1) | Ni(2)–N(2) | 2.036(4) |
| Ni(1)–O(1) | 2.030(3) | Ni(2)–N(11) | 2.095(4) |
| Ni(1)–O(1′) | 2.133(3) | Ni(2)–N(12′) | 2.085(4) |
| Ni(1)–O(3) | 2.013(4) | C(41)–O(3) | 1.277(6) |
| Ni(1)–O(11) | 2.117(3) | C(41)–O(4) | 1.229(8) |
| Ni(1)–O(w) | 2.072(5) | C(6)–O(1) | 1.390(6) |
| Ni(1)–N(1) | 2.083(4) | C(6)–O(2) | 1.410(7) |
| O(1)–Ni(1)–O(1′) | 80.6(1) | O(1)–Ni(2)–N(11) | 109.0(2) |
| O(1)–Ni(1)–O(3) | 171.0(1) | O(1)–Ni(2)–N(12′) | 155.1(2) |
| O(1)–Ni(1)–O(11) | 82.1(1) | O(11)–Ni(2)–O(11′) | 83.2(1) |
| O(1)–Ni(1)–O(w) | 94.7(2) | O(11)–Ni(2)–N(2) | 154.7(2) |
| O(1)–Ni(1)–N(1) | 78.2(2) | O(11)–Ni(2)–N(11) | 77.1(2) |
| O(1′)–Ni(1)–O(3) | 99.6(2) | O(11)–Ni(2)–N(12′) | 106.7(1) |
| O(1′)–Ni(1)–O(11) | 76.6(1) | O(11′)–Ni(2)–N(2) | 104.9(2) |
| O(1′)–Ni(1)–O(w) | 92.7(2) | O(11′)–Ni(2)–N(11) | 157.0(2) |
| O(1′)–Ni(1)–N(1) | 158.8(2) | O(11′)–Ni(2)–N(12′) | 74.5(2) |
| O(3)–Ni(1)–O(11) | 89.2(1) | N(2)–Ni(2)–N(11) | 98.0(2) |
| O(3)–Ni(1)–O(w) | 94.3(2) | N(2)–Ni(2)–N(12′) | 98.5(2) |
| O(3)–Ni(1)–N(1) | 101.3(2) | N(11)–Ni(2)–N(12′) | 95.9(2) |
| O(11)–Ni(1)–O(w) | 169.2(2) | Ni(1)–O(1)–Ni(1′) | 97.9(1) |
| O(11)–Ni(1)–N(1) | 100.4(2) | Ni(1)–O(1)–Ni(2) | 99.0(1) |
| O(w)–Ni(1)–N(1) | 89.0(2) | Ni(1)–O(11)–Ni(2) | 96.6(1) |
| O(1)–Ni(2)–O(11) | 80.1(2) | Ni(1)–O(11)–Ni(2′) | 104.0(1) |
| O(1)–Ni(2)–O(11′) | 78.6(1) | Ni(1′)–O(1)–Ni(2) | 100.6(1) |
| O(1)–Ni(2)–N(2) | 78.1(2) | Ni(2)–O(11)–Ni(2′) | 95.2(1) |

[a] Primed atoms are related to the unprimed ones by the symmetry transformation $-x + 1$, $y$, $-z + 1/2$.

Table 3. Details for the hydrogen bonding of complex $[Ni_4(O_2CMe)_2\{(2\text{-py})_2C(OH)O\}_4(H_2O)_2](ClO_4)_2$ (**1**).[a]

| D–H···A | D···A [Å] | H···A [Å] | DHA [°] | Symmetry operator of A |
|---|---|---|---|---|
| O(w)–H(wA)···O(4)[b] | 2.670 | 1.990 | 171.8 | $x$, $y$, $z$ |
| O(w)–H(wB)···O(2′)[b] | 2.997 | 2.495 | 122.4 | $-x + 1$, $y$, $-z + 1/2$ |
| O(12)–H(O12)···O(3)[b] | 2.698 | 2.012 | 177.2 | $x$, $y$, $z$ |
| O(2)–H(O2)···O(7)[c] | 3.096 | 2.521 | 176.1 | $-x + 1/2$, $y + 1/2$, $-z + 1/2$ |

[a] A = acceptor; D = donor. [b] Intramolecular hydrogen bonds. [c] O(7) is a perchlorate oxygen atom.

tance of 2.032(3) Å, whereas the two other bonds are longer [average distance 2.121(3) Å]. The cube deviates from the ideal geometry. The internal cube angles (RO–Ni–OR) at the metal vertices average 80.2(2)°, whereas the corresponding angles at the alkoxide corners (Ni–OR–Ni) are much larger averaging 98.9(1)°. The Ni···Ni vectors in the cluster reflect the different Ni–O (alkoxide-type) bond lengths, with the Ni(1)···Ni(2′)/Ni(1′)···Ni(2) [3.272(1) Å] and Ni(2)···Ni(2′) [3.060(1) Å] distances being the longest and the shortest, respectively. The shortest Ni···Ni distance corresponds to the smallest Ni–O–Ni [95.2(1)°] and the largest O–Ni–O [83.2(1)°] internal cube angles, whereas the longest Ni···Ni distance corresponds to the larger Ni–O–Ni [average 102.3(1)°] and the smaller O–Ni–O [average 77.6(1)°] angles. Average Ni–N, Ni–O (alkoxide-type), and Ni–O (acetate) bond lengths of 2.075(4), 2.091(3), and 2.013(4) Å, respectively, lie well within the range of reported

Table 4. Selected interatomic distances [Å] and angles [°] for $[Ni_4(O_2CMe)_3\{(2\text{-py})_2C(OH)O\}_4](ClO_4)\cdot 2H_2O\cdot 2EtOH$ (**3**·$2H_2O$·2EtOH).

| | | | |
|---|---|---|---|
| Ni(1)···Ni(2) | 3.258(2) | Ni(3)–O(1) | 2.106(6) |
| Ni(1)···Ni(3) | 3.038(2) | Ni(3)–O(11) | 2.100(7) |
| Ni(1)···Ni(4) | 3.173(2) | Ni(3)–O(31) | 2.045(7) |
| Ni(2)···Ni(3) | 3.195(2) | Ni(3)–N(2) | 2.084(9) |
| Ni(2)···Ni(4) | 2.970(2) | Ni(3)–N(12) | 2.058(9) |
| Ni(3)···Ni(4) | 3.286(2) | Ni(3)–N(32) | 2.103(9) |
| Ni(1)–O(1) | 2.025(6) | Ni(4)–O(11) | 2.092(6) |
| Ni(1)–O(21) | 2.075(6) | Ni(4)–O(21) | 2.044(6) |
| Ni(1)–O(31) | 2.105(7) | Ni(4)–O(31) | 2.201(7) |
| Ni(1)–N(1) | 2.088(8) | Ni(4)–O(42) | 2.016(8) |
| Ni(1)–N(21) | 2.043(9) | Ni(4)–O(61) | 1.993(9) |
| Ni(1)–N(31) | 2.079(9) | Ni(4)–N(22) | 2.085(9) |
| Ni(2)–O(1) | 2.162(6) | C(101)–O(61) | 1.25(2) |
| Ni(2)–O(11) | 2.037(7) | C(101)–O(62) | 1.23(2) |
| Ni(2)–O(21) | 2.099(7) | C(91)–O(51) | 1.269(14) |
| Ni(2)–O(41) | 2.021(8) | C(91)–O(52) | 1.234(14) |
| Ni(2)–O(51) | 2.030(7) | C(81)–O(41) | 1.277(15) |
| Ni(2)–N(11) | 2.079(9) | C(81)–O(42) | 1.220(15) |
| O(1)–Ni(1)–N(31) | 158.6(3) | Ni(1)–O(1)–Ni(2) | 102.1(3) |
| O(21)–Ni(1)–N(1) | 154.9(3) | Ni(1)–O(1)–Ni(3) | 94.7(3) |
| O(31)–Ni(1)–N(21) | 155.7(3) | Ni(1)–O(21)–Ni(2) | 102.6(3) |
| O(1)–Ni(2)–O(41) | 167.2(3) | Ni(1)–O(21)–Ni(4) | 100.8(3) |
| O(11)–Ni(2)–O(51) | 166.2(3) | Ni(1)–O(31)–Ni(3) | 94.1(3) |
| O(21)–Ni(2)–N(11) | 162.2(3) | Ni(1)–O(31)–Ni(4) | 94.9(3) |
| O(1)–Ni(3)–N(12) | 154.4(3) | Ni(2)–O(1)–Ni(3) | 96.9(2) |
| O(11)–Ni(3)–N(32) | 154.3(3) | Ni(2)–O(11)–Ni(3) | 101.1(3) |
| O(31)–Ni(3)–N(2) | 156.9(3) | Ni(2)–O(11)–Ni(4) | 92.0(3) |
| O(11)–Ni(4)–N(22) | 162.6(3) | Ni(2)–O(21)–Ni(4) | 91.6(3) |
| O(21)–Ni(4)–O(61) | 166.9(4) | Ni(3)–O(11)–Ni(4) | 103.2(3) |
| O(31)–Ni(4)–O(42) | 166.2(3) | Ni(3)–O(31)–Ni(4) | 101.4(3) |

Table 5. Selected interatomic distances [Å] and angles [°] for $[Ni_4(O_2CMe)_3\{(2\text{-py})_2C(OH)O\}_4](O_2CMe)\cdot 6H_2O\cdot MeCN$ (**5**·$6H_2O$·MeCN).

| | | | |
|---|---|---|---|
| Ni(1)···Ni(2) | 3.189(1) | Ni(3)–O(1) | 2.112(2) |
| Ni(1)···Ni(3) | 3.267(1) | Ni(3)–O(21) | 2.173(2) |
| Ni(1)···Ni(4) | 3.026(1) | Ni(3)–O(31) | 2.052(2) |
| Ni(2)···Ni(3) | 2.976(1) | Ni(3)–O(42) | 2.009(3) |
| Ni(2)···Ni(4) | 3.285(1) | Ni(3)–O(61) | 2.012(3) |
| Ni(3)···Ni(4) | 3.178(1) | Ni(3)–N(31) | 2.073(3) |
| Ni(1)–O(1) | 2.076(2) | Ni(4)–O(11) | 2.039(2) |
| Ni(1)–O(11) | 2.117(2) | Ni(4)–O(21) | 2.083(2) |
| Ni(1)–O(21) | 2.026(2) | Ni(4)–O(31) | 2.085(2) |
| Ni(1)–N(1) | 2.028(3) | Ni(4)–N(12) | 2.087(3) |
| Ni(1)–N(11) | 2.089(3) | Ni(4)–N(22) | 2.087(3) |
| Ni(1)–N(21) | 2.077(3) | Ni(4)–N(32) | 2.038(3) |
| Ni(2)–O(1) | 2.040(2) | C(81)–O(41) | 1.268(4) |
| Ni(2)–O(11) | 2.175(2) | C(81)–O(42) | 1.251(4) |
| Ni(2)–O(31) | 2.097(2) | C(83)–O(51) | 1.280(4) |
| Ni(2)–O(41) | 2.020(2) | C(83)–O(52) | 1.221(5) |
| Ni(2)–O(51) | 2.043(2) | C(85)–O(61) | 1.282(5) |
| Ni(2)–N(2) | 2.088(3) | C(85)–O(62) | 1.219(5) |
| O(1)–Ni(1)–N(21) | 155.5(1) | Ni(1)–O(1)–Ni(2) | 101.6(1) |
| O(11)–Ni(1)–N(1) | 155.4(1) | Ni(1)–O(1)–Ni(3) | 102.5(1) |
| O(21)–Ni(1)–N(11) | 157.4(1) | Ni(1)–O(11)–Ni(2) | 96.0(1) |
| O(1)–Ni(2)–O(51) | 164.4(1) | Ni(1)–O(11)–Ni(4) | 93.4(1) |
| O(11)–Ni(2)–O(41) | 166.5(1) | Ni(1)–O(21)–Ni(3) | 102.1(1) |
| O(31)–Ni(2)–N(2) | 162.3(1) | Ni(1)–O(21)–Ni(4) | 94.8(1) |
| O(1)–Ni(3)–N(31) | 162.0(1) | Ni(2)–O(1)–Ni(3) | 91.6(1) |
| O(21)–Ni(3)–O(42) | 166.0(1) | Ni(2)–O(11)–Ni(4) | 102.4(1) |
| O(31)–Ni(3)–O(61) | 165.5(1) | Ni(2)–O(31)–Ni(3) | 91.6(1) |
| O(11)–Ni(4)–N(22) | 158.6(1) | Ni(2)–O(31)–Ni(4) | 103.6(1) |
| O(21)–Ni(4)–N(32) | 155.5(1) | Ni(3)–O(21)–Ni(4) | 96.6(1) |
| O(31)–Ni(4)–N(12) | 154.9(1) | Ni(3)–O(31)–Ni(4) | 100.4(1) |

 © 2006 Wiley-VCH Verlag GmbH & Co. KGaA, Weinheim 

Table 6. Established and possible hydrogen bonds for $[Ni_4(O_2CMe)_3\{(2\text{-py})_2C(OH)O\}_4](O_2CMe)\cdot 6H_2O\cdot MeCN$ (**5**·$6H_2O$·MeCN).[a]

| D–H···A | D···A [Å] | H···A [°] | DHA [°] | Symmetry operator of A |
|---|---|---|---|---|
| O(2)–H(O2)···O(62) | 2.710 | 1.945 | 169.8 | *x*, *y*, *z* |
| O(12)–H(O12)···O(51) | 2.718 | 1.981 | 167.0 | *x*, *y*, *z* |
| O(22)–H(O22)···O(61) | 2.716 | 1.975 | 166.0 | *x*, *y*, *z* |
| O(32)–H(O32)···O(52) | 2.666 | 1.974 | 162.3 | *x*, *y*, *z* |
| O(W1)–H(OW1A)···O(W6) | 2.720 | 1.969 | 161.3 | *x*, *y*, *z* |
| O(W1)–H(OW1B)···O(62) | 2.900 | 1.951 | 163.5 | *x*, *y*, *z* |
| O(W2)–H(OW2A)···O(71)[b] | 2.628 | 1.614 | 154.4 | –*x* + 1, –*y* + 1, –*z* + 1 |
| O(W2)–H(OW2B)···O(W3) | 2.451 | 1.625 | 157.4 | –*x*, –*y* + 1, –*z* + 1 |
| O(W3)···O(W4) | 2.526 | | | –*x*, –*y* + 1, –*z* + 1 |
| O(W3)···O(W3) | 2.863 | | | –*x*, –*y* + 1, –*z* + 1 |
| O(W4)···O(72)[b] | 2.388 | | | –*x* + 1, –*y* + 1, –*z* + 1 |
| O(W5)···O(52) | 3.151 | | | *x*, *y*, *z* |
| O(W5)···O(W5A) | 2.983 | | | –*x* + 1, –*y*, –*z* |
| O(W5A)···O(41) | 2.880 | | | *x*, *y*, *z* |
| O(W5A)···O(52) | 2.897 | | | *x*, *y*, *z* |
| O(W5A)···O(W5A) | 2.964 | | | –*x* + 1, –*y*, –*z* |
| O(W6)···O(W6) | 2.755 | | | –*x* + 1, –*y* + 1, –*z* + 1 |
| O(W6)···O(71)[b] | 2.414 | | | *x*, *y*, *z* |

[a] A = acceptor; D = donor. [b] These oxygen atoms belong to the acetate counterion.

values for the corresponding bond lengths of other tetranuclear cubane $Ni^{II}$clusters.[6a,7a,10,14]

There is an amount of hydrogen bonding in **1** (Table 3). The donors are the aqua ligands and the hydroxy groups of all the $(2\text{-py})_2C(OH)O^-$ ligands. A notable feature here is that both uncoordinated and coordinated oxygen atoms of the terminal acetate ligands participate in intracubane hydrogen bonds; of interest is also the fact that the hydroxy oxygen atom O(2) acts both as a donor and an acceptor.

The cation $[Ni_4(O_2CMe)_3\{(2\text{-py})_2C(OH)O\}_4]^+$ present in complex **3**·$2H_2O$·2EtOH also has a cubane structure (Figure 5), with the $\eta^1{:}\eta^3{:}\eta^1\mu_3$ $(2\text{-py})_2C(OH)O^-$ ligands (Figure 3) supplying the O atoms at the alternate sites of the heterocubane. However, its structure is different from the structure of the cation present in **1**. There are no solvate ligands and a third acetate is present. Two acetates are coordinated to each of Ni(2) and Ni(4). The third acetate acts as an 1,3-bridge ($\eta^1{:}\eta^1{:}\mu_2$) between Ni(2) and Ni(4); thus, one face of the cube is capped by the $\mu_2$-bridging acetate which lies across the face diagonally. The metal centers that are bridged by the acetate ion have the shortest metal–metal distance [Ni(2)···Ni(4) 2.970(2) Å]. There are two distinct nickel sites in **3**·$2H_2O$.2EtOH. Two [Ni(1), Ni(3)] have an $O_3N_3$ coordination sphere, while for the other two [Ni(2),Ni(4)] the coordination environment is $O_5N$. Three Ni–O (alkoxide-type) distances are realized for Ni(1), Ni(2), and Ni(4). One bond is short with an average of 2.035(6) Å, one bond is relatively long with an average distance of 2.156(7) Å, while the third bond is of intermediate strength [average Ni–O distance of 2.089(7) Å]. For Ni(3) one bond is rather short to a distance of 2.045(7) Å, whereas the two other bonds are longer [2.106(6), 2.100(7) Å]. As in **1**, the $\{Ni_4O_4\}$ cube deviates from the ideal geometry. Since all the hydrogen atoms of this complex were not located by difference maps, we can not comment on the hydrogen bonds.

The molecular structure of the cation $[Ni_4(O_2CMe)_3\{(2\text{-py})_2C(OH)O\}_4]^+$ present in complex **5**·$6H_2O$·MeCN (Figure 6) is almost identical to that of the tetranuclear cation with the same formula in complex **3**·$2H_2O$·2EtOH. Clearly, the replacement of the $ClO_4^-$ counterion by the $MeCO_2^-$ counterion and the change of the lattice solvate molecules have very little structural effect. The crystal structure is stabilized by a series of strong or relatively strong hydrogen bonds with water solvate molecules as donors.

The molecular structure of the cations $[Ni_4(O_2CMe)_3\{(2\text{-py})_2C(OH)O\}_4]^+$ of complexes **3**·$2H_2O$·2EtOH and **5**·$6H_2O$·MeCN is very similar to that of the same cation present in complex $[Ni_4(O_2CMe)_3\{(2\text{-py})_2C(OH)O\}_4](ClO_4)\cdot 8\cdot 25H_2O$.[7a]

Complexes **1**, **3**·$2H_2O$·2EtOH and **5**·$6H_2O$·MeCN join a family of polynuclear $Ni^{II}$ complexes with $(2\text{-py})_2CO$-based ligands, which currently comprises 12 clusters. The eight previously characterized clusters (solvate molecules are not indicated) are $[Ni_9(OH)_2(O_2CMe)_8\{(2\text{-py})_2CO_2\}_4]$,[6f] $[Ni_9(N_3)_2(O_2CMe)_8\{(2\text{-py})_2CO_2\}_4]$,[6f] $[Ni_4(O_2CMe)_3\{(2\text{-py})_2C(OH)O\}_4](ClO_4)$,[7a] $[Ni_4(O_2CMe)_4\{(2\text{-py})_2C(OH)O\}_4]$,[7b] $[Ni_4\{(2\text{-py})_2C(OH)O\}_2\{(2\text{-py})_2C(OEt)O\}_2(CH_3CONHO)_2]Cl_2$,[7b] where $CH_3CONHO^-$ is the acetohydroxamate(–1) ion, $[Ni_4\{N(CN)_2\}_2(O_2CMe)_2\{(2\text{-py})_2C(OH)O\}_4]$,[6a] $\{K[Ni_6(CO_3)(N_3)_6(O_2CMe)_3\{(2\text{-py})_2C(CH_2CN)O\}_3]\}_2[K_2(H_2O)_2]$,[15] where $(2\text{-py})_2C(CH_2CN)O^-$ is the monoanion of a ligand generated in situ by the reaction of MeCN and $(2\text{-py})_2CO$ in the presence of *tert*-butoxide, $[Ni_4(N_3)_4\{(2\text{-py})_2C(OH)O\}_4]$,[9h] and $[Ni_4(N_3)_2\{(2\text{-py})_2C(OH)O\}_2\{(2\text{-py})_2C(OMe)O\}_2(H_2O)_2](ClO_4)_2$.[9i] From the tetranuclear clusters in the above list, only complexes $[Ni_4(O_2CMe)_3\{(2\text{-py})_2C(OH)O\}_4](ClO_4)$,[7a] $[Ni_4\{N(CN)_2\}_2(O_2CMe)_2\{(2\text{-py})_2C(OH)O\}_4]$,[6a] and the clusters **1**, **3**·$2H_2O$·2EtOH, **5**·$6H_2O$·MeCN reported in this work have a cubane structure.

### *$[Ni_4(O_2CMe)_4\{(2\text{-py})_2C(OH)O\}_4]\cdot 2MeCN$ (4·2MeCN)*

A partially labeled plot of the tetranuclear molecule of compound **4** is shown in Figure 7. Selected interatomic dis-

 © 2006 Wiley-VCH Verlag GmbH & Co. KGaA, Weinheim 

tances and angles are listed in Table 7, while hydrogen bonding details are summarized in Table 8.

Table 7. Selected interatomic distances [Å] and angles [°] for $[Ni_4(O_2CMe)_4\{(2\text{-py})_2C(OH)O\}_4]\cdot 2MeCN$ (**4**·2MeCN).[a]

| | | | |
|---|---|---|---|
| Ni(1)···Ni(1′) | 3.178(1) | Ni(2)–O(1) | 2.023(3) |
| Ni(1)···Ni(2) | 3.089(1) | Ni(2)–O(3′) | 2.101(3) |
| Ni(1)···Ni(2′) | 3.273(1) | Ni(2)–O(5) | 2.025(3) |
| Ni(2)···Ni(2′) | 5.515(1) | Ni(2)–O(11) | 2.157(3) |
| Ni(1)–O(1) | 2.108(3) | Ni(2)–N(2) | 2.124(4) |
| Ni(1)–O(3) | 2.061(3) | Ni(2)–N(12) | 2.089(3) |
| Ni(1)–O(11) | 2.039(3) | C(41)–O(3) | 1.303(5) |
| Ni(1)–O(11′) | 2.091(3) | C(41)–O(4) | 1.206(6) |
| Ni(1)–N(1) | 2.051(3) | C(43)–O(5) | 1.262(5) |
| Ni(1)–N(11) | 2.116(4) | C(43)–O(6) | 1.229(6) |
| O(1)–Ni(1)–O(3) | 161.9(1) | Ni(1)–O(1)–Ni(2) | 96.8(1) |
| O(11)–Ni(1)–N(1) | 158.6(1) | Ni(1)–O(11)–Ni(2) | 94.8(1) |
| O(11′)–Ni(1)–N(11) | 153.2(1) | Ni(1)–O(11)–Ni(1′) | 100.6(1) |
| O(1)–Ni(2)–N(12) | 155.8(1) | Ni(1′)–O(11)–Ni(2) | 100.8(1) |
| O(3′)–Ni(2)–N(2) | 166.8(1) | Ni(1)–O(3)–Ni(2′) | 103.7(1) |
| O(5)–Ni(2)–O(11) | 162.7(1) | | |

[a] Primed atoms are related to the unprimed ones by the symmetry transformation $-x, -y + 2, -z$.

Table 8. Details for the hydrogen bonding of complex $[Ni_4(O_2CMe)_4\{(2\text{-py})_2C(OH)O\}_4]\cdot 2MeCN$ (**4**·2MeCN).[a]

| D–H···A | D···A [Å] | H···A [Å] | DHA [°] | Symmetry operator of A |
|---|---|---|---|---|
| O(2)–H(O2)···O(6)[b] | 2.659 | 1.992 | 171.0 | $x, y, z$ |
| O(12)–H(O12)···O(1′)[b] | 2.656 | 1.872 | 167.7 | $-x, -y + 2, -z$ |

[a] A = acceptor; D = donor. [b] Intramolecular hydrogen bonds.

Complex **4**·2MeCN crystallizes in monoclinic space group $P2_1/n$. Its structure consists of centrosymmetric tetranuclear $[Ni_4(O_2CMe)_4\{(2\text{-py})_2C(OH)_2O\}_4]$ molecules and lattice MeCN molecules; the latter will not be further discussed. The four $Ni^{II}$ ions are located at four vertices of a defect dicubane (two cubanes sharing one face and each missing one vertex, Figure 8) and bridged by means of O atoms from the $(2\text{-py})_2C(OH)O^-$ ligands and two $\eta^2{:}\mu_2$ acetate ions (Figure 9). Peripheral ligation is provided by two O atoms of two monodentate ($\eta^1$, Figure 9) acetates and the N atoms of the eight 2-pyridyl rings. Atoms O(11)/O(11′) of two $(2\text{-py})_2C(OH)O^-$ ligands are triply bridging with distances to $Ni^{II}$ ions of 2.039(3), 2.091(3), and 2.157(3) Å. Atoms O(1)/O(1′) of the last two $(2\text{-py})_2C(OH)O^-$ ligands are doubly bridging forming one strong bond to Ni(2)/Ni(2′) [2.023(3) Å] and one weaker bond to Ni(1)/Ni(1′) [2.108(3) Å]. The bridging Ni–$O_{acetate}$ distances [2.061(3), 2.101(3) Å] are slightly asymmetric. The Ni–O bond lengths for the bridging acetate oxygen are longer than the Ni(2)–O(5) distance [2.025(3) Å] exhibited by the terminal acetate. One O atom of each $(2\text{-py})_2C(OH)O^-$ ligand remains protonated and unbound to the metal ions. Therefore, two $(2\text{-py})_2C(OH)O^-$ ligands adopt the $\eta^1{:}\eta^3{:}\eta^1{:}\mu_3$ coordination mode and the other two bind with the $\eta^1{:}\eta^2{:}\eta^1{:}\mu_2$ mode. Ni(1) and Ni(2) are also bridged by the O(3) atom of the $\eta^2{:}\mu_2$ acetate ligand. In the centrosymmetric tetramer two types of octahedrally coordinated $Ni^{II}$ ions can be distinguished, Ni(1) and Ni(2). The two chromophores are Ni(1)($O_{alkoxo}$)$_3$($O_{acetate}$)$N_2$ and Ni(2)($O_{alkoxo}$)$_2$($O_{acetate}$)$_2N_2$.

Complex **4** is the 13th member in the above-mentioned family of structurally characterized $Ni^{II}$ clusters with $(2\text{-py})_2CO$-based ligands.[6a,f,7a,b,9h,i,15] Within this family, complexes **4**, $[Ni_4(O_2CMe)_4\{(2\text{-py})_2C(OH)O\}_4]$ (as the tetraethanol solvate),[7b] $[Ni_4\{(2\text{-py})_2C(OH)O\}_2\{(2\text{-py})_2C(OEt)O\}_2(CH_3CONHO)_2]Cl_2$,[7b] $[Ni_4(N_3)_4\{(2\text{-py})_2C(OH)O\}_4]$,[9h] and $[Ni_4(N_3)_2\{(2\text{-py})_2C(OH)O\}_2\{(2\text{-py})_2C(OMe)O\}_2(H_2O)_2](ClO_4)_2$[9i] have a defect dicubane structural motif. Complex **4** has a remarkable structural similarity with compound $[Ni_4(O_2CMe)_4\{(2\text{-py})_2C(OH)O\}_4]\cdot 4EtOH$;[7b] only the crystal packing of this cluster differs.

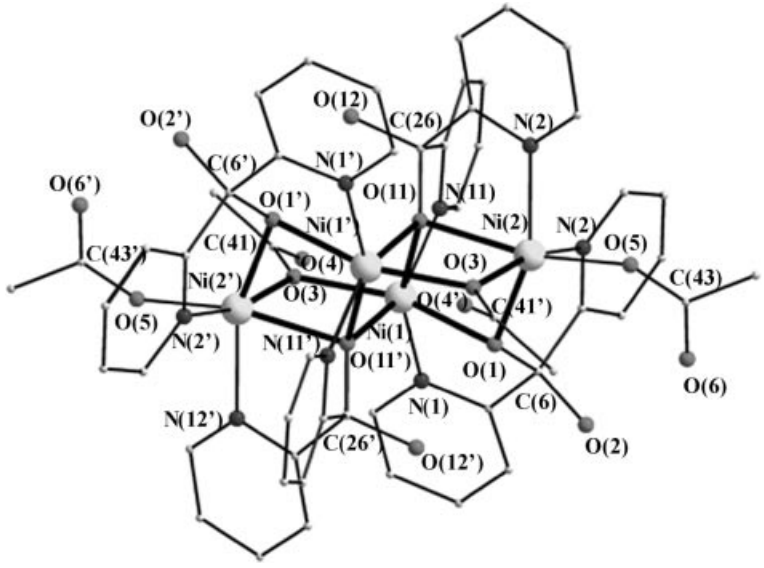


Figure 7. Partially labeled ORTEP plot of the tetranuclear molecule present in complex **4**·2MeCN. Primed and unprimed atoms are related by the crystallographic inversion center. The defect dicubane core has been highlighted.

 © 2006 Wiley-VCH Verlag GmbH & Co. KGaA, Weinheim 

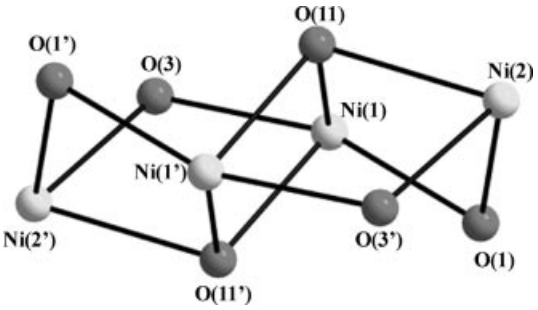


Figure 8. Labeled plot of the defect dicubane core present in complex **4**·2MeCN. Atoms O(3) and O(3′) originate from the $\eta^2$:$\mu_2$ acetates, while atoms O(1), O(1′), O(11), and O(11′) are the deprotonated oxygens of the $(2\text{-py})_2C(OH)O^-$ ligands.

Figure 9. The crystallographically established coordination modes of the acetate ligands present in complex **4**·2MeCN.

Tetranuclear $Ni^{II}$ clusters with the defect dicubane unit have been reported,[7b,9h,i,16] but these are significantly less than the $Ni^{II}$ cubanes.

## IR Spectra

The prepared complexes exhibit medium to strong intensity bands in the 3605–3150 $cm^{-1}$ region, assignable to ν(OH) vibrations of the $(2\text{-py})_2C(OH)_2$, $(2\text{-py})_2C(OH)O^-$, $H_2O$, and EtOH ligands/lattice molecules.[6a,9a] The broadness and relatively low frequencies of these bands are both indicative of hydrogen bonding.

The spectrum of **2**·$H_2O$ exhibits a strong band at 1686 $cm^{-1}$, assigned to ν(C=O) and suggesting that a certain amount of the organic ligand is present in its ketone form. This mode is situated at the same wavenumber (1684 $cm^{-1}$) in the spectrum of free $(2\text{-py})_2CO$, confirming the nonparticipation of the ketone group in the coordination in this complex. The spectra of **1** and **3**–**5** do not exhibit bands in the region expected for ν(C=O) vibrations, with the nearest IR absorptions at ca. 1600 $cm^{-1}$ assigned as a 2-pyridyl stretching mode raised from 1582 $cm^{-1}$ on coordination, as observed earlier[17] upon complex formation involving hydration of di-2-pyridyl ketone.[17]

Several bands appear in the 1600–1400 $cm^{-1}$ range in the spectra of the complexes. Contributions from the $MeCO_2^-$ $\nu_{as}(CO_2)$ and $\nu_s(CO_2)$ modes would be expected in this region, but overlap with the stretching vibrations of the 2-pyridyl rings and $\delta(CH_3)$ renders assignments tentative and application of the spectroscopic criterion of Deacon and Phillips[18] extremely difficult.

The IR spectra of **1**–**3** exhibit medium or strong bands at ca. 1100 and 620 $cm^{-1}$, because of the $\nu_3(F_2)$ and $\nu_4(F_2)$ modes of the uncoordinated $T_d$ $ClO_4^-$, respectively.[19] The $\nu_3(F_2)$ band is broadened and split, indicating the crystallographically established (at least for **1** and **2**) involvement of the $ClO_4^-$ ion in hydrogen bonding.[20]

## Magnetic Studies

Solid-state dc magnetic susceptibility measurements were performed on polycrystalline samples of the representative complexes **1** and **4**, under a constant field of 0.5 T in the temperature range of 1.9 to 300 K.

The exchange coupling of four $S = 1$ centers results in $n = 3^4 = 81$ molecular magnetic states that are split into 3 singlets ($S = 0$), 6 triplets ($S = 1$), 6 quintets ($S = 2$), 3 septets ($S = 3$), and 1 nonet ($S = 4$). Depending upon the actual topology, these states can be degenerate (the case of a perfect tetrahedron with a single exchange coupling constant) or the degeneracy can be partially removed.

The structural parameters of **1** suggest a lower symmetry than $T_d$. The magnetic analyses were carried out using a 2-*J* model and assuming that the tetranuclear structure results from the association of two planar, doubly-bridged dimeric units as shown in Figure 10. The intradimer interaction (noted $J_1$) is between Ni(1) and Ni(1′) on the one hand and between Ni(2) and Ni(2′) on the other hand, while the interdimer one is noted $J_2$. The spin Hamiltonian for such a model, reflecting the $S_4$ symmetry, is given by Equation (7).

$$\hat{H}(\mathbf{S}_4) = -J_1(\vec{S}_1\cdot\vec{S}_{1'} + \vec{S}_2\cdot\vec{S}_{2'}) - J_2(\vec{S}_1\cdot\vec{S}_2 + \vec{S}_1\cdot\vec{S}_{2'} + \vec{S}_{1'}\cdot\vec{S}_2 + \vec{S}_{1'}\cdot\vec{S}_{2'}) + \mu_B B g_{iso}(\vec{S}_1 + \vec{S}_{1'} + \vec{S}_2 + \vec{S}_{2'}) \quad (7)$$

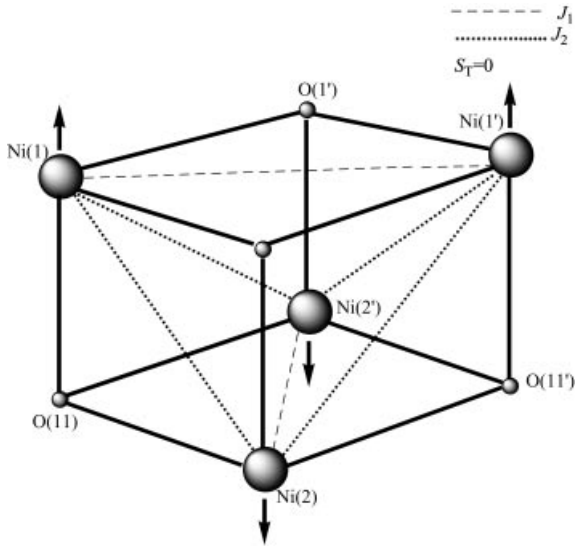


Figure 10. Core representation of the cation of **1** showing the coupling scheme used in the magnetic model and the relative orientation of the $Ni^{II}$ spins in the ground state. The numbering scheme from Figure 4 has been used.

 © 2006 Wiley-VCH Verlag GmbH & Co. KGaA, Weinheim 

The Hamiltonian matrix in the basis set of coupled kets $|S_1S_{1'}S_{11'}S_2S_{2'}S_{22'}SM\rangle$ is already diagonal, so that the energy levels are given[21] by a simple formula [Equation (8)], where the last, constant term can be omitted.

$$\varepsilon_{B=0}(S) = \left\langle S_{11'}S_{22'}SM \left| \hat{H}(S_4) \right| S_{11'}S_{22'}SM \right\rangle = -(J_2/2)[S(S+1) - S_{11'}(S_{11'}+1) - S_{22'}(S_{22'}+1)] - (J_1/2)[S_{11'}(S_{11'}+1) + S_{22'}(S_{22'}+1)] + (J_1/2)[S_1(S_1+1) + S_{1'}(S_{1'}+1) + S_2(S_2+1) + S_{2'}(S_{2'}+1)] \quad (8)$$

The addition of the Zeeman term results in the formula given by Equation (9), where a single, isotropic $g_{iso}$-factor common to all magnetic centers occurs.

$$\varepsilon_B(S,M) = \varepsilon_{B=0}(S) + \mu_B g_{iso} MB \quad (9)$$

The identification of the van Vleck coefficients is now an easy task, so that one can applythe van Vleck equation (with a vanishing second-order term) to end up with an analytical formula [Equation (10)] for the mean magnetic susceptibility, where the physical constants in the reduced Curie constant $C_0 = N_A\mu_0\mu_B^2/k$ adopt their usual meaning.

$$\overline{\chi}_{mol} = C_0 \frac{g_{iso}^2}{T} \frac{\sum_S \sum_{M=-S}^{+S} M^2 \exp[-\varepsilon_{B=0}(S)/kT]}{\sum_S \exp[-\varepsilon_{B=0}(S)/kT]} \quad (10)$$

Figure 11 shows plots of the experimental data for **1** in the form of $\mu_{eff}$ (effective magnetic moment) per complex, $\chi_{mol}$ and $\chi_{mol}^{-1}$ vs. $T$, respectively. The value of $\mu_{eff}$ at 300 K is 6.13 $\mu_B$ per complex. As the temperature is lowered, $\mu_{eff}$ experiences a slight increase, reaching a maximum value of 6.57 $\mu_B$ at 30 K, followed by a much sharper decline at lower temperatures, 2.48 $\mu_B$ at 1.9 K. The best fit parameters ($R$ = 0.055) are found to be $J_1$ = 13.7 cm$^{-1}$, $J_2$ = –1.4 cm$^{-1}$, and $g_{iso}$ = 2.14. Since the fit with $J$ constants is sufficient, there is no need to add $D$ to the model, risking an overparameterization. The experimental data show that complex **1** can be described as two ferromagnetically coupled $Ni_2$ pairs that, in turn, are coupled antiferromagnetically. The zero-field energy levels of **1** are shown in the inset of Figure 11. One can observe that the width of the energy band is less than $\Delta\varepsilon$ <100 cm$^{-1}$. This means that at ambient temperature a Curie law holds true owing to a uniform population of all energy levels. Upon cooling down, some "magnetically less productive states" (singlets, triplets, quintets) are depopulated and, thus, the overall "magnetic productivity" is raised; under the term "magnetic productivity" we mean the contribution of the state $g^2M^2\exp[\varepsilon_B = {}_0(S)/kT]$ to the susceptibility function and/or the effective magnetic moment. This point explains the maximum of $\mu_{eff}$ at 30 K. However, the ground state is $S$ = 0, because of the antiferromagnetic coupling between the two dimeric units. Consequently, the magnetic susceptibility exhibits a turning point on cooling (at 5.0 K), below which it drops to zero. Low-temperature data bring no evidence for the presence of a paramagnetic impurity in **1**. It can not be excluded that the zero-field splitting of the $S \geq 1$ states occurs, as the $D$ values (the axial zero-field splitting parameter), ranging between $D/k$ = –10 and +10 K, are typical for mononuclear $Ni^{II}$ complexes on departure from the octahedral geometry.[22] The involvement of the local anisotropy through the axial zero-field splitting parameter led to a rather slight improvement of the data-fit ($R$ = 0.0082) with magnetic parameters $J_1$ = 11.7 cm$^{-1}$, $J_2$ = –1.3 cm$^{-1}$, $g_{iso}$ = 2.16, and $D_{Ni}$ = –2.8 cm$^{-1}$. The obtained $D_{Ni}$ parameter lies at the limit of its detection from the susceptibility data; moreover, it has been obtained by assuming all the $D$ tensors are collinear, the negligible $g$-tensor anisotropy, and neglect of the pair-interaction $D_{Ni–Ni}$ parameters (the asymmetric exchange) that are inconsistent approximations.[22]

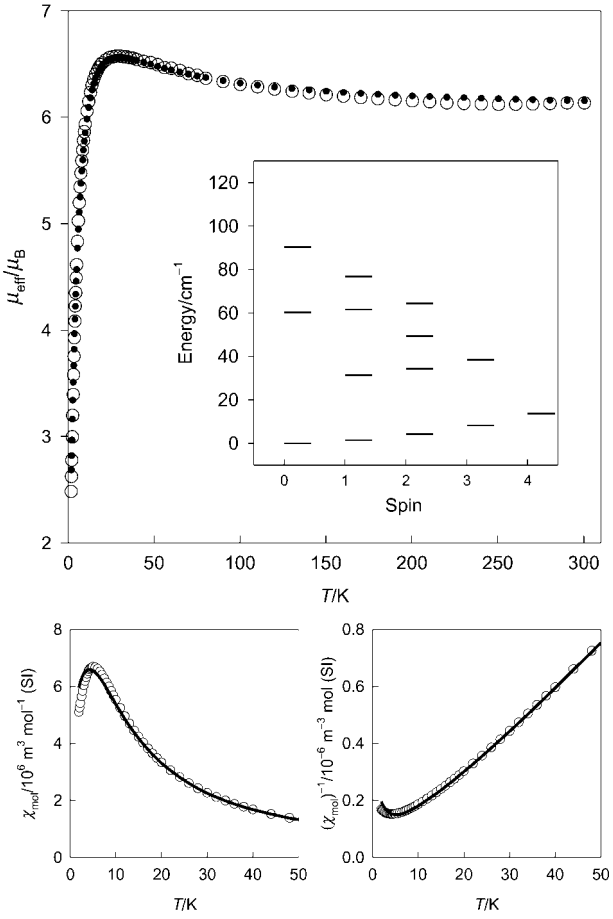


Figure 11. Plots of experimental (open circles) $\mu_{eff}$ (left), $\chi_{mol}$ (right up) and $\chi_{mol}^{-1}$ (right bottom) vs. $T$ per molecule of **1**. The filled circles and the solid lines are the fits to the experimental data (see text for details). Inset: calculated energy levels for individual total spins.

The lowest temperature data (below 5 K) can suffer from eventual saturation effects; when the magnetization approaches saturation, the apparent susceptibility $\chi = \mu_0 M/B$ decreases substantially [the true differential susceptibility, $\tilde{\chi} = \mu_0(\partial M/\partial B)$, as measured by the alternating-current susceptometer, then drops to zero]. Finally, some molecular field correction, accounting for the weak intercluster inter-

 © 2006 Wiley-VCH Verlag GmbH & Co. KGaA, Weinheim 

actions can contribute to the low-temperature data. All of these effects are assumed to be of secondary importance and they do not alter the main conclusion for **1**, i.e. that the intradimer coupling is of ferromagnetic nature, whereas the interdimer interaction is antiferromagnetic.

It should be mentioned at this point that the most important parameter in the magnetostructural correlation of tetranuclear nickel(II) clusters possessing the $\{Ni_4(\mu_3\text{-}OR)_4\}^{4+}$ cubane core has been reported[6a,10c,14e–h,14k–14n] to be the average Ni–O–Ni angle of a cubane face. A ferromagnetic exchange interaction is observed for Ni–O–Ni angles lower than ca. 99° and the $J$ value increases as the angle decreases. On the other hand, Ni–O–Ni angles in the vicinity of, and larger than, 99° lead to an antiferromagnetic interaction and the $|J|$ value increases as the angle increases. Accordingly, a linear correlation between $J$ and the Ni–O–Ni angle has been reported.[14e] The $J_1$ and $J_2$ values for **1** are in line with the previous studies mentioned above. The mean Ni–O–Ni angle for the pairs described by $J_1$ is 96.6°, thus the coupling is predicted to be ferromagnetic, and indeed, it is ($J_1$ = 13.7 cm$^{-1}$). The value of the ferromagnetic parameter $J_1$ matches satisfactorily the linear dependence reported.[14e,h,l] The mean Ni–O–Ni value of 100.0° for the remaining four faces of the cube justifies the weak antiferromagnetic value of $J_2$ (–1.4 cm$^{-1}$).

Magnetically, the closest precedents of complex **1** are the cubanes $[Ni_4(O_2CMe)_3\{(2\text{-py})_2C(OH)O\}_4](ClO_4)$[7a] and $[Ni_4(O_2CCMe_3)_4(Mq)_4]$ (Mq = 1,8-hydroxyquinaldinate);[14n] their behavior was interpreted on the basis of two pairs of ferromagnetically coupled dimers that couple antiferromagnetically to give a diamagnetic ground state.

Variable-temperature magnetic data for complex **4** are presented in Figure 12. As the temperature is lowered, $\mu_{eff}$ experiences a very slight increase from $\mu_{eff}$ = 5.71 $\mu_B$ at 300 K (it practically has a constant value), reaching a broad maximum of $\mu_{eff}$ = 5.79 $\mu_B$ at 90 K, followed by a much sharper decline at lower temperatures, down to $\mu_{eff}$ = 1.33 $\mu_B$ at 1.9 K. Considering the cluster topology and core connectivity, the magnetic data were analyzed with the spin Hamiltonian given in Equation (11) [the spin numbering follows the Ni$^{II}$ ions in Figure 8],

$$\hat{H} = -J_1(\vec{S}_1 \cdot \vec{S}_{1'}) - J_2(\vec{S}_1 \cdot \vec{S}_{2'} + \vec{S}_{1'} \cdot \vec{S}_2) - J_3(\vec{S}_1 \cdot \vec{S}_2 + \vec{S}_{1'} \cdot \vec{S}_{2'}) + \mu_B B g_{iso}(\vec{S}_1 + \vec{S}_{1'} + \vec{S}_2 + \vec{S}_{2'}) \quad (11)$$

where $J_1$ is assigned to the Ni(1)···Ni(1′) interaction of the central pair, $J_2$ to the Ni(1)···Ni(2′) [Ni(1′)···Ni(2)] interaction, and $J_3$ to the Ni(1)···Ni(2) [Ni(1′)···Ni(2′)] exchange interaction. The above Hamiltonian cannot be taken to a diagonal form so that we are left with the diagonalization of its matrix elements and a numerical finding of the van Vleck coefficients that enter the formula for the magnetic susceptibility.[23] The best-fit parameters ($R$ = 0.030) are: $J_1$ = –5.0 cm$^{-1}$, $J_2$ = –4.8 cm$^{-1}$, $J_3$ = 15.3 cm$^{-1}$ with $g$ = 2.00. The involvement of the local anisotropy through the axial zero-field splitting parameter $D_{Ni}$ led only to a slight improvement of the data-fit ($R$ = 0.018) with magnetic parameters $J_1$ = –5.3 cm$^{-1}$, $J_2$ = –4.6 cm$^{-1}$, $J_3$ = 15.7 cm$^{-1}$, $g$ = 2.00, and $D_{Ni}$ = –2.0 cm$^{-1}$.

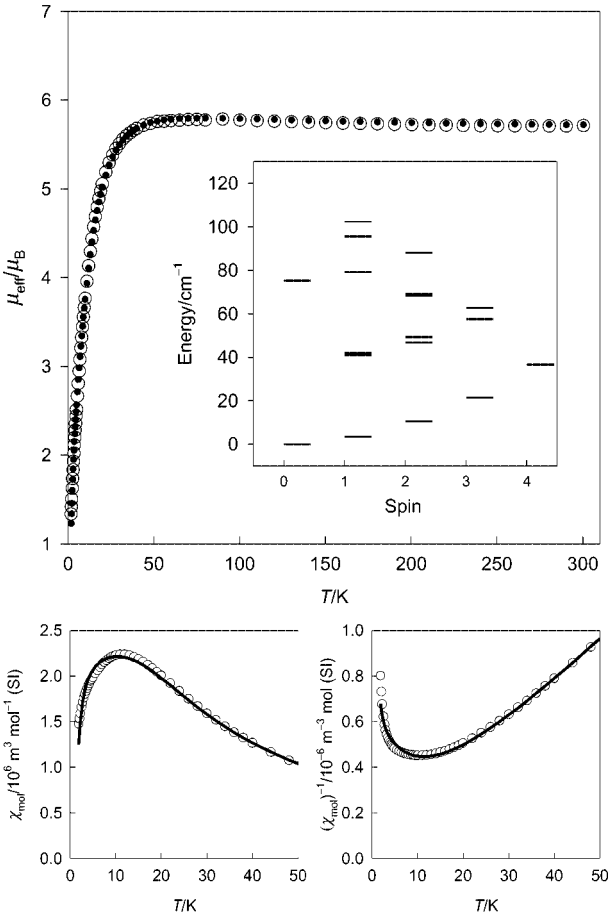


Figure 12. Plots of experimental (open circles) $\mu_{eff}$ (left), $\chi_{mol}$ (right up) and $\chi_{mol}^{-1}$ (right bottom) vs. $T$ per molecule of **4**. The filled circles and the solid lines are the fits to the experimental data (see text for details). Inset: calculated energy levels for individual total spins.

The calculated zero-field, total spin energy levels of complex **4** are shown in the inset of Figure 12. Approaching room temperature, all the levels are equally populated, so that we end up with Curie law behavior. On cooling, however, some magnetically less productive states are depopulated and, thus, the overall magnetic productivity rises. This explains the shallow maximum of $\mu_{eff}$ at about 90 K. Upon further cooling below 40 K, the $S$ = 4, $S$ = 3, $S$ = 2, and $S$ = 1 states are gradually depopulated and, therefore, the effective magnetic moment drops to zero. Because of the $S$ = 0 ground state, a turning point exists at 11 K in the $\chi_{mol}$ vs. $T$ curve upon cooling.

The signs of the $J$ values are in line with the already mentioned magnetostructural correlation for nickel(II) clusters. The double oxygen bridge [Ni(1)–O(1)–Ni(2) and Ni(1)–O(11)–Ni(2)], which mediates the positive $J_3$ exchange interaction, has angles of 96.8 and 94.8° that are known to lead to ferromagnetic interactions.[16a] The other two weak antiferromagnetic exchange interactions of –5.0 ($J_1$) and –4.8 ($J_2$) are associated with angles in the range

 © 2006 Wiley-VCH Verlag GmbH & Co. KGaA, Weinheim 

100.6–103.7°; such angles are expected to lead to weak antiferromagnetic interactions.[24] In the three previously characterized[16a,16b] tetranuclear defect dicubane $Ni^{II}$ clusters *possessing exclusively oxygen monoatomic bridges*, ferromagnetic exchange interactions have been observed leading to a $S = 4$ ground state. However, in the present case of **4**, competing ferromagnetic and antiferromagnetic interactions are observed as a result of the two different types of Ni–O–Ni angle values, those at 94.8 and 96.8°, and those between 100.6 and 103.7°. This result further emphasizes the sensitivity of both ferromagnetic and antiferromagnetic exchange interactions with respect to the Ni–O–Ni angles.

## Conclusions and Perspectives

The further use of di-2-pyridyl ketone in nickel(II) acetate chemistry has provided access to five new complexes, four tetranuclear and one mononuclear. The structure of **2** is novel in the coordination chemistry of di-2-pyridyl ketone, because this complex constitutes the first example of any metal, in which both the ketone and the *gem*-diol forms coexist as ligands. Complexes **1** and **3**–**5** are valuable additions to the chemistry of tetranuclear $Ni^{II}$ clusters; with their structural characterization, and bearing in mind the relevant literature,[7a,7b] the cubane and the defect dicubane topologies can now be considered as general structural motifs in $Ni^{II}/MeCO_2^-/(2\text{-py})_2CO$ chemistry. For two clusters (**1**, **4**) under investigation we have derived the exchange couplings between $Ni^{II}$ ions. In both cases, the coupling is mediated by the μ-oxygen bridges and one can draw some correlations between the coupling sign and the Ni–O–Ni angles; as has been shown previously, there is a clear trend with ferromagnetic coupling observed for small Ni–O–Ni angles and antiferromagnetic couplings at higher angles. Although **1** and **4** have been found to possess an $S = 0$ ground state, the bridging modes of $(2\text{-py})_2C(OH)O^-$ nevertheless suggest possibilities for other $Ni_x$ species that might exist (e.g. clusters containing $SO_4^{2-}$ instead of $MeCO_2^-$) and that may have high-spin ground states.

Analogues of compounds **1** and **3**–**5** with pivalates or benzoates are not known, at least to date, and it is currently not evident whether the preparation and stability of such cubanes are dependent on the particular nature of the carboxylate ligand. The two terminal acetates present in the structures of **1** and **3**–**5** and the aqua ligands in **1** could have future utility as sites for facile incorporation of other monodentate ligands by metathesis or as a means to access higher-nuclearity species by using bis(monodentate) bridging aromatic heterocycles or α,ω-dicarboxylates. Work is in progress to clarify these matters.

## Experimental Section

**Materials and Physical Measurements:** All manipulations were performed under aerobic conditions using materials and solvents (Merck, Aldrich) as received. Elemental analyses (C, H, N) were performed by the University of Ioannina (Greece) Microanalytical Service using an EA 108 Carlo Erba analyzer. IR spectra (4000–450 $cm^{-1}$) were recorded with a Perkin–Elmer PC 16 FT-IR spectrometer with samples prepared as KBr pellets. Magnetic susceptibility measurements in the 1.9–300 K range under a field of 0.5 T were performed with a Quantum Design SQUID-based MPMSXL-5-type magnetometer. The magnetometer was calibrated with a palladium rod sample (Materials Research Corporation, measured purity 99.9985%). The measurements were carried out on polycrystalline samples. Data were corrected for diamagnetic contributions using Pascal's constants; the temperature-independent paramagnetism of the $Ni^{II}$ ion was considered to be $Na = 2.5 \cdot 10^{-9}\ m^3\ mol^{-1}$ (SI units).

**CAUTION**: Although no such tendency was observed during the present work, perchlorate salts are potentially explosive and should be handled with care and in small quantities.

**$[Ni_4(O_2CMe)_2\{(2\text{-py})_2C(OH)O\}_4(H_2O)_2](ClO_4)_2$ (1):** A solution of $(2\text{-py})_2CO$ (0.100 g, 0.54 mmol) in $H_2O$ (3 mL) was added to an aqueous solution (6 mL) of $Ni(O_2CMe)_2 \cdot 4H_2O$ (0.200 g, 0.80 mmol) and $NaClO_4$ (0.099 g, 0.81 mmol). The resulting green solution was stirred for about 10 min and was then allowed to slowly concentrate by solvent evaporation at room temperature for a period of 8–10 d. Well-formed green needles appeared that were collected by filtration, washed with $Me_2CO$ (2 × 3 mL) and dried in air. Yield (based on the ligand): 0.121 g (64%). $C_{48}H_{46}Cl_2N_8Ni_4O_{22}$ (1392.67): calcd. C 41.39, H 3.34, N 8.05; found C 41.60, H 3.40, N 7.89. Crystals of the product were also obtained by layering the initial aqueous reaction solution with a double volume of $Me_2CO$ (18 mL). IR data (KBr pellet): $\tilde{\nu}$ = 3420 $cm^{-1}$ (s, broad), 3051 (w), 2923 (w), 1604 (s), 1576 (s), 1470 (sh), 1430 (s), 1342 (w), 1290 (w), 1260 (w), 1220 (m), 1122 (s), 1082 (s), 1048 (m), 1022 (sh), 960 (m), 904 (w), 806 (w), 782 (sh), 768 (m), 682 (m), 626 (m), 598 (w), 516 (w), 470 (w) $cm^{-1}$.

**$[Ni(O_2CMe)\{(2\text{-py})_2C(OH)_2\}\{(2\text{-py})_2CO\}](ClO_4) \cdot H_2O$ ($2 \cdot H_2O$):** An aqueous, green solution (5 mL) containing $Ni(O_2CMe)_2 \cdot 4H_2O$ (0.062 g, 0.25 mmol) and $NaClO_4$ (0.061 g, 0.50 mmol) were slowly added to a solution of $(2\text{-py})_2CO$ (0.092 g, 0.50 mmol) in $H_2O$ (2.5 mL). A noticeable color change from green to mauve occurred. The resulting mauve solution was stirred for about 10 min and was then allowed to slowly concentrate by solvent evaporation at room temperature for a period of 5–7 d. An approximately 3:1 mixture of brown-red and mauve crystals formed. The crystals were carefully collected by filtration. The two products were readily separable manually, and the brown-red and mauve crystals proved by single-crystal X-ray crystallography to be complexes $2 \cdot H_2O$ and $[Ni\{(2\text{-py})_2C(OH)O\}\{(2\text{-py})_2C(OH)_2\}]_2[Ni\{(2\text{-py})_2C(OH)O\}_2](ClO_4)_2 \cdot 7H_2O$,[11] respectively. Yields for $2 \cdot H_2O$ (based on $Ni^{II}$) as high as 0.085 g (55%) were obtained. A batch of brown-red crystals was used for analyses and IR spectroscopy. $C_{24}H_{23}ClN_4NiO_{10}$ (621.62): calcd. C 46.40, H 3.74, N 9.02; found C 46.51, H 3.60, N 8.86. IR data (KBr pellet): $\tilde{\nu}$ = 3604 $cm^{-1}$ (m), 3476 (m, broad), 3352 (m, broad), 3082 (w), 3005 (w), 2910 (w), 1686 (s), 1650 (m), 1602 (s), 1574 (m), 1464 (sh), 1442 (s), 1430 (sh), 1318 (s), 1288 (m), 1272 (w), 1232 (m), 1168 (m), 1156 (m), 1104 (s, broad), 1088 (s), 1062 (sh), 1022 (m), 944 (m), 914 (m), 828 (m), 806 (m), 778 (sh), 760 (s), 690 (m), 668 (s), 644 (sh), 624 (s), 576 (m), 512 (w) $cm^{-1}$.

**$[Ni_4(O_2CMe)_3\{(2\text{-py})_2C(OH)O\}_4](ClO_4) \cdot 2H_2O \cdot 2EtOH$ ($3 \cdot 2H_2O \cdot 2EtOH$):** A solution of $(2\text{-py})_2CO$ (0.092 g, 0.50 mmol) in EtOH (10 mL) was added dropwise to a slurry of $NaClO_4$ (0.031 g, 0.25 mmol) in the same solvent (15 mL). The obtained slurry was added to a green solution of $Ni(O_2CMe)_2 \cdot 4H_2O$ (0.124 g,

 © 2006 Wiley-VCH Verlag GmbH & Co. KGaA, Weinheim 

0.50 mmol) in EtOH (20 mL). Solid $NaClO_4$ soon dissolved. The resulting solution was stirred for 45 min at room temperature and allowed to stand undisturbed in a closed flask for 2 d. Well-formed green crystals appeared, which were collected by filtration, washed with ice-cold EtOH (1 mL) and $Et_2O$ (2 × 3 mL) and dried in vacuo with silica gel. Yield (based on $Ni^{II}$): 0.120 g (71%). The dried solid analyzed as EtOH-free **3**·2$H_2O$. $C_{50}H_{49}ClN_8Ni_4O_{20}$ (1352.36): calcd. C 44.40, H 3.66, N 8.29; found C 44.51, H 3.49, N 8.25. The obtained crystals were good diffractors of X-rays, as long as they were kept in contact with the mother liquor to prevent EtOH loss. IR data for the dried sample (KBr pellet): $\tilde{\nu}$ = 3425 $cm^{-1}$ (m, broad), 3085 (w, broad), 3017 (w), 2928 (w), 1590 (s, broad), 1443 (sh), 1430 (s), 1341 (w), 1296 (w), 1263 (w), 1218 (m), 1162 (sh), 1082 (s, broad), 1050 (sh), 1012 (sh), 958 (m), 804 (w), 760 (m, broad), 680 (m), 618 (m), 543 (w), 500 (w), 465 (w) $cm^{-1}$.

**$[Ni_4(O_2CMe)_4\{(2\text{-py})_2C(OH)O\}_4]$·2MeCN (4·2MeCN):** An almost colorless solution of $(2\text{-py})_2CO$ (0.100 g, 0.54 mmol) in MeCN (10 mL) was added dropwise to a pale green slurry of $Ni(O_2CMe)_2$·4$H_2O$ (0.135 g, 0.54 mmol) in the same solvent (15 mL). The color of the reaction mixture did not change. The mixture was refluxed for 1 h and 45 min, a small quantity of undissolved green material removed by filtration and the filtrate layered with $Et_2O$ (50 mL). Slow mixing gave X-ray quality green crystals of the product. The crystals were collected by filtration, washed with ice-cold MeCN (1 mL) and $Et_2O$ (2 × 2 mL), and dried in vacuo with silica gel. Yield (based on $Ni^{II}$): 0.128 g (74%). The dried solid analyzed satisfactorily as MeCN-free **4**. $C_{52}H_{48}O_{16}N_8Ni_4$ (1275.92): calcd. C 48.95, H 3.80, N 8.78; found C 48.99, H 3.67, N 8.86. Crystals of the same product could also be isolated, by allowing the initial MeCN solution to slowly evaporate at room temperature. The crystals of **4**·2MeCN were found to lose solvent rapidly, and they were kept in the mother liquor until a suitable crystal had been found for X-ray crystallography. IR data for the dried sample (KBr pellet): $\tilde{\nu}$ = 3418 $cm^{-1}$ (m, broad), 3072 (m), 3025 (w), 2983 (w), 2806 (m, broad), 1638 (sh), 1602 (s), 1574 (s), 1454 (sh), 1438 (sh), 1412 (s), 1370 (m), 1306 (s), 1262 (w), 1210 (s), 1154 (m), 1120 (sh), 1098 (s), 1066 (s), 1046 (sh), 1020 (s), 958 (m), 926 (w), 900 (w), 806 (m), 782 (sh), 764 (s), 684 (s), 656 (s), 640 (sh), 602 (m), 536 (sh), 508 (m), 478 (m) $cm^{-1}$.

**$[Ni_4(O_2CMe)_3\{(2\text{-py})_2C(OH)O\}_4](O_2CMe)$·6$H_2O$·MeCN (5·6$H_2O$·MeCN):** EtOH (15 mL) and MeCN (5 mL) were added to a solid mixture containing $Ni(O_2CMe)_2$·4$H_2O$ (0.124 g, 0.50 mmol), $(2\text{-py})_2CO$ (0.092 g, 0.50 mmol), and LiOH·$H_2O$ (0.021 g, 0.50 mmol). Most of the quantities of the solids dissolved upon reflux for 30 min and a cloudy green "solution" was obtained. This was filtered and the solvents were then evaporated under reduced pressure at 35 °C. The obtained residue was dissolved in MeCN (8 mL), filtered and the closed reaction flask containing the filtrate was stored in the refrigerator (ca. 5 °C) for a period of one month. X-ray quality green needles formed, which were collected by filtration, washed with $Et_2O$ (3 mL), and dried in air. Yield (based on $Ni^{II}$): 0.080 g (46%). The air-dried solid analyzed satisfactorily as MeCN-free **5**·6$H_2O$. $C_{52}H_{60}O_{22}N_8Ni_4$ (1384.04): calcd. C 45.12, H 4.38, N 8.10; found C 44.91, H 4.41, N 8.02. The crystals of the

Table 9. Crystal data and structure refinement for $[Ni_4(O_2CMe)_2\{(2\text{-py})_2C(OH)O\}_4(H_2O)_2](ClO_4)_2$ (**1**), $[Ni(O_2CMe)\{(2\text{-py})_2C(OH)_2\}\{(2\text{-py})_2CO\}](ClO_4)$·$H_2O$ (**2**·$H_2O$), and $[Ni_4(O_2CMe)_3\{(2\text{-py})_2C(OH)O\}_4](ClO_4)$·2$H_2O$·2EtOH (**3**·2$H_2O$·2EtOH).

| | **1** | **2**·$H_2O$ | **3**·2$H_2O$·2EtOH |
|---|---|---|---|
| Empirical formula | $C_{48}H_{46}Cl_2Ni_4N_8O_{22}$ | $C_{24}H_{23}ClNiN_4O_{10}$ | $C_{54}H_{61}ClNi_4N_8O_{22}$ |
| Mol. mass | 1392.67 | 621.62 | 1444.40 |
| Color and habit | green needles | brown-red prisms | green prisms |
| Crystal size [mm] | 0.10 × 0.20 × 0.30 | 0.08 × 0.18 × 0.30 | 0.08 × 0.40 × 0.55 |
| Crystal system | monoclinic | monoclinic | triclinic |
| Space group | *C*2/*c* | $P2_1$ | $P\bar{1}$ |
| *a* [Å] | 23.258(7) | 9.700(1) | 11.964(7) |
| *b* [Å] | 12.097(4) | 14.183(1) | 13.238(7) |
| *c* [Å] | 21.312(7) | 10.252(1) | 19.26(1) |
| *α* [°] | 90 | 90 | 96.37(2) |
| *β* [°] | 116.97(1) | 108.15(1) | 93.22(2) |
| *γ* [°] | 90 | 90 | 99.38(2) |
| *V* [Å$^3$] | 5344(3) | 1340.3(2) | 2982(3) |
| *Z* | 4 | 2 | 2 |
| $\rho_{calcd.}$ [g $cm^{-3}$] | 1.731 | 1.540 | 1.609 |
| *T* [°*C*] | 25 | 25 | 25 |
| *λ* [Mo-$K_a$] [Å] | 0.71073 | | 0.71073 |
| *λ* [Cu-$K_a$] [Å] | | 1.54180 | |
| *μ* [$mm^{-1}$] | 1.578 | 2.523 | 1.374 |
| *F* (000) | 2848 | 640 | 1492 |
| $2\theta_{max}$ [°] | 50.00 | 134.78 | 44.98 |
| Index ranges | $-27 \le h \le 0$ | $0 \le h \le 10$ | $-11 \le h \le 11$ |
| | $-14 \le k \le 0$ | $-16 \le k \le 13$ | $0 \le k \le 14$ |
| | $-21 \le l \le 25$ | $-12 \le l \le 11$ | $-18 \le l \le 20$ |
| No. of reflections collected | 4750 | 3663 | 6186 |
| No. of independent reflections/$R_{int.}$ | 4645/0.0290 | 3360/0.0205 | 5861/0.0363 |
| Data with $I > 2\sigma(I)$ | 3479 | 3360 | 4417 |
| Parameters refined | 479 | 462 | 772 |
| $[\Delta/\sigma]_{max}$ | 0.029 | 0.011 | 0.017 |
| Goodness-of-fit on $F^2$ | 1.126 | 1.061 | 1.027 |
| $[R_1]$[a] | 0.0488 | 0.0363 | 0.0711 |
| $wR_2$[b] | 0.1200 | 0.0994 | 0.1788 |
| Residuals [e Å$^{-3}$] | 0.918/–0.348 | 0.409/–0.366 | 0.936/–0.591 |

[a] $R_1 = \Sigma(|F_o| - |F_c|)/\Sigma(|F_o|)$. [b] $wR_2 = \{\Sigma[w(F_o^2 - F_c^2)^2]/\Sigma[w(F_o^2)^2]\}1/2$.

 © 2006 Wiley-VCH Verlag GmbH & Co. KGaA, Weinheim 

product were found to lose MeCN readily, and they were maintained in the mother liquor for X-ray crystallography. IR data for the analytically pure sample (KBr pellet): $\tilde{\nu}$ = 3406 $cm^{-1}$ (m, broad), 3149 (w, broad), 3065 (w, broad), 2925 (w), 2851 (w), 1625 (sh), 1573 (s, broad), 1429 (s, broad), 1402 (m), 1335 (w), 1293 (w), 1215 (m), 1160 (w), 1120 (w), 1080 (m), 1049 (sh), 957 (w), 795 (sh), 770 (m), 675 (m), 660 (sh), 604 (w), 516 (w), 462 (w) $cm^{-1}$.

**X-ray Crystallographic Studies:** Crystals of **1**, **3**·2$H_2O$·2EtOH, **4**·2MeCN, and **5**·6$H_2O$·MeCN were mounted in capillaries filled with drops of mother liquor, while crystals of **2**·$H_2O$ were stable and mounted in air. Diffraction measurements for **1**, **3**·2$H_2O$·2EtOH, **4**·2MeCN, and **5**·6$H_2O$·MeCN were made on a Crystal Logic Dual Goniometer diffractometer using graphite–monochromated $M_o$-$K_\alpha$ radiation. The X-ray data set for **2**·$H_2O$ was collected with a $P2_1$ Nicolet diffractometer upgraded by Crystal Logic using graphite–monochromated Cu-$K_\alpha$ radiation. Complete crystal data and parameters for data collection and refinement are listed in Table 9 and Table 10. Unit cell dimensions were determined and refined by using the angular settings of 25 automatically centered reflections in the ranges 11° < 2$\theta$ < 23° (for **1**, **3**·2$H_2O$·2EtOH, **4**·2MeCN, and **5**·6$H_2O$·MeCN) and 22° < 2$\theta$ < 54° (for **2**·$H_2O$). Intensity data were recorded using the $\theta$-2$\theta$ scan method. Three standard reflections monitored every 97 reflections showed less than 3% variation and no decay. Lorentz, polarization, and $\Psi$-scan absorption (for **2**·$H_2O$, **3**·2$H_2O$·2EtOH, and **4**·2MeCN) were applied using the Crystal Logic software package. The structures were solved by direct methods using SHELXS-86[25a] and refined by full-matrix least-squares techniques on $F^2$ with SHELXL-97.[25b] For complexes **2**·$H_2O$ and **3**·2$H_2O$·2EtOH, the reflections to parameters ratio is relatively low. For the former a full data set was collected for a quarter of the sphere of reflections to 2$\theta$ = 135° (for Cu radiation). When the structure was solved it proved to belong to the noncentrosymmetric monoclinic space group $P2_1$. The collection of additional data was continued for a second quarter of the reflections sphere only until 2$\theta$ = 95°, because the complex is mononuclear and its structural characterization was valuable mainly in terms of our synthetic efforts. For the latter the data collection was stopped at 2$\theta$ = 45° (for Mo radiation), because the molecular structure of the cation present in **3**·2$H_2O$·2EtOH is almost identical to that of the cation with the same formula in complex **5**·6$H_2O$·MeCN, for which a full data set to 2$\theta$ = 50° had already been collected. For all the structures the ordered non-hydrogen atoms were refined anisotropically. In the case of **1**, the chlorine atoms and one of the perchlorate oxygen atoms were found to be disordered and refined anisotropically over two positions with occupation factors fixed at 0.50. Three of the perchlorate oxygen atoms of **2**·$H_2O$ were found to be disordered and refined in two orientations with occupation factors summing one. In the structure of **3**·2$H_2O$·2EtOH the solvate molecules were refined isotropically, while the methyl group of one of the acetate ligands was found to be disordered and refined isotropically over two positions with occupation factors summing one. The non-hydrogen atoms of the MeCN solvate molecules of **4**·2MeCN were refined isotropically. For **1**, **2**·$H_2O$, **4**·2MeCN, and **5**·6$H_2O$·MeCN, all hydrogen atoms were located by difference maps and were refined isotropically, ex-

Table 10. Crystal data and structure refinement for $[Ni_4(O_2CMe)_4\{(2\text{-py})_2C(OH)O\}_4]$·2MeCN (**4**·2MeCN) and $[Ni_4(O_2CMe)_3\{(2\text{-py})_2C(OH)O\}_4](O_2CMe)$·6$H_2O$·MeCN (**5**·6$H_2O$·MeCN).

| | **4**·2MeCN | **5**·6$H_2O$·MeCN |
|---|---|---|
| Empirical formula | $C_{56}H_{54}Ni_4N_{10}O_{16}$ | $C_{54}H_{63}Ni_4N_9O_{22}$ |
| Mol. mass | 1357.94 | 1424.97 |
| Color and habit | greenish prisms | green needles |
| Crystal size [mm] | 0.15×0.25×0.50 | 0.10×0.20×0.50 |
| Crystal system | monoclinic | triclinic |
| Space group | $P2_1/n$ | $P\bar{1}$ |
| $a$ [Å] | 10.343(5) | 11.793(4) |
| $b$ [Å] | 12.644(7) | 12.863(5) |
| $c$ [Å] | 22.39(1) | 20.531(8) |
| $\alpha$ [°] | 90 | 74.87(2) |
| $\beta$ [°] | 95.30(2) | 85.48(1) |
| $\gamma$ [°] | 90 | 79.70(2) |
| $V$ [Å$^3$] | 2915(3) | 2956.3(2) |
| $Z$ | 2 | 2 |
| $\rho_{calcd.}$ [g $cm^{-3}$] | 1.547 | 1.601 |
| $T$ [°C] | 25 | 25 |
| $\lambda$ [Mo-$K_a$] [Å] | 0.71073 | 0.71073 |
| $\mu$ [$mm^{-1}$] | 1.350 | 1.342 |
| $F$ (000) | 1400 | 1476 |
| $2\theta_{max}$ [°] | 50.00 | 50.00 |
| Index ranges | $-12 \le h \le 0$ | $-14 \le h \le 0$ |
| | $-15 \le k \le 0$ | $-15 \le k \le 15$ |
| | $-26 \le l \le 26$ | $-24 \le l \le 24$ |
| No. of reflections collected | 5441 | 10956 |
| No. of independent reflections/$R_{int.}$ | 5138/0.0228 | 10402/0.0110 |
| Data with $I > 2\sigma(I)$ | 3685 | 8546 |
| Parameters refined | 447 | 943 |
| $[\Delta/\sigma]_{max}$ | 0.019 | 0.014 |
| Goodness-of-fit on $F^2$ | 1.052 | 1.044 |
| $[R_1]$[a] | 0.0427 | 0.0420 |
| $wR_2$[b] | 0.1104 | 0.1058 |
| Residuals [e Å$^{-3}$] | 0.941/–0.487 | 0.959/–0.939 |

[a] $R_1 = \Sigma(|F_o| - |F_c|)/\Sigma(|F_o|)$. [b] $wR_2 = \{\Sigma[w(F_o^2 - F_c^2)^2]/\Sigma[w(F_o^2)^2]\}^{1/2}$.

 © 2006 Wiley-VCH Verlag GmbH & Co. KGaA, Weinheim 

cept those of the acetate ligands which were introduced at calculated positions as riding on bonded atoms; no hydrogen atoms for the water solvate molecule of **2**·$H_2O$ were included in the refinement. All hydrogen atoms of **3**·2$H_2O$·2EtOH were introduced at calculated positions as riding on their respective bonded atoms. CCDC-278891, -278892, -278893, -278894, and CCDC-278895 contain the supplementary crystallographic data for this paper. These data can be obtained free of charge from The Cambridge Crystallographic Data Centre via www.ccdc.cam.ac.uk/data_request/cif.

**Note Added in Proof** (March 22, 2006): After this paper had been submitted, the single-crystal X-ray structure of complex **1** was published. The complex was prepared in MeOH under reflux; however, no magnetic studies for this cluster were reported (Y.-M. Li, J.-J. Zhang, R.-B. Fu, S.-C. Xiang, T.-L. Sheng, D.-Q. Yuan, X.-H. Huang, X.-T. Wu, *Polyhedron*, DOI: 10.1016/j.poly.2005.11.002).

## Acknowledgments

S. P. P. thanks the European Social Fund (EST), the Operational Program for Educational and Vocational Training II (EPEAK II), and particularly the Program PYTHAGORAS (Grant b.365.037) for funding of this work. Slovak grant agencies (VEGA 1/2453/05, APVT 20-005204), the Polish Ministry of Science and Computerization, and the 6th Framework Programme EU NoE MAGMANet are also acknowledged.

[1] For excellent reviews, see: a) R. E. P. Winpenny, *Adv. Inorg. Chem.* **2001**, *52*, 1–111; b) R. E. P. Winpenny, *J. Chem. Soc., Dalton Trans.* **2002**, 1–10.

[2] S. Mukhopadhyay, S. K. Mandal, S. Bhaduri, W. H. Armstrong, *Chem. Rev.* **2004**, *104*, 3981–4026.

[3] a) R. Sessoli, H. L. Tsai, A. R. Schake, S. Wang, J. B. Vincent, K. Folting, D. Gatteschi, G. Christou, D. N. Hendrickson, *J. Am. Chem. Soc.* **1993**, *115*, 1804–1816; b) R. Sessoli, D. Gatteschi, A. Caneschi, M. A. Novak, *Nature* **1993**, *365*, 141–143.

[4] For excellent reviews concerning SMMs, see: a) G. Christou, D. Gatteschi, D. N. Hendrickson, R. Sessoli, *MRS Bull.* **2000**, *25*, 66–71; b) D. Gatteschi, R. Sessoli, *Angew. Chem. Int. Ed.* **2003**, *42*, 268–297.

[5] For a comprehensive reference list of 3d-metal SMMs, see: G. Christou, *Polyhedron* **2005**, *24*, 2065–2075.

[6] Recent, representative references from our group: a) G. S. Papaefstathiou, A. Escuer, F. A. Mautner, C. Raptopoulou, A. Terzis, S. P. Perlepes, R. Vicente, *Eur. J. Inorg. Chem.* **2005**, 879–893; b) A. K. Boudalis, B. Donnadieu, V. Nastopoulos, J. M. Clemente-Juan, A. Mari, Y. Sanakis, J.-P. Tuchagues, S. P. Perlepes, *Angew. Chem.* **2004**, *43*, 2266–2270; c) C. J. Milios, E. Kefalloniti, C. P. Raptopoulou, A. Terzis, R. Vicente, N. Lalioti, A. Escuer, S. P. Perlepes, *Chem. Commun.* **2003**, 819–821; d) G. S. Papaefstathiou, A. Escuer, M. Font-Bardia, S. P. Perlepes, X. Solans, R. Vicente, *Polyhedron* **2002**, *21*, 2027–2032; e) N. Lalioti, C. P. Raptopoulou, A. Terzis, A. E. Aliev, I. P. Gerothanassis, E. Manessi-Zoupa, *Angew. Chem. Int. Ed.* **2001**, *40*, 3211–3214; f) G. S. Papaefstathiou, A. Escuer, R. Vicente, M. Font-Bardia, X. Solans, S. P. Perlepes, *Chem. Commun.* **2001**, 2414–2415; g) G. S. Papaefstathiou, S. P. Perlepes, A. Escuer, R. Vicente, M. Fond-Bardia, X. Solans, *Angew. Chem. Int. Ed.* **2001**, *40*, 884–886.

[7] a) M.-L. Tong, S.-L. Zheng, J.-X. Shi, Y.-X. Tong, H. K. Lee, X.-M. Chen, *J. Chem. Soc., Dalton Trans.* **2002**, 1727–1734; b) S. B. Jedner, H. Schwöppe, H. Nimir, A. Rompel, D. A. Brown, B. Krebs, *Inorg. Chim. Acta* **2002**, *340*, 181–186; c) M.-L. Tong, H. K. Lee, Y.-X. Tong, X.-M. Chen, T. C. W. Mak, *Inorg. Chem.* **2000**, *39*, 4666–4669.

[8] For a review, see: G. S. Papaefstathiou, S. P. Perlepes, *Inorg. Chem.* **2002**, *23*, 249–274.

[9] a) E. Katsoulakou, V. Bekiari, C. P. Raptopoulou, A. Terzis, P. Lianos, E. Manessi-Zoupa, S. P. Perlepes, *Spectrochim. Acta Part A* **2005**, *61*, 1627–1638; b) C. Kanaras, B. L. Westcott, G. Crundwell, J. B. Updegraff III, M. Zeller, A. D. Hunter, S. O. Sommerer, *Z. Kristallogr.* **2004**, *219*, 1–2; c) K. N. Crowder, S. J. Garcia, R. L. Burr, J. M. North, M. H. Wilson, B. L. Conley, P. E. Fanwick, P. S. White, K. D. Sienerth, R. M. Granger II, *Inorg. Chem.* **2004**, *43*, 72–78; d) A. K. Boudalis, F. Dahan, A. Bousseksou, J.-P. Tuchagues, S. P. Perlepes, *Dalton Trans.* **2003**, 3411–3418; e) E. Katsoulakou, N. Lalioti, C. P. Raptopoulou, A. Terzis, E. Manessi-Zoupa, S. P. Perlepes, *Inorg. Chem. Commun.* **2002**, *5*, 719–723; f) Z. E. Serna, M. K. Urtiaga, M. G. Barandika, R. Cortés, S. Martin, L. Lezama, M. I. Arriortua, T. Rojo, *Inorg. Chem.* **2001**, *40*, 4550–4555; g) G. S. Papaefstathiou, A. Escuer, C. P. Raptopoulou, A. Terzis, S. P. Perlepes, R. Vicente, *Eur. J. Inorg. Chem.* **2001**, 1567–1574; h) Z. E. Serna, M. G. Barandika, R. Cortés, M. K. Urtiaga, G. E. Barberis, T. Rojo, *J. Chem. Soc., Dalton Trans.* **2000**, 29–34; i) Z. E. Serna, L. Lezama, M. K. Urtiaga, M. I. Arriortua, M. G. Barandika, R. Cortés, T. Rojo, *Angew. Chem. Int. Ed.* **2000**, *39*, 344–347; j) G. Yang, S.-L. Zheng, X.-M. Chen, H. K. Lee, Z.-Y. Zhou, T. C. W. Mak, *Inorg. Chim. Acta* **2000**, *303*, 86–93; k) A. C. Deveson, S. L. Heath, C. J. Harding, A. K. Powell, *J. Chem. Soc., Dalton Trans.* **1996**, 3173–3178; l) A. N. Papadopoulos, V. Tangoulis, C. P. Raptopoulou, A. Terzis, D. P. Kessisoglou, *Inorg. Chem.* **1996**, *35*, 559–565; m) S. R. Breeze, S. Wang, J. E. Greedan, N. P. Raju, *Inorg. Chem.* **1996**, *35*, 6944–6951.

[10] a) E.-C. Yang, W. Wernsdorfer, S. Hill, R. S. Edwards, M. Nakano, S. Maccagnano, L. N. Zakharov, A. L. Rheingold, G. Christou, D. N. Hendrickson, *Polyhedron* **2003**, *22*, 1727–1733; b) R. S. Edwards, S. Maccagnano, E.-C. Yang, S. Hill, W. Wernsdorfer, D. Hendrickson, G. Christou, *J. Appl. Phys.* **2003**, *93*, 7807–7809; c) M. Moragues-Cánovas, M. Helliwell, L. Ricard, E. Riviére, W. Wernsdorfer, E. Brechin, T. Mallah, *Eur. J. Inorg. Chem.* **2004**, 2219–2222.

[11] C. G. Efthymiou, C. P. Raptopoulou, A. Terzis, E. G. Bakalbassis, S. P. Perlepes, manuscript in preparation.

[12] a) V. Tangoulis, C. P. Raptopoulou, S. Paschalidou, E. G. Bakalbassis, S. P. Perlepes, A. Terzis, *Angew. Chem. Int. Ed. Engl.* **1997**, *36*, 1083–1085; b) A. Tsohos, S. Dionyssopoulou, C. P. Raptopoulou, A. Terzis, E. G. Bakalbassis, S. P. Perlepes, *Angew. Chem. Int. Ed.* **1999**, *38*, 983–985.

[13] a) Z. E. Serna, R. Cortés, M. K. Urtiaga, M. G. Barandika, L. Lezama, M. I. Arriortua, T. Rojo, *Eur. J. Inorg. Chem.* **2001**, 865–872; b) J. M. Seco, M. Quirós, M. J. González Garmendia, *Polyhedron* **2000**, *19*, 1005–1013.

[14] a) J. E. Andrew, A. B. Blake, *J. Chem. Soc. A* **1969**, 1556–1560; b) J. A. Bertrand, A. P. Ginsberg, R. I. Kaplan, C. E. Kirkwood, R. L. Martin, R. C. Sherwood, *Inorg. Chem.* **1971**, *10*, 240–246; c) W. Vreugdenhil, J. G. Haasnoot, J. Reedijk, A. L. Spek, *Inorg. Chim. Acta* **1987**, *129*, 205–216, and references cited therein; d) K. S. Murray, *Adv. Inorg. Chem.* **1995**, *43*, 261–358; e) M. A. Halcrow, J.-S. Sun, J. C. Huffman, G. Christou, *Inorg. Chem.* **1995**, *34*, 4167–4177; f) M. S. El Fallah, E. Rentschler, A. Caneschi, D. Gatteschi, *Inorg. Chim. Acta* **1996**, *247*, 231–235; g) A. Escuer, M. Fonta-Bardia, S. B. Kumar, X. Solans, R. Vicente, *Polyhedron* **1999**, *18*, 909–914; h) J. M. Clemente-Juan, B. Chansou, B. Donnadieu, J.-P. Tuchagues, *Inorg. Chem.* **2000**, *39*, 5515–5519; i) A. K. Sah, G. P. Rao, P. K. Saarenketo, K. Rissanen, *Chem. Lett.* **2001**, 1296–1297; j) V. G. Kessler, S. Golih, M. Kritikos, O. N. Korsak, E. E. Knyazeva, I. F. Moskovskaya, B. V. Romanovsky, *Polyhedron* **2001**, *20*, 915–922; k) C. Boskovic, E. Rusanov, H. Stoeckli-Evans, H. U. Güdel, *Inorg. Chem. Commun.* **2002**, *5*, 881–886; l) S. Mukherjee, T. Weyhermüller, E. Bothe, K. Wieghardt, P. Chaudhuri, *Eur. J. Inorg. Chem.* **2003**, 863–875; m) T. K. Paine, E. Rentschler, T. Weyhermüller, P. Chaudhuri, *Eur. J. Inorg. Chem.*

 © 2006 Wiley-VCH Verlag GmbH & Co. KGaA, Weinheim 

**2003**, 3167–3178; n) G. Aromi, A. S. Batsanov, P. Christian, M. Helliwell, O. Roubeau, G. A. Timco, R. E. P. Winpenny, *Dalton Trans.* **2003**, 4466–4471; o) G. Chaboussant, R. Basler, H.-U. Güdel, S. Ochsenbein, A. Parkin, S. Parsons, G. Rajaraman, A. Sieber, A. A. Smith, G. A. Timco, R. E. P. Winpenny, *Dalton Trans.* **2004**, 2758–2766; p) A. J. Blake, E. K. Brechin, A. Codron, R. O. Could, C. M. Grant, S. Parsons, J. M. Rawson, R. E. P. Winpenny, *J. Chem. Soc. Chem. Commun.* **1995**, 1983–1985.

[15] M.-L. Tong, M. Monfort, J. M. Clemente Juan, X.-M. Chen, X.-H. Bu, M. Ohba, S. Kitagawa, *Chem. Commun.* **2005**, 233–235.

[16] a) P. King, R. Clérac, W. Wernsdorfer, C. E. Anson, A. K. Powell, *Dalton Trans.* **2004**, 2670–2676; b) J. M. Clemente-Juan, E. Coronado, J. R. Galán-Mascarós, C. J. Gómez-Garzia, *Inorg. Chem.* **1999**, *38*, 55–63; c) T. K. Karmakar, S. K. Chandra, J. Ribas, G. Mostafa, T. H. Lu, B. K. Ghosh, *Chem. Commun.* **2002**, 2364–2365.

[17] P. K. Byers, A. J. Canty, L. M. Engelhardt, J. M. Patrick, A. H. White, *J. Chem. Soc., Dalton Trans.* **1985**, 981–986.

[18] G. B. Deacon, R. J. Phillips, *Coord. Chem. Rev.* **1980**, *33*, 227–250.

[19] K. Nakamoto, *Infrared and Raman Spectra of Inorganic Chemistry and Coordination Compounds*, 4th ed., Wiley, New York, **1986**, pp. 130–138.

[20] G. Christou, S. P. Perlepes, E. Libby, K. Folting, J. C. Huffman, R. J. Webb, D. N. Hendrickson, *Inorg. Chem.* **1990**, *29*, 3657–3666.

[21] R. Boča, *Theoretical Foundations of Molecular Magnetism*, Elsevier, Amsterdam, **1999**.

[22] R. Boča, *Coord. Chem. Rev.* **2004**, *248*, 757–815.

[23] R. Boča, Program *Polymagnet-2002*, Slovak Technical University, Bratislava, **2002**.

[24] S. Wörl, H. Pritzkow, I. O. Fritsky, R. Krämer, *Chem. Commun.* **2005**, 27–29.

[25] a) G. W. Sheldrick, *SHELXS-86*, Program for the Solution of Crystal Structures, University of Göttingen, **1986**; b) G. W. Sheldrick, *SHELXL-97*, Crystal Structure Refinement Program, University of Göttingen, **1997**.

Received: October 7, 2005
Published Online: April 4, 2006

 © 2006 Wiley-VCH Verlag GmbH & Co. KGaA, Weinheim 

DOI: 10.1002/ejic.200500904

# Syntheses, Structures and Characterisation of Two $Cu^{II}$ Polymers with 8-Connected Topologies Based on Highly Connected SBUs

**Jian Zhang,[a] Yao Kang,[a] Jie Zhang,[a] Zhao-Ji Li,[a] Ye-Yan Qin,[a] and Yuan-Gen Yao*[a]**

**Keywords:** Coordination polymers / Copper / Hydrothermal synthesis / Magnetic properties / N ligands

Two hydrothermally synthesised 3D metal-coordination polymers, namely [Cu(isonicotinate)(nicotinate)]$_n$ (**1**), with an 8-connected CsCl topology, and [$Cu_2$($\mu_3$-OH)(isonicotinate)$_2$-(BDC)$_{0.5}$]$_n$ (**2**), with an unusual 8-connected $3^5.4^{11}.5^8.6^4$ topology, demonstrate that highly connected SBUs can be employed in the construction of complicated frameworks. The temperature-dependent magnetic susceptibilities for the two complexes were also determined.
(© Wiley-VCH Verlag GmbH & Co. KGaA, 69451 Weinheim, Germany, 2006)

## Introduction

Recent studies on inorganic/organic hybrid materials, especially in the area of metal–ligand coordination framework polymers, have enriched crystal engineering and have provided a wide range of inorganic networks in the solid state.[1] A large number of the lowly connected network topologies depicted by Wells[2] are commonly found in framework materials such as zeolites and in coordination polymers.[3] However, highly connected topologies are still a major challenge to chemists because the construction of such systems is severely hampered by the available number of coordination sites at the metal centres and the steric demand of the organic ligands. Yaghi et al. have developed a SBU (secondary building unit) strategy to direct the assembly of metal–organic frameworks (MOFs), which has been widely used for understanding and predicting structural topologies.[4] Most recently, Champness et al. have successfully obtained a series of highly connected topologies by selecting high coordinate lanthanide metals and flexible 4,4′-bipyridine-*N*,*N*′-dioxide ligands.[5] Although a large number of crystalline materials constructed from SBUs and linkers have been reported, the construction of highly connected topologies based on highly connected SBUs are extremely rare.[6] Compared with complexes with d- or f-block metal nodes, complexes with metal cluster nodes generally have weak metal–metal interactions and some interesting physical properties, such as luminescence and magnetism. We report here two novel polymers, namely [Cu(isonicotinate)(nicotinate)]$_n$ (**1**) and [$Cu_2$($\mu_3$-OH)(isonicotinate)$_2$(BDC)$_{0.5}$]$_n$ (**2**; BDC = 1,3-benzenedicarboxylate), which exhibit 8-connected CsCl and non-CsCl topologies, respectively.

[a] State Key Laboratory of Structural Chemistry, Fujian Institute of Research on the Structure of Matter, The Chinese Academy of Sciences,
Fuzhou, Fujian 350002, China
Fax: +86-591-8371-4946
E-mail: yyg@ms.fjirsm.ac.cn

## Results and Discussion

### X-ray Crystal Structure of [Cu(isonicotinate)(nicotinate)]$_n$ (1)

The single-crystal X-ray structure of complex **1** reveals that it adopts a 3D structure consisting of dimetallic clusters bridged by both nicotinate and isonicotinate ligands. Each $Cu^{II}$ cation exhibits a distorted trigonal-bipyramidal geometry with an $N_2O_3$ coordination sphere from three nicotinate ligands and two isonicotinate ligands (Figure 1 and Table 1). Nicotinate acts as a $\mu_3$-ligand with its carboxylate group bridging two Cu atoms that are separated by 4.330 Å. As shown in Figure 2 (a), the nicotinate ligands bridge the dinuclear copper clusters to form a 2D sheet parallel to the *bc* plane. The isonicotinate ligand bridges the Cu centres through one O donor and one N donor to form a zigzag chain in a head-to-tail manner. These chains are also linked by the carboxylate group of nicotinate ligands to form another 2D sheet almost parallel to the *ab* plane (Figure 2, b). In other words, each dinuclear copper cluster binds to four nicotinate ligands and four isonicotinate ligands simultaneously.

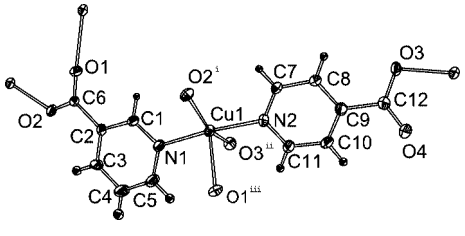


Figure 1. An ORTEP drawing of the molecular structure of complex **1**. For definition of i, ii and iii see footnote a in Table 1.

 © 2006 Wiley-VCH Verlag GmbH & Co. KGaA, Weinheim 

Table 1. Selected bond lengths [Å] and angles [°] for **1** and **2**.

| | | | |
|---|---|---|---|
| Complex **1**[a] | | | |
| Cu1–O2$^{i}$ | 1.955(4) | Cu1–N2 | 2.037(5) |
| Cu1–O3$^{ii}$ | 1.999(4) | Cu1–O1$^{iii}$ | 2.248(5) |
| Cu1–N1 | 2.031(5) | | |
| O2$^{i}$–Cu1–O3$^{ii}$ | 152.4(2) | N1–Cu1–N2 | 174.2(2) |
| O2$^{i}$–Cu1–N1 | 91.1(2) | O2$^{i}$–Cu1–O1$^{iii}$ | 115.24(18) |
| O3$^{ii}$–Cu1–N1 | 89.3(2) | O3$^{ii}$–Cu1–O1$^{iii}$ | 92.34(18) |
| O2$^{i}$–Cu1–N2 | 94.5(2) | N1–Cu1–O1$^{iii}$ | 86.9(2) |
| O3$^{ii}$–Cu1–N2 | 86.4(2) | N2–Cu1–O1$^{iii}$ | 89.4(2) |
| Complex **2**[b] | | | |
| Cu1–O3$^{i}$ | 1.9687(14) | Cu2–O6$^{iii}$ | 1.9062(14) |
| Cu1–O7 | 2.0015(14) | Cu2–O7$^{iii}$ | 1.9659(14) |
| Cu1–N2$^{ii}$ | 2.0045(17) | Cu2–O7 | 1.9702(15) |
| Cu1–O1 | 2.0431(14) | Cu2–N1 | 1.9828(16) |
| Cu1–O5 | 2.1844(15) | Cu2–Cu2$^{iii}$ | 3.0057(6) |
| O3$^{i}$–Cu1–O7 | 91.78(6) | N2$^{ii}$–Cu1–O5 | 88.79(6) |
| O3$^{i}$–Cu1–N2$^{ii}$ | 91.38(6) | O1–Cu1–O5 | 100.61(6) |
| O7–Cu1–N2$^{ii}$ | 176.31(6) | O6$^{iii}$–Cu2–O7$^{iii}$ | 94.14(6) |
| O3$^{i}$–Cu1–O1 | 157.30(6) | O6$^{iii}$–Cu2–O7 | 169.31(6) |
| O7–Cu1–O1 | 87.20(6) | O7$^{iii}$–Cu2–O7 | 80.43(6) |
| N2$^{ii}$–Cu1–O1 | 89.15(6) | O6$^{iii}$–Cu2–N1 | 89.49(7) |
| O3$^{i}$–Cu1–O5 | 102.09(6) | O7$^{iii}$–Cu2–N1 | 169.15(6) |
| O7–Cu1–O5 | 92.42(6) | O7–Cu2–N1 | 97.53(6) |

[a] Symmetry codes: (i) $1 - x$, $1/2 + y$, $-1/2 - z$; (ii) $2 - x$, $-1/2 + y$, $1/2 - z$; (iii) $x$, $1/2 - y$, $1/2 + z$. [b] Symmetry codes: (i) $1 - x$, $1 - y$, $-z$; (ii) $1/2 - x$, $1/2 + y$, $1/2 - z$; (iii) $1/2 - x$, $1/2 - y$, $-z$.

According to the concept of SBUs, this structure can be reduced to a schematic that rationalizes the structure as the assembly of $[Cu_2(CO_2)_2O_2N_4]$ SBUs, as shown in Figure 2 (c). Each SBU has eight vertices to eight adjacent SBUs. By treating the SBU as a single node and connecting the nodes according to the connectivity defined by nicotinate and isonicotinate ligands, a CsCl-like 3D network sustained by 8-connected nodes is formed, as illustrated in Figure 3. Although there is only one type of node in this net, there are two different links, identified by two different node–node distances (8.351 and 10.774 Å). The isonicotinate ligand defines the longer node–node distance and connects the nodes into a (4,4) 2D net, while the nicotinate ligand defines the shorter node–node distance and connects the nodes into another (4,4) 2D net parallel to the *bc* plane. These two types of nets intersect at an angle of 75.65° to generate the distorted CsCl net. To the best of our knowledge, this is the first transition metal complex with this unusual CsCl topology.

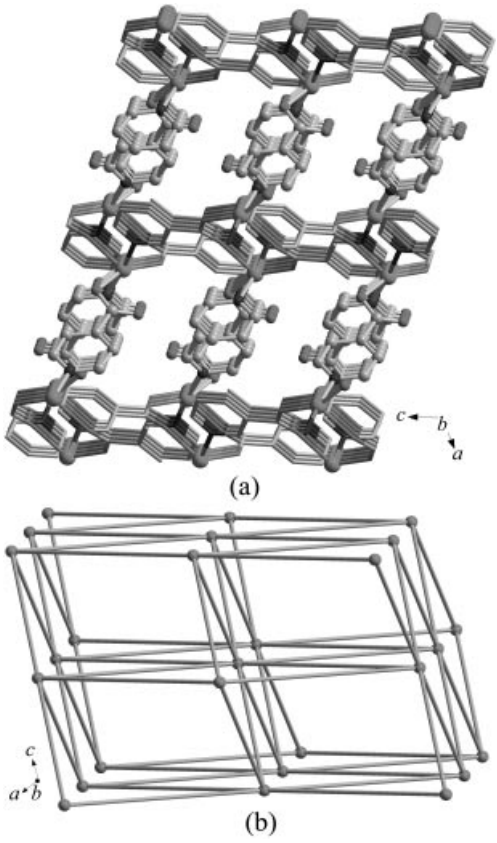


Figure 3. (a) The 3D packing structure of **1**; (b) schematic representation of the distorted CsCl net in complex **1**.

### X-ray Crystal Structure of $[Cu_2(\mu_3\text{-OH})(isonicotinate)_2(BDC)_{0.5}]_n$ (2)

The single-crystal X-ray diffraction study showed that complex **2** consists of tetranuclear $Cu^{II}$ clusters linked by isonicotinate and the BDC ligand. As shown in Figure 4, the tetranuclear cluster contains two independent Cu centres: one Cu centre (Cu1) has a distorted trigonal-bipy-

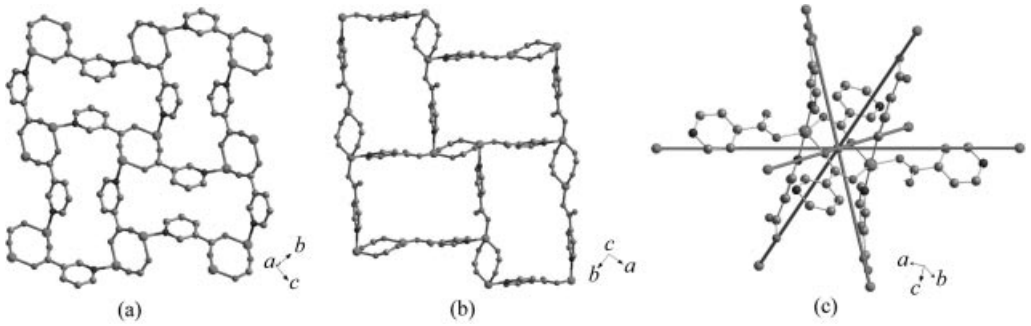


Figure 2. (a) View of the 2D (4,4) net constructed from dimetallic clusters and nicotinate ligands; (b) view of the 2D (4,4) net constructed from dimetallic clusters and isonicotinate ligands; (c) view of the 8-connected SBU in complex **1**, illustrating the connections to eight neighbours.

 © 2006 Wiley-VCH Verlag GmbH & Co. KGaA, Weinheim 

ramidal geometry and is bound by one BDC ligand, three different isonicotinate ligands and one hydroxide ion, whereas the other Cu centre (Cu2) has a distorted square-pyramidal geometry and is bound by one BDC ligand, two independent isonicotinate ligands and two hydroxide ions. A pair of $CuO_4N$ square-pyramidal polyhedra share an edge with each other and a corner with two $CuO_4N$ trigonal-bipyramidal polyhedra through two $\mu_3$-hydroxy groups (Figure 5, e). The centre of inversion is situated in the middle of the two $\mu_3$-hydroxy groups. The four copper ions, which lie on a plane, form an approximate parallelogram. Two $\mu_3$-hydroxy groups bridge four Cu centres with an adjacent Cu···Cu separation in the range of 3.006 to 3.342 Å.

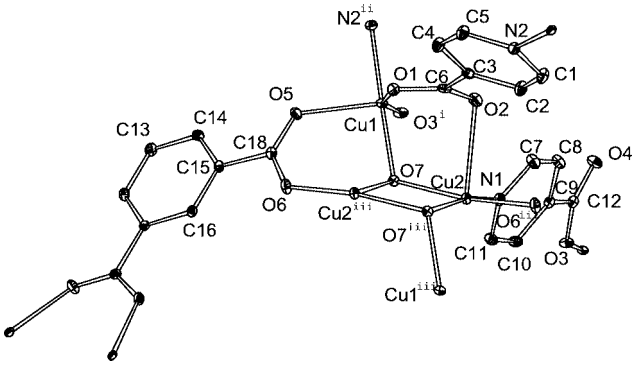


Figure 4. An ORTEP drawing of the molecular structure of complex **2**. For definition of i, ii and iii see footnote b in Table 1.

The asymmetric unit of **2** also contains two independent isonicotinate ligands, each of which has different coordination modes: one isonicotinate ligand acts as a $\mu_3$-bridge and links the tetranuclear clusters to form a 2D sheet parallel to *bc* plane (Figure 5, a), while the other isonicotinate ligand binds through one O donor and one N donor to bridge the tetranuclear clusters and form a 1D double-chain (Figure 5, b). At the same time, the BDC ligand acts as a $\mu_4$-bridge and links the tetranuclear clusters to form a 1D zigzag chain (Figure 5, c). In other words, each tetranuclear copper cluster binds to two BDC ligands and eight isonicotinate ligands simultaneously (Figure 5, d).

Four Cu polyhedra and four carboxylate carbon atoms represent a 10-connected inorganic SBU, as illustrated in Figure 5 (e). Although ten bridging ligands ligate each SBU, each SBU is connected to only eight nearest neighbours because two pairs of isonicotinate ligands form "double bridges". By treating the SBU as a single node and connecting the nodes according to the connectivity defined by the BDC and isonicotinate ligands (the double bridge being considered as one connection), a non-CsCl 3D network sustained by 8-connected nodes is then formed, as illustrated in Figure 6. This net is clearly different from other reported network topologies containing 8-connected nodes[5,6c] and adopts an unprecedented $3^5.4^{11}.5^8.6^4$ topology.[9] The asymmetric unit of **2** contains one BDC ligand and two independent isonicotinate ligands such that three different node–node distances (9.726, 10.362 and 10.940 Å) can be iden-

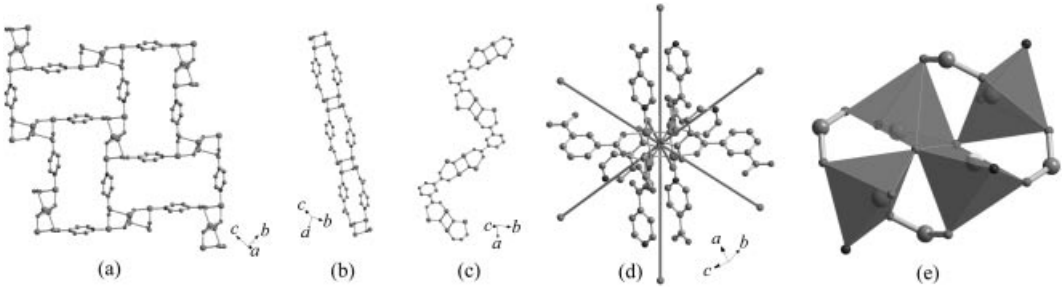


Figure 5. (a) View of the 2D (4,4) net constructed from tetranuclear clusters and isonicotinate ligands; (b) view of the 1D double-chain constructed from tetranuclear clusters and the second independent isonicotinate ligands; (c) view of the 1D zigzag chain constructed from tetranuclear clusters and BDC ligands; (d) view of the 10-connected SBU in complex **2**, illustrating the connections to eight neighbours; (e) view of the SBU in complex **2**, illustrating the four Cu polyhedra.

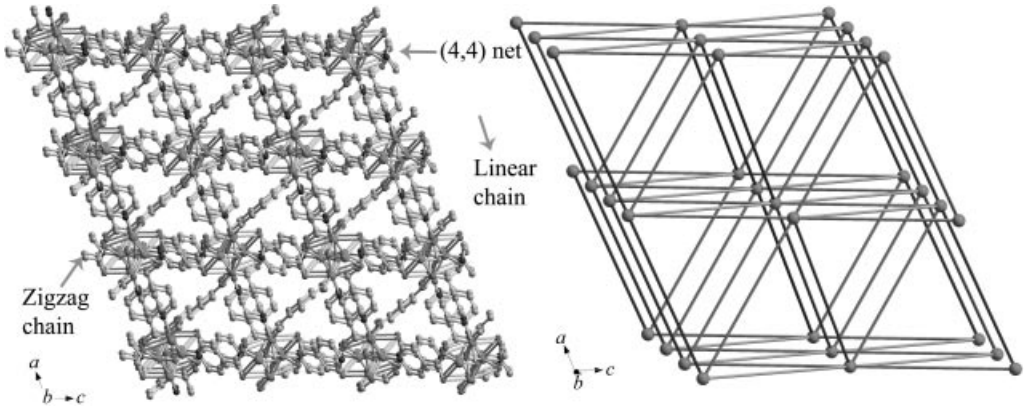


Figure 6. Left: the 3D packing structure of **2**; right: schematic representation of the $3^5.4^{11}.5^8.6^4$ topology in complex **2**.

 © 2006 Wiley-VCH Verlag GmbH & Co. KGaA, Weinheim 

tified. Each node, which is located at the symmetrical centre, links six neighbours in one plane, and the angles between the adjacent nodes are 54.251°, 65.904° and 59.845°, respectively.

The structure of **2** is completely different from the CsCl net and the other two previously known non-CsCl eight-connected nets. As shown in Figure 7, the parallel (4,4) nets of all nets are cross-linked by zigzag chains, although the detailed connection modes are different: in CsCl, the zigzag chain in the inter-layer region bridges the diagonal of a single window in the (4,4) net (Figure 7, a), in the $3^3 4^{15} 5^8 6^2$ topological net the zigzag chains bridge the edges of one (4,4) net and the diagonal of the next (Figure 7, b),[5b] and in the third net the zigzag chains bridge the diagonal of two neighbouring windows (Figure 7, c),[6c] whereas in **2** the zigzag chain is out of a plane and bridges two zigzag chains in two (4,4) nets, which, moreover, are alternately arranged on the two sides of the (4,4) net.

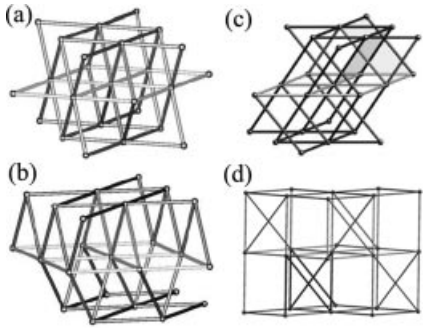


Figure 7. Difference between the four eight-connected nets: (a) CsCl-type net; (b) the $3^3 4^{15} 5^8 6^2$ topological net; (c) the self-penetrating eight-connected net; (d) the $3^5.4^{11}.5^8.6^4$ topology in complex **2**.

## Magnetic Properties

The variable-temperature magnetic susceptibility of **1** was measured in the temperature range from 300 to 2 K (Figure 8), at a magnetic field strength of 5000 G. The $\chi_m T$ value at room temperature is 0.42 $cm^3 K mol^{-1}$, which is slightly bigger than the value of 0.375 $cm^3 K mol^{-1}$ expected for a noncoupled $Cu^{II}$ ion with $g = 2$. Upon cooling, the $\chi_m T$ product decreases smoothly, thus indicating that a predominantly antiferromagnetic interaction exists in **1**. The $1/\chi_m$ vs. $T$ (Curie) plot is linear. Fitting this curve to the Curie–Weiss law gives a Curie constant, $C$, of 0.454 $cm^3 K mol^{-1}$ and a Weiss constant, $\theta$, of –18.13 K, which is a further indication of the weak antiferromagnetic interactions in **1**. According to the crystal structure of **1**, it can be assumed that the superexchange interactions between $Cu^{II}$ ions through the bridging carboxylate groups are weak, which may lead to such a magnetic behaviour.

The Cu···Cu distance in **2**, which is much shorter than that in **1**, implies a weak Cu···Cu interaction. The variable-temperature magnetic susceptibility measurements of a powdered sample of complex **2** were performed in the temperature range 300–2 K. The magnetic behaviour of complex **2** is shown in Figure 9 in the form of $\chi_M T$ and $\chi_M^{-1}$ vs. $T$ plots. The $\chi_M T$ value at room temperature is 1.50 $cm^3 K mol^{-1}$ per tetramer, which is consistent with the spin-only value for four uncoupled $S = 1/2$ centres with $g = 2$. Upon cooling, $\chi_M T$ decreases rapidly down to about 40 K, showing a dominant antiferromagnetic interaction between paramagnetic $Cu^{II}$ ions. A Curie–Weiss fitting above 50 K give a Weiss constant of –90 K; this large negative value demonstrates a strong antiferromagnetic coupling. The pathway of antiferromagnetic interactions may be between the adjacent copper centres (Cu···Cu = 3.006 to 3.342 Å) bridged by a $\mu_3$-hydroxy group. The decrease of $\chi_M T$ is less pronounced between 40 and 20 K, tending to a small plateau at a value (ca. 0.7 $cm^3 K mol^{-1}$) close to that expected for two uncoupled electrons resulting from an antiferromagnetically coupled tetranuclear $Cu^{II}$ compound. Below 20 K, a rapid decrease appears due to further intra- and inter-tetramer antiferromagnetic interactions.

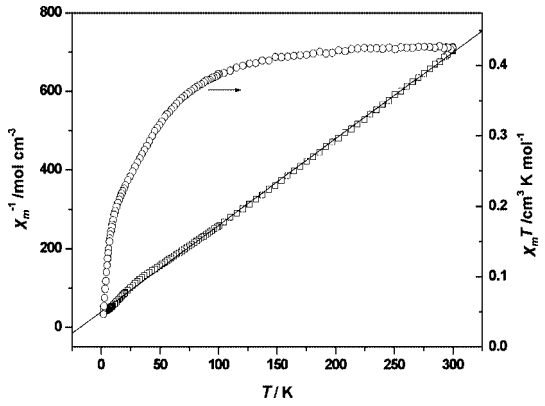


Figure 8. Plots of the temperature dependence (from 300 to 2 K) of $\chi_m T$ and $\chi_m^{-1}$ for **1**.

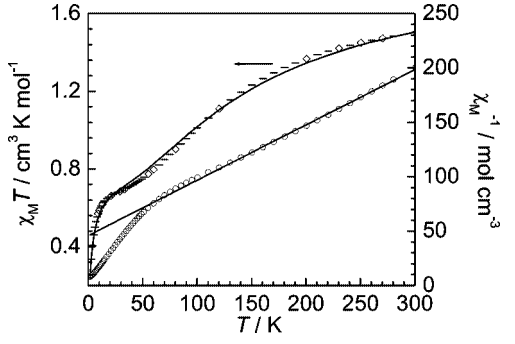


Figure 9. Plots of the temperature dependence (from 300 to 2 K) of $\chi_m T$ and $\chi_m^{-1}$ for **2**.

Considering the butterfly arrangement of the $Cu^{II}$ ions in **2**, the experimental magnetic susceptibility data were analysed with the modified analytical expression derived by combining the tetramer model with $S = 1/2 \cdot [H = -J_1(S_1 + S_2)\cdot(S_3 + S_4) - J_2 S_3 \cdot S_4]$ by Murugavel[10] and inter-tetramer interactions ($J$) under the molecular-field approximation.[11] The best fitting for the experimental data gives $J_1 = -56.7\ cm^{-1}$, $J_2 = -114.9\ cm^{-1}$, $g = 2.25$ and $zj' =$

 © 2006 Wiley-VCH Verlag GmbH & Co. KGaA, Weinheim 

$-3.38\ cm^{-1}$. The agreement factor $R = \Sigma[(\chi_M T)_{obs} - (\chi_M T)_{calc}]^2/\Sigma(\chi_M T)_{obs}^2$ is $3.93 \times 10^{-4}$.

## Conclusion

In summary, two 8-connected nets of a CsCl-type and an unusual $3^5.4^{11}.5^8.6^4$ topology have been structural characterised. The size of the SBUs increases from dinuclear to tetranuclear and their connections also increase from eight-connected to ten-connected. We have confirmed that SBUs can adopt highly connected nodes that can be employed for the construction of highly connected frameworks.

## Experimental Section

**General Remarks:** All the syntheses were performed in Teflon-lined stainless-steel autoclaves under autogenous pressure. Reagents were purchased commercially and were used without further purification. Elemental C,N,H analyses were performed on an EA1110 CHNS-0 CE elemental analyzer. IR (KBr pellet) spectra were recorded with a Nicolet Magna 750FT-IR spectrometer. Variable-temperature magnetic susceptibilities in the temperature range 2–300 K were performed with a model CF-1 superconducting extracting sample magnetometer with the powdered sample kept in the capsule for weighing. All data were corrected for diamagnetism of the ligands estimated from Pascal's constants.

**$[Cu(isonicotinate)(nicotinate)]_n$ (1):** An aqueous mixture (15 mL) containing $CuNO_3{\cdot}3H_2O$ (0.24 g, 1 mmol), isonicotinic acid (0.123 g, 1 mmol) and nicotinic acid (0.123 g, 1 mmol) was placed in a Parr Teflon-lined stainless-steel bomb, which was sealed and placed in a programmable furnace. The temperature was raised to 160 °C over 4 h and held at that temperature for 60 h, then cooled over 60 h to 80 °C and finally cooled down to room temperature over 12 h. The resulting rectangular blue crystals were collected (0.1 g, 32.49% yield). This compound is stable in air and is insoluble in water and common organic solvents. $C_{12}H_8CuN_2O_4$ (307.74): calcd. C 46.91, H 2.63, N 9.12; found C 47.05, H 2.66, N 8.98. IR (solid KBr pellet): $\tilde{\nu}$ = 3434 (w), 3119 (s), 1651 (w), 1629 (vs), 1398 (vs), 1385 (s), 693 (w), 613 (w) $cm^{-1}$.

**$[Cu_2(\mu_3\text{-}OH)(isonicotinate)_2(BDC)_{0.5}]_n$ (2):** A mixture containing $Cu(OH)_2{\cdot}CuCO_3$ (0.44 g, 2 mmol), 1,3-benzenedicarboxylic acid (0.1 g, 0.6 mmol), isonicotinic acid (0.123 g, 1 mmol) and distilled water (10 mL) was placed in a Teflon-lined stainless-steel bomb, which was sealed and placed in a programmable furnace. The temperature was raised to 160 °C over 4 h and held at that temperature for 60 h, then cooled over 60 h to 80 °C and finally cooled down to room temperature over 12 h. The blue prismatic crystals were collected (0.1 g, 64% yield). This complex is stable in air and is insoluble in water and common organic solvents. $C_{16}H_{11}Cu_2N_2O_7$ (470.35): calcd. C 40.95, H 2.36, N 5.97; found C 41.05, H 2.66, N 5.98. IR (solid KBr pellet): $\tilde{\nu}$ = 3314 (w), 3108 (s), 1614 (s), 1559 (m), 1401 (vs), 1087 (m), 751 (m), 728 (m) $cm^{-1}$.

**X-ray Crystallographic Study:** X-ray intensities of complexes **1** and **2** were collected on a Siemens Smart CCD diffractometer equipped with a graphite-monochromated Mo-$K_\alpha$ radiation source ($\lambda$ = 0.71073 Å) at 293(2) K. Empirical absorption corrections were applied to the data using the SADABS program.[7] The structures were solved by direct methods and refined by full-matrix least-squares on $F^2$ using the SHELXTL-97 program.[8] All of the non-hydrogen atoms were refined anisotropically. The H atoms bonded to C atoms were positioned geometrically and refined using a riding model. Crystallographic data and other pertinent information for **1** and **2** are summarised in Table 2. Selected bond lengths and angles are listed in Table 1.

Table 2. Crystallographic data for **1** and **2**.

| | **1** | **2** |
|---|---|---|
| Empirical formula | $C_{12}H_8CuN_2O_4$ | $C_{16}H_{11}Cu_2N_2O_7$ |
| Temperature [K] | 293(2) | 293(2) |
| Crystal colour | blue | blue |
| Crystal size | $0.30 \times 0.25 \times 0.22$ | $0.30 \times 0.08 \times 0.05$ |
| Formula weight | 307.74 | 470.35 |
| Crystal system | monoclinic | monoclinic |
| Space group | $P2_1/c$ | $C2_1/c$ |
| $a$ [Å] | 9.5505(5) | 17.922(2) |
| $b$ [Å] | 11.6346(4) | 12.550(1) |
| $c$ [Å] | 11.9841(6) | 16.492(2) |
| $\beta$ [°] | 113.083(2) | 111.309(4) |
| $V$ [Å$^3$] | 1225.01(10) | 3456.0(7) |
| $Z$ | 4 | 8 |
| Density (calculated) | 1.669 | 1.808 |
| Abs. coeff. [mm$^{-1}$] | 1.793 | 2.504 |
| $F$(000) | 620 | 1880 |
| Reflections collections | 3439 | 12983 |
| Independent reflection | 2143 [$R$(int) = 0.0405] | 3927 [$R$(int) = 0.0194] |
| Goodness-of-fit on $F^2$ | 1.070 | 1.070 |
| $R1$,$wR2$ [$I > 2\sigma(I)$] | 0.0601, 0.1356 | 0.0259, 0.0597 |
| $R1$,$wR2$ (all data) | 0.0923, 0.1614 | 0.0298, 0.0616 |

CCDC-272139 (for **1**) and -272140 (for **2**) contain the supplementary crystallographic data for this paper. These data can be obtained free of charge from The Cambridge Crystallographic Data Centre via www.ccdc.cam.ac.uk/data_request/cif.

## Acknowledgments

This work was supported by grants from the State Key Basic Research and Development Plan of China (001CB108906), the NNSF of China (nos. 29733090 and 20173063) and the NSF of Fujian Province (E0020001).

[1] For recent reviews, see for example: a) C. Janiak, *Dalton Trans.* **2003**, 2781–2804; b) B. Moulton, M. J. Zaworotko, *Chem. Rev.* **2001**, *101*, 1629–1658; c) L. Carlucci, G. Ciani, D. M. Proserpio, *Coord. Chem. Rev.* **2003**, *246*, 247–289.

[2] a) A. F. Wells, *Three-Dimensional Nets and Polyhedra*; Wiley-Interscience: New York, **1977**; b) A. F. Wells, *Further Studies of Three-Dimensional Nets*; ACA Monograph 8; American Crystallographic Association, **1979**.

[3] See for example: a) S. R. Batten, R. Robson, *Angew. Chem. Int. Ed.* **1998**, *37*, 1460–1494; b) O. M. Yaghi, M. O'Keeffe, N. W. Ockwig, H. K. Chae, M. Eddaoudi, J. Kim, *Nature* **2003**, *423*, 705–714; c) S. R. Batten, *CrystEngCommun* **2001**, *3*, 67–72; d) A. J. Blake, N. R. Champness, P. Hubberstey, W. S. Li, M. A. Withersby, M. Schröder, *Coord. Chem. Rev.* **1999**, *183*, 117–138; e) O. V. Dolomanov, D. B. Cordes, N. R. Champness, A. J. Blake, L. R. Hanton, G. B. Jameson, M. Schröder, C. Wilson, *Chem. Commun.* **2004**, 642–643; f) J. Zhang, Y. Kang, R.-B. Zhang, Z.-J. Li, J.-K. Cheng, Y.-G. Yao, *CrystEngCommun* **2005**, *7*, 177–178; g) J. Zhang, Z.-J. Li, Y. Kang, J. K. Cheng, Y.-G. Yao, *Inorg. Chem.* **2004**, *43*, 8085–8091.

[4] a) H. Li, M. Eddaoudi, M. O'Keeffe, O. M. Yaghi, *Nature* **1999**, *402*, 276–279; b) N. L. Rosi, J. Eckert, M. Eddaoudi, D. T. Vodak, J. Kim, M. O'Keeffe, O. M. Yaghi, *Science* **2003**, *300*, 1127–1129; c) M. Eddaoudi, D. B. Moler, H. Li, B. Chen,

 © 2006 Wiley-VCH Verlag GmbH & Co. KGaA, Weinheim 

T. M. Reineke, M. O'Keeffe, O. M. Yaghi, *Acc. Chem. Res.* **2001**, *34*, 319–330.

[5] a) D.-L. Long, A. J. Blake, N. R. Champness, C. Wilson, M. Schröder, *Angew. Chem. Int. Ed.* **2001**, *40*, 2443–2447; b) D.-L. Long, R. J. Hill, A. J. Blake, N. R. Champness, P. Hubberstey, D. M. Proserpio, C. Wilson, M. Schröder, *Angew. Chem. Int. Ed.* **2004**, *43*, 1851–1854; c) R. J. Hill, D.-L. Long, A. J. Blake, N. R. Champness, P. Hubberstey, M. Schröder, *Acc. Chem. Res.* **2005**, *38*, 335–348.

[6] a) X. M. Zhang, R. Q. Fang, H. S. Wu, *J. Am. Chem. Soc.* **2005**, *127*, 7670–7671; b) L. Pan, H. Liu, X. Lei, X. Huang, D. H. Olson, N. J. Turro, J. Li, *Angew. Chem. Int. Ed.* **2003**, *42*, 542–546; c) X.-L. Wang, C. Qin, E.-B. Wang, Z.-M. Su, L. Xu, S. R. Batten, *Chem. Commun.* **2005**, 4789–4790.

[7] *SADABS*, G. M. Sheldrick, University of Göttingen, Germany. **1996**.

[8] Siemens, *SHELXTL* (Version 5.05). Siemens Analytical X-ray Instruments Inc., Madison, Wisconsin, USA. **1994**.

[9] O. V. Dolomanov, A. J. Blake, N. R. Champness, M. Schröder, *J. Appl. Crystallogr.* **2003**, *36*, 1283–1284.

[10] R. Murugavel, M. Sathiyendiran, R. Pothiraja, M. G. Walawalkar, T. Mallah, E. Riviére, *Inorg. Chem.* **2004**, *43*, 945–953. (Note: a $1/kT$ term is missing in the $\chi_M T$ expression).

[11] R. L. Carlin, *Magnetochemistry*, Springer, Berlin, **1986**.

Received: October 12, 2005
Published Online: March 30, 2006

 © 2006 Wiley-VCH Verlag GmbH & Co. KGaA, Weinheim 

DOI: 10.1002/ejic.200500950

# Reactivity of Polyiodides Towards 1,3-Bis(4-pyridyl)propane (bpp): A New CuI Cluster Polycatenane Framework and a Novel 2D AgI Cluster Motif

**Yunyin Niu,[a] Yinglin Song,[b] Ning Zhang,[a] Hongwei Hou*[a] Deji Che,[a] Yaoting Fan,[a] Yu Zhu,[a] and Chunying Duan[c]**

**Keywords:** Clusters / Copper / Iodine / Lead / Organic–inorganic hybrid composites / Silver

The solution-phase reactions of metal iodides or iodine with 1,3-bis(4-pyridyl)propane (bpp) yields four new organic–inorganic hybrid frameworks, namely $[(CuI)_4(bpp)_4]_n$ (**1**), $[(AgI)_6(bpp)]_n$ (**2**), $[PbI_2(bpp)]_n$ (**3**), and $[I_3(bppH)]$ (**4**), each of which adopts a different structural motif. For example, complex **1** is a 2D "open" coordination polymeric cluster consisting of a $CuI_2Cu$ rhomboid cluster core coordinated by *anti-anti* and *anti-gauche* bpp interactions to produce an interpenetrating 2D (4,4) polycatenane net; **2** is a novel bpp inclusion compound with a unique 2D polymeric hexagonal prism-shaped $[Ag_6I_6]_n$ cluster motif; compound **3** is also a 2D "open" supramolecular cluster made from $[PbI_2]_n$ "ribbons" and bpp bridges; compound **4** is a triiodide made up of organic $[bppH]^+$ cations and a $I_3^-$ anion chain. The clusters **1**–**3** obtained from the reaction between polyiodide complexes and an organic ligand suggest that this simple synthetic approach is likely to be applicable to the construction of polymeric clusters. The third-order NLO effects of **1** were studied by Z-scan techniques. The polymeric cluster exhibits good nonlinearities and the effective third-order NLO refractive index ($n_2$) value is $2.56\times10^{-12}$ esu which is comparable to those of most cluster monomers and polymers.
(© Wiley-VCH Verlag GmbH & Co. KGaA, 69451 Weinheim, Germany, 2006)

## Introduction

The construction of supramolecular polymeric networks has been of great interest in recent years, not only due to their intriguing architectures and topologies[1] but also for their potential properties as functional solid materials in catalysis,[2] optics,[3] and magnetism.[4] In addition to the main driving forces of metal–ligand coordination and hydrogen bonding, weak interactions and other subtle factors such as molecular entanglement[5] and halogen–halogen interactions[6] can also have a dramatic effect on the assembly of extended porous topologies. Polycatenation can be regarded as regularly repeated infinite versions of the closed molecular loops via a topological Hopf link − the whole catenated array has a higher dimensionality than the component motifs for a possible combination of interlocking or interweaving covalent, mechanical, and coordination bonds.[5c,7] Since no genuine example of an organic polycatenane has been characterized, a number of metal-based molecular rings have been used as building blocks for the construction of polycatenanes. According to Fujita,[8] transition-metal-directed self-assembly is a designable and highly efficient catenane synthesis pathway, and the configuration of the bridging ligands plays an important role in the self-assembly of metal-based catenanes.

Polyiodides are well-known for their ability to form a vast diversity of extended networks with unique conducting and optical properties.[9] Studies have shown that their structures and macroscopic physical properties can be understood through the level of halogen–halogen interactions between three fundamental building blocks: the Lewis acid acceptor $I_2$, and the Lewis base donors $I^-$ or $I_3^-$, and "guest" building blocks (e.g. metal iodides). These building blocks can be catenated easily and a large variety of polyiodides can be synthesized. The synthesis methods can be described simply as the addition of iodine to an iodide in an appropriate reaction medium, such as $I_3^-$: $I_2(s) + I^-(aq) \rightarrow I_3^-(aq)$. Recently, the reaction between monovalent metal halides MI ($M = Cu^+$, $Ag^+$) and $I^-$ attracted our attention because the solubility of MI increases in mixed solvents (such as $THF/H_2O$ and $CH_3CN/H_2O$) upon addition of excess KI. This increase in solubility may be a consequence of the formation of a metal diiodide anion: $MI(s) + I^- \rightarrow MI_2^-$. More importantly, the active intermediate $MI_2^-$ ion is a good iodine source for cluster construction, and its self-assembly reaction with rigid and flexible bispyridyl ligands is an effective route for the preparation of novel polymeric complexes containing iodine clusters. The systematic incorporation of a metal iodide and organic spacer-based molecular rings within polymeric cluster networks allows for the

[a] Department of Chemistry, Zhengzhou University, Henan 450052, P. R. China
E-mail: houhongw@zzu.edu.cn
Fax: +86-371-6776-1744
[b] Department of Applied Physics, Harbin Institute of Technology, Heilongjiang 150001, P. R. China
[c] State Key Laboratory of Coordination Chemistry, Coordination Chemistry Institute, Nanjing University, Nanjing 210093, P. R. China

 © 2006 Wiley-VCH Verlag GmbH & Co. KGaA, Weinheim 

modulation of their structural and physical properties. With this method we have previously obtained a 2D "open" polymer $[AgI(bpe)]_n$ [bpe = 1,2-bis(4-pyridyl)ethane][10] and a unique 1D coordination polymeric cluster $\{[AgI(inh)]_6(KI)\}_n$ with hexagonal cluster units centered by $\mu_6$-I.[11]

Herein we use bpp as a bridging ligand due to its networking ability[12] and its variable configurations (*anti-anti*, *anti-gauche*, and *gauche-gauche*; Figure 1), and report the formation of four bpp-based compounds by self-assembly with polyiodide species (Scheme 1): **1**–**3** are cluster compounds and **4** is a triiodide. The good nonlinear optical effects of cluster **1** are also presented.

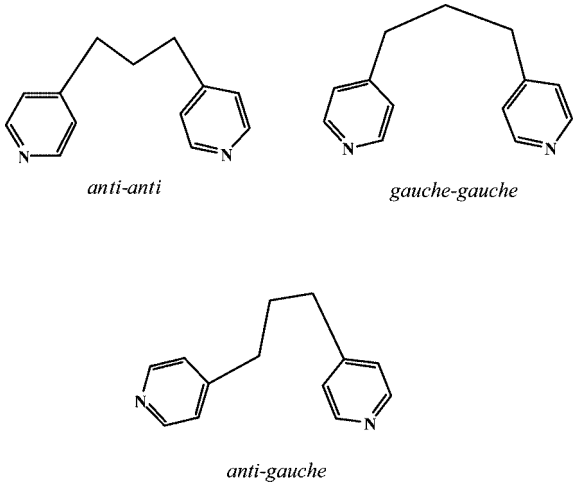


Figure 1. Three main coordination configurations of bpp.

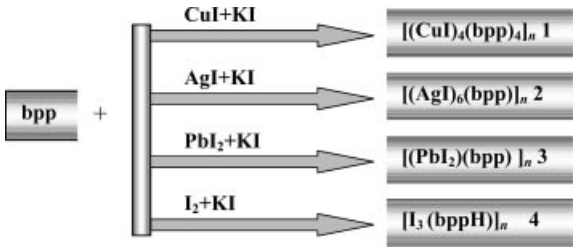


Scheme 1. Schematic view of the reactivity of polyiodides toward bpp under distinct conditions.

## Results and Discussion

### Preparation of Compounds

As far as the use of insoluble inorganic metal salts in coordination chemistry is concerned, their solubility is a crucial question to the related preparation procedure. Several strategies have been employed to circumvent this practical problem. Firstly, the use of an appropriate solvent. For example, THF is a superior solvent to dissolve $HgI_2$ as the solubility of $HgI_2$ in THF is about 20 times better than that in ethanol. More than ten $HgI_2$ coordination polymers have been obtained with the method.[13] The second procedure is solid-state reaction at low temperature. When an insoluble salt such as CuI or AgI is mixed and ground with $Bu_4NBr$ (or $Et_4NBr$) and $MoS_4^{2-}$, the mixture reacts easily at room temperature or low temperature to give a soluble product in organic solvents. About six polymeric clusters with novel motifs have been synthesized with the method.[14] The third method involves finding a soluble precursor complex. When the concentration of $X^-$ (X = $Cl^-$, $Br^-$, and $I^-$) increases to a certain level, the solubility of MX increases due to the formation of polyhalide anion complexes $MX_2^-$. This method has been used unintentionally by the addition of NaI, KI, HI, $Bu_4NI$, or $Ph_4PI$,[15] and moreover, we found a small quantity of water is helpful for accelerating the dissolution. Many insoluble metal iodides such as CuI, AgI, $PbI_2$, $HgI_2$, etc. can be dissolved efficiently by this method, and several interesting metal–iodine clusters have been found.[10,11] In this contribution, complex **1** was prepared as light-yellow crystals by the addition of a DMF solution of bpp to a THF/$H_2O$ solution of CuI in excess KI. The product is insoluble in common organic solvents and stable in air.

Compound **2** was obtained by a similar procedure to that of **1**, except that the mixed solvent THF/$CH_3CN$/$H_2O$ was used; the use of a single solvent (such as THF or $CH_3CN$) never gave a perfect crystal. Complex **2** was only obtained when the solvent evaporation was conducted in the dark and the solution was nearly dry.

For **3**, the dissolution of $PbI_2$ may obey the following well-known equation: $PbI_2 + 2KI \rightarrow K_2(PbI_4)$. Slow evaporation of the solution gives **3** as a colorless crystal. Compound **3** is also the first example of a $PbI_2$ coordination polymer obtained by the polyiodide reaction.

Compound **4** was obtained without a metal polyiodide. The formation of $I_3^-$ shows its special stability in $CH_3OH$/$H_2O$.[9a] The N-protonation of bpp may be a result of protonation by the mixed solvents.

### Crystal Structure of $[(CuI)_4(bpp)_4]_n$ (1)

In the structure of $[(CuI)_4(bpp)_4]_n$ (**1**), $Cu^I$ adopts a distorted $CuI_2N_2$ tetrahedral coordination sphere and binds two pyridines from bpp and two bridging iodide counterions (Figure 2). Both the bridging iodides are also bound to another symmetry-related $Cu^I$ center to form a $Cu(\mu_2\text{-}I)_2Cu$ rhombohedron. A similar unit is also present in dissociated dimeric molecules[16a,16b] and its self-assembly products with multitopic ligands.[16c–16j] Due to the flexibility of both the Cu–I–Cu and I–Cu–I angles, this $CuI_2Cu$ rhomboid unit can adapt to a given coordination geometry produced by the ligands.[16b] In **1**, these metallic $CuI_2Cu$ subunits connect alternately two couples of didentate bpp ligands to form a one-dimensional double-bridged polymeric chain which propagates along the *a* or *b* crystallographic direction. The doubly bridging iodides lie above and below the planes of the chain rings. An interesting feature of **1** is the parallelity of the $CuI_2Cu$ metallacycles. All these cycles retain a plane perpendicular to the double-bridge surfaces, which shows that the bpp ligands have no evident impact on the $CuI_2Cu$ configuration. On the other hand, the flexible

 © 2006 Wiley-VCH Verlag GmbH & Co. KGaA, Weinheim 

trimethylene spacer decreases the rigidity of the chain to cater for the parallelity of the $CuI_2Cu$ rings. From this point of view, cluster **1** is a typical example of metal-directed self-assembly.

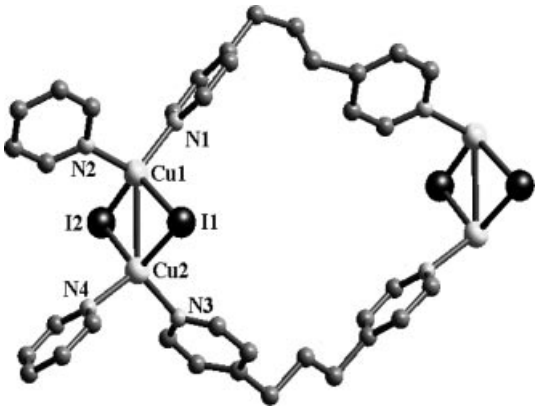


Figure 2. The elliptic molecular ring with approximate dimensions of $12.56 \times 10.79$ Å$^2$ in **1**.

Another noteworthy aspect of this structure is the existence of the interweaving linkages. In the doubly bridged chains, two such subunits and two bpp ligands with distinct conformations (*anti-anti* and *anti-gauche*) form an elliptic molecular ring with approximate dimensions of $12.56 \times 10.79$ Å$^2$. As mentioned above, there are two groups of equivalent chains extended along the *a* and *b* axes, respectively. Each closed elliptic circuit is penetrated by the same loop from another chain at the loosest point with a Hopf link (Figure 3, top), leaving no residual space for solvent inclusion. These two groups of interweaving chains display 2D "open" vertical interpenetration (Figure 3, bottom) to give a uniform (4,4) net containing square intermolecular boxes with approximate dimensions of $12.56 \times 12.56$ Å$^2$. The catenated coordination rings indicate an ideal separation between the ligands in each molecular ring, whereas catenation does not take place if the elliptical rings possess no voids in their cavities due to the possible excessive flexibility or the entanglement of the ligands. Compound **1** also emphasizes that optimized ligand conformations are essential for the self-assembly of catenanes.[8] Thus, this net is clearly different from other reported network topologies containing $CuI_2Cu$ rhomboids[16g,16h] and represents the first uniform net of [2]-catenane nodes.

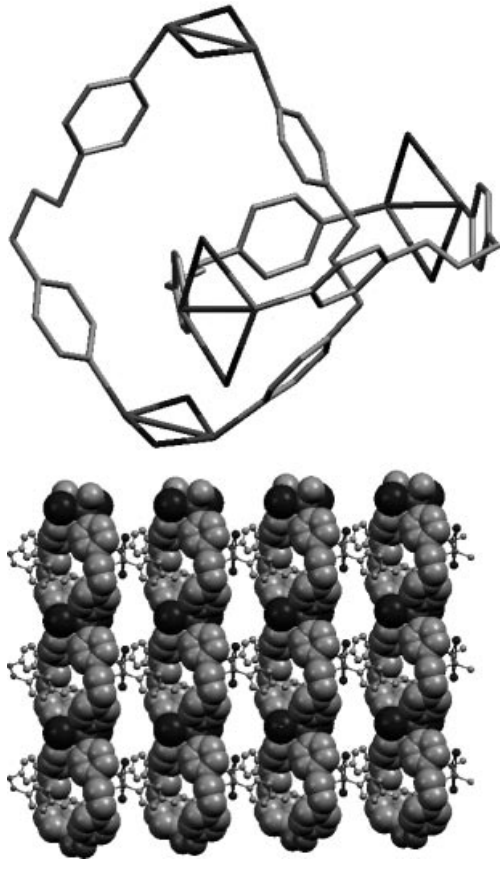

Figure 3. Solid-state structure of **1**. Top: The catenation of two individual $[(CuI)_2(bpp)_2]_n$ chains showing the Hopf links. Bottom: View along the *c*-direction the infinite interlocking 2D (4,4) lattice in **1** showing [2]-catenane nodes. The two individual polymeric chains are perpendicular to each other and are shown in capped-stick and space-filling representations, respectively.

### Crystal Structure of $[(AgI)_6(bpp)]_n$ (2)

The X-ray single-crystal structural analysis showed that compound **2** crystallizes in the monoclinic system with space group *C*2/*c*. A portion of the cluster is shown in Figure 4. The structure of **2** is made up of isolated bpp units and the infinite polymeric cluster $[(AgI)_6]_n$.

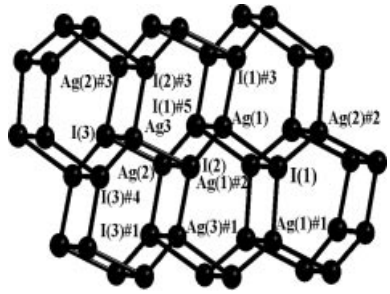


Figure 4. View of the two-dimensional $[AgI]_{6n}$ double layer in $[(AgI)_6(bpp)]_n$ (**2**).

In the polymeric structure, each silver atom is covalently bonded to three iodines at 2.77–2.87 Å in the same layer (Figure 4). The bond angles are in the range 102–114°. The iodine and silver atoms can therefore form six-membered rings but don't link up to form flat sheets. A fourth strong Ag–I covalent force with distances of 2.88–2.97 Å holds the layers together. This interaction prevents the layers from slipping over each other, which is different from the graphite lattice structure. The cluster can also be seen as a double layer (6,3) net motif composed of an edge-sharing $Ag_6I_6$ hexagonal prism-shaped cell. A section of the double layer of **2** is shown in Figure 5. There have been a series of polymeric metal(I) halide clusters reported;[17] comparing the crystallographic data available for different classes of silver

 © 2006 Wiley-VCH Verlag GmbH & Co. KGaA, Weinheim 

iodide clusters in the Cambridge Structural Database (CSD) and search results from the Chemical Abstracts database with SciFinder Scholar®, we see that compound **2** is the first example of a 2D bilayer AgI cluster motif.

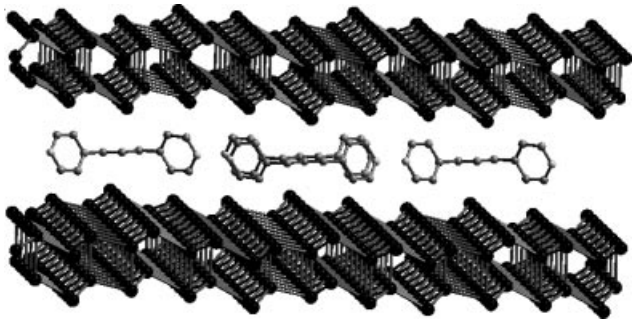

Figure 5. View showing the alternating $[AgI]_{6n}$ bilayer and bpp layer in **2**.

There is a closely related example for **2**, namely the triazine-based coordination polymer $[Cu_2I_2(tri)]_n$ (tri = triazine).[17b] In $[Cu_2I_2(tri)]_n$, the $[CuI]_n$ layer is also an undulating hexagonal net, with each six-membered ring adopting a boat conformation, but the fourth position of the tetrahedral copper center is occupied by a triazine nitrogen and triazine ligands link $[CuI]_n$ layers to give alternating copper(I) iodide and triazine layers. Because of the existence of bridging triazine layers, the longer distances between neighboring $[CuI]_n$ monolayers (minimum Cu–I distance is 6.2–7.1 Å) eliminate the possible Cu···I interlayer interactions. In **2**, the uncoordinated bpp is more like a cluster cutter and isolates the $[AgI]_n$ double layer unit from the metal polyiodide phase. The $[AgI]_n$ double layers are much more regular than $[CuI]_n$ in $[Cu_2I_2(tri)]_n$, so this structure can be considered to be a novel topological type for monovalent $M^I$ halide polymeric clusters.

### Crystal Structure of $[PbI_2(bpp)]_n$ (3)

An ORTEP drawing with the atom-numbering scheme of **3** is shown in Figure 6. The geometry around the lead atom is a distorted octahedron involving the nitrogen atom from pyridyl donors and the iodine atoms. Around the lead the four Pb–I distances range from 3.15 to 3.31 Å and the Ag–N distance is 2.64 Å. Each Pb also has a supramolecular interaction with a nitrogen atom from another bpp at a distance of 2.80 Å. The polymeric structure is comprised of $[PbI_2]_n$ "staircase clusters" and bpp bridges. The bpp ligands link cluster ribbons to form a 2D "open" motif spreading out in the *ab* plane. The bpp molecules stack along the *a*-axis with a stacking distance of 4.54 Å (to the neighboring equivalent pyridyl ring), forming a two-column structure between the $[PbI_2]_n$ ribbons. Each bpp ligand adopts an *anti-anti* configuration and the two pyridyl rings have a dihedral angle of 58.6°. The nearest Pb–Pb distance along the *a*-axis is equal to the repetition distance of bpp. The 2D sheets stack along the *c*-direction in an ABAB pattern, with the equivalent interlayer Pb–Pb separation distance being 11.92 Å. These 2D sheets are similar to those observed in $[PbX_2(4,4'\text{-bipy})]_n$,[18a] $[PbI_2(C_{12}H_{10}N_4)]_{2n}\cdot 0.5n(C_{12}H_{10}N_4)$,[18b] and $[PbI_2(L)]_n$ [L = *N*,*N*′-bis(3-pyridylmethyl)-1,4-biphenylenedimethyleneimine].[18c]

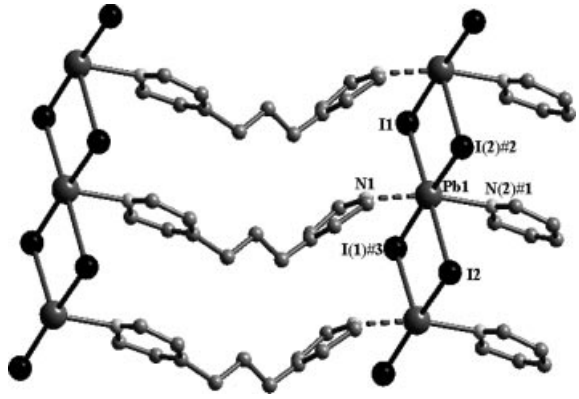


Figure 6. The 2D sheet structure of **3** formed by association of $[PbI_2]_n$ "staircase clusters" through supramolecular Pb···N interactions.

### Crystal Structure of $[I_3(bppH)]$ (4)

The structure of **4** is made up of organic $[bppH]^+$ cations and $I_3^-$ anion chains (Figure 7). The crystal packing is dominated by noncovalent donor–acceptor interactions involving both N–H···N (2.66 Å) hydrogen bonding between $bppH^+$ cations and I···I interactions between $I_3^-$ anions. The triiodide ion is nearly linear (I2–I1–I3 = 178.12°) and asymmetric, and has *d*(I–I) distances of 2.901 and 2.921 Å. The triiodide ions are stacked in zigzag patterns with weak $I_3^-\cdots I_3^-$ interactions (3.69 Å). It is believed that the large linear deformation of the $I_3^-$ ion is a result of the different environments in the solid state. Packing effects and electrostatic interactions may be considered to explain the induced asymmetry of $I_3^-$ here.[9a] In **4**, all these interactions are considerably shorter than the sums of the van der Waals contact distances for the atoms involved (N: 1.55–1.61 Å; I: 1.98–2.00 Å).[19] The *anti-anti* configuration of bpp is also retained.

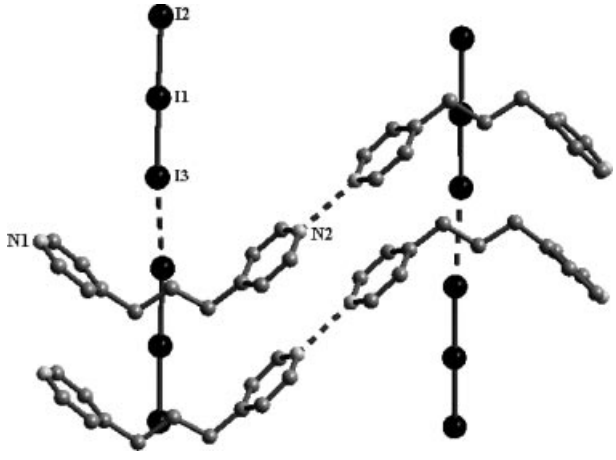


Figure 7. Crystal structure of polyiodide **4**.

 © 2006 Wiley-VCH Verlag GmbH & Co. KGaA, Weinheim 

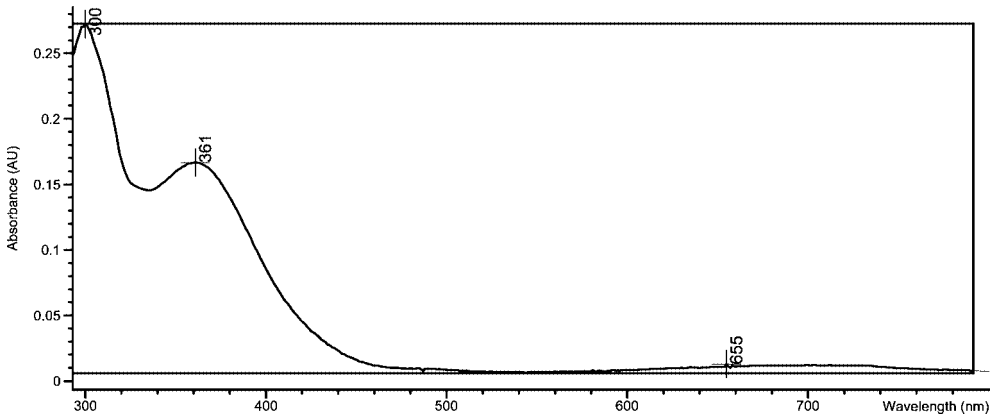


Figure 8. UV/Vis spectra of compound **1**.

### *Third-Order NLO Properties of 1*

#### *UV/Vis Spectra of 1*

In the ground state UV/Vis spectra (Figure 8) of **1**, two strong absorption peaks at 300 and 361 nm in the near ultraviolet (UV) wavelength range are attributed to the charge-transfer excitation between $Cu^+$ and $I^-$ ions of the cluster segment, perhaps the HOMO (mostly iodide in character) to LUMO (mostly metal) cluster-centered transition suggested by ab initio calculations.[20] In the visible region, there is a weak linear absorption at 655 nm assigned to d-d ligand field (LF) transition.[21]

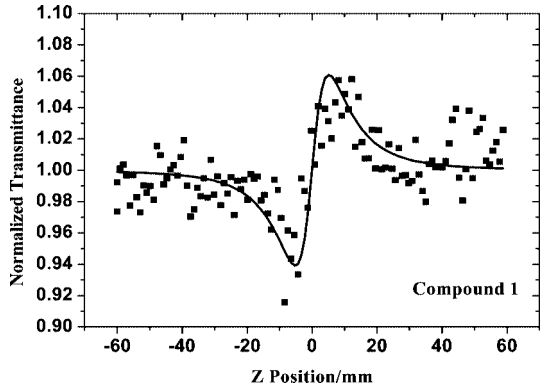


Figure 9. *Z*-scan measurement of the cluster **1** in $1.28\times10^{-4}$ M DMF solution.

#### *Nonlinear Effects of 1*

A preliminary study of the third-order NLO properties of **1** was carried out by the *Z*-scan method in a $1.28\times10^{-4}$ M DMF solution. The compound exhibits strong nonlinear optical behavior at 532 nm and the nonlinear optical properties are dominated by nonlinear refraction. The *Z*-scan data of the compound are given in Figure 9. The filled boxes are the experimental data measured under an open aperture. The nonlinear refractive components of the compound were assessed by dividing the normalized *Z*-scan data obtained in an open-aperture configuration. An effective third-order nonlinear refractive index, $n_2$, can be derived from the difference between normalized transmittance values at valley and peak positions ($\Delta T_{V-P}$) by using Equation (1), where $\Delta T_{V-P}$ is the difference between normalized transmittance values at valley and peak positions, $\alpha_0$ is the linear coefficient, $L$ is the sample thickness, $I$ is the peak irradiation intensity at focus, and $\lambda$ is the wavelength of the laser. The effective third-order NLO refractive index was calculated to be $2.56\times10^{-12}$ esu. The data show that the cluster has a positive sign for refractive nonlinearity, and the valley–peak pattern of the normalized transmitted curve obtained in the closed-aperture configuration shows the characteristic self-focusing behavior of propagating light in the sample.

$$n_2^{eff} = \frac{\lambda\alpha_0}{0.812\pi I\left(1-e^{-\alpha_0 L}\right)}\Delta T_{V-P} \quad (1)$$

Although this value of $n_2$ was obtained with a dilute solution of **1**, it is better than many best known third-order materials in neat solid form, such as $SiO_2$ ($2\times10^{-20}$ $m^2W^{-1}$) and CdS ($2.5\times10^{-18}$ $m^2W^{-1}$),[22] $SrLaGa_3O_7$ ($11.1\times10^{-20}$ $m^2W^{-1}$) and $Ca_2Ga_2SiO_7$ ($6.5\times10^{-20}$ $m^2W^{-1}$).[23] In particular, the $n_2$ value is also comparable to that of some clusters, including monomers, oligomers, and polymers in solution, such as the nest-shaped cluster $[MoOS_3Cu_3I(py)_5]$ ($3.0\times10^{-17}$ $m^2W^{-1}$),[24] the hexagonal prism cluster $[W_2S_8Ag_4(AsPh_3)_4]$ ($5.9\times10^{-17}$ $m^2W^{-1}$),[25] and the 2D microporous cluster $[MoS_4Cu_6I_4(py)_4]_n$ ($2.5\times10^{-17}$ $m^2W^{-1}$).[26] We speculate that the NLO properties of **1** are enhanced, in part, by the planar skeleton and the $Cu^I$–bpp molecular rings in the cluster. The heavy-atom effects of the planar "open" structures in **1** may allow better spin–orbital couplings, and thus intersystem crossing at the excited states.[27] In addition, the use of heavy atoms such as Cu and I may introduce more sublevels into the energy hierarchy and provide more allowed electronic transitions for the initial excited state in

 © 2006 Wiley-VCH Verlag GmbH & Co. KGaA, Weinheim 

**1**. The increased numbers of allowed electronic transitions probably enhance the nonlinear optics. On the other hand, these planar clusters have higher symmetry than other clusters. This higher symmetry, as in the phthalocyanine systems,[28] may decrease the probability of ground-state electronic transitions and gives a smaller absorption cross-section, $\sigma_g$, and a larger $\sigma_e/\sigma_g$ ($K_\alpha$) ratio. Our recent results have also shown that sometimes the metal core and peripheral ligands may have a complimentary effect on the strength of the NLO properties.[29] This presentation is the first report on the coordination chemistry of metallic polyiodides where the systematic incorporation of metal iodide and organic ligand-based molecular rings into polymeric cluster networks allows for the fine modulation of their structural and optical properties. In addition, although the concentration of coordination polymeric clusters in solution is apparently limited by their poor solubility, larger nonlinear index values may be expected if higher concentrations are attained.

## Conclusions

The metal halides CuI, AgI, and $PbI_2$ form three different polymeric networks with bpp depending upon the coordination geometry of the metals and the reaction condition. In **2** bpp isn't coordinated to the Ag atoms, presumably due to the additional structural rigidity and stability of the 2D $(AgI)_n$ polymer sheet. The use of mixed organic solvents (THF/$CH_3CN$/$H_2O$) shows that the formation of **2** is also sensitive to the experimental conditions.[12d,12e] The choice of bpp as ligand is of great importance in determining the cluster skeleton (0D $[Cu_2I_2]$ for **1**, 1D $[PbI_2]_n$ for **3**, and 2D $[(AgI)_6]_n$ for **2**) and the final topology of the supramolecular arrays.

In summary, we have prepared and characterized the first uniform polycatenane (4,4) net with good NLO properties. The current work shows that this metallic polyiodides approach, which incorporates a metal-organic molecular ring or altering cluster skeletons into polymeric species, is perhaps a promising research direction in the search for better NLO materials. Further systematic investigation will focus on the influence of assembly conditions on the diversity of cluster networks and the design and construction of better NLO materials like the planar "open" coordination polymeric cluster **1**. Studies are under way to extend this facile method to other metal polyiodide anions, and to further probe their structure/properties relationship.

## Experimental Section

**Genaral:** 1,3-Bis(4-pyridyl)propane (bpp) was obtained from Aldrich. Other chemicals were obtained from commercial sources and used as received. All solvents were pre-dried with activated molecular sieves and refluxed over the appropriate drying agents under argon. The IR spectrum was recorded with a Shimazu IR435 spectrometer as KBr disk (4000–400 $cm^{-1}$). UV/Vis spectra of **1** were measured with a HP 8453 ultraviolet-visible spectrophotometer. The C, H, and N microanalyses were performed with a Perkin–Elmer 240C instrument.

**Preparation of $[(CuI)_4(bpp)_4]_n$ (1):** A DMF solution of bpp (19.8 mg, 0.1 mmol) was added to a stirring colorless solution of CuI (19 mg, 0.1 mmol) dissolved in 10 mL of THF/$H_2O$ (volume ratio of 1:5) in the presence of excess KI (99.6 mg, 0.6 mmol). The solution was then filtered and slowly evaporated in a vial at room temperature. Light-yellow crystals of **1** suitable for X-ray analysis were obtained after several days in about 22% yield. $C_{52}H_{56}Cu_4I_4N_8$ (1554.8): calcd. C 40.17, H 3.63, N 7.21; found C 40.36, H 3.70, N 7.20. IR (KBr): $\tilde{\nu}$ = 1608(vs), 1423 (s), 1218 (m), 809 (m) $cm^{-1}$. UV/Vis (DMF): $\lambda_{max}$ ($\log\varepsilon$) = 300.0 nm (3.327), 361.0 (3.115), 655.0 (2.004).

**Preparation of $[(AgI)_6(bpp)]_n$ (2):** Compound **2** was obtained by a similar reaction procedure from bpp, AgI, and KI (molar ratio = 1:1:6) in THF/$CH_3CN$/$H_2O$ at room temperature. Upon slow evaporation in the dark, colorless needles of **2** were harvested in 47% yield when the solution was nearly dry. $C_{13}H_{14}Ag_6I_6N_2$ (1606.9): calcd. C 9.74, H 0.88, N 1.75; found C 9.56, H 0.76, N 1.24. IR (KBr): $\tilde{\nu}$ = 3428 (sh), 3139 (sh), 2983 (w), 1710 (w), 1620 (s), 1400 (s), 1177 (w), 814 (w), 619 (w), 545 (w) $cm^{-1}$.

**Preparation of $[PbI_2(bpp)]_n$ (3):** Compound **3** was obtained by a similar reaction procedure from bpp, $PbI_2$, and KI (molar ratio = 1:1:2) in DMF/$H_2O$ at room temperature. A colorless polymer **3** was harvested in 25% yield after 1 month. $C_{13}H_{14}I_2N_2Pb$ (659.25): calcd. C 23.64, H 2.14, N 4.24; found C 23.56, H 2.20, N 4.24. IR (KBr): $\tilde{\nu}$ = 2940 (w), 1606 (s), 1425 (w), 1221 (w), 1010 (m), 815 (m), 514 (w) $cm^{-1}$.

**Preparation of $[I_3(bppH)]$ (4):** Compound **4** was obtained by a similar reaction procedure from bpp, $I_2$, and KI (molar ratio = 1:1:2) in $CH_3OH$/$H_2O$ at room temperature. Needle-shaped, dark-red crystals of **4** were obtained in 32% yield after 1 d. $C_{13}H_{15}I_3N_2$ (579.97): calcd. C 26.92, H 2.61, N 4.83; found C 26.86, H 2.56, N

Table 1. Selected bond lengths [Å] and angles [°] for **1**.[a]

| | | | | | |
|---|---|---|---|---|---|
| Cu1–N2 | 2.048(6) | Cu1–N1#1 | 2.067(6) | Cu1–I1 | 2.6521(12) |
| Cu2–I1 | 2.6031(11) | Cu2–N3#1 | 2.058(6) | Cu1–I2 | 2.6690(11) |
| Cu2–I2 | 2.6756(11) | Cu2–N4 | 2.061(7) | N1–Cu1#2 | 2.067(6) |
| N2–Cu1–N1#1 | 113.3(2) | N2–Cu1–I1 | 104.22(17) | N1–Cu1–I1 | 109.55(17) |
| N2–Cu1–Cu2 | 112.85(19) | N1#1–Cu1–Cu2 | 133.88(16) | N1#1–Cu1–I2 | 107.16(17) |
| I1–Cu1–Cu2 | 57.50(3) | I2–Cu1–Cu2 | 59.06(3) | N2–Cu1–I2 | 106.8(2) |
| N4–Cu2–I1 | 111.4(2) | N3#1–Cu2–I2 | 104.21(18) | I1–Cu1–I2 | 115.96(4) |
| N4–Cu2–I2 | 106.2(2) | N3#1–Cu2–N4 | 108.4(3) | N3#1–Cu2–I1 | 108.73(19) |
| Cu2–I1–Cu1 | 63.28(3) | I1–Cu2–I2 | 117.44(4) | N3#1–Cu2–Cu1 | 130.71(17) |
| N4–Cu2–Cu1 | 120.64(19) | Cu1–I2–Cu2 | 62.11(3) | I1–Cu2–Cu1 | 59.23(3) |
| I2–Cu2–Cu1 | 58.83(3) | C5–N1–Cu1#2 | 122.4(5) | C1–N1–Cu1#2 | 120.8(5) |

[a] Symmetry transformations used to generate equivalent atoms: #1: $x + 1, y, z$; #2: $x - 1, y, z$.

 © 2006 Wiley-VCH Verlag GmbH & Co. KGaA, Weinheim 

Table 2. Selected bond lengths [Å] and angles [°] for **2**.[a]

| | | | | | | | |
|---|---|---|---|---|---|---|---|
| Ag(1)–I(1) | 2.853(3) | Ag(1)–I(2) | 2.860(3) | Ag(1)–I(1)#5 | 2.891(3) | Ag(1)–I(1)#3 | 2.841(3) |
| I(1)–Ag(1)#1 | 2.841(3) | I(1)–Ag(1)#2 | 2.891(3) | Ag(2)–I(2) | 2.971(4) | Ag(2)–I(3) | 2.770(3) |
| Ag(2)–I(3)#1 | 2.782(3) | Ag(2)–I(1)#5 | 2.870(4) | I(1)–Ag(2)#2 | 2.870(4) | I(2)–Ag(3) | 2.839(3) |
| I(3)–Ag(2)#3 | 2.782(3) | Ag(3)–I(3)#4 | 2.821(3) | Ag(3)–I(2)#3 | 2.867(3) | I(3)–Ag(3) | 2.888(3) |
| I(2)–Ag(3)#1 | 2.867(3) | I(3)–Ag(3)#4 | 2.821(3) | | | | |
| Ag(1)#1–I(1)–Ag(1) | 106.49(11) | Ag(1)#1–I(1)–Ag(2)#2 | 106.68(10) | Ag(1)–I(1)–Ag(2)#2 | 113.43(10) | Ag(1)#1–I(1)–Ag(1)#2 | 72.88(8) |
| Ag(1)–I(1)–Ag(1)#2 | 72.70(8) | Ag(2)#2–I(1)–Ag(1)#2 | 64.70(11) | Ag(3)–I(2)–Ag(1) | 98.43(9) | Ag(3)–I(2)–Ag(3)#1 | 106.17(10) |
| Ag(1)–I(2)–Ag(3)#1 | 104.59(9) | Ag(1)–I(2)–Ag(2) | 63.80(10) | Ag(3)–I(2)–Ag(2) | 65.35(9) | Ag(2)–I(3)–Ag(2)#3 | 110.49(13) |
| Ag(2)#3–I(3)–Ag(3) | 67.22(10) | Ag(3)#1–I(2)–Ag(2) | 65.04(9) | Ag(2)–I(3)–Ag(3) | 67.34(10) | Ag(2)–I(3)–Ag(3)#4 | 115.38(11) |
| Ag(2)#3–I(3)–Ag(3)#4 | 102.44(10) | Ag(3)#4–I(3)–Ag(3) | 77.48(10) | I(1)#3–Ag(1)–I(1) | 106.49(11) | I(1)#3–Ag(1)–I(2) | 112.37(10) |
| I(1)#3–Ag(1)–Ag(2) | 130.65(11) | I(2)–Ag(1)–I(1)#5 | 117.17(11) | I(1)–Ag(1)–I(2) | 105.77(9) | I(1)#3–Ag(1)–I(1)#5 | 107.37(9) |
| I(2)–Ag(1)–Ag(2) | 59.86(10) | I(1)#5–Ag(1)–Ag(2) | 57.31(10) | I(1)–Ag(1)–I(1)#5 | 107.05(9) | I(3)#1–Ag(2)–I(1)#5 | 105.09(12) |
| I(3)–Ag(2)–I(3)#1 | 110.49(13) | I(3)–Ag(2)–I(1)#5 | 98.41(11) | I(1)–Ag(1)–Ag(2) | 122.73(10) | I(3)#1–Ag(2)–I(2) | 113.85(11) |
| I(3)–Ag(2)–I(2) | 113.38(11) | I(3)#1–Ag(2)–Ag(1) | 127.79(13) | I(1)#5–Ag(2)–Ag(1) | 57.99(9) | I(3)–Ag(2)–Ag(1) | 120.28(11) |
| I(1)#5–Ag(2)–Ag(3) | 122.49(12) | I(2)–Ag(2)–Ag(1) | 56.34(10) | I(3)–Ag(2)–Ag(3) | 58.13(8) | I(2)#3–Ag(3)–I(3) | 113.84(10) |
| I(1)#5–Ag(2)–Ag(3)#1 | 129.68(13) | I(3)#1–Ag(2)–Ag(3) | 131.71(15) | I(1)#5–Ag(2)–I(2) | 114.33(12) | I(2)–Ag(3)–Ag(2) | 59.37(9) |
| I(2)–Ag(2)–Ag(3)#1 | 55.87(9) | I(2)–Ag(2)–Ag(3) | 55.29(9) | I(3)–Ag(2)–Ag(3)#1 | 131.66(15) | I(3)#4–Ag(3)–I(3) | 102.52(10) |
| I(3)#4–Ag(3)–I(2)#3 | 103.72(10) | I(2)–Ag(3)–I(2)#3 | 106.17(10) | I(3)#1–Ag(2)–Ag(3)#1 | 58.00(8) | I(2)#3–Ag(3)–Ag(2) | 130.65(13) |
| I(3)#4–Ag(3)–Ag(2) | 125.29(13) | I(2)–Ag(3)–I(3) | 113.87(10) | I(3)#4–Ag(3)–I(2) | 116.53(11) | I(3)#4–Ag(3)–Ag(2)#3 | 112.97(12) |
| I(3)–Ag(3)–Ag(2)#3 | 54.78(9) | I(3)–Ag(3)–Ag(2) | 54.53(9) | I(2)–Ag(3)–Ag(2)#3 | 130.47(14) | I(2)#3–Ag(3)–Ag(2)#3 | 59.09(9) |

[a] Symmetry transformations used to generate equivalent atoms: #1: $x$, $y + 1$, $z$; #2: $-x + 1/2$, $y + 1/2$, $-z + 1/2$; #3: $x$, $y - 1$, $z$; #4: $-x + 1/2$, $-y - 1/2$, $-z + 1$; #5: $-x + 1/2$, $y - 1/2$, $-z + 1/2$; #6: $-x$, $y$, $-z + 1/2$.

Table 3. Selected bond lengths [Å] and angles [°] for **3** and **4**.[a]

| | | | | | | | |
|---|---|---|---|---|---|---|---|
| Compound **3** | | | | | | | |
| Pb(1)–N(2)#1 | 2.64(3) | Pb(1)–I(1) | 3.154(2) | Pb(1)–I(2)#2 | 3.165(2) | Pb(1)–I(2) | 3.280(2) |
| Pb(1)–I(1)#3 | 3.315(2) | I(1)–Pb(1)#2 | 3.315(2) | I(2)–Pb(1)#3 | 3.165(2) | N(2)–Pb(1)#4 | 2.64(3) |
| N(2)#1–Pb(1)–I(1) | 98.0(7) | N(2)#1–Pb(1)–I(2)#2 | 91.7(6) | I(1)–Pb(1)–I(2)#2 | 93.06(5) | N(2)#1–Pb(1)–I(2) | 81.5(7) |
| I(1)–Pb(1)–I(2) | 177.27(5) | I(2)#2–Pb(1)–I(2) | 89.63(5) | N(2)#1–Pb(1)–I(1)#3 | 87.6(6) | I(1)–Pb(1)–I(1)#3 | 89.18(5) |
| I(2)#2–Pb(1)–I(1)#3 | 177.71(6) | I(2)–Pb(1)–I(1)#3 | 88.12(5) | Pb(1)–I(1)–Pb(1)#2 | 89.18(5) | Pb(1)#3–I(2)–Pb(1) | 89.63(5) |
| Compound **4** | | | | | | | |
| I(1)–I(3) | 2.9012(10) | I(1)–I(2) | 2.9204(10) | N(1)–C(1) | 1.333(10) | N(1)–C(5) | 1.343(9) |
| N(2)–C(13) | 1.338(9) | N(2)–C(9) | 1.342(9) | | | | |
| I(3)–I(1)–I(2) | 178.11(3) | C(1)–N(1)–C(5) | 118.2(7) | C(13)–N(2)–C(9) | 119.9(7) | N(1)–C(1)–C(2) | 122.2(8) |
| C(4)–C(3)–C(2) | 116.9(7) | N(1)–C(5)–C(4) | 122.5(7) | C(3)–C(6)–C(7) | 108.6(6) | C(6)–C(7)–C(8) | 113.7(6) |
| C(11)–C(8)–C(7) | 109.3(6) | C(12)–C(11)–C(10) | 117.0(6) | | | | |

[a] Symmetry transformations used to generate equivalent atoms in **3**: #1: $x$, $y - 1$, $z$; #2: $x + 1$, $y$, $z$; #3: $x - 1$, $y$, $z$; #4: $x$, $y + 1$, $z$.

Table 4. Crystal data, data collection, and structure-refinement parameters for **1**–**4**.

| Compound | $[(CuI)_4(bpp)_4]_n$ (**1**) | $[(AgI)_6(bpp)]_n$ (**2**) | $[PbI_2(bpp)]_n$ (**3**) | $[I_3(bppH)]$ (**4**) |
|---|---|---|---|---|
| Formula | $C_{52}H_{56}Cu_4I_4N_8$ | $C_{13}H_{14}Ag_6I_6N_2$ | $C_{13}H_{14}I_2N_2Pb$ | $C_{13}H_{15}I_3N_2$ |
| Formula weight | 1554.81 | 1606.88 | 659.25 | 579.97 |
| Crystal system | tetragonal | monoclinic | monoclinic | orthorhombic |
| Space group | $P4_12_12$ | $C2/c$ | $P2_1$ | $Pbca$ |
| $a$ [Å] | 12.5555(2) | 29.891(6) | 4.5429(9) | 17.245(3) |
| $b$ [Å] | 12.5555(2) | 4.5617(9) | 15.305(3) | 9.4476(19) |
| $c$ [Å] | 36.437(7) | 23.470(5) | 11.925(2) | 21.811(4) |
| $\beta$ [°] | 90 | 123.37(3) | 95.00(3) | 90 |
| Volume [Å$^3$] | 5743.9(16) | 2672.7(9) | 825.9(3) | 3553.5(12) |
| $Z$ | 4 | 4 | 2 | 8 |
| $\rho_{calcd.}$ [Mg m$^{-3}$] | 1.798 | 3.993 | 2.651 | 2.168 |
| $\mu$ [mm$^{-1}$] | 3.651 | 11.245 | 13.937 | 5.265 |
| $F(000)$ | 3008 | 2824 | 588 | 2128 |
| Temperature [K] | 291(2) | 291(2) | 291(2) | 291(2) |
| $\lambda$ (Mo-$K_\alpha$) [Å] | 0.71073 | 0.71073 | 0.71073 | 0.71073 |
| Reflections collected | 10600 | 3371 | 2130 | 8775 |
| Independent reflections | 10284 | 2046 | 1994 | 2977 |
| Goodness-of-fit on $F^2$ | 1.027 | 1.137 | 1.075 | 1.137 |
| Final $R_1$,[a] $wR_2$[b] | 0.0448, 0.0741 | 0.0870,0.2626 | 0.0951, 0.2475 | 0.0514, 0.1060 |
| $R$ indices (all data) | 0.1074, 0.0862 | 0.1030, 0.2813 | 0.0951, 0.2475 | 0.0845, 0.1172 |
| Largest peak, hole [e Å$^{-3}$] | 0.002, 0.000 | 2.318, –3.230 | 6.436, –2.119 | 0.990, –0.973 |

[a] $R_1 = \Sigma||F_o| - |F_c||/\Sigma|F_o|$. [b] $wR_2 = [\Sigma w(|F_o^2| - |F_c^2|)^2/\Sigma w|F_o^2|^2]^{1/2}$. $w = 1/[\sigma^2(F_o)^2 + 0.0297P^2 + 27.5680P]$, where $P = (F_o^2 + 2F_c^2)/3$.

 © 2006 Wiley-VCH Verlag GmbH & Co. KGaA, Weinheim 

4.75. IR (KBr): $\tilde{\nu}$ = 3029 (w), 2922 (w), 1616 (s), 1501 (w), 1406 (w), 1351 (w), 1223 (w), 1029 (m), 816 (m), 618 (w), 552 (w), 442 (w) $cm^{-1}$.

**Nonlinear Optical Measurements:** The optical measurements were performed with linearly polarized 8-ns pulses at 532 nm generated from a frequency-doubled Q-switched Nd:YAG laser. This wavelength is of paramount practical importance in the field of optical limiting as well as the design and fabrication of resonance cavities of lasers. The spatial profiles of the pulses were nearly Gaussian after a spatial filter was employed. A DMF solution of compound **1** was placed in a 1-mm-thick quartz cell for optical limiting measurements. Crystalline samples of **1** are stable toward oxygen, moisture, and laser light. The laser pulse was focused into the cells containing the non-linear medium with a 250-mm focal length lens. The laser beam was divided into two beams. One was used to monitor the incident laser energy meter and the other was focused onto the sample cell. The input and the output energies of the beams were measured with an energy meter (Laser Precision Rjp-735), which were linked to a computer by an IEEE interface.[30,31] The experimental data were collected utilizing a single shot at a rate of 1 pulse per minute to avoid the influence of thermal effects.

**X-ray Crystallography:** Crystallographic data for the title compounds were collected using Mo-$K_\alpha$ radiation ($\lambda$ = 0.71073 Å) on a Rigaku RAXIS-IV image plate area detector. The data were corrected for Lorentz and polarization factors and for absorption by using empirical scan data. The structure was solved with the SHELX program,[32] and refined by full-matrix least-squares methods based on $F^2$, with anisotropic thermal parameters for the non-hydrogen atoms. The hydrogen atoms were located theoretically and not refined. Selected bond lengths and bond angles for **1** (Table 1), **2** (Table 2), and **3** and **4** (Table 3) are given below. Crystal data are summarized in detail in Table 4.

CCDC-252911 (for **1**), -287706 (for **2**), -287707 (for **3**), and -287708 (for **4**) contain the supplementary crystallographic data for this paper. These data can be obtained free of charge from The Cambridge Crystallographic Data Center via www.ccdc.cam.ac.uk/data_request/cif.

## Acknowledgments

This research was funded by the National Natural Science Foundation (grant no. 20371042), the Henan Province Excellent Young Foundation (grant no. 2005002800), and the China Postdoctoral Science Foundation (2003033525). The author also thanks one of the referees, Prof. Richard E. Marsh, and Guang Yang for their helpful comments.

[1] a) J. M. Lehn, *Supramolecular Chemistry: Concepts and Perspectives*, VCH, Weinheim, **1995**, p. 89; b) A. J. Blake, N. R. Champness, P. Hubberstey, W. S. Li, M. A. Withersby, M. Schroder, *Coord. Chem. Rev.* **1999**, *183*, 117–138; c) S. Kitagawa, R. Kitaura, S. I. Noro, *Angew. Chem. Int. Ed.* **2004**, *43*, 2334–2375.
[2] M. Fujita, Y. J. Kwon, S. Washizu, K. Ogura, *J. Am. Chem. Soc.* **1994**, *116*, 1151–1152.
[3] O. R. Evans, W. Lin, *Acc. Chem. Res.* **2002**, *35*, 511–522.
[4] O. Kahn, *Acc. Chem. Res.* **2000**, *33*, 647–657.
[5] a) B. F. Hoskins, R. Robson, D. A. Slizys, *J. Am. Chem. Soc.* **1991**, *119*, 2952–2953; b) S. R. Batten, R. Robson, *Angew. Chem. Int. Ed.* **1998**, *37*, 1460–1494; c) L. Carlucci, G. Ciani, D. M. Proserpio, *Coord. Chem. Rev.* **2003**, *246*, 247–289.
[6] a) S. L. Price, A. J. Stone, J. Lucas, R. S. Rowland, A. E. Thornley, *J. Am. Chem. Soc.* **1994**, *116*, 4910–4918; b) G. R. Desiraju, *Angew. Chem. Int. Ed. Engl.* **1995**, *34*, 2311–2327.
[7] a) C. Hamers, O. Kocian, F. M. Raymo, J. F. Stoddart, *Adv. Mater.* **1998**, *10*, 1366–1369; b) F. M. Raymo, J. F. Stoddart, *Chem. Rev.* **1999**, *99*, 1643–1664; c) H. F. Zhu, J. Fan, T. A. Okamura, W. Y. Sun, N. Ueyama, *Cryst. Growth Des.* **2005**, *5*, 289–294.
[8] M. Fujita, *Acc. Chem. Res.* **1999**, *32*, 53–61.
[9] a) P. H. Svensson, L. Kloo, *Chem. Rev.* **2003**, *103*, 1649–1684; b) L. M. Castro-Castro, M. G. Arnold, *Inorg. Chem.* **2004**, *43*, 4537–4539.
[10] Y. Y. Niu, H. W. Hou, Y. Zhu, *J. Cluster Sci.* **2003**, *14*, 483–493.
[11] Y. Y. Niu, Y. L. Song, H. W. Hou, Y. Zhu, *Inorg. Chem.* **2005**, *44*, 2553–2559.
[12] a) M. J. Plater, M. R. S. J. Foreman, T. Gelbrich, S. J. Coles, M. B. Hursthouse, *J. Chem. Soc., Dalton Trans.* **2000**, 3065–3073; b) S. A. Barnett, N. R. Champness, *Coord. Chem. Rev.* **2003**, *246*, 145–168; c) A. Erxleben, *Coord. Chem. Rev.* **2003**, *246*, 203–228; d) K. Jin, X. Huang, L. Pang, J. Li, A. Appel, S. Wherland, *Chem. Commun.* **2002**, 2872–2873; e) L. Carlucci, G. Ciani, M. Moret, D. M. Proserpio, S. Rizzato, *Chem. Mater.* **2002**, *14*, 12–16.
[13] a) H. W. Hou, Y. L. Song, H. Xu, Y. Wei, Y. T. Fan, Y. Zhu, L. Li, C. Du, *Macromolecules* **2003**, *36*, 999–1008; b) Y. Y. Niu, Y. L. Song, J. Wu, H. W. Hou, Y. Zhu, *Inorg. Chem. Commun.* **2004**, *7*, 471–474; c) Y. Y. Niu, Y. L. Song, H. W. Hou, Y. Zhu, *Inorg. Chim. Acta* **2003**, *355*, 151–156.
[14] Y. Y. Niu, H. G. Zheng, H. W. Hou, X. Q. Xin, *Coord. Chem. Rev.* **2004**, *248*, 169–183.
[15] a) S. Myllyviita, R. Sillanpaa, *J. Chem. Soc., Dalton Trans.* **1994**, 2125–2128; b) B. Corradi, M. R. Cramarossa, T. Manfredini, L. P. Battaglia, G. Pelosi, A. Saccani, F. Sandrolini, *J. Chem. Soc., Dalton Trans.* **1993**, 3587–3591; c) G. Helgesson, S. Jagner, *J. Chem. Soc., Dalton Trans.* **1990**, 2413; d) M. A. S. Goher, A. K. Hafez, T. C. W. Mak, *Polyhedron* **2001**, *20*, 2583–2587.
[16] a) K. R. Kyle, C. K. Ryu, J. A. DiBenedetto, P. C. Ford, *J. Am. Chem. Soc.* **1991**, *113*, 2954–2965; b) M. Vitale, P. C. Ford, *Coord. Chem. Rev.* **2001**, *219–221*, 3–16; c) A. Pfitzner, S. Reiser, H. J. Deiseroth, *Z. Anorg. Allg. Chem.* **1999**, *625*, 2196–2201; d) C. M. Fitchett, P. J. Steel, *New J. Chem.* **2000**, *24*, 945–947; e) L. R. Hanton, K. Lee, *J. Chem. Soc., Dalton Trans.* **2000**, 1161–1166; f) X. Y. Liu, *Chem. Commun.* **1998**, 1149–1150; g) I. M. Müller, T. Röttgers, W. S. Sheldrick, *Chem. Commun.* **1998**, 823–824; h) N. R. Brooks, A. J. Blake, N. R. Champness, P. A. Cooke, P. Hubberstey, D. M. Proserpio, C. Wilson, M. Schröder, *J. Chem. Soc., Dalton Trans.* **2001**, 456–465; i) S. R. Batten, J. C. Jeffery, M. D. Ward, *Inorg. Chim. Acta* **1999**, *292*, 231; j) S. Hu, M. L. Tong, *Dalton Trans.* **2005**, 1165–1167.
[17] a) G. Helgesson, S. Jagner, *J. Chem. Soc., Dalton Trans.* **1990**, 2413–2420; b) A. J. Blake, N. R. Brooks, N. R. Champness, P. A. Cooke, A. M. Deveson, D. Fenske, P. Hubberstey, W. S. Li, M. Schröder, *J. Chem. Soc., Dalton Trans.* **1999**, 2103–2110; c) Q. X. Liu, F. B. Xu, Q. S. Li, X. S. Zeng, X. B. Leng, Y. L. Chou, Z. Z. Zhang, *Organometallics* **2003**, *22*, 309–314; d) M. Massaux, M. T. L. Bihan, R. Chevalier, *Acta Crystallogr., Sect. B* **1977**, *33*, 2084–2091.
[18] a) Y. J. Shi, Y. Xu, Y. Zhang, B. Huang, D. R. Zhu, C. M. Jin, H. G. Zhu, Z. Yu, X. T. Chen, X. Z. You, *Chem. Lett.* **2001**, 678–679; b) Y. J. Shi, L. H. Li, Y. Z. Li, Y. Xu, X. T. Chen, Z. L. Xue, X. Z. You, *Inorg. Chem. Commun.* **2002**, *5*, 1090–1094; c) L. Y. Kong, Z. H. Zhang, T. Okamura, M. J. Fei, W. Y. Sun, N. Ueyama, *Chem. Lett.* **2004**, *33*, 1572–1573.
[19] J. I. Jay, C. W. Padgett, R. D. B. Walsh, T. W. Hanks, W. T. Pennington, *Crystal Growth Des.* **2001**, *1*, 501–507.
[20] V. W. W. Yam, K. K. W. Lo, *Chem. Soc. Rev.* **1999**, *28*, 323–334.
[21] X. H. Bu, H. Liu, M. Du, K. M. C. Wong, V. W. W. Yam, *Inorg. Chim. Acta* **2002**, *333*, 32–40.
[22] J. L. Bredas, C. Adant, P. Tackx, A. Persoons, *Chem. Rev.* **1994**, *94*, 243–278.

 © 2006 Wiley-VCH Verlag GmbH & Co. KGaA, Weinheim 

[23] Z. Burshtein, Y. Kostoulas, H. M. Van, *J. Opt. Soc. Am. B* **1997**, *14*, 2477–2487.
[24] P. Ge, S. H. Tang, W. Ji, S. Shi, H. W. Hou, D. L. Long, X. Q. Xin, S. F. Lu, Q. J. Wu, *J. Phys. Chem. B* **1997**, *101*, 27–31.
[25] G. Sakane, T. Shibahare, H. W. Hou, X. Q. Xin, S. Shi, *Inorg. Chem.* **1995**, *34*, 4785–4789.
[26] H. W. Hou, Y. T. Fan, C. X. Du, Y. Zhu, W. L. Wang, X. Q. Xin, M. K. M. Low, W. Ji, H. G. Ang, *Chem. Commun.* **1999**, 647–648.
[27] S. Shi, W. Ji, S. H. Tang, J. P. Lang, X. Q. Xin, *J. Am. Chem. Soc.* **1994**, *116*, 3615–3616.
[28] Y. P. Sun, J. E. Riggs, *Int. Rev. Phys. Chem.* **1999**, *18*, 43–90.
[29] H. W. Hou, Y. L. Wei, Y. L. Song, L. W. Mi, M. S. Tang, L. K. Li, Y. T. Fan, *Angew. Chem. Int. Ed.* **2005**, *44*, 6067–6074.
[30] M. Sheik-Bahae, A. A. Said, T. H. Wei, D. J. Hangan, E. W. Van Stryland, *IEEE J. Sel. Top. Quantum Electron.* **1990**, *26*, 760–769.
[31] M. Sheik-Bahae, A. A. Said, E. W. Van Stryland, *Opt. Lett.* **1989**, *14*, 955–957.
[32] G. M. Sheldrick, SHELXTL-93, University of Göttingen, Germany, **1993**.

Received: October 27, 2005
Published Online: March 31, 2006

 © 2006 Wiley-VCH Verlag GmbH & Co. KGaA, Weinheim 

DOI: 10.1002/ejic.200501016

# (Diphosphane monosulfide)platinum(II) Complexes for Hydroformylation Reactions: Their Catalytic Activity and a High-Pressure NMR Mechanistic Study

**Antonio Lofù,[a] Piero Mastrorilli,*[a] Cosimo F. Nobile,[a] Gian P. Suranna,[a] Piero Frediani,[b] and Jonathan Iggo[c]**

**Keywords:** Heteroditopic ligands / Hydroformylation / NMR spectroscopy / P,S ligands / Platinum

The neutral complexes of formula [$\kappa^2P,S$-(dppmS)Pt($CH_3$)(Cl)] (**1**), [$\kappa^2P,S$-(dppeS)Pt($CH_3$)(Cl)] (**2**) and [$\kappa^2P,S$-(dpppS)Pt($CH_3$)(Cl)] (**3**) [dppmS = $Ph_2PCH_2P(S)Ph_2$; dppeS = $Ph_2P(CH_2)_2P(S)Ph_2$; dpppS = $Ph_2P(CH_2)_3P(S)Ph_2$] are active catalyst precursors for the hydroformylation of 1-octene in methyl isobutyl ketone. The order of reactivity found is **3** > **2** > **1**. Surprisingly, the cationic complexes [$\kappa^2P,S$-(dppeS)Pt($CH_3$)($CH_3CN$)]$BF_4$ (**4a**) and [{$\kappa P,\mu$-$\kappa S$-(dppeS)Pt($CH_3$)}$_2$][$BF_4$]$_2$ (**5**) are less active than the analogous neutral complex **2**. High-pressure NMR studies revealed that, at 20 °C under 1 to 50 bar of syngas, and in the presence of $SnCl_2$, both **2** and **4a** react immediately to form the same acetyl complex (**8**). However, in the absence of $SnCl_2$, the methyl carbonyl complex [$\kappa^2P,S$-(dppeS)Pt($CH_3$)(CO)]$^+$ (**9**), which is formed from **4a** and CO, does not undergo insertion to give the acetyl complex, even under 50 bar of syngas. Thus, the role of $SnCl_2$ is not only to create a vacant site for CO coordination and to lower the energy barrier for the hydrogenolysis, but also to assist migration of the alkyl group in the CO insertion step. High-pressure NMR studies of the working reaction solution, under steady-state conditions, found no evidence for intermediates in which the phosphane sulfide group shows hemilabile behaviour during catalysis.

(© Wiley-VCH Verlag GmbH & Co. KGaA, 69451 Weinheim, Germany, 2006)

## Introduction

Hydroformylation of alkenes is one of the most important catalytic reactions in industry, which runs plant processes with Co- or Rh-based catalysts.[1] On the other hand, there is an increasing interest in platinum-catalysed olefin hydroformylation, mainly devoted to the optimisation of chemo- and regioselectivity of the reaction and the synthesis of linear aldehydes.[2]

Since Parshall's pioneering work using $PtCl_2$ in the ionic liquid [$(NEt_4)SnCl_3$],[3] many catalytic systems,[4–7] including some specifically suited to enantioselective catalysis,[8–15] have been developed. A common feature of all these systems is the use of $SnCl_2$ in combination with the $Pt^{II}$ salt or complex. Several mechanistic studies on the catalytic cycle[16–19] and on the role of the $SnCl_2$[20,21] have appeared, and these have concluded that the $SnCl_2$ generates trichlorostannate species by reaction with chloroplatinum(II) catalyst precursors and promotes the hydrogenolysis of the Pt–acetyl intermediate. The use of chelating diphosphanes brings about considerable activity enhancement, especially in the case of dppb,[22] and Scrivanti et al. have performed a mechanistic study intended to explain why the seven-membered metallacycle is the most efficient.[23]

Heteroditopic ligands are chelating compounds endowed with different chemical functionalities capable of coordinating to a metal centre. The very different *trans* effects produced by the dissimilar donor atoms in these ligands offer the potential to introduce widely different activity and selectivity at selected coordination sites in metal complexes and has resulted in such ligands receiving increasing attention in the field of organometallic chemistry and catalysis.[24] Interest in P^S heteroditopic ligands[25–31] is driven by the ability of sulfur to coordinate strongly to soft metal centres.[32,33] In the framework of our studies into the coordination chemistry of heteroditopic ligands,[34,35] we recently became interested in the monosulfides of diphosphane ligands (P^PS)[36] and have studied the synthesis and reactivity of neutral and cationic methyl complexes of platinum(II) with the P^PS heteroditopic ligands dppmS and dppeS.[37]

The heteroditopic behaviour of the diphosphane monosulfide (P^PS) ligands has recently been exploited in Rh- and Ir-catalysed methanol carbonylation.[38,39] Considerably less attention has been paid to the use of Pt complexes

[a] Department of Water Engineering and of Chemistry (DIAC) Polytechnic of Bari, and C.N.R. ICCOM-Sezione di Bari, 4 Via Orabona, 70125 Bari, Italy
Fax: +39-080-596-3611
E-mail: p.mastrorilli@poliba.it
[b] Department of Organic Chemistry, University of Florence, 13 Via della Lastruccia, 50019 Sesto Fiorentino (FI), Italy
[c] Department of Chemistry, University of Liverpool, P. O. Box 147, L69 7ZD Liverpool, UK

 © 2006 Wiley-VCH Verlag GmbH & Co. KGaA, Weinheim 

of heteroditopic ligands as catalysts for olefin hydroformylation.[7,40,41] Here we report our results using both neutral and cationic methylplatinum complexes of diphosphane monosulfide ligands in combination with $SnCl_2$ as catalysts for the hydroformylation of 1-octene. In particular, we have focused our interest on the roles of the heteroditopic ligand and the cocatalyst, and on the effects of chelating ring size in/on the catalytic reaction. The study has been complemented by high-pressure NMR experiments aimed at gaining insights into the reaction mechanism.

## Results and Discussion

### Synthesis

The neutral and cationic methylplatinum(II) complexes of diphosphane monosulfides used in this study are depicted in Figure 1. Neutral complexes of general formula [$\kappa^2$*P*,*S*-(P^PS)Pt($CH_3$)Cl] [P^PS: $Ph_2PCH_2P(S)Ph_2$, dppmS (**1**); $Ph_2P(CH_2)_2P(S)Ph_2$, dppeS (**2**); $Ph_2P(CH_2)_3P(S)Ph_2$, dpppS, (**3**)] were synthesised by reaction of [(cod)Pt($CH_3$)(Cl)] (cod = 1,5-cyclooctadiene) with one equivalent of the relevant ligand.[37] Reaction of **2** with silver tetrafluoroborate in MeCN affords the cationic complex [$\kappa^2$*P*,*S*-(dppeS)Pt($CH_3$)($CH_3CN$)][$BF_4$] (**4a**), in which the chloride is replaced with acetonitrile. The cationic dimer [{$\kappa$*P*,$\mu$-$\kappa$*S*-(dppeS)Pt($CH_3$)}$_2$][$BF_4$]$_2$ (**5**), in which the sulfur atoms bridge the two platinum atoms, is obtained quantitatively on heating solid **4a** at 363 K under vacuum, as described previously.[37] Reaction of [(cod)Pt($CH_3$)(Cl)] with two equivalents of dpppS affords [*trans*-($\kappa$*P*-dpppS)$_2$Pt($CH_3$)(Cl)] (**6**) in high yield, in which the two dpppS ligands are coordinated through the phosphorus atoms only.

### Hydroformylations

Preformed complexes **1**–**6** were used as catalyst precursors for the hydroformylation of 1-octene (Scheme 1) in the presence of five equivalents of $SnCl_2 \cdot 2H_2O$ as cocatalyst, in methyl isobutyl ketone as solvent (Table 1). Alternatively, catalysts were formed in situ from [(cod)Pt($CH_3$)Cl] or [(cod)$PtCl_2$] and the appropriate ligand (this experimental procedure has been validated; compare entries 4 and 7 with entries 3 and 6 of Table 1). The progress of the reaction was monitored by gas consumption. The reaction times of all catalytic tests were kept below 4 h in order to minimise the formation of side products deriving from aldol condensation between formed aldehydes and between aldehyde and solvent. In all tests, the amount of condensation products was less than 10%, while the regioselectivity towards normal aldehyde ranged from 79 to 91%.

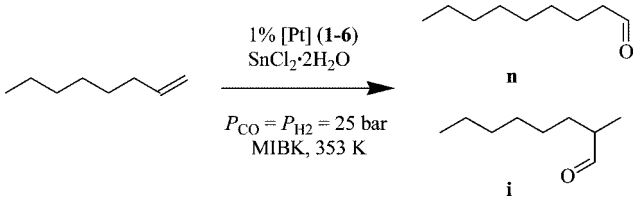


Scheme 1. Hydroformylation of 1-octene.

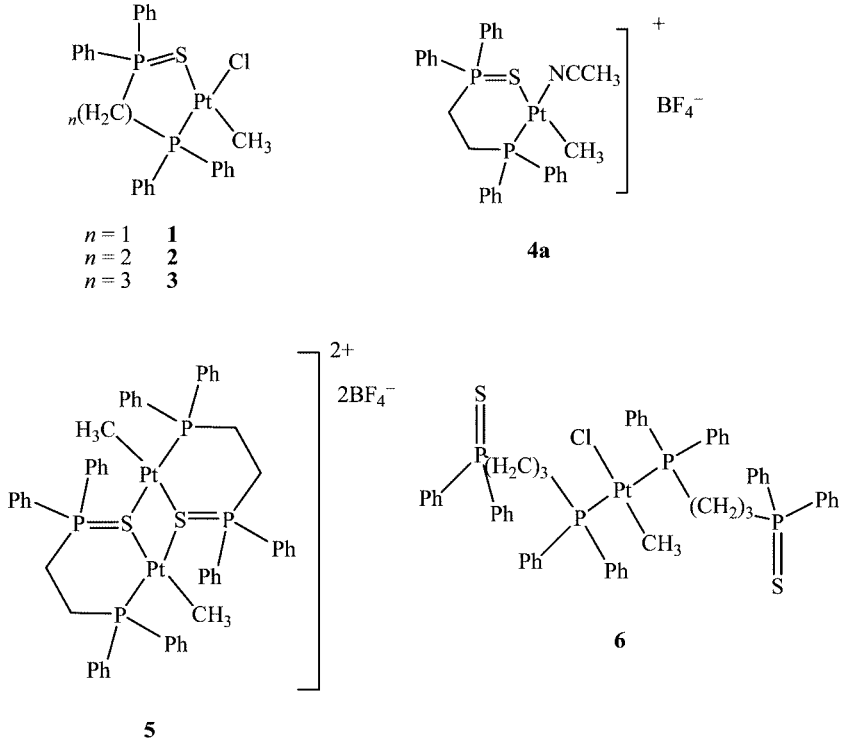


Figure 1. Cationic and neutral complexes used in catalysis.

 © 2006 Wiley-VCH Verlag GmbH & Co. KGaA, Weinheim 

Table 1. Platinum-catalysed hydroformylation of 1-octene.[a]

| Entry | Catalyst | *t* [h] | Conversion [%] | Yield of aldehydes [%] | Regioselectivity[b] [%] | TOF[c] [$h^{-1}$] |
|---|---|---|---|---|---|---|
| 1 | **1** | 4 | 63 | 25 | 81 | 6 |
| 2 | dppe + [(cod)Pt($CH_3$)Cl] | 4 | 100 | 39 | 77 | 10 |
| 3 | **2** | 3.5 | 100 | 56 | 85 | 16 |
| 4 | dppeS + [(cod)Pt($CH_3$)Cl] | 3 | 100 | 49 | 84 | 16 |
| 5 | dppp + [(cod)Pt($CH_3$)Cl] | 1 | 100 | 50 | 66 | 50 |
| 6 | **3** | 1.25 | 100 | 60 | 79 | 48 |
| 7 | dpppS + [(cod)Pt($CH_3$)Cl] | 1 | 100 | 54 | 82 | 54 |
| 8 | dppb + [(cod)Pt($CH_3$)Cl] | 1 | 100 | 51 | 76 | 51 |
| 9 | **6** | 4 | 76 | 70 | 91 | 18 |
| 10 | dppb + [(cod)Pt($CH_3$)Cl] (2:1 mol/mol) | 4 | 100 | 46 | 81 | 12 |
| 11 | dppeS + [(cod)$PtCl_2$] | 2 | 100 | 33 | 75 | 17 |
| 12[d] | dppeS + [(cod)$PtCl_2$] | 2.5 | 90 | 60 | 85 | 24 |
| 13 | dppp + [(cod)$PtCl_2$] | 1 | 100 | 38 | 50 | 38 |
| 14 | **4a** | 3.5 | 52 | 27 | 87 | 8 |
| 15 | **5** | 3.5 | 52 | 32 | 89 | 9 |
| 16[e] | **4a** | 4 | 3 | 0 | – | – |

[a] Reaction conditions: olefin (1-octene: 5.8 mmol), olefin/Pt/Sn = 100:1:5; $T$ = 353 K, $P(CO) = P(H_2)$ = 25 bar; solvent: methyl isobutyl ketone (5.8 mL). The reaction times are those required to reach the stated conversions. [b] Selectivity: *n*-nonanal/total aldehydes. [c] TOF: Turn over frequency as (mol aldehydes)(mol Pt)$^{-1}$(time)$^{-1}$. [d] Pt/$SnCl_2$ = 1:1. [e] Reaction performed in the absence of $SnCl_2$.

### Effect of Ring Size

In agreement with previous reports on the effect of chelate ring size in diphosphaneplatinum(II)-based catalytic systems,[42] we found a pronounced increase in both activity and selectivity as the ring size is increased. Thus, **1** (five-membered platinacycle) affords incomplete substrate conversion after 4 h, and 25% yield in nonanals (Table 1, entry 1), whereas with **2** (six-membered platinacycle) we observed complete conversion after 3.5 h with a 56% yield in nonanals (entry 3). Complete conversion after 1.25 h and 60% yield in aldehydes (Table 1, entry 6) was observed with **3**, thereby clearly demonstrating the beneficial effects of a larger metallacycle. This effect has previously been reported and ascribed to a lowering in the activation energy for the hydrogenolysis step.[22,23]

### Effect of the Heteroditopic Ligand

The performance of catalyst systems incorporating heteroditopic P^PS ligands is comparable with that of analogous systems containing P^P ligands that give equally sized platinacycles, although the P^P complexes were found to be more stable under hydroformylation conditions, no Pt black being observed in the products at the end of the reaction, in contrast to the P^PS-containing systems.[43] Thus, using catalysts formed in situ from [(cod)Pt($CH_3$)Cl] and the appropriate ligand the P^PS ligands give slightly more regio- and chemoselective catalyst systems (compare entries 1 and 2, 4 and 5, and 7 and 8 of Table 1), although the P^P ligands show comparable or greater activity. Replacement of a diphosphane by a diphosphane monosulfide ligand on the catalyst precursor will reduce the electronic density at the metal centre, which should favour Markovnikoff-type hydride attack on the olefin to give the linear Pt–alkyl intermediate and account for the observed increase in the *n*:*iso* ratio. The diminished electron density on Pt might also be expected to retard hydrogenolysis thereby lowering the activity of the catalyst, and this is indeed observed.

### Effect of Ligand/Metal Ratio

We have also investigated the effect of the ligand/metal ratio using both P^PS and P^P ligands. Thus, with [*trans*-(κ*P*-dpppS)$_2$Pt($CH_3$)Cl] (**6**) as the catalyst precursor the reaction gave the highest chemoselectivity towards hydroformylation products (70% aldehydes), the remainder being octane and internal octenes, with the highest regioselectivity towards *n*-nonanal (91%). However, the catalytic activity was lower, with conversion of 76% in 4 h (Table 1, entry 9) compared to that obtained using a ligand/metal ratio of 1 (Table 1, entry 6). A similar behaviour was observed for the P^P system using a mixture of [(cod)Pt($CH_3$)Cl] and 1,4-bis(diphenylphosphanyl)butane (dppb) as catalyst precursor (Table 1, entries 8 and 10). Once again, activity is lower and selectivity to linear product higher. This is not surprising as the 2:1 ligand to metal ratio may lead to the blocking of coordination sites, thereby reducing the activity,[5,42] and increase the steric hindrance at the metal, thus improving the regioselectivity.[5,44]

### Role of $SnCl_2$

Given that cationic $Pt^{II}$ species are normally invoked in the catalytic cycle, and the role of the $SnCl_2$ is widely believed to be the generation of such cationic species by abstraction of $Cl^-$ to form $SnCl_3^-$, we tested the mono- and dinuclear cationic complexes **4a** and **5** in the catalysis and were surprised to find that these complexes gave much lower activity and productivity than **2** (27% and 32% yield of nonanals after 3.5 h for **4a** and **5**, respectively, see en-

 © 2006 Wiley-VCH Verlag GmbH & Co. KGaA, Weinheim 

tries 14 and 15 of Table 1) even though $SnCl_2$ was present in the reactions. The similar catalytic activities exhibited by **4a** and **5** suggest the formation of the same active species from these cationic precursors, i.e. MeCN is not retained at Pt and does not interfere in the catalysis. In the absence of $SnCl_2$ cocatalyst (Table 1, entry 16) **4a** is almost inactive. Thus, independent of the charge on the $Pt^{II}$ precursor, the addition of $SnCl_2$ is necessary to trigger the hydroformylation,[5,15] and the formation of $SnCl_3^-$ (which is possible starting from **2** but not from **4a** or **5** since chloride is not available in the latter systems) further increases the reaction rate.

Interestingly, using [(cod)$PtCl_2$] as the platinum source (and 5 equiv. of $SnCl_2$) affords catalyst systems that are less chemo- and regioselective than those using [(cod)Pt-($CH_3$)Cl], from which only one equivalent of $SnCl_3^-$ can be obtained by halide abstraction, as the Pt source (compare entries 4 and 11 and 5 and 13 of Table 1). However, using equimolar amounts of Sn and Pt (Table 1, entry 12) and [(cod)$PtCl_2$] as the Pt source affords higher chemo-and regioselectivities, similar to those obtained using **2** with a Sn/Pt molar ratio of 5:1. This seems to indicate a detrimental effect of a Sn/Pt molar ratio higher than 1 when using [(cod)$PtCl_2$] as the Pt source.

### Summary of the Catalytic Results

The use of heteroditopic P^PS ligands in Pt/Sn olefin hydroformylation systems affords catalysts that compare favourably with analogous systems that use P^P ligands. No significant variation in regioselectivity was observed using cationic vs. neutral complexes as catalyst precursors, thus indicating that regioselectivity is established in a $Pt^{II}$ intermediate that is identical for both cationic and neutral catalyst precursors. For both P^P and P^PS systems, activity is related to ring size, with seven-membered rings giving the most active systems. The correlation of activity with ring size is consistent with a chelating structure being maintained in the rate-determining steps of the catalysis, although it has been suggested that the dppb may, alternatively, form oligomeric/polymeric metal species.[23] The presence of $SnCl_2$ is essential to the generation of effective catalyst systems from both neutral and cationic precursors, thus indicating that the role of $SnCl_2$ is more than simply the generation of an active site at Pt by removal of $Cl^-$. However, the presence of excess $SnCl_3^-$ is detrimental to the catalysis under our conditions.

### High-Pressure NMR Study

A high-pressure NMR study of the reaction was performed using both a HP-NMR bubble column reactor developed in Liverpool[45] and conventional sapphire tubes with the aim of gaining additional insight into the mechanistic differences responsible for the reactivities of the neutral (**2**) and cationic (**4a**) complexes. Except where otherwise stated, [$D_6$]acetone was used as solvent for this study since the catalytic reaction is known to proceed smoothly in ketonic solvents.

### HP-NMR Behaviour of the Catalyst Precursors 2 and 4a

Compound **2** is poorly soluble in acetone. However, upon addition of $SnCl_2$ (Sn/Pt = 5:1), rapid dissolution of the solids occurred, accompanied by a colour change from pale straw yellow to dark orange, indicating the formation of a new species (**7a**; Scheme 2), which we propose to be the $SnCl_2$ adduct of **2**. Thus, the $^1H$ NMR spectrum of **7a** (Table 2, entry 2) shows a resonance at $\delta_H$ = 0.43 ppm, which can be assigned to a methyl group directly bound to Pt. The $^{31}P\{^1H\}$ NMR spectrum of **7a** shows resonances at similar chemical shifts to those of **2** in $CD_2Cl_2$. However, the $^3J_{P,P}$, $^2J_{P,Pt}$ and $^1J_{P,Pt}$ coupling constants are significantly different from those of **2**, clearly indicating the formation of a new methylplatinum complex. The chemical shifts and coupling constants (Table 2, entry 2) indicate that the methyl group remains *trans* to the phosphane sulfide donor. Thus, Tóth et al. have reported a $^1J_{P,Pt}$ value of 1628–1836 Hz for $CH_2PPh_2$ *trans* to methyl in the structurally similar diphosphane complexes [(BDPP)Pt($CH_3$)(L)] (L = Cl, $SnCl_3$),[18] to be compared with $^1J_{P,Pt}$ = 3869 Hz in **7a**. We can suggest at least three possibilities for the group occupying the fourth coordination site at Pt in **7a**: i) acetone, in which case $SnCl_3^-$ is present as the counterion; ii) $SnCl_3^-$ directly bonded to platinum; or iii) Pt-bound $SnCl_2$. We can discount the latter hypothesis since, in an otherwise identical experiment but using one equivalent of $SnCl_2$, complex **7a** was again obtained in high yield.

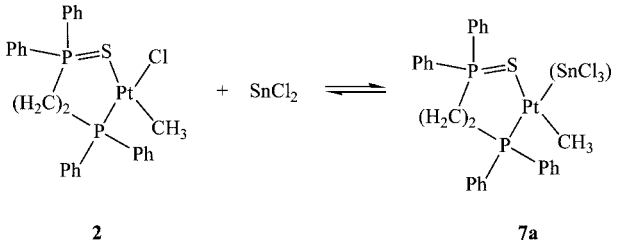


**2** **7a**

Scheme 2.

In an attempt to differentiate the remaining possibilities we measured the $^{31}P\{^1H\}$NMR spectrum of **4a** in [$D_6$]acetone since we believed that acetone would displace the coordinated MeCN to give [Pt(dppeS)($CH_3$)(acetone)]$^+$, the cation of the first hypothesis, as a result of mass action. In this experiment, in addition to the resonances of **4a** and its dimer **5**,[37] two new resonances were observed in the $^{31}P\{^1H\}$NMR spectrum at chemical shifts, and with coupling constants, different to those of **2** + $SnCl_2$ reported above (compare entries 2 and 3 in Table 2). We assign these resonances to the new complex [Pt(dppeS)($CH_3$)(acetone)]$^+$ (**4b**). The larger value of $^1J_{P,Pt}$ (5003 Hz in **4b** vs. 4606 Hz in **2**) confirms the displacement of the acetonitrile by acetone, a ligand with a weaker *trans* influence. These observations allow us to exclude **4b** or **5** as the complex **7a** and

 © 2006 Wiley-VCH Verlag GmbH & Co. KGaA, Weinheim 

Table 2. Main $^{31}P\{^1H\}$ NMR spectroscopic data for the complexes (80 MHz, [$D_6$]acetone if not otherwise specified, 290 K).

| Entry | | Complex formed | $\delta_P$ | $\delta_{PS}$ | $^3J_{P,P}$ | $^2J_{P,Pt}$ | $^1J_{P,Pt}$ | Other data |
|---|---|---|---|---|---|---|---|---|
| 1[37] | **2** in $CH_2Cl_2$ | | 10.1 | 36.6 | 8 | 58 | 4606 | poorly soluble in acetone |
| 2 | **2** + $SnCl_2$ | [(dppeS)Pt($CH_3$)($SnCl_3$)] (**7a**) | 10.4 | 36.7 | 18 | 74 | 3869 | $^1$H NMR: $\delta_{CH_3}$ = 0.43 ppm (d, $^3J_{H,P}$ = 6, $^2J_{H,Pt}$ = 76 Hz) |
| 3 | **4a** in acetone | [(dppeS)Pt($CH_3$)(acetone)]$^+$ (**4b**) (plus **4a** and **5**) | 6.2 | 39.4 | 5 | 56 | 5003 | |
| 4 | **2** +$SnCl_2$ + $^{13}$CO (4.5 bar) | [(dppeS)Pt{C(O)$CH_3$}(L)]$^{n+}$ (**8**) | –1.4 | 38.8 | 17 | 83 | 4001 | $^1$H NMR: $\delta_{CH_3}$ = 1.77 ppm (s). $^{13}C\{^1H\}$ NMR: $\delta_{CO}$ = 224 ppm (s, $^1J_{C,Pt}$ = 815 Hz) |
| 5 | **2** + $SnCl_2$ + syngas (50 bar) | **8** | –1.4 | 38.8 | 16 | 83 | 4005 | |
| 6[37] | **4a** in $CH_2Cl_2$ | **5** | 16.1 | 38 | | | 4331 | |
| | | (plus **4a**) | 7.6 | 39.7 | 7 | 55 | 4695 | |
| 7 | **4a** + $SnCl_2$ | [(dppeS)Pt($CH_3$)($SnCl_2$)]$^+$ (**7b**) | 9.6 | 35.6 | 17 | 72 | 4036 | |
| 8 | **4a** + $SnCl_2$ + syngas (50 bar) | **8** | –1.4 | 38.8 | 16 | 83 | 3995 | |
| 9 | **4a** + $^{13}$CO (6.7 bar) | [(dppeS)Pt($CH_3$)(CO)]$^+$ (**9**) | 10.8 | 40.5 | 12 | 59 | 3367 | $^1$H NMR: $\delta_{CH_3}$ = 0.57 ppm (d, $^3J_{H,P}$ = 6.4 Hz. $^{13}C\{^1H\}$ NMR: $\delta_{CO}$ = 177 ppm (d, $^2J_{C,P}$ = 147 Hz) |
| 10 | **4a** + syngas (50 bar) | **9** | 10.8 | 40.5 | n.d. | 59 | 3367 | |
| 11[a] | **2** (or **4a**) + $SnCl_2$ + 1-octene + syngas (50 bar) | **10** | 0.0 | 38.7 | n.d. | n.d. | 4208 | |
| | | plus **11** | 9.0 | 40.6 | n.d. | n.d. | 4001 | |

[a] At 353 K; n.d. = not determinable.

support the hypothesis of $SnCl_3^-$ directly bonded to platinum. Moreover, the reduction of $^1J_{P,Pt}$, from 4606 Hz in **2** to 3869 Hz in **7a** is consistent with displacement of chloride by $SnCl_3^-$, a ligand with a stronger *trans* influence. However, the $^{119}Sn\{^1H\}$ spectrum of **7a** shows no resonance in the region $\delta$ = –300 to +300 ppm over the temperature range 298–213 K, which suggests that the $SnCl_3^-$ ligand is involved in a fluxional process.[46] Support for this hypothesis is the marked broadness of the $^{31}P\{^1H\}$ signal of the P *trans* to this site ($\Delta\nu_{1/2}$ = 110 Hz, $T$ = 290 K).

Finally, reaction of an acetone solution of **4a** (comprising **4a**, **4b** and **5**) with $SnCl_2$ gives a bright yellow solution of a new complex (**7b**) quantitatively (by $^{31}P\{^1H\}$ NMR spectroscopy; Table 2, entry 7). The NMR spectroscopic data for **7b** are similar to those of **7a** with the exception of $^1J_{P,Pt}$, which increases from 3869 Hz in **7a** to 4036 Hz in **7b**, thus indicating that **7a** and **7b** have a similar overall structure but a different ligand, of similar *trans* influence, occupying the fourth coordination site at Pt. Since $Cl^-$ is not present in acetone solutions of **4a**, thereby precluding the formation of $SnCl_3^-$, we suggest this ligand is $SnCl_2$,[47] i.e. **7a** is the adduct formed between [Pt(dppeS)($CH_3$)Cl] (**2**) and $SnCl_2$, and **7b** its cationic analogue [Pt(dppeS)($CH_3$)($SnCl_2$)]$^+$. Again, no clear $^{119}$Sn NMR resonance could be observed in the case of **7b**, presumably due to fluxionality, as confirmed by the broadness of the $^{31}P\{^1H\}$ NMR signals.

Both **7a** and **7b** react under 50 bar of syngas at 290 K to give **8** (quantitatively by $^{31}P\{^1H\}$ NMR spectroscopy), which is an acyl complex derived from CO insertion into the Pt–$CH_3$ bond (Table 2, entries 5 and 8). In a separate experiment, **7a** was treated with $^{13}$CO (4.5 bar) at 290 K in a sapphire tube. After pressurizing with $^{13}$CO, the dark-orange colour of **7a** progressively lightened as $^{13}$CO diffused into solution to become straw yellow after about 20 min, when $^{31}P\{^1H\}$ NMR spectroscopy confirmed the formation of **8**. The $^1$H NMR spectrum (Table 2, entry 4) shows the disappearance of the Pt–C$H_3$ signal of **7a** to be replaced by a sharp doublet at $\delta$ = 1.77 ppm attributable to the methyl group of the acyl moiety ($^2J_{C,H}$ = 5 Hz).[48] In agreement with this assignment, the $^{13}C\{^1H\}$ NMR spectrum of this sample shows a sharp singlet at $\delta_C$ = 224 ppm flanked by platinum satellites, as expected for a Pt–$^{13}$C(O)$CH_3$ group. The magnitude of the $^1J_{P,Pt}$ coupling constant (4001 Hz) is not consistent with the acetyl group occupying the site *trans* to P, for which Tóth has reported a value of about 1400 Hz for the analogous diphosphane complexes [(BDPP)Pt(COMe)L]$^{n+}$ (L = Cl, $n$ = 0;L = CO, $n$ = 1). Therefore, we propose that the acetyl group is *trans* to the sulfur donor,[18] a disposition also observed in related dppeS–Rh complexes.[38]

The identity of the ligand occupying the fourth coordination site on Pt is more difficult to establish. The value of $^1J_{P,Pt}$ in **8** is significantly smaller than that observed in **4b** (5003 Hz), which seems to exclude acetone. No signal attributable to a Pt–CO group is observed in the $^{13}C\{^1H\}$ NMR spectrum, coupling between phosphorus and $^{13}$CO is not observed, and the $^{31}$P NMR chemical shift and coupling constants are unchanged on purging the solution with nitrogen,[49] observations that exclude both tightly bound and labile CO as the ligand at the fourth site on Pt. Starting from **4a**, $SnCl_3^-$ cannot be present, which therefore excludes $SnCl_3^-$. However, an identical $^{31}P\{^1H\}$ NMR spectrum is obtained starting from **2** and one equivalent of $SnCl_2$, when $SnCl_2$ is presumably reacted (Figure 2). Thus we cannot assign with certainty the ligand occupying the fourth site on Pt in **8**. This contrasts with the analogous P^P acylplatinum(II) system[18,19] in which the fourth coordination site is occupied by CO even at low pressure.

 © 2006 Wiley-VCH Verlag GmbH & Co. KGaA, Weinheim 

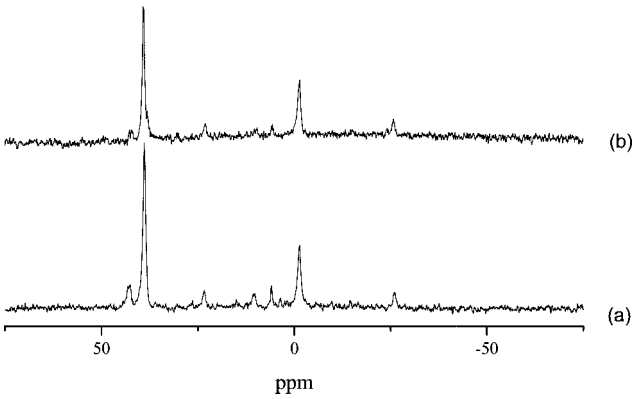


Figure 2. $^{31}P\{^{1}H\}$ HP-NMR spectra of the acyl complex **8** obtained from **2** (a) or **4a** (b) (entries 5 and 8 of Table 2 respectively).

The ready formation of the acetyl complex **8** from the reaction of either **2** or **4a** with CO in the presence of $SnCl_2$ (Scheme 3) contrasts with our previous report of the formation of $[Pt(dppeS)(CH_3)(CO)][BF_4]$ (**9**), which is inert to methyl migration in $CH_2Cl_2$, in the absence of $SnCl_2$.[37] We have confirmed this result for **4a** in acetone (Scheme 4), which gives **9** even under 6.7 bar of $^{13}CO$ or 50 bar of syngas (Table 2, entries 9 and 10). The dependence of the CO insertion reaction on $SnCl_2$ for P^PS ligand complexes contrasts with the situation for $Pt^{II}$ complexes of diphosphane[18,19,50] or P^N ligands,[24] for which no such requirement is reported. The reluctance of CO to insert into the Pt–alkyl bond in the absence of $SnCl_2$ provides a ready explanation for the initially surprising inactivity of the cationic complex **4a** in olefin hydroformylation in the absence of a co-catalyst (entry 6 of Table 1).

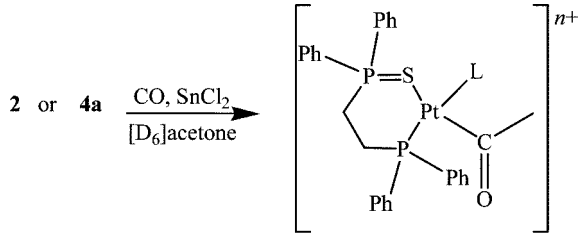


**8**

Scheme 3.

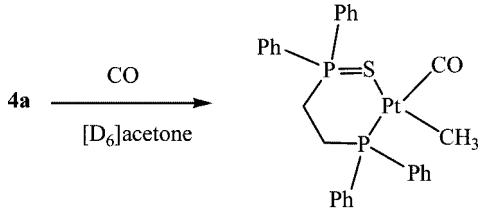


**9**

Scheme 4.

## HP-NMR Behaviour of the Working Catalyst

The understanding of the chemistry of the catalyst precursors outlined above provides a firm basis for an HP-NMR study of the working catalyst. Figure 3 shows the $^{31}P\{^{1}H\}$ HP-NMR spectra, recorded in our bubble column reactor at 353 K and 50 bar of syngas, of solutions prepared from either **2** or **4a** (0.010 M), $SnCl_2$ (5 equiv.) and 1-octene (100 equiv.). The spectra of both solutions show resonances of the same two species (**10** and **11**). The similarity of the $^{31}P\{^{1}H\}$ NMR spectroscopic data of **10** and **8** (Table 2, entries 4 and 11) allow us to formulate **10** as the acyl complex $[Pt(dppeS)\{C(O)(C_8H_{17})\}(L)]^{n+}$, in which an octyl chain derived from octene is present, as required by the catalysis. The close similarity of $^{1}J_{P,Pt}$ in **8** and **10** is consistent with the same L in both complexes. The identity of **11** ($\delta_P$ = 9.0, $\delta_{PS}$ = 40.6 ppm; $^{1}J_{P,Pt}$ = 4001 Hz) is less certain. The significant difference in the $^{31}P\{^{1}H\}$ NMR spectra of **10** and **11** is not consistent with **11** also being an acyl complex, with **10** and **11** being the acyls derived from the *n*- and *iso*-alkyl intermediates. The similarity in the $^{31}P\{^{1}H\}$ NMR spectroscopic data of **11** with those of the methyl complexes **7a** and **7b** suggests **11** as the octyl intermediate $[Pt(dppeS)(C_8H_{17})(L)]^{n+}$ (Scheme 5). The resonances of **10** and **11** were not observed in an analogous experiment using **4a** as the catalyst precursor in the absence of $SnCl_2$, consistent with **10** and **11** being intimately associated with the working catalyst (the lack of reactivity in the absence of $SnCl_2$ is discussed above). Furthermore we changed the reacting gas from $CO/H_2$ to $H_2$ (50 bar), in order to convert the working catalyst into a hydride species, but we observed only the slow disappearance of the resonances of both **10** and **11**. Furthermore, no high-field signals, ascribable to hydrides, were observed in the $^{1}H$ HP-NMR spectrum, consistent with our attribution of these complexes to the nonanoyl- and octylplatinum(II) resting states.

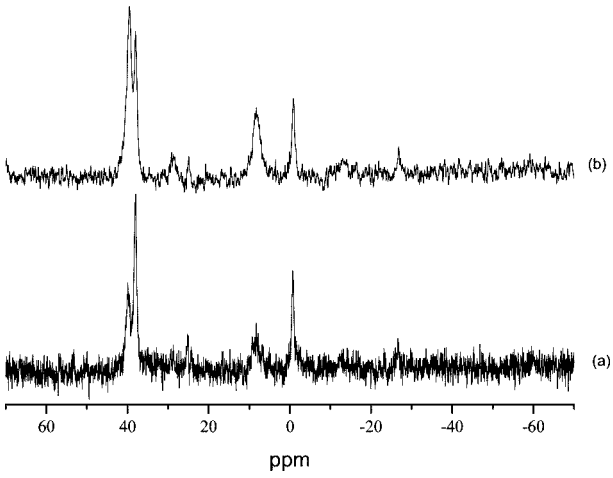


Figure 3. In situ $^{31}P\{^{1}H\}$ HP-NMR spectra showing the steady state of catalytic reactions using **2** (a) or **4a** (b).

The observation of both resting states is consistent with both CO insertion and hydrogenolysis being slow in this catalytic system, since the use of a bubble column reactor allows us to eliminate artifacts resulting from poor gas delivery to the reaction.

 © 2006 Wiley-VCH Verlag GmbH & Co. KGaA, Weinheim 

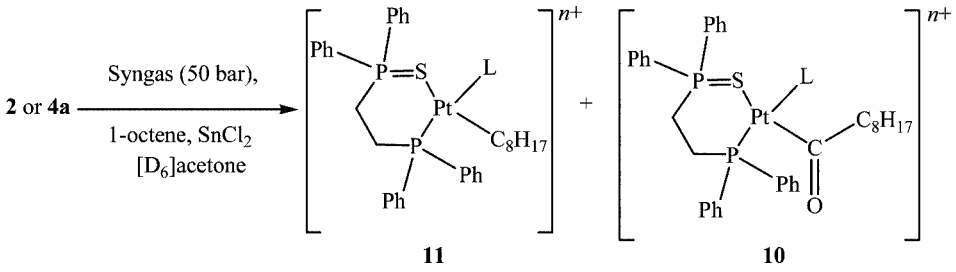


**11** **10**

Scheme 5.

## Conclusions

Complexes **1**, **2** and **3** in the presence of $SnCl_2$ are active catalyst precursors for the hydroformylation of 1-octene with yields ranging from 25 to 60% and regioselectivity in linear aldehyde higher than 79%. The reactivity is dependent on the ring size of the platinacycle, with the seven-membered ring being the most active. Tin halides have been shown to fulfil three essential roles in the Pt/diphosphane monosulfide/$SnCl_2$ catalysed hydroformylation of higher alkenes: (i) removal of halide from the platinum centre as $SnCl_3^-$, which can then (ii) function as a labile ligand, and (iii) for diphosphane-monosulfide-based catalyst systems, tin(II) chloride plays an essential additional role in activating the alkyl complex for the CO insertion step, presumably by coordination to the CO oxygen. The observation of both the alkyl and acyl intermediates in solutions of the working catalyst, and in the absence of the gas delivery problems that are often encountered in sapphire NMR tubes, indicates that, at least for the diphosphane monosulfide studied here, there are two slow steps in the reaction. It is interesting to note that tin halides appear to play a role in accelerating *both* slow steps.

## Experimental Section

All reactions (at least two replicates) were carried out under nitrogen using standard Schlenk techniques. Methyl isobutyl ketone was refluxed with a little $KMnO_4$, washed with aq. $NaHCO_3$, dried over $CaCl_2$ and purified by passing through a small column of activated alumina and freshly distilled prior to use. 1-Octene was purchased from Acros and purified by percolation through a short plug of neutral alumina prior to use.

$SnCl_2{\cdot}2H_2O$ was purchased from Carlo–Erba and used as received. The ligand dpppS was prepared by adapting the procedure published for dppmS or dppeS.[36] Complexes **1**, **2**, **3**, **4a** and **5** were synthesised as described.[37] Anhydrous $SnCl_2$ for the mechanistic study was purchased from Aldrich. $CDCl_3$ was purchased from Aldrich and [$D_6$]acetone from Cambridge.

C,H,S elemental analyses were carried out with a Eurovector CHNS-O Elemental Analyser. IR spectra were recorded with a Bruker Vector 22 instrument. Chromatographic analyses were carried out on Hewlett–Packard 6890 instruments using a 19091Z-236 HP-1 methylsiloxane capillary column (60.0 m × 250 μm × 1.00 μm) or a HP 19091J-413 HP-5 phenylmethyl siloxane column (30.0 m × 320 μm × 0.25 μm; injector temperature: 553 K; FID temperature: 553 K; carrier: nitrogen). GCMS data (EI = 70 eV) were acquired with an HP 6890 instrument using an HP 19091S-433 HP-5MS 5% phenylmethylsiloxane column (30.0 m × 250 μm × 0.25 μm) coupled with an HP 5973 mass spectrometer (injector temperature: 553 K; carrier: helium; 70 eV). $^1H$, $^{13}C\{^1H\}$, $^{31}P\{^1H\}$ and $^{119}Sn\{^1H\}$ NMR spectra were recorded with a Bruker Avance 400 MHz. HPNMR spectra were recorded with a Bruker AM200SWB spectrometer using a home built HP-NMR bubble column reactor.

**Synthesis of [κ²*P,S*-(dpppS)Pt(CH₃)Cl] (3):** A solution containing an equimolar amount of dpppS (129 mg) in $CH_2Cl_2$ (10 mL) was added dropwise over about 2 h to a solution of [(cod)Pt($CH_3$)Cl] (102.6 mg, 0.290 mmol) in $CH_2Cl_2$ (5 mL) and the mixture stirred vigorously at room temperature overnight. The solvent was then evaporated to about one fifth of the volume and addition of diethyl ether caused the precipitation of a pale-yellow powder. Filtration followed by washing with diethyl ether (3 × 5 mL) and drying under vacuo afforded **3** in high yield (180 mg, 90%). M.p. 493 K (dec.). $C_{28}H_{29}ClP_2PtS$ (690.07): calcd. C 48.73, H 4.24, S 4.65; found C 48.43, H 4.38, S 4.32. IR (KBr): $\tilde{\nu}$ = 3051 $cm^{-1}$ (m), 2882 (m), 1481 (m), 1435 (vs), 1136 (vs), 927 (s), 834 (s), 743 (vs), 690 (vs), 582 (s, P=S, str.), 518 (s), 275 (m, Pt–Cl). LC-MS: exact mass calcd. for $C_{28}H_{29}ClP_2PtS$: 689.08 amu; APCI; found 724.7 $[M + Cl]^-$. $^1H$ NMR (400 MHz, $CDCl_3$, 298 K): $\delta$ = 0.79 [dd, $^3J_{H,P}$ = 3.2, $^4J_{H,PS}$ = 1.2, $^3J_{Pt,H}$ = 74 Hz, 3 H, $CH_3$], 1.76–1.97 (m, 2 H, $CH_2$), 2.91–3.00 (m, 2 H, $CH_2$), 3.04–3.14 (m, $CH_2$), 7.35–7.50 (m, 6 H, $H_{arom.}$), 7.50–8.09 (m, 14 H, $H_{arom.}$) ppm. $^{13}C\{^1H\}$ NMR (101 MHz, $CDCl_3$, 298 K): $\delta$ = –3.4 (d, $^2J_{P,C}$ = 6, $^1J_{Pt,C}$ = 640 Hz, $CH_3$), 18.3 (s, $CH_2$) 24.6 (d, $J_{P,C}$ = 40 Hz, *C*$H_2$P), 28.9 (m, *C*$H_2$PS), 128.1–133.3 ($C_{arom.}$) ppm. $^{31}P\{^1H\}$ NMR (162 MHz, $CDCl_3$, 298 K): $\delta$ = 4.3 (s, $^1J_{P,Pt}$ = 4565 Hz, $PPh_2$), 37.3 (s, $^2J_{Pt,PS}$ = 49 Hz, $Ph_2PS$) ppm. $^{195}Pt\{^1H\}$NMR (86 MHz, $CDCl_3$, 298 K): $\delta$ = –4337.5 ppm (dd, $^1J_{Pt,P}$ = 4565, $^2J_{Pt,PS}$ = 49 Hz) ppm.

**Synthesis of [*trans*-(κ*P*-dpppS)₂Pt(CH₃)Cl] (6):** A solution of two equivalents of dpppS (139 mg, 0.312 mmol) in $CH_2Cl_2$ (10 mL) was added dropwise over about 2 h to a solution of [(cod)Pt($CH_3$)Cl] (55.43 mg, 0.156 mmol) in $CH_2Cl_2$ (10 mL) and the mixture stirred vigorously at room temperature overnight. The solvent was then evaporated to about one fifth of the volume and addition of diethyl ether caused the precipitation of a white powder. Filtration followed by washing with diethyl ether (3 × 5 mL) and drying under vacuo afforded **6** in high yield (159 mg, 90%). M.p. 508 K (dec.). $C_{55}H_{55}ClP_4PtS_2$ (1134.6): calcd. C 58.22, H 4.89, S 5.65; found C 58.37, H 4.92, S 5.61. IR (KBr): $\tilde{\nu}$ = 3052 $cm^{-1}$ (m), 2935 (m), 1480 (m), 1435 (vs), 1102 (vs), 953 (s), 803 (m), 749 (s), 691 (vs), 610 (s, free P=S), 493 (s), 276 (m, Pt–Cl). LC-MS: exact mass calcd. for $C_{55}H_{55}ClP_4PtS_2$: 1133.20 amu; APCI; found 1097.2 $[M - Cl]^+$. $^1H$ NMR (400 MHz, $CDCl_3$, 298 K): $\delta$ = –0.10 (t, $^3J_{H,P}$ = 4, $^2J_{H,Pt}$ = 73 Hz, 3 H, $CH_3$), 2.03–2.17 (m, 4 H, $CH_2$), 2.68–2.84 (m, 8 H, $2CH_2$), $\delta$ = 7.29–7.85 (m, 40 H, $H_{arom}$) ppm. $^{13}C\{^1H\}$ NMR

 © 2006 Wiley-VCH Verlag GmbH & Co. KGaA, Weinheim 

(101 MHz, $CDCl_3$, 298 K): $\delta$ = –12.8 (t, $^2J_{C,P}$ = 6, $^1J_{C,Pt}$ = 659 Hz, $CH_3$), 18.2 (s, $CH_2$), 26.7 (m *C*$H_2$–P), 33.5 (m, *C*$H_2$P*S*), 128.2–133.7 ($C_{arom}$) ppm. $^{31}P\{^1H\}$ NMR (162 MHz, $CDCl_3$, 298 K): $\delta$ = 41.9 (s, $Ph_2PS$), 21.5 (s, $^1J_{P,Pt}$ = 3050 Hz, $Ph_2P$) ppm. $^{195}Pt\{^1H\}$ NMR (86 MHz, $CDCl_3$, 298 K): $\delta$ = –4578.4 ppm (t, $^1J_{Pt,P}$ = 3059 Hz) ppm.

**Hydroformylation Experiments:** In a typical experiment using preformed catalysts, a solution of the platinum complex (0.058 mmol), 1-octene (5.8 mmol) and $SnCl_2{\cdot}2H_2O$ (0.29 mmol) in 5.8 mL of methyl isobutyl ketone was transferred under nitrogen into a 50-mL stainless steel autoclave. The reaction vessel was pressurised to 50 bar total pressure ($CO/H_2$ = 1:1) and the magnetically stirred mixture was heated to 353 K in a thermostated apparatus. The reaction was monitored by following the drop in pressure.

For the "in situ" procedure, the ligand, dissolved when possible in about 1.5 mL of methyl isobutyl ketone, was added to a solution of the platinum precursor in about 1.5 mL of methyl isobutyl ketone and the mixture was kept under vigorous stirring for 30 min. After this time $SnCl_2{\cdot}2H_2O$, 1-octene and methyl isobutyl ketone (up to 5.8 mL of solvent) were added to the solution. The pressure was monitored throughout the reaction. After cooling and venting of the gas, the pale-yellow solution was immediately analysed by GLC. Conversion of 1-octene and yield of aldehydes were calculated using dodecane as internal standard.

**HP-NMR Experiments:** In a typical experiment, a solution of 0.058 mmol of the desired Pt complex, together with the specified amounts of $SnCl_2$ and 1-octene (Table 2) in $[D_6]$acetone (6 mL) were injected into the HP-NMR bubble column reactor against a counter stream of $N_2$, CO or syngas, as appropriate. The reactor was sealed, pressurised, and heated to the desired temperature (Table 2), upon which the $^{31}P\{^1H\}$ NMR spectrum of the sample was recorded.

## Acknowledgments

We thank Dr. G. Ciccarella for LC/MS measurements. The Italian MURST (PRIN 2004 project, prot. 2004030719) and COSTD30 (fellowship for STSM to A. L.) are gratefully acknowledged for financial support.

[1] G. W. Parshall, S. D. Ittel, *Homogeneous Catalysis*, 2nd edition, Wiley Interscience, **1992**, p. 106.
[2] G. Petöcz, Z. Berente, T. Kégl, L. Kollár, *J. Organomet. Chem.* **2004**, *689*, 1188–1193.
[3] G. W. Parshall, *J. Am. Chem. Soc.* **1972**, *94*, 8716–8719.
[4] C. Y. Hsu, M. Orchin, *J. Am. Chem. Soc.* **1975**, *97*, 3553.
[5] I. Schwager, J. F. Knifton, *J. Catal.* **1976**, *45*, 256–267.
[6] P. Meessen, D. Vogt, W. Keim, *J. Organomet. Chem.* **1998**, *551*, 165–170.
[7] L. A. Van der Veen, P. K. Keeven, P. C. J. Kamer, P. W. N. M. van Leeuwen, *J. Chem. Soc., Dalton Trans.* **2000**, 2105–2112.
[8] P. Haelg, G. Consiglio, P. Pino, *J. Organomet. Chem.* **1985**, *296*, 281–290.
[9] G. Parrinello, J. K. Stille, *J. Am. Chem. Soc.* **1987**, *109*, 7122–7127.
[10] G. Consiglio, S. C. A. Nefkens, A. Borer, *Organometallics* **1991**, *10*, 2046–2051.
[11] S. Gladiali, D. Fabbri, L. Kollár, *J. Organomet. Chem.* **1995**, *491*, 91–96.
[12] A. Scrivanti, S. Zeggio, V. Beghetto, U. Matteoli, *J. Mol. Catal. A* **1995**, *101*, 217–220.
[13] A. Scrivanti, V. Beghetto, A. Bastianini, U. Matteoli, G. Menchi, *Organometallics* **1996**, *15*, 4687–4694.
[14] J. F. Cámer, A. Aaliti, N. Ruiz, A. M. M. Bultó, C. Claver, C. J. Cardin, *J. Organomet. Chem.* **1997**, *530*, 199–209.
[15] L. Dahlenburg, S. Mertel, *J. Organomet. Chem.* **2001**, *630*, 221–243.
[16] M. Gómez, G. Muller, D. Sainz, J. Sales, X. Solans, *Organometallics* **1991**, *10*, 4036–4045.
[17] G. Cavinato, G. De Munno, M. Lami, M. Marchionna, L. Toniolo, D. Viterbo, *J. Organomet. Chem.* **1994**, *466*, 277–282.
[18] I. Tóth, T. Kégl, C. J. Elsevier, L. Kollár, *Inorg. Chem.* **1994**, *33*, 5708–5712.
[19] T. Kégl, L. Kollár, L. Radics, *Inorg. Chim. Acta* **1997**, *265*, 249–254.
[20] G. K. Anderson, H. C. Clark, J. A. Davies, *Inorg. Chem.* **1983**, *22*, 427–433.
[21] H. J. Ruegg, P. S. Pregosin, A. Scrivanti, L. Toniolo, C. Botteghi, *J. Organomet. Chem.* **1986**, *316*, 233–241.
[22] Y. Kawabata, T. Hayashi, I. Ogata, *J. Chem. Soc., Chem. Commun.* **1979**, 462–463.
[23] A. Scrivanti, C. Botteghi, L. Toniolo, A. Berton, *J. Organomet. Chem.* **1988**, *344*, 261–275.
[24] G. P. C. M. Dekker, A. Buijs, C. J. Elsevier, K. Vrieze, P. W. N. M. van Leeuwen, W. J. J. Smeets, A. L. Spek, Y. F. Wang, C. H. Stam, *Organometallics* **1992**, *11*, 1937–1948.
[25] S. O. Grim, J. D. Mitchell, *Inorg. Chem.* **1977**, *16*, 1762–1770.
[26] R. Colton, J. Ebner, B. F. Hoskins, *Inorg. Chem.* **1988**, *27*, 1993–1999.
[27] J. Browning, G. W. Bushnell, K. R. Dixon, R. W. Hilts, *J. Organomet. Chem.* **1993**, *452*, 205–218.
[28] T. C. Blagborough, R. Davis, P. Ivison, *J. Organomet. Chem.* **1994**, *467*, 85–94.
[29] S. M. Aucott, A. M. Z. Slawin, J. D. Woollins, *Eur. J. Inorg. Chem.* **2002**, 2408–2418.
[30] S. M. Aucott, A. M. Z. Slawin, J. D. Woollins, *Polyhedron* **2003**, *22*, 361–368.
[31] D. E. Berry, J. Browning, K. R. Dixon, R. W. Hilts, *Can. J. Chem.* **1988**, *66*, 1272–1282.
[32] J. R. Dilworth, N. Wheatley, *Coord. Chem. Rev.* **2000**, *199*, 89–158.
[33] R. Romeo, L. Monsù Scolaro, M. R. A. Plutino, F. N. Romeo, A. Del Zotto, *Eur. J. Inorg. Chem.* **2002**, 629–638.
[34] I. Brassat, U. Englert, W. Keim, D. Keitel, S. Killat, G. P. Suranna, R. Wang, *Inorg. Chim. Acta* **1998**, *280*, 150–162.
[35] I. Brassat, W. Keim, S. Killat, M. Moethrath, P. Mastrorilli, C. F. Nobile, G. P. Suranna, *J. Mol. Catal. A* **2000**, *157*, 41–58.
[36] G. P. Suranna, P. Mastrorilli, C. F. Nobile, W. Keim, *Inorg. Chim. Acta* **2000**, *305*, 151–156.
[37] P. Mastrorilli, C. F. Nobile, G. P. Suranna, F. P. Fanizzi, G. Ciccarella, U. Englert, Q. Li, *Eur. J. Inorg. Chem.* **2004**, 1234–1242.
[38] M. J. Baker, M. F. Giles, A. Guy, M. J. Taylor, R. J. Watt, *J. Chem. Soc., Chem. Commun.* **1995**, 197–198.
[39] L. Gonsalvi, H. Adams, G. J. Sunley, E. Ditzel, A. Haynes, *J. Am. Chem. Soc.* **2002**, *124*, 13597–13612.
[40] S. Gladiali, E. Alberico, S. Pulacchini, L. Kollár, *J. Mol. Catal. A* **1999**, *143*, 155–162.
[41] D. D. Ellis, G. Harrison, A. G. Orpen, P. Hirihattaya, P. G. Pringle, J. G. de Vries, H. Oevering, *J. Chem. Soc., Dalton Trans.* **2000**, 671–675.
[42] T. Hayashi, Y. Kawabata, T. Isoyama, I. Ogata, *Bull. Chem. Soc. Jpn.* **1981**, *54*, 3438–3446.
[43] As expected, no Pt black formed in the reaction carried out with complex **6**, in which the Pt atom is bound to two P atoms.
[44] F. Ancillotti, M. Lami, M. Marchionna, *J. Mol. Catal.* **1990**, *58*, 331–344.
[45] J. A. Iggo, D. Shirley, N. C. Tong, *New J. Chem.* **1998**, *22*, 1043–1045.
[46] Over this temperature range the combination of broadening of the $^{119}Sn$ signal and its inherent weakness presumably precludes its observation.
[47] It is known that solvated $SnCl_2$ can act as a donor ligand toward transition metals. See, for instance: F. A. Cotton, G. Wil-

 © 2006 Wiley-VCH Verlag GmbH & Co. KGaA, Weinheim 

kinson, *Advanced Inorganic Chemistry*, 4th edition, Wiley, New York, p. 380.
[48] There is a noticeable difference in the $^1$H NMR chemical shift of the methyl group of **8** when it is prepared using one ($\delta$ = 1.68 ppm) or five ($\delta$ = 1.77 ppm) equivalents of $SnCl_2$. This difference may be due to an interaction of excess tin chloride with the acyl oxygen (see ref.[20]) resulting in a downfield shift of the $CH_3$ signal.
[49] Complex **8** is stable with respect to CO deinsertion on purging the solution with $N_2$.
[50] A. Scrivanti, A. Berton, L. Toniolo, C. Botteghi, *J. Organomet. Chem.* **1986**, *314*, 369–383.

Received: November 15, 2005
Published Online: April 4, 2006

 © 2006 Wiley-VCH Verlag GmbH & Co. KGaA, Weinheim 

DOI: 10.1002/ejic.200501064

# Luminescence Modulation of a Terbium Complex with Anions and Its Application as a Reagent

Dengqing Zhang,[a] Mei Shi,[a] Zhiqiang Liu,[a] Fuyou Li,*[a] Tao Yi,[a] and Chunhui Huang*[a]

**Keywords:** Luminescence modulations / Fluoride anions / Terbium complexes

A terbium complex $Tb(PMIP)_3(PhCN)$, namely tris(1-phenyl-3-methyl-4-isobutyl-5-pyrazolone)-terbium-(pyrazino[2,3-*f*][1,10]phenanthroline-2,3-dicarbonitrile), was synthesized as a reagent for anions. Compared with $Tb(PMIP)_3(H_2O)_2$, the fluorescent quantum yield of $Tb(PMIP)_3(PhCN)$ was reduced because the triplet energy level of PhCN (20920 $cm^{-1}$) is a little higher than that of $^5D_4$ of $Tb^{3+}$ (20400 $cm^{-1}$) and lower than that of PMIP (23000 $cm^{-1}$). This resulted in a back-energy transfer from $Tb^{3+}$ to PhCN. Interestingly, the photoluminescent properties of $Tb(PMIP)_3(PhCN)$ drastically depend on the nature of the anions added into the solution. When apropos equivalents of fluoride (or acetate) anions were added into the $CH_3CN$ solution of $Tb(PMIP)_3(PhCN)$, the replacement of PhCN with fluoride (or acetate) anions took place and the above back-energy transfer was prohibited, which resulted in a fluorescence enhancement of the terbium complex. After excessive equivalents of fluoride (or acetate) anions were added, the replacement of PMIP with fluoride (or acetate) anions prohibited the ligand PMIP sensitized energy transfer of the terbium complex, resulting in the fluorescence quenching of the system. However, in the aqueous solution, the terbium complex shows a remarkable selectivity of fluoride anions over the other anions. As a reagent, its sensitivity is about $10^{-8}$ mol·$L^{-1}$ for the fluoride anions.
(© Wiley-VCH Verlag GmbH & Co. KGaA, 69451 Weinheim, Germany, 2006)

## Introduction

Anion recognition and sensing are of current interest because of their importance in biological, environmental, and chemical systems.[1–4] The construction of anion chemosensors is essentially composed of two units, the binding site and the signaling subunit, which may be covalently linked (binding site-signaling submit approach)[5–8] or not (displacement approach).[9] The interaction with the anion and the change in color or fluorescence are in principle reversible. However, development of fluorescent reagents has emerged as a research area of significant importance.[1,10,11] In these systems, anion signaling using fluorescence or color changes can also be observed using irreversible reactions.[12] The underlying idea of these irreversible systems is to take advantage of the selective reactivity that certain anions may display. Hence, the use of an anion-induced reagent system usually has high selectivity and also an accumulative effect is directly related with the anion concentration. Fluoride, the smallest anion, has unique biological and chemical properties, and its recognition and detection are of growing interest because it is associated with dental care[13] and the treatment of osteoporosis.[14] As a result, there is a need to develop new sensitive methods for fluoride detection. Most of the emerging detection methods have focused on the specific Lewis acid-base interaction, such as the strong affinity of a boron atom towards the fluoride anion,[15–19] or the designed hydrogen bonding with the fluoride anion.[20,21] These binding events have been converted into an electrochemical[22] or fluorescent change,[23–26] or more directly, colorimetric change seen by the naked eye.[27,28] However, the reported fluorescent reagents for fluoride anions is quite limited.[29–31]

In the past decade, the synthesis, characterization, and application of luminescent lanthanide complexes have been the focus of much attention.[32–35] On the basis of the unique photophysical properties of lanthanide cations (long luminescence lifetime and very sharp emission band),[36,37] lanthanide complexes as luminescent materials were paid particular attention in the immunoassay[38] and organic light-emitting diode (OLED).[39–42] Recently, some luminescent lanthanide complexes have been used as a chemosensor for anions.[43–50] For example, Ziessel et al. reported that several lanthanide complexes were engineered from a ligand consisting of a single P=O fragment and two methylene linked bipyridine subunits for nitrate anion detection.[49,50] It is well known that fluoride anions bind tightly with lanthanide ions, and some work has reported on the influence of fluoride anions on the luminescence property of crown-based lanthanide complexes by exchanging coordinated water with fluoride anions.[51,52] In this paper, a new terbium complex $Tb(PMIP)_3(PhCN)$ (see Scheme 1) was designed and synthesized as a reagent for detecting anions by another mechanism. Here, PMIP and PhCN stand for

[a] Laboratory of Advanced Materials, Fudan University, Shanghai, 200433, P. R. China

 © 2006 Wiley-VCH Verlag GmbH & Co. KGaA, Weinheim 

the anion of 4-isobutyl-3-methyl-1-phenyl-5-pyrazolone and pyrazino[2,3-*f*][1,10]phenanthroline-2,3-dicarbonitrile, respectively. The photophysical studies of $Tb(PMIP)_3(PhCN)$ showed that the luminescent properties of this complex could be modulated upon addition of the different anions.

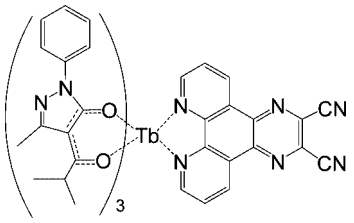


Scheme 1. Chemical structure of $Tb(PMIP)_3(PhCN)$.

## Results and Discussion

### Structure Characterization of $Gd(PMIP)_3(H_2O)_2$·$Gd(PMIP)_3(C_2H_5OH)(H_2O)$ (A)

The structure of the gadolinium complex **A** was characterized by X-ray crystallography. An ORTEP diagram for the asymmetric unit is shown in Figure 1. Details of the crystal data and data collection parameters for **A** are given in Table 1. It can be seen form Figure 1 that a common repeating unit exists for the two molecules of $Gd(PMIP)_3(H_2O)_2$ and $Gd(PMIP)_3(C_2H_5OH)(H_2O)$. In $Gd(PMIP)_3(H_2O)_2$, the geometry around the central ions can be described as a distorted bicapped-trigonal prism where the trigonal prism is composed of six oxygen atoms (O9, O10, O12, O13, O15, O16). Among them, O9 and O10 are from one β-diketone, O12 and O13 are from the other two β-diketones, and O15 and O16 are from two water molecules. Another two oxygen atoms (O11, O14) cap the two quadrilateral faces O9–O10–O12–O16 and O9–O15–O13–O16, respectively. The average Gd–O distance is 2.42 Å [2.31(2)–2.53(3)], which is a little smaller than the sum of the radii of $Gd^{3+}$ (1.05 Å, eight coordinated) and $O^{2-}$ (1.42 Å). Furthermore, the structure of $Gd(PMIP)_3(C_2H_5OH)(H_2O)$ is the same as that of $Gd(PMIP)_3(H_2O)_2$ except for an ethanol molecule occurring in place of the water molecule, the coordination geometry is that of distorted a bicapped-trigo-

Table 1. Crystal data, collection and structure refinement parameters for complex **A**.

| | $Gd(PMIP)_3(H_2O)_2Gd(PMIP)_3(C_2H_5OH)(H_2O)$ |
|---|---|
| Empirical formula | $C_{87}H_{108}Gd_2N_{12}O_{18}$ |
| $M_r$ [g mol$^{-1}$] | 1924.35 |
| Crystal system | triclinic |
| Space group | $P\bar{1}$ |
| Crystal size [mm] | 0.40 × 0.25 × 0.18 |
| $a$ [Å] | 13.2931(2) |
| $b$ [Å] | 18.0432(2) |
| $c$ [Å] | 18.7608(3) |
| $\alpha$ [°] | 77.3215(5) |
| $\beta$ [°] | 86.4151(5) |
| $\gamma$ [°] | 89.7183(7) |
| $V$ [Å$^3$] | 4381.29(11) |
| $Z$ | 2 |
| $\rho_{calcd.}$ [g cm$^{-3}$] | 1.459 |
| $\mu$ [mm$^{-1}$] | 1.574 |
| $F$ (000) | 1972 |
| $R_1$ [$I > 2\sigma(I)$] | 0.0422 |
| $wR_2$ [$I > 2\sigma(I)$] | 0.0684 |
| $R_1$ (all data) | 0.1134 |
| $wR_2$ (all data) | 0.0826 |
| GOF | 0.938 |

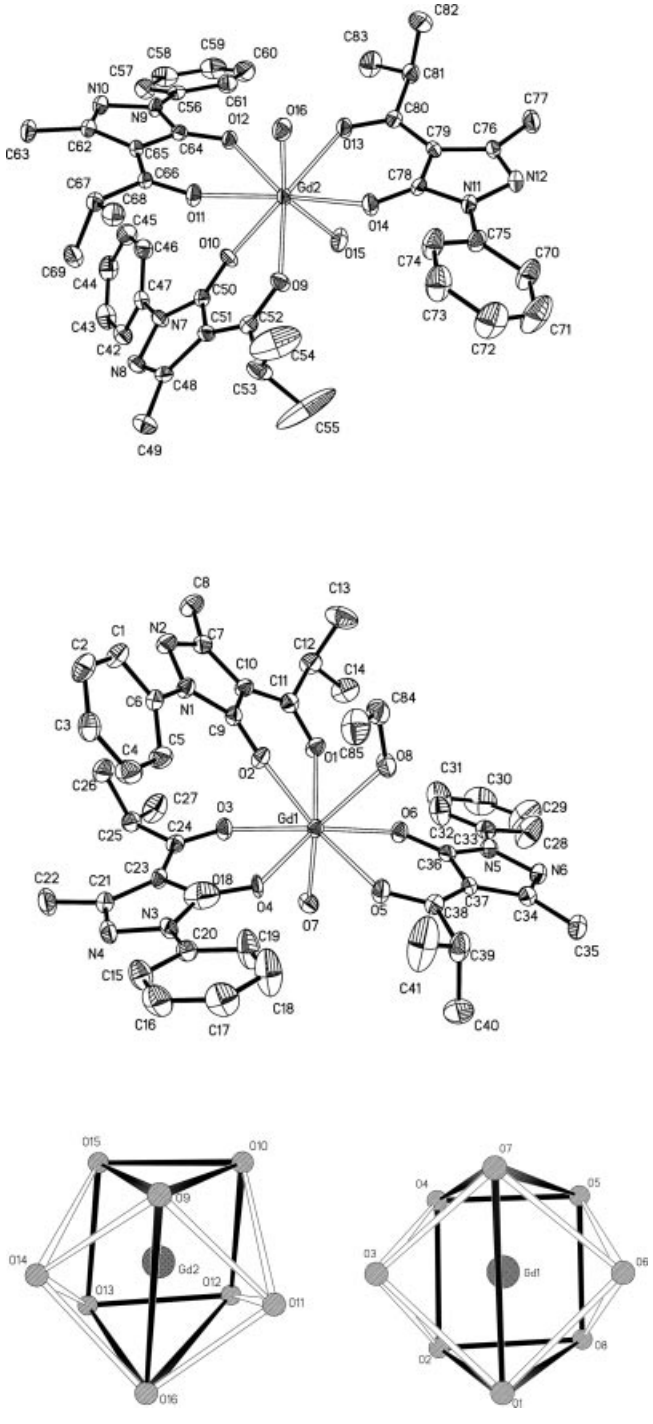


Figure 1. ORTEP diagram of **A** with the thermal ellipsoids drawn at the 30% probability level and the H atoms removed for clarity.

 © 2006 Wiley-VCH Verlag GmbH & Co. KGaA, Weinheim 

nal prism, as illustrated in Figure 1. Moreover, an independent $C_2H_5OH$ solvent molecule exists in the unit cell.

### UV/Vis Spectra

UV/Vis absorption spectra of the ligands (PMIP and PhCN) and $Tb(PMIP)_3(PhCN)$ in $CH_3CN$ solution are shown in Figure 2. The maximum absorption band of PMIP at 263 nm is attributed to a singlet-singlet π-π* enol absorption of the β-diketonate. The ligand PhCN has two absorption bands at 264 and 306 nm, which are attributed to n-π* and singlet-singlet π-π* absorption, respectively. Compared with the spectrum of PMIP, the absorption maximum of $Tb(PMIP)_3(PhCN)$ is red-shifted by 5 nm, which is agreement with the enlargement of the conjugated structure of ligands after coordinating to the terbium ion. It can be seen from Figure 2 that the spectral shape of $Tb(PMIP)_3(PhCN)$ in $CH_3CN$ is similar to that of PMIP, indicating that the coordination of the terbium ion does not significantly influence the singlet-state energy of PMIP. The molar absorption coefficients ($\varepsilon$) of PMIP, PhCN, and $Tb(PMIP)_3(PhCN)$ are calculated as $2.55\times10^4$, $6.11\times10^4$, and $9.61\times10^4$ $L\cdot mol^{-1}\cdot cm^{-1}$, respectively, revealing that the two ligands and the terbium complex have a strong ability to absorb light.

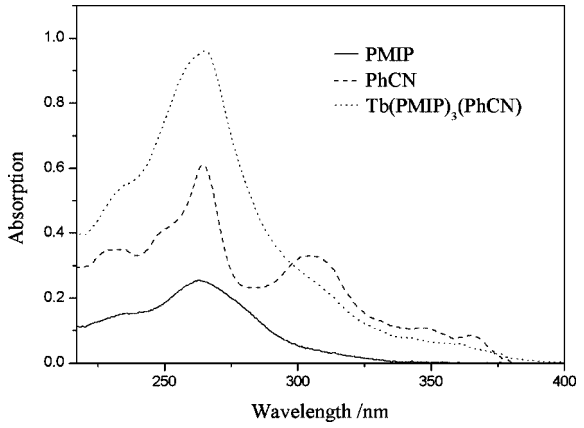


Figure 2. UV/Vis spectra of PMIP, PhCN, and $Tb(PMIP)_3(PhCN)$ in $CH_3CN$ ($1.0\times10^{-5}$ $mol\cdot L^{-1}$).

### Fluorescence Characteristics

The fluorescence spectrum of $Tb(PMIP)_3(PhCN)$ in $CH_3CN$ solution (see Figure 3) shows characteristic emission bands of $Tb^{3+}$ ($\lambda_{ex}$ = 280 nm) centered at 489, 544, 584, and 612 nm resulting from the deactivation of the $^5D_4$ excited state to the corresponding ground state $^7F_J$ ($J$ = 6, 5, 4, 3) of the $Tb^{3+}$ ion. The strongest emission is centered around 544 nm and corresponds to the hypersensitive transition of $^5D_4\rightarrow{}^7F_5$. The excitation spectrum of $Tb(PMIP)_3$-(PhCN) overlays the absorption wavelength range of PMIP well, indicating that the emission of $Tb(PMIP)_3(PhCN)$ originates mainly from the energy absorbed by PMIP. We also investigated the emission spectrum of $Tb(PMIP)_3$-(PhCN) in the different solvents, such as $CHCl_3$, DMF, and DMSO, the similarity of the emission patterns in these solvents suggests that there are no solvent-dependent structural changes.

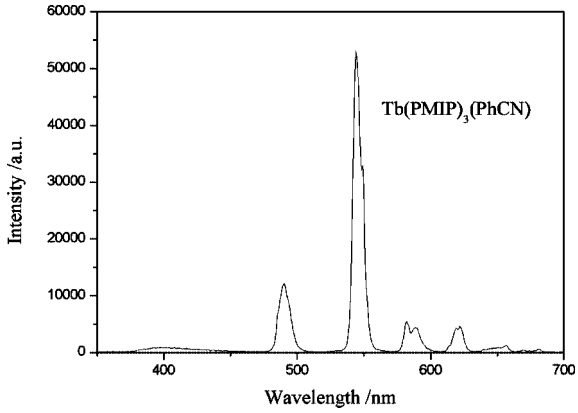


Figure 3. The luminescence spectrum of $Tb(PMIP)_3(PhCN)$ at 298 K in $CH_3CN$.

### Phosphorescence Spectra

Since the first excited energy level of the $Gd^{3+}$ ion ($^6P_{7/2}$) is high, the energy absorbed by the ligand in the $Gd^{3+}$ complex usually cannot be transferred to the $Gd^{3+}$ ion. Therefore the phosphorescence emission from the $Gd^{3+}$ complex can be considered as ligand-localized phosphorescence emission, and then the energy level of $^3$π-π* of the ligand can be deduced. At room temperature, the phosphorescent emission spectrum of the $Gd^{3+}$ complex is very weak, however at a lower temperature (77 K), the ligand-localized phosphorescent spectrum can be observed. Herein, the gadolinium complexes $Gd(NO_3)_3(PhCN)$ and **A** were synthesized for triplet-energy level measurements. The phosphorescent spectra of **A** and $Gd(NO_3)_3(PhCN)$ at 77 K are shown in Figure 4. The emission bands of **A** and $Gd(NO_3)_3(PhCN)$ peak at 464 nm (21552 $cm^{-1}$) and 502 nm (19920 $cm^{-1}$), respectively. By referring to the lower wavelength emission edges of the corresponding phosphorescent

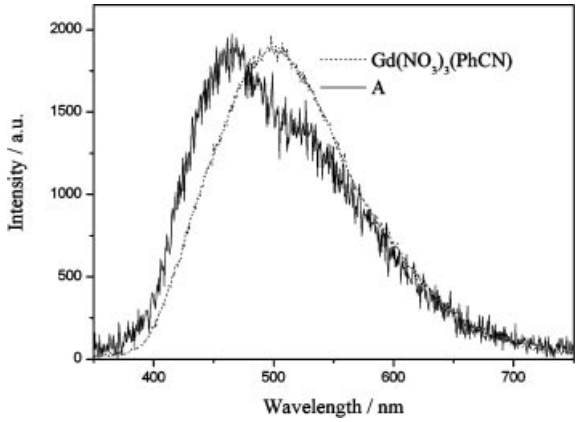


Figure 4. Phosphorescent spectra of **A** and $Gd(NO_3)_3(PhCN)$ at 77 K.

 © 2006 Wiley-VCH Verlag GmbH & Co. KGaA, Weinheim 

spectra, the energies of zero-phonon transition of the triplet states ($^3\pi\pi^*$) at about 435 nm (23000 $cm^{-1}$) and 478 nm (20920 $cm^{-1}$) were obtained for PMIP and PhCN, respectively.

### Photophysical Properties of the Terbium Complexes

By using Rhodamine 6G in ethanol ($1\times10^{-6}$ mol·$L^{-1}$, $\varphi_{ref}$ = 0.92) as a reference, the overall luminescence quantum yields ($\varphi_{overall}$) of $Tb(PMIP)_3(PhCN)$ and $Tb(PMIP)_3(H_2O)_2$ in $CH_3CN$ were measured to be 0.15% and 2.97% according to the well-known method.[53] The luminescence lifetimes ($\tau$) were also investigated for $Tb(PMIP)_3(PhCN)$ and $Tb(PMIP)_3(H_2O)_2$ in $CH_3CN$. The measured luminescent decay can be described by monoexponential kinetics, and the luminescence lifetimes of $Tb(PMIP)_3(PhCN)$ and $Tb(PMIP)_3(H_2O)_2$ are 95.5 and 341.1 μs, respectively.

In order to understand the influence of the ligand modification on the photophysical property of $Tb(PMIP)_3(PhCN)$, the efficiency of energy transfer ($\varphi_{transfer}$) from the ligand to $Tb^{3+}$ and the probability of the terbium emission ($\varphi_{Ln}$) were investigated for $Tb(PMIP)_3(PhCN)$ and $Tb(PMIP)_3(H_2O)_2$ on the basis of the method developed by Selvin et al.[54] The overall quantum yield ($\varphi_{overall}$) can be defined as Equation (1).

$$\varphi_{overall} = \varphi_{transfer}\varphi_{Ln} \quad (1)$$

When a lanthanide complex is mixed with an acceptor of known quantum yield and very short fluorescence lifetime (ns), the efficiency of energy transfer between them ($\varphi_{ET}$) and the probability of lanthanide emission ($\varphi_{Ln}$) are calculated from both the fluorescence decay lifetime and intensity measurements, see Equation(2) and (3).

$$\varphi_{ET} = 1 - (\tau_{da}/\tau_d) \quad (2)$$

$$\varphi_{Ln} = \varphi_a(I_{da}/I_{ad})/(1/\varphi_{ET} - 1) = \varphi_a I_{da}(\tau_d - \tau_{ad})/(I_{ad}\tau_{ad}) \quad (3)$$

Here $\tau_{ad}$ and $\tau_d$ are the excited state lifetime of the lanthanide complex in the presence and absence of the acceptor, respectively; $\varphi_a$ is the fluorescence quantum yield of the acceptor; $I_{da}$ is the integral area under the residual lanthanide emission in the presence of the acceptor; and $I_{ad}$ is the integral area of the fluorescent emission part of the acceptor.

Here, Rhodamine 6G was used as the acceptor in ethanol ($\varphi_a$ = 0.92 and $\tau < 10$ ns). For example, in a mixture solution consisting of $Tb(PMIP)_3(PhCN)$ (10 μM) and Rhodamine 6G (1.25 μM), the emission lifetime of the $Tb^{III}$ complex ($\lambda_{em}$ = 544 nm) decreased from 95.5 to 80.0 μs, indicating that 16.2% of the energy was transferred from $Tb(PMIP)_3(PhCN)$ to Rhodamine 6G. From these measurements and Equation (3), the probability of $Tb^{3+}$ emission ($\varphi_{Ln}$) in $Tb(PMIP)_3(PhCN)$ was determined to be 1.1% (Table 2). In combination with the overall quantum yield ($\varphi_{overall}$) of $Tb(PMIP)_3(PhCN)$, the efficiency of energy transfer ($\varphi_{transfer}$) from the ligand to $Tb^{3+}$ was calculated to be 14.2% (see Table 2) according to Equation (1). Similarly, the efficiency of energy transfer ($\varphi_{transfer}$) of 56.3% and the probability of $Tb^{3+}$ emission ($\varphi_{Ln}$) of 5.3% were obtained for $Tb(PMIP)_3(H_2O)_2$.

With $\varphi_{Ln}$ and $\tau_d$ determined in acetonitrile, radiative and nonradiative decay rates of the $Tb^{III}$ complex were calculated from Equation (4).

$$k_{rad} = \varphi_{Ln}/\tau_d k_{nr} = (1 - \varphi_{Ln})/\tau_d \quad (4)$$

Taking 1.1% of $\varphi_{Ln}$ and 95.5 μs of $\tau_d$ into account, the radiative and norradiative decay rates of $Tb(PMIP)_3(PhCN)$ were calculated as 111 and $1.04\times10^4$ $s^{-1}$, respectively (see Table 2). Similarly, the radiative and nonradiative decay rates of $Tb(PMIP)_3(H_2O)_2$ were determined as 151 and $2.71\times10^3$ $s^{-1}$ (see Table 2), respectively.

To elucidate the energy transfer process of the terbium complex, the energy levels of the relevant electronic states should be estimated. By referring to their wavelengths at the UV/Vis absorbance edges, the singlet-energy levels of PMIP and PhCN were estimated to be 32260 $cm^{-1}$ (310 nm) and 29410 $cm^{-1}$ (340 nm), respectively. In combination with the triplet-energy levels of PMIP and PhCN, the schematic energy level diagram and the energy transfer process are shown in Figure 5.

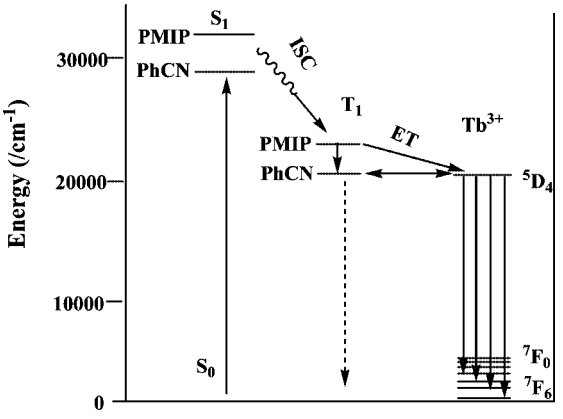


Figure 5. Schematic energy level diagram and the energy transfer process in the system of $Tb(PMIP)_3(PhCN)$. $S_1$: the first excited singlet state, $T_1$: the first excited triplet state.

Generally, the sensitization pathway in luminescent terbium complexes consists of the excitation of the ligands from the ground state to their excited singlet states, and

Table 2. Photophyscical properties of $Tb(PMIP)_3(PhCN)$ and $Tb(PMIP)_3(H_2O)_2$ in $CH_3CN$.

| System | $\lambda_{max}^{PL}$ [nm] | $\tau$ [μs] | $\varphi_{overall}$ [$\times10^3$] | $\varphi_{Ln}$ [%] | $\varphi_{transfer}$ [%] | $k_{rad}$ [$s^{-1}$] | $k_{nr}$ [$s^{-1}$] |
|---|---|---|---|---|---|---|---|
| $Tb(PMIP)_3(H_2O)_2$ | 544 | 341.1 | 29.7 | 5.3 | 56.3 | 151 | $2.71\times10^3$ |
| $Tb(PMIP)_3(PhCN)$ | 544 | 95.5 | 1.5 | 1.1 | 14.2 | 111 | $1.04\times10^4$ |
| $Tb(PMIP)_3(PhCN) + 3F^-$ | 544 | 114.9 | 10.5 | 3.7 | 28.4 | 321 | $8.4\times10^3$ |

 © 2006 Wiley-VCH Verlag GmbH & Co. KGaA, Weinheim 

subsequently through the intersystem crossing of the ligands to their triplet states, following the energy transfer from the triplet state of the ligand to the central ion. In this process the 4f electrons of the $Tb^{3+}$ ion are excited to the $^5D_J$ manifold ion from the ground state, finally the $Tb^{3+}$ ion emits when the 4f electrons undergo a transition from the excited state of $^5D_4$ to the ground state.[55,56] We noticed that the energy gaps $\Delta E$ ($^1\pi\pi^*$-$^3\pi\pi^*$) between the $^1\pi\pi^*$ and $^3\pi\pi^*$ levels are 9260 and 8490 $cm^{-1}$ for PMIP and PhCN, respectively (see Figure 5). According to Reinhoudt's empirical rule that the intersystem crossing process will be effective when $\Delta E$ ($^1\pi\pi^*$-$^3\pi\pi^*$) is at least 5000 $cm^{-1}$,[57] the intersystem crossing processes are effective for PMIP and PhCN. On the other hand, the triplet-energy level of PMIP ($\approx$23000 $cm^{-1}$) is higher than that of $^5D_4$ (20400 $cm^{-1}$) for $Tb^{3+}$, and their energy gap $\Delta E$ ($^3\pi\pi^*$-$^5D_4$) between the ligand- and metal-centered level is 2600 $cm^{-1}$. According to Latva's empirical rule,[58] an optimal ligand-to-metal transfer process for $Tb^{III}$ is when $\Delta E$ ($^3\pi\pi^*$-$^5D_0$) $> 2000$ $cm^{-1}$. It can be concluded that the transfer process is also effective from PMIP to $Tb^{3+}$ and that PMIP is suitable as a sensitizer for $Tb^{III}$. On the contrary, the $^3\pi\pi^*$ state (ca. 20920 $cm^{-1}$) of PhCN is so close to $^5D_4$ (20400 $cm^{-1}$) of $Tb^{3+}$, giving $\Delta E$ ($^3\pi\pi^*$-$^5D_0$) = 520 $cm^{-1}$, which is too low to prevent the back-energy transfer from the $Tb^{3+}$ excited state to the triplet state of PhCN. Moreover, the triplet energy level of PhCN is lower than that of PMIP, and the energy transfer from PMIP to PhCN may occur. Therefore, it is not difficult to understand the fact that $Tb(PMIP)_3(PhCN)$ exhibits a lower fluorescence quantum yield ($\varphi_{overall}$) (0.15%) compared to that (2.97%) of $Tb(PMIP)_3(H_2O)$.

### Fluorescence Modulation of the Complex with Anions

The fluorescence modulation of $Tb(PMIP)_3(PhCN)$ with anions was investigated by the fluorescence titration experiments in $CH_3CN$. Figure 6 shows the titration curves of the spectral parameters of $Tb(PMIP)_3(PhCN)$ against the [anion]/[$Tb(PMIP)_3(PhCN)$] ratio in acetonitrile. Interestingly, a different fluorescent modulation of $Tb(PMIP)_3$-(PhCN) was observed upon addition of the different anions. For example, a slight variation of the luminescent properties of $Tb(PMIP)_3(PhCN)$ was observed upon addition of other anions such as $ClO_4^-$, $NO_3^-$, or $NO_2^-$. When one equivalent of $Cl^-$, $Br^-$, or $I^-$ was added, the fluorescent intensity of $Tb(PMIP)_3(PhCN)$ reached the maximum (see Figure 6), and then it was almost unchanged with further addition of $Cl^-$, $Br^-$, or $I^-$. Similarly, Mahajan et al. reported that the luminescence intensity of tris(β-diketonate) europium ($\lambda_{em}$ = 611 nm) was enhanced twofold when three equivalents of $Cl^-$ were added.[47] Generally, the coordination number of the $Tb^{III}$ complexes in solution is nine.[59] The coordination number of $Tb^{3+}$ in $Tb(PMIP)_3(PhCN)$ is eight, implying that the complex can bond one anion to form a coordination of nine, hence, the increasing fluorescent emission was observed upon addition of one equivalent of the anions. Because of their weak bonding ability to the terbium ion, $Cl^-$, $Br^-$, and $I^-$ had difficultly in displacing the ligands PhCN and PMIP, which was confirmed by the fact that there was no obvious change in the luminescent emission of $Tb(PMIP)_3(PhCN)$ with further addition of $Cl^-$, $Br^-$, or $I^-$ (see Figure 6).

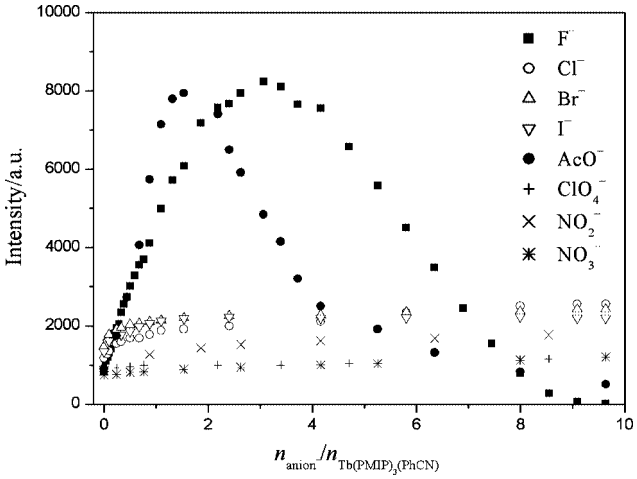


Figure 6. Fluorescent titrations of $Tb(PMIP)_3(PhCN)$ ($1.0\times10^{-5}$ mol·$L^{-1}$) in $CH_3CN$ upon addition of $F^-$, $Cl^-$, $Br^-$, $I^-$, $ClO_4^-$, $NO_3^-$, $NO_2^-$, and $AcO^-$.

It is well known that the lanthanide complex receptor prefers smaller (harder) $F^-$ (or $AcO^-$) to larger (softer) $Cl^-$, $Br^-$, or $I^-$. In fact, a special fluorescent modulation of $Tb(PMIP)_3(PhCN)$ was observed upon addition of fluoride and acetate anions. For example, Figure 7 shows fluorescent spectral changes of $Tb(PMIP)_3(PhCN)$ in $CH_3CN$ solution (10 μM) upon addition of tetra-*n*-butylammonium fluoride ($Bu_4NF$). Upon addition of the fluoride anion, the characteristic terbium emission ($\lambda_{ex}$ = 280 nm) greatly increased along with an increase of the emission intensity of PhCN centred at 400 nm (see Figure 7, a). When $Bu_4NF$ reached about three equivalents of $Tb(PMIP)_3(PhCN)$ (see Figure 7, a), this change became saturated with a fluorescent quantum yield of 1.05%. Under these conditions, the efficiency of energy transfer ($\varphi_{transfer}$) and the probability of $Tb^{3+}$ emission ($\varphi_{Ln}$) for this mixture were measured to be 28.4% and 3.7%, respectively (see Table 2). It can be seen from Table 2 that the mixture exhibited a higher energy transfer efficiency ($\varphi_{transfer}$) and larger probability of $Tb^{3+}$ emission compared with $Tb(PMIP)_3(PhCN)$. Because of its strong bonding ability, the fluoride anions were able to substitute one solvent molecule and one PhCN molecule that were weakly coordinated to $Tb^{III}$ in the complex, and so $Tb^{III}$ reached a coordination number of nine, revealing that the back-energy transfer from $^5D_4$ of $Tb^{3+}$ and the triplet state of PMIP to the triplet state of PhCN was restrained (see Figure 5); consequently, both the probability of $Tb^{3+}$ emission ($\varphi_{Ln}$) and the fluorescent quantum yield of the mixture were improved. However, further addition of a large excess of $Bu_4NF$ caused a decrease of the characteristic fluorescent emission of $Tb^{3+}$, and the emission was quenched completely when nine equivalents of $Bu_4NF$ were added (see Figure 7b). These changes can be interpreted as the follow-

 © 2006 Wiley-VCH Verlag GmbH & Co. KGaA, Weinheim 

ing: upon addition of more fluoride anions, PMIP ligands were completely replaced by fluoride anions, resulting in the breakage of the ligand-sensitized energy transfer from PMIP to $Tb^{3+}$, consequently reducing the fluorescent quantum yield of the complex. Compared with the fluoride anion, the acetate anion exhibited a similar modulation behavior for the fluorescent emission of the terbium complex (see Figure 6). From the above results, we can see that the addition of fluoride and acetate anions affects the quantum yield of $Tb^{3+}$ emission and modulates the energy transfer path, which finally results in the modulation of the overall emission quantum yield.

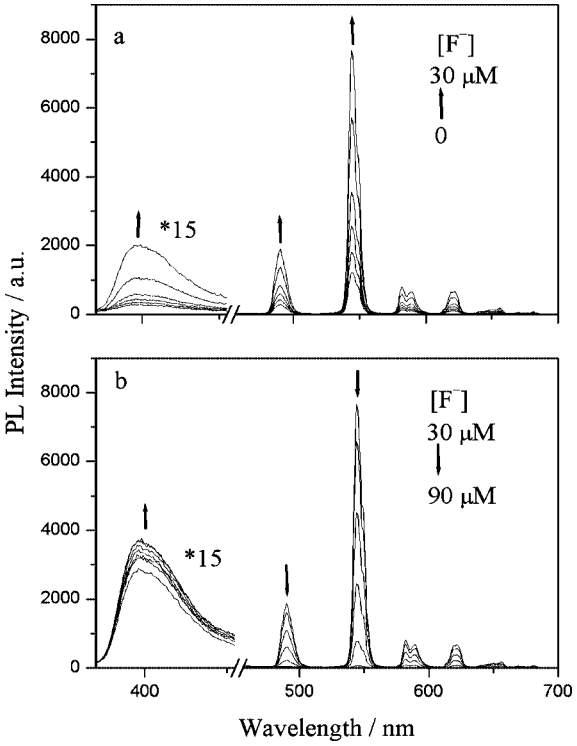


Figure 7. Fluorescent titrations of $Tb(PMIP)_3(PhCN)$ ($1.0\times10^{-5}$ mol·L$^{-1}$) upon addition of $Bu_4NF$.

However, when $Tb(PMIP)_3(PhCN)$ was dissolved in the mixture of $CH_3CN/H_2O$ (9:1 v/v), only a decrease in fluorescent emission of the complex was observed upon addition of fluoride and acetate anions. Under these conditions, the coordinating water molecules can compete with PhCN fragments and gradually remove them from the first coordination sphere of $Tb^{3+}$, then back-energy transfer from the $Tb^{3+}$ excited state to the triplet state of PhCN was broken. In fact, the complex exhibited more intense fluorescent emission ($\varphi$ = 0.62%) in $CH_3CN/H_2O$ (9:1 v/v). When further fluoride anions were added, PMIP was replaced by fluoride anions, resulting in the breakage of the ligand-sensitized energy transfer from PMIP to $Tb^{3+}$ (see Figure 5), and then the fluorescence of $Tb^{3+}$ was quenched. However, fluorescent quenching to different degrees was observed for $Tb(PMIP)_3(PhCN)$ upon addition of the different anions (see Figure 8). Consequently, the complex showed a remarkable selectivity of fluoride anions over the other anions, which may be explained by the small size, the high surface charge density of the fluoride anion and its strong affinity to $Tb^{3+}$.[60] Even in this situation, the solution is very clear and transparent, the observable sensitivity is about $10^{-8}$ mol·L$^{-1}$ of fluoride anions.

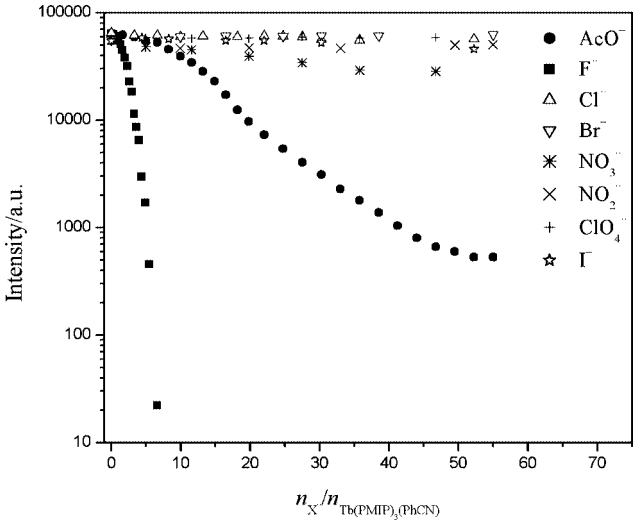


Figure 8. Fluorescent titrations of $Tb(PMIP)_3(PhCN)$ ($1.0\times10^{-5}$ mol·L$^{-1}$) in $CH_3CN/H_2O$ (9:1 v/v) upon addition of $F^-$, $Cl^-$, $Br^-$, $I^-$, $ClO_4^-$, $NO_3^-$, $NO_2^-$, and $AcO^-$.

## Conclusions

In summary, we have designed and synthesized a novel lanthanide-based luminescent reagent $Tb(PMIP)_3(PhCN)$ for anions. By using $Tb^{3+}$ as the fluorophore, $Tb(PMIP)_3$-(PhCN) displays high selective fluorescent modulation on the fluoride and acetate anions in acetonitrile. The large fluorescent enhancement at first and then fluorescence quenching were observed for the terbium complex upon addition of fluoride and acetate anions. However, in aqueous solution, $Tb(PMIP)_3(PhCN)$ shows a unique fluorescent quenching upon addition of fluoride, indicating its remarkable selectivity for fluoride anions over the other anions. At the same time, the reason for the fluorescence modulation with the anions was described. This system is particularly useful relative to other molecules because it allows detection of traces of fluoride and acetate anions by luminescence monitoring at a terbium center.

## Experimental Section

**General:** Diaminomaleonitrile and tetrabutylammonium fluoride trihydrate were obtained from Acros. $TbCl_3\cdot6H_2O$, $Gd(NO_3)_3\cdot6H_2O$, and 1-phenyl-3-methyl-4-isobutyl-5-pyrazolone were purchased from Shanghai Sinopharm Chemical Reagent Co. Ltd., Phenanthroline-5,6-dione was synthesized according to the literature.[61] The complexes $Tb(PMIP)_3(H_2O)_2$ and $Gd(PMIP)_3(H_2O)_2\cdot Gd(PMIP)_3(C_2H_5OH)(H_2O)$ (**A**) were synthesized according to a similar method reported previously[62] and characterized by elemental analyses. Moreover, the structure of the complex **A** was characterized by X-ray crystallography. UV/Visible absorption

 © 2006 Wiley-VCH Verlag GmbH & Co. KGaA, Weinheim 

spectra were recorded with a UV 2550 spectrophotometer of Shimadzu. The element analyses were performed with Vario EL III O-Element analyzer. $^1$HNMR spectra were recorded with a Mercury Plus 400NB NMR spectrometer. The luminescence and phosphorescence spectra were measured with an Edinburgh LFS920 fluorescence spectrophotometer and LP-920 laser flash photolysis spectrophotometer, respectively. For the phosphorescence measurements, the fourth harmonic 266 nm of the pulsed GCR-4 Nd:YAG Laser (Spectra-Physics, USA) with 30 Hz repetition rate and 6 ns pulse width was used as the excitation source, and the experiments were completed at 77 K in ethanol/methanol (1:1 v/v). Fluorescence lifetimes were recorded with a single photon counting spectrometer from Edinburgh LFS920 fluorescence spectrophotometer with microsecond pulse lamp as the excitation source. The data were analyzed by an iterative convolution of the luminescence decay profile with the instrument response function using a software package provided by Edinburgh Instruments.

**Synthesis of Pyrazino[2,3-*f*][1,10]phenanthroline-2,3-dicarbonitrile (PhCN):** PhCN was synthesized according to a similar method reported previously.[63] 2,3-Diaminomaleonitrile (6.0 mmol) was added to a solution consisting of 1,10-phenanthroline-5,6-dione (1.0 g, 4.8 mmol) and absolute ethanol (30 mL) in a 50 mL flask. The reaction mixture was refluxed for 3 h and then cooled to room temperature. The solution was concentrated to ca. 10 mL with a rotary evaporator and the solid product was filtered. After recrystallization from ethanol twice, the desired pale yellow powder (1.0 g) was obtained with a yield of 74%. $^1$HNMR (400 MHz, $CDCl_3$): $\delta$ = 7.93 (q, 2 H), 9.4–9.46 (d, 2 H), 9.46–9.52 (d, 2 H) ppm. $C_{16}H_6N_6$(282.26): calcd. C 68.08, H 2.14, N 29.77; found C 68.00, H 2.10, N 30.02.

**Synthesis of Tb(PMIP)$_3$(PhCN) and Gd(NO$_3$)$_3$(PhCN):** The complexes Tb(PMIP)$_3$(PhCN) and Gd(NO$_3$)$_3$(PhCN) were synthesized according to a previous literature procedure.[64]

**Tb(PMIP)$_3$(PhCN):** Ethanol (10 mL), 4-isobutyl-3-methyl-1-phenyl-5-pyrazolone (3.0 mmol), and triethylamine (3 mmol) were added to a 25 mL side-arm flask. The mixture was stirred for 10 minutes, and then PhCN and $TbCl_3{\cdot}6H_2O$ (1.0 mmol) were added to the flask. The reaction mixture was refluxed for 3 h whilst stirring, and then cooled to room temperature. The solvent was removed under reduced pressure and the residue was washed with water. The crude product was then recrystallized from an ethanol/water mixture (8:2 v/v) to afford the desired product (1.42 g) with a yield of 80%. $C_{58}H_{51}N_{12}O_6Tb$ (1771.03): calcd. C 59.49, H 4.39, N 14.35; found C 59.30, H 4.41, N 14.19.

**Gd(NO$_3$)$_3$(PhCN):** $Gd(NO_3)_3{\cdot}6H_2O$ (0.25 mmol) was added dropwise whilst stirring to an ethanol solution (10 mL) containing PhCN (0.25 mmol), and then the reaction mixture was refluxed for 4 h. The resulting solution was filtered and a white powder was obtained by recrystallization from an ethanol solution, 117 mg, yield 75%. $C_{16}H_6N_9O_9Gd$ (625.52): calcd. C 30.72, H 0.97, N 20.15; found C 30.65, H 0.91, N 20.10.

**Crystallography:** The crystal of complex **A** was mounted on a glass fiber and transferred to a Bruker SMART CCD area detector. Crystallographic measurements were carried out using a Bruker Apex II CCD diffractometer, $\sigma$ scans, graphite-monochromated Mo-$K_a$ radiation ($\lambda$ = 0.71073 Å) under room temperature. The structures were solved by direct methods and refined by full-matrix least-squares on $F^2$ values using the program SHELXS-97.[65] All non-hydrogen atoms were refined anisotropically. Hydrogen atoms were calculated in ideal geometries. For the full-matrix least-squares refinements [$I > 2\sigma(I)$], the unweighted and weighted agreement factors of $R_1 = \Sigma(F_o - F_c)/\Sigma F_o$ and $wR_2 = [\Sigma w(F_o^2 - F_c^2)^2/\Sigma wF_o^4]^{1/2}$ were used. The crystal data and details of the structure determinations are summarized in Table 1.

CCDC-288368 contains the supplementary crystallographic data for this paper. These data can be obtained free of charge from The Cambridge Crystallographic Data Centre via www.ccdc.cam.ac.uk/data_request/cif.

**Fluorescence Modulation:** Fluorescence modulations were carried out in the following manner: the solution of Tb(PMIP)$_3$(PhCN) in a 1.0 cm quartz cuvette was titrated with the concentrated solutions of tetrabutylammonium salts of different anions (X = $F^-$, $Cl^-$, $Br^-$, $I^-$, $ClO_4^-$, $NO_3^-$, $NO_2^-$, and $AcO^-$) by a micro sample injector. In order to account for the dilution effect, the volume of these concentrated solutions was negligible. The concentration of Tb(PMIP)$_3$(PhCN) in all experiments was $1.0 \times 10^{-5}$ mol·L$^{-1}$.

## Acknowledgments

The authors thank the National Science Foundation of China (Grant 20490210 and 20501006), National Basic Research 973 Program (2006CB601103), Shanghai Sci. Tech. Comm. (05DJ14004), and China Postdoctoral Science Foundation for financial support.

[1] R. Martínez-Máñez, F. Sancenón, *Chem. Rev.* **2003**, *103*, 4419–4476.
[2] P. D. Beer, P. A. Gale, *Angew. Chem. Int. Ed.* **2001**, *40*, 486–516.
[3] C. Suksai, T. Tuntulani, *Chem. Soc. Rev.* **2003**, *32*, 192–202.
[4] T. Gunnlaugsson, J. P. Leonard, *Chem. Commun.* **2005**, 3114–3131.
[5] R. A. Bissell, P. de Silva, H. Q. N. Gunaratne, P. L. M. Lynch, G. E. M. Maguire, K. R. A. S. Sandanayake, *Chem. Soc. Rev.* **1992**, *21*, 187–195.
[6] D. Parker, J. H. Yu, *Chem. Commun.* **2005**, 3141–3143.
[7] R. S. Dickins, T. Gunnlaugsson, D. Parker, R. D. Peacock, *Chem. Commun.* **1998**, 1643–1644.
[8] T. Gunnlaugsson, J. P. Leonard, K. Sénéchal, A. J. Harte, *J. Am. Chem. Soc.* **2003**, *125*, 12062–12063.
[9] S. L. Wiskur, H. Ait-Haddou, J. J. Lavigne, E. V. Anslyn, *Acc. Chem. Res.* **2001**, *34*, 963–972.
[10] A. P. de Silva, H. Q. N. Gunaratne, T. Gunnlaugsson, A. J. M. Huxley, C. P. McCoy, J. T. Rademacher, T. E. Rice, *Chem. Rev.* **1997**, *97*, 1515–1566.
[11] B. Liu, H. Tian, *Chem. Commun.* **2005**, 3156–3158.
[12] J. V. Ros-Lis, M. D. Marcos, R. Martínez-Máñez, K. Rurack, J. Soto, *Angew. Chem. Int. Ed.* **2005**, *44*, 4405–4407 and references cited therein.
[13] K. L. Kirk, *Biochemistry of the Halogens and Inorganic Halides*, Plenum Press, New York, **1991**, 58.
[14] M. Kleerekoper, *Endocrinol. Metab. Clin. North Am.* **1998**, *27*, 441.
[15] S. Yamaguchi, S. Akiyama, K. Tamao, *J. Am. Chem. Soc.* **2001**, *123*, 11372–11375.
[16] Y. Kubo, M. Yamamoto, M. Ikeda, M. Takeuchi, S. Shinkai, S. Yamaguchi, K. Tamao, *Angew. Chem. Int. Ed.* **2003**, *42*, 2036–2040.
[17] S. Solé, F. P. Gabbaï, *Chem. Commun.* **2004**, 1284–1285.
[18] V. C. Williams, W. E. Piers, W. Clegg, M. R. J. Elsegood, S. Collins, T. B. Marder, *J. Am. Chem. Soc.* **1999**, *121*, 3244–3245.
[19] Z. Q. Liu, M. Shi, F. Y. Li, Q. Fang, Z. H. Chen, T. Yi, C. H. Huang, *Org. Lett.* **2005**, *7*, 5481–5484.
[20] P. Anzenbacher Jr, K. Jursíková, J. L. Sessler, *J. Am. Chem. Soc.* **2000**, *122*, 9350–9351.
[21] H. Miyaji, W. Sato, J. L. Sessler, V. M. Lynch, *Tetrahedron Lett.* **2000**, *41*, 1369–1373.
[22] H. Yamamoto, A. Ori, K. Ueda, C. Dusemund, S. Shinkai, *Chem. Commun.* **1996**, 407–408.

 © 2006 Wiley-VCH Verlag GmbH & Co. KGaA, Weinheim 

[23] J. S. Wu, J. H. Zhou, P. F. Wang, X. H. Zhang, S. K. Wu, *Org. Lett.* **2005**, *7*, 2133–2136.
[24] S. Arimori, M. G. Davidson, T. M. Fyles, T. G. Hibbert, T. D. James, G. I. Kociok-Kohn, *Chem. Commun.* **2004**, *14*, 1640–1641.
[25] G. X. Xu, M. A. Tarr, *Chem. Commun.* **2004**, *9*, 1050–1051.
[26] C. R. Copper, N. Spencer, T. D. James, *Chem. Commun.* **1998**, 1365–1366.
[27] C. Dusemund, K. R. A. S. Sandanayake, S. J. Shinkai, *J. Chem. Soc., Chem. Commun. Chem. Soc., Chem. Commun.* **1995**, 333–334.
[28] H. Miyaji, W. Sato, J. L. Sessler, *Angew. Chem. Int. Ed.* **2000**, *39*, 1777–1780.
[29] S. Xu, K. C. Chen, H. Tian, *J. Mater. Chem.* **2005**, *15*, 2676–2680.
[30] C. J. Ward, P. Patel, T. D. James, *Chem. Lett.* **2001**, 406–407.
[31] A. B. Descalzo, D. Jiménez, J. El Haskouri, D. Beltrán, P. Amorós, M. D. Marcos, R. Martínez-Máñez, J. Soto, *Chem. Commun.* **2002**, 562–563.
[32] T. Gunnlaugsson, D. A. Mac Donaill, D. Parker, *J. Am. Chem. Soc.* **2001**, *123*, 12866–12876.
[33] S. Torelli, D. Imbert, M. Cantuel, G. Bernardinelli, S. Delahaye, A. Hauser, J.-C. G. Bünzli, C. Piguet, *Chem. Eur. J.* **2005**, *11*, 3228–3242.
[34] J. Zhang, P. D. Badger, S. J. Geib, S. Petoud, *Angew. Chem. Int. Ed.* **2005**, *44*, 2508–2512.
[35] H. Tsukube, S. Shinoda, *Chem. Rev.* **2002**, *102*, 2389–2404.
[36] J. C. G. Bünzli, *In Lanthanide Probes in Life, Chemical and Earth Sciences* (Eds.: J. C. G. Bünzli, G. R. Choppin), Elsevier, Amsterdam, **1989**.
[37] C. H. Huang (Ed.), *Chemistry of Rare Earth Complexes*, Science Press, Beijing, **1997**.
[38] I. A. Hemmila (Ed.), *Applications of Fluorescence in Immunoassays*, Wiley, New York, **1991**.
[39] J. Wang, R. Wang, J. Yang, Z. Zheng, M. D. Carducci, T. Cayon, N. Peyghambarian, G. E. Jabbour, *J. Am. Chem. Soc.* **2001**, *123*, 6179–6180.
[40] S. F. Li, G. Y. Zhong, W. H. Zhu, F. Y. Li, J. F. Pan, W. Huang, H. Tian, *J. Mater. Chem.* **2005**, *15*, 3221–3228.
[41] J. Kido, Y. Okamoto, *Chem. Rev.* **2002**, *102*, 2357–2368.
[42] M. Shi, F. Y. Li, T. Yi, D. Q. Zhang, H. M. Hu, C. H. Huang, *Inorg. Chem.* **2005**, *44*, 8929–8936.
[43] D. Parker, *Coord. Chem. Rev.* **2000**, *205*, 109–130.
[44] H. Shinoda, H. Tamiaki, *Coord. Chem. Rev.* **2002**, *226*, 227–234.
[45] T. Gunnlaugsson, J. P. Leonard, *Chem. Commun.* **2005**, 3114–3131.
[46] D. Parker, J. H. Yu, *Chem. Commun.* **2005**, 3141–3143.
[47] R. K. Mahajan, I. Kaur, R. Kaur, S. Uchida, A. Onimaru, S. Shinoda, H. Tsukube, *Chem. Commun.* **2003**, 2238–2239.
[48] K. Hanaoka, K. Kikuchi, H. Kojima, Y. Urano, T. Nagano, *J. Am. Chem. Soc.* **2004**, *126*, 12470–12476.
[49] L. J. Charbonnière, R. Ziessel, M. Montalti, L. Prodi, N. Zaccheroni, C. Boehme, G. Wipff, *J. Am. Chem. Soc.* **2002**, *124*, 7779–7788.
[50] M. Montalti, L. Prodi, N. Zaccheroni, L. Charbonnière, L. Douce, R. Ziessel, *J. Am. Chem. Soc.* **2001**, *123*, 12694–12695.
[51] N. Sabbatini, S. Perathoner, G. Lattanzi, S. Dellonte, V. Balzani, *J. Phys. Chem.* **1987**, *91*, 6136–6139.
[52] J. P. Cross, A. Dadabhoy, P. G. Sammes, *J. Lumin.* **2004**, *110*, 113–124.
[53] B. G. Huth, G. I. Farmer, M. R. Kagan, *J. Appl. Phys.* **1969**, *40*, 5145–5147.
[54] M. Xiao, P. R. Selvin, *J. Am. Chem. Soc.* **2001**, *123*, 7067–7073.
[55] M. Tanaka, G. Yamagughi, J. Shiokawa, C. Yamanaka, *B Chem. Soc. Jpn.* **1970**, *43*, 549–550.
[56] A. V. Hayes, H. G. Drickamer, *J. Chem. Phys.* **1982**, *76*, 114–125.
[57] F. J. Steemers, W. Verboom, D. N. Reinhoudt, E. B. van der Tol, J. W. Verhoeven, *J. Am. Chem. Soc.* **1995**, *117*, 9408–9414.
[58] M. Latva, H. Takalo, V. M. Mukkala, C. Matachescu, J. C. Rodriguez-Ubis, J. Kankare, *J. Lumin.* **1997**, *75*, 149–169.
[59] S. I. Klink, L. Grave, D. N. Reinhoudt, F. C. J. M. van Veggel, *J. Phys. Chem. A* **2000**, *104*, 5457–5468.
[60] J. Burgess, J. Kijowski, *Advances in Inorganic Chemistry and Radiochemistry*, Academic Press, **1981**.
[61] X. H. Zou, B. H. Ye, H. Li, J. G. Liu, Y. Xiong, L. N. Ji, *J. Chem. Soc., Dalton Trans.* **1999**, 1423–1428.
[62] H. Xin, M. Shi, X. C. Gao, Y. Y. Huang, Z. L. Gong, D. B. Nie, H. Cao, Z. Q. Bian, F. Y. Li, C. H. Huang, *J. Phys. Chem. B* **2004**, *108*, 10796–10800.
[63] P. P. Sun, J. P. Duan, J. J. Lih, C. H. Cheng, *Adv. Funct. Mater.* **2003**, *13*, 683–691.
[64] H. Xin, F. Y. Li, M. Shi, Z. Q. Bian, C. H. Huang, *J. Am. Chem. Soc.* **2003**, *125*, 7166–7167.
[65] G. M. Sheldrick, *SHELXTL-Plus V5.1 Software Reference Manual*, Bruker AXS Inc., Madison, WI, **1997**.

Received: November 29, 2005
Published Online: March 30, 2006

 © 2006 Wiley-VCH Verlag GmbH & Co. KGaA, Weinheim 

DOI: 10.1002/ejic.200501102

# Oxidorhenium(V) Complexes of a Family of Bipyridine-Like Ligands Including Pyridyltriazines and Pyrazinyltriazine: Oxygen-Atom Transfer, Metal Redox and Correlations

**Samir Das[a] and Animesh Chakravorty*[a,b]**

**Keywords:** N ligands / Oxido ligands / Nitrogen heterocycles / Reduction potentials / Rhenium

The title ligands (general abbreviation L) are bipyridine (bpy), its dimethyl (mbpy) and diphenyl (pbpy) derivatives, phenanthroline (phen), 5,6-diphenyl-3-(2-pyridyl)-1,2,4-triazine (ppyt) and its dimethyl (mpyt) and pyrazinyl (ppzt) analogues. The concerned oxido complexes are $[ReOCl_3(L)]$, $[ReOBr_3(ppyt)]$ and $[ReOBr_3(ppzt)]$. The chloro and bromo complexes of ppyt and ppzt were prepared by reacting these ligands with $[ReOX_3(AsPh_3)_2]$ (X = Cl, Br). The X-ray structures of $[ReOCl_3(ppyt)]$ and $[ReOCl_3(ppzt)]$ reveal that the $ReCl_3$ fragment is meridionally disposed and that the L ligand is *N*,*N*-coordinated such that the pyridine/pyrazine nitrogen lies *trans* to the oxido oxygen atom. The Re–O lengths [1.656(10)/1.625(9) Å] correspond to approximate triple bonding. The rate of oxygen-atom transfer from $[ReOX_3(L)]$ to triphenylphosphane in solution follows second-order kinetics and is associated with a large and negative entropy of activation (approx. $-30\ cal\,K^{-1}\,mol^{-1}$). The initial attack is believed to involve the phosphane lone pair and Re≡O $\pi^*$-orbitals. Electron withdrawal from the $Re^{V}O$ moiety by varying X or L facilitates oxygen-atom transfer. Thus, the rates follow the orders Br < Cl; mbpy < bpy < phen < pbpy << mpyt < ppyt < ppzt. The reduction potential of the quasireversible $Re^{VI}O/Re^{V}O$ couple displays similar trends and the logarithmic rate constant of oxygen-atom transfer is found to correlate linearly with the reduction potential.

(© Wiley-VCH Verlag GmbH & Co. KGaA, 69451 Weinheim, Germany, 2006)

## Introduction

The oxygen-atom transfer ability of the oxidorhenium(V) moiety $Re^{V}O$ has been known for a long time,[1,2] and the nature and scope of the process have attracted significant recent attention.[3–9] In this laboratory we have been concerned[10] with the design and reactivity of $Re^{V}O$ complexes incorporating *N*,*N*-chelation by pyridyl ligands where the second nitrogen site belongs either to an acyclic function, such as an imine[11–13] or azo[13–16] group, or to a heterocyclic moiety. The scope of the latter alternative is potentially wide because of the many interesting variations possible in the form of aza-aromatic ligands.

Although a beginning in this direction was recently made with pyridylazole ligands,[17,18] the logical starting point would be the familiar didentate pyridyl aza-aromatic, viz. bipyridine (bpy). This has prompted us to examine the $Re^{V}O$ chemistry of bpy and certain bpy-like ligands including pyridyltriazine and pyrazinyltriazine. Very little is currently known about rhenium binding by the latter two ligands (vide infra).

[a] Department of Inorganic Chemistry, Indian Association for the Cultivation of Science,
Kolkata 700 032, India
Fax: +91-33-2473-2805
E-mail: icac@mahendra.iacs.res.in
[b] Jawaharlal Nehru Centre for Advanced Scientific Research, Bangalore 560 064, India

The oxygen-atom transfer potency of the family of $Re^{V}O$ complexes is estimated using triphenylphosphane as a model oxophile. The systematics in the rate of oxygen-atom transfer, which spans nearly two orders of magnitude, are scrutinized in terms of electron withdrawal and metal reduction potential.

## Results and Discussion

### The $Re^{V}O$ Family

The ligand family used here consists of **1**–**4**, each member being abbreviated as shown below. The family spans three distinct types of bpy modifications: simple substitution (as in **1**), augmented conjugation (as in **2**) and incorporation of nitrogen hetero atoms (as in **3** and **4**).

The nine oxido complexes (Table 1) of **1**–**4** are of coordination type **5**, abbreviated as $[ReOX_3(L)]$, where X = Cl or Br.

The complexes of **1** and **2** (X = Cl) were conveniently synthesised as yellow solids following a method previously used for bpy.[19] The pink chelates $[ReOCl_3(L)]$ (L = **3** and **4**) were prepared by the 1:1 reaction of $[ReOCl_3(AsPh_3)_2]$ with L in benzene at room temperature. The use of the arsane precursor is crucial for optimum yield. When $[ReOCl_3(PPh_3)_2]$ is employed the initially formed oxido com-

 © 2006 Wiley-VCH Verlag GmbH & Co. KGaA, Weinheim 

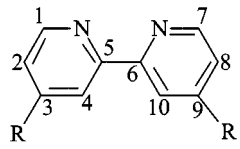

| R | |
|---|---|
| H | bpy |
| Me | mbpy |
| Ph | pbpy |

**1**

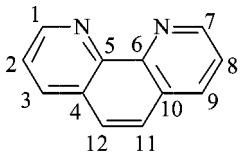

phen

**2**

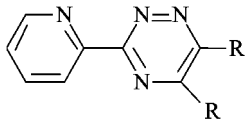

| R | |
|---|---|
| Me | mpyt |
| Ph | ppyt |

**3**

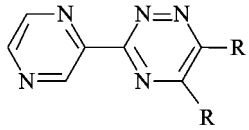

| R | |
|---|---|
| Ph | ppzt |

**4**

Table 1. The type **5** oxido complexes, their $Re^{VI}O/Re^{V}O$ reduction potential (in Volt vs. SCE) and oxygen-atom transfer rate to $PPh_3$.

| Complex | $E_{½}$ [V] ($\Delta E_p$ [mV])[a] | $10^3k$ [$M^{-1}s^{-1}$][b,c] |
|---|---|---|
| $[ReOCl_3(bpy)]$ (**5a**) | 1.45 (100) | 1.60(0.03) |
| $[ReOCl_3(mbpy)]$ (**5b**) | 1.44 (80) | 1.30(0.04) |
| $[ReOCl_3(pbpy)]$ (**5c**) | 1.48 (100) | 2.52(0.04) |
| $[ReOCl_3(phen)]$ (**5d**) | 1.47 (100) | 2.21(0.03) |
| $[ReOCl_3(ppyt)]$ (**5e**) | 1.61 (90) | 25.01(0.02) |
| $[ReOBr_3(ppyt)]$ (**5f**) | 1.58 (90) | 13.34(0.05) |
| $[ReOCl_3(mpyt)]$ (**5g**) | 1.53 (130) | 10.45(0.05) |
| $[ReOCl_3(ppzt)]$ (**5h**) | 1.68 (90) | 62.58(0.04) |
| $[ReOBr_3(ppzt)]$ (**5i**) | 1.65 (100) | 36.64(0.06) |

[a] In acetonitrile; $\Delta E_p$ is peak-to-peak separation. [b] In dichloromethane, temperature: 303 K. [c] Least-squares deviations are given in parentheses.

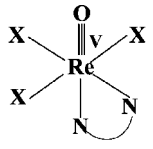

**5**

plex reacts with the liberated phosphane (vide infra), which affects the yield and purity of the product.

The use of $[ReOBr_3(AsPh_3)_2]$ in place of the chloro precursor gives the bromo system $[ReOBr_3(L)]$ for L = ppyt and ppzt. Attempted synthesis of the iodo analogue from $[ReOI_3(AsPh_3)_2]$ furnished only unstable products. However, in the presence of $ArNH_2$ in the reaction mixture the imido system $[Re(NAr)I_3(L)]$ could be isolated, which is a possible intermediate in the formation of the $Re^{V}O$ analogue.[20]

Selected spectroscopic data for $[ReOX_3(L)]$ are collected in the Experimental Section. The species uniformly display an Re≡O stretch near 1000 $cm^{-1}$ and two absorption bands in the visible region around 500 and 750 nm, which are of diagnostic value in rate studies (vide infra). The complexes are diamagnetic ($5d^2$) and show well-resolved $^1H$ NMR spectra, which have been assigned.

Of the complexes listed in Table 1, $[ReOCl_3(bpy)]$[19,21] and $[ReOCl_3(phen)]$[22] have been reported before. The analytical[23] and coordination[24,25] chemistry of ppyt complexes has been well-documented, but the only reported rhenium complex is $[Re(CO)_3Cl(ppyt)]$,[26] which has recently been structurally characterised in this laboratory.[20] There is no report of rhenium complexes of mpyt and ppzt, which have otherwise been only sparsely studied as ligands.[25,27]

## Structure

The X-ray structures of $[ReOCl_3(ppyt)]$ (**5e**) and $[ReOCl_3(ppzt)]$ (**5h**) were determined. Molecular views are shown in Figures 1 and 2, respectively, and selected bond parameters are listed in Table 2. In the distorted octahedral $ReOCl_3N_2$ coordination sphere the chloride ligands are meridionally disposed. In both molecules the coordinated nitrogen of the triazine ring is N2 and not N4, as also observed in copper[24b] and ruthenium[27] chelates of ppyt/ppzt. The coordinated pyridine nitrogen in **5e** and pyrazine nitrogen in **5h** lie *trans* to the oxido ligand. In both cases the chloride ligands and the triazine N2 atom define a good equatorial plane (mean deviation: 0.03 Å) from which the Re atom is displaced by 0.32 (**5e**) and 0.37 Å (**5h**) towards the oxygen atom. The chelate ring in both cases is satisfactorily planar (mean deviation of about 0.06 Å). The two heterocyclic rings deviate significantly from coplanarity, the dihedral angles being 6.9° (**5e**) and 13.3° (**5h**).

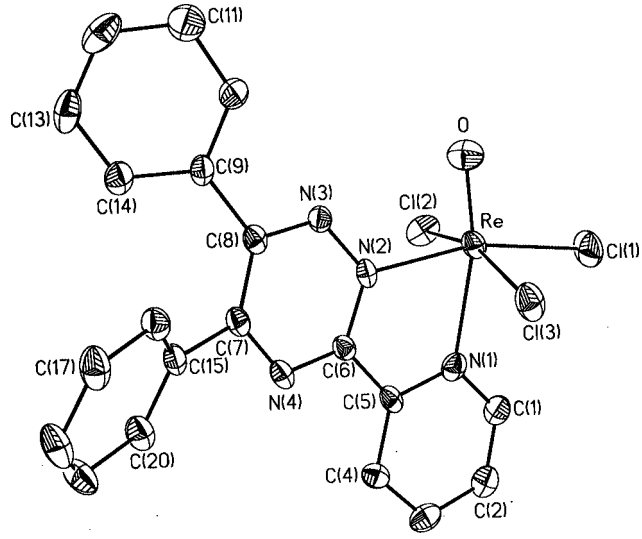


Figure 1. Molecular view and atom labelling scheme for $[ReOCl_3(ppyt)]$ (**5e**). All non-hydrogen atoms are represented by 30% thermal probability ellipsoids. Hydrogen atoms have been omitted for clarity.

 © 2006 Wiley-VCH Verlag GmbH & Co. KGaA, Weinheim 

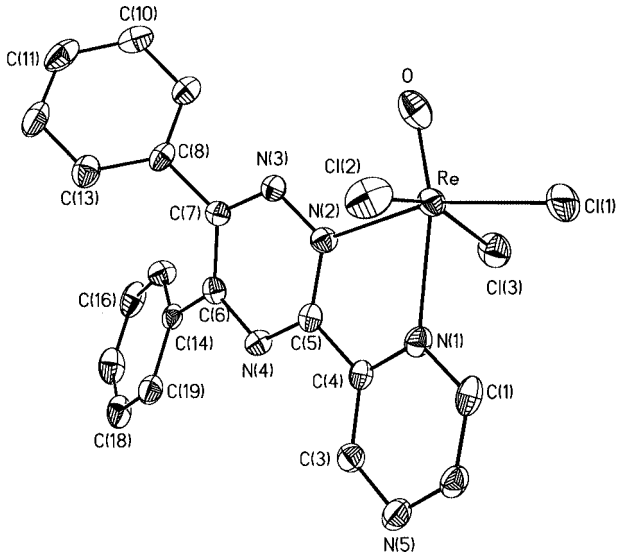


Figure 2.Molecular view and atom labelling scheme for [ReOCl$_3$(ppzt)] (**5h**). All non-hydrogen atoms are represented by 30% thermal probability ellipsoids. Hydrogen atoms have been omitted for clarity.

Table 2. Selected bond length [Å] and angles [°] for **5e** and **5h**.

| | **5e** | **5h** |
|---|---|---|
| Re–O | 1.656(10) | 1.625(9) |
| Re–N(1) | 2.262(11) | 2.296(8) |
| Re–N(2) | 2.104(9) | 2.124(7) |
| Re–Cl(1) | 2.313(4) | 2.318(3) |
| Re–Cl(2) | 2.332(3) | 2.345(3) |
| Re–Cl(3) | 2.363(3) | 2.363(3) |
| N(2)–N(3) | 1.327(13) | 1.330(10) |
| O–Re–N(2) | 90.5(4) | 90.9(3) |
| N(2)–Re–N(1) | 73.1(4) | 71.9(3) |
| N(2)–Re–Cl(1) | 164.4(3) | 162.1(2) |
| O–Re–Cl(2) | 99.3(4) | 100.3(3) |
| O–Re–Cl(3) | 97.8(4) | 99.5(3) |
| N(2)–Re–Cl(3) | 85.8(3) | 87.4(2) |
| Cl(1)–Re–Cl(3) | 88.77(14) | 87.53(13) |
| O–Re–N(1) | 163.5(4) | 162.9(3) |
| O–Re–Cl(1) | 104.8(4) | 106.8(3) |
| N(1)–Re–Cl(1) | 91.6(3) | 90.3(2) |
| N(2)–Re–Cl(2) | 91.4(3) | 92.1(2) |
| N(1)–Re–Cl(3) | 80.2(3) | 79.9(2) |
| Cl(2)–Re–Cl(3) | 162.76(14) | 160.17(11) |

The Re–O length, which corresponds to approximate triple bonding,[28] is somewhat longer in **5e** [1.656(10) Å] than in **5h** [1.625(9) Å]. The Re–N1 bond lying *trans* to Re≡O is longer than the Re–N2 bond by around 0.17 Å. Significantly, the shorter Re–O bond in **5h** is associated with a longer Re–N1 bond. The structure of the bpy complex of type **5**, viz. [ReOBr$_3$(bpy)], is known.[29] Here, the Re–O distance is significantly longer [1.689(8) Å] than those in **5e** and **5h**.

### Oxygen-Atom Transfer

The [ReOX$_3$(L)] (X = Cl, Br) complexes are uniformly reactive towards triphenylphosphane in solution, furnishing a violet solution from which paramagnetic phosphane oxide complexes of type [Re$^{III}$(OPPh$_3$)X$_3$(L)] have been isolated. Characterisation data for two representative species are set out in the Experimental Section. The observed room-temperature magnetic moments (1.5–1.7 $\mu_B$) are much lower than the idealised spin-only value for the $t_{2g}^4$ configuration due to strong orbital coupling, as is common for trivalent rhenium. As expected, the $^1$H NMR spectra of the complexes are paramagnetically shifted.[14,17,19,30]

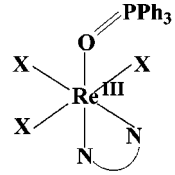


**6**

Although no direct structural characterisation was possible due to lack of single crystals, our previous work[11–18,31] on related systems strongly supports the gross geometry of the phosphane oxide complexes to be **6**.

The rate of the reaction of Equation (1) was determined spectrophotometrically in dichloromethane solution.

$$Re^{V}OX_3(L) + PPh_3 \xrightarrow{k} Re^{III}(OPPh_3)X_3(L) \quad (1)$$

Selected rate data are listed in Tables 1 and 3. A representative time-evolution spectrum characterised by isosbestic points is shown in Figure 3. Under pseudo-first-order con-

Table 3. Variable-temperature rate constants for the reaction [ReOCl$_3$(L)] with PPh$_3$ in dichloromethane solution.[a,b]

| | $T$ [K] | [PPh$_3$] [M] | $10^4 k_{obs}$ [s$^{-1}$] | $10^3 k$ [M$^{-1}$ s$^{-1}$] |
|---|---|---|---|---|
| ppyt | 293 | 0.012 | 1.452 | 12.08(0.05) |
| | | 0.015 | 1.814 | |
| | | 0.019 | 2.300 | |
| | 298 | 0.012 | 2.000 | 16.72(0.02) |
| | | 0.015 | 2.509 | |
| | | 0.019 | 3.177 | |
| | 303 | 0.012 | 3.001 | 25.01(0.02) |
| | | 0.015 | 3.750 | |
| | | 0.019 | 4.752 | |
| | 308 | 0.012 | 3.935 | 32.80(0.03) |
| | | 0.015 | 4.920 | |
| | | 0.019 | 6.232 | |
| ppzt | 293 | 0.012 | 4.300 | 35.38(0.09) |
| | | 0.015 | 5.375 | |
| | | 0.019 | 6.808 | |
| | 298 | 0.012 | 5.958 | 49.65(0.08) |
| | | 0.015 | 7.448 | |
| | | 0.019 | 9.434 | |
| | 303 | 0.012 | 7.510 | 62.58(0.04) |
| | | 0.015 | 9.388 | |
| | | 0.019 | 11.891 | |
| | 308 | 0.012 | 10.501 | 87.51(0.02) |
| | | 0.015 | 13.126 | |
| | | 0.019 | 16.627 | |

[a] Initial concentrations of [ReOCl$_3$(ppyt)] and [ReOCl$_3$(ppzt)] are $5.43 \times 10^{-5}$ M and $4.65 \times 10^{-5}$ M, respectively. [b] Least-squares deviations are given in parentheses.

 © 2006 Wiley-VCH Verlag GmbH & Co. KGaA, Weinheim 

ditions (excess $PPh_3$), the rate is proportional to the concentration of the oxido complex, and the observed rate constant, $k_{obs}$, is proportional to the concentration of $PPh_3$. The reaction is thus second order in nature, see Equation (2).

$$\text{rate} = k_{obs}[ReOX_3(L)] = k[ReOX_3(L)][PPh_3] \quad (2)$$

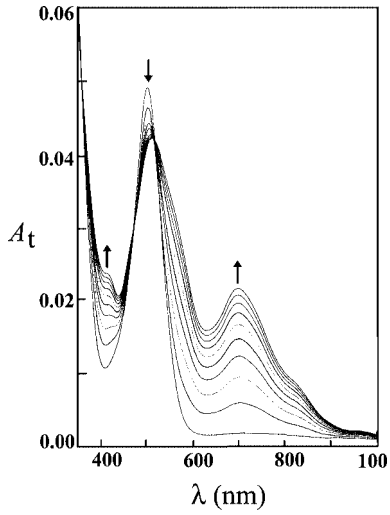


Figure 3. Time evolution spectra for the reaction of $[ReOCl_3(ppyt)]$ and $PPh_3$ in dichloromethane solution at 303 K ($A_t$ is absorbance).

Rates for all the complexes were determined at 303 K (Table 1), although in the cases of $[ReOCl_3(ppyt)]$ (**5e**) and $[ReOCl_3(ppzt)]$ (**5h**) variable-temperature studies were also made (Table 3). In both cases the rate constant, $k$, was found to obey the Eyring equation. The activation parameters $\Delta H^{\ddagger}$ and $\Delta S^{\ddagger}$ are as follows: 11.66(0.26) kcal mol$^{-1}$ and –27.48(0.88) cal K$^{-1}$ mol$^{-1}$ for **5e** and 9.94(0.28) kcal mol$^{-1}$ and –31.95(0.95) cal K$^{-1}$ mol$^{-1}$ for **5h**. The large and negative entropy of activation implies close association of $[ReOX_3(L)]$ and $PPh_3$ in the transition state, as in the model **7**,[10,17] where initial attack involves the phosphane lone pair and Re≡O π*-orbitals.

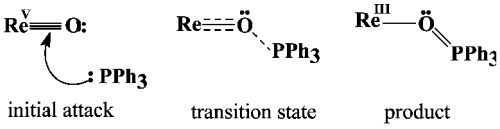


**7**

### Electron Withdrawal, Rate and Reduction Potential

The observed trend of reactivity is qualitatively consistent with the reaction model. Electron withdrawal from the $Re^{V}O$ moiety due to variation of X or due to modification of L is expected to favour the initial nucleophilic attack and thereby facilitate oxygen-atom transfer. This is systematically observed. We note that $[ReOCl_3(ppyt/ppzt)]$ is nearly twice as reactive as $[ReOBr_3(ppyt/ppzt)]$, in line with the higher electronegativity of Cl. Again, the rate trend $[ReOCl_3(mbpy)] < [ReOCl_3(bpy)] < [ReOCl_3(pbpy)]$ correctly reflects the electron-withdrawal power of the substituent (Me < H < Ph). The $[ReOCl_3(phen)]$ complex fits between the bpy and pbpy species. An increase in the number of nitrogen hetero atoms is a very effective instrument for achieving electron withdrawal.[32] Accordingly, the rate of oxygen-atom transfer in the case of $[ReOCl_3(ppzt)]$ is 2.5 and 25 times faster than that for $[ReOCl_3(ppyt)]$ and $[ReOCl_3(pbpy)]$, respectively (Table 1).

While electron withdrawal from the $Re^{V}O$ moiety by ligand variation facilities oxygen-atom transfer, it is also expected to make metal oxidation more difficult. Fortunately, the $[ReOX_3(L)]$ complexes are uniformly electroactive in acetonitrile solution, exhibiting a quasi-reversible one-electron oxidative response near 1.5 V vs. SCE assigned to the $Re^{VI}O/Re^{V}O$ couple. Representative voltammograms are shown in Figure 4 and reduction potential data are listed in Table 1.

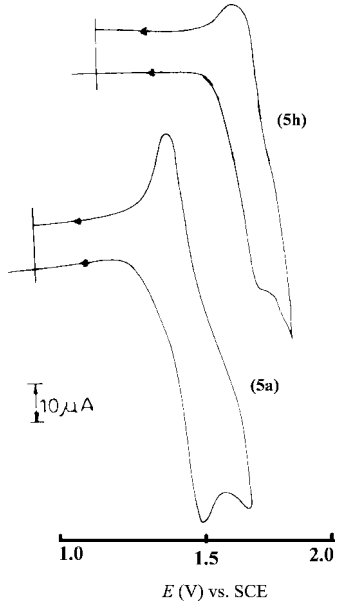


Figure 4. Cyclic voltammograms of $[ReOCl_3(bpy)]$ (**5a**) and $[ReOCl_3(ppzt)]$ (**5h**) in acetonitrile solution at platinum working electrode (scan rate: 100 mV s$^{-1}$).

The data of Table 1 reveal that the rate of oxygen-atom transfer rapidly increases with $E_{1/2}$ of the $Re^{VI}O/Re^{V}O$ couple. Indeed, there is a satisfactory linear correlation (correlation constant 0.99) between the logarithmic rate constant and the reduction potential (Figure 5). All the complexes except **5g** lie virtually on the least-squares line itself. The slope of the line is about 16. Evidently, a single linear equation of this type cannot encompass all $Re^{V}O$ complexes but it is gratifying to note that within a group where the L ligands belong to the same type (two six-membered N-heterocycles connected by a single bond) a simple correlation does exist.

 © 2006 Wiley-VCH Verlag GmbH & Co. KGaA, Weinheim 

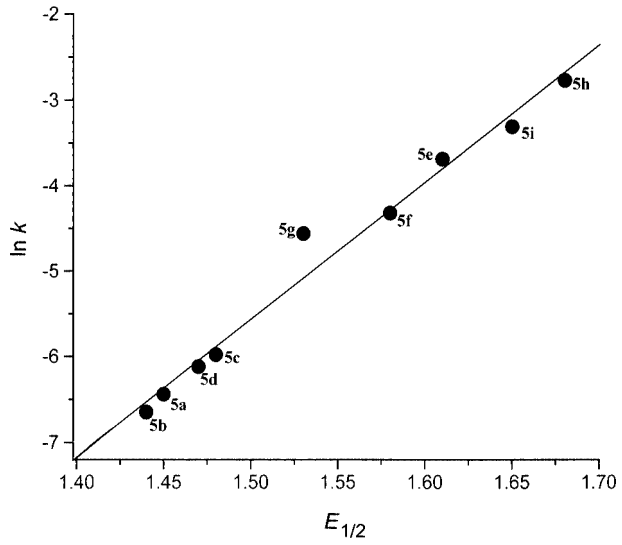


Figure 5. Plot of logarithmic rate constant vs. $Re^{VI}O/Re^{V}O$ reduction potential at 303 K.

## Conclusion

In our search for reactive $Re^{V}O$ complexes of *N*,*N*-chelating heterocyclic ligands (L) the rhenium chemistry of the pyridyl- and pyrazinyltriazine heterocycles ppyt, mpyt and ppzt has been developed in the form of the complexes [$ReOX_3$(L)] (X = Cl, Br), two of which have been structurally characterised.

These undergo strongly associative oxygen-atom transfer to $PPh_3$ ($\Delta S^{\ddagger} \approx -30$ cal $K^{-1}$ $mol^{-1}$). The rate of transfer has also been determined for other [$ReOCl_3$(L)] complexes (L = bpy, mbpy, pbpy and phen). The oxygen-atom transfer rates span nearly two orders of magnitude for the whole family examined here.

Consistent with the proposed reaction model based on nucleophilic attack of the $PPh_3$ lone pair on π*(Re≡O) orbitals, the transfer rate increases systematically with increasing electron withdrawal from $Re^{V}O$ due to variation of X (Cl > Br) or L (ppzt > ppyt > mpyt >> pbpy > phen > bpy > mbpy).

A second molecular parameter also responsive to electron withdrawal is the voltammetric $Re^{VI}O/Re^{V}O$ reduction potential, which shows the same trends as above. Indeed, the logarithmic rate of transfer correlates linearly with the $Re^{VI}O/Re^{V}O$ reduction potential within the present family of [$ReOX_3$(L)] complexes.

## Experimental Section

**Materials:** The complexes [$ReOX_3(AsPh_3)_2$][33] and [$ReOCl_3(Me_2S)(OPPh_3)$][19] and the triazine ligands[25,27] were prepared by reported methods. The purification and drying of dichloromethane and acetonitrile for spectral and electrochemical work was done as before.[34] Tetrahydrofuran and benzene ware dried using standard methods. All other chemicals and solvent were of reagent grade and were used as received.

**Physical Measurements:** UV/Vis spectral measurements were carried out with a Shimadzu UVPC 1601 spectrometer fitted with thermostatted cell compartments. $^1$H NMR spectra were recorded with a Bruker FT 300 MHz spectrometer. The atom numbering scheme used in $^1$H NMR is the same as in crystallography. Electrochemical measurements were performed under nitrogen with a CH 620A electrochemical analyzer, using a platinum working electrode. The supporting electrolyte was tetraethylammonium perchlorate (TEAP), and potentials are referred to the standard calomel electrode (SCE). Room-temperature magnetic susceptibilities of powders were measured with a model 155 PAR vibrating sample magnetometer. Microanalyses (C,H,N) were performed using a Perkin–Elmer 2400 series II elemental analyzer. Mass spectra were measured with Q-TOF mass spectrometer.

**Synthesis of Complexes:** The complex [$ReOCl_3$(bpy)] (**5a**) was synthesised from [$ReOCl_3(Me_2S)(OPPh_3)$] and bpy by a reported procedure.[19] We found the procedure to be suitable for synthesis of **5b**–**5d** as well with some modifications. Details are given below for [$ReOCl_3$(phen)] (**5d**).

**[$ReOCl_3$(phen)] (5d):** A suspension of [$ReOCl_3(Me_2S)(OPPh_3)$] (84 mg, 0.13 mmol) and phen (30 mg, 0.15 mmol) in 10 mL of tetrahydrofuran was stirred for 5 h. Filtration and washing with diethyl ether (5 × 5 mL) gave 43 mg (0.09 mmol, 68%) of yellowish **5d** in pure form. $C_{12}H_8Cl_3N_2ORe$ (488.78): calcd. C 29.49, H 1.64, N 5.73; found C 29.40, H 1.69, N 5.78. UV/Vis ($CH_2Cl_2$ solution: $\lambda_{max}$ (ε) = 270 nm (56500 $M^{-1}cm^{-1}$), 410 (4150), 456 (5690), 795 (160). IR (KBr): $\tilde{\nu}$ = 989 $cm^{-1}$ ($\nu_{Re=O}$). $^1$H NMR (300 MHz, $CDCl_3$, 298 K): δ = 10.03 (d, *J* = 5.20 Hz, H1), 9.31 (d, *J* = 8.10 Hz, H7), 8.98 (d, *J* = 5.01 Hz, H3), 8.62 (t, *J* = 7.62 Hz, H2), 8.60 (d, *J* = 7.98 Hz, H9), 8.55 (d, *J* = 5.32 Hz, H12), 8.52 (d, *J* = 5.30 Hz, H11), 8.30 (t, *J* = 8.02 Hz, H8) ppm.

**[$ReOCl_3$(mbpy)] (5b):** Yield: 44 mg (69%.) $C_{12}H_{12}Cl_3N_2ORe$ (492.81): calcd. C 29.25, H 2.45, N 5.68 found C 29.30, H 2.40, N 5.60. UV/Vis ($CH_2Cl_2$ solution): $\lambda_{max}$ (ε) = 299 (47400), 458 (7670), 795 (225). IR (KBr): $\tilde{\nu}$ = 984 $cm^{-1}$ ($\nu_{Re=O}$). $^1$H NMR (300 MHz, [$D_6$]DMSO, 298 K): δ = 8.92 (s, H4), 8.55 (s, H10), 8.40 (d, *J* = 5.85 Hz, H1), 8.10 (d, *J* = 6.06 Hz, H7), 7.48 (d, *J* = 6.03 Hz, H2), 7.40 (d, *J* = 5.79 Hz, H8), 4.70 (s, 3 H, 3-Me), 3.65 (s, 3 H, 9-Me) ppm.

**[$ReOCl_3$(pbpy)] (5c):** Yield: 52 mg (65%). $C_{22}H_{16}Cl_3N_2ORe$ (616.96): calcd. C 42.79, H 2.59, N 4.53; found C 42.70, H 2.53, N 4.58. UV/Vis ($CH_2Cl_2$ solution): $\lambda_{max}$ (ε) = 326 nm (50000 $M^{-1}cm^{-1}$), 465 (13100), 774 (253). IR (KBr): $\tilde{\nu}$ = 987 $cm^{-1}$ ($\nu_{Re=O}$). $^1$H NMR (300 MHz, $CDCl_3$, 298 K): δ = 9.08 (s, H4), 8.60 (d, *J* = 8.10 Hz, H1), 8.55 (d, *J* = 8.16 Hz, H2), 8.00–7.50 (m, 13 H, H3, H8, H10, 2Ph) ppm.

**The Complexes 5e–5i:** These complexes were prepared in 75–85% yield by the same general procedure based on the reaction of [$ReOX_3(AsPh_3)_2$] with L in benzene at room temperature. Details are given here for a representative case.

**[$ReOCl_3$(ppyt)] (5e):** The ligand ppyt (34 mg, 0.11 mmol) was added to a suspension of [$ReOCl_3(AsPh_3)_2$] (100 mg, 0.11 mmol) in 25 mL of benzene. The resulting mixture was stirred for 1 h at room temperature to produce a pink solution. The solvent was then removed under reduced pressure. The solid mass thus obtained was repeatedly washed with *n*-hexane to remove the liberated $AsPh_3$. The solid was then dissolved in 5 mL of dichloromethane and subjected to chromatography on a silica gel column (10 × 1 cm, 60–120 mesh) prepared in toluene. The pink complex was eluted with pure dichloromethane. Solvent removal from the eluate under reduced pressure afforded [$ReOCl_3$(ppyt)] in pure form, which was dried under vacuo over fused calcium chloride. Yield: 53 mg (78%). $C_{20}H_{14}Cl_3N_4ORe$ (618.93): calcd. C 38.81, H 2.28, N 9.05; found C 38.87, H 2.21, N

 © 2006 Wiley-VCH Verlag GmbH & Co. KGaA, Weinheim 

9.09. UV/Vis ($CH_2Cl_2$ solution): $\lambda_{max}$ ($\varepsilon$) = 306 nm (35400 $M^{-1}cm^{-1}$), 508 (13800), 736 (550). IR (KBr): $\tilde{\nu}$ = 1000 $cm^{-1}$ ($\nu_{Re\equiv O}$). $^1H$ NMR (300 MHz, $CDCl_3$, 298 K): $\delta$ = 8.91 (d, $J$ = 9.09 Hz, H1), 8.52 (d, $J$ = 7.41 Hz, H4), 8.14 (t, $J$ = 7.20 Hz, H3), 7.94 (t, $J$ = 7.74 Hz, H18), 7.72 (d, $J$ = 7.98 Hz, 2 H, H10, H14), 7.64 (d, $J$ = 7.05 Hz, 2 H, H16, H20), 7.59 (t, $J$ = 7.95 Hz, 2 H, H11, H13), 7.53 (t, $J$ = 6.93 Hz, 2 H, H17, H19), 7.44 (t, $J$ = 7.79 Hz, H12), 7.37 (t, $J$ = 6.60 Hz, H2) ppm.

**[ReOBr$_3$(ppyt)] (5f):** Yield: 60 mg (80%). $C_{20}H_{14}Br_3N_4ORe$ (752.28): calcd. C 31.93, H 1.88, N 7.45; found C 31.90, H 1.93, N 7.40. UV/Vis ($CH_2Cl_2$ solution): $\lambda_{max}$ ($\varepsilon$) = 302 nm (34300 $M^{-1}cm^{-1}$), 514 (10900), 726 (1050). IR (KBr): $\tilde{\nu}$ = 996 $cm^{-1}$ ($\nu_{Re\equiv O}$). $^1H$ NMR (300 MHz, $CDCl_3$, 298 K): $\delta$ = 8.92 (d, $J$ = 5.82 Hz, H1), 8.51 (d, $J$ = 7.89 Hz, H4), 8.14 (t, $J$ = 7.77 Hz, H3), 7.72 (d, $J$ = 7.41 Hz, 2 H, H10, H14), 7.63 (d, $J$ = 7.08 Hz, 2 H, H16, H20), 7.58 (t, $J$ = 8.88 Hz, 2 H, H11, H13), 7.53 (t, $J$ = 8.22 Hz, 2 H, H17, H19), 7.42 (t, $J$ = 7.68 Hz, H12), 7.42 (t, $J$ = 7.74 Hz, H18), 7.34 (t, $J$ = 5.24 Hz, H2) ppm.

**[ReOCl$_3$(mpyt)] (5g):** Yield: 41 mg (75%). $C_{10}H_{10}Cl_3N_4ORe$ (494.79): calcd. C 24.27, H 2.04, N 11.32; found C 24.30, H 2.08, N 11.40. UV/Vis ($CH_2Cl_2$ solution): $\lambda_{max}$ ($\varepsilon$) = 300 nm (32900 $M^{-1}cm^{-1}$), 496 (6800), 701 (950). IR (KBr): $\tilde{\nu}$ = 994 $cm^{-1}$ ($\nu_{Re\equiv O}$). $^1H$ NMR (300 MHz, $CDCl_3$, 298 K): $\delta$ = 8.74 (d, $J$ = 5.02 Hz, H1), 7.92 (t, $J$ = 7.77 Hz, H3), 7.76 (d, $J$ = 7.74 Hz, H4), 7.60 (t, $J$ = 5.90 Hz, H2), 2.68 (s, 3 H, 7-Me), 2.64 (s, 3 H, 8-Me) ppm.

**[ReOCl$_3$(ppzt)] (5h):** Yield: 57 mg (83%). $C_{19}H_{13}Cl_3N_5ORe$ (619.92): calcd. C 36.81, H 2.11, N 11.30; found C 36.86, H 2.17, N 11.35. UV/Vis ($CH_2Cl_2$ solution): $\lambda_{max}$ ($\varepsilon$) = 310 nm (36400 $M^{-1}cm^{-1}$), 523 (13800), 737 (540). IR (KBr): $\tilde{\nu}$ = 1004 $cm^{-1}$ ($\nu_{Re\equiv O}$). $^1H$ NMR (300 MHz, $CDCl_3$, 298 K): $\delta$ = 9.95 (s, H3), 8.85 (d, $J$ = 6.00 Hz, H2), 7.95 (d, $J$ = 4.20 Hz, 2 H, H9, H13), 7.88 (d, $J$ = 7.20 Hz, H1), 7.74 (d, $J$ = 7.80 Hz, 2 H, H15, H19), 7.65 (t, $J$ = 6.90 Hz, 2 H, H10, H12), 7.54 (t, $J$ = 10.80 Hz, 2 H, H16, H18), 7.45 (t, $J$ = 7.80 Hz, H11), 7.45 (t, $J$ = 7.80 Hz, H17) ppm.

**[ReOBr$_3$(ppzt)] (5i):** Yield: 64 mg (85%). $C_{19}H_{13}Br_3N_5ORe$ (753.27): calcd. C 30.30, H 1.74, N 9.30; found C 30.25, H 1.70, N 9.24. UV/Vis ($CH_2Cl_2$ solution): $\lambda_{max}$ ($\varepsilon$) = 310 nm (35100 $M^{-1}cm^{-1}$), 531 (10600), 739 (850). IR (KBr): $\tilde{\nu}$ = 999 $cm^{-1}$ ($\nu_{Re\equiv O}$). $^1H$ NMR (300 MHz, $CDCl_3$, 298 K): $\delta$ = 9.75 (s, H3), 8.81 (d, $J$ = 4.76 Hz, H2), 8.60 (d, $J$ = 4.88 Hz, H1), 7.74 (d, $J$ = 7.59 Hz, 2 H, H9, H13), 7.66 (d, $J$ = 6.42 Hz, 2 H, H15, H19), 7.56 (t, $J$ = 7.80 Hz, 2 H, H10, H12), 7.52 (t, $J$ = 6.42 Hz, 2 H, H16, H18), 7.48 (t, $J$ = 5.90 Hz, H11), 7.46 (t, $J$ = 7.44 Hz, H17) ppm.

**Complexes [Re(OPPh$_3$)Cl$_3$(L)]:** These were prepared in 75–80% yield by the same general procedure based on the reaction of [ReOX$_3$(L)] with triphenylphosphane in benzene at room temperature. Details are given below for a representative case and data for a second compound prepared analogously follow.

**[Re(OPPh$_3$)Cl$_3$(ppyt)]:** $PPh_3$ (68 mg, 0.28 mmol) was added to a solution of [ReOCl$_3$(ppyt)] (80 mg, 0.13 mmol) in 25 mL of dichloromethane. The resulting solution was magnetically stirred for 4 h at room temperature and during this time the colour of the solution changed from pink to violet. It was then subjected to chromatography on a silica gel column. Excess $PPh_3$ was eluted with benzene. A violet band was eluted with a benzene/acetonitrile (25:2) mixture. The solvent was removed under reduced pressure and the violet complex so obtained was dried under vacuo over fused calcium chloride. Yield: 90 mg (75%). $C_{38}H_{29}Cl_3N_4OPRe$ (881.22): calcd. C 51.80, H 3.32, N 6.35; found C 51.72, H 3.39, N 6.30. UV/Vis ($CH_2Cl_2$ solution): $\lambda_{max}$ ($\varepsilon$) = 289 nm (31300 $M^{-1}cm^{-1}$), 532 (8700), 701 (5150). IR (KBr): $\tilde{\nu}$ = 1119 $cm^{-1}$ ($\nu_{O=P}$). $^1H$ NMR (300 MHz, $CDCl_3$, 298 K): $\delta$ = 25.99 (t, $J$ = 9.00 Hz, H2), 10.19 (t, $J$ = 7.50 Hz, H12), 9.58 (d, $J$ = 8.40 Hz, 2 H, H16, H20), 9.50 (t, $J$ = 7.50 Hz, 2 H, H11, H13), 8.22 (d, $J$ = 7.80 Hz, H1), 8.10 (d, $J$ = 8.10 Hz, 2 H, H10, H14), 7.73 (t, $J$ = 7.20 Hz, H18), 7.17 [d, $J$ = 7.20 Hz, 6 H, $o$-H($PPh_3$)], 6.77 [t, $J$ = 7.50 Hz, 3 H, $p$-H($PPh_3$)], 5.06 (t, $J$ = 7.50 Hz, 2 H, H17, H19), 4.00 [t, $J$ = 7.80 Hz, 6 H, $m$-H($PPh_3$)], 2.79 (d, $J$ = 4.80 Hz, H4), –17.01 (t, $J$ = 9.00 Hz, H3) ppm. $E_{1/2}$ ($Re^{IV}/Re^{III}$ couple): 0.33 V ($\Delta E_p$ = 70 mV). $\mu$ (in powder): 1.51 $\mu_B$ (298 K). Q-TOF-MS: $m/z$ 881.30.

**[Re(OPPh$_3$)Br$_3$(ppzt)]:** Yield: 104 mg (79%). $C_{37}H_{28}Br_3N_5OPRe$ (1015.56): calcd. C 43.76, H 2.78, N 6.96; found C 43.70, H 2.73, N 6.83. UV/Vis ($CH_2Cl_2$ solution): $\lambda_{max}$ ($\varepsilon$) = 300 nm (32900 $M^{-1}cm^{-1}$), 525 (8400), 665 (5900). IR (KBr): $\tilde{\nu}$ = 1121 $cm^{-1}$ ($\nu_{O=P}$). $^1H$ NMR (300 MHz, $CDCl_3$, 298 K): $\delta$ = 42.83 (d, $J$ = 7.11 Hz, H1), 21.98 (s, H3), 8.78 (t, $J$ = 7.62 Hz, 2 H, H10, H12), 8.62 (d, $J$ = 7.08 Hz, 2 H, H9, H13), 7.93 (t, $J$ = 6.87 Hz, H11), 7.68 (d, $J$ = 7.89 Hz, H2), 7.41 [d, $J$ = 6.72 Hz, 6 H, $o$-H($PPh_3$)], 6.96 [t, $J$ = 6.96 Hz, 3 H, $p$-H ($PPh_3$)], 6.27 (t, $J$ = 6.36 Hz, H17), 6.13 [t, $J$ = 8.03 Hz, 6 H, $m$-H($PPh_3$)], 5.67 (t, $J$ = 7.44 Hz, 2 H, H16, H18), 4.61 (d, $J$ = 7.74 Hz, 2 H, H15, H19) ppm. $E_{1/2}$ ($Re^{IV}/Re^{III}$ couple): 0.58 V ($\Delta E_p$ = 90 mV). $\mu$ (in powder): 1.67 $\mu_B$ (298 K). Q-TOF-MS: $m/z$ 1015.34.

**Rate Measurement:** The representative case of the reaction of [ReOCl$_3$(ppyt)] with $PPh_3$ will be described. A known excess of $PPh_3$ was added to a solution of [ReOCl$_3$(ppyt)] ($5.43 \times 10^{-5}$ M) in dichloromethane at the desired temperature, and the thermostatted reaction was followed spectrophotometrically (quartz cell; path length: 1 cm) by measuring the absorbance ($A_\alpha$) of the peak at 710 nm as a function of time ($t$). The absorbance ($A_\alpha$) at the end of the reaction (24 h) was also measured. Values of $k_{obs}$ and $k$ were obtained from the slopes of the linear plots of $-[\ln(A_\alpha - A_t)]$ vs. $t$ and $k_{obs}$ vs. [$PPh_3$] respectively. The activation enthalpy and entropy parameters were determined from the linear plot of $-\ln(kh/k_BT)$ vs. $T^{-1}$ using the Eyring equation, see Equation (3).

$$k = (k_BT/h)\exp(-\Delta H^{\ddagger}/RT)\exp(\Delta S^{\ddagger}/R) \quad (3)$$

**Crystal Structure Determination:** Single crystals of the complexes [ReOCl$_3$(ppyt)] (**5e**) and [ReOCl$_3$(ppzt)] (**5h**) were grown by slow diffusion of hexane into dichloromethane solutions of the respective compounds. Data were collected on a Nicolet R3m/V four-circle diffractometer with graphite-monochromated Mo-$K_\alpha$ radiation ($\lambda$ = 0.71073 Å) by the $\omega$-scan technique in the range $3° \leq 2\theta < 50°$. All data were corrected for Lorentz-polarisation and absorption.[35] The metal atoms were located from Patterson maps and the rest of the non-hydrogen atoms emerged from successive Fourier syntheses. The structures were then refined by a full-matrix least-squares procedure on $F^2$. All non-hydrogen atoms were refined anisotropically. All hydrogen atoms were included in calculated positions. Calculations were performed using the SHELXTL™ V 5.03 program package.[36]

**Data for 5e:** $C_{20}H_{14}Cl_3N_4ORe$, monoclinic, $P2_1/n$, $a$ = 8.920(2), $b$ = 15.021(3), $c$ = 15.558(3) Å, $\beta$ = 92.05(3)°, $V$ = 2083.2(3) Å$^3$, $Z$ = 4, 3111 unique reflections ($R_{int}$ = 0.0000). Final residuals $R_1$ = 0.0556 and $wR_2$ = 0.1405 [$I > 2\sigma(I)$].

**Data for 5h:** $C_{19}H_{13}Cl_3N_5ORe$, monoclinic, $P2_1/c$, $a$ = 9.274(2), $b$ = 16.418(3), $c$ = 13.732(3) Å, $\beta$ = 98.70(3)°, $V$ = 2066.8(7) Å$^3$, $Z$ = 4, 3617 unique reflections ($R_{int}$ = 0.0648). Final residuals $R_1$ = 0.0472 and $wR_2$ = 0.1154 [$I > 2\sigma(I)$].

 © 2006 Wiley-VCH Verlag GmbH & Co. KGaA, Weinheim 

CCDC-292211 and -292212 contain the supplementary crystallographic data for this paper. These data can be obtained free of charge from The Cambridge Crystallographic Data Centre via www.ccdc.cam.ac.uk/data_request/cif.

## Acknowledgments

We thank the Department of Science and Technology and the Council of Scientific and Industrial Research, New Delhi for financial support.

[1] G. Rouschias, G. Wilkinson, *J. Chem. Soc. A* **1967**, 993–1000.
[2] J. F. Rowbottom, G. Wilkinson, *J. Chem. Soc., Dalton Trans.* **1972**, 826–830.
[3] G. Lante, J. H. Espenson, *Inorg. Chem.* **2000**, *39*, 4809–4814.
[4] S. B. Symore, S. N. Brown, *Inorg. Chem.* **2000**, *39*, 325–332.
[5] C. Zhang, I. A. Guzei, J. H. Espenson, *Inorg. Chem.* **2001**, *40*, 2437–2438.
[6] Y. Wang, G. Lante, J. H. Espenson, *Inorg. Chem.* **2002**, *41*, 1272–1280.
[7] B. D. Sherry, A. T. Radosevich, F. D. Toste, *J. Am. Chem. Soc.* **2003**, *125*, 6076–6077.
[8] J. J. K. Smith, K. A. Nolin, H. P. Gunterman, F. D. Toste, *J. Am. Chem. Soc.* **2003**, *125*, 4056–4057.
[9] M. M. Abu-Omar, *Chem. Commun.* **2003**, 2102–2111.
[10] A. Chakravorty, *Eur. J. Inorg. Chem.* **2005**, 4863–4875.
[11] B. K. Dirghangi, M. Menon, A. Pramanik, A. Chakravorty, *Inorg. Chem.* **1997**, *36*, 1095–1101.
[12] S. Das, I. Chakraborty, A. Chakravorty, *Inorg. Chem.* **2003**, *42*, 6545–6555.
[13] S. Bhattacharyya, I. Chakraborty, B. K. Dirghangi, A. Chakravorty, *Inorg. Chem.* **2001**, *40*, 286–293.
[14] a) S. Banerjee, S. Bhattacharyya, B. K. Dirghangi, M. Menon, A. Chakravorty, *Inorg. Chem.* **2000**, *39*, 6–13; b) I. Chakraborty, S. Bhattacharyya, S. Banerjee, B. K. Dirghangi, A. Chakravorty, *J. Chem. Soc., Dalton Trans.* **1999**, 3747–3753; c) S. Bhattacharyya, S. Banerjee, B. K. Dirghangi, M. Menon, A. Chakravorty, *J. Chem. Soc., Dalton Trans.* **1999**, 155–159.
[15] S. Das, I. Chakraborty, A. Chakravorty, *Polyhedron* **2003**, *22*, 901–907.
[16] S. Bhattacharyya, I. Chakraborty, B. K. Dirghangi, A. Chakravorty, *Chem. Commun.* **2000**, 1813–1814.
[17] J. Gangopadhyay, S. Sengupta, S. Bhattacharyya, I. Chakraborty, A. Chakravorty, *Inorg. Chem.* **2002**, *41*, 2616–2622.
[18] S. Sengupta, J. Gangopadhyay, A. Chakravorty, *Dalton Trans.* **2003**, 4635–4643.
[19] J. C. Bryan, R. E. Stenkamp, J. H. Tulip, J. M. Mayer, *Inorg. Chem.* **1987**, *26*, 2283–2288.
[20] S. Das, Ph. D. Thesis, Jadavpur University, Jadavpur Kolkata, India, **2005**.
[21] a) S. Fortin, A. L. Beauchamp, *Inorg. Chem.* **2000**, *39*, 4886–4893; b) M. C. Chakravorti, *J. Inorg. Nucl. Chem.* **1975**, *37*, 1991–1993.
[22] a) R. D. Swarnakar, D. K. Chakraborty, *Indian J. Chem.* **1972**, *10*, 528–531; b) V. I. Belova, Y. K. Syrkin, D. K. Chakrabarti, B. N. Ivanov-Emin, *Z. Strukt. Khim.* **1968**, *9*, 73–78.
[23] a) A. A. Schilt, P. J. Taylor, *Anal. Chem.* **1970**, *42*, 220–224; b) H. Katano, H. Kuboyama, M. Senda, *J. Electroanal. Chem.* **2000**, *483*, 117–123; c) C. D. Chriswell, A. A. Schilt, *Anal. Chem.* **1974**, *46*, 992–996; d) P. L. Croot, K. A. Hunter, *Anal. Chim. Acta* **2000**, *406*, 289–302; e) J. Almong, B. Glattstein, *J. Forensic Sci.* **1997**, *42*, 993–996; f) S. Comment, M. Bonfanti, A. Gallusser, *J. Can. Soc. Forensic Sci.* **1998**, *31*, 79–94.
[24] a) J. Zhang, F. C. Anson, *J. Electroanal. Chem.* **1993**, *348*, 81–97; b) R. Uma, M. Palaniandavar, R. Butcher, *J. Chem. Soc., Dalton Trans.* **1996**, 2061–2066; c) S. S. Chen, R. C. Kapoor, *Chem. Environ. Res.* **1992**, *1*, 67–72; d) R. Hage, J. H. Van Diemen, G. Ehrlich, J. G. Haasnoot, D. J. Stufkene, T. L. Shoeck, J. G. Vos, J. Reedijk, *Inorg. Chem.* **1990**, *29*, 988–993; e) J. Granifo, *Polyhedron* **1995**, *14*, 1593–1599.
[25] R. Hage, J. G. Haasnoot, J. Reedijk, *Inorg. Chim. Acta* **1990**, *172*, 19–23.
[26] J. Granifo, *Polyhedron* **1996**, *15*, 203–209.
[27] H. Deng, J. Cai, H. Xu, H. Zhang, L. N. Ji, *Dalton Trans.* **2003**, 325–330.
[28] I. Chakraborty, B. K. Panda, J. Gangopadhyay, A. Chakravorty, *Inorg. Chem.* **2005**, *44*, 1054–1060 and references cited therein.
[29] B. Machura, J. O. Dziegielewski, R. Kruszynski, T. J. Bartczak, J. Kusz, *Polyhedron* **2003**, *22*, 2573–2580.
[30] F. Tisato, F. Refosco, C. Bolzati, A. Cagnolini, S. Gatto, G. Bandoli, *J. Chem. Soc., Dalton Trans.* **1997**, 1421–1428.
[31] a) M. Menon, S. Choudhury, A. Pramanik, A. K. Deb, S. K. Chandra, N. Bag, S. Goswami, A. Chakravorty, *J. Chem. Soc., Chem. Commun.* **1994**, 57–58; b) M. Menon, A. Pramanik, N. Bag, A. Chakravorty, *Inorg. Chem.* **1994**, *33*, 403–404.
[32] R. T. Morrison, R. N. Boyd, *Organic Chemistry*, 4th ed., Allyn and Bacon, Boston, **1983**.
[33] N. P. Johnson, C. J. L. Lock, G. Wilkinson, *J. Chem. Soc.* **1964**, 1054–1066.
[34] a) G. K. Lahiri, S. Bhattacharya, B. K. Ghosh, A. Chakravorty, *Inorg. Chem.* **1987**, *26*, 4324–4331; b) D. T. Sawyer, J. L. Roberts Jr, *Experimental Electrochemistry for Chemists*, Wiley, New York, **1974**, p. 167.
[35] A. C. T. North, D. C. Philips, F. S. Mathews, *Acta Crystallogr., Sect. A* **1968**, *24*, 351–359.
[36] G. M. Sheldrick, *SHELXTL V 5.03*; Bruker Analytical X-ray Systems: Madison, WI, **1994**; Part Number 269-015900.

Received: December 8, 2005
Published Online: April 4, 2006

 © 2006 Wiley-VCH Verlag GmbH & Co. KGaA, Weinheim 

DOI: 10.1002/ejic.200501111

# Relationship Between the Nearest-Neighbor Exchange Coupling Constants and the Number of Exchange Interactions in the Cyano-Bridged $MnMo_6(CN)_{18}$ Cluster: Density Functional Theory Calculations

**Yi-Quan Zhang*[a] and Cheng-Lin Luo[a]**

**Keywords:** Molecular magnetism / Density functional calculations / Broken symmetry / Cyano-bridged clusters / Single-molecule studies

A theoretical density functional study of the relationship between the nearest-neighbor MnMo constants and the number of exchange interactions in the cyano-bridged $K[(Me_3tacn)_6MnMo_6(CN)_{18}](ClO_4)_3$ cluster is presented. Two approaches (the first approach consisted of evaluating the exchange coupling constant $J_{ij}$ between two paramagnetic metal centers *i* and *j* in the hexanuclear molecule by calculating the energy differences between the highest and broken-symmetry spin states of a model molecule in which metal atoms except for *i* and *j* are substituted by diamagnetic $Y^{III}$ cations, and the second is to calculate the different spin-state energies of hexanuclear complexes and use the Heisenberg Hamiltonian to obtain the exchange coupling constants between different metal centers) show that the antiferromagnetic coupling interactions between nearest neighbors weaken with the increase of the number of exchange interactions. The various $\theta$ angles have an influence on the interactions between the nearest-neighbor MoMn but do not change the trend between $J_{12}$ and the number of exchange interactions. Moreover, Kahn's qualitative theory succeeded in being applied to interpret the trend.

(© Wiley-VCH Verlag GmbH & Co. KGaA, 69451 Weinheim, Germany, 2006)

## Introduction

In recent years, the synthesis and study of single-molecule magnets with high total spin that can be used to store potential data have received much attention.[1–14] In these single-molecule magnets, much attention is focused on developing cyano-bridged cluster systems, for which the parameters S and D are more readily adjusted by substitution of various metal ions.[5–14] Long and coworkers found that the absolute nearest-neighbor constants *J* always diminish as the number of exchange interactions increases for a series of cyano-bridged $Mn^{II}$–$Cr^{III}$,[5,6] $Mn^{III}$–$Cr^{III}$,[7–9] $Mo^{III}$–$Ni^{II}$,[10] and $Cr^{III}$–$Ni^{II}$ [11,12] complexes. It was demonstrated that the interactions between the nearest-neighbor $Mn^{III}$ and $Cr^{III}$ decrease with the increase of the number of exchange interactions when we investigated the magnetism of the cyano-bridged $\{Cr[CNMn(salen)(H_2O)]_6\}^{3+}$ [7,8] cluster and the linear trinuclear $[(5\text{-Brsalen})_2(H_2O)_2Mn_2Cr(CN)_6]$[9] cluster.[13] For the cyano-bridged single-molecule cluster $K[(Me_3tacn)_6MnMo_6(CN)_{18}](ClO_4)_3$,[14] which has a substantial increase in the nearest-neighbor MnMo interactions compared to those of the above MnCr complexes, we want to know whether the above trend also exists. and whether the MoMnMo angle has an influence on the interactions between the nearest neighbors. Kahn's qualitative theory[15,16] was used to interpret the relationship. Finally, we will discuss the relationship between the calculated spin-density populations on $Mn^{II}$ or $Mo^{III}$ and the number of exchange interactions.

## Computational Methodology

### Description of the Complexes and Models

In calculations, we used model $\mathbf{A^6}$ $[(Me_3tacn)_6MnMo_6(CN)_{18}]^{2+}$, which is a polynuclear cluster in which six $[(Me_3tacn)Mo(CN)_3]$ units surround a central $Mn^{II}$ ion (see Figure 1) and was directly taken from complex $K[(Me_3tacn)_6MnMo_6(CN)_{18}](ClO_4)_3$[14] and not optimized. The bridges are of the Mo–CN–Mn type and, therefore, the Mn atom with an $N_6$ coordination sphere is in a high-spin configuration. Models $\mathbf{A^1}$, $\mathbf{A^2}$, $\mathbf{A^3}$, $\mathbf{A^4}$, and $\mathbf{A^5}$ (the superscript numbers denote the number of exchange interactions) (see Figure 2) were used to investigate the relationship between the nearest-neighbor exchange coupling constants $J_{12}$ and the number of exchange interactions. To investigate the relationship between $J_{12}$ and the $\theta$ angle (we use $\theta$ to represent the MoMnMo angle), we obtained three different structures that all include two of the exchange interactions $\mathbf{A^2}$, $\mathbf{A^{2'}}$, and $\mathbf{A^{2''}}$ (see Figure 3). The $\theta$ angles for $\mathbf{A^2}$, $\mathbf{A^{2'}}$, and $\mathbf{A^{2''}}$ are 86.38°, 113.33°, and 154.92°, respectively. All the mod-

[a] School of Physical Science and Technology, Nanjing Normal University,
Nanjing 210097, China
E-mail: zhangyiquan@pine.njnu.edu.cn

 © 2006 Wiley-VCH Verlag GmbH & Co. KGaA, Weinheim 

els were directly taken from model **A**$^{6}$, and not optimized because small changes to the experimental structures could result in significant deviations for the coupling constants. To easily perceive the topology of the metal framework, we used sticks for the carbons of the tacn ligands and the terminal CN ligands in Figure 1, Figure 2, and Figure 3.

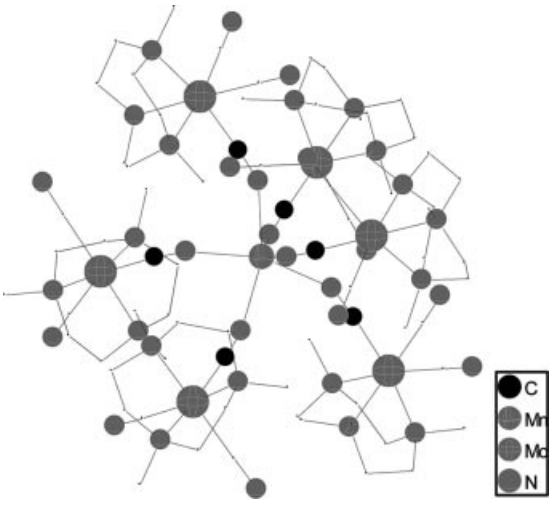


Figure 1. Structure of model **A**$^{6}$ ($MnMo_6$).

**Calculation on Exchange Coupling Constant**

There are two different approaches to calculating the exchange coupling constants for the polynuclear complexes.[17–19] In all calculations, the spin-orbit coupling is not considered, so the magnetic anisotropy does not need to be considered. The first approach consisted of evaluating the exchange coupling constant $J_{ij}$ between two paramagnetic metal centers $i$ and $j$ in the hexanuclear molecule by calculating the energy difference between the highest and broken-symmetry spin states of a model molecule in which metal atoms except for $i$ and $j$ are substituted by diamagnetic $Y^{III}$ cations. This approach was used to calculate the exchange coupling interactions of hexanuclear complexes in many papers and proved to give good results compared to the experimental ones.[17–20] The second approach is to calculate the different spin-state energies of hexanuclear complexes and use the Heisenberg Hamiltonian to obtain the exchange coupling constants between different metal centers.[17–21] It is a more rigorous approach in evaluating $J$ for polynuclear complexes than the first one. How to use these two approaches will be interpreted thoroughly below.

For the first approach, the magnetic interactions between $Mn^{II}$ and $Mo^{III}$ metal ions were studied on the basis of density functional theory (DFT) coupled with the broken-symmetry approach (BS).[22–24] The exchange coupling constants $J$ were evaluated by calculating the energy difference

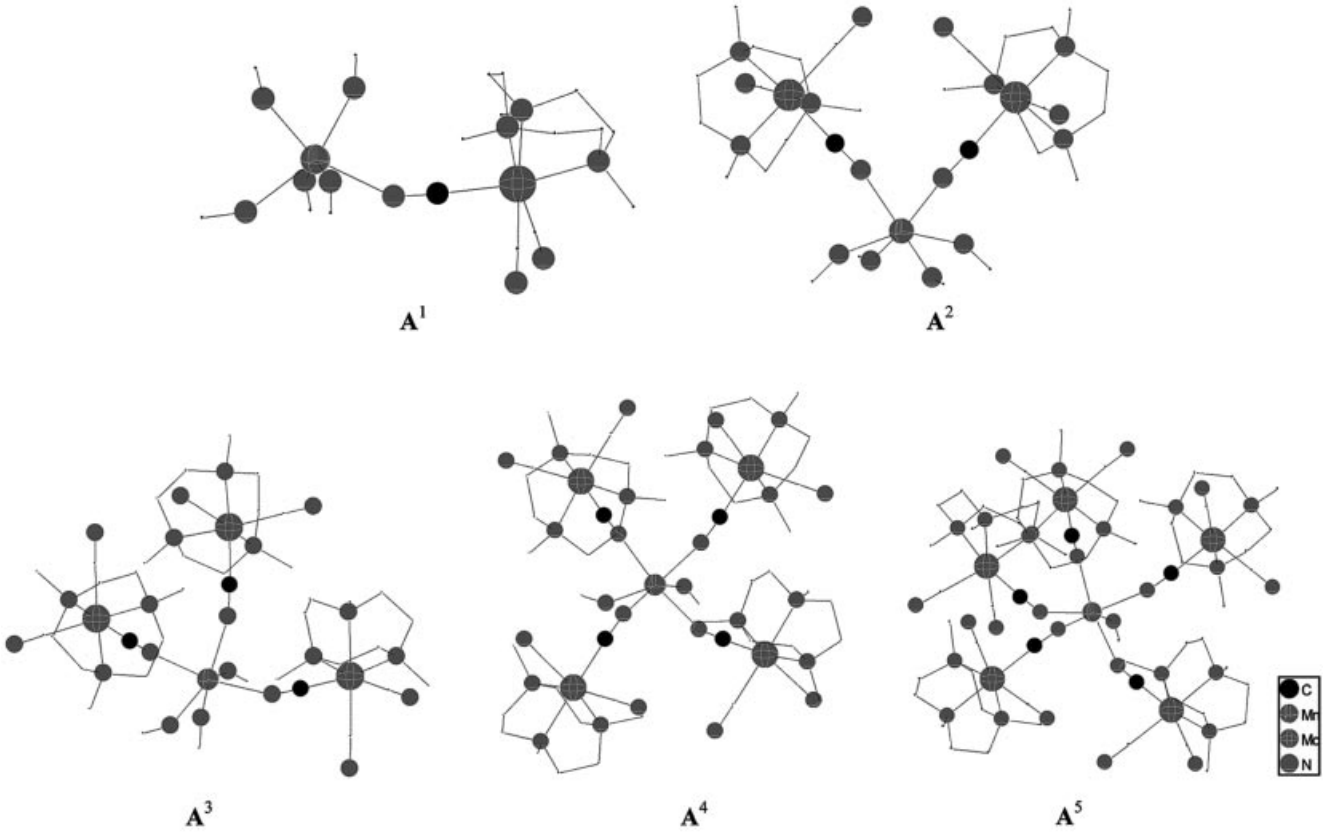


Figure 2. Structure of models **A**$^{1}$ (MnMo), **A**$^{2}$ ($MnMo_2$), **A**$^{3}$ ($MnMo_3$), **A**$^{4}$ ($MnMo_4$), and **A**$^{5}$ ($MnMo_5$).

 © 2006 Wiley-VCH Verlag GmbH & Co. KGaA, Weinheim 

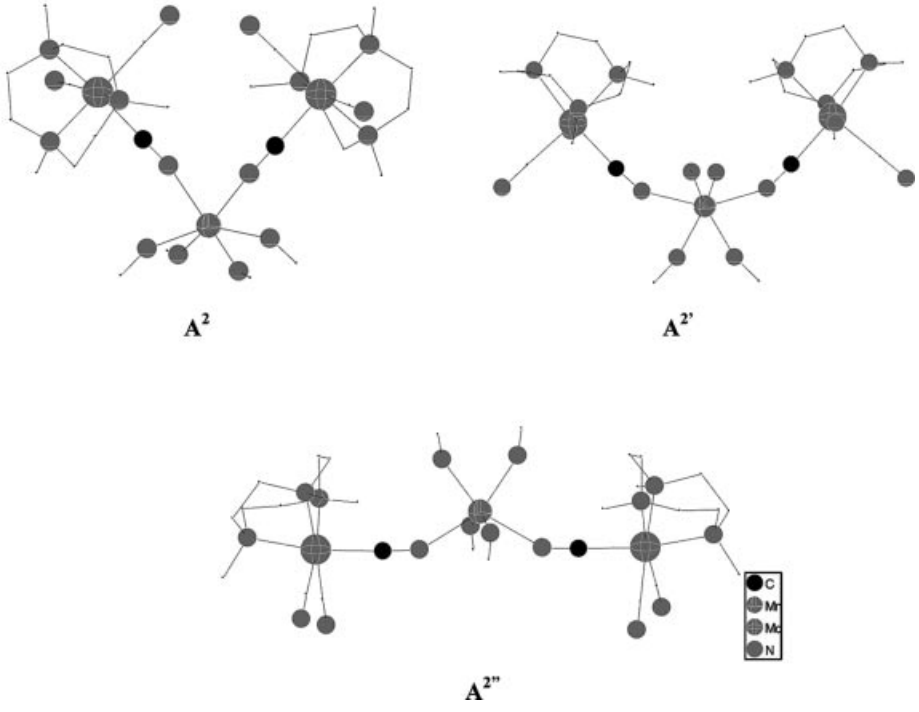


Figure 3. Structure of models **A²** ($\theta$ = 86.38°), **A²′** ($\theta$ = 113.33°), and **A²″** ($\theta$ = 154.92°).

between the high-spin state ($E_{HS}$) and the broken-symmetry state ($E_{BS}$). Assume the spin Hamiltonian is defined as Equation (1).

$$\hat{H} = -2J\hat{S}_1 \cdot \hat{S}_2 \quad (1)$$

If the spin-projected approach is used, the equation proposed by Noodleman[22–24] to extract the $J$ value for a binuclear transition-metal complex is thus Equation (2).

$$J = \frac{E_{BS} - E_{HS}}{4S_1S_2} \quad (2)$$

while with the nonprojected approach:[25]

$$2J = \frac{E_{BS} - E_{HS}}{2S_1S_2 + S_2} \quad (3)$$

where $S_1$ and $S_2$ are the total spins of two interacting paramagnetic centers and $S_1 > S_2$ is assumed for heterodinuclear complexes.

However, Equation (3) corresponds strictly to the limit of complete overlap between the magnetic orbitals and such a hypothesis is not sustained,[26] although it can give good $J$ results compared to the experimental ones.[25,27,28]

For all models, where $S_1$ = 5/2 for $Mn^{II}$ and $S_2$ = 3/2 for $Mo^{III}$, from Equation (2) we get Equation (4).

$$J = (E_{BS} - E_{HS})/15 \quad (4)$$

The second approach is more rigorous. If one neglects the spin-orbit coupling effects, the Hamiltonian for a general extended structure is indicated in Equation (5).

$$\hat{H} = \sum_{i>j} -2J_{ij}\hat{S}_i\hat{S}_j \quad (5)$$

where $\hat{S}_i$ and $\hat{S}_j$ are the spin operators of the different paramagnetic centers. The $J_{ij}$ values are the coupling constants between all the paramagnetic centers. In our paper, we only consider the exchange interactions between nearest neighbors. This fact together with the presence of additional symmetry elements in the structure normally result in a reduced set of $J_{ij}$ values.

When using single-determinant methods such as DFT, the calculated energies are related to the diagonal matrix elements of the Heisenberg Hamiltonian. An alternative way to describe the system is by considering an Ising Hamiltonian as a special case of a Heisenberg Hamiltonian in which only the diagonal terms are kept. Thus, we can consider that the wave functions obtained with the single-determinant methods are eigenfunctions of an Ising Hamiltonian that is formulated with the same $J$ values as the original Heisenberg Hamiltonian because their diagonal terms are identical. For that reason, the $J$ values obtained with single-determinant methods are directly comparable to those obtained from experimental data.[19] So we can use the single-dominant method DFT to obtain the $J$ values from calculating the energy differences between two spin-states. A thorough description of this approach can be found in refs.[17–19,21]

For **A²**, which includes three magnetic centers, the magnetic coupling constants $J_{12}$ between each nearest-neighbor $Mo^{III}$–$Mn^{II}$ pair are the same for the symmetry of the complete structure. Moreover, we only need the nearest-neighbor coupling constant. So, the $J_{12}$ can be extracted by

 © 2006 Wiley-VCH Verlag GmbH & Co. KGaA, Weinheim 

calculating the energies of two spin-states: **1** with $S = 1/2$, and **2** with $S = 11/2$, which are shown in Figure 4. The equation to extract $J_{12}$ is thus Equation (6).

$$J_{12} = (E_1 - E_2)/35 \quad (6)$$

Figure 4. Two spin states: **1** with $S = 1/2$ (left), **2** with $S = 11/2$ (right) for model $\mathbf{A^2}$.

To obtain all the nearest-neighbor constants $J_{12}$ for the modeled structures $\mathbf{A^3}$, $\mathbf{A^4}$, $\mathbf{A^5}$, and $\mathbf{A^6}$, we also only need to calculate the energy of two spin-states for each model. Two spin-states for each model are as follows: **1** with $S = 1/2$ and **2** with $S = 11/2$ for $\mathbf{A^2}$, **1** with $S = 2$ and **2** with $S = 14/2$ for $\mathbf{A^3}$, **1** with $S = 7/2$ and **2** with $S = 17/2$ for $\mathbf{A^4}$, **1** with $S = 5$ and **2** with $S = 10$ for $\mathbf{A^5}$, and **1** with $S = 13/2$ and **2** with $S = 23/2$ for $\mathbf{A^6}$. For all these **1** states, only the spins on $Mn^{II}$ are flipped. The equations to extract $J_{12}$ values for all of the models are as follows:
For model $\mathbf{A^3}$, Equation (7) is thus:

$$J_{12} = (E_1 - E_2)/50 \quad (7)$$

For model $\mathbf{A^4}$, Equation (8) is thus:

$$J_{12} = (E_1 - E_2)/65 \quad (8)$$

For model $\mathbf{A^5}$, Equation (9) is thus:

$$J_{12} = (E_1 - E_2)/80 \quad (9)$$

For model $\mathbf{A^6}$, Equation (10) is thus:

$$J_{12} = (E_1 - E_2)/95 \quad (10)$$

DFT calculations have been performed using the Amsterdam Density Functional (ADF, version 2004.01[29–31]) package for four models. Illas et al.[32] showed the strong dependence of the calculated $J$ with respect to the exchange-correlation functionals chosen. Several exchange-correlation functionals will be used to evaluate $J$. In the calculations of $J$ using ADF, the local density approximation (LDA) made use of the Vosko, Wilk, and Nusair[33] (VWN) local correlation functional. A series of generalized gradient approximation (GGA): Perdew-Wang 1991 (PW91),[34] Perdew-Burke-Ernzerhof (PBE),[35] and the recently developed OPTX-Perdew (Operdew)[36,37] and OPTX-Perdew–Burke–Ernzerhof (OPBE)[35–37] functionals were examined. Basis set TZV2P [a basis set of triple-ζ quality[38] supplemented with two p orbitals ("polarization functions")] was applied for all of the metals (Mo, Mn) and basis set DZP (a basis set of double-ζ quality[38] supplemented with one polarization function) for the other atoms (C, N, and H). The inner core shells of C(1s), N(1s), Mn(1s, 2s, 2p), Y(1s, 2s, 2p, 3s, 3p), and Mo(1s, 2s, 2p, 3s, 3p) were treated by the frozen core approximation. The accuracy parameter (accint) for the numerical integration grid was set to 4.0 for all of the complexes. The convergence standard of the system energy was set to be smaller than $10^{-6}$ eV, reaching a precision required for the evaluation of $J$.

## Results and Discussion

### Relationship Between $J$ and the Number of Exchange Interactions

The relationship between the nearest-neighbor exchange coupling constants $J_{12}$ and the number of exchange interactions is shown in Figure 5. Two approaches show that the absolute $J_{12}$ values decrease with the increase of the number of exchange interactions. The second approach gives better results than the first one for $\mathbf{A^2}$, $\mathbf{A^{2'}}$, and $\mathbf{A^{2''}}$. However, the two approaches give similar results for $\mathbf{A^3}$, $\mathbf{A^4}$, $\mathbf{A^5}$, and $\mathbf{A^6}$. This is because the decrease of the absolute $J_{12}$ values with the increase of the number of exchange interactions will reduce the differences between the results using the two approaches. Moreover, this is of conceptual importance, as the

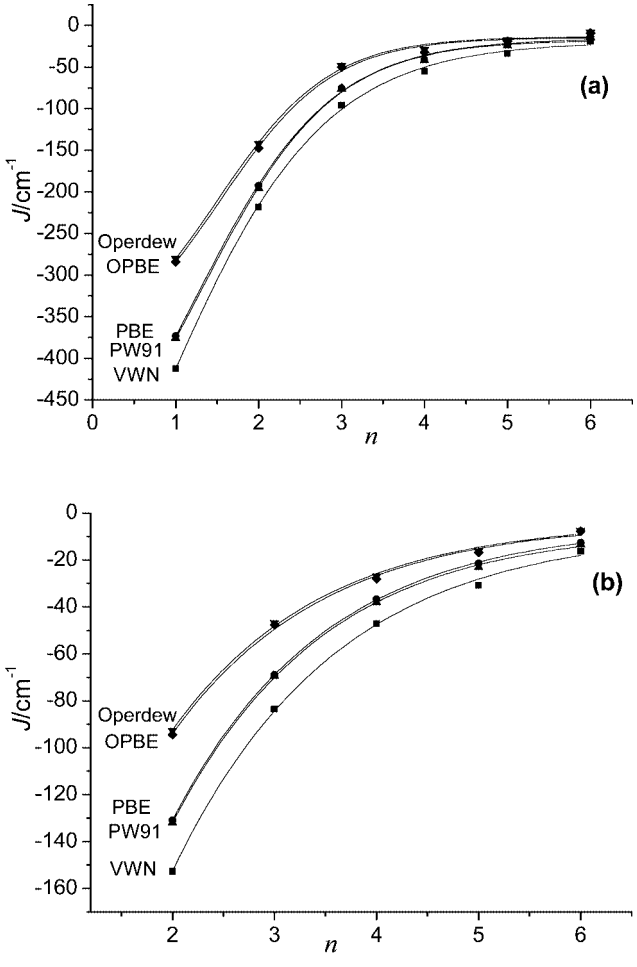


Figure 5. Relationship between the nearest-neighbor interaction constant $J_{12}$ ($cm^{-1}$) and the number of exchange interactions $n$ with several functionals [VWN (■), PW91 (●), PBE (▲), Operdew (▼), and OPBE (♦)] for the models of complex **I**. (a) The relationship using the first approach; (b) the relationship using the second approach.

 © 2006 Wiley-VCH Verlag GmbH & Co. KGaA, Weinheim 

Table 1. Experimental $J_{12}$ value for the complete structure and calculated $J_{12}$ values ($cm^{-1}$) for models **A**$^{1}$, **A**$^{2}$, **A**$^{2'}$, **A**$^{2''}$, **A**$^{3}$, and **A**$^{6}$ using two approaches with different functionals in ADF.

| | Approach | VWN | PW91 | PBE | Operdew | OPBE | Experiment |
|---|---|---|---|---|---|---|---|
| **A**$^{1}$ | first | –412.3 | –373.2 | –375.7 | –280.1 | –284.2 | |
| **A**$^{2}$ | first | –218.0 | –192.5 | –195.8 | –142.0 | –147.2 | |
| | second | –152.7 | –130.9 | –132.0 | –92.7 | –94.4 | |
| **A**$^{2'}$ | first | –208.2 | –183.2 | –184.8 | –133.0 | –136.3 | |
| | second | –147.9 | –127.3 | –128.3 | –89.4 | –91.4 | –6.7[10] |
| **A**$^{2''}$ | first | –164.4 | –132.8 | –133.9 | –84.6 | –87.7 | |
| | second | –123.1 | –98.4 | –99.2 | –62.4 | –64.4 | |
| **A**$^{3}$ | first | –95.8 | –75.4 | –76.1 | –48.1 | –50.1 | |
| | second | –83.6 | –68.9 | –69.5 | –46.7 | –47.7 | |
| **A**$^{6}$ | first | –18.7 | –13.4 | –14.8 | –8.6 | –9.0 | |
| | second | –16.3 | –12.6 | –13.5 | –7.4 | –7.7 | |

changes in $J_{12}$ values with the number of Mo atoms has to do with the fact that one new $t_{2g}$ orbital is incorporated in the exchange interaction for the first three Mo atoms, then the addition of new atoms does not introduce new orbital interactions, as reflected in the small slopes between $n = 3$ and $n = 6$. From Figure 5, the consistent behavior between the calculated $J_{12}$ values and the experimental value becomes better in the sequence: LDA (VWN), GGA (PW91, PBE), GGA (Operdew, OPBE), which was also found in our previous paper,[13] and the differences between the calculated $J_{12}$ values using the two approaches decrease with the increase of the number of exchange interactions for all of the functionals. From Table 1, the calculated $J_{12}$ values of model **A**$^{6}$, which is the most similar to the complete structure using two approaches with Operdew and OPBE functionals, have good agreement with the experimental result.[14]

The nearest-neighbor exchange coupling constants $J_{12}$ calculated using different functionals with two approaches for models **A**$^{2}$, **A**$^{2'}$, and **A**$^{2''}$ are shown in Table 1 where the absolute $J_{12}$ values calculated using two approaches with all the functionals all decrease with the increase of the $\theta$ angle. From Table 1, we also found that the increase of the $J_{12}$ values from **A**$^{2}$ to **A**$^{2'}$ is very small but large from **A**$^{2'}$ to **A**$^{2''}$. However, all the $J_{12}$ values of models **A**$^{2}$, **A**$^{2'}$, and **A**$^{2''}$ are between those of **A**$^{1}$ and **A**$^{3}$ and thus, the different $\theta$ angles do not change the trend between $J_{12}$ and the number of exchange interactions.

### Qualitative Analysis of the Exchange Interaction

According to Kahn's theory,[15,16] the exchange coupling constant $J$ is expressed in Equation (11) ($\hat{H} = -2J\hat{S}_1 \cdot \hat{S}_2$).

$$J_{ab} \approx K_{ab} - S_{ab}(\Delta^2 - \delta^2)^{1/2} \quad (11)$$

The positive term $K_{ab}$ represents the ferromagnetic contribution $J_F$, favoring parallel alignment of the spins and a triplet ground state, while the negative term $-S_{ab}(\Delta^2 - \delta^2)^{1/2}$ is the antiferromagnetic contribution $J_{AF}$, favoring antiparallel alignment of the spins and a singlet ground state. $S_{ab}$ is the overlap integrals between **a** and **b**. $\delta$ is the initial energy gap between the magnetic orbitals, and $\Delta$ the energy gap between the molecular orbitals derived from them. When several electrons are present on each center, $n_A$ on one side, $n_B$ on the other, $J$ can be described by the sum of the different "orbital pathways" $J_{ab}$, defined as above for pairs of orbitals **a** and **b** located on each site, weighted by the number of electrons [Equation (12)].

$$J = \sum_{a,b} J_{ab}/n_A n_B \quad (12)$$

Some authors[39,40] have recently shown that magnetic orbitals **a** and **b** are well represented by the localized orbitals of the broken-symmetry solution (they call them BS-OMSO[41]). There are 15 different contributions to the exchange coupling constant in each $Mo^{III}$–$Mn^{II}$ pair; the inappropriate orientation of some of the magnetic orbitals involved allows us to discard most of them. The ferromagnetic contributions are not considered because the antiferromagnetic coupling interactions for all the complexes are dominant. Moreover, as usual, the changes in the $J_{AF}$ term are more important and these contributions usually control the magnetostructural correlations, especially for those whose intramolecular interactions are antiferromagnetic. Hence, we only consider the changes in the $J_{AF}$ term. Among the important antiferromagnetic contributions, the most relevant ones are those involving two $t_{2g}$ orbitals ($d_{xy}$ and $d_{xz}$) of the $Mo^{III}$, which are directed toward the bridging ligands because of the good overlap with the appropriate $t_{2g}$ orbitals ($d_{xy}$ and $d_{xz}$) of the $Mn^{II}$. The mean overlap integral $S_{ij}$ between the four orbitals of the $Mo^{III}$ and $Mn^{II}$ can be expressed as Equation (13).

$$S_{ij} = 1/4(d_{xy}d_{xy} + d_{xy}d_{xz} + d_{xz}d_{xy} + d_{xz}d_{xz}) \quad (13)$$

Figure 6 gives the relationship between $J_{12}$ and $S_{ij}$ obtained using Equation (13) and the PW91 functional with the increase of the number of the exchange interaction. The absolute $J_{12}$ values decrease with the decrease of the $S_{ij}$ in accordance with Kahn's qualitative theory. Therefore, we can conclude that the increase of the number of exchange interactions will decrease the overlap integral $S_{ij}$ and lead to the decrease of the absolute $J_{12}$ values. This conclusion can be verified by investigating the relationship between $J_{12}$ and the spin-density populations on $Mo^{III}$ and $Mn^{II}$ with the increase of the number of exchange interactions. Because the spin-density populations on several $Mo^{II}$ are al-

 © 2006 Wiley-VCH Verlag GmbH & Co. KGaA, Weinheim 

most the same, we only use the spin-density population on one $Mo^{III}$. The spin-density populations on $Mo^{III}$ and $Mn^{II}$ were obtained with Mulliken Population Analysis[42] calculated using the PW91 functional in the ADF2004.01 package in the high-spin (HS) states. The relationship is shown in Figure 7 where the spin populations on $Mo^{III}$ and $Mn^{II}$ increase with the decrease of the absolute $J_{12}$. From Kahn's theory, the increase of the spin populations on $Mo^{III}$ and $Mn^{II}$ will decrease the $S_{ij}$ and then lead to the decrease of the absolute $J_{12}$. Moreover, we also found that the various spin populations on $Mn^{II}$ were much smaller than those on $Mo^{III}$. These results were calculated using the first approach. The second approach also gives the same trend between $J_{12}$ and the spin-density populations on $Mo^{III}$ and $Mn^{II}$ in the high-spin states.

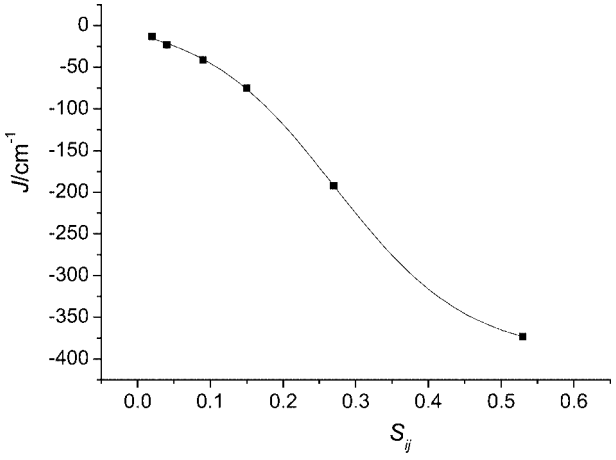


Figure 6. Relationship between the nearest-neighbor interaction constant $J_{12}$ ($cm^{-1}$) and the mean overlap integral $S_{ij}$ with the increase of the number of exchange interactions using the PW91 functional.

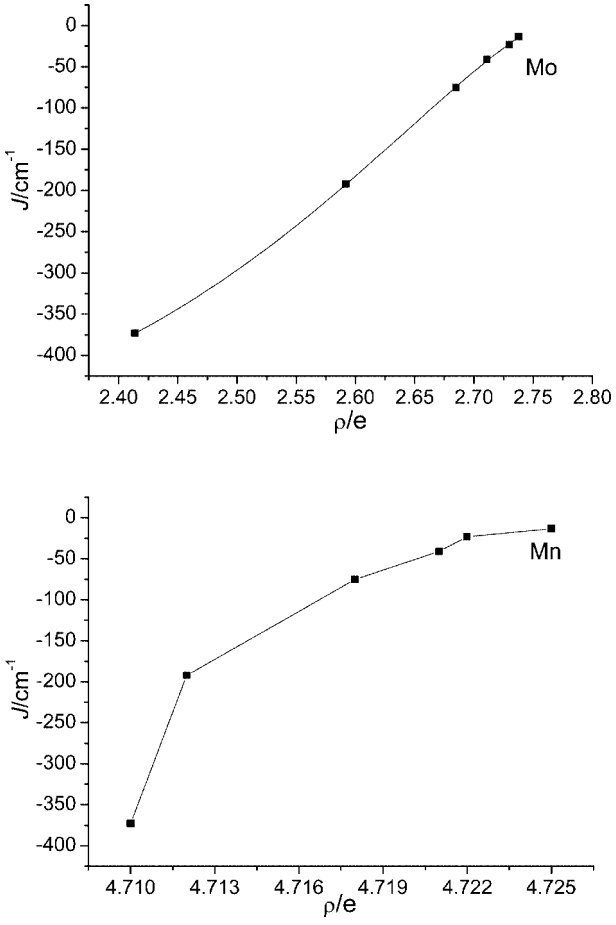


Figure 7. Relationship between the nearest-neighbor interaction constant $J_{12}$ ($cm^{-1}$) and the spin-density populations $\rho$ on $Mo^{III}$ (top) and $Mn^{II}$ (bottom) in the high-spin states with the PW91 functional using the first approach.

## Conclusions

Two approaches were used to investigate the magnetic coupling interactions between the nearest-neighbor $Mo^{III}$ and $Mn^{II}$. From our calculations, both approaches show that the antiferromagnetic interactions between nearest-neighbors decrease with the increase of the number of exchange interactions for our studied $Mo^{III}$–$Mn^{II}$ system. The trend is rationalized by using Kahn's theory through the overlap integral $S_{ij}$ and the spin-density populations on $Mo^{III}$ and $Mn^{II}$ in the HS states successfully. The absolute $J_{12}$ values calculated using two approaches with all the functionals all decrease with the increase of the $\theta$ angle, and the decrease of the absolute $J_{12}$ values from $\mathbf{A^2}$ to $\mathbf{A^{2'}}$ is very small but large from $\mathbf{A^{2'}}$ to $\mathbf{A^{2''}}$. However, all the $J_{12}$ values of models $\mathbf{A^2}$, $\mathbf{A^{2'}}$, and $\mathbf{A^{2''}}$ are between those of $\mathbf{A^1}$ and $\mathbf{A^3}$ and, thus, the different $\theta$ angles do not change the trend between $J_{12}$ and the number of exchange interactions.

## Acknowledgments

This project is supported by the Natural Science Foundation of Jiangsu Province of China, the Natural Science Foundation of University of Jiangsu Province of China (Grant No. 05KJB150055), and the Natural Science Foundation of Nanjing Normal University of China (Grant No. 111080B142).

[1] O. Kahn, C. J. Martinez, *Science* **1998**, *279*, 44–48.
[2] R. Sessoli, D. Gatteschi, A. Caneschi, M. A. Novak, *Nature* **1993**, *365*, 141–143.
[3] Y. Q. Zhang, C. L. Luo, Z. Yu, *New J. Chem.* **2005**, *29*, 1285–1290.
[4] Y. Q. Zhang, C. L. Luo, Z. Yu, *Int. J. Quantum Chem.* **2005**, *102*, 165–173.
[5] J. L. Heinrich, J. J. Sokol, A. G. Hee, J. R. Long, *J. Solid State Chem.* **2001**, *159*, 293–301.
[6] L. Toma, R. Lescouezec, J. Vaissermann, F. S. Delgado, C. Ruiz-Perez, R. Carrasco, J. Cano, F. Lloret, M. Julve, *Chem. Eur. J.* **2004**, *10*, 6130–6145.
[7] H. J. Choi, J. J. Sokol, J. R. Long, *J. Phys. Chem. Solids* **2004**, *65*, 839–844.
[8] X. Shen, B. Li, J. Zou, Z. Xu, *Transition Met. Chem.* **2002**, *27*, 372–376.
[9] H. J. Choi, J. J. Sokol, J. R. Long, *Inorg. Chem.* **2004**, *43*, 1606–1608.
[10] M. P. Shores, J. J. Sokol, J. R. Long, *J. Am. Chem. Soc.* **2002**, *124*, 2279–2292.
[11] P. A. Berseth, J. J. Sokol, M. P. Shores, J. L. Heinrich, J. R. Long, *J. Am. Chem. Soc.* **2000**, *122*, 9655–9662.

 © 2006 Wiley-VCH Verlag GmbH & Co. KGaA, Weinheim 

[12] T. Mallah, C. Auberger, M. Verdaguer, P. J. Veillet, *Chem. Soc., Chem. Commun.* **1995**, 61–62.
[13] Y. Q. Zhang, C. L. Luo, *J. Phys. Chem. A*, in press.
[14] J. J. Sokol, A. G. Hee, J. R. Long, *J. Am. Chem. Soc.* **2002**, *124*, 7656–7657.
[15] O. Kahn, B. J. Briat, *Chem. Soc. Faraday Trans.* **1976**, *72*, 268–281.
[16] J. J. Girerd, Y. Journaux, O. Kahn, *Chem. Phys. Lett.* **1981**, *82*, 534–538.
[17] E. Ruiz, J. Cano, S. Alvarez, A. Caneschi, D. Gatteschi, *J. Am. Chem. Soc.* **2003**, *125*, 6791–6794.
[18] E. Ruiz, A. Rodríguez-Fortea, P. Alemany, S. Alvarez, *Polyhedron* **2001**, *20*, 1323–1327.
[19] E. Ruiz, M. Llunell, P. Alemany, *J. Solid State Chem.* **2003**, *176*, 400–411.
[20] E. Ruiz, A. Rodríguez-Fortea, J. Cano, S. Alvarez, P. Alemany, *J. Comput. Chem.* **2003**, *24*, 982–989.
[21] O. Kahn, *Molecular Magnetism*, VCH Publishers, New York, **1993**, pp. 211–236.
[22] L. Noodleman, *J. Chem. Phys.* **1981**, *74*, 5737–5743.
[23] L. Noodleman, E. J. Baerends, *J. Am. Chem. Soc.* **1984**, *106*, 2316–2327.
[24] L. Noodleman, D. A. Case, *Adv. Inorg. Chem.* **1992**, *38*, 423–432.
[25] E. Ruiz, J. Cano, S. Awarez, P. Alemany, *J. Comput. Chem.* **1999**, *20*, 1391–1400.
[26] R. Caballol, O. Castell, F. Illas, I. de P. R. Moreira, J. P. Malrieu, *J. Phys. Chem. A* **1997**, *101*, 7860–7866.
[27] E. Ruiz, P. Alemany, S. Alvarez, J. Cano, *Inorg. Chem.* **1997**, *36*, 3683–3688.
[28] A. Rodríguez-Fortea, P. Alemany, S. Alvarez, E. Ruiz, *Chem. Eur. J.* **2001**, *7*, 627–637.
[29] F. M. te Velde, G. Bickelhaupt, S. J. A. van Gisbergen, C. Fonseca Guerra, E. J. Baerends, J. G. Snijders, T. Ziegler, *J. Comput. Chem.* **2001**, *22*, 931–967.
[30] C. Fonseca Guerra, G. J. G. Snijders, F. M. te Velde, E. J. Baerends, *Theor. Chem. Acc.* **1998**, *99*, 391–403.
[31] ADF2004.01, SCM, Theoretical Chemistry, Vrije Universiteit, Amsterdam, The Netherlands, http://www.scm.com.
[32] F. Illas, I. de P. R. Moreira, J. M. Bofill, M. Filatov, *Phys. Rev. B* **2004**, *70*, 132414.
[33] S. H. Vosko, L. Wilk, M. Nusair, *Can. J. Phys.* **1980**, *58*, 1200.
[34] J. P. Perdew, J. A. Chevary, S. H. Vosko, K. A. Jackson, M. R. Pederson, D. J. Singh, C. Fiolhais, *Phys. Rev. B* **1992**, *46*, 6671–6687.
[35] J. P. Perdew, K. Burke, M. Ernzerhof, *Phys. Rev. Lett.* **1996**, *77*, 3865–3868.
[36] N. C. Handy, A. J. Cohen, *Mol. Phys.* **2001**, *99*, 403–412.
[37] J. P. Perdew, *Phys. Rev. B* **1986**, *33*, 8822–8824.
[38] A. Schaefer, C. Huber, R. Ahlrichs, *J. Chem. Phys.* **1994**, *100*, 5829–5835.
[39] F. Fabrizi de Biani, E. Ruiz, J. Cano, J. J. Novoa, S. Alvarez, *Inorg. Chem.* **2000**, *39*, 3221–3229.
[40] C. Blanchet-Boiteux, J. M. Mouesca, *Theor. Chem. Acc.* **2000**, *104*, 257–264.
[41] C. Desplanches, E. Ruiz, A. Rodríguez-Fortea, *J. Am. Chem. Soc.* **2002**, *124*, 5197–5205.
[42] A. Szabo, N. S. Ostlund, *Modern Quantum Chemistry*, McGraw-Hill, New York, **1989**.

Received: December 13, 2005
Published Online: April 10, 2006

 © 2006 Wiley-VCH Verlag GmbH & Co. KGaA, Weinheim 

DOI: 10.1002/ejic.200600094

# Reactivity of the Inversely Polarised Arsaalkenes R–As=C(NMe$_2$)$_2$ {R = [($\eta^5$-C$_5$Me$_5$)(CO)$_2$Fe], *t*BuC(O)} Towards Vinylidene Complexes [$\eta^5$-(C$_5$H$_5$)(CO)(NO)W=C=C(H)R] (R = Ph, *t*Bu)

**Lothar Weber,*[a] Philipp Bayer,[a] Gabriel Noveski,[a] Hans-Georg Stammler,[a] and Beate Neumann[a]**

**Keywords:** Arsaalkenes / Heteroallene ligands / Vinylidene complexes / Tungsten

The reaction of the vinylidene complexes [(C$_5$H$_5$)(CO)(NO)W=C=C(H)R] (**10a**: R = *t*Bu; **10b**: R = Ph) with the arsaalkene *t*BuC(O)–As=C(NMe$_2$)$_2$ (**11**) afforded the novel $\eta^2$-1-arsaallene complexes [$\eta^2$-{*t*BuC(O)–As=C=C(H)R}W(CO)(NO)C$_5$H$_5$] (**13**: R = *t*Bu; **15**: R = Ph). Similarly, treatment of **10a** with the ferrioarsaalkene [(C$_5$Me$_5$)(CO)$_2$Fe–As=C(NMe$_2$)$_2$] (**12**) led to the formation of [$\eta^2$-{[(C$_5$Me$_5$)(CO)$_2$Fe]–As=C=C(H)*t*Bu}W(CO)(NO)(C$_5$H$_5$)] (**14**), whereas combination of **12** and **10b** yielded the carbene complex [(C$_5$H$_5$)(CO)(NO)W=C(NMe$_2$)C(Ph)=C(H)NMe$_2$] (**16**) in high yield instead of the anticipated arsaallene complex. The novel compounds **13**, **14**, **15** and **16** were characterised by elemental analyses and by means of spectroscopy (IR, $^1$H, $^{13}$C NMR). Moreover, the molecular structures of **14** and **15** were elucidated by X-ray diffraction analyses.

(© Wiley-VCH Verlag GmbH & Co. KGaA, 69451 Weinheim, Germany, 2006)

## Introduction

A considerable number of heteroallenes showing cumulated P=C and C=X bond systems[1] (X = CR$_2$,[2] NR,[2b,3] O,[2a,2d,4] PR[5]) have been described in the literature. Only those having bulky substituents at the phosphorus atom could be isolated and fully characterised. In some cases coordination to transition-metal complex fragments provides additional stability to such heterocumulenes.

In contrast to this, the chemistry of heterocumulenes with $\lambda^3$,$\sigma^2$-arsenic atoms is only poorly developed. The first stable arsaallene **2** has been synthesised from arsaalkene **1** and fluorenone in an organolithium-mediated condensation (Scheme 1).[6]

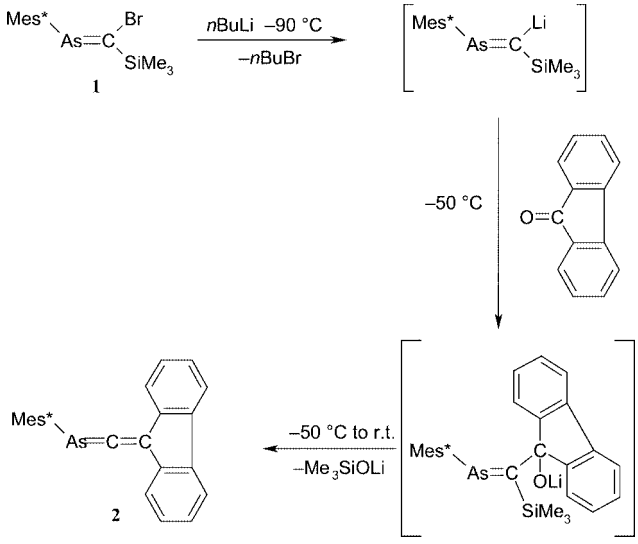


Scheme 1. Synthesis of arsaallene **2**.

The first and only arsaphosphaallene Mes*P=C=AsMes* (**5**) was synthesised from the reaction of phosphaalkene Mes*P=CBr$_2$ (**3a**) (Mes* = 2,4,6-*t*Bu$_3$C$_6$H$_2$) with *n*-butyllithium followed by the addition of Mes*AsF$_2$ to give intermediate **4a**. Treatment of the latter with *n*-butyllithium and LiF elimination led to the heterocumulene[7] (Scheme 2). Similarly, the stable 1,3-diarsaallene **6** was synthesised from Mes*As=CBr$_2$ (**3b**) and Mes*AsF$_2$[8] (Scheme 2).

During the course of our studies on inversely polarised arsaalkenes of the type R–As=C(NMe$_2$)$_2$ we disclosed their properties to act as nucleophilic arsanediyl transfer reagents. Reaction of phosphavinylidene complexes [(C$_5$H$_5$)(CO)$_2$M=P=C(SiMe$_3$)$_2$] (M = Mo, W) with [Cp*(CO)$_2$Fe–As=C(NMe$_2$)$_2$], *t*BuC(O)–As=C(NMe$_2$)$_2$ or MesC(O)–As=C(NMe$_2$)$_2$ [Mes = 2,4,6-(CH$_3$)$_3$C$_6$H$_2$] afforded complexes **7** featuring novel $\eta^3$-2-phospha-1-arsaallyl ligands[9] (Scheme 3).

Employment of the less bulky arsaalkene 4-EtC$_6$H$_4$–As=C(NMe$_2$)$_2$ gave rise to the formation of complexes **8** and **9** depending upon the stoichiometry of the reaction[9b,9c] (Scheme 4).

[a] Fakultät für Chemie der Universität Bielefeld,
Universitätsstrasse 25, 33615 Bielefeld, Germany
Fax: +49-521-106-6146
E-mail: lothar.weber@uni-bielefeld.de

 © 2006 Wiley-VCH Verlag GmbH & Co. KGaA, Weinheim 

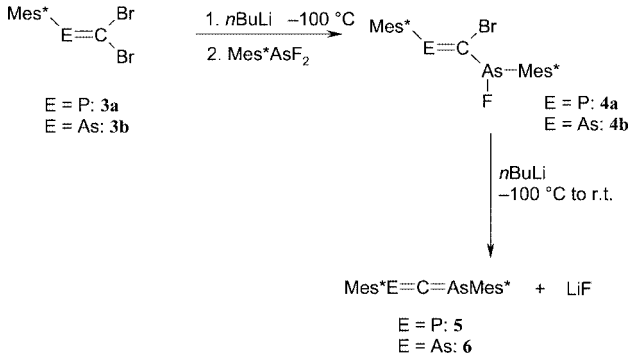


Scheme 2. Synthesis of heteroallenes **5** and **6**.

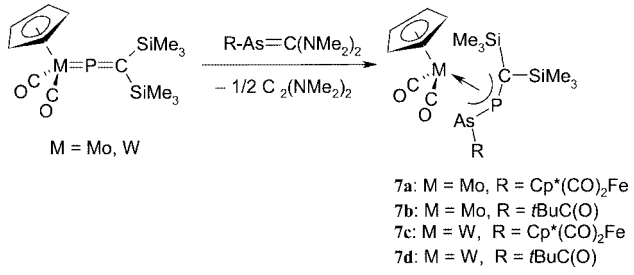


Scheme 3. Formation of 2-phospha-1-arsaallyl complexes **7a**–**d**.

In order to explore the scope and limitations of inversely polarised arsaalkenes to formally act as a source for arsanediyl species, we extended our investigations from phosphavinylidene to the related vinylidene complexes.

## Results and Discussion

Treatment of complex [Cp(CO)(NO)W=C=C(H)*t*Bu] (**10a**)[10] with an equimolar amount of arsaalkenes R–As=C(NMe$_2$)$_2$ {**11**: R = *t*BuC(O);[9b] **12**: R = [Cp*(CO)$_2$-Fe][11]} in diethyl ether solution in the range of –30 °C to 20 °C afforded the crystalline $\eta^2$-1-arsaallene complexes **13** (50% yield) and **14** (73% yield), respectively. Purification of the products was effected by column chromatography on Florisil with diethyl ether (for **13**) or pentane (for **14**) as eluents. In case of product **14**, two isomers could be distinguished by NMR spectroscopy (Scheme 5).

The air- and moisture-sensitive complexes are well soluble in saturated hydrocarbons, ethereal and aromatic solvents. Tetrakis(dimethylamino)ethene was formed as a by-product. After removal of solvent from the reaction mixture, a few drops of the alkene were distilled off and identified by comparison of the $^1$H and $^{13}$C NMR spectra with those of an authentic sample.

In the $^1$H NMR spectrum of **13**, singlets at $\delta$ = 1.24, 1.25, 4.81 and 7.86 ppm were assigned to the protons of the two different *tert*-butyl groups, the Cp ligand and the exocyclic methylene group, respectively. These data and the absence of resonances because of the C(NMe$_2$)$_2$ fragment indicate the combination of the vinylidene unit of **10a** and the arsanediyl group of **11** to the novel ligand in product **13**. In the precursor molecule **10a** the protons of the $C_5H_5$ ring are much more deshielded ($\delta$ = 5.81, 5.83 ppm), whereas the signal of the hydrogen atom at the vinylidene unit was observed at significantly higher field ($\delta$ = 5.69,

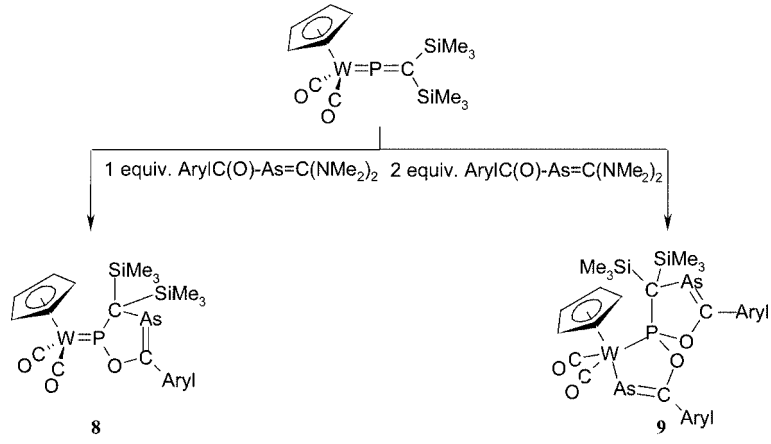


Scheme 4. Synthesis of complexes **8** and **9** (Aryl = 4-Et$C_6H_4$).

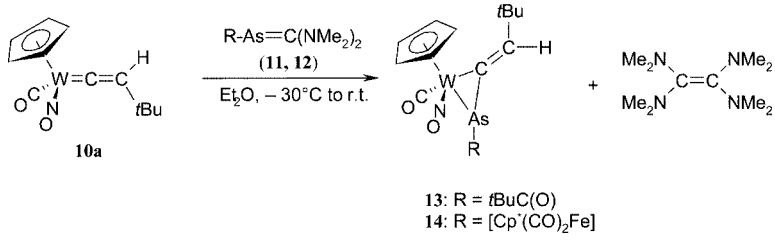


Scheme 5. Formation of the 1-arsaallene complexes **13**, **14**.

 © 2006 Wiley-VCH Verlag GmbH & Co. KGaA, Weinheim 

5.73 ppm). In the $^{13}C\{^1H\}$ NMR spectrum of **13**, singlets at $\delta$ = 174.8 and 158.3 ppm were assigned to the carbon atoms in β and α positions, respectively, of the arsaallene ligand. In **10a** these carbon atoms give rise to resonances at $\delta$ = 139.5, 140.0 and 338.4, 338.7 ppm. In the unsupported arsaallene **2**, singlets at $\delta$ = 255.8 and 129.1 ppm are due to the α- and β-C atoms, respectively, of the heteroallenic skeleton. The strong high-field shift of the α-C signal in going from **10a** to **13** points to the $\eta^2$-ligation of the As=C bond to the metal atom. The $^{13}C$ NMR signals of the terminal CO ligand and the acylic carbonyl group were observed at $\delta$ = 216.7 and 227.5 ppm, respectively. The significant low-field shift of the resonance of the CO ligand compared to precursor **10a** ($\delta$ = 210.8, 211.8 ppm) points to an improved donor capacity of the heteroallene ligand over the vinylidene system. This is also evident from the $\nu$(CO) bands in the IR spectrum of **13** ($\tilde{\nu}$ = 1982 $cm^{-1}$) and **10a** ($\tilde{\nu}$ = 2002 $cm^{-1}$).

Singlets in the $^1H$ NMR spectrum of the ferrioarsaallene complex **14** at $\delta$ = 1.35, 1.41; 1.51, 1.59; 5.08, 5.33 and 8.01, 8.03 ppm are readily assigned to the *tert*-butyl, methyl, cyclopentadienyl and vinylic protons, respectively, of two isomers. In the $^{13}C\{^1H\}$ NMR spectrum of **14**, the signals of the α-C atoms appeared as singlets at $\delta$ = 175.7 and 178.8 ppm with $^{13}C$-$^{183}W$ coupling constants of 109 and 118 Hz. Singlets at $\delta$ = 156.08 and 156.14 ppm were assigned to the carbon atoms in β-position. Carbonyl resonances at $\delta$ = 219.3 and 219.9 ppm are due to the W–CO unit whereas singlets at $\delta$ = 216.1, 216.9, 217.1 and 217.7 are due to the carbonyliron moieties.

An analogous treatment of vinylidene complex **10b** with pivaloylarsaalkene **11** afforded the thermolabile complex **15** as orange crystals in 29% yield (Scheme 6).

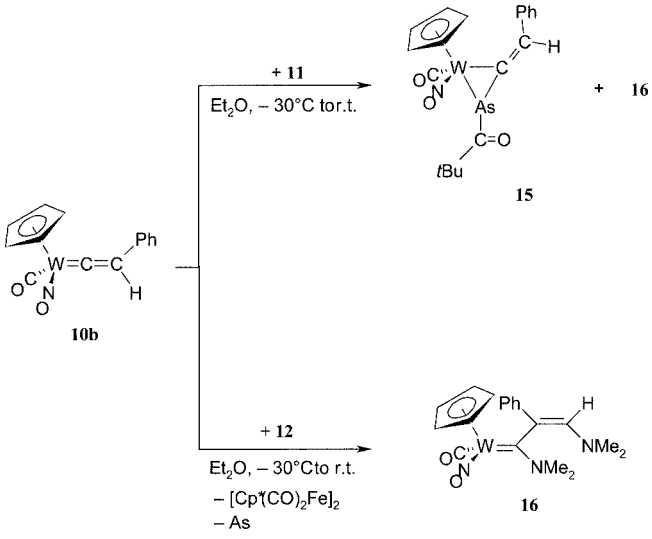


Scheme 6. Reaction of **10b** with arsaalkenes **11** and **12**.

In sharp contrast to this, reaction of **10b** with ferrioarsaalkene **12** did not lead to the expected arsaallene system. Instead, carbene complex **16** was isolated as red crystals in 69% yield. Elemental arsenic and complex $[Cp^*Fe(CO)_2]_2$ were obtained in 82% yield. According to the NMR spectra, product **15** was generated as one single isomer. Singlets in the $^1H$ NMR spectrum of **15** at $\delta$ = 1.24, 4.72 and 8.69 ppm are attributed to the hydrogen atoms at the *tert*-butyl group, the $C_5H_5$ ring and the vinylic unit, respectively. The carbon atoms of the arsaallene in α- and β-positions give rise to singlets at $\delta$ = 183.3 and 144.7 ppm, respectively. The resonances of the carbonyl ligand and the acylic CO group were observed as singlets at $\delta$ = 221.9 and 223.0 ppm, respectively. In comparison to precursor **10b** [$\tilde{\nu}$(CO) = 2010; $\tilde{\nu}$(NO) = 1654 $cm^{-1}$], the bands of the corresponding vibrations in **15** are bathochromically shifted [$\tilde{\nu}$(CO) = 1960; $\tilde{\nu}$(NO) = 1634 $cm^{-1}$].

The $^{13}C\{^1H\}$ NMR spectrum of **16** displays a singlet at $\delta$ = 260.8 ppm for the carbene carbon atom. This chemical shift is in good agreement with the corresponding signals of the aminocarbene complexes **17** ($\delta$ = 259.3; 259.7 ppm) or **18** ($\delta$ = 262.0 ppm).[12]

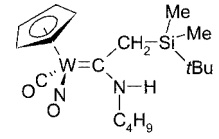


**17**

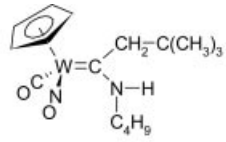


**18**

The methyl groups of the $Me_2N$ unit attached to the carbene centre are chemically and magnetically not equivalent giving rise to singlets at $\delta$ = 3.33 and 3.73 ppm in the $^1H$ NMR spectrum and $\delta$ = 44.4 and 49.3 ppm in the $^{13}C\{^1H\}$ NMR spectrum of **16**. Singlets at $\delta$ = 2.92 ppm in the $^1H$ NMR spectrum and $\delta$ = 42.6 ppm in the $^{13}C\{^1H\}$ spectrum are assigned to the $Me_2N$ group at the γ-carbon atom. The signal of the hydrogen atom at the C=C double bond was observed as a singlet at $\delta$ = 5.65 ppm. $^{13}C$ NMR singlets at $\delta$ = 140.6 and 118.8 ppm are due to the carbon atoms β-C and γ-C, respectively, of this double bond. A $^{13}C$ NMR singlet at $\delta$ = 233.2 ppm is attributed to the carbonyl ligand. This resonance is markedly low-field shifted in comparison to those of precursor **10b** and complex **15**, which reflects the pronounced donor capacity of the aminocarbene ligand. Accordingly, the $\nu$(CO) band in the IR spectrum of **16** is registered at $\tilde{\nu}$ = 1899 $cm^{-1}$, whereas the band for the nitrosyl stretching vibration appears at $\tilde{\nu}$ = 1768 $cm^{-1}$ and is hypsochromically shifted relative to those of **10b** [$\tilde{\nu}$(NO) = 1654 $cm^{-1}$] and **15** [$\tilde{\nu}$(NO) = 1634 $cm^{-1}$].

### X-ray Structural Investigations

Single crystals of **14** suitable for X-ray diffraction analysis were grown from diethyl ether at –30 °C.

The analysis (Figure 1, Table 1) displays a molecule with a distorted piano-stool geometry [As(1)–W(1)–C(6) =

 © 2006 Wiley-VCH Verlag GmbH & Co. KGaA, Weinheim 

67.8(1)°, C(6)–W(1)–N(1) = 93.2(2)°, N(1)–W(1)–C(7) = 92.7(1)°], with the nearly linear carbonyl and nitrosyl ligands [W(1)–C(6)–O(2) = 174.4(3)°, W(1)–N(1)–O(1) = 174.3(3)°]. The most interesting part of the molecule is the 1-arsaallene ligand, which is unsymmetrically linked to the metal atom in an $\eta^2$-fashion by bonds W(1)–As(1) [2.7145(3) Å] and W(1)–C(7) [2.165(3) Å]. The latter bond is significantly shorter than the W(1)–C distances of the [$C_5H_5W$] part of the molecule [2.353(3)–2.390(3) Å].

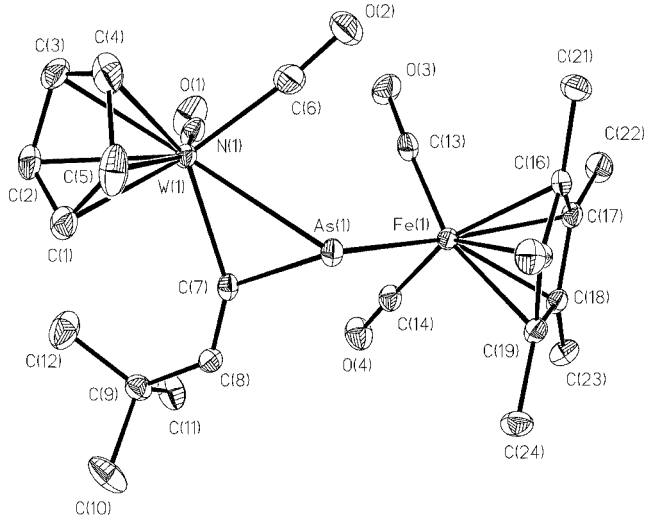


Figure 1. Molecular structure of **14** in the crystal. Selected bond lengths [Å] and angles [°]: W(1)–C(6) 2.004(4), W(1)–N(1) 1.809(3), W(1)–C(7) 2.165(3), W(1)–As(1) 2.7145(3), W(1)–C(1-5) 2.353(3)–2.390(3), As(1)–C(7) 1.911(3), As(1)–Fe(1) 2.4416(5), C(7)–C(8) 1.348(4); W(1)–C(6)–O(2) 174.4(3), W(1)–N(1)–O(1) 174.3(3), W(1)–C(7)–As(1) 52.4(1), W(1)–C(7)–C(8) 147.8(2), C(7)–W(1)–As(1) 44.4(1), C(7)–W(1)–N(1) 92.7(1), N(1)–W(1)–C(6) 93.2(1), C(6)–W(1)–As(1) 67.8(1), W(1)–As(1)–Fe(1) 119.5(2), W(1)–As(1)–C(7) 52.4(1), As(1)–C(7)–C(8) 129.0(2), Fe(1)–As(1)–C(7) 112.9(1).

The bond length W(1)–C(7) is comparable to that in complex **19** [2.178(7) Å][13] but much smaller than in the ($\eta^3$-2-phospha-1-arsaallyl)tungsten complex **7d** [2.439(2) Å].[9b]

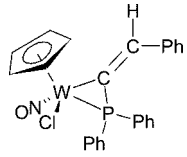


**19**

Thus, the situation of a π-complex involving the W-atom and As=C double bond is not reflected satisfactorily by the structural data of **14**. Moreover, inspection of W=C bond lengths in a series of (carbene)tungsten complexes [1.859(4)–2.23(2) Å][14] reveals some WC multiple bonding in our new complex. The separation W(1)–As(1) [2.7145(3) Å] is similar to the endocyclic bonds W(2)–As(1) [2.697(5) Å] and W(2)–As(2) [2.696(4) Å] determined in the diarsene complex **20**, whereas the exocyclic contacts W(1)–As(1) [2.638(5) Å] and W(3)–As(2) [2.626(5) Å] are slightly shorter.[15] The endocyclic bond length As(1)–C(7) [1.911(3) Å] may be envisaged as a multiple bond elongated

Table 1. Crystal data and data collection parameters.

| Compound | **14** | **15** |
|---|---|---|
| Empirical formula | $C_{24}H_{30}AsFeNO_4W$ | $C_{19}H_{20}AsNO_3W$ |
| $M_r$ [g mol$^{-1}$] | 711.11 | 569.13 |
| Crystal dimensions [mm] | 0.18×0.15×0.09 | 0.26×0.18×0.06 |
| Crystal system | monoclinic | monoclinic |
| Space group | $P2_1/n$ | $P2_1/a$ |
| $a$ [Å] | 11.728(2) | 12.8229(13) |
| $b$ [Å] | 14.886(2) | 7.3004(6) |
| $c$ [Å] | 14.900(2) | 20.8001(15) |
| $\beta$ [°] | 102.46(1) | 97.066(7) |
| $V$ [Å$^3$] | 2540.0(5) | 1932.4(3) |
| $Z$ | 4 | 4 |
| $\rho_{calcd.}$ [g cm$^{-3}$] | 1.860 | 1.956 |
| $\mu$ [mm$^{-1}$] | 6.418 | 7.694 |
| $F$(000) | 1384 | 1088 |
| $\theta$ [°] | 2.01–30.00 | 2.96–30.19 |
| No. reflections collected | 65907 | 81988 |
| Unique reflections | 7397 | 8259 |
| $R_{int}$ | 0.0560 | not defined |
| Refined parameters | 297 | 227 |
| Gof | 1.062 | 1.186 |
| $R_F$ [$I > 2\sigma(I)$] | 0.0278 | 0.0427 |
| $wR$ ($F^2$) [all data] | 0.0559 | 0.1173 |
| $\Delta\rho_{max/min}$ [e· Å$^{-3}$] | 1.831 (0.81 Å from W1)/ –0.968 | 1.352 (1.04 Å from W1)/ –2.221 |
| Remarks | | Crystals are twinned (ratio 42:58) by a rotation of 180° about 001. $R$(int) is not defined because of this twinning. |

by π-coordination. Generally, unsupported As=C bond lengths in acyclic arsaalkenes range from 1.789(3) Å in (*Z*)-Mes*As=C(Br)SiMe$_3$[6] to 1.867(9) Å in *t*Bu–As=C(F)-NEt$_2$.[16] For the As=C distance in 1-arsaallene **2** an even shorter value [1.754(2) Å] was determined.[6] The iron–arsenic bond of 2.4416(5) Å in **14** is markedly longer than in the 2-phospha-1-arsaallyl complex **7a** [2.4098(4) Å][9b] or in the ferrioarsacyclobutene **21** [2.396(1)].[11]

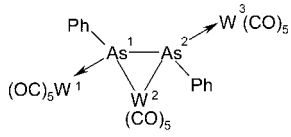


**20**

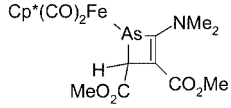


**21**

The carbon–carbon double bond C(7)–C(8) [1.348(4) Å] in **14** is lengthened with respect to the one in **2** [1.314(3) Å].[6] The angle As(1)–C(7)–C(8) of 129.0(2)° is strongly compressed when compared with the one in 1-arsaallene **2** [169.72(19)°]. Carbon atom C(8) is located in the plane defined by the atoms W(1), As(1) and C(7). Thereby the As atom is roughly placed in a *trans* disposition to the

 © 2006 Wiley-VCH Verlag GmbH & Co. KGaA, Weinheim 

nitrosyl ligand, whereas C(7) and the carbonyl group are *trans*-oriented.

Single crystals of complex **15** were grown from a diethyl ether solution at –30 °C. As given with compound **14**, the X-ray analysis displays an arsaallene ligand attached to the metal centre whereby a three-membered metalloheterocycle of atoms W(1), As(1) and C(1) is formed (Figure 2, Table 1).

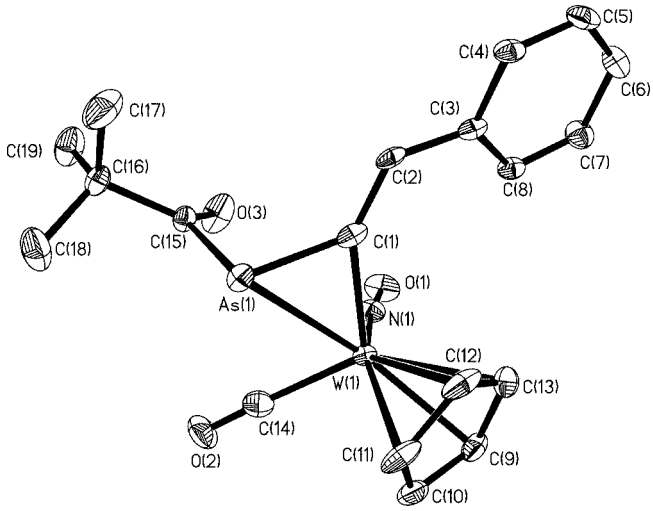


Figure 2. Molecular structure of **15** in the crystal. Selected bond lengths [Å] and angles [°]: W(1)–C(14) 2.034(7), W(1)–N(1) 1.806(5), W(1)–C(1) 2.134(6), W(1)–As(1) 2.690(1), W(1)–C(9-13) 2.336(6)–2.388(7), As(1)–C(1) 1.909(6), As(1)–C(15) 2.065(6), C(15)–O(3) 1.207(7), C(1)–C(2) 1.360(9), C(2)–C(3) 1.472(9), O(2)–C(14) 1.137(8), N(1)–O(1) 1.216(7); N(1)–W(1)–C(14) 88.3(3), N(1)–W(1)–C(1) 93.0(2), C(14)–W(1)–As(1) 73.3(2), N(1)–W(1)–As(1) 110.8(2), W(1)–As(1)–C(15) 101.2(2), C(1)–As(1)–C(15) 95.4(2), As(1)–C(15)–C(16) 114.5(4), As(1)–C(15)–O(3) 122.4(5), C(16)–C(15)–O(3) 123.0(6), As(1)–C(1)–C(2) 131.6(5), C(1)–C(2)–C(3) 129.6(6), W(1)–C(14)–O(2) 176.8(6), W(1)–N(1)–O(1) 174.0(5), W(1)–C(1)–C(2) 145.2(5).

The structural parameters of **15** are essentially the same as in complex **14**, with bond lengths of W(1)–As(1) = 2.690(1) Å, W(1)–C(1) = 2.134(6) Å and As(1)–C(1) = 1.909(6) Å. The single bond length As(1)–C(15) of 2.065(6) Å is on the upper end of the range 1.97–2.00 Å, usually determined for such single bonds, and matches well with the corresponding bond in **7d** [2.063(2) Å]. In precursor *t*BuC(O)–As=C(NMe$_2$)$_2$ the respective As–C(O) bond is considerably shorter [1.938(4) Å],[17] which may be due to some π-delocalisation with the As=C bond. The angle As(1)–C(1)–C(2) [131.6(5)°] is comparable to that in **14**. Atoms As(1), C(1) and C(2) constitute a plane to which vector As(1)–C(15) forms an angle of 100.4°. The phenyl ring is twisted out of the plane through the atoms As(1), C(1), C(2) and C(3) by 18.9°.

## Mechanistic Considerations

In line with previous observations concerning the electrophilicity of the α-C atom in vinylidene complexes it is conceivable that the formation of complexes **13**–**15** is initiated by the nucleophilic attack of arsaalkenes **11** or **12** by their As atom on this C atom of **10a**,**b** to give adduct **A**. Ring closure and extrusion of the carbene lead to the final products **13**, **14** and **15** (Scheme 7).

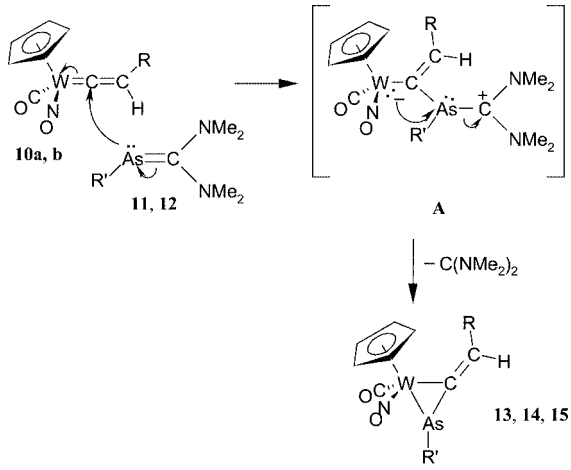


Scheme 7. Proposed mechanism for the formation of **13**, **14** and **15** {R = Ph, *t*Bu; R′ = *t*BuC(O), [Cp*(CO)$_2$Fe]}.

The formation of the aminocarbene complex **16** may be initiated by the electrophilic attack of arsaalkene **12** through its electrophilic carbon atom at the nucleophilic β-C atom of **10b** affording zwitterion **B**, from which a ferrioarsanediyl moiety is liberated to give the cyclopropanediyl complex **C**. Dissociation of a dimethylamide ion and ring opening afford carbene **D**. The addition of the dimeth-

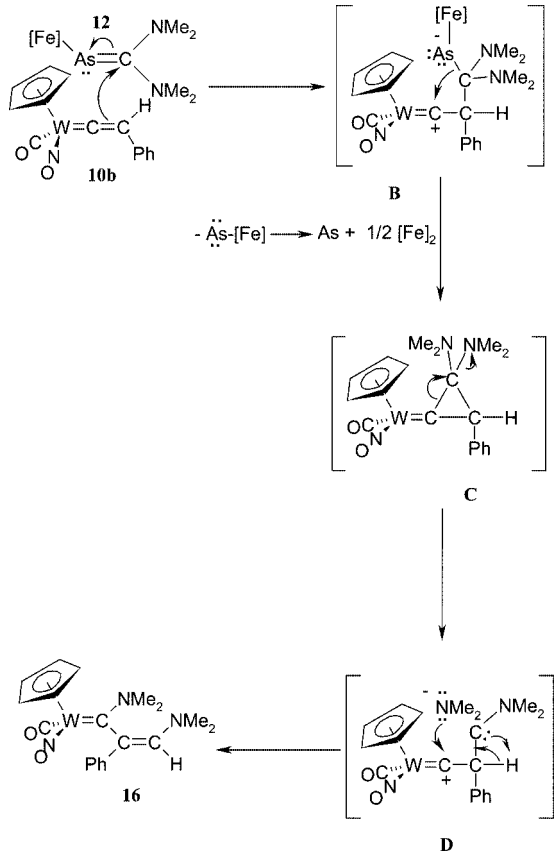


Scheme 8. Proposed mechanism for the formation of **16**.

 © 2006 Wiley-VCH Verlag GmbH & Co. KGaA, Weinheim 

ylamide ion at the α-C atom and a 1,2-hydrogen shift give the final product **16** (Scheme 8).

## Conclusions

The previously observed transition-metal-induced cleavages of inversely polarised arsaalkenes to give cyclotriarsanes,[18] an $\eta^2$-diarsene complex[19] or $\eta^3$-1-arsa-2-phosphaallyl complexes[9] were extended to the smooth generation of $\eta^2$-1-arsaallene complexes **13**, **14** and **15**, which underline the ability of arsaalkenes to act as convenient sources for arsanediyl (arsinidene) units under mild conditions.

## Experimental Section

**General:** All manipulations were performed under dry, oxygen-free nitrogen using standard Schlenk techniques. Solvents were rigorously dried with an appropriate drying agent and freshly distilled under $N_2$ before use. The following compounds were prepared according to literature procedures: $[Cp(CO)_2(NO)W]$,[20] $[Cp^*(CO)_2Fe–As=C(NMe_2)_2]$ (**12**),[11] $Me_3Si–As=C(NMe_2)_2$.[11] IR spectra: Bruker FTIR VECTOR 22. $^1H$, $^{13}C$ NMR spectra in $C_6D_6$ at room temperature; Bruker AM Avance DRX 500 ($^1H$: 500.13 Hz; $^{13}C$: 125.75 MHz); reference: $SiMe_4$. Florisil (Merck), pivaloyl chloride, phenylacetylene and *tert*-butylacetylene were purchased commercially.

**Improved Synthesis of 10a and 10b:** A solution of *n*BuLi (1.6 M) in hexane (12.5 mL, 20 mmol) was added dropwise to a chilled solution (–30 °C) of *tert*-butylacetylene (1.64 g, 20 mmol) or phenylacetylene (2.04 g, 20 mmol) in diethyl ether (60 mL). The solution of R–C≡CLi was slowly warmed up to 20 °C, then transferred into a dropping funnel and added dropwise to a solution of $[Cp(CO)_2(NO)W]$ (5.02 g, 15 mmol) in cold diethyl ether (–30 °C, 100 mL). After stirring at –30 °C for 5 h, the solution was warmed up to 0 °C and concentrated HCl (3 mL), diluted with oxygen-free water (50 mL), was added. The organic phase was separated, washed with saturated aqueous sodium hydrogen carbonate (30 mL) and saturated aqueous sodium chloride (30 mL). After removal of solvents under reduced pressure, compounds **10a** (5.72 g, 98%) and **10b** (5.89 g, 96%) were isolated as red solids. The spectroscopic data of the products are identical to those reported in the literature.[10]

**[Cp(CO)(NO)W{η²-*t*BuC(O)AsC=C(H)*t*Bu}] (13):** A chilled solution (–30 °C) of arsaalkene **11** (1.81 mmol) in diethyl ether (20 mL) was added dropwise to a well-stirred cold solution (–30 °C) of complex **10a** (0.70 g, 1.81 mmol) in diethyl ether (25 mL). It was slowly warmed to ambient temperature and stirring was continued for 12 h. The reaction mixture was freed from solvent and volatile components. The black residue was dissolved with diethyl ether (10 mL), then Florisil (5 g) was added and the slurry was concentrated to dryness. The coated Florisil was transferred on top of a column ($d$ = 1.5 cm, $l$ = 6 cm) charged with Florisil (20 g). A yellow zone was eluted with diethyl ether. Removal of the solvent from the eluate afforded yellow microcrystalline **13** (0.50 g, 50%). IR (KBr): $\tilde{\nu}$ = 1982 (C≡O), 1693 (C=O), 1649 (N=O) $cm^{-1}$. $^1H$ NMR: $\delta$ = 1.24 (s, 9 H, *t*Bu), 1.25 (s, 9 H, *t*Bu), 4.81 (s, 5 H, Cp), 7.86 (s, 1 H, *t*BuC*H*) ppm. $^{13}C\{^1H\}$ NMR: $\delta$ = 25.5 [s, $(CH_3)_3C$], 26.6 [s, $(CH_3)_3C$], 37.8 [s, $(CH_3)C$], 51.2 [s, $(CH_3)_3C$], 96.0 (s, Cp), 158.3 (s, $C_\beta$), 174.8 (s, $C_\alpha$), 216.7 (s, C≡O), 227.5 (s, C=O) ppm. $C_{17}H_{24}AsNO_3W$ (569.15): calcd. C 37.18, H 4.40, N 2.55; found C 36.88, H 4.15, N 2.99.

**[Cp(CO)(NO)W{η²-[Cp*(CO)₂Fe]AsC=C(H)*t*Bu}] (14):** Analogously, combination of **12** (0.76 g, 1.81 mmol) in diethyl ether (20 mL) with **10a** (0.70 g, 1.81 mmol) in diethyl ether (25 mL) at –30 °C and similar work up (Florisil, pentane) afforded dark red crystalline **14** (0.94 g, 73%). IR (KBr): $\tilde{\nu}$ = 1973, 1943, 1917 (C≡O), 1620 (N=O) $cm^{-1}$. $^1H$ NMR [two isomers (2:1)]; first isomer: $\delta$ = 1.41 (s, 9 H, *t*Bu), 1.59 (s, 15 H, $Me_5C_5$), 5.08 (s, 5 H, Cp), 8.01 (s, 1 H, *t*BuC*H*) ppm; second isomer: $\delta$ = 1.35 (s, 9 H, *t*Bu), 1.51 (s, 15 H, $Me_5C_5$), 5.33 (s, 5 H, Cp), 8.03 (s, 1 H, *t*BuC*H*) ppm. $^{13}C\{^1H\}$ NMR ($C_6D_6$): $\delta$ = 9.4 (s, $C_5Me_5$), 9.5 (s, $C_5Me_5$), 30.6 [s, $C(CH_3)_3$], 31.5 [s, $C(CH_3)_3$], 36.3 [s, $C(CH_3)_3$], 37.9 (s, $C(CH_3)_3$), 95.1 (s, $C_5Me_5$), 95.7 (s, $C_5Me_5$), 96.3 (s, $C_5H_5$), 96.8 (s, $C_5H_5$), 156.1 (s, $C_\beta$), 156.1 (s, $C_\beta$), 175.7 (s, $C_\alpha$, $J_{CW}$ = 109 Hz), 178.8 (s, $C_\alpha$, $J_{CW}$ = 118 Hz), 216.1 (s, FeCO), 216.9 (s, FeCO), 217.1 (s, FeCO), 217.7 (s, FeCO), 219.3 (s, WCO), 219.9 (s, WCO). $C_{24}H_{30}AsFeNO_4W$ (711.11) calcd. C 40.54, H 4.25, N 1.97; found C 40.54, H 4.35, N 2.00.

**[Cp(CO)(NO)W{η²-*t*BuC(O)AsC=C(H)Ph}] (15):** A chilled solution (–30 °C) of arsaalkene **11** (1.81 mmol) in diethyl ether (20 mL) was added dropwise to a well-stirred cold solution (–30 °C) of complex **10b** (0.74 g, 1.81 mmol) in diethyl ether (25 mL). Stirring at –30 °C was continued for 4 h before the reaction mixture was slowly warmed to room temperature. The solvent was removed in vacuo and the brown residue was dissolved in diethyl ether (10 mL). Florisil (5 g) was added and the slurry was concentrated to dryness. As described before, the crude material was chromatographed on a Florisil column ($d$ = 1.5 cm, $l$ = 6 cm) charged with Florisil (20 g). An orange zone was eluted with a pentane/diethyl ether mixture (5:1). Removal of solvents from the eluate afforded orange crystalline thermolabile **15** (0.30 g, 29%). IR (KBr): $\tilde{\nu}$ = 1960 (C≡O), 1634 (br., N=O, C=O) $cm^{-1}$. $^1H$ NMR ($C_6D_6$): $\delta$ = 1.24 (s, 9 H, *t*Bu), 4.72 (s, 5 H, Cp), 7.08 (t, $J_{(H,H)}$ = 7.5 Hz, 1 H, Ph), 7.20 (t, $J_{(H,H)}$ = 7.5 Hz, 2 H, Ph), 7.60 (d, $J_{(H,H)}$ = 7.5 Hz, 2 H, Ph), 8.69 (s, 1 H, PhC*H*) ppm. $^{13}C\{^1H\}$ NMR ($C_6D_6$): $\delta$ = 31.0 [s, $(CH_3)_3C$], 38.4 [s, $(CH_3)_3C$], 96.5 (s, Cp), 127.2 (s, Ph), 128.4 (s, Ph), 128.5 (s, Ph), 142.1 (s, Ph), 144.7 (s, $C_\beta$), 183.3 (s, $C_\alpha$), 221.9 (s, C=O), 223.0 (s, C≡O) ppm. $C_{19}H_{20}AsNO_3W$ (569.13): calcd. C 40.10, H 3.54, N 2.46; because of the pronounced thermolability of the compound it was not possible to obtain reliable elemental analyses. A second, orange zone was diluted with diethyl ether to obtain a few crystals of compound **16**.

**Cp(CO)(NO)W=C(NMe₂)C(C₆H₅)=C(H)NMe₂ (16):** A chilled solution (–30 °C) of arsaalkene **12** (0.76 g, 1.81 mmol) in diethyl ether (20 mL) was added dropwise to a well-stirred cold solution (–30 °C) of complex **10b** (0.74 g, 1.81 mmol) in diethyl ether (25 mL). It was slowly warmed to ambient temperature and stirring was continued for 12 h. The reaction mixture was freed from solvent and volatile components. The black residue was dissolved with diethyl ether (10 mL) and filtered. The residue was identified as elemental arsenic. Florisil (5 g) was then added to the solution and the slurry was concentrated to dryness. The coated Florisil was transferred on top of a column ($d$ = 1.5 cm, $l$ = 6 cm) charged with Florisil (20 g). A deep red zone was eluted with pentane. Removal of the solvent from the eluate afforded black microcrystalline $[Cp^*Fe(CO)_2]_2$ (0.45 g, 82%). A second, orange zone was eluted with diethyl ether. Removal of solvents to the beginning of crystallisation and storage at –30 °C yielded **16** (0.64 g, 69%) as red crystals. IR (KBr): $\tilde{\nu}$ = 1899 (C≡O), 1768 (N=O) $cm^{-1}$. $^1H$ NMR ($CDCl_3$): $\delta$ = 2.92 (s, 6 H, $NMe_2$), 3.33 (s, 3 H, $NMe_2$), 3.73 (s, 3 H, $NMe_2$), 5.41 (s, 5 H, Cp), 5.65 (s, 1 H, PhC=C*H*), 6.89 (d, $J_{(H,H)}$

 © 2006 Wiley-VCH Verlag GmbH & Co. KGaA, Weinheim 

= 7.5 Hz, 2 H, Ph), 7.02 (t, $J_{(H,H)}$ = 6.9 Hz, 1 H, Ph), 7.20 (t, $J_{(H,H)}$ = 7.5 Hz, 2 H, Ph) ppm. $^{13}C\{^1H\}$ NMR ($CDCl_3$): $\delta$ = 42.6 (s, $NMe_2$), 44.4 (s, $NMe_2$), 49.3 (s, $NMe_2$), 96.0 (s, Cp), 118.8 (s, $C_\gamma$) 124.3 (s, Ph), 128.4 (s, Ph), 128.6 (s, Ph), 129.3 (s, Ph), 140.6 (s, $C_\beta$), 233.2 (s, CO), 260.8 (s, $C_\alpha$) ppm. $C_{19}H_{23}N_3O_2W$ (509.26): calcd. C 44.81, H 4.55, N 8.25; found C 44.77, H 4.43, N 8.28.

**X-ray Crystallography:** Crystallographic data were collected with a Nonius Kappa CCD diffractometer with Mo-$K_\alpha$ (graphite monochromator, $\lambda$ = 0.71073 Å) at 100 K. Crystallographic programs used for structure solution and refinement were from SHELXS-97,[21] SIR-97[22] and SHELXL-97.[21] The structures were solved by direct methods and were refined by using full-matrix least squares on $F^2$ of all unique reflections with anisotropic thermal parameters for all non-hydrogen atoms. Hydrogen atoms were included at calculated positions with $U$(H) = 1.2$U_{eq}$ for $CH_2$ groups and $U$(H) = 1.5$U_{eq}$ for $CH_3$ groups. Crystal data of the compounds are listed in Table 1. CCDC-297420 (for **14**) and -297421 (for **15**) contain the supplementary crystallographic data for this paper. These data can be obtained free of charge from The Cambridge Crystallographic Data Centre via www.ccdc.cam.ac.uk/data_request/cif.


[1] For reviews on phosphacumulenes –P=C=X see: a) R. Appel in *Multiple Bonds and Low Coordination in Phosphorus Chemistry* (Eds.: M. Regitz, O. J. Scherer), Georg Thieme Verlag, Stuttgart, Germany, **1990**, pp. 181–191; b) K. Dillon, F. Mathey, J. F. Nixon, *Phosphorus: The Carbon Copy*, John Wiley & Sons, Chichester, **1998**, pp. 147–163; c) J. Escudié, H. Ranaivonjatovo, L. Rigon, *Chem. Rev.* **2000**, *100*, 3639–3696.

[2] a) R. Appel, P. Fölling, B. Josten, M. Siray, V. Winkhaus, F. Knoch, *Angew. Chem.* **1984**, *96*, 620–621; *Angew. Chem. Int. Ed. Engl.* **1984**, *23*, 619–620; b) M. Yoshifuji, K. Toyota, K. Shibayama, N. Inamoto, *Tetrahedron Lett.* **1984**, *25*, 1809–1812; c) M. Yoshifuji, K. Toyota, N. Inamoto, K. Hirotsu, T. Higuchi, S. Nagase, *Phosphorus, Sulfur, Silicon Relat. Elem.* **1985**, *25*, 237–243; d) R. Appel, V. Winkhaus, F. Knoch, *Chem. Ber.* **1986**, *119*, 2446–2472; e) R. Mathieu, A. M. Caminade, J. P. Majoral, J. C. Daran, *J. Am. Chem. Soc.* **1986**, *108*, 8007–8010; f) R. Appel, F. Knoch, V. Winkhaus, *J. Organomet. Chem.* **1986**, *307*, 93–95; g) V. Winkhaus, PhD Thesis, University of Bonn, **1987**; h) G. Märkl, S. Reitinger, *Tetrahedron Lett.* **1988**, *29*, 463–466; i) M. Yoshifuji, S. Sasaki, N. Inamoto, *Tetrahedron Lett.* **1989**, *30*, 839–842; j) M. Yoshifuji, Y. Yoshimura, K. Toyota, *Chem. Lett.* **1990**, 827–830; k) S. J. Goede, L. de Vries, F. Bickelhaupt, *Bull. Soc. Chim. Fr.* **1993**, *130*, 185–188; l) M. Hafner, T. Wegemann, M. Regitz, *Synthesis* **1993**, 1247–1252; m) G. Märkl, W. Bauer, *Tetrahedron Lett.* **1993**, *34*, 2915–2918; n) M. Yoshifuji, M. Shibata, K. Toyota, I. Miyahara, K. Hirotsu, *Heteroat. Chem.* **1994**, *5*, 195; o) M. van der Sluis, J. B. M. Wit, F. Bickelhaupt, *Organometallics* **1996**, *15*, 174–180; p) R. Streubel, H. Wilkens, P. G. Jones, *Chem. Commun.* **1998**, 1761–1762; q) R. Streubel, H. Wilkens, F. Ruthe, P. G. Jones, *Z. Anorg. Allg. Chem.* **1999**, *625*, 102–106; r) K. Toyota, A. Nakamura, M. Yoshifuji, *Chem. Commun.* **2002**, 3012–3013; s) S. Ito, K. Kimura, M. Yoshifuji, *Bull. Chem. Soc. Jpn.* **2003**, *76*, 405–412; t) M. Chentit, H. Sidorenkova, S. Choua, M. Geoffroy, Y. Ellinger, G. Bernardelli, *J. Organomet. Chem.* **2001**, *634*, 136–144.

[3] a) O. I. Kolodiazhnyi, *Zh. Obshch. Khim.* **1982**, *52*, 2361; b) O. I. Kolodiazhnyi, *Tetrahedron Lett.* **1982**, *23*, 4933–4936; c) O. I. Kolodiazhnyi, *Phosphorus, Sulfur, Silicon Relat. Elem.* **1983**, *18*, 39–42; d) O. I. Kolodiazhnyi, *Zh. Obshch. Khim.* **1983**, *53*, 1226; e) X.-G. Zhou, L. B. Zhang, R.-F. Cai, Q.-J. Wu, L. H. Weng, Z.-E. Huang, *J. Organomet. Chem.* **2000**, *604*, 260–266.

[4] a) R. Appel, P. Fölling, W. Schuhn, F. Knoch, *Tetrahedron Lett.* **1986**, *27*, 1661–1664; b) R. Appel, C. Porz, F. Knoch, *Chem. Ber.* **1986**, *119*, 2748–2755; c) R. Appel, W. Paulen, *Angew. Chem.* **1983**, *95*, 807–808; *Angew. Chem. Int. Ed. Engl.* **1983**, *22*, 785–786.

[5] a) M. Yoshifuji, K. Toyota, N. Inamoto, *J. Chem. Soc., Chem. Commun.* **1984**, 689–690; b) H. H. Karsch, H. U. Reisacher, G. Müller, *Angew. Chem.* **1984**, *96*, 619–620; *Angew. Chem. Int. Ed. Engl.* **1984**, *23*, 618–619; c) H. H. Karsch, F. H. Köhler, H. U. Reisacher, *Tetrahedron Lett.* **1984**, *25*, 3687–3690; d) M. Gouygou, C. Tachon, R. El Ouatib, O. Ramarijaona, G. Etemad-Moghadam, M. Koenig, *Tetrahedron Lett.* **1989**, *30*, 177–178; e) M. Yoshifuji, S. Sasaki, N. Inamoto, *J. Chem. Soc., Chem. Commun.* **1989**, 1732–1733; f) K. Toyota, A. Nakamura, M. Yoshifuji, *Chem. Commun.* **2002**, 3012–3013.

[6] M. Bouslikhane, H. Gornitzka, H. Ranaivonjatovo, J. Escudié, *Organometallics* **2002**, *21*, 1531–1533.

[7] H. Ranaivonjatovo, H. Ramdane, H. Gornitzka, J. Escudié, J. Satge, *Organometallics* **1998**, *17*, 1631–1633.

[8] M. Bouslikhane, H. Gornitzka, J. Escudié, H. Ranaivonjatovo, H. Ramdane, *J. Am. Chem. Soc.* **2000**, *122*, 12880–12881.

[9] a) L. Weber, P. Bayer, H.-G. Stammler, B. Neumann, *Chem. Commun.* **2005**, 1595–1597; b) L. Weber, P. Bayer, S. Uthmann, T. Braun, H.-G. Stammler, B. Neumann, *Eur. J. Inorg. Chem.* **2006**, *1*, 137–143; c) L. Weber, P. Bayer, T. Braun, H.-G. Stammler, B. Neumann, *Organometallics* **2006**, *25*, 1786–1794.

[10] J. Ipaktschi, G. J. Demuth-Eberle, F. Mirzaei, B. G. Müller, J. Beck, M. Serafin, *Organometallics* **1995**, *14*, 3335–3341.

[11] L. Weber, O. Kaminski, H.-G. Stammler, B. Neumann, *Chem. Ber.* **1996**, *129*, 223–226.

[12] J. Ipaktschi, S. Uhlig, A. Dülmer, *Organometallics* **2001**, *20*, 4840–4846.

[13] J. Ipaktschi, T. Klotzbach, A. Dülmer, *Organometallics* **2000**, *19*, 5281–5286.

[14] U. Schubert in: *Transition Metal Carbene Complexes*, VCH, Weinheim, **1973**, p. 103.

[15] H. Lang, G. Huttner, B. Sigwarth, U. Weber, L. Zsolnai, I. Jibril, O. Orama, *Z. Naturforsch., B: Chem. Sci.* **1986**, *41*, 191–206.

[16] T. Albers, J. Grobe, D. Le Van, B. Krebs, M. Läge, *Z. Naturforsch., B: Chem. Sci.* **1995**, *50*, 94–100.

[17] S. Uthmann, PhD Thesis, University of Bielefeld, **1999**.

[18] L. Weber, G. Dembeck, P. Lönnecke, H.-G. Stammler, B. Neumann, *Organometallics* **2001**, *20*, 2288–2293.

[19] L. Weber, M. H. Scheffer, H.-G. Stammler, B. Neumann, *Inorg. Chim. Acta* **1999**, *291*, 311–316.

[20] R. J. Angelici, *Inorg. Synth.* **1990**, *28*, 186.

[21] G. M. Sheldrick, *SHELX-97, program for crystal structure refinement*, University of Göttingen, **1997**.

[22] A. Altomare, M. C. Burla, M. Camalli, B. Carrozini, G. L. Cascarone, C. Giacovazzo, A. Guagliardi, A. G. G. Moliterni, G. Polidori, R. Rizzi, *J. Appl. Crystallogr.* **1999**, *32*, 115–119.


Received: February 2, 2006
Published Online: April 10, 2006

 © 2006 Wiley-VCH Verlag GmbH & Co. KGaA, Weinheim 

DOI: 10.1002/ejic.200500679

# Synthesis and Characterization of Zirconium and Hafnium Aryloxide Compounds and Their Reactivity Towards Lactide and ε-Caprolactone Polymerization

**Kun-Chun Hsieh,[a] Wen-Yi Lee,[a] Li-Feng Hsueh,[a] Hon Man Lee,[a] and Jui-Hsien Huang*[a]**

**Keywords:** Hafnium aryloxide / Zirconium aryloxide / Lactide / Caprolactone / Hafnium / Zirconium

Reactions of 2 equiv. pyrrole with $[C_4H_3N(CH_2NMe_2)\text{-}2]_2M(NEt_2)_2$ in toluene generated tetra-pyrrolyl metal compounds $[C_4H_3N(CH_2NMe_2)\text{-}2]_2M(C_4H_4N)_2$ (**3**, M = Zr; **4**, M = Hf) in moderate yields. Similarly, treatment of metal amides $[C_4H_3N(CH_2NMe_2)\text{-}2]_2M(NEt_2)_2$ with 2,6-dimethylphenol or 2,6-diisopropylphenol in heptane resulted in the elimination of diethylamine along with the formation of the corresponding metal alkoxides $[C_4H_3N(CH_2NMe_2)\text{-}2]_2M(OR)_2$ (**5**, M = Zr, R = $C_6H_3$-2,6-$Me_2$; **6**, M = Hf, R = $C_6H_3$-2,6-$Me_2$; **7**, M = Zr, R = $C_6H_3$-2,6-*i*$Pr_2$; **8**, M = Hf, R = $C_6H_3$-2,6-*i*$Pr_2$) in moderate yields. All the new compounds were characterized by $^1H$ and $^{13}C$ NMR spectroscopy and the structures of **3**, **4**, **6**, **7**, and **8** have also been determined by X-ray crystallographic studies. The aryloxides and the substituted pyrrolyl ligands in both compounds **5** and **6** show fluxionality as observed by $^1H$ NMR signals. A kinetic study on the ring-opening polymerization of lactide exhibits a first-order reaction of lactide monomer with compound **8**. The catalytic properties of all the metal complexes have been studied for the ring-opening polymerization of ε-caprolactone.
(© Wiley-VCH Verlag GmbH & Co. KGaA, 69451 Weinheim, Germany, 2006)

## Introduction

Poly-ε-caprolactone (PCL) and polylactide (PLA) are considered as biodegradable polyesters for medical and ecological applications.[1–4] PCL and PLA are mainly synthesized by ring-opening polymerization using $Sn(OR)_2$ as catalysts.[5–8] However, the study of polyesters generated from ring-opening polymerization using non-tin metal alkoxides as catalysts has just started to attract researchers' attention. Among those metal alkoxides, aluminum,[9–15] lithium,[16,17] titanium,[18–21] and some lanthanide metals[22–27] have been studied by different groups. We have previously examined the ring-opening polymerization of ε-caprolactone and lactide with aluminum alkoxides supported by monoanionic bidentate ketiminate ligands.[28] Herein we report the synthesis and characterization of zirconium and hafnium metal complexes containing substituted pyrrolyl ligands and their applications as catalysts on the ring-opening polymerization of ε-caprolactone and lactide.

## Results and Discussion

### Synthesis of Compounds 1–8

The zirconium and hafnium amide complexes $[C_4H_3N(CH_2NMe_2)\text{-}2]_2M(NEt_2)_2$ (**1**, M = Zr; **2**, M = Hf) were prepared following the published procedures (see experimental section) by treatment of $M(NEt_2)_4$ with 2 equiv. of substituted pyrrolyl ligands (Scheme 1). Reactions of 2 equiv. pyrrole with **1** and **2** in toluene generated tetrapyrrolyl metal compounds $[C_4H_3N(CH_2NMe_2)\text{-}2]_2M(C_4H_4N)_2$ (**3**, M = Zr; **4**, M = Hf) in moderate yields. Similarly, treatment of metal amides **1** and **2** with a stoichiometric amount of 2,6-dimethylphenol or 2,6-diisopropylphenol in heptane resulted in the elimination of diethylamine with the formation of the corresponding metal alkoxides $[C_4H_3N(CH_2NMe_2)\text{-}2]_2M(OR)_2$ (**5**, M = Zr, R = $C_6H_3$-2,6-$Me_2$; **6**, M = Hf, R = $C_6H_3$-2,6-$Me_2$; **7**, M = Zr, R = $C_6H_3$-2,6-*i*$Pr_2$; **8**, M = Hf, R = $C_6H_3$-2,6-*i*$Pr_2$) in moderate yields (Scheme 1). The resulting metal alkoxide compounds **3**–**8** were characterized by $^1H$ and $^{13}C$ NMR spectroscopy.

### Molecular Structures for Compounds 3, 4, 6, 7, and 8

Compounds **3**, **4**, **6**, **7**, and **8** were structurally characterized and selected bond lengths and angles are listed in Table 1. The molecular geometries are shown in Figure 1, Figure 2, Figure 3, Figure 4, and Figure 5 where the molecular geometries are highly dependent on the steric hindrance of the ligands. Compounds **3**, **4**, **6**, and **8** all contain solvent molecules in their unit cells. For compound **4**, there are two independent molecules in the asymmetrical unit. However, the bond lengths and angles of the two molecules are very similar; therefore, only one molecule is discussed

[a] Department of Chemistry, National Changhua University of Education,
Changhua, Taiwan 500

 © 2006 Wiley-VCH Verlag GmbH & Co. KGaA, Weinheim 

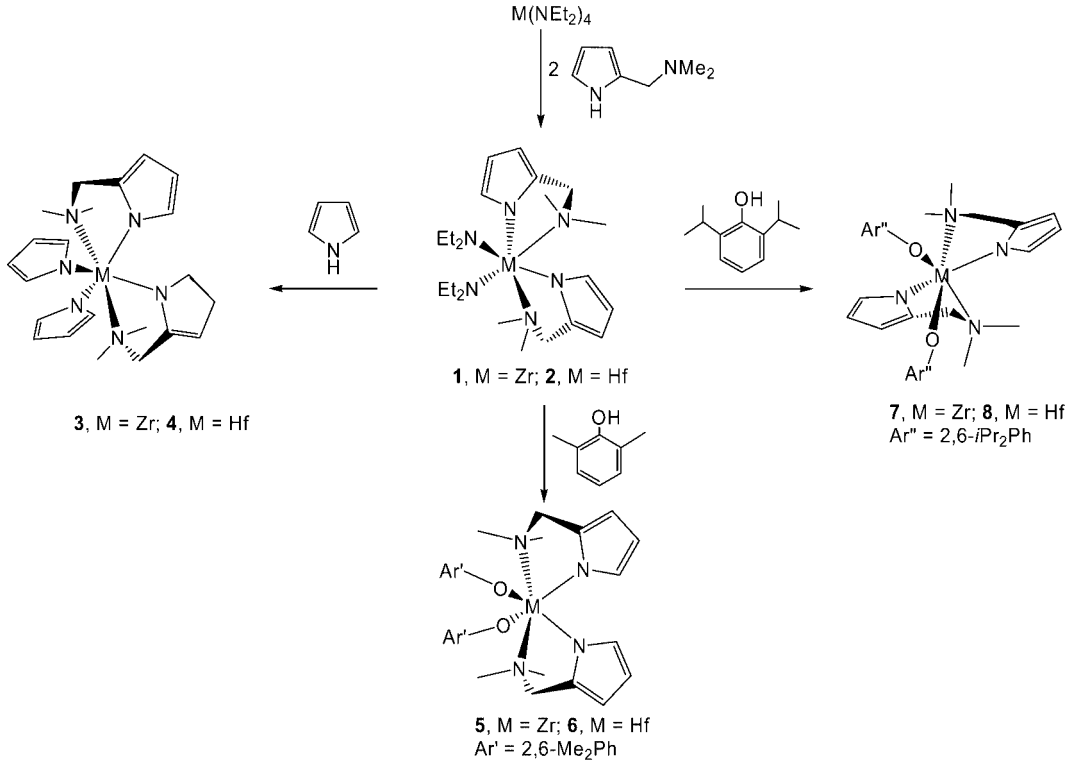


Scheme 1.

Table 1. Selected bond lengths [Å] and angles [°] for compounds **3**, **4**, **6**, **7**, and **8**.

| | | | |
|---|---|---|---|
| | **3** | | |
| Zr(1)–N(1) | 2.1445(16) | Zr(1)–N(2) | 2.3824(16) |
| Zr(1)–N(3) | 2.1393(16) | Zr(1)–N(4) | 2.3957(16) |
| Zr(1)–N(5) | 2.1611(16) | Zr(1)–N(6) | 2.1577(16) |
| N(1)–Zr(1)–N(6) | 143.09(6) | N(3)–Zr(1)–N(5) | 143.47(6) |
| N(2)–Zr(1)–N(4) | 163.05(6) | N(1)–Zr(1)–N(2) | 71.07(6) |
| N(3)–Zr(1)–N(4) | 72.62(6) | | |
| | **4** | | |
| Hf(1)–N(1) | 2.134(6) | Hf(1)–N(2) | 2.381(6) |
| Hf(1)–N(3) | 2.133(7) | Hf(1)–N(4) | 2.359(6) |
| Hf(1)–N(5) | 2.140(6) | Hf(1)–N(6) | 2.112(7) |
| N(1)–Hf(1)–N(5) | 143.5(2) | N(2)–Hf(1)–N(4) | 162.1(2) |
| N(3)–Hf(1)–N(6) | 143.8(2) | N(1)–Hf(1)–N(2) | 73.2(2) |
| N(3)–Hf(1)–N(4) | 70.6(2) | | |
| | **6** | | |
| Hf(1)–N(1) | 2.190(5) | Hf(1)–N(2) | 2.391(5) |
| Hf(1)–N(3) | 2.182(5) | Hf(1)–N(4) | 2.389(5) |
| Hf(1)–O(1) | 1.975(4) | Hf(1)–O(2) | 1.945(5) |
| N(1)–Hf(1)–N(2) | 71.87(18) | N(3)–Hf(1)–N(4) | 71.8(2) |
| N(4)–Hf(1)–N(2) | 159.24(19) | N(1)–Hf(1)–O(1) | 142.54(19) |
| O(2)–Hf(1)–N(3) | 139.59(18) | | |
| | **7** | | |
| Zr(1)–O(1) | 1.924(2) | Zr(1)–N(1) | 2.535(3) |
| Zr(1)–N(2) | 2.137(3) | | |
| N(1)–Zr(1)–N(2) | 69.68(10) | O(1)–Zr(1)–N(1A) | 168.04(10) |
| N(2)–Zr(1)–N(2A) | 141.17(15) | | |
| | **8** | | |
| Hf(1)–O(1) | 1.9446(16) | Hf(1)–N(1) | 2.162(2) |
| Hf(1)–N(2) | 2.508(2) | | |
| N(1)–Hf(1)–N(2) | 70.87(7) | O(1A)–Hf(1)–N(2) | 170.47(7) |
| N(1)–Hf(1)–N(1A) | 140.28(11) | | |

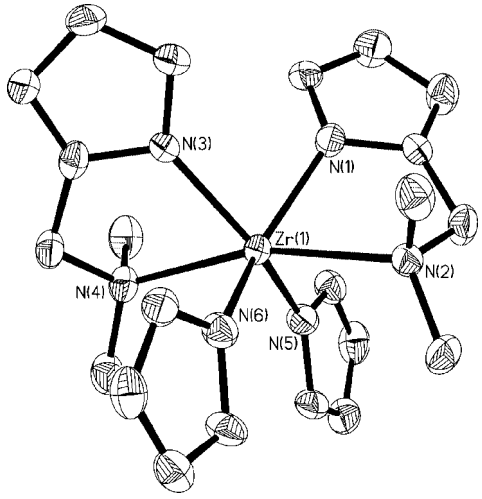


Figure 1. The molecular structure for compound **3**; thermal ellipsoids were drawn at 50% probability level. Toluene and hydrogen atoms were omitted for clarity.

here. The structures for compounds **3**, **4**, and **6**, with less steric congestion, are quite similar and show a highly distorted octahedral geometry, which can also be described as an *anti*-trigonal prism. The two nitrogen atoms of the dimethylamino fragments in compounds **4** and **6** have *trans* positions with bond angles of 162.1(2)° and 159.24(19)°, respectively. The sterically congested compounds **7** and **8** exhibit regular octahedral geometries. For the sterically congested compound **8**, the aryloxide ligands are *trans* to the dimethylamino fragments and the two pyrrolyl fragments are *trans* to each other; where the bond angles of the three axes for the octahedral geometry are 170.47(7)°,

 © 2006 Wiley-VCH Verlag GmbH & Co. KGaA, Weinheim 

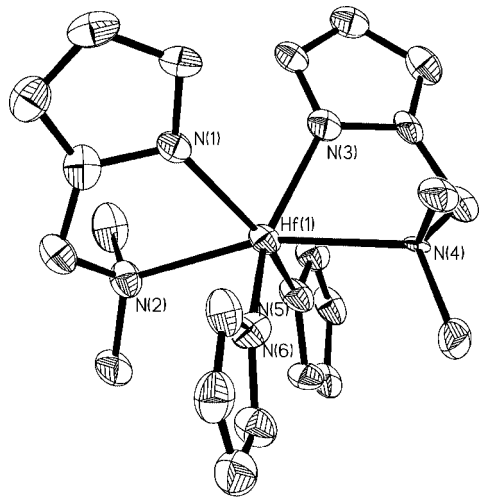


Figure 2. One of two independent molecular structures of compound **4**; thermal ellipsoids were drawn at 50% probability level. Toluene and hydrogen atoms were omitted for clarity.

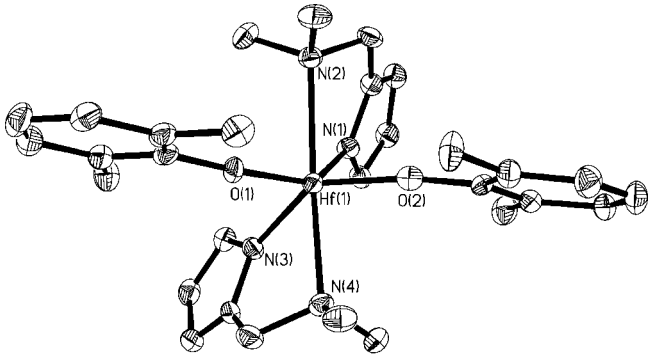


Figure 3. The molecular structure for compound **6**; thermal ellipsoids were drawn at 50% probability level. Methylene chloride molecule and hydrogen atoms were omitted for clarity.

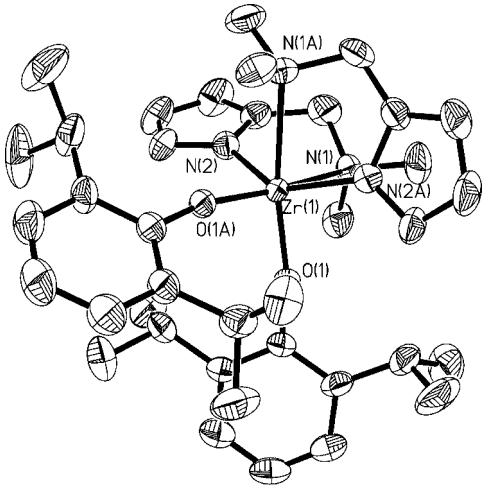


Figure 4. The molecular structure for compound **7**; thermal ellipsoids were drawn at 30% probability level. Hydrogen atoms were omitted for clarity.

170.47(7)°, and 140.28(11)°, respectively. The bond lengths of metal to pyrrolyl nitrogen atoms and metal to dimethylamino nitrogen atoms are very similar despite the differences in steric effect for compounds **4**, **6**, and **8**.[29–34]

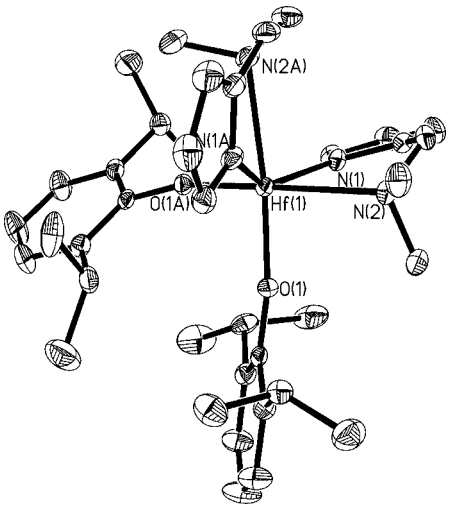


Figure 5. The molecular structure for compound **8**; thermal ellipsoids were drawn at 50% probability level. Methylene chloride and hydrogen atoms were omitted for clarity.

### NMR Study of the Structures in Solution

For compounds **3** and **4**, the $^1$H NMR spectra of the 2-[(dimethylamino)methyl] fragments at room temperature exhibit sharp singlets for the methylene and methyl protons at $\delta$ = 3.60 and 2.43 ppm for **3** and $\delta$ = 3.18 and 1.87 ppm for **4**. The proton-coupled $^{13}$C NMR spectra of the methylene fragments for compounds **3** and **4** both show a triplet resonance at $\delta$ = 62.6 and 62.5 ppm with $^1J_{CH}$ coupling constants of 136 and 139 Hz, respectively. In the solid-state structures of **3** and **4**, there is nonsymmetrical geometry; the $NMe_2$ and the $NCH_2$ of the substituted pyrrolyl ligands, and the NCH and CCHC of the pyrrolide anion should have different resonance signals. However, the room temperature NMR spectroscopic data for **3** and **4** indicate either the solution structures are different from the solid ones and/or equilibria are occurring. In order to elucidate eventual dynamic phenomena (rotation of the pyrrolide anions) and/or the *cis*/*trans* isomerization of the complex, a variable temperature NMR investigation and $^1$H–$^1$H NOESY spectra were carried out. The results show the resonance signals for the substituted pyrrolyl ligands and pyrrolides remain unchanged at 250 K, which indicates a fast rotation of the pyrrolide anions and a fast equilibrium of the *cis*/*trans* isomerization must exist at the same time.

The bulkiness of the aryloxide groups indeed affects the M–O bond rotation rate and the fluxionality of the substituted pyrrolyl ligands. The methyl fragments of the aryloxides and the dimethylaminomethyl groups in compounds **5** and **6** show broad $^1$H NMR signals at room temperature. Use of bulkier 2,6-diisopropylphenyl groups in compounds **7** and **8** results in greater stereorigidity of the molecular structures in which the methyl groups of the isopropyl fragments were split into four doublet signals, whereas the methyl groups of the dimethylamino fragments were split into two singlets. For compound **6**, $^1$H, $^{13}$C and $^1$H–$^{13}$C HSQC NMR spectra were recorded in the range of 320–250 K in $CDCl_3$ with a 300 MHz NMR spectrometer in

 © 2006 Wiley-VCH Verlag GmbH & Co. KGaA, Weinheim 

order to resolve its structure in solution at various temperatures. Variable temperature $^1$H NMR spectra of compound **6** are shown in Figure 6. The $^1$H and $^1$H–$^{13}$C HSQC NMR spectra clearly identified that the methyl groups of aryloxides and dimethylamino fragments appeared as sharp singlets at $\delta$ = 2.22 and 2.46 ppm, respectively, at 320 K. The methylene protons of the $CH_2NM_2$ fragments also show a sharp singlet at 320 K. The methyl groups of the aryloxides and dimethylamino fragments were split into complicated singlets at $\delta$ = 2.45, 2.58, 2.51, 2.30, 2.02, and 1.40 when the temperature was lowered to 250 K. Similarly, the methylene protons of the $CH_2NM_2$ fragments showed splitting of signal from a sharp singlet at $\delta$ = 3.87 to a complicated overlapping of two doublets and a broad singlet when the temperatures were lowered from 320 to 250 K. The observed patterns at 250 K are indicative of complex solution dynamics. As far as the $NCH_2$ signal is concerned, the splitting of the singlet at room temperature into two doublets and a singlet at low temperature could indicate that two isomers, namely *cis* and *trans*, may be present in solution at low temperature. The two doublets may result from a solution structure similar to the solid state one (the *cis* form) and the singlet may result from a more symmetrical solution structure such as a more symmetrical pseudo-$C_2$ symmetry of *trans* geometry (the *trans* form with the phenoxide anions in an axial arrangement and the bidentate ligands in the equatorial plane with an unpredictable mutual arrangement). Interestingly, in accordance with this, six methyl resonances are observed and assignable to (i) the two nonequivalent methyls of the phenoxide anions; (ii) the two nonequivalent $NMe_2$ methyls of the *cis* isomers; and (iii) the $NMe_2$ moiety and the two equivalent methyls of the reasonably freely rotating phenoxide of the *trans* isomer. A $^1$H NOESY experiment of **6** was performed at 250 K; however, because of the complication of methyl resonances we are unable to determine the *cis* and *trans* forms of **6**.[35]

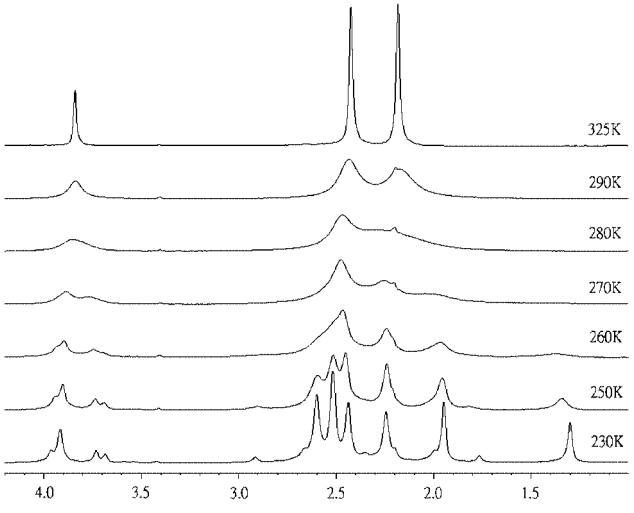


Figure 6. Variable $^1$H NMR spectra of compound **6** in $CDCl_3$ using a 300 MHz NMR spectrometer. Spectra ranges are drawn in the range of $\delta$ = 1.0–4.2.

### Kinetic Study of Lactide Polymerization Initiated by 8

The reactions of **8** with *rac* lactides proceeded in $CDCl_3$ at 70 °C and were monitored with a $^1$H NMR spectrometer. The consumptions of lactide were measured from the integration of the $^1$H NMR signals. Plots of ln([lactide]$_0$/[lactide]) versus time give straight lines (Figure 7), indicating the lactide polymerization is first-order with respect to the monomer.[36]

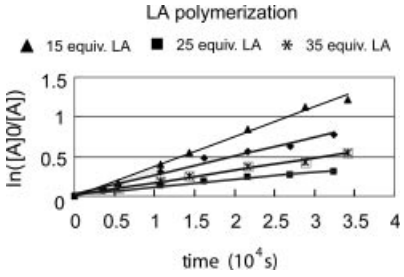


Figure 7. Plot of ln([lactide]$_0$/[lactide]) vs. time for the reaction of **8** with *rac* lactide in $CDCl_3$ at 70 °C.

### Polymerization of ε-Caprolactone

Polymerizations of ε-caprolactone by using zirconium or hafnium complexes as catalysts have been seen in the literature.[37–39] Here we use the synthesized metal complexes as catalysts to study their reactivity toward ε-caprolactone. All the compounds have been studied as catalysts for the ring-opening polymerization of ε-caprolactone. The results of polymerization studies of ε-caprolactone initiated by compounds **3**–**8** are shown in Table 2. It is found that compounds **3**–**8** catalyzed the ring-opening polymerization of ε-caprolactone to give a moderate molecular weight of PCL (range 11000–53000) with a rather broad molecular weight distribution (PDI = 1.38–2.63). There are no noticeable differences toward the ring-opening polymerization relating to metals (Zr or Hf) or bulkiness of the substituted aryloxides and pyrrolyl ligands of compounds **3**–**8**.

Table 2. Ring-opening polymerization of ε-caprolactone initiated by complexes **3**–**8**.

| Entry | Catalyst | [M]/[cata] | *T* (°C) | Yield (%) | Mn | PDI |
|---|---|---|---|---|---|---|
| 1 | **3** | 100 | 25 | 96 | 18457 | 2.63 |
| 2 | **3** | 100 | 65 | 98 | 15612 | 2.38 |
| 3 | **4** | 100 | 25 | 99 | 52962 | 1.45 |
| 4 | **4** | 100 | 65 | 97 | 26416 | 2.10 |
| 5 | **5** | 100 | 50 | 76 | 21219 | 1.55 |
| 6 | **6** | 100 | 50 | 75 | 17727 | 1.38 |
| 7 | **7** | 100 | 50 | 93 | 14764 | 1.38 |
| 8 | **8** | 100 | 50 | 94 | 10907 | 1.23 |

## Experimental Section

**General Procedure:** All reactions were performed under dry nitrogen using standard Schlenk techniques or in a glovebox. Toluene, heptane, diethyl ether, and tetrahydrofuran were dried by refluxing over sodium benzophenone ketyl. $CH_2Cl_2$ was dried with $P_2O_5$.

 © 2006 Wiley-VCH Verlag GmbH & Co. KGaA, Weinheim 

All solvents were distilled and stored in solvent reservoirs which contained 4 Å molecular sieves and were purged with nitrogen. $^1$H and $^{13}$C NMR spectra were recorded with a Bruker AC 200 or an Avance 300 spectrometer. Chemical shifts for $^1$H and $^{13}$C spectra were recorded in ppm relative to the residual protons and $^{13}$C of $CDCl_3$ ($\delta$ = 7.24, 77.0) and $C_6D_6$ ($\delta$ = 7.16, 128.0). Elemental analyses were performed with a Heraeus CHN-OS Rapid Elemental Analyzer at the Instrument Center, NCHU. $[C_4H_3N(CH_2NMe_2)\text{-}2]_2Zr(NEt_2)_2$, $[C_4H_3N(CH_2NMe_2)\text{-}2]_2Hf(NEt_2)_2$,[40,41] $C_4H_3NH(CH_2NMe_2)\text{-}2$,[42,43] and $M(NEt_2)_4$ (M = Zr, Hf)[44] were prepared according to previously reported procedures.

**$[C_4H_3N(CH_2NMe_2)\text{-}2]_2Zr(NC_4H_4)_2$ (3):** Pyrrole (0.1 mL, 1.44 mmol) was added to a solution of $[C_4H_3N(CH_2NMe_2)\text{-}2]_2Zr(NEt_2)_2$ (0.345 g, 0.72 mmol) in toluene (15 mL) at 0 °C with a micro syringe. The solution was stirred at room temperature for 10 h after the addition was completed. The volatiles were removed under vacuum, and the residue was recrystallized from a toluene solution to yield 0.181 g of colorless crystals in 53.9% yield. $^1$H NMR ($CDCl_3$): $\delta$ = 2.43 (s, 12 H, N*Me*$_2$), 3.60 (s, 4 H, C*H*$_2$N), 5.97 (m, 2 H, pyrrolyl C*H*), 6.17 (m, 6 H, pyrrolyl C*H*), 6.70 (m, 4 H, pyrrolyl C*H*), 6.97 (m, 2 H, pyrrolyl C*H*) ppm. $^{13}$C NMR ($CDCl_3$): $\delta$ = 47.1 (q, $J_{CH}$ = 138 Hz, N*Me*$_2$), 62.6 (t, $J_{CH}$ = 136 Hz, *C*H$_2$N), 104.2 (d, $J_{CH}$ = 167 Hz, pyrrolyl *C*H), 109.2 (d, $J_{CH}$ = 168 Hz, pyrrolyl *C*H), 125.5 (d, $J_{CH}$ = 179 Hz, pyrrolyl *C*H), 127.7 (d, $J_{CH}$ = 190 Hz, pyrrolyl *C*H), 135.9 (s, pyrrolyl *C*$_{ipso}$) ppm. One pyrrolyl carbon resonance was not observed because of overlapping ($\delta$ = 109.2 ppm). $C_{22}H_{30}N_6Zr$ (467.74): calcd. C 56.25, H 6.44, N 17.89; found C 55.83, H 6.53, N 17.85.

**$[C_4H_3N(CH_2NMe_2)\text{-}2]_2Hf(NC_4H_4)_2$ (4):** This compound was prepared in a manner analogous to that described for the synthesis of **3** using $[C_4H_3N(CH_2NMe_2)\text{-}2]_2Hf(NEt_2)_2$ (1.0 g, 1.76 mmol) and pyrrole (0.248 mL, 3.52 mmol) as starting material. Colorless crystals of **4** were obtained from a toluene solution (0.812 g, 83% yield). $^1$H NMR ($C_6D_6$): $\delta$ = 1.87 (s, 12 H, N*Me*$_2$), 3.18 (s, 4 H, C*H*$_2$N), 6.12 (m, 2 H, pyrrolyl C*H*), 6.40 (m, 4 H, pyrrolyl C*H*), 6.49 (m, 4 H, pyrrolyl C*H*), 6.68 (m, 2 H, pyrrolyl C*H*) ppm. $^{13}$C NMR ($C_6D_6$): $\delta$ = 46.5 (q, $J_{CH}$ = 138 Hz, N*Me*$_2$), 62.5 (t, $J_{CH}$ = 139 Hz, *C*H$_2$N), 105.6 (d, $J_{CH}$ = 166 Hz, pyrrolyl *C*H), 110.4 (d, $J_{CH}$ = 168 Hz, pyrrolyl *C*H), 111.0 (d, $J_{CH}$ = 171 Hz, pyrrolyl *C*H), 126.9 (d, $J_{CH}$ = 180 Hz, pyrrolyl *C*H), 128.5 (d, $J_{CH}$ = 181 Hz, pyrrolyl *C*H), 136.1 (s, pyrrolyl *C*$_{ipso}$) ppm.

**$[C_4H_3N(CH_2NMe_2)\text{-}2]_2Zr(OC_6H_3Me_2\text{-}2,6)_2$ (5):** A solution of 2,6-dimethylphenol (0.254 g, 2.08 mmol) in heptane (15 mL) was added to a heptane solution (20 mL) of $[C_4H_3N(CH_2NMe_2)\text{-}2]_2Zr(NEt_2)_2$ (0.50 g, 1.04 mmol) dropwise over 10 min. The solution was stirred at room temperature for 3 h after the addition was completed. The volatiles were removed under vacuum, and the residue was recrystallized from a dichloromethane solution to yield 0.45 g of colorless crystals in 73.8% yield. $^1$H NMR ($CDCl_3$): $\delta$ = 2.23 (br. s, 12 H, N*Me*$_2$), 2.47 (br. s, 12 H, Ph-*Me*), 3.87 (br. s, 4 H, C*H*$_2$N), 5.29 (s, 2 H, C*H*$_2$Cl$_2$), 6.02 (m, 2 H, pyrrolyl C*H*), 6.16 (m, 2 H, pyrrolyl C*H*), 6.70 (m, 2 H, pyrrolyl C*H*), 6.93 (m, 4 H, *Ph*), 7.33 (br., 2 H, *Ph*) ppm. $^{13}$C NMR ($CDCl_3$): $\delta$ = 17.8 (q, $J_{CH}$ = 126 Hz, Ph-*Me*), 48.2 (q, $J_{CH}$ = 140 Hz, N*Me*$_2$), 61.6 (t, $J_{CH}$ = 137 Hz, *C*H$_2$N), 104.5 (d, $J_{CH}$ = 168 Hz, pyrrolyl *C*H), 108.2 (d, $J_{CH}$ = 166 Hz, pyrrolyl *C*H), 120.2 (d, $J_{CH}$ = 162 Hz, *Ph*), 126.5 (s, Ph *C*$_{ipso}$), 128.6 (d, $J_{CH}$ = 158 Hz, *Ph*), 128.8 (d, $J_{CH}$ = 180 Hz, pyrrolyl *C*H), 136.3 (s, pyrrolyl *C*$_{ipso}$), 159.2 (s, Ph *C*$_{ipso}$) ppm. $C_{30}H_{40}N_4O_2Zr{\cdot}CH_2Cl_2$ (664.82): calcd. C 56.00, H 6.37, N 8.43; found C 55.72, H 6.54, N 8.43.

**$[C_4H_3N(CH_2NMe_2)\text{-}2]_2Hf(OC_6H_3Me_2\text{-}2,6)_2$ (6):** This compound was prepared in a manner analogous to that described for the synthesis of **5** using $[C_4H_3N(CH_2NMe_2)\text{-}2]_2Hf(NEt_2)_2$ (1.0 g, 1.76 mmol) and 2,6-dimethylphenol (0.429 g, 3.52 mmol) as starting material. Colorless crystals of **6** were obtained from a $CH_2Cl_2$ solution (0.74 g, 63.2% yield). $^1$H NMR ($CDCl_3$): $\delta$ = 2.25 (br. s, 12 H, Ph-*Me*), 2.50 (br. s, 12 H, N*Me*$_2$), 3.90 (br. s, 4 H, C*H*$_2$N), 5.29 (s, 2 H, C*H*$_2$Cl$_2$), 6.09 (m, 2 H, pyrrolyl C*H*), 6.22 (m, 2 H, pyrrolyl C*H*), 6.69 (m, 2 H, pyrrolyl C*H*), 6.95 (m, 4 H, *Ph*), 7.39 (br., 2 H, *Ph*) ppm. $^{13}$C NMR ($CDCl_3$): $\delta$ = 17.9 (q, $J_{CH}$ = 128 Hz, Ph-*Me*), 48.4 (q, $J_{CH}$ = 145 Hz, N*Me*$_2$), 53.5 (t, $J_{CH}$ = 177 Hz, *C*H$_2$Cl$_2$), 61.6 (t, $J_{CH}$ = 137 Hz, *C*H$_2$N), 105.1 (d, $J_{CH}$ = 166 Hz, pyrrolyl *C*H), 109.1 (d, $J_{CH}$ = 166 Hz, pyrrolyl *C*H), 120.0 (d, $J_{CH}$ = 161 Hz, *Ph*), 126.8 (s, Ph *C*$_{ipso}$), 128.6 (d, $J_{CH}$ = 155 Hz, *Ph*), 129.4 (d, $J_{CH}$ = 179 Hz, pyrrolyl *C*H), 136.5 (s, pyrrolyl *C*$_{ipso}$), 159.0 (s, Ph *C*$_{ipso}$) ppm. $C_{30}H_{40}HfN_4O_2{\cdot}CH_2Cl_2$ (752.09): calcd. C 49.51, H 5.63, N 7.45; found C 49.80, H 5.65, N 7.48.

**$[C_4H_3N(CH_2NMe_2)\text{-}2]_2Zr(OC_6H_3iPr_2\text{-}2,6)_2$ (7):** This compound was prepared in a manner analogous to that described for the synthesis of **5** using $[C_4H_3N(CH_2NMe_2)\text{-}2]_2Zr(NEt_2)_2$ (1.0 g, 2.08 mmol) and 2,6-diisopropylphenol (0.74 g, 4.16 mmol) as starting material. Colorless crystals of **7** were obtained from a $CH_2Cl_2$ solution (0.85 g, 59.2% yield). $^1$H NMR ($CDCl_3$): $\delta$ = 0.72 (d, 6 H, CH*Me*$_2$), 0.82 (d, 6 H, CH*Me*$_2$), 1.27 (d, 6 H, CH*Me*$_2$), 1.47 (d, 6 H, CH*Me*$_2$), 2.12 (s, 6 H, N*Me*$_2$), 2.31 (s, 6 H, N*Me*$_2$), 3.45 (d, 2 H, C*H*$_a$H$_b$NMe$_2$), 3.51 (m, 2 H, C*H*Me$_2$), 4.00 (m, 2 H, C*H*Me$_2$), 4.21 (d, 2 H, CH$_a$*H*$_b$NMe$_2$), 5.27 (s, C*H*$_2$Cl$_2$), 6.00 (d, 2 H, pyrrolyl C*H*), 6.13 (d, 2 H, pyrrolyl C*H*), 6.85 (m, 4 H, pyrrolyl + phenyl C*H*), 7.07 (m, 2 H, phenyl C*H*), 7.38 (m, 2 H, phenyl C*H*) ppm. $^{13}$C NMR ($CDCl_3$): $\delta$ = 23.0 (q, $J_{CH}$ = 126 Hz, CH*Me*$_2$), 24.2 (q, $J_{CH}$ = 122 Hz, CH*Me*$_2$), 25.56 (q, $J_{CH}$ = 127 Hz, CH*Me*$_2$), 25.61 (q, $J_{CH}$ = 127 Hz, CH*Me*$_2$), 25.63 (d, $J_{CH}$ = 123 Hz, *C*HMe$_2$), 26.8 (d, $J_{CH}$ = 123 Hz, *C*HMe$_2$), 47.2 (q, $J_{CH}$ = 137 Hz, N*Me*$_2$), 50.3 (q, $J_{CH}$ = 140 Hz, N*Me*$_2$), 54.3 (t, $J_{CH}$ = 177 Hz, *C*H$_2$Cl$_2$), 61.9 (t, $J_{CH}$ = 135 Hz, *C*H$_2$N), 105.3 (d, $J_{CH}$ = 165 Hz, pyrrolyl *C*H), 108.3 (d, $J_{CH}$ = 167 Hz, pyrrolyl *C*H), 121.2 (d, $J_{CH}$ = 161 Hz, phenyl *C*H), 123.6 (d, $J_{CH}$ = 151 Hz, phenyl *C*H), 123.7 (d, $J_{CH}$ = 151 Hz, phenyl *C*H), 127.7 (d, $J_{CH}$ = 180 Hz, pyrrolyl *C*H), 135.8 (s, phenyl *C*$_{ipso}$), 136.1 (s, pyrrolyl *C*$_{ipso}$), 139.2 (s, phenyl *C*$_{ipso}$), 155.8 (s, phenyl *C*$_{ipso}$). $C_{38}H_{56}N_4O_2Zr{\cdot}0.5CH_2Cl_2$ (734.57): calcd. C 62.95, H 7.82, N 7.63; found C 62.31, H 8.09, N 7.34.

**$[C_4H_3N(CH_2NMe_2)\text{-}2]_2Hf(OC_6H_3iPr_2\text{-}2,6)_2$ (8):** This compound was prepared in a manner analogous to that described for the synthesis of **5** using $[C_4H_3N(CH_2NMe_2)\text{-}2]_2Hf(NEt_2)_2$ (0.3 g, 0.53 mmol) and 2,6-diisopropylphenol (0.19 g, 1.06 mmol) as starting material. Colorless crystals of **8** were obtained from a $CH_2Cl_2$ solution (0.20 g, 44% yield). $^1$H NMR ($CDCl_3$): $\delta$ = 0.67 (d, 6 H, CH*Me*$_2$), 0.78 (d, 6 H, CH*Me*$_2$), 1.24 (d, 6 H, CH*Me*$_2$), 1.45 (d, 6 H, CH*Me*$_2$), 2.13 (s, 6 H, N*Me*$_2$), 2.31 (s, 6 H, N*Me*$_2$), 3.47 (m, 4 H, C*H*$_a$H$_b$NMe$_2$ + C*H*Me$_2$), 3.96 (m, 2 H, C*H*Me$_2$), 4.15 (m, 2 H, CH$_a$*H*$_b$NMe$_2$), 6.02 (m, 2 H, pyrrolyl C*H*), 6.12 (m, 2 H, pyrrolyl C*H*), 6.83 (m, 4 H, pyrrolyl + phenyl C*H*), 7.03 (m, 2 H, phenyl C*H*), 7.33 (s, 2 H, phenyl C*H*) ppm. $^{13}$C NMR ($CDCl_3$): $\delta$ = 22.8 (q, $J_{CH}$ = 127 Hz, CH*Me*$_2$), 24.3 (q, $J_{CH}$ = 126 Hz, CH*Me*$_2$), 25.5 (d, $J_{CH}$ = 131 Hz, CH*Me*$_2$), 25.7 (q, $J_{CH}$ = 123 Hz, CH*Me*$_2$), 25.8 (d, $J_{CH}$ = 126 Hz, *C*HMe$_2$), 26.6 (d, $J_{CH}$ = 126 Hz, *C*HMe$_2$), 47.2 (q, $J_{CH}$ = 141 Hz, N*Me*$_2$), 50.7 (q, $J_{CH}$ = 141 Hz, N*Me*$_2$), 61.9 (t, $J_{CH}$ = 137 Hz, *C*H$_2$N), 105.8 (d, $J_{CH}$ = 167 Hz, pyrrolyl *C*H), 109.0 (d, $J_{CH}$ = 167 Hz, pyrrolyl *C*H), 120.9 (d, $J_{CH}$ = 160 Hz, phenyl *C*H), 123.6 (d, $J_{CH}$ = 155 Hz, phenyl *C*H), 123.7 (d, $J_{CH}$ = 155 Hz, phenyl *C*H), 128.7 (d, $J_{CH}$ = 181 Hz, pyrrolyl *C*H), 136.1 (s, phenyl *C*$_{ipso}$), 136.4 (s, pyrrolyl *C*$_{ipso}$), 139.1 (s, phenyl *C*$_{ipso}$), 155.5 (s, phenyl *C*$_{ipso}$). $C_{38}H_{56}HfN_4O_2{\cdot}CH_2Cl_2$ (864.30): calcd. C 54.20, H 6.76, N 6.48; found C 54.13, H 6.63, N 6.06.

 © 2006 Wiley-VCH Verlag GmbH & Co. KGaA, Weinheim 

Table 3. The summary of data collections for compounds **3**, **4**, **6**, **7**, and **8**.

| | **3**·0.5$C_7H_8$ | **4**·0.75$C_7H_8$ | **6**·$CH_2Cl_2$ | **7** | **8**·$CH_2Cl_2$ |
|---|---|---|---|---|---|
| Empirical formula | $C_{25.5}H_{34}N_6Zr$ | $C_{27.25}H_{36}HfN_6$ | $C_{31}H_{42}Cl_2HfN_4O_2$ | $C_{38}H_{56}N_4O_2Zr$ | $C_{39}H_{58}Cl_2HfN_4O_2$ |
| Formula mass | 515.81 | 626.11 | 752.08 | 692.09 | 864.28 |
| $T$ [K] | 293 | 150(2) | 150(2) | 298(2) | 150(2) |
| Crystal system | triclinic | triclinic | triclinic | monoclinic | monoclinic |
| Space group | $P\bar{1}$ | $P\bar{1}$ | $P\bar{1}$ | $C2/c$ | $P2/n$ |
| $a$ [Å] | 9.5756(6) | 9.6927(15) | 11.253(3) | 20.950(2) | 10.7842(3) |
| $b$ [Å] | 10.8727(7) | 17.163(3) | 12.453(3) | 10.8831(10) | 10.9035(3) |
| $c$ [Å] | 13.1039(9) | 18.581(3) | 13.726(4) | 18.3747(18) | 17.5344(5) |
| $\alpha$ [°] | 94.1730(10) | 64.774(3) | 113.833(4) | 90 | 90 |
| $\beta$ [°] | 111.0280(10) | 84.135(3) | 97.283(4) | 113.258(2) | 107.8480(10) |
| $\gamma$ [°] | 95.7100(10) | 74.502(2) | 111.359(4) | 90 | 90 |
| $V$ [Å$^3$]/$Z$ | 1258.44(14)/2 | 2694.3(7)/4 | 1551.6(7)/2 | 3849.1(6)/4 | 1962.56(10)/2 |
| $D_{calcd}$ [mg/m$^3$] | 1.361 | 1.543 | 1.610 | 1.194 | 1.463 |
| $\mu$ [mm$^{-1}$] | 0.461 | 3.898 | 3.568 | 0.321 | 2.831 |
| Reflections collected | 7996 | 16456 | 15047 | 12112 | 20865 |
| No. of independent reflections | 5548 [$R$(int) = 0.025] | 11773 [$R$(int) = 0.0403] | 6813 [$R$(int) = 0.0478] | 4394 [$R$(int) = 0.0752] | 4526 [$R$(int) = 0.0408] |
| Final $R$ indices [$I > 2\sigma(I)$] | $R_1$ = 0.0285 | $R_1$ = 0.0428 | $R_1$ = 0.0428 | $R_1$ = 0.0414 | $R_1$ = 0.0270 |
| | $wR_2$ = 0.0578 | $wR_2$ = 0.0953 | $wR_2$ = 0.1337 | $wR_2$ = 0.0623 | $wR_2$ = 0.0475 |
| $R$ indices (all data) | $R_1$ = 0.0398 | $R_1$ = 0.0800 | $R_1$ = 0.0490 | $R_1$ = 0.1158 | $R_1$ = 0.0335 |
| | $wR_2$ = 0.0606 | $wR_2$ = 0.1031 | $wR_2$ = 0.1379 | $wR_2$ = 0.0.0722 | $wR_2$ = 0.0480 |
| Largest diff. peak and hole [e/Å$^3$] | 0.576 and –0.431 | 2.087 and –2.927 | 4.065 and –1.930 | 0.379 and –0.734 | 2.070 and –1.651 |

**X-ray Structure Determination of Compounds 3, 4, 6, 7, and 8:** The crystals were sealed in glass fibers under nitrogen and transferred to a goniostat. Data were collected with a Bruker SMART CCD diffractometer with graphite-monochromated Mo-$K_\alpha$ radiation with a radiation wavelength of 0.71073 Å at 293(2) K. Structural determinations were made using the SHELXTL package of programs. A SADABS absorption correction was made. All refinements were carried out by full-matrix least-squares using anisotropic displacement parameters for all non-hydrogen atoms. All the hydrogen atoms are placed with the use of a riding model. The crystal data are summarized in Table 3.

CCDC-279540 (for **3**), -279541 (for **4**), -279543 (for **6**), -279542 (for **7**), and -279544 (for **8**) contain the supplementary crystallographic data for this paper. These data can be obtained free of charge from The Cambridge Crystallographic Data Centre via www.ccdc.cam.ac.uk/data_request/cif.

**Kinetic Study of *rac*-Lactide Polymerization Initiated by 8:** Compound **8** and lactides were placed in a J-Young NMR tube and $CDCl_3$ (0.5 mL) was added. The solution was placed in a preheated oil bath (70 °C) and reactions were monitored by a $^1$H NMR spectrometer constantly.

**General Procedure for the Polymerization of ε-Caprolactone:** General procedures for ε-caprolactone polymerization catalyzed by the new zirconium and hafnium complexes are as follows. In a glovebox, the monomer (ε-caprolactone) and catalyst were placed in separate Schlenk flasks and then moved out of the glovebox. Toluene (10 mL) was added with a syringe to the catalyst and heated to the desired temperature followed by the addition of the monomer. The reactions proceeded in the desired conditions and were quenched with methanol. Solids were obtained by filtration, washed with methanol to remove excess metal catalysts, and dried under vacuum.

## Acknowledgments

We thank the National Science Council of Taiwan for financial support and the National Changhua University of Education for purchasing the Bruker CCD X-ray diffractometer.

[1] Y. Ikada, H. Tsuji, *Macromol. Rapid. Commun.* **2000**, *21*, 117–132.
[2] O. Dechy-Cabaret, B. Martin-Vaca, D. Bourissou, *Chem. Rev.* **2004**, *104*, 6147–6176.
[3] B. J. O'Keefe, M. A. Hillmyer, W. B. Tolman, *J. Chem. Soc., Dalton Trans.* **2001**, 2215–2224.
[4] K. M. Stridsberg, M. Ryner, A.-C. Albertsson, *Adv. Polym. Sci.* **2002**, *157*, 41–65.
[5] D. W. Grijpma, A. J. Pennings, *Polym. Bull.* **1991**, *25*, 335–341.
[6] H. R. Kricheldorf, J. Meier-Haack, *Macromol. Chem.* **1993**, *194*, 715–725.
[7] A. Kowalski, A. Duda, S. Penczek, *Macromolecules* **2000**, *33*, 689–695.
[8] M. Ryner, K. Stridsberg, A.-C. Albertsson, H. von Schenck, M. Svensson, *Macromolecules* **2001**, *34*, 3877–3881.
[9] B.-T. Ko, C.-C. Lin, *Macromolecules* **1999**, *32*, 8296–8330.
[10] C.-H. Huang, F.-C. Wang, B.-T. Ko, T.-L. Yu, C.-C. Lin, *Macromolecules* **2001**, *34*, 356–361.
[11] C.-T. Chen, C.-A. Huang, B.-H. Huang, *Macromolecules* **2004**, *37*, 7968–7973.
[12] L. M. Alcazar-Roman, B. J. O'Keefe, M. A. Hillmyer, W. B. Tolman, *Dalton Trans.* **2003**, 3082–3087.
[13] P. Arndt, A. Spannenberg, W. Baumann, S. Becke, U. Rosenthal, *Eur. J. Inorg. Chem.* **2001**, 2885–2890.
[14] D. Chakraborty, E. Y.-X. Chen, *Organometallics* **2002**, *21*, 1438–1442.
[15] H.-L. Chen, B.-T. Ko, B.-H. Huang, C.-C. Lin, *Organometallics* **2001**, *20*, 5076–5083.
[16] K. C. Hultzsch, T. P. Spaniol, J. Okuda, *Organometallics* **1997**, *16*, 4845–4856.
[17] T. Kitayama, H. Yamaguchi, T. Kanzawa, T. Hirano, *Polym. Bull.* **2000**, *45*, 97–104.
[18] D. Takeuchi, T. Nakamura, T. Aida, *Macromolecules* **2000**, *33*, 725–729.
[19] Y. Takashima, Y. Nakayama, T. Hirao, H. Yasuda, A. Harada, *J. Organomet. Chem.* **2004**, *689*, 612–619.
[20] Y. Takashima, Y. Nakayama, K. Watanabe, T. Itono, N. Ueyama, A. Nakamura, H. Yasuda, A. Harada, *Macromolecules* **2002**, *35*, 7538–7544.
[21] D. Takeuchi, T. Aida, *Macromolecules* **2000**, *33*, 4607–4609.
[22] H.-X. Li, Z.-G. Ren, Y. Zhang, W.-H. Zhang, J.-P. Lang, Q. Shen, *J. Am. Chem. Soc.* **2005**, *127*, 1122–1123.

 © 2006 Wiley-VCH Verlag GmbH & Co. KGaA, Weinheim 

[23] Y. Shen, Z. Shen, Y. Zhang, K. Yao, *Macromolecules* **1996**, *29*, 8289–8295.
[24] M. Yamashita, Y. Takemoto, E. Ihara, H. Yasuda, *Macromolecules* **1996**, *29*, 1798–1806.
[25] C. Villiers, P. Thuery, M. Ephritikhine, *Eur. J. Inorg. Chem.* **2004**, *23*, 4624–4632.
[26] T. J. Woodman, M. Schormann, D. L. Hughes, M. Bochmann, *Organometallics* **2004**, *23*, 2972–2979.
[27] J.-L. Chen, Y.-M. Yao, Y.-J. Luo, L.-Y. Zhou, Y. Zhang, Q. Shen, *J. Organomet. Chem.* **2004**, *689*, 1019–1024.
[28] R.-C. Yu, C.-H. Hung, J.-H. Huang, H.-Y. Lee, J.-T. Chen, *Inorg. Chem.* **2002**, *41*, 6450–6455.
[29] S. Venne-Dunker, G. Kehr, R. Fröhlich, G. Erker, *Organometallics* **2003**, *22*, 948–958.
[30] J. M. Taski, G. Parkin, *Organometallics* **2002**, *21*, 587–589.
[31] R. Vollmerhaus, R. Tomaszewski, P. Shao, N. J. Taylor, K. J. Wiacek, S. P. Lewis, A. Al-Humydi, S. Collins, *Organometallics* **2005**, *24*, 494–507.
[32] V. Passarelli, F. Benetollo, P. Zanella, *Eur. J. Inorg. Chem.* **2004**, 1714–1723.
[33] K.-C. Hsieh, J.-C. Chang, T.-Y. Lee, C.-H. Hu, C.-H. Hung, H.-M. Lee, J.-H. Huang, *Inorg. Chim. Acta* **2004**, *357*, 3517–3524.
[34] R. D. Roger, R. V. Bynum, J. L. Atwood, *J. Cryst. Spect. Res.* **1984**, *14*, 21–28.
[35] We thank one of the reviewers who gave us very helpful suggestions on the solution NMR spectra of these complexes.
[36] An abstract has been published previously: J.-H. Huang, K.-C. Hsieh, H.-M. Lee, 228th ACS National Meeting, Philadelphia, PA, USA, **2004**, Inorg-221.
[37] D. Thomas, P. Arndt, N. Peulecke, A. Spannenberg, R. Kempe, U. Rosenthal, *Eur. J. Inorg. Chem.* **1998**, 1351–1357.
[38] C. Miola-Delaite, T. Hamaide, R. Spitz, *Macromol. Chem. Phys.* **1999**, *200*, 1771–1778.
[39] P. Dobrzynski, *J. Polym. Sci., Part A: Polym. Chem.* **2002**, *40*, 3129–3143.
[40] J.-H. Huang, L.-S. Chi, R.-C. Yu, G. J. Jiang, W.-T. Yang, G.-H. Lee, S.-M. Peng, *Organometallics* **2001**, *20*, 5788–5791.
[41] K.-C. Hsieh, W.-Y. Lee, C.-L. Lai, C.-H. Hu, H. M. Lee, J.-H. Huang, S.-M. Peng, G.-H. Lee, *J. Organomet. Chem.* **2004**, *689*, 3362–3369.
[42] W. Herz, K. Dittmer, S. J. Cristol, *J. Am. Chem. Soc.* **1947**, *69*, 1698–1700.
[43] I. T. Kim, R. L. Elsenbaumer, *Tetrahedron Lett.* **1998**, *39*, 1087–1090.
[44] D. C. Bradley, I. M. Thomas, *J. Chem. Soc.* **1960**, 3857–3861.

Received: July 28, 2005
Published Online: March 30, 2006

 © 2006 Wiley-VCH Verlag GmbH & Co. KGaA, Weinheim 

DOI: 10.1002/ejic.200500983

# Facile and Selected-Control Synthesis of β-$MnO_2$ Nanorods and Their Magnetic Properties

**Guangli Wang,[a] Bo Tang,*[a] Linhai Zhuo,[a] Jiechao Ge,[a] and Mei Xue[a]**

**Keywords:** β-Manganese dioxide / Nanostructures / Hydrothermal synthesis / Magnetic properties

Single crystal β-$MnO_2$ nanorods were successfully synthesized employing a facile in-situ redox precipitation hydrothermal process. The effects of various experimental conditions on the morphology of the products were investigated. The mechanism of formation of the nanorods was investigated and discussed based on the experimental results. The magnetic measurement of the nanorods with a diameter of 25–40 nm and a length of 240–440 nm indicates that the Néel magnetic transition temperature is about 6 K higher than that of the bulk β-$MnO_2$ crystal.
(© Wiley-VCH Verlag GmbH & Co. KGaA, 69451 Weinheim, Germany, 2006)

## 1. Introduction

One-dimensional (1D) nanocrystals such as nanorods, nanowires, and nanotubes have been the focus of considerable interest.[1–3] As a consequence of their low dimensionality and quantum confinement effect, they can show unique electronic, optical, and magnetic properties that are anomalous when compared to the bulk materials.[4–7] Manganese dioxide can form many kinds of polymorph, such as α-, β-, γ-, and δ-types, each offering distinctive properties and applications. Applications include as molecular sieves, ion sieves, in catalysis, as cathode materials for secondary rechargeable batteries, and as new magnetic materials.[8–12] Bach et al.[13] have especially pointed out that the electrochemical properties of $MnO_2$ strongly depend on parameters such as powder morphology, crystalline structure, and bulk density. One-dimensional nanostructures are the smallest structures known for the efficient transport of electrons, and they may provide the possibility of detecting the theoretical operating limits of a lithium battery.[14–15] $MnO_2$ also possesses an interesting magnetic structure.[16–20] To date we have found nothing in the literature on the magnetic properties of nanosized $MnO_2$. Therefore, development of a controllable synthesis method for one-dimensional $MnO_2$ nanostructures was deemed very important to be able to explore their novel properties as well as examine potential applications for $MnO_2$. Much effort has been put into preparing nanocrystalline $MnO_2$ with different crystallographic forms; such as nanorod-shaped and nanofibrous α- and Tokorokite-type $MnO_2$,[21] β-$MnO_2$ nanorods,[22] γ-$MnO_2$ nanowires,[23] and δ-$MnO_2$ nanofibers.[24] Although Li et al. have reported on the hydrothermal synthesis of α-$MnO_2$ nanowires and β-$MnO_2$ nanorods by oxidizing $MnSO_4$ with $KMnO_4$ or $K_2S_2O_8$, respectively,[22] the control of both morphology and the phase of the one-dimensional β-$MnO_2$ nanostructures using the direct reaction route is still challenging.

In this paper, we report a facile in-situ redox precipitation hydrothermal synthesis method for the selected control synthesis of single-crystal β-$MnO_2$ nanorods. The effects of various experimental conditions on the morphology and particle size of the products were studied. The mechanism of formation of the nanorods was investigated and discussed. The magnetic properties of the as-obtained nanorods with diameters of 25–40 nm and lengths of 240–440 nm were characterized.

## 2. Results and Discussion

### 2.1. Characterization

X-ray powder diffraction (XRD) patterns reveal the phase and purity of the as-obtained products. As shown in Figure 1, all of the reflection peaks can be indexed to a pure tetragonal phase of β-$MnO_2$ [JCPDS 24-0735, space group $P4_2/mnm$(136)] with lattice constants $a$ = 4.3998 Å and $c$ = 2.8695 Å. The sharp peaks indicate that the product is perfectly crystallized. No other impurity peaks were observed, demonstrating the high purity of the products obtained under current experimental conditions.

A typical TEM image of the as-prepared sample is shown in Figure 2 (a), which indicates that the final product consists of nanorods with diameters of 25–40 nm and lengths ranging from 240 to 440 nm. More detailed structural information for these nanorods was obtained from

[a] College of Chemistry, Chemical Engineering and Materials Science, Shandong Normal University,
Jinan, Shandong 250014, P. R. China
Fax: +86-531-86180017
E-mail: tangb@sdnu.edu.cn

 © 2006 Wiley-VCH Verlag GmbH & Co. KGaA, Weinheim 

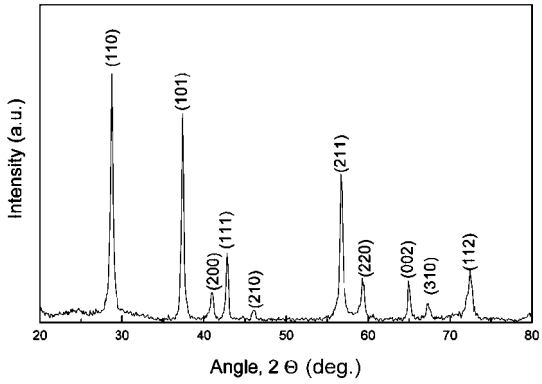


Figure 1. XRD pattern of the as-obtained product.

high-resolution transmission electron microscopy (HRTEM) images and selected area diffraction (SAED) patterns. The HRTEM image (Figure 2, b) of an individual nanorod shows that the nanorod is structurally uniform with an interplanar spacing of about 0.315 nm, which corresponds to the (110) plane of tetragonal β-$MnO_2$. Selected area electron diffraction patterns taken from the individual nanorod (shown in the inset image in Figure 2, b) reveal its single crystal nature, and can be indexed to the [001] zone axis of tetragonal β-$MnO_2$.

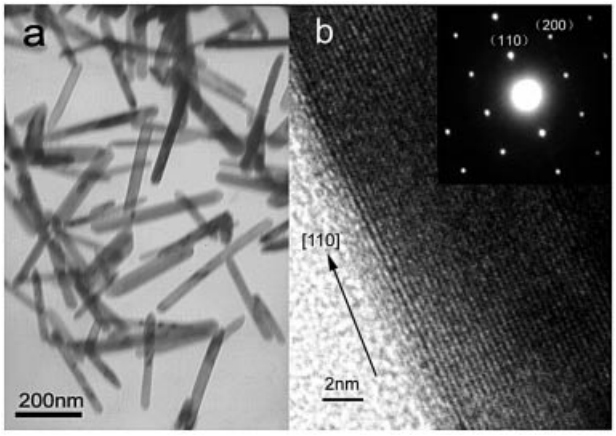


Figure 2. The (a) TEM image and (b) HRTEM and SAED (inset image) patterns of the as-prepared sample.

A typical room temperature X-ray photoelectron spectrum of the as-synthesized sample is shown in Figure 3. Only the peaks of Mn(2p3/2, 2p1/2) and O1s can be observed. The binding energies of Mn(2p3/2) and Mn(2p1/2) are 642.32 and 653.95 ev, respectively, which are well in accordance with $MnO_2$ [Mn(2p3/2) = 642.1 ev and Mn(2p1/2) = 653.8 ev].[25] The estimated relative ratio of O to Mn is 2.16:1, which is caused by the interference of oxygen in the air for the XPS study.

## 2. 2. The Effect of Reaction Conditions on the Morphology and Particle Size of the Products

### *2. 2. 1. The Effects of Ammonia on the Morphology and Particle Size of the Products*

It was found that the concentration of ammonia as well as the way the ammonia was added had significant effects on the morphology of the products. Uniform nanorods were obtained (as shown in Figure 2, a) when ammonia was added dropwise. Pouring ammonia into the mixture of $Mn(NO_3)$ and $H_2O_2$ led to the product being composed of big rod-like structures (200–400 nm in diameter and more than 10 μm in length) and nanoparticles (Figure 4, a). The concentration of ammonia also significantly affected the morphology of the products. In our synthetic system, the concentrations of $Mn(NO_3)_2$ and $H_2O_2$ were kept constant and ammonia was added dropwise with different concentrations. As the concentration of ammonia was varied (0.25, 0.5, 1, 2 M) the morphology changed from a spindle morphology (Figure 4, b), to nanorods (Figure 2, a), a mixture of nanorods and nanoparticles (Figure 4, c), and finally to nanoparticles (Figure 4, d). From the above results, we can see that the precipitator ammonia in our synthetic system has significant effects on the morphology of the products.

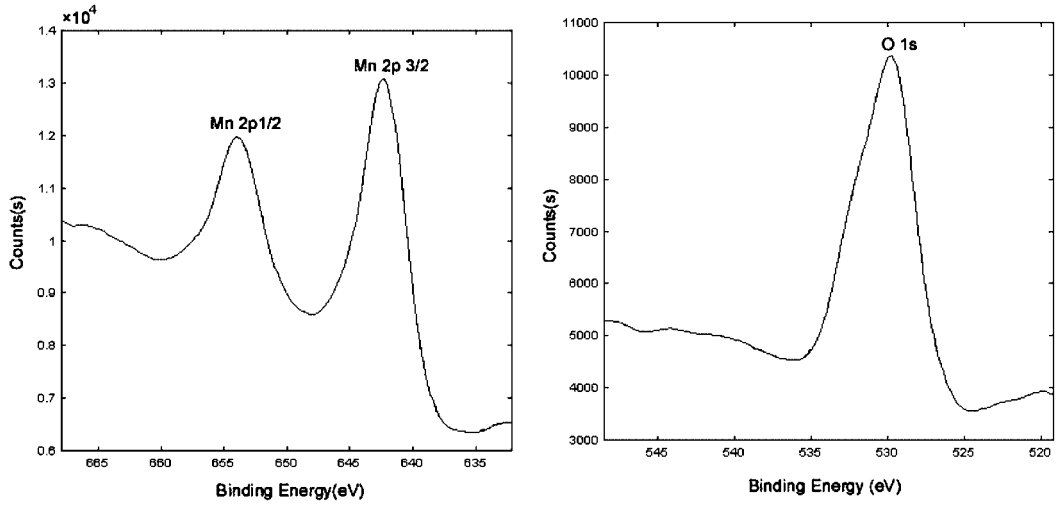


Figure 3. Room temperature X-ray photoelectron spectra of the as-obtained sample.

 © 2006 Wiley-VCH Verlag GmbH & Co. KGaA, Weinheim 

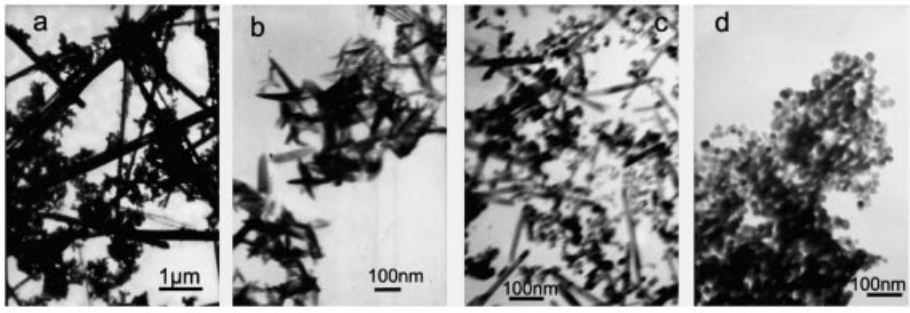


Figure 4. (a) 0.5 M ammonia was added by pouring, (b–d) ammonia was added dropwise with different concentrations; (b) 0.25 M; (c) 1 M; (d) 2 M.

#### *2.2.2. Effects of $H_2O_2$ on the Morphology of the Products*

Increasing the amount of $H_2O_2$ to 2 mL, while the other experimental conditions were kept constant, led to a morphology of the products similar to that shown in Figure 4 (a). The as-obtained products are composed of rod-like structures (400–500 nm in diameter and 10–20 μm in length) and nanoparticles.

#### *2.2.3. Effects of Temperature on the Morphology of the Products*

Temperature also affected the morphology and particle size of the final products. At a lower temperature such as 130 °C, only nanoparticles could be obtained (Figure 5, a). Upon increasing the temperature to 140 °C, we obtained a mixture of nanoparticles and nanorods (Figure 5, b). Nanorods could be obtained in the temperature range 180–250 °C. The TEM image in part c of Figure 5 shows that $MnO_2$ obtained at 180 °C consists of uniform nanorods with a diameter of 15–30 nm and lengths of 150–200 nm, whereas the product obtained at 210 °C is on average 20–30 nm in diameter and has a length of 200–300 nm as shown in part d of Figure 5. Upon increasing the temperature to 250 °C, the product was found to consist of uniform nanorods with a diameter of 25–40 nm and lengths of up to 240–440 nm as shown in Figure 2 (a). From the above results, we can see that the diameter and length of the nanorods increase slightly with increasing temperature. It is apparent that higher temperatures favor the anisotropic growth of the crystals and nanorod formation.

The phases of nanorods obtained in the temperature range 180–250 °C were examined by the X-ray powder diffraction technique, which demonstrated that all the phases were pure β-$MnO_2$. In contrast to solution-based methods for the growth of one-dimensional nanostructures in which the problem of phase control of the products often exists,[22] the present synthetic process can be performed over a wide range of hydrothermal reaction temperatures.

### 2.3. Possible Growth Mechanism of the Nanorods

The chemical reaction can be formulated as:

$$Mn^{2+} + H_2O_2 + 2\ NH_3{\cdot}H_2O \rightarrow MnO_2{\cdot}xH_2O + 2\ NH_4^+ + H_2O \quad (1)$$

$$MnO_2{\cdot}xH_2O \xrightarrow[\text{reaction}]{\text{hydrothermal}} MnO_2 + x\ H_2O \quad (2)$$

As illustrated in the chemical equation above, when ammonia was added to the mixture of hydrogen peroxide and manganese nitrate, the precipitation and oxidation reaction occurred together [Equation (1)], accompanied by the decomposition of hydrogen peroxide. After the in-situ redox precipitation process, we obtained $MnO_2{\cdot}xH_2O$. In the hydrothermal process, $MnO_2{\cdot}xH_2O$ dehydrated to $MnO_2$ [Equation (2)]. In order to investigate the growth process of

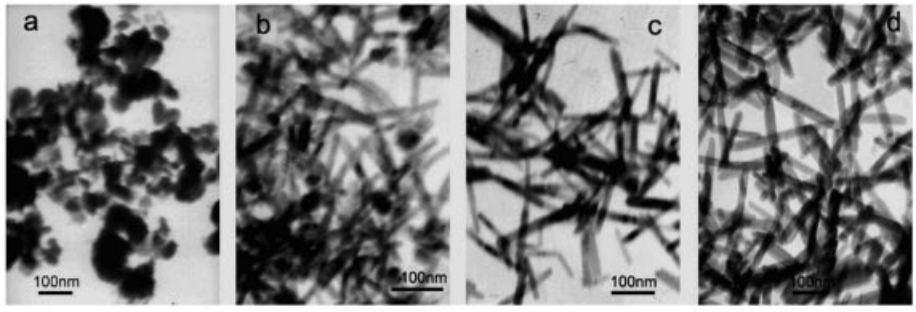


Figure 5. The products obtained at different hydrothermal reaction temperatures for 12 h: (a) 130 °C; (b) 140 °C; (c) 180 °C; (d) 210 °C.

 © 2006 Wiley-VCH Verlag GmbH & Co. KGaA, Weinheim 

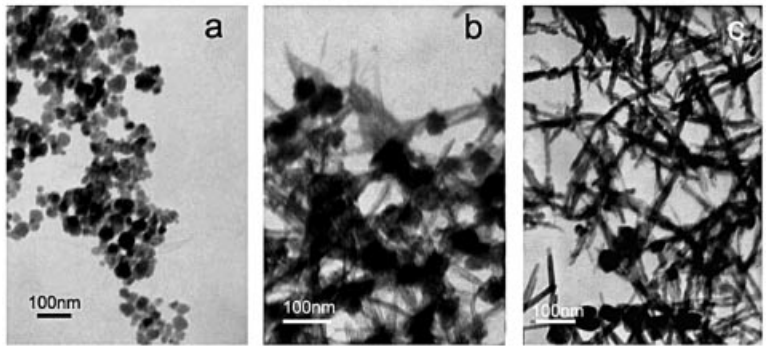


Figure 6. TEM image of the as-obtained samples at different hydrothermal reaction times: (a) 5 min; (b) 15 min; (c) 1 h.

the nanorods, we carried out the hydrothermal reaction at 250 °C for different periods of time. Figure 6 (a) shows the TEM image of the sample obtained after heating for 5 min, there are only nanoparticles with a diameter of 15–60 nm. The sample was characterized by XRD, but no peak was detected, indicting that crystallization did not occur for these nanoparticles. Figure 6 (b) shows the samples obtained after heating for 15 min, which indicates that there are nanoparticles with diameters of 40–60 nm and a few short nanorods. The smaller nanoparticles in Figure 6 (a) are not seen in Figure 6 (b). After heating for 1 h, the amount of nanorods is more than that shown in Figure 6 (b), and the amount of nanoparticles has dramatically decreased (Figure 6, c). The TEM image of the product obtained after heating for 12 h indicates that the product is composed of nanorods and the nanoparticles are no longer seen (Figure 2, a). The above study demonstrates that the nanorods are grown from the small nanoparticles. We believe that the mechanism of formation of the $MnO_2$ nanorods follows the Ostwald ripening process.[26]

## 3. Magnetic Property of the As-Synthesized β-$MnO_2$ Nanorods

The magnetic properties of the as-synthesized β-$MnO_2$ nanorods with a diameter of 25–40 nm and a length of 240–440 nm were characterized. Figure 7 shows the magnetization vs. temperature curve of the as-synthesized β-$MnO_2$ nanorods at an applied field of 1000 Oe. A kink is observed at 98 K in Figure 7, which corresponds to the Néel magnetic transition temperature $T_N$. This temperature is higher than that of the bulk $MnO_2$ crystal ($T_N$ = 92 K),[27–28] which may be because of the special morphology and the effect of surface spins of the as-obtained nanorods.[29–30] Strangely, a discontinuity is seen in the temperature range 30–50 K in Figure 7. From the XRD and XPS studies, we know that the products we obtained were of high purity. So the reason for the discontinuity cannot be any impurity in the products, but may be caused by the special morphology and uncompensated surface spins of the nanorods.[29,31–32] At 293 K, a nearly linear M–H curve (Figure 8) reveals that a superparamagnetic state exists at this temperature.

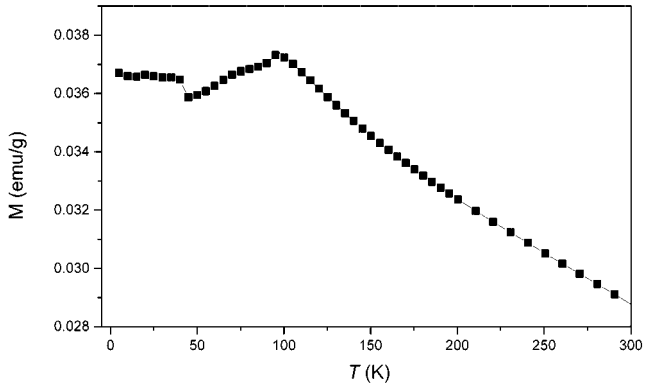


Figure 7. Magnetization vs. temperature curve of the as-obtained nanorods at an applied field of 1000 Oe.

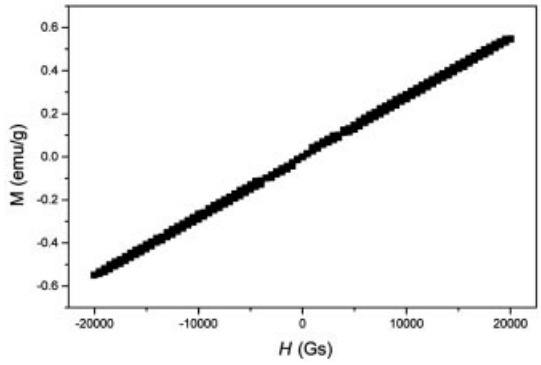


Figure 8. The magnetization vs. applied magnetic field of the as-obtained nanorods.

## 4. Conclusion

In summary, a simple in-situ redox precipitation hydrothermal synthesis method has been developed to synthesize single-crystal β-$MnO_2$ nanorods. The reactant ammonia and peroxide hydrogen as well as the hydrothermal reaction temperatures can greatly influence the morphology of the final products. Compared to the previous solution-based methods for the growth of 1D nanostructures in which the problem of phase control of products often exists, the present synthetic process can be performed over a wide range of hydrothermal temperatures. The magnetic measurements

 © 2006 Wiley-VCH Verlag GmbH & Co. KGaA, Weinheim 

indicate that the Néel temperature of the as-synthesized β-$MnO_2$ single crystals is about 98 K, which is about 6 K higher than that of the bulk β-$MnO_2$ crystals. The nanorod materials produced also may show possible novel electronic and catalytic properties induced by their dimensionality.

## Experimental Section

$MnO_2$ nanorods were obtained by an in-situ redox precipitation hydrothermal synthesis method. In a typical experiment, hydrogen peroxide (1 mL, 30%) was added to an aqueous solution of manganese nitrate (12 mL, 0.3 mol/L) whilst stirring to form a homogeneous solution, then ammonia (5 mL, 0.5 mol/L) was added to the mixture dropwise. Upon the addition of ammonia, the precipitation of $Mn^{2+}$ by ammonia to $Mn(OH)_2$ and the oxidization of $Mn(OH)_2$ by $H_2O_2$ were achieved immediately accompanied by the decomposition of $H_2O_2$. A brown suspension of $MnO_2{\cdot}xH_2O$ precipitated during the in-situ redox precipitation reaction. The resulting suspension was transferred into a 20-mL Teflon-lined autoclave up to 80% of the total volume. The sealed autoclave was heated at 250 °C for 12 h. The resulting black solid product was collected, washed several times with distilled water and absolute ethanol, centrifuged, and dried under vacuum at 60 °C for 3 h.

The phase and purity of the products were identified using X-ray powder diffraction (XRD) patterns collected with a Japan Rigaku Dmax-γA X-ray diffractometer with Cu-$K_\alpha$ radiation ($\lambda$ = 1.54178 Å). A scan rate of 4°/min was applied to record the patterns in the $2\theta$ range from 10 to 80°.The morphology and particle size of the products were determined with a Hitachi Model H-800 transmission electron microscope (TEM) operated at 200 kv. Structural information for the nanocrystals was obtained from selected area diffraction (SAED) patterns and high-resolution transmission electron microscopy (HRTEM) images obtained using a JEOL-2010F transmission electron microscope at an acceleration voltage of 200 kv. Electron diffraction patterns were obtained from samples during HRTEM measurements. X-ray photoelectron spectra were collected with a PHI5300 model XPS spectrometer with an Al-$K_\alpha$ radiation source. Magnetic properties were investigated with a superconducting quantum interference device (SQUID) magnetometer (MPMS-7).

## Acknowledgments

This work was supported by the Program for New Century Excellent Talents in University (NCET-04-0651), the National Natural Science Foundation of China (Nos. 90401019 and 20335030) and the Excellent Young and Middle-aged Scientist Foundation of Shandong Province in China (No. 2004BS04002).

[1] W. U. Huynh, J. J. Dittmer, A. P. Alivisatos, *Science* **2002**, *295*, 2425–2427.
[2] Y. Xia, P. Yang, Y. Sun, Y. Wu, B. Mayers, B. Gates, Y. Yin, F. Kim, H. Yan, *Adv. Mater.* **2003**, *15*, 353–389.
[3] J. Wang, Q. W. Chen, B. Y. Hou, Z. M. Peng, *Eur. J. Inorg. Chem.* **2004**, 1165–1168.
[4] S. W. Chung, J. Y. Yu, J. R. Heath, *Appl. Phys. Lett.* **2000**, *76*, 2068–2070.
[5] N. R. Jana, L. Gearheart, C. J. Murphy, *Chem. Commun.* **2001**, 617–618.
[6] Y. Y. Wu, H. Q. Yan, M. Huang, B. Messer, J. H. Song, P. D. Yang, *Chem. Eur. J.* **2002**, *8*, 1260–1268.
[7] A. B. Panda, S. Acharya, S. Efrima, *Adv. Mater.* **2005**, *17*, 2471–2474.
[8] M. M. Thackeray, *Prog. Solid State Chem.* **1997**, *25*, 1–71.
[9] B. Ammundsen, J. Paulsen, *Adv. Mater.* **2001**, *13*, 493–496.
[10] L. Hueso, N. Mathur, *Nature* **2004**, *427*, 301–302.
[11] A. R. Armstrong, P. G. Bruce, *Nature* **1996**, *381*, 499–500.
[12] Q. Feng, H. Kanoh, K. Ooj, *J. Mater. Chem.* **1999**, *9*, 319–334.
[13] S. Bach, M. Henry, N. Baffer, J. Livage, *J. Solid State Chem.* **1990**, *88*, 325–333.
[14] J. T. Hu, T. W. Odom, C. M. Lieber, *Acc. Chem. Res.* **1999**, *32*, 435–445.
[15] M. H. Huang, S. Mao, H. Feick, H. Q. Yan, Y. Y. Wu, H. Kind, E. Weber, R. Russo, P. D. Yang, *Science* **2001**, *292*, 1897–1899.
[16] H. Kawamura, *J. Appl. Phys.* **1988**, *63*, 3086–3088.
[17] H. Sato, K. Wakiya, T. Enoki, T. Kiyama, Y. Wakabayashi, H. Nakao, Y. Murakami, *J. Phys. Soc. Jpn.* **2001**,*70*, 37–40.
[18] N. Yamamoto, T. Endo, M. Shimada, T. Takada, *Jap. J. Appl. Phys.* **1974**, *13*, 723–725.
[19] A. Yoshinori, *J. Phys. Soc. Jpn.* **1959**, *14*, 807–821.
[20] J. E. Greedan, N. P. Raju, A. S. Wills, C. Morin, S. M. Shaw, *Chem. Mater.* **1998**, *10*, 3058–3067.
[21] a) D. C. Golden, C. C. Chen, J. B. Dixon, *Science* **1986**, *231*, 717–718; b) R. N. DeGuzman, Y. F. Shen, E. J. Neth, S. L. Suib, C. L. young, S. Levine, J. M. Newsam, *Chem. Mater.* **1994**, *6*, 815–821; c) Y. F. Shen, R. P. Zerger, S. L. Suib, L. McCurdy, D. I. Potter, C. L. young, *Science* **1993**, *260*, 511–515; d) X. Wang, Y. D. Li, *Chem. Commun.* **2002**, 764–765; e) N. Kijima, H. Yasuda, T. Sato, Y. Yoshimura, *J. Solid State Chem.* **2001**, *159*, 94–102.
[22] X. Wang, Y. D. Li, *J. Am. Chem. Soc.* **2002**, *124*, 2880–2881.
[23] a) Y. Xiong, Y. Xie, Z. Li, C. Wu, *Chem. Eur. J.* **2003**, *9*, 1645–1651; b) Z. Y. Yuan, Z. L. Zhang, G. Du, T. Ren, B. Su, *Chem. Phys. Lett.* **2003**, *378*, 349–353.
[24] F. A. Al-Sagheer, M. I. Zaki, *Colloids Surf. A* **2000**, *173*, 193–203.
[25] J. Chastain, *Handbook of X-ray Photoelectron Spectroscopy*, 2nd ed., Perkin–Elmer Corporation, Wellesley, MA, **1992**, p. 79.
[26] A. R. Roosen, W. C. Carter, *Phys. A* **1998**, *261*, 232–247.
[27] A. Yoshinori, *J. Phys. Soc. Jpn.* **1959**, *14*, 807–821.
[28] N. Ohama, Y. Hamaguchi, *J. Phys. Soc. Jpn.* **1971**, *30*, 1311–1318.
[29] J. Park, E. Kang, C. J. Bac, J. G. Park, H. J. Noh, J. Y. Kim, J. H. Park, M. P. Park, T. Hyeon, *J. Phys. Chem. B* **2004**, *108*, 13594–13598.
[30] K. Woo, H. J. Lee, *J. Magn. Magn. Mater.* **2004**, *272–276*, 1155–1158.
[31] G. H. Lee, S. H. Huh, J. W. Jeong, B. J. Choi, S. H. Kim, H. C. Ri, *J. Am. Chem. Soc.* **2002**, *124*, 12094–12095.
[32] W. S. Seo, H. H. Jo, K. Lee, B. Kim, S. J. Oh, T. Park, *Angew. Chem. Int. Ed.* **2004**, *43*, 1115–1117.

Received: November 4, 2005
Published Online: March 30, 2006

 © 2006 Wiley-VCH Verlag GmbH & Co. KGaA, Weinheim 

EurJIC
European Journal of Inorganic Chemistry

Issue 12/2006

Pages 2321–2520

*Papers available ahead of print in Early View at www.interscience.wiley.com*

*Earliest available Table of Contents:*
*Automatically, free of charge by e-mail through*
*www.interscience.wiley.com/alerts*

## COVER PICTURE

**The cover picture shows** the structural changes in tertiary carboxamide groups induced by coordination of the electrically neutral nitrogen atom to a metal ion. Changing the hybridization from $sp^2$ to $sp^3$ results in pyramidalization at the nitrogen atom. This is expressed by the parameter $\chi_N$ which ranges from 0° ($sp^2$) to 60° ($sp^3$). Werner complexes with relatively weak $M-N^{amide}$ bonds are known with $\chi_N$ values between 30° and 47°. Full $sp^3$ hybridization with complete lifting of the resonance and a value of 58° for $\chi_N$ is achieved in a complex in which the copper(II) ion is in the centre of the tetraazamacrocyclic amide ligand *tert*-butoxycarbonyl-alanyl-cyclam. Details of its synthesis and structure are discussed in the article by R. Alsfasser et al. on p. 2357 ff.

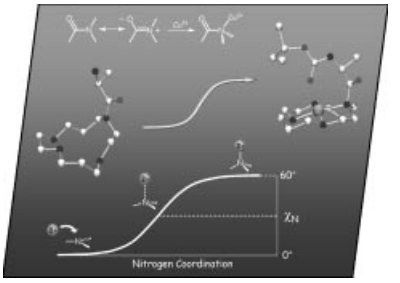


## MICROREVIEW

**Contents**

**2333** **Y. Kobuke***

Artificial Light-Harvesting Systems by Use of Metal Coordination

**Keywords:** Energy conversion / Complementary coordination / Porphyrinoids / Phthalocyanines / Perylenebisimide / Bi(ter)pyridyl complex

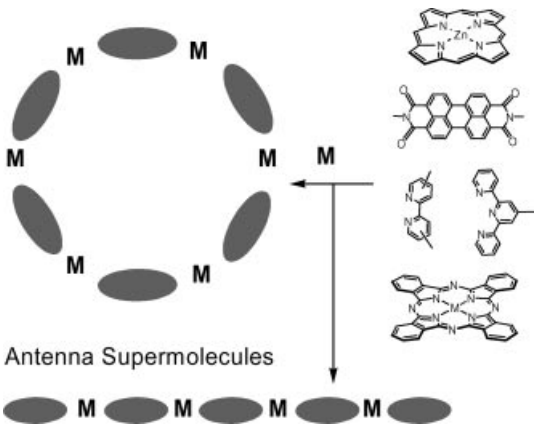


 © 2006 Wiley-VCH Verlag GmbH & Co. KGaA, Weinheim 

# SHORT COMMUNICATION


**2353** **O. M. Abu-Salah,* M. H. Jáfar, A. R. Al-Ohaly, K. A. Al-Farhan, H. S. Al-Enzi, O. V. Dolomanov, J. A. K. Howard**

Synthesis and Structural Characterization of a Halide-Free Rhombohedral Silver-Alkynyl Cage Complex $[Ag_{14}(C_2tBu)_{12}][BF_4]_2$

**Keywords:** Silver / Clusters / Silver alkynyls / Alkynyl cluster / Cationic silver complex / Silver cage complex / Rhombohedral silver cage


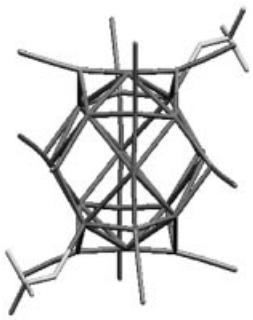

# FULL PAPERS


**2357** **C. Schickaneder, F. W. Heinemann, R. Alsfasser***

Copper(II) Complexes of the Tetraazamacrocyclic Tertiary Amide Ligand Alanyl-Cyclam

**Keywords:** Copper / Cyclam / Bioinorganic chemistry / Electrophilic activation / Winkler−Dunitz parameters


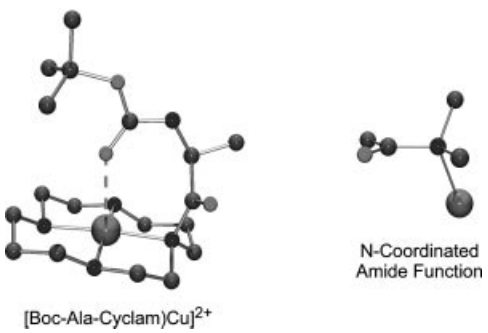



**2364** **X. Zheng, C. Liu, Y. Xie***

An Analogous Solution-Liquid-Solid (ASLS) Growth Route to InP Hollow Spheres and a Honeycomb-Like Macroporous Framework

**Keywords:** Materials science / Mesoporous materials / Semiconductors / Synthesis design


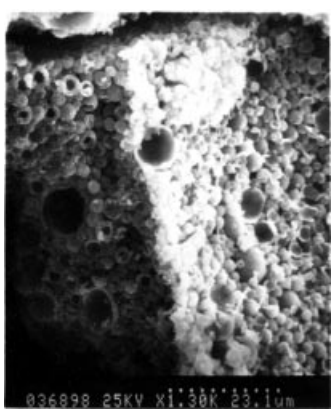


**2370** **L. Bertolo, S. Tamburini,* P. A. Vigato, W. Porzio, G. Macchi, F. Meinardi**

Tris(tropolonato)phenanthroline Lanthanide(III) Complexes as Photochemical Devices

**Keywords:** Lanthanides / N ligands / O ligands / Molecular devices / Donor−acceptor systems / Time-resolved spectroscopy / Infrared emitters


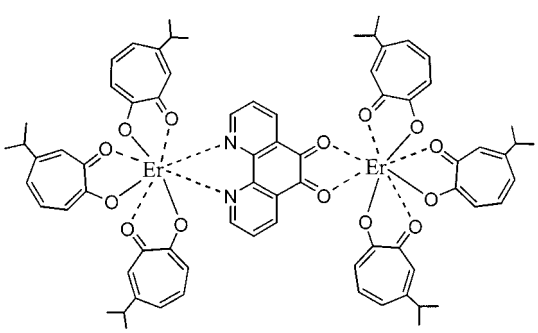

**2377** **H.-J. Holdt,* H. Müller, M. Pötter, A. Kelling, U. Schilde, I. Starke, M. Heydenreich, E. Kleinpeter**

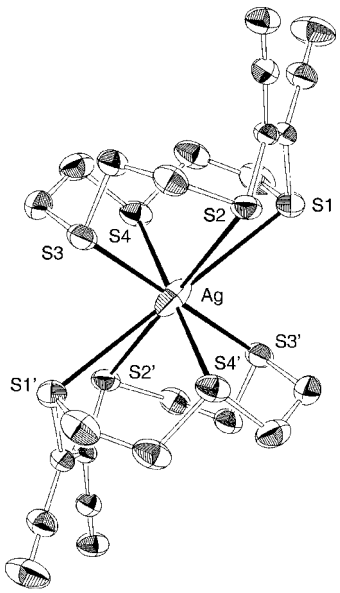


The First Sandwich Complex with an Octa(thioether) Coordination Sphere: Bis(maleonitrile-tetrathia-12-crown-4)silver(I)

**Keywords:** Crown compounds / S ligands / Sandwich complexes / Silver

**2385** **D. Walther,* L. Böttcher, J. Blumhoff, S. Schebesta, H. Görls, K. Schmuck, S. Rau, M. Rudolph**

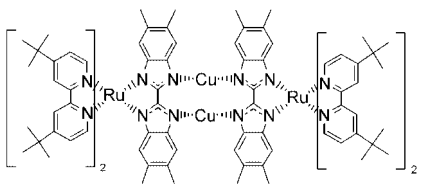


Tetranuclear Complexes Containing a Luminescent $Ru_2M_2$ Core [M = $Cu^I$, (allyl)$Pd^{II}$]: Synthesis, Structures and Electrochemical Properties

**Keywords:** Copper / Luminescence / N ligands / Palladium / Ruthenium

**2393** **V. Cappello, J. Baumgartner, A. Dransfeld, M. Flock,* K. Hassler***

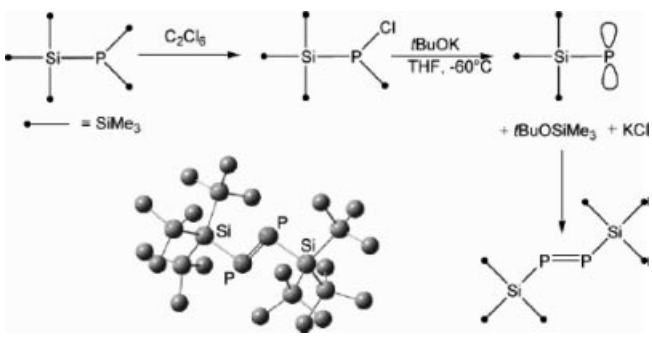


Hypersilylphosphanylidene: A Facile Low-Temperature Generation and Formation of Bis(hypersilyl)diphosphene and the Bis(hypersilyl)triphosphaallyl Anion

**Keywords:** Ab initio calculations / Carbene homologues / Phosphanes / Silicon

**2406** **S. J. Lei, K. B. Tang*, Y. X. Qi, Z. Fang, H. G. Zheng**

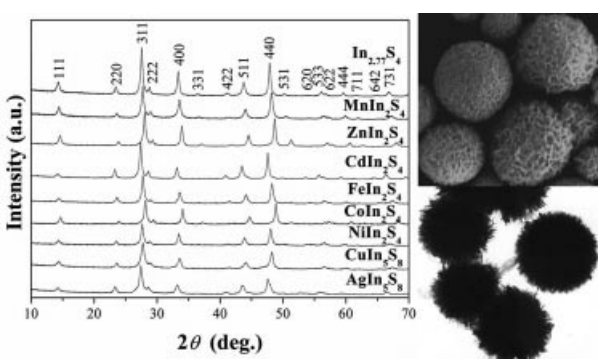


A Self-Sacrificing Template Route to Spinel $M^{II}In_2S_4$ ($M^{II}$ = Mn, Zn, Cd, Fe, Co, Ni) and $M^{I}In_5S_8$ ($M^{I}$ = Cu, Ag) Porous Microspheres

**Keywords:** Solvothermal synthesis / Spinel phases / Microporous materials / Semiconductors

 © 2006 Wiley-VCH Verlag GmbH & Co. KGaA, Weinheim 

**2411** **C.-Y. Sun, S. Gao,* L.-P. Jin***

Hydrothermal Syntheses, Architectures and Magnetic Properties of Six Novel $Mn^{II}$ Coordination Polymers with Mixed Ligands

**Keywords:** Coordination polymers / Magnetic properties / Manganese / Microporous materials / Organic−inorganic hybrid composites

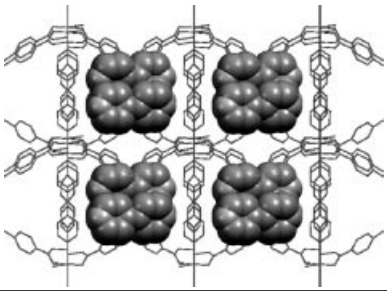

**2422** **P. Pelagatti,* A. Bacchi, M. Balordi, S. Bolaño, F. Calbiani, L. Elviri, L. Gonsalvi,* C. Pelizzi, M. Peruzzini, D. Rogolino**

Octahedral $Ru^{II}$ Complexes with [PNO] Hydrazonic Ligands: Synthesis, Structure, Reactivity and Catalytic Activity in the Addition of Benzoic Acid to Alkynes

**Keywords:** Tridentate ligands / Ruthenium / Homogeneous catalysis / Enol esters / Mass spectrometry

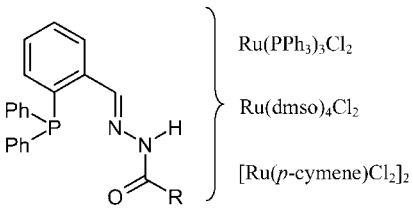


**2437** **C. H. Zhou, Y. Y. Wang,* D. S. Li, L. J. Zhou, P. Liu, Q. Z. Shi**

Polymers or Supramolecules Generated From a New V-Shaped Bis-monodentate Ligand and the Effect of Steric Hindrance on Coordination Modes of the Ligand

**Keywords:** Dipyridylamine / Helical structure / Density functional study / Silver / Copper

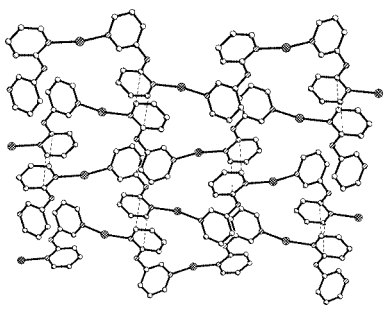

**2447** **H.-H. Li, Z.-R. Chen, J.-Q. Li,* C.-C. Huang, Y.-F. Zhang, G.-X. Jia**

Synthesis and Characterization of Two Silver Iodides with One- and Three-Dimensional Hybrid Structures Constructed From Ag···Ag Interactions and Organic Templates

**Keywords:** Coordination polymers / Iodine / Organic-inorganic hybrid composites / Silver

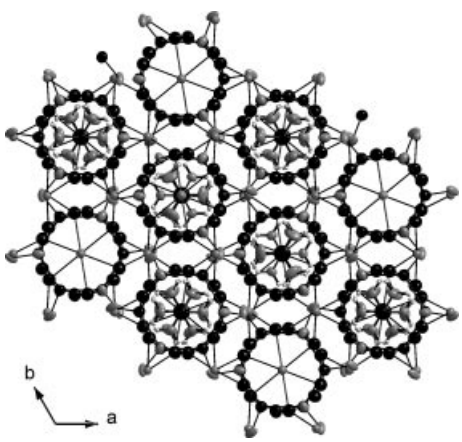


**2454** **B.-Q. Xie, Y. Qian,* S. Zhang, S. Fu, W. Yu**

A Hydrothermal Reduction Route to Single-Crystalline Hexagonal Cobalt Nanowires

**Keywords:** Cobalt / Hydrothermal synthesis / Magnetic properties / Nanostructures

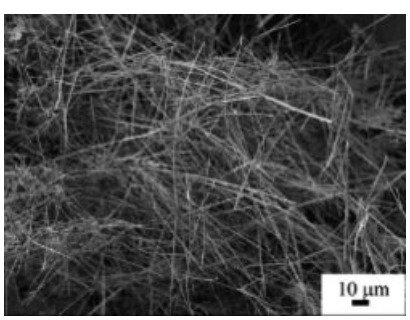


 © 2006 Wiley-VCH Verlag GmbH & Co. KGaA, Weinheim 

**2460** **C. Makedonas, C. A. Mitsopoulou***

The Relationship Between Aromaticity and Charge-Transfer Transitions: A Combined Study of Square-Planar Metal Complexes Based on DFT, NMR and Nucleus-Independent Chemical Shifts

**Keywords:** Aromaticity / Density functional calculations / N ligands / S ligands / Transition metals

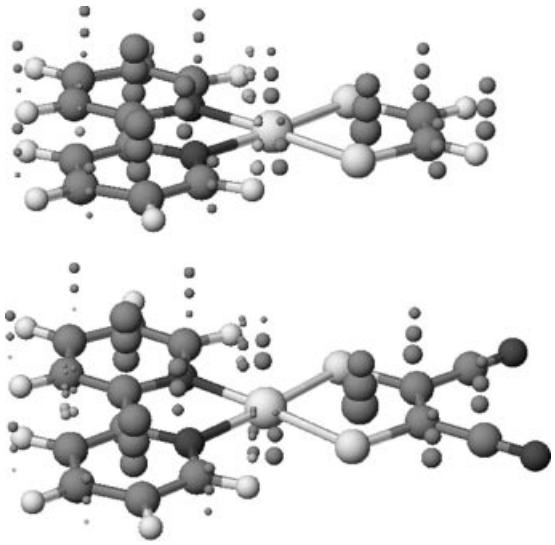

**2469** **L. Yao, X. Zeng, M. Ge,* W. Wang, Z. Sun, L. Du, D. Wang**

First Experimental Observation of Gas-Phase Nitrosyl Thiocyanate

**Keywords:** Gas phase generation / Nitrosyl thiocyanate / Photoelectron spectroscopy / Time-of-flight mass spectrometer

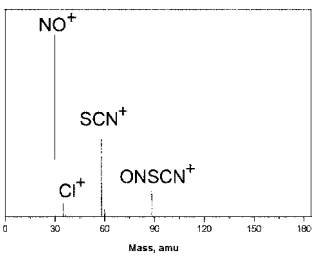


**2476** **K. Meelich, M. Galanski,* V. B. Arion, B. K. Keppler**

Bis(2-amino alcohol-κ*N*)dicarboxylatoplatinum(II) Complexes − Elegant Synthesis via Ring-Opening of Bis(2-amino alcoholato-κ$^2$*N*,*O*)-platinum(II) Species with Dicarboxylic Acids

**Keywords:** Bioinorganic chemistry / Platinum / N,O ligands / Antitumor agents / Drug design

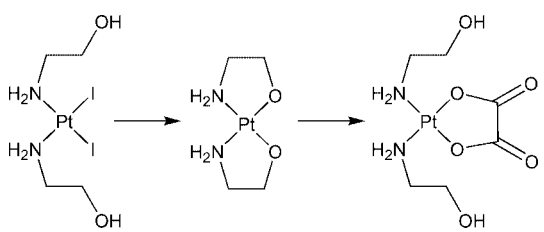


**2484** **S. Iwatsuki,* E. Isomura, A. Wada, K. Ishihara,* K. Matsumoto***

$^{195}$Pt NMR Spectra of Head-to-Head and Head-to-Tail Amidato-Bridged Platinum(III) Dinuclear Complexes

**Keywords:** Platinum / $^{195}$Pt NMR / α-Pyridone / α-Pyrrolidone / Pivalamide / NMR spectroscopy

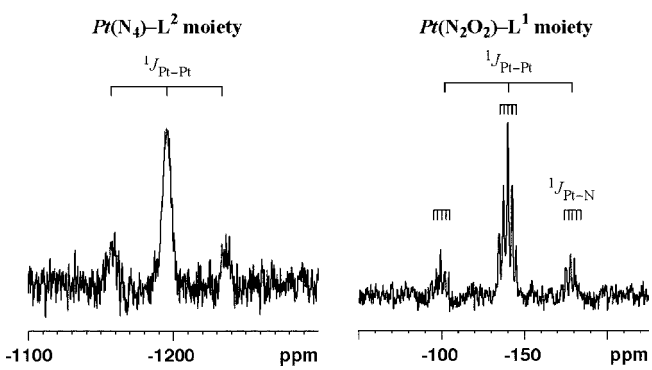


 © 2006 Wiley-VCH Verlag GmbH & Co. KGaA, Weinheim 

**2491** **X. He, C.-Z. Lu,* C.-D. Wu, L.-J. Chen**

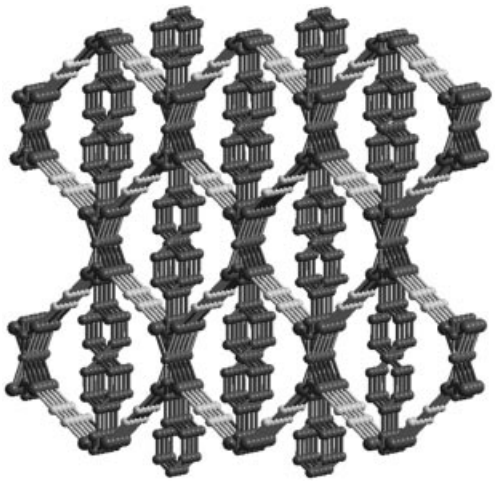

A Series of One- to Three-Dimensional Copper Coordination Polymers Based on N-Heterocyclic Ligands

**Keywords:** Coordination polymers / Copper / Luminescence / Nitrogen heterocycles / Organic–inorganic hybrid composites

**2504** **M. Kato, A. K. Sah, T. Tanase,* M. Mikuriya**

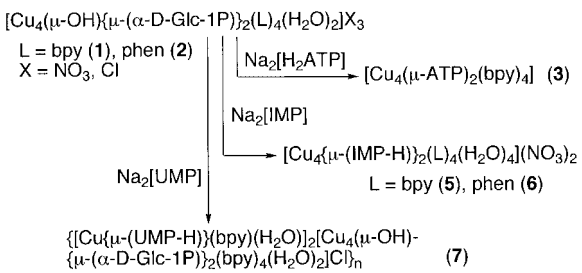


Transformation of a Tetranuclear Copper(II) Complex Bridged by Sugar Phosphates into Nucleotide-Containing $Cu_4$ Aggregations

**Keywords:** Coordination chemistry / Copper / Nucleic acids / Carbohydrates / Clusters

# CORRECTION

**2515** **S. Gautron, N. Lassauque, C. Le Berre, P. Serp, L. Azam, R. Giordano, G. Laurenczy, D. Thiébaut, P. Kalck***

Analysis of the Synergistic Effect of Carbonylplatinum Complexes on the Iridium-Catalysed Carbonylation of Methanol to Acetic Acid

**Keywords:** Homogeneous catalysis / Carbonylation / Iridium / Platinum / Reaction mechanism

 © 2006 Wiley-VCH Verlag GmbH & Co. KGaA, Weinheim 

DOI: 10.1002/ejic.200600161

# Artificial Light-Harvesting Systems by Use of Metal Coordination

**Yoshiaki Kobuke*[a]**

**Keywords:** Energy conversion / Complementary coordination / Porphyrinoids / Phthalocyanines / Perylenebisimide / Bi(ter)pyridyl complex

Construction of artificial light-harvesting systems by metal coordination is reviewed. Light absorbing dyes include porphyrin, phthalocyanine, perylenebisimide and polypyridyl metal complexes. The supramolecular assemblies are obtained by ligand coordination to metal ions in the center or exterior of the chromophores. Supermolecules of discrete structures even in the solution phase are focused on, and methodologies to acquire large association constants are discussed. Complementary or multitopic coordination to the $Zn^{2+}$ ion gives satisfactory results in obtaining stable and discrete supramolecular structures while maintaining the singlet excited state. Fast energy transfers among the chromophore units are analyzed satisfactorily to examine the properties of light-harvesting antennae. Use of transition-metal ions provides strong coordination, but intersystem crossing of the singlet excited state to the triplet becomes significant. Photophysical properties of such triplet excited species are reported in a limited number of cases and their properties are discussed in view of the light-harvesting antenna function.

(© Wiley-VCH Verlag GmbH & Co. KGaA, 69451 Weinheim, Germany, 2006)

## 1. Introduction

Photosynthetic oxidation-reduction reactions start at the reaction center by ejecting an electron from the photoexcited primary electron donor, the chlorophyll dimer of the so-called special pair or monomeric chlorophyll in more evolved systems to the primary electron acceptor. This reaction center is surrounded by a large number of light-harvesting antenna chlorophylls in order to make the maximum use of the incoming photons. When a photon hits one of the chlorophyll molecules, the excitation energy must be transferred to the far reaction center without losing the energy. There are several decay processes to lose the singlet excited state: intersystem crossing to the corresponding triplet state, emission through fluorescence, and nonemissive internal conversions. Since the lifetime of the singlet excited chlorophylls is generally of the order of nanoseconds, the energy transfer must take place with time constants faster than the order of a nanosecond.

An artificial light-harvesting system is interesting from various viewpoints. Understanding the way that nature per-

[a] Graduate School of Materials Science, Nara Institute of Science and Technology,
8916-5 Takayama, Ikoma, Nara 630-0192, Japan,
Fax: +81-743-72-6119
E-mail: kobuke@ms.naist.jp

*Yoshiaki Kobuke obtained his Bachelor degree from the Department of Synthetic Chemistry, Faculty of Engineering in 1964 at Kyoto University, where he worked under the supervision of Prof. Ryohei Oda. He joined the group of Prof. Junji Furukawa at the same Department as a graduate student in 1964. His thesis work for which he received his Ph.D. in Engineering was on the study of mechanisms of stereospecific polymerization and endo-exo stereoselectivities of Diels–Alder reactions. In 1969 he joined the Department of Synthetic Chemistry, Faculty of Engineering at Kyoto University as an Assistant Professor and collaborated with Prof. Junji Furukawa. In the period of 1972–1973 he joined the group of Prof. Robert Burns Woodward as a research associate in the Department of Chemistry at Harvard University for the total syntheses of Vitamin B12 and erythromycin. After the retirement of Prof. Furukawa in 1977, he collaborated with Prof. Iwao Tabushi. In 1980 he was promoted to Associate Professor. In 1990, he was appointed to Professor in the Department of Materials Science, Faculty of Engineering at Shizuoka University. The main research target was the synthesis of artificial ion channels and their characterization by single channel current observations. In 1998 he moved to the Graduate School of Materials Science, Nara Institute of Science and Technology. During 1998–2003 he was a project leader of CREST (Core Research for Evolutionary Science and Technology from the Japan Science and Technology Corporation). His research interest is artificial photosynthesis focusing on its initial events, i.e. antenna function and charge separation. Studies on novel two photon absorbing materials and artificial ion channels are under way.*

**MICROREVIEWS:** This feature introduces the readers to the authors' research through a concise overview of the selected topic. Reference to important work from others in the field is included.

 © 2006 Wiley-VCH Verlag GmbH & Co. KGaA, Weinheim 

forms intricate functions should be of profound interest. In the case of light-harvesting antenna, visually aesthetic crystallographic structures are already known. Their well-organized structure is thought to correlate closely with the functions they perform. If we succeed in establishing the nature of the structure-function relationship, we will obtain the method by which the photo-excited energy is stored in molecules or molecular systems, and transferred with minimum loss. This knowledge can then be applied not only to the construction of artificial photosynthetic systems and solar energy conversion systems, but also to the development of photonic and electronic materials by the use of chromophores having expanded π-electronic systems.

An artificial light-harvesting system may best be achieved by mimicking the purple bacterial system, since the structure-function relationship may be understood best in the simplest way. Therefore, macrocyclic arrangements of porphyrins and other chromophores will be the first choice. Covalent linking is the most classical and productive method. There are numerous examples reported, and also review articles.[1–5] Alternatively, a supramolecular approach to this target may have special importance, since the natural structure is one of the best examples as will soon be explained. In this article, the author will focus on the supramolecular approach to the construction of a light-harvesting system. As a requisite to clear discussions based on structural information, the species having discrete structures in solution will be treated. In view of strong coordination and definite coordination angle, metal coordination may play the most important role.[6–16]

Nature uses only the singlet excited state for photosynthesis and specially protects against the formation of the triplet state. This does not necessarily mean that the artificial systems should use the singlet excited species. The triplet excited species have longer lifetimes and the $[Ru(bpy)_3]^{2+}$ complex and its derivatives have been successfully used for dye-sensitized solar cells. However, the detailed analysis of the triplet energy transfer processes is accompanied by added difficulties compared with that for the singlet species. Therefore many potential complexes are prepared by using transition-metal ions, without mentioning the photophysical properties. Here, discussion will focus on supermolecules and the measurement of their photophysical properties.

## 2. Natural Light-Harvesting Systems

In order to achieve effective charge separation, Nature has designed a most sophisticated molecular system for the reaction center. It is not clever to place such a system in all the light-receiving spots so the reaction center is instead accompanied by a large number of light-harvesting devices in the surrounding space. This system resembles a central factory system appropriate for mass production, and is maintained by the supply of light harvesting devices of simple structure for the unitary function.

The arrangement of a bacterial photosynthetic system was first analyzed by X-ray crystallography in 1995.[17–22] The light-harvesting complex LH2 from purple bacteria is composed of B800 and B850. B800 contains nine bacteriochlorophylls arranged in a planar circle form. In contrast, B850 contains 18 bacteriochlorophylls in a barrel form arranged perpendicularly to B800. The light energy absorbed by B800 is transferred to B850 according to the cascading energy transfer. The excitation energy travels further to other B850s and finally reaches LH1. Here, 30 bacteriochlorophylls are arranged in a barrel form similar to B850, except for having one open exit. In addition, LH1 contains the reaction center in the central space. Therefore, the excitation energy reaching LH1 is transferred effectively to the special pair initiating the charge separation. The arrangements of B850, LH1, and interestingly even the special pair are given by coordination of the imidazolyl side chains in transmembrane helices to the central $Mg^{2+}$ ion in the bacteriochlorophyll. The energy transfer rates in the supramolecular arrangements (Figure 1) are as fast as the order of picoseconds within lifetimes of the order of nanoseconds.[23–30]

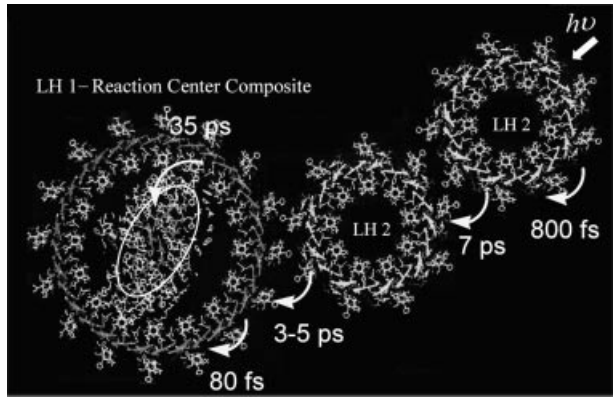


Figure 1. Scheme of light harvesting in photosynthetic purple bacteria.[22]

As seen above, the light-harvesting system of bacteria employs very regular arrangements of bacteriochlorophylls. This is not general for all the light-harvesting antenna systems. Antennae in plants and cyanobacteria, both being very similar, seem to use a totally different architecture.[31–35] Figure 2 shows the crystallographic structure of cyanobacterial photosystem I as a trimer, which represents the existing form also in vivo. The monomer contains a large number of chromophores of 90 chlorophyll *a* molecules and 22 carotenoids. This is a core antenna system and is accompanied further by separately existing antenna components, which are normally associated with photosystem II. It must be noted that a plant employs almost the same architecture as cyanobacteria. It is remarkable that the system employed by cyanobacteria 2.5 billion years ago is still effective even 1 billion years after plants first evolved. Almost no evolutional change of the structure may signify that the perfect form of the antenna system has been arrived at. However, it seems extremely difficult to extract a simple constitutional principle from the apparently random architecture.

 © 2006 Wiley-VCH Verlag GmbH & Co. KGaA, Weinheim 

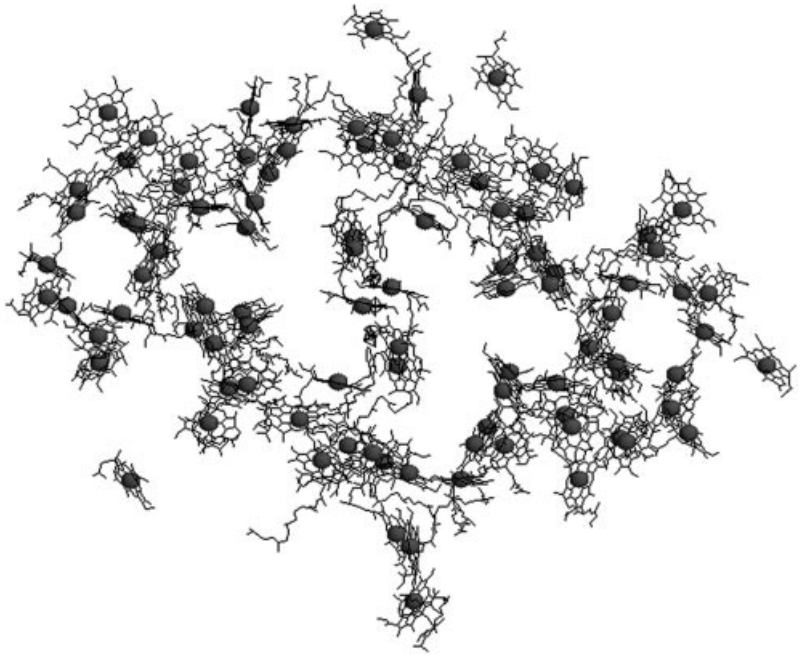

Figure 2. Crystal structure of cyanobacterial photosystem I. Prepared from Brookhaven Data Bank file 1JB0.[31]

## 3. Chromophores

In light-harvesting devices, incoming light energy must be captured efficiently by one of the chromophores distributed widely in the surrounding space and transferred efficiently to the reaction center. For this purpose, nature employs chlorophyll-*a* and -*b* or the corresponding bacteriochlorophylls as the light-absorbing unit. They have extinction coefficients as large as $10^5$–$10^6$ $cm^{-1}$ $M^{-1}$ near the regions at 400 and 600 nm. Chromophores closely related to chlorophyll derivatives are porphyrin and phthalocyanine. Recently, the use of perylenebisimide has been demonstrated to be excellent for such purposes. Ruthenium tris-bipyridine or bis-terpyridine have unique characteristics for such purposes and are widely used for photocurrent generation systems. The typical characteristics of these chromophores are compared in Table 1. Figure 3 shows the absorption spectra at the same extinction coefficient scale for easy comparison of their relative magnitudes.

The photosynthetic reaction is conducted through the singlet excited state and its conversion to the triplet is strictly protected by several mechanisms. It is important to

Table 1. Photochemical characteristics of typical chromophores used for natural and artificial antenna systems.

| Compounds[a] | Fluorescence quantum yield | Fluorescence lifetime [ns] | Phosphorescence quantum yield | Phosphorescence lifetime [μs] | Ref. |
|---|---|---|---|---|---|
| Chl *a* | 0.3 | 6.1 | | | [36] |
| Chl *b* | 0.117 | | | | [37] |
| BChl *a* | 0.18 | 3.1 | | | [38] |
| BChl *c* (monomer) | 0.29 | 6.5 | | | [38] |
| BChl *c* (aggregate) | 0.5 | 3.3 | | | [38] |
| $H_2TPP$ | 0.13 | 6.3 | 0.87 | | [39] |
| ZnTPP | 0.033 | 1.92 | | | [40] |
| MgTPP | 0.15 | 9 | 0.8 | | [41,42] |
| $H_2Pc$ | 0.6 | 5.5 | | 0.28[b] | [43,44] |
| ZnPc | 0.3 | 3 | 0.1[b] | 1100[b] | [43] |
| MgPc | 0.84 | 5.7 | $5\cdot10^{-6}$[b] | 1000[b] | [45] |
| Perylenebisimide, $(OAr)_4$ | 0.92 | 6.1 | | | [46] |
| $[Ru(bpy)_3]^{2+}$ | | | 0.042 | 0.63 | [47] |
| $[Ru(tpy)_2]^{2+}$ | | | $<5\cdot10^{-6}$ | – | [48] |
| $[Ru(4'\text{-Phtpy})_2]^{2+}$ | | | $4\cdot10^{-5}$ | 0.001 | [48] |
| $[Ru(4'\text{-Cltpy})_2]^{2+}$ | | | $<1\cdot10^{-5}$ | 0.0002 | [48] |

[a] Chl = chlorophyll, BChl = bacteriochlorophyll, $H_2TPP$ = tetraphenylporphyrin, ZnTPP = zinc tetraphenylporphyrin, MgTPP = magnesium tetraphenylporphyrin, $H_2Pc$ = phthalocyanine, ZnPc = zincphthalocyanine, MgPc = magnesiumphthalocyanine, perylenebisimide = 1,6,7,12-tetraarylperylenebisimide, $[Ru(bpy)_3]^{2+}$ = [ruthenium tris(bipyridine)]$^{2+}$, $[Ru(tpy)_2]^{2+}$ = [ruthenium bis(terpyridine)]$^{2+}$, $[Ru(4'\text{-Phtpy})_2]^{2+}$ = [ruthenium bis(4′-phenylterpyridine)]$^{2+}$, $[Ru(4'\text{-Cltpy})_2]^{2+}$ = [ruthenium bis(4′-chloroterpyridine)]$^{2+}$. [b] From ref.[49] (77 K).

 © 2006 Wiley-VCH Verlag GmbH & Co. KGaA, Weinheim 

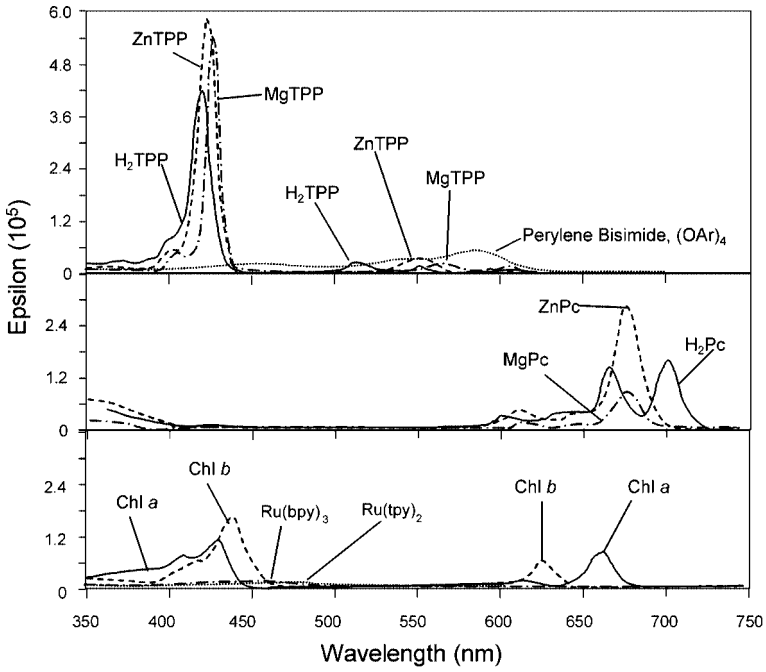


Figure 3. Comparison of absorption spectra of chromophores in Table 1 at the same scale of extinction coefficient, with the same codes as used in Table 1.[46,48,50]

transfer the singlet excitation energy within the lifetime. Therefore, close inter-chromophore distances are critical to ensure the successful fast excitation energy transfers, as observed for the B850 and LH1 systems. The close interchromophoric distance induces strong exciton interaction as shown schematically in Figure 4. Face-to-face interaction induces a blue shift of the absorption wavelength, while head-to-tail interaction shifts the absorption band to a longer wavelength.[51] The excited state of the face-to-face interaction tends to lose its excitation energy through internal conversion to the vibrational energy and decay without fluorescence emission. On the other hand, excitons with a head-to-tail orientation can maintain the excited state and transfer the excitation energy within the lifetime. By using the red shift of the absorption wavelength, a vectorial energy transfer pathway can be constructed.

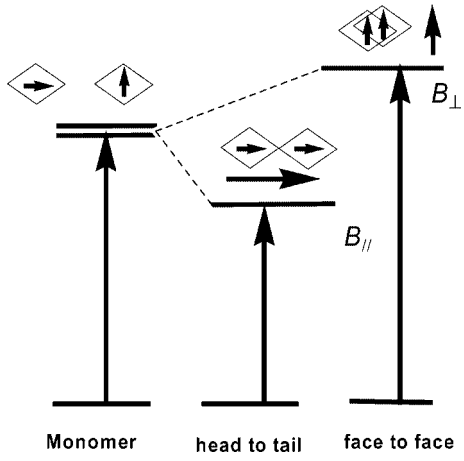


Figure 4. Exciton interaction of transition dipoles.[51]

## 4. Methods of Coordination Assembly

The assembly formation sometimes induces the formation of an energy sink, where the singlet excitation energy is lost through internal conversion to vibrational states. Random assembly of chromophores induces this kind of unfavorable defect formation, and for this reason regular arrangement of the chromophores is desirable. There are several methods to assemble chromophores through supramolecular assembling.

Coordination to metal ions provides the strongest intermolecular forces among others such as hydrogen bonds, ionic interactions, and π-π stacking interactions. It is important to obtain chromophore assemblies of discrete structure for the discussion based on a clear molecular basis. From this viewpoint, metal coordination provides the best intermolecular force for chromophore assembly. Other intermolecular forces are also used in combination with metal coordination, but are hardly expected to obtain supermolecules of discrete structure in solution by using their weak intermolecular forces alone.[52,53]

The nature of metal ions has a large effect on the characteristics of the resulting metal-coordinated chromophore assemblies. Metal ions of typical groups and $d^{10}$ transition-metal ions do not have much influence on the singlet excited state. However, transition-metal ions having odd electron spins tend to quench the singlet excitation energy through interaction with their odd spin. Therefore, the use of paramagnetic transition-metal ions for the assembly formation must be primarily avoided. The former class of metal ions, however, in general provides only a weak ligand field with small stability constants and allows equilibrium with free ligands. Assemblies have been obtained with due consider-

 © 2006 Wiley-VCH Verlag GmbH & Co. KGaA, Weinheim 

ation of the above characteristics and limitations. The modes of complexation will be classified into two types as illustrated in Figure 5.

Type I: Coordination of the chromophore's ligand to metallochromophore.

Type II: Coordination of the chromophore's ligand to external metal ions.

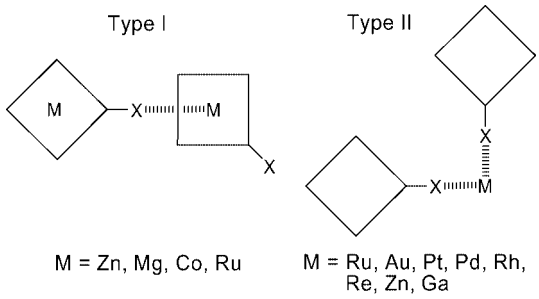


Figure 5. Mode of assembly formation by coordination, with the square and X representing chromophore and coordinating ligand, respectively.

As chromophores containing metal ions, porphyrin and phthalocyanine provide the most typical examples for Type I assembly formation. Chlorophyll employs $Mg^{2+}$ but artificial systems use $Zn^{2+}$ as the most typical substitute, since $Zn^{2+}$ has a $d^{10}$ electronic configuration without odd spin. $Zn^{2+}$ complexes are practically stable toward heat, acidic condition, and oxidation. The artificial system prefers $Zn^{2+}$ in most cases based on these properties, although its fluorescence quantum yield is inferior to $Mg^{2+}$ systems. Since $Zn^{2+}$ cannot provide a strong ligand field, the stability constant is not inherently very large, unless multitopic or complementary coordination is designed. Unique ideas have therefore been developed for obtaining stable assemblies.

When transition-metal ions are incorporated into the central core of porphyrins and phthalocyanines, even mono-axial coordination can afford large stability constants. However, the intersystem crossing of singlet to the triplet states occurs and light harvesting through the triplet pathway must become the main route.

When the assembly inducing metal ion locates outside the chromophore, the flexibility of the molecular design for assembly formation increases. Chelation may be powerful for obtaining stable complexes. Nanoparticles developed recently may also be interesting.

## 5. Porphyrin with an Inner-Ring Metal Ion

Central metals accommodated in the macrocyclic structure allow one or two axial coordinations of ligand depending on the metal ion species. Penta-coordinating $Zn^{2+}$ accepts only one axial coordination. Neutral nitrogen ligands generally afford large stability constants, but simple monocoordination is not strong enough to maintain the discrete structure under μM concentrations for which special molecular designs are required. Kobuke proposed the idea of complementary coordination of an imidazolyl substituent of one porphyrin to the $Zn^{2+}$ center of another porphyrin, whose imidazolyl coordinated back to $Zn^{2+}$ in the original porphyrin.[54,55] The stability constant reaches $10^{11}$ $M^{-1}$ in nonpolar solvents. The factor that contributes most to such a large stability constant is the complementarity of the imidazolyl–Zn–porphyrin. Compared with other potential ligands such as pyridyl, imidazolyl has the following advantages (see Figure 6):

(1) High basicity leading to high coordination ability.

(2) Smaller angle strain from the ideal (vertical to the macrocyclic plane) coordination angle.

(3) Smaller steric hindrance from substituents at positions α to the ligating N atom.

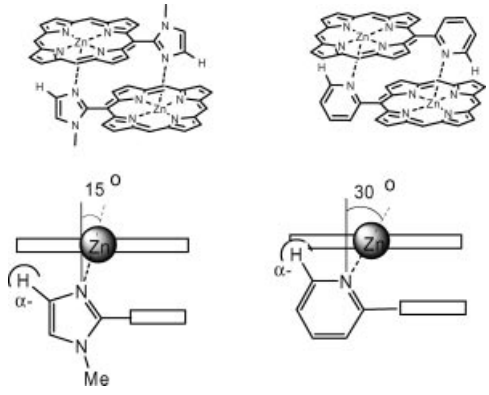


Figure 6. Complementary coordination of imidazolyl and pyridyl to $Zn^{2+}$, where the rectangle denotes porphyrin.

This motif can be applied to the formation of linear and macrocyclic species, both of which are regarded as excellent light harvesting antennae. Firstly, in order to obtain linear porphyrin arrays based on complementary coordination, two imidazolyl–Zn–porphyrin units were connected directly at their *meso* positions, as shown in compound **1**. Since the coordination grows to both sides opposite to each other, the successive complementary coordination leads to a linear multi-porphyrin array **2** (Figure 7A).[56] The molecular weight was extremely high reflecting the large stability constant of the complementary coordination and the number of the longest porphyrin unit reached 800 porphyrin units with a distribution peak of 160 units. However, the coordination bond is cleaved and regenerated by adding and eliminating coordinating solvents, respectively. An example was shown by GPC elution curves (A) and (B) in part B of Figure 7. A mixture of *meso*-*meso*-linked bisporphyrin **1** and monoimidazolylporphyrin **3** showed the corresponding two peaks in $CHCl_3$ (A). When methanol was added to the chloroform solution, followed by evaporation to cleave and regenerate the coordination, bisporphyrin oligomers terminated by monomeric porphyrins **4** were obtained (B).

It is noteworthy that this linear assembly does not induce fluorescence quenching. Evaluation of the energy transfer rate along the one-dimensional array is not as easy as in the degenerated array of the ring. Therefore, fluorescence-quenching Mn–porphyrins were attached at both the terminals of the linear array by using hetero-complementary coordination of imidazolyl–Mn–porphyrin **5** to the terminal

 © 2006 Wiley-VCH Verlag GmbH & Co. KGaA, Weinheim 

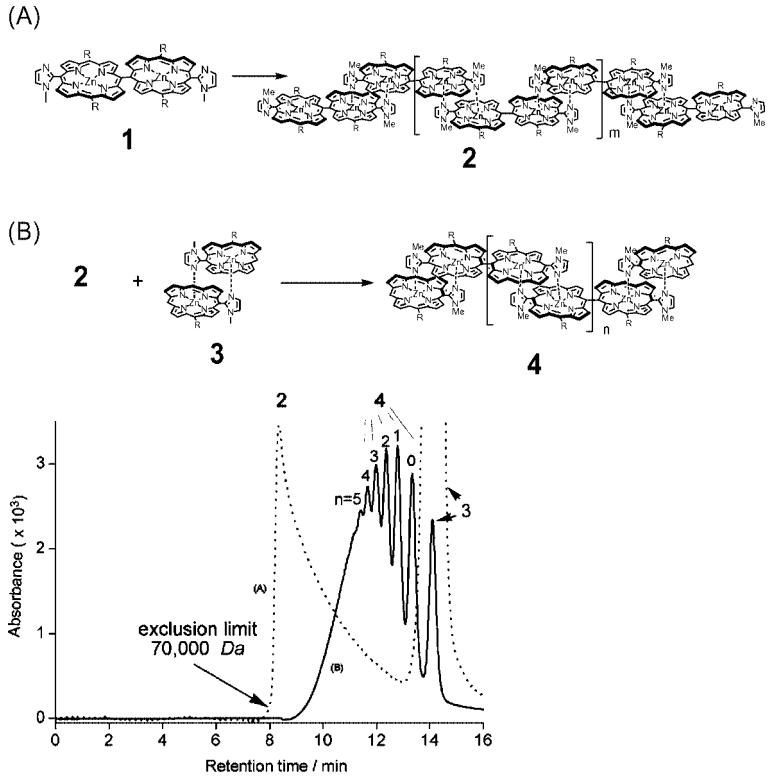


Figure 7. (A) Linear array formation of bis(imidazolylzincporphyrin) and (B) linear array with terminal monoimidazolylporphyrins and its GPC characterization.[56]

imidazolyl–Zn–porphyrin (Figure 8).[57] It is possible to design the array **6** of 200 Zn-porphyrin arrays terminated by Zn–Mn hetero-coordination by considering the relative strength of hetero Mn–Zn and homo Zn–Zn and Mn–Mn complementary coordinations. Under such conditions, photoexcitation of any porphyrin in the terminal 130 arrays leads to quenching by the terminal Mn–porphyrins, suggesting that rapid and efficient energy transfer is occurring along the linear array.

The linear porphyrin arrays are characterized by two important properties: no fluorescence quenching on array formation and efficient energy transfer along the array. Photocurrent generation by use of a dye-modified flat electrode may provide interesting applications for fields other than the conventional surface-coated porous semiconductor materials. In the former case, the efficient light-harvesting system becomes critical to compensate for the decreased surface area. Imidazolyl–Zn–porphyrin appended with an ω-mercaptoalkyl group is employed as a key element connecting the Au electrode surface and the porphyrin arrays.[58,59] Porphyrin appended with thiol **7** can modify the Au surface simply by a dipping process and an imidazolyl–Zn–porphyrin array can grow by a simple immersion procedure into a solution of *meso*-*meso*-coupled imidazolyl-zinc-porphyrin dimer **8**. After rinsing, the complementary coordination pair can be immobilized by covalent linking of *meso*-allyl ether substituents by a ring-closing metathesis reaction.[60,61] This series of procedures can be repeated until multi-porphyrin layers **9** are accumulated as detected by the gradual increase in the characteristic porphyrin absorption

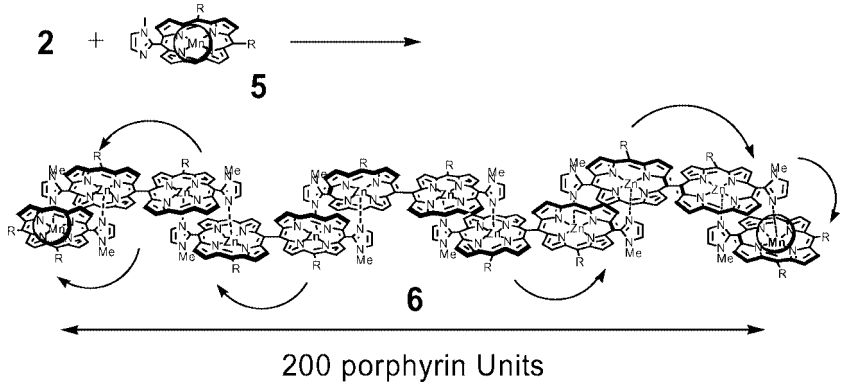


Figure 8. Hetero linear array formation from Zn and Mn porphyrins.[57]

 © 2006 Wiley-VCH Verlag GmbH & Co. KGaA, Weinheim 

(Figure 9).[62] Light-induced cathodic current was increased as a function of the accumulated amount of the porphyrin, suggesting the light harvesting effect.

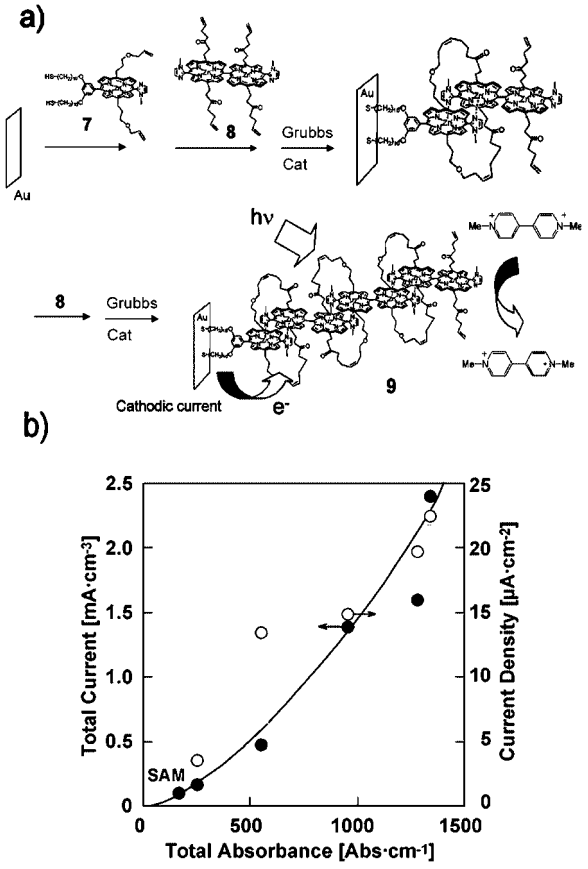


Figure 9. (a) Multiporphyrin array formation on a Au surface and metathesis linking. (b) Dependence of photocurrent on surface grafting.[62]

Two imidazolyl-zinc-porphyrins were then connected through a *m*-phenylene group to adjust the dihedral angle between two porphyrins to 120°, so that bifunctional bis-(imidazolyl–Zn–porphyrin) **10** may be organized into macrocycles, most optimistically to a strain-free hexamer (Figure 10).[63,64] The results were not so simple, but the newly developed reorganization procedure opened up a path to interesting supramolecular methodology leading selectively to macrocyclization. Here, the dynamic nature of imidazolyl-to-zinc coordination plays a critical role. Coordination under normal concentrations (>mM) leads to oligomerization rather than macrocyclization, since the latter process is entropically unfavorable. Then the mixture **11** is first subjected to equilibrium conditions by the addition of coordinating additives, usually MeOH, under high dilution. The successive solvent evaporation leads almost quantitatively to a mixture of macrocycles. The hexamer **12** was accompanied by an equal amount of pentamer **13**, suggesting that the balance of enthalpy and entropy governs the product distribution. Enthalpically, there is no choice of pentamer formation, since it leads to angular strain from the ideal 120°. Entropically a smaller ring is favored, since the encountering probability of two terminal imidazolyl–Zn–porphyrins becomes smaller for a larger ring. In the case of the *m*-phenylene-bridged bisporphyrin, the competition seems equally high for pentamer and hexamer, but far less so for tetramer and heptamer.

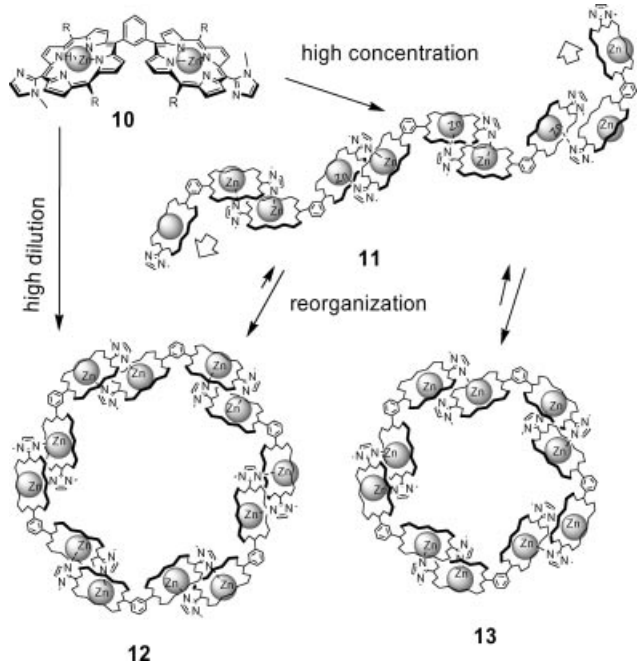


Figure 10. *m*-Phenylene-connected bis(imidazolyl)zincporphyrin and coordination organization.[63]

The assembled macrocycles never lose the fluorescence properties and maintain almost the same quantum yield and lifetime in their fluorescence emission. The energy hopping time constants through the coordination dimer units were determined by the analysis of anisotropy depolarization of the transient absorption spectra after polarized light excitation.[65] At the same time, exciton-exciton annihilation rates were obtained from pump-power dependence on the transient absorption. The coincident time constants from two methods were 8.3 and 5.3 ps for the pentamer and hexamer, respectively (Figure 11). The size-dependent rate constants may represent the effect of orientation factors. Considering the fluorescence lifetime of 2.2 ns, rapid energy transfer should take place 300–400 times during its excited state lifetime. These combined properties prove the excellent light-harvesting antenna models of the B850 type not only in their structure, but also in their function.

When three porphyrins are connected through *m*-phenylene groups and imidazolyls are appended at molecular terminals as in **14**, the self-complementary coordination results in a macrocyclic trimer **15** with a high selectivity under similar reorganization conditions. In this case, the competitive formation of dimer or tetramer is hardly observed because of two unfavorable strain energies. It is interesting that this macrocyclic trimer, which contains three coordination-free zinc-porphyrins, can accommodate tripodal ligand **16** in its hole by multitopic and cooperative coordination (Figure 12).[66] Then, UV and fluorescence titration of this macrocycle with tetrapyridyl ligand **17** in toluene suggested

 © 2006 Wiley-VCH Verlag GmbH & Co. KGaA, Weinheim 

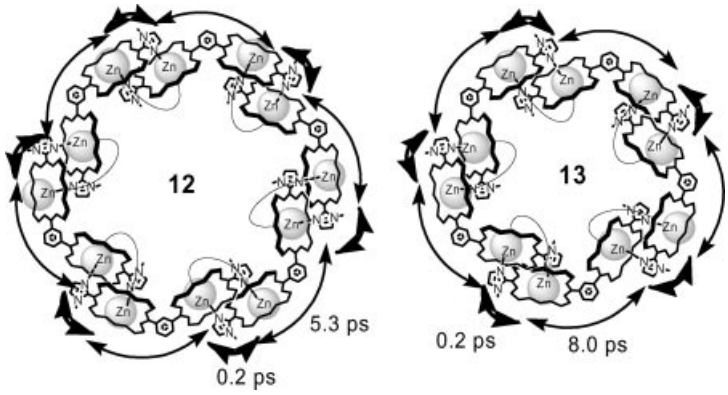


Figure 11. Macrocyclic hexamer and pentamer with excited energy hopping times. The metathesized links in the rear positions are abbreviated.[65]

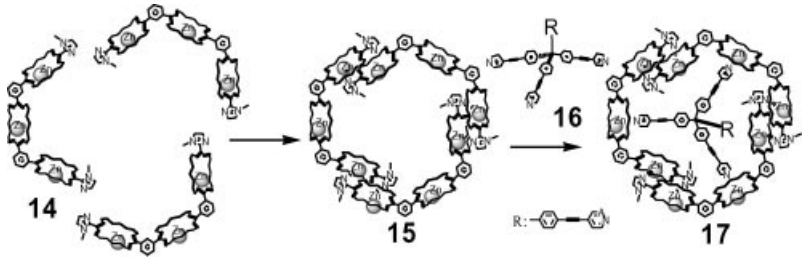


Figure 12. Macrocyclic trimer of trisporphyrin accommodating a tripodal pyridyl ligand.[66]

a stable 1:1 complex with a stability constant of $8 \cdot 10^8$ M$^{-1}$. When an electron acceptor is appropriately substituted at the fourth arm, the macrocycle can be regarded as a model of an LH1-type antenna.

4-Pyrazolylporphyrin instead of 2-(1-methylimidazolyl)-porphyrin can afford the cyclic trimer according to its angular requirement for coordination.[67,68] The trimer formation is somewhat cooperative, but its stability constant is estimated to be $9.0 \cdot 10^8$ M$^{-2}$ in dichloromethane at 22 °C. In accord with this stability constant, NMR and UV spectra of the trimer species are temperature and concentration dependent in the μM–mM concentration range.

Introduction of an ester group at the *ortho*-position of *para*-phenyl substituent increases the stability constant up to $6.0 \cdot 10^{13}$ M$^{-2}$ through the contribution of additional hydrogen bonding. These trimers have shown similar fluorescence quantum yields and lifetimes to the starting monomeric porphyrin, suggesting no significant perturbation in their $S_1$ states despite the strong interaction in the $S_2$ states.

Placement of a nitrogen atom at the 3-position in *meso*-pyridyl derivatives such as the 3-pyridyl or 5-(2-aminopyrimidyl) substituent results in the macrocyclic structure to satisfy the angular dependency.[69,70] The crystal structure suggests the macrocyclic tetramer **18** and **19** as shown in Figure 13, while the structure in solution shows a dynamic equilibrium between the cyclotetramer and other forms depending on other *meso*-substituents, as well as concentration and temperature. Thermochromic change is associated with complexation/decomplexation dynamics in solution at the concentration ca. $1 \cdot 10^{-4}$ M.

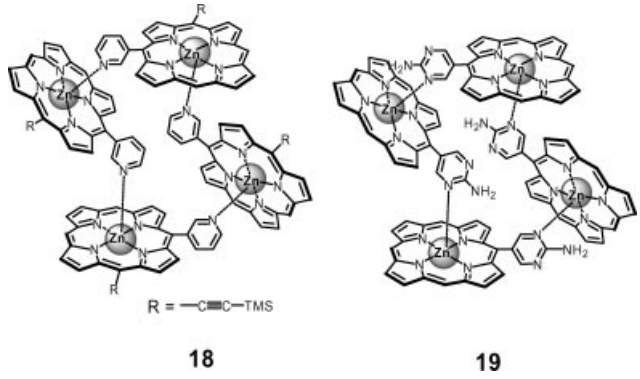


Figure 13. Cyclic tetramer formation from *m*-pyridyl- and pyrimidylzincporphyrins.[69,70]

The control of coordination angle is important for performing the desired cooperativity. The 2,6-dicarbamoylpyridine unit has internal hydrogen bonds to adopt a conformation that orients two arms approximately perpendicular to one another. A rectangular macrocycle **20** using a complementary coordination of the pyridyl unit to zincporphyrin was obtained (Figure 14). The stability constant was evaluated in $CHCl_3$ as $2 \cdot 10^8$ M$^{-1}$, from which the effective molarity was calculated as 6 M on the basis of the intrinsic binding constant for zinc-pyridine interaction.[71]

Two zincporphyrin units were connected by using this angle-constraining 2,6-dicarbamoylpyridine unit, **21**. Then tetrapyridyl free-base porphyrin **22**, in which intramolecular hydrogen bonds constrain the rotation of the pyridyl li-

 © 2006 Wiley-VCH Verlag GmbH & Co. KGaA, Weinheim 

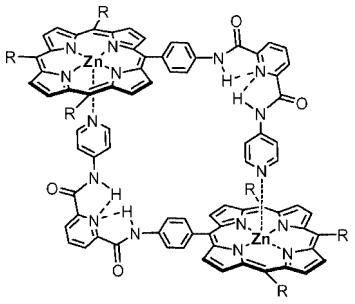

**20**

Figure 14. Adjustment of coordination angle by hydrogen bonding.[71]

gands, assembled two units of the zincporphyrin by multitopic coordination into a 2:1 mixture of **21** and **22** (Figure 15).[72] The multitopic coordination interaction afforded the stability constant of $2.0 \pm 0.5 \times 10^6$ M$^{-1}$ for each binding event. The overall arrangement constructed a photosynthetic model containing four zincporphyrin units around the free-base porphyrin. The fluorescence intensity of the 2:1 complex **23** showed biphasic decay with a faster component of 490 ps along with a 1330-ps component of the **21**. The energy transfer occurred from **21** to **22** with the rate constant of $2 \cdot 10^9$ s$^{-1}$ and with a quantum yield of 73%. There are several examples of multitopic coordination of pyridyl-appended porphyrins to antenna macrocycles according to covalent approaches.[73–75]

A three-dimensional (3D) box formation is produced by cooperative coordinations. When two porphyrins are connected at the *meso* position, orthogonal conformation is favored by steric repulsion. When 5-(*p*-pyridyl)porphyrin is coupled at the 1-*meso* position, the product becomes a chiral mixture. The mixture is organized by self-coordination to a chiral mixture of three-dimensional bisporphyrin tetramers through homochiral self-sorting processes. The 3D box is favored by its rigidity and is more stable than the monocyclic tetramer from monopyridylporphyrin.[76,77] ω-Pyridyl(phenylene)$_n$-appended zincporphyrins gave similar porphyrin boxes. The energy hopping rates among the unit porphyrins for these box-type assemblies were analyzed by time-resolved spectroscopic methods in conjunction with polarization anisotropy measurements. The data were analyzed by assuming an exciton coherence length of L = 2 for the *meso*-*meso*-coupled dimer. The time constant was explained by a Förster-type incoherent energy hopping model. Therefore, the excitation energy hopping times between the dimeric zincporphyrin units were 48, 98, and 361 ps for **24a**, **24b**, and **24c**, respectively, showing exciton-exciton distance dependence by the bridging (phenylene)$_n$ units (Figure 16).[78]

When porphyrins are connected through a mono- or bisalkynylene unit, two porphyrins prefer to adopt a planar conformation due to a beneficial π-conjugation effect despite the rotational freedom around the triple bond. The zinc complex of bisporphyrin with *meso*-pyridyl functionalities, **25**, self-assembles by coordination to a box-shaped cyclic tetramer **26**, where two conformers, perpendicular and planar, are allowed (Figure 17).[79] In the case of the monoalkynylene-bridge, a planar conformer was the exclusive product reflecting the conformational preference at the monomer level. In the case of the bisalkynylene-bridge, on the contrary, the perpendicular conformer becomes predominant probably because of effective cancellation of the dipole moment, which is induced by the directions of the pyridyl groups in the tetramer.

As discussed earlier, the use of transition-metal ions in the porphyrin metal center cannot be the method of singlet energy harvesting. Although many studies on the structure formation are reported, photophysical studies on the triplet states are rare due to the inherent difficulty of the studies. The following few reports identify the decay processes after the excitation.

Scandola reported on the photophysical behavior of the system of a pentad porphyrin arising from coordination of tetra-*m*-pyridylporphyrin to four Ru(CO)TPP units (**27**)

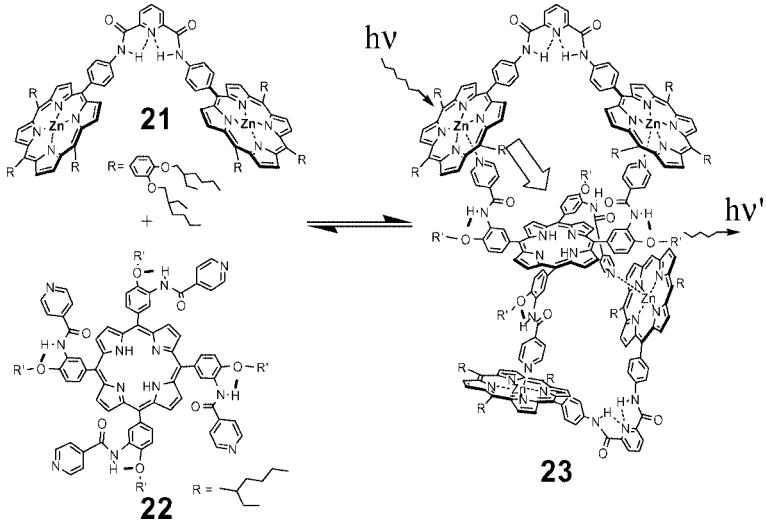


Figure 15. Complementary 2:1 complexation of zinc- and free base porphyrins and internal energy transfer.[72]

 © 2006 Wiley-VCH Verlag GmbH & Co. KGaA, Weinheim 

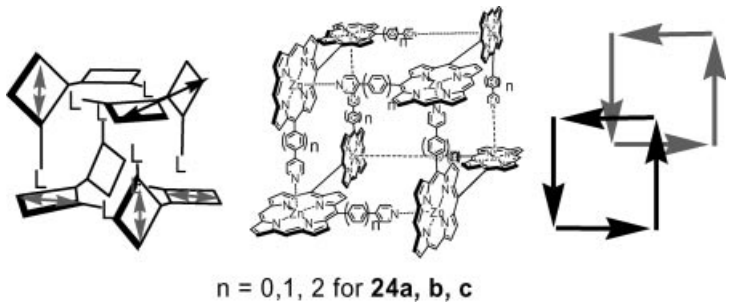


Figure 16. Box formation from *meso-meso* coupled bisporphyrin appended with pyridyl ligand and exciton energy transfer in the box assembly.[77,78]

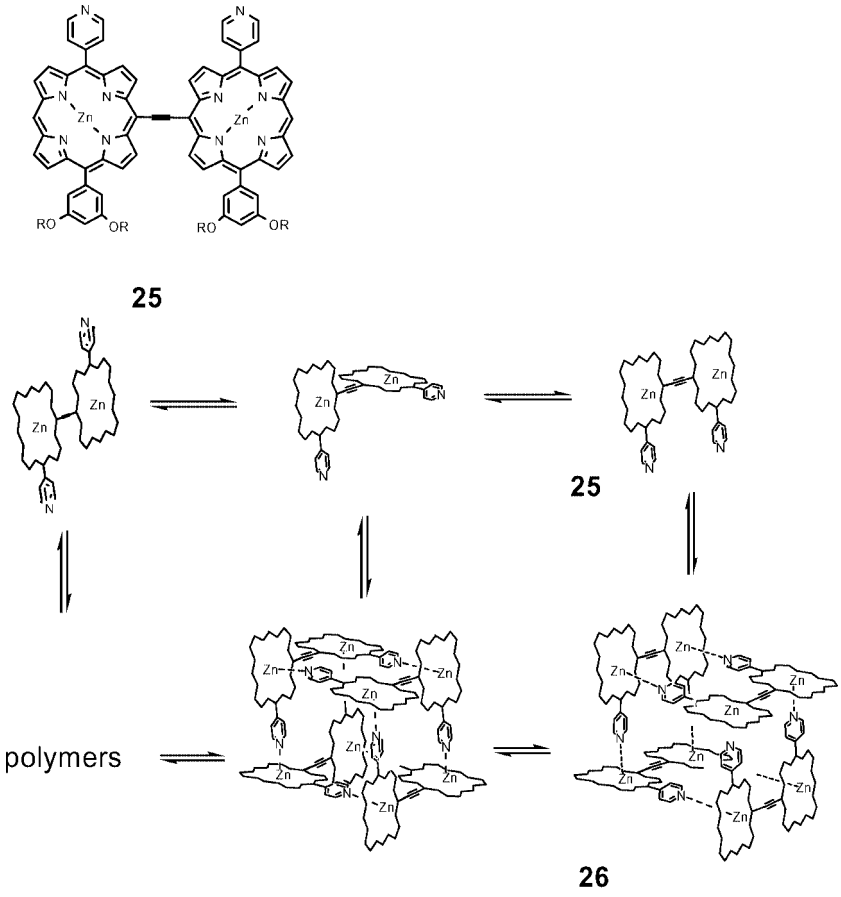


Figure 17. Acetylene-linked bis(pyridylporphyrin) and its coordination organization.[79]

(Figure 18).[80] The lifetime of the free-base porphyrin is shortened significantly to 0.5 ns from around 9 ns for TPP because of the efficient (95%) Ru-facilitated intersystem crossing to $^3$*Fb by spin-orbit perturbation. Excitation of the Ru porphyrin part leads also to $^3$*Ru with a much faster time constant (<30 ps) with 100% efficiency, then followed by irreversible energy transfer to $^3$*FbRu again with 100% efficiency due to the large driving force from Fb$^3$*Ru to $^3$*FbRu. The triplet energy transfer rate was estimated to be in the range $10^8$–$10^9$ $s^{-1}$. When zinc porphyrin is used as the axial ligating unit, the higher energy level of $^3$*Zn makes the energy difference between $^3$*ZnRu and Zn$^3$*Ru smaller and the equilibrium between two triplet states is established prior to deactivation.

Ruthenium porphyrin was connected by another chromophore, pyridyl-substituted perylenebisimide to afford a side-to-face supramolecular array of chromophores (**28**).[81] The absorption spectrum covers the full range of 350–620 nm with an extinction coefficient larger than $10^4$ $M^{-1}$ $cm^{-1}$. The photophysical properties obtained by using nano- and femtosecond time-resolved techniques are summarized in Figure 19. When the perylenebisimide (PBI) part (585 nm) is irradiated, the characteristic strong fluorescence ($\lambda_{max}$ = 620 nm) of the parent PBI is completely

 © 2006 Wiley-VCH Verlag GmbH & Co. KGaA, Weinheim 

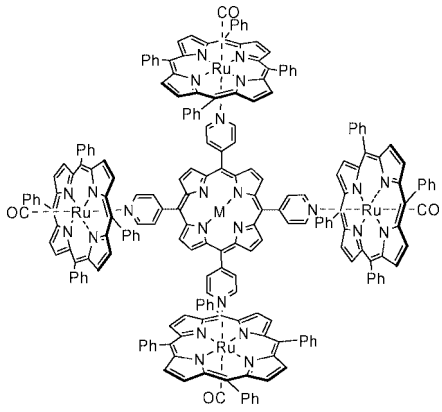

**27** M = $H_2$, Zn

Figure 18. Axial coordination of tetrakis(pyridyl)porphyrin to four $Ru^{2+}$(CO)porphyrins.[80]

quenched ($\Phi$ = 0.001), compared with $\Phi$ = 0.96 for free PBI. The spectral change was characterized by the rise of the typical absorption band of the radical anion of PBI near 780 nm, associated with the formation of the Ru(TPP)CO radical cation. The change, with a time constant of 5.6 ps, clearly shows electron transfer from Ru(TPP)CO to $^1$*PBI. Excitation of the Ru(TPP)CO part (530 nm, although accompanied with PBI excitation), on the other hand, leads to the formation of $^3$*Ru(TPP)CO by fast intersystem crossing within 1 ps. Then energy transfer occurs from $^3$*Ru to PBI to generate a new species of $^3$*PBI. The triplet species of $^3$*PBI with a lifetime of 9.8 μs in deaerated $CH_2Cl_2$ is therefore obtainable by the irradiation of the Soret band region of the Ru(TPP)CO site.

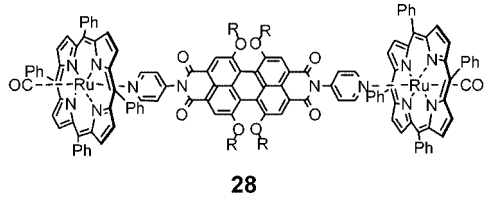

**28**

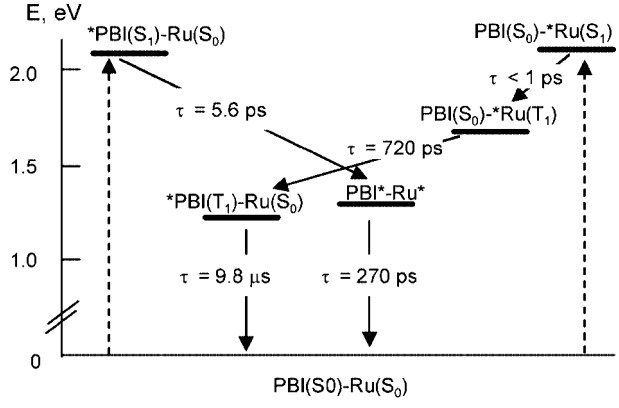


Figure 19. Formation of perylenebisimide-$Ru^{2+}$porphyrin and photophysical pathways.[81]

## 6. Porphyrin with an Outer-Ring Metal Ion

The use of transition-metal ions from external sources is a powerful tool for obtaining various self-assemblies and has been well documented. Fujita and Ogura introduced first an elegant way of coordination organization, in which the combination of *cis*-coordination transition-metal ions and linear bridging ligands gave the most thermodynamically stable macrocycles after equilibrium.[82–85] When a porphyrin is employed as the component of the linear bridging ligand, macrocycles composed of porphyrin units are easily obtained. Alessio has already addressed these examples focusing on this methodology in his review.[11] However, the resulting assembly in most cases loses its fluorescence and photophysical studies through phosphorescence emission are rather limited.

Scandola examined the effect of external Ru complexes, which connect pyridyl-porphyrins, on the quenching of the porphyrin singlet. It was found that two mechanisms are operative in the adducts and that their contributions are dependent on the type of Ru complex. One is an enhanced intersystem crossing from Por($S_1$) to Por($T_1$) by interaction with centers of Type I Ru complexes (Figure 20).[86] The singlet quenching is proportional to the number of Ru centers. The other mechanism is singlet-triplet energy transfer from Por($S_1$) to Ru($T_1$) of the centers of Type II Ru complexes and provides an additional channel. The latter contribution depends on the energy level of the Ru($T_1$) state in the coordination environment at the Ru center. The energy levels of Ru($T_1$) with weak field ligands, such as DMSO, are low compared with the ones with strong field ligands, such as CO. The fluorescence lifetimes of the compounds **29**–**31** are reasonably explained by these mechanisms.

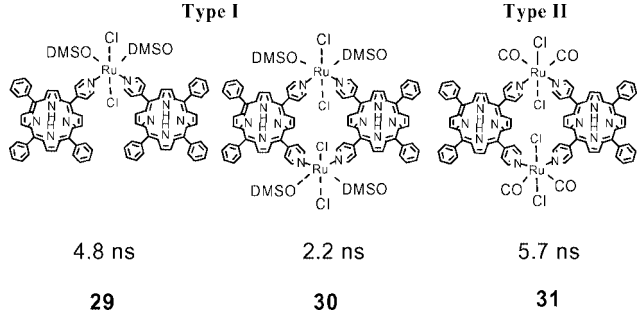


Figure 20. Organization of porphyrin by using external $Ru^{2+}$ coordination.[86]

The square porphyrin nonamer **33** is formed in solution by the addition of *trans*-coordinating bis(benzonitrile)$Pd^{2+}$ dichloride to a stoichiometric mixture of one central X-shaped unit (porphyrin **32a**), four T-shaped units (porphyrin **32b**), and four L-shaped units (porphyrin **32c**) (Figure 21).[87,88] The fluorescence emission of the solution mixture is quenched to greater than 90%. In accord with this observation, the fluorescence lifetime is shortened from 12 ns (the average lifetime for the initial mixture) to less than 1 ns. The claim of a light-harvesting effect must await analysis of how the triplet excited state behaves.

 © 2006 Wiley-VCH Verlag GmbH & Co. KGaA, Weinheim 

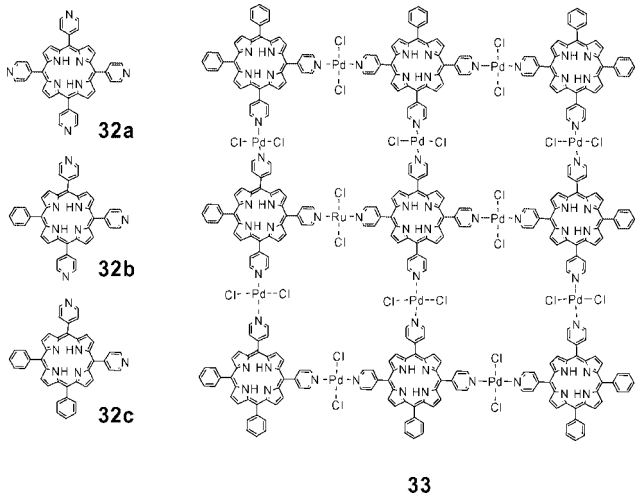


Figure 21. 2D porphyrin array by using *trans*-$Pd^{2+}$ complex.[87]

Rhenium tetramers of free-base and $Zn^{2+}$ porphyrins **34a** and **34b** may be a rare example of fluorescent metallamacrocycles (Figure 22).[89] Into this host cavity, tetrakis(4-pyridyl)porphyrin is incorporated as in **35** with a stability constant of $4 \cdot 10^7$ $M^{-1}$ by apparently cooperative multitopic coordination. The host emission is quenched by this incorporation without emission from the central guest.

As a chelating ligand, 8-hydroxyquinoline (oxine) is interesting, since quenching-free metal ions such as $Al^{3+}$ and $Ga^{3+}$ are known to give very stable octahedral complexes. Therefore, the *meso*-oxinyl-appended porphyrin was synthesized and its *fac*-tris(oxinylporphynyl) gallium complex **36** was obtained. In the complex, three porphyrins are arranged like a pinwheel. The center-to-center distances between two porphyrin units a-b, b-c, and c-a in Figure 23 were 15, 17, and 18.5 Å, respectively.[90,91] The fluorescence intensity was increased in the coordination complex compared with the free porphyrin. The fluorescence anisotropy decay analyzed the energy transfer rate between three porphyrin components as ca. 10 ps. Considering the fluorescence lifetime of 8.6 ns, the energy is stored in the trisporphyrin complex that allows an energy transfer 800 times to neighboring porphyrins in its excited lifetime. The introduction of two oxinyl groups at the facing *meso*-positions extends the coordination organization further to a dendritic structure **37**. Even in such a large assembly, the fluorescence intensity was larger than that of the starting free porphyrin.

As a quenching-free external metal ion, $Zn^{2+}$ may also be used for chelation organization. For this class of porphyrin assembly, Groves synthesized mono- and bisphenanthrolinyl-porphyrins, **38** and **39**, respectively.[92] Addition of the $Zn^{2+}$ ion to **38** induced a red shift of the Soret band by head-to-tail interaction of porphyrins of orthogonal orientation (Figure 24). For the case of **39**, a larger shift and

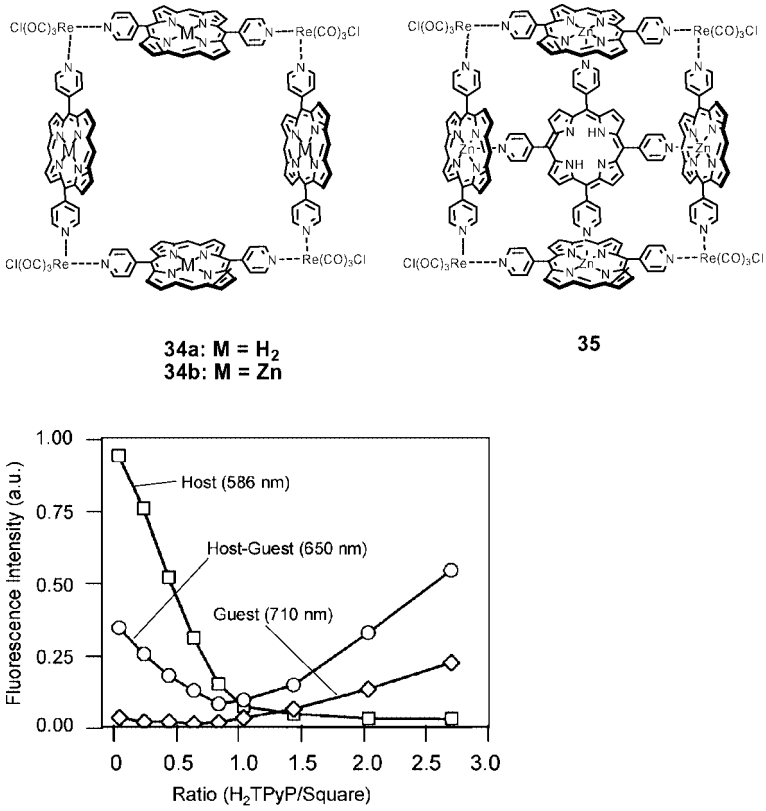


Figure 22. Fluorescence emission change on guest complexation into $Re^{2+}$-organized porphyrin square.[89]

 © 2006 Wiley-VCH Verlag GmbH & Co. KGaA, Weinheim 

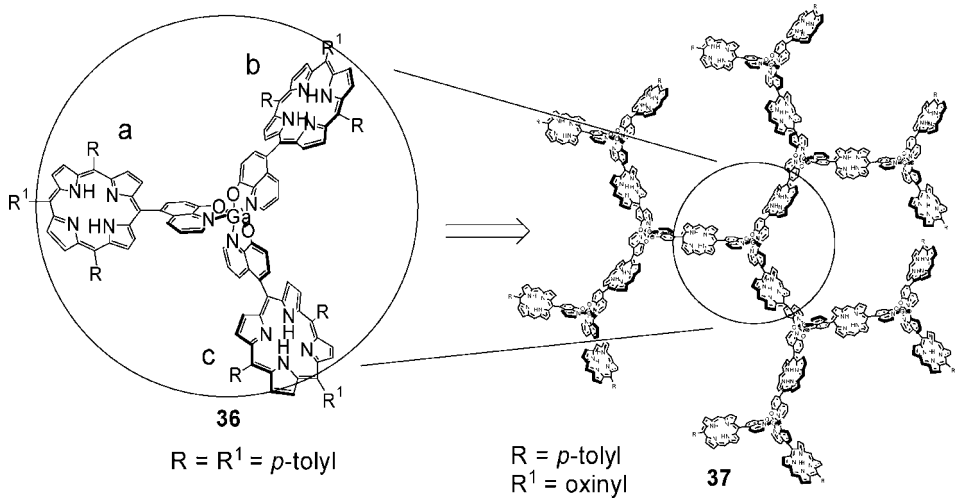


Figure 23. $Ga^{3+}$-organized oxinylzincporphyrin pinwheel and its dendritic growth.[90,91]

broadening of the Soret band were observed to show the development of exciton interaction. The average chain length of oligomer **40** was estimated from the complexation rate constant and estimated as 12.3 ± 0.5. The oligomeric products are potentially fluorescent.

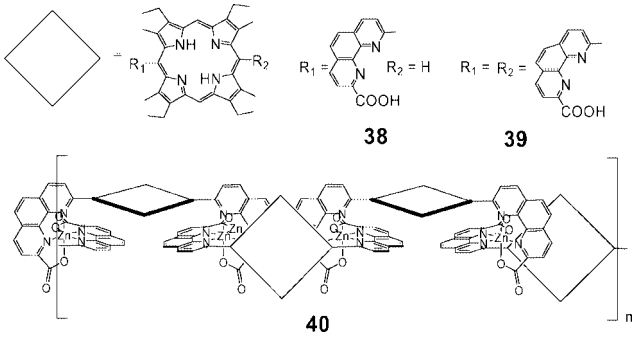


Figure 24. Mono- and bis(phenanthrolinyl)porphyrins and their $Zn^{2+}$ complexation.[92]

The use of a flat electrode surface instead of a porous semiconductor one for a dye-sensitized solar cell may provide an interesting possibility. The problems arising from the decreased surface area must, however, be overcome. Gold nanoparticles have attracted wide interest in view of physical properties that are different from bulk materials. Nano-sized particles should have large surface areas that can be modified by appropriate functionalities. The surface can be modified and protected by alkanethiolate. Therefore, an ω-porphyrin-bearing alkanethiolate with or without simple alkanethiolate was employed to modify the gold nanoparticles so as to afford **41** and **42** (Figure 25).[93]

The fluorescence of porphyrin gold particles **41** and **42** showed a double exponential decay. The lifetime of the parent compound (9.5 ns in THF) was perturbed to contain short major components 0.15 ns (86%) and 0.17 ns (97%), for **41** and **42**, respectively. The average lifetimes are therefore calculated as 1.4 ns for **41** and 0.41 ns for **42**. This means that the fluorescence of the porphyrin is significantly quenched even on the surface of gold nanoparticles. However, the degree of quenching is smaller compared with the case in which the same porphyrin is modified on a two-dimensional Au(111) surface, the latter fluorescence lifetime being 0.04 ns. A fewer number of gold atoms on the 3D surface of nanoparticles compared with the planar Au(111) electrode surface is involved in energy transfer quenching. The decay rate ($7.7 \cdot 10^9$ $s^{-1}$) of the absorption at 460 nm agreed with the rise of the excited plasmon band at about 600 nm. This means that any electron-transfer system faster than 130 ps can compete favorably with this energy transfer quenching.[94–96]

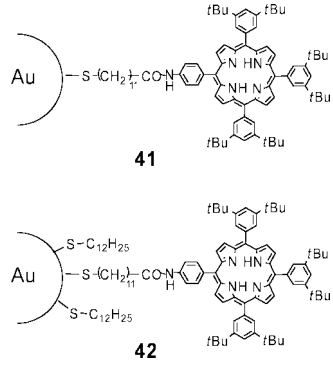


Figure 25. Porphyrin grafting on gold nanoparticle.[93]

The gold nanoparticles coated with a porphyrin-alkanethiolate **43** monolayer as in **44** were then treated with fullerene. Broad absorption appeared in the 700–800 nm region as a sign of a charge-transfer absorption band due to the π-complex formation between porphyrin and $C_{60}$. At the same time, these nanoparticles (**45**) were clusterized in solution as shown in **46** (Figure 26) and deposited on a $SnO_2$ electrode. The photocurrent action spectrum shows that the IPCE value increases with high concentrations of $C_{60}$ and reaches ca. 30% at 490 nm. The excited singlet state porphyrin is quenched efficiently by $C_{60}$ via electron transfer in the porphyrin-$C_{60}$ complex rather than energy transfer to gold nanoparticles.

 © 2006 Wiley-VCH Verlag GmbH & Co. KGaA, Weinheim 

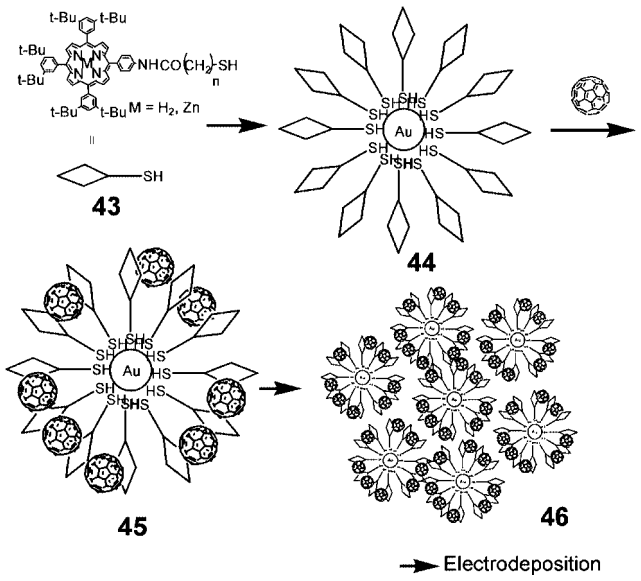


Figure 26. High order organization of porphyrin and fullerene with gold nanoparticles.[96]

The photoinduced charge separation is facilitated in the supramolecular complex of the porphyrin and $C_{60}$. The reduced $C_{60}$ injects the electron into the conduction band of $SnO_2$ nanocrystallites, or the electron is relayed through hopping among the $C_{60}$ molecules in the cluster. On the other hand, the oxidized porphyrin is regenerated by electron-transfer reduction with iodide in the electrolyte.[97]

## 7. Phthalocyanine

Compared with porphyrins, phthalocyanines have higher extinction coefficients in the Q-band region at longer wavelengths and emit fluorescence with much higher quantum yields. The metal-assisted organization of phthalocyanine in the past resulted in most cases in the quenching of singlet excitation energy. The author has been interested in incorporating phthalocyanine into supramolecular systems by using metal coordination. The first example is the use of the strategy of complementary coordination of an imidazolyl-zinc-porphyrin. Here the phthalocyanine unit is connected to the porphyrin as the *meso*-substituent. Two phthalocyanines are then connected through a complementary porphyrin dimer as **47**.[98] The absorption spectrum is a sum of two chromophores and covers a wide range of the visible region, just like the natural chlorophyll chromophores, but with an even larger extinction coefficient as illustrated in Figure 27. Excitation of any absorption range of porphyrin and phthalocyanine falls into the $S_1$(Q) state of phthalocyanine via efficient energy transfer to the lowest excited state. The fluorescence quantum yield from this state is as high as 0.71. Overall, the supermolecule is regarded as an excellent antenna composite having broad and strong absorption bands of both $S_2$ of porphyrin and $S_1$ of phthalocyanine and with a high fluorescence quantum yield from the lowest excited state of phthalocyanine.

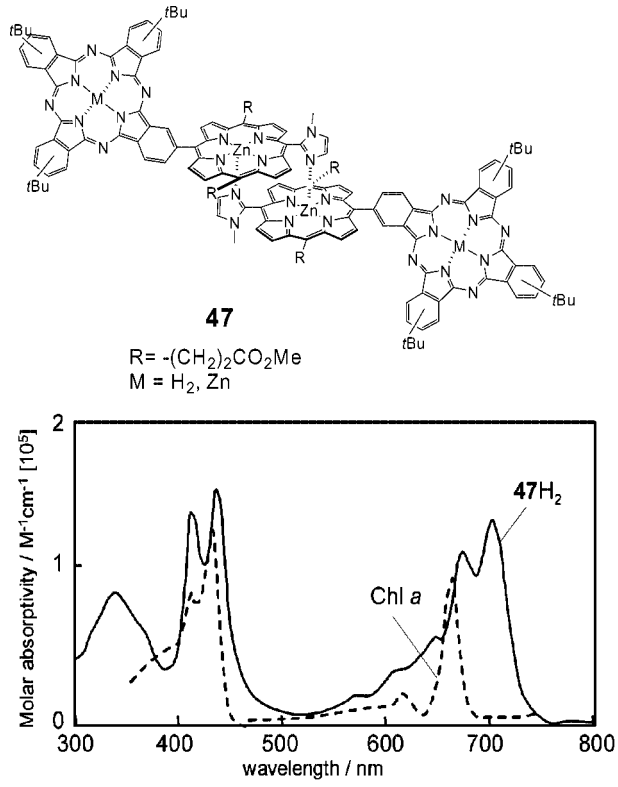


Figure 27. Complementary dimer formation of imidazolylzincporphyrin with phthalocyanine and comparison of the absorption spectrum with that of chlorophyll *a*.[98]

The above method is interesting in that phthalocyanines are brought into a highly fluorescent supermolecule. At the same time, it is challenging to develop a methodology to organize phthalocyanines themselves. Applying the same methodology as for porphyrins, an imidazolyl substituent was introduced at one of the benzo-groups of metallophthalocyanine.[99] A very stable dimer **48** (Figure 28) was formed with use of $Zn^{2+}$ or $Mg^{2+}$-phthalocyanine, as observed by NMR, UV/visible and mass spectra. The Q-bands split by exciton interaction in the dimer converge into a single band on titrating with *N*-methylimidazole through a clear isosbestic point. That a large excess of competitive ligand was required to cleave the coordination bond reflects the large stability constant. The values were evaluated as large as $1.4 \cdot 10^{11}$–$1.1 \cdot 10^{12}$ $M^{-1}$ for $Zn^{2+}$- and $Mg^{2+}$-phthalocyanines. The interaction of complementary coordination of imidazolyl-to-$Zn^{2+}$ or $Mg^{2+}$ was confirmed by characteristic higher-field shifts of the imidazolyl and the half of the ring protons that face each other to the large π-electronic system of phthalocyanine. The fluorescence of this dimer is not quenched on this assembly formation. The fluorescence quantum yields of the dimers from Zn(*t*Bu)$_3$, Zn(OBu)$_6$, and Mg(*t*Bu)$_3$-phthalocyanines were 0.26, 0.45, and 0.76, respectively. These values were almost identical to those of the starting monomeric species. The coordination organization of imidazolyl-porphyrin has thus been introduced into the field of phthalocyanine. A new version of supramolecular chemistry in the field of phthalocyanine will be interesting.

 © 2006 Wiley-VCH Verlag GmbH & Co. KGaA, Weinheim 

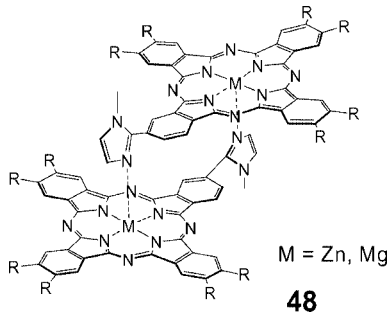


Figure 28. Complementary coordination of imidazolyl-M-(Zn,Mg)$^{2+}$-phthalocyanine.[99]

## 8. Perylenebisimide

As briefly overviewed in the general characteristics of chromophores, perylenebisimide shows excellent properties in light absorption and emission. The high aggregation tendency through the overlap of planar π-orbitals can be reduced when bulky substituents such as tetraaryloxy groups are introduced at the 1, 6, 7, and 12-positions.[100–104] According to the coordination organization proposed by Fujita, linear ligands were prepared most easily by introducing ligands at the imide nitrogen atoms of perylenebisimide. Then M(dppp), where dppp represents 1,3-bis(diphenylphosphanyl)propane, afforded in quantitative yields macrocyclotetramers **49** of perylenebisimides appended with various aryloxy groups with use of M = $Pt^{2+}$ and $Pd^{2+}$ (Figure 29).[105] These complexes remain intact at concentrations as low as ca. $10^{-6}$ M. Even if transition-metal ions are used in this case, the fluorescence quantum yield of the starting perylenebisimide in the square remained largely intact at a level of nearly 90%.

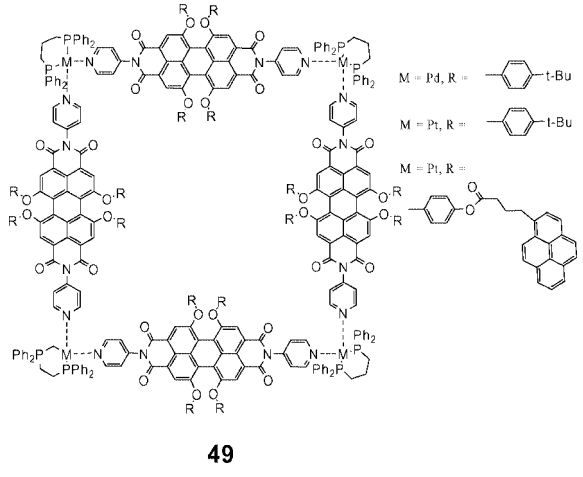


Figure 29. Macrocyclo-tetramerization of pyridyl-appended tetraaryloxyperylenebisimide by $Pd^{2+}$ or $Pt^{2+}$ complex.[105]

When pyrene is introduced at the 1, 6, 7, and 12 positions as the aryloxy substituent, the square has a large number of chromophores, 16 pyrene and four perylenebisimide chromophores, appropriate for light harvesting to cover a wide range of wavelengths with high molar extinction coefficients. Photophysical measurements were undertaken by steady state and time-resolved emission and transient absorption spectroscopy. Compared with the simple phenyl-substituted square, efficient (90%) and fast (0.2 ns) energy transfer from the pyrene to the perylenebisimide chromophores quenched almost completely the pyrenyl fluorescence. At the same time, very fast and efficient (>94%) electron transfer from pyrene to perylene reduced significantly the fluorescence from the perylene.

When bis(terpyridyl)-functionalized perylenebisimide **50** was subjected to self-assembly by metal coordination, linear metallo-supramolecular polymers (**51**) could be obtained (Figure 30).[106–109] Isothermal titration calorimetry studies of the terpyrydine ligand with various transition-metal ions established that $Zn^{2+}$ afforded a very stable bis(terpyridyl) complex with the successive stability constants $K_1 > 10^8$ M$^{-1}$ and $K_2 > 10^{10}$ M$^{-1}$, demonstrating a clear tendency for stable 2:1 complex formation. The complexes exhibited intense red fluorescence ($\lambda_{max}$ = 620 nm) with the quantum yield of ca. 0.9. The complexation with $Zn^{2+}$ has virtually no effect on the fluorescence quantum yield, although the use of $Fe^{2+}$ for the assembly formation induces a quenching down to $\Phi_{fl} < 0.1$. Likewise, fluorescence lifetimes of $Zn^{2+}$ dimer and polymer complexes were the same as that of the uncomplexed ligand, showing no electronic interaction between $Zn(tpy)_2$ and perylene sites. The complex showed reversibility of the binding event within a short timescale less than 1 min.

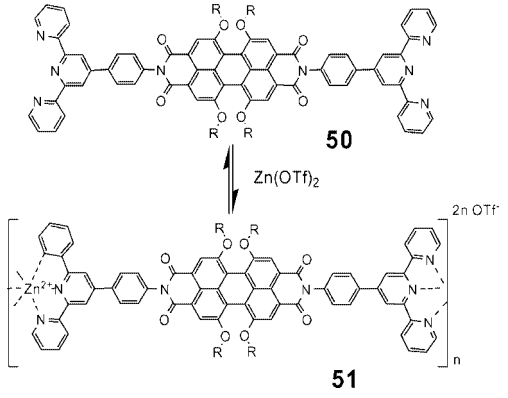


Figure 30. Bis(tpy)-connected polymerization of tetraaryloxyperylenebisimide.[106]

The process was monitored by fluorescence anisotropy titration. When fluorescence anisotropy $r$ is plotted as a function of the $Zn^{II}$/perylene monomer ratio, the $r$ value increased almost linearly to a maximum of $r$ = 0.133 at a 1:1 ratio of $Zn^{2+}$/**50**. The observations are compatible with the reversibility of the assembly formation, since the anisotropy decay due to the rotational diffusion of polymer must be slower. In the linear rigid coordination polymer, the transition-dipole moments align along the N–N axis of the perylenebisimide unit, and energy transfer within the perylenebisimide units along the same polymeric chain will not induce the anisotropy decrease. After 1:1 stoichiometry, a fragmentation process leading to the oligomeric units occurs and the anisotropy tends to decrease again, but never reaches the value of the monomer unit.

 © 2006 Wiley-VCH Verlag GmbH & Co. KGaA, Weinheim 

The dynamic character of ligand exchange was tested in solution by mixing two different perylenebisimide ligands **I** and **II** in a 1:1 molar ratio.[110] These ligands have the same molecular length and differ only in their alkyl groups at the phenoxy substituents. $^{1}H$ and $^{31}P$ NMR spectra after the equilibrium suggested the formation of an ideal statistical mixture. Mass spectra proved the existence of all the molecular squares **A**, **B**, **C**, **D**, **E**, and **F** (Figure 31) in the resulting solution.

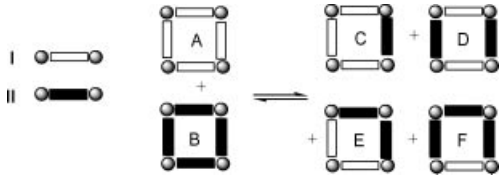


Figure 31. Ligand exchange equilibrium after mixing two molecular squares.[110]

## 9. Polypyridyl Metal Complexes

Bipyridyl (bpy), terpyridyl (tpy), phenanthrolyl (phen) metal complexes belong to this class and afford stable complexes with various metal ions. The ruthenium tris(bpy) complex and its derivatives play important roles on dye-sensitized solar cells.

The emission quantum yield from $^{3}MLCT$ of $Ru(bpy)_3$ is relatively high at 0.04, but $[Ru(tpy)_2]^{2+}$ emits with a low quantum yield of $1\cdot10^{-5}$ with a lifetime of 250 ps. The terpyridine complex is characterized by a directed connection and its large stability constant. When two tpy units are connected through a *m*-phenylene group its complexation with $Ru^{2+}$ ion affords automatically a macrocyclic hexamer of the $[Ru(tpy)_2]^{2+}$ complex **52** (Figure 32).[111] When carbazole is substituted as the central connecting unit, pentameric macrocycles are self-assembled by complexation with $Zn^{2+}$, $Ru^{2+}$, and $Fe^{2+}$ ions (**53**).[112] Although carbazole itself is highly fluorescent, the pentamacrocyclic $Ru^{2+}$ complex does not show fluorescence at all. On the other hand, the $Zn^{2+}$ macrocycle shows a strong emission at 560 nm. The macropentacyclic $[M(tpy)_2]^{2+}$ complexes were used for coating of nanocrystalline $TiO_2$ in a Grätzel-type solar cell device. The $Ru^{2+}$ complex gave the highest photoconversion efficiency ($\eta$) of the cell, $\eta$ being 1.53, 0.73, and 0.49% for the $Ru^{2+}$, $Zn^{2+}$. and $Fe^{2+}$ cases, respectively.

The $[Ru(tpy)_2]^{2+}$ complex is suitable for connecting other chromophores in a linear fashion. When $Ru(tpy)_2$ connects porphyrins as in **54**, the energy absorbed by the porphyrin is transferred to the lowest triplet state with 100% efficiency (Figure 33).[113] Triplet energy transfer from $^{3}PAu\text{-}Ru\text{-}PH_2$ to $PAu\text{-}Ru\text{-}^{3}PH_2$ with a center-to-center separation of 21 Å was examined. The energy transfer was mediated by the interposed Ru complex by an exchange mechanism at 77 K with a rate constant of $2.5\cdot10^{7}\ s^{-1}$, which is as fast as the arylene-connected case.

Hanan reports that the lifetime of $^{3}MLCT$ emission from $[Ru(tpy)_2]^{2+}$ increases significantly by the introduction of

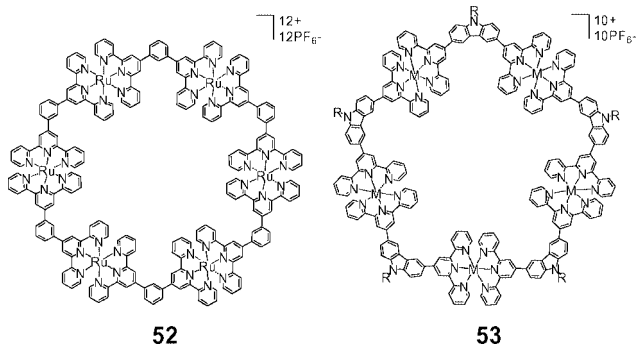


Figure 32. Macrohexamer and pentamer of $[Ru(tpy)_2]^{2+}$.[111,112]

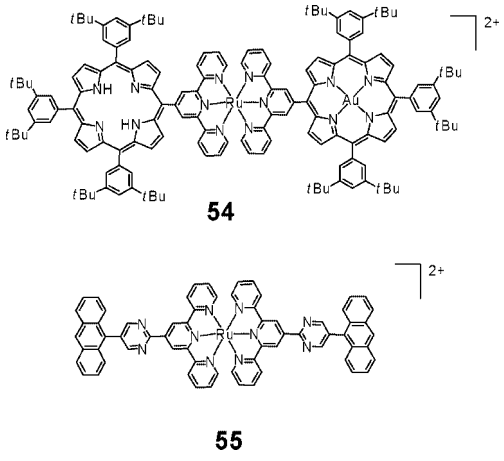


Figure 33. Connection of porphyrins through $[Ru(tpy)_2]^{2+}$ complex and $[Ru^{2+}(anthracenyl\text{-}tpy)_2]^{2+}$ complex.[113,114]

an anthracene moiety as in **55**.[114] The luminescence decay lasts up to 1.8 μs at room temperature. The phenomenon is explained by the equilibrium between the initially formed $^{3}MLCT$ state of $[Ru(tpy)_2]^{2+}$ and the low-lying anthracene-based triplet states. Introduction of organic chromophores having triplet excited states of energies close to the $^{3}MLCT$ is claimed to be an efficient way to prolong the short excited-state lifetime of the $[Ru(tpy)_2]^{2+}$.

The dendritic Ru(biscarbazolyl-phenanthroline)$_3$ complex **56** shows a red shift of absorption and emission maxima compared to $Ru(phen)(bpy)_2$ **57** (Figure 34).[115] The excitation spectrum resembles the absorption spectrum and

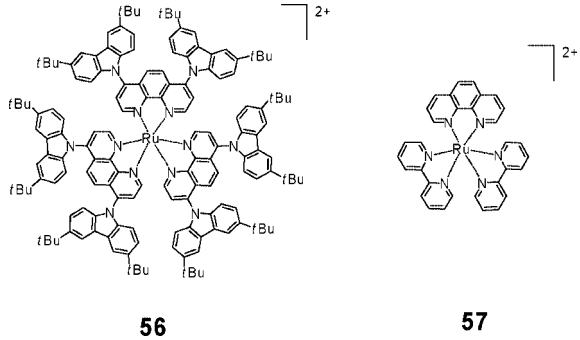


Figure 34. Ru(biscarbazolyl-phenanthroline)$_3$ and $Ru(phen)(bpy)_2$ complexes.[115]

 © 2006 Wiley-VCH Verlag GmbH & Co. KGaA, Weinheim 

the fluorescence from the carbazolyl part is completely quenched. These properties suggest its potential usefulness for the antenna function.

## 10. Conclusion and Outlook

The research on light-harvesting antenna has been much inspired by very aesthetic X-ray crystallographic structures of antenna complexes of the photosynthetic purple bacteria. The energy degeneracy of each component in the ring structure is important for transferring the energy efficiently to targets in any direction. Many chromophores having large extinction coefficients in the visible wavelength region have been organized into macrocyclic structures. New supramolecular methodologies have been developed and have succeeded in providing macrocycles of not only 2D but also 3D arrangements. Photophysical studies have elucidated the rate of the fast excitation energy hopping process by anisotropy decay after polarized light excitation and also by exciton-exciton annihilation. In the development of artificial antenna complexes, noncyclic systems are important too. Linear arrays without loss of excitation energy have also been developed. In order to obtain stable supramolecular complexes, transition-metal ions have been frequently used. In most cases, intersystem crossing leads to the triplet state. The analysis of such systems becomes difficult in most cases and awaits further photophysical studies.

## Acknowledgments

We thank our collaborators and co-workers, whose work is reported in this article. This work has been supported by Grants-in-Aid for Scientific Research (A) (No. 15205020) and Scientific Research on Priority Areas (No. 15036248), Reaction Control of Dynamic Complexes from the Ministry of Education, Culture, Sports, Science, and Technology of the Japanese Government.

[1] A. K. Burrell, D. L. Officer, P. G. Plieger, D. C. W. Reid, *Chem. Rev.* **2001**, *101*, 2751–2796.
[2] D. Holten, D. F. Bocian, J. S. Lindsey, *Acc. Chem. Res.* **2002**, *35*, 57–69.
[3] D. Kim, A. Osuka, *Acc. Chem. Res.* **2004**, *37*, 735–745.
[4] M.-S. Choi, T. Yamazaki, I. Yamazaki, T. Aida, *Angew. Chem. Int. Ed.* **2004**, *43*, 150–158.
[5] H. Imahori, *J. Phys. Chem. B* **2004**, *108*, 6130–6143.
[6] J. C. Chambron, V. Heitz, J.-P. Sauvage in *The Porphyrin Handbook* (Eds.: K. M. Kadish, K. M. Smith, R. Guilard), Academic Press, New York, **1999**, vol. 6, chapter 40, pp. 1–42.
[7] S. Takagi, H. Inoue in *Molecular and Supramolecular Photochemistry* (Eds.: V. Ramamurthy, K. S. Schanze), Marcel Decker, New York, **1999**, vol. 4, chapter 6, pp. 251–342.
[8] J. K. M. Sanders in *The Porphyrin Handbook* (Eds.: K. M. Kadish, K. M. Smith, R. Guilard), Academic Press, New York, **2000**, vol. 3, pp. 347–368.
[9] M. Tabata, J. Nishimoto in *The Porphyrin Handbook* (Eds.: K. M. Kadish, K. M. Smith, R. Guilard), Academic Press, New York, **2000**, vol. 9, pp. 221–419.
[10] J. Wojaczynski, L. Latos-Grazynski, *Coord. Chem. Rev.* **2000**, *204*, 113–171.
[11] E. Iengo, E. Zangrando, E. Alessio, *Eur. J. Inorg. Chem.* **2003**, 2371–2384.
[12] P. D. Harvey in *The Porphyrin Handbook* (Eds.: K. M. Kadish, K. M. Smith, R. Guilard), Academic Press, New York, **2003**, vol. 18, pp. 63–249.
[13] K. Ogawa, Y. Kobuke in *Encyclopedia of Nanoscience and Nanotechnology* (Ed.: H. S. Nalwa), American Scientific Publishers, Stevenson Ranch, California, **2003**, vol. 10, 1–30.
[14] T. S. Balaban, "Light-Harvesting Nanostructures", in *Encyclopedia of Nanoscience and Nanotechnology* (Ed.: H. S. Nalwa), American Scientific Publishers, Stevenson Ranch, CA, **2004**, vol. 4, pp. 505–559.
[15] A. Satake, Y. Kobuke, *Tetrahedron* **2005**, *61*, 13–41.
[16] Y. Kobuke, *Structure and Bonding*, in press.
[17] S. Karrasch, P. A. Bullough, R. Ghosh, *EMBO J.* **1995**, *14*, 631–638.
[18] G. McDermott, S. M. Prince, A. A. Freer, A. M. Hawthornthwaite-Lawless, M. Z. Papiz, R. J. Cogdell, N. W. Isaacs, *Nature* **1995**, *374*, 517–521.
[19] M. Z. Papiz, S. M. Prince, T. Howard, R. J. Cogdell, N. W. Isaacs, *J. Mol. Biol.* **2003**, *326*, 1523–1538.
[20] R. J. Cogdell, N. W. Isaacs, A. A. Freer, T. D. Howard, A. T. Gardiner, S. M. Prince, M. Z. Pappiz, *FEBS Lett.* **2003**, *555*, 35–39.
[21] S. Bahatyrova, R. N. Frese, C. A. Siebert, J. D. Olsen, K. O. van der Werf, R. Van Grondelle, R. A. Niederman, P. A. Bullough, C. Otto, C. N. Hunter, *Nature* **2004**, *430*, 1058–1062.
[22] X. Hu, A. Damjanovic, T. Ritz, K. Schulten, *Proc. Natl. Acad. Sci. USA* **1998**, *95*, 5935–5941.
[23] A. P. Shreve, J. K. Trautman, H. A. Frank, T. G. Owens, A. C. Albrecht, *Biochim. Biophys. Acta* **1991**, *1058*, 280–288.
[24] R. Jimenez, S. N. Dikshit, S. E. Bradforth, G. R. Fleming, *J. Phys. Chem.* **1996**, *100*, 6825–6834.
[25] L. M. P. Beekman, F. van Mourik, M. R. Jones, H. M. Visser, C. N. Hunter, R. van Grondelle, *Biochem.* **1994**, *33*, 3143–3147.
[26] S. Hess, M. Chachisvilis, K. Timpmann, M. R. Jones, C. N. Hunter, V. Sundström, *Proc. Natl. Acad. Sci. USA* **1995**, *92*, 12333–12337.
[27] X. Hu, T. Ritz, A. Damjanovic, K. Schulten, *J. Phys. Chem. B* **1997**, *101*, 3854–3871.
[28] C. Jungas, J.-L. Ranck, J.-L. Rigaud, P. Joliot, A. Vermeglio, *EMBO J.* **1999**, *18*, 534–542.
[29] A. W. Roszak, T. D. Haward, J. Southall, A. T. Gardiner, C. J. Law, N. W. Isaacs, R. J. Cogdell, *Science* **2003**, *302*, 1969–1972.
[30] S. Scheuring, F. Francia, J. Busselez, B. A. Melandri, J.-L. Rigaud, D. Levy, *J. Biol. Chem.* **2004**, *279*, 3620–3626.
[31] P. Jordan, P. Fromme, H. T. Witt, O. Klukas, W. Saenger, N. Krauss, *Nature* **2001**, *411*, 909–917.
[32] B. R. Green, W. W. Parson (Eds.), "Light-Harvesting Antennas", in *Advances in Photosynthesis and Respiration* (Ed.: Govindjee), vol. 13, Kluwer Academic Publishers, **2003**.
[33] Z. Liu, H. Yan, K. Wang, T. Kuang, J. Zhang, L. Gui, X. An, W. Chang, *Nature* **2004**, *428*, 287–292.
[34] N. Nelson, A. Ben-Shem, *Bioessays* **2005**, *27*, 914–922.
[35] D. L. Andrews (Ed.), *Energy Harvesting Materials*, World Scientific, Hackensack, NJ, **2005**.
[36] M. A. Palacios, F. L. de Weerd, J. A. Ihalainen, R. van Grondelle, H. V. Amerongen, *J. Phys. Chem. B* **2002**, *106*, 5782–5787.
[37] G. Weber, F. W. J. Teale, *Faraday Trans.* **1957**, *53*, 646–655.
[38] T. P. Causgrove, P. Cheng, D. C. Brune, R. E. Blankenship, *J. Phys. Chem.* **1993**, *97*, 5519–5524.
[39] D. J. Quimby, F. R. Longo, *J. Am. Chem. Soc.* **1975**, *97*, 5111–5117.
[40] K. Kamioka, R. A. Cormier, T. W. Lutton, J. S. Connolly, *J. Am. Chem. Soc.* **1992**, *114*, 4414–4415.
[41] D. Kim, J. Terner, T. G. Spiro, *J. Am. Chem. Soc.* **1986**, *108*, 2097–2099.
[42] J. S. Lindsey, J. N. Woodford, *Inorg. Chem.* **1995**, *34*, 1063–1069.
[43] P. G. Seybold, M. Gouterman, *J. Mol. Spectrosc.* **1969**, *31*, 1–13.

 © 2006 Wiley-VCH Verlag GmbH & Co. KGaA, Weinheim 

[44] R. O. Loutfy, E. R. Menzel, *J. Am. Chem. Soc.* **1980**, *102*, 4967–4970.
[45] D. F. O'Shea, M. A. Miller, H. Matsueda, J. S. Lindsey, *Inorg. Chem.* **1996**, *35*, 7325–7338.
[46] R. Dobrawa, M. Lysetska, P. Ballester, M. Grüne, F. Würthner, *Macromolecules* **2005**, *38*, 1315–1325.
[47] L. J. Henderson Jr, F. R. Fronczek, W. R. Cherry, *J. Am. Chem. Soc.* **1984**, *106*, 5876–5879.
[48] M. Maestri, N. Armaroli, V. Balzani, E. C. Constable, A. M. W. C. Thompson, *Inorg. Chem.* **1995**, *34*, 2759–2767.
[49] G. Ferraudi in *Phthalocyanines, Properties and Applications* (Eds.: C. C. Leznoff, A. B. P. Lever), Wiley-VCH, New York, **1989**, vol. 1, chapter 4, pp. 291–340.
[50] H. Du, R. A. Fuh, J. Li, A. Corkan, J. S. Lindsey, *Photochem. Photobiol.* **1998**, *68*, 141–142.
[51] M. Kasha, H. R. Rawls, M. A. El-Bayyoumi, *Pure Appl. Chem.* **1965**, *11*, 371–392.
[52] Y. Kobuke, K. Ogawa, *Bull. Chem. Soc. Jpn.* **2003**, *76*, 689–708.
[53] Y. Kobuke, *J. Porphyrins Phthalocyanines* **2004**, *8*, 156–174.
[54] Y. Kobuke, H. Miyaji, *J. Am. Chem. Soc.* **1994**, *116*, 4111–4112.
[55] Y. Kobuke, H. Miyaji, *Bull. Chem. Soc. Jpn.* **1996**, *69*, 3563–3569.
[56] K. Ogawa, Y. Kobuke, *Angew. Chem. Int. Ed.* **2000**, *39*, 4070–4073.
[57] D. Furutsu, A. Satake, Y. Kobuke, *Inorg. Chem.* **2005**, *44*, 4460–4462.
[58] A. Nomoto, Y. Kobuke, *Chem. Commun.* **2002**, 1104–1105.
[59] A. Nomoto, H. Mitsuoka, H. Ozeki, Y. Kobuke, *Chem. Commun.* **2003**, 1074–1075.
[60] A. Ohashi, A. Satake, Y. Kobuke, *Bull. Chem. Soc. Jpn.* **2004**; *77*, 365–374.
[61] T. M. Trnka, R. H. Grubbs, *Acc. Chem. Res.* **2001**, *34*, 18–29.
[62] M. Morisue, S. Yamatsu, N. Haruta, Y. Kobuke, *Chem. Eur. J.* **2005**, *11*, 5563–5574.
[63] R. Takahashi, Y. Kobuke, *J. Am. Chem. Soc.* **2003**, *125*, 2372–2373.
[64] R. Takahashi, Y. Kobuke, *J. Org. Chem.* **2005**, *70*, 2745–2753.
[65] I.-W. Hwang, D. M. Ko, T. K. Ahn, D. Kim, F. Ito, Y. Ishibashi, S. R. Khan, Y. Nagasawa, H. Miyasaka, C. Ikeda, R. Takahashi, K. Ogawa, A. Satake, Y. Kobuke, *Chem. Eur. J.* **2005**, *11*, 3753–3761.
[66] Y. Kuramochi, A. Satake, Y. Kobuke, *J. Am. Chem. Soc.* **2004**, *126*, 8668–8669.
[67] C. Ikeda, N. Nagahara, N. Yoshioka, H. Inoue, *New J. Chem.* **2000**, *24*, 897–902.
[68] C. Ikeda, Y. Tanaka, T. Fujihara, Y. Ishii, T. Ushiyama, K. Yamamoto, N. Yoshioka, H. Inoue, *Inorg. Chem.* **2001**, *40*, 3395–3405.
[69] A. Tsuda, S. Sakamoto, K. Yamaguchi, T. Aida, *J. Am. Chem. Soc.* **2003**, *125*, 15722–15723.
[70] T. S. Balaban, R. Goddard, M. Linke-Schaetzel, J.-M. Lehn, *J. Am. Chem. Soc.* **2003**, *125*, 4233–4239.
[71] P. Ballester, A. Costa, P. M. Deya, A. Frontera, R. M. Gomila, A. I. Oliva, J. K. M. Sanders, C. A. Hunter, *J. Org. Chem.* **2005**, *70*, 6616–6622.
[72] R. A. Haycock, A. Yartsev, U. Michelsen, V. Sundström, C. A. Hunter, *Angew. Chem. Int. Ed.* **2000**, *39*, 3616–3619.
[73] E. Iengo, E. Zangrando, E. Alessio, J.-C. Chambron, V. Heitz, L. Flamigni, J.-P. Sauvage, *Chem. Eur. J.* **2003**, *9*, 5879–5887.
[74] S. Anderson, H. L. Anderson, A. Bashall, M. AcParlin, J. K. M. Sanders, *Angew. Chem. Int. Ed. Engl.* **1995**, *34*, 1096–1099.
[75] S. Rucareanu, O. Mongin, A. Schuwey, N. Hoyler, A. Gossauer, W. Amrein, H.-U. Hediger, *J. Org. Chem.* **2001**, *66*, 4973–4988.
[76] I.-W. Hwang, H. S. Cho, D. H. Jeong, D. Kim, A. Tsuda, T. Nakamura, A. Osuka, *J. Phys. Chem. B* **2003**, *107*, 9977–9988.
[77] A. Tsuda, T. Nakamura, S. Sakamoto, K. Yamaguchi, A. Osuka, *Angew. Chem. Int. Ed.* **2002**, *41*, 2817–2821.
[78] I.-W. Hwang, T. Kamada, T. K. Ahn, D. M. Ko, T. Nakamura, A. Tsuda, A. Osuka, D. Kim, *J. Am. Chem. Soc.* **2004**, *126*, 16187–16198.
[79] A. Tsuda, H. Hu, R. Tanaka, T. Aida, *Angew. Chem. Int. Ed.* **2005**, *44*, 4884–4888.
[80] A. Prodi, M. T. Indelli, C. J. Kleverlaan, F. Scandola, E. Alessio, T. Gianferrara, L. G. Marzilli, *Chem. Eur. J.* **1999**, *5*, 2668–2679.
[81] A. Prodi, C. Chiorboli, F. Scandola, E. Iengo, E. Alessio, R. Dobrawa, F. Würthner, *J. Am. Chem. Soc.* **2005**, *127*, 1454–1462.
[82] M. Fujita, J. Yazaki, K. Ogura, *J. Am. Chem. Soc.* **1990**, *112*, 5645–5647.
[83] M. Fujita, K. Ogura, *Bull. Chem. Soc. Jpn.* **1996**, *69*, 1471–1482.
[84] M. Fujita, *Chem. Soc. Rev.* **1998**, *27*, 417–425.
[85] M. Fujita, *Acc. Chem. Res.* **1999**, *32*, 53–61.
[86] A. Prodi, C. J. Kleverlaan, M. T. Indelli, F. Scandola, E. Alessio, E. Iengo, *Inorg. Chem.* **2001**, *40*, 3498–3504.
[87] C. M. Drain, F. Nifiatis, A. Vasenko, J. D. Batteas, *Angew. Chem. Int. Ed.* **1998**, *37*, 2344–2347.
[88] T. Milic, J. C. Garno, J. D. Batteas, G. Smeureanu, C. M. Drain, *Langmuir* **2004**, *20*, 3974–3983.
[89] R. V. Slone, J. T. Hupp, *Inorg. Chem.* **1997**, *36*, 5422–5423.
[90] I. V. Rubtsov, Y. Kobuke, H. Miyaji, K. Yoshihara, *Chem. Phys. Lett.* **1999**, *308*, 323–328.
[91] Y. Kobuke, H. Miyaji, K. Ogawa, *J. Supramol. Chem.* **2002**, *14*, 159–170.
[92] K. P. McNaughton, J. T. Groves, *Org. Lett.* **2003**, *5*, 1829–1832.
[93] H. Imahori, M. Arimura, T. Hanada, Y. Nishimura, I. Yamazaki, Y. Sakata, S. Fukuzumi, *J. Am. Chem. Soc.* **2001**, *123*, 335–336.
[94] T. Hasobe, H. Imahori, P. V. Kamat, S. Fukuzumi, *J. Am. Chem. Soc.* **2003**, *125*, 14962–14963.
[95] H. Imahori, Y. Kashiwagi, Y. Endo, T. Hanada, Y. Nishimura, I. Yamazaki, Y. Araki, O. Ito, S. Fukuzumi, *Langmuir* **2004**, *20*, 73–81.
[96] T. Hasobe, H. Imahori, P. V. Kamat, T. K. Ahn, S. K. Kim, D. Kim, A. Fujimoto, T. Hirakawa, S. Fukuzumi, *J. Am. Chem. Soc.* **2005**, *127*, 1216–1228.
[97] H. Imahori, A. Fujimoto, S. Kang, H. Hotta, K. Yoshida, T. Umeyama, Y. Matano, S. Isoda, M. Isosomppi, N. V. Tkachenko, H. Lemmetyinen, *Chem. Eur. J.* **2005**, *11*, 7265–7275.
[98] K. Kameyama, A. Satake, Y. Kobuke, *Tetrahedron Lett.* **2004**, *45*, 7617–7620.
[99] K. Kameyama, M. Morisue, A. Satake, Y. Kobuke, *Angew. Chem. Int. Ed.* **2005**, *44*, 2–5.
[100] G. Seybold, C. Wagenblast, *Dyes Pigm.* **1989**, *71*, 303–317.
[101] R. Gvishi, R. Reisfeld, Z. Burshtein, *Chem. Phys. Lett.* **1993**, *213*, 338–344.
[102] D. Dotcheva, M. Klapper, K. Mullen, *Macromol. Chem. Phys.* **1994**, *195*, 1905–1911.
[103] F. Würthner, C. Thalacker, A. Sautter, *Adv. Mater.* **1999**, *11*, 754–758.
[104] F. Würthner, C. Thalacker, A. Sautter, *Angew. Chem. Int. Ed.* **2000**, *39*, 1243–1245.
[105] C.-C. You, F. Würthner, *J. Am. Chem. Soc.* **2003**, *125*, 9716–9725.
[106] R. Dobrawa, F. Würthner, *Chem. Commun.* **2002**, 1878–1879.
[107] F. Würthner, *Chem. Commun.* **2004**, 1564–1579.
[108] R. Dobrawa, M. Lysetska, P. Ballester, M. Grüe, F. Würthner, *Macromolecules* **2005**, *38*, 1315–1325.
[109] R. Dobrawa, F. Würthner, *J. Polymer Sci. A Polymer Chem.* **2005**, *43*, 4981–4995.
[110] F. Würthner, A. Sautter, D. Schmid, P. J. A. Weber, *Chem. Eur. J.* **2001**, *7*, 894–902.
[111] G. R. Newkome, T. J. Cho, C. N. Moorefield, G. R. Baker, R. Cush, P. S. Russo, *Angew. Chem. Int. Ed.* **1999**, *38*, 3717–3721.

 © 2006 Wiley-VCH Verlag GmbH & Co. KGaA, Weinheim 

[112] S.-H. Hwang, P. Wang, C. N. Moorefield, L. A. Godínez, J. Manríquez, E. Bustosc, G. R. Newkome, *Chem. Commun.* **2005**, 4672–4674.
[113] L. Flamigni, F. Barigelletti, N. Armaroli, B. Ventura, J.-P. Collin, J.-P. Sauvage, J. A. G. Williams, *Inorg. Chem.* **1999**, *38*, 661–667.
[114] R. Passalacqua, F. Loiseau, S. Campagna, Y.-Q. Fang, G. S. Hanan, *Angew. Chem. Int. Ed.* **2003**, *42*, 1608–1611.
[115] N. D. McClenaghan, R. Passalacqua, F. Loiseau, S. Campagna, B. Verheyde, A. Hameurlaine, W. Dehaen, *J. Am. Chem. Soc.* **2003**, *125*, 5356–5365.

Received: February 23, 2006
Published Online: May 17, 2006

 © 2006 Wiley-VCH Verlag GmbH & Co. KGaA, Weinheim 

DOI: 10.1002/ejic.200600128

# Synthesis and Structural Characterization of a Halide-Free Rhombohedral Silver-Alkynyl Cage Complex $[Ag_{14}(C_2tBu)_{12}][BF_4]_2$

**Omar M. Abu-Salah,*[a] Mohammed H. Ja'far,[a] Abdel Razzak Al-Ohaly,[a] Khalid A. Al-Farhan,[a] Hamda S. Al-Enzi,[a] Oleg V. Dolomanov,[b] and Judith A. K. Howard[b]**

**Keywords:** Silver / Clusters / Silver alkynyls / Alkynyl cluster / Cationic silver complex / Silver cage complex / Rhombohedral silver cage

The novel cationic complex $[Ag_{14}(C_2tBu)_{12}]^{2+}$ has been synthesized by four reactions: reaction of $[Ag(C_2tBu)]_n$ and $AgBF_4$ in acetone in a 6:1 mole ratio, that of $HC{\equiv}CtBu$ and $AgBF_4$ in water in the absence of a base, treatment of $[AgC_2tBu]_n$ with $HBF_4$ in acetone or that of $\{[Ag_3(C_2tBu)_2][BF_4]\}_n$ with $[Ag(C_2tBu)]_n$ in a 1:4 mole ratio. Single-crystal X-ray studies showed it to be a hexacapped cube of silver(I) atoms, with twelve $\eta^1$, $\mu^3$-$C_2tBu$ ligands.
(© Wiley-VCH Verlag GmbH & Co. KGaA, 69451 Weinheim, Germany, 2006)

## Introduction

Since the pioneering work of Nast[1] on acetylide complexes, dramatic developments in the field, parallel to the advances in organometallic chemistry, have been accomplished. The versatile mode of bonding of the alkynyl ligand resulted in numerous polynuclear alkynyl complexes.[2,3] Different aspects of the subject have been reviewed extensively.[2,4] Luminescence properties, particularly of mixed-metal platinum(II)-copper(I) and -silver(I) alkynyl complexes have been studied widely.[5] In the field of pure coinage metal alkynyls, new aspects of organometallic chemistry emerged when bis(phenylethynyl) metallates $[M(C_2Ph)_2]^-$ (M = Cu, Ag, Au) were treated with metal phenylacetylide polymers $[M(C_2Ph)]_n$ (M = Cu, Ag, Au). Consecutive steps of ethynylation and condensation of the formed anionic and cationic moieties resulted in the formation of homonuclear $[Ag_5(C_2Ph)_6]^-$ and heteronuclear $[Au_2Cu(C_2Ph)_4]^-$, $[Au_3M_2(C_2Ph)_6]^-$ (M = Cu, Ag), $[Ag_6Cu_7(C_2Ph)_{14}]^-$ and $[AuAg_6Cu_6(C_2Ph)_{14}]^-$ complexes.[6] Extension of ethynylation reactions to neutral complexes resulted in the complexes $[Au_2Ag_2(C_2Ph)_4(PPh_3)_2]$, $[Ag_2Cu_2(C_2Ph)_4(PPh_3)_4]$, $[AuAg(C_2Ph)_2]_n$, $[AuCu(C_2Ph)_2]_n$ and $[AgCu(C_2Ph)_2]_n$.[6i,7] Silver cages of various structures encapsulating the dianion $C_2^{2-}$, which is isoelectronic with $CN^-$, have been reported.[8] Recently anion-templated, rhombohedral silver-alkynyl cages $[Ag_{14}(C_2tBu)_{12}X]^+$ (X = F, Cl, Br) were synthesized and structurally identified.[9] Earlier we reported the synthesis and structure of the novel cationic silver alkynyl polymer $[Ag_3(C_2tBu)_2]_n[BF_4]_n$.[10] We now report new aspects of the chemistry resulting from the synthesis of halide-free rhombohedral silver alkynyl complex $[Ag_{14}(C_2tBu)_{12}][BF_4]_2$ and its structure.

[a] Chemistry Department, College of Science, King Saud University,
P. O. Box 2455, Riyadh 11451, Saudi Arabia
Fax: + 966-1-4675992,
E-mail: omrsalah@ksu.edu.sa
[b] Chemistry Department, Durham University,
South Road, Durham DH1 3LE, UK
E-mail: J.A.K.Howard@durham.ac.uk

## Results and Discussion

The addition of $AgBF_4$ to $[Ag(C_2tBu)]_n$ in a 1:6 mole ratio in acetone gave a clear solution. Normal workup resulted in the slow precipitation of colourless crystals of $[Ag_{14}(C_2tBu)_{12}][BF_4]_2$. Elemental analysis agrees very well with this formulation. The infrared spectrum has a strong $\nu(C{\equiv}C)$ signal at 2036 $cm^{-1}$. This frequency is dramatically lower than that of the linear complex $[Ag(C_2Ph)_2]^-$[6i] (by ca. 50 $cm^{-1}$), which indicates a bridging mode of bonding. A very strong band at 1077 $cm^{-1}$ was assigned to $BF_4^-$.

Single-crystal X-ray structure determination showed that the fourteen silver atoms are arranged in a hexacapped cube of silver atoms (rhombohedral dodecahedron) with twelve $\eta^1$, $\mu^3$-alkynyl ligands, each pair of alkynyl groups are almost linearly bonded to each capping silver atom, and every ligand bridges two nearby silver atoms on each edge of the cube (Figure 1).

This metal cage is similar to the cage of $[Ag_{14}(C_2tBu)_{12}X][BF_4]$ (X = F, Cl, Br), in which the $X^-$ anion is located at the centre of the cage.[9] We found, however, that halide ions are not a prerequisite to the formation and stability of the cage as claimed by other workers.[9] Unlike the case in complexes $[Ag_{14}(C_2tBu)_{12}X][BF_4]$,[9a,9b] the $BF_4^-$ anions are unambiguously located here. There is a weak Ag···F interaction [2.499(4) Å]. The $^{19}F$ NMR spectrum showed two reso-

 © 2006 Wiley-VCH Verlag GmbH & Co. KGaA, Weinheim InterScience 

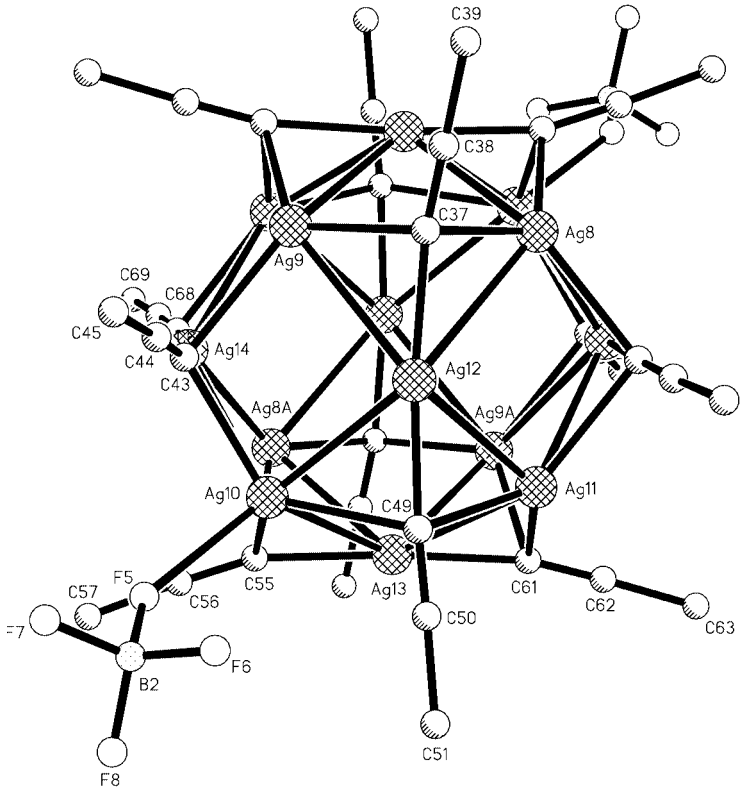


Figure 1. Structure of $[Ag_{14}(C_2tBu)_{12}][BF_4]_2$. Methyl groups of tertiary butyl groups have been omitted for clarity.

nances characteristic for $BF_4^-$ at –151.62 and –151.57 ppm.[9a,9b]

The most interesting finding that emerges from the comparison of the encapsulated halide-anion $Ag_{14}$ cages[9a,9b] with the present anion-free $Ag_{14}$ cage is that the encapsulated fluoride anion shrinks the $Ag_{14}$ cage, while the bromide ion expands it. The mean Ag–Ag bond length in the anion-free cage is 2.9747(7) Å, which is almost equal to the corresponding value in the chloride-encapsulated cage [2.971(2) Å], but is 0.015 Å shorter and 0.064 Å longer than the corresponding bond lengths in the bromide- and fluoride-encapsulated cages, respectively.

This cationic cluster represents the highest homoleptic finite polynuclear monosubstituted alkynyl complex to be synthesized and structurally identified. Although neutral ligands and anions[11,12] are known to depolymerize monosubstituted alkynyl coinage metal polymers $[M(C_2R)]_n$ (M = Cu, Ag, Au), this reaction represents the first cationic depolymerization reaction for these polymers.

The same complex was also prepared by the reaction of $HC_2tBu$ and $AgBF_4$ in water by using different mole ratios in the absence of a base. The reactions in aqueous $NH_3$, which afford $[Ag(C_2R)]_n$, are well known for the identification of monosubstituted alkynes; nevertheless, no report has been documented for the reaction in the absence of a base. If the above reaction is carried out in ether, the cationic polymer $[Ag_3(C_2tBu)_2]_n[BF_4]_n$[10] is obtained. On the other hand, using $AgNO_3$ with $HC_2tBu$ in water results in the formation of the neutral polymer $[Ag_3(C_2tBu)_2NO_3]_n$, which was reported recently.[9b] The other product of the above reactions is $HBF_4$ [Equation (1), Equation (2)]:

$$7\ AgBF_4 + 6\ HC{\equiv}C\text{–}tBu \rightarrow \frac{1}{2}\{[Ag_{14}(C_2tBu)_{12}][BF_4]_2\} + 6\ HBF_4 \quad (1)$$

$$3\ AgBF_4 + 2\ HC{\equiv}C\text{–}tBu \rightarrow \frac{1}{n}\{[Ag_3(C_2tBu)_2][BF_4]\}_n + 2\ HBF_4 \quad (2)$$

The acid was determined by titration and by measuring the pH of the solution. This implies that these complexes are stable in strongly acidic media.

A third procedure for the synthesis of the same complex is the reaction of $HBF_4$ with $[Ag(C_2tBu)]_n$ in acetone. The product was identified by usual methods and by comparison with an authentic sample. If excess acid is used, $\{[Ag_3(C_2tBu)_2][BF_4]\}_n$ is obtained [Equation (3), Equation (4)]:

$$HBF_4 + \frac{7}{n}[Ag(C_2tBu)]_n \rightarrow \frac{1}{2}\{[Ag_{14}(C_2tBu)_{12}][BF_4]_2\} + HC_2tBu \quad (3)$$

$$HBF_4 + \frac{3}{n}[Ag(C_2tBu)]_n \rightarrow \frac{1}{n}\{[Ag_3(C_2tBu)_2][BF_4]\}_n + HC_2tBu \quad (4)$$

A fourth route for the same complex involves the reaction of $\{[Ag_3(C_2tBu)_2][BF_4]\}_n$ and $[Ag(C_2tBu)]_n$ in acetone in a 1:4 mole ratio [Equation (5)]:

 © 2006 Wiley-VCH Verlag GmbH & Co. KGaA, Weinheim 

$$\frac{1}{n}\{[Ag_3(C_2tBu)_2][BF_4]\}_n + \frac{4}{n}[Ag(C_2tBu)]_n \rightarrow \frac{1}{2}\{[Ag_{14}(C_2tBu)_{12}][BF_4]_2\} \quad (5)$$

The cage structure of the complex indicates without doubt that a halide template is not necessary for the formation and stability of such cages. The different reactions described for the synthesis of the complex might be of general use in the synthesis of homo- and heteronuclear group 11 metal-alkynyl cluster complexes.

## Experimental Section

**Synthesis of $[Ag_{14}(C_2tBu)_{12}][BF_4]_2$**

**Method 1:** Silver tetrafluoroborate, $AgBF_4$ (98 mg, 0.5 mmol), was added to a suspension of $[Ag(C_2tBu)]_n$ (567 mg, 3.0 mmol) in acetone(20 mL). The reaction mixture was stirred for 24 h and then filtered. The solution was concentrated to a small volume and was left for crystallization. Colourless crystals of $[Ag_{14}(C_2tBu)_{12}][BF_4]_2$ (540 mg, 81%) were obtained in two crops; m.p. 187–190 °C. IR (KBr disc):$\tilde{\nu}$ = 2036 (vs) $cm^{-1}$ (C≡C). $^1H$ NMR (400 MHz, [D$_6$]-acetone, TMS): $\delta$ = 1.46 ppm. $C_{72}H_{108}Ag_{14}B_2F_8$ (2657.41): calcd. C 32.68, H 4.12; found C 32.58, H 4.04.

**Method 2:** *tert*-Butylacetylene (1.96 mL, 16.0 mmol) was added to $AgBF_4$ (389 mg, 2.0 mmol) in water (20 mL) in an ice bath. The mixture became turbid within a few minutes, and a white, floating precipitate formed. After stirring for 12 h, the white precipitate of $[Ag_{14}(C_2tBu)_{12}][BF_4]_2$ was filtered off and dried (224 mg, 59%); m.p. 190 °C. IR (KBr disc):$\tilde{\nu}$ = 2037 (vs) $cm^{-1}$ (C≡C). $C_{72}H_{108}Ag_{14}B_2F_8$ (2657.41): calcd.: Ag 56.62; found C 32.20, H 4.15, Ag 57.80, measured pH 1.79.

**Method 3:** Tetrafluoroboric acid, $HBF_4$ (0.103 mL, 0.46 mmol), was added to a suspension of $[Ag(C_2tBu)]_n$ (567 mg, 3.0 mmol) in acetone (25 mL) with stirring in a nitrogen atmosphere at room temperature. A clear solution was obtained within 10 min. The filtrate was concentrated to half volume. Addition of hexane (30 mL) effected the precipitation of colourless crystals of $[Ag_{14}(C_2tBu)_{12}][BF_4]_2$ (470 mg, 77%). IR (KBr disc):$\tilde{\nu}$ = 2037 (vs) $cm^{-1}$ (C≡C); identical in all respects to an authentic sample described above.

**Method 4:** Silver *tert*-butylacetylide (378 mg, 2.0 mmol) was added to solution of $\{[Ag_3(C_2tBu)_2][BF_4]\}_n$ (287 mg, 0.5 mmol) in acetone (25 mL). A clear solution was obtained within 15 min. Filtration and addition of hexane gave $[Ag_{14}(C_2tBu)_{12}][BF_4]_2$ (400 mg, 60%). IR (KBr disc): $\tilde{\nu}$ = 2037 (vs) $cm^{-1}$ (C≡C); $C_{72}H_{108}Ag_{14}B_2F_8$ (2657.41): found C 32.56, H 4.05; identical in all respects to an authentic sample described above.

**Reaction between *tert*-Butylacetylene and Silver Nitrate**

*tert*-Butylacetylene, $HC_2tBu$ (1.96 mL, 16.0 mmol), was added to $AgNO_3$ (340 mg, 2.0 mmol) in water (20 mL) in an ice bath. The mixture became turbid within a few minutes, and a white precipitate formed. After stirring for 12 h, the white precipitate of $[Ag_3(C_2tBu)_2(NO_3)]_n$ was filtered off, washed with water and dried (220 mg, 60%). IR (KBr disc): $\tilde{\nu}$ = 2023.5 (vs) $cm^{-1}$ (C≡C); ref.[9b] 2022 $cm^{-1}$. $C_{12}H_{18}Ag_3NO_3$ (547.88): calcd. C 26.31, H 3.31, N 2.56; Ag 59.06; found C 26.00, H 3.19, N 2.69, Ag 58.80.

**Crystal Data:** $[C_{72}H_{108}Ag_{14}B_2F_8]$ $M$ = 2657.38, triclinic, P$\bar{1}$, $a$ = 13.725(1), $b$ = 13.793(1), $c$ = 24.466(2) Å, $\alpha$ = 95.16(1), $\beta$ = 94.33(1), $\gamma$ = 106.99(1)°, $V$ = 4386.3(6) Å$^3$, $Z$ = 2, $D_{calcd.}$ = 2.012 g cm$^{-3}$, $\mu$ (Mo-$K_\alpha$) = 3.10 mm$^{-1}$, $T$ = 120(2) K, colourless block; 52607 measured reflections, 23128 independent ($R_{int}$ = 0.046 after semiempirical absorption correction), least-squares refinement of 924 parameters against $F^2$, $R(F)$ = 0.051 on 14969 independent reflections with $I>2\sigma(I)$, w$R(F^2)$ = 0.122 on all data. The structure contains two independent clusters, both at inversion centres. In one cluster, two Ag atoms are ordered, whereas twelve are disordered between two sets of positions in a 4:1 ratio (distances between alternative positions of the same atoms are 0.40 to 0.57 Å); six ethynyl ligands are disordered by a rotation around the quaternary C atom (which remains ordered), probably in concert with the disorder of the metal core. There is also rotational disorder of *t*Bu groups and monodentate $BF_4$ ligands. The second cluster is ordered, except for rotational disorder of two *t*Bu groups. CCDC-290250 contains the supplementary crystallographic data for this paper. These data can be obtained free of charge from The Cambridge Crystallographic Data Centre via www.ccdc.cam.ac.uk/data_request/cif.

## Acknowledgments

The authors are grateful to Research Centre, College of Science, King Saud University for financial support (Chem/1417/12). H. S. A. thanks King Abdul Aziz City for Science and Technology for financial support. Dr. Andrei S. Batsanov is thanked for helpful advice.

[1] R. Z. Nast, *Z. Naturforsch. Teil B* **1953**, *8*, 381.
[2] R. Nast, *Coord. Chem. Rev.* **1982**, *47*, 89.
[3] a) R. W. M ten Hoedt, J. G. Nolts, G. van Koten, A. L. Spek, *J. Chem. Soc., Dalton Trans.* **1978**, 1800; b) L. Naldini, F. Demartin, M. Manasero, M. Sansoni, G. Rassu, M. A. Zorodda, *J. Organomet. Chem.* **1985**, *279*, C42; c) O. M. Abu-Salah, M. I. Bruce, M. R. Churchill, B. G. De Boer, *J. Chem. Soc., Chem. Commun.* **1974**, 688; d) A. J. Carty, S. A. MacLaughlin, N. J. Taylor, *J. Am. Chem. Soc.* **1981**, *103*, 2456; e) J. Fornies, E. Lalinda, *J. Chem. Soc., Dalton Trans.* **1996**, 2587; f) D. M. P. Mingos, J. Yau, S. Menzer, D. I. Williams, *Angew. Chem.* **1995**,*107*, 2065; *Angew. Chem. Int. Ed. Engl.* **1995**, *34*, 1894; g) I. Ara, J. R. Berenguer, E. Eguizabal, J. Fornies, J. Gomez, E. Lalinde, *J. Organomet. Chem.* **2003**, *670*, 221; h) J. Diez, M. P. Gamasa, J. Gimeno, A. Aguire, S. Garcia-Granda, *Organometallics* **1991**, *10*, 380; i) M. P. Gamasa, J. Gimeno, E. Lastra, X. Solans, *J. Organomet. Chem.* **1988**, *346*, 277.
[4] a) M. I. Bruce, *Chem. Rev.* **1991**, *91*, 197; b) H. Lang, *Angew. Chem.* **1994**, *106*, 569; *Angew. Chem. Int. Ed. Engl.* **1994**, *33*, 547; c) S. Lotz, P. H. VamRooyen, R. Meyer, *Adv. Organomet. Chem.* **1995**, *37*, 219; d) H. Lang, K. Koher, S. Blaer, *Coord. Chem. Rev.* **1995**, *143*, 113; e) V. W.-W. Yam, K. K. W. Lo, K. M. Wong, *J. Organomet. Chem.* **1999**, *578*, 3; f) H. Lang, D. S. A. George, G. Rheinwald, *Coord. Chem. Rev.* **2000**, *206*, 101; g) H. Lang, A. Del Villar, *J. Organomet. Chem.* **2003**, *670*, 45.
[5] a) K. M.-C. Wong, C.-K. Hui, K.-L. Yu, V. W.-W. Yam, *Coord. Chem. Rev.* **2002**, *229*, 123, and references cited therein; b) V. W.-W. Yam, *J. Organomet. Chem.* **2004**, *689*, 1393.
[6] a) O. M. Abu-Salah, A. R. Al-Ohaly, C. B. Knobler, *J. Chem. Soc., Chem. Commun.* **1985**, 1502; b) O. M. Abu-Salah, A. R. Al-Ohaly, *J. Chem. Soc., Dalton Trans.* **1988**, 2297; c) O. M. Abu-Salah, A. R. A-Ohaly, Z. F. Mutter, *J. Organomet. Chem.* **1990**, *389*, 427; d) O. M. Abu-Salah, A. R. Al-Ohaly, Z. F. Mutter, *J. Organomet. Chem.* **1990**, *391*, 267; e) O. M. Abu-Salah, M. S. Hussain, E. O. Schlemper, *J. Chem. Soc., Chem. Commun.* **1988**, 212; f) O. M. Abu-Salah, *Polyhedron* **1992**, *11*, 951; g) M. Ul-Haque, W. Horne, O. M. Abu-Salah, *J. Crystallogr. Spec. Res.* **1992**, *22*, 421; h) K. A. Al-Farhan, O. M. Abu-Salah, M. Makhalalati, M. H. Ja'far, *Acta Crystallogr. Sect. C* **1995**, *51*, 1089; i) O. M. Abu-Salah, *J. Orgnomet. Chem.*

 © 2006 Wiley-VCH Verlag GmbH & Co. KGaA, Weinheim 

**1998**, *565*, 216; j) M. S. Hussain, M. Ul-Haque, O. M. Abu-Salah, *J. Clust. Sci.* **1996**, *7*, 168.
[7] a) O. M. Abu-Salah, C. B. Knobler, *J. Organomet. Chem.* **1986**, *302*, C10; b) O. M. Abu-Salah, *J. Organomet. Chem.* **1990**, *387*, 123.
[8] a) G. C. Guo, Q. J. Wang, G. D. Zhou, T. C. W. Mak, *J. Chem. Soc., Chem. Commun.* **1998**, 339; b) G. C. Guo, G. D. Zhou, T. C. W. Mak, *J. Am. Chem. Soc.* **1999**, *121*, 3136; c) X. L. Zhao, T. C. W. Mak, *Dalton Trans.* **2004**, 3212; d) X. L. Zhao, T. C. W. Mak, *Dalton Trans.* **2005**, 1865.
[9] a) D. Rais, J. Yau, D. M. P. Mingos, R. Vilar, A. J. P. White, D. J. Williams, *Angew. Chem.* **2001**, *113*, 3572; *Angew. Chem. Int. Ed.* **2001**, *40*, 3464; b) D. Rais, D. M. P. Mingos, R. Vilar, A. J. P. White, D. J. Williams, *J. Organomet. Chem.* **2002**, *652*, 87; c) D. M. P. Mingos, R. Vilar, D. Rais, *J. Organomet. Chem.* **2002**, *641*, 126.
[10] K. A. Al-Farhan, M. H. Ja'far, O. M. Abu-Salah, *J. Organomet. Chem.* **1999**, *579*, 59.
[11] a) G. E. Coates, C. Parkin, *J. Inorg. Nucl. Chem.* **1961**, *22*, 59; b) G. E. Coates, C. Parkin, *J. Chem. Soc.* **1962**, 3220.
[12] a) O. M. Abu-Salah, A. R. Al-Ohaly, *Inorg. Chim. Acta* **1983**, *77*, L159; b) O. M. Abu-Salah, *J. Organomet. Chem.* **1984**, *270*, C26; c) O. M. Abu-Salah, A. R. Al-Ohaly, H. A. Al-Qahtani, *Inorg. Chim. Acta* **1986**, *117*, L29.

Received: January 17, 2006
Published Online: May 3, 2006

 © 2006 Wiley-VCH Verlag GmbH & Co. KGaA, Weinheim 

DOI: 10.1002/ejic.200600055

# Copper(II) Complexes of the Tetraazamacrocyclic Tertiary Amide Ligand Alanyl-Cyclam

**Christian Schickaneder,[a] Frank W. Heinemann,[a] and Ralf Alsfasser*[b]**

**Keywords:** Copper / Cyclam / Bioinorganic chemistry / Electrophilic activation / Winkler–Dunitz parameters

Hydrogen bonding to the electrically neutral tertiary carboxamide nitrogen atom of peptidyl-prolyl groups is known to facilitate the C–N bond rotation during peptide and protein folding. Since metal complexes with nitrogen-coordinated tertiary amide ligands are formally analogous, they may be used to model this so-called electrophilic activation. In this paper we report on the synthesis of a monoacylated cyclam complex, [(Boc-Ala-cyclam)Cu]$(CF_3SO_3)_2$ (**8**; Boc: *tert*-butyloxycarbonyl, Ala: alanine, cyclam: 1,4,8,11-tetraazacyclotetradecane). It contains a fully $sp^3$-hybridized metal-bound amide nitrogen atom. The resonance is completely cancelled and the observed C–N distance of 147 pm is consistent with a single bond. These features are exceptional among Werner-type complexes and define the maximal possible electrophilic distortion of an amide bond.

(© Wiley-VCH Verlag GmbH & Co. KGaA, 69451 Weinheim, Germany, 2006)

## Introduction

The activation of tertiary carboxamides towards hydrolytic cleavage and C–N bond rotation is a topic of considerable interest. Two catchwords are the hydrolysis of β-lactam antibiotics[1] and the *cis*-*trans* isomerization about peptidyl–prolyl bonds in proteins.[2] The latter is often the slow step during protein folding and supposed to play an important role as a functional switch in different processes such as enzymatic substrate recognition[3] or neurodegenerative protein aggregation.[4] Isomerases, PPIases, are known to facilitate the amide rotation. How exactly they operate is not known, although different means to lower the rotational barrier have been discussed.[5] Particularly interesting for coordination chemists is a motif observed in the catalytic centre of cyclophilines,[6] and in histidyl peptides:[7] hydrogen bonding to the amide nitrogen atom is proposed to stabilize the pyramidal transition state structure at the nitrogen atom. This is formally analogous to the coordination of a metal ion as it has been proposed to explain the effect of siver(I) ions on the rotational barrier of dimethylacetamide.[8] An illustration of an arginine hydrogen bond in comparison with a coordinated metal center is shown in Scheme 1.

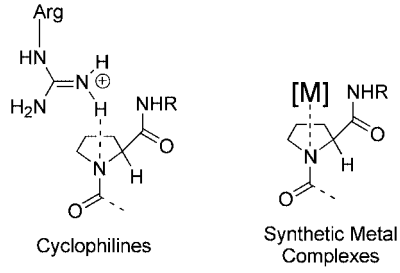


Scheme 1. Electrophilic activation of a tertiary amide group; hydrogen bonding in peptides and proteins (left), or metal coordination (right).

Based on this analogy, Lectka and colleagues have suggested that metal complexes could be developed into synthetic catalysts to trigger biological proline switches.[9] This perspective is highly interesting but suffers from the lack of information on coordination complexes containing nitrogen-bound tertiary carboxamide ligands. We have therefore started a systematic study of these unusual compounds.[10] Here we describe the synthesis and structural properties of copper(II) complexes with macrocyclic alanyl-cyclam ligands. Our aim was to place a metal ion in close proximity to an amide nitrogen atom in order to achieve full pyramidalization and complete cancellation of resonance. This limiting case is an important missing piece required for a quanitative understanding of the electrophilic amide activation.

[a] Institut für Anorganische Chemie, Universität Erlangen-Nürnberg,
Egerlandstr. 1, 91058 Erlangen, Germany
[b] Institut für Anorganische Chemie, Universität Freiburg,
Albertstr. 21, 79104 Freiburg, Germany
Fax: +49-761-2036012
E-mail: ralf.alsfasser@ac.uni-freiburg.de

 © 2006 Wiley-VCH Verlag GmbH & Co. KGaA, Weinheim 

## Results and Discussion

### Synthesis

Our first aim was to prepare a cyclam ligand in which one of the amine functions is converted into a tertiary amide. Prior to monoacylation, three of the cyclam nitrogen atoms had to be protected. Scheme 2 shows the synthesis of triple-protected cyclam. We have synthesized the tris(*tert*-butoxycarbonyl) (Boc) and tris(benzoxycarbonyl) (Cbz) derivatives **1** and **2** according to a slightly modified route reported by Brandes et al.[11] The yields of 35–50% after flash column chromatography on silica gel were moderate in both cases. Coupling with *N*-*tert*-butoxycarbonyl-(*S*)-alanine [Boc-(*S*)-Ala-OH] was achieved by the well-established DCC/HOBt (DCC = dicyclohexylcarbodiimide, HOBt = *N*-hydroxybenzotriazole) method.[12] We have applied this method earlier to the synthesis of ruthenium-modified 1,4,7,10-tetraazacyclodecane (cyclen) ligands.[13] The isolated yields were moderate in the case of Boc-(*S*)-Ala-cyclam-$Boc_3$ (**3**, 70%) and low in the case of Boc-(*S*)-Ala-cyclam-$Cbz_3$ (**4**, 26%). The structures and the synthesis of both compounds are shown in Scheme 2.

Acid deprotection of Boc-(*S*)-Ala-cyclam-$Boc_3$ was achieved with aqueous HCl in dioxane.[13] Scheme 3 shows the structure of the tris(hydrochloride) salt **5** which was characterized by an X-ray structure analysis (Figure 1). In order to facilitate binding of a copper(II) ion inside the macrocyclic ring and to enhance the solubility of the ligand in organic aprotic solvents, we attempted to remove most of the HCl. An interesting and revealing result was obtained with a ligand sample obtained by passing an $NH_3$ stream through a suspension of **5** in chloroform. The soluble product was isolated and reacted with copper(II) triflate in acetonitrile. Unfortunately, we were not able to obtain single crystals of the complex formed. However, its IR spectrum shows a shift of the carbonyl band from 1625 $cm^{-1}$ to 1592 $cm^{-1}$. This clearly indicates that the metal ion does not bind to the amide nitrogen atom which would cause a high energy shift due to the reduced amide resonance.[14] We propose the structure **6** shown in Scheme 3 with a bidentate ethylenediammine part of the cyclam ligand and two chloride ions coordinated to the copper(II) ion. This is based on the analogy to observations in related acylated triazacyclononane complexes by Houser et al.[15] and supported by C,H,N,S elemental analysis data. The shift of the carbonyl IR band indicates that the amide oxygen atom may also coordinate.

We concluded from the results summarized in Scheme 3 that complete removal of HCl from the ligand **5** is a prerequisite for the coordination of the tertiary amide nitrogen atom in copper complexes. Since this required a strong base, NaOH in dichloromethane was applied to prepare the acid-free ligand. Subsequent reaction with $Cu(CF_3SO_3)_2$ in acetonitrile and layering with diethyl ether yielded a violet material with elemental analysis data indicating the constitution $[(Ala\text{-}cyclam)(H_2O)Cu](CF_3SO_3)_2 \cdot 0.25Et_2O$. There is no evidence for the presence of chloride in the sample and an IR band at 1756 $cm^{-1}$ is consistent with a nitrogen-bound amide ligand. However, a second IR band at 1592 $cm^{-1}$ with a shoulder at 1649 $cm^{-1}$ indicates that a mixture of N- and O-coordinated tertiary amide complexes is present and we were not able to separate these species. It is not yet clear whether trace impurities of chloride or an unknown coordination mode involving the free amine function of the amino acid moiety is responsible for this behaviour.

Our failure to obtain well-defined N-coordinated amide complexes from the protonated ligand **5** reflects the difficulties involved in the synthesis of such compounds. Even though the cyclam framework should strongly favour coordination of a copper(II) ion within the ring, the system avo-

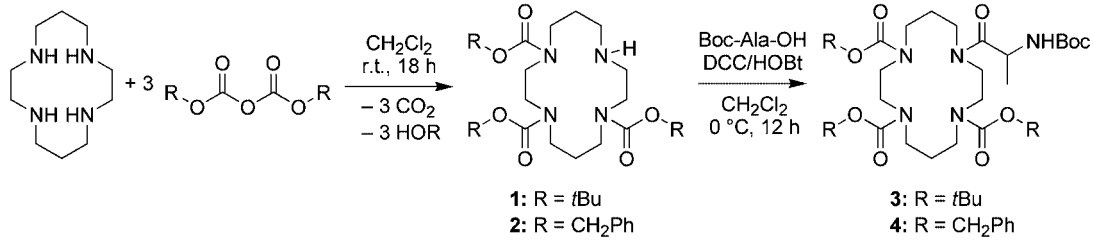


Scheme 2. Synthesis of the Boc- and Cbz-protected Boc-(*S*)-alanylcyclam derivatives Boc-(*S*)-Ala-cyclam-$Boc_3$ (**3**) and Boc-(*S*)-Ala-cyclam-$Cbz_3$ (**4**).

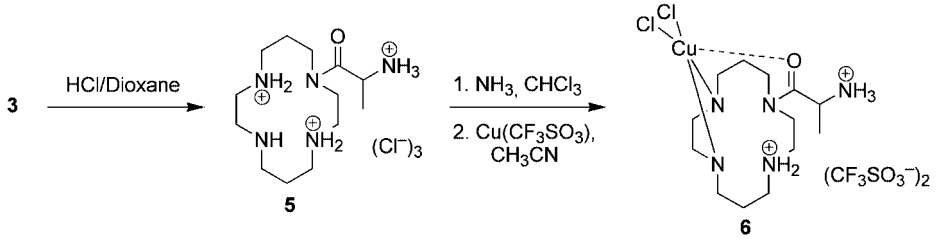


Scheme 3. Acid deprotection of Boc-(*S*)-Ala-cyclam-$Boc_3$ (**3**) and the reaction of Ala-cyclam·3HCl (**5**) with copper(II) triflate.

 © 2006 Wiley-VCH Verlag GmbH & Co. KGaA, Weinheim 

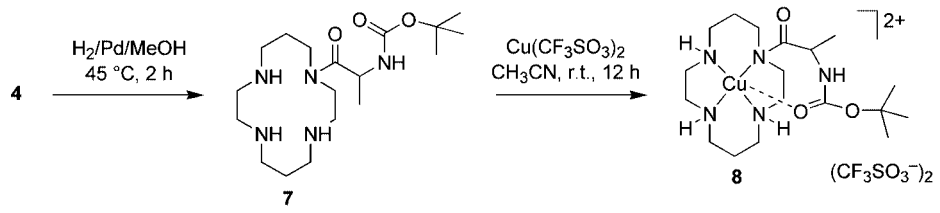


Scheme 4. Hydrogenation of the Cbz-protected compound **4** to the free ligand **7** and synthesis of the copper complex [{Boc-(*S*)-Ala-cyclam}Cu]$(CF_3SO_3^-)_2$ (**8**).

ids coordination of the weak amide donor. It is therefore not surprising that amide nitrogen coordination was unknown before the 1990s and has been categorically ruled out in several important older articles on amide complexes.[16] We reasoned that in our case a protecting group would be preferable which can be removed without protonation of the ligand. The Cbz function turned out to be a good choice.[17] It is cleaved off by hydrogenation in the presence of a palladium catalyst in methanol. This and the following reaction of Boc-(*S*)-Ala-cyclam (**7**) with $Cu(CF_3SO_3)_2$ is shown in Scheme 4. The copper complex [{Boc-(*S*)-Ala-cyclam}Cu]$(CF_3SO_3)_2$ (**8**) was obtained with a yield of 74%. Its composition was confirmed by C,H,N,S elemental analysis and FAB mass spectrometry. The IR spectrum shows two bands at 1742 $cm^{-1}$ for the amide function and 1658 $cm^{-1}$ for the Boc protecting group. The blue shift of the amide band is in excellent agreement with our data on a $Cu(CF_3SO_3)_2$ of dipicolyl-*N*-boc-glycylamide[10a] and confirms amide nitrogen coordination in the bulk sample. An X-ray structure analysis of the complex is discussed below.

### X-ray Structure Analyses

Single crystals were obtained from the ligand tris(hydrochloride) salt **5** and the copper complex **8**. An ORTEP plot representing the structure of the cation in **5** is shown in Figure 1. All hydrogen atoms were localized in the electron density map. The alanyl nitrogen atom N5 and the two cyclam atoms N2 and N4 are positively charged. Hydrogen bonds between those ammonium functions and the chloride ions loosely connect individual molecules in a three-dimensional network. Most important for our study is the geometry of the tertiary amide function. Deviations from planarity are most conveniently described by two quantitative parameters defined by Winkler and Dunitz.[18] One is the twist angle $\tau$ between the C1–C10 and the C12–O1 axes which ranges from 0° to 90°. The second is the pyramidalization $\chi_N$ at the nitrogen atom. It varies between 0° for a planar environment and ca. 60° for a fully pyramidal geometry. We will later discuss how the binding of metal ions deplanarize an amide group and how this activation affects the C–N bond length. In this context, ligand structures are useful for comparison. The C11–N1 bond length in **5** of 135.7 pm and the small twist angle $\tau$ = 9.3° are typical for an undistorted amide function. Interestingly, a significant pyramidalization at the nitrogen atom of $\chi_N$ = 17.7° is observed. This is larger than in related dipicolylamide derivatives[10b] although not unusual for carboxamides. Large deviations from planarity are possible because the energy barrier for out-of-plane wagging is rather low.[19] An examination of amide structures by Gilli et al. reveals that $\chi_N$ can reach values of over 20° without a significant elongation of the C–N bond.[20] Much effort of organic chemists focused on the effects of distortion on non-planar amides which model different stages during the C–N-bond rotation.[21] It was shown that geometric strain can enforce significant twisting and pyramidalization. However, the effects on the C–N bond lengths are generally rather small and the variety of different compounds having the amide group as a part of an acyclic, cyclic, or polycyclic structure make quantitative correlations difficult. An examination of different structures leads to the conclusion that the amide C–N bond is only affected when $\chi_N$ reaches values of ca. 30°. This has not been specifically addressed by other authors but it is interesting in the context of our observations on metal complexes. We will show below that the latter provide a better basis for quantitative structure correlations since their amide groups are not forced into a rigid structure which may obscure changes in the C–N bond length. A key compound in our studies is the copper complex **8** which contains a fully pyramidalized amide nitrogen atom.

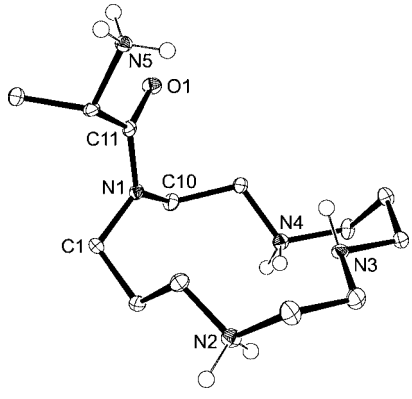


Figure 1. ORTEP plot at 50% probability of the cation Ala-cyclam·$3H^+$ (**5**) (hydrogen atoms except for NH are omitted for clarity); selected bond lengths [pm], angles [°], $\tau$ [°], and $\chi_N$ [°]: C11–N1 135.7(2), C11–O1 123.3(2); C1–N1–C10 118.1(2), C1–N1–C11 124.3(2), C10–N1–C11 115.3(2); $\tau$ = 9.3; $\chi_N$ = 17.7.

Compound **8** crystallizes in the acentric space group $P2_1$ with two independent complexes **A** and **B** in the asymmetric unit. They are depicted in Figure 2. In complex **8A** the copper ion is bound in the center of the cyclam ligand which

 © 2006 Wiley-VCH Verlag GmbH & Co. KGaA, Weinheim 

coordinates in the typical *trans*-III mode[22] with one five-membered chelate ring in the δ, one in the λ, and both six-membered rings in the chair configuration. The Boc protecting group is weakly bound at a distance Cu1–O2 of 248.8 pm and a triflate ion is positioned in the apical position of a distorted octahedron with a long contact of Cu1–O63 of 278.9 pm. The second complex **8B** also has a *trans*-III type cyclam ligand but one of the six-membered chelate rings is in the rare boat form.[23] As a consequence, the proton H20b of the central methylene group is only 270.5 pm away from the copper centre and there is no room for an apical triflate ion. The coordinated Boc group compensates for the lack of σ-donation and binds at a distance of Cu2–O5 of 230.5 pm, which is 13.3 pm shorter than the corresponding contact in **8A**. However, the coordinated tertiary amide function is not much affected by these differences.

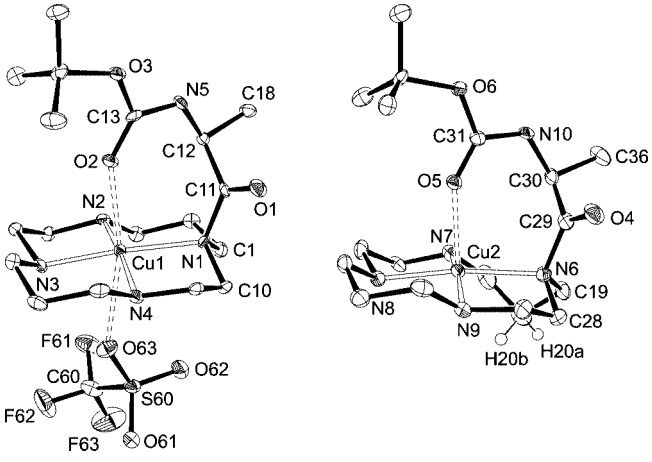


Figure 2. ORTEP plots at 50% probability of the two complexes **A** and **B** observed in the structure of [{Boc-(*S*)-Ala-cyclam}Cu]$(CF_3SO_3)_2$ (**8**) (hydrogen atoms except for those located at C20 in complex **B**, and the three non-coordinating triflate ions are omitted for clarity); selected distances [pm], angles [°], $\tau$ [°], and $\chi_N$ [°] of **A**: Cu1–N1 212.7(3), Cu1–N2 201.2(3), Cu1–N3 202.1(3), Cu1–N4 200.5(3), Cu1–O2 248.8(2), Cu1–O63 278.9, C11–N1 146.9(4), C11–O1 120.2(4); N1–Cu1–N2 95.3(2), N1–Cu1–N3 175.7(2), N1–Cu1–N4 86.7(2), N1–Cu1–O2 92.4(2), N2–Cu1–N3 86.7(2), N2–Cu1–N4 170.3(2), N2–Cu1–O2 92.7(2), N3–Cu1–N4 90.7(2), N3–Cu1–O2 91.4(2), N4–Cu1–O2 96.7(2), Cu1–N1–C1 112.4(2), Cu1–N1–C10 100.6(2), Cu1–N1–C11 112.8(2), C1–N1–C10 109.8(3), C1–N1–C11 112.8(2), C10–N1–C11 109.3(2); $\tau$ = 35.8; $\chi_N$ = 58.5; selected distances [pm], angles [°], $\tau$ [°], and $\chi_N$ [°] of **B**: Cu2–N6 214.7(3), Cu2–N7 203.1(3), Cu2–N8 200.9(3), Cu2–N9 202.1(3), Cu2–O5 230.5(2), Cu2–H20b 270.5, C29–N6 146.2(5), C29–O4 119.9(5); N6–Cu2–N7 96.3(2), N6–Cu2–N8 172.02(2), N6–Cu2–N9 85.3(2), N6–Cu2–O5 92.2(2), N7–Cu2–N8 85.5(2), N7–Cu2–N9 165.7(2), N7–Cu2–O5 97.3(2), N8–Cu2–N9 91.1(2), N8–Cu2–O5 93.3.4(2), N9–Cu–O5 96.8(2), Cu2–N6–C19 112.5(2), Cu2–N6–C28 102.6(2), Cu2–N6–C29 109.2(2), C19–N6–C28 110.4(3), C19–N6–C29 110.9(3), C28–N6–C29 111.1(2); $\tau$ = 30.6; $\chi_N$ = 56.9.

The stereochemistry of the amino acid part is in both cases (*S*) at the stereogenic α-carbon atom and (*Rp*) with respect to the chiral plane defined by the amide function. This implies that the methyl group is *exo* with respect to the seven-membered chelate ring formed by the coordinating Boc group and is analogous to the situation in a cadmium(II) complex of dipicolyl-Boc-alanylamide.[10a] The Cu–N(amide) distances (**8A**: 212.7 pm; **8B**: 214.7) are not much longer than the contacts between the copper ion and the secondary amine group which have typical values of 200–203 pm. A comparison with the few known copper(II) complexes with N-coordinated tertiary amide ligands shows that the Cu–N(amide) bond in **8** is unusually short. A recently published diisopropyl-triazacyclononane acetamide copper(II) chloride complex by Watkinson et al. has a Cu–N distance of 251.1 pm[24] and a paper by Schröder et al. reports on a related triazacyclononane derivative with a distance of 261.1 pm.[25] The closest contact observed in a dipicolylamide derivative is 216.4 pm in a copper(II) triflate complex from our group.[10c] The short Cu–N(amide) distance in **8** corresponds to a fully pyramidalized nitrogen atom as is evident from the pyramidalization parameter $\chi_N$ of almost 60° (**8A**: 58.5°; **8B**: 56.9°). Again, these values are exceptional in that they are the highest observed in Werner-type complexes to date.

In accord with this finding the C–N distance of 146 pm is typical for a single bond (147 pm[26]) and indicates that the amide resonance[27] is completely cancelled. It is interesting to compare this result with the situation in Schröder's complex with its long Cu–N(amide) distance of 261.1 pm which is significantly larger than the sum of the ionic radii of a six-coordinate $Cu^{2+}$ ion (87 pm) and the van der Waals radius of a nitrogen atom (160 pm).[26] This weak electrostatic interaction suffices to induce a significant pyramidalization at the nitrogen atom ($\chi_N$ = 30°), whereas the C–N distance of 135.7 pm is typical for an undistorted organic carboxamide. Further support for this interpretation is provided by Schindler et al.[28] who described the pyramidalization of a secondary amide group located 282.7 pm above the copper(II) ion the apical position of a square-pyramidal complex. These data are very important and confirm that with our new complex **8** Werner-type nitrogen-coordinated tertiary carboxamide complexes now span the whole range of electrophilic amide activation.

## Conclusions

With the crystallographic characterization of **8**, we have shown that forcing a metal center into a macrocyclic cyclam ring with a neutral amide N-donor produces a completely non-resonant tertiary carboxamide. The complex defines an upper limit for nitrogen pyramidalization and C–N bond elongation achievable by purely electrophilic activation without geometric strain. In this respect, it complements the generation of a purely organic amino ketone in Kirby's most twisted amide, 3,5,7-trimethyl-1-azaadamantan-2-one.[29]

## Experimental Section

**General Methods:** Spectra were recorded with the following instruments: IR: Mattson Polaris FT IR. UV/Vis: Varian Cary 1G spectrophotomer. $^1H$ and $^{13}C$ NMR: Bruker Avance DPX 300. All chemical shifts are referenced to TMS ($CDCl_3$) or TSP ($D_2O$) as

 © 2006 Wiley-VCH Verlag GmbH & Co. KGaA, Weinheim 

internal standards, with high frequency shifts recorded as positive. MS: Varian MAT 212 (FD, FAB) and Micromass ZabSpec (FAB) mass spectrometer. Elemental analysis: Carlo Erba Elemental Analyser 1106 (C,H,N), and Carlo Erba Elemental Analyser 1108 (C,H,N,S). All reactions except for the syntheses of cyclam-$Boc_3$ (**1**) and cyclam-$Cbz_3$ (**2**) were carried out in absolute solvents under dry nitrogen. The subsequent workup was performed under ambient laboratory conditions unless stated otherwise. The synthesis of cylam-$Boc_3$ is a slight modification of a literature procedure.[11] Absolute solvents ($CH_2Cl_2$, $Et_2O$, $CH_3CN$) were purchased from Fluka, stored under nitrogen and used without further purification. All other chemicals and deuterated solvents were obtained from Aldrich.

**Syntheses**

**Cyclam-$Boc_3$ (1):** A solution of di-*tert*-butyl pyrocarbonate ($Boc_2O$, 2.72 g, 12.5 mmol) in 150 mL of $CH_2Cl_2$ was added dropwise at room temperature over a period of 6 h to a stirred solution of cyclam (1.00 g, 5.00 mmol) in 300 mL of $CH_2Cl_2$. Stirring was continued for 12 h and the solvent stripped by rotary evaporation. The oily residue was dissolved in a minimum amount of diethyl ether. Rapid stripping of all solvent and drying under vacuum yielded a pale-yellow foam which was re-dissolved in $CH_2Cl_2$/$CH_3OH$ (95:5) and purified by flash column chromatography on silica; using the solvent as the eluent yielded 1.08 g (2.13 mmol, 51.1%) of cyclam-$Boc_3$ as a colourless, hygroscopic solid. FD-MS [$CHCl_3$; $C_{25}H_{48}N_4O_6$ (500.68)]: *m*/*z* = 501 [$M^+$]. $^1$H NMR ($CDCl_3$): $\delta$ = 1.45 (s, 27 H, Boc), 1.70 (m, 2 H, cyclam), 1.92 (m, 2 H, cyclam), 2.61 (t, 2 H, cyclam), 2.78 (t, 2 H, cyclam), 3.27–3.39 (m, 12 H, cyclam) ppm.

**Boc-(*S*)-Ala-cyclam-$Boc_3$ (3):** Boc-Ala-OH (1.02 g, 5.40 mmol), **1** (2.45 g, 4.90 mmol), *N*-hydroxybenzotriazole (0.71 g, 5.22 mmol), and $NEt_3$ (1.41 mL, 9.98 mmol) were dissolved in 300 mL of $CH_2Cl_2$ and the mixture was stirred with cooling at 0 °C. Dicyclohexylcarbodiimide (1.76 g, 8.47 mmol) in 20 mL of $CH_2Cl_2$ was added in one portion. The solution was warmed slowly to room temperature after which stirring was continued for 12 h. The resulting mixture was filtered and the volume of the filtrate was reduced to 1/2 by rotary evaporation. Filtration was repeated after storage at –18 °C overnight. The filtrate was washed 3 times with aqueous 5% $NaHCO_3$ and 3 times with saturated aqueous NaCl, dried with solid $MgSO_4$ and filtered. All solvent was removed by rotary evaporation and the residue purified by flash column chromatography on silica gel using $CH_2Cl_2$/$CH_3OH$ (95:5) as the eluent. All solvent was removed by rotary evaporation and the solid residue dissolved in a minimum amount of diethyl ether. Rapid stripping of the solvent and drying under vacuum yielded 2.42 g (3.60 mmol, 73.5%) of **3** as a colourless hygroscopic solid. $C_{33}H_{61}N_5O_9$·0.33$H_2O$ (671.87+6.00): calcd. C 58.47, H 9.17, N 10.33; found C 58.65, H 10.59, N 10.33. FD-MS ($CHCl_3$): *m*/*z* = 672 [$M^+$]. $^1$H NMR ($CDCl_3$): $\delta$ = 1.31 (t, 3 H, $^{\beta}CH_3$), 1.45 (m, 36 H, Boc), 1.74 (m, 4 H, cyclam), 3.14–3.69 (m, 16 H, cyclam), 4.56 (m, 1 H, $^{\alpha}$CH), 5.19–5.50 (m, 1 H, NH) ppm.

**(*S*)-Ala-cyclam·3HCl (5):** Compound **3** (2.42 g, 3.60 mmol) was treated with 15 mL of a cold 4 N HCl/dioxane solution with stirring at 0 °C. Stirring was continued without further cooling for 12 h. The product Boc-Ala-cyclam·3HCl·4$H_2O$ formed 1.36 g (3.00 mmol, 83.4%) of a colourless precipitate which was collected on a glass filter funnel, washed with hot ethanol (3 × 50 mL) and diethyl ether (3 × 20 mL), and dried under vacuum. $C_{13}H_{29}N_5O$·3HCl·4$H_2O$ (452.79): calcd. C 34.45, H 8.83, N 15.46; found C 34.39, H 9.15, N 15.29. $^1$H NMR ($D_2O$): $\delta$ = 1.46 (d, 3 H, $^{\beta}CH_3$), 2.22 (m, 4 H, cyclam), 2.92–4.00 (m, 16 H, cyclam), 4.40 (q, 1 H, $^{\alpha}$CH) ppm. IR (KBr): $\tilde{\nu}$ = 3178 ($NH_3^+$), 1646 (amide) $cm^{-1}$.

**[(Boc-Ala-cyclam$H_2$)$CuCl_2$]($CF_3SO_3$)$_2$ (6):** Tris(hydrochloride) salt **5** (2.51 g, 6.02 mmol) was suspended in 100 mL of $CHCl_3$ and the solution cooled to 0 °C. A slow stream of $NH_3$ gas was passed through the reaction mixture. After 1.5 h, the mixture was warmed to room temperature. Precipitated ammonium chloride was filtered off, the filtrate concentrated to dryness and the residue treated with 50 mL of $CH_2Cl_2$. Insoluble material was removed by filtration and all solvent by rotary evaporation. Drying under vacuum afforded a colourless resin (1.62 g). This compound (1.31 g) was dissolved in 200 mL of $CH_3CN$. A solution of Cu($CF_3SO_3$)$_2$ in 150 mL of $CH_3CN$ was added dropwise with stirring over a period of 1 h. The reaction mixture turned deep blue. Stirring was continued at room temperature for 12 h. The solution was concentrated to dryness and the residue re-dissolved in a minimum amount of $CH_3CN$. Layering with diethyl ether and storage at –18 °C overnight afforded the product **6** as a blue precipitate which was isolated by filtration and dried under vacuum [2.46 g, 3.49 mmol, 72.2% based on Cu($CF_3SO_3$)$_2$]. $C_{15}H_{31}Cl_2CuF_6N_5O_7S_2$ (706.01): calcd. C 25.52, H 4.43, N 9.92, S 9.08; found C 25.42, H 4.34, N 9.63, S 8.92. IR (KBr): $\tilde{\nu}$ = 3244 (R–$NH_3^+$), 1592 (amide) $cm^{-1}$. UV/Vis ($CH_3CN$): $\lambda_{max}$ (lg$\varepsilon$) = 619 (2.17 $M^{-1}cm^{-1}$) nm. FAB-MS (nitrobenzyl alcohol): *m*/*z* = 483 [M – 2 HCl – $CF_3SO_3$]$^+$.

**[(Ala-cyclam)($H_2O$)Cu]($CF_3SO_3$)$_2$·0.25$Et_2O$:** A mixture of **5** (450 mg, 1.08 mmol) and excess $NaOH^{(s)}$ was suspended in ca. 50 mL of $CH_2Cl_2$ at room temperature. The suspension was stirred for 24 h. Insoluble material was removed by filtration and the clear filtrate concentrated to dryness. Drying under vacuum afforded the free base as a colourless oily residue. It was dissolved in 50 mL of $CH_3CN$ and Cu($CF_3SO_3$)$_2$ (340 mg, 0.94 mmol) was added in small portions to the stirred solution. Stirring was continued for 12 h. The mixture was filtered and the clear blue filtrate layered with $Et_2O$. Upon storage at –18 °C the product precipitated as a violet oily residue. Separation and drying under vacuum afforded the product (446 mg, 0.73 mmol, 77.7%) as a violet solid. FD-MS ($CH_3CN$): *m*/*z* = 484 [MH – $CF_3SO_3$]$^+$. $C_{15}H_{29}CuF_6N_5O_7S_2$·1$H_2O$·0.25$Et_2O$ (651.10+18.53): calcd. C 28.70, H 5.04, N 10.46; found C 28.60, H 4.78, N 10.17. IR (KBr): $\tilde{\nu}$ = 3342, 3226 ($NH_3^+$), 1756, 1649 (shoulder), 1592 $cm^{-1}$.

**cyclam-$Cbz_3$ (2):** A solution of dibenzyl pyrocarbonate ($Cbz_2O$, 7.20 g, 25.00 mmol) in 500 mL of $CH_2Cl_2$ was added dropwise at room temperature over a period of 6 h to a stirred solution of cyclam (2.00 g, 10.00 mmol) in 200 mL of $CH_2Cl_2$. Stirring was continued for 12 h and the solvent stripped by rotary evaporation. The oily residue was dissolved in a minimum amount of dichloromethane and the pale yellow solution was filtered through silica gel. The filtrate which contained benzyl alcohol was discarded and the compound was eluted with methanol. All solvent was removed by rotary evaporation and drying under vacuum. The residue was re-dissolved in a minimum amount of $CH_2Cl_2$/$CH_3OH$ (98:2) and purified by flash column chromatography on silica using the solvent as the eluent. The colourless, oily compound was repeatedly treated with small quantities of diethyl ether which was stripped under vacuum until formation of a foam; 1.80 g (2.99 mmol, 35.9%) of the product **2** was obtained as a highly hygroscopic, colourless resin. FD-MS [$CHCl_3$; $C_{34}H_{42}N_4O_6$ (602.72)]: *m*/*z* = 603 [$M^+$]. $^1$H NMR ($CDCl_3$): $\delta$ = 1.64 (m, 2 H, cyclam), 1.93 (m, 2 H, cyclam), 2.55 (m, 2 H, cyclam), 2.76 (m, 2 H, cyclam), 3.10–3.52 (m, 12 H, cyclam), 5.03 (s, 2 H, Ph-$CH_2$), 5.12 (s, 4 H, Ph-$CH_2$), 7.33 (m, 15 H, $C_6H_5$) ppm.

**Boc-Ala-cyclam-$Z_3$ (4):** Boc-Ala-OH (0.62 g, 3.28 mmol), **2** (1.79 g, 2.97 mmol), *N*-hydroxybenzotriazole (0.43 mg, 3.17 mmol), and

 © 2006 Wiley-VCH Verlag GmbH & Co. KGaA, Weinheim 

$NEt_3$ (0.85 mL, 6.06 mmol) were dissolved in 150 mL of $CH_2Cl_2$ and the mixture stirred with cooling at 0 °C. Dicyclohexylcarbodiimide (1.07 g, 5.14 mmol) in 10 mL of $CH_2Cl_2$ was added in one portion. The solution was warmed slowly to room temperature after which stirring was continued for 12 h. The resulting mixture was filtered and the volume of the filtrate was reduced to 1/2 by rotary evaporation. Filtration was repeated after storage at –18 °C overnight. The filtrate was washed 3 times with aqueous 5% $NaHCO_3$ and 3 times with saturated aqueous NaCl, dried with solid $MgSO_4$ and filtered. All solvent was removed by rotary evaporation and the residue purified by flash column chromatography on silica gel using $CH_2Cl_2/CH_3OH$ (95:5) as eluent. All solvent was removed by rotary evaporation and the solid residue dissolved in a minimum diethyl ether. Drying under vacuum yielded 595 mg (0.77 mmol, 25.9%) of **4** as a colourless hygroscopic solid. $C_{42}H_{55}N_5O_9 \cdot 0.5Et_2O$ (773.91+37.06): calcd. C 65.16, H 7.46, N 8.64; found C 65.46, H 8.27, N 8.90. FD-MS ($CHCl_3$): *m*/*z* = 774 [$M^+$]. $^1H$ NMR ($CDCl_3$): $\delta$ = 1.26 (m, 3 H, $^{\beta}CH_3$), 1.43 (2 s, 9 H, Boc), 1.71 (m, 4 H, cyclam), 3.05–3.75 (m, 16 H, cyclam), 4.45 (m, 1 H, $^{\alpha}CH$), 4.86–5.19 (m, 7 H, Ph-$CH_2$ + NH), 7.13–7.45 (m, 15 H, $C_6H_5$) ppm.

**Boc-Ala-cyclam (7):** A solution of **2** (315 mg, 0.41 mmol) in absolute methanol was transferred to a flask containing catalytic amounts of Pd/C and equipped with a hydrogen inlet, a reflux condenser, a magnetic stir bar, and a mineral oil bubbler. Nitrogen was passed over the suspension for 15 min. The mixture was heated to 45 °C in an oil bath and a slow stream of $H_2$ was applied for 2 h. The flask was then flushed with $N_2$ and the suspension filtered through Celite at room temperature. Rotary evaporation of the solvent and drying under vacuum yielded 116 mg (0.31 mmol, 76.0%) of **4** as a hygroscopic resin. It was characterized by $^1H$ NMR spectroscopy and used without further purification. $^1H$ NMR ($CDCl_3$): $\delta$ = 1.29 (m, 3 H, $^{\beta}CH_3$), 1.42 (s, 9 H, Boc), 1.59–2.00 (m, 6 H, cyclam), 2.45–3.12 (m, 10 H, cyclam), 3.19–3.80 (m, 4 H, cyclam), 4.59 (m, 1 H, $^{\alpha}CH$ ), 5.41 (m, 1 H, NH) ppm.

**[(Boc-Ala-cyclam)Cu]($CF_3SO_3$)$_2$ (8):** Boc-Ala-cyclam (116 mg, 0.31 mmol) was dissolved in 25 mL of absolute acetonitrile and a solution of anhydrous $Cu(CF_3SO_3)_2$ (112 mg, 0.31 mmol) in 25 mL of absolute acetonitrile was added dropwise with stirring over a period of 30 min. The blue solution gradually turned deep purple. Stirring was continued at room temperature overnight and all solvent removed by evaporation under vacuum. The crude product was re-dissolved in $CH_2Cl_2$ and insoluble materials were removed by filtration. Drying of the filtrate under vacuum yielded the product as a deep purple solid; yield 209 mg (0.29 mmol, 92.0%). $C_{20}H_{37}CuF_6N_5O_9S_2 \cdot 2CH_2Cl_2$ (903.11): calcd. C 29.26, H 4.58, N 7.76; found C 29.34, H 4.60, N 8.05. IR (KBr): $\tilde{\nu}$ = 1742 (amide); 1658 (Boc) $cm^{-1}$. UV/Vis ($CH_3CN$): $\lambda_{max}$ (lg$\varepsilon$) = 540.4 (1.89 $M^{-1}cm^{-1}$) nm. FAB-MS (nitrobenzyl alcohol): *m*/*z* = 583 [M – $CF_3SO_3$]$^+$.

**X-ray Structure Analyses:** Colorless blocks of Ala-Cyclam·3HCl (**5**) were obtained by precipitation from diethyl ether/ethanol and recrystallization of the solid from $D_2O$ upon slow evaporation of the solvent at room temperature. The copper complex salt **8**·1/8$H_2O$ crystallized upon slow concentration of a dichloromethane/acetonitrile solution. Details of the X-ray structure analyses are summarized in Table 1. Suitable single crystals were embedded in protective perfluoropolyether oil and data were collected at 100 K with a Bruker-Nonius KappaCCD diffractometer using Mo-$K_\alpha$ radiation ($\lambda$ = 0.71073 Å, graphite monochromator). Images were taken using $\varphi$- and $\omega$-rotations with a rotation angle of 2.0° for **5** and 1.8° for **8**·1/8$H_2O$. An irradiation time of 80 s per frame was applied for **5** and 432 s per frame for **8**·1/8$H_2O$. Lorentz and polarization corrections were applied. Semi-empirical absorption corrections based on equivalent reflections were made using the program SADABS.[30] All structures were solved by direct methods and refined using full-matrix least-squares procedures on $F^2$ using the program package SHELXTL NT 6.12.[31] All non-hydrogen atoms were refined anisotropically. One of the triflate ions in **8**·1/8$H_2O$ was disordered. Two positions with occupation factors of 0.75 and 0.25 were refined. All hydrogen atoms in **5** were located in the difference Fourier map and refined with isotropic displacement parameters being 1.2 or 1.5 times *U*(eq) of the corresponding C or N atom. All hydrogen atoms in **8**·1/8$H_2O$ (except for those of the water which were located in the difference Fourier map and not refined) were geometrically positioned with isotropic displacement parameters being 1.2 or 1.5 times *U*(eq) of the corresponding C, N or O atom. CCDC-262792 (**5**) and -262793 (**8**·1/8$H_2O$) contain the supplementary crystallographic data for this paper. These data can be obtained free of charge from The Cambridge Crystallographic Data Centre via www.ccdc.cam.ac.uk/data_request/cif.

Table 1. Details of the crystal structure analyses.

| Compound | **5** | **8**·1/8$H_2O$ |
|---|---|---|
| Empirical formula | $C_{13}H_{32}Cl_3N_5O$ | $C_{20}H_{37.25}CuF_6N_5O_{9.125}S_2$ |
| Formula mass | 380.79 | 735.46 |
| Temperature [K] | 100(2) | 100(2) |
| Wavelength [Å] | 0.71073 | 0.71073 |
| Crystal system | orthorhombic | monoclinic |
| Space group | $P2_12_12_1$ | $P2_1$ |
| *a* [Å] | 11.491(2) | 11.762(2) |
| *b* [Å] | 12.262(2) | 13.274(1) |
| *c* [Å] | 13.605(1) | 19.890(2) |
| $\alpha$ [°] | 90 | 90 |
| $\beta$ [°] | 90 | 103.380(6) |
| $\gamma$ [°] | 90 | 90 |
| Volume [Å$^3$] | 1901.3(5) | 3021.1(6) |
| Z | 4 | 4 |
| Calculated density [Mg/m$^3$] | 1.330 | 1.617 |
| Absorption coefficient [mm$^{-1}$] | 0.491 | 0.953 |
| *F*(000) | 816 | 1521 |
| Crystal size[mm] | 0.24×0.23×0.14 | 0.23×0.15×0.05 |
| $\theta$ range [°] | 3.43–28.28 | 3.42–27.10 |
| Index ranges | $-15 \le h \le 15$ | $-14 \le h \le 14$ |
| | $-16 \le k \le 15$ | $-17 \le k \le 16$ |
| | $-18 \le l \le 18$ | $-25 \le l \le 25$ |
| Reflections collected/unique | 28742/4702 | 56796/12866 |
| Refinement method | based on $F^2$ | based on $F^2$ |
| Data/restraints/parameters | 4702/0/295 | 12866/1/830 |
| Goodness-of-fit on $F^2$ | 1.069 | 0.925 |
| Final *R* indices [$I > 2\sigma(I)$] | *R*1 = 0.0318 | *R*1 = 0.0430 |
| | *wR*2 = 0.0635 | *wR*2 = 0.0773 |
| *R* indices (all data) | *R*1 = 0.0428 | *R*1 = 0.0799 |
| | *wR*2 = 0.0668 | *wR*2 = 0.0874 |
| Largest diff. peak/hole [e·Å$^{-3}$] | 0.251/–0.289 | 0.601/–0.514 |

## Acknowledgments

Financial support from the Bayerischer Forschungsverbund Prionen is greatfully acknowledged.

[1] a) Z. Wang, W. Fast, A. M. Valentine, S. J. Benkovic, *Curr. Opin. Chem. Biol.* **1999**, *3*, 614; b) J. D. Garrity, B. Bennett, M. W. Crowder, *Biochemistry* **2005**, *44*, 1078.
[2] G. Fischer, T. Aumüller, *Rev. Physiol. Biochem. Pharmacol.* **2003**, *148*, 105.

 © 2006 Wiley-VCH Verlag GmbH & Co. KGaA, Weinheim 

[3] a) A. H. Andreotti, *Biochemistry* **2003**, *42*, 9515; b) K. K.-S. Ng, W. I. Weis, *Biochem.* **1998**, *37*, 17977.
[4] E. Cohen, A. Taraboulos, *EMBO J.* **2003**, *22*, 404.
[5] a) C. Dugave, L. Demange, *Chem. Rev.* **2003**, *103*, 2475; b) G. Fischer, *Chem. Soc. Rev.* **2000**, *29*, 119.
[6] a) S. Hur, T. C. Bruice, *J. Am. Chem. Soc.* **2002**, *124*, 7303; b) G. Li, Q. Cui, *J. Am. Chem. Soc.* **2003**, *125*, 15028.
[7] U. Reimer, N. E. Mokdad, M. Schutkowski, G. Fischer, *Biochemistry* **1997**, *36*, 13802.
[8] a) P. A. Temussi, F. Quadrifoglio, *J. Chem. Soc., Chem. Commun.* **1968**, 844; b) W. E. Waghorn, A. J. I. Ward, T. G. Clune, B. G. Cox, *J. Chem. Soc., Faraday Trans. 1* **1980**, *76*, 1131.
[9] a) C. Cox, T. Lectka, *Acc. Chem. Res.* **2000**, *33*, 849; b) C. Cox, D. Feraris, N. N. Murthy, T. Lectka, *J. Am. Chem. Soc.* **1996**, *118*, 5332.
[10] a) N. Niklas, F. Hampel, G. Liehr, A. Zahl, R. Alsfasser, *Chem. Eur. J.* **2001**, *7*, 5135; b) N. Niklas, F. W. Heinemann, F. Hampel, R. Alsfasser, *Angew. Chem.* **2002**, *114*, 3535; *Angew. Chem. Int. Ed.* **2002**, *41*, 3386; c) N. Niklas, F. W. Heinemann, F. Hampel, T. Clark, R. Alsfasser, *Inorg. Chem.* **2004**, *43*, 4663.
[11] S. Brandès, C. Gros, F. Denat, P. Pullumbi, R. Guilard, *Bull. Soc. Chim. Fr.* **1996**, *133*, 65.
[12] W. König, R. Geiger, *Chem. Ber.* **1970**, *103*, 788.
[13] B. Geißer, B. König, R. Alsfasser, *Eur. J. Inorg. Chem.* **2001**, 1543.
[14] a) R. B. Penland, S. Mizushima, C. Curran, J. V. Quagliano, *J. Am. Chem. Soc.* **1957**, *79*, 1575; b) P. Maslak, J. J. Sczepanski, M. Parvez, *J. Am. Chem. Soc.* **1991**, *113*, 1991; c) D. P. Failie, T. C. Woon, W. A. Wickramasinghe, A. C. Willis, *Inorg. Chem.* **1994**, *33*, 6425.
[15] A. Mondal, E. L. Klein, M. A. Khan, R. P. Houser, *Inorg. Chem.* **2003**, *42*, 5462.
[16] a) H. C. Freeman, *Inorg. Biochem.* **1973**, *1*, 121; b) H. Sigel, R. B. Martin, *Chem. Rev.* **1982**, *82*, 385.
[17] For other applications of Cbz-protected macrocyclic ligands see, for example: R. Reichenbach-Klinke, M. Zabel, B. König, *Dalton Trans.* **2003**, 141.
[18] F. K. Winkler, J. D. Dunitz, *J. Mol. Biol.* **1971**, *59*, 169.
[19] K. B. Wiberg in: The *Amide Linkage: Structural Aspects in Chemistry, Biochemistry and Material Science* (Eds.: A. Greenberg, C. M. Breneman, J. F. Liebman), John Wiley & Sons, Hoboken, **2003**, p. 33.
[20] G. Gilli, V. Bertolasi, F. Bellucci, V. Ferretti, *J. Am. Chem. Soc.* **1986**, *108*, 2420.
[21] a) A. Greenberg, C. A. Venanzi, *J. Am. Chem. Soc.* **1993**, *115*, 6951; b) Y. Otani, O. Nagae, Y. Naruse, S. Inagaki, M. Ohno, K. Yamaguchi, G. Yamamoto, M. Uchiyama, T. Ohwada, *J. Am. Chem. Soc.* **2003**, *125*, 15191; c) T. Ohwada, T. Achiwa, I. Okamoto, K. Shudo, *Tetrahedron Lett.* **1998**, *39*, 865; d) G. Yamamoto, N. Tsubai, H. Murakami, Y. Mazaki, *Chem. Lett.* **1997**, 1295; e) A. J. Kirby, I. V. Komarov, N. Feeder, *J. Chem. Soc., Perkin Trans. 2* **2001**, 522.
[22] a) B. Bosnich, C. K. Poon, M. L. Tobe, *Inorg. Chem.* **1965**, *4*, 1102; b) X. Liang, P. J. Sadler, *Chem. Soc. Rev.* **2004**, *33*, 246.
[23] M. A. Donnelly, M. Zimmer, *Inorg. Chem.* **1999**, *38*, 1650.
[24] K. F. Sibbons, M. Al-Hashimi, M. Motevalli, J. Wolowska, M. Watkinson, *Dalton Trans.* **2004**, 3163.
[25] A. J. Blake, I. A. Fallis, R. O. Gould, S. Parsons, S. A. Ross, M. Schröder, *J. Chem. Soc., Chem. Commun.* **1994**, 2467.
[26] N. Wiberg, *Hollemann/Wiberg: Lehrbuch der Anorganischen Chemie*, W. de Gruyter, Berlin, **1995**.
[27] L. Pauling, *The Nature of the Chemical Bond*, Cornell University Press, Cornell, **1948**.
[28] M. Schatz, M. Leibold, S. P. Foxon, M. Weitzer, F. W. Heinemann, F. Hampel, O. Walter, S. Schindler, *Dalton Trans.* **2003**, 1480.
[29] A. J. Kirby, I. V. Komarov, P. D. Wothers, N. Feeder, *Angew. Chem. Int. Ed. Engl.* **1998**, *37*, 785.
[30] Bruker-AXS, Inc., *SADABS*, Madison, WI, USA, **2002**.
[31] a) Bruker-AXS, Inc., *SHELXTL NT 6.12*, Madison, WI, USA, **2002**; b) H. D. Flack, *Acta Crystallogr., Sect. A* **1983**, *39*, 876.

Received: January 19, 2006
Published Online: April 18, 2006

 © 2006 Wiley-VCH Verlag GmbH & Co. KGaA, Weinheim 

DOI: 10.1002/ejic.200500937

# An Analogous Solution-Liquid-Solid (ASLS) Growth Route to InP Hollow Spheres and a Honeycomb-Like Macroporous Framework

Xiuwen Zheng,[a,b] Changzeng Liu,[a] and Yi Xie*[b]

**Keywords:** Materials science / Mesoporous materials / Semiconductors / Synthesis design

Hollow spheres and a honeycomb-like macroporous framework structure of InP have been successfully fabricated by employing Au/In core/shell composite colloid droplets formed in situ as the template and catalyst for a simple analogous solution-liquid-solid (ASLS) growth route. SEM images show that the morphology of the obtained InP is mostly micrometer-scale hollow spheres (>80 %) accreted with honeycomb-like structures (<5 %). These hollow spheres have well-defined voids and homogeneous walls, and the surface of the obtained InP hollow spheres is porous, which indicates that the building blocks are InP nanoparticles formed by solidification on the surface of Au/In core/shell droplets. A possible growth mechanism for the micrometer hollow spheres and honeycomb-like macroporous framework is proposed.
(© Wiley-VCH Verlag GmbH & Co. KGaA, 69451 Weinheim, Germany, 2006)

## Introduction

Over the past decade, hollow microspheres and highly porous inorganic materials with well-defined pore sizes have become an important area of research.[1] The main thrust of these intensive investigations stems from their wide application,[2] such as small containers for microencapsulation, catalysis, controlled delivery, artificial cells, light fillers, acoustic insulation, photonic crystals, optical devices, etc.[3] Porous spherical beads can also be used to improve the properties of materials by increasing the accessible surface. Macroporous materials with pore sizes > 50 nm and with well-defined and controllable porosity have attracted particular interest because of their unique optical, catalytic, and mechanical properties.[4] Macroporous supports can be designed to provide optimal flow and improved efficiencies in catalysis and large-molecule separation processes, as well as to permit immobilization and stabilization of large guest molecules.[5] Due to the importance of these specific morphologies and assemblies, notable progress has been made in structural, compositional, and morphological control, in processing aspects of porous solids, and new applications of these materials. Some important synthetic strategies have also been reported for the control and preparation of these peculiar hollow microspheres and ordered three-dimensional macroporous framework. Among these methods, templating techniques are the most appropriate and versatile method to produce hollow spheres and macroporous materials. The templates used include polystyrene latex spheres,[4a,6] liquid crystals,[7] surfactant vesicles,[8] macroporous active carbon,[9] emulsions,[4b] etc. So far, various hollow spheres and macroporous materials have been fabricated by this universally applied template-directed synthesis, including oxides,[4a,6] graphite and diamond,[10] semiconductor Si,[11] CdS,[1a] and metals.[1f]

Recently, III–V semiconductor nanoparticles, which are well-known electronic and optoelectronic materials, have received renewed interest due to their technological importance.[12] InP is an especially intriguing target for research because of its extensive use in the sources and detectors in fiber optic communications and high-speed electronic applications. Several new strategies have been developed to synthesize InP nanocrystals with different morphologies, such as high-quality InP nanocrystals obtained in a noncoordinating solvent[13] or aqueous solution,[14] InP nanowires or nanotubes by a laser ablation process by a vapor-liquid-solid (VLS) growth mechanism,[15] or a solution-phase synthesis by a solution-liquid-solid (SLS) mechanism,[16] with the goal of lowering the processing temperature and avoiding complex reactions and toxic precursors. In addition, the widespread research into porous III–V semiconductors is fuelled by the exhibition of new properties and a large potential for applications in nonlinear optical materials.[17] The porosity of a III–V compound induces bandgap widening and further results in blue and ultraviolet luminescence.[18] For example, two-dimensionally nanostructured porous GaP membranes exhibit a strongly enhanced optical second harmonic generation in comparison with the bulk materials.[19] Our group has made significant progress towards the synthesis of III–V semiconductors, such as InP,[20] GaP,[14] and InAs,[21] with desired morphologies by simple and effective solvothermal methods. Up to now,

[a] Department of Chemistry, Normal University of Linyi, Linyi, Shandong 276000, P. R.China
[b] Nanomaterials and Nanochemistry, Hefei National Laboratory for Physical Sciences at Microscale and Department of Chemistry, University of Science & Technology of China, Hefei, Anhui 230026, China
E-mail: yxielab@ustc.edu.cn


© 2006 Wiley-VCH Verlag GmbH & Co. KGaA, Weinheim

most effort has been focused on the formation of one-dimensional III–V semiconductors. One of the most important growth mechanisms for one-dimensional nanostructures is the VLS mechanism in chemical vapor deposition (CVD) or laser ablation using Au as the catalyst.[15] Recently, the VLS mechanism was extended in solution for the preparation of InAs quantum rods with controlled lengths and diameters by applying a nanocrystalline gold catalyst to the reaction of $InCl_3$ with tris(trimethylsilyl)arsane [$As(TMS)_3$] at 360 °C,[22] which can also be considered as an improved SLS route.[16] A detailed investigation of these reported methods helped us find that there is one common factor, namely the existence of alloy liquid droplets that serve as a nucleation catalyst for the formation of one-dimensional nanostructures at the given elevated temperature, such as the In–Au alloy liquid droplets in the formation of InP and InAs nanowires.[15,22] The essence of the catalytic functions of these liquid droplets is the existence of supersaturation, which supports the whisker growth at the liquid/solid interface. However, a high reaction temperature is a prerequisite for the formation of In–Au alloy liquid droplets in all these reports. We therefore wondered what the results would be if the temperature is too low to form the In–Au alloy in a given reaction system. In order to find the answer to this question we decided to exploit an analogous SLS (ASLS) growth route to synthesize InP spherical assemblies, which can be considered as an extension of the SLS method. The latter has traditionally been applied to grow 1D III–V semiconductors containing low-melting-point metals such as indium by decomposition of indium-containing organometallic complexes as intermediate and catalyst for the directed growth of III–V one-dimensional structures.[16] In our approach, to obtain a solution-controllable synthesis of InP with the desired hollow sphere morphology we introduced gold nanoparticles (formed by reduction of $HAuCl_4$ in solution) into the classical SLS system[16,20,21] and controlled the system temperature at 200 °C. The in-situ formed gold nanoparticles act as a colloidal template for the synthesis of spherical assemblies.

## Results and Discussion

The XRD patterns (Figure 1a) of the samples agree well with the bulk InP reflection,[23] thus indicating the same cubic zinc blende lattice structure. Judging from the XRD pattern, the products have very high crystallinity under the given experimental conditions. No component of the Au catalyst can be detected in Figure 1a, thus indicating that its content is less than the resolution limit of XRD. SEM images, as shown in Figures 2a and b, give a general view of the obtained InP micrometer hollow spheres under low magnification. Many collapsed and hemispherical hollow spheres can also be seen in Figure 2a, thus indicating the hollow structure of the spheres. Figures 2c and d display images of typical, collapsed hemispheres, from which it can be seen that the obtained hollow spheres are about 3–6 μm in diameter with a wall thickness of 1 μm. The opening and collapse are probably due to decomposition of the templates when washing with dilute HCl. Figure 3 displays the SEM images of the obtained InP hollow spheres at high magnification; the porous nature of the surface can clearly be seen. Figure 3 also confirms that the building blocks of the InP hollow spheres are InP nanoparticles. Interestingly and surprisingly, some ordered honeycomb-like macroporous networks are also found to accrete with the hollow spheres, as shown in Figure 4. The pore diameter of the ordered honeycomb-like macroporous network is approximately 2–5 μm. A key feature of these networks is the interconnectedness of their pores; an SEM image at high magnification (Figure 4b, arrowed) shows that some of the voids

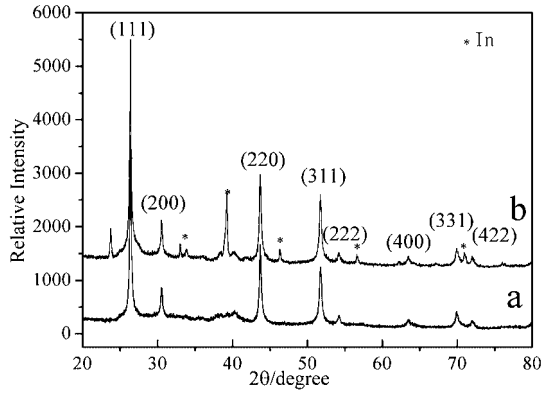


Figure 1. XRD pattern of obtained InP samples (a) after HCl treatment and (b) without HCl treatment, indicating the presence of In.

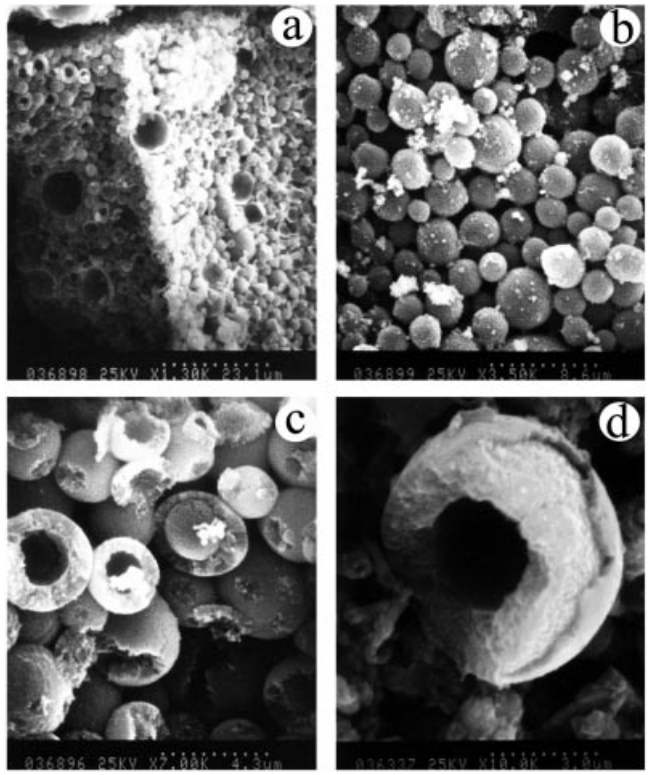


Figure 2. SEM images of obtained InP micrometer hollow spheres: (a) and (b) show the obtained InP micrometer hollow spheres at low magnification and (c) and (d) show the collapsed and broken InP spheres at high magnification, indicating their hollow nature.

 © 2006 Wiley-VCH Verlag GmbH & Co. KGaA, Weinheim 

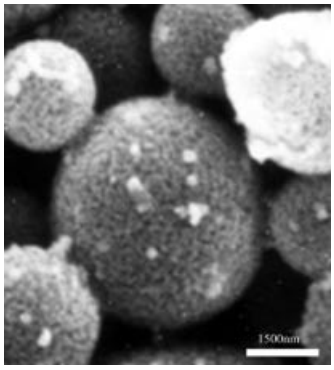


Figure 3. SEM images of obtained InP hollow spheres at high magnification, showing the porous surface structure.

are connected to their neighbors by smaller windows. Such microstructures allow these macroporous networks to be filled with different liquid precursor solutions in the second templating process. These small windows play important roles in the fabrication of the desired morphologies as they provide the necessary channels to allow the precursor solution to flow through and form a shell throughout the entire void. The arrow in Figure 4c shows some InP spheres inlaid in the macroporous network, which further prove the proposed formation mechanism.

XPS spectra were recorded to identify the surface composition of the as-prepared products. The bonding energies obtained from the XPS analysis were corrected for specimen charging by referencing the C 1s line to 287.60 eV. Figure 5a shows the XPS survey spectra of InP. No obvious impurities (besides the Au catalyst and trace amounts of adsorbed $O_2$) can be detected in the samples, thus indicating that the products have high purity and the level of impurities is lower than the resolution limit of XPS (1 at%). The typical high-resolution spectra of In 3d and P 2p are shown in Figure 5b. The binding energy values are 443.74 eV for In $3d_{5/2}$ and 451.38 eV for In $3d_{3/2}$. The P 2p core shows two peaks, one at 128.88 eV corresponding to P from InP and the other at 132.95 eV (arrowed) corresponding to oxidized P species due to exposure to the air. The peak areas of these high-resolution scans were measured and used to calculate the In/P ratio for the product. The quantification of the peaks gives an atomic ratio of In/P of 0.43:0.53. The excess P perhaps comes from the added P raw materials. All of the observed binding energy values for In 3d and P 2p coincide with the reported data within the experimental errors.[24]

In both the reported VLS route and its extension in solution, the noble metal Au and the in-situ formed alloy species function as catalysts for the nucleation and further direct the growth of 1D nanostructures. Thus, the reaction temperature must be higher than the eutectic temperature of the alloy. Once formed, the In–Au alloy liquid droplets dissolve the reactants and the subsequent supersaturation supports one-dimensional structure growth at the liquid/solid interface.[15,22] In our approach, however, the obtained product is spherical rather than the usual one-dimensional nanostructure. Our reaction temperature (200 °C) is lower than that of the melting point of bulk gold and higher than that of the melting point of In and $P_4$ (157 and 44.1 °C, respectively), therefore the Au–In alloy cannot form. Banin has reported that InAs nanorods do not yield one-dimensional growth at a lower reaction temperature of 300 °C, which indicates that reaction temperatures of at least 360 °C are required for the onset of Au melting.[22] This value is consistent with theoretical studies that predict a melting temperature for $Au_{146}$ (diameter ca. 1.6 nm) of ca. 350 °C, increasing to ca. 480 °C for $Au_{459}$ (diameter ca. 2.5 nm).[25] The current low temperature (200 °C) may not suffice to activate the gold particles as catalysts to direct the growth of the one-dimensional nanoscale material. However, the reduced liquid In becomes coated on the newly formed Au nanoparticles due to the physical tendency to reach the lowest energy level and forms Au/In core/shell droplets. These droplets further serve as a second template for the nucleation of InP nanoparticles, therefore the function of the Au/In core/shell droplets is as a template for a spherical structure[16] rather than a nucleation catalyst for the formation of a one-dimensional structure.[15,22] In the region of scattered Au/In core/shell beads, however, the $P_4$ molecules in solution will react with the In on the surface of Au/In beads (Path 1 in Scheme 1). Thereafter, the formed InP nanoparticles solidify to form a compact InP layer on the surface of the Au/In core/shell droplets, which blocks the further

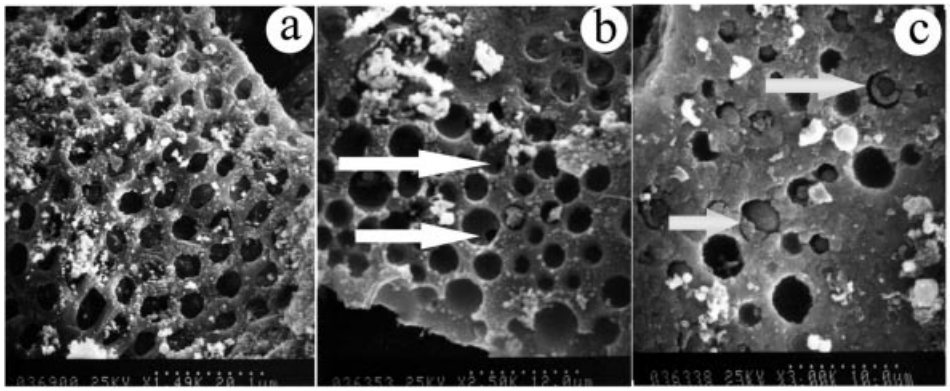


Figure 4. (a)–(c) SEM images of obtained InP honeycomb-like macroporous network(<5%). The arrow in (c) shows some InP spheres inlayed in the macroporous network.

 © 2006 Wiley-VCH Verlag GmbH & Co. KGaA, Weinheim 

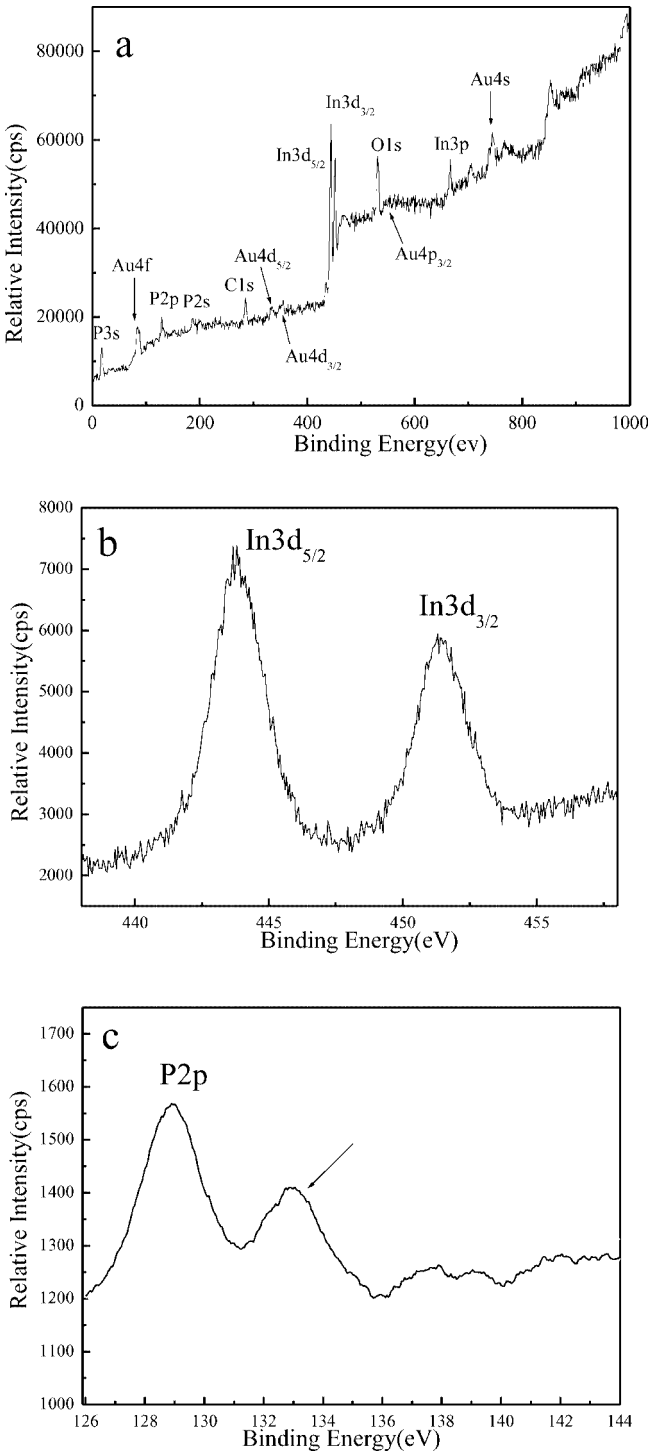


Figure 5. XPS spectra: (a) InP survey spectra, showing the presence of Au catalyst; (b) In 3d; (c) P 2p, with an arrow indicating the oxidized P species.

reaction of $P_4$ with In molecules in the beads. As a result, when removing the unreacted In by treatment with dilute HCl solution, the inner Au cores separate from the outermost InP shells and finally produce InP hollow spheres (>80%). Upon removal of the support, some collapsed hollow spheres are formed. The presence of In before the HCl treatment was observed by XRD, as shown in Figure 1b. However, it is reasonable to propose that in the dense and thick regime of Au/In beads, which array in order, $P_4$ molecules in solution filter into and fill the void spaces among the beads of the crystalline array. The reaction of $P_4$ with In molecules and subsequent solidification form a compact InP layer on the surface of the Au/In core/shell beads. This process is similar to the formation of InP hollow spheres. However, due to the highly aggregated nature of the array of Au/In beads, the solidification of the InP spheres connects each other into a compact whole containing unreacted In. After the removal of residual In, an ordered three-dimensional porous structure with an array of interconnected spherical pores is formed (Path 2 in Scheme 1, <5%). In addition, some InP spheres inlaid in the macropores are also found (Figure 4c, arrowed), which further demonstrates the template effect of the Au/In core/shell droplets. This large surface area endows InP with many promising applications in separation and adsorption. Moreover, the periodical pores can also serve as cavities to accommodate diverse guest molecules. Scheme 1 outlines the schematic process of the formation of the desired morphology.

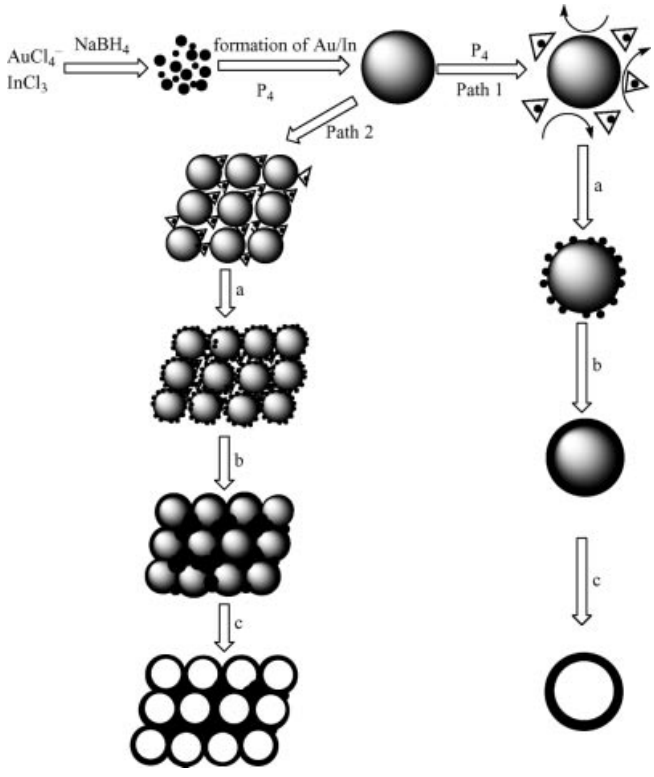


Scheme 1. Schematic illustration of the formation of InP micrometer hollow spheres and the honeycomb-like macroporous network: (a) reaction of $P_4$ with In on the surface of Au/In beads; (b) solidification of InP nanoparticles on the surface of Au/In beads, which leads to the formation of a core/shell structure. (c) removal of In by HCl, leading to the formation of InP hollow spheres or a macroporous network (a triangle represents $P_4$ molecules). The predominant Path 1 gives the hollow spheres and Path 2 leads to the honeycomb-like macroporous network.

 © 2006 Wiley-VCH Verlag GmbH & Co. KGaA, Weinheim 

A series of comparison experiments were performed to determine the effect of synthetic conditions on the formation of InP hollow spheres and macroporous networks. Detailed investigation helped us determine that the ratio of In/Au is important for controlling the synthesis of InP nanocrystals with different assemblies, and that the optimal molar ratio of In/Au for the formation of these InP hollow spheres and network is 25:1. At this molar ratio the product is mainly microporous hollow spheres (>80%) with a small amount of a three-dimensional ordered macroporous network. We also found that it is difficult to obtain the desired hollow spheres morphology if the molar ration of In/Au is too far above or below this ratio. For example, the obtained products are mainly irregular particles with a small quantity of rough spherical products at a ratio of 50:1. These particles resemble an irregular stack that shows some morphological similarity to that of Figure 2b. However, the amount of obtained microscale spherical structures is less than 10%. With a reduction of the ratio, for example to 10:1, the obtained products are poorly crystalline particles.

In order to understand the formation mechanism of InP hollow spheres, the reaction was carried out without the addition of P; all other experimental conditions and parameters were kept constant. The obtained In/Au composite beads are spherical, as shown in Figures 6a and b, and gold nanoparticles exhibiting high contrast can be discerned in the cores of many of them (Figure 6b), which provides firm evidence for our proposed mechanism.

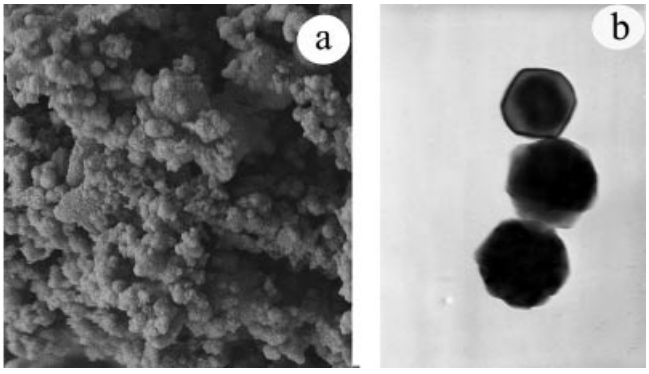


Figure 6. Obtained Au/In spherical composite particles: (a) SEM image, (b) TEM images; gold nanoparticles exhibiting high contrast can be discerned in the cores.

As is well known, it is very important to select appropriate solvents for the design of solid-state compounds by a solvothermal route.[20,26] Based on our control experiments, we found that ethylenediamine plays an important role in the formation of InP particles under our conditions as it can disperse yellow phosphorus to form a brown dispersion and readily dissolve $KBH_4$, which means that it increases the surface area of the reactants and promotes the reaction at given temperatures.[20] When other solvents were used, such as ethanol, benzene, DMF, or pyridine, the reaction either did not take place or the products could not be identified. Strongly polarizing solvents such as ethylenediamine at the appropriate temperature provide conditions that are adequate to greatly enhance solubility, diffusion, and crystallization.

The same route has also been applied to the synthesis of GaP, using $GaCl_3$ instead of $InCl_3{\cdot}4H_2O$ as the source. The obtained GaP micrometer spheres, with a diameter of ca. 3–4 μm, are shown in Figure 7. Some spheres with small openings in the surface can also be observed (inset in Figure 7), thus indicating that the obtained GaP spheres have a hollow structure. However, at the given temperature (200 °C) the obtained GaP hollow spheres are very poorly crystalline.

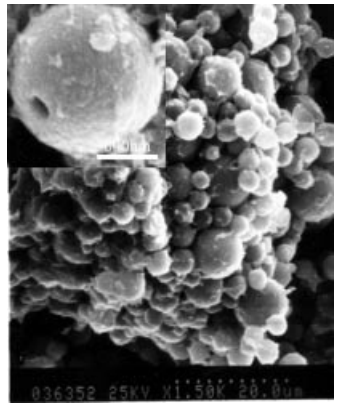

Figure 7. GaP micrometer-sized hollow spheres obtained in the same approach; the inset shows the small openings in the surface of GaP spheres, which indicate the hollow structure of the obtained GaP spheres.

## Conclusions

In summary, we have demonstrated an effective analogous solution-liquid-solid (ASLS) growth route to mesoscale InP hollow spheres accreted with honeycomb-like structures, in which the Au/In core/shell droplets formed in situ serve as the template and catalyst. These hollow spheres have well-defined voids and homogeneous walls. The surface of the InP hollow spheres obtained is porous, which further indicates that the building blocks are InP nanoparticles formed by solidification on the surface of Au/In core/shell droplets. A systematic investigation has shown that the correct ratio of indium/noble metal is a prerequisite for the synthesis of InP novel structures, and that the optimal ratio is 25:1. The same experimental process has been applied to GaP hollow spheres and will be extended to other important metal phosphides with desired morphologies.

## Experimental Section

Analytical-grade reagents and solvents were purchased from Shanghai Chemistry Co. Ltd and used without further treatment. Typical procedure: 40 mL of ethylenediamine, 1.11 g of $InCl_3{\cdot}4H_2O$, 0.5 g of yellow phosphorus, 2 mL of an ethanol solution of $HAuCl_4$ (0.0758 M) and 1.6 g of $KBH_4$ were placed in a 50-mL Teflon-lined autoclave. The autoclave was maintained at 200 °C

 © 2006 Wiley-VCH Verlag GmbH & Co. KGaA, Weinheim 

for 10 h, and then cooled to room temperature naturally. The black products were filtered off and washed with absolute alcohol and dilute aqueous HCl (1 M). Finally, the products were dried in vacuo at 50 °C for 1 h. The key to the fabrication of InP hollow spheres and macroporous network is the control of the In/Au ratio. During the formation of the desired InP hollow spheres, the influence of this ratio was investigated in detail and control experiments were performed with different molar ratios of In/Au, such as 120:1, 100:1, 80:1, 50:1, 25:1, and 10:1. In addition, in order to understand the formation mechanism, different solvents, such as ethanol, benzene, DMF, and pyridine were selected to investigate the optimal experimental conditions.

The final products were characterized by various techniques. X-ray powder diffraction (XRD) was carried out with a Rigaku D/max rA X-ray diffractometer with Cu-$K_\alpha$ radiation ($\lambda$ = 1.54178 Å). A scan rate of 0.05° per second was applied to record the pattern in the $2\theta$ range of 20–85°. The morphology and size of as-prepared products were determined from SEM images, which were recorded with an X-650 scanning electronic microanalyzer. To obtain further evidence for the purities and compositions of the as-prepared products, the X-ray photoelectron spectra were recorded with an ESCALab MKII X-ray photoelectron spectrometer, using Mg-$K_\alpha$ radiation as the exciting source.

## Acknowledgments

Financial support from the Chinese National Foundation of Natural Sciences and the Chinese Ministry of Education are gratefully acknowledged.

[1] a) Z. B. Lei, J. M. Li, Y. X. Ke, Y. G. Zhang, H. Wang, G. F. He, *J. Mater. Chem.* **2001**, *11*, 1778–1780; b) K. Kamata, Y. N. Xia, *J. Am. Chem. Soc.* **2003**, *125*, 2384–2385; c) Y. Hu, J. F. Chen, W. M. Chen, X. H. Lin, X. L. Li, *Adv. Mater.* **2003**, *15*, 726–729; d) O. D. Velev, A. M. Lenhoff, E. W. Kaler, *Science* **2000**, *287*, 2240–2243; e) P. Jiang, J. F. Bertone, V. L. Colvin, *Science* **2001**, *291*, 453–457; f) L. B. Xu, L. D. Tung, L. Spinu, A. A. Zakhidov, R. H. Baughman, J. B. Wiley, *Adv. Mater.* **2003**, *15*, 1562–1564.

[2] a) *Hollow and Solid Spheres and Microspheres: Science and Technology Associated with their Fabrication and Application* (Eds.: D. L. Wilcox, M. Berg, T. Bernat, D. Kelleman, J. K. Cochran), MRS proceedings, vol. 372, Materials' Research Society, Pittsburgh, PA, **1994**; b) H. Huang, E. E. Remsen, *J. Am. Chem. Soc.* **1999**, *121*, 3805–3806; c) E. Mathlowitz, J. S. Jacob, Y. S. Jong, G. P. Carino, D. E. Chickering, P. Chaturvedl, C. A. Santos, K. Vijayaraghavan, S. Mongtgomery, M. Bassett, C. Morrell, *Nature* **1997**, *386*, 410–414; d) M. Ohmori, E. Matijevic, *J. Colloid Interface Sci.* **1992**, *150*, 594–597.

[3] a) M. Nogami, R. Nagao, C. Wong, *J. Phys. Chem. B* **1998**, *102*, 5772–5775; b) O. Kalinina, E. Kumacheva, *Chem. Mater.* **2001**, *13*, 35–38; c) E. Litovsky, S. M. Hapiro, A. Shavit, *J. Am. Ceram. Soc.* **1996**, *79*, 1366–1376.

[4] a) Y. Hotta, P. C. A. Alberius, L. Bergström, *J. Mater. Chem.* **2003**, *13*, 496–501; b) A. Imhof, D. J. Pine, *Nature* **1997**, *389*, 948–951; c) M. E. Davis, *Nature* **2002**, *417*, 813–821.

[5] a) F. C. Meldrum, R. Seshadri, *Chem. Commun.* **2000**, 29–30; b) N. A. Melosh, P. Lipic, F. S. Bates, F. Wudl, G. D. Stucky, G. H. Fredrickson, B. F. Chemelka, *Macromolecules* **1999**, *32*, 4332–4342.

[6] a) Z. Y. Zhong, Y. D. Yin, B. Gates, Y. N. Xia, *Adv. Mater.* **2000**, *12*, 206–209; b) G. Gundiah, C. N. R. Rao, *Solid State Sci.* **2000**, *2*, 877–882.

[7] P. V. Braun, S. I. Stupp, *Mater. Res. Bull.* **1999**, *34*, 463–469.

[8] H. T. Schmidt, A. E. Ostafin, *Adv. Mater.* **2002**, *14*, 532–535.

[9] Z. B. Lei, J. M. Li, Y. X. Ke, Y. G. Zhang, H. C. Zhang, F. Q. Li, J. Y. Xing, *J. Mater. Chem.* **2001**, *11*, 2930–2933.

[10] a) A. A. Zakhidov, R. H. Baughman, Z. Iqbal, C. X. Cui, I. Khayrullin, S. O. Dantas, J. Marti, V. G. Ralchenko, *Science* **1998**, *282*, 897–901; b) Z. B. Lei, Y. G. Zhang, H. Wang, Y. X. Ke, J. M. Li, F. Q. Li, J. Y. Xing, *J. Mater. Chem.* **2001**, *11*, 1975–1977.

[11] A. Blanco, E. Chomski, S. Grabtchak, M. Ibisate, S. John, S. W. Leonard, C. Lopez, F. Meseguer, H. Miguez, J. P. Mondia, G. A. Ozin, O. Toader, H. M. Driel, *Nature* **2000**, *405*, 437–440.

[12] a) T. J. Trentler, K. M. Hickman, S. C. Goel, A. M. Viano, P. C. Gibbons, W. E. Buhro, *Science* **1995**, *270*, 1791–1794; b) E. P. A. M. Bakkers, M. A. Verheijen, *J. Am. Chem. Soc.* **2003**, *125*, 3440–3441; c) M. S. Gudiksen, L. J. Lauhon, J. Wang, D. C. Smith, C. M. Lieber, *Nature* **2002**, *415*, 617–620.

[13] a) D. Battaglia, X. G. Peng, *Nano Lett.* **2002**, *2*, 1027–1030; b) S. P. Ahrenkiel, O. L. Mićić, A. Miedaner, C. J. Crutis, J. M. Nedeliković, A. J. Nozik, *Nano. Lett.* **2003**, *3*, 833–837.

[14] S. M. Gao, J. Lu, N. Chen, Y. Zhao, Y. Xie, *Chem. Commun.* **2002**, 3064–3065.

[15] a) M. S. Gudiksen, J. F. Wang, C. M. Lieber, *J. Phys. Chem. B* **2001**, *105*, 4062–4064; b) E. P. A. M. Bakkers, M. A. Verheijen, *J. Am. Chem. Soc.* **2003**, *125*, 3440–3441.

[16] T. J. Trentier, K. M. Hickman, S. C. Goel, A. M. Viano, P. C. Gibbons, W. E. Buhro, *Science* **1995**, *270*, 1791–1794.

[17] I. M. Tiginyanu, I. V. Kravetsky, S. Langa, G. Marowsky, J. Monecke, H. Föll, *Phys. Stat. Sol.* **2003**, *197*, 549–555.

[18] H. Föll, S. Langa, J. Carstensen, M. Christophersen, I. M. Tiginyanu, *Adv. Mater.* **2003**, *15*, 183–198.

[19] I. M. Tiginyanu, I. V. Kravetsky, J. Monecke, W. Cordts, G. Marowsky, H. L. Hartnagel, *Appl. Phys. Lett.* **2000**, *77*, 2415–2417.

[20] P. Yan, W. Z. Wang, F. Y. Liu, Y. T. Qian, *J. Mater. Chem.* **1999**, *9*, 1831–1833.

[21] Y. Xie, P. Yan, J. Lu, W. Z. Wang, Y. T. Qian, *Chem. Mater.* **1999**, *11*, 2619–2622.

[22] S. Kan, T. Mokari, E. Rothenberg, U. Banin, *Nat. Mater.* **2003**, *2*, 155–158.

[23] JCPDS file no. 32-452.

[24] C. D.Wagner, W. W.Riggs, L. E. Davis, J. F. Moulder, G. E. Muilenberg, *Handbook of X-ray Photoelectron Spectroscopy*, Perkin–Elmer Corporation, Physical Electronics Division, USA, **1979**.

[25] a) C. L. Cleveland, W. D. Luedtke, U. Landman, *Phys. Rev. Lett.* **1998**, *81*, 2036–2039; b) C. L. Cleveland, W. D. Luedtke, U. Landman, *Phys. Rev. B* **1999**, *60*, 5065–5077.

[26] W. S. Sheldrick, M. Wachhold, *Angew. Chem. Int. Ed. Engl.* **1997**, *36*, 206–224.

Received: October 23, 2005
Published Online: April 11, 2006

 © 2006 Wiley-VCH Verlag GmbH & Co. KGaA, Weinheim 

DOI: 10.1002/ejic.200501061

# Tris(tropolonato)phenanthroline Lanthanide(III) Complexes as Photochemical Devices

**Laura Bertolo,[a] Sergio Tamburini,*[a] Pietro Alessandro Vigato,[a] William Porzio,[b] Giorgio Macchi,[c] and Francesco Meinardi[c]**

**Keywords:** Lanthanides / N ligands / O ligands / Molecular devices / Donor–acceptor systems / Time-resolved spectroscopy / Infrared emitters

The tris-tropolonato erbium(III) complexes [Er(hino)$_3$(phen)] and [{Er(hino)$_3$}$_2$(pdon)] (H-hino = 2-hydroxy-6-isopropylcyclohepta-2,4,6-trien-1-one; phen = 1,10-phenanthroline; pdon = 1,10-phenanthroline-5,6-dione) have been prepared by reaction of [Er(hino)$_3$]$_n$ with the appropriate chelating ligand in alcoholic solution. The complexes were characterized by elemental analyses, TG, ESI MS, $^1$H NMR, and IR spectroscopy, also by comparison with the properties of the analogous Eu$^{III}$ and Yb$^{III}$ complexes. The ESI-MS spectroscopy of the complex with the ditopic ligand pdon parallels the other physico-chemical data (IR, NMR), confirming the occurrence of a dinuclear entity. All the investigated Er$^{III}$ complexes show efficient NIR emissions at about 1550 nm upon excitation at 355 nm in the UV ligand absorption band, emerging as possible candidate as active material for the realization of plastic amplifiers for telecommunications.
(© Wiley-VCH Verlag GmbH & Co. KGaA, 69451 Weinheim, Germany, 2006)

## Introduction

Lanthanide complexes with distinct magnetic and optical properties are currently of interest for use in applications involving the fabrications of novel materials, both as active layer in optoelectronic devices and probes in biological systems.[1–5]

Among a wealth of stimulating applications the recent developments of (i) new phosphors for lighting,[6] (ii) high-efficiency electroluminescent devices for light-emitting diodes,[7] (iii) contrast agents for medical magnetic resonance imaging,[8] (iv) NMR shift reagents for cations for transport processes of alkali metal ions through biological membranes,[9] (v) luminescent probes for analytes,[10] (vi) labels for proteins and amino acids,[11] (vii) light-emitting sensors in fluoroimmunoassays,[12] (viii) tags for time-resolved luminescent microscopy,[13] (ix) magnetically addressable liquid crystals,[14] (x) magnetic alloys for refrigeration,[15] (xi) precursors for superconducting materials,[16] (xii) specific redox reagents for chemical transformation[17] or molecular-based information storage,[18] and (xiii) acidic catalysts for sophisticated organic transformations[19,20] or for the cleavage of phosphodiester bridges in RNA[21] fully justify the efforts made to control the metallic sites and to selectively introduce lanthanides into organized assemblies. For more than two decades, systematic investigations of the subtle interplay between the structural control of the coordination sphere and the associated metal-centred electronic properties have led to the design of lanthanide-containing devices whose function can be judiciously addressed and tuned.

The use of optical properties of these metal ions are quite attractive and promising. However, these photophysical properties of these ions depend markedly on their environment. To optimize efficient emissions, for instance, chromophoric ligands have been often employed to transfer absorbed energy efficiently to the appropriate lanthanide ion.

Remarkably, these ligands must be capable of protecting the lanthanide(III) centre from solvent molecules, which can quench emission.

A variety of multidentate cyclic and acyclic ligands, designed to encapsulate the lanthanide ions, have been synthesized and successfully used. Thus, using ligands with appropriate coordination geometry, and/or coordinating anions, it is possible to obtain suitable structure quite effective in keeping solvent and water molecules away from lanthanide(III) centres.

The design and synthesis of lanthanide complexes with charged and/or neutral chelating organic ligands offers the possibility to obtain stable compounds with quite particular optical properties. A relevant aspect of this research consists in the possibility to optimize these properties of a particular lanthanide(III) ion by suitable choice of ligands.

The recent interest towards Organic Light-Emitting Diodes (OLED) based on organolanthanide complexes[22] stems on the fact of the observed peculiar mechanism of

[a] Istituto di Chimica Inorganica e delle Superfici – C.N.R., Corso Stati Uniti 4, 35127 Padova, Italy
[b] Istituto per lo studio delle Macromolecole del C.N.R., Via E. Bassini 15, 20133 Milano
[c] Dipartimento di Scienza dei Materiali Università di Milano Bicocca, Via Cozzi 53 20125 Milano
E-mail: sergio.tamburini@icis.cnr.it

 © 2006 Wiley-VCH Verlag GmbH & Co. KGaA, Weinheim 

emission in regions different according to the lanthanide. Specifically the ligand acting as antenna, absorbs the light, and then transfers the energy towards the coordinate metal ion ($Er^{3+}$), poorly absorbing in the visible, while efficiently emitting in the near infrared (NIR) region. With the aim to enhance the luminescence efficiency of these materials, the accurate choice of peculiar ligands assumes crucial relevance due to both the window of use and the stability. Quite recently, a versatile approach to the development of lanthanide complexes that emit in the NIR based on tropolone (H-$L_T$) as ligand has been found.[23] Upon deprotonation, tropolones can be used as seven-membered ring, bidentate oxygen-donor chelators that allow direct coordination of the chromophoric group to the $Ln^{III}$ cation. Their hard Lewis base character is suitable for forming strong bonds with $Ln^{III}$. Furthermore, tropolone has a good electronic structure to act as an antenna because the energy of its triplet state (16800 $cm^{-1}$) is compatible for efficient energy transfer to the low accepting levels of several $Ln^{III}$ ions that emit in the NIR such as $Nd^{III}$, $Er^{III}$, $Ho^{III}$, and $Tm^{III}$. In the past, $[Ln(L_T)_3]$ and $M[Ln(L_T)_4]$ ($M = NH_4^+$, $Na^+$) complexes have been prepared.[24] Upon changing the counterion to $K^+$, the complexes $K[Ln(L_T)_4](dmf)$ have been prepared and fully characterized also by X-ray diffraction investigations.[23] In these complexes the coordination around the lanthanide cation has been described as a distorted dodecahedron. Quantitative luminescence measurements indicated that the tropolonato ligands are able to sensitize several lanthanide cations that emit in the NIR domain.[23]

Other studies have been successfully carried out on tris-β-diketonato lanthanide complexes containing also functionalized dipyridine or phenanthroline ligands that are known as very good sensitizers and many excellent papers have been published consequently.[25] In particular, the addition of the phenanthroline ligand acts to saturate the coordination number of $Ln^{III}$ ions and also to improve the fluorescence intensity, volatility and stability of the $Ln^{III}$ complexes[26]

In order to enhance the optical properties we have used as ligand 2-hydroxy-4-isopropylcyclohepta-2,4,6-trien-1-one (4-isopropyltropolone, also known as hinokitiol or β-thujaplicin) (H-hino) and prepared the tris-tropolonato complexes [Er(hino)$_3$(phen)], and [{Er(hino)$_3$}$_2$(pdon)] by reaction of H-hino with $ErCl_3 \cdot 6H_2O$ and 1,10-phenanthroline or 1,10-phenanthroline-5,6-dione in methanol, respectively, in the presence of NaOH. Furthermore, 1,10-phenanthroline-5,6-dione was successfully used as appropriate ditopic ligand for dinuclear lanthanide complexation. In fact, it permits to coordinate two lanthanide(III) ions in the opposite side of the molecule by the $N_2$ and $O_2$ donor atoms allowing an interesting interaction between the two coordinated metal ions. In particular, [{Er(hino)$_3$}$_2$(pdon)] was obtained following a procedure similar to that employed for the phenanthroline analogue. The complexes were characterized by $^1$H NMR, ESI MS and IR spectroscopy and elemental analysis, moreover a photophysical characterization in solution was performed. All the complexes display an absorption in the UV region, while the subsequent emission in the NIR region (≈ 1550 nm) is quite interesting and comparable with the best emitter compounds up to now reported. This paper reports the physicochemical properties arising from this molecular aggregation.

## Results and Discussion

### Synthesis of the Complexes

The tris-tropolonato lanthanide(III) complexes of $Er^{III}$, $Eu^{III}$, and $Yb^{III}$ have been prepared accordingly to Scheme 1.

In particular the tris-tropolonato $Ln^{III}$ complexes obtained by reaction of a methanolic solution of 4-isopropyltropolone (H-hino) with NaOH and the appropriate lanthanide(III) trichloride hexahydrate and recovered from a water/methanol solution, show only trace of water or methanol according to elemental analyses and thermogravimetric and IR investigations. Furthermore, the complexes are stable in air for long periods of time. We suppose that, in order to complete the high coordination number required by these lanthanides(III) ions, the complexes are in the form $[Ln(hino)_3]_n$ ($n$ = 2 or 3). NMR spectra in $CD_3OD$ or $CDCl_3$ show in fact the correct pattern [shifted depending on the paramagnetism of lanthanide(III) metal ion] of the tropolonato ligand with very small amount of free water. Only the $[Eu(hino)_3]_n$ complex in $(CD_3)_2SO$ shows a double pattern of the tropolonato ligand, indicating the different role of the oxygens bridging the $Eu^{III}$ ions.

This is not a very surprising result; many β-diketonate complexes, for instance, can loose a solvent molecule coordinated to the central metal ion giving rise to an easy oligomerization through oxygen bridges of the chelating ligands. The lack of quenching in the fluorescence of these complexes (vide postea) is an additional proof of the absence of water in the coordination environment of the erbium(III) ion.

This dimeric or trimeric complexes can easily turn into the monomeric one in the presence of the chelating ligand 1,10-phenanthroline. The resulting complex [Er(hino)$_3$(phen)]·$H_2O$ is soluble in a variety of solvents, such as MeOH, EtOH, $CHCl_3$, $CH_2Cl_2$, $CH_3CN$, DMSO, but insoluble in $H_2O$ and *i*PrOH. The IR spectra of the complex show the characteristic strong absorption bands at ($cm^{-1}$) 1588 (νC=O), 1504 (νAr, C=C), 1239–1240 (νC–O). Thermogravimetric analyses indicate a 1.71% weight loss at 92 °C, in agreement with the loss of one non-coordinated water molecule. Again the presence of water only in the crystalline framework and not directly bonded to the central metal ion is proved by the photophysical behaviour (vide postea).

The complex appears to be monomeric with the metal ion in an octacoordinated environment.

A further functionalization of the periphery of the chelating nitrogen-containing ligands was introduced in order to allow them to serve as dinucleating ligands towards equal

 © 2006 Wiley-VCH Verlag GmbH & Co. KGaA, Weinheim 

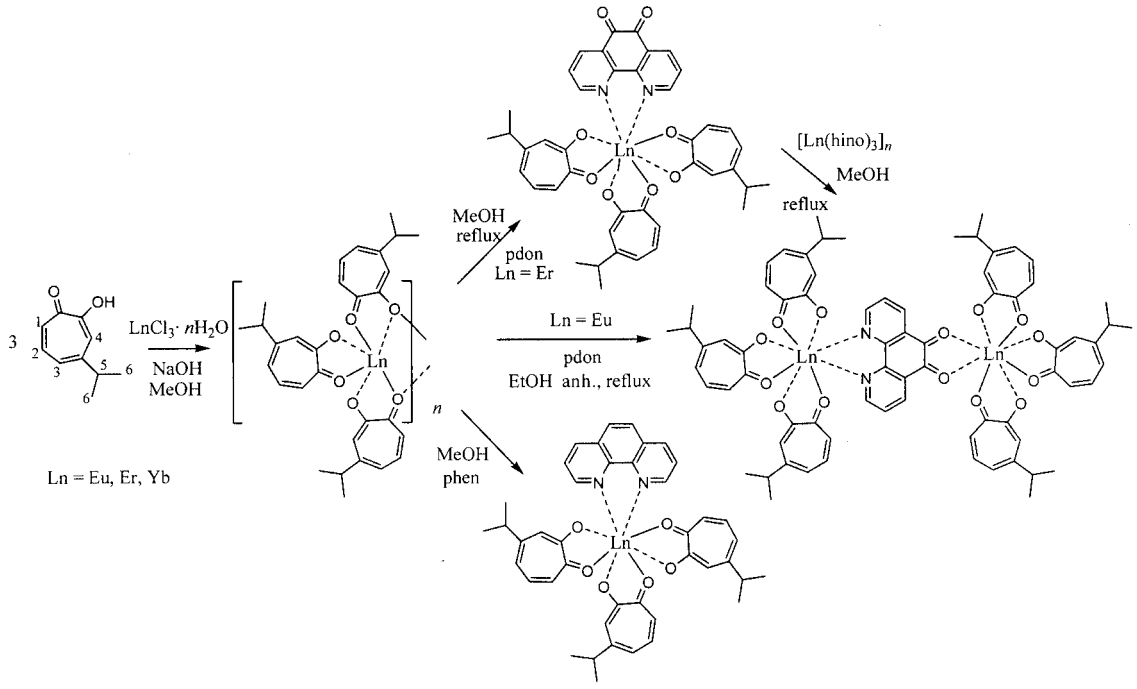


Scheme 1.

or different lanthanide(III) ions. 1,10-Phenanthroline-5,6-dione (pdon) is a suitable ditopic ligand: it contains two well separated coordinating sites, one containing two nitrogen atoms and one containing two oxygen atoms, both suitable for lanthanide(III) complexation. Thus, the reaction of $[Er(hino)_3]_n$ with pdon in anhydrous methanol in a 1:1 molar ratio under reflux affords $[Er(hino)_3(pdon)]\cdot 0.2H_2O$ with the lanthanide(III) ion coordinated to the two nitrogen atoms of the functionalized phenanthroline. In fact, $^1H$ NMR experiments performed in $CD_3OD$ of diamagnetic yttrium and lutetium complexes[27] $[Ln(hino)_3(pdon)]$ show a significant downfield proton shift of CH-N (from 8.95 to 9.12 ppm) and the corresponding upfield shift of CH-C=O (from 8.55 to 8.45 ppm) with respect to the free pdon. This mononuclear complex, by reaction of $[Er(hino)_3]_n$ in anhydrous methanol in a 1:1 ratio under reflux gives rise to the homodinuclear $[\{Er(hino)_3\}_2(pdon)]\cdot H_2O$. Elemental and thermogravimetric analyses of the mononuclear and dinuclear complexes agree with the proposed formulations, whereas IR spectra show nearly the same pattern, with the characteristic strong absorption bands at ($cm^{-1}$) 1688–1689 (νC=O, pdon), 1588 (νC=O), 1504–1505 (νAr, C=C), 1239–1240 (νC–O). The NMR spectra of $[Er(hino)_3(pdon)]\cdot 0.2H_2O$ and $[\{Er(hino)_3\}_2(pdon)]\cdot H_2O$ in $(CD_3)_2SO$ have the same pattern as well, but in the spectrum of the dinuclear complex, the peaks related to the protons of 4-isopropyltropolone are of double intensity (with respect to the pdon proton intensity) compared to those present in the spectrum of the mononuclear complex, therefore showing the presence of six 4-isopropyltropolonate units to one of 1,10-phenanthroline-5,6-dione in the dinuclear complex.

It must be noted that, under anhydrous conditions, using the precursor $[Eu(hino)_3]_n$ and pdon in a 1:1 molar ratio, only the homodinuclear complex $[\{Eu(hino)_3\}_2(pdon)]$ was obtained. This complex, shows the same IR spectrum as that of the related $Er^{III}$ complexes above reported, but a different NMR pattern system, in which the peaks of the two $Eu(hino)_3$ units are shifted each other, as inferred by 2D COSY and NOESY experiments: peaks at $\delta$ = 7.32 (4-H), 6.81 (1-H), 5.94 (3-H), 4.51 (2-H), 2.37 (5-H), 0.86 (6-H) are related to one 4-isopropyltropolonate unit, and peaks at $\delta$ = 4.86 (3′-H), 3.49 (4′-H), 3.28 (1′-H), 3.09 (2′-H), 1.33 (5′-H), 0.08 (6′-H) to the other unit, while the signals at $\delta$ = 8.97, 8.36, and 7.65 correspond to the protons of 1,10-phenanthroline-5,6-dione.

Population of gas phase ions generated by ESI-MS was studied to prove the presence of polynuclear complexes. The structural assignments of such ions are supported by their characteristic isotopic distributions particularly affected by the presence of erbium and europium atoms ($^{166}Er/^{167}Er/^{168}Er$ of 1:1.5:1.25) ($^{151}Eu/^{153}Eu$ of 1:1.1) and exact mass measurements.

The spectra of $[Ln(hino)_3(phen)]$ and $[Ln(hino)_3(pdon)]$, (Ln = Er and Eu) parallel each other and shows a fragmentation pattern consistent with the proposed formulation. In particular, it is interesting to note that, under the experimental conditions used for the spectra acquisition (1% HCOOH in $MeCN/H_2O$, 1:1 solution), the detected peaks are due to species ranging from $[Ln(hino)_2]^+$ to $[Ln(hino)_3\text{-}(H\text{-}hino)_3]^+$, $[Ln(hino)(L)]^{\cdot+}$, and $[Ln(hino)_3(L)]^+$ (L = phen, pdon). Thus, while for $[Er(hino)_3(phen)]$ the parent peak is clearly detectable at the appropriate *m*/*z* value, the

 © 2006 Wiley-VCH Verlag GmbH & Co. KGaA, Weinheim 

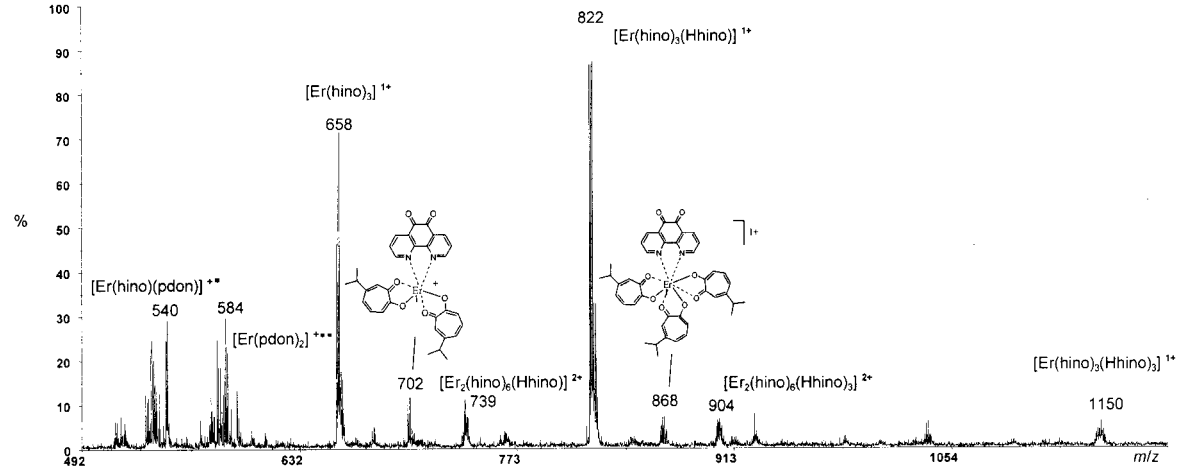


Figure 1. ESI mass spectrum in the positive mode of the methanolic solution of $[Er(hino)_3(pdon)]$.

parent peak of the dinuclear complex $[\{Ln(hino)_3\}_2(pdon)]$ was not detected probably owing to the particular experimental condition adopted.

As an example, the mass spectrum of $[\{Eu(hino)_3\}_2$-(pdon)] is reported in Figure 1; the most relevant species present in solution are indicated. The obtained data clearly show the rearrangement of the starting complex, this favouring the formation of complexes with a progressively higher number of tropolonato ligands about the central metal ion. This is certainly due to the high affinity of this particular α-diketone towards lanthanide(III) ions.

## Photophysical Properties

All the investigated $Er^{III}$ complexes in anhydrous DMSO dilute solution display strong and broad UV absorption band due to transitions between the electronic states of the organic ligand. On the contrary the UV/Vis absorption peaks arising from transition between the $Er^{3+}$ ground and excited states are only barely recognizable because of their small oscillator strength. In particular, as shown in Figure 2 (A) for the $[Er(hino)_3(pdon)]$ complex, only the $^2H_{11/2}$–$^4I_{15/2}$ transition gives rise to a detectable absorption peak at 520 nm.

Upon optical excitation in the absorption bands of the ligand, the characteristic $Er^{3+}$ emission due to the transition $^4I_{13/2}$–$^4I_{15/2}$ can be easily observed [Figure 2, (A)] indicating that an efficient energy-transfer process between the ligand and the manifold of $Er^{3+}$ excited state takes place. The quantum yield (QY) of the IR emission is nearly the same of the corresponding peak observed in a $[Er(Q)_3]$[28] (HQ = 8-hydroxyquinoline), i.e. of the order of few $10^{-4}$, in agreement with the data reported for similar tropolonate-based complexes.[23] The emission bandwidth is about 60 nm, significantly larger than the corresponding one in Er-doped silica, suggesting a high inhomogeneous disorder of $Er^{3+}$ surroundings, which hinder any possible differences among different complexes.

Deeper insight about the processes involved in the IR emission of these complexes can be obtained from time-resolved measurements. In such a way it is possible to evaluate independently the efficiency of the ligand→$Er^{3+}$ energy transfer and the efficiency of the $Er^{3+}$ photoluminescence (PL) quenching processes. Indeed, the PL intensity immediately after the excitation pulse [PL($t$ = 0)] depends only on the efficiency of the energy transfer, because the quenching of the $Er^{3+}$ excited states occurs in a relatively long timescale. On the other hand, the lifetime of the $Er^{3+}$ PL is strongly affected by the presence of non-radiative decay channels but is not related to the efficiency of $Er^{3+}$ excitation processes that take place within few ns. In Figure 3 the PL decay trace is showed for the $[Er(hino)_3(pdon)]$ complex with the corresponding fit obtained using a single exponential function. The found lifetime ($\tau_{tot}$) for the $[Er(hino)_3(pdon)]$ complex is 2.12 μs, while it is not possible to observe any PL rise time. This confirms that the excitation of the $Er^{3+}$ is extremely fast. The agreement between experimental and fitted data is perfect indicating that all the $Er^{3+}$ ions experiment the same mean local environment. Quite similar measurements have been obtained for all the studied complexes, and the corresponding lifetimes and PL efficiencies are reported in Table 1.

Because the radiative lifetime ($\tau_{rad}$) of the $Er^{3+}$ $^4I_{13/2}$–$^4I_{15/2}$ transition is around 10 ms,[29] i.e. about $10^4$ time longer the PL-detected decay time, the origin of the low efficiency of the 1550 nm emission has to be ascribed completely to the presence of fast quenching processes as usual for all the $Er^{3+}$ complexes. Indeed the $^4I_{13/2}$–$^4I_{15/2}$ transition is nearly resonant with both the first overtone of the O–H stretching vibration and the second overtone of the C–H one. By contrast the indirect excitation pathway of the $Er^{3+}$ ion seems to be rather efficient because: i) no 1550 μm PL rise time is detectable, at least in the employed timescale, and ii) the QY evaluated from the ratio between radiative and total PL lifetime (QY = $\tau_{tot}/\tau_{rad}$) and that obtained from the comparison of the integrated PL of tropolone-based complexes and of $[Er(Q)_3]$ are in good agreement. As a confirmation, it should be pointed out that in all considered complexes the distance between the Er atom and the closest H atom (C–H bond), belonging to phenanthroline ligand, has been

 © 2006 Wiley-VCH Verlag GmbH & Co. KGaA, Weinheim 

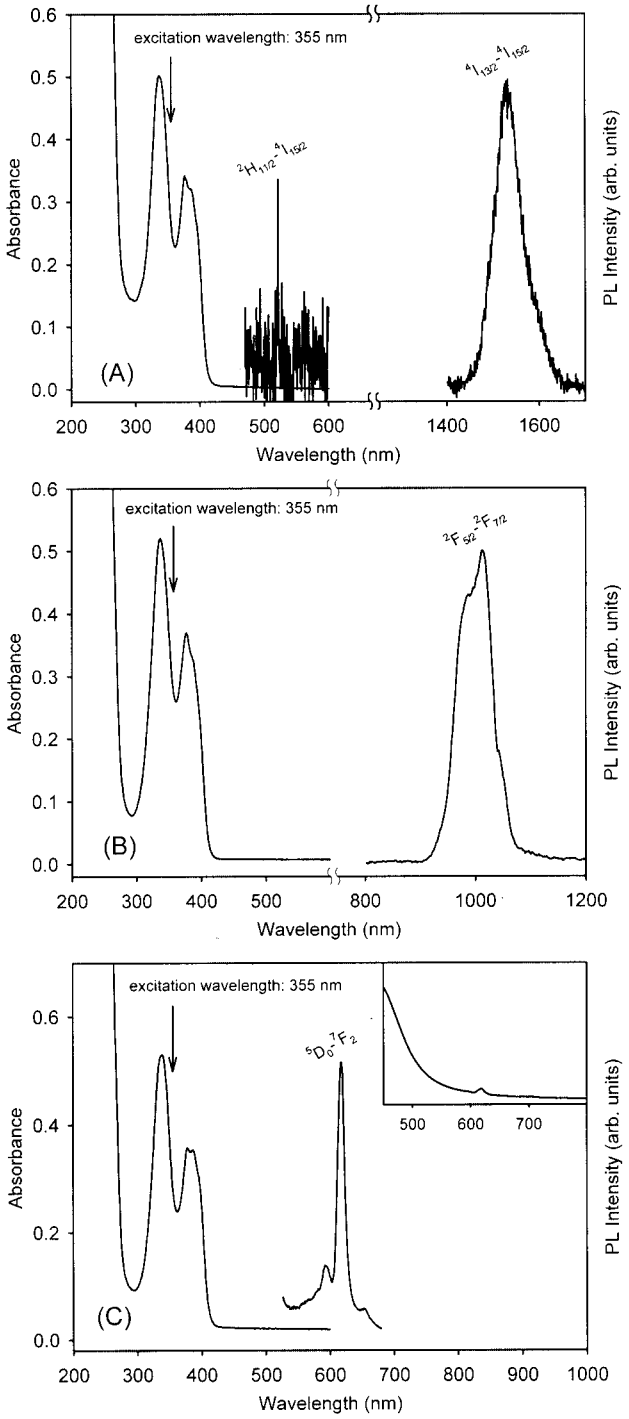


Figure 2. Absorption (left) and emission (right) spectra of the $[Er(hino)_3(pdon)]$, $[Yb(hino)_3]_n$ and $[Eu(hino)_3]_n$ complexes in DMSO at room temperature [(A), (B), and (C)] respectively. The absorption spectrum in the region of the $^2H_{12/2}$–$^4I_{15/2}$ $Er^{3+}$ transition (520 nm) has been multiplied by 100. In the panel (C) the broad PL from the ligand has been subtracted (the recoded spectrum is reported in the inset).

evaluated, from molecular modelling calculations, near to 0.41 nm; hence accounting for a reduced PL in NIR region.

It is interesting to outline that the measured PL decay times ($\tau > 2.10$ μs) are systematically longer in the studied complexes than in $[Er(Q)_3]$ ($\tau = 1.80$ μs), while the PL

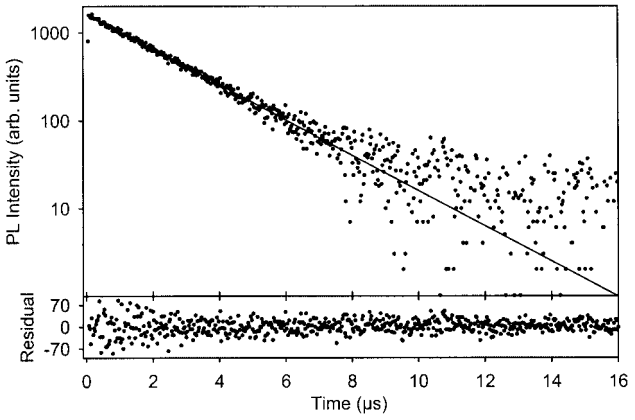


Figure 3. PL decay trace of the $[Er(hino)_3(pdon)]$ complex in DMSO (dots) recorded at 1550 nm complex at room temperature. The continuous line is the fit obtained with a single exponential function. The PL lifetime is 2.12 μs.

Table 1. Main optical data of the studied $Er^{III}$ complexes. All the reported efficiencies have been normalized to the values of $[Er(Q)_3]$ which has been set to 100.

| | Lifetime | Relative transfer efficiency | Relative total efficiency |
|---|---|---|---|
| $[Er(Q)_3]$ | 1.80 μs | 100 | 100 |
| $[\{Er(hino)_3\}_2(pdon)]$ | 2.11 μs | 107 | 125 |
| $[Er(hino)_3(pdon)]$ | 2.12 μs | 91 | 108 |
| $[Er(hino)_3(phen)]$ | 2.15 μs | 106 | 127 |
| $[Er(hino)_3]_n$ | 2.15 μs | 91 | 108 |

($t = 0$) is larger in this reference complex (see Table 1). This behaviour can be tentatively explained assuming that the bond length between the ligand and the rare earth ion are longer in the tropolone-based complexes than in $[Er(Q)_3]$, because both $Er^{3+}$ excitation and PL quenching involve energy-transfer processes which strongly depend on the distance ($R$) between donor and acceptor moieties (the transfer rate is proportional $1/R^6$ or to $e^{-R}$ for the Förster and Dexter mechanisms, respectively). Moreover, also the ability of the synthesized complexes to shield the $Er^{3+}$ ion from water molecules should be rather good, being the O–H vibration of these latter another source of non-radiative decay channels.

In Figure 2 (B, C) also typical absorption/emission spectra of the $[Yb(hino)_3]_n$ and $[Eu(hino)_3]_n$ complexes have been reported. In the case of $Yb^{III}$ complexes, upon the excitation of the ligand at 355 nm, the emission at around 1 μm due to the $^2F_{5/2}$–$^2F_{7/2}$ rare-earth transition is rather strong. Even if quantitative measurements have been not performed, the QY of these complexes is about two order of magnitude larger than in the corresponding $Er^{III}$ complexes. The $^2F_{5/2}$–$^2F_{7/2}$ PL decay is again a single exponential with a lifetime as long as 70–80 μs, which suggest the lack of any efficient quenching process in agreement with the observed high emission efficiency. On the contrary in the $Eu^{III}$ complexes the sharp emission of the lanthanide at 615 nm, even if still detectable, is extremely week and partially overlapped to the low energy tail of the ligand PL

 © 2006 Wiley-VCH Verlag GmbH & Co. KGaA, Weinheim 

[Figure 2 (C)]. In particular, in the tropolone-based complexes only the first $Eu^{3+}$ optical transition ($^5D_0$–$^7F_2$) is nearly resonant with the first triplet excited state of the ligand at about 16800 $cm^{-1}$ (595 nm). However, due to its small oscillator strength, this transition can not be excited efficiently via energy transfer.

## Conclusions

The erbium(III) derivatives $[Er(hino)_3]_n$, $[Er(hino)_3(phen)]$, $[Er(hino)_3(pdon)]$, and $[\{Er(hino)_3\}_2(pdon)]$ containing the tropolonato moiety and designed to test the IR emission on varying the chemical surrounds at the metal(III) ion were synthesized and characterized by IR, NMR, thermogravimetry, and both absorption and emission spectroscopy. The PL efficiency at 1550 nm has been measured for the whole series; values larger than that for $[Er(Q)_3]$ were observed, even though they were still affected by quenching due to the relatively short distances between the C–H bonds and the Er atom. However the longer lifetimes with respect to the $[Er(Q)_3]$ complex indicate that in tropolone complexes the number of such short distances should be diminished and and/or their values have been augmented, encouraging to design new ligands where H atoms are placed more far away. The absence of water molecules coordinated to europium(III) ion in $[Eu(hino)_3]_n$ is remarkable and somewhat unexpected. Owing to this and the high stability in the solid state and the easy formation of the phenanthroline adduct $[Eu(hino)_3(phen)]$, it is an excellent starting complex for the preparation of more sophisticated tropolonato-containing complexes.

## Experimental Section

**Materials:** The solvents, the inorganic and organic compounds and the lanthanide chloride hydrates were commercial products, supplied by Aldrich, Riedel-de Haën, Carlo–Erba, or Fluka. They were used as received, without further purification. 4-Isopropyltropolone is a TCI-GR product.

**Preparation of $[Ln(hino)_3]$ (Ln = Er, Yb, Eu):** To a methanolic (40 mL) solution of 4-isopropyltropolone (H-hino) (0.3 mmol), NaOH in methanol was added in a 1:1 ratio. Then $LnCl_3{\cdot}6H_2O$ (Ln = Er, Yb, Eu) (0.1 mmol) was added, and the resulting solution was stirred for 4 h. The solution was reduced in volume and water was added. The precipitate formed was collected by filtration, washed with water and dried in vacuo.

**$[Er(hino)_3]_n$:** IR ($cm^{-1}$): $\tilde{\nu}$ = 1588 (νC=O), 1504 (νAr, C=C), 1239 (νC–O). $C_{30}H_{33}ErO_6$ (656.83): calcd C 54.86, H 5.06; found C 54.80, H 5.17. $^1H$ NMR [$(CD_3)_2SO$, paramagnetic]: $\delta$ = 7.45, 5.45, 3.48, 1.39, 1.07, 0.31, –1.26, –2.83, –3.63, –3.90, –7.34, –10.25 ppm.

**$[Yb(hino)_3]_n$:** IR ($cm^{-1}$): $\tilde{\nu}$ = 1588 (νC=O), 1505 (νAr, C=C), 1241 (νC–O). $C_{30}H_{33}O_6Yb$ (662.61): calcd. C 62.29, H 5.75; found C 60.91, H 5.74. $^1H$ NMR [$(CD_3)_2SO$, paramagnetic]: $\delta$ = 13.06, 8.34, 7.21, 6.57, 5.97, 5.03, 3.28, 2.77, 0.79, 0.63, –0.05, –1.17, –3.42, –7.46, –9.20 ppm.

**$[Eu(hino)_3]_n$:** IR ($cm^{-1}$): $\tilde{\nu}$ = 1588 (νC=O), 1504 (νAr, C=C), 1239 (νC–O). $C_{30}H_{33}EuO_6$ (641.53): calcd. C 56.17, H 5.19; found C 55.92, H 5.02. $^1H$ NMR [$(CD_3)_2SO$, paramagnetic]: $\delta$ = 7.28, 6.79, 5.90, 5.87, 4.82, 4.47, 3.46, 3.09, 2.29, 1.28, 0.78, 0.01 ppm.

**Preparation of $[Er(hino)_3(phen)]$:** To a methanolic solution of 4-isopropyltropolone (40 mL, 0.3 mmol), NaOH in methanol was added in a 1:1 ratio. Then $ErCl_3{\cdot}6H_2O$ (0.1 mmol), was added. The resulting solution was added to a methanolic solution (20 mL) of 1,10-phenanthroline (phen) (0.1 mmol) and stirred for 4 h. The solution was reduced in volume and water was added. The precipitate formed was collected by filtration, washed with water and dried in vacuo.

**$[Er(hino)_3(phen)]{\cdot}1H_2O$:** IR ($cm^{-1}$): $\tilde{\nu}$ = 1588 (νC=O), 1504 (νAr C=C), 1240 (νC–O). $C_{42}H_{43}ErN_2O_7$ (855.05): calcd. C 59.00, H 5.07, N 3.28; found C 59.14, H 4.88, N 3.00. These values are in agreement with thermogravimetric data. $^1H$ NMR [$(CD_3)_2SO$, paramagnetic]: $\delta$ = 9.09, 8.49, 7.99, 7.77, 0.38, –1.34, –2.84, –3.17, –3.77, –7.58, –10.53 ppm.

**Preparation of $[Er(hino)_3(pdon)]$:** $Er(hino)_3$ in anhydrous methanol (40 mL) was added to 1,10-phenanthroline-5,6-dione dissolved in anhydrous methanol (20 mL) in a 1:1 molar ratio, and the resulting solution was refluxed overnight. After refluxing, a brown precipitate appears, that was centrifuged off. The clear solution was evaporated to dryness and the solid was washed with diethyl ether, filtered and dried in vacuo.

**$[Er(hino)_3(pdon)]{\cdot}0.2H_2O$:** IR ($cm^{-1}$): $\tilde{\nu}$ = 1588 (νC=O), 1504 (νC=C Ar), 1240 (νC–O). $C_{42}H_{39.1}ErN_2O_{8.2}$ (870.32): calcd. C 57.00, H 4.67, N 3.17; found C 56.52, H 4.56, N 2.91. $^1H$ NMR [$(CD_3)_2SO$], paramagnetic: $\delta$ = 8,96, 8.36, 7.65, 4.02, 0.37, –1.35, –2.85, –3.85, –7.63, –10.54 ppm.

**Preparation of $[\{Er(hino)_3\}_2(pdon)]$:** $Er(hino)_3$ in anhydrous methanol was added to $[Er(hino)_3(pdon)]$ dissolved in anhydrous methanol in a 1:1 molar ratio, and the solution was refluxed for 1 day. The solution was reduced in volume and diethyl ether was added. The precipitate now formed was collected by filtration and dried in vacuo.

**$[\{Er(hino)_3\}_2(pdon)]{\cdot}H_2O$:** IR ($cm^{-1}$): $\tilde{\nu}$ = 1588 (νC=O), 1505 (νC=C, Ar), 1239 (νC–O). $C_{72}H_{74}Er_2N_2O_{15}$ (1541.85): calcd. C 56.09, H 4.84, N 1.82; found C 55.48, H 4.71, N 1.66. $^1H$ NMR ($(CD_3)_2SO$), paramagnetic: $\delta$ = 8.97 (2 H, pdon), 8.36 (2 H, pdon), 7.66 (2 H, pdon), 3.14, 1.05, 0.34, –1.29, –2.82, –3.69, –3.88, –7.46, –10.42 ppm.

**Preparation of $[\{Eu(hino)_3\}_2(pdon)]$:** $Eu(hino)_3$ dried in vacuo at 100° was dissolved in anhydrous ethanol and 1,10-phenanthroline-5,6-dione in anhydrous ethanol was added in a 1:1 molar ratio. The solution was refluxed for 3 h under nitrogen, then it was reduced in volume. Diethyl ether was added and the precipitate formed was filtered and dried in vacuo.

**$[\{Eu(hino)_3\}_2(pdon)]$:** IR ($cm^{-1}$): $\tilde{\nu}$ = 1588 (νC=O), 1503 (νC=C Ar), 1239 (νC–O). $C_{72}H_{72}Eu_2N_2O_{14}$ (1493.24): calcd. C 57.91, H 4.86, N 1.88; found C 56.79, H 4.59, N 2.21. $^1H$ NMR [$(CD_3)_2SO$, paramagnetic]: $\delta$ = 8.97 (2 H, pdon), 8.36 (2 H, pdon), 7.65 (2 H, pdon), 7.32 (4-H), 6.81 (1-H), 5.94 (3-H), 4.86 (3′-H), 4.51 (2-H), 3.49 (4′-H), 3.28 (1′-H), 3.09 (2′-H), 2.37 (5-H), 1.33 (5′-H), 0.86 (6-H), 0.08 (6′-H) ppm.

**Physico-Chemical Measurements:** Elemental analyses were carried out with a Fison 1108 analyzer. IR spectra were recorded as KBr pellets with a Mattson FTIR spectrometer. NMR spectra ($^1H$, $^{13}C$) were recorded with a Bruker AMX300 spectrometer equipped with direct and inverse broad-band multinuclear probes. The $T_1$ longitudinal relaxation times and the mixing times of NOESY experiments of the paramagnetic europium complex were measured using the

 © 2006 Wiley-VCH Verlag GmbH & Co. KGaA, Weinheim 

standard inversion recovery pulse sequence. All ESI-MS spectra measurements were performed with a LCQ mass spectrometry (Finnigam) in methanol solutions of the samples ($10^{-5}$ M) eluted with MeCN/$H_2O$ (1:1) solution with 1% of HCOOH. The water content in the prepared samples was evaluated by thermal analysis curves using a Netzsch STA 429 thermoanalytical equipment. The tests were performed under nitrogen (flux rate 250 mL/min; heating rate 5 °C min$^{-1}$) and in air under the same conditions. Neutral alumina (Carlo–Erba product) was used as reference material.

All the optical characterizations have been performed in anhydrous DMSO dilute solution. As reference, also [Er(Q)$_3$] [tris(8-hydroxyquinolinato)erbium(III)] solutions, which is currently the benchmark for non-fluorinated organolanthanide and coordination complexes, have been prepared. UV/Vis absorption measurements have been done with a Cary 50 (Varian) spectrophotometer. NIR photoluminescence (PL) measurements have been carried out by exciting the samples with the third harmonic of a pulsed ND:YAG laser ($\lambda_{exc}$ = 355 nm, pulse duration ca. 10 ns, repetition rate 20 kHz, power ca. 1 mW). The laser beam was focused on the samples with a cylindrical lens (spot dimension about 7×0.5 mm$^2$) in order to minimize the complex degradation. The PL emission was detected with a Hamamatsu R5509-73 photomultiplier (or with a Spex 2000 CCD in the case of emissions in the visible) coupled with a Cornerstone (Oriel) monochromator (bandwidth 20 nm). The PL spectra and PL decay traces have been recorded in photon counting mode with a Ortec 9353 multichannel scaler. The overall time resolution is better than 30 ns.

## Acknowledgments

We thank Mr. V. Corrado and Mrs. A. Moresco for technical assistance. We thank Italian MIUR for partial support by FIRB project no. RBNE019H9K for financial support.

[1] N. Sabbatini, M. Guardigli, J. M. Lehn, *Coord. Chem. Rev.* **1993**, *123*, 201–228.
[2] J.-C. G. Bünzli, G. R. Choppin, *Lanthanide Probes in Life, Chemical, and Earth Sciences: Theory and Practice*, Elsevier, Amsterdam, **1989**.
[3] A. Døssing, *Eur. J. Inorg. Chem.* **2005**, 1425–1434.
[4] a) J.-C. G. Bünzli, C. Piguet, *Chem. Rev.* **2002**, *102*, 1897–1928; b) J. C. G. Bünzli, C. Piguet, *Chem. Soc. Rev.* **2005**, *34*, 1048–1077.
[5] a) D. Parker, R. S. Dickins, H. Puschmann, C. Crossland, J. A. K. Howard, *Chem. Rev.* **2002**, *102*, 1977–2010; b) S. Faulkner, J. L. Matthews, *Comprehensive Coordination Chemistry II* (Eds.: J. A. McCleverty, T. J. Meyer), Elsevier, Amsterdam, **2004**, vol. 9, pp. 913–944.
[6] T. Jüstel, H. Nikol, *Adv. Mater.* **2000**, *12*, 527–530.
[7] S. Capecchi, O. Renault, D.-G. Moon, M. Halim, M. Etchells, P. J. Dobson, O. V. Salata, V. Christou, *Adv. Mater.* **2000**, *12*, 1591.
[8] a) *The Chemistry of Contrast Agents in Medical Magnetic Resonance Imaging* (Eds.: A. E. Merbach, E. Toth), Wiley, Chichester, **2001**; b) P. Caravan, J. J. Ellison, T. J. McMurry, R. B. Lauffer, *Chem. Rev.* **1999**, *99*, 2293.
[9] J. Ren, A. D. Sherry, *Inorg. Chim. Acta* **1996**, *246*, 331–341; M. Botta, U. Casellato, C. Scalco, S. Tamburini, P. Tomasin, P. A. Vigato, S. Aime, A. Barge, *Chem. Eur. J.* **2002**, *8*, 3917–3926.
[10] D. Parker, *Coord. Chem. Rev.* **2000**, *205*, 109; I. Hemmilä, V. Laitala, *J. Fluorine Chem.* **2005**, *15*, 529–542.
[11] V. W. W. Yam, K. K. W. Lo, *Coord. Chem. Rev.* **1999**, *184*, 157.
[12] a) I. Hemmilä, T. Ståhlberg, P. Mottram, *Bioanalytical Applications of Labeling Technologies* (Ed.: Wallac Oy), Turku, **1995**; b) G. Mathis, in: *Rare Earths* (Eds.: R. Saez Puche, P. Caro), Editorial Complutense S. A., Madrid, **1998**, 285–298; c) I. Hemmilä, V. M. Mukkala, *Crit. Rev. Clin. Lab. Sci.* **2001**, *38*, 441–519.
[13] L. J. Charbonnière, R. Ziessel, *J. Alloys Compd.* **2004**, *374*, 283–288.
[14] a) K. Binnemans, Y. G. Galyametdinov, R. Van Deun, D. W. Bruce, S. R. Collinson, A. P. Polishchuk, I. Bikchantaev, W. Haase, A. V. Prosvirin, L. Tinchurina, U. Litvinov, A. Gubajdullin, A. Rakhmatullin, K. Uytterhoeven, L. Van Meervelt, *J. Am. Chem. Soc.* **2000**, *122*, 4335; b) Y. G. Galyametdinov, L. V. Malykhina, W. Haase, K. Driesen, K. Binnemans, *Liq. Cryst.* **2002**, *29*, 1581–1584.
[15] a) V. K. L. Pecharsky, K. A. Gschneidner Jr, *J. Magn. Magn. Mater.* **1999**, *200*, 44; b) K. Ahn, A. O. Pecharsky, K. A. Gschneidner, V. K. Pecharsky, *J. Appl. Phys.* **2005**, 97.
[16] a) L. G. Hubert-Pfalzgraf, *New J. Chem.* **1995**, *19*, 727; b) F. A. Gleizes, M. Julve, N. Kuzmina, A. Alikhanyan, F. Lloret, I. Malkerova, J. L. Sanz, F. Senocq, *Eur. J. Inorg. Chem.* **1998**, 1169.
[17] a) G. A. Molander, *Chem. Rev.* **1992**, *92*, 29; b) G. A. Molander, C. R. Harris, *Chem. Rev.* **1996**, *96*, 307; c) P. G. Steel, *J. Chem. Soc., Perkin Trans. 1* **2001**, 2727.
[18] T. Gross, F. Chevalier, J. S. Lindsey, *Inorg. Chem.* **2001**, *40*, 4762.
[19] a) J. Inanaga, Y. Sugimoto, T. Hanamoto, *New J. Chem.* **1995**, *19*, 707; b) S. Kobayashi, *Top. Organomet. Chem.* **1999**, *2*, 63.
[20] a) H. Sasai, T. Suzuki, N. Itoh, K. Tanaka, T. Date, K. Okamura, M. Shibasaki, *J. Am. Chem. Soc.* **1993**, *115*, 10372; b) H. Sasai, M. Hiroi, Y. M. A. Yamada, M. Shibasaki, *Tetrahedron Lett.* **1997**, *38*, 6031; c) E. Emori, T. Arai, H. Sasai, M. Shibasaki, *J. Am. Chem. Soc.* **1998**, *120*, 4043; d) K. Yamakoshi, S. J. Harwood, M. Kanai, M. Shibasaki, *Tetrahedron Lett.* **1999**, *40*, 2565.
[21] D. M. Epstein, L. L. Chappell, H. Khalili, R. M. Supkowski, W. DeWitt Horrocks Jr, J. R. Morrow, *Inorg. Chem.* **2000**, *39*, 2130.
[22] a) K. Kuriki, Y. Koike, Y. Okamoto, *Chem. Rev.* **2002**, *102*, 2347; b) J. Kido, Y. Okamoto, *Chem. Rev.* **2002**, *102*, 2357; c) R. Van Deun, P. Nockemann, C. Görller-Walrand, K. Binnemans, *Chem. Phys. Lett.* **2004**, *397*, 447–450.
[23] J. Zhang, P. D. Badger, S. J. Geib, S. Petoud, *Angew. Chem. Int. Ed.* **2005**, *44*, 2508–2512.
[24] E. L. Muetterties, C. M. Wright, *J. Am. Chem. Soc.* **1965**, *87*, 4706–4717.
[25] J. Kido, Y. Okamoto, *Chem. Rev.* **2002**, *102*, 2357–2368.
[26] J. Kido, H. Hayase, K. Hongawa, K. Nagai, K. Okuyama, *Appl. Phys. Lett.* **1994**, *33*, 863.
[27] U. Casellato, L. Bertolo, S. Tamburini, P. A. Vigato, unpublished results.
[28] R. Pizzoferrato, L. Lagonigro, T. Ziller, A. Di Carlo, R. Paolesse, F. Mandoj, A. Ricci, C. Lo Sterzo, *Chem. Phys.* **2004**, *300*, 217–225.
[29] W. J. Miniscalco, *J. Lightw. Technol.* **1991**, *9*, 234–250.

Received: November 28, 2005
Published Online: April 11, 2006

 © 2006 Wiley-VCH Verlag GmbH & Co. KGaA, Weinheim 

DOI: 10.1002/ejic.200501109

# The First Sandwich Complex with an Octa(thioether) Coordination Sphere: Bis(maleonitrile-tetrathia-12-crown-4)silver(I)

**Hans-Jürgen Holdt,*[a] Holger Müller,[a] Matthias Pötter,[a] Alexandra Kelling,[a] Uwe Schilde,[a] Ines Starke,[b] Matthias Heydenreich,[b] and Erich Kleinpeter[b]**

*Dedicated to Professor Eberhard Hoyer on the occasion of his 75th birthday*

**Keywords:** Crown compounds / S ligands / Sandwich complexes / Silver

The new tetrathiacrown ethers maleonitrile-tetrathia-12-crown-4 ($mn12S_4$) and maleonitrile-tetrathia-13-crown-4 ($mn13S_4$) have been prepared and characterised by X-ray crystallographic analysis. These crown ethers form 2:1, 3:2 and 1:1 complexes with AgY (Y = $BF_4$, $PF_6$). The crystal structures of $[Ag(mn12S_4)_2]BF_4$ (**3a**), $[Ag(mn13S_4)_2]BF_4$ (**4a**) and $[Ag_2(mn13S_4)_3](PF_6)_2$ (**6b**) have been determined. Compound **3a** contains the centrosymmetric sandwich complex cation $[Ag(mn12S_4)_2]^+$ where each $mn12S_4$ ligand is coordinated to the Ag centre in an *endo* manner through all four S atoms. The 2:1 complex $[Ag(mn12S_4)_2]^+$ is the first sandwich complex with a tetrathiacrown ether and the first complex with an octa(thioether) coordination sphere. The crystal structure of compound **4a** also reveals a 2:1 complex. This complex, $[Ag(mn13S_4)_2]^+$, exhibits a half-sandwich structure. One $mn13S_4$ ligand coordinates to $Ag^+$ by all four S donor atoms and the other $13S_4$ crown by only one S atom. Compound **6b** contains a dinuclear Ag complex. The Ag complexes **3a**,**b**–**8a**,**b** were also studied by electrospray ionisation mass spectrometry. Collision-induced dissociation (CID) was used to compare the relative stability of 2:1 complexes $[AgL_2]^+$ and 1:1 complexes $[AgL]^+$ (L = $mn12S_4$, $mn13S_4$). The $^{13}C$ NMR chemical shifts of 2:1 and 1:1 Ag complexes and their corresponding free ligands were also estimated and compared. The free energy of the barrier of ring inversion ($\Delta G^{\ddagger}$) for $[Ag(mn12S_4)_2]^+$ was determined to be 64 kJ mol$^{-1}$.
(© Wiley-VCH Verlag GmbH & Co. KGaA, 69451 Weinheim, Germany, 2006)

## Introduction

The classical crown ether, 12-crown-4 ($12O_4$), forms sandwich complexes with a number of metal ions.[1] In these complexes, for example $[Na(12O_4)_2]Cl·5H_2O$,[2] $[Mn(12O_4)_2][Br_3]_2$,[3] $[Li(12O_4)_2][PPh_2]$,[4] $[Ag(12O_4)_2][AsF_6]$,[5] $[Fe(12O_4)_2][PF_6]_2$,[6] $[In(12O_4)][SbCl_6]·3CH_3CN$,[7] and $[Zn(12O_4)_2][ZnCl_3H_2O]_2$,[8] the metal ion is coordinated to eight oxygen atoms to form an octa(oxygen) coordination sphere which is not accessible with acyclic ligands. In early studies of crown ether chemistry the structures of bis(12-crown-4)–metal ion sandwich complexes and the properties of the coordinated metal ions were of interest. Later, the ability of 12-crown-4 to coordinate metal ions in sandwich structures was used to separate cations from carbanions in an organometallic compound, such as in the substituted cyclopentadienide salt $[Li(12\text{-crown-}4)_2][1,2,4\text{-}(Me_3Si)_3C_5H_2]$,[9] to stabilize salts, such as $[Na(12O_4)_2][\{(CO)_5Mo\}_2Sn(Cl)_2]$,[10] to synthesise new inorganic polymers, such as $[Cd(12O_4)_2][Cd_2(SCN)_6]$,[11] and to construct novel molecular conductors from supramolecular cations.[12] 12-Crown-4 generally forms sandwich complexes because its cavity (1.2–1.4 Å[13]) is too small to accommodate the metal ion. Moreover, free 12-crown-4 is already preorganized for the formation of sandwich complexes. The global minimum of 12-crown-4 has been shown to be the so-called "square" conformation, which has four identical *gauche*,*gauche*,*anti* conformations for the individual O–C–C–O groups. 12-Crown-4 also adopts a "square" conformation in the solid state.[14] In this conformation all four oxygen atoms are orientated in an endodentate fashion,[15] which is perfect for a sandwich structure.[16]

The cavities of the analogous tetrathia-12-crown-4[17] ($12S_4$) and tetraaza-12-crown-4[18] ($12N_4H_4$) are also too small to accommodate a metal ion, although so far there are no known sandwich complexes with these tetradentate macrocycles. In the case of tetrathia-12-crown-4, this is because of the exodentate orientation of all four sulfur atoms in the free ligand.[17]

For the synthesis of sandwich complexes with tetradentate $S_4$- or $N_4$-crown ether compounds, preorganized derivatives are necessary. With the help of 2,11-diaza[3.3](2,6)-

[a] Institut für Chemie, Anorganische Chemie, Universität Potsdam,
Postfach 601553, 14415 Potsdam
Fax: +49-331-977-5055
E-mail: holdt@chem.uni-potsdam.de
[b] Institut für Chemie, Analytische Chemie, Universität Potsdam, Postfach 601553, 14415 Potsdam

 © 2006 Wiley-VCH Verlag GmbH & Co. KGaA, Weinheim 

pyridinophane ($12N_4H_2$, Scheme 1), Krüger et al. have synthesised $Fe^{II}$,[19a] $Fe^{III}$[19a] and $Co^{II}$[19b] sandwich-like complexes with $N_8$ coordination spheres. The rigid pyridinophane $12N_4H_2$ is a preorganized macrocyclic $N_4$ ligand that forces a metal ion in a sandwich complex to have a coordination number of eight.

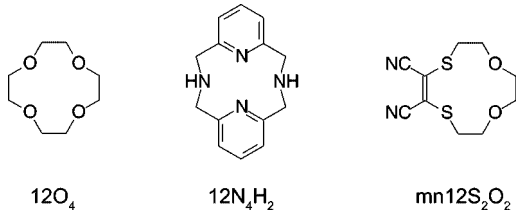


Scheme 1. Tetradentate macrocycles for 2:1 complexes (macrocycle/metal ion) with coordination number eight: 12-crown-4 ($12O_4$), 2,11-diaza[3.3](2,6)pyridinophane ($12N_4H_2$), maleonitrile-dithia-12-crown-4 ($mn12S_2O_2$).

Approaches to the preorganisation of twelve-membered $S_4$ macrocycles for sandwich complexation have, until now, not been carried out. However, tetrathiacrown ethers with larger cavities, for example with thirteen and fourteen members, have been modified at their periphery with different groups (cyclohexyl, phenyl, methyl, benzo, hydroxy) to preorganize the macrocyclic ligands for the "in-cavity" complexation.[20]

Previously, we have found that 1,4-dithiacrown ethers are stabilized in endodentate conformations by incorporating the rigid maleonitrile unit between the two sulfur atoms. The resulting maleonitrile-dithiacrown ethers[21] are preorganized $S_2O_n$ coronands ($n$ = 2–5) for the complexation of $Ag^+$,[22a,22b,23a] $Tl^+$,[22c] $Cs^+$,[21c] $Na^+$,[22d] $HgCl_2$,[22c,23b] and $MCl_3$ (M = Sb, Bi)[22d] in "in-cavity" sandwich or half-sandwich structures with mixed ether/thioether coordination spheres. The twelve-membered maleonitrile-dithia-12-crown-4 ($mn12S_2O_2$, Scheme 1) forms a sandwich complex $[Ag(mn12S_2O_2)_2]^+$ with $Ag^+$.[22a] The overall environment surrounding $Ag^I$ in $[Ag(mn12S_2O_2)_2]^+$ is that of a distorted cubic $S_4O_4$ set of donors. In this paper we report on the synthesis of the maleonitrile-tetrathiacrown ethers $mn12S_4$ and $mn13S_4$ (Scheme 2). These new tetrathiacrown ethers are preorganized $S_4$ macrocycles for the preparation of sandwich and half-sandwich complexes. Maleonitrile-tetrathia-12-crown-4 ($mn12S_4$) forms the sandwich complex $[Ag(mn12S_4)_2]^+$ with $Ag^I$, which is the first complex with an octa(thioether) coordination sphere.

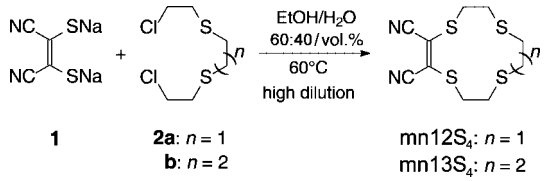


Scheme 2. Synthesis of the maleonitrile-tetrathiacrown ethers $mn12S_4$ and $mn13S_4$.

## Results and Discussion

Using the high-dilution technique, the maleonitrile-tetrathiacrown ethers $mn12S_4$ and $mn13S_4$ were obtained by treating disodium 1,2-dicyanoethene-1,2-dithiolate[24] (**1**) with 1,8-dichloro-3,6-dithiaoctane[25] (**2a**) and 1,9-dichloro-3,7-dithianonane[25] (**2b**), respectively, in ethanol/water solution (Scheme 2). The dichlorides **2a** and **2b** were prepared by chlorination of the corresponding diols with $SOCl_2$ in $CHCl_3$ and were cyclized with the dithiolate **1** without isolation.

The crystal structures of the two new tetrathiacrown ethers were obtained by X-ray crystallographic analysis; details of data collection and refinement are given in the Experimental Section. The crystal structure of $mn12S_4$ is shown in Figure 1 from two different views. The rigid maleonitrile fragment forces the orientation of the sulfur atoms

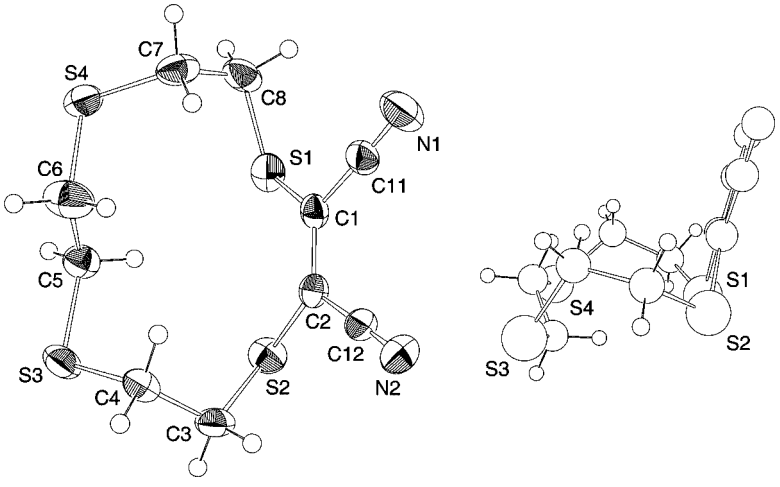


Figure 1. T7o different views of the molecular structure of maleonitrile-tetrathiacrown ether $mn12S_4$. Selected torsion angles [°] of free $mn12S_4$ and of coordinated $mn12S_4$ (in square brackets) in $[Ag(mn12S_4)_2]^+$ (Figure 3): S1–C1–C2–S2 1.68(18) [–0.7(3)], C1–C2–S2–C3 –135.65(12) [–137.37(19)], C2–S2–C3–C4 71.47(12) [65.8(19)], S2–C3–C4–S3 69.07(13) [69.2(2)], C3–C4–S3–C5 –92.51(12) [–162.59(17)], C4–S3–C5–C6 –67.56(15) [61.2(2)], S3–C5–C6–S4 –176.83(10) [64.8(2)], C5–C6–S4–C7 –106.43(10) [–151,46(19)], C6–S4–C7–C8 104.79(13) [148.49(19)], S4–C7–C8–S1 –68.65(14) [–66.4(2)], C7–C8–S1–C1 –68.38(13) [–57.7(2)], C8–S1–C1–C2 150.33(13) [139.36(19)].

 © 2006 Wiley-VCH Verlag GmbH & Co. KGaA, Weinheim 

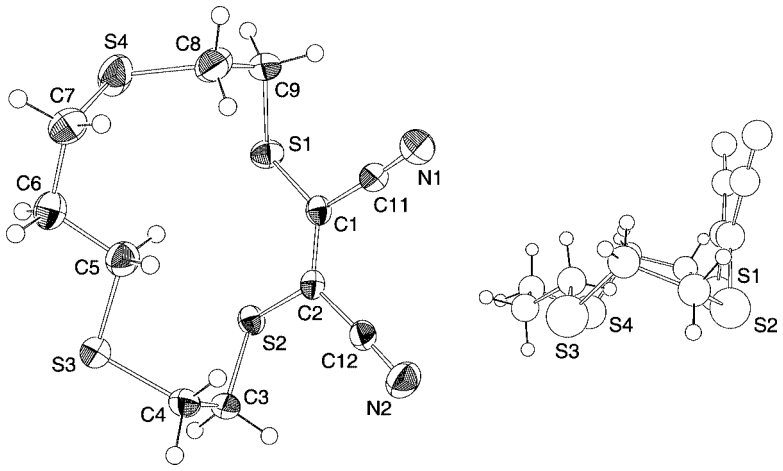


Figure 2. Two different views of the molecular structure of maleonitrile-tetrathiacrown ether mn13$S_4$. Selected torsion angles [°] of free mn13$S_4$ and of coordinated mn13$S_4$ (in square brackets) in the half-sandwich complex [Ag(mn13$S_4$){mn13$S_4$(A)-κ$^1$-S4A}]$^+$: S1–C1–C2–S2 –2.2(3) [–2.0(2)], C1–C2–S2–C3 –148.29(19) [–146.12(17)], C2–S2–C3–C4 61.8(2) [62.76(18)], S2–C3–C4–S3 61.8(2) [65.93(19)], C3–C4–S3–C5 –101.7(2) [–162.76(16)], C4–S3–C5–C6 –169.01(19) [76.69(19)], S3–C5–C6–C7 –174.14(19) [88.1(2)], C5–C6–C7–S4 67.9(3) [–92.8(2)], C6–C7–S4–C8 –107.1(2) [–73.67(19)], C7–S4–C8–C9 148.76(19) [163.15(16)], S4–C8–C9–S1 –67.5(2) [–62.9(2)], C8–C9–S1–C1 –71.8(2) [–62.67(19)], C9–S1–C1–C2 157.60(19) [145.28(17)].

S1 and S2 toward the macrocyclic ring centre (endodentate orientation). Sulfur atom S4 is in a half endo-/half exodentate position, while S3 is fully exodentate.

The preferred conformers of both mn12$S_4$ and mn13$S_4$ were also studied by molecular modelling in the gas state.[26] Two of the three most stable conformations of mn12$S_4$ show orientations for the S-donor atoms as observed in the crystal structure. In conclusion, both the results of the X-ray crystallographic analysis and of the molecular modelling reveal that free mn12$S_4$ adopts preferred conformations in which three of the four S donor atoms are already in an endodentate orientation. Similar positions for the sulfur atoms were also observed in free mn13$S_4$; in the corresponding crystal structure (see Figure 2), S1, S2 and S3 proved to be orientated in an endodentate fashion, and only S4 is exodentate.

$Ag^I$ complexes of the studied tetrathiacrown ethers were obtained by mixing a solution of the crown ether in chloroform with a methanolic solution of $AgBF_4$ or $AgPF_6$. The macrocycles and silver salts were allowed to react in 2:1, 3:2 and 1:1 molar ratios, yielding the $Ag^I$ complexes of corresponding compositions (**3a**,**b**–**8a**,**b**; Scheme 3). The IR spectra of these new $Ag^I$ complexes show the typical ligand and anion bands (see Experimental Section); there is no hint of a coordination of the nitrile groups or anions to the silver cation. Therefore, the silver ions in compounds **3a**,**b**–**8a**,**b** should only be coordinated by the S atoms of the ligands. The crystal structures of the compounds [Ag(mn12$S_4$)$_2$]$BF_4$ (**3a**), [Ag(mn13$S_4$)$_2$]$BF_4$ (**4a**) and [$Ag_2$(mn13$S_4$)$_3$]($PF_6$)$_2$ (**6b**) were determined by X-ray crystallographic analysis; the corresponding data are summarised in the Experimental Section.

Compound **3a** contains the centrosymmetric complex cation [Ag(mn12$S_4$)$_2$]$^+$, with $Ag^I$ sandwiched between the two mn12$S_4$ molecules. Each mn12$S_4$ ligand is coordinated to the $Ag^I$ centre in an *endo* manner through all four S

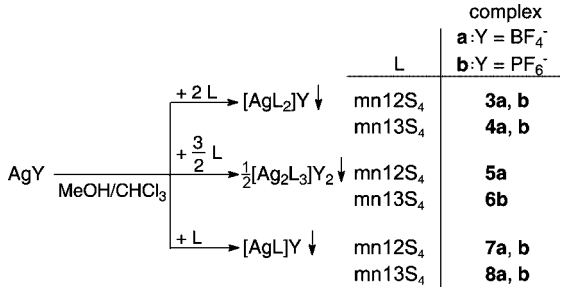


Scheme 3. Synthesis of the $Ag^I$ complexes.

atoms. Two tetradentate mn12$S_4$ macrocycles force the $Ag^I$ centre to have a closed octa(thioether) coordination sphere. The $S_8$ set of donors exhibits a distorted cubic geometry. The Ag–S bond lengths in the centrosymmetric cation [Ag(mn12$S_4$)$_2$]$^+$ are of different lengths, with four of them being shorter [2.5861(7), 2.7804(6) Å] than the other ones [3.2664(7), 3.2137(7) Å]. This kind of gradation is typical of $Ag^I$ complexes with $S_8$ coordination spheres. For example, in the centrosymmetrical sandwich complex bis(tetraethylcyclotetraarsathiane)silver(I) [Ag{*cyclo*-($C_2H_5AsS$)$_4$}$_2$]$^+$, four Ag–S distances are short [2.716(7), 2.767(5) Å] and four long [3.218(6), 3.328(9) Å].[27] Also, in the recently synthesised complex bis(η$^4$-cyclooctasulfur)silver(I) [Ag(η$^4$-$S_8$)$_2$]$^+$, four Ag–S distances are shorter (2.68–2.99 Å) than the other four (3.20–3.31 Å).[28] In the three complexes [Ag(mn12$S_4$)$_2$]$^+$, [Ag{*cyclo*-($C_2H_5AsS$)$_4$}$_2$]$^+$ and [Ag(η$^4$-$S_8$)$_2$]$^+$ the four short Ag–S distances lie in a plane.

In the sandwich complex [Ag(mn12$S_4$)$_2$]$^+$, the $Ag^+$ ion is located 1.6543(4) Å above the best least-squares plane of the four mn12$S_4$ S atoms. The sandwich complexation of the $Ag^+$ ion by two mn12$S_4$ molecules is possible because the $Ag^+$ ion cannot be accommodated in the cavity of a single crown mn12$S_4$ (1.0–1.25 Å). Moreover, the free mn12$S_4$ S atoms already assume orientations which should

 © 2006 Wiley-VCH Verlag GmbH & Co. KGaA, Weinheim 

be favourable for sandwich complexation. This expectation is confirmed by similar conformations of the free and coordinated mn12$S_4$ in the solid state. A comparative conformation analysis reveals only distinct differences for the C(4)$H_2$–S3–C(5)$H_2$–C(6)$H_2$ group, namely *a*, $g^-$ and *a* in the free and $g^-$, $g^-$ and $g^-$ in the coordinated ligand (see caption of Figure 3). The bis(maleonitrile-tetrathia-12-crown-4)silver(I) complex is the first sandwich complex with a tetrathiacrown ether and the first complex with an octa(thioether) coordination sphere.

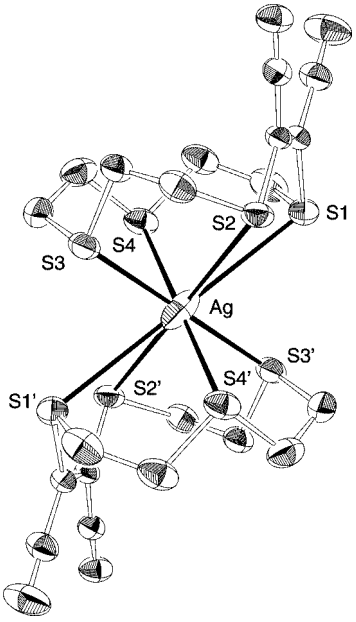


Figure 3. Molecular structure of the sandwich complex cation $[Ag(mn12S_4)_2]^+$ in compound **3a**. Selected bond lengths [Å]: Ag–S1 3.2664(7), Ag–S2 3.2137(7), Ag–S3 2.5861(7), Ag–S4 2.7804(6). For selected torsion angles see caption of Figure 1.

The crystal structure of $[Ag(mn13S_4)_2]BF_4$ (**4a**) reveals a 2:1 complex of the thirteen-membered maleontrile-tetrathia-13-crown-4 with silver(I) (Figure 4). As opposed to the sandwich complex $[Ag(mn12S_4)_2]^+$, the $[Ag(mn13S_4)_2]^+$ complex exhibits only a half-sandwich structure. One mn13$S_4$ ligand coordinates silver(I) by all four S-donor atoms and the other mn13$S_4$ molecule by only one S atom, resulting in an overall $S_5$ environment around $Ag^I$ with a distorted square-pyramidal coordination geometry. The Ag–S bond lengths [2.5020(5)–2.9475(6) Å] are normal for penta(thioether)-coordinated $Ag^+$ ions (2.550–2.995 Å[29]). In the present complex the $Ag^I$ is located only 0.9881(3) Å above the best least-squares plane of the fourfold-coordinated mn13$S_4$, which means that the $Ag^+$ ion dips markedly into the mn13$S_4$ cavity and more than half of its coordination sphere is already shielded. Thus, the second mn13$S_4$ ligand in this complex can only act as a monodentate ligand. The mn13$S_4$ cavity (1.3–1.45 Å) is too large to form a sandwich complex with silver(I), so the twelve-membered homolog mn12$S_4$ is the only one with the right cavity dimensions for preparing sandwich complexes.

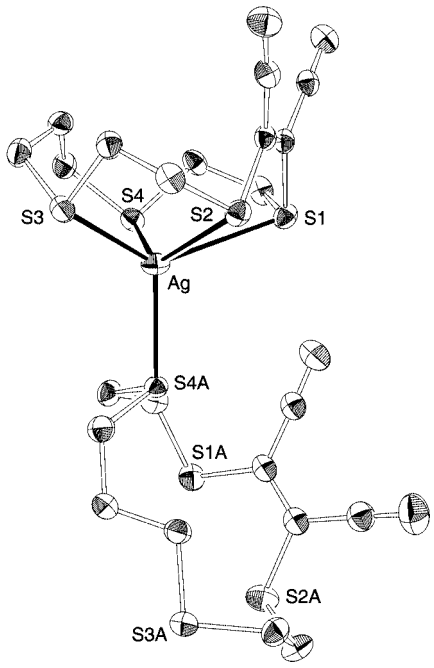


Figure 4. Molecular structure of the half-sandwich complex $[Ag(mn13S_4)\{mn13S_4(A)\text{-}\kappa^1\text{-}S4A\}]^+$ in compound **4a**. Selected bond lengths [Å]: Ag–S1 2.9475(6), Ag–S2 2.8100(6), Ag–S3 2.5508(6), Ag–S4 2.5647(6), Ag–S4A 2.5020(5). For selected torsion angles of the fourfold coordinated mn13$S_4$ molecule see the caption of Figure 2.

$[Ag_2(mn13S_4)_3](PF_6)_2$ (**6b**) contains the dinuclear $Ag^I$ complex $[\{Ag1(mn13S_4)\}\{Ag2[mn13S_4(B)]\}\{\mu_2\text{-}mn13S_4\text{-}(A)\text{-}\kappa^1\text{-}S4A,\text{-}\kappa^1\text{-}S3A\}]$ (see Figure 5). The two half-sandwich moieties $[Ag1(mn13S_4)]^+$ and $[Ag2\{mn13S_4(B)\}]^+$ are connected by the third mn13$S_4$ molecule through the S atoms S4A and S3A. Both $Ag^I$ centres therefore have a distorted square-pyramidal coordination geometry, as was already observed for the $Ag^I$ centre in the complex $[Ag(mn13S_4)_2]^+$.

Electrospray ionisation was used to study the complexes **3a**,**b**, **4a**,**b**, **7a**,**b** and **8a**,**b**. Both $[AgL_2]^+$ and $[AgL]^+$ complexes are observed in the mass spectra with different intensities (see Table 1). The loss of the anions ($PF_6^-$ and $BF_4^-$) seems to be the dominant ionisation process.[30] Additionally, the mn12$S_4$ and mn13$S_4$ ligands form 3:2 complexes **5a** and **6b** but with very low ion intensities (total ion current $< 50$ counts) in the mass spectra.

Collision-induced dissociation (CID) measurements were carried out to compare the relative stability of the $[AgL_2]Y$ and $[AgL]Y$ complexes. The $[AgL_2]Y$ complexes decompose easily by the elimination of one ligand ion. Increasing the collisional energy lowers the relative abundance of the peak of the $[AgL_2]^+$ complex ion, but raises the relative abundance of the peak of the $[AgL]^+$ complex ion. The collision voltage was gradually increased until the relative intensity of the 1:1 complex ion as well as that of the 2:1 complex ion was only 50%: the collision voltages thus obtained give an estimate of the dissociation energies of the corresponding complexes, which are generally higher for the $[AgL]^+$ complexes (22–25 eV) than for the corresponding $[AgL_2]^+$

 © 2006 Wiley-VCH Verlag GmbH & Co. KGaA, Weinheim 

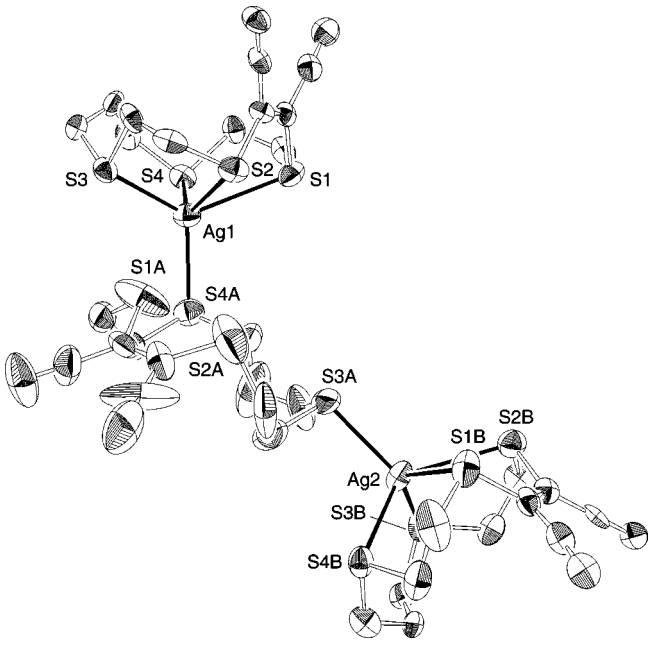


Figure 5. Molecular structure of the dinuclear complex $[\{Ag1(mn13S_4)\}\{Ag2(mn13S_4(B))\}\{\mu_2\text{-}mn13S_4(A)\text{-}\kappa^1\text{-}S4A\text{-}\kappa^1\text{-}S3A\}]^{2+}$ in compound **6b**. Selected bond lengths [Å]: Ag1–S1 2.888(3), Ag1–S2 2.908(3), Ag1–S3 2.556(3), Ag1–S4 2.597(3), Ag1–S4A 2.484(3), Ag2–S1B 2.840(3), Ag2–S2B 2.904(3), Ag2–S3B 2.581(3), Ag2–S4B 2.613(3), Ag2–S3A 2.540(4).

complexes (0–6 eV). Obviously, under electrospray conditions the tetrathiacrown ethers $mn12S_4$ and $mn13S_4$ form much more stable 1:1 complexes than 2:1 complexes.[31] Only minor differences in the CID measurements were observed in the fragmentation of the [AgL] complexes with $mn12S_4$ and $mn13S_4$. In the CID experiments of the $[AgL]^+$ ions, fragmentation occurred in the same way, mainly involving cleavage of the bond between the sulfur atoms and the carbon atom attached to the ethylene unit.

$^{13}C$ NMR spectroscopic investigations of both the complexes **3a**, **4a**, **7a** and **8a** and the free ligands $mn12S_4$ and $mn13S_4$ in solution ([$D_3$]nitromethane) showed no evidence for any equilibrium formation in the case of the complexes or of conformational changes in the case of the free ligands; only one set of signals could be observed at room temperature. The complexation with silver ions changed the chemical shifts of all signals with respect to those of the free ligands. Except for the C atoms in the γ-position to the double bond, the 12-membered complexes **3a** and **7a** and the 13-membered complexes **4a** and **8a**, the difference of the chemical shifts is larger in the 1:1 complex than in the 1:2 complex. Also, the direction of the complex-induced difference of chemical shifts is always the same. However, the signals of the C atoms in the γ-position in the 1:2 complexes are always found downfield with regard to the 1:1 complexes (see Tables 2 and 3).

Table 2. $^{13}C$ NMR chemical shifts and shift differences [ppm] of the 12-membered tetrathiacrown ether $mn12S_4$.

| | $mn12S_4$ | **7a** | $\Delta\delta$(**7a** – $mn12S_4$) | **3a** | $\Delta\delta$(**3a** – $mn12S_4$) |
|---|---|---|---|---|---|
| C=C | 125.2 | 125.7 | +0.5 | 125.7 | +0.5 |
| C≡N | 114.2 | 112.8 | –1.4 | 113.3 | –0.9 |
| C-5 | 38.5 | 35.2 | –3.3 | 36.5 | –2.0 |
| C-6 | 34.7 | 33.7[a] | –1.0 | 35.0 | +0.3 |
| C-7 | 35.9 | 34.0[a] | –1.9 | 35.3 | –0.6 |

[a] Or reversed.

Table 3. $^{13}C$ NMR chemical shifts and shift differences [ppm] of the 13-membered tetrathiacrown ether $mn13S_4$.

| | $mn13S_4$ | **8a** | $\Delta\delta$(**8a** – $mn13S_4$) | **4a** | $\Delta\delta$(**4a** – $mn13S_4$) |
|---|---|---|---|---|---|
| C=C | 124.1 | 124.2 | +0.1 | 124.4 | +0.3 |
| C≡N | 114.0 | 112.7 | –1.3 | 113.3 | –0.7 |
| C-3 | 37.8 | 35.3[a,b] | –2.5 | 36.4 | –1.4 |
| C-2 | 33.5 | 34.3[a] | +0.8 | 34.7 | +1.2 |
| C-13 | 33.2 | 35.2[b] | +2.0 | 34.8 | +1.6 |
| C-12 | 30.3 | 26.5 | –3.8 | 28.4 | –1.9 |

[a] Or reversed. [b] Or reversed.

The $^1H$ NMR spectra of **7a** and **8a** show strongly broadened lines at room temperature. The low-temperature spectra of these compounds gave significant splitting of all groups of signals only in the case of **7a**, which permitted the determination of the free energy of the barrier of ring inversion ($\Delta G^{\ddagger}_{338}$ = 64 kJ mol$^{-1}$). The coalescence temperature of **8a** is very close to room temperature, and cooling to the melting point of the solution gave an insufficient splitting of the signals to estimate the difference of the chemical shifts. Thus, the barrier of ring inversion in **7a** is higher than in the 1:2 complex $[Ag(mn12S_2O_2)_2]^+$, which was determined previously to be 51 kJ mol$^{-1}$.[32] The presence of four S atoms, as well as a generally stronger bonding of the cation in the 1:1 complex **7a**, led us to expect such a behaviour. In general, the complexation in 12-membered ring systems leads to a strongly increased barrier of the ring inversion by fixing the donor atoms. As a comparison, the barriers for cyclododecane (ca. 29 kJ mol$^{-1}$),[33] substituted cyclododecanes (ca. 34–37 kJ mol$^{-1}$)[34] and cyclododecene (ca. 29 and 40 kJ mol$^{-1}$)[35] should be highlighted.

Table 1. Positive-ion ES-MS data for the 2:1 complexes recorded in MeCN solution. Cone voltage: 20 V; collision energy: 3 eV.

| Complex | Ions (*m*/*z*, %) | |
|---|---|---|
| $[Ag(mn12S_4)_2]BF_4$ (**3a**) | $[Ag(mn12S_4)_2]^+$ (684, 100) | $[Ag(mn12S_4)]^+$ (395, 50) |
| $[Ag(mn13S_4)_2]BF_4$ (**4a**) | $[Ag(mn13S_4)_2]^+$ (711, 80) | $[Ag(mn13S_4)]^+$ (410, 100) |
| $[Ag(mn12S_4)_2]PF_6$ (**3b**) | $[Ag(mn12S_4)_2]^+$ (684, 20) | $[Ag(mn12S_4)]^+$ (395, 100) |
| $[Ag(mn13S_4)_2]PF_6$ (**4b**) | $[Ag(mn13S_4)_2]^+$ (711, 100) | $[Ag(mn13S_4)]^+$ (410, 95) |

 © 2006 Wiley-VCH Verlag GmbH & Co. KGaA, Weinheim 

## Conclusion

The maleonitrile-tetrathia-12-crown-4 is the first preorganized tetradentate thiacrown ether that forms sandwich complexes with the coordination number eight. At present we are investigating the complexing properties of $mn12S_4$ and $mn13S_4$ for other metal ions.

## Experimental Section

**General:** All operations were performed under dry argon using standard equipment and vacuum techniques. Solvents were dried by standard methods and distilled prior to use. 1,8-Dichloro-3,6-dithiaoctane,[25] 1,9-dichloro-3,7-dithianonane[25] and disodium (*Z*)-1,2-dicyanoethene-1,2-dithiolate[24] were prepared according to published procedures. Elemental analyses (C, H, N, S) were performed with an Elementar Vario EL elemental analyzer. NMR spectra were recorded with a Bruker Avance 500 or an Avance 300 spectrometer. For preparing the complex solutions, 15 mg was dissolved in 0.7 mL of deuterated chloroform or [$D_3$]nitromethane. Chemical shifts are referenced to TMS (for $^1H$) or to the solvent ($^{13}C$). All 1D and 2D COSY and HMQC pulse sequences were taken from the standard Bruker software. IR spectra were recorded with a Thermo Nicolet NEXUS FTIR instrument. UV/Vis measurements were carried out with an Analytik Jena Specord S 100 spectrophotometer with sealed quartz cuvettes. The ESI and CID spectra were recorded with a Micromass Q-TOF$_{micro}$ mass spectrometer in positive electrospray mode.

**Synthesis of Maleonitrile-tetrathiacrown Ethers $mn12S_4$ and $mn13S_4$:** A solution of disodium (*Z*)-1,2-dicyanoethene-1,2-dithiolate (11.72 g, 63 mmol) in water (0.8 L) was added to a solution of 1,8-dichloro-3,6-dithiaoctane (13.14 g, 60 mmol; synthesis of $mn12S_4$) or 1,9-dichloro-3,7-dithianonane (13.98 g, 60 mmol; synthesis of $mn13S_4$) in ethanol (1.2 L). The solution was stirred at 60 °C for 60 h and the polymeric reaction products were filtered off. The filtrate was concentrated, the residue dissolved in chloroform, the solution washed twice with water and dried with magnesium sulfate. The drying agent was removed by filtration and the filtrate concentrated in vacuo. The residual brown oil was chromatographed on a silica gel 60 gravity column (3 cm diameter × 50 cm length), and was eluted with chloroform to give the maleonitrile-tetrathiacrown ether.

**1,4,7,10-Tetrathiacyclododec-2-ene-2,3-dicarbonitrile ($mn12S_4$):** Yield: 3.4 g (18.7%). $R_f$ = 0.49 (chloroform). M.p. 182 °C (chloroform). IR (KBr): $\tilde{\nu}$ = 2222 m, 2208 m (C≡N); 1504 m (C=C) $cm^{-1}$. UV (chloroform): $\lambda_{max}$ (log $\varepsilon$) = 316 sh, 347 (3.97) nm. $^1H$ NMR ($CDCl_3$): $\delta$ = 2.88 [m, 4 H, C(6)$H_2$], 2.96 [s, 4 H, C(8)$H_2$], 3.37 [m, 4 H, C(5)$H_2$] ppm. $^{13}C$ NMR: See Table 2. ESI(HR)-MS: *m*/*z* calcd. for $C_{10}H_{12}N_2S_4$ $[M]^+$ 287.9883; found 287.9881. $C_{10}H_{12}N_2S_4$ (288.46): calcd. C 41.64, H 4.19, N 9.71, S 44.46; found C 42.38, H 4.24, N 9.62, S 44.47.

**1,4,7,10-Tetrathiacyclotridec-5-ene-5,6-dicarbonitrile ($mn13S_4$):** Yield: 3.05 g (16%). $R_f$ = 0.33 (chloroform). M.p. 152–153 °C (chloroform). IR (KBr): $\tilde{\nu}$ = 2221 m, 2209 m (C≡N); 1507 m (C=C) $cm^{-1}$. UV (chloroform): $\lambda_{max}$ (log $\varepsilon$) = 297 sh, 347 (4.09) nm. $^1H$ NMR ($CDCl_3$): $\delta$ = 1.79 [m, 2 H, C(12)$H_2$], 2.73 [t, $^3J_{H,H}$ = 7.4 Hz, 4 H, C(13)$H_2$], 2.87 [m, 4 H, C(2)$H_2$], 3.35 [m, 4 H, C(3)$H_2$] ppm. $^{13}C$ NMR: See Table 3. ESI(HR)-MS: *m*/*z* calcd. for $C_{11}H_{15}N_2S_4$ $[M + H]^+$ 303.0118; found 303.0133. $C_{11}H_{14}N_2S_4$ (302.49): calcd. C 43.68, H 4.67, N 9.26, S 42.40; found C 44.04, H 4.54, N 9.14, S 41.92.

**Synthesis of $Ag^I$ Complexes 3a,b–8a,b:** A methanolic solution of AgY (Y = $BF_4$, $PF_6$) was added to a stirred solution of the maleonitrile-tetrathiacrown ether in chloroform. After a few seconds, yellow crystals formed and were isolated by filtration.

**$[Ag(mn12S_4)_2]BF_4$ (3a):** Formed from $mn12S_4$ (28.8 mg, 0.1 mmol) in $CHCl_3$ (2 mL) and $AgBF_4$ (9.7 mg, 0.05 mmol) in MeOH (1 mL). Yield: 68 mg (88%). M.p. 194–196 °C. IR (KBr): $\tilde{\nu}$ = 2222 m, 2212 m (C≡N); 1510 m (C=C); 1083 s, 1061 s, 1052 s (B–F) $cm^{-1}$. $^1H$ NMR ($CD_3NO_2$): $\delta$ = 3.18 [s, 4 H, C(8)$H_2$], 3.21 [m, 4 H, C(6)$H_2$], 3.56 [m, 4 H, C(5)$H_2$] ppm. $^{13}C$ NMR: See Table 2. ESI(HR)-MS: *m*/*z* calcd. for $C_{20}H_{24}AgN_4S_8$ $[M - BF_4]^+$ 682.8818; found 682.8812. $C_{20}H_{24}AgBF_4N_4S_8$ (771.59): calcd. C 31.13, H 3.14, N 7.26, S 33.24; found C 30.51, H 3.00, N 6.92, S 32.35.

**$[Ag(mn12S_4)_2]PF_6$ (3b):** Formed from $mn12S_4$ (28.8 mg, 0.1 mmol) in $CHCl_3$ (2 mL) and $AgPF_6$ (12.6 mg, 0.05 mmol) in MeOH (2 mL). Yield: 52 mg (63%). M.p. 193 °C. IR (KBr): $\tilde{\nu}$ = 2222 m, 2213 m (C≡N); 1512 m (C=C); 835 s, 558 m (P–F) $cm^{-1}$. ESI(HR)-MS: *m*/*z* calcd. for $C_{20}H_{24}AgN_4S_8$ $[M - PF_6]^+$ 682.8818; found 682.8825. $C_{20}H_{24}AgF_6N_4PS_8$ (829.75): calcd. C 28.95, H 2.92, N 6.75, S 30.91; found C 28.63, H 2.78, N 6.48, S 31.30.

**$[Ag(mn13S_4)_2]BF_4$ (4a):** Formed from $mn13S_4$ (30.2 mg, 0.1 mmol) in $CHCl_3$ (2 mL) and $AgBF_4$ (9.7 mg, 0.05 mmol) in MeOH (1 mL). Yield: 71 mg (88%). M.p. 190–191 °C. IR (KBr): $\tilde{\nu}$ = 2217 m, 2209 m (C≡N); 1512 m, 1504 m (C=C); 1069 s, 1052 s, 1035 s (B–F) $cm^{-1}$. $^1H$ NMR ($CD_3NO_2$): $\delta$ = 2.06 [m, 2 H, C(12)$H_2$], 3.02 [t, $^3J_{H,H}$ = 6.1 Hz, 4 H, C(13)$H_2$], 3.24 [m, 4 H, C(2)$H_2$], 3.59 [m, 4 H, C(3)$H_2$]. $^{13}C$ NMR: See Table 3. ESI(HR)-MS: *m*/*z* calcd. for $C_{22}H_{28}AgN_4S_8$ $[M - BF_4]^+$ 710.9131; found 710.9136. $C_{22}H_{28}AgBF_4N_4S_8$ (799.64): calcd. C 33.04, H 3.53, N 7.01, S 32.07; found C 32.90, H 3.42, N 6.63, S 32.59.

**$[Ag(mn13S_4)_2]PF_6$ (4b):** Formed from $mn13S_4$ (30.2 mg, 0.1 mmol) in $CHCl_3$ (2 mL) and $AgPF_6$ (12.6 mg, 0.05 mmol) in MeOH (2 mL). Yield: 57 mg (66%). M.p. 193–195 °C. IR (KBr): $\tilde{\nu}$ = 2225 m, 2216 m, 2210 m (C≡N); 1514 m, 1505 m (C=C); 840 s, 558 m (P–F) $cm^{-1}$. ESI(HR)-MS: *m*/*z* calcd. for $C_{22}H_{28}AgN_4S_8$ $[M - PF_6]^+$ 710.9131; found 710.9140. $C_{22}H_{28}AgF_6N_4PS_8$ (857.80): calcd. C 30.80, H 3.29, N 6.53, S 29.90; found C 30.77, H 3.20, N 6.44, S 30.34.

**$[Ag_2(mn12S_4)_3](BF_4)_2$ (5a):** Formed from $mn12S_4$ (21.6 mg, 0.075 mmol) in $CHCl_3$ (2 mL) and $AgBF_4$ (9.7 mg, 0.05 mmol) in MeOH (1 mL). Yield: 31 mg (33%). M.p. 172–185 °C. IR (KBr): $\tilde{\nu}$ = 2223 m, 2213 m (C≡N); 1511 m, 1502 m (C=C); 1053 s, 1037 s (B–F) $cm^{-1}$. ESI(HR)-MS: *m*/*z* calcd. for $C_{30}H_{36}Ag_2BF_4N_6S_{12}$ (< 1) $[M - BF_4]^+$ 1164.7781; found 1164.7758. $C_{30}H_{36}Ag_2B_2F_8N_6S_{12}$ (1254.7): calcd. C 28.72, H 2.89, N 6.70, S 30.66; found C 28.12, H 2.55, N 6.35, S 31.40.

**$[Ag_2(mn13S_4)_3](PF_6)_2$ (6b):** Formed from $mn13S_4$ (22.65 mg, 0.075 mmol) in $CHCl_3$ (2 mL) and $AgPF_6$ (12.6 mg, 0.05 mmol) in MeOH (2 mL). Yield: 42 mg (40%). M.p. 194.5–195.5 °C. IR (KBr): $\tilde{\nu}$ = 2223 m, 2211 m (C≡N); 1510 m, 1503 m (C=C); 845 s, 558 m (P–F) $cm^{-1}$. ESI(HR)-MS: *m*/*z* calcd. for $C_{33}H_{44}Ag_2F_6N_6PS_{12}$ (< 1) $[M - PF_6 + 2\ H]^+$ 1266.8020; found 1266.8044. $C_{33}H_{42}Ag_2F_{12}N_6P_2S_{12}$ (1413.12): calcd. C 28.05, H 3.00, N 5.95, S 27.22; found C 27.81, H 2.92, N 5.83, S 28.40.

**$[Ag(mn12S_4)]BF_4$ (7a):** Formed from $mn12S_4$ (14.4 mg, 0.05 mmol) in $CHCl_3$ (1 mL) and $AgBF_4$ (9.7 mg, 0.05 mmol) in MeOH (1 mL). Yield: 18 mg (75%). M.p. 169–172 °C. IR (KBr): $\tilde{\nu}$ = 2227 m, 2215 m (C≡N); 1511 m, 1504 m (C=C); 1056 s (B–F) $cm^{-1}$. $^1H$ NMR: See text. $^{13}C$ NMR: See Table 2. ESI(HR)-MS: *m*/*z* calcd. for $C_{10}H_{12}AgN_2S_4$ $[M - BF_4]^+$ 394.8934; found 394.8959.

 © 2006 Wiley-VCH Verlag GmbH & Co. KGaA, Weinheim 

$C_{10}H_{12}AgBF_4N_2S_4$ (483.13): calcd. C 24.86, H 2.50, N 5.80, S 26.54; found C 24.62, H 2.34, N 5.63, S 27.20.

**[Ag(mn12S$_4$)]PF$_6$ (7b):** Formed from mn12S$_4$ (14.4 mg, 0.05 mmol) in $CHCl_3$ (1 mL) and $AgPF_6$ (12.6 mg, 0.05 mmol) in MeOH (2 mL). Yield: 18 mg (67%). M.p. 169.5–172 °C. IR (KBr): $\tilde{\nu}$ = 2226 m, 2216 m (C≡N); 1512 m, 1504 m (C=C); 839 s, 558 m (P–F) cm$^{-1}$. ESI(HR)-MS: *m/z* calcd. for $C_{10}H_{12}AgN_2S_4$ $[M - PF_6]^+$ 394.8934; found 394.8928. $C_{10}H_{12}AgF_6N_2PS_4$ (541.29): calcd. C 22.19, H 2.23, N 5.18, S 23.69; found C 22.25, H 2.13, N 5.13, S 24.48.

**[Ag(mn13S$_4$)]BF$_4$ (8a):** Formed from mn13S$_4$ (15.1 mg, 0.05 mmol) in $CHCl_3$ (1 mL) and $AgBF_4$ (9.7 mg, 0.05 mmol) in MeOH (1 mL). Yield: 21 mg (85%). M.p. 158–161 °C. IR (KBr): $\tilde{\nu}$ = 2224 m, 2214 m (C≡N); 1510 m, 1503 m (C=C); 1054 s (B–F) cm$^{-1}$. $^1$H NMR: See text. $^{13}$C NMR: See Table 3. ESI(HR)-MS: *m/z* calcd. for $C_{11}H_{14}AgN_2S_4$ $[M - BF_4]^+$ 408.9091; found 408.9115. $C_{11}H_{14}AgBF_4N_2S_4$ (497.16): calcd. C 26.58, H 2.84, N 5.63, S 25.79; found C 26.32, H 2.73, N 5.48, S 26.38.

**[Ag(mn13S$_4$)]PF$_6$ (8b):** Formed from mn13S$_4$ (15.1 mg, 0.05 mmol) in $CHCl_3$ (1 mL) and $AgPF_6$ (12.6 mg, 0.05 mmol) in MeOH (2 mL). Yield: 19 mg (68%). M.p. 167–168 °C. IR (KBr): $\tilde{\nu}$ = 2225 m, 2214 m (C≡N); 1510 m, 1502 m (C=C); 840 s, 558 m (P–F) cm$^{-1}$. ESI(HR)-MS: *m/z* calcd. for $C_{11}H_{14}AgN_2S_4$ $[M - PF_6]^+$ 408.9091; found 408.9109. $C_{11}H_{14}AgF_6N_2PS_4$ (555.32): calcd. C 23.79, H 2.54, N 5.04, S 23.09; found C 24.08, H 2.48, N 5.01, S 23.7.

**Electrospray Ionisation:** The ligand and complex solutions ($10^{-5}$ M) for the ESI investigations were prepared with $CH_3CN$ or $CH_3NO_2$. All samples were injected (5–25 μL min$^{-1}$) with a Harvard syringe pump. The capillary voltage was set to 2.5 kV, with a cone voltage of between 15 and 35 V. The source temperature was 80 °C and the desolvation temperature 150 °C. The cone and desolvation gases (nitrogen) were delivered at 50 and 360 μL h$^{-1}$, respectively (Table 2). For MS/MS, after selection of the appropriate precursor ion, argon was used as the collision gas (approx. $5 \times 10^{-5}$ mbar) and the gas cell was maintained between 3 and 40 eV. Elemental compositions were determined by accurate mass measurement with a standard deviation of less than 5 ppm.

**X-ray Structure Determinations for mn12S$_4$, mn13S$_4$, 3a, 4a and 6b:** Crystals of mn12S$_4$ and mn13S$_4$ suitable for the X-ray structure determination were obtained by slow crystallisation from a chloroform solution in a refrigerator at 6 °C. Single crystals of **3a** were selected from a nitromethane solution after standing at 6 °C for 4 d. A solution of **4a** was placed in the narrow region of a crystallisation tube and carefully covered with a heptane layer. After 5 d, yellow crystals, which were suitable for X-ray analysis, were obtained. Crystals of **6b** were grown at 6 °C from a methanol/nitromethane solution during a six-week period. The crystals were mounted on a glass fibre. Diffraction data for mn12S$_4$, mn13S$_4$, **3a** and **6b** were collected with a STOE IPDS-2 diffractometer (Table 4). Data for **4a** were collected with a STOE four-circle instrument. All measurements were performed at 210(2) K using graphite-monochromated Mo-$K_\alpha$ radiation ($\lambda$ = 0.71073 Å). Spherical absorption corrections were applied for mn12S$_4$ and mn13S$_4$. For **4a**, an empirical absorption correction was performed. The structures were solved by direct methods (SHELXS-97)[36] and refined by full-matrix least-squares on $F^2$ using all reflections (SHELXL-97).[37] All non-hydrogen atoms were refined anisotropically. The hydrogen atoms were calculated in their expected positions and refined using a riding model. The packing of **3a** contains disordered tetrafluoroborate anions and two solvate molecules (nitromethane) with small occupancy factors, from which only one solvate molecule could be satisfactorily refined. Therefore only one was involved in the refinement; the other ones were disregarded with the SQUEEZE instruction of the PLATON[38] program. CCDC-266947 to -266951 (for mn12S$_4$, mn13S$_4$, **3a**, **4a** and **6b**,

Table 4. Crystallographic data for the structural analyses of compounds mn12S$_4$, mn13S$_4$, **3a**, **4a**, and **6b**.

| | mn12S$_4$ | mn13S$_4$ | **3a**·2CH$_3$NO$_2$ | **4a** | **6b**·2CH$_3$NO$_2$ |
|---|---|---|---|---|---|
| Empirical formula | $C_{10}H_{12}N_2S_4$ | $C_{11}H_{14}N_2S_4$ | $C_{22}H_{30}AgBF_4N_6O_4S_8$ | $C_{22}H_{28}AgBF_4N_4S_8$ | $C_{35}H_{48}Ag_2F_{12}N_8O_4P_2S_{12}$ |
| Formula mass | 288.46 | 302.48 | 893.67 | 799.64 | 1535.21 |
| Crystal system | monoclinic | monoclinic | triclinic | triclinic | monoclinic |
| Space group | $P2_1/c$ | $P2_1/c$ | $P\bar{1}$ | $P\bar{1}$ | $P2_1$ |
| *a* [Å] | 7.9925(5) | 9.1375(8) | 8.4720(8) | 9.0222(6) | 9.2270(3) |
| *b* [Å] | 17.7229(9) | 9.3531(5) | 10.8770(10) | 9.4131(8) | 32.9208(17) |
| *c* [Å] | 9.5906(6) | 16.6903(15) | 12.7790(11) | 18.4532(14) | 9.3795(3) |
| *α* [°] | 90 | 90 | 66.830(6) | 83.591(7) | 90 |
| *β* [°] | 105.572(5) | 95.761(7) | 73.070(6) | 89.939(6) | 96.779(3) |
| *γ* [°] | 90 | 90 | 73.370(6) | 81.332(6) | 90 |
| *V* [Å$^3$] | 1308.65(13) | 1419.21(19) | 1015.78(16) | 1539.4(2) | 2829.20(19) |
| *Z* | 4 | 4 | 1 | 2 | 2 |
| $D_{calcd.}$ [g cm$^{-3}$] | 1.464 | 1.416 | 1.461 | 1.725 | 1.802 |
| *F*(000) | 600 | 632 | 413 | 808 | 1540 |
| *Θ* range [°] | 2.30–24.99 | 2.24–24.99 | 1.77–25.00 | 2.20–27.49 | 1.24–22.50 |
| Index range | $-9 \le h \le 9$ | $-10 \le h \le 10$ | $-10 \le h \le 10$ | $0 \le h \le 11$ | $-9 \le h \le 9$ |
| | $-20 \le k \le 20$ | $-11 \le k \le 11$ | $-12 \le k \le 12$ | $-12 \le k \le 12$ | $-35 \le k \le 35$ |
| | $-11 \le l \le 11$ | $-19 \le l \le 19$ | $-15 \le l \le 15$ | $-20 \le l \le 23$ | $-10 \le l \le 10$ |
| Reflections collected | 19147 | 8242 | 10580 | 7391 | 26971 |
| Independent reflections | 2300 | 2489 | 3573 | 6969 | 7373 |
| Data/restraints/parameters | 2300/0/146 | 2489/0/155 | 3573/0/226 | 6969/0/362 | 7373/3/688 |
| $R_1$, $wR_2$ [$I > 2\sigma(I)$] | 0.0234, 0.0601 | 0.0343, 0.0816 | 0.0305, 0.0878 | 0.0277, 0.0766 | 0.0517, 0.1059 |
| $R_1$, $wR_2$ (all data) | 0.0285, 0.0618 | 0.0442, 0.0847 | 0.0358, 0.0895 | 0.0377, 0.0807 | 0.0771, 0.1144 |
| *S* | 1.039 | 1.042 | 1.060 | 1.027 | 0.953 |
| $\Delta\rho_{min.}$, $\Delta\rho_{max.}$ [e Å$^{-3}$] | –0.203, 0.039 | –0.522, 1.070 | –0.488, 0.371 | –0.771, 1.246 | –0.632, 1.092 |

 © 2006 Wiley-VCH Verlag GmbH & Co. KGaA, Weinheim 

respectively) contain the supplementary crystallographic data for this paper. These data can be obtained free of charge from The Cambridge Crystallographic Data Centre via www.ccdc.cam.ac.uk/data_request/cif.

## Acknowledgments

This work was supported by the Deutsche Forschungsgemeinschaft.

[1] G. W. Gokel, *Crown Ethers and Cryptands*, The Royal Society of Chemistry, Cambridge, **1994**.
[2] F. P. van Remoortere, F. P. Boer, *Inorg. Chem.* **1974**, *13*, 2071–2078.
[3] B. B. Hughes, R. C. Haltiwanger, C. G. Pierpont, M. Hampton, G. L. Blackmer, *Inorg. Chem.* **1980**, *19*, 1801–1803.
[4] H. Hope, M. M. Olmstead, P. P. Power, X. Xu, *J. Am. Chem. Soc.* **1984**, *106*, 819–821.
[5] P. G. Jones, T. Gries, H. Grützmacher, H. W. Roesky, J. Schimkowiak, G. M. Sheldrick, *Angew. Chem.* **1984**, *96*, 357–358; *Angew. Chem. Int. Ed. Engl.* **1984**, *23*, 376–377.
[6] K. Meier, G. Rihs, *Angew. Chem.* **1985**, *97*, 879–880; *Angew. Chem. Int. Ed. Engl.* **1985**, *24*, 858–859.
[7] H. von Arnim, K. Dehnicke, K. Maczek, D. Fenske, *Z. Naturforsch., Teil B* **1993**, *48*, 1331–1340.
[8] P. C. Junk, M. K. Smith, J. W. Steed, *Polyhedron* **2001**, *20*, 2979–2988.
[9] H. Chen, P. Jutzi, W. Leffers, M. M. Olmsted, P. P. Power, *Organometallics* **1991**, *10*, 1282–1286.
[10] B. Schiemenz, B. Antelmann, G. Huttner, L. Zsolnai, *Z. Anorg. Allg. Chem.* **1994**, *620*, 1760–1767.
[11] H. Zhang, X. Wang, H. Zhu, W. Xiao, B. K. Teo, *J. Am. Chem. Soc.* **1997**, *119*, 5463–5464.
[12] S. Nishihara, N. Takamatsu, T. Akutagawa, T. Hasegawa, T. Nakamura, *Synth. Met.* **2001**, *121*, 1806–1807.
[13] D. A. Laidler, J. F. Stoddart, in *Crown Ethers and Analogues* (Eds.: S. Patai, Z. Rappoport), John Wiley and Sons, Chichester, **1989**, pp. 1–59.
[14] I. L. Toner, in *Crown Ethers and Analogues* (Eds.: S. Patai, Z. Rappoport), John Wiley and Sons, Chichester, **1989**, pp. 77–205.
[15] R. E. DeSimone, M. D. Glick, *J. Am. Chem. Soc.* **1976**, *98*, 762–767.
[16] J. Dale, *Isr. J. Chem.* **1980**, *20*, 3–11.
[17] a) R. E. Wolf Jr, J. R. Hartman, J. M. E. Storey, B. M. Foxman, S. R. Cooper, *J. Am. Chem. Soc.* **1987**, *109*, 4328–4335; b) P. Bultinck, A. Huyghebaert, C. Van Alsenoy, A. Goeminne, *J. Phys. Chem. A* **2001**, *105*, 11266–11275.
[18] G. A. Melson, in *Coordination Chemistry of Macrocyclic Compounds* (Ed.: G. A. Melson), Plenum Press, New York, London, **1979**, p. 17–144.
[19] a) W. O. Koch, A. Barbieri, M. Grodzicki, V. Schünemann, A. X. Trautwein, H.-J. Krüger, *Angew. Chem.* **1996**, *108*, 484–486; *Angew. Chem. Int. Ed. Engl.* **1996**, *35*, 422–424; b) W. O. Koch, J. T. Kaiser, H.-J. Krüger, *Chem. Commun.* **1997**, 2237–2238.
[20] a) V. B. Pett, G. H. Leggett, T. H. Cooper, P. R. Reed, D. Situmeang, L. A. Ochrymowycz, D. B. Rorabacher, *Inorg. Chem.* **1988**, *27*, 2164–2169; b) J. M. Desper, S. H. Gellmann, *J. Am. Chem. Soc.* **1990**, *112*, 6732–6734; c) J. M. Desper, S. H. Gellmann, R. E. Wolf Jr, S. R. Copper, *J. Am. Chem. Soc.* **1991**, *113*, 8663–8671; d) A. Y. Nazarenko, R. M. Izatt, J. D. Lamb, J. M. Desper, B. E. Matysik, S. H. Gellmann, *Inorg. Chem.* **1992**, *31*, 3990–3993; e) L. Aronne, B. C. Dunn, J. R. Vyryan, C. W. Souvignier, M. J. Mayer, T. A. Howard, C. A. Salhi, S. N. Goldie, L. A. Ochrymowycz, D. B. Rorabacher, *Inorg. Chem.* **1995**, *34*, 357–369; f) P. Comba, A. Fath, A. Kühner, B. Nuber, *J. Chem. Soc., Dalton Trans.* **1997**, 1889–1898.
[21] a) H.-J. Holdt, J. Teller, *Z. Chem.* **1988**, *28*, 249–250; b) H.-J. Holdt, *Pure Appl. Chem.* **1993**, *65*, 477–482; c) H.-J. Drexler, H. Reinke, H.-J. Holdt, *Z. Anorg. Allg. Chem.* **1998**, *624*, 1376–1380.
[22] a) H.-J. Drexler, H. Reinke, H.-J. Holdt, *Chem. Ber.* **1996**, *129*, 807–814; b) H.-J. Drexler, M. Grotjahn, E. Kleinpeter, H.-J. Holdt, *Inorg. Chim. Acta* **1999**, *285*, 305–308; c) H.-J. Drexler, Dissertation, University of Rostock, **1997**; d) H.-J. Drexler, I. Starke, M. Grotjahn, H. Reinke, E. Kleinpeter, H.-J. Holdt, *Z. Naturforsch., Teil B* **1999**, *54*, 799–806.
[23] a) J. W. Sibert, S. J. Lange, C. Stern, B. M. Hoffmann, A. G. M. Barrett, *J. Chem. Soc., Chem. Commun.* **1994**, 1751–1752; b) J. W. Sibert, S. J. Lange, D. J. Williams, A. G. M. Barrett, B. M. Hoffmann, *Inorg. Chem.* **1995**, *34*, 2300–2305.
[24] G. Bähr, G. Schleitzer, *Chem. Ber.* **1957**, *90*, 438–443.
[25] E. J. Gasson, H. McCombie, A. H. Williams, F. N. Woodward, *J. Chem. Soc.* **1948**, 44–46.
[26] A. Holzberger, H.-J. Holdt, E. Kleinpeter, *J. Phys. Org. Chem.* **2004**, *17*, 257–265.
[27] T. Häusler, W. S. Sheldrick, *Z. Naturforsch., Teil B* **1994**, *49*, 1215–1222.
[28] T. S. Cameron, A. Decken, I. Dionne, M. Fang, I. Krossing, J. Passmore, *Chem. Eur. J.* **2002**, *8*, 3386–3401.
[29] a) H. W. Roesky, H. Hofmann, P. G. Jones, W. Pinkert, G. M. Sheldrick, *J. Chem. Soc., Dalton Trans.* **1983**, 1215–1216; b) E. Sekido, K. Suzuki, K. Hamada, *Anal. Sci.* **1987**, *3*, 505–508; c) C. R. Lucas, S. Liu, M. J. Newlands, J.-P. Charland, E. J. Gabe, *Can. J. Chem.* **1990**, *68*, 644–649.
[30] a) W. Henderson, C. Evans, *Inorg. Chim. Acta* **1999**, 183–192; b) M. Y. Combariza, R. W. Vachet, *J. Am. Soc. Mass Spectrom.* **2002**, *13*, 813–825.
[31] a) H. Lavanant, E. Hecquet, Y. Hoppilliard, *Int. J. Mass Spectrom* **1999**, *187*, 11–23; b) M. Satterfield, J. S. Brodbelt, *Inorg. Chem.* **2001**, *40*, 5393–5400.
[32] E. Kleinpeter, M. Grotjahn, K. D. Klika, H.-J. Drexler, H.-J. Holdt, *J. Chem. Soc., Perkin Trans. 2* **2001**, 988–993.
[33] M. Oki, in *Methods in Stereochemical Analysis*, vol. 4 ("Applications of Dynamic NMR Spectroscopy to Organic Chemistry") (Ed.: A. P. Marchand), VCH Publishers, Deerfield Beach, **1985**, p. 321.
[34] V. V. Kolochkov, P. P. Chernov, A. M. Polozov, V. L. Antonovskii, G. N. Koshel, T. N. Antonova, A. V. Aganov, *Zh. Org. Khim.* **1990**, *26*, 387–392.
[35] F. A. L. Anet, T. N. Rawdah, *Tetrahedron Lett.* **1979**, *20*, 1943–1946.
[36] G. M. Sheldrick, *SHELXS-97 – Program for Crystal Structure Solution*, Göttingen, **1997**.
[37] G. M. Sheldrick, *SHELXL-97 – Program for Crystal Structure Refinement*, Göttingen, **1997**.
[38] A. L. Spek, *PLATON – A Multipurpose Crystallographic Tool*, Utrecht, **2005**.

Received: December 12, 2005
Published Online: April 25, 2006

 © 2006 Wiley-VCH Verlag GmbH & Co. KGaA, Weinheim 

DOI: 10.1002/ejic.200501130

# Tetranuclear Complexes Containing a Luminescent $Ru_2M_2$ Core [M = $Cu^I$, (allyl)$Pd^{II}$]: Synthesis, Structures and Electrochemical Properties

**Dirk Walther,*[a] Lars Böttcher,[a] Jörg Blumhoff,[a] Sebastian Schebesta,[a] Helmar Görls,[a] Katrin Schmuck,[a] Sven Rau,[a] and Manfred Rudolph[a]**

**Keywords:** Copper / Luminescence / N ligands / Palladium / Ruthenium

The reaction between $[(tbbpy)_2Ru(tmbiH_2)](PF_6)_2$ (tbbpy = 4,4′-di-*tert*-butyl-2,2′-bipyridine; $tmbiH_2$ = 5,5′,6,6′-tetramethyl-2,2′-dibenzimidazole) and LiMe/CuI affords the tetranuclear complex **1** containing the dication $[\{(tbbpy)_2Ru(tmbi)\}_2Cu_2]^{2+}$. The X-ray structure of **1** shows that the two $[(tbbpy)_2Ru(tmbi)]$ units coordinate the two Cu atoms in a twofold monodentate manner. Each copper atom is surrounded by two N-donor atoms of different ruthenium(II) units with N–Cu–N angles of 167.3°. The Cu···Cu separation (2.72 Å) indicates intranuclear contacts. LiMe/$[(allyl)PdCl]_2$ reacts with the starting Ru complex to form **2**, which contains the tetranuclear dication $[\{(tbbpy)_2Ru(tmbi)\}_2\{Pd(\eta^3\text{-allyl})\}_2]^{2+}$. Its crystal structure shows that the $Ru^{II}$ units act as twofold monodentate ligands as well. Each $Pd^{II}$ is in an essentially planar coordination environment containing two nitrogen atoms of two different dibenzimidazolates in the *cis* position with the $\eta^3$-bonded allyl group occupying the two remaining positions. In contrast to **1**, where the Ru–Cu–Cu–Ru unit forms an essentially planar structure, a strongly bent structure is formed in compound **2**. ESI mass spectra of **1** and **2** clearly show that the tetranuclear complexes are present in solution as well. Both complexes are luminescent. In addition, **2** catalyses the Heck coupling at 120 °C in *N*,*N*-dimethylacetamide. In contrast to **1** and **2**, the homodinuclear complex $[(tbbpy)_2Ru(tmbi)Ru(tbbpy)_2]$ (**3**) contains the dibenzimidazolate as a twofold chelating ligand that forms two five-membered chelate rings with the Ru centres. Electrochemical measurements of **2** show two reversible, one-electron oxidation steps, the difference between which ($\Delta E$ = 89 mV) is distinctly larger than the pure entropic effect. Furthermore, four reduction steps are observed, the first two of which are fully reversible.
(© Wiley-VCH Verlag GmbH & Co. KGaA, 69451 Weinheim, Germany, 2006)

## Introduction

The construction of oligonuclear metal complexes containing at least two different metals on the opposite side of bridging ligands is an area of general interest not only from synthetic, structural or theoretical points of view but also due to their potential catalytic properties, which often may be different from the related mononuclear species.[1,2] Of special interest in this field is the development of supramolecular combinations consisting of both a photo-redoxactive metal unit ($M^1$) and a reactive metal ($M^2$) connected by bridging ligands that allow electronic communication between the metal centers (for a review see ref.[3]). In these complexes the unit $M^1$ may act as a sensor of reactions at the reactive metal $M^2$. Furthermore, such systems are interesting candidates for studying directional photoelectron transfer processes between the different metals. In addition, in this type of complex the reactivity of $M^2$ may not only be tuned by steric or electronic influences of the $M^1$ units but also by light.[4] An attractive application of this effect would be the development of new photoswitchable catalysts.

We report here on the synthesis, structures and spectroscopic and electrochemical measurements of the two tetranuclear complexes **1** and **2** consisting of two peripheral photoactive $(tbbpy)_2Ru^{II}$ fragments ("$M^1$"), a tetramethyldibenzimidazolate bridging ligand, and either $Cu^I$ or (allyl)$Pd^{II}$ as reactive metal centres ("$M^2$"). In these combinations the bridging system is expected to allow electronic communication between the metals on each side.

## Results and Discussion

### Syntheses and Structures of Complexes 1 and 2

Very recently we have described the new ruthenium complex $[(tbbpy)_2Ru(tmbiH_2)](PF_6)_2$ (tbbpy = 4,4′-di-*tert*-butyl-2,2′-bipyridine; $tmbiH_2$ = 5,5′,6,6′-tetramethyl-2,2′-dibenzimidazole), which is easily accessible by a microwave-assisted reaction.[5] In contrast to the unsubstituted derivative, $[(tbbpy)_2Ru(tmbiH_2)](PF_6)_2$ is more soluble in organic solvents due to the presence of ten methyl groups at the periphery of the complex. Furthermore, the complex contains a free coordination side and should therefore be able

[a] Institut für Anorganische und Analytische Chemie der Friedrich-Schiller-Universität,
Lessingstraße 8, 07743 Jena, Germany
Fax: +49-3641-948-172
E-mail: Dirk.Walther@uni-jena.de

 © 2006 Wiley-VCH Verlag GmbH & Co. KGaA, Weinheim 

to act as a "metalloligand" after deprotonation, analogous to similar systems (for typical Ru complexes of this type see refs.[5–15]).

The copper(I) complex **1** was obtained as follows. Treatment of $[(tbbpy)_2Ru(tmbiH_2)](PF_6)_2$ in THF with a mixture of copper iodide and methyllithium (molar ratio 1:2) dissolved in diethyl ether at –78 °C resulted in a dark-red solution from which **1** was obtained as a crystalline brown solid after workup. Its electrospray mass spectrum (ESI-MS) performed in $CHCl_3/CH_3OH$ reveals one major peak at *m*/*z* 2123 corresponding to the composition $[\{(tbbpy)_2Ru(tmbi)\}_2Cu_2(PF_6)]^+$, which suggests a structure of the dication according to Figure 1. The calculated isotopic pattern for this tetranuclear species agrees well with the experimentally found one.

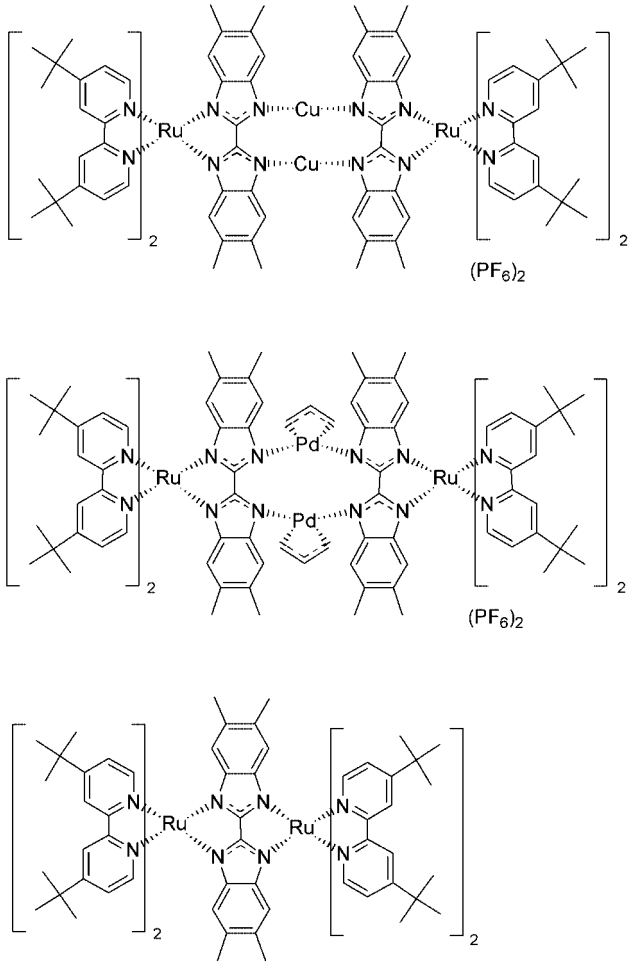


Figure 1. The cations of complexes **1**, **2** and **3**.

The $^1H$ NMR spectrum of **1** in $CDCl_3$ shows the typical resonances for the $[Ru(tbbpy)_2(tmbi)]$ moiety[5,6] although it gives little additional structural information about **1**. It displays two singlets for the methyl protons of the *tert*-butyl groups at $\delta$ = 1.34 and 1.47 ppm, and two singlets for the methyl protons of the bridging ligand at $\delta$ = 2.01, and 2.30 ppm in the expected intensity ratio of 3:3:1:1. The protons for the 2,2′-bipyridine system show the expected set of six signals for H3, H3′, H5, H5′, H6, H6′, respectively. Furthermore, two resonances are observed for the aromatic protons of the bridging tmbi at $\delta$ = 5.36 and 7.66 ppm. In comparison with the mononuclear complex $[(tbbpy)_2Ru(tmbiH_2)](PF_6)_2$, the corresponding signals in **1** are only slightly low-field shifted.

We succeeded in growing single crystals of the complex **1**, which crystallizes with the anions $PF_6^-$ and $Cl^-$ and with some solvent molecules. Figure 2 shows the solid-state structure of the dication of **1** determined by a low-temperature X-ray analysis and contains relevant bond lengths and angles in the caption.

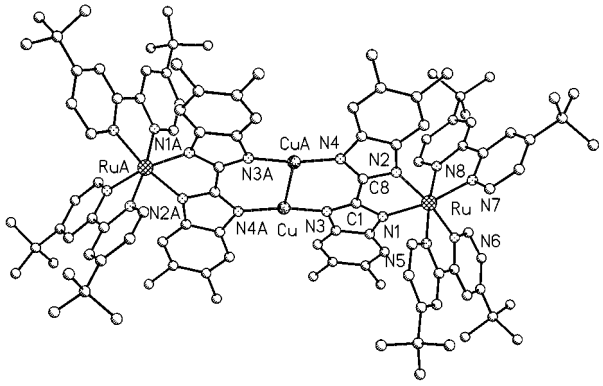


Figure 2. Molecular structure of the dication of complex **1** (the H atoms have been omitted for clarity). Selected bond lengths [Å]: Cu–CuA 2.720(1), Cu–N3 1.852(5), Cu–N4A 1.850(5), Ru–N1 2.087(5), Ru–N2 2.076(5), Ru–N5 2.036(5), Ru–N6 2.041(5), Ru–N7 2.054(6), Ru–N8 2.046(5), C1–C8 1.436(8). Symmetry transformations used to generate equivalent atoms: A $-x+1$, $-y+1$, $-z+1$.

The most remarkable feature is that the two metalloligands do not act as chelating ligands for $Cu^I$ but bind the two Cu atoms in a monodentate manner resulting in an N–Cu–N coordination for each copper(I) centre. There is no additional interaction with the anions. The considerable deviation of the N–Cu–N angles (167.3°) from linearity may be explained by the influence of the other $Cu^I$ centre, which is in close proximity. The Cu···Cu separation is 2.72 Å, which suggests intramolecular contacts (van der Waals radii: 2.8 Å[16]). The Ru···Ru separation is 11.36 Å. Furthermore, the bridging imidazolato rings are essentially planar, and their C–N bond lengths are equal within the experimental error. Since the benzene rings do not lie in this plane, the two tetramethyldibenzimidazolate systems have a boat form with an angle of 163.9° for the centroids of C1–C8, C4–C5 and C11–C12, and C1A–C8A, C4A–C5A and C11A–C12A, respectively.

In addition, the atoms N3–Cu–N4A–N3A–CuA–N4 lie in a plane with extremely small deviations of the Cu atoms from this plane (0.012 Å). The nitrogen atoms N1 and N2, which are coordinated to the $[(tbbpy)_2Ru]$ fragment, lie above this plane (Cu–N3–N1 = 166.6°); the other pair of nitrogen atoms N1A and N2A, which are coordinated to the $[(tbbpy)_2Ru(A)]$ moiety, lies below this plane resulting in a chair arrangement of the eight nitrogen atoms of the two bridging ligands. The unidentate coordination of bridging imidazolates has already been described for a number

 © 2006 Wiley-VCH Verlag GmbH & Co. KGaA, Weinheim 

of complexes with other metals, although not with $Cu^{I}$.[1,7] For example, a similar coordination mode for a disilver complex containing π-acidic [2-(phenylazo)pyridine]$_2$Ru fragments at the periphery and the unsubstituted diimidazolate as bridging ligand was recently described by Goswami et al.[7] Furthermore, in a hexametallic $Cu^{II}$ complex containing two $Cu^{II}$ centres and four (bipy)$_2$Ru(bimidazolate) units the diimidazolates also act as monodentate ligands.[8]

Although **1** is coordinatively unsaturated, it does not react with triphenylphosphane. Furthermore, in the solid state no reaction with air was observed.

Treatment of [Ru(tbbpy)$_2$(tmbiH$_2$)](PF$_6$)$_2$ in THF with two equivalents of methyllithium at –78 °C and subsequent treatment with a slight excess of dimeric (allyl)palladium(II) chloride resulted in a dark-red/violet solution from which reddish-brown crystals of **2** were obtained. The ESI mass spectrum performed in $CHCl_3$/$CH_3OH$ showed an envelope of peaks at *m*/*z* 2292 that match well with the isotopic distribution calculated for the fragment ion [{(tbbpy)$_2$-Ru(tmbi-H)}$_2${Pd(allyl)$_2$}(PF$_6$)]$^+$. This indicates that a tetranuclear complex similar to **1** is present in solution as well. The $^1$H NMR spectrum of **2** in $CD_2Cl_2$ shows the typical pattern for the [Ru(tbbpy)$_2$(tmbi)] fragments, with the methyl proton signals at $\delta$ = 1.37 and 1.53 ppm and the methyl protons of the dibenzimidazolate at $\delta$ = 2.03 and 2.33 ppm. In comparison with **1**, these signals and the resonances for the bipy protons and for the aryl signal H7 are shifted slightly downfield.

Single crystals of **2** suitable for an X-ray determination were grown from a mixture of dichloromethane and methanol in the presence of a small amount of water by slow diffusion of dichloroethane into this mixture. Under these conditions, the tetranuclear diaction [{(tbbpy)$_2$Ru-(tmbi-H)}$_2${Pd(allyl)$_2$}]$^{2+}$ crystallizes with both the PF$_6^-$ and the Cl$^-$ anions and with different solvent molecules. Figure 3 shows the molecular structure of the dication and contains relevant bond lengths and angles in the caption.

The two halves of the molecule form an extremely unsymmetrical structure. Similar to complex **1**, the (tbpby)$_2$-Ru(tmbi) metalloligand coordinates in a twofold monodentate manner to the two $Pd^{II}$ centres. Each $Pd^{II}$ is in a distorted planar coordination environment formed by two nitrogen atoms of two different dibenzimidazolates in *cis* positions while the $\eta^3$-bonded allyl group occupies the two remaining positions. The two $C_2PdN_2$ planes are not parallel to each other but are strongly twisted, with a torsion angle of 46.9°. The Pd···Pd separation of 3.06 Å is rather short, suggesting a weak interaction between these metals. The intramolecular Ru···Ru separation is 8.308 Å. In contrast to complex **1**, where the Ru–Cu–Cu–Ru atoms form a planar structure, in compound **2** a strongly bent structure is found. The centroids of the two Pd atoms and the two Ru centres form an angle of 90.7°.

Other bond lengths and angles are in good agreement with typical values found for similar complexes (Figure 3). It is interesting to note that a long-known tetranuclear Pd complex in which four (allyl)$Pd^{II}$ moieties are connected via two dibenzimidazolate bridges has a related structure.[17] In this compound, each of the two imidazolates coordinates an (allyl)$Pd^{II}$ unit to form a chelate ring whereas the other two Pd centres are monodentately coordinated. Although no X-ray studies have been carried out, other mixed complexes containing Pd and Rh may have a similar tetranuclear arrangement.[17] Additionally, related structures have been found in a tetranuclear rhodium carbonyl complex with diimidazolate bridges[18] and in the complex [($\eta^6$-*p*-cumene)ClRu(μ-bbzim)Rh(norbornadiene)$_2$].[1]

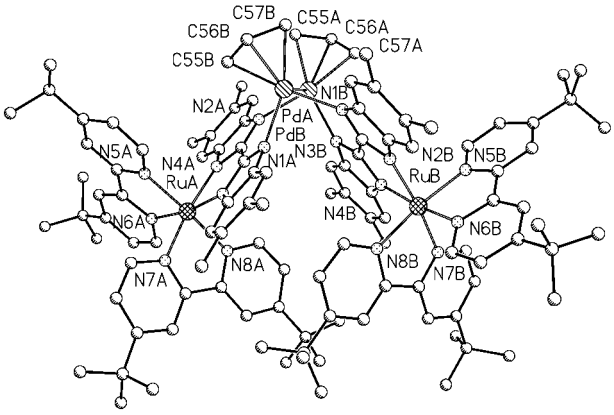


Figure 3. Molecular structure of the dication of complex **2** (the H atoms, the anions PF$_6^-$ and Cl$^-$, and some atom labels have been omitted for clarity). Selected bond lengths [Å]: PdA–N2A 2.092(6), PdA–N3B 2.085(6), PdB–N1A 2.091(5), PdB–N1B 2.111(5), PdA–C55A 2.128(9), PdA–C56A 2.089(9), PdA–C57A 2.096(10), RuA–N4A 2.082(6), RuA–N5A 2.047(6), RuA–N6A 2.049(6), RuA–N7A 2.048(5), RuA–N8A 2.049(6), C1A–C8A 1.450(9), PdB–C55B 2.124(8), PdB–C56B 2.113(12), PdB–C57B 2.153(8), RuB–N4B 2.086(5), RuB–N5B 2.052(5), RuB–N6B 2.045(5), RuB–N7B 2.036(5), RuB–N8B 2.040(5), C1B–C8B 1.460(10).

In contrast to the observed ligand behaviour in these complexes, the structurally similar oxalamidinate ligands act as normal twofold didentate bridging ligands towards $Pd^{II}$ and Cu, forming five-membered chelate rings.[19–22]

The homodinuclear ruthenium tetramethyldibenzimidazolate complex **3** has been prepared using standard procedures.[9] The fully characterised compound was isolated as a mixture of the *rac* and *meso* diastereomers, which exhibit slightly different $^1$H NMR signals. In contrast to both **1** and **2**, the dibenzimidazolato ligand in **3** acts as a twofold chelating ligand. The X-ray crystal structure of its *meso* form (not depicted; see Experimental Section) shows the two Ru centres on the opposite side of the diimidazolate bridging ligand with bond lengths and angles that are typical for such chelate complexes, althoughr with one exception: the bridging tetramethyldibenzimidazolate ligand is kinked within the central C–C bond.[9]

### Electronic Spectra and Catalytic Behaviour of 1–3

The electronic spectra of **1** in THF show an absorption band in the visible region at $\lambda$ = 519 nm which can be attributed to a $^3$MLCT transition from $Ru^{II}$ to the bipy ligand. While the starting compound − the deprotonated

 © 2006 Wiley-VCH Verlag GmbH & Co. KGaA, Weinheim 

metalloligand $[(tbbpy)_2Ru(tmbi)]^-$ is not luminescent, coordination of $Cu^I$ switches on emission resulting in an emission band at $\lambda$ = 705 nm. The lifetime of the excited state in THF at room temperature (93 ns) (Table 1) is significantly shorter than that in the protonated compound $[(tbbpy)_2Ru(tmbiH_2)]^{2+}$ (lifetime in THF of 363 ns). We have recently observed a similar behaviour with the unsubstituted dibenzimidazolate complex $[(tbbpy)_2Ru(bbim)]$, which acts as a cation-driven molecular switch due to the formation of emitting systems by reacting with metal ions in solution.[6]

Table 1. Optical and electrochemical data of the complexes **1**–**3** at room temperature.

| | Complex **1** | Complex **2** | Complex **3** |
|---|---|---|---|
| Absorption $\lambda_{max}$ [nm][a] | 519 | 524 | 515 |
| Emission $\lambda_{max}$ [nm][b] | 705 | 653 | 707 |
| Lifetime [ns][c] | 93[d] | 244[d] | 60[e] |
| $E^{[f]}_{1/2}$ (ox) [V] | dec. | +0.146, +0.235 | +0.215, +0.51 |
| $E^{[f]}_{1/2}$ (red) [V] | dec. | –1.989, –2.036 | –1.963, –2.027 |
| | | –2.313, –2.385 | –2.260, –2.338 |

[a] ±2 nm in THF. [b] ±4 nm in THF. [c] ±10%. [d] In THF. [e] In acetonitrile. [f] ±0.004 V in acetonitrile.

In the electronic spectrum of **2** in THF (Table 1) the lowest absorption maximum appears at $\lambda$ = 524 nm which is only slightly shifted compared with **1**. In contrast, a larger difference was observed in the emission spectra in THF, where the emission maximum was found at $\lambda_{em}$ = 653 nm, which represents a hypsochromic shift of 52 nm. In addition, the lifetime of the excited state of 244 ns is significantly longer than that for **1**. A more detailed study of the interesting photophysical behaviour of complex **2** will be described in detail in a separate publication.[23]

The homodinuclear complex **3** has the lowest absorption maximum in THF at $\lambda$ = 515 nm and emits at 707 nm, which compares well with the unsubstituted derivatives.[9]

Preliminary investigations of the catalytic behaviour of **1** and **2** show only low activity of **1** in the catalytic oxidation of 3,5-di-*tert*-butylcatechol to form the *o*-quinone. Complex **2** catalyses the Heck reaction of aryl bromides with substituted aryl olefins. An investigation of the reaction between 4-bromoacetophenone and *n*-butyl acrylate, which is usually chosen as a standard reaction to evaluate the catalyst productivity, at 120 °C in (*N*,*N*-dimethylacetamide) with sodium acetate as the base resulted in 86% conversion after two hours (turnover number: 4300 mol conversion per mol catalyst). At 80 °C the catalysis proceeded slowly, with 37% conversion after 11 h (TON = 1850). In the microwave-assisted Heck coupling 83% conversion was observed after 1 h (TON = 4150; programme 10 s at 175 W, then 1 h at 65 W).

### Electrochemistry of Complexes 2 and 3

Due to the decomposition of **1** during the electrochemical measurements the electrochemistry of this complex could not be studied. In contrast, the palladium complex **2** is stable under these conditions and could be investigated electrochemically (Table 1). For comparison, the dimeric ruthenium complex $[(tbbpy)_2Ru(\mu\text{-}tmbi)Ru(tbbpy)_2]$ (**3**) was also investigated. Complex **3** exhibits two chemically reversible one-electron oxidation steps. The half-wave potentials were found to be at +0.215 and +0.51 V with respect to the ferrocene/ferrocenium couple and the diffusion coefficient of the complex, $D_{LRu–RuL}$, amounts to about $5 \times 10^{-6}$ cm$^2$ s$^{-1}$. Formally the two one-electron steps may be attributed to the oxidation of both the ruthenium(II) centres in the complex. The relatively large difference of these potentials ($\Delta E$ = 295 mV) shows that there is a remarkable electronic communication between the Ru centres.

At first glance the reduction of complex **3** ("LRu–RuL") shown in Figure 4 seems also to proceed in two separate reduction steps at about –2 and –2.3 V, respectively. However, a more detailed analysis of the frequency dependence of the peak heights and peak shapes (using the diffusion coefficient estimated from the oxidation process) revealed that each peak is actually formed by two overlapping one-electron steps. A comparison of experimental square-wave voltammograms (solid line) and those simulated on the basis of the mechanism (M1; open circles) is shown in Figure 4.

$$\begin{aligned}
&LRu-RuL + e^- \rightleftharpoons LRu-RuL^- \quad (E_1^0 = -1.963\ V)\\
&LRu-RuL^- + e^- \rightleftharpoons L^-Ru-RuL^- \quad (E_2^0 = -2.027\ V)\\
&L^-Ru-RuL^- + e^- \rightleftharpoons L^-Ru-RuL^{2-} \quad (E_3^0 = -2.260\ V)\\
&L^-Ru-RuL^{2-} + e^- \rightleftharpoons L^{2-}Ru-RuL^{2-} \quad (E_4^0 = -2.338\ V)
\end{aligned} \tag{M1}$$

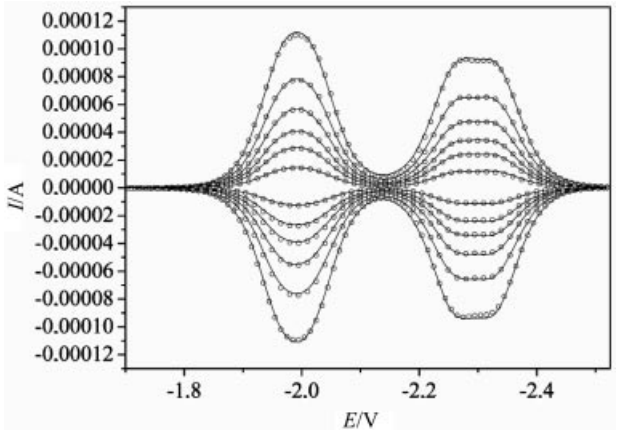


Figure 4. Comparison of experimental (solid line) and simulated (open circles) cyclic square-wave voltammograms for the reduction of a 1.1 mM solution of complex **3** at a mercury drop electrode in acetonitrile. The voltammograms refer to square-wave frequencies of 50, 200, 400, 800, 1500 and 3000 Hz (with increasing peak height) and the potential scale is referenced to the ferrocene/ferrocenium couple. The simulations were executed on the basis of the mechanism M1 with LRu–RuL = complex **3**.

The one-electron steps can be attributed here to the stepwise reduction of the two $(tbbpy)_2Ru$ units involved in the complex assuming fully reversible charge-transfer reactions and identical diffusion coefficients for all species. The dif-

 © 2006 Wiley-VCH Verlag GmbH & Co. KGaA, Weinheim 

ference $|E_2^0–E_1^0|$ = 64 mV and $|E_4^0–E_3^0|$ = 78 mV is distinctly greater than the limiting value of 35.6 mV resulting from a pure entropic effect. A communication of the complex centres through the bridging ligand is therefore clearly visible in the cathodic charge-transfer processes. Of course, the electronic coupling is even larger if both reduction steps refer to the same $(tbbpy)_2Ru$ moiety ($|E_3^0–E_1^0|$ = 297 mV and $|E_4^0–E_2^0|$ = 311 mV, respectively).

The oxidation of complex **2** by cyclic square-wave voltammetry is shown in Figure 5. This figure reveals that the oxidation of the complex is similar to that reported above for **3**, but in contrast to the latter compound both one-electron steps are no longer well separated. For this reason, reliable results can be evaluated only by subjecting the experimental data to a fitting procedure. The values of the half-wave potentials retrieved for the best fit are +0.146 and +0.235 V, respectively, which is a difference of 89 mV. This value is smaller than that reported above for complex **3** but still distinctly larger than that expected for a pure entropic effect.

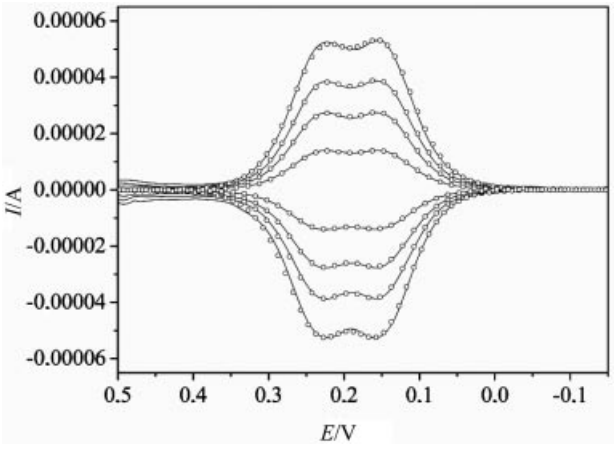


Figure 5. Comparison of experimental (solid line) and simulated (open circles) cyclic square-wave voltammograms for the oxidation of a 1.9 mM solution of complex **2** at a platinum disc electrode in acetonitrile. The voltammograms refer to square-wave frequencies of 50, 200, 400 and 800 Hz (with increasing peak height) and the potential scale is referenced to the ferrocene/ferrocenium couple. The simulations were executed for a reversible E–E mechanism using the standard potentials reported in the text.

The close relationship to the electrochemistry of the LRu–RuL complex **3** also becomes visible when looking at the reduction of **2** using the cyclic square-wave voltammograms (depicted in Figure 6) or at the experiment referring to the highest square-wave frequency ($f_{sw} \geq 200$ Hz) in Figure 7. Figure 6 reveals that the first two one-electron steps proceed in a fully reversible way analogously to that indicated by the first two reactions in (M1) when replacing LRu–RuL by LRu-$^{Pd}$-RuL as a symbol for complex **2**. The half-wave potentials of these processes (evaluated from the data fitting shown in Figure 6) were estimated to be at $E_1°$ = –1.989 and $E_2°$ = –2.036 V, respectively, which means that $|E_2^0–E_1^0|$ is 47 mV. That means that the deviation from the ideal peak shape of an uncoupled system is hardly visible and is only detectable by fitting current curves referring to different time windows.

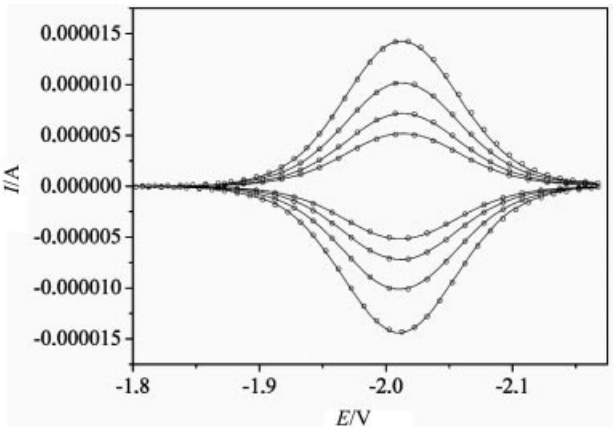


Figure 6. Comparison of experimental (solid line) and simulated (open circles) cyclic square-wave voltammograms for the reduction of a 0.6 mM solution of complex **2** at a mercury-drop electrode in acetonitrile. The voltammograms refer to square wave frequencies of 25, 50, 100 and 200 Hz (with increasing peak height) and the potential scale is referenced with respect to the ferrocene/ferrocenium couple. The simulations were executed taking the first two reactions of the mechanism shown in M2 into consideration.

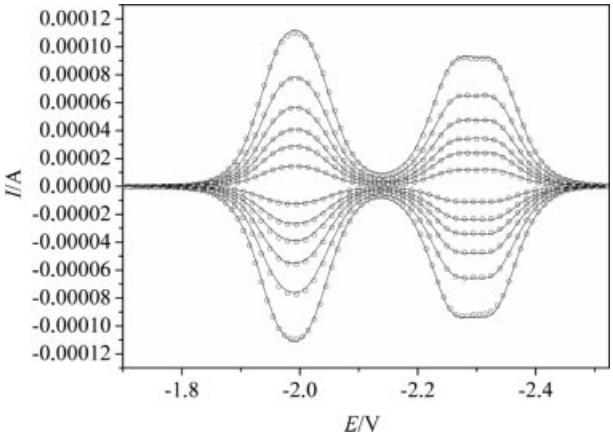


Figure 7. Comparison of experimental (solid line) and simulated (open circles) cyclic square-wave voltammograms for the reduction of a 0.6 mM solution of **2** at a mercury drop electrode in acetonitrile. The voltammograms refer to square wave frequencies of 25, 50, 100 and 200 Hz (with increasing peak height) and the potential scale is referenced with respect to the ferrocene/ferrocenium couple. The simulations were executed taking the reactions M2, M3 and M4 into consideration.

The most striking difference in the electrochemistry of the LRu-$^{Pd}$-RuL complex **2** compared to that of the LRu–RuL complex **3** becomes visible when looking at the low-frequency experiments shown in Figure 7. While the current response of the high-frequency experiment ($f_{sw}$ = 200 Hz) is, at least qualitatively, very similar to the voltammograms of the LRu–RuL complex depicted in Figure 4, an additional shoulder is more and more noticeable at around –2.05 V upon decreasing the square-wave frequency (i.e. more time is needed before the re-oxidation process to the

 © 2006 Wiley-VCH Verlag GmbH & Co. KGaA, Weinheim 

starting product takes place). Integrating the cathodic and anodic current in these curves reveals that virtually no charge is lost in the course of the re-oxidation processes. Combining this result with the fact that the first two one-electron steps appear (chemically and electrochemically) fully reversible in Figure 6 gives rise to the conclusion that (after receiving three or four electrons) complex **2** slowly decomposes to another product which is reoxidized and gives the additional shoulder at about –2.05 V. Interestingly, the latter value is very close to one of the reversible half-wave potentials of the deprotonated complex [(tbbpy)$_2$-Ru(tmbi)].[9] This complex exhibits two chemically reversible one-electron reduction steps at –2.07 and –2.364 V, respectively. It therefore appears reasonable to assume that the additional shoulder results from the re-oxidation of reduced [(tbbpy)$_2$Ru(tmbi)] species formed by decomposition of the three- or fourfold reduced complex **3**. Indeed, the experimental square-wave voltammograms shown in Figure 7 (solid lines) are in very good agreement with the simulated ones (open circles) obtained on the basis of a reaction scheme similar to M1

$$\begin{aligned}
&LRu-\overset{Pd}{\underset{Pd}{}}-RuL+e^- \rightleftharpoons LRu-\overset{Pd}{\underset{Pd}{}}-RuL^- \quad (E_1^0 = -1.989\ V)\\
&LRu-\overset{Pd}{\underset{Pd}{}}-RuL^- + e^- \rightleftharpoons L^-Ru-\overset{Pd}{\underset{Pd}{}}-RuL^- \quad (E_2^0 = -2.036\ V)\\
&L^-Ru-\overset{Pd}{\underset{Pd}{}}-RuL^- + e^- \rightleftharpoons L^-Ru-\overset{Pd}{\underset{Pd}{}}-RuL^{2-} \quad (E_3^0 = -2.313\ V)\\
&L^-Ru-\overset{Pd}{\underset{Pd}{}}-RuL^{2-} + e^- \rightleftharpoons L^{2-}Ru-\overset{Pd}{\underset{Pd}{}}-RuL^{2-} \quad (E_4^0 = -2.385\ V)
\end{aligned} \qquad (M2)$$

but includes the decomposition reaction. (Actually, it cannot really be distinguished from the experimental data whether the decomposition reaction starts with the third or only after the fourth reduction step. For convenience, only one follow-up reaction has been taken into consideration.)

$$L^{2-}Ru-\overset{Pd}{\underset{Pd}{}}-RuL^{2-} \rightarrow RuL^{2-} + RuL^{2-} \qquad (M3)$$
$$(k \approx 1\ s^{-1})$$

In the backward scan the re-oxidation proceeds simultaneously by two pathways: firstly, as indicated in M2, and secondly, as re-oxidation of the decomposition products.

$$\begin{aligned}
&RuL^- + e^- \rightleftharpoons RuL^{2-} \quad (E_{2'}^0 = -2.358\ V)\\
&RuL + e^- \rightleftharpoons RuL^- \quad (E_{1'}^0 = -2.075\ V)
\end{aligned} \qquad (M4)$$

The fact that the half-wave potentials $E_{1'}^0$ and $E_{2'}^0$ retrieved by the fitting routine are, within the experimental error, in agreement with those reported above for the deprotonated complex [(tbbpy)$_2$Ru(tmbi)] is a strong indication that the latter species is really formed by the follow-up reaction (M3).

## Conclusions

The tetranuclear complexes **1** and **2** are built up by connecting two (tbbpy)$_2$Ru$^{II}$(tetramethyldiimidazolate) fragments by either Cu$^{I}$ centres or two (allyl)Pd$^{II}$ fragments. In these complexes the dibenzimidazolates act as twofold monodentate ligands resulting in 10-membered metallamacrocycles, which are luminescent at room temperature. Electrochemical measurements show that there is an electronic communication between the Ru centres in **2**. Complex **2** is a good catalyst for the Heck reaction in the dark.

## Experimental Section

**General Procedures:** Infrared spectra were recorded with a Perkin–Elmer 2000 FT-IR, $^1$H NMR spectra were recorded with a Bruker 400 MHz/200 MHz spectrophotometer and UV/Vis spectra were obtained with a Varian Cary 1 UV/Vis or Shimadzu UV 3100 UV/Vis-NIR. The mass spectra were recorded with a SSQ 170, Finnigan Mat spectrometer. Electrospray mass spectra were recorded with a Finnnigan MAT, MAT 95 XL. Values quoted for *m*/*z* are for the most intense peak of the isotope envelope. The measured isotopic pattern for complexes **1** and **2** are in good agreement with the isotopic pattern calculated using the program ICIS (version 8.2.1, Finnigan). Emission spectra were recorded with a Perkin–Elmer LS50B spectrometer equipped with a Hamamatsu R928 red-sensitive detector.

All manipulations were carried out by using modified Schlenk techniques under an atmosphere of argon. Prior to use, THF, diethyl ether and *n*-pentane were dried with potassium hydroxide and distilled from over sodium/benzophenone. Methyllithium (1.6 M solution in diethyl ether, Fluka), 4-bromoacetophenone (Fluka) and sodium acetate (Aldrich) were used as received; [(tbbpy)$_2$Ru-(tbbpy)$_2$Cl$_2$] and [(tbbpy)$_2$Ru(tmbiH$_2$)](PF$_6$)$_2$ was prepared according to a literature procedure.[5]

**Complex 1:** A stirred suspension of bis(4,4′-di-*tert*-butyl-2,2′-bipyridine)-5,6,5′,6′-tetramethyl-2,2′-dibenzimidazolatoruthenium(II) hexafluorophosphate (298 mg, 0.24 mmol) in 30 mL of THF at –78 °C was treated dropwise with a an equimolar amount of lithium dimethylcuprate, prepared by reaction of CuI with MeLi in diethyl ether. The reaction mixture was than stirred for 36 h at room temperature. After filtration the solvent was evaporated and the remaining substance was dried in vacuo. Yield: 266 mg (96%). $^1$H NMR (CDCl$_3$, 200 MHz): $\delta$ = 1.34, 1.47 (s, each 36 H, *tert*-butyl), 2.01, 2.30 (s, each 12 H, CH$_3$ of benzimidazolate), 5.36 (s, 4 H, Ar-H4), 7.15 (dd, $^3J$ = 6.2, $^4J$ = 1.8 Hz, 4 H, bipy-H5′), 7.40 (dd, $^3J$ = 6.2, $^4J$ = 2.0 Hz, 4 H, bipy-H5), 7.66 (s, 4 H, aryl-H7), 7.75 (d, $^3J$ = 6.0 Hz, 4 H, bipy-H6′), 7.91 (d, $^3J$ = 6.2 Hz, 4 H, bipy-H6), 8.13 (d, $^4J$ = 1.4 Hz, 4 H, bipy-H3′), 8.20 (d, $^4J$ = 1.8 Hz, 4 H, bipy-H3) ppm. MS (Micro-ESI in CH$_2$Cl$_2$/methanol): *m*/*z* 2123 [M – PF$_6$]$^+$, 990 [M/2 + H – 2PF$_6$]$^+$. Absorption (THF): $\lambda_{max}$ = 519 nm (intensity = 19526 L mol$^{-1}$ cm$^{-1}$). Emission (THF): $\lambda_{em}$ = 705 nm ($\lambda_{ex}$ = 520 nm); lifetime of the first excited state: 93 ns in THF at room temperature.

Recrystallization from THF/CH$_2$Cl$_2$ resulted in a complex of the composition **1**·2THF·CH$_2$Cl$_2$. C$_{117}$H$_{146}$Cl$_2$CuF$_{12}$N$_{16}$O$_2$Pd$_2$P$_2$Ru$_2$ (2498.4): calcd. C 56.24, H 5.89, N 8.97; found C 55.91, H 5.98, N 8.64. Single crystals of the composition [{(tbbpy)$_2$Ru(tmbi)}$_2$-Cu$_2$](PF$_6$)$_{1.5}$Cl$_{0.5}$·CH$_2$Cl$_2$·2 CH$_3$OH·H$_2$O, were grown from a solution in dichloromethane and methanol in the presence of a small amount of water.

**Complex 2:** A stirred suspension of bis(4,4′-di-*tert*-butyl-2,2′-bipyridine)-5,6,5′,6′-tetramethyl-2,2′-dibenzimidazolatoruthenium(II) hexafluorophosphate (500 mg, 0.41 mmol) in about 20 mL of THF

 © 2006 Wiley-VCH Verlag GmbH & Co. KGaA, Weinheim 

was treated dropwise with 0.4 mL of a solution of methyllithium in diethyl ether (1.6 M). Then, (allyl)palladium(II) chloride dimer (100 mg, 0.27 mmol) dissolved in 10 mL of THF was added dropwise at –78 °C. Stirring for about 20 h and evaporation of most the solvent at 0 °C in vacuo gave a dark red precipitate which was dissolved in dichloromethane. After subsequent filtration to remove the lithium salt and evaporation of most of the solvent, complex **2** crystallized as a red, microcrystalline compound. Yield: 432 mg (70%). MS (Micro-ESI in $CHCl_3$/methanol): *m/z* 2292 $[M + H - PF6]^+$, 1073 $[M/2 - 2PF_6]^+$. Absorption (THF): $\lambda_{max}$ = 524 nm (intensity = 13431 $L\,mol^{-1}\,cm^{-1}$). Emission (THF): $\lambda_{em}$ = 653 nm ($\lambda_{ex}$ = 524 nm); lifetime of the first excited state: 244 ns in THF at room temperature. $^1H$ NMR ($CD_2Cl_2$, 200 MHz): $\delta$ = 1.37, 1,53 (each s, *tert*-butyl), 2.03, 2.33 (each s, $CH_3$ of benzimidazolate), 3.10, 3.70, 4.20 (broad, m, allyl), 5.41 (s, aryl-H4), 7.40 (m, Ar-H), 7.5–7.6 (m, bipy-5 + aryl-H7), 7.84, 7.87 (each s, bipy-H6, bipy-H6′), 8.22, 8.29 (each d, bipy-H3 and bipy-H3′) ppm. Recrystallization from $CH_2Cl_2$ resulted in a complex with the composition **2**·4$CH_2Cl_2$. $C_{118}H_{146}Cl_8F_{12}N_{16}P_2Pd_2Ru_2$ (2776.4): calcd. C 51.03, H 5,30, N 8.07; found C 51.29, H 5.59, N 7.75. Single crystals were grown from a mixture of dichloromethane and methanol in the presence of a small amount of water by slow diffusion of dichloroethane into this mixture.

**Complex 3:** Complex 3 was obtained by employing the method described for homologous dinuclear dibenzimidazole complexes[9] using $[Ru(tbbpy)_2Cl_2]$ (233 mg, 0.33 mmol) and $tmbiH_2$ (50 mg, 0.165 mmol). After obtaining the pure fractions recrystallization from acetone/water (50:50) yielded the pure complex. Crystals suitable for X-ray diffraction were grown from acetone/water at –20 °C. Under these conditions the *meso* isomer crystallized. Absorption maximum ($CH_3CN$) at $\lambda_{max}$ = 512 nm, emission maximum ($CH_3CN$) at $\lambda_{em}$ = 709 nm. $^1H$ NMR (200 MHz, $CDCl_3$): $\delta$ = 8.23 (d, *J* = 4.9 Hz, 6 H), 8.16 (m, 8 H), 7.84–7.80 (m, 4 H), 7.72 (d, *J* = 6.8 Hz, 2 H), 7.44–7.37 (m, 6 H), 7.10 (s, 2 H), 2.15 (s, 12 H), 1.45 (s, 36 H), 1.31 (s, 36 H) ppm. MS (ESI in MeOH) *m/z* 781 [M/2 – $2PF_6$] 1562 $[M - 2PF_6]^+$; 1707 $[M - PF_6)]^+$ with the expected isotopic pattern. [**3**(acetone)$_4$($H_2O$)$_2$]. $C_{102}H_{140}F_{12}N_{12}O_6P_2Ru_2$ (2122.2): calcd. C 57.77, H 6.65, N 7.92; found C 57.85, H 6.42, N 7.74. Single crystals of the composition [{$(tbbpy)_2Ru(tmbi)_2$}-$(PF_6)_2$] were grown from acetonitrile at –20 °C.

**Crystal Structure Determination:** The intensity data for the compounds were collected on a Nonius KappaCCD diffractometer using graphite-monochromated Mo-$K_\alpha$ radiation. Data were corrected for Lorentz-polarization effects and for absorption effects.[24–26] The structures were solved by direct methods (SHELXS[27]) and refined by full-matrix least-squares techniques against $F_o^2$ (SHELXL-97[28]). The hydrogen atoms were included at calculated positions with fixed thermal parameters. All non-hydrogen atoms were refined anisotropically.[28] XP (SIEMENS Analytical X-ray Instruments, Inc.) was used for structure representations.

**Crystal Data for 1:**[29] $C_{108}H_{128}N_{16}Cu_2Ru_2{\cdot}1.5PF_6{\cdot}0.5Cl{\cdot}4CH_2Cl_2{\cdot}2CH_3OH{\cdot}H_2O$, $M_r$ = 2635.46 $g\,mol^{-1}$, red-brown prism, size 0.04 × 0.04 × 0.04 $mm^3$, triclinic, space group $P\bar{1}$, *a* = 12.5919(3), *b* = 13.9697(4), *c* = 19.6388(5) Å, *α* = 100.022(2)°, *β* = 93.575(1)°, *γ* = 94.941(1)°, *V* = 3378.7(2) $Å^3$, *T* = –90 °C, *Z* = 1, $\rho_{calcd.}$ = 1.295 $g\,cm^{-3}$, $\mu$(Mo-$K_\alpha$) = 7.78 $cm^{-1}$, multi-scan, $transm._{min.}$ = 0.7326, $transm._{max.}$ = 0.8678, *F*(000) = 1359, 21202 reflections in *h*(–16/16), *k*(–18/17), *l*(–25/24), measured in the range 7.13° ≤ *Θ* ≤ 27.46°, completeness $\Theta_{max}$ = 91.9%, 14231 independent reflections, $R_{int}$ = 0.040, 10166 reflections with $F_o > 4\sigma(F_o)$, 734 parameters, 0 restraints, $R_{1obs}$ = 0.089, $wR_{2obs}$ = 0.218, $R_{1all}$ = 0.130, $wR_{2all}$ = 0.256, GOOF = 1.027, largest difference peak and hole: 3.510/–1.553 e $Å^{-3}$.

**Crystal Data for 2:**[29] $C_{114}H_{138}N_{16}Pd_2Ru_2{\cdot}1.5PF_6{\cdot}0.5Cl{\cdot}1.5C_2H_4Cl_2{\cdot}CH_3OH{\cdot}8H_2O$, $M_r$ = 2707.12 $g\,mol^{-1}$, red-brown prism, size 0.06 × 0.06 × 0.05 $mm^3$, triclinic, space group $P\bar{1}$, *a* = 16.0071(2), *b* = 18.3010(2), *c* = 29.0031(4) Å, *α* = 107.518(1)°, *β* = 95.968(1)°, *γ* = 93.112(1)°, *V* = 8025.5(2) $Å^3$, *T* = –90°C, *Z* = 2, $\rho_{calcd.}$ = 1.120 $g\,cm^{-3}$, $\mu$(Mo-$K_\alpha$) = 5.36 $cm^{-1}$, multi-scan, $transm._{min.}$ = 0.8426, $transm._{max.}$ = 0.9778, *F*(000) = 2798, 42423 reflections in *h*(–20/19), *k*(–23/21), *l*(–28/37), measured in the range 2.51° ≤ *Θ* ≤ 27.49°, completeness $\Theta_{max}$ = 86.3%, 31794 independent reflections, $R_{int}$ = 0.026, 23991 reflections with $F_o > 4\sigma(F_o)$, 1498 parameters, 0 restraints, $R_{1obs}$ = 0.087, $wR_{2obs}$ = 0.258, $R_{1all}$ = 0.114, $wR_{2all}$ = 0.290, GOOF = 1.027, largest difference peak and hole: 2.862/–1.560 e $Å^{-3}$.

**Crystal Data for 3:**[29] $C_{90}H_{112}F_{12}N_{12}P_2Ru_2{\cdot}3C_2H_3N$, $M_r$ = 1977.16 $g\,mol^{-1}$, red-brown prism, size 0.04 × 0.04 × 0.03 $mm^3$, triclinic, space group $P\bar{1}$, *a* = 15.6447(5), *b* = 17.4399(4), *c* = 19.9816(5) Å, *α* = 74.301(2)°, *β* = 80.793(2)°, *γ* = 67.123(2)°, *V* = 4826.4(2) $Å^3$, *T* = –90°C, *Z* = 2, $\rho_{calcd.}$ = 1.361 $g\,cm^{-3}$, $\mu$ (Mo-$K_\alpha$) = 4.22 $cm^{-1}$, *F*(000) = 2056, 33338 reflections in *h*(–20/19), *k*(–22/21), *l*(–25/24), measured in the range 2.48° ≤ *Θ* ≤ 27.51°, completeness $\Theta_{max}$ = 98.6%, 21886 independent reflections, $R_{int}$ = 0.042, 14398 reflections with $F_o > 4\sigma(F_o)$, 1150 parameters, 0 restraints, $R_{1obs}$ = 0.060, $wR_{2obs}$ = 0.128, $R_{1all}$ = 0.109, $wR_{2all}$ = 0.153, GOOF = 1.027, largest difference peak and hole: 0.811/–0.620 e $Å^{-3}$.

**Heck Reactions:** In a typical experiment, 6.25 mmol of 4-bromoacetophenone and 7 mmol of anhydrous sodium acetate as base were placed in a 25-mL two-necked flask equipped with a stirring bar, reflux condenser and septum. The flask was degassed under vacuum and purged with argon to ensure an inert reaction atmosphere. Then, 10 mL of *N*,*N*-dimethylacetamide as solvent, 0.5 g of diethylene glycol/dibutyl ether as GC standard and 6.75 mmol of *n*-butyl acrylate were added through the septum. The reaction mixture was thoroughly stirred and heated to the appropriate reaction temperature at which it was held for 5 min followed by treatment with the catalyst solution containing complex **2** (1.25 μmol in 0.5 mL of THF). After the appropriate time interval the reaction mixture was hydrolyzed with 2 mL of distilled water and extracted with 2 mL of $CH_2Cl_2$. The organic phase was dried with $K_2CO_3$ and stored at –25 °C until GC analysis for determination of the yield. The microwave-assisted Heck coupling was carried out using a Microwave Laboratory Systems MLS EM-2 microwave system (microwave set-up: 10 s at 175 W then 1 h at 65 W).

**Electrochemical Measurements:** Square-wave voltammetric measurements were conducted using a three-electrode technique with a home-built computer-controlled instrument based on the PCI-6110E data acquisition board (National Instruments). The experiments were performed in acetonitrile containing 0.25 M tetrabutylammonium perchlorate under a blanket of solvent-saturated argon. The ohmic resistance, which had to be compensated for, was determined by measuring the impedance of the system at potentials where the faradaic current was negligibly small. The internal reference electrode was an Ag/AgCl electrode in acetonitrile containing 0.25 M tetrabutylammonium chloride. However, for convenience all potentials are reported with respect to the ferrocene/ferrocenium couple. The working electrode was either a hanging mercury drop ($m_{Hg-drop}$ = 3.8–4.4 mg) produced by the CGME instrument or a 1.5 mm platinum disk electrode (both from Bioanalytical Systems, Inc.,West Lafayette, USA; experimental errors for *E* = ±0.004 V; and for $\Delta E_{1/2}$ = ±0.001 V). The electrochemical experiments were

 © 2006 Wiley-VCH Verlag GmbH & Co. KGaA, Weinheim 

evaluated by fitting theoretical current curves to experimental ones using the freely available DigiElch software (DigiElch can be freely downloaded from www.DigiElch.de). The theoretical background of the simulation method used in this program has been given in a series of accompanying papers.[30] We assumed in all simulations that the diffusion coefficients of the complexes do not depend on the charge of the complex.

## Acknowledgments

Financial support from the Deutsche Forschungsgemeinschaft (SFB, 436) is gratefully acknowledged.

[1] D. Carmona, J. Ferrer, A. Mendoza, F. J. Lahoz, L. A. Oro, *Organometallics* **1995**, *14*, 2066.
[2] M. P. Garcia, A. M. Lopez, M. A. Esteruelas, F. J. Lahoz, L. A. Oro, *Organometallics* **1991**, *10*, 127.
[3] V. Balzani, A. Credi, M. Venturi, *Molecular Devices and Machines*, Wiley-VCH, Weinheim, **2003**.
[4] M. Saito, Y. Nishibayashi, S. Uemura, *Organometallics* **2004**, *23*, 4012.
[5] S. Rau, B. Schäfer, A. Grüßing, S. Schebesta, K. Lamm, J. Vieth, H. Görls, D. Walther, M. Rudolph, U. W. Grummt, E. Birkner, *Inorg. Chim. Acta* **2004**, *357*, 4496.
[6] S. Rau, T. Büttner, C. Temme, M. Ruben, H. Görls, D. Walther, M. Duati, S. Fanni, G. Vos, *Inorg. Chem.* **2000**, *39*, 1621.
[7] P. Majumdar, K. K. Kamar, S. Goswami, A. Castineiras, *Chem. Commun.* **2001**, 1292–1293.
[8] K. K. Kamar, L. R. Falvello, P. E. Fanwick, J. Kim, S. Goswami, *Dalton Trans.* **2004**, 1827.
[9] S. Rau, M. Ruben, T. Büttner, C. Temme, S. Dautz, H. Görls, M. Rudolph, D. Walther, A. Brotkorb, M. Duati, C. O'Connor, J. G. Vos, *J. Chem. Soc., Dalton Trans.* **2000**, 3649.
[10] S. Rau, B. Schäfer, S. Schebesta, A. Grüßing, W. Poppitz, D. Walther, M. Duati, W. R. Browne, J. G. Voss, *Eur. J. Inorg. Chem.* **2003**, 1503.
[11] M. Haga, *Inorg. Chim. Acta* **1980**, *45*, L183.
[12] M. Haga, *Inorg. Chim. Acta* **1983**, *75*, 29.
[13] A. M. Bond, M. Haga, *Inorg. Chem.* **1986**, *25*, 4507.
[14] M. Haga, T. Matsamura-Inoue, S. Yamabe, *Inorg. Chem.* **1987**, *26*, 4148.
[15] D. P. Rillema, R. Sahai, P. Matthews, A. K. Edwards, R. J. Shaver, L. Morgan, *Inorg. Chem.* **1990**, *29*, 167.
[16] M. A. Carvajal, S. Alvarez, J. J. Novoa, *Chem. Eur. J.* **2004**, *10*, 2117.
[17] R. Usón, J. Gimeno, L. A. Oro, J. M. Martinez del Ilardya, J. A. Cabeza, *J. Chem. Soc., Dalton Trans.* **1983**, 1729 and references cited therein.
[18] W. Kaiser, R. B. Saillant, W. N. Butler, P. G. Rasmusen, *Inorg. Chem.* **1976**, *15*, 2688.
[19] D. Walther, T. Döhler, N. Theyssen, H. Görls, *Eur. J. Inorg. Chem.* **2001**, 2049.
[20] L. Böttcher, D. Walther, H. Görls, *Z. Anorg. Allg. Chem.* **2003**, *629*, 1208.
[21] K. Lamm, M. Stollenz, M. Meyer, H. Görls, D. Walther, *J. Organomet. Chem.* **2003**, *681*, 24.
[22] S. Rau, K. Lamm, H. Görls, J. Schöffel, D. Walther, *J. Organomet. Chem.* **2004**, *689*, 3582.
[23] B. Dietzek, W. Kiefer, J. Blumhoff, L. Böttcher, S. Rau, D. Walther, U. Uhlemann, M. Schmitt, J. Popp, *Chem. Eur. J.* (manuscript submitted).
[24] COLLECT, Data Collection Software; Nonius B. V., Netherlands, **1998**.
[25] Z. Otwinowski, W. Minor, "*Processing of X-ray Diffraction Data Collected in Oscillation Mode*", in *Methods in Enzymology*, vol. 276, Macromolecular Crystallography, Part A (Eds.: C. W. Carter, R. M. Sweet), pp. 307–326, Academic Press, **1997**.
[26] SORTAV, R. H. Blessing, *Acta Crystallogr., Sect. A* **1995**, *51*, 33.
[27] G. M. Sheldrick, *Acta Crystallogr., Sect. A* **1990**, *46*, 467.
[28] G. M. Sheldrick, *SHELXL-97* (release 97-2), University of Göttingen, Germany, **1997**.
[29] CCDC-279790 (for **1**), -279791 (for **2**) and -286988 (for **3**) contain the supplementary crystallographic data for this paper. These data can be obtained free of charge from The Cambridge Crystallographic Data Centre via www.ccdc.cam.ac.uk/data_request/cif.
[30] See: M. Rudolph, *J. Comput. Chem.* **2005**, *26*, 1193 and references cited therein.

Received: December 21, 2005
Published Online: April 11, 2006

 © 2006 Wiley-VCH Verlag GmbH & Co. KGaA, Weinheim 

DOI: 10.1002/ejic.200600028

# Hypersilylphosphanylidene: A Facile Low-Temperature Generation and Formation of Bis(hypersilyl)diphosphene and the Bis(hypersilyl)triphosphaallyl Anion

**Vittorio Cappello,[a] Judith Baumgartner,[a][‡] Alk Dransfeld,[a][‡‡] Michaela Flock,*[a][‡‡] and Karl Hassler*[a]**

*Dedicated to Prof. Dr. Reint Eujen on the occasion of his 60th birthday*

**Keywords:** Ab initio calculations / Carbene homologues / Phosphanes / Silicon

The reaction of hypersilyl(trimethylsilyl)chlorophosphane $(SiMe_3)_3SiP(SiMe_3)Cl$ (**1**) with *t*BuOK in THF at –60 °C proceeds by Si–P bond cleavage of the trimethylsilyl group and formation of $tBuOSiMe_3$/KCl and bis(hypersilyl)phosphanylidene. The phosphanylidene dimerizes to form bis(hypersilyl)diphosphene (**2**) in excellent yields (≥95%). X-ray diffraction experiments reveal the simultaneous presence of two rotamers in the solid state that differ in their SiSiPP torsion angles. Ab initio calculations for the parent diphosphene $(SiH_3)_3SiP{=}PSi(SiH_3)_3$ at the DFT/6-31+G(d) level predict an energy difference of 2.3 kJ mol$^{-1}$. A *cis* arrangement of the two $Si(SiH_3)_3$ groups raises the energy by about 45 kJ mol$^{-1}$. In the UV/Vis spectrum the $n \rightarrow \pi^*$ excitation is observed at 622 nm, which is in excellent agreement with the ab initio results. In the Raman spectrum, the P=P stretching vibration is easily identified as a strong line at 591 cm$^{-1}$. When a solution of **1** in THF is added to a solution of KO*t*Bu in THF, maintaining an excess of KO*t*Bu during the reaction, the deep-violet bis(hypersilyl)triphosphenide anion $[HypPPPHyp]^-$ (**4**) forms in excellent yields. This anion is also formed when **2** is treated with KO*t*Bu. Compound **2** can be derivatized with 2,3-dimethylbutadiene to give a cyclic diphosphane **5** by [4+2] addition. When a solution of **2** in toluene is heated to 110 °C for 4 h, bis(hypersilyl)cyclotriphosphane ($Hyp_2P_3H$, **6**) is formed, besides some $HypPH_2$ as a byproduct. As an aid for the interpretation of $^{31}P$ NMR spectra, equilibrium structures and phosphorus chemical shifts have been calculated at the DFT and MP2 level for a large number of molecules with phosphorus-containing backbones, which are closely related to those described in the present work. Calculations for disilyldiphosphenes reveal a close correlation between PPSi bond angles and $^{31}P$ NMR chemical shifts, which is useful for predicting NMR spectra.

(© Wiley-VCH Verlag GmbH & Co. KGaA, 69451 Weinheim, Germany, 2006)

## Introduction

Over the last two decades a great deal of effort has been devoted to the synthesis of double-bonded systems composed of the heavier elements of group V, such as diphosphenes (RP=PR) and diarsenes (RAs=AsR).[1] Large organic substituents R such as mesityl, supermesityl (2,4,6-tri-*tert*-butylphenyl) or $CH(SiMe_3)_2$ have been used for kinetic stabilisation of the double bonds. Various reactions of these double bonds, such as electrophilic additions or cycloadditions, have also been investigated.

The first disilyldiphosphene, SupP=PSup (Sup = supersilyl = Si*t*Bu$_3$) was obtained by Wiberg in 2002 from the reaction of $PCl_3$ with NaSup. It is formed via $SupPCl_2$ and SupClPPClSup as intermediate products; no crystals suitable for an X-ray investigation could be grown.[2] The same reaction also afforded the bis(supersilyl)triphosphaallyl anion $[SupPPPSup]^-$ a few years earlier, probably via the dianion $[SupPPPPSup]^{2-}$.[3] About ten years before, the synthesis of $[SupAsAsAsSup]^-$ had been described by Jutzi.[4] Both anions could be characterised unambiguously by X-ray diffraction experiments. It is of some note that less bulky silyl groups such as $tBuMe_2Si$ also possess the capability to stabilize unusual structural motifs, for instance SiSi double bonds.[5]

It is a common feature of the chemistry of double bonds between main group elements of period three (and higher) that reactions almost invariably happen at the double bond and not at the substituents, which have to be chosen to be as chemically inert as possible, otherwise they themselves will react with the double bond. The question therefore arises whether substituents can be designed that are large

[a] Institute of Inorganic Chemistry, University of Technology, Stremayrgasse 16, 8010 Graz, Austria
E-mail: michaela.flock@tugraz.at
karl.hassler@tugraz.at
[‡] X-ray structure analysis
[‡‡] Ab initio calculations
Supporting information for this article is available on the WWW under http://www.eurjic.org or from the author.

 © 2006 Wiley-VCH Verlag GmbH & Co. KGaA, Weinheim 

enough to stabilize double bonds but at the same time are sufficiently reactive to allow reactions to be initiated without (at least in the first step) affecting the double bonds. Our experience with oligosilanes led us to the conclusion that oligosilyl groups should be good candidates for this type of substituents for two reasons. First, silyl groups such as $t$Bu$_3$Si can be used successfully for the stabilisation of double bonds (as Wiberg has shown), which supports the idea that oligosilyl groups can serve the same purpose. Second, SiSi bonds readily undergo cleavage reactions under relatively mild conditions, even at low temperatures. In the present publication we explore a method that can be used for the preparation of oligosilylphosphanylidenes, bis(oligosilyl)diphosphenes and bis(oligosilyl)triphosphaallyl anions. The method can probably be used for organo-substituted phosphanylidenes as well. The hypersilyl group Si(SiMe$_3$)$_3$ (denoted as Hyp) was chosen to demonstrate the feasibility of the reactions because it is easily and quickly accessible in large quantities. We will report on the results using other oligosilyl groups in a forthcoming paper.

## Results and Discussion

One of the problems one faces when attempting to prepare silylated diphosphenes is that silyl groups are excellent leaving groups in phosphorus chemistry. For instance, SiMe$_3$ groups are routinely used for the preparation of organodiphosphenes RP=PR by elimination of chlorotrimethylsilane from RPCl$_2$ and RP(SiMe$_3$)$_2$.[6] The question therefore is whether the reaction rates of oligosilyl groups differ sufficiently from those of trimethylsilyl groups to open new paths to tailored diphosphenes. A slower reaction rate of the hypersilyl group would make the synthesis of the hypersilylphosphanylidene and of bis(hypersilyl)diphosphene an accessible goal. Silylphosphanylidenes such as H$_3$SiP are computed to prefer the triplet ground state by 122 kJ mol$^{-1}$ (CASSCF/6-31G** level).[7] At the QCISD(T)/6-311++G(3df2p)//UMP2/6-31G** level, this energy reduces to 107 kJ mol$^{-1}$.[7b] The triplet structure is stable towards rearrangement into the phosphasilene with a barrier of 170 kJ mol$^{-1}$ and a relative energy of the product of 61 kJ mol$^{-1}$. Therefore, a migration of the trimethylsilyl group in triplet (SiMe$_3$)$_3$SiP to form (SiMe$_3$)$_2$Si=P(SiMe$_3$) is unlikely to occur.

### Synthesis

As reported elsewhere, (SiMe$_3$)$_3$SiP(SiMe$_3$)$_2$ reacts with C$_2$Cl$_6$ to form a stable chlorodisilylphosphane **1**, as shown in Scheme 1.[8]

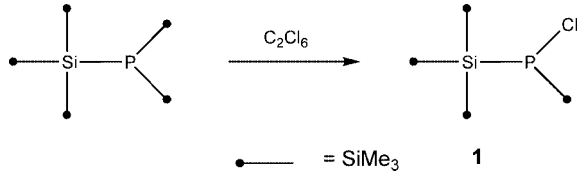


Scheme 1.

A solution of **1** in toluene does not decompose at room temperature or if heated at 90 °C for 2 h, but does so in refluxing toluene (110 °C) with formation of chlorotrimethylsilane and a plethora of compounds, although without any indications of a PP double bond. In contrast, the pure, colourless chlorodisilylphosphane turns light green at 20 °C over a period of a week, and bis(hypersilyl)diphosphene (**2**) can be identified in the reaction mixture by $^{31}$P NMR spectroscopy along with bis(hypersilyl)bicyclotetraphosphane (**3**), as shown in Scheme 2.

From the $^{31}$P NMR spectrum it follows that **2** and **3** form in a ratio of about 2:1, with **2** giving a single line at $\delta$ = 735.0 ppm (as compared to $\delta$ = 818.1 ppm for SupP=PSup). The spectrum of **3** is of first-order ($A_2X_2$) and consists of two triplets at $\delta$ = –329.2 and –155.0 ppm with a $^1J_{P,P}$ coupling constant of 161.8 Hz, which clearly demonstrates that it is the *exo*/*exo* isomer that is formed exclusively. The *exo*/*endo* isomer is expected to give more signals, and the formation of the *endo*/*endo* isomer is extremely unlikely due

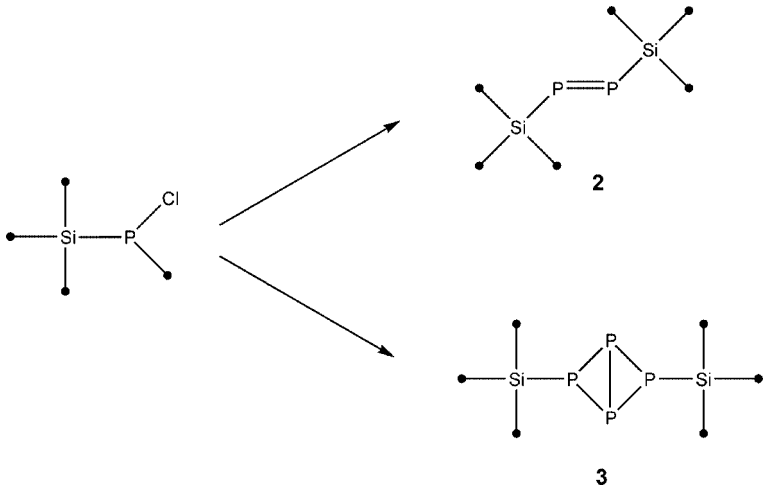


Scheme 2.

 © 2006 Wiley-VCH Verlag GmbH & Co. KGaA, Weinheim 

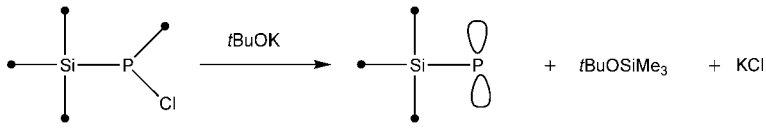


Scheme 3.

to the steric interactions of the large hypersilyl groups. It is worth noting that the analogous supersilyl compound $Sup_2P_4$ has also been observed by Wiberg in the reaction between $SupPCl_2$ and NaSup ($\delta$ = –334.4 and –139.1 ppm, $^1J_{P,P}$ = 170.5 Hz).[2]

Besides **2** and **3**, the decomposition of **1** also affords trihypersilylheptaphosphane ($P_7Hyp_3$) as well as a second $P_n$ cage or polycycle of as-yet-unknown structure with second-order resonances between $\delta$ = –90 and –220 ppm as minor by-products.

The observed reaction products suggest that under these conditions the diphosphene is formed by dimerisation via HypClP–P($SiMe_3$)Hyp and subsequent elimination of chlorotrimethylsilane. A possible reaction pathway leading to the formation of the diphosphane would be the insertion of hypersilylphosphanylidene (formed from **1** by 1,1-elimination of chlorotrimethylsilane) into the PCl bond of **1**. The occurrence of reaction products such as $Hyp_2P_4$ and $Hyp_3P_7$ indicates that under these conditions the SiP bond of the hypersilyl group also takes part in the reaction, albeit with a much lower reaction rate.

These considerations led us to the expectation that the dimerisation of hypersilylphosphanylidene to form the diphosphene would be the preferred reaction if the phosphanylidene could be generated quickly and in quantitative yield. This is easily achieved by reaction of **1** with KO*t*Bu, to form the phosphanylidene, *t*BuOSi$Me_3$ and KCl, as shown in Scheme 3. Previously we have shown that KO*t*Bu can indeed be used to cleave an SiP bond of $P(SiMe_3)_3$,[9] and that the reaction with $HypP(SiMe_3)_2$ proceeds quickly and selectively with formation of *t*BuOSi$Me_3$ and HypP($SiMe_3$)K.[8] The reaction rate of the hypersilyl group is much slower.

When a solution of KO*t*Bu in THF is added to a solution of HypPCl($SiMe_3$) in THF very slowly at –60 °C to avoid any local excess of the reagent, light-green **2** forms quantitatively (≥95%, by $^{31}$P NMR) without any noticeable by-products. Compound **2** crystallises readily from pentane. The exclusive formation of the diphosphene **2** strongly supports the idea that the reaction indeed proceeds via hypersilylphosphanylidene. Compared to other methods described in the literature that can be used to prepare phosphanylidenes, its generation from RP($SiMe_3$)Cl and KO*t*Bu can be achieved at much lower temperatures. For instance, the phosphoranylidenephosphane $tBu_2P$–P=P$Br(tBu)_2$ decomposes at 20 °C to give the phosphanylphosphanylidene $tBu_2PP$, which has been trapped with 2,3-dimethylbutadiene.[10] The generation of phosphanylidenes from three-membered rings requires even higher temperatures of up to 140 °C.[11]

During these experiments we noticed that if the two solutions are mixed very quickly, the colour immediately changes to a dark-brown, which then slowly turns into a dark-violet. We therefore reversed the reaction sequence described above, adding the solution of HypPCl($SiMe_3$) to the solution of KO*t*Bu, maintaining an excess of KO*t*Bu throughout the whole procedure. In this way potassium 1,3-bis(hypersilyl)triphosphenide (**4**) can be obtained almost quantitatively (≥90%, by $^{31}$P NMR), as shown in Scheme 4.

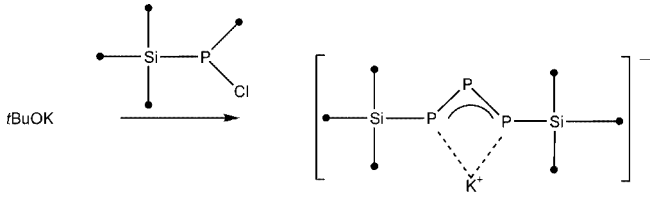


Scheme 4.

The $^{31}$P NMR spectrum of **4** consists of a triplet at $\delta$ = 705.5 ppm and a doublet at $\delta$ = 197.5 ppm with a coupling constant of 540.4 Hz; values of $\delta$ = 732.5, 212.5 ppm and 552.6 Hz have been reported for the analogous supersilyl derivative.[3] Attempts to crystallise **4** as the [18-crown-6·K]$^+$ salt were not successful.[12] Our experiments showed that treating HypP=PHyp with KO*t*Bu also led to the formation of **4**. Whether the reaction starts with SiP or SiSi bond cleavage remains unknown; the mechanism is under investigation.

### Derivatisation of 2 and 4

When 2,3-dimethylbutadiene is added to a solution of **2** in toluene, the green colour disappears slowly with formation of the [4+2] cycloaddition product **5**, which was identified by NMR spectroscopy. The $^{31}$P nuclei give a singlet at $\delta$ = –137.6 ppm, and the $^{29}$Si NMR spectrum consists of two pseudotriplets at $\delta$ = –9.8 ($SiMe_3$ groups) and –89.5 ppm (see also Experimental Section). The reaction proceeds quantitatively.

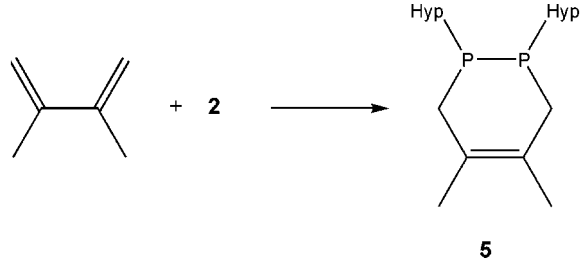


 © 2006 Wiley-VCH Verlag GmbH & Co. KGaA, Weinheim 

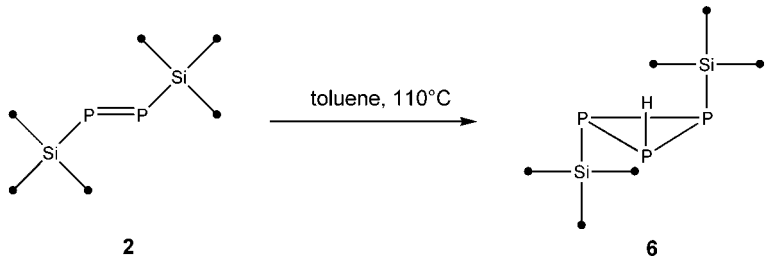


2 6

When **4** reacts with trifluoroacetic acid, bis(hypersilyl)cyclotriphosphane $Hyp_2P_3H$ (**6**) forms almost quantitatively, along with some hypersilylphosphane $HypPH_2$. We were not able to obtain crystals suitable for X-ray diffraction, therefore **6** was characterised by $^{31}P$ NMR spectroscopy, including 2D-COSY experiments. Remarkably, **6** also forms when a solution of **2** in toluene is refluxed for several hours. Here again, the major by-product is hypersilylphosphane, which cannot be removed quantitatively by sublimation in vacuo as **6** decomposes slowly upon raising the temperature. A solution of **2** in THF does not decompose, even if held under reflux for 6 h.

The $^{31}P$ and $^{31}P\{^1H\}$ NMR spectra and the COSY spectrum of the cyclotriphosphane are illustrated in Figure 1 (left and right, respectively). The $^{31}P\{^1H\}$ NMR spectrum exhibits signals of an AMP spin system [$\delta_A(P^1)$ = –233.0, $\delta_M(P^2)$ = –241.3, $\delta_P(P^3)$ = –260.9 ppm; $^1J_{P^1,P^2}$ = –142.1, $^1J_{P^1,P^3}$ = –202.3, $^1J_{P^2,P^3}$ = –182.7 Hz]. The larger coupling between $P^1$ and $P^3$ indicates a *cis* orientation of the substituents H and Hyp. In the proton-coupled spectrum, the AMP spin system extends to AMPX [$^1J_{P^1,H}$ = 141.1Hz, $^2J_{P^2,H}$ = 10.0, $^2J_{P^3,H}$ < 3 Hz]. A calculated $^{31}P\{^1H\}$ spectrum assuming negative values for all P–P coupling constants is also included as (c) in Figure 1 (left).

## X-ray Crystallography

An ORTEP plot of the molecular structure of **2** in the crystal as well as the numbering of the atoms is presented in Figure 2; selected bond lengths, bond angles and torsion angles are collected in Table 1. As expected, it is the *trans* isomer that is formed by dimerisation of the phosphanylidene. Surprisingly, two stereoisomers **A** and **B** that differ by a rotation of the hypersilyl group around the PSi bond are observed in the crystal. If viewed along an axis joining the two central Si atoms of the hypersilyl groups, the trimethylsilyl groups in isomer **A** are in a staggered arrangement with dihedral angles between 55° and 65°. The molecule possesses an inversion centre. In isomer **B**, the arrangement of the trimethylsilyl groups is almost eclipsed with the dihedral angles alternating between 5° and 120°, giving approximately a $C_s$-symmetric isomer with differences between the PSiSi and SiSiSi bond angles on both sides of the molecule being smaller than about 2° (Table 1). As described later on, the ab initio calculations for $(SiH_3)_3SiP{=}PSi(SiH_3)_3$ also predict two minima on the potential energy surface corresponding to **A** and **B**. At the level employed for these calculations [B3LYP/6-31+G(d)], **B** becomes a transition structure for $(SiMe_3)_3SiP{=}PSi(SiMe_3)_3$. Obviously, it is stabilized in the crystal due to packing effects.

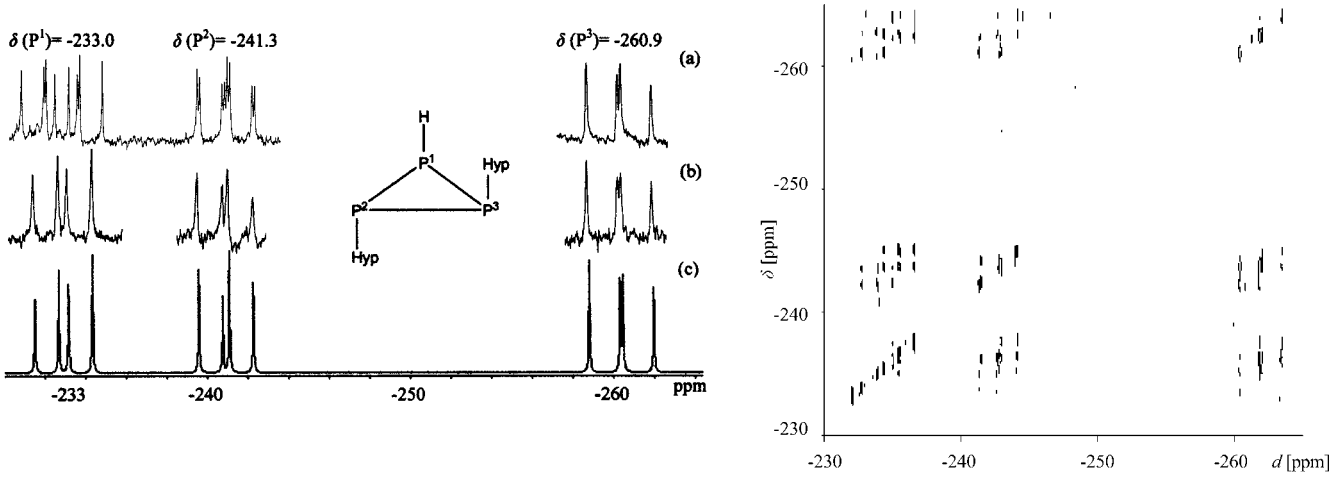


Figure 1. Left: Proton-coupled (a), decoupled (b) and calculated (c) $^{31}P$ NMR spectrum of bis(hypersilyl)cyclotriphosphane (**6**). Right: $^{31}P$ COSY spectrum of **6**.

 © 2006 Wiley-VCH Verlag GmbH & Co. KGaA, Weinheim 

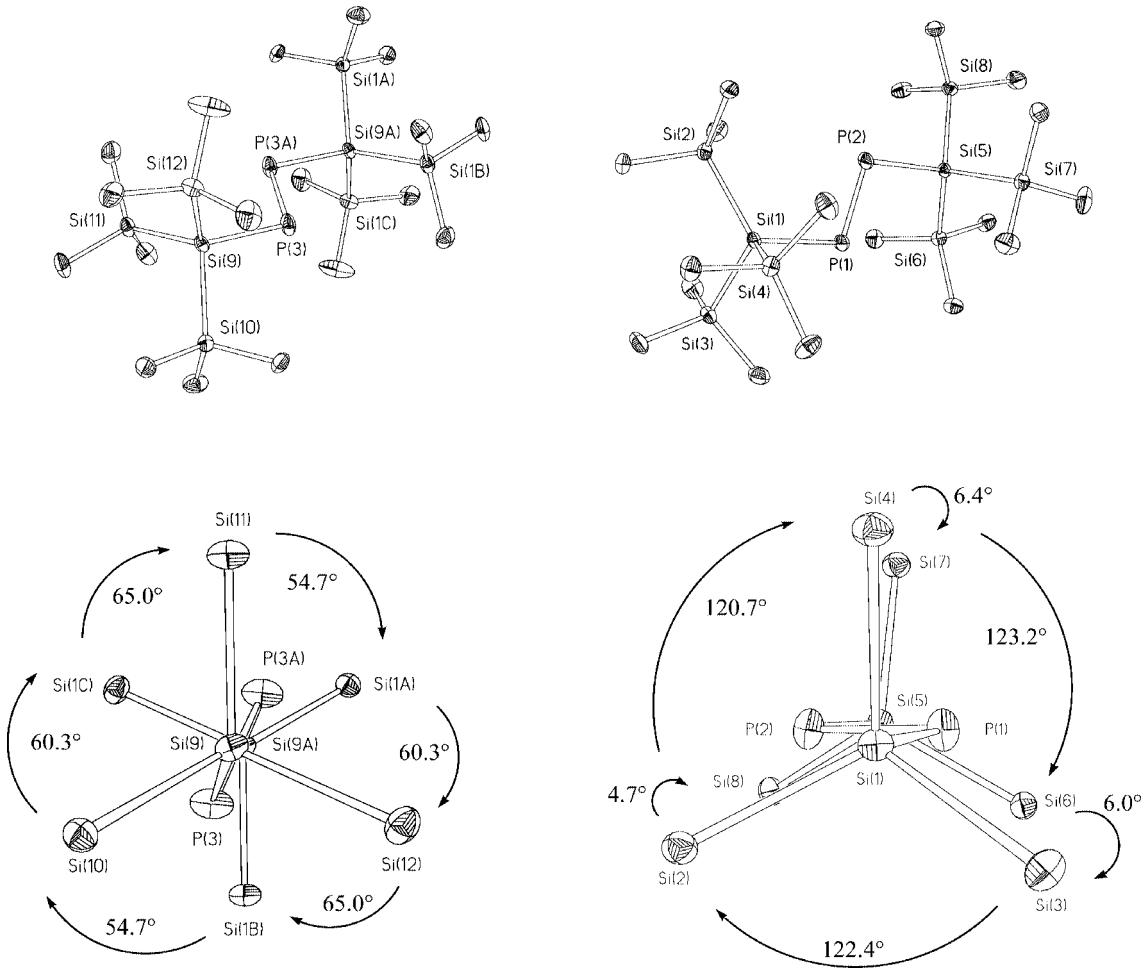


Figure 2. ORTEP plots of the two conformers of bis(hypersilyl)diphosphene in the crystal (top) and projections showing the different dihedral angles between the $SiMe_3$ groups (bottom). Isomer **A** is on the left and isomer **B** on the right side.

Table 1. Selected bond lengths [pm], bond angles [°] and dihedral angles [°] for the two isomers **A** and **B** of bis(hypersilyl)diphosphene.

| | Isomer **A** | Isomer **B** |
|---|---|---|
| PP | 203.0(2) | 202.2(2) |
| PSi | 228.0(2) | 227.0(2), 226.9(2) |
| SiSi | 234.6(2), 235.0(2), 235.3(2) | 234.6(2), 234.6(1), 235.0(2)<br>234.4(2), 234.9(2), 235.5(2) |
| PPSi | 102.7(1) | 103.2(1), 100.9(1) |
| PSiSi | 106.0(1), 104.4(1), 115.6(1) | 100.9(1), 104.7(1), 114.1(1)<br>103.1(1), 106.7(1), 113.5(1) |
| SiSiSi | 107.8(1), 110.9(1), 111.6(1) | 111.0(1), 111.6(1), 113.7(1)<br>111.0(1), 109.9(1), 112.3(1) |
| SiPPSi | 180.0 | –178.2(2) |

The P=P bond lengths of isomer **A** [203.0(2) pm] and **B** [202.2(2) pm] are almost identical, which is also the case for the PSi and SiSi bonds. Moreover, all distances are in the range that is considered normal for P=P, P–Si and Si–Si bonds and need no further discussion.

## Raman and UV Spectra

As diphosphenes possess absorptions in the UV and visible range (usually assigned as π–π* and n–π* transitions), the Raman spectra obtained with excitation sources in the visible or UV range are expected to show resonance or preresonance effects. The two main effects are an intensity enhancement as well as the appearance of an overtone progression for the P=P stretching vibration. So far, wavenumbers for the P=P stretch have been determined for $(Me_3Si)_3CP{=}PC(SiMe_3)_3$ (595 $cm^{-1}$) and ArP=PAr [Ar = 2,4,6-tri-*tert*-butylphenyl (610 $cm^{-1}$) and 2,6-bis(*m*-xylyl)-phenyl (622 $cm^{-1}$)].[13] There seems to be only a limited amount of mixing between the P=P and P–C stretching vibrations despite the fact that they are quite close to each other. This was concluded from a normal coordinate analysis (NCA) of MeP=PMe and $(Me_3Si)_3CP{=}PC(SiMe_3)_3$ by treating the methyl group as a point mass of 15.[14] So far, no NCA for a diphosphene based on an ab initio force field has been reported in the literature.

 © 2006 Wiley-VCH Verlag GmbH & Co. KGaA, Weinheim 

The Raman spectrum of bis(hypersilyl)diphosphene in the wavenumber range 50–900 $cm^{-1}$ is presented in Figure 3. The green 532-nm line of a frequency-doubled Nd:YAG laser (10 mW) was used to excite the sample. Its interpretation is rather straightforward, even without a NCA.

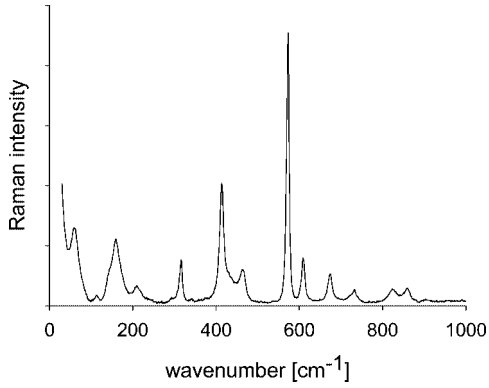


Figure 3. Raman spectrum of solid bis(hypersilyl)diphosphene in the wavenumber range 50–900 $cm^{-1}$.

The strongest line in this range, at 591 $cm^{-1}$, is clearly the P=P stretch, with the symmetric $SiC_3$ stretch at 626 $cm^{-1}$ being quite close. Nevertheless, there is negligible kinetic coupling between these two modes because the SiC bonds are separated from the P=P double bond by two SiSi bonds. This is not the case for the PSi and SiSi modes, which are expected on the low-wavenumber side in the range 300–500 $cm^{-1}$. They are observed at 481 and 450 $cm^{-1}$ [$\nu_{as}(SiSi_3)$], 431 $cm^{-1}$ [$\nu$(PSi)] and 332 and 323 $cm^{-1}$ [$\nu_s(SiSi_3)$]. The SiSiC and CSiC deformations of the trimethylsilyl groups fall in the range 50–240 $cm^{-1}$. No line splittings due to the presence of the two isomers **A** and **B** is observed as their spectra are expected to differ very little. This is confirmed by the ab initio results for the parent molecule $(SiH_3)_3SiP{=}PSi(SiH_3)_3$ (see next section).

For corroboration of the assignments given above, a normal coordinate analysis was carried out for $(H_3Si)_3SiP{=}PSi(SiH_3)_3$ and $(Me_3Si)_3SiP{=}PSi(SiMe_3)_3$ employing the Hessian matrices obtained from ab initio calculations (see next section). The Hessian matrix gives the force constants defined as displacements of Cartesian coordinates and has to be transformed into a force field described in terms of symmetry coordinates that themselves are linear combinations of displacements of internal coordinates such as bond lengths, bond angles and torsion angles. These calculations, known to spectroscopists as Wilson's FG method,[15] were performed using an enlarged version of the program ASYM40.[16] ASYM40 needs the Hessian matrix and the atomic coordinates of the equilibrium geometry as input data as well as the symmetry coordinates, which were chosen according to standard methods described in the literature.[17] Calculated PP, SiP and SiSi stretching force constants are summarised in Table 2. The P=P force constant is predicted as 326 and 332 $N\,m^{-1}$ for $(H_3Si)_3SiP{=}PSi(SiH_3)_3$ and $(Me_3Si)_3SiP{=}PSi(SiMe_3)_3$, respectively. The force constant for a PP single bond, for instance in $(SiMe_3)_2PP(SiMe_3)_2$, is considerably smaller, a value of 195 $N\,m^{-1}$ being obtained from ab initio calculations on this molecule.[18] Furthermore, the calculations of the potential energy distributions (PED) show that $\nu$(P=P) is indeed a group vibration in these diphosphenes, with *f*(PP) contributing as much as 86% to $\nu$(P=P) in $(H_3Si)_3SiP{=}PSi(SiH_3)_3$ and 97% in $(Me_3Si)_3SiP{=}PSi(SiMe_3)_3$. Coupling with other modes can be largely neglected.

Table 2. Experimental and calculated wavenumbers [$cm^{-1}$] for the PP and in-phase SiP and SiSi stretching vibrations and calculated force constants [$N\,m^{-1}$] for the rotational conformers **A**, **B** and **C** of $H_9Si_4P{=}PSi_4H_9$ [B3LYP/6-311+G(d)] and **A** of $Me_9Si_4P{=}PSi_4Me_9$ [B3LYP/6-311+G(d)].

| | $(H_3Si)_3SiP{=}PSi(SiH_3)_3$ | | | $(Me_3Si)_3SiP{=}PSi(SiMe_3)_3$ | |
|---|---|---|---|---|---|
| | **A** | **B** | **C** | **A** | |
| | calcd. | calcd. | calcd. | calcd. | exp. |
| $\nu$(P=P) | 603 | 599 | 597 | 604 | 591 |
| $\nu$(PSi) | 415 | 416 | 391 | 433 | 431 |
| $\nu_s(SiSi_3)$ | 314 | 314 | 278 | 331 | 332 |
| $\nu_{as}(SiSi_3)$ | 437 | 433 | 424 | 479 | 481 |
| *f*(P=P) | 326 | | | 332 | |
| *f*(PSi) | 153 | | | 157 | |
| *f*(SiSi) | 157 | | | 157 | |

The UV/Vis spectrum of **2** (solution in *n*-hexane) is presented in Figure 4 for three different concentrations. The absorption maxima corresponding to $\pi\rightarrow\pi^*$ and $n\rightarrow\pi^*$ excitations appear at 400 and 622 nm, respectively, the latter of which causes the green colour (see section on ab initio calculations).

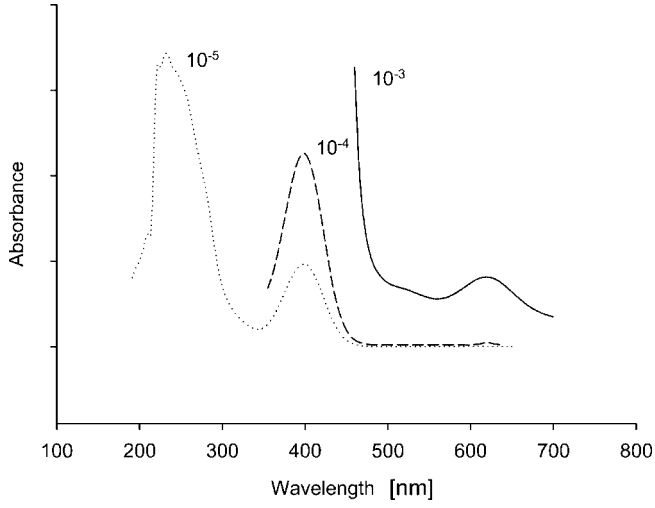


Figure 4. UV/Vis spectrum of bis(hypersilyl)diphosphene (**2**) for concentrations of $10^{-5}$, $10^{-4}$ and $10^{-3}$ M.

## Ab initio Calculations

### *Bis(hypersilyl)diphosphene*

Hyp–P=P–Hyp (**2**) is, with 82 atoms, computationally quite demanding. For our calculations at the B3LYP/6-31+G(d) level, we first used a smaller model created by replacing the hypersilyl groups by $Si(SiH_3)_3$.

 © 2006 Wiley-VCH Verlag GmbH & Co. KGaA, Weinheim 

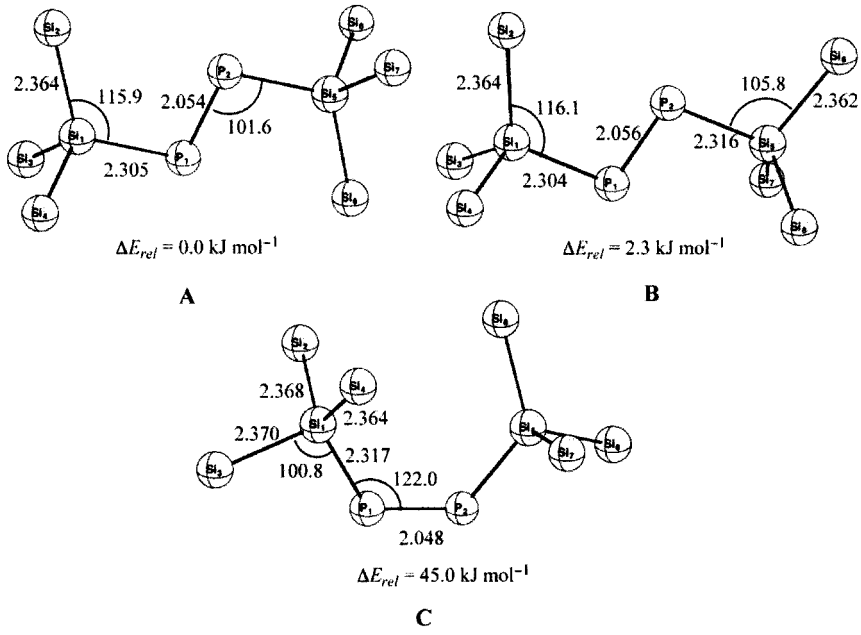


Figure 5. Rotational isomers of $(H_3Si)_3Si–P=P–Si(SiH_3)_3$ at the B3LYP/6-31+G(d) level of theory. The hydrogen atoms have been omitted for clarity.

Three minima were located on the potential energy surface (PES), as depicted in Figure 5.

The low-energy minima **A** and **B** have the Si–P=P–Si backbone in a *trans* orientation corresponding to the structures identified by X-ray spectroscopy. The energy separation ($\Delta E_{rel}$ = 2.3 kJ mol$^{-1}$) is quite small. The $SiH_3$ groups in **A** are oriented *trans* to each other and the conformer possesses a centre of inversion. The reason for the higher stability of this geometric arrangement can be identified by NBO analyses. Negative hyperconjugation occurs between the P lone pair and the respective antibonding Si–Si orbital if the $SiH_3$ group is oriented *cis* to the P=P double bond. Rotation of one $Si(SiH_3)_3$ group around the P–Si bond until the $H_3Si–Si–P–P$ angle is 180° yields the $C_s$-symmetric minimum **B**, destroys one of the LP(P)→σ*(Si–Si) interactions and consequently diminishes the stability.

The negative hyperconjugation also affects the bond lengths and angles. The P–Si bond length shrinks by 0.01 Å and the respective P–Si–Si angle becomes wider. For the full geometry data, see the Supporting Information.

A *cis* orientation of the Si–P=P–Si backbone is quite unfavourable and only one minimum, **C**, with a relative energy of 45.0 kJ mol$^{-1}$ was located on the PES.

The P=P stretching vibrations of the three minima [603 (**A**), 599 (**B**) and 597 cm$^{-1}$ (**C**)] are too close to discern the conformers by Raman spectroscopy. The same is true for the ν(PSi), $\nu_s(SiSi_3)$ and $\nu_{as}(SiSi_3)$ vibrations listed in Table 2.

As the synthesised diphosphene is light-green, we calculated UV/Vis spectra with time-dependent B3LYP and 6-311+G(d) basis sets. The global minimum has a strong absorption band at 358 nm ($f$ = 0.27) corresponding to a π → π* excitation. The HOMO–LUMO transition, corresponding to an n → π* excitation, is found at 562 nm but should not be visible as the oscillator strength is 0.00. However, the oscillator strength of the same transition for minimum **B** at 583 nm is calculated to be 0.0002. There is also a strong π → π* transition at 367 nm ($f$ = 0.21). Minimum **C** shows a similar behaviour, with a weak n →π* excitation at 586 nm ($f$ = 0.0002) and a strong π → π* transition at 359 nm ($f$ = 0.13).

Upon replacment of $Si(SiH_3)_3$ by the full hypersilyl group $Si\{Si(CH_3)_3\}_3$, only structure **A** corresponds to a minimum, while **B** becomes a transition structure at the B3LYP/6-31+G(d) level used. Due to space limitations, we were unable to perform MP2 calculations, which might predict **B** to be a minimum structure, too. The geometric parameters change slightly due to the larger hypersilyl groups. The P=P distance remains at 2.054 Å, but the P–Si bonds elongate by 0.01 Å and the SiPP bond angles become 4° wider. The characteristic Raman frequencies are close to the values of the smaller model, as shown in Table 2.

As expected, the n → π* excitation drifts to larger wavelengths, namely 632 nm. However, as for the smaller model, this HOMO–LUMO transition for **A** is not visible ($f$ = 0.0), although the π → π* excitation at 409 nm is quite strong ($f$ = 0.24).

### *Bis(hypersilyl)triphosphenide*

We also performed ab initio calculations for the bis(hypersilyl)triphosphenide anion at the same level of theory [B3LYP/6-31+G(d)], including calculations of $^{31}P$ chemical shifts. The $C_2$-optimised structure is shown in Figure 6. The Si–Si–P bond angle is only 3° wider in the $Hyp_2P_3$ anion than in $[(H_3Si)_3Si]_2P_3$ and about 8° wider than in the parent $(H_3Si)_2P_3$ (**10a**; see next section). Nevertheless, the P–P–P angle of the allylic backbone is roughly identical for R = Hyp (Figure 6) and $Si(SiH_3)_3$ (106.1°), and only 3° narrower

 © 2006 Wiley-VCH Verlag GmbH & Co. KGaA, Weinheim 

than in the parent. Even though the formal cone angle of hypersilyl is approximately 180°, the P–P–Si arrangement is far from linear. Therefore, investigations of the variation of the steric effect of R are of ongoing interest. A comparison of the DFT-calculated NMR chemical shifts (Figure 6) shows that the values are much too positive. When the correction factor 0.84, which is described in the section "$^{31}$P NMR Shift Calculations", is considered, the shift of the signal of the central phosphorus atom is $\delta$ = 695 ppm, in agreement with the observed value of $\delta$ = 705 ppm. For the terminal phosphorus atoms, which have a direct contact with the counterion, the correction leads to a value of $\delta$ = 229 ppm, which differs by only about 11 ppm from the experimental value.

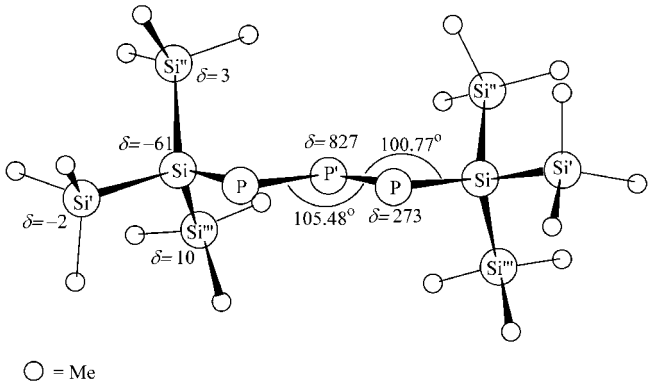


Figure 6. Optimized $C_2$ geometry for bis(hypersilyl)triphosphenide.

### *Geometries of Model Compounds*

To gain a deeper understanding of the steric and electronic influences of the substituents on the structures of molecules with phosphorus-containing backbones, geometry optimisations at the B3LYP/6-31+G* level of theory were performed for **7**–**12**, as shown in Figure 7. The model compounds, which are closely related to compounds **2**–**6**

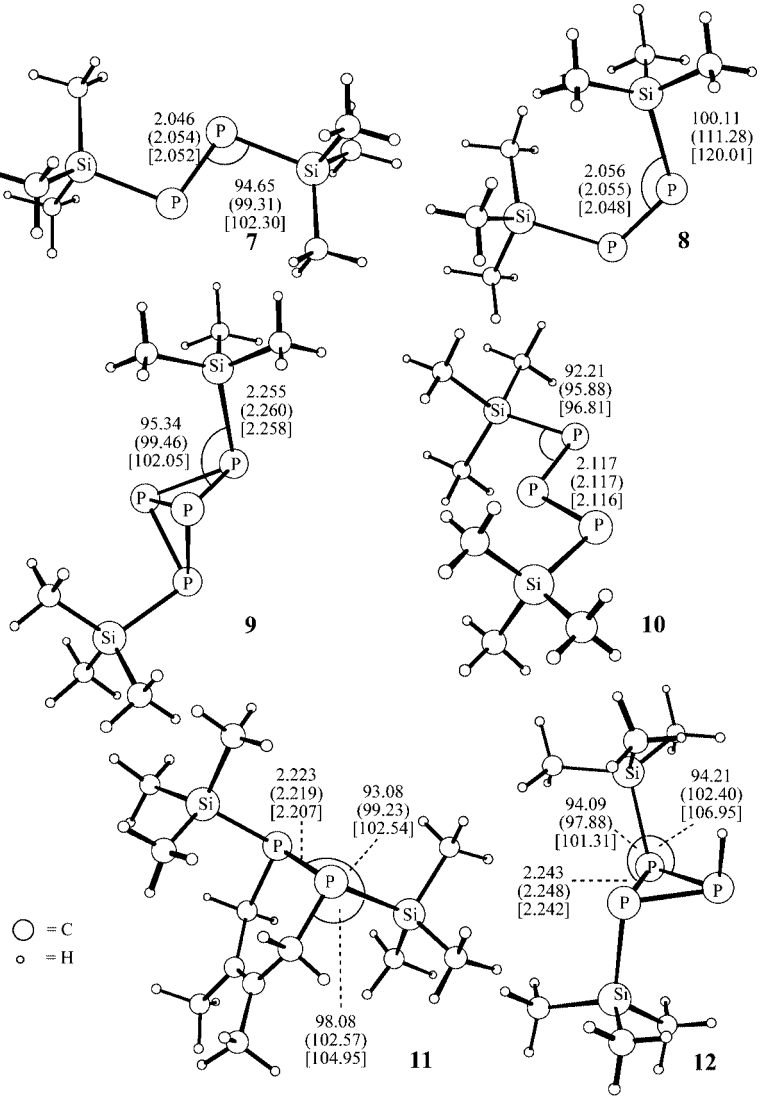


Figure 7. Ab initio (B3LYP/6-31+G*) optimised geometries of molecules with phosphorus-containing backbones (**7**–**12**). Structures for R = H and R = $SiH_3$ are not depicted. Values are given for R = H, with those for R = $SiH_3$ in parentheses and for R = $Si(CH_3)_3$ in square brackets.

 © 2006 Wiley-VCH Verlag GmbH & Co. KGaA, Weinheim 

described previously, were *trans*-RP=PR (R = H, **7a**; R = $SiH_3$, **7b**; R = $SiMe_3$, **7c**), *cis*-RP=PR (**8a**–**8c**), $R_2P_4$ (**9a**–**9c**), $[R_2P_3]^-$ (**10a**–**10c**), $R_2(PCH_2CHMe)_2$ (**11a**–**11c**) and $R_2P_3H$ (**12a**–**12c**). The backbones in this set vary from common tricoordinate phosphorus (**9**, **11** and **12**) through phosphorus in an allyl anion framework (**10**) to the P=P double bond in **7** and **8**.

The selected R groups differ only slightly in their inductive effects towards phosphorus, as seen by the Mulliken charges of $RPH_2$, which are –0.03 for R = H, –0.05 for $SiH_3$ and –0.06 for $SiMe_3$. The π-conjugation effect, as expressed by the bond angle sum, Σ$\alpha$, at $PH_2$[19] is difficult to separate from steric influences measured by the cone angle, $\gamma$, of R with P as the cone point.[20] The average cone angles (80.24° for R = H, 94.32° for $SiH_3$ and 125.16° for $SiMe_3$) derived from the //B3LYP/6-31+G* geometries suggest that silyl and trimethylsilyl should show distinctly different steric effects.

In the bicyclotetraphosphanes **9** as well as in the cyclotriphosphanes **12** the substituents R are attached to a $P_3$ ring. The $SiH_3$ substituent has the largest elongating effect on the $P^\alpha$–P bond, and the R–$P^\alpha$–P angle increases from H through $SiH_3$ to $SiMe_3$ (see Figure 7), paralleling the increase of the cone angles. While the R–$P^\alpha$–P and R–$P^\alpha$–C bond angles increase similarly in the six-membered ring **11**, the P–P bond length shrinks with silylation (H: 2.223; $SiH_3$: 2.219; $SiMe_3$: 2.207 Å). The allyl anions **10a**–**10c** with a delocalised π-conjugation show astonishing population effects on the phosphorus atom attached to R with charges –0.27 (H), –0.29 ($SiH_3$) and –0.21 ($SiMe_3$). H and $SiH_3$ behave more similarly than $SiH_3$ and $SiMe_3$. In contrast, the charges of the central P atom follow the trend of the inductive effect (–0.36, –0.16 and –0.18, respectively). The P–P bond length is almost unaffected by the substituents, and the P–P–P angle is smaller in the silyl derivatives, with a range of 107.30–108.58°. Counterion effects on the geometry of the triphosphaallyl anion have been discussed elsewhere.[3]

Compared to the allyl bond length, the P=P double bond is modified slightly more by the substituents, with values of 2.046, 2.054 and 2.052 Å for the *trans*-diphosphenes **7a**–**7c** and 2.056, 2.055 and 2.048 Å for the *cis*-diphosphenes **8a**–**8c**. Substantial changes are obtained for the R–P–P angles, which are 94.65°, 99.32° and 102.30° for the *trans* isomers.

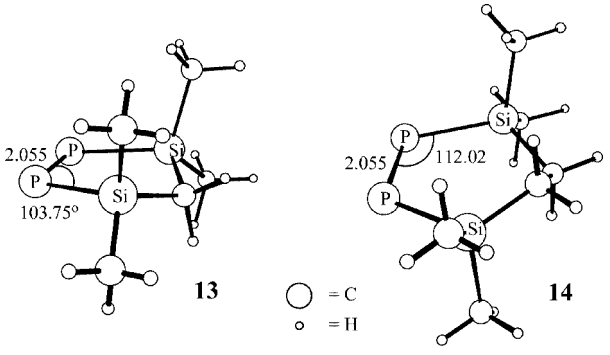


Figure 8. Geometries for model compounds **13** and **14**.

Due to the steric interaction between the substituents, these values are much larger for the *cis* isomers (106.11°, 111.28° and 120.01°). It is also noteworthy that the R–P–P–R torsion angles always differ by less than 1° from 180° (*trans*) or 0° (*cis*), even in *cis*-$Me_3SiP$=$PSiMe_3$.

The model compounds also include two silylated cyclic diphosphenes, which possess a *cis* geometry of the double bond, as shown in Figure 8.

### *$^{31}$P NMR Shift Calculations*

The $^{31}$P chemical shifts of supersilyldiphosphene and hypersilyldiphosphene differ by a striking 83 ppm. The difference is much smaller for other isostructural hypersilyl and supersilyl compounds such as $R_2P_4$ or $R_2P_3H$ and the allyl anion $[R_2P_3]^-$, at less than 25–30 ppm. As both SupP=PSup and HypP=PHyp are too large for high-quality MP2 shift calculations, we have performed a series of calculations for smaller diphosphenes as a test for the accuracy of the DFT calculations. Table 3 lists the chemical shifts for a series of selected diphosphenes (including cyclic derivatives with a *cis* arrangement) calculated at the DFT and various MP2 levels. We employed the B3LYP method with the 6-31G* basis set and the MP2 method with the three basis sets 6-31G* and McLean–Chandler's 6-311G* and 6-311+G**, labelled B3LYP-A, MP2-A, MP2-B and MP2-C further on. From the correlation analysis, the equation $\delta_{^{31}P(MP2\text{-}C)} = 0.84 \times \delta_{^{31}P(DFT\text{-}A)}$, which has a negligible intercept and squared correlation coefficient, *cc*, of 0.984, is obtained. Thus, $^{31}$P chemical shifts can be reliably estimated with this equation from DFT results. The correlation also extends to tetracoordinate phosphorus, as shown by including calculations for $[PH_3PH_2]^+$.

The DFT-A calculations with $C_1$ symmetry predict $\delta_{^{31}P}$ = 917 ppm for HypP=PHyp and 1071 ppm for SupP=PSup. The difference of 154 ppm becomes 129 ppm when taking into account the correlation mentioned above, thus increasing the agreement with the experimental difference (83 ppm).

We next turned to the question as to whether differing PPSi bond angles can cause large shift differences. The DFT-A calculations provide values of 104.55°/104.54° for HypP=PHyp (somewhat larger than the experimental values, see Table 1) and 106.47°/106.60° for SupP=PSup. To search for a bond angle–chemical shift relationship, DFT-A calculations were performed for ten *cis*- and twenty *trans*-RP=PR molecules. The predicted $\delta_{^{31}P}$ values are plotted as functions of the R–P=P angle, $\alpha$, for a large variety of R groups, such as H, F, Cl, $CF_3$,$CH_3$, *t*Bu, $NH_2$, $NMe_2$, $SiH_3$ and $SiMe_3$, in Figure 9. Several cyclic diphosphenes with PC, PN and PSi bonds are also included (see Table 3). In agreement with previous investigations,[21] a regression analysis confirms the impression that there is no general relationship that is valid for all substituents ($cc < 0.2$). Nevertheless, some subsets do display interesting trends that are useful for predicting phosphorus shifts. The data points for the substituents H, F, $SiH_3$, $SiMe_3$, Hyp and Sup correlate nicely with the calculated bond angles with the linear fit $\delta_{^{31}P} = 37 + 2866\alpha$ ($cc = 0.966$). Small changes of the PPSi

 © 2006 Wiley-VCH Verlag GmbH & Co. KGaA, Weinheim 

Table 3. Chemical shifts at the DFT and MP2 levels for *cis*-R–P=P–R and the $H_3P^*PH_2^+$ cation.

| R | DFT-A[a,b] | MP2-A[a] | MP2-B[a] | MP2-C[a] |
|---|---|---|---|---|
| H | 587 | 395 | 488 | 466 |
| Cl | 698 | 470 | 555 | 540 |
| F | 754 | 574 | 672 | 660 |
| $CH_3$ | 595 | 425 | 516 | 500 |
| *t*Bu | 640 | 474 | 562 | 554 |
| $SiH_3$ | 791 | 545 | 632 | 616 |
| $SiMe_3$ | 875 | 605 | 694 | 680 |
| $CF_3$ | 583 | 409 | 481 | 476 |
| *cyclo*-(NH)–P=P*–$(CH_2)_2$[c] | 299 | 207 | 270 | 272 |
| *cyclo*-(NH)–P*=P–$(CH_2)_2$[c] | 484 | 363 | 444 | 437 |
| *cyclo*-P=P–$(CH_2)_3$[c] | 570 | 424 | 509 | 497 |
| *cyclo*-P=P–$(CH_2)_4$[c] | 526 | 403 | 487 | 478 |
| *cyclo*-(NH)–P=P–(NH)–$(CH_2)$[c] | 366 | 267 | 336 | 337 |
| *cyclo*-(NMe)–P=P–(NMe)–$(CH_2)$[c] | 369 | 273 | 340 | 342 |
| $H_3PP^*H_2^+$ | –187 | –201 | –187 | –192 |
| $H_3P^*PH_2^+$ | –111 | –117 | –109 | –107 |

[a] All molecules optimised without symmetry constraints at the B3LYP/6-31G* level. Chemical shifts calculated for these geometries at the GIAO/B3LYP/6-31G* (DFT-A) and GIAO/MP2(fc) with 6-31G* (MP2-A), 6-311G* (MP2-B) and 6-311+G** (MP2-C) levels. Reference $PH_3$ with the same NMR methods at the //B3LYP/6-31+G* level has magnetic shieldings of 585.6 (DFT-A), 646.2 (MP2-A), 613.6 (MP2-B), 607.1 (MP2-C) and a chemical shift of $\delta$ = –240 ppm. [b] The slope and squared correlation coefficient, *cc*, between $\delta_{^{31}P(DFT\text{-}A)}$ and the higher levels of NMR calculation are: $\delta_{^{31}P(MP2\text{-}A)} = 0.77\delta_{^{31}P(DFT\text{-}A)} - 31$ ppm, with $r = 0.989$; $\delta_{^{31}P(MP2\text{-}B)} = 0.86\delta_{^{31}P(DFT\text{-}A)} + 0$ ppm, with $r = 0.988$; and $\delta_{^{31}P(MP2\text{-}C)} = 0.84\delta_{^{31}P(DFT\text{-}A)} + 0$ ppm, with $r = 0.984$. [c] Cyclic compounds with a *cis* arrangement of the P=P double bond; otherwise *trans* conformer.

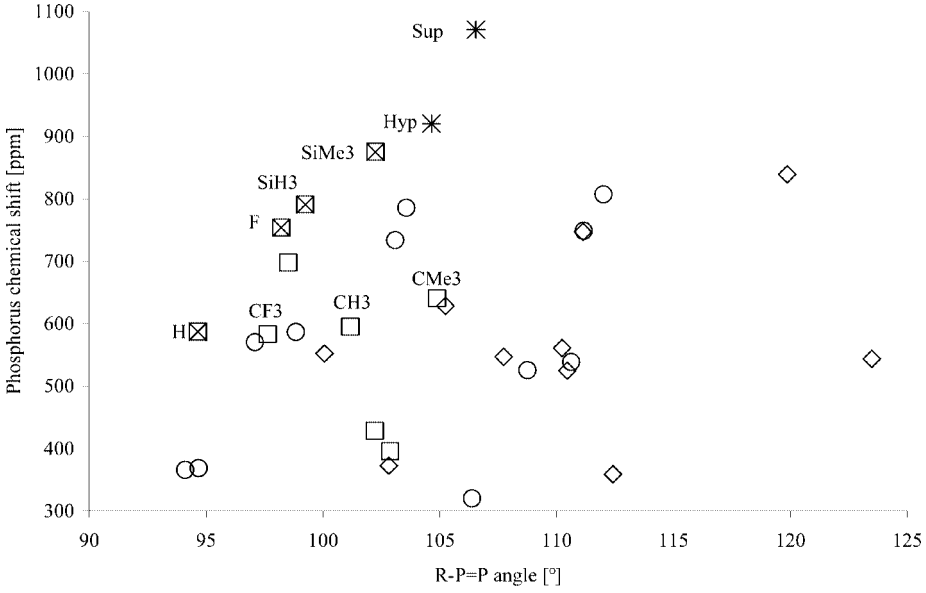


Figure 9. Relation between the R–P=P angle and chemical shifts of phosphorus at ab initio/NMR level DFT-A for *trans* (squares), *cis* (diamonds) and cyclic (circles) diphosphenes. A cross denotes the *trans*-disilylated molecules and the additional cross (forming an asterisk) marks the molecules that are known experimentally.

bond angles of *trans*-disilyldiphosphenes cause a large change of the phosphorus shift, which is different from the *trans* carbon analogues, as shown for the substituents H, $CF_3$, $CH_3$ and $CMe_3$. Here, a difference of the bond angles of more than 10° (see also Table 3) causes a shift change of no more than 50 ppm. As is to be expected, the P=P–R angle and the bulkiness of R correlate so that the shift also correlates with the calculated cone angles, which are 92.9°, 123.2°, 175.9° and 211.2° for $SiH_3$, $SiMe_3$, Hyp and Sup, respectively.

Remarkably, the chemical-shift changes for the *cis* isomers per unit angle change are much smaller. For the *cis* series with H, F, $SiH_3$ and $SiMe_3$, the calculated bond angles are 100.2°, 105.2°, 111.1° and 119.9°, with shift values of $\delta$ = 552, 628, 747 and 839 ppm, respectively, which gives a linear fit $\delta_{^{31}P} = -923 + 15\alpha$ (*cc* = 0.982). In the corresponding alkyl series H, $CF_3$, $CH_3$ and $CMe_3$, the shift is almost independent of the bond angle: all values are between $\delta$ = 525 and 552 ppm with bond angles between 100° and 123°. The shift values for *cis*- and *trans*-$(H_2N)$-P=P$(NH_2)$ and -$(Me_2N)$P=P$(NMe_2)$ do not fit into these correlations as they are much lower (between $\delta$ = 350 and 400 ppm). This is consistent with previous phosphorus NMR investigations that an increased electronegativity of

 © 2006 Wiley-VCH Verlag GmbH & Co. KGaA, Weinheim 

the atom attached to the phosphorus atom causes an upfield shift.[21] In diphosphenes with P–C or P–Si bonds, β-alkylation, i.e. replacing $CH_3$ or $SiH_3$ by $CH_2R$ and $SiH_2R$, always increases $\alpha$ as the cone angle of the substituent becomes larger and a downfield shift occurs. With the amino-substituted *cis*-diphosphenes $(H_2N)P{=}P(NH_2)$ and $(Me_2N)P{=}P(NMe_2)$ the opposite effect is observed; an upfield shift of about 20 ppm is predicted by the ab initio calculations.

The *cis*-E–P=P–E group in the cyclic compounds shows similar small effects of the bond angle on $\delta_{^{31}P}$. In agreement with a positive angle vs. shift correlation, $\delta_{^{31}P}$ of the six-membered rings increases compared to the corresponding five-membered rings.

All carbon-substituted diphosphenes are predicted to possess phosphorus resonances in the range between $\delta$ = 525 and 641 ppm, which does not overlap with the range for silyl-substituted diphosphenes [$\delta$ = 734 ppm for *cyclo*-1,2-diphospha-3,5-disilacyclopent-1-ene and $\delta$ = 875 ppm for *trans*-$(Me_3Si)P{=}P(SiMe_3)$]. Similarly, the amino-substituted diphosphenes show up with distinguishable chemical shifts in the range $\delta$ = 325–425 ppm, at higher field than the alkyldiphosphenes.

## Conclusions

Along with the synthesis of the first example of a bis(oligosilyl)diphosphene, several synthetic refinements for the generation of phosphorus–phosphorus double bonds have been developed. The concentration-dependent product formation in the reaction of Hyp–PCl–$SiMe_3$ with KO*t*Bu indicates the intermediacy of a hypersilylphosphanylidene. The green colour of the diphosphene is in agreement with the weak n–π* absorption band at 632 nm obtained from DFT calculations. Geometries and GIAO/MP2 as well as GIAO/B3LYP chemical-shift calculations have been performed for the H-, $SiH_3$-, and $SiMe_3$-substituted parents of the experimentally investigated molecules. The relation (*cc* = 0.984; 16 examples with a P=P bond) between the large basis set MP2 and B3LYP/6-31G* results provide an equation [$\delta_P$(MP2-C) = 0.84 × $\delta_P$(B3LYP)] with a negligible intercept. The correction factor has been successfully applied to the bare triphosphaallyl anion, resulting in differences of less than 32 ppm with respect to the NMR spectroscopic data of the complex of the anion with $K(THF)_n$ (**4**). The R–P=P bond angle vs. chemical shift relationship for 33 molecules with an –P=P– moiety has been analysed: *trans*-R–P=P–R shows larger shifts with larger angles (approximately 40 ppm per degree), although little effect is seen for *cis*-R–P=P–R (including endocyclic moieties), probably due to compensation resulting from geometric constraints. While previous model computations only considered R = H and $SiH_3$ (as placeholder for supersilyl) the present set expands the scope to $SiMe_3$ and, in special cases, to hypersilyl, $Si(SiMe_3)$. The change of geometric parameters from the $SiH_3$ to the $SiMe_3$ substituent is most obvious in *cis*-R–P=P–R, with a widening of the P=P–Si angle by 9°. In the other compounds considered this angle changes by only 2° ($P_3$-allyl) or 5° (cyclo-$P_3$). This is in agreement with NMR shifts of cyclotriphosphanes with R = H, Me, *i*Pr, and *t*Bu, which exemplify steric effects reflected in NMR signals.[22]

## Experimental Section

**General Remarks:** All syntheses and manipulations were carried out under either $N_2$ or Ar using standard Schlenk techniques. Solvents were distilled from sodium, potassium, sodium/potassium alloy or $LiAlH_4$ prior to use. Elemental analyses were performed with a Heraeus Vario Elementar.

**Ab Initio Calculations:** The B3LYP/6-31+G* method was used for geometry optimisation, examining all stationary points by analytical frequency calculations with the Gaussian 98 program package.[23] For selected minimum geometries the magnetic shielding was calculated with the GIAO approach at the B3LYP/6-31G* and MP2 level with the basis sets 6-31G*, 6-311G* and 6-311+G**, and transformed into chemical shifts (see Table 3). The UV spectra were obtained by time-dependent DFT calculations with the hybrid B3LYP functional and 6-311+G(d) basis set.

**Spectroscopy:** NMR spectra were recorded with a Bruker MSL 300 or a Varian Unity Inova 300 spectrometer. The $^{29}Si$ and $^{31}P$ NMR spectra were measured for solutions in THF or toluene in 10-mm tubes with capillaries of $D_2O$ serving as external lock. $^{31}P$-$^{31}P$ COSY spectra were recorded at 25 °C from a solution in $C_6D_6$ using 4096 × 4096 data points and a sweep width of 10582 Hz, The time required for an experiment was about 11 h. Raman spectra were recorded with a JobinYvon T64000 triple monochromator equipped with a CCD detector and a frequency-doubled Nd:YAG laser operating at 532 nm with a power of 10 mW. Samples were placed in 1-mm capillaries and sealed under dry, oxygen-free nitrogen. The UV/Vis spectrum of a solution of bis(hypersilyl)diphosphene in *n*-hexane was measured with a Perkin–Elmer Lamda 2S spectrometer in the range 200–700 nm.

**X-ray Structure Analysis of 2:** The crystal was mounted onto the tip of a glass fibre and data collection was performed with a Bruker-AXS SMART APEX CCD diffractometer using graphite-monochromated Mo-$K_\alpha$ radiation ($\lambda$ = 0.71073 Å). The data was reduced to $F_o^2$ and corrected for absorption effects with SAINT[24] and SADABS,[25] respectively. The structure was solved by direct methods and refined by full-matrix least-squares methods (SHELXL-97).[26] All non-hydrogen atoms were refined with anisotropic displacement parameters and were located in positions calculated to correspond to standard bond lengths and angles. The diagrams were drawn with 30% probability thermal ellipsoids, with all hydrogen atoms omitted for clarity. Selected data are collected in Table 4. CCDC-291188 contains the supplementary crystallographic data for this paper. These data can be obtained free of charge from The Cambridge Crystallographic Data Centre via www.ccdc.cam.ac.uk/data_request/cif.

**Synthesis of Bis(hypersilyl)diphosphene (2):** Solid $C_2Cl_6$ (0.21 g, 0.87 mmol) was added to a solution of $HypP(SiMe_3)_2$ (0.31 g, 0.73 mmol) in 20 mL of toluene and the reaction mixture was stirred at room temperature overnight. The solvent and all volatile reaction products such as $C_2Cl_4$ and $ClSiMe_3$ were then carefully removed by concentration in vacuo. The oily residue of pure **1** was dissolved in 20 mL of THF and a solution of *t*BuOK (0.09 g, 0.76 mmol) in 10 mL of THF was added dropwise at –70 °C. The colour slowly changed to light-green. The mixture was stirred for another 2 h and then warmed to room temperature. The solvent

 © 2006 Wiley-VCH Verlag GmbH & Co. KGaA, Weinheim 

Table 4. Crystal data and structure refinement for bis(hypersilyl)-diphosphene.

| | |
|---|---|
| Empirical formula | $C_{27}H_{81}P_3Si_{12}$ |
| Formula mass | 835.91 |
| $T$ [K] | 100(2) |
| Wavelength [Å] | 0.71073 |
| Crystal system | triclinic |
| Space group | $P\bar{1}$ |
| $a$ [Å] | 9.3084(19) |
| $b$ [Å] | 13.495(3) |
| $c$ [Å] | 23.693(5) |
| $\alpha$ [°] | 94.59(3) |
| $\beta$ [°] | 100.94(3) |
| $\gamma$ [°] | 107.23(3) |
| $V$ [Å$^3$] | 2761.3(10) |
| $Z$ | 2 |
| $\rho_{calcd.}$ [g cm$^{-3}$] | 1.005 |
| Absorption coefficient [mm$^{-1}$] | 0.385 |
| $F$(000) | 912 |
| Crystal size [mm] | 0.45 × 0.28 × 0.16 |
| $\theta$ range [°] | 1.60–26.37 |
| | $-11 < h < 11$ |
| | $-16 < k < 16$ |
| | $-29 < l < 29$ |
| Reflections collected/unique | 22108/11119 [$R$(int) = 0.0509] |
| Completeness to $\theta$ = 22.00° | 98.4% |
| Absorption correction | SADABS |
| Refinement method | full-matrix least squares on $F^2$ |
| Data/restraints/parameters | 11119/0/406 |
| Goodness-of-fit on $F^2$ | 1.006 |
| Final $R$ indices [$I > 2\sigma(I)$] | $R_1$ = 0.0593, $wR_2$ = 0.1346 |
| $R$ indices (all data) | $R_1$ = 0.0989, $wR_2$ = 0.1443 |
| Largest diff. peak/hole [e Å$^{-3}$] | 0.524/–0.315 |

was removed by evaporation in vacuo and replaced with pentane. Light-green crystals of **2** (0.19 g, 95%) with a quality suitable for X-ray diffraction were obtained at –30 °C. $C_{18}H_{54}P_2Si_8$ (557.32): calcd. C 38.79, H 9.77; found C 37.90, H 9.52. $^{31}$P NMR: $\delta$ = +735.0 ppm. $^{29}$Si NMR: $\delta$ = –56.7 (pseudo-t, $|^1J_{P,Si} + {}^2J_{P,Si}|$ = 46.0 Hz), –9.9 (pseudo-t, $|^2J_{P,Si} + {}^3J_{P,Si}|$ = 7.1 Hz, $SiMe_3$) ppm.

**Synthesis of Potassium hypersilyltriphosphenide (4):** *t*BuOK (0.22 g, 1.96 mmol) was dissolved in 10 mL of THF and a solution of **1** (0.73 g, 1.88 mmol) in 20 mL of THF was added dropwise at –60 °C over a period of 30 min. The colour of the reaction mixture turned dark brown. After completion, the reaction mixture was warmed to room temperature, whereby the colour changed to deep violet. According to the $^{31}$P NMR spectrum, **4** formed almost quantitatively (>95%) with traces of $HypPH_2$ (<5%) as a by-product. Attempts to crystallise **4** as the [18-crown-6·K]$^+$ salt failed. $^{31}$P NMR: $\delta$ = +705.5 (t), +197.5 (d) ppm.

**Reaction of Bis(hypersilyl)diphosphene with 2,3-Dimethylbutadiene. Formation of 5:** Compound **2** (0.06 g, 0.11 mmol) was dissolved in 1 mL of THF and the solution was transferred into an NMR tube. 2,3-Dimethylbutadiene (0.073 g, 0.188 mmol) was then added. After 1 h at room temperature, the green colour had disappeared. According to the NMR spectra, the [4+2] cycloaddition product **5** had formed almost quantitatively (≥95%). No attempt to crystallise the compound was made. $^{31}$P NMR: $\delta$ = –137.3 (s) ppm. $^{29}$Si NMR: $\delta$ = –89.5 (pseudo-t, $|^1J_{P,Si} + {}^2J_{P,Si}|$ = 37.0 Hz), –9.8 (pseudo-t, $|^2J_{P,Si} + {}^3J_{P,Si}|$ = 10.6 Hz, $SiMe_3$) ppm.

**Thermal Decomposition of Bis(hypersilyl)diphosphene. Formation of 6:** Compound **2** (0.06 g, 0.11 mmol) was dissolved in 10 mL of toluene and refluxed for 4 h. After this period, the green colour had disappeared completely and the signal of **2** could no longer be detected in the $^{31}$P NMR spectrum as **6** had formed almost quantitatively, along with some $HypPH_2$. Not unexpectedly, **6** also formed when **4** was treated with HypCl. Removal of the toluene by concentration in vacuo gave an oily residue, which turned out to be impossible to purify so no crystals could be grown, despite the use of different solvents. Attempts to purify **6** by sublimation failed due to decomposition, therefore no elemental analysis was carried out. $^{31}$P NMR: $\delta$ = –233.0 (q), –241.3 (q), –260.9 (q) ppm. For a discussion of the spectra, see Synthesis section.

**Supporting Information** (see also the footnote on the first page of this article): Cartesian coordinates of the $(H_3Si)_3SiP{=}PSi(SiH_3)_3$ minima obtained by B3LYP/6-31+G(d) calculations with Gaussian98.

## Acknowledgments

The authors gratefully acknowledge financial support of projects P 16112 (K. H.) and P 16912 (M. F.) by the Fonds zu Förderung der wissenschaftlichen Forschung (FWF), Vienna.

[1] See, for instance: *Multiple Bonding and Low Coordination in Phosphorus Chemistry* (Eds.: M. Regitz, O. J. Scherer), Georg Thieme, Stuttgart, **1990**.
[2] N. Wiberg, A. Wörner, H.-W. Lerner, K. Karaghiosoff, *Z. Naturforsch., Teil B* **2002**, *57*, 1027.
[3] N. Wiberg, A. Wörner, H.-W. Lerner, K. Karaghiosoff, D. Fenske, G. Baum, A. Dransfeld, P. v. R. Schleyer, *Eur. J. Inorg. Chem.* **1998**, 833.
[4] P. Jutzi, U. Meyer, *Phosphorus Sulfur* **1988**, *40*, 275.
[5] M. Kira, T. Maruyama, C. Kabuto, K. Ebata, H. Sakurai, *Angew. Chem. Int. Ed. Engl.* **1994**, *33*, 1489.
[6] See for instance the review: M. Yoshifuji, K. Toyota, "Synthesis of Multiply Bonded Phosphorus Compounds Using Silylphosphines and Silylphosphides", in *Chemistry of Organic Silicon Compounds 3* (Eds.: Z. Rappoport, Y. Apeloig), John Wiley, Chichester, UK, **2001**, pp. 491.
[7] a) P. Chaquin, A. Gherbi, D. Masure, A. Sevin, *J. Mol. Struct.: Theochem.* **1996**, *369*, 85; b) M. T. Nguyen, A. Van Keer, L. G. Vanquickenborne, *J. Org. Chem.* **1996**, *61*, 7077.
[8] V. Cappello, J. Baumgartner, A. Dransfeld, K. Hassler, *Eur. J. Inorg. Chem.*, submitted.
[9] U. Englich, K. Hassler, K. Ruhlandt-Senge, F. Uhlig, *Inorg. Chem.* **1998**, *37*, 3532.
[10] G. Fritz, T. Vaahs, H. Fleischer, E. Matern, *Angew. Chem. Int. Ed. Engl.* **1989**, *28*, 315.
[11] E. Niecke, R. Rüger, B. Krebs, M. Dartmann, *Angew. Chem. Int. Ed. Engl.* **1983**, *22*, 552.
[12] During the preparation of the manuscript, we learned that a lithium salt of the bis(hypersilyl)triphosphenide anion has been characterised by X-ray diffraction in the group of Klinkhammer in Mainz.
[13] a) H. Hamaguchi, M. Tasumi, M. Yoshifuji, T. Hashida, N. Inamoto, *Chem. Lett.* **1984**, *3*, 463; b) H. Hamaguchi, M. Tasumi, M. Yoshifuji, N. Inamoto, *J. Am. Chem. Soc.* **1984**, *106*, 508; c) T. Copeland, M. P. Shea, M. C. Milliken, R. C. Smith, J. D. Protasiewicz, M. C. Simpson, *Anal. Chim. Acta* **2003**, *496*, 155.
[14] I. A. Garbuzova, L. A. Leites, S. S. Bukalov, *J. Mol. Struct.* **1997**, *410*, 467.
[15] E. B. Wilson Jr, J. C. Decius, P. C. Cross, *Molecular Vibrations*, McGraw-Hill, New York, **1955**.
[16] ASYM 40, update of program ASYM 20: L. Hedberg, I. M. Mills, *J. Mol. Spectrosc.* **1993**, *160*, 117.
[17] S. J. Cyvin, J. Brunvoll, B. N. Cyvin, I. Elvebredd, G. Hagen, *Mol. Phys.* **1968**, *14*, 43.
[18] K. Hassler, G. Tekautz, unpublished results.

 © 2006 Wiley-VCH Verlag GmbH & Co. KGaA, Weinheim 

[19] M. N. Glukhovtsev, A. Dransfeld, P. v. R. Schleyer, *J. Phys. Chem.* **1996**, *100*, 13447.
[20] The cone angle is defined as the rigid angle between the tangent at the van der Waals radius of the most remote atom at one side of the cone and the tip of the cone and the line between the atom at the tip of the cone and the atom attached to this atom. See: C. A. Tolman, *Chem. Rev.* **1977**, *77*, 313.
[21] a) J. R. Van Wazer, J. H. Letcher, "Interpretation of $^{31}$P NMR Chemical Shifts", in *Topics in Phosphorus Chemistry*, vol. 5 (Eds.: M. M. Crutchfield, C. H. Dungan), Wiley, New York, **1967**; b) P. v. R. Schleyer, A. Dransfeld, *Magn. Res. Chem.* **1998**, *36*, 29.
[22] J. Hahn, M. Baudler, C. Krüger, T. Yi-Hung, *Z. Naturforsch., Teil B* **1982**, *37*, 797.
[23] M. J. Frisch, G. W. Trucks, H. B. Schlegel, G. E. Scuseria, M. A. Robb, J. R. Cheeseman, V. G. Zakrzewski, J. A. Montgomery Jr, R. E. Stratmann, J. C. Burant, S. Dapprich, J. M. Millam, A. D. Daniels, K. N. Kudin, M. C. Strain, O. Farkas, J. Tomasi, V. Barone, M. Cossi, R. Cammi, B. Mennucci, C. Pomelli, C. Adamo, S. Clifford, J. Ochterski, G. A. Petersson, P. Y. Ayala, Q. Cui, K. Morokuma, P. Salvador, J. J. Dannenberg, D. K. Malick, A. D. Rabuck, K. Raghavachari, J. B. Foresman, J. Cioslowski, J. V. Ortiz, A. G. Baboul, B. B. Stefanov, G. Liu, A. Liashenko, P. Piskorz, I. Komaromi, R. Gomperts, R. L. Martin, D. J. Fox, T. Keith, M. A. Al-Laham, C. Y. Peng, A. Nanayakkara, M. Challacombe, P. M. W. Gill, B. Johnson, W. Chen, M. W. Wong, J. L. Andres, C. Gonzalez, M. Head-Gordon, E. S. Replogle, J. A. Pople, *Gaussian 98, Revision A.11*, Gaussian, Inc., Pittsburgh, PA, **2001**.
[24] *SAINTPLUS: Software Reference Manual*, Version 6.45, Bruker-AXS, Madison, WI, **1997–2003**.
[25] R. H. Blessing, *Acta Crystallogr., Sect. A* **1995**, 51, 33–38. *SADABS*, Version 2.1, Bruker AXS, **1998**.
[26] G. M. Sheldrick, *SHELX-97, Programs for Crystal Structure Analysis*, release 97-2, University of Göttingen, Germany, **1998**.

Received: January 18, 2006
Published Online: April 11, 2006

 © 2006 Wiley-VCH Verlag GmbH & Co. KGaA, Weinheim 

DOI: 10.1002/ejic.200501112

# A Self-Sacrificing Template Route to Spinel $M^{II}In_2S_4$ ($M^{II}$ = Mn, Zn, Cd, Fe, Co, Ni) and $M^{I}In_5S_8$ ($M^{I}$ = Cu, Ag) Porous Microspheres

**Shuijin Lei,[a,b] Kaibin Tang*[a,b] Yunxia Qi,[a,b] Zhen Fang,[a,b] and Huagui Zheng[b]**

**Keywords:** Solvothermal synthesis / Spinel phases / Microporous materials / Semiconductors

A facile, self-sacrificing template route has been developed to synthesize spinel $M^{II}In_2S_4$ ($M^{II}$ = Mn, Zn, Cd, Fe, Co, Ni) and $M^{I}In_5S_8$ ($M^{I}$ = Cu, Ag) porous microspheres. The BET surface areas of the products are around 70 $m^2g^{-1}$. The urchin-like $In_{2.77}S_4$ microspheres precursor acts as both starting material and template to confine the growth of the final products. The phase structures and morphologies of the products were characterized by X-ray diffraction, scanning electron microscopy, transmission electron microscopy, and electron diffraction. Possible formation process and growth mechanism for the porous structure are proposed based on the experimental results.
(© Wiley-VCH Verlag GmbH & Co. KGaA, 69451 Weinheim, Germany, 2006)

## Introduction

Porous solid materials are of practical significance as useful supports due to their interconnected pore structure, large surface area, and small pore size.[1,2] Recently, the preparation and investigation of nano-/micro-sized porous spheres has attracted considerable attention because of their technical applications in catalysis, drug-delivery systems, separation techniques, photonics, as well as piezoelectric and other dielectric devices.[3,4] Rapid solvent removal,[5] porogen leaching,[6] double-emulsification,[7,8] and solution-induced phase separation[9] have been used to fabricate porous microspheres based on an emulsion–solvent evaporation method. However, these methods are rather complicated for repeatable production and subtle manipulation.

In recent years, multinary chalcogenide compounds have been the subject of intense research,[10,11] and considerable progress has been made in the synthesis and characterization of ternary semiconductor crystallites.[12,13] Various ternary semiconducting compounds with formula $A^{II}B^{III}{}_2X^{VI}{}_4$ have been of special interest due to their unusual properties (e.g. wide transparency intervals, high value of non-linear susceptibility combined with natural birefringence) and potential applications (e.g. electro-photographic films, switches, optical filters, photodetectors, magnetic field control lasers, light modulators, optoelectronics, and Schottky diodes).[14–18] The type I-III-VI ternary semiconductors $CuIn_5S_8$ and $AgIn_5S_8$ are also of great technological and scientific interest because of their possible application in semiconductor devices and optical and quantum electronics.[19]

Both $M^{II}In_2S_4$ and $M^{I}In_5S_8$ show n-type conductivity and crystallize in the spinel-type cubic structure with the space group $Fd\bar{3}m$. There are theoretical and practical reasons to believe that they can all be used as an absorber layer material for a p-n junction solar cell.[18,20,21] Many efforts have been made to study the magnetic, optical, electrical, and semiconducting properties of $M^{II}In_2S_4$[22–26] and the electrical and optical properties of $M^{I}In_5S_8$.[19,27,28]

Conventionally, $M^{II}In_2S_4$ and $M^{I}In_5S_8$ powders are prepared by solid-state reaction methods under high temperature and vacuum conditions for a long time.[19,29,30] Recently, many methods such as metal-organic chemical vapor deposition (MOCVD),[31] chemical vapor transport,[32] precipitation,[33] hydrothermal/solvothermal techniques,[26,34] and a chemical spraying route[18] have been reported for the preparation of $M^{II}In_2S_4$. As for the synthesis of $M^{I}In_5S_8$, spray deposition,[35] pulsed-laser deposition,[36] sequential deposition,[37] and thermal-deposition[38] methods have also been reported. However, the complicated synthesis process and the requirements for special instruments or harsh conditions in these processes are the main disadvantages of these methods. To the best of our knowledge, the extensively applicable self-sacrificing template method has not been reported to be applicable for the fabrication of porous microspheres of a series of $M^{II}In_2S_4$ and $M^{I}In_5S_8$ compounds.

In this paper, we report the successful devolepment of a rational self-sacrificing template route to prepare spinel $M^{II}In_2S_4$ ($M^{II}$ = Mn, Zn, Cd, Fe, Co, Ni) and $M^{I}In_5S_8$ ($M^{I}$ = Cu, Ag) porous microspheres at low temperature (180 °C). The precursor $In_{2.77}S_4$ was obtained by a convenient mixed-solvent/thermal method at 160 °C in an "aqueous solution/water-immiscible organic solvent" system

[a] Nanomaterial and Nanochemistry, Hefei National Laboratory for Physical Sciences at Micro-scale, University of Science and Technology of China,
Hefei, Anhui 230026, P. R. China
Fax: +86-551-360-1791
E-mail: kbtang@ustc.edu.cn
[b] Department of Chemistry, University of Science and Technology of China,
Hefei, Anhui 230026, P. R. China

 © 2006 Wiley-VCH Verlag GmbH & Co. KGaA, Weinheim 

using $InCl_3{\cdot}4H_2O$ and thiourea (Tu) as the starting materials and a water-immiscible organic solvent (WIOS) plus distilled water as the solvent.

## Results and Discussion

Figure 1 shows the XRD patterns of the as-obtained samples. The XRD pattern of the precursor is shown in Figure 1a; it can be indexed to the cubic spinel structure $In_{2.77}S_4$ with lattice constant $a$ = 10.74 Å, consistent with reported values (JCPDS card file No. 88-2495: $a$ = 10.72 Å). The XRD patterns shown in Figure 1b–i can be indexed to cubic spinel structure $MnIn_2S_4$ (JCPDS card file No. 85-1229), $ZnIn_2S_4$ (48-1778), $CdIn_2S_4$ (27-0060), $FeIn_2S_4$ (80-0608), $CoIn_2S_4$ (79-1015), $NiIn_2S_4$ (79-1016), $CuIn_5S_8$ (24-0361), and $AgIn_5S_8$ (24-1477). All nine XRD patterns are very similar as they have the same crystal structure. No characteristic peaks for other impurities, such as metal sulfides ($In_2S_3$) are observed. The composition of the samples was further analyzed by ICP. The results reveal that the molar ratio of $M^{II}$ ($M^{II}$ = Mn, Zn, Cd, Fe, Co, Ni) to In and S, and $M^{I}$ ($M^{I}$ = Cu, Ag) to In and S is 1:2.03:4.08, 1:1.95:4.03, 1:1.99:4.05, 1:2.02:4.08, 1:2.02:4.07, 1:1.96:3.99, 1:4.91:7.96, and 1:4.96:8.03, respectively.

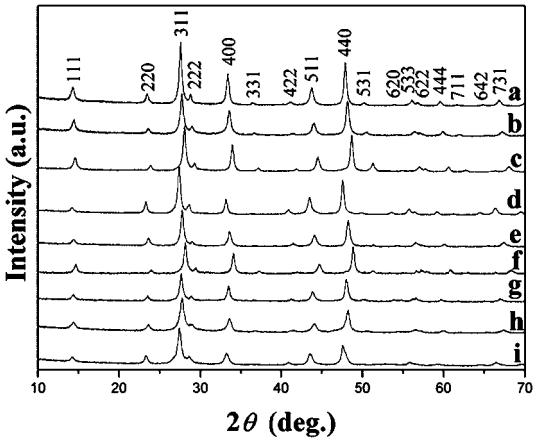


Figure 1. XRD patterns of the as-prepared $In_{2.77}S_4$ precursor (a), $MnIn_2S_4$ (b), $ZnIn_2S_4$ (c), $CdIn_2S_4$ (d), $FeIn_2S_4$ (e), $CoIn_2S_4$ (f), $NiIn_2S_4$ (g), $CuIn_5S_8$ (h), and $AgIn_5S_8$ (i).

Figures 2a and b show SEM images of the as-synthesized precursor $In_{2.77}S_4$ sample, and reveal that the product consists of large-scale porous spheres with a large size distribution (1–6 μm in diameter). It is obvious that the sphere is built up by many interconnected slightly bending flakes with a thickness of about 60 nm, which entangle together to form a network on the surface of the sphere (Figure 2b). Figure 2c is the TEM image of this sample and the inset is the high-magnification TEM image of the surface of the porous microspheres. These images further confirm the spherical urchin-like architecture of the product and the flakes on the surface can also be clearly observed. The corresponding ED patterns in Figure 2d show several diffraction rings, which can be characterized as the (111), (220), (311), (400), (511), and (440) planes (from inner to outer) and further reveal the cubic spinel structure of the product.

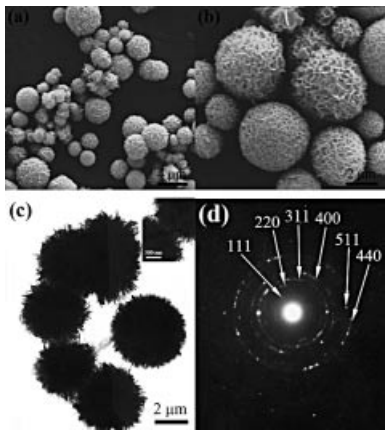


Figure 2. (a), (b) SEM images of the as-prepared $In_{2.77}S_4$ precursor. (c) TEM image of the as-prepared $In_{2.77}S_4$ precursor (inset: TEM image at high magnification). (d) Corresponding ED patterns.

Figure 3 shows an SEM image of the as-synthesized $MnIn_2S_4$ sample using the $In_{2.77}S_4$ precursor as the reactant. It can be seen that the product also consists of porous microspheres, on the surface of which a network of interconnected bending flakes has formed (the SEM image at high magnification is shown in the inset). The TEM images shown in Figures 3b and c also show evidence for the morphological structure, and the corresponding ED patterns (inset of Figure 3b) also reveal that the $MnIn_2S_4$ product has a cubic spinel structure.

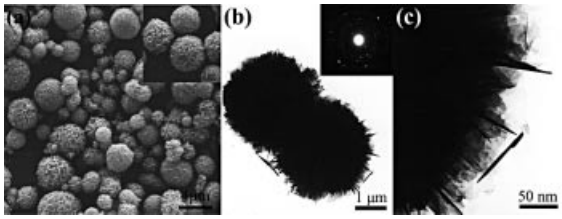


Figure 3. (a) SEM and (b), (c) TEM images of the as-synthesized $MnIn_2S_4$ sample [inset of (a): SEM image at high magnification; inset of (b): corresponding ED patterns].

The SEM images of the other samples, viz. $ZnIn_2S_4$, $CdIn_2S_4$, $FeIn_2S_4$, $CoIn_2S_4$, $NiIn_2S_4$, $CuIn_5S_8$, and $AgIn_5S_8$, are displayed in Figures 4a–h. They all have the same morphology (porous microspheres) as those in Figure 2, which implies that these $M^{II}In_2S_4$ ($M^{II}$ = Mn, Zn, Cd, Fe, Co, Ni) and $M^{I}In_5S_8$ ($M^{I}$ = Cu, Ag) products still keep the morphology of the $In_{2.77}S_4$ precursor. It is therefore reasonable to deduce that the precursor $In_{2.77}S_4$ porous microspheres play a critical role in the formation of the morphology of the final products.

The surface areas of the as-prepared representative products were determined by the BET method. The BET surface areas of the $In_{2.77}S_4$ precursor and $MnIn_2S_4$, $ZnIn_2S_4$, $FeIn_2S_4$, and $CuIn_5S_8$ are 73.6906, 63.6089, 73.4746, 66.9709, and 62.4300 $m^2 g^{-1}$.

 © 2006 Wiley-VCH Verlag GmbH & Co. KGaA, Weinheim 

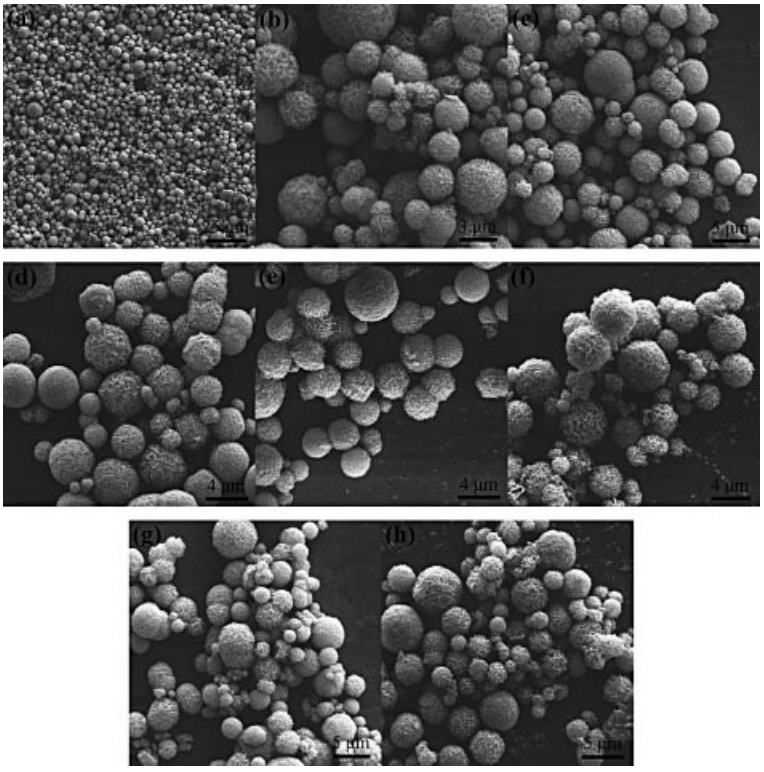


Figure 4. SEM images of as-synthesized (a), (b) $ZnIn_2S_4$, (c) $CdIn_2S_4$, (d) $FeIn_2S_4$, (e) $CoIn_2S_4$, (f) $NiIn_2S_4$, (g) $CuIn_5S_8$, and (h) $AgIn_5S_8$.

Based on the experiments, a possible formation process of $M^{II}In_2S_4$ and $M^{I}In_5S_8$ in this reaction system can be proposed. The reaction of Tu with $H_2O$ can release $S^{2-}$ ions,[39,40] which react with metal ions ($Mn^{2+}$, $Zn^{2+}$, $Cd^{2+}$, $Fe^{2+}$, $Co^{2+}$, $Ni^{2+}$, $Cu^{+}$, $Ag^{+}$) to produce $M^{II}S$ or $M_2^{I}S$. The subsequent reaction of $In_{2.77}S_4$ with $M^{II}S$ or $M_2^{I}S$ results in the formation of $M^{II}In_2S_4$ or $M^{I}In_5S_8$. These processes can be summarized as follows:

$NH_2CSNH_2$ (Tu) + 2 $H_2O \rightarrow H_2S + 2\ NH_3 + CO_2$

$M^{2+} + S^{2-} \rightarrow M^{II}S$ or $M^{+} + S^{2-} \rightarrow M^{I}{}_2S$

$In_2S_3$ ($In_{2.77}S_4$) + $M^{II}S \rightarrow M^{II}In_2S_4$ or 5 $In_2S_3$ ($In_{2.77}S_4$) + $M^{I}{}_2S \rightarrow 2\,M^{I}In_5S_8$

Actually, the spinel structure $In_{2.77}S_4$ can be represented by $(In_{1-x})(In_2)S_4$. When it reacts with metal sulfides, some metal atoms (Mn, Zn, Cd, Fe, Co, Ni, Cu, Ag) occupy part of the tetrahedral sites and the rest of the metal atoms occupy part of the octahedral sites to form the $(M^{II}{}_xIn_{1-x})$-$(M^{II}{}_{1-x}In_{1+x})S_4$ or $(M^{I}{}_{1/2-x}In_{1/2+x})(M^{I}{}_xIn_{2-x})S_4$ spinel structure.

Interestingly, if the $In_{2.77}S_4$ precursor is replaced by the appropriate amount of $InCl_3{\cdot}4H_2O$ and Tu, directly mixed with the metal ($M^{II}$ or $M^{I}$) salt, and loaded into an autoclave, then the product was not pure $M^{II}In_2S_4$ or $M^{I}In_5S_8$. For the synthesis of $MnIn_2S_4$ only $In_{2.77}S_4$ is obtained here, whereas in other procedures unreacted $M^{II}S$ and $M^{I}{}_2S$ impurities still exist, which increases the reaction time and the amount of Tu needed.

The amount of distilled water is also a crucial factor for the formation of pure $M^{II}In_2S_4$ or $M^{I}In_5S_8$. When the volume of distilled water in the reaction system reached 1 mL, $In(OH)_3$ impurities could be observed, which may result from the hydrolysis of the $In_{2.77}S_4$ precursor.

From the above analyses, it can be seen that the $In_{2.77}S_4$ precursor may serve as a "self-sacrificing template" to confine the formation of the $M^{II}In_2S_4$ and $M^{I}In_5S_8$ porous microspheres. To investigate the template effect of the $In_{2.77}S_4$ precursor, some contrast experiments were performed. During the preparation of the $In_{2.77}S_4$ precursor, increasing of the volume of distilled water to 10–40 mL caused the formation of $In_{2.77}S_4$ porous microspheres (marked with arrow I) and smooth microspheres (marked with arrow II) simultaneously, as shown in Figure 5a. When this $In_{2.77}S_4$ precursor was used as the reactant, the obtained $M^{II}In_2S_4$ and $M^{I}In_5S_8$ samples also consisted of porous microspheres (marked with arrow I) and smooth microspheres (marked with arrow II), as shown in Figures 5b and c. The final products still kept the morphology of the precursor, which confirmed the self-sacrificing template effect of the $In_{2.77}S_4$ precursor.

A possible growth mechanism for the porous architecture of the $In_{2.77}S_4$ precursor and obtained $M^{II}In_2S_4$ and $M^{I}In_5S_8$ can also be tentatively proposed. During the synthesis of the $In_{2.77}S_4$ precursor, small $In_{2.77}S_4$ spheres are formed first in the "aqueous solution/water-immiscible organic solvent" system because of the interfacial tension. Subsequently, the $[In(Tu)_n]Cl_3$ complex solution[41] reacts on the surface of the spheres to form $In_{2.77}S_4$ flakes in different directions. These flakes then collide with each other and yield an entangled network morphology. Upon interleaving,

 © 2006 Wiley-VCH Verlag GmbH & Co. KGaA, Weinheim 

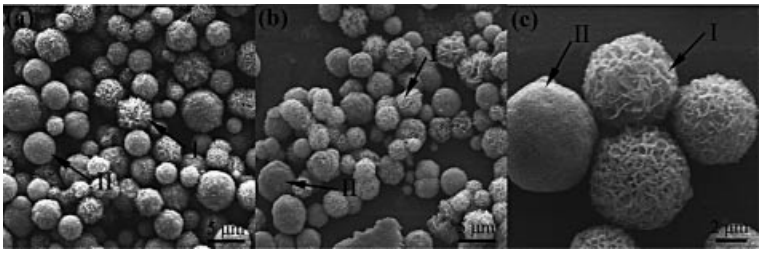


Figure 5. SEM images of (a) as-prepared $In_{2.77}S_4$ precursor with the amount of distilled water increased to 10–40 mL and (b), (c) the $MnIn_2S_4$ sample produced using a mixture of porous and smooth microspheres of $In_{2.77}S_4$ as the reactant.

these newly formed thin flake interfaces become strongly undulated, which results in a slight bending of the flakes in order to relax the strain due to the elongation of the flakes.[42] This process continues until the spheres become completely covered, thereby minimizing the interfacial free energy, to finally give the $In_{2.77}S_4$ porous spheres.[43] Subsequent reaction of the metal salts and Tu on the interface of the $In_{2.77}S_4$ porous spheres gives the final $M^{II}In_2S_4$ and $M^{I}In_5S_8$ porous microspheres. When the amount of distilled water is increased in the preparation of the $In_{2.77}S_4$ precursor, the volume of the aqueous solution increases and many of the initial $In_{2.77}S_4$ spheres are unable to form an interface with the water-immiscible organic solvent, which results in the coexistence of smooth and porous $In_{2.77}S_4$ spheres (Figure 5a). Actually, our experiments showed that the smooth $In_{2.77}S_4$ microspheres occur in the product when the volume of distilled water is above 10 mL. All the obtained $In_{2.77}S_4$ samples consist of porous microspheres and smooth microspheres when the volume of distilled water is in the range 10–40 mL.

## Conclusions

In summary, porous microspheres of the ternary semiconductors $M^{II}In_2S_4$ ($M^{II}$ = Mn, Zn, Cd, Fe, Co, Ni) and $M^{I}In_5S_8$ ($M^{I}$ = Cu, Ag) have been successfully synthesized by a simple self-sacrificing template method using $In_{2.77}S_4$ porous microspheres as the starting material. The possible formation process for the product and a growth mechanism for the porous architecture have been tentatively proposed and discussed in detail. This novel synthesis is performed under ambient conditions and can be easily operated. It is expected to be extendable to the synthesis of other ternary inorganic compounds.

## Experimental Section

**General:** All chemical reagents were of analytical grade, purchased from Shanghai Chemical Reagent Company and used without further purification.

**Preparation of the Precursor $In_{2.77}S_4$ Porous Microspheres:** In a typical procedure, 2 mmol of $InCl_3{\cdot}4H_2O$ (0.586 g) and a slight excess of Tu (0.25 g) were put into a Teflon-lined autoclave of 60 mL capacity and dissolved in 2–3 mL of distilled water to form a solution. The autoclave was then filled with a water-immiscible organic solvent (WIOS, e.g. benzene, toluene, hexane, cyclohexane) up to 90% of the total volume, sealed, and maintained at 160 °C for 12 h. After cooling to room temperature naturally, the final products were filtered off, washed with absolute ethanol and distilled water several times, and then dried under vacuum at 60 °C for 4 h. An orange-red powder was obtained.

**Preparation of $M^{II}In_2S_4$ ($M^{II}$ = Mn, Zn, Cd, Fe, Co, Ni) and $M^{I}In_5S_8$ ($M^{I}$ = Cu, Ag) Porous Microspheres:** A given amount of divalent metal salt [$MnCl_2{\cdot}4H_2O$, $Zn(CH_3COO)_2{\cdot}2H_2O$, $CdCl_2{\cdot}2.5H_2O$, $FeSO_4{\cdot}7H_2O$, $CoCl_2{\cdot}6H_2O$, $NiCl_2{\cdot}6H_2O$] or univalent metal salt (CuCl or $AgNO_3$), the $In_{2.77}S_4$ precursor, Tu, and 2–3 drops of distilled water were loaded into the Teflon-lined autoclave, which was then filled with WIOS up to 90% of the total volume, sealed, and maintained at 180 °C for 20 h. After cooling to room temperature naturally, the products were filtered off, washed with absolute ethanol and distilled water several times to remove impurities, and dried in vacuo at 60 °C for 4 h.

**Sample Characterization:** The X-ray powder diffraction (XRD) patterns were recorded with a Philips X'pert PRO SUPER diffractometer with Cu-$K_\alpha$ radiation ($\lambda$ = 1.541874 Å). Direct elemental analysis was performed by inductively coupled plasma-atomic emission spectrometry (ICP-AES) using an Atomscan Advantage (Thermo Jarrell Ash Corporation) instrument. The SEM images were taken with an X-650 scanning electronic microanalyzer. The TEM images and electron diffraction (ED) patterns were obtained with a Hitachi H-800 transmission electron microscope, at an accelerating voltage of 200 kV. For TEM investigation, one or two drops of the solution containing the as-prepared composites were deposited onto an amorphous carbon film supported on a copper grid and allowed to dry at room temperature in air. The surface areas of the samples were evaluated from nitrogen adsorption data by the Brunauer–Emmett–Teller (BET) technique at 77 K with a Micromeritics ASAP 2000 analyzer.

## Acknowledgments

Financial support by the National Natural Science Foundation of China, the 973 Projects of China, and the Program for New Century Excellent Talents in university (NCET) is gratefully acknowledged.

[1] H. Bu, J. Rong, Z. Yang, *Macromol. Rapid Commun.* **2002**, *23*, 460.
[2] P. Jiang, K. S. Hwang, D. M. Mittleman, J. F. Bertone, V. L. Colvin, *J. Am. Chem. Soc.* **1999**, *121*, 11630.
[3] U. Meyer, A. Larsson, H. P. Hentze, R. A. Caruso, *Adv. Mater.* **2002**, *14*, 1768.
[4] A. Stein, *Microporous Mesoporous Mater.* **2001**, *44*, 227.
[5] R. Jeyanthi, B. C. Thanoo, R. C. Metha, P. D. Deluca, *J. Controlled Release* **1996**, *38*, 235.

 © 2006 Wiley-VCH Verlag GmbH & Co. KGaA, Weinheim 

[6] Y. Senuma, S. Franceschin, J. G. Hilborn, P. Tissieres, I. Bisson, P. Frey, *Biomaterials* **2000**, *21*, 1135.
[7] D. A. Edwards, J. Hanes, G. Caponetti, J. Hrkach, A. BenJebria, M. L. Eskew, J. Mintzes, D. Deaver, N. Lotan, R. Langer, *Science* **1997**, *276*, 1868.
[8] G. Crotts, T. G. Park, *J. Controlled Release* **1995**, *35*, 91.
[9] Y. Hong, C. Y. Gao, Y. C. Shi, J. C. Shen, *Polym. Adv. Technol.* **2005**, *16*, 622.
[10] F. J. Disalvo, *Science* **1990**, *247*, 649.
[11] a) W. S. Sheldrick, M. Wachhold, *Angew. Chem. Int. Ed. Engl.* **1997**, *36*, 206; b) C. L. Bowes, G. A. Ozin, *Adv. Mater.* **1996**, *8*, 13; c) G. A. Ozin, *Adv. Mater.* **1992**, *4*, 612.
[12] B. F. Levine, *Phys. Rev. B: Condens. Matter* **1973**, *7*, 2600.
[13] R. K. Route, R. S. Feigelson, R. J. Raymakers, *J. Cryst. Growth* **1976**, *33*, 239.
[14] N. Bottka, J. Stankeiwicz, W. Giriat, *J. Appl. Phys.* **1981**, *52*, 4189.
[15] R. N. Bekimbetov, Yu. V. Rud, M. A. Tiarov, *Fiz. Tekhn. Poluprvodn.* **1987**, *21*, 1051; *Chem. Abstr.* **1987**, *107*, 125271y.
[16] a) B. L. Gelmont, V. I. Ivanov-Omskii, I. T. Postolaki, V. A. Smirnov, *Fiz. Tekhn. Poluprvodn.* **1986**, *20*, 508; *Chem. Abstr.* **1986**, *105*, 32220z; b) B. L. Gelmont, V. I. Ivanov-Omskii, I. T. Postolaki, V. A. Smirnov, *Sov. Phys. Semicond.* **1986**, *20*, 318.
[17] A. N. Georgobiani, S. I. Radustan, I. M. Tiginyanu, *Sov. Phys. Semicond.* **1985**, *19*, 121.
[18] a) R. K. Sharma, S. T. Lakshmikumar, G. Singh, A. C. Rastogi, *Mater. Chem. Phys.* **2005**, *92*, 240; b) R. K. Sharma, G. Singh, A. C. Rastogi, *Solar Energy Mater. Solar Cells* **2004**, *82*, 217; c) R. K. Sharma, A. C. Rastogi, S. Kohli, T.-W. Kang, G. Singh, *Phys. B (Amsterdam, Neth.)* **2004**, *351*, 45.
[19] N. S. Orlova, I. V. Bondnar, E. A. Kudritskaya, *Cryst. Res. Technol.* **1998**, *33*, 37.
[20] I. Konovalov, O. Tober, M. Winker, K. Otte, *Sol. Energy Mater.* **2001**, *67*, 49.
[21] I. Konovalov, O. Tober, *Barrier Height in Cu-In-S Solar Cells On Cu Tape (CISCuT)*, Rome, Italy, October 7–11, 2002, Conference "Photovoltaic in Europe" Proceeding, WIP-Munich and ETA-Florence, **2002**, p. 401.
[22] a) N. N. Niftiev, O. B. Tagiev, *Solid State Commun.* **1992**, *81*, 693; b) N. N. Niftiev, *Solid State Commun.* **1994**, *92*, 781; c) N. N. Niftiev, *Fiz. Tekhn. Poluprvodn.* **2002**, *36*, 836; *Chem. Abstr.* **2002**, *137*, 302649v; d) N. N. Niftiev, O. B. Tagiev, *Fiz. Tekhn. Poluprvodn.* **2004**, *38*, 164; *Chem. Abstr.* **2004**, *140*, 397688f; e) N. N. Niftiev, *Fiz. Tekhn. Poluprvodn.* **2004**, *38*, 166; *Chem. Abstr.* **2004**, *140*, 397689g.
[23] V. V. Ursaki, F. J. Manjn, I. M. Tiginyanu, V. E. Tezlevan, *J. Phys. C* **2002**, *14*, 6801.
[24] N. Romeo, A. Dallaturca, R. Braglia, G. Sberveglieri, *Appl. Phys. Lett.* **1973**, *22*, 21.
[25] S. I. Radautsan, I. M. Tiginyanu, *Jpn. J. Phys. Suppl.* **1993**, *32–33*, 5.
[26] Z. B. Lei, W. S. You, M. Y. Liu, G. H. Zhou, T. Takata, M. Hara, K. Domen, C. Li, *Chem. Commun.* **2003**, *17*, 2142.
[27] A. F. Qasrawi, N. M. Gasanly, *Cryst. Res. Technol.* **2001**, *36*, 457.
[28] a) G. Delgado, A. J. Mora, C. Pineda, T. Tinoco, *Mater. Res. Bull.* **2001**, *36*, 2507; b) N. M. Gasanly, A. Serpenguzel, A. Aydinli, O. Gurlu, I. Yilmaz, *J. Appl. Phys.* **1999**, *85*, 3198.
[29] a) M. Eibschufz, H. Hermon, S. Shtrikman, *Solid State Commun.* **1967**, *5*, 529; b) C. M. Yagnik, H. B. Mathur, *Solid State Commun.* **1967**, *5*, 841; c) S. Schlein, A. Wold, *J. Solid State Chem.* **1972**, *4*, 286; d) T. Kanomata, H. Ido, T. Kaneko, *J. Phys. Soc. Jpn.* **1973**, *34*, 554.
[30] a) M. Robbins, M. A. Miksovsky, *Mater. Res. Bull.* **1971**, *6*, 359; b) R. S. Roth, H. S. Parker, W. S. Brower, *Mater. Res. Bull.* **1973**, *8*, 333.
[31] J. Mcaleese, P. O'Brien, D. Otway, *J. Chem. Vap. Depos.* **1998**, *4*, 94.
[32] R. Nitsche, *J. Cryst. Growth* **1971**, *9*, 238.
[33] M. A. Sriram, P. H. McMichael, A. Waghray, P. N. Kumta, *J. Mater. Sci.* **1998**, *33*, 4333.
[34] a) X. Y. Chen, Z. J. Zhang, X. F. Zhang, J. W. Liu, Y. T. Qian, *J. Cryst. Growth* **2005**, *277*, 524; b) Q. Y. Lu, J. Q. Hu, K. B. Tang, Y. T. Qian, G. E. Zhou, X. M. Liu, *Chem. Lett.* **1999**, *6*, 481; c) J. Q. Hu, B. Deng, W. X. Zhang, K. B. Tang, Y. T. Qian, *Inorg. Chem.* **2001**, *40*, 3130; d) J. Lu, Y. Xie, G. A. Du, X. C. Jiang, L. Y. Zhu, X. J. Wang, Y. T. Qian, *J. Mater. Chem.* **2002**, *12*, 103; e) R. B. Zheng, X. G. Yang, H. M. Hu, Y. T. Qian, *Mater. Res. Bull.* **2004**, *39*, 933.
[35] M. Gorska, R. Beaulieu, J. J. Loferski, B. Roessler, *Thin Solid Films* **1980**, *67*, 341.
[36] I. V. Bodnar, V. F. Gremenok, V. Y. Rud, *Semiconductors* **1999**, *33*, 740.
[37] L. Makhova, R. Szargan, I. Konovalov, *Thin Solid Films* **2005**, *472*, 157.
[38] A. F. Qasrawi, T. S. Kayed, I. Ercan, *Mater. Sci. Eng., B* **2004**, *113*, 73.
[39] I. K. Ostrovskaya, G. A. Kitaev, A. A. Velijanov, *Russ. J. Phys. Chem.* **1976**, *50*, 956.
[40] G. E. Kitaev, T. P. Sokolva, *Russ. J. Inorg. Chem.* **1970**, *15*, 167.
[41] N. N. Golovnev, A. S. Primakov, I. I. Golovneva, *Zh. Neorg. Khim.* **1995**, *40*, 973; *Chem. Abstr.* **1995**, *123*, 210012q.
[42] M. Remskar, Z. Skraba, F. Cléton, R. Sanjinés, F. Lécy, *Appl. Phys. Lett.* **1996**, *69*, 351.
[43] L. Y. Zhu, Y. Xie, X. W. Zheng, X. Liu, G. E. Zhou, *J. Cryst. Growth* **2004**, *260*, 494.

Received: December 13, 2005
Published Online: April 20, 2006

 © 2006 Wiley-VCH Verlag GmbH & Co. KGaA, Weinheim 

DOI: 10.1002/ejic.200501155

# Hydrothermal Syntheses, Architectures and Magnetic Properties of Six Novel $Mn^{II}$ Coordination Polymers with Mixed Ligands

**Chang-Yan Sun,[a] Song Gao,*[b] and Lin-Pei Jin*[a]**

**Keywords:** Coordination polymers / Magnetic properties / Manganese / Microporous materials / Organic–inorganic hybrid composites

Six novel manganese(II) coordination polymers, namely $[Mn(oba)(4,4'\text{-bpy})]_n \cdot n(4,4'\text{-bpy})$ (**1**), $[Mn(oba)(phen)(H_2O)]_n$ (**2**), $[Mn_2(oba)_2(2,2'\text{-bpy})_2(H_2O)_2]_n \cdot nH_2oba$ (**3**), $[Mn_2(cca)_2(4,4'\text{-bpy})_2]_n \cdot 2n(4,4'\text{-bpy})$ (**4**), $[Mn(cca)(phen)]_n$ (**5**) and $[Mn(cca)(2,2'\text{-bpy})]_n \cdot 0.25nH_2O$ (**6**) [$H_2oba$ = 4,4′-oxybis(benzoic acid); 4,4′-bpy = 4,4′-bipyridine; phen = 1,10-phenanthroline; 2,2′-bpy = 2,2′-bipyridine; $H_2cca$ = *p*-carboxycinnamic acid] have been synthesised under hydrothermal conditions. Complexes **1** and **4** possess 3D microporous metal-organic frameworks with free 4,4′-bpy ligands in the channels. The $Mn^{II}$ ions in complex **2** are bridged into 1D infinite double-chain structures, and those in complex **3** are bridged into 1D zigzag chains. Hydrogen bonds cause the formation of 3D supramolecular networks for complexes **2** and **3**. Complex **5** is a complicated 3D metal-organic framework, and the $Mn^{II}$ ions in complex **6** are linked into 2D layers with cavities; interpenetration of these 2D layers results in the formation of a 3D supramolecular network. Magnetic susceptibility measurements indicate that complex **2** displays a weak ferromagnetic interaction between the $Mn^{II}$ ions with the following parameters: $J$ = 0.462(3) $cm^{-1}$, $g$ = 2.0387(6), $zJ'$ = –0.0062(3) $cm^{-1}$ and $R = 8.0 \times 10^{-6}$. Complex **4** shows antiferromagnetic coupling between the $Mn^{II}$ ions with $J$ = –0.718(4) $cm^{-1}$, $g$ = 1.986(4) and $R = 2.3 \times 10^{-4}$.
(© Wiley-VCH Verlag GmbH & Co. KGaA, 69451 Weinheim, Germany, 2006)

## Introduction

Manganese-based coordination compounds have received considerable interest in the fields of supramolecular chemistry, crystal engineering and materials chemistry. This interest arises not only from their remarkable magnetochemical properties,[1] but also from their rich biochemistry.[2] Furthermore, due to their low cost and toxicity, manganese coordination compounds are growing in importance as homogeneous catalysts.[3] As far as we know, the current focus is on the construction of molecule-based magnetic materials. The main approach is to employ short bridging ligands to connect manganese ions. These short ligands, such as azide,[4] cyanide[5] and oxalate,[6] efficiently mediate the magnetic coupling. Long bridging ligands, because of their large separation and thus their inefficiency in transmitting magnetic interactions, have seldom been used to construct manganese coordination compounds.

It is well-known that the topology of coordination compounds depends both on the coordination geometry of the metal centres and on the coordination behaviour of the organic ligands. When long bridging ligands are used to connect metal ions, their versatile coordination modes may lead to new architectures with novel topologies and interesting properties.

4,4′-Oxybis(benzoic acid) ($H_2oba$) is a typical example of long V-shaped ligands. Its coordination chemistry has been studied and some coordination polymers have been obtained.[7] Because of its two oxo carboxylate groups, $H_2oba$ can coordinate to metal ions in didentate, tridentate, tetradentate, pentadentate and hexadentate modes. *p*-Carboxycinnamic acid ($H_2cca$) also has two oxo carboxylate groups. There is only one cobalt(II) complex known with $H_2cca$,[8] and we are interested in the architecture of metal complexes with this asymmetrical functional carboxylate ligand.

The choice of a suitable co-ligand often has a significant effect on the formation and structure of metal complexes. 4,4′-Bipyridine (4,4′-bpy) has been demonstrated to be one of the most important rigid linear co-ligands and has been extensively used to connect metal ions.[9] Chelating N-containing aromatic ligands, such as 2,2′-bipyridine (2,2′-bpy) and 1,10-phenanthroline (phen), can not only affect the coordination geometry of metal ions but also bring about π-π stacking interactions, which are important for the construction of supramolecular networks.[10]

Taking into account the above-mentioned aspects, we report here the syntheses, structures and magnetic properties

[a] School of Chemistry, Beijing Normal University, Beijing 100875, P. R. China
Fax: +86-105-880-2075
E-mail: lpjin@bnu.edu.cn
[b] State Key Laboratory of Rare Earth Materials Chemistry and Applications, College of Chemistry and molecular Engineering, Peking University, Beijing 100871, P. R. China
Supporting information for this article is available on the WWW under http://www.eurjic.org or from the author.

 © 2006 Wiley-VCH Verlag GmbH & Co. KGaA, Weinheim 

of six novel $Mn^{II}$ coordination compounds, namely $[Mn(oba)(4,4'\text{-bpy})]_n \cdot n(4,4'\text{-bpy})$ (**1**), $[Mn(oba)(phen)(H_2O)]_n$ (**2**), $[Mn_2(oba)_2(2,2'\text{-bpy})_2(H_2O)_2]_n \cdot nH_2oba$ (**3**), $[Mn_2(cca)_2\ (4,4'\text{-bpy})_2]_n \cdot 2n(4,4'\text{-bpy})$ (**4**), $[Mn(cca)(phen)]_n$ (**5**) and $[Mn(cca)(2,2'\text{-bpy})]_n \cdot 0.25nH_2O$ (**6**). All six coordination polymers contain long spacers (oba/cca) and co-ligands (4,4′-bpy/phen/2,2′-bpy), and possess very different structures, ranging from 1D chains to 2D layers and 3D metal-organic frameworks.

## Results and Discussion

### Description of the Structures

#### *[Mn(oba)(4,4′-bpy)]$_n$·n(4,4′-bpy) (1)*

Complex **1** is a 3D porous coordination polymer containing channels with guest 4,4′-bpy molecules. There is only one metal environment in complex **1**, as shown in Figure 1. Each $Mn^{II}$ ion is coordinated to four oxygen atoms of four oba ligands and two nitrogen atoms of two 4,4′-bpy ligands, and is located in a slightly distorted octahedral geometry. The average Mn–N bond length is 2.322 Å and the Mn–O bond lengths are in the range 2.147–2.162 Å. Each oba ligand in complex **1** is severely bent at the ether-oxygen site (C–O–C = 118.6°) and adopts a bis(bridging didentate) mode, linking four $Mn^{II}$ ions (see Scheme 1a). All $Mn^{II}$ ions are connected by oba ligands into 2D pillar-like layers. The nearest Mn···Mn distance in these layers is 4.835 Å. The 4,4′-bpy ligands bridge these layers into a 3D porous framework with channels of about 11 × 14 Å (based on the distance between metal ions), as shown in Figure 2. The channels are big enough to accommodate free 4,4′-bpy molecules.

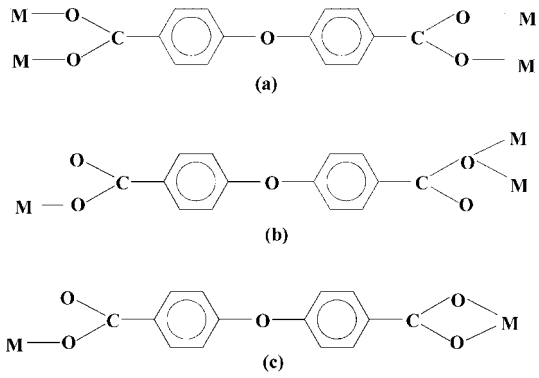


Scheme 1. The coordination modes of the oba ligands in complexes **1**–**3**.

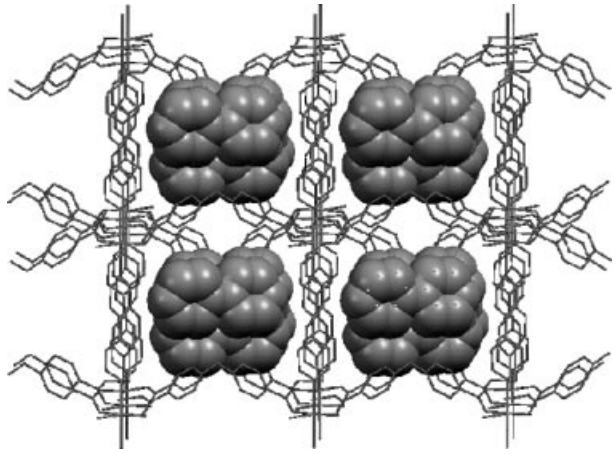

Figure 2. The 3D porous framework of complex **1** viewed along the *c* axis, with space-filling models representing the free 4,4′-bpy molecules.

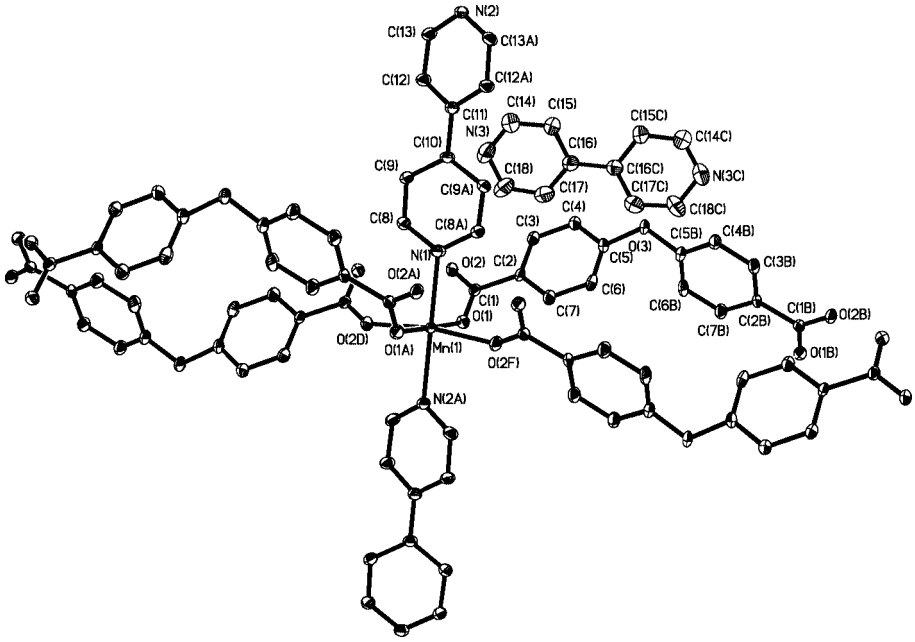


Figure 1. The coordination environment of the $Mn^{II}$ ion in complex **1** with 30% thermal ellipsoids. All hydrogen atoms have been omitted for clarity.

 © 2006 Wiley-VCH Verlag GmbH & Co. KGaA, Weinheim 

### *[Mn(oba)(phen)($H_2O$)]$_n$ (2)*

Figure 3 shows the coordination environment of the $Mn^{II}$ ions in complex **2**. The coordination geometry around each $Mn^{II}$ ion is $N_2O_4$, with three oxygens from three oba ligands, one oxygen from a coordinated water molecule and two nitrogens from one phen ligand, and can be described as a distorted octahedron. The average Mn–N bond length is 2.271 Å and the Mn–O bond lengths are in the range 2.107–2.158 Å. The oba ligands are also bent (C–O–C: 118.6°), as in complex **1**. The coordination modes in complexes **1** and **2**, however, are different as each oba ligand in complex **2** adopts a tridentate mode, linking three $Mn^{II}$ ions, as shown in Scheme 1b. This coordination mode has not been reported before. The bridging carboxylate oxygen atoms cause the formation of the building blocks of $Mn_2O_2$ cores, in which the Mn···Mn distance is 3.387 Å (Mn–O–Mn angle: 101.81°). These cores are interconnected by oba ligands into 1D double-chain structures. A similar structure has been reported for [Zn(bpndc)(phen)($H_2O$)]$_n$.[11] There are hydrogen bonds between the coordinated water molecules and the uncoordinated carboxylate oxygen atoms (O···O distances of 2.697 and 2.740 Å). In addition, weak π-π stacking interactions exist between phen molecules of neighbouring chains, with an average distance of 3.53 Å. Both the hydrogen bonds and π-π stacking interactions result in the formation of a 3D supramolecular network with channels of about 3 × 13 Å. This is small and means that it is unable to incorporate any guest molecules.

### *[$Mn_2$(oba)$_2$(2,2′-bpy)$_2$($H_2O$)$_2$]$_n$·n$H_2$oba (3)*

There are two kinds of crystallographically different $Mn^{II}$ ions in complex **3**, as shown in Figure 4. Both Mn(1) and Mn(2) are coordinated to three oxygen atoms of two oba ligands, one from a coordinated water molecule and two nitrogen atoms of a 2,2′-bpy ligand, but their bond lengths and bond angles are different. The average Mn(1)–N bond length is 2.261 Å and the Mn(1)–O bond lengths are in the range 2.085–2.408 Å, while the average Mn(2)–N bond length is 2.242 Å and the Mn(2)–O bond lengths are in the range 2.095–2.363 Å. Mn(1) and Mn(2) are bridged by an oba ligand with a distance of 14.365 Å. There are three kinds of oba ligands in complex **3**, two of which coordinate in a tridentate mode linking two $Mn^{II}$ ions (see Scheme 1c). They are bent at the ether-oxygen sites (C–O–C = 118.4° and 119.9°), and connect the $Mn^{II}$ ions into 1D infinite zigzag chains (the Mn···Mn distance within a chain is 14.365 Å). The third kind of oba ligand is protonated and does not coordinate to $Mn^{II}$. It is also bent at the ether-oxygen sites, with a C–O–C angle of 120.2°. There are hydrogen bonds between the coordinated water molecules and the coordinated oba/free $H_2$oba ligands (O···O distances of

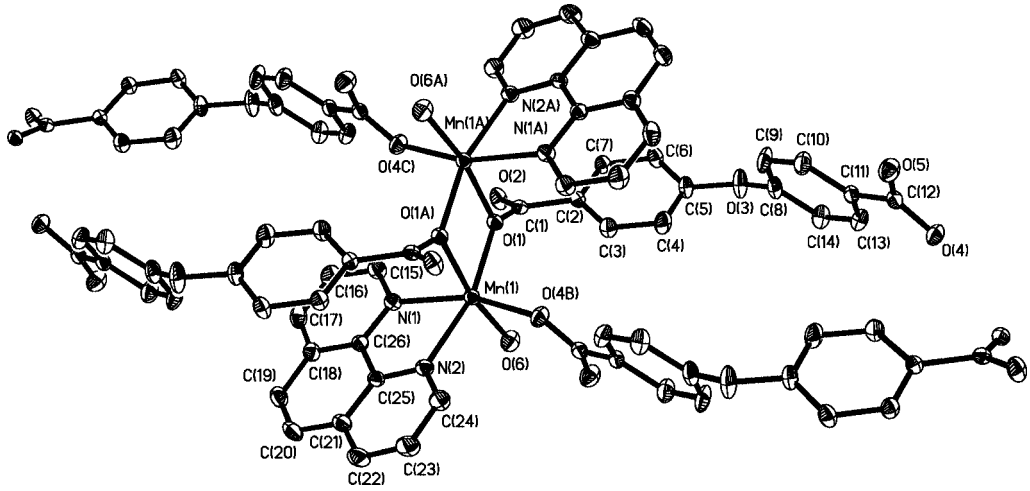


Figure 3. The coordination environment of the $Mn^{II}$ ion in complex **2** with 30% thermal ellipsoids. All hydrogen atoms have been omitted for clarity.

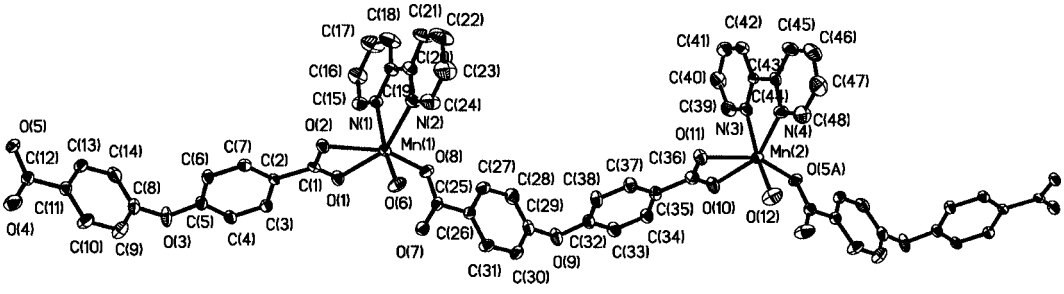


Figure 4. The coordination environments of the $Mn^{II}$ ions in complex **3** with 30% thermal ellipsoids. Free $H_2$oba ligands and all hydrogen atoms have been omitted for clarity.

 © 2006 Wiley-VCH Verlag GmbH & Co. KGaA, Weinheim 

2.896, 2.753 and 2.855 Å), forming a 3D supramolecular network, as shown in Figure 5.

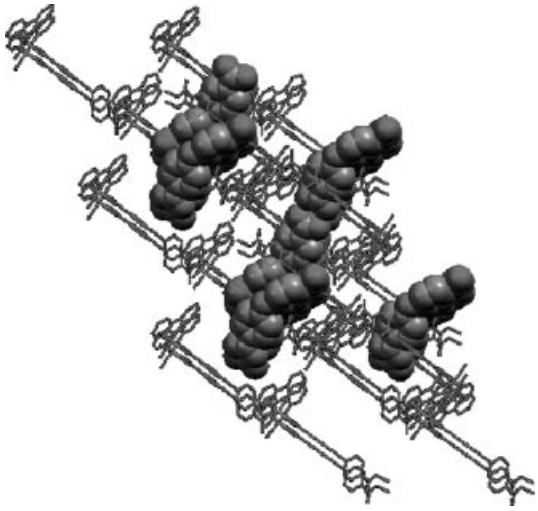

Figure 5. The 3D supramolecular network of complex **3** viewed along the *a* axis, with space-filling models representing the free $H_2$oba ligands.

### *[Mn$_2$(cca)$_2$(4,4′-bpy)$_2$]$_n$·2n(4,4′-bpy) (4)*

Complex **4** possesses a 3D porous metal-organic framework whose channels contain free 4,4′-bpy molecules. Similar to complex **3**, there are two types of $Mn^{II}$ environments (see Figure 6). Both Mn(1) and Mn(2) are coordinated to four oxygen atoms of four cca ligands and two nitrogen atoms of two 4,4′-bpy molecules, and are located in slightly distorted octahedra. However, their bond lengths and angles are different. The Mn(1)–N bond length is 2.275 Å and the Mn(1)–O bond lengths are in the range 2.152–2.173 Å, while the Mn(2)–N bond length is 2.299 Å and the Mn(2)–O bond lengths are in the range 2.166–2.197 Å. Mn(1) and Mn(2) are bridged by two carboxylate groups of two cca ligands with a distance of 5.112 Å. Each cca ligand in complex **4** adopts a tetradentate mode, linking four $Mn^{II}$ ions (see Scheme 2a). All $Mn^{II}$ ions are connected by cca ligands into 2D pillar-like layers. These layers are interconnected by 4,4′-bpy ligands, resulting in the formation of a 3D porous framework with channels of about 11 × 11 Å, similar to those in complex **1**. These channels contain free 4,4′-bpy molecules.

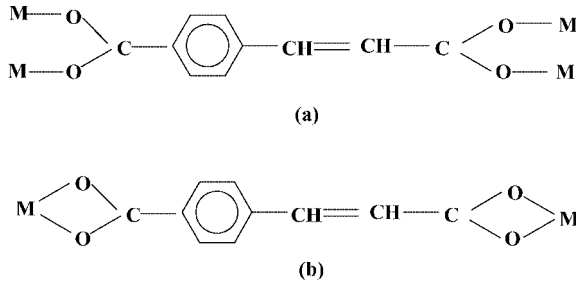


Scheme 2. The coordination modes of the cca ligands in complexes **4**–**6**.

### *[Mn(cca)(phen)]$_n$ (5)*

There is only one metal environment in complex **5**, as shown in Figure 7. Each $Mn^{II}$ ion is placed in a distorted octahedron, which is completed by four oxygen atoms of four cca ligands and two nitrogen atoms of one phen molecule with the same Mn–N distance. The Mn–N bond length is 2.317 Å and the Mn–O bond lengths are in the range 2.094–2.203 Å. Each cca ligand adopts a tetradentate mode, linking four $Mn^{II}$ ions (see Scheme 2a). The nearest Mn···Mn distance is 4.587 Å. All $Mn^{II}$ ions are linked by cca ligands into a 3D metal-organic framework with 1D channels. However, chelating phen ligands occupy the diagonal position, which greatly decreases the dimension of the

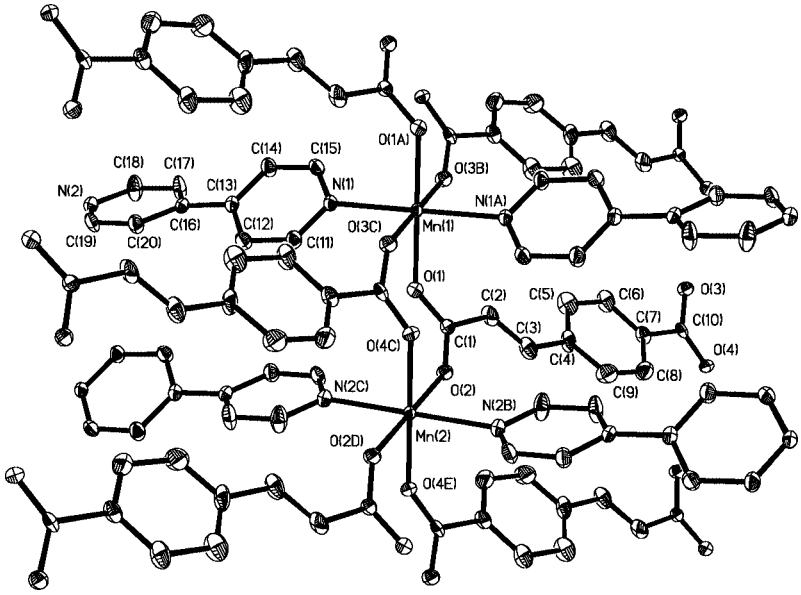


Figure 6. The coordination environments of the $Mn^{II}$ ions in complex **4** with 30% thermal ellipsoids. All hydrogen atoms have been omitted for clarity.

 © 2006 Wiley-VCH Verlag GmbH & Co. KGaA, Weinheim 

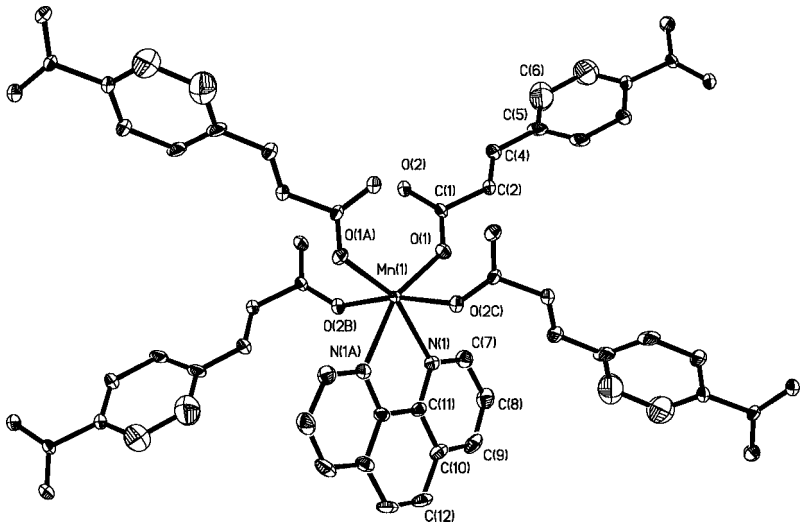


Figure 7. The coordination environment of the $Mn^{II}$ ion in complex **5** with 30% thermal ellipsoids. All hydrogen atoms have been omitted for clarity.

channels. All phen rings are parallel to each other, and the nearest face-to-face distance is 3.29 Å, indicating the presence of π-π stacking interactions.

### *[Mn(cca)(2,2′-bpy)]$_n$·0.25n$H_2O$ (6)*

Because of the disorder of the cca ligands, there are four types of $Mn^{II}$ environment. Figure 8 shows one of them, and the others can be found in the Supporting Information (Figures S1–S3). Each $Mn^{II}$ ion is coordinated to four oxygen atoms of three cca ligands and two nitrogen atoms of one 2,2′-bpy molecule. The cca ligands in complex **6** adopt two kinds of coordination modes, namely bis(bridging didentate) and bis(chelating didentate) (see Scheme 2). The dinuclear species $[Mn_2(cca)_2(2,2'\text{-bpy})_2]$, which has a metal–metal distance of 4.462 Å, can be regarded as a secondary building block. These moieties are linked by cca ligands into 2D grid-like layers with cavities of about 12 × 13 Å, and the 2D layers are interpenetrated, resulting in the formation of a 3D supramolecular network in which weak π-π stacking interactions between 2,2′-bpy molecules (the nearest distance is 3.29 Å) further stabilize the supramolecular structure.

It is obvious from the above descriptions that the carboxylate ligands and the co-ligands have significant effects on the formation and architecture of the resulting complexes. The structures of these six complexes can be simplified as shown in Scheme 3. Although complexes **1**, **2** and **3** contain the same carboxylate ligand oba, they possess different structures. In complex **1**, both V-shaped oba and linear 4,4′-bpy ligands work as bridging ligands, resulting in the formation of a 3D porous structure. The free 4,4′-bpy ligands may be one of the important factors for the construction of the porous structure as they might function as templates and occupy the pores, thus preventing further interpenetration. Complexes **2** and **3** possess infinite 1D chains, which may be attributed to the existence of the terminal ligands phen/2,2′-bpy/$H_2O$. These terminal ligands occupy the coordination sites of the metal ions and prevent the

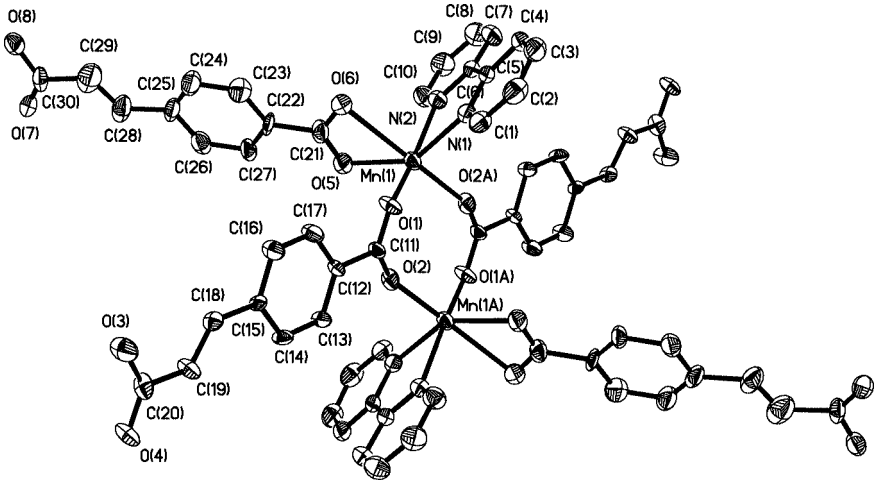


Figure 8. The coordination environment of the $Mn^{II}$ ion in complex **6** with 30% thermal ellipsoids. All hydrogen atoms have been omitted for clarity.

 © 2006 Wiley-VCH Verlag GmbH & Co. KGaA, Weinheim 

structures from extending into higher dimensions. Complex **2** has a double-chain structure while complex **3** has a single-chain structure because the oba ligands adopt different coordination modes in the two complexes (see Scheme 1 i and b). When the oba ligand is replaced by cca, we obtain the box-like structure of complex **4**. Both cca and 4,4′-bpy are bridging ligands that link metal ions into a 3D porous structure. The presence of free 4,4′-bpy works as template, promoting the formation of the 3D porous structure. However, with the terminal ligand phen, complex **5** possesses a 3D metal-organic framework due to the tetradentate bridging ligand cca, and in complex **6** the introduction of 2,2′-bpy as a ligand leads to 2D grid-like layers, where hydrogen bond and π-π stacking interactions result in a 3D supramolecular network.

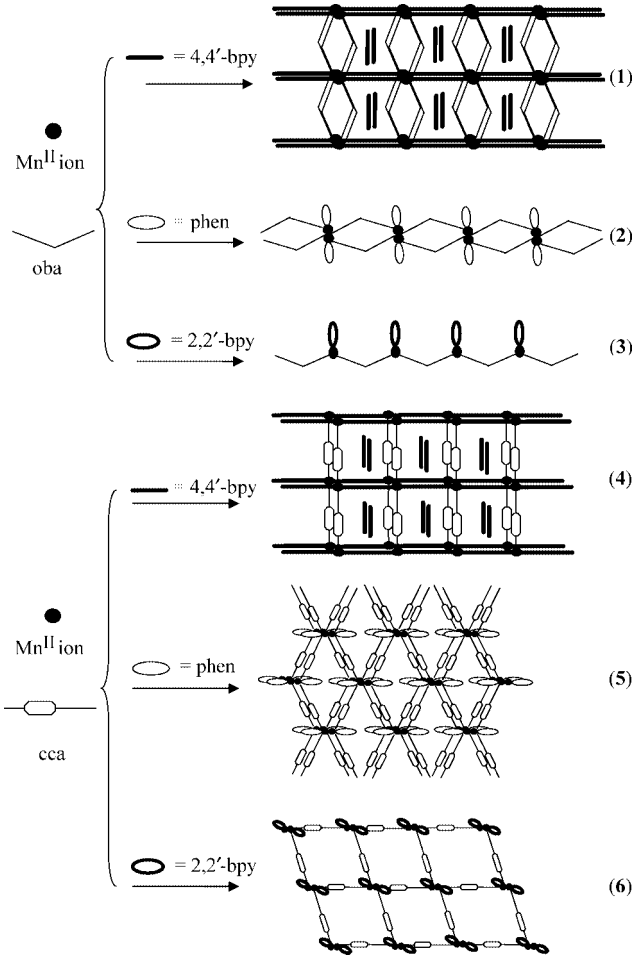


Scheme 3. A simplified representation of the structures of complexes **1**–**6**.

Both oba and cca have two *exo* carboxylate groups, but there are some differences in their complexes. Comparing complexes **1** and **4**, although they are both 3D porous structures they are quite different: complex **1** possesses dumbbell-like channels while complex **4** possesses regular rhombus channels. This is because oba is V-shaped whereas cca is nearly linear. The introduction of phen and 2,2′-bpy as ligands in the $Mn^{II}$/oba and $Mn^{II}$/cca systems results in different structures. Complexes **2** and **3** are infinite 1D chains, while complex **5** possesses a complicated 3D structure and complex **6** is made up of 2D grid-like layers when only coordination bonds are considered. The existence of coordinated water molecules in complexes **2** and **3** is one important factor for the formation of the chain structures. The V-shaped oxo carboxylate ligand oba is also fundamental for the construction of chains in the presence of terminal ligands such as phen and 2,2′-bpy,[7a,7b,7e] while the linear ligand cca contributes to higher dimensionalities in complexes **5** and **6**, thus showing that the shape of the ligands plays an important role in the architecture of coordination polymers.

## Magnetic Properties

### *Magnetic Properties of Complex 2*

The $\chi_m^{-1}$ and $\chi_m T$ vs. $T$ plots (2–300 K) of complex **2** are shown in Figure 9. The magnetic susceptibility data (10 to 300 K) of complex **2** obey the Curie–Weiss law very well, with a Weiss constant, $\theta$, of +3.2 K and a Curie constant, $C$, of 4.554(1) $cm^3 K mol^{-1}$. The value of $C$ is consistent with one spin-only $Mn^{II}$ ion with $S = 5/2$ and $g = 2.040$. The positive Weiss constant and the increase of $\chi_m T$ upon cooling are typical of a ferromagnetic coupling between the $Mn^{II}$ ions. Based on the structural data, the magnetic susceptibility data of complex **2** can be analysed by using a $Mn_2$ dimer model with an intradimer interaction $J$ and including the contribution of the intermolecular interaction $zJ'$. Assuming an isotropic exchange, the exchange Hamiltonian $H = -2JS_1S_2$, with $S_1 = S_2 = 5/2$, and the expression for magnetic susceptibility may be used to fit the data.[12] The least-squares fit of the experimental data in the whole temperature range gives the following parameters: $J$ = 0.462(3) $cm^{-1}$, $g$ = 2.0387(6), $zJ'$ = –0.0062(3) $cm^{-1}$, and $R = 8.0 \times 10^{-6}$.

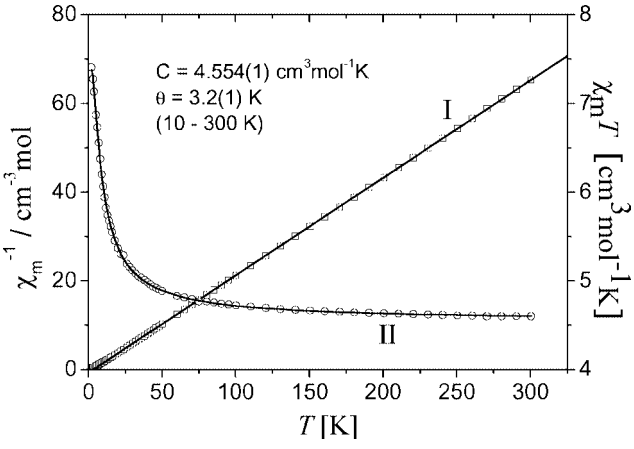


Figure 9. Temperature dependence of $\chi_m^{-1}$ and $\chi_m T$ for complex **2**. Line I is the fit of the Curie–Weiss law and line II is the fit using a dimer model (see text).

 © 2006 Wiley-VCH Verlag GmbH & Co. KGaA, Weinheim 

Clearly, a weak ferromagnetic interaction is observed in the doubly (μ-O)-carboxylate bridged $Mn^{II}$ dimer, while some structurally similar $Mn^{II}$ dimers show weak antiferromagnetic coupling between the $Mn^{II}$ ions (Table 1).[13] The ferromagnetic coupling in complex **2** may be mainly due to the smaller Mn–O–Mn angle, which facilitates ferromagnetic coupling as in some azido- or chloro-bridged $Mn^{II}$ dimers.[14]

Table 1. Comparison of the magnetic coupling constant $J$ and structural parameters for $Mn^{II}_2(\mu\text{-}O)_2$ complexes.

| Compd. | $J$ [$cm^{-1}$] | Mn···Mn [Å] | Mn–O–Mn [°] | Ref. |
|---|---|---|---|---|
| A | –0.631 | 3.712(2) | 109.1(3), 109.8(3) | [13a] |
| B | –0.655 | 3.726(4) | 108.9(3) | [13a] |
| C | –0.785 | 3.460(1) | 105.04(7), 102.77(7) | [13b] |
| D | +0.462 | 3.387(12) | 101.81(7) | this work |

### *Magnetic Properties of Complex 3*

The $\chi_m^{-1}$ and $\chi_m T$ vs. $T$ plots (2–300 K) of complex **3** are shown in Figure 10. The magnetic susceptibility data (2 to 300 K) of complex **3** obey the Curie–Weiss law very well with a very small Weiss constant of 0.09 K and a Curie constant of 9.004(1) $cm^3\,K\,mol^{-1}$. The value of $C$ is consistent with two non-interacting spin-only $Mn^{II}$ ions with $S$ = 5/2 and $g$ = 2.029. The very small Weiss constant suggests essentially no magnetic coupling between the $Mn^{II}$ ions, which is consistent with the long separation between the $Mn^{II}$ ions in this complex. The peak around 50 K might arise from the effect of oxygen.[15]

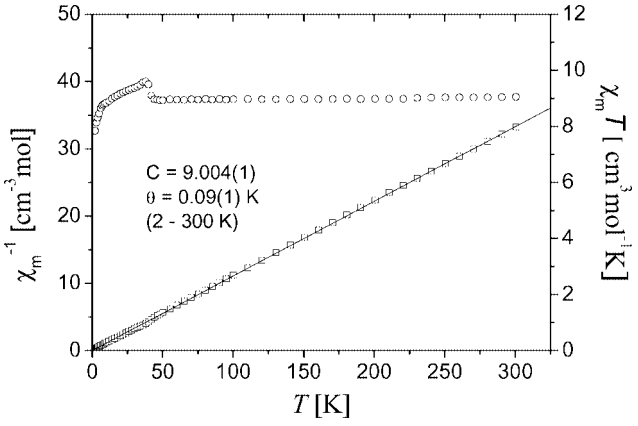


Figure 10. Temperature dependence of $\chi_m^{-1}$ and $\chi_m T$ for complex **3**. The line is the fit of the Curie–Weiss law.

### *Magnetic Properties of Complex 4*

The $\chi_m^{-1}$ and $\chi_m$ vs. $T$ plots (2–300 K) of complex **4** are shown in Figure 11. The magnetic susceptibility data (20 to 300 K) of complex **4** obey the Curie–Weiss law very well with a Weiss constant of –15.8 K and a Curie constant of 8.8355(7) $cm^3\,K\,mol^{-1}$. The value of $C$ is consistent with two non-interacting spin-only $Mn^{II}$ ions with $S$ = 5/2 and $g$ = 2.0098. The negative Weiss constant and the peak in the $\chi_m$ curve for the complex are typical of antiferromagnetic coupling between the $Mn^{II}$ ions. Based on the structural data, complex **4** can be viewed as a 1D uniform chain along the $a$ axis. Consequently, the magnetic susceptibility data of complex **4** can be analysed by using a 1D Fisher model with an intradimer interaction $J$. Assuming isotropic exchange, the exchange Hamiltonian is $H = -2JS_iS_j$ with $S_i = S_j$ = 5/2 and the expression of magnetic susceptibility may be used to fit the data.[16] The least-squares fit of the experimental data in the whole temperature range gives the following parameters: $J$ = –0.718(4) $cm^{-1}$, $g$ = 1.986(4), and $R = 2.3 \times 10^{-4}$. The $J$ value falls in the range for other carboxylato-bridged $Mn^{II}$ compounds.[17]

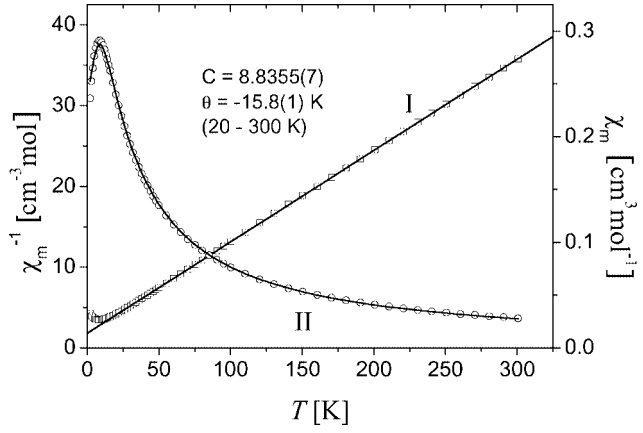


Figure 11. Temperature dependence of $\chi_m^{-1}$ and $\chi_m$ for complex **4**. Line I is the fit of the Curie–Weiss law and line II is the fit using a 1D Fisher model.

## Conclusions

In summary, microporous $Mn^{II}$ coordination polymers (complexes **1** and **4**) are formed by using the V-shaped ligand oba or the linear ligand cca with the rigid ligand 4,4′-bpy. The free 4,4′-bpy ligand acts as a template and also occupies the pore, thus preventing interpenetration. The introduction of terminal ligands such as 2,2′-bpy and phen leads to the formation of 1D chains for complexes **2** and **3**; hydrogen bonds mould these chains into 3D supramolecular networks. In complex **6**, the $Mn^{II}$ ions are coordinated by cca and 2,2′-bpy into 2D layers that interpenetrate to form a 3D supramolecular network. A weak ferromagnetic interaction is observed in the doubly (μ-O)-carboxylate-bridged $Mn^{II}$ dimer in complex **2**, which may be mainly due to the smaller Mn–O–Mn angle.

## Experimental Section

**General Remarks:** All reagents were used as received without further purification. The C, H, N microanalyses were carried out with a Vario EL elemental analyzer. The IR spectra were recorded with a Nicolet Avatar 360 FT-IR spectrometer using the KBr pellet technique. The magnetic susceptibilities were obtained for crystalline

 © 2006 Wiley-VCH Verlag GmbH & Co. KGaA, Weinheim 

Table 2. Crystal data and structure refinement parameters for complexes **1**–**6**.

| | **1** | **2** | **3** | **4** | **5** | **6** |
|---|---|---|---|---|---|---|
| Chemical formula | $C_{34}H_{24}MnN_4O_5$ | $C_{26}H_{18}MnN_2O_6$ | $C_{62}H_{46}Mn_2N_4O_{17}$ | $C_{60}H_{44}Mn_2N_8O_8$ | $C_{24}H_{14}N_2O_4Mn$ | $C_{20}H_{14.50}MnN_2O_{4.25}$ |
| Crystal system | monoclinic | triclinic | triclinic | triclinic | monoclinic | monoclinic |
| Space group | *P*2/*c* | $P\bar{1}$ | $P\bar{1}$ | $P\bar{1}$ | *C*2/*c* | *C*2/*c* |
| Formula weight | 623.51 | 509.36 | 1228.91 | 1114.91 | 449.31 | 405.78 |
| *a* [Å] | 13.251(4) | 7.699(2) | 11.317(4) | 10.224(2) | 21.897(7) | 15.009(2) |
| *b* [Å] | 11.742(4) | 11.671(4) | 16.036(5) | 11.723(2) | 11.677(4) | 19.383(2) |
| *c* [Å] | 9.317(3) | 13.477(4) | 17.986(6) | 12.227(2) | 7.396(2) | 13.926(2) |
| *α* [°] | 90 | 82.295(5) | 64.910(6) | 65.980(3) | 90 | 90 |
| *β* [°] | 90.195(7) | 83.799(5) | 87.609(6) | 71.305(3) | 100.311(6) | 114.709(2) |
| *γ* [°] | 90 | 73.086(5) | 76.789(6) | 84.622(4) | 90 | 90 |
| *V* [Å$^3$] | 1449.6(8) | 1145.1(6) | 2872.3(16) | 1266.7(4) | 1860.6(10) | 3680.8(8) |
| *Z* | 2 | 2 | 2 | 1 | 4 | 8 |
| *F*(000) | 642 | 522 | 1264 | 574 | 916 | 1660 |
| $D_c$ [g cm$^{-3}$] | 1.428 | 1.477 | 1.421 | 1.462 | 1.604 | 1.464 |
| *T* [K] | 293(2) | 293(2) | 293(2) | 293(2) | 293(2) | 293(2) |
| *θ* range [°] | 1.73–26.39 | 2.26–26.43 | 1.25–25.01 | 1.90–25.01 | 1.89–26.49 | 1.83–26.35 |
| *μ* [mm$^{-1}$] | 0.506 | 0.623 | 0.516 | 0.566 | 0.747 | 0.747 |
| GOF | 1.025 | 1.042 | 1.003 | 1.013 | 1.127 | 1.046 |
| Final *R* indices | $R_1$ = 0.0544 | $R_1$ = 0.0408 | $R_1$ = 0.0593 | $R_1$ = 0.0509 | $R_1$ = 0.0573 | $R_1$ = 0.0360 |
| [$I > 2\sigma(I)$] | $wR_2$ = 0.1118 | $wR_2$ = 0.0934 | $wR_2$ = 0.1392 | $wR_2$ = 0.1140 | $wR_2$ = 0.1600 | $wR_2$ = 0.0838 |

Table 3. Selected bond lengths [Å] and angles [°] for complexes **1**–**3**.

| | | | |
|---|---|---|---|
| **1**[a] | | | |
| Mn(1)–O(1) | 2.162(2) | Mn(1)–N(1) | 2.333(4) |
| Mn(1)–O(2)#1 | 2.147(2) | Mn(1)–N(2)#4 | 2.311(4) |
| O(1)–Mn(1)–N(1) | 89.08(6) | O(2)#2–Mn(1)–O(1) | 86.48(9) |
| O(1)–Mn(1)–N(2)#4 | 90.92(6) | O(2)#1–Mn(1)–N(1) | 94.41(6) |
| O(1)#3–Mn(1)–O(1) | 178.16(13) | O(2)#1–Mn(1)–N(2)#4 | 85.59(6) |
| O(2)#1–Mn(1)–O(1) | 93.66(9) | N(2)#4–Mn(1)–N(1) | 180.0 |
| O(2)#1–Mn(1)–O(2)#2 | 171.18(12) | | |
| **2**[b] | | | |
| Mn(1)–O(1) | 2.156(2) | Mn(1)–O(6) | 2.159(2) |
| Mn(1)–O(1)#2 | 2.208(2) | Mn(1)–N(1) | 2.251(2) |
| Mn(1)–O(4)#1 | 2.107(2) | Mn(1)–N(2) | 2.290(2) |
| O(1)–Mn(1)–O(1)#2 | 78.19(7) | O(4)#1–Mn(1)–O(6) | 87.36(7) |
| O(1)–Mn(1)–O(6) | 91.32(7) | O(4)#1–Mn(1)–N(2) | 88.55(7) |
| O(1)–Mn(1)–N(1) | 95.32(7) | O(4)#1–Mn(1)–N(1) | 161.31(7) |
| O(1)–Mn(1)–N(2) | 164.77(7) | O(6)–Mn(1)–O(1)#2 | 169.16(7) |
| O(1)#2–Mn(1)–N(1) | 91.55(7) | O(6)–Mn(1)–N(1) | 92.13(7) |
| O(1)#2–Mn(1)–N(2) | 92.05(7) | O(6)–Mn(1)–N(2) | 98.78(7) |
| O(4)#1–Mn(1)–O(1) | 103.36(7) | N(1)–Mn(1)–N(2) | 73.06(7) |
| O(4)#1–Mn(1)–O(1)#2 | 92.39(7) | | |
| **3**[c] | | | |
| Mn(1)–O(1) | 2.157(3) | Mn(2)–O(5)#1 | 2.095(4) |
| Mn(1)–O(2) | 2.407(3) | Mn(2)–O(10) | 2.179(4) |
| Mn(1)–O(6) | 2.176(4) | Mn(2)–O(11) | 2.363(4) |
| Mn(1)–O(8) | 2.085(4) | Mn(2)–O(12) | 2.176(4) |
| Mn(1)–N(1) | 2.274(4) | Mn(2)–N(3) | 2.248(5) |
| Mn(1)–N(2) | 2.249(4) | Mn(2)–N(4) | 2.236(4) |
| O(1)–Mn(1)–O(2) | 56.98(12) | O(5)#1–Mn(2)–O(10) | 96.02(15) |
| O(1)–Mn(1)–O(6) | 101.89(15) | O(5)#1–Mn(2)–O(11) | 151.78(14) |
| O(1)–Mn(1)–N(1) | 91.62(15) | O(5)#1–Mn(2)–O(12) | 87.94(16) |
| O(1)–Mn(1)–N(2) | 151.88(16) | O(5)#1–Mn(2)–N(3) | 99.51(16) |
| O(6)–Mn(1)–O(2) | 84.01(14) | O(5)#1–Mn(2)–N(4) | 110.32(16) |
| O(6)–Mn(1)–N(1) | 161.44(14) | O(10)–Mn(2)–O(11) | 57.73(13) |
| O(6)–Mn(1)–N(2) | 90.36(16) | O(10)–Mn(2)–N(3) | 92.40(16) |
| O(8)–Mn(1)–O(1) | 100.70(14) | O(10)–Mn(2)–N(4) | 151.33(17) |
| O(8)–Mn(1)–O(2) | 156.97(14) | O(12)–Mn(2)–O(10) | 98.30(18) |
| O(8)–Mn(1)–O(6) | 96.62(15) | O(12)–Mn(2)–O(11) | 86.20(16) |
| O(8)–Mn(1)–N(1) | 93.25(15) | O(12)–Mn(2)–N(3) | 166.28(16) |
| O(8)–Mn(1)–N(2) | 102.93(16) | O(12)–Mn(2)–N(4) | 93.89(18) |
| N(1)–Mn(1)–O(2) | 92.99(14) | N(3)–Mn(2)–O(11) | 92.34(15) |
| N(2)–Mn(1)–O(2) | 100.09(15) | N(4)–Mn(2)–N(3) | 72.76(17) |
| N(2)–Mn(1)–N(1) | 72.09(16) | N(4)–Mn(2)–O(11) | 97.61(16) |

[a] Symmetry transformations used to generate equivalent atoms: #1 –*x*, –*y*, –*z* + 1; #2 *x*, –*y*, *z* + 1/2; #3 –*x*, *y*, –*z* + 3/2; #4 *x*, *y* – 1, *z*. [b] Symmetry transformations used to generate equivalent atoms: #1 –*x* + 1, –*y*, –*z* + 2; #2 –*x* + 1, –*y*, –*z* + 1. [c] Symmetry transformations used to generate equivalent atoms: #1 *x* – 1, *y* + 1, *z* + 1; #2 *x* + 1, *y* – 1, *z* – 1.

 © 2006 Wiley-VCH Verlag GmbH & Co. KGaA, Weinheim 

samples using a Quantum Design MPMS SQUID magnetometer. The experimental susceptibilities were corrected for the sample holder and the diamagnetism contributions estimated from Pascal's constants.

**Synthesis of $[Mn(oba)(4,4'\text{-bpy})]_n \cdot n(4,4'\text{-bpy})$ (1):** A mixture of $H_2oba$ (0.026 g, 0.1 mmol), $Mn(OAc)_2 \cdot 4H_2O$ (0.024 g, 0.1 mmol), 4,4′-bpy·$2H_2O$ (0.019 g, 0.1 mmol), NaOH solution (0.3 mL, 0.65 M) and deionized water(5 mL) was sealed in a Teflon-lined stainless-steel vessel (25 mL) and heated at 180 °C for 72 h. The vessel was then cooled slowly to room temperature. Yellow crystals were isolated by filtration, and washed with water and ethanol. Yield: 0.011 g (17.6%). $C_{34}H_{24}MnN_4O_5$ (623.51): calcd. C 65.44, H 3.85, N 8.98; found C 65.82, H 3.93, N 8.80. IR (KBr pellet): $\tilde{\nu}$ = 3439 $cm^{-1}$ (s), 3072 (w), 1648 (m), 1602 (s), 1560 (m), 1532 (m), 1496 (w), 1413 (m), 1386 (s), 1240 (s), 1159 (m), 1097 (w), 1071 (w), 1011 (w), 879 (w), 803 (m), 785 (m), 695 (w).

**Synthesis of $[Mn(oba)(phen)(H_2O)]_n$ (2):** The synthesis of complex **2** followed a similar procedure as for complex **1** but with phen·$H_2O$ (0.020 g, 0.1 mmol) instead of 4,4′-bpy·$2H_2O$. Yield: 0.040 g (78.5%). $C_{26}H_{18}MnN_2O_6$ (509.36): calcd. C 61.25, H 3.53, N 5.50; found C 60.88, H 3.67, N 5.53. IR (KBr pellet): $\tilde{\nu}$ = 3317 $cm^{-1}$ (m), 3049 (w), 1602 (s), 1553 (m), 1519 (m), 1496 (m), 1429 (m), 1384 (s), 1335 (s), 1238 (s), 1160 (m), 1137 (w), 1102 (w), 1047 (w), 1011 (w), 876 (w), 849 (m), 786 (m), 698 (w).

**Synthesis of $[Mn_2(oba)_2(2,2'\text{-bpy})_2(H_2O)_2]_n \cdot nH_2oba$ (3):** The synthesis of complex **3** followed a similar procedure as for complex **1** but with 2,2′-bpy (0.016 g, 0.1 mmol) instead of 4,4′-bpy·$2H_2O$. Yield: 0.032 g (52.1%). $C_{62}H_{46}Mn_2N_4O_{17}$ (1228.9): calcd. C 60.59, H 3.74, N 4.56; found C 60.38, H 3.84, N 4.81. IR (KBr pellet): $\tilde{\nu}$ = 3462 $cm^{-1}$ (m), 3044 (w), 1596 (s), 1565 (m), 1499 (w), 1401 (s), 1316 (w), 1229 (s), 1165 (m), 1100 (w), 1061 (w), 1016 (w), 877 (m), 783 (m), 764 (m), 644 (w).

**Synthesis of $[Mn_2(cca)_2(4,4'\text{-bpy})_2]_n \cdot 2n(4,4'\text{-bpy})$ (4):** A mixture of $H_2cca$ (0.02 g, 0.1 mmol), $Mn(OAc)_2 \cdot 4H_2O$ (0.024 g, 0.1 mmol), 4,4′-bpy·$2H_2O$ (0.038 g, 0.2 mmol), NaOH solution (0.3 mL, 0.65 M) and deionized water (5 mL) was sealed in a Teflon-lined stainless-steel vessel (25 mL) and heated at 140 °C for 72 h. The vessel was then cooled slowly to room temperature. Yellow crystals were isolated by filtration, and washed with water and ethanol. Yield: 0.020 g (35.9%). $C_{60}H_{44}Mn_2N_8O_8$ (1114.9): calcd. C 64.58, H 3.95, N 10.05; found C 64.20, H 4.12, N 9.97. IR (KBr pellet): $\tilde{\nu}$ = 3442 $cm^{-1}$ (s), 1638 (m), 1588 (s), 1550 (s), 1492 (m), 1417 (m),

Table 4. Selected bond lengths [Å] and angles [°] for complexes **4**–**6**.

| | | | |
|---|---|---|---|
| **4**[a] | | | |
| Mn(1)–O(1) | 2.173(3) | Mn(2)–O(2) | 2.166(2) |
| Mn(1)–O(3)#1 | 2.152(2) | Mn(2)–O(4)#2 | 2.197(3) |
| Mn(1)–N(1) | 2.278(3) | Mn(2)–N(2)#6 | 2.299(3) |
| O(1)–Mn(1)–N(1) | 87.10(10) | O(2)–Mn(2)–O(2)#4 | 180.0 |
| O(1)–Mn(1)–N(1)#3 | 92.90(10) | O(2)–Mn(2)–O(4)#2 | 89.43(10) |
| O(1)#3–Mn(1)–O(1) | 180.0 | O(2)–Mn(2)–O(4)#5 | 90.57(9) |
| O(3)#1–Mn(1)–O(1) | 91.57(10) | O(2)–Mn(2)–N(2)#6 | 88.95(11) |
| O(3)#1–Mn(1)–O(1)#3 | 88.43(10) | O(2)–Mn(2)–N(2)#7 | 91.05(11) |
| O(3)#1–Mn(1)–O(3)#2 | 180.0 | O(4)#2–Mn(2)–O(4)#5 | 179.998(1) |
| O(3)#1–Mn(1)–N(1) | 91.76(10) | O(4)#2–Mn(2)–N(2)#6 | 86.45(10) |
| O(3)#1–Mn(1)–N(1)#3 | 88.24(10) | O(4)#2–Mn(2)–N(2)#7 | 93.55(11) |
| N(1)#3–Mn(1)–N(1) | 180.0 | N(2)#6–Mn(2)–N(2)#7 | 180.0 |
| **5**[b] | | | |
| Mn(1)–O(1) | 2.094(3) | Mn(1)–N(1) | 2.317(4) |
| Mn(1)–O(2)#2 | 2.203(3) | | |
| O(1)–Mn(1)–O(1)#1 | 113.4(2) | O(2)#2–Mn(1)–O(2)#3 | 168.3(2) |
| O(1)–Mn(1)–O(2)#2 | 86.1(1) | O(2)#2–Mn(1)–N(1) | 85.6(1) |
| O(1)–Mn(1)–O(2)#3 | 100.3(1) | O(2)#3–Mn(1)–N(1) | 84.9(1) |
| O(1)–Mn(1)–N(1) | 87.9(1) | O(2)#2–Mn(1)–N(1)#1 | 84.9(1) |
| O(1)–Mn(1)–N(1)#1 | 158.1(1) | O(2)#3–Mn(1)–N(1)#1 | 85.6(1) |
| O(1)#1–Mn(1)–O(2)#2 | 100.3(1) | N(1)–Mn(1)–N(1)#1 | 71.4(2) |
| O(1)#1–Mn(1)–O(2)#3 | 86.1(1) | | |
| **6**[c] | | | |
| Mn(1)–O(1) | 2.12(4) | Mn(1)–O(6) | 2.51(2) |
| Mn(1)–O(2)#3 | 2.08(2) | Mn(1)–N(1) | 2.245(2) |
| Mn(1)–O(5) | 2.15(2) | Mn(1)–N(2) | 2.290(2) |
| O(1)–Mn(1)–O(5) | 94.4(1) | O(2)#3–Mn(1)–N(2) | 87.8(7) |
| O(1)–Mn(1)–O(6) | 87.3(1) | O(5)–Mn(1)–O(6) | 55.2(3) |
| O(1)–Mn(1)–N(1) | 95.0(8) | O(5)–Mn(1)–N(1) | 145.1(3) |
| O(1)–Mn(1)–N(2) | 164.4(8) | O(5)–Mn(1)–N(2) | 92.1(5) |
| O(2)#3–Mn(1)–O(1) | 101.9(1) | N(1)–Mn(1)–O(6) | 91.7(4) |
| O(2)#3–Mn(1)–O(5) | 116.6(5) | N(2)–Mn(1)–O(6) | 84.8(7) |
| O(2)#3–Mn(1)–O(6) | 168.6(8) | N(1)–Mn(1)–N(2) | 71.86(7) |
| O(2)#3–Mn(1)–N(1) | 94.2(5) | | |

[a] Symmetry transformations used to generate equivalent atoms: #1 $-x, -y, -z + 1$; #2 $x, y + 1, z$; #3 $-x, -y + 1, -z + 1$; #4 $-x + 1, -y + 1, -z + 1$; #5 $-x + 1, -y, -z + 1$; #6 $x + 1, y, z - 1$; #7 $-x, -y + 1, -z + 2$; #8 $x, y - 1, z$. [b] Symmetry transformations used to generate equivalent atoms: #1 $-x, y, -z + 3/2$; #2 $x, -y, z - 1/2$; #3 $-x, -y, -z + 2$; #4 $-x + 1/2, -y - 1/2, -z + 2$. [c] Symmetry transformations used to generate equivalent atoms: #1 $x + 1/2, y + 1/2, z$; #2 $-x + 1/2, -y + 1/2, -z + 1$; #3 $-x + 1, -y + 1, -z + 1$; #4 $-x, -y + 1, -z$; #5 $x - 1/2, y - 1/2, z$.

 © 2006 Wiley-VCH Verlag GmbH & Co. KGaA, Weinheim 

1376 (s), 1225 (m), 1074 (w), 1001 (w), 864 (w), 817 (m), 794 (m), 721 (w), 628 (m), 605 (w).

**Synthesis of [Mn(cca)(phen)]$_n$ (5):** The synthesis of complex **5** followed a similar procedure as for complex **4** except that phen·$H_2O$ (0.020 g, 0.1 mmol) was used instead of 4,4′-bpy·$2H_2O$ and the temperature was 160 °C. Yield: 0.022 g (48.9%). $C_{24}H_{14}MnN_2O_4$ (449.31): calcd. C 62.07, H 3.29, N 6.58; found C 61.75, H 3.43, N 6.86. IR (KBr pellet): $\tilde{\nu}$ = 3439 $cm^{-1}$ (s), 1649 (s), 1606 (m), 1509 (m), 1425 (m), 1381 (s), 1099 (w), 987 (w), 851 (m), 789 (m), 730 (m), 636 (w).

**Synthesis of [Mn(cca)(2,2′-bpy)]$_n$·0.25$n$$H_2O$ (6):** The synthesis of complex **6** followed a similar procedure as for complex **4** except that 2,2′-bpy (0.016 g, 0.1 mmol) was used instead of 4,4′-bpy·$2H_2O$ and the temperature was 120 °C. Yield: 0.017 g (41.9%). $C_{20}H_{14.50}MnN_2O_{4.25}$ (405.78): calcd. C 59.15, H 3.57, N 6.90; found C 58.91, H 3.81, N 6.82. IR (KBr pellet): $\tilde{\nu}$ = 3431 $cm^{-1}$ (m), 3025 (m), 1646 (s), 1616 (s), 1536 (s), 1473 (m), 1439 (s), 1390 (s), 1312 (m), 1245 (m), 1171 (m), 1098 (w), 1016 (m), 984 (m), 862 (m), 763 (m), 737 (m), 647 (m), 625 (w).

**X-ray Crystallographic Study:** Diffraction intensities for the six complexes were collected at 293 K on a Bruker SMART 1000 CCD diffractometer employing graphite-monochromated Mo-$K_\alpha$ radiation ($\lambda$ = 0.71073 Å). Semi-empirical absorption correction was applied using the SADABS program. The structures were solved by direct methods and refined by full-matrix least-squares on $F^2$ using the SHELXS-97 and SHELXL-97 programs, respectively.[18] Non-hydrogen atoms were refined anisotropically. Hydrogen atoms were placed in geometrically calculated positions. The crystallographic data for complexes **1** to **6** are listed in Table 2, and selected bond lengths and angles in Tables 3 and 4.

CCDC-293769 to -293774 (for **1**–**6**, respectively) contain the supplementary crystallographic data for this paper. These data can be obtained free of charge from the Cambridge Crystallographic Data Centre via www.ccdc.cam.ac.uk/data_request/cif.

**Supporting Information** (see footnote on the first page of this article): The other three kinds of coordination environments of the $Mn^{II}$ ion in complex **6**.

## Acknowledgments

This work was supported by the National Natural Science Foundation of China (grant nos. 20331010, 20501003 and 20490210).

[1] a) E. Q. Gao, S. Q. Bai, Z. He, C. H. Yan, *Inorg. Chem.* **2005**, *44*, 677–682; b) H. Oshio, M. Nihei, S. Koizumi, T. Shiga, H. Nojiri, M. Nakano, N. Shirakawa, M. Akatsu, *J. Am. Chem. Soc.* **2005**, *127*, 4568–4569; c) A. J. Tasiopoulos, W. Wernsdorfer, K. A. Abboud, G. Christou, *Angew. Chem. Int. Ed.* **2004**, *43*, 6338–6342; d) G. Rajaraman, M. Musugesu, E. C. Sanudo, M. Soler, W. Wernsdorfer, M. Helliwell, C. Muryn, J. Raftery, S. J. Teat, G. Christou, E. K. Brechin, *J. Am. Chem. Soc.* **2004**, *126*, 15445–15457; e) D. J. Price, S. R. Batten, B. Moubaraki, K. S. Murray, *Chem. Commun.* **2002**, 762–763; f) S. Wang, M. S. Wemple, H. L. Tsai, K. Folting, J. C. Huffman, K. S. Hagen, D. N. Hendrickson, G. Christou, *Inorg. Chem.* **2000**, *39*, 1501–1513; g) H. Andres, R. Basler, H. U. Gudel, G. Aromi, G. Christou, H. Buttner, B. Ruffle, *J. Am. Chem. Soc.* **2000**, *122*, 12469–12477.

[2] a) K. N. Ferreira, T. M. Iverson, K. Maghlaoui, J. Barber, S. Iwata, *Science* **2004**, *303*, 1831–1838; b) A. W. Rutherford, A. Boussac, *Science* **2004**, *303*, 1782–1784; c) S. Mukhopadhyay, S. K. Mandal, S. Bhaduri, W. H. Armstrong, *Chem. Rev.* **2004**, *104*, 3981–4026; d) G. C. Dismukes, *Chem. Rev.* **1996**, *96*, 2909–2926.

[3] a) K. B. Jensen, E. Johansen, F. B. Larsen, C. J. McKenzie, *Inorg. Chem.* **2004**, *43*, 3801–3803; b) J. Brinksma, R. Hage, J. Kerschner, B. L. Feringa, *Chem. Commun.* **2000**, 537–538; c) W. Zhang, J. L. Loebach, S. B. Wilson, E. N. Jacobsen, *J. Am. Chem. Soc.* **1990**, *112*, 2801–2803.

[4] a) A. Escuer, F. A. Mautner, M. A. S. Goher, M. A. M. Abu-Youssef, R. Vicente, *Chem. Commun.* **2005**, 605–607; b) C. M. Liu, S. Gao, D. Q. Zhang, Y. H. Huang, R. G. Xiong, Z. L. Liu, F. C. Jiang, D. B. Zhu, *Angew. Chem. Int. Ed.* **2004**, *43*, 990–994; c) E. Q. Gao, S. Q. Bai, Y. F. Yue, Z. M. Wang, C. H. Yan, *Inorg. Chem.* **2003**, *42*, 3642–3649; d) M. A. M. Abu-Youssef, A. Escuer, M. A. S. Goher, F. A. Mautner, G. J. Reiß, R. Vicente, *Angew. Chem. Int. Ed.* **2000**, *39*, 1624–1626; e) R. Cortés, M. Drillon, X. Solans, L. Lezama, T. Rojo, *Inorg. Chem.* **1997**, *36*, 677–683; f) G. D. Munno, M. Julve, G. Viau, F. Lloret, J. Faus, D. Viterbo, *Angew. Chem. Int. Ed. Engl.* **1996**, *35*, 1807.

[5] a) Y. Z. Zhang, S. Gao, Z. M. Wang, G. Su, H. L. Sun, F. Pan, *Inorg. Chem.* **2005**, *44*, 4534–4545; b) F. Karadas, E. J. Schelter, A. V. Prosvirin, J. Bacsa, K. R. Dunbar, *Chem. Commun.* **2005**, 1414–1416; c) R. Lescouëzec, J. Vaissermann, L. M. Toma, R. Carrasco, F. Lloret, M. Julve, *Inorg. Chem.* **2004**, *43*, 2234–2236; d) T. Kashiwagi, S. Ohkoshi, H. Seino, Y. Mizobe, K. Hashimoto, *J. Am. Chem. Soc.* **2004**, *126*, 5024–5025; e) M. Ohha, N. Usuki, N. Fukita, H. Ōkawa, *Angew. Chem. Int. Ed.* **1999**, *38*, 1795–1798.

[6] a) E. Coronado, J. R. Galán-Mascarós, C. J. Gómez-García, C. Martí-Gastaldo, *Inorg. Chem.* **2005**, *44*, 6197–6202; b) E. Coronado, J. R. Galán-Mascarós, C. J. Gómez-García, V. Laukhin, *Nature* **2000**, *408*, 447–449; c) R. Pellaux, H. W. Schmalle, R. Huber, P. Fischer, T. Hauss, B. Ouladdiaf, S. Decurtins, *Inorg. Chem.* **1997**, *36*, 2301–2308; d) S. G. Carling, C. Mathonière, P. Day, K. M. A. Malik, S. J. Coles, M. B. Hursthouse, *J. Chem. Soc., Dalton Trans.* **1996**, 1839–1843.

[7] a) Z. B. Han, X. N. Cheng, X. M. Chen, *Cryst. Growth Des.* **2005**, *5*, 695–700; b) Y. Z. Zheng, G. F. Liu, B. H. Ye, X. M. Chen, *Z. Anorg. Allg. Chem.* **2004**, *630*, 296–300; c) Y. B. Wang, Z. M. Wang, C. H. Yan, L. P. Jin, *J. Mol. Struct.* **2004**, *692*, 177–186; d) M. Kondo, Y. Irie, Y. Shimizu, M. Miyazawa, H. Kawaguchi, A. Nakamura, T. Naito, K. Maeda, F. Uchida, *Inorg. Chem.* **2004**, *43*, 6139–6141; e) X. M. Chen, G. F. Liu, *Chem. Eur. J.* **2002**, *8*, 4811–4817; f) G. F. Liu, Z. P. Qiao, H. Z. Wang, X. M. Chen, G. Yang, *New J. Chem.* **2002**, *26*, 791–795; g) J. Tao, J. X. Shi, M. L. Tong, X. X. Zhang, X. M. Chen, *Inorg. Chem.* **2001**, *40*, 6328–6330.

[8] H. Kumagai, Y. Oka, K. Inoue, M. Kurmoo, *J. Chem. Soc., Dalton Trans.* **2002**, 3442–3446.

[9] a) X. Q. Lu, J. J. Jiang, C. L. Chen, B. S. Kang, C. Y. Su, *Inorg. Chem.* **2005**, *44*, 4515–4521; b) B. Q. Ma, K. L. Mulfort, J. T. Hupp, *Inorg. Chem.* **2005**, *44*, 4912–4914; c) R. Pothiraja, M. Sathiyendiran, R. J. Butcher, R. Murugavel, *Inorg. Chem.* **2005**, *44*, 6314–6323; d) S. Kraft, E. Hanuschek, R. Beckhaus, D. Haase, W. Saak, *Chem. Eur. J.* **2005**, *11*, 969–978; e) M. I. Khan, E. Yohannes, R. C. Nome, S. Ayesh, V. O. Golub, C. J. O'Connor, R. J. Doedens, *Chem. Mater.* **2004**, *16*, 5273–5279; f) R. Lin, J. H. K. Yip, K. Zhang, L. L. Koh, K. Y. Wong, K. P. Ho, *J. Am. Chem. Soc.* **2004**, *126*, 15852–15869.

[10] a) B. Gómez-Lor, E. Gutiérrez-Puebla, M. Iglesias, M. A. Monge, C. Ruiz-Valero, N. Snejko, *Chem. Mater.* **2005**, *17*, 2568–2573; b) F. Li, Z. Ma, Y. L. Wang, R. Cao, W. H. Bi, X. Li, *CrystEngComm* **2005**, *7*, 569–574; c) B. H. Ye, M. L. Tong, X. M. Chen, *Coord. Chem. Rev.* **2005**, *249*, 545–565; d) X. L. Wang, C. Qin, E. B. Wang, L. Xu, Z. M. Su, C. W. Hu, *Angew. Chem. Int. Ed.* **2004**, *43*, 5036–5040; e) N. Hao, E. H. Shen, Y. G. Li, E. B. Wang, C. W. Hu, L. Xu, *Eur. J. Inorg. Chem.* **2004**, 4102–4107; f) L. Y. Zhang, G. F. Liu, S. L. Zheng, B. H. Ye, X. M. Zhang, X. M. Chen, *Eur. J. Inorg. Chem.* **2003**, 2965–2971.

 © 2006 Wiley-VCH Verlag GmbH & Co. KGaA, Weinheim 

[11] C. Y. Sun, L. P. Jin, *J. Mol. Struct.* **2005**, *733*, 63–68.
[12] W. Wojciechowski, *Inorg. Chim. Acta* **1967**, *1*, 318.
[13] a) H. Iikura, T. Nagata, *Inorg. Chem.* **1998**, *37*, 4702–4711; b) J. Kim, J. M. Lim, M. C. Suh, H. Yun, *Polyhedron* **2001**, *20*, 1947–1951.
[14] a) Z. H. Ni, H. Z. Kou, L. Zheng, Y. H. Zhao, L. F. Zhang, R. J. Wang, A. L. Cui, O. Sato, *Inorg. Chem.* **2005**, *44*, 4728–4736; b) G. A. van Albada, A. Mohamadou, W. L. Driessen, R. Gelder, S. Tanase, J. Reedijk, *Polyhedron* **2004**, *23*, 2387–2391.
[15] Oxygen Contamination, MPMS Application Note 1014–210, *Quantum Design*, **1997**.
[16] R. L.Carlin, *Magnetochemistry*, Springer-Verlag, **1986**, p170.
[17] S. Durot, C. Policar, G. Pelosi, F. Bisceglie, T. Mallah, J. P. Mahy, *Inorg. Chem.* **2003**, *42*, 8072–8080.
[18] G. M. Sheldrick, *SHELXTL-97*, *Program for the Refinement of Crystal Structures*, University of Göttingen, Germany, **1997**.
Received: December 30, 2005
Published Online: April 18, 2006

 © 2006 Wiley-VCH Verlag GmbH & Co. KGaA, Weinheim 

DOI: 10.1002/ejic.200600016

# Octahedral $Ru^{II}$ Complexes with [PNO] Hydrazonic Ligands: Synthesis, Structure, Reactivity and Catalytic Activity in the Addition of Benzoic Acid to Alkynes

**Paolo Pelagatti,*[a] Alessia Bacchi,[a] Marcella Balordi,[a] Sandra Bolaño,[b][‡] Francesca Calbiani,[a] Lisa Elviri,[a] Luca Gonsalvi,*[b] Corrado Pelizzi,[a] Maurizio Peruzzini,[b] and Dominga Rogolino[a]**

**Keywords:** Tridentate ligands / Ruthenium / Homogeneous catalysis / Enol esters / Mass spectrometry

A series of $Ru^{II}$ complexes containing [(H)PNO] hydrazonic ligands were synthesised using different ruthenium sources such as $[Ru(PPh_3)_3Cl_2]$, $[Ru(dmso)_4Cl_2]$ and $[Ru(p\text{-cymene})Cl_2]_2$. The complexes were characterised by $^1H$ NMR, $^{31}P\{^1H\}$ NMR, IR, FAB-MS, microanalysis and in some cases by X-ray diffraction analysis on a single crystal. The ligands show a great variety of different coordinating behaviours such as $\kappa^3$-(H)PNO, $\kappa^2$-(H)PN, $\kappa^1$-(H)P and $\kappa^3$-PNO, depending on the ruthenium precursor and on the synthetic experimental conditions. The complexes *trans*-$[Ru(\kappa^3\text{-(H)PNO})(PPh_3)Cl_2]$ reacted with dmso to give the bis-chelate complex $[Ru(\kappa^3\text{-PNO})_2]$, $[Ru(dmso)_4]Cl_2$, $OPPh_3$, HCl and $Me_2S$, through an oxygen-transfer reaction from dmso to $PPh_3$. A catalytic version of this reaction was also developed. The complexes obtained from $[Ru(PPh_3)_3Cl_2]$ were tested as homogeneous pre-catalysts for the coupling between benzoic acid and terminal alkynes to give the corresponding enol esters. High stereo- and regio-selectivity, up to 100 % (determined by $^1H$ NMR), in favour of the (*Z*)-*anti*-Markovnikov products (*Z*)-alk-1-en-1-yl benzoate was observed. An ESI-MS monitoring of the catalytic couplings revealed that the enol ester formation occurs through an intermolecular attack of an external carboxylate anion onto a vinylidene–Ru intermediate of the type $[Ru(PNO)(PPh_3)(C{=}CH{-}C_4H_9)Cl]$.
(© Wiley-VCH Verlag GmbH & Co. KGaA, 69451 Weinheim, Germany, 2006)

## Introduction

The use of potentially tridentate [PNO] ligands in the synthesis of transition-metal complexes is scarcely described in the literature.[1] However, $Ru^{II}$ complexes with [PNO] ligands have been shown to be active catalysts in the transfer hydrogenation of ketones,[2] and some of us have reported that [Pd(PNO)(OAc)] and [Pd(PNO)Cl] complexes [PNO = acylhydrazones] promote the catalytic homogeneous hydrogenation of alkenes[3] and the semi-hydrogenation of terminal alkynes,[4] respectively. The use of [PNO] ligands for the preparation of homogeneous catalysts containing *soft* transition metals, is based on two assumptions: *i*) that the chelating PN unit stabilizes the metal fragment under the catalytic conditions and *ii*) that the labile M–O bond makes reactive the metal complex exerting, at the same time, a control upon the accessibility at the metal for an incoming substrate. This last feature can be determinant for the selectivity of the catalytic process. When the [PNO] ligand is protic, as in the case of the acyl hydrazones, a further control on the hemilability of the ligand, from a $\kappa^3$-(H)PNO coordination to a $\kappa^2$-(H)PN one, as well as on the nucleophilicity of the metal, can be exerted as a function of the anionic or neutral character of the ligand.[5]

As our ongoing research on the use of protic [PNO] acyl hydrazones as ligands in the synthesis of transition-metal-containing complexes,[5] we have undertaken a study on the coordinating behaviour of 2-(diphenylphosphanyl)benzaldehyde benzoylhydrazone (Hbidf) and 2-(diphenylphosphanyl)benzaldehyde acetylhydrazone (Haidf) (Scheme 1), towards $Ru^{II}$.

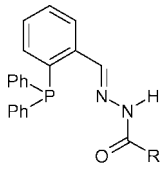


R = Ph **Hbidf**
Me **Haidf**

Scheme 1.

[a] Dipartimento di Chimica Generale ed Inorganica, Chimica Analitica, Chimica Fisica, Università degli Studi di Parma, Parco Area delle Scienze 17/A, 43100 Parma, Italy
E-mail: paolo.pelagatti@unipr.it
[b] Istituto di Chimica dei Composti Organometallici, Consiglio Nazionale delle Ricerche (ICCOM-CNR), via Madonna del Piano 10, 50019 Sesto Fiorentino, Firenze, Italy
E-mail: l.gonsalvi@iccom.cnr.it
[‡] Current address: Universidad de Vigo, Facultad de Ciencias (Químicas), Campus Universitario, 36310 Lagoas Marcosende, Vigo, Spain
Supporting information for this article is available on the WWW under http://www.eurjic.org or from the author.

 © 2006 Wiley-VCH Verlag GmbH & Co. KGaA, Weinheim 

The two ligands have been reacted with $[Ru(PPh_3)_3Cl_2]$ under different reaction conditions, in order to isolate neutral or ionic complexes containing the ligands in either protonated or deprotonated form. All the complexes have been fully characterised by a number of analytical and spectroscopic techniques and, in several cases, by X-ray diffraction analysis on a single crystal. In order to elucidate the reactivity shown by the complexes of the type $[Ru(\kappa^3\text{-}HPNO)(PPh_3)Cl_2]$ with dmso, the syntheses and the characterisations of various Ru complexes obtained by reactions of Hbidf with $[Ru(dmso)_4Cl_2]$ and $[Ru(p\text{-cymene})Cl_2]_2$ are also reported.

Ruthenium is certainly one of the mostly used transition metals in homogeneous catalysis.[6] The Ru-promoted coupling between benzoic acid and terminal alkynes (Scheme 2) is an elegant way to produce vinyl esters, which find industrial applications as polymerising substrates[7] and acylating reagents for the synthesis of amides[8] and halogenated ketones;[9] other applications include cyclopropanation,[10] 1,3-dipolar cycloaddition,[11] asymmetric hydrogenation[12] and hydroformylation reactions.[13]

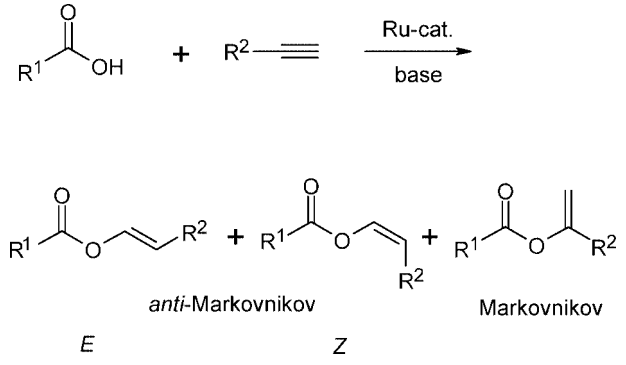


Scheme 2.

The first report describing this reaction dates back to 1983[14] and deals with the use of $Ru_3(CO)_{12}$ in the coupling of aliphatic and aromatic carboxylic acids to di- and monosubstituted acetylenes. Later on, the process has been developed by Mitsudo,[15] Dixneuf[16] and Verpoort,[17] although other groups have been and are still involved in the field.[18] From the literature it can be inferred that the combination of monodentate phosphanes with different Ru sources generally yields to the Markovnikov product,[15,16a,16b,19] although in some cases the selectivity can be switched to the *anti*-Markovnikov product by replacing inorganic bases with organic (coordinating) ones, such as pyridine derivatives.[18] The same trend has been described by Dixneuf replacing mono- with chelating phosphanes[16d] and by Verpoort adding phosphanes to N-heterocyclic carbene complexes.[17d] With this in our mind, we have argued that the high chelation degree of the acyl hydrazones could induce a good selectivity towards the *anti*-Markovnikov products, thus leading to the formation of the less commonly obtained isomer. In order to test this hypothesis and because of the lack of data concerning the use of pre-catalysts containing tridentate ligands for this particular coupling reaction, we have decided to test the complexes deriving from the combinations of Hbidf and Haidf with $[Ru(PPh_3)_3Cl_2]$ as pre-catalysts in the addition of benzoic acid to terminal alkynes. Aiming at detecting the organometallic intermediates involved in the catalytic cycle, an ESI-MS study has been performed. ESI-MS technique allows for the detection of species at low concentration in solution and this makes it attractive to define the mechanism of metal-promoted catalytic transformations. It has been successfully employed in different reactions, such as the reduction of ketones,[20] epoxidations,[21] olefins polymerisation[22] and C–H bonds activation.[23] To the best of our knowledge, this is the first report dealing with the application of such a technique for the study of the addition of carboxylic acids to alkynes.

## Results and Discussion

Selected spectroscopic data ($^{31}P\{^1H\}$NMR, $^1H$ NMR and FT-IR) of the complexes reported in this work are collected in Table 1.

### Ru Complexes Obtained from $[Ru(PPh_3)_3Cl_2]$

The free ligands Hbidf and Haidf react with a stoichiometric amount of $[Ru(PPh_3)_3Cl_2]$ in dichloromethane at room temperature, leading to the neutral dichloride complexes *trans*-$[Ru(\kappa^3\text{-}(H)PNO)(PPh_3)Cl_2]$, which were isolated as purple solids in good yields (**1** and **2** in Scheme 3, respectively).

The neutral hydrazones coordinate in a tridentate fashion by means of the P, $N_{imine}$ and O donors. The neutral behaviour of the ligands is indicated by the IR stretching bands of the N–H bonds (3148 and 3145 $cm^{-1}$ for **1** and **2**, respectively), while the involvement of the carbonyl group in the coordination is pointed out by the shift to lower wavenumbers of the C=O stretching band (1629 $cm^{-1}$ for both complexes) with respect to the free ligands (1652 and 1678 $cm^{-1}$ for Hbidf and Haidf, respectively). The octahedral coordinations are completed by a $PPh_3$ molecule and by two chloride ligands. The FAB-MS spectra and the elemental analyses confirm the proposed stoichiometries. The complexes **1** and **2** are poorly soluble in chloroform, dichloromethane, THF, toluene, acetonitrile and methanol, while they readily dissolve in strongly coordinating solvents, like dmso and dmf. Based on the reactivity of **1** observed in warm acetonitrile (vide infra), we suppose that the solution of **1** and **2** in dmso or dmf occurs by breaking of a Ru–Cl bond and formation of the cationic complexes $[Ru(\kappa^3\text{-}(H)PNO)(PPh_3)(S)Cl]Cl$ (**1a** and **2a**, S = dmso or dmf). The $^1H$ NMR spectra of the freshly prepared samples recorded in $[D_6]$dmso show singlets belonging to the hydrazonic protons at $\delta$ = 14.11 and 13.65 ppm for **1a** and **2a**, respectively, while the HC=N protons give rise to doublets at $\delta$ = 9.14 ppm and 8.69 ppm, respectively. The somewhat high $^4J_{PH}$ values of 7.5 and 7.7 Hz for **1a** and **2a**, respectively, corresponding to the couplings between the iminic protons

 © 2006 Wiley-VCH Verlag GmbH & Co. KGaA, Weinheim 

Table 1. Selected spectroscopic signals of the Ru complexes.

| Complex | $^{31}P\{^1H\}$ NMR[a] | | | $^1H$ NMR [$\delta$][a] | | IR [$cm^{-1}$][b] | |
|---|---|---|---|---|---|---|---|
| | $PPh_2$ | $PPh_3$ | $^2J_{PP}$ [Hz] | N–H | HC=N [$^4J_{PH}$] | ν(NH) | ν(C=O) |
| **1** | | | | | | 3148 (w) | 1629 (s) |
| **1a**[c] | 63 | 39.1 | 32 | 14.11 | 9.14 (7.5) | | |
| **1b**[c] | 49 | 32 | 26.5 | | 9.14 (8.2) | | |
| **1c** | 54 | 34 | 30 | | | | |
| **2** | | | | | | 3145 (w) | 1629 (s) |
| **2a**[c] | 65.3 | 40.8 | 31 | 13.65 | 8.69 (7.7) | | |
| **2b**[c] | 53.1 | 33.9 | 28 | | | | |
| **3** | 56.1 | 38.6 | 24 | – | 9.06 (8.1) | absent | absent |
| **4** | 54.9 | 37.4 | 24 | – | 8.85 (br) | absent | absent |
| **5** | 59.3 | 40 | 29 | n.d. | 9.24 (8.1) | 3168 (w) | 1624 (s) |
| **6** | 56.4 | 35.6 | 27 | 14.31 | 8.88 (br) | 3180 (w) | 1625 (s) |
| **7** | 57.9 | 38.3 | 24 | n.d. | 9.12 (7.2) | 3259 (w) | 1612 (m) |
| **8** | 55.5 | 37.7 | 28 | 10.53 | 7.69 (br) | 3267 (w) | 1630 (m) |
| **9** | 54.8 | 38.3 | 22 | – | 9.04 (8.1) | absent | absent |
| **10** | 50.4 | 30.8 | br. s | – | 8.87 (br) | absent | absent |
| **12** | 57.7 (s) | | | – | 9.18 (s) | absent | absent |
| **13** | 45.5 (s) | | | 11.24 | 9.15 (s) | 3294 (w) | 1674 (s) |
| **14** | 61 (s) | | | 10.34 | 8.53 (s) | 3156 (w) | 1594 (s) |
| **15** | 29.6 | | | 10.31 | 9.08 (s) | 3311 (w) | 1696 (s) |

[a] $CD_2Cl_2$. [b] KBr disks. [c] $[D_6]$dmso.

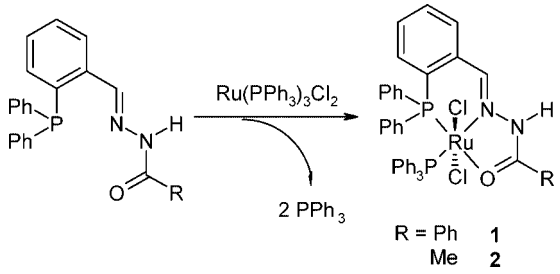


Scheme 3.

and the P atoms of the $PPh_3$ (as established by heteronuclear $^1H$-$^{31}P$ correlation), are indicative of a $PPh_3$ molecule *trans* to the HC=N function.[24] The chloride ligand and dmso occupy the apices of the octahedron. The stereoselectivity of the reaction is indicated by $^{31}P\{^1H\}$-NMR spectroscopy by two doublets centred at 63 and 39.1 ppm for **1a** and 65.3 and 40.8 ppm for **2a**. The more shielded signals are generated by the $PPh_3$ ligands, while the signals at lower fields are generated by the hydrazonic phosphorus nuclei.[24] The small $^2J_{PP}$ values of 32 and 31 Hz for **1a** and **2a**, respectively, are in agreement with a *cis* arrangement of the two P atoms. The isolation of the cationic complexes **1a** and **2a** is not possible because of their reactivity with dmso, as shown by NMR spectroscopy. In fact, on keeping the NMR sample of **1a** at room temperature overnight, two additional $^{31}P\{^1H\}$-NMR doublets appear, centred at $\delta$ = 49 and 32 ppm ($^2J_{PP}$ = 26.5 Hz). Moreover, two small singlets at $\delta$ = 53 and 27 ppm are also visible (see Supporting Information; see also the footnote on the first page of this article). When the tube is warmed at 50 °C for 6 hours, the new signals grow at the expenses of those belonging to the starting complex, and an additional pair of doublets centred at $\delta$ = 54 and 34 ppm ($^2J_{PP}$ = 30 Hz) appears. After 16 hours at 50 °C, the main signals are still those of **1a**, but the singlets at $\delta$ = 53 and 27 ppm have grown considerably while the other two pairs of doublets have diminished. Finally, after 48 hours the spectrum shows only the singlets at $\delta$ = 55 and 29 ppm. The low $^2J_{PP}$ values of the two transient pairs of doublets indicate the formation of two labile Ru complexes containing two mutually *cis* phosphanes, while the final singlets are ascribable to $OPPh_3$ (singlet at $\delta$ = 29 ppm[25]) and to the bis-chelate complex $[Ru(bidf)_2]$ (**12**, singlet at $\delta$ = 55 ppm). The presence of **12** is confirmed by ESI-MS analysis of the warm dmso solution by a cluster at $m/z$ = 917. Complex **12** can be prepared by reaction between $[Ru(PPh_3)_3Cl_2]$ or $[Ru(dmso)_4Cl_2]$ with a twofold excess of Hbidf (vide infra) in the presence of a base. Its $^{31}P\{^1H\}$-NMR spectrum shows a singlet at $\delta$ = 57.7 ppm, which is in good agreement with the value observed for the in situ formed complex. On the basis of the aforementioned observations we propose that the **1** → **12** transformation occurs in agreement with Scheme 4.

Although the detection of $(CH_3)_2S$ is made difficult by its volatility, a singlet at $\delta$ = 2.08 ppm is observed during $^1H$ NMR monitoring of the reaction. The same technique has allowed the detection of $[Ru(dmso)_4Cl_2]$: by repeating the **1** → **12** transformation in dmso, after the complete removal of the solvent, the $^1H$ NMR spectrum of the solid residue recorded in $CDCl_3$ shows, apart from the signals ascribable to **12**, singlets in the region 3.47–2.25 ppm, indicative of the presence of a mixture of *trans*- and *cis*-$[Ru(dmso)_4Cl_2]$.[26] The **1** → **12** transformation must necessarily occur through the transfer of a PNO ligand from a Ru nucleus to another one. Thus, the changes observed in the $^{31}P\{^1H\}$-NMR spectrum of **1a** in dmso may be tentatively explained as follows (Scheme 4): dmso reacts with **1a** causing the displacement of the C=O group of the ligand giving rise to $[Ru(\kappa^2\text{-}(H)PN)(PPh_3)(dmso)_2Cl]Cl$ (**1b**). Complex **1b** gives rise to the pair of doublets at $\delta$ = 49 and 32 ppm, where the more shielded signal is due to $PPh_3$ while the other is due to the $PPh_2$ moiety. The chemical shift of 49 ppm is similar to that found for **13** ($\delta$ =45.5 ppm, vide

 © 2006 Wiley-VCH Verlag GmbH & Co. KGaA, Weinheim 

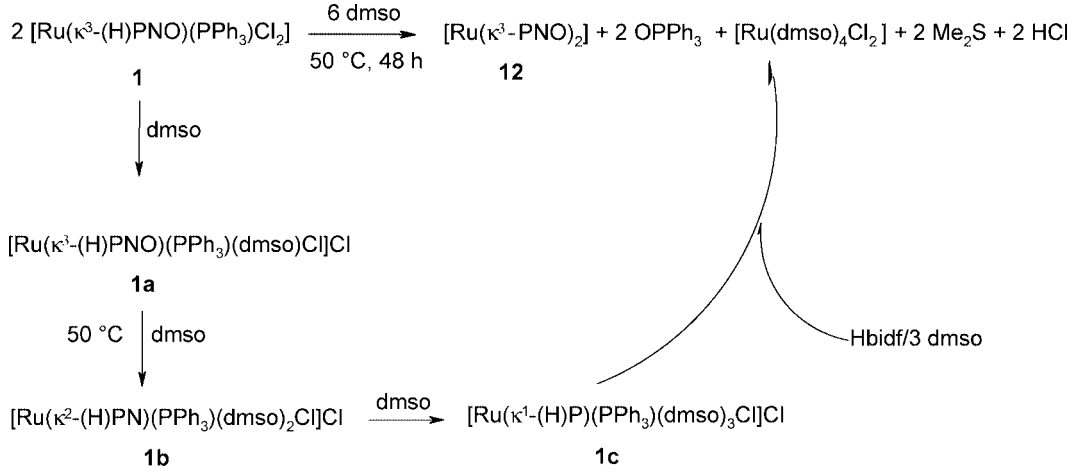


Scheme 4.

infra), where Hbidf coordinates in a (H)PN bidentate fashion. The simple isomerisation of **1b** due, for example, to the shift of $PPh_3$ from the plane to an apex of the octahedron is ruled out by the $^1H$ NMR monitoring of the process: the HC=N function of **1b** gives rise to a doublet centred at $\delta$ = 9.14 ppm with a $^4J_{PH}$ of 8.02 Hz, indicative of a $PPh_3$ *trans* to the imine function. The reaction continues with the decoordination of the imine nitrogen from ruthenium which is replaced by an additional molecule of dmso (probably favoured by the *trans* effect of $PPh_3$), with formation of complex **1c** in which the neutral ligand coordinates in an unidentate fashion through the P atom, giving rise to the pair of doublets at $\delta$ = 54 and 34 ppm. Although one would expect a decrease of the chemical shift on passing from **1b** to **1c** due to the loss of the chelation ring,[27] a chemical shift around 50 ppm is not unusual for Ru complexes containing coordinated monophosphanes and dmso.[28] Moreover, the ability of Hbidf to coordinate Ru in a P-monodentate mode is confirmed by the complex [($\eta^6$-*p*-cymene)-Ru($\kappa^1$-(H)P)$Cl_2$]·3/2 $CHCl_3$ (**15**, vide infra) obtained by the reaction of Hbidf with [Ru(*p*-cymene)$Cl_2$]$_2$. Finally, **1c** further transforms, through a not yet defined pathway, into [Ru(dmso)$_4Cl_2$], $OPPh_3$, $(CH_3)_2S$, HCl and **12**. $PPh_3$ oxidation then occurs through the dmso reduction to dimethyl sulfide. The metal ion-mediated deoxygenation of coordinated sulfoxides has been observed with different metals.[29] The most intensively studied systems are based on oxorhenium[30] and oxomolybdenum compounds,[25,31] the last also being good models of the enzymes belonging to the dmso reductase class.[32] To the best of our knowledge, the only article dealing with the deoxygenation of dmso promoted by ruthenium has been reported by James, describing the reaction of $RuCl_3$·3 $H_2O$ with dmso at high temperatures in the presence of HCl or HBr;[33] in those cases however, although dimethyl sulfide complexes were isolated, the nature of the reductants remained unknown. Interestingly, the oxygen transfer from dmso to $PPh_3$ promoted by **1** can be made catalytic by dissolving the complex in dmso and heating the solution at 100 °C in the presence of a 100-fold excess of $PPh_3$; the reaction is complete within 20 hours as indicated by $^{31}P\{^1H\}$-NMR spectroscopy (disappearance of the $PPh_3$ signal at –7.5 ppm in favour of the $OPPh_3$ signal at $\delta$ = 26.8 ppm). A similar behaviour is conjecturable also for complex **2**, although its reactivity in dmso has not been investigated in details. It is worth noting that this step-by-step ligand decoordination probably corresponds to the reversed way the ligand approaches the metal, a process not always easy to envision with polydentate ligands. The key-role played by dmso in the **1** → **12** transformation is evidenced by the different reactivity shown by **1** in acetonitrile at 50 °C. After 4 hours an almost clear solution has been obtained and the work-up has led to the cationic monochelate complex [Ru($\kappa^3$-(H)PNO)($PPh_3$)($CH_3CN$)Cl]Cl (**11**). The neutral character of the ligand is clearly pointed out by the IR and $^1H$ NMR spectra with a weak band at 3173 $cm^{-1}$ and a singlet at $\delta$ = 10.48 ppm, respectively. The coordinated acetonitrile gives rise to a weak IR band at 2273 $cm^{-1}$ and a singlet at $\delta$ = 1.31 ppm in the $^1H$ NMR spectrum. Complex **11** decomposes within 24 hours in solution and within 24–48 hours in the solid state, without evidencing the formation of **12**.

Treatment of a toluene suspension of **1** or **2** with an excess of triethylamine in the presence of acetonitrile, leads to the isolation of the neutral monochloride complexes [Ru($\kappa^3$-PNO)($PPh_3$)($CH_3CN$)Cl] (**3** and **4** in Scheme 5) as yellow solids in good yields. The reactions occur with the substitution of a chloride ligand (precipitated as $Et_3NHCl$) with an acetonitrile molecule.

The anionic character of the ligand is indicated by the disappearance of the spectroscopic signals of the N–H and C=O bonds.[5] The coupling constants between the P nuclei are again small (24 Hz) to indicate a *cis* arrangement of the $PPh_3$ and $PPh_2$ moieties, while the iminic protons give rise to doublets with appreciable $^4J_{PH}$ values indicative of a HC=N group *trans* to a $PPh_3$[24] (Table 1). The coordinated acetonitrile gives a singlet at $\delta$ = 1.21 ppm in both complexes. The FAB-MS spectrum of **3** shows a cluster centred at *m*/*z* = 806 corresponding to the [Ru($\kappa^3$-PNO)($PPh_3$)Cl]$^+$ fragment, while in the FAB-MS spectrum of **4** the molecular peak is visible at *m*/*z* = 786. By slow evaporation of a

 © 2006 Wiley-VCH Verlag GmbH & Co. KGaA, Weinheim 

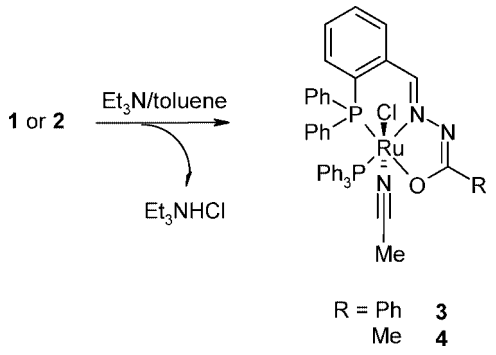


Scheme 5.

dichloromethane/acetonitrile mixture of **4**, crystals suitable for X-ray diffraction have been collected, and the structure of the complex has been unequivocally confirmed. Compound **4** crystallises with the inclusion of two water molecules in the asymmetric unit, which take part in the packing interactions. In **4** the Ru atom is hexacoordinate by the tridentate deprotonated PNO (aidf$^-$) ligand, one triphenylphosphane, *trans* to the N donor, one chloride and one acetonitrile molecule, *trans* each other, in an irregular octahedral geometry. The molecular structure is shown in Figure 1, along with the labelling scheme, while the most relevant geometric features are collected in Table 2.

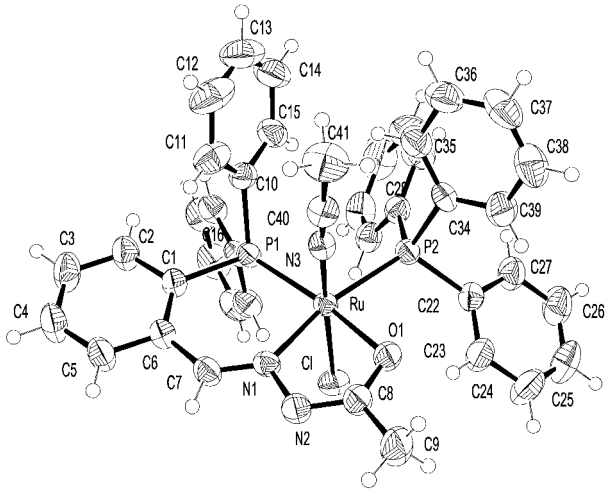


Figure 1. Perspective view and labelling scheme of compound **4**. Rings C16–C21 and C28–C33 are labelled only on the *ipso* carbon for clarity. Thermal ellipsoids at the 50% level.

The tridentate PNO coordination of aidf$^-$ gives rise to two chelation rings, which are both planar within 0.06 Å. The planarity of the six-membered chelation ring containing P1 contrasts with the behaviour generally observed in the family of the similar Pd(aidf) and Pd(bidf) complexes,[3,5c] where the chelation ring is puckered and the phosphorus donor is remarkably out of the average ring plane (values ranging between 0.38 and 0.52 Å). In fact, in the Pd series the Pd–P distances range from 2.184 to 2.212 Å, while in **4** the Ru–P bond is significantly longer [2.2951(3) Å], and can accommodate for ring planarity. By contrast, even if the Ru–O bond [2.1177(5) Å] is longer than the Pd–O bond (2.065 Å) in the [Pd(aidf)(OAc)] analogue,[3] the ligand bond lengths along the five-membered chelation ring are very close to those observed in the palladium complex, from which they do not deviate by more than 0.013 Å. The molecular association in the crystal is based on dimeric aggregates composed by two complexes related by a crystallographic twofold axis, linked by two water molecules which act as hydrogen-bond donors towards chloride and nitrogen as shown in Figure 2 [O2···N2: 2.883(2) Å, O2–H···N2: 149.7(6)°; O2···Cl(i): 2.232(1) Å, O2–H···Cl(i): 152.6(4)°, i: $y, x, 1-z$]. This pattern is conserved in the related structure of **6**.

The dichloride complexes **1** and **2** suspended in a dichloromethane/acetonitrile mixture react with an excess of $KPF_6$ or $NaBPh_4$ leading to the cationic monochloride complexes [Ru($\kappa^3$-(H)PNO)($PPh_3$)($CH_3CN$)Cl][X] [HPNO = Hbidf, X = $PF_6$ (**5**), X = $BPh_4$ (**7**); HPNO = Haidf, X = $PF_6$ (**6**), X = $BPh_4$ (**8**)] and precipitation of KCl or NaCl, respectively (Scheme 6).

As can be inferred from Table 1, the spectroscopic characterisation indicates that the ligands have not varied their coordinating behaviour with respect to the dichloride precursors, and that the $PPh_3$ ligands are still *trans* to the HC=N moieties [the $^{31}P\{^1H\}$-NMR signals range from 55.5 to 59.3 ppm for the $PPh_2$ moiety, and from 35.6 to 40.0 ppm for the $PPh_3$ ligand, with $^2J_{PP}$ values ranging from 24.6 to 29 Hz; the $^4J_{PH}$ values range from 7.2 to 8.1 Hz]. The apices of the octahedron are occupied by the residual chloride and by an acetonitrile molecule, whose presence is confirmed by IR (stretching band in the region 2265–2281 cm$^{-1}$) and $^1H$ NMR spectroscopy (singlets ranging from 0.43 to 1.70 ppm). The [$PF_6$]$^-$ anions originate, in the $^{31}P\{^1H\}$-NMR spectra, multiplets centred at –141.1 and –145.5 ppm, for **5** and **6**, respectively, while in the IR spectra they give rise to an intense band at 845 cm$^{-1}$. The presence of the [$BPh_4$]$^-$ anion in **7** and **8** is pointed out by IR bands at about 850 cm$^{-1}$. The structure of **6** has been unequivocally established by X-ray diffraction analysis conducted on a single crystal grown in a $CH_2Cl_2$/*n*-pentane mixture. In compound **6**, the [Ru(Haidf)]$^+$ cation (Figure 3) is arranged identically to the related deprotonated neutral complex **4**.

The comparison between the two molecules (Figure 4, Table 2) may help to investigate the effect of protonation on [Ru(aidf)($PPh_3$)($CH_3CN$)Cl]. The protonation of the hydrazonic nitrogen N2 seems to localize a larger double-bond character on the carbonylic bond, which shortens by 0.055 Å, while at the same time the adjacent C(O)–N bond elongates by 0.016 Å. Moreover, in the cationic complex **6** the Ru–O bond is longer than in **4** by 0.028 Å, while Ru–P bond is slightly shorter (0.017 Å). The shortening of the Ru–P bond is accompanied by a slight distortion from planarity of the six-membered chelation ring, as P1 deviates by 0.14 Å from the ring plane. The [Ru(Haidf)]$^+$ cations are assembled in dimeric units (Figure 5) by N–H···Cl hydrogen bonds [N2···Cl(ii): 3.300(6) Å, N2–H···Cl(ii): 149(7)°,

 © 2006 Wiley-VCH Verlag GmbH & Co. KGaA, Weinheim 

Table 2. Bond lengths [Å] and angles [°] for compounds **4**, **6**, **12**·dmso·$H_2O$, **15**·1.5$CHCl_3$, with standard uncertainties in parentheses. In **15**·1.5$CHCl_3$ $C_T$ denotes the centroid of the *p*-cymene ring.

| | | | | | |
|---|---|---|---|---|---|
| Compound **4** | | | | | |
| Ru–N(3) | 1.995(2) | P(1)–C(1) | 1.845(2) | N(1)–Ru–P(2) | 166.42(4) |
| Ru–N(1) | 2.075(1) | C(1)–C(6) | 1.405(3) | O(1)–Ru–P(2) | 89.30(4) |
| Ru–O(1) | 2.118(1) | C(6)–C(7) | 1.457(3) | P(1)–Ru–P(2) | 100.60(2) |
| Ru–P(1) | 2.2950(5) | N(3)–Ru–N(1) | 89.26(6) | N(3)–Ru–Cl | 171.58(5) |
| Ru–P(2) | 2.3688(5) | N(3)–Ru–O(1) | 84.94(6) | N(1)–Ru–Cl | 85.66(4) |
| Ru–Cl | 2.4222(5) | N(1)–Ru–O(1) | 77.13(5) | O(1)–Ru–Cl | 87.368(4) |
| N(1)–C(7) | 1.290(2) | N(3)–Ru–P(1) | 90.07(5) | P(1)–Ru–Cl | 96.89(2) |
| N(1)–N(2) | 1.406(2) | N(1)–Ru–P(1) | 92.97(4) | P(2)–Ru–Cl | 93.25(2) |
| N(2)–C(8) | 1.310(3) | O(1)–Ru–P(1) | 168.94(4) | | |
| O(1)–C(8) | 1.295(2) | N(3)–Ru–P(2) | 90.10(5) | | |
| Compound **6** | | | | | |
| Ru–N(3) | 2.001(6) | P(1)–C(1) | 1.845(6) | N(1)–Ru–P(2) | 165.2(1) |
| Ru–N(1) | 2.073(5) | C(1)–C(6) | 1.410(9) | O(1)–Ru–P(2) | 87.8(1) |
| Ru–O(1) | 2.147(4) | C(6)–C(7) | 1.44(1) | P(1)–Ru–P(2) | 103.48(6) |
| Ru–P(1) | 2.278(2) | N(3)–Ru–N(1) | 87.0(2) | N(3)–Ru–Cl | 172.2(2) |
| Ru–P(2) | 2.385(2) | N(3)–Ru–O(1) | 84.9(2) | N(1)–Ru–Cl | 86.7(1) |
| Ru–Cl | 2.398(2) | N(1)–Ru–O(1) | 77.6(2) | O(1)–Ru–Cl | 89.2(1) |
| N(1)–C(7) | 1.277(8) | N(3)–Ru–P(1) | 89.0(2) | P(1)–Ru–Cl | 95.72(6) |
| N(1)–N(2) | 1.411(7) | N(1)–Ru–P(1) | 91.3(1) | P(2)–Ru–Cl | 90.47(6) |
| N(2)–C(8) | 1.325(8) | O(1)–Ru–P(1) | 167.6(1) | | |
| O(1)–C(8) | 1.241(7) | N(3)–Ru–P(2) | 94.4(2) | | |
| Compound **12**·dmso·$H_2O$ | | | | | |
| Ru–N(3) | 2.030(3) | N(2)–C(8) | 1.316(4) | N(1)–Ru–O(2) | 95.6(1) |
| Ru–N(1) | 2.034(3) | N(3)–C(33) | 1.288(4) | O(1)–Ru–O(2) | 80.65(9) |
| Ru–O(1) | 2.109(2) | N(3)–N(4) | 1.419(4) | N(3)–Ru–P(1) | 94.58(8) |
| Ru–O(2) | 2.120(2) | N(4)–C(34) | 1.310(4) | N(1)–Ru–P(1) | 90.67(8) |
| Ru–P(1) | 2.2503(9) | C(1)–C(6) | 1.411(4) | O(1)–Ru–P(1) | 166.22(7) |
| Ru–P(2) | 2.2553(9) | C(6)–C(7) | 1.463(5) | O(2)–Ru–P(1) | 93.35(7) |
| P(1)–C(1) | 1.829(3) | C(27)-C(32) | 1.425(4) | N(3)–Ru–P(2) | 90.79(8) |
| P(2)–C(27) | 1.826(3) | C(32)–C(33) | 1.458(5) | N(1)–Ru–P(2) | 94.90(8) |
| O(1)–C(8) | 1.288(4) | N(3)–Ru–N(1) | 171.9(1) | O(1)–Ru–P(1) | 93.28(7) |
| O(2)–C(34) | 1.292(4) | N(3)–Ru–O(1) | 96.3(1) | O(2)–Ru–P(2) | 166.49(7) |
| N(1)–C(7) | 1.292(4) | N(1)–Ru- = (1) | 77.7(1) | P(1)–Ru–P(2) | 90.05(3) |
| N(1)–N(2) | 1.409(3) | N(3)–Ru–O(2) | 78.0(1) | | |
| Compound **15**·1.5$CHCl_3$ | | | | | |
| Ru–$C_T$ | 1.698(1) | P–C(21) | 1.857(9) | $C_T$–Ru–P | 132.3(1) |
| Ru–C(31) | 2.27(2) | N(1)–C(7) | 1.231(16) | $C_T$–Ru–Cl(2) | 125.6(1) |
| Ru–C(28) | 2.28(2) | N(1)–N(2) | 1.39(2) | P–Ru–Cl(2) | 85.0(2) |
| Ru–P | 2.374(5) | N(2)–C(8) | 1.31(3) | $C_T$–Ru–Cl(1) | 124.3(1) |
| Ru–Cl(2) | 2.380(4) | O–C(8) | 1.26(3) | P–Ru–Cl(1) | 89.1(2) |
| Ru–Cl(1) | 2.422(5) | C(1)–C(6) | 1.35(2) | Cl(2)–Ru–Cl(1) | 86.0(1) |
| P–C(1) | 1.81(2) | C(6)–C(7) | 1.47(2) | | |

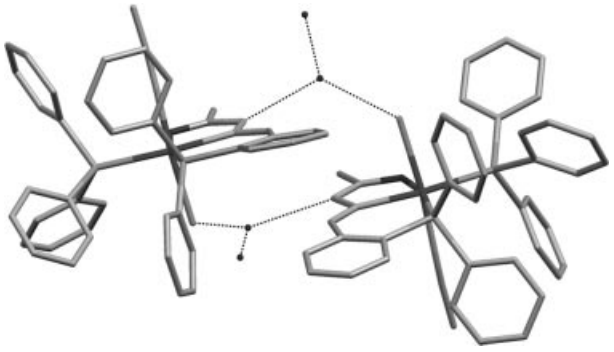

Figure 2. Association in dimers bridged by hydrogen-bonded water molecules in the crystal structure of **4**.

ii: $1-x$, $-y$, $1-z$]; this arrangement recalls the one observed in **4**, where the insertion of a water molecule provides the bridging element, here constituted by the protonated –NH. In the case of **6** the dimer is centrosymmetric.

Repeated attempts aimed at obtaining the dicationic complexes of the type [Ru($\kappa^3$-(H)PNO)($PPh_3$)($CH_3CN)_2$]-[$X_2$] by removal of the second chloride from the complexes **5**–**8** using several halogen scavengers such as $KPF_6$, $NaBPh_4$, $AgCF_3SO_3$ and $TlPF_6$, have failed due to extensive decompositions or isolation of unknown products, irrespective of the amount of scavenger employed.

However, bis-acetonitrile Ru complexes have been obtained by treatment of the cationic mono-chloride complexes **6** and **7** with an excess of $Et_3N$ in the presence of

 © 2006 Wiley-VCH Verlag GmbH & Co. KGaA, Weinheim 

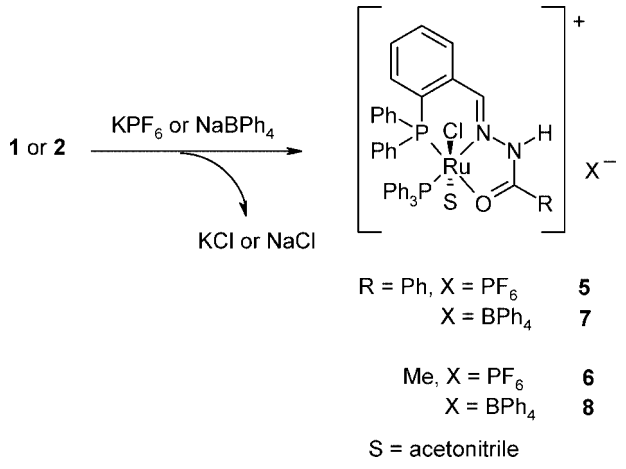


Scheme 6.

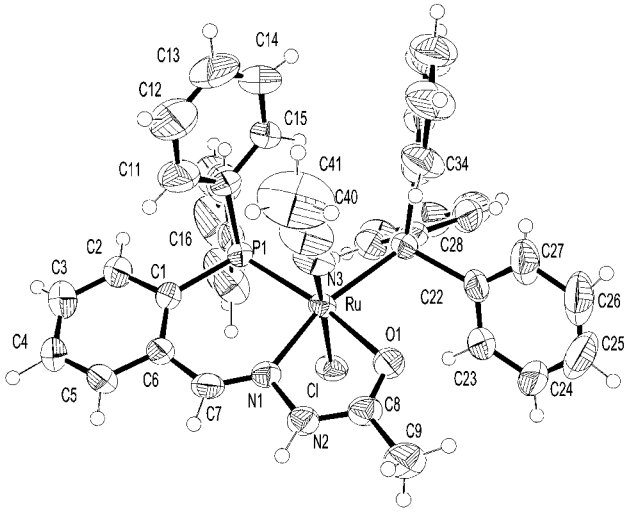


Figure 3. Perspective view and labelling scheme of compound **6**. Rings C16–C21, C28–C33 and C34–C39 are labelled only on the *ipso* carbon for clarity. Thermal ellipsoids at the 50% level. The $PF_6^-$ anion has been omitted.

Figure 4. Superimposition of the molecular structure of **4** ($aidf^-$, grey) and **6** (Haidf, black) showing the geometric effects due to protonation of the PNO ligand.

acetonitrile. This procedure leads to the neutral complexes *trans*-[Ru($\kappa^3$-PNO)($PPh_3$)($CH_3CN$)$_2$][X] [PNO = bidf, X = $BPh_4$ (**9**); PNO = aidf, X = $PF_6$ (**10**)] in good yields (Scheme 7).

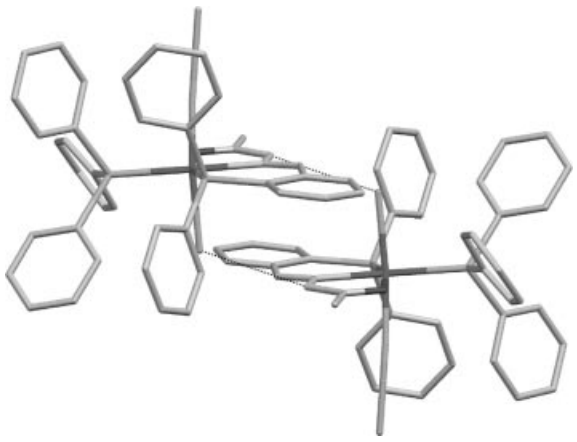

Figure 5. Association in hydrogen-bonded dimers in the crystal structure of **6**.

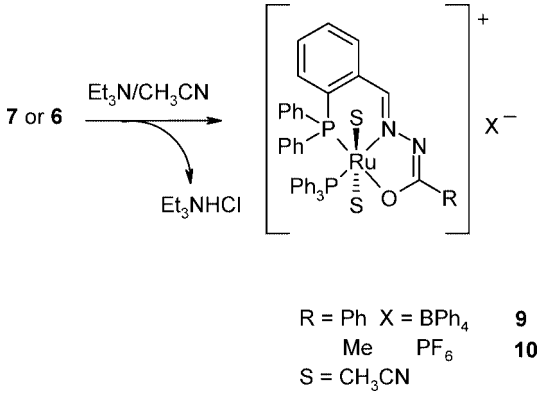


Scheme 7.

The disappearance of the spectroscopic signals of the N–H and C=O bonds agrees with the anionic character of the ligand, while the NMR spectroscopic data similar to those of the precursors indicate that $PPh_3$ has not moved from its *trans* disposition with respect to the imine moiety (Table 1). The entering of the second molecule of acetonitrile is indicated by $^1$H NMR spectroscopy with the appearance of an additional singlet at $\delta$ = 2.37 and 2.34 ppm for **9** and **10**, respectively. These complexes are significantly unstable both in solution and in the solid state.

### Ru Complexes Obtained from [Ru(dmso)$_4$Cl$_2$]

In order to understand the nature of the Ru species involved in the **1** → **12** transformation observed in dmso, the ligand Hbidf has been reacted with [Ru(dmso)$_4$Cl$_2$]. In refluxing EtOH/NaOH [Ru(dmso)$_4$Cl$_2$] reacts with a twofold excess of Hbidf leading to the formation of the bis-chelate octahedral complex [Ru(bidf)$_2$] (**12**) in good yield (Scheme 8). In complex **12** two deprotonated ligands coordinate Ru in a PNO fashion.

The disappearance of the spectroscopic signals of the N–H and C=O bonds is indicative of the deprotonation that occurred in both ligands, while the presence of a singlet at $\delta$ = 57.7 ppm in the $^{31}$P{$^1$H}-NMR spectrum is in agree-

 © 2006 Wiley-VCH Verlag GmbH & Co. KGaA, Weinheim 

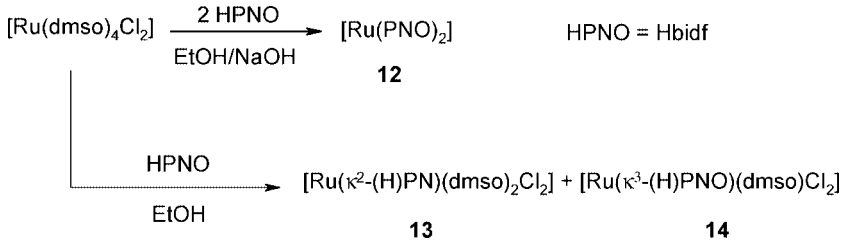


Scheme 8.

ment with two magnetically equivalent phosphorus nuclei. The HC=N proton resonates as a singlet at $\delta$ = 9.18 ppm in the $^1$H NMR spectrum recorded in $CDCl_3$, as expected in the absence of a $PPh_3$ ligand. The CI-MS spectrum exhibits a cluster centred at *m/z* = 916 (molecular peak). The structure of **12** has been unequivocally established by X-ray diffraction analysis on a single crystal obtained from a dmso solution of **13** (vide infra) and is shown in Figure 6. Compound **12** crystallises as a 1:1:1 dmso/$H_2O$ solvate. The principal geometric features are reported in Table 2. The most relevant feature in the geometry of [Ru(bidf)$_2$] is that the steric hindrance due to the bis-chelation produces significant distortions in the planarity of the two coordinated [PNO] ligands. In fact in both ligands the P atom deviates remarkably from the chelation plane (0.64 and 0.59 Å, respectively), and the Ru–P distances are significantly shorter [Ru–P1: 2.2503(9), Ru–P2: 2.2553(9) Å] than in the previous mono-chelated complexes (Table 2). By contrast, the five-membered chelation rings are planar within 0.09 Å, and the bond lengths along the ring are in agreement with those observed in the neutral mono-chelate **4**. The mutual arrangement of the two ligands in **12**·dmso·$H_2O$ favours a remarkable intramolecular π–π stacking between the rings belonging to the ligands main backbone and the diphenylphosphane rings, with C···C separation ranging between 3.3 and 3.9 Å.

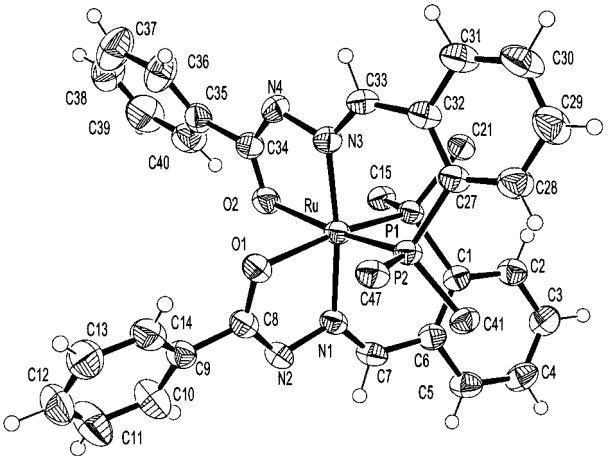


Figure 6. Perspective view and labelling scheme of compound **12**·dmso·$H_2O$. Rings C15–C20, C21–C26, C41–C46 and C47–C52 are represented only by the *ipso* carbon for clarity. Thermal ellipsoids at the 50% level.

The reaction between Hbidf and [Ru(dmso)$_4$Cl$_2$] has been repeated without a base. When the reaction is carried out at room temperature with a Ru/Hbidf = 1:1 molar ratio, a complex mixture of different products forms, whose separation and identification has not been possible so far. A clearer picture is instead obtained when the reaction is performed in refluxing ethanol. Two different Ru$^{II}$ complexes, [Ru(κ$^2$-(H)PN)(dmso)$_2$Cl$_2$] (**13**) and [Ru(κ$^3$-(H)PNO)-(dmso)Cl$_2$] (**14**) form as shown in Scheme 8. In complex **13** the neutral ligand coordinates the metal in a PN bidentate fashion, as evidenced by IR [ν(N–H) = 3249 cm$^{-1}$, ν(C=O) = 1674 cm$^{-1}$] and $^1$HNMR (singlet at $\delta$ = 11.24 ppm) spectroscopy.[4] Two chlorides and two dmso molecules complete the octahedron, as evidenced by the IR [two strong bands at 1088 and 1019 cm$^{-1}$ due to the ν(S=O) and δ(C–H), respectively] and $^1$H NMR (four singlets in the region 3.65–2.84 ppm) spectra as well as by microanalysis. The $^{31}$P{$^1$H}-NMR spectrum shows a singlet at $\delta$ = 45.5 ppm. From a dmso solution of **13** crystals suitable for X-ray analysis have been collected. The diffractometric analysis shows the formation of the bis-chelate complex **12**; this further mono-chelate → bis-chelate transformation is not surprising, because compound **13** is structurally similar to **1b**, a proposed intermediate in the dmso-promoted **1** → **12** transformation.

In complex **14** the neutral ligand coordinates in a PNO fashion as clearly indicated by the IR bands of the N–H (3156 cm$^{-1}$) and C=O (1594 cm$^{-1}$) groups. The hydrazonic proton gives rise to a singlet at $\delta$ = 10.34 ppm in the $^1$H NMR spectrum recorded in $CDCl_3$, while the $^{31}$P{$^1$H}-NMR spectrum shows a singlet at $\delta$ = 61 ppm. The octahedron is completed by two chlorides and a dmso molecule, while a half dmso molecule is outside of the coordination sphere [the $^1$H NMR spectrum recorded in $CDCl_3$ shows four singlets in the region 3.48–2.48 ppm, while the IR spectrum shows strong bands at 1095 and 1023 cm$^{-1}$, attributable to the ν(S=O) and δ(C–H) of the dmso, respectively]. Owing to the lack of structural information, a detailed stereochemical description of the complexes **13** and **14** is not possible at present.

### Ru Complex Obtained from [Ru(*p*-cymene)Cl$_2$]$_2$

[Ru(*p*-cymene)Cl$_2$]$_2$ reacts with Hbidf in chloroform at room temperature, leading to the isolation of [(η$^6$-*p*-cymene)Ru(κ$^1$-(H)P)Cl$_2$]·3/2 $CHCl_3$ (**15**), where the ligand uses only the P atom to bind to ruthenium. The pseudo-octahedral coordination is completed by a η$^6$-coordinated *p*-cymene molecule and by two chloride ligands. The IR

 © 2006 Wiley-VCH Verlag GmbH & Co. KGaA, Weinheim 

spectrum shows the presence of the N–H and of the C=O groups with two bands at 3311 and 1696 $cm^{-1}$, respectively. The neutral character of the ligand is further substantiated by $^1H$ NMR spectroscopy with a singlet at $\delta$ = 10.31 ppm; the HC=N proton corresponds to a singlet at $\delta$ = 9.08 ppm, while the *p*-cymene protons resonate at the expected chemical shifts (in the range 5.47–5.33 ppm). The $^{31}P\{^1H\}$-NMR spectrum recorded in $CDCl_3$ shows a singlet at $\delta$ = 29.6 ppm. The structure of **15** has been unambiguously elucidated by X-ray diffraction analysis conducted on a crystal collected from a chloroform/diethyl ether mixture which was cooled to –20 °C. The molecular structure is reported in Figure 7, and the most important geometric parameters are listed in Table 2. The neutral Hbidf ligand is coordinated to the Ru atom only by the P donor [Ru–P bond 2.376(5) Å], while the remaining potential N and O donors point away from the metal. The NH is instead on the same side as the P atom, in the opposite conformation with respect to the one observed in the tridentate complexes. The Ru centre completes its pseudo-octahedral coordination by two chloride atoms and the $\eta^6$-*p*-cymene. The conformation of the neutral ligand allows for a favourable contact between the NH and the CH group and one of the coordinated Cl [(N2)H···Cl1: 2.910(5), (C7)H···Cl1: 2.655(5) Å], thus strongly differentiating the intramolecular environment of the two chloride atoms.

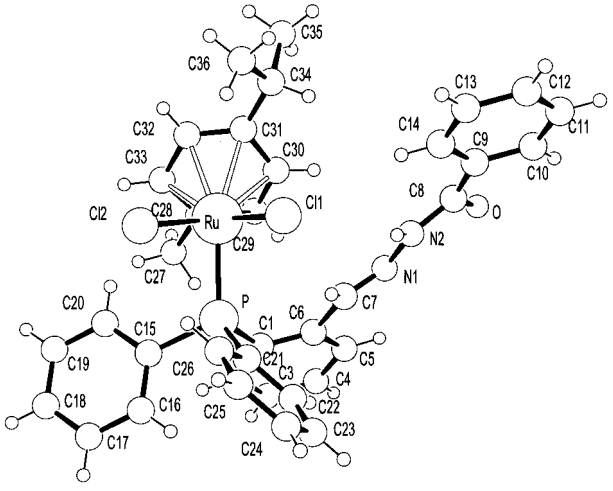


Figure 7. Perspective view and labelling scheme of the ball-and-stick structure of **15**·1.5$CHCl_3$. $\eta^6$-Coordination of the *p*-cymene ligand is represented by empty sticks.

### Addition of Benzoic Acid to Terminal Alkynes

The Ru-catalysed coupling of alkynes with carboxylic acids (Scheme 2) is an elegant way to obtain enol esters, which are starting materials for several important chemical transformations.[7–13] One of the major goals of this catalysis is the development of stereo- and regio-selective processes leading exclusively to one of the three possible enol ester isomers (Scheme 2), thus the preparation of selective catalysts is certainly desirable. Literature data show that the Markovnikov products are those usually produced using several Ru-catalysts containing monodentate ligands.[15,16a,b,19] However, high selectivity towards (*Z*)-alk-1-en-1-yl benzoate (*anti*-Markovnikov product) has been achieved in the coupling of phenylacetylene with 1-hexyne using allyl–$Ru^{II}$ complexes containing chelating diphosphanes such as dppp or dppb.[16d] The same type of selectivity has been achieved by adding coordinating bases, such as pyridines, to *half-sandwich* $Ru^{II}$ complexes containing monodentate phosphanes,[18] or adding monophosphanes to N-hetherocyclic carbene complexes.[17d] As we wanted to test whether the chelation of the acyl hydrazones could determine a good selectivity towards (*Z*)-alk-1-en-1-yl benzoate, we have tested the complexes **1**–**4**, **6**, **7**, **9** and **10** as pre-catalysts in the addition of benzoic acid to phenylacetylene. To the best of our knowledge, this is the first report dealing with Ru complexes containing tridentate ligands employed as pre-catalysts in such a catalytic transformation. The experimental conditions have been kept constant for every catalytic run: toluene as solvent (for concentrations of about $10^{-3}$ M all the complexes are perfectly soluble), $Na_2CO_3$ as base (Ru/base molar ratio = 1:5), $T$ = 120 °C and 1% of catalyst loading. The yields of the reactions (referred to the isolated enol esters) have been checked after 16 hours. The catalytic results are collected in Table 3.

As can be deduced from Entries 1 and 2, the dichloride complexes **1** and **2** are completely inactive in the coupling between 1-hexyne and benzoic acid. This is not unexpected, as it can be imputed to the strongly bound chloride ligands.[8,16a,b,19,34] The substitution of a chloride with a more labile acetonitrile molecule, like in the case of the mono-chloride complexes **3** and **4**, leads to a moderate catalytic activity with 35% and 49% yields (Entries 3 and 4), respectively. However, high stereo- and regio-selectivity in favour of (*Z*)-alk-1-en-1-yl benzoate have been reached in both cases (94% an 99%, respectively). The amount of the Markovnikov product remains very low and no traces of (*E*)-alk-1-en-1-yl benzoate have been detected. The cationic complexes **6** and **7** (Entries 5 and 6) lead to similar yields, but again accompanied by excellent selectivities towards the *Z*-*anti*-Markovnikov product. Finally, the cationic complexes **9** and **10** show catalytic activities comparable to those of the mono-chloride complexes, with a slightly diminished selectivity (10% of the Markovnikov product has been obtained in both cases, Entries 7 and 8). Under the experimental conditions applied, with the only exception of the dichlorides **1** and **2**, the tested Ru complexes result more active than $[Ru(PPh_3)_3Cl_2]$ (Entry 13) which, moreover, leads exclusively to the Markovnikov product. From an inspection of Entries 1–8 of Table 3, it can be inferred that the removal of a chloride ligand is necessary to have catalytic activity accompanied by a good selectivity (compare Entries 1 and 2 with Entries 3 and 4), while the removal of the second chloride ligands does not bring to any improvement of the final yield, but instead provokes a slight decrease in selectivity (compare Entries 3–6 with Entries 7 and 8). The importance of having a vacant coordination site is confirmed by the inertness of the complexes observed in coordinating solvents such as dmso, dmf and acetonitrile;

 © 2006 Wiley-VCH Verlag GmbH & Co. KGaA, Weinheim 

Table 3. Catalytic results for the addition of benzoic acid to terminal alkynes.[a]

| Entry | Ru complex | Alkyne | Yield [%][b] | *Z-anti*-M [%][c] | M [%][c] |
|---|---|---|---|---|---|
| 1 | **1** | 1-hexyne | – | | |
| 2 | **2** | 1-hexyne | – | | |
| 3 | **3** | 1-hexyne | 35 | 94 | 6 |
| 4 | **4** | 1-hexyne | 49 | 99 | 1 |
| 5 | **6** | 1-hexyne | 44 | 100 | – |
| 6 | **7** | 1-hexyne | 53 | 95 | 5 |
| 7 | **9** | 1-hexyne | 56 | 90 | 10 |
| 8 | **10** | 1-hexyne | 49 | 90 | 10 |
| 9 | **7** | phenylacetylene | 36 | 81 | 19 |
| 10 | **7** | *p*-tolylacetylene | 33 | 98 | 2 |
| 11 | **7** | *tert*-butylacetylene | 25 | 86 | 14 |
| 12 | **7** | 1-octyne | 56 | 94 | 6 |
| 13 | $[Ru(PPh_3)_3Cl_2]$ | 1-hexyne | 19 | – | 100 |

[a] Conditions: solvent = toluene; $T$ = 120 °C; Ru/benzoic acid/alkyne/$Na_2CO_3$ = 1:100:100:5. [b] Referred to the isolated product. [c] Determined by $^1H$ NMR spectroscopy.

no traces of enol esters have been detected even after 24 hours of reaction. From the lengthening of the Ru–O bond observed in the solid structure of **6** with respect to the same bond length found in **4**, one could expect a higher catalytic activity for the complexes containing protonated ligands, such as **6** and **7**, on the basis of a hemilabile behaviour of the acyl hydrazones, from a $\kappa^3$-(H)PNO coordination to a $\kappa^2$-(H)PN one. However, these pre-catalysts behave similarly to the complexes containing anionic ligands **3**, **4**, **9** and **10**, and this suggests that the acyl hydrazones remain tridentate throughout the catalytic cycle. An explanation of this levelling effect could certainly reside in the deprotonation of the ligand induced by the excess of $Na_2CO_3$ which forces the acyl hydrazones to an anionic PNO coordination in all cases.

The study of the catalytic behaviour of complex **7** has been extended to other terminal alkynes, such as 1-octyne, phenylacetylene, *p*-tolylacetylene and *tert*-butylacetylene.

Whereas with 1-octyne the catalytic performance is similar to the one observed with 1-hexyne (56% conversion with 94% of *Z-anti*-Markovnikov product and 6% of Markovnikov product, Entry 12), conversions not higher than 36% and lower selectivities have been obtained with the aryl alkynes, (Entries 9 and 10) and with the bulkier *t*Bu-acetylene (Entry 11). Whilst with *t*Bu-acetylene the lower yield can be imputed to steric factors, more difficult is to explain the lower reactivity of the aryl alkynes. Noteworthy is the fact that traces of dimerisation products have been detected neither with phenylacetylene nor with *p*-tolylacetylene, as instead described with Ru–alkylidene complexes bearing N-heterocyclic carbene ligands.[17c] A possible explanation could reside in the bulkiness of the phenyl ring attached to the triple C–C bond of the alkyne which hampers the vinylidene formation (vide infra), but elucidation of this point needs further studies.

## ESI-MS Study

ESI-MS technique has been successfully employed in several metal-catalysed transformations like, for example, reduction of ketones,[20] epoxidations,[21] olefins polymerisation[22] and C–H bonds activation[23] for the detection of the metal-containing intermediates involved in the catalytic cycles. To the best of our knowledge, no report dealing with the use of such a technique for the study of the addition of carboxylic acids to alkynes has appeared in the literature. Mechanistic studies conducted on diphosphanes containing complexes,[15d] have evidenced the formation of a vinylidene intermediate as active catalyst, which undergoes an intermolecular attack of a carboxylate anion to generate the final enol ester. We have therefore undertaken an ESI-MS study aimed at detecting the key intermediates involved in the enol ester synthesis catalysed by our Ru–PNO complexes; complex **5** $[Ru(Hbidf)(PPh_3)(CH_3CN)Cl][PF_6]$ has been chosen as a model. Initially, we have collected the ESI(+) spectrum of a $10^{-3}$ M toluene solution of **5** at room temperature; this shows a predominant cluster centred at $m/z$ = 813 accounting for $[Ru(bidf)(PPh_3)(CH_3CN)]^+$, and minor clusters at $m/z$ = 849 and $m/z$ = 772 accounting for $[Ru(Hbidf)(PPh_3)(CH_3CN)Cl]^+$ and $[Ru(bidf)(PPh_3)]^+$, respectively. The solution has then been heated at 120 °C for 40 minutes and a new ESI(+) spectrum has been collected. This shows again the clusters centred at $m/z$ = 813 and 772, indicating that the complex is preserved under these conditions (Figure 8, a). A small cluster at $m/z$ = 917 shows the presence of **12**, although the isotope pattern points out the presence of a second unknown species with similar mass which tangles the signal up.

To a freshly prepared toluene solution of **5** heated at 120 °C benzoic acid and $Na_2CO_3$ have been added (Ru/acid/$Na_2CO_3$ = 1:5:5 molar ratio); the ESI(+) spectrum shows the disappearance of the signal at $m/z$ = 813 in favour of a cluster centred at $m/z$ = 894 corresponding to the fragment $[Ru(Hbidf)(PPh_3)(C_6H_5COO)]^+$, where a carboxylate anion is coordinated to Ru; the clusters at $m/z$ = 772 and 917 are still visible (Figure 8, b). Subsequently, to a freshly prepared toluene solution of **5** heated at 120 °C 1-hexyne has been added (Ru/alkyne = 1:5 molar ratio); the collected ESI(+) spectrum shows the disappearance of the signal at $m/z$ = 813 and the appearance of a cluster at $m/z$ = 854, corresponding to $[Ru(bidf)(PPh_3)(C{=}CH{-}C_4H_9)]^+$ (Figure 8, c); the cluster at $m/z$ = 800 can be tentatively assigned

 © 2006 Wiley-VCH Verlag GmbH & Co. KGaA, Weinheim 

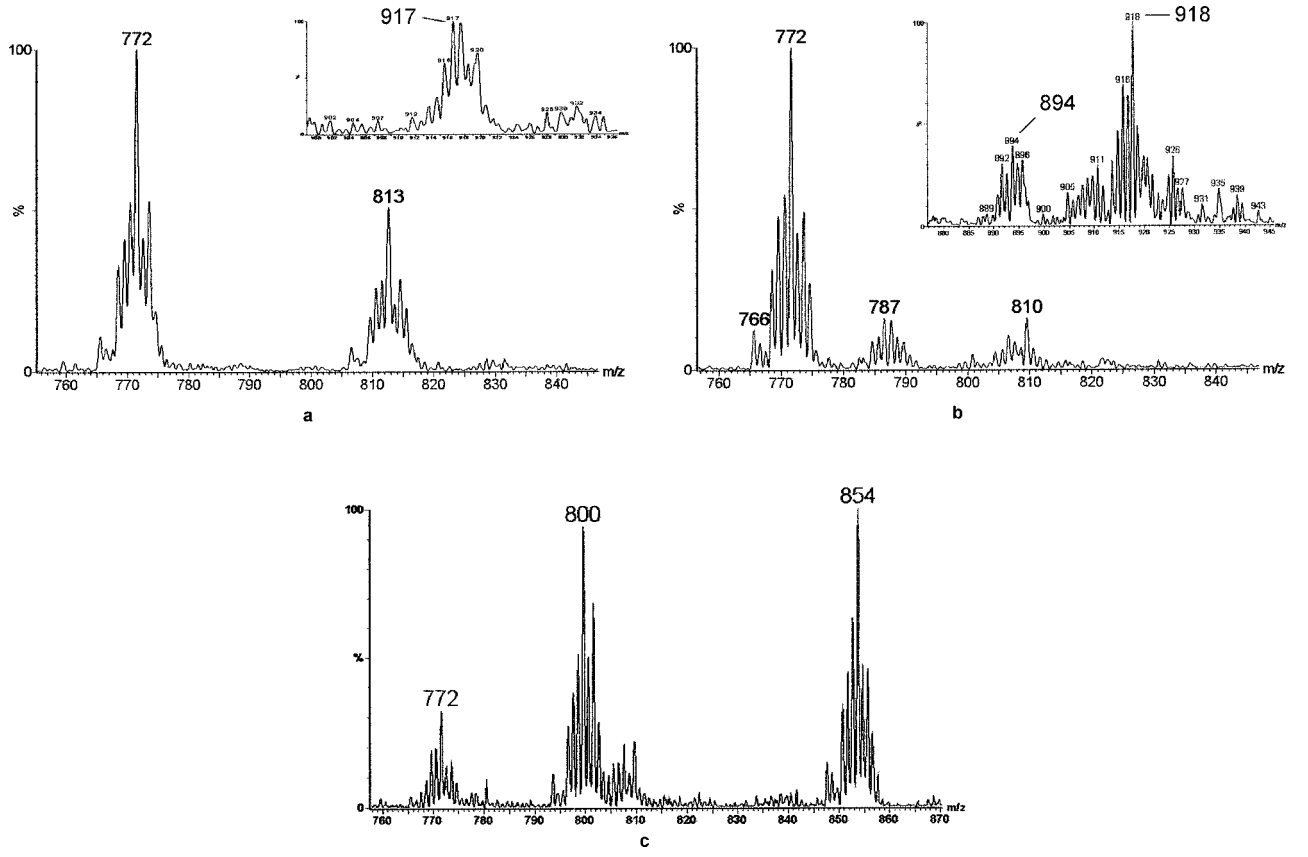


Figure 8. ESI(+) spectra of toluene solutions of **5**: **a**) after one hour at 120 °C; **b**) after the addition of benzoic acid/$Na_2CO_3$; **c**) after the addition of 1-hexyne.

to the loss of butadiene from the vinylidene species, with formation of the cation $[Ru(bidf)(PPh_3)(C_2H_4)]^+$. This last signal however quickly disappears leaving the signal at *m*/*z* = 854. The formation of the vinylidene intermediate is then independent from the presence of benzoic acid. In fact, the addition of 1-hexyne to a toluene solution containing the carboxylate intermediate leads to the immediate disappearance of the signal at *m*/*z* = 894 in favour of that at *m*/*z* = 854. Although the ESI-MS experiments does not give conclusive evidences of the reaction mechanism governing the studied catalytic process, several observations are in favour of the intermolecular nucleophilic attack of the carboxylate anion onto the vinylidene complex $[Ru(bidf)(PPh_3)(C{=}CH{-}C_4H_9)Cl]$, such as: *i*) the formation of the vinylidene intermediate which occurs independently on the presence of the carboxylate ion, *ii*) that the signal of the carboxylate complex quickly disappears in favour of that of the vinilydene intermediate after the addition of the alkyne, and *iii*) that no signal deriving from vinylidene species containing a carboxylate anion has been detected. Unfortunately, repeated attempts aimed at the isolation or detection of $[Ru(PNO)(PPh_3)(C{=}CH{-}C_4H_9)Cl]$ species have been so far unsuccessful.

The observation of ESI-MS signals attributable to the bis-chelate complex **12** can be one of the reasons of the incomplete conversion of the alkyne substrates, as its formation, through a not defined pathway, can in principle account for catalyst deactivation.

## Conclusions

In this work we have reported the synthesis and the full characterisation of several new octahedral $Ru^{II}$ complexes obtained by reaction of $[Ru(PPh_3)_3Cl_2]$ with two protic [PNO] ligands. Depending on the experimental conditions, different coordination modes to Ru can be created, giving rise to neutral or cationic complexes of general formula *trans*-$[Ru(\kappa^3\text{-HPNO})(PPh_3)Cl_2]$, $[Ru(\kappa^3\text{-PNO})(PPh_3)(CH_3CN)Cl]$, $[Ru(\kappa^3\text{-HPNO})(PPh_3)(CH_3CN)Cl][X]$ (X = $PF_6$ or $BPh_4$) and $[Ru(\kappa^3\text{-PNO})(PPh_3)(CH_3CN)_2][X]$. The complexes of the type *trans*-$[Ru(\kappa^3\text{-HPNO})(PPh_3)Cl_2]$ show an interesting reactivity with dmso which leads to the formation of bis-chelate complexes of the type $[Ru(\kappa^3\text{-PNO})_2]$. Such unusual conversion, monitored by $^{31}P\{^1H\}$ spectroscopy, occurs through the stepwise decoordination of the three donors of the [PNO] ligand induced by dmso. Then, the initial detachment of the amide oxygen leads to the formation of intermediate species where the ligands are $\kappa^2$-(H)PN coordinated; subsequently, the nitrogen decoordination leads to P-monodentate behaviour and, finally, a PNO ligand transfer from two different ruthenium atoms takes

 © 2006 Wiley-VCH Verlag GmbH & Co. KGaA, Weinheim 

place with formation of the bis-chelate complex [Ru($\kappa^3$-PNO)$_2$], [Ru(dmso)$_4$Cl$_2$], $Me_2S$, $OPPh_3$ and HCl. The deoxygenation of dmso occurs by oxygen transfer to a $PPh_3$ molcule. Model systems of the spectroscopically detected intermediates have been obtained by reaction of an HPNO ligand with [Ru(dmso)$_4$Cl$_2$] and [Ru(*p*-cymene)Cl$_2$]$_2$. A catalytic version of the oxygen transfer reaction from dmso to $PPh_3$ has also been developed.

Most of the complexes containing $PPh_3$ promote the catalytic coupling between benzoic acid and terminal alkynes in toluene/$Na_2CO_3$ at 120 °C, with 1% of catalyst loading. The reactions proceed with high stereo- and regioselectivity, up to 100% as established by $^1$HNMR, towards the formation of the *anti*-Markovnikov product. Important mechanistic details come from the ESI-MS study applied for the first time to this ruthenium-catalysed coupling reaction: the enol esters form thanks to an intermolecular nucleophilic attack of a uncoordinated carboxylate anion onto a Ru–vinylidene intermediate of the type [Ru(PNO)($PPh_3$)(C=CH–$C_4H_9$)Cl].

## Experimental Section

**General:** All reactions were performed under dry nitrogen employing standard Schlenk techniques. Solvents were dried prior to use and stored under nitrogen. Elemental analysis (C, H, N and S) were performed with a Carlo Erba Mod. EA 1108 apparatus. Infrared spectra were recorded with a Nicolet 5PCFT-IR spectrophotometer in the 4000–400 cm$^{-1}$ range by using KBr disks. $^1$H NMR spectra were obtained with a Bruker 300 FT spectrometer using $SiMe_4$ as internal standard, while $^{31}$P{$^1$H} NMR spectra were recorded with a Bruker AMX 400 FT using $H_3PO_4$ 85% as external standard. Heterocorrelated $^{31}$P-$^1$H NMR spectra were measured with a Bruker Avance 400 MHz. All spectra were collected at 298 K. FAB-MS spectra were performed with a Micromass Autoespec mass spectrometer, employing *m*-nitrobenzyl alcohol as matrix. A Quattro LC triple quadrupole instrument (Micromass, Manchester, UK) equipped with an electrospray interface and a Masslynx v. 3.4 software (Micromass) was used for ESI-MS data acquisition and processing. The nebulizing gas (nitrogen, 99.999% purity) and the desolvation gas (nitrogen, 99.998% purity) were delivered at a flow-rate of 80 and 500 L/h, respectively. ESI-MS analyses were performed by operating the mass spectrometer in positive (PI) ion mode, acquiring mass spectra over the scan range *m*/*z* 100–1300, using a step size of 0.1 Da and a scan time of 1.2 seconds. The operating parameters of the interface were as follows: source temperature 70 °C, desolvation temperature 70 °C, ES(+) voltage 3.0 kV, cone voltage 30 and 50 V, rf lens 0.3 V.

2-(Diphenylphosphanyl)benzaldehyde benzoylhydrazone (**Hbidf**) and 2-(diphenylphosphanyl)benzaldehyde acetylhydrazone (**Haidf**) were synthesised as previously reported.[4b] [Ru($PPh_3$)$_3$Cl$_2$] was synthesised by a literature reported method.[35]

***trans*-[Ru(Hbidf)($PPh_3$)Cl$_2$]·$CH_2Cl_2$ (1):** The ligand (250 mg, 0.613 mmol) was dissolved in 15 mL of $CH_2Cl_2$ at room temperature. After 10 minutes of stirring [Ru($PPh_3$)$_3$Cl$_2$] (590 mg, 0.617 mmol) was added and the resulting purple solution was stirred for 5 hours at room temperature. The solvent was partially removed in vacuo, and the solution was cooled to –18 °C for a night. A purple powder was filtered off, washed with *n*-hexane and diethyl ether and then dried under vacuum. Yield: 430 mg (83%). M.p. 160 °C (dec.). $C_{44}H_{36}Cl_2N_2OP_2Ru$·$CH_2Cl_2$ (927.642): calcd. C 58.25, H 4.10, N 3.02; found C 58.85, H, 4.11, N 3.02. $^1$H NMR ([D$_6$]dmso): $\delta$ = 8.02–6.94 (m, 34 H, Ph), 5.20 (s, 2 H, $CH_2Cl_2$) ppm. FAB-MS: *m*/*z* = 842 [M – $CH_2Cl_2$]$^+$, 807 [M – $CH_2Cl_2$ – Cl]$^+$.

***trans*-[Ru(Haidf)($PPh_3$)Cl$_2$]·1/2 $CH_2Cl_2$ (2):** As for **1** but using ligand **Haidf** (150 mg, 0.433 mmol). Yield: 310 mg (91%). M.p. 160 °C (dec.). $C_{39}H_{34}Cl_2N_2OP_2Ru$·1/2$CH_2Cl_2$ (823.105): calcd. C 57.75, H 4.26, N 3.41; found C 58.38, H 4.16, N 3.40. $^1$H NMR ([D$_6$]dmso): $\delta$ = 7.75–6.87 (m, 29 H, Ph), 5.21 (s, 1 H, $CH_2Cl_2$), 2.25 [s, 3 H, $CH_3C$(O)] ppm. FAB-MS: *m*/*z* = 780 [M – $CH_2Cl_2$ + H$^+$]$^+$, 745 [M – $CH_2Cl_2$ – Cl]$^+$, 709 [M – $CH_2Cl_2$ – HCl – Cl]$^+$.

**[Ru(bidf)($PPh_3$)($CH_3CN$)Cl] (3):** Complex **1** (320 mg, 0.380 mmol) was dispersed in 20 mL of toluene at room temperature. $NEt_3$ (262 μL, 1.900 mmol) and $CH_3CN$ (1 mL) were added, and the purple solution was stirred at room temperature overnight. A yellow solid was filtered off, washed with water and *n*-hexane and then dried under vacuum. Yield: 260 mg (81%). M.p. 180 °C (dec.). $C_{46}H_{41}ClN_3OP_2Ru$ (850.325): calcd. C 62.25, H 4.52, N 4.96; found C 65.90, H 4.98, N 4.65. $^1$H NMR ($CD_2Cl_2$): $\delta$ = 8.16 (dd, 2 H, Ph), 7.30 (t, 2 H, Ph), 7.28–7.14 (m, 28 H, Ph), 7.12 (t, 1 H, Ph), 6.58 (t, 2 H, Ph), 1.21 (s, 3 H, $CH_3CN$) ppm. FAB-MS: *m*/*z* = 806 [M – $CH_3CN$]$^+$, 771 [M – $CH_3CN$ – Cl]$^+$.

**[Ru(aidf)($PPh_3$)($CH_3CN$)Cl] (4):** As for **3** but starting from complex **2**. Yellow solid. Yield: 130 mg (81%). M.p. 174 °C (dec.). $C_{41}H_{36}ClN_3OP_2Ru$ (785.23): calcd. C 62.86, H 4.60, N 5.36; found C 62.98, H 4.75, N 4.95. $^1$H NMR ($CD_2Cl_2$): $\delta$ = 7.80 (t, 2 H, Ph), 7.58–7.11 (m, 24 H, Ph), 6.95 (t, 1 H, Ph), 6.54 (t, 2 H, Ph), 2.36 [s, 3 H, $CH_3C$(O)], 1.21 (s, 3 H, $CH_3CN$) ppm. FAB-MS: *m*/*z* = 786 [M + H$^+$]$^+$, 744 [M – $CH_3CN$]$^+$. For slow evaporation of a dichloromethane/acetonitrile mixture, crystals suitable for X-ray analysis were collected.

**[Ru(Hbidf)($PPh_3$)($CH_3CN$)Cl][$PF_6$] (5):** Complex **1** (250 mg, 0.297 mmol) was dispersed in 45 mL of $CH_2Cl_2$ at room temperature. After 15 minutes of stirring $KPF_6$ (280 mg, 1.521 mmol) and $CH_3CN$ (1 mL) were added. The solution was stirred overnight at room temperature, then filtered and the resulting orange solution was concentrated under vacuum, treated with *n*-hexane and refrigerated at –18 °C. An orange powder was filtered off, washed with *n*-hexane and dried under vacuum. Yield: 210 mg (71%). M.p. 170 °C (dec.). $C_{46}H_{39}ClF_6N_3OP_3Ru$ (993.271): calcd. C 55.65, H 3.93, N 4.23; found C 55.34, H 3.89, N 4.31. IR (cm$^{-1}$): $\tilde{\nu}$ = 2281 (w, $CH_3C{\equiv}N$), 845 (vs, PF). $^1$H NMR ($CD_2Cl_2$): $\delta$ = 8.01 (d, 2 H, Ph), 7.70 (m, 1 H, Ph), 7.63–7.23 (m, 28 H, Ph), 7.18 (t, 1 H, Ph), 6.40 (t, 2 H, Ph), 1.63 (s, 3 H, $CH_3CN$) ppm. $^{31}$P{$^1$H}NMR ($CD_2Cl_2$): $\delta$ = –141.1 (m, 1 P, $PF_6$) ppm. FAB-MS: *m*/*z* = 806 [M – $PF_6$ – $CH_3CN$]$^+$, 771 [M – $PF_6$ – $CH_3CN$ – HCl]$^+$.

**[Ru(Haidf)($PPh_3$)($CH_3CN$)Cl][$PF_6$]·$CH_2Cl_2$ (6):** As for **5** but starting from complex **2**. Yield: 160 mg (69%). M.p. 170 °C (dec.). $C_{41}H_{37}ClF_6N_3OP_3Ru$·$CH_2Cl_2$ (1016.133): calcd. C 49.65, H 4.14, N 4.14; found C 50.00, H 3.91, N 4.48. IR (cm$^{-1}$): $\tilde{\nu}$ = 2273 (w, $CH_3C{\equiv}N$), 845 (vs, PF). $^1$H NMR ($CD_2Cl_2$): $\delta$ = 8.88 (br., 1 H, CH=N), 7.88 (t, 2 H, Ph), 7.72–7.03 (m, 25 H, Ph), 6.33 (t, 2 H, Ph), 5.20 (s, 2 H, $CH_2Cl_2$), 2.38 [s, 3 H, $CH_3C$(O)] 1.70 (s, 3 H, $CH_3CN$) ppm. $^{31}$P{$^1$H}NMR ($CD_2Cl_2$): $\delta$ = –145.5 (m, 1 P, $PF_6$) ppm. FAB-MS: *m*/*z* = 786 [M – $CH_2Cl_2$ – $PF_6$]$^+$, 745 [M – $CH_2Cl_2$ – $PF_6$ – $CH_3CN$]$^+$, 709 [M – $CH_2Cl_2$ – $PF_6$ – $CH_3CN$ – HCl]$^+$. From a refrigerated dichloromethane /*n*-pentane mixture, crystals suitable for X-ray analysis were collected.

**[Ru(Hbidf)($PPh_3$)($CH_3CN$)Cl][$BPh_4$] (7):** As for **6** but starting from complex **1** and using $NaBPh_4$ instead of $KPF_6$. Yield: 180 mg (81%). M.p. 146–148 °C. $C_{70}H_{59}BClN_3OP_2Ru$ (1167.544): calcd. C

 © 2006 Wiley-VCH Verlag GmbH & Co. KGaA, Weinheim 

72.04, H 5.06, N 3.60; found C 72.45, H 5.74, N 3.48. IR ($cm^{-1}$): $\tilde{\nu}$ = 2269 (w, $CH_3C{\equiv}N$), 843 (w, BP). $^1H$ NMR ($CD_2Cl_2$): $\delta$ = 8.03 (d, 2 H, Ph), 7.83–6.84 (m, 50 H, Ph), 6.39 (t, 2 H, Ph), 1.23 (s, 3 H, $CH_3CN$) ppm. FAB-MS: *m*/*z* = 848 $[M - BPh_4]^+$, 807 $[M - BPh_4 - CH_3CN]^+$, 771 $[M - BPh_4 - CH_3CN - HCl]^+$.

**[Ru(Haidf)(PPh$_3$)(CH$_3$CN)Cl][BPh$_4$] (8):** As for **7** but starting from complex **2**. Yield: 50 mg (70%). M.p. 152–154 °C. $C_{65}H_{57}BClN_3OP_2Ru{\cdot}1/4CH_2Cl_2$ (1171.747): calcd. C 69.65, H 5.03, N 3.38; found C 69.68, H 5.15, N 3.74. IR ($cm^{-1}$): $\tilde{\nu}$ = 2265 (w, $CH_3C{\equiv}N$), 851 (w, BP). $^1$HNMR ($CDCl_3$): $\delta$ = 7.83–6.84 (m, 47 H, Ph), 6.53 (t, 2 H, Ph), 2.23 [s, 3 H, $CH_3C(O)$], 0.43 (s, 3 H, $CH_3C{\equiv}N$) ppm. FAB-MS: *m*/*z* = 786 $[M - BPh_4]^+$, 745 $[M - BPh_4 - CH_3CN]^+$, 709 $[M - BPh_4 - CH_3CN - HCl]^+$.

***trans*-[Ru(bidf)(PPh$_3$)(CH$_3$CN)$_2$][BPh$_4$] (9):** Complex **7** (110 mg, 0.094 mmol) was dissolved in 20 mL of tolune at room temperature. To the resulting yellow solution acetonitrile (3 mL) and $NEt_3$ (75 μL, 0.539 mmol) were added and then it was left stirring at room temperature overnight. The solvent was completely removed under vacuum obtaining a sticky pale orange solid, which was washed with water and repeatedly triturated with *n*-hexane. The bright orange powder was finally filtered off, washed with diethyl ether and dried under vacuum. Yield: 90 mg (82%). M.p. 150–154 °C. Due to the instability of the complex, irreproducible microanalyses have been obtained. IR ($cm^{-1}$): $\tilde{\nu}$ = 2273 (w, $CH_3C{\equiv}N$), 873 (w, BP). $^1$H NMR ($CD_2Cl_2$): $\delta$ = 8.21 (d, 2 H, Ph), 7.70 (t, 1 H, Ph), 7.46–7.05 (m, 49 H, Ph), 6.55 (t, 2 H, Ph), 2.37 (s, 3 H, $CH_3C{\equiv}N$), 1.29 (s, 3 H, $CH_3C{\equiv}N$) ppm. FAB-MS: *m*/*z* = 771 $[M - BPh_4 - 2CH_3CN]^+$.

***trans*-[Ru(aidf)(PPh$_3$)(CH$_3$CN)$_2$][PF$_6$] (10):** As for **9** but starting form complex **8**. Yield: 50 mg (76%). M.p. 137–142 °C. Due to the instability of the complex, irreproducible microanalyses have been obtained. IR ($cm^{-1}$): $\tilde{\nu}$ = 2281 (w, $CH_3C{\equiv}N$), 835 (vs, PF). $^1$H NMR ($CD_2Cl_2$): $\delta$ = 7.72 (t, 2 H, Ph), 7.61 (t, 2 H, Ph), 7.48–7.12 (m, 22 H, Ph), 7.05 (t, 2 H, Ph), 6.51 (t, 2 H, Ph), 2.34 [s, 3 H, $CH_3C(O)$], 1.44 (s, 3 H, $CH_3C{\equiv}N$), 1.27 (s, 3 H, $CH_3C{\equiv}N$) ppm. $^{31}P\{^1H\}$NMR ($CD_2Cl_2$): $\delta$ = –150 (m, 1 P, $PF_6$) ppm.

**[Ru(Hbidf)(PPh$_3$)(CH$_3$CN)Cl]Cl (11):** Complex **1** (100 mg, 0.12 mmol) was treated with $CH_3CN$ and the mixture was heated at 50 °C for 4 hours. The initial purple mixture became an almost clear orange solution. After filtration the resulting orange solution was dried under vacuum, obtaining an orange powder. Yield: 60 mg (57%). $C_{46}H_{37}Cl_2N_3OP_2Ru$ (881.746): calcd. C 62.16, H 4.25, N 4.57; found C 62.38, H 4.46, N 4.57. IR ($cm^{-1}$): $\tilde{\nu}$ = 2273 (w, $CH_3C{\equiv}N$). $^1$H NMR ($CD_2Cl_2$): $\delta$ = 7.88–6.86 (m, 32 H, Ph), 6.55 (t, 2 H, Ph), 1.31 (s, 3 H, $CH_3C{\equiv}N$) ppm.

**[Ru(bidf)$_2$]·2H$_2$O (12). Method A:** Hbidf (100 mg, 0.244 mmol) was dissolved in ethanol (25 mL) by warming. 1 M NaOH solution was added until a pH ≈ 8 (checked by litmus paper), obtaining a pale yellow solution. $[Ru(dmso)_4Cl_2]$ (59.3 mg, 0.122 mmol) was dissolved in ethanol (10 mL) and added to the ligand solution. After 2 h of reflux the solvent was partially removed under vacuum and the resultant clear solution was refrigerated at –20 °C. The soformed solid was filtered off, washed with cold ethanol and vacuum dried. Yield: 84 mg (75%).

**Method B:** Hbidf (140 mg, 0.343 mmol) was dissolved in 5 mL of $CH_2Cl_2$ at room temperature. A KOH solution (3.75 mL , 0.21 M) was added, and the resulting pale yellow solution was stirred at room temperature for 1 hour. $[Ru(PPh_3)_3Cl_2]$ (160 mg, 0.167 mmol) previously dissolved in 15 mL of $CH_2Cl_2$ was added, and the mixture stirred at room temperature for 3 hours. The solution was then filtered and the solvent partially removed under vacuum. After cooling at –18 °C a yellow solid formed, which was filtered off, washed with diethyl ether and vacuum dried. Yield: 99 mg (63%) M.p. 253–258 °C. $C_{52}H_{40}N_4O_2P_2Ru{\cdot}2H_2O$ (951.966): calcd. C 65.60, H 4.65, N 5.88; found C 65.26, H 4.76, N 5.59. $^1$H NMR ($CDCl_3$): $\delta$ = 7.66 (d, 4 H, Ph), 7.19–6.77 (m, 38 H, Ph) ppm. CI-MS: *m*/*z* = 916 $[M - H_2O]^+$.

**[Ru(Hbidf)(dmso)$_2$Cl$_2$] (13) and [Ru(Hbidf)(dmso)Cl$_2$]·1/2dmso·H$_2$O (14):** $[Ru(dmso)_4]Cl_2$ (59.3 mg, 0.122 mmol) was dissolved in ethanol (15 mL). An equimolar amount of Hbidf dissolved in ethanol (15 mL) was added, and the resulting solution was refluxed for 1 h. A yellow solid precipitated (**13**), which was filtered off, washed with ethanol and vacuum dried for several hours. Yield: 31 mg (35%). M.p. 227 °C (dec.). $C_{30}H_{33}Cl_2N_2O_3PRuS_2$ (736.675): calcd. C 48.91, H 4.51, N 3.80, S, 8.70; found C 48.86, H 4.47, N 3.86; S, 8.78. IR ($cm^{-1}$): $\tilde{\nu}$ = 1088 (vs, S=O); 1019 (s, $\rho C–H)_{dmso}$. $^1$H NMR ($CDCl_3$): $\delta$ = 7.92 (d, 2 H, Ph), 7.79–7.20 (m, 17 H, Ph), 3.65 (s, 3 H, dmso), 3.45 (s, 3 H, dmso), 3.03 (s, 3 H, dmso), 2.84 (s, 3 H, dmso) ppm. By slow evaporation of a dmso solution of **13** crystals of **12**·dmso·H$_2$O suitable for X-ray analysis were collected (see crystallograhic analysis).

After the filtration of **13**, the resulting solution was treated with *n*-hexane observing the precipitation of an orange solid (**14**), which was filtered off, washed with *n*-hexane and vacuum dried. Yield: 34 mg (40%). M.p. 228 °C (dec.). $C_{29}H_{32}Cl_2N_2O_{3.5}PRuS_{1.5}$ (715.625): calcd. C 48.67, H 4.51, N 3.91, S 6.72; found C 48.21, H 4.71, N 4.22, S 7.14. IR ($cm^{-1}$): $\tilde{\nu}$ = 1095 (vs, S=O), 1023 (s, $\rho C–H)_{dmso}$. $^1$H NMR ($CDCl_3$): $\delta$ = 7.78–7.35 (m, 19 H, Ph), 3.48 (s, 3 H, dmso), 2.95 (s, 3 H, dmso) ppm.

**[Ru(Hbidf)(*p*-cymene)Cl$_2$]·2CHCl$_3$ (15):** Hbidf (50 mg, 0.122 mmol) was dissolved in 40 mL of chloroform and $[Ru(p\text{-cymene})Cl_2]_2$ (75 mg, 0.122 mmol) was added. The mixture was stirred at room temperature for 2.5 hours obtaining a deep red solution, which was reduced in volume and treated with diethyl ether. A brown solid precipitated (25 mg) whose characterisation was not possible. From the mother liquors refrigerated at –20 °C, brown crystals suitable for X-ray analysis were collected. Yield: 46.5 mg (40%). M.p. 220 °C (dec.). $C_{36}H_{35}Cl_2N_2OPRu{\cdot}2CHCl_3$ (953.395): calcd. C 47.87, H 3.90, N 2.90; found C 48.20, H 3.80, N 2.30. $^1$H NMR ($CDCl_3$): $\delta$ = 8.07 (d, 2 H, Ph), 7.62–7.03 (m, 17 H, Ph), 5.47 (d, 2 H, *p*-cymene), 5.33 (d, 2 H, *p*-cymene), 2.94 [m, 1 H, C*H*-$(CH_3)_2$], 1.75 [s, 3 H, $CH(CH_3)_2$], 1.28 [s, 3 H, $CH(CH_3)_2$] ppm.

**X-ray Analysis:** Mo-$K_\alpha$ radiation ($\lambda$ = 0.71073 Å), $T$ = 293 K, on a SMART AXS 1000 diffractometer equipped with CCD detector was used for compounds **4** and **6** and **12**·dmso·H$_2$O, while Cu-$K_\alpha$ radiation ($\lambda$ = 1.54178 Å), $T$ = 293 K, with a Siemens AED diffractometer equipped with scintillation detector was employed for **15**·1.5CHCl$_3$, which showed a significant crystal decay over the data collection (47% intensity loss, correction applied). Lorentz, polarisation, and absorption corrections were applied.[36] Structures were solved by direct methods using SIR97[37] and refined by full-matrix least-squares on all $F^2$ using SHELXL97[38] implemented in the WingX package.[39] Hydrogen atoms were partly located on Fourier difference maps and refined isotropically, partly introduced in calculated positions. Anisotropic displacement parameters were refined for all non-hydrogen atoms in **4**, **6** and **12**·dmso·H$_2$O, but only for Ru and its coordination environment for **15**·1.5CHCl$_3$. In **12**·dmso·H$_2$O the dmso presents a disorder on the S atom. Final geometries have been analysed with SHELXL97[36] and PARST97,[40] and extensive use was made of the Cambridge Crystallographic Data Centre packages.[41] Table 4 summarises crystal data and structure determination results.

 © 2006 Wiley-VCH Verlag GmbH & Co. KGaA, Weinheim 

Table 4. Crystal data and structure refinement for structure analyses.

| | **4** | **6** | **12**·dmso·$H_2O$ | **15**·1.5 $CHCl_3$ |
|---|---|---|---|---|
| Empirical formula | $C_{41}H_{40}ClN_3O_3P_2Ru$ | $C_{41}H_{37}ClF_6N_3OP_3Ru$ | $C_{54}H_{48}N_4O_4P_2RuS$ | $C_{38}H_{37}Cl_{6.50}N_2OPRu$ |
| Formula weight | 821.22 | 931.17 | 1012.03 | 900.16 |
| Wavelength | 0.71073 Å | 0.71073 Å | 0.71073 Å | 1.54100 Å |
| Crystal system | tetragonal | orthorhombic | monoclinic | hexagonal |
| Space group | $P4_32_12$ | *Pcab* | $P2_1/c$ | *R*-3 |
| Unit cell dimensions [Å, °] | $a$ = 14.430(1) | $a$ = 18.334(1) | $a$ = 11.114(2) | $a$ = 41.520(8) |
| | $b$ = 14.430(1) | $b$ = 20.599(1) | $b$ = 21.271(4) $\beta$ = 95.89(1) | $b$ = 41.520(8) |
| | $c$ = 37.134(2) | $c$ = 21.621(1) | $c$ = 20.280(4) | $c$ = 13.270(4) |
| Volume [$Å^3$] | 7732.2(9) | 8165.4(7) | 4769(2) | 19811(8) |
| $Z$ | 8 | 8 | 4 | 18 |
| Density (calculated) [$mg/m^3$] | 1.411 | 1.515 | 1.410 | 1.358 |
| Absorption coefficient [$mm^{-1}$] | 0.599 | 0.631 | 0.491 | 7.090 |
| $F(000)$ | 3376 | 3776 | 2088 | 8217 |
| $\Theta$ range for data collection [°] | 1.51–27.10 | 1.76–28.42 | 1.39–28.49 | 3.55–64.77 |
| Reflections collected | 84143 | 86434 | 28916 | 7243 |
| Independent reflections | 8525 [$R$(int) = 0.0314] | 9617 [$R$(int) = 0.0720] | 10731 [$R$(int) = 0.0523] | 6370 [$R$(int) = 0.0835] |
| Data/restraints/parameters | 8525/6/480 | 9617/0/615 | 10731/2/775 | 6370/5/222 |
| Goodness-of-fit on $F^2$ | 1.180 | 1.203 | 0.875 | 0.780 |
| Final $R$ indices [$I > 2\sigma(I)$] ($R_1$, $wR_2$) | 0.0296, 0.0631 | 0.0709, 0.1465 | 0.0454, 0.0963 | 0.1135, 0.3044 |
| $R$ indices (all data) ($R_1$, $wR_2$) | 0.0343, 0.0655 | 0.1205, 0.1593 | 0.0918, 0.1114 | 0.2530, 0.3526 |
| Largest $\Delta F$ max./min. [e·$Å^{-3}$] | 0.472/–0.516 | 0.539/–0.518 | 0.981/–0.675 | 0.964/–0.506 |

CCDC-294363 (for **4**), -294364 (for **6**), -294365 (for **12**·dmso·$H_2O$) and -294366 (for **15**·1.5 $CHCl_3$) contain the supplementary crystallographic data for this paper. These data can be obtained free of charge from The Cambridge Crystallographic Data Centre via www.ccdc.cam.ac.uk/data_request/cif.

**Catalytic Reactions**

**Addition of Benzoic Acid to Terminal Alkynes:** A toluene solution (7 mL) containing the catalyst (0.01 mmol) and the alkyne (1 mmol) was added at room temperature to a toluene solution (6 mL) of benzoic acid containing solid $Na_2CO_3$ (0.05 mmol). The resulting mixture was heated to 120 °C and stirred for 16 hours, then dried under vacuum; the residual solid was treated with 5 mL of $CH_2Cl_2$ and the precipitate was filtered off. Solid $NaHCO_3$ (1 mmol) was added, and the mixture was washed with $H_2O$ three times; the organic layer was dried by anhydrous $Na_2SO_4$ and reduced in volume by vacuum and then filtered through silica gel to remove the catalyst. The solution was finally dried under vacuum and analysed by $^1H$ NMR spectroscopy.

**Oxygen Transfer from Dmso to $PPh_3$:** Compound **1** (11 mg, 0.012 mmol) was dissolved in 8 mL of nitrogen-saturated dmso and $PPh_3$ (326 mg, 1.243 mmol) was added. The yellow solution was refluxed under nitrogen and small samples were withdrawn at regular intervals, added of $CDCl_3$ and analysed by $^{31}P\{^1H\}$-NMR spectroscopy.

**Supporting Information** (see footnote on the first page of this article): $^{31}P\{^1H\}$-NMR spectra of complex **1** recorded in [$D_6$]dmso.

## Acknowledgments

Dr P. Barbaro (ICCOM-CNR) is gratefully thanked for running the heterocorrelated $^{31}P$-$^1H$ spectra, while Dr. Maria Carmen Rodriguez Argüelles (University of Vigo, Spain) is thanked for FAB-MS measurements. SB thanks Xunta de Galicia for a postdoctoral grant. The authors thank ECRF and "Firenze Hydrolab" Project for access to Bruker Avance 400 MHz and the Centro Interfacoltà di Misure G. Casnati of the University of Parma for the instrument facilities.

[1] a) M. Alvarez, N. Lugan, R. Mathieu, *J. Chem. Soc., Dalton Trans.* **1994**, 2755–2760; b) J. R. Dilworth, S. D. Howe, A. J. Hutson, J. R. Miller, J. Silver, R. M. Thompson, M. Harman, M. B. Hursthouse, *J. Chem. Soc., Dalton Trans.* **1994**, 3553–3562; c) K. K. Hii, S. D. Perera, B. L. Shaw, *J. Chem. Soc., Dalton Trans.* **1994**, 3589–3596; d) P. Bhattacharyya, J. Parr, A. M. Z. Slawin, *J. Chem. Soc., Dalton Trans.* **1998**, 3609–3614; e) P. Bhattacharyya, M. L. Loza, J. Parr, A. M. Z. Slawin, *J. Chem. Soc., Dalton Trans.* **1999**, 2917–2921; f) J. D. G. Correia, A. Domingos, A. Paulo, I. Santos, *J. Chem. Soc., Dalton Trans.* **2000**, 2477–2482; g) J. W. Faller, G. Mason, J. Parr, *J. Organomet. Chem.* **2001**, *626*, 181–185; h) K. Nakajima, S. Ishibashi, M. Inamo, M. Kojima, *Inorg. Chim. Acta* **2001**, *325*, 36–44; i) G. Sanchez, F. Momblona, J. L. Serrano, L. Garcia, E. Perez, J. Perez, G. Lopez, *J. Coord. Chem.* **2002**, *55*, 917–923; j) M. Ahmad, S. D. Perera, B. L. Shaw, M. Thornton-Pett, *J. Chem. Soc., Dalton Trans.* **2002**, 1954–1962; k) S. R. Korupoju, R.-Y. Lai, Y.-H. Liu, S.-M. Peng, S.-T. Liu, *Inorg. Chim. Acta* **2005**, *358*, 3003–3008.

[2] a) H. Yang, M. Alvarez, N. Lugan, R. Mathieu, *J. Chem. Soc., Chem. Commun.* **1995**, 1721–1722; b) H. Yang, M. Alvarez-Gressier, N. Lugan, R. Mathieu, *Organometallics* **1997**, *16*, 1401–1409; c) H. L. Kwong, W. S. Lee, T. S. Lai, W. T. Wong, *Inorg. Chem. Commun.* **1999**, *2*, 66–69; d) H. Dai, X. Hu, H. Chen, C. Bai, Z. Zheng, *Tetrahedron: Asymmetry* **2003**, *14*, 1467–1472.

[3] P. Pelagatti, A. Bacchi, M. Carcelli, M. Costa, A. Fochi, P. Ghidini, E. Leporati, M. Masi, C. Pelizzi, G. Pelizzi, *J. Organomet. Chem.* **1999**, *583*, 94–105.

[4] a) A. Bacchi, M. Carcelli, M. Costa, P. Pelagatti, C. Pelizzi, G. Pelizzi, *Gazz. Chim. Ital.* **1994**, *124*, 429–435; b) A. Bacchi, M. Carcelli, M. Costa, A. Leporati, E. Leporati, P. Pelagatti, C. Pelizzi, G. Pelizzi, *J. Organomet. Chem.* **1997**, *535*, 107–120.

[5] a) P. Pelagatti, A. Bacchi, C. Bobbio, M. Carcelli, M. Costa, C. Pelizzi, C. Vivorio, *Organometallics* **2000**, *19*, 5440–5446; b) P. Pelagatti, A. Bacchi, C. Bobbio, M. Carcelli, M. Costa, A. Fochi, C. Pelizzi, *J. Chem. Soc., Dalton Trans.* **2002**, 1–7; c) P. Pelagatti, A. Bacchi, M. Carcelli, M. Costa, H.-W. Frühauf, K. Goubitz, C. Pelizzi, M. Triclistri, K. Vrieze, *Eur. J. Inorg. Chem.* **2002**, 439–446.

[6] C. Bruneau, P. H. Dixneuf, *Ruthenium Catalysts and Fine Chemistry*, Springer GmbH, Berlin, Germany, **2004**.

 © 2006 Wiley-VCH Verlag GmbH & Co. KGaA, Weinheim 

[7] J. P. Monthéard, M. Camps, G. Seytre, J. Guillet, J. C. Dubois, *Angew. Makromol. Chem.* **1978**, *72*, 45–55.
[8] E. Bruneau, M. Neveux, Z. Kabouche, C. Ruppin, P. H. Dixneuf, *Synlett* **1991**, 755–763.
[9] a) R. C. Cambie, R. C. Hayward, J. L. Jurlina, P. S. Rutledge, P. D. Woodgate, *J. Chem. Soc., Perkin Trans. 1* **1978**, 126–130; b) S. Torii, T. Inokuchi, S. Misima, T. Kobayashi, *J. Org. Chem.* **1980**, *45*, 2731–2735; c) S. Stavber, B. Sket, B. Zajc, M. Zupan, *Tetrahedron* **1989**, *45*, 6003–6010; d) A. D. Cort, *J. Org. Chem.* **1991**, *56*, 6708–6709.
[10] a) A. Demonceau, E. Saive, Y. de Froidmont, A. F. Noels, A. J. Hubert, *Tetrahedron Lett.* **1992**, *33*, 2009–2012; b) W. B. Motherwell, L. R. Roberts, *J. Chem. Soc., Chem. Commun.* **1992**, 1582–1583.
[11] a) L. F. Tietze, A. Montenbruck, C. Schneider, *Synlett* **1994**, 509–510; b) M. C. Pirrung, Y. R. Lee, *Tetrahedron Lett.* **1994**, *35*, 6231–6234.
[12] K. E. Koenig, G. L. Bachman, B. E. Vineyard, *J. Org. Chem.* **1980**, *45*, 2362–2365.
[13] a) N. Sakai, K. Nozaki, K. Massima, H. Takaya, *Tetrahedron: Asymmetry* **1992**, *3*, 583–586; b) C. G. Arena, F. Nicolò, D. Drommi, G. Bruno, F. Faraone, *J. Chem. Soc., Chem. Commun.* **1994**, 2251–2252.
[14] M. Rotem, Y. Shvo, *Organometallics* **1983**, *2*, 1689–1691.
[15] a) T. Mitsudo, Y. Hori, Y. Watanabe, *J. Org. Chem.* **1985**, *50*, 1566–1568; b) T. Mitsudo, Y. Hori, Y. Yamakawa, Y. Watanabe, *Tetrahedron Lett.* **1986**, *27*, 2125–2126; c) T. Mitsudo, Y. Hori, Y. Yamakawa, Y. Watanabe, *J. Org. Chem.* **1987**, *52*, 2230–2239.
[16] a) C. Ruppin, P. H. Dixneuf, *Tetrahedron Lett.* **1986**, *27*, 6323–6324; b) C. Ruppin, P. Dixneuf, *Tetrahedron Lett.* **1988**, *29*, 5365–5368; c) H. Doucet, J. Höfer, C. Bruneau, P. H. Dixneuf, *J. Chem. Soc., Chem. Commun.* **1993**, 850–851; d) H. Doucet, B. Martin-Vaca, C. Bruneau, P. H. Dixneuf, *J. Org. Chem.* **1995**, *60*, 7247–7255; e) H. Doucet, N. Derrien, Z. Kabouche, C. Bruneau, P. H. Dixneuf, *J. Organomet. Chem.* **1997**, *551*, 151–157.
[17] a) T. Opstal, F. Verpoort, *Tetrahedron Lett.* **2002**, *43*, 9259–9263; b) B. De Clercq, F. Verpoort, *J. Organomet. Chem.* **2003**, *672*, 11–16; c) K. Melis, D. De Vos, P. Jacobs, F. Verpoort, *J. Organomet. Chem.* **2003**, *671*, 131–136; d) K. Melis, F. Verpoort, *J. Mol. Catal. A* **2003**, *194*, 39–47.
[18] L. J. Goossen, J. Paetzold, D. Koley, *Chem. Commun.* **2003**, 706–707.
[19] M. Neveux, B. Seller, F. Hagerdon, C. Bruneau, P. H. Dixneuf, *J. Organomet. Chem.* **1993**, *451*, 133–138.
[20] a) K. Everaere, A. Mortreux, M. Bulliard, J. Brussee, A. van der Gen, G. Nowogroki, J.-F. Carpentier, *Eur. J. Org. Chem.* **2001**, 275–291; b) C. A. Sandoval, T. Ohkuma, K. Muñiz, R. Noyori, *J. Am. Chem. Soc.* **2003**, *125*, 13490–13503; c) P. Pelagatti, M. Carcelli, F. Calbiani, C. Cassi, L. Elviri, C. Pelizzi, U. Rizzotti, D. Rogolino, *Organometallics* **2005**, *24*, 5836–5844.
[21] D. Feichtinger, D. A. Plattner, *Chem. Eur. J.* **2001**, *7*, 591–599.
[22] D. Feichtinger, D. A. Plattner, P. Chen, *J. Am. Chem. Soc.* **1998**, *120*, 7125–7126.
[23] G. Gerdes, P. Chen, *Organometallics* **2004**, *23*, 3031–3036.
[24] a) P. Crochet, J. Gimeno, S. García-Granada, J. Borge, *Organometallics* **2001**, *20*, 4369–4377; b) P. Crochet, J. Gimeno, J. Borge, S. García-Granada, *New J. Chem.* **2003**, *27*, 414–420.
[25] S. M. O. Quintal, H. I. S. Nogueira, V. Félix, M. G. B. Drew, *J. Chem. Soc., Dalton Trans.* **2002**, 4479–4487.
[26] a) I. P. Evans, A. Spencer, G. Wilkinson, *J. Chem. Soc., Dalton Trans.* **1973**, 204; b) E. Alessio, G. Mestroni, G. Nardin, W. M. Attia, M. Calligaris, G. Sava, S. Zorzet, *Inorg. Chem.* **1988**, *27*, 4099–4106.
[27] P. E. Garrou, *Chem. Rev.* **1981**, *81*, 229–266.
[28] a) R. F. R. Jazzar, M. F. Mahon, M. K. Whittlesey, *Organometallics* **2001**, *20*, 3745–3751; b) T. Suárez, B. Fontal, M. Reyes, F. Bellandi, R. R. Contreras, E. Millán, P. Cancines, D. Paredes, *Transition Met. Chem.* **2003**, *28*, 217–219.
[29] V. Y. Kukushkin, *Coord. Chem. Rev.* **1995**, *139*, 375–407.
[30] a) J. C. Bryan, R. E. Stenkamp, T. H. Tulip, J. M. Mayer, *Inorg. Chem.* **1987**, *26*, 2283–2288; b) N. Koshino, J. H. Espenson, *Inorg. Chem.* **2003**, *42*, 5735–5742.
[31] a) A. M. Khenkin, R. Neumann, *J. Am. Chem. Soc.* **2002**, *124*, 4198–4199; b) F. J. Arnáiz, R. Aguado, M. R. Pedrosa, M. A. Maestro, *Polyhedron* **2004**, *23*, 537–543; c) K. Most, S. Köpke, F. Dall'Antonia, N. C. Mösch-Zanetti, *Chem. Commun.* **2004**, 1676–1677; d) A. Lehtonen, R. Sillanpää, *Polyhedron* **2005**, *24*, 257–265.
[32] J. P. McNamara, I. H. Hillier, T. S. Bhachu, C. D. Garner, *Dalton Trans.* **2005**, 3572–3579.
[33] J. S. Jaswal, S. J. Rettig, B. R. James, *Can. J. Chem.* **1990**, *68*, 1808–1817.
[34] J. Höfer, H. Doucet, C. Bruneau, P. H. Dixneuf, *Tetrahedron Lett.* **1991**, *32*, 7409–7410.
[35] P. S. Hallman, T. A. Stephenson, G. Wilkinson, *Inorg. Synth.* **1970**, *12*, 237–240.
[36] a) SAINT: SAX, Area Detector Integration, Siemens Analytical instruments INC., Madison, Wisconsin, USA; b) SADABS: Siemens Area Detector Absorption Correction Software, Sheldrick G., 1996, University of Goettingen, Germany; c) SMART for WNT/2000 version 5.622, Smart Software Reference Manual; Bruker Advanced X-ray Solution, Inc.: Madison, WI, **2001**.
[37] A. Altomare, M. C. Burla, M. Cavalli, G. Cascarano, C. Giacovazzo, A. Gagliardi, A. G. Moliterni, G. Polidori, R. Spagna, Sir97: A New Program For Solving And Refining Crystal Structures, **1997**, Istituto di Ricerca per lo Sviluppo di Metodologie Cristallografiche, CNR, Bari.
[38] G. Sheldrick, Shelxl97. Program for structure refinement. University of Göttingen, Germany, **1997**.
[39] L. J. Farrugia, *J. Appl. Crystallogr.* **1999**, *32*, 837.
[40] M. Nardelli, *J. Appl. Crystallogr.* **1995**, *28*, 659.
[41] a) F. H. Allen, O. Kennard, R. Taylor, *Acc. Chem. Res.* **1983**, *16*, 146; b) I. J. Bruno, J. C. Cole, P. R. Edgington, M. Kessler, C. F. Macrae, P. McCabe, J. Pearson, R. Taylor, *Acta Crystallogr., Sect. B* **2002**, *58*, 389.

Received: January 9, 2006
Published Online: April 20, 2006

 © 2006 Wiley-VCH Verlag GmbH & Co. KGaA, Weinheim 

DOI: 10.1002/ejic.200600052

# Polymers or Supramolecules Generated From a New V-Shaped Bis-monodentate Ligand and the Effect of Steric Hindrance on Coordination Modes of the Ligand

**Caihua Zhou,[a,b] Yaoyu Wang,*[a] Dongsheng Li,[a,b] Lijun Zhou,[a] Ping Liu,[a] and Qizhen Shi [a]**

**Keywords:** Dipyridylamine / Helical structure / Density functional study / Silver / Copper

A new V-shaped bis-monodentate ligand L (L = 2,3′-dipyridylamine) (**1**) has been designed and synthesized by alkylation reaction of pyridylamine. An investigation of the charge distributions of the coordination atoms and single-point energy calculations of four conformers of ligand L based on the geometry of conformers optimized by the DFT (density functional theory) method was carried out. The results show that the four conformers of ligand L take on two stable and two less stable configurations. Theory forecasts that two relatively stable configurations present in complexes as probable coordination motifs of the ligand, and that steric hindrance of pyridine nitrogen atoms in isomers will affect its coordination ability together with the electronic factor. This forecast has been demonstrated by the coordination chemistry of ligand L, that is, configuration (a) and (b) of the ligand occur in the following reported complexes, which combines with $Ag^{I}$ or $Cu^{II}$ through two coordination modes (bidentate bridging or a monodentate mode) resulting in coordination polymers $\{[Ag(L)_2]NO_3\}_n$ (**2**), $[Cu_2(L)_2(maa)_4]_n$ (maa = methacrylic acid) (**3**), and the mononuclear molecule $[Cu(L)_4](ClO_4)_2 \cdot 2CH_3CH_2OH$ (**4**). The ligand assumes different coordination modes in the three complexes because of different levels of steric hindrance of the pyridine nitrogen atoms in the conformers. Interestingly, polymers **2** and **3** assume a 1D helical structure and a linear framework, respectively, and **4** has a 2D supramolecular architecture induced from hydrogen bond interactions. In addition, the magnetic properties of **3** have been explored, which shows a strong antiferromagnetic interaction.

(© Wiley-VCH Verlag GmbH & Co. KGaA, 69451 Weinheim, Germany, 2006)

## Introduction

Crystal engineering of coordination polymers and supramolecules have attracted a lot of attention due to their potential as functional materials, as well as their intriguing compositions and topologies. Considerable progress has been made on theoretical forecasting and practical approaches aimed at controlling the topology structure and geometry of the networks.[1–3] However, the general and precise principles for the solid structures of the target products are still subjective because the self-assembly process is highly influenced by several factors such as the structure of ligands, the coordination preference of metal ions, the coordination behavior of counterions, and the solvent system.[4–6] The chemical structure of the organic ligands including the molecular angle, length, and relative orientation of the donor groups plays an extremely important role in dictating polymer topology. So far, much of the research has been concentrated on the exploitation of angular ligands with a molecular angle, such as ligands with a T-shape, V-shape etc, in the construction of versatile coordination polymer architectures.[7–9] Especially, bidentate bridging ligands with a V-shaped structure have been widely used to construct coordination frameworks with a helical structure because of its flexional characteristic and the configuration stability of binding metal ions.[10,11] On the basis of the V-shaped *exo*-bidentate ligand, 2,2′-bis(4-pyridyleneoxy)-1,1′-binaphthalene[12] and 4,4′-oxy-bis(benzoate),[13] several novel helical complexes have been prepared.

With this background in mind, our research has focused on designing new V-shaped ligands and investigating the rational control of their self-assembly with metal centers. In our previous work, we successfully constructed helical structural supramolecular complexes [14] using the V-shaped 3,4′-dipyridylamine ligand. Continuing our investigations on the coordination properties of V-shaped dipyridylamine ligands, we designed another new V-shaped bis-monodentate 2,3′-dipyridylamine ligand. Particularly, this V-shaped molecule is an isomer of the well-documented molecule 2,2′-dipyridylamine, which is widely used as a chelate

[a] Department of Chemistry and Shaanxi Key Laboratory of Physico-inorganic Chemistry, Northwest University, Xi'an 710069, P. R. China
Fax: +86-29-88373398,
E-mail: wyaoyu@nwu.edu.cn
[b] Department of Chemistry and Chemical Engineering, Yan'an University, Yan'an 716000, P. R. China

 © 2006 Wiley-VCH Verlag GmbH & Co. KGaA, Weinheim 

ligand in its amine form, or as a tridentate ligand in its deprotonated form.[15,16] In order to investigate the possible coordination modes of 2,3′-dipyridylamine compared to 2,2′-dipyridylamine, we explored the electronic effect of coordination atoms, the single-point energy calculations of four conformers of 2,3′-dipyridylamine based on the geometry of four conformers optimized by the DFT method. According to these guidelines, we used 2,3′-dipyridylamine as the ligand to coordinate with $Ag^{I}$ and $Cu^{II}$, and obtained two 1D polymers with a helical or linear structure and one 2D supramolecule. Herein, we report the syntheses, crystal structures, and characterization of properties of ligand (**1**) and three complexes, namely $\{[Ag(L)_2]NO_3\}_n$ (**2**), $[Cu_2(L)_2(maa)_4]_n$ (**3**), and $[Cu(L)_4](ClO_4)_2 \cdot 2CH_3CH_2OH$ (**4**). At the same time, the magnetic properties of **3** have also been studied.

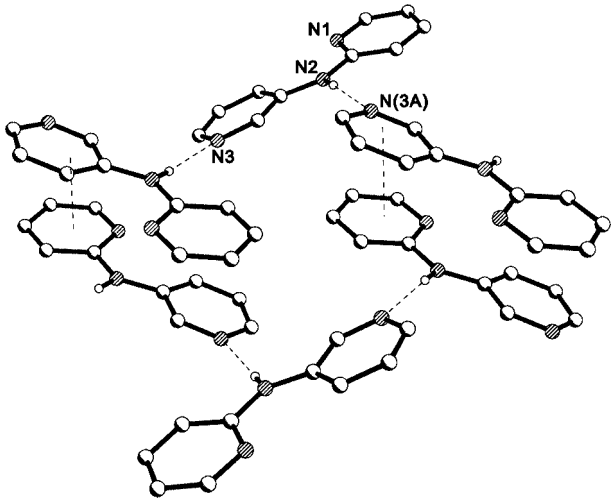


Figure 1. Perspective view of N–H···N hydrogen bonds and π-π stacking interactions in ligand **1**. [N2–N(3A) 3.0949(18) Å; N2–H···N(3A) 168.1(1)°; the distance between the centers of the pyridyl rings is 3.48(8) Å, the angle is 12.5427(4)° between two planes].

## Results and Discussion

### Description of the Structures

#### *Ligand 1*

The single-crystal X-ray structural analysis shows that ligand **1** crystallizes in an orthorhombic system. From the crystal structure of the ligand, it can be seen that the ligand forms zigzag chains in the solid state, and the molecules are held together by a series of N–H···N hydrogen bonds [N2–N(3A) 3.0949(18) Å; N2–H···N(3A) 168.1(1)°]. The two pyridine rings in the ligand are twisted with a dihedral angle of 12.5427(4)°, the ligand molecules are associated in pairs, in a head-to-tail arrangement showing π-π stacking interactions [the distance between the centers of the pyridyl rings is 3.48(8) Å, the dihedral angle is 12.5427(4)°], and give rise to a two-dimensional supramolecular structure (Figure 1).

In addition, single-point energy calculations and charge distributions for four conformers of the ligand have been carried out at DFT levels. Two stable and two less stable configurations have been obtained by structural optimization of the four conformers; the electronic layouts of the four conformers are shown in Figure 2. Single point energies of conformers (a), (b), (c), and (d) are –550.46003, –550.46214, –550.40317, and –550.40293 hartree, and the HOMO–LUMO energy gaps are 0.17477, 0.17273, 0.16899, and 0.16735 eV, respectively. These data reveal that configurations (a) and (b) are relatively more stable than (c) and (d). From the charge layouts of the four conformers, it can be seen that N1 and N3 each have an approximately equal donor electron ability in the four conformational isomers

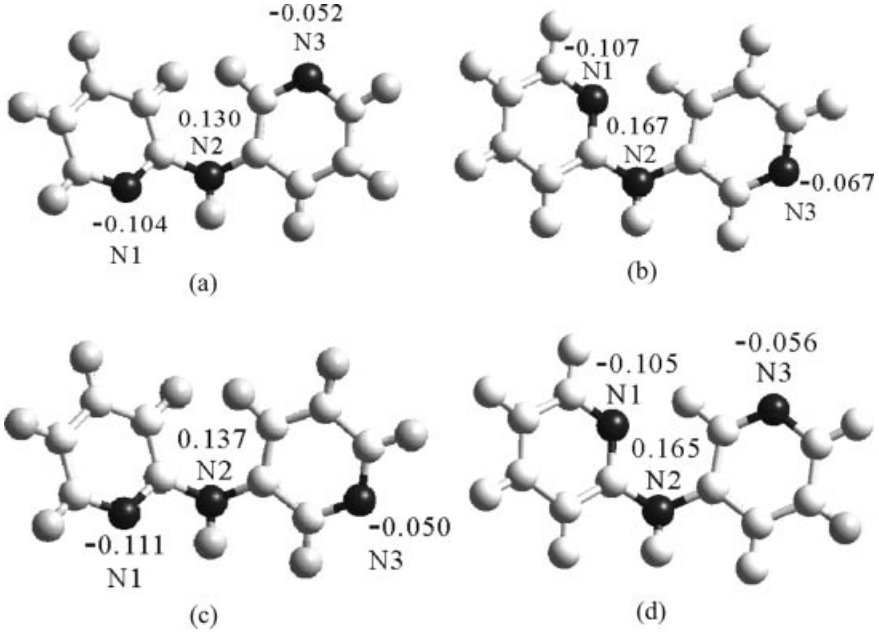


Figure 2. The four optimized conformations of the ligand **1**, as well as the calculated electron distributions.

 © 2006 Wiley-VCH Verlag GmbH & Co. KGaA, Weinheim 

(but each N1's donor electron ability is slightly stronger than that of each N3), if only considering their electronic effect.[17] However, we can see that the steric hindrance of N1 in configuration (b) and (d) is obviously larger than in configuration (a) and (c). Considering steric hindrance might affect the coordination ability of N1 in different configurations, we further investigated the coordination properties of ligand **1** with transition metal ions by experimental means. Fortunately, the experimental results prove this estimation. In the three synthetic complexes, we find that the ligand only takes on the coordination motifs of configuration (a) and (b). Configuration (b) presents in complex **4**, which combines with metal ions in a monodentate mode, and configuration (a) appears in polymers **2** and **3**, which links with metal ions in a bidentate bridging mode. Therefore, the difference in the coordination ability of N1 between configuration (a) and (b) mainly results from the difference in the steric hindrance of N1.

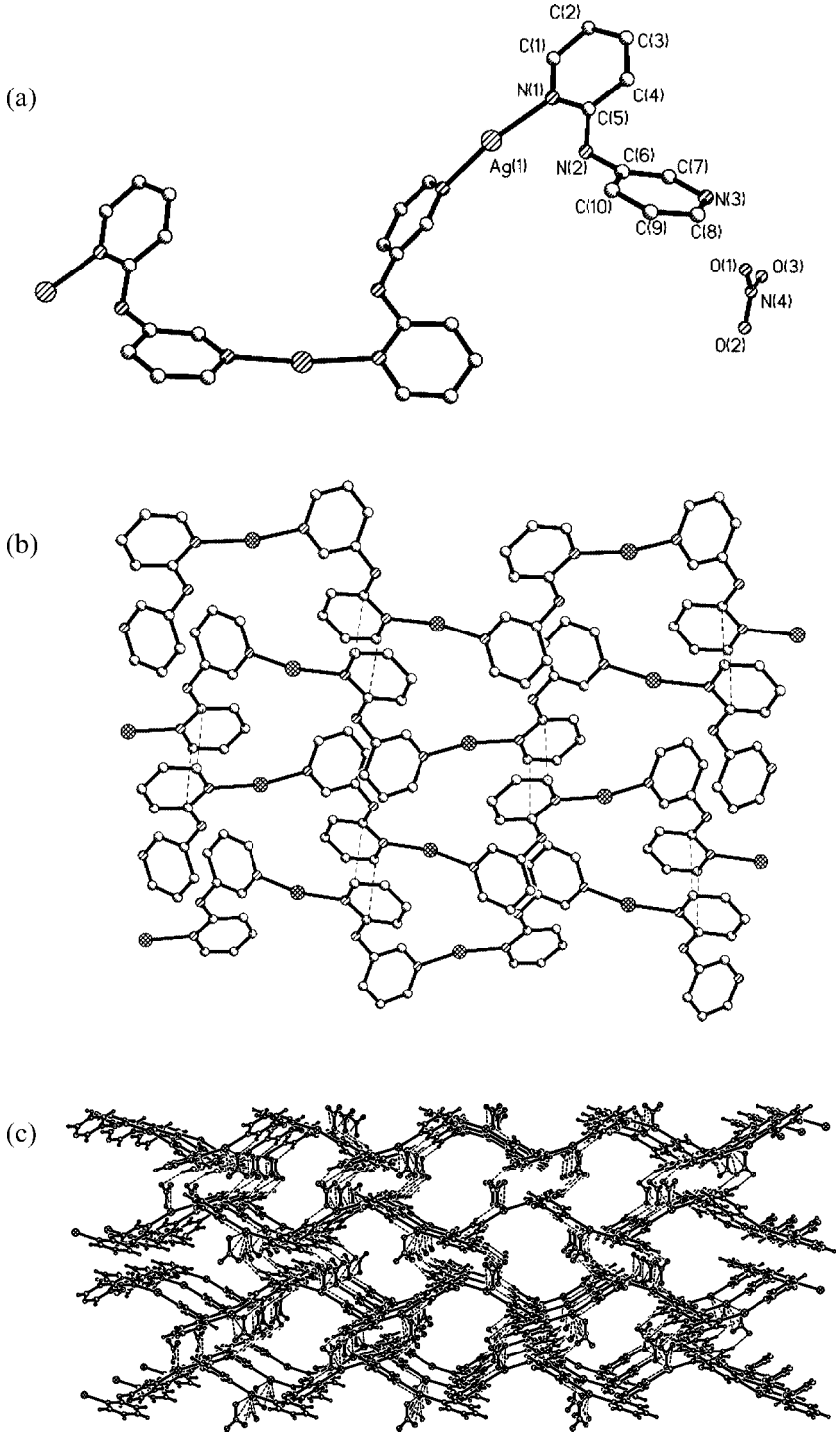


Figure 3. (a) The helical chain of **2**; (b) π-π packing interactions between helical chains; (c) the 3D structure formed by hydrogen-bonding and Ag···O weak interactions between adjacent layers.

 © 2006 Wiley-VCH Verlag GmbH & Co. KGaA, Weinheim 

### *{[Ag(L)$_2$]NO$_3$}$_n$ (2)*

The single-crystal X-ray data shows the structure of **2** consists of one-dimensional (1D) cationic polymeric $\{[Ag(L)_2]\}^+_n$ chains and uncoordinated $NO_3^-$ anions. The ligand adopts a *N*,*N*-bidentate bridging coordination mode by using two pyridine nitrogen atoms to coordinate to the $Ag^I$ centers forming a 1D helical chain (Figure 3, a). The bond angle of N1–Ag1–N(3A) is 165.09(6)°, and the bond lengths of Ag1–N1 and Ag1–N(3A) are 2.193(2) and 2.196(2) Å, respectively, which are the typical values for $Ag^I$–$N_{py}$ coordination distances.[18–21] The helices, parallel to the [010] direction, are generated around a twofold screw axis presented in the space group $P2_1/n$. Pyridine rings through centers of inversion from adjacent helical chains indicate significant π-π stacking interactions. Pyridine rings involving π-π stacking are absolutely parallel and the distances between their centroids are 3.769(6) and 3.593(8) Å, (Figure 3, b). Not only do the intermolecular π-π stacking interactions stabilize the helical frameworks but they also produce a two-dimensional layer parallel to the crystallographic *bc* plane, the same as most reported similar helical structures.[22,23]

A striking feature of **2** is the stacking pattern in the solid state. The packing diagram of **2** shows that the $NO_3^-$ counterions are sandwiched between two layers, and every layer interacts with other close layers by two groups of C–H···O hydrogen bonds between uncoordinated oxygen atoms of $NO_3^-$ and carbon atoms of the pyridine rings [C–O 3.310(2), 3.250(2) Å, C–H···O 146.63(1), and 150.35(3)°] and Ag···O weak interactions, resulting in a 3D supramolecular structure (Figure 3c).

### *[Cu$_2$(L)$_2$(maa)$_4$]$_n$ (3)*

The structure of **3** consists of linear dinuclear one-dimensional polymeric $[Cu_2(L)_2(maa)_4]_n$ chains (Figure 4, a). The basal unit of the chain is a dinuclear $Cu^{II}$ subunit of the paddle-wheel type, the two copper atoms are located at equivalent sites in the dinuclear unit. Each copper atom has a square pyramid coordination environment, with four oxygen atoms from four methacrylic groups, forming an equatorial plane, and one pyridyl nitrogen atom, occupying an axis place. The axial Cu–N distance is longer than the average Cu–O bond length. So the coordination geometry around the copper(II) atom can be regarded as a distorted square pyramid, and the Jahn–Teller effect in the polymer manifests itself as an asymmetric elongation along the axial direction. In the structure of **3**, four methacrylic acid groups are bound to the copper(II) atoms in the form of a symmetrical bridging mode (*syn*,*syn*-$\eta^1$:$\eta^1$:$\mu_2$), thus forming a $Cu_2(maa)_4$ paddle-wheel type linked by L ligands. Just as those reported coordination polymers containing the paddle-wheel type,[24,25] the bridging ligand is located in an axial position in the paddle-wheel type structure. On the other hand, this big paddle-wheel type group hinders further torsion of the two pyridine rings of the bridging ligand, and

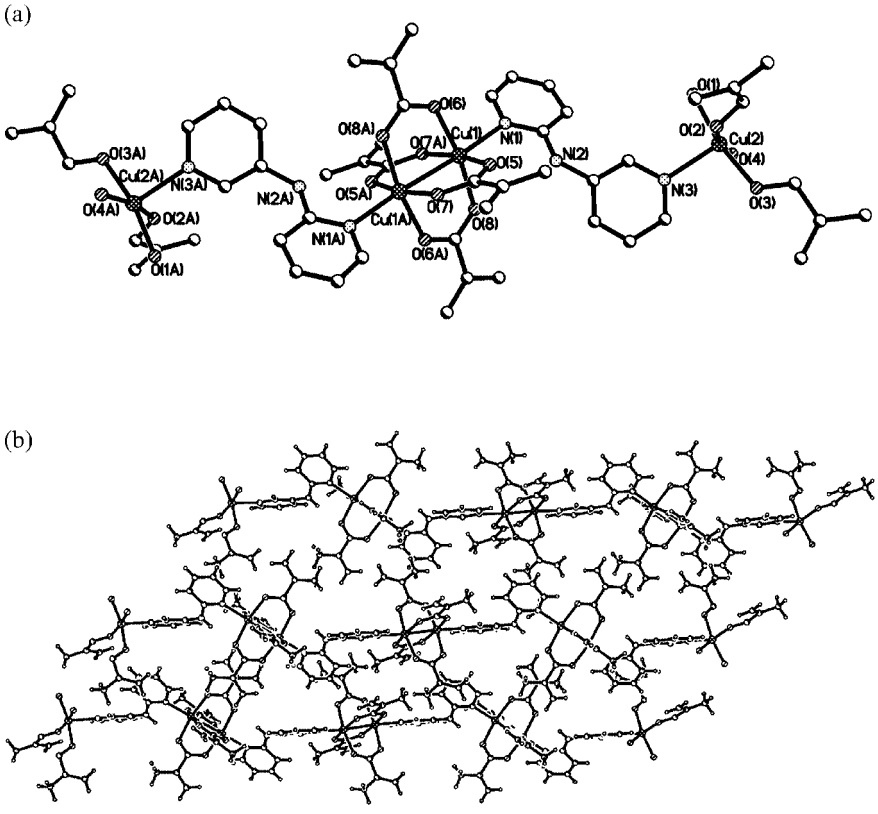


Figure 4. (a) Repeat units of the infinite coordination polymer of **3**; (b) The two-dimensional network of **3** viewed along the *a* axis.

 © 2006 Wiley-VCH Verlag GmbH & Co. KGaA, Weinheim 

causes the formation of a neutral one-dimensional linear chain rather than a helical chain. The chains self-organize and produce a two-dimensional supramolecular structure (Figure 4b) through C–H···O [C···O 3.513(5) Å, C–H···O 159.18(2)°] hydrogen bonds and C–H···π interaction [C–H···π 3.012(6) Å].

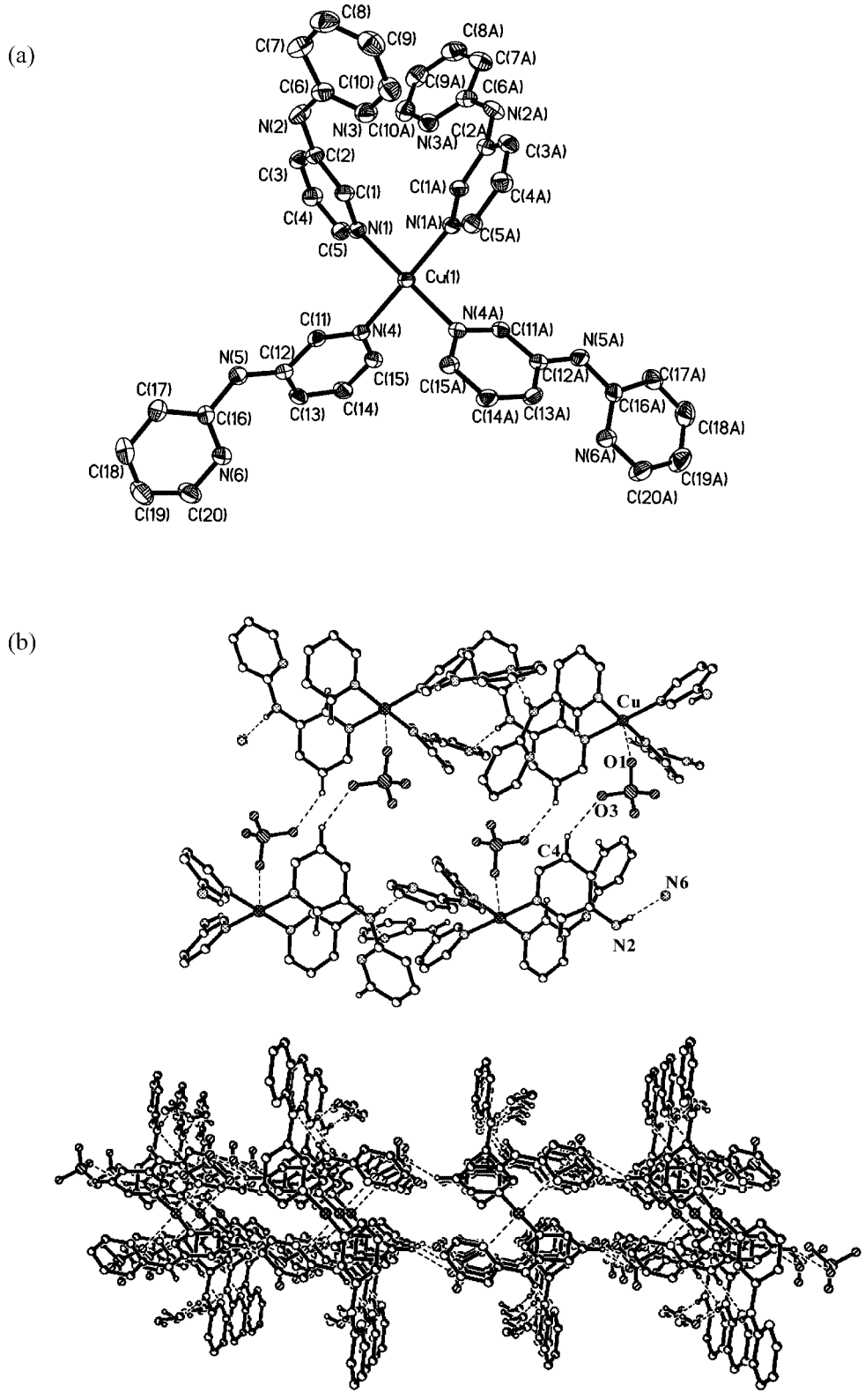


Figure 5. (a) ORTEP views showing the metal environment in the cation of **4**; (b) Perspective view of hydrogen-bonding and Cu–O weak interactions in **4** (top), and 2D packing view along the *b* axis (bottom).

 © 2006 Wiley-VCH Verlag GmbH & Co. KGaA, Weinheim 

### *[Cu(L)$_4$](ClO$_4$)$_2$·2CH$_3$CH$_2$OH (4)*

Single-crystal X-ray diffraction analysis reveals that **4** is a neutral, mononuclear molecule with the $Cu^{II}$ atom in a square coordination geometry with four pyridine nitrogen atoms of the four different dipyridylamine ligands (Figure 5, a). From the data about the N–Cu–N bond angles [89.14(14), 90.23(10), 90.23(10), and 90.42(13)°] and the Cu–N bond lengths [2.011(2), 2.011(2), 2.019(2), and 2.019(2) Å], it can be seen that the $Cu^{II}$ ions together with the four nitrogen atoms form a perfect square geometry, and this ideal quadrangle structure is rare in the coordination geometry of $Cu^{II}$. A twofold rotary axis along the *b* axis direction presenting in space group *C*2/*c* is the typically symmetrical operation of **4**. The dihedral angles between two pyridine planes are about 28.106(2), 28.106(2), 23.418(2), and 23.418(2)° in the four ligands respectively, which are obviously larger than the free ligand **1**. This indicates that the ligand coordinated to the metal $Cu^{II}$ promoted flexion of the $\sigma_{C-N}$ bond. Interestingly, the four ligands all adopt a monodentate coordination mode and they all present in **4** as configuration (b), which further proves the theoretical judgment that the coordination ability of N1 atoms in configuration (b) has been reduced by a steric barrier. Two O atoms of the uncoordinated $ClO_4^-$ anions form the acceptors of C(4)–H···O(3) [C–O 3.277(5) Å, C–H···O 140.36(2)°] intermolecular hydrogen bonds and $Cu^{II}$···O(1) weak interactions, which link the discrete units to form a 2D supramolecular structure together with the N(2)–H···N(6) [N–N 3.130(4) Å, N–H···N 176.69(3)°] intermolecular hydrogen bonds (Figure 5, b). In this complex, the uncoordinated $ClO_4^-$ anions are an essential part of the structure, which act as a key linker in the 2D supramolecular structure, similar to $BF_4^-$ in the reported complex $[(CH_3OH)_2Co(L)_4](BF_4)_4$.[26] However, the ethonal molecule present in complex **4** only functioned as an acceptor of intramolecular hydrogen bonds between the oxygen atoms of ethonal and amino nitrogen atoms of the ligand, which has little influence on the extended structure of complex **4**.

It is worth noting that **4** has a higher stability than the organic ligand owing to the fact that the single point energy (–2397.66179 hartree) of **4** is far lower than that of **1**. The HOMO–LUMO energy gap of **4** is 0.1332 eV, and the ligand has a high contribution to the front orbit of **4**. In addition, comparing this new ligand with 2,2′-dipyridylamine, we find that there are several differences between them: (i) 2,3′-dipyridylamine is a monodentate or bidentate ligand, and 2,2′-dipyridylamine is a chelate or monodentate ligand[27] in their amine form; (ii) 2,3′-dipyridylamine is an asymmetrical V-shaped molecule that may produce different conformers in complexes, and 2,2′-dipyridylamine is a symmetrical molecule that generally has three coordination modes, *syn-syn*, *syn-anti*, and *anti-anti*;[28] (iii) the *syn-syn* conformation of 2,2′-dipyridylamine builds many linear conformations of metal complexes in its deprotonated form,[29] and 2,3′-dipyridylamine can not form linear chains of metal atoms.

### IR Spectra and TGA Analysis

IR spectra of the three complexes and the L ligand were recorded as KBr pellets in the range 4000–400 $cm^{-1}$. Ligand **1** shows a broad band at 3535 $cm^{-1}$, which can be assigned as the stretch absorption of ν(N–H). The next group of bands appears at 3071 $cm^{-1}$, corresponding to stretching vibrations of ν(C–H). Skeletal vibration of the pyridine ring shows a strong band at 1503 $cm^{-1}$. Because of the formation of intermolecular coordination bonds and hydrogen bonds, these absorption peaks are significantly shifted to lower frequencies in three complexes. In **2**, ν(N–H), ν(C–H), and the pyridine ring skeleton exhibit at 3448, 3017, and 1484 $cm^{-1}$, respectively; there is a strong absorption appearing at 1355.15 $cm^{-1}$ for the noncoordinated anions of nitrate ($NO_3^-$). While in **3** the three characteristic peaks appear at 3526, 2923, and 1496 $cm^{-1}$. Another characteristic absorption for **3** is concerned with the values of asymmetric and symmetric stretching frequencies for the $COO^-$ groups. The difference between $\nu_{as}$(COO) and $\nu_s$(COO) in comparison to the corresponding values in ionic species is currently employed to determine a characteristic coordination mode of the carboxylate group.[30] For **3**, the complex shows strong bands corresponding to $\nu_{as}$(COO) and $\nu_s$(COO) at 1601 and 1415 $cm^{-1}$, respectively. The $\Delta\nu$ is 186 $cm^{-1}$, close to the corresponding values for the sodium methacrylic (178 $cm^{-1}$), indicating that the methacrylic groups coordinate to metal ions in a symmetrical bridging mode (*syn*,*syn*-$\eta^1$:$\eta^1$:$\mu_2$), in agreement with the paddle-wheel type structure of **3**. The IR spectra of **4** is similar to **2**, ν (N–H), ν (C–H), and the pyridine ring skeleton exhibit at 3621, 3206, and 1501 $cm^{-1}$, respectively. There is a slight red shift in **4** compared to **2** and **3** because of the more conjugated pyridine rings presenting in **4**. Meanwhile, a strong absorption band appears at 1131 $cm^{-1}$ for the noncoordinated $ClO_4^-$ anions. The bands appearing below 600 $cm^{-1}$ may be assigned to the M–N frequencies for the three complexes.

The thermogravimetric analysis (TGA) reveals the weight loss of **2** occurs in two stages. The first stage occurs between 208.7 and 428.6 °C with a weight loss of 66.99%, which is equivalent to the loss of the ligands (calculated to be 66.83%). The total thermal effect of decomposition and oxidation of the ligand causes an exothermic peak at 216.5 C. When the temperature is above 440 °C, the $AgNO_3$ begins to decompose and metal silver is the final product, which constitutes 20.86% (calculated to be 20.93%). In contrast to **2**, the TGA shows that the weight of **3** remains almost unchanged from 40 to 180 °C. In the temperature range 180–400 °C, the complex undergoes a large weight loss of 76.67%, which represents weight loss from L and the methacrylic groups (calculated to be 79.12%). The DSC curve shows an exothermic peak at 218.4 °C, and the final product is CuO in 21.33% yield (calculated to be 20.88%). Complex **4** has undergone two steps of weight loss. The first weight loss occurs at 50–180 °C, corresponding to the loss of ethanol molecules. The higher temperature for the release of ethanol molecules is due to the strong hydrogen bonds involving ethanol molecules in

 © 2006 Wiley-VCH Verlag GmbH & Co. KGaA, Weinheim 

**4**. At this step, the experimental percentage weight loss is 8.01% (calculated to be 8.85%). The following steps of weight loss represent the pyrolysis of the organic ligand. The residues above 500 °C have a composition of CuO, and the observed residue percentage is 7.31% (calculated to be 7.69%).

### Magnetic Properties

Variable-temperature magnetic susceptibility measurements over a 5–300 K range were carried out for **3**. The temperature dependence of magnetic susceptibilities $\chi_M$ and $\chi_M T$ of complex **3** is shown in Figure 6. It should be noted that polymer **3** exhibits two types of magnetic exchange interaction between two $Cu^{II}$ ions; one is through short bridges via the methacrylic groups and the other is through a long bridge via L. Actually, because of the long L ligand fragment, the possibility of overlap of the magnetic orbital through the C and N atoms of L is negligible. Hence, the $Cu_2(maa)_4$ unit of paddle-wheel type plays an important role in the magnetic properties of polymer **3**. This type of antiferromagnetic interaction is strong because unpaired electron density from both Cu ions is transferred to the same orbital of the bridging methacrylic groups. The $\chi_M$ curve is typical for a very strong antiferromagnetic coupling with a small amount of paramagnetic impurities: the molar magnetic susceptibility decreases to a minimum and then suddenly increases when the temperature is lowered, attaining a maximum. The magnetic datafit to a Bleaney–Bowers equation,[31,32] which was derived from the spin Hamiltonian $H = -JS_1S_2$. The best-fit parameters are $-2J = 316\ cm^{-1}$, $g = 2.09$, and $R = 6.8 \cdot 10^{-4}$ ($R = \Sigma[(\chi_M T)_{obs} - (\chi_M T)_{calc}]^2/\Sigma[(\chi_M T)_{obs}]^{1/2}$). In contrast to the reported dinuclear $Cu^{II}$ carboxylates, such as $Cu_2(C_{10}H_9O_2)_4(C_2H_5OH)_2$ ($-2J = 242\ cm^{-1}$),[33] $Cu_2(C_7H_{15}COO)_4$ ($-2J = 320\ cm^{-1}$), and $Cu_2(C_7H_{15}COO)_4(C_6H_7N)_2$ ($-2J = 300\ cm^{-1}$),[34] polymer **3** ($-2J = 316\ cm^{-1}$) shows a considerably stronger antiferromagnetic interaction.

## Conclusions

In summary, a new V-shaped ligand **1** has been designed and synthesized. Density functional calculations at the B3LYP level of theory provide a satisfactory forecast for coordination properties of the ligand with metal ions. That is, two relatively stable conformers of the ligand combine with metal ions by different coordination modes. On the basis of ligand **1**, we have synthesized three novel complexes, $\{[Ag(L)_2]NO_3\}_n$ (**2**), $[Cu_2(L)_2(maa)_4]_n$ (maa = methacrylic acid) (**3**), and $[Cu(L)_4](ClO_4)_2 \cdot 2CH_3CH_2OH$ (**4**). Interestingly, polymers **2** and **3** assume a 1D helical structure and a linear framework, respectively, and **4** has a 2D supramolecular structure. Although the two relatively stable configurations of the ligand have very similar single-point energies and charge distributions, they form different coordination modes in the three complexes. These results indicate that the steric factors of the N atoms play important roles in the coordination modes of the dipyridylamine ligand, which may help us to understand the influence of organic spacers in determining the type and topology of the product.

## Experimental Section

**Physical Measurements:** Elemental analyses (C,H,N) were determined with a Perkin–Elmer 240C elemental analyzer. Infrared spectra on KBr pellets were recorded with a Bruker EQUINOX-55 spectrometer in the range of 4000–400 $cm^{-1}$. Thermal analyses were performed with a Netzsch STA 449C microanalyzer with a heating rate of 10 °C·$min^{-1}$ under air. Magnetic measurements were carried out on a polycrystalline sample with a SQUID magnetometer operating in the 5–300 K temperature range with an applied field of 5 kOe. Diamagnetic corrections were estimated from Pascal constants. $^1H$ NMR spectra were recorded with a Varian INOVA 400-MHz spectrometer. Electronic spectra were recorded with a Cary 300 Bio UV/Visible spectrophotometer. Mass spectra were obtained with a JEOL HX-110 HF double focusing spectrometer operating in the positive ion detection mode.

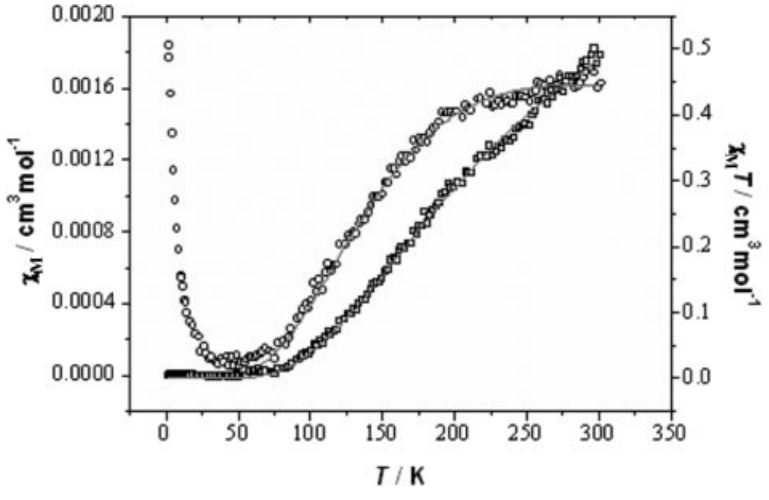


Figure 6. Plot of $\chi_M$ (○) (left scale) and $\chi_M T$ (□) (right scale) per $Cu^{II}$ ion vs. $T$ for **3**. The solid lines represent the best fit to the modified Bleaney–Bowers expression.

 © 2006 Wiley-VCH Verlag GmbH & Co. KGaA, Weinheim 

**The Synthesis of Ligand 1:** The reagents and solvents were purchased from commercial sources (Aldrich) and used as received. The 2,3′-dipyridylamine ligand was obtained as follows (Scheme 1): 2-aminopyridine (2.80 g, 34.8 mmol) and NaOBu (6.90 g, 72.9 mmol) were added to a 200 mL flask under nitrogen. Then the solution of 3-bromopyridine (3.44 mL, 34.8 mmol) and dry benzene (100 mL) were added to the container. The resulting solution was stirred for 72 h under reflux, and then cooled to room temperature. The original product was filtered and washed with dry benzene and water several times. The final product was purified by column chromatography on silica gel (dichloromethane/hexane, 1:1) to afford a colorless crystalline solid (4.16 g, 69.82%). $C_{10}H_9N_3$ (171.20): calcd. C 70.17, H 5.263, N 24.54; found C 69.98, H 5.210, N 24.66. IR (KBr): $\tilde{\nu}_{max}$ = 3535 (s), 3434 (s), 3294 (s), 3172 (s), 3071 (m), 3000 (m), 1643 (m), 1592 (m), 1503 (s), 1476 (s), 1421 (s), 1270 (m), 1210 (m), 1051 (s), 902 (m), 824 (m), 732.44 (s), 677 (m), 574 (w) $cm^{-1}$. UV/Vis ($\lambda$/nm): 320, 260, 220. MS (FAB): *m/z* (%) = 171.2 (L). $^1H$ NMR ($CDCl_3$): $\delta$ = 8.59 (s, 1 H, 1-H), 7.05 (s, 1 H, 2-H), 8.02 (d, 1 H, $^3J$ = 4.4 Hz, 3-H), 7.54 (dd, 1 H, $^3J$ = 5.8, $^3J$ = 5.4, 4-H), 7.27 (d, 1 H, $^3J$ = 5.8 Hz, 5-H), 6.80 (d, 2 H, $^3J$ = 6.3 Hz, 6-H), 8.25 (d, 2 H, $^3J$ = 3 Hz, 7-H) ppm.

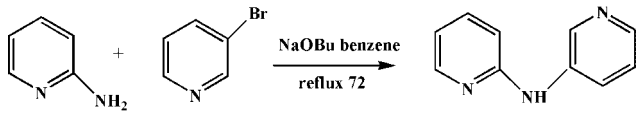


Scheme 1. The preparation of ligand 2,3′-dipyridylamine.

**The Synthesis of the Complexes**

The formation of **2**, **3**, and **4** with experimental conditions are shown in Scheme 2, their syntheses are given in the sequel.

**{[Ag(L)$_2$]NO$_3$}$_n$ (2):** A solution of silver(I) nitrate (16.9 mg, 0.1 mmol) in $CH_2Cl_2$ (10 mL) was added to a solution of L (17.1 mg, 0.1 mmol) in $CH_2Cl_2$ (10 mL). The reaction mixture was stirred at 25 °C for 1 h, and then the solvent was removed under reduced pressure. The resulting white powder was partially dissolved in acetonitrile (5 mL) ($CH_3CN$). The mixture was filtered,

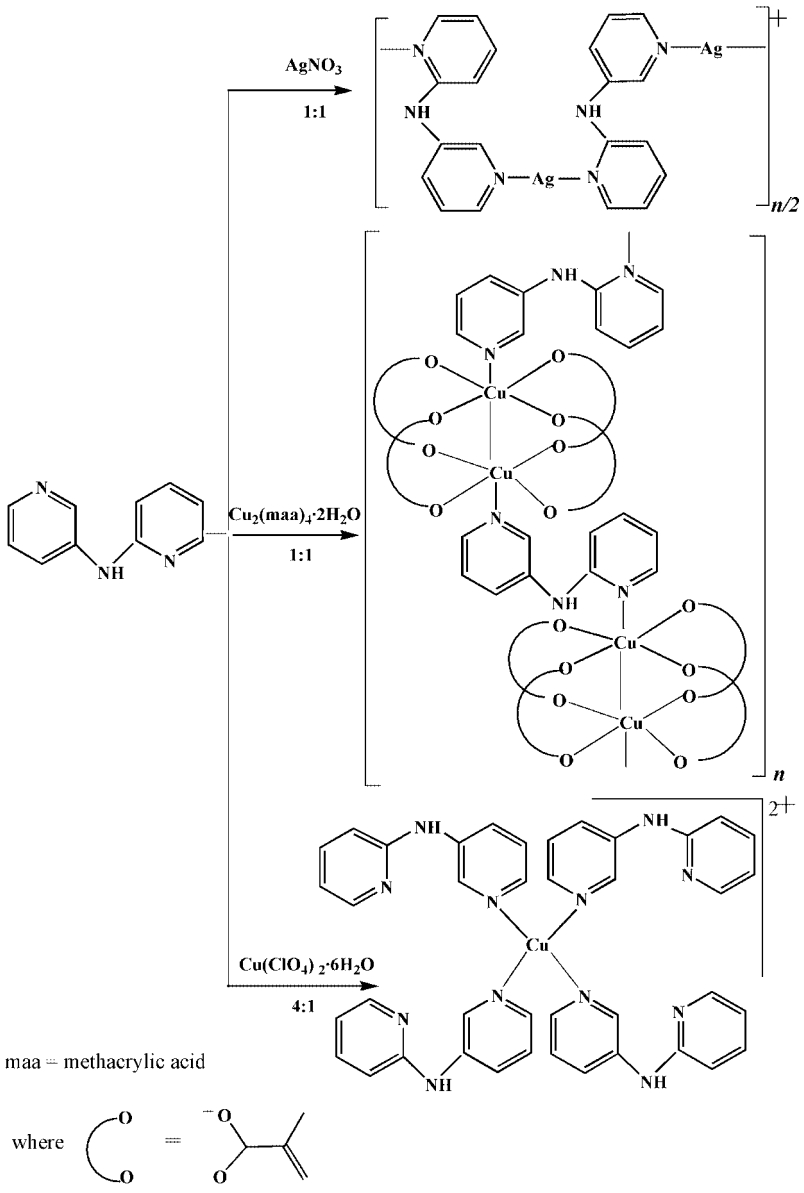


Scheme 2. The formation of **2**, **3**, and **4** with experimental conditions.

 © 2006 Wiley-VCH Verlag GmbH & Co. KGaA, Weinheim 

Table 1. Crystal data and structure refinements for **1**–**4**.

| Complex | **1** | **2** | **3** | **4** |
|---|---|---|---|---|
| Empirical formula | $C_{10}H_9N_3$ | $C_{10}H_8AgN_4O_3$ | $C_{26}H_{29}Cu_2N_3O_8$ | $C_{44}H_{48}Cl_2CuN_{12}O_{10}$ |
| Formula mass | 171.20 | 340.07 | 638.68 | 1039.38 |
| Temperature [K] | 273(2) | 273(2) | 273(2) | 296(2) |
| Crystal system | orthorhombic | monoclinic | triclinic | monoclinic |
| Space group | *Pbca* | $P2_1/n$ | $P\bar{1}$ | $C2/c$ |
| *a* [Å] | 9.2018(3) | 8.293(3) | 9.092(8) | 27.767(4) |
| *b* [Å] | 11.9210(5) | 14.174(4) | 9.229(8) | 10.7067(14) |
| *c* [Å] | 15.6331(6) | 9.751(3) | 17.335(15) | 18.144(2) |
| α [°] | 90 | 90 | 93.786(13) | 90 |
| *β* [°] | 90 | 101.064(5) | 91.981(15) | 115.891(9) |
| *γ* [°] | 90 | 90 | 97.735(14) | 90 |
| *V* [Å$^3$] | 1714.87(11) | 1125.0(6) | 1437(2) | 4852.6(11) |
| *Z* | 8 | 4 | 2 | 4 |
| $D_{calcd.}$[g·cm$^{-3}$] | 1.326 | 2.008 | 1.572 | 1.423 |
| *μ* [mm$^{-1}$] | 0.084 | 1.798 | 0.829 | 0.629 |
| *F* [000] | 720 | 668 | 714 | 21562 |
| *θ* [°] | 2.61–25.09 | 2.57–29.15 | 2.23–29.19 | 1.63–25.10 |
| Data/restraints/parameters | 1521/0/119 | 2769/0/164 | 6693/0/357 | 4315/0/314 |
| Goodness-of-fit on $F^2$ | 1.043 | 1.045 | 0.999 | 1.073 |
| $R_1$ $wR_2$[a] [$I > 2\sigma(I)$] | 0.0417, 0.1069 | 0.0220, 0.0581 | 0.0455, 0.1268 | 0.0474, 0.1205 |

[a] $R_1 = \Sigma(||F_o| - |F_c|)/\Sigma|F_o|$; $wR_2 = [\Sigma w(F_o^2 - F_c^2)^2/\Sigma w(F_o^2)^2]^{1/2}$.

and diethyl ether vapor was diffused into this solution. After several days, suitable single crystals for X-ray diffraction could be obtained from the acetonitrile solution. Yield: 83.98% (28.56 mg). $C_{10}H_8AgN_4O_3$ (340.07): calcd. C 35.19, H 2.34, N 16.42; found C 35.13, H 2.40, N 16.67.

**$[Cu_2(L)_2(maa)_4]_n$ (3):** $Cu_2(maa)_4{\cdot}2H_2O$ was prepared according to a similar method reported previously in the literature.[35] A methanol solution (20 mL) of L (17.1 mg, 0.1 mmol) was slowly added to a solution of $Cu_2(maa)_4{\cdot}2H_2O$ (50.4 mg, 0.1 mmol) dissolved in methanol/ethanol (20 mL, v/v = 1:1). The resultant solution was allowed to evaporate slowly for several days at room temperature, and block-shaped green crystals of **1** were obtained. Yield: 66.82% (42.63 mg). $C_{26}H_{29}Cu_2N_3O_8$ (638.68): calcd. C 50.13, H 5.48, N 10.96; found: C 50.12, H 5.45, N 10.94.

**$[Cu(L)_4](ClO_4)_2{\cdot}2CH_3CH_2OH$ (4):** The solution of $Cu(ClO_4)_2{\cdot}6H_2O$ (37.05 mg, 0.1 mmol) in ethanol (10 mL) was carefully layered on top of a solution of L (68.4 mg, 0.4 mmol) in chloroform (10 mL) in a test tube. After several days at room temperature, yellow green single crystals appeared at the boundary between ethanol and chloroform with a yield of 63.66% (66.17 mg). $C_{44}H_{48}Cl_2CuN_{12}O_{10}$ (1039.38): calcd. C 50.85, H 4.65, N 16.17; found C 50.87, H 4.60, N 16.14.

**Crystal Data Collection and Refinement:** Diffraction experiments for **1**, **2**, **3**, and **4** were carried out with Mo-$K_\alpha$ radiation using a Bruker SMART APEXCCD diffractometer at 273(2) K for **1**, **2**, **3**, and 296(2) K for **4**. A summary of the crystallographic data and structure refinement is given in Table 1, and selected bond lengths and angles of the four complexes are listed in Table 2. All structures were solved by direct methods and refined with the full-matrix least-squares technique on $F^2$ using the SHELXS-97[36] and SHELXL-97[37] programs. All non-hydrogen atoms were refined anisotropically.

X-ray crystallographic data in CIF format for the structures reported in this paper have been deposited with the Cambridge Crystallographic Data Centre, CCDC-277949 (for **1**), -277950 (for **2**), -277951 (for **3**), and -294858 (for **4**). These data can be obtained free of charge from The Cambridge Crystallographic Data Centre via www.ccdc.cam.ac.uk/data_request/cif.

Table 2. Selected bond lengths [Å] and angles [°] for **1**–**4**.

| | | | |
|---|---|---|---|
| Ligand **1** | | | |
| C(6)–N(3) | 1.324(2) | C1–N(1) | 1.329(2) |
| C(10)–N(3) | 1.339(2) | C(5)–N(1) | 1.350(2) |
| C(1)–N(2)–C(7) | 129.87(13) | | |
| Complex **2** | | | |
| Ag(1)–N(1) | 2.193(2) | Ag(1)–N(3A) | 2.196(2) |
| N(1)–Ag(1)–N(3A) | 165.09(6) | | |
| Complex **3** | | | |
| Cu(1)–O(7)A | 1.960(3) | Cu(1)–O(8) | 1.970(3) |
| Cu(1)–O(6) | 1.964(3) | Cu(1)–O(5) | 1.970(3) |
| Cu(1)–N(1) | 2.193(3) | Cu(1)–Cu(1A) | 2.6280(19) |
| Cu(2)–N(3) | 2.183(3) | Cu(2)–Cu(2A) | 2.6416(18) |
| O(7A)–Cu(1)–O(6) | 89.64(12) | O(6)–Cu(1)–O(8) | 168.32(10) |
| O(6)–Cu(1)–O(5) | 90.33(12) | O(8)–Cu(1)–O(5) | 88.27(12) |
| O(7A)–Cu(1)–N(1) | 94.32(11) | O(6)–Cu(1)–N(1) | 93.92(12) |
| O(4)–Cu(2)–N(3) | 98.89(13) | O(1)–Cu(2)–N(3) | 96.92(12) |
| O(3)–Cu(2)–N(3) | 95.11(12) | O(2)–Cu(2)–N(3) | 93.12(13) |
| Complex **4** | | | |
| Cu(1)–N(1) | 2.011(2) | Cu(1)–N(1A) | 2.011(2) |
| Cu(1)–N(4) | 2.019(2) | Cu(1)–N(4A) | 2.019(2) |
| N(1)–Cu(1)–N(1A) | 89.14(14) | N(1)–Cu(1)–N(4) | 90.23(10) |
| N(1A)–Cu(1)–N(4A) | 90.23(10) | N(4)–Cu(1)–N(4A) | 90.42(13) |

Symmetry code: A: $x-1/2$, $-y+1/2$, $-z$ for **1**, $-x+3/2$, $y-1/2$, $-z+1/2$ for **2**, $-x+2$, $-y+2$, $-z$ for **3** and $-x+1$, $y$, $-z+3/2$ for **4**.

**Calculation Details:** The single-point energy and the orbit calculations based on the geometry of the free ligand and complex **4** were optimized by the DFT method using the B3LYP/LanL2DZ basis set in the Gaussian 03 program.[38] The data analyses were performed with Hyperchem 7.5 and GaussView 3.0.

## Acknowledgments

This work was supported by the National Natural Science Foundation of China (Grant No. 20471048) and TRAPOYT.

 © 2006 Wiley-VCH Verlag GmbH & Co. KGaA, Weinheim 

[1] D. M. Shin, I. S. Lee, Y. K. Chung, *Inorg. Chem.* **2003**, *42*, 8838–8846.
[2] Z. B. Han, X. N. Cheng, X. M. Chen, *Cryst. Growth Des.* **2005**, *5*, 695–700.
[3] L. F. Anne-Marie, A. L. David, J. L. Paul, M. Z. Alexandra, D. B. Walker, *J. Am. Chem. Soc.* **2005**, *127*, 12612–12619.
[4] C. M. Zaleski, E. C. Depperman, C. D. Samara, M. Alexiou, D. P. Kessissoglou, M. L. Kirk, *J. Am. Chem. Soc.* **2005**, *127*, 12862–12872.
[5] B. Moulton, J. Lu, M. J. Zaworotko, *J. Am. Chem. Soc.* **2001**, *123*, 9924–9925.
[6] B. E. Villarroya, C. Tejel, M. M. Rohmer, O. A. Luis, *Inorg. Chem.* **2005**, *44*, 6536–6544.
[7] C. Y. Su, Y. P. Cai, C. L. Chen, M. D. Smith, W. Kaim, H. C. Loye, *J. Am. Chem. Soc.* **2003**, *125*, 8595–8613.
[8] Y. L. Jack, A. R. Karren, N. Christine, *Inorg. Chem.* **2001**, *40*, 4516–4517.
[9] H. Gudbjartson, K. Biradha, K. M. Poirier, M. J. Zaworotko, *J. Am. Chem. Soc.* **1999**, *121*, 2599–2600.
[10] K. Biradha, C. Seward, M. J. Zaworotko, *Angew. Chem. Int. Ed.* **1999**, *38*, 492–495.
[11] C. L. Chen, H. Y. Tan, J. H. Yao, C. Y. Su, *Inorg. Chem.* **2005**, *44*, 8510–8520.
[12] R. H. Wang, L. J. Xu, X. S. Li, Y. M. Li, M. C. Hong, A. S. C. Chan, *Eur. J. Inorg. Chem.* **2004**, 1595–1599.
[13] X. M. Chen, G. F. Liu, *Chem. Eur. J.* **2002**, *8*, 4811–4817.
[14] C. H. Zhou, H. Y. Zhu, Y. Y. Wang, D. S. Li, Q. Z. Shi, *J. Mol. Struct.* **2005**, *779*, 61–67.
[15] Y. J. Kang, C. Seward, D. T. Song, S. N. Wang, *Inorg. Chem.* **2003**, *42*, 2789–2797.
[16] M. M. Rohmer, M. Be'nard, *J. Am. Chem. Soc.* **1998**, *120*, 9372–9373.
[17] Y. B. Xie, J. R. Li, C. Zhang, X. H. Bu, *Cryst. Growth Des.* **2005**, *5*, 1743–1749.
[18] V. J. Catalano, M. A. Malwitz, A. O. Etogo, *Inorg. Chem.* **2004**, *43*, 5714–5724.
[19] D. A. McMorran, P. J. Steel, *Chem. Commun.* **2002**, 2120–2121.
[20] M. C. Hong, Y. J. Zhao, W. P. Su, R. Cao, M. Fujita, Z. Y. Zhou, A. S. C. Chan, *Angew. Chem. Int. Ed.* **2000**, *39*, 2468–2470.
[21] D. A. McMorran, P. J. Steel, *Chem. Commun.* **2002**, 2120–2121.
[22] G. H. Cui, J. R. Li, J. L. Tian, X. H. Bu, S. R. Batten, *Cryst. Growth Des.* **2005**, *5*, 1775–1780.
[23] H. L. Zhu, Y. X. Tong, X. M. Chen, *J. Chem. Soc., Dalton Trans.* **2000**, 4182–4186.
[24] X. J. Luan, Y. Y. Wang, L. J. Zhou, C. H. Zhou, Q. Z. Shi, *J. Mol. Struct.* **2005**, *750*, 63–68.
[25] M. Taybani, K. Feghali, S. Gambrotta, G. P. A. Yap, *Inorg. Chem.* **2001**, *40*, 1399–1401.
[26] H. Amouri, L. Mimassi, M. N. Rager, B. E. Mann, C. Guyard-Duhayon, L. Raehm, *Angew. Chem.* **2005**, *117*, 4619–4622; *Angew. Chem. Int. Ed.* **2005**, *44*, 4543–4546.
[27] S. Kar, N. Chanda, S. M. Mobin, F. A. Urbanos, R. J. Aparicio, G. K. Lahiri, *Inorg. Chem.* **2005**, *44*, 1571–1579.
[28] J. T. Sheu, C. C. Lin, I. Chao, C. C. Wang, S. M. Peng, *Chem. Commun.* **1996**, 315–316.
[29] F. A. Cotton, L. M. Daniels, C. A. Murillo, I. Pascual, *J. Am. Chem. Soc.* **1997**, *119*, 10223–10224.
[30] G. B. Deacon, R. J. Phillips, *Coord. Chem. Rev.* **1980**, *33*, 227–238.
[31] B. Bleaney, K. D. Bowers, *Proc. R. Soc. London, Ser. A* **1952**, *214*, 451–465.
[32] O. Kahn, *Molecular Magnetism*, VCH, Weinheim, Germany, **1993**.
[33] F. P. W. Agterberg, H. A. J. Provo Kluit, W. L. Driessen, H. Oevering, W. Buijs, M. T. Lakin, A. L. Spek, J. Reedijk, *Inorg. Chem.* **1997**, *36*, 4321–4328.
[34] C. C. Hadjikostas, G. A. Katsoulos, M. P. Sigalas, C. A. Tsipis, *Inorg. Chim. Acta* **1990**, *67*, 165–168.
[35] Y. Y. Wang, Q. Shi, Q. Z. Shi, Y. C. Gao, Z. Y. Zhou, *Chin. Sci. Bull.* **1998**, *43*, 2512–2516.
[36] G. M. Sheldrick, *SHELXS 97*, Program for Crystal Structure Solution, University of Göttingen, Germany, **1997**.
[37] G. M. Sheldrick, *SHELXL 97*, Program for Crystal Structure Refinement, University of Göttingen, Germany, **1997**.
[38] M. J. Frisch, G. W. Trucks, H. B. Schlegel, G. E. Scuseria, M. A. Robb, J. R. Cheeseman, V. G. Zakrzewski, J. A. Montgomery, R. E. Stratmann, J. C. Burant, S. Dapprich, J. M. Millam, A. D. Daniels, K. N. Kudin, M. C. Strain, O. Farkas, J. Tomasi, V. Barone, M. Cossi, R. Cammi, B. Mennuci, C. Pomelli, C. Adamo, S. Clifford, J. Ochterski, G. A. Petersson, P. Y. Ayala, Q. Cui, K. Morokuma, D. K. Malick, A. D. Rabuck, K. Raghavachari, J. B. Foresman, J. Cioslowski, J. V. Oritz, B. B. Stefanov, G. Liu, A. Liashenko, P. Piskorz, I. Komaromi, R. Gomperts, R. L. Martin, D. J. Fox, T. Keith, M. A. Al-Laham, C. Y. Peng, A. Nanayakkara, C. Gonzalez, M. Challacombe, P. M. W. Gill, B. G. Johnson, W. Chen, M. W. Wong, J. L. Andres, M. Head-Gordon, E. S. Replogle, J. A. Pople, *GAUSSIAN03, Revision C.02*; Gaussian, Inc., Pittsburgh, PA, **2003**.

Received: January 18, 2006
Published Online: April 20, 2006

 © 2006 Wiley-VCH Verlag GmbH & Co. KGaA, Weinheim 

DOI: 10.1002/ejic.200600057

# Synthesis and Characterization of Two Silver Iodides with One- and Three-Dimensional Hybrid Structures Constructed From Ag···Ag Interactions and Organic Templates

**Hao-Hong Li,[a] Zhi-Rong Chen,[a] Jun-Qian Li,*[a,b] Chang-Cang Huang,[a] Yong-Fan Zhang,[a] and Gui-Xiao Jia[a]**

**Keywords:** Coordination polymers / Iodine / Organic-inorganic hybrid composites / Silver

Two new organically templated silver iodides, namely $[(bmph)(Ag_5I_7)]_n$ (**1**) and $[(Hteda)_4(Ag_{12}I_{16})]_n$ (**2**), have been synthesized with $bmph^{2+}$ and teda [$bmph^{2+}$ = 1,6-bis(4-methylpyridinio)hexane, Hteda = protonated triethylenediamine] as structure-directing agents. Complex **1** consists of a one-dimensional polymer that can be described as edge-sharing $AgI_4$ tetrahedra, whereas **2** is the first example of a three-dimensional Ag/I framework based on Ag···Ag weak interactions and an organic template. Electrostatic interactions between the organic countercations and inorganic moieties are present and contribute to the crystal packing. Both compounds have been further characterized by IR spectroscopy, elemental analysis, TGA, and optical limiting measurements.

(© Wiley-VCH Verlag GmbH & Co. KGaA, 69451 Weinheim, Germany, 2006)

## Introduction

There has been remarkable progress and interest in the synthesis and characterization of hybrid organic-inorganic molecular materials owing to their enormous variety of intriguing structural topologies and their fascinating properties, as well as their potential applications in many fields, such as catalysis, materials science, medicine, and magnetochemistry,[1] and the optical properties of polymer hybrids have attracted particular interest from chemists recently.[2] Among the various families of hybrid functional materials, the family of metal halides is an important one. As a branch of the metal halides, silver(I) halides occupy an important position.

In general, predicting the structures of self-assembled $Ag^I$ compounds is difficult because the silver ion is known to adopt a myriad of bonding modes and coordination geometries. So far, considerable progress has been made towards the goal of obtaining specific architectures, such as the recently reported [4 × 5] $Ag_{20}$ grid,[3a] an $Ag_{10}$ quadruple helicate,[3a] and a chiral $Ag^I$ diamondoid polymer,[3a,3b] all of which were prepared on the basis of rational design principles. Most of the reports involve metal-organic compounds that have variable dimensions and topologies, and compounds that contain organic-inorganic hybrid $Ag^I$/amino systems are much less common and only zero- or one-dimensional structures are known.[4] A recent advance in this system is to design the coordination frameworks of silver(I) halides by incorporating various organic structure-directing agents (SDA). It is noteworthy that the introduction of new organic template agents always leads to a dramatic structural change of the basic inorganic phases.[5] It seems that the structure of the inorganic moiety becomes more complicated when the space volume of the SDA increases. Furthermore, the inorganic structure can be different even with the same SDA. In all, the coordination chemistry of silver halides is versatile and the study in this field is in the ascendant. We aim to probe the impact of organic quaternary ammonium cations on the structure of the inorganic moiety. In this paper, we report the preparation, crystal structures, and some physical properties of the one-dimensional hybrid complex $[(bmph)(Ag_5I_7)]_n$ and the first three-dimensional Ag/I coordination polymer $[(Hteda)_4(Ag_{12}I_{16})]_n$, assembled from $bmph^{2+}$ [$bmph^{2+}$ = 1,6-bis(4-methylpyridinio)hexane] and $Hteda^+$ ($Hteda^+$ = protonated triethylenediamine) with $Ag^I$ (Scheme 1).

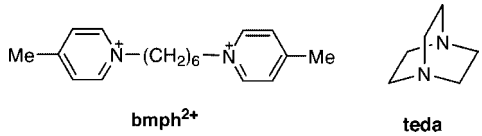


$bmph^{2+}$ teda

Scheme 1. Structure of the two SDAs.

[a] College of Chemistry and Chemical Engineering, Fuzhou University,
Fuzhou, Fujian 350002, P. R. China
E-mail: jqli@fzu.edu.cn
Fax: +86-591-8789-3239
[b] State Key Laboratory of Structural Chemistry, Fujian Institute of Research on the Structure of Matter, Chinese Academy of Science,
Fujian, Fuzhou 350002, P. R. China

 © 2006 Wiley-VCH Verlag GmbH & Co. KGaA, Weinheim 

## Results and Discussion

### Preparation of the Complexes

Variation of the SDA leads to the formation of two silver(I) inorganic components with different stoichiometries. They present dissimilar dimensions whose structures differ greatly in their linkage modes. Colorless block crystals of complexes **1** and **2** crystallize in a weakly acidic environment with pH = 5.0. In particular, **1** must be synthesized by slow condensation of diethyl ether into the DMF solution. The two complexes grow in solutions enriched with NaI, otherwise the crystals are of low quality or even do not form. Overall, many factors determine the anionic substructures, including the concentration and molar ratio of the starting materials, nature of the solvent, and, most importantly, the size, shape, and charge of the counterions.

### Crystal Structures

#### *[(bmph)(Ag$_5$I$_7$)]$_n$ (1)*

According to the structural analysis, the crystal structure of **1** shows a one-dimensional arrangement constructed from $(bmph)^{2+}$ fragments and $(Ag_5I_7)_n^{2-}$ chains, which are held together by electrostatic forces. The $(bmph)^{2+}$ units are discrete, but the inorganic moiety $(Ag_5I_7)_n^{2-}$ is polymeric and exists in the crystal as an extended chain along the *a* axis [Figure 1(a)]. In other words, this structure is a one-dimensional infinite polymeric anion accompanied by discrete cations. It should be mentioned that the chain is almost linear. As shown in Figure 1(b), the $(Ag_5I_7)_n^{2-}$ chain can be discussed in terms of an $Ag_5I_{10}$ building block in which each silver atom has an $I_4$ donor set and tetrahedral geometry when the Ag···Ag interactions are not taken into account. The $Ag_5I_{10}$ building block can be described as the result of five edge-sharing $AgI_4$ tetrahedra and

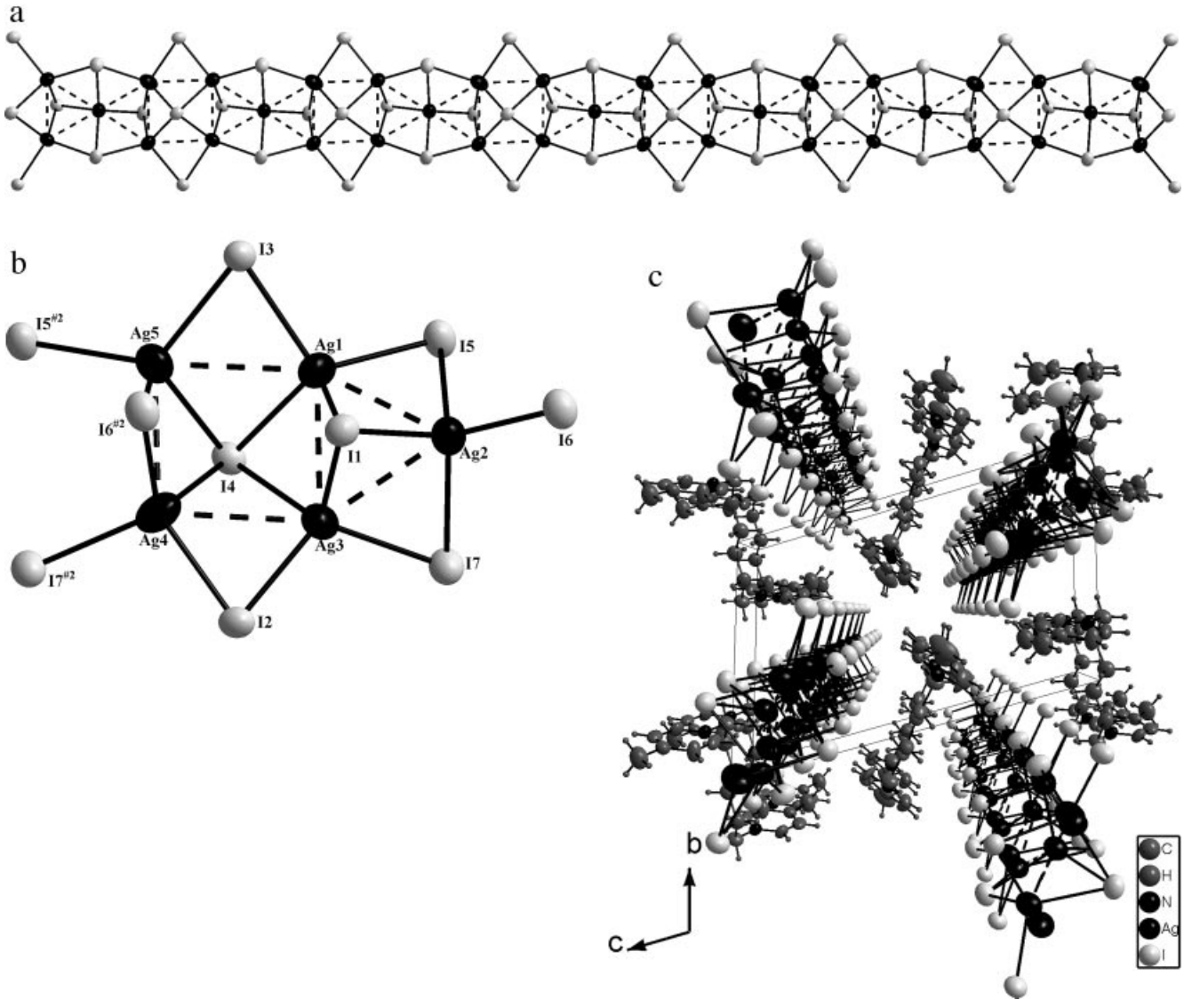


Figure 1. (a) View of the 1D zigzag chain structure of $[Ag_5I_7]_n^{2-}$ along the *a* axis. (b) Diagram of the $Ag_5I_{10}$ building block. (c) Packing diagram of **1** showing SDA molecules contained in the cavities formed by the inorganic chains.

 © 2006 Wiley-VCH Verlag GmbH & Co. KGaA, Weinheim 

argentophilic interactions. The infinite chain is built up by *cis*-edge-sharing $Ag_5I_{10}$ building blocks, where the shared edges are I(5)–I(6) and I(6)–I(7).

Ag···Ag interactions have been found in many silver complexes, and the term argentophilicity has been adopted to describe this metal–metal interaction. The attraction between $d^{10}$–$d^{10}$ closed-shell metal atoms promotes the aggregation of silver(I) centers, as supported by spectroscopic and structural evidence.[6] In this work the Ag···Ag distances in **1** range from 3.038(3) [Ag(2)–Ag(4)#1, Ag(4)–Ag(2)#2] to 3.361(3) Å [Ag(3)–Ag(4)], which are longer than that of metallic silver (2.88 Å) but shorter than the van der Waals radius sum of silver (3.44 Å).[7] The Ag···Ag separations [3.312(2)–3.556(3) Å] in $[(Et_4N)_3Ag_6(\mu\text{-}2Br)_6(\mu\text{-}4Br)_3]_n$[8] suggest that weak Ag···Ag interactions may exist. Compounds possessing argentophilicity can be potentially used in silver-containing antibacterial agents.[9]

This polymeric anion contains several very interesting features, the most extraordinary of which is the local environment of the Ag(4) atom. This atom is surrounded by I(2), I(4), I(6)#2, and I(7)#2, although in order to form stable polyanions the distances of Ag(4)–I(4) and Ag(4)–I(7)#2 [3.007(3) and 3.067(3) Å, respectively] are relatively long in comparison with the normal Ag–I distance. The $Ag(4)I_4$ tetrahedron is therefore highly distorted with Ag–I lengths ranging from 2.779(2) to 3.067(3) Å. The distorted pseudo-tetrahedron of $Ag(4)I_4$ can also be extracted from the data of I(2)–Ag(4)–I(6)#2 [125.83(9)°], I(2)–Ag(4)–I(7)#2 [103.16(7)°], and I(2)–Ag(4)–I(4) [96.31(7)°], and furthermore, because Ag(4) is pseudo-tetrahedral, it leads to the tetrahedron of corner-shared Ag(5) to be distorted with three short and one long Ag–I distances [2.826(2), 2.859(2), 2.933(2), and 3.000(3) Å, respectively].

The stacking of **1** is intimately associated with the role played by the electrostatic interaction between the $(bmph)^{2+}$ cations and the silver halide polyanions in the crystal. As can be seen from Figure 1(c), groups of $(bmph)^{2+}$ cations girdle the columnar stacks, and it is this slippage and kinking of the stacks that leads to the recombinatorial structure of the compound, thus forming a so-called organic-inorganic hybrid structure.

### *$[(Hteda)_4(Ag_{12}I_{16})]_n$ (2)*

The single-crystal X-ray analysis reveals that the crystal structure of complex **2** represents a three-dimensional arrangement. As shown in Figure 2, the basic structural unit of **2** is an $Ag_{12}I_{12}$@I building block [Figure 2(a)]. If the terminal I(1) atoms are eliminated, the $Ag_{12}I_6$@I unit forms a quasi-hexagonal antiprism [Figure 2(b)] in which the top and bottom $Ag_3I_3$ hexagons are not coplanar but take on a chair-like configuration. The Ag–I–Ag angles in this $Ag_3I_3$ chair-like arrangement are 116.61(5)° and I–Ag–I angles are 120.70(4)°, so the hexagon is distorted to a small extent. An $IAg_6$ octahedron in the middle of the $Ag_{12}I_6$@I hexagonal antiprism links two $Ag_3I_3$ hexagons through $\mu_3$-I(2) and Ag···Ag interactions. This $IAg_6$ octahedron is greatly distorted, with Ag(2A) and Ag(2A)#6 occupying the axial positions and Ag(2A)#1, Ag(2A)#2, Ag(2A)#3, and Ag(2A)#4 comprising the equatorial plane [symmetry transformations: #1: $-y$, $x-y$, $z$; #2: $x-y$, $x$, $-z$; #3: $y$, $-x+y$, $-z$; #4: $-x+y$, $-x$, $z$; #6: $-x$, $-y$, $-z$; Ag(2) is distorted therefore only Ag(2A) is discussed]. The $\mu_6$-I(3) atom is located at the center of the octahedron (on a $\bar{3}$ site) and is σ-bonded to six Ag atoms, with six equivalent contacts with Ag(2A) of 2.872(3) Å. These values are much shorter than that in $\{I@[AgI(inh)]_6\}$(3.09 Å).[10] The Ag···Ag distances in **2** range from 2.915(3) Å [Ag(1)–Ag(2A)] to 3.286(4) Å [Ag(2A)–Ag(2A)#2], thereby indicating that weak Ag···Ag interactions may exist. The peripheral terminal I(1) atoms bond with Ag(2A) to complete its tetrahedral coordination geometry.

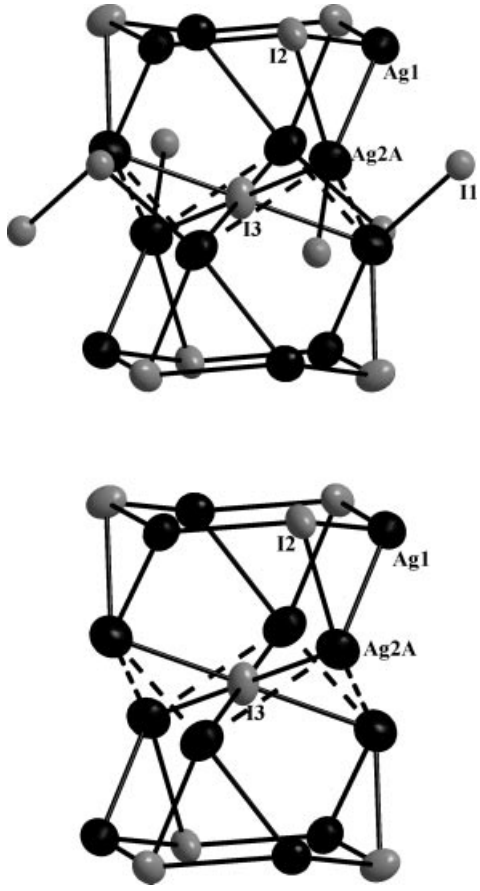


Figure 2. (a) Structure of the $Ag_{12}I_{12}$@I building block. (b) View of the $Ag_{12}I_6$@I quasi-hexagonal antiprism.

Although a series of monomeric $Ag_6$ octahedral clusters[11] and polymeric $Ag_6$ octahedral units centered by anions such as $\mu_6$-I,[10] $\mu_6$-$C_2^{2-}$, $\mu_6$-F, $\mu_3$-F, and $\mu_3$-$CF_3SO_3$[12] have been reported, this $Ag_{12}I_{12}$@I hexagonal prism cluster centered by $\mu_6$-I was unknown until now. The hexagonal surfaces of the hexagonal prism are parallel to the *ab* plane, and each $Ag_{12}I_{12}$@I building block links six $Ag_{12}I_{12}$@I prisms through $\mu_2$-I(4) into a three-dimensional arrangement (Figure 3). The triethylenediamine-based countercations arrange in a parallel fashion between the $Ag_{12}I_{12}$@I hexagonal prism building blocks and play an important structural direction role. The half-protonation of

 © 2006 Wiley-VCH Verlag GmbH & Co. KGaA, Weinheim 

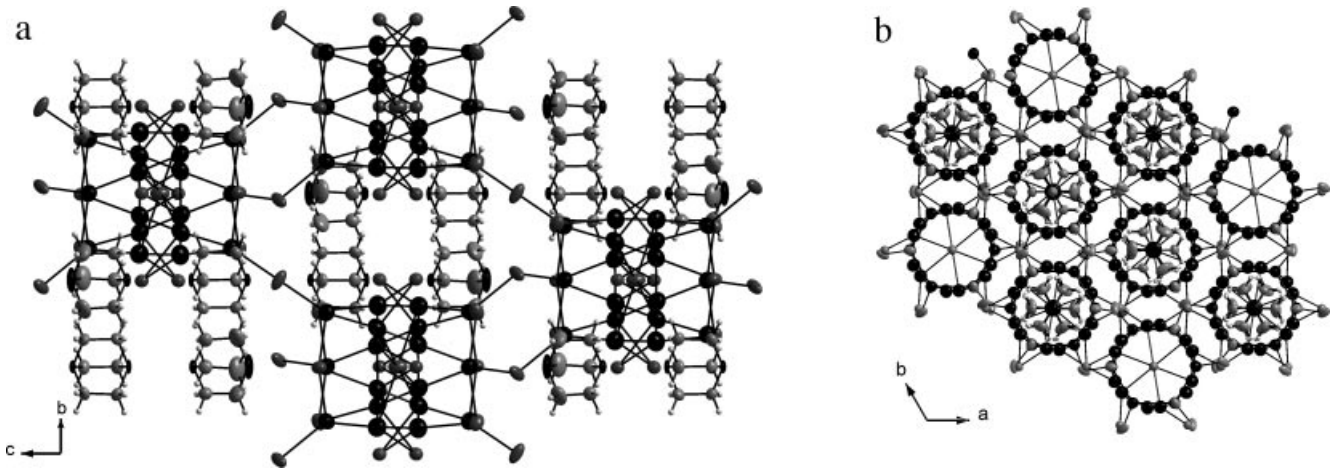


Figure 3. 3D perspective view of **1** based on $Ag_{12}I_{12}$@I building blocks [(a): side view; (b): top view].

triethylenediamine was determined from the charge-balance requirements, although, to our disappointment, the hydrogen atom of the protonated amine could not be found in the Fourier map. The organic cations line up with intermolecular N···N contacts of about 2.8 Å, which clearly indicate H-bonding distances.

A particularly obvious feature of the polymeric structure is the charge-balanced $Hteda^+$ cations trapped within the cavity of the three-dimensional cavities, which act as the nut and bolt of the tube-like combination (Figure 3). It is worth noting that the formation of the 3D polymeric cluster could be a good illustration of a cation-induced self-assembly reaction. In addition, although there are many examples of self-assembly induced or controlled by cations {such as $[(Et_3NC_6H_{12}NEt_3)_2(Ag_5I_7)]_n$ (unpublished work) and $[Ag^{II}(tmc)(BF_4)]_\infty^+$},[13] complex **2** represents the first three-dimensional product of an Ag/I assembly induced by a cation.

It is known that the formation of anionic complexes of the type $[Ag_lX_k]^{(k-l)-}$ is strongly dependent on the countercation and the nature of the halide.[14] In the case of iodide, the ions $[AgI_3]^{2-}$, $[Ag_2I_4]^{2-}$, and $[Ag_4I_8]^{4-}$ have been reported.[3] To the best of our knowledge, polymer **1** is a new example of a 1D Ag/I coordination polymer, and, more importantly, **2** is the first example of a three-dimensional product of Ag/I assembly based on weak Ag···Ag interactions and an organic template.

### Optical Limiting Effect Measurement

The optical limiting results of **1** and **2** are depicted in Figure 4. The result shows that the present compounds exhibit a good optical limiting capacity. The response of the composite is linear to the input energy intensity at the beginning, obeying Beer's law. However, as input energy intensity increases, the light transmittance starts to deviate from the linear response expected due to Beer's law when the input light fluence rises to 0.86 and 0.62 $J\,cm^{-2}$ for **1** and **2**, respectively. The limiting threshold can be defined as the incident fluence at which the solution transmittance falls to 50% of the linear transmittance. The limiting threshold value of **1** and **2** was measured as 1.12 and 0.7 $J\,cm^{-2}$ according to the experimental data. A lower limiting threshold and saturation level provide a greater safety margin for device protection. A comparison of this new compound

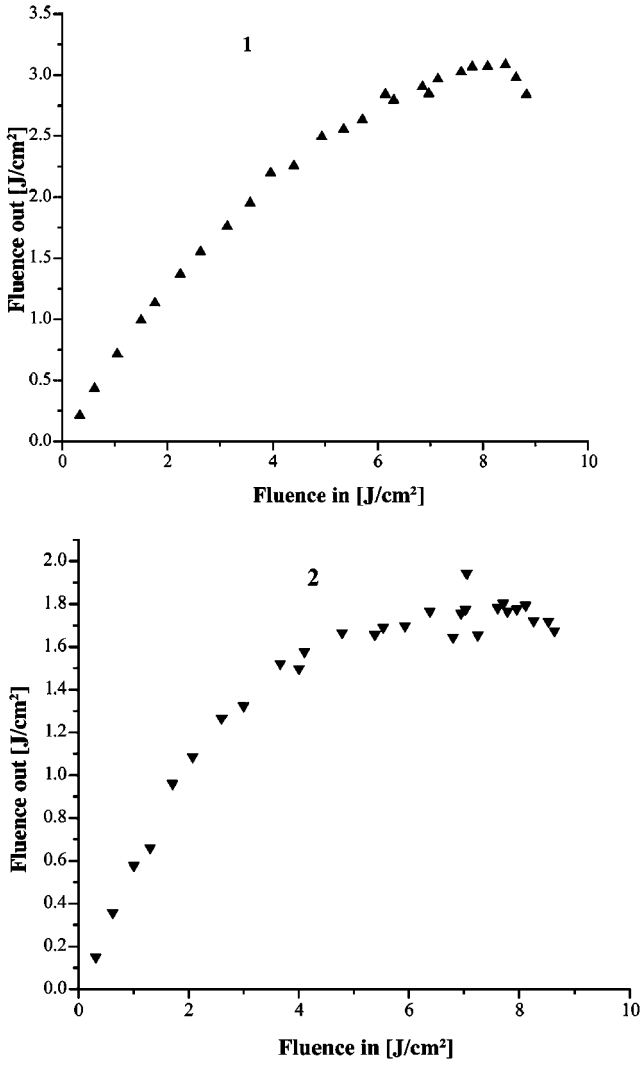


Figure 4. Optical limiting effect of $[(bmph)(Ag_5I_7)]_n$ (**1**) and $[(Hteda)_4(Ag_{12}I_{16})]_n$ (**2**) in a $1.0\times10^{-5}$ M DMF solution.

 © 2006 Wiley-VCH Verlag GmbH & Co. KGaA, Weinheim 

Table 1. Limiting thresholds of polymeric compounds measured at 532 nm with ns laser pulses.

| Polymeric compound | Structure type | Solvent | Limiting threshold [J cm$^{-2}$] | Ref. |
|---|---|---|---|---|
| $C_{60}$ | | toluene | 1.6 | [15a] |
| {I@[AgI(inh)]$_6$} | 1D polymer | DMF | 0.53 | [9] |
| {[La(Me$_2$SO)$_8$][(μ-WSe$_4$)$_3$Ag$_3$]}$_n$ | 1D polymer | DMF | 0.7 | [15b] |
| [MoS$_4$Cu$_6$I$_4$(py)$_4$]$_n$ | 2D microporous | DMSO | 0.6 | [15c] |
| [Et$_4$N]$_2$[MoS$_4$Cu$_6$(CN)$_4$]$_n$ | 3D cross-framework | DMF | 0.28 | [15d] |
| [(bmph)(Ag$_5$I$_7$)]$_n$ | 1D polymer | DMF | 1.12 | this work |
| [(Hteda)$_4$(Ag$_{12}$I$_{16}$)]$_n$ | 3D cross-framework | DMF | 0.7 | this work |

with other well-known optical limiting materials will be interesting. Table 1 gives the limiting thresholds of **1**, **2**, polymeric clusters, and $C_{60}$.[15] It is clear that the limiting performance of **1** in DMF solution is two times better than that displayed by $C_{60}$. It has been universally accepted that the assembly of monomeric cluster units into a polymer will bring an enhancement of the optical limiting effect.[16] Among the structure–optical limiting (OL) property correlation of clusters and polymers, the heavy atom effect also plays an important role.[2] So, as far as this work is concerned, the heavier atoms Ag and I, together with the polymeric aggregation, play a vital role in determining its OL properties. The successful synthesis of coordination polymeric clusters containing a polyiodide complex paves the way for the quick and facile preparation of novel OL materials.

### Thermogravimetric Analysis

The thermogravimetric analysis (TGA) results for **1** show that the weight loss between 40 and 240 °C is 1.76%, which might correspond to the loss of DMF solvent molecules absorbed on the crystal surface. This complex is thermally stable until around 260 °C, and then loses 30.38% of its weight in the temperature range 260–450 °C. Because isolated $(bmph)^{2+}$ molecules take the role of countercations, the framework collapses during the removal of the organic components. This stage can be attributed to the loss of (bmph)·$I_2$ (calcd. 30.85%).

The polymeric cluster **2** shows remarkable thermal stability. Thermal gravimetric analysis for **2** shows no weight loss up to 310 °C. Weight loss under heating starts at 355 °C and finishes at 980 °C.

## Conclusions

Two organically templated hybrid silver iodides, namely [(bmph)(Ag$_5$I$_7$)]$_n$ (**1**) and [(Hteda)$_4$(Ag$_{12}$I$_{16}$)]$_n$ (**2**), have been obtained as good quality single crystals by a direct method. Structural analyses indicate that both compounds consist of uncoordinated structure-directing molecules and an inorganic moiety that is tuned by organic SDAs. Complex **1** presents a one-dimensional chain structure, whereas the inorganic moiety of **2** is the first example of an Ag/I coordination polymer based on Ag···Ag weak interactions and an organic template. Both compounds possess optical limiting activity.

## Experimental Section

**General Remarks:** All chemicals except bmph·$I_2$ were of reagent grade quality from commercial sources and were used without further purification. C, H, N analyses were carried out with a Vario EL III element analyzer. IR spectra were recorded with a Nicolet Co. Magna-IR 750 spectrometer as KBr pellets in the region 4000–400 cm$^{-1}$. Thermal stability (TG-DTA) studies from room temperature to 800 °C (for **1**) and 1200 °C (for **2**) under nitrogen with a heating rate of 10 °C min$^{-1}$ were performed with a Perkin–Elmer TGA 7 instrument. The optical limiting behaviors were investigated by fluence-dependent transmittance measurements. Radiation with a wavelength of 532 nm was provided by a Q-switched Nd:YAG laser with a pulse duration of 8 ns.

**Synthesis of bmph·$I_2$:** bmph·$I_2$ was prepared as reported in the literature:[17]

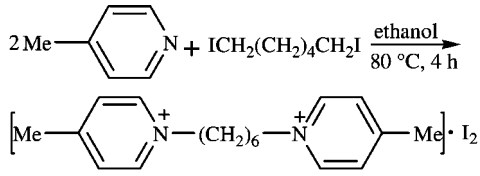


Table 2. Crystal data and structure refinement for **1** and **2**.

| | **1** | **2** |
|---|---|---|
| Empirical formula | $C_{18}H_{26}Ag_5I_7N_2$ | $C_{12}H_{24}Ag_6I_8N_4$ |
| Formula mass | 1698.06 | 1886.77 |
| Crystal system | triclinic | hexagonal |
| Space group | $P\bar{1}$ | $R\bar{3}c$ |
| $a$ [Å] | 8.5704(17) | 13.3373(19) |
| $b$ [Å] | 11.886(2) | 13.3373(19) |
| $c$ [Å] | 18.170(4) | 63.537(13) |
| $\alpha$ [°] | 103.93(3) | 90.00 |
| $\beta$ [°] | 98.16(3) | 90.00 |
| $\gamma$ [°] | 102.05(3) | 120.00 |
| $V$ [Å$^3$] | 1720.4(6) | 9788(3) |
| $Z$ | 2 | 12 |
| $D_c$ [g cm$^{-3}$] | 3.278 | 3.841 |
| $\mu$ [mm$^{-1}$] | 9.087 | 11.111 |
| $F$(000) | 1508 | 9960 |
| Reflections, total | 13669 | 30308 |
| Reflections, unique | 6830 | 2510 |
| Reflections, observed | 3574 | 1570 |
| Goodness-of-fit on $F^2$ | 0.964 | 0.925 |
| No. of parameters refined | 289 | 101 |
| $R_1$ [$I > 2\sigma(I)$][a] | 0.0589 | 0.0396 |
| $wR_2$ [$I > 2\sigma(I)$][b] | 0.1364 | 0.1131 |
| Residual electron density [e Å$^3$] | 2.213, –2.280 | 2.847, –2.788 |

[a] $R_1 = \Sigma(|F_o| - |F_c|)/\Sigma|F_o|$. [b] $wR_2 = [w(F_o^2 - F_c^2)^2/w(F_o^2)^2]^{1/2}$.

 © 2006 Wiley-VCH Verlag GmbH & Co. KGaA, Weinheim 

Table 3. Selected bond lengths [Å] and angles [°] for **1** and **2**.

| | | | |
|---|---|---|---|
| Compound **1**[a] | | | |
| Ag(1)–I(1) | 2.866(2) | Ag(1)–I(3) | 2.827(2) |
| Ag(1)–I(4) | 2.968(2) | Ag(1)–I(5) | 2.942(2) |
| Ag(2)–I(1) | 2.867(2) | Ag(2)–I(5) | 2.872(2) |
| Ag(2)–I(7) | 2.891(2) | Ag(2)–I(6) | 2.856(2) |
| Ag(3)–I(1) | 2.887(2) | Ag(3)–I(2) | 2.814(2) |
| Ag(3)–I(4) | 2.967(2) | Ag(3)–I(7) | 2.860(2) |
| Ag(4)–I(2) | 2.779(2) | Ag(4)–I(4) | 3.067(3) |
| Ag(4)–I(6)#2 | 2.839(3) | Ag(4)–I(7)#2 | 3.007(3) |
| Ag(5)–I(3) | 2.826(2) | Ag(5)–I(4) | 3.000(3) |
| Ag(5)–I(6)#2 | 2.859(2) | Ag(5)–I(5)#2 | 2.933(2) |
| Ag(1)–Ag(2) | 3.086(2) | Ag(1)–Ag(3) | 3.124(2) |
| Ag(1)–Ag(5) | 3.333(2) | Ag(2)–Ag(4)#1 | 3.038(3) |
| Ag(2)–Ag(5)#1 | 3.140(2) | Ag(2)–Ag(3) | 3.177(2) |
| Ag(3)–Ag(4) | 3.361(3) | Ag(4)–Ag(2)#2 | 3.038(3) |
| Ag(4)–Ag(5) | 3.149(3) | Ag(5)–Ag(2)#2 | 3.140(2) |
| Ag(1)–I(1)–Ag(2) | 65.14(6) | Ag(1)–I(1)–Ag(3) | 65.78(6) |
| Ag(1)–I(4)–Ag(5) | 67.90(6) | Ag(1)–I(4)–Ag(4) | 95.36(7) |
| Ag(2)–I(1)–Ag(3) | 67.03(6) | Ag(2)–I(5)–Ag(1) | 64.11(5) |
| Ag(2)–I(5)–Ag(5)#1 | 65.49(5) | Ag(2)–I(6)–Ag(5)#1 | 66.66(6) |
| Ag(2)–I(7)–Ag(4)#1 | 61.98(6) | Ag(3)–I(4)–Ag(5) | 103.71(7) |
| Ag(3)–I(4)–Ag(4) | 67.66(6) | Ag(3)–I(7)–Ag(2) | 67.05(6) |
| Ag(3)–I(7)–Ag(4)#1 | 126.93(7) | Ag(3)–I(4)–Ag(1) | 63.52(5) |
| Ag(4)–I(2)–Ag(3) | 73.86(6) | Ag(4)#1–I(6)–Ag(2) | 64.48(7) |
| Ag(4)#1–I(6)–Ag(5)#1 | 67.11(7) | Ag(5)–I(3)–Ag(1) | 72.26(6) |
| Ag(5)–I(4)–Ag(4) | 62.53(6) | Ag(5)#1–I(5)–Ag(1) | 126.38(6) |
| I(1)–Ag(1)–I(5) | 110.94(6) | I(1)–Ag(1)–I(4) | 107.63(7) |
| I(1)–Ag(1)–Ag(2) | 57.43(5) | I(1)–Ag(1)–Ag(3) | 57.43(5) |
| I(1)–Ag(2)–I(5) | 113.02(7) | I(1)–Ag(2)–I(7) | 105.71(7) |
| I(1)–Ag(3)–I(4) | 107.10(6) | I(2)–Ag(3)–I(7) | 113.48(7) |
| I(2)–Ag(3)–I(1) | 110.02(7) | I(2)–Ag(3)–I(4) | 97.83(6) |
| I(2)–Ag(4)–I(6)#2 | 125.83(9) | I(2)–Ag(4)–I(7)#2 | 103.16(7) |
| I(2)–Ag(4)–Ag(2)#2 | 153.07(9) | I(2)–Ag(4)–I(4) | 96.31(7) |
| I(3)–Ag(1)–I(1) | 119.02(8) | I(3)–Ag(1)–I(5) | 106.24(7) |
| I(3)–Ag(1)–I(4) | 98.48(6) | I(3)–Ag(5)–I(6)#2 | 114.42(8) |
| I(3)–Ag(5)–I(5)#2 | 114.64(7) | I(3)–Ag(5)–I(4) | 97.75(6) |
| I(5)–Ag(1)–I(4) | 114.22(7) | I(5)–Ag(2)–I(7) | 111.57(8) |
| I(5)#2–Ag(5)–I(4) | 111.91(7) | I(6)–Ag(2)–I(1) | 103.37(7) |
| I(6)–Ag(2)–I(5) | 109.02(7) | I(6)–Ag(2)–I(7) | 113.92(7) |
| I(6)#2–Ag(4)–I(7)#2 | 111.00(7) | I(6)#2–Ag(4)–I(4) | 109.35(8) |
| I(6)#2–Ag(5)–I(5)#2 | 107.27(7) | I(6)#2–Ag(5)–I(4) | 110.70(7) |
| I(7)–Ag(3)–I(1) | 105.99(7) | I(7)–Ag(3)–I(4) | 121.97(8) |
| I(7)#2–Ag(4)–I(4) | 109.80(8) | | |
| Compound **2**[b] | | | |
| Ag(1)–I(4) | 2.8115(12) | Ag(1)–I(2) | 2.8121(14) |
| Ag(1)–I(2)#1 | 2.8630(14) | Ag(1)–I(1) | 2.9108(14) |
| Ag(2A)–I(1) | 2.779(3) | Ag(2A)–I(3) | 2.872(3) |
| Ag(2A)–I(2)#2 | 2.792(3) | Ag(2A)–I(1)#3 | 2.928(3) |
| Ag(2A)#1–I(3) | 2.872(3) | Ag(2A)#2–I(1) | 2.928(3) |
| Ag(2A)#2–I(3) | 2.872(3) | Ag(2A)#3–I(2) | 2.792(3) |
| Ag(2A)#3–I(3) | 2.872(3) | Ag(2A)#4–I(3) | 2.872(3) |
| Ag(2A)#6–I(3) | 2.872(3) | Ag(1)–Ag(2A)#2 | 2.915(3) |
| Ag(2A)–Ag(2A)#2 | 3.286(4) | | |
| Ag(1)–I(2)–Ag(1)#4 | 116.60(5) | Ag(1)#5–I(4)–Ag(1) | 131.01(6) |
| Ag(1)–I(1)–Ag(2A)#2 | 59.89(5) | Ag(1)#3–Ag(2A)–I(1)#3 | 59.76(6) |
| Ag(2A)–I(3)–Ag(2A)#1 | 110.21(5) | Ag(2A)–I(1)–Ag(1) | 95.75(6) |
| Ag(2A)–I(1)–Ag(2A)#2 | 70.25(10) | Ag(2A)#2–I(3)–Ag(2A)#3 | 110.21(5) |
| Ag(2A)#2–I(3)–Ag(2A)#5 | 110.21(5) | Ag(2A)#2–I(3)–Ag(2A)#4 | 180.00(9) |
| Ag(2A)#2–I(3)–Ag(2A) | 69.79(5) | Ag(2A)#2–I(3)–Ag(2A)#1 | 69.79(5) |
| Ag(2A)#3–I(2)–Ag(1) | 97.91(7) | Ag(2A)#3–I(2)–Ag(1)#4 | 62.04(6) |
| Ag(2A)#3–I(3)–Ag(2A)#5 | 110.21(5) | Ag(2A)#3–I(3)–Ag(2A)#4 | 69.79(5) |
| Ag(2A)#3–I(3)–Ag(2A) | 69.79(5) | Ag(2A)#3–I(3)–Ag(2A)#1 | 180.00(16) |
| Ag(2A)#4–I(3)–Ag(2A) | 110.21(5) | Ag(2A)#4–I(3)–Ag(2A)#1 | 110.21(5) |
| Ag(2A)#5–I(3)–Ag(2A)#4 | 69.79(5) | Ag(2A)#5–I(3)–Ag(2A) | 180.00(9) |
| Ag(2A)#5–I(3)–Ag(2A)#1 | 69.79(5) | I(1)–Ag(2A)–I(3) | 107.44(8) |
| I(1)–Ag(2A)–I(1)#3 | 113.29(9) | I(2)–Ag(1)–I(2)#1 | 120.70(5) |
| I(2)–Ag(1)–I(1) | 111.94(4) | I(2)#1–Ag(1)–I(1) | 112.10(4) |
| I(2)#2–Ag(2A)–I(3) | 105.89(9) | I(2)#2–Ag(2A)–I(1)#3 | 113.70(8) |
| I(3)–Ag(2A)–I(1)#3 | 103.52(9) | I(4)–Ag(1)–I(2) | 108.06(4) |
| I(4)–Ag(1)–I(2)#1 | 98.05(4) | I(4)–Ag(1)–I(1) | 103.47(4) |

[a] Symmetry transformations used to generate equivalent atoms: #1: $x + 1, y, z$; #2: $x - 1, y, z$; #3: $-x, -y, -z + 1$; #4: $-x, -y, -z$. [b] Symmetry transformations used to generate equivalent atoms: #1: $-y, x - y, z$; #2: $x - y, x, -z$; #3: $y, -x + y, -z$; #4: $-x + y, -x, z$; #5: $-x, -y, -z$.

 © 2006 Wiley-VCH Verlag GmbH & Co. KGaA, Weinheim 

**Synthesis of $[(bmph)(Ag_5I_7)]_n$ (1):** A suspension of AgI (0.234 g, 1.0 mmol), NaI (0.225 g. 1.5 mmol), and bmph·$I_2$ (0.262 g, 0.5 mmol) in DMF (10 mL) was stirred at 60 °C for 40 min. During the course of stirring, a small amount of NaI was added until the solution became colorless and clear. The resultant solution was adjusted to pH = 5.0 with 10% HI solution. After filtration, diethyl ether (10 mL) was slowly condensed into the solution. Colorless block crystals of **1** were isolated with a yield of 0.132 g (38.9%, based on Ag) after 4 d. $C_{18}H_{26}Ag_5I_7N_2$ (1698.1): calcd. C 12.73, H 1.54, N 1.64; found C 12.75, H 1.52, N 1.65. IR: $\tilde{\nu}$ = 3049 (m), 2932 (s), 2854 (m), 2445 (s), 1790 (s), 1637 (s), 1571 (m), 1510 (m), 1465 (s), 1384 (s), 1365 (s),1304 (w), 1256 (m), 1177 (s), 1115 (w), 1031 (m), 835 (s), 811 (s), 731 (m), 700 (m) $cm^{-1}$.

**Synthesis of $[(Hteda)_4(Ag_{12}I_{16})]_n$ (2):** A mixture of AgI (0.117 g, 0.5 mmol), NaI (0.225 g. 1.5 mmol), and teda (0.247 g, 2.2 mmol) in 10 mL of DMF was stirred until it became colorless and clear and was then adjusted to pH = 5.0 with 10% HI solution. Colorless crystals of **2** were isolated with a yield of 54.3% after 5 d. $C_{12}H_{26}Ag_6I_8N_4$ (1888.8): calcd. C 7.63, H 1.39, N 2.97; found C 7.69, H 1.35, N 2.80. IR: $\tilde{\nu}$ = 3437 (s), 2968 (m), 2890 (w), 2788 (m), 2637 (m), 1685 (w), 1637 (s), 1459 (s), 1177 (s), 1051 (m), 983 (s), 897 (s), 844 (s), 788 (s), 599 (s) $cm^{-1}$.

**X-ray Crystallography:** X-ray data for both complexes were collected at 293(2) K with a Rigaku Weissenbery IP diffractometer using graphite-monochromated Mo-$K_\alpha$ radiation [$\lambda$ = 0.71069 Å]. Correction for Lp factors and multi-scan absorption corrections were applied. The structures were solved by direct methods and refined by full-matrix least-squares techniques on $F^2$ using SHELXTL-97.[18] All non-hydrogen atoms of **1** and **2** were treated anisotropically. CH hydrogen atoms were generated geometrically. Experimental X-ray data are listed in Table 2, and selected bond lengths and angles are given in Table 3. CCDC-289211 (**1**) and -280903 (**2**) contain the supplementary crystallographic data for this paper. These data can be obtained free of charge from The Cambridge Crystallographic Data Centre via www.ccdc.cam.ac.uk/data_request/cif.

## Acknowledgments

We acknowledge support of this research by the Key Project of Fujian Province (2005HZ01-2-6), the PhD Programs Foundation of the Ministry of Education of China (20050386003), and the Foundation of the Education Committee of Fujian Province (JB04016 and JB04017).

[1] a) O. M. Yaghi, H. Li, C. Davis, D. Richardson, T. L. Groy, *Acc. Chem. Res.* **1998**, *31*, 474–484; b) A. K. Cheetham, *Science* **1994**, *264*, 794–795; c) M. T. Pope, A. Müller, *Angew. Chem. Int. Ed. Engl.* **1991**, *30*, 34–38; d) C. L. Hill, *Chem. Rev.* **1998**, *98*, 1–2; e) C.-D. Wu, C.-Z. Lu, X. Lin, D.-M. Wu, S.-F. Lu, H.-H. Zhuang, J.-S. Huang, *Chem. Commun.* **2003**, 1284–1285.

[2] Y.-Y. Niu, H.-G. Zheng, H.-W. Hou, X.-Q. Xin, *Coord. Chem. Rev.* **2004**, *248*, 169–183.

[3] a) P. N. W. Baxter, J. M. Lehn, G. Baumand, D. Fenske, *Chem. Eur. J.* **2000**, *6*, 4510–4517; b) A. J. Blake, N. R. Champness, P. A. Cooke, J. E. B. Nicolson, C. Wilson, *J. Chem. Soc., Dalton Trans.* **2000**, 3811–3819.

[4] a) S. Olson, G. Helgesson, S. Jagner, *Inorg. Chim. Acta* **1994**, *217*, 15–20; b) W.-Z. Chen, F.-H. Liu, *J. Organomet. Chem.* **2003**, *673*, 5–12; c) N. W. Alcock, S. J. Archibald, D. H. Busch, *Acta Crystallogr., Sect. E* **2003**, *59*, m1110; d) H. J. Keller, B. Keppler, H. Pritzkow, *Acta Crystallogr., Sect. B* **1982**, *38*, 1603–1605; e) C. J. Gilmore, P. A. Tucker, P. Woodward, *J. Chem. Soc. A* **1971**, 1337–1341; f) Y.-J. Zhao, W.-P. Su, R. Cao, M.-C. Hong, *Acta Crystallogr., Sect. C* **1999**, *55*, e122–e124; g) K. Peters, H. G. Schnering, W. Ott, H. M. Seidenspinner, *Acta Crystallogr., Sect. C* **1984**, *40*, 789–790; h) M. M. Thackeray, J. Coetzer, *Acta Crystallogr., Sect. B* **1975**, *31*, 2341–2342; i) J. Coetzer, *Acta Crystallogr., Sect. B* **1975**, *31*, 2115–2116; j) H. H. Li, Z. R. Chen, C. C. Huang, Y. G. Ren, Q. H. Chen, *Chin. J. Struct. Chem.* **2004**, *23*, 288–291; k) H. H. Li, Z. R. Chen, C. C. Huang, G. C. Xiao, Y. G. Ren, *Chin. J. Struct. Chem.***2004**, *23*, 1009–1012; l) G. A. Bowmaker, Effendy, B. W. Skelton, N. Somers, A. H. White, *Inorg. Chim. Acta* **2005**, *358*, 4307–4326.

[5] D. J. Chestnut, A. Kusnetzow, R. R. Birge, *Inorg. Chem.* **1999**, *38*, 2663–2671.

[6] a) C.-M. Che, Z. Mao, V. M. Miskowski, M.-C. Tse, C.-K. Chan, K.-K. Cheung, D. L. Phillips, K.-H. Leung, *Angew. Chem. Int. Ed.* **2000**, *39*, 4084–4088; b) C.-M. Che, M.-C. Tse, M. C. W. Chan, K.-K. Cheung, D. L. Phillips, K.-H. Leung, *J. Am. Chem. Soc.* **2000**, *122*, 2464–2468; c) K.-H. Leung, D. L. Phillips, M.-C. Tse, C.-M. Che, V. M. Miskowski, *J. Am. Chem. Soc.* **1999**, *121*, 4799–4803.

[7] A. Bondi, *J. Phys. Chem.* **1964**, *68*, 441–451.

[8] M.-C. Hong, R. Cao, W.-P. Su, F.-L. Jiang, *Chin. J. Struct. Chem.* **1999**, *9*, 384–392.

[9] K. Nomiya, S. Takahashi, R. Noguchi, *J. Chem. Soc., Dalton Trans.* **2000**, 2091–2097.

[10] Y.-Y. Niu, Y.-L. Song, H. W. Hou, Y. Zhu, *Inorg. Chem.* **2005**, *44*, 2553–2559.

[11] a) V. W. W. Yam, E. C. C. Cheng, N. Y. Zhu, *New J. Chem.* **2002**, *26*, 279–284; b) H. Dietrich, W. Storck, G. J. Manecke, *J. Chem. Soc., Chem. Commun.* **1982**, 1036–1037; c) C. E. Briant, R. G. Smith, D. M. P. Mingos, *J. Chem. Soc., Chem. Commun.* **1984**, *9*, 586–588; d) C.-W. Liu, I. J. Shang, J.-C. Wang, T.-C. Keng, *Chem. Commun.* **1999**, 995–996.

[12] a) G.-C. Guo, Q.-G. Wang, G.-D. Zhou, T. C. W. Mak, *Chem. Commun.* **1998**, 339–341; b) Q.-M. Wang, T. C. W. Mak, *J. Am. Chem. Soc.* **2000**, *122*, 7608–7609; c) Q.-M. Wang, T. C. W. Mak, *Chem. Commun.* **2000**, 1435–1436.

[13] Q.-M. Wang, T. C. W. Mak, *Chem. Commun.* **2001**, 807–808.

[14] F. A. Cotton, G. Wilkinson, C. A. Murillo, M. Bochmann, *Advanced Inorganic Chemistry*, 6th ed., Wiley, New York, **1999**.

[15] a) R. L. McLean, M. C. Sutherland, D. M. Brant, P. A. Brandelik, T. Pottenger, *Opt. Lett.* **1993**, *18*, 858–860; b) Q.-F. Zhang, W.-H. Leung, X.-Q. Xin, H.-K. Fun, *Inorg. Chem.* **2000**, *39*, 417–426; c) H.-W. Hou, Y.-T. Fan, C.-X. Du, Y. Zhu, W.-L. Wang, X.-Q. Xin, M. K. M. Low, W. Ji, H. G. Ang, *Chem. Commun.* **1999**, 647–648; d) C. Zhang, Y.-L. Song, Y. Xu, H.-K. Fun, G.-Y. Fang, Y.-X. Wang, X.-Q. Xin, *J. Chem. Soc., Dalton Trans.* **2000**, 2823–2829.

[16] Q.-F. Zhang, Y.-Y. Niu, W.-H. Leung, Y.-L. Song, I. D. Williams, X.-Q. Xin, *Chem. Commun.* **2001**, 1126–1127.

[17] S. Huang, R.-G. Xie, *Preparation Manual of Organic Synthesis Reagents*, Sichuan University Press, ChengDu, **1988**.

[18] G. M. Sheldrick, *SHELXT 97, Program for Crystal Structure Refinement*, University of Göttingen, Germany, **1997**.

Received: January 20, 2006
Published Online: April 20, 2006

 © 2006 Wiley-VCH Verlag GmbH & Co. KGaA, Weinheim 

DOI: 10.1002/ejic.200600061

# A Hydrothermal Reduction Route to Single-Crystalline Hexagonal Cobalt Nanowires

By-Qin Xie,[a,b] Yitai Qian,*[a,b] Shuyuan Zhang,[a] Shenquan Fu,[a] and Weichao Yu[b]

**Keywords:** Cobalt / Hydrothermal synthesis / Magnetic properties / Nanostructures

Hexagonal close-packed (hcp) cobalt nanowires with diameters of 150–300 nm and lengths of up to several hundreds of micrometers have been synthesized by a hydrothermal reduction method. These cobalt nanowires were generated by the reduction of cobalt(II) citrate complexes by hypophosphite ($H_2PO_2^-$) in basic solution at 160 °C. High-resolution TEM and SAED reveal that the as-prepared Co nanowires have a single-crystalline structure with a [001] growth direction. The room-temperature hysteresis loop of these nanowires shows a ferromagnetic behavior with enhanced coercivity. A formation mechanism for these Co nanowires is proposed.
(© Wiley-VCH Verlag GmbH & Co. KGaA, 69451 Weinheim, Germany, 2006)

## Introduction

Magnetic nanomaterials have attracted considerable interest due to their novel properties and many applications in magnetic recording media, sensors and other devices.[1–4] In particular, nanocrystalline Co has sparked intensive studies not only due to its multiple crystal structures (hcp, fcc, and ε), but also because of its structure-dependent magnetic and electronic properties.[5] It has been reported that the anisotropic high magnetic coercivity of hcp-Co is the preferred structure for permanent magnet applications, as compared with the more symmetric low coercivity fcc phase used for soft magnetic applications.[6] A series of possible techniques have been applied for the structure-controlled synthesis of Co nanocrystals. For example, ε-Co nanoparticles (2–17 nm) have been synthesized in a mixture of an organic solvent and surfactant by the pyrolysis of carbonyl compounds[6,7] or a solution-phase metal salt reduction.[8,9] Thermodynamically stable hcp-Co nanorods have been obtained by the decomposition of [Co($\eta^3$-$C_8H_{13}$)($\eta^4$-$C_8H_{12}$)] in the presence of oleic acid and a long amine ligand.[10]

Anisotropic magnetic nanoparticles are expected to exhibit interesting properties because of their shape anisotropy,[11,12] and an hcp-Co nanowire array has been fabricated by an electrochemical deposition technique using polycarbonate membranes,[13] porous AAO,[14] and mesoporous silica films[15] as templates. However, most Co nanowires obtained by electrodeposition techniques are either very wide in diameter (380–420 nm) or polycrystalline.

Wet chemical methods have proved to be very effective for the production of single-crystalline, low-dimensional hexagonal cobalt nanocrystals. For example, hcp-Co nanodisks and their assembly of ribbons have been prepared by rapid decomposition of carbonylcobalt in the presence of trioctylphosphane (TOP) and oleic acid (OA),[16] and a superlattice of monodisperse hcp-Co nanorods and nanowires has been selectively synthesized by the decomposition of organometallic precursors in the presence of a mixture of long-chain amines and acid molecules.[17] A surfactant-assisted hydrothermal reduction route has been used to synthesize hexagonal cobalt nanobelts (diameter: 200–500 nm) in a mixed solvent of water and ethanol.[18] Up to now, the preparation of shape-anisotropic magnetic nanomaterials by wet chemical methods has mainly been achieved in a hot organic solvent containing a surfactant. However, recent studies have shown that low-dimensional magnetic nanostructures (such as Ni nanobelts[19] and nanoflowers[20] and $Fe_2O_3$ nanorod arrays[21]) can be formed in aqueous solution under properly controlled conditions even without the presence of surfactants. Herein, we report a facile hydrothermal method to synthesize single-crystalline hcp-Co nanowires, in which citrate salts have been introduced as a complexing reagent and shape modifier to control the growth process. The chemical reduction can be formulated as follows:

$$[Co(C_6H_5O_7)_2]^{4-} + H_2PO_2^- + 3\ OH^- \rightarrow Co + 2\ C_6H_5O_7^{3-} + HPO_3^{2-} + 2\ H_2O$$

## Results and Discussion

The crystalline nature of the phase and its purity were determined by X-ray diffraction (XRD). A representative

[a] Hefei National Laboratory for Physical Science at Microscale, University of Science and Technology of China,
Hefei, Anhui 230026, People's Republic of China
Fax: +86-551-360-7402
E-mail: ytqian@ustc.edu.cn
[b] University of Science and Technology of China, Department of Chemistry,
Hefei, Anhui 230026, People's Republic of China

 © 2006 Wiley-VCH Verlag GmbH & Co. KGaA, Weinheim 

XRD pattern of the as-prepared product is shown in Figure 1a. All the diffraction peaks can be well indexed to hexagonal-phase cobalt, with lattice constants of $a$ = 2.506 and $c$ = 4.072 Å, which is consistent with the standard values reported in JCPDS 05-0727 (space group $P6_3/mmc$). No characteristic peaks due to the impurities of cobalt oxides or hydroxides were detected, which indicates that the nanostructures obtained by the present synthetic route consist of a pure hcp phase. In addition, the relative intensity of the peaks corresponding to the (002)/(100) and (002)/(101) planes is significantly higher than the standard values, which indicates a different growth tropism of the products. X-ray energy dispersive (EDS) microanalysis (shown in Figure 1b) of the Co nanowires indicated that the sample is essentially pure Co. Only a very small amount of oxygen (element ratio: 0.54%) was detected, which was possibly from slight oxidation of the surface. Considering that the experiment was carried out in air, it is not difficult to explain this.

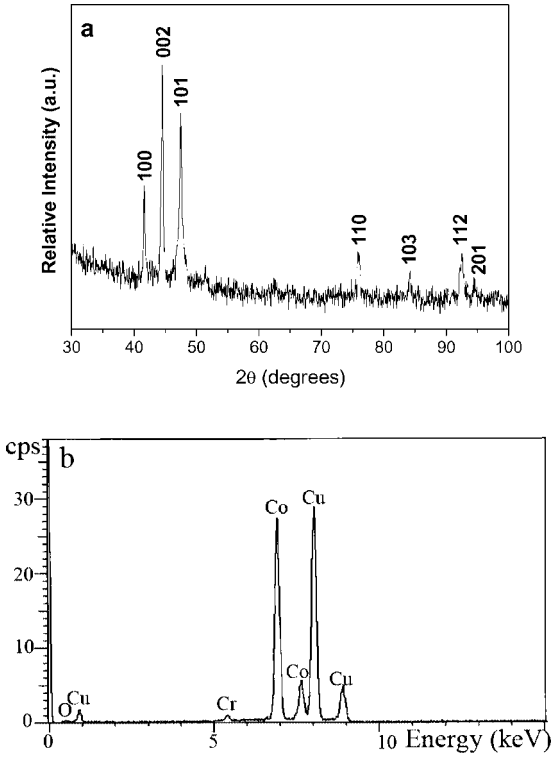


Figure 1. (a) XRD pattern of the final product obtained at 160 °C after 20 h. (b) EDS pattern of the final product (Cr and Cu signals can be attributed to the copper microgrid supporting the sample).

The morphologies and structures of the as-prepared products were examined by SEM and TEM. SEM observation (in Figure 2a) shows that the products consist of a large quantity of wire-like nanostructures. The nanowires range from several tens to several hundreds of micrometers in length. Figures 2b and c are TEM images that show the morphology of the nanowires. Each nanowire has a uniform width over its entire length, and the typical diameter of the wires is in the range 150–300 nm. Figure 2c displays the twist feature of a nanowire with an "M" shape, thus indicating the flexibility of the nanowire.

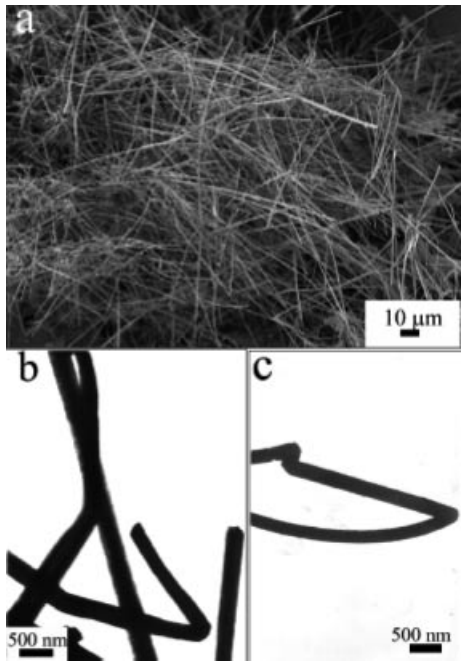


Figure 2. SEM and TEM images of the sample: (a) typical SEM image of the as-prepared Co nanowires; (b) and (c) TEM images of the Co nanowires, displaying the twist feature of the nanowire (c).

A more detailed study of the nanowires was performed by high-resolution TEM (HRTEM). Figure 3a shows a TEM image of an individual Co nanowire with a diameter of 200 nm. Figure 3b is a typical selected-area electron diffraction (SAED) pattern that was recorded from this nanowire. These pattern spots demonstrate the single-crystalline nature of this Co nanowire. Figure 3c is an HRTEM image recorded near the edge of this Co nanowire. The fringe spacing of 2.04 Å corresponding to the separation of the {002} planes of hcp-Co can be seen from Figure 3c; this also shows that the nanowire is single-crystalline. Further studies of both the HRTEM image and SAED patterns confirm that the single-crystalline nanowire grows along the [001] direction. The preferential crystal growth direction along the $c$ axis is the magnetic easy axis of hexagonal cobalt crystals.[22]

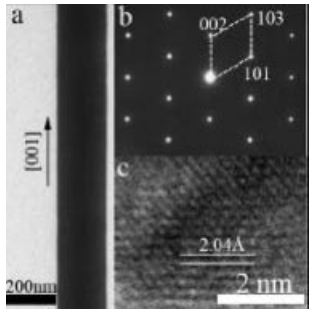


Figure 3. (a) Typical nanowire with a diameter of 200 nm. (b) SAED pattern recorded from this nanowire. (c) HRTEM image taken from the edge of this nanowire.

 © 2006 Wiley-VCH Verlag GmbH & Co. KGaA, Weinheim 

To investigate the nucleation and growth process of these nanowires, the evolution of the Co nanostructures was studied at various growth stages of the hydrothermal reaction by XRD and SEM techniques. Figure 4 shows the XRD patterns of samples that were taken after hydrothermal treatment for 6, 12, and 18 h. After heating for 6 h, the blue color of the mixture had disappeared and a large amount of grey solid product had formed. The XRD pattern (shown in Figure 4a) of the sample obtained at this stage indicates that hexagonal-phase cobalt had been produced. The SEM image (Figure 5a) shows that the sample is composed of cobalt particles and that they aggregate, driven by their natural magnetism. When the hydrothermal reaction time was extended to 12 h, the diffraction peaks of cobalt strengthened (Figure 4b). The SEM image (Figure 5b) reveals that radial nanowires were generated on the particles, and the surfaces of nanowires were covered with large numbers of nanoparticles. The inset of Figure 5b shows a magnified view of this radial structure. This image distinctly demonstrates that the Co nanowires grow from the particles. After 18 h, the diffraction peak of (002) planes has clearly strengthened, as shown in Figure 4c, which indicates that the sample has preferential tropism. The SEM image shown in Figure 5c shows that most of the products evolve into nanowires with smooth surfaces. After 20 h, the yield of cobalt nanowires was above 90%.

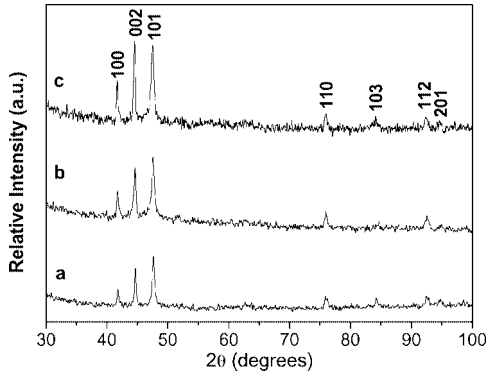


Figure 4. XRD patterns of the as-prepared samples at various growth stages of the hydrothermal process: (a) 6 h, (b) 12 h, and (c) 18 h.

On the basis of previous investigations on the evolution of cobalt nanowires, we found that this growth mode is very similar to the recent reports for the growth of one-dimensional metals in solution.[19,23] Under the present conditions, the formation of Co nanowires can also be attributed to nucleation and continuous growth by Ostwald ripening. In this mechanism, the small particles are generated by reduction of the cobalt(II) citrate complex by $H_2PO_2^-$ in basic solution in the initial stage of the hydrothermal process. In a subsequent step, the larger particles will grow at the expense of the smaller nanoparticles through the Ostwald ripening process. In the presence of citrate, most particles grow into nanowires. Finally, the nanoparticles are gradually consumed, resulting in the formation of long nanowires (shown in Figure 2a).

The presence of citrate ions is crucial for the formation of Co nanowires. Control experiments have shown that without citrate ions, only Co particles (diameter ca. 500 nm) are obtained (Figure 6a), and at a low concentration of citrate ions (0.04 M), the product (shown in Figure 6b) is a flower-like aggregation of plates (width 200 nm). In addition, we also found that by keeping all other reaction conditions the same, wire-like structures can be obtained in the presence of either citric acid or potassium citrate, but cannot be obtained in the presence of other complexing reagents such as tartrate and ethylenediamine tetraacetate. This indicates that citrate anions play a crucial role in the formation of Co nanowires. Furthermore, the different stability and structures of the Co complex precursors may affect the reaction conditions for the formation of wire-like structures, as reported for the ligand-mediated synthesis of shape-controlled materials.[20,24]

Citrate is an important biological ligand for metal ions and at high concentrations (ca. 0.2 mM) forms strong complexes with metal ions such as $Ag^+$, $Ca^{2+}$, $Mg^{2+}$, $Ni^{2+}$, and $Zn^{2+}$.[25] Citrate has been used as a shape modifier for the synthesis of ZnO complex structures[26] and Ag nanowires.[27] Citrate plays two major roles in our system. First, citrate ions can coordinate with cobalt ions to form $[Co(C_6H_5O_7)_2]^{4-}$ complexes in the excess citrate solution,[28,29] which decreases the free $Co^{2+}$ concentration in solution and results in the slow generation of Co nanoparticles. The relatively slow reaction rate may be favorable for the subsequent growth of Co nanostructures along the easy magnetic axis of the hexagonal cobalt, namely the [001] direction. In addition, citrate may bind to certain crystal faces of the cobalt particles through its $COO^-$ and OH functions. An FT-IR spectrum of the sample, hydrothermally treated in 0.2 M citrate solution for 12 h and unwashed before measurement, is shown in Figure 6c. It exhibits the characteristic absorption for the carbonyl groups of the citrate carbox-

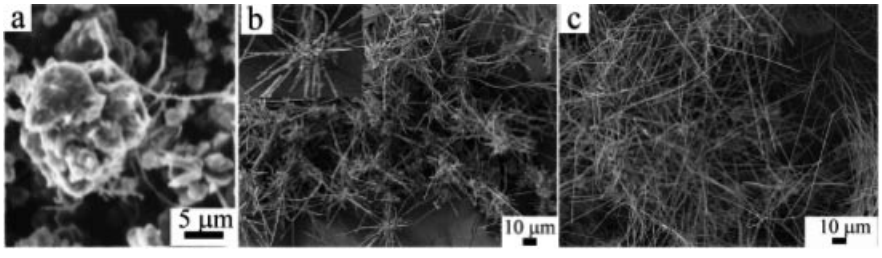


Figure 5. SEM images of the samples obtained at 160 °C after a hydrothermal treatment of (a) 6 h, (b) 12 h, and (c) 18 h.

 © 2006 Wiley-VCH Verlag GmbH & Co. KGaA, Weinheim 

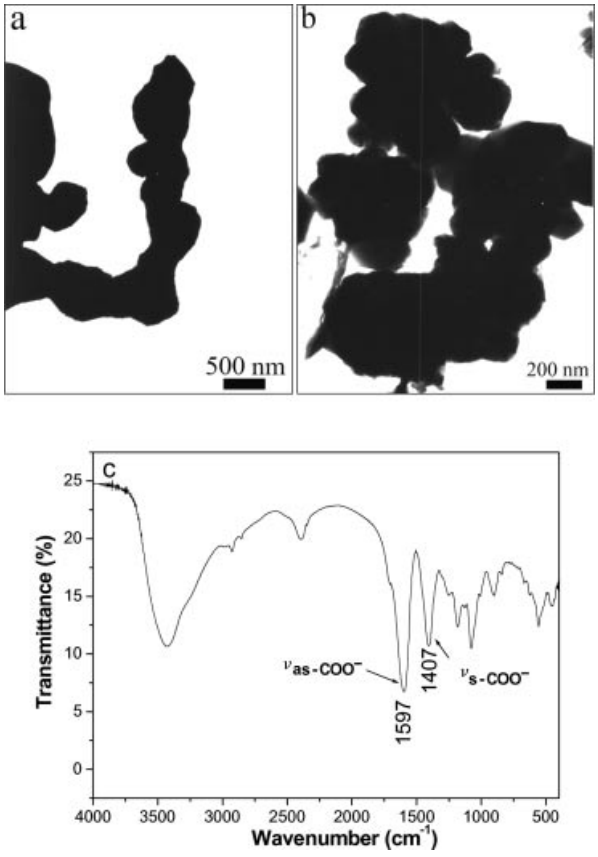


Figure 6. TEM images of products from syntheses with no sodium citrate (a) and 0.04 M sodium citrate solution (b). (c) FT-IR spectrum of the sample hydrothermally treated in 0.2 M citrate solution for 12 h and unwashed before measurement.

ylate ligands in the asymmetric and symmetric vibration regions. The asymmetric stretching vibrations $\nu_{as\text{-}COO^-}$ appear at 1597 cm$^{-1}$ and the symmetric stretching vibration $\nu_{s\text{-}COO^-}$ at 1407 cm$^{-1}$. The bands are shifted to lower frequencies compared to those of free citric acid, which suggests some interaction between metal and citrate ligand. These interactions could force the nanoparticles to grow along only one axis. In this case, citrate plays a similar role to that in the formation of Ag nanowires.[27]

Other reaction conditions, such as the concentration of NaOH in the reaction system and the reaction temperature, are also important factors in determining the shape of the final product. We found that a low concentration of NaOH solution (1 M) led to the formation of bamboo-like nanostructures with an average diameter of 300 nm (shown in Figure 7a). The reaction at a higher concentration of NaOH solution (4 M) produced Co dendrites (Figure 7b). Furthermore, if the other reaction conditions were maintained and the reaction temperature was reduced to less than 140 °C, the product was only aggregated particles. A higher temperature (such as 180 °C) resulted in wider wire-like structures and even some dendritic Co crystals. A temperature between 140 and 160 °C is therefore optimal for the growth of Co nanowires.

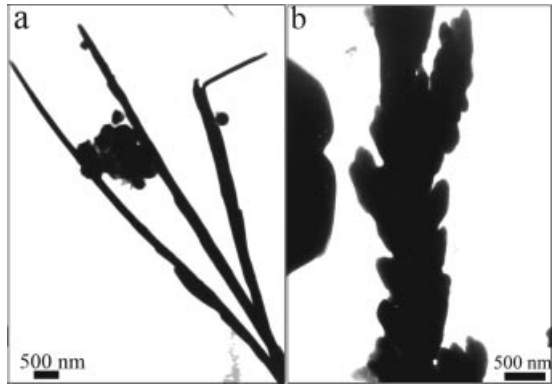


Figure 7. TEM images of the samples prepared at different NaOH concentrations: (a) 1 M NaOH solution, (b) 4 M NaOH solution.

The $M/H$ hysteresis loop (Figure 8) of the powdered Co nanowires measured at room temperature (300 K) shows a ferromagnetic behavior. The coercivity ($H_c$) and saturation magnetization ($M_s$) values are 166.8 Oe and 133.1 emu g$^{-1}$, respectively. The saturation magnetization is reduced relative to the bulk value (168 emu g$^{-1}$).[30] Surface oxidation at grain boundaries has been shown to cause a decrease in saturation magnetization.[30,31] Under the present experimental conditions, such a surface oxidation could be the reason for the decrease of $M_s$. In addition, although the

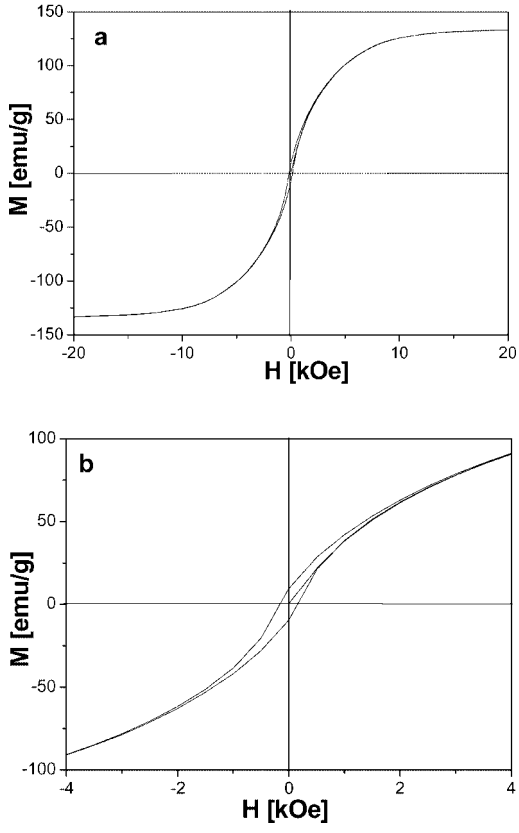


Figure 8. (a) Magnetic hysteresis loop of as-prepared cobalt nanowires measured at room temperature (300 K). (b) Enlargement of (a) at low field.

 © 2006 Wiley-VCH Verlag GmbH & Co. KGaA, Weinheim 

sample was washed before the measurement, a very small quantity of citrate molecules adsorbed on the Co nanowires could quench the magnetic moment through electron exchange between the ligand and surface atoms, which would partly result in the reduction of saturation magnetization.[32] Compared to the value for bulk material (a few tens of oersteds),[33] Co nanowires exhibit enhanced coercivity, which may be attributed to the small size and anisotropic shape of the nanowires. However, the coercivity value is much lower than that of the 2D and 3D superlattice of nanorods (740, 3200, and 7200 Oe)[17] or nanobelts (410.6 Oe)[18] with smaller sizes. Because a higher coercivity is an important factor for high-density information storage, further experiments are in progress to improve the coercivity of these nanowires.

## Conclusions

In summary, we have reported a simple hydrothermal reduction route for the synthesis of hexagonal Co nanowires in high yield. Citrate salts are introduced as a reagent and shape modifier to control the growth of Co nanostructures. The effects of the reaction temperature and the concentration of sodium citrate and NaOH have also been discussed. The as-prepared Co nanowires show ferromagnetism with a greater coercivity ($H_c$) than the bulk materials. Such a simple and environmentally friendly synthetic route may be extended to the fabrication of one-dimensional structures of other transition metals or their alloys.

## Experimental Section

All the reagents used were of analytical grade (purchased from Shanghai Chemical Industrial Co.) In a typical procedure for the preparation of cobalt nanowires, 10 mmol of $Na_3C_6H_5O_7{\cdot}2H_2O$, 2 mmol of $CoCl_2{\cdot}6H_2O$, and 10 mmol of $NaH_2PO_2$ were dissolved in 40 mL of distilled water, and then NaOH (10 M, 10 mL) aqueous solution was added with constant magnetic stirring. The final concentration of the raw materials in solution was 40 mM $Co^{II}$, 0.2 M citrate, 0.2 M $NaH_2PO_2$, and 2 M NaOH. The mixture was stirred for 10 min and then transferred into a 55-mL Teflon-lined autoclave. The autoclave was sealed and maintained in a furnace at 160 °C for 20 h, and then cooled to room temperature naturally. The grey powders were collected and washed with alcohol and distilled water several times and then dried in a vacuum oven at 60 °C for 5 h.

The X-ray diffraction (XRD) pattern was recorded with a Rigaku (Japan) D/max-rA X-ray diffractometer equipped with graphite-monochromated Cu-$K_\alpha$ radiation ($\lambda$ = 0.154187 nm). The SEM images were obtained with a field emission scanning electron microscope (FESEM, JEOL-6300F) or a Hitachi X-650 SEM. The TEM images were captured with a Hitachi Model H-800 instrument at an acceleration voltage of 200 kV. The high-resolution transmission electron microscopy (HRTEM) images and the corresponding selected area electron diffraction (SAED) pattern were taken with a JEOL 2010 high-resolution transmission electron microscope with X-ray energy-dispersive spectroscopy (EDS) performed at 200 kV. The FT-IR spectrum was recorded with a Bruker Vector-22 FT-IR spectrometer from 4000 to 400 $cm^{-1}$ at room temperature on KBr mulls. The magnetic measurement of the sample was carried out with a superconducting quantum interference device (SQUID) magnetometer (Quantum Design MPMS XL-7) with 6.4 mg of sample sealed in a small cylindrical vessel.

## Acknowledgments

Financial support from the National Natural Science Foundation of China and the 973 Project of China are appreciated. The authors thank Dr. Li Pi for recording the SQUID experiment.

[1] M. Zheng, L. Menon, H. Zeng, Y. Liu, S. Bandyopadhyay, R. D. Kirby, D. J. Sellmyer, *Phys. Rev. B* **2000**, *62* 12282–12286.
[2] K. Liu, K. Nagodawithana, P. C. Searson, C. L. Chien, *Phys. Rev. B* **1995**, *51*, 7381–7384.
[3] V. Tzitzios, D. Niarchos, M. Gjoka, N. Boukos, D. Petridis, *J. Am. Chem. Soc.* **2005**, *127*, 13756–13757.
[4] D. Weller, A. Moser, *IEEE Trans. Magn.* **1999**, *35*, 4423–4439.
[5] V. F. Puntes, K. M. Krishnan, A. P. Alivisatos, *Science* **2001**, *291*, 2115–2117.
[6] D. P. Dinepa, M. G. Bawendi, *Angew. Chem. Int. Ed.* **1999**, *38*, 1788–1791.
[7] V. F. Puntes, K. M. Krishnan, P. Alivisatos, *Appl. Phys. Lett.* **2001**, *78*, 2187–2189.
[8] S. H. Sun, C. B. Murray, *J. Appl. Phys.* **1999**, *85*, 4325–4330.
[9] J. Legrand, A. T. Ngo, C. Petit, M.-P. Pileni, *Adv. Mater.* **2001**, *13*, 58–62.
[10] F. Dumestre, B. Chaudret, C. Amiens, M.-C. Fromen, M.-J. Casanove, P. Renaud, P. Zurcher, *Angew. Chem. Int. Ed.* **2002**, *41*, 4286–4289.
[11] S.-J. Park, S. Kim, S. Lee, Z. G. Khim, K. Char, T. Hyeon, *J. Am. Chem. Soc.* **2000**,*122*, 8581.
[12] H. Zheng, M. Zheng, R. Skomski, D. J. Sellmyer, Y. Liu, L. Menon, S. Bandyopadhyay, *J. Appl. Phys.* **2000**, *87*, 4718–4720.
[13] S. H. Ge, C. Li, X. Ma, W. Li, L. Xi, C. X. Li, *J. Appl. Phys.* **2001**, *90*, 509–511.
[14] J. Qin, J. Nogués, M. Mikhaylova, A. Roig, J. S. Muñoz, M. Muhammed, *Chem. Mater.* **2005**,*17*, 1829–1835.
[15] H. M. Luo, D. H. Wang, J. B. He, Y. F. Lu, *J. Phys. Chem. B* **2005**,*109*, 1919–1922.
[16] V. F. Puntes, D. Zanchet, C. K. Erdonmez, A. P. Alivisatos, *J. Am. Chem. Soc.* **2002**, *124*, 12874–12880.
[17] F. Dumestre, B. Chaudret, C. Amiens, M. Respaud, P. Fejes, P. Renaud, P. Zurcher, *Angew. Chem. Int. Ed.* **2003**, *42*, 5213–5216.
[18] Q. Xie, Z. Dai, W. W. Huang, J. B. Liang, C. L. Jiang, Y. T. Qian, *Nanotechnology* **2005**, *16*, 2958–2962.
[19] Z. P. Liu, S. Li, Y. Yang, S. Peng, Z. K. Hu, Y. T. Qian, *Adv. Mater.* **2003**, *15*, 1946–1948.
[20] X. M. Ni, Q. B. Zhao, H. G. Zheng, B. B. Li, J. M. Song, D. E. Zhang, X. J. Zhang, *Eur. J. Inorg. Chem.* **2005**, *23*, 4788–4793.
[21] L. Vayssieres, C. Sathe, S. M. Butorin, D. K. Shuh, J. Nordgren, J. H. Guo, *Adv. Mater.* **2005**, *17*, 2320–2323.
[22] D. F. Wan, X. L. Ma, *Magnetic Physics*, Publishing House of the Electronics Industry, Beijing, **1999**, p.178.
[23] Y. L. Wang, T. Herricks, Y. N. Xia, *Nano Lett.* **2003**, *3*, 1163–1166.
[24] X. G. Peng, *Adv. Mater.* **2003**, *15*, 459–463.
[25] J. A. Parkinson, H. Z. Sun, P. J. Sadler, *Chem. Commun.* **1998**, *8*, 881–882.
[26] Z. R. Tian, J. A. Voigt, J. Liu, B. Mckenzie, M. J. Mcdermott, M. A. Rodriguez, H. Konishi, H. F. Xu, *Nat. Mater.* **2003**, *2*, 821–826.
[27] K. K. Caswell, C. M. Bender, C. J. Murphy, *Nano Lett.* **2003**, *3*, 667–669.
[28] C. Bresson, L. Bion, C. Moulin, C. Lamouroux, *Radiochim. Acta* **2005**, *93*, 672–682.

 © 2006 Wiley-VCH Verlag GmbH & Co. KGaA, Weinheim 

[29] M. Matzapetakis, M. Dakanali, C. P. Raptopoulou, V. Tangoulis, A. Terzis, N. Moon, J. Giapintzakis, A. Salifoglou, *J. Biol. Inorg. Chem.* **2000**, *5*, 469–474.
[30] G. Dumpich, T. P. Krome, B. Hausmans, *J. Magn. Magn. Mater.* **2002**, *248*, 241–247.
[31] B. Hausmanns, T. P. Krome, G. Dumpich, *J. Appl. Phys.* **2003**, *93*, 8095–8097.
[32] D. A. van Leeuwen, J. M. van Ruitenbeek, L. J. de Jongh, A. Ceriotti, G. Pacchioni, O. D. Häberlen, N. Rösch, *Phys. Rev. Lett.* **1994**, *73*, 1432–1435.
[33] H. Q. Cao, Z. Xu, H. Sang, D. Sheng, C. Y. Tie, *Adv. Mater.* **2001**, *13*, 121–123.

Received: January 21, 2006
Published Online: April 11, 2006

 © 2006 Wiley-VCH Verlag GmbH & Co. KGaA, Weinheim 

DOI: 10.1002/ejic.200600114

# The Relationship Between Aromaticity and Charge-Transfer Transitions: A Combined Study of Square-Planar Metal Complexes Based on DFT, NMR and Nucleus-Independent Chemical Shifts

**Christodoulos Makedonas[a] and Christiana A. Mitsopoulou*[a]**

*Dedicated to the memory of Professor Dimitris F. Katakis*

**Keywords:** Aromaticity / Density functional calculations / N ligands / S ligands / Transition metals

The aromaticity of square-planar metal complexes, in this case mixed diiminodithiolate complexes of group VIII metals, has been investigated by $^{1}H$ and $^{1}H$-$^{15}N$ NMR spectroscopy, both experimentally and theoretically, as well as NICS indices. The electron-donating/-attracting ability of the substituent group and the metal ion interact with each other and control the aromaticity of the chelated rings and, as a consequence, the extent of the delocalization in the molecular plane. Evolution of the nucleus-independent chemical shift (NICS) of the ligands upon complexation is consistent with the change in their electron distribution. At the same time, and in analogy with the EMF in closed circuits, a positive difference of the NICS value ($\Delta_{NICS}$) between two points (where HOMO and LUMO are located) can be envisioned as the driving force for charge-transfer transitions.

(© Wiley-VCH Verlag GmbH & Co. KGaA, 69451 Weinheim, Germany, 2006)

## Introduction

Despite the lack of a unique and precise definition, the concept of aromaticity is one of the most frequently used in organic chemistry[1] and nowadays in inorganic and organometallic chemistry as well.[2] Aromaticity is associated with the widely understood concept of electron delocalization, but until recently was mainly related to cyclic π-systems. Today, the Hückel $(4n+2)$ π-electron rule is known to be just an ideal case and aromaticity is no longer limited to fully conjugated organic rings or even nonmetals. The terms σ-aromaticity, δ-aromaticity, and even σ/δ-antiaromaticity that are currently in use imply the contribution of highly or not delocalized σ-, π-, and δ-type (referring to the symmetry) molecular orbitals.[3] Moreover, the concept of multiple (π- *and* δ-) aromaticity has been introduced for metal heterocyclic compounds, such as planar bis- and tris(dithiolene) complexes,[4,5] while a 3D aromaticity of relevant complexes has also been proved.[6] The former not only explains the peculiar properties of this class of compounds but also the "non-innocent" character of the dithiolene ligand. The latter has a significant role over a wide range of chemistry since complexes with ligands of this class are widely applicable in bioinorganic chemistry[4c] and catalysis,[4d] and as magnetic and non-linear optics materials.[4e] Here, one should stress that aromaticity/antiaromaticity in all the aforementioned systems will not manifest itself exactly the same way as in organic chemistry. Many specific deviations are expected. Nevertheless, it is believed that the overall chemical bonding picture and most of the molecular properties of these compounds should be explainable using the concepts of aromaticity and antiaromaticity.

With all this in mind, we tried to "measure" the aromaticity, or more accurately, the existence or not of significant diatropic ring currents, of a different class of compounds that bear dithiolate ligands, namely the mixed α-diiminodithiolate complexes. The latter have attracted researchers' attention since their first introduction by Miller and Dance[7] due to their interesting chemistry and their potential applications as new materials and photosensitizers.[8–11] The combination of a good π*-donor (the dithiolate ligand) and a good π*-acceptor (the diimine) leads to systems that possess intriguing properties, namely photoluminescence in solution, electrical conductivity in the solid state, large molecular hyperpolarizabilities, and large excited oxidation potentials. These properties are the result of the existence of a mixed metal-ligand-to-ligand charge transfer (MMLL′CT) band in the low-energy region of the UV/Vis/NIR spectrum, as has been indicated both experimentally[8] and theoretically.[11d]

As aromaticity is not defined exactly, since it is not a directly measurable quantity, we had to use one of the in-

[a] Inorganic Chemistry Laboratory, Department of Chemistry, National and Kapodistrian University of Athens, Panepistimiopolis, Zografou 15771, Greece
Fax: +30-210-832-2828
E-mail: cmitsop@chem.uoa.gr

 InterScience © 2006 Wiley-VCH Verlag GmbH & Co. KGaA, Weinheim 

dices available in the literature. Some of the main criteria on which aromatic behavior are based are the geometrical indices, $^1$H NMR chemical shifts, ASE (aromatic stabilization energy) on the basis of homodesmotic reactions, the exaltation of magnetic susceptibility ($\Lambda$), and HOMA (harmonic oscillator model of aromaticity),[12] none of which, however, has proved to be generally applicable.[13] On the contrary, the NICS (nucleus-independent chemical shift), which is a magnetism-based index,[14] is not only widely used to characterize the aromaticity and antiaromaticity of organic rings[15] but it is also well accepted as one of the most efficient tools for the understanding and interpretation of ring currents[16] of organic compounds, boranes and fullerenes,[17] and inorganic[18] and organometallic[2] complexes. NICS values have been defined by Schleyer et al.[14] based on the absolute magnetic shieldings computed at the ring center at the ab initio, density functional, and semi-empirical (MNDO) levels; the signs are reversed to conform to the NMR chemical shift convention (negative upfield and positive downfield). Significantly negative NICS values in the interior positions of rings or cages indicate aromaticity or diatropic ring currents, whereas positive values denote antiaromaticity or paratropic ring currents.[14] Moreover, the σ-contribution can be separated from the π-contribution by using NICS(1) instead of NICS(0) values.[16a] NICS(1) refers to the location 1 Å above the center of the ring plane, where local contributions of σ-bonds are reduced in favor of the π-effects.

The above examples of the application of NICS encouraged us to undertake a systematic study, firstly to find out if mixed diiminodithiolate complexes have an aromatic character and, as a consequence, gain some hints about their electronic structure, and secondly to reveal the role of the metal atom or the substituents on the chelating ligands in the extent of delocalization of the electron current. To the best of our knowledge, although there are a few papers[2b,2c] dealing with NICS in coordination compounds, this is the first attempt at a systematic use of NICS as a probe of the change of "aromatic" delocalization in mixed-ligand metal complexes by changing the metal ion or the substituents on the conjugated rings.

## Results and Discussion

The compounds employed for this study are displayed in Scheme 1. The selection of these ten compounds was done as follows. First of all, in the formal oxidation state +2 the mixed diiminodithiolate complexes have a square-planar coordination and two planar didentate ligand systems. In other words, compounds **1**–**5** and **10** contain the metal ion as a link between two planar ligands, forming a coplanar compound with five-membered conjugated rings. The metal ion is part of a delocalized π-electron system. This delocalized system is mainly composed of the metal $d_{xz}$ orbitals, the sulfur $3p_z$, the nitrogen $2p_z$, and the carbon $p_z$ orbitals.

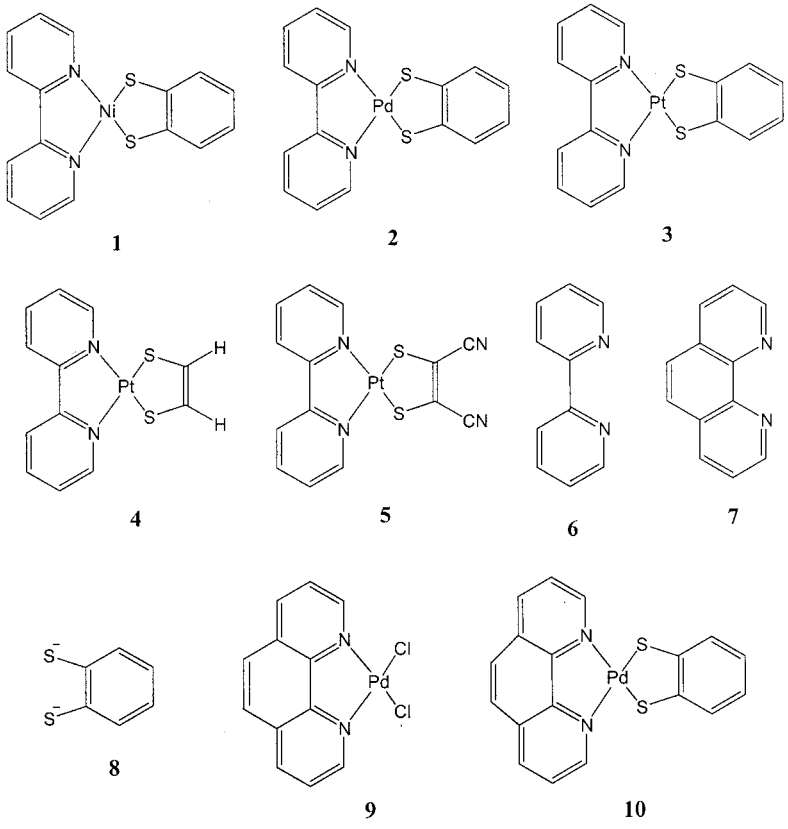


Scheme 1.

 © 2006 Wiley-VCH Verlag GmbH & Co. KGaA, Weinheim 

Complexes **1**–**3** consist of an aromatic α-diimine and an aromatic dithiolate ligand coordinated to a formally $d^8$ metal atom. Both ligands are characterized by their medium-strength π*-donating/-accepting ability and are suitable for the investigation of the metal's role. Thus, changes in the diatropic ring currents of the chelated ligands induced by tuning the metal ion will be discussed.

The next series of compounds, **3**–**5**, were employed in order to determine the substituents' effect on the dithiolate chelate ring. The dithiolate ligand in these complexes acts as a strong σ-donor, whereas its π*-donating role is reduced along the series $edt^{2-} > bdt^{2-} > mnt^{2-}$.[8,11d] The influence of the substituents' π*-accepting ability on the MMLL′CT band and the complexes' electron properties is very well established.[7–11] Finally, based on compounds **7**–**10** we will try to reveal the way that ring currents arise upon complexation.

Selected structural data for compounds **1**–**10**, optimized by DFT, are collected in Table 1 along with the available experimental data. From a close inspection of the data we can see that the DFT M–X bond lengths systematically exceed the corresponding X-ray values by about 0.04 Å, which is generally anticipated. All other parameters are in accordance with the experimental ones, thus revealing the overall agreement between theory and experiment.

Since ring currents are very sensitive to geometrical characteristics, a closer inspection of the structural data is necessary. Firstly, in the series **1**–**5** and **10** the M–N bonds are longer than those observed in M–diimine complexes, while the M–S bonds are shorter by 0.02 Å than the M–S bond of M–dithiolene complexes.[2b] This is consistent with the significant *trans* influence in similar compounds.[8d] Secondly, the C–S bond lengths in these complexes are in close agreement with the typical S–C($sp^2$) distance (1.751 Å), indicating that the observed delocalization in similar dithiolene complexes (S–C = 1.704 Å) is not seen in the mixed diiminodithiolate ones.

Focusing on the central metal's structural role, a comparison of the M–N and M–S bond lengths in the series **1**–**3** must be made. Inspection of the data collected in Table 1 shows that the above bond lengths are sensitive to the nature of the metal. Thus, the M–N bond lengths increase in the order Ni–N < Pt–N < Pd–N; Ni has a significantly smaller bonding radius than Pd and Pt. According to the contribution of each fragment and the relative energies of the bonding orbitals (Table 2), we can conclude that the better overlap between the metal atom and the dithiolate ligand in Pd complexes reduces the electron density of the M–N bonds. On the other hand, as both $Pd^{2+}$ and $Pt^{2+}$ have almost the same radius (86 and 85 pm, respectively), they can successively overlap with both conjugated ligands, thus providing the series Ni–S > Pd–S ≈ Pt–S on passing from Ni to Pt.

For chelated five-membered rings, the C–C bond should be an indicator of the cyclic electron delocalization. Thus, for a dithiolate ring the C–C bond length changes from 1.341 Å for **4** to 1.365 Å for **5** and 1.402 Å for **3**, which is close to the bond length in benzene [1.40 Å; for comparison, ($sp^2$)C=C($sp^2$) = 1.331 Å]. According to the above bond lengths the degree of bond delocalization decreases in the order **3** > **5** > **4**, thereby indicating that diatropic ring currents are reinforced by the presence of π*-accepting substituents on the dithiolate ring, in accordance with the benzene derivatives. Here, it could be argued that a C–C bond is expected to be the longest in the case of **3** since the benzene ring would try to achieve its aromatic sextet as much as possible by following the Clar rule; although this is generally true, the overall assignment must be considered to be correct as it is completely consistent with the π*-accepting ability of the substituents. The last assertion has also been stated for dithiolene complexes.[2b,2c] In the series **3**–**5**, the C–C bond lengths in the diimine-containing conjugated ring are nearly constant (1.466 Å). Thus, these bonds are practically unaffected by the substituents on the dithiolate

Table 1. Comparison of selected calculated bond lengths [Å] and angles [°] for the compounds under study with experimental values from X-ray analysis.

| | M | M–N | M–S | C–S | C=N | C=C$^{dith.}$ | C=C$^{diim.}$ | $\varphi_{diim.}$ | $\varphi_{dith.}$ |
|---|---|---|---|---|---|---|---|---|---|
| **1** | exp.[20] | 1.937(2) | 2.144(3) | 1.755(3) | 1.358(3) | 1.395(3) | 1.472(3) | 83.31(8) | 90.18(3) |
| | calcd. | 1.970 | 2.178 | 1.765 | 1.358 | 1.401 | 1.467 | 82.26 | 90.18 |
| **2** | exp.[20] | 2.071(2) | 2.245(1) | 1.762(2) | 1.353(3) | 1.396(3) | 1.474(3) | 79.41(6) | 88.67(2) |
| | calcd. | 2.120 | 2.286 | 1.774 | 1.358 | 1.401 | 1.476 | 77.85 | 88.16 |
| **3** | exp.[21] | 2.050(5) | 2.248(2) | 1.761(6) | 1.367(8) | 1.373(8) | 1.464(8) | 80.1(2) | 89.0(1) |
| | calcd. | 2.095 | 2.299 | 1.771 | 1.363 | 1.402 | 1.466 | 78.00 | 88.26 |
| **4** | exp.[22] | 2.049(4) | 2.250(1) | 1.743(7) | 1.362(7) | 1.346(14) | 1.469(10) | 79.26(16) | 88.67(6) |
| | calcd. | 2.092 | 2.302 | 1.754 | 1.365 | 1.341 | 1.462 | 78.10 | 88.05 |
| **5** | calcd. | 2.099 | 2.296 | 1.759 | 1.362 | 1.365 | 1.469 | 78.04 | 88.44 |
| **6** | exp.[23c] | – | – | – | 1.35(3) | – | 1.50(3) | – | – |
| | calcd. | – | – | – | 1.341 | – | 1.500 | – | – |
| **7** | exp.[23a,23b] | – | – | – | 1.362(8) | – | 1.441(8) | – | – |
| | calcd. | – | – | – | 1.350 | – | 1.459 | – | – |
| **8** | calcd. | – | – | 1.771 | – | 1.454 | – | – | – |
| **9** | calcd. | 2.082 | – | – | 1.363 | – | 1.430 | 80.15 | – |
| **10** | exp.[11d] | 2.096(8) | 2.261(3) | 1.787(10) | 1.368(12) | 1.376(13) | 1.437(13) | 80.2(3) | 89.17(10) |
| | calcd. | 2.128 | 2.283 | 1.775 | 1.364 | 1.401 | 1.434 | 78.69 | 88.49 |

 © 2006 Wiley-VCH Verlag GmbH & Co. KGaA, Weinheim 

ligands. However, in the series **1**–**3** the C–C bond lengths in the diimine-containing conjugated ring decrease in the order **2** > **1** ≈ **3**, while the corresponding bond for the dithiolate ring remains practically the same (1.401 Å). This observation reveals the significant role of the metal in determining the extent of delocalization. Complexes **2** and **10** have identical structural characteristics, as anticipated, since bpy and phen have almost the same σ-donating and π*-accepting behavior.

Finally, the Pd–N bond of **9** is shorter than that of **10** due to the weaker *trans* influence of the chlorine atoms, whereas the phenanthroline moiety **7** is slightly affected by complexation (changes of ±0.015 Å in bond lengths). On the other hand, the C–C bond lengths of benzedithiolate **8** (1.454 Å) are more benzene-like after complexation (1.401 Å in **10**).

Considering the data in Table 2, one could suppose that the HOMO–LUMO gap can be used as an index of aromaticity.[19] However, this is quite a complicated task for the

Table 2. Contribution of different fragments to the valence orbitals of the complexes. HOMOs and LUMOs are shown in bold.

| MO | *E* [eV] | Diimine | Dithiolate[a] | Metal |
|---|---|---|---|---|
| | | **1** | | |
| | | unoccupied | | |
| $39a_1$ | –0.98 | 70.1 | 21.9 | 8.0 |
| $33b_2$ | –1.59 | 11.0 | 38.0 | 51.0 |
| $8a_2$ | –1.77 | 99.1 | 0.1 | 0.8 |
| $11b_1$ | –2.08 | 99.0 | 0.1 | 1.0 |
| **$10b_1$** | **–2.93** | **91.4** | **5.3** | **3.3** |
| | | occupied | | |
| **$9b_1$** | **–4.67** | **6.5** | **84.2** | **9.3** |
| $7a_2$ | –5.14 | 0.7 | 89.1 | 10.3 |
| $38a_1$ | –6.25 | 1.2 | 14.6 | 84.2 |
| $6a_2$ | –6.67 | 2.4 | 60.4 | 37.2 |
| $8b_1$ | –6.71 | 5.3 | 33.5 | 61.2 |
| $32b_2$ | –6.81 | 6.1 | 65.7 | 28.2 |
| | | **2** | | |
| | | unoccupied | | |
| $39a_1$ | –0.67 | 65.7 | –9.4 | 43.7 |
| $33b_2$ | –1.71 | 9.2 | 48.2 | 42.6 |
| $8a_2$ | –1.79 | 99.0 | 0.2 | 0.8 |
| $11b_1$ | –2.08 | 99.0 | 0.3 | 0.8 |
| **$10b_1$** | **–2.93** | **92.4** | **4.6** | **3.0** |
| | | occupied | | |
| **$9b_1$** | **–4.69** | **5.8** | **85.4** | **8.8** |
| $7a_2$ | –5.14 | 0.8 | 89.1 | 10.1 |
| $38a_1$ | –6.28 | 8.6 | 39.0 | 52.3 |
| $6a_2$ | –6.75 | 1.8 | 75.9 | 22.3 |
| $8b_1$ | –6.89 | 5.0 | 55.6 | 39.4 |
| $32b_2$ | –7.22 | 18.1 | 60.8 | 21.1 |
| | | **3** | | |
| | | unoccupied | | |
| $39a_1$ | –0.66 | 59.9 | 2.3 | 37.8 |
| $33b_2$ | –1.06 | 6.5 | 46.6 | 46.9 |
| $8a_2$ | –1.8 | 98.2 | 0.5 | 1.3 |
| $11b_1$ | –2.04 | 98.1 | 0.5 | 1.4 |
| **$10b_1$** | **–2.92** | **87.4** | **7.2** | **5.4** |
| | | occupied | | |
| **$9b_1$** | **–4.63** | **10.0** | **79.9** | **10.0** |
| $7a_2$ | –5.13 | 1.7 | 83.7 | 14.6 |
| $38a_1$ | –6.4 | 6.7 | 24.2 | 69.1 |
| $6a_2$ | –6.73 | 3.3 | 70.0 | 26.7 |
| $8b_1$ | –6.82 | 7.6 | 51.9 | 40.5 |
| $37a_1$ | –7.27 | 3.4 | 53.1 | 43.5 |
| | | **4** | | |
| | | unoccupied | | |
| $33a_1$ | –0.58 | 57.1 | 4.6 | 38.4 |
| $28b_2$ | –1.01 | 12.6 | 44.9 | 42.4 |
| $7a_2$ | –1.69 | 98.4 | 0.4 | 1.3 |
| $10b_1$ | –1.92 | 98.1 | 0.5 | 1.4 |
| **$9b_1$** | **–2.81** | **84.6** | **9.7** | **5.6** |
| | | occupied | | |
| **$8b_1$** | **–4.50** | **12.7** | **78.0** | **9.3** |
| $6a_2$ | –5.68 | 3.0 | 67.4 | 29.6 |
| $32a_1$ | –6.35 | 7.7 | 23.9 | 68.4 |
| $7b_1$ | –7.04 | 11.6 | 25.8 | 62.6 |
| $31a_1$ | –7.26 | 4.3 | 52.9 | 42.8 |
| $27b_2$ | –7.36 | 17.6 | 62.2 | 20.1 |

Table 2. *(continued)*.

| MO | *E* [eV] | Diimine | Dithiolate[a] | Metal |
|---|---|---|---|---|
| | | **5** | | |
| | | unoccupied | | |
| $9a_2$ | –1.60 | 3.8 | 94.4 | 1.8 |
| $33b_2$ | –1.89 | 10.0 | 46.1 | 43.9 |
| $8a_2$ | –2.37 | 96.5 | 2.5 | 0.9 |
| $11b_1$ | –2.59 | 98.3 | 0.4 | 1.2 |
| **$10b_1$** | **–3.49** | **90.4** | **5.0** | **4.5** |
| | | occupied | | |
| **$9b_1$** | **–5.51** | **7.5** | **81.1** | **11.4** |
| $7a_2$ | –6.53 | 2.8 | 67.0 | 30.2 |
| $37a_1$ | –7.15 | 7.8 | 21.0 | 71.2 |
| $8b_1$ | –7.63 | 7.9 | 49.3 | 42.8 |
| $36a_1$ | –8.17 | 2.0 | 52.3 | 45.7 |
| $32b_2$ | –8.20 | 18.4 | 61.2 | 20.3 |
| | | **9** | | |
| | | unoccupied | | |
| 78 ($a_2$) | –1.16 | 99.5 | 0.0 | 0.5 |
| 77 ($b_1$) | –1.80 | 98.9 | 0.1 | 1.0 |
| 76 ($b_2$) | –2.42 | 17.6 | 31.0 | 51.4 |
| 75 ($a_2$) | –2.98 | 99.3 | 0.1 | 0.6 |
| **74 ($b_1$)** | **–3.18** | **96.6** | **0.7** | **2.7** |
| | | occupied | | |
| **73 ($a_2$)** | **–6.27** | **2.1** | **72.8** | **25.0** |
| 72 ($a_1$) | –6.51 | –4.5 | 74.2 | 30.3 |
| 71 ($b_1$) | –6.51 | 6.8 | 63.7 | 29.5 |
| 70 ($b_2$) | –6.61 | –1.0 | 96.8 | 4.2 |
| 69 ($a_1$) | –6.81 | 15.7 | 24.9 | 59.3 |
| 68 ($b_1$) | –7.83 | **78.8** | 13.8 | 7.4 |
| | | **10** | | |
| | | unoccupied | | |
| $9a_2$ | –0.90 | 99.5 | 0.0 | 0.5 |
| $12b_1$ | –1.56 | 99.0 | 0.3 | 0.8 |
| $35b_2$ | –1.69 | 11.8 | 46.6 | 41.7 |
| $8a_2$ | –2.73 | 99.3 | 0.2 | 0.5 |
| **$11b_1$** | **–2.89** | **92.8** | **4.3** | **2.9** |
| | | occupied | | |
| **$10b_1$** | **–4.66** | **5.4** | **85.6** | **9.0** |
| $7a_2$ | –5.11 | 0.9 | 88.8 | 10.3 |
| $41a_1$ | –6.25 | 2.8 | 33.9 | 63.4 |
| $6a_2$ | –6.72 | 1.7 | 75.9 | 22.3 |
| $9b_1$ | –6.84 | 9.1 | 52.7 | 38.1 |
| $40a_1$ | –7.22 | 4.7 | 48.3 | 47.0 |

[a] In the case of **9** this denotes the contribution of the two Cl atoms.

 © 2006 Wiley-VCH Verlag GmbH & Co. KGaA, Weinheim 

complexes under study as both the HOMO and LUMO are located in different parts of the complex (on the dithiolate ring and the diimine ring, respectively). Thus, proceeding with our analysis of the delocalization of the ring currents in M(diimine)(dithiolate) complexes by studying the NMR data and NICS indices, a cage of sampling points was built around every molecule at distances of 0, 0.5, and 1 Å above the ring plane. The grid of points includes the NICS(0) and NICS(1), as calculated by definition. NICS(0) and NICS(1) constants for all compounds under investigation are displayed in Table 3, and the $^1$H NMR frequencies of selected nuclei are shown in Table 4. The selected sampling points are indicated in Figure 1.

Table 3. NICS(0)/NICS(1) values for the center of the selected rings.[a]

| | A | B | C | D | E |
|---|---|---|---|---|---|
| **1** | +0.27/–1.18 | –10.32/–5.29 | –4.22/–7.71 | – | –7.99/–9.31 |
| **2** | +1.58/–1.21 | –7.21/–3.77 | –4.93/–7.97 | – | –7.79/–9.00 |
| **3** | –1.14/–3.27 | –7.56/–4.61 | –4.59/–7.39 | – | –7.79/–9.09 |
| **4** | –1.84/–3.53 | –7.41/–4.41 | –4.05/–6.87 | – | – |
| **5** | –0.93/–2.89 | –10.31/–5.61 | –5.30/–8.09 | – | – |
| **6** | – | – | –5.43/–9.07 | – | – |
| **7** | +7.30/ +2.34 | – | –7.37/–10.41 | –5.81/–8.34 | – |
| **8** | – | – | – | – | –4.30/–6.31 |
| **9** | +2.36/ +0.88 | – | –7.47/–10.24 | – | – |
| **10** | +2.52/–0.45 | –6.70/–3.20 | –6.14/–9.36 | –6.21/–8.24 | –7.40/–8.70 |

[a] NICS/NICS(1) of benzene: –7.92/–9.93.

Table 4. $^1$H NMR chemical shifts in [D$_6$]DMSO.

| | H1-H1′ | H2-H2′ | H3-H3′ | H4-H4′ |
|---|---|---|---|---|
| **1** | 8.66 | 8.25 | – | 6.72 |
| **2** | 8.67 | 8.32 | – | 6.75 |
| **3** | 9.28 | 8.41 | – | 6.80 |
| **4** | 9.36 | 8.08 | – | – |
| **5** | 9.12 | 8.52 | – | – |
| **6** | 8.69 | 7.94 | – | – |
| **7** | 9.01 | 8.93 | 8.28 | – |
| **8** | – | – | – | 6.55 |
| **9** | 9.27 | 8.97 | 8.29 | – |
| **10** | 9.10 | 8.47 | 7.98 | 6.90 |

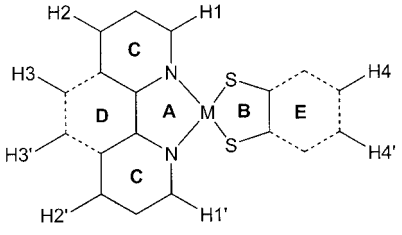


Figure 1. Sampling grid of NICS values and selected nuclei.

Specific proton nuclei were selected as indicators for the electron delocalization for the following reasons. For both bipyridine and phenanthroline complexes, H1-H1′ are close to the chelated ring – they are coupled through two bonds to the nitrogen atom and three to the metal atom – whereas protons H2-H2′ (for bpy), H3-H3′ (for phen), and H4-H4′ (for bdt) lie furthest from the metal atom and, as a result, are the most effective indicators of alterations in the π-electron current.

Based on NICS values in the ring centers (Table 3), the aromaticity of the dithiolate ring (B) is only marginal (maximum of around –5 ppm vs. around –10 ppm for benzene) while the diimine ring (A) is not aromatic (maximum NICS about –3 ppm). The nonaromatic character of the diimine ring (A) can be explained by the large difference in electronegativity between nitrogen (3.04), carbon (2.55), and the metal (2.28 for Pt and 2.20 for Pd), which leads to localization of electron density on the nitrogen atom; on the other hand, delocalization is observed in the dithiolate ring (B) due to the similar electronegativities of carbon (2.55) and sulfur (2.58). Moreover, differences in NICS values are observed with changes of metal or the substituents, thereby providing us with the opportunity to monitor changes of the diatropic current in the complexes. Thus, in the series **3**–**5** the NICS(1) values of the dithiolate ring (B) decrease in the order **5** > **3** > **4**, thereby indicating the enhanced ring diatropicity in the presence of substituents with a relatively high electron-withdrawing ability. The reverse order is found for the diimine ring, as the NICS values for (A) decrease from **4** to **3** and **5**. The electron-withdrawing groups on the dithiolate ring tend to stabilize the HOMO, thus increasing the HOMO–LUMO gap, as has been proved experimentally[8] and further supported by our calculations.[11] This stabilization has its origin in the better overlap of the central metal atom with the dithiolate ligand and causes the shielding of the latter. Moreover, the NICS(1) values of (C) (considering also the free ligand) decrease in the order **6** > **5** > **3** > **4**, in accordance with the HOMO stabilization (Table 2).

At this point we should comment on the reverse direction of $^1$H NMR and NICS(1) values that is observed on moving from free bipyridine ligand to the coordinated one. According to the NICS(1) values of (C), diatropic ring currents on the pyridine moieties diminish as a consequence of σ-donation of electron density to the metal atom through the nitrogen atoms. On the other hand, the $^1$H NMR chemical shifts (H2-H2′, Table 4) indicate that the protons of complexed bipyridine are more deshielded than those of the free ligand due to the paratropic effect of the metal atom. The asymmetrical charge-distribution in the valence orbitals of the metal atom is responsible to a large extent for the strong diamagnetic shift of the nucleus bound to it.[24] The resulting paramagnetic moment deshields the metal atom, but shields the other nucleus as in a synergic procedure. For the complexes under study, this is clearly demonstrated by the $^{15}$N NMR chemical shifts, which upon complexation are shielded from $\delta$ = 313.13 ppm for free phenanthroline to $\delta$ = 240.45 ppm for **10** (Figure 2). As a result, the rest of the bipyridine molecule is deshielded, with the effect being more apparent for the H1-H1′ nuclei (Table 4); since complexation has taken place, the $^1$H NMR and NICS(1) values are in total accordance within the series **5** > **3** > **4** provided that relativistic effects for heavy metals (i.e. Pt) are taken

 © 2006 Wiley-VCH Verlag GmbH & Co. KGaA, Weinheim 

into account even for the NICS values. In this class of complexes, the bipyridine also acts as a weak π*-acceptor, with its vacant π-orbitals interacting with filled metal d-orbitals. As H1-H1′ is deshielded in the series **4** > **3** > **5**, we expect the metal atom to be deshield in the same order. Our results are in close agreement with those reported by Bereman and Purrington et al. in their extensive study of various dithiolene complexes.[22]

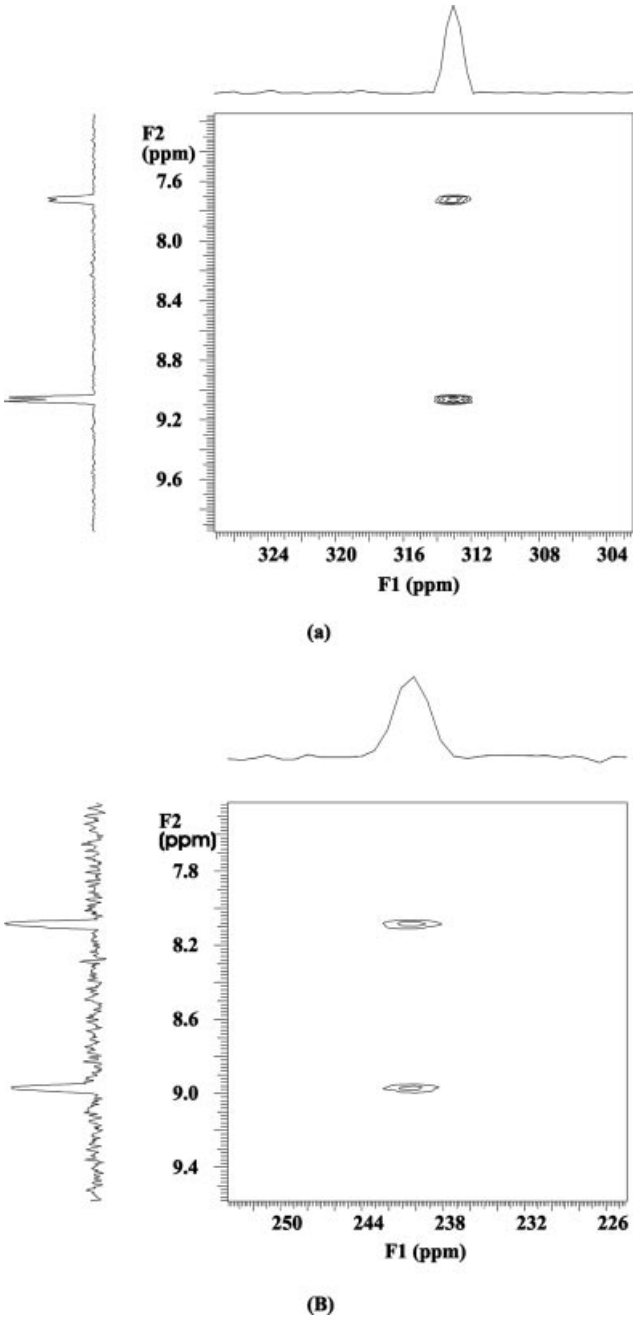


Figure 2. $^{1}H$-$^{15}N$ HMBC spectra of 1,10-phenanthroline (a) and Pd(phen)(bdt) (b).

The role of the central metal is revealed by studying the series **1**–**3**. First of all, the diatropic ring current of the dithiolate (bdt) chelate ring (B) decreases in the order **1** > **3** > **2** while the corresponding one for the (bpy) diimine conjugated ring (A) decreases in the order **3** > **2** ≈ **1**, in accordance with the energy of the MMLL′CT of these complexes. The former order was derived by Lauterbach and Fabian for a series of bis(dithiolenes).[2b] As a matter of fact, based on NICS(1) values for the bpy ring (–3.27 ppm) and the bdt ring (–4.61 ppm) complex **3** can be considered as aromatic, as opposed to **1** and **2**, where only the dithiolate ring (–5.29 and –3.77 ppm, respectively) is considered marginally aromatic. The conjugated electronic system of complex **3** appears more delocalized than the corresponding ones of **1** and **2**. The above differences can only be due to the metal atom since both chelating ligands are the same for all three complexes. Ni has not only the smallest bonding radius but also low-lying π-orbitals that could interact with the dithiolate ones; the dithiolate ligand is a π*-donor to the metal atom. Thus, the dithiolate ring in **1** is more aromatic or, more accurately, diatropic (–5.29 ppm) than the other two complexes. Due to Ni's smaller size, the overlap with the diimine orbitals is quite as effective and, as a consequence, the five-membered diimine ring is paratropic (–1.18 ppm). Pt enhances the aromaticity of both rings, as compared to Pd, probably due to the extension of its 5d orbital in spaces, which causes a better overlap with the ligand's valence orbitals, as supported by the extended delocalization of valence orbitals (Table 2).

Based on NICS(1) values for the benzenedithiolate ligand (E) (Table 3), we can conclude that its aromaticity decreases in the order **1** > **3** ≈ **2** due to its proximity to another aromatic ring. The $^{1}H$ NMR chemical shifts change very slowly in the direction **3** > **2** > **1** due to the paramagnetic influence of the central metal.

Finally, we determined the changes of diatropic and paratropic currents upon complexation by applying a procedure completely analogous to that of the synthesis, namely **7** → **9** → **10** ← **8**. First of all, phenanthroline is a highly aromatic compound, with the diimine rings being more aromatic than the benzenoid one, as is also observed in phenanthrene.[14] Complex **9** also possesses an aromatic phenanthroline ligand, but the benzenoid ring (D) is slightly more aromatic after coordination, whereas the chelated five-membered ring is slightly paratropic (+0.88 ppm). The $^{1}H$ NMR chemical shifts are, in general, consistent with the above discussion apart from a slight deviation of H1-H1′ due to the paratropic effect of the metal atom.

Complex **10** results from coordination of **8** to **9**, and several changes are induced in the ring currents. First of all, the aromaticity of the whole phenanthroline ligand is reduced, which is also confirmed by the $^{1}H$ NMR chemical shifts. NICS(1) of the diimine five-membered ring indicates a slight diatropic current (–0.45 ppm) but still the ring is not aromatic. On the other hand, the conjugated dithiolate ring is more diatropic (–3.20 ppm) and its aromaticity is marginal, while the aromaticity of the benzenoid ring (E) is maximized (–6.31 ppm for the free bdt to –8.70 ppm for the coordinated one). This behavior is expected since the interaction of the metal atom with the good σ-donor/π*-donor $bdt^{2-}$ focuses electron density on the dithiolate and benzenedithiolate ring, thereby reducing ring currents in the

 © 2006 Wiley-VCH Verlag GmbH & Co. KGaA, Weinheim 

diimine rings. Moreover, the aforementioned complexation route is in favor of the delocalization of the conjugated electronic system. A graphic representation of selected NICS values is shown in Figure 3.

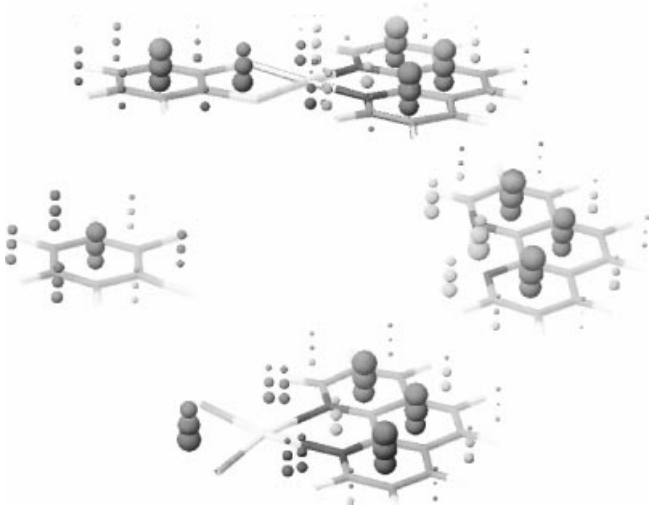

Figure 3. Graphic representation of NICS values for the selected grid for Pd(phen)(bdt), $Pd(phen)Cl_2$, phen, and $bdt^{2-}$. Dark grey spheres: diatropicity. Light grey: paratropicity.

Summarizing the effects on **10**, we suggest that a motion of diatropicity from the diimine to the dithiolate ligand is observed in a manner that is opposite to the route the electron cloud follows during the mixed metal-ligand-to-ligand transition. In that sense, the positive difference of the NICS value ($\Delta_{NICS}$) between two points where the orbitals involved in the charge-transfer transition are located can be envisioned as a difference in electron distribution and, in analogy with the EMF (electromotive force), in close circuits, as the driving force for charge-transfer transitions.

The aforementioned conclusions suggest that NICS values are not only probes for the extent of aromatic electron delocalization in cyclic conjugated systems[3a] but also in square-planar bis(chelated) metal complexes. Moreover, the evolution of the NICS during complexation is consistent with the evolution of the diatropicity of the rings and implies, at the same time, the direction of the charge-transfer transition.

## Conclusions

In the present report, structural aspects, $^1H$- and $^1H$-$^{15}N$ NMR data, as well as NICS constants are employed in order to determine the aromaticity of the mixed-ligand complexes of the type M(diimine)(dithiolate). The following are the principal results and conclusions of this investigation:

1) All complexes and ligands were fully optimized in the gas phase, giving structures in accordance with those anticipated or crystallographically determined.

2) The aromaticity of the dithiolate chelate ring is marginal, whereas the relative diimine chelate ring can be generally characterized as nonaromatic.

3) The aromatic diimine ligands lose some of their diatropicity upon complexation, an effect which is not immediately obvious from the $^1H$ NMR chemical shifts due to the presence of the metal atom but is revealed by NICS(1) values.

4) Aromatic substituents on dithiolate ligands enhance their aromaticity upon complexation as a direct consequence of the complexes' electronic properties and the Clar rules.

5) Electron-withdrawing groups as substituents on the coordinated dithiolate ring tend to enhance its diatropicity and have the opposite effect on the chelated diimine ring.

6) The role of the central metal is significant in determining the aromaticity of the complexes as it is part of the delocalized π-electron system.

The most important conclusion is:

7) In light of the diatropicity changes induced by complexation and the MMLL′CT transition which characterize these complexes, the difference in NICS values between the chelated rings (where the valence orbitals are located) can be regarded as an electronic analogue of the EMF and is the driving force of the transition. This conclusion can be applied in every case, and $\Delta_{NICS}$ for charge-transfer transitions could be analogous to $\Delta E°$ for oxidative processes.

## Experimental Section

**General:** All reactions and manipulations were conducted under argon using standard Schlenk techniques. Solvents were purified by standard procedures prior to use.[25] The chemicals 1,10-phenanthroline (phen), 2,2′-bipyridine (bpy), 1,2-benzenedithiol ($H_2bdt$), disodium maleonitriledithiolate ($Na_2mnt{\cdot}2H_2O$), [$PdCl_2$(phen)], [$PtCl_2$(bpy)], were purchased from Aldrich and used as received. The complexes [Pt(bpy)(bdt)],[20,21] [Pt(bpy)(mnt)],[8d] [Pt(bpy)(edt)],[22] [Pd(bpy)(bdt)],[20] [Ni(bpy)(bdt)],[20] and [Pd(phen)(bdt)][11a,11d] were prepared according to literature procedures. Their physical properties are consistent with those reported. $^1H$ NMR and $^1H$-$^{15}N$ HMBC spectra were recorded with Varian UNITYplus spectrometers operating at 300 and 600 MHz, respectively. Chemical shifts are reported in ppm downfield from tetramethylsilane (TMS), using the solvent peaks as an internal reference.

**Computational Methods:** DFT[26] quantum chemical calculations were carried out using the 1998 release of the GAUSSIAN suite of programs.[27] The functional used throughout this study is B3LYP (BLYP was also tested and does not influence our results in a qualitative way), which consists of a hybrid exchange functional as defined by Becke's three-parameter equation[28] and the Lee–Yang–Parr correlation functional.[29] The ground-state geometries were obtained in the gas phase by full geometry optimization, starting from structural data,[20–22,24] and were regularized in order to satisfy the $C_{2v}$ symmetry. The VeryTight option was used in all cases, which demands tighter convergence criteria than the default ones, while numerical integration was performed using the UltraFine option, which requests a pruned (99,590) grid. The optimum structures located as minima on the potential energy surfaces were verified by the absence of imaginary frequencies. No imaginary frequencies were found apart from two cases. 2,2′-bipyridine at the $C_{2v}$ symmetry is a first-order saddle point that corresponds to the transition state that links the two energy minima at the potential energy surface through rotation of the C1–C1′ bond. We preferred to use this structure because it is the one which the compound has during the complexes' formation. Every attempt to optimize

 © 2006 Wiley-VCH Verlag GmbH & Co. KGaA, Weinheim 

[$PdCl_2$(phen)] in the $C_{2v}$ point group by employing basis sets with a quality superior to double-ζ was unsuccessful, giving a second-order saddle point. Optimization of the same complex with the selected basis sets under no symmetry constraint yielded a structure that is essentially equivalent (based on geometrical and NICS criteria) to that derived previously. Therefore, in our analysis we will use the first structure for uniformity reasons. The derived wavefunctions were found to be free from internal instabilities. The basis set used for all non-metal atoms was the well-known valence triple-zeta 6-311+G*.[30] The quasi-relativistic Stuttgardt–Dresden effective core potential of the type ECP28MWB and ECP60MWB was used when the central metal was Pd and Pt, respectively.[31] In the case of the Ni complex, a small core potential of the type ECP10MDF was used.[31] The core potentials were complemented by the respective valence basis sets. For all other calculations related to the investigation an additional diffuse and a polarization function was added to the hydrogen atoms. Preliminary calculations showed that the addition of a p-type polarization function to the metals' valence basis sets[2b] gave practically the same results and its addition was not selected in order to avoid further computational cost. NICS constants were calculated with the gauge-independent atomic orbital method (GIAO).[32] Finally, Mulliken population analysis was performed with the AOMix program.[33]

## Acknowledgments

Financial support by the Greek Ministry of Education and the program EPEAEK "Pythagoras I" is gratefully acknowledged. We are very grateful to Dr. D. Fox from Gaussian Inc., and Prof. P. von Ragué-Schleyer for their valuable help in the beginning of our calculations and Dr. D. Argyropoulos from Varian Inc. for recording some of the NMR spectra.

[1] a) V. I. Minkin, M. N. Glukhovtsev, B. Ya. Simkin, *Aromaticity and Antiaromaticity – Electronic and Structural Aspects*, Wiley, New York, **1994**; b) Special issue on aromaticity: P. v. R. Schleyer (Guest Ed.), *Chem. Rev.* **2001**, *101*, 1115–1566.

[2] a) P. v. R. Schleyer, H. Jiao, N. J. R. van Eikema Hommes, V. G. Malkin, O. L. Malkina, *J. Am. Chem. Soc.* **1997**, *119*, 12669–12670; b) C. Lauterbach, J. Fabian, *Eur. J. Inorg. Chem.* **1999**, 1995–2004; c) G. Liu, Q. Fang, C. Wang, *J. Mol. Struct. (THEOCHEM)* **2004**, *679*, 115–120.

[3] a) C. S. Wannere, C. Corminboeuf, Z. X. Wang, M. D. Modrich, R. B. King, P. v. R. Schleyer, *J. Am. Chem. Soc.* **2005**, *127*, 5701–5705; b) A. I. Boldyrev, L. S. Wang, *Chem. Rev.* **2005**, *105*, 3716–3757.

[4] a) G. N. Schrauzer, V. R. Mayweg, *J. Am. Chem. Soc.* **1966**, *88*, 3235–3242; b) U. T. Mueller-Westerhoff, B. Vance, in *Comprehensive Coordination Chemistry* (Ed.: G. Wilkinson), Pergamon, Oxford, **1987**, vol. 2, pp. 595–631; c) J. H. Enemark, J. J. A. Cooney, J. J. Wang, R. H. Holm, *Chem. Rev.* **2004**, *104*, 1175–1200; d) C. Mitsopoulou, J. Konstantatos, D. Katalis, E. J. Vrachnou, *Mol. Catal.* **1991**, 67 137–146; e) S. Curreli, P. Deplano, C. Faulmann, A. Ienco, C. Mealli, M. L. Mercuri, L. Pilia, G. Pintus, A. Serpe, E. F. Trogu, *Inorg. Chem.* **2004**, *43*, 5069–5079.

[5] D. Argyropoulos, C.-A. Mitsopoulou, D. Katakis, *Inorg. Chem.* **1996**, *35*, 5549–5554.

[6] D. Argyropoulos, E. Lyris, C.-A. Mitsopoulou, D. Katakis, *J. Chem. Soc., Dalton Trans.* **1997**, 615.

[7] T. R. Miller, I. G. Dance, *J. Am. Chem. Soc.* **1973**, *95*, 6970–6979.

[8] a) M. Hissler, I. E. McGarrah, W. B. Connick, D. K. Geiger, S. D. Cummings, R. Eisenberg, *Coord. Chem. Rev.* **2000**, *208*, 115–137; b) S. D. Cummings, R. Eisenberg, *J. Am. Chem. Soc.* **1996**, *118*, 1949–1960; c) S. D. Cummings, L.-T. Cheng, R. Eisenberg, *Chem. Mater.* **1997**, *9*, 440–450; d) J. A. Zuleta, M. S. Burberry, R. Eisenberg, *Coord. Chem. Rev.* **1990**, *97*, 47–64.

[9] a) K. Kubo, M. Nakano, H. Tamura, G.-E. Matsubayashi, *Inorg. Chim. Acta* **2002**, *336*, 120; b) G. Matsubayashi, M. Nakano, H. Tamura, *Coord. Chem. Rev.* **2002**, *226*, 143; c) A. Islam, H. Sugihara, K. Hara, L. P. Singh, R. Katoh, M. Yanakida, Y. Takahashi, S. Murata, H. Arakawa, *Inorg. Chem.* **2001**, *40*, 5371.

[10] a) V. E. Kaasjager, E. Bouwman, S. Gorter, J. Reedijk, C. A. Grapperhaus, J. H. Reibenspies, J. J. Smee, M. Y. Darensbourg, A. Derecskei-Kovacs, L. M. Thomson, *Inorg. Chem.* **2002**, *41*, 1837; b) Y. Zhang, K. D. Ley, K. S. Schanze, *Inorg. Chem.* **1996**, *35*, 7102; c) K. Base, M. T. Tierney, A. Fort, J. Muller, M. W. Grinstaff, *Inorg. Chem.* **1999**, *38*, 287d) Y.-D. Chen, Y.-H. Qin, L.-Y. Zhang, L.-X. Shi, Z.-N. Chen, *Inorg. Chem.* **2004**, *43*, 1197–1205; e) Y.-D. Chen, L.-Y. Zhang, L.-X. Shi, Z.-N. Chen, *Inorg. Chem.* **2004**, *43*, 7493–7501.

[11] a) C. Makedonas, C.-A. Mitsopoulou, *J. Inorg. Biochem.* **2001**, *86*, 326; b) C. Makedonas, C.-A. Mitsopoulou, *Eur. J. Inorg. Chem.* **2006**, 590–598; c) C. Makedonas, C.-A. Mitsopoulou, *Spectrochim. Acta Part A* **2006**, *64*, 918–930; d) C. Makedonas, C.-A. Mitsopoulou, F. J. Lahoz, A. I. Balana, *Inorg. Chem.* **2003**, *42*, 8853–8865.

[12] P. v. R. Schleyer, *Chem. Rev.* **2001**, *101*, 1115 and references cited therein.

[13] a) W. J. Hehre, R. T. McIver, J. A. Pople, P. v. R. Schleyer, *J. Am. Chem. Soc.* **1974**, *96*, 7162–7163; b) L. Radom, *J. Chem. Soc., Chem. Commun.* **1974**, 403–404; c) T. M. Krygowski, M. Cyrañski, *Tetrahedron* **1996**, *52*, 1713–1722.

[14] P. v. R. Schleyer, C. Maerker, A. Drausfeld, H. Jiao, N. J. R. van Eikema Hommes, *J. Am. Chem. Soc.* **1996**, *118*, 6317–6318.

[15] a) G. Subramanian, P. v. R. Schleyer, H. Jiao, *Angew. Chem. Int. Ed. Engl.* **1996**, *35*, 2638–2641; b) H. Jiao, P. v. R. Schleyer, R. B. Beno, K. N. Houk, R. Warmuth, *Angew. Chem. Int. Ed. Engl.* **1997**, *36*, 2761–2764; c) A. A. Fokin, H. Jiao, P. v. R. Schleyer, *J. Am. Chem. Soc.* **1998**, *120*, 9364–9365; d) T. Zywietz, H. Jiao, P. v. R. Schleyer, A. de Meijere, *J. Org. Chem.* **1998**, *63*, 3417; e) S. Patchkovskii, W. Thiel, *J. Mol. Mod.* **2000**, *6*, 67–75.

[16] a) P. v. R. Schleyer, M. Manoharan, Z.-X. Wang, B. Kiran, H. Jiao, R. Puchta, N. J. R. v. E. Hommes, *Org. Lett.* **2001**, *3*, 2465–2468; b) M. K. Cyrañski, T. M. Krygowski, A. R. Katritzky, P. v. R. Schleyer, *J. Org. Chem.* **2002**, *67*, 1333–1338; c) R. W. A. Havenith, H. Jiao, L. W. Jenneskens, J. H. van Lenthe, M. Sarobe, P. v. R. Schleyer, M. Kataoka, A. Necula, L. T. Scott, *J. Am. Chem. Soc.* **2002**, *124*, 2363–2370.

[17] a) M. Bühl, *Chem. Eur. J.* **1998**, *4*, 734–739; b) M. L. McKee, Z. X. Wang, P. v. R. Schleyer, *J. Am. Chem. Soc.* **2000**, *122*, 4781–4793; c) A. Hirsch, Z. Chen, H. Jiao, *Angew. Chem. Int. Ed.* **2000**, *39*, 3915–3917; d) M. Bühl, A. Hirsch, *Chem. Rev.* **2001**, *101*, 1153–1183.

[18] P. v. R. Schleyer, B. Kiran, D. V. Simon, T. S. Sorensen, *J. Am. Chem. Soc.* **2000**, *122*, 510–513.

[19] a) Z. Zhou, R. G. Parr, J. F. Garst, *Tetrahedron Lett.* **1988**, *29*, 4843–4846; b) Z. Zhou, R. G. Parr, *J. Am. Chem. Soc.* **1989**, *111*, 7371–7379.

[20] T. M. Cocker, R. E. Bachman, *Inorg. Chem.* **2001**, *40*, 1550–1556.

[21] W. B. Connick, H. B. Gray, *J. Am. Chem. Soc.* **1997**, *119*, 11620–11627.

[22] C. E. Keefer, R. D. Bereman, S. T. Purrington, B. W. Knight, P. D. Boyle, *Inorg. Chem.* **1999**, *38*, 2294–2302.

[23] a) S. Nishigaki, H. Yoshioka, K. Nakatsu, *Acta Crystallogr., Sect. B* **1978**, *34*, 875–879; b) Y.-D. Tian Duan, X.-X. Xu, X.-Z. You, *Acta Crystallogr., Sect. C* **1995**, *51*, 2309–2312; c) L. L. Merritt, E. D. Schroeder, *Acta Crystallogr.* **1956**, *12*, 801–804.

[24] H. Günther, *NMR Spectroscopy – Basic Principles, Concepts and Applications in Chemistry*, 2nd ed., John Wiley & Sons, Chichester, **1995**.

 © 2006 Wiley-VCH Verlag GmbH & Co. KGaA, Weinheim 

[25] D. D. Perrin, W. L. F. Armarego, *Purification of Laboratory Chemicals*, 3rd ed., Pergamon Press, New York, **1988**.
[26] R. G. Parr, W. Yang, *Density Functional Theory of Atoms and Molecules*, Oxford University Press, Oxford, **1989**.
[27] M. J. Frisch, G. W. Trucks, H. B. Schlegel, G. E. Scuseria, M. A. Robb, J. R. Cheeseman, V. G. Zakrzewski, J. A. Montgomery Jr, R. E. Stratmann, J. C. Burant, S. Dapprich, J. M. Millam, A. D. Daniels, K. N. Kudin, M. C. Strain, O. Farkas, J. Tomasi, V. Barone, M. Cossi, R. Cammi, B. Mennucci, C. Pomelli, C. Adamo, S. Clifford, J. Ochterski, G. A. Petersson, P. Y. Ayala, Q. Cui, K. Morokuma, D. K. Malick, A. D. Rabuck, K. Raghavachari, J. B. Foresman, J. Cioslowski, J. V. Ortiz, A. G. Baboul, B. B. Stefanov, G. Liu, A. Liashenko, P. Piskorz, I. Komaromi, R. Gomperts, R. L. Martin, D. J. Fox, T. Keith, M. A. Al-Laham, C. Y. Peng, A. Nanayakkara, M. Challacombe, P. M. W. Gill, B. Johnson, W. Chen, M. W. Wong, J. L. Andres, C. Gonzalez, M. Head-Gordon, E. S. Replogle, J. A. Pople, *Gaussian 98*, Revision A.9, Gaussian, Inc., Pittsburgh PA, **1998**.
[28] A. D. Becke, *J. Chem. Phys.* **1993**, *98*, 5648–5652.
[29] C. Lee, W. Yang, R. G. Parr, *Phys. Rev. B* **1988**, *37*, 785–789.
[30] a) A. D. McLean, G. S. Chandler, *J. Chem. Phys.* **1980**, *72*, 5639–5648; b) R. Krishnan, J. S. Binkley, R. Seeyer, J. A. Pople, *J. Chem. Phys.* **1980**, *72*, 650–654.
[31] D. Andrae, U. Haeussermann, M. Dolg, H. Stoll, H. Preuss, *Theor. Chim. Acta* **1990**, *77*, 123–141.
[32] a) K. Wolinski, J. F. Hilton, P. Pulay, *J. Am. Chem. Soc.* **1990**, *112*, 8251–8260; b) J. L. Dodds, R. McWeeny, A. J. Sadlej, *Mol. Phys.* **1977**, *34*, 1779–1791; c) R. Ditchfield, *Mol. Phys.* **1974**, *27*, 789; d) R. McWeeny, *Phys. Rev.* **1962**, *126*, 1028–1034.
[33] a) S. I. Gorelsky, *AOMix program*, revisions 4.7 and 5.1 http://www.sg-chem.net/aomix/; b) S. I. Gorelsky, A. B. P. Lever, *J. Organomet. Chem.* **2001**, *635*, 187–196.

Received: February 8, 2006
Published Online: April 18, 2006

 © 2006 Wiley-VCH Verlag GmbH & Co. KGaA, Weinheim 

DOI: 10.1002/ejic.200600163

# First Experimental Observation of Gas-Phase Nitrosyl Thiocyanate

Li Yao,[a,b] Xiaoqing Zeng,[a,b] Maofa Ge,*[a] Weigang Wang,[a,b] Zheng Sun,[a] Lin Du,[a,b] and Dianxun Wang[a]

**Keywords:** Gas phase generation / Nitrosyl thiocyanate / Photoelectron spectroscopy / Time-of-flight mass spectrometer

The unstable nitrosyl thiocyanate molecule has been generated in the gas phase for the first time from an in situ heterogeneous reaction at low temperature. The product was detected and characterized by a photoelectron spectrometer-photoionization mass spectrometer (PES-PIMS). The electronic and geometric structures of the molecule were investigated with the help of quantum chemical calculations at the B3LYP, CBS-QB3, and CCSD(T) levels. The joint spectroscopic and theoretical studies provided evidence for the formation of nitrosyl thiocyanate, and indicated that the molecule adopts an open-chain, bent structure with the NO and SCN groups bonding by a relatively strong interaction.
(© Wiley-VCH Verlag GmbH & Co. KGaA, 69451 Weinheim, Germany, 2006)

## Introduction

The generation and spectroscopy of sulfur–nitrogen compounds, which are known to be extremely unstable and highly reactive, is one of the very active areas of chemistry.[1,2] The thiocyanate group, SCN, is ambidentate and has the potential to bond through sulfur or nitrogen forming RSCN or RNCS type molecules. In vivo thiocyanate originates from smoking cigarettes and dietary items that contain or generate nitriles. It forms during detoxification of cyanide and normally occurs in blood at a concentration less than 2 mg per 100 mL.[3] Given the biochemical significance of NO/$NO^+$, nitrosyl thiocyanate, ONSCN, (**1**) is a species of potential biochemical interest.

ONSCN is a highly unstable blood-red compound known only in solution, which is formed by mixing a very acidic solution of sodium nitrite with a solution of potassium thiocyanate.[4] At room temperature ONSCN decomposes into NO and $(SCN)_2$ and shows the typical nitrosyl and thiocyanate group reactions [see Equation (1) and (2)].

$$H^+ + HNO_2 + SCN^- \rightleftharpoons ONSCN + H_2O \quad (1)$$

$$2\ ONSCN \rightleftharpoons 2\ NO + (SCN)_2 \quad (2)$$

[a] State Key Laboratory for Structural Chemistry of Unstable and Stable Species, Institute of Chemistry, Chinese Academy of Sciences,
Beijing 100080, People's Republic of China
Fax: +86-10-62559373
E-mail: gemaofa@iccas.ac.cn
[b] Graduate University of Chinese Academy of Sciences,
Beijing 100080, People's Republic of China
Supporting information for this article is available on the WWW under http://www.eurjic.org or from the author.

Despite the instability, it is widely used as a nitrosating agent in organic chemistry and biochemistry.[5,6] However, its structure is unknown since it is very unstable at high concentration and room temperature. Westwood et al. pointed out that potential media for generating and investigating **1** are the dilute gas-phase or an inert low-temperature matrix, which would provide important information on its full electronic and geometric characterization.[7]

The calculated results predicted that **1** has planar, bent structures and that isomer ON–SCN (**1a**) is more stable than ON–NCS (**1b**),[7–9] in agreement with the notion that S–nitrosation is more favourable through a soft-soft interaction, characterized by a large charge transfer from the nucleophile to the electrophile.[7,8,10]

On the other hand, there has been interest in simple, often transient, species containing triatomic pseudohalide groups e.g. –SCN, –NCO, –NNN. Recently several of these have been detected and spectroscopically characterized. Klapötke et al. have successfully isolated nitrosyl azide ON–$N_3$ at low temperature.[11] They studied the reaction of AgOCN with $ClNO_2$, ClNO, and BrNO by means of gas-phase IR spectroscopy, and proposed a reaction mechanism involving the formation of two neutral intermediates OCN–$NO_2$ and OCN–NO.[12] Our group recently reported the in situ generation of ONNCO in the gas phase and the subsequent characterization by photoelectron spectroscopy.[13] Thiazyl thiocyanide NS–SCN has been produced by an online process using NSCl passed over heated AgSCN and monitored by gas-phase FTIR spectroscopy.[14] Westwood and colleagues tried to observe the very interesting NS–NCO molecule from the reaction of $NSCl_{(g)}/AgNCO_{(s)}$, but in fact they observed another species, $S_2N_2CO$, recorded by HeI photoelectron, photoionization mass and mid-infrared spectroscopy.[15] The unexpected result has prompted them

 © 2006 Wiley-VCH Verlag GmbH & Co. KGaA, Weinheim 

to carried out an ab initio study of some isomers of $CN_2OS$,[7] which also includes the ONSCN compound.

In this work we report the first gas phase generation and characterization of the unstable molecule **1** and its investigation by HeI photoelectron spectroscopy−photoionization mass spectroscopy and quantum chemical calculations.

## Results and Discussion

### Molecular Geometries

Given that both the thiocyanate and isothiocyanate exist for the $CH_3$ derivatives, we have performed an identical calculation for the molecules **1a** and **1b**. As shown by ab initio calculations[7–9], **1a** and **1b** both have planar, bent structures. Each molecule has, in principle, two rotational isomers, the *cis* and *trans* isomers. The calculated structural parameters are compiled in Table 1 (Figure 1).

Table 1. Calculated structures of planar nitrosyl thiocyanate.[a]

| | *cis*-**1a** | *trans*-**1a** | *cis*-**1b** | *trans*-**1b** |
|---|---|---|---|---|
| *r*(O–N) | 1.136 | 1.142 | 1.140 | 1.154 |
| *r*(N–S) or *r*(N–N) | 2.081 | 2.043 | 1.686 | 1.552 |
| *r*(S–C) | 1.667 | 1.676 | 1.567 | 1.561 |
| *r*(C–N) | 1.160 | 1.158 | 1.213 | 1.219 |
| (S–C–N) | 174.5 | 179.6 | 178.7 | 176.7 |
| (O–N–S) or (O–N–N) | 115.2 | 114.4 | 115.3 | 112.4 |
| (N–S–C) or (N–N–C) | 95.35 | 94.45 | 116.3 | 119.6 |

[a] Bond lengths in Å and angles in degrees at B3LYP/6-311++G(3d) level.

All calculations predict **1a** to be the more stable in the gas phase. According to the CCSD(T)/6-311++G(3d) level of theory, the more stable *cis*-**1a** isomer gives a total energy less than that of *cis*-**1b** by 11.2 kcal mol$^{-1}$.

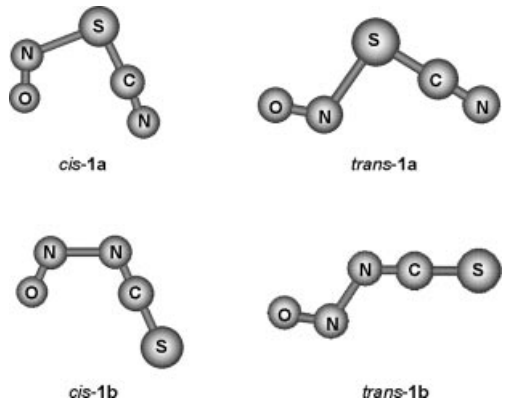


Figure 1. Stable conformers of nitrosyl thiocyanate.

Figure 2 shows a limited 3D plot of the potential energy surface, which indicates that both the *cis* and *trans* conformers of **1a** lie in a deep well with respect to the N–S coordinate and need only rotate around the long N–S bond with a low barrier. At the CBS-QB3 level the energy gap between the *cis* and *trans* conformers is calculated to be 2.0 kcal mol$^{-1}$, and the transition state resides just 4.5 kcal mol$^{-1}$ above the *trans* conformer.

In several molecules containing triatomic pseudohalide groups e.g. –SCN, –NCO, –NNN, etc., it has been established that the atoms are not colinear. When combining the SCN ligand with NO, the SCN angle shows a deviation of about 5° from linearity, which is similar to those of XSCN (X = CN[16], SCN[17], Cl[18], Br[18]). Comparing the predicted NO bond with experimentally determined bond lengths of similar molecules, we find that the predicted O–N bond of **1** (1.136–1.154 Å) lies between the diatomic NO (1.151 Å)[19] and ClNO (1.139 Å)[20], favoring ClNO slightly. However, on considering the linearity from the

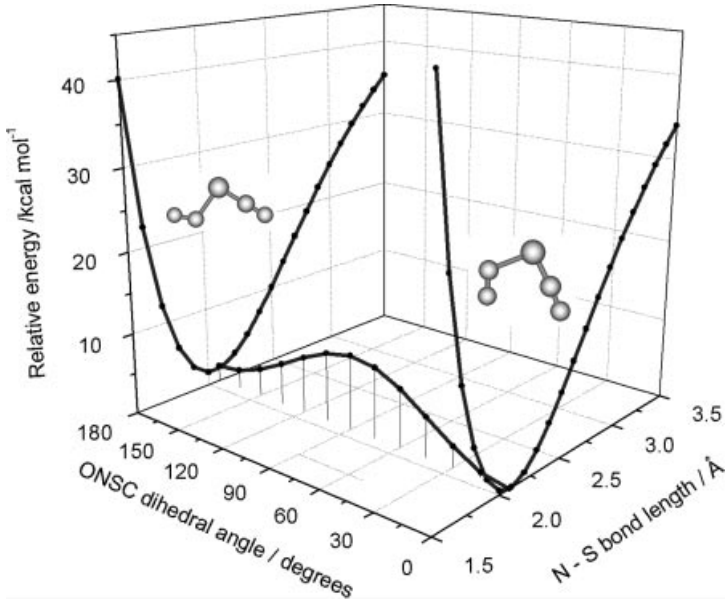


Figure 2. Calculated [B3LYP/6-311++G(3d)] potential-energy surfaces for the *cis* and *trans* conformers along the N–S coordinate together with the interconnecting surface obtained by torsion of the N–S bond in **1a**.

 © 2006 Wiley-VCH Verlag GmbH & Co. KGaA, Weinheim 

point of the whole molecule **1a** the calculated N–S bond length (2.043–2.081 Å) is much longer than that of $S_2N_2$ (1.65 Å)[21] and NSCN (1.49 Å)[22], and the NSC angle (95.35–94.45°) is much smaller than the NSC in NSCN[22] (109.3°) and ∠SSC in $(SCN)_2$[17] (108.2°). These data indicate that a strong interaction exists between the NO and SCN groups.

### Photoionization Mass Spectroscopy

The HeI photoionization mass spectrum (Figure 3) observed at –60 °C is relatively simple. The main peaks in the spectrum are $NO^+$, $SCN^+$, $ON–SCN^+$, and $Cl^+$, respectively, with the dominant feature being the $NO^+$ peak. Since there are no NO, SCN, and Cl photoelectron peaks in the PE spectrum (Figure 4), it is suggested that the signals of $NO^+$, $SCN^+$, and $Cl^+$ come from the dissociation of parent ions. For some molecules, HeI photoionization produces a fragmentation ion distribution similar to that of electron-impact ionization.[23] This may be rationalized by a similar energy deposition mechanism for the two methods, as the interaction energies (some tens of electronvolts) are comparable. The dominant fragment ions $NO^+$ and $X^+$ (X = SCN) in the HeI photoionization mass spectra are analogous to those of other ONX molecules (X = Cl, $CH_3$) in the electron impact spectra. They mostly result from the direct dissociation of the parent ions $ONX^+$. Although there is no parent ion peak for ClNO in the photoionization mass spectra of the products, the PE bands of the ClNO molecule appear in the photoelectron spectrum (Figure 4). This indicates that the signals of $Cl^+$ and a part of $NO^+$ originate from the dissociation of $ClNO^+$, which is very unstable and dissociates to $Cl^+$/NO or $NO^+$/Cl once it is formed. This also agrees with the electron impact mass spectrum of ClNO, which also shows no $ClNO^+$ peak. In a word, we demonstrated that we generated **1** under our experimental conditions though we could not distinguish

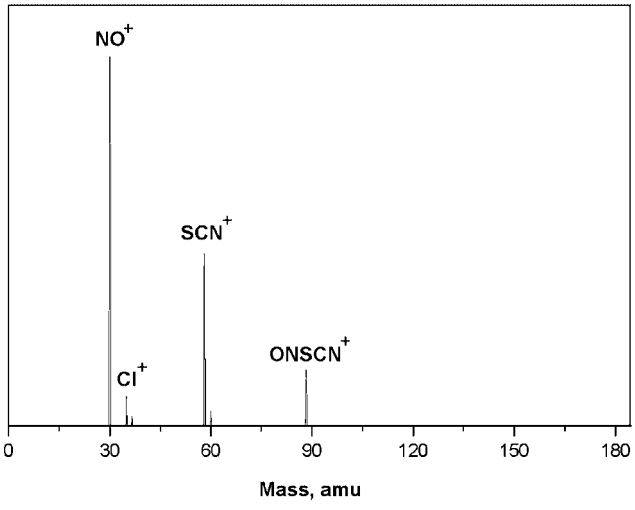


Figure 3. The HeI photoionization mass spectrum of nitrosyl thiocyanate.

**1a** and **1b** isomers from a photoionization mass spectroscopy study.

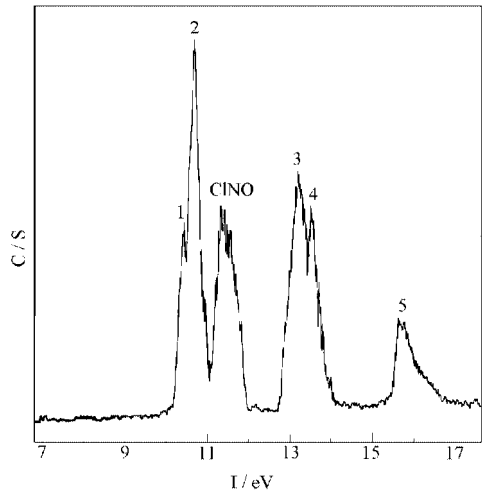


Figure 4. The HeI photoelectron spectrum of nitrosyl thiocyanate.

### Photoelectron Spectroscopy

The HeI photoelectron spectrum of **1** recorded at –60 °C is shown in Figure 4. It does not show any of the decomposing products but only the reactant ClNO[20] with an unnumbered band between 11.0 and 12.0 eV. The reaction was also monitored simultaneously by photoionization mass spectroscopy. The PE spectrum clearly shows a group of distinct bands below 11 eV, another group in the 12.5–14 eV range, and one additional band above 15 eV. In previous photoelectron spectroscopy experiments, XSCN (X = Cl, Br), instead of XNCS, was produced by passing gaseous halogen over solid AgSCN.[18] Our photoelectron spectroscopic experimental results also agree better with the ROVGF and CBS-QB3 calculations on **1a** than those on **1b** (see Table 2), though we cannot completely exclude the existence of **1b**. There is no noticeable difference between the orbital energies of the two most stable conformers of *cis*- and *trans*-**1a**. So our discussion is reduced to the analysis of the slightly more stable conformer *cis*-**1a** only. The experimental and calculated ionization energies for the *cis*- and *trans*-**1a** are collected in Table 2. It is noted that the ROVGF results are in good agreement with the experimental data.[13,24]

The unstable nitrosyl thiocyanate (**1**) can be characterized by its three groups of bands, which can be attributed to the lone electron pair of sulfur, the π system, and the S–C bond. Therefore, the study of these bands may reflect the extent and character of the intramolecular interactions. The electronic structure of the SCN group can be explained in two ways. One can assume a single S–C bond and a triple C≡N bond. In this case the appearance of two new bands resulting from the C≡N π bonds is expected in the low-energy region of the spectrum. Another interpretation is that the SCN unit is considered as a two perpendicular four-electron three-centre π system, which suggests four

 © 2006 Wiley-VCH Verlag GmbH & Co. KGaA, Weinheim 

Table 2. Experimental and computed ionization energies (eV) for the isomers of **1**.

| Exp. $I_v$ | Calcd. *cis*-**1a** | | *trans*-**1a** | | *cis*-**1b** | *trans*-**1b** |
|---|---|---|---|---|---|---|
| 10.45 | 10.338[a] | 10.485[b] | 10.440[a] | 10.407[b] | 9.840[a] | 10.154[a] |
| 10.65 | 10.733[a] | | 10.686[a] | | 10.195[a] | 10.198[a] |
| 13.20 | 13.423[a] | | 13.455[a] | | 12.673[a] | 12.389[a] |
| | 13.454[a] | | 13.485[a] | | 13.792[a] | 14.070[a] |
| 13.46 | 13.716[a] | | 13.767[a] | | 13.868[a] | 14.148[a] |
| 15.68 | 15.604[a] | | 15.732[a] | | 15.543[a] | 15.733[a] |

[a] According to $C_s$ symmetry using the ROVGF/6-311++G(3d) method. [b] According to $C_s$ symmetry using the CBS-QB3 method.

new bands in the spectrum: the high-energy bonding in- and out-of-plane π orbitals [$\pi_b(a')$ and $\pi_b(a'')$] and the low-energy nonbonding in- and out-of-plane π orbitals [$\pi_{nb}(a')$ and $\pi_{nb}(a'')$]. If the molecule is linear, the perpendicular MO pairs are degenerate. In the case of the strongly bent ONSCN, we would expect, using HeI radiation, to observe ionization from the six highest filled molecular orbitals. The appearance of all the $\pi_{SCN}$ bands is expected on the basis of the calculations. And the S lone pair in the SCN group is a part of the π system. The additional bands of a pσ type orbital ($\sigma_{SCN}$, localized mainly on N) and a σ type orbital (S–C bonding) are expected in the photoelectron spectrum.

The shape and intensity of the first group of bands suggest that it should be attributed to two ionization processes. Consistent with analogous molecules XSCN (X = H[25], $CH_3$[26], Cl[18], Br[18], I[27]), the first two bands are assigned to the nonbonding in- and out-of-plane π orbitals [$\pi_{nb}(a')$ and $\pi_{nb}(a'')$] partially localized on the pseudohalide group. In the molecule ONNCO[13], the first two orbitals $\pi_{nb}(a')$ and $\pi_{nb}(a'')$ are distributed fairly evenly over the whole molecule, whereas for *cis*-**1a** there is a dominant S 3p involvement in the first two π orbitals as indicated by the two relatively low ionization potentials. These are also supported by the quantum chemical calculated results. The first band of ONNCO at 10.71 eV is attributed to an in-plane combination of a strong antibonding $\pi_{NO}$ and nonbonding $\pi_{NCO}$ with the same a′ symmetry.[13] Therefore, the first ionization process of ON–SCN can easily be assigned by combining the NO and SCN moieties.

The vertical ionization potential of the first band (10.45 eV) is in good agreement with the calculated ionization energy of *cis*-**1a** (10.338 eV by ROVGF method and 10.485 eV by CBS-QB3). It is a structureless band and can be compared to the first PE band of $CH_3NO$[28] at 9.70 eV and ONCN[29] at 11.50 eV. The HOMO 18a′ (Figure 5) for this ionization process can be described as an in-plane combination of nonbonding $\pi_{SCN}$ and antibonding $\pi_{NO}$. It also shows that an interaction may exist between both of the moieties. The second band at 10.65 eV is sharp and characteristic of a nonbonding orbital with considerable lone-pair character. It derives from the ionization of the 4a′′ orbital and coincides with the calculation value of 10.733 eV. This band is ascribed to the nonbonding out-of-plane $\pi_{SCN}$ [$\pi_{nb}(a'')$], mainly localized on the sulfur atom. This orbital can also be regarded as the antisymmetric combination of the out-of-plane sulfur lone-pair and $\pi_{CN}$ orbital.

An interesting and important feature for PE spectra of compounds containing SCN is that the energetic order of the first two highest occupied orbitals is $\pi_{nb}(a'') < \pi_{nb}(a')$, such as for XSCN (X = H, $CH_3$, Cl, Br, I).[18,25–27] However, this trend is reversed in ONSCN, as is the case in ONNCO.[13] Because of the extensive incorporation of the $\pi_{NO}$ antibonding character into the 18a′, with $\pi_{nb}(a')$ character, its ionization becomes less energetic. Compared with analogous molecules XSCN (X = $CH_3$, Cl, Br, I)[18,26,27] the separation of $\pi_{nb}(a')$ and $\pi_{nb}(a'')$ is also quite narrow. The obvious decrease of the separation of nonbonding π orbitals ($\pi_{nb}$) in *cis*-**1a** reflects the direct interaction between the $\pi_{SCN}$ and $\pi_{NO}$ moieties. This interaction is so strong that it shifts the $\pi_{nb}(a')$ band causing the exchange in the sequence of the $\pi_{nb}(a')$ and $\pi_{nb}(a'')$ bands.

The two bands between 12.5–14.0 eV come from the ionization of the two bonding π orbitals (a′ and a′′) and a terminal –SCN pσ type orbital, as considerable mixing between orbitals of the same symmetry often occurs for the XSCN molecule.[18,26,27] Combining our calculated ROVGF results and the assignments of the PE spectrum of other XSCN molecules, we assigned the third band as arising from the ionizations of the in-plane bonding $\pi_{CN}$ orbital 17a′ and out-of-plane bonding $\pi_{SCN}$ orbital 3a′′, and the fourth band at 13.46 eV as arising from the ionization of the 16a′ pσ type orbital. This is in good agreement with the calculation value 13.716 eV, which is also in good agreement with the corresponding experimental values of the PE band from pσ type orbitals in ClSCN[18] at 13.66 eV and BrSCN[18] at 13.43 eV.

The PE band at 15.68 eV is the ionization of the 15a′ orbital, which is in agreement with the calculated value 15.604 eV. The primary MO character is $\sigma_{(S-C)}$ bonding with considerable s character on all the atoms; similar bands occur in the PE spectrum of HSCN[25] (Figure 5).

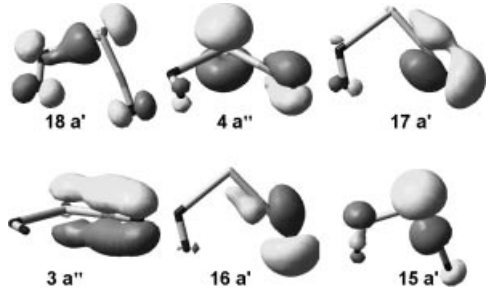


Figure 5. Characters of the first six highest occupied molecular orbitals for *cis*-**1a**.

Based on the above discussion, we consider the photoelectron spectrum shown in Figure 4 to be that of **1** and the assignment of the photoelectron spectroscopic bands is reasonably supported by previous studies on analogous molecules, as well as the ROVGF and CBS-QB3 calculations. From the experimental PE spectra of **1** and some thiocyanate with similar symmetry, a clear correlation of the respective bands can be seen. One important difference

 © 2006 Wiley-VCH Verlag GmbH & Co. KGaA, Weinheim 

is the inversion in the sequence of the $\pi_{nb}(a')$ and $\pi_{nb}(a'')$ bands, which has relations with the interaction between the $\pi_{SCN}$ and $\pi_{NO}$ moieties in **1**. However, the isomers **1a** and **1b** cannot be reliably distinguished by our photoelectron spectroscopy experiment. It is hoped that this study could stimulate further experimental work to enable the different isomers of this important unstable species to be distinguished.

## Conclusions

The unstable molecule **1** has been generated in the gas phase for the first time by means of an online reaction of gaseous nitrosyl chloride with silver thiocyanate at low temperature. Using the home-made PES-PIMS we have obtained the photoelectron and mass spectra of **1**. With the help of theoretical studies, the electronic and geometric structures of **1** were investigated by photoelectron spectroscopy. The assignment of the photoelectron spectroscopic bands is reasonably supported by previous studies on analogous molecules, as well as by the ROVGF and CBS-QB3 calculations. Both the spectroscopic and theoretical investigations have proved the formation of **1**, and suggest that the molecule adopts an open-chain, bent structure. It is indicated that the NO and SCN moieties bond by means of a relatively strong interaction, which is related to the inversion of the first two π orbitals. This fact proves that our home-made PES-PIMS can be used as a powerful tool for the investigation of transient species in the gas phase.

## Experimental Section

Over the past decades, ultraviolet photoelectron spectroscopy (UPS) has established itself as one of the important techniques used to obtain a direct measure of atomic and molecular energy levels. Moreover, some groups using photoelectron spectroscopy have made great progress and extended the application to transient or unstable species. Using photoelectron spectroscopy and infrared matrix isolation spectroscopy, Dyke et al. studied the thermal decomposition of organic azides.[30–32] By combining HeI photoelectron spectroscopy with mid-infrared absorption and mass spectroscopy, Westwood and colleagues investigated ground, excited, and ionic states of various small unstable molecules.[33–35]

To improve our ability of studying the transient species, our group has built a photoelectron spectrometer-photoionization mass spectrometer (PES-PIMS) as described elsewhere.[23] A schematic diagram of the PES-PIMS is shown in Figure 6. The modification of the spectrometer was based on the HeI photoelectron spectrometer. An important feature of our experiment is the measurement of both mass and PE spectra. The ions are produced by soft ionization of transient species with HeI (21.2 eV) radiation. The ions formed are transferred by a set of electrostatic lenses. The field-free drift region has a length of 120 cm. A dual MCP is used to detect charged particles. The signal is recorded using a 500 MHz digital oscilloscope (Tektronix, TDS2024) and then transferred to a PC for storage and analysis.

The photoelectron spectrum was recorded on a double chamber UPS machine-II,[36,37] which was built specifically to detect transient species at a resolution of about 30 meV as indicated by the $Ar^+(^2P_{2/3})$ photoelectron band. Experimental vertical ionization energies (Iv in eV) are calibrated by simultaneous addition of a small amount of argon and methyl iodide to the sample.

When the mass spectra are measured, pulsed positive voltages are applied to the repelling and attracting electrodes, and then the cation is extracted into the time-of-flight drift region. Proper pulsed voltages $U_1$ and $U_2$ are chosen to meet the requirement of the first spatial focus to pursue the high mass resolution. The optimum mass resolution can reach 410 at $m/z$ = 254. When the photoelectrons are collected, both $U_1$ and $U_2$ are set to 0. Hence, the photoelectron can fly directly to the energy analyzer through the electron path. Thus, the photoelectron and photoionization mass spectra can be recorded within a few seconds.

In general, we can observe the electronic structure by the photoelectron spectrum and the dissociation of molecular ions by mass spectra with this experimental apparatus. The joint spectrometer is characterized by at least two advantageous features. Firstly, the reaction conditions can be optimized online to improve the yield of the desired species. It can be used to investigate not only general gaseous samples but also transient species produced by gas-solid reactions or microwave discharge etc. Other inlet modifications with high-temperature furnaces or low-temperature cells can also be easily attached to the spectrometer. Secondly, with the advances of fast detection and high sensitivity TOFMS will help us to resolve some problems of photoelectron spectroscopy in complicated systems.

### Generation and Detection of ONSCN

The intermediate **1** was generated at –60 °C by passing gaseous ClNO over finely powdered AgSCN, similarly for producing other

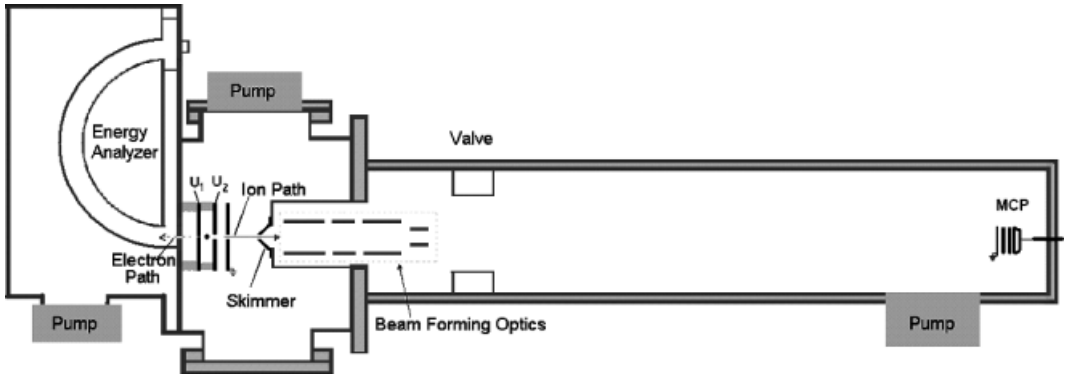


Figure 6. Schematic diagram of the experimental apparatus PES-PIMS. It mainly consists of an ultraviolet photoelectron spectrometer and a home-made time-of-flight mass spectrometer (TOFMS). The photo source (HeI) in the ionization region is marked with a dot.

 © 2006 Wiley-VCH Verlag GmbH & Co. KGaA, Weinheim 

unstable species like ONNCO[13] and NSSCN[14]. The reaction was monitored simultaneously in situ by photoelectron and photoionization mass spectra. The reaction is be represented by Equation (3).

$$ClNO\ (g) + AgSCN(s) \xrightarrow{-60\ ^{o}C} ONSCN\ (g) + AgCl\ (s) \quad (3)$$

AgSCN (ACROS) was dried in vacuo ($10^{-4}$ Torr) for 2 h at 60 °C before the experiment was performed. ClNO was prepared as reported[38] and identified by photoelectron[20] and photoionization mass spectroscopy.

**Quantum Chemical Calculations**

On the basis of the previous theoretical discussions on the isomers of $CN_2OS$[7], we have only considered the four most stable isomers, *cis*- and *trans*-**1a**, *cis*- and *trans*-**1b**, which are related to our experiment. The geometries were optimized at the B3LYP/6-311++G(3d) level, which is a hybrid functional method based on the Becke's three-parameter nonlocal exchange functional[39], with the nonlocal correlation due to Lee, Yang, and Parr.[40] To determine the barrier between the *cis* and *trans* rotamers, the potential energy surface scans for internal rotation around the N–S bond were carried out at the B3LYP/6-311++G(3d) level before the appropriate transition states were optimized at the CBS-QB3 level.[41] The ionization energies for *cis* and *trans* isomers were calculated at the ab initio level according to Cederbaum's outer valence Green's function (OVGF) [42] method at the 6-311++G(3d) basis set, and by taking the difference between the energy of the neutral atom and the ion (CBS-QB3 calculation). All the calculations were performed using the Gaussian 03 program package.[43]

**Supporting Information** (see footnote on the first page of this article): HeI photoionization mass spectra of ClNO, and reaction products of $NOCl_{(g)}/AgSCN_{(s)}$ at room temperature are included.

## Acknowledgments

This project was supported by the Chinese Academy of Sciences (Hundred talents fund) and the National Natural Science Foundation of China (Contract No. 20577052, 20473094, 50372071, 20503035). Li Yao, Xiaoqing Zeng, Weigang Wang and Lin Du would like to thank the Chinese Academy of Sciences for the receipt of scholarships during the period of this work.

[1] W. J. Middleton, *J. Am. Chem. Soc.* **1966**, *88*, 3842–3844.
[2] M. Takahashi, R. Okasaki, N. Inamoto, T. Sugarawa, H. Iwamura, *J. Am. Chem. Soc.* **1992**, *114*, 1830–1837.
[3] R. G. Guy, *The Chemistry of Cyanates and their Thio Derivatives* (Ed.: S. Patai); Wiley: New York, **1977**, part II, pp. 819–886.
[4] E. Jones, C. G. Munkley, E. D. Phillips, G. Stedman, *J. Chem. Soc., Dalton Trans.* **1996**, *9*, 1915–1920.
[5] E. G. DeMaster, B. J. Quast, R. A. Mitchell, *Biochem. Pharmacol.* **1997**, *53*, 581–585.
[6] E. Iglesias, *J. Org. Chem.* **2003**, *68*, 2689–2697.
[7] T. Pasinszki, N. P. C. Westwood, *J. Chem. Soc. Farad. Trans.* **1996**, *92*, 333–341.
[8] K. A. Jørgensen, S.-O. Lawesson, *J. Am. Chem. Soc.* **1984**, *106*, 4687–4691.
[9] K. A. Jørgensen, S.-O. Lawesson, *J. Chem. Soc., Perkin Trans. 2* **1985**, 231–235.
[10] K. A. Jørgensen, M. T. M. Ei-Wassimy, S.-O. Lawesson, *Acta Chem. Scand. B* **1983**, *37*, 785–790.
[11] a) A. Schulz, I. C. Tornieporth-Oetting, T. M. Klapötke, *Angew. Chem. Int. Ed. Engl.* **1993**, *32*, 1610–1612; b) A. Schulz, T. M. Klapötke, *Chem. Ber.* **1995**, *128*, 201–203.
[12] T. M. Klapötke, A. Schulz, *Inorg. Chem.* **1996**, *35*, 7897–7904.
[13] X. Q. Zeng, M. F. Ge, Z. Sun, D. X. Wang, *Inorg. Chem.* **2005**, *44*, 9283–9287.
[14] Z. Ajji, D. Y. Naima, M. N. Odeh, A. W. Allaf, *Spectrochim. Acta Part A* **1999**, *55*, 1753–1756.
[15] R. H. DeLaat, L. Durham, E.-G. Livingstone, N. P. C. Westwood, *J. Phys. Chem.* **1993**, *97*, 11216–11220.
[16] P. Rosmus, H. Stafast, H. Bock, *Chem. Phys. Lett.* **1975**, *34*, 275–280.
[17] D. C. Frost, C. Kirby, W. M. Lau, C. B. MacDonald, C. A. McDowell, N. P. C. Westwood, *Chem. Phys. Lett.* **1980**, *69*, 1–5.
[18] D. C. Frost, C. B. MacDonald, C. A. McDowell, N. P. C. Westwood, *J. Am. Chem. Soc.* **1981**, *103*, 4423–4427.
[19] K. P. Huber, G. Herzberg, *Constants of Diatomic Molecules*, Van Nonstrand Reinhold: New York, **1979**.
[20] M. I. Abbas, J. M. Dyke, A. Morris, *J. Chem. Soc., Faraday Trans. 2* **1976**, *72*, 814–819.
[21] R. H. Findlay, M. H. Palmer, A. J. Downs, R. G. Egdell, R. Evans, *Inorg. Chem.* **1980**, *19*, 1307–1314.
[22] A. W. Allaf, R. L. Johnston, R. J. Suffolk, *Chem. Phys. Lett.* **1995**, *233*, 33–35.
[23] L. Yao, W. G. Wang, X. Q. Zeng, M. F. Ge, L. Du, Z. Sun, D. X. Wang, F. Liang, H. B. Qu, H. Y. Li, *Anal. Instrum.* **2006**, *1*, 5–9.
[24] G. Bajor, T. Veszprémi, E. H. Riague, J.-C. Guillemin, *Chem. Eur. J.* **2004**, *10*, 3649–3656.
[25] S. Cradock, E. A. V. Ebsworth, J. D. Murdoch, *J. Chem. Soc., Faraday Trans. 2* **1972**, *68*, 86–100.
[26] B. J. M. Neijzen, C. A. DeLange, *J. Electron. Spectrosc. Relat. Phenom.* **1980**, *18*, 179–188.
[27] H. Leung, R. J. Suffolk, J. D. Watts, *Chem. Phys.* **1986**, *109*, 289–300.
[28] D. C. Frost, W. M. Lau, C. A. McDowell, N. P. C. Westwood, *J. Phys. Chem.* **1982**, *86*, 3577–3581.
[29] O. Walter, L. S. Cederbaum, B. Solouki, P. Rosmus, H. Bock, *J. Phys. Chem.* **1985**, *89*, 1384–1387.
[30] J. M. Dyke, G. Levita, A. Morris, J. S. Ogden, *Chem. Eur. J.* **2005**, *11*, 1665–1676.
[31] N. Hooper, L. J. Beeching, J. M. Dyke, A. Morris, J. S. Ogden, A. A. Dias, M. L. Costa, M. T. Barros, M. H. Cabral, A. M. Moutinho, *J. Phys. Chem. A* **2002**, *106*, 9968–9975.
[32] J. M. Dyke, A. P. Groves, A. Morris, J. S. Ogden, A. A. Dias, A. M. Oliveira, M. L. Costa, M. T. Barros, M. H. Cabral, A. M. Moutinho, *J. Am. Chem. Soc.* **1997**, *119*, 6883–6887.
[33] T. Pasinszki, N. P. C. Westwood, *J. Electron Spectrosc. Relat. Phenom.* **2000**, *108*, 63–73.
[34] T. Pasinszki, N. P. C. Westwood, *J. Phys. Chem. A* **2001**, *105*, 1244–1253.
[35] T. Pasinszki, N. P. C. Westwood, *J. Am. Chem. Soc.* **1995**, *117*, 8425–8430.
[36] H. Q. Zhao, D. X. Wang, G. Z. Xu, *Anal. Instrum.* **1992**, *4*, 23–26.
[37] X. J. Zhu, M. F. Ge, J. Wang, Z. Sun, D. X. Wang, *Angew. Chem. Int. Ed.* **2000**, *39*, 1940–1943.
[38] A. Obermeyer, H. Borrmann, A. Simon, *J. Am. Chem. Soc.* **1995**, *117*, 7887–7890.
[39] A. D. Becke, *J. Chem. Phys.* **1993**, *98*, 5648–5652.
[40] C. Lee, W. Yang, R. G. Parr, *Phys. Rev. B* **1988**, *37*, 785–789.
[41] J. A. Montgomery Jr, M. J. Frisch, J. W. Ochterski, G. A. Petersson, *J. Chem. Phys.* **1999**, *110*, 2822–2827.
[42] J. V. Ortiz, *J. Chem. Phys.* **1988**, *89*, 6348–6352.
[43] M. J. Frisch, G. W. Trucks, H. B. Schlegel, G. E. Scuseria, M. A. Robb, J. R. Cheeseman, J. A. Montgomery Jr, T. Vreven, K. N. Kudin, J. C. Burant, J. M. Millam, S. S. Iyengar, J. Tomasi, V. Barone, B. Mennucci, M. Cossi, G. Scalmani, N. Rega, G. A. Petersson, H. Nakatsuji, M. Hada, M. Ehara, K. Toyota, R. Fukuda, J. Hasegawa, M. Ishida, T. Nakajima, Y. Honda,

 © 2006 Wiley-VCH Verlag GmbH & Co. KGaA, Weinheim 

O. Kitao, H. Nakai, M. Klene, X. Li, J. E. Knox, H. P. Hratchian, J. B. Cross, C. Adamo, J. Jaramillo, R. Gomperts, R. E. Stratmann, O. Yazyev, A. J. Austin, R. Cammi, C. Pomelli, J. W. Ochterski, P. Y. Ayala, K. Morokuma, G. A. Voth, P. Salvador, J. J. Dannenberg, V. G. Zakrzewski, S. Dapprich, A. D. Daniels, M. C. Strain, O. Farkas, D. K. Malick, A. D. Rabuck, K. Raghavachari, J. B. Foresman, J. V. Ortiz, Q. Cui, A. G. Baboul, S. Clifford, J. Cioslowski, B. B. Stefanov, G. Liu, A. Liashenko, P. Piskorz, I. Komaromi, R. L. Martin, D. J. Fox, T. Keith, M. A. Al-Laham, C. Y. Peng, A. Nanayakkara, M. Challacombe, P. M. W. Gill, B. Johnson, W. Chen, M. W. Wong, C. Gonzalez, J. A. Pople, *Gaussian 03*, Gaussian, Inc., Pittsburgh, PA, **2003**.

Received: February 23, 2006
Published Online: April 18, 2006

 © 2006 Wiley-VCH Verlag GmbH & Co. KGaA, Weinheim 

DOI: 10.1002/ejic.200600193

# Bis(2-amino alcohol-κ*N*)dicarboxylatoplatinum(II) Complexes – Elegant Synthesis via Ring-Opening of Bis(2-amino alcoholato-κ$^2$*N*,*O*)platinum(II) Species with Dicarboxylic Acids

**Kristof Meelich,[a] Markus Galanski,*[a] Vladimir B. Arion,[a] and Bernhard K. Keppler[a]**

**Keywords:** Bioinorganic chemistry / Platinum / N,O ligands / Antitumor agents / Drug design

Synthesis and purification of bis(2-amino alcohol-κ*N*)dicarboxylatoplatinum(II) complexes is problematic because of the use of light-sensitive silver(I) salts and the competing ring-closing side-reactions, especially after release of the chloro- or iodo ligands of the dihalogeno starting platinum(II) species. A novel synthetic procedure, namely selective synthesis of doubly ring-closed bis(2-amino alcoholato-κ$^2$*N*,*O*)platinum(II) compounds as the purification step and subsequent coordination of dicarboxylates in the absence of silver(I) via a ring-opening reaction, yielded a series of new complexes, which were characterized by elemental analysis, NMR spectroscopy, and X-ray crystallography. Exemplarily, the ring-opening of bis(2-aminoethanolato-κ$^2$*N*,*O*)platinum(II) was performed in the NMR tube by means of oxalic acid and investigated by $^1$H and $^{195}$Pt NMR spectroscopy. The reaction was found to be highly efficient: within 3 h complete transformation to the dicarboxylatoplatinum(II) complex was observed. Contrary, when sodium oxalate was used, no reaction could be detected at all during a period of one day.

(© Wiley-VCH Verlag GmbH & Co. KGaA, 69451 Weinheim, Germany, 2006)

## Introduction

Cisplatin, carboplatin, and oxaliplatin are the only metal-based chemotherapeutic drugs routinely used in the clinics in the fight against cancer (Figure 1).[1–4] In nearly 50% of all tumor therapies, platinum complexes are involved; in the case of testicular cancer, cisplatin demonstrates extraordinary tumor-inhibiting properties with real cure rates beyond 90%. Nevertheless, severe toxic side-effects and success of platinum complexes in only a limited number of solid tumors led to extensive attempts in the synthesis of a plethora of new platinum compounds.[5–7] In this context, hydrolysis of the administered drug was decreased by the use of dicarboxylato ligands (e.g., 1,1-cyclobutanedicarboxylate in carboplatin) resulting in significantly reduced systemic toxicity. Research has also focused on improving the solubility of the drugs for example by using oxalate (e.g., oxaliplatin) instead of chloro ligands (Figure 1).

Additionally, monodentate 2-amino alcohol or hydroxyethyl-substituted bidentate diamine ligands have been introduced in the drug development process in order (i) to increase the solubility, (ii) to further use the functional group for subsequent derivatization,[8,9] or (iii) to take advantage of the OH groups as donor or acceptor for hydrogen bonds with the DNA, the primary target of anticancer platinum complexes.[10,11]

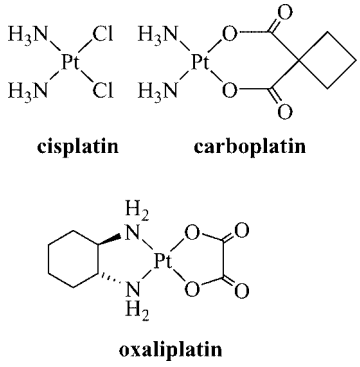


Figure 1. Chemical structures of established platinum-based anticancer drugs in world-wide clinical use.

Synthesis of bis(2-amino alcohol-κ*N*)platinum(II) complexes with dicarboxylato ligands, which would combine both structural features, is a logical consequence of the aforementioned considerations and seems to be straightforward from the chemical point of view. But only one publication by Khokhar et al. deals with this type of complex.[12] This is explainable by a set of problems arising during the synthetic procedure. Here we present an elegant and novel strategy in the preparation of bis(2-amino alcohol-κ*N*)dicarboxylatoplatinum(II) complexes as well as their characterization by elemental analysis, NMR spectroscopy, and X-ray crystallography. As the purification step, doubly ring-closed bis(2-amino alcoholato-κ$^2$*N*,*O*)platinum(II) com-

[a] Institute of Inorganic Chemistry, University of Vienna, Waehringer Strasse 42, 1090 Vienna, Austria
Fax: +43-1-4277-52680
E-mail: markus.galanski@univie.ac.at

Supporting information for this article is available on the WWW under http://www.eurjic.org or from the author.

 © 2006 Wiley-VCH Verlag GmbH & Co. KGaA, Weinheim 

plexes were prepared, now allowing us to omit silver(I) salts in the very last reaction step.

## Results and Discussion

In almost every case, dicarboxylatoplatinum(II) compounds have been synthesized starting from dichloro- or diiodoplatinum(II) complexes (Figure 2) followed by release and precipitation of the halide through addition of silver(I) salts (predominantly $AgNO_3$ or $Ag_2SO_4$). After filtration, the activated platinum species is brought to reaction with the respective sodium dicarboxylate (commercially available or synthesized in situ via addition of NaOH). A second variant is based directly on the use of silver dicarboxylates, offering the advantage that separation from $NaNO_3$ or $Na_2SO_4$ in the case of highly soluble dicarboxylatoplatinum(II) compounds is not required. However, in both instances reactions including light-sensitive silver salts are inherently problematic especially in the last reaction step.[13] In the case of a slight excess of $Ag^+$, difficulties in the purification of the reaction product can be expected. Furthermore, $Ag^+$ itself is biologically active, leading to false positive or false negative results during the evaluation of the anticancer properties.

Consequently, one strategy is to take substoichiometric amounts of the silver salt,[14,15] which then could lead to a contamination with monochloro- or monoiodoplatinum(II) species, depending on the solubility of the target platinum compounds. Additionally, and this is a characteristic feature of bis(2-amino alcohol-κ*N*)platinum(II) complexes, intramolecular ligand exchange reactions leading to singly and doubly ring-closed analogues must be taken into consideration. This facet has been studied in detail by NMR spectroscopy and was published recently in the case of (*SP*-4–2)-bis(2-aminoethanol-κ*N*)dichloroplatinum(II) and (*OC*-6–22)-bis(2-aminoethanol-κ*N*)tetrachloroplatinum(IV).[16] For activated platinum complexes (no halogeno ligand), an effective ring-closing side reaction should logically be expected.

In order to circumvent these synthetic difficulties, namely to avoid the use of silver salts in the very last reaction step

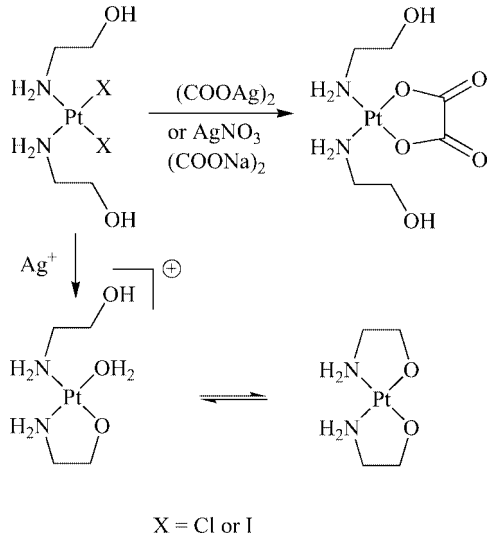


Figure 2. General synthesis of dicarboxylatoplatinum(II) complexes [e.g., (*SP*-4–2)-bis(2-aminoethanol-κ*N*)oxalatoplatinum(II)]; in the case of amino alcohol ligands, undesired side reactions to the singly and doubly ring-closed species are observed.

and to suppress side reactions as much as possible, a novel and elegant synthetic strategy was evaluated for its general applicability in the preparation of bis(2-amino alcohol-κ*N*)-dicarboxylatoplatinum(II) complexes. The basis of this procedure is the selective synthesis of the doubly ring-closed platinum species **2a**–**d** (which are in the above-mentioned synthetic pathway one of the unwanted side products) directly starting from the diiodoplatinum(II) compounds **1a**–**d** (Figure 3).

This is in contrast to our previously published pathway, where the dichloro analogues have been used.[17] Release of the iodo ligands is thereby accomplished (i) in the presence of substoichiometric amounts of $AgNO_3$ and (ii) additionally by the use of a basic anion exchanger (IRA 402), which further accelerates the ring formation process by a high pH value. The doubly ring-closed platinum(II) complexes **2a**–**d** were isolated and characterized by elemental analysis, NMR spectroscopy and in the case of **2c**(***S***) and **2d**(***S***) (*S*-enantiomers of complexes **2c** and **2d**) by X-ray diffraction

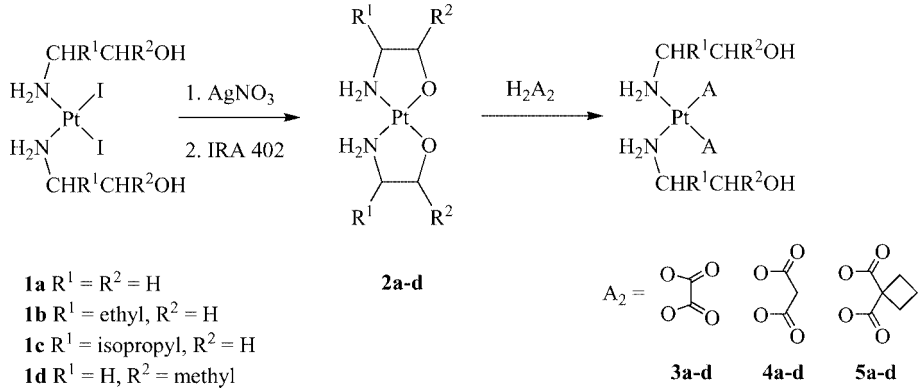


Figure 3. Synthesis of the target bis(2-amino alcohol-κ*N*)dicarboxylatoplatinum(II) complexes **3a**–**5d** via ring-opening with dicarboxylic acids (stereochemistry omitted).

 © 2006 Wiley-VCH Verlag GmbH & Co. KGaA, Weinheim 

analysis (Figure S1 and S2, Table S1 and S2, Supporting Information). The analytical data are in agreement with recently published results.[16] Most indicative for the success of the ring-closing reaction are the $^{1}H$ and $^{13}C$ chemical shifts of the methylene (**2a**–**c**) or methine (**2d**) group as well as the $^{195}Pt$ satellites of the C*H*R$^{2}$OPt protons. The latter, deriving from a $^{3}J(^{1}H,^{195}Pt)$ coupling are only visible in the case of the ring-closed complexes. In proton NMR spectra, the C*H*R$^{2}$OPt protons display an upfield shift in **2a**–**c** (e.g., **2a**, 2.97 ppm, corresponding dichloro complex, 3.76 ppm).

Typically, for the *C*HR$^{2}$OPt carbon atoms of **2a**–**d** resonances in the region between $\delta$ = 69.3 and 75.1 ppm can be detected. This is about 10 ppm downfield from the signals of the analogous ring-opened dichloro complexes (e.g., **2a**, 69.3 ppm, corresponding dichloro complex, 60.8 ppm). As could be shown earlier, addition of HCl or DCl results in the formation of the dichloro counterparts.[18] But addition of NaCl to the doubly ring closed species even in a 35-fold excess (without decrease of the pH value) shifts the equilibrium slightly towards the mono- but not to the dichloro complex (Figure S3). Consequently, **2a**–**d** have been used as starting complexes for the synthesis of compounds **3a**–**5d** via direct reaction with oxalic-, malonic-, and 1,1-cyclobutanedicarboxylic acid in water without addition of any other reagent. The products **3a**–**5d** were characterized by elemental analysis, NMR spectroscopy, and X-ray single crystal diffraction (**3a** and **5a**). Products **3a**–**d** were investigated by $^{1}H$ and $^{13}C$ NMR spectroscopy, whereas in the case of the analogous dicarboxylates **4a**–**5d** only $^{1}H$ NMR spectra have been performed for comparison.

In analogy to the reactions with HCl and NaCl, ring-opening could only be performed by means of dicarboxylic acids. When the respective sodium salt (e.g., sodium oxalate) was used, no reaction could be observed at all during a period of 24 h, as could be demonstrated by $^{1}H$ NMR spectroscopy (Figure S4). Formation of the bis(2-amino alcohol-κ*N*)dicarboxylatoplatinum(II) complexes **3a**–**5d** can best be judged by significant changes in $^{1}H$ NMR spectra. An apparent downfield shift of C*H*R$^{2}$OH proton resonances from 2.97–3.41 ppm in **2a**–**d** to 3.74–4.11 ppm in **3a**–**5d** was detected in conjunction with loss of the $^{3}J(^{1}H,^{195}Pt)$ coupling. Within the series of dicarboxylates (e.g., **3a**, **4a**, and **5a**, the same amine ligand, but different dicarboxylato ligand) the C*H*R$^{2}$OH chemical shifts showed marginal deviations within 0.04 ppm. In $^{13}C$ NMR spectra of the oxalato complexes **3a**–**d** noteworthy changes were observed for *C*HR$^{2}$OH carbon atoms (between $\delta$ = 60.5 and 66.9 ppm) in comparison to the ring-closed species **2a**–**d** (between $\delta$ = 69.3 and 75.1 ppm). Furthermore, in oxalato complexes **3a**–**d** $^{13}C$OO signals of the coordinated carboxylato ligands were detected in a narrow range at $\delta$ = 169.2 and 169.3 ppm (oxalic acid, 161.9 ppm; sodium oxalate, 173.8 ppm). The elemental analysis data of all new complexes were found in accordance with the expected values, proving their identity as well.

For complexes **3a** and **5a** it was possible to determine their solid-state structure by X-ray diffraction. Structural features of the square-planar platinum(II) complex **3a** are revealed in Figure 4. Selected bond lengths and angles are given in Table 1.

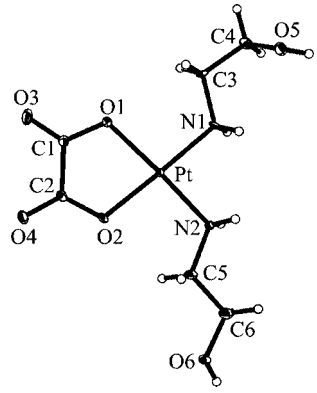


Figure 4. ORTEP diagram of **3a** displaying thermal ellipsoids at 50% probability.

Table 1. Bond lengths [Å] and angles [°] in the platinum(II) coordination polyhedron of **3a** and **5a**.

| atom1–atom2 | **3a** | atom1–atom2 | **5a** |
|---|---|---|---|
| Pt–O1 | 2.032(5) | Pt–O3 | 2.012(2) |
| Pt–O2 | 2.033(5) | Pt–O5 | 2.023(2) |
| Pt–N1 | 2.050(6) | Pt–N1 | 2.027(2) |
| Pt–N2 | 2.038(6) | Pt–N2 | 2.037(2) |
| C1–O1 | 1.311(9) | C5–O3 | 1.305(3) |
| C1–O3 | 1.248(9) | C5–O4 | 1.228(3) |
| C2–O2 | 1.293(9) | C10–O5 | 1.296(3) |
| C2–O4 | 1.238(9) | C10–O6 | 1.233(3) |
| atom1–atom2–atom3 | | atom1–atom2–atom3 | |
| O1–Pt–O2 | 82.0(2) | O3–Pt–O5 | 91.17(8) |
| N1–Pt–N2 | 86.6(3) | N1–Pt–N2 | 91.19(10) |

A projection of the molecule of **5a** on the coordination plane through PtN1N2O3O5 is shown in Figure 5. Selected bond lengths and angles are listed in Table 1. In **5a** the Pt atom has a square-planar coordination geometry. The Pt–O bond lengths are 2.012(2) and 2.023(2) Å, while the Pt–N bonds are 2.027(2) and 2.037(2) Å. These parameters are comparable with those in Pt(EtNH$_2$)$_2$(1,1-cyclobutanedicarboxylato)·H$_2$O [Pt–O 2.000(4) and 2.015(4) Å, Pt–N 1.992(5) and 2.020(5) Å].[19] As expected the C–O bonds (involving coordinated oxygens) at 1.305(3) and 1.296(3) Å are significantly longer than the two C=O bonds [C5–O4 1.228(3) and C10–O6 1.233(3) Å]. The angles inside the cyclobutane ring vary between 87.69(19) and 89.2(2)°, in agreement with those reported for Pt{*trans*-(–)-1,2-cyclohexanediamine}(1,1-cyclobutanedicarboxylate).[20] The mean deviation of the four atoms forming the four-membered ring from the best plane through C6, C7, C8, and C9 does not exceed 0.129 Å. The dihedral angle between the cyclobutane ring and the Pt coordination plane is ca. 70.9°. The two ethanolamine ligands and the cyclobutane ring are all on the same side of the Pt coordination plane. The six-membered malonate chelate cycle has a boat conformation. The mean deviation of O3, C5, O5, and C10 from the best plane through these four atoms is 0.0041 Å, with Pt and C6

 © 2006 Wiley-VCH Verlag GmbH & Co. KGaA, Weinheim 

atoms on the same side of the plane with deviations of 0.6858 and 0.6290 Å. The two carbonyl oxygen atoms O4 (deviation –0.4585 Å) and O6 (deviation –0.4667 Å) are oriented towards the other side of the plane. Of note is also the intramolecular hydrogen bond O1–H1···O3 [O1–H1 0.84, H1···O3 2.457, O1···O3 3.159 Å, ∠O1H1O3 141.72°] (see Figure 5).

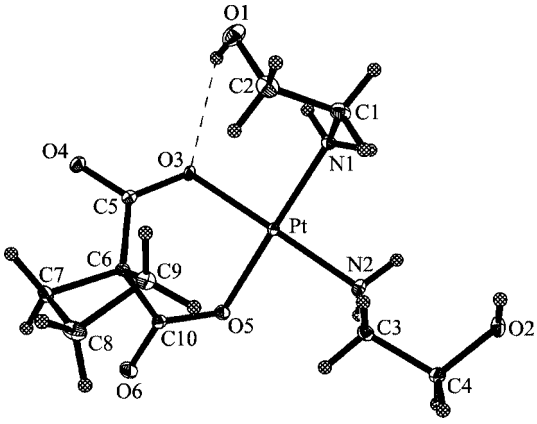


Figure 5. ORTEP diagram of **5a** displaying thermal ellipsoids at 50% probability.

Additionally, ring-opening of **2a** and formation of the dicarboxylatoplatinum(II) complex **3a** were studied directly in the NMR tube (Figure 6). As can be deduced from the $^{1}H$ and $^{195}Pt$ NMR spectra the reaction of oxalic acid with **2a** was very efficient. Three hours after mixing of **2a** (10.0 mg, 0.032 mmol) with oxalic acid (3.0 mg, 0.033 mmol) dissolved in 0.6 mL of $D_2O$, the dicarboxylato complex **3a** was formed and was detected as the sole species in both $^{1}H$ and $^{195}Pt$ NMR spectra (note that this is in clear contrast to the reaction with sodium oxalate, where no ring-opening could be observed at all during a period of 24 h; compare Figure S4). Ring-opening and dicarboxylate formation is reflected by significant downfield shifts of $^{1}H$ and $^{195}Pt$ resonances. In the case of $CH_2N$ protons, chemical shift differences are consequently smaller (**2a**, 2.27 ppm; **3a**, 2.67 ppm) than for $CH_2O$ protons (**2a**, 2.98 ppm; **3a**, 3.76 ppm) since the oxygen atom is released from the platinum(II) center (Figure 6).

Unresolved $^{195}Pt$ satellites deriving from a $^{3}J(^{1}H,^{195}Pt)$ coupling were detected for $CH_2N$ and $CH_2OPt$ protons (marked with asterisks in Figure 6) at the base of the respective resonances. In **3a** the $CH_2OH$ signals do not display such satellites, further proving the ring-opening reaction. Moreover, a remarkable downfield shift in the $^{195}Pt$ NMR spectra from –621 (**2a**) to –255 ppm (**3a**) finally documents the success of the conversion from **2a** to **3a**.

## Conclusions

The synthesis of bis(2-amino alcohol-κ*N*)dicarboxylatoplatinum(II) complexes was advantageously performed via a ring-opening reaction of the respective bis(2-amino alcoholato-κ$^2$*N*,*O*)platinum(II) species with dicarboxylic acids. This novel synthetic strategy is independent from the use of light-sensitive silver(I) salts in the last reaction step, which could cause problems during the purification and isolation of the target compounds. As could be exemplarily shown by $^{1}H$ and $^{195}Pt$ NMR spectroscopy for the reaction of bis(2-aminoethanolato-κ$^2$*N*,*O*)platinum(II) with oxalic acid, the transformation to the dicarboxylato complex is considerably fast and efficient. In contrast, reaction with sodium oxalate did not result in any detectable product during a period of one day.

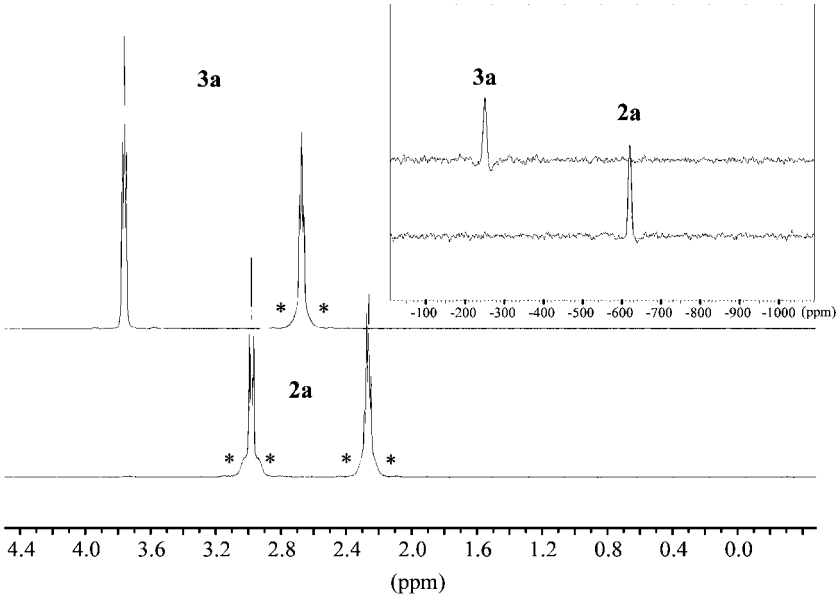


Figure 6. $^{1}H$ and $^{195}Pt$ (small insert) NMR spectra of the conversion of **2a** to **3a** through addition of an equivalent amount of oxalic acid; reaction was directly performed in the NMR tube, $^{195}Pt$ satellites are marked with asterisks.

 © 2006 Wiley-VCH Verlag GmbH & Co. KGaA, Weinheim 

## Experimental Section

All chemicals were purchased from commercial suppliers; $K_2PtCl_4$ was obtained from Johnson Matthey. Deionized water (reverse osmosis) was doubly distilled before use. All reactions were carried out under protection from light and for stirring a glass-coated magnetic stirrer was used. The $^1H$, $^{13}C$, and $^{195}Pt$ NMR spectra were recorded with a Bruker DPX 400 (Ultrashield™ Magnet) at 400.13, 100.62, and 86.11 MHz, respectively at 25 °C, using standard pulse programs. $^{195}Pt$ chemical shifts were referenced relative to external $K_2PtCl_4$. The elemental analyses were performed using a Perkin–Elmer 2400 CHN Elemental Analyzer by the microlaboratory of the Institute of Physical Chemistry, University of Vienna.

(*SP*-4–2)-Bis(2-aminoethanol-κ*N*)diiodoplatinum(II), **1a**, (*SP*-4–2)-bis[(*S*)-2-amino-1-butanol-κ*N*]diiodoplatinum(II), **1b(*S*)**, and (*SP*-4–2)-bis[(*R*)-2-amino-1-butanol-κ*N*]diiodoplatinum(II), **1b(*R*)**, were synthesized as described elsewhere.[16]

**(*SP*-4–2)-Bis[(*S*)-2-amino-3-methyl-1-butanol-κ*N*]diiodoplatinum(II) [1c(*S*)]:** $K_2PtCl_4$ (5.997 g, 14.45 mmol) was dissolved in water (50 mL) and treated with KI (12.0 g, 72.29 mmol). After stirring for 30 min at room temperature, a solution of (*S*)-2-amino-3-methyl-1-butanol (3.428 g, 33.23 mmol) in water (10 mL) was added in small portions and the brown reaction mixture was stirred for 10 h at room temperature. Precipitation of a yellow solid was completed by cooling the mixture for 12 h at 4 °C. The product was filtered off, washed with cold water (three times, 2 mL), and dried in vacuo over $P_4O_{10}$. Yield: 4.408 g (47%). $C_{10}H_{26}I_2N_2O_2Pt$ (655.21): calcd. C 18.33, H 4.00, N 4.27; found C 18.37, H 3.87, N 4.15.

**(*SP*-4–2)-Bis[(*R*)-2-amino-3-methyl-1-butanol-κ*N*]diiodoplatinum(II) [1c(*R*)]:** The synthesis was carried out as described for **1c(*S*)**, starting from $K_2PtCl_4$ (1.574 g, 3.79 mmol). Yield: 1.760 g (71%). $C_{10}H_{26}I_2N_2O_2Pt$ (655.21): calcd. C 18.33, H 4.00, N 4.27; found C 18.38, H 3.80, N 4.17.

**(*SP*-4–2)-Bis[(*S*)-1-amino-2-propanol-κ*N*]diiodoplatinum(II) [1d(*S*)]:** $K_2PtCl_4$ (618 mg, 1.49 mmol) was dissolved in water (ca. 5 mL) and treated with KI (1.235 g, 7.44 mmol). After stirring for 30 min at room temperature, a solution of (*S*)-1-amino-2-propanol (224 mg, 2.98 mmol) in water (1 mL) was added dropwise. The mixture was stirred for 3 h at room temperature. Precipitation of a yellow solid could be observed, which was completed by cooling for 1 h at 4 °C. The product was filtered off, washed with ice-cold water (three times, 1 mL), and dried in vacuo over $P_4O_{10}$. Yield: 640 mg (72%). $C_6H_{18}I_2N_2O_2Pt$ (599.11): calcd. C 12.03, H 3.03, N 4.68; found C 12.08, H 2.86, N 4.48.

**(*SP*-4–2)-Bis[(*R*)-1-amino-2-propanol-κ*N*]diiodoplatinum(II) [1d(*R*)]:** The synthesis was carried out as described for **1d(*S*)**, starting from $K_2PtCl_4$ (2.100 g, 5.06 mmol). Yield: 2.078 g (69%).

**(*SP*-4–2)-Bis(2-aminoethanolato-κ²*N*,*O*)platinum(II) (2a): 1a** (5.660 g, 9.91 mmol) was suspended in water (80 mL), mixed with $AgNO_3$ (3.198 g, 18.83 mmol), and stirred for 24 h at room temperature. AgI was filtered off and the clear solution was mixed with a preconditioned basic anion exchange resign, IRA 402 (the commercially available chloride form was treated with 2 M NaOH for 30 min and washed with deionized water until a pH of 7). After stirring for 12 h at room temperature, the liquid was decanted from the resign, which was washed three times with water. The combined aqueous solutions were filtered and thereafter concentrated to ca. 1 mL under reduced pressure at 30 °C. Crystallization of the product occurred at room temperature and was completed at 4 °C. The white product was isolated by filtration, rinsed with a few drops of ice-cold water, and dried in vacuo over $P_4O_{10}$. Yield: 1.337 g (45%). $C_4H_{12}N_2O_2Pt$ (315.23): calcd. C 15.24, H 3.84, N 8.89; found C 15.33, H 3.68, N 8.69. $^1H$ NMR ($D_2O$): $\delta$ = 2.97 (t, $^3J_{H,H}$ = 5.4 Hz, 4 H, C$H_2$O), 2.25 (t, $^3J_{H,H}$ = 5.5 Hz, 4 H, C$H_2$N) ppm. $^{13}C$ NMR ($D_2O$): $\delta$ = 69.3 (2 C, *C*$H_2$O), 50.8 (2 C, *C*$H_2$N) ppm.

**(*SP*-4–2)-Bis[(*S*)-2-amino-1-butanolato-κ²*N*,*O*]platinum(II) [2b(*S*)]: 1b(*S*)** (2.860 g, 4.56 mmol) was suspended in water (60 mL), treated with $AgNO_3$ (1.405 g, 8.27 mmol), and stirred for 24 h. After filtration of AgI, the clear solution was treated with preconditioned IRA 402 as described for **2a**; the reaction was stirred for 48 h. After removal of the ion exchange resign and filtration, the solution was concentrated until a solid product appeared. Precipitation was completed first at room temperature and later at 4 °C. The white product was isolated by filtration, rinsed with a few drops of ice-cold water, and dried in vacuo over $P_4O_{10}$. Yield: 745 mg (48%). $C_8H_{20}N_2O_2Pt$ (371.33): calcd. C 25.88, H 5.43, N 7.54; found C 26.05, H 5.21, N 7.47. $^1H$ NMR ($H_2O/D_2O$, 9:1): $\delta$ = 3.01 (m, 2 H, C$H_2$O), 2.88 (m, 2 H, C$H_2$O), 2.48 (m, 2 H, C*H*N), 1.53 (m, 2 H, $CH_3CH_2$), 1.34 (m, 2 H, $CH_3CH_2$), 0.80 (t, $^3J_{H,H}$ = 7.3 Hz, 6 H, C$H_3$) ppm. $^{13}C$ NMR ($H_2O/D_2O$, 9:1): $\delta$ = 73.0 (2 C, *C*$H_2$O), 64.1 (2 C, *C*HN), 22.9 (2 C, $CH_3CH_2$), 10.8 (2 C, *C*$H_3$) ppm.

**(*SP*-4–2)-Bis[(*R*)-2-amino-1-butanolato-κ²*N*,*O*]platinum(II) [2b(*R*)]:** The synthesis was carried out as described for **2b(*S*)**, starting from **1b(*R*)** (1.260 g, 2.01 mmol). Yield: 366 mg (52%). $C_8H_{20}N_2O_2Pt$ (371.33): calcd. C 25.88, H 5.43, N 7.54; found C 25.99, H 5.14, N 7.50. $^1H$ NMR ($H_2O/D_2O$, 9:1): $\delta$ = 3.06 (m, 2 H, C$H_2$O), 2.94 (m, 2 H, C$H_2$O), 2.54 (m, 2 H, C*H*N), 1.59 (m, 2 H, $CH_3CH_2$), 1.42 (m, 2 H, $CH_3CH_2$), 0.86 (t, $^3J_{H,H}$ = 7.6 Hz, 6 H, C$H_3$) ppm. $^{13}C$ NMR ($H_2O/D_2O$, 9:1): $\delta$ = 72.9 (2 C, *C*$H_2$O), 64.1 (2 C, *C*HN), 22.9 (2 C, $CH_3CH_2$), 10.8 (2 C, *C*$H_3$) ppm.

**(*SP*-4–2)-Bis[(*S*)-2-amino-3-methyl-1-butanolato-κ²*N*,*O*]platinum(II) [2c(*S*)]: 1c(*S*)** (2.058 g, 3.14 mmol) was suspended in water (70 mL), treated with $AgNO_3$ (1.024 g, 6.03 mmol), and stirred for 24 h. After filtration of AgI, the clear solution was treated with preconditioned IRA 402 as described for **2a**; the reaction was stirred for 48 h. After removal of the ion exchange resign and filtration, the solution was concentrated until a solid product appeared. Precipitation was completed first at room temperature and later at 4 °C. The white product was isolated by filtration, rinsed with a few drops of ice-cold water, and dried in vacuo over $P_4O_{10}$. Yield: 103 mg (8%). $C_{10}H_{24}N_2O_2Pt{\cdot}H_2O$ (417.40): calcd. C 28.77, H 6.28, N 6.71; found C 28.78, H 6.02, N 6.68. $^1H$ NMR ($D_2O$): $\delta$ = 3.09 (m, 2 H, C$H_2$O), 2.99 (m, 2 H, C$H_2$O), 2.30 (m, 2 H, C*H*N), 1.62 [m, 2 H, $(CH_3)_2CH$], 0.85 (d, $^3J_{H,H}$ = 7.8 Hz, 12 H, C$H_3$) ppm. $^{13}C$ NMR ($D_2O$): $\delta$ = 71.9 (2 C, *C*$H_2$O), 68.5 (2 C, *C*HN), 28.8 [2 C, *C*$H(CH_3)_2$], 20.4 (2 C, *C*$H_3$), 18.9 (2 C, *C*$H_3$) ppm.

**(*SP*-4–2)-Bis[(*R*)-2-amino-3-methyl-1-butanolato-κ²*N*,*O*]platinum(II) [2c(*R*)]:** The synthesis was carried out as described for **2c(*S*)**, starting from **1c(*R*)** (1.700 g, 2.59 mmol). Yield: 112 mg (11%). $C_{10}H_{24}N_2O_2Pt{\cdot}H_2O$ (417.40): calcd. C 28.77, H 6.28, N 6.71; found C 28.78, H 6.02, N 6.68. $^1H$ NMR ($D_2O$): $\delta$ = 3.06 (m, 2 H, C$H_2$O), 2.97 (m, 2 H, C$H_2$O), 2.29 (m, 2 H, C*H*N), 1.60 [m, 2 H, $(CH_3)_2CH$], 0.84 (t, $^3J_{H,H}$ = 7.8 Hz, 12 H, C$H_3$) ppm. $^{13}C$ NMR ($D_2O$): $\delta$ = 71.8 (2 C, *C*$H_2$O), 68.4 (2 C, *C*HN), 28.6 [2 C, *C*$H(CH_3)_2$], 20.2 (2 C, *C*$H_3$), 18.7 (2 C, *C*$H_3$) ppm.

**(*SP*-4–2)-Bis[(*S*)-1-amino-2-propanolato-κ²*N*,*O*]platinum(II) [2d(*S*)]: 1d(*S*)** (3.026 g, 5.05 mmol) was suspended in water (80 mL), treated with $AgNO_3$ (1.647 g; 9.70 mmol), and stirred for 24 h. After filtration of AgI, the clear solution was treated with preconditioned IRA 402 as described for **2a**; the reaction was stirred for 48 h. After removal of the ion exchange resign and filtration, the solution was concentrated until a solid product appeared. Precipitation was completed first at room temperature and later at 4 °C. The white

 © 2006 Wiley-VCH Verlag GmbH & Co. KGaA, Weinheim 

product was isolated by filtration, rinsed with a few drops of ice-cold water, and dried in vacuo over $P_4O_{10}$. Yield: 186 mg (10%). $C_6H_{16}N_2O_2Pt·1.5H_2O$ (370.30): calcd. C 19.46, H 5.17, N 7.56; found C 19.60, H 4.87, N 7.33. $^1$H NMR ($D_2O$): $\delta$ = 3.42 (m, 2 H, C*H*O), 2.28 (dd, $^3J_{H,H}$ = 3.5 Hz, $^3J_{H,H}$ = 11.5 Hz, 2 H, C$H_2$N), 2.01 (dd, $^3J_{H,H}$ = 11.4 Hz, 2 H, C$H_2$N), 1.03 (d, $^3J_{H,H}$ = 6.0 Hz, 6 H, C$H_3$) ppm. $^{13}$C NMR ($D_2O$): $\delta$ = 75.2 (2 C, *C*HO), 55.3 (2 C, *C*$H_2$N), 17.7 (2 C, *C*$H_3$) ppm.

**(*SP*-4-2)-Bis[(*R*)-1-amino-2-propanolato-κ$^2$*N*,*O*]platinum(II) [2d(*R*)]:** The synthesis was carried out as described for **2d(*S*)**, starting from **1d(*R*)** (2.022 g, 3.37 mmol). Yield: 429 mg (39%). $C_6H_{16}N_2O_2Pt$ (343.28): calcd. C 20.99, H 4.70, N 8.16; found C 20.76, H 4.99, N 7.86. $^1$H NMR ($D_2O$): $\delta$ = 3.41 (m, 2 H, C*H*O), 2.27 (dd, $^3J_{H,H}$ = 3.4 Hz, $^3J_{H,H}$ = 11.5 Hz, 2 H, C$H_2$N), 2.00 (dd, $^3J_{H,H}$ = 10.7 Hz, 2 H, C$H_2$N), 1.03 (d, $^3J_{H,H}$ = 6.3 Hz, 6 H, C$H_3$) ppm. $^{13}$C NMR ($D_2O$): $\delta$ = 75.1 (2 C, *C*HO), 54.9 (2 C, *C*$H_2$N), 17.6 (2 C, *C*$H_3$) ppm.

**(*SP*-4-2)-Bis(2-aminoethanol-κ*N*)oxalatoplatinum(II) (3a): 2a** (122 mg, 0.39 mmol) and oxalic acid dihydrate (50 mg, 0.40 mmol) were dissolved in water (2 mL) and stirred for 20 h at room temperature. The solution was filtered and reduced in a hood air stream until crystallization of colorless needles occurred. The product was separated and dried in vacuo over $P_4O_{10}$. Yield: 140 mg (89%). $C_6H_{14}N_2O_6Pt$ (405.26): calcd. C 17.78, H 3.48, N 6.91; found C 17.82, H 3.28, N 6.73. $^1$H NMR ($D_2O$): $\delta$ = 3.76 (t, $^3J_{H,H}$ = 5.3 Hz, 4 H, C$H_2$O), 2.68 (m, 4 H, C$H_2$N) ppm. $^{13}$C NMR ($D_2O$): $\delta$ = 169.3 (2 C, *C*OO), 60.5 (2 C, *C*$H_2$O), 48.3 (2 C, *C*$H_2$N) ppm.

**(*SP*-4-2)-Bis[(*S*)-2-amino-1-butanol-κ*N*]oxalatoplatinum(II) [3b(*S*)]: 2b(*S*)** (49 mg, 0.13 mmol) and oxalic acid dihydrate (17 mg, 0.13 mmol) were dissolved in water (1 mL) and stirred for 18 h at room temperature. The solution was filtered and concentrated under reduced pressure over $P_4O_{10}$ until a crystalline product appeared, which was washed with water (two times with 0.5 mL) and dried in vacuo over $P_4O_{10}$. Yield: 28 mg (46%). $C_{10}H_{22}N_2O_6Pt$ (461.37): calcd. C 26.03, H 4.81, N 6.07; found C 25.98, H 4.70, N 5.94. $^1$H NMR ($D_2O$): $\delta$ = 3.92 (dd, $^3J_{H,H}$ = 3.6 Hz, $^3J_{H,H}$ = 12.0 Hz, 2 H, C$H_2$O), 3.63 (dd, $^3J_{H,H}$ = 5.1 Hz, $^3J_{H,H}$ = 12.0 Hz, 2 H, C$H_2$O), 2.59 (m, 2 H, C*H*N), 1.72 (m, 2 H, $CH_3CH_2$), 1.54 (m, 2 H, $CH_3CH_2$), 0.89 (t, $^3J_{H,H}$ = 7.5 Hz, 6 H, C$H_3$) ppm. $^{13}$C NMR ($D_2O$): $\delta$ = 169.3 (2 C, *C*OO), 62.4 (2 C, *C*$H_2$O), 59.1 (2 C, *C*HN), 24.3 (2 C, *C*$H_2CH_3$), 9.9 (2 C, *C*$H_3$) ppm.

**(*SP*-4-2)-Bis[(*R*)-2-amino-3-methyl-1-butanol-κ*N*]oxalatoplatinum(II) [3c(*R*)]: 2c(*R*)** (76 mg, 0.19 mmol) and oxalic acid dihydrate (24 mg, 0.19 mmol) were dissolved in water (5 mL) and stirred for 48 h at room temperature. The solution was concentrated under reduced pressure at 35 °C to ca. 1 mL and stored at room temperature for 12 h. A white product was isolated and dried in vacuo. Yield: 75 mg (81%). $C_{12}H_{26}N_2O_6Pt$ (489.44): calcd. C 29.45, H 5.35, N 5.72; found C 29.44, H 5.13, N 5.59. $^1$H NMR ($D_2O$): $\delta$ = 4.02 (dd, $^3J_{H,H}$ = 3.7 Hz, $^3J_{H,H}$ = 12.0 Hz, 2 H, C$H_2$O), 3.73 (dd, $^3J_{H,H}$ = 5.6 Hz, $^3J_{H,H}$ = 12.0 Hz, 2 H, C$H_2$O), 2.45 (m, 2 H, C*H*N), 1.99 [m, 2 H, $(CH_3)_2CH$], 0.91 (d, $^3J_{H,H}$ = 6.8 Hz, 6 H, C$H_3$), 0.87 (d, $^3J_{H,H}$ = 6.8 Hz, 6 H, C$H_3$) ppm. $^{13}$C NMR ($D_2O$): $\delta$ = 169.3 (2 C, *C*OO), 63,2 (2 C, *C*HN), 61.5 (2 C, *C*$H_2$O), 29.4 [2 C, *C*$H(CH_3)_2$], 18.9 (2 C, *C*$H_3$), 18.1 (2 C, *C*$H_3$) ppm.

**(*SP*-4-2)-Bis[(*R*)-1-amino-2-propanol-κ*N*]oxalatoplatinum(II) [3d(*R*)]: 2d(*R*)** (157 mg, 0.46 mmol) and oxalic acid dihydrate (58 mg, 0.46 mmol) were dissolved in water (5 mL) and stirred for 48 h at room temperature. The solution was reduced to 1 mL and stored at room temperature for 12 h. A white precipitate was separated from the residual solution and dried in vacuo. Yield: 79 mg (40%). $C_8H_{18}N_2O_6Pt$ (433.32): calcd. C 22.17, H 4.19, N 6.46; found: C 22.40, H 3.97, N 6.31. $^1$H NMR ($D_2O$): $\delta$ = 4.07 (m, 2 H, C*H*O), 2.65 (m, 2 H, C$H_2$N), 2.41 (m, 2 H, C$H_2$N), 1.11 (d, $^3J_{H,H}$ = 6.4 Hz, 6 H, C$H_3$) ppm. $^{13}$C NMR ($D_2O$): $\delta$ = 169.2 (2 C, *C*OO), 66.9 (2 C, *C*HO), 53.2 (2 C, *C*$H_2$N), 20.1 (2 C, *C*$H_3$) ppm.

**(*SP*-4-2)-Bis(2-aminoethanol-κ*N*)malonatoplatinum(II) (4a): 2a** (200 mg, 0.63 mmol) and malonic acid (66 mg, 0.65 mmol) were dissolved in water (10 mL) and stirred for 24 h at room temperature. The colorless solution was filtered and the solvent was removed slowly under reduced pressure over $CaCl_2$. A white crystalline product was isolated and dried in vacuo over $P_4O_{10}$. Yield: 230 mg (86%). $C_7H_{16}N_2O_6Pt$ (419.30): calcd. C 20.05, H 3.85, N 6.68; found C 20.18, H 3.69, N 6.53. $^1$H NMR ($H_2O/D_2O$, 9:1): $\delta$ = 3.75 (t, $^3J_{H,H}$ = 5.2 Hz, 4 H, C$H_2$O), 3.57 (s, 2 H, C$H_2$COO), 2.64 (m, 4 H, C$H_2$N) ppm.

**(*SP*-4-2)-Bis[(*R*)-2-amino-1-butanol-κ*N*]malonatoplatinum(II) [4b(*R*)]: 2b(*R*)** (200 mg, 0.54 mmol) and malonic acid (56 mg, 0.55 mmol) were dissolved in water (10 mL) and stirred for 24 h at 40 °C. The solution was filtered and the solvent was removed under reduced pressure at 40 °C. The residual yellow oil was treated with diethyl ether (15 mL) for 30 s in an ultra sonic bath, then the solvent was immediately evaporated. This procedure was repeated five times. The solid product was dried in vacuo, recrystallized from acetone/ethanol (3:1), and finally dried in vacuo. Yield: 82 mg (32%). $C_{11}H_{24}N_2O_6Pt$ (475.40): calcd. C 27.79, H 5.09, N 5.89; found C 27.58, H 4.80, N 5.65. $^1$H NMR ($H_2O/D_2O$, 9:1): $\delta$ = 3.92 (m, 2 H, C$H_2$O), 3.60 (m, 2 H, C$H_2$O), 3.58 (s, 2 H, C$H_2$COO), 2.58 (s, 2 H, C*H*N), 1.71 (m, 2 H, C$H_2CH_3$), 1.53 (m, 2 H, C$H_2CH_3$), 0.87 (m, 6 H, C$H_3$) ppm. $^{13}$C NMR ($H_2O/D_2O$, 9:1): $\delta$ = 178.4 (2 C, $CH_2COO$), 62.6 (2 C, *C*$H_2$O), 58.7 (2 C, *C*HN), 48.0 (1 C, *C*$H_2$COO), 24.3 (2 C, *C*$H_2CH_3$), 9.9 (2 C, *C*$H_3$) ppm.

**(*SP*-4-2)-Bis[(*R*)-2-amino-3-methyl-1-butanol-κ*N*]malonatoplatinum(II) [4c(*R*)]:** Malonic acid (52 mg, 0.51 mmol) was dissolved in water (10 mL). To this solution **2c(*R*)** (200 mg, 0.48 mmol) was added and the mixture was stirred for 24 h at 35 °C. The solution was filtered, the solvent was removed, and the residual yellow paste-like solid was treated with ether as described for **4b(*R*)**. A white solid product was isolated and dried in vacuo. Yield: 103 mg (43%). $C_{13}H_{28}N_2O_6Pt$ (503.45): calcd. C 31.01, H 5.61, N 5.56; found C 31.23, H 5.39, N 5.33. $^1$H NMR ($H_2O/D_2O$, 9:1): $\delta$ = 4.01 (dd, $^3J_{H,H}$ = 3.8 Hz, $^3J_{H,H}$ = 11.9 Hz, 2 H, C$H_2$O), 3.70 (dd, $^3J_{H,H}$ = 6.0 Hz, $^3J_{H,H}$ = 12.1 Hz, 2 H, C$H_2$O), 3.57 (s, 2 H, C$H_2$COO), 2.46 (m, 2 H, C*H*N), 2.04 [m, 2 H, C$H(CH_3)_2$], 0.91 (d, $^3J_{H,H}$ = 7.1 Hz, 6 H, C$H_3$), 0.86 (d, $^3J_{H,H}$ = 6.8 Hz, 6 H, C$H_3$) ppm.

**(*SP*-4-2)-Bis[(*R*)-1-amino-2-propanol-κ*N*]malonatoplatinum(II) [4d(*R*)]: 2d(*R*)** (175 mg, 0.51 mmol) and malonic acid (53 mg, 0.51 mmol) were dissolved in water (10 mL) and stirred for 24 h at room temperature. The solution was filtered and lyophilized. A white product was isolated and dried in vacuo over $P_4O_{10}$. Yield: 216 mg (95%). $C_9H_{20}N_2O_6Pt$ (447.34): calcd. C 24.16, H 4.51, N 6.26; found C 23.86, H 4.56, N 6.05. $^1$H NMR ($H_2O/D_2O$, 9:1): $\delta$ = 4.11 (m, 2 H, C*H*O), 3.56 (s, 2 H, C$H_2$COO), 2.63 (m, 2 H, C$H_2$N), 2.38 (m, 2 H, C$H_2$N), 1.12 (d, $^3J_{H,H}$ = 6.4 Hz, 6 H, C$H_3$) ppm.

**(*SP*-4-2)-Bis(2-aminoethanol-κ*N*)cyclobutane-1,1-dicarboxylatoplatinum(II) (5a): 2a** (200 mg, 0.63 mmol) and cyclobutane-1,1-dicarboxylic acid (91 mg, 0.63 mmol) were dissolved in water (10 mL) and stirred for 48 h at room temperature. The solution was concentrated in a hood air stream until crystallization could be observed. The colorless product was collected and dried in vacuo over $P_4O_{10}$. Yield: 220 mg (75%). $C_{10}H_{20}N_2O_6Pt$ (459.35): calcd. C 26.15, H 4.39 N 6.10; found C 26.22, H 4.16, N 5.98. $^1$H NMR ($D_2O$): $\delta$ =

 © 2006 Wiley-VCH Verlag GmbH & Co. KGaA, Weinheim 

3.74 (t, $^3J_{H,H}$ = 5.3 Hz, 4 H, C$H_2$O), 2.78 (t, $^3J_{H,H}$ = 7.8 Hz, 4 H, C$H_2$C$H_2$C$H_2$), 2.66 (m, 4 H, C$H_2$N), 1.81 (m, 2 H, $CH_2CH_2CH_2$) ppm.

**(*SP*-4–2)-Bis[(*R*)-2-amino-1-butanol-κ*N*]cyclobutane-1,1-dicarboxylatoplatinum(II) [5b(*R*)]: 2b(*R*)** (205 mg, 0.55 mmol) and cyclobutane-1,1-dicarboxylic acid (86 mg, 0.60 mmol) were dissolved in water (10 mL) and stirred for 48 h at 40 °C. The solvent was evaporated in a hood air stream at 40 °C. A white solid was isolated, washed with water twice, and dried in vacuo over $P_4O_{10}$. Yield: 151 mg (53%). $C_{14}H_{28}N_2O_6Pt$ (515.46): calcd. C 32.62, H 5.47, N 5.43; found C 32.01, H 5.07, N 5.26. $^1$H NMR ($D_2O$): $\delta$ = 3.92 (m, 2 H, C$H_2$O), 3.62 (m, 2 H, C$H_2$O), 2.76 (m, 4 H, C$H_2$CH$_2$C$H_2$), 2.58 (m, 2 H, C*H*N), 1.87–1.67 (m, 4 H, C$H_2$CH$_3$), 1.53 (m, 2 H, CH$_2$C$H_2$CH$_2$), 0.88 (t, $^3J_{H,H}$ = 7.4 Hz, 6 H, C$H_3$) ppm.

**(*SP*-4–2)-Bis[(*R*)-2-amino-3-methyl-1-butanol-κ*N*]cyclobutane-1,1-dicarboxylatoplatinum(II) [5c(*R*)]: 2c(*R*)** (160 mg, 0.38 mmol) and cyclobutane-1,1-dicarboxylic acid (58 mg, 0.40 mmol) were dissolved in water (10 mL) and stirred for 48 h at 40 °C. The solution was reduced in a hood air stream at 40 °C to ca. 2 mL, which led to the precipitation of a white solid. The latter was filtered off, washed with water (two times with 0.5 mL), and dried in vacuo over $P_4O_{10}$. Yield: 109 mg (52%). $C_{16}H_{32}N_2O_6Pt$ (543.51): calcd. C 35.36, H 5.93, N 5.15; found C 35.13, H 5.65, N 5.00. $^1$H NMR ($D_2O$): $\delta$ = 4.01 (dd, $^3J_{H,H}$ = 3.9 Hz, $^3J_{H,H}$ = 12.0 Hz, 2 H, C$H_2$O), 3.70 (dd, $^3J_{H,H}$ = 5.9 Hz, $^3J_{H,H}$ = 12.0 Hz, 2 H, C$H_2$O), 2.74 (m, 4 H, C$H_2$CH$_2$C$H_2$), 2.46 (m, 2 H, C*H*N), 2.06 [m, 2 H, C*H*(CH$_3$)$_2$], 1.80 (m, 2 H, CH$_2$C$H_2$CH$_2$), 0.92 (d, $^3J_{H,H}$ = 6.8 Hz, 6 H, C$H_3$), 0.86 (d, $^3J_{H,H}$ = 7.1 Hz, 6 H, C$H_3$) ppm.

**(*SP*-4–2)-Bis[(*R*)-1-amino-2-propanol-κ*N*]cyclobutane-1,1-dicarboxylatoplatinum(II) [5d(*R*)]: 2d(*R*)** (182 mg, 0.53 mmol) and cyclobutane-1,1-dicarboxylic acid (80 mg, 0.55 mmol) were dissolved in water (10 mL) and stirred for 48 h at room temperature. The solvent was removed in a hood air stream. This yielded a slightly yellow paste-like solid, which was dissolved in ethanol (4 mL). Upon addition of acetone (30 mL), a white solid precipitated. After 12 h the product was separated, washed with acetone (5 mL), and dried in vacuo over $P_4O_{10}$. Yield: 180 mg (70%). $C_{12}H_{24}N_2O_6Pt$ (487.41): calcd. C 29.57, H 4.96, N 5.75; found C 29.66, H 4.72, N 5.63. $^1$H NMR ($D_2O$): $\delta$ = 4.09 (m, 2 H, C*H*O), 2.76 (m, 4 H, C$H_2$CH$_2$C$H_2$), 2.64 (m, 2 H, C$H_2$N), 2.41–2.30 (m, 2 H, C$H_2$N), 1.80 (m, 2 H, CH$_2$C$H_2$CH$_2$), 1.12 (d, $^3J_{H,H}$ = 6.6 Hz, 6 H, C$H_3$) ppm.

Table 2. Crystallographic data for **3a** and **5a**.

| Complex | **3a** | **5a** |
|---|---|---|
| Empirical formula | $C_6H_{14}N_2O_6Pt$ | $C_{10}H_{20}N_2O_6Pt$ |
| *Fw* | 405.28 | 459.37 |
| Space group | *C*2/*c* | P$\bar{1}$ (No. 2) |
| *a* [Å] | 17.453(4) | 8.0934(16) |
| *b* [Å] | 8.0475(16) | 8.2393(16) |
| *c* [Å] | 16.371(3) | 10.253(2) |
| *a* [deg] | | 92.81(3) |
| *β* [deg] | 119.35(3) | 92.05(3) |
| *γ* [deg] | | 104.30(3) |
| *V*( [Å]$^3$) | 2004.3(7) | 660.9(2) |
| *Z* | 8 | 2 |
| *λ* [Å] | 0.71073 | 0.71073 |
| $\rho_{calcd}$ (g cm$^{-3}$) | 2.686 | 2.308 |
| Crystal size ([mm$^3$]) | 0.22×0.20×0.10 | 0.30×0.25×0.18 |
| *T* [K] | 100 | 120 |
| *μ* [cm$^{-1}$] | 14.015 | 10.640 |
| $R_1$[a] | 0.0290 | 0.0187 |
| $wR_2$[b] | 0.0806 | 0.0476 |
| GOF[c] | 1.120 | 1.026 |

[a] $R_1 = \Sigma||F_o| - |F_c||/\Sigma|F_o|$. [b] $wR_2 = \{\Sigma[w(F_o^2 - F_c^2)^2]/\Sigma[w(F_o^2)^2]\}^{1/2}$. [c] GOF = $\{\Sigma[w(F_o^2 - F_c^2)^2]/(n - p)\}^{1/2}$, where *n* is the number of reflections and *p* is the total number of parameters refined.

X-ray diffraction measurements were performed with Nonius Kappa CCD and Bruker X8APEX II CCD diffractometers for **2c(*S*)**, **2d(*S*)**, **3a**, and **5a**, respectively. Single crystals were positioned at 35, 30, 37.5, and 30 mm from the detector and 747, 371, 673, and 379 frames were measured, each for 10, 15, 40, and 8 s over 1, 2, 1, and 2° scan width [complexes **2c(*S*)**, **2d(*S*)**, **3a**, and **5a**, respectively]. The data were processed using Denzo-SMN software.[21] Crystal data, data collection parameters, and structure refinement details for **2c(*S*)** and **2d(*S*)** are given in Table S2, whereas those for **3a** and **5a** are given in Table 2. The structures were solved by direct methods and refined by full-matrix least-squares techniques. Non-hydrogen atoms were refined with anisotropic displacement parameters. H atoms were calculated and allowed to ride. Computer programs: structure solution, SHELXS-97,[22] refinement, SHELXL-97,[23] molecular diagrams, ORTEP,[24] computer: Pentium II; scattering factors.[25]

CCDC-298141 (for **2c*S***), -298142 [for **2d(*S*)**], -298144 (for **3a**), and -298143 (for **5a**) contain the supplementary crystallographic data for this paper. These data can be obtained free of charge from The Cambridge Crystallographic Data Centre via www.ccdc.cam.ac.uk/data_request/cif.

**Supporting Information** (see also the footnote on the first page of this article): ORTEP drawings and Tables with bond lengths, angles, and crystallographic data of **2c(*S*)** and **2d(*S*)**. NMR spectra for the reaction of **2a** with NaCl and sodium oxalate.

## Acknowledgments

We are thankful to Prof. G. Giester and Mr. A. Roller for the collection of X-ray data. The support of the FWF (Fonds zur Foerderung der wissenschaftlichen Forschung), the Austrian Council for Research and Technology Development, Faustus Forschung Translational Drug Development AG and COST (European Cooperation in the Field of Scientific and Technical Research) is gratefully acknowledged.

[1] B. Rosenberg, *Interdiscip. Sci. Rev.* **1978**, *3*, 134–147.
[2] B. Lippert (Ed.), *Cisplatin: Chemistry and Biochemistry of a Leading Anticancer Drug*, Verlag Helvetica Chimica Acta, Zürich, Wiley-VCH, Weinheim, **1999**.
[3] M. A. Jakupec, M. Galanski, B. K. Keppler, *Rev. Physiol. Biochem. Pharmacol.* **2003**, *146*, 1–54.
[4] M. Galanski, M. A. Jakupec, B. K. Keppler in *Metal Compounds in Cancer Chemotherapy* (Eds.: J. M. Pérez, M. A. Fuertes, C. Alonso), Research Signpost, Kerala, **2005**, p. 155–185.
[5] M. A. Fuertes, J. Castilla, C. Alonso, J. M. Perez, *Curr. Med. Chem. Anti-Cancer Agents* **2002**, *2*, 539–551.
[6] M. Galanski, M. A. Jakupec, B. K. Keppler, *Curr. Med. Chem.* **2005**, *12*, 2075–2094.
[7] M. Galanski, Recent Patents Anti-Cancer Drug Discov., **2005**, in press.
[8] L. Cai, K. Lim, S. Ren, R. S. Cadena, W. T. Beck, *J. Med. Chem.* **2001**, *44*, 2959–2965.
[9] M. Galanski, W. Zimmermann, M. Berger, C. Baumgartner, G. Giester, B. K. Keppler, *Eur. J. Inorg. Chem.* **2002**, 417–421.
[10] E. R. Jamieson, S. J. Lippard, *Chem. Rev.* **1999**, *99*, 2467–2498.
[11] D. Wang, S. J. Lippard, *Nat. Rev. Drug Discovery* **2005**, *4*, 307–320.
[12] A. R. Khokhar, Q. Xu, R. A. Newman, Z. H. Siddik, *J. Inorg. Biochem.* **1991**, *43*, 57–63.

 © 2006 Wiley-VCH Verlag GmbH & Co. KGaA, Weinheim 

[13] A. V. Chuchuryukin, P. A. Chase, A. M. Mills, M. Lutz, A. L. Spek, G. P. M. van Klink, G. van Koten, *Inorg. Chem.* **2006**, *45*, 2045–2054.
[14] M. Galanski, B. K. Keppler, B. Nuber, *Angew. Chem. Int. Ed. Engl.* **1995**, *34*, 1103–1104.
[15] M. Galanski, A. Yasemi, S. Slaby, M. A. Jakupec, V. B. Arion, M. Rausch, A. A. Nazarov, B. K. Keppler, *Eur. J. Med. Chem.* **2004**, *39*, 707–714.
[16] M. Galanski, C. Baumgartner, V. B. Arion, B. K. Keppler, *Eur. J. Inorg. Chem.* **2003**, 2619–2625.
[17] M. Galanski, C. Baumgartner, K. Meelich, V. B. Arion, M. Fremuth, M. A. Jakupec, P. Schluga, C. G. Hartinger, N. Graf von Keyserlingk, B. K. Keppler, *Inorg. Chim. Acta* **2004**, *357*, 3237–3244.
[18] M. Galanski, W. Zimmermann, C. Baumgartner, B. K. Keppler, *Eur. J. Inorg. Chem.* **2001**, 1145–1149.
[19] F. D. Rochon, L. M. Gruia, *Inorg. Chim. Acta* **2000**, *306*, 193–204.
[20] P. Bitha, G. O. Morton, T. S. Dunne, E. F. Delos Santos, Y. Lin, S. R. Boone, R. C. Haltiwanger, C. G. Pierpont, *Inorg. Chem.* **1990**, *29*, 645–652.
[21] Z. Otwinowski, W. Minor in *Methods in Enzymology*, vol. 276 ("Macromolecular Crystallography, Part A) (Eds.: C. W. Carter Jr., R. M. Sweet), Academic Press, New York, **1997**, p. 307–326.
[22] G. W. Sheldrick, *SHELXS-97, Program for Crystal Structure Solution*, University of Göttingen, Germany, **1997**.
[23] G. W. Sheldrick, *SHELXL-97, Program for Crystal Structure Refinement*, University of Göttingen, Germany, **1997**.
[24] C. K. Johnson, Report ORNL-5138, OAK Ridge National Laboratory, OAK Ridge, TN, **1976**.
[25] *International Tables for X-ray Crystallography* (Ed.: A. J. C. Wilson), Kluwer Academic Press, Dordrecht, The Netherlands, **1992**, vol. C, Tables 4.2.6.8 and 6.1.1.4.

Received: March 3, 2006
Published Online: April 18, 2006

 © 2006 Wiley-VCH Verlag GmbH & Co. KGaA, Weinheim 

DOI: 10.1002/ejic.200500954

# $^{195}$Pt NMR Spectra of Head-to-Head and Head-to-Tail Amidato-Bridged Platinum(III) Dinuclear Complexes

Satoshi Iwatsuki,*[a] Eigo Isomura,[b] Atsushi Wada,[b] Koji Ishihara,*[b,c] and Kazuko Matsumoto*[b,d]

**Keywords:** Platinum / $^{195}$Pt NMR / α-Pyridone / α-Pyrrolidone / Pivalamide / NMR spectroscopy

$^{195}$Pt chemical shifts and $^{1}J_{Pt-Pt}$ coupling constants were measured for a series of head-to-head (HH) and head-to-tail (HT) amidato-bridged *cis*-diammineplatinum(III) dinuclear complexes involved in the axial water substitution reactions with halide ions ($X^-$ = $Cl^-$, $Br^-$): HH-$[Pt_2(NH_3)_4(\mu\text{-amidato})_2L^1L^2]^{n+}$ ≡ $[L^1\text{–}Pt(N_2O_2)\text{–}Pt(N_4)\text{–}L^2]^{n+}$ (amidato = α-pyridonato, α-pyrrolidonato, and pivalamidato) and HT-$[Pt_2(NH_3)_4(\mu\text{-}\alpha\text{-pyridonato})_2L^1L^2]^{n+}$ ≡ $[L^1\text{–}Pt(N_3O)\text{–}Pt(N_3O)\text{–}L^2]^{n+}$; the diaqua ($L^1$, $L^2$ = $H_2O$, $n$ = 4), the aquahalo ($L^1$ = $X^-$, $L^2$ = $H_2O$, $n$ = 3), and the dihalo complexes ($L^1$, $L^2$ = $X^-$, $n$ = 2). The $^{195}$Pt NMR spectroscopic data were considered in relation to the lability in the axial ligand substitution reaction and the electron distribution along the Pt–Pt bond. The NMR spectroscopic data suggested different electron distributions along the Pt–Pt bonds in all the HH dimers and in the HT aquahalo dimers, such as $[L^1\text{–}Pt^{IV}(N_2O_2)\text{–}Pt^{II}(N_4)\text{–}L^2]^{n+}$ and $[X\text{–}Pt^{IV}(N_3O)\text{–}Pt^{II}(N_3O)\text{–}OH_2]^{3+}$, respectively. Relative shifts of the $^{195}$Pt NMR signals for each substitution step indicate that the replacement of the axial water ligand by $X^-$ affects more effectively the electron density of the opposite Pt atom than that of the substituted one.

(© Wiley-VCH Verlag GmbH & Co. KGaA, 69451 Weinheim, Germany, 2006)

## Introduction

Head-to-head (HH) and head-to-tail (HT) amidato-bridged platinum(III) dinuclear complexes having a metal–metal bond between the two $d^7$ platinum atoms have two inorganic axial ligands, and the substitution reactions at the axial sites are well known synthetically[1–3] and kinetically.[4–8]

The two platinum atoms in the HH complex are not equivalent, that is, one is coordinated by two amidate oxygen atoms and two ammine nitrogen atoms [$Pt(N_2O_2)$], whereas the other is coordinated by four nitrogen atoms [$Pt(N_4)$]. On the other hand, the HT complex has two equivalent Pt atoms [$Pt(N_3O)$].

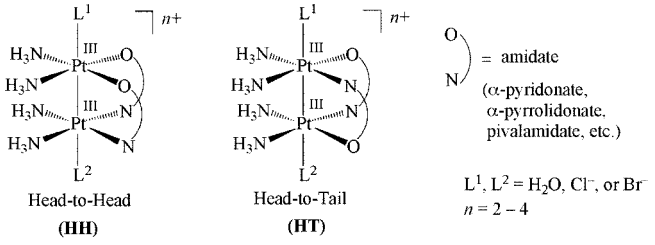


The axial ligand substitution with halide ion ($X^-$ = $Cl^-$, $Br^-$) on both the HH and HT diaqua $Pt^{III}$ complexes occurs consecutively in two steps [Equations (1) and (2)].[4–6]

$$[(H_2O)Pt(NH_3)_2(\mu\text{-amidato})_2Pt(NH_3)_2(OH_2)]^{4+} + X^- \overset{\text{step 1}}{\rightleftharpoons} [(H_2O)Pt(NH_3)_2(\mu\text{-amidato})_2Pt(NH_3)_2(X)]^{3+} + H_2O \quad (1)$$

$$[(H_2O)Pt(NH_3)_2(\mu\text{-amidato})_2Pt(NH_3)_2(X)]^{3+} + X^- \overset{\text{step 2}}{\rightleftharpoons} [(X)Pt(NH_3)_2(\mu\text{-amidato})_2Pt(NH_3)_2(X)]^{2+} + H_2O \quad (2)$$

In step 1 [Equation (1)] for the reaction of the diaqua $Pt^{III}$ dinuclear complexes, deprotonation of the aqua ligands occurs preferentially on the $Pt(N_4)$ atom and substitution occurs on the $Pt(N_2O_2)$ atom in HH diaqua $Pt^{III}$ complexes, whereas deprotonation occurs on one of the two equivalent $Pt(N_3O)$ atoms and substitution occurs on the other $Pt(N_3O)$ atom in HT diaqua $Pt^{III}$ complexes. There are two parallel reaction paths in step 1 for both HH and

[a] Graduate School of Science and Engineering, Waseda University,
Okubo, Shinjuku-ku, Tokyo 169-8555, Japan
E-mail: s-iwatsuki@aoni.waseda.jp
[b] Department of Chemistry, School of Science and Engineering, Waseda University,
Okubo, Shinjuku-ku, Tokyo 169-8555, Japan
Fax: +81-3-3208-2735
E-mail: ishi3719@waseda.jp
kmatsu@waseda.jp
[c] Materials Research Laboratory for Bioscience and Photonics, Graduate School of Science and Engineering, Waseda University,
Okubo, Shinjuku-ku, Tokyo 169-8555, Japan
[d] Advanced Research Institute for Science and Engineering, Waseda University,
Okubo, Shinjuku-ku, Tokyo 169-8555, Japan
Supporting information for this article is available on the WWW under http://www.eurjic.org or from the author.

 InterScience © 2006 Wiley-VCH Verlag GmbH & Co. KGaA, Weinheim 

HT complexes ($k_1$ and $k_1^{\#}$ in Scheme 1), because the diaqua complex exists in equilibrium with the aquahydroxo complex, and both complexes undergo substitution with $X^-$.[4–8] In step 2 [Equation (2)], there are three possible pathways (Scheme 2), and step 2 proceeds by either one or two paths of the three, depending on the axial ligand ($X^-$). One of the three paths is the direct substitution path (**A**), the second path (**B**) is by dissociation of the water molecule on the $Pt(N_4)$ atom or on the $Pt(N_3O)$ atom, and the third (**C**) is the unusual path of $OH^-$ replacement.[4–6] The substitution lability of the second step is influenced strongly by the first halide ligand on the opposite axial site, which is explained as follows: the extent of the charge localization in the Pt–Pt bond in the dinuclear complex {the contribution of $[X–Pt^{IV}(NH_3)_2(\mu\text{-amidato})_2Pt^{II}(NH_3)_2–OH_2]^{3+}$ as compared to $[X–Pt^{III}(NH_3)_2(\mu\text{-amidato})_2Pt^{III}(NH_3)_2–OH_2]^{3+}$} depends largely on the electron-donating ability of the first substituted ligand ($X^-$), which is reflected in the reaction mechanisms examined so far for several amidato-bridged $Pt^{III}$ dinuclear complexes. The different extent of the Pt–Pt bond polarization leads to variations of the substitution lability and coordination stability of the axial aqua ligand, thus affecting the substitution reaction mechanism. When $X^-$ is less electron-donating, paths **A** and **C** or only path **A** take place in the reactions of the HT α-pyridonato-bridged and HH α-pyrrolidonato-bridged complexes, whereas paths **A** and **B** are preferred in these complexes when $X^-$ is more electron-donating, though paths **A** and **B** are preferred irrespective of $X^-$ in the reaction of the HH α-pyridonato-bridged complex.[4–6] In contrast, however, paths **A** and **C** are involved in the reaction of the HH pivalamidato-bridged complex for more electron-donating $X^-$ (Scheme 2 and Table 1).[6]

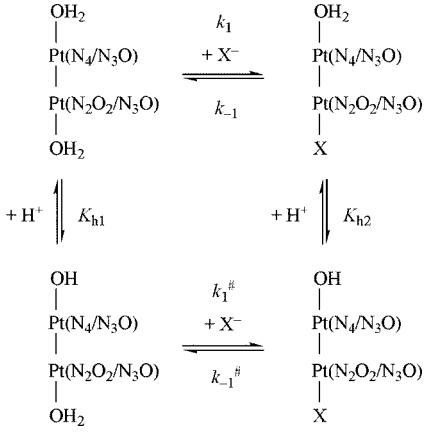


Scheme 1. Reaction paths in step 1 for the reaction of the HH and HT amidato-bridged $Pt^{III}$ dimer with $X^-$ ($X^-$ = $Cl^-$ or $Br^-$).

In this paper we present the systematic [195]Pt NMR spectroscopic data for a series of the HH and HT amidato-bridged *cis*-diammineplatinum(III) dinuclear complexes involved in the axial water substitution reactions with halide ions ($X^-$ = $Cl^-$, $Br^-$): HH-$[Pt_2(NH_3)_4(\mu\text{-amidato})_2L^1L^2]^{n+}$ (amidato = α-pyridonato, α-pyrrolidonato, and pivalamidato) and HT-$[Pt_2(NH_3)_4(\mu\text{-α-pyridonato})_2L^1L^2]^{n+}$; the diaqua ($L^1$, $L^2$ = $H_2O$, $n$ = 4), the aquahalo ($L^1$ = $X^-$, $L^2$ = $H_2O$, $n$ = 3), and the dihalo complexes ($L^1$, $L^2$ = $X^-$, $n$ = 2). The electron localization and consequently the axial ligand substitution must be reflected in the [195]Pt NMR spectroscopic data. The exceptional reactivity observed for the second step (step 2) of the HH pivalamidato-bridged $Pt^{III}$ dinuclear complex (Scheme 2 and Table 1) may be reflected in and related to the chemical shift and the Pt–Pt coupling constant of the [195]Pt NMR spectra.

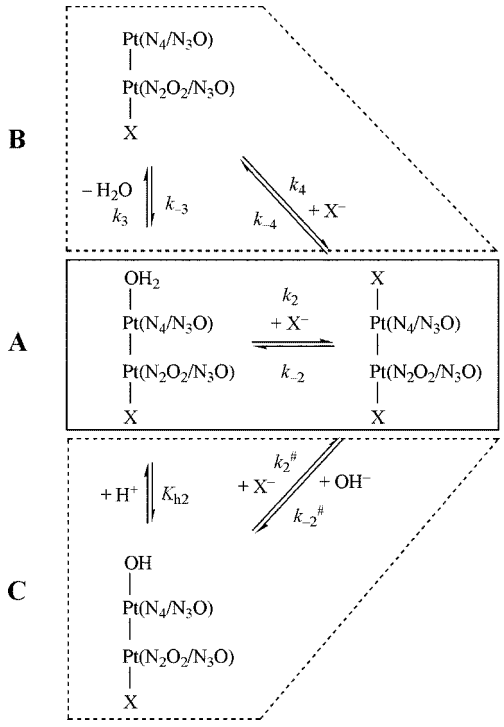


Scheme 2. Three possible reaction paths in step 2 for the reaction of the HH and HT amidato-bridged $Pt^{III}$ dimer with $X^-$ (= $Cl^-$ or $Br^-$).

Table 1. Reaction paths in step 2 (**A**, **B**, and **C** in Scheme 2) for the reactions of HH and HT $Pt^{III}$ dimers with halide ions.[a]

| $Pt^{III}$ dimer | $X^-$ = $Cl^-$ | $X^-$ = $Br^-$ |
|---|---|---|
| α-Pyridonato-bridged HH | **A** and **B** | **A** and **B** |
| α-Pyrrolidonato-bridged HH | **A** | **A** and **B** |
| Pivalamidato-bridged HH | **A** | **A** and **C** |
| α-Pyridonato-bridged HT | **A** and **C** | **A** and **B** |

[a] Refs.[4–6]

## Results and Discussion

### Assignment of [195]Pt NMR Signals

Figure 1 shows the [195]Pt NMR spectra of the HH diaqua complex bridged by α-pyridonate {the HH-$[Pt_2(NH_3)_4(\mu\text{-α-pyridonato})_2(OH_2)_2]^{4+}$ complex}. A set of two signals at higher and lower fields both with a couple of satellite signals due to Pt–Pt coupling was successfully assigned to $Pt(N_4)$ and $Pt(N_2O_2)$, respectively, based on the multiplicity

 © 2006 Wiley-VCH Verlag GmbH & Co. KGaA, Weinheim 

of the lines [9 for $Pt(N_4)$ and 5 for $Pt(N_2O_2)$ because of $^{195}Pt$–$^{14}N$ coupling]. Similar assignable signals were observed for all the other HH α-pyridonato-bridged $Pt^{III}$ dimers, that is, the aquachloro (Figure 2), aquabromo (Figure S1), dichloro (Figure S2), and dibromo complexes (Figure S3). The signal of the $Pt(N_2O_2)$ moiety of all the HH α-pyridonato-bridged $Pt^{III}$ dimers is always observed at a lower field, and the $Pt(N_4)$ signal at a higher field. For the HH α-pyrrolidonato-bridged and the pivalamidato-bridged complex systems, the signal assignments similar to those of α-pyridonato-bridged dimers are applied to the aquahalo and dihalo complexes. The $^{195}Pt$ NMR signals for the α-pyrrolidonato-bridged and the pivalamidato-bridged HH diaqua complexes could not be assigned; the Pt–Pt coupling was observed with no distinguishable Pt–N couplings such as those mentioned above (Figures S12 and S13). Therefore, the assignment for these diaqua dimers was performed according to the result of the HH α-pyridonato-bridged diaqua complex. The $^{195}Pt$ chemical shifts ($\delta_{Pt}$) and Pt–Pt coupling constants ($^1J_{Pt-Pt}$) for the present HH amidato-bridged $Pt^{III}$ dinuclear complexes are summarized in Table 2.

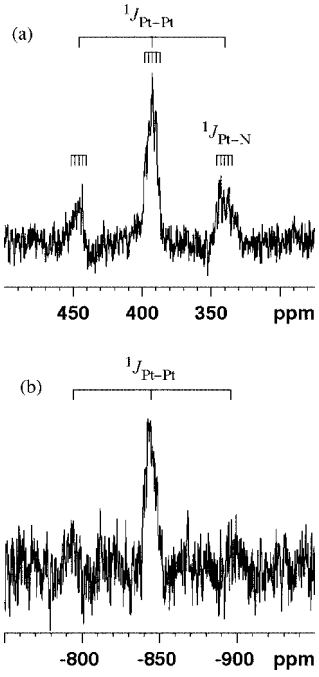


Figure 1. $^{195}Pt$ NMR signals of the $Pt(N_2O_2)$ (a) and the $Pt(N_4)$ (b) moieties in the HH α-pyridonato-bridged diaqua dimer in $DClO_4$ (1.2 M)/$D_2O$.

The HT α-pyridonato-bridged $Pt^{III}$ dimer complexes with the same axial ligands (the diaqua, dichloro, and dibromo dimers) showed a single $^{195}Pt$ NMR signal (Figure S14), as the two platinum atoms are equivalent: $[L^1$–$Pt(N_3O)$–$Pt(N_3O)$–$L^2]^{n+}$ where $L^1 = L^2$. On the other hand, the HT aquahalo complexes afforded two different $^{195}Pt$ signals (Figures S15 and S16) that have similar Pt–Pt (a couple of satellite) and Pt–N couplings [a multiplicity of 7 due to $Pt(N_3O)$ moieties] to those of the HH complexes. Therefore, the assignment of these HT aquahalo dimers was

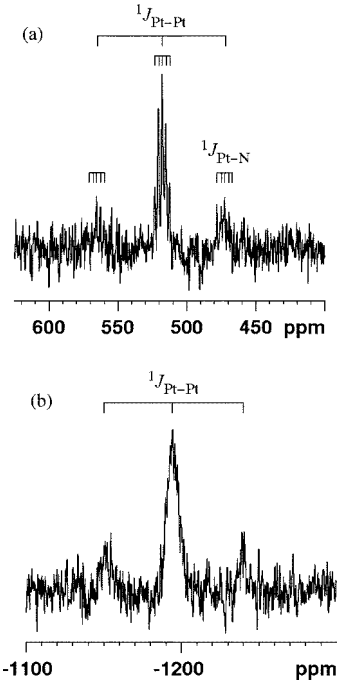


Figure 2. $^{195}Pt$ NMR signals of the $Pt(N_2O_2)$ (a) and the $Pt(N_4)$ (b) moieties in the HH α-pyridonato-bridged aquachloro dimer in $DClO_4$ (1.2 M)/$D_2O$.

done based on the results of the corresponding HH amidato-bridged $Pt^{III}$ aquahalo complexes; a lower-field signal was assigned to $X$–$Pt(N_3O)$, while a higher-field signal was assigned to $Pt(N_3O)$–$OH_2$. In Table 2 the $\delta_{Pt}$ and $^1J_{Pt-Pt}$ values obtained for the HT α-pyridonato-bridged $Pt^{III}$ dimers are also listed.

The $^{195}Pt$ NMR spectra of the HH and HT amidato-bridged $Pt^{III}$ aquahydroxo complexes could not be measured because of the gradual decomposition of the complexes in less acidic aqueous solution for a prolonged measuring time (> ca. 8 h).

In general, the $^{195}Pt$ chemical shifts of $Pt^{IV}$ complexes tend to be at lower fields than those of $Pt^{II}$ complexes (Table S1).[9,10] Therefore, the HH amidato-bridged $Pt^{III}$ dimer seems to be polarized close to $[L^1$–$Pt^{IV}(N_2O_2)$–$Pt^{II}(N_4)$–$L^2]^{n+}$ ($L^1$, $L^2$ = $H_2O$, $Cl^-$, or $Br^-$). Our previous studies on the reaction of the diaqua complex, $[H_2O$–$Pt^{IV}(N_2O_2)$–$Pt^{II}(N_4)$–$OH_2]^{4+}$, with $X^-$ showed that the first substitution always occurs at the $Pt^{IV}(N_2O_2)$ atom and the acid dissociation occurs preferentially at the axial $H_2O$ ligand of the $Pt^{II}(N_4)$ atom.[5,6] It is known that $Pt^{II}$ complexes are usually inert for substitution, and $Pt^{IV}$ complexes are even more inert.[11] In the HH amidato-bridged $Pt^{III}$ dimer, however, the axial site of the $Pt(N_2O_2)$ atom having $Pt^{IV}$ character is more substitution-active than that of the $Pt(N_4)$ atom having $Pt^{II}$ character, which suggests that both the $Pt(N_2O_2)$ and the $Pt(N_4)$ atoms still have a $Pt^{III}$ character to a substantial extent in the polarized $Pt^{III}$ complexes. In all these complexes, deprotonation occurs preferentially at the $H_2O$–$Pt^{II}(N_4)$ moiety having a shorter Pt–$OH_2$ bond, whereas the first substitution occurs at the $Pt^{IV}(N_2O_2)$ atom having a longer Pt–$OH_2$ bond.

 © 2006 Wiley-VCH Verlag GmbH & Co. KGaA, Weinheim 

Table 2. $^{195}$Pt NMR chemical shifts of the head-to-head (HH) and head-to-tail (HT) amidato-bridged $Pt^{III}$ dinuclear complexes and the lantern-type complexes.[a]

| Type | Bridging ligand | $L^1$–Pt–Pt–$L^2$ | $\delta_{Pt}$ [ppm] (assignment) | | $\Delta\delta$ ($\delta_{center}$) [ppm] | $^1J_{Pt-Pt}$ [Hz] | Path in step 2 |
|---|---|---|---|---|---|---|---|
| HH | α-pyridonate | $H_2O/H_2O$ | 393 [$Pt(N_2O_2)$] | –844 [$Pt(N_4)$] | 1237 (–226) | 8886 | |
| | | $Cl^-/Cl^-$ | 129 [$Pt(N_2O_2)$] | –948 [$Pt(N_4)$] | 1077 (–410) | 6636 | |
| | | $Br^-/Br^-$ | –32 [$Pt(N_2O_2)$] | –988 [$Pt(N_4)$] | 956 (–510) | 6306 | |
| | | $Cl^-/H_2O$ | 518 [$Pt(N_2O_2)$] | –1194 [$Pt(N_4)$] | 1712 (–338) | 7774 | **A + B** |
| | | $Br^-/H_2O$ | 643 [$Pt(N_2O_2)$] | –1391 [$Pt(N_4)$] | 2034 (–374) | 7574 | **A + B** |
| | α-pyrrolidonate | $H_2O/H_2O$ | 266[b] | –889[b] | 1155 (–312) | 9482 | |
| | | $Cl^-/Cl^-$ | 3 [$Pt(N_2O_2)$] | –1081 [$Pt(N_4)$] | 1084 (–539) | 7132 | |
| | | $Br^-/Br^-$ | –140 [$Pt(N_2O_2)$] | –1195 [$Pt(N_4)$] | 1055 (–668) | 6682 | |
| | | $Cl^-/H_2O$ | 328 [$Pt(N_2O_2)$] | –1288 [$Pt(N_4)$] | 1616 (–480) | 8096 | **A** |
| | | $Br^-/H_2O$ | 439 [$Pt(N_2O_2)$] | –1545 [$Pt(N_4)$] | 1984 (–553) | 7940 | **A + B** |
| | pivalamidate | $H_2O/H_2O$ | 222[b] | –989[b] | 1212 (–384) | 9262 | |
| | | $Cl^-/Cl^-$ | 8 [$Pt(N_2O_2)$] | –1190 [$Pt(N_4)$] | 1198 (–591) | 7216 | |
| | | $Br^-/Br^-$ | –108 [$Pt(N_2O_2)$] | –1327 [$Pt(N_4)$] | 1219 (–718) | 6902 | |
| | | $Cl^-/H_2O$ | 284 [$Pt(N_2O_2)$] | –1383 [$Pt(N_4)$] | 1667 (–550) | 8234 | **A** |
| | | $Br^-/H_2O$ | 394 [$Pt(N_2O_2)$] | –1672 [$Pt(N_4)$] | 2066 (–639) | 8086 | **A + C** |
| HT | α-pyridonate | $H_2O/H_2O$ | –265 | | 0 (–265) | | |
| | | $Cl^-/Cl^-$ | –433 | | 0 (–433) | | |
| | | $Br^-/Br^-$ | –529 | | 0 (–529) | | |
| | | $Cl^-/H_2O$ | –102 (Pt–Cl)[c] | –652 (Pt–$OH_2$)[c] | 550 (–377) | 7564 | **A + C** |
| | | $Br^-/H_2O$ | 20 (Pt–Br)[c] | –900 (Pt–$OH_2$)[c] | 920 (–440) | 7260 | **A + B** |
| Lantern[d] | hydrogenphosphate | $H_2O/H_2O$ | 1796 | | 0 (1796) | | |
| | | $Cl^-/Cl^-$ | 1822 | | 0 (1822) | | |
| | | $Br^-/Br^-$ | 1744 | | 0 (1744) | | |
| | | $Cl^-/H_2O$ | 1713 (Pt–Cl) | 1886 (Pt–$OH_2$) | 173 (1800) | 5342 | |
| | | $Br^-/H_2O$ | 1550 (Pt–Br) | 1973 (Pt–$OH_2$) | 423 (1761) | 5349 | |
| | sulfate | $H_2O/H_2O$ | 1756 | | 0 (1756) | | |
| | | $Cl^-/Cl^-$ | 1720 | | 0 (1720) | | |
| | | $Br^-/Br^-$ | 1592 | | 0 (1592) | | |
| | | $Cl^-/H_2O$ | 1638 (Pt–Cl) | 1809 (Pt–$OH_2$) | 170 (1724) | 3464 | |
| | | $Br^-/H_2O$ | 1440 (Pt–Br) | 1866 (Pt–$OH_2$) | 427 (1653) | 3472 | |

[a] Relative to aqueous $H_2PtCl_6$ ($\delta$ = 0 ppm) or $K_2PtCl_4$ ($\delta$ = –1622 ppm) as external references. [b] The signals could not be assigned experimentally. [c] The assignments are performed based on the trends of the chemical shift change in the HH complex systems. [d] Refs.[15,16]

### $^{195}$Pt Chemical Shifts and $^1J_{Pt-Pt}$ Coupling Constants

Variations of the $^{195}$Pt chemical shift for the diaqua, dichloro, and dibromo complexes of HH-[$L^1$–$Pt(N_2O_2)$–$Pt(N_4)$–$L^2$]$^{n+}$ and HT-[$L^1$–$Pt(N_3O)$–$Pt(N_3O)$–$L^2$]$^{n+}$ ($L^1$ = $L^2$) are shown in Figure 3. For the HH diaqua and dihalo complexes, both of the $Pt(N_2O_2)$ and the $Pt(N_4)$ signals shift to higher field, when both of the axial aqua ligands are changed to $Cl^-$ and $Br^-$, though the $\Delta\delta$ (= $\delta_{Pt(N_2O_2)}$ – $\delta_{Pt(N_4)}$) values are almost constant (Table 2). A similar tendency is observed for the chemical shift of the $Pt(N_3O)$ signal in the HT complex. On the other hand, when only the aqua ligand on the $Pt(N_2O_2)$ atom in the HH diaqua dimer is changed to $Cl^-$ and $Br^-$, the $Pt(N_2O_2)$ signals shift to much lower fields and the $Pt(N_4)$ signals shift to much higher fields, compared to those of the diaqua, dichloro (Figure 4a), and dibromo complexes (Figure 4b). The X–$Pt(N_3O)$ and $H_2O$–$Pt(N_3O)$ signals of the HT dimer shift similarly (Figure 4). These indicate that the Pt–Pt bonds in the monosubstituted (aquahalo) complexes are more polarized as X–$Pt^{IV}(N_2O_2/N_3O)$–$Pt^{II}(N_4/N_3O)$–$OH_2$, compared to those of the $Pt^{III}$ dimer complexes having the same axial ligands (the diaqua and dihalo complexes).

Variation of the Pt–Pt coupling constants with the axial ligands is depicted in Figure 5. The coupling constants in each HH dimer system tend to decrease in the order: $H_2O$–$Pt(N_2O_2)$–$Pt(N_4)$–$OH_2$ > Cl–$Pt(N_2O_2)$–$Pt(N_4)$–$OH_2$ > Br–$Pt(N_2O_2)$–$Pt(N_4)$–$OH_2$ > Cl–$Pt(N_2O_2)$–$Pt(N_4)$–Cl > Br–$Pt(N_2O_2)$–$Pt(N_4)$–Br. In all of the HH aquahalo and dihalo complexes, the coupling constants decrease in the order: pivalamidato-bridged dimer > α-pyrrolidonato-bridged di-

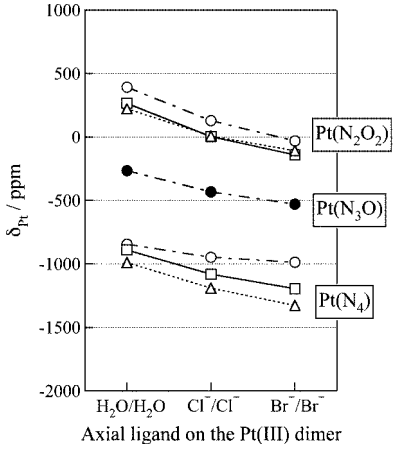


Figure 3. Dependence of $\delta_{Pt}$ on the axial ligands in the diaqua, dichloro, and dibromo complexes of the HH α-pyridonato-bridged (○), α-pyrrolidonato-bridged (□), and pivalamidato-bridged (Δ) dimers [$Pt(N_2O_2)$ and $Pt(N_4)$] and the HT α-pyridonato-bridged (●) dimer [$Pt(N_3O)$].

 © 2006 Wiley-VCH Verlag GmbH & Co. KGaA, Weinheim 

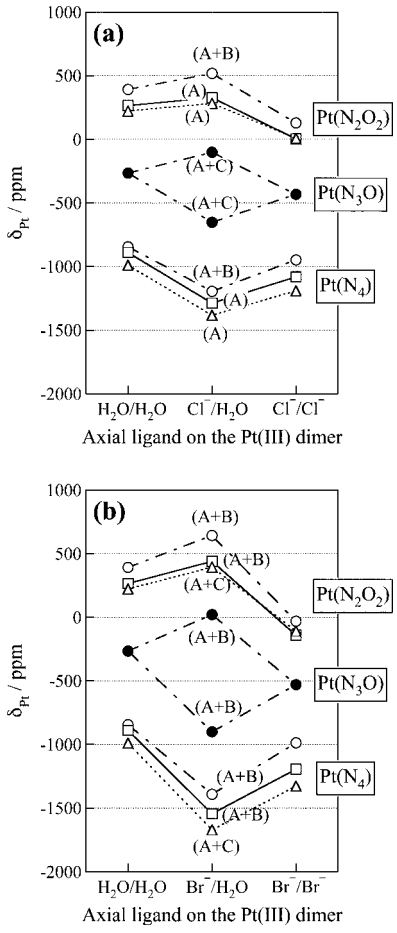


Figure 4. Dependence of $\delta_{Pt}$ on the axial ligands in the diaqua, aquahalo, and dihalo complexes for the reaction systems with $Cl^-$ (a) and $Br^-$ (b); HH α-pyridonato-bridged (○), α-pyrrolidonato-bridged (□), and pivalamidato-bridged (Δ) dimers [$Pt(N_2O_2)$ and $Pt(N_4)$] and HT α-pyridonato-bridged (●) dimer [$Pt(N_3O)$].

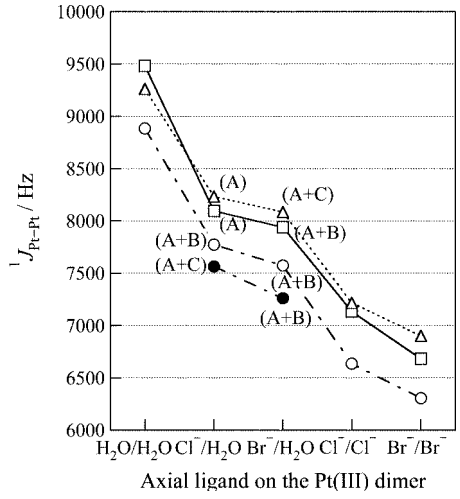


Figure 5. Dependence of $^1J_{Pt-Pt}$ on the axial ligands in the HH α-pyridonato-bridged (○), α-pyrrolidonato-bridged (□), and pivalamidato-bridged (Δ) dimers and the HT α-pyridonato-bridged (●) dimer.

mer > α-pyridonato-bridged dimer, but for the HH diaqua complexes the order is different, that is, the coupling constant of the pivalamidato-bridged dimer is smaller than that of the α-pyrrolidanato-bridged dimer.

### $^{195}$Pt NMR Spectroscopic Data and Ligand Substitution Mechanism

Both of the $^{195}$Pt NMR chemical shifts and the Pt–Pt coupling constants should be taken into account to understand the electronic structure of the Pt–Pt bonds and the mechanism of the axial substitution reactions. The deprotonation and the substitution lability of the diaqua dimers mentioned earlier in this paper suggest that the $L^2$–$Pt(N_4)$ bond having a higher-field chemical shift would be stronger and less labile than the $L^1$–$Pt(N_2O_2)$ bond having a lower-field shift in each complex, that is, the diaqua, aquahalo, and dihalo complexes. In other words, the Pt atom having the stronger axial Pt–L bond would give the higher-field chemical shift in the present HH amidato-bridged dimer complexes. Thus, both of the $L^1$–$Pt(N_2O_2)$ and the $L^2$–$Pt(N_4)$ bonds become stronger in the order: diaqua dimer < dichloro dimer < dibromo dimer. On the other hand, the Pt–Pt bond becomes weaker in the same order, based on the Pt–Pt coupling constants in Figure 5.

In the aquachloro complexes $\{[Cl–Pt(N_2O_2)–Pt(N_4)–OH_2]^{3+}\}$, all of the axial bonds, $Cl–Pt(N_2O_2)$, Pt–Pt, and $Pt(N_4)–OH_2$ bonds, would be strengthened in the order: α-pyridonato-bridged dimer < α-pyrrolidonato-bridged dimer < pivalamidato-bridged dimer, as the resonance fields (opposite order in the chemical shifts) and the coupling constants increase in the same order (Figure 4a and Figure 5). The same is true for a series of aquabromo dimers (Figure 4b and Figure 5). These orders of the axial bond strengths in the aquahalo dimers explain the variation of the axial water substitution mechanism in step 2 (Scheme 2) among the HH dimer systems. (1) For the HH dimer + $Cl^-$ systems, the reaction of the HH α-pyridonato-bridged aquachloro dimer proceeds through paths **A** and **B**, while the reactions of the α-pyrrolidonato-bridged and the pivalamidato-bridged aquachloro dimers proceed only by path **A**, because the $H_2O–Pt(N_4)$ bond in the former dimer is relatively weak compared to that of the latter. (2) For the HH dimer + $Br^-$ systems, both of the α-pyridonato-bridged and α-pyrrolidonato-bridged aquabromo dimers prefer paths **A** and **B**, because of the weaker $H_2O–Pt(N_4)$ bonds. In contrast, however, the pivalamidato-bridged dimer reacts with $Br^-$ by paths **A** and **C** in step 2. The exceptional behavior would be because deprotonation of the $H_2O$ ligand at the $Pt(N_4)$ atom is easier owing to the stronger $H_2O–Pt(N_4)$ bond. This is strongly supported by the highest field in the chemical shifts and the coupling constant of the pivalamidato-bridged aquabromo dimer among the present HH dimer + $Br^-$ systems (Figures 4b and 5).

The p$K_a$ values of the diaqua complexes are reported to be 1.71, 1.74, and 2.88 for the α-pyridonato-bridged dimer, the α-pyrrolidonato-bridged dimer, and the pivalamidato-

 © 2006 Wiley-VCH Verlag GmbH & Co. KGaA, Weinheim 

bridged dimer, respectively,[6,12] which is the opposite of the result expected from the chemical shift data of these diaqua complexes. The $^{1}J_{Pt–Pt}$ values of the diaqua dimers, which would involve the effects of all of the axial bonds as well as of the equatorial (bridging) ligands, decrease in the order: α-pyrrolidonato-bridged dimer > pivalamidato-bridged dimer > α-pyridonato-bridged dimer (Figure 4). These differences would be explained by: the chemical shifts and the coupling constants reflect the electronic distributions around the Pt atoms in the $H_2O$–$Pt(N_2O_2)$–$Pt(N_4)$–$OH_2$ moiety, while p$K_a$ reflects the Pt–$OH_2$ bond strength. It seems that the effects of both the bridging ligands and the axial ligands are important in determining the substitution reaction path.

The exceptional reactivity of the HH pivalamidato-bridged $Pt^{III}$ dinuclear complex (Scheme 2 and Table 1), as mentioned above, could not be explicitly reflected in the chemical shift and coupling constant of the $^{195}$Pt NMR spectroscopy. This may suggest that not only electronic effects that are reflected in the NMR spectroscopic data but also (dynamic) steric effects due to bridging ligands, complementary ligands, solvent, etc. contribute significantly and complicatedly to the determination of the ligand substitution mechanism for the present systems. That is, the $^{195}$Pt NMR spectroscopic data would be reproduced by detailed DFT calculations including solvent effect, relativistic effect, etc.,[13] but the calculations do not serve the ligand substitution mechanism.

### Comparison Between the Amidato-Bridged $Pt^{III}$ Dinuclear Complexes and the Lantern-Type $Pt^{III}$ Dinuclear Complexes

In Table 2, the $^{195}$Pt chemical shifts of the lantern-type complexes are at much lower field than those of the amidato-bridged complexes, and the $\Delta\delta$ values of the aquahalo lantern-type complexes are much smaller than those of the amidato-bridged aquahalo dimers, that is, much less electron localization occurs in the lantern-type complexes, suggesting that the reactivities of the two-type complexes are different. Indeed, the axial ligand substitution occurs in two steps in the present amidato-bridged complexes, whereas it is one step in the hydrogenphosphato-bridged lantern-type complex.[14] In the amidato-bridged diaqua complexes, the two Pt centers behave differently and independently, because the electron distribution along the Pt–Pt bond of the intermediate (the aquahalo complex) after step 1 of the amidato-bridged complexes is very different from that of the original diaqua complex. This fact and the $^{195}$Pt NMR spectroscopic data again support the higher flexibility of the Pt–Pt bond in the amidato-bridged complexes compared to those of the lantern-type complexes, as mentioned in the previous report.[14] In Table 2, two opposite assignments of $^{195}$Pt NMR for the same complex, $[(L)Pt(\mu\text{-}HPO_4)_4Pt(OH_2)]^{n-}$ (L = $Cl^-$, $Br^-$, $SCN^-$, $NO_2^-$, $CN^-$, $NH_3$, etc.) are reported by Appleton et al.: (a) a higher field is assigned to Pt–L and a lower field to Pt–$OH_2$ for L = $Cl^-$, $Br^-$, and $SCN^-$, and (b) a lower field is assigned to Pt–L and a higher field to Pt–$OH_2$ for L = $NO_2^-$, $CN^-$, and $NH_3$.[15,16] All of the assignments of the aquahalo amidato-bridged complexes, which are based on the Pt–N coupling pattern of HH α-pyridonato-bridged complexes, are consistent with assignment (b). Table 2 and Figure 4 show that axial ligand substitution has much more influence on the opposite Pt atom [$Pt(N_4)$] than the Pt atom directly coordinated with $X^-$ [$Pt(N_2O_2)$].

## Conclusions

$^{195}$Pt NMR spectroscopic data (the chemical shifts and Pt–Pt coupling constants) were systematically obtained for a series of HH and HT bis(amidato-bridged) platinum(III) dinuclear complexes existing in the axial water ligand substitution reactions with $Cl^-$ and $Br^-$. Polarization of the Pt–Pt bond is observed in the $^{195}$Pt NMR spectra for the HH amidato-bridged diaqua $Pt^{III}$ dinuclear complex similarly to the HH aquahalo $Pt^{III}$ complexes, that is, the Pt–Pt bond is polarized approximately to $[H_2O–Pt^{IV}(N_2O_2)–Pt^{II}(N_4)–OH_2]^{4+}$. The first substitution of $H_2O$ on the $Pt^{IV}(N_2O_2)$ atom with $X^-$ enhances the electron localization to form the more polarized aquahalo complex having very different axial Pt–$OH_2$ bond lengths from that of the original diaqua complex. More pronounced electron localization was observed for the HT complex. The second substitution of the $H_2O$ ligand on the $Pt^{II}(N_4)$ atom in $[X–Pt^{IV}(N_2O_2)–Pt^{II}(N_4)–OH_2]^{3+}$ with $X^-$ reduces the electron polarization to an extent similar to the diaqua complex.

## Experimental Section

**Materials:** *cis*-$[Pt(NH_3)_2Cl_2]$ was prepared from $K_2[PtCl_4]$ (Tanaka Kikinzoku Kogyo K. K., Tokyo) according to Dhara's method.[17] α-Pyridone (97+%, Wako Pure Chemical Industries Ltd., Osaka) was recrystallized twice from water. Reagent grade α-pyrrolidone (Kanto Chemical Co. Inc., Tokyo) was purified once by vacuum distillation. Pivalamide (98%, Kanto) was recrystallized twice from water. HT-$[(NO_3)Pt(NH_3)_2(\mu\text{-}C_5H_4NO)_2Pt(NH_3)_2(NO_3)](NO_3)_2\cdot 0.5H_2O$ (HT α-pyridonato-bridged dimer), HH-$[(H_2O)Pt(NH_3)_2(\mu\text{-}C_5H_4NO)_2Pt(NH_3)_2(NO_3)](NO_3)_3\cdot 2H_2O$ (HH α-pyridonato-bridged dimer), HH-$[(H_2O)Pt(NH_3)_2(\mu\text{-}C_4H_6NO)_2Pt(NH_3)_2(H_2O)](NO_3)_4\cdot 2H_2O$ (HH α-pyrrolidonato-bridged dimer), and HH-$[(H_2O)Pt(NH_3)_2(\mu\text{-}C_5H_{10}NO)_2Pt(NH_3)_2(H_2O)](NO_3)_4\cdot 2H_2O$ (HH pivalamidato-bridged dimer) were prepared according to the literature.[18–21] Sodium chloride (99.99%, Aldrich) and sodium bromide (99.99%, Aldrich) were used without further purification. The NMR sample solution was prepared by using $D_2O$ (99.9 atom-%, Isotec) and [D]perchloric acid (68 wt.-% in $D_2O$, Aldrich).

**Measurements:** The $^{195}$Pt NMR spectra were recorded with a Bruker Avance 400 spectrometer operating at 85.9 MHz at ambient temperature (20 ± 2 °C). The chemical shift was referenced to $H_2PtCl_6$ ($\delta$ = 0 ppm) or $K_2PtCl_4$ ($\delta$ = –1622 ppm) as external standards. The sample solution was prepared by using an acidic $D_2O$ solution ($DClO_4/D_2O$) to suppress deprotonation of the diaqua complexes; acid dissociation constants: $-\log K_{h1}$ = 1.98 (HT α-pyridonato-bridged dimer),[4] 1.71 (HH α-pyridonato-bridged dimer),[5]

 © 2006 Wiley-VCH Verlag GmbH & Co. KGaA, Weinheim 

1.74 (HH α-pyrrolidonato-bridged dimer),[6,12] and 2.88 (HH pivalamidato-bridged dimer).[6] The concentration of the platinum(III) dimer ($C_{Pt}$) was adjusted to appropriately 5–40 mM according to the solubility of each compound in $D_2O$. The concentration of halide ion ($C_X$) in the monohalo and dihalo complex solutions was adjusted considering each equilibrium constant ($K_1^X$, $K_2^X$); $\log K_1^{Cl}$ = 5.27 and $\log K_2^{Cl}$ = 3.83 (HT α-pyridonato-bridged dimer + $Cl^-$),[4] $\log K_1^{Br}$ = 5.53 and $\log K_2^{Br}$ = 4.44 (HT α-pyridonato-bridged dimer + $Br^-$),[4] $\log K_1^{Cl}$ = 5.93 and $\log K_2^{Cl}$ = 3.71 (HH α-pyridonato-bridged dimer + $Cl^-$),[5] $\log K_1^{Br}$ = 6.20 and $\log K_2^{Br}$ = 4.55 (HH α-pyridonato-bridged dimer + $Br^-$),[5] $\log K_1^{Cl}$ = 5.61 and $\log K_2^{Cl}$ = 3.73 (HH α-pyrrolidonato-bridged dimer + $Cl^-$),[6] $\log K_1^{Br}$ = 5.50 and $\log K_2^{Br}$ = 4.68 (HH α-pyrrolidonato-bridged dimer + $Br^-$),[6] $\log K_1^{Cl}$ = 5.04 and $\log K_2^{Cl}$ = 3.21 (HH pivalamidato-bridged dimer + $Cl^-$),[6] and $\log K_1^{Br}$ = 5.93 and $\log K_2^{Br}$ = 3.91 (HH pivalamidato-bridged dimer + $Br^-$).[6]

**Supporting Information** (see footnote on the first page of this article): $Pt^{195}$ NMR chemical shifts of $Pt^{IV}$ and $Pt^{II}$ complexes (Table S1) and $^{195}Pt$ NMR spectra of all the other HH and HT $Pt^{III}$ dimers measured in this study except for the spectra shown in Figures 1 and 2 (Figures S1–S16).

## Acknowledgments

We wish to express our thanks for financial supports from the 21COE "Practical Nano-Chemistry" project from MEXT, Japan and from the Waseda University Grant for Special Research Projects (2004A-131).

[1] K. Matsumoto, M. Ochiai, *Coord. Chem. Rev.* **2002**, *231*, 229–238, and references therein.
[2] K. Matsumoto, K. Sakai, *Adv. Inorg. Chem.* **2000**, *49*, 375–427, and references therein.
[3] B. Lippert, *Coord. Chem. Rev.* **1999**, *182*, 263–295, and references therein.
[4] N. Saeki, Y. Hirano, Y. Sasamoto, I. Sato, T. Toshida, S. Ito, N. Nakamura, K. Ishihara, K. Matsumoto, *Eur. J. Inorg. Chem.* **2001**, 2081–2088.
[5] N. Saeki, Y. Hirano, Y. Sasamoto, I. Sato, T. Toshida, S. Ito, N. Nakamura, K. Ishihara, K. Matsumoto, *Bull. Chem. Soc. Jpn.* **2001**, *74*, 861–868.
[6] K. Shimazaki, H. Sekiya, H. Inoue, N. Saeki, N. Nakamura, K. Ishihara, K. Matsumoto, *Eur. J. Inorg. Chem.* **2003**, 1785–1793.
[7] N. Saeki, N. Nakamura, T. Ishibashi, M. Arime, H. Sekiya, K. Ishihara, K. Matsumoto, *J. Am. Chem. Soc.* **2003**, *125*, 3605–3616.
[8] M. Arime, K. Ishihara, K. Matsumoto, *Inorg. Chem.* **2004**, *43*, 309–316.
[9] R. J. Goodfellow in *Multinuclear NMR* (Ed.: J. Mason), Plenum Press, New York, **1987**.
[10] *Studies in Inorganic Chemistry*, vol. 13 ("Transition Metal Nuclear Magnetic Resonance") (Ed.: P. S. Pregosin), Elsevier, Amsterdam, **1991**.
[11] F. A. Cotton, R. G. Wilkinson, *Advanced Inorganic Chemistry*, 5th ed., John Wiley & Sons, New York, **1988**.
[12] The acid dissociation constant for the HH α-pyrrolidonato-bridged dimer was redetermined at $I$ = 2.0 M and 25 °C by spectrophotometry.
[13] K. Matsumoto, S. Arai, M. Ochiai, W. Chen, A. Nakata, H. Nakai, S. Kinoshita, *Inorg. Chem.* **2005**, *44*, 8552–8560.
[14] S. Iwatsuki, C. Mizushima, N. Morimoto, S. Muranaka, K. Ishihara, K. Matsumoto, *Inorg. Chem.* **2005**, *44*, 8097–8104.
[15] T. G. Appleton, J. R. Hall, D. W. Neale, *Inorg. Chim. Acta* **1985**, *104*, 19–31.
[16] T. G. Appleton, J. R. Hall, D. W. Neale, S. F. Ralph, *Inorg. Chim. Acta* **1983**, *77*, L149–L151.
[17] S. C. Dhara, *Indian J. Chem.* **1970**, *8*, 193–194.
[18] K. Matsumoto, Y. Nakai, J. Matsunami, K. Mizuno, T. Abe, R. Somazawa, J. Kinoshita, H. Shimura, *J. Am. Chem. Soc.* **1998**, *120*, 2900–2907.
[19] L. S. Hollis, S. J. Lippard, *Inorg. Chem.* **1983**, *22*, 2605–2614.
[20] K. Sakai, K. Matsumoto, *J. Am. Chem. Soc.* **1989**, *111*, 3074–3075.
[21] K. Sakai, K. Matsumoto, *J. Mol. Catal.* **1991**, *67*, 7–18.

Received: October 28, 2005
Published Online: April 18, 2006

 © 2006 Wiley-VCH Verlag GmbH & Co. KGaA, Weinheim 

DOI: 10.1002/ejic.200500978

# A Series of One- to Three-Dimensional Copper Coordination Polymers Based on N-Heterocyclic Ligands

Xiang He,[a] Can-Zhong Lu*[a] Chuan-De Wu,[a] and Li-Juan Chen[a]

**Keywords:** Coordination polymers / Copper / Luminescence / Nitrogen heterocycles / Organic–inorganic hybrid composites

A family of copper coordination polymers containing different N-heterocyclic ligands, namely $[Cu(CN)(dmpyz)]_n$ (**1**), $[Cu_2(CN)_2(imz)]_n$ (**2**), $[Cu_3(CN)(trz)_2]_n$ (**3**), $[Cu_6(CN)_6(dmtrz)_3]_n$ (**4**), $[Cu_2(CN)(5\text{-metta})]_n$ (**5**), $[Cu_2(CN)(5\text{-phtta})]_n$ (**6**), and $\{[Cu_6(CN)_6(dmtrz)]_2[Cu_2(CN)_2(dmtrz)_2]\}_n$ (**7**) has been prepared and structurally characterized by X-ray crystallography. The crystal structures of **1** and **2** are 1D chain frameworks. Compound **3** is a twofold interpenetrating 2D supramolecular framework in which the cyanide groups act as bridging ligands to link the copper centers into an unusual bilayer motif with large channels. Compounds **4**–**6** all possess 3D networks. Compound **4** is constructed by two parts: 2D rectangular-grid layers and $\{Cu_2(CN)_2(dmtrz)_2\}$ building blocks. Compound **5** is built up by X-shaped chains that connect each other in an ABAB arrangement to generate the 3D network. The structure of **6** is a 3D network including one-dimensional square-grid channels, with a shortest Cu2···Cu2A (A: $-x + 1, -y + 1, -z$) distance of about 2.347(1) Å. Compound **7** features a peculiar 3D + 1D network in which 1D guest metal-organic polymer chains are filled in an unusual 3D architecture constructed by double helical host tubes. Compounds **1**–**7** show a systematic variation in dimensionality from 1D to 3D to 3D + 1D. The luminescence properties of these compounds have been also studied.
(© Wiley-VCH Verlag GmbH & Co. KGaA, 69451 Weinheim, Germany, 2006)

## Introduction

Considerable attention has been paid to the study of metal coordination polymers not only because these polymers may possess intriguing architectures but also because of their potential applications in the fields of catalysis, molecular-based magnets, electrical conductivity, and zeolite-like materials.[1–3] Among these metal coordination polymers, copper cyanide systems have received special interest due to their fascinating structural frameworks, physical and chemical properties, and potential applications in many fields.[4–7] When studied from a coordination chemistry viewpoint, the structural variety of copper cyanide coordination polymers might be the result of two main factors. Firstly, the cyanide group is a versatile ligand that can act as a monodentate ligand as well as a $\mu_2$-, $\mu_3$-, or $\mu_4$-bridging ligand to generate interesting compounds that may exhibit intriguing topological architectures.[8,9] Secondly, the copper atom has versatile coordination properties and normally adopts three-, four-, five-, or six-coordination to form diverse geometries; the ligand geometry also plays an important role in controlling the structural dimensionalities and stereochemistry of the copper center.[10] On the other hand, from a synthetic chemistry viewpoint, cyanide-containing systems may be prepared either by assembling cyanometalates and metal complexes or by multicomponent self-assembly of cyanide, metal ions, and multidentate ligands. Although the majority of synthetic processes in these systems still follow the conventional solution route, attention has recently turned to solvothermal techniques.[11] To understand the construction of supramolecular architectures further, it is important to continue the investigations on the effect of organic ligands when fabricating multidimensional polymers. We are currently interested in using CuCN, $K_3Fe(CN)_6$, and a series of five-membered N-heterocyclic ring ligands (Scheme 1) as precursors to obtain some homometallic cyanide-bridged coordination polymeric compounds under hydrothermal conditions. In this article we report seven copper polymeric compounds, namely $[Cu(CN)(dmpyz)]_n$ (**1**), $[Cu_2(CN)_2(imz)]_n$ (**2**), $[Cu_3(CN)(trz)_2]_n$ (**3**), $[Cu_6(CN)_6(dmtrz)_3]_n$ (**4**) $[Cu_2(CN)(5\text{-metta})]_n$ (**5**), $[Cu_2(CN)(5\text{-phtta})]_n$ (**6**), and $\{[Cu_6(CN)_6(dmtrz)]_2[Cu_2(CN)_2(dmtrz)_2]\}_n$ (**7**), which exhibit variation dimensionalities.

[a] State Key Laboratory of Structural Chemistry, Fujian Institute of Research on the Structure of Matter, the Chinese Academy of Sciences,
Fuzhou, Fujian 350002, China
Fax: +86-591-8371-4946
E-mail: czlu@ms.fjirsm.ac.cn
Supporting information for this article is available on the WWW under http://www.eurjic.org or from the author.

 © 2006 Wiley-VCH Verlag GmbH & Co. KGaA, Weinheim 

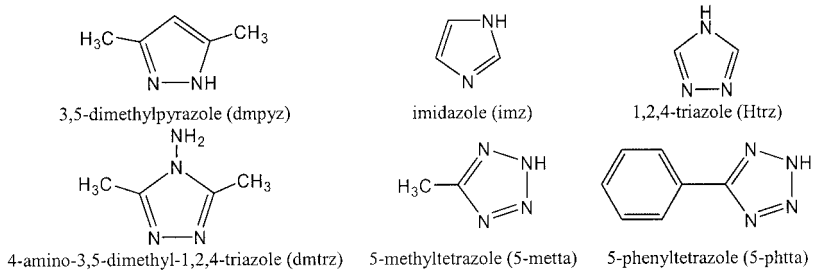


Scheme 1.

## Results and Discussion

### Synthetic Considerations

In order to study the overall factors affecting the structural frameworks of the cyanide-bridged systems, we varied the reaction conditions (including reagent, temperature, and metal/ligand ratio). Firstly, we used $K_3Fe(CN)_6$ as a precursor instead of KCN to provide $CN^-$, based on the following consideration: (1) free cyanide might be released from the dissociation of ferricyanide anions under hydrothermal conditions; (2) the slow release of $CN^-$ might play an important role in the formation of various compounds; (3) cyanide-bridged iron(II)–copper(I) dimetallic compounds might be obtained under appropriate conditions.[12] Secondly, different kinds of N-heterocyclic ligands have an important impact on the final structures of the compounds obtained. Thirdly, the role of temperature in determining the structures of the products can be observed. Under hydrothermal conditions, we used $K_3Fe(CN)_6$ as a precursor to successfully obtain these new cyanide-bridged copper coordination polymers. Compound **7** is obtained at 180 °C, while at a lower temperature of 140 °C, violet, plate-like crystalline $K[Cu(CN)_3]_n{\cdot}H_2O$[13,14] is obtained instead of compound **7**. Interestingly, varying the composition of the reaction mixture gives **4** instead of **7**. During the synthesis of compound **3**, when $CuCl_2$ is used instead of CuCN under otherwise identical reaction conditions compound **3** is again obtained. The design and synthesis of novel coordination architectures controlled by varying the reaction conditions (including temperature,[15] metal/ligand ratio,[16] and counteranions[17]) are of great interest in coordination chemistry.

### Crystal Structures

#### *[Cu(CN)(dmpyz)]$_n$ (1)*

As shown in Figure 1, the structure exhibits a backbone constructed by a zigzag {Cu(CN)} chain. Each $Cu^I$ ion is in a trigonal-planar geometry, defined by one nitrogen atom from the 3,5-dimethylpyrazole ligand [Cu(1)–N(1) = 1.988(7) Å] and two cyanide groups [Cu(1)–X(6) = 1.870(11), Cu(1)–X(7) = 1.986(8) Å; X(6)–Cu(1)–X(7A) = 125.0(4)°], which bridge neighboring copper atoms to form the parent chain. The distance between the aromatic rings of the 3,5-dimethylpyrazole ligands from adjacent chains is 3.221 Å, which indicates the presence of a π–π stacking interaction.

#### *[Cu$_2$(CN)$_2$(imz)]$_n$ (2)*

The structure of **2** is similar to that of **1**, as shown in Figure 2. This compound contains two coordination modes for the $Cu^I$ ions: one is coordinated by three cyanide groups [Cu(1)–X(1) = 1.916(5), Cu(1)–X(2) = 1.920(4) Å; X(1)–Cu(1)–X(2) = 119.94(14)°], and the other is nonlinearly coordinated by one cyanide group and one imidazole ligand [Cu(2)–X(3) = 1.843(6), Cu(2)–N(4) = 1.877(5) Å; N(4)–Cu(2)–X(3) = 170.1(3)°]. The structure also exhibits a backbone constructed from a zigzag {Cu(CN)} chain, with [Cu(CN)(imz)] groups projecting from the chain as side-arms.

#### *[Cu$_3$(CN)(trz)$_2$]$_n$ (3)*

The structure of **3** is an interesting twofold interpenetrated 2D supramolecular framework. As shown in Figure 3, the structure of **3** possesses six unique metal sites. Three metal centers [Cu(2), Cu(3), and Cu(5)] are all in distorted trigonal geometries. However, the detailed coordination environment of these copper atoms is different as Cu(2) and Cu(5) are coordinated by two triazole ligands and one $\mu_2$-bridging cyanide group while Cu(3) is coordinated by two triazole ligands and one $\mu_3$-1,2κC:3κN cyanide group, with Cu–X bond lengths ranging from 1.881(10) to 1.889(9) Å, and a Cu(3)–$N_{CN}$ bond length of 1.886(10) Å. Cu(1) is in a tetrahedral geometry and is coordinated by two triazole ligands and two $\mu_3$-1,2κC:3κN cyanide groups [Cu(1)–C(3) = 2.221(11) Å], the Cu(1)–C(3) bond being much longer than that to the $\mu_2$-bridging cyanide group. The remaining sites [Cu(4) and Cu(6)] are in linear geometries and are coordinated by two triazole ligands with N–Cu–N bond angles of 178.1(4)° and 176.7(4)°, respectively.

The $\{Cu_2N_4\}$ ring formed by atoms Cu(3) and Cu(5) [or Cu(1) and Cu(2)] and the 1- and 2-nitrogen donors of the trz ligands is nonplanar, and the dihedral angle between the Cu(3)Cu(5)N(6)N(7) and Cu(3)Cu(5)N(6B)N(7B) moieties is 20.85(12)°. Cu(3) and Cu(5) are bridged by two trz ligands with a Cu···Cu separation of 3.5316(16) Å, and these ligands bond through their $N^4$ sites to Cu(4) to form a two-coordinate linear geometry, which means that the deprotonated triazole binds in a $\mu_3$-bridging mode to link the copper

 © 2006 Wiley-VCH Verlag GmbH & Co. KGaA, Weinheim 

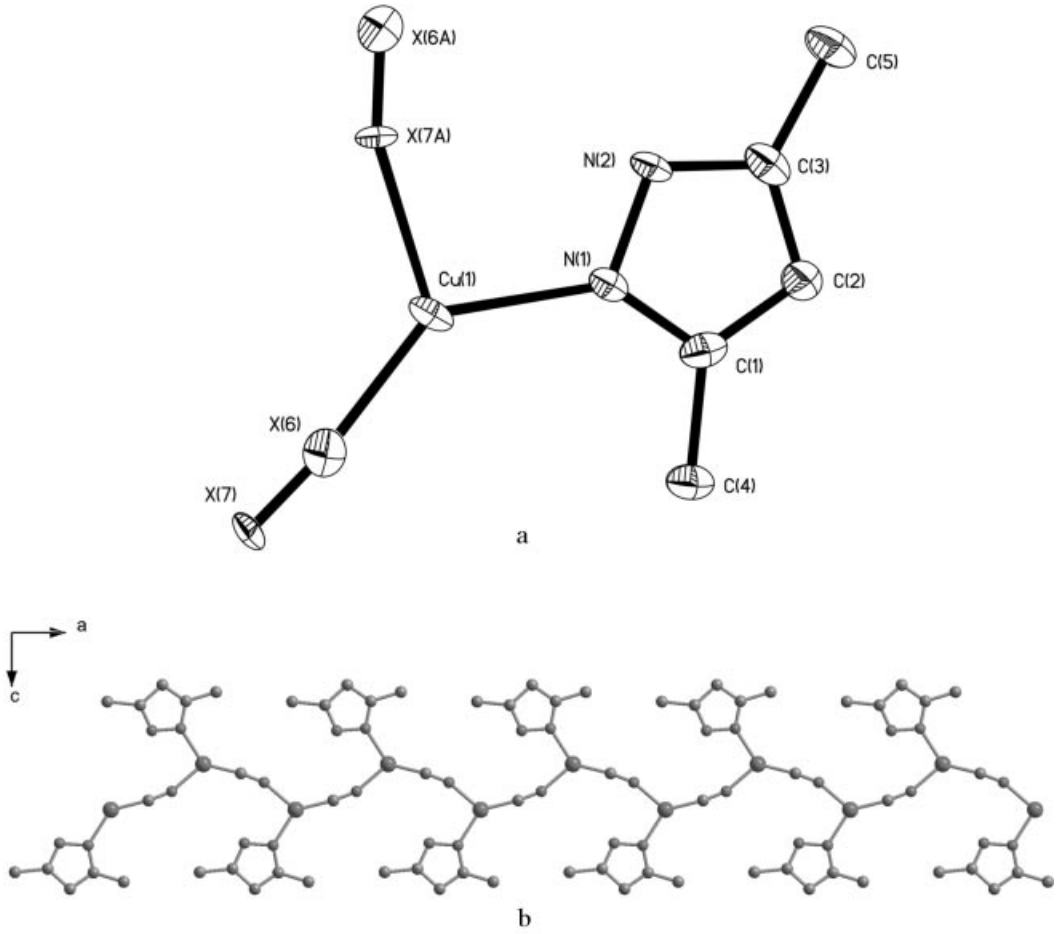


Figure 1. (a) ORTEP representation of the polymeric structure of **1**, showing the coordination environments of the Cu centers (30% probability thermal ellipsoids; hydrogen atoms have been omitted for clarity). Atoms from the disordered CN bridging groups are labeled as X. (b) Schematic view of the chain of **1** viewed along the *b* axis.

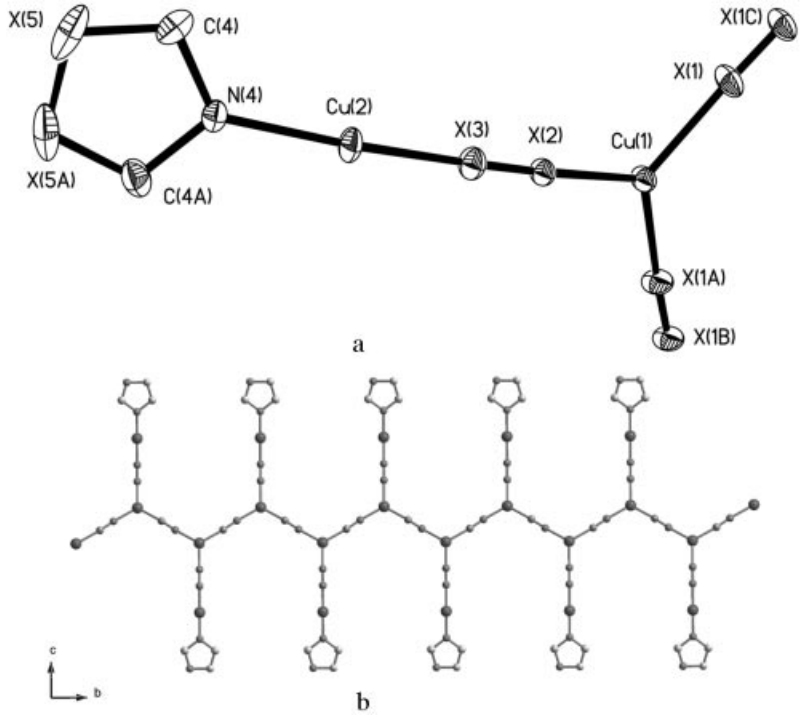


Figure 2. (a) ORTEP representation of the polymeric structure of **2**, showing the coordination environments of the Cu centers (30% probability thermal ellipsoids; hydrogen atoms have been omitted for clarity). Atoms from the disordered CN bridging groups are labeled as X. (b) Schematic view of the chain of **2** viewed along the *a* axis.

 © 2006 Wiley-VCH Verlag GmbH & Co. KGaA, Weinheim 

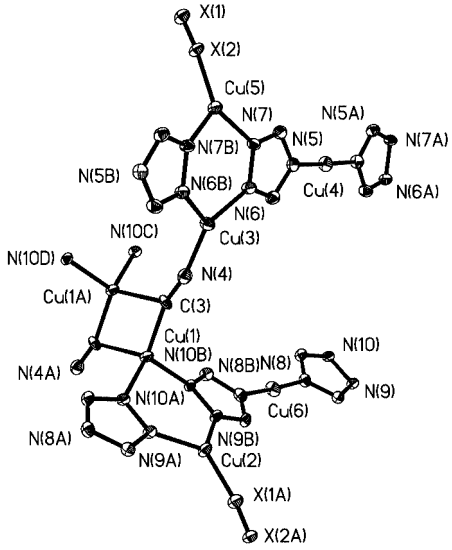


Figure 3. ORTEP representation of the polymeric structure of **3**, showing the coordination environments of the Cu centers (30% probability thermal ellipsoids; hydrogen atoms have been omitted for clarity). Atoms from the disordered CN bridging groups are labeled as X.

ions into linear chains along the *b* axis, with Cu(4), Cu(3), and Cu(5) in one chain and Cu(6), Cu(2), and Cu(1) in the other. In addition, the cyanide groups not only act as $\mu_2$-bridges to link these chains into a wave-like layer structure but also as $\mu_3$-bridges to link Cu(1) and Cu(6) from two different layers together to form an unusual bilayer motif (Figure 4a), which exhibits large channels with dimensions of approximately $11.69 \times 13$ Å$^2$ along the *b* axis. These bilayers pass through each other to generate the interpenetrating 2D network (Figure 4b). In addition, there are π–π stacking interactions between adjacent aromatic rings of triazole ligands with a separation of about 3.299 Å.

Although several types of double-layered architectures have been reported by the assembly of T-shaped or rectangular building blocks,[18–20] this ring-shaped network, to the best of our knowledge, is unprecedented. A view along the *b* axis shows that the actual crystal structure of **3** is a twofold interpenetrating 2D supramolecular framework (Figure S1). This is consistent with the fact that crystal structures with such large cavities are stabilized either by inclusion of suitable guests or by interpenetrating lattices.[21]

### *[Cu$_6$(CN)$_6$(dmtrz)$_3$]$_n$ (4)*

The 3D network of compound **4** is made up of two parts: one is a 2D rectangular grid layer and the other is a $\{Cu_2(CN)_2(dmtrz)_2\}$ building block. As shown in Figure 5, the crystal structure has six crystallographically independent Cu atoms bridged by cyanide groups and dmtrz ligands. The copper atoms adopt two kinds of coordination modes, namely three- and four-coordination. Cu(2), Cu(3), Cu(6), and Cu(1) are in distorted trigonal geometries, of

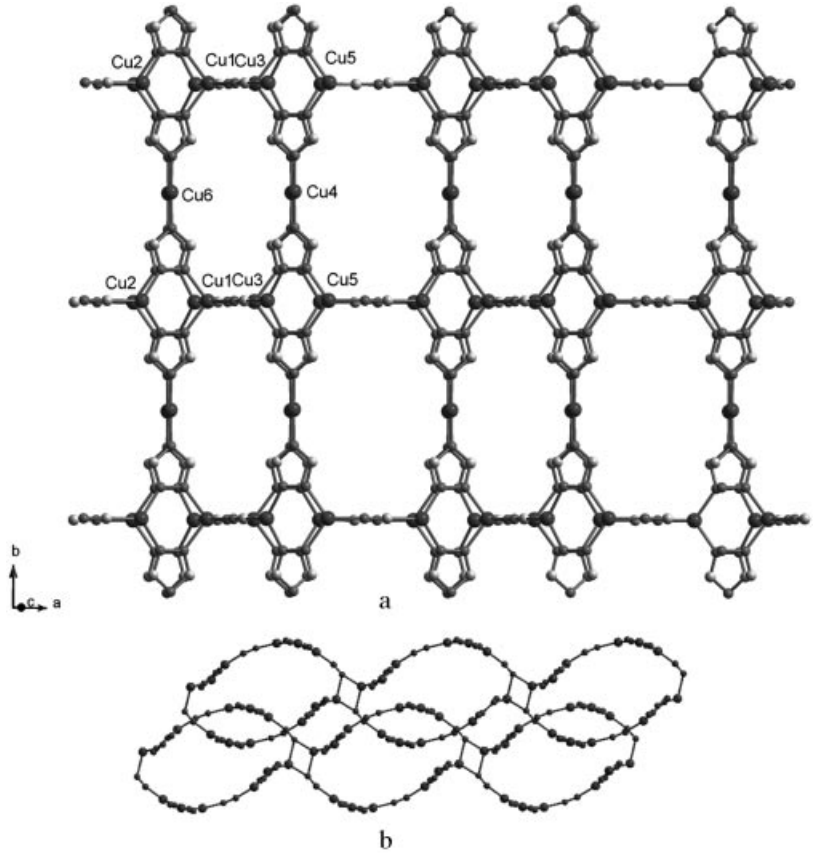


Figure 4. (a) Layer structure of compound **3**. (b) Interpenetrating 2D network constructed by the bilayers, with a large channel of approximately $11.69 \times 13$ Å$^2$, viewed along the *b* axis.

 © 2006 Wiley-VCH Verlag GmbH & Co. KGaA, Weinheim 

which the former three are three-coordinated by two dmtrz ligands [Cu–$N_{dmtrz}$ = 1.967(3)–2.014(3) Å] and one $\mu_2$-bridging cyanide group, with Cu–X bond lengths ranging from 1.888(4) to 1.895(4) Å, while Cu1 is coordinated by three cyanide groups, two of the being in $\mu_2$-bridging modes [Cu–X = 1.899(4)–1.992(4) Å] and the other in a $\mu_3$-bridging mode [Cu(1)–N(14) = 1.896(3) Å]. Cu(4) and Cu(5) are both in tetrahedral geometries and are coordinated to four cyanide groups. However, the coordination environments of these two copper atoms are different as Cu(4) is coordinated by two $\mu_3$-bridging [Cu(4)–C(20) = 2.055(4), Cu(4)–C(20A) = 2.142(4) Å] and two $\mu_2$-bridging cyanide groups [Cu(4)–X = 1.967(3)–2.007(3) Å], while Cu(5) is coordinated by three $\mu_3$-bridging and one $\mu_2$-bridging cyanide groups.

In the $\{Cu_2(CN)_2(dmtrz)_2\}$ building block (Figure 6a), the $\{Cu_2N_4\}$ ring formed by the *endo* Cu atoms and the 1- and 2-nitrogen donors of the dmtrz ligands is almost planar, with a dihedral angle between the Cu(2)Cu(3)N(5)N(6) and Cu(2)Cu(3)N(1)N(2) planes of 5.23(7)°. The adjacent Cu(2)Cu(3)N(5)N(6)N(1)N(2) and Cu(6)Cu(6A)N(9)N(10)N(9A)N(10A) ring planes in this building block are nearly parallel, with a dihedral angle of 3.519°.

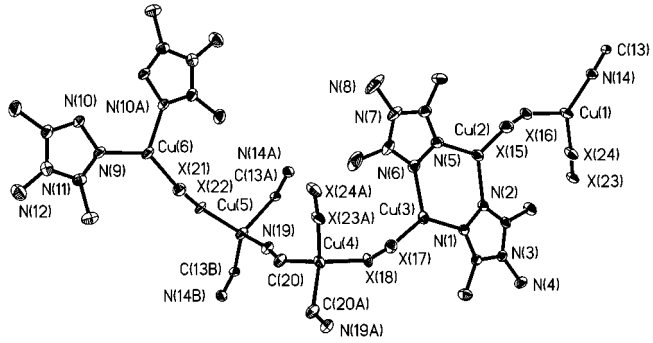


Figure 5. ORTEP representation of the polymeric structure of **4**, showing the coordination environments of the Cu centers (30% probability thermal ellipsoids; hydrogen atoms have been omitted for clarity). Atoms from the disordered CN bridging groups are labeled as X.

The structure consists of 2D rectangular grid layers (Figure 6b), parallel to the *ab* plane, constructed by six-mem-

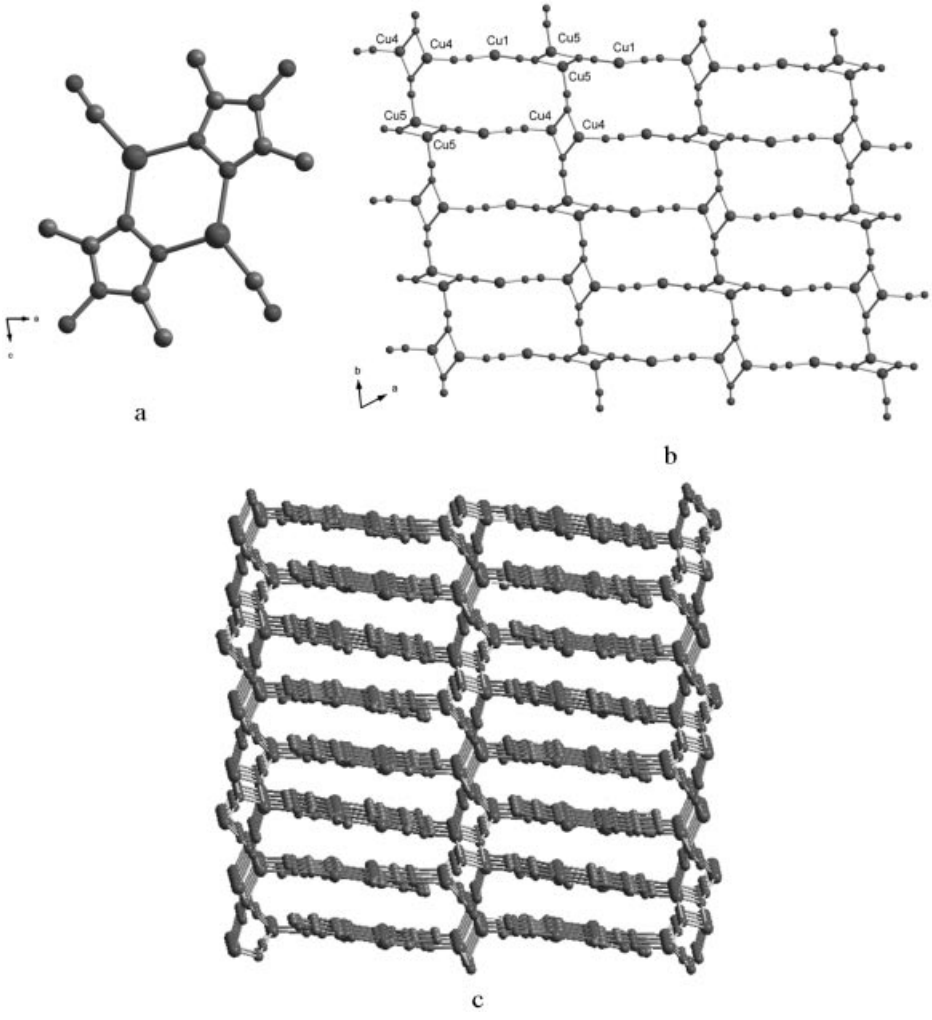


Figure 6. (a) $\{Cu_2(CN)_2(dmtrz)_2\}$ building block. (b) 2D rectangular grid layers. (c) 3D framework of compound **4** constructed by parallel 2D rectangular grid layers linked by the $\{Cu_2(CN)_2(dmtrz)_2\}$ building block.

 © 2006 Wiley-VCH Verlag GmbH & Co. KGaA, Weinheim 

bered nonplanar centrosymmetric rings of metal atoms in which the metal centers are bridged by cyanide groups. These rings all adopt a chair conformation for the Cu4–Cu1–Cu5–Cu4′–Cu1′–Cu5′ unit, with a ring size of $8.9 \times 8.0$ Å$^2$. The strong Cu···Cu interaction, with a separation of 2.442(8) Å, is double-bridged by two cyanide groups. Although the shortest known $Cu^I$···$Cu^I$ separation is 2.412(1) Å,[22] the Cu···Cu distance in the present compound is notably shorter than those found in other $Cu^I$ compounds[23] that show strong Cu···Cu interactions.

The parallel 2D rectangular grid layers are linked by $\{Cu_2(CN)_2(dmtrz)_2\}$ building blocks to form a 3D framework (Figure 6c and Figure S2); π–π stacking interactions are present between adjacent $\{CuN_4\}$ planes in compound **4**, with a plane–plane separation of about 3.327 Å and a centroid–centroid distance of 3.407 Å.

### *[Cu$_2$(CN)(5-metta)]$_n$ (5)*

The structure of **5** is a 3D supramolecular framework composed of X-shaped one-dimensional chains. As shown in Figure 7, the structure consists of two crystallographically independent Cu atoms that adopt two kinds of coordination modes, namely three- and four-coordination. Cu(1) trigonally coordinates to two N atoms from different 5-metta ligands and one N atom from a $\mu_3$-bridging cyanide group, while Cu(2) is tetrahedrally coordinated by two N atoms from two 5-metta ligands and two C atoms from different $\mu_3$-bridging cyanide groups. The X-shaped one-dimensional chains are formed by copper atoms bridged by 5-metta ligands in a $\mu_4$-tetrazolyl mode with a Cu2···Cu2B

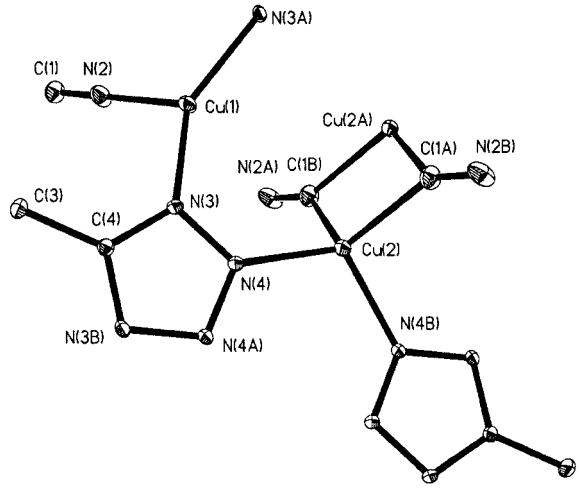


Figure 7. ORTEP representation of the polymeric structure of **5**, showing the coordination environments of the Cu centers (30% probability thermal ellipsoids; hydrogen atoms have been omitted for clarity). Atoms from the disordered CN bridging groups are labeled as X.

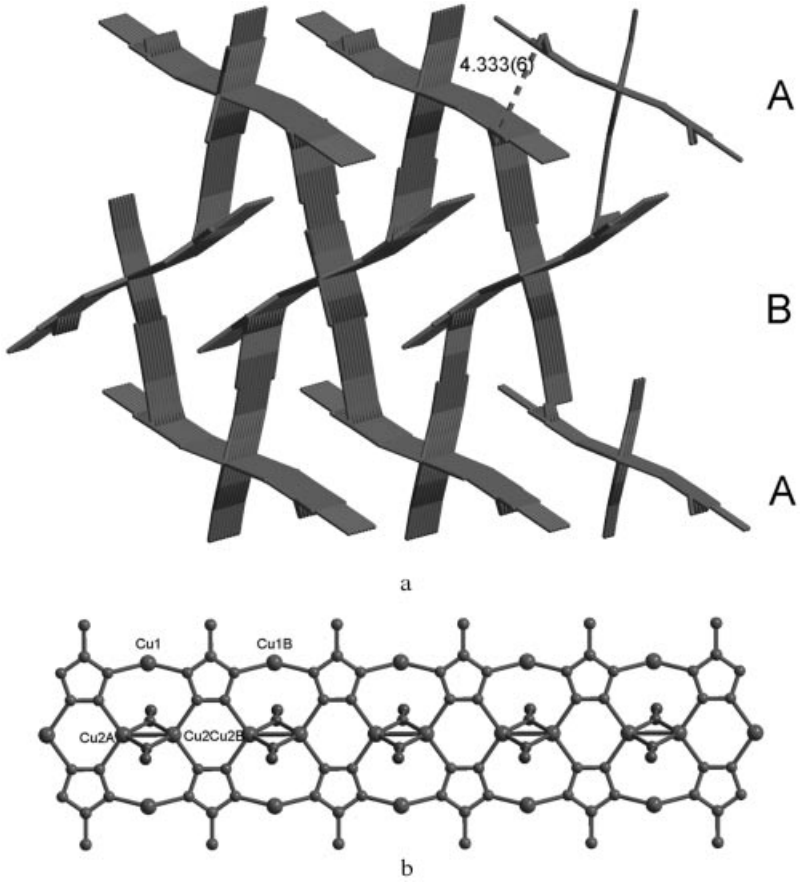


Figure 8. (a) 3D structure constructed by the X-shaped one-dimensional chains. (b) One-dimensional chain bridged by 5-metta ligands and cyanide groups [Cu2···Cu2A (A: $x + 1$, $y + 1$, $z$) = 2.347(1) Å].

 © 2006 Wiley-VCH Verlag GmbH & Co. KGaA, Weinheim 

(B: $x$, $y$, $-z + 1$) distance of 3.586(1) Å and a Cu1···Cu1B (B: $x$, $y$, $-z + 1$) distance of 5.933(7) Å and two cyanide groups doubly bridging Cu2···Cu2A (A: $-x + 1$, $-y + 1$, $-z$) with a distance of 2.347(1) Å. Rare examples with such short values have been found for other $Cu^{I}$ compounds.[24] The adjacent chains are parallel to each other in the same layer, with a Cu···Cu distance of 4.333(6) Å, while they are linked by a cyanide group between adjacent layers (Figure 8). These X-shaped chains connect to each other in an ABAB arrangement to generate an interesting 3D network (Figure S3); π–π stacking interactions between adjacent aromatic rings of tetrazole also exist in compound **5**, with a plane–plane separation of about 3.370 Å.

### *[Cu$_2$(CN)(5-phtta)]$_n$ (6)*

The structure of **6** is a 3D network (Figure 9). There is one crystallographically independent $Cu^{I}$ center, which adopts three-coordination in a distorted trigonal geometry, coordinated by two $\mu_4$-5-phtta ligands and one $\mu_2$-cyanide group [$N_{phtta}$–Cu(1) = 1.966(2)–2.0867(18), X–Cu(1) = 1.876(2) Å; N(X)–Cu(1)–N(X) = 102.88(7)–140.47(9)°]. The 5-phtta ligands bind in a $\mu_4$-tetrazolyl mode to bridge four copper atoms to form a one-dimensional chain with a Cu···Cu separation of 3.512(2) and 3.794(2) Å along the $c$ axis (Figure 10a). Each chain is bridged by a cyanide group to form a square-grid structure that exhibits large channels with approximate dimensions of 8.472 × 9.259 Å$^2$, although the effective pore size is partly reduced by the phenyl groups of the 5-phtta ligands Furthermore, these one-dimensional chains are linked to each other by cyanide groups to form the 3D framework (Figure 10b and Figure S4).

### *{[Cu$_6$(CN)$_6$(dmtrz)]$_2$[Cu$_2$(CN)$_2$(dmtrz)$_2$]}$_n$ (7)*

The crystal structure of **7** is comprised of two distinct and crystallographically independent polymeric motifs packed together to form a 3D architecture, which comprises interesting double helical host tubes filled by 1D metal-organic polymeric chains as guests, i.e. {[$Cu_6(CN)_6$(dmtrz)]$_n$}$_2$ (**A**) and [$Cu_2(CN)_2$(dmtrz)$_2$]$_n$ (**B**).

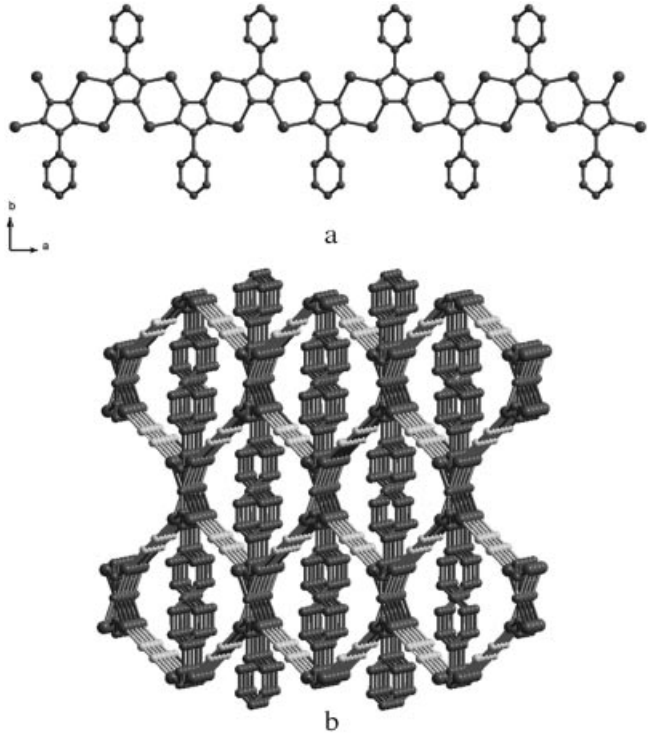


Figure 10. (a) One-dimensional chain constructed by 5-phtta ligands. (b) 3D structure of compound **6**.

The crystal structure has six crystallographically independent Cu atoms bridged by cyanide groups and a dmtrz ligand in polymer **A** (Figure 11). The copper atoms adopt two kinds of coordination modes, namely two- and three-coordination. Cu4, Cu5, and Cu6 are in linear geometries, coordinated by two $\mu_2$-bridging cyanide groups [Cu–X = 1.839(4)–1.866(4) Å; X–Cu–X = 166.3(2)–170.4(2)°], while Cu7 and Cu8 are in distorted trigonal geometries and are coordinated by three $\mu_2$-bridging cyanide groups [Cu–X = 1.895(4)–1.993(4) Å; X–Cu–X = 111.21(18)–133.42(18)°], while Cu3 is also in a distorted trigonal geometry and is

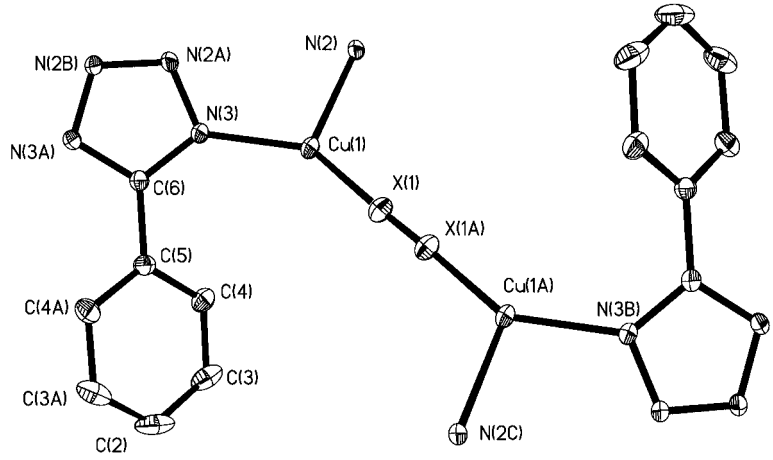


Figure 9. ORTEP representation of the polymeric structure of **6**, showing the coordination environments of the Cu centers (30% probability thermal ellipsoids; hydrogen atoms have been omitted for clarity). Atoms from the disordered CN bridging groups are labeled as X.

 © 2006 Wiley-VCH Verlag GmbH & Co. KGaA, Weinheim 

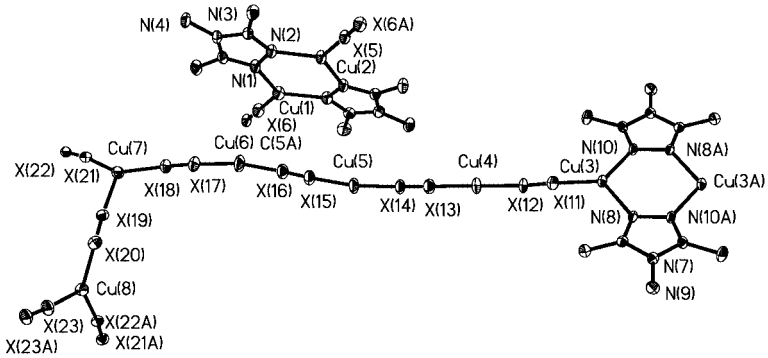


Figure 11. ORTEP representation of the polymeric structure of **7**, showing the coordination environments of the Cu centers (30% probability thermal ellipsoids; hydrogen atoms have been omitted for clarity). Atoms from the disordered CN bridging groups are labeled as X.

coordinated by two dmtrz ligands [Cu3–$N_{dmtrz}$ = 1.967(3)–2.014(3) Å] and one $\mu_2$-bridging cyanide group [Cu3–X11 = 1.886(4) Å] The host polymer **A** consists of two kinds of helical chains, namely mode I and mode II (Figure 12a). Six copper atoms bridged by six cyanide ions form a honeycomb-shaped helical chain (mode I) when viewed along the *b* axis. The unclosed Cu–CN linkage in this structure gives rise to two types of helices with opposite chiralities (Figure S5). The left- and right-handed helices are coupled with each other to form helical tubes of approximately $4.99 \times 5.00$ Å$^2$ with opposite chirality (calculated from opposite metal ion centers of the hexagon; Figure 12b). The helical chain along the $2_1$ screw axis has a long pitch of 12.898(1) Å (Figure 13a). The helical chain of mode II is composed of 22 copper atoms bridged by 20 cyanide ions and four dmtrz ligands to form a distorted hexagon. To the best of our knowledge, this is the first compound constructed from such a long chain of cyanide-bridged copper atoms. The left- and right-handed helical chains of mode II form helical channels of $42.26 \times 4.99$ Å$^2$ with opposite chirality (calculated from the opposite metal ions of the hexagon). The long pitch of the helical chain along the $2_1$ screw axis is 59.985(6) Å (Figure 13b). Two chemically independent polymers **A** interweave to form a 3D architecture with double-stranded helical channels along two spiral directions (Figure S6).

There are two crystallographically independent Cu atoms bridged by cyanide groups and dmtrz ligand in polymer **B**

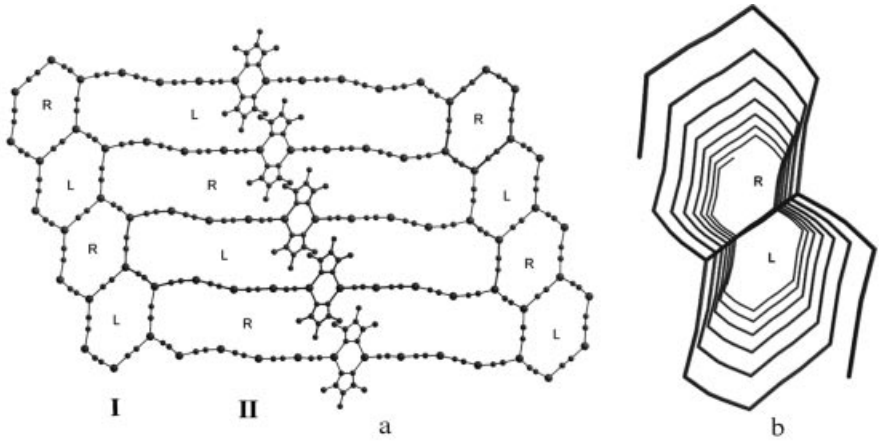


Figure 12. (a) Two kinds of helical chains (modes I and II) in polymer **A**. (b) Right- and the left-handed helical tubes of mode I.

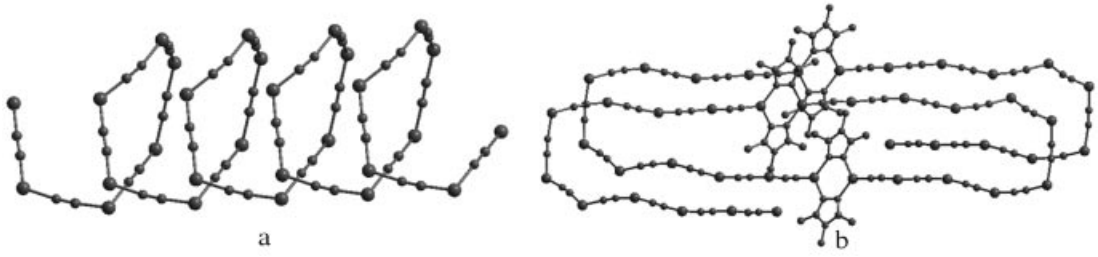


Figure 13. (a) Structure of a helical chain of mode I with a pitch of 12.898(1) Å running along the screw axis. (b) Structure of a helical chain of mode II with a pitch of 59.985(6) Å running along the screw axis.

 © 2006 Wiley-VCH Verlag GmbH & Co. KGaA, Weinheim 

(Figure 14). Cu1 and Cu2 are in distorted trigonal geometries and are coordinated by two dmtrz ligands [Cu–$N_{dmtrz}$ = 1.967(3)–2.014(3) Å] and one $\mu_2$-bridging cyanide group [Cu–X = 1.885(5)–1.897(6) Å], with Cu···Cu separations of 3.652(1) Å. These building blocks are linked further by cyanide ions to form cable-like linear chains. The polymers **B** are present in the helical channels with opposite chirality constructed by helical chains of mode II. The guest polymers play an important role in the formation of double-stranded helical channels through specific host–guest interactions (Figure 15).

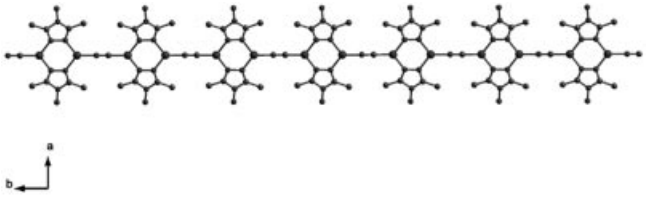

Figure 14. One-dimensional chain of polymer **B**.

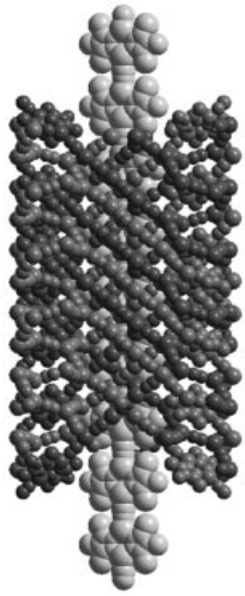

Figure 15. One-dimensional chain of polymer **B** filled in the mode II helical channel of polymer **A**.

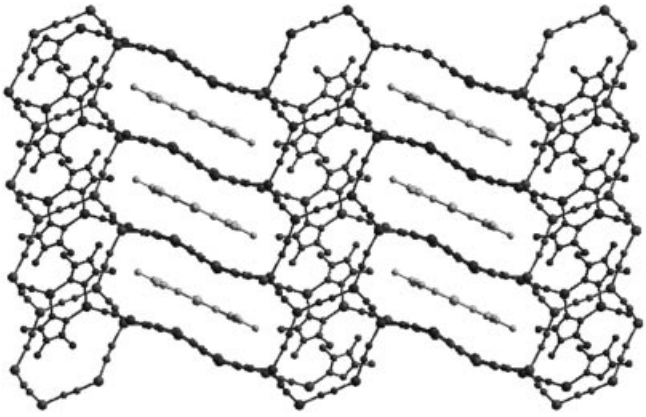

Figure 16. 3D + 1D structure of compound **7**, with the 1D polymer **B** filled in the two independent helical 3D polymers **A**.

Two independent helical substructures of polymer **A** $\{[Cu_6(CN)_6(dmtrz)]_n\}$ interweave into a 3D network with double-stranded helical channels that host 1D linear polymers **B** $\{[Cu_2(CN)_2(dmtrz)_2]_n\}$ to form a novel 3D supramolecular architecture (Figure 16).

This compound is interesting in that it contains two supramolecular isomers in the same crystal, infinite double helices with large channels in the spiral direction, and two kinds of helical channels with opposite chirality constructed by helical chains I and II in the same polymer.

### Summary of the Structures

A series of compounds of a new copper cyanide/organoamine family have been synthesized by a hydrothermal method and structurally characterized. Compounds **1** and **2** contain a one-dimensional network. In contrast to the two one-dimensional chains mentioned above, compound **1** does not contain side-arms but has only N-heterocyclic ligands directly bound to the parent chains, whereas compound **2** has side arms, which represent an extra part with an additional {Cu(CN)} subunit. The cyanide groups only adopt $\mu_2$-bridging modes in these compounds.

The 2D compound **3**, in which triazole ligands and cyanide groups all act as bridging ligands to link the copper atoms into a 2D structure, is obtained with the $\mu_3$-bridging triazole ligand. This structure can be compared with that of **4**, which contains $\mu_2$-dmtrz ligands instead of $\mu_3$-triazole ligands, and therefore contains structurally different dimensionalities. The steric demands of the bulky substituents on the 3-, 4-, and 5-positions may be the cause of the change of coordination number around the copper atom. It has previously been pointed out that the use of triazole derivatives gives interesting coordination compounds.[5]

Compounds **5** and **6**, in which the cyanide groups exhibit two different coordination modes in a 3D structure, are obtained with the $\mu_4$-bridging tetrazole ligand. In the structures of compounds **5** and **6**, which contain the polycyclic N-heterocyclic ligands 5-metta and 5-phtta, respectively, all the ligands are $\mu_4$-bridging and link four copper atoms. Steric effects might be the major factors controlling the structures of these compounds, although the different coordination modes of the cyanide groups also affect the structural framework.

Although they contain the same ligand, two different structures are present in compounds **4** and **7**. One is a 3D network and the other is a 3D + 1D network. It can be seen that the different arrangement of the cyanide groups results in different dimensionalities. In compound **7**, all the cyanide groups adopt a $\mu_2$-bridging coordination mode, while $\mu_2$-bridging and $\mu_3$-bridging modes are found in compound **4**. The versatility of the connectivity motifs linking the copper atoms therefore provides a rich structural chemistry.

### Photoluminescent Properties

It is well known that numerous mono- and polynuclear $Cu^I$ compounds show excellent luminescence properties.

 © 2006 Wiley-VCH Verlag GmbH & Co. KGaA, Weinheim 

Metal-to-ligand charge-transfer is the most common assignment of the lowest electronic excited state, although copper-centered emission, ligand-centered emission, and interligand charge-transfer are also possible.[25] We have studied the luminescence properties of compounds **1**–**7** (Figure 17). The emission spectra have a maximum at 523, 622, 508, 589, 505, and 481 nm, with an excitation maximum at 307, 348, 345, 316, 352, and 352 nm for **1**, **2**, **3**, **4**, **6**, and **7**, respectively. The emission may be tentatively assigned to a metal-to-ligand charge transfer (MLCT: Cu→CN) because the oxidation state of the copper atoms bridged by cyanide ions in these compounds is +1 and this is also consistent with the results of the IR spectra and is similar to the situation in other cyanide complexes.

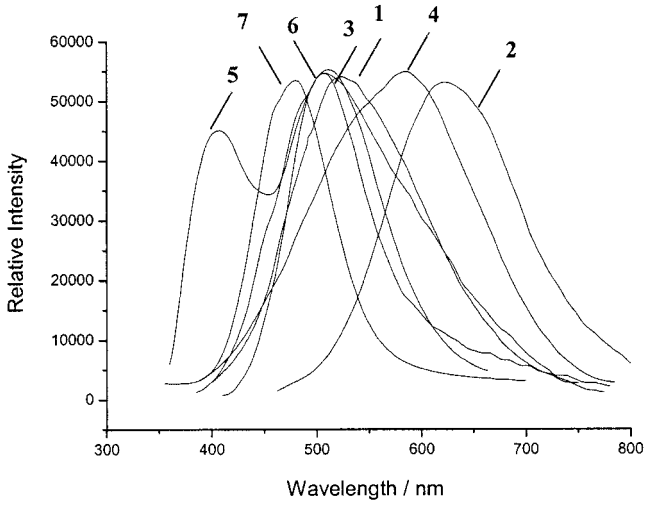


Figure 17. Emission spectra of compounds **1**–**7** measured in the solid state at room temperature.

The emission spectrum of compound **5** has a low-energy transition at around 408 nm and a high-energy one at around 502 nm, with an excitation maximum at 338 nm. The high-energy transition can be assigned as metal-to-ligand transfer (MLCT: Cu→CN), whereas the low-energy transition may be attributed to intraligand (π–π*) fluorescence in the 5-metta ligands, which is in reasonable agreement with literature examples.[26–28]

### IR Spectra

The IR bands corresponding to the CN stretching vibrations for compounds **1**–**7** appear in the range 2080–2158 $cm^{-1}$, which is typical for bridging cyanide groups and higher than that of terminal cyanide ions (approx. 2050 $cm^{-1}$).[29] For compounds **1**, **5**, and **6** there is only one $\nu$(CN) absorption, thus indicating the existence of one type of cyanide group in the crystal lattice, while there are two absorptions in compounds **2**–**4** and **7**, thus indicating the existence of two types of cyanide groups. Although the cyanide groups are only in $\mu_2$-bridging modes in compounds **2** and **7**, the reason for the two absorptions might be the different distances of the $Cu^I$–C/N bond as the coordination number around copper(I) atoms increases. For cyanide-bridged $Cu^I$ compounds, $Cu^I$–C/N distances are found to increase with coordination number around the copper(I) atoms. For instance, the $Cu^I$–C/N distances range from 1.82–1.86 Å for nearly linear two-coordinate systems whereas they increase to 1.92–1.98 Å in three-coordinate systems; $\nu$(CN) increases as the $Cu^I$–CN distances decreases. This trend has also been observed for other compounds.[30,31]

## Conclusions

We have obtained seven new copper cyanide/N-heterocycle compounds with a variety of one-, two-, three-, and one/three-dimensional frameworks by a hydrothermal method. We have found that organic ligands with specific geometric requirements affect the structure of these compounds. Triazole and tetrazole ligands bridge the copper centers to propagate a variety of structural styles that form multi-dimensional networks, while pyrazole and imidazole serve as terminal ligands that restrict the spatial extension of the structure. Other factors, such as the subtle interplay of metal coordination preferences, ligand type, spatial extension, and steric constraints, also play important roles in the formation of novel multidimensional open framework materials. The successful isolation of seven compounds demonstrates that it is possible to apply $K_3Fe(CN)_6$ as a precursor and other N-heterocyclic ligands to prepare coordination compounds with various structures under hydrothermal conditions. Some compounds display strong fluorescence emissions at different wavelengths, and these might be used as new emitting materials. The structure–function relationships of such components will begin to emerge and will provide further guidelines for synthetic methodologies.

## Experimental Section

**General Remarks:** All syntheses were performed in poly(tetrafluoroethylene)-lined stainless steel autoclaves under autogenous pressure. Reagents were purchased commercially and were used without further purification. Elemental analyses for C and H were performed with an EA1110 CHNS-0 CE elemental analyzer. IR spectra (KBr pellets) were recorded with a Nicolet Magna 750FT-IR spectrometer. Fluorescence data were collected with an Edinburgh FL-FS920 TCSPC system.

**General Method for the Preparation of Compounds 1–6:** A mixture of CuCN (0.27 g, 3 mmol), $K_3Fe(CN)_6$ (0.32 g, 1 mmol), and the corresponding N-heterocyclic ligand (1 mmol; Scheme 1) in 15 mL of $H_2O$ was stirred at room temperature for 20 min, then the mixture was transferred into a 25-mL Teflon-lined stainless steel vessel and the mixture was heated at 180 °C under autogenous pressure for 3 d. After the reaction mixture had slowly cooled to room temperature, suitable crystals for X-ray diffraction were produced, which were collected by filtration and washed with distilled water and dried in air.

 © 2006 Wiley-VCH Verlag GmbH & Co. KGaA, Weinheim 

**$[Cu(CN)(dmpyz)]_n$ (1):** Colorless prism-like crystals, (0.23 g; yield: 43%, based on Cu). $C_6H_8CuN_3$ (185.69): calcd. C 38.81, H 4.34, N 22.63; found C 38.92, H 4.36, N 22.71. IR (solid KBr pellet): $\tilde{\nu}$ = 339 (s), 2106 (s), 1570 (m), 1470 (m), 1284 (m), 1153 (m), 1037 (m), 978 (w), 779 (m), 679 (m), 654 (m), 579 (m), 445 (w), 427 (w) $cm^{-1}$.

**$[Cu_2(CN)_2(imz)]_n$ (2):** Colorless needle-like crystals (0.16 g; yield: 42%, based on Cu). $C_5H_4Cu_2N_4$ (247.19): calcd. C 24.29, H 1.63, N 22.66; found C 24.60, H 1.02, N 23.28. IR (solid KBr pellet): $\tilde{\nu}$ = 3346 (s), 3149 (m), 2146 (m), 2108 (s), 1635 (w), 1543 (m), 1508 (m), 1427 (m), 1257 (m), 1070 (s), 843 (w), 762 (m), 714 (m), 650 (m), 607 (m) $cm^{-1}$.

**$[Cu_3(CN)(trz)_2]_n$ (3):** Colorless prism-like crystals (0.11 g; yield: 30%, based on Cu). $C_5H_4Cu_3N_7$ (352.77): calcd. C 17.02, H 1.14, N 27.79; found C 17.32, H 1.48, N 27.42. IR (solid KBr pellet): $\tilde{\nu}$ = 3130 (m), 2102 (s), 2090 (s), 2069 (m), 1713 (m), 1506 (s), 1279 (s), 1205 (m), 1155 (s), 1066 (m), 1016 (m), 877 (m), 854 (m), 679 (m) $cm^{-1}$.

**$[Cu_6(CN)_6(dmtrz)_3]_n$ (4):** Colorless prism-like crystals (0.17 g; yield: 40%, based on Cu). $C_{18}H_{24}N_{18}Cu_6$ (873.79): calcd. C 24.74, H 2.77, N 28.85; found C 24.33, H 2.45, N 28.62. IR (solid KBr pellet): $\tilde{\nu}$ = 3552 (m), 3421 (m), 3049 (m), 2102 (vs), 2080 (vs), 1628 (m), 1421 (s), 1342 (m), 1205 (m), 1142 (m), 1051 (m), 847 (s), 777 (w), 723 (s), 633 (w), 559 (m) $cm^{-1}$.

**$[Cu_2(CN)(5\text{-metta})]_n$ (5):** Colorless prism-like crystals (0.10 g; yield: 30%, based on Cu). $C_3H_3N_5Cu_2$ (236.18): calcd. C 15.26, H 1.28, N 29.65; found C 15.67, H 1.46, N 29.82. IR (solid KBr pellet): $\tilde{\nu}$ = 2953 (w), 2484 (w), 2081 (s), 1497 (s), 1375 (m), 1254 (m), 1176 (m), 1147 (m), 1111 (w), 1049 (m), 710 (m) $cm^{-1}$.

**$[Cu_2(CN)(5\text{-phtta})]_n$ (6):** Colorless prism-like crystals (0.16 g; yield: 36%, based on Cu). $C_8H_5N_5Cu_2$ (298.25): calcd. C 32.22, H 1.69, N 23.48; found C 32.54, H 1.93, N 24.09. IR (solid KBr pellet): $\tilde{\nu}$ = 3421 (m), 3078 (m), 2133 (s), 1525 (m), 1454 (s), 1379 (m), 1159 (m), 1078 (m), 928 (w), 789 (m), 741 (s), 717 (s), 546 (w), 519 (w) $cm^{-1}$.

**Preparation of $\{[Cu_6(CN)_6(dmtrz)]_2[Cu_2(CN)_2(dmtrz)_2]\}_n$ (7):** This compound was synthesized by a procedure analogous to that described above but with CuCN (5.6 mmol), $K_3Fe(CN)_6$ (1 mmol), and dmtrz (1 mmol). Colorless platelike crystals (0.21 g; yield: 31%, based on Cu). $C_{30}H_{32}Cu_{14}N_{30}$ (1702.4): calcd. C 21.17, H 1.89, N 24.68; found C 21.39, H 2.14, N 24.96. IR (solid KBr pellet): $\tilde{\nu}$ = 3365 (m), 3323 (m), 3278 (m), 2158 (s), 2108 (s), 1616 (m), 1543 (m), 1419 (m), 1394 (m), 1263 (w), 1049 (w), 887 (m), 779 (m), 744 (m), 660 (w) $cm^{-1}$.

**X-ray Crystallographic Study:** Suitable single crystals of the compounds were carefully selected and glued to thin glass fibers with epoxy resin. Crystal structure measurements for compounds **1**–**7** were performed with a Rigaku Mercury CCD diffractometer with graphite-monochromated Mo-$K_\alpha$ radiation ($\lambda$ = 0.71073 Å) at room temperature. The structures were solved by direct methods and refined on $F^2$ with the SHELXL-97 program.[32] For all compounds the $\mu_2$-bridging cyanide group between two $Cu^I$ atoms indicated disorder with respect to the C and N termini; this disorder was treated by adopting 50% C and N occupancies at those sites. The disordered C/N positions are labeled as X. All non-hydrogen atoms were refined with anisotropic displacement parameters, and the hydrogen atoms were treated as riding atoms using the SHELX-97 default parameters. For **2**, the imidazole hydrogen atoms were neither found nor calculated, and the disorder was treated by assuming half occupancies of the C and N atoms. The crystallographic data and details of refinements for compounds **1**–**7** are summarized in Table 1; selected bond lengths and angles are listed in Table 2. CCDC-284132 (**1**), -284133 (**2**), -284136 (**3**), -284137 (**4**), -284138 (**5**), -284139 (**6**), and -284140 (**7**) contain the supplementary crystallographic data for this paper. These data can be obtained free of charge from The Cambridge Crystallographic Data Centre via www.ccdc.cam.ac.uk/data_request/cif.

Table 1. Crystal and structural refinement data for compounds **1**–**7**.

| Compound | **1** | **2** | **3** | **4** | **5** | **6** | **7** |
|---|---|---|---|---|---|---|---|
| Empirical formula | $C_6H_8CuN_3$ | $C_5H_4Cu_2N_4$ | $C_5H_4Cu_3N_7$ | $C_{18}H_{24}Cu_6N_{18}$ | $C_3H_3Cu_2N_5$ | $C_8H_5Cu_2N_5$ | $C_{30}H_{32}Cu_{14}N_{30}$ |
| Formula mass | 185.69 | 247.19 | 352.77 | 873.79 | 236.18 | 298.25 | 1702.42 |
| Crystal system | orthorhombic | orthorhombic | monoclinic | triclinic | orthorhombic | monoclinic | monoclinic |
| Space group | *Pnma* | *Pnma* | *C*2/*m* | $P\bar{1}$ | *Pbam* | *C*2/*c* | *C*2/*c* |
| *a* [Å] | 8.777(2) | 6.9901(6) | 14.0944(3) | 11.1042(2) | 7.2307(5) | 11.123(9) | 42.347(15) |
| *b* [Å] | 6.6410(19) | 8.5874(7) | 11.2119(3) | 11.2046(3) | 13.4943(11) | 12.780(9) | 8.569(3) |
| *c* [Å] | 12.716(3) | 13.0732(11) | 13.0843(4) | 13.7862(2) | 5.9352(5) | 8.133(6) | 14.490(5) |
| $\alpha$ [°] | 90 | 90 | 90 | 69.565(9) | 90 | 90 | 90 |
| $\beta$ [°] | 90 | 90 | 113.684(2) | 74.161(10) | 90 | 125.231(8) | 108.758(6) |
| $\gamma$ [°] | 90 | 90 | 90 | 65.069(9) | 90 | 90 | 90 |
| *V* [Å$^3$] | 741.2(3) | 784.74(11) | 1893.50(9) | 1441.48(5) | 579.12(8) | 944.3(13) | 4979(3) |
| *Z* | 4 | 4 | 8 | 2 | 4 | 4 | 4 |
| $D_{calcd.}$ [g·cm$^{-3}$] | 1.664 | 2.075 | 2.475 | 2.013 | 2.709 | 2.098 | 2.271 |
| *F*(000) | 376 | 472 | 1360 | 864 | 456 | 584 | 3312 |
| Absorption coefficient [mm$^{-1}$] | 2.867 | 5.351 | 6.649 | 4.392 | 7.249 | 4.470 | 5.903 |
| $\theta$ range for data collection [°] | 2.82–25.03 | 3.12–27.48 | 1.70–25.02 | 3.18–27.48 | 4.13–27.48 | 3.01–27.47 | 3.01–27.49 |
| Reflections collected | 1711 | 5686 | 2923 | 11297 | 4169 | 3511 | 18598 |
| Unique reflections | 695 | 953 | 1752 | 6529 | 724 | 1080 | 5684 |
| *R*(int) | 0.0368 | 0.0225 | 0.0260 | 0.0235 | 0.0303 | 0.0244 | 0.0443] |
| Parameters | 61 | 60 | 151 | 379 | 54 | 70 | 337 |
| Goodness-of-fit on $F^2$ | 1.006 | 1.018 | 1.079 | 1.052 | 1.055 | 1.054 | 1.095 |
| $R_1$[a] | 0.0697 | 0.0389 | 0.0514 | 0.0394 | 0.0203 | 0.0220 | 0.0448 |
| $wR_2$ [$I > 2\sigma(I)$][b] | 0.1560 | 0.1064 | 0.1163 | 0.0937 | 0.0543 | 0.0651 | 0.1221 |
| $R_1$[a] | 0.0800 | 0.0420 | 0.0558 | 0.0550 | 0.0211 | 0.0243 | 0.0519 |
| $wR_2$ (all data) | 0.1618 | 0.1085 | 0.1192 | 0.1024 | 0.0549 | 0.0663 | 0.1269 |

[a] $R_1 = \Sigma(|F_o| - |F_c|)/\Sigma|F_o|$. [b] $wR_2 = [\Sigma w(F_o^2 - F_c^2)^2/\Sigma w(F_o^2)^2]^{0.5}$.

 © 2006 Wiley-VCH Verlag GmbH & Co. KGaA, Weinheim 

Table 2. Selected bond lengths [Å] and angles [°] for compounds **1**–**7**. Symmetry transformations used to generate equivalent atoms are given as footnotes.

| | | | | | |
|---|---|---|---|---|---|
| Compound **1**[a] | | | | | |
| Cu(1)–X(6) | 1.870(11) | Cu(1)–X(7)$^{I}$ | 1.986(8) | X(6)–Cu(1)–X(7)$^{I}$ | 125.0(4) |
| Cu(1)–N(1) | 1.988(7) | X(6)–Cu(1)–N(1) | 136.6(4) | N(1)–Cu(1)–X(7)$^{I}$ | 98.4(3) |
| Compound **2**[b] | | | | | |
| N(1)–Cu(1) | 1.920(4) | N(4)–Cu(2) | 1.877(5) | X(2)–Cu(1)–X(1) | 119.94(14) |
| X(2)–Cu(1) | 1.916(5) | X(3)–Cu(2)–N(4) | 170.1(3) | X(1)$^{I}$–Cu(1)–X(1) | 120.1(3) |
| X(3)–Cu(2) | 1.843(6) | | | | |
| Compound **3**[c] | | | | | |
| Cu(1)–C(3)$^{I}$ | 1.955(10) | Cu(5)–N(7) | 2.000(6) | N(9)$^{III}$–Cu(2)–N(9) | 112.0(3) |
| Cu(1)–N(10) | 2.016(6) | Cu(5)–N(2)$^{VI}$ | 1.888(9) | N(4)–Cu(3)–N(6) | 123.34(19) |
| Cu(1)–C(3)$^{II}$ | 2.221(11) | Cu(6)–N(8) | 1.867(6) | N(6)–Cu(3)–N(6)$^{IV}$ | 112.3(4) |
| Cu(2)–X(1) | 1.882(10) | C(3)$^{I}$–Cu(1)–N(10) | 114.3(2) | N(5)$^{II}$–Cu(4)–N(5)$^{V}$ | 178.0(4) |
| Cu(2)–N(9) | 1.973(6) | N(10)–Cu(1)–N(10)$^{III}$ | 108.3(3) | X(2)$^{VI}$–Cu(5)–N(7) | 124.27(18) |
| Cu(3)–N(4) | 1.887(10) | C(3)$^{I}$–Cu(1)–C(3)$^{II}$ | 107.5(3) | N(7)$^{VI}$–Cu(5)–N(7) | 110.2(3) |
| Cu(3)–N(6) | 1.977(6) | N(10)–Cu(1)–C(3)$^{II}$ | 105.9(2) | N(8)–Cu(6)–N(8)$^{VI}$ | 176.7(4) |
| Cu(4)–N(5)$^{II}$ | 1.864(6) | X(1)–Cu(2)–N(9) | 123.41(17) | | |
| Compound **4**[d] | | | | | |
| Cu(1)–N(14) | 1.895(3) | Cu(5)–X(22) | 1.993(3) | X(23)$^{I}$–Cu(4)–X(18) | 104.79(14) |
| Cu(1)–X(24) | 1.898(4) | Cu(5)–C(13)$^{III}$ | 2.015(4) | X(23)$^{I}$–Cu(4)–C(20) | 112.50(16) |
| Cu(1)–X(16) | 1.991(4) | Cu(5)–C(13)$^{IV}$ | 2.258(4) | X(18)–Cu(4)–C(20) | 110.66(14) |
| Cu(2)–X(15) | 1.896(4) | Cu(6)–X(21) | 1.908(4) | X(18)–Cu(4)–C(20)II | 111.78(15) |
| Cu(2)–N(5) | 1.966(3) | Cu(6)–N(9) | 1.986(3) | C(20)–Cu(4)–C(20)$^{II}$ | 108.86(13) |
| Cu(2)–N(2) | 2.007(3) | N(14)–Cu(1)–X(24) | 135.01(15) | N(19)–Cu(5)–X(22) | 107.06(14) |
| Cu(3)–X(17) | 1.889(4) | N(14)–Cu(1)–X(16) | 114.28(14) | N(19)–Cu(5)–C(13)$^{III}$ | 112.37(15) |
| Cu(3)–N(1) | 1.972(3) | X(24)–Cu(1)–X(16) | 110.55(15) | X(22)–Cu(5)–C(13)$^{III}$ | 117.16(14) |
| Cu(3)–N(6) | 2.014(3) | X(15)–Cu(2)–N(5) | 128.34(16) | N(19)–Cu(5)–C(13)$^{IV}$ | 105.42(14) |
| Cu(4)–X(23)$^{I}$ | 1.967(3) | X(15)–Cu(2)–N(2) | 121.42(14) | X(22)–Cu(5)–C(13)$^{IV}$ | 106.64(14) |
| Cu(4)–X(18) | 2.007(3) | N(5)–Cu(2)–N(2) | 110.19(12) | C(13)$^{III}$–Cu(5)–C(13)$^{IV}$ | 107.44(11) |
| Cu(4)–C(20) | 2.055(4) | X(17)–Cu(3)–N(1) | 130.91(14) | X(21)–Cu(6)–N(9) | 132.72(15) |
| Cu(4)–C(20)$^{II}$ | 2.142(4) | X(17)–Cu(3)–N(6) | 118.08(14) | X(21)–Cu(6)–N(10)$^{V}$ | 117.13(15) |
| Cu(5)–N(19) | 1.979(3) | N(1)–Cu(3)–N(6) | 110.87(12) | N(9)–Cu(6)–N(10)$^{V}$ | 110.11(12) |
| Compound **5**[e] | | | | | |
| Cu(1)–N(3) | 1.978(1) | N(3)–Cu(1)–N(3)$^{II}$ | 141.89(8) | N(4)–Cu(2)–C(1)IV | 102.41(8) |
| Cu(1)–N(2) | 1.993(2) | N(3)–Cu(1)–N(2) | 109.03(4) | N(4)–Cu(2)–C(1)$^{V}$ | 114.74(9) |
| C(1)–Cu(2)$^{I}$ | 2.096(2) | N(2)–C(1)–Cu(2)$^{I}$ | 145.61(5) | C(1)$^{IV}$–Cu(2)–C(1)$^{V}$ | 111.86(8) |
| N(4)–Cu(2) | 2.011(1) | N(4)$^{III}$–Cu(2)–N(4) | 111.16(8) | N(4)–Cu(2)–Cu(2)$^{VI}$ | 124.42(4) |
| Cu(2)–C(1)$^{IV}$ | 2.096(2) | | | | |
| Compound **6**[f] | | | | | |
| X(1)–Cu(1) | 1.877(2) | C(6)–N(3)–Cu(1) | 131.67(14) | X(1)–Cu(1)–N(2) | 114.73(9) |
| N(2)–Cu(1) | 2.088(1) | N(2)$^{I}$–N(3)–Cu(1) | 120.13(12) | N(3)–Cu(1)–N(2) | 102.91(7) |
| N(3)–Cu(1) | 1.967(2) | X(1)–Cu(1)–N(3) | 140.46(9) | | |
| Compound **7**[g] | | | | | |
| X(5)–Cu(2) | 1.885(5) | X(11)–Cu(3) | 1.886(4) | N(2)–Cu(2)–N(2)$^{II}$ | 110.99(19) |
| X(12)–Cu(4) | 1.846(3) | X(13)–Cu(4) | 1.857(5) | X(11)–Cu(3)–N(8) | 123.60(15) |
| X(14)–Cu(5) | 1.839(4) | X(15)–Cu(5) | 1.855(4) | X(11)–Cu(3)–N(10) | 127.48(15) |
| X(16)–Cu(6) | 1.844(4) | X(17)–Cu(6) | 1.866(4) | N(8)–Cu(3)–N(10) | 108.59(12) |
| X(18)–Cu(7) | 1.927(4) | X(19)–Cu(7) | 1.993(4) | X(12)–Cu(4)–X(13) | 168.8(2) |
| X(20)–Cu(8) | 1.895(4) | X(23)–Cu(8) | 1.905(4) | X(14)–Cu(5)–X(15) | 170.4(2) |
| X(21)–Cu(7) | 1.916(4) | Cu(8)–X(22)$^{I}$ | 1.971(4) | X(16)–Cu(6)–X(17) | 166.3(2) |
| N(1)–Cu(1) | 1.992(3) | X(6)–Cu(1)–N(1) | 124.82(9) | X(21)–Cu(7)–X(18) | 133.42(18) |
| N(2)–Cu(2) | 1.970(3) | X(6)–Cu(1)–N(1)$^{II}$ | 124.82(9) | X(21)–Cu(7)–X(19) | 111.59(17) |
| N(6)–Cu(1) | 1.897(6) | N(1)–Cu(1)–N(1)$^{II}$ | 110.35(19) | X(18)–Cu(7)–X(19) | 111.21(18) |
| N(8)–Cu(3) | 1.993(3) | X(5)–Cu(2)–N(2) | 124.51(9) | X(20)–Cu(8)–X(23) | 124.9(2) |
| N(10)–Cu(3) | 2.001(3) | X(5)–Cu(2)–N(2)$^{II}$ | 124.51(9) | X(20)–Cu(8)–X(22)$^{I}$ | 118.52(16) |
| | | | | X(23)–Cu(8)–X(22)$^{I}$ | 115.85(19) |

[a] I: *x* – 1/2, *y*, –*z* + 3/2. [b] I: –*x* + 2, –*y*, –*z*. [c] I: *x* – 1/2, *y* – 1/2, *z* – 1; II: –*x* + 1/2, –*y* + 1/2, –*z* + 2; III: *x*, –*y*, *z*; IV: *x*, –y + 1, *z*; V: –*x* + 1/2, *y* + 1/2, –*z* + 2; VI: *x* – 1/2, *y* + 1/2, *z*. [d] I: *x*, *y*, *z* + 1; II: –*x* + 2, –*y* + 1, –*z* + 1; III: *x* + 1, *y* – 1, *z* + 1; IV: –*x* + 1, –*y* + 1, –*z*; V: –*x* + 1, –*y*, –*z* + 2. [e] I: –*x* + 1/2, *y* – 1/2, –*z*; II: *x*, *y*, –*z*; III: –*x* + 1, –*y* + 1, *z*; IV: *x* + 1/2, –*y* + 1/2, *z*; V: –*x* + 1/2, *y* + 1/2, –*z*; VI: –*x* + 1, –*y* + 1, –*z*. [f] I: –*x* + 1/2, –*y* + 1/2, –*z* + 2. [g] I: *x*, –*y* – 3, *z* + 1/2; II: –*x*, *y*, –*z* – 1/2.

 © 2006 Wiley-VCH Verlag GmbH & Co. KGaA, Weinheim 

**Supporting Information** (see footnote on the first page of this article): Packing diagram of **3**–**6** and additional figure of **7**.

## Acknowledgments

This work was supported by the 973 program of the MOST (001CB108906), the National Science Foundation of China (20425313, 90206040, 20333070, and 20303021), the NSF of Fujian, and the Chinese Academy of Sciences.

[1] L. Toma, R. Lescouezec, J. Vaissermann, F. S. Delgado, C. Ruiz-Perez, R. Carrasco, J. Cano, F. Lloret, M. Julve, *Chem. Eur. J.* **2004**, *10*, 6130–6145.
[2] M. Verdaguer, A. Bleuzen, V. Marvaud, J. Vaissermann, M. Seuleiman, C. Desplanches, A. Scuiller, C. Train, R. Garde, G. Gelly, C. Lomenech, I. Rosenman, P. Veillet, C. Cartier, F. Villain, *Coord. Chem. Rev.* **1999**, *190*, 1023–1047.
[3] M. Ohba, H. Okawa, *Coord. Chem. Rev.* **2000**, *198*, 313–328.
[4] T. Korzeniak, K. Stadnicka, R. Pelka, M. Balanda, K. Tomala, K. Kowalski, B. Sieklucka, *Chem. Commun.* **2005**, 2939–2941.
[5] L. Yi, B. Ding, B. Zhao, P. Cheng, D. Z. Liao, S. P. Yan, Z. H. Jiang, *Inorg. Chem.* **2004**, *43*, 33–43.
[6] J. M. Zheng, S. R. Batten, M. Du, *Inorg. Chem.* **2005**, *44*, 3371–3373.
[7] P. V. Bernhardt, F. Bozoglian, B. P. Macpherson, *Coord. Chem. Rev.* **2005**, *249*, 1902–1916.
[8] D. F. Shriver, *Struct. Bonding (Berlin)* **1966**, *1*, 32–58.
[9] H. Zhang, J. Cai, X. L. Feng, B. H. Ye, X. Y. Li, L. N. Ji, *J. Chem. Soc., Dalton Trans.* **2000**, 1687–1688.
[10] D. J. Chesnut, A. Kusnetzow, R. Birge, J. Zubieta, *Inorg. Chem.* **1999**, *38*, 5484–5494.
[11] E. Colacio, J. M. Dominguez-Vera, F. Lloret, J. M. M. Sanchez, R. Kivekas, A. Rodriguez, R. Sillanpaa, *Inorg. Chem.* **2003**, *42*, 4209–4214.
[12] a) E. Colacio, R. Kivekas, F. Lloret, M. Sunberg, J. S. Varela, M. Bardaji, A. Laguna, *Inorg. Chem.* **2002**, *41*, 5141–5149; b) E. Colacio, A. Debdoubi, R. Kivekas, A. Rodriguez, *Eur. J. Inorg. Chem.* **2005**, 2860–2868.
[13] D. T. Cromer, A. C. Larson, *Acta Crystallogr., Sect. B* **1972**, *28*, 858–861.
[14] Crystallographic data for $K[Cu(CN)_3]_n \cdot H_2O$: mononclinic, space group $P2_1/c$, $a$ = 12.034(2), $b$ = 8.2249(15), $c$ = 7.4987(14) Å, $\beta$ = 96.637(4)°, $V$ = 737.3(2) Å$^3$, $Z$ = 4, $\rho$ = 2.363 g cm$^{-3}$, $F(000)$= 504, $\mu$(Mo-$K_\alpha$) = 6.259 mm$^{-1}$, GOF = 1.129. Of 2442 total reflections collected, 1285 were unique [$R$(int)= 0.0477] $R_1$ ($wR_2$) = 0.0867 (0.1734) for 91 parameters. CCDC-284904 contains the supplementary crystallographic data for this paper. These data can be obtained free of charge from The Cambridge Crystallographic Data Centre via www.ccdc.cam.ac.uk/data_request/cif.
[15] P. M. Forster, A. R. Burbank, C. Livage, G. Férey, A. K. Cheetham, *Chem. Commun.* **2004**, 368–369.
[16] A. J. Blake, N. R. Brooks, N. R. Champness, P. A. Cooke, A. M. Deveson, D. Fenske, P. Hubberstey, W.-S. Li, M. Schröder, *J. Chem. Soc., Dalton Trans.* **1999**, 2103–2110.
[17] J. R. Black, N. R. Champness, W. Levason, G. Reid, *J. Chem. Soc., Chem. Commun.* **1995**, 1277–1278.
[18] a) A. Rujiwatra, C. J. Kepert, M. J. Rosseinsky, *Chem. Commun.* **1999**, 375–376; b) M. Kondo, T. Yoshitomi, K. Seki, H. Matsuzaka, S. Kitagawa, *Angew. Chem. Int. Ed. Engl.* **1997**, *36*, 1725–1727.
[19] M. J. Zaworotko, *Chem. Commun.* **2001**, 1–2.
[20] Z.-Y. Fu, X.-T. Wu, J.-C. Dai, L.-M. Wu, C.-P. Cui, S.-M. Hu, *Chem. Commun.* **2001**, 1856–1857.
[21] a) J.-C. Dai, X.-T. Wu, Z.-Y. Fu, S.-M. Hu, W.-X. Du, C.-P. Cui, L.-M. Wu, H.-H. Zhang, R.-Q. Sun, *Chem. Commun.* **2002**, 12–13; b) R. E. Melendez, C. V. K. Sharma, M. J. Zaworotko, C. Bauer, R. D. Rogers, *Angew. Chem. Int. Ed. Engl.* **1996**, *35*, 2213–2215.
[22] R. I. Papasergio, C. L. Raston, A. H. White, *J. Chem. Soc., Dalton Trans.* **1987**, 3085–3091.
[23] C. M. Che, Z. Mao, V. M. Miskowski, M. C. Tse, C. K. Chan, K. K. Cheung, D. L. Phillips, K. H. Leung, *Angew. Chem. Int. Ed.* **2000**, *39*, 4084–4086.
[24] J. Beck, J. Strahle, *Angew. Chem. Int. Ed. Engl.* **1985**, *24*, 409–410.
[25] M. Vitale, P. C. Ford, *Coord. Chem. Rev.* **2001**, *219*, 3–16.
[26] M. Henary, J. L. Wootton, S. I. Khan, J. I. Zink, *Inorg. Chem.* **1997**, *36*, 796–801.
[27] B. W. Pfennig, A. B. Bocarsly, *J. Phys. Chem.* **1992**, *96*, 226–233.
[28] C. Dlaz, A. Arancibia, *Inorg. Chim. Acta* **1998**, *269*, 246–263.
[29] K. Nakamoto, *Infrared and Roman Spectra of Inorganic Coordination Compounds*, 4th ed., Wiley, New York, **1986**, p. 272.
[30] G. A. Bowmaker, J. C. Effendy, C. E. Reid, F. Rickard, B. W. Skelton, A. H. White, *J. Chem. Soc., Dalton Trans.* **1998**, 2139–2146.
[31] D. J. Chesnut, A. Kusnetzow, R. Birge, J. Zubieta, *J. Chem. Soc., Dalton Trans.* **2001**, 2581–2586.
[32] G. M. Sheldrick, *SHELXS97, Program for Solution of Crystal Structures*, University of Göttingen, Germany, **1997**.

Received: November 3, 2005
Published Online: April 20, 2006

 © 2006 Wiley-VCH Verlag GmbH & Co. KGaA, Weinheim 

DOI: 10.1002/ejic.200600009

# Transformation of a Tetranuclear Copper(II) Complex Bridged by Sugar Phosphates into Nucleotide-Containing $Cu_4$ Aggregations

**Merii Kato,[a] Ajay Kumar Sah,[a] Tomoaki Tanase,*[a] and Masahiro Mikuriya[b]**

**Keywords:** Coordination chemistry / Copper / Nucleic acids / Carbohydrates / Clusters

Reaction of $[Cu_4(\mu\text{-OH})\{\mu\text{-}(\alpha\text{-D-Glc-1P})\}_2(L)_4(H_2O)_2]X_3$ (**1a**: L = bpy, X = $NO_3$, α-D-Glc-1P = α-D-glucopyranose-1-phosphate) with $Na_2[H_2ATP]$ (ATP = adenosine 5′-triphosphate) readily afforded the ATP-bridged tetranuclear copper(II) complex $[Cu_4(\mu\text{-ATP})_2(bpy)_4]$ (**3**), which was characterized by X-ray crystallographic analysis to consist of four linearly dispersed $\{Cu^{II}(bpy)\}^{2+}$ fragments bridged by two triphosphate groups of the ATP tetravalent anions. The sugar and adenine base parts of the ATP moieties are away from the copper(II) centers, but the structure was stabilized by weak intramolecular π–π stacking between the ATP purine ring and two bpy ligands and intermolecular hydrogen bonding between the adenine base pairs. The variable-temperature magnetic susceptibility of complex **3** exhibited only weak antiferromagnetic couplings between the four linearly dispersed $Cu^{II}$ ions. A similar reaction of **1a** or **2** (L = phen, X = $NO_3$) with $Na_2$[IMP] (IMP = inosine 5′-monophosphate) yielded a different type of tetracopper(II) complex formulated as $[Cu_4\{\mu\text{-(IMP-H)}\}_2(L)_4(H_2O)_4](NO_3)_2$ [L = bpy (**5**), phen (**6**)], in which the IMP moieties are deprotonated at the N-1 position of the nucleobase, forming IMP-H trianions, and four $\{Cu(bpy)(H_2O)\}^{2+}$ fragments are connected through the N-1, N-7, and O-6 atoms of the nucleobase and the monodentate 5′-phosphate group. Reaction of **1b** (L = bpy, X = Cl) with $Na_2$[UMP] (UMP = uridine 5′-monophosphate) resulted in a polymeric compound formulated as $\{[Cu\{\mu\text{-(UMP-H)}\}(bpy)(H_2O)]_2[Cu_4(\mu\text{-OH})\{\mu\text{-}(\alpha\text{-D-Glc-1P})\}_2(bpy)_4(H_2O)_2]Cl\}_n$ (**7**). The N-3 deprotonated $[UMP\text{-}H]^{3-}$ anions connect $\{Cu(bpy)(H_2O)\}^{2+}$ fragments through the N-3 nitrogen atom and the phosphate oxygen atoms to afford $C_2$-helical coordination polymers and the tetracopper(II) complex cations, $[Cu_4(\mu\text{-OH})\{\mu\text{-}(\alpha\text{-D-Glc-1P})\}_2(bpy)_4(H_2O)_2]^{3+}$, are incorporated between the polymer chains with a $C_2$-chiral arrangement of the $\{Cu_4(\mu\text{-OH})(\mu\text{-}PO_4)_2(bpy)_4(H_2O)_2\}$ framework constrained to the *Λ*-form through inter- and intramolecular stacking interactions between the bpy ligands.
(© Wiley-VCH Verlag GmbH & Co. KGaA, 69451 Weinheim, Germany, 2006)

## Introduction

The interaction of metal ions with nucleotides and polynucleotides (DNA and RNA) has been extensively studied with a variety of bioinorganic interests, concerning metalloenzymes that promote cleavage of nucleotide phosphate ester bonds, such as DNA polymerase I ($Mg^{2+}$, $Mn^{2+}$, $Zn^{2+}$), P1 nuclease ($Zn^{2+}$), and RNase H ($Mg^{2+}$, $Mn^{2+}$), and so forth,[1] a number of bioenergetic processes coupled with phosphoryl transfer reactions of high-energy nucleotides, usually adenosine triphosphate (ATP), mediated by metal ions ($Mg^{2+}$, $Mn^{2+}$, etc.),[2] and the action of $Pt^{II}$ complexes as anticancer drugs,[3] and so on. To elucidate the nucleotide–metal interaction in such biological processes, a number of binary and ternary transition-metal complexes involving nucleotides have been reported; however, most are mononuclear complexes or polymeric compounds containing mononuclear metal centers.[4] Whereas nucleotides are potentially ambivalent with their multiple metal-binding sites, phosphate groups, hydroxy groups of the sugar moiety, and nitrogen and oxygen atoms of the nucleobase, studies of discrete, multinuclear transition-metal complexes with nucleotides have been extremely scarce thus far. As to the complexes of nucleotides having di- and triphosphate groups, successfully isolated multimetallic complexes are only two examples with dinuclear $Zn^{2+}$ and $Cu^{2+}$ systems, $[Zn_2(\mu\text{-}H_2ATP)_2(bpy)_2]$ (**8**)[5] and $[Cu_2(\mu\text{-}H_2ATP)_2(phen)_2]$ (**9**)[6] (bpy = 2,2′-bipyridyl, phen = 1,10-phenanthroline). The reason for the lack of studies may not only be the difficulty of getting crystalline compounds because of their ambivalent properties, but also the fact that most divalent metal ions catalyze the nonenzymatic hydrolysis of the nucleotide phosphate groups. Notably, one of the best characterized DNA cleavage reactions is that promoted by $[Cu(phen)_2]^{2+}$.[7] Even for thermodynamically stable nucleoside monophosphate esters, a very restricted number of structures are available for multinuclear transition-metal complexes, $[Cu_4\{\mu\text{-(IMP-H)}\}(phen)_4(H_2O)_2](NO_3)_2$ (**6**, IMP-H = N-1 deprotonated inosine 5′-monophosphate),[8] $[\{Ru(\mu\text{-AMP})(\eta^6\text{-}p\text{-}MeC_6H_4iPr)\}_3]$ (AMP = adenosine 5′-monophosphate),[9] $Na_2[Mo_5O_{15}(\mu\text{-HAMP})_2]$,[10] and

[a] Department of Chemistry, Faculty of Science, Nara Women's University,
Kitauoya-higashi-machi, Nara 630-8285, Japan
Fax: +81-742-20-3399
E-mail: tanase@cc.nara-wu.ac.jp
[b] Department of Chemistry, School of Science and Technology, Kwansei Gakuin University,
2-1 Gakuen, Sanda-shi, Hyogo 669-1337, Japan

 © 2006 Wiley-VCH Verlag GmbH & Co. KGaA, Weinheim 

$[Mo_2(\eta^5\text{-}C_5H_5)_4(\mu\text{-dGMP})_2]$ (dGMP = 2′-deoxyguanosine 5′-monophosphate),[11] and for dicopper(II) complexes involving the $\{LCu(\mu\text{-}OPO)_2CuL\}$ eight-membered macrocycles with nucleoside 5′-monophosphates [L = bpy, phen, and bis(2-pyridyl)amine].[12]

Recently, we synthesized a tetranuclear copper(II) complex bridged by α-D-glucose-1-phosphate (α-D-Glc-1P) dianions, $[Cu_4(\mu\text{-OH})\{\mu\text{-}(\alpha\text{-D-Glc-1P})\}_2(L)_4(H_2O)_2]X_3$ [L = bpy, X = $NO_3$ (**1a**), Cl (**1b**), Br (**1c**); L = phen, X = $NO_3$ (**2**)] (Figure 1a).[13] Complex **2** was structurally characterized as the first example of a transition-metal complex containing free sugar monophosphates, in which four $\{Cu(phen)\}^{2+}$ fragments are held together by a hydroxo bridge and two phosphate groups of α-D-Glc-1P moieties to result in a trapezoidal $Cu^{II}_4$ framework with the D-glucopyranosyl pendants away from the metal centers.[13] In the crystal structure of **2**, two $C_2$-chiral structures with respect to the arrangement of bpy ligands, *Δ* (cation A) and *Λ* (cation B), were observed in a 1:1 ratio; both are coupled to a different orientation of α-D-glucopyranosyl pendants, upward and downward, respectively (Figure 1b, c). In addition, complex **1a** was found to readily undergo a phosphate ester exchange reaction and be transformed into an ATP-stabilized tetracopper(II) complex, $[Cu_4(\mu\text{-ATP})_2(bpy)_4]$ (**3**). These results prompted us to investigate the reactions of **1** and **2** with several nucleotides. In the present study, we wish to report the full details of synthesis and characterization of **3**, together with those for $[Cu_4\{\mu\text{-}(IMP\text{-}H)\}_2(L)_4(H_2O)_4](NO_3)_2$ [L = bpy (**5**), phen (**6**)] and the polymeric compound formulated as $\{[Cu\{\mu\text{-}(UMP\text{-}H)\}(bpy)(H_2O)]_2[Cu_4(\mu\text{-OH})\{\mu\text{-}(\alpha\text{-D-Glc-1P})\}_2(bpy)_4(H_2O)_2]Cl\}_n$ (**7**, UMP-H = N-3 deprotonated uridine 5′-monophosphate). Although the structure of **3** was briefly reported,[13a] the detailed ATP-bridging structure in **3** compared with related compounds and its magnetic property are presented in this report. The present reaction may also provide an efficient route to a series of tetranucler ternary $Cu^{II}$ complexes with IMP moieties and diimine auxiliary ligands. In addition, the structure of **7** revealed an interesting chiral influence transfer from the $C_2$-helical structure of the polymer $\{[Cu\{\mu\text{-}(UMP\text{-}H)\}(bpy)(H_2O)]^-\}_n$ to the $C_2$-chiral structure of the tetranuclear $Cu^{II}$ units involved in **7**, $[Cu_4(\mu\text{-OH})\{\mu\text{-}(\alpha\text{-D-Glc-1P})\}_2(bpy)_4(H_2O)_2]^{3+}$, through inter- and intramolecular bpy–bpy stacking interactions.

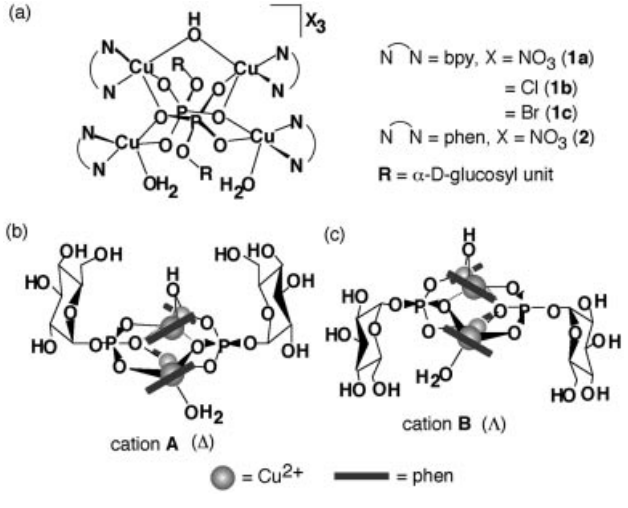


Figure 1. (a) Structure of **1a**–**c** and **2**. Schematic structures for (b) cation **A** and (c) cation **B** involved in **2**. Gray bars represent the phen ligands which are arranged in *Δ* and *Λ* configurations with respect to the pseudo-$C_2$ axis for cations **A** and **B**, respectively.

## Results and Discussion

### Synthesis and Structure of $[Cu_4(\mu\text{-ATP})_2(bpy)_4]$ (3)

When the tetranuclear copper(II) complex bridged by a sugar phosphate, $[Cu_4(\mu\text{-OH})\{\mu\text{-}(\alpha\text{-D-Glc-1P})\}_2(bpy)_4(H_2O)_2](NO_3)_3$ (**1a**), was treated with $Na_2[H_2ATP]$ in a 1:2 ratio at room temperature, a phosphate ester exchange reaction readily proceeded to result in the formation of an ATP-bridged tetracopper(II) complex, $[Cu_4(\mu\text{-ATP})_2(bpy)_4]$ (**3**), in good yield (56%) and crystalline form (Scheme 1).

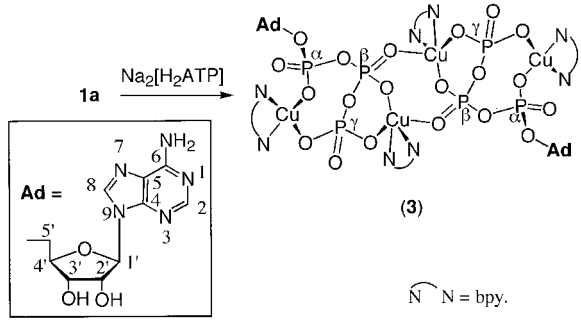


Scheme 1.

The IR spectrum showed the presence of ATP anions and bpy ligands, and the CD spectral pattern around the d–d transition region for $Cu^{II}$ ions is quite different from that of the starting complex **1a**, indicating an introduction of ATP on the tetranuclear centers. From the mother liquor, a very small amount of a pyrophosphate-bridged dicopper complex, $[Cu_2(\mu\text{-}P_2O_7)(bpy)_2(H_2O)_2]$ (**4**),[14] was obtained, suggesting that hydrolytic cleavage of the triphosphate group occurred to a small extent during the reaction. It should be noted that complex **3** was not obtained just by mixing $Cu(NO_3)_2{\cdot}3H_2O$ with $Na_2[H_2ATP]$ and bpy, demonstrating that the tetranuclear $Cu^{II}$ centers of **1a** provide a suitable platform to stabilize the triphosphate unit of ATP.

The structure of **3** was determined by X-ray crystallographic analysis; an ORTEP plot with the atomic numbering scheme is given in Figure 2a and selected bond lengths and angles are listed in Table 1. The structure consists of four linearly dispersed $\{Cu^{II}(bpy)\}^{2+}$ fragments bridged by two ATP tetravalent anions with interatomic distances of Cu1···Cu2 = 3.444(1) Å, Cu3···Cu4 = 3.4523(8) Å, and Cu2···Cu4 = 5.0613(7) Å. The triphosphate group of ATP exclusively connects two $Cu^{II}$ ions, each ligated by a bpy ligand, to afford the square-planar dicopper(II) unit, $\{Cu_2(\mu\text{-ATP})(bpy)_2\}$. The adenine bases and D-ribofuranosyl parts are away from the metal centers without any inter-

 © 2006 Wiley-VCH Verlag GmbH & Co. KGaA, Weinheim 

actions. The two dinuclear fragments are further connected through the axial coordination of β-phosphate oxygen atoms [Cu2–O23 = 2.263(4) Å, Cu4–O10 = 2.247(4) Å], resulting in a characteristic eight-membered puckered ring of the central part (Figure 2b). Whereas metal complexes with ATP could provide useful insights to elucidate bioenergetic processes, characterized examples are still rare and most are mononuclear species[15] and their sodium salts.[16] In particular, those containing multimetallic centers are strictly limited; the only available structures with multinuclear transition-metal ions are the dinuclear complexes $[Zn_2(\mu\text{-}H_2ATP)_2(bpy)_2]$ (**8**)[5] and $[Cu_2(\mu\text{-}H_2ATP)_2(phen)_2]$ (**9**),[6] and with the present complex **3** the first crystal structure of a tetranuclear transition-metal complex with ATP anions is available. Both complexes **8** and **9** possess an essentially identical structure with the triphosphate group chelating to a metal ion through the three α-, β-, and γ-phosphate oxygen atoms in a facial mode, and another γ-phosphate oxygen atom attached to the other metal ion, forming an $[MOPO]_2$ eight-membered macrocycle. The metal centers adopt an $[N_2O_4]$ octahedral geometry. In contrast, in the present structure, the bridging behavior of the ATP triphos-

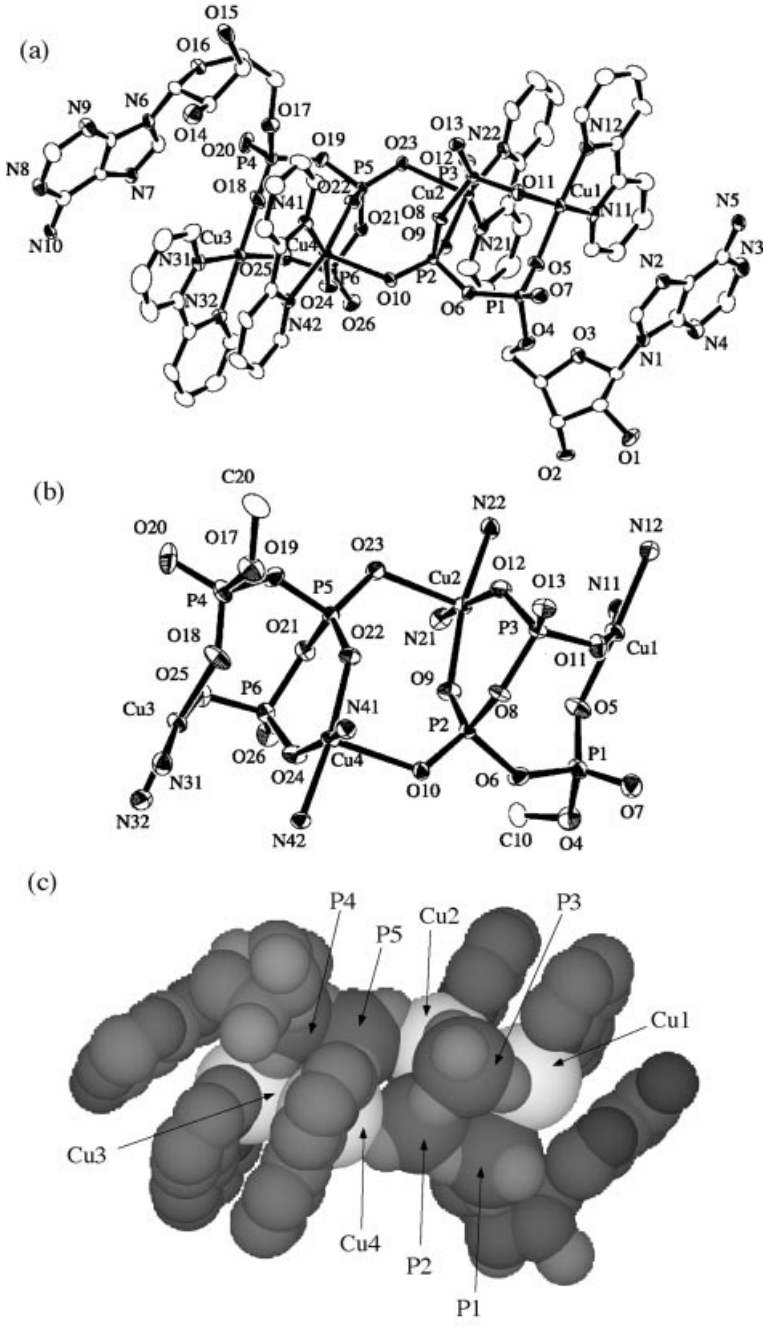


Figure 2. (a) ORTEP plot of **3** with hydrogen atoms omitted for clarity. (b) Core structure of **3**; the adenosine parts and the carbon atoms of bpy ligands are omitted. (c) Perspective drawing of **3** with van der Waals radii.

 © 2006 Wiley-VCH Verlag GmbH & Co. KGaA, Weinheim 

Table 1. Selected bond lengths [Å] and angles [°] for complex **3**.

| | | | |
|---|---|---|---|
| Cu1–O5 | 1.943(4) | Cu3–O18 | 1.922(4) |
| Cu1–O11 | 1.951(4) | Cu3–O25 | 1.919(4) |
| Cu1–N11 | 1.983(5) | Cu3–N31 | 2.021(4) |
| Cu1–N12 | 1.978(4) | Cu3–N32 | 2.006(5) |
| Cu2–O9 | 1.982(4) | Cu4–O10 | 2.247(4) |
| Cu2–O12 | 1.934(4) | Cu4–O22 | 1.935(4) |
| Cu2–O23 | 2.263(4) | Cu4–O24 | 1.921(4) |
| Cu2–N21 | 1.980(4) | Cu4–N41 | 2.011(4) |
| Cu2–N22 | 1.973(5) | Cu4–N42 | 2.032(4) |
| P1–O4 | 1.582(4) | P4–O17 | 1.580(4) |
| P1–O5 | 1.496(5) | P4–O18 | 1.501(5) |
| P1–O6 | 1.592(4) | P4–O19 | 1.600(4) |
| P1–O7 | 1.487(4) | P4–O20 | 1.471(5) |
| P2–O6 | 1.611(5) | P5–O19 | 1.602(5) |
| P2–O8 | 1.583(3) | P5–O21 | 1.577(4) |
| P2–O9 | 1.488(4) | P5–O22 | 1.503(4) |
| P2–O10 | 1.490(3) | P5–O23 | 1.487(3) |
| P3–O8 | 1.644(3) | P6–O21 | 1.637(4) |
| P3–O11 | 1.519(4) | P6–O24 | 1.520(5) |
| P3–O12 | 1.512(5) | P6–O25 | 1.534(4) |
| P3–O13 | 1.497(4) | P6–O26 | 1.482(4) |
| O5–Cu1–O11 | 91.0(2) | O18–Cu3–O25 | 92.8(2) |
| N11–Cu1–N12 | 82.0(2) | N31–Cu3–N32 | 80.5(2) |
| O9–Cu2–O12 | 93.7(2) | O10–Cu4–O22 | 92.5(2) |
| O9–Cu2–O23 | 97.5(1) | O10–Cu4–O24 | 91.6(2) |
| O12–Cu2–O23 | 88.4(2) | O22–Cu4–O24 | 95.2(2) |
| N21–Cu2–N22 | 81.5(2) | N41–Cu4–N42 | 80.2(2) |
| O5–P1–O6 | 109.4(2) | O18–P4–O19 | 110.7(2) |
| O6–P2–O8 | 103.4(2) | O19–P5–O21 | 102.8(2) |
| O6–P2–O9 | 109.4(2) | O19–P5–O22 | 109.1(2) |
| O8–P2–O9 | 111.2(2) | O21–P5–O22 | 111.3(2) |
| O8–P3–O11 | 106.5(2) | O21–P6–O24 | 106.4(2) |
| O8–P3–O12 | 106.7(2) | O21–P6–O25 | 105.1(2) |
| O11–P3–O12 | 111.8(2) | O24–P6–O25 | 110.7(2) |
| Cu1–O5–P1 | 132.8(2) | Cu3–O18–P4 | 135.0(3) |
| P1–O6–P2 | 133.6(3) | P4–O19–P5 | 131.0(3) |
| P2–O8–P3 | 128.7(2) | P5–O21–P6 | 129.4(2) |
| Cu2–O9–P2 | 133.7(2) | Cu4–O22–P5 | 131.8(2) |
| Cu4–O10–P2 | 124.0(2) | Cu2–O23–P5 | 118.1(2) |
| Cu1–O11–P3 | 123.4(3) | Cu4–O24–P6 | 131.5(2) |
| Cu2–O12–P3 | 128.8(3) | Cu3–O25–P6 | 116.2(3) |

phate group in the dimeric unit of **3** is remarkably different, as two $Cu^{II}$ ions are held together by the bridges from α- and β-phosphate oxygen atoms [Cu1–O5 = 1.943(4) Å, Cu3–O18 = 1.922(4) Å; Cu2–O9 = 1.982(4) Å, Cu4–O22 = 1.935(4) Å] and from two oxygen atoms of the γ-phosphate unit [Cu1–O11 = 1.951(4) Å, Cu2–O12 = 1.934(4) Å; Cu3–O25 = 1.919(4) Å, Cu4–O24 = 1.921(4) Å], resulting in an unprecedented bridging structure of the ATP triphosphate group (Figure 2b). While the triphosphate backbones are folded, as indicated by the angles P1–P2–P3 = 86.11(4)° and P4–P5–P6 = 88.23(5)°, like complexes **8** and **9**, strain involved in the triphosphate parts of **3** might be released to some extent, in comparison with those in the dimers of **8** and **9** and the mononuclear complexes.[5,6,15] In complex **3**, the eight-membered chelate ring by the α- and γ-phosphate oxygen atoms is fused with the six-membered chelate ring by the β- and γ-oxygen atoms, which should be contrasted with two fused six-membered chelate rings from α-/β- and β-/γ-phosphate oxygen atoms in **8** and **9**. The $\{Cu_4(\mu\text{-}P_3O_{10})_2(bpy)_4\}$ core structure, except the adenosine moieties, possesses a pseudocentrosymmetry; the outer two copper ions (Cu1, Cu3) take an $[N_2O_2]$ square-planar geometry and the inner two (Cu2, Cu4) are in an $[N_2O_3]$ square-pyramidal environment with usual bond lengths and angles. It should be noted that, by using the $HADP^{2-}$ anion, a related tetranuclear copper(II) complex, $[Cu_4(\mu\text{-HADP})_2(NO_3)_2(bpy)_2(H_2O)_2]^{2+}$, was prepared and involves a central eight-membered macrocycle very similar to that of **3** (ADP = adenosine 5′-diphosphate).[17]

The adenosine residues take *anti*–C2′*–endo* conformation without any direct interaction with metal ions, but weak intramolecular π–π stacking between the purine ring and two bpy ligands is observed, as in complexes **8** and **9**.[5,6] The adenine–bpy and bpy–bpy intramolecular stacking interactions in **3** (Figure 2c) enhance its stability and may prevent coordination of the adenosine moieties to the metal centers. In the lattice packing, the N-7 imino and the N-6 amino groups of the adenine base are hydrogen-bonded to the same functional pair of ATP anchoring on the neighboring molecule [N2···N10* = 2.870(6) Å, N5···N7* = 2.980(6) Å; the atoms with * are generated by a symmetry operation of $x - 1$, $y$, $z + 1$], these hydrogen-bonding networks further stabilizing the ATP moieties trapped onto the tetracopper(II) aggregation.

The temperature-dependent magnetic susceptibility data for complex **3** are shown as plots of $\chi_M$ and $\mu_{eff}$ versus $T$ over a range of 4.5–300 K (Figure 3), indicating a very weak antiferromagnetic interaction with $\mu_{eff}$ per $Cu_4$ of 4.24 $\mu_B$ (300 K) and 3.22 $\mu_B$ (4.5 K). The magnetic susceptibility data were fitted by a theoretical expression derived from the van Vleck equation with the $J_1$ and $J_2$ spin-exchange coupling constants [Equation (1)] to afford the best-fitted values of $g = 2.33$, $J_1 = -1.2$ cm$^{-1}$, and $J_2 = -3.1$ cm$^{-1}$. The results clearly demonstrate that antiferromagnetic spin-exchange couplings are not effective in the triphosphate-bridged dimer and interdimers, which was consistent with the structural features involving no effective pathway for metal-to-metal magnetic interactions.

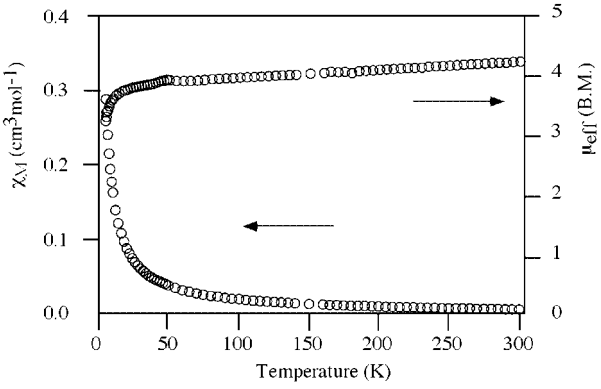


Figure 3. Plots of magnetic susceptibility ($\chi_M$) and $\mu_{eff}$ vs. $T$ for **3**.

### Synthesis and Structure of $[Cu_4\{\mu\text{-(IMP-H)}\}_2(L)_4(H_2O)_4](NO_3)_2$ [L = bpy (5), phen (6)]

The tetranuclear copper complexes **1a** and **2** readily reacted with $Na_2$[IMP] in water to yield green block-shaped

 © 2006 Wiley-VCH Verlag GmbH & Co. KGaA, Weinheim 

crystals of $[Cu_4\{\mu\text{-}(IMP\text{-}H)\}_2(L)_4(H_2O)_4](NO_3)_2$ [L = bpy (**5**) 64%; phen (**6**) 26%], where the abbreviation of IMP-H represents the N-1 deprotonated inosine 5′-monophosphate trianion (Scheme 2). The IR spectral patterns of **5** and **6** are very similar, indicating the presence of IMP and nitrate anions as well as the diimine ligands. The circular dichroism spectra of **5** and **6** also resemble each other, suggesting incorporation of the nucleotide moieties into the tetranuclear $Cu^{II}$ centers. The ESI mass spectra for aqueous solutions containing **5** and **6** exhibit divalent cationic peaks corresponding to $\{Cu_4(IMP\text{-}H)_2(L)_4\}^{2+}$ at 783.16 for **5** (L = bpy) and 831.14 for **6** (L = phen).

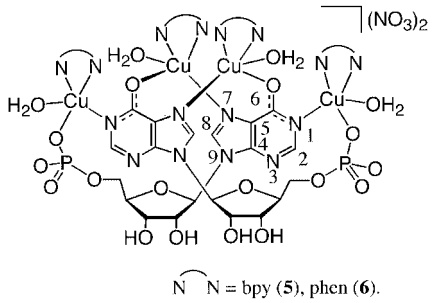


Scheme 2.

A detailed structure of **6** was determined by low-temperature X-ray crystallography using a CCD detector. As the present crystallographic structure for **6**·21.5$H_2O$ is almost identical within the experimental errors to the structure for **6**·14$H_2O$ reported by Bau,[8] except for the number of identified solvent water molecules, we wish to describe the structural features briefly as follows. An ORTEP plot for the complex cation of **6** with the atomic numbering scheme is given in Figure 4 and some selected bond lengths and angles are listed in Table 2. In the complex cation of **6**, four $\{Cu(phen)(H_2O)\}^{2+}$ fragments are held together by two inosine monophosphate anions to result in a pseudo-$C_2$-symmetrical structure [Cu1···Cu2 = 3.431(1) Å, Cu1···Cu3 = 4.232(1) Å, Cu2···Cu4 = 4.254(1) Å]. Each inosine monophosphate moiety is deprotonated at the N-1 position of the nucleobase and bridges four $Cu^{II}$ ions

Table 2. Selected bond lengths [Å] and angles [°] for complex **6**.

| | | | |
|---|---|---|---|
| Cu1–O5 | 1.943(4) | Cu3–O18 | 1.922(4) |
| Cu1–O1 | 2.175(4) | Cu2–O2 | 2.193(4) |
| Cu1–O21 | 1.980(4) | Cu2–O11 | 1.955(4) |
| Cu1–N2 | 2.018(4) | Cu2–N6 | 2.018(4) |
| Cu1–N11 | 2.010(5) | Cu2–N13 | 2.010(4) |
| Cu1–N12 | 2.015(4) | Cu2–N14 | 2.022(5) |
| Cu3–O3 | 2.225(4) | Cu4–O4 | 2.227(5) |
| Cu3–O16 | 1.943(4) | Cu4–O26 | 1.946(4) |
| Cu3–N7 | 2.021(5) | Cu4–N3 | 2.042(5) |
| Cu3–N15 | 2.024(5) | Cu4–N17 | 2.030(5) |
| Cu3–N16 | 2.023(5) | Cu4–N18 | 2.017(5) |
| P1–O15 | 1.623(4) | P2–O25 | 1.612(4) |
| P1–O16 | 1.534(4) | P2–O26 | 1.531(4) |
| P1–O17 | 1.520(4) | P2–O27 | 1.514(4) |
| P1–O18 | 1.508(4) | P2–O28 | 1.502(4) |
| O11–C13 | 1.263(7) | O21–C23 | 1.272(7) |
| N3–C13 | 1.365(7) | N7–C23 | 1.367(7) |
| N3–C14 | 1.350(8) | N7–C24 | 1.345(8) |
| O1–Cu1–O21 | 93.5(2) | O2–Cu2–O11 | 91.8(2) |
| O1–Cu1–N2 | 92.9(2) | O2–Cu2–N6 | 92.1(2) |
| O21–Cu1–N2 | 96.5(2) | O11–Cu2–N6 | 95.8(2) |
| N11–Cu1–N12 | 82.1(2) | N13–Cu2–N14 | 82.2(2) |
| O3–Cu3–O16 | 97.7(2) | O4–Cu4–O26 | 99.7(2) |
| O3–Cu3–N7 | 99.0(2) | O4–Cu4–N3 | 98.4(2) |
| O16–Cu3–N7 | 90.6(2) | O26–Cu4–N3 | 92.9(2) |
| N15–Cu3–N16 | 81.5(2) | N17–Cu4–N18 | 81.7(2) |
| O15–P1–O16 | 101.6(2) | O25–P2–O26 | 101.1(2) |
| Cu2–O11–C13 | 127.3(4) | Cu1–O21–C23 | 125.6(3) |
| Cu3–O16–P1 | 131.5(3) | Cu4–O26–P2 | 129.1(2) |

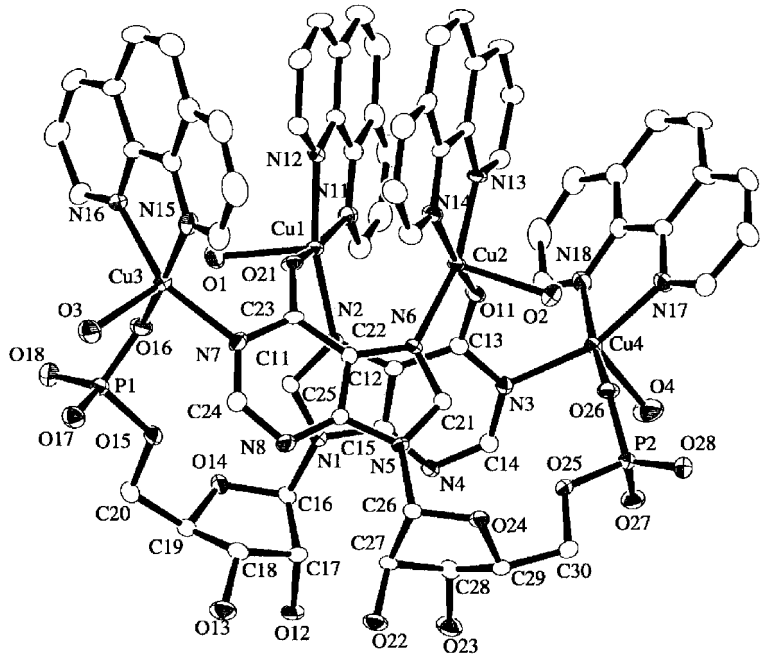


Figure 4. ORTEP plot of **6** with hydrogen atoms omitted for clarity.

 © 2006 Wiley-VCH Verlag GmbH & Co. KGaA, Weinheim 

through the deprotonated N-1 nitrogen atom [Cu3–N7 = 2.021(5) Å, Cu4–N3 = 2.042(5) Å], the oxygen atom at C-6 position [Cu1–O21 = 1.980(4) Å, Cu2–O11 = 1.955(4) Å], the N-7 nitrogen atom [Cu1–N2 = 2.018(4) Å, Cu2–N6 = 2.018(4) Å], and the monodentate phosphate oxygen atom [Cu3–O16 = 1.943(4) Å, Cu4–O26 = 1.946(4) Å]. There is no interaction between the D-ribose units and the metal centers. All four $Cu^{II}$ ions take an $[N_3O_2]$ square-pyramidal coordination geometry with the water at its apical site (av. Cu–O = 2.205 Å). The structural features are essentially identical to those already reported.[8]

### Transformation of 1b to $[Cu\{\mu\text{-}(UMP\text{-}H)\}(bpy)(H_2O)]_2[Cu_4(\mu\text{-}OH)\{\mu\text{-}(\alpha\text{-}D\text{-}Glc\text{-}1P)\}_2(bpy)_4(H_2O)_2]Cl$ (7)

When complex **1b** was treated with uridine 5′-monophosphate disodium salt ($Na_2$[UMP]) in water, blue crystals formulated as $[Cu\{\mu\text{-}(UMP\text{-}H)\}(bpy)(H_2O)]_2[Cu_4(\mu\text{-}OH)\{\mu\text{-}(\alpha\text{-}D\text{-}Glc\text{-}1P)\}_2(bpy)_4(H_2O)_2]Cl$ (**7**) were obtained in moderate yield (30%) (Scheme 3), which were characterized by elemental analysis, IR, UV/Vis, and CD spectroscopic data, and X-ray crystallographic analysis. The X-ray crystal structure revealed that compound **7** is composed of a dis-

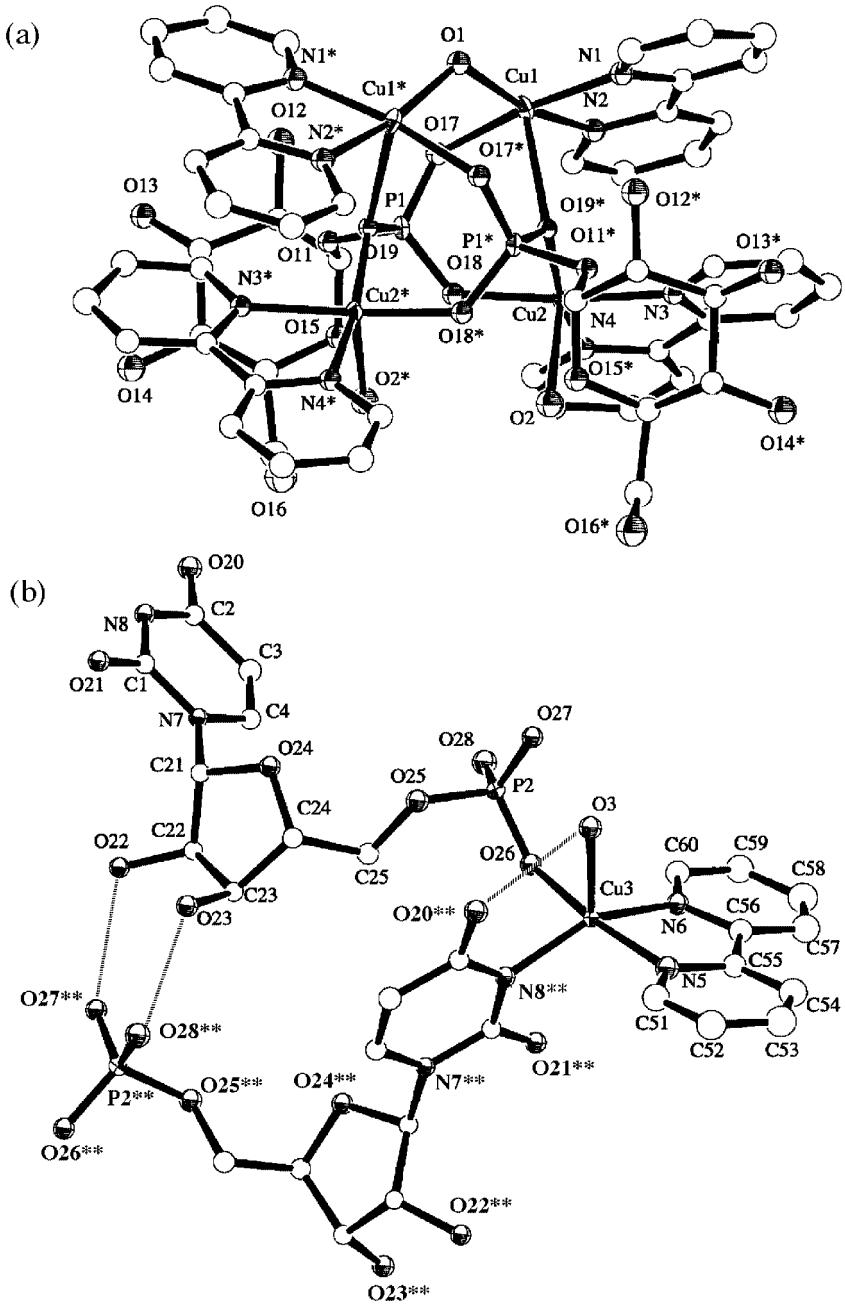


Figure 5. ORTEP diagrams for (a) the tetracopper(II) unit, $[Cu_4(\mu\text{-}OH)\{\mu\text{-}(\alpha\text{-}D\text{-}Glc\text{-}1P)\}_2(bpy)_4(H_2O)_2]^{3+}$, and (b) the polymer part, $\{[Cu\{\mu\text{-}(UMP\text{-}H)\}(bpy)(H_2O)]^-\}_n$, of **7**. Hydrogen atoms are omitted for clarity and hydrogen-bonding interactions are indicated by dotted thin lines.

 © 2006 Wiley-VCH Verlag GmbH & Co. KGaA, Weinheim 

Table 3. Selected bond lengths [Å] and angles [°] for complex **7**.[a]

| | | | |
|---|---|---|---|
| Cu1–O1 | 1.911(5) | Cu3–O3 | 2.360(7) |
| Cu1–O17 | 1.967(7) | Cu3–O26 | 1.917(7) |
| Cu1–O19* | 2.455(6) | Cu3–N5 | 2.015(9) |
| Cu1–N1 | 1.988(9) | Cu3–N6 | 1.997(9) |
| Cu1–N2 | 2.005(9) | Cu3–N8** | 2.033(8) |
| Cu2–O2 | 2.270(9) | P2–O25 | 1.598(8) |
| Cu2–O18 | 1.961(7) | P2–O26 | 1.517(8) |
| Cu2–O19* | 1.938(6) | P2–O27 | 1.520(7) |
| Cu2–N3 | 2.007(8) | P2–O28 | 1.523(7) |
| Cu2–N4 | 2.003(8) | O20–C2 | 1.27(1) |
| P1–O11 | 1.608(7) | O21–C1 | 1.25(1) |
| P1–O17 | 1.512(8) | N8–C1 | 1.33(1) |
| P1–O18 | 1.517(8) | N8–C2 | 1.38(1) |
| P1–O19 | 1.534(6) | | |
| O1–Cu1–O17 | 90.7(3) | O3–Cu3–O26 | 93.9(3) |
| O1–Cu1–O19* | 99.6(3) | O3–Cu3–N5 | 86.5(3) |
| O1–Cu1–N1 | 97.5(3) | O3–Cu3–N6 | 109.4(3) |
| O1–Cu1–N2 | 165.9(4) | O3–Cu3–N8** | 97.1(3) |
| O17–Cu1–O19* | 89.1(2) | O26–Cu3–N5 | 171.5(3) |
| O17–Cu1–N1 | 171.4(3) | O26–Cu3–N6 | 91.0(3) |
| O17–Cu1–N2 | 92.0(3) | O26–Cu3–N8** | 92.3(3) |
| O19*–Cu1–N1 | 87.0(3) | N5–Cu3–N6 | 80.9(4) |
| O19*–Cu1–N2 | 94.3(3) | N5–Cu3–N8** | 96.1(3) |
| N1–Cu1–N2 | 80.6(4) | N6–Cu3–N8** | 153.0(3) |
| O2–Cu2–O18 | 95.7(3) | | |
| O2–Cu2–O19* | 95.2(3) | | |
| O2–Cu2–N3 | 95.6(3) | | |
| O2–Cu2–N4 | 99.0(3) | | |
| O18–Cu2–O19* | 91.9(3) | | |
| O18–Cu2–N3 | 166.9(3) | | |
| O18–Cu2–N4 | 90.5(3) | | |
| O19*–Cu2–N3 | 93.8(3) | | |
| O19*–Cu2–N4 | 165.3(3) | | |
| N3–Cu2–N4 | 81.1(3) | | |
| O11–P1–O17 | 108.6(4) | O25–P2–O26 | 107.2(4) |
| O11–P1–O18 | 105.1(4) | O25–P2–O27 | 102.5(4) |
| O11–P1–O19 | 103.8(4) | O25–P2–O28 | 108.1(4) |
| O17–P1–O18 | 112.5(4) | O26–P2–O27 | 114.6(4) |
| O17–P1–O19 | 112.4(4) | O26–P2–O28 | 109.5(4) |
| O18–P1–O19 | 113.6(4) | O27–P2–O28 | 114.2(4) |
| Cu1–O1–Cu1* | 122.0(6) | | |
| Cu1–O19*–Cu2 | 104.2(2) | | |

[a] Symmetry equivalents: *: $-x + 1, y, -z$; **: $-x + 1/2, y + 1/2, -z - 1$.

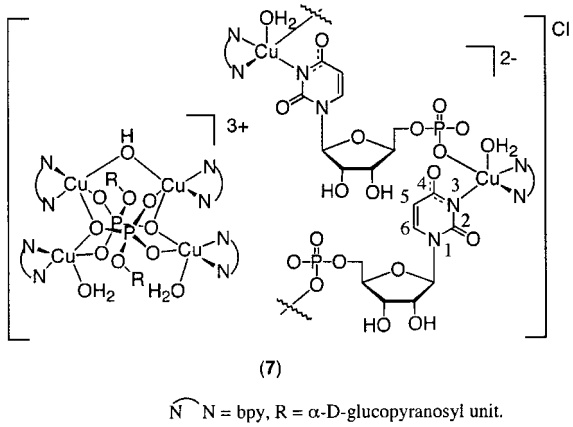


Scheme 3.

crete tetranuclear $[Cu_4(\mu\text{-}OH)\{\mu\text{-}(\alpha\text{-D-Glc-1P})\}_2(bpy)_4(H_2O)_2]^{3+}$ cation (Figure 5a), a coordination polymer with a $[Cu\{\mu\text{-}(UMP\text{-}H)\}(bpy)(H_2O)]^-$ monoanionic unit (Figure 5b), and a chloride anion, in a 1:2:1 ratio. Selected bond lengths and angles are listed in Table 3.

In the polymeric structure of $\{[Cu\{\mu\text{-}(UMP\text{-}H)\}(bpy)(H_2O)]^-\}_n$ (Figure 5b), the uridine 5′-monophosphate moieties are deprotonated at the N-3 position of the nucleobase to form the $[UMP\text{-}H]^{3-}$ trianions, which connect mononuclear $Cu^{II}$ ions through the N-3 deprotonated nitrogen atom [Cu3–N8** = 2.033(8) Å] and the phosphate oxygen atom in a monodentate fashion [Cu3–O26 = 1.917(7) Å]. The Cu3···Cu3** interatomic distance is 12.170(2) Å. The $Cu^{II}$ center is further ligated by two nitrogen atoms of bpy [Cu3–N5 = 2.015(9) Å, Cu3–N6 = 1.997(9) Å] and a water oxygen atom [Cu3–O3 = 2.360(7) Å] to complete a square-pyramidal $[N_3O_2]$ coordination geometry. The Cu atom deviates toward the apical O3 atom by 0.224(4) Å from the basal mean plane, and consequently the geometrical structure is deformed, with a $\tau$ value of 0.31.[18] On the basis of the N–C and O–C bond lengths, the negative charge generated upon N-3 deprotonation should be delocalized in the neighboring O-4 and O-2 oxygen atoms, and notably, the O-4 oxygen atom is hydrogen-bonded to the apical water ligand [O3···O20** = 2.76(1) Å], and the O-2 oxygen atom weakly interacts with the Cu ion at the sixth semi-coordination site [Cu3···O21** = 2.732(7) Å]. These structural features may contribute to fix the uracil base orientation with respect to the copper center. The polymeric structure is further supported by the intrapolymer hydrogen-bonding interaction between the two hydroxy groups of the D-ribofuranosyl unit and the two oxygen atoms of the phosphate group [O22···O27** = 2.68(1) Å, O23···O28** = 2.57(1) Å]. The overall structure of the polymer possesses a $C_2$-helical symmetry along the *b* axis, as illustrated in Figure 6.

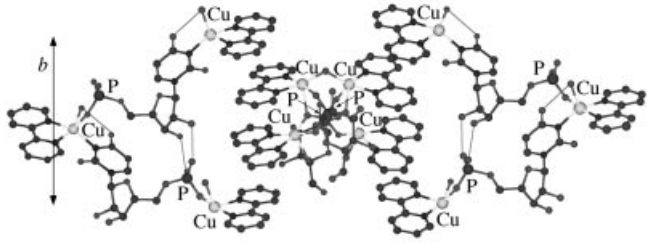


Figure 6. Perspective drawing for a part of the packing structure of **7** viewed vertically to the *b*-axis, showing the stacking interactions between the bpy ligands bound to the polymeric and the tetranuclear $Cu^{II}$ units.

The tetracopper(II) complex cation (Figure 5a), $[Cu_4(\mu\text{-}OH)\{\mu\text{-}(\alpha\text{-D-Glc-1P})\}_2(bpy)_4(H_2O)_2]^{3+}$, has a crystallographically imposed $C_2$ symmetry with the axis passing through the O1 atom and the middle point between the Cu1 and Cu1* atoms, and is comprised of four $Cu^{II}$ ions bridged by a hydroxo and two α-D-glucose-1-phosphate dianions together with auxiliary ligations of four bpy and two water molecules. The tetracopper framework is trapezoidal in which the upper two Cu atoms are connected by μ-OH and

 © 2006 Wiley-VCH Verlag GmbH & Co. KGaA, Weinheim 

two μ-1,3-OPO′ bridges, the basal two Cu atoms by two μ-1,3-OPO′ bridges, and the upper and basal Cu pairs by μ-1,1-O and μ-1,3-OPO′ bridges of the phosphate groups [Cu1···Cu1* = 3.342(3) Å, Cu1···Cu2 = 3.480(2) Å, Cu2···Cu2* = 4.366(2) Å]. An intramolecular π–π stacking interaction between the bpy ligands bound to the upper and basal metal ions is observed, as in complex **2** with phen ligands. The structure is essentially similar to those observed in the crystal structure of **2**,[13] except the $C_2$-chiral structures of the $\{Cu_4(\mu\text{-}OH)(\mu\text{-}PO_4)_2(L)_4(H_2O)_2\}$ core depending on the orientation of sugar pendants. Without any chiral molecules other than the sugar phosphate as in **2**, two enantiomeric structures arose (Figure 1b, c) presumably to avoid steric repulsive interaction between the sugar pendants and phen moieties and to increase the π–π stacking stabilization of phen ligands. In the present case of **7**, the observed $C_2$ configuration is *Λ* with downward orientation of the sugar pendants; the C-6 hydroxymethyl groups of the sugar residues are away from the upper $Cu_2(\mu\text{-}OH)$ unit. Namely, only one $C_2$-chiral structure of the tetracopper complex cation is stabilized through interaction with the coordination polymers containing the chiral biomolecule UMP linkers. As shown in Figure 6, the $\{[Cu\{\mu\text{-}(UMP\text{-}H)\}(bpy)(H_2O)]^-\}_n$ coordination polymers adopt a $C_2$-helical secondary structure along the *b*-axis with a pitch of 11.866(2) Å, and between the polymers, the tetracopper(II) cations are well trapped, with an intermolecular π–π stacking interaction between the bpy ligands and their $C_2$-chiral configuration regulated to be *Λ*. The present structural system could be regarded as an interesting chiral transfer mechanism mediated not by direct hydrophilic interaction between the chiral nucleotide and sugar phosphate, but by amplified hydrophobic stacking interaction between the bpy ligands.

## Conclusions

The present study revealed that tetracopper(II) complexes, $[Cu_4(\mu\text{-}OH)\{\mu\text{-}(\alpha\text{-D-Glc-1P})\}_2(L)_4(H_2O)_2]^{3+}$ [L = bpy (**1**), phen (**2**)], were readily transformed into different types of nucleotide-containing coordination compounds with tetranuclear $Cu^{II}$ aggregations, $[Cu_4(\mu\text{-}ATP)_2(bpy)_4]$ (**3**), $[Cu_4\{\mu\text{-}(IMP\text{-}H)\}_2(L)_4(H_2O)_4]^{2+}$ [L = bpy (**5**), phen (**6**)], and $\{[Cu\{\mu\text{-}(UMP\text{-}H)\}(bpy)(H_2O)]_2[Cu_4(\mu\text{-}OH)\{\mu\text{-}(\alpha\text{-D-Glc-1P})\}_2(bpy)_4(H_2O)_2]Cl\}_n$ (**7**). The structural analyses for the obtained compounds provided molecular-based important information concerning the ternary systems with $Cu^{II}$, nucleotide, and diimine ligand. In complex **3**, the triphosphate group of ATP exclusively assembles tetranuclear $Cu^{II}$ ions in an unprecedented fashion and the adenine nucleobase is protected from metal binding by intramolecular stacking with a bpy moiety and intermolecular hydrogen bonding between the adenine base pairs. In addition, the crystal structure of **7** interestingly demonstrated that the $C_2$-helical structure of the polymer $\{[Cu\{\mu\text{-}(UMP\text{-}H)\}(bpy)(H_2O)]^-\}_n$ regulated the $C_2$-chiral structure of the tetranucler $Cu^{II}$ complex cation, $[Cu_4(\mu\text{-}OH)\{\mu\text{-}(\alpha\text{-D-Glc-1P})\}_2(bpy)_4(H_2O)_2]^{3+}$, through inter- and intramolecular bpy–bpy stacking interactions.

## Experimental Section

**Materials:** All reagents were of the best commercial grade and used as received. Complexes **1a**·$10H_2O$, **1b**·$14H_2O$, and **2**·$6H_2O$ were prepared according to the methods already reported.[13] The following abbreviations are used: adenosine 5′-triphosphate disodium salt, $Na_2[H_2ATP]$; uridine 5′-monophosphate disodium salt, $Na_2[UMP]$; inosine 5′-monophosphate disodium salt, $Na_2[IMP]$.

**Measurements:** Electronic absorption spectra were recorded with a Shimadzu UV-3100 spectrometer and circular dichroism spectra with a Jasco J-720 spectropolarimeter. IR spectra were measured in KBr pellets with a Jasco FTIR 410 spectrometer. The electrospray mass spectra were recorded with an Applied Biosystems model Mariner. Variable-temperature magnetic susceptibility measurements were carried out with an MPMS-5S Quantum Design SQUID magnetometer over a range of 4.5–300 K and the obtained magnetic susceptibility data were corrected for diamagnetism using Pascal's constants. Considering an idealized $C_i$-symmetrical structure of **3**, the four exchange parameters, $J_1$–$J_4$, were introduced to simplify the Heisenberg spin exchange Hamiltonian to $\boldsymbol{H} = -2J_1(\boldsymbol{S}_1\cdot\boldsymbol{S}_3 + \boldsymbol{S}_2\cdot\boldsymbol{S}_4) - 2J_2\boldsymbol{S}_1\cdot\boldsymbol{S}_2 - 2J_3(\boldsymbol{S}_1\cdot\boldsymbol{S}_4 + \boldsymbol{S}_2\cdot\boldsymbol{S}_3) - 2J_4\boldsymbol{S}_3\cdot\boldsymbol{S}_4$, where $J_3$ and $J_4$ were set to zero because of their long interatomic distances.

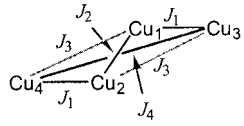


The magnetic susceptibility data were fitted by a theoretical expression derived from the van Vleck equation with the resulting energy matrix [Equation (1)], in which $A = J_1 + (1/2)J_2$, $B = -J_1 + (1/2)J_2$, $C = -(1/2)J_2 - (J_1^2 + J_2^2)^{1/2}$, $D = -(1/2)J_2 + (J_1^2 + J_2^2)^{1/2}$, and $E = (4J_1^2 + J_2^2 - 2J_1J_2)^{1/2}$. The values of *p* (ratio of paramagnetic impurity) and *Nα* (temperature-independent paramagnetism) were estimated to be 0 and $60\times10^{-6}$ emu mol$^{-1}$ per $Cu^{II}$ ion, respectively.

$$\chi_M = (1-p)\left(\frac{N\mu_B^2g^2}{kT}\right)\frac{10\exp(A/kT)+2\exp(B/kT)+2\exp(C/kT)+2\exp(D/kT)}{5\exp(A/kT)+3\exp(B/kT)+3\exp(C/kT)+3\exp(D/kT)+\exp((-A-E)/kT)+\exp((-A+E)/kT)} + p\left(\frac{N\mu_B^2g^2}{kT}\right)+4N\alpha \quad (1)$$

**Preparation of $[Cu_4(\mu\text{-}ATP)_2(bpy)_4]\cdot15H_2O$ (3·15$H_2O$):** $Na_2[H_2ATP]$ (32 mg, 0.058 mmol) in $CH_3OH$ (3 mL) was added to an aqueous solution (5 mL) of **1a**·$10H_2O$ (50 mg, 0.027 mmol). The reaction mixture was stirred at room temperature for 12 h, and was concentrated under reduced pressure to about 1 mL. Slow concentration of the solution afforded block-shaped blue crystals of $[Cu_4(\mu\text{-}ATP)_2(bpy)_4]\cdot15H_2O$ (**3**·15$H_2O$) in 56% yield (33 mg), which were collected and dried under vacuum. $C_{60}H_{90}Cu_4N_{18}O_{41}P_6$ (2159.50): calcd. C 33.37, H 4.20, N 11.67; found C 33.62, H 4.15, N 11.49. IR (KBr): $\tilde{\nu}$ = 3366 (br), 1653 (w), 1603 (m), 1448 (w), 1248 (s), 1100 (s), 985 (m), 906 (w) cm$^{-1}$. UV/Vis ($H_2O$): $\lambda_{max}$ ($\varepsilon$) = 680 ($1.93\times10^2$ M$^{-1}$cm$^{-1}$) nm. CD ($H_2O$): $\lambda_{max}$ ($\Delta\varepsilon$) = 744 ($-1.27\times10^{-1}$), 597 ($8.15\times10^{-2}$ M$^{-1}$cm$^{-1}$) nm.

 © 2006 Wiley-VCH Verlag GmbH & Co. KGaA, Weinheim 

**Preparation of $[Cu_4\{\mu\text{-(IMP-H)}\}_2(L)_4(H_2O)_4](NO_3)_2\cdot nH_2O$ (5: L = bpy, $n$ = 15; 6: L = phen, $n$ = 20):** Complex **1a**·10$H_2O$ (61 mg, 0.030 mmol) was dissolved in $H_2O$ (10 mL) and a portion of $Na_2$[IMP] (28 mg, 0.070 mmol) was added to the solution. The reaction mixture was stirred at room temperature for 12 h and was concentrated under reduced pressure to about 2 mL. Slow concentration of the solution afforded green crystals of $[Cu_4(\mu\text{-IMP})_2(bpy)_4(H_2O)_4](NO_3)_2\cdot 15H_2O$ (**5**·15$H_2O$), which were collected and dried under vacuum (yield 64%, 44 mg). $C_{60}H_{92}Cu_4N_{18}O_{41}P_2$ (2037.62): calcd. C 35.37, H 4.55, N 12.37; found C 35.45, H 4.04, N 11.92. IR (KBr): $\tilde{\nu}$ = 3389 (br), 1604 (s), 1385 (s), 1109 (br), 977 (m), 771 (s) $cm^{-1}$. UV/Vis ($H_2O$): $\lambda_{max}$ ($\varepsilon$) = 671 ($2.43\times10^2$ $M^{-1}cm^{-1}$) nm. CD ($H_2O$): $\lambda_{max}$ ($\Delta\varepsilon$) = 693 ($7.00\times10^{-1}$ $M^{-1}cm^{-1}$) nm. MS (ESI): $m/z$ (%) = 783.16 [calcd. for $\{Cu_4(IMP\text{-}H)_2(bpy)_4\}^{2+}$ 783.02]. A similar procedure but using complex **2**·6$H_2O$ (59 mg, 0.032 mmol) and $Na_2$[IMP] (30 mg, 0.075 mmol) gave green crystals of $[Cu_4\{\mu\text{-(IMP-H)}\}_2(phen)_4(H_2O)_4](NO_3)_2\cdot 20H_2O$ (**6**·20$H_2O$) in 26% yield (16 mg). $C_{68}H_{102}Cu_4N_{18}O_{46}P_2$ (2223.78): calcd. C 36.73, H 4.62, N 11.34; found C 36.76, H 4.61, N 11.57. IR (KBr): $\tilde{\nu}$ = 3414 (br), 1608 (s), 1384 (s), 1106 (br), 980 (m), 772 (s) $cm^{-1}$. UV/Vis ($H_2O$): $\lambda_{max}$ ($\varepsilon$) = 677 ($3.01\times10^2$ $M^{-1}cm^{-1}$) nm. CD ($H_2O$): $\lambda_{max}$ ($\Delta\varepsilon$) = 692 ($4.63\times10^{-1}$ $M^{-1}cm^{-1}$) nm. MS (ESI): $m/z$ (%) = 831.14 [calcd. for $\{Cu_4(IMP\text{-}H)_2(phen)_4\}^{2+}$ 831.02]. The same compound with a different number of solvent water molecules, **6**·14$H_2O$, was prepared according to a different procedure.[8]

**Preparation of $[Cu\{\mu\text{-(UMP-H)}\}(bpy)(H_2O)]_2[Cu_4(\mu\text{-OH})\{\mu\text{-}(\alpha\text{-D-Glc-1P})\}_2(bpy)_4(H_2O)_2]Cl\cdot 9H_2O$ (7·9$H_2O$):** A portion of $Na_2$[UMP] (28 mg, 0.076 mmol) was added to an aqueous solution (5 mL) containing **1b**·14$H_2O$ (106 mg, 0.059 mmol). After stirring for 12 h, the solution was concentrated under reduced pressure to about 2 mL. Slow concentration of the solution afforded blue crystals of $[Cu\{\mu\text{-(UMP-H)}\}(bpy)(H_2O)]_2[Cu_4(\mu\text{-OH})\{\mu\text{-}(\alpha\text{-D-Glc-1P})\}_2(bpy)_4(H_2O)_2]Cl\cdot 9H_2O$ (**7**·9$H_2O$), which were collected and dried under vacuum (yield 30% based on Cu, 32 mg). $C_{90}H_{117}ClCu_6N_{16}O_{50}P_4$ (2763.62): calcd. C 39.11, H 4.27, N 8.11; found C 39.10, H 4.20, N 8.40. IR (KBr): $\tilde{\nu}$ = 3400 (br), 1637 (s), 1447 (s), 1117 (br), 986 (m), 774 (m) $cm^{-1}$. UV/Vis ($H_2O$): $\lambda_{max}$ ($\varepsilon$) = 658 ($2.66\times10^2$ $M^{-1}cm^{-1}$) nm. CD ($H_2O$): $\lambda_{max}$ ($\Delta\varepsilon$) = 708 ($-1.86\times10^{-2}$), 601 ($0.58\times10^{-2}$), 465 ($0.24\times10^{-2}$ $M^{-1}cm^{-1}$) nm.

**Crystallographic Studies:** Slow concentration of aqueous solutions afforded X-ray-quality crystals of **3**·20.5$H_2O$, **6**·21.5$H_2O$, and **7**·22$H_2O$, which were quickly coated with Paraton N oil and mounted on a glass fiber at low temperature. Crystal data and experimental conditions are summarized in Table 4. All data were collected at –120 °C with a Rigaku AFC8R/Mercury CCD diffractometer equipped with graphite-monochromated Mo-$K_\alpha$ radiation using a rotating-anode X-ray generator. A total of 2160 oscillation images, covering the whole sphere of $2\theta < 55°$, were collected with exposure rates of 120 (**3**, **6**) and 128 (**7**) s/° by the $\omega$-scan method ($-62° < \omega < 118°$) with $\Delta\omega = 0.25°$. The crystal-to-detector ($70\times70$ mm) distance was set to 60 mm. The data were processed using the Crystal Clear 1.3.5 program (Rigaku/MSC)[19] and corrected for Lorentz polarization and absorption effects. The structures of complexes **3**, **6**, and **7** were solved by direct methods (SIR-92/97 for **3** and **7**; DIRDIF94 Patty for **6**),[20,21] and refined on $F^2$ with full-matrix least-squares techniques with SHELXL-93/97.[22] In the refinement of **3**, all non-hydrogen atoms, except the solvent water oxygen atoms, were refined with anisotropic thermal parameters. The solvent water O atoms were refined isotropically. The carbon- and nitrogen-bound hydrogen atoms were placed in ideal positions, and the hydrogen atoms of the D-ribose hydroxy groups were determined from difference Fourier syntheses (H atom bound to O1 was not determined). All hydrogen atoms were fixed in the refinement. In the refinement of **6**, all non-hydrogen atoms, except the nitrate anions and the solvent water oxygen atoms, were refined with anisotropic thermal parameters. The solvent water O atoms were refined isotropically. The two nitrate anions were disordered and refined with the four-site model at special positions, each possessing 0.5 occupancy. The carbon-bound hydrogen atoms were placed at ideal positions, and the hydrogen atoms of the D-ribose hydroxy groups were determined from difference Fourier syntheses. All hydrogen atoms were fixed in the refinement. In the refinement of **7**, the Cu, Cl, and P atoms were refined anisotropically and other non-hydrogen atoms were refined with isotropic temperature factors. The positions of C–H hydrogen atoms were calculated and

Table 4. Experimental and crystallographic data for **3**·20.5$H_2O$, **6**·21.5$H_2O$, and **7**·22$H_2O$.

| | **3**·20.5$H_2O$ | **6**·21.5$H_2O$ | **7**·22$H_2O$ |
|---|---|---|---|
| Empirical formula | $C_{60}H_{97}Cu_4N_{18}O_{46.5}P_6$ | $C_{68}H_{103}Cu_4N_{18}O_{47.5}P_2$ | $C_{90}H_{143}ClCu_6N_{16}O_{63}P_4$ |
| $M_r$ [g mol$^{-1}$] | 2254.55 | 2248.79 | 2997.81 |
| Crystal system | triclinic | orthorhombic | monoclinic |
| Space group | $P\bar{1}$ (No.1) | $C222_1$ (No. 20) | $C2$ (No. 5) |
| $a$ [Å] | 10.9106(2) | 19.3511(8) | 33.349(1) |
| $b$ [Å] | 12.7652(4) | 24.339(1) | 11.8659(4) |
| $c$ [Å] | 17.4061(2) | 40.127(2) | 16.1861(5) |
| $\alpha$ [°] | 76.852(6) | 90 | 90 |
| $\beta$ [°] | 72.075(6) | 90 | 101.7562(4) |
| $\gamma$ [°] | 84.895(7) | 90 | 90 |
| $V$ [Å$^3$] | 2245.7(1) | 18899(1) | 6270.7(4) |
| $Z$ | 1 | 8 | 2 |
| $T$ [°C] | –120.0 | –120 | –120 |
| $\mu$(Mo-$K_\alpha$) [cm$^{-1}$] | 11.49 | 10.28 | 11.76 |
| $D_{calcd.}$ [g cm$^{-3}$] | 1.667 | 1.581 | 1.588 |
| $2\theta$ range [°] | $6 < 2\theta < 55$ | $6 < 2\theta < 55$ | $6 < 2\theta < 55$ |
| No. of observations [$I > 2\sigma(I)$] | 9142 | 9959 | 5794 |
| No. of variables | 1112 | 1118 | 395 |
| $R$[a] | 0.037 | 0.051 | 0.074 |
| $wR_2$[b] | 0.100 | 0.148 | 0.196 |
| Gof | 1.01 | 1.00 | 1.05 |

[a] $R = \Sigma||F_o| - |F_c||/\Sigma|F_o|$. [b] $wR_2 = \{\Sigma[w(F_o^2 - F_c^2)^2]/\Sigma w(F_o^2)^2\}^{1/2}$.

 © 2006 Wiley-VCH Verlag GmbH & Co. KGaA, Weinheim 

were fixed in the refinement. The O–H hydrogen atoms were not determined. The Cl atom is disordered at two positions with each having 0.25 occupancy. The absolute configurations for the structures of **3**, **6**, and **7** were determined by using the chiral carbon centers of the sugar moieties, α-D-glucose and/or D-ribose units, as internal references, which was further confirmed by consistency with Flack parameters. All calculations were carried out with a Pentium PC with the Crystal Structure package 3.6[23] and a Silicon Graphics O2 station with the teXsan crystallographic software package.[24] CCDC-239857 (for **3**), -294065 (for **6**), and -294066 (for **7**) contain the supplementary crystallographic data for this paper. These data can be obtained free of charge from The Cambridge Crystallographic Data Centre via www.ccdc.cam.ac.uk/data_request/cif.

## Acknowledgments

This work was partially supported by a Grant-in-Aid for Scientific Research from the Ministry of Education, Culture, Supports, Science, and Technology of Japan. A. K. S. is grateful to the Japan Society for the Promotion of Science (JSPS) for providing a fellowship and research grant.

[1] a) D. E. Wilcox, *Chem. Rev.* **1996**, *96*, 2435–2458; b) J. A. Cowan, *Chem. Rev.* **1998**, *98*, 1067–1088; c) B. L. Vallee, D. S. Auld, *Biochemistry* **1993**, *32*, 6493–6500; d) D. E. Fenton, H. Okawa, *J. Chem. Soc., Dalton Trans.* **1993**, 1349–1357; e) N. Strater, W. N. Lipscomb, T. Klabunde, B. Krebs, *Angew. Chem. Int. Ed.* **1996**, *35*, 2024–2055; f) L. S. Beese, T. A. Steitz, *EMBO J.* **1991**, *10*, 25–33; g) T. A. Steitz, S. J. Smerdon, J. Jager, C. M. Joyce, *Science* **1994**, *266*, 2022–2025; h) T. A. Steitz, J. Steitz, *Proc. Natl. Acad. Sci. U S A* **1993**, *90*, 6498–6502.

[2] a) J. E. Walker, *Angew. Chem. Int. Ed.* **1998**, *37*, 2308–2319; b) P. D. Boyer, *Angew. Chem. Int. Ed.* **1998**, *37*, 2296–2307; c) J. A. Adams, *Chem. Rev.* **2001**, *101*, 2271–2290; d) G. M. Blackburn, M. J. Gait (Eds.), *Nucleic Acids in Chemistry and Biology*, 2nd ed., Oxford University Press, New York, **1996**; e) D. Voet, J. G. Voet, *Biochemistry*, John Wiley & Sons, Inc., NewYork, **1995**.

[3] a) S. J. Lippard, J. M. Berg, *Principles of Bioinorganic Chemistry*, University Science Books, CA, **1994**; b) J. P. Whitehead, S. J. Lippard, *Metal Ions in Biological Systems* (Eds.: A. Sigel, H. Sigel), Marcel Dekker, Basel, **1996**, vol. 32, chapter 20; c) S. E. Sheman, D. Gibson, A. H.-J. Wang, S. J. Lippard, *Science* **1985**, *230*, 412–417; d) S. E. Sheman, D. Gibson, A. H.-J. Wang, S. J. Lippard, *J. Am. Chem. Soc.* **1988**, *110*, 7368–7381.

[4] a) K. Aoki, *Metal Ions in Biological Systems* (Eds.: A. Sigel, H. Sigel), Marcel Dekker, Basel, **1996**, vol. 32, chapter 4; b) H. Sigel, *Chem. Soc. Rev.* **1993**, *22*, 255–267.

[5] a) P. Orioli, R. Cini, D. Donati, S. Mangani, *Nature* **1980**, *283*, 691–693; b) P. Orioli, R. Cini, D. Donati, S. Mangani, *J. Am. Chem. Soc.* **1981**, *103*, 4446–4452.

[6] W. S. Sheldrick, *Angew. Chem. Int. Ed.* **1981**, *20*, 460–461.

[7] a) D. S. Sigman, A. Mazumder, D. M. Perrin, *Chem. Rev.* **1993**, *93*, 2295–2316; b) G. Pratviel, J. Bernadou, B. Meunier, *Angew. Chem. Int. Ed.* **1995**, *3*, 746–769; c) W. K. Pogozelski, T. D. Tullius, *Chem. Rev.* **1998**, *98*, 1089–1108; d) K. J. Humphreys, K. D. Karlin, S. E. Rokita, *J. Am. Chem. Soc.* **2002**, *124*, 6009–6019; e) K. J. Humphreys, K. D. Karlin, S. E. Rokita, *J. Am. Chem. Soc.* **2002**, *124*, 8055–8066; f) S. Dhar, D. Senapati, P. K. Das, P. Chattopadhyay, M. Nethaji, A. R. Chakravarty, *J. Am. Chem. Soc.* **2003**, *125*, 12118–12124.

[8] R. W. Gellert, B. E. Fischer, R. Bau, *J. Am. Chem. Soc.* **1980**, *102*, 7812–7815.

[9] S. Korn, W. S. Sheldrick, *J. Chem. Soc., Dalton Trans.* **1997**, 2191–2200.

[10] L. Y. Kuo, M. G. Kanatzidis, M. Sabat, A. L. Tipton, T. J. Marks, *J. Am. Chem. Soc.* **1991**, *113*, 9027–9045.

[11] M. Inoue, T. Yamase, *Bull. Chem. Soc. Jpn.* **1996**, *69*, 2863–2868.

[12] a) K. Aoki, *J. Am. Chem. Soc.* **1978**, *100*, 7106–7108; b) K. Aoki, *J. Chem. Soc., Chem. Commun.* **1979**, 589–591; c) K. Aoki, H. Yamazaki, *J. Chem. Soc. Jpn.* **1988**, 611–620; d) R. Cini, G. Giorgi, *Inorg. Chim. Acta* **1987**, *137*, 87–90; e) G. Giorgi, R. Cini, *Inorg. Chim. Acta* **1988**, *151*, 153–161; f) B. E. Fischer, R. Bau, *Inorg. Chem.* **1978**, *17*, 27–34; g) C.-Y. Wei, B. E. Fischer, R. Bau, *J. Chem. Soc., Chem. Commun.* **1978**, 1053–1055.

[13] a) M. Kato, T. Tanase, *Inorg. Chem.* **2005**, *44*, 8–10; b) M. Kato, A. K. Sah, T. Tanase, M. Mikuriya, submitted for publication.

[14] P. E. Kruger, R. P. Doyle, M. Julve, F. Lloret, M. Nieuwenhuyzen, *Inorg. Chem.* **2001**, *40*, 1726–1727.

[15] a) R. Cini, L. G. Marzilli, *Inorg. Chem.* **1988**, *27*, 1855–1856; b) M. Sabat, R. Cini, T. Haromy, M. Sundaralingam, *Biochemistry* **1985**, *24*, 7827–7833; c) R. Cini, M. C. Burla, A. Nunzi, G. P. Polidori, P. F. Zanazzi, *J. Chem. Soc., Dalton Trans.* **1984**, 2467–2476; d) R. Cini, M. Sabat, M. Sundaralingam, M. C. Burla, A. Nunzi, G. Polidori, P. F. Zanazzi, *J. Biomol. Struct. Dyn.* **1983**, *1*, 633–637.

[16] For example: a) R. Cini, C. Pifferi, *J. Chem. Soc., Dalton Trans.* **1999**, 699–710; b) Y. Sugawara, N. Kamiya, H. Iwasaki, T. Ito, Y. Satow, *J. Am. Chem. Soc.* **1991**, *113*, 5440–5445, and references therein.

[17] W. S. Sheldrick, *Z. Naturforsch* **1982**, *37b*, 863–871.

[18] A. W. Addison, T. N. Rao, *J. Chem. Soc., Dalton Trans.* **1984**, 1349–1356.

[19] *Crystal Clear 1.3.5, Operating Software for the CCD Detector System*, Rigaku, Molecular Structure Corp., Tokyo, **2003**.

[20] a) A. Altomare, M. Burla, M. Camalli, G. Cascarano, C. Giacovazzo, A. Guagliardi, A. Moliterni, G. Polidori, R. Spagna, *J. Appl. Crystallogr.* **1999**, *32*, 115–119; b) A. Altomare, G. Cascarano, C. Giacovazzo, A. Guagliardi, M. Burla, G. Polidori, M. Camalli, *J. Appl. Crystallogr.* **1994**, *27*, 435–436.

[21] P. T. Beurskens, G. Admiraal, G. Beurskens, W. P. Bosman, R. de Gelder, R. Israel, J. M. M. Smits, *DIRDIF-94 program system*, Technical Report of the Crystallography Laboratory, University of Nijmegen, The Netherlands, **1994**.

[22] a) G. M. Sheldrick, *SHELXL-93, Program for Crystal Structure Refinement*, University of Göttingen, Göttingen, Germany, **1993**; b) G. M. Sheldrick, *SHELXL-97, Program for the Refinement of Crystal Structures*, University of Göttingen, Göttingen, Germany, **1997**.

[23] *Crystal Structure 3.6, Crystal Structure Analysis Package*, Rigaku and Molecular Structure Corp., Tokyo, **2003**.

[24] *teXsan: Crystal Structure Analysis Package*, Molecular Structure Corp., Tokyo, **1999**.

Received: January 6, 2006
Published Online: April 11, 2006

 © 2006 Wiley-VCH Verlag GmbH & Co. KGaA, Weinheim 

DOI: 10.1002/ejic.200600307

# Analysis of the Synergistic Effect of Carbonylplatinum Complexes on the Iridium-Catalysed Carbonylation of Methanol to Acetic Acid

**Samuel Gautron,[a,b] Nicolas Lassauque,[a] Carole Le Berre,[a] Philippe Serp,[a] Laurent Azam,[a] Roberto Giordano,[a] Gábor Laurenczy,[c] Daniel Thiébaut,[b] and Philippe Kalck*[a]**

**Keywords:** Homogeneous catalysis / Carbonylation / Iridium / Platinum / Reaction mechanism

*In Figure 4 on page 1124 of the original article,*[1] *the formulas appearing at the top right and centre left must be interchanged; the correct Figure 4 appears on the following page. The Supporting Information has been changed accordingly.*

*The Authors*

[a] Laboratoire de Catalyse, Chimie Fine et Polymères, Ecole Nationale Supérieure des Ingénieurs en Arts Chimiques et Technologiques (ENSIACET),
118 Route de Narbonne, 31077 Toulouse Cedex4, France
E-mail: Philippe.Kalck@ensiacet.fr
[b] ACETEX, AATF1, Usine de Pardies,
B. P. 17 Pardies, 64150 Mourenx, France
[c] Ecole Polytechnique Fédérale de Lausanne, Institut des Sciences et Ingénierie Chimiques, BCH-LCOM,
1015 Lausanne, Switzerland

Supporting information for this article is available on the WWW under http://www.eurjic.org or from the author.

 © 2006 Wiley-VCH Verlag GmbH & Co. KGaA, Weinheim 

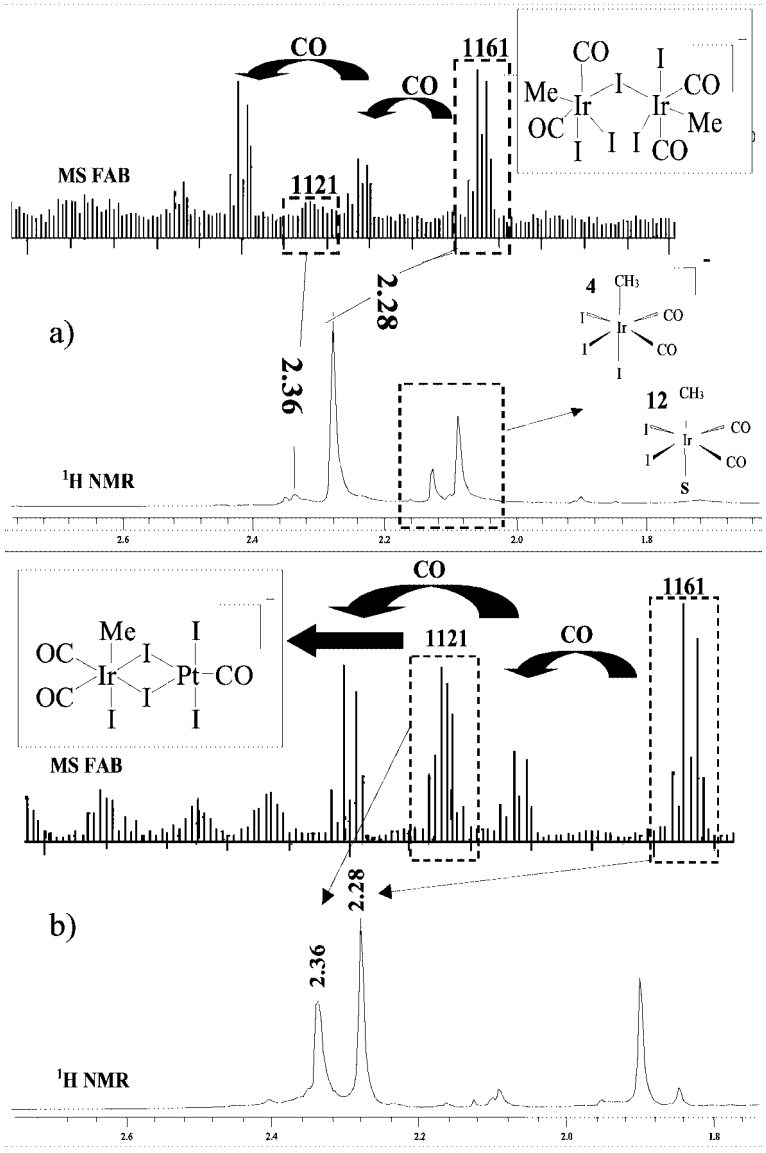


Figure 4. Detection of $[IrI(CH_3)(CO)_2(\mu\text{-}I)_2PtI_2(CO)]^-$ and $[Ir_2I_4(\mu\text{-}I)(CH_3)_2(CO)_4]^-$ by tandem NMR and FAB/MS experiments: top (Ir/Pt = 9.5:1), bottom (Ir/Pt = 5.3:1).

[1] S. Gautron, N. Lassauque, C. Le Berre, P. Serp, L. Azam, R. Giordano, G. Laurenczy, D. Thiébaut, P. Kalck, *Eur. J. Inorg. Chem.* **2006**, 1121–1126.

Received: April 5, 2006
Published Online: April 28, 2006

 © 2006 Wiley-VCH Verlag GmbH & Co. KGaA, Weinheim 

EurJIC
European Journal of Inorganic Chemistry

Issue 13/2006

Pages 2521–2712

*Papers available ahead of print in Early View at www.interscience.wiley.com*

*Earliest available Table of Contents:*
*Automatically, free of charge by e-mail through*
*www.interscience.wiley.com/alerts*

## COVER PICTURE

**The cover picture shows** the structure and IR spectrum of a novel triple-decker complex $(C_5H_5)Fe(B_6C)Fe(C_5H_5)$ obtained by density functional calculations. Similar results on a series of $(C_nH_n)M(B_6X)M(C_nH_n)$ (M = Fe, Ru, Mn, Re; X = B, C, N; $n$ = 5, 6) complexes containing planar hexacoordinate carbon or other nonmetal atoms at the centers of the $B_6X$ middle-deckers were also obtained. Natural orbital analyses indicate that the nonmetal centers X follow the octet rule in these complexes, and effective d−π coordination interactions exist between the partially filled Fe 3d orbitals and the delocalized π orbitals of the three parallel ligands. This work provides strong theoretical evidence to facilitate future experimental characterization of the long-sought planar hexacoordinate carbon atom and expands the structural domain of traditional sandwich-type transition-metal complexes. Details are discussed in the article by S.-D. Li et al. on p. 2567 ff.

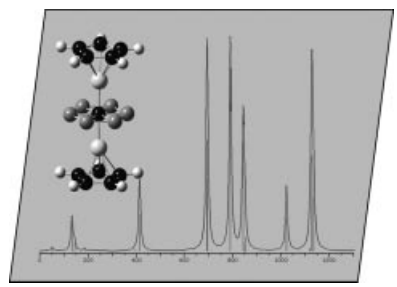

## MICROREVIEW

**Contents**

**2533** **O. A. Efremova, Y. V. Mironov,* V. E. Fedorov**

Design of Cyano-Bridged Coordination Polymers Based on Tetrahedral Rhenium Cluster Cyanide Complexes and 3d Transition Metals

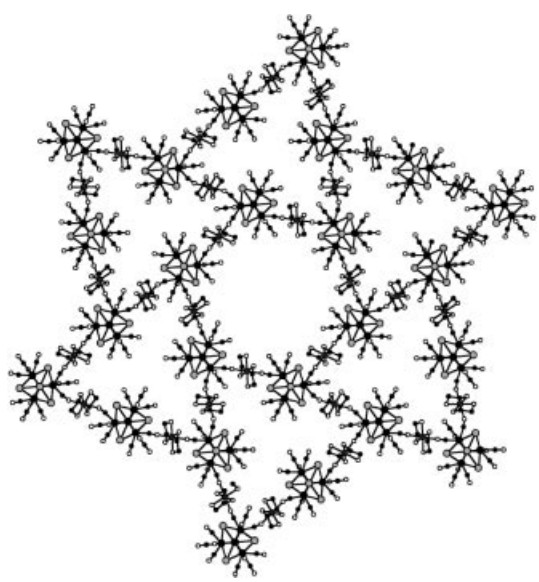

**Keywords:** Cluster compounds / Cyanides / N ligands / Rhenium / Transition metals

 © 2006 Wiley-VCH Verlag GmbH & Co. KGaA, Weinheim 

# SHORT COMMUNICATIONS


**2551** **R. J. Deeth***

A Theoretical Rationale for the Formation, Structure and Spin State of Pentacyanochromate(II)

**Keywords:** Density functional theory / Ligand field theory / Angular overlap model / COSMO / Solvation effects


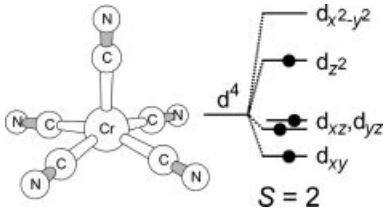



**2556** **C.-O. Turrin, A. Maraval, G. Magro, V. Maraval, A.-M. Caminade,* J.-P. Majoral***

First Example of Dendrons as Topological Amplifiers

**Keywords:** Dendrons / Dendrimers / Macrocycles / Phosphorus / NMR spectroscopy


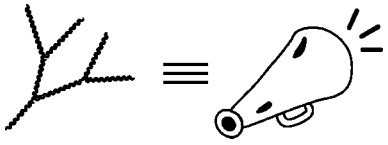


**2561** **S. Otto,* A. Chanda, P. V. Samuleev, A. D. Ryabov***

DFT-Verified Crystallographic Mechanism of Cycloplatination

**Keywords:** Platinum / C-H activation / Metallacycles / X-ray diffraction / Density functional calculations


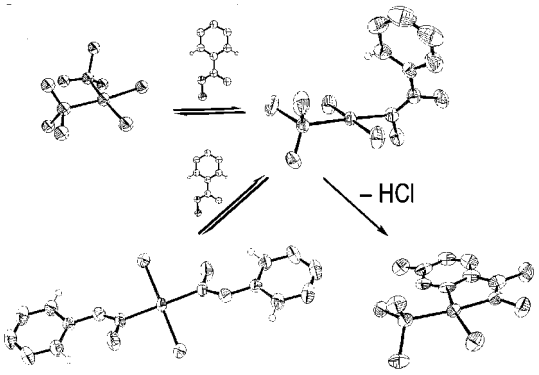


# FULL PAPERS


**2567** **S.-D. Li,* C.-Q. Miao, G.-M. Ren, J.-C. Guo**

Triple-Decker Transition-Metal Complexes $(C_nH_n)M(B_6C)M(C_nH_n)$ (M = Fe, Ru, Mn, Re; $n$ = 5, 6) Containing Planar Hexacoordinate Carbon Atoms

**Keywords:** Planar hexacoordinate carbon / Triple-decker transition-metal complexes / Density functional theory / Geometric structures / Electronic structure / IR spectroscopy


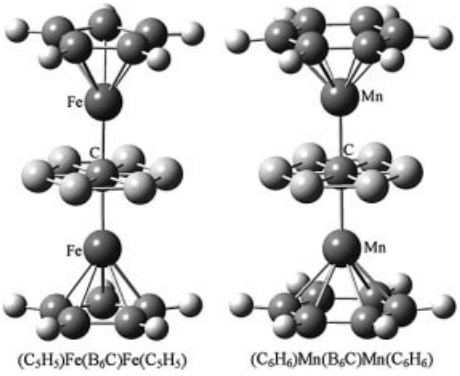

**2572** **D. Ortiz de Zárate, A. Gómez-Moratalla, C. Guillem, A. Beltrán, J. Latorre, D. Beltrán, P. Amorós***

High-Zirconium-Content Nano-Sized Bimodal Mesoporous Silicas

**Keywords:** Mesoporous materials / Zirconia / Surfactants / Nanoparticles / Bimodal porous materials

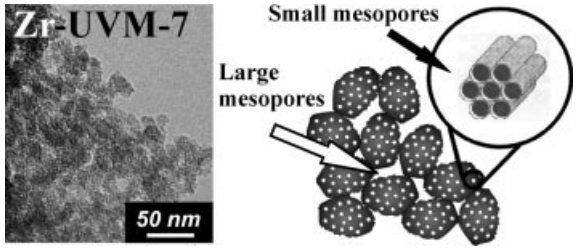


**2582** **L. Medei, L. Orian, O. V. Semeikin, M. G. Peterleitner, N. A. Ustynyuk, S. Santi,* C. Durante, A. Ricci, C. Lo Sterzo***

A Joint Experimental and Computational Study on the Electronic Communication in Diethynylaryl-Bridged $(\eta^5\text{-}C_5H_5)Fe(\eta^2\text{-dppe})$ and $(\eta^5\text{-}C_5H_5)Fe(CO)_2$ Units

**Keywords:** Mixed-valence compounds / Iron / Electron transfer / Electronic communication / Ethynylaryl bridging ligand

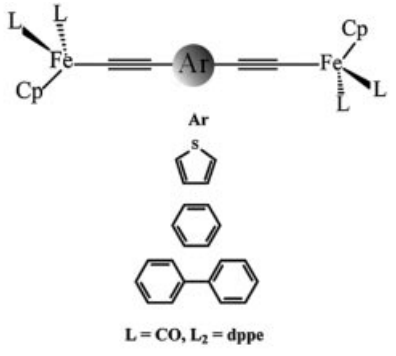


**2598** **J. W. Han, K. I. Hardcastle, C. L. Hill***

Redox-Active Coordination Polymers from Esterified Hexavanadate Units and Divalent Metal Cations

**Keywords:** Polyoxometalates / Coordination polymers / Vanadium

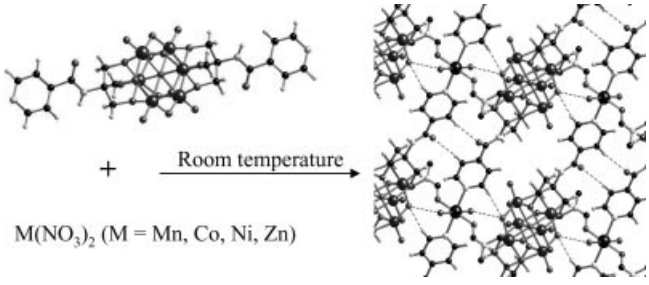


**2604** **G. Gachot, P. Pellon, T. Roisnel, D. Lorcy***

Redox-Active 17- and 19-Membered Metallamacrocycles Incorporating Tetrathiafulvalene

**Keywords:** Metallamacrocycle / Tetrathiafulvalene / Diphosphane ligands / Molybdenum / Tungsten

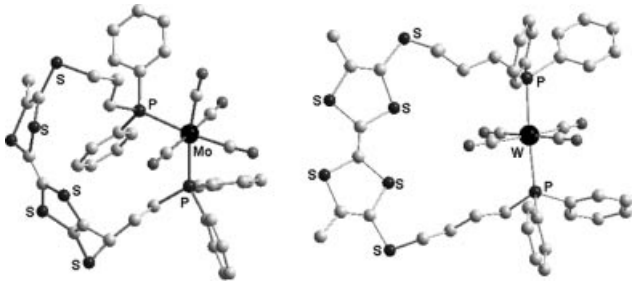


 © 2006 Wiley-VCH Verlag GmbH & Co. KGaA, Weinheim 

## 2612

**M. Reithofer, M. Galanski,* A. Roller, B. K. Keppler**

An Entry to Novel Platinum Complexes: Carboxylation of Dihydroxoplatinum(IV) Complexes with Succinic Anhydride and Subsequent Derivatization

**Keywords:** Antitumor agents / Bioinorganic chemistry / Carboxylate ligands / Drug design / Platinum

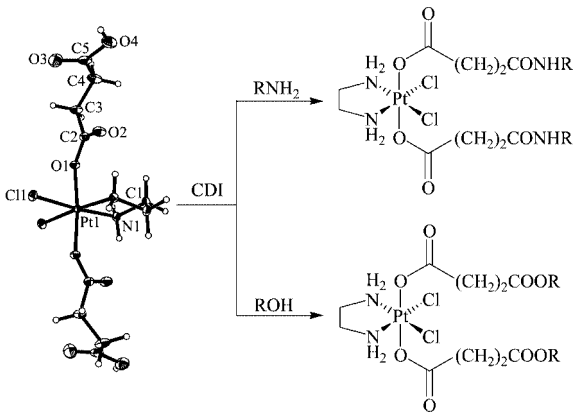


## 2618

**M. J. Richardson,* J. H. Johnston, T. Borrmann**

Monomeric and Polymeric Amines as Dual Reductants/Stabilisers for the Synthesis of Gold Nanocrystals: A Mechanistic Study

**Keywords:** Amines / Nanostructures / Phase diagram / Colloids

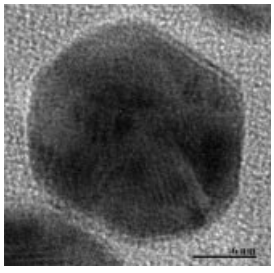

## 2624

**J. A. Mata, S. Maria, J.-C. Daran, R. Poli***

Synthesis and Characterization of $MoOI_2(PMe_3)_3$ and Use of $MoOX_2(PMe_3)_3$ (X = Cl, I) in Controlled Radical Polymerization

**Keywords:** Molybdenum / Oxido ligands / Phosphane ligands / Halide exchange / Atom transfer radical polymerization

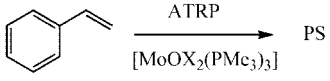


## 2634

**V. Gallo, M. Latronico, P. Mastrorilli,* C. F. Nobile, G. Ciccarella, U. Englert**

Stepwise Sulfuration of the Terminal Phosphido Complex *trans*-$[PtCl(PHCy_2)_2(PCy_2)]$: Synthesis of $[Pt(\kappa^2S,S'\text{-}PS_2Cy_2)(PHCy_2)_2]Cl$ and $[Pt(\kappa^2S,S'\text{-}PS_2Cy_2)\{\kappa P\text{-}P(S)Cy_2\}(PHCy_2)]$ and Crystal Structure of $[Pt(\kappa^2\text{-}S,S\text{-}PCy_2S_2)(\kappa\text{-}S\text{-}PCy_2S_2)(PHCy_2)]$

**Keywords:** Platinum / Terminal phosphides / Phosphanyl sulfides / Phosphanyldithioates / Phosphorus

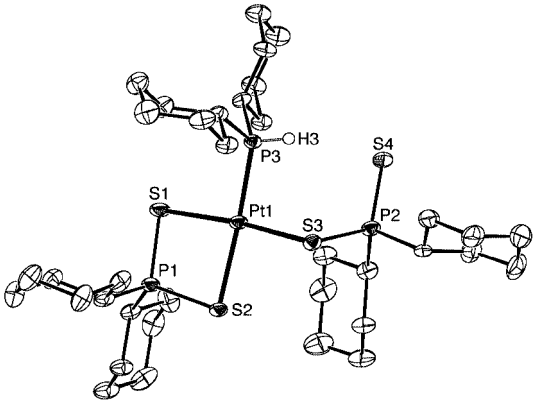


 © 2006 Wiley-VCH Verlag GmbH & Co. KGaA, Weinheim 

**2642** **I. D. Kostas,* B. R. Steele,* A. Terzis, S. V. Amosova, A. V. Martynov, N. A. Makhaeva**

New Palladium Complexes with S- or Se-Containing Schiff-Base Ligands as Efficient Catalysts for the Suzuki−Miyaura Cross-Coupling Reaction of Aryl Bromides with Phenylboronic Acid under Aerobic Conditions

**Keywords:** Homogeneous catalysis / Suzuki / C−C coupling / Schiff bases / Tridentate ligands

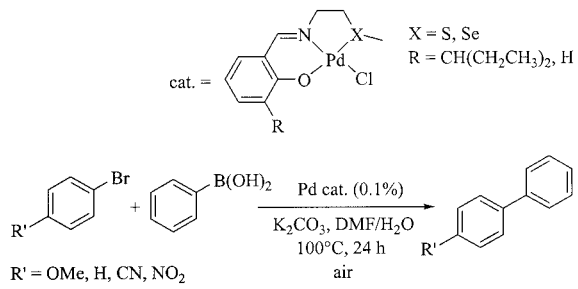


**2647** **J. V. Ros-Lis, R. Martínez-Máñez,* J. Soto, C. McDonagh, A. Guckian**

A Prospective Study of the Use of the $[Os(tpy)_2]^{2+}$ (tpy = 2,2′;6′:2″-Terpyridine) Core as Signalling Scaffolding for the Development of Chemical Sensors

**Keywords:** Chemosensors / Osmium terpyridines / Macrocyclic ligands / Fluorescent probes / Thin films

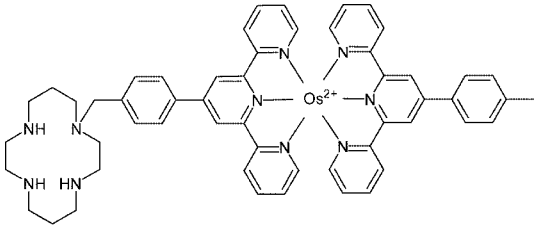

**2656** **B. Sreenivasulu, F. Zhao, S. Gao, J. J. Vittal***

Synthesis, Structures and Catecholase Activity of a New Series of Dicopper(II) Complexes of Reduced Schiff Base Ligands

**Keywords:** Biomimetic studies / Copper / Reduced Schiff-base complexes / Tridentate ligands / Catecholase activity / Magnetic properties

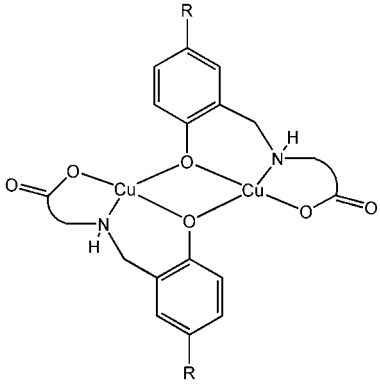


**2671** **G. S. Matouzenko,* D. Luneau, G. Molnár, N. Ould-Moussa, S. Zein, S. A. Borshch, A. Bousseksou, F. Averseng**

A Two-Step Spin Transition and Order−Disorder Phenomena in the Mononuclear Compound $[Fe(Hpy\text{-}DAPP)](BF_4)_2$

**Keywords:** Density functional calculations / Iron / Magnetic properties / Mössbauer spectroscopy / N ligands / Spin crossover

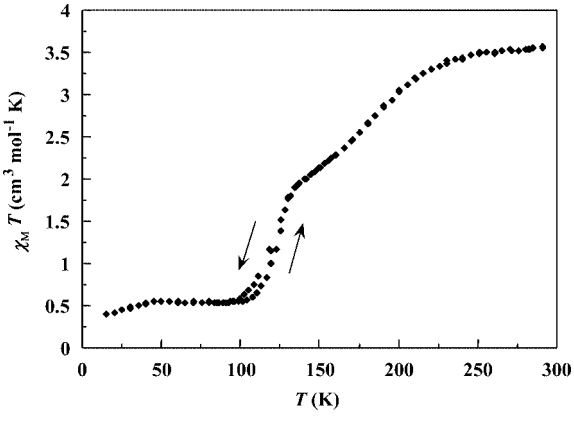


 © 2006 Wiley-VCH Verlag GmbH & Co. KGaA, Weinheim 

**2683** **A. Noor, W. Kretschmer, R. Kempe***

Synthesis and Structure of Trialkyltantalum Complexes Stabilized by Aminopyridinato Ligands

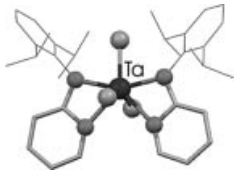


**Keywords:** Amido ligands / Aminopyridinato ligands / N ligands / Olefin polymerization / Tantalum

**2690** **E. Garribba,* G. Micera,* E. Lodyga-Chruscinska, D. Sanna**

Oxovanadium(IV) Complexes with Pyrazinecarboxylic Acids: The Coordinating Properties of Ligands with the ($N_{aromatic}$, $COO^-$) Donor Set

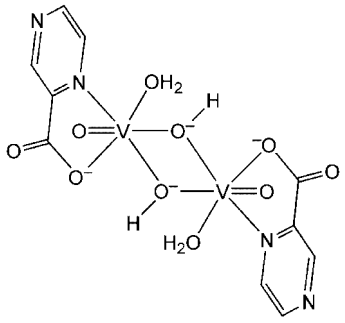

**Keywords:** Vanadium / N,O ligands / Isomers / Magnetic properties / EPR spectroscopy

**2701** **M. Jurić, P. Planinić, N. Brničević,* D. Milić, D. Matković-Čalogović, D. Pajić, K. Zadro**

New Heterometallic ($Cu^{II}$ and $Cr^{III}$) Complexes − First Crystal Structure of an Oxalate-Bridged Ferromagnetically Coupled [$Cu^{II}Cr^{III}Cu^{II}$] System

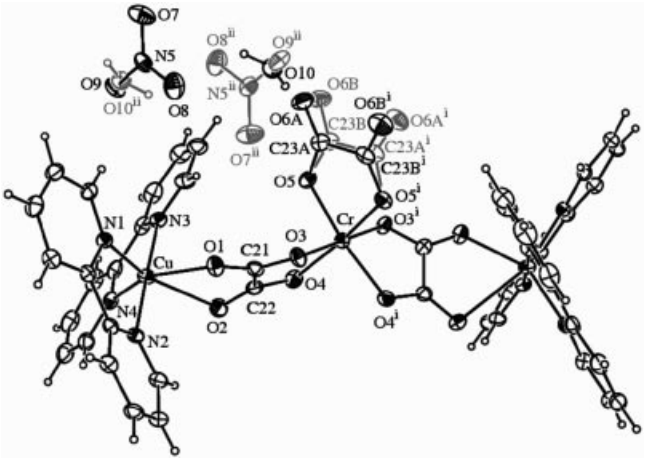


**Keywords:** Crystal structure / Copper complexes / Chromium complexes / Oxalate bridges / Ferromagnetic interaction

DOI: 10.1002/ejic.200600178

# Design of Cyano-Bridged Coordination Polymers Based on Tetrahedral Rhenium Cluster Cyanide Complexes and 3d Transition Metals

**Olga A. Efremova,[a] Yuri V. Mironov,*[a] and Vladimir E. Fedorov[a]**

**Keywords:** Cluster compounds / Cyanides / N ligands / Rhenium / Transition metals

This microreview surveys some novel possibilities in the design of coordination polymers using the tetrahedral rhenium cluster chalcocyanide complexes $[Re_4Q_4(CN)_{12}]^{4-}$ (Q = S, Se, Te) and 3d transition metals. The large number of cyano groups in the cluster complexes $[Re_4Q_4(CN)_{12}]^{4-}$, their ambidentate character and their strong ability to form cyano-bridged structures lead to the formation of a wide variety of coordination polymers with different architectures that depend on the reaction conditions. The diversity of the coordination environment of the transition metals has been used as one of the most important factors to control the dimensionality of the crystal structures of the target compounds.
(© Wiley-VCH Verlag GmbH & Co. KGaA, 69451 Weinheim, Germany, 2006)

## 1. Introduction

Tetranuclear cluster complexes are well known for most of the transition metals.[1–4] These compounds contain the $M_4Q_4$ cluster core as the main structural fragment, which can be represented as two interpenetrating $M_4$ and $Q_4$ tetrahedra. In these $M_4Q_4$ cluster cores, the inner $\mu_3$-Q ligands are most often chalcogenide ions. In this paper we will review only those tetrahedral rhenium cluster chalcocyanide complexes that have the stoichiometry $[Re_4Q_4(CN)_{12}]$ (Q = $S^{2-}$, $Se^{2-}$ and $Te^{2-}$) where each rhenium atom is additionally coordinated by three outer-sphere CN ligands. Within the framework of the ion-covalent model the formal oxidation state of rhenium in similar clusters is 4+ (the $d^3$ configuration), therefore there are six covalent metal–metal bonds in the $Re_4$ tetrahedron (two electrons for each edge of the tetrahedron).

Significant progress in the developing chemistry of $Re_4$ cluster compounds was achieved after synthesis of the chalcogenide-halide clusters $[Re_4Q_4(TeX_2)_4X_8]$ (Q = S, Se, Te; X = Cl;[5] Q = Te, X = Br[6]). The tellurium-containing complex $[Re_4Te_4(TeCl_2)_4Cl_8]$ was prepared by the reaction of $ReCl_5$ with elemental tellurium at 350 °C. Complexes with Q = S and Se were synthesised by the reaction of $ReCl_5$ with mixtures of elemental tellurium and sulfur or selenium, respectively, at 400 °C.

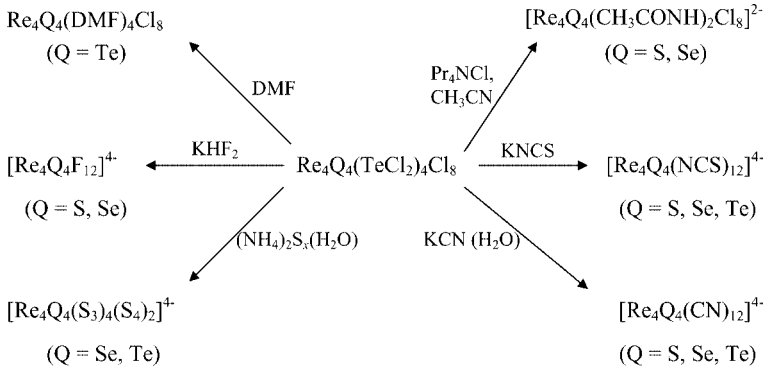


Scheme 1.

[a] Nikolaev Institute of Inorganic Chemistry, Siberian Branch of the Russian Academy of Sciences,
3, Acad. Lavrentiev pr., 630090 Novosibirsk, Russia
Fax: +7-383-330-9489
E-mail: yuri@che.nsk.su

**MICROREVIEWS:** This feature introduces the readers to the authors' research through a concise overview of the selected topic. Reference to important work from others in the field is included.

 © 2006 Wiley-VCH Verlag GmbH & Co. KGaA, Weinheim 

Table 1. Labels for the CN ligand couples taking part in binding with transition metal cations.

| Label | Binding type | Label | Binding type |
|---|---|---|---|
| *gem*-CN groups | 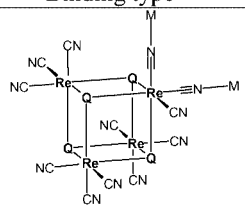 | *ortho*-CN groups | 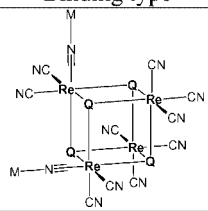 |
| *sym*-CN groups | 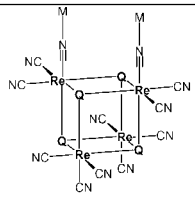 | *meta*-CN groups | 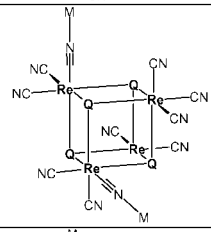 |
| | | *para*-CN groups | 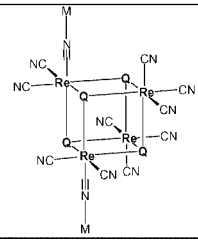 |

*Olga Efremova graduated from the Natural Science Department of the Novosibirsk State University in 2005. Because of her excellent academic record during her education at the University she was awarded several Fellowships. Her diploma work was devoted to the synthesis and study of the structure and properties of coordination polymers based on tetrahedral chalcocyanide rhenium cluster complexes. At present, Olga is working in the group of Prof. Yuri Mironov in the Laboratory of Prof. Fedorov (Nikolaev Institute of Inorganic Chemistry, Russian Academy of Sciences) where she is continuing her experimental studies as a PhD student. Her current research is devoted to the development of different approaches to the design of nanomaterials with different dimensionalities using cluster anionic complexes and 3d or 4f transition metal cations possessing tailored ligand environment as building blocks. She teaches students of the Natural Science Department of NSU.*

*Yuri Mironov graduated from the Natural Science Department of the Novosibirsk State University in 1981 and received his PhD from the Institute of Inorganic Chemistry of the Russian Academy of Sciences in 1990. In 2000 he received his highest scientific degree − Doctor of Chemical Sciences − and habilitated as Professor of Chemistry. He is an experienced researcher in coordination and cluster chemistry. His research interests cover the realm of synthesis, reactivity, structures and properties of cluster halides, chalcogenides and chalcohalides of the early transition metals (V, Nb, Mo, W, Re). Prof. Mironov and his students have synthesised and characterised more than two hundred new cluster compounds and published about a hundred articles. He has been awarded several grants from different foreign foundations, like the Alexander von Humboldt Foundation (with Prof. W. S. Sheldrick, Bochum University, Germany) and the NSF (with Prof. J. A. Ibers, Northwestern University, USA), and has also received a Korean Fellowship (with Prof. S.-J. Kim, Ewha Womans University, Seoul, Korea).*

*Vladimir Fedorov graduated from the Leningrad Institute of Technology and obtained his Dipl. Ing. in 1959. The same year he went as an engineer to the plant of advanced ceramics and composites in Novosibirsk where he spent three years. From 1963 to 1966 he studied inorganic, coordination and solid-state chemistry at the Natural Science Department of the Novosibirsk State University, where he completed his thesis and received his PhD. From 1966 to the present day V. Fedorov has been working at the Nikolaev Institute of Inorganic Chemistry, Russian Academy of Sciences (Novosibirsk). Further research in cluster chemistry led to the award of his highest scientific degree − Doctor of Chemical Sciences − in 1990. He then habilitated the position of Full Professor of Inorganic Chemistry. Currently he is head of the laboratory of synthesis of cluster compounds and materials and a lecturer at the Natural Sciences Department of the Novosibirsk State University, where he teaches cluster chemistry of the transition metals. The main research interests of Prof. Fedorov lie in cluster, coordination and medical chemistry, including the synthesis and design of materials, the study of crystal and electronic structures, and the investigation of different physico-chemical properties of solids and solutions. Prof. Fedorov's studies have resulted in more than 350 scientific publications, two monographs and several patents.*

 © 2006 Wiley-VCH Verlag GmbH & Co. KGaA, Weinheim 

The $[Re_4Q_4(TeCl_2)_4Cl_8]$ compounds are insoluble both in water and common organic solvents but readily react with various compounds in aqueous solution or organic solvents or even with the solvents themselves upon heating or occasionally at room temperature. All such transformations proceed with the replacement of the outer-sphere ligands ($TeCl_2$ or $Cl^-$) of the cluster complexes, resulting in the formation of compounds with different outer ligands (fluoride, polysulfide, thiocyanate, cyanide, acetamide, DMF etc.; see Scheme 1).[7–12]

The cyanide complexes $[Re_4Q_4(CN)_{12}]^{4-}$ are of particular interest among these compounds. Due to their ambidentate character, the CN groups can serve as bridging ligands to give polymeric compounds of different dimensionalities. Such an approach has been applied for the preparation of coordination polymers based on $Re_6$[13–19] cluster chalcocyanides and very recently was successfully used for $W_6$[20] and $Nb_6$[21–22] cyano complexes. $Re_4$ cluster complexes have 12 CN ligands (three for each Re atom), in contrast to the six CN ligands (one for each Re atom) in $M_6$ cluster complexes. This difference leads to a greater variety of coordination complexes of $Re_4$ chalcocyanides with transition metals. In recent years, we have carried out systematic studies of the synthesis of cyano-bridged coordination polymers based on the tetrahedral rhenium cluster complexes $[Re_4Q_4(CN)_{12}]^{4-}$ (Q = S, Se or Te) and 3d metal complexes. The use of polydentate ligands in the coordination sphere of transition metals offers additional possibilities for controlling the dimensionality of the resulting cyano-bridged compounds.

For the convenience of structure description in cases where two transition metal cations are coordinated by one cluster anion we offer the following labels for the CN ligand couples that take part in binding (Table 1).

One of the important experimental factors for the reactions mentioned below is the reaction medium. The compounds described in this review were obtained either in aqueous solution or in aqueous ammonia solution.

## 2. The Interaction of $[Re_4Q_4(CN)_{12}]^{4-}$ Anions with Aqua Complexes of Transition Metals

The reaction of water solutions of $K_4[Re_4Te_4(CN)_{12}]$ and $CuCl_2$ in a gel based on sodium silicate leads to the cluster complex $[Cu_4(\mu_3\text{-}OH)_4][Re_4(\mu_3\text{-}Te)_4(CN)_{12}]$ (**1**).[23] The structure of this compound contains layers built up from tetranuclear $[Cu_4(\mu_3\text{-}OH)_4]^{4+}$ cations and $[Re_4Te_4(CN)_{12}]^{4-}$ cluster anions (Figure 1). Eight of the twelve $CN^-$ ligands of the cluster anion coordinate copper atoms in the layer; the four remaining $CN^-$ ligands are directed perpendicular to the layer and are bonded to the OH groups of cations from adjacent layers. In the $[Cu_4(\mu_3\text{-}OH)_4]^{4+}$ cation, which is synthesised by a self-assembly reaction, the four copper atoms and four $OH^-$ groups form a cubane-like structure with two short and four long Cu–Cu distances of 2.99 and 3.18 Å, respectively.

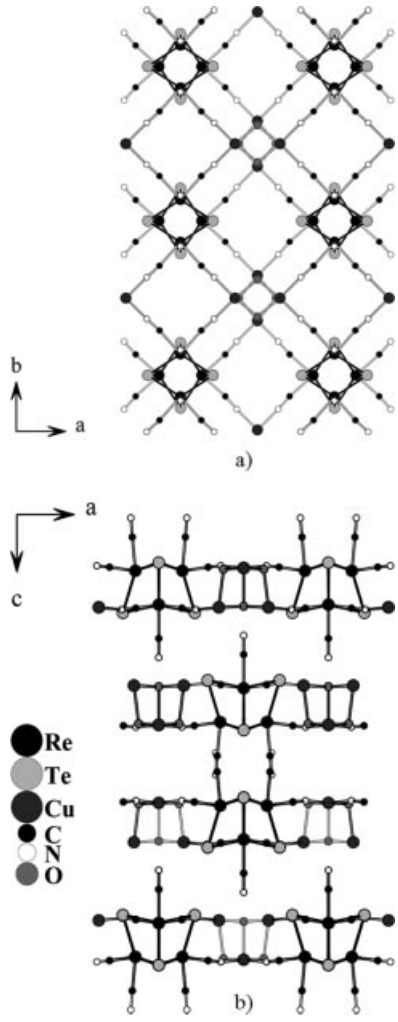


Figure 1. a) The covalent layer in **1** (projection along the *ab* plane). b) The packing of the layers (projection along the *ac* plane). Hydrogen atoms have been omitted for clarity in this figure and others.

If the reaction of $K_4[Re_4Te_4(CN)_{12}]$ and $CuCl_2$ is carried out in 1 M hydrochloric acid solution the three-dimensional cluster complex $[\{Cu(H_2O)_2\}\{Cu(H_2O)_2\}Re_4Te_4(CN)_{12}]$ (**2**) is formed.[11] There are two copper cations with different coordination environments in the structure of this compound. The Cu1 cation is coordinated by four nitrogen atoms of CN groups and by two oxygen atoms of water molecules to form a two-dimensional network in which the cluster units are linked through Re–C≡N–Cu–N≡C–Re bridges, whereas the Cu2 cation is coordinated by two nitrogen atoms of CN groups and two oxygen atoms of water molecules to give a square-planar environment of the Cu2 atoms (Figure 2). The Cu2 cation bridges two-dimensional networks to give a complicated three-dimensional packing.

The ions $Cd^{2+}$ and $Mn^{2+}$ give two related cluster complexes, namely $[\{Cd(H_2O)_2\}\{Cd(H_2O)_4\}Re_4Te_4(CN)_{12}]$ (**3**) and $[\{Mn(H_2O)_2\}\{Mn(H_2O)_4\}Re_4Te_4(CN)_{12}]$ (**4**).[11] They are isostructural to the copper complex **2** although, unlike the Cu2 cation, Cd2 and Mn2 demand an octahedral environment. Such a coordination preference results in disordering of the M2 cations over two crystallographically

 © 2006 Wiley-VCH Verlag GmbH & Co. KGaA, Weinheim 

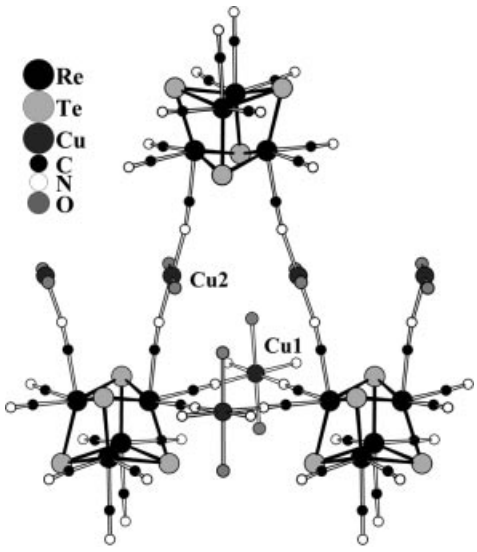


Figure 2. A fragment of the crystal structure of compound **2**.

equivalent positions with equal contributions in complexes **3** and **4**. This cation is coordinated by two nitrogen atoms of CN groups and four oxygen atoms of water molecules. M2–M2 dimers are present in the structure, with two water molecules and a cluster anion coordinated as bridges (Figure 3).

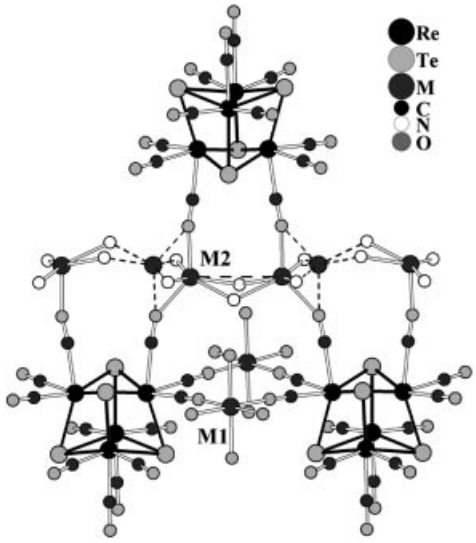


Figure 3. The M(2)···M(2) dimers in the structures of **3** and **4**. The second, disordered positions of M(2) are shown by dashed bond lines.

## 3. The Interaction of $[Re_4Q_4(CN)_{12}]^{4-}$ Anions with Amino Complexes of Transition Metals

The interaction of cluster anions with amino complexes of metal cations such as $Ni^{2+}$, $Cd^{2+}$ and $Cu^{2+}$ gives different products to those obtained with aqua complexes.

The compound $[\{Ni(NH_3)_5\}_2\{Re_4Te_4(CN)_{12}\}]\cdot 3.4H_2O$ (**5**) was prepared from $NiCl_2$ and $K_4[Re_4Te_4(CN)_{12}]$ in aqueous ammonia solution.[24] The molecular structure of this compound contains two $[Ni(NH_3)_5]^{2+}$ cations bonded to one cluster anion through the nitrogen atoms of the *gem*-CN groups. The coordination polyhedron of the Ni atoms is practically a regular octahedron (Figure 4).

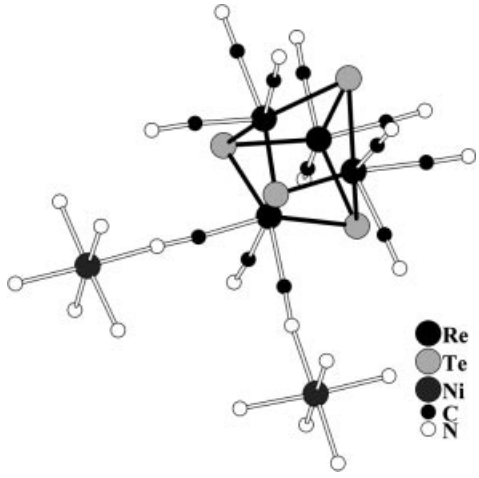


Figure 4. View of the $[\{Ni(NH_3)_5\}_2Re_4Te_4(CN)_{12}]$ molecule in **5**.

The use of $CdSO_4$ instead of $NiCl_2$ leads to the formation of a compound formulated as $[\{Cd(NH_3)_5\}\{Cd(NH_3)_3\}\{Re_4Te_4(CN)_{12}\}]\cdot 4H_2O$ (**6**).[24] This compound contains two types of cations: a terminal $[Cd(NH_3)_5]^{2+}$ cation and a bridging $[Cd(NH_3)_3]^{2+}$ one. Whereas the $[Cd(NH_3)_5]^{2+}$ cations are coordinated by only one cyanide group, the $[Cd(NH_3)_3]^{2+}$ cations are coordinated by three CN groups of different cluster anions to form a chain-like structure (Figure 5).

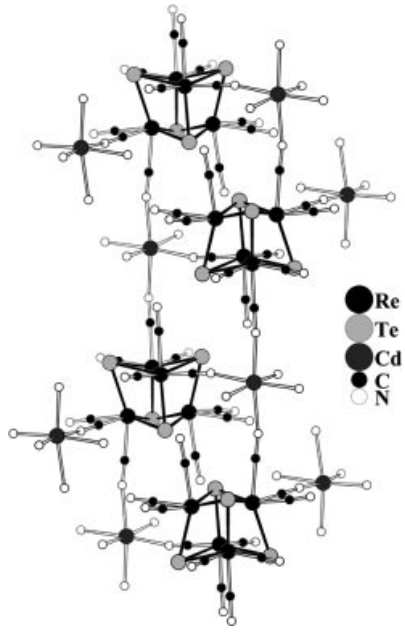


Figure 5. A fragment of the crystal structure of **6**.

The reaction of aqueous $K_4[Re_4Q_4(CN)_{12}]$ solutions with an ammonia solution of $CuCl_2$ give the complexes $[\{Cu(NH_3)_3\}_2\{Re_4Q_4(CN)_{12}\}]\cdot nH_2O$ [Q = S (**7**), Se (**8**)] (Figure 6) and $[\{Cu(NH_3)_3\}_{1.7}\{Cu(NH_3)_4\}_{0.3}Re_4Te_4(CN)_{12}]$

 © 2006 Wiley-VCH Verlag GmbH & Co. KGaA, Weinheim 

(**9**).[25] In compounds **7** and **8** the $[Re_4Q_4(CN)_{12}]^{4-}$ cluster units are linked by cyanide bridging ligands through $[Cu(NH_3)_3]^{2+}$ to give chains that extend along the *c* axis. In the case of Q = Te these chains have a discrete character because some of the copper atoms are coordinated by four ammonia molecules (Figure 7). These copper cations have a distorted square-pyramidal coordination environment formed by three ammonia molecules and the N atom of the CN ligand in the equatorial plane, and additionally by the N atom of the CN ligand in the apical position.

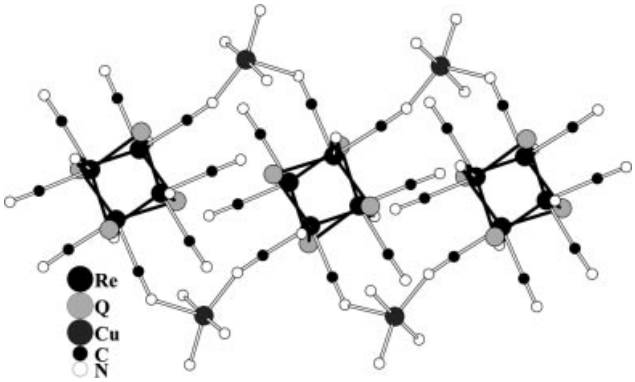


Figure 6. A fragment of the crystal structure of compound **7**.

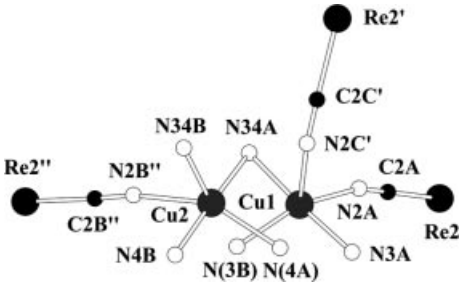


Figure 7. Disordering of the Cu atoms over two positions in the crystal structure of compound **9**.

Compounds **7**–**9** have a one-dimensional topology similar to **6**. However, there are several differences. For instance, the Cd atoms have an octahedral coordination environment whereas the Cu atoms have a square-pyramidal environment, and in **6** only half of the Cd atoms are bridged linking three clusters at once.

The reaction of an aqueous $K_4[Re_4Te_4(CN)_{12}]\cdot 5H_2O$ solution with a $ZnCl_2$ ammonia solution leads to formation of $[\{Zn(H_2O)_2\}\{Zn(H_2O)_4\}Re_4Te_4(CN)_{12}]$ (**10**), which has a structure similar to that of compounds **3** and **4**. Compound **10** dissolves when ammonia is added and can be recrystallised by removing this ammonia.[26]

Thus, the formation of compounds **5**–**9** can be considered as stages in the formation of **2**–**4**. In this scheme, the polymeric complex **10** is the final product.

## 4. The Interaction of $[Re_4Q_4(CN)_{12}]^{4-}$ Anions with Amino Complexes of Transition Metals in the Presence of Polydentate N-Donor Ligands

One of the most convenient and effective ways to change the dimensionality of structures is by using polydentate ligands, which can effectively block coordination sites around the transition metal cations and thus control the number of coordination sites available for binding with CN groups. Partial or complete blocking of coordination sites allows the directional regulation of structure dimensionality. A wide assortment of polydentate ligands having N-donor atoms, such as ethylenediamine (en), diethylenetriamine (dien), triethylenetetraamine (trien) and *threo*-tetraaminobutane (*threo*-tab), have been used for such a purpose. These ligands can block two, three or four coordination sites around the transition metal, and also can behave as bridges.

### 4.1. Complexes with Ethylenediamine

The interaction of $M^{2+}$ transition metal cations having different coordination numbers [$n$ = 6 (Ni, Zn, Cu) and 5 (Cu)] with bidentate ethylenediamine in water or aqueous ammonia solution leads to the formation of complexes with different M/en ratios. This can be described by the stepwise complex formation shown in Equations (1), (2) and (3) (L = $H_2O$, $NH_3$).

$$[ML_n]^{2+} + en \rightarrow [ML_{n-2}(en)]^{2+} + 2L \quad (1)$$

$$[ML_{n-2}(en)]^{2+} + en \rightarrow [ML_{n-4}(en)_2]^{2+} + 2L \quad (2)$$

$$[ML_{n-4}(en)_2]^{2+} + en \rightarrow [M(en)_3]^{2+} + 2L \quad (3)$$

Generally, all cationic forms coexist simultaneously in solution and can interact with cluster anions to give compounds of different stoichiometry. The predominance of one form or another depends on the ligand concentration, i.e. the M/en ratio in solution, and the stability constants of the corresponding complexes; the form that reacts with the cluster anion to give the solid depends on these factors and its solubility too.

#### *4.1.1. Compounds Containing $[Ml_{n-2}(en)]^{2+}$*

The interaction of $K_4[Re_4Se_4(CN)_{12}]$ with an equimolar mixture of $CuCl_2$ and en in aqueous ammonia solution leads to the formation of $[\{Cu(en)\}\{Cu(NH_3)(en)\}Re_4Se_4(CN)_{12}]\cdot 5H_2O$ (**11**)[27] in which the chemical form $[CuL_3(en)]^{2+}$ (L = CN and $NH_3$; $n$ = 5) is observed. There are two copper cations in the structure of this compound, both of which have a distorted square-pyramidal environment but different coordination compositions. The Cu1 cation is coordinated by two amino groups of an en molecule and three nitrogen atoms of CN ligands of different cluster anions, whereas Cu2 bridges only two cluster anions so it is coordinated by two N atoms of CN ligands, en and ammonia molecules. As a result this compound has a complicated polymeric structure in which two infinite chains directed along *b* axes are linked through Re–CN–Cu1 bridges (Figure 8).

 © 2006 Wiley-VCH Verlag GmbH & Co. KGaA, Weinheim 

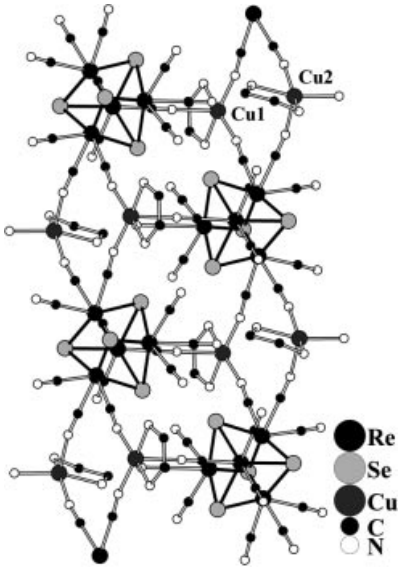


Figure 8. A fragment of the structure of complex **11**.

### *4.1.2. Compounds Containing a Mixture of $[ML_{n-2}(en)]^{2+}$ and $[ML_{n-4}(en)_2]^{2+}$*

A mixture of chemical forms corresponding to the first and the second steps of complex formation, in a 1:1 ratio, was observed in complexes $[Ni(NH_3)_4(en)][\{Ni(NH_3)(en)_2\}Re_4Te_4(CN)_{12}]\cdot 2H_2O$ (**12**) and $[Zn(NH_3)_2(en)_2][\{Zn(NH_3)_2(en)\}Re_4Te_4(CN)_{12}]\cdot H_2O$ (**13**) (L = $NH_3$ and CN).

Compound **12** was obtained from an aqueous ammonia solution containing $K_4[Re_4Te_4(CN)_{12}]$, $NiCl_2$ and ethylenediamine (Ni/en ratio of 1:1.5).[28] The structure of **12** is ionic, with an $[Ni(NH_3)_4(en)]^{2+}$ cation and an $[\{Ni(NH_3)(en)_2\}Re_4Te_4(CN)_{12}]^{2-}$ anion (Figure 9). The $[Ni(NH_3)_4(en)]^{2+}$ cation corresponds to the $[ML_{n-2}(en)]^{2+}$ chemical form in Equation (1) for an octahedral environment. At the same time, the $[\{Ni(NH_3)(en)_2\}Re_4Te_4(CN)_{12}]^{2-}$ anion can be described as the result of substitution of an ammonia molecule by the $[Re_4Te_4(CN)_{12}]^{4-}$ cluster anion in the coordination environment of a *cis*-$[Ni(NH_3)_2(en)_2]^{2+}$ complex cation.

Compound **13** also has an ionic structure, with an *cis*-$[Zn(NH_3)_2(en)_2]^{2+}$ cation corresponding to the $[ML_{n-4}(en)_2]^{2+}$ ($n$ = 6) chemical form and a $[\{Zn(NH_3)_2(en)\}Re_4Te_4(CN)_{12}]_n^{2n-}$ anion, which has a zigzag chain-like structure (Figure 10).[26] Once again, the anion formation can be viewed as the result of substitution of *cis*-ammonia molecules by nitrogen atoms of two different cluster anions in the $[ML_{n-2}(en)]^{2+}$ chemical form.

It should be noted that only these two compounds out of the whole series of tetrahedral rhenium cluster complexes including $[ML_{n-4}(en)_2]^{2+}$ units contain *cis*-$[ML_2(en)_2]^{2+}$ cations. An analysis of the structural data of all compounds deposited in the CCDC (CSD v.5.25) shows that the number of *trans*-$[ML_2(en)_2]^{2+}$ complexes is much higher than that of *cis*-$[ML_2(en)_2]^{2+}$ complexes. Apparently, *trans*-$[ML_2(en)_2]^{2+}$ complexes are energetically more stable than the *cis*-$[ML_2(en)_2]^{2+}$ form. However, the isolation of this form from solution has proved to be possible upon crystallisation with cluster anions.

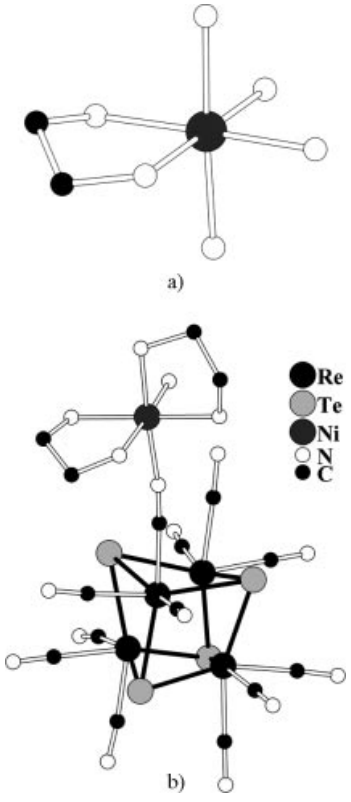


Figure 9. Structure of the complex $[Ni(NH_3)_4(en)]^{2+}$ cation (a) and the $[\{Ni(NH_3)(en)_2\}Re_4Te_4(CN)_{12}]^{2-}$ anion (b) in compound **12**.

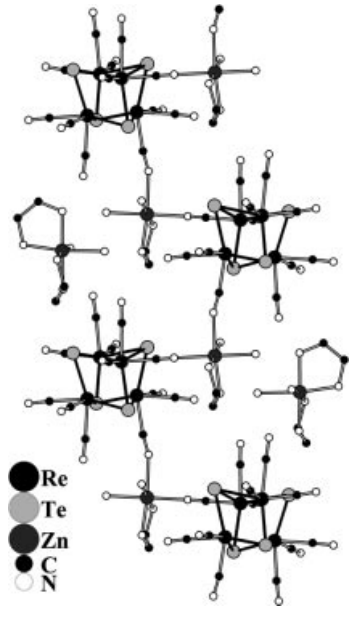


Figure 10. A fragment of structure of **13**.

### *4.1.3. Compounds Containing Only $[ML_{n-4}(en)_2]^{2+}$*

All compounds synthesised in the presence of ethylenediamine with an M/en ratio of 1:2 contain *trans*-$[ML_{n-4}(en)_2]$ units. Such complexes are known with bridging $\{M(en)_2\}$

 © 2006 Wiley-VCH Verlag GmbH & Co. KGaA, Weinheim 

(M = $Ni^{2+}$, $Cu^{2+}$ and $Zn^{2+}$) groups or terminal $\{Cu(en)_2\}$ ($n$ = 5) groups coordinated to CN ligands of the cluster anion.

The compound $[\{Cu(en)_2\}_2Re_4S_{3.83}Te_{0.17}(CN)_{12}]\cdot H_2O$ (**14**) has a polymeric grid structure in which the $[Re_4S_{3.83}Te_{0.17}(CN)_{12}]^{4-}$ cluster anions are situated at the cross-points of this lattice and are linked by $[Cu(en)_2]^{2+}$ cationic units, as depicted in Figure 11. Each Cu atom in the cationic part has a [4+2] coordination environment: it is coordinated by four $NH_2$ groups of two ethylenediamine units in the equatorial plane and by two N atoms of CN ligands of different cluster anions with longer Cu–N distances (2.367 and 2.759 Å).[29]

The isostructural compounds $[\{Ni(en)_2\}_2Re_4Se_4(CN)_{12}]\cdot 3.25H_2O$ (**15**)[18] and $[\{Zn(en)_2\}_2Re_4S_{3.60}Te_{0.41}(CN)_{12}]\cdot 3.75H_2O$ (**16**)[29] have a polymeric grid structure with $[Re_4Q_4(CN)_{12}]^{4-}$ cluster anions at the cross-points and $[M(en)_2]^{2+}$ moieties on the edges (Figure 12). However, two of these lattices are arranged differently. In the case of **14** four CN groups of two rhenium atoms (2+2) take part in binding; whereas in of **15** and **16** four CN ligands belonging to three Re atoms (2+1+1) of the cluster anion are involved in formation of the polymeric structure. In this context, the different bridging modes have a crucial influence on the packing characteristics. The bent bridging modes in **14** result in the formation of wavy layers (Figure 13, a), whereas the tentatively flat binding of **15** and **16** generates approximately planar layers (Figure 13, b).

The compound of composition $[Ni(NH_3)_2(en)_2][\{Ni(en)_2\}_3\{Re_4Te_4(CN)_{12}\}_2]\cdot 38H_2O$ (**17**) was obtained under the same reaction conditions as those of **15**. However, the structure of this compound differs dramatically. Figure 14 shows the structure of the $[\{Ni(en)_2\}_3\{Re_4Te_4(CN)_{12}\}_2]^{2-}$ anion, in which $[Re_4Te_4(CN)_{12}]^{4-}$ clusters are linked by $\{Ni(en)_2\}^{2+}$ units to form hexagonal layers. There are two types of channels in this structure: large hexagonal and smaller triangular ones, which are filled with water molecules and $[Ni(NH_3)_2(en)_2]^{2+}$ counterions. The volume of the large cavity is 1590 $Å^3$ and the volume of each of the two smaller ones is 640 $Å^3$. The total available volume for solvent per unit cell is 2870 $Å^3$, corresponding to about 37% of the unit cell volume. Compound **17** is the first example of a highly porous structure derived from the tetrahedral $Re_4Q_4$ cluster core. The en molecules coordinated to the Ni atoms make the framework in **17** robust and prevent its collapse after dehydration. Indeed, powder diffraction studies of samples left in air for weeks at room temperature and after heating to 120 °C (a temperature at which the material is completely dehydrated according to thermal analysis) indicate that the original crystal structure remains essentially unchanged. The walls of the large channels of the framework in **17** are decorated by twelve N atoms from the terminal CN ligands of the $[Re_4Te_4(CN)_{12}]^{4-}$ cluster anion in every sheet. This feature makes this robust framework an attractive matrix for inclusion of molecules or ions of corresponding size and shape based on "host–guest" prin-

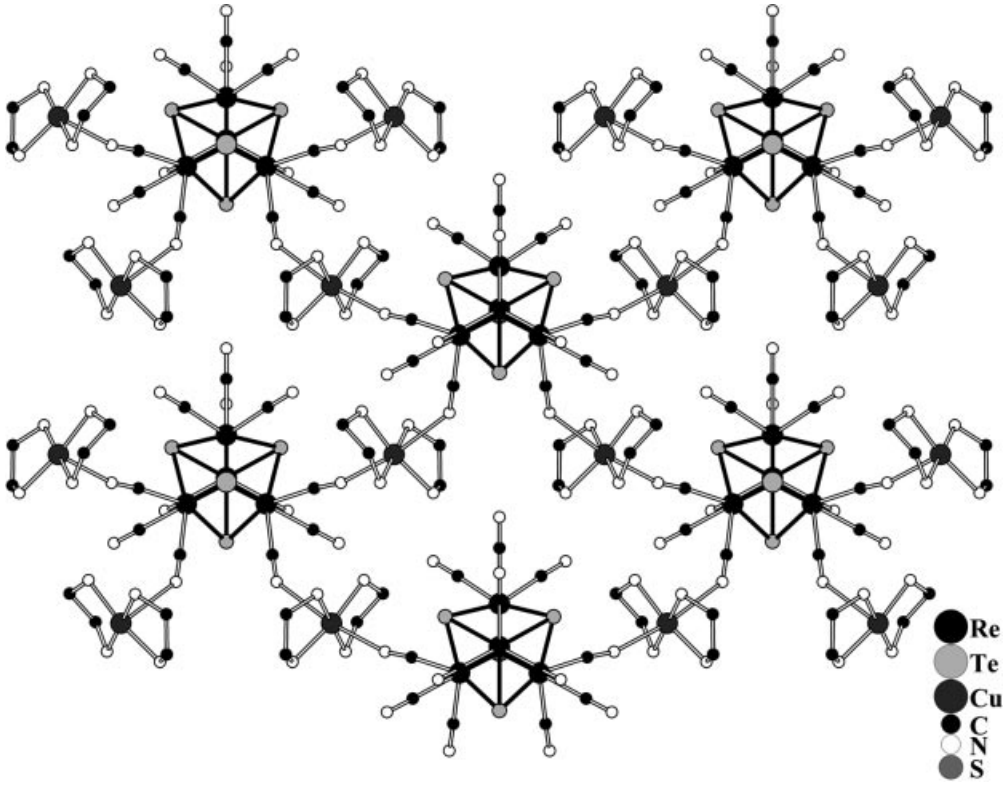


Figure 11. A fragment of the layer in compound **14**.

 © 2006 Wiley-VCH Verlag GmbH & Co. KGaA, Weinheim 

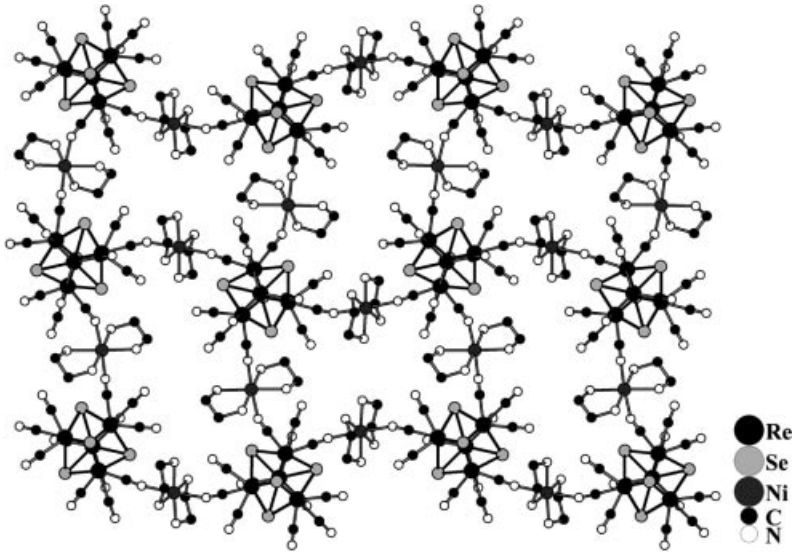


Figure 12. A fragment of the layer in compound **15**.

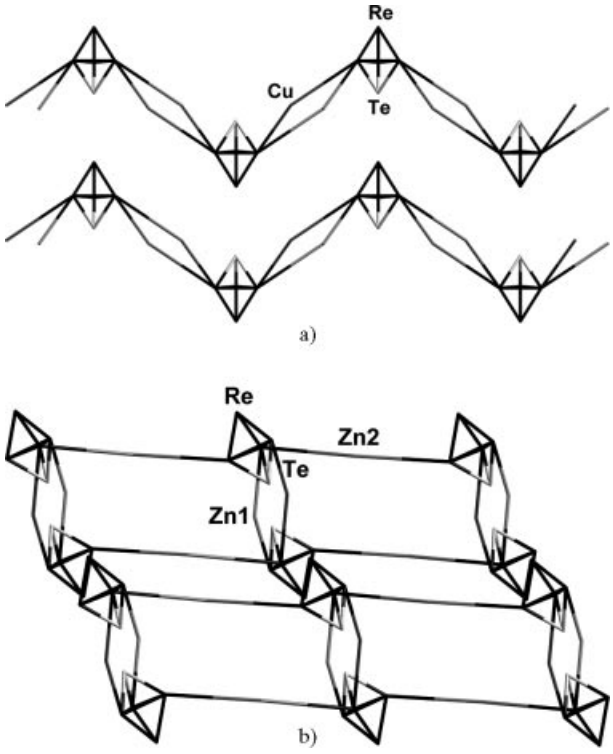


Figure 13. Views of the stacking of layers in **14** (a) and **16** (b) using a stick model.

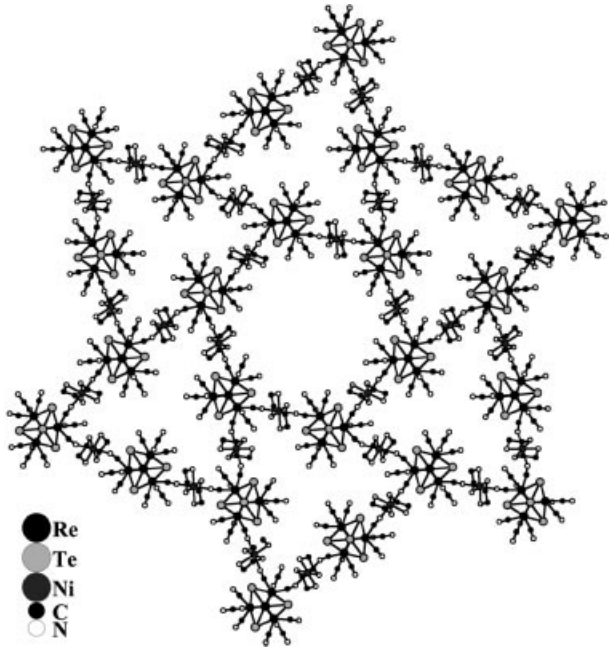


Figure 14. View down the *c* axis of the crystal packing of the $[\{Ni(en)_2\}_3\{Re_4Te_4(CN)_{12}\}_2]^{2-}$ polymeric anion in **17**.

ciples. The N atoms directed into the channel are able to form both covalent bonds, with any N-acceptor atoms such as transition metals, and hydrogen bonds, with H-containing molecules such as alcohols, to guest molecules.[30] Apparently, the reason for formation of such differently arranged structures as that of **15** and **17** is the different cluster core composition ($Re_4Se_4$ in **15** and $Re_4Te_4$ in **17**).

The use of $[Cu(en)_2Cl_2]$ instead of $[Ni(en)_2Cl_2]$, which was used for the synthesis of **15** and **17**, gives the formation of the molecular compounds $[\{Cu(en)_2\}_2Re_4Q_4(CN)_{12}]\cdot 5H_2O$ [$Q_4 = Te_4$ (**18**),[31] $STe_3$ (**19**)[32]], which have different structures. In these compounds the $[Re_4Q_4(CN)_{12}]^{4-}$ cluster anions are coordinated by two $\{Cu(en)_2\}^{2+}$ units in opposite directions (Figure 15). To put it another way, every *trans*-$\{Cu(en)_2\}$ unit is linked to only one CN ligand of the cluster anion, which means that *n* in this case is equal to 5; this results in the formation of a molecular structure.

 © 2006 Wiley-VCH Verlag GmbH & Co. KGaA, Weinheim 

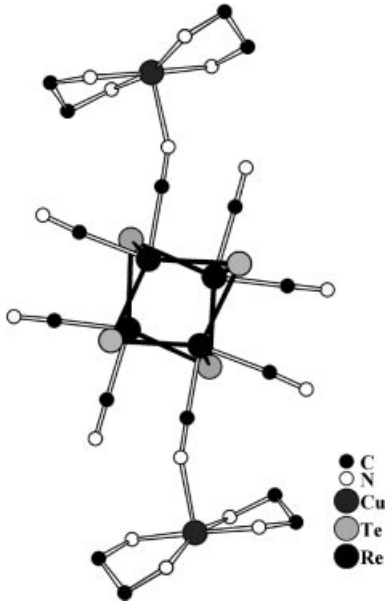


Figure 15. View of the $[\{Cu(en)_2\}_2Re_4Te_4(CN)_{12}]$ molecule in **18**.

Thus, the interaction of $[Re_4Q_4(CN)_{12}]^{4-}$ (Q = S, Se, Te) cluster anions with $Ni^{2+}$, $Cu^{2+}$ and $Zn^{2+}$ metal cations in the presence of a chelate ligand such as ethylenediamine leads to the formation of compounds with various structures made up of cluster anions and cationic units corresponding to the different chemical forms that coexist in solutions containing a transition metal salt and en.

### 4.2. Complexes with Diethylenetriamine

The diethylenetriamine ligand can block one, two or three coordination sites around a transition metal cation. It can also bridge two cations. Table 2 shows the labels of three different coordination modes of the dien molecule.

Table 2. Labels of the coordination modes of the dien molecule.

| Labeling | Coordination mode |
|---|---|
| (1,2,3)-mode | 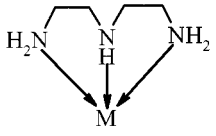 |
| (1)-(3)-mode | 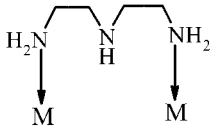 |
| (1,2)-(3)-mode | 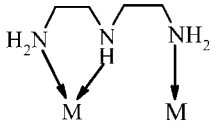 |

All three coordination modes have been found in complexes containing tetrahedral chalcocyanide rhenium cluster anions and transition metal cations bonded with dien. The (1,2,3)-coordination mode is present in all compounds but the bridging mode only exists in compounds with a dien/M molar ratio greater than 1. A possible reason for this situation is that the $K_1$ stability constant of $[M(dien)]^{2+}$ (M = Ni, Cu and Zn) is higher than the $K_2$ constant.

#### *4.2.1. Complexes with Only the (1,2,3)-Coordination Mode*

Five complexes containing $\{ML_{n-3}(dien)\}$ cationic units (where L is either ammonia molecules or nitrogen atoms of CN ligands) have been obtained by the reaction of $M^{2+}$ cations (M = Ni, Cu or Zn) with $[Re_4Q_4(CN)_{12}]^{4-}$ (Q = S, Se, Te) cluster anions in the presence of diethylenetriamine (M/dien = 1:1) in aqueous ammonia solution.

The $[Ni(NH_3)_3(dien)]^{2+}$ chemical form was observed in the ionic compound $[Ni(NH_3)_3(dien)]_2[Re_4Se_4(CN)_{12}]\cdot 5.5H_2O$ (**20**), which contains *fac*-$[Ni(NH_3)_3(dien)]^{2+}$ cations (Figure 16). The compound $[\{Ni(NH_3)_2(dien)\}_2Re_4Te_4(CN)_{12}]\cdot 2.5H_2O$ (**21**) can be considered the result of an ammonia molecule substitution in a *fac*-$[Ni(NH_3)_3(dien)]^{2+}$ cationic unit by the nitrogen atom of a CN ligand (Figure 17).[28]

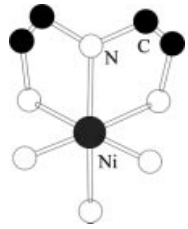


Figure 16. Structure of the complex $[Ni(NH_3)_3(dien)]^{2+}$ cation in compound **20**.

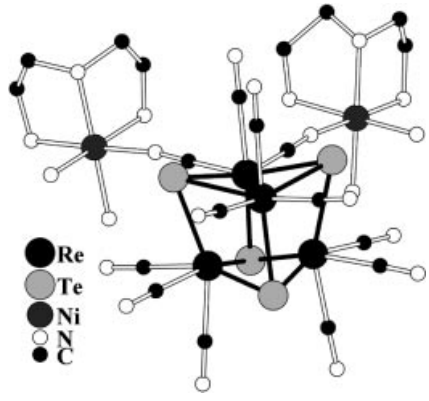


Figure 17. View of the $[\{Ni(NH_3)_2(dien)\}_2Re_4Te_4(CN)_{12}]$ molecule in **21**.

At the same time, the formation of compounds $[\{Cu(NH_3)(dien)\}_2Re_4S_{3.64}Te_{0.36}(CN)_{12}]\cdot 3H_2O$ (**22**)[29] and $[\{Cu(NH_3)(dien)\}_2Re_4Se_4(CN)_{12}]\cdot 2.5H_2O$ (**23**)[33] can be presented as the result of coordination of a CN ligand to a $[Cu(NH_3)(dien)]^{2+}$ unit with a square-planar structure. The structures of **22** and **23** have only one distinction: in the case of **22** *gem*-CN ligands are bonded to two cationic units, whereas in **23** these bridging ligands have an *ortho* orientation (Figure 18).

 © 2006 Wiley-VCH Verlag GmbH & Co. KGaA, Weinheim 

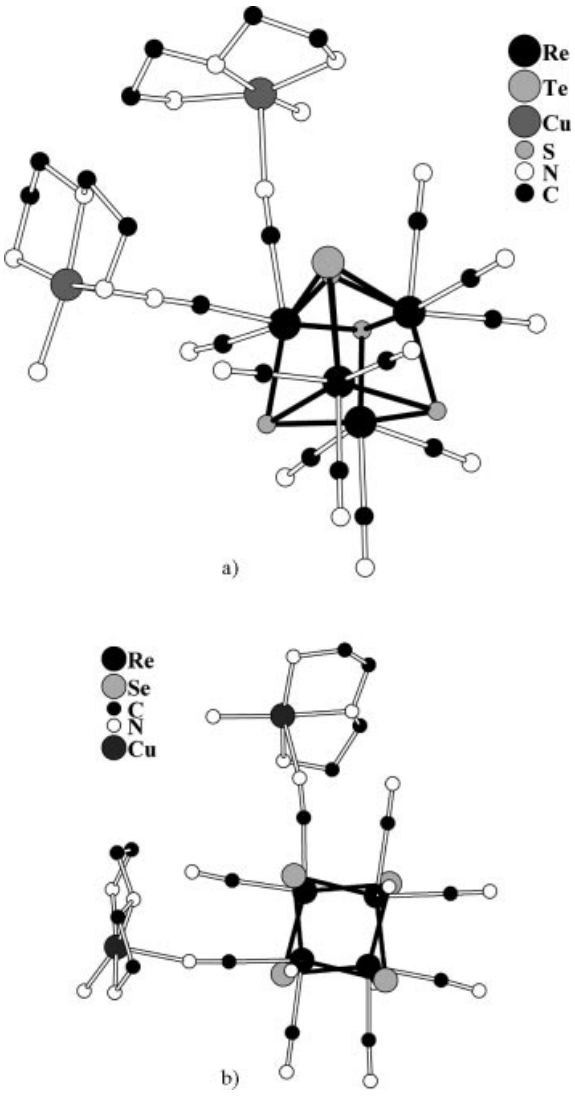


Figure 18. View of the $[\{Cu(dien)(NH_3)\}_2Re_4S_{3.45}Te_{0.55}(CN)_{12}]$ molecule in compound **22** (a) and $[\{Cu(dien)(NH_3)\}_2Re_4Se_4(CN)_{12}]$ molecule in compound **23** (b).

The next step of complication can be viewed in $[\{Cu(dien)\}_2Re_4Te_4(CN)_{12}]\cdot 9H_2O$ (**24**).[27] This compound has a chain-like structure in which the cluster anions are linked to each other through two complex $\{Cu(dien)\}^{2+}$ cations. An alternation of the -2Cu(dien)-cluster-2Cu(dien)- fragments gives rise to a coordination-chain polymer whose structure is shown in Figure 19. Thus, the formation of this compound can be considered as a two-step process. First, the molecular complex $[\{Cu(NH_3)(dien)\}_2Re_4Te_4(CN)_{12}]$, similar to that described for **22**, is formed, and in the next step these molecular units are condensed by means of substitution of an ammonia molecule in the equatorial plane of the copper cation by a nitrogen atom from an adjacent cluster anion.

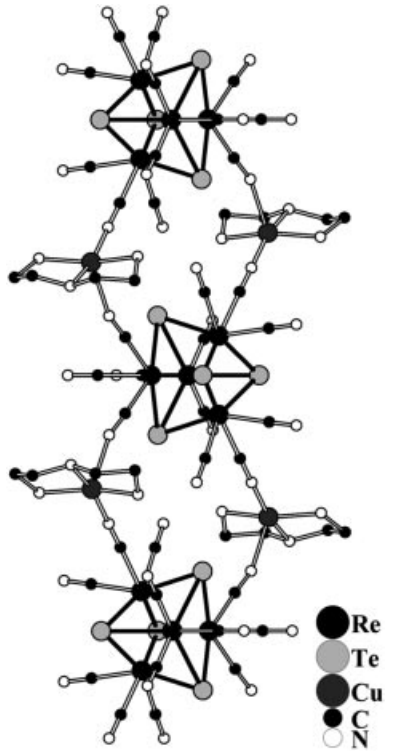


Figure 19. A fragment of the chain in structure of **24**.

We have described above analogous chain structures for compounds **7** and **8** in which the cluster anions are linked to each other by two cationic $\{Cu(NH_3)_3\}^{2+}$ fragments. In the ammonium analog, four CN groups of one cluster anion involved in the formation of the polymeric structure are coordinated to two Re atoms [2 + 2], whereas the bridging CN ligands in the compound with dien are coordinated to three Re atoms [2 + 1 + 1].

#### *4.2.2. A Complex with the (1,3)-Coordination Mode*

Decreasing the dien/$M^{2+}$ ratio leads to the formation of complexes in which dien molecules exhibit bridged coordi-

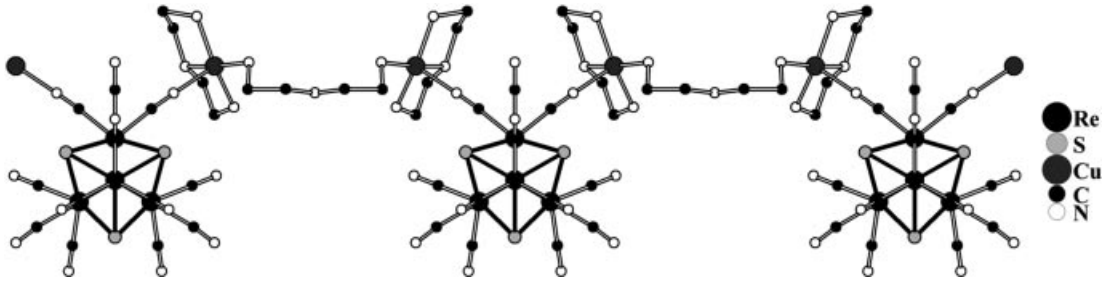


Figure 20. Chain fragment of the structure of compound **25**.

 © 2006 Wiley-VCH Verlag GmbH & Co. KGaA, Weinheim 

nation modes along with the (1,2,3)-coordination mode. The (1,3)-coordination mode has been found only in the case of $[\{Cu_2(dien)_3\}Re_4S_4(CN)_{12}]$ (**25**),[33] which has a polymeric structure where the $[Re_4S_4(CN)_{12}]^{4-}$ cluster anions are bridged by $[(dien)Cu\text{-}dien\text{-}Cu(dien)]^{4+}$ cationic chains (Figure 20). Each Cu atom in the cationic chain-like building blocks is coordinated by one dien molecule with (1,2,3)-coordination mode and one amino group of bridged dien molecule with (1)-(3)-coordination mode. On the other hand the formation of this compound can be also considered as a result of two-step process. On the first step the formation of $[\{Cu(NH_3)(dien)\}_2Re_4S_4(CN)_{12}]$ takes place analogously to that described for **22**. And then these molecular units are linked by dien molecules which substitute ammonia molecule in equatorial plane of copper cation by terminal amino groups.

### *4.2.3. The Complexes with (1,2)-(3)-Coordination Mode*

The two isostructural compounds $[\{Cu_2(dien)_3\}Re_4Q_4(CN)_{12}]\cdot nH_2O$ [Q = Se (**26**) and Te (**27**)] have been synthesised following the same synthetic procedure.[33] It is very interesting to note that both these compounds have a compositions similar to that of **25**, but their structures are sufficiently different. Whereas compound **25** has a chain-like polymeric structure, **26** and **27** are molecular (Figure 21) and consist of $[Re_4Q_4(CN)_{12}]^{4-}$ (Q = Se, Te) cluster anions and non-binding $[Cu_2(dien)_3]^{4+}$ cationic units, the structure of which differs noticeably from the corresponding cation in **25**. Both Cu atoms in **25** are crystallographically equivalent and are coordinated by N atoms of CN ligands of different clusters. In **26** and **27**, however, the Cu atoms exhibit different coordination environments: one Cu atom has a similar arrangement to the Cu atom in compound **25**, whereas the second Cu atom is coordinated by three N atoms of one dien ligand and by two N atoms of another dien ligand, in a (1,2)-(3)-mode, which bridges the two Cu atoms of the cationic unit through its third N atom. Such a coordination type prevents the formation of a polymeric structure. A comparison of **26** and **27** with **25** shows that the structure of the latter can be transformed into the structure of **26** and **27** by the rupture of one Cu–NC bond and the formation of a new bond with the middle amino group of the bridging dien ligand.

The composition of $[\{Zn_2(dien)_3\}Re_4Te_4(CN)_{12}]\cdot 6H_2O$ (**28**)[26] is similar to that of **26** and **27**. However, its molecular structure looks like **26** and **27** only partially. The structure of the $[Zn_2(dien)_3]^{4+}$ cationic unit is analogous to $[Cu_2(dien)_3]^{4+}$ in **26** and **27**, but it is bonded to the cluster cation through not one but two CN ligands, i.e. in this case both metal cations are coordinated by nitrogen atoms of CN ligands (Figure 22). Thus, there are interesting structural transitions between **25** and **26** (or **27**), and then **28**, in which the dimensionality initially decreases from 1D to 0D due to the rupture of an M–NC bond, with an adjustment of the cluster cation and the formation of a new bond inside one molecular unit.

If the $Cu^{2+}$ concentration is reduced the isostructural compounds $[K(H_2O)_2]_2[\{Cu_3(dien)_4\}\{Re_4Q_4(CN)_{12}\}_2]\cdot 8H_2O$ [Q = Se (**29**) and Te (**30**)] can be obtained.[33] The anionic unit of this structure is provided by the complex $[\{Cu_3(dien)_4\}\{Re_4Te_4(CN)_{12}\}_2]^{2-}$ (Figure 23), in which two $[Re_4Te_4(CN)_{12}]^{4-}$ cluster anions are bridged by the cation $[Cu_3(dien)_4]^{6+}$, which can be described as [(dien)Cu-(dien)-Cu(dien)-Cu(dien)]. There are two symmetry-equivalent Cu atoms, each coordinated by three N atoms of one dien ligand, one N atom of the bridging dien ligand [(1,2)-(3)-coordination mode], and by one N atom of a CN ligand of the $[Re_4Q_4(CN)_{12}]^{4-}$ anion. The third Cu atom lies at the centre of this cation and is symmetrically coordinated by four N atoms of two bridging dien ligands and at the same time by two additional *trans*-situated N atoms of CN ligands of two different anions (Figure 23). Thus, this Cu atom is octahedrally coordinated and bridges the $[\{Cu_3(dien)_4\}\{Re_4Te_4(CN)_{12}\}_2]^{2-}$ anionic units to construct the polymeric structure. The negative charge of this one-dimensional network is compensated by $K^+$ cations.

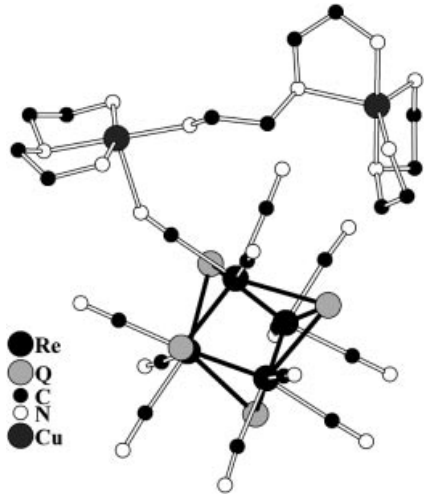


Figure 21. View of the $[\{Cu_2(dien)_3\}Re_4Se_4(CN)_{12}]$ molecule in compound **26** and **27**.

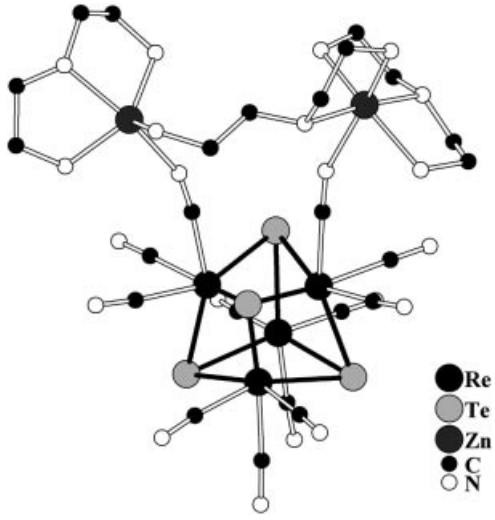


Figure 22. View of the $[\{Zn_2(dien)_3\}Re_4Te_4(CN)_{12}]$ molecule in compound **28**.

 © 2006 Wiley-VCH Verlag GmbH & Co. KGaA, Weinheim 

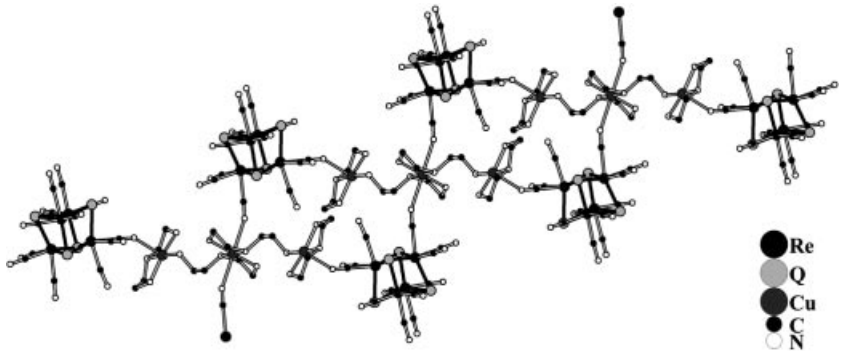


Figure 23. Anionic connectivity pattern in the crystal structure of compounds **29** and **30**.

Thus, the interaction of $[Re_4Q_4(CN)_{12}]^{4-}$ (Q = S, Se, Te) cluster anions with $Ni^{2+}$, $Cu^{2+}$, and $Zn^{2+}$ in the presence of the tridentate ligand diethylenetriamine leads to the formation of a number of complex cluster compounds containing different cationic units: mononuclear $\{M(NH_3)_{n-4}(dien)\}$ or polynuclear $\{M_2(dien)_3\}^{4+}$ and $\{Cu_3(dien)_4\}^{6+}$. The obtained complexes allow us to trace the structural connection between the compounds formed in this system. The parameters affecting the structural type are:

*Ratio of reagents*: When the M/dien ratio is 1:1 compounds with a (1,2,3)-coordination mode of dien are formed. The M/cluster anion ratio is also important. Although in all these reactions the concentration of $M^{2+}$ ions was sufficient to form complexes containing only $M^{2+}$ cations, two compounds (**29** and **30**) were obtained that crystallise with additional $K^+$ cations. This may be due to structural factors: these compounds contain longer oligomeric cations $\{Cu_3(dien)_4\}^{6+}$.

*The cluster core composition*: The influence of this parameter is obvious in the case of **25**, **26**, and **27**, where, on going from Q = S to Q = Se and Te, the structure changes from chain-like to molecular.

*The coordination polyhedron of the transition metal cation*: The $Ni^{2+}$ cation prefers a rigid octahedral environment, $Cu^{2+}$ a square-pyramidal [4+1] or distorted octahedral [4+2] environment, and $Zn^{2+}$, with $n$ = 5 or 6, can have various coordination polyhedra.

Compounds **25**–**30** are of particular interest because they contain cations ($Cu^{2+}$, $Zn^{2+}$) with bridging coordination modes of the dien molecule. Such coordination modes have not previously been observed in M complexes; in all similar complexes three N atoms of the dien ligand are always coordinated to one M atom as, for example, in $[Cu(dien)]_3[Fe(CN)_6]_2 \cdot 6H_2O$.[34] There are only two known examples of metal compounds (both Ag-containing complexes) with bridging dien ligands.[35] Compound **23** is the first example in which the (1,3)-coordination of dien is realized.

### 4.3. Complexes with Triethylenetetraamine

Complexes have also been obtained with the next member of this homologous series, namely triethylenetetraamine. The interaction of $Cu^{2+}$ with $[Re_4Q_4(CN)_{12}]^{4-}$ ($Q_4$ = $Se_4$, $Te_4$, $STe_3$) cluster anions in the presence of trien leads to the formation of complexes formulated as $[\{Cu(trien)\}_2Re_4Q_4(CN)_{12}] \cdot nH_2O$ ($Q_4 = Se_4$ (**31**),[27] $Te_4$ (**32**),[36] $STe_3$ (**33**)[32]). *trien* is present in these compounds as a tetradentate ligand occupying four coordination sites. The fifth coordination site is occupied by a nitrogen atom of a bridging CN ligand (Figure 24). In the structures of the compounds, two crystallographically independent $[Cu(trien)]^{2+}$ cations are bonded by the nitrogen atoms of the *meta*-CN ligands of one $[Re_4Q_4(CN)_{12}]^{4-}$ anion. Thus, the formation of these complexes can be considered as a result of coordination of CN groups of the cluster anion to two $[Cu(trien)]^{2+}$ complex cations. It should be noted that this chemical form is the most stable in solution.

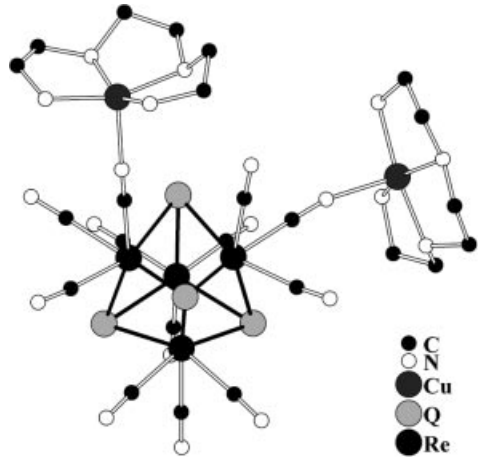


Figure 24. View of the $[\{Cu(trien)\}_2Re_4Q_4(CN)_{12}]$ molecule in compounds **31**–**33**.

Several examples of compounds containing a $[Cu(trien)]^{2+}$ complex cation with a square-pyramidal copper atom, namely [CuL(trien)] compounds (L = $SCN^-$,[37] $NCS^-$,[38] $I^-$,[39] $N(CN)_2^-$,[40]) and also three recently obtained $[Cu(NH_3)(trien)]_2[Re_6Q_8(CN)_6] \cdot nH_2O$ (Q = S, Se, Te)[41] complexes have been described in the literature. In all these cases the coordination environment of the copper atoms is formed by a triethylenetetraamine molecule in the equatorial plane with an L ligand or $NH_3$ molecule in the apical positions with structures close to those of **31**–**33**.

 © 2006 Wiley-VCH Verlag GmbH & Co. KGaA, Weinheim 

The reaction of $Ni^{2+}$ with $[Re_4Q_4(CN)_{12}]^{4-}$ (Q = S, Se) cluster anions in the presence of trien leads to the formation of $[Ni(NH_3)_2(trien)][\{Ni(NH_3)(trien)\}Re_4Se_4(CN)_{12}]\cdot 2.5H_2O$ (**34**) and $[\{Ni(trien)\}_2Re_4S_4(CN)_{12}]\cdot 3H_2O$ (**35**), which have various crystal structures. The *trien* ligand in these complexes is also tetradentate, occupying four coordination sites in the Ni atom environment; two more coordination sites are occupied either by ammonia molecules or by nitrogen atoms of CN ligands.[28] The $[Ni(NH_3)_2(trien)]^{2+}$ chemical form is observed in **34**. The structure of the $[\{Ni(NH_3)(trien)\}Re_4Se_4(CN)_{12}]^{2-}$ anion (Figure 25) can be viewed as the result of substitution of an ammonia molecule in $[Ni(NH_3)_2(trien)]^{2+}$ by a nitrogen atom of a CN ligand. However, there is a difference in the conformations of the trien ligands in the cationic and anionic complexes. In **35**, the nitrogen atoms of the CN ligands of various cluster anions substitute two ammonia molecules in $[Ni(NH_3)_2(trien)]^{2+}$, binding each other and giving a 1D structure (Figure 26, a). It should be noted that **35** also shows conformational disorder (Figure 26, b and c), the reason for which seems to be the presence of various chemical forms in solution corresponding to different coordination types of triethylenetetraamine.

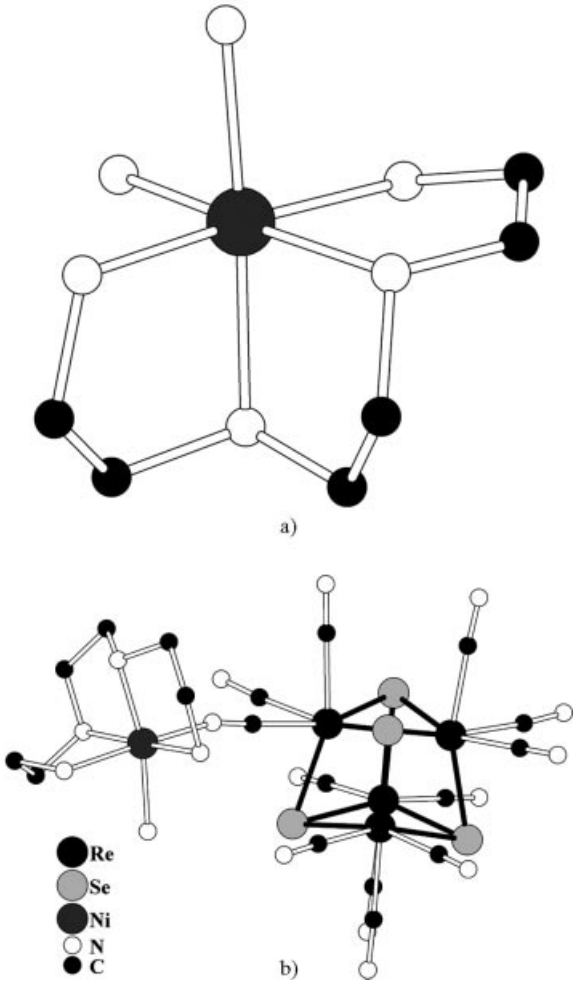


Figure 25. Structure of the complex $[Ni(NH_3)_2(trien)]^{2+}$ cation (a) and $[\{Ni(NH_3)(trien)\}Re_4Se_4(CN)_{12}]^{2-}$ anion (b) in compound **34**.

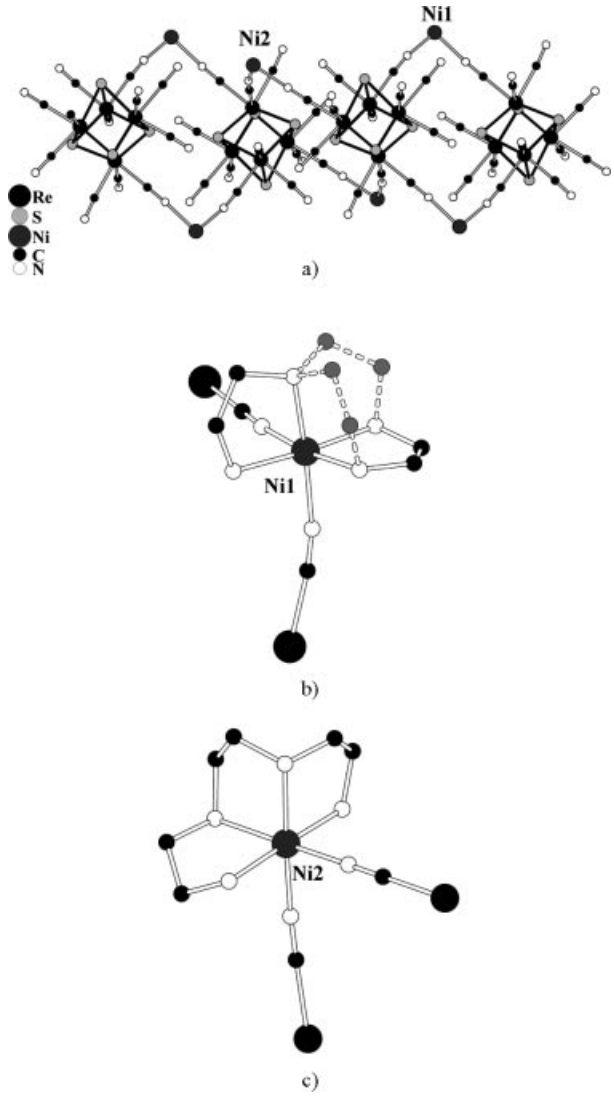


Figure 26. a) A fragment of the structure of **35**; trien ligands have been omitted for clarity. b) The coordination environment of the Ni1 cations. c) The coordination environment of the Ni2 cations.

The chain-like structure of **35** is similar to that of **24**. Based on these two compounds, the connection between ligand denticity, the coordination number of the metal cation, and the formation of a certain structural type can be traced easily. In **24**, the dien molecule occupies three coordination sites in the copper atom environment such that the copper atoms have $n = 5$. Correspondingly, there are two coordination sites open for bonding to CN ligands. An analogous situation is observed in **35** with only one difference: the trien molecule occupies four coordination sites in the environment of nickel atoms with $n = 6$.

### 4.4. Complexes with *threo*-Tetraaminobutane

(1,2*S*,3*S*,4)-Tetraaminobutane, like triethylenetetraamine, has four amino groups, however, this ligand coordinates preferably in a bis-didentate mode with a metal–metal separation of about 7 Å. The bis-didentate coordination mode

 © 2006 Wiley-VCH Verlag GmbH & Co. KGaA, Weinheim 

arises from steric constraints, which prevent binding of the four amino donor atoms to the same metal centre. As has been shown previously,[42] this results in the formation of chiral {...(*threo*-tab)-Cu-(*threo*-tab)...}$_n$ oligomeric species with a linear chain structure and square-planar {$CuN_4$} units. Additional binding of a bridging unit to the axial positions of the $Cu^{2+}$ centres would thus provide a route to new, two-dimensional and chiral metal organic frameworks with an open structure. The bridging unit would serve as a spacer, and its size and structure could be used to adjust the distance between individual {[Cu(*threo*-tab)]$^{2+}$}$_\infty$ strands.

This strategy has been exploited by using [$Re_4Q_4(CN)_{12}$]$^{4-}$ clusters as bridging units to interlink linear [{Cu(*threo*-tab)}$^{2+}$]$_\infty$ strands. The crystalline solids [{Cu(*threo*-tab)}$_2$$Re_4Te_4(CN)_{12}$]·6.5$H_2O$ (**36**) and [{$Cu_2(NH_3)$(*threo*-tab)$_2$}$Re_4Te_4(CN)_{12}$]·4$H_2O$ (**37**) were prepared by direct combination of *threo*-tab, $Cu^{2+}$, and the rhenium cluster anion in aqueous ammonia solution.[43,44]

There is a clear influence of the individual steric properties of the bridging units possessing different compositions on the grid structure. In the [$Re_4Te_4(CN)_{12}$]$^{4-}$ ion, for example, the high number of cyano ligands enables different types of Cu-cluster-Cu interactions, and two of them are realized in **36** and **37**. The nitrogen atoms of four CN ligands of the cluster anion take part in binding in compound **36**, and this mode of binding means that all copper atoms are coordinated by CN ligands; at the same time, all copper atoms are equal and have a distorted octahedral [4+2] environment formed by nitrogen atoms (Figure 27).

In compound **37**, two of the twelve CN groups of the cluster anions take part in binding. In this case, only every second copper atom is coordinated by a CN ligand; the remaining copper atoms are coordinated by ammonia molecules. Half of the copper atoms are in a [4+2] environment and the others are in a [4+1] environment. The one-dimensional {...*threo*-tab-Cu-*threo*-tab-Cu-*threo*-tab...}$_\infty$ strands formed by $Cu^{2+}$ cations and *threo*-tab molecules have a complicated zigzag structure (Figure 28).

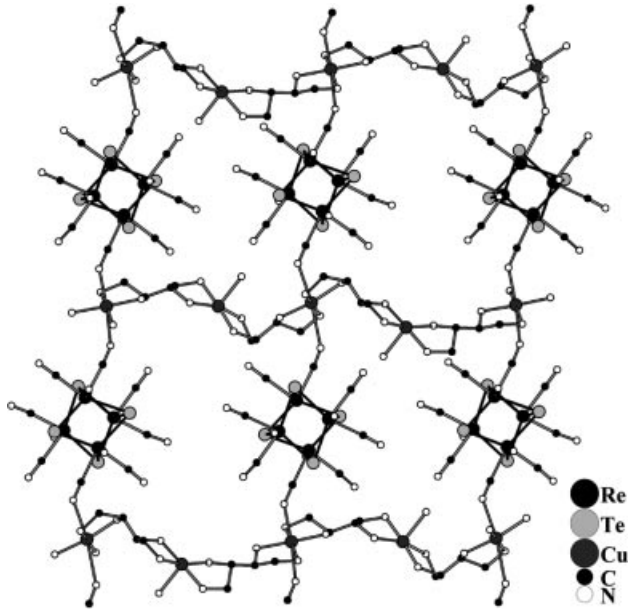


Figure 28. A fragment of the [{$Cu_2(NH_3)$(*threo*-tab)$_2$}$Re_4Te_4(CN)_{12}$] polymer layer in **37**.

The third type of packing is realized in the compound [{Cu($NH_3$)(*threo*-tab)}]$_2$[$Re_4S_{3.4}Te_{0.6}(CN)_{12}$]·1.25$H_2O$ (**38**),[44] which contains undulating, infinite {...*threo*-tab-Cu-*threo*-tab...}$_\infty$ chains that are weakly bonded to cluster anions. The nearest Cu–N(CN ligand) distance is 2.95 Å. In this case, the cluster anions are situated in voids formed by chain packing. The $Cu^{2+}$ cations have a typical five-coordinate environment with four nitrogen atoms from *threo*-tab and an ammonia molecule (Figure 29).

The question as to what caused the structures to be so different in these systems was answered when it was found that in the case of tetrahedral rhenium complexes the structure of the formed coordination polymer depends on two factors, namely the method of synthesis and the cluster core structure.[44]

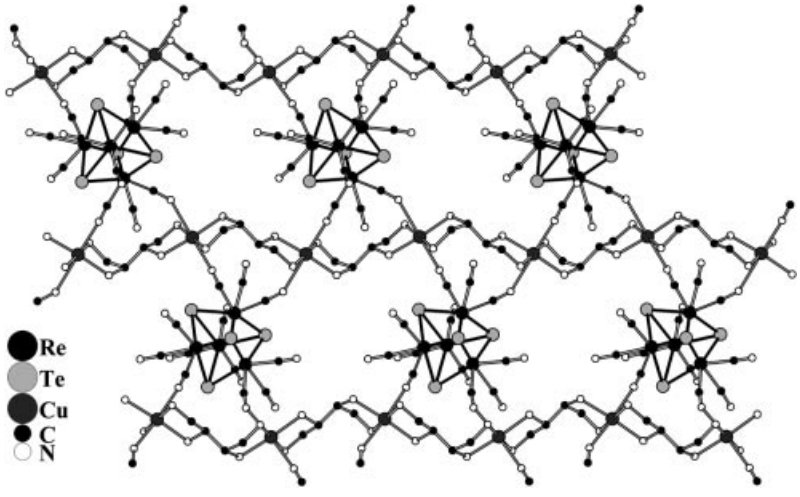


Figure 27. A fragment of the [{Cu(*threo*-tab)}$_2$$Re_4Te_4(CN)_{12}$] polymer layer in **36**.

 © 2006 Wiley-VCH Verlag GmbH & Co. KGaA, Weinheim 

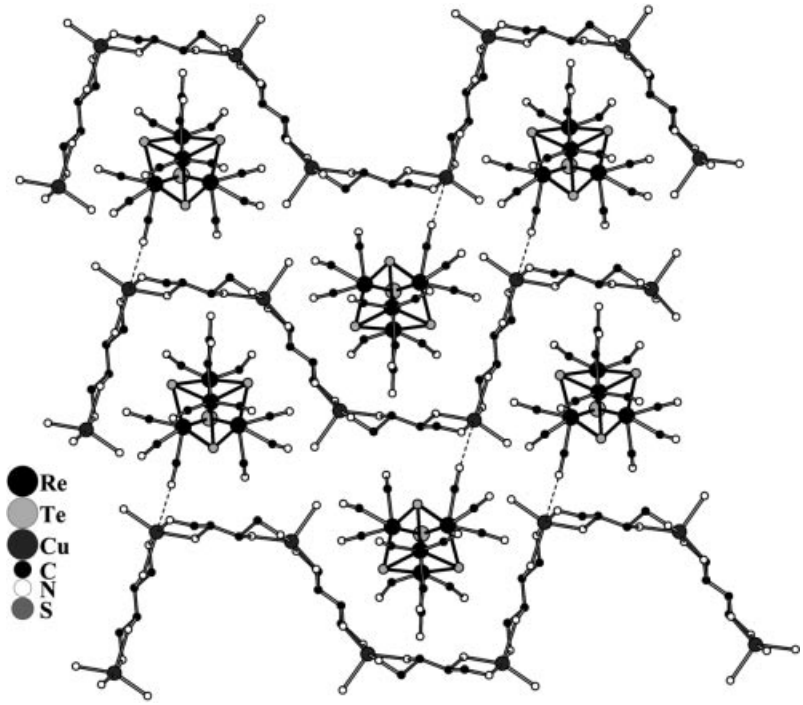


Figure 29. Mutual arrangement of {...(*threo*-tab)-Cu-(*threo*-tab)-Cu-(*threo*-tab)...} chains and location of the cluster anions in **38** (the shortest distances between the N atoms of the CN groups in the cluster anions and the Cu atoms in the polymer chains are shown as dashed lines).

### 4.5. Complexes Containing $Re_4S_{4-x}Te_x$ Cluster Cores

According to the single crystal diffraction analyses, compounds **14**, **16**, **19**, **22**, **33** and **38** contain mixed S/Te chalcogenide ligands in the cluster core $\{Re_4S_{4-x}Te_x\}$. The starting cluster compound $K_4[Re_4S_{4-x}Te_x(CN)_{12}]$ has been synthesised accidentally during preparation of the cluster $K_4[Re_4S_4(CN)_{12}]$ from $[Re_4S_4(TeCl_2)_4Cl_8]$ by boiling with KCN as described for $K_4[Re_4Se_4(CN)_{12}]\cdot 6H_2O$.[11] According to elemental analysis, the compound obtained contains tellurium. This could be due to a sulfur shortage during the preparation of $[Re_4S_4(TeCl_2)_4Cl_8]$ from $ReCl_5$, S and Te.[10]

In compounds **14**, **16** and **22** there are two different cluster anions, with compositions $[Re_4S_4(CN)_{12}]^{4-}$ and $[Re_4S_3Te(CN)_{12}]^{4-}$. In the latter cluster one sulfur atom is substituted by a tellurium atom. In the structures of all three compounds the $Re_4S_4$ and $Re_4S_3Te$ cluster cores are ordered in such a way that three positions of the $Q_4$ tetrahedron are equivalent and occupied by only sulfur atoms; the fourth position is occupied by either a sulfur or a tellurium atom.

It should be noted that in all three structures the metal cations are bound to the CN groups that are closest to the tellurium atom position. To understand the reason for this density functional theory calculations have been carried out on different $[Re_4S_3Q(CN)_{12}]^{4-}$ (Q = S, Se, Te) cluster anions with the ADF program.[45] According to these calculations, there are several types of CN ligands in these cluster anions. Considering each Re atom to be octahedrally coordinated, without taking Re–Re bonds into account (Scheme 2), there are three CN groups bonded to the $ReS_3$ fragment (type 1). The remaining CN ligands are coordinated to three $ReS_2Q$ (Q = Se, Te) fragments. Within the $ReS_2Q(CN)_3$ units, one CN group is more distant from the Q atom than the other two groups (these ligands are denoted types 2 and 3, respectively). For CN ligands of types 1 and 2 the changes are negligible, but for six CN groups of the third type they are considerable and increase with a decrease of the electronegativity of the chalcogen atoms. The increase of negative charge on the N atoms of type 3 results in a considerable preference for the metal ions to coordinate to these atoms.

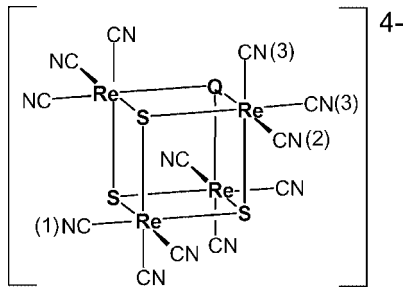


Scheme 2.

All copper atoms in compound **14** are coordinated by CN groups of type 3 to give a polymeric structure (Scheme 3, a). This differs slightly from compound **16**, in which the Zn1 atoms are coordinated by two CN groups of type 3 whereas the Zn2 cations are linked to CN groups of both types 2 and 3. To put it another way, only three of the four bridging CN ligands of one cluster anion are of type 3, while the fourth one is of type 2 (Scheme 3, b). In molecular

 © 2006 Wiley-VCH Verlag GmbH & Co. KGaA, Weinheim 

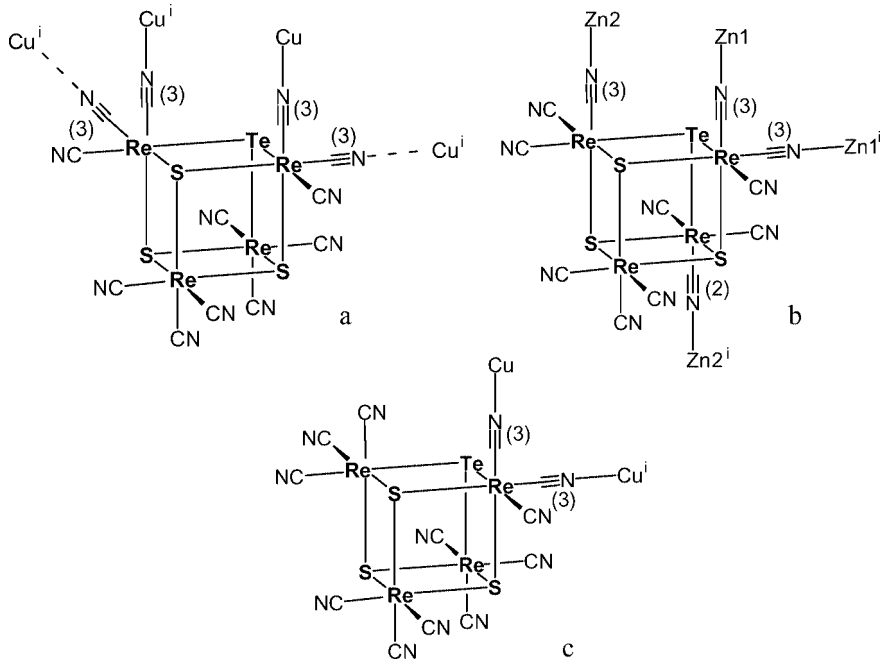


Scheme 3.

compound **22**, two bridging CN groups also belong to type 3 (Scheme 3, c).

It was also interesting to study the behaviour of the $\{Re_4STe_3\}$ cluster core in similar systems. For this, the cluster salt $K_4[Re_4STe_3(CN)_{12}]\cdot 5H_2O$ (**I**) was synthesised and characterised.[32] However, in compounds **19** and **33** the expected ordering of sulfur positions was not observed. The sulfur atoms are disordered over two (**19**) or four (**33**) of the apexes of the tetrahedron. One of the possible reasons for this might be the cluster core composition of the starting materials, which could contain $\{Re_4S_2Te_2\}$ and $\{Re_4Te_4\}$ clusters as well as $\{Re_4STe_3\}$.

## 5. Conclusions

Throughout this microreview we have mainly reported the isolation and characterisation of various complexes based on tetranuclear rhenium cluster anions $[Re_4Q_4(CN)_{12}]^{4-}$ (Q = S, Se, Te) and transition metal cations, the coordination sites of which are fully or partially occupied by water molecules or N-donor ligands, particularly ammonia, ethylenediamine, diethylenetriamine, triethylenetetraamine and chiral *threo*-tetraaminobutane. The structures of all compounds have been confirmed by single-crystal X-ray analysis.

We should emphasise, again, that the composition and structure of the obtained compounds are determined by several parameters, namely:

1) the reagent ratio: $M^{2+}$ cation/polydentate ligand or $M^{2+}$ cation/cluster anion;
2) the $M^{2+}$ cation coordination environment;
3) the coordination number and coordination polyhedron of the $M^{2+}$ cations;
4) the cluster core composition.

It has been shown that the reaction of chalcocyanide rhenium cluster complexes $[Re_4Q_4(CN)_{12}]^{4-}$ with cations of 3d-transition metals ($Ni^{2+}$, $Cu^{2+}$, $Zn^{2+}$) in the presence of chelating ligands gives many complex compounds with various structures (ionic, molecular or polymeric). Complicated cluster complexes with polymeric structures containing bridging polydentate ligands, namely diethylenetriamine and *threo*-tetraaminobutane, were obtained for the first time.

We have also introduced a new and straightforward synthetic pathway to heterometallic and chiral coordination polymers. The use of oligonuclear bridging units has proved to be of particular interest because it allows the design of open networks with sufficiently large voids for host–guest interactions. More importantly, the use of the chiral, bisdidentate *threo*-tab ligand guarantees the formation of a chiral crystal structure which has the ideal prerequisites for the coating of suitable surfaces with a chiral monolayer.

Complexes containing mixed-ligand $\{Re_4S_{4-x}Te_x\}$ cluster cores have been obtained and characterised for the first time. Their structural data supplement previous research and show that six CN groups of the cluster anion can be activated for interaction with metal cations by substituting one sulfur atom by a tellurium atom in the $Re_4S_4$ cluster core; these groups are those nearest to the Te atom.

## Acknowledgments

This work was supported by the Russian Foundation for Basic Research (grants 05-03-32123 and 05-03-08090).

[1] Y. V. Mironov, V. E. Fedorov, *Russ. Chem. Bull. Int. Ed.* **2002**, *51*, 569–580.

 © 2006 Wiley-VCH Verlag GmbH & Co. KGaA, Weinheim 

[2] I. V. Kalinina, V. P. Fedin, *Russ. J. Coord. Chem.* **2003**, *29*, 597–615.
[3] S. Harris, *Polyhedron* **1989**, *8*, 2843–2882.
[4] T. Saito, *J. Chem. Soc., Dalton Trans.* **1999**, 97–105.
[5] Y. V. Mironov, E. Albrecht-Schmitt, J. A. Ibers, *Inorg. Chem.* **1997**, *36*, 944–946.
[6] E. S. Lang, U. Abram, J. Strähle, *Z. Anorg. Allg. Chem.* **1996**, *622*, 251–253.
[7] Y. V. Mironov, S. S. Yarovoi, D. Y. Naumov, N. V. Kuratieva, S. V. Kozlova, A. Simon, V. E. Fedorov, *Eur. J. Inorg. Chem.* **2005**, 2476–2479.
[8] Y. V. Mironov, M. A. Pell, T. E. Albrecht-Schmitt, J. A. Ibers, *Inorg. Chem.* **2001**, *40*, 5472–5474.
[9] Y. V. Mironov, *Polyhedron* **2000**, *19*, 437–439.
[10] Y. V. Mironov, T. E. Albrecht-Schmitt, J. A. Ibers, *Z. Kristallogr.* **1997**, *212*, 308.
[11] Y. V. Mironov, A. V. Virovets, W. S. Sheldrick, V. E. Fedorov, *Polyhedron* **2001**, *20*, 969–974.
[12] Y. V. Mironov, *Eur. J. Inorg. Chem.* **1999**, 997–999.
[13] N. G. Naumov, A. V. Virovets, M. N. Sokolov, S. B. Artemkina, V. E. Fedorov, *Angew. Chem. Int. Ed.* **1998**, *37*, 1943–1945.
[14] L. G. Beauvais, M. P. Shores, J. R. Long, *Chem. Mater.* **1998**, *10*, 3783–3786.
[15] M. V. Bennett, L. G. Beauvais, M. P. Shores, J. R. Long, *J. Am. Chem. Soc.* **2001**, *123*, 8022–8032.
[16] Y. Kim, S.-M. Park, W. Nam, S.-J. Kim, *Chem. Commun.* **2001**, 1470–1471.
[17] S. B. Artemkina, N. G. Naumov, A. V. Virovets, V. E. Fedorov, *Eur. J. Inorg. Chem.* **2005**, 142–146.
[18] M. S. Tarasenko, A. Y. Ledneva, N. G. Naumov, D. Y. Naumov, V. E. Fedorov, *J. Cluster Sci.* **2005**, *16*, 353–365.
[19] N. G. Naumov, M. S. Tarasenko, A. V. Virovets, Y. Kim, S. J. Kim, V. E. Fedorov, *Eur. J. Inorg. Chem.* **2006**, 298–303.
[20] S. Jin, F. J. DiSalvo, *Chem. Mater.* **2002**, *14*, 3448–3457.
[21] B. B. Yan, H. J. Zhou, A. Lachgar, *Inorg. Chem.* **2003**, *42*, 8818–8822.
[22] Z. H. Yan, C. S. Day, A. Lachgar, *Inorg. Chem.* **2005**, *44*, 4499–4505.
[23] Y. V. Mironov, A. V. Virovets, S. B. Artemkina, V. E. Fedorov, *Angew. Chem. Int. Ed.* **1998**, *37*, 2507–2509.
[24] Y. V. Mironov, O. Oeckler, A. Simon, V. E. Fedorov, *Eur. J. Inorg. Chem.* **2001**, 2751–2753.
[25] Y. V. Mironov, O. A. Efremova, V. E. Fedorov, O. Oecler, A. Simon, C. Vicent, R. Lusar, *Russ. Chem. Bull. Int. Ed.* **2003**, *52*, 1698–1701.
[26] Y. V. Mironov, O. A. Efremova, D. Y. Naumov, V. E. Fedorov, *Russ. Chem. Bull. Int. Ed.* in press.
[27] Y. V. Mironov, O. A. Efremova, S. F. Solodovnikov, N. G. Naumov, W. S. Sheldrick, A. Perrin, V. E. Fedorov, *Russ. Chem. Bull. Int. Ed.* **2004**, *53*, 2129–2134.
[28] O. A. Efremova, Y. V. Mironov, N. V. Kuratieva, V. E. Fedorov, *Russ. J. Coord. Chem*. in press.
[29] O. A. Efremova, Y. V. Mironov, D. Y. Naumov, S. G. Kozlova, V. E. Fedorov, *Polyhedron* **2006**, *25*, 1233–1238.
[30] K. A. Brylev, Y. V. Mironov, N. G. Naumov, V. E. Fedorov, J. A. Ibers, *Inorg. Chem.* **2004**, *43*, 4833–4838.
[31] Y. V. Mironov, V. E. Fedorov, I. Ijjaali, J. A. Ibers, *Inorg. Chem.* **2001**, *40*, 6320–6323.
[32] O. A. Efremova, Y. V. Mironov, D. Y. Naumov, V. E. Fedorov, *J. Struct. Chem*. in press.
[33] Y. V. Mironov, O. A. Efremova, D. Y. Naumov, W. S. Sheldrick, V. E. Fedorov, *Eur. J. Inorg. Chem.* **2003**, 2591–2595.
[34] H.-Z. Kou, D.-Z. Liao, P. Cheng, Z.-H. Jiang, S.-P. Yan, G.-L. Wang, X.-K. Yao, H.-G. Wang, *J. Chem. Soc., Dalton Trans.* **1997**, 1503–1506.
[35] E. C. Plappert, D. M. P. Mingos, S. E. Lawrence, D. J. Williams, *J. Chem. Soc., Dalton Trans.* **1997**, 2119–2123.
[36] O. A. Efremova, Y. V. Mironov, D. Y. Naumov, V. E. Fedorov, *J. Struct. Chem.* **2005**, *46*, 973–977 (in Russian).
[37] G. Marongiu, E. C. Lingafelter, P. Paoletti, *Inorg. Chem.* **1969**, *8*, 2763–2767.
[38] G. Marongiu, M. Gannas, *J. Chem. Soc., Dalton Trans.* **1979**, 41–44.
[39] V. Manriquez, M. Campos Vallette, N. Lara, N. Gonzalez Tejeda, O. Wittke, G. Diaz, S. Diaz, R. Munoz, L. Kriskovic, *J. Chem. Crystallogr.* **1996**, *26*, 15–22.
[40] J. Luo, X. G. Zhou, L. H. Weng, X. F. Hou, *Acta Crystallogr. Sect. C* **2003**, *59*, m392–m395.
[41] K. A. Brylev, N. G. Naumov, G. Peris, R. Lusar, V. E. Fedorov, *Polyhedron* **2003**, *22*, 3383–3387.
[42] A. Zimmer, D. Kuppert, T. Weihermüller, I. Müller, K. Hegetschweiler, *Chem. Eur. J.* **2001**, *7*, 917–931.
[43] Y. V. Mironov, N. G. Naumov, K. A. Brylev, O. A. Efremova, V. E. Fedorov, K. Hegetschweiler, *Angew. Chem. Int. Ed.* **2004**, *43*, 1297–1300.
[44] Y. V. Mironov, N. G. Naumov, K. A. Brylev, O. A. Efremova, V. E. Fedorov, K. Hegetschweiler, *Russ. J. Coord. Chem.* **2005**, *31*, 269–281.
[45] Amsterdam Density Functional (ADF) program, release 2002.02; Vrije Universteit, Amsterdam, The Netherlands, **2002**.

Received: February 28, 2006
Published Online: May 18, 2006

 © 2006 Wiley-VCH Verlag GmbH & Co. KGaA, Weinheim 

DOI: 10.1002/ejic.200600137

# A Theoretical Rationale for the Formation, Structure and Spin State of Pentacyanochromate(II)

**Robert J. Deeth*[a]**

**Keywords:** Density functional theory / Ligand field theory / Angular overlap model / COSMO / Solvation effects

The pentacyanochromate(II) complex is unusual in two respects. Firstly, it is one of the few homoleptic cyanide species with a high-spin ground state. Secondly, it was synthesised during an attempt to make the hexacoordinate complex. A combination of qualitative ligand field theory and quantitative density functional theory including solvation effects is applied to rationalise these observations. The spin state depends on the d orbital energy differences and how the promotion energy, PE, associated with a change in spin state compares to the d–d spin pairing energy, SPE. The calculations show that PE > SPE for octahedral $[Cr^{II}(CN)_6]^{4-}$, hence it has a spin triplet $S = 1$ ground state, while PE < SPE for $[Cr^{II}(CN)_5]^{3-}$, hence it is high spin with $S = 2$. The hexacyanide is stabilised in aqueous solution by solvation. In less polar solvents such as acetonitrile, the unfavourable electrostatic interactions dominate and the reaction stops at the pentacyano complex. In both complexes, the cyanide behaves as a strong-field ligand and is both a good σ donor and π acceptor.

(© Wiley-VCH Verlag GmbH & Co. KGaA, 69451 Weinheim, Germany, 2006)

## Introduction

Ligand Field Theory (LFT)[1] classifies the cyanide ligand as strong field and, therefore, the normal expectation is for homoleptic complexes to exhibit low-spin configurations. Octahedral cyanide complexes are invariably low spin, but there are some interesting exceptions for other coordination numbers. For example, low-spin (i.e. $S = 1$) $[Cr(CN)_6]^{4-}$ can be synthesised from aqueous solution providing excess cyanide is present but in acetonitrile, pentacyanochromate(II) is produced with magnetic properties consistent with a high-spin $S = 2$ $d^4$ configuration. Both the higher spin state and lower coordination number were not anticipated.[2]

An explanation of this behaviour is amenable to computation. This communication describes the first detailed computational study of $[Cr(CN)_5]^{3-}$ and $[Cr(CN)_6]^{4-}$ using both qualitative ligand field theory (LFT) and quantitative density functional theory (DFT) calculations. Theory successfully explains not only why $[Cr(CN)_5]^{3-}$ is high spin, but also why the change in medium from aqueous solution to acetonitrile causes the reaction to stop at coordination number five.

## Results and Discussion

Hexacyanochromate(II) is extremely air sensitive[3] which goes some way to explain the relative lack of experimental data. However, the crystal structure of $Na_4[Cr(CN)_6]\cdot(H_2O)_{10}$ has been reported some years ago[4] and $[Cr(CN)_6]^{4-}$ remains of interest in the context of molecular magnets.[2,5] Indeed, it was in the search for new molecular magnetic materials that Nelson et al.[2] attempted a non-aqueous route to $[Cr^{II}(CN)_6]^{4-}$ which resulted in the unexpected preparation of the very interesting pentacyanochromate(II) anion. Their work highlighted two intriguing aspects of the chemistry of $[Cr(CN)_5]^{3-}$. Firstly, why does the system display a high-spin $S = 2$ state given that high-field ligands such as cyanide are conventionally associated with low-spin configurations? Secondly, why is a pentacyano complex isolated from the non-aqueous synthetic procedure rather than the expected hexacoordinate complex, which can be made in aqueous solution provided an excess of cyanide is present?

In principle, modern computational chemistry should be able to address these issues quantitatively although, apart from an early Xα study,[6] there appears to be no other computational work on either $[Cr^{II}(CN)_6]^{4-}$ nor $[Cr^{II}(CN)_5]^{3-}$.

The spin state is a balance between one-electron (orbital) and two-electron (interelectronic repulsion) effects. The d–d interelectron repulsion term favours a high-spin configuration (maximum quantum mechanical exchange, minimal spin pairing energy, SPE) while the one-electron term relates to d orbital splittings and favours low-spin configurations (minimum electronic promotion energy, PE). Note that, depending on the symmetry, low spin need not necessarily imply diamagnetic properties. For example, the low-spin configuration for octahedral $d^4$ species is $t_{2g}^4$ which still has two unpaired electrons. Critically, the d orbital

[a] Department of Chemistry, University of Warwick, Coventry CV4 7AL, United Kingdom
E-mail: r.j.deeth@warwick.ac.uk

 © 2006 Wiley-VCH Verlag GmbH & Co. KGaA, Weinheim 

splittings are ligand- and geometry-dependent while, to a first approximation, the spin-pairing energy is not.

The X-ray crystallographic study of $(NEt_4)_3[Cr^{II}(CN)_5]$·MeCN·1/8THF reveals four chromium complexes in the unit cell displaying geometries which are distorted to varying degrees away from either ideal square-pyramidal (SPY) or trigonal-bipyramidal (TBP) structures.[2] The question then is how the promotion energy for pentacoordinate systems compares to $\Delta_{oct}$.

The d orbital energies can be conveniently expressed in terms of the Angular Overlap Model (AOM).[7] For an octahedral complex of "linear ligator" ligands like cyanide, $\Delta_{oct} = 3e_\sigma - 4e_\pi$, where $e_\sigma$ and $e_\pi$ are respectively the AOM parameters describing M–CN σ and π bonding. The expressions for individual d orbital energies are given in Equations (1), (2), (3) and (4) for SPY and (5), (6) and (7) for TBP and include group theory labels appropriate to $C_{4v}$ and $D_{3h}$ symmetry, respectively. In Equations (1)–(4), $\alpha$ refers to the angle between the apical and equatorial ligands.

$$E(d_{x^2-y^2}) = E(b_1) = 3/4(1 - \cos 2\alpha)^2 \cdot e_\sigma(eq) + (\sin^2 2\alpha) \cdot e_\pi(eq) \quad (1)$$

$$E(d_{z^2}) = E(a_1) = 1/4(1 + 3\cos 2\alpha)^2 \cdot e_\sigma(eq) + e_\sigma(ax) + 3(\sin^2 2\alpha) \cdot e_\pi(eq) \quad (2)$$

$$E(d_{xy}) = E(b_2) = 4(\cos^2 2\alpha) \cdot e_\pi(eq) \quad (3)$$

$$E(d_{xz}, d_{yz}) = E(e) = 3/2(\sin^2 2\alpha) \cdot e_\sigma(eq) + 2(\cos^2 2\alpha) \cdot e_\pi(eq) + e_\pi(ax) \quad (4)$$

$$E(d_{z^2}) = E(a_1) = 3/4e_\sigma(eq) + 2e_\sigma(ax) \quad (5)$$

$$E(d_{x^2-y^2}, d_{xy}) = E(e') = 9/8e_\sigma(eq) + 3/2e_\pi(ax) \quad (6)$$

$$E(d_{xz}, d_{yz}) = E(e'') = 1/2e_\pi(eq) + 2e_\pi(ax) \quad (7)$$

The relevant orbital energy differences corresponding to the promotion energy which must be overcome for a high-spin $d^4$ configuration are shown in Figure 1.

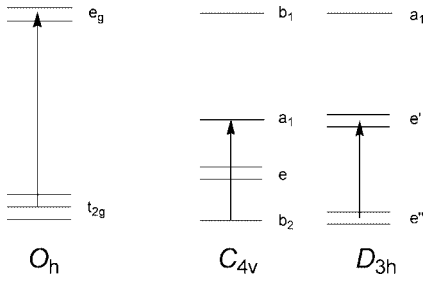


Figure 1. Qualitative d orbital energy level diagrams for octahedral ($O_h$), SPY ($C_{4v}$) and TBP ($D_{3h}$) symmetries illustrating the high-spin promotion energy for a $d^4$ configuration.

Figure 1 is not drawn to scale. A numerical comparison can be based on Equations 1–7. Hence, the promotion energies, PE, are Equations (8), (9), and (10).

$$PE(O_h) = 3e_\sigma - 4e_\pi \quad (8)$$

$$PE(C_{4v}) = 0.83e_\sigma(eq) + e_\sigma(ax) + 0.35e_\pi(eq) - 3.53e_\pi(eq) = 0.65e_\sigma(eq) + e_\sigma(ax) - 3.18e_\pi(eq) \quad (9)$$

$$PE(D_{3h}) = 9/8e_\sigma(eq) - 1/2\{e_\pi(eq) + e_\pi(ax)\} \quad (10)$$

In arriving at these expressions, the angle $\alpha$ between apical and equatorial cyanides in the SPY structure has been taken as 100° and cyanide was assumed to be a π acceptor (i.e. $e_\pi < 0$). We return to the latter issue below.

Assuming $e_\lambda(ax) = e_\lambda(eq)$, λ = σ, π, Equations (8)–(10) collapse to Equations (11), (12), and (13)].

$$PE(O_h) = 3e_\sigma - 4e_\pi \quad (11)$$

$$PE(C_{4v}) = 1.65e_\sigma - 3.18e_\pi \quad (12)$$

$$PE(D_{3h}) = 1.13e_\sigma - e_\pi \quad (13)$$

This is a very crude assumption because the AOM parameters will vary strongly with distance. Nevertheless, the difference between $O_h$ and $C_{4v}$ or $D_{3h}$ promotion-energies expressions is so great that the assertion that the promotion energies for pentacoordinate symmetries would be substantially less than for an octahedral complex seems secure. The observation of high-spin $[Cr(CN)_5]^{3-}$ is thus simply a function of the coordination number and symmetry. Cyanide may continue to be a strong-field ligand in the sense that the AOM parameter values could be identical in all symmetries. That is, strong-field ligands do not necessarily have to be associated with low-spin electronic configurations – e.g. the tetrahedral complex $[Mn(CN)_4]^{2-}$ is high spin consistent with the well-known result that the tetrahedral splitting $\Delta_{tet} \approx 1/2\ \Delta_{oct}$.

However, while LFT can easily rationalise why $[Cr(CN)_5]^{3-}$ is high spin, it cannot address the issue of why is forms in the first place. For this we require a more sophisticated quantum mechanical approach like DFT.

DFT has effectively revolutionised the application of quantum chemistry to transition-metal systems,[8] but it is by no means a perfect model. In particular, current functionals may not give a good description of spin state energy differences.[9–13] Our experience with $Fe^{II}$ and $Fe^{III}$ complexes shows that although there can be large numerical differences, most pure functionals give the correct qualitative trend.[9] Others have focussed on tuning the amount of exact exchange in the B3LYP functional to give more accurate results for spin-crossover systems.[11,13] The present problem is less delicate, which probably means that almost any gradient corrected functional will be at least qualitatively reasonable. To test this, the DFT protocol was first validated against $[Cr(CN)_6]^{4-}$, which is known to be a low-spin, $t_{2g}^4$ $S = 1$ system (see Table 1).

In octahedral symmetry, high-spin $[Cr(CN)_6]^{4-}$ has a $^5E_g$ state, which is expected to display a strong Jahn–Teller distortion hence the second optimisation in $D_{4h}$ symmetry which allows for an orbitally-nondegenerate state leading to the expected elongated octahedral structure. Similarly, the

 © 2006 Wiley-VCH Verlag GmbH & Co. KGaA, Weinheim 

Table 1. Optimised Cr–CN distances and relative total energies (including solvation) for $[Cr(CN)_6]^{4-}$ in $O_h$ symmetry unless otherwise stated. $E_{tot}$ is total DFT energy and equals the sum of the electronic energy, $E_{el}$, and the COSMO solvation energy, $E_{sol}$. $\Delta E$ is the energy difference between $E_{tot}$ for that entry and $E_{tot}$ for the octahedral, $S = 1$ state.

| $S$ | Cr–CN [Å] | $E_{tot}$ [kJ·mol$^{-1}$] | $\Delta E$ [kJ·mol$^{-1}$] | $E_{el}$ [kJ·mol$^{-1}$] | $E_{sol}$ [kJ·mol$^{-1}$] |
|---|---|---|---|---|---|
| 2 | 2.23 | –11797.09 | +169 | –9164.82 | –2632.27 |
| 2 | 2.11, 2.61[a] | –11832.87[a] | +90[a] | –9217.93[a] | –2614.94[a] |
| 1 | 2.04 | –11957.43 | 0 | –9234.30 | –2723.13 |
| 1 | 2.03, 2.03, 2.07[b] | –11966.56 | –9[b] | –9241.16[b] | –2725.40[b] |
| 0 | 2.02 | –11890.43 | +73 | –9160.40 | –2730.03 |

[a] $D_{4h}$ Symmetry, axial elongation. [b] $D_{2h}$ symmetry.

spin triplet state in octahedral symmetry is $^3T_{2g}$ and is also formally Jahn–Teller active. However, compared to the $^5E_g$ case, the Jahn–Teller effect for the $^3T_{2g}$ state is much more complicated but since it is dominated by π effects, it is also much weaker. A complete analysis has not been attempted. Instead, the geometry was reoptimised in $D_{2h}$ symmetry as an example of one possible distortion mode. Finally, the spin singlet state is clearly going to be higher than the $S = 1$ state and, although in $O_h$ symmetry, this too is formally orbitally degenerate, only the octahedral geometry has been computed.

The DFT results in Table 1 are in good agreement with experiment. They correctly predict the spin-triplet $S = 1$ ground state with an optimised Cr–CN bond length (in $O_h$ symmetry) only about 0.03 Å longer than the average Cr–CN distance reported for $Na_4[Cr(CN)_6]\cdot 10H_2O$.[4] Note that in the absence of solvation, the optimised Cr–C distance for octahedral, $S = 1$ hexacyanochromate(II) extends 0.08 Å to 2.12 Å. In the gas phase, many occupied orbitals have physically unreasonable positive energies. This leads to an expansion of the Cr–C bond. The solvation field stabilises the anionic charge, lowers the orbital energies and generates a better optimal structure.

Further vindication that DFT (with solvation) describes these systems well can be seen in Table 2 where DFT data for $[Cr(CN)_5]^{3-}$ are presented.

For both symmetries, the spin state energies increase quintet < triplet < singlet. The $^5B_1$ state in $C_{4v}$ and the $^5A_1$ state in $D_{3h}$ are orbitally non-degenerate, and thus Jahn–Teller inactive as is the $^3A_1$ state in $C_{4v}$ derived from the $b_2^2e^2$ configuration. The remaining triplet and the two singlet states are much higher in energy and, even though some are orbitally degenerate, the effect is not large enough to alter the overall conclusion that the predicted DFT ground state of $[Cr(CN)_5]^{3-}$ is a spin quintet.

The computed structures are also reasonable, although compared to $[Cr(CN)_6]^{4-}$ DFT now gives somewhat shorter Cr–C distances than observed for $[Cr(CN)_5]^{3-}$. Both SPY and TBP structures are predicted to have virtually identical energies consistent with the somewhat distorted structures observed in the crystal structure and with the general notion that five-coordinate systems are not rigid.

DFT can also be applied to explain the relative stabilities of $[Cr^{II}(CN)_6]^{4-}$ vs. $[Cr^{II}(CN)_5]^{3-}$. The data in Table 1 and Table 2 clearly demonstrate the critical importance of the environment of the complex. Thus, the reaction energy for the process

$$[Cr(CN)_5]^{3-} + CN^- \rightarrow [Cr(CN)_6]^{4-}$$

is –87 kJ·mol$^{-1}$ when the COSMO solvation energies are included, but an enormous +794 kJ·mol$^{-1}$ from just the electronic energies alone. Obviously, there is a strong repulsive interaction when trying to bring a monoanion like cyanide up to a complex which already carries three negative charges, but because the solvation energy is proportional to $Z^2$, the additional solvation energy of a tetraanion vs. a trianion amounts to an extra 1100–1200 kJ·mol$^{-1}$, which is sufficient to overcome this repulsive term. Because the solvation energy depends on $(1 - 1/\varepsilon)$, where $\varepsilon$ is the dielectric constant, large solvation energies are associated with a high dielectric constant. Acetonitrile is simply not polar enough to support the reaction hence the hexacyano complex cannot form.

Having established that the relative spin states are well described (with and without solvation energies) and seen that the complex formed depends strongly on the solvent,

Table 2. DFT results for $[Cr(CN)_5]^{3-}$ for different spin states ($S$) and symmetries – $C_{4v}$ for SPY and $D_{3h}$ for TBP. Bond lengths in Å, energies in kJ·mol$^{-1}$. $E_{tot}$ is total DFT energy and equals the sum of the electronic energy, $E_{el}$, and the COSMO solvation energy, $E_{sol}$. $\Delta E$ is the energy difference between $E_{tot}$ for that entry and the lowest $E_{tot}$ overall. Experimental data[2] in parentheses.

| Symmetry | $S$ | Cr–$C_{ax}$ | Cr–$C_{eq}$ | $C_{ax}$–Cr–$C_{eq}$ | $E_{tot}$ | $\Delta E$ | $E_{el}$ | $E_{sol}$ |
|---|---|---|---|---|---|---|---|---|
| $C_{4v}$ | 2 | 2.14 | 2.08 | 101 | –9980.87 | 3 | –8442.11 | –1538.76 |
| | 2 | (2.23) | (2.12) | (100) | | | | |
| $C_{4v}$ | 1 | 1.98 | 2.02 | 95.2 | –9943.53 | 41 | –8363.30 | –1580.23 |
| $C_{4v}$ | 0 | 1.94 | 2.00 | 97.7 | –9854.66 | 130 | –8275.92 | –1578.74 |
| $D_{3h}$ | 2 | 2.07 | 2.09 | – | –9984.20 | 0 | –8445.02 | –1539.18 |
| $D_{3h}$ | 1 | 2.01 | 2.01 | – | –9880.40 | 104 | –8319.32 | –1561.08 |
| $D_{3h}$ | 0 | 1.97 | 1.96 | – | –9857.02 | 127 | –8275.47 | –1581.55 |
| $C_{\infty v}$[a] | – | – | – | – | –1886.33 | – | –1583.47 | –302.86 |

[a] Data for isolated $CN^-$.

 © 2006 Wiley-VCH Verlag GmbH & Co. KGaA, Weinheim 

the issue of whether cyanide is always a "strong-field" ligand requires an assessment of whether the fundamental nature of the Cr–CN bonding changes radically with coordination number. In the spirit of LFT, let us use the DFT structures and orbital energies as the basis of a ligand-field analysis.

The octahedral complex is our starting point. Although the electronic spectrum of $[Cr(CN)_6]^{4-}$ has been reported,[3] no assignments were offered due to the broad nature of the diffuse reflectance bands. The DFT estimate of ca. 32000 $cm^{-1}$ may be compared to the values in Table 3, which also include computed results for other hexacyanides.

Table 3. Experimental[14] and calculated $\Delta_{oct}$ values [$cm^{-1}$] for hexacyanometallate complexes.

| Complex | $\Delta_{oct}$ | $\Delta_{oct}$ (calcd.) |
|---|---|---|
| $[Cr(CN)_6]^{3-}$ | 26600 | 29815 |
| $[Cr(CN)_6]^{4-}$ | – | 31989 |
| $[Mn(CN)_6]^{3-}$ | 34000 | 32400 |
| $[Mn(CN)_6]^{4-}$ | 30000 | 33777 |
| $[Fe(CN)_6]^{3-}$ | 34950 | 35614 |
| $[Fe(CN)_6]^{4-}$ | 33800 | 36426 |

It appears that the DFT spherical configuration orbital energy differences (see Computational Details section) generally overestimate $\Delta_{oct}$. Experimentally, one normally sees larger values for higher metal oxidation states. Hence, given an experimental value for $[Cr^{III}(CN)_6]^{3-}$ of 26600 $cm^{-1}$ and a threshold value at which a first-row octahedral $d^4$ species switches from quintet to triplet spin of about 23500 $cm^{-1}$,[15] $\Delta_{oct}$ for $[Cr(CN)_6]^{4-}$ should lie between 23500 and 26600 $cm^{-1}$. The DFT estimate is ca. 32000 $cm^{-1}$.

For the Cr(II) complex $\Delta_{oct}$ is probably quite close to that for $Cr^{III}$. Because both are low spin, the lower oxidation state, which has more d electrons, has a larger ligand field stabilisation energy (LFSE) at least in terms of $\Delta_{oct}$ values. Hence, the $M^{II}$–C bond lengths are actually shorter than the $M^{III}$–C distances despite the latter's higher formal oxidation state and smaller ionic radius. The relative change in LFSE increases from 20% for the $d^5/d^6$ $Fe^{III}/Fe^{II}$ couple to 25% for $d^4/d^5$ $Mn^{III}/Mn^{II}$ to 33% for the $d^3/d^4$ $Cr^{III}/Cr^{II}$, which correlates reasonably well with bond–length contractions of 0.02, 0.05 and 0.05 Å, respectively. Given the large percentage change in $\Delta_{oct}$, the decrease in Cr–C distance and the DFT prediction that $\Delta_{oct}$ for $M^{II}$ gets larger relative to that for $M^{III}$ in the series Fe < Mn < Cr, the assertion that $\Delta_{oct}$ for $[Cr^{II}(CN)_6]^{4-}$ and $[Cr^{III}(CN)_6]^{3-}$ are about the same seems reasonable.

While a better theoretical treatment along the lines of, say, ligand field DFT,[16] time-dependent DFT[17] or CASPT2[18] may provide better quantitative agreement with experiment, the precise value of $\Delta_{oct}$ is not important for the present analysis because the errors seems to be propagated more or less systematically between $[Cr^{II}(CN)_6]^{4-}$ and $[Cr^{II}(CN)_5]^{3-}$. The aim is to see whether the AOM parameter values deduced from the DFT orbital energies of $[Cr(CN)_6]^{4-}$ generate AOM d orbital energies for $[Cr(CN)_5]^{3-}$, which in turn agree with the DFT equivalents. If so, then the ligand-field strength is essentially the same in both complexes.

Of course, as $\Delta_{oct} = 3e_\sigma - 4e_\pi$, unique values for both AOM parameters cannot be extracted from a single value of $\Delta_{oct}$. By applying a small tetragonal distortion to the molecule, the "d" orbitals will split, which will provide three degrees of freedom but now there are four parameters, $e_\sigma$(eq), $e_\sigma$(ax), $e_\pi$(eq) and $e_\pi$(ax). The number of free variables can be halved if the distance dependence is established. Lengthening the Cr–C bonds, $r$, from 2.038 to 2.078 Å lowers the computed $\Delta_{oct}$ from 31989 to 29233 $cm^{-1}$. Assuming all AOM parameters depend on $r^{-m}$ yields $m$ = 4.6, which is close enough to the electrostatic theory value of $m$ = 5. Applying an axial elongation to the two ligands on the $z$ axis ($r_{ax}$ = 2.078, $r_{eq}$ = 2.038 Å) gives a "d" orbital sequence of $b_{2g} < e_g < a_{1g} < b_{1g}$ and because in the AOM $E(b_{2g}) = e_\pi(eq)$, $E(e_g) = 2e_\pi(eq) + 2e_\pi(ax)$, and $|e_\pi(eq)| > |e_\pi(ax)|$ because $r_{eq}$ is shorter, the DFT calculations are consistent with $e_\pi < 0$ – i.e. cyanide is behaving as a π acceptor. Assuming $m$ = 5, the $e_g - b_{2g}$ and $b_{1g} - a_{1g}$ DFT orbital energy differences equate to effective AOM parameter values of $e_\sigma$ = 8767 and $e_\pi$ = –1398 $cm^{-1}$ at the octahedral geometry.

The optimised $C_{4v}$ structure for $[Cr(CN)_5]^{3-}$ has $r_{ax}$ = 2.14 and $r_{eq}$ = 2.08 Å corresponding to $e_\sigma$(ax) = 6869, $e_\pi$(ax) = –1095, $e_\sigma$(eq) = 7918 and $e_\pi$(eq) = –1263 $cm^{-1}$. Substituting these values into Equations (1)–(4) with $\alpha$ = 101° gives the energy difference between the highest and lowest energy d functions, $d_{x^2-y^2}(b_1)$ and $d_{xy}$, of 26222 $cm^{-1}$ vs. the DFT spherical configuration estimate of 28136 $cm^{-1}$. Hence, the assumption that cyanide remains a strong ligand generates quite good agreement with the DFT electronic structure.

Moreover, using the AOM parameter values for $r$ = 2.038 Å in Equations (11)–(13) yields rough promotion energies of ca. 32000, 19000 and 11000 $cm^{-1}$ for $O_h$, $C_{4v}$ and $D_{3h}$ symmetries, respectively, the former clearly being more than, while the latter two are clearly less than the spin crossover threshold of 23500 $cm^{-1}$.

## Conclusions

A combination of AOM and DFT arguments and calculations provides a simple explanation for the high-spin quintet ground state of $[Cr(CN)_5]^{3-}$ – the cost of promoting an electron to give an $S$ = 2 state is less than the cost of spin pairing. The reverse applies in octahedral symmetry and a triplet $S$ = 1 configuration results. In both cases, the combination of the BP86 functional and COSMO solvation provides a DFT protocol which successfully predicts good structures and the correct order of spin state energies. COSMO is critical for obtaining good structural data but does not alter the predicted lowest energy spin state. Spin contamination is minimal.

Given the highly charged species involved, the COSMO aqueous solvation energies are large and predict that the

 © 2006 Wiley-VCH Verlag GmbH & Co. KGaA, Weinheim 

formation of hexacyanochromate(II) from the pentacyanide precursor is favourable by 79 kJ·mol$^{-1}$. However, the "raw" electronic energies show that the powerful electrostatic interactions disfavour the process by over 700 kJ·mol$^{-1}$ and hence in less polar media such as acetonitrile, there is insufficient solvation energy to form the tetraanionic species.

An AOM ligand-field analysis based on DFT orbital energies for $[Cr(CN)_6]^{4-}$ suggests that cyanide is both a strong σ donor and reasonably strong π acceptor with typical $e_\sigma$ and $e_\pi$ values around 8500 and –1400 cm$^{-1}$, respectively. Assuming that cyanide remains a strong-field ligand for pentacyanochromate(II) yields AOM-derived d orbital energies in good agreement with their DFT counterparts. However, due to the change in coordination number and symmetry, even a strong-field ligand cannot force the ground state to a lower spin degeneracy.

Strong M–CN binding results in relatively large changes in energy as a function of coordination number and/or symmetry. Hence, the theoretical predictions tolerate larger errors and are more robust. In particular, DFT, in conjunction with a treatment of the environment, provides a reasonable basis for describing the chemistry of Cr(II)–cyanide complexes and, most likely, metallocyanides in general.

## Computational Details

All DFT calculations employed ADF version 2005.[19] After some preliminary testing, the Becke Perdew (BP86) functional was chosen in conjunction with triple-ζ plus polarisation basis sets (TZP) and frozen cores[20] up to 2p for the metals and 1s for C and N. Geometries were optimised with full point group symmetry as appropriate in the presence of a COSMO solvation field as implemented in ADF, with atomic radii C: 1.4 Å, N: 1.5 Å[21] and M: 2.58 Å. Where appropriate, all calculations were run spin-unrestricted, and the extent of spin contamination monitored by the calculation of $<S^2>$, which was generally within 0.03 of the ideal value except for $S = 1$, where the worst case was $<S^2> = 2.05$ for Cr systems and 2.08 for $[Mn(CN)_6]^{3-}$, and for $S = 2$, where the worst case was $<S^2> = 6.08$. Orbital energy differences were computed at the relevant optimised geometry using "spherical configurations", which we have used successfully in the past[22,23] and is a modification of the Average Over Configuration approach implemented in ADF and recently described by Atansov and Daul.[24] The five molecular orbitals, which are predominantly d antibonding in character, are identified and then assigned populations of $m/5$ where $m$ is the notional number of d electrons for the idealised metal oxidation state. A spin-restricted single-point calculation is then run to SCF convergence. Angular Overlap Model (AOM) expressions were derived from Figgis and Hitchman.[7]

## Acknowledgments

R. J. D. acknowledges access to the EPSRC Chemical Database Service, Daresbury Laboratory, UK.

[1] C. J. Ballhausen, *Introduction to Ligand Field Theory*, McGraw-Hill, New York, **1962**.
[2] K. J. Nelson, I. D. Giles, W. W. Shum, A. M. Arif, J. S. Miller, *Angew. Chem., Int. Ed.* **2005**, *44*, 3129–3132.
[3] J. P. Eaton, D. Nicholls, *Transition Met. Chem.* **1981**, *6*, 203–208.
[4] E. Ljungstroem, *Acta Chem. Scand.* **1977**, *31*, 104–108.
[5] S. M. Holmes, G. S. Girolami, *Mol. Cryst Liq. Cryst. Sci. Technol., Sect. A* **1997**, *305*, 279–290.
[6] V. A. Nasluzov, A. V. Kondratenko, K. M. Neyman, G. L. Gutsev, *Chem. Phys. Lett.* **1988**, *146*, 253–258.
[7] B. N. Figgis, M. A. Hitchman, *Ligand Field Theory and Its Applications*, John Wiley & Sons Ltd., New York, **2000**.
[8] T. Ziegler, *Can. J. Chem.* **1995**, *73*, 743–761.
[9] R. J. Deeth, N. Fey, *J. Comput. Chem.* **2004**, *25*, 1840–1848.
[10] O. Salomon, M. Reiher, B. A. Hess, *J. Chem. Phys.* **2002**, *117*, 4729–4737.
[11] M. Reiher, O. Salomon, B. A. Hess, *Theor. Chem. Acc.* **2001**, *107*, 48–55.
[12] M. Reiher, *Inorg. Chem.* **2002**, *41*, 6928–6935.
[13] H. Paulsen, A. X. Trautwein, *J. Phys. Chem. Solids* **2004**, *65*, 793–798.
[14] J. J. Alexander, H. B. Gray, *J. Am. Chem. Soc.* **1968**, *90*, 4260–4271.
[15] A. B. P. Lever, *Inorganic Electronic Spectroscopy*, 2nd ed., Elsevier, New York, **1984**.
[16] A. Atanasov, C. A. Daul, C. Rauzy, in *Optical Spectra and Chemical Bonding in Inorganic Compounds*, vol. 1, vol. 106, Springer Verlag, Berlin, **2004**, pp. 97–125.
[17] A. Rosa, E. J. Baerends, S. J. A. van Gisbergen, E. van Lenthe, J. A. Groeneveld, J. G. Snijders, *J. Am. Chem. Soc.* **1999**, *121*, 10356–10365.
[18] C. Ribbing, B. Gilliams, K. Pierloot, B. O. Roos, G. Karlstrom, *J. Chem. Phys.* **1998**, *109*, 3145–3152.
[19] E. J. Baerends, A. Bérces, C. Bo, P. M. Boerrigter, L. Cavallo, L. Deng, R. M. Dickson, D. E. Ellis, L. Fan, T. H. Fischer, C. Fonseca Guerra, S. J. A. van Gisbergen, J. A. Groeneveld, O. V. Gritsenko, F. E. Harris, P. van den Hoek, H. Jacobsen, G. van Kessel, F. Kootstra, E. van Lenthe, V. P. Osinga, P. H. T. Philipsen, D. Post, C. C. Pye, W. Ravenek, P. Ros, P. R. T. Schipper, G. Schreckenbach, J. G. Snijders, M. Sola, D. Swerhone, G. te Velde, P. Vernooijs, L. Versluis, O. Visser, E. van Wezenbeek, G. Wiesenekker, S. K. Wolff, T. K. Woo, T. Ziegler, *Scientific Computing and Modelling NV*, Free University, Amsterdam, Amsterdam, **2005**.
[20] E. J. Baerends, D. E. Ellis, P. Ros, *Theor. Chim. Acta* **1972**, *27*, 339.
[21] C. C. Pye, T. Ziegler, *Theor. Chem. Acc.* **1999**, *101*, 396.
[22] R. J. Deeth, *Faraday Discuss.* **2003**, *124*, 379–391.
[23] R. J. Deeth, D. L. Foulis, B. J. Williams-Hubbard, *Dalton Trans.* **2003**, 3949–3955.
[24] M. Atanasov, C. A. Daul, *C. R. Chim.* **2005**, *8*, 1421–1433.

Received: February 17, 2006
Published Online: May 9, 2006

 © 2006 Wiley-VCH Verlag GmbH & Co. KGaA, Weinheim 

DOI: 10.1002/ejic.200600217

# First Example of Dendrons as Topological Amplifiers

**Cédric-Olivier Turrin,[a] Alexandrine Maraval,[a] Germinal Magro,[a] Valérie Maraval,[a] Anne-Marie Caminade,*[a] and Jean-Pierre Majoral*[a]**

*Dedicated to the memory of our friend, the late Professor Marcial Moreno-Mañas*

**Keywords:** Dendrons / Dendrimers / Macrocycles / Phosphorus / NMR spectroscopy

A phosphorus-containing dendron was synthesized and grafted to a tetraphosphorus macrocycle. The presence of such bulky substituents allowed for the first time the amplification of topological differences in the macrocycle. These differences become detectable by $^{31}P$ NMR spectroscopy, with the appearance of several signals for the phosphorus atoms included in the macrocycle.

(© Wiley-VCH Verlag GmbH & Co. KGaA, 69451 Weinheim, Germany, 2006)

## Introduction

Dendrons,[1] also called dendritic wedges,[2] play an important role in dendritic macromolecular science, generally as large building blocks for the convergent synthesis of dendrimers[3] or dendronized polymers,[4] and for the elaboration of complex dendritic architectures.[5] Besides these classical uses of dendrons, their very particular topological features have already found more original applications, for instance in steric protection responsible for site isolation,[6] in new modes of self-organization,[7] in enantiomer separation of dendronized molecular knots,[8] as light harvesting antenae,[9] or as rotaxane stoppers.[10] However, to the best of our knowledge, dendrons were never used as amplifiers of local topological phenomena. We thought that such big, ramified, and conical substituents could facilitate the detection of previously undetectable phenomena, by amplifying the local difference.

Being interested since a long time in the synthesis and applications of dendrimers[11] and dendrons,[5,12] generally based on phosphorus,[13,14] we decided to test this assumption by grafting dendrons to compounds in which stereoisomers must exist but were never detected. We previously reported the synthesis of a series of phosphorus macrocycles,[15] obtained quantitatively by condensation reactions between 2 equiv. of phosphorylated dialdehydes and 2 equiv. of phosphodihydrazides.[16] These compounds appeared as the most suitable objects to confirm or invalidate our hypothesis about the role of dendrons as topological amplifiers. More precisely, we used macrocycle **1**,[17] constituted of 4 tetracoordinate phosphorus atoms ($P^{IV}$), two of them being included in O–P–O linkages, the two others in N–P–N linkages. The four $P^{IV}$ atoms are functionalized by an azide group as noncyclic substituent. This macrocycle possesses 4 asymmetric phosphorus centres, which can be easily functionalized through the reactivity of the azide groups (Figure 1).

Obviously, the presence of diastereoisomers in macrocycle **1** can be anticipated, and the zero value found for its optical rotation strongly suggests a 50:50 ratio for the stereoisomers on each phosphorus atom. If the macrocycle is relatively planar or if it is flexible, five diasteroisomers should be present; if the macrocycle exists in stable bent forms, as shown by the X-ray diffraction structure of a related macrocycle,[18] nine diasteroisomers should exist. However, the existence of such diastereoisomers was never detected previously. Even $^{31}P$ NMR spectroscopy, which is very useful for the detection of topological differences in constraint small cycles,[19] is inefficient with unconstraint large cycles such as **1**. The $^{31}P$ NMR spectrum of this 36-membered ring is shown in Figure 1; the 4 phosphorus atoms give two sharp singlets, one for the O–P–O linkages ($P_c$) and one for the N–P–N linkages ($P'_c$).

In a first attempt to detect the presence of diastereoisomers, a small but relatively hindered compound was grafted to the macrocycle. We used a Staudinger reaction between the azide groups and the functionalized phosphane **2**.[20] The creation of the P=N double bond occurs easily with the azide groups connected to the O–P–O linkages, and more slowly with the azide groups connected to the N–P–N linkages, as shown by $^{31}P$ NMR spectroscopy after 1 h. Indeed, the singlet corresponding to the O–P–O linkage has

[a] Laboratoire de Chimie de Coordination du CNRS,
205 route de Narbonne, 31077 Toulouse Cedex 4, France
Fax: + 33-5-61-55-30-03
E-mail: caminade@lcc-toulouse.fr
majoral@lcc-toulouse.fr

 © 2006 Wiley-VCH Verlag GmbH & Co. KGaA, Weinheim 

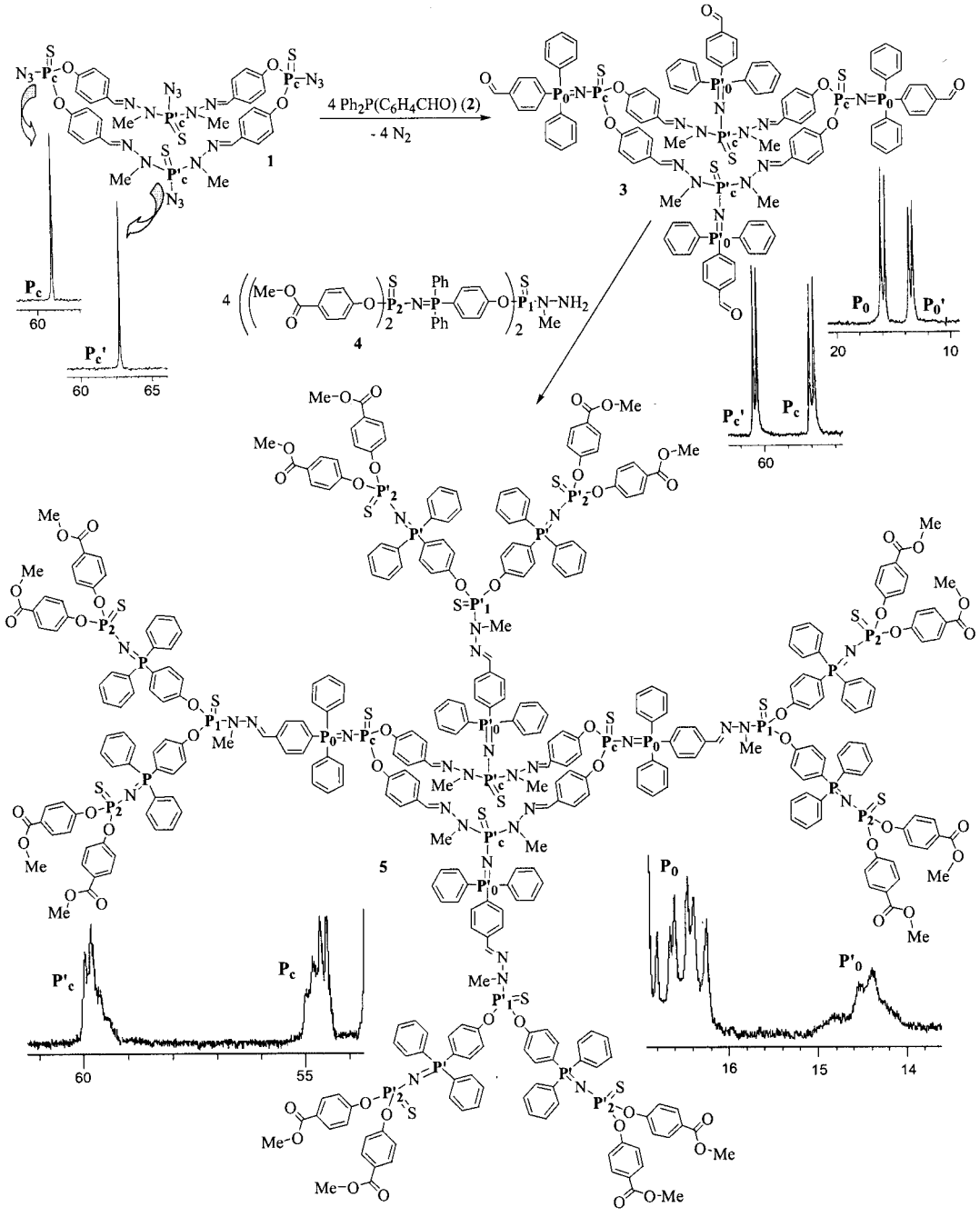


Figure 1. Synthesis of the macrocycle substituted by 4 dendrons and detection of diastereoisomers by $^{31}P$ NMR spectroscopy. Only the parts of the spectrum corresponding to $P_c$–N=$P_0$ and $P'_c$–N=$P'_0$ are shown for compound **5**. The spectra were recorded at 25 °C for **1** and **3**, at 80 °C for **5**.

disappeared on behalf of two doublets at $\delta$ = 16.2 ppm (P=N) and 55.7 ppm (P=S), whereas the singlet corresponding to the N–P–N linkages remains unchanged. This difference in the reactivity of both types of azide groups could be ascribed to a higher electron-withdrawing influence of the O–Aryl groups compared to the N–Me substituents, favouring the reaction.[21] However, the macrocycle **3** is finally isolated in nearly quantitative yield after reaction overnight. The $^{31}P$ NMR spectrum gives two sets of two sharp doublets corresponding to two types of P=N–P=S linkages as expected.[22] No trace of diastereoisomers could be detected even with these relatively bulky substituents (Figure 1).

In order to graft dendrons on the 4 aldehyde groups of **3** (one for each phosphorus atom included in the macrocycle), it was necessary to build a dendron possessing one $NH_2$ group at the core, preferably pertaining to an hydrazine or hydrazide linkage to ensure the stability of the future CH=N bond. The size of the dendron is also of crucial importance, because it must be large enough to induce de-

 © 2006 Wiley-VCH Verlag GmbH & Co. KGaA, Weinheim 

tectable differences, but not too large to allow the signals of the macrocycle to be still detectable. For this purpose, we synthesized the second-generation dendron **4**, obtained by a Staudinger reaction between $H_2NNMeP(S)(OC_6H_4PPh_2)_2$[23] and $N_3P(S)(OC_6H_4CO_2Me)_2$, synthesized according to a method we reported previously[24] (Scheme 1).

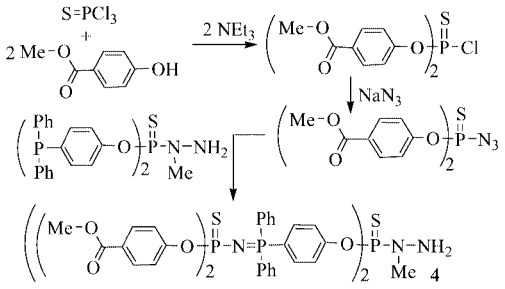

Scheme 1.

In the last step, 4 equiv. of the dendron **4** are condensed with the aldehyde groups of macrocycle **3**, to afford the second-generation dendrimer **5**, (Figure 1) as shown by the disappearance of the signal corresponding to the CHO group by $^1H$, $^{13}C$ NMR, and IR spectroscopy. The $^{31}P$ NMR spectrum of compound **5** at room temperature gives relatively sharp signals as expected for the phosphorus atoms pertaining to the dendrons (a single singlet for $P_1$ and $P'_1$, a single doublet for $P_2$ and $P'_2$, and a single doublet for P and P′, not shown in Figure 1). Indeed, no particular steric hindrance or lock of bonds is foreseeable around these phosphorus atoms. However, broad signals are observed for the P=N–P=S linkages in which the P=S group is part of the macrocycle, in contrast to the 4 sharp doublets obtained for the same atoms in macrocycle **3**. Such behaviour is generally characteristic of a "frozen" internal structure; we have observed previously such a phenomenon for high-generation polycationic phosphorus dendrimers,[25] but never for such small generations. Variable-temperature $^{31}P$ NMR experiments carried out in DMSO up to 80 °C improved only slightly the definition of the signals. A slightly better resolution is observed for the P=N groups linked to the macrocycle ($P_0$ and $P'_0$), compared to the P=S groups included in the macrocycle ($P_c$ and $P'_c$), whose degree of freedom is smaller. The better resolution observed for $P_0$ compared to $P'_0$ is presumably due to the higher degree of freedom of $P_c$ compared to $P'_c$. Indeed, all the X ray structure determinations carried out up to now for $P_cN(Me)NC{=}CHC_6H_4OP'_c$ linkages have shown that all atoms from $P_c$ to O lie in a same plane, whereas $P'_c$ is out of this plane.[26] At least 3 sharp doublets can be distinguished for $P_0$, which might correspond to the three main topological features expected; indeed, the dendron connected to $P_0$ can be surrounded with either zero, one or two dendrons, in the half space to which it belongs, defined by the average plane of the macrocycle (Figure 2). In form **A**, the dendrons linked to $P_c$ and $P'_c$ have two interactions, thus inducing a large modification of angles at the level of the $S{=}P_c{-}N{=}P_0$ and $S{=}P'_c{-}N{=}P'_0$ linkages. The same level of modification of angles occurs for the $S{=}P'_c{-}N{=}P'_0$ linkage in form **B**, and for the $S{=}P_c{-}N{=}P_0$ linkage in form **C**. Dendrons having a single interaction should induce a moderate modification of angles, for the $S{=}P'_c{-}N{=}P'_0$ linkage in forms **C** and **D**, and for the $S{=}P_c{-}N{=}P_0$ linkage in forms **B** and **D**. Finally, no interaction should occur for dendrons linked to the $S{=}P'_c{-}N{=}P'_0$ linkage in forms **B** and **E**, and for dendrons linked to the $S{=}P_c{-}N{=}P_0$ linkage in forms **C** and **E**. It is known that $^{31}P$ NMR chemical shifts are sensitive to modification of the angles around the phosphorus atom.[19] The minimization of interactions between the end groups of the dendrons linked to some diastereoisomers of the macrocycle necessitates modification of the angles at the level of their "root" ($P_c{-}N{=}P_0$ and $P'_c{-}N{=}P'_0$ linkages), which is translated into variation of the chemical shift. Thus, one may attribute the phenomenon observed here by $^{31}P$ NMR spectroscopy to the existence of diastereoisomers. It demonstrates without any ambiguity that our assumption concerning the role of dendrons as amplifiers of local phenomena was correct, and could be usefully applied to other systems.

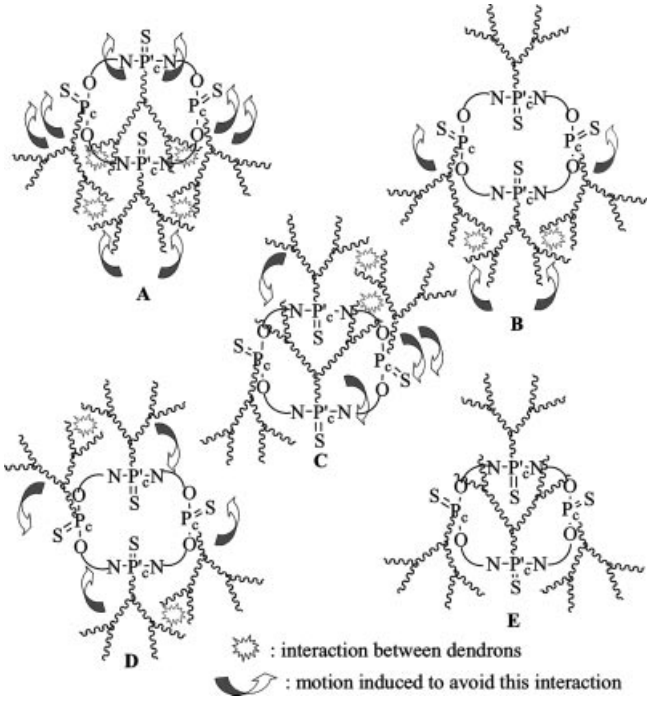


Figure 2. Schematization of the five diastereoisomers of compound **5**, showing the interactions between dendrons, and the movement to avoid these interactions, which modify the angles around the $P_c$ (and $P_0$), and $P'_c$ (and $P'_0$) phosphorus atoms.

## Experimental Section

**General:** All manipulations were carried out with standard high-vacuum and dry-argon techniques. The solvents were freshly dried and distilled (THF and diethyl ether with sodium/benzophenone, pentane and $CH_2Cl_2$ with phosphorus pentoxide). Classical $^1H$, $^{13}C$, $^{31}P$ NMR spectra were recorded with Bruker AC 200, AC 250, DPX 300, or AMX 400 spectrometers. References for NMR chemical shifts are 85% $H_3PO_4$ for $^{31}P$ NMR, $SiMe_4$ for $^1H$ and

 © 2006 Wiley-VCH Verlag GmbH & Co. KGaA, Weinheim 

$^{13}C$ NMR spectroscopy. The attribution of $^{13}C$ NMR signals has been done using $J_{mod}$, two-dimensional HMBC, and HMQC, broad-band or CW $^{31}P$ decoupling experiments when necessary. The numbering used for NMR assignments is depicted in Figure 3. IR analyses were recorded with Perkin–Elmer FT 1725x. Elemental analyses were performed by the Service d'Analyse du LCC, Toulouse, France. Compounds **1**,[17] **2**,[20] and $H_2NNMeP(S)(OC_6H_4PPh_2)_2$[23] were synthesized according to methods previously reported.

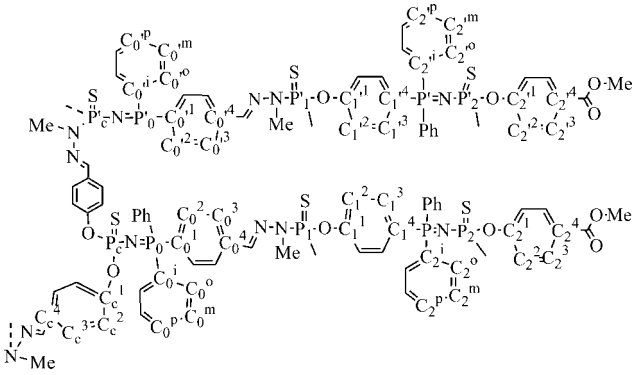

Figure 3. Numbering scheme used for NMR assignments.

**Synthesis and Characterization of 3:** To a solution containing 51 mg (0.050 mmol) of **1** in dichloromethane (5 mL) at room temp. was added 67 mg (0.23 mmol, slight excess) of $Ph_2P(C_6H_4CHO)$. The reaction mixture was stirred at room temp. overnight and concentrated to dryness. The crude residue was washed with a THF/pentane mixture to afford **3** as a white powder in 92% yield (95 mg). $^{31}P\{^1H\}$NMR (81.015 MHz, $CDCl_3$): $\delta$ = 13.4 (d, $^2J_{PP}$ = 27 Hz, $P'_c$ = N), 15.8 (d, $^2J_{PP}$ = 32 Hz, $P_c$=N), 55.9 (d, $^2J_{PP}$ = 32 Hz, $P_0$=S), 60.8 (d, $^2J_{PP}$ = 27 Hz, $P'_0$=S) ppm. $^1H$ NMR (200.132 MHz, $CDCl_3$): $\delta$ = 3.14 (br. d, $^3J_{HP}$ = 7.5 Hz, 12 H, NMe), 6.94–7.91 (m, 76 H, CH=N, $H_{arom}$), 9.91 (s, 2 H, CHO), 9.95 (s, 2 H, CHO) ppm. $^{13}C\{^1H\}$ NMR (62.896 MHz, $CDCl_3$): $\delta$ = 32.65 (d, $^2J_{CP}$ = 9.4 Hz, NMe), 121.57 (br. s, $C_c^2$), 126.96 (s, $C_c^3$), 127.66 (d, $^1J_{CP}$ = 108.5 Hz, $C_0^i$), 128.60 (d, $^3J_{CP}$ = 12.0 Hz, $C_0^m$), 128.81 (d, $^3J_{CP}$ = 12.3 Hz, $C_0'^m$), 129.07 (d, $^3J_{CP}$ = 12.0 Hz, $C_0'^3$), 129.11 (d, $^1J_{CP}$ = 108.4 Hz, $C_0'^i$), 129.25 (d, $^3J_{CP}$ = 11.6 Hz, $C_0^3$), 131.19 (s, $C_0^p$, $C_0'^p$), 132.62 (d, $^2J_{CP}$ = 11.0 Hz, $C_0^o$), 132.80 (d, $^2J_{CP}$ = 12.0 Hz, $C_0'^o$), 132.90 (s, $C_c^4$), 133.33 (d, $^2J_{CP}$ = 11.8 Hz, $C_0^2$), 133.52 (d, $^2J_{CP}$ = 11.8 Hz, $C_0'^2$), 134.21 (s, $C_0^4$), 134.44 (s, $C_0'^4$), 135.21 (d, $^1J_{CP}$ = 102.2 Hz, $C_0^1$), 136.47 (d, $^1J_{CP}$ = 101.8 Hz, $C_0'^1$), 138.51 (d, $^3J_{CP}$ = 10.0 Hz, CH=N), 151.57 (d, $^2J_{CP}$ = 9.6 Hz, $C_c^1$), 191.70 (s, CHO) ppm. $C_{108}H_{92}N_{12}O_8P_8S_4$ (2062.02): calcd. C 62.91, H 4.50, N 8.15; found C 63.02, H 4.61, N 7.92.

**Synthesis and Characterization of 4:** To a solution containing 663 mg (1.1 mmol, slight excess) of $H_2NNMeP(S)(OC_6H_4PPh_2)_2$ in dichloromethane (10 mL) at room temp. was added 815 mg (2 mmol) of $N_3P(S)(OC_6H_4CO_2Me)_2$. The reaction mixture was stirred at room temp. overnight and concentrated to dryness. The crude residue was flash-chromatographed on silica gel (dichloromethane as eluent) to afford **4** as a white powder in 90% yield (1.28 g). $^{31}P\{^1H\}$NMR (81.015 MHz, $CDCl_3$): $\delta$ = 16.1 (d, $^2J_{PP}$ = 30.6 Hz, P), 53.8 (d, $^2J_{PP}$ = 30.6 Hz, $P_2$), 68.51 (s, $P_1$) ppm. $^1H$ NMR (250.133 MHz, $CDCl_3$): $\delta$ = 3.19 (d, $^3J_{HP}$ = 10.8 Hz, 3 H, NMe), 3.87 (s, 12 H, OMe), 7.17–7.94 (m, 44 H, $H_{arom}$) ppm. $^{13}C\{^1H\}$ NMR (62.896 MHz, $CDCl_3$): $\delta$ = 41.35 (d, $^2J_{CP}$ = 13.7 Hz, NMe), 52.11 (s, OMe), 121.13 (dd, $^3J_{CP}$ = 6.3 Hz, $^3J_{CP}$ = 15.3 Hz, $C_1^2$), 121.40 (d, $^3J_{CP}$ = 5.8 Hz, $C_2^2$), 125.02 (dd, $^1J_{CP}$ = 108.3 Hz, $^3J_{CP}$ = 4.6 Hz, $C_1^4$), 128.15 (dd, $^1J_{CP}$ = 108.2 Hz, $^3J_{CP}$ = 4.4 Hz, $C_2^i$), 128.80 (d, $^2J_{CP}$ = 12.3 Hz, $C_2^m$), 131.06 (s, $C_2^3$), 132.68 (d, $^2J_{CP}$ = 11.7 Hz, $C_2^o$), 132.85 (s, $C_2^p$), 132.91 (s, $C_2^4$), 134.75 (d, $^2J_{CP}$ = 12.0 Hz, $C_1^3$), 154.16 (d, $^2J_{CP}$ = 7.9 Hz, $C_1^1$), 155.75 (d, $^2J_{CP}$ = 8.2 Hz, $C_2^1$), 166.61 (s, C=O) ppm. IR (KBr): $\tilde{\nu}$ = 1718 $cm^{-1}$ (CO). $C_{69}H_{61}N_4O_{14}P_5S_3$ (1421.31): calcd. C 58.31, H 4.33, N 3.94; found C 58.42, H 4.51, N 3.80.

**Synthesis and Characterization of $N_3P(S)(OC_6H_4CO_2Me)_2$:** To a solution containing 4.000 mL (39.3 mmol) of $PSCl_3$ in THF (100 mL) at –95 °C was added dropwise a solution of 15.584 g (82.7 mmol, slight excess) of methyl 4-hydroxybenzoate and 16.5 mL (82.7 mmol, slight excess) of triethylamine in THF (150 mL). The reaction mixture was allowed to reach room temperature overnight and the white precipitate was filtered off. After solvent removal under reduced pressure, the crude oil was dissolved in acetone (50 mL) and treated with 5.850 g (90 mmol, slight excess) of sodium azide at room temperature for 2 d. The precipitate was removed by filtration, and after solvent removal under reduced pressure, the azide was extracted from the crude oily product with pentane. Evaporation of pentane afforded the expected compound as a white powder in 75% yield (12.00 g). $^{31}P\{^1H\}$ NMR (81.015 MHz, $CDCl_3$): $\delta$ = 61.3 (s) ppm. $^1H$ NMR (250.133 MHz, $CDCl_3$): $\delta$ = 3.89 (s, 6 H, OMe), 7.27 (d, $^3J_{HH}$ = 7.6 Hz, 4 H, $H_{arom}$), 8.06 (d, $^3J_{HH}$ = 7.6 Hz, 4 H, $H_{arom}$) ppm. $^{13}C\{^1H\}$ NMR (62.896 MHz, $CDCl_3$): $\delta$ = 52.33 (s, OMe), 121.17 (d, $^3J_{CP}$ = 4.4 Hz, $C_b$), 128.23 (s, $C_d$), 131.66 (s, $C_c$), 153.22 (d, $^2J_{CP}$ = 8.0 Hz, $C_a$), 165.96 (s, C=O) ppm. $C_{16}H_{14}N_3O_6PS$ (407.34): calcd. C 47.18, H 3.46, N 10.32; found C 47.19, H 3.52, N 10.19.

**Synthesis and Characterization of 5:** To a solution containing 65 mg (0.032 mmol) of **3** in dichloromethane (5 mL) at room temp. was added 182 mg (0.128 mmol) of **4**. The reaction mixture was stirred at room temp. overnight and the residue was precipitated with diethyl ether, filtered and washed twice with 20 mL of diethyl ether to afford **5** as a white powder in 95% yield (230 mg). $^{31}P\{^1H\}$ NMR (161.975 MHz, $CDCl_3$): $\delta$ = 14–15 (m, $P'_0$=N), 16.3 (d, $^2J_{PP}$ = 31 Hz, $P_0$=N), 16.5 (d, $^2J_{PP}$ = 31 Hz, $P_0$=N), 16.7 (d, $^2J_{PP}$ = 31 Hz, $P_0$=N), 17.05 (d, $^2J_{PP}$ = 30 Hz, P=N, P′=N), 53.2 (d, $^2J_{PP}$ = 30.0 Hz, $P_2$=S, $P'_2$=S), 54.6 (d, $^2J_{PP}$ = 31 Hz, $P_c$=S), 54.9 (m, $P_c$=S), 59.3–60.0 (m, $P'_c$=S), 63.2 (s, $P_1$, $P'_1$) ppm. $^1H$ NMR (400.130 MHz, $CDCl_3$): $\delta$ = 3.21 (br. s, 12 H, $P'_0$-NMe), 3.37 (br. s, 12 H, $P_1$-NMe and $P'_1$-NMe), 3.84 (s, 48 H, $CO_2Me$), 7.02–7.98 (m, 256 H, CH=N, $H_{arom}$) ppm. $^{13}C\{^1H\}$ NMR (100.613 MHz, $CDCl_3$): $\delta$ = 33.23–33.86 (m, NMe), 52.53 (s, OMe), 121.78 (d, $^3J_{CP}$ = 4.8 Hz, $C_2^2$, $C_2'^2$, $C_c^2$), 122.05 (dd, $^3J_{CP}$ = 5.2 Hz, $^3J_{CP}$ = 12.9 Hz, $C_1^2$, $C_1'^2$), 125.85 (d, $^1J_{CP}$ = 108.2 Hz, $C_1'^4$, $C_1^4$), 128.35 (d, $^1J_{CP}$ = 108.1, $C_2^i$, $C_2'^i$), 128.53 (s, $C_c^3$), 128.96 (s, $C_2^4$, $C_2'^4$), 129.24 (br. d, $^3J_{CP}$ = 13.1 Hz, $C_0^m$, $C_2^m$, $C_0^3$, $C_0'^m$, $C_2'^m$, $C_0'^3$), 131.48 (s, $C_2^3$, $C_0^p$, $C_2'^3$, $C_0'^p$), 133.05 (br. d, $^2J_{CP}$ = 10.8 Hz, $C_0^o$, $C_2^o$, $C_0'^o$, $C_2'^o$), 133.34 (br. s, $C_0^4$, $C_2^p$, $C_0'^4$, $C_2'^p$), 133.80 (br. s, $C_0^2$, $C_0'^2$), 135.18 (d, $^2J_{CP}$ = 11.9 Hz, $C_1^3$, $C_1'^3$), 138.81–139.68 (m, CH=N), 152.17 (br. s, $C_c^1$), 154.25 (br. s, $C_1^1$, $C_1'^1$), 156.15 (d, $^2J_{CP}$ = 8.9 Hz, $C_2^1$, $C_2'^1$), 166.92 (s, C=O) ppm. IR (KBr): $\tilde{\nu}$ = 1718 $cm^{-1}$ (CO). $C_{384}H_{328}N_{28}O_{60}P_{28}S_{16}$ (7675.2): calcd. C 60.09, H 4.31, N 5.11; found C 60.01, H 4.40, N 5.01.


[1] C. J. Hawker, J. M. J. Fréchet, *J. Am. Chem. Soc.* **1990**, *112*, 7638–7647.
[2] J. S. Moore, Z. Xu, *Macromolecules* **1991**, *24*, 5893–5894.
[3] S. M. Grayson, J. M. J. Fréchet, *Chem. Rev.* **2001**, *101*, 3819–3868.
[4] A. Zhang, L. Okrasa, T. Pakula, A. D. Schlueter, *J. Am. Chem. Soc.* **2004**, *126*, 6658–6666.
[5] A. M. Caminade, A. Maraval, J. P. Majoral, *Eur. J. Inorg. Chem.* **2006**, 887–901 (Microreview).


 © 2006 Wiley-VCH Verlag GmbH & Co. KGaA, Weinheim 

[6] E. M. Harth, S. Hecht, B. Helms, E. Malmström, J. M. J. Fréchet, C. J. Hawker, *J. Am. Chem. Soc.* **2002**, *124*, 3926–3938.
[7] X. Zeng, G. Ungar, Y. Liu, V. Percec, A. E. Dulcey, J. K. Hobbs, *Nature* **2004**, *428*, 157–160.
[8] J. Recker, W. M. Müller, U. Müller, T. Kubota, Y. Okamoto, M. Nieger, F. Vögtle, *Chem. Eur. J.* **2002**, *8*, 4434–4442.
[9] G. M. Stewart, M. A. Fox, *J. Am. Chem. Soc.* **1996**, *118*, 4354–4360.
[10] D. B. Amabilino, P. R. Ashton, V. Balzani, C. L. Brown, A. Credi, J. M. J. Fréchet, J. W. Leon, F. M. Raymo, N. Spencer, J. F. Stoddart, M. Venturi, *J. Am. Chem. Soc.* **1996**, *118*, 12012–12020.
[11] a) N. Launay, A. M. Caminade, R. Lahana, J. P. Majoral, *Angew. Chem. Int. Ed. Engl.* **1994**, *33*, 1589–1592; b) N. Launay, A. M. Caminade, J. P. Majoral, *J. Am. Chem. Soc.* **1995**, *117*, 3282–3283.
[12] V. Maraval, R. Laurent, B. Donnadieu, M. Mauzac, A. M. Caminade, J. P. Majoral, *J. Am. Chem. Soc.* **2000**, *122*, 2499–2511.
[13] J. P. Majoral, A. M. Caminade, *Chem. Rev.* **1999**, *99*, 845–880.
[14] J. P. Majoral, A. M. Caminade, V. Maraval, *Chem. Commun.* **2002**, 2929–2942.
[15] A. M. Caminade, J. P. Majoral, *Chem. Rev.* **1994**, *94*, 1183–1213.
[16] F. Gonce, A. M. Caminade, F. Boutonnet, J. P. Majoral, *J. Org. Chem.* **1992**, *57*, 970–975.
[17] J. Mitjaville, A. M. Caminade, R. Mathieu, J. P. Majoral, *J. Am. Chem. Soc.* **1994**, *116*, 5007–5008.
[18] M. Badri, J. P. Majoral, A. M. Caminade, M. Delmas, A. Gaset, A. Gorgues, J. Jaud, *J. Am. Chem. Soc.* **1990**, *112*, 5618–5623.
[19] L. D. Quin, J. G. Verkade, Eds, *Phosphorus-31 NMR Spectral Properties in Compounds Characterization and Structural Analysis*, VCH Publishers, New York, **1994**.
[20] G. P. Schiemenz, H. Haack, *Justus Liebigs Ann. Chem.* **1973**, 1480–1493.
[21] J. E. Leffler, T. D. Temple, *J. Am. Chem. Soc.* **1967**, *89*, 5235–5246.
[22] C. Galliot, C. Larré, A. M. Caminade, J. P. Majoral, *Science* **1997**, *277*, 1981–1984.
[23] L. Brauge, G. Magro, A. M. Caminade, J. P. Majoral, *J. Am. Chem. Soc.* **2001**, *123*, 6698–6699.
[24] G. Magro, B. Donnadieu, A. M. Caminade, J. P. Majoral, *Chem. Eur. J.* **2003**, *9*, 2151–2159.
[25] J. Leclaire, Y. Coppel, A. M. Caminade, J. P. Majoral, *J. Am. Chem. Soc.* **2004**, *126*, 2304–2305.
[26] M. L. Lartigue, B. Donnadieu, C. Galliot, A. M. Caminade, J. P. Majoral, J. P. Fayet, *Macromolecules* **1997**, *30*, 7335–7337.

Received: March 10, 2006
Published Online: May 18, 2006

 © 2006 Wiley-VCH Verlag GmbH & Co. KGaA, Weinheim 

DOI: 10.1002/ejic.200600320

# DFT-Verified Crystallographic Mechanism of Cycloplatination

**Stefanus Otto,*[a][‡] Arani Chanda,[b] Pavel V. Samuleev,[c] and Alexander D. Ryabov*[b]**

**Keywords:** Platinum / C-H activation / Metallacycles / X-ray diffraction / Density functional calculations

Two key intermediates in the mechanistic cycle of cycloplatination of aryl oximes by $Pt^{II}$ complexes were crystallographically characterized. *trans*-[$PtCl_2(SOMe_2)$(*N*-acetophenone oxime)] is an active precursor on the C–H cleavage reaction coordinate. The formation of *trans*-[$PtCl_2$(*N*-benzaldehyde oxime)$_2$] accounts for the rate retardation by excess oxime. DFT calculations support the crystallographic evidence that provides unequivocal proof for the electrophilic nature of cycloplatination.

(© Wiley-VCH Verlag GmbH & Co. KGaA, 69451 Weinheim, Germany, 2006)

Disclosure of mechanisms of cyclometalation by transition-metal complexes is a difficult task.[1a] Cyclometalation is a multistep event that should include (i) ligand coordination to a metal center through its usually N, P, O, or S donor site (X), and (ii) a stepwise metal-involved cleavage of the C–H bond (Scheme 1).

Step (i) is an intermolecular ligand substitution, which may occur through associative, dissociative, or interchange pathways. Step (ii) is a combination of intramolecular ligand substitution and C–H cleavage. Options for the C–H cleavage include oxidative addition/reductive elimination, electrophilic substitution, or multicentered activation (σ-bond metathesis).[1a,1b] Agostic interactions[2] are also often included in a mechanistic picture.[3] Consequently, extensive efforts are required for the unequivocal understanding of cyclometalation mechanisms. A complicating factor is that mechanistic studies are often performed with excess incoming ligand X~C–H and may result in the binding of more than one ligand to the metal center.

All stated above apply to cycloplatination by the $Pt^{II}$ sulfide and sulfoxide complexes [$PtCl_2(SR_2)_2$] or [$PtCl_2(SOR_2)_2$]. These metalating agents are very convenient for performing various cycloplatination reactions,[4] and the use of chiral sulfoxides SORR′ allows for the synthesis of platinacycles with the planar[5a] and central carbon chirality.[5b] We recently reported on the mechanism of cycloplatination of aryl oximes by [$PtCl_2(SR_2)_2$] or *cis*-[$PtCl_2(SOR_2)_2$] (R = Me) as shown in Scheme 2.[6] Evidence was presented that the cycloplatination is a multistep process and the principal reaction steps were recognized. The key intermediate was identified as complex **A**, which supports the views of other authors.[7] The formation of dichlorobis(*N*-oxime)platinum(II) **B** was postulated to account for the rate retardation by excess acetophenone oxime. Our deductions were based on kinetic and $^1$H NMR spectroscopic data that may leave room for alternative interpretations. In this communication, we report X-ray crystallographic data for the compounds matching the intermediates **A** and **B**. They are complexes **1** and **2**, respectively. Although mechanistic chemists should apply caution when using solid-state information for the interpretation of kinetic data obtained in solution, the structures of complexes **A** and **B** are exceptionally mechanistically informative towards the dynamics of intramolecular C–H bond activation by $Pt^{II}$. The mech-

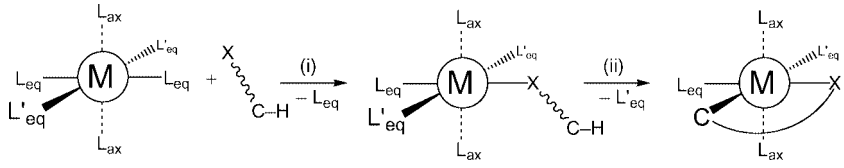


Scheme 1. General scheme for cyclometalation by octahedral or square-planar ($L_{ax}$ = 0) transition metal complexes. Here $L_{eq}$ and $L_{ax}$ are equatorial and axial ligands, respectively.

[a] Department of Chemistry, University of the Free State, P. O. Box 339, Bloemfontein 9300, South Africa
[b] Department of Chemistry, Carnegie Mellon University, 4400 Fifth Av., Pittsburgh, PA 15213, USA
E-mail: ryabov@andrew.cmu.edu
[c] Department of Chemistry, M. V. Lomonosov Moscow State University, 119899 Moscow, Russia
[‡] Current address: Sasol Technology R & D, P. O. Box 1, Sasolburg 1947, South Africa, E-mail: Fanie.Otto@sasol.com
Supporting information for this article is available on the WWW under http://www.eurjic.org or from the author.

 © 2006 Wiley-VCH Verlag GmbH & Co. KGaA, Weinheim 

anistic conclusions made were verified, supported, and refined by theoretical analysis of key participants in Scheme 2 with DFT calculations.

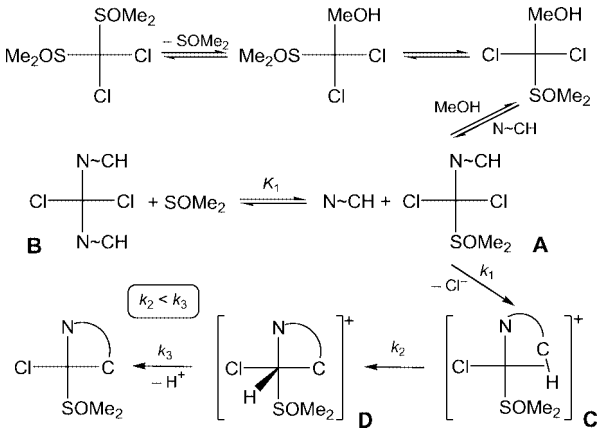


Scheme 2. Mechanism of cycloplatination of aryl oximes by *cis*-$[PtCl_2(dmso)_2]$ suggested in ref.[6]

Compounds **1** and **2** were synthesized according to Equations (1) and (2), respectively, and characterized by $^1H$ NMR spectroscopy, analytical data, and X-ray crystallography. Crystal structures of **1** and **2** are displayed in Figure 1. Both complexes exhibit a square-planar geometry. The N-atom of the acetophenone oxime is in *trans* position relative to the sulfur atom of dmso in complex **1**. The phenyl plane of the oxime ligand is orientated almost perpendicularly to the metal plane with a Cl(1)–Pt–N–C(10) torsion angle of 69.1°. The phenyl ring is in the axial position with a closest Pt···C(16) contact of 3.153 Å [Pt···H(16) 2.852 Å]. The Pt–S(1) and Pt–N(1) bond lengths of 2.206(3) and 2.051(9) Å, respectively, are within normal ranges for bonds of this type. The Pt–Cl(1) and Pt–Cl(2) bond lengths of 2.287(3) and 2.293(3) Å, respectively, do not differ significantly and are within expected ranges.

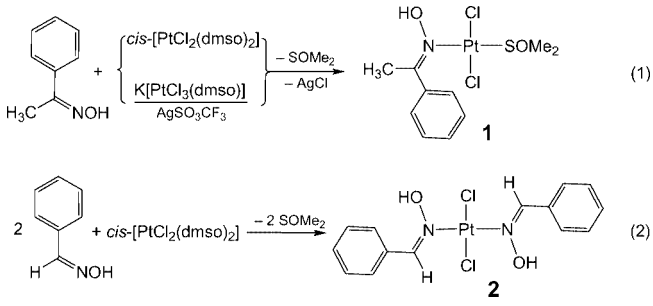


Compound **2** crystallizes with the inversion center in the triclinic space group $P\bar{1}$ resulting in a mutually *trans* configuration of the oxime and chloro ligands with the oxime ligands located in the coordination plane. The hydroxy group is directed towards a chloro ligand, typical of many oxime complexes of Pd and Pt.[8] There is a Cl···H–O interaction, with Cl···O and Cl···H separations of 3.056 and 2.408 Å, respectively. The Pt–Cl(1) and Pt–N(1) bond lengths of 2.3053(19) and 2.021(6) Å, respectively, are within normal ranges for complexes of this type.

Crystallographically characterized species **1** and **2** do prove unambiguously the existence of the proposed intermediates **A** and **B**, respectively, shown in Scheme 2. Importantly, both structural and DFT (see below) data provide evidence why complex **B** is not on the reaction coordinate. In contrast, **A** is adequately pre-organized for subsequent metalation of the C–H bond. The azomethine unit geometry is an essential feature. Data in Figure 1 confirm the (*E*) and (*Z*) configuration of the C=N unit in complexes **1** and **2**, respectively. To avoid any confusion, all assignments are made for imaginary free aryl oximes, which are *not* bound to $Pt^{II}$. The (*Z*) geometry in **2** implies that the *trans*-bis(oxime)platinum(II) unit should be unreactive towards cyclometalation. The *ortho* C–H bonds are located too far from the metal center with a shortest Pt···H–C(16) distance of 4.916 Å. In contrast to **2**, the geometry at the C=N unit in

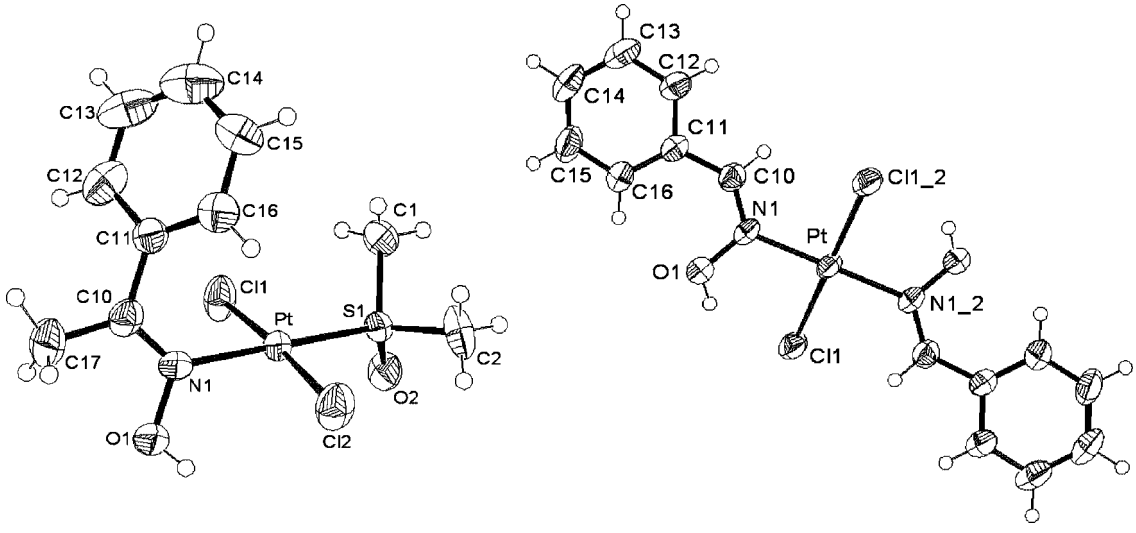


Figure 1. ORTEP diagrams of **1** (left) and **2** (right) at 30% probability level. Hydrogen atoms are of arbitrary size. Selected bond lengths [Å]: **1**: Pt–Cl(1) 2.287(3), Pt–Cl(2) 2.293(3), Pt–N(1) 2.051(9), Pt–S(1) 2.206(3); **2**: Pt–Cl(1) 2.3053(19), Pt–N(1) 2.021(6).

 © 2006 Wiley-VCH Verlag GmbH & Co. KGaA, Weinheim 

the mono(aryl oxime) complex **1** is (*E*) resulting in **1** being much better arranged for the subsequent C–H bond activation. In fact, different geometries at the C=N moiety in monomeric bis- and mono(oxime) complexes of $Pt^{II}$ is a notable observation because the aspect of geometric isomerization at the C=N bonds was rather confusing. This is understandable because the geometry of ligands in free and cyclometalated states may be different. For example, azomethines are sometime involved in (*E*) → (*Z*) isomerization during cyclometalation.[4j] As in the case of **1**, the binding of the (*E*) form of the aryl oxime delivers its *ortho* C–H bond to the proximity of the metal center. The Pt···C(16) separation is only 3.153 Å. For comparison, $Pt^{II}$ is further away from the C–H bond of the Cp ring in *trans*-[$PtCl_2(CpFeC_5H_4CMe{=}NPh)$dmso] and therefore an additional external base is needed to facilitate the C–H bond cleavage.[9] Note that cycloplatination of **1** occurs spontaneously in methanol without basic co-catalyst.

Assuming that the short Pt···C(16) separation is evidence that complex **1** is on the reaction coordinate, several comments could be made based on mutual atom arrangement in **1**. The C(16) atom is located right above the Pt–N bond and H(16) is directed at Cl(2). Therefore, there is a favorable setup of all key groups involved in cycloplatination for an easy conversion of **A** into **C** (Scheme 2). Essential is just the dissociation of chloride Cl(2) that gives intermediate **C**. Based on the data reported here, elsewhere,[6,10,11] and the results of DFT analysis of this particular system (see below) we suggest a first DFT-verified "crystallographic" mechanism of cycloplatination by *cis*-[$PtCl_2(SOMe_2)_2$] (Figure 2), which actually involves all major steps of the "kinetic" mechanism in Scheme 2. A strength of the "crystallographic" mechanism is that ***all*** the compounds in Figure 2 have now been characterized by X-ray crystallography including the starting complex *cis*-[$PtCl_2(SOMe_2)_2$] and the incoming aryl oxime.

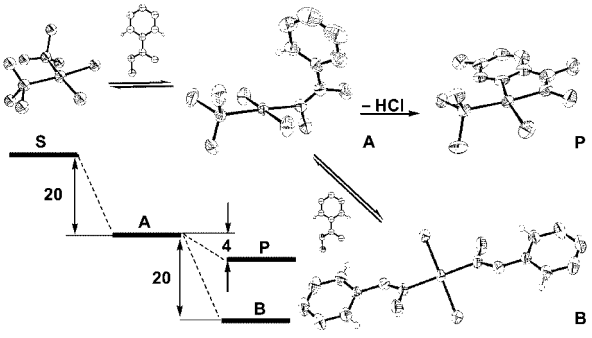


Figure 2. "Crystallographic" mechanism of cycloplatination of aryl oximes by *cis*-[$PtCl_2(SOMe_2)_2$]. X-ray data for $Pt^{II}$ complexes **S** and **P** are from ref.[10] and ref.[6], respectively; structures **A** and **B** are reported in this work. A structure of (*E*)-acetophenone oxime was published by Gieren, et al.[11] At the bottom left is the DFT-calculated diagram with energies in kcal mol$^{-1}$.

The geometries of all structures in Figure 2 are optimized using Becke's three-parameter hybrid potential (B3LYP) with LANL2DZ basis set as provided by Gaussian 03.[12] Optimizations are done in the absence of any solvent. The optimized geometries are in general agreement with the experimental bond lengths/angles. Longer Pt–Cl and Pt–S but shorter Cl···HO bond lengths (all by 0.1–0.2 Å) were, however, observed. Substitution of the S- by the N-donor ligand to form intermediate **A** is energetically favorable (ca. 20 kcal mol$^{-1}$), as well as the second exergonic substitution leading to **B**. As a result, *Z* configured intermediate **B** is in a deep energy well and its C–H bonds are inaccessible for cycloplatination (Figure 2).

Our theoretical simulations indicate that the C–H bond activation (**A** → **P**) ***never*** occurs when both chloride ions are bound to $Pt^{II}$. In other words, there is no C–H breaking pathway through an axial agostic contact. The evidence for the C–H bond activation begins to emerge after enforced dissociation of chloride as shown in Figure 3. Here, complex **A′** is generated by removing one chloride ion from the DFT-optimized structure of **A**. Geometry optimization of **A′** results in **C′**, which matches nicely the postulated intermediate **C** in Scheme 2. Remarkably, the C–H bond carbon atom in **C′** aligns itself *in the metal plane* and is almost ideally *trans* to the chloro ligand with a C···Pt–Cl angle of 165°. Hence, the in-plane disposition of the C–H bond is absolutely crucial for the reaction to happen. The Pt–C distance changes from 3.153 Å (in **A**) to 2.519 Å in **C′** to become finally 2.021 Å in **P**. The Mulliken charge on the carbon atom varies drastically as well, viz. –0.304 (**A**) → –0.449 (**C′**) → –0.193 (**P**), indicating a major development of a carbanion character of the C–H bond carbon atom in high-energy intermediate **C′**. Elongation of the $C^1$–$C^2$ bond (1.438 vs. average 1.410 Å for other aryl C–C bonds of **C′**, Figure 3) supports also the "carbanionic" hypothesis. This also shows that the hydrogen atom should dissociate rather as proton in an electrophilic substitution sequence. DFT calculations show that the cycloplatination of the C–H bond (**A** → **P**) is 4–5 kcal mol$^{-1}$ favorable when the leaving HCl is allowed to interact with product **P**.[13] If the energies of **P** and HCl are calculated separately, the cycloplatination reaction is ca. 10 kcal mol$^{-1}$ endergonic. This scenario may be different in the presence of methanol as solvent where H-bonding should play a significant role. Apparently, the chloro ligand is somehow involved in the stabilization of the leaving hydrogen atom. Mechanistic options are either chloride interacts with $H^+$ as a base, thus precluding reverse

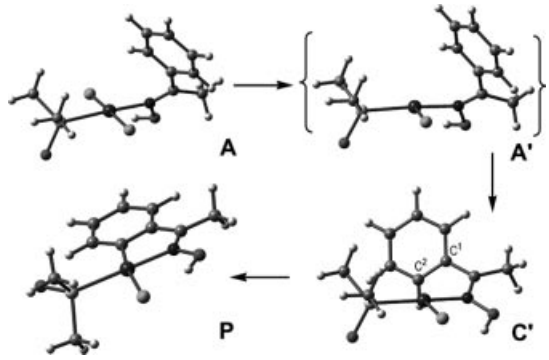


Figure 3. DFT-optimized structures of intermediates **A**, **C′**, and product **P**, see text for details.

 © 2006 Wiley-VCH Verlag GmbH & Co. KGaA, Weinheim 

protonolysis of the Pt–C bond of **P**, or its role is a compensation of a positive charge of intermediate **D** in Scheme 2.

In conclusion, a combination of kinetic and X-ray structural data plus theoretical DFT information generated a unified, self-consistent detailed mechanistic picture of the electrophilic C–H bond cyclometalation by platinum(II). The DFT routine filled elegantly the mechanistic gaps, about which kinetics and crystallography are usually silent.

## Experimental Section

**Chemicals:** Acetophenone oxime (Acros), benzaldehyde oxime (Acros), $SOMe_2$ (Merck) and $AgSO_3CF_3$ (Aldrich) were used as received, methanol (Riedel–de Haën) was of analytical grade and was freshly distilled from $CaH_2$ under dinitrogen prior to use.

**NMR Measurements:** The $^1H$ NMR spectra were recorded at 295 K as $CD_3OD$ or $CDCl_3$ solutions with either a Bruker 300 MHz or a Varian Unity 300 spectrometer operating at 299.78 MHz; the spectra were calibrated relative to TMS at $\delta = 0$ ppm.

**Preparation of Complexes:** $K[PtCl_3(SOMe_2)]$ and *cis*-$[PtCl_2(SOMe_2)_2]$ were prepared according to literature procedures.[14,15]

***trans*-[PtCl$_2${HO–N=C(CH$_3$)C$_6$H$_5$}(SOMe$_2$)] (1). (a)** A homogeneous solution of *cis*-$[PtCl_2(SOMe_2)_2]$ (104 mg, 0.246 mmol) was prepared in methanol (30 mL) by gently heating with effective stirring for 2 h. Acetophenone oxime (35 mg, 0.26 mmol) in methanol (5 mL) was added at ambient temperature and the solution was stirred for 30 min. The reaction mixture was concentrated to 20 mL under a flow of nitrogen and left at 15 °C to crystallize by slow evaporation of methanol. Crystals of **1** suitable for X-ray diffraction were obtained. **(b)** $AgSO_3CF_3$ (64 mg, 0.25 mmol), dissolved in methanol (5 mL), was added to a solution of $K[PtCl_3(SOMe_2)]$ (100 mg, 0.239 mmol), also in methanol (25 mL). The resulting mixture was stirred for 15 min to facilitate the precipitation of AgCl and was subsequently filtered to yield a clear solution. Acetophenone oxime (34 mg, 0.25 mmol) in methanol (5 mL) was added at ambient temperature and the solution was stirred for 10 min. Evaporation of the methanol resulted in isolation of **1** in almost quantitative yield. $^1H$ NMR ($CDCl_3$): $\delta$ = 2.50 (s, 3 H, $CCH_3$), 3.24 (t, $^3J_{PtH}$ 19 Hz, 6 H, $SCH_3$), 7.50 (m, 3 H, 2-H, 4-H, 6-H), 7.90 (m, 2 H, 3-H, 5-H), 8.00 (s, 1 H, OH) ppm. $C_{10}H_{15}Cl_2NO_2PtS$ (477.98): calcd. C 25.1, H 3.2, N 2.9; found C 25.4, H 3.6, N 2.7.

***trans*-[PtCl$_2$(HO–N=CHC$_6$H$_5$)$_2$] (2):** Benzaldehyde oxime (592 mg, 4.89 mmol) was added to a solution of $K[PtCl_3(SOMe_2)]$ (210 mg, 0.50 mmol) in methanol (25 mL) and the reaction mixture was subsequently refluxed for 4 d. The reaction progress was monitored by $^1H$ NMR spectroscopy as described previously.[6] Yield 119 mg (48%). $^1H$ NMR ($CDCl_3$): $\delta$ = 7.4–7.6 (m, 6 H, 2× 2-H, 2× 4-H, 2× 6-H), 7.93 (m, 4 H, 2× 3-H, 2× 5-H), 8.19 (t, $^3J_{PtH}$ = 22 Hz, 2 H, 2× CH), 9.56 (s, 2 H, 2× OH) ppm. $C_{14}H_{14}Cl_2N_2O_2Pt$ (507.01): calcd. C 33.1, H 2.8, N 5.5; found C 33.4, H 3.0, N 5.4.

**Crystallography:** The data collections were carried out with a Siemens SMART CCD diffractometer using Mo-$K_\alpha$ radiation ($\lambda$ = 0.71073 Å) and ω-scans at 293(2) K. After completion of the data collection, the first 50 frames were repeated to check for decay, of which none was observed. All reflections were merged and integrated using SAINT[16] and were corrected for Lorentz, polarization and absorption effects using SADABS.[17] The structure was solved by the heavy-atom method and refined through full-matrix least-squares cycles using the SHELXL97[18] software package with $\Sigma(|F_o| - |F_c|)^2$ being minimized. All non-H atoms were refined with anisotropic displacement parameters while the H atoms were placed in geometrically idealized positions and constrained to ride on their parent atoms (aromatic C–H 0.93 Å, aliphatic C–H 0.96 Å, O–H 0.82 Å). For both structures the minimum and maximum residual electron densities were located within 1 Å of the platinum nuclei indicating no physical meaning. The crystal data and details of the data collection and refinement are given in Table S1 with selected geometrical parameters in Table S2. Crystallographic data have been deposited with the Cambridge Crystallographic Data Center as supplementary publications CCDC-290273 and -290274 (**2** and **1**, respectively). These data can be obtained free of charge from The Cambridge Crystallographic Data Centre via www.ccdc.cam.ac.uk/data_request/cif.

**Supporting Information** (see also the footnote on the first page of this article): Crystal data and structure refinement parameters, bond lengths and bond angles in Tables S1 and S2.

## Acknowledgments

The University of Lund, Sweden, is thanked for the use of their diffractometer. The University of the Free State is acknowledged for financial support.

[1] a) A. D. Ryabov, *Chem. Rev.* **1990**, *90*, 403; b) M. Lersch, M. Tilset, *Chem. Rev.* **2005**, *105*, 2471.
[2] M. Brookhart, M. L. H. Green, L. L. Wong, *Progr. Inorg. Chem.* **1988**, *36*, 1.
[3] See for example: a) P. S. Pregosin, F. Wombacher, *Magn. Reson. Chem.* **1991**, *29*, S106; b) A. Albinati, F. Lianza, B. Muller, P. S. Pregosin, *Inorg. Chim. Acta* **1993**, *208*, 119; c) M. J. Ingleson, M. F. Mahon, A. S. Weller, *Chem. Commun.* **2004**, 2398; d) R. Romeo, M. R. Plutino, A. Romeo, *Helv. Chim. Acta* **2005**, *88*, 507; e) R. H. Crabtree, *J. Organomet. Chem.* **2004**, *689*, 4083; f) D. L. Davies, S. M. A. Donald, S. A. Macgregor, *J. Am. Chem. Soc.* **2005**, *127*, 13754.
[4] a) P. R. R. Ranatunge-Bandarage, B. H. Robinson, J. Simpson, *Organometallics* **1994**, *13*, 500; b) Y. J. Wu, Y. H. Liu, X. L. Cui, H. Z. Yuan, X. A. Mao, *Polyhedron* **1996**, *15*, 3315; c) A. D. Ryabov, G. M. Kazankov, I. M. Panyashkina, O. V. Grozovsky, O. G. Dyachenko, V. A. Polyakov, L. G. Kuz'mina, *J. Chem. Soc., Dalton Trans.* **1997**, 4385; d) L. Ding, D. P. Zou, Y. J. Wu, *Polyhedron* **1998**, *17*, 2511; e) M. D. Meijer, A. W. Kleij, M. Lutz, A. L. Spek, G. van Koten, *J. Organomet. Chem.* **2001**, *640*, 166; f) M. D. Meijer, E. de Wolf, M. A. L. Lutz, G. Spek, P. M. van Klink, G. van Koten, *Organometallics* **2001**, *20*, 4198; g) M. D. Meijer, A. W. Kleij, B. S. Williams, D. Ellis, M. Lutz, A. L. Spek, G. P. M. van Klink, G. van Koten, *Organometallics* **2002**, *21*, 264; h) S. Perez, C. Lopez, A. Caubet, X. Solans, M. Font-Bardia, *New J. Chem.* **2003**, *27*, 975–982; i) A. Caubet, C. Lopez, X. Solans, M. Font-Bardia, *J. Organomet. Chem.* **2003**, *669*, 164; j) M. Crespo, M. Font-Bardia, J. Granell, M. Martinez, X. Solans, *Dalton Trans.* **2003**, 3763; k) C. Lopez, A. Caubet, S. Perez, X. Solans, M. Font-Bardia, *Chem. Commun.* **2004**, 540.
[5] a) A. D. Ryabov, I. M. Panyashkina, V. A. Polyakov, J. A. K. Howard, L. G. Kuz'mina, M. S. Datt, C. Sacht, *Organometallics* **1998**, *17*, 3615; b) A. D. Ryabov, I. M. Panyashkina, V. A. Polyakov, A. Fischer, *Organometallics* **2002**, *21*, 1633.
[6] A. D. Ryabov, S. Otto, P. V. Samuleev, V. A. Polyakov, L. Alexandrova, G. M. Kazankov, S. Shova, M. Revenco, J. Lipkowski, M. H. Johansson, *Inorg. Chem.* **2002**, *41*, 4286.
[7] Y. Wu, S. Huo, J. Gong, X. Cui, L. Ding, K. Ding, C. Du, Y. Liu, M. Song, *J. Organomet. Chem.* **2001**, *637–639*, 27.
[8] a) A. D. Ryabov, G. M. Kazankov, A. K. Yatsimirsky, L. G. Kuz'mina, O. Y. Burtseva, N. V. Dvortsova, V. A. Polyakov, *In-*

 © 2006 Wiley-VCH Verlag GmbH & Co. KGaA, Weinheim 

*org. Chem.* **1992**, *31*, 3083; b) A. D. Ryabov, L. G. Kuz'mina, V. A. Polyakov, G. M. Kazankov, E. S. Ryabova, M. Pfeffer, R. van Eldik, *J. Chem. Soc., Dalton Trans.* **1995**, 999.
[9] Y. J. Wu, L. Ding, H. X. Wang, Y. H. Liu, H. Z. Yuan, X. A. Mao, *J. Organomet. Chem.* **1997**, *535*, 49.
[10] R. Melanson, F. D. Rochon, *Can. J. Chem.* **1975**, *53*, 2371–2374.
[11] A. Gieren, T. Huebner, C. Ruiz-Perez, *Chem.-Ztg.* **1986**, *110*, 73–76.
[12] M. J. Frisch, G. W. Trucks, H. B. Schlegel, G. E. Scuseria, M. A. Robb, J. R. Cheeseman, J. A. Montgomery Jr, T. Vreven, K. N. Kudin, J. C. Burant, J. M. Millam, S. S. Iyengar, J. Tomasi, V. Barone, B. Mennucci, M. Cossi, G. Scalmani, N. Rega, G. A. Petersson, H. Nakatsuji, M. Hada, M. Ehara, K. Toyota, R. Fukuda, J. Hasegawa, M. Ishida, T. Nakajima, Y. Honda, O. Kitao, H. Nakai, M. Klene, X. Li, J. E. Knox, H. P. Hratchian, J. B. Cross, V. Bakken, C. Adamo, J. Jaramillo, R. Gomperts, R. E. Stratmann, O. Yazyev, A. J. Austin, R. Cammi, C. Pomelli, J. W. Ochterski, P. Y. Ayala, K. Morokuma, G. A. Voth, P. Salvador, J. J. Dannenberg, V. G. Zakrzewski, S. Dapprich, A. D. Daniels, M. C. Strain, O. Farkas, D. K. Malick, A. D. Rabuck, K. Raghavachari, J. B. Foresman, J. V. Ortiz, Q. Cui, A. G. Baboul, S. Clifford, J. Cioslowski, B. B. Stefanov, G. Liu, A. Liashenko, P. Piskorz, I. Komaromi, R. L. Martin, D. J. Fox, T. Keith, M. A. Al-Laham, C. Y. Peng, A. Nanayakkara, M. Challacombe, P. M. W. Gill, B. Johnson, W. Chen, M. W. Wong, C. Gonzalez, J. A. Pople, *Gaussian 03*, release B.05, Wallingford, CT, USA, **2004**.
[13] In the optimised structure, HCl is H-bonded to the oxygen atom of coordinated dimethyl sulfoxide.
[14] V. Y. Kukushkin, A. J. L. Pombeiro, C. M. P. Ferreira, L.-I. Elding, *Inorg. Synth.* **2002**, *33*, 189–196.
[15] J. H. Price, A. N. Williamson, R. F. Schramm, B. B. Wayland, *Inorg. Chem.* **1972**, *11*, 1280.
[16] SAINT: *Siemens Analytical X-ray Instruments Inc*., Madison, Wisconsin, USA, **1995**.
[17] G. M. Sheldrick, University of Göttingen, Göttingen, Germany, **1996**.
[18] G. M. Sheldrick, *SHELXL97*, University of Göttingen, Göttingen, **1997**.

Received: March 21, 2006
Published Online: May 17, 2006

 © 2006 Wiley-VCH Verlag GmbH & Co. KGaA, Weinheim 

DOI: 10.1002/ejic.200600118

# Triple-Decker Transition-Metal Complexes $(C_nH_n)M(B_6C)M(C_nH_n)$ (M = Fe, Ru, Mn, Re; $n$ = 5, 6) Containing Planar Hexacoordinate Carbon Atoms

**Si-Dian Li,*[a] Chang-Qing Miao,[a] Guang-Ming Ren,[a] and Jin-Chang Guo[a]**

**Keywords:** Planar hexacoordinate carbon / Triple-decker transition-metal complexes / Density functional theory / Geometric structures / Electronic structure / IR spectroscopy

A density functional theory investigation is presented in this work on a new class of triple-decker complexes $(C_nH_n)M(B_6X)M(C_nH_n)$ (M = Fe, Ru, Mn, Re; X = B, C, N; $n$ = 5, 6) containing almost perfect planar hexacoordinate carbon atoms and other planar hexacoordinate nonmetals at the centers of the $B_6X$ middle-deckers. Effective d–π coordination interactions between the partially filled 3d orbitals of the transition-metal center and the delocalized π orbitals of the three parallel ligands maintain the stabilities of these triple-decker complexes. The strong IR absorption peaks of $(C_nH_n)M(B_6X)M(C_nH_n)$ complexes mainly originate from the in-plane and off-plane vibrations of their planar hexacoordinate nonmetal centers. The results obtained in this work provide a possible new approach to characterize planar hexacoordinate carbon-containing systems in future experiments and expand the structural domain of transition-metal complexes by introducing inorganic $B_6X$ middle-deckers into traditional sandwich-type structures.
(© Wiley-VCH Verlag GmbH & Co. KGaA, 69451 Weinheim, Germany, 2006)

## Introduction

As a challenge to tetrahedral carbon, which has dominated organic chemistry and biochemistry for over 130 years, planar tetracoordinate carbon (ptC) was first proposed by Hoffmann et al.[1] about 30 years ago and was recently observed in gas phases in $D_{4h}$ $Al_4C^-$,[2] $C_{2v}$ $Al_3XC$, $Al_3XC^-$ (X = Si, Ge),[3,4] and $[CAl_4]^{2-}$.[5] The smallest anion with a ptC at its center is $D_{2h}$ $C_5^{2-}$, which has been incorporated in various neutral molecules.[6] Theoretical studies on planar coordinate carbon atoms also include planar pentacoordinate carbon atoms (ppCs) in $B_3C_2H_2C$ and extended systems[7] and planar hexacoordinate carbon atoms (phCs) in the $B_6C^{2-}$ dianion.[8] Designing and characterizing new forms of planar coordinate C atoms remains a huge challenge in chemistry. In a series of recent works at density functional theory (DFT) level, our group developed a strategy to incorporate planar coordinate group IV elements at the centers of various hydrometal polygons, including ptC in $M_4H_4C$ (M = Cu, Ni),[9] ppC in $Cu_5H_5X$ (X = B, C, N, O),[10] planar pentacoordinate silicon (ppSi) in $M_5H_5X$ (M = Pd, Pt; X = Si, Ge),[11] and planar hexacoordinate silicon (phSi) in $Cu_6H_6X$ (X = Si, Ge) complexes.[12] Employing $B_6C^{2-}$ as an aromatic ligand, in a recent communication,[13] we incorporated quasi-phCs in a new class of sandwich-type complexes $(B_6C)_2M$ (M = Mn, Fe, Co, Ni). In this work at DFT level, we introduce $B_6C^{2-}$ to a novel class of triple-decker complexes $(C_nH_n)M(B_6C)M(C_nH_n)$ (M = Fe, Ru, Mn, Re; $n$ = 5, 6) that contain almost perfect phCs at the centers of the $B_6C$ middle-deckers. Similar results are also obtained for their isoelectronic complexes with planar hexacoordinate boron (phB) or planar hexacoordinate nitrogen (phN) centers. In the triple-decker[14] and multi-decker[15] complexes reported before, the hexanuclear benzene-centered tris(alkynyl triple-decker) complex[14] is particularly interesting, in which the three ligands around the benzene core are typical triple-decker complexes with a $C_2B_3$ ring as the middle-decker. However, to the best of our knowledge, there have been no triple-decker complexes with phCs, phBs, or phNs reported to date in the literature.

## Theoretical Method

As the phC-containing $B_6C^{2-}$ unit[8] is a 6π-electron aromatic dianion, while $C_5H_5^-$ is a 6π-electron monoanion, to meet the 18-electron requirements of the two $Fe^{II}$ centers, the most possible triple-decker structure of a dinuclear neutral $(C_5H_5)Fe(B_6C)Fe(C_5H_5)$ would contain a $B_6C^{2-}$ middle-decker to balance the overall molecular charge of the system, while the two $C_5H_5^-$ rings serve as terminal ligands, with the whole complex possessing a $C_{2v}$ symmetry. But a singlet $C_{2v}$ $(C_5H_5)Fe(B_6C)Fe(C_5H_5)$ turned out to be a transition state with one imaginary frequency. Relaxing the system in the imaginary vibrational mode leads to a slightly distorted $C_2$ structure that is a true minimum. The initially optimized structures with $C_2$ symmetries obtained at the hybrid DFT-B3LYP/6-31+G(d) level were refined comparatively with the bigger bases of 6-311+G(d,p) and 6-

[a] Institute of Materials Sciences and Department of Chemistry, Xinzhou Teachers' University, Xinzhou 034000, Shanxi, P. R. China

 © 2006 Wiley-VCH Verlag GmbH & Co. KGaA, Weinheim 

311+G(3df,p) and the optimized results turned out to be quite insensitive to the bases employed. When $C_5H_5^-$ terminal ligands are replaced with two neutral benzene molecules $C_6H_6$, two $Mn^I$ centers are required to replace $Fe^{II}$ to follow the 18-electron rule. Natural bond orbital (NBO) analyses[16] and zero-point energy (ZPE) corrections were performed in the frequency analyzing processes. Results obtained at B3LYP/6-311+G(d,p) level are presented in this work hereafter for the first-row transition-metal complexes. For heavy transition-metal complexes, we choose the basis of 6-31+G(d,p) for nonmetal atoms and Lanl2dz[17] (which contains an effective core potential for transition metals) for the second- and third-row transition metals. Figure 1 depicts the optimized structures that are true minima on their potential energy surfaces and Table 1 tabulates their geometrical and electronic properties. Figure 2 shows the typical molecular orbitals (MOs) of $C_2$ $(C_5H_5)Fe(B_6C)$-$Fe(C_5H_5)$ involving Fe 3d orbitals and the delocalized π orbitals of the three parallel ligands and Figure 3 demonstrates the calculated IR spectra of $C_2$ $(C_5H_5)Fe(B_6C)$-$Fe(C_5H_5)$ and $C_2$ $(C_6H_6)Mn(B_6C)Mn(C_6H_6)$ to facilitate future spectroscopic investigations. All the calculations in this work were performed using the Gaussian 03 program.[18]

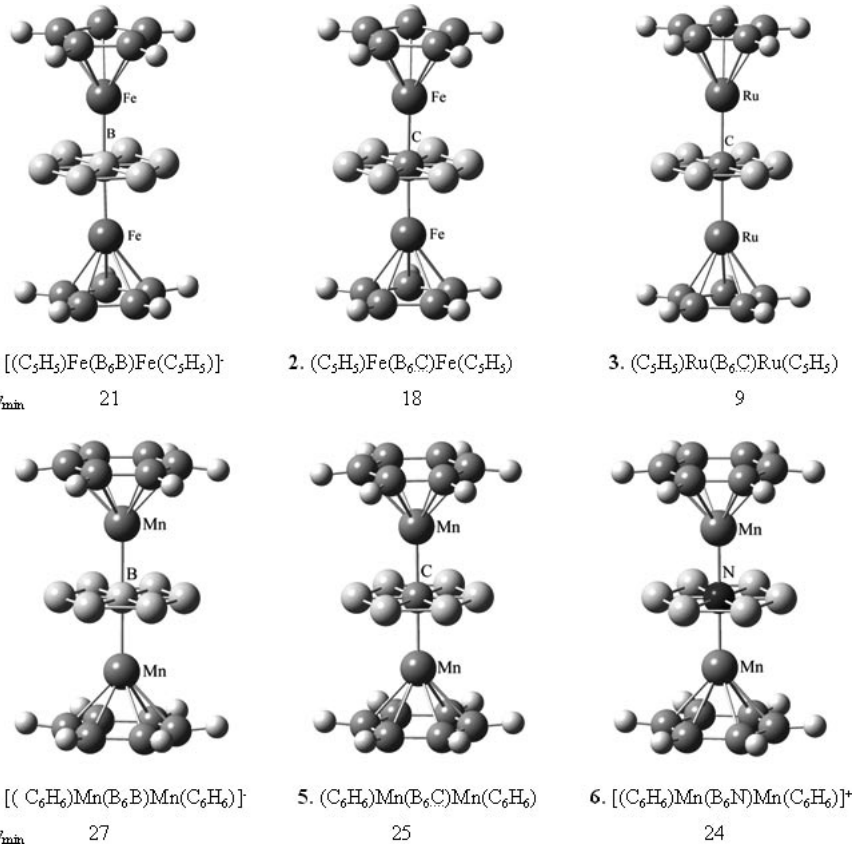


**1**. $[(C_5H_5)Fe(B_6B)Fe(C_5H_5)]^-$ $\tilde{\nu}_{min}$ 21

**2**. $(C_5H_5)Fe(B_6C)Fe(C_5H_5)$ 18

**3**. $(C_5H_5)Ru(B_6C)Ru(C_5H_5)$ 9

**4**. $[(C_6H_6)Mn(B_6B)Mn(C_6H_6)]^-$ $\tilde{\nu}_{min}$ 27

**5**. $(C_6H_6)Mn(B_6C)Mn(C_6H_6)$ 25

**6**. $[(C_6H_6)Mn(B_6N)Mn(C_6H_6)]^+$ 24

Figure 1. Optimized structures of $(C_nH_n)M(B_6X)M(C_nH_n)$ triple-decker complexes (M = Fe, Ru, Mn, Re; X = B, C, N; $n$ = 5, 6) containing planar hexacoordinate nonmetal centers, with the lowest vibrational frequencies $\tilde{\nu}_{min}$ ($cm^{-1}$) indicated.

Table 1. Averaged bond lengths $r$ [Å], M–phX–M bond angles $\theta$, HOMO energies $E_{HOMO}$ [eV], HOMO–LUMO energy gaps $\Delta E_{gap}$ [eV], and natural atomic charges $q_{phX}$ (|e|), and total Wiberg bond indices $WBI_{phX}$ of the phX centers of typical $(C_nH_n)M(B_6X)M(C_nH_n)$ complexes at DFT-B3LYP level.

| $(C_nH_n)M(B_6X)M(C_nH_n)$ | $r_{M-C}$ | $r_{M-B}$ | $r_{M-phX}$ | $r_{B-B}$ | $\theta$ | $E_{HOMO}$ | $\Delta E_{gap}$ | $q_{phX}$ | $WBI_{phX}$ |
|---|---|---|---|---|---|---|---|---|---|
| $(C_5H_5)Fe(B_6B)Fe(C_5H_5)^-$ | 2.059 | 2.510 | 1.913 | 1.624 | 177.2° | –1.82 | 3.53 | –0.68 | 3.92 |
| $(C_5H_5)Fe(B_6C)Fe(C_5H_5)$ | 2.057 | 2.474 | 1.884 | 1.603 | 177.8° | –5.70 | 3.52 | –0.96 | 3.85 |
| $(C_5H_5)Fe(B_6N)Fe(C_5H_5)^+$ | 2.064 | 2.464 | 1.845 | 1.619 | 177.9° | –9.68 | 3.47 | –1.12 | 3.01 |
| $(C_5H_5)Ru(B_6C)Ru(C_5H_5)$ | 2.190 | 2.606 | 2.047 | 1.612 | 179.1° | –5.76 | 3.59 | –1.02 | 3.73 |
| $(C_5H_5)Ru(B_6B)Ru(C_5H_5)^-$ | 2.197 | 2.620 | 2.046 | 1.638 | 178.7° | –1.88 | 3.45 | –0.73 | 3.91 |
| $(C_6H_6)Mn(B_6B)Mn(C_6H_6)^-$ | 2.092 | 2.542 | 1.956 | 1.624 | 180.0° | –1.76 | 3.73 | –0.57 | 3.92 |
| $(C_6H_6)Mn(B_6C)Mn(C_6H_6)$ | 2.104 | 2.500 | 1.919 | 1.603 | 180.0° | –5.36 | 3.72 | –0.90 | 3.89 |
| $(C_6H_6)Mn(B_6N)Mn(C_6H_6)^+$ | 2.124 | 2.472 | 1.871 | 1.618 | 180.0° | –9.12 | 3.50 | –1.08 | 3.05 |
| $(C_6H_6)Re(B_6C)Re(C_6H_6)$ | 2.217 | 2.587 | 2.012 | 1.626 | 180.0° | –4.83 | 3.25 | –1.02 | 3.75 |

 © 2006 Wiley-VCH Verlag GmbH & Co. KGaA, Weinheim 

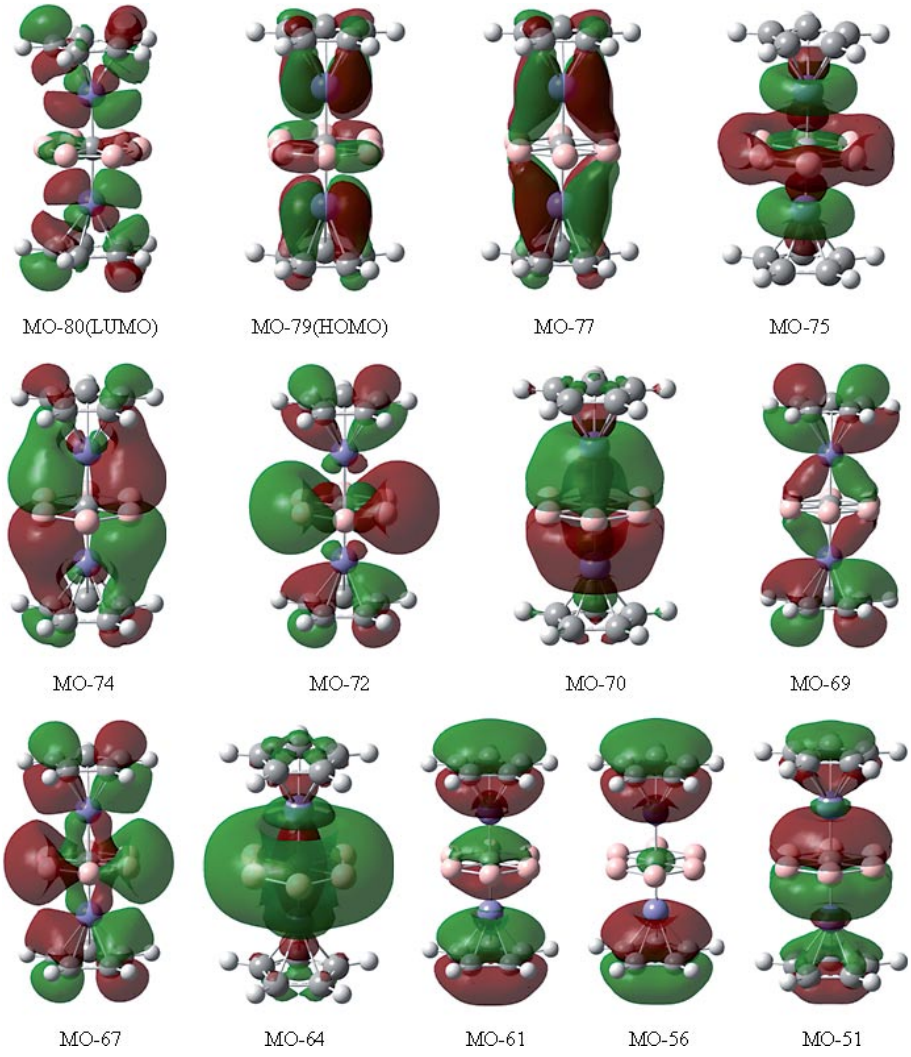


Figure 2. Typical MO pictures of $C_2$ $(C_5H_5)Fe(B_6C)Fe(C_5H_5)$ involving Fe 3d and the delocalized π orbitals of the three parallel ligands. For doubly degenerate orbitals, only one of them is depicted.

## Results and Discussion

As shown in Figure 1, all the triple-decker structures possess a real lowest vibrational frequency corresponding to rotations of the three parallel ligands about the M–phX–M molecular axis (with the two $C_nH_n$ terminal ligands rotating clockwise while the $B_6X$ middle-decker rotates anticlockwise) with a small energy barrier of about 2 kcal/mol, similar to the lowest-energy rotary vibrational modes of the well-known sandwich-type $(C_5H_5)_2Fe$ and $(C_6H_6)_2Cr$. But a singlet $C_2$ $(C_5H_5)Fe(B_6N)Fe(C_5H_5)^+$ monocation turned out to be a transition state with one imaginary frequency at 62i $cm^{-1}$ (an up-and-down movement of the $B_6$ ring along the Fe–phN–Fe axis). Structural analyses indicate that the three quasiplanar ligands intervened by two Fe atoms in the prototypic $C_2$ $(C_5H_5)Fe(B_6C)Fe(C_5H_5)$ are almost perfectly parallel to one another, with the three axial atoms of Fe, phC, and Fe being nearly collinear with the bond angle of $\theta_{Fe–phC–Fe}$ = 177.8° and the averaged bond lengths of $r_{Fe–C}$ = 2.057 Å, $r_{Fe–B}$ = 2.474 Å, $r_{Fe–phC}$ = 1.884 Å, and $r_{B–B}$ = 1.603 Å. All the $(C_nH_n)M(B_6X)M(C_nH_n)$ complexes (M = Fe, Ru; X = B, C, N; $n$ = 5, 6) possess very similar triple-decker structures featured with the $B_6X$ middle-deckers, which are almost perfect hexagons with phX atoms located at their geometrical centers and approximately equal B–B and phX–B bond lengths ($r_{B–B} \approx r_{phX–B}$). The B–B bond lengths in the middle-deckers of these complexes (see Table 1 for details) are slightly longer than the corresponding B–B distance of 1.594 Å in free $B_6C^{2-}$.[8] The calculated Fe–C bond lengths of 2.057 Å in $(C_5H_5)Fe(B_6C)Fe(C_5H_5)$ turned out to be very close to the corresponding measured values of 2.064 Å in ferrocene $(C_5H_5)Fe(C_5H_5)$,[19] while the Fe–phC distances of 1.884 Å are 0.224 Å longer than the corresponding Fe–phC distance in half-sandwich-type $(B_6C)Fe$.[13] This suggests that a triple-decker $(C_5H_5)Fe(B_6C)Fe(C_5H_5)$ complex could be constructed by inserting a half-sandwich-type $(B_6C)Fe$ into a ferrocene molecule $(C_5H_5)Fe(C_5H_5)$. The middle-decker $B_6C^{2-}$ in structure **2** acts as a bridge to link two half-sandwich-type $(C_5H_5)Fe$ together by forming two Fe–phC inter-

 © 2006 Wiley-VCH Verlag GmbH & Co. KGaA, Weinheim 

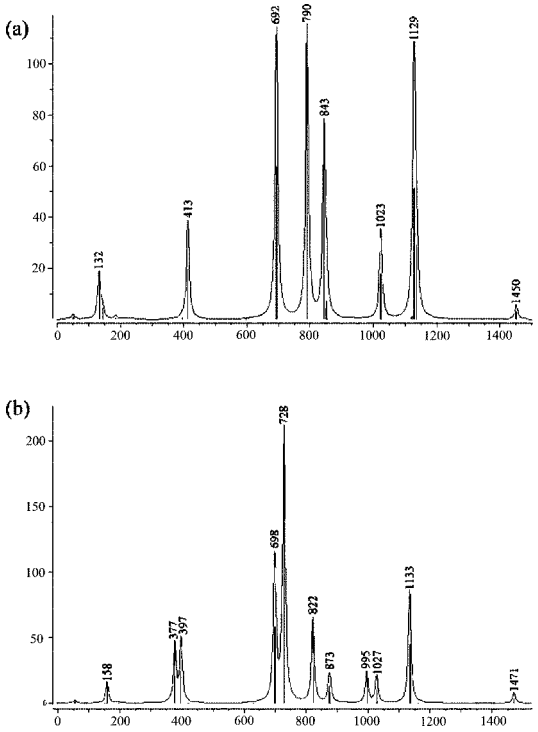


Figure 3. Calculated IR spectra (in $cm^{-1}$) of $C_2$ $(C_5H_5)Fe(B_6C)Fe(C_5H_5)$ (a) and $C_2$ $(C_6H_6)Mn(B_6C)Mn(C_6H_6)$ (b).

actions. Heavy transition-metal complexes $(C_5H_5)Ru(B_6X)Ru(C_5H_5)$ (X = C, B) with $C_2$ symmetries were confirmed to be transition states. With the $C_2$ symmetry constraints removed during structural optimization, these structures were slightly distorted to $C_1$ symmetries with the lowest frequencies ($\tilde{\nu}_{min}$) of 9 and 16 $cm^{-1}$ for X = C and B, respectively.

A triple-decker $(C_6H_6)Mn(B_6C)Mn(C_6H_6)$ (**5**) with a phC center and two neutral $C_6H_6$ terminal ligands has the averaged bond lengths of $r_{Mn-C}$ = 2.104 Å, $r_{Mn-phC}$ = 1.919 Å, $r_{Mn-B}$ = 2.500 Å, and $r_{B-B}$ = 1.603 Å. The three ligands are almost perfectly parallel to one another and the Mn–C distances of 2.104 Å are well in line with the measured Cr–C distance of $r_{Cr-C}$ = 2.15 Å in $D_{6h}$ $(C_6H_6)_2Cr$. With two $C_6H_6$ terminal ligands, both phB and phN can be stabilized at the centers of the $B_6X$ middle-deckers, as indicated in Figure 1 for structures **4** and **6**, which have bond lengths of $r_{Mn-phB}$ = 1.956 Å and $r_{B-B}$ = 1.624 Å in **4** and $r_{Mn-phN}$ = 1.871 Å and $r_{B-B}$ = 1.618 Å in **6**. A triple-decker $(C_6H_6)Re(B_6C)Re(C_6H_6)$ also turned out to be a stable singlet species with $\tilde{\nu}_{min}$ = 16 $cm^{-1}$.

The stabilities of the phC-containing $C_2$ $(C_5H_5)Fe(B_6C)Fe(C_5H_5)$ and $C_2$ $(C_6H_6)Mn(B_6C)Mn(C_6H_6)$ are supported by the negative thermodynamic quantity changes of the following processes starting from stable reactants [Equation (1)].

$$(C_5H_5)_2Fe(D_5) + (B_6C)Fe(C_{6v}) = (C_5H_5)Fe(B_6C)Fe(C_5H_5)(C_2) \quad (1)$$

$$(C_6H_6)_2Mn^+(D_{6h}) + (B_6C)Mn^-(C_{6v}) = (C_6H_6)Mn(B_6C)Mn(C_6H_6)(C_2) \quad (2)$$

In Equation (2), the monocation $(C_6H_6)_2Mn^+$ with $\tilde{\nu}_{min}$ = 32 $cm^{-1}$ and monoanion $(B_6C)Mn^-$ with $\tilde{\nu}_{min}$ = 301 $cm^{-1}$ are isoelectronic with $D_{6h}$ $(C_6H_6)_2Cr$ and $C_{6v}$ $(B_6C)Fe$,[13] respectively. With ZPE corrections included, $\Delta E(1)$ = –124.8, $\Delta H(1)$ = –122.8, $\Delta G(1)$ = –87.1, and $\Delta E(2)$ = –596.2, $\Delta H(2)$ = –594.9, $\Delta G(2)$ = –554.0 kJ/mol. These negative values indicate that the desired products are favored in thermodynamics relative to the corresponding reactants. Detailed kinetic studies are beyond the reach of available computing resources at this stage.

NBO analyses indicate that all the component atoms in these complexes follow the octet rule. For example, atoms in $(C_5H_5)Fe(B_6C)Fe(C_5H_5)$ (**1**) possess the total Wiberg bond indices (WBIs) of $WBI_{phC}$ = 3.85, $WBI_C$ = 3.96, $WBI_B$ = 3.50, $WBI_H$ = 0.94, and $WBI_{Fe}$ = 2.98, respectively. The middle-decker $B_6C$ in the complex has the bond orders of $WBI_{B-B}$ = 1.14 and $WIB_{B-phC}$ = 0.56, well in line with the corresponding bond orders of $WBI_{B-B}$ = 1.29 and $WIB_{B-phC}$ = 0.63 in free $B_6C^{2-}$.[8] The slight bond-order difference is well compensated for by two extra phC–Fe interactions in vertical directions with $WBI_{phC-Fe}$ = 0.20 and $WBI_{phC}$ = 3.85 to satisfy the bonding requirement of the central carbon atom. It is also interesting to notice that the phC centers in $(C_5H_5)Fe(B_6C)Fe(C_5H_5)$ (**2**), $(C_5H_5)Ru(B_6C)Ru(C_5H_5)$ (**3**), and $(C_6H_6)Mn(B_6C)Mn(C_6H_6)$ (**5**) carry approximately unitary negative charges, with $q_{phC}$ = –0.96|e|, –1.02|e|, and –0.90|e|, respectively. This implies that the phC centers possess approximately an extra electron in triple-decker complexes. It is this extra electron, which occupies the delocalized phC $2p_z$ orbital perpendicular to the $B_6C$ middle-decker, that helps to stabilize the phC center in the complex (see Figure 2), similar to the situation of three $sp^2$ hybrids plus a doubly occupied $2p_z$ orbital in ptC-containing systems.[1,6d,9]

NBO analyses help to understand the bonding nature of these triple-decker structures. As indicated in Table 1, all these complexes possess negative HOMO energies and their HOMO–LUMO energy gaps are greater than 3.25 eV. Orbital coefficients and the MO pictures shown in Figure 2 indicate that both the degenerate HOMO(MO-79) and MO-77 of $(C_5H_5)Fe(B_6C)Fe(C_5H_5)$ mainly involve the contributions from Fe $3d_{xy}$ and $3d_{x^2-y^2}$, while MO-75, MO-70, and MO-64 are mostly composed of different interactions between Fe $3d_{z^2}$ and the delocalized π or σ orbitals of the $B_6C^{2-}$ middle-decker. The degenerate MO-74 consists almost purely of the delocalized π orbital of the middle-decker $B_6C^{2-}$. Fe $3d_{xz}$ and $3d_{yz}$ orbitals mainly participate in the formations of the degenerate MO-72, MO-69, and MO-67, while MO-61, MO-56, and MO-51 originate almost purely from the out-of-phase or in-phase interactions between the totally delocalized π orbitals of the three parallel ligands (MO-51 also involves the in-phase contribution from Fe $3d_{z^2}$). It is these d–π and π–π interactions that work together to maintain the stabilities of these triple-decker structures. MO-80, the lowest unoccupied molecular orbital with a negative orbital energy of –2.18 eV, is mainly composed of the out-of-phase overlap between Fe $3d_{yz}$ and the delocalized π orbitals of the $C_5H_5^-$ ligands.

 © 2006 Wiley-VCH Verlag GmbH & Co. KGaA, Weinheim 

Frequency analyses indicate that the two strong IR absorptions of $C_2$ $(C_5H_5)Fe(B_6C)Fe(C_5H_5)$ at 692 $cm^{-1}$ and 1129 $cm^{-1}$ in Figure 3 (a) mainly originate from two in-plane vibrations of the phC center within the $B_6$ ring, while the other strong peak at 790 $cm^{-1}$ corresponds to an off-plane movement of the phC center perpendicular to its $B_6$ ligand. The unsymmetrical off-plane swings of the 10 H atoms in $C_5H_5$ ligands produce the IR absorption at 843 $cm^{-1}$ and their in-plane movements result in the absorption peak at 1023 $cm^{-1}$. The weak peak at 132 $cm^{-1}$ is the result of the up-and-down movements of the $B_6$ ring along the molecular axis; meanwhile, the peak at 413 $cm^{-1}$ corresponds to unsymmetrical swings of the two $C_5H_5$ ligands and the weakest peak at 1450 $cm^{-1}$ originates from their in-plane twisting vibrations. As shown in Figure 3 (b), similar vibrational modes exist for $C_2$ $(C_6H_6)Mn(B_6C)Mn(C_6H_6)$, with the off-plane vibrational mode of the phC center shifted to 728 $cm^{-1}$ while all the other absorption bands are basically maintained. The obvious correspondence in IR spectra between Figure 3a and Figure 3 (b) indicates that these complexes vibrate in similar vibrational modes that are closely related with the triple-decker geometries they possess.

## Summary

In summary, planar hexacoordinate nonmetal centers following the octet rule have been stabilized in triple-decker complexes $(C_nH_n)M(B_6X)M(C_nH_n)$ (M = Fe, Ru, Mn, Re; X = B, C, N; $n$ = 5, 6) in which the hexagonal $B_6X$ middle-deckers are well maintained, the metal–ligand ($M–C_nH_n$) distances possess normal M–C coordination bond lengths, and phX centers carry approximately unitary natural charges. It is the effective coordination interactions between the partially filled 3d orbitals of the transition-metal centers and the delocalized π orbitals of the three parallel ligands that help to stabilize these triple-decker structures. The strong IR absorptions of these complexes mainly originate from the in-plane and off-plane vibrational modes of their phX centers. As a complement to the initial proposal of $B_6C^{2-}$,[8] this work has introduced phCs and other nonmetal centers phXs at the centers of inorganic $B_6X$ middle-deckers to transition-metal triple-decker complexes, providing a possible new approach to synthesize phC-containing systems in future experiments.

## Acknowledgments

This work was jointly supported by the Natural Science Foundation of China (No. 20573088) and Shanxi Natural Science Foundation (No. 20021029).

[1] R. Hoffmann, R. W. Alder, C. F. Wilcox Jr, *J. Am. Chem. Soc.* **1970**, *92*, 4992.
[2] X. Li, L.-S. Wang, A. I. Boldyrev, J. Simons, *J. Am. Chem. Soc.* **1999**, *121*, 6033.
[3] L. S. Wang, A. I. Boldyrev, X. Li, J. Simons, *J. Am. Chem. Soc.* **2000**, *122*, 7681.
[4] X. Li, H.-J. Zhai, L.-S. Wang, *Chem. Phys. Lett.* **2002**, *357*, 415.
[5] X. Li, H.-F. Zhang, L.-S. Wang, G. D. Geske, A. I. Boldyrev, *Angew. Chem. Int. Ed.* **2000**, *39*, 3630.
[6] a) G. Merino, M. A. Mendez-Rojas, A. Vela, *J. Am. Chem. Soc.* **2003**, *125*, 6026; b) G. Merino, M. A. Mendez-Rojas, H. I. Beltran, C. Corminboeuf, T. Herine, A. Vela, *J. Am. Chem. Soc.* **2004**, *126*, 16160; c) N. Perez, T. Herine, R. Barthel, G. Seifert, A. Vela, M. A. Mendez-Rojas, G. Merino, *Org. Lett.* **2005**, *7*, 1509; d) P. M. Esteves, M. B. P. Ferreira, R. J. Correa, *J. Am. Chem. Soc.* **2005**, *127*, 8680.
[7] Z.-X. Wang, P. v. R. Schleyer, *Science* **2001**, *292*, 2465.
[8] K. Exner, P. v. R. Schleyer, *Science* **2000**, *290*, 1937.
[9] S.-D. Li, G.-M. Ren, C.-Q. Miao, J.-C. Guo, *Angew. Chem. Int. Ed.* **2004**, *43*, 1371.
[10] S.-D. Li, C.-Q. Miao, G.-M. Ren, *Eur. J. Inorg. Chem.* **2004**, 2232.
[11] S.-D. Li, C.-Q. Miao, *J. Phys. Chem. A* **2005**, *109*, 7594.
[12] S.-D. Li, G.-M. Ren, C.-Q. Miao, *Inorg. Chem.* **2004**, *43*, 6331.
[13] S.-D. Li, J.-C. Guo, C.-Q. Miao, G.-M. Ren, *Angew. Chem. Int. Ed.* **2005**, *44*, 2158.
[14] H. Yao, M. Sabat, R. N. Grimes, *Organometallics* **2002**, *21*, 2833.
[15] J. Wang, P. H. Acioli, J. Jelinek, *J. Am. Chem. Soc.* **2005**, *127*, 2812.
[16] a) J. E. Carpenter, F. Weinhold, *J. Mol. Struct. (Theochem)* **1988**, *169*, 41; b) J. P. Foster, F. Weinhold, *J. Am. Chem. Soc.* **1980**, *102*, 7211.
[17] a) P. J. Hay, W. R. Wadt, *J. Chem. Phys.* **1985**, *82*, 270; b) P. J. Hay, W. R. Wadt, *J. Chem. Phys.* **1985**, *82*, 299; c) T. H. Dunning Jr, P. J. Hay in *Modern Theoretical Chemistry* (Ed.: H. F. Schaefer III), Plenum, New York, **1976**, vol. 3, pp. 1–28.
[18] M. J. Frisch, G. W. Trucks, H. B. Schlegel, G. E. Scuseria, M. A. Robb, J. R. Cheeseman, J. A. Montgomery Jr, T. Vreven, K. N. Kudin, J. C. Burant, J. M. Millam, S. S. Iyengar, J. Tomasi, V. Barone, B. Mennucci, M. Cossi, G. Scalmani, N. Rega, G. A. Petersson, H. Nakatsuji, M. Hada, M. Ehara, K. Toyota, R. Fukuda, J. Hasegawa, M. Ishida, T. Nakajima, Y. Honda, O. Kitao, H. Nakai, M. Klene, X. Li, J. E. Knox, H. P. Hratchian, J. B. Cross, C. Adamo, J. Jaramillo, R. Gomperts, R. E. Stratmann, O. Yazyev, A. J. Austin, R. Cammi, C. Pomelli, J. W. Ochterski, P. Y. Ayala, K. Morokuma, G. A. Voth, P. Salvador, J. J. Dannenberg, V. G. Zakrzewski, S. Dapprich, A. D. Daniels, M. C. Strain, O. Farkas, D. K. Malick, A. D. Rabuck, K. Raghavachari, J. B. Foresman, J. V. Ortiz, Q. Cui, A. G. Baboul, S. Clifford, J. Cioslowski, B. B. Stefanov, G. Liu, A. Liashenko, P. Piskorz, I. Komaromi, R. L. Martin, D. J. Fox, T. Keith, M. A. Al-Laham, C. Y. Peng, A. Nanayakkara, M. Challacombe, P. M. W. Gill, B. Johnson, W. Chen, M. W. Wong, C. Gonzalez, J. A. Pople, *Gaussian 03*, Revision A.1, Gaussian, Inc., Pittsburgh, PA, **2003**.
[19] A. Haaland, *Acc. Chem. Res.* **1979**, *12*, 415.

Received: February 9, 2006
Published Online: April 10, 2006

 © 2006 Wiley-VCH Verlag GmbH & Co. KGaA, Weinheim 

DOI: 10.1002/ejic.200501140

# High-Zirconium-Content Nano-Sized Bimodal Mesoporous Silicas

David Ortiz de Zárate,[a] Andrés Gómez-Moratalla,[a] Carmen Guillem,[a] Aurelio Beltrán,[a] Julio Latorre,[a] Daniel Beltrán,[a] and Pedro Amorós*[a]

**Keywords:** Mesoporous materials / Zirconia / Surfactants / Nanoparticles / Bimodal porous materials

Silica-based nanoparticulated bimodal mesoporous materials with high Zr content ($43 \geq Si/Zr \geq 4$) have been synthesized by a one-pot surfactant-assisted procedure from a hydroalcoholic medium using a cationic surfactant (CTMABr = cetyltrimethylammonium bromide) as structure-directing agent, and starting from molecular atrane complexes of Zr and Si as hydrolytic inorganic precursors. This preparative technique allows optimization of the dispersion of the Zr guest species in the silica walls. The bimodal mesoporous nature of the final high surface area nano-sized materials is confirmed by XRD, TEM, and $N_2$ adsorption–desorption isotherms. The small intraparticle mesopore system (with pore sizes around 2–3 nm) is due to the supramolecular templating effect of the surfactant, while the large mesopores (around 12–24 nm) have their origin in the packing voids generated by aggregation of the primary nanometric mesoporous particles. The basicity of the reaction medium seems to be a key parameter in the definition of this last pore system. The effects induced by the progressive incorporation of Zr atoms on the mesostructure have been examined, and the local environment of the Zr sites in the framework has been investigated by UV/Vis spectroscopy. Observations based on the consequences of post-treatments of the as-synthesized materials with HCl/ethanol mixtures corroborate that the atrane method leads to Zr-rich materials showing enhanced site accessibility and high chemical homogeneity throughout the pore walls.
(© Wiley-VCH Verlag GmbH & Co. KGaA, 69451 Weinheim, Germany, 2006)

## Introduction

Silicon/zirconium mixed oxides, $(SiO_2)_{1-x}(ZrO_2)_x$, have attracted considerable attention for a long time because of their mechanical (low thermal-expansion coefficient) and chemical (resistance to alkaline attack) properties.[1–7] Moreover, they are also interesting materials in catalysis. Indeed, they exhibit catalytic activity due to both their moderate acidity and oxidizing capability, and also can be used as catalyst supports.[8] However, the possibility for industrial applications has been limited because these materials generally show low surface area and no size selectivity.[9,10] Hence, the search for improved-performance (high surface area) catalysts stimulated the preparation of $(SiO_2)_{1-x}(ZrO_2)_x$ solids in the form of particulated xerogels, which was approached through a diversity of sol-gel routes starting from alkoxide precursors.[11–13] The structure of these xerogels was studied some time ago by SAXS and WAXS techniques,[14] which revealed a very open architecture (involving interconnected 3D pore systems) that has been recently referred to as optimal for catalytic applications.[15] In practice, the $(SiO_2)_{1-x}(ZrO_2)_x$ particulated xerogels are high surface area catalysts displaying strong acidity and showing satisfactory activity in a diversity of organic reactions (cumene dealkylation, alcohol dehydration, alkene isomerization).[16–18]

However, the use of these $(SiO_2)_{1-x}(ZrO_2)_x$ xerogels as catalysts presents a certain limitation derived from their lack of size selectivity.[9,10] Until now, the most promising strategies to overcome this problem have been those conceived to incorporate Zr atoms into the frameworks of molecular sieves or high surface area silica-based materials.[19–21] Thus, there are reports on Zr-containing materials derived from both microporous solids (such as zeolites and also ALPOS)[22–25] and mesoporous silicas (Zr-MCM-41, Zr-MCM-48, Zr-HMS, Zr-MSU, Zr-SBA-15),[26–39] which simultaneously display high surface area and size selectivity. Hence, a diversity of both small and large substrates could be processed with the help of such a variety of Zr-containing molecular sieves.

In short, the preparative procedures implemented for incorporating zirconium in silica-based porous matrices can be referred to as one-pot (cohydrolysis) methods[26,32,34–36,38,39] or postsynthesis (grafting) treatments.[33,37] Independent of the synthesis strategy used, an important condition for having very active supported zirconia catalysts (high-Zr-content materials) lies in site isolation: the Zr atoms must be isolated and well dispersed throughout the silica walls, thus avoiding the formation of $ZrO_2$ domains.[40] In fact, while the preparation of doped mesoporous silicas is straightforward and usually leads to a relatively homogeneous distribution of cations, the situation changes when high dopant loads are required, and we must

[a] Institut de Ciència dels Materials (ICMUV), Universitat de València,
P. O. Box 2085, 46071 València, Spain
Fax: +34-96-3543633
E-mail: pedro.amoros@uv.es

 InterScience © 2006 Wiley-VCH Verlag GmbH & Co. KGaA, Weinheim 

face a complex chemistry plagued with problems, which often results in the absence of chemical homogeneity, phase segregation or mesostructure collapse.[41] Careful manipulation of the templating chemistry is thus required.

The origin of these problems lies in the different hydrolytic reactivity of elements such as Si and Zr (unequal hydrolysis and condensation reaction rates).[36,41] In practice, zirconium species usually hydrolyze faster than silicon precursors. In most cases, this results in partial segregation of $ZrO_2$ domains (together with a decrease of the Zr/Si molar ratio in the resulting mixed oxide with respect to the mother solution). Insofar as the catalysts' efficacy substantially depends on their purity and chemical homogeneity, phase segregation must be avoided. The goal of a variety of one-pot (cohydrolysis) synthesis procedures developed over the past few years was to circumvent this reactivity problem. Among the alternatives described, we can emphasize the utilization of Zr-complexing precursor species,[36,42] the use of single-source molecular precursors,[43] the optimization of the inorganic precursors and the pH,[44] the use of microwaves in the processing,[34] the application of hydrothermal post-treatments,[39] or chemical control based on adjusting the reaction conditions.[35] In this context, our group reported on how [using the atrane route,[45,46] that is to say starting from kinetically inert molecular atrane precursors (complexes of Si and Zr containing triethanolamine-derived ligands)] it is possible to orchestrate the Zr and Si hydrolytic reaction rates, thus leading to thermally stable Zr-MCM-41 porous silicas whose composition ranges from doped silicas to very-high-Zr-content materials ($\infty \geq Si/Zr \geq 0.3$).[36]

It should be emphasized that the main concern in these previous valuable investigations is the heteroelement (Zr) incorporation. Less attention has been paid to the site accessibility and connectivity in these silica-based catalysts, which also is a key for catalytic efficiency.[15] A strategy to deal with the site accessibility problem that recently has attracted interest is conceptually based on the consequences of decreasing the mesoporous particle size in the nanoparticle range.[15] This necessarily implies, at first, the shortening of the mesopore length, whereas the particle packing would generate supplementary interparticle porosity. The one-pot synthesis of functionalized (with inorganic elements and/or organic groups) nanoparticulated bimodal porous silicas was initially described by Pauly et al.[47] (Al-HMS materials) and El Haskouri et al.[48,49] (M-UVM-7 solids, M = Al, Ti, V, and Zr; HPNOs), who used in their processes a single surfactant (non-ionic, HMS; cationic, M-UVM-7, and HPNOs). In order to find applications, Pauly et al. demonstrated the benefits of this nanoparticle-based architecture by showing how the use of Al-HMS (average particle size $< 200$ nm) instead of Al-MCM-41 improves the yield in the catalytic alkylation of 2,4-di-*tert*-butylphenol with cinnamyl alcohol.[47] A two-step process for obtaining similar materials has recently been reported.[50] In any case, it must be noted that, until now, the heteroelement amounts which have been possible to incorporate into these nanoparticulated catalysts have not been too high (in the zirconia-supported materials we are dealing with, the upper limit was established at Si/Zr = 50 in ref.[48] vs. Si/Zr = 20 in ref.[50], although in this last case there is insufficient analytical information).

As mentioned in this Introduction, following previous work on related materials, we recently succeeded in synthesizing a novel family of nanoparticulated bimodal mesoporous pure and doped silicas, and published some of our preliminary results as a short communication.[48] On this basis, insofar as the interest on improved zirconia catalysts remains, we considered the possibility of transferring the mentioned nanoparticulated organization from the already explored limit of doped silicas up to the field of truly $(SiO_2)_{1-x}(ZrO_2)_x$ mixed oxides. We have succeeded in this aim, and this work describes the one-pot reproducible surfactant-assisted procedure that has allowed us to synthesize high-Zr-content nanoparticulated bimodal mesoporous silicas displaying high chemical homogeneity (good dispersion of the active sites) and a considerable amount of accessible Zr centers. The resulting Zr-UVM-7 solids bring together high heteroelement contents, the size selectivity provided by the surfactant-generated mesopores, and the high accessibility typical of xerogels. The effects of the presence of Zr atoms on the mesostructure have been examined, and the main features characterizing the Zr sites in the framework have been elucidated.

## Results and Discussion

### Synthesis Strategy

Bimodal mesoporous materials of the UVM-7 type that are rich in Zr atoms have been synthesized through a one-pot approach using CTABr as surfactant in a $TEAH_3$/water medium (CTABr = cetyltrimethylammonium bromide; $TEAH_3$ = triethanolamine) (see Exp. Sect.). Summarized in Table 1 are the main synthesis variables and physical data concerning the Zr-UVM-7 materials prepared in this way.

Our synthesis strategy has been designed both to overcome problems associated with the great reactivity differences that characterize the most usual Zr and Si precursor species (because of the lower electronegativity of Zr and its tendency to exhibit multiple coordination states) and to preserve, as far as possible, the nanoparticulated bimodal porous organization typical of UVM-7 silicas.[48] As mentioned above, this protocol is a modification of the so-called "atrane route", a simple preparative technique whose main points have been described previously in detail.[45] In fact, such a method has allowed us to successfully prepare a diversity of unimodal mesoporous single and mixed oxides, including the Zr-MCM-41 materials,[36] working under strongly basic conditions (pH = 11–12).[51–56] In contrast, in the case we are dealing with, the synthesis pH was buffered at ca. 9. It has been proven that these comparatively mild basic conditions favor the nucleation and growth of silica-based small nanoparticles,[48] thus avoiding the formation of relatively large particles typical of the MCM-41-like materials. In any case, the presence of atrane complexes

 © 2006 Wiley-VCH Verlag GmbH & Co. KGaA, Weinheim 

Table 1. Selected physicochemical properties of Zr-UVM-7 materials.

| | Si/Zr | | $a_0$ | $\Delta_0$ | BET area | Pore size | | Pore vol. | | Wall thickness |
|---|---|---|---|---|---|---|---|---|---|---|
| | Gel | Solid[a] | [nm][b] | [nm][c] | [$m^2$/g] | Small pore [nm][d] | Large pore [nm][d] | Small pore [$cm^3$/g][d] | Large pore [$cm^3$/g][d] | [nm][e] |
| 1 | 50 | 43 | 4.73 | 0.58 | 1146 | 2.99 | 24.2 | 1.03 | 1.58 | 1.74(2) |
| 2 | 25 | 19 | 4.62 | 0.52 | 1036 | 2.80 | 14.6 | 0.83 | 0.99 | 1.82(2) |
| 3 | 12 | 11 | 4.54 | 0.48 | 1001 | 2.75 | 12.1 | 0.79 | 0.66 | 1.79(2) |
| 4 | 5 | 4 | 4.55 | 0.47 | 846 | 2.70 | 12.6 | 0.63 | 0.68 | 1.85(2) |

[a] Si/Zr molar ratio in the porous samples estimated from EPMA. [b] Cell parameter calculated assuming a hexagonal cell [$a_0 = 2 \cdot d(100)/3^{1/2}$]. [c] Shrinkage after calcination (from XRD) defined as $\Delta_0 = a_0$(as-synthesized) – $a_0$(mesoporous). [d] Calculated from the adsorption branch of the isotherms and using the BJH model. [e] Pore wall thickness defined as $a_0$ – BJH small pore size.

in solution at the working pH, before and after water addition, has been confirmed by FAB-MAS. This study has been carried out firstly on independent Si- or Zr-containing solutions in which the reagent proportions are the same used in the preparation of the Zr-UVM-7 porous materials described in this work. In the absence of water, the majority species for both Si and Zr solutions correspond to M(TEA)-$(TEAH_2)$ [M = Si (100%) or Zr (100%)] monomers, and only in the Si case have additional entities been detected [$Si_2(TEA)_2TEAH$ and $Si_3(TEA)_4$], in very low proportions (12 and 15%, respectively). The relative intensities have been calculated without considering the peaks associated with the dissolvent. In contrast to previous experiments carried out at pH = 11,[36] the presence of oligomers is now practically negligible. Immediately after water addition, and independent of the pH ($9 < pH < 11$), both the Si and Zr atrane complexes remain in solution as monomers, $M(TEA)^+$ and M(TEA)OH (M = Si or Zr) being the majority hydrolyzed species. Later, the corresponding FAB signals progressively disappear as the sol evolves to gel. On the other hand, it must be emphasized that additional FAB-MAS experiments carried out on solutions containing both elements (Si and Zr) reveal (before and after water addition) the presence of the same species as in the independent solutions, which allows us to reasonably conclude that formation of binary (containing both Si and Zr entities) atrane complexes can be discarded. Thus, the precursor solution appears to mainly consist of a random intimate mixture of independent Zr and Si molecular monomeric fragments. In conclusion, although the proportion of oligomer species in the absence of water is dependent on the basicity of the medium, the use in the present case of moderately basic conditions (pH ≈ 9) to favor the formation of nanoparticulated materials does not seem to alter the nature of the Si and Zr species in hydroalcoholic solution (with regard to previous synthesis in more basic media). In other words, irrespective of the nature (condensation degree) of the starting atranes (pH-dependent), the hydrolyzed species become similar. In this way, the already studied role played by $TEAH_3$ in order to orchestrate the hydrolytic reactions of the Si and Zr precursor species[36] is preserved in the current synthesis of the Zr-UVM-7 solids. Finally, once the hydrolytic reactions have been completed, the total concentration of soluble silica can be accounted for by $Si(OH)_4$ and $(HO)_3SiO^-$ species in an approximate ratio of 10:1.6,[57,58] while the majority Zr species should be the $Zr(OH)_5^-$ monomer.[59] The subsequent condensation processes will proceed from these monomeric entities. In this sense, we can refer to a recent study on the condensation processes involving silicon and zirconium alkoxides, which demonstrates the formation of copolymerized tridimensional products in reaction media rich in water.[60] Then, the condensation processes of the hydrolyzed units must provide charged (anionic) binary (Si and Zr) oligomers that could match (by displacement of $Br^-$ anions) with cationic surfactant aggregates [$(CTMA)_{mm}^+$] following an $S^+I^-$ mechanism.

As mentioned above, the pH constitutes the key parameter to obtain nanoparticulated materials of this type. The working conditions (pH ≈ 9) have been selected in order to achieve high hydrolysis and condensation reaction rates and also low silica back solution.[57] Thus, silica polymerization is fastest at pH values in the range of 8–9, and the silica solubility reaches a minimum at pH ≈ 8.[57,58] Under these conditions, we favor (1) supersaturation, a necessary condition for the formation of a large number of small primary mesoporous nanoparticles, and (2) limited particle growth, as a consequence of the low silica solubility. Moreover, the incorporation of Zr helps to decrease the solubility. It is well known that the presence of heteroelements (such as Al or Zr) in the silica framework, even in low proportions, increases in a significant way the insolubility of the resulting doped or mixed oxides with regard to those of the respective individual oxides.[57] This property of Si/Zr mixed oxides has been exploited to prepare alkali-resistant filtration membranes based on mesoporous Zr-MCM-48 materials.[61]

Once the primary particles have been formed, the generation of a large pore system (see below) should be a consequence of their aggregation, which mainly implies the establishment of Si–O–Si interparticle covalent links (which might be kinetically favored in the presence of $Zr^{IV}$).[43] Moreover, as occurs in the case of xerogels, the presence of Zr favors the interparticle condensation reactions and leads to clusters more dense than those originated by the analogous pure silica derivatives.[14] This behavior may be attributed to the development of cross-linking through Zr centers between individual particles (Zr–O–Si or Zr–O–Zr bridges), as expected from the affinity of Zr atoms for higher oxygen coordination environments. Particle aggregation is a sol-gel process, which probably is the result of base-catalyzed interparticle collisions.[57] In short, the Zr incorporation into the silica walls helps to promote the nucleation of very insolu-

 © 2006 Wiley-VCH Verlag GmbH & Co. KGaA, Weinheim 

ble small nano-sized mesoporous particles, which in turn favors the stabilization of the UVM-7-like organization.

### Characterization

We have used EPMA both to determine the real amounts of Zr incorporated into the framework and also to check the chemical homogeneity of the resulting solids [a relevant objective of our work was to preserve, under the new working conditions, good dispersion of the heteroelement (Zr) in the walls of the resulting materials, which usually is achieved through the atrane route]. Summarized in Table 1 are the corresponding Si/Zr molar ratio values (averaged from data of about 50 different particles) of the resulting solids. EPMA shows that the reported Zr-UVM-7 materials contain Si/Zr molar ratios similar to those present in the mother solutions. This fact indicates that, in general, there is no preferential incorporation of Zr or Si into the final porous walls. However, we observe a certain increase of the Zr proportion in the case of the solids prepared from the precursor solutions having the lowest Zr contents (Si/Zr = 50 and 25). This result could be associated with the comparatively low solubility of the Zr-containing species (with regard to the pure silica ones), the effect of which should decrease as the amount of well-dispersed Zr centers increases. On the other hand, EPMA also shows that all Zr-UVM-7 samples are chemically homogeneous (have regular distributions of Zr and Si atoms) at the micrometer level (spot area $\approx$ 1 μm) with a constant and well-defined composition. Hence, the Zr-UVM-7 solids can be considered as monophasic products. In fact, segregation of extra-framework crystalline $ZrO_2$ can be practically discarded even for the samples having the highest Zr content (although formation of $ZrO_2$-like amorphous nanodomains might progress as the Zr content increases). This result is consistent with the absence of zirconia peaks in the high-angle region of the XRD patterns. In short, according to our initial hypothesis, we can conclude that the use of atrane precursors results in the harmonization of the rates of the hydrolytic processes involving the corresponding Si and Zr species, which facilitates the incorporation of relatively high amounts of the heteroelement (Zr). Indeed, the amounts of Zr which are incorporated into Zr-UVM-7 solids are higher than those usually achieved in other related silica-based materials prepared from conventional Si and Zr sources (for a given Si/Zr initial ratio). Even more, as mentioned above, the use of the atrane route allows very-high-Zr-content porous silicas to be obtained, but the nanoparticulated organization of the material we are looking for is lost when the Si/Zr molar ratio becomes smaller than 4:1.

The TEM images in Figure 1 clearly show that the UVM-7-like organization is maintained in the compositional range of 43 $\geq$ Si/Zr $\geq$ 4. All solids present a continuous nanometric array constructed from aggregates of nano-sized mesoporous particles, which include two different pore systems: (1) the first one can be related to the porogen effect of the surfactant-templating micelles, which generates the small intraparticle regular mesopores organized in a short-range hexagonal-ordering array, and (2) the second one consists of large cage-like interparticle pores and corresponds to the voids appearing as a consequence of the collision and aggregation of the primary nanoparticles. According to its origin, this second pore system presents a nonordered character similar to that defining the cross-linked network in nanoparticulated xerogels.[62,63]

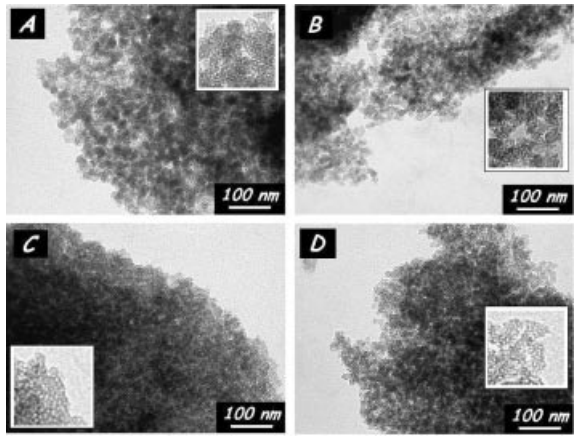


Figure 1. Representative TEM images of Zr-UVM-7 materials: (A) Sample 1 (Si/Zr = 43), (B) Sample 2 (Si/Zr = 19), (C) Sample 3 (Si/Zr = 11), and (D) Sample 4 (Si/Zr = 4). The insets show enlarged (×3) TEM images.

On the other hand, a careful analysis of the TEM images allows certain tendencies in the variation of both the particle morphology and the progress of the cluster-like aggregation with the Zr content to be established. Thus, the average particle size slightly decreases as the Zr content increases. The progressive Zr incorporation also favors the formation of denser aggregates, reflecting a more efficient packing of the primary nanoparticles. Such an evolution of the mesostructure can be firstly related to the solubility decrease induced by the Zr incorporation. Thus, the particle growth decreases as the insolubility of the nanoparticles increases. Moreover, the ability of Zr atoms to increase their coordination number favors the interparticle connectivity (based on Si–O–Si covalent bonds) through (additional) Zr–O–Zr or Zr–O–Si links. This results in an interparticle shrinkage similar to that observed in xerogels.[14] These tendencies can be better appreciated by comparing a pure UVM-7 silica with a Zr-containing derivative (Figure 2). The micrographs in Figure 2 clearly show how the incorporation of Zr atoms also involves a change in the particle morphology. Indeed, while the UVM-7 pure silica exhibits aggregates defined by regular elliptical nanoparticles, these primary building blocks in the Zr-UVM-7 materials present an irregular and angular shape. It is well known that, independently of the particle size (nano- or micrometric Stöber-like silica particles), the incorporation of Zr (or another heteroelement) strongly affects the regular growth of the silica spheres, thus leading to irregular particles. A similar morphologic evolution with the Zr content was described previously for Zr-containing silica xerogels.[14]

 © 2006 Wiley-VCH Verlag GmbH & Co. KGaA, Weinheim 

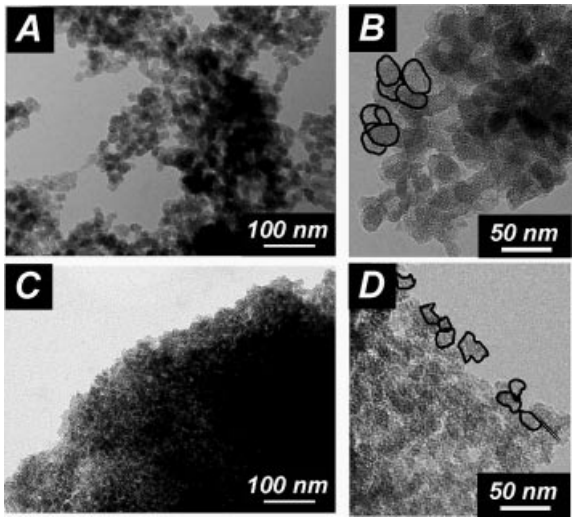


Figure 2. Comparative TEM micrographs of (Zr-free) UVM-7 silica (A and B) and Zr-UVM-7 Sample 3 (C and D).

The characteristics of the intraparticle mesopore array have been further studied by XRD with results that fully correlate to TEM observations. All materials (as-synthesized and calcined) display XRD patterns with at least one strong diffraction peak in the low-angle region, which is characteristic of mesostructured solids. The low-angle region of the XRD patterns corresponding to the mesoporous (calcined) samples is shown in Figure 3. In all these last cases, apart from the intense peak at low $2\theta$ values [associated with the (100) reflection if a basic hexagonal cell is assumed],[64] we can observe a broad signal of relatively low intensity that can be indexed to the overlapped (110) and (200) reflections of the typical hexagonal cell. The observation of this last unresolved broad signal is characteristic of an MCM-41-like short-range hexagonal intraparticle mesopore topology. We can also notice the decrease of the relative intensity of this broad signal with the Zr content (it appears as a shoulder on the main peak for samples in which Si/Zr $\leq$ 19). Such an evolution is indicative of a progressive lowering of order in the mesopore array as the Zr amount incorporated into the silica walls increases. The lattice parameter value remains practically unchanged in the range of 43 $\geq$ Si/Zr $\geq$ 4 for both the as-synthesized (about $5.20 \pm 0.13$ nm) and porous (about $4.64 \pm 0.10$ nm) materials. Assuming the effective incorporation of Zr atoms in the silica framework, this result might seem a priori unreasonable [even more so when compared to the values of the $a_0$ parameter of the mesostructured (5.13 nm) and calcined (4.91 nm) UVM-7 pure silica]. To understand this behavior, it is necessary to consider two opposite phenomena: (1) cell expansion due to the replacement of Si atoms with Zr ones, and (2) strong intraparticle network-shrinkage associated with the cross-linking ability of Zr, which is enhanced after calcination. As shown in Table 1, the contraction of the $a_0$ parameter upon calcination for the Zr-containing materials (about $0.51 \pm 0.07$ nm) is significantly higher than that observed for the Zr-free UVM-7 silica (0.22 nm).[65] It must be emphasized that this significant shrinkage is similar to those observed in the cases of Zr-MCM-41[36] and (pure) $ZrO_2$[66] mesoporous solids prepared through surfactant-assisted procedures.

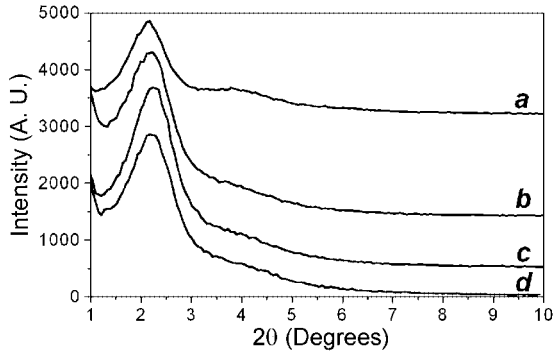


Figure 3. Low-angle XRD patterns of Zr-UVM-7 materials: (a) Sample 1 (Si/Zr = 43), (b) Sample 2 (Si/Zr = 19), (c) Sample 3 (Si/Zr = 11), and (d) Sample 4 (Si/Zr = 4).

The $N_2$ adsorption–desorption isotherms gathered in Figure 4 corroborate that the bimodal pore system typical of nanoparticulated UVM-7 silicas is maintained in the Zr-UVM-7 (43 $\geq$ Si/Zr $\geq$ 4) materials. The curves show, in all cases, two well-defined adsorption steps (at intermediate and high partial pressures). The adsorption at $P/P_0$ values in the range of 0.25–0.50 can be related to capillary condensation of nitrogen inside the cylindrical intraparticle surfactant-templated mesopores. The second adsorption at $P/P_0 > 0.65$ corresponds to the filling of the large cage-like interparticle voids. Application of the BJH model (see Figure 5) allows independent analysis of the evolution with the Zr content of the two pore systems.

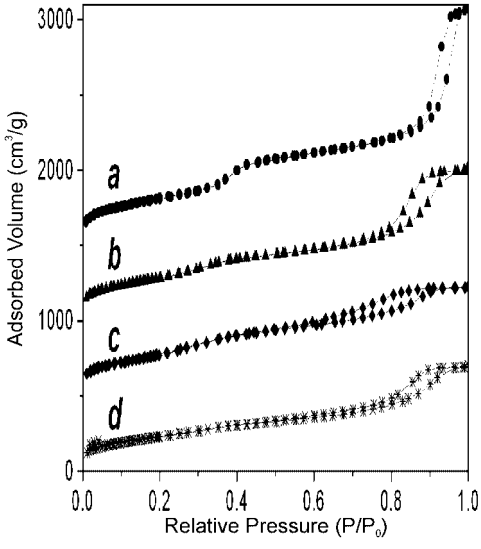


Figure 4. $N_2$ adsorption–desorption isotherms for Zr-UVM-7 materials: (a) Sample 1 (Si/Zr = 43), (b) Sample 2 (Si/Zr = 19), (c) Sample 3 (Si/Zr = 11), and (d) Sample 4 (Si/Zr = 4).

 © 2006 Wiley-VCH Verlag GmbH & Co. KGaA, Weinheim 

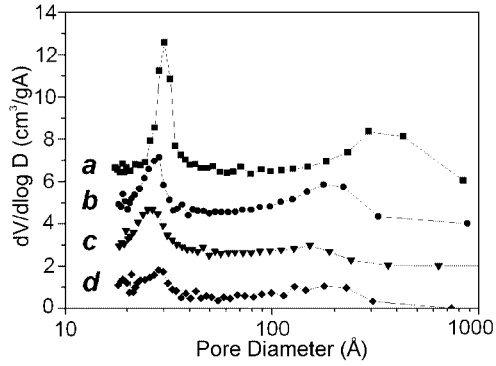


Figure 5. BJH pore size distributions for Zr-UVM-7 materials: (a) Sample 1 (Si/Zr = 43), (b) Sample 2 (Si/Zr = 19), (c) Sample 3 (Si/Zr = 11), and (d) Sample 4 (Si/Zr = 4).

Indeed, the pore size and volume associated with the intraparticle small mesopores gradually decrease with the Zr content (see Table 1), a result which is consistent with an effective heteroelement incorporation into the silica walls. The intraparticle shrinkage commented on above could account for such a BJH pore and volume evolution. On the other hand, we observe similar tendencies for the pore size and volume associated with the interparticle pores in the case of oxides (doped or mixed) with intermediate Zr loads ($43 \geq Si/Zr > 11$). Later, as the Zr content increases ($11 \geq Si/Zr \geq 4$), the pore size and volume seem to be stabilized. At this point, it can be interesting to compare these results with those concerning the interparticle pore system (pore size = 50–60 nm) corresponding to pure (Zr-free) UVM-7 silicas.[48] We can conclude that Zr centers seem to be very effective for interconnecting different nanoparticles (with the consequent pore-size reduction) even for low heteroelement contents. Thus, the incorporation of small amounts of Zr (Si/Zr = 43) already implies a reduction of the large pore size in about 50% with regard to the pure UVM-7 silica. This reduction continues more smoothly until significant Zr contents ($Si/Zr \geq 11$) are reached, for which we might consider that the size and volume of the interparticle pore system is roughly stabilized (about 12.5 nm and 0.67 $cm^3/g$). This general behavior suggests that, in the presence of moderate proportions of interparticle Zr binding sites, the cage-like pore system is controlled by the nanoparticle packing efficiency (physical aspects related to the size and shape of the particles) rather than by the heteroelement amount.

The high BET surface area, characteristic of UVM-7 and MCM-41 materials, is maintained in the whole compositional range studied (Table 1). Incorporation of Zr leads to a small and gradual decrease of the BET area. Insofar as the major surface area corresponds to the intraparticle mesopore system, this evolution must be attributed to disorder induced by Zr in the surfactant-templated pore array. This is a general tendency already observed for M-MCM-41-like samples,[38] which has to be related to the relative lowering of the $S^+I^-$-matching capability of the heteroelement-containing silica oligomers. However, this BET surface area decrease does not necessarily imply a significant loss of porosity, and it could be related to a great extent with the gradual increase of the density of the samples as Zr atoms replace Si ones. Also, the thickness of the pore walls (defined as $Wt = a_0$ – BJH pore size) shows a certain tendency to increase with the Zr content, which should be correlated with the effective incorporation of Zr into the walls.

Once it is unambiguously confirmed that our materials retain the nanometric architecture typical of the UVM-7 silicas, it is possible to gain insight into the characteristics of the local environment and dispersion of the Zr centers in the silica walls with the help of UV/Vis spectroscopy. The diffuse-reflectance UV/Vis spectra corresponding to the anhydrous (i) and hydrated (ii) Zr-UVM-7 compositions we are dealing with (the spectrum of bulk $ZrO_2$ has also been included for comparative purposes) are shown in Figure 6.

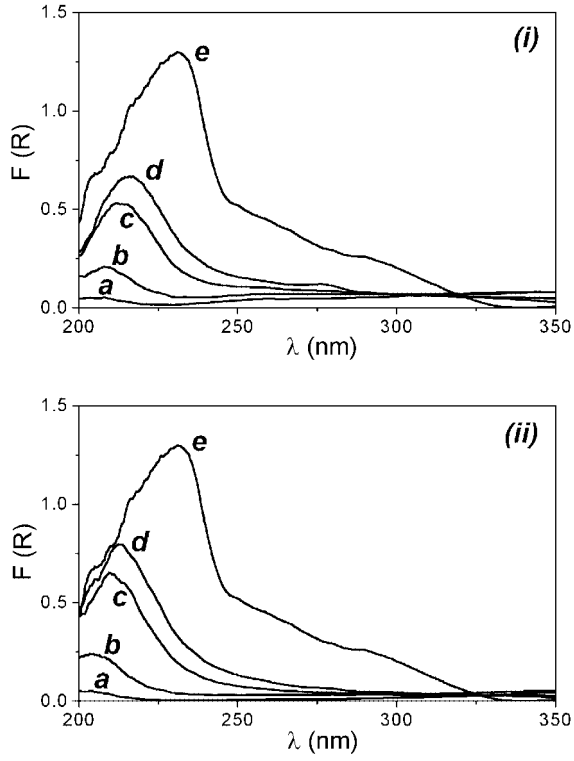


Figure 6. Diffuse-reflectance UV/Vis spectra of (i) anhydrous and (ii) hydrated Zr-UVM-7 samples. (a) Sample 1 (Si/Zr = 43), (b) Sample 2 (Si/Zr = 19), (c) Sample 3 (Si/Zr = 11), (d) Sample 4 (Si/Zr = 4), and (e) $ZrO_2$.

In all cases, the spectra display an intense absorption band at about 210–217 nm whose intensity monotonically increases as the Si/Zr ratio decreases. As can be seen, the spectrum of $ZrO_2$ is clearly different: the most intense absorption band is complex and its maximum appears at comparatively low energy values (about 230–240 nm); moreover it exhibits additional bands in the range of 250–350 nm. The intense adsorption band in the spectra of Zr-UVM-7-related materials is usually attributed to ligand-to-metal charge transfer from oxide entities to isolated $Zr^{IV}$ cations in a tetrahedral environment.[67] This band presents a gradual red-shift as the Zr content increases, but the absorption maximum always falls at wavelengths lower than that corre-

 © 2006 Wiley-VCH Verlag GmbH & Co. KGaA, Weinheim 

sponding to pure zirconia, that is to say the band-gap energies for the Zr-UVM-7 materials are larger than for $ZrO_2$.[68] This result further corroborates the lack of extra-framework bulk $ZrO_2$ as a segregate phase in the Zr-UVM-7 samples, and also indicates the presence of isolated Zr centers (or highly dispersed zirconia-based clusters or nanodomains) in the pore walls. FTIR spectroscopic data offer further evidence in this sense. Thus, the relative intensity of the band at ca. 970 $cm^{-1}$, which is usually related to vibrational modes involving Si–O–Zr linkages,[69] clearly increases with the Zr content. Moreover, the detection of a certain UV/Vis absorption in the range of 250–350 nm has been recognized as characteristic of nanoscopic regions containing Zr–O–Zr bonds in related materials.[34] It must be noted that the spectrum of bulk $ZrO_2$ presents, at least, two rather intense adsorption bands in this range. In the case of the Zr-UVM-7 solids, we cannot detect any absorption in this spectral range until reaching the Zr content corresponding to a molar ratio of Si/Zr = 11. Even in the case of the spectrum of the highest-Zr-content material (Si/Zr = 4), we can observe only a small shoulder at ca. 250–275 nm. We cannot disregard, therefore, the presence of a certain proportion of Zr–O–Zr-containing nanodomains in this last sample of high Zr content. Such a shoulder can be better appreciated in the spectrum of the anhydrous Si/Zr = 4 sample. The thermal treatment carried out to eliminate water probably favors a certain intra- and interparticle condensation leading to the formation of new Zr–O–Zr bonds. As discussed above, this observation correlates to the ability of Zr centers to adopt different coordination environments.

Concerning the potential catalytic applications of these materials, it seems relevant to evaluate the proportion of Zr sites that are reagent-accessible. In general, this variable is highly dependent on the synthesis approach used. Thus, when comparing cohydrolysis processes to grafting techniques, we find that, although cohydrolysis usually leads to higher chemical homogeneity, it has an associated drawback: the loss of a significant part of the incorporated, potentially active centers, which are buried inside the pore walls (that is to say inaccessible for the reagents). Then, assuming that the mesoscopic organization of the material is maintained, we can consider that only those Zr centers close to the pore surface should be accessible to different substrates. Our approach to estimating the proportion of Zr-accessible sites in the Zr-UVM-7 materials is based on evaluating the effects of using an alternative procedure for removing the surfactant from the as-synthesized samples. Thus, we chemically extracted the surfactant with the help of HCl/ethanol mixtures. This process has a double effect: it obviously provokes the exchange between $CTMA^+$ species and protons, but also favors the leaching of accessible Zr atoms in the form of chloride complexes. Thus, we observe in all cases that the Zr content, as measured by EPMA, decreases after extraction (see Table 2).

In all samples, at least 1/3 of the Zr centers are accessible under the experimental conditions we have used. Moreover, the proportion of accessible Zr centers increases with the Zr content [from about 40% (Si/Zr = 43) to about 60% (Si/Zr = 4)]. At first glance, this evolution might suggest that there is a certain progressive (with the Zr content) loss of chemical homogeneity of the pore walls, which would result in enrichment in Zr of the surface with regard to the core walls. However, these results must be carefully considered, because the leaching of superficial Zr centers (or $ZrO_2$ nanodomains in the Zr-richest samples) also favors a progressive attack on partially buried Zr species. In practice, this degradation will progress continuously, leading to an enhanced elimination of Zr (internal and a priori inaccessible) cations of the inorganic walls. This process really is very similar to the well-known dealumination and desilication reactions carried out on zeolites to favor the generation of additional hierarchical porosity.[70,71] A possible consequence of the progressive formation of new disordered pores should be mesostructure degradation (partial or total). In fact, a preliminary study (XRD and $N_2$ adsorption–desorption) carried out on chemically extracted samples shows that the process induces significant changes in the (UVM-7) organization of the resulting materials. Thus, according to the XRD patterns in Figure 7, the intraparticle short-range hexagonal ordering mesopore system is maintained only up to Sample 3 (initial molar ratio: Si/Zr = 11), and it practically disappears for the Zr-richest material (Sample 4).

Table 2. Analytical data for Zr-UVM-7 samples before and after treatment with HCl/ethanol.

| Sample | Si/Zr calcined | Si/Zr chemically extracted | Accessible Zr sites (%) |
|---|---|---|---|
| 1 | 43 | 66 | 35 |
| 2 | 19 | 34 | 41 |
| 3 | 11 | 24 | 50 |
| 4 | 4 | 11 | 60 |

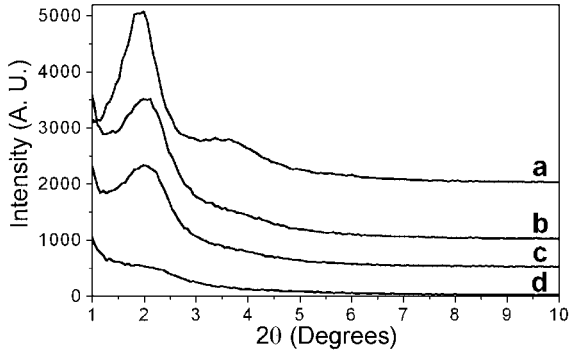


Figure 7. Low-angle XRD patterns of the chemically extracted Zr-UVM-7 materials: (a) Sample 1 (Si/Zr = 66), (b) Sample 2 (Si/Zr = 34), (c) Sample 3 (Si/Zr = 24), and (d) Sample 4 (Si/Zr = 11).

On the other hand, we only observe (see Figure 8) UVM-7-like isotherms (with two well-differentiated adsorption steps) up to Sample 2 (initial molar ratio: Si/Zr = 19). Indeed, as the Zr content increases, the first adsorption step (associated with the intraparticle mesopores) progressively disappears, and the second adsorption step (typical of interparticle voids) in the isotherms evolves to wide pore-size distributions.

 © 2006 Wiley-VCH Verlag GmbH & Co. KGaA, Weinheim 

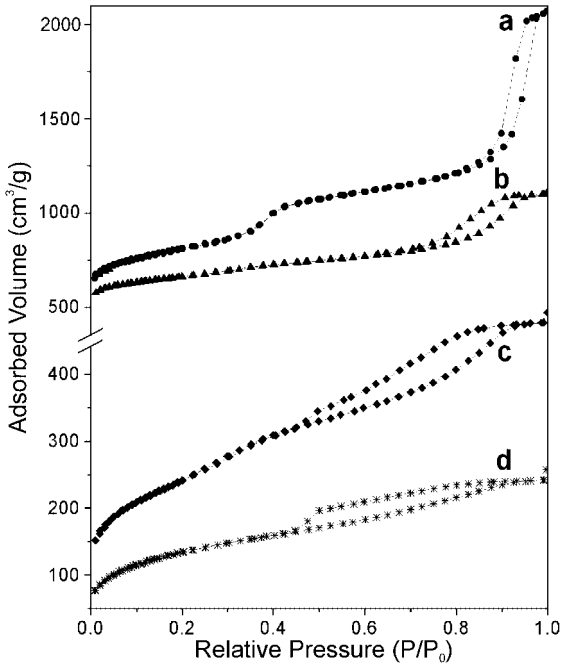


Figure 8. $N_2$ adsorption–desorption isotherms of the chemically extracted Zr-UVM-7 materials: (a) Sample 1 (Si/Zr = 66), (b) Sample 2 (Si/Zr = 34), (c) Sample 3 (Si/Zr = 24), and (d) Sample 4 (Si/Zr = 11).

According to XRD and porosimetry data, we can conclude that the UVM-7-like architecture in chemically extracted materials is preserved only in the compositional range of $43 \geq Si/Zr > 19$ (initial molar ratio values). On the basis of this observation, and taking into account both the proportion of accessible Zr sites estimated for the samples in this range (from 35 to 40%, Table 2) and their wall thickness (Table 1), it is possible to propose a rough structural model for estimating the degree of chemical homogeneity of the pore walls. Then, assuming the existence of a silica-based framework constructed from $Q^4$ centers [*d*(Si–O) = 0.16 nm], about six silica chains are necessary to achieve a wall thickness of ca. 1.7–1.8 nm (Figure 9). Under the reasonable hypothesis that in the low-Zr-content silicas ($Si/Zr > 19$) only the Zr sites located in the more external chains should be eliminated by the treatment with HCl/ethanol mixtures, the proportion of accessible Zr centers for a homogeneous heteroelement dispersion is 1/3, a value very close to those observed for Samples 1 and 2 (35% and 41%, respectively). In any case, although a slight Zr surface enrichment cannot be completely disregarded, we can conclude that the atrane method leads to mesoporous materials with high chemical homogeneity throughout the pore walls. In contrast, an appreciable Zr enrichment of the surface has been detected for mesoporous materials synthesized from conventional reagents.[35] Dealing with the surfactant-exchanged materials in the compositional range of $11 \geq Si/Zr > 4$, it is interesting to point out that, as occurs for zeolites, the gradual degradation of the mesostructure by Zr leaching to induce additional hierarchic porosity may be controlled to increase the material accessibility. In this regard, additional work is currently in progress.

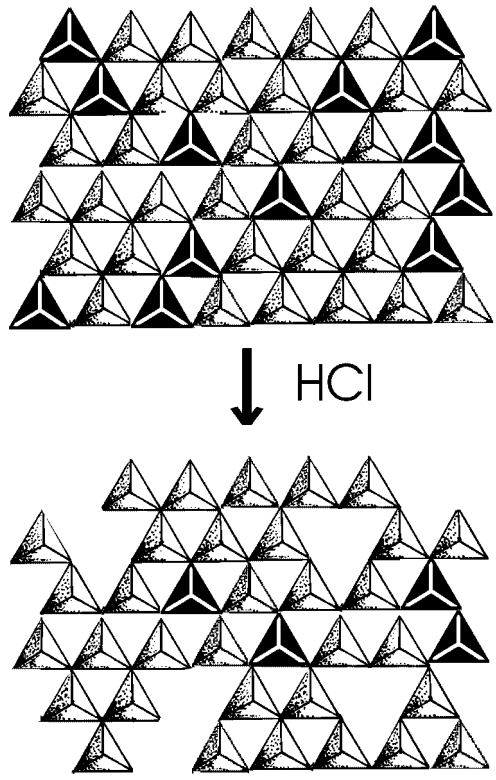


Figure 9. Scheme of the pore wall. Grey and white positions in the framework correspond to Zr and Si sites, respectively.

## Conclusions

In short, we reported here on how, starting from kinetically inert atrane precursors, it is possible to synthesize high-zirconium-content nano-sized bimodal porous silicas by using a cationic surfactant-assisted procedure under controlled pH conditions. The resulting Zr-UVM-7 silica-based materials maintain the typical array of the parent pure silica: aggregates of nano-sized mesoporous particles defining a large interparticle pore system resulting from the imperfect packing of the primary building blocks. The effects of the Zr atoms on the UVM-7 pore morphology are explained on the basis of both the modification of the silica solubility by incorporation of Zr centers into the oligomers and the ability of the Zr atoms to expand their coordination number. The latter aspect favors a significant decrease of the textural porosity with regard to Zr-free UVM-7 materials. Once more, the atrane method proves to be a very efficient tool to achieve a good dispersion of the heteroelement guest species in the silica framework.

## Experimental Section

**Chemicals:** All the synthesis reagents were analytically pure, and were used as received from Aldrich. The Si and Zr primary sources were tetraethyl orthosilicate (TEOS) and zirconium isopropoxide

 © 2006 Wiley-VCH Verlag GmbH & Co. KGaA, Weinheim 

(ZrP), respectively. 2,2′,2′′-Nitrilotriethanol or triethanolamine [$N(CH_2–CH_2–OH)_3$, $TEAH_3$] was used for obtaining Si and Zr atrane complexes. The templating agent was cetyltrimethylammonium bromide (CTMABr).

**Synthesis:** The method was a modification of the so-called "atrane route".[36,45,46] The nano-sized Zr-UVM-7 materials were synthesized through a one-pot surfactant-assisted procedure in a homogeneous hydroalcoholic reaction medium (water/$TEAH_3$). The cationic surfactant (CTMABr) acted as a structure-directing agent or supramolecular template (and consequently, as porogen after template extraction). Although the Si and Zr primary sources were commercial alkoxides, the real hydrolytic precursors in this strategy were Si and Zr atranes (relatively inert complexes that include $TEAH_3$-related ligand species).[36,45,46] Together with its complexing ability, the presence of the polyalcohol ($TEAH_3$) was a key because it kept the reaction medium buffered (pH ≈ 9), favoring the formation of nanoparticulated materials.[47,48] Details of a typical synthesis leading to Sample 2 (see Table 1) can be described as follows: (1) Preparation of an adequate mixture of atrane precursors from commercial alkoxides. TEOS (32.1 mL, 0.144 mol) and ZrP (2.56 mL of a 70% in weight solution, 0.0058 mol) were slowly added to liquid $TEAH_3$ (66.9 mL, 0.51 mol) and heated at 150 °C to give atrane complexes. (2) Addition of the structure-directing (porogen) agent. After cooling of the previous solution to 90 °C, CTMABr surfactant (13.68 g, 0.0375 mol) was added. (3) Mesostructure formation. The solution containing the atrane complexes and the template was cooled to 60 °C and mixed with water (240 mL, 13.33 mol). After a few seconds, a white powder appeared. The resulting suspension was allowed to age at room temperature for 24 h. The final (mesostructured) powder was filtered off, washed with water and ethanol, and air-dried. (4) Surfactant removal. In order to open the pore system, the as-synthesized solid was heated at 500 °C under static air for 5 h. In all cases, the molar ratio of the reagents in the mother liquor was adjusted to (2–$x$)Si/$x$Zr/7$TEAH_3$/0.52CTMABr/180$H_2O$ (where $x$ = 0.04, 0.08, 0.15, and 0.33). On the other hand, in order to evaluate the proportion of internal and external (accessible) Zr sites, we used an alternative procedure to remove the surfactant from the as-synthesized samples. Indeed, the surfactant was chemically extracted from some selected samples using an HCl/ethanol solution (about 1 g of powder, 15 mL of HCl 35%, and 150 mL of ethanol 96%) by maintaining the suspension of the mesostructured solid in the solution, while stirring at room temperature for 24 h. The final (porous) material was separated by filtration, washed with ethanol, and air-dried.

**Physical Measurements:** All solids were characterized by electron probe microanalysis (EPMA) using a Philips SEM-515 instrument. The Si/Zr molar ratio values averaged from EPMA data corresponding to about 50 different particles of each sample are summarized in Table 1. Fast atomic bombardment (FAB) coupled to mass spectrometry (MAS) analysis of the precursor solutions was performed to investigate the nature of the atrane precursors (before and after water addition). X-ray powder diffraction (XRD) data were recorded with a Seifert 3000TT $\theta$-$\theta$ diffractometer using Cu-$K_\alpha$ radiation. Low-angle XRD patterns were collected in steps of 0.02° (2$\theta$) over the angular range of 0.65–10° (2$\theta$) for 25 s/step. To detect the presence of some crystalline bulk phase, additional patterns were recorded with a larger scanning step [0.05° (2$\theta$)] over the angular range of 10–70° (2$\theta$) and a lower acquisition time (10 s/step). An electron microscopy study (TEM) was carried out with a JEOL JEM-1010 instrument operating at 100 kV and equipped with a CCD camera. The specimens for TEM analysis were prepared from powders by conventional crushing in an agate mortar, and dispersing the resulting small crystallites in dodecane. Microparticles were then deposited on holey carbon microgrids under ambient conditions. Surface area, pore size, and volume values were calculated from nitrogen adsorption–desorption isotherms (–196 °C) recorded with a Micromeritics ASAP-2010 instrument. Calcined samples were degassed at 130 °C and $10^{-6}$ Torr for 15 h prior to measurement. Surface areas were estimated according to the BET model,[72] and pore size dimensions were calculated by using the BJH method (measures at $P/P_0 < 0.55$ and $P/P_0 > 0.55$ values have been used to characterize the intrananoparticle and the internanoparticle pore systems, respectively).[73] Room-temperature diffuse-reflectance spectra were registered using a Shimadzu UV/Vis 2501PC instrument equipped with an integrated sphere coated with $BaSO_4$, which also is used as standard. IR spectra (KBr pellets) were registered with an FTIR Perkin–Elmer 1750 spectrophotometer.

## Acknowledgments

This work was supported by the Spanish Ministerio de Educación y Ciencia (under grants MAT2002-04329-C03-02 and MAT2003-08568-C03-01) and the Generalitat Valenciana (grant GRUPOS03/099 and GV2004-B-745). D. O. Z. thanks the Spanish Ministerio de Educación y Ciencia for a doctoral grant.

[1] R. C. Garvie, R. H. Hannik, R. T. Pascoe, *Nature* **1975**, *258*, 703–704.
[2] A. Paul, *Chemistry of Glasses*, Chapman and Hall, London, **1982**.
[3] M. Nogami, M. Tomozawa, *J. Am. Ceram. Soc.* **1986**, *69*, 99–102.
[4] M. Palladino, F. Pirini, M. Beghi, P. Chirulo, G. Cogliati, L. Costa, *J. Non-Cryst. Solids* **1992**, *147–148*, 335–339.
[5] F. Garbassi, L. Balducci, R. Ungarelli, *J. Non-Cryst. Solids* **1998**, *223*, 190–199.
[6] T. Lopez, F. Tzompantzi, J. Navarrete, R. Gomez, J. L. Boldu, E. Muñoz, O. Novaro, *J. Catal.* **1999**, *181*, 285–293.
[7] H. Yang, R. Lu, L. Shen, L. Song, J. Zhao, Z. Wang, W. Li, *Mater. Lett.* **2003**, *57*, 2572–2579.
[8] K. Tanabe, M. Misono, Y. Ono, H. Hattori, *Stud. Surf. Sci. Catal.* **1989**, *51*, 1–5.
[9] K. Tanabe, T. Yamaguchi, *Catal. Today* **1994**, *20*, 185–198.
[10] T. Yamaguchi, *Catal. Today* **1994**, *20*, 199–218.
[11] R. Takahashi, K. Nakanishi, N. Soga, *J. Ceram. Soc. Jpn.* **1998**, *106*, 772–777.
[12] H. Hayashi, H. Suzuki, S. Kaneko, *J. Sol-Gel Sci. Technol.* **1998**, *12*, 87–94.
[13] Z. G. Wu, Y. X. Zhao, D. S. Liu, *Microporous Mesoporous Mater.* **2004**, *68*, 127–132.
[14] O. Stachs, V. Petkov, Th. Gerber, *J. Appl. Crystallogr.* **1997**, *30*, 670–674.
[15] D. R. Rolison, *Science* **2003**, *299*, 1698–1701.
[16] H. J. M. Bosman, E. C. Kruissink, J. Van der Spoel, F. Van der Brink, *J. Catal.* **1994**, *148*, 660–672.
[17] J. B. Miller, S. E. Rankin, E. I. Ko, *J. Catal.* **1994**, *148*, 673–682.
[18] J. R. Sohn, H. J. Jang, *J. Mol. Catal.* **1991**, *64*, 349–360.
[19] X. Gao, J. L. G. Fierro, I. E. Wachs, *Langmuir* **1999**, *15*, 3169–3178.
[20] Z. Dang, B. G. Anderson, Y. Amenomiya, B. A. Morrow, *J. Phys. Chem.* **1995**, *99*, 14437–14443.
[21] C. Contescu, *J. Catal.* **1995**, *157*, 244–258.
[22] G. Wang, X. Wang, S. Yu, *Stud. Surf. Sci. Catal.* **1994**, *83*, 67–74.
[23] M. K. Dongare, P. Singh, P. Moghe, P. Ratnasamy, *Zeolites* **1991**, *11*, 690–693.

 © 2006 Wiley-VCH Verlag GmbH & Co. KGaA, Weinheim 

[24] B. Rakshe, V. Ramaswamy, S. G. Hegde, R. Vetrivel, A. V. Ramaswamy, *Catal. Lett.* **1997**, *45*, 41–50.
[25] A. Brait, M. E. Davis, *Appl. Catal., A* **2000**, *204*, 117–127.
[26] A. Tuel, S. Gontier, R. Teissier, *Chem. Commun.* **1996**, 651–652.
[27] S. Gontier, A. Tuel, *Appl. Catal., A* **1996**, *143*, 125–135.
[28] D. J. Jones, J. Jiménez-Jiménez, A. Jiménez-López, P. Maireles-Torres, P. Olivera-Pastor, E. Rodriguez-Castellón, J. Rozière, *Chem. Commun.* **1997**, 431–432.
[29] A. Tuel, *Microporous Mesoporous Mater.* **1999**, *27*, 151–169.
[30] M. S. Morey, G. D. Stucky, S. Schwarz, M. Fröba, *J. Phys. Chem. B* **1999**, *103*, 2037–2041.
[31] M. L. Occelli, S. Biz, A. Auroux, *Appl. Catal., A* **1999**, *183*, 231–239.
[32] K. Chaudhari, R. Bal, T. K. Das, A. Chandwadkar, D. Srinavas, S. Sivasanker, *J. Phys. Chem. B* **2000**, *104*, 11066–11074.
[33] X. X. Wang, F. Lefebvre, J. Patarin, J. M. Basset, *Microporous Mesoporous Mater.* **2001**, *42*, 269–276.
[34] B. L. Newalkar, J. Olanrewaju, S. Komarneni, *J. Phys. Chem. B* **2001**, *105*, 8356–8360.
[35] M. S. Wong, H. C. Huang, J. Y. Ying, *Chem. Mater.* **2002**, *14*, 1961–1973.
[36] J. El Haskouri, S. Cabrera, C. Guillem, J. Latorre, A. Beltrán, D. Beltrán, M. D. Marcos, P. Amorós, *Chem. Mater.* **2002**, *14*, 5015–5022.
[37] X.-X. Wang, L. Veyre, F. Lefebvre, J. Patarin, J.-M. Basset, *Microporous Mesoporous Mater.* **2003**, *66*, 169–179.
[38] A. Infantes-Molina, J. Mérida-Robles, P. Maireles-Torres, E. Finocchio, G. Busca, E. Rodríguez-Castellón, J. L. G. Fierro, A. Jiménez-López, *Microporous Mesoporous Mater.* **2004**, *75*, 23–32.
[39] S.-Y. Chen, L.-Y. Jang, S. Cheng, *Chem. Mater.* **2004**, *16*, 4174–4180.
[40] C. Flego, L. Carluccio, C. Rizzo, C. Perego, *Catal. Commun.* **2001**, *2*, 43–48.
[41] G. J. A. A. Soler-Illia, C. Sanchez, B. Lebeau, J. Patarin, *Chem. Rev.* **2002**, *102*, 4093–4138.
[42] A. Tarafdar, A. B. Panda, P. Pramanik, *Microporous Mesoporous Mater.* **2005**, *84*, 223–228.
[43] J. W. Kriesel, M. S. Sander, T. Don Tilley, *Adv. Mater.* **2001**, *13*, 331–335.
[44] G. J. A. A. Soler-Illia, E. L. Crepaldi, D. Grosso, C. Sanchez, *J. Mater. Chem.* **2004**, *14*, 1879–1886.
[45] S. Cabrera, J. El Haskouri, C. Guillem, J. Latorre, A. Beltrán, D. Beltrán, M. D. Marcos, P. Amorós, *Solid State Sci.* **2000**, *2*, 405–420.
[46] P. Amorós, A. Beltrán, D. Beltrán, S. Cabrera, J. El Haskouri, M. D. Marcos, Patent WO 01-72635.
[47] T. R. Pauly, Y. Liu, T. J. Pinnavaia, S. J. L. Billinge, T. P. Rieker, *J. Am. Chem. Soc.* **1999**, *121*, 8835–8842.
[48] J. El Haskouri, D. Ortiz de Zárate, C. Guillem, J. Latorre, M. Caldés, A. Beltrán, D. Beltrán, A. B. Descalzo, G. Rodríguez, R. Martínez, M. D. Marcos, P. Amorós, *Chem. Commun.* **2002**, 330–331.
[49] J. El Haskouri, D. Ortiz de Zárate, F. Pérez-Pla, A. Cervilla, C. Guillem, J. Latorre, M. D. Marcos, A. Beltrán, D. Beltrán, P. Amorós, *New J. Chem.* **2002**, *26*, 1093–1095.
[50] M.-C. Chao, H.-P. Lin, C.-Y. Mou, B.-W. Cheng, C.-F. Cheng, *Catal. Today* **2004**, *97*, 81–87.
[51] S. Cabrera, J. El Haskouri, S. Mendioroz, C. Guillem, J. Latorre, A. Beltrán, D. Beltrán, M. D. Marcos, P. Amorós, *Chem. Commun.* **1999**, 1679–1680.
[52] S. Cabrera, J. El Haskouri, J. Alamo, A. Beltrán, D. Beltrán, S. Mendioroz, M. D. Marcos, P. Amorós, *Adv. Mater.* **1999**, *11*, 379–381.
[53] S. Cabrera, J. El Haskouri, A. Beltrán, D. Beltrán, M. D. Marcos, P. Amorós, *Solid State Sci.* **2000**, *2*, 513–518.
[54] J. El Haskouri, S. Cabrera, M. Gutierrez, A. Beltrán, D. Beltrán, M. D. Marcos, P. Amorós, *Chem. Commun.* **2001**, 309–310.
[55] J. El Haskouri, S. Cabrera, M. Caldés, C. Guillem, J. Latorre, A. Beltrán, D. Beltrán, M. D. Marcos, P. Amorós, *Chem. Mater.* **2002**, *14*, 2637–2643.
[56] J. El Haskouri, S. Cabrera, C. J. Gómez-García, C. Guillem, J. Latorre, A. Beltrán, D. Beltrán, M. D. Marcos, P. Amorós, *Chem. Mater.* **2004**, *16*, 2805–2813.
[57] R. K. Iler, *The Chemistry of Silica – Solubility, Polymerization, Colloid and Surface Properties, and Biochemistry*, John Wiley & Sons, New York, **1979**.
[58] S. A. Greenberg, D. Sinclair, *J. Phys. Chem.* **1955**, *59*, 435–440.
[59] C. F. Baes, R. E. Mesmer, *The Hydrolysis of Cations*, Wiley, New York, **1976**.
[60] D.-Y. Shin, S.-M. Han, K.-N. Kim, *J. Ceram. Processing Res.* **2004**, *5*, 70–75.
[61] N. Nishiyama, H. Saputra, D.-H. Park, Y. Egashira, K. Ueyama, *J. Membr. Sci.* **2003**, *218*, 165–171.
[62] L. Chu, M. I. Tejedor-Tejedor, M. A. Anderson, *Microporous Mater.* **1997**, *8*, 207–213.
[63] I. C. Tilgner, P. Fischer, F. M. Bohnen, H. Rehage, W. F. Maier, *Microporous Mater.* **1995**, *5*, 77–90.
[64] C. T. Kresge, M. E. Leonowicz, W. J. Roth, J. C. Vartuli, J. S. Beck, *Nature* **1992**, *359*, 710–712.
[65] L. Huerta, C. Guillem, J. Latorre, A. Beltrán, D. Beltrán, P. Amorós, *Sol. State Sci.* **2005**, *7*, 405–414.
[66] G. Pacheco, E. Zhao, A. García, A. Sklyarov, J. J. Fripiat, *J. Mater. Chem.* **1998**, *8*, 219–226.
[67] R. A. Schoonheydt in *Characterization of Heterogeneous Catalysts* (Ed.: F. Delannay), Marcel Dekker, New York, **1984**.
[68] W. N. Delgass, G. L. Haller, R. Kellerman, J. H. Lunsford, *Spectroscopy in Heterogeneous Catalysis*, Academic Press, New York, **1979**.
[69] M. Andrianainarivelo, R. Corriu, D. Leclercq, P. H. Mutin, A. Vioux, *J. Mater. Chem.* **1996**, *6*, 1665–1671.
[70] J. Scherzer, *ACS Symp. Ser.* **1984**, *248*, 157–158.
[71] J. C. Groen, L. A. A. Peffer, J. A. Moulijn, J. Pérez-Ramírez, *Chem. Eur. J.* **2005**, *11*, 4983–4994.
[72] S. Brunauer, P. H. Emmett, E. Teller, *J. Am. Chem. Soc.* **1938**, *60*, 309–319.
[73] E. P. Barrett, L. G. Joyner, P. P. Halenda, *J. Am. Chem. Soc.* **1951**, *73*, 373–380.

Received: December 22, 2005
Published Online: April 21, 2006

 © 2006 Wiley-VCH Verlag GmbH & Co. KGaA, Weinheim 

DOI: 10.1002/ejic.200600024

# A Joint Experimental and Computational Study on the Electronic Communication in Diethynylaryl-Bridged ($\eta^5$-$C_5H_5$)Fe($\eta^2$-dppe) and ($\eta^5$-$C_5H_5$)-Fe$(CO)_2$ Units

**Laura Medei,[a] Laura Orian,[b] Oleg V. Semeikin,[c] Mikhail G. Peterleitner,[c] Nikolai A. Ustynyuk,[c] Saverio Santi,*[b] Christian Durante,[b] Antonella Ricci,[d] and Claudio Lo Sterzo*[d]**

**Keywords:** Mixed-valence compounds / Iron / Electron transfer / Electronic communication / Ethynylaryl bridging ligand

A family of bimetallic complexes [$Cp(CO)_2Fe$–C≡C–Ar–C≡C–$Fe(CO)_2Cp$] {Cp = $C_5H_5$; **6a**–**g**: Ar = $C_4H_2S$ (**a**), 3-($C_4H_9$)-$C_4HS$ (**b**), 3-($C_{16}H_{33}$)-$C_4HS$ (**c**), $C_6H_4$ (**d**), 2,5-bis-($OC_4H_9$)-$C_6H_2$ (**e**), 2,5-bis($OC_8H_{17}$)-$C_6H_2$ (**f**), ($C_6H_4$)$_2$ (**g**)} was prepared by the three-step Pd-catalysed *extended one-pot* (EOP) synthetic protocol from $Bu_3Sn$–C≡CH, X–Ar–X (X = I, Br) and $Cp(CO)_2FeI$. Complexes **6a**,**d**,**g** were then exposed to ultraviolet irradiation in the presence of an equivalent amount of 1,2-bis(diphenylphosphanyl)ethane (dppe) to form the corresponding bimetallic complexes [Cp(dppe)Fe–C≡C–Ar–C≡C–Fe(dppe)Cp] (**7a**,**d**,**g**). Compounds **6a**–**g** and **7a**,**d**,**g** were characterised by cyclic voltammetry (CV). The most significant electrochemical information comes from the oxidation of the dppe derivatives. The $\Delta E°$ separations between the subsequent reversible waves suggest that the efficiency of the metal–metal electronic coupling decreases in the order **7a** > **7d** > **7g**. Complexes **7a** and **7g** were also chemically oxidised with [$Fe(Cp^*)]_2[BF_4]$ {$Cp^*$ = $C_5(CH_3)_5$} and $[Fe(Cp)]_2[BF_4]$ respectively, and the near infrared (NIR) spectra of the mixed-valence species **7a**$^+$ and **7g**$^+$ were recorded. A strong intervalence transition (IT) band was observed only for the radical cation **7a**$^+$. While this finding confirms the existence of an electronic interaction between the two termini when a 2,5-thiophene group is present in the spacer, the NIR spectrum of **7g**$^+$ reveals a reduced efficiency in conveying electrons when the $C_4H_2S$ moiety is replaced by a 4,4′-biphenyl. In order to rationalise and quantify the extent of electronic communication, ruled by geometrical and electronic factors, density functional computational results on selected [Cp $(PH_3)_2$Fe] and [$Cp(CO)_2Fe$] binuclear model complexes are reported.

(© Wiley-VCH Verlag GmbH & Co. KGaA, 69451 Weinheim, Germany, 2006)

## Introduction

Highly ethynylated organic or organometallic compounds are currently providing new opportunities in projecting materials to be used in electronics, optics and ceramics.[1]

The attention devoted to such compounds arises from unique chemical and physical properties due to *facile* electron transfer along rod-like unsaturated molecular chains (eventually) incorporating metal centres.[2] The possibilities of extended delocalisation through the π networks can hardly influence physical properties such as polarisability, conductivity, and so forth, making these complexes suitable as active components in optoelectronic devices.[3]

We have recently disclosed a new one-pot route to poly(acetylide)s and poly(metallaacetylide)s based on palladium-catalysed carbon–carbon and metal–carbon bond formation (Scheme 1).[4]

By this procedure, named *extended one-pot* (EOP), a great variety of organic co- and homopolymers can be straightforwardly obtained with few steps and very good yields, with no need to isolate intermediate compounds (see path $a_1$ and path b in Scheme 1). Moreover, taking advantage of a new performance of Pd catalysts we discovered, allowing the formation of metal–carbon bonds, also organometallic oligomers and polymers can be conveniently accessed by this procedure[4a,4b,5] (path $a_2$ in Scheme 1).

With such versatile synthetic methodology at our disposal, we pursued our study by aiming for the valuation of the electrochemical and optical properties of some spacers

[a] Istituto CNR di Metodologie Chimiche (IMC-CNR), Sezione Meccanismi di Reazione Dipartimento di Chimica, Box 34, Roma 62, Università "La Sapienza",
Piazzale Aldo Moro 5, 00185 Roma, Italy
[b] Dipartimento di Scienze Chimiche, Università degli Studi di Padova,
Via Marzolo 1, 35131 Padova, Italy
E-mail: saverio.santi@unipd.it
[c] A. N. Nesmeyanov Institute of Organoelement Compounds (INEOS), Russian Academy of Science,
Vavilov Street 28, Moscow 119991, Russian Federation
[d] Dipartimento di Scienze degli Alimenti, Facoltà di Agraria, Università degli Studi di Teramo,
Via Carlo R. Lerici 1, 64023 Mosciano Sant'Angelo (Teramo), Italy
E-mail: closterzo@unite.it

Supporting information for this article is available on the WWW under http://www.eurjic.org or from the author.

 © 2006 Wiley-VCH Verlag GmbH & Co. KGaA, Weinheim 

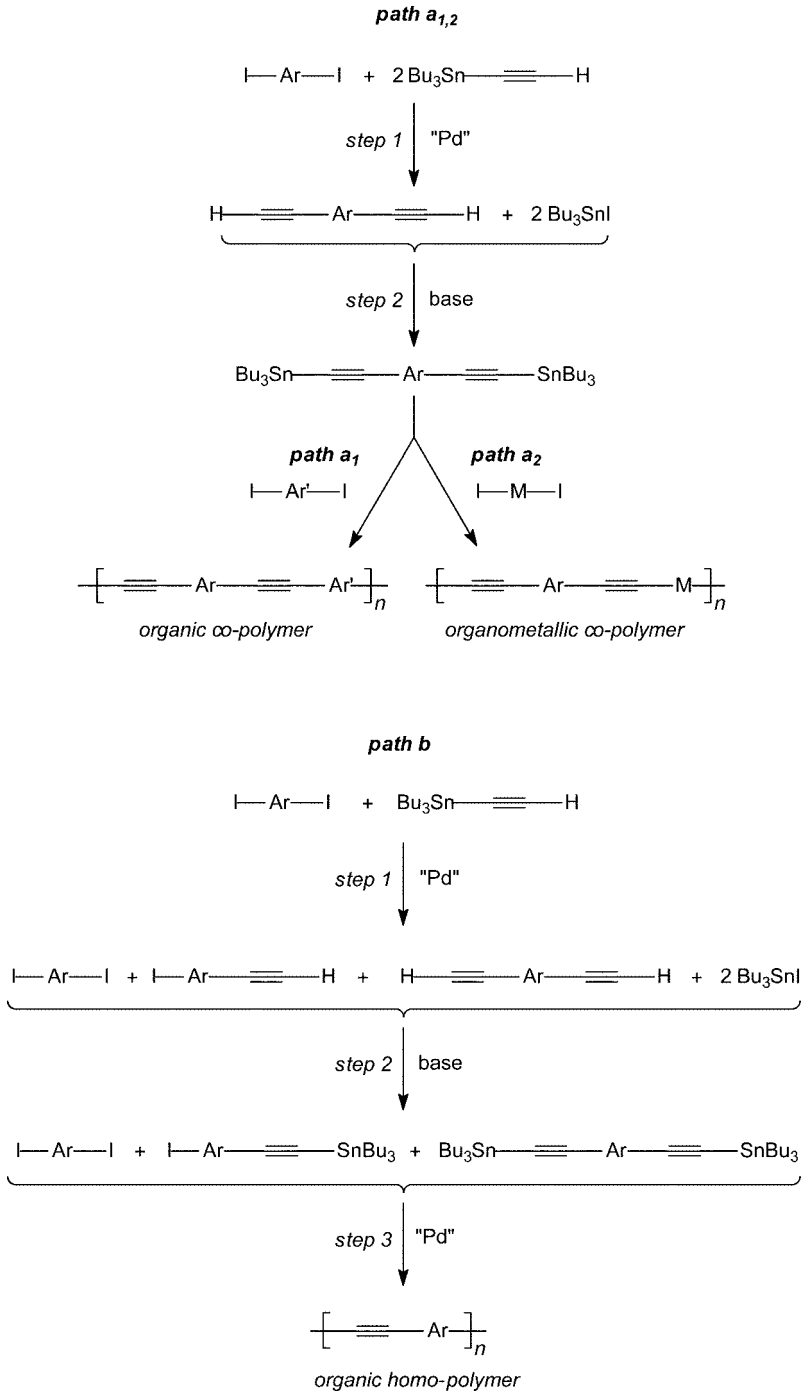


Scheme 1.

commonly used as building blocks in the preparation of opto- and electroactive polymers. To achieve this purpose, insertion of different spacers between two iron centres [CpFe(dppe)-] was planned, in order to exploit the electronic interaction between the metallic nuclei in a given redox state and the bridging ligand.

Actually, depending on both the redox state of the molecule and its structure, electron transfer and magnetic exchange can occur along the intermetallic bridge.

Several compounds with different metallic termini, that is iron and rhenium, bridged by unsaturated all-carbon chains ($C_4$ to $C_{20}$),[6a–6j], or iron, ruthenium and osmium, bridged by σ-acetylides intercalated by different aryl cores,[6k–6m] have been prepared and evaluated for their physical properties by other authors. Elegant studies on the possibility of tuning the electronic communication by lengthening the polyalkynyl bridging ligand and/or by changing the metallic termini have been presented by

 © 2006 Wiley-VCH Verlag GmbH & Co. KGaA, Weinheim 

Lapinte,[7] Gladysz[8] and Bruce[9] and their co-workers. In a few cases aryl cores have been intercalated in the hydrocarbon spacer.[7g,7h,7k,7l,7o,7p,7s]

In this paper new binuclear $Fe^{II}$ compounds incorporating aromatic groups are presented. Aromatic groups to be introduced between iron centres have been chosen in order to keep the rigid-rod geometry of the carbon chain, to increase the chemical stability of the compounds and to maintain a high level of electronic coupling. The availability of compounds that differ for the aryl core in their bridge and the metal ancillary ligands allows discussion of the effects of structural and electronic molecular features on the extent of metal–metal communication. Particularly interesting are the effects on the metal–metal interaction resulting from (i) the replacement of a thiophenyl core by a phenyl core, a structural change in the bridge which does not greatly affect the intermetallic distance, (ii) the insertion of a 4,4′-biphenyl core, which significantly increases the length of the hydrocarbon linker and (iii) the presence of different ancillary ligands, that is CO and dppe.

The physical–chemical study was performed by electrochemical (CV) and spectroscopic techniques [IR, near infrared (NIR), UV/Vis] on selected synthesised dppe complexes.

Cyclic voltammetry (CV) results give information on the stability of the oxidation products but are not sufficient to determine the extent of electronic coupling between the metal termini. Actually, in a typical redox process involving symmetric bimetallic complexes, the separation between the two subsequent reversible waves, in the chemical and electrochemical sense, $\Delta E°$, allows a quantitative estimate of the thermodynamic stability of the intermediate oxidation state with respect to disproportionation (i.e., the comproportionation constant $K_c$).[10] $\Delta E°$ is only a qualitative indicator of an interaction between the two sites. According to the classification proposed by Robin and Day,[10a] $\Delta E°$ values close to zero are characteristic of noninteracting metal sites, that is of class I complexes. Small $\Delta E°$ separations correspond to a weak interaction between the metals and this situation is described by a mixed-valence state involving trapped-valence systems (class II). Finally, larger $\Delta E°$ values correspond to a stabilisation of the mixed-valence complexes involving the totally delocalised class III systems. Although the larger the conjugation along the intermetallic bridge is, the easier the transfer of electronic information between metal centres is, the greater $\Delta E°$ tends to be, the more CV separations are influenced by other factors, in particular the medium (solvent and support electrolyte), which can modify the electrostatic interaction in the dications.[10n] Thus, the CV analysis should always be integrated with spectroscopic investigation, in particular in the NIR region where mixed-valence species typically absorb.

While CV provides no information on the thermodynamic stability in the carbonylated species because of the irreversible nature of their waves, the dppe derivatives are studied in detail. In particular, the two dppe-substituted compounds, including the thiophenyl core and the 4,4′-biphenyl core respectively, exhibit very different reversible electrochemical behaviour. Thus they were also chemically oxidised and their products were studied by near infrared (NIR) spectroscopy. A quenching of the NIR absorption band, which is characteristic of mixed-valence species, occurs when the thiophenyl core is replaced by the 4,4′-biphenyl moiety.

Theoretical calculations, based on state-of-the-art density functional theory (DFT) methods, were carried out on selected $(PH_3)_2$ and $(CO)_2$ model derivatives and provided (i) reliable structures for the title complexes, for which crystallographic data are not available yet, (ii) a detailed description of the electronic structure of the neutral and radical cation species, and (iii) prediction and interpretation of the experimental NIR bands based on the model radical cations.

## Results and Discussion

The synthesis of dppe-substituted bimetallic compounds **7a**–**g** (Scheme 2) was first attempted using the EOP synthetic strategy outlined in path $a_2$ of Scheme 1; however, all the attempts to couple CpFe(dppe)I (**4**) with the different in situ generated $Bu_3Sn–C≡C–Ar–C≡C–SnBu_3$ (**3a**–**g**) in the presence of Pd failed (step 3 of path $a_2$). The failure in the formation of the Fe–C≡C bond was probably due to the strong electron-donating effect of dppe groups on the metal, which decreases the electrophilicity of the Fe–I bond, a basic requirement for oxidative addition to the Pd catalyst, thus the disclosure of the coupling process leading from **4** and **3a**–**g** to **7a**–**g**.[7j,11]

As direct EOP formation of **7a**–**g** proved not to be possible, we decided first to form the (CO)-substituted bimetallic compounds **6a**–**g**, then to subject these compounds to photolytic substitution in the presence of dppe as reported for similar compounds.[7d,12]

### Synthesis of (CO)-Substituted Bimetallic Compounds 6a–g

In Scheme 2 the EOP route to the bimetallic compounds **6a**–**g** and the subsequent conversion into the dppe derivatives **7a**–**g** are outlined. The EOP transformations were performed in dioxane solvent using 2–4% of $Pd^0$ catalyst (single addition at the beginning of step 1). While step 1 and step 2 were rapidly accomplished (20–30 min overall time) with quantitative formation of **3a**–**g**, the accomplishment of step 3 was revealed to be a critical event because of the delicate nature of the bimetallic complexes **6a**–**g**. Although the reaction temperature was lowered to 50–80 °C, with consequent prolongation of reaction times, monitoring of the reaction progress by $^1H$ NMR revealed that formation of the expected product was always accompanied by unidentified side products and a small amount of starting materials always remained.

Isolation of products **6a**–**g** was not straightforward. Chromatographic separation proved to be always detrimental, therefore products had to be isolated and purified by repeated crystallisation (see Experimental Section), which affected the yields of recovered products.

 © 2006 Wiley-VCH Verlag GmbH & Co. KGaA, Weinheim 

### Synthesis of (dppe)-Substituted Bimetallic Compounds 7a,d,g

Complexes **6a**,**d**,**g** were subjected to ultraviolet irradiation (Scheme 2) to obtain the corresponding dppe-substituted bimetallic complexes. All reactions were carried out in distilled benzene using an equivalent amount per iron centre of 1,2-bis(diphenylphosphanyl)ethane, which readily replaces all the carbonyl groups.

Concerning the recovery of products in a pure form, chromatographic purification proved always too aggressive, and isolation of complexes **7a**,**d**,**g** was achieved only by repeated cycles of precipitation from hexane and following dissolution of residues in toluene (or benzene), which allowed free dppe to be removed. By this method, products could be isolated and obtained in a satisfactory pure state, but the numerous cycles of precipitation/dissolution caused the yields to be drastically decreased.

### Cyclic Voltammetry (CV)

The CV at the platinum electrode, at scan rate 0.1 $V s^{-1}$, of a 2-mM solution of complex **7a** in $CH_2Cl_2$ in the presence of 0.1 M $nBu_4NPF_6$ exhibits two reversible (in the chemical and electrochemical sense) one-electron waves at $E_{pa}$ =

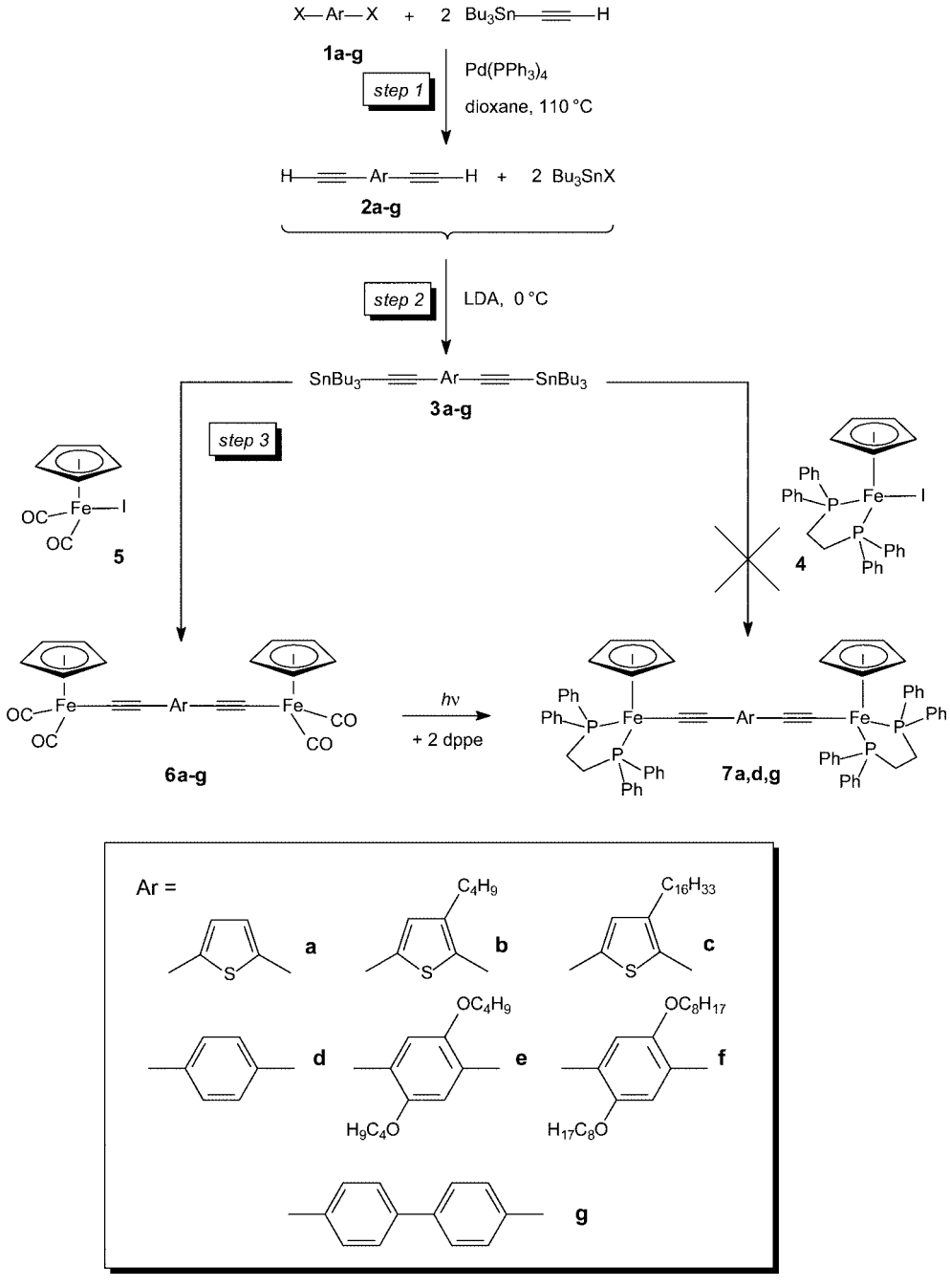


Scheme 2.

 © 2006 Wiley-VCH Verlag GmbH & Co. KGaA, Weinheim 

Table 1. Cyclic voltammetric data for $[Cp(dppe)Fe–C\equiv C–Ar–C\equiv C–Fe(dppe)Cp]^+[BF_4^-]$.[a]

| Complex | Ligand $L_2$ | Spacer Ar | $\Delta E^0 = E_2^0 - E_1^0$[b] | $E_1^0(0/+1)$[b] | $E_{pa}–E_{pc}$[c] | $E_2^0(+1/+2)$[b] | $E_{pa}–E_{pc}$[c] |
|---|---|---|---|---|---|---|---|
| **7a** | dppe | | 0.29 | –0.19 | 56 | 0.10 | 70 |
| **7d** | dppe | | 0.22 | 0.09 | 60 | 0.31 | 60 |
| **7g** | dppe | 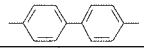 | – | 0.04 | 70 | – | – |

[a] Solvent $CH_2Cl_2$/0.2 M $nBu_4NBF_4$; potential scan rate 0.1 V s$^{-1}$ at a 0.5-mm diameter platinum disk electrode; $T$ = 20 °C. [b] Volts vs. SCE. [c] Data are in mV.

–0.16 V and 0.14 V versus saturated calomel electrode (SCE), current ratio ($i_{pa}/i_{pc}$) = 1 (Figure 1, a). These two waves correspond to the formation of **7a**$^+$ and **7a**$^{2+}$. The anodic and cathodic peak separations ($E_{pa}–E_{pc}$) are 56 and 70 mV at scan rate 0.1 V s$^{-1}$ (Table 1).

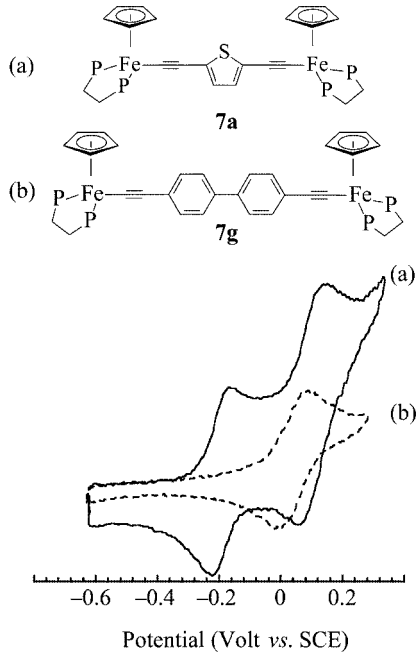


Figure 1. Cyclic voltammetric scan at a 0.5-mm diameter platinum disk electrode, $T$ = 20 °C. Solvent $CH_2Cl_2$/0.1 M $nBu_4NBF_4$; scan rate of 0.1 V s$^{-1}$; (a) solid line, 1 mM **7a**; (b) dashed line, 1 mM **7g**.

Similarly the CV of complex **7d** in the same conditions is characterised by two reversible one-electron waves in the oxidation scan from 1.5 to –1.5 V ($E_{pa}$ = 0.12 V and 0.34 V vs. SCE) and shows a wave separation $\Delta E°$ of 0.22 V and peak separations ($E_{pa}–E_{pc}$) of 60 mV (Table 1). On the contrary, the CV of complex **7g** (Figure 1, b) reveals only one reversible wave at $E_{pa}$ = 0.08 V with ($E_{pa}–E_{pc}$) = 70 mV and current ratio ($i_{pa}/i_{pc}$) = 1 (Table 1).

The low values of the oxidation potentials show that these binuclear complexes are electron-rich compounds. More interesting the quite large wave separations found for complexes **7a** and **7d** ($\Delta E°$ = 0.29 V and 0.22 V, respectively) reveal a significant degree of metal–metal interaction when the 2,5-thiophene and 1,4-phenylene groups are present in the diethynylaryl spacer. The presence of a single wave in the CV of complex **7g** suggests that the intercalation of a 4,4′-biphenyldiyl spacer drastically reduces the electronic communication between the metal sites.

We have also measured by CV the CO-substituted precursors **6a**–**g**. Such compounds are unstable in redox cycles, as expected from the absence of the bidentate phosphane ligands, which guarantee the reversibility of the process for **7a**,**d**,**g**. As a consequence, the possibility of obtaining analogous information about their electrical behaviour and the metal–metal electronic interaction is compromised. The CVs of all (CO)-substituted complexes (except for **6c**, this compound is very weakly soluble in most of the commonly used solvents) are characterised in the anodic scan by two irreversible waves. The CV in Figure 2 (a) is representative of the anodic scan of complexes **6a**,**b** and **6d**–**g**; in Table 2 the values of $E_p$ are reported. The first waves correspond to the formation of $[Cp(CO)_2Fe–C\equiv C–Ar–C\equiv C–Fe(CO)_2Cp]^+$ in the range of $E_p$ = 0.84–1.15 V; potentials as high as expected on the basis of the electron-poor nature of the $CpFe(CO)_2$ moiety. Concerning the second oxidation waves, they cannot be definitely assigned to the formation of $[Cp(CO)_2Fe–C\equiv C–Ar–C\equiv C–Fe(CO)_2Cp]^{2+}$ because of the irreversible nature of the preceding peaks. It is easily seen from Figure 2 that the height of the second oxidation peak is noticeably smaller than that of the first oxidation peak. The CVs at higher scan rates up to 100 V s$^{-1}$ did not

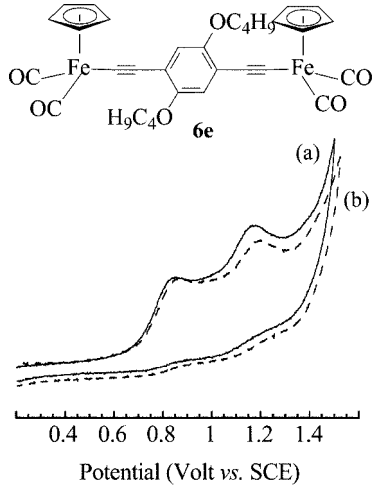


Figure 2. Cyclic voltammetric scan of 1 mM **6e** at a 0.5-mm diameter platinum disk electrode, $T$ = 20 °C. Solvent $CH_2Cl_2$/0.1 M $nBu_4NBF_4$; (a) solid line, scan rate of 0.1 V s$^{-1}$; (b) dashed line, scan rate 0.5 V.

 © 2006 Wiley-VCH Verlag GmbH & Co. KGaA, Weinheim 

allow unequivocal analysis of the variation of the intensity of the second waves because of the intrinsic slowness of the corresponding electron transfer. However, by increasing the scan rate from 0.1 to 0.5 $V s^{-1}$, the intensity of this wave, $i \times v^{-1/2}$ ($v$ = scan rate), decreases (Figure 2, b). One can suggest that the second oxidation process does not correspond to the oxidation of the radical cation of the neutral ethynylaryl binuclear complexes, but rather indicates the oxidation of other intermediates formed at the potential of the first wave. In this context, the separation between the two subsequent waves does not furnish sound information on the electronic interaction between the $CpFe(CO)_2$ units.

Table 2. Cyclic voltammetric data for $[Cp(CO)_2Fe–C\equiv C–Ar–C\equiv C–Fe(CO)_2Cp]^+[BF_4^-]$.[a]

| Complex | Ligand $L_2$ | Spacer Ar | R | $E_1^0(0/+1)$ [b] | $E_2^0(+1/+2)$ [b] |
|---|---|---|---|---|---|
| **6a** | $(CO)_2$ | | / | 0.84 | 1.33 |
| **6b** | $(CO)_2$ | | $C_4H_9$ | 0.90 | 1.21 |
| **6d** | $(CO)_2$ | | / | 0.89 | 1.31 |
| **6e** | $(CO)_2$ | | $C_4H_9$ | 0.85 | 1.18 |
| **6f** | $(CO)_2$ | | $C_8H_{17}$ | 0.87 | 1.14 |
| **6g** | $(CO)_2$ | 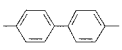 | / | 1.15 | 1.32 |

[a] Solvent $CH_2Cl_2$/0.2 M $nBu_4NBF_4$; potential scan rate 0.1 $V s^{-1}$ at a 0.5-mm diameter platinum disk electrode; $T$ = 20 °C. [b] Volts vs. SCE.

## IR, UV/Vis, NIR Analysis

The mixed-valence radical cation **7a**$^+$ was generated at room temperature in $CH_2Cl_2$ by chemical oxidation of a 3.4-mM wine-coloured solution of the neutral complex with 1 equiv. of decamethylferrocenium tetrafluoroborate, $[Fe(Cp^*)]_2[BF_4]$ {$Cp^* = C_5(CH_3)_5$}. The resulting solution was deep-blue coloured.

The IR analysis of **7a**$^+$ shows a single vibration mode for the C≡C stretches (1981 $cm^{-1}$), at an intermediate frequency between those found for **7a** (2031 $cm^{-1}$) and **7a**$^{2+}$ (1929 $cm^{-1}$). Averaging of the vibration modes of the triple bonds is expected in homobimetallic class III complexes containing a polyalkynyl bridge, as the unpaired electron is fully delocalised and the resulting structure is symmetrical.

Conversely, for the previously reported [Cp*(dppe) Fe–C≡C–Ar–C≡C–Fe(dppe)Cp*] analogue (Ar = 2,5-$C_4H_2S$), Lapinte and co-workers[7h] found that the two metal sites are not equivalent on the basis of the presence of two separate C≡C vibration modes in the IR spectrum (1983 and 1927 $cm^{-1}$), predicting that the unpaired electron is partially localised on the IR time scale ($10^{-13}$ s). Alternatively, in this latter case, the lower energy band could not be a consequence of a symmetry breaking associated with the localisation of the odd electron. Possibly this band could be due to a Fermi coupling or to a harmonic combination with another absorption mode at lower energy.[13] These results reveal that substitution of the Cp* with the Cp groups in the metal sites renders more efficient the electronic coupling between the metal groups, the difference presumably coming from the metal/carbon ratio in the frontier orbitals because of the presence of the methyl groups.

The NIR spectrum of **7a**$^+$ (Figure 3) displays a band with a maximum at 5640 $cm^{-1}$ and a shoulder at 6500 $cm^{-1}$.

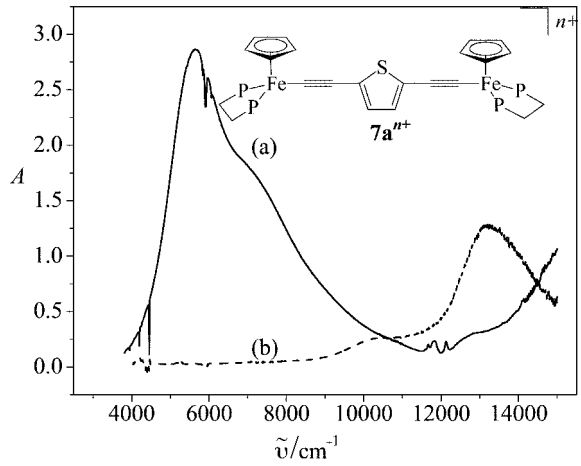


Figure 3. NIR spectra in $CH_2Cl_2$ at 20 °C of (a) 3.41 mM **7a**$^+$ and (b) **7a**$^{2+}$; optical path, $b$ = 0.100 cm.

The bands in this spectral region are considered diagnostic for an intervalence transfer process.[10] A detailed theoretical overview on the presence of two or more bands, as previously discussed for the closely related Cp* derivatives[7h] and other mixed-valence complexes,[8a] is given by Meyer et al.[11] As shown in Figure 4, the deconvolution of the spectrum has been satisfactorily obtained by considering three Gaussian components (5500, 6500, 7900 $cm^{-1}$) and the tail of the UV/Vis absorption. The effect of the polarity and ionic strength of the medium, which is generally employed to distinguish between class II and class III behaviour, was tested. The spectra of **7a**$^+$ in $CH_3CN$ ($\varepsilon$ = 37.5) and $CH_2Cl_2$ ($\varepsilon$ = 10.7) are almost identical, that is no variation of the band energy and shape was observed. Moreover, there is no dependence of the band energy and shape on ionic strength up to an electrolyte concentration of 0.2 M in $[nBu_4N][BF_4]$.[6i,7h,10] The analysis of the bands gives a bandwidth for the lower energy band **I** (Figure 4), $\Delta\tilde{\nu}_{1/2}$ = 1000 $cm^{-1}$, which is much below the theoretical value (3630 $cm^{-1}$) predicted by the Hush equation for a localised mixed-valence (class II) symmetric system,[14] $\Delta\tilde{\nu}_{1/2} = (2310\tilde{\nu}_c)^{1/2}$ $cm^{-1}$, where $\tilde{\nu}_c$ is the frequency of the maximum. By analogy with the data reported by Lapinte and co-workers on the Cp* analogues,[7h] band **I** of **7a**$^+$ could be an intervalence transfer (IT) transition and **7a**$^+$ is assigned to class III, at least on the timescale of the NIR spectroscopy ($10^{-14}$ s). The value of the $H_{ab}$ parameter,[14,15] calculated using the formula $H_{ab}$ ($cm^{-1}$) = $\tilde{\nu}_{max}/2$, is 2750 $cm^{-1}$.

 © 2006 Wiley-VCH Verlag GmbH & Co. KGaA, Weinheim 

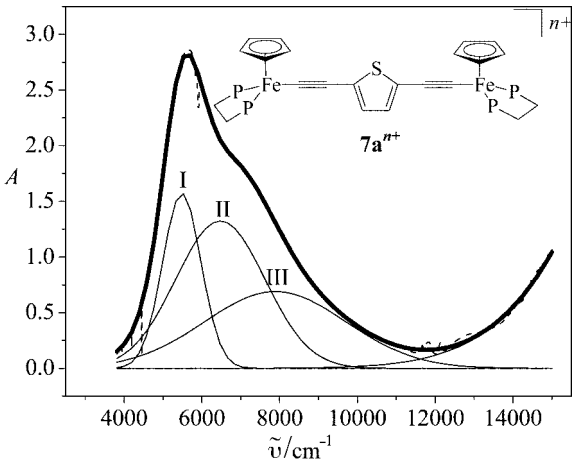


Figure 4. Gaussian deconvolution of the NIR bands of **7a**$^+$ (dashed line, experimental curve; solid lines, deconvoluted bands **I**, **II**, **III**; bold line, the sum of **I**, **II**, **III** components).

The addition either in $CH_3CN$ or $CH_2Cl_2$ of a second equivalent of ferrocenium, whose oxidation potential is sufficiently high to oxidise the second metal group forming a green solution of **7a**$^{2+}$, causes the disappearance of the bands of the monocation and the appearance of a less intense absorption at 13100 cm$^{-1}$ (Figure 3), likely because of a ligand-to-metal charge transfer (LMCT) transition. Under the same condition, we have found that $Cp_2Fe^+$ and $Cp^*_2Fe^+$ show bands at 13600 and 12900 cm$^{-1}$ respectively.

Also the oxidation of **7g** was monitored by NIR spectroscopy (Figure 5). The oxidation with 1 equiv. of ferrocenium gives a green solution whose spectrum in this region presents a very weak band at about 6000 cm$^{-1}$ and a more intense band at 12500 cm$^{-1}$, which could be assigned to the IT process of **7g**$^+$ and to an LMCT transition of the dication **7g**$^{2+}$, respectively, indicating that the mixed-valence state is not stable with respect to the disproportionation to the **7g** and **7g**$^{2+}$ states, in agreement with the presence of a single oxidation wave in the CV of complex **7g**.

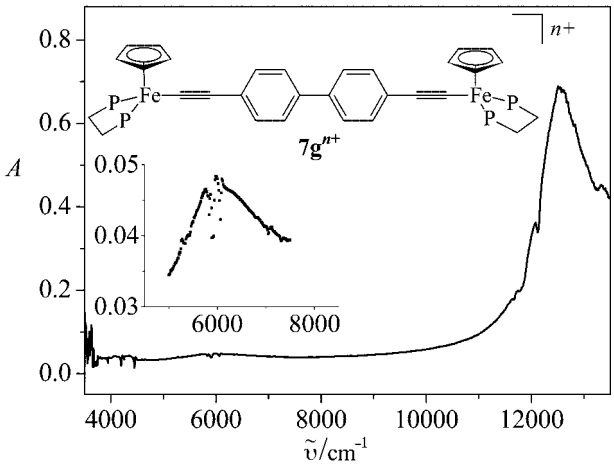


Figure 5. NIR spectra in $CH_2Cl_2$ at 20 °C of 3.4 mM **7g** oxidised with 1 equiv. of ferrocenium.

The couple **7a**/**7a**$^+$ was also studied in the UV/Vis spectroscopic region. The solution of **7a** in $CH_2Cl_2$ presents a very strong absorption at $\lambda$ = 410 nm, a wavelength quite similar to that reported for the Cp* analogue (418 nm), and attributed to a metal-to-ligand charge transfer (MLCT) transition.[7h] The spectrum of the deep-blue solution of **7a**$^+$ is totally different from its precursor **7a**. In fact, two new strong bands appears at 612 and 765 nm, which are responsible for the deep-blue colour of the mixed-valence species. They might be ascribed to LMCT transitions, similarly to what Lapinte and co-workers previously proposed for the absorptions at 588 and 653 nm of the Cp* mixed-valence analogous species.[7h] In that case, the intense MLCT transition observed for the neutral complex is still present in the spectrum of the monocation at a slightly red-shifted wavelength (423 nm), indicating that the characteristic absorptions of both $Fe^{II}$ and $Fe^{III}$ metal groups coexist (trapped valence, class II). On the contrary, in the UV/Vis spectrum of **7a**$^+$ the MLCT band, which is characteristic of a $Fe^{II}$ species, is absent, clearly showing that in **7a**$^+$ the valence is delocalised on the very fast UV/Vis timescale ($10^{-15}$ s).

## Density Functional Theory (DFT) Analysis

In order to gain insight on the factors ruling the extent of electronic communication and possibly to deconvolute the effects due to the structural parameters (i.e., metal–metal distance) from those related to the peculiar electronic features (i.e., the nature of the bridge and the nature of the ancillary ligands), we investigated systematically selected model complexes by DFT calculations.[16]

DFT optimisations were performed at B3LYP/LANL2DZ,6-31G** level of theory without any restriction in symmetry and tight conditions (see Computational Details) for neutral and oxidised $PH_3$ analogues of **7a**$^{0/+1}$, **7d**$^{0/+1}$ and **7g**$^{0/+1}$, which differ in the nature of the conjugated spacer. A *transoid* conformation of the metal centres is found to be more stable for $PH_3$-**7a** and $PH_3$-**7d**. Instead, in the fully optimised $PH_3$-**7g** the phenyl rings are oriented in distorted *cisoid* conformation.[17] It is worth noticing that the orientation of the metal fragments is such that the plane of the aromatic cores bisects the dihedral angle P–Fe–P. Consequently the conformation calculated for $PH_3$-**7g** is directly related to the torsion angle between the two phenyl rings. The calculated geometries of the neutral complexes are shown in Figure 6 (I–III). Significant interatomic distances and bond angles are reported in Table 3. In several cases the crystallographic data of structurally similar compounds are indicated and the good agreement with the analogous computed parameters enhances our confidence in the quality of the optimised geometries. A distinct alternation of single and multiple bonds is predicted in the three complexes. The average bond length of the alkyne units of the linkers is 1.232 Å, a value that nicely compares to the triple bond length in acetylene, that is 1.212 Å. The localised double bonds of the rings have an average value of 1.386 Å, which is also comparable to the ethylene double bond length (1.320 Å).

 © 2006 Wiley-VCH Verlag GmbH & Co. KGaA, Weinheim 

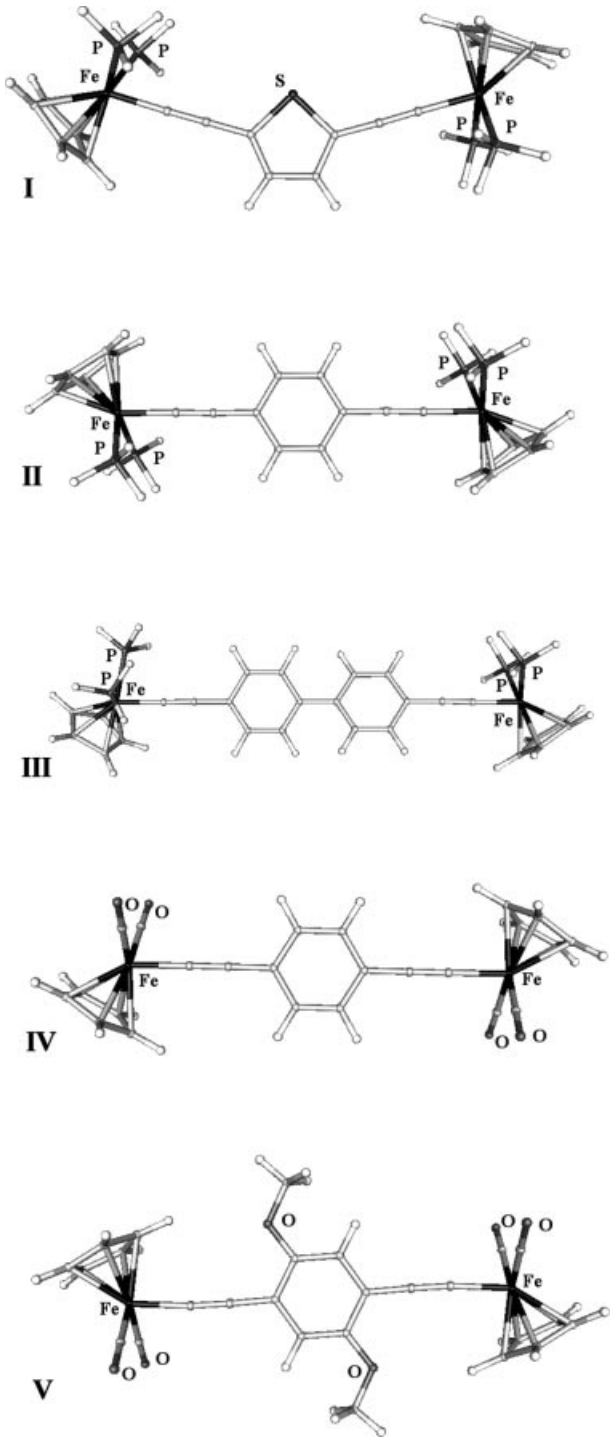


Figure 6. Calculated molecular structures of neutral model complexes: $PH_3$-**7a** (I), $PH_3$-**7d** (II), $PH_3$-**7g** (III), **6d** (IV) and $CH_3O$-**6e** (V). Heteroatoms are labelled for sake of clarity.

The ground-state electronic structures of $PH_3$-**7a**, $PH_3$-**7d** (the electronic structure of this complex was previously reported by Lapinte et al.[7o]) and $PH_3$-**7g** exhibit similar features.

Several authors have reported their theoretical studies on polyalkynyl- and alkynylaryl-bridged bimetallic complexes; thus the bonding between group 8 metal centres and acetylides is well documented.[18] A qualitative fragment analysis reveals that the cationic $[Cp(PH_3)_2Fe]^+$ fragments bond by strong σ-type interactions between unoccupied high-lying metallic frontier orbitals and low-lying occupied orbitals of the bridge (electron donation from the bridge to the metal fragments). Metal–carbon π-type interactions occur between occupied metal frontier orbitals and unoccupied carbon levels (weak π-type back-donation). The Kohn–Sham HOMOs are mainly localised on the metal centres and the ethynyl groups, and, to a less extent, on the aromatic rings. They result from out-of-phase combination of metal dπ orbitals and out-of-plane π orbitals of the linker; they exhibit *anti* bonding character between adjacent multiple bonds. The LUMO and LUMO+1 are almost degenerate and localised on the metal fragments. The topologies of Kohn–Sham frontier orbitals of $PH_3$-**7d** are shown in Figure 7.

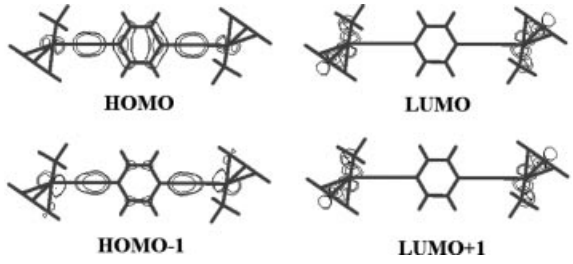


Figure 7. Top view of the contour plot of the frontier Kohn–Sham MOs of $PH_3$-**7d**. Contour values are ±0.035, ±0.04 and ±0.05 (e/bohr$^3$)$^{1/2}$.

A rather large energy gap separates the occupied and empty orbital sets in $PH_3$-**7a**, $PH_3$-**7d** and $PH_3$-**7g** (see Figure 8). The HOMO–LUMO gap in $PH_3$-**7d** is larger by about 0.2 eV than that of $PH_3$-**7a** (3.50 vs. 3.30 eV), and this is mainly due to the fact that the energy of HOMO of $PH_3$-**7d** is lower than that of HOMO of $PH_3$-**7a**. The HOMO–LUMO gap of $PH_3$-**7g** is 3.69 eV.

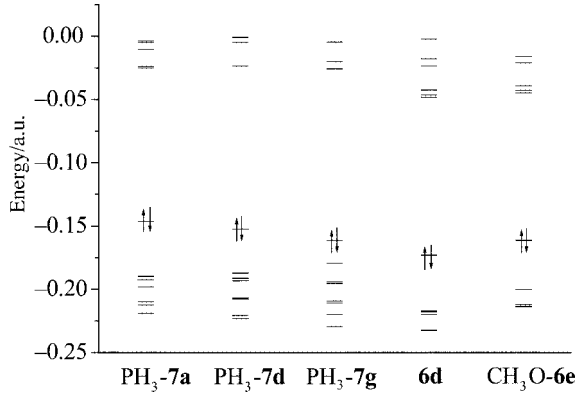


Figure 8. Frontier MOs for complexes $PH_3$-**7a**, $PH_3$-**7d**, $PH_3$-**7g**, **6d** and $CH_3O$-**6e**. HOMOs are indicated by double occupancy arrows; bold lines indicate almost degenerate energy levels.

Upon oxidation no significant conformational changes are observed. Both in $PH_3$-**7a**$^+$ and $PH_3$-**7d**$^+$ the metal units

 © 2006 Wiley-VCH Verlag GmbH & Co. KGaA, Weinheim 

Table 3. Selected interatomic distances [Å] and angles [°] for the neutral and oxidised complexes $PH_3$-**7a**$^{0/+1}$, $PH_3$-**7d**$^{0/+1}$ and $PH_3$-**7g**$^{0/+1}$.

| $PH_3$-**7a**$^{0/+1}$ | | $PH_3$-**7d**$^{0/+1}$ | | $PH_3$-**7g**$^{0/+1}$ | |
|---|---|---|---|---|---|
| Fe1–Fe2 | 11.315 | Fe1–Fe2 | 12.008 | Fe1–Fe2 | 16.342 |
| | *11.234* | | *11.853* | | *16.197* |
| Fe–P[a] | 2.206 | Fe–P[a] | 2.200 (2.187[b]) | Fe–P[a] | 2.203 |
| | *2.221* | | *2.221* | | *2.219* |
| Fe–$C_\alpha$ [a] | 1.915 | Fe–$C_\alpha$ | 1.918 | Fe–$C_\alpha$ | 1.917 |
| | *1.856* | | *1.860* | | *1.868* |
| Fe–Q[a] | 1.771 | Fe–Q[a] | 1.768 (1.738[b]) | Fe–Q[a] | 1.769 |
| | *1.773* | | *1.772* | | *1.773* |
| $C_\beta$–C[a,c] | 1.408 | $C_\beta$–C[a,c] | 1.426 (1.42[d]) | $C_\beta$–C[a,c] | 1.426 |
| | *1.378* | | *1.399* | | *1.405* |
| $C_\alpha \equiv C_\beta$ [a,e] | 1.233 | $C_\alpha \equiv C_\beta$ [a,e] | 1.232 (1.23[d]) | $C_\alpha \equiv C_\beta$ [a,e] | 1.231 |
| | *1.247* | | *1.244* | | *1.242* |
| | | | | 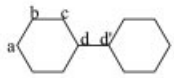 | |
| S–$C_a$ | 1.765 | $C_a$–$C_b$ | 1.412 | $C_a$–$C_b$ | 1.411 |
| | *1.766* | | *1.426* | | *1.421* |
| $C_a$–$C_b$ | 1.384 | $C_b$–$C_c$ | 1.388 | $C_b$–$C_c$ | 1.389 |
| | *1.386* | | *1.376* | | *1.380* |
| $C_b$–$C_c$ | 1.416 | $C_c$–$C_d$ | 1.412 | $C_c$–$C_d$ | 1.407 |
| | *1.413* | | *1.426* | | *1.418* |
| | | | | $C_d$–$C_{d'}$ | 1.481 |
| | | | | | *1.461* |
| | | | | θ[f] | 34.5 |
| | | | | | *24.2* |
| γ[g] | 178.2 | γ[g] | 180.0 | γ[g] | 33.8 |
| | *170.8* | | *180.0* | | *24.5* |

[a] Average values. [b] X-ray data of $(\eta^5\text{-}C_5Me_5)(\eta^2\text{-dppe})Fe\text{–}C\equiv C\text{–}C_6H_5$.[7j] [c] Single $C_\beta$–C bond in the ethynyl bridge. [d] Average crystallographic values of $[Fe(\eta^5\text{-}C_5Me_5)(\eta^2\text{-dppe})(C\equiv C)]_3(\mu\text{-}1,3,5\text{-}C_6H_3)$.[7o]. [e] Triple $C_\alpha \equiv C_\beta$ bond in the ethynyl bridge. [f] Torsion angle between the two rings, around the bond $C_d$–$C_{d'}$. [g] By indicating the centroids of the Cp rings as Q and Q′, a torsion angle $\gamma$ can be defined as Q–Fe1–Fe2–Q′, so that $\gamma = 0$ corresponds to a *cis* conformation of the metal termini and $\gamma = 180$ indicates a *trans* conformation.

are still oriented *trans* with respect to the bridging ligand, while in $PH_3$-**7g**$^+$ the *cisoid* conformation is still more stable. Upon going from the neutral to the corresponding oxidised species, the Fe–$C_\alpha$ bond and the bond between $C_\beta$ and the adjacent carbon atom of the aryl core shorten, while the alkyne bond $C_\alpha \equiv C_\beta$ elongates. The cation $PH_3$-**7a**$^+$ is generated by removal of one electron from the HOMO of the neutral parent compound. In $PH_3$-**7d**$^+$ and $PH_3$-**7g**$^+$ there is a rearrangement of the energy levels, because their HOMOs (118β and 138β) correspond to HOMOs–1 of the neutral parent complexes. The trend in stability, based on the HOMO–LUMO gap, is inverted in the series of cations, $PH_3$-**7a**$^+$ being the most stable, as expected on the basis of the lower resonance energy of the thiophenyl unit compared to that of the phenyl unit, because of the mixing of sulfur d orbitals with carbon pπ orbitals. The HOMOs of the cations $PH_3$-**7d**$^+$ and $PH_3$-**7g**$^+$ are characterised by an in-phase contribution of metal dπ orbitals disposed in an *anti* bonding fashion with respect to the out-of-plane pπ orbitals of the linker. While the extent of delocalisation is large in $PH_3$-**7a**$^+$, the contribution of p(π) carbon orbitals of the phenyls to HOMO is poorer both in $PH_3$-**7d**$^+$ and $PH_3$-**7g**$^+$. The Kohn–Sham HOMOs of $PH_3$-**7a**$^+$, $PH_3$-**7d**$^+$ and $PH_3$-**7g**$^+$ are shown in Figure 9.

The effect of replacing the ancillary ligands $PH_3$ with CO groups was investigated theoretically on the couple **6d**$^{0/+1}$ by direct comparison with $PH_3$-**7d**$^{0/+1}$. In addition, the influence of alkoxy groups on the phenyl core was explored by calculating the electronic structures of the methoxy analogues of **6e**$^{0/+1}$, to be compared with those of **6d**$^{0/+1}$. The full geometry optimisations of **6d**$^{0/+1}$ and of $CH_3O$-**6e**$^{0/+1}$ were calculated at B3LYP/LANL2DZ,6-31G** level of

 © 2006 Wiley-VCH Verlag GmbH & Co. KGaA, Weinheim 

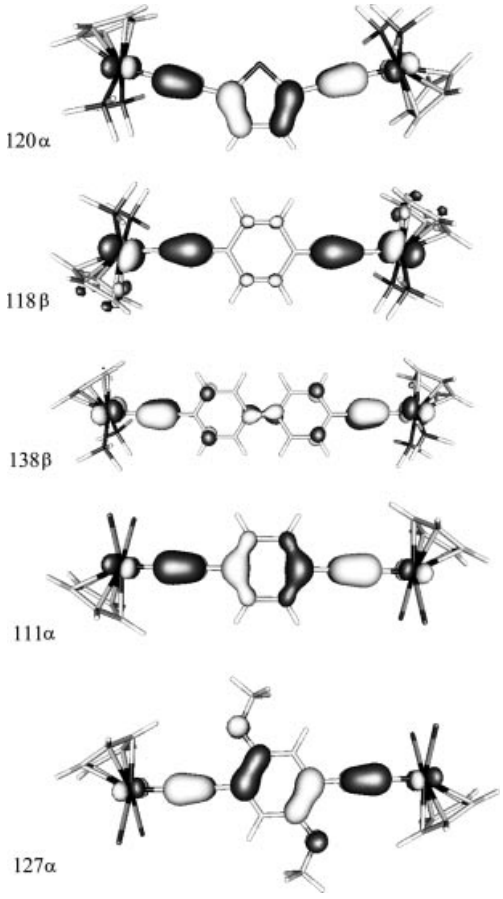


Figure 9. Kohn–Sham HOMOs of $PH_3$-**7a**$^+$, $PH_3$-**7d**$^+$, $PH_3$-**7g**$^+$, **6d**$^+$ and $CH_3O$-**6e**$^+$. Surface values are 0.04 $(e/bohr^3)^{1/2}$.

theory. The neutral species are shown in Figure 6 (IV, V) and their significant structural data are reported in Table 4. The full optimisations converged in both neutral complexes with a *trans* conformation of the metal groups. As for the $PH_3$ neutral derivatives, the calculations predict a distinct alternation of adjacent single and multiple bonds (see Table 4). In particular, a contraction of the alkyne bond length $C_\alpha{\equiv}C_\beta$ is observed compared to the $PH_3$-substituted species, which is a consequence of the electron density loss of the metal (1.225 vs. 1.232 Å).

Another effect of replacing the phosphanes with carbonyl groups is a reduction in energy of the frontier orbitals, as expected on the basis of the electron-poorer nature of the metal centres in the carbonylated complexes due to backbonding from the occupied metal orbitals to the empty π* of the carbonyl ligands (Figure 8). The HOMOs of **6d** and $CH_3O$-**6e**, resulting from out-of-phase combination of metal dπ orbitals and out-of-plane π orbitals of the linker, are strongly localised on the bridge, with minor metal contribution, and show *anti* bonding character between adjacent multiple bonds. The LUMOs and LUMOs+1 are almost degenerate and localised on the end-capping termini. The HOMO–LUMO gap of $CH_3O$-**6e** (3.17 eV) is smaller that that of **6d** (3.39 eV) and this is mainly the result of the destabilisation of the HOMO of the former complex, caused by the presence of the methoxy substituents (Figure 8). The variation in bond lengths occurring upon oxidation is reported in Table 4. No rearrangements of the frontier electronic levels are observed: the electron is removed from the HOMO of the neutral parent compound, as found for $PH_3$-**7a**.

Table 4. Selected interatomic distances [Å] and angles [°] for the neutral and oxidised complexes **6d**$^{0/+1}$ and $CH_3O$-**6e**$^{0/+1}$.

| | **6d** | **6d**$^+$ | | $CH_3O$-**6e** | $CH_3O$-**6e**$^+$ |
|---|---|---|---|---|---|
| Fe1–Fe2 | 11.970 | 11.851 | Fe1–Fe2 | 11.930 | 11.858 |
| Fe–$C_{CO}$[a] | 1.770 | 1.786 | Fe–$C_{CO}$[b] | 1.768 | 1.783 |
| Fe–$C_\alpha$[a] | 1.911 | 1.873 | Fe–$C_\alpha$[a] | 1.906 | 1.878 |
| Fe–Q[a] | 1.778 | 1.775 | Fe–Q[b] | 1.778 | 1.774 |
| $C_\beta$–C[a,b] | 1.426 | 1.395 | $C_\beta$–C[a,b] | 1.422 | 1.394 |
| $C_\alpha{\equiv}C_\beta$[a,c] | 1.225 | 1.240 | $C_\alpha{\equiv}C_\beta$[a,c] | 1.224 | 1.236 |
| | | | | 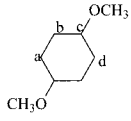 | |
| $C_a$–$C_b$ | 1.411 | 1.429 | O–$C_c$[a] | 1.372 | 1.344 |
| $C_b$–$C_c$ | 1.388 | 1.373 | $C_a$–$C_b$ | 1.416 | 1.448 |
| $C_c$–$C_d$ | 1.411 | 1.429 | $C_b$–$C_c$ | 1.392 | 1.384 |
| | | | $C_c$–$C_d$ | 1.409 | 1.414 |
| γ[d] | 121.9 | 174.8 | γ[d] | 174.9 | 179.5 |

[a] Average values. [b] Single $C_\beta$–C bond in the ethynyl bridge. [c] Triple $C_\alpha{\equiv}C_\beta$ bond in the ethynyl bridge. [d] By indicating the centroids of the Cp rings as Q and Q′, a torsion angle $\gamma$ can be defined as Q–Fe1–Fe2–Q′, so that $\gamma = 0$ corresponds to a *cis* conformation of the metal termini and $\gamma = 180$ indicates a *trans* conformation.

 © 2006 Wiley-VCH Verlag GmbH & Co. KGaA, Weinheim 

Table 5. Mulliken spin densities.

| | $PH_3$-**7a**$^+$ | $PH_3$-**7d**$^+$ | **6d**$^+$ | $PH_3$-**7g**$^+$ | $CH_3O$-**6e**$^+$ |
|---|---|---|---|---|---|
| Fe1 | 0.197 | 0.244 | 0.102 | 0.219 | 0.065 |
| Fe2 | 0.192 | 0.244 | 0.102 | 0.218 | 0.065 |
| $C_{\alpha 1}$ [a] | 0.144 | 0.106 | 0.212 | 0.079 | 0.211 |
| $C_{\beta 1}$ [b] | 0.027 | 0.073 | 0.033 | 0.076 | –0.001 |
| $C_{\alpha 2}$ [a] | 0.143 | 0.106 | 0.212 | 0.079 | 0.211 |
| $C_{\beta 2}$ [b] | 0.030 | 0.073 | 0.033 | 0.076 | –0.001 |
| S | – | – | – | – | – |
| P [c] | 0.046 | –0.002 | – | –0.002 | – |
| $C_{CO}$ | –0.0008 | – | –0.005 | – | –0.004 |
| $O_{CO}$ | – | – | –0.006 | – | –0.005 |
| $O_{CH_3O}$ | – | – | – | – | 0.045 |
| | – | | | | |
| | | 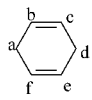 | 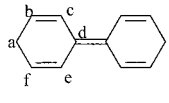 | 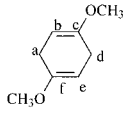 | |
| $C_a$ [c] | 0.124 | 0.073 | 0.129 | 0.045 | 0.167 |
| $C_b$ [c] | 0.053 | 0.016 | 0.021 | 0.022 | 0.096 |
| $C_c$ [c] | 0.057 | 0.018 | 0.018 | 0.006 | –0.076 |
| $C_d$ [c] | 0.126 | 0.073 | 0.129 | 0.057 | 0.167 |
| $C_e$ [c] | – | 0.016 | 0.021 | 0.005 | 0.096 |
| $C_f$ [c] | – | 0.018 | 0.018 | 0.022 | –0.076 |

[a] Alkyne carbon atom linked to iron. [b] Alkyne carbon atom linked to the aromatic ring. [c] Carbon atom of the aromatic core; the labelling is reported in the schemes above.

The extent of delocalisation of the unpaired electron in the radical cations was estimated on the basis of Mulliken spin densities, which are reported in Table 5.

The distribution of the spin density is symmetric in all the radical cations, although symmetry was not taken into account in the calculations. The spin density is well delocalised on the iron centres and on the $C_\alpha$ atoms in $PH_3$-**7a**$^+$ and in $PH_3$-**7d**$^+$. In $PH_3$-**7a**$^+$ the spin density is distributed also on the carbon atoms adjacent to S in the thiophenyl core, while in both $PH_3$-**7d**$^+$ and $PH_3$-**7g**$^+$ the spin density values on the phenyl rings are rather small. In **6d**$^+$ and $CH_3O$-**6e**$^+$ the significant decrease of the spin density on the metals as compared to $PH_3$-**7d**$^+$ is accompanied by its increase on the two α carbons and on two carbon atoms of the rings (see Table 5).

The extent of delocalisation is in favour of a stronger metal–metal interaction,[7m] and decreases in the $PH_3$ derivatives in the order $PH_3$-**7a**$^+$ > $PH_3$-**7d**$^+$ > $PH_3$-**7g**$^+$, in agreement with the trend based on the experiments.

To investigate the presence and the nature of the NIR absorptions of these model di-iron cations we have carried out time-dependent density functional theory (TDDFT) calculations,[19] which have been recently employed with success for mixed-valence organometallic species.[20] The level of theory is B3LYP/LANL2DZ,6-31+G* (see Computational Details). The lowest excitation energy computed for $PH_3$-**7a**$^+$ in the NIR region is 8560 cm$^{-1}$ (0.47), with an error comparable to those reported in a similar analysis.[20a] It corresponds to the lowest energy deconvoluted experimental absorption at 5500 cm$^{-1}$. The detailed composition is shown in Table 6. Its most relevant components involve the couples of levels 120α–121α and 119β–120β, that is the highest occupied α/β levels and the lowest unoccupied α/β levels respectively (pictures of the couples of MOs involved in the calculated excitation energies are given in the Supporting Information), which have significant contributions from d orbitals of both iron centres and p(π) carbon orbitals of the bridge.

In the case of $PH_3$-**7d**$^+$, an absorption is computed at 6859 cm$^{-1}$ ($f$ = 0.62) corresponding mainly to the HOMO (118β)–LUMO (119β) transition. The experimental spectrum of the Cp* analogue of **7d**$^+$ exhibits a single band at 4960 cm$^{-1}$.[7l] Also in this case the couple of orbitals involved in the monoelectronic transition are delocalised all over the molecular backbone.

By TDDFT calculations we also found an allowed low-energy absorption for $PH_3$-**7g**$^+$ at 5216 cm$^{-1}$ ($f$ = 0.83) assigned mainly to HOMO (138β)–LUMO (139β) and HOMO–1 (137β)–LUMO (139β) transitions. This excitation energy in the NIR region corresponds to the weak

 © 2006 Wiley-VCH Verlag GmbH & Co. KGaA, Weinheim 

Table 6. NIR vertical excitation energies.

| | $PH_3$-**7a**$^+$ | $PH_3$-**7d**$^+$ | $PH_3$-**7g**$^+$ | **6d**$^+$ | $CH_3O$-**6e**$^+$ |
|---|---|---|---|---|---|
| HOMO–LUMO gap | 1.525 eV[a] | 1.452 eV[b] | 0.886 eV[c] | 1.474 eV[d] | 1.451 eV[e] |
| Excitation energy | | | | | |
| [nm] | 1168 | 1458 | 1917 | 871 | 809 |
| [$cm^{-1}$] | (8562) | (6859) | (5216) | (11481) | (12361) |
| Oscillator strength | 0.47 | 0.62 | 0.83 | 0.52 | 0.39 |
| Composition[f] | 120α → 121α | 119α → 122α | 139α → 140α | 111α → 112α | 126α → 128α |
| | (0.296) | (0.258) | (0.239) | (0.277) | (0.101) |
| | 108β → 120β | 107β → 119β | 132β → 139β | 111α → 116α | 127α → 128α |
| | (–0.104) | (–0.107) | (0.200) | (0.133) | (–0.300) |
| | 116β → 123β | 111β → 119β | 135β → 140β | 108β → 111β | 126β → 127β |
| | (–0.161) | (–0.160) | (–0.149) | (–0.174) | (0.935) |
| | 119β → 120β | 115β → 122β | 138β → 139β | 110β → 111β | |
| | (1.006) | (–0.171) | (0.865) | (0.904) | |
| | | 118β → 119β | | | |
| | | (0.996) | | | |

[a] The HOMO is 120α, the LUMO is 120β. [b] The HOMO is 118β, the LUMO is 119β. [c] The HOMO is 138β, the LUMO is 139β. [d] The HOMO is 111α, the LUMO is 111β. [e] The HOMO is 127α, the LUMO is 127β. [f] The most relevant monoelectronic transitions are indicated; values in brackets are the CI coefficients.

absorption experimentally detected for **7g**$^+$ around 6000 $cm^{-1}$. It should be noted that in $PH_3$-**7d**$^+$ and $PH_3$-**7g**$^+$ the strongest NIR absorptions have an important contribution from the HOMO–LUMO transition and are thus shifted toward lower frequencies, as compared to that of $PH_3$-**7a**$^+$. Most importantly, no charge transfer character between the metal termini is observed, as reported recently for other organometallic binuclear systems,[20a] but these NIR absorptions are better interpreted as allowed electronic transitions between filled and empty delocalised frontier levels. The oscillator strengths increase with the length of the alkynylaryl bridge, as already noticed in previous theoretical studies.[20c,20d]

TDDFT calculations on the carbonylated model cations **6d**$^+$ and $CH_3O$-**6e**$^+$ do not reveal any low-energy transition. In the former an absorption is predicted at 11481 $cm^{-1}$ ($f$ = 0.52), while in the latter the calculated excitation energy is 12361 $cm^{-1}$ ($f$ = 0.39). In both cases the transitions involve the highest occupied α/β levels and the lowest unoccupied α/β levels, as for $PH_3$-**6a**$^+$. Also in these species no metal–metal charge transfer character is observed.

## Conclusions

The combination of the EOP synthetic protocol and the Pd-catalysed metal–carbon bond formation procedure offers suitable synthetic access to a large family of bimetallic complexes (**6a**–**g**) characterised by the presence of different conjugated (bis-ethynyl)aromatic spacers bridging two iron centres. Our EOP synthetic route represents a complementary approach to alkynylaryl-bridged bimetallic complexes with respect to Lapinte's method.[7q] In our procedure the straightforward formation of the bis(tributylethynyltin)aromatic derivatives **3a**–**g** and their direct in situ use to form complexes **6a**–**g** prevent the formation and isolation of the corresponding bis(trimethylsilylethynyl) derivatives as required by Lapinte's procedure.[7u]

Although substitution of carbonyls with dppe is conveniently performed only in some cases, the dppe derivatives of such organometallic assembly (**7a**,**d**,**g**) proved to be a useful manifold to study the electrical and optical properties of the conjugated spacer and the interaction between the metal centres, and thus, in perspective, the properties of polymeric materials incorporating such building blocks in the backbone.

On the basis of the electrochemical and optical properties of complexes **7a**,**d**,**g**, a correlation between the extent of the metal–metal electronic interaction and the nature of the diethynylaryl bridge can be pointed out. In fact, the $\Delta E°$ separations between the two subsequent reversible waves increase in the order **7a** > **7d** > **7g**, as does the efficiency of the metal–metal electronic coupling. The previously reported [Cp*(dppe)Fe–C≡C–Ar–C≡C–Fe(dppe)-Cp*] analogue (Ar = 2,5-$C_4H_2S$) displayed a somewhat more pronounced $\Delta E°$ (0.35 V) than **7a**. This indicates a higher thermodynamic stability of the corresponding monocationic intermediate with respect to disproportionation, probably due to the electron-donating effect of the methyl substituents of Cp*, which stabilise the positive charge on the metal groups. A similar trend can be established on the basis of the spectroscopic results for the mixed-valence species **7a**$^+$, **7d**$^+$ and **7g**$^+$. In the case of **7a**$^+$, the IR data, the shape and the solvent effect of the NIR band and the UV/Vis spectrum indicate unambiguously that the cation is a delocalised (class III) mixed-valence system on the timescale of $10^{-15}$ s. The comparison with the analogous 2,5-bis{[$\eta^5$-$C_5(CH_3)_5$]Fe($\eta^2$-dppe)($\sigma^1$-C≡C)}-$C_4H_2S$, which is valence-trapped on the IR timescale, highlights the important effect of replacing Cp* with Cp in the metal termini. On the basis of its electrochemical behaviour and the spectroscopic data reported in the literature, **7d**$^+$ can also be assigned to class III. The analysis of **7g**$^+$ is less clear-cut, because of the low stability of this mixed-valence cation in solution. $PH_3$-**7g**$^+$ has a certain extent of delocalisation, but the metal–metal interaction is hampered with respect to $PH_3$-**7d**$^+$ because of the increase of the distance and the greater flexibility of the bridge. DFT calculations support the experimental findings and allow deconvolution

 © 2006 Wiley-VCH Verlag GmbH & Co. KGaA, Weinheim 

of geometric effects, such as the intermetallic distance ($PH_3$-**7d**$^+$ vs. $PH_3$-**7g**$^+$), from electronic effects, that is the different nature of the incorporated aryl core ($PH_3$-**7a**$^+$ vs. $PH_3$-**7d**$^+$), on the extent of electronic delocalisation. On the basis of the computational results on the carbonylated model cation **6d**$^+$ a less efficient electron delocalisation is observed with respect to the corresponding $PH_3$ analogue (**6d**$^+$ vs. **7d**$^+$). In addition, in the presence of the methoxy substituents on the aryl core in $CH_3O$-**6e**$^+$ the spin density decreases further on the iron centres and moves to the phenyl ring ($CH_3O$-**6e**$^+$ vs. **6d**$^+$).

TDDFT calculations predict that NIR absorptions, which are a sort of fingerprint of mixed-valence species, occur only in $PH_3$-**7a**$^+$, $PH_3$-**7d**$^+$ and $PH_3$-**7g**$^+$, and that they do not exhibit dominant charge transfer character between the metal termini, but are better described as allowed electronic transitions between filled and empty frontier levels.

Finally the efficiency of the dialkynyl–thiophenyl unit in conveying electron information is further recognised and associated to the large extent of delocalisation in the radical cations bearing this aryl core.[6l,6m] Work is in progress to employ this functional unit, intercalated also by different metal centres, in larger molecular wires.

## Experimental Section

**General:** All manipulations were carried out under argon using Schlenk techniques. Dioxane and benzene were dried and distilled respectively over Na and Na/K alloy, and argon-saturated prior to use. The following chemicals were prepared according to the published procedure: 1,4-diiodo-2,5-dioctyloxybenzene,[4] 1,4-diiodo-2,5-dibutoxybenzene,[4] 2,5-diiodo-3-hexadecylthiophene[4] and 2,5-diiodo-3-butylthiophene.[4] Other chemicals were used as received. Routine NMR spectra were recorded with a AC-300 P Bruker spectrometer (300, 121 and 75 MHz respectively for $^1H$, $^{31}P$, $^{13}C$). Chemical shifts are given in parts per million (ppm) relative to tetramethylsilane (TMS) for $^1H$ NMR and $^{13}C$ NMR spectra and 85% $H_3PO_4$ for $^{31}P$ NMR spectroscopy. Cyclic voltammograms [except the ones of complexes **6d**,**g** and **7a**,**d**, performed by Dr. Mikhail G. Peterleitner of Nesmeyanov Institute of Organoelement Compounds (INEOS), Russian Academy of Science, Moscow] were recorded with an AMEL 500 potentiostat. Transmittance FTIR spectra were recorded with a Nicolet FT 510 instrument in the solvent subtraction mode, using a 0.1-mm $CaF_2$ cell. NIR spectra were recorded with a Bruker Equinox55 FTIR spectrometer equipped with an optical fibre for NIR measurements on liquids. Elemental analyses were performed by the Servizio Microanalisi of the Dipartimento di Chimica of Università di Roma "La Sapienza".

**2,5-Bis[($\eta^5$-$C_5H_5$)Fe(CO)$_2$($\sigma^1$-C≡C)]C$_4$H$_2$S (6a). Step 1:** In a Schlenk tube $Bu_3SnC{\equiv}CH$ (0.962 g, 3.05 mmol), 2,5-diiodothiophene (0.500 g, 1.49 mmol) and $Pd(PPh_3)_4$ (40 mg, 0.035 mmol) were stirred in dioxane (30 mL) at 110 °C for 20 min.

**Step 2:** The brown solution was then cooled (ca. 0 °C) and LDA (1.8 mL, 2 M) was slowly added.

**Step 3:** This mixture was left for about 30 min at room temperature, ($\eta^5$-$C_5H_5$)Fe(CO)$_2$I (0.914 g, 3.01 mmol) was added and the resulting dark solution was heated (50 °C) for 7 h, then filtered through a thin Celite layer and dried under vacuum. The residue was dissolved in a small amount of $CH_2Cl_2$ and then precipitated with pentane. After filtration and repeated washings with pentane, a dark brown powder (0.533 g, 74% yield) was obtained. IR ($CH_2Cl_2$): 2095 (w) $\tilde{\nu}_{C\equiv C}$, 2044 (s), 2000 (s) $\tilde{\nu}_{CO}$ cm$^{-1}$. $^1H$ NMR ($CDCl_3$): $\delta$ = 6.60 (2 H, thioph.), 5.02 (10 H, Cp) ppm. Spectroscopic data correspond to the reported data.[4]

**2,5-Bis[($\eta^5$-$C_5H_5$)Fe(CO)$_2$($\sigma^1$-C≡C)]-3-($C_4H_9$)-C$_4$HS (6b):** This complex was prepared as described for **6a**, from $Bu_3SnC{\equiv}CH$ (0.837 g, 2.55 mmol), 2,5-diiodo-3-butylthiophene (0.500 g, 1.28 mmol) and $Pd(PPh_3)_4$ (30 mg, 0.03 mmol) in dioxane (30 mL), LDA (1.5 mL, 2 M) and ($\eta^5$-$C_5H_5$)Fe(CO)$_2$I (0.799 g, 2.55 mmol). Step 3 was accomplished by stirring at 70 °C for 10 h. After repeated precipitation cycles from $CH_2Cl_2$/pentane the product (0.352 g, 51% yield) was recovered as described for **6a** as a coffee-brown powder. IR ($CH_2Cl_2$): 2095 (w) $\tilde{\nu}_{C\equiv C}$, 2042 (s), 1997 (s) $\tilde{\nu}_{CO}$ cm$^{-1}$. $^1H$ NMR ($C_6D_6$): $\delta$ = 7.73 (thioph.), 4.04 (Cp), 2.85, 1.70–0.80 ($C_4H_9$) ppm. $^{13}C$ NMR ([$D_7$]DMF): $\delta$ = 213.2, 141.9, 131.3, 128.4, 107.3, 89.5, 85.9, 71.7, 66.3, 31.8, 21.7, 13.1 ppm. $C_{26}H_{20}Fe_2O_4S$ (540.20): calcd. C 57.81, H 3.73; found C 57.60, H 3.83.

**2,5-Bis[($\eta^5$-$C_5H_5$)Fe(CO)$_2$($\sigma^1$-C≡C)]-3-($C_{16}H_{33}$)-C$_4$HS (6c):** This complex was prepared as described for **6a**, from $Bu_3SnC{\equiv}CH$ (0.586 g, 1.79 mmol), 2,5-diiodo-3-hexadecylthiophene (0.500 g, 0.89 mmol) and $Pd(PPh_3)_4$ (16 mg, 0.01 mmol) in dioxane (30 mL), LDA (1.1 mL, 2 M) and ($\eta^5$-$C_5H_5$)Fe(CO)$_2$I (0.559 g, 1.78 mmol). Step 3 was accomplished by stirring at 65 °C for 23 h. After repeated precipitation cycles from $CH_2Cl_2$/methanol the product (0.09 g, 15% yield) was recovered as described for **6a** as a coffee-brown powder. IR ($CH_2Cl_2$): 2096 (w) $\tilde{\nu}_{C\equiv C}$, 2042 (s), 1997 (s) $\tilde{\nu}_{CO}$ cm$^{-1}$. $^1H$ NMR ($C_6D_6$): $\delta$ = 7.52 (thioph.), 4.08 (Cp), 1.70–0.80 ($C_{16}H_{33}$) ppm. $^{13}C$ NMR ($CDCl_3$): $\delta$ = 249.6, 230.2, 158.8, 121.6, 90.6, 85.3, 31.9, 29.7, 29.4, 22.7, 22.3, 14.1 ppm. $C_{38}H_{44}Fe_2O_4S$ (708.52): calcd. C 64.42, H 6.26; found C 64.30, H 6.15.

**1,4-Bis[($\eta^5$-$C_5H_5$)Fe(CO)$_2$($\sigma^1$-C≡C)]C$_6$H$_4$ (6d):** This complex was prepared as described for **6a**, from $Bu_3SnC{\equiv}CH$ (0.985 g, 3.00 mmol), 1,4-diiodobenzene (0.500 g, 1.5 mmol) and $Pd(PPh_3)_4$ (35 mg, 0.03 mmol) in dioxane (25 mL), LDA (1.8 mL, 2 M) and ($\eta^5$-$C_5H_5$)Fe(CO)$_2$I (0.940 g, 3.00 mmol). Step 3 was accomplished by stirring at 60 °C for 6 h. After repeated precipitation cycles from $CH_2Cl_2$/pentane the product (0.406 g, 57% yield) was recovered as described for **6a** as a dark yellow powder. IR ($CH_2Cl_2$): 2107 (w) $\tilde{\nu}_{C\equiv C}$, 2043 (s), 1996 (s) $\tilde{\nu}_{CO}$ cm$^{-1}$. $^1H$ NMR ($C_6D_6$): $\delta$ = 7.56 (benzene), 4.06 (Cp) ppm. $^{13}C$ NMR ([$D_7$]DMF): $\delta$ = 213.6, 131.7–124.9, 115.6, 91.1, 85.9 ppm. $C_{24}H_{14}Fe_2O_4$ (478.07): calcd. C 60.30, H 2.95; found C 60.53, H 2.91.

**1,4-Bis[($\eta^5$-$C_5H_5$)Fe(CO)$_2$($\sigma^1$-C≡C)]-2,5-bis($OC_4H_9$)C$_6$H$_2$ (6e):** This complex was prepared as described for **6a**, from $Bu_3SnC{\equiv}CH$ (0.692 g, 2.11 mmol), 1,4-diiodo-2,5-dibutoxybenzene (0.500 g, 1.05 mmol) and $Pd(PPh_3)_4$ (25 mg, 0.02 mmol) in dioxane (25 mL), LDA (1.3 mL, 2 M) and ($\eta^5$-$C_5H_5$)Fe(CO)$_2$I (0.661 g, 2.11 mmol). Step 3 was accomplished by stirring at 50 °C for 7 h. After repeated precipitation cycles from $CH_2Cl_2$/hexane the product (0.320 g, 49% yield) was recovered as described for **6a** as a coffee-brown powder. IR ($CH_2Cl_2$): 2106 (w) $\tilde{\nu}_{C\equiv C}$, 2041 (s), 1994 (s) $\tilde{\nu}_{CO}$ cm$^{-1}$. $^1H$ NMR ($C_6D_6$): $\delta$ = 7.72 (benzene), 4.19 (Cp), 3.75 ($OCH_2$), 1.62–0.92 [$OCH_2(CH_2)_2CH_3$] ppm. $^{13}C$ NMR ([$D_7$]DMF): $\delta$ = 213.6, 130.4, 116.8, 86.5, 68.0, 19.1, 13.3 ppm. $C_{32}H_{30}Fe_2O_6$ (622.28): calcd. C 61.77, H 4.86; found C 61.90, H 4.81.

**1,4-Bis[($\eta^5$-$C_5H_5$)Fe(CO)$_2$($\sigma^1$-C≡C)]-2,5-bis($OC_8H_{17}$)C$_6$H$_2$ (6f):** This complex was prepared as described for **6a**, from $Bu_3SnC{\equiv}CH$ (0.896 g, 2.73 mmol), 1,4-diiodo-2,5-dioctyloxybenzene (0.800 g, 1.36 mmol) and $Pd(PPh_3)_4$ (32 mg, 0.03 mmol) in dioxane (25 mL),

 © 2006 Wiley-VCH Verlag GmbH & Co. KGaA, Weinheim 

LDA (1.7 mL, 2 M) and ($\eta^5$-$C_5H_5$)Fe(CO)$_2$I (0.855 g, 2.73 mmol). Step 3 was accomplished by stirring at 80 °C for 12 h. After repeated precipitation cycles from $CH_2Cl_2$/methanol the product (0.521 g, 52% yield) was recovered as described for **6a** as a brown powder. IR ($CH_2Cl_2$): 2106 (w) $\tilde{\nu}_{C\equiv C}$, 2042 (s), 1996 (s) $\tilde{\nu}_{CO}$ cm$^{-1}$. $^1$H NMR ($C_6D_6$): $\delta$ = 4.20 (Cp), 3.70 (OC$H_2$), 1.50–0.90 [OCH$_2$(C$H_2$)$_6$C$H_3$] ppm. $^{13}$C NMR ($CDCl_3$): $\delta$ = 212.5, 154.0–110.0, 85.4, 69.2, 29.4–22.6, 14.1 ppm. $C_{40}H_{46}Fe_2O_6$ (734.50): calcd. C 65.41, H 6.31; found C 65.32, H 6.27.

**4,4′-Bis[($\eta^5$-$C_5H_5$)Fe(CO)$_2$($\sigma^1$-C≡C)]($C_6H_4$)$_2$ (6g):** This complex was prepared as described for **6a**, from $Bu_3SnC{\equiv}CH$ (1.031 g, 3.14 mmol), 4,4′-dibromobiphenyl (0.500 g, 1.57 mmol) and $Pd(PPh_3)_4$ (37 mg, 0.03 mmol) in dioxane (30 mL), LDA (1.9 mL, 2 M) and ($\eta^5$-$C_5H_5$)Fe(CO)$_2$I (0.984 g, 3.14 mmol). Step 3 was accomplished by stirring at 80 °C for 9 h. After repeated precipitation cycles from $CH_2Cl_2$/pentane the product (0.728 g, 84% yield) was recovered as described for **6a** as a dark orange powder. IR ($CH_2Cl_2$): 2106 (w) $\tilde{\nu}_{C\equiv C}$, 2041 (s), 1994 (s) $\tilde{\nu}_{CO}$ cm$^{-1}$. $^1$H NMR ($C_6D_6$): $\delta$ = 7.66–7.01 (biph), 4.10 (Cp) ppm. $^{13}$C NMR ([$D_7$]-DMF): $\delta$ = 213.6, 136.2–125.5, 115.3, 92.5, 86.0 ppm. $C_{30}H_{18}Fe_2O_4$ (554.16): calcd. C 65.02, H 3.27; found C 65.15, H 3.29.

**2,5-Bis[($\eta^5$-$C_5H_5$)Fe(dppe)($\sigma^1$-C≡C)]$C_4H_2S$ (7a):** A rust colour mixture of 2,5-bis[($\eta^5$-$C_5H_5$)Fe(CO)$_2$($\sigma^1$-C≡C)]$C_4H_2S$ (**6a**) (0.247 g, 0.51 mmol) and 1,2-bis(diphenylphosphanyl)ethane (0.406 g, 1.02 mmol) in benzene (200 mL) was exposed to ultraviolet irradiation for 2 h at room temperature. The dark brown reaction mixture was then filtered and dried under vacuum. The black residue was washed with hexane, dissolved in toluene and precipitated with hexane. This treatment was repeated three times to isolate a crystalline black powder (0.137 g, 23% yield). IR ($CH_2Cl_2$): 2052 (w) $\tilde{\nu}_{C\equiv C}$ cm$^{-1}$. $^1$H NMR ($C_6D_6$): $\delta$ = 7.96, 740–6.90, 4.21 (Cp), 2.50–0.40 ppm. $^{13}$C NMR ($C_6D_6$): $\delta$ = 142.7–128.0, 114.2, 99.7, 81.7, 30.2, 28.6 ppm. $^{31}$P NMR ($C_6D_6$): $\delta$ = 106.9 ppm. $C_{70}H_{60}Fe_2P_4S$ (1168.90): calcd. C 71.93, H 5.17; found C 72.05, H 5.09.

**1,4-Bis[($\eta^5$-$C_5H_5$)Fe(dppe)($\sigma^1$-C≡C)]$C_6H_4$ (7d):** A yellow-orange mixture of 1,4-bis[($\eta^5$-$C_5H_5$)Fe(CO)$_2$($\sigma^1$-C≡C)]$C_6H_4$ (**6d**) (0.200 g, 0.42 mmol) and 1,2-bis(diphenylphosphanyl)ethane (0.345 g, 0.42 mmol) in benzene (200 mL) was exposed to ultraviolet irradiation for 3.5 h at room temperature. The dark red reaction mixture was then filtered and dried under vacuum. The residue was washed with hexane, dissolved in toluene and precipitated with hexane. This treatment was repeated ten times, and the pure complex (0.056 g, 12% yield) was finally recovered as a crystalline black powder. IR ($CH_2Cl_2$): 2065 (w) $\tilde{\nu}_{C\equiv C}$ cm$^{-1}$. $^1$H NMR ($C_6D_6$): $\delta$ = 7.98, 7.69, 6.99, 4.28 (Cp), 2.68–0.90 ppm. $^{31}$P NMR ($C_6D_6$): $\delta$ = 107.1 ppm. $C_{72}H_{62}Fe_2P_4$ (1162.87): calcd. C 74.37, H 5.37; found C 74.64, H 5.81.

**4,4′-Bis[($\eta^5$-$C_5H_5$)Fe(dppe)($\sigma^1$-C≡C)]($C_6H_4$)$_2$ (7g):** A brick-red mixture of 4,4′-bis[($\eta^5$-$C_5H_5$)Fe(CO)$_2$($\sigma^1$-C≡C)]($C_6H_4$)$_2$ (**6d**) (0.150 g, 0.26 mmol) and 1,2-bis(diphenylphosphanyl)ethane (0.222 g, 0.54 mmol) in benzene (200 mL) was exposed to ultraviolet irradiation for 2 h at room temperature. The yellow-orange reaction mixture was then filtered and dried under vacuum. The light-orange residue was washed with hexane, dissolved in toluene and precipitated with hexane. This treatment was repeated ten times, and the pure product (0.060 g, 19% yield) was finally recovered as a dark yellow powder. IR ($CH_2Cl_2$): 2059 (w) $\tilde{\nu}_{C\equiv C}$ cm$^{-1}$. $^1$H NMR ($C_6D_6$): $\delta$ = 8.01, 7.25–6.90, 4.30 (Cp), 2.57–0.43 ppm. $^{13}$C NMR ([$D_7$]DMF, ppm): $\delta$ = 133.5–120.3, 105.2, 84.8, 78.6, 66.9, 29.9 ppm. $^{31}$P NMR ($C_6D_6$): $\delta$ = 107.1 ppm. $C_{78}H_{66}Fe_2P_4$ (1238.97): calcd. C 75.62, H 5.37; found C 75.40, H 5.11.

**[{Fe($\eta^5$-$C_5H_5$)($\eta^2$-dppe)(C≡C)}$_2${2,5-$C_4H_2S$}][$BF_4$] (7a$^+$):** [Fe($\eta^5$-$C_5Me_5$)$_2$][$BF_4$] (0.0033 g, 0.0081 mmol, 0.95 equiv.) was added at room temperature to a stirred solution of [{Fe($\eta^5$-$C_5H_5$)($\eta^2$-dppe)(C≡C)}$_2${2,5-$C_4H_2S$}] (**7a**) (0.01 g, 0.0085 mmol) in $CH_2Cl_2$ (10 mL). The wine-coloured mixture immediately became blue and was stirred at room temperature for 1.5 h. The solution was filtered through Celite, reduced in vacuo to about 2 mL, and hexane (15 mL) was added, allowing precipitation of a blue solid. After decantation of supernatant pale yellow liquid, the precipitate was washed several times with 5 mL of hexane, and dried under vacuum yielding the pure [{Fe($\eta^5$-$C_5H_5$)($\eta^2$-dppe)(C≡C)}$_2${2,5-$C_4H_2S$}]-[$BF_4$] as blue microcrystals (0.0102 g, 95%). IR ($CH_2Cl_2$): 2059 (s) $\tilde{\nu}_{C\equiv C}$ cm$^{-1}$. $C_{70}H_{60}BF_4Fe_2P_4S$ (1255.70): calcd. C 66.96, H 4.82; found C 66.64, H 4.63.

**Computational Details:** Full geometry optimisations with tight conditions were performed at B3LYP level of theory, as implemented in Gaussian03.[21] The hybrid functional is Becke's three-parameter nonlocal exchange functional[22] with the local correlation functional of Lee, Yang and Parr et al.[23] The choice of this functional is motivated by the successful results obtained in geometry calculations of both neutral and charged similar complexes[7p] and by its performance reported in very recent studies on the electronic coupling in mixed-valence organometallic complexes.[20a,24] In both spin-restricted and spin-unrestricted calculations the 6-31G** basis set was used for S, P, O, C and H and the standard LANL2DZ-ECP was employed for Fe (B3LYP/LANL2DZ, 6-31G**).[25] This choice is suitable for accurate results at an acceptable computational expenditure. In charged species the total spin values do not show significant spin contamination for doublet ion states. TDDFT excitation energies were calculated at B3LYP level of theory; standard LANL2DZ-ECP basis set was used for Fe and 6-31+G* was employed for all the other atoms (B3LYP/LANL2DZ, 6-31+G*).[25]

**Supporting Information** (see footnote on the first page of this article): UV/Vis spectra of **7a** and **7a$^+$**; B3LYP/LANL2DZ,6-31G**-optimised geometries of the studied model complexes, and pictures of MOs involved in the NIR transitions.

## Acknowledgments

This work was supported by the Consiglio Nazionale delle Ricerche (CNR, Roma) within the CNR/RAS (Russian Academy of Science, Moscow) bilateral agreement for financial support and by the Ministero dell'Istruzione, dell'Università e della Ricerca (MIUR) within the PRIN 2003 research project. We are grateful to Patrizia Gentili (Università "La Sapienza", Roma) for her very useful cooperation. CINECA (Consorzio Interuniversitario di Calcolo del Nord-Est, Casalecchio di Reno, Italia) is greatly acknowledged for the generous allocation of their computational facilities.

[1] a) D. W. Bruce, D. O'Hare, *Inorganic Materials*, Wiley, Chichester, England, **1992**; b) Y. Sun, N. J. Taylor, A. J. Carty, *Organometallics* **1992**, *11*, 4293; c) D. L. Lichtenberger, S. K. Renshaw, A. Wong, C. Tagge, *Organometallics* **1993**, *12*, 3522; d) T. Bartik, B. Bartik, M. Brady, R. Dembinsky, J. A. Gladysz, *Angew. Chem. Int. Ed. Engl.* **1996**, *35*, 969; e) H. Lang, *Angew. Chem. Int. Ed. Engl.* **1994**, *33*, 547; f) U. H. F. Bunz, F. Beer, *Organometallics* **1995**, *14*, 2490; g) J. E. C. Wiegelmann-Kreiter, U. H. F. Bunz, *Organometallics* **1995**, *14*, 4449; h) P. F. Schwab, M. D. Lewin, J. Michl, *Chem. Rev.* **1999**, *99*, 1863; i) T. Yamamoto, *Bull. Chem. Soc. Jpn.* **1999**, *72*, 621–638 and references cited therein; j) U. H. F. Bunz, *Chem. Rev.* **2000**, *100*, 1605–

 © 2006 Wiley-VCH Verlag GmbH & Co. KGaA, Weinheim 

1644; k) T. Yamamoto, *Synlett* **2003**, *4*, 425; l) K. D. Demadis, C. M. Hartshorn, T. J. Meyer, *Chem. Rev.* **2001**, *101*, 2655.

[2] a) D. L. Zeckel, K. C. Hultzsch, R. Rulkens, D. Balaishis, Y. Ny, J. K. Pudelsky, A. J. Lough, I. Manners, D. A. Foucher, *Organometallics* **1996**, *15*, 1972; b) M. J. Irwin, G. Jia, N. C. Payne, R. J. Puddenphatt, *Organometallics* **1996**, *15*, 51; c) M. Altmann, U. H. F. Bunz, *Angew. Chem. Int. Ed. Engl.* **1995**, *34*, 569; d) A. A. Dembeck, P. J. Fagan, M. Marsi, *Macromolecules* **1993**, *26*, 2292; e) A. Kohler, H. F. Wittmann, R. H. Friend, M. S. Khan, J. Lewis, *Synth. Met.* **1996**, *77*, 147; f) Y. Ni, R. Rulkens, I. Manners, *J. Am. Chem. Soc.* **1996**, *118*, 4102; g) G. Tomos, P. Nugara, M. V. Laksmikantham, M. P. Lava, *Synth. Met.* **1993**, *53*, 271.

[3] a) S. Takahashi, Y. Takai, H. Morimoto, K. Sonogashira, N. Hagihara, *Mol. Cryst. Liq. Cryst.* **1982**, *32*, 139; b) D. Posselt, W. Badur, M. Steiner, M. Baumgarten, *Synth. Met.* **1993**, *55–57*, 3299; c) M. Hmyene, A. Yassar, M. Escorne, A. Percheron-Guegan, F. Garnier, *Adv. Mater.* **1994**, *6*, 564; d) W. L. Blau, H. J. Byrne, D. J. Cardin, A. P. Davey, *J. Mater. Chem.* **1991**, *1*, 245; e) N. J. Long, *Angew. Chem. Int. Ed. Engl.* **1995**, *34*, 21.

[4] a) E. Antonelli, P. Rosi, C. Lo Sterzo, E. Viola, *J. Organomet. Chem.* **1999**, *578*, 210; b) P. Altamura, G. Giardina, C. Lo Sterzo, M. V. Russo, *Organometallics* **2001**, *20*, 4360; c) G. Giardina, P. Rosi, A. Ricci, C. Lo Sterzo, *J. Polym. Sci., Part A: Polym. Chem.* **2000**, *38*, 2603; d) R. Pizzoferrato, M. Berliocchi, A. Di Carlo, P. Lugli, M. Venanzi, A. Micozzi, A. Ricci, C. Lo Sterzo, *Macromolecules* **2003**, *36*, 2215; e) A. La Groia, A. Ricci, M. Bassetti, D. Masi, C. Bianchini, C. Lo Sterzo, *J. Organomet. Chem.* **2003**, *683*, 406; f) A. Micozzi, M. Ottaviani, G. Giardina, A. Ricci, R. Pizzoferrato, T. Ziller, D. Compagnone, C. Lo Sterzo, *Adv. Synth. Catal.* **2005**, *347*, 143.

[5] a) E. Viola, C. Lo Sterzo, R. Crescenzi, G. Frachey, *J. Organomet. Chem.* **1995**, *493*, C9–C13; b) E. Viola, C. Lo Sterzo, F. Trezzi, *Organometallics* **1996**, *15*, 4352.

[6] a) W. Beck, B. Niemer, M. Wieser, *Angew. Chem. Int. Ed. Engl.* **1993**, *32*, 923; b) A. D. Hunter, *Organometallics* **1989**, *8*, 118; c) E. A. Maatta, D. D. Devore, *Angew. Chem. Int. Ed. Engl.* **1988**, *27*, 569; d) J. P. Collmann, J. T. McDevitt, C. R. Leidner, G. T. Yee, J. B. Torrance, W. A. Little, *J. Am. Chem. Soc.* **1987**, *109*, 4606; e) S. J. Davis, B. F. J. Johnson, M. S. Fhan, J. Lawis, *J. Chem. Soc., Chem. Commun.* **1991**, 187; f) M. S. Khan, S. J. Davies, A. K. Kakkar, D. Schwartz, B. Lin, B. F. G. Johnson, J. Lewis, *J. Organomet. Chem.* **1992**, *424*, 87; g) H. Fyfe, M. Mlekuz, D. Zargarian, N. J. Taylor, T. B. Marder, *J. Chem. Soc., Chem. Commun.* **1991**, 188; h) O. J. Stang, R. Tykwinsky, *J. Am. Chem. Soc.* **1992**, *114*, 4411; i) J. Kiesewetter, G. Poignant, V. Guerchais, *J. Organomet. Chem.* **2000**, *595*, 81; j) T. L. Stott, M. O. Wolf, *Coord. Chem. Rev.* **2003**, *246*, 89; k) O. Lavastre, M. Even, P. H. Dixneuf, A. Pacreau, J. P. Vairon, *Organometallics* **1996**, *15*, 1530; l) M. C. B. Colbert, J. Lewis, N. J. Long, P. R. Raithby, M. Younus, A. J. P. White, D. J. Williams, N. N. Payne, L. Yellowlees, D. Beljonne, N. Chawdhury, R. H. Friend, *Organometallics* **1998**, *17*, 3034; m) Y. Zhu, D. B. Millet, M. O. Wolf, S. J. Rettig, *Organometallics* **1999**, *18*, 1930.

[7] a) N. Le Narvor, C. Lapinte, *Organometallics* **1995**, *14*, 634; b) N. Le Narvor, L. Toupet, C. Lapinte, *J. Am. Chem. Soc.* **1995**, *117*, 7129; c) F. Coat, C. Lapinte, *Organometallics* **1996**, *15*, 477; d) F. Coat, M. A. Guillevic, L. Toupet, F. Paul, C. Lapinte, *Organometallics* **1997**, *16*, 5988; e) N. Le Narvor, C. Lapinte, *C. R. Acad. Sci., Ser. IIc: Chim.* **1998**, 745; f) M. Guillemot, L. Toupet, C. Lapinte, *Organometallics* **1998**, *17*, 1928; g) T. Weyland, K. Costuas, A. Mari, J.-F. Halet, C. Lapinte, *Organometallics* **1998**, *17*, 5569; h) S. Le Stang, F. Paul, C. Lapinte, *Organometallics* **2000**, *19*, 1035–1043; i) F. Paul, W. E. Meyer, L. Toupet, H. Jiao, H. J. A. Gladysz, C. Lapinte, *J. Am. Chem. Soc.* **2000**, *122*, 9405; j) R. Denis, L. Toupet, F. Paul, C. Lapinte, *Organometallics* **2000**, *19*, 4240; k) T. Weyland, K. Costuas, L. Toupet, J.-F. Halet, C. Lapinte, *Organometallics* **2000**, *19*, 4228; l) T. Weyland, I. Ledoux, S. Brasselet, J. Zyss, C. Lapinte, *Organometallics* **2000**, *19*, 5235; m) H. Jiao, K. Costuas, J. A. Gladysz, J.-F. Halet, M. Guillemot, L. Toupet, F. Paul, C. Lapinte, *J. Am. Chem. Soc.* **2003**, *125*, 9511; n) J. Courmarcel, G. Le Gland, L. Toupet, F. Paul, C. Lapinte, *J. Organomet. Chem.* **2003**, *670*, 108; o) T. Weyland, C. Lapinte, G. Frapper, M. J. Calhorda, J.-F. Halet, L. Toupet, *Organometallics* **1997**, *16*, 2024; p) K. M.-C. Wong, S. C.-F. Lam, C.-C. Ko, N. Zhu, V. W.-W. Yam, S. Roué, C. Lapinte, S. Fathallah, K. Costuas, S. Kahlal, J.-F. Halet, *Inorg. Chem.* **2003**, *42*, 7086; q) K. Costuas, F. Paul, L. Toupet, J.-F. Halet, C. Lapinte, *Organometallics* **2004**, *23*, 2053; r) S. Roué, C. Lapinte, T. Bataille, *Organometallics* **2004**, *23*, 2558; s) F. de Montigny, G. Argouarch, K. Costuas, J.-F. Halet, T. Roisnel, L. Toupet, C. Lapinte, *Organometallics* **2005**, *24*, 4558; t) M. I. Bruce, K. Costuas, T. Davin, B. G. Ellis, J.-F. Halet, C. Lapinte, P. J. Low, M. E. Smith, B. W. Skelton, L. Toupet, A. H. White, *Organometallics* **2005**, *24*, 3864; u) F. de Montigny, G. Argouarch, K. Costuas, J.-F. Halet, T. Roisnel, L. Toupet, C. Lapinte, *Organometallics* **2005**, *24*, 4558.

[8] a) M. Brady, W. Weng, Y. Zhou, J. W. Seyler, A. J. Amoroso, A. M. Arif, M. Böhme, G. Frenking, J. A. Gladysz, *J. Am. Chem. Soc.* **1997**, *119*, 775; b) T. B. Peters, J. C. Bowling, A. M. Arif, J. A. Gladysz, *Organometallics* **1999**, *18*, 3261; c) R. Dembinski, T. Bartik, B. Bartik, M. Jaeger, J. A. Gladysz, *J. Am. Chem. Soc.* **2000**, *122*, 810; d) W. E. Meyer, A. J. Amoroso, C. R. Horn, M. Jaeger, J. A. Gladysz, *Organometallics* **2001**, *20*, 1115; e) C. Herrmann, J. Neugebauer, J. A. Gladysz, M. Reiher, *Inorg. Chem.* **2005**, *44*, 6174; f) F. Zhuravlev, J. A. Gladysz, *Chem. Eur. J.* **2004**, *10*, 6510.

[9] a) M. I. Bruce, L. I. Denisovich, P.-J. Low, S. M. Peregudova, N. A. Ustynyuk, *Mendeleev Commun.* **1996**, 200; b) M. I. Bruce, P. J. Low, K. Costuas, J.-F. Halet, S. P. Best, G. A. Heath, *J. Am. Chem. Soc.* **2000**, *122*, 1949; c) M. I. Bruce, M. Ke, P. J. Low, B. W. Skelton, A. H. White, *Organometallics* **1998**, *17*, 3539; d) M. I. Bruce, B. C. Hall, B. D. Kelly, P. J. Low, B. K. Skelton, A. H. White, *J. Chem. Soc., Dalton Trans.* **1999**, 3719; e) M. I. Bruce, P. Hinterding, E. R. T. Tiekink, B. W. Skelton, A. H. White, *J. Organomet. Chem.* **1993**, *450*, 209.

[10] a) M. B. Robin, P. Day, *Adv. Inorg. Chem. Radiochem.* **1967**, *10*, 247; b) C. Creutz, H. Taube, *J. Am. Chem. Soc.* **1969**, *91*, 3988; c) C. Creutz, *Prog. Inorg. Chem.* **1983**, *30*, 1; d) D. E. Richardson, H. Taube, *Coord. Chem. Rev.* **1984**, *60*, 107; e) R. J. Crutchley, *Adv. Inorg. Chem.* **1994**, *41*, 273; f) M. D. Ward, *Chem. Soc. Rev.* **1995**, *24*, 121; g) S. Barlow, D. O'Hare, *Chem. Rev.* **1997**, *97*, 637; h) P. Chen, T. J. Meyer, *Chem. Rev.* **1998**, *98*, 1439; i) F. Paul, C. Lapinte, *Coord. Chem. Rev.* **1998**, *178*, 431; j) D. P. Arnold, G. A. Heath, D. A. James, *J. Porphyrins Phthalocyanines* **1999**, *3*, 5; k) C. J. Atwood, W. E. Geiger, *J. Am. Chem. Soc.* **2000**, *122*, 5477; l) A. Ceccon, S. Santi, L. Orian, A. Bisello, *Coord. Chem. Rev.* **2004**, *248*, 683; m) S. Santi, A. Ceccon, F. Carli, L. Crociani, A. Bisello, M. Tiso, A. Venzo, *Organometallics* **2002**, *21*, 2679; n) F. Barrière, N. Camire, W. E. Geiger, U. T. Mueller-Westerhoff, R. Sanders, *J. Am. Chem. Soc.* **2002**, *124*, 7262.

[11] a) J. K. Stille, *Angew. Chem. Int. Ed. Engl.* **1986**, *25*, 508; b) T. N. Mitchell in *Metal-Catalyzed Cross-Coupling Reaction* (Eds.: F. Diederich, P. J. Stang), Wiley-VCH, Weinheim, Germany, **1988**; c) V. Farina, V. Krishnamurthy, W. J. Scott, *The Stille Reaction*, John Wiley & Sons, Inc., New York, **1998**.

[12] R. B. King, L. W. Houk, K. H. Pannell, *Inorg. Chem.* **1969**, *8*, 1042.

[13] C. Lapinte, private communication.

[14] a) G. C. Allen, N. S. Hush, *Prog. Inorg. Chem.* **1967**, *8*, 357; b) N. S. Hush, *Prog. Inorg. Chem.* **1967**, *8*, 391.

[15] Z. Bao, Z. Y. Che, L. Yu, *Macromolecules* **1993**, *26*, 5281.

[16] R. G. Parr, W. Yang, *Density Functional Theory of Atoms and Molecules*, **1989**, Oxford University Press.

[17] As previously described,[7o] the orientation of the $FeCp(PH_3)_2$ fragments relative to the plane of the aromatic core has a negligible influence on the structural and electronic features of these complexes. In a conformational study on $PH_3$-**7a** at the em-

 © 2006 Wiley-VCH Verlag GmbH & Co. KGaA, Weinheim 

ployed level of theory we found no significant energy difference between the conformers, i.e., less than 0.3 kcal mol$^{-1}$. In addition, a full geometry optimisation was carried out on the model complex dHpe-**7a** (dHpe = $PH_2CH_2CH_2PH_2$) in order to investigate the effect of replacing a chelating ligand with two $PH_3$ ligands. The results, included in the Supporting Information, do not show a significant difference.

[18] a) D. L. Lichtenberger, S. K. Renshaw, *Organometallics* **1993**, *12*, 3522; b) G. Frapper, M. Kertesz, *Inorg. Chem.* **1993**, *32*, 732; c) J. E. McGrady, T. Lovell, R. Stranger, M. G. Humphrey, *Organometallics* **1997**, *16*, 4004.

[19] M. E. Casida, C. Jamorski, K. C. Casida, D. R. Salahub, *J. Chem. Phys.* **1998**, *108*, 4439.

[20] a) F. A. Cotton, C. Y. Liu, C. A. Murillo, D. Villagran, X. Wang, *J. Am. Chem. Soc.* **2004**, *126*, 14822; b) C. E. Powell, M. P. Cifuentes, J. P. Morrall, R. Stranger, M. G. Humphrey, M. Samoc, B. Luther-Davies, G. A. Heath, *J. Am. Chem. Soc.* **2003**, *125*, 602; c) F. C. Grozema, L. P. Candeias, M. Swart, P. Th. van Duijnen, J. Wildeman, G. Hdziioanou, L. D. A. Siebbeles, J. M. Warman, *J. Chem. Phys.* **2002**, *117*, 11366; d) J. Cornil, D. Beljonne, J. L. Bredas, *J. Chem. Phys.* **1995**, *103*, 834.

[21] M. J. Frisch, G. W. Trucks, H. B. Schlegel, G. E. Scuseria, M. A. Robb, J. R. Cheeseman, V. G. Zakrzewski, J. A. Montgomery Jr, R. E. Stratmann, J. C. Burant, S. Dapprich, J. M. Millam, A. D. Daniels, K. N. Kudin, M. C. Strain, O. Farkas, J. Tomasi, V. Barone, M. Cossi, R. Cammi, B. Mennucci, C. Pomelli, C. Adamo, S. Clifford, J. Ochterski, G. A. Petersson, P. Y. Ayala, Q. Cui, K. Morokuma, N. Rega, P. Salvador, J. J. Dannenberg, D. K. Malick, A. D. Rabuck, K. Raghavachari, J. B. Foresman, J. Cioslowski, J. V. Ortiz, A. G. Baboul, B. B. Stefanov, G. Liu, A. Liashenko, P. Piskorz, I. Komaromi, R. Gomperts, R. L. Martin, D. J. Fox, T. Keith, M. A. Al-Laham, C. Y. Peng, A. Nanayakkara, M. Challacombe, P. M. W. Gill, B. Johnson, W. Chen, M. W. Wong, J. L. Andres, C. Gonzalez, M. Head-Gordon, E. S. Replogle, J. A. Pople, *Gaussian03*, Revision A.11.3, Gaussian, Inc., Pittsburgh, PA, **2002**.

[22] A. D. Becke, *Phys. Rev. A* **1988**, *38*, 3098.

[23] C. Lee, W. Yang, R. G. Parr, *Phys. Rev. B* **1988**, *37*, 785.

[24] M. Bühl, W. Thiel, *Inorg. Chem.* **2004**, *43*, 6377.

[25] a) P. J. Hay, W. R. Wadt, *J. Chem. Phys.* **1985**, *82*, 270; b) P. J. Hay, W. R. Wadt, *J. Chem. Phys.* **1985**, *82*, 284; c) P. J. Hay, W. R. Wadt, *J. Chem. Phys.* **1985**, *82*, 299; d) Basis sets were obtained from the Extensible Computational Chemistry Environment Basis Set Database, Version 4/17/03, as developed and distributed by the Molecular Science Computing Facility, Environmental and Molecular Sciences Laboratory, which is part of the Pacific Northwest Laboratory, P.O. Box 999, Richland, WA 99352, USA, and funded by the US Department of Energy. The Pacific Northwest Laboratory is a multiprogram laboratory operated by the Battelle Memorial Institute for the US Department of Energy under contract DE-AC06-76RLO 1830.

Received: January 11, 2006
Published Online: May 2, 2006

 © 2006 Wiley-VCH Verlag GmbH & Co. KGaA, Weinheim 

DOI: 10.1002/ejic.200600096

# Redox-Active Coordination Polymers from Esterified Hexavanadate Units and Divalent Metal Cations

Jong Woo Han,[a] Kenneth I. Hardcastle,[a] and Craig L. Hill*[a]

**Keywords:** Polyoxometalates / Coordination polymers / Vanadium

The redox-active bis(pyridyl)-capped hexavanadate $[V_6O_{13}\{(OCH_2)_3C(4\text{-}CONHC_5H_4N)\}_2]^{2-}$ (**1**) reacts with divalent first-row transition-metal cations ($Mn^{II}$, $Co^{II}$, $Ni^{II}$, or $Zn^{II}$) to yield crystalline linear zwitterionic coordination polymers (**1**M). The zwitterionic coordination chains are connected to each other by hydrogen bonds to form a 3D network. Microporous channels are formed along the packing axes of the 2D networks. All four compounds exhibit almost identical cell parameters, space group ($P\bar{1}$) and crystal morphology. The materials have been characterized by X-ray crystallography, $^1H$ and $^{51}V$ NMR, IR, UV/Vis, elemental analysis, and TGA. All compounds **1**M are reversibly reduced by chemical reductants such as phenylhydrazine and $NaBH_4$ in $CCl_4$ in which the hexavanadates are insoluble.
(© Wiley-VCH Verlag GmbH & Co. KGaA, 69451 Weinheim, Germany, 2006)

## Introduction

Supramolecular coordination chemistry as a means to construct sophisticated solid materials has been a topic of intense research.[1] Recently, coordination polymers based on organic polyoxometalate (POM) derivatives and metal ions have attracted increasing attention because of the extensive and diverse properties of POMs.[2] In coordination polymers, POM units are generally formed under hydrothermal conditions, so it is difficult to relate the final structure and composition to the starting materials.[3] There are examples of applying preformed complete[4] or lacunary POMs[5] as ligands to metal ions to construct coordination polymers. However, the coordination modes of the POM oxo groups in the coordination polymers are complex and not defensibly predictable. By using pre-formed organic POM derivatives with a well-defined coordination mode as linking ligands, one can expect to design the morphologies and properties of the products from an understanding of the geometrical possibilities from the building units. Recently, coordination polymers using pre-formed organic POM derivatives have been reported. The first supramolecular coordination network materials[6] with pre-formed organic POM derivatives were reported by Stein et al. using organic POM derivatives with aniline moieties, $[W_6O_{25}H(AsC_6H_4\text{-}4\text{-}NH_2)_2]^{5-}$ and $[Mo_{12}O_{46}(AsC_6H_4\text{-}NH_2)_4]^{4-}$. In these materials, both the aniline moieties and POM oxo groups are coordinated to transition-metal ions. Stein et al. reported another coordination network assembled with $Cu^{II}$, (4,4′-bipyridyl)ethylene, and a preformed POM derivative, $[Mo_{12}O_{46}(AsC_6H_4NH_2)_4]^{4-}$.[7] In the network, the POM derivative behaves as a non-coordinating anion. Presumably because of the weak coordinating ability of the aniline, the coordination modes of the POM building units are complicated. More recently, Hasenknopf et al. reported the assembly of the polyoxomolybdate $[MnMo_6O_{18}\{(OCH_2)_3CNHCO(4\text{-}C_5H_4N)\}_2]^{3-}$ and $[PdCl_2(PhCN)_2]$, that yields a transparent and birefringent gel.[8] The design and construction of materials based on a redox-active building block with a pre-defined coordination mode and transformation into a crystalline coordination material would constitute an advance.

Here we report the preparation of a pyridine-terminated bis(trialkoxo)hexavanadate complex, $[V_6O_{13}\{(OCH_2)_3C(4\text{-}CONHC_5H_4N)\}_2]^{2-}$ (**1**), and the assembly of **1** with divalent transition-metal cations, M = $Mn^{II}$, $Co^{II}$, $Ni^{II}$, or $Zn^{II}$, to form POM-based coordination polymers. We are interested in the hexavanadate units esterified in a linear fashion with two chelating triols, $[V_6O_{13}\{(OCH_2)_3CR\}_2]^{2-}$, because the alkoxy groups of the chelating (triester)$V_3$ units are quite stable to hydrolysis,[9] and bis(triester)$V_6$ units can be extensively and reversibly reduced.[10] Unfortunately, the terminal R groups on the triester "caps" of the compounds reported to date, R = $CH_3$, $CH_2CH_3$, $NO_2$, and $CH_2OH$, bind metal ions poorly if at all.[10,11] Complex **1** can be viewed as a tunable, redox-active analogue of organic linking molecules such as 4,4′-bipyridine. A larger goal of this study, which we document, is the reversible reduction of POM-based open-framework coordination networks, and in particular oxidative regeneration (re-oxidation) by air. The latter phenomenon typically implies the ability of the POM-based

[a] Department of Chemistry, Emory University, Atlanta, GA 30322, USA
E-mail: chill@emory.edu
Supporting information for this article is available on the WWW under http://www.eurjic.org or from the author.

 © 2006 Wiley-VCH Verlag GmbH & Co. KGaA, Weinheim 

material to catalyze air-based oxidations, an area of considerable interest in context with removal of pollutants, decontamination of toxic agents, environmental remediation, and green chemistry.[12–14]

## Results and Discussion

The triol derivative $(HOCH_2)_3CNHCO(4\text{-}C_5H_4N)$ was prepared by the reaction of $(HOCH_2)_3CNH_2$ and isonicotinoyl chloride hydrochloride, $(4\text{-}C_5H_4N)COCl{\cdot}HCl$, in DMA under $N_2$ in the presence of $K_2CO_3$ at 60 °C for 72 h. The bis(pyridyl)-capped hexavanadate **1** was prepared by the reaction of $(HOCH_2)_3CNHCO(4\text{-}C_5H_4N)$ with $[(n\text{-}C_4H_9)_4N]_3[H_3V_{10}O_{28}]$[15] in DMA under $N_2$ at 80 °C for 60 h, a modification of the method used by Zubieta and co-workers for the $\text{-}CH_3$, $\text{-}CH_2CH_3$, $\text{-}NO_2$, and $\text{-}CH_2OH$ derivatives,[10] and characterized by various spectroscopic methods and X-ray crystallography. Coordination polymers, $[M(DMF)_2(H_2O)_2(V_6O_{13}\{(OCH_2)_3CCONH(4\text{-}C_5H_4N)\}_2)]_n$ (M = Mn, Co, Ni, or Zn), were synthesized in 70–80% yield, by adding the appropriate transition-metal ion, dissolved either in methanol or in acetonitrile, to the stock solution of **1** in DMF and storing the solution at room temperature for 4–7 d. Regardless of the molar ratio of metal ion/**1**, zwitterionic (1:1 = divalent metal ion/**1**) compounds were obtained. In the case of **1**Ni and **1**Zn, single crystals suitable for X-ray diffraction were obtained by carefully layering the stock solution of **1** with a solution of the metal ion. In the case of **1**Mn and **1**Co, the formation of the product was relatively slow, so dilute solutions of each metal ion and the solution of **1** were mixed and the resulting solution was left undisturbed at room temperature for 4 d to afford single crystals suitable for X-ray diffraction.

All four coordination polymers **1**M (M = Mn, Co, Ni, or Zn) are nearly isostructural and exhibit almost identical unit cell parameters, space group ($P\bar{1}$) and crystal morphology. The metal atom, M, is in a symmetry-unique position in all four coordination polymers. This d-electron-containing metal center is located in a crystallographic inversion center and is six-coordinate with 2 DMF, 2 water, and 2 pyridine ligands all *trans* to each other (Figure 1). The divalent transition-metal ions and the pyridine-terminated triesterified polyoxovanadates form one-dimensional (1D) coordination chains. Interestingly, the 1D coordination chains are connected to each other by weak hydrogen bonds involving C–H moieties of the pyridine units to form microporous channels. Four different types of hydrogen bonds connect the 1D chains in a direction nearly parallel to the crystallographic *c* axis to form a two-dimensional (2D) network (Figure 2): (1) a relatively strong hydrogen bond between a coordinated water molecule and a bridging oxo group of the POM (O–O distance ca. 2.7 Å), weak hydrogen bonds between either pyridine hydrogen atoms and (2) bridging oxo groups of the POM (O–O distance ca. 3.3 Å) or (3) a terminal oxo group of the POM (O–O distance ca. 3.7 Å), and (4) hydrogen bonds between pyridine hydrogen atoms and carbonyl oxygen atoms of amide units (N–O distance ca. 3.7 Å). The 2D networks, in turn, are linked to each other in a direction nearly parallel to the crystallographic *a* axis by hydrogen bonds between a methyl hydrogen atom of the coordinated DMF molecule and a terminal oxo group (O–O distance ca. 3.4 Å) of the POM. Microporous channels are formed along the crystallographic *c* axis of the 2D networks (Figure 3).

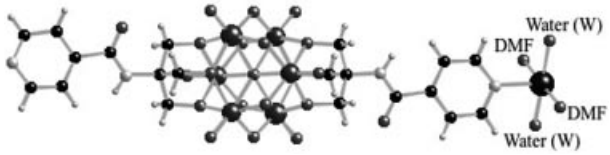


Figure 1. Structure of the repeating coordination unit of **1**Co. Selected distances [Å] and angles [°]: Co–O(DMF) 2.065(3), Co–O(W) 2.067(2), Co–N(pyridine) 2.157(2); O(DMF)–Co–O(W) 88.91(10), O(DMF)–Co–N(pyridine) 86.69(11), O(W)–Co–N(pyridine) 90.84(10).

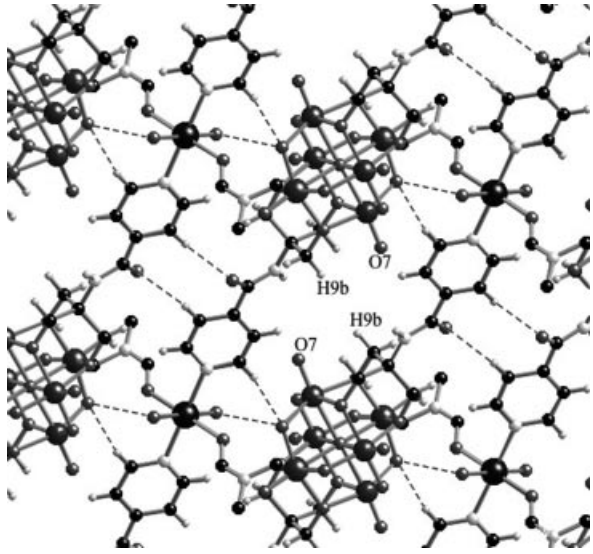


Figure 2. View parallel to the *a* axis. DMF molecules and some hydrogen atoms are omitted for clarity. Longest dimension (O7–O7) 5.54 Å, shortest dimension (H9b–H9b) 2.76 Å.

Bond valence sum (BVS) calculations[16] confirm that all six symmetry-distinct vanadium atoms in the hexavanadate unit are in the +5 oxidation state (values 5.0–5.1). The infrared and UV/Vis spectroscopic data are also consistent with vanadium(V).[17]

All the product polymers are slightly soluble (0.04–0.2 mM in the repeating unit) in polar aprotic solvents such as DMSO, DMF and $CH_3CN$ and insoluble in non-coordinating solvents such as dichloroethane and chloroform. Both the $^1H$ and $^{51}V$ NMR spectra of **1**Zn and **1**Mn (see Figures S1 and S2 in the Supporting Information) clearly show that only the signals for the monomer are observed, and that these signals have effectively identical chemical shifts to that for **1** only. Expectedly, the $^1H$ NMR spectra of the polymers with paramagnetic centers (**1**M; M = Mn, Co, or Ni) exhibit broader signals than those of **1**Zn. Dissolution clearly involves dissociation of the pyridine–metal coordination bond in **1**M. The slow kinetics of formation/

 © 2006 Wiley-VCH Verlag GmbH & Co. KGaA, Weinheim 

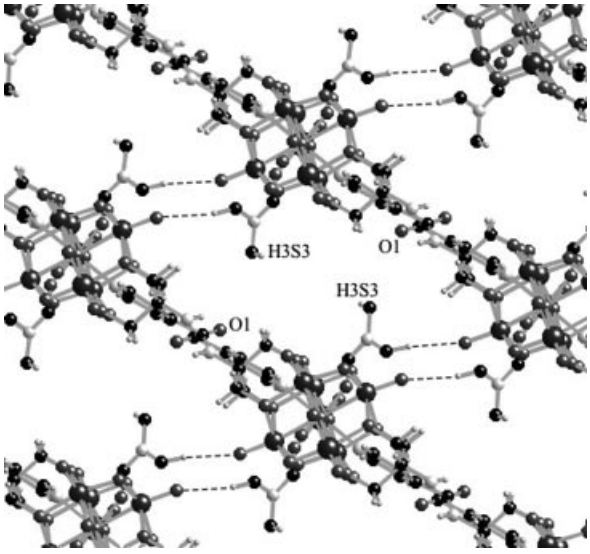


Figure 3. View parallel to the crystallographic *c* axis. Longest dimension (O1–O1) 8.89 Å, shortest dimension (H3S1–H3S1) 4.27 Å. Channel-filling DMF molecules and some hydrogen atoms are omitted for clarity.

crystallization as well as solubilization of all compounds **1**M precluded quantification of the dissociation equilibrium constants: $K$ = [soluble monomer]. Dynamic light scattering (DLS) was attempted in order to corroborate the findings but the low solubility of dissociated monomers precluded acquisition of acceptable data.[18]

Thermogravimetric analysis (TGA) shows that the polymers **1**M are thermally less stable than the monomeric hexavanadate **1**. The polymers lose 20–30% of their total weight from 30 to 160 °C which correlates with the loss of the DMF molecules in the pores and the two DMF molecules coordinated to the metal ion in each formula unit. The differential scanning calorimetry (DSC) data supports the implications of TGA data. The IR spectra of **1**Zn at different temperatures were obtained to confirm the stability of the compound (see Figure S5).

The phase purity of the bulk material was evaluated by X-ray powder diffraction pattern (XRPD). The measured XRPD pattern matches well with that of the calculated one from the single crystal data (see Figure S6). Unfortunately, XRPD data of all compounds **1**M dried under vacuum ($10^{-2}$ Torr for 2 d) indicated loss of crystallinity, consistent with the complete loss of framework structure upon the evacuation of the channel-occupying solvent molecules.

All compounds **1**M are reversibly reduced by chemical reductants such as phenylhydrazine and $NaBH_4$ in tetrachloromethane in which the compounds **1**M are insoluble. Reduction by $NaBH_4$ is much slower than that by phenylhydrazine. The reduced compounds **1**M are reoxidized without decomposition by any of the following: $O_2$, $Br_2$, $Ce^{IV}$, and $S_2O_8^{2-}$ (reoxidation by $O_2$ is very slow but accelerated in the presence of HCl vapor). The reduction and reoxidation of the hexavanadate unit can be easily detected from the distinctive change in color (red in fully oxidized state and blue in reduced species) and by the characteristic $\nu_{V-O-V}$ stretch for the fully oxidized hexavanadate unit at 790–810 $cm^{-1}$ that shifts to a lower energy (750 $cm^{-1}$) upon reduction. The shift to a lower frequency upon reduction is consistent with protonation. Zubieta and co-workers documented longer V–O distances relative to those of fully oxidized hexavanadate units and protonated oxygen atoms by BVS calculations in the X-ray structure of the reduced forms of tris(alkoxo)hexavanadates.[19] The number of reduced vanadium atoms in the bis(triester)hexavanadate unit reproducibly determined by titration with $Br_2$ averages 2.5.

## Conclusions

In conclusion, we have prepared a new class of POM-based supramolecular materials composed of the linear pyridine-terminated redox-active esterified hexavanadate units and divalent transition-metal cations ($Mn^{II}$, $Co^{II}$, $Ni^{II}$, or $Zn^{II}$). The terminal linking groups on the triester "cap" of the bis(triester)$V_6$ units, the metal composition of the POM units and the linking cations should all be independently variable affording a fairly diverse family of redox-active open-framework materials.

## Experimental Section

**General Methods and Materials:** All chemicals were obtained from Aldrich. Dimethylacetamide (DMA) was dried with molecular sieves (3 Å) before use. Other chemicals were used as received. $^1H$ and $^{13}C$ NMR spectra were recorded either with a Varian INOVA 400 MHz instrument or a Mercury 300 MHz instrument. $^{51}V$ NMR spectra were recorded with a Varian Unity 600 MHz instrument. $^1H$ and $^{13}C$ NMR spectra were referenced to the deuterated solvent itself, and chemical shifts are reported relative to $(CH_3)_4Si$. $^{51}V$ NMR spectra were referenced externally by the sample replacement method to a 10 mM solution of $H_4PVMo_{11}O_{40}$ in 0.60 M NaCl ($\delta$ = –533.6 ppm relative to neat $VOCl_3$), and chemical shifts are reported relative to $VOCl_3$. IR spectra were recorded with a Nicolet 510 FT-IR instrument. Electronic absorption spectra were collected with a Hewlett-Packard 8452A UV/Vis spectrophotometer. Thermal gravimetric analyses (TGA) were performed with an ISI TGA 1000 instrument under $N_2$ flow from 25 to 400 °C at a rate of 10 °C/min. Differential scanning calorimetry (DSC) data were recorded with an ISI DSC 100 instrument under $N_2$ flow from 25 to 400 °C at a rate of 10 °C/min. Elemental analyses for C, H, and N were conducted by Atlantic Microlab, Norcross, GA, and elemental analyses for all other elements were conducted either by Desert Analytics, Tucson, AZ or by Kanti Lab Ltd., Mississauga, Ontario.

**Preparation of $(HOCH_2)_3CNHCO(4\text{-}C_5H_4N)$:** A solid mixture of $K_2CO_3$ (6.08 g, 44.0 mmol) and $(HOCH_2)_3CNH_2$ (2.42 g, 20.0 mmol) was added to a solution of isonicotinoyl chloride hydrochloride, $(4\text{-}C_5H_4N)COCl{\cdot}HCl$ (3.81 g, 21.4 mmol) in 30 mL of DMA under $N_2$. The resulting yellow solution and $K_2CO_3$ pellets were stirred under $N_2$ at 60 °C for 72 h. During the reaction, a decrease of the amount of $K_2CO_3$ pellets and the formation of a fine powder was observed. After the reaction batch was cooled to room temperature, the fine powder was filtered with a fine fritted glass filter. Acetone (150 mL) was added to the filtrate. After 1 d, the resulting crystalline material (needle morphology; isonicotinic acid, confirmed by $^1H$ NMR and IR) was filtered off, and the fil-

 © 2006 Wiley-VCH Verlag GmbH & Co. KGaA, Weinheim 

trate was concentrated to about 25 mL. Acetone (100 mL) was added to the concentrated solution. After 1 d, the resulting crystalline material was filtered off, and the filtrate was concentrated under vacuum to about 4 mL. To this concentrate was added 20 mL of acetone. After 1 d, a crystalline solid was obtained (2.8 g, 62%). The product was used for further reaction without additional purification. [Note 1: A small amount of isonicotinic acid (2–5% based on the integration of the $^1$H NMR spectrum of the product) observed in the product could be removed by repeated (2–3 times) crystallization in DMA/acetone. Note 2: When the product was used for further reaction without additional purification, the impurity was successfully removed during the crystallization of the subsequent material, **1**.] $^1$H NMR ([D$_6$]DMSO): $\delta$ = 3.68 (d, 12 H), 4.67 (t, 6 H), 7.49 (s, 1 H), 7.69 (d, 2 H), 8.69 (d, 2 H) ppm. $^{13}$C NMR ([D$_6$]DMSO): $\delta$ = 60.47 ($HOCH_2$), 63.78 (CNH), 122.16 (β-Py), 143.02 (γ-Py), 150.66 (α-Py), 166.19 (CO) ppm. $C_{10}H_{14}N_2O_4$ (226.23): calcd. C 53.09, H 6.23, N 12.38; found C 52.58, H 6.13, N 12.13. IR (KBr, 400–4000 cm$^{-1}$): $\tilde{\nu}$ = 3422 (s, br.), 3261 (w), 3097 (w), 3028 (w), 2920 (m), 2849 (w), 1733 (w), 1641 (s), 1607 (w), 1581(m), 1552 (m), 1493 (w), 1453 (w), 1418 (w), 1374 (w), 1054 (m), 1024 (m), 962 (w), 895 (w), 845 (w), 757 (w), 700 (m) cm$^{-1}$.

**Preparation of [(*n*-$C_4H_9)_4N]_2[V_6O_{13}\{(CH_2O)_3CNHCO(4$-$C_5H_4N)\}_2]$·1.8DMF {[(*n*-$C_4H_9)_4N]_2$1·1.8DMF}:** The bis(pyridyl)-capped hexavanadate **1** was prepared by a modification of the method reported by Zubieta and co-workers.[10] DMA (62 mL) was transferred to the solid mixture of $(HOCH_2)_3CNHCO(4$-$C_5H_4N)$ (1.21 g, 5.40 mmol) and $[(n$-$C_4H_9)_4N]_2[H_3V_{10}O_{28}]$ (3.01 g, 1.80 mmol). An orange solution resulted and the flask was wrapped with aluminum foil to protect the solution from potential photoreduction; stirring was continued under $N_2$ at 80–90 °C for 60 h. After the reaction batch was cooled to room temperature, the resulting deep reddish brown solution was filtered with a fine fritted glass filter. The filtrate was added to 180 mL of diethyl ether in ca. 1-mL portions using a Pasteur pipette. The dark brown precipitate was filtered and washed with diethyl ether. The pure product was obtained by repeated (normally two) crystallization [dimethylformamide (DMF)/acetonitrile/ether = 2:1:6]. After filteration and washing with diethyl ether, the resulting crystalline product was dried under vacuum at room temperature for 1 d. The yield (2.1 g, 45%) was calculated based on the amount of vanadium. The amount of the solvent in the crystal was confirmed by TGA. $^1$H NMR ([D$_6$]DMSO): $\delta$ = 0.92 (t, 24 H), 1.30 (sext, 16 H), 1.55 (quint, 16 H), 3.15 (t, 16 H), 5.27 (d, 12 H), 7.69 (d, 4 H), 8.05 (s, 2 H), 8.67 (d, 4 H) ppm. $^{13}$C NMR ([D$_6$]DMSO): $\delta$ = 14.20, 19.89, 23.75, 53.92 (CNH), 58.17, 82.71 ($HOCH_2$), 122.35 (β-Py), 142.66 (γ-Py), 150.61 (α-Py), 166.49 (CO) ppm. $^{51}$V NMR ([D$_6$]DMSO): $\delta$ = –494.9 ppm. $C_{57.4}H_{106.6}N_{7.8}O_{22.8}V_6$ (**1**·1.8DMF, 1576.73): calcd. C 43.71, H 6.82, N 6.93, V 19.40; found C 43.61, H 6.80, N 6.95, V 19.49. UV/Vis (DMF): $\lambda_{max}$ (ε) = 360 (6000 M$^{-1}$ cm$^{-1}$) nm. IR (KBr, 400–4000 cm$^{-1}$): $\tilde{\nu}$ = 3345 (m, br.), 3272 (w), 2962 (m), 2934 (m, sh), 2876 (m), 1730 (w), 1669 (s), 1597 (w), 1540 (m), 1486 (m), 1407 (w), 1384 (w), 1322 (m), 1280 (w), 1188 (w), 1153 (w), 1102 (s),1050 (s), 953(s), 811 (s), 798 (m), 723 (s), 639 (m), 583 (m), 515 (w), 460 (w), 417 (m) cm$^{-1}$.

### Preparation of Coordination Polymers

**General Preparation:** A 10.2 mM stock solution of **1** was used for the preparation of the polymers. The stock solution was prepared by dissolving 1.60 g (1.02 mmol) of **1** in 100 mL of DMF. Coordination polymers were synthesized by adding the appropriate transition-metal ions dissolved either in methanol or in acetonitrile to the stock solution of **1** (yield 70–80%). In the case of **1**Ni and **1**Zn, single crystals suitable for X-ray diffraction study were obtained by careful layering of a stock solution of **1** with the solution of each metal ion. In the case of **1**Mn and with **1**Co, dilute solutions of each metal ion and a solution of **1** were mixed, and the resulting solution was left undisturbed at room temperature for several days. Single crystals suitable for X-ray diffraction analysis were produced. Samples for elemental analysis were dried under vacuum for 2 d. The crystalline materials appeared to lose crystallinity when dried (the crystals lose luster when dried).

**Preparation of $[Co(H_2O)_2(DMF)_2(V_6O_{13}\{(CH_2O)_3CNHCO(4$-$C_5H_4N)\}_2)]_n$ (1Co):** A solution of $Co(NO_3)_2$ (5.2 mM) in acetonitrile and a stock solution of **1** (diluted from 10.2 mM to 5.1 mM) were mixed and left undisturbed for several days to form crystals suitable for X-ray diffraction. $C_{38.6}H_{69.4}CoN_{10.3}O_{29.2}V_6$ (**1**Co·4.2DMF, 1509.61): calcd. C 30.72, H 4.64, Co 3.91, N 9.47, V 20.27; found C 30.18, H 4.75, Co 4.01, N 9.44, V 19.5. The amount of solvent was consistent with the TGA data. IR (KBr, 400–4000 cm$^{-1}$): $\tilde{\nu}$ = 3399 (m, br.), 3261 (m), 2928 (m), 2860 (w), 1653 (s), 1543 (m), 1495 (w), 1438 (w), 1417 (w), 1386 (m), 1324 (w), 1283 (w), 1255 (w), 1101 (m), 1049 (m), 957 (s), 810 (m), 800 (m),720 (m), 622 (w), 618 (w), 583 (w), 417 (m) cm$^{-1}$.

**Preparation of $[Mn(H_2O)_2(DMF)_2(V_6O_{13}\{(CH_2O)_3CNHCO(4$-$C_5H_4N)\}_2)]_n$ (1Mn):** Complex **1**Mn was prepared according to the same procedure as described above for **1**Co except using $Mn(NO_3)_2$·$x$H$_2$O ($x$ = 4–6) (in calculations $x$ was taken as 6) in methanol as a metal source instead of $Co(NO_3)_2$·6H$_2$O in acetonitrile. $C_{33.8}H_{58.2}MnN_{8.6}O_{27.6}V_6$ (**1**Mn·2.6DMF, 1387.26): calcd. C 29.25, H 4.23, Mn 3.96, N 8.68, V 22.04; found C 28.68, H 4.33, Mn 4.25, N 8.55, V 21.6. The amount of solvent was consistent with the TGA data. IR (KBr, 400–4000 cm$^{-1}$): $\tilde{\nu}$ = 3251 (m, br.), 3060 (w), 2929 (w), 2867 (w), 1654 (s), 1545 (m), 1496 (w), 1438 (w), 1417 (w), 1387 (w), 1323 (w), 1284 (w), 1255 (w), 1187 (w), 1101 (m), 1050 (s), 958 (s), 809 (s), 795 (m), 718 (s), 641 (m), 586 (w), 515 (w), 420 (m) cm$^{-1}$.

**Preparation of $[Ni(H_2O)_2(DMF)_2(V_6O_{13}\{(CH_2O)_3CNHCO(4$-$C_5H_4N)\}_2)]_n$ (1Ni):** Single crystals suitable for X-ray diffraction were prepared by a solution diffusion method as follows. DMF (1.0 mL) was layered on top of 1.0 mL of a stock solution of **1** (10.2 mM) in a 5-mL test tube. To the layered DMF solution, 1.5 mL of a solution of $Ni(NO_3)_2$·6H$_2$O in acetonitrile (6.6 mM) was carefully added. After several days, single crystals suitable for X-ray diffraction were obtained. $C_{32.6}H_{55.4}N_{8.2}NiO_{27.2}V_6$ (**1**Ni·2.2DMF, 1361.78): calcd. C 28.75, H 4.10, N 8.44, Ni 4.26, V 22.47; found C 28.15, H 4.22, N 8.23, Ni 4.11, V 21.91. The amount of solvent was consistent with the TGA data. IR (KBr, 400–4000 cm$^{-1}$): $\tilde{\nu}$ = 3423 (m, br.), 2929 (w), 2863 (w), 1650 (s), 1541 (m), 1495 (w), 1436 (w), 1417 (w), 1384 (w), 1325 (w), 1282 (w), 1101(m), 1049(m), 958(s), 811(m), 723(m), 645 (w), 586 (w), 555 (w), 417(m) cm$^{-1}$.

**Preparation of $[Zn(H_2O)_2(DMF)_2(V_6O_{13}\{(CH_2O)_3CNHCO(4$-$C_5H_4N)\}_2)]_n$ (1Zn):** Single crystals suitable for X-ray diffraction were prepared according to the same method described for the crystallization of **1**Ni. $C_{31.4}H_{53.6}N_{7.8}O_{26.8}V_6Zn$ (**1**Zn·1.8DMF, 1340.25): calcd. C 28.16, H 4.04, N 8.16, V 22.84, Zn 4.78; found C 28.51, H 3.80, N 8.16, V 20.9, Zn 4.5. The amount of solvent was consistent with the TGA data. IR (KBr, 400–4000 cm$^{-1}$): $\tilde{\nu}$ = 3418 (s, br.), 3026 (w), 2921 (w), 2866 (w), 1733 (w), 1655 (s), 1539 (m), 1494 (w), 1451 (w), 1420 (w), 1385 (w), 1327 (w), 1282 (w), 1100 (m), 1066 (m), 1047 (s), 960 (s), 810 (s), 792 (s), 699 (s), 646 (m), 584 (w), 569 (w), 420 (m) cm$^{-1}$.

**X-ray Crystallography:** Suitable crystals of **1** and **1**M (M = Mn, Co, Ni, or Zn) were coated with Paratone N oil, suspended on a small fiber loop, and placed in a cooled nitrogen stream at 100 K

 © 2006 Wiley-VCH Verlag GmbH & Co. KGaA, Weinheim 

of a Bruker D8 SMART APEX CCD sealed tube diffractometer with graphite-monochromated Mo-$K_\alpha$ (0.71073 Å) radiation. Redundant data were measured using a series of combinations of $\varphi$ and $\omega$ scans with 10 s frame exposures and 0.3° frame widths. Data collection, indexing, and initial cell refinements were handled using SMART software.[20] Frame integration and final cell refinements were carried out using SAINT software.[21] The final cell parameters were determined from least-squares refinements, and the SADABS program[22] was used to carry out absorption corrections. The structures were solved by direct methods and difference Fourier techniques. All atoms were refined anisotropically, except where noted (see data deposited in the crystal structure data base). The final *R*1 scattering factors and anomalous dispersion corrections were taken from the *International Tables for X-ray Crystallography*.[23] Additional details for **1** and **1**Co are provided in Table 1 (see crystallographic details for **1**Mn, **1**Ni, and **1**Zn in the crystal structure data base). CCDC-229734 to -229738 contain the supplementary crystallographic data for the structures reported upon in this paper. These data can be obtained free of charge from The Cambridge Crystallographic Data Centre via www.ccdc.cam.ac.uk/data_request/cif.

Table 1. Crystallographic data and structure refinement for **1** and **1**Co.

| | **1** | **1**Co |
|---|---|---|
| Empirical formula | $C_{61}H_{115}N_9O_{24}V_6$ | $C_{41.30}H_{75.70}CoN_{11.10}O_{30.10}V_6$ |
| Formula mass | 1664.26 | 1586.96 |
| Crystal system | monoclinic | triclinic |
| Space group | $P2_1/n$ | $P\bar{1}$ |
| *a* [Å] | 16.0689(9) | 11.6301(7) |
| *b* [Å] | 15.6178(9) | 11.7707(7) |
| *c* [Å] | 17.2400(1) | 13.4852(8) |
| *α* [°] | 90 | 91.801(1) |
| *β* [°] | 115.118 (1) | 112.050(1) |
| *γ* [°] | 90 | 109.797(1) |
| *V* [Å$^3$] | 3917.4(4) | 1583.06(16) |
| Z | 2 | 1 |
| $D_{calcd.}$ [mg/m$^3$] | 1.411 | 1.646 |
| $\mu$ [mm$^{-1}$] | 0.762 | 1.195 |
| Reflections collected | 69186 | 28163 |
| Independent reflections | 14310 | 11210 |
| *R*(int) | 0.0476 | 0.0567 |
| GOF on $F^2$ | 1.014 | 1.032 |
| $R1$ [$I > 2\sigma(I)$] | 0.0674 | 0.0780 |
| $wR2$ [$I > 2\sigma(I)$] | 0.1920 | 0.2263 |

**Reduction and Reoxidation of 1M:** To **1**M suspended in $CCl_4$, where **1**M is completely insoluble, either chemical reductant, $NaBH_4$ or phenylhydrazine, was added, and the suspension was stirred for 36 h or 24 h, respectively. The reduction of **1**M can be easily observed from the distinctive change in the color of **1**M (red in fully oxidized state and blue in reduced state). Reduced **1**M was reoxidized in a separate reaction by $O_2$, $Br_2$, $Ce^{IV}$, or $S_2O_8^{2-}$.

**Titration of Reduced 1Zn with $Br_2$:** The number of reduced vanadium atoms in the bis(triester)hexavanadate unit was evaluated by titration with $Br_2$. To phenylhydrazine hydrochloride (104 mg, 0.720 mmol), suspended in 6.0 mL of chloroform, triethylamine (100 mL, 0.720 mmol) was added to obtain a homogeneous solution. Solid **1**Zn (160 mg, 0.120 mmol of repeating unit) was suspended in 10.0 mL of chloroform. To the suspension, the phenylhydrazine solution was added, and the mixture was stirred for 24 h. The initial red solid turned bluish green over the reaction period. The powder was then filtered and washed with methanol (2 × 5 mL) and diethyl ether (2 × 5 mL) and was suspended in 10.0 mL of tetrachloromethane ($CCl_4$). To this suspension, 0.10 M of $Br_2$ in $CCl_4$ was added slowly until the decoloration of $Br_2$ was no longer observed. The titration gives reproducible values within the experimental error (< 0.1 mL). An average of 3.0 mL of the $Br_2$ solution was added in the titrations. Therefore, the number of reduced vanadium atoms in the hexavanadate unit averages 2.5.

**Supporting Information** (see footnote on the first page of this article): $^1$H and $^{51}$V NMR of **1**Zn, $^1$H NMR of **1**Mn, TGA of monomer and **1**Zn, DSC of monomer and **1**Zn, FT-IR of **1**Zn as a function of temperature, simulated and measured powder X-ray diffraction pattern, cyclic voltammetry data of **1** and analogous compounds.

## Acknowledgments

This work is financially supported by ARO (Army Research Office) and DARPA (contract to TDA Research Corporation).

[1] a) S. Kitagawa, R. Kitaura, S. Noro, *Angew. Chem. Int. Ed.* **2004**, *43*, 2334–2375; b) O. M. Yaghi, M. O'Keeffe, N. W. Ockwig, H. K. Chae, M. Eddaoudi, J. Kim, *Nature* **2003**, *423*, 705–714; c) B. Moulton, M. J. Zaworotko, *Chem. Rev.* **2001**, *101*, 1629–1658; d) B. J. Holliday, C. A. Mirkin, *Angew. Chem. Int. Ed.* **2001**, *40*, 2022–2043; e) M. Eddaoudi, D. B. Moler, H. Li, B. Chen, T. M. Reineke, M. O'Keeffe, O. M. Yaghi, *Acc. Chem. Res.* **2001**, *34*, 319–330; f) P. J. Hagrman, D. Hagrman, J. Zubieta, *Angew. Chem. Int. Ed.* **1999**, *38*, 2639–2684.

[2] a) M. T. Pope, in: *Comprehensive Coordination Chemistry II*, Elsevier Ltd., Oxford, UK **2004**, vol. 4, pp. 635–678; b) C. L. Hill, in: *Comprehensive Coordination Chemistry II*, Elsevier Ltd., Oxford, UK, **2004**, vol. 4, pp. 679–759; c) A. Müller, S. Roy, *Coord. Chem. Rev.* **2003**, *245*, 153–166; d) T. Yamase, M. T. Pope, *Polyoxometalate Chemistry for Nano-Composite Design*, Kluwer Academic/Plenum Publishers, New York, NY, **2002**; e) C. L. Hill (Guest Ed.), *Chem. Rev.* **1998**, *98*, 1–389.

[3] a) G. Yucesan, V. Golub, C. J. O'Connor, J. Zubieta, *Dalton Trans.* **2005**, 2241–2251; b) M. I. Khan, E. Yohannes, R. C. Nome, S. Ayesh, V. O. Golub, C. J. O'Connor, R. J. Doedens, *Chem. Mater.* **2004**, *16*, 5273–5279; c) E. Burkholder, V. Golub, C. J. O'Connor, J. Zubieta, *Inorg. Chem.* **2004**, *43*, 7014–7029; d) Y. Li, G. De, M. Yuan, E. Wang, R. Huang, C. Hu, N. Hu, H. Jia, *Dalton Trans.* **2003**, 331–334; e) G. Luan, Y. Li, S. Wang, E. Wang, Z. Han, C. Hu, N. Hu, H. Jia, *Dalton Trans.* **2003**, 233–235; f) E. Burkholder, V. Golub, C. J. O'Connor, J. Zubieta, *Chem. Commun.* **2003**, 2128–2129; g) R. C. Finn, R. S. Rarig Jr, J. Zubieta, *Inorg. Chem.* **2002**, *41*, 2109–2123; h) M. I. Khan, E. Yohannes, D. Powell, *Inorg. Chem.* **1999**, *38*, 212–213.

[4] a) H. An, Y. Li, E. Wang, D. Xiao, C. Sun, L. Xu, *Inorg. Chem.* **2005**, *44*, 6062–6070; b) J. Y. Niu, D.-J. Guo, J.-P. Wang, J.-W. Zhao, *Cryst. Growth Des.* **2004**, *4*, 241–247; c) J. Y. Niu, Q. Wu, J.-P. Wang, *J. Chem. Soc. Dalton Trans.* **2002**, 2512–2516.

[5] a) P. Mialane, L. Lisnard, A. Mallard, J. Marrot, E. Antic-Fidancev, P. Aschehoug, D. Vivien, F. Schéresse, *Inorg. Chem.* **2003**, *42*, 2102–2108; b) N. Honma, K. Kusaka, T. Ozeki, *Chem. Commun.* **2002**, 2896–2897; c) M. Sadakane, M. H. Dickman, M. T. Pope, *Angew. Chem. Int. Ed.* **2000**, *39*, 2914–2916; d) K. Wassermann, M. H. Dickman, M. T. Pope, *Angew. Chem. Int. Ed. Engl.* **1997**, *36*, 1445–1448.

[6] B. J. S. Johnson, S. A. Geers, W. W. Brennessel, V. G. Young Jr, A. Stein, *Dalton Trans.* **2003**, 4678–4681.

[7] B. J. S. Johnson, R. C. Schroden, C. Zhu, V. G. Young Jr, A. Stein, *Inorg. Chem.* **2002**, *41*, 2213–2218.

[8] S. Favette, B. Hasenknopf, J. Vaissermann, P. Gouzerh, C. Roux, *Chem. Commun.* **2003**, 2664–2665.

[9] Y. Hou, C. L. Hill, *J. Am. Chem. Soc.* **1993**, *115*, 11823–11830.

 © 2006 Wiley-VCH Verlag GmbH & Co. KGaA, Weinheim 

[10] Q. Chen, D. P. Goshorn, C. P. Scholes, X. L. Tan, J. Zubieta, *J. Am. Chem. Soc.* **1992**, *114*, 4667–4681.
[11] a) P. Gouzerh, A. Proust, *Chem. Rev.* **1998**, *98*, 77–112; b) Q. Chen, J. Zubieta, *Coord. Chem. Rev.* **1992**, *114*, 107–167.
[12] a) I. V. Kozhevnikov, *NATO Sci. Ser., II* **2003**, *98*, 351–380.; b) J. B. Moffat, *Metal-Oxygen Clusters: The Surface and Catalytic Properties of Heteropolyoxometalates*, Kluwer Academic/Plenum Publishers, New York, NY, **2001**; c) R. Neumann, *Prog. Inorg. Chem.* **1998**, *47*, 317–370; d) T. Okuhara, N. Mizuno, M. Misono, *Adv. Catal.* **1996**, *41*, 113–252; e) C. L. Hill, C. M. Prosser-McCartha, *Coord. Chem. Rev.* **1995**, *143*, 407–455.
[13] a) O. A. Kholdeeva, M. N. Timofeeva, G. M. Maksimov, R. I. Maksimovskaya, W. A. Neiwert, C. L. Hill, *Inorg. Chem.* **2005**, *44*, 666–672; b) O. A. Kholdeeva, M. P. Vanina, M. N. Timofeeva, R. I. Maksimovskaya, T. A. Trubitsina, M. S. Melgunov, E. B. Burgina, J. Mrowiec-Bialon, A. B. Jarzebski, C. L. Hill, *J. Catal.* **2004**, *226*, 363–371; c) N. M. Okun, T. M. Anderson, K. I. Hardcastle, C. L. Hill, *Inorg. Chem.* **2003**, *42*, 6610–6612; d) N. M. Okun, T. M. Anderson, C. L. Hill, *J. Mol. Catal. A* **2003**, *197*, 283–290; e) N. M. Okun, T. M. Anderson, C. L. Hill, *J. Am. Chem. Soc.* **2003**, *125*, 3194–3195; f) J. T. Rhule, W. A. Neiwert, K. I. Hardcastle, B. T. Do, C. L. Hill, *J. Am. Chem. Soc.* **2001**, *123*, 12101–12102; g) L. Xu, E. Boring, C. Hill, *J. Catal.* **2000**, *195*, 394–405.
[14] C. L. Hill, *Nature* **1999**, *401*, 436–437.
[15] V. W. Day, W. G. Klemperer, D. J. Maltbie, *J. Am. Chem. Soc.* **1987**, *109*, 2991–3002.
[16] N. E. Brese, M. O'Keeffe, *Acta Crystallogr., Sect. B* **1991**, *47*, 192–197.
[17] Distinctive features in IR and UV/Vis spectra for the reduced hexavanadate units (from $V^{V}$ to $V^{IV}$) have been documented by Zubieta and co-workers in their extensive studies on the hexavanadate derivatives. See ref.[10]
[18] In any event, the sizes of dissociated monomers, and aggregates of up to ca. 10 or more monomers, at these concentration, are likely below the lower limit for size distribution quantification by DLS. The intensity of light scattering is proportional to the concentration in solution and the cube of the size of the molecule.
[19] IR and crystallographic studies on the reduced forms of tris(alkoxo)hexavanadate units by Zubieta et al. shows that the protonation of the bridging oxo group in the reduced species lengthens the V–O bonds and results in the low energy shift of the $\nu_{V-O-V}$ stretch. See ref.[10]
[20] *SMART*, version 5.624 ed., Bruker AXS, Inc., Madison, WI, **2002**.
[21] *SAINT*, version 6.45A ed., Bruker AXS, Inc., Madison, WI, **2002**.
[22] *SADABS*, version 2.10 ed., University of Göttingen, Göttingen, Germany, **2003**.
[23] A. J. C. Wilson, *International Tables for X-ray Crystallography*, Kynoch Academic Publishers, Dordrecht, Netherlands, **1992**, vol. C.

Received: February 2, 2006
Published Online: April 27, 2006

 © 2006 Wiley-VCH Verlag GmbH & Co. KGaA, Weinheim 

DOI: 10.1002/ejic.200600101

# Redox-Active 17- and 19-Membered Metallamacrocycles Incorporating Tetrathiafulvalene

Grégory Gachot,[a] Pascal Pellon,[a] Thierry Roisnel,[a] and Dominique Lorcy*[a]

**Keywords:** Metallamacrocycle / Tetrathiafulvalene / Diphosphane ligands / Molybdenum / Tungsten

Redox-active 17- and 19-membered metallamacrocycles were prepared thanks to the chelating ability of bis[(diphenylphosphane)alkylthio]TTF towards the $M(CO)_4$ fragment (M = Mo, W). The TTF unit can adopt either a *cis* or a *trans* configuration as can the phosphorus atoms coordinated to the metal center. Moreover, an element of planar chirality is generated by the *trans* isomer of the TTF. Thus, the reaction affords six stereoisomers as evidenced by $^{31}P$ NMR and X-ray crystallographic analyses. The electrochemical properties of the title compounds have been investigated by cyclic voltammetry. Within the 19-membered metallamacrocycles, no significant influence of the two redox moieties was detected, whereas in the 17-membered metallamacrocycles, the oxidized TTF modifies the redox behavior of the metal center. Two crystalline complexes obtained with tetracyanoquinodimethane (TCNQ) and the tungsten 17- and 19-membered metallamacrocycles are reported. Comparison of the crystal structures shows that these metallamacrocycles appear to be rather flexible even with strained structures.

(© Wiley-VCH Verlag GmbH & Co. KGaA, 69451 Weinheim, Germany, 2006)

## Introduction

Various cyclophanes or cage molecules incorporating one or more electroactive units such as a tetrathiafulvalene core (TTF) have been studied with the aim of creating, through intramolecular or intermolecular interactions, nanoelectronic devices.[1] Among the electroactive macrocycles described so far, none of them contain a metallic fragment. Association of the TTFs with one appropriate metal will lead to a macrocycle with multiple redox sites and the possibility of interaction between the inorganic and organic moieties.[2] Various potential applications can be envisioned for these hybrid molecules, as molecular materials or in catalytic systems as it is well known that the steric and electronic properties of the ligand have an enormous effect on the reactivity of metal complexes.[3] A simple route toward the formation of large metallamacrocycles involves the coordination of a bidentate α,ω-diphosphane ligand to the transition metal center.[4] Therefore, we have studied the ability of bis-substituted [(diphenylphosphanyl)propylthio]-TTF **1**[5] to form metal carbonyl complexes upon chelation of the $Mo(CO)_4$ and $W(CO)_4$ fragments. Moreover, we also present the synthesis of the diphosphanyl ligand **2** where the phosphane moieties are linked to the donor core through a longer spacer group such as a thiobutyl one and the influence of this longer chain on the structural and electrochemical properties of the metallamacrocycles. Comparison of the effect of the length of the spacer group on the molecular structure and the redox behavior will then be discussed. Another interesting feature that will be presented is the influence of the complexation with TCNQ on the conformation of these metallamacrocycles.

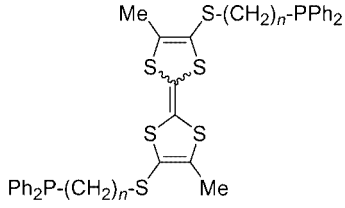


**1** *n* = 3 *cis*/*trans*
**2** *n* = 4 *cis*/*trans*

## Results and Discussion

The synthesis of the ligand **2** was accomplished as depicted in Scheme 1 according to the chemical pathway used for the synthesis of bis[(diphenylphosphanyl)propylthio]-TTF **1** using the preformed TTF derivative **3** as the starting material.[5] The methodology consists first of the synthesis of the bis[(boronatodiphenylphosphanyl)butylthio]TTF **5**. The use of phosphane–borane substituents in the synthesis of the target TTFs presents several advantages as they are very stable compared to phosphane derivatives towards the

[a] UMR 6226 "Sciences Chimiques de Rennes" CNRS-Université de Rennes 1,
Campus de Beaulieu, Bât 10A, 35042 Rennes cedex, France
Fax: +33-22323-67-38
E-mail: dominique.lorcy@univ-rennes1.fr

 © 2006 Wiley-VCH Verlag GmbH & Co. KGaA, Weinheim 

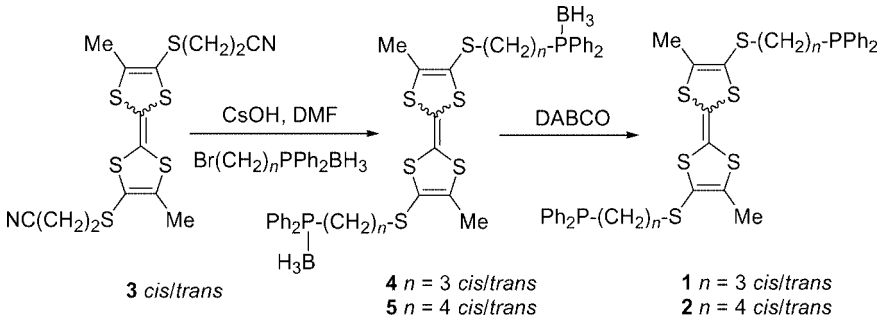


Scheme 1.

usual oxidizing or electrophilic reagents, and very easy to handle and to purify.[6,7] The bis(cyanoethylthioTTF) **3** was treated with cesium hydroxide and reacted with the bromobutyldiphenylphosphane–borane leading to TTF **5**. Decomplexation of the phosphane–borane complex was performed in the presence of DABCO under an inert atmosphere to give the bis[(diphenylphosphanyl)butylthio]TTF **2**.[8] These TTFs **1**–**2** should be kept under an inert atmosphere to avoid the formation of the corresponding phosphane oxides. Note that all these TTFs **1**–**5** are obtained as a mixture of the *cis* and *trans* isomers and attempts to separate these isomers are worthless as TTFs are prone to isomerization in solution upon light exposure or in the presence of traces of acid.[9,10]

In order to form metal carbonyl complexes with these TTF ligands, we used *cis*-$M(CO)_4(C_5H_{10}NH)_2$ derivatives (M = Mo, W) where the two labile piperidine ligands can be easily replaced by other ligands such as two phosphanes.[11] As mentioned earlier for monosubstituted phosphanylTTF derivatives, the metal carbonyl complexation can be realized directly from the phosphane–borane TTF complexes,[12] in a one-pot procedure by a two-step chemical synthesis: firstly decomplexation of the phosphane–borane complex in the presence of DABCO and then addition of one equivalent of *cis*-$M(CO)_4(C_5H_{10}NH)_2$ in the medium where the bis[(diphenylphosphanyl)alkylthio]TTFs were formed. The solution was warmed at 80 °C for 2 h. Actually, because of the flexibility of the alkylthio spacer groups, two types of metal carbonyl complexes were obtained, the expected metallamacrocycles **6**–**9** (Scheme 2) but also polymeric derivatives resulting respectively from an intramolecular and an intermolecular complexation. The mononuclear metallamacrocycles formed can be easily isolated after column chromatography upon silica gel in an overall yield of 20–33%.

Analysis of the fraction containing the mononuclear complexes by $^{31}P$ NMR, after the chromatographic separation, reveals the presence of four signals for each of the four investigated derivatives **6**–**9** (Table 1). Indeed, besides the *cis*/*trans* isomerism of the TTF core, the phosphorus atoms can also be either *cis* or *trans* coordinated to the metal center. For the tungsten metallamacrocyles **6** and **8**, a small doublet due to the coupling of the phosphorus atom with the $^{183}W$ isotope is associated with the four singlets. Thanks to the coupling constant, it is possible to distinguish the *cis*-P–W–P isomers from the *trans*-P–W–P ones.[13] Indeed, the phosphorus atoms resonate at high field for **6** and **8** with $^1J_{PW}$ = 230 Hz characteristic for the *cis*-P–W–P isomers while the two signals observed at low field for **6** and **8** exhibit a $^1J_{PW}$ = 279 Hz characteristic for the *trans*-P–W–P one. For the molybdenum metallamacrocycles, by analogy with previous results on monodiphenylphosphanylpropylthioTTF (P–TTF) *cis* coordinated to the $Mo(CO)_4$, *cis*-$Mo(CO)_4$-$(P–TTF)_2$,[12] where the phosphorus atoms resonated at $\delta$ = 26.6 ppm, the singlets observed at high field for **7** and **9** can be attributed to *cis*-P–Mo–P isomers while the signals observed at low field for **7** and **9** are assigned to the *trans* isomers.

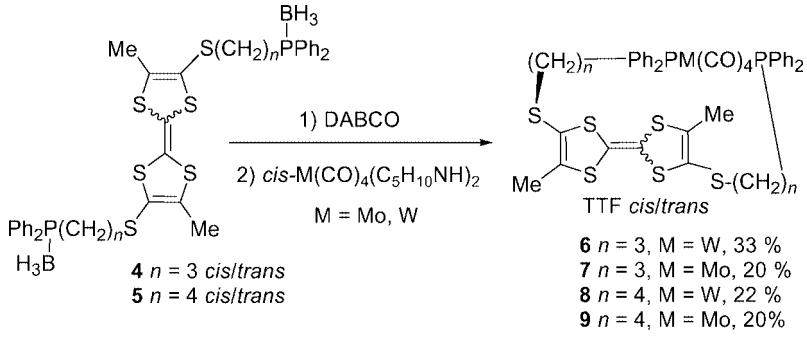


Scheme 2.

 © 2006 Wiley-VCH Verlag GmbH & Co. KGaA, Weinheim 

Table 1. $^{31}P$ chemical shifts for compounds **6**–**9** in $CDCl_3$ solution.

| Compound (metal, *n*) | $\delta$ = $^{31}P$ ppm ($^1J_{PW}$ [Hz]) |
|---|---|
| **6** (W, 3) | 5.9 (230), 6.9 (230), 13.5 (279), 14.6 (279) |
| **7** (Mo, 3) | 24.2, 24.7, 38.4, 39.3 |
| **8** (W, 4) | 8.0 (230), 8.6 (230), 14.8 (279), 14.9 (279) |
| **9** (Mo, 4) | 25.5, 25.7, 39.0, 39.1 |

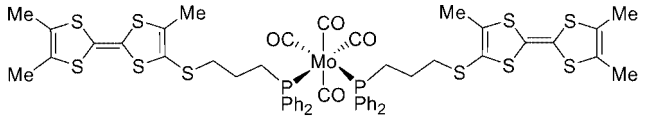

*cis*-$Mo(CO)_4$(P-TTF)$_2$

Interestingly, the intensity of the various signals observed indicates that a majority of the *trans* isomers on the metal center are formed in all the cases with an estimated *trans* P–M–P/*cis* P–M–P ratio of 5:2. The obtention of *cis*/*trans* isomers on the metal center, starting from the *cis*-$M(CO)_4$-(piperidine)$_2$ derivatives (M = Mo, W), finds its origin in the temperature used to form these metallamacrocycles.[11] Indeed, when the reaction was performed at 50 °C, no isomerization occurs as previously observed for monosubstituted TTF but the reaction rate is very low, while at 80 °C substitution of the two piperidine ligands occurs, especially for the *cis*-$W(CO)_4$(piperidine)$_2$ derivative, but also isomerization on the metallic center. The TTF core can also adopt either a *cis* or *trans* configuration. The presence of isomers on the TTF moiety is not surprising as we started from a mixture of *cis* and *trans* isomers for both TTFs **4** and **5**. Moreover, the *trans* form of the TTF introduces an element of planar chirality. Therefore, as depicted in Scheme 3, six stereoisomers can be envisioned for each metallamacrocycle, **6**–**9**, corresponding to the following isomers: (i) **a** *cis* TTF/*trans* P–M–P, (ii) **b** *cis* TTF/*cis* P–M–P, (iii) **c** *trans* (R)TTF/*cis* P–M–P and **c′** *trans* (S)TTF/*cis* P–M–P and (iv) **d** *trans* (R)TTF/*trans* P–M–P, and **d′** *trans* (S)TTF/*trans* P–M–P, hence the four $^{31}P$ NMR signals since the enantiomers **c/c′** and **d/d′** can not be distinguished in this way.

Crystals of the metallamacrocyles **6**, **7**, and **8** were isolated from a mixture of dichloromethane and methanol. The crystal structure determinations reveal that in the case of the macrocycles **6** (*n* = 3, M = W) and **8** (*n* = 4, M = W), the isomers **a** (*cis* TTF/*trans* P–W–P), were isolated (Figure 1), while for **7** (*n* = 3, M = Mo) the two enantiomeric forms **7 c/c′** [*trans* (R/S) TTF/*cis* P–Mo–P] (Figure 2) were crystallized in the racemic mixture.

All the TTF moieties adopt a boat conformation within these metallacyclophanes where both dithiole rings are folded along the S···S vector with asymmetric folding angles, which are more pronounced for the most strained 17-membered metallamacrocycles **6a** (17 and 28°) and **7c/c′** (19 and 36°) than for the 19-membered metallamacrocycle **8a** (9 and 11°). Comparison of the crystal structure of **6a** (*n* = 3) with **8a** (*n* = 4), where the difference is only due to the length of the spacer group between the TTF and the phosphorus atoms, shows that in both cases, the W–P distances and P–W–P interligand angles are similar and in the

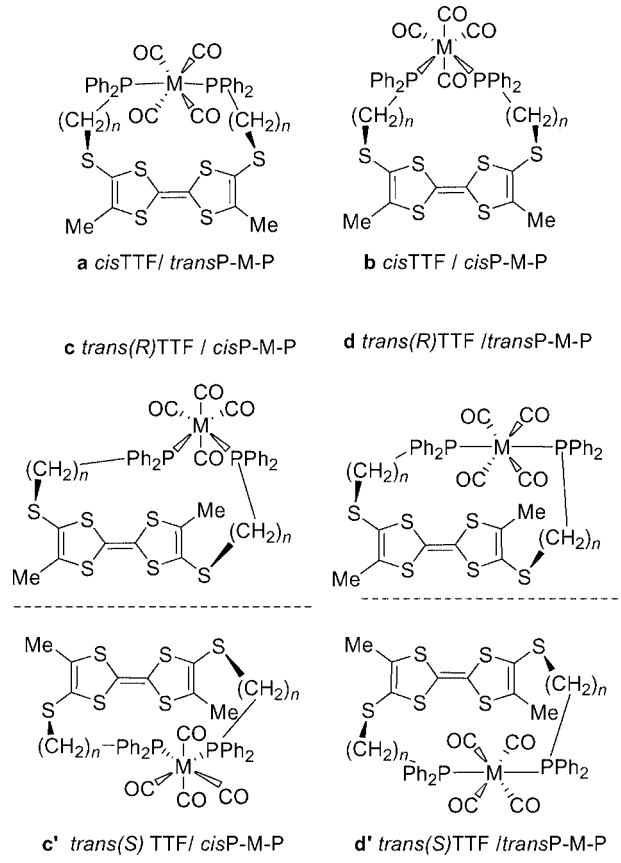


Scheme 3.

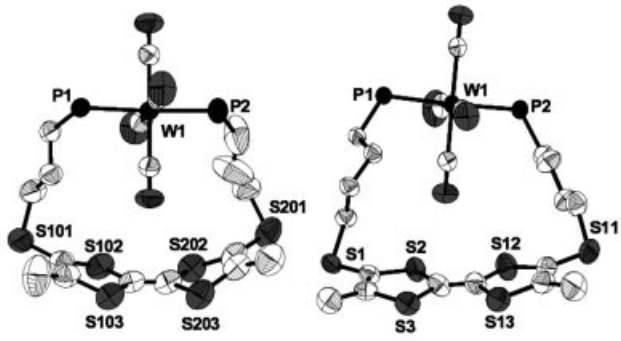


Figure 1. Molecular structure of (left) **6a** and (right) **8a**. The hydrogen atoms and the phenyl rings are not shown for clarity (thermal ellipsoids set at 50% probability). Selected bond lengths [Å] and angles [°]: W(1)–P(1) 2.4636(12), W(1)–P(2) 2.4644(14), P(1)–W(1)–P(2) 177.36(5) for **6a** and: W(1)–P(1) 2.4717(8), W(1)–P(2) 2.4652(8), P(1)–W(1)–P(2) 176.20(2) for **8a**.

usual range. Therefore, constrains brought by the formation of the metallamacrocycle are more effective on the fulvalene skeleton than on the inorganic part. Analysis of the crystals **6a** and **8a**, dissolved in $CDCl_3$, by $^{31}P$ NMR reveals that the isomers **a** (*cis* TTF/*trans* P–W–P) exhibit only one set of signals at $\delta$ = 13.5 ppm for **6a** and at $\delta$ = 14.8 ppm for **8a**. The same $CDCl_3$ solution left under ambient light exposure and analyzed again one day later exhibits this time two sets of signals caused by the presence of the *cis* and *trans* TTF isomers.[9]

 © 2006 Wiley-VCH Verlag GmbH & Co. KGaA, Weinheim 

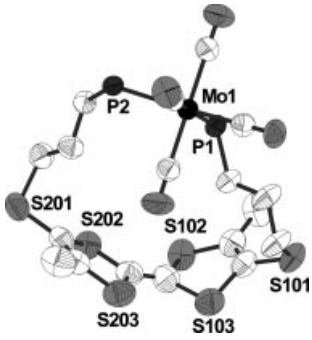


Figure 2. Molecular structure of **7c**. The hydrogen atoms and the phenyl rings are not shown for clarity (thermal ellipsoids set at 50% probability). Selected bond lengths [Å] and angles [°]: Mo(1)–P(1) 2.5386(13), Mo(1)–P(2) 2.5666(12), P(1)–Mo(1)–P(2) 99.85(4).

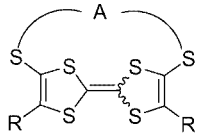


TTF *cis*/*trans*

14-membered ring : R = Ar, A = $(CH_2)_6$
R = Ar, A = $CH_2C_6H_4CH_2$
R = H, A = $CH_2C_6H_4CH_2$
R = $CO_2Me$, A = $CH_2C_6H_4CH_2$
18-membered ring : R = Me, A = $(CH_2)_{10}$
20-membered ring : R = Me, A = $(CH_2)_{12}$

The redox properties of the metallacyclophanes **6**–**9** were studied by cyclic voltammetry and peak potentials of the various complexes are collected in Table 2 together with the data for the starting ligands TTF **1** and **2**. In order to obtain an insight into the effect of the ligand environment on the redox potentials of the metal center, we also added to Table 2 the data for complexes $Mo(CO)_4(PPh_3)_2$ and $W(CO)_4(PPh_3)_2$. It is worth noting that *cis*-$M(CO)_4(PPh_3)_2$ and *trans*-$M(CO)_4(PPh_3)_2$ (M = Mo, W) present almost identical $E°$ values [15] and exhibit cyclic voltammograms which are partially reversible for the molybdenum complex and irreversible for the tungsten one because of the loss of carbon monoxide on the metallic center upon oxidation.[15] Concerning the various metallamacrocycles, two oxidation waves are observed. The first reversible oxidation step corresponds to the oxidation of the TTF in its radical cation while the second oxidation process is due to the concomitant oxidation of the TTF radical cation into the dication and the oxidation of the metallic center. However, this process is not fully reversible due to the loss of the carbonyl ligand upon oxidation (Figure 3). This concomitant oxidation of the organic and inorganic moieties was also observed on phosphane TTF linked to a metal via a nonconjugated spacer group, such as *cis*-$Mo(CO)_4(P–TTF)_2$.[12] Within the metallamacrocycles of the same size, the nature of the metal center, Mo or W, does not modify the redox potentials. Moreover, comparison of the first redox potentials of the complexes with those of the starting ligands (**1** and **2**) shows that there is no significant influence of the cyclization despite the strained structures described above. Interestingly, comparison can also be made with TTF cyclophanes where fully covalent bridges of various lengths link the two dithiole moieties leading to 14-, 18-, and 20-membered rings.[16–18] Indeed, among those cyclophanes, the most constrained one with the shortest bisthioalkyl link ($–S(CH_2)_6S–$[16] and $–SCH_2C_6H_4CH_2S–$[16,17]) were found to exhibit a single irreversible oxidation wave, while by contrast, longer links [$–S(CH_2)_{10–12}S$][18] or the redox active metallamacrocycles described here display a first fully reversible oxidation wave. The lack of reversibility of the redox system on the 14-membered TTF cyclophanes was attributed to the severe bending of the TTF core as for instance the *cis*-substituted TTF with a bisthiohexyl bridge, [$–S(CH_2)_6S$], is folded by 47 and 34° along the S···S vector.[16b] Although, in **6**–**9**, the metallic fragment with the CO ligands brings a novel inner constraint to the TTF unit, the bridge is long enough to enable the two typical redox waves of a TTF core.

Table 2. Oxidation potentials V vs. SCE, Pt-working electrode with $nBu_4NPF_6$ (0.1 M) in $CH_2Cl_2$, scanning rate 0.1 V/s.

| Compound (metal, *n*) | $E^1$ | $E_{pa}^2$ / $E_{pc}^2$ |
|---|---|---|
| $W(CO)_4(PPh_3)_2$ | 0.87[a] | |
| $Mo(CO)_4(PPh_3)_2$ | 0.85/0.76 | |
| **6** (W, 3) | 0.45 | 0.93/.0.82 |
| **7** (Mo, 3) | 0.47 | 0.91/.0.82 |
| **8** (W, 4) | 0.41 | 0.88/0.77 |
| **9** (Mo, 4) | 0.41 | 0.85/0.76 |
| **1** (*n* = 3) | 0.46 | 0.86/0.80 |
| **2** (*n* = 4)[14] | 0.39 | 0.82[a] |

[a] Irreversible process.

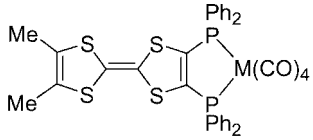


[P2][M(CO)4] (M = Mo, W)

Considering the second redox process, the comparison of the anodic peak potential $E_{pa}^2$ in the complexes **6**–**9** with the value of the noncyclic $Mo(CO)_4(PPh_3)_2$ and $W(CO)_4(PPh_3)_2$ shows a significant positive shift of $E_{pa}^2$ in the 17-membered cyclic compounds **6** and **7** (+60 mV for Mo, W) while the $E_{pa}^2$ potentials are almost identical in the less-constrained **8** and **9** molecules. This indicates that through-space interactions occur between the two−organic and organometallic−redox moieties in the smallest metallamacrocycles. This effect on $E_{pa}^2$ is most probably due to electrostatic repulsion and the close proximity of the TTF dication to the bound metal. Note that by contrast, when the phosphane is directly linked to the TTF core, as in [P2][$M(CO)_4$] (M = Mo, W), oxidation of the coordinated metallic center occurs at a more positive potential than the $TTF^+/TTF^{2+}$ redox system because of even stronger electrostatic interactions.[19] In this case the donating ability of the TTF core within the complexes was also significantly decreased as a positive shift of about 200 mV was observed, while in our metallamacrocycle **6**–**9** the redox properties of the donor are conserved.

 © 2006 Wiley-VCH Verlag GmbH & Co. KGaA, Weinheim 

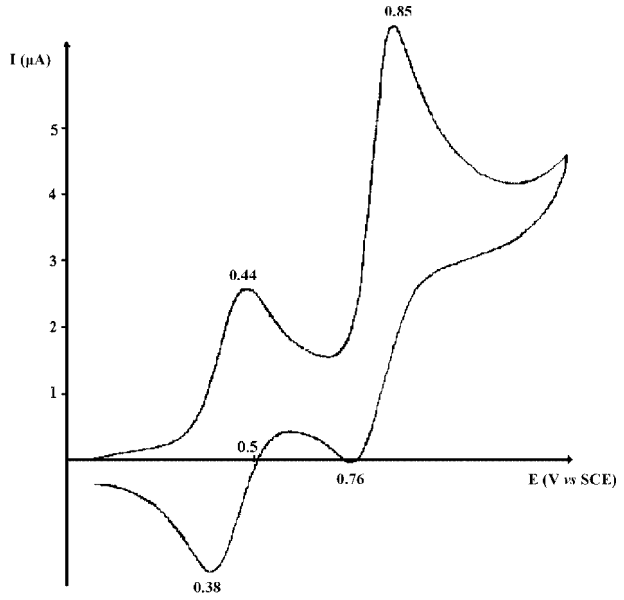


Figure 3. Cyclic voltammogram of **9**, $n$Bu$_4$NPF$_6$ (0.1 M) in $CH_2Cl_2$, scanning rate 0.1 V/s.

Formation of charge transfer salts with TCNQ depends on the relative redox potentials of the donor ($E_D^1$) and TCNQ ($E_A^1$ = 0.18 V vs. SCE). These metallamacrocycles with their first redox potentials above 0.40 V are a rather borderline case as precursors of such charge transfer salts since $E_D^1$-$E_A^1 > 0.22$ V. Indeed, it is known that a partial or full charge transfer is only possible when $E_D^1$-$E_A^1 < 0.25$ V.[20–21] Mixing a dichloromethane solution of the metallamacrocycles **6** or **8** with an acetonitrile solution of TCNQ afforded deep purple shiny single crystals after slow evaporation. X-ray crystal structure determinations reveal a stoichiometry of two metallamacrocycles for one TCNQ in each case with inclusion of acetonitrile, that is (**6**)$_2$(TCNQ)·(CH$_3$CN)$_3$ and (**8**)$_2$(TCNQ)·(CH$_3$CN)$_2$. The former complex with **6** ($n$ = 3) crystallizes in the triclinic system, space group $P\bar{1}$, with molecule **6** in a general position in the unit cell, one TCNQ located on an inversion center, one acetonitrile disordered on an inversion center, and one acetonitrile in a general position. Complex (**8**)$_2$(TCNQ)·(CH$_3$CN)$_2$ crystallizes in a triclinic system, space group $P\bar{1}$, with molecule **8** in a general position in the unit cell, TCNQ located on an inversion center with only one acetonitrile in a general position. In the solid state, the TCNQ molecule is, in each case, sandwiched by two TTF cores of the metallamacrocycles in a ···DAD··· (D = **6** or **8** and A = TCNQ) motif. The TCNQ ring overlaps the central C=C bond of the TTF core and the interplanar separations between the donor and the acceptor are 3.48 and 3.53 Å for (**6**)$_2$(TCNQ)·(CH$_3$CN)$_3$ and (**8**)$_2$(TCNQ)·(CH$_3$CN)$_2$, respectively (Figure 4). Using the empirical formula of Kistenmacher, which correlates the bond lengths to the formal charge of the TCNQ in various charge transfer salts,[22] we found that in both complexes the TCNQ is neutral. This is supported by the EPR analyses carried out on the crystals and no EPR signal was observed from room to liquid helium temperature. This is also confirmed by the diamagnetic behavior found in the whole temperature range by SQUID susceptibility measurements. Therefore, both complexes, (**6**)$_2$(TCNQ)·(CH$_3$CN)$_3$ and (**8**)$_2$(TCNQ)·(CH$_3$CN)$_2$, are neutral donor/acceptor complexes. Concerning (**8**)$_2$(TCNQ)·(CH$_3$CN)$_2$, the DAD motifs form stacks with a lateral slip between two neighboring TTF cores with S···S distances at 4.499(9) Å, while for (**6**)$_2$(TCNQ)·(CH$_3$CN)$_3$ the DAD motifs are isolated from each other by the inorganic moieties of the macrocycles (Figure 5).

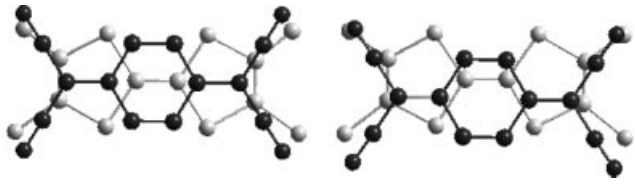

Figure 4. TTF/TCNQ overlap in (**6a**)$_2$(TCNQ)·(CH$_3$CN)$_3$ (left) and (**8a**)$_2$(TCNQ)·(CH$_3$CN)$_2$ (right).

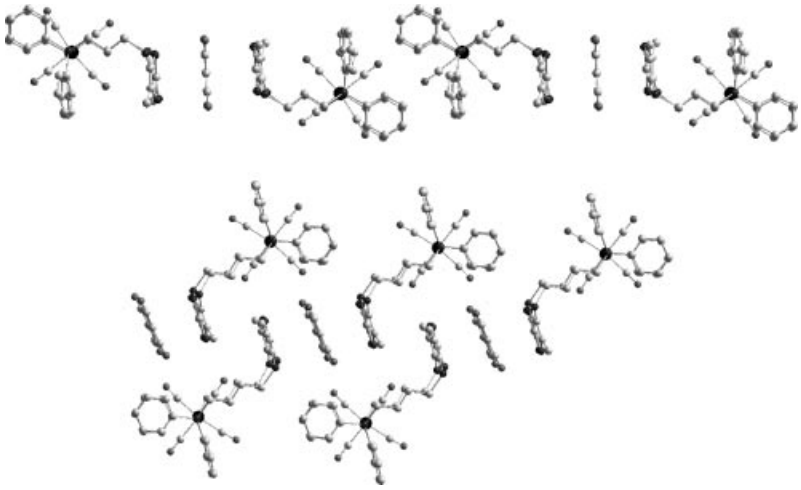

Figure 5. Stacking arrangement of (**6a**)$_2$(TCNQ)·(CH$_3$CN)$_3$ (top) and (**8a**)$_2$(TCNQ)·(CH$_3$CN)$_2$ (bottom).

 © 2006 Wiley-VCH Verlag GmbH & Co. KGaA, Weinheim 

Also noticeable, among the six possible stereoisomers for each metallamacrocycle **6** and **8** present in the starting solution for the elaboration of the TCNQ complexes, the isomers that crystallized within these complexes are the isomers **a** (*cis* TTF/*trans* P–W–P), which were independently crystallographically characterized and described above. The complexation with TCNQ has a significant influence on the conformation of the metallamacrocycles **6a** and **8a** as depicted in Figure 6. Comparison of the molecular structures shows that the TTF core for the 17-membered metallamacrocycle **6a** is more planar within the complex as the folding angles along the S···S vector for the dithiole rings are smaller (11 and 15° instead of 17 and 28°). The planarization of the TTF core in $(\mathbf{6a})_2(TCNQ)\cdot(CH_3CN)_3$ brings the metal closer to the TTF core with a distance of about 5.85 vs. 6.25 Å in the starting complex. Contrariwise, for the 19-membered metallamacrocycle **8a**, the folding angles are in the same range (10 and 10° instead of 11 and 9°). Actually, the difference brought by the complexation on **8a** lies in the location of the metal in relation to the TTF core. Indeed, within the complex $(\mathbf{8a})_2(TCNQ)\cdot(CH_3CN)_2$ the side chain with the metallic moiety is located in a plane perpendicular to the plane of the TTF core, while before complexation the chain with the metallic fragment was located more on the side of the TTF (Figure 6).

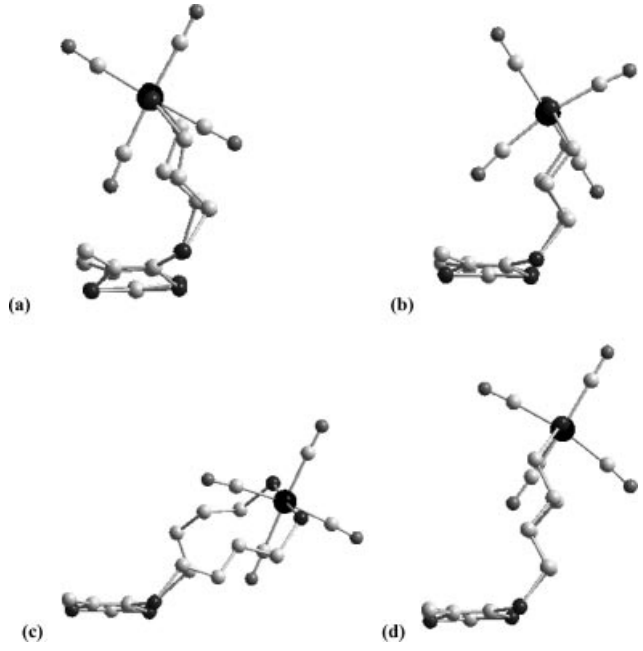


Figure 6. Side view of the metallamacrocycles, (a) **6a**, (b) $(\mathbf{6a})_2(TCNQ)\cdot(CH_3CN)_3$, (c) **8a**, (d) $(\mathbf{8a})_2(TCNQ)\cdot(CH_3CN)_2$.

Analysis of the bond lengths of the metallamacrocycles within the TCNQ complexes shows that in both cases the bond lengths of the TTF core are in the usual range for neutral TTF moieties with the central C=C bond lengthened by 1.340 Å, but still within the range for the neutral TTF core. Similarly, the W–P distances are not significantly modified (Table 3). On the contrary, the P–W–P angles are altered and for **6a** it amounts to 169.16(3)° instead of 177.36(5)° and for **8a** 176.20(2)° instead of 172.58(4)°, accounting for the consequences of the complexation with TCNQ (Table 3). Therefore, even with a constrained structure such as **6a** these metallamacrocyles remain flexible and the planarization of the TTF core, within the TCNQ complexes, induces a transfer of the constraints onto the metallic fragment.

Table 3. Significant bond lengths [Å] and angles [°].

| Compound | *d* W–P | *d* C=C | Angle P–W–P | Folding angles along S···S vector |
|---|---|---|---|---|
| **6a** | 2.4636(12) | 1.310(9) | 177.36(5) | 17 |
| | 2.4644(14) | | | 28 |
| $(\mathbf{6a})_2(TCNQ)$ | 2.4655(10) | 1.340(6) | 169.16(3) | 11 |
| | 2.4697(9) | | | 15 |
| **8a** | 2.4652(8) | 1.312(6) | 176.20(2) | 9 |
| | 2.4717(8) | | | 11 |
| $(\mathbf{8a})_2(TCNQ)$ | 2.4550(12) | 1.340(9) | 172.58(4) | 10 |
| | 2.4606(12) | | | 10 |

## Conclusions

In this study, redox active 17- and 19-membered metallamacrocycles incorporating one TTF unit have been synthesized through the coordination of the bidentate [(diphenylphosphanyl)alkylthio]TTFs to the $Mo(CO)_4$ and $W(CO)_4$ fragments. As a consequence of the possible *cis*/*trans* isomerization of the TTF core and the metallic fragment six stereoisomers were formed. As evidenced by the X-ray diffraction studies, the central TTF unit in these metallamacrocycles is not planar, however it is significantly less folded in the 19-membered ring than in the 17-membered ring. Nevertheless, the bending of the TTF is not sufficient to negate the electron-donating ability of this redox unit. Furthermore, in the 17-membered metallamacrocycles, the close proximity of the metallic fragment to the TTF produces electrostatic interactions as evidenced by the shift of the oxidation peak potentials of the metallic fragment to more positive potentials. Two TCNQ complexes with the 17- and 19-membered metallamacrocycles (M = W) have been obtained and crystallographically analyzed. Although no charge transfer was observed, comparison of the crystal structures provide valuable information on the relative flexibility of these strained structures. An attractive feature of these metallamacrocycles lies in the modification of the TTF core upon oxidation which should modify the molecular organization in the neighborhood of the metal fragment and attempts at isolating cation radical salts are currently under way.

## Experimental Section

$^1H$ NMR and $^{31}P$ NMR spectra were recorded with a Bruker AC 300P spectrometer. Chemical shifts are reported in ppm referenced to TMS for $^1H$ NMR and to $H_3PO_4$ for $^{31}P$ NMR spectroscopy. Elemental analyses were obtained from the Laboratoire Central de Microanalyse du CNRS, Lyon. Mass spectra were recorded with

 © 2006 Wiley-VCH Verlag GmbH & Co. KGaA, Weinheim 

a ZABSpec TOF instrument by the Centre Régional de Mesures Physiques de l'Ouest, Rennes. $CH_2Cl_2$ was distilled from $P_2O_5$. Toluene was dried with sodium wire. Chromatography was performed using silica gel Merck 60 (70–260 mesh). $Mo(CO)_6$ and 1,4-diazabicyclo[2.2.2]octane (DABCO) were purchased from ACROS Organics, $W(CO)_6$ was purchased from Aldrich. $M(CO)_4(NHC_5H_{10})_2$ was prepared from $M(CO)_6$ according to published procedures.[11] Cyclic voltammetry was carried out in dichloromethane, containing 0.1 M $nBu_4NPF_6$ as the supporting electrolyte. Voltammograms were recorded at 0.1 $Vs^{-1}$ on a platinum disk electrode ($A$ = 1 $mm^2$). The potentials were measured vs. a saturated calomel electrode. TTF **2** was prepared following known procedures.[5]

**General Procedure for the Synthesis of Complexes 6–9:** To a solution of the TTF **4** or **5** (0.5 mmol) in dried, degassed toluene (30 mL) DABCO (112 mg, 1 mmol) was added under argon. The mixture was stirred for 4 h at 50 °C after which $M(CO)_4(NHC_5H_{10})_2$ (0.5 mmol) in degassed $CHCl_3$ (10 mL) was added. The resulting solution was stirred at 80 °C for 2 h and then the solvent was removed under reduced pressure. The solid residue was dissolved in $CH_2Cl_2$, washed with water, and dried with $Na_2SO_4$. The solvent was removed and chromatography of the residue over silica gel (3:1 $CH_2Cl_2$/PE) afforded the complexes **6**–**9** as a mixture of isomers.

**Complex 6:** Yield 170 mg (33%). $^1$H NMR ($CDCl_3$): $\delta$ = 1.20–1.40 (4 m, 4 H), 1.99, 2.01, 2.09, 2.14 (4 s, 6 H), 2.25–2.64 (4 m, 4 H), 2.70–3.0 (4 m, 4 H), 7.19–7.70 (m, 20 H) ppm. $^{31}$P NMR ($CDCl_3$): $\delta$ = 5.9 ($^1J_{PW}$ = 230 Hz), 6.9 ($^1J_{PW}$ = 230 Hz), 13.5 ($^1J_{PW}$ = 279 Hz), 14.6 ($^1J_{PW}$ = 279 Hz) ppm. $C_{42}H_{38}O_4P_2S_6W$: HRMS calcd. 1044.0075; found 1044.0075. $C_{42}H_{38}O_4P_2S_6W{\cdot}CH_3OH$: calcd. C 47.95, H 3.90, S 17.84; found C 47.58, H 3.80, S 17.53.

**Complex 7:** Yield 100 mg (20%). $^1$H NMR ($CDCl_3$): $\delta$ = 1.20–1.40 (4 m, 4 H), 1.98, 2.02, 2.14, 2.16 (4 s, 6 H), 2.25–2.64 (4 m, 4 H), 2.70–3.0 (4 m, 4 H), 7.19–7.70 (m, 20 H) ppm. $^{31}$P NMR ($CDCl_3$): $\delta$ = 24.2, 24.7, 38.4, 39.3 ppm. $C_{42}H_{38}MoO_4P_2S_6$: HRMS calcd. 957.9626; found 957.9626.

**Complex 8:** Yield 120 mg (22%). $^1$H NMR ($CDCl_3$): $\delta$ = 1.18–1.80 (4 m, 8 H), 2.00, 2.02, 2.10, 2.12 (4 s, 6 H), 2.41–2.62 (4 m, 8 H), 7.15–7.50 (m, 20 H) ppm. $^{31}$P NMR ($CDCl_3$): $\delta$ = 8.0 ($^1J_{WP}$ = 230 Hz), 8.6 ($^1J_{WP}$ = 230 Hz), 14.8 ($^1J_{WP}$ = 279 Hz), 14.9 ($^1J_{WP}$ = 279 Hz) ppm. $C_{44}H_{42}O_4P_2S_6W$: HRMS calcd. 1072.0392; found 1072.0395.

**Complex 9:** Yield 100 mg (20%). $^1$H NMR ($CDCl_3$): $\delta$ = 1.18–1.40 (4 m, 4 H), 1.40–1.55 (4 m, 4 H), 1.92–2.09 (4 s, 6 H), 2.38–2.62 (4 m, 8 H), 7.12–7.49 (m, 20 H) ppm. $^{31}$P NMR ($CDCl_3$): $\delta$ = 25.5, 25.7, 39.0, 39.1 ppm. $C_{44}H_{42}MoO_4P_2S_6$: HRMS calcd. 985.9940; found 985.9946.

Crystallization of the derivatives **6**, **7**, and **8** from $CH_2Cl_2$/MeOH afforded prisms of complexes **6a**, **7c/c′**, and **8a** that were suitable for X-ray crystal structure analyses.

**Single-Crystal Structure Determination:** A single crystal of each compound was carefully selected under a polarizing microscope and glued to a thin fiber glass. Single crystal data collection was performed at room temperature with a Nonius KappaCCD diffractometer (Centre de Diffractométrie, Université de Rennes, France), with Mo-$K_\alpha$ radiation ($\lambda$ = 0.71073 Å). A crystal-to-detector distance of 25.0 mm was used for all the crystals and the data collection strategy (determination and optimization of the goniometer positions) was performed with the help of the COLLECT program.[23] Experimental details of the data collection are summarized in Table 4.

The integration process and data reduction was carried out using the DENZO-SCALEPACK[24] program. Numerical absorption corrections were performed using the multiscan procedure[25a] implemented in the WinGX program suite.[25b] Structure determination was performed with the direct methods solving program SIR97,[26] which revealed all the non-hydrogen atoms. SHELXL 97[27] was used to refine the structure. Finally, hydrogen atoms were placed geometrically and held in the riding mode in the least-square

Table 4. Crystallographic data.

| Structure parameter | **6a** | **7c/c′** | **8a** | (**6a**)$_2$(TCNQ)·($CH_3CN$)$_3$ | (**8a**)$_2$(TCNQ)·($CH_3CN$)$_2$ |
|---|---|---|---|---|---|
| Empirical formula | $C_{42}H_{38}O_4P_2S_6W_1$ | $C_{42}H_{38}MoO_4P_2S_6$ | $C_{44}H_{42}O_4P_2S_6W_1$ | $C_{51}H_{44.5}N_{3.5}O_4P_2S_6W$ | $C_{52}H_{47}N_3O_4P_2S_6W$ |
| Molecular weight | 1044.87 | 956.96 | 1072.93 | 1208.55 | 1216.05 |
| Color | orange | yellow | orange | purple | purple |
| Cryst. system | triclinic | monoclinic | triclinic | triclinic | triclinic |
| Space group | $P\bar{1}$ | $P21/c$ | $P\bar{1}$ | $P\bar{1}$ | $P\bar{1}$ |
| $a$ [Å] | 10.4523(2) | 13.0628(2) | 10.4360(1) | 12.31580(10) | 12.1689(3) |
| $b$ [Å] | 12.1755(2) | 17.6849(4) | 12.5218(1) | 15.0526(2) | 12.9499(4) |
| $c$ [Å] | 18.1465(4) | 19.7180(4) | 18.1813(3) | 16.5610(3) | 18.5932(5) |
| $\alpha$ [°] | 79.438(1) | 90 | 79.8321(5) | 68.7400(10) | 101.823(2) |
| $\beta$ [°] | 78.558(1) | 105.2488(10) | 84.1490(5) | 69.4250(10) | 92.619(2) |
| $\gamma$ [°] | 80.787(1) | 90 | 85.6027(5) | 85.3210(10) | 109.5750(10) |
| $V$ [Å$^3$] | 2206.69(7) | 4394.77(15) | 2322.21(5) | 2675.01(6) | 2681.27(13) |
| $Z$ | 2 | 4 | 2 | 2 | 2 |
| $F$(000) | 1044 | 1960 | 1076 | 1214 | 1224 |
| $D_{calcd.}$ [g/cm$^3$] | 1.573 | 1.446 | 1.535 | 1.501 | 1.506 |
| $M$ [mm$^{-1}$] | 3.014 | 0.696 | 2.867 | 2.499 | 2.493 |
| Data collected | 42143 | 44160 | 46842 | 52690 | 41261 |
| Independent data | 10104 | 9658 | 13458 | 11779 | 11380 |
| $R_{int}$ | 0.0611 | 0.0985 | 0.0829 | 0.082 | 0.0836 |
| Observed data [$I > 2\sigma(I)$] | 8380 | 5587 | 11327 | 9492 | 9154 |
| Parameters refined | 497 | 497 | 515 | 625 | 615 |
| $R(F)$ | 0.0426 | 0.0532 | 0.0386 | 0.0383 | 0.0459 |
| $wR(F^2)$ | 0.1137 | 0.1578 | 0.1005 | 0.0799 | 0.1058 |
| GoF | 1.044 | 1.02 | 1.052 | 1.05 | 1.085 |
| Residual $d$ [e·Å$^{-3}$] | 1.305/–1.198 | 0.676/–0.589 | 1.408/–1.501 | 0.921/–0.882 | 1.717/–1.46 |

 © 2006 Wiley-VCH Verlag GmbH & Co. KGaA, Weinheim 

refinement procedure. The last cycles of the refinement included atomic positions for all the atoms, anisotropic displacement parameters for all the non-hydrogen atoms, and isotropic displacement parameters for all the hydrogen atoms.

CCDC-297239 to -297243 [for **6a**, (**6a**)$_2$(TCNQ)·(CH$_3$CN)$_3$, **7c/c′**, **8a**, and (**8a**)$_2$(TCNQ)·(CH$_3$CN)$_2$, respectively] contain the supplementary crystallographic data for this paper. These data can be obtained free of charge from the Cambridge Crystallographic Data Centre via www.ccdc.cam.ac.uk/data_request/cif.


[1] a) J. O. Jeppesen, M. B. Nielsen, J. Becher, *Chem. Rev.* **2004**, *104*, 5115–5131; b) A. R. Pease, J. O. Jeppesen, J. F. Stoddart, Y. Luo, C. P. Collier, J. R. Heath, *Acc. Chem. Res.* **2001**, *34*, 433–444.

[2] a) E. Coronado, P. Day, *Chem. Rev.* **2004**, *104*, 5419–5448; b) E. Coronado, J. R. Galán-Mascarós, C. J. Gómes-Garcia, V. Laukhin, *Nature* **2000**, *408*, 447–449.

[3] P. C. J. Kamer, P. W. N. M. Van Leeuwen, J. N. H. Reek, *Acc. Chem. Res.* **2001**, *34*, 895–904.

[4] C. A. Bessel, P. Aggarwal, A. C. Marschilok, K. Takeuchi, *Chem. Rev.* **2001**, *101*, 1031–1066, and cited references.

[5] P. Pellon, E. Brulé, N. Bellec, K. Chamontin, D. Lorcy, *J. Chem. Soc., Perkin Trans. 1* **2000**, 4409–4412.

[6] P. Pellon, *Tetrahedron Lett.* **1992**, *33*, 4451–4452.

[7] Y. Gourdel, A. Ghanimi, P. Pellon, M. Le Corre, *Tetrahedron Lett.* **1993**, *34*, 1011–1012.

[8] H. Brisset, Y. Gourdel, P. Pellon, M. Le Corre, *Tetrahedron Lett.* **1993**, *34*, 4523–4526.

[9] R. Ballardini, V. Balzani, J. Becher, A. Di Fabio, M. T. Gandolfi, G. Mattersteig, M. B. Nielsen, F. M. Raymo, S. T. Rowan, J. F. Stoddart, A. J. P. White, D. J. Williams, *J. Org. Chem.* **2000**, *65*, 4120–4126.

[10] A. Souizi, A. Robert, P. Batail, L. Ouahab, *J. Org. Chem.* **1987**, *52*, 1610–1611.

[11] D. Darensbourg, R. L. Kump, *Inorg. Chem.* **1978**, *17*, 2680–2682.

[12] P. Pellon, G. Gachot, J. Le Bris, S. Marchin, R. Carlier, D. Lorcy, *Inorg. Chem.* **2003**, *42*, 2056–2060.

[13] L. Hirsivaara, M. Haukka, J. Pursiainen, *J. Inorg. Chem. Commun.* **2000**, *3*, 508–510.

[14] The lack of reversibility for the second oxidation process for **2** is ascribed to the presence of the phosphane moieties on the TTF which thanks to the thiobutyl chain can reduce the dication species in the medium.

[15] A. M. Bond, D. J. Darensbourg, E. Mocellin, B. J. Stewart, *J. Am. Chem. Soc.* **1981**, *103*, 6827–6832.

[16] a) F. Bertho-Thoraval, A. Robert, A. Souizi, K. Boubekeur, P. Batail, *J. Chem. Soc., Chem. Commun.* **1991**, 843–845; b) K. Boubekeur, P. Batail, F. Bertho-Thoraval, A. Robert, *Acta Crystallogr., Sect. C* **1991**, *47*, 1109–1111.

[17] J. Lau, P. Blanchard, A. Riou, M. Jubault, M. P. Cava, J. Becher, *J. Org. Chem.* **1997**, *62*, 4936–4942.

[18] K. Boubekeur, C. Lenoir, P. Batail, R. Carlier, A. Tallec, M. P. Le Paillard, D. Lorcy, A. Robert, *Angew. Chem. Int. Ed. Engl.* **1994**, *33*, 1379–1381.

[19] N. Avarvari, D. Martin, M. Fourmigué, *J. Organomet. Chem.* **2002**, *643–644*, 292–300.

[20] R. C. Wheland, *J. Am. Chem. Soc.* **1976**, *98*, 3926–3930.

[21] J. B. Torrance, *Acc. Chem. Res.* **1979**, *12*, 79–86.

[22] T. J. Kistenmacher, T. J. Emge, A. N. Bloch, D. O. Cowan, *Acta Crystallogr. Acta Crystallogr., Sect. B* **1982**, *38*, 1193–1199.

[23] Nonius, *COLLECT*, KappaCCD software, Nonius BV, Delft, The Netherlands, **1998**.

[24] Z. Otwinowski, W. Minor in *Enzymology* (Eds.: C. W. Carter Jr, R. M. Sweet), Academic Press, New York, **1997**, vol. 276, pp. 307–326.

[25] a) R. H. Blessing, *Acta Crystallogr., Sect. A* **1995**, *51*, 33; b) L. J. Farrugia, *J. Appl. Crystallogr.* **1999**, *32*, 837.

[26] A. Altomare, M. C. Burla, M. Camalli, G. Cascarano, C. Giacovazzo, A. Guagliardi, A. G. G. Moliterni, G. Polidori, R. Spagna, *J. Appl. Crystallogr.* **1999**, *32*, 115–119.

[27] G. M. Sheldrick, *SHELX97*, Program for the Refinement of Crystal Structures, University of Göttingen, Germany, **1997**.


Received: February 3, 2006
Published Online: May 2, 2006

 © 2006 Wiley-VCH Verlag GmbH & Co. KGaA, Weinheim 

DOI: 10.1002/ejic.200600108

# An Entry to Novel Platinum Complexes: Carboxylation of Dihydroxoplatinum(IV) Complexes with Succinic Anhydride and Subsequent Derivatization

**Michael Reithofer,[a] Markus Galanski,*[a] Alexander Roller,[a] and Bernhard K. Keppler[a]**

**Keywords:** Antitumor agents / Bioinorganic chemistry / Carboxylate ligands / Drug design / Platinum

An improved carboxylation method of (*OC*-6-33)-dichloro-(ethane-1,2-diamine)dihydroxyplatinum(IV) based on succinic anhydride is reported. Reaction of the uncoordinated carboxylic acid with simple amines and alcohols leads to the corresponding amides and esters in the presence of 1,1′-carbonyldiimidazole. The resulting new complexes are characterized by IR, $^{1}H$, $^{13}C$, $^{15}N$, and $^{195}Pt$ NMR spectroscopy, mass spectrometry, and elemental analysis. This reaction provides an entry to a new class of kinetically inert platinum(IV) complexes.
(© Wiley-VCH Verlag GmbH & Co. KGaA, 69451 Weinheim, Germany, 2006)

## Introduction

Cisplatin, *cis*-diamminedichloroplatinum(II) (Figure 1),[1,2] is a highly effective platinum-based anticancer agent that is used in nearly 50% of all tumor therapies all over the world. Cisplatin alone, or in combination with other antineoplastic drugs, is used against a series of solid tumors, including ovarian cancer, non-small cell lung cancer, and head and neck cancer. Cure rates above 90% have been reported in the case of testicular germ-cell cancer, depending on the point of diagnosis; it is thus one of the few anticancer drugs with real curative potential. Nevertheless, severe adverse effects such as a dose-limiting nephrotoxicity, peripheral neuropathy, tinnitus, and hearing loss in the high frequency range are known.[3] Additionally, acquired or intrinsic resistance of tumors to cisplatin therapy narrows the use of this drug.[4] After evaluation of thousands of platinum compounds in preclinical settings during the last 40 years, the second- and third-generation platinum complexes carboplatin [*cis*-diammine(1,1-cyclobutanedicarboxylato)-platinum(II)] and oxaliplatin [(*trans*-*R*,*R*-cyclohexane-1,2-diamine)platinum(II)] were successfully introduced into clinical practice.[5,6]

Besides platinum(II) complexes, which have to be administered intravenously due to their instability in the gastrointestinal tract, platinum(IV) complexes have also been investigated, thereby opening up the possibility of an oral absorption. In this context it has to be mentioned that, in principle, an orally administrable drug offers some advantages in the clinical routine, such as a reduction of the hospitalization costs and a better acceptance of chemotherapy by the patient. From the chemical point of view, octahedrally coordinated platinum(IV) complexes exhibit a higher coordination number than their square-planar platinum(II) counterparts, and therefore variation in the ligand sphere is more easily accessible. This is of great significance in order to fine-tune important properties such as lipophilicity, stability, reduction behavior, and biological activity.[7] Platinum(IV) complexes are kinetically inert and therefore show a significantly decreased reactivity. It is generally accepted that platinum(IV) complexes act as prodrugs by extra- or intracellular reduction to the more reactive platinum(II) complexes upon release of the axial ligands (activation by reduction).[8,9] The first platinum(IV) complexes, tetraplatin and iproplatin (Figure 1), which were investigated in phase-I clinical trials both showed an unfavorable pharmacokinetic behavior in vivo. Tetraplatin (two axial chloro ligands; reduction potential: –90 mV)[10] displays a high systemic

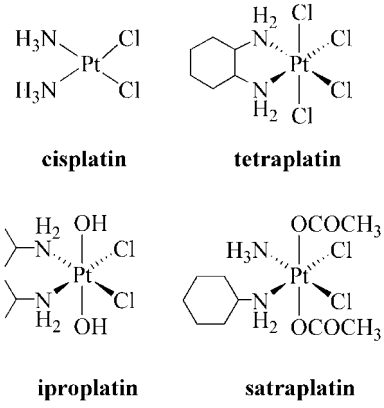


Figure 1. Chemical structures of the anticancer drug cisplatin and of tumor inhibiting platinum(IV) complexes in clinical evaluation. Tetraplatin and iproplatin were abandoned.

[a] Institute of Inorganic Chemistry, University of Vienna, Waehringer Strasse 42, 1090 Vienna, Austria
Fax: +43-1-4277-52680
E-mail: markus.galanski@univie.ac.at

 © 2006 Wiley-VCH Verlag GmbH & Co. KGaA, Weinheim 

toxicity due to a very fast reduction of the platinum(IV) complex in the blood stream, whereas iproplatin (two axial hydroxy ligands; reduction potential: –730 mV) was found to be inactive because it is not reduced fast enough to the more (re)active platinum(II) species in the body. A breakthrough was reached with the synthesis of satraplatin (Figure 1), which contains two carboxylate ligands in the axial positions. Satraplatin is currently being investigated in phase-III clinical trials in hormone refractory prostate cancer.[11] The reduction potential (which is most influenced by the axial ligands) of satraplatin adopts an average value with –250 mV, but the lipophilicity of this complex also seems to be in an appropriate range. Very recently, a close analogue to satraplatin, namely LA-12, a platinum(IV) complex with a bulky and hydrophobic 1-adamantylamine ligand instead of cyclohexylamine, entered clinical phase I trials.[12,13] LA-12 shows high cytotoxic potential in leukemia, melanoma, and colorectal cancer cells and has been found to overcome acquired resistance to cisplatin in human ovarian A2780cisR cells.[14]

The success of satraplatin is a direct consequence of progress in the synthesis and derivatization of platinum(IV) complexes. Some years ago, the design of platinum(IV) coordination compounds was limited to oxidation of the corresponding platinum(II) species with hydrogen peroxide or chlorine gas:[15,16] selective ligand substitution was difficult to perform since platinum(IV) complexes are kinetically inert (substitution of chloride for hydroxide, for example works under comparatively drastic conditions in the presence of hydrochloric acid at high temperature). With the knowledge that hydroxide coordinated to platinum(IV) has nucleophilic properties and therefore can be carboxylated with classical agents known from synthetic organic chemistry, a new class of platinum(IV) complexes was accessible, which resulted in the development of satraplatin. Carboxylation of *trans*-dihydroxoplatinum(IV) by anhydrides, pyrocarbonates, isocyanates, and even by carboxylic acid chlorides in the presence of pyridine has recently been described in the literature,[17–21] leading to numerous new and interesting platinum(IV) derivatives. Very recently, the carboxylation with cyclic anhydrides (succinic, maleic, glutaric, and phthalic anhydride) under different reaction conditions was reported. Carboxylation in $CH_2Cl_2$ over 1–2 days,[22] reaction in DMSO at 70 °C with a considerably large amount (3.3 g) of the dihydroxoplatinum(IV) starting complex,[23] and the unsuccessful use of molten phthalic anhydride[24] have been reported. The yields were reported to be in the range of 40 to 70%. The use of cyclic anhydrides offers a further advantage, besides the fact that novel platinum(IV) compounds are prepared: it provides an uncoordinated carboxylic acid moiety for subsequent derivatization, although in only one case has derivatization to the amide been described; amine-modified estrogens were coupled to the uncoordinated carboxylic acid by the use of a common peptide coupling reagent, namely diisopropylcarbodiimide/4-(dimethylamino)pyridine.

Here we report an improved carboxylation method based on succinic anhydride. Additionally, reaction of the uncoordinated carboxylic acid with simple amines and alcohols, leading to the corresponding amides and esters in the presence of 1,1′-carbonyldiimidazole, is described. The platinum(IV) complexes have been synthesized for the first time and were characterized in detail by multinuclear NMR spectroscopy.

## Results and Discussion

Derivatization of kinetically inert platinum(IV) complexes is an attractive entry to novel platinum compounds. Besides the well-established carboxylation of hydroxide coordinated to the $Pt^{IV}$ center, derivatization of peripheral hydroxo groups in diaminetetrachloroplatinum(IV) complexes has also been reported.[25] With the use of cyclic anhydrides, a further functional group is now accessible in the axial position. In order to set up a general reaction procedure, synthesis of the bis(carboxylato)platinum(IV) complex **2** was improved and subsequent derivatization of the uncoordinated carboxylic acid group was evaluated (Figure 2).

The starting (*OC*-6-33)-dichloro(ethane-1,2-diamine)dihydroxoplatinum(IV) complex **1** was prepared by reaction of $K_2PtCl_4$ with ethane-1,2-diamine; the dichloroplatinum(II) compound was then oxidized with hydrogen peroxide. The carboxylation reaction with succinic anhydride was performed in DMF at 70 °C, affording **2** in a good yield of 85%. This is in clear contrast to the synthetic procedures described recently. The use of DMSO at higher temperatures seems to be especially problematic since it often leads to decomposition of the platinum complexes. The subsequent derivatization of **2** was carried out in DMF by activation of the carboxylic acid with 1,1′-carbonyldiimidazole (CDI). The formed imidazolide was used directly without isolation for the next reaction step. Contrary to our synthetic procedure, Lippard and co-workers have used another typical peptide coupling reagent, namely diisopropylcarbodiimide/4-(dimethylamino)pyridine, which could cause problems in the workup of the reaction mixture and may lead to unfavorable side-reactions. Reaction of the imidazolide with amines afforded the corresponding amides, whereas the use of alcohols, which were converted in part to the alkoxides by catalytic amounts of sodium, produced the esters. In the case of ethanolamine (in the absence of a strong base), only the amide was produced, thus demonstrating the selectivity of the reaction.

The new complexes **2**, **3a**–**c**, **4a**, and **4b** were characterized in detail by elemental analysis, IR, $^1H$, $^{13}C$, $^{15}N$, and $^{195}Pt$ NMR spectroscopy, mass spectrometry, and also by X-ray diffractometry in the case of **2**. The carboxylation of **1** and its subsequent derivatization to the amide or ester can be followed by significant changes in the infrared spectra. The *trans*-dihydroxoplatinum(IV) starting complex exhibits a characteristic very sharp and intense O–H stretch at 3483 $cm^{-1}$, which disappears after carboxylation with succinic anhydride. As a result, two C=O stretches, at 1654 $cm^{-1}$ for the coordinated carboxylato moiety and at 1719 $cm^{-1}$ for the uncoordinated carboxylic acid group, are

 © 2006 Wiley-VCH Verlag GmbH & Co. KGaA, Weinheim 

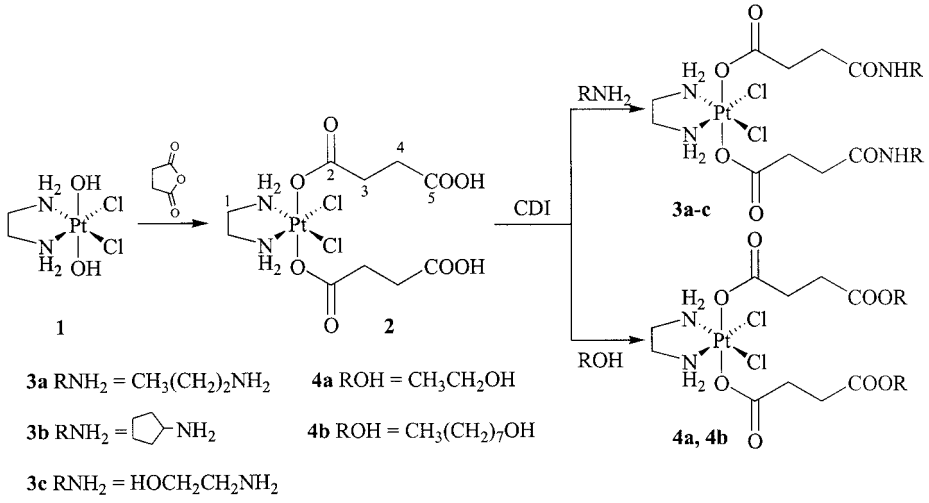


Figure 2. Synthesis of novel bis(carboxylato)platinum(IV) complexes and NMR numbering scheme.

detectable. The shift of the C=O band of the coordinated carboxylate to smaller wavenumbers is in good agreement with previously published data for analogous complexes (1633–1669 $cm^{-1}$).[19] Derivatization with amines, leading to complexes **3a**–**c**, is reflected by two characteristic absorptions (1633–1640 and 1664–1675 $cm^{-1}$) for the coordinated carboxylate and the amide C=O stretch, respectively, whereas the ester formation is accompanied by C=O absorption bands in the range of 1650 and 1658 $cm^{-1}$ for the PtOC=O stretch and between 1739 and 1745 $cm^{-1}$ for the C=O stretch of the ester moiety. Remarkably, in the case of ethanolamine the amide formation (vs. ester formation) could be confirmed by infrared spectroscopy.

$^{1}H$, and $^{195}Pt$ as well as gradient-enhanced two-dimensional $^{1}H$,$^{13}C$- and $^{1}H$,$^{15}N$-COSY NMR spectra of complexes **2**, **3a**–**c**, **4a**, and **4b** were acquired in [$D_7$]DMF. The ligand sphere around the platinum center can best be judged by the chemical shift of the $^{195}Pt$ nucleus, which spans a wide range of several thousand ppm, depending on the coordinated atoms, the geometry, and the oxidation state of the metal center. The $^{195}Pt$ resonances of the novel platinum(IV) complexes were found between $\delta$ = 2621 and 2630 ppm, which is indicative of a *cis*,*cis*,*trans*-$Pt^{IV}N_2Cl_2O_2$ ligand sphere (Table 1). These values are in good agreement with literature data {$\delta$ = 2658 ppm for [$PtCl_2$(en)-($OCOCH_3$)$_2$]}.[26] As expected, the $^{195}Pt$ chemical shifts as well as the $^{1}H$ ($\delta$ = 8.88–8.92 ppm) and $^{15}N$ resonances ($\delta$ = –3.3 to –4.2 ppm) of the coordinated amine moiety are not significantly influenced by derivatization at the uncoordinated carboxylic acid group. Nevertheless, a trend in the $^{195}Pt$ and $^{1}H$ (of the $NH_2$ group) chemical shifts seems to be obvious. In the $^{13}C$ NMR spectra, two resonances for the quaternary carbon atoms of the coordinated carboxylate (C-2 at around $\delta$ = 180 ppm and C-5 in the region between $\delta$ = 169.9 and 172.3 ppm) are detected, with an apparent upfield shift of C-5 upon derivatization of the uncoordinated carboxylic acid. Amide formation, especially in the case of the bifunctional ethanolamine, was verified by significant $^{1}H$ and $^{15}N$ shift differences. In complexes **3a**–**c** the proton resonances of the amide protons are found at around $\delta$ = 7.96 ppm, with $^{15}N$ chemical shifts in the region between $\delta$ = 90 and 109 ppm (typical region for amide nitrogens: $\delta$ = 63–113 ppm). Values between $\delta$ = 1 and 3 ppm ($^{1}H$) and –15 to +15 ppm ($^{15}N$) are found in the free amines, thus demonstrating the success of amide formation. In both **3a**–**c** and **4a**/**4b**, long-range shift correlation signals between the derivatized C=O quaternary carbon atom and the amine- or alcohol-derived residue could also be detected, additionally proving the amide or ester formation. Furthermore, these cross peaks in the two-dimensional shift correlated spectra allowed us unequivocally to distinguish between the two $^{13}C$=O resonances.

Table 1. $^{1}H$, $^{13}C$, $^{15}N$, and $^{195}Pt$ NMR spectroscopic data for the new complexes **2**, **3a**–**c**, **4a**, and **4b**.

| | $^{1}H$ | | $^{13}C$ | | $^{15}N$ | | $^{195}Pt$ |
|---|---|---|---|---|---|---|---|
| | N$H_2$ | N*H* | C-2 | C-5 | *N*$H_2$ | *N*H | |
| **2** | 8.93 | – | 180.0 | 172.3 | –3.8 | – | 2630 |
| **3a** | 8.89 | 7.95 | 180.3 | 170.0 | –3.3 | 94.6 | 2622 |
| **3b** | 8.88 | 7.94 | 180.3 | 169.9 | –3.7 | 108.5 | 2622 |
| **3c** | 8.88 | 7.98 | 180.2 | 170.3 | –4.2 | 90.1 | 2621 |
| **4a** | 8.92 | – | 179.7 | 170.8 | –3.6 | – | 2629 |
| **4b** | 8.92 | – | 179.7 | 170.9 | –3.5 | – | 2628 |

Crystals suitable for X-ray diffraction analysis were grown by vapor diffusion of diethyl ether into a solution of **2** in acetone. The result of the X-ray diffraction study of complex **2**·2($CH_3$)$_2$CO is shown in Figure 3. Crystal data, data collection parameters and structure-refinement details are given in the Experimental Section. The compound crystallizes in the monoclinic space group *P*2/*c*, with the platinum atom lying on a twofold rotation axis that also goes through the center of the C–C bond of the ethane-1,2-diamine ring. The platinum(IV) atom has an octahedral coordination geometry with ethane-1,2-diamine and two chloro ligands bound in the equatorial plane and two succinic acids coordinated in a monodentate fashion in the axial positions. The Pt–N1, Pt–Cl1, and Pt–O1 bond lengths

 © 2006 Wiley-VCH Verlag GmbH & Co. KGaA, Weinheim 

[2.0541(10), 2.3175(5), and 2.0113(12) Å, respectively] are well comparable with those in *cis,trans*-[Pt(en)$Cl_2$-($OCOCH_3$)$_2$] [2.040(5), 2.315(1), and 2.017(5) Å, respectively].[27] A five-membered chelate ring, with a bite angle of 83.66(6)°, is formed upon coordination of ethane-1,2-diamine to $Pt^{IV}$. A zigzag arrangement of the ligand atoms alternately above and below the mean least-squares plane through $PtCl_2N_2$ is observed. The dihedral angle $\Theta_{N1-C1-C1^i-N1^i}$ (superscript i denotes $-x + 1$, $y$, $1/2 - z$), which serves as a measure of the deviation of the corresponding chelate ring from planarity, is –55.8°.

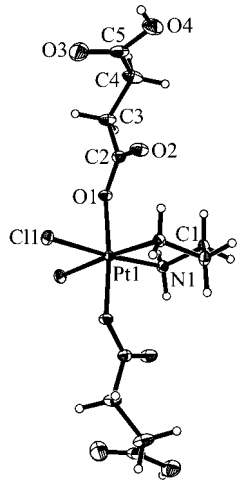


Figure 3. ORTEP diagram of **2** displaying thermal ellipsoids at 50% probability (the solvent molecule has been omitted). Selected bond lengths [Å] and angles [°]: Pt–N1 2.0541(10), Pt–Cl1 2.3175(5), Pt–O1 2.0113(12), O1–C2 1.3095(16), C2–O2 1.2235(16), C2–C3 1.5122(19), C3–C4 1.519(2), C4–C5 1.497(2), C5–O3 1.234(2), C5–O4 1.3070(18); O1–C2–O2 126.42(13), O3–C5–O4 123.13(15).

## Conclusions

It has been demonstrated that carboxylation of (*OC*-6-33)-dichloro(ethane-1,2-diamine)dihydroxoplatinum(IV) with succinic anhydride results in a platinum complex with coordinated carboxylato ligands, which contains further uncoordinated carboxylic acid groups for subsequent derivatization. Improved reaction conditions have allowed synthesis of this new complex in a pleasingly high yield of 85%. Reaction of the uncoordinated carboxylic acid with simple amines and alcohols, which leads to the corresponding amides and esters in the presence of 1,1′-carbonyldiimidazole, has been shown to be generally applicable to this kind of platinum complex, and provides entry to a new class of kinetically inert platinum(IV) complexes with potentially useful anticancer properties.

## Experimental Section

All chemicals were obtained from commercial suppliers and were used as received. The $^1$H, $^{195}$Pt and two-dimensional $^1$H,$^{13}$C- and $^1$H,$^{15}$N-COSY NMR spectra were recorded with a Bruker Avance DPX 400 spectrometer (Ultrashield™ Magnet) at 400.13, 86.11, 100.62, and 40.55 MHz, respectively, in [$D_7$]DMF at 25 °C, using standard pulse programs; two-dimensional spectra were measured in a gradient-enhanced mode. $^{15}$N and $^{195}$Pt chemical shifts are referenced relative to external $NH_4Cl$ and $K_2PtCl_4$, respectively. Half-height line widths of $^{195}$Pt resonances are given in parentheses. IR spectra were measured in a KBr matrix (4000–400 $cm^{-1}$) with a Perkin–Elmer Spectrum 2000 FT-IR spectrometer. Mass spectra (ESI-MS) were recorded with a Bruker $ESQUIRE_{3000}$ ion-trap mass spectrometer in the negative- as well as in the positive-ion mode. The elemental analyses were performed with a Perkin–Elmer 2400 CHN elemental analyzer by the microlaboratory of the Institute of Physical Chemistry, University of Vienna. Silica gel 60 (Fluka) was used for column chromatography. (*OC*-6-33)-Dichloro-(ethane-1,2-diamine)dihydroxoplatinum(IV) (**1**) was synthesized according to standard literature procedures by mixing equivalent amounts of ethane-1,2-diamine and $K_2PtCl_4$ in aqueous solution and subsequent oxidation with $H_2O_2$.[16]

**(*OC*-6-33)-Bis(3-carboxypropanoato)dichloro(ethane-1,2-diamine)-platinum(IV) (2):** Succinic anhydride (114 mg, 1.139 mmol) was added to a suspension of **1** (100 mg, 0.278 mmol) in DMF (2 mL) and the reaction mixture was stirred at 70 °C for 24 h. During this time the solid material dissolved to form a yellow-brown solution. DMF was then removed under reduced pressure. The residue was dissolved in acetone and filtered to give a clear, yellow solution. This solution was concentrated under reduced pressure, and subsequent addition of diethyl ether led to precipitation of a pale-yellow solid. The product was dried in vacuo. Yield: 131.5 mg (85%). $C_{10}H_{18}Cl_2N_2O_8Pt$ (560.24): calcd. C 21.44, H 3.24, N 5.00; found C 21.72, H 3.18, N 4.89. ESI-MS: *m*/*z* 561.1 [M + $H^+$]$^+$, 583.1 [M + $Na^+$]$^+$, 598.1 [M + $K^+$]$^+$, 559.1 [M – $H^+$]$^-$. IR: $\tilde{\nu}$ = 3445 ($\nu_{COO-H}$), 3202 ($\nu_{N-H}$), 3039–2927 ($\nu_{C-H}$), 1719, 1654 ($\nu_{as\ C=O}$) $cm^{-1}$. $^1$H NMR: $\delta$ = 12.52 (s, 2 H, COO*H*), 8.93 (s, $^2J_{H,Pt}$ = 52.7 Hz, 4 H, N$H_2$), 3.15 (s, 4 H, 1-H), 2.70 (m, 4 H, 3-H/4-H), 2.67 (m, 4 H, 3-H/4-H) ppm. $^{13}$C NMR: $\delta$ = 180.0 (C-2), 172.3 (C-5), 47.6 (C-1), 28.1, 29.5 (C-3/C-4) ppm. $^{15}$N NMR: $\delta$ = –3.8 ppm. $^{195}$Pt NMR: $\delta$ = 2630 (420 Hz) ppm. Crystals suitable for X-ray data collection were grown by vapor diffusion of diethyl ether into a solution of **2** in acetone.

**(*OC*-6-33)-Dichloro(ethane-1,2-diamine)bis{(4-propylamino)-4-oxobutanoato}platinum(IV) (3a):** 1,1′-Carbonyldiimidazole (CDI; 237.3 mg, 1.464 mmol) in DMF (16 mL) was added to a solution of **2** (400 mg, 0.714 mmol) in DMF (8 mL) and the mixture heated to 60 °C. After 10 min stirring, the solution was cooled down to room temperature and $CO_2$ was removed by flushing with argon. Propylamine (120.8 μL, 1.464 mmol) in DMF (24 mL) was added to the solution and stirred for 24 h at room temperature. DMF was then removed under reduced pressure to form a yellow-brown oil. The crude product was purified by column chromatography (EtOAc/MeOH, 4:1) to yield a white powder. Yield: 253.1 mg (55%). $C_{16}H_{32}Cl_2N_4O_6Pt$ (642.43): calcd. C 29.91, H 5.02, N 8.72; found C 30.12, H 4.89, N 8.67. ESI-MS: *m*/*z* 643.1 [M + $H^+$]$^+$, 665.1 [M + $Na^+$]$^+$, 681.0 [M + $K^+$]$^+$, 641.1 [M – $H^+$]$^-$, 677 [M + $Cl^-$]$^-$. IR: $\tilde{\nu}$ = 3300, 3206 ($\nu_{N-H}$), 2963, 2929–2873 ($\nu_{C-H}$), 1664, 1640 ($\nu_{as\ C=O}$) $cm^{-1}$. $^1$H NMR: $\delta$ = 8.89 (br. s, 4 H, N$H_2$), 7.95 (br. s, 2 H, N*H*), 3.25 [q, $^3J_{H,H}$ = 6.3 Hz, 4 H, 6-H], 3.16 (br. s, 4 H, 1-H), 2.66 (t, $^3J_{H,H}$ = 7.0 Hz, 4 H, 3-H/4-H), 2.55 (t, $^3J_{H,H}$ = 7.0 Hz, 4 H, 3-H/4-H), 1.62 (m, 4 H, 7-H), 1.03 (t, $^3J_{H,H}$ = 7.4 Hz, 6 H, 8-H) ppm. $^{13}$C NMR: $\delta$ = 180.3 (C-2), 170.0 (C-5), 47.5 (C-1), 39.1 (C-6), 30.0, 30.5 (C-3/C-4), 21.0 (C-7), 9.4 (C-8) ppm. $^{15}$N NMR: $\delta$ = 94.6 (*N*H), –3.3 (*N*$H_2$) ppm. $^{195}$Pt NMR: $\delta$ = 2622 (440 Hz) ppm.

 © 2006 Wiley-VCH Verlag GmbH & Co. KGaA, Weinheim 

**(*OC*-6-33)-Dichlorobis{(4-cyclopentylamino)-4-oxobutanoato}-(ethane-1,2-diamine)platinum(IV) (3b):** The synthesis was carried out as described for **3a**. The crude product was purified by column chromatography (EtOAc/MeOH, 4:1) and recrystallized from MeOH to yield a white powder. Yield: 102.3 mg (21%). $C_{20}H_{36}Cl_2N_4O_6Pt$ (694.51): calcd. C 34.59, H 5.22, N 8.07; found C 34.56, H 5.02, N 7.89. ESI-MS: *m/z* 717.1 $[M + Na^+]^+$, 733.0 $[M + K^+]^+$, 693.1 $[M - H^+]^-$. IR: $\tilde{\nu}$ = 3251, 3199 ($\nu_{N-H}$), 2947–2865 ($\nu_{C-H}$), 1664, 1638 ($\nu_{as\ C=O}$) $cm^{-1}$. $^1H$ NMR: $\delta$ = 8.88 (br. s, 4 H, N*H*$_2$), 7.94 (d, $^3J_{H,H}$ = 6.8 Hz, 2 H, N*H*), 4.23 (m, 2 H, 6-H), 3.17 (br. s, 4 H, 1-H), 2.65 (t, $^3J_{H,H}$ = 7.1 Hz, 4 H, 3-H/4-H), 2.52 (t, $^3J_{H,H}$ = 7.1 Hz, 4 H, 3-H/4-H), 1.99 (m, 4 H, 7-H), 1.82 (m, 4 H, 8-H), 1.68 (m, 4 H, 8-H), 1.60 (m, 4 H, 7-H) ppm. $^{13}C$ NMR: $\delta$ = 180.3 (C-2), 169.6 (C-5), 49.1 (C-6), 47.6 (C-1), 30.9 (C-7), 30.0, 30.5 (C-3/C-4), 21.9 (C-8) ppm. $^{15}N$ NMR: $\delta$ = 108.5 (*N*H), –3.7 (*N*H$_2$) ppm. $^{195}Pt$ NMR: $\delta$ = 2622 (433 Hz) ppm.

**(*OC*-6-33)-Dichloro(ethane-1,2-diamine)bis{[4-(2-hydroxyethyl)-amino]-4-oxobutanoato}platinum(IV) (3c):** The synthesis was carried out as described for **3a**. The crude product was purified by column chromatography (MeOH) to yield a pale-yellow powder. Yield: 87.7 mg (38%). $C_{14}H_{28}Cl_2N_4O_8Pt$ (646.38): calcd. C 26.01, H 4.37, N 8.67; found C 25.81, H 4.07, N 8.43. ESI-MS: *m/z* 669.3 $[M + Na^+]^+$, 645.2 $[M - H^+]^-$. IR: $\tilde{\nu}$ = 3592, 3530 ($\nu_{O-H}$), 3309, 3213 ($\nu_{N-H}$), 1675, 1633 ($\nu_{as\ C=O}$) $cm^{-1}$. $^1H$ NMR: $\delta$ = 8.88 (br. s, N*H*$_2$), 7.98 (br. s, 2 H, N*H*), 4.88 (br. s, 2 H, O*H*), 3.70 (m, 4 H, 7-H), 3.42 (m, 4 H, 6-H), 3.16 (br. s, 4 H, 1-H), 2.67 (t, $^3J_{H,H}$ = 6.8 Hz, 4 H, 3-H/4-H), 2.57 (t, $^3J_{H,H}$ = 6.8 Hz, 4 H, 3-H/4-H) ppm. $^{13}C$ NMR: $\delta$ = 180.2 (C-2), 170.3 (C-5), 59.1 (C-7), 47.6 (C-1), 40.3 (C-6), 30.4, 29.9 (C-3/C-4) ppm. $^{15}N$ NMR: $\delta$ = 90.1 (*N*H), –4.2 (*N*H$_2$) ppm. $^{195}Pt$ NMR: $\delta$ = 2621 (440 Hz) ppm.

**(*OC*-6-33)-Dichloro(ethane-1,2-diamine)bis{(4-ethoxy)-4-oxobutanoato}platinum(IV) (4a):** CDI (59.3 mg, 0.365 mmol) in abs. DMF (4 mL) was added to a solution of **2** (100 mg, 0.178 mmol) in abs. DMF (2 mL) and heated to 60 °C. After 10 min stirring, the solution was cooled down to room temperature and $CO_2$ was removed by flushing with argon. Sodium ethanolate (4 mg of Na in 10 mL of abs. ethanol) in abs. ethanol was added to the solution and stirred for 24 h at room temperature. Ethanol and DMF were removed under reduced pressure to form a yellow-brown oil. The crude product was purified by column chromatography (EtOAc/MeOH, 7:1) to yield a white powder. Yield: 41.5 mg (38%). $C_{14}H_{26}Cl_2N_2O_8Pt$ (616.35): calcd. C 27.28, H 4.25, N 4.55; found C 27.58, H 4.09, N 4.50. ESI-MS: *m/z* 616.1 $[M + H^+]^+$, 639.1 $[M + Na^+]^+$, 655.0 $[M + K^+]^+$, 615.2$[M - H^+]^-$. IR: $\tilde{\nu}$ = 3203 ($\nu_{N-H}$); 2985, 2929 ($\nu_{C-H}$); 1739, 1654 ($\nu_{as\ C=O}$) $cm^{-1}$. $^1H$ NMR: $\delta$ = 8.92 (t, $^2J_{H,Pt}$ = 53.6 Hz, 4 H, N*H*$_2$), 4.25 (q, $^3J_{H,H}$ = 7.1 Hz, 4 H, 6-H), 3.16 (br. s, 4 H, 1-H), 2.73 (m, 4 H, 3-H/4-H), 2.68 (m, 4 H, 3-H/4-H), 1.37 (t, $^3J_{H,H}$ = 7.1 Hz, 6 H, 7-H) ppm. $^{13}C$ NMR: $\delta$ = 179.7 (C-2), 170.8 (C-5), 58.4 (C-6), 47.6 (C-1), 28.2, 29.3 (C-3/C-4), 12.1 (C-7) ppm. $^{15}N$ NMR: $\delta$ = –3.6 ppm. $^{195}Pt$ NMR: $\delta$ = 2629.1 (460 Hz) ppm.

**(*OC*-6-33)-Dichloro(ethane-1,2-diamine)bis{(4-octyloxy)-4-oxobutanoato}platinum(IV) (4b):** The synthesis was carried out as described for **4a**. The crude product was purified by column chromatography (EtOAc) to yield a white powder. Yield: 143.9 mg (34%). $C_{26}H_{50}Cl_2N_2O_8Pt$ (784.67): calcd. C 39.80, H 6.42, N 3.57; found C 39.69, H 6.26, N 3.49. ESI-MS: *m/z* 807.3 $[M + Na^+]^+$, 823.2 $[M + K^+]^+$, 783.3 $[M - H^+]^-$. IR: $\tilde{\nu}$ = 3210 ($\nu_{N-H}$), 2958, 2927, 2856 ($\nu_{C-H}$), 1745, 1650 ($\nu_{as\ C=O}$) $cm^{-1}$. $^1H$ NMR: $\delta$ = 8.92 (br. s, 4 H, N*H*$_2$), 4.21 (t, $^3J_{H,H}$ = 6.7 Hz, 4 H, 6-H), 3.16 (br. s, 4 H, 1-H), 2.74 (m, 4 H, 3-H/4-H), 2.69 (m, 4 H, 3-H/4-H), 1.77 (m, 4 H, 7-H), 1.46 (br. s, 20 H, 8-H to 12-H), 1.04 (t, $^3J_{H,H}$ = 6.6 Hz, 6 H, 13-H) ppm. $^{13}C$ NMR: $\delta$ = 179.7 (C-2), 170.9 (C-5), 62.6 (C-6), 47.7 (C-1), 29.5, 28.1 (C-3/C-4), 26.9 (C-7), 30.1, 27.5$_2$, 27.4$_8$, 24.1, 20.8 (C-8 to C-12), 12.0 (C-13) ppm. $^{15}N$ NMR: $\delta$ = –3.5 ppm. $^{195}Pt$ NMR: $\delta$ = 2628 (420 Hz) ppm.

X-ray diffraction measurements were performed on a Bruker X8APEX II CCD diffractometer at 100 K. Single crystals were positioned 37.5 mm from the detector and 813 frames were measured, each for 80 s over a 1° scan. The data were processed using the Denzo-SMN software package.[28] Crystal data, data collection parameters, and structure-refinement details for **2**·2$CH_3COCH_3$ are given in Table 2. The structures were solved by direct methods and refined by full-matrix least-squares techniques. Non-hydrogen atoms were refined with anisotropic displacement parameters. H atoms were calculated and allowed to ride. Computer programs: structure solution: SHELXS-97;[29] refinement: SHELXL-97;[30] molecular diagrams: ORTEP.[31] Computer: PC, Pentium II; scattering factors taken from the literature.[32]

Table 2. Crystallographic data for **2**·2$CH_3COCH_3$.

| | |
|---|---|
| Empirical formula | $C_{16}H_{30}Cl_2N_2O_{10}Pt$ |
| Fw | 676.41 |
| Space group | *P*2/*c* |
| *a* [Å] | 15.128(3) |
| *b* [Å] | 7.9108(16) |
| *c* [Å] | 10.745(2) |
| $\beta$ [°] | 110.72(3) |
| *V* [Å$^3$] | 1202.8(4) |
| *Z* | 2 |
| $\lambda$ [Å] | 0.71073 |
| $\rho_{calcd.}$ [g cm$^{-3}$] | 1.868 |
| Crystal size [mm] | 0.18 × 0.10 × 0.04 |
| *T* [K] | 100 |
| $\mu$ [cm$^{-1}$] | 61.06 |
| $R_1$[a] | 0.0108 |
| $wR_2$[b] | 0.0259 |
| GOF[c] | 1.061 |

[a] $R_1 = \Sigma||F_o| - |F_c||/\Sigma|F_o|$. [b] $wR_2 = \{\Sigma[w(F_o^2 - F_c^2)^2]/\Sigma[w(F_o^2)^2]\}^{1/2}$. [c] GOF = $\{\Sigma[w(F_o^2 - F_c^2)^2]/(n - p)\}^{1/2}$, where *n* is the number of reflections and *p* is the total number of parameters refined.

CCDC-297226 contains the supplementary crystallographic data for this paper. These data can be obtained free of charge from The Cambridge Crystallographic Data Center via www.ccdc.cam.ac.uk/data_request/cif.

## Acknowledgments

The support of the FWF (Fonds zur Förderung der wissenschaftlichen Forschung), Faustus Forschungs Compagnie Translational Cancer Research GmbH, and COST (European Co-operation in the Field of Scientific and Technical Research) is gratefully acknowledged. We are thankful to Prof. Arion for the discussion of X-ray data.

[1] B. Rosenberg, *Interdiscip. Sci. Rev.* **1978**, *3*, 134–147.
[2] *Cisplatin: Chemistry and Biochemistry of a Leading Anticancer Drug* (Ed.: B. Lippert), Verlag Helvetica Chimica Acta, Zürich, Switzerland and Wiley-VCH, Weinheim, Germany), **1999**.
[3] P. J. O'Dwyer, J. P. Stevenson, S. W. Johnson, *Drugs* **2000**, *59 (Suppl. 4)*, 19–27.
[4] L. R. Kelland, *Drugs* **2000**, *59 (Suppl. 4)*, 1–8.
[5] M. A. Jakupec, M. Galanski, B. K. Keppler, *Rev. Physiol. Biochem. Pharmacol.* **2003**, *146*, 1–54.

 © 2006 Wiley-VCH Verlag GmbH & Co. KGaA, Weinheim 

[6] M. Galanski, M. A. Jakupec, B. K. Keppler, in *Metal Compounds in Cancer Chemotherapy* (Eds.: J. M. Pérez, M. A. Fuertes, C. Alonso), Research Signpost, Kerala, **2005**, p. 155.
[7] M. Galanski, M. A. Jakupec, B. K. Keppler, *Curr. Med. Chem.* **2005**, *12*, 2075–2094.
[8] M. D. Hall, T. W. Hambley, *Coord. Chem. Rev.* **2002**, *232*, 49–67.
[9] M. D. Hall, R. C. Dolman, T. W. Hambley, *Met. Ions Biol. Syst.* **2004**, *42*, 297–322.
[10] S. Choi, C. Filotto, M. Bisanzo, S. Delaney, D. Lagasee, J. L. Whitworth, A. Jusko, C. Li, N. A. Wood, J. Willingham, A. Schwenker, K. Spaulding, *Inorg. Chem.* **1998**, *37*, 2500–2504.
[11] T. Latif, L. Wood, C. Connell, D. C. Smith, D. Vaughn, D. Lebwohl, D. Peereboom, *Invest. New Drugs* **2005**, *23*, 79–84.
[12] J. Turanek, A. Kasna, D. Zaluska, J. Neca, V. Kvardova, P. Knotigova, V. Horvath, L. Sindlerova, A. Kozubik, P. Sova, A. Kroutil, F. Zak, A. Mistr, *Anti-Cancer Drugs* **2004**, *15*, 537–543.
[13] F. Zak, J. Turanek, A. Kroutil, P. Sova, A. Mistr, A. Poulova, P. Mikolin, Z. Zak, A. Kasna, D. Zaluska, J. Neca, L. Sindlerova, A. Kozubik, *J. Med. Chem.* **2004**, *47*, 761–763.
[14] A. Kozubik, V. Horvath, L. Svihalkova-Sindlerova, K. Soucek, J. Hofmanova, P. Sova, A. Kroutil, F. Zak, A. Mistr, J. Turanek, *Biochem. Pharmacol.* **2005**, *69*, 373–383.
[15] G. B. Kauffman, *Inorg. Synth.* **1963**, *7*, 236–238.
[16] E. J. Bulten, F. Verbeek, U. S. Patent 4482569, **1984**.
[17] C. M. Giandomenico, M. J. Abrams, B. A. Murrer, J. F. Vollano, M. I. Rheinheimer, S. B. Wyer, G. E. Bossard, J. D. Higgins, *Inorg. Chem.* **1995**, *34*, 1015–1021.
[18] M. Galanski, B. K. Keppler, *Met.-Based Drugs* **1995**, *2*, 57–63.
[19] M. Galanski, B. K. Keppler, *Inorg. Chem.* **1996**, *35*, 1709–1711.
[20] M. Galanski, B. K. Keppler, *Inorg. Chim. Acta* **1997**, *265*, 271–274.
[21] W. H. Ang, I. Khalaila, C. S. Allardyce, L. Juillerat-Jeanneret, P. J. Dyson, *J. Am. Chem. Soc.* **2005**, *127*, 1382–1383.
[22] A. Alvarez-Valdes, J. M. Perez, I. Lopez-Solera, R. Lannegrand, J. M. Continente, P. Amo-Ochoa, M. J. Camazon, X. Solans, M. Font-Bardia, C. Navarro-Ranninger, *J. Med. Chem.* **2002**, *45*, 1835–1844.
[23] K. R. Barnes, A. Kutikov, S. J. Lippard, *Chem. Biol.* **2004**, *11*, 557–564.
[24] W. H. Ang, S. Pilet, R. Scopelliti, F. Bussy, L. Juillerat-Jeanneret, P. J. Dyson, *J. Med. Chem.* **2005**, *48*, 8060–8069.
[25] M. Galanski, W. Zimmermann, M. Berger, C. Baumgartner, G. Giester, B. K. Keppler, *Eur. J. Inorg. Chem.* **2002**, 417–421.
[26] A. R. Khokhar, Y. Deng, Y. Kido, Z. H. Siddik, *J. Inorg. Biochem.* **1993**, *50*, 79–87.
[27] L. T. Ellis, H. M. Er, T. W. Hambley, *Aust. J. Chem.* **1995**, *48*, 793–806.
[28] Z. Otwinowski, W. Minor in *Methods in Enzymology*, vol. 276 ("Macromolecular Crystallography", part A) (Eds.: C. W. Carter Jr., R. M. Sweet), Academic Press, New York, **1997**, p. 307–326.
[29] G. M. Sheldrick, *SHELXS-97, Program for Crystal Structure Solution*, University of Göttingen, Germany, **1997**.
[30] G. M. Sheldrick, *SHELXL-97, Program for Crystal Structure Refinement*, University of Göttingen, Germany, **1997**.
[31] C. K. Johnson, Rep. ORNL-5138, OAK Ridge National Laboratory, OAK Ridge, TN, **1976**.
[32] *International Tables for X-ray Crystallography* (Ed.: A. J. C. Wilson), Kluwer Academic Press, Dordrecht, The Netherlands, **1992**, vol. C, Tables 4.2.6.8 and 6.1.1.4.

Received: February 7, 2006
Published Online: April 26, 2006

 © 2006 Wiley-VCH Verlag GmbH & Co. KGaA, Weinheim 

DOI: 10.1002/ejic.200600154

# Monomeric and Polymeric Amines as Dual Reductants/Stabilisers for the Synthesis of Gold Nanocrystals: A Mechanistic Study

**Michael J. Richardson,*[a] James H. Johnston,[a] and Thomas Borrmann[a]**

**Keywords:** Amines / Nanostructures / Phase diagram / Colloids

Uniform, monodisperse gold nanocrystals have been prepared in a single-step synthesis by the addition of secondary and tertiary alkylamines, or a cationic polymer containing these moieties, to dilute solutions of gold tetrachloraurate. The acidic pH resulted in the formation of quaternary ammonium sites, scavenging loosely bound chloride ions from the tetrachloraurate species, lowering the overall potential and reducing $Au^{III}$ to nanocrystalline $Au^0$. The secondary amino groups then served to stabilise the particles, preventing aggregation and collapse of the colloidal system. Addition of further capping groups was thus not required. The particles were characterised by UV/Visible spectroscopy, HR-TEM, X-ray diffraction, electrochemical potential and pH measurements (Eh-pH) and FTIR.
(© Wiley-VCH Verlag GmbH & Co. KGaA, 69451 Weinheim, Germany, 2006)

## Introduction

Nanoscale metallic particles exhibit characteristics at variance with those of the bulk metal.[1] Increased surface area, susceptibility towards Brownian motion and restricted plasmon oscillation are observed. Interaction with electromagnetic radiation (Mie theory) and biological systems allows for potential applications in the next generation of data storage disks,[2] photovoltaic and photochemical devices, catalysis and antimicrobial surfaces.[3]

In general, nanocrystalline gold is prepared either by physical means, for example vapour deposition, or chemically through the reduction of tetrachlorauric acid. The latter is now accepted as being more flexible, due to the remarkable influence that the type and molar ratio of reductant to $Au^{III}$, in addition to reaction time and temperature, exert over the size and shape of the particles formed.[4] The reductant supplies the necessary electrons to affect the reduction from the ionic through to the metallic state. Use of trisodium citrate provides particle sizes of 1.6 to 140 nm with a relatively narrow size distribution, tuneable according to the molar excess of reductant present.[5] Sodium borohydride in conjunction with either an alkanethiol capping group[6] or a branched polyamine[7] to ensure the stability of the colloidal system, provides particles of 6 to 20 nm. Interestingly, glucose in the presence of sodium hydroxide has been shown to reduce $Au^{III}$ to $Au^0$.[8] Alternatively, photochemical reduction may be employed[9] with the incoming photons generating the necessary electrons.

However, due to the precarious stability of the Au–Cl–$H_2O$ system (Figure 1) weaker reductants may be employed to initiate the transition to the metallic state. While $AuCl_4^-$ is stable over a wide pH range (0–7.5), any slight reduction in electrochemical potential will result in destabilisation of the system with a subsequent transition to $AuCl_2^-$ at 920 mV. Further lowering of the overall potential will then cause a further redistribution of electrons, favouring $Au^0$ as the stable species. This change in potential may result from a change in concentration of one or more species present, the addition of a new compound, a deviation in temperature or pH.

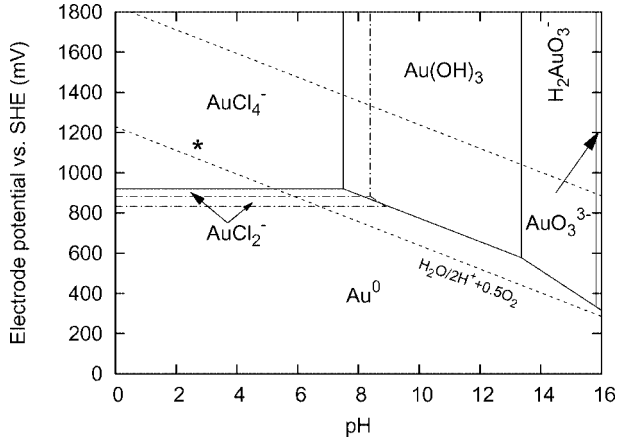


Figure 1. Pourbaix diagram for the Au–Cl–$H_2O$ system at 298 K.[10] $a_{Au} = 10^{-3}$ and $a_{Cl} = 1$ (—), $a_{Cl} = 5$ (– · – ·), chloride treated as electro-inactive. Water metastability region (- - -) calculated assuming standard conditions. The resting potential for the $AuCl_4^-$ used in the present study is indicated at *.

While commonly used for the steric stabilisation of nanocrystals, polymeric amines have recently received attention for their potential role as dual reductants/stabilisers.[11,12] In a few studies the mechanistic route is reasonably clear, for

[a] School of Chemical and Physical Sciences, Victoria University, P. O. Box 600, Wellington, New Zealand
Fax: +64-4-463-5237
E-mail: michael.richardson@vuw.ac.nz


© 2006 Wiley-VCH Verlag GmbH & Co. KGaA, Weinheim

example the degradation of *N*,*N*-dimethylacetoacetamide,[12] however in many it is not. This is particularly so when the amine is relatively stable towards oxidation compared to the metal complex that is to be reduced. Oxidation to an imine has been suggested,[13] however, no evidence of this route has yet been published. Furthermore, it is not difficult to disprove this hypothesis (see below).

Due to the difficulties in observing individual proton chemical shifts in highly branched polymers, an initial investigation was made into the ability of simple primary, secondary and tertiary amines to reduce $AuCl_4^-$, or at least destabilise the system such that metallic $Au^0$ would become the favoured species. In the present work, primary, secondary and tertiary amino groups are investigated as potential dual reductants/stabilisers for the synthesis of nanocrystalline gold. This allows some conclusions to be drawn regarding the use of cationic alkylamino polymers containing these groups.

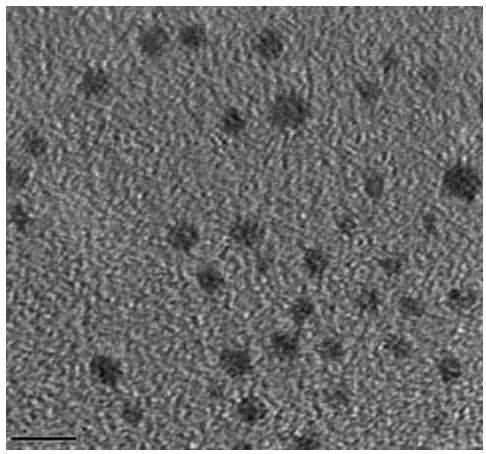

Figure 2. HR TEM of seed gold nanocrystals prepared with diethylamine. The scale bar represents 5 nm.

## Results and Discussion

**Monomeric Amines:** No reaction was observed between the primary amines, methylamine, ethylamine, and $AuCl_4^-$, either when heated to boiling or left under ambient conditions for several days. However, the secondary amine, diethylamine, reacted relatively slowly with the gold complex over 48 hours to form stable seed nanocrystals of 1.7 nm mean diameter, standard deviation 0.2 nm (Figure 2). The tertiary amine, trimethylamine, reacted relatively quickly to form nanocrystals within one hour; however, these began to aggregate immediately.

Examination of the proton nuclear magnetic resonance (NMR) spectrum of trimethylamine before and after nanocrystal formation showed a partial splitting of the single peak at $\delta$ = 3.35 ppm into two tiers of peaks over the range 2.20 to 3.60 ppm. It is believed that this is due to partial coordination of the gold to the nitrogen, as no coupling constants were able to be distinguished. A similar effect was observed for diethylamine, with the exception that coupling constants of 7 Hz were observed, consistent with methylene protons (Figure 3). By contrast, the proton NMR spectrum of ethylamine was found to be unchanged after addition of $AuCl_4^-$ (save for the expected shift of the triplet and quartet peaks due to the change in pH).

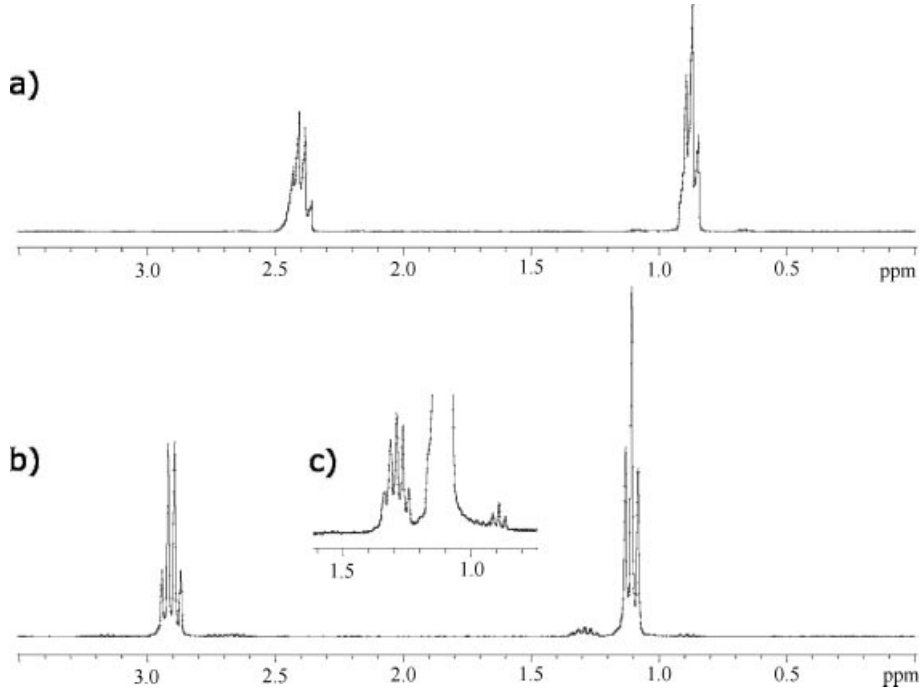


Figure 3. $^1$H NMR spectra of a) diethylamine, b) nanocrystalline gold prepared with diethylamine, c) expansion of spectrum b) showing the 7 Hz coupling-constant multiplet downfield of the triplet.

 © 2006 Wiley-VCH Verlag GmbH & Co. KGaA, Weinheim 

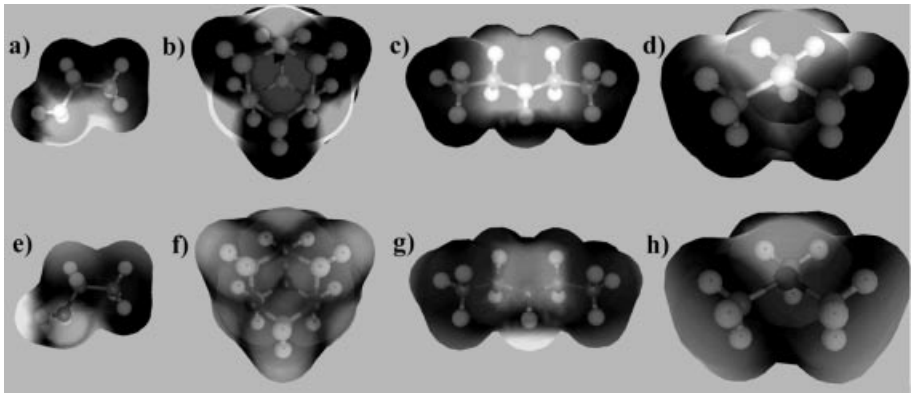


Figure 4. Molecular models of a) ethylamine (–0.18), b) hexamethylenetetramine (–0.20), c) diethylamine (–0.16) and d) trimethylamine (–0.13) showing the Van der Waals shell shaded white in areas of high electrostatic potential. Models on the second row represent e) ethylamine, f) hexamethylenetetramine, g) diethylamine and h) trimethylamine, respectively, redrawn to show areas of low electrostatic potential shaded white. Nitrogen charge in parentheses.

Length of the alkyl chain was also found to affect the ability of the amine to form nanocrystalline gold from the $AuCl_4^-$ solution. When the primary chain length was increased linearly to eight methylene (octylamine) units, colloid formation was observed. When the alkyl chain was cyclised (cyclohexylamine), however, no reaction was observed. Conversely, a longer alkyl chain in the secondary amines (dipropylamine, dibutylamine, dioctylamine) resulted in the formation of flakes of metallic gold. No reaction was observed with a shorter secondary amine chain length (dimethylamine). For the tertiary amines, the use of triethylamine rather than trimethylamine, while decreasing the volume of amine from 10 to 2 μL resulted in a colloid, which was stable for several days. The colloid was unstable with a greater volume of amine. No nanocrystal formation was observed with hexamethylenetetramine.

The differences in reactivity of the amino groups may be attributed to a combination of steric hinderence and extent of charge separation, in addition to their slightly different levels of basicity. Molecular modelling of the charge on the nitrogen and the steric hinderence (Figure 4) suggests that compounds better suited to interaction with gold nanocrystals are those with a charge on the nitrogen greater than than –0.16, in addition having the areas of minimum and maximum charge well separated. Access to the nitrogen atom is necessary if nanocrystal growth is to proceed. For example, addition of pyridine resulted in immediate formation of an unstable colloid, while the sterically hindered 1-methylpyridine provided a colourless solution – indicative of reduction to monoatomic gold. Gold colloid formation was not observed with the remaining amines.

Potential dissociation of the ammonium ion is also likely to affect formation of the nanocrystals. Diethylamine (as the ammonium ion) has the highest p$K_a$ (10.94) while ethylamine and trimethylamine have p$K_a$ values of 10.64 and 10.72, respectively.[15] While the increase in reactivity observed for longer chained secondary amines may be explained by their higher p$K_a$, only a minimal change in p$K_a$ in the primary amines is observed as the chain length is increased. Greater intramolecular interaction, exemplified by the increase in boiling point from 16.6 to 176 °C as the chain length is increased from one to eight methylene units, is expected to take an additional role.

The aromatic amines aniline, methoxyanilinesulfonate and benzylamine were also found to react readily with the $AuCl_4^-$ to form polyaniline (for the former) and nanocrystalline gold, in a similar fashion to that previously observed for 2-methoxyaniline[16] and pyrrole.[17] However, due to the ease of oxidation of these compounds relative to those discussed above, no further work was continued with these compounds.

While the above constitutes only an introductory investigation into the use of saturated monomeric amines as dual reductant/stabilising functional groups, it may tentatively be concluded that for short alkyl chains it is the tertiary amines that are the most effective at reducing $Au^{III}$, followed by longer chained secondary amines. However, secondary amines are more effective at providing the necessary coordination required for stabilisation of the nanocrystals as they are formed.

**Polymeric Amines:** No reaction was observed with polyacrylamide or polyvinylpyrrolidone containing primary and tertiary amino groups, respectively. The branched polyethylenimine (PEI) containing primary, secondary and tertiary amino groups reacted over a period of three hours to form the characteristic deep red colloid, stable over several months. Previous studies have confirmed its stabilising effect on nanocrystalline gold.[7] Due to the success observed with PEI, the remainder of the study focused on the use of this polyamine for nanocrystal synthesis.

Figure 5 shows the increase in the UV/Visible band at 525 nm associated with the transverse plasmon resonance[18] for these colloids (denoted type I, for the purposes of distinguishing the various colloids in the paper presented here). The mean particle size measured was 11 nm, with a standard deviation of 4 nm. Figure 6 and Figure 7 show the crystalline particles formed, together with a typical X-ray diffraction pattern. Type II colloids were prepared fortuitously when investigating the effect of temperature on formation of type I particles. On reaching 70 °C the solution

 © 2006 Wiley-VCH Verlag GmbH & Co. KGaA, Weinheim 

rapidly underwent a colour change to deep red, which on examination under HR TEM showed that reduction had occurred and nanocrystals had formed. For comparison, similar colloids (denoted type III) were also synthesised according to the method of Sun[7] using $NaBH_4$ as reductant. Interestingly, the particles appeared more encumbered by the PEI used to stabilise the colloids when the reducing agent had been used, relative to the type I and II colloids.

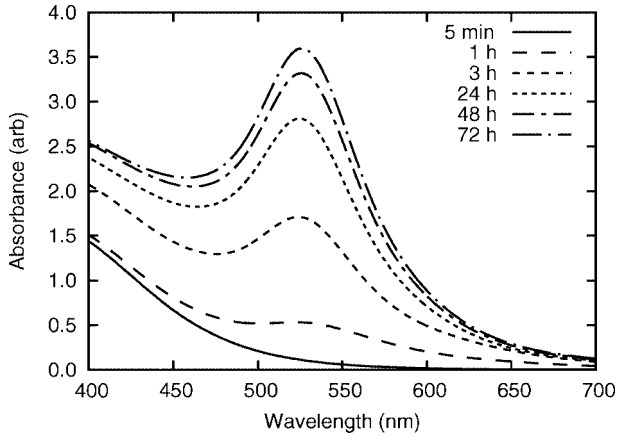


Figure 5. UV/Visible spectra of gold colloids (type I) prepared with PEI (N/Au ratio of 33:1) over the first three days, showing the development of the peak at 525 nm.

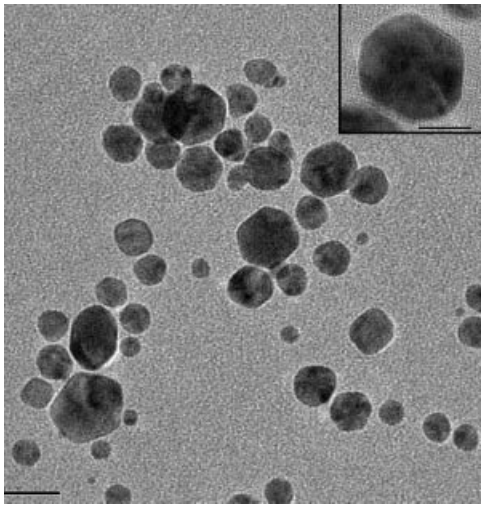

Figure 6. HR TEM of gold nanocrystals prepared with polyethylenimine (type I, N/Au 33:1). The scale bar represents 20 nm for the main picture, 10 nm for the inset.

Use of a lower concentration of PEI, measured as the average number of amino groups present, resulted in the formation of some metallic gold (though none at the nanometer scale) which settled rapidly to the bottom of the vial Figure 7. With a 1:1 N/Au ratio, the colloid aggregated within several hours – a minimum ratio of 33:1 was required to ensure stability of the system. As the ratio of N to Au was increased from 33:1 to 330:1, a gradual colour change from red to blue was observed in the colloidal system. This is seen in the UV/Visible spectra (Figure 8) as a broadening towards higher wavelengths of the principle absorbance

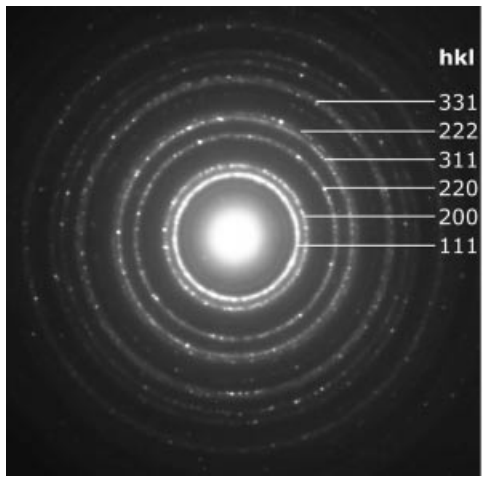


Figure 7. Typical diffraction pattern of multi-crystalline nanoparticulate gold prepared with PEI (type I, 33:1 N/Au, camera height = 80 cm).

peak. The change in absorbance was due in part to a slightly higher mean particle size; however, a greater tendency towards aggregation into larger "clumps" of 50 to 100 nm, was the over-riding factor. Increasing the N/Au ratio further had no noticeable effect. However, if the ratio of N/Au was kept at 33:1 and the colloid aged for up to four months, then a decrease in size distribution (standard deviation 1 nm) and concurrent increase in mean particle size (13 nm) due to Ostwald ripening, is observed. A corresponding shift in absorbance to longer wavelengths was also noted.

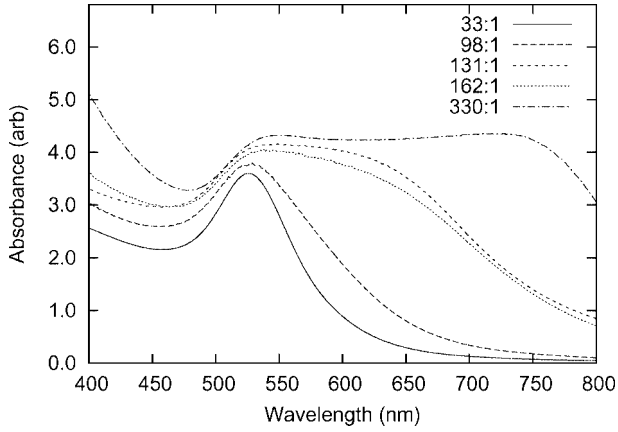


Figure 8. UV/Visible spectra of type I colloids at increasing molar ratios of amino nitrogen to gold, after four days.

The mechanism by which the reduction occurs is likely to be complex and remains unresolved at present. It has been postulated that the amino groups on the polymer are oxidised to imino moieties,[13] and indeed this is the obvious source of electrons by which the reduction of $Au^{III}$ could take place. No evidence for the required carbon–nitrogen double bond has been published, however. NMR analysis of the PEI–colloid system before and after synthesis of the colloid should show the appearance of a proton bound to a carbon with a carbon–nitrogen double bond. However,

 © 2006 Wiley-VCH Verlag GmbH & Co. KGaA, Weinheim 

proton and HSQC NMR spectra lack such a peak in the polymer both before and after reduction of the $Au^{III}$, confirming the absence of the imine group.

It has also been suggested that the loss of the peak at 1570 $cm^{-1}$ in the IR spectrum after ten days[13] attributed to the N–H bending vibration, is evidence for the oxidation of the amino groups. Considering that nanocrystal formation is observed in less than three hours and is essentially complete within 24 hours, this is unlikely. Furthermore, the expected concurrent appearance of the carbon–nitrogen double-bond at 1700 $cm^{-1}$ is not observed. Oxidation of the amino groups to nitrate was eliminated as a possibility by the negative "Brown Ring" test.[14]

However, some suggestions towards a mechanism must be made. Formation of type I and II particles is believed to proceed initially through transfer of protons from the acidic gold solution to the nitrogen groups of the polymer to form quaternary ammonium sites, the resulting cationic species attracting the chloride ions initially complexed to the gold. In order to test the hypothesis that this "doping" of the amino groups on the polymer was required for the reduction, parallel experiments were conducted where the polymer was first treated with excess chloride before addition of the gold. Upon subsequent addition of $AuCl_4^-$ no reaction was observed. This suggests that availability of the nitrogen lone electron pairs, as cationic quaternary ammonium sites under acid pH, is requisite to formation of the nanocrystals. Revisiting the secondary and tertiary amines, a similar effect was found, with no reduction of the tetrachloraurate.

The main difficulty is locating the source of the electrons required for reduction of $Au^{III}$ to $Au^0$. Analysis of the oxidation–reduction potential (ORP) of the $H_2O$–PEI–$AuCl_4^-$ system with various concentrations of PEI, corresponding to multiples of the number of moles of chloride ion present, shows that at a molar ratio of nitrogen to gold ions of approximately 1:1, a lowering of the potential is observed (Figure 9). A slight reduction in pH is observed concurrently, followed by an increase to a pH of 7.3. Due to the potential of the system initially being in that where water is

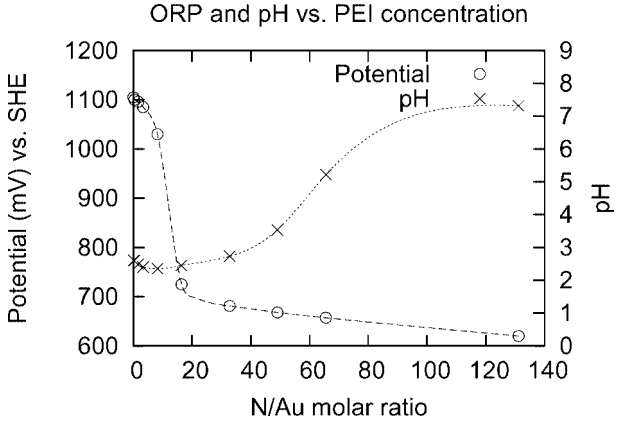


Figure 9. Oxidation–reduction potential vs. the standard hydrogen electrode (SHE) and pH as a function of the molar ratio of polymeric amino nitrogen to gold.

only metastable (Figure 1) some water may have been oxidised concurrently with the initial stages of nanocrystal formation. Nanoparticulate gold is known to catalyse the reduction of oxygen to peroxide[19] thus it is possible that the equivalent oxidation may also be thus affected. The resulting protons would lead to the observed lower pH, simultaneously providing the electrons required for the reduction of the gold. Once all required electrons have been provided and the reaction with the gold species is complete, the presence of additional, excess amino groups only serves to increase the overall system pH.

## Conclusions

Crystalline gold nanocrystals of 6 to 100 nm diameter have been prepared using both monomeric and polymeric amines in a dual reductant/stabilising role, the latter containing both primary, secondary and tertiary amino groups. The secondary groups were found to be the most amenable to the synthesis and stabilisation of the nanocrystals, while the tertiary amines were able to reduce the $Au^{III}$ but unable to stabilise the colloid. The mechanism by which reduction takes place is expected to be complex, but is believed to involve the formation of quaternary ammonium sites on the monomer or polymer, together with possible oxidation of water to provide the necessary electrons. A significant advantage of the processes used to form the nanocrystals is the simplicity of the synthesis (one pot, one step). This allows ready scale-up of the synthesis. Additionally, the three compounds used are relatively benign at the concentrations used, leaving no undesirable by-products for disposal or further treatment.

## Experimental Section

### Synthesis of Colloids

**Monomeric Amines:** $HAuCl_4$ (40 μL, 1.24 wt.-%) was added to Millipore water (5 mL, 15 MΩ·$cm^{-1}$) with rapid stirring. After one min, the amine [methylamine (40 wt.-%, aqueous), ethylamine (70 wt.-%, aqueous), octylamine, cyclohexylamine, benzylamine, ethylenediamine, phenylethylamine, 1,1,3,3-tetramethylguanidine, dimethylamine (26 wt.-%, aqueous), diethylamine, dipropylamine, dibutylamine, dioctylamine, aniline, methoxyanilinesulfonate, pyrrole, pyridine, 1-methylpyridine, trimethylamine (25 wt.-%, aqueous), triethylamine, hexamethylenetetramine](1 to 10 μL) was added and stirring continued for a further minute before leaving to stand for 2 to 72 hours. A duplicate sample of the diethylamine-Au colloid was evaporated to dryness before dispersion in $D_2O$ in preparation for $^1H$ NMR analysis (300 MHz, $D_2O$, 25 °C): $\delta$ = 1.11 (t, $J_{H,H}$ = 7 Hz), 1.29 (m, $J_{H,H}$ = 7 Hz), 2.90 (m, $J_{H,H}$ = 7 Hz), in addition to a further sample of the trimethylamine-Au colloid (300 MHz, $D_2O$, 25 °C): $\delta$ = 2.42 (s), 2.49 (s), 2.55 (s), 2.60 (s), 2.67 (s), 2.73 (s), 2.80 (s), 2.83 (s), 2.87 (s), 2.91 (s), 2.97 (s), 3.05 (s), 3.22 (s), 3.24 (s), 3.53 (s) ppm.

**Polymeric Amines:** Stock solutions of surfactant were prepared using dry polyethylenimine (PEI) (A: 18 wt.-%, B: 0.18 wt.-%, average Mw 25000, Aldrich), polyvinylpyrrolidone (C: 1 wt.-%), polyacrylamide (D: 1 wt.-%) and Millipore water (15 MΩ·$cm^{-1}$).

 © 2006 Wiley-VCH Verlag GmbH & Co. KGaA, Weinheim 

Type I nanocrystals were prepared by the addition of $HAuCl_4$ (40 μL, 1.24 wt.-%) to Millipore water (5 mL) with rapid stirring, followed by the required amount of solution A to D. The reaction mixture was left to stand for a minimum of 24 hours in a sealed vial, whereupon a characteristic colour change to deep red was observed. NMR samples were prepared by evaporating to dryness a duplicate volume (5 mL) of the PEI–Au colloid, prior to redispersion in $D_2O$. $^1H$ NMR (300 MHz, $D_2O$, 25 °C): $\delta$ = 4.74 (s), 4.67 (s), 4.61 (s), 4.41 (s), 3.33 (m), 3.21 (s), 3.17 (m), 3.02 (m), 2.83 (m), 2.28 (s), 2.13 (s), 2.06 (s), 2.00 (s), 1.85 (s), 1.80 (s) ppm. $^{13}C$ NMR (from HSQC at 300 MHz, $D_2O$, 25 °C): $\delta$ = 35.5 (s), 36.7 (s), 43.9 (s), 44.0 (s), 45.1 (s), 49.7 (s), 72.9 (s), 138.1 (s), 153.5 (s) ppm. Type II nanocrystals were formed in the same manner as type I, with the PEI/$HAuCl_4$ solution being heated momentarily to 70 °C. The vial was cooled to ambient temperature prior to further analysis. Type III nanocrystals were prepared according to the method of Sun (2003).[7] $HAuCl_4$ (80 μL, 1.24 wt.-%) was added to a 15 mL glass vial containing water (10 mL) and a magnetic stirring bar. After stirring rapidly for one min, PEI (20 μL, 18 wt.-%) was added to the mixture, whereupon a colour change to faint red was noted. After a further minute of stirring, $NaBH_4$ (2.0 M in dimethyl ether/ethylene glycol, Aldrich) was added dropwise until a colour change to deep red was observed.

### Analysis

High-resolution transmission electron micrographs (HR TEM) and diffraction patterns were recorded with a Jeol 2010 instrument at 200 keV acceleration voltage with the samples mounted on carbon-coated copper grids (200 mesh). Ultra-violet/visible (UV/Visible) spectra were measured using matched quartz curvettes and a Varian Cary 100 system. A Bruker Tensor 27 system attached to a Pike Technologies single-reflectance horizontal-attenuated total reflectance (ATR) attachment was used to obtain Fourier Transform infra-red (FTIR) spectra. pH and oxidation–reduction potentials (ORP) were measured using Mettler Toledo and Hanna probes, respectively, with a Hanna 8521 instrument. $^1H$ and gradient heteronuclear single quantum correlation (HSQC) nuclear magnetic resonance (NMR) spectra were recorded on a Varian Inova spectrometer at 300 MHz.

### Molecular Modelling

Modelling of the charge density on the compounds was undertaken using the Polak Ribiere conjugate gradient algorithm, on HyperChem. 7.5 (Gainesville, Florida). Rendering of the molecular models was achieved using Ghemical 1.91[20] and the Massively Parallel Quantum Chemistry system (MPQC).[21]

## Acknowledgments

Funding from the School of Chemical and Physical Sciences, Victoria University is gratefully acknowledged. The authors would also like to thank Dr. Richard Tilley and Mr. David Flynn for their valuable assistance with HR TEM sample preparation and analysis.

[1] G. Schmid, B. Corain, *Eur. J. Inorg. Chem.* **2003**, 3081–3098.
[2] R. D. Tilley, S. Saito, *Langmuir* **2003**, *19*, 5115–5120.
[3] H. J. Lee, S. Y. Yeo, S. H. Jeong, *J. Mater. Sci.* **2003**, *38*, 2199–2204.
[4] K. Kurihara, J. Kizling, P. Stenius, J. Fendler, *J. Am. Chem. Soc.* **1983**, *105*, 2574–2579.
[5] G. Frens, *Nature Phys. Sci.* **1973**, *241*, 20–22.
[6] M. Brust, M. Walker, D. Bethell, D. J. Schiffrin, R. Whyman, *J. Chem. Soc., Chem. Commun.* **1994**, 801–802.
[7] X. P. Sun, Z. L. Zhang, B. L. Zhang, X. D. Dong, S. J. Dong, E. K. Wang, *Chin. Chem. Lett.* **2003**, *14*, 866–869.
[8] J. C. Liu, G. W. Qin, P. Raveendran, Y. Ikushima, *Chem. Eur. J.* **2006**, *12*, 2131–2138.
[9] K. Esumi, A. Suzuki, N. Aihara, K. Usui, K. Torigoe, *Langmuir* **1998**, *14*, 3157–3159.
[10] G. H. Kelsall, N. J. Welham, M. A. Diaz, *J. Electroanal. Chem.* **1993**, *361*, 13–24.
[11] H. Zhu, Z. Pan, E. Hagaman, C. Liang, S. Overbury, S. Dai, *J. Colloid Interface Sci.* **2005**, *287*, 360–365.
[12] J. H. Song, Y.-J. Kim, J.-S. Kim, *Curr. Appl. Phys.* **2006**, *6*, 216–218.
[13] P. Kuo, C. Chen, M. Jao, *J. Phys. Chem. B* **2005**, *109*, 9445–9450.
[14] A. I. Vogel, *Vogel's Qualitative Inorganic Analysis*, 6th ed. (revised by G. Svehla), Longman Scientific & Technical, Essex, **1987**.
[15] J. McMurray, *Organic Chemistry*, 3rd Ed., Brooks/Cole, Pacific Grove, **1992**.
[16] Y. Tan, Y. Li, D. Zhu, *Synth. Met.* **2003**, *135–136*, 847–848.
[17] J.-E. Park, M. Atobe, T. Fuchigami, *Electrochim. Acta* **2006**, *51*, 849–854.
[18] T. J. Norman, C. D. Grant, D. Magana, J. Z. Zhang, *J. Phys. Chem. B* **2002**, *106*, 7005–7012.
[19] C. R. Raj, A. I. Abdelrahman, T. Ohsaka, *Electrochem. Commun.* **2005**, *7*, 888–893.
[20] T. Hassinen, M. Perakyla, *J. Comput. Chem.* **2001**, *22*, 1229–1242.
[21] C. L. Janssen, I. B. Nielson, M. L. Leininger, E. F. Valeev, E. T. Seidl, *The Massively Parallel Quantum Chemistry Program (MPQC)*, Version 2.3.0, Sandia National Laboratories, Livermore, California, **2004**.

Received: February 22, 2006
Published Online: April 26, 2006

 © 2006 Wiley-VCH Verlag GmbH & Co. KGaA, Weinheim 

DOI: 10.1002/ejic.200600156

# Synthesis and Characterization of $MoOI_2(PMe_3)_3$ and Use of $MoOX_2(PMe_3)_3$ (X = Cl, I) in Controlled Radical Polymerization

**José A. Mata,[a] Sébastien Maria,[a] Jean-Claude Daran,[a] and Rinaldo Poli*[a]**

**Keywords:** Molybdenum / Oxido ligands / Phosphane ligands / Halide exchange / Atom transfer radical polymerization

Complex $MoOCl_2(PMe_3)_3$ smoothly reacts with NaI in acetone to produce $MoOI_2(PMe_3)_3$ in good yields. The geometry of the compound is *mer-cis* octahedral, that is, identical to that of the dichloride precursor, as shown by NMR spectroscopy and by an X-ray crystallographic study. Electrochemical investigations of $MoOX_2(PMe_3)_3$ show irreversible oxidation waves at $E_{p,a}$ = +0.18 and +0.39 V for X = Cl and I, respectively. A study of the halide exchange between $MoOCl_2(PMe_3)_3$ and NaI, or between $MoOI_2(PMe_3)_3$ and $Bu_4NCl$, shows two equilibrated isomers for the mixed halide intermediate $MoOICl(PMe_3)_3$. The diiodide complex rapidly exchanges the iodo ligands with chloride upon dissolution in chloroform at room temperature, and with bromide from (1-bromoethyl)benzene (BEB) under more forcing conditions. The equilibrium favors the softer halide (I) on C and the harder one (Cl or Br) on $Mo^{IV}$. Both oxido compounds catalyze the atom transfer radical polymerization (ATRP) of styrene in combination with the BEB initiator, yielding polymers with quite narrow molecular weight distributions (down to 1.11). The apparent polymerization rate constant is approximately doubled in the presence of 1 equiv. of the $Al(OiPr)_3$ cocatalyst. On the other hand, the system is not capable of efficiently controlling the radical chain growth for methyl acrylate polymerization.
(© Wiley-VCH Verlag GmbH & Co. KGaA, 69451 Weinheim, Germany, 2006)

## Introduction

In recent years, a number of coordination and organometallic compounds based on different transition metals have been proven capable of controlling the radical polymerization of activated olefins. The phenomenon is accomplished by maintaining the active radical concentration at very low levels through a fast reversible equilibrium with a dormant species, thereby reducing the incidence of bimolecular terminations. The equilibrium may implicate a halogen atom transfer (see Scheme 1), thus the term atom transfer radical polymerization (ATRP).[1,2] In this respect, the process corresponds to a transition-metal-catalyzed multiple insertion of olefins into the carbon–halogen bond of the initiator molecule. A metal complex, however, may also yield a dormant species by reversibly forming a metal–carbon bond (see Scheme 2). This process is termed, somewhat inappropriately, stable free radical polymerization (SFRP). Indeed, the stable transition-metal complex acting as a spin trap need not possess a radical character. We have recently proposed a new term for this process, organometallic radical polymerization (OMRP), because it involves the reversible formation of a metal–carbon bond.[3]

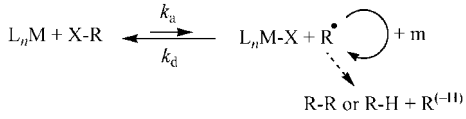


Scheme 1.

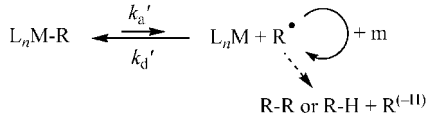


Scheme 2.

The various metals so far shown to be effective include $Ti^{III}$,[4] $Mo^{III}$,[5,6] $Re^{V}$,[7] $Fe^{II}$,[8,9] $Ru^{II}$,[10] $Ni^{II}$,[11] $Ni^{0}$,[12] and $Cu^{I}$.[13] Although no system currently appears to parallel the activities and practical advantages of certain $Cu^{I}$ complexes, the investigation of other metal systems is useful in order to shine additional light on the mechanistic details of the process. For instance, by using $CpMoCl_2L_2$ complexes (L = tertiary phosphanes or $L_2$ = diene), we have demonstrated how the two trapping processes in Schemes 1 and 2 may simultaneously take place when the polymerization is carried out under ATRP conditions.[5] Furthermore, the use of $MoX_3(PMe_3)_3$ catalysts (X = Cl, Br, I) has revealed that the oxidized metal complex (ATRP spin trap) need not be a thermodynamically stable species in order for the catalyst to ensure good control.[14] In fact, whereas the $Mo^{IV}$ complexes $MoX_3Y(PMe_3)_3$ (X, Y = Cl, Br) could be isolated

[a] Laboratoire de Chimie de Coordination, UPR CNRS 8241 lié par convention à l'Université Paul Sabatier et à l'Institut National Polytechnique de Toulouse,
205 Route de Narbonne, 31077 Toulouse Cedex, France
Fax: +33-561553003
E-mail: poli@lcc-toulouse.fr

 © 2006 Wiley-VCH Verlag GmbH & Co. KGaA, Weinheim 

and fully characterized, no such complex containing an iodo ligand was shown to exist, because it would decompose by an internal redox process to an $Mo^{III}$ complex and $I_2$. As a further example, a comparison of the rates of halide exchange between various ATRP catalysts [i.e. $MoX_3(PMe_3)_3$, $CpMoCl_2(RN{=}CHCH{=}NR)$ (R = *i*Pr), $RuCl_2(PPh_3)_3$] and initiator molecules, in the presence and in the absence of $Al(O{i}Pr)_3$, has revealed two possible mechanisms for this exchange process.[15,16]

The results of DFT calculations have shown that the Mo–X and Mo–R bond strengths decrease upon raising the metal oxidation state, the computed values suggesting that the $Mo^{III/IV}$ redox couple is ideally placed to insure appropriate equilibrium positions for both ATRP and SFRP processes. Indeed, no radical polymerization occurs in the presence of the complex $CpMo(CH_2SiMe_3)_2(\eta^4\text{-}C_4H_6)$, showing that this particular $Mo^{III}$–R bond is too strong.[5] On the other hand, preliminary evidence, which will be reported separately, has indicated the possible implication of $Mo^{IV/V}$ couples in ATRP. For this reason, we have decided to test some typical $Mo^{IV}$ coordination compounds as ATRP catalysts. In this paper, we report our results obtained by using a well-known $Mo^{IV}$ coordination compound, $MoOCl_2(PMe_3)_3$. In addition, we also report the results obtained with the related compound $MoOI_2(PMe_3)_3$, whose synthesis and characterization is reported here for the first time. Our interest in this compound was twofold. From the point of view of ATRP catalysis, we have shown that some iodo derivatives of certain $Mo^{III}$ ATRP catalysts, for example, $CpMoI_2(RN{=}CHCH{=}NR)$ (R = *i*Pr) are more active than the corresponding chloro derivatives.[15] From the coordination chemistry point of view, we have demonstrated the incompatibility between iodo ligands and $Mo^{IV}$ in complexes of type $MoX_nY_{4-n}(PMe_3)_3$ (vide supra).[14] Yet, stable iodide derivatives of molybdenum in higher oxidation states do exist when the metal electronic deficiency is satisfied by strong donor ligands (e.g. $Cp^*Mo^{IV}I_4^-$ and $Mo^{V}OI_4^-$).[17,18] Therefore, it was of interest to see whether compound $MoOI_2(PMe_3)_3$ would be stable, to investigate its redox properties, and to test its catalytic properties in ATRP.

## Results and Discussion

### Syntheses and Characterization

The new complex $MoOI_2(PMe_3)_3$ was obtained by halide exchange from the dichloride precursor as described in Scheme 3. The reaction is driven by the precipitation of the less soluble NaCl and is relatively rapid at room temperature. The spectroscopic properties of the isolated compound indicate an identical structure to that of the precursor. In particular, the $^{31}P$ NMR spectrum shows two types of phosphane ligands in a 2:1 ratio, whereas the virtual triplet pattern for the $^1H$ NMR resonance of the two equivalent $PMe_3$ ligands establishes their mutual *trans* arrangement (the spectral parameters are collected in Table 1). This clearly identifies the *mer* arrangement of the $Mo(PMe_3)_3$ moiety. The $^{31}P$ NMR spectrum is qualitatively different in [$D_6$]acetone and in $C_6D_6$. Whereas the doublet/triplet pattern expected for an $AX_2$ spin system is relatively unperturbed in the former solvent, a more complex pattern, which is indicative of second-order coupling for an $AB_2$ system, is evident in $C_6D_6$ (see Figure 1). This difference is caused by the closer proximity of the two $^{31}P$ resonances in $C_6D_6$. The values reported in Table 1 result from the successful simulation of the spectrum.

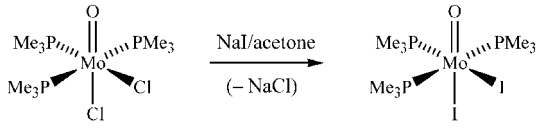


Scheme 3.

Table 1. $^1H$ and $^{31}P\{^1H\}$ NMR parameters ($\delta$ in ppm, $J$ in Hz) for compounds $MoOXY(PMe_3)_3$ (X, Y = Cl or I).

| Compound | Solvent | $\delta_H$ ($J_{HP}$)[a] | $\delta_P$ ($J_{PP}$) |
|---|---|---|---|
| $MoOCl_2(PMe_3)_3$ | [$D_6$]acetone | 1.68 (d, 8.4) | 2.0 (t, 22) |
| | | 1.63 (t, 3.9) | –5.2 (d, 22) |
| $MoOBr_2(PMe_3)_3$ | [$D_6$]acetone | 1.73 (d, 8.7) | –2.8 (t, 22) |
| | | 1.73 (t, 4.0) | –9.4 (d, 22) |
| $MoOI_2(PMe_3)_3$ | [$D_6$]acetone | 1.91 (t, 4.0) | –12.5 (t, 20) |
| | | 1.80 (d, 8.7) | –15.7 (d, 20) |
| $MoOI_2(PMe_3)_3$ | $C_6D_6$ | 1.73 (t, 4.1) | –14.98 (t, 22.2) |
| | | 1.36 (d, 8.4) | –16.40 (d, 22.2) |
| $MoOClI(PMe_3)_3$, **A**[b] | [$D_6$]acetone | 1.71 (d, 8.4) | 2.2 (t, 20) |
| | | 1.80 (t, 3.9) | –8.4 (d, 20) |
| $MoOClI(PMe_3)_3$, **B**[b] | [$D_6$]acetone | n.i.[d] | –9.7 (t, 20) |
| | | n.i.[d] | –12.0 (d, 20) |
| $MoOBrI(PMe_3)_3$, **A′**[c] | [$D_6$]acetone | 1.84 (t, 4.0) | –3.6 (t, 23) |
| | | 1.74 (d, 8.7) | –11.0 (d, 23) |
| $MoOBrI(PMe_3)_3$, **B′**[c] | [$D_6$]acetone | n.i.[d] | –10.3 (t, 22) |
| | | n.i.[d] | –13.8 (d, 22) |

[a] vt: virtual triplet. [b] **A**: I *trans* to O; **B**: Cl *trans* to O (see Scheme 5). [c] **A′**: I *trans* to O; **B′**: Cl *trans* to O (see Scheme 6). [d] Not identified.

The relative *cis* arrangement of the two iodo ligands is unambiguously confirmed by the single-crystal X-ray diffraction study, but is also indicated by the NMR monitoring of the halide exchange process, notably by the presence of *two* different stereoisomers for the mixed halide complex (vide infra). When using a sufficiently large excess of NaI (>5 equiv.), the isolated product is devoid of any mixed halide impurity. It is also devoid of the known[19] $Mo^{III}$ complex $MoI_3(PMe_3)_3$, a problem that often affects its dichloride precursor $MoOCl_2(PMe_3)_3$.[20] Indeed, the latter is usually obtained from $MoCl_4(THF)_2$ and $PMe_3$ in the presence of water,[21] giving a product whose color (varying from blue to green) depends on the level of contamination by yellow $MoCl_3(PMe_3)_3$. By replacing the $Mo^{IV}$ tetrachloride precursor with the bis(ether) complex, $MoCl_4(Et_2O)_2$,[22] we have obtained a blue material that is also contaminated by minor amounts of the $Mo^{III}$ trichloride complex, as evidenced by $^1H$ NMR spectroscopy. A better synthesis of pure $MoOCl_2(PMe_3)_3$ is that reported by Galindo et al., from $MoO_2Cl_2(MeOCH_2CH_2OMe)$ and $PMe_3$.[23] Our synthesis of $MoOI_2(PMe_3)_3$ was carried out from a dichloride precursor obtained by the latter procedure.

 © 2006 Wiley-VCH Verlag GmbH & Co. KGaA, Weinheim 

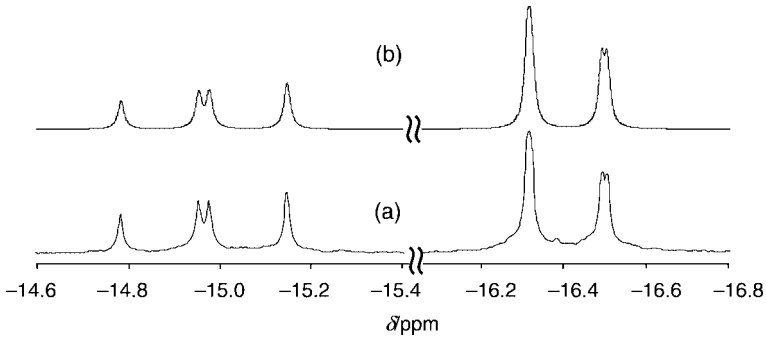


Figure 1. Experimental (a) and simulated (b) $^{31}P$ NMR spectrum of $MoOI_2(PMe_3)_3$ in $C_6D_6$.

A view of the molecule resulting from the X-ray diffraction study is shown in Figure 2. Selected geometric parameters are collected in Table 2. The thermal ellipsoids are well behaved, showing no evidence for positional disorder, in agreement with the NMR evidence for the absence of $MoI_3(PMe_3)_3$. In addition, the presence of iodide in the oxido position would have a notable effect on the refined Mo=O distance, whereas the experimental value of 1.685(4) Å is quite short. Moreover, this distance is identical within experimental error to the distance reported for the corresponding complex *cis-mer*-$MoOCl_2(PMe_2Ph)_3$ [1.675(3) Å].[20] Therefore, these results show that there is no compositional I/O disorder, contrary to previous reports for the dichloro analogues.[20] The Mo–P distances [2.494–2.513 Å] are within the normal range for related compounds.

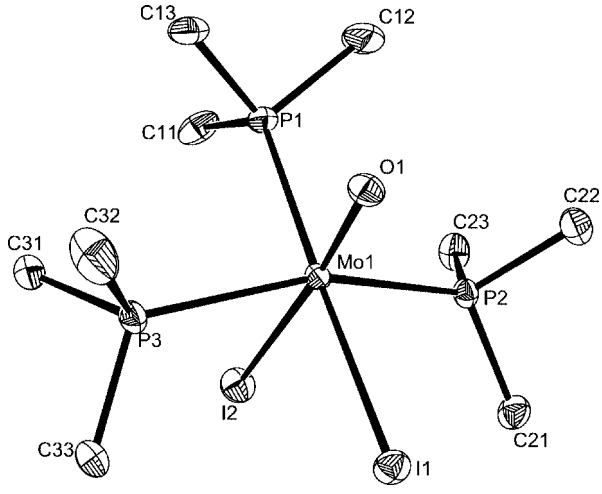


Figure 2. ORTEP view of $MoOI_2(PMe_3)_3$. The ellipsoids are drawn at the 50% probability level.

From a benzene/*n*-pentane solution of $MoOCl_2(PMe_3)_3$ set aside for several days, crystals of compound $[MoOCl(PMe_3)(OPMe_3)]_2(\mu\text{-}O)$ were obtained, possibly by adventitious contact with air and moisture. As the resulting structure is more accurately determined and is in a different crystal system than one reported previously for the same compound,[24] we report it here but do not comment on it any further. No analogous compound was obtained from the corresponding oxido diiodide complex.

Table 2. Selected bond lengths [Å] and angles [°] for compound $MoOI_2(PMe_3)_3$.

| | | | |
|---|---|---|---|
| Mo(1)–P(1) | 2.4939(15) | Mo(1)–O(1) | 1.685(4) |
| Mo(1)–P(2) | 2.5073(14) | Mo(1)–I(1) | 2.8634(6) |
| Mo(1)–P(3) | 2.5130(15) | Mo(1)–I(2) | 2.9207(6) |
| O(1)–Mo(1)–P(1) | 82.16(15) | P(1)–Mo(1)–P(2) | 93.80(5) |
| O(1)–Mo(1)–P(2) | 99.94(15) | P(1)–Mo(1)–P(3) | 92.38(5) |
| O(1)–Mo(1)–P(3) | 102.79(15) | P(2)–Mo(1)–P(3) | 157.06(5) |
| O(1)–Mo(1)–I(1) | 93.43(15) | P(1)–Mo(1)–I(1) | 175.50(4) |
| O(1)–Mo(1)–I(2) | 172.20(15) | P(1)–Mo(1)–I(2) | 90.08(4) |
| P(2)–Mo(1)–I(1) | 87.84(4) | P(3)–Mo(1)–I(1) | 87.70(4) |
| P(2)–Mo(1)–I(2) | 79.76(3) | P(3)–Mo(1)–I(2) | 78.16(4) |
| I(1)–Mo(1)–I(2) | 94.343(17) | | |

The existence and stability of the $MoOI_2(PMe_3)_3$ compound [cf. the nonexistence of $MoI_4(PMe_3)_3$][14] indicates that the oxido ligand is a much stronger electron donor than two iodo ligands toward the Mo center, raising the energy of the LUMO and thereby making the metal center a less powerful oxidizing agent. Indeed, qualitative MO considerations lead to the expectation of an interaction as shown in Scheme 4, where the energy of the $d_{xz}$ and $d_{yz}$ orbitals of the pseudo-$t_{2g}$ set (octahedral coordination environment) is raised through the π-donation mechanism.

An electrochemical investigation of compounds $MoOX_2(PMe_3)_3$ yields irreversible oxidation processes at $E_{p,a}$ = +0.18 and +0.39 V for X = Cl and I, respectively (see Figure 3). The lack of reversibility indicates the occurrence of a fast chemical process after oxidation to the cationic $Mo^V$ complex $[MoOX_2(PMe_3)_3]^+$, probably involving solvent coordination. The voltammogram recorded on the chloride complex shows that a new and broad cathodic peak is generated after the oxidation peak (this feature is not observed during the first cathodic scan prior to the oxidation peak). In the presence of chloride ions, the oxidation peak shifted slightly toward less positive potentials, but the overall shape of the voltammogram was otherwise unaffected. This result can be rationalized by a follow-up coordination of $Cl^-$ to $[MoOCl_2(PMe_3)_3]^+$, with generation of the putative ATRP spin trap, $MoOCl_3(PMe_3)_3$. The same phenomenon was previously observed by us for the oxidation of $MoX_3(PMe_3)_3$ in the presence of $X^-$ (X = Cl, Br) and verified by an independent study of the isolated $MoX_4(PMe_3)_3$ products.[14] In the present case, a similar verification is impossible because, to the best of our knowl-

 © 2006 Wiley-VCH Verlag GmbH & Co. KGaA, Weinheim 

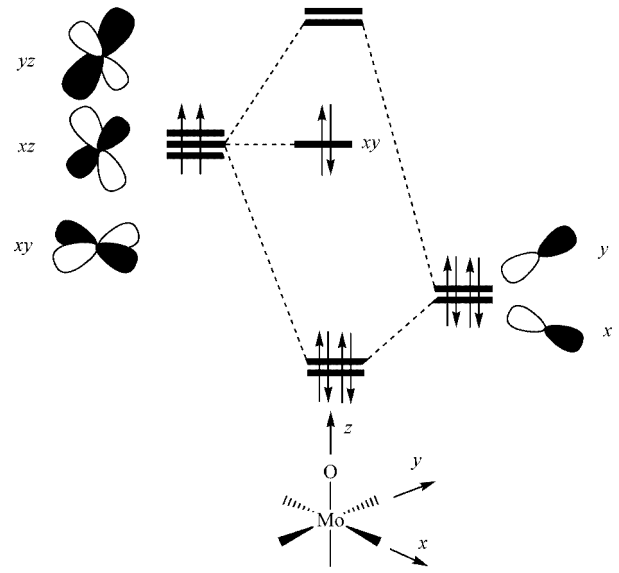


Scheme 4.

edge, complex $MoOCl_3(PMe_3)_3$ is nonexistent. Indeed, the voltammetric response in the presence of $Cl^-$ shows that such a compound is unstable under the conditions of the CV experiment (THF solution) and decomposes in a similar way to that of the $[MoOCl_2(PMe_3)_3]^+$ complex.

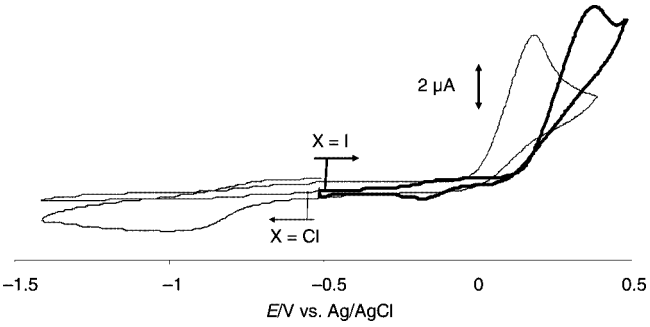


Figure 3. Cyclic voltammogram of $MoOX_2(PMe_3)_3$ in THF. Thinner curve: X = Cl; thicker curve: X = I. $C_{Mo} = 4 \times 10^{-3}$ M. Scan rate = 100 mV/s.

Concerning the voltammogram of the diiodide complex, the greater oxidation potential relative to the dichloride analogue parallels the corresponding shift for the $Mo^{III}$ complexes $MoX_3(PMe_3)_3$ upon going from X = Cl to I.[14] Note the presence of a small reversible wave at about –0.1 V in this voltammogram. This corresponds to the oxidation of $I^-$ to $I_3^-$ (as verified by the deliberate addition of $I^-$ to the solution) and grows with the time lapse between the solution preparation and the voltammetric study. Even upon rapidly recording the voltammogram (as in the example shown in Figure 3), this feature could not be completely eliminated, suggesting the establishment of a slow ligand substitution equilibrium between iodide and THF. The other important observation is that the oxidation of $I^-$ occurs at a less positive potential relative to the oxidation of the (oxido)$Mo^{IV}$ complex. This has implications for the ATRP process (vide infra).

It is interesting to compare the oxidation potentials of $MoOX_2(PMe_3)_3$ with those of the corresponding $MoX_4(PMe_3)_3$. Because of its nonexistence, the $E_{1/2}$ for the oxidation of $MoI_4(PMe_3)_3$ could not be established, but those of the analogous $MoX_4(PMe_3)_3$ complexes are –0.15 V (X = Cl) and –0.06 V (X = Br), allowing extrapolation to a value of about +0.05 for X = I. Thus, we can observe that the replacement of two X ligands by one O ligand has the effect of raising the oxidation potential by about 0.3 V. This change can be related to a lower energy of the HOMO for the oxido compound (Scheme 4), resulting from the greater electronegativity of the oxygen atom. In other words, there is less electron donation by one O atom relative to two I atoms by the σ-bonding mechanism.

## NMR Study of the Halide Exchange Reactions

The conversion of the dichloride to the diiodide complex was monitored by $^1H$ and $^{31}P$ NMR in the presence of NaI in [$D_6$]acetone. Figure 4 shows representative $^{31}P\{^1H\}$ NMR spectra recorded during the transformation. The resonance values for the different compounds are collected in Table 1. Given the *mer-cis* coordination, there are two possible stereoisomers for the mixed halide intermediate, **A** and **B** (see Scheme 5). A *mer-trans* or a *fac* arrangement would only allow a single stereoisomer. The monitoring clearly shows the preferential formation of isomer **A**. The structural assignment of **A** and **B** as shown in Scheme 5 is strongly suggested by the $\delta_P$ resonance pattern, especially the chemical shift of the unique P nucleus, which is expected to be most sensitive to the nature of the *trans*-halide ligand. This resonance shifts very little during the first substitution for isomer **A**, whereas it shifts by a large amount for isomer **B**, to a position close to that observed for the final product. The two mutually *trans*-P nuclei (*cis* to both halide coordination positions), on the other hand, shift gradually with the halide substitution.

A preferential formation of **A** would seem consistent with kinetic control of the halide exchange, as the oxido ligand should exert a stronger *trans* effect relative to the $PMe_3$ ligand. However, the conversion in the opposite direction, which occurs in the presence of $Bu_4N^+Cl^-$ in [$D_6$]acetone, again yields isomer **A** as the *major* intermediate. If the exchange process had been under kinetic control, the prevalence of isomer **B** was expected. Therefore, we conclude that the halide exchange process is under thermodynamic control and that the position *trans* to the oxido ligand is preferentially occupied by the softer iodo ligand.

In order to gain further insight on this issue, we have also carried out a reaction between $MoOI_2(PMe_3)_3$ and NaBr in [$D_6$]acetone. The reaction qualitatively follows the same pathway (see Scheme 6). The use of a small excess amount of NaBr (about 1.3 equiv.) leads to rapid equilibration (4 h at room temperature) with the two mixed halide intermediates having structures **A′** and **B′**, the former being predominant, plus a small amount of the corresponding dibromide.

 © 2006 Wiley-VCH Verlag GmbH & Co. KGaA, Weinheim 

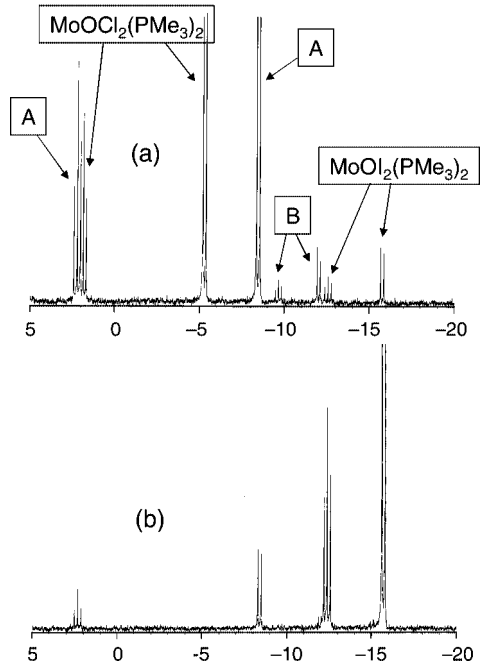


Figure 4. Room-temperature $^{31}P\{^1H\}$ NMR spectra of $MoOCl_2(PMe_3)_3$ (50 mg, 0.12 mmol) and NaI in [$D_6$]acetone (0.6 mL). (a) After 5 h with 1 equiv. NaI; (b) 2.5 h after spectrum (a) with excess NaI.

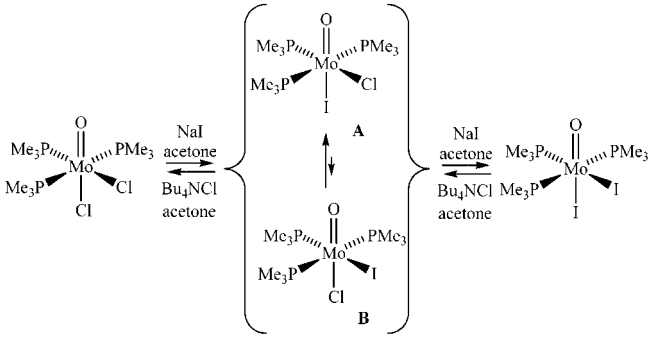


Scheme 5.

Treatment with an excess of NaBr increases the amount of dibromide product. The $^{31}P$ resonance of the unique $PMe_3$ ligand shifts from $\delta$ = –12.5 ppm for the diiodide complex to $\delta$ = –3.6 ppm for **A′** and only to $\delta$ = –10.3 ppm for **B′**. The same nucleus resonates at $\delta$ = –2.8 ppm for the dibromide complex. Once again, the *trans* position to the oxido ligand shows a thermodynamic preference for the softer iodo ligand.

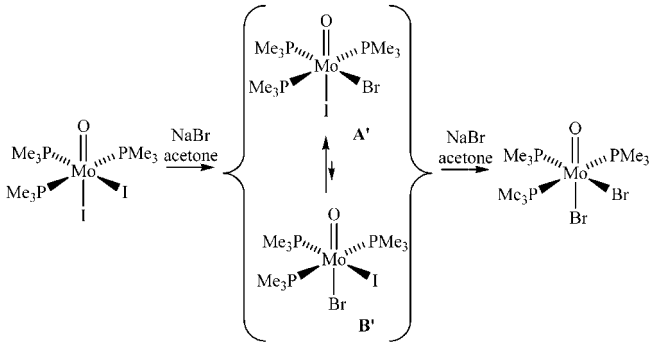


Scheme 6.

It is interesting to note that complex $MoOI_2(PMe_3)_3$ rapidly undergoes halide exchange when dissolved in chloroform (about 50% in 30 min at room temperature). The NMR monitoring indicates the intermediate formation of the mixed halide isomers **A** (major) and **B** (very minor), though the exchange is eventually complete. In dichloromethane, this exchange is much slower, as no significant amount of mixed halide species (**A**) is formed after 20 h of stirring at room temperature. This phenomenon could either take place by an internal nucleophilic substitution assisted by solvent coordination to the metal center, as we have recently pointed out for other transition-metal complexes,[16] or by reversible atom transfer. In the latter case, the phenomenon would suggest that this system could serve as a good catalyst in atom transfer radical polymerization. This has indeed been verified experimentally (vide infra).

As $MoOI_2(PMe_3)_3$ rapidly exchanges its halogen atoms with chloroform, we have also tested the halogen exchange with the initiator molecule used in ATRP, namely (1-bromoethyl)benzene, $PhCH(Br)CH_3$ (BEB). The reaction (Scheme 7) was monitored by $^1H$ NMR, as the C*H* proton is very sensitive to the nature of the halogen atom. At 90 °C in [$D_8$]toluene and using a stoichiometric BEB/Mo ratio (same conditions used for the ATRP experiments, vide infra), the exchange process is essentially complete after 40 min (see Figure 5). A slower exchange is also observed at room temperature. $^{31}P$ NMR monitoring shows that the reaction proceeds through the same intermediates seen

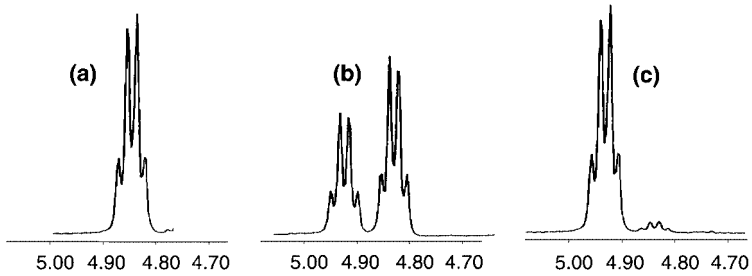


Figure 5. $^1H$ NMR monitoring of the halogen exchange between $MoOI_2(PMe_3)_3$ and BEB in [$D_8$]toluene at 90 °C ([Mo] = [BEB] ≈ 0.1 mol/L). (a) $t$ = 0 min. (b) $t$ = 20 min. (c) $t$ = 40 min.

 © 2006 Wiley-VCH Verlag GmbH & Co. KGaA, Weinheim 

when using NaBr, namely $MoOBrI(PMe_3)_3$ (**A′** and **B′**, the former being predominant). The quantitative nature of the exchange illustrates the thermodynamic preference for placing the heavier halogen on the carbon atom and the lighter one on the metal atom. On the basis of Pearson's HSAB theory,[25] this result may be interpreted in terms of a harder character for the $Mo^{IV}$ center with respect to carbon.

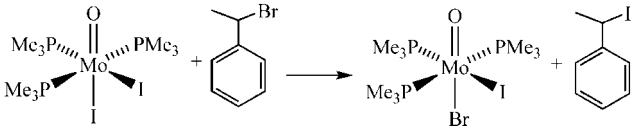

Scheme 7.

### Controlled Radical Polymerizations

Complexes $MoOX_2(PMe_3)_3$ were tested as catalysts for the controlled radical polymerization of styrene and methyl acrylate under ATRP conditions. The experimental conditions and apparent polymerization rates for the styrene polymerization are summarized in Table 3. In each case, the first-order monomer consumption rate was verified by the linearity of the $\ln([M]_0/[M])$ versus time plot, indicating that the concentration of active radical remains constant throughout the polymerization process, as expected for a controlled process. The polymerization was carried out both in the absence and in the presence of an equivalent amount of the $Al(OiPr)_3$ cocatalyst, whose effectiveness in ATRP seems quite general. In fact, it has been demonstrated that the apparent polymerization rates increase by factors up to 10 or more when 1 equiv. of this compound is used in conjunction with a variety of different catalysts based on Group 6–11 metals, including $CpMoCl_2(i\text{PrN=CH–CH=N}i\text{Pr})$,[6] $MoX_3(PMe_3)_3$,[14] $ReIO_2(PPh_3)_2$,[7] $CpFeX(CO)_2$ (X = Br, I),[8] $RuCl_2(PPh_3)_3$,[10] $NiBr_2(PPh_3)_2$,[11] $Ni(PPh_3)_4$,[12] and CuBr/bipy.[13] The proposed mode of action of this cocatalyst consists of a shift of the atom transfer equilibrium, caused by the stronger interaction of the Al Lewis acid with the halogen lone pairs in the more polarized Mo–X bond, relative to the C–X bond of the initiator/dormant species.[16] Table 3 shows that $Al(OiPr)_3$ is also effective in conjunction with the $MoOX_2(PMe_3)_3$ catalysts, although by a smaller margin. In each case, the apparent polymerization rate approximately doubles when 1 equiv. of $Al(OiPr)_3$ is added. Note also that the diiodide system is about twice as fast as the dichloride system.

Table 3. ATRP of styrene using $MoOX_2(PMe_3)_3$ (X = Cl, I) catalysts.[a]

| Entry | X | Mo/I/Al/S[b] | $k_{app}$ [$min^{-1}$] |
|---|---|---|---|
| 1 | Cl | 1:1:–:200 | $2.18\times10^{-4}$ |
| 2 | Cl | 1:1:1:200 | $4.38\times10^{-4}$ |
| 3 | I | 1:1:–:200 | $4.26\times10^{-4}$ |
| 4 | I | 1:1:1:200 | $9.54\times10^{-4}$ |

[a] All polymerizations were carried out in toluene at 90 °C. [b] I: initiator (BEB); Al: $Al(OiPr)_3$ cocatalyst; S: styrene.

For each dihalide catalyst and in the absence of $Al(OiPr)_3$, the experimentally determined number-average molecular weights ($M_n$) of the polymer grow linearly with the monomer conversion and correspond closely to the theoretical molecular weights on the basis of the monomer/initiator ratio (see Figure 6a, c). These characteristics are as expected for a controlled radical polymerization process. Furthermore, the polydispersity indexes (PDI = $\bar{M}_w/\bar{M}_n$) are quite low, down to 1.11. These are the lowest PDIs reported to date for an Mo-based catalyst, underlining the excellent level of control exerted by these oxidomolybdenum(IV) complexes. At high conversions, the experimental $M_n$ value is slightly lower than the theoretical one for the dichloride system, whereas it is slightly higher for the diiodide system. The former effect could result from the slight intervention of chain transfer processes, whereas the latter one could find a rationalization in an initiator efficiency slightly lower than 100% ($f < 1$). In the presence of $Al(OiPr)_3$, the dichloride catalyst appears to insure a less effective control, as the PDIs are higher (about 1.3 at 75% conversion), although $M_n$ still grows linearly with conversion (see Figure 6b), and the monomer consumption follows first-order kinetics. In addition, the experimental $M_n$ value is about two times larger than the calculated one (i.e. $f \approx 0.5$). The diiodide catalyst also controls the polymerization a little less effectively in the presence of $Al(OiPr)_3$, but $f$ remains close to 1 (see Figure 6d). At the moment, we are not able to rationalize why the nature of the halogen has such a large effect on the initiator efficiency, and only for the experiments carried out in the presence of $Al(OiPr)_3$.

The putative coordination compounds produced by the atom transfer process could not be characterized. From the electrochemical study, we have established that the oxidation potential of complex $MoOCl_2(PMe_3)_3$ is less positive than those of the free $Cl^-$ or $Br^-$ ions.[14] Therefore, the oxidized complex $[MoOCl_2(PMe_3)_3]^+$ is compatible with the presence of these ions or, in other words, complex $MoOCl_2X(PMe_3)_3$ (X = Cl, Br) is predicted to be a stable system from the redox point of view. Nonetheless, the electrochemical study indicates instability for $MoOCl_3(PMe_3)_3$, at least in the THF solvent used for the cyclic voltammetric investigation. On the other hand, the free iodide ion is oxidized at a less positive potential than both complexes $MoOX_2(PMe_3)_3$ (X = Cl, I). This means that the putative ATRP spin trap, namely an (oxido)$Mo^V$ complex of type $MoOX_2Y(PMe_3)_3$, is thermodynamically unstable when either X or Y is an iodine atom, relative to an internal redox process leading to the reduction of $Mo^V$ to $Mo^{IV}$ and oxidation of $I^-$. This observation might seem inconsistent with the ability of $MoOI_2(PMe_3)_3$, in combination with a bromide initiator, to catalyze the ATRP of styrene with a controlled chain growth. However, our recently published investigation of the $MoI_3(PMe_3)_3$ ATRP catalyst, for which the same apparent contradiction was observed, provides the basis to rationalize this phenomenon.[14] In essence, the oxidized $MoOI_2Br(PMe_3)_3$ complex is capable of efficiently acting as a spin trap for the growing radical chain for kinetic reasons, its decomposition being a bimolecular reaction

 © 2006 Wiley-VCH Verlag GmbH & Co. KGaA, Weinheim 

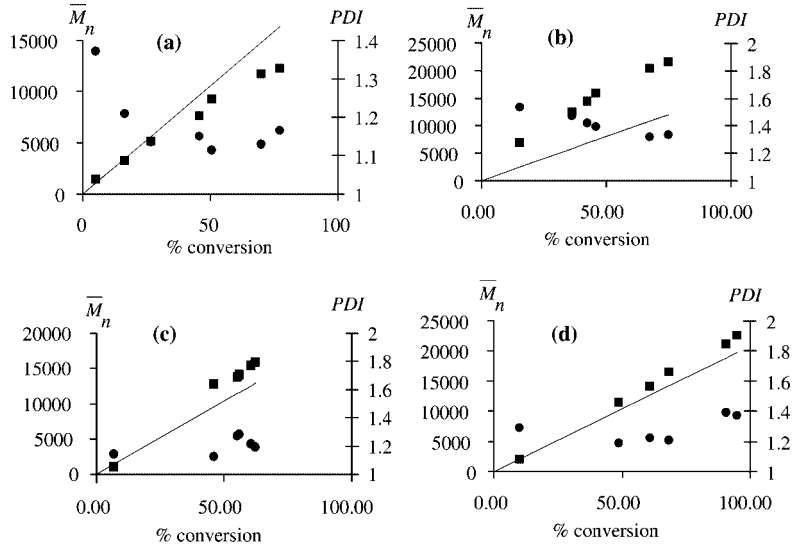


Figure 6. $M_n$ vs. conversion and PDI for the ATRP of styrene catalyzed by $MoOX_2(PMe_3)_3$ (X = Cl, I). Conditions are given in Table 3 (Entries 1–4). Squares: experimental $M_n$; circles: PDI; straight line: theoretical $M_n$. (a) X = Cl, no Al(O*i*Pr)$_3$ (Entry 1); (b) X = Cl, with Al(O*i*Pr)$_3$ (Entry 2); (c) X = I, no Al(O*i*Pr)$_3$ (Entry 3); (d) X = I, with Al(O*i*Pr)$_3$ (Entry 4).

and involving a greater activation barrier than the radical trapping process.

The polymerization of methyl acrylate was not well controlled by these (oxido)$Mo^{IV}$ complexes. Initial experiments carried out with each dihalide complex at 90 °C with ethyl 2-iodopropionate as an initiator gave very fast polymerizations, with greater than 90% conversion after the first 300 min. The reaction was therefore repeated at a lower temperature (35 °C). Even under these conditions, however, the polymerization process remained quite fast. With complex $MoOCl_2(PMe_3)_3$ the conversion was initially high and slowed down at later times (the monomer decay did not follow a first-order rate law), reaching about 60% conversion in 6 d. With complex $MoOI_2(PMe_3)_3$, the process was even faster, reaching 100% conversion in about 18 h. In both cases, the molecular weights were much larger than expected on the basis of a controlled process, and the PDIs were quite high (>1.5), see for instance Figure 7 for the chloride system. This behavior is consistent with an atom transfer process that is not sufficiently shifted toward the dormant species. Further studies under different conditions (nature of the initiator, different cocatalysts) will need to be carried out in order to optimize this process.

In order to check whether the OMRP equilibrium also plays a role in the ATRP catalyzed by $MoOX_2(PMe_3)_3$, the polymerization of styrene was also carried out using AIBN as a thermal initiator in the presence of these compounds. After heating at 100 °C for 30 min to decompose most of the initiator, the temperature was set to 80 °C for the rest of the experiment. The polymerizations were not controlled, with conversions reaching 30% within the first 4 h and then increasing slowly to 65% over the next 4 d. There was no first-order monomer consumption, and the PDIs remained consistently high throughout the experiment. These results are typical of an uncontrolled free radical process. Only a minor retardation effect was noted in the presence of the

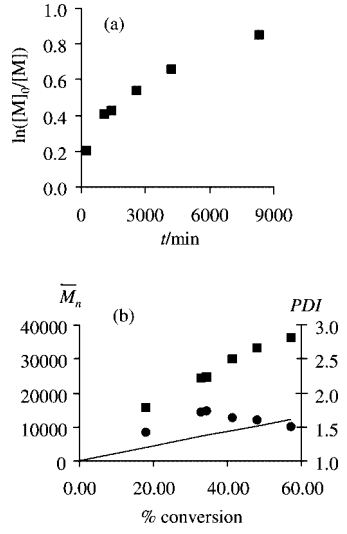


Figure 7. Polymerization of methyl acrylate catalyzed by $MoOCl_2(PMe_3)_3$ at 35 °C. Conditions: Mo/I/Al/MA = 1:1:1:250 [MA: methyl acrylate; I (initiator): ethyl 2-iodopropionate; Al: Al(O*i*Pr)$_3$]. (a) Kinetics plot. (b) $M_n$ vs. conversion and PDI. Squares: experimental $M_n$; circles: PDI; straight line: theoretical $M_n$.

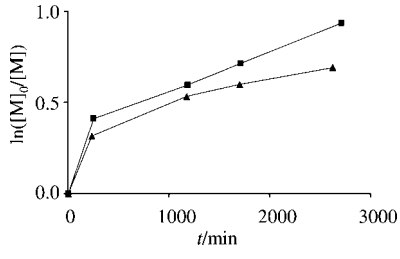


Figure 8. Polymerization of styrene in toluene (30%, v/v) in the presence of AIBN as initiator (styrene/AIBN = 250) at 80 °C. Squares: without Mo complex; triangles: with $MoOI_2(PMe_3)_3$ (AIBN/Mo = 1:1).

 © 2006 Wiley-VCH Verlag GmbH & Co. KGaA, Weinheim 

metal complexes (e.g. see Figure 8). This suggests the possibility of a radical-trapping process by the $MoOX_2(PMe_3)_3$ complex, but the stability of the adduct is insufficient. In conclusion, the $MoOX_2(PMe_3)_3$ complexes are not capable of efficiently trapping the reactive radical of polystyrene and form sufficiently persistent dormant species.

## Conclusions

The current investigation has shown, for the first time, the ability of $Mo^{IV}$ complexes to function as ATRP catalysts. Both the well-known dichloro complex and its newly developed diiodo analogue are equally capable of producing polystyrenes with rather narrow polydispersities. The diiodide catalyst gives higher apparent polymerization rates, and the rate is further doubled in the presence of 1 equiv. of $Al(OiPr)_3$ for each catalyst. We could not isolate and characterize the metallic spin traps, which are expected to be $Mo^{V}$ complexes of the formula $MoOX_2Y(PMe_3)_3$ (X, Y = Cl, Br, I). The electrochemical studies indicate instability for these complexes, at least in THF. In addition, the iodide-containing system is thermodynamically unstable with respect to an intramolecular redox process. However, as we have recently demonstrated for a related catalyst,[14] it is not necessary for the spin trap to be a thermodynamically stable compound. It remains capable of performing the radical-trapping function, thereby regulating the concentration of the active organic radical, for kinetic reasons. We are now interested in testing these oxidomolybdenum(IV) complexes as well as other similar compounds in the polymerization (under ATRP and SFRP conditions) of other monomers.

## Experimental Section

**General:** All manipulations were carried out under dry and oxygen-free argon with standard Schlenk techniques. Styrene was washed with aqueous NaOH (10%), neutralized with water, dried with $MgSO_4$ and then distilled at 25 °C under reduced pressure. Toluene and pentane were purified by distillation under argon after drying with sodium/benzophenone ketyl. $CH_2Cl_2$ was purified with $P_4O_{10}$ and distilled under argon. 1-Bromo-1-phenylethane [or (1-bromoethyl)benzene, BEB] and $Al(OiPr)_3$ were purchased from Aldrich Chemical Co., and used as received. Complex $MoOCl_2(PMe_3)_3$ was prepared according to the literature.[21,23] A slight modification of the procedure described in ref.[21] with use of complex $MoCl_4(EtO)_2$ instead of $MoCl_4(THF)_2$ as starting material gave the product in the form of a blue solid containing a small percentage of the $MoCl_3(PMe_3)_3$ byproduct, as shown by $^1H$ NMR spectroscopy.[20] The procedure described in ref.[23] afforded a pure product (deep blue solid) in 70% yield.

**Physical Measurements:** The cyclic voltammograms were obtained with an EG&G 362 potentiostat connected to a Macintosh computer through MacLab hardware/software. The electrochemical cell was fitted with an Ag/AgCl reference electrode, a platinum disk working electrode and a platinum wire counter electrode. $[Bu_4N]PF_6$ (about 0.1 M) was used as supporting electrolyte. The ferrocene standard was added to each solution and measured at the end of the experiments. Its potential was $E_{1/2}$ = +0.50 V under our experimental conditions. NMR spectra were recorded with a Bruker DRX 400 MHz spectrometer. The peak positions are reported with positive shifts in ppm downfield of TMS, as calculated from residual solvent peaks. Digital simulation of the $^{31}P$ NMR spectrum was carried out with MestReC.[26] The molecular weight distribution, $\bar{M}_n$ and $\bar{M}_w/\bar{M}_n$ of the polymers, was measured by size-exclusion chromatography (SEC) using THF as eluent (1 mL/min) at room temperature on a 300 × 7.5 mm PLgel 5-μm Mixed-D column (Polymer Laboratories), equipped with multiangle light scattering (miniDawn Tristar, Wyatt Technology Corp.) and refractive index (RI2000, Soparès) detectors.

**Synthesis of $MoOI_2(PMe_3)_3$:** An excess of NaI (795 mg, 5.3 mmol) was added to a solution of $MoOCl_2(PMe_3)_3$ (435 mg, 1.06 mmol) in freshly distilled THF (15 mL). The solution was then stirred at 50 °C for 2 h to achieve completion, although after 10 min it was possible to observe the formation of a white precipitate of NaCl. After removing the volatiles under reduced pressure, the crude residue was redissolved in toluene (15 mL) to eliminate the insoluble salts of NaI and NaCl. Then pentane (25 mL) was added to the toluene solution to precipitate complex $MoOI_2(PMe_3)_3$ as an emerald-green solid, which was filtered and washed with pentane (2 × 10 mL). Yield 314 mg, 50%. Single crystals for X-ray diffraction were obtained by slow diffusion of pentane into a concentrated solution of the product in toluene. The NMR properties are collected in Table 1. $C_9H_{27}I_2MoOP_3$ (593.98): calcd. C 18.20, H 4.58; found C 18.30, H 4.28. The compound was soluble and stable in THF, acetone, and aromatic hydrocarbons. It dissolved in $CDCl_3$ but gave rise to rapid halogen exchange in this solvent.

**X-ray Structural Studies:** A single crystal of each compound was mounted under inert perfluoropolyether on the tip of a glass fiber and cooled in the cryostream of either a Stoe IPDS diffractometer [for $MoOI_2(PMe_3)_3$] or an Oxford-Diffraction XCALIBUR CCD diffractometer [for $\{MoCl_2O(PMe_3)(OPMe_3)\}_2O$]. The structures were solved by direct methods (SIR97)[27] and refined by least-squares procedures on $F^2$ using SHELXL-97.[28] All H atoms attached to carbon atoms were introduced in idealized positions and treated as riding models. The absolute structure for $MoOI_2(PMe_3)_3$ was confirmed by the refinement of Flack's enantiopole parameter[29,30] and by careful examination of the sensitive reflections. The drawing of the molecules was realized with the help of ORTEP32.[31] Crystal data and refinement parameters are shown in Table 4. CCDC-294667 and -294668 contain the supplementary crystallographic data for this paper. These data can be obtained free of charge from The Cambridge Crystallographic Data Centre via www.ccdc.cam.ac.uk/data_request/cif.

**Controlled Radical Polymerizations:** All ATRP polymerization reactions were conducted according to the same experimental procedure. A typical procedure is described as a representative example. $MoOCl_2(PMe_3)_3$ (54 mg, 0.13 mmol) was added to a 25-mL Schlenk tube equipped with a stirring bar. Styrene (3 mL, 26 mmol), toluene (6 mL), and (1-bromoethyl)benzene (17.7 μL, 0.13 mmol) were added to the reaction flask by a syringe after a 20-min Ar purge. The Schlenk tube was immersed in an oil bath heated at 90 °C. Aliquots were withdrawn periodically for monitoring. All OMRP polymerization reactions were conducted according to the same experimental procedure. A typical procedure is described as a representative example. $MoOI_2(PMe_3)_3$ (21 mg, 0.035 mmol) and AIBN (2.9 mg, 0.018 mmol) were added to a 15-mL Schlenk tube equipped with a stirring bar. Styrene (1 mL, 8.7 mmol) and toluene (2 mL) were added to the reaction flask by a syringe after a 20-min Ar purge. The Schlenk tube was immersed during 30 min in an oil bath heated at 100 °C and at 80 °C for the

 © 2006 Wiley-VCH Verlag GmbH & Co. KGaA, Weinheim 

Table 4. Crystal data and structure refinement.

| Compound | $MoOI_2(PMe_3)_3$ | $[MoCl_2O(PMe_3)(OPMe_3)]_2O$ |
|---|---|---|
| Empirical formula | $C_9H_{27}I_2MoOP_3$ | $C_{12}H_{36}Cl_4Mo_2O_5P_4$ |
| Formula mass | 593.96 | 717.97 |
| Temperature [K] | 180(2) | 180(2) |
| Wavelength [Å] | 0.71073 | 0.71073 |
| Crystal system | orthorhombic | monoclinic |
| Space group | $P2_12_12_1$ | $P2_1/c$ |
| $a$ [Å] | 9.9624(8) | 16.6058(18) |
| $b$ [Å] | 10.6370(10) | 11.8087(12) |
| $c$ [Å] | 18.8084(19) | 16.099(2) |
| $\beta$ [°] | | 113.384(11) |
| Volume [Å$^3$] | 1993.1(3) | 2897.7(6) |
| $Z$ | 4 | 4 |
| Density (calcd.) [Mg/m$^3$] | 1.979 | 1.646 |
| $\mu$ [mm$^{-1}$] | 3.982 | 1.474 |
| $F$(000) | 1128 | 1440 |
| Crystal size [mm] | $0.38 \times 0.32 \times 0.28$ | $0.14 \times 0.09 \times 0.08$ |
| θ range [°] | 2.17–26.09 | 2.85–26.37 |
| Reflections collected | 19690 | 21350 |
| Unique refl. ($R_{int}$) | 3874 (0.0455) | 5900 (0.0663) |
| Completeness to θ [%] | 98.1 (26.09°) | 99.8 (26.37°) |
| Absorption correction | semiempirical | semiempirical |
| Max. and min. trans. | 0.4148 and 0.2387 | 0.8737 and 0.8359 |
| Refinement method | full-matrix least squares on $F^2$ | full-matrix least squares on $F^2$ |
| Data/restraints/parameters | 3874/0/154 | 5900/0/256 |
| Goodness-of-fit on $F^2$ | 1.087 | 0.782 |
| Final $R$ indices [$I > 2\sigma(I)$] | $R_1 = 0.0287$, $wR_2 = 0.0816$ | $R_1 = 0.0379$, $wR_2 = 0.0554$ |
| $R$ indices (all data) | $R_1 = 0.0295$, $wR_2 = 0.0822$ | $R_1 = 0.0899$, $wR_2 = 0.0648$ |
| Absolute structure parameter | 0.00(2) | |
| Residual density [e/Å$^3$] | 0.951 and –1.437 | 0.557 and –0.470 |

remainder of the reaction. Aliquots were withdrawn periodically for monitoring. The yield of polymer, and thus the percentage conversion, for each withdrawn aliquot was calculated by the mass ratio before and after the complete removal of solvent and residual monomer by evaporation, until achievement of constant weight.

## Acknowledgments

We are grateful to the CNRS for support of this work and to Sandrine Vincendeau for technical assistance. J. A. M. thanks the Ministerio de Educación y Ciencia of Spain for a post-doctoral fellowship. S. M. thanks the Conseil Régional de Bourgogne and the CNRS for a BDI fellowship.

[1] K. Matyjaszewski, J. H. Xia, *Chem. Rev.* **2001**, *101*, 2921–2990.
[2] M. Kamigaito, T. Ando, M. Sawamoto, *Chem. Rev.* **2001**, *101*, 3689–3745.
[3] R. Poli, *Angew. Chem. Int. Ed.*, in press.
[4] Y. Kabachii, S. Kochev, L. Bronstein, I. Blagodatskikh, P. Valetsky, *Polym. Bull.* **2003**, *50*, 271–278.
[5] E. Le Grognec, J. Claverie, R. Poli, *J. Am. Chem. Soc.* **2001**, *123*, 9513–9524.
[6] F. Stoffelbach, D. M. Haddleton, R. Poli, *Eur. Polym. J.* **2003**, *39*, 2099–2105.
[7] Y. Kotani, M. Kamigaito, M. Sawamoto, *Macromolecules* **1999**, *32*, 2420–2424.
[8] Y. Kotani, M. Kamigaito, M. Sawamoto, *Macromolecules* **1999**, *32*, 6877–6880.
[9] V. C. Gibson, R. K. O'Reilly, W. Reed, D. F. Wass, A. J. P. White, D. J. Williams, *Chem. Commun.* **2002**, 1850–1851.
[10] T. Ando, M. Kamigaito, M. Sawamoto, *Macromolecules* **2000**, *33*, 6732–6737.
[11] H. Uegaki, Y. Kotani, M. Kamigaito, M. Sawamoto, *Macromolecules* **1997**, *30*, 2249–2253.
[12] H. Uegaki, M. Kamigaito, M. Sawamoto, *J. Polym. Sci., Part A: Polym. Chem.* **1999**, *37*, 3003–3009.
[13] J. Guo, Z. Han, P. Wu, *J. Mol. Catal. A: Chem.* **2000**, *159*, 77–83.
[14] S. Maria, F. Stoffelbach, J. Mata, J.-C. Daran, P. Richard, R. Poli, *J. Am. Chem. Soc.* **2005**, *127*, 5946–5956.
[15] F. Stoffelbach, R. Poli, *Chem. Commun.* **2004**, 2666–2667.
[16] R. Poli, F. Stoffelbach, S. Maria, J. Mata, *Chem. Eur. J.* **2005**, *11*, 2537–2548.
[17] J. U. Desai, J. C. Gordon, H.-B. Kraatz, V. T. Lee, B. E. Owens-Waltermire, R. Poli, A. L. Rheingold, C. B. White, *Inorg. Chem.* **1994**, *33*, 3752–3769.
[18] J. C. Gordon, S. P. Mattamana, R. Poli, P. E. Fanwick, *Polyhedron* **1995**, *14*, 1339–1342.
[19] F. A. Cotton, R. Poli, *Inorg. Chem.* **1987**, *26*, 1514–1518.
[20] K. Yoon, G. Parkin, A. L. Rheingold, *J. Am. Chem. Soc.* **1991**, *113*, 1437–1438.
[21] E. Carmona, A. Galindo, L. Sanchez, A. J. Nielson, G. Wilkinson, *Polyhedron* **1984**, *3*, 347–352.
[22] F. Stoffelbach, D. Saurenz, R. Poli, *Eur. J. Inorg. Chem.* **2001**, 2699–2703.
[23] T. Robin, F. Montilla, A. Galindo, C. Ruiz, J. Hartmann, *Polyhedron* **1999**, *18*, 1485–1490.
[24] F. A. Cotton, L. M. Daniels, S. Herrero, *Acta Crystallogr., Sect. C: Cryst. Struct. Commun.* **1999**, *55*, IUC9900018.
[25] J. E. Huheey, E. A. Keiter, R. L. Keiter, *Inorganic Chemistry – Principles of Structure and Reactivity*, 4th ed., Harper & Row, New York, **1993**.
[26] *MestReC*, v. 446, Mestrelab Research, Santiago de Compostela, Spain, **2005**.

 © 2006 Wiley-VCH Verlag GmbH & Co. KGaA, Weinheim 

[27] A. Altomare, M. Burla, M. Camalli, G. Cascarano, C. Giacovazzo, A. Guagliardi, A. Moliterni, G. Polidori, R. Spagna, *J. Appl. Crystallogr.* **1999**, *32*, 115–119.
[28] G. M. Sheldrick, *SHELXL97, Program for Crystal Structure Refinement*, University of Göttingen, Göttingen, Germany, **1997**.
[29] H. D. Flack, *Acta Crystallogr., Sect. A: Found. Crystallogr.* **1983**, *39*, 876–881.
[30] G. Bernardinelli, H. D. Flack, *Acta Crystallogr., Sect. A: Found. Crystallogr.* **1985**, *41*, 500–511.
[31] L. J. Farrugia, *J. Appl. Crystallogr.* **1997**, *30*, 565.

Received: February 22, 2006
Published Online: April 21, 2006

 © 2006 Wiley-VCH Verlag GmbH & Co. KGaA, Weinheim 

DOI: 10.1002/ejic.200600174

# Stepwise Sulfuration of the Terminal Phosphido Complex *trans*-[PtCl(PHCy$_2$)$_2$(PCy$_2$)]: Synthesis of [Pt(κ$^2$*S*,*S*′-PS$_2$Cy$_2$)(PHCy$_2$)$_2$]Cl and [Pt(κ$^2$*S*,*S*′-PS$_2$Cy$_2$){κ*P*-P(S)Cy$_2$}(PHCy$_2$)] and Crystal Structure of [Pt(κ$^2$-*S*,*S*-PCy$_2$S$_2$)(κ-*S*-PCy$_2$S$_2$)(PHCy$_2$)]

**Vito Gallo,[a] Mario Latronico,[a,b] Piero Mastrorilli,*[a] Cosimo Francesco Nobile,[a] Giuseppe Ciccarella,[c] and Ulli Englert[d]**

**Keywords:** Platinum / Terminal phosphides / Phosphanyl sulfides / Phosphanyldithioates / Phosphorus

The terminal phosphido complex *trans*-[PtCl(PHCy$_2$)$_2$(PCy$_2$)] (**1**) has been prepared, exploiting the reversibility of the reaction with HCl, by action of 1,8-diazabicyclo[5.4.0]undec-7-ene (DBU) on [PtCl(PHCy$_2$)$_3$]Cl, and its reactivity towards elemental sulfur studied. The first product obtained by reaction of **1** with 1 equiv. of sulfur is *trans*-[PtCl(PHCy$_2$)$_2${κ*P*-P(S)Cy$_2$}] (**2**), which rapidly isomerises in halogenated solvents into *cis*-[PtCl(PHCy$_2$)$_2${κ*P*-P(S)Cy$_2$}] (**3**). Further addition of sulfur causes the formation of a mixture of [Pt(κ$^2$*S*,*S*′-PS$_2$Cy$_2$)(PHCy$_2$)$_2$]Cl (**4**) and [Pt(κ$^2$*S*,*S*′-PS$_2$Cy$_2$){κ*P*-P(S)Cy$_2$}(PHCy$_2$)] (**5**), which could be selectively synthesised; the first upon sulfuration of pure **3** and the second by reaction of **4** with 1 equiv. of sulfur in the presence of DBU. Complex **5** can be further sulfurated to [Pt(κ$^2$*S*,*S*′-PCy$_2$S$_2$)(κ*S*-PCy$_2$S$_2$)(PHCy$_2$)] (**6**), which is fluxional in solution and was also characterised by single-crystal X-ray diffraction.
(© Wiley-VCH Verlag GmbH & Co. KGaA, 69451 Weinheim, Germany, 2006)

## Introduction

Terminal phosphides are interesting albeit rare ligands, the reactivity of which depends mainly on the characteristics of the lone pair on the phosphorus atom. The first terminal phosphido complexes were prepared in 1968 by reaction of CpFe(CO)$_2^-$ or CpMo(CO)$_3^-$ with P(C$_6$F$_5$)$_2$Cl to give Cp(CO)$_2$Fe[P(C$_6$F$_5$)$_2$] and Cp(CO)$_3$Mo[P(C$_6$F$_5$)$_2$], respectively.[1] From then on, a number of terminal phosphido complexes have been prepared mainly by two routes: (i) the reaction of diorganometal phosphides with a metal species;[2–16] (ii) the deprotonation of a coordinated phosphane bearing at least a P–H bond by means of an appropriate base {1,8-diazabicyclo[5.4.0]undec-7-ene (DBU),[17–19] methoxide, OH$^-$,[20–24] *t*BuO$^-$,[25–29] [N(SiMe$_3$)$_2$]$^-$,[30–32] NEt$_3$,[33] BuLi[34]} that, in some instances, was previously coordinated onto the metal atom.[35–39]

The reactivity of terminal phosphido complexes is determined by the presence of the lone pair on the phosphorus atom, which renders such molecules highly nucleophilic. Such high nucleophilicity has been exploited for the synthesis of phosphido-bridged heterodimetallic species,[40] and is also responsible for the ease of protonation of the three-coordinate phosphorus atom[13,20,41–43] as well as for its reactivity with MeI.[41,43–47]

The typical reaction of coordinated terminal phosphides with chalcogens transforms the trivalent into a pentavalent phosphorus atom bound to the chalcogen as in Scheme 1.

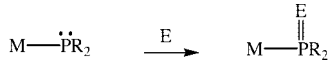


Scheme 1. Typical addition of chalcogens E to coordinated terminal phosphides.

Such reactivity is shown by Ir(CO)(Cl)$_2$(PEt$_3$)$_2$(PF$_2$) (reaction with O$_2$, S$_8$ or Se),[48] (η$^5$-C$_5$H$_5$)Ru(PEt$_3$)$_2$(PPh$_2$) (reaction with O$_2$),[25] (η$^5$-C$_5$H$_5$)Re(NO)(PPh$_3$)$_2$(PR$_2$) (R = Ph, *t*Bu, reaction with O$_2$),[28] (η$^5$-C$_5$H$_5$)Fe(CO)$_2$[P(CF$_3$)$_2$] (reaction with S$_8$),[49] (η$^5$-C$_5$H$_5$)M(CO)$_3$(PCl$_2$) (M = Cr, reaction with S$_8$; M = W, reaction with S$_8$, Se)[50] and (η$^5$-C$_5$H$_5$)M(CO)$_2$(L)(PPh$_2$) (L = CO or PMe$_3$, M = Mo, reaction with S$_8$; M = W, reaction with S$_8$, Se).[41,51]

We have recently described the synthesis and characterisation of *trans*-[PtCl(PHCy$_2$)$_2$(PCy$_2$)Cl] (**1**) obtained by reaction of *cis*-PtCl$_2$(PHCy$_2$)$_2$ with LiPCy$_2$.[52] Complex **1** is stable under inert gases but reacts promptly with dry dioxygen to give the hydrogen-bound bis(phosphinito) complex [PtCl(PHCy$_2$){P(O)Cy$_2$}$_2$H][53] and with hydrogen peroxide to give *trans*-[PtCl(PHCy$_2$)$_2${κ*P*-P(O)Cy$_2$}Cl].[54]

[a] Dipartimento di Ingegneria delle Acque e di Chimica, Polytechnic of Bari,
Via Orabona 4, 70125 Bari, Italy
[b] Dipartimento di Ingegneria e Fisica dell'Ambiente,
Viale dell'Ateneo Lucano 10, 85100 Potenza, Italy
[c] Dipartimento di Ingegneria dell'Innovazione, University of Lecce,
Via Monteroni, 73100 Lecce, Italy
[d] Institut für Anorganische Chemie der RWTH,
Landoltweg. 1, 52074 Aachen, Germany
Supporting information for this article is available on the WWW under http://www.eurjic.org or from the author.

 © 2006 Wiley-VCH Verlag GmbH & Co. KGaA, Weinheim 

Herein we describe the stepwise sulfuration of **1** leading to the compounds *trans*-[PtCl(PHCy$_2$)$_2${κ*P*-P(S)Cy$_2$}] (**2**), *cis*-[PtCl(PHCy$_2$)$_2${κ*P*-P(S)Cy$_2$}Cl] (**3**), [Pt(κ$^2$*S*,*S*′-PS$_2$Cy$_2$)(PHCy$_2$)$_2$]Cl (**4**), [Pt(κ$^2$*S*,*S*′-PCy$_2$S$_2$)(PHCy$_2$){κ*P*-P(S)Cy$_2$}] (**5**) and [Pt(κ$^2$*S*,*S*′-PCy$_2$S$_2$)(κ*S*-PCy$_2$S$_2$)(PHCy$_2$)] (**6**).

## Results and Discussion

### Reversible Protonation of 1

Reaction of *trans*-[PtCl(PHCy$_2$)$_2$(PCy$_2$)] (**1**) with gaseous HCl results in the fast and complete protonation of the coordinated terminal phosphide with formation of the cationic Pt$^{II}$ complex [PtCl(PHCy$_2$)$_3$]Cl (**7**). In order to test the reversibility of the protonation reaction of **1**, a toluene suspension of **7** was treated with DBU, leading to the quantitative formation of **1** as the only soluble product, so that the reaction sequence shown in Scheme 2 represents the most convenient way for preparing **1**.

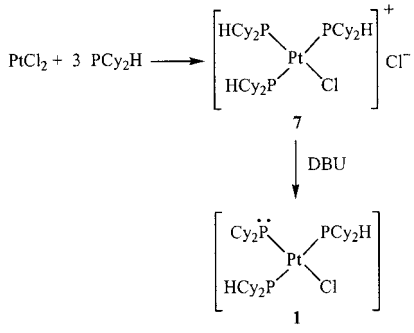


Scheme 2.

### Reaction with $S_8$

Reaction of **1** with sulfur carried out in toluene at room temperature using an S/Pt molar ratio of 1.0 resulted in the formation of the *P*-bound thiophosphinito complex *trans*-[PtCl(PHCy$_2$)$_2${κ*P*-P(S)Cy$_2$}] (**2**).[54] Dissolving **2** in halogenated solvents, the irreversible isomerisation into the thermodynamically favoured *cis* complex **3** took place as indicated in Scheme 3. This isomerisation was completed in 5 min by heating the reaction mixture at 40 °C.

When an excess of sulfur (S/Pt molar ratio of 8) was treated with **1** in toluene, the reaction led, after 1 h, to a mixture of two new sulfur-containing platinum complexes, **4** and **5**, along with *cis*-PtCl$_2$(PHCy$_2$)$_2$ and dicyclohexylphosphane sulfide P(S)HCy$_2$ (Scheme 4).

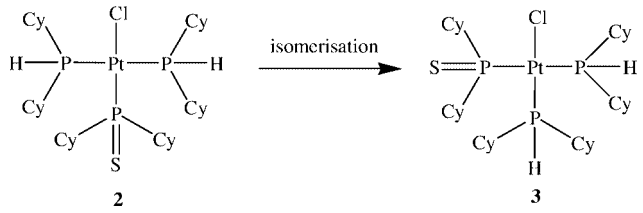


Scheme 3.

Complex **4**, which incorporates two S atoms, showed two $^{31}$P{$^1$H} NMR signals in CDCl$_3$ at $\delta$ = 136.6 ($^2J_{P,Pt}$ = 151 Hz) and $\delta$ = 2.0 ($^1J_{P,Pt}$ = 3048 Hz), which support a structure in which the sulfur atoms are bound to the phosphide P atom and chelate the platinum atom. The remaining coordination sites are occupied by two PHCy$_2$ ligands, mutually *cis*. Accordingly, the $^{195}$Pt{$^1$H} NMR spectrum in CDCl$_3$ consists of a triplet ($^1J_{Pt,P}$ = 3048 Hz) of doublets ($^2J_{Pt,P}$ = 151 Hz) centred at $\delta$ = –4596 ppm. Compound **4** can be therefore formulated as [Pt(κ$^2$*S*,*S*′-PS$_2$Cy$_2$)(PHCy$_2$)$_2$]Cl, a dithiophosphinato complex of Pt$^{II}$. ESI-MS analysis confirmed this formulation by comparison of the measured isotope pattern centred at 852.35 Da with that calculated on the basis of the natural abundances.

Recording the $^{31}$P{$^1$H} and $^1$H NMR spectra of **4** in different solvents, we noticed that the resonance of (PS$_2$Cy$_2$) remained almost unchanged ($\delta$ = 134–138 ppm), whilst the chemical shift of the coordinated PHCy$_2$ ligand ranged from $\delta$ = –5.9 to 10.0 ppm ($^{31}$P) and from $\delta$ = 4.3 to 6.8 ppm ($^1$H) (Table 1).

Table 1. $^{31}$P{$^1$H} and $^1$H NMR spectroscopic data of **4** in different solvents.

| | *P*S$_2$ | *P*H | P*H* |
|---|---|---|---|
| C$_6$D$_6$ | 134 | –5.9 | 6.83 |
| CDCl$_3$ | 137 | 2.0 | 5.15 |
| CD$_2$Cl$_2$ | 139 | 9.3 | 4.32 |
| CD$_3$CN | 140 | 10.0 | 4.43 |

Such behaviour could be explained invoking a hydrogen bond interaction between the P–H of the cationic complex and the chloride anion, an interaction already found for [PtCl(PCy$_2$H)$_3$]Cl.[54] In order to confirm such a hypothesis we have compared the $^{35}$Cl NMR spectra recorded in CD$_2$Cl$_2$ before and after the addition of CD$_3$OD as a hydrogen bond breaker. No signal could be observed in the $^{35}$Cl NMR spectrum recorded in CD$_2$Cl$_2$, as expected for a

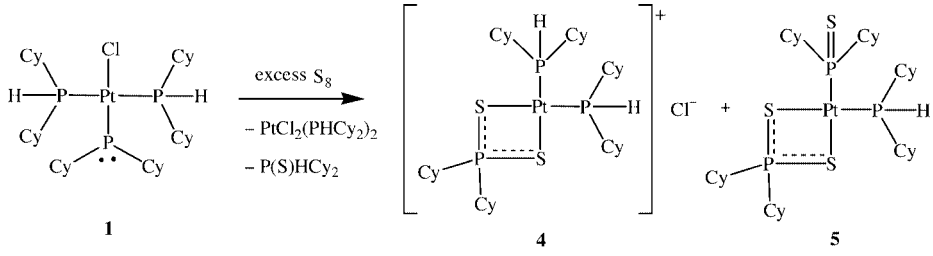


Scheme 4.

 © 2006 Wiley-VCH Verlag GmbH & Co. KGaA, Weinheim 

quadrupolar nucleus surrounded by an asymmetric electron cloud. However, the addition of a few drops of $CD_3OD$ caused the rupture of the ion pairs, leaving the chloride anion in a nearly symmetric solvation sphere, and permitted the observation of a broad $^{35}Cl$ NMR signal centred at $\delta$ = –18 ppm after the same number of scans (Figure 1).

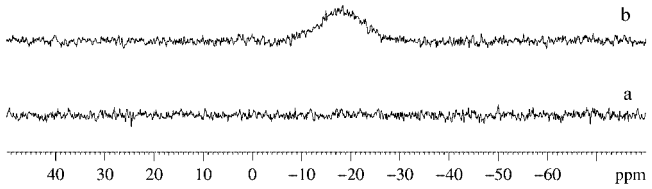


Figure 1. $^{35}Cl$ NMR spectrum of **4** (39 MHz, 295 K); a) in $CD_2Cl_2$; b) after the addition of a few drops of $CD_3OD$.

Pure **4** could be isolated from the reaction of **3** with 1 equiv. $S_8$ in dichloromethane at room temperature and showed IR bands ascribable to PH (2272 $cm^{-1}$) and $PS_2$ stretchings (591, 553 $cm^{-1}$).

Complex **5** incorporates three atoms of S and gives in $C_6D_6$ three $^{31}P\{^1H\}$ NMR signals flanked by $^{195}Pt$ satellites at $\delta$ = 127.2, 48.4 and 38.9 ppm. Of these, that at $\delta$ = 38.9 ppm can be attributed to a coordinated $PHCy_2$ ligand (proton-coupled spectrum gave $^1J_{P,H}$ = 424 Hz) and that at $\delta$ = 48.4 ppm can be attributed, on the basis of its chemical shift and $^1J_{P,Pt}$ value (2977 Hz), to a *P*-bound $P(S)Cy_2$ ligand *cis* to $PHCy_2$. The remaining signal at $\delta$ = 127.2 ppm is flanked by satellites from which a $^2J_{P,Pt}$ value of 137 Hz was extracted and can be attributed to a chelating dithiophosphinate ligand, $PS_2Cy_2$. The $^{195}Pt\{^1H\}$ NMR spectrum consists of a doublet of doublets of doublets centred at $\delta$ = –4522 ppm and the proposed structure for **5** is [Pt($\kappa^2$*S*,*S*′-$PS_2Cy_2$){κ*P*-$P(S)Cy_2$}($PHCy_2$)].

Complex **5** could be obtained in high yield by treating **4** with $S_8$ in the presence of DBU as proton scavenger, and showed P=S (of the thiophosphinite ligand) and PH IR stretchings at 597 and 2366 $cm^{-1}$ respectively. Comparison of the IR features of complexes **2**, **4** and **5** allowed us to assign the $\nu PS_2$ bands of **5** at 556 ($\nu_{sym.}$) and 597 ($\nu_{asym.}$). Such assignments are consistent with those reported for $R_2PS_2$ complexes.[55–57]

A mechanism for the reaction of **1** with excess sulfur in $CH_2Cl_2$ is depicted in Scheme 5. The initially formed **2** par-

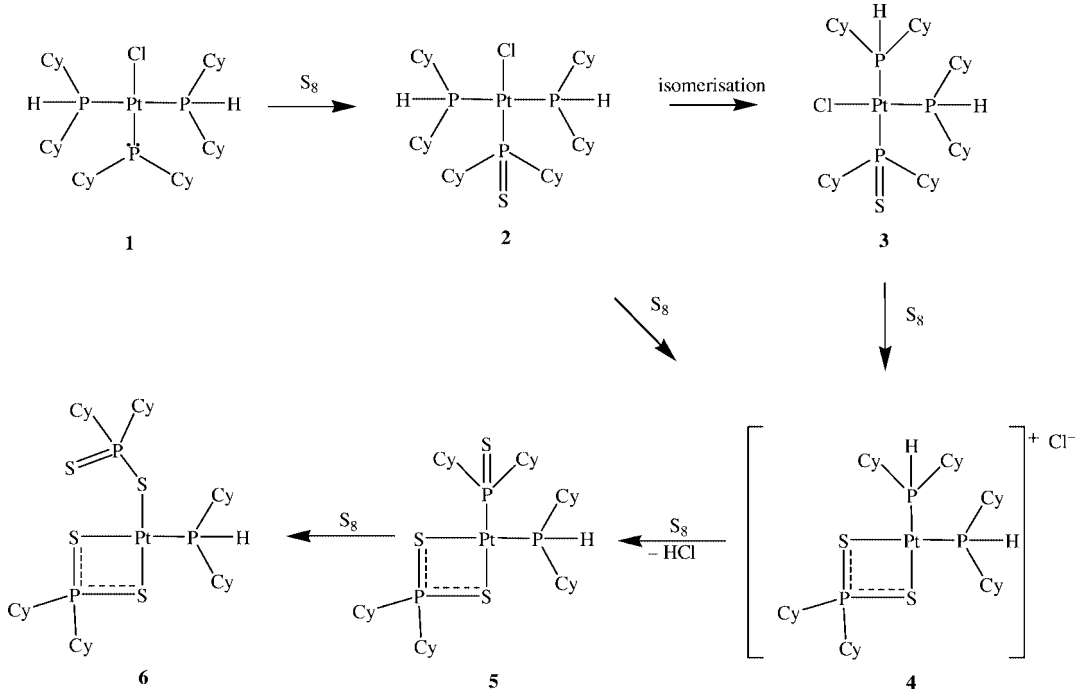


Scheme 5. Stepwise sulfuration of **1**.

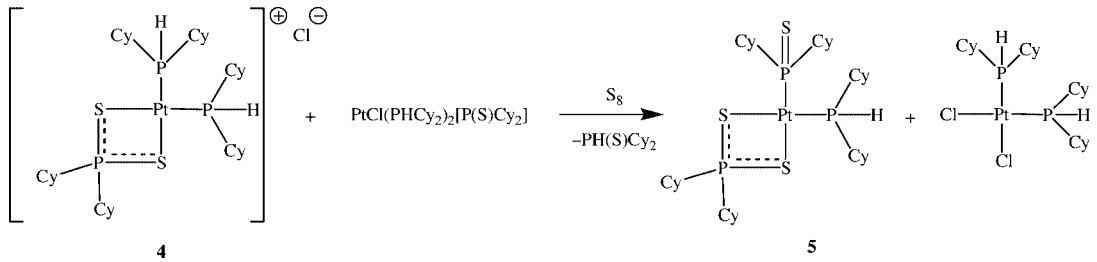


Scheme 6.

 © 2006 Wiley-VCH Verlag GmbH & Co. KGaA, Weinheim 

tially isomerises into **3**. Both **2** and **3** can incorporate one more S atom yielding **4**. The subsequent sulfuration of **4** into **5** requires a proton scavenger, as confirmed by the lack of reaction between **4** and $S_8$ in the absence of DBU.

In the reaction medium, possible proton scavengers are the thiophosphinite complexes **2** and **3**, whose products of HCl formal addition are P(S)HCy$_2$ and Pt(PHCy$_2$)$_2$Cl$_2$, effectively found as byproducts (Scheme 6).

Compound **5** reacted slowly (several weeks) with elemental sulfur in toluene solution to give the bis(dithiophosphinato)phosphane product Pt(κ$^2$*S*,*S*-PCy$_2$S$_2$)(κ*S*-PCy$_2$S$_2$)(PHCy$_2$) (**6**, Scheme 5), which precipitated from the reaction medium.

Complex **6** showed IR bands in the PS region (650–500 cm$^{-1}$) attributable to bidentate (620 and 527 cm$^{-1}$) and unidentate (598 and 559 cm$^{-1}$) PCy$_2$S$_2$ ligands (Table 2).[55,58]

Table 2. Characteristic IR bands in the PS region.

| Complex | P(S)Cy$_2$ | PS$_2$Cy$_2$ Bidentate | | PS$_2$Cy$_2$ Monodentate | |
|---|---|---|---|---|---|
| | $\nu$ | $\nu_{sym.}$ | $\nu_{asym.}$ | $\nu_{sym.}$ | $\nu_{asym.}$ |
| **2** | 579 | | | | |
| **3** | 577 | | | | |
| **4** | | 553 | 591 | | |
| **5** | 597 | 556 | 597 | | |
| **6** | | 559 | 598 | 527 | 620 |
| **8** | | 561 | 595 | | |

The $^{31}$P{$^1$H} NMR spectrum of **6** in C$_6$D$_6$ showed three resonances at $\delta$ = 124.8, 81.8 and 2.5 ppm ascribable to bidentate PCy$_2$S$_2$, unidentate PCy$_2$S$_2$ and PHCy$_2$, respectively. Complexes of the general formula M(PS$_2$)$_2$(P) (where PS$_2$ represents a dithiophosphinato and P a tertiary phosphane) have long been known as the reaction products between M(PS$_2$)$_2$ and P in polar solvents[55] and, in fact, we could prepare **6** in high yield also starting from [Pt(κ$^2$*S*,*S*′-PCy$_2$S$_2$)$_2$] (**8**) and 1 equiv. of PHCy$_2$ in toluene.

As already noticed for related complexes,[59–61] dynamic $^{31}$P{$^1$H} and $^{195}$Pt{$^1$H} NMR experiments (Figures 2 and 3) demonstrated the existence, for compound **6**, of a rapid interchange of bidentate and unidentate dithiophosphinates (Scheme 7).

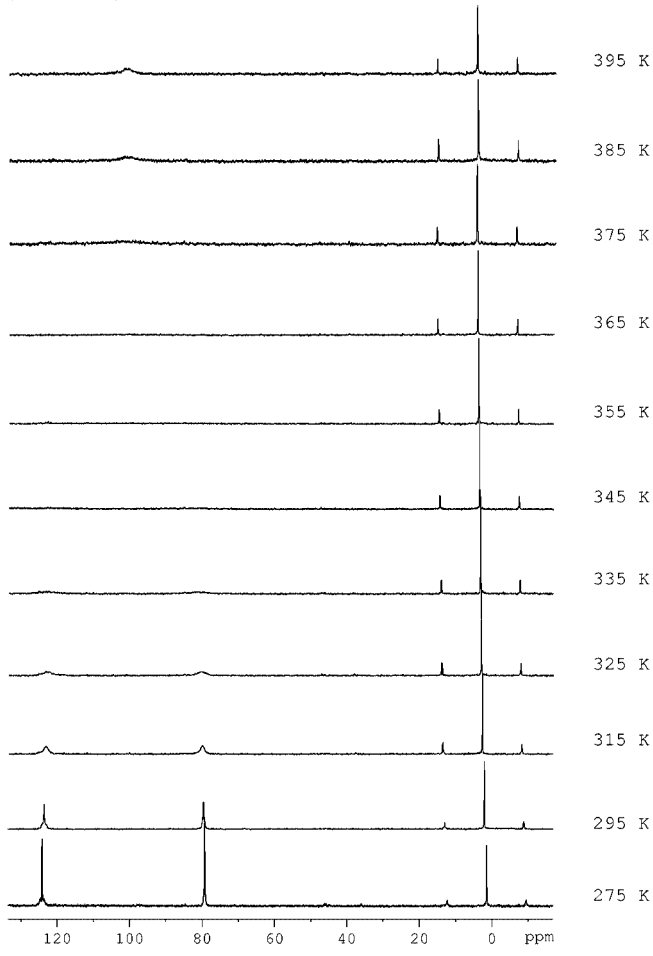


Figure 2. Variable-temperature $^{31}$P{$^1$H} NMR spectra of **6** in 1,2-dichlorobenzene.

Accordingly, the $^{31}$P EXSY experiment showed an intense exchange cross-peak between the signals at $\delta$ = 124.8 ppm (bidentate PS$_2$Cy$_2$) and $\delta$ = 81.8 ppm (uniden-

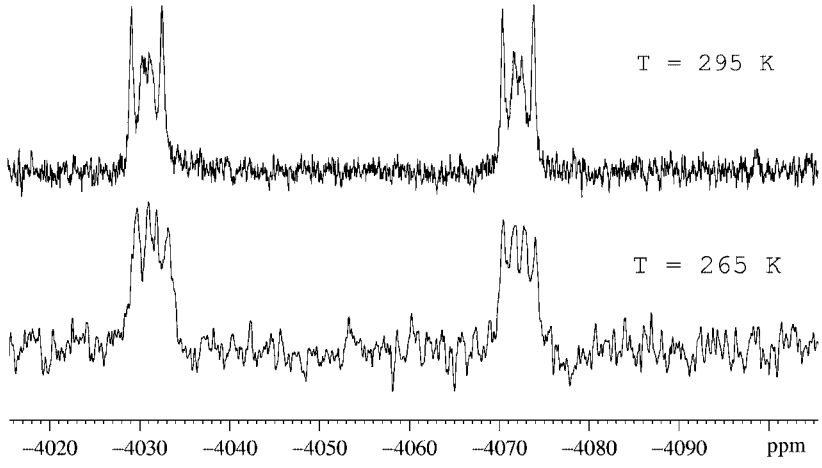


Figure 3. Variable-temperature $^{195}$Pt{$^1$H} NMR spectra of **6** in CDCl$_3$.

 © 2006 Wiley-VCH Verlag GmbH & Co. KGaA, Weinheim 

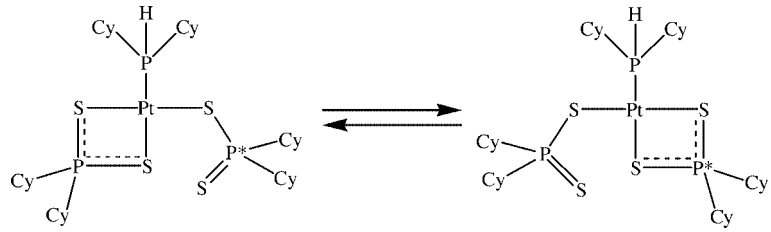

Scheme 7.

tate $PS_2Cy_2$) (Figure 4). Variable-temperature $^{31}P\{^1H\}$ NMR spectra allowed us to calculate an activation $\Delta G^{\ddagger}$ value of 59 ± 1 kJ/mol. Such a value is fully consistent with those obtained in the related complexes $Pt(Me_2PS_2)(PPh_3)$ ($\Delta G^{\ddagger}$ = 56 kJ/mol),[60,62] $Pt(Me_2PS_2)(PPh_2C_6F_5)$ ($\Delta G^{\ddagger}$ = 55 kJ/mol)[62] and $Pt\{(OEt)_2PS_2\}(PPh_3)$ ($\Delta G^{\ddagger}$ = 52 kJ/mol).[60,61]

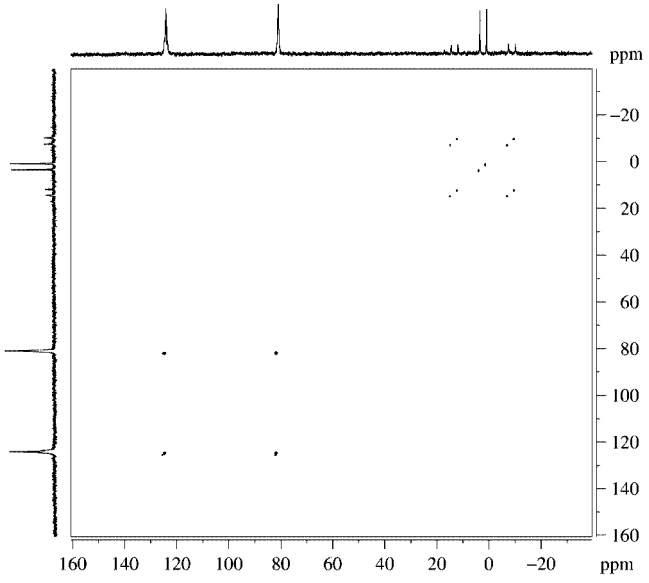


Figure 4. $^{31}P$ EXSY spectrum of **6** in $C_6D_6$.

Yellow crystals of **6** suitable for single-crystal X-ray diffraction were deposited upon slow concentration of a toluene solution. Complex **6** crystallises in the monoclinic space group $P2_1/c$ with one complex molecule in the asymmetric unit. The molecular structure, depicted in Figure 5, is characterised by a distorted square-planar geometry around the Pt atom. The Pt atom is bound to two $PCy_2S_2^-$ ligands, one of which is chelating whereas the other one is unidentate. The Pt–S(1) [2.3419(16) Å] and Pt–S(3) [2.3024(15) Å] bond lengths are shorter than Pt–S(2) [2.4134(15) Å], as expected on the basis of the different *trans* influences of P and S. The structure of **6** resembles that found for the related complex $Pt[(OEt)_2PS_2]_2(PPh_3)$.[61] Both complexes show one uncoordinated sulfur atom at a Pt···S distance of more than 4 Å. The interaction between H(3) and the sulfur atom S(4) not coordinated to Pt is certainly weak: the interatomic distance amounts to 2.91 Å, to be compared with several intra- and intermolecular C–H···S contacts in the range between 2.8 and 3.0 Å. Selected bond lengths and angles are listed in Table 3.

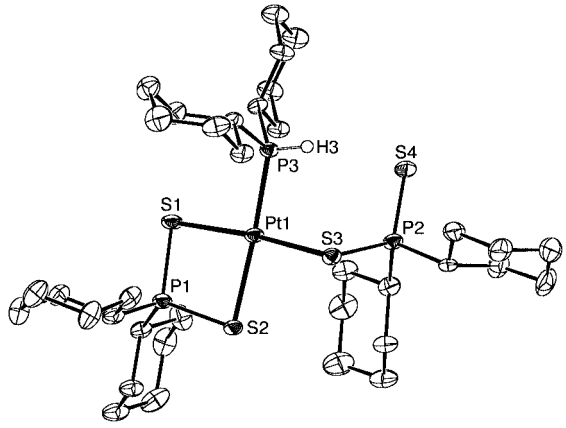


Figure 5. Displacement ellipsoid plot of **6**.[63] Ellipsoids are scaled to 50% probability. Only the phosphorus-bonded hydrogen atom is shown with arbitrary radius; the other H atoms are omitted for clarity.

Table 3. Selected bond lengths [Å] and angles [°] for **6**.

| | |
|---|---|
| Pt(1)–P(3) | 2.2136(15) |
| Pt(1)–S(3) | 2.3024(15) |
| Pt(1)–S(1) | 2.3419(16) |
| Pt(1)–S(2) | 2.4134(15) |
| S(1)–P(1) | 2.024(2) |
| S(2)–P(1) | 2.017(2) |
| S(3)–P(2) | 2.062(2) |
| S(4)–P(2) | 1.964(2) |
| P(3)–Pt(1)–S(3) | 91.20(5) |
| P(3)–Pt(1)–S(1) | 93.89(5) |
| S(3)–Pt(1)–S(1) | 173.92(5) |
| P(3)–Pt(1)–S(2) | 176.44(6) |
| S(3)–Pt(1)–S(2) | 90.58(5) |
| S(1)–Pt(1)–S(2) | 84.16(5) |
| P(1)–S(1)–Pt(1) | 86.17(7) |
| P(1)–S(2)–Pt(1) | 84.44(7) |
| P(2)–S(3)–Pt(1) | 108.61(8) |
| P(3)–H(3)–S(4) | 136 |

## Conclusion

We have demonstrated that the sulfuration of complex **1** occurs stepwise, and involves first the terminal phosphide giving rise to the formation of complexes **2**, **3** and **4** and

 © 2006 Wiley-VCH Verlag GmbH & Co. KGaA, Weinheim 

subsequently one of the coordinated PHCy$_2$ ligands with formation of products **5** and **6**.

## Experimental Section

**General:** All manipulations were carried out under pure argon, using freshly distilled and oxygen-free solvents. Dicyclohexylphosphane (Strem) and $PtCl_2$ (Acros) were used as received. Complexes **2** and **7** were prepared as described elsewhere.[54] Melting points were determined with Gallenkamp equipment and are uncorrected. C, H and S elemental analyses were carried out with a Eurovector CHNS-O Elemental Analyser. Cl elemental analysis was performed by potentiometric titration using a Metrohm DMS Titrino. Infrared spectra were recorded with a Bruker Vector 22 spectrometer. All the ESI-MS spectra were recorded with an Agilent LC-MS SL series instrument adopting the following general conditions: electrospray, positive ions, flow rate 0.200 mL/min, drying gas flow 4.0 L/min, nebuliser pressure 25 psi, drying gas temperature 300 °C, capillary voltage 4000 V, mass range $m/z$ = 400–1400. $CH_2Cl_2$ solutions of the complexes were infused with a Cole-Parmer syringe pump. The isotopic pattern was calculated by the Isotope Pattern Viewer software available free of charge from the www.surfacespectra.com Web site. NMR spectra were recorded with a BRUKER Avance DRX400 spectrometer; frequencies are referenced to $Me_4Si$ ($^1$H and $^{13}$C), 85% $H_3PO_4$ ($^{31}$P), $H_2PtCl_6$ ($^{195}$Pt) and aqueous 1 M NaCl ($^{35}$Cl). The reported temperatures of variable-temperature NMR experiments were calibrated from the chemical shift difference of the signals in the $^1$H NMR spectrum of a standard sample of methanol. The uncertainty in the $\Delta G^{\ddagger}_{Tc}$ value (±1 kJ/mol) was estimated on the basis of the assumption that there is an error of 5 °C in the determination of the coalescence temperature. 2D $^{31}$P EXSY spectra were recorded with a gradient-selected NOESY pulse program from Bruker (noesygpph) with a mixing time of 10 or 50 ms and a relaxation delay of 1.0 s. The spectra were phased to give positive peaks along the diagonal.

***trans*-[Pt(PHCy$_2$)$_2$(PCy$_2$)Cl] (1):**[52] DBU (131 μL, 0.86 mmol) was added to a suspension of **7** (0.74 g, 0.86 mmol in 15 mL of toluene) and the mixture stirred at room temperature for 5 min. The resulting yellow suspension was filtered and pure **1** was obtained as a yellow solid after solvent evaporation (0.63 g, 0.77 mmol, 89%).

**Isomerisation of *trans*-[Pt(PHCy$_2$)$_2${P(S)Cy$_2$}Cl] (2) into *cis*-[Pt(PHCy$_2$)$_2${P(S)Cy$_2$}Cl] (3):** A dichloromethane solution of **2** was stirred at room temperature for 1 h. Pure **3** was obtained after evaporation of the solvent under reduced pressure. The complex is very soluble in halogenated solvents, fairly soluble in toluene, and scarcely soluble in hexane. $C_{36}H_{68}ClP_3PtS$ (856.44): calcd. C 50.49, H 8.00, Cl 4.14, S 3.74; found C 50.92, H 7.85, Cl 4.35, S 3.72. LC-MS: exact mass calcd. for $C_{36}H_{68}ClP_3PtS$: 855.36 amu; found 856 [M + H]$^+$. M.p. 186 °C (dec.). IR (Nujol mull): $\tilde{\nu}_{max}$ = 2272 (w, PH), 1344 (w), 1297 (m), 1268 (m), 1201 (m), 1176 (m), 1115 (m), 1074 (w), 1005 (s), 918 (m), 895 (m), 870 (m), 848 (m), 819 (w), 736 (s), 577 (s, P=S), 511 (m), 411 (w), 400 (w), 388 (w), 298 (m, Pt–Cl), 227 (m) cm$^{-1}$. $^1$H NMR (400 MHz, $CDCl_3$, 295 K): $\delta$ = 5.39 (m, $^1J_{P,H}$ = 383 Hz, P*H trans* Cl), 5.22 [m, $^1J_{P,H}$ = 373, $^2J_{H,Pt}$ = 67 Hz, P*H trans* P(S)] ppm. $^{31}$P{$^1$H} NMR (162 MHz, $CDCl_3$, 295 K): $\delta$ = 67.4 [dd, $^1J_{P,Pt}$ = 1733, $^2J_{P,P}$ = 252, $^2J_{P,P}$ = 16 Hz, P(S)], 11.6 (br. s, $^1J_{P,Pt}$ = 3540, P *trans* Cl), 10.9 [dd, $^1J_{P,Pt}$ = 2822, $^2J_{P,P}$ = 252, $^2J_{P,P}$ = 14 Hz, P *trans* P(S)] ppm. $^{195}$Pt{$^1$H} NMR (86 MHz, $CDCl_3$, 295 K): $\delta$ = –5329 (ddd, $^1J_{P,Pt}$ = 3540, $^1J_{P,Pt}$ = 2822, $^1J_{P,Pt}$ = 1733 Hz) ppm.

**[Pt(κ$^2$*S*,*S*′-PS$_2$Cy$_2$)(PHCy$_2$)$_2$]Cl (4):** A dichloromethane solution of sulfur (9.0 mg, in 2 mL) was slowly added to a stirred $CH_2Cl_2$ solution of **3** (0.230 g, 0.268 mmol in 5 mL) at room temperature. After 2 h, the solvent was removed under reduced pressure and the residue was treated with toluene (5 mL). Addition of *n*-hexane caused the precipitation of **4** as a yellow solid, which was isolated by filtration, washed with *n*-hexane and dried under vacuum. Yield: 0.170 g (71%). The complex was very soluble in halogenated solvents and toluene and scarcely soluble in *n*-hexane. $C_{36}H_{68}ClP_3PtS_2$ (888.51): calcd. C 48.66, H 7.71, Cl 3.99, S 7.22; found 48.45, H 7.83, Cl 4.05, S 6.95. LC-MS: exact mass calcd. for the cationic $C_{36}H_{68}P_3PtS_2$: 852.36 amu; found 852. M.p. 214 °C (dec.). IR (Nujol mull): $\tilde{\nu}_{max}$ = 2274 (w, P–H), 1345 (w), 1296 (m), 1268 (m), 1201 (w), 1172 (m), 1120 (m), 1074 (w), 1005 (s), 918 (s), 888 (m), 850 (m), 820 (m), 752 (w), 727 (m), 591 (m, $\nu$PS$_2$), 553 (s, $\nu$PS$_2$), 515 (m), 466 (s), 406 (m) cm$^{-1}$. $^1$H NMR (400 MHz, $CDCl_3$, 295 K): $\delta$ = 4.19 (m, $^1J_{P,H}$ = 402, $^2J_{Pt,H}$ = 88 Hz, P*H*) ppm. $^{31}$P{$^1$H} NMR (162 MHz, $CDCl_3$, 295 K): $\delta$ = 136.6 (s, $^2J_{P,Pt}$ = 151 Hz, *P*S$_2$Cy$_2$), 2.0 (s, $^1J_{P,Pt}$ = 3048 Hz, *P*HCy$_2$) ppm. $^{35}$Cl NMR (39 MHz, $CD_2Cl_2$, 295 K): $\delta$ = –18 (br.) ppm. $^{195}$Pt{$^1$H} NMR (86 MHz, $CDCl_3$, 295 K): $\delta$ = –4596 (td, $^1J_{P-Pt}$ = 3048, $^2J_{P-Pt}$ = 151 Hz) ppm.

**[Pt(κ$^2$*S*,*S*′-PS$_2$Cy$_2$){κ*P*-P(S)Cy$_2$}(PHCy$_2$)] (5):** DBU (30 μL, 0.202 mmol) was added to a stirred dichloromethane solution (5 mL) containing **4** (0.180 g, 0.202 mmol) and sulfur (7.5 mg). After 10 min, the solvent was removed under reduced pressure and the residue was treated with toluene (5 mL). The resulting suspension was filtered and **5** was obtained as a white solid (0.16 g, 89% yield) after evaporation of the filtrate under reduced pressure. The complex is very soluble in toluene and halogenated solvents, and scarcely soluble in hexane and methanol. $C_{36}H_{67}P_3PtS_3$ (884.11): calcd. C 48.91, H 7.64, S 10.88; found C 48.67, H 7.54, S 11.08. LC-MS: exact mass calcd. for $C_{36}H_{67}P_3PtS_3$: 883.33 amu; found 884 [M + H]$^+$. M.p. 248–250°°C. IR (Nujol mull): $\tilde{\nu}_{max}$ = 2366 (w, PH), 1342 (w), 1328 (w), 1296 (m), 1175 (m), 1111 (m), 1075 (m), 1025 (s), 1002 (s), 889 (m), 848 (s), 817 (m), 756 (m), 736 (s), 597 (s, $\nu$P=S and $\nu$PS$_2$), 556 (s, $\nu$PS$_2$), 510 (m), 467 (w), 403 (m), 400 (m), 352 (w), 316 (m) cm$^{-1}$. $^1$H NMR (400 MHz, $C_6D_6$, 295 K): $\delta$ = 5.24 (br. d, $^1J_{P,H}$ = 424, $^2J_{Pt,H}$ = 72 Hz) ppm. $^{31}$P{$^1$H} NMR (162 MHz, $C_6D_6$, 295 K): $\delta$ = 127.2 (br., $^2J_{P,Pt}$ = 137 Hz, PS$_2$Cy$_2$), 48.4 [br., $^1J_{P,Pt}$ = 2977 Hz, P(S)Cy$_2$], 38.9 (br., $^1J_{P,Pt}$ = 3977 Hz, PHCy$_2$) ppm. $^{195}$Pt{$^1$H} NMR (86 MHz, $C_6D_6$, 295 K): $\delta$ = –4522 (ddd, $^1J_{P,Pt}$ = 3977, $^1J_{P,Pt}$ = 2977, $^2J_{P,Pt}$ = 137 Hz) ppm.

**[Pt(κ$^2$*S*,*S*′-PCy$_2$S$_2$)(κ*S*-PCy$_2$S$_2$)(PHCy$_2$)] (6):** A toluene solution of PHCy$_2$ (0.180 mmol in 2 mL) was slowly added to an orange toluene suspension of **8** (0.133 g, 0.184 mmol in 5 mL). After 10 min, the obtained yellow suspension was filtered, the filtrate was concentrated to dryness and the resulting yellow solid was washed with *n*-hexane (3 × 2 mL). Yield: 0.128 g, 76%. Complex **6** is very soluble in halogenated solvents, slightly soluble in toluene and scarcely soluble in *n*-hexane. $C_{36}H_{67}P_3PtS_4$ (916.18): calcd. C 47.19, H 7.37, S 14.0; found C 47.25, H 7.45, S 14.4. LC-MS: exact mass calcd. for $C_{48}H_{90}OP_4Pt_2$: 915.30 amu; found 916 [M + H]$^+$, 718 [M – PHCy$_2$ + H]$^+$. M.p. 208–210 °C. IR (Nujol mull): $\tilde{\nu}_{max}$ = 2367 (w, P–H), 1297 (w), 1267 (w), 1178 (m), 1113 (m), 1075 (w), 999 (m), 919 (w), 885 (m), 849 (m), 819 (m), 748 (m), 620 (s, $\nu$ of unidentate PS$_2$), 598 (m, $\nu$ of bidentate PS$_2$), 559 (s, $\nu$ of bidentate PS$_2$), 527 (m, $\nu$ of unidentate PS$_2$), 473 (w), 356 (w), 310 (w) cm$^{-1}$. $^1$H NMR (400 MHz, $C_6D_6$, 295 K): $\delta$ = 5.94 (br. m, $^1J_{P,H}$ = 417 Hz, P*H*) ppm. $^{31}$P{$^1$H} NMR (162 MHz, $C_6D_6$, 295 K): $\delta$ = 124.8 (br. s, $^2J_{P,Pt}$ = 195 Hz, κ$^2$*S*,*S*′-PCy$_2$S$_2$), 81.8 (br. s, κ*S*-PCy$_2$S$_2$), 2.5 (s, $^1J_{P,Pt}$ = 3551 Hz, PHCy$_2$) ppm. $^{195}$Pt{$^1$H} NMR (86 MHz, $CDCl_3$, 265 K): $\delta$ = –4052 (ddd, $^1J_{P,Pt}$ = 3551, $^2J_{P,Pt}$ = 184, $^2J_{P,Pt}$ = 116 Hz) ppm.

**Pt(κ$^2$*S*,*S*′-PCy$_2$S$_2$)$_2$ (8):** Dicyclohexylphosphane sulfide,[64] prepared by addition of 1 equiv. of elemental sulfur to a toluene solu-

 © 2006 Wiley-VCH Verlag GmbH & Co. KGaA, Weinheim 

tion of $PHCy_2$ at room temperature, was converted into $P(Cy)_2S_2Na$ by further reaction with 1 equiv. of sulfur and subsequent deprotonation by NaH. $NaP(Cy_2S_2)$ (0.193 g, 0.678 mmol)[65] was then poured into an ethanol suspension of $K_2PtCl_4$ (0.141 g, 0,339 mmol in 5 mL) and the mixture was vigorously stirred at room temperaturefor 24 h. Complex **8** was isolated by filtration as a pale orange solid, washed with *n*-hexane (4×2 mL) and dried under vacuum. Yield: 0.181 g, 74%. The complex is fairly soluble in halogenated solvents and insoluble in hexane and ethanol. $C_{24}H_{44}P_2PtS_4$ (717.90): calcd. C 40.15, H 6.18, S 17.87; found C 40.65, H 6.31, S 18.05. LC-MS: exact mass calcd. for $C_{24}H_{44}P_2PtS_4$: 717.14 amu; found 718 $[M + H]^+$. M.p. 279 °C (dec.). IR (Nujol mull): $\tilde{\nu}_{max}$ = 1266 (w), 1180 (m), 1113 (w), 1078 (w), 1023 (w), 1001 (m), 887 (m), 850 (w), 818 (w), 742 (m), 595 (m, *ν* of bidentate $PS_2$), 561 (s, *ν* of bidentate $PS_2$), 524 (w), 401 (w), 298 (m) $cm^{-1}$. $^{31}P\{^1H\}$ NMR (162 MHz, $CDCl_3$ 295 K): $\delta$ = 134.5 (s, $^2J_{P,Pt}$ = 279 Hz) ppm. $^{195}Pt\{^1H\}$ NMR (86 MHz, $CDCl_3$, 295 K): $\delta$ = –3025 (t, $^2J_{P,Pt}$ = 279 Hz) ppm.

**X-ray Data Collection, Structure Solution and Refinement of 6:** Crystal data, parameters for intensity data collection and convergence results are compiled in Table 4. A pale yellow platelet of approximate dimensions 0.30×0.20×0.20 mm was studied at 110 K with a BRUKER-AXS SMART APEX diffractometer. An empirical absorption correction (min. trans. 0.40, max. trans. 0.52) was applied before averaging symmetry-equivalent data [*R*(int) = 0.0815]. After merging, 11370 independent reflections remained for the structure solution by direct methods.[66] The structure model was completed by Fourier difference syntheses and refined with full-matrix least squares on $F^2$.[67] CCDC-299582 contains the supplementary crystallographic data for this paper. These data can be obtained free of charge from The Cambridge Crystallographic Data Centre via www.ccdc.cam.ac.uk/data_request/cif.

Table 4. Crystal data and structure refinement for **6**.

| | |
|---|---|
| Empirical formula | $C_{36}H_{67}P_3PtS_4$ |
| Formula mass | 916.14 |
| Temperature [K] | 110(2) |
| Wavelength [Å] | 0.71073 |
| Crystal system | monoclinic |
| Space group | $P2_1/c$ |
| Unit cell dimensions: | |
| *a* [Å] | 15.731(2) |
| *b* [Å] | 11.1000(16) |
| *c* [Å] | 27.258(3) |
| *β* [°] | 121.060(5) |
| *V* [Å$^3$] | 4077.2(9) |
| *Z* | 4 |
| $D_{calcd.}$ [Mg/m$^3$] | 1.492 |
| Absorption coeff. [mm$^{-1}$] | 3.788 |
| *θ* range for data coll. [°] | 2.25–29.70 |
| Reflections measured | 51300 |
| Independent reflections | 11370 |
| Observed reflections [$I > 2\sigma(I)$] | 8705 |
| Data/parameters | 11370/397 |
| Goodness-of-fit on $F^2$ | 1.102 |
| $R$[a] [$I > 2\sigma(I)$] | 0.0581 |
| $wR_2$[b] (all data) | 0.1208 |
| Largest diff. peak/hole [e/Å$^3$] | 1.934/–2.962 |

[a] $R = \Sigma||F_o| - |F_c||/\Sigma|F_o|$. [b] $wR_2 = [\Sigma w(F_o^2 - F_c^2)^2/\Sigma w(F_o^2)^2]^{1/2}$.

**Supporting Information** (see footnote on the first page of this article): $^{31}P\{^1H\}$ NMR spectra of **3**, **4**, **5** and **8**, $^{195}Pt\{^1H\}$ NMR spectrum of **8**, ESI-MS spectra of **3**, **4**, **5**, **6** and **8**.

## Acknowledgments

The Italian M.I.U.R. (PRIN 2004, project 2004030719_005) is gratefully acknowledged for financial support.

[1] M. Cook, M. Green, D. Kirkpatrick, *J. Chem. Soc. A* **1968**, 1507–1510.
[2] R. T. Baker, J. F. Whitney, S. S. Wreford, *Organometallics* **1983**, *2*, 1049–1051.
[3] L. Weber, K. Reizig, R. Boese, *Chem. Ber.* **1985**, *118*, 1193–1203.
[4] W. E. Buhro, M. H. Chillsholm, K. Folting, J. C. Hoffman, *J. Am. Chem. Soc.* **1987**, *109*, 905–906.
[5] M. D. Fryzuk, K. Bhangu, *J. Am. Chem. Soc.* **1988**, *110*, 961–963.
[6] M. D. Fryzuk, K. Joshi, *Organometallics* **1989**, *8*, 722–726.
[7] S. Atlan, F. Nief, L. Ricard, *Bull. Soc. Chim. Fr.* **1995**, *132*, 649–651.
[8] D. G. Dick, D. W. Stephan, *Organometallics* **1991**, *10*, 2811–2816.
[9] K. Izod, P. O'Shaughnessy, J. M. Sheffield, W. Glegg, S. T. Liddle, *Inorg. Chem.* **2000**, *39*, 4741–4748.
[10] E. Hey-Hawkins, M. F. Lappert, J. L. Atwood, S. G. Bott, *J. Chem. Soc., Dalton Trans.* **1991**, 939–948.
[11] E. Urnezius, S. J. Klippenstein, J. D. Protasiewitcz, *Inorg. Chim. Acta* **2000**, *297*, 181–190.
[12] R. Melenkivitz, D. J. Mindiola, G. L. Hillhouse, *J. Am. Chem. Soc.* **2002**, *124*, 3846–3847.
[13] L. Dahlenburg, N. Höck, H. Berke, *Chem. Ber.* **1988**, *121*, 2083–2093.
[14] H. Schäfer, *Z. Anorg. Allg. Chem.* **1979**, *459*, 157–169.
[15] J. C. T. R. Burckett-St. Laurent, R. J. Haines, C. R. Nolte, N. D. C. T. Steen, *Inorg. Chem.* **1980**, *19*, 577–587.
[16] P. J. Domaille, B. M. Foxman, T. J. McNeese, S. S. Wreford, *J. Am. Chem. Soc.* **1980**, *102*, 4114–4120.
[17] D. S. Bohle, T. C. Jones, C. E. F. Rickard, W. R. Roper, *Organometallics* **1986**, *5*, 1612–1619.
[18] D. S. Bohle, G. R. Clark, C. E. F. Rickard, W. R. Roper, M. J. Taylor, *J. Organomet. Chem.* **1988**, *348*, 385–409.
[19] F. Cecconi, G. A. Ghilardi, S. Midollini, S. Moneti, A. Orlandini, G. Scapacci, *Inorg. Chim. Acta* **1991**, *189*, 105–110.
[20] G. Bonnet, O. Lavastre, J. C. Leblanc, C. Moïse, *New J. Chem.* **1988**, *12*, 551–552.
[21] P. Oudet, M. M. Kubicki, C. Moïse, *Organometallics* **1994**, *13*, 4278–4284.
[22] G. Boni, P. Sauvageot, E. Marpeaux, C. Moïse, *Organometallics* **1995**, *14*, 5652–5656.
[23] C. Barre, M. M. Kubicki, J. C. Leblanc, C. Moïse, *Inorg. Chem.* **1990**, *29*, 5244–5246.
[24] G. Bonnet, M. M. Kubicki, C. Moise, R. Lazzaroni, P. Salvadori, G. Vitulli, *Organometallics* **1992**, *11*, 964–967.
[25] J. G. Planas, J. A. Gladysz, *Inorg. Chem.* **2002**, *41*, 6947–6949.
[26] G. T. Crisp, G. Salem, F. S. Stephens, S. B. Wild, *J. Chem. Soc., Chem. Commun.* **1987**, 600–602.
[27] W. Malisch, N. Gunzelmann, K. Thirase, M. Neumayer, *J. Organomet. Chem.* **1998**, *571*, 215–222.
[28] W. E. Buhro, B. D. Zwick, S. Georgiou, J. P. Hutchinson, J. A. Gladysz, *J. Am. Chem. Soc.* **1988**, *110*, 2427–2439.
[29] B. D. Zwick, M. A. Dewey, D. A. Knight, W. E. Buhro, A. M. Arif, J. A. Gladysz, *Organometallics* **1992**, *11*, 2673–2685.
[30] A. Handler, P. Peringer, E. P. Müller, *J. Chem. Soc., Dalton Trans.* **1990**, 3725–3727.
[31] D. K. Wicht, I. V. Kourkine, I. Kovacik, D. S. Glueck, T. E. Concolino, G. P. A. Yap, C. D. Incarvito, A. L. Rheingold, *Organometallics* **1999**, *18*, 5381–5394.
[32] M. A. Zhuravel, D. S. Glueck, L. N. Zakharov, A. L. Rheingold, *Organometallics* **2002**, *21*, 3208–3214.
[33] S. M. Rocklage, R. R. Schrock, M. R. Churchill, H. J. Wasserman, *Organometallics* **1982**, *1*, 1332–1338.

 © 2006 Wiley-VCH Verlag GmbH & Co. KGaA, Weinheim 

[34] F. Maassarani, M. F. Davidson, I. C. M. Wehman-Ooyevaar, D. M. Grove, M. A. van Koten, W. J. J. Smeets, A. L. Spek, G. van Koten, *Inorg. Chim. Acta* **1995**, *235*, 327–338.
[35] H. C. Aspinall, S. R. Moore, A. K. Smith, *J. Chem. Soc., Dalton Trans.* **1992**, 153–156.
[36] R. D. Simpson, R. G. Bergman, *Organometallics* **1992**, *11*, 3980–3993.
[37] D. K. Wicht, S. N. Paisner, B. N. Lew, D. S. Glueck, G. P. A. Yap, L. M. Liable-Sands, A. L. Rheingold, C. M. Haar, S. P. Nolan, *Organometallics* **1998**, *17*, 652–660.
[38] D. K. Wicht, D. S. Glueck, L. M. Liable-Sands, A. L. Rheingold, *Organometallics* **1999**, *18*, 5130–5140.
[39] D. K. Wicht, I. Kovacik, D. S. Glueck, L. M. Liable-Sands, C. D. Incarvito, A. L. Rheingold, *Organometallics* **1999**, *18*, 5141–5151.
[40] G. Boni, M. M. Kubicki, C. Moïse in *Metal Cluster in Chemistry* (Eds.: P. Braunstein, L. A. Oro, P. R. Raithby), Wiley-VCH, Weinheim, **1999**, vol. 1, pp. 115–123.
[41] W. Malisch, R. Maisch, I. J. Colquhoun, W. McFarlane, *J. Organomet. Chem.* **1981**, *220*, C1–C6.
[42] C. W. Allen, E. A. V. Ebsworth, S. G. Henderson, D. W. H. Rankin, H. E. Robertson, B. Turner, J. D. Whitelock, *J. Chem. Soc., Dalton Trans.* **1986**, 1333–1338.
[43] F. Cecconi, C. A. Ghiraldi, S. Midollini, S. Moneti, A. Orlandini, G. Scapacci, *Inorg. Chim. Acta* **1991**, *189*, 105–110.
[44] F. Maassarani, M. F. Davidson, I. C. M. Wehman-Ooyevaar, D. M. Grove, M. A. van Koten, W. J. J. Smeets, A. L. Spek, G. van Koten, *Inorg. Chim. Acta* **1995**, *235*, 327–338.
[45] M. D. Fryzuk, K. Joshi, *Organometallics* **1989**, *8*, 722–726.
[46] W. Malisch, M. Kuhn, *J. Organomet. Chem.* **1974**, *73*, C1–C4.
[47] G. T. Crisp, G. Salem, F. S. Stephens, S. B. Wild, *J. Chem. Soc., Chem. Commun.* **1987**, 600–601.
[48] E. A. V. Ebsworth, R. O. Gould, N. T. Mcmanus, D. W. H. Rankin, M. D. Walkinshaw, J. D. Whitelock, *J. Organomet. Chem.* **1983**, *249*, 227–242.
[49] R. C. Dobbie, P. R. Mason, *J. Chem. Soc., Dalton Trans.* **1973**, 1124–1128.
[50] W. Malisch, R. Alsmann, *Angew. Chem. Int. Ed. Engl.* **1976**, *15*, 769–770.
[51] W. Malisch, R. Maisch, A. Meyer, D. Greissinger, E. Gross, I. J. Colquhoun, W. McFarlane, *Phosphorus, Sulfur, Silicon Relat. Elem.* **1983**, *18*, 299–302.
[52] P. Mastrorilli, C. F. Nobile, F. P. Fanizzi, M. Latronico, C. Hu, U. Englert, *Eur. J. Inorg. Chem.* **2002**, 1210–1218.
[53] P. Mastrorilli, M. Latronico, C. F. Nobile, G. P. Suranna, F. P. Fanizzi, U. Englert, G. Ciccarella, *Dalton Trans.* **2004**, 1117–1119.
[54] P. Mastrorilli, C. F. Nobile, M. Latronico, V. Gallo, U. Englert, F. P. Fanizzi, O. Sciacovelli, *Inorg. Chem.* **2005**, *44*, 9097–9104.
[55] J. M. C. Alison, T. A. Stephenson, R. O. Gould, *J. Chem. Soc. A* **1971**, 3690–3696.
[56] D. F. Steele, T. A. Stephenson, *J. Chem. Soc., Dalton Trans.* **1973**, 2124–2130.
[57] J. S. Casas, M. S. García-Tasende, A. Sánchez, J. Sordo, M. Vázquez-López, E. E. Castellano, J. Zukerman-Schpector, *Inorg. Chim. Acta* **1993**, *209*, 137–142.
[58] D. F. Steele, T. A. Stephenson, *J. Chem. Soc., Dalton Trans.* **1973**, 2124–2130.
[59] M. C. Cornock, T. A. Stephenson, *J. Chem. Soc., Dalton Trans.* **1977**, 501–505.
[60] J. M. C. Alison, T. A. Stephenson, *J. Chem. Soc., Dalton Trans.* **1973**, 254–263.
[61] J. P. Fackler Jr, L. D. Thompson, I. J. B. Lin, T. A. Stephenson, R. O. Gould, J. M. C. Alison, A. J. F. Fraser, *Inorg. Chem.* **1982**, *21*, 2397–2403.
[62] D. F. Steele, T. A. Stephenson, *J. Chem. Soc., Dalton Trans.* **1973**, 2124–2130.
[63] A. L. Spek, *PLATON, A Multipurpose Crystallographic Tool*, Utrecht University, Utrecht, The Netherlands, **2001**.
[64] M. M. Rauhut, H. A. Currier, V. P. Wystrach, *J. Org. Chem.* **1961**, *26*, 5133–5135.
[65] $^{31}$P NMR (162 MHz, $C_6D_6$, 295 K): $\delta$ = 82.5 ppm. $^{1}$H NMR (400 MHz, $C_6D_6$, 295 K): $\delta$ = 5.95 (br. m, $^{1}J_{P-H}$ = 421 Hz) ppm.
[66] G. M. Sheldrick, *SHELXS97, Program for Crystal Structure Solution*, University of Göttingen, **1997**.
[67] G. M. Sheldrick, *SHELXL97, Program for Crystal Structure Refinement*, University of Göttingen, **1997**.

Received: February 27, 2006
Published Online: April 21, 2006

 © 2006 Wiley-VCH Verlag GmbH & Co. KGaA, Weinheim 

DOI: 10.1002/ejic.200600180

# New Palladium Complexes with S- or Se-Containing Schiff-Base Ligands as Efficient Catalysts for the Suzuki–Miyaura Cross-Coupling Reaction of Aryl Bromides with Phenylboronic Acid under Aerobic Conditions

**Ioannis D. Kostas,*[a] Barry R. Steele,*[a] Aris Terzis,[b] Svetlana V. Amosova,[c] Alexander V. Martynov,[c] and Natalia A. Makhaeva[c]**

**Keywords:** Homogeneous catalysis / Suzuki / C–C coupling / Schiff bases / Tridentate ligands

Four palladium chelate complexes with S- or Se-containing substituted salicylaldehyde Schiff-base derivatives have been synthesized. Spectroscopic and crystallographic data indicate that, in the complexes, the deprotonated salicylaldehyde ligand is bound to the metal in an O,N,S (or Se)-tridentate coordination mode, forming one six- and one five-membered chelate ring. The complexes are thermally and air stable and efficiently catalyze the Suzuki–Miyaura cross-coupling of aryl bromides with phenylboronic acid in air.

(© Wiley-VCH Verlag GmbH & Co. KGaA, 69451 Weinheim, Germany, 2006)

## Introduction

Palladium-catalyzed carbon–carbon coupling reactions have now become essential tools for the organic synthetic chemist,[1] and one of the most important of these is the Suzuki–Miyaura cross-coupling of aryl halides with organoboronic acids.[1,2] This reaction now represents a key process for the synthesis of biaryls, which play an important role as intermediates in organic synthesis and as functional groups in natural products.[3] Intensive research efforts are being made into finding ways of improving and expanding the scope of this process, and one aspect that has received particular attention is the development of new ligands. As a consequence, a large number of phosphorus ligands,[4] and phosphane-free ligands,[5] have been reported that are applicable to the conventional thermal Suzuki–Miyaura reaction.

We have previously reported several nitrogen- and/or sulfur-containing phosphorus ligands and their applications to transition-metal homogeneous catalysis.[6] However, as efficient catalysis under phosphane-free conditions represents a challenge of high current importance, our interest has focused on the development of new phosphane-free ligands and recently, for the first time, we used thiosemicarbazones as effective catalyst precursors for palladium-catalyzed coupling reactions under aerobic conditions.[7] In a previous paper, we reported a synthetic route for the preparation of chalcogen (S,Se,Te)-containing substituted salicylaldehyde Schiff-base derivatives.[8] Taking into account the potential of these Schiff bases as tridentate ligands,[9] in this paper we report the synthesis of palladium complexes with S- or Se-containing Schiff-base ligands, two crystal structures of which were determined by X-ray analysis. These phosphane-free systems were applied to the Suzuki–Miyaura coupling of aryl bromides with phenylboronic acid under aerobic conditions.

[a] National Hellenic Research Foundation, Institute of Organic and Pharmaceutical Chemistry,
Vas. Constantinou 48, 116 35 Athens, Greece
E-mail: ikostas@eie.gr
bsteele@eie.gr
[b] Institute of Materials Science, NCSR Democritos,
153 10 Aghia Paraskevi Attikis, Greece
[c] A. E. Favorsky Irkutsk Institute of Chemistry, Siberian Branch of the Russian Academy of Sciences,
Favorsky Str. 1, 664033 Irkutsk, Russia

## Results and Discussion

### Synthesis and Characterization of the Palladium Complexes with S- or Se-Containing Schiff-Base Ligands

The synthesis of the palladium complexes **3a**–**d** is outlined in Scheme 1. Chalcogen-containing Schiff bases 2-(1-ethylpropyl)-6-({[2-(methylsulfanyl)ethyl]imino}methyl)-benzenol ("emSib", **2a**), 2-({[2-(methylsulfanyl)ethyl]imino}-methyl)benzenol ("mSib", **2b**), 2-(1-ethylpropyl)-6-({[2-(methylselanyl)ethyl]imino}methyl)benzenol ("emSEib", **2c**), and 2-({[2-(methylselanyl)ethyl]imino}methyl)benzenol ("mSEib", **2d**) were prepared by treatment of salicylaldehyde derivative **1a** or salicylaldehyde **1b** with 2-(methylsulfanyl)- or 2-(methylselanyl)ethylamine (or their hydrochlorides), according to a procedure recently published by us.[8] In the $^1$H NMR spectra of **2a**–**d**, the signal of the phenolic proton at $\delta$ = 13.30 ppm (**2b**,**d**) or 13.50 ppm (**2a**,**c**) is consistent with hydrogen bonding between the hydroxy and the nitrogen of the imine group.[10] The syntheses of the palladium complexes **3a**–**d** were achieved by the reaction of li-

 © 2006 Wiley-VCH Verlag GmbH & Co. KGaA, Weinheim 

gands **2a**–**d** with $Li_2PdCl_4$, prepared in situ from $PdCl_2$ and LiCl. Spectroscopic studies indicate that the ligands are bound to palladium in an O,N,S (or Se)-terdentate coordination mode. In the $^1H$ NMR spectra of **3a**–**d**, the signal of the phenolic proton is absent because of deprotonation and complex formation. In the $^1H$ and $^{13}C\{^1H\}$ NMR spectra of **3a**–**d**, the $CH_2N$ and $XCH_3$ resonances are shifted to low field compared to the corresponding resonances in the free ligands, indicating Pd–N as well as Pd–X coordination (Table 1).

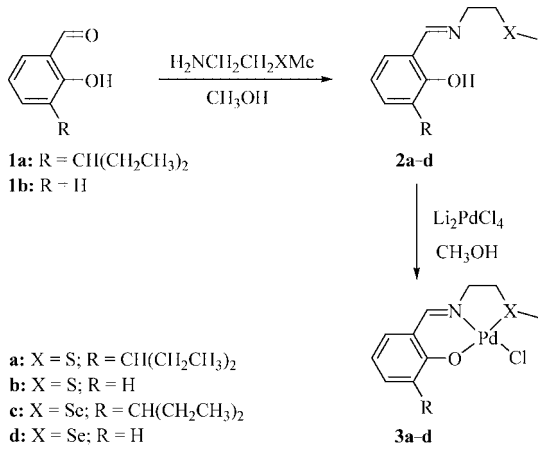


Scheme 1. Synthesis of the palladium complexes [PdCl(emSib)] (**3a**), [PdCl(mSib)] (**3b**), [PdCl(emSEib)] (**3c**), and [PdCl(mSEib)] (**3d**).

Yellow-orange crystals of complexes **3a** and **3c** suitable for X-ray determination were obtained by slow diffusion of diethyl ether through a diluted solution of the complexes in dichloromethane. The two complexes are isostructural and, for that reason, only the structure of **3c** is presented here. As shown in Figure 1, the monoanionic ligand is coordinated to palladium in a terdentate fashion by the phenoxy oxygen, the azomethine nitrogen and the selenium atom, forming one six- and one five-membered chelate ring. In both complexes, the coordination geometry at the metal center can be regarded as slightly distorted square-planar, and the four Pd–heteroatom distances have normal values, according to the selected data presented in Table 2.

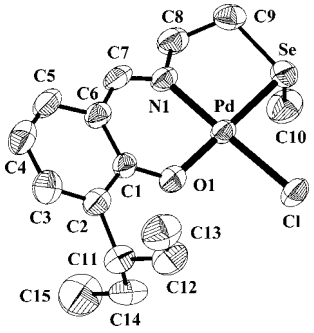


Figure 1. Labeled ORTEP diagram of **3c** with 50% thermal probability ellipsoids (hydrogen atoms have been omitted for clarity).

Table 2. Selected bond lengths [Å] and angles [°] in complexes **3a** and **3c**.

| **3a** | | **3c** | |
|---|---|---|---|
| Pd–N(1) | 1.971(3) | Pd–N(1) | 1.985(4) |
| Pd–O(1) | 2.002(3) | Pd–O(1) | 2.017(4) |
| Pd–S | 2.257(2) | Pd–Se | 2.365(1) |
| Pd–Cl | 2.322(1) | Pd–Cl | 2.323(2) |
| N(1)–Pd–O(1) | 92.3(1) | N(1)–Pd–O(1) | 92.3(2) |
| N(1)–Pd–S | 87.5(1) | N(1)–Pd–Se | 88.0(1) |
| O(1)–Pd–S | 177.9(1) | O(1)–Pd–Se | 177.0(1) |
| N(1)–Pd–Cl | 177.4(1) | N(1)–Pd–Cl | 177.1(1) |
| O(1)–Pd–Cl | 89.9(1) | O(1)–Pd–Cl | 90.3(1) |
| S–Pd–Cl | 90.3(1) | Cl–Pd–Se | 89.5(1) |

## Suzuki–Miyaura Coupling Reactions Catalyzed by Palladium Complexes with S- or Se-Containing Schiff-Base Ligands under Aerobic Conditions

Complexes **3a**–**d** were applied to the Suzuki–Miyaura reaction of phenylboronic acid with some representative aryl bromides (from electron-rich to electron-poor) at 100 °C for 24 h, in DMF, using $K_2CO_3$ as base, without addition of free ligand or any promoting additive (Scheme 2, Table 3). All reactions were performed in air. As it is known that addition of water enhances the activity of the catalyst,[4b,7b] catalysis was performed in the presence of a small amount of water (close to 1 equiv. with respect to the substrates). Catalysts seem to be air stable at 100 °C, and palladium-black, which could indicate the degradation of the catalysts, was not observed. The reaction was performed using a 1:1000 catalyst/aryl halide molar ratio. As expected, the catalytic activity depended on the halide, while electron-withdrawing groups on the aryl ring increased the reaction rate. According to the GC and GC–MS analysis of the reaction mixtures resulting from the coupling of 4-substituted aryl halides, homocoupling of phenylboronic acid to give unsubstituted biphenyl was observed in a low yield (3–4%) only for the substrate with an electron-donating group. For the deactivated 4-bromoanisole, the reaction proceeded with conversions to the coupled product, MeO–$C_6H_4$–Ph,

Table 1. Comparative NMR spectroscopic data of the ligands **2a**–**d** and their corresponding palladium complexes **3a**–**d** for the groups $CH_2N$ and $XCH_3$ (X = S or Se).

| Ligand/complex | $CH_2N$ | | $XCH_3$ (X = S or Se) | |
|---|---|---|---|---|
| | $^1H$ NMR [ppm] | $^{13}C$ NMR [ppm] | $^1H$ NMR [ppm] | $^{13}C$ NMR [ppm] |
| **2a**[8]/**3a** | 3.79/4.04–3.81 | 58.7/63.4 | 2.14/2.65 | 15.8/21.0 |
| **2b**/**3b** | 3.78/4.28–3.95 | 58.8/63.6 | 2.12/2.53 | 15.9/19.6 |
| **2c**[8]/**3c** | 3.86/4.30–4.05 | 59.7/65.6 | 2.01/2.52 | 4.5/12.7 |
| **2d**/**3d** | 3.87/4.40–4.21 | 59.7/65.6 | 2.02/2.45 | 4.7/11.6 |

 © 2006 Wiley-VCH Verlag GmbH & Co. KGaA, Weinheim 

in the range 21–25% (entries 1–4), and for the nonactivated bromobenzene in the range 40–45% (entries 5–8). The narrow ranges for the yields for entries 1–4 and also 5–8 do not permit conclusions to be drawn concerning the influence of the bulky substituent $CHEt_2$ on the salicylaldehyde moiety or on the effect of replacing sulfur with selenium on the catalytic activity of the complexes. For the activated 4-bromobenzonitrile (entries 9–12) and 1-bromo-4-nitrobenzene (entries 13–16), the reaction proceeded with high or even quantitative yield. The results in these entries provide evidence that the presence of the $CHEt_2$ group on the aryl ring, situated away from the coordination sphere around the metal, does not significantly influence the activity of the complex. This observation is not in contrast with that broadly accepted concerning the increased reactivity of a ligand by the presence of a bulky electron-donating group, thereby making the ligand more electron-rich, because in our systems the ligand is in an anionic form. On the other hand, the presence of a selenium donor in the complex was found to promote its catalytic activity slightly compared to the sulfur analogue. For comparison purposes, coupling of 4-bromobenzonitrile with phenylboronic acid was also achieved by using $Li_2PdCl_4$ or $Pd(OAc)_2$ as catalysts under the same reaction conditions as those described above. The reactions proceeded with 95% ($Li_2PdCl_4$ as catalyst) and 92% [$Pd(OAc)_2$ as catalyst] yields of coupling product, but, in contrast to complexes **3a**–**d**, unsubstituted biphenyl was also observed (5% and 8%, respectively) because of homocoupling of phenylboronic acid. Although it is known that these simple palladium compounds may produce nanoparticles under these reaction conditions,[11] it remains to be established whether this is the case for the complexes reported here.

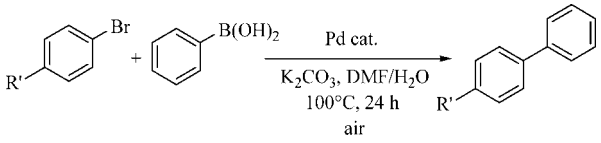


Scheme 2. Suzuki–Miyaura cross-coupling of aryl bromides with phenylboronic acid catalyzed by palladium complexes **3a**–**d**, in air.

Table 3. Suzuki–Miyaura cross-coupling of aryl bromides with phenylboronic acid catalyzed by palladium complexes **3a**–**d**, in air.

| Entry[a] | Catalyst | R′ | Conversion[b] (%) |
|---|---|---|---|
| 1 | **3a** | OMe | 21 (3)[c] |
| 2 | **3b** | OMe | 25 (4)[c] |
| 3 | **3c** | OMe | 23 (4)[c] |
| 4 | **3d** | OMe | 25 (4)[c] |
| 5 | **3a** | H | 45 |
| 6 | **3b** | H | 40 |
| 7 | **3c** | H | 40 |
| 8 | **3d** | H | 42 |
| 9 | **3a** | CN | 79 |
| 10 | **3b** | CN | 80 |
| 11 | **3c** | CN | 96 |
| 12 | **3d** | CN | 96 |
| 13 | **3a** | $NO_2$ | 90 |
| 14 | **3b** | $NO_2$ | 94 |
| 15 | **3c** | $NO_2$ | 100 |
| 16 | **3d** | $NO_2$ | 100 |

[a] Reaction conditions: ArBr (2.0 mmol), $PhB(OH)_2$ (3.0 mmol), $K_2CO_3$ (4.0 mmol), $H_2O$ (3.3 mmol), Pd complex in DMF (0.5 mM, 4 mL), 100 °C, 24 h; ArBr/Pd = 1000:1. [b] Conversion to coupled product R′-$C_6H_4$–Ph, based on aryl bromide (GC, decane as internal standard). [c] Conversion to unsubstituted biphenyl because of homocoupling of phenylboronic acid.

## Conclusions

We have shown that new palladium chelate complexes with S- or Se-containing substituted salicylaldehyde Schiff-base derivatives, in which the ligand is bound to the metal in an O,N,S (or Se)-terdentate coordination mode, can serve as efficient catalysts for the Suzuki–Miyaura cross-coupling of aryl bromides with phenylboronic acid under mild reaction conditions. Se-containing ligands are slightly more active than the S-containing analogues. Although the activity is not as high as some other palladium systems, these phosphane-free catalysts are thermally and air stable, and offer the advantage of the successful coupling of aryl bromides and the synthesis of biaryls under aerobic conditions.

## Experimental Section

**General:** 3-(1-Ethylpropyl)-2-hydroxybenzenecarbaldehyde (**1a**),[12] 2-(methylsulfanyl)ethylamine,[13] and 2-(methylselanyl)ethylamine[8] were prepared by known procedures. Syntheses of ligands emSib (**2a**) and emSEib (**2c**) have been described by us elsewhere.[8] Ligands mSib (**2b**) and mSEib (**2d**) were prepared according to the same procedure. All other chemicals were commercially available. Coupling reactions were performed on a Radleys Carousel Reactor™ with 12 tubes of about 45 mL in two stacked aluminum blocks. The lower block was placed on a heater–stirrer and maintained at a constant temperature by means of a thermostat, while water circulated in the upper block, which served to cool the tops of the tubes. NMR measurements were made using a Bruker AC 300 (300.13 MHz and 75.47 MHz for $^1H$ and $^{13}C\{^1H\}$, respectively). Distinction of the CH, $CH_2$, and $CH_3$ carbons in the $^{13}C\{^1H\}$ NMR spectra was performed by DEPT NMR experiments. Gas chromatography was undertaken using a Varian Star 3400 CX with a 30 m × 0.53 mm DB5 column. Electron impact gas chromatography–mass spectrometry was carried out using a Varian Saturn 2000 with a 30 m × 0.25 mm DB5-MS column. Elemental analyses for C, H, N were carried out on a Perkin–Elmer PE 2400 II instrument.

**2-({[2-(Methylsulfanyl)ethyl]imino}methyl)benzenol ("mSib", 2b):**[14] Reaction of salicylaldehyde **1b** (2.01 g, 16.48 mmol) with 2-(methylsulfanyl)ethylamine (1.50 g, 16.48 mmol) in MeOH (15 mL) yielded **2b** (3.09 g, 96%). $^1H$ NMR (300.13 MHz, $CDCl_3$): $\delta$ = 13.31 (s, 1 H, OH), 8.35 (s, 1 H, C*H*=N), 7.30 (m, 2 H, ArH), 6.95 (d, $^3J$ = 8.5 Hz, 1 H, ArH), 6.87 (t, $^3J$ = 7.3 Hz, 1 H, ArH), 3.78 (t, $^3J$ = 6.7 Hz, 2 H, $CH_2$N), 2.81 (t, $^3J$ = 6.7 Hz, 2 H, $CH_2$S), 2.12 (s, 3 H, S$CH_3$) ppm. $^{13}C\{^1H\}$ NMR (75.47 MHz, $CDCl_3$): $\delta$ = 165.9 (*C*H=N), 161.0 (*C*-OH), 132.3, 131.3, 118.5, and 116.9 (ArC), 58.8 ($CH_2$N), 34.9 ($CH_2$S), 15.9 (S$CH_3$) ppm.

**2-({[2-(Methylselanyl)ethyl]imino}methyl)benzenol ("mSEib", 2d):**[15] Reaction of salicylaldehyde **1b** (1.05 g, 8.61 mmol) with 2-(methylselanyl)ethylamine (1.19 g, 8.62 mmol) in MeOH (10 mL) yielded **2d** (1.98 g, 95%). $^1H$ NMR (300.13 MHz, $CDCl_3$): $\delta$ =

 © 2006 Wiley-VCH Verlag GmbH & Co. KGaA, Weinheim 

13.30 (s, 1 H, OH), 8.37 (s, 1 H, C*H*=N), 7.30 (m, 2 H, ArH), 6.96 (d, $^3J$ = 8.5 Hz, 1 H, ArH), 6.88 (t, $^3J$ = 7.3 Hz, 1 H, ArH), 3.87 (t, $^3J$ = 6.7 Hz, 2 H, C$H_2$N), 2.84 (t, $^3J$ = 6.7 Hz, 2 H, C$H_2$Se), 2.02 (s, 3 H, SeC$H_3$) ppm. $^{13}$C{$^1$H} NMR (75.47 MHz, $CDCl_3$): $\delta$ = 165.5 (*C*H=N), 161.1 (*C*-OH), 132.3, 131.4, 118.6, and 117.0 (ArC), 59.7 (*C*$H_2$N), 25.9 (*C*$H_2$Se), 4.7 (Se*C*$H_3$) ppm.

**Typical Procedure for the Preparation of the Palladium Complexes 3a–d:** $PdCl_2$ (0.10 g, 0.56 mmol) was stirred with LiCl (0.075 g, 1.76 mmol) in MeOH (10 mL). Ligand **2a** (0.15 g, 0.56 mmol) was added to the dark brown-red solution formed, yielding a yellow-orange suspension after stirring at room temperature overnight. The reaction mixture was allowed to settle and an orange solid was isolated by filtration in air, washed with small amounts of methanol and diethyl ether, and recrystallized from dichloromethane/ether yielding **3a**.

**[PdCl(emSib)] (3a):** Reaction of ligand **2a** with $Li_2PdCl_4$, prepared in situ from $PdCl_2$ and LiCl in MeOH, in the quantities indicated above, yielded **3a** (0.18 g, 79%). $^1$H NMR (300.13 MHz, $CDCl_3$): $\delta$ = 7.37 (s, 1 H, C*H*=N), 7.16 (d, $^3J$ = 7.5 Hz, 1 H, ArH), 6.84 (d, $^3J$ = 7.5 Hz, 1 H, ArH), 6.54–6.49 (m, 1 H, ArH), 4.04–3.96 and 3.90–3.81 (m, m, 2 H, C$H_2$N), 3.13–3.07 and 3.03–2.95 (m, m, 2 H, C$H_2$S), 2.65 (s, 3 H, SC$H_3$), 2.58–2.50 [m, 1 H, C*H*(C$H_2$C$H_3$)$_2$], 1.73–1.54 [m, 4 H, CH(C$H_2$C$H_3$)$_2$], 0.81–0.75 [m, 6 H, CH(CH$_2$C$H_3$)$_2$] ppm. $^{13}$C{$^1$H} NMR (75.47 MHz, $CDCl_3$): $\delta$ = 163.02 (ArC), 160.50 (*C*H=N), 135.91, 133.61, 132.06, 118.38, and 115.07 (ArC), 63.35 (*C*$H_2$N), 41.87 [*C*H(CH$_2$CH$_3$)$_2$], 37.60 (*C*$H_2$S), 26.99 and 26.79 [CH(*C*$H_2$CH$_3$)$_2$], 20.97 (S*C*$H_3$), 12.24 and 12.07 [CH(CH$_2$*C*$H_3$)$_2$] ppm. $C_{15}H_{22}ClNOPdS$ (406.28): calcd. C 44.35, H 5.46, N 3.45; found C 44.56, H 5.53, N 3.77.

**[PdCl(mSib)] (3b):** Reaction of ligand **2b** (0.12 g, 0.62 mmol) with $Li_2PdCl_4$, prepared in situ from $PdCl_2$ (0.10 g, 0.56 mmol) and LiCl (0.075 g, 1.76 mmol) in MeOH (10 mL), yielded **3b** (0.15 g, 79%). $^1$H NMR (300.13 MHz, [D$_6$]DMSO): $\delta$ = 8.19 (s, 1 H, C*H*=N), 7.39–7.29 (m, 2 H, ArH), 6.80 (d, $^3J$ = 8.5 Hz, 1 H, ArH), 6.61–6.56 (m, 1 H, ArH), 4.28–4.19 and 4.03–3.95 (m, m, 2 H, C$H_2$N), 2.98–2.89 and 2.74–2.66 (m, m, 2 H, C$H_2$S), 2.53 (s, 3 H, SC$H_3$) ppm. $^{13}$C{$^1$H} NMR (75.47 MHz, [D$_6$]DMSO): $\delta$ = 163.43 (ArC), 160.78 (*C*H=N), 135.32, 134.93, 119.60, 119.47, and 114.94 (ArC), 63.60 (*C*$H_2$N), 36.33 (*C*$H_2$S), 19.57 (S*C*$H_3$) ppm. $C_{10}H_{12}ClNOPdS$ (336.14): calcd. C 35.73, H 3.60, N 4.17; found C 36.15, H 3.96, N 4.59.

**[PdCl(emSEib)] (3c):** Reaction of ligand **2c** (0.18 g, 0.58 mmol) with $Li_2PdCl_4$, prepared in situ from $PdCl_2$ (0.10 g, 0.56 mmol) and LiCl (0.075 g, 1.76 mmol) in MeOH (10 mL), yielded **3c** (0.17 g, 68%). $^1$H NMR (300.13 MHz, $CDCl_3$): $\delta$ = 7.34 (s, 1 H, C*H*=N), 7.16 (d, $^3J$ = 7.5 Hz, 1 H, ArH), 6.84 (d, $^3J$ = 7.5 Hz, 1 H, ArH), 6.54–6.49 (m, 1 H, ArH), 4.30–4.20 and 4.14–4.05 (m, m, 2 H, C$H_2$N), 3.16–3.01 (m, 2 H, C$H_2$Se), 2.52 (s, 3 H, SeC$H_3$), 2.50–2.44 [m, 1 H, C*H*(CH$_2$CH$_3$)$_2$], 1.69–1.58 [m, 4 H, CH(C$H_2$CH$_3$)$_2$], 0.83–0.76 [m, 6 H, CH(CH$_2$C$H_3$)$_2$] ppm. $^{13}$C{$^1$H} NMR (75.47 MHz, $CDCl_3$): $\delta$ = 163.08 (ArC), 160.82 (*C*H=N), 135.52, 133.32, 132.25, 118.51, and 114.78 (ArC), 65.61 (*C*$H_2$N), 41.64 [*C*H(CH$_2$CH$_3$)$_2$], 28.99 (*C*$H_2$Se), 26.95 and 26.70 [CH(*C*$H_2$CH$_3$)$_2$], 12.66 (Se*C*$H_3$), 12.24 and 12.07 [CH(CH$_2$*C*$H_3$)$_2$] ppm. $C_{15}H_{22}ClNOPdSe$ (453.18): calcd. C 39.76, H 4.89, N 3.09; found C 39.58, H 5.01, N 3.38.

**[PdCl(mSEib)] (3d):** Reaction of ligand **2d** (0.15 g, 0.62 mmol) with $Li_2PdCl_4$, prepared in situ from $PdCl_2$ (0.10 g, 0.56 mmol) and LiCl (0.075 g, 1.76 mmol) in MeOH (10 mL), yielded **3d** (0.12 g, 56%). $^1$H NMR (300.13 MHz, [D$_6$]DMSO): $\delta$ = 8.13 (s, 1 H, C*H*=N), 7.36–7.28 (m, 2 H, ArH), 6.79 (d, $^3J$ = 8.0 Hz, 1 H, ArH), 6.59–6.54 (m, 1 H, ArH), 4.40–4.21 (m, 2 H, C$H_2$N), 2.94–2.85 and 2.73–2.66 (m, m, 2 H, C$H_2$Se), 2.45 (s, 3 H, SeC$H_3$) ppm. $^{13}$C{$^1$H} NMR (75.47 MHz, [D$_6$]DMSO): $\delta$ = 163.76 (ArC), 161.04 (*C*H=N), 135.16, 134.93, 119.44, and 114.58 (Ar), 65.57 (*C*$H_2$N), 28.53 (*C*$H_2$Se), 11.58 (Se*C*$H_3$) ppm. $C_{10}H_{12}ClNOPdSe$ (383.03): calcd. C 31.36, H 3.16, N 3.66; found C 30.98, H 2.90, N 4.07.

**General Procedure for the Suzuki–Miyaura Cross-Coupling Reactions:** A mixture of aryl bromide (2.0 mmol), $PhB(OH)_2$ (0.366 g, 3.0 mmol), $K_2CO_3$ (0.553 g, 4.0 mmol), water (60 μL, 3.3 mmol), and a stock solution of palladium complex **3a–d** in DMF (0.5 mM, 4 mL, $2\times10^{-3}$ mmol) was heated at 100 °C for 24 h, and then cooled to room temperature. After addition of water and extraction with dichloromethane, the organic phase was washed with brine, dried with $Na_2SO_4$, filtered, passed through Celite, and analyzed by GC and GC–MS. All the biaryls prepared were known compounds.[4b]

**X-ray Crystallographic Study of 3a and 3c:** Slow crystallization from $CH_2Cl_2/Et_2O$ yielded yellow-orange crystals of **3a** ($0.20\times0.25\times0.55$ mm) and **3c** ($0.10\times0.20\times0.50$ mm), which were mounted in air. Diffraction measurements were made on a Crystal Logic Dual Goniometer diffractometer using graphite-monochromated Mo radiation. Unit cell dimensions were determined and refined by using the angular settings of 25 automatically centered reflections in the range $11 < 2\theta < 23°$ and they appear in Table 4. Intensity data were recorded using a $\theta$–$2\theta$ scan. Three standard reflections monitored every 97 reflections showed less than 3% variation and no decay. Lorentz, polarization, and absorption corrections were applied using Crystal Logic software. The structures were solved by direct methods using SHELXS-86[16] and refined by full-matrix least-squares methods on $F^2$ with SHELXL-97.[17] All non-hydrogen atoms were refined anisotropically. Hydrogen atoms were located by difference maps and were refined isotropically (except those on C13 and C15 in **3a**, which were introduced at calculated positions as riding on bonded atoms). Crystal data and experimental details for the crystals of compounds **3a** and **3c** are given in Table 4.

Table 4. X-ray experimental data of compounds **3a** and **3c**.

| | **3a** | **3c** |
|---|---|---|
| Empirical formula | $C_{15}H_{22}ClNOPdS$ | $C_{15}H_{22}ClNOPdSe$ |
| Formula mass | 406.25 | 453.15 |
| Crystal system | monoclinic | monoclinic |
| Space group | $P2_1/c$ | $P2_1/c$ |
| $a$ [Å] | 13.469(6) | 13.404(7) |
| $b$ [Å] | 8.425(3) | 8.468(5) |
| $c$ [Å] | 15.056(6) | 15.204(9) |
| $\beta$ [°] | 94.54(2) | 93.59(2) |
| $V$ [Å$^3$] | 1703(1) | 1722(2) |
| Z | 4 | 4 |
| $D_{calcd.}$ [g cm$^{-3}$] | 1.584 | 1.748 |
| $F(000)$ | 824 | 896 |
| $\mu$ [mm$^{-1}$] | 1.364 | 3.341 |
| $T$ [K] | 298 | 298 |
| $\lambda$ [Å] | 0.71073 | 0.71073 |
| Radiation | Mo-$K_\alpha$ | Mo-$K_\alpha$ |
| $\theta$ limits | 2.77/25.00 | 2.68/25.00 |
| No. of data with $I > 2\sigma(I)$ | 2446 | 2176 |
| No. of variables | 245 | 269 |
| $R$ | 0.0369 | 0.0397 |
| $Rw$ | 0.0950 | 0.1043 |
| Gof | 1.034 | 1.051 |
| Largest peak in final difference [e Å$^{-3}$] | 0.804/–0.710 | 1.419/–0.693 |

 © 2006 Wiley-VCH Verlag GmbH & Co. KGaA, Weinheim 

CCDC-298854 (for **3a**) and -298855 (for **3c**) contain the supplementary crystallographic data for this paper. These data can be obtained free of charge from The Cambridge Crystallographic Data Centre via www.ccdc.cam.ac.uk/data_request/cif.

## Acknowledgments

Financial support of this work by the Greek General Secretariat for Research and Technology and the Russian Academy of Sciences is gratefully acknowledged.

[1] Recent selected books: a) J. Tsuji, *Palladium Reagents and Catalysts*, John Wiley & Sons, Chichester, **1995**; b) F. Diederich, P. J. Stang, *Metal-Catalyzed Cross-Coupling Reactions*, Wiley-VCH, Weinheim, **1998**; c) M. T. Reetz, *Transition Metal Catalysed Reactions* (Eds.: S. G. Davies, S.-I. Murahashi), Blackwell Science, Oxford, **1999**; d) N. Miyaura, *Cross-Coupling Reactions*, Springer, Berlin, **2002**.

[2] Recent selected reviews: a) N. Miyaura, A. Suzuki, *Chem. Rev.* **1995**, *95*, 2457–2483; b) S. P. Stanforth, *Tetrahedron* **1998**, *54*, 263–303; c) A. Suzuki, *J. Organomet. Chem.* **2002**, *653*, 83–90; d) N. Miyaura, *Top. Curr. Chem.* **2002**, *219*, 11–59; e) A. F. Littke, G. C. Fu, *Angew. Chem. Int. Ed.* **2002**, *41*, 4176–4211; f) A. Zapf, M. Beller, *Top. Catal.* **2002**, *19*, 101–109; g) R. B. Bedford, C. S. J. Cazin, D. Holder, *Coord. Chem. Rev.* **2004**, *248*, 2283–2321; h) F. Bellina, A. Carpita, R. Rossi, *Synthesis* **2004**, 2419–2440; i) A. C. Frisch, M. Beller, *Angew. Chem. Int. Ed.* **2005**, *44*, 674–688.

[3] G. Bringmann, C. Gunther, M. Ochse, O. Schupp, S. Tasler in *Progress in the Chemistry of Organic Natural Products* (Eds.: W. Hertz, H. Falk, G. W. Kirby, R. Moore), Springer, New York, **2001**, vol. 82, pp. 1–293.

[4] Recent selected papers: a) R. B. Bedford, C. S. J. Cazin, M. B. Hursthouse, M. E. Light, V. J. M. Scordia, *Dalton Trans.* **2004**, 3864–3868; b) M. an der Heiden, H. Plenio, *Chem. Eur. J.* **2004**, *10*, 1789–1797; c) A. Zapf, R. Jackstell, F. Rataboul, T. Riermeier, A. Monsees, C. Fuhrmann, N. Shaikh, U. Dingerdissen, M. Beller, *Chem. Commun.* **2004**, 38–39; d) K. W. Anderson, S. L. Buchwald, *Angew. Chem. Int. Ed.* **2005**, *44*, 6173–6177; e) T. E. Barder, S. D. Walker, J. R. Martinelli, S. L. Buchwald, *J. Am. Chem. Soc.* **2005**, *127*, 4685–4696; f) W.-M. Dai, Y. Zhang, *Tetrahedron Lett.* **2005**, *46*, 1377–1381; g) D. Liu, W. Gao, Q. Dai, X. Zhang, *Org. Lett.* **2005**, *7*, 4907–4910; h) M. Dochnahl, M. Doux, E. Faillard, L. Ricard, P. Le Floch, *Eur. J. Inorg. Chem.* **2005**, 125–134; i) C. Bianchini, G. Lenoble, W. Oberhauser, S. Parisel, F. Zanobini, *Eur. J. Inorg. Chem.* **2005**, 4794–4800; j) R. C. Smith, C. R. Bodner, M. J. Earl, N. C. Sears, N. E. Hill, L. M. Bishop, N. Sizemore, D. T. Hehemann, J. J. Bohn, J. D. Protasiewicz, *J. Organomet. Chem.* **2005**, *690*, 477–481; k) J. Gong, G. Liu, C. Du, Y. Zhu, Y. Wu, *J. Organomet. Chem.* **2005**, *690*, 3963–3969.

[5] Recent selected papers: a) C. W. K. Gstöttmayr, V. P. W. Böhm, E. Herdtweck, M. Grosche, W. A. Herrmann, *Angew. Chem. Int. Ed.* **2002**, *41*, 1363–1365; b) J. S. Zhou, G. C. Fu, *J. Am. Chem. Soc.* **2004**, *126*, 1340–1341; c) I. J. S. Fairlamb, A. R. Kapdi, A. F. Lee, G. Sánchez, G. López, J. L. Serrano, L. García, J. Pérez, E. Pérez, *Dalton Trans.* **2004**, 3970–3981; d) I. J. S. Fairlamb, A. R. Kapdi, A. F. Lee, *Org. Lett.* **2004**, *6*, 4435–4438; e) R. A. Gossage, H. A. Jenkins, P. N. Yadav, *Tetrahedron Lett.* **2004**, *45*, 7689–7691; f) A. Mukherjee, A. Sarkar, *Tetrahedron Lett.* **2005**, *46*, 15–18; g) A. I. Moncada, M. A. Khan, L. M. Slaughter, *Tetrahedron Lett.* **2005**, *46*, 1399–1403; h) C. Song, Y. Ma, Q. Chai, C. Ma, W. Jiang, M. B. Andrus, *Tetrahedron* **2005**, *61*, 7438–7446; i) T. Mino, Y. Shirae, M. Sakamoto, T. Fujita, *J. Org. Chem.* **2005**, *70*, 2191–2194; j) C.-L. Chen, Y.-H. Liu, S.-M. Peng, S.-T. Liu, *Organometallics* **2005**, *24*, 1075–1081.

[6] Recent selected papers: a) I. D. Kostas, *J. Organomet. Chem.* **2001**, *626*, 221–226; b) I. D. Kostas, *J. Organomet. Chem.* **2001**, *634*, 90–98; c) I. D. Kostas, *Inorg. Chim. Acta* **2003**, *355*, 424–427; d) I. D. Kostas, B. R. Steele, A. Terzis, S. V. Amosova, *Tetrahedron* **2003**, *59*, 3467–3473; e) I. D. Kostas, B. R. Steele, F. J. Andreadaki, V. A. Potapov, *Inorg. Chim. Acta* **2004**, *357*, 2850–2854; f) I. D. Kostas, K. A. Vallianatou, J. Holz, A. Börner, *Appl. Organomet. Chem.* **2005**, *19*, 1090–1095.

[7] a) D. Kovala-Demertzi, P. N. Yadav, M. A. Demertzis, J. P. Jasinski, F. J. Andreadaki, I. D. Kostas, *Tetrahedron Lett.* **2004**, *45*, 2923–2926; b) I. D. Kostas, F. J. Andreadaki, D. Kovala-Demertzi, C. Prentjas, M. A. Demertzis, *Tetrahedron Lett.* **2005**, *46*, 1967–1970.

[8] S. V. Amosova, N. A. Makhaeva, A. V. Martynov, V. A. Potapov, B. R. Steele, I. D. Kostas, *Synthesis* **2005**, 1641–1648.

[9] A. D. Garnovskii, I. S. Vasil′chenko, *Usp. Khim.* **2002**, *71*, 1064–1089.

[10] G. C. Percy, D. A. Thornton, *J. Inorg. Nucl. Chem.* **1972**, *34*, 3369–3376.

[11] M. T. Reetz, J. G. De Vries, *Chem. Commun.* **2004**, 1559–1563.

[12] a) R. X. Wang, X. Z. You, Q. J. Merg, E. A. Minz, X. R. Bu, *Synth. Commun.* **1994**, *24*, 1757–1760; b) S. Matsui, M. Mitani, J. Saito, Y. Tohi, H. Makio, N. Matsukawa, Y. Takagi, K. Tsuru, M. Nitabaru, T. Nakano, H. Tanaka, N. Kashiwa, T. Fujita, *J. Am. Chem. Soc.* **2001**, *123*, 6847–6856.

[13] J. Okuda, T. Eberle, T. P. Spaniol, V. Piquet-Fauré, *J. Organomet. Chem.* **1999**, *591*, 127–137.

[14] **2b** is a known compound but no NMR spectroscopic data were reported: S. Dhar, D. Senapati, P. K. Das, P. Chattopadhyay, M. Nethaji, A. R. Chakravarty, *J. Am. Chem. Soc.* **2003**, *125*, 12118–12124.

[15] **2d** was isolated as a viscous oil and used for complex formation without further purification. Analogous (butyl)Se- or (hexyl) Se-containing Schiff bases are known: a) H. Liang, J. Wu, Y. Liu, L. Yang, L. Hu, S. Qu, *Biol. Trace Elem. Res.* **2003**, *92*, 181–188; b) C.-Y. Yang, Y. Liu, J. Wu, R. Li, Y.-J. Hu, S.-S. Qu, *J. Pharm. Pharmacol.* **2004**, *56*, 1127–1133.

[16] G. M. Sheldrick, *SHELXS-86, Structure Solving Program*, University of Göttingen, Germany, **1986**.

[17] G. M. Sheldrick, *SHELXL-97, Crystal Structure Refinement*, University of Göttingen, Germany, **1997**.

Received: February 28, 2006
Published Online: April 26, 2006

 © 2006 Wiley-VCH Verlag GmbH & Co. KGaA, Weinheim 

DOI: 10.1002/ejic.200501122

# A Prospective Study of the Use of the $[Os(tpy)_2]^{2+}$ (tpy = 2,2′;6′:2′′-Terpyridine) Core as Signalling Scaffolding for the Development of Chemical Sensors

**Jose V. Ros-Lis,[a] Ramón Martínez-Máñez,*[a] Juan Soto,[a] Colette McDonagh,*[b] and Adrian Guckian[b]**

**Keywords:** Chemosensors / Osmium terpyridines / Macrocyclic ligands / Fluorescent probes / Thin films

The heteroleptic osmium(II) complex $[Os(L^1)(Me\text{-}phtpy)][PF_6]_2$ ($L^1$ = 1-[4′-*p*-tolyl-(2,2′:6′,2′′-terpyridyl)]-1,4,8,11-tetraazacyclotetradecane, Me-phtpy = 4′-*p*-tolyl-2,2′:6′,2′′-terpyridine) has been prepared, characterized and its potential use for chemical sensing purposes studied. The complex contains a polyazacycloalkane as "binding site" and a $Os(tpy)_2^{2+}$ core that acts as a "signalling subunit". The emission intensity of the osmium complex was quenched in acetonitrile/water (1:1 v/v) by $Cu^{2+}$ and $Ni^{2+}$. Potentiometric titrations of $[Os(L^1)(Me\text{-}phtpy)]^{2+}$ in the presence of $Cu^{2+}$ were carried out in order to determine thermodynamic binding constants in acetonitrile/water (70:30 v/v, 0.1 mol·dm$^{-3}$ tetrabutylammonium perchlorate). With $Cu^{2+}$ the receptor $[Os(L^1)(Me\text{-}phtpy)]^{2+}$ forms the complex $\{Cu[Os(L^1)(Me\text{-}phtpy)]\}^{4+}$ at neutral pH. Moreover it undergoes two stepwise protonation processes at acid pH related to the partial protonation of the cyclam core and forms two hydroxo complexes at basic pH. The $Ni^{2+}$ complexes of the osmium receptor $[Os(L^1)(Me\text{-}phtpy)]^{2+}$ are able to act as an anion fluorogenic chemosensor in acetonitrile/water mixtures. A displacement of the quenching effect to more acidic pH in the $Ni^{2+}$–$[Os(L^1)(Me\text{-}phtpy)]^{2+}$ system was observed for anions in the order ATP > AMP > chloride. A prospective study of the use of the $[Os(L^1)(Me\text{-}phtpy)]^{2+}$ complex as a fluorogenic sensor for oxygen was also carried out by incorporation of the complex in sol-gel silica films made with TEOS and MTEOS. Significant quenching of the osmium fluorescence by oxygen was observed. The oxygen response of the films showed good stability and repeatability. The study suggested that the $Os(tpy)_2^{2+}$ core might act as suitable signalling scaffolding in chemical sensing systems of cations, anions and gases.

(© Wiley-VCH Verlag GmbH & Co. KGaA, 69451 Weinheim, Germany, 2006)

## Introduction

The development of new chemosensors for the selective sensing of cations and anions based on the covalent or non-covalent coupling of binding sites and signalling subunits is an area of interest. These programmed molecular systems, when appropriately designed, are capable of transducing guest binding processes into suitable signalling events such as changes in colour, fluorescence or redox properties of the formed molecular ensemble. Among different output signals, those based on changes in emission properties are especially attractive and a number of different fluorogenic chemosensors have been described for anion[1] and cation[2] sensing. Both all-organic and metal-based fluorogenic subunits have been widely used. Among metal-based luminescent systems, the complexes of ruthenium and rhenium are well known and have been used as signalling subunits in a considerable number of reported chemosensors.[3] In fact, the polypyridyl complexes of $d^6$ metal cations, with their strong metal-to-ligand charge transfer absorptions and emitting excited states, are good candidates as signalling reporters. In this sense, the most widely used metal-based signalling framework has been the $Ru(bpy)_3^{2+}$ core.[4] In contrast, the analogous $Ru(tpy)_2^{2+}$ scaffolding has been used as a signalling unit in very few cases.[5–10] $Ru(tpy)_2^{2+}$ might show certain advantages versus $Ru(bpy)_3^{2+}$, that is, it is relatively easy to functionalise the terpyridine core. The most serious drawback in using the $Ru(tpy)_2^{2+}$ scaffolding is its usually very low quantum yield when compared with that found for the $Ru(bpy)_3^{2+}$ systems. In order to maintain the use of the terpyridine framework but in an attempt to enhance the emission properties of the signalling unit at room temperature, we have moved in this paper from ruthenium to osmium as an alternative metal centre. Thus, for instance, the quantum yield at room temperature of the Ru(tolyl-tpy)$_2^{2+}$ complex (tolyl-tpy = bis[4′-(*p*-tolyl)-2,2′:6′,2′′-terpyridine]) is $3.2 \times 10^{-5}$, whereas that observed with osmium as the metal centre, Os(tolyl-tpy)$_2^{2+}$, is more than 500 times larger ($\varphi$ = 0.021).[11] Although the osmium–terpyridine complexes have received less consideration than other metal–terpyridine systems, their photophysical properties

[a] Instituto de Química Molecular Aplicada, Departamento de Química, Universidad Politécnica de Valencia, Camino de Vera s/n, 46022 Valencia, Spain
E-mail: rmaez@qim.upv.es
[b] National Centre for Sensor Research, Dublin City University, Dublin 9, Ireland

 © 2006 Wiley-VCH Verlag GmbH & Co. KGaA, Weinheim 

are well known because of comparative studies with the ruthenium analogues.[12]

Some of us have previously reported ruthenium bis-terpyridine functionalised systems as chemosensors for metal cations and anions.[6–10] However, and as far as we know, there are very few examples of the use of the $Os(tpy)_2^{2+}$ core as a signalling subunit for chemosensing purposes. As part of our interest in the development of chemical sensors for cations,[13] anions[14] and neutral guests,[15] we report here a prospective use of the osmium–terpyridine scaffolding as signalling reporter for the fluorogenic sensing of metal cations, anions and gases.

## Results and Discussion

### Synthesis and Characterisation

The ligand $L^1$ was synthesised following previously reported procedures[7] by reaction of 4′-[(4-bromomethyl)-phenyl]-2,2′:6′,2′′-terpyridine with an excess of cyclam in dichloromethane in the presence of $NEt_3$ at 30 °C for 24 h. Equimolar amounts of $L^1$ and [Os(Me-phtpy)$O_2$OH·-$(NO_3)_2$] (Me-phtpy = 4′-*p*-tolyl-2,2′:6′,2′′-terpyridine) were reacted in a THF/water (1:1 v/v) mixture in the presence of hydrazine hydrate as reductant to yield a complex mixture containing several Os–tpy derivatives. The desired heteroleptic derivative $[Os(L^1)(Me\text{-}phtpy)][PF_6]_2$ was isolated from the reaction mixture by column chromatography in silica using a mixture of acetonitrile/water/saturated aqueous solution of $KNO_3$ (85:10:5 v/v/v) as eluent and further precipitation with ammonium hexafluorophosphate (see Scheme 1). The high-resolution FAB mass spectrum of the $[Os(L^1)(Me\text{-}phtpy)][PF_6]_2$ complex showed peaks at *m*/*z* 1325, 1180 and 1033 corresponding to $[Os(L^1)(Me\text{-}phtpy)][PF_6]_2$, $[Os(L^1)(Me\text{-}phtpy)][PF_6]$ and $[Os(L^1)(Me\text{-}phtpy)]$ fragments, respectively. The high-resolution FAB mass spectra also showed the expected isotopic distribution of peaks corresponding to the Os(192), Os(190) and Os(189) isotopes. The $^1H$ NMR spectra of the osmium complex were also in agreement with the proposed formulation.

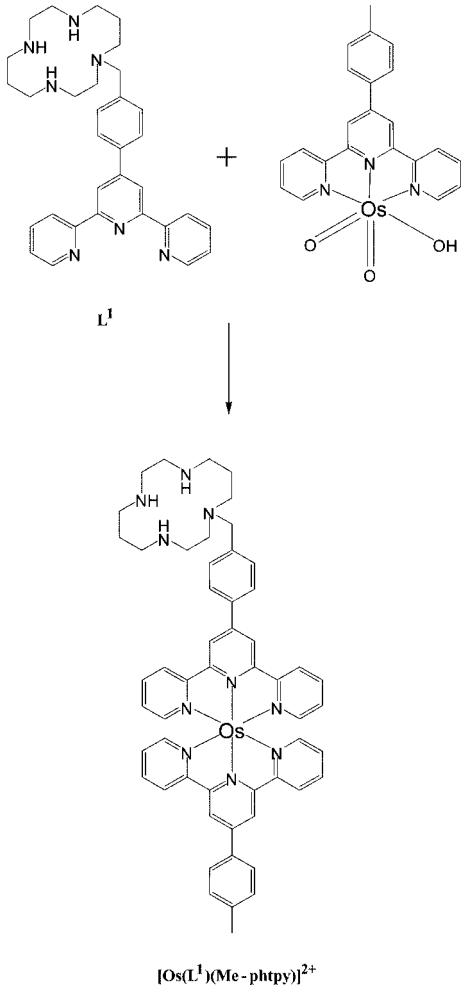


Scheme 1. $L^1$ and synthesis of $[Os(L^1)(Me\text{-}phtpy)]^{2+}$.

### Fluorogenic Sensing of Metal Cations

The synthesised osmium(II) complex $[Os(L^1)(Me\text{-}phtpy)]^{2+}$ contains a polyazacycloalkane as "binding site" and an $Os(tpy)_2^{2+}$ core able to act as a "signalling subunit". In the first step, the studies shown below were carried out to identify the effect that the coordination of metal cations on the cyclam fragment has on the emission properties of the signalling osmium–terpyridine reporter. The electronic spectrum of the $[Os(L^1)(Me\text{-}phtpy)]^{2+}$ complex is as expected for an $Os(tpy)_2^{2+}$ chromophore[11] with two bands in the visible region because of the spin-allowed d→π metal-to-ligand charge transfer (MLCT) transition ($\lambda_{max}$ = 470 nm) and the spin-forbidden MLCT band ($\lambda_{max}$ = 670 nm).

The studies below were performed in acetonitrile–water mixtures because of the insolubility in pure water of the $[Os(L^1)(Me\text{-}phtpy)][PF_6]_2$ complex in a wide pH range. Excitation at 670 nm resulted in the emission at 740 nm. This emission of the $[Os(L^1)(Me\text{-}phtpy)]^{2+}$ complex remains unaltered within 5% in the 2–12 pH interval (see Figure 1). This behaviour is similar to that found for some ruthenium–terpyridine–polyamine analogues.[8] This indicates that in these systems there are no pH-dependent PET processes from the lone pair of the cyclam nitrogens to the photoexcited fluorophore as is usually found in polyazaalkanes bearing polycyclic aromatic hydrocarbons as signalling units.[2]

Steady-state fluorescence experiments as a function of the pH in the presence of equimolar amounts of metal cations $M^{2+}$ ($M^{2+}$ = $Cu^{2+}$, $Zn^{2+}$, $Cd^{2+}$, $Hg^{2+}$, $Pb^{2+}$ and $Ni^{2+}$) resulted in noticeable changes only in the presence of $Cu^{2+}$ and $Ni^{2+}$, whereas the emission intensity versus pH profile stayed unaltered in the presence of the remaining cations. The metal cation $Cu^{2+}$ induced an important quenching of the $Os(tpy)_2^{2+}$ emission in the 3–12 pH range, whereas $Ni^{2+}$ gave a similar quenching at basic pH (see Figure 1). This behaviour is significantly different to that found for the

 © 2006 Wiley-VCH Verlag GmbH & Co. KGaA, Weinheim 

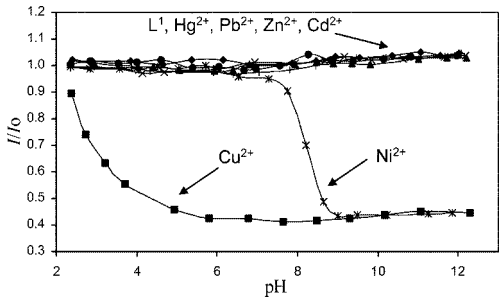


Figure 1. Emission intensity of the system [Os(L$^1$)(Me-phtpy)]$^{2+}$–M$^{2+}$–H$^+$ as a function of the pH in acetonitrile/water (70:30 v/v) mixture, [{Os(L$^1$)(Me-phtpy)}$^{2+}$] = $10^{-4}$ mol·dm$^{-3}$, in the presence of 1 equiv. of metal cation ($\lambda_{ex}$ = 670 nm, $\lambda_{em}$ = 740 nm).

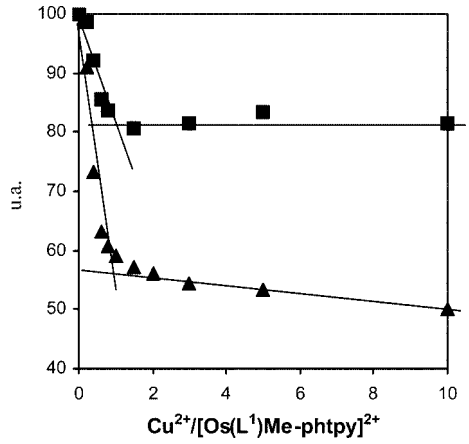


Figure 2. Steady-state fluorescence intensity (▲) and contribution of the lifetime of the free [Os(L$^1$)(Me-phtpy)]$^{2+}$ to the global decay (■) as a function of the Cu$^{2+}$ equivalents in acetonitrile/water (70:30 v/v) mixture.

analogous [Ru(L$^1$)(Me-tpy)]$^{2+}$ compound (Me-tpy = 4′-methyl-2,2′:6′,2′′-terpyridine),[9] for which quenching was observed in a narrower pH window (5–9 pH range). In recent years a certain number of fluorogenic molecular probes for copper and nickel have been reported.[16–18] When compared with them, the complex [Os(L$^1$)(Me-phtpy)]$^{2+}$ shows some advantages; it displays fluorogenic sensing properties in mixed aqueous solutions and shows emission properties in the far end of the visible window where usually few fluorescence interferences are found.

Additional time-resolved emission studies of the ligand [Os(L$^1$)(Me-phtpy)]$^{2+}$ in the presence of Cu$^{2+}$ were carried out in acetonitrile and in acetonitrile/water (70:30 v/v) solutions at neutral pH. In both cases the concentration of the osmium complex was $3\times10^{-5}$ M. The ligand [Os(L$^1$)(Me-phtpy)]$^{2+}$ shows a monoexponential decay in both acetonitrile and acetonitrile/water mixtures with lifetime values of 107 ns and 112 ns, respectively. In the presence of certain amounts of Cu$^{2+}$, a biexponential decay was observed. One of the species has the same lifetime as [Os(L$^1$)(Me-phtpy)]$^{2+}$, whereas the other showed significantly shorter lifetime values of 22 and 28 ns respectively for acetonitrile and acetonitrile/aqueous solutions. This second lifetime was assigned to the formation of Cu$^{2+}$–[Os(L$^1$)(Me-phtpy)]$^{2+}$ complexes. In fact, when we compare the intensity of steady-state fluorescence and the contribution of the 107 ns component to the global decay, we observe that they follow the same tendency (see Figure 2), which is in agreement with the assignment of the 25 ns species to the copper complex that induced the quenching of the fluorescence of the Os(tpy)$_2^{2+}$ core. Upon increasing amounts of Cu$^{2+}$, in water, the lifetime at 112 ns does not undergo significant changes. On the contrary, when only acetonitrile is employed as solvent, the lifetime at 108 ns decreases to a value lower than 95 ns in the presence of an excess of Cu$^{2+}$. This suggests that in acetonitrile the free Cu$^{2+}$ displays some kind of additional interaction with the fluorogenic group that is avoided in the presence of water, probably because of a stronger solvation of the metal. The curves in Figure 2 also reach an asymptotic behaviour between 1 and 2 equiv., suggesting the formation of [Os(L$^1$)(Me-phtpy)]$^{2+}$:Cu$^{2+}$ 1:1 complexes.

In order to obtain more information about the nature of the cation–ligand interaction, we have performed additional coordination studies for the Cu$^{2+}$–[Os(L$^1$)(Me-phtpy)]$^{2+}$ system by the use of potentiometric titrations.

## Potentiometric Studies

The protonation and coordination behaviour of the [Os(L$^1$)(Me-phtpy)]$^{2+}$ complex was studied by potentiometric titrations with KOH of previously acidified acetonitrile/aqueous solutions (70:30 v/v, 0.1 mol·dm$^{-3}$ tetrabutylammonium perchlorate) of [Os(L$^1$)(Me-phtpy)][PF$_6$]$_2$. The resulting protonation constants are shown in Table 1. For comparison purposes, the protonation constants of the ligand L$^1$[9] are also included in Table 1. Os$^{II}$–terpyridine complexes are very stable and kinetically inert, therefore titration experiments could be carried out without observing demetallation on the Os(tpy)$_2^{2+}$ framework. L$^1$ gives rise to five protonation constants in acetonitrile/aqueous solutions. The first two correspond to protonation of the cyclam fragment whereas the remaining three are more difficult to assign and might correspond to either protonation of the terpyridine or the cyclam units. The existence of a large number of protonation sites in L$^1$ makes the last two protonations too acidic and those constant values could not be determined. For the [Os(L$^1$)(Me-phtpy)]$^{2+}$ complex only three protonations were observed. This is in agreement with the results found for cyclam in acetonitrile/water (70:30 v/v) mixtures, in which only three protonation processes (log $K$ = 11.6, 9.49 and 2.01, respectively) were found.[9] The protonation constants for the [Os(L$^1$)(Me-phtpy)]$^{2+}$ complex are very close to those reported for the analogous Ru-containing complex [Ru(L$^1$)(Me-tpy)]$^{2+}$.[9] This was an expected behaviour that indicated that the simple modification of the metal centre in the M–terpyridine core does not significantly affect the protonation of the anchored cyclam unit.

 © 2006 Wiley-VCH Verlag GmbH & Co. KGaA, Weinheim 

Table 1. Logarithms of the protonation constants of $L^1$ and $[Os(L^1)(Me\text{-}phtpy)]^{2+}$ in acetonitrile/water (70:30 v/v) (298 K, 0.1 mol·dm$^{-3}$ tetrabutylammonium perchlorate).

| Reaction | log$\beta$ |
|---|---|
| $[Os(L^1)(Me\text{-}phtpy)]^{2+} + H^+ \leftrightarrows [Os(L^1)(Me\text{-}phtpy)H]^{3+}$ | 10.42(3) |
| $[Os(L^1)(Me\text{-}phtpy)H]^{3+} + H^+ \leftrightarrows [Os(L^1)(Me\text{-}phtpy)H_2]^{4+}$ | 18.90(4) |
| $[Os(L^1)(Me\text{-}phtpy)H_2]^{3+} + H^+ \leftrightarrows [Os(L^1)(Me\text{-}phtpy)H_3]^{5+}$ | 23.81(5) |
| $[L^1H]^+ + H^+ \leftrightarrows [L^1H_2]^{2+}$ | 19.34(4) |
| $[L^1H_2]^{2+} + H^+ \leftrightarrows [L^1H_3]^{3+}$ | 23.95(3) |
| $[L^1H_3]^{3+} + H^+ \leftrightarrows [L^1H_4]^{4+}$ | 26.89(3) |
| $[L^1H_4]^{4+} + H^+ \leftrightarrows [L^1H_5]^{5+}$ | 29.51(2) |

Table 2 shows the stability constants obtained for the formation of $Cu^{2+}$ complexes with $[Os(L^1)(Me\text{-}phtpy)]^{2+}$ in acetonitrile/water (70:30 v/v) mixtures from potentiometric titrations with KOH of previously acidified solutions of 1:1 mixtures of $Cu^{2+}$ and $[Os(L^1)(Me\text{-}phtpy)][PF_6]_2$. The distribution diagram of $[Os(L^1)(Me\text{-}phtpy)]^{2+}$–$H^+$–$Cu^{2+}$ is shown in Figure 3. The receptor $[Os(L^1)(Me\text{-}phtpy)]^{2+}$ forms the complex $\{Cu[Os(L^1)(Me\text{-}phtpy)]\}^{4+}$ that exists at neutral pH (see Figure 3). This complex undergoes two stepwise protonation processes at acid pH and forms two hydroxo complexes at basic pH. The hydroxo complexes are formed by $OH^-$ coordination to the $Cu^{2+}$ centre to give most likely an octahedral configuration, whereas protonation processes at acidic pH involve the partial protonation of the cyclam subunit. The logarithm of the stability constant for the formation of the $\{Cu[Os(L^1)(Me\text{-}phtpy)]\}^{4+}$ complex is 14.2. This value is very close to that found for the formation of the analogous ruthenium complex $\{Cu[Ru(L^1)(Me\text{-}tpy)]\}^{4+}$ (log$K$ = 13.30), in agreement with the almost identical nature of the receptor.[9] The constant for the formation of the $\{Cu[Os(L^1)(Me\text{-}phtpy)]\}^{4+}$ complex can be compared with that found, under similar conditions (acetonitrile/water, 70:30), for the formation of the complex $[Cu(tmfcyclam)]^{2+}$ (log$K$ = 19.06), where tmfcyclam is a cyclam-substituted derivative [tmfcyclam = 1,4,8,11-tetrakis(ferrocenylmethyl)-tetraazacyclotetradecane].[9] Despite the somewhat different nature of both coordination sites in these complexes, the lower stability constants found for the former with $Cu^{2+}$ are in agreement with the electrostatic repulsions imposed by the $Os(tpy)_2^{2+}$ core on the $Cu^{2+}$–cyclam coordination process.

Table 2. Logarithms of the stability constants of the system $[Os(L^1)(Me\text{-}phtpy)]^{2+}$–$H^+$–$Cu^{2+}$ in acetonitrile/water (70:30 v/v) (298 K, 0.1 mol·dm$^{-3}$ tetrabutylammonium perchlorate).

| Reaction | log$\beta$ |
|---|---|
| $[Os(L^1)(Me\text{-}phtpy)]^{2+} + Cu^{2+} + 2H^+ \leftrightarrows$ $[Os(L^1)(Me\text{-}phtpy)CuH_2]^{6+}$ | 24.38(9) |
| $[Os(L^1)(Me\text{-}phtpy)]^{2+} + Cu^{2+} + H^+ \leftrightarrows$ $[Os(L^1)(Me\text{-}phtpy)CuH]^{5+}$ | 20.64(8) |
| $[Os(L^1)(Me\text{-}phtpy)]^{2+} + Cu^{2+} \leftrightarrows$ $[Os(L^1)(Me\text{-}phtpy)Cu]^{4+}$ | 14.20(8) |
| $[Os(L^1)(Me\text{-}phtpy)]^{2+} + Cu^{2+} + H_2O \leftrightarrows$ $[Os(L^1)(Me\text{-}phtpy)Cu(OH)]^{3+} + H^+$ | 5.01(5) |
| $[Os(L^1)(Me\text{-}phtpy)]^{2+} + Cu^{2+} + 2H_2O \leftrightarrows$ $[Os(L^1)(Me\text{-}phtpy)Cu(OH)_2]^{2+} + 2H^+$ | –5.45(7) |

From the stability constants obtained from potentiometric methods and emission studies shown in Figure 1 it is possible to determine which species are responsible for the quenching observed in the interaction of $Cu^{2+}$ with the $Os(tpy)_2^{2+}$ signalling unit. This can be seen in Figure 3, which shows both the distribution diagram and the emission intensity versus pH profile for the $[Os(L^1)(Me\text{-}phtpy)]^{2+}$–$H^+$–$Cu^{2+}$ system. It can be observed that the quenching of the emission of the $Os(tpy)_2^{2+}$ core is related to the formation of $Cu^{2+}$–$[Os(L^1)(Me\text{-}phtpy)]^{2+}$ complexes independently of the nature of the species formed. Neither the partial coordination of the cyclam macrocycle by the protons to form $\{Cu[Os(HL^1)(Me\text{-}phtpy)]\}^{5+}$ and $\{Cu[Os(H_2L^1)(Me\text{-}phtpy)]\}^{6+}$ nor the coordination of $OH^-$ to the $Cu^{2+}$ cation to form $\{Cu(OH)[Os(L^1)(Me\text{-}phtpy)]\}^{3+}$ and $\{Cu(OH)_2[Os(L^1)(Me\text{-}phtpy)]\}^{2+}$ produce significant changes in the emission intensity of the $Os(tpy)_2^{2+}$ core. The enhancement at acid pH is due to demetallation of the $Cu^{2+}$ to recover the emissive $[Os(L^1)(Me\text{-}phtpy)]^{2+}$ species.

This behaviour contrasts significantly with that observed for the $Cu^{2+}$–$[Ru(L^1)(Me\text{-}tpy)]^{2+}$ system, for which the quenching of the emission intensity of the $Ru(tpy)_2^{2+}$ core was only found at neutral pH and attributed to the existence of the $\{Cu[Ru(L^1)(Me\text{-}tpy)]\}^{4+}$ complex in the solution.[9] In that case, the partial protonation of the macrocycle or $Cu^{II}$ coordination with $OH^-$ induced the recuperation of the emission intensity. In our system the different complexes formed have no effect on the emission of the $Os(tpy)_2^{2+}$ core in the $[Os(L^1)(Me\text{-}phtpy)]^{2+}$–$H^+$–$Cu^{2+}$ system, suggesting that the deactivation path should be different to that of $Ru(tpy)_2^{2+}$ in the analogous $[Ru(L^1)(Me\text{-}tpy)]^{2+}$–$H^+$–$Cu^{2+}$ ensemble. For the latter, a deactivation by energy transfer (ET) mechanisms was suggested, bearing in mind that photoelectron transfer (PET) processes were unlikely because of the large difference between the reduction of the $Cu(cyclam)^{2+}$ fragment and the oxidation of the $Ru^{II}$ core.

From a simple thermodynamic cycle the free energy associated to a photoelectron transfer from the excited state of the Os or Ru complex to the Cu–cyclam core can be calculated from the redox potentials of the metal–terpyridine and copper–cyclam cores and the $\lambda_{em}$ from the excited state of the metal–terpyridine group by using the equation: $\Delta G = -F[E_{Cu^{II}/Cu^{I}} - E_{M^{III}/M^{II}}] - hcN_A/\lambda_{em}$ where M = Os or Ru. The oxidation of the $Ru^{II}$ core in $[Ru(Me\text{-}tpy)_2]^{2+}$ is +1.3 V versus SCE, whereas the oxidation of the $Os^{II}$ metal centre in $[Os(L^1)(Me\text{-}phtpy)]^{2+}$ is found at +0.84 V versus SCE. Additionally, the $\lambda_{em}$ for the Os and Ru complexes is 740 and 670 nm, respectively. Unfortunately, the Os system did not show any defined reduction peak for the $Cu^{II}$–cyclam core. Nevertheless, it might be possible to get some conclusion from the comparison between the oxidation potentials and $\lambda_{em}$ from the Ru and Os complexes. Thus, from the above equation it can be observed that a reduction in the oxidation potential of the $M(tpy)_2^{2+}$ core would favour the occurrence of photoelectron transfer processes, whereas a reduction of the energy of the excited state (longer $\lambda_{em}$) would disfavour this. When we move from Ru to Os there

 © 2006 Wiley-VCH Verlag GmbH & Co. KGaA, Weinheim 

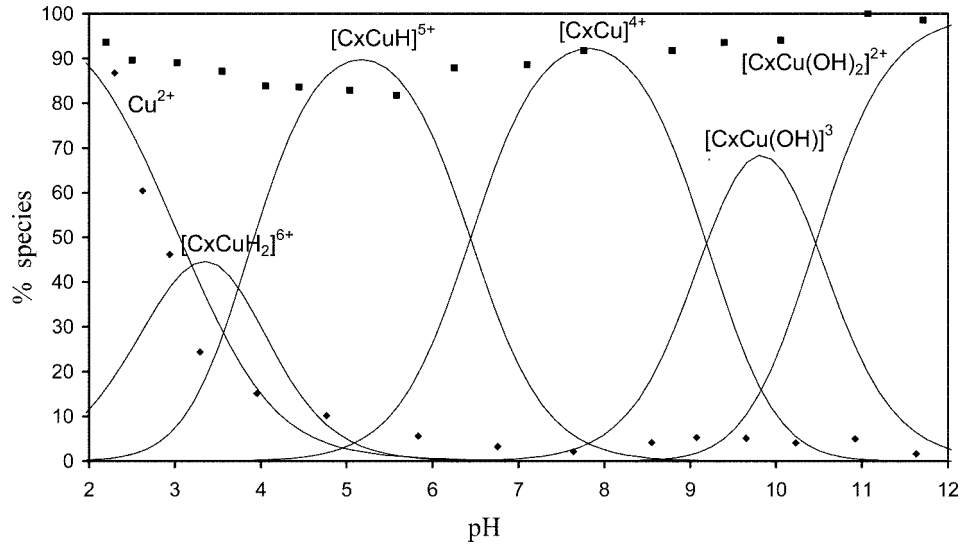


Figure 3. Species distribution diagram of the system [Os(L$^1$)(Me-phtpy)]$^{2+}$–H$^+$–Cu$^{2+}$ in acetonitrile/water (70:30 v/v) from the data of Table 2. The experimental values of intensity of fluorescence of [Os(L$^1$)(Me-phtpy)]$^{2+}$ (■) and [Os(L$^1$)(Me-phtpy)]$^{2+}$–Cu$^{2+}$ (♦) [Cx = Os(L$^1$)(Me-phtpy)] are also included.

is a fall in the oxidation potential of almost 500 mV that is not compensated by the difference in $\lambda_{em}$ from the excited states of Os and Ru ($\lambda_{em}$ at 740 and 670 nm), which correspond to an energy of only 180 mV. This indicates that a PET process from the excited state of the M(tpy)$_2^{2+}$ core to the Cu$^{II}$–cyclam moiety is thermodynamically more favourable to occur for Cu$^{2+}$–[Os(L$^1$)(Me-phtpy)]$^{2+}$ than for the analogous ruthenium Cu$^{2+}$–[Ru(L$^1$)(Me-phtpy)]$^{2+}$ complex.

Attempts to determine stability constants from potentiometric titrations for the Ni$^{2+}$–[Os(L$^1$)(Me-phtpy)]$^{2+}$ system were unsuccessful, most likely because of the presence of kinetically slow coordination processes. Nevertheless, the Ni$^{2+}$ cation would be expected to form similar complexes to those found for Cu$^{2+}$, that is, the formation of the {Ni[Os(L$^1$)(Me-phtpy)]}$^{4+}$ complex at near neutral pH and the formation of hydroxo complexes and protonation of the cyclam macrocycle at basic and acidic pH, respectively. Assuming this general behaviour it might tentatively be suggested that the quenching in the case of the Ni$^{2+}$ cations occurs in the pH range where the square-planar 1:1 {Ni[Os(L$^1$)(Me-phtpy)]}$^{4+}$ complex and the corresponding hydroxo complexes exist in solution.

## Anion Sensing

As we have found above, the complex [Os(L$^1$)(Me-phtpy)]$^{2+}$ can protonate in acetonitrile/water media to give highly positively charged species. We believed that some of these formed species in mixed aqueous environments might be used as chemosensors for the fluorogenic sensing of anions. In order to check this possibility, certain anions were added to acidified solutions of [Os(L$^1$)(Me-phtpy)]$^{2+}$ and the emission of the Os(tpy)$_2^{2+}$ core monitored at different pH values. Unfortunately, the emission versus pH profile of the [Os(L$^1$)(Me-phtpy)]$^{2+}$ complex remained unaltered in the presence of the anions studied (Br$^-$, Cl$^-$, phosphate, sulfate, ATP, ADP and GMP). As an alternative, we also carried out similar studies with the Cu$^{2+}$–[Os(L$^1$)(Me-phtpy)]$^{2+}$ systems. However, unfortunately no change in the emission intensity of the Os(tpy)$_2^{2+}$ core was observed at any pH in the presence of the above-mentioned anions. This might be because, as we have found above, to observe a recovery of emission intensity in the Cu$^{2+}$–[Os(L$^1$)(Me-phtpy)]$^{2+}$ system it appears necessary to remove the copper from the macrocycle, whereas none of the anions is able to produce an interaction strong enough to take out the Cu$^{2+}$ from the cyclam.

The research in this section has been completed by studying the effect that the presence of anions has on the emission behaviour of the Ni$^{2+}$–[Os(L$^1$)(Me-phtpy)]$^{2+}$ system (see Figure 4). As can be seen, the anions ATP, ADP and chloride show a remarkable behaviour and are able to significantly change the emission intensity versus pH profile of the Ni$^{2+}$–[Os(L$^1$)(Me-phtpy)]$^{2+}$ ensemble. Other anions (Br$^-$, phosphate, sulfate and GMP) are not shown but they did not induce significant emission changes. In all cases the Ni$^{2+}$ quenching effect is shifted to the acidic range, suggesting these anions stabilise the formation of the nickel complex. In fact, the interaction of the Ni$^{2+}$–[Os(L$^1$)(Me-phtpy)]$^{2+}$ complex with anions would reduce the neat charge of complex. This would decrease the repulsion with the protonated cyclam core at acidic pH, resulting in a stabilization of the Ni$^{2+}$–[Os(L$^1$)(Me-phtpy)]$^{2+}$ system in a wider pH range with the concomitant fluorescence quenching due to the presence of the Ni$^{2+}$ cation in the cyclam core. On the contrary, it seems that the anions are not able to produce an extra stabilisation of Cu$^{2+}$ in the macrocycle because the quenching effect of Cu$^{2+}$ is not shifted in the presence of anions (see above). The pH value at which the

 © 2006 Wiley-VCH Verlag GmbH & Co. KGaA, Weinheim 

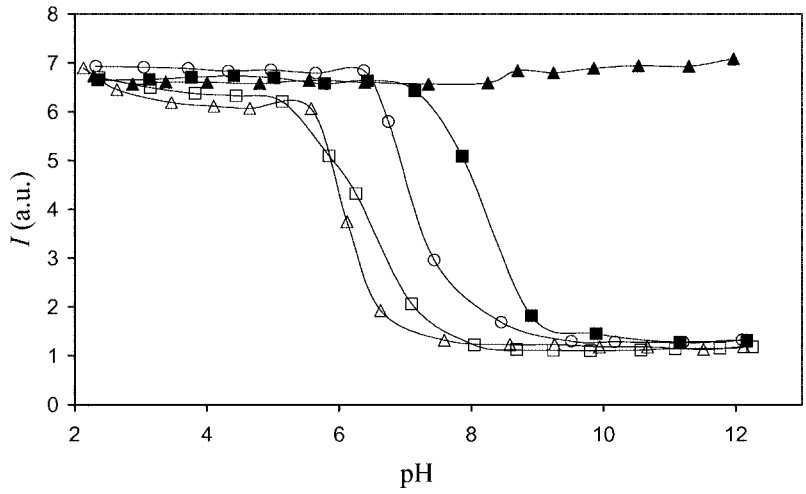


Figure 4. Emission intensity of the system $[Os(L^1)(Me\text{-}phtpy)]^{2+}$–$Ni^{2+}$–$H^+$–$A^{n-}$ as a function of the pH in acetonitrile/water (70:30 v/v) mixture, $[\{Os(L^1)(Me\text{-}phtpy)\}^{2+}] = 10^{-4}$ mol·dm$^{-3}$, in the presence of 1 equiv. of anion unless otherwise noted ($\lambda_{ex}$ = 670 nm, $\lambda_{em}$ = 740 nm). $[Os(L^1)(Me\text{-}phtpy)]^{2+}$ (▲), $Ni^{2+}$ (■), chloride (○), ADP, (□) and ATP (△).

demetallation is produced (about 4 units lower than in the case of $Ni^{2+}$) is probably too low and the compensation of charge with anions is too weak to produce a significant effect in the fluorescence emission.

Selectivity can, for example, be achieved by changing the pH. For instance, addition of anions to the $Ni^{2+}$–$[Os(L^1)(Me\text{-}phtpy)]^{2+}$ system at pH 6.5 would result in a significant quenching only in the presence of ATP and ADP anions. A displacement of the quenching effect to more acidic pH is observed for anions in the order ATP > AMP > chloride. A similar sequence would also be expected (ATP > ADP > chloride) in relation with the strength of the interaction of these anions with the $\{Ni[Os(L^1)(Me\text{-}phtpy)]\}^{4+}$ complex. This is a somewhat attractive behaviour that indicated that the $Ni^{2+}$ complex of the $[Os(L^1)(Me\text{-}phtpy)]^{2+}$ system acts as an anion fluorogenic chemosensor in mixed aqueous environments.

## Oxygen Sensing

Finally, we have also tested the oxygen-sensing properties of the osmium complex $[Os(L^1)(Me\text{-}phtpy)]^{2+}$. There are a certain number of examples in the literature of the use of ruthenium–polypyridyl complexes for the detection of oxygen both in air[19] and as dissolved oxygen in water.[20] These studies are usually carried out either by immobilising the complex in polymer films or in sol-gel-derived films. In these systems the oxygen concentration is proportional to the degree of quenching of the ruthenium complex emission in the presence of oxygen. In most of the cases the complexes used for the preparation of oxygen sensors are $Ru(bipy)_3^{2+}$. On the contrary, there are very few examples of oxygen sensors using osmium complexes.[21]

Thus, we have performed studies directed to test the use of the $[Os(L^1)(Me\text{-}phtpy)]^{2+}$ complex as a gas-phase oxygen

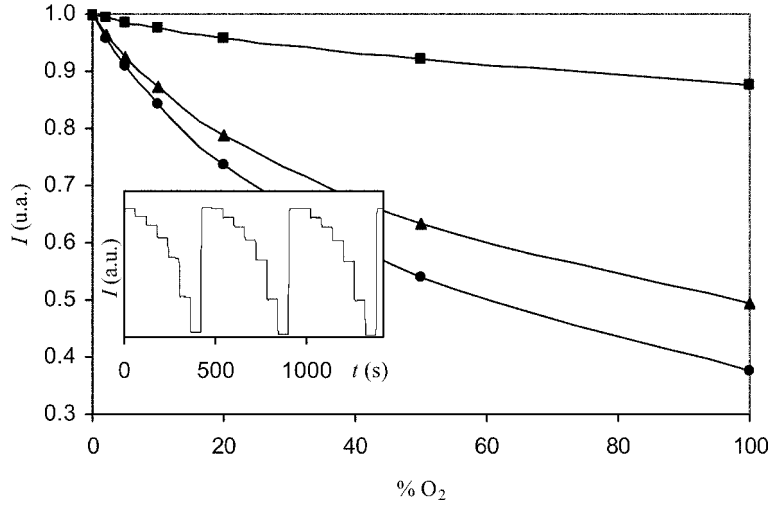


Figure 5. Emission intensity in different $N_2$:$O_2$ mixtures. MTEOS (■), MTEOS/TEOS, 1:1 (▲), TEOS (●).

 © 2006 Wiley-VCH Verlag GmbH & Co. KGaA, Weinheim 

sensor. The studies have been carried out using sol-gel silica films in which the osmium complex has been immobilised. Additionally, in order to study the influence of the sol-gel matrix we have used two different silica precursors, tetraethoxysilane (TEOS) and methyl tryethoxysilane (MTEOS). These precursors have a different number of hydrolysable positions and different speed of hydrolysis. Furthermore, the MTEOS precursor has a methyl group that increases the hydrophobicity of the final matrix. The emission intensity of the [Os(L$^1$)(Me-phtpy)]$^{2+}$ complex in the presence of different $O_2/N_2$ mixtures ($\lambda_{ex}$ = 470 nm, $\lambda_{em}$ = 740 nm) was measured and it was observed that oxygen produced a significant quenching of the osmium fluorescence. Figure 5 plots the emission intensity of the osmium core as a function of the concentration of oxygen for three different films made with TEOS, MTEOS and TEOS/MTEOS in 1:1 molar ratio. Table 3 shows the characteristics of the films prepared. As can be seen in Figure 5 and Table 3, the choice of precursor has a significant effect on the sensor response. Thus, films made with TEOS display a larger quenching (63% of the original emission intensity) in the presence of oxygen than that found for films with MTEOS (13% of the original osmium emission). As can also be seen in Table 3, the response time (time for the intensity to drop to 90% of the original value for a certain concentration of $O_2$) for films fabricated with TEOS was approximately 10 times larger than for the films made with MTEOS. This is most likely due to the presence of silanol groups in the former films that are able to retain some water in the structure hence slowing the sensor response time. The presence of the hydrophobic $CH_3$ groups in the matrix made with MTEOS avoids this effect and enhances the accessibility of the gas in the films, resulting in shorter response times. The films prepared showed a good stability and repeatability, indicating a very reversible process (see inset of Figure 5).

Table 3. Response parameters of the films.

| Film | Quenching $O_2$ [%] | Response time 90% [s] |
|---|---|---|
| MTEOS | 13 | 6.7 |
| MTEOS/TEOS, 1:1 | 52 | 4.4 |
| TEOS | 63 | 44.1 |

## Conclusions

A new osmium bis-terpyridine derivative attached to a cyclam receptor unit has been prepared and its ability to act as a fluorogenic chemosensor has been studied. The osmium complex [Os(L$^1$)(Me-phtpy)]$^{2+}$ is able to act as a fluorogenic sensor of copper and nickel in mixed aqueous environments, whereas the emission of the osmium–terpyridine core remains unaltered in the presence of other metal cations. Additionally, changes in the emission of the nickel complex have shown to be capable of sensing anions such as ATP, ADP and chloride in mixed aqueous solutions. Finally we have demonstrated good gas-phase oxygen sensitivity of sol-gel-based thin films in which the complex has been immobilised. All these studies indicate that osmium–terpyridine systems might behave as suitable and versatile signalling subunits for different sensing purposes.

## Experimental Section

**General Remarks:** [Os(Me-phterpy)$O_2$OH·$(NO_3)_2$], 4′-[4-methylphenyl]-2,2′:6′,2′′-terpyridine and 1-[4′-*p*-tolyl-(2,2′:6′,2′′-terpyridyl)]-1,4,8,11-tetraazacyclotetradecane (L$^1$) were prepared according to published methods. All other reagents were obtained from commercial sources and were used as received.

**Synthesis of [Os(L$^1$)(Me-phtpy)][$PF_6$]$_2$:** The synthesis of the osmium complex [Os(L$^1$)(Me-phtpy)]$^{2+}$ was carried out following a general procedure described previously.[22] A mixture of L$^1$ (195.06 mg, 0.35 mmol), [Os(Me-phterpy)$O_2$OH·$(NO_3)_2$] (238.6 mg, 0.35 mmol) and hydrazine hydrate (0.65 mL) as a reducing agent in water/THF (1:1 v/v) were heated to 50 °C for 10 min. Ammonium hexafluorophosphate was added to the resulting deep red solution and the THF was eliminated under reduced pressure until the appearance of a precipitate that was filtered. This precipitate was purified by column chromatography over silica using acetonitrile/aqueous/saturated $KNO_3$ aqueous solution 85:10:5 as eluent. The product was finally isolated as its $PF_6^-$ salt (19 mg, 4.1% yield). The osmium complexes are toxic and they should be handled carefully. $^1$H NMR (300 MHz, $CD_3CN$, 25 °C) $\delta$ = 2.5–3.5 (m), 4.1 (s, 2 H), 7.13–7.20 (m, 4 H), 7.368 (t, 4 H), 7.61–7.70 (m, 4 H), 7.864 (t, 4 H), 8.137 (d, 2 H), 8.282 (d, 2 H), 8.699 (t, 4 H), 9.082 (s, 2 H), 9.109 (s, 2 H). FAB$^+$: 1325 [Os(L$^1$)(Me-phtpy)]$^{2+}$·2$PF_6^-$, 1180 [Os(L$^1$)(Me-phtpy)]$^{2+}$·$PF_6^-$, 1033 [Os(L$^1$)(Me-phtpy)]$^{2+}$. High resolution FAB$^+$ $C_{54}H_{57}F_{12}N_{10}OsP_2$ (192) calcd. 1327.36662, found 1327.36961. $C_{54}H_{57}F_{12}N_{10}OsP_2$ (190) calcd. 1325.36358, found 1325.35995. $C_{54}H_{57}F_{12}N_{10}OsP_2$ (189) calcd. 1324.36328, found 1324.38587.

**Preparation of the Films for Oxygen Sensing:** Aqueous HCl (0.1 M) and the corresponding Si precursor were added to [Os(L$^1$)(Me-phtpy)][$PF_6$]$_2$ (20 mg, 15 μM) solved in acetonitrile (see Table 4). The solution was stirred for 30 min at room temperature and aged in the oven at 70 °C for several hours. Glass slides were coated by dip coating (3 mm·s$^{-1}$), and the films aged in the oven at 70 °C for 24 h.

Table 4. Details for the preparation of the oxygen-sensing films.

| TEOS [%] | ACN [mL] | HCl [mL] | MTEOS [mL] | TEOS [mL] | Oven [h] |
|---|---|---|---|---|---|
| 0 | 3.280 | 0.630 | 1.800 | – | 1 |
| 50 | 2.995 | 0.536 | 0.847 | 0.946 | 4 |
| 100 | 2.840 | 0.563 | – | 1.800 | 5 |

**Physical Measurements and Instrumentation:** Photochemical data were obtained with a FS900CDT steady-state T-Geometry Fluorometer from Edinburgh Analytical Instruments. $^1$H NMR spectra were recorded with a Varian Gemini spectrometer. Potentiometric titrations were carried out in acetonitrile/water (70:30, v/v, 0.1 mol·dm$^{-3}$ tetrabutylammonium perchlorate) under nitrogen using a vessel water-thermostatted at 25.0 ± 0.1 °C. The tritant was added by means of a Crison microburette 2031. Further details of the potentiometric experiments have been published previously.[23] The concentrations of the metal ions were determined using standard methods. The computer program SUPERQUAD[24] was used to calculate the protonation and stability constants. The titration curves for each system (about 250 experimental points, correspond-

 © 2006 Wiley-VCH Verlag GmbH & Co. KGaA, Weinheim 

ing to at least three titration curves; pH range investigated 2.5–10.2; ligand and metal ions concentration about $1.0\times10^{-3}$ mol·dm$^{-3}$) could be treated either as a single set or as separate entities without significant variation in the values of the stability constants. Finally, the sets of data were merged together and treated simultaneously to give the quoted stability constants.

Oxygen sensitivity was measured employing a Nichia blue LED (470 nm) as an excitation source and S1223 photodiode from Hamamatsu as detector placed at 90° to the LED. Appropriate optical filters were used to isolate the excitation from the emission light. Oxygen/nitrogen mixtures were delivered using computer-controlled mass-flow controllers from Kinetic Systems, Dublin, Ireland.

## Acknowledgments

We thank the Ministerio de Ciencia y Tecnología (projects REN2002-04237-C02-01 and MAT2003-08568-C03-02) and UPV (project PPI-06-03) for support. J. V. R.-L. thanks the Ministerio de Educación y Ciencia for a Doctoral Fellowship.

[1] An exhaustive compilation can be found in: R. Martínez-Máñez, F. Sancenón, *Chem. Rev.* **2003**, *103*, 4419–4476; R. Martínez-Máñez, F. Sancenón, *J. Fluoresc.* **2005**, *15*, 267–285.

[2] See for example: a) A. P. de Silva, H. Q. N. Gunaratne, T. Gunnlaugsson, A. J. M. Huxley, C. P. McCoy, J. T. Rademacher, T. E. Rice, *Chem. Rev.* **1997**, *97*, 1515–1566; b) B. Valeur, I. Leray, *Coord. Chem. Rev.* **2000**, *205*, 3–40.

[3] a) S. S. Sun, A. J. Lees, *Chem. Commun.* **2000**, 1687–1688; b) P. D. Beer, V. Timoshenko, M. Maestri, P. Passaniti, V. Balzani, *Chem. Commun.* **1999**, 1755–1756; c) S. S. Sun, J. A. Anspach, A. J. Lees, P. Y. Zavalij, *Organometallics* **2002**, *21*, 685–693; d) D. B. MacQueen, K. S. Schanze, *J. Am. Chem. Soc.* **1991**, *113*, 6108–6110; e) D. I. Yoon, C. A. Berg-Brennan, H. Lu, J. J. Hupp, *Inorg. Chem.* **1992**, *31*, 3192–3194; f) Y. Shen, B. P. Sullivan, *Inorg. Chem.* **1995**, *34*, 6235–6236; g) J. D. Lewis, J. N. Moore, *Dalton Trans.* **2004**, *9*, 1376–1385; h) V. W. Yam, A. S. Kai, *Chem. Commun.* **1998**, 109–110.

[4] a) P. D. Beer, O. Kocian, R. J. Mortimer, C. Ridgway, *J. Chem. Soc., Chem. Commun.* **1995**, 1799–1800; b) S. C. Rawle, P. Moore, N. W. Alcock, *J. Chem. Soc., Chem. Commun.* **1994**, 684–687; c) P. D. Beer, F. Szemes, V. Balzani, C. M. Sala, M. G. B. Drew, S. W. Dent, M. Maestri, *J. Am. Chem. Soc.* **1997**, *119*, 11864–11875; d) M. J. Deetz, B. D. Smith, *Tetrahedron Lett.* **1998**, *39*, 6841–6844; e) P. Anzenbacher, D. S. Tyson, K. Jursikova, F. N. Castellano, *J. Am. Chem. Soc.* **2002**, *124*, 6232–6233; f) M. S. Vickers, K. S. Martindale, P. D. Beer, *J. Mater. Chem.* **2005**, *15*, 2784–2790.

[5] a) F. Barigelletti, L. Flamigni, G. Calogero, L. Hammarstrom, J. P. Sauvage, J. P. Collin, *Chem. Commun.* **1998**, *21*, 2333–2334; b) F. Barigelletti, L. Flamigni, M. Guardigli, J. P. Sauvage, J. P. Collin, A. Sour, *Chem. Commun.* **1996**, 1329–1330.

[6] M. E. Padilla-Tosta, J. M. Lloris, R. Martínez-Máñez, M. D. Marcos, M. A. Miranda, T. Pardo, F. Sancenon, J. Soto, *Eur. J. Inorg. Chem.* **2001**, 1475–1482.

[7] M. E. Padilla-Tosta, J. M. Lloris, R. Martínez-Máñez, T. Pardo, J. Soto, A. Benito, M. D. Marcos, *Inorg. Chem. Commun.* **2000**, *3*, 45–48.

[8] Y. Al Shihadeh, A. Benito, J. M. Lloris, R. Martínez-Máñez, J. Soto, *Transition Met. Chem.* **2002**, *27*, 307–310.

[9] M. E. Padilla-Tosta, J. M. Lloris, R. Martínez-Máñez, A. Benito, J. Soto, T. Pardo, M. A. Miranda, M. D. Marcos, *Eur. J. Inorg. Chem.* **2000**, 741–748.

[10] M. E. Padilla-Tosta, J. M. Lloris, R. Martínez-Máñez, T. Pardo, F. Sancenón, J. Soto, M. D. Marcos, *Eur. J. Inorg. Chem.* **2001**, 1221–1226.

[11] J. P. Sauvage, J. P. Collin, J. C. Chambron, S. Guillerez, C. Coudret, V. Balzani, F. Barigelletti, L. De Cola, L. Flamigni, *Chem. Rev.* **1994**, *94*, 993–1019.

[12] a) J. P. Collin, S. Guillerez, J. P. Sauvage, F. Barigelletti, L. Flamigni, L. De Cola, V. Balzani, *Coord. Chem. Rev.* **1991**, *111*, 291–296; b) J. C. Chambron, C. Coudret, J. P. Sauvage, *New J. Chem.* **1992**, *16*, 361–367; c) F. Barigelletti, L. Flamigni, V. Balzani, J. P. Collin, J. P. Sauvage, A. Sour, E. C. Constable, A. M. W. Thompson, A. M. W. Cargill, *J. Chem. Soc., Chem. Commun.* **1993**, 942–944; d) F. Barigelletti, L. Flamigni, V. Balzani, J. P. Collin, J. P. Sauvage, A. Sour, E. C. Constable, A. M. W. Thompson, *Coord. Chem. Rev.* **1994**, *132*, 209–214.

[13] a) F. Sancenón, R. Martínez-Máñez, J. Soto, *Chem. Commun.* **2001**, 2262–2263; b) A. B. Descalzo, R. Martínez-Máñez, R. Radeglia, K. Rurack, J. Soto, *J. Am. Chem. Soc.* **2003**, *125*, 3418–3419; c) J. V. Ros-Lis, R. Martínez-Máñez, K. Rurack, F. Sancenón, J. Soto, M. Spieles, *Inorg. Chem.* **2004**, *43*, 5183–5185; d) J. V. Ros-Lis, M. D. Marcos, R. Martínez-Máñez, K. Rurack, J. Soto, *Angew. Chem. Int. Ed.* **2005**, *44*, 4405–4407.

[14] a) F. Sancenón, A. B. Descalzo, R. Martínez-Máñez, M. A. Miranda, J. Soto, *Angew. Chem. Int. Ed.* **2001**, *40*, 2640–2643; b) F. Sancenón, R. Martínez-Máñez, J. Soto, *Angew. Chem. Int. Ed.* **2002**, *41*, 1416–1419; c) A. B. Descalzo, D. Jiménez, J. El Haskouri, D. Beltrán, P. Amorós, M. D. Marcos, R. Martínez-Máñez, J. Soto, *Chem. Commun.* **2002**, 562–563; d) J. V. Ros-Lis, R. Martínez-Máñez, J. Soto, *Chem. Commun.* **2002**, 2248–2249; e) A. B. Descalzo, D. Jiménez, M. D. Marcos, R. Martínez-Máñez, J. Soto, J. El Haskouri, C. Guillem, D. Beltrán, P. Amorós, M. V. Borrachero, *Adv. Mater.* **2002**, *14*, 966–969; f) F. Sancenón, R. Martínez-Máñez, M. A. Miranda, M.-J. Seguí, J. Soto, *Angew. Chem. Int. Ed.* **2003**, *42*, 647–650; g) D. Jiménez, R. Martínez-Máñez, F. Sancenón, J. V. Ros-Lis, A. Benito, J. Soto, *J. Am. Chem. Soc.* **2003**, *125*, 9000–9001; h) B. García-Acosta, X. Albiach-Martí, E. García, L. Gil, R. Martínez-Máñez, K. Rurack, F. Sancenón, J. Soto, *Chem. Commun.* **2004**, 774–775; i) R. Casasús, M. D. Marcos, R. Martínez-Máñez, J. V. Ros-Lis, J. Soto, L. A. Villaescusa, P. Amorós, D. Beltrán, C. Guillem, J. Latorre, *J. Am. Chem. Soc.* **2004**, *126*, 8612–8613; j) A. B. Descalzo, K. Rurack, H. Weisshoff, R. Martínez-Máñez, M. D. Marcos, P. Amorós, K. Hoffmann, J. Soto, *J. Am. Chem. Soc.* **2005**, *127*, 184–200; k) M. Comes, G. Rodríguez-López, M. D. Marcos, R. Martínez-Máñez, F. Sancenón, J. Soto, L. A. Villaescusa, P. Amorós, D. Beltrán, *Angew. Chem. Int. Ed.* **2005**, *44*, 2918–2922; l) C. Coll, R. H. Labrador, R. Martínez-Máñez, J. Soto, F. Sancenón, M.-J. Seguí, E. Sánchez, *Chem. Commun.* **2005**, 3033–3035; m) F. García, J. M. García, B. García-Acosta, R. Martínez-Máñez, F. Sancenón, J. Soto, *Chem. Commun.* **2005**, 2790–2792.

[15] a) J. V. Ros-Lis, B. García, D. Jiménez, R. Martínez-Máñez, F. Sancenón, J. Soto, F. Gonzalvo, M. C. Valldecabres, *J. Am. Chem. Soc.* **2004**, *126*, 4064–4065; b) M. Comes, M. D. Marcos, R. Martínez-Máñez, F. Sancenón, J. Soto, L. A. Villaescusa, P. Amorós, D. Beltrán, *Adv. Mater.* **2004**, *16*, 1783–1786; c) J. V. Ros-Lis, R. Martínez-Máñez, J. Soto, *Org. Lett.* **2005**, *7*, 2337–2339; d) M. Comes, M. D. Marcos, R. Martínez-Máñez, M. C. Millán, J. V. Ros-Lis, F. Sancenón, J. Soto, L. A. Villaescusa, *Chem. Eur. J.* **2005**, *12*, 2162–2170.

[16] a) R. Martínez, A. Espinosa, A. Tárraga, P. Molina, *Org. Lett.* **2005**, *7*, 5869–5872; b) L. L. Zhou, H. Sun, X. H. Zhang, S. K. Wu, *Spectrochim. Acta, Part A* **2004**, *61*, 61–65.

[17] a) M. Shamsipur, T. Poursaberi, A. R. Karami, M. Hosseini, A. Momeni, N. Alizadeh, M. Yousefi, M. R. Ganjali, *Anal. Chim. Acta* **2004**, *501*, 55–60; b) M. K. Amini, T. Momeni-Isfahani, J. H. Khorasani, M. Pourhossein, *Talanta* **2004**, *63*, 713–720.

[18] a) N. Shao, Y. Zhang, S. Cheung, R. Yang, W. Chan, T. Mo, K. Li, F. Liu, *Anal. Chem.* **2005**, *77*, 7294–7303; b) M. Shamsi-

 © 2006 Wiley-VCH Verlag GmbH & Co. KGaA, Weinheim 

pur, T. Poursaberi, A. Avanes, H. Sharghi, *Spectrochim. Acta, Part A* **2006**, *63*, 9–14; c) Y. D. Cao, Q. Y. Zheng, C. F. Chen, Z. T. Huang, *Tetrahedron Lett.* **2003**, *44*, 4751–4755; d) S. Ressalan, C. S. P. Iyer, *J. Lumin.* **2005**, *11*, 121–129.

[19] a) C. S. Burke, O. McGaughey, J.-M. Sabatie, H. Barry, A. K. McEvoy, C. McDonagh, B. D. MacCraith, *Analyst* **2005**, *130*, 41–45; b) G. O′Keeffe, B. D. MacCraith, A. K. McEvoy, C. M. McDonagh, J. F. McGilp, *Sens. Actuators, B* **1995**, *29*, 226–230; c) B. D. MacCraith, G. O′Keeffe, A. K. McEvoy, C. M. McDonagh, J. F. McGilp, B. O'Kelly, J. O'Mahony, M. Cavanagh, *Opt. Eng.* **1994**, *33*, 3861–3866; d) P. Kiernan, C. McDonagh, B. D. MacCraith, K. Mongey, *J. Sol-Gel Sci. Technol.* **1994**, *2*, 513–517; e) B. D. MacCraith, G. O'Keeffe, C. M. McDonagh, A. K. McEvoy, *Electron. Lett.* **1994**, *30*, 888–889; f) B. D. MacCraith, C. M. McDonagh, G. O′Keeffe, E. T. Keyes, J. G. Vos, B. O′Kelly, J. F. Brendan, *Analyst* **1993**, *118*, 385–388.

[20] a) C. M. McDonagh, C. Kolle, A. K. McEvoy, D. L. Dowling, A. A. Cafolla, S. J. Cullen, B. D. McCraith, *Sens. Actuators, B* **2001**, *74*, 124–130; b) P. Lavin, C. M. McDonagh, B. D. McCraith, *J. Sol-Gel Sci. Technol.* **1998**, *13*, 641–645; c) C. M. McDonagh, A. M. Shields, A. K. McEvoy, B. D. McCraith, J. F. Gouin, *J. Sol-Gel Sci. Technol.* **1998**, *13*, 207–211; d) C. M. McDonagh, B. D. McCraith, A. K. McEvoy, *Anal. Chem.* **1998**, *70*, 45–50; e) A. K. McEvoy, C. M. McDonagh, B. D. McCraith, *J. Sol-Gel Sci. Technol.* **1997**, *8*, 1121–1125; f) A. K. McEvoy, C. M. McDonagh, B. D. McCraith, *Analyst* **1996**, *121*, 785–788.

[21] J. N. Demas, B. A. DeGraff, *Coord. Chem. Rev.* **2001**, *221*, 317–351; S. B. Bambot, G. Rao, M. Romauld, G. M. Carter, J. Sipior, E. Terpetchnig, J. R. Lakowicz, *Biosens. Bioelectron.* **1995**, *10*, 643–652.

[22] J. P. Collin, S. Guillerez, J. P. Sauvage, *Inorg. Chem.* **1990**, *29*, 5009–5010.

[23] J. M. Lloris, R. Martínez-Máñez, T. Pardo, J. Soto, M. E. Padilla-Tosta, *J. Chem. Soc., Dalton Trans.* **1998**, 2635–2642.

[24] P. Gans, A. Sabatini, A. Vacca, *J. Chem. Soc., Dalton Trans.* **1985**, 1195–1200.

Received: December 19, 2005
Published Online: April 21, 2006

 © 2006 Wiley-VCH Verlag GmbH & Co. KGaA, Weinheim 

DOI: 10.1002/ejic.200600022

# Synthesis, Structures and Catecholase Activity of a New Series of Dicopper(II) Complexes of Reduced Schiff Base Ligands

**Bellam Sreenivasulu,[a] Fei Zhao,[b] Song Gao,[b] and Jagadese J. Vittal*[a]**

**Keywords:** Biomimetic studies / Copper / Reduced Schiff-base complexes / Tridentate ligands / Catecholase activity / Magnetic properties

A series of dinuclear $Cu^{II}$ complexes of reduced Schiff bases from substituted salicylaldehydes and amino acids have been synthesized and characterized. They are: $[Cu_2(RScp11)_2(H_2O)_2]$ {$H_2RScp11$ = 1-[(2-hydroxy-5-R-benzyl)amino]cyclopentane-1-carboxylic acid; R = H (**1**), Cl (**2**), $CH_3$ (**3**), OH (**4**)}, $[Cu_2(RSch11)_2(H_2O)_x]$ {$H_2RSch11$ = 1-[(2-hydroxy-5-R-benzyl)amino]cyclohexane-1-carboxylic acid; R = H and *x* = 1 (**5**), R = Cl and *x* = 2 (**6**), R = $CH_3$ and *x* = 2 (**7**)}, $[Cu_2(RSch12)_2(H_2O)_2]$ {$H_2RSch12$ = 2-[(2-hydroxy-5-R-benzyl)amino]cyclohexane-1-carboxylic acid; R = H (**8**), $CH_3$ (**10**) and $[Cu_2(ClSch12)_2]\cdot 2H_2O$ (**9**)}, $[Cu_2(Diala5)_2(H_2O)_2]\cdot H_2O$ [$H_3$Diala5 = *N*-(2,5-dihydroxybenzyl)-L-alanine] (**11**), $[Cu_2(Diala4)_2(H_2O)_2]\cdot H_2O$ [$H_3$Diala4 = *N*-(2,4-dihydroxybenzyl)-L-alanine] (**12**), and $[Cu_2(Diala3)_2(H_2O)_2]\cdot H_2O$ [$H_3$Diala3 = *N*-(2,3-dihydroxybenzyl)-L-alanine] (**13**). They were isolated and characterized by chemical and spectroscopic methods. Single crystal X-ray crystallographic studies have revealed that $[Cu_2(Scp11)_2(MeOH)_2]$ (**1a**), $[Cu_2(ClScp11)_2(DMF)(H_2O)]\cdot MeCN$ (**2a**), $[Cu_2(MeScp11)_2(MeOH)_2]\cdot 2MeOH$ (**3a**), $[Cu_2(ClSch11)_2(MeOH)_2]\cdot 2MeOH$ (**6a**), $[Cu_2(ClSch12)_2]\cdot 2MeOH$ (**9a**), and $[Cu_2(Diala4)_2(DMSO)_2]\cdot 2DMSO\cdot 2$acetone (**12a**) have 1D hydrogen-bonded polymeric structures while **4** has a 3D hydrogen-bonded network structure. Complex **8** displays a 2D coordination polymeric network structure. The complexes **1**–**13** have been investigated as functional models for the catechol oxidase by employing 3,5-di-*tert*-butylcatechol as a model substrate. Electron-withdrawing substituents reduced the activity while electron-donating substituents enhanced the activity. Variable-temperature magnetic studies conducted on compound **8** suggest the presence of strong inter-dimer antiferromagnetic coupling.

(© Wiley-VCH Verlag GmbH & Co. KGaA, 69451 Weinheim, Germany, 2006)

## Introduction

Among the well-known representatives of Type III copper proteins, catechol oxidase with active dicopper(II) sites is a ubiquitous enzyme in living systems for catalyzing the oxidation of a wide range of *ortho*-diphenols to *ortho*-diquinones. The subsequent auto polymerization of the highly active quinones into polyphenolic catechol melanins is considered to be responsible for the defense mechanism observed in plants against pathogens or pests.[1] In fact, the two copper atoms of dicopper(II) bio-active centers present in different metalloenzymes are found to act cooperatively within the proximity of ca. 3.5 Å with each $Cu^{II}$ center coordinated by three histidine donors.[2,3] As confirmed by the recent X-ray crystal structure analysis, catechol oxidase in the *met* oxidized form contains dicopper centers with a Cu···Cu distance of 2.9 Å.[3] Modeling the features of bio-relevant dinuclear active sites through synthetic analogues basically involves the judicious design of binucleating ligands to meet the conditions such as bridging mode controlling the metal–metal distance, steric-electronic properties, and geometry around the metal centers.[4] Consequently, dinuclear copper(II) complexes of the binucleating ligands have been extensively documented as bimetallic catalysts due to their potential ability to mimic the functions of the so-called catechol oxidase.[2,4–5]

Our research group has been interested in the coordination chemistry of reduced Schiff-base ligands, *N*-(2-hydroxybenzyl)-amino acids, which have the potential to form dinuclear complexes through a bridging phenolate group. In addition, these ligands can also afford the choice of coordination environments that determine the nature of metal ions that can be bound within the closest proximity. Apart from the studies illustrating interesting solid-state supramolecular transformation of $Cu^{II}$ and $Zn^{II}$ complexes,[6] and the novel helical stair-case structure in the $Ni^{II}$ complex,[7] our research group has reported several dicopper(II) complexes derived from reduced Schiff bases as functional models for catechol oxidase.[8] Very recently, we have also demonstrated that the dicopper(II) complexes containing the weakly coordinating sulfonate donor group are more active

[a] Department of Chemistry, National University of Singapore, Science Drive 3, Singapore 117543
Fax: +65-6779-1691
E-mail: chmjjv@nus.edu.sg
[b] College of Chemistry and Molecular Engineering, Peking University,
Beijing 100871, P. R. China
Supporting information for this article is available on the WWW under http://www.eurjic.org or from the author.

 © 2006 Wiley-VCH Verlag GmbH & Co. KGaA, Weinheim 

catalysts towards the oxidation of 3,5-DTBC compared to their carboxylate analogues.[9]

In this paper, we report a new series of dicopper(II) complexes of reduced Schiff-base ligands formed between various substituted salicylaldehydes and aminocyclopentane/cyclohexanecarboxylic acids and L-alanine (Scheme 1). Our previous studies discussing the effect of chelating side arms[8] and the weakly coordinating sulfonate group[9] on the activity, prompted us to investigate and evaluate the activity of these closely related yet distinct series of dicopper(II) complexes with substituted phenyl rings under similar experimental conditions. Despite the plethora of reports on catecholase activity of various dicopper(II) complexes, studies modulating the activity in terms of electronic properties via substituted bridging phenolates have not been well documented.[10] Such an investigation of the structure-reactivity patterns is essential to enhance the mechanistic understanding of the parameters affecting the catecholase activity. In this paper, we present the salient structural features and the details of catecholase activity of the dicopper(II) complexes of various reduced Schiff-base ligands containing the substituted phenolate moiety. Further, variable temperature magnetic studies of a selected complex have also been discussed.

## Results and Discussion

Copper complexes **1**–**13** have been synthesized in good yields by the complexation of $Cu^{II}$ salts with the corresponding reduced Schiff-base ligands according to the procedures described in the experimental section. Owing to their poor solubility in common solvents except in DMF and DMSO, our attempts to obtain single crystals of the

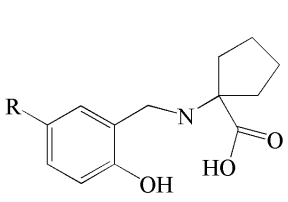

R = H, $H_2$Scp11
R = Cl, $H_2$ClScp11
R = Me, $H_2$MeScp11
R = OH, $H_2$(OH)Scp11

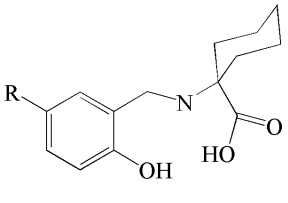

R = H, $H_2$Sch11
R = Cl, $H_2$ClSch11
R = Me, $H_2$MeSch11

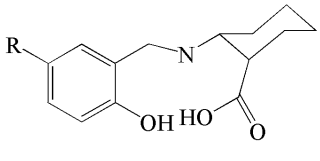

R = H, $H_2$Sch12
R = Cl, $H_2$ClSch12
R = Me, $H_2$MeSch12

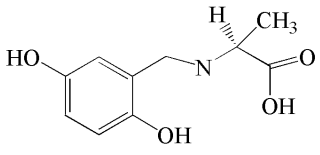

$H_3$Diala5

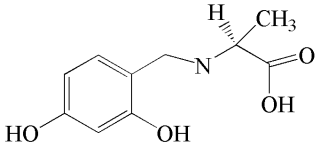

$H_3$Diala4

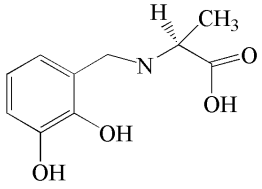

$H_3$Diala3

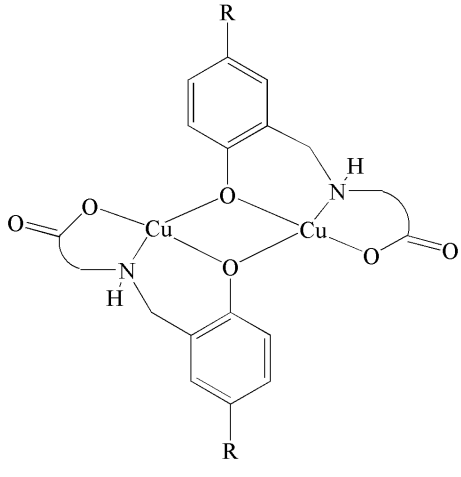

R = H, Cl, OH, $CH_3$

Scheme 1. Ligands and schematic diagram of dicopper(II) complex.

 © 2006 Wiley-VCH Verlag GmbH & Co. KGaA, Weinheim 

bulk as such were not successful. However, the single crystals obtained were different from the bulk due to lattice and coordinated solvents in the case of $[Cu_2(Scp11)_2(MeOH)_2]$ (**1a**), $[Cu_2(ClScp11)_2(DMF)(H_2O)]\cdot MeCN$ (**2a**), $[Cu_2(MeScp11)_2(MeOH)_2]\cdot 2\,MeOH$ (**3a**), $[Cu_2(ClSch11)_2(MeOH)_2]\cdot 2\,MeOH$ (**6a**), $[Cu_2(ClSch12)_2]\cdot 2\,MeOH$ (**9a**), and $[Cu_2(Diala4)_2(DMSO)_2]\cdot 2\,DMSO\cdot 2\,acetone$ (**12a**); however, complexes **4** and **8** afforded single crystals that were the same as the bulk during single crystal growth.

The IR absorption bands of the newly synthesized complexes **1**–**13** in the range of 3398–3458 $cm^{-1}$ indicate the presence of coordinated or lattice water molecules in the compounds.[11a,11c] This can be further supported by the weight loss observed in thermo gravimetric (TG) analysis. The sharp bands observed in the range of 2927–2960 $cm^{-1}$ are due to ν(N–H). The absorption bands observed in the region of 1597–1640 and 1360–1460 $cm^{-1}$ are due to the asymmetric [$\nu_{as}COO^-$] and symmetric [$\nu_sCOO^-$] stretching frequencies of the carboxylate group, respectively. The difference (Δν) between the asymmetric and symmetric stretching frequencies of carboxylate groups can be used to determine their binding mode in the metal complexes.[11a] In general, Δν for monodentate carboxylate is greater than 200 $cm^{-1}$ and for a bridging carboxylate Δν is less than 200 $cm^{-1}$.[12] This observation has been confirmed for the 2D coordination polymeric structure in **8** showing the bridging ($\Delta\nu$ = 115) mode of carboxylate.

The initial weight loss in TG of **4** in the temperature range of 134–177 °C corresponds to the two water molecules coordinated to the $Cu^{II}$ ions, which is corroborated by the crystal structure of **4**. The complex **8** showed weight loss for all six water molecules in the temperature range 80–119 °C and the crystal structure of **8** contains two aqua ligands and four lattice water molecules. The loss of metal bound water molecules along with lattice waters is similar to the observed behavior during the solid-state supramolecular transformations via thermal dehydration.[6a–b] The TG of the bulk **1**–**3**, **5**–**7**, and **9**–**10** showed weight loss in the temperature range of 60–168 °C due to the loss of two metal-bound aqua ligands. The observed dehydration temperature below 120 °C for **11** and **12**, and 130 °C for **13** also suggests similar behavior of metal bound aqua ligands as in **8**. Thus, in the light of the observed thermal dehydration behavior, UV/Vis, IR, and ESI-MS studies the molecular formulae of the bulk have been proposed.

## Solution Studies

The structural behavior of the complexes **1**–**13** in solution has been investigated using UV/Vis, ESI-MS spectroscopic techniques.

### *UV/Vis Spectroscopy*

Electronic spectra of the complexes **1**–**13** recorded in DMF solution and Nujol mull are shown in Table 1. The absorption bands observed in the range 620–703 nm correspond to *d-d* transitions and the strong bands at 358–402 nm are due to ligand-to-metal charge transfer. For an octahedral geometry the expected $^2E_g$ to $^2T_{2g}$ transition takes place at around 800 nm. This band will undergo a significant blue shift when the octahedral geometry distorts to a square pyramidal and square planar structure.[13] For the reduced Schiff base copper(II) complexes with square pyramidal geometry, the *d-d* transitions and charge transfer transitions generally occur in the range 620–720 and 360–450 nm, respectively.[8–9,14a–14d]

The medium intensity bands occurring in the range 356–401 nm are due to phenolate-to-copper(II) charge transfer.[14a–14d] As the present complexes contain the *para* substituents on the bridging phenolate, definitive assignment of CT bands can be provided based on the electronic effects induced by the substituents. Electron-donating groups are expected to decrease the Lewis acidity of the copper center thus shifting the phenoxo-to-copper CT band to lower energies while electron-withdrawing groups are expected to increase the Lewis acidity and shift the phenolate-to-copper CT bands to higher energies.[10a,14d] Accordingly, we observe the electron-donating *para* $-CH_3$ group shifting the LMCT band to lower energy and the electron-withdrawing *para* –OH and –Cl groups causing the shift of the LMCT

Table 1. Summary of the UV/Vis spectroscopic data of **1**–**13**.

| Complex | Absorption bands (DMF) | | (Nujol) | |
|---|---|---|---|---|
| | *d-d* (ε)[a] | CT(ε) | *d-d* | CT |
| $[Cu_2(Scp11)_2(H_2O)_2]$, **1** | 705 (150) | 380 (1780) | 695 | 378 |
| $[Cu_2(ClScp11)_2(H_2O)_2]$, **2** | 702 (170) | 356 (1340) | 690 | 360 |
| $[Cu_2(MeScp11)_2(H_2O)_2]$, **3** | 703 (170) | 394 (2050) | 697 | 392 |
| $[Cu_2(OHScp11)_2(H_2O)_2]$, **4** | 703 (1010) | 364 (1520) | 696 | 370 |
| $[Cu_2(Sch11)_2](H_2O)$, **5** | 703 (1890) | 380 (2800) | 698 | 388 |
| $[Cu_2(ClSch11)_2(H_2O)_2]$, **6** | 704 (180) | 370 (1190) | 691 | 378 |
| $[Cu_2(MeSch11)_2(H_2O)_2]$, **7** | 702 (1860) | 400 (1410) | 696 | 398 |
| $[\{Cu_2(Sch12)_2\}_2Cu_2(Sch12)_2(H_2O)_2]\cdot 4H_2O$, **8** | 704 (530) | 381 (1430) | 700 | 382 |
| $[Cu_2(ClSch12)_2]\cdot 2H_2O$, **9** | 623 (240) | 368 (1680) | 628 | 370 |
| $[Cu_2(MeSch12)_2(H_2O)_2]$, **10** | 702 (180) | 401 (2440) | 697 | 399 |
| $[Cu_2(Diala5)_2(H_2O)_2]\cdot H_2O$, **11** | 703 (160) | 364 (1740) | 695 | 368 |
| $[Cu_2(Diala4)_2(H_2O)_2]\cdot H_2O$, **12** | 702 (210) | 368 (2120) | 704 | 364 |
| $[Cu_2(Diala3)_2(H_2O)_2]\cdot H_2O$, **13** | 703 (210) | 372 (920) | 702 | 379 |

[a] ($M^{-1}\,cm^{-1}$).

 © 2006 Wiley-VCH Verlag GmbH & Co. KGaA, Weinheim 

band to higher energy. On the basis of the crystal structure of **9a**, the geometry around the copper(II) centers in **9** is assumed to have a square-planar geometry. The observed *d-d* transitions in **9** at 623 nm also indicate square planar $Cu^{II}$ centers. This behavior is similar to that recorded for the structurally well-characterized square planar copper(II) complexes.[13] The electronic spectra of **1**–**13** do not change much in DMF solution and Nujol mull, and appear to indicate that the coordination number and geometry observed in the solid state are retained in solution.

### *ESI-MS Studies*

The structural behavior of the complexes **1**–**13** in solution has been investigated by ESI mass spectral analysis. ESI mass spectra of the complexes were recorded in MeOH except for **2**, **7**, and **9** for which the spectra were recorded in a 1:1 solvent mixture of MeOH and DMSO because of a solubility problem. As indicated by the masses of both positive and negative ions in the spectra, all the complexes are found to exist in solution mainly as dicopper(II) species. For example, the positive ion ESI masses observed for **8** shows the existence of dicopper(II) species predominantly in solution as $[Cu_2(Sch12)_2Na]^+$ (643, 100). The other less intense peaks found were $[Cu(Sch12)Na]^+$ (333, 27); $[Cu_3(Sch12)_3Na]^+$ (954, 55); $[Cu_4(Sch12)_4Na]^+$ (1267, 25); $[Cu_5(Sch12)_5Na]^+$ (1574, 20). Our attempts to obtain consistent electrochemical data using CV were unsuccessful owing to the solubility problem. Nonetheless, it maybe noted that the concentration levels in methanolic solutions were just enough for the activity studies.

## General Description of Crystal Structures

The crystal structures of complexes **1a**, **2a**, **3a**, **4**, **6a**, **8**, **9a**, and **12a** were determined by single-crystal X-ray crystallographic analysis. In all these complexes, the reduced Schiff-base ligands display a tridentate coordination mode while bridging the two copper ions through phenolate oxygen atoms forming $Cu_2O_2$ cores with a Cu···Cu distance of ca. 3 Å. The crystal structure of **9a** displayed $Cu^{II}$ centers with a square-planar geometry while the other complexes contain square pyramidal $Cu^{II}$ centers.

In all the square pyramidal complexes, the basal plane of the square pyramid is completed by the coordination of each $Cu^{II}$ to the two bridging phenolate oxygen atoms, imine nitrogen, and carboxylate oxygen. The Cu–O bond lengths due to the coordination of each $Cu^{II}$ to the bridging phenolate and carboxylate oxygen atoms in the basal plane fall in the range of 1.934(2)–2.002(3) and 1.876(2)–1.982(7) Å, respectively, while the bond lengths due to Cu–N (imine nitrogen) are observed in the range of 1.950(2)–2.004(8) Å. The apical position is occupied by solvents. A crystallographic center of inversion is present in the dimeric structure of **1a**, **3a**, **4**, **6a**, and **9a**. Selected bond lengths and angles as well as hydrogen bond parameters have been compiled in Table 2 and Table 3 respectively.

With respect to the ligands, **1a**, **2a**, **3a**, and **4** contain a 1-aminocyclopentanecarboxylate side arm but different

Table 2. Selected bond lengths and bond angles for the complexes.

| | | | |
|---|---|---|---|
| Complex **1a** | | | |
| Cu(1)–O(2) | 1.945(2) | O(2)–Cu(1)–O(1)[a] | 102.78(9) |
| Cu(1)–O(1)[a] | 1.958(2) | O(1)–Cu(1)–Cu(1)[a] | 39.44(6) |
| Cu(1)–O(1) | 1.961(2) | N(1)–Cu(1)–Cu(1)[a] | 131.92(8) |
| Cu(1)–N(1) | 1.983(3) | C(1)–O(1)–Cu(1)[a] | 133.7(2) |
| Cu(1)–O(4) | 2.213(2) | C(1)–O(1)–Cu(1) | 118.4(2) |
| Cu(1)–Cu(1)[a] | 3.0245(7) | Cu(1)[a]–O(1)–Cu(1) | 101.04(9) |
| Complex **2a** | | | |
| Cu(1)–O(4) | 1.949(2) | O(4)–Cu(1)–N(1) | 68.2(1) |
| Cu(1)–N(1) | 1.962(3) | O(4)–Cu(1)–O(2) | 102.4(1) |
| Cu(1)–O(2) | 1.964(3) | N(1)–Cu(1)–O(2) | 82.5(1) |
| Cu(1)–O(1) | 2.002(3) | O(4)–Cu(1)–O(1) | 79.2(1) |
| Cu(1)–O(8) | 2.230(3) | N(1)–Cu(1)–O(1) | 93.5(1) |
| Cu(1)–Cu(2) | 3.0428(6) | O(2)–Cu(1)–O(1) | 165.7(1) |
| Complex **3a** | | | |
| Cu(1)–O(2) | 1.939(2) | O(2)–Cu(1)–O(1)[a] | 102.02(7) |
| Cu(1)–O(1)[a] | 1.944(2) | O(2)–Cu(1)–O(1) | 174.04(7) |
| Cu(1)–O(1) | 1.960(2) | O(1)[a]–Cu(1)–O(1) | 79.33(7) |
| Cu(1)–N(1) | 1.961(2) | O(1)[a]–Cu(1)–N(1) | 171.71(7) |
| Cu(1)–Cu(1)[a] | 3.0056(5) | O(2)–Cu(1)–Cu(1)[a] | 141.57(5) |
| | | O(1)–Cu(1)–N(1) | 93.79(7) |
| Complex **4** | | | |
| Cu(1)–O(2) | 1.920(2) | O(2)–Cu(1)–O(1) | 178.97(8) |
| Cu(1)–O(1) | 1.930(2) | O(2)–Cu(1)–O(1)[a] | 102.10(8) |
| Cu(1)–O(1)[a] | 1.934(2) | O(1)–Cu(1)–O(1)[a] | 78.48(8) |
| Cu(1)–N(1) | 1.973(2) | O(2)–Cu(1)–N(1) | 84.57(9) |
| Cu(1)–O(4) | 2.660(3) | O(1)–Cu(1)–N(1) | 94.67(9) |
| Cu(1)–Cu(1)[a] | 2.9923(7) | O(1)[a]–Cu(1)–N(1) | 165.21(9) |
| | | O(1)[a]–Cu(1)–O(4) | 105.32(8) |
| Complex **6a** | | | |
| Cu(1)–O(2) | 1.940(2) | O(2)–Cu(1)–O(1)[a] | 103.62(6) |
| Cu(1)–O(1)[a] | 1.951(1) | O(2)–Cu(1)–N(1) | 83.76(7) |
| Cu(1)–N(1) | 1.968(2) | O(1)[a]Cu(1)–N(1) | 169.91(7) |
| Cu(1)–O(1) | 1.972(1) | O(2)–Cu(1)–O(1) | 173.62(6) |
| O(1)–Cu(1)[a] | 1.951(1) | O(1)[a]–Cu(1)–O(1) | 78.49(6) |
| Cu(1)–Cu(1)[a] | 3.0382(5) | O(2)–Cu(1)–Cu(1)[a] | 142.78(5) |
| Complex **8** | | | |
| Cu(1)–O(2) | 1.91(1) | O(2)–Cu(1)–O(1)[a] | 94.9(5) |
| Cu(1)–O(1) | 1.95(1) | O(1)–Cu(1)–O(1)[a] | 76.8(6) |
| Cu(1)–O(1)[a] | 1.97(1) | O(1)[a]–Cu(1)–N(1) | 154.7(6) |
| Cu(1)–N(1) | 1.98(1) | O(1)[a]–Cu(1)–O(6) | 111.8(5) |
| Cu(1)–O(6) | 2.35(1) | O(5)–Cu(2)–O(4)[b] | 96.8(5) |
| Cu(2)–O(5) | 1.93(2) | O(4)[b]–Cu(2)–O(4) | 76.1(5) |
| Cu(2)–O(9) | 2.51(1) | O(4)[b]–Cu(2)–N(2) | 161.0(6) |
| Cu(2)–O(4)[b] | 1.96(1) | C(15)–O(4)–Cu(2)[b] | 133.4(10) |
| O(1)–Cu(1)[a] | 1.97(1) | Cu(2)[b]–O(4)–Cu(2) | 103.9(5) |
| O(4)–Cu(2)[b] | 1.96(1) | O(7)[c]–Cu(3)–O(7) | 78.1(6) |
| Cu(3)–O(7)[c] | 1.96(1) | O(7)[c]–Cu(3)–N(3) | 163.4(6) |
| O(7)–Cu(3)[c] | 1.96(1) | Cu(3)[c]–O(7)–Cu(3) | 101.9(6) |
| $Cu^{I}$–Cu(1A) | 3.074(4) | O(7)[c]–Cu(3)–O(11) | 95.0(5) |
| Cu(3)–Cu(3)[c] | 3.056(4) | | |
| Complex **9a** | | | |
| Cu(1)–O(2) | 1.876(2) | O(2)–Cu(1)–O(1) | 164.48(9) |
| Cu(1)–O(1) | 1.926(2) | O(2)–Cu(1)–O(1)[a] | 95.72(8) |
| Cu(1)–O(1)[a] | 1.949(2) | O(1)–Cu(1)–O(1)[a] | 76.90(9) |
| Cu(1)–N(1) | 1.950(2) | O(2)–Cu(1)–N(1) | 95.98(9) |
| Cu(1)–Cu(1)[a] | 3.0350(7) | O(1)[a]–Cu(1)–N(1) | 165.17(9) |
| | | O(2)–Cu(1)–Cu(1)[a] | 132.51(6) |

 © 2006 Wiley-VCH Verlag GmbH & Co. KGaA, Weinheim 

Table 2. *(continued)*

| Complex **12a** | | | |
|---|---|---|---|
| Cu(1)–O(5) | 1.982(7) | O(5)–Cu(1)–O(1) | 102.3(3) |
| Cu(1)–O(1) | 1.999(7) | O(5)–Cu(1)–N(2) | 84.1(3) |
| Cu(1)–N(2) | 2.004(8) | O(1)–Cu(1)–N(2) | 169.1(3) |
| Cu(1)–O(4) | 2.005(7) | O(5)–Cu(1)–O(4) | 168.9(3) |
| Cu(1)–O(9) | 2.300(7) | O(1)–Cu(1)–O(4) | 77.4(3) |
| Cu(1)–Cu(2) | 3.0225(8) | N(2)–Cu(1)–O(4) | 94.7(3) |
| | | O(5)–Cu(1)–O(9) | 97.8(3) |
| | | O(1)–Cu(1)–O(9) | 93.4(3) |
| | | N(2)–Cu(1)–O(9) | 94.5(3) |
| | | O(4)–Cu(1)O(9) | 93.3(3) |

[a] Symmetry transformations used to generate equivalent atoms: $-x+1, -y+1, -z+1$ (**1a**); $-x+1, -y+1, -z+1$ (**3a**); $-x+1, -y+1, -z+1$ (**4**); $-x+1, -y+1, -z+1$ (**6a**); $-x+1, -y+1, -z+1$ (**8**); $-x+1, -y+1, -z+1$ (**9a**). [b] $-x, -y, -z$ (**8**). [c] $-x+1, -y+1, -z$ (**8**).

substituents on the 5-position of the benzene ring; H in **1a**, Cl in **2a**, $CH_3$ in **3a**, and OH in **4a**. All these complexes, **1a**, **2a**, **3a**, and **4** display $Cu^{II}$ centers with a distorted square pyramidal geometry ($\tau$ = 0.168, 0.043, 0.038, 0.228, and 0.003, respectively).[15] The common 1-aminocyclopentanecarboxylate side arm of the ligands in **1a**, **2a**, **3a**, and **4** resulted in the formation of five-membered rings. The complex **1a** as a methanol adduct crystallized with two methanol molecules in the monoclinic system with space group *C*2/*c* with a Cu···Cu separation of 3.0245(7) Å. The apical positions of the square pyramid of the two $Cu^{II}$ atoms are occupied by methanol molecules in *trans* fashion (Figure 1). Complementary MeOH···O=C (O4–H4···O2) and N–H···O=C (N1–H1···O3) intermolecular hydrogen bonding generates a 1D polymeric structure in **1a** in the solid state (Figure 2).

Table 3. Hydrogen bond parameters.

| D–H | *d*(D–H) | *d*(H···A) | ∠DHA | *d*(D···A) | A | Symmetry |
|---|---|---|---|---|---|---|
| Compound **1a** | | | | | | |
| N1–H1 | 0.80(3) | 2.35(4) | 148(4) | 3.053(3) | O3 | $x-1, y, z-1/2$ |
| O4–H4 | 0.72(4) | 1.97(4) | 174(5) | 2.691(4) | O2 | $x-1, y, z-1/2$ |
| Compound **2a** | | | | | | |
| O7–H7A | 0.73(6) | 2.26(4) | 162(6) | 2.961(9) | N4S | $x+1, y, z$ |
| O7–H7B | 0.81(6) | 1.92(4) | 177(5) | 2.728(4) | O3 | $x-1, y-1, z-1$ |
| Compound **3a** | | | | | | |
| N1–H1 | 0.87(3) | 2.10(3) | 159(3) | 2.932(3) | O5 | $-x,-y+1,-z+1$ |
| O4–H4 | 0.76(4) | 2.05(4) | 163(3) | 2.785(3) | O3 | $x+1, y, z$ |
| O5–H5 | 0.78(6) | 2.14(5) | 156(5) | 2.864(4) | O2 | |
| Compound **4** | | | | | | |
| N1–H1 | 0.84(3) | 2.39(3) | 143(3) | 3.100(3) | O3 | $x-1, y-1, -z$ |
| O4–H4A | 0.68(4) | 2.10(4) | 162(4) | 2.753(3) | O3 | $x-1, y-1, -z$ |
| O4–H4B | 0.75(4) | 2.20(4) | 146(4) | 2.849(4) | O5 | $x-2, -y, 1-z$ |
| O5–H5 | 0.72(4) | 2.05(4) | 173(4) | 2.770(4) | O4 | $x+1, y, z$ |
| C13–H13B | 0.98 | 2.58 | 144 | 3.420(3) | O2 | $x-1, y-1, -z$ |
| Compound **6a** | | | | | | |
| N1–H1 | 1.01(3) | 1.92(3) | 167(2) | 2.905(3) | O5 | |
| O4–H4 | 0.71(3) | 2.08(3) | 171(4) | 2.775(2) | O3 | $x-1, y, z$ |
| O5–H5 | 0.75(3) | 2.11(3) | 169(3) | 2.851(3) | O2 | $-x+2, -y+1, -z+1$ |
| Compound **8** | | | | | | |
| N1–H1 | 0.81(17) | 2.38(16) | 157(19) | 3.14(1) | O5 | |
| N2–H2 | 0.8(2) | 2.4(2) | 164(18) | 3.18(2) | O8 | |
| N3–H3 | 0.85(18) | 2.13(19) | 170(15) | 2.97(2) | O12 | |
| O11–H11C | 0.9(3) | 1.9(3) | 165(26) | 2.83(3) | O12 | |
| O11–H11D | 0.9(2) | 2.0(2) | 164(27) | 2.84(2) | O6 | |
| O12–H12C | 0.9(3) | 1.9(3) | 168(18) | 2.75(2) | O2 | |
| O13–H13C | 0.9(3) | 2.0(3) | 153(12) | 2.88(3) | O9 | |
| O13–H13D | 0.9(3) | 2.02(18) | 161(12) | 2.89(3) | O3 | |
| Compound **9a** | | | | | | |
| N1–H1 | 0.84(4) | 2.03(4) | 171(3) | 2.866(4) | O1S | |
| O1S–H1S | 0.79(4) | 1.89(4) | 166(5) | 2.667(4) | O3 | $-x+1, -y+1, -z$ |
| Compound **12a** | | | | | | |
| N1–H1 | 0.92 | 2.11 | 153 | 2.96(1) | O11 | |
| N2–H2 | 0.92 | 2.08 | 146 | 2.89(1) | O12 | |
| O7–H7 | 0.83 | 1.87 | 164 | 2.68(1) | O3 | $x+1, y+1, z$ |
| O8–H8A | 0.83 | 1.93 | 154 | 2.70(1) | O6 | $x-1, y-1, z$ |

 © 2006 Wiley-VCH Verlag GmbH & Co. KGaA, Weinheim 

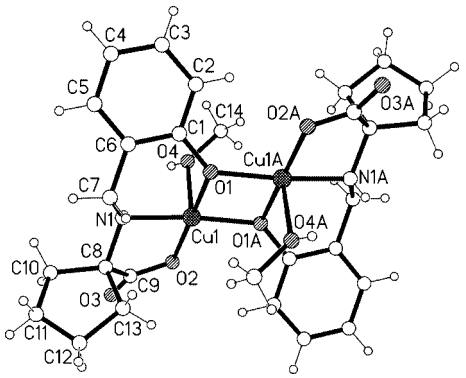


Figure 1. A perspective view of the dimer **1a** (symmetry equivalent positions: $-x+1$, $-y+1$, $-z+1$).

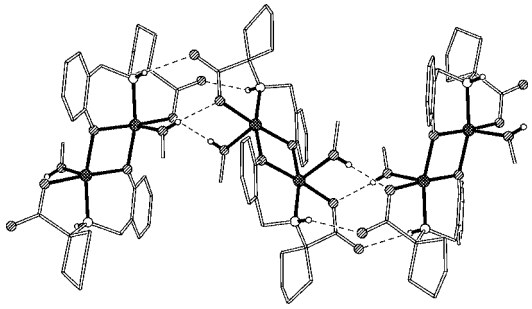

Figure 2. A view showing a portion of the 1D hydrogen-bonded structure in **1a**.

In **2a** the two copper atoms in the dimer are separated by a distance of 3.0428(6) Å. The apical site of the square pyramid is occupied by DMF [Cu(1)–O(8), 2.230(3) Å] with Cu(1) and the aqua ligand [Cu(2)–O(7), 2.299(3) Å] with Cu(2) in *trans* to each other. Each dimer is associated with two molecules of acetonitrile solvent in the asymmetric unit. There are very weak interactions between the carbonyl oxygen atoms and the copper atoms [Cu(1)···O3(1 – *x*, 1 – *y*, 1 – *z*), 2.885 Å and Cu(2)···O6(1 – *x*, *y*, *z*), 2.922 Å] that are about the sum of the van der Waals radii, 2.9 Å. These Cu···O interactions generate a 1D polymer along the *b*-axis sustained by hydrogen bonds between carboxylate oxygen and the aqua ligand, O(7) H(7B)···O(3). Further O(7)–H(7A)···N(4S) hydrogen bonds have also been observed.

The complex **3a** displays square pyramidal geometry at each $Cu^{II}$ center with a Cu···Cu distance of 3.0056(5) Å. The apical sites of the square pyramid at each $Cu^{II}$ center are occupied by methanol molecules in *trans* fashion with a Cu···O distance of 2.59 Å. Packing of dimers along the *a* axis displays a 1D hydrogen-bonded polymer in **3a** supported by intermolecular hydrogen bonds generated between imine H atoms and methanol oxygen [N–H···O(5)], methanolic hydrogen, and carboxylate oxygen atoms [O(4)–H(4)···O(3) and O(5)–H(5)···O(2)] as well as weak interactions of neighboring carboxylate oxygen atoms with each $Cu^{II}$ ion (Cu···O, 2.885 Å) in *syn-anti* fashion.

In the crystal structure of **4** the two lattice water molecules are in close interaction with $Cu^{II}$ atoms [Cu–O, 2.66(3) Å] occupying the apical positions to complete the square pyramidal geometry around each $Cu^{II}$ center (Figure 3) with a Cu···Cu distance of 2.9924(8) Å. Intermolecular hydrogen bonds generated by the hydroxy group on the phenolate moiety with the aqua ligand (O4–H4B···O5, O5–H5···O4) and carboxylate oxygen atom (O4–H4A···O3) and by the imine hydrogen with another carboxylate oxygen (N1–H1···O3) have resulted in a 3D hydrogen-bonded network in **4** as shown in Figure 4.

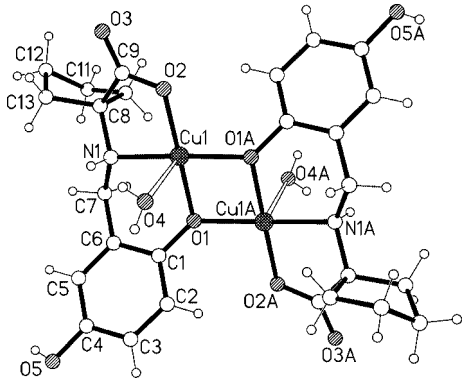


Figure 3. A perspective view of the dimer **4** (symmetry equivalent positions: $-x+1$, $-y+1$, $-z+1$).

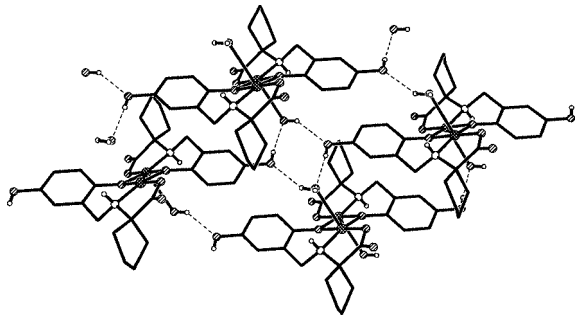

Figure 4. Packing diagram of **4**.

The compound **6** crystallized in triclinic space group $P\bar{1}$ with two methanol molecules in the crystal lattice and **6a** is isomorphous to **3a**, i.e. the arrangement of molecules in the crystal lattice, but not isostructural. The hydrogen bonding pattern in **6a** is also similar to that observed in **3a**. The solid-state crystal packing along the *b* axis revealed that the complex is a 1D polymer that resulted from weak Cu···O interactions and intermolecular hydrogen bonding. Further, carboxylate oxygen atoms of the neighboring dimeric units maintain weak interactions with each $Cu^{II}$ ion (Cu···O, 2.95 Å) in *syn-anti* mode. In addition to these interactions, crystal packing also reveals that N–H hydrogen atoms are involved in the intermolecular hydrogen bonding to methanolic oxygen atoms [N(1)–H(1)···O(5)] and the methanolic hydrogen atoms maintain intermolecular hydrogen bonds to carboxylate oxygen atoms [O(4)–H(4)···O(3) and O(5)–H(5)···O(2)].

In the crystal structure of **8** for $Z = 3$ in the triclinic space group $P\bar{1}$, there are three independent $Cu^{II}$–Sch12 units and each one is near an inversion center (1/2, 1/2, 1/2), (0,0,0), and (1/2, 1/2, 0) as illustrated in Figure 5. Of

 © 2006 Wiley-VCH Verlag GmbH & Co. KGaA, Weinheim 

these Cu3 has an aqua ligand in the apical position. The O9 of the carboxylate group from this unit is bonded to Cu2 with the Cu2–O9 distance of 2.51(1) Å. Similarly, O6 occupies the apical axial position of the Cu1 [Cu1–O6, 2.36(1) Å] with a distorted square pyramidal geometry. On the other hand, the oxygen atom of the third carboxylate group, O3, is only involved in hydrogen bonding to a hydrogen atom, H13D of lattice water. The axial bonding of the carbonyl oxygen atoms O6 and O9 from neighboring dimeric units to Cu1 and Cu2 centers produces a 2D coordination polymeric structure and the interdimer connectivity leads to the formation of a 2D (4, 4) network structure as shown in Figure 6 and these (4, 4) nets are well known in coordination polymeric structures.[16]

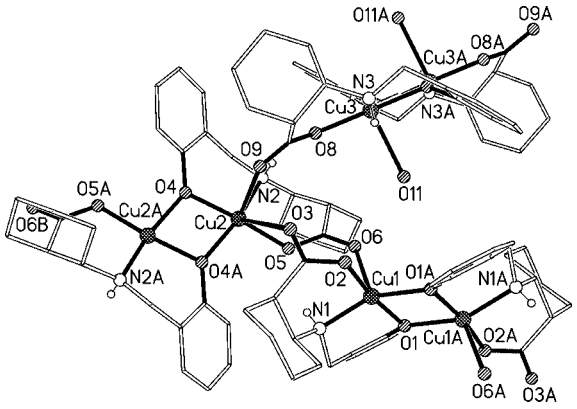


Figure 5. Perspective view of the unit cell contents in **8**. The lattice water molecules are omitted for clarity.

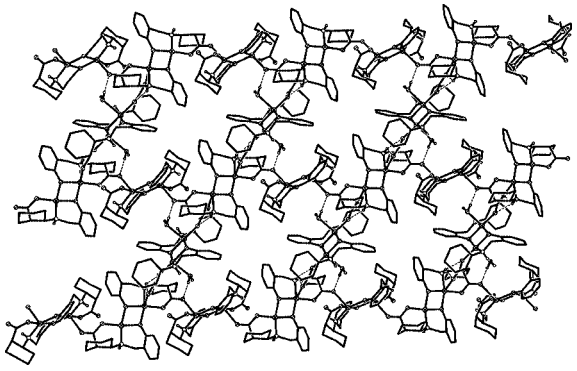

Figure 6. Portion of packing diagram of **8** showing the 2D connectivity. The hydrogen atoms and lattice water molecules have been omitted for clarity.

In this series, the only compound that displays a square-planar geometry at the $Cu^{II}$ atoms is **9a**. The unit cell contains two methanol molecules involved in hydrogen bonding via imine nitrogen [N(1)–H(1)···O(1S)] and carboxylate oxygen [O(1S)–H(1S)···O(3)], which lead to the formation of a 1D polymeric structure. The hydrogen bond lengths observed in the solid-state packing of **9a** are found to vary between 1.90 and 2.38 Å. Table 3 contains selected hydrogen bond parameters. These hydrogen bonds are considered to be normal as compared to the available literature on N–H···O and O–H···O hydrogen bond parameters.[17]

The dimer **12a** crystallized with four DMSO molecules of which two are bonded at the apical positions of each $Cu^{II}$ in the dimer and two are hydrogen-bonded to the imine hydrogen atoms through N–H···O interactions. The two DMSO molecules are disposed in *anti* fashion probably due to the bulkiness of the axial substitution. This causes the dimer to have a pseudo-center of inversion which is unprecedented in these types of structure having chiral reduced Schiff-base ligands.[6] A ribbon-like 1D hydrogen-bonded polymeric structure is produced by complementary O–H···O bonds between phenolic hydrogen and oxygen atoms of the carboxylate group. All these polymers are aligned parallel to the (1$\bar{1}$0) plane. Acetone molecules filled the empty cavities between these strands.

### Magnetic Studies of $[\{Cu_2(Sch12)_2\}_2Cu_2(Sch12)_2(H_2O)_2]\cdot 4H_2O$ (8)

It is evident from the previous section that only complexes **4** and **8** furnished the single crystals that represent the structures of the bulk. Further, the inter-dimer connectivity in **8** generated an interesting 2D (4, 4) coordination polymeric network structure. Hence, we investigated the variable temperature magnetic moments for **8** in order to understand the inter-dimer magnetic coupling interactions mediated by *syn-anti* carboxylate bridging.

The temperature dependences of $\chi_m$ and $\chi_m T$ for crystalline samples of **8** per $Cu_2$ unit are presented in Figure 7. On lowering the temperature, $\chi_m$ decreases gradually, there is an increase below ca. 70 K; while the $\chi_m T$ value even at 330 K (0.383 $cm^3 mol^{-1} K$) is quite small compared with the expected value 0.75 $cm^3 mol^{-1} K$ for two noninteracting $Cu^{II}$ ions, upon cooling it decreases rapidly to a value close to zero at 2 K. The increase of $\chi_m$ at low temperature should be due to trace paramagnetic impurity ($\rho$). Overall, the data suggest a strong antiferromagnetic coupling between the adjacent Cu ions in **8**. The coupling between the dinuclear moiety in the 2D layer of **8** is negligible, as expected, because of both the *syn-anti* carboxylate bridging

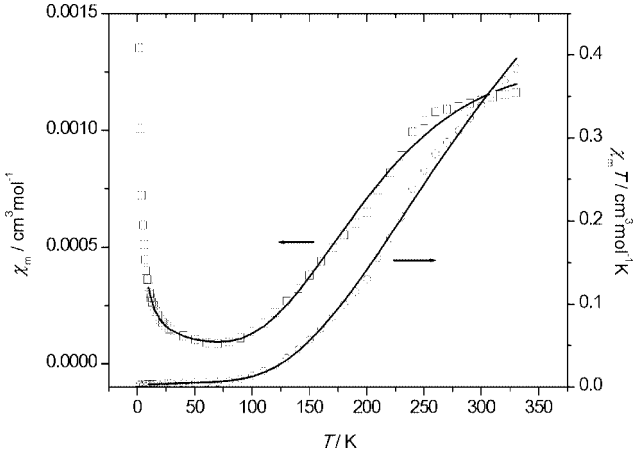


Figure 7. The temperature dependences of $\chi_m$ and $\chi_m T$ in the range of 2–350 K for **8**. The solid lines represent the fit using a $Cu_2$ dimer model.

 © 2006 Wiley-VCH Verlag GmbH & Co. KGaA, Weinheim 

mode and the orthogonal relationship of the planes of the neighboring $Cu_2O_2$.[14b] Therefore, the magnetic data of **8** can be analyzed by fitting the susceptibilities to an equation calculated using an $H = -2JS_1S_2$ Hamiltonian for a dimer plus impurity of the monomer model.[14e–14f] The parameters have their usual meanings. As shown in Figure 7, a reasonable fit was obtained with the results: $J = -230(3)\ cm^{-1}$, $g = 2.29(2)$, $\rho = 0.0056$; $N_\alpha = 4.9\times10^{-6}$ with $R = 1.4\times10^{-3}$ $\{R = \sum[(\chi_m)_{obs} - (\chi_m)_{calc}]^2/\sum[(\chi_m)_{obs}]^2\}$.

### Catecholase Biomimetic Studies

In order to gain deeper insight into the various parameters that determine the copper-mediated substrate oxidations and bimetallic reactivity both in natural metalloenzymes and in synthetic analogues, quite a number of mono- and dinuclear copper(II) complexes have been investigated as biomimetic catalysts for catechol oxidation.[18–23] In all these investigations, a common and convenient model substrate, 3,5-DTBC was used due to its low redox potentials.[20] Some of the crucial factors dictating the catecholase activity can now be highlighted based on many investigations correlating various structural parameters of the dicopper(II) complexes with their activity; viz., the distance between the $Cu^{II}$ centers,[24] the nature of the bridging group between the copper ions,[25] electronic properties of the complexes,[10,26] and the geometric changes of the dicopper core.[27] Furthermore, the factors such as the number of donor sites, nature of the donors, and the rigidity of the ligand or the bridging moiety imposing strain in the complex have also been found to play a vital role.[28] However, the studies correlating the activity with electronic effects due to substituents on the bridging phenolate have not been well explored.[10] Since the present series of complexes contain both electron-donating and -withdrawing substituents on the phenyl ring we have attempted to investigate their activity.

On the basis of the chemical and spectroscopic characterizations of the complexes **1**–**13** and the crystal structures of selected compounds, all these complexes are characterized by active $Cu_2O_2$ centers with a Cu···Cu distance of ca. 3 Å, which is favorable for the efficient binding of the substrate. Minor changes observed in the UV/Vis spectra recorded in DMF solution compared to Nujol mull indicate that the coordination number and geometry of **1**–**13** are retained in solution. Further, ESI-MS studies confirm the existence of copper(II) dimers in solution. Subsequently, all the complexes exhibit significant activity due to the presence of active dicopper(II) cores. The course of oxidation of 3,5-DTBC catalyzed by **8** is shown in Figure 8. The kinetic parameters have been determined by applying the Michaelis–Menten approach. A linear relationship for the initial rates and the concentration of the complexes has been obtained for **1**–**13**, which shows a first-order dependence of the rate on the catalyst concentration. An example of a Lineweaver–Burk plot[18f] is given in Figure 9 for **8**. Kinetic parameters of the complexes are given in Table 4.

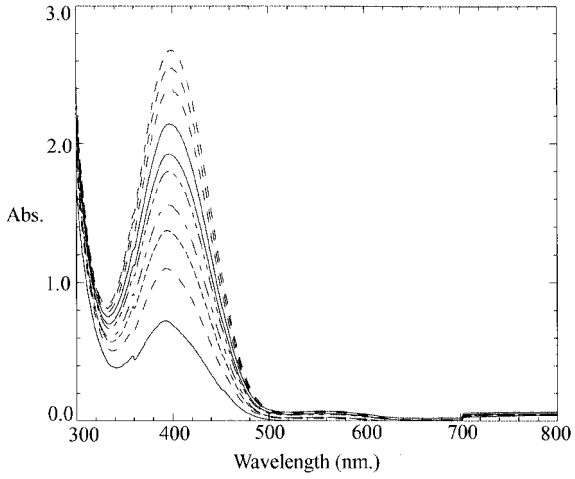


Figure 8. Oxidation of 3,5-DTBC by **8** monitored by UV/Vis spectroscopy. Higher concentrations were used only to emphasize the bands for the oxidation process.

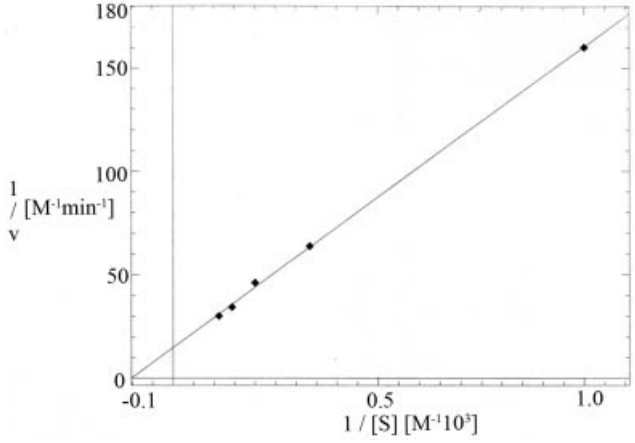


Figure 9. Lineweaver–Burk plot for the catalysis by **8**.

Table 4. Kinetic parameters for the oxidation of 3,5-DTBC by the complexes **1**–**13**.[a]

| Complex | Substituent (R) | $K_{cat}$ [$h^{-1}$] | $K_m$ [mM] | $V_{max}$ [$10^6\ Ms^{-1}$] |
|---|---|---|---|---|
| **1** | –H | 850(28) | 22.3(4) | 30.2(6) |
| **2** | –Cl | 694(32) | 26.2(3) | 22.4(1) |
| **3** | $-CH_3$ | 1003(59) | 15.4(6) | 34.3(6) |
| **4** | –OH | 773(30) | 20.6(7) | 26.7(3) |
| **5** | –H | 863(28) | 18.5(5) | 30.2(1) |
| **6** | –Cl | 785(49) | 20.3(8) | 24.5(5) |
| **7** | $-CH_3$ | 1080(30) | 14.6(3) | 36.1(2) |
| **8** | –H | 2006(44) | 9.2(1) | 68.5(4) |
| **9** | –Cl | 883(33) | 17.7(3) | 29.3(3) |
| **10** | $-CH_3$ | 3120(28) | 4.3(1) | 104.6(6) |
| **11** | *para* –OH | 595(27) | 21.4(4) | 22.3(7) |
| **12** | *meta* –OH | 513(21) | 28.6(4) | 19.4(8) |
| **13** | *ortho* –OH | 460(14) | 31.3(3) | 17.6(5) |

[a] The values were obtained from three measurements.

It is obvious from Table 4 that the activity of **1**–**4** follows the order **3** > **1** > **4** > **2** with **3** showing higher activity ($K_{cat}$ = 1003 $h^{-1}$). Further, the activity of **2** has noticeably

 © 2006 Wiley-VCH Verlag GmbH & Co. KGaA, Weinheim 

decreased due to the strong electron-withdrawing nature of *Cl* when compared to the activity of **4** containing the *–OH* group.[29] Thus, with respect to the substituents on the bridging phenolate, the activity of the corresponding complexes followed the order: $CH_3 > H > OH > Cl$. A similar trend (**7** > **5** > **6**) has been observed (Table 4) for $Cu^{II}$ complexes of RSch11 ligands, **5**–**7**. Among **8**–**10**, the *methyl*-substituted **10** exhibited significantly higher activity ($K_{cat}$ = 3120 $h^{-1}$) while *chloro*-substituted **9** with $Cu^{II}$ in a square-planar geometry showed a lower activity ($K_{cat}$ = 883 $h^{-1}$) following a similar trend. Earlier investigations on the activity of copper(II) systems have shown that the square planar copper(II) complexes are weak catechol-oxidase catalysts.[19,22,24d,28,31] However, reports are also available on square planar dicopper(II) complexes showing very high activity.[18f,25] On the same grounds, **9** with a similar geometry exhibiting significant activity can be another example for the latter.

The six-membered chelate rings facilitate strain-free substrate binding compared to the five-membered rings[9,18f,28] by offering a flexible and relaxed coordination sphere at $Cu^{II}$ centers thus enhancing the activity of **8** compared to the activities of **1** ($K_{cat}$ = 850 $h^{-1}$), and **5** ($K_{cat}$ = 863 $h^{-1}$) forming five-membered rings. Furthermore, it is also the formation of six-membered rings that significantly enhanced the activity of **10** ($K_{cat}$ = 3120 $h^{-1}$) compared to **3** ($K_{cat}$ = 1003 $h^{-1}$) or **7** ($K_{cat}$ = 1080 $h^{-1}$) which contain five-membered rings. It may be noted that these complexes (**3**, **7**, and **10**) have *para* methyl phenyl rings.

In the case of **11**–**13** containing Diala ligands, the trend in $K_{cat}$ is **11** > **12** > **13** (Table 4). The activity of **11** ($K_{cat}$ = 595 $h^{-1}$) with a *para*-hydroxy bridging phenolate is found to be higher than that of **12** ($K_{cat}$ = 513 $h^{-1}$) and **13** ($K_{cat}$ = 460 $h^{-1}$) containing *meta*- and *ortho*-hydroxy bridging phenolate moieties, respectively. These variations in the activity maybe attributed to the differences in the steric match[18,27,28] caused by the respective changes in the position of the *–OH* group on the bridging phenolate. Further, comparing the activity ($K_{cat}$ = 666 $h^{-1}$), under similar experimental conditions, of our previously reported unsubstituted complex $[Cu_2(L\text{-}Sala)_2(H_2O)]$[8] with the activity ($K_{cat}$ = 595 $h^{-1}$) of the present *para* hydroxy-substituted **11** it is obvious that the decrease in the activity of **11** can be attributed to the effect of the electron-withdrawing *-OH* group on the phenyl ring of the ligand.

The kinetic data for **1**–**13** presented in Table 4 shows that the substitution of phenolate by electron-donating substituents increased the activity while the substitution by electron-withdrawing groups decreased the activity. In the absence of electrochemical data for **1**–**13**, it is difficult to conclude that the catalytic efficiency is solely governed by the electronic influence of the substituents except envisaging a rough correlation. Moreover, no clear and direct correlation has been established so far between the rates of reaction, redox potentials, and electronic effects of the complexes.[10,26,28] However, other factors such as geometry, steric factors, and interactions between the substrate and catalyst can also influence the overall efficiency. It should also be noted that the exact Cu···Cu separation in solid-state structures need not be retained in the solution, and direct correlation between the Cu···Cu distance and catalytic activity need not be expected. However, based on the information regarding the geometries and molecular species obtained from the solution studies involving the techniques such as UV/Vis spectroscopy and ESI-MS at least some correlations can be achieved.

Recently, Wegner et al. reported the most active catalyst among the known functional model complexes so far, with a turnover number or $K_{cat}$ of 9927 $h^{-1}$.[5h] When compared mainly with the turnover numbers of 1188 $h^{-1}$, 2804 $h^{-1}$, and 5470 $h^{-1}$, reported by Monzani et al.,[31–32] Meyer et al., [27] and Mukherjee et al.[25a] respectively, and with the other lower to moderate turnover values,[5,10,18–19,22–30] the observed turnover rates of 460 to 3120 $h^{-1}$ may suggest moderate to high catalytic activity of the present complexes. However, all activity studies on the model complexes synthesized so far have only achieved turnover numbers of about several thousand-fold lower when compared to the turnover number of native enzymes[31,26a] (for example catechol oxidase from sweet potatoes has been found to be highly active with a $K_{cat}$ of 2293 $s^{-1}$ especially towards catechol).[33] The current high activity in **10** ($K_{cat}$ = 3120 $h^{-1}$) observed among the present model catalysts has been found to be ca. 2600-fold slower towards the oxidation of 3,5-DTBC when compared to the natural enzyme. Finally, these findings suggest that significant differences in the catalytic ability of dicopper(II) complexes can be induced by the judicious choice of different sets of binucleating ligands.

## Summary

A new series of dicopper(II) complexes **1**–**13** containing reduced Schiff-base ligands formed between different substituted salicylaldehydes and amino acids have been synthesized and characterized by physicochemical and spectroscopic methods. On the basis of the single-crystal X-ray crystallographic studies of selected compounds, it can be suggested that all the complexes contain $Cu_2O_2$ cores with a Cu···Cu distance of ca. 3 Å. In view of the interesting 2D coordination polymeric structure, variable temperature magnetic studies carried out on **8** suggested the presence of strong intradimer antiferromagnetic coupling.

The catecholase activity of the complexes **1**–**4**, **5**–**7**, **8**–**10**, and **11**–**13** containing 1-aminocyclopentane-1-carboxylate, 1-aminocyclohexane-1-carboxylate, 2-aminocyclohexane-1-carboxylate, and L-alanine side chains, respectively, in the corresponding reduced Schiff-base ligands has been evaluated and systematically compared. It has been found that the presence of electron-withdrawing groups decreased the activity while the electron-donating groups enhanced the activity of the complexes. Under similar experimental conditions the activity shown by the current series of dicopper(II) complexes can be considered moderate to high as observed in our previous results.[8–9]

 © 2006 Wiley-VCH Verlag GmbH & Co. KGaA, Weinheim 

## Experimental Section

### Materials and Physical Measurements

All the chemicals were purchased from commercial sources and used as received for syntheses. All the solvents used were of reagent grade. The yields are reported with respect to the metal salts.

The $^1$H NMR spectra were recorded with a Bruker ACF 300FT-NMR spectrometer using TMS as an internal reference at 25 °C and the infrared spectra (KBr pellet) were recorded using a FTS 165 Bio-Rad FTIR spectrometer in the range 4000–400 cm$^{-1}$. The electronic transmittance spectra were recorded with a Shimadzu UV-2501/PC UV/Vis spectrometer in DMF and Nujol mull. ESI-MS spectra were recorded using a Finnigan MAT LCQ Mass Spectrometer using the syringe-pump method. The elemental analyses were performed in the Micro Analytical Laboratory, Department of Chemistry, National University of Singapore. Water present in the compounds was determined using a SDT 2960 TGA Thermal Analyzer with a heating rate of 10 °C min$^{-1}$ using a sample size of 7–10 mg per sample run. Room-temperature magnetic susceptibility measurements were carried out with a Johnson–Mathey Magnetic Susceptibility balance with Hg[Co(SCN)$_4$] as the standard. Variable temperature magnetic studies were made using a Quantum Design MPMS-XL5 SQUID magnetometer operating in an applied field of 5 kOe. Corrections for diamagnetism were made using Pascal's constants. Optical rotation was measured on the specified solutions in a 0.1-dm cell at 27 °C using a Perkin–Elmer model 341 polarimeter. The concentration of the solutions was 5.5 mg mL$^{-1}$ for both the ligands (in MeOH) and complexes (in DMSO). The optical rotation of the ligands was recorded at the wavelength of 365 nm where as for the complexes the measurements were conducted at the wavelength of the D line (578 nm) of sodium.

### Ligands

All the ligands except $H_3$Diala5, $H_3$Diala4, and $H_3$Diala3 have been synthesized using the same molar quantities according to the procedure described for $H_2$Scp11 in our earlier report.[6c]

**1-[(5-Chloro-2-hydroxybenzyl)amino]cyclopentane-1-carboxylic Acid ($H_2$ClScp11):** This compound was prepared from 1-aminocyclopentane-1-carboxylic acid and 5-chlorosalicylaldehyde. Yield: 0.92 g (73%). m.p. 271–272 °C. $C_{13}H_{16}ClNO_3$ (269.7): calcd. C 57.8, H 5.9, N 5.2; found C 57.2, H 6.0, N 5.7. IR (KBr): $\tilde{\nu}$ = 2966 m (NH), 1566 s $\upsilon_{as}$(COO$^-$), 1384 s $\upsilon_s$(COO$^-$), 1276 s (phenolic CO) cm$^{-1}$. $^1$H NMR (CD$_3$OD): $\delta$ = 1.83–2.28 (m, 8 H, -C$_5$H$_8$), 4.12 (s, 2 H, benzylic), 6.83–7.36 (m, 3 H, Ar-H). $^{13}$C NMR (CD$_3$OD): $\delta$ = 25.9, 37.3, 47.5, 48.1, and 48.4 (-C$_5$H$_8$), 72.9 (benzylic), 119.4, 122.3, 127.4, 129.1, 129.5, and 160.6 (aromatic), 182.7 (-COOH). EI-MS: *m*/*z* (%) = 269.2.

**1-[(2-Hydroxy-5-methylbenzyl)amino]cyclopentane-1-carboxylic Acid ($H_2$MeScp11):** This compound was prepared from 1-aminocyclopentane-1-carboxylic acid and 5-methylsalicylaldehyde. Yield: 0.92 g (76%). m.p. 272–273 °C. $C_{14}H_{19}NO_3$ (249.3): calcd. C 67.4, H 7.6, N 5.6; found C 67.0, H 7.7, N 5.9. IR (KBr): $\tilde{\nu}$ = 3447 m (OH), 2956 m (NH), 1571 s $\upsilon_{as}$(COO$^-$), 1383 s $\upsilon_s$(COO$^-$), 1277 s (phenolic CO) cm$^{-1}$. $^1$H NMR (CD$_3$OD): $\delta$ = 1.89–2.11 (m, 8 H, -C$_5$H$_8$), 2.35 (s, Ar–CH$_3$), 3.62 (s, 2 H, benzylic), 6.53–6.83 (m, 3 H, Ar-H). $^{13}$C NMR (CD$_3$OD): $\delta$ = 20.6 (Ar–CH$_3$), 24.3, 26.1, 37.6, 47.4, and 48.2 (-C$_5$H$_8$), 72.8 (benzylic), 118.4, 126.0, 127.1, 129.6, 130.6, and 160.3 (aromatic), 184.0 (-COOH). ESI-MS: *m*/*z* (%) = 249.2.

**1-[(2,5-Dihydroxybenzyl)amino]cyclopentane-1-carboxylic Acid ($H_2$(OH)Scp11):** This compound was prepared from 1-aminocyclopentane-1-carboxylic acid and 5-hydroxysalicylaldehyde. Yield: 0.75 g (63%). m.p. 263–264 °C. $C_{13}H_{17}NO_4$ (251.6): calcd. C 62.1, H 6.8, N 5.5; found C 62.0, H 6.9, N 5.6. IR (KBr): $\tilde{\nu}$ = 3398 m (OH), 2960 m (NH), 1582 s $\upsilon_{as}$(COO$^-$), 1390 s $\upsilon_s$(COO$^-$), 1276 s (phenolic CO) cm$^{-1}$. $^1$H NMR (CD$_3$OD): $\delta$ = 1.73–2.11 (m, 8 H, -C$_5$H$_8$), 3.83 (s, 2 H, benzylic), 6.43–6.51 (m, 3 H, Ar-H). $^{13}$C NMR (CD$_3$OD): $\delta$ = 24.7, 26.1, 36.0, 37.6, and 40.9 (-C$_5$H$_8$), 72.7 (benzylic), 117.6, 118.7, 119.6, 126.3, 148.2, and 159.6 (aromatic), 184.1 (-COOH). ESI-MS: *m*/*z* (%) = 251.

**1-[(2-Hydroxybenzyl)amino]cyclohexane-1-carboxylic Acid ($H_2$Sch11):** This compound was prepared from 1-aminocyclohexane-1-carboxylic acid and salicylaldehyde. Yield: 1.06 g (90%). m.p. 296–297 °C. $C_{14}H_{19}NO_3$ (249.3): calcd. C 67.4, H 7.6, N 5.6; found C 67.4, H 7.7, N 5.5. IR (KBr): $\tilde{\nu}$ = 2941 m (NH), 1577 s $\upsilon_{as}$(COO$^-$), 1388 s $\upsilon_s$(COO$^-$), 1272 s (phenolic CO) cm$^{-1}$. $^1$H NMR (CD$_3$OD): $\delta$ = 1.43–2.03 (m, 10 H, -C$_6$H$_{10}$), 3.70 (s, 2 H, benzylic), 6.41–7.02 (m, 4 H, Ar-H). $^{13}$C NMR (CD$_3$OD): $\delta$ = 23.0, 27.0, 34.5, 37.1, 48.1, and 48.4 (-C$_6$H$_{10}$), 64.3 (benzylic), 117.7, 118.3, 127.0, 129.3, 130.0, and 162.5 (aromatic), 182.8 (-COOH). ESI-MS: *m*/*z* (%) = 249.2

**1-[(5-Chloro-2-hydroxybenzyl)amino]cyclohexane-1-carboxylic Acid ($H_2$ClSch11):** This compound was prepared from 1-aminocyclohexane-1-carboxylic acid and 5-chlorosalicylaldehyde. Yield: 0.88 g (66%). m.p. 290–291 °C. $C_{14}H_{18}ClNO_3$ (283.7): calcd. C 59.3, H 6.4, N 4.9; found C 59.0, H 6.5, N 4.9. IR (KBr): $\tilde{\nu}$ = 3462 m (OH), 2940 m (N–H), 1568 s $\upsilon_{as}$(COO$^-$), 1495 s $\upsilon_s$(COO$^-$), 1273 s (phenolic CO) cm$^{-1}$. $^1$H NMR (CD$_3$OD): $\delta$ = 1.41–2.03 (m, 10 H, -C$_6$H$_{10}$), 3.70 (s, 2 H, benzylic), 6.60–7.01 (m, 4 H, Ar-H). $^{13}$C NMR (CD$_3$OD): $\delta$ = 23.4, 26.9, 34.3, 37.0, 46.1, and 48.2, (-C$_6$H$_{10}$), 64.61 (benzylic), 119.6, 121.7, 128.2, 128.9, 129.4, and 161.5 (aromatic), 182.2 (-COOH). ESI-MS: *m*/*z* (%) = 283.7.

**1-[(2-Hydroxy-5-methylbenzyl)amino]cyclohexane-1-carboxylic Acid ($H_2$MeSch11):** This compound was prepared from 1-aminocyclohexane-1-carboxylic acid and 5-methylsalicylaldehyde. Yield: 0.81 g (66%). m.p. 295–296 °C. $C_{15}H_{21}NO_3$ (263.3): calcd. C 68.4, H 8.0, N 5.3; found C 67.9, H 8.0, N 5.4. IR (KBr): $\tilde{\nu}$ = 3450 m (OH), 2932 m (NH), 1624 s $\upsilon_{as}$(COO$^-$), 1381 s $\upsilon_s$(COO$^-$), 1262 s (phenolic CO) cm$^{-1}$. $^1$H NMR (CD$_3$OD): $\delta$ = 1.40–2.17 (m, 10 H, -C$_6$H$_{10}$), 2.38 (CH$_3$), 3.71 (s, 2 H, benzylic), 6.60–6.88 (m, 4 H, Ar-H). $^{13}$C NMR (CD$_3$OD): $\delta$ = 20.5 (Ar–CH$_3$), 23.3, 26.8, 34.3, 37.0, 47.2, and 48.2, (-C$_6$H$_{10}$), 64.4 (benzylic), 117.0, 125.3, 128.8, 129.7, 130.3, and 156.8 (aromatic), 182.71 (-COOH). ESI-MS: *m*/*z* (%) = 263.3.

**2-[(2-Hydroxybenzyl)amino]cyclohexane-1-carboxylic Acid ($H_2$Sch12):** This compound was prepared from 2-aminocyclohexanecarboxylic acid and salicylaldehyde. Yield: 1.05 g (89%). m.p. 238–239 °C. $C_{14}H_{19}NO_3$ (249.3): calcd. C 67.4, H 7.7, N 5.6; found C 67.0, H 7.6, N 5.5. IR (KBr): $\tilde{\nu}$ = 2853 m (N–H), 1580 s $\upsilon_{as}$(COO$^-$), 1461 s $\upsilon_s$(COO$^-$), 1263 s (phenolic CO) cm$^{-1}$. $^1$H NMR (CD$_3$OD): $\delta$ = 1.38–2.07 (m, 8 H, -C$_6$H$_{10}$), 2.62 (t, 1 H, HC–N), 3.01 (t, 1 H, HC–COO$^-$), 4.06 (s, 2 H, benzylic), 6.53–7.05 (m, 4 H, Ar-H). $^{13}$C NMR (CD$_3$OD): $\delta$ = 24.0, 25.1, 28.2, 29.2, 48.1, and 48.4 (-C$_6$H$_{10}$), 57.4 (benzylic), 116.4, 119.1, 125.8, 129.4, 129.6, and 164.5 (aromatic), 182.3 (-COOH). ESI-MS: *m*/*z* (%) = 249.3.

**2-[(5-Chloro-2-hydroxybenzyl)amino]cyclohexane-1-carboxylic Acid ($H_2$ClSch12):** This compound was prepared from 2-aminocyclohexanecarboxylic acid and 5-chlorosalicylaldehyde. Yield: 0.18 g (64%). m.p. 233–234 °C. $C_{14}H_{18}ClNO_3$ (283.7): calcd. C 59.3, H 6.4, N 4.9; found C 59.1, H 6.4, N 4.8. IR (KBr): $\tilde{\nu}$ = 2940 m (NH), 1579 s $\upsilon_{as}$(COO$^-$), 1449 s $\upsilon_s$(COO$^-$), 1268 s (phenolic CO) cm$^{-1}$. $^1$H NMR (CD$_3$OD): $\delta$ = 1.34–2.10 (m, 8 H, -C$_6$H$_{10}$), 2.61 (t, 1 H, HC–N), 2.98 (t, 1 H, HC–COO$^-$), 3.96 (s, 2 H, benzylic), 6.54–7.01 (m,

 © 2006 Wiley-VCH Verlag GmbH & Co. KGaA, Weinheim 

3 H, Ar-H). $^{13}$C NMR ($CD_3OD$): $\delta$ = 21.4, 22.2, 25.5, 26.3, 44.5, and 45.4 (-$C_6H_{10}$), 55.3 (benzylic), 117.0, 117.4, 117.7, 124.4, 126.3, and 161.5 (aromatic), 179.2 (-COOH). ESI-MS: *m*/*z* (%) = 283.3.

**2-[(2-Hydroxy-5-methylbenzyl)amino]cyclohexane-1-carboxylic Acid ($H_2$MeSch12):** This compound was prepared from 2-aminocyclohexanecarboxylic acid and 5-methylsalicylaldehyde. Yield: 60%. m.p. 285–286 °C. $C_{15}H_{21}NO_3$ (263.3): calcd. C 68.4, H 8.0, N 5.3; found C 68.1, H 8.0, N 5.0. IR (KBr): $\tilde{\nu}$ = 2941 m (N–H), 1632 s $\upsilon_{as}(COO^-)$, 1459 s $\upsilon_s(COO^-)$, 1272 s (phenolic CO) cm$^{-1}$. $^1$H NMR ($CD_3OD$): $\delta$ = 1.34–2.17 (m, 8 H, -$C_6H_{10}$), 2.37 (Ar–$CH_3$), 2.57 (t, 1 H, HC–N), 2.97 (t, 1 H, HC–$COO^-$), 3.96 (s, 2 H, benzylic), 6.55–6.87 (m, 3 H, aromatic). $^{13}$C NMR ($CD_3OD$): $\delta$ = 20.5 ($CH_3$), 25.1, 28.0, 29.1, 37.0, 47.1, and 48.4 (-$C_6H_{10}$), 57.1 (benzylic), 117.4, 117.8, 123.4, 127.4, 130.2, and 159.3 (aromatic), 182.0 (-COOH). ESI-MS: *m*/*z* (%) = 263.4.

The ligands $H_3$Diala5, $H_3$Diala4, and $H_3$Diala3 were synthesized as described below.

***N*-(2,5-Dihydroxybenzyl)-L-alanine ($H_3$Diala5):** A mixture of L-alanine (0.9 g, 10.1 mmol) and NaOH (0.4 g, 10.1 mmol) in methanol (20 mL) was stirred for 20 min to get a clear solution. To this was added 2,5-dihydroxybenzaldehyde (1.4 g, 10.1 mmol). After stirring for 1 h, the resulting yellow solution was cooled in an ice bath and then treated with $NaBH_4$ (0.42 g, 11.11 mmol). The yellow color slowly disappeared. After 45 min, the pH of the solution was brought to 5 by adding acetic acid. Upon stirring for 40 min, a pale-brown solid separated out. Filtration followed by washing with methanol (2 × 5 mL), diethyl ether (2 × 5 mL), and then drying under vacuum afforded pure $H_3$Diala5. Yield: 1.82 g (85%). m.p. 268–270 °C. $C_{10}H_{13}NO_4$ (211.2): calcd. C 56.8, H 6.2, N 6.6; found C 56.3, H 6.3, N 6.5. IR (KBr): $\tilde{\nu}$ = 3438 m (OH), 2487 m (NH), 1635 s $\upsilon_{as}(COO^-)$, 1511 s $\upsilon_s(COO^-)$, 1285 s (phenolic CO) cm$^{-1}$. $^1$H NMR ([D$_6$]DMSO): $\delta$ = 1.31 (m, 3 H, $CH_3$), 3.21 (m, 1 H, -CH), 3.92 (m, 2 H, benzylic), 6.61–6.72 (m, 3 H, Ar-H). $^{13}$C NMR: $\delta$ = 15.7 ($CHCH_3$), 45.5 (benzylic), 56.2 (-$CHCH_3$), 116.0, 116.2, 116.9, 120.3, 148.6, and 149.6 (aromatic), 171.3 (-COOH). ESI-MS: *m*/*z* (%) = 211.4. $[\alpha]_D^{27}$: 7.4 (*c* = 5.5 mg mL$^{-1}$, MeOH).

***N*-(2,4-Dihydroxybenzyl)-L-alanine ($H_3$Diala4):** This ligand was synthesized according to the same procedure as $H_3$Diala4 except that 2,4-dihydroxybenzaldehyde was used instead of 2,5-dihydroxybenzaldehyde. Yield: 1.65 g (77%). m.p. 288–290 °C. $C_{10}H_{13}NO_4$ (211.2): calcd. C 56.8, H 6.2, N 6.6; found C 56.3, H 6.3, N 6.5. IR (KBr): $\tilde{\nu}$ = 3267 m (OH), 3085 m (NH); 1623 s $\upsilon_{as}(COO^-)$, 1522 s $\upsilon_s(COO^-)$, 1216 s (phenolic CO) cm$^{-1}$. $^1$H NMR ([D$_6$]DMSO): $\delta$ = 1.29 (d, 3 H, -$CH_3$), 3.20 (m, 1 H, -CH), 3.91 (s, 2 H, benzylic), 7.01–6.21 (m, 3 H, Ar-H). $^{13}$C NMR: $\delta$ = 15.4 ($CHCH_3$), 45.7 (benzylic), 56.6 (-$CHCH_3$), 116.1, 116.2, 117.0, 120.2, 148.7, and 149.5 (aromatic), 172.1 (-COOH). ESI-MS: *m*/*z* (%) = 211.3. $[\alpha]_D^{27}$: 8.0 (*c* = 5.5 mg mL$^{-1}$, MeOH).

***N*-(2,3-Dihydroxybenzyl)-L-alanine ($H_3$Diala3):** This ligand was prepared according to the same procedure as $H_3$Diala3 except that 2,3-dihydroxybenzaldehyde was used instead of 2,5-dihydroxybenzaldehyde. Yield: 1.41 g (66%). m.p. 262–264 °C. $C_{10}H_{13}NO_4$ (211.2): calcd. C 56.8, H 6.2, N 6.6; found C 56.7, H 6.0, N 6.4. IR (KBr): $\tilde{\nu}$ = 3367 m (OH), 3085 m (NH), $\upsilon_{as}(COO^-)$ 1623 s, 1522 s $\upsilon_s(COO^-)$, 1216 s (phenolic CO) cm$^{-1}$. $^1$H NMR ([D$_6$]DMSO): $\delta$ = 1.30 (d, 3 H, -$CH_3$), 3.26 (m, 1 H, -CH), 3.96 (s, 2 H, benzylic), 6.78–6.62 (m, 3 H, aromatic). $^{13}$C NMR: $\delta$ = 15.5 ($CHCH_3$), 45.8 (benzylic), 56.7 (-$CHCH_3$), 116.1, 116.2, 116.4, 120.6, 148.3, and 149.1 (aromatic), 170.5 (-COOH). ESI-MS: *m*/*z* (%) = 211.2. $[\alpha]_D^{27}$: 8.4 (*c* = 5.5 mg mL$^{-1}$, MeOH).

**Complexes**

The compound **[$Cu_2$(Scp11)$_2$($H_2O$)$_2$] (1)** was synthesized according to the procedure described earlier.[6c] Weight loss (60–115 °C) as per TGA: 5.1% [calculated for 2 $H_2O$: 5.7%]. $\mu_B$ = 1.55 B. M. Slow diffusion of methanol into a slightly turbid solution of **1** in water afforded single crystals of [$Cu_2$(Scp11)$_2$(MeOH)$_2$] (**1a**).

**[$Cu_2$(ClScp11)$_2$($H_2O$)$_2$] (2):** A clear solution containing of $H_2$Clscp11 (0.13 g, 0.5 mmol) and NaOH (0.04 g, 1.0 mmol) in methanol (20 mL) was obtained after stirring the mixture for 15 min. To this was added solid copper(II) acetate monohydrate in portions (0.10 g, 0.5 mmol). After stirring for another 2 h, a green solid separated out and was filtered off, washed with methanol (4 mL), diethyl ether (4 mL), and then in air. Yield: 0.31 g (88%). $C_{26}H_{32}Cl_2Cu_2N_2O_8$ (698.5): calcd. C 44.7, H 4.6, N 4.0; found C 45.1, H 4.7, N 3.7. IR (KBr): $\tilde{\nu}$ = 3400 m (OH), 2955 m (NH), 1619 s $\upsilon_{as}(COO^-)$, 1375 s $\upsilon_s(COO^-)$, 1266 s (phenolic CO) cm$^{-1}$. Weight loss (65–145 °C) as per TGA: 5.5% [calculated for 2 $H_2O$: 5.2%]. $\mu_B$ = 1.64 BM. Slow diffusion of acetonitrile into a saturated solution of **2** in DMF furnished dark green single crystals of [$Cu_2$(ClScp11)$_2$(DMF)($H_2O$)]·MeCN (**2a**).

**[$Cu_2$(MeScp11)$_2$($H_2O$)$_2$] (3):** To a clear solution of $H_2$MeScp11 (0.12 g, 0.5 mmol) and NaOH (0.04 g, 1.0 mmol) in a mixture of methanol (10 mL) and water (10 mL) was added copper(II) acetate monohydrate (0.10 g, 0.5 mmol) in portions. A green solid obtained after stirring for 2 h was filtered off, washed with water (2 × 2 mL), methanol (2 × 2 mL) and diethyl ether (2 × 2 mL) and then dried in air. Yield: 0.28 g (85%). $C_{28}H_{38}Cu_2N_2O_8$ (657.7): calcd. C 51.1, H 5.8, N 4.3; found C 51.2, H 5.9, N 4.1. IR (KBr): $\tilde{\nu}$ = 3399 m (OH), 2960 m (NH), 1621 s $\upsilon_{as}(COO^-)$, 1369 s $\upsilon_s(COO^-)$, 1264 s (phenolic CO) cm$^{-1}$. Weight loss (40–102 °C) as per TGA: 5.9% [calculated for 2 $H_2O$: 5.5%]. $\mu_B$ = 1.43 BM. Slow diffusion of methanol into a saturated solution of **3** in DMSO afforded single crystals of [$Cu_2$(MeScp11)$_2$(MeOH)$_2$]·2MeOH (**3a**).

**[$Cu_2$(OHScp11)$_2$($H_2O$)$_2$] (4):** A suspension of $H_2$(OH)Scp11 (0.04 g, 0.16 mmol) in methanol (6 mL) was allowed to slowly diffuse into a clear solution of copper(II) acetate monohydrate (0.03 g, 0.16 mmol) in water (3 mL) in a test tube. Dark brownish green single crystals of **4** were obtained after 2 days. Yield: 76% (0.08 g). $C_{26}H_{34}Cu_2N_2O_{10}$ (661.6): calcd. C 47.2, H 5.2, N 4.2; found C 47.1, H 5.2, N 4.2. IR (KBr): $\tilde{\nu}$ = 3481 m (OH), 2954 m (NH); 1625 s $\upsilon_{as}(COO^-)$, 1366 s $\upsilon_s(COO^-)$, 1264 s (phenolic CO) cm$^{-1}$. Weight loss (134–177 °C) as per TGA: 5.8% [calculated for 2 $H_2O$: 5.4%]. $\mu_B$ = 1.41 BM.

**[$Cu_2$(Sch11)$_2$]·($H_2O$) (5):** To a clear solution of $H_2$Sch11 (0.12 g, 0.50 mmol) and NaOH (0.04 g, 1.0 mmol) in methanol (20 mL) was added a solution of copper(II) acetate monohydrate (0.10 g, 0.50 mmol) in methanol (5 mL) and the solution was stirred for 3 h. The resulting green product was filtered, washed with methanol (2 × 2 mL), diethyl ether (2 × 2 mL), and then dried in air. Yield: 0.06 g (90%). $C_{28}H_{36}Cu_2N_2O_7$ (639.7): calcd. C 52.6, H 5.7, N 4.4; found C 52.4, H 5.7, N 4.3. IR (KBr): $\tilde{\nu}$ = 3435 m (OH), 2930 m (N–H), 1640 s $\upsilon_{as}(COO^-)$, 1373 s, $\upsilon_s(COO^-)$, 1272 s (phenolic CO) cm$^{-1}$. Weight loss (33–99 °C) as per TGA: 2.7% [calculated for $H_2O$: 2.8%]. $\mu_B$ = 1.57 BM.

**[$Cu_2$(ClSch11)$_2$($H_2O$)$_2$] (6):** To a clear solution of $H_2$ClSch11 (0.14 g, 0.50 mmol) and NaOH (0.04 g, 1.0 mmol) in methanol (20 mL) was added copper(II) acetate monohydrate (0.10 g, 0.5 mmol) and the solution was stirred for 1.5 h. The green product was filtered off, washed with methanol (2 × 2 mL), diethyl ether (2 × 2 mL), and then dried in air. Yield: 0.32 g (88%). $C_{28}H_{36}Cl_2Cu_2N_2O_8$ (726.6): calcd. C 46.3, H 5.0, N 3.9; found C

 © 2006 Wiley-VCH Verlag GmbH & Co. KGaA, Weinheim 

46.7, H 5.0, N 3.5. IR (KBr): $\tilde{\nu}$ = 3447 m (OH), 2937 m (N–H), 1622 s $\upsilon_{as}(COO^-)$, 1382 s $\upsilon_s(COO^-)$, 1266 s, (phenolic CO) $cm^{-1}$. Weight loss (65–168 °C) as per TGA: 4.4% [calculated for $2H_2O$: 4.9%]. $\mu_B$ = 1.32 BM. Slow diffusion of methanol into a saturated solution of **6** in DMSO afforded dark green single crystals of $[Cu_2(ClSch11)_2(MeOH)_2]\cdot 2MeOH$ (**6a**).

**$[Cu_2(MeSch11)_2(H_2O)_2]$ (7):** A clear solution of copper(II) acetate monohydrate in methanol (5 mL) was added to a clear solution containing a mixture of $H_2$MeSch11 (0.26 g, 1.0 mmol) and NaOH (0.08 g, 2.00 mmol) in methanol (20 mL). Upon stirring this reaction mixture for 1.5 h, the resulting greenish product obtained was filtered, washed with methanol (4 mL), diethyl ether (4 mL), and then dried in air. Yield: 0.46 g (67%). $C_{30}H_{42}Cu_2N_2O_8$ (685.7): calcd. C 52.5, H 6.2, N 4.1; found C 53.2, H 6.2, N 4.1. IR (KBr): $\tilde{\nu}$ = 3436 m (OH), 2932 m (NH), 1624 s $\upsilon_{as}(COO^-)$, 1381 s $\upsilon_s(COO^-)$, 1262 s (phenolic CO) $cm^{-1}$. Weight loss (68–127 °C) as per TGA: 5.5% [calculated for $2H_2O$: 5.2%]. $\mu_B$ = 1.40 BM.

**$[\{Cu_2(Sch12)_2\}_2Cu_2(Sch12)_2(H_2O)_2]\cdot 4H_2O$ (8):** The ligand $H_2$Sch21 (0.12 g, 0.50 mmol) along with NaOH (0.04 g, 1.0 mmol) was added to a solvent mixture of water (15 mL) and acetonitrile (15 mL) and stirred for 15 min to obtain a clear solution. To this was added copper(II) nitrate trihydrate (0.12 g, 0.50 mmol) and the solution was stirred for another 3.5 h. The clear dark-green solution obtained was filtered. Dark green single crystals were formed from the clear filtrate upon slow evaporation for 4–5 days. Yield: 0.26 g (79%). $C_{84}H_{114}N_6O_{24}Cu_6$ (1973.1): calcd. C 51.1, H 5.8, N 4.3; found C 51.4, H 5.7, N 4.2. IR (KBr): $\tilde{\nu}$ = 3429 m (OH), 2928 m (NH), $\upsilon_{as}(COO^-)$ 1597 s 1360 s $\upsilon_s$ $(COO^-)$, 1265 s (phenolic CO) $cm^{-1}$. Weight loss (64–119 °C) as per TGA: 5.9% [calculated for $6H_2O$: 5.5%]. $\mu_B$ = 1.31 BM.

**$[Cu_2(ClSch12)_2]\cdot 2H_2O$ (9):** To a clear solution of $H_2$ClSch12 (0.14 g, 0.5 mmol) and NaOH (0.04 g, 1.0 mmol) in methanol (10 mL) was added water (10 mL) followed by the addition solid copper(II) nitrate trihydrate (0.12 g, 0.5 mmol) and the mixture was stirred for 1.5 h. The dark green product obtained was filtered, washed with water (2 × 2 mL), methanol (2 × 2 mL) and diethyl ether (4 mL) and then dried in air. Yield: 0.31 g (85%). $C_{28}H_{36}Cl_2Cu_2N_2O_8$ (726.6): calcd. C 46.3, H 5.0, N 3.9; found C 47.0, H 5.2, N 4.0. IR (KBr): $\tilde{\nu}$ = 3396 m (OH), 3115 m (NH), 1603 s $\upsilon_{as}(COO^-)$, 1384 s $\upsilon_s(COO^-)$, 1264 s (phenolic CO) $cm^{-1}$. Weight loss (80–146 °C) as per TGA: 5.8% [calculated for $2H_2O$: 5.0%]. $\mu_B$ = 1.25 BM. A clear saturated solution of **9** in the solvent mixture of methanol/dichloromethane (1:1) afforded single crystals of $[Cu_2(ClSch12)_2]\cdot 2MeOH$, **9a** upon slow evaporation for 3 days.

**$[Cu_2(MeSch12)_2(H_2O)_2]$ (10):** A clear solution of $H_2$MeSch12 (0.26 g, 1.0 mmol) and NaOH (0.08 g, 2.0 mmol) in methanol (20 mL) was obtained on stirring the mixture for 15 min. To this was added solid copper(II) nitrate trihydrate (0.24 g, 1.0 mmol) in one portion. The reaction mixture was stirred for another 1 h. The greenish product obtained was filtered, washed with methanol, $Et_2O$, and then dried in air. Yield: 0.48 g (70%). $C_{30}H_{42}Cu_2N_2O_8$ (685.7): calcd. C 52.5, H 6.17, N 4.1; found C 52.4, H 6.25, N 4.1. IR (KBr): $\tilde{\nu}$ = 3458 m (OH), 2936 m (NH), 1601 s $\upsilon_{as}(COO^-)$, 1396 s $\upsilon_s(COO^-)$, 1262 s (phenolic CO) $cm^{-1}$. Weight loss (60–107 °C) as per TGA: 5.2% [calculated for $2H_2O$: 5.3%]. $\mu_B$ = 1.34 BM.

**$[Cu_2(Diala5)_2(H_2O)_2]\cdot H_2O$ (11):** To a clear solution of copper(II) acetate monohydrate (0.20 g, 1 mmol) in water (20 mL) $H_3$Diala5 (0.21 g, 1 mmol) was added directly and stirred for 3 h. The green solid obtained after stirring for 3 h was filtered, washed with methanol (2 × 2 mL), diethyl ether (2 × 2 mL), and then dried in air. Yield: 0.38 g (63%). $C_{20}H_{28}Cu_2N_2O_{11}$ (599.5): calcd. C 40.1, H 4.7, N 4.6; found C 40.2, H 4.8, N 4.2. IR (KBr): $\tilde{\nu}$ = 3406 m (OH), 2920 m (NH), 1611 s $\upsilon_{as}(COO^-)$, 1462 s $\upsilon_s(COO^-)$, 1299 s (phenolic CO) $cm^{-1}$. $[a]_D^{27}$: 97.4 ($c$ = 5.5 mg$mL^{-1}$, DMSO). Weight loss (24–101 °C) as per TGA: 8.6% [calculated for $3H_2O$: 9.0%]. $\mu_B$ = 1.51 BM.

**$[Cu_2(Diala4)_2(H_2O)_2]\cdot H_2O$ (12):** To the clear solution of copper acetate (0.20 g, 1 mmol) in methanol (20 mL) $H_3$Diala4 (0.21 g, 1 mmol) was added directly and stirred. The green precipitate that formed after 10 min was subjected to further stirring for 3.5 h and then filtered off, washed with methanol, $Et_2O$, and dried in air. Yield: 0.36 g (61%). $C_{20}H_{28}Cu_2N_2O_{11}$ (599.5): calcd. C 40.1, H 4.7, N 4.6; found C 40.1, H 4.5, N 4.4. IR (KBr): $\tilde{\nu}$ = 3406 m (OH), 2920 m (NH), 1611 s $\upsilon_{as}(COO^-)$, 1462 s $\upsilon_s(COO^-)$, 1299 s (phenolic CO) $cm^{-1}$. $[a]_D^{27}$: 32.4 ($c$ = 5.5 mg$mL^{-1}$, DMSO). Weight loss (23–106 °C) as per TGA: 8.2% [calculated for $3H_2O$: 9.0%]. $\mu_B$ = 1.25 BM. Slow diffusion of acetone into a saturated solution of **12** in DMSO afforded dark-green single crystals of $[Cu_2(Diala4)_2(DMSO)_2]\cdot 2DMSO\cdot 2$acetone (**12a**).

**$[Cu_2(Diala3)_2(H_2O)_2]\cdot H_2O$ (13):** To a clear solution of copper acetate (0.40 g, 2 mmol) in methanol (30 mL) $H_3$Diala3 (0.42 g, 2 mmol) was added directly and stirred. The dark-green solution was stirred for 5 h. The mixture was reduced to a small volume and then precipitated with excess of diethyl ether. The green product was dried in air. Yield: 0.82 g (68%). $C_{20}H_{28}Cu_2N_2O_{11}$ (599.5): calcd. C 40.1, H 4.7, N 4.6; found C 40.0, H 4.6, N 4.4. IR (KBr): $\tilde{\nu}$ = 3406 m (OH), 2920 m (NH), 1611 s $\upsilon_{as}(COO^-)$, 1462 s $\upsilon_s(COO^-)$; 1299 s (phenolic CO) $cm^{-1}$. $[a]_D^{27}$: 40.7 ($c$ = 5.5 mg$mL^{-1}$, DMSO). Weight loss (80–131 °C) as per TGA: 8.6% [calculated for $3H_2O$: 9.0%]. $\mu_B$ = 1.91 BM.

**Catecholase Activity and Kinetics Measurements:** The catecholase activity of the complexes **1**–**13** described here in has been measured by the reaction with model substrate 3,5-DTBC at 25 °C. The growth of absorption maximum at $\lambda_{max}$ = 390 nm, characteristic of the product of oxidation 3, 5-DTBQ, was measured as a function of time. For this purpose, $10^{-4}$ mol$dm^{-3}$ solutions of **1**–**13** were treated with 50 equivalents of 3,5-DTBC. The reaction was carried out in methanol because of the satisfactory solubility of 3,5-DTBC and 3,5-DTBQ. The course of the reaction was followed by UV/Vis spectroscopy. The UV/Vis spectra of the original solution directly after the addition and after 10, 20, 30, 40, 50, 60, 75, 90, 105, and 120 min were recorded and corrected for volume changes. The increase in the absorption due to the formation of DTBQ at 390 nm indicated significant catalytic activity for all the complexes. Kinetic parameters on the rate of catechol oxidation were determined by reaction of $1\,10^{-3}$ to $1.3\,10^{-2}$ M solutions of DTBC with $10^{-4}$ solutions of complexes in methanol. A kinetic treatment on the basis of the Michaelis–Menten approach was applied and the results were evaluated from Lineweaver–Burk double reciprocal plots. The errors in the kinetic parameters were obtained from at least three measurements.

**X-ray Crystallography:** The diffraction experiments were carried out with a Bruker AXS SMART CCD diffractometer. The program SMART[34a] was used for collecting frames of data, indexing reflections, and determining lattice parameters, SAINT[34a] for integration of the intensity of reflections and scaling, SADABS[34b] for absorption correction and SHELXTL[34c] for space group and structure determination, least-squares refinements on $F^2$. All the hydrogen atom positions of the imine groups, methanol, and water molecules were located and their positional parameters were refined in the least-squares cycles. One of the carbon atoms in **2a** (C12 with occupancies 0.65/0.35) and **3a** (C11 with occupancies 0.6/0.4) were found to be disordered. Selected crystallographic data

 © 2006 Wiley-VCH Verlag GmbH & Co. KGaA, Weinheim 

Table 5. X-ray crystallographic data and structure refinement details.

| Complex | **1a** | **2a** | **3a** | **4** |
|---|---|---|---|---|
| Formula | $C_{28}H_{38}Cu_2N_2O_8$ | $C_{31}H_{40}Cl_2Cu_2N_4O_8$ | $C_{32}H_{50}Cu_2N_2O_{10}$ | $C_{26}H_{34}Cu_2N_2O_{10}$ |
| Formula wt. | 657.68 | 794.65 | 749.82 | 661.63 |
| $T$ [K] | 223(2) | 223(2) | 223(2) | 223(2) |
| Crystal system | monoclinic | triclinic | triclinic | triclinic |
| Space group | $C2/c$ | $P\bar{1}$ | $P\bar{1}$ | $P\bar{1}$ |
| $a$ [Å] | 16.5064(8) | 11.2530(6) | 7.7219(5) | 7.7024(8) |
| $b$ [Å] | 14.5462(7) | 12.3363(7) | 10.4139(7) | 8.8514(9) |
| $c$ [Å] | 14.1803(7) | 13.9093(8) | 11.599(28) | 9.835(1) |
| $\alpha$ [°] | 90 | 107.662(1) | 106.958(1) | 76.240(2) |
| $\beta$ [°] | 124.930 | 105.555(1) | 106.312(1) | 89.220(2) |
| $\gamma$ [°] | 90 | 98.783(1) | 96.710(1) | 81.352(2) |
| $V$ [Å$^3$] | 2791.4(2) | 1713.9(2) | 836.0(1) | 643.7(1) |
| $Z$ | 4 | 2 | 1 | 1 |
| $\mu$ [mm$^{-1}$] | 1.577 | 1.451 | 1.331 | 1.716 |
| Reflections collected | 8047 | 9753 | 4902 | 3806 |
| Independent reflections | 2460 | 5943 | 2948 | 2266 |
| $R_{int}$ | 0.0313 | 0.0196 | 0.0135 | 0.0164 |
| GooF | 1.010 | 1.034 | 1.054 | 1.053 |
| Final $R$ [$I>2\sigma$], $R_1$[a] | 0.0372 | 0.0479 | 0.0316 | 0.0337 |
| $wR_2$[b] | 0.0902 | 0.1212 | 0.0828 | 0.0831 |
| Complex | **6a** | **8** | **9a** | **12a** |
| Formula | $C_{32}H_{48}Cl_2Cu_2N_2O_{10}$ | $C_{28}H_{38}Cu_2N_2O_8$ | $C_{30}H_{40}Cl_2Cu_2N_2O_8$ | $C_{34}H_{58}Cu_2N_2O_{14}S_4$ |
| Formula wt. | 817.7 | 657.68 | 754.62 | 974.14 |
| $T$ [K] | 223(2) | 223(2) | 223(2) | 223(2) |
| Wavelength [Å] | 0.71073 | 0.71073 | 0.71073 | 0.71073 |
| Crystal system | triclinic | triclinic | triclinic | triclinic |
| Space group | $P\bar{1}$ | $P\bar{1}$ | $P\bar{1}$ | $P1$ |
| $a$ [Å] | 7.7614(3) | 12.3573(11) | 7.4698(9) | 9.5244(7) |
| $b$ [Å] | 10.8014(4) | 14.1055(14) | 9.9411(12) | 10.8149(8) |
| $c$ [Å] | 11.8232(4) | 14.1822(15) | 11.2134(14) | 12.0257(9) |
| $\alpha$ [°] | 108.395(2) | 104.195(2) | 72.522(3) | 96.841(2) |
| $\beta$ [°] | 107.969(2) | 110.017(2) | 79.596(3) | 102.547(2) |
| $\gamma$ [°] | 95.718(2) | 104.945(3) | 88.363(3) | 111.801(2) |
| $V$ [Å$^3$] | 873.10(6) | 2087.2(4) | 780.9(2) | 1095.0(1) |
| $Z$ | 1 | 3 | 1 | 1 |
| $\mu$ [mm$^{-1}$] | 1.429 | 1.582 | 1.586 | 1.225 |
| Reflections collected | 7693 | 17670 | 6432 | 6278 |
| Independent reflections | 5003 | 10780 | 4305 | 4545 |
| $R_{int}$ | 0.0206 | 0.0239 | 0.0216 | 0.0162 |
| GooF | 0.921 | 1.019 | 1.084 | 1.078 |
| Final $R$ [$I > 2\sigma$], $R_1$[a] | 0.0398 | 0.0376 | 0.0521 | 0.0444 |
| $wR_2$[a] | 0.0856 | 0.0734 | 0.1146 | 0.1136 |

[a] $R_1 = \Sigma||F_o| - |F_c||/\Sigma|F_o|$. [b] $wR_2 = [\Sigma w(F_o^2 - F_c^2)^2/\Sigma w(F_o^2)^2]^{1/2}$.

and refinement details are displayed in Table 5. The structure of **12a** can also be solved in the centrosymmetric space group $P\bar{1}$ with the methyl group of the alanine part of the ligand disordered. However, the optical activity of **12** containing the optically active Diala4 ligand is comparable to those of **11** and **13** and therefore, the chiral space group was retained.

CCDC-277306 to -277313 (for **1a**, **2a**, **3a**, **4**, **6a**, **8**, **9a**, and **12a**, respectively) contain the supplementary crystallographic data discussed in this paper. These data can be obtained free of charge from The Cambridge Crystallographic Data Centre via www.ccdc.cam.ac.uk/data_request/cif.

**Supporting Information** (see also the footnote on the first page of this article): Structure diagrams, thermogravimetric curves, UV/Vis spectra of the oxidation of 3,5-DTBC, Lineweaver–Burk plots (1/v vs. 1/[S]) and ESI-MS data (total number of pages: 25).

## Acknowledgments

We gratefully acknowledge the financial support from NUS (R143-000-252-112), and from NSFC (20125104, 20490210).

[1] a) H. S. Mason, *Nature* **1956**, *177*, 79–81; b) J. R. Walker, P. H. Ferrar, *Biotechnol. Genet. Eng. Rev.* **1998**, *15*, 457–498; c) R. H. Holm, E. I. Solomon, *Chem. Rev.* **1996**, *96*, 2239–3042.

[2] a) C. X. Zhang, H.-C. Liang, K. J. Humphreys, K. D. Karlin in *Advances in Catalytic Activation of Dioxygen by Metal Complexes* (Ed.: L. I. Simandi), Kluwer Academic Publishers, Dordrecht, **2003**, pp. 79–121; b) K. D. Karlin, Z. Tyeklar, *Bioinorganic Chemistry of Copper*, Chapman & Hall, New York, **1993**.

[3] a) C. Gerdermann, C. Eicken, B. Krebs, *Acc. Chem. Res.* **2002**, *35*, 183–191; b) C. Eicken, F. Zippel, K. Buldt-Karentzopoulos, B. Krebs, *FEBS Lett.* **1998**, *436*, 293–299.

 © 2006 Wiley-VCH Verlag GmbH & Co. KGaA, Weinheim 

[4] a) E. I. Solomon, U. M. Sundaram, T. E. Machonkin, *Chem. Rev.* **1996**, *96*, 2563–2605; b) W. B. Tolman, *Acc. Chem. Res.* **1997**, *30*, 227–237; c) E. A. Lewis, W. B. Tolman, *Chem. Rev.* **2004**, *104*, 1047–1076; d) L. M. Miricia, X. Ottenwaelder, T. D. P. Stack, *Chem. Rev.* **2004**, *104*, 1013–1045; e) L. Q. Hatcher, K. D. Karlin, *J. Biol. Inorg. Chem.* **2004**, *9*, 669–683; f) A. L. Gavrilova, B. Bosnich, *Chem. Rev.* **2004**, *104*, 349–383.

[5] See for example, a) K. D. Karlin, *Science* **1993**, *261*, 701–708; b) J. Reedjik, *Bioinorganic Catalysis* (Ed.: J. Reedjik), 2nd ed., Dekker, New York, **1999**; c) T. N. Sorrell, *Tetrahedron* **1989**, *45*, 3–68; d) P. A. Vigato, S. Tamburini, D. E. Fenton, *Coord. Chem. Rev.* **1990**, *106*, 25–170; e) N. Kitajima, *Adv. Inorg. Chem.* **1992**, *39*, 1–77; f) P. Gentschev, M. Luken, N. Moller, A. Rompel, B. Krebs, *Inorg. Chem. Commun.* **2001**, *4*, 753–756; g) R. Wegner, M. Dubs, H. Gorls, C. Robl, B. Schonecker, E.-G. Jager, *Steroids* **2002**, *67*, 835–849; h) R. Wegner, M. Gottschaldt, P. Wolfgang, E.-G. Jager, D. Klemm, *J. Mol. Catal. A* **2003**, *201*, 93–118 and references cited therein; i) C. Belle, J. L. Pierre, *Eur. J. Inorg. Chem.* **2003**, 4137–4146; j) B. Krebs, M. Merkel, A. Rompel, *J. Argent. Chem. Soc.* **2004**, *92*, 1–15 and references cited therein; k) J. Kaizer, R. Csonka, G. Speir, M. Giorgi, M. Reglier, *J. Mol. Catal. A* **2005**, *235*, 81–87; l) C. H. Lee, S. T. Wong, T. S. Lin, C. Y. Mou, *J. Phys. Chem. B* **2005**, *109*, 775–784; m) I. A. Koval, C. Belle, K. Selmeczi, C. Philouze, S. A. Eric, A. M. Schuitema, P. Gamez, J. L. Pierre, J. Reedjik, *J. Biol. Inorg. Chem.* **2005**, *10*, 739–750.

[6] a) J. D. Ranford, J. J. Vittal, D. Wu, *Angew. Chem. Int. Ed. Engl.* **1998**, *37*, 1114–1116; b) J. D. Ranford, J. J. Vittal, D. Wu, X. Yang, *Angew. Chem. Int. Ed.* **1999**, *38*, 3498–3501; c) B. Sreenivasulu, J. J. Vittal, *Crystal Growth Des.* **2003**, *3*, 635–637.

[7] B. Sreenivasulu, J. J. Vittal, *Angew. Chem. Int. Ed.* **2004**, *43*, 5769–5772.

[8] C. T. Yang, M. Vetrichelvan, X. D. Yang, B. Moubaraki, K. S. Murray, J. J. Vittal, *Dalton Trans.* **2004**, 113–121.

[9] B. Sreenivasulu, M. Vetrichelvan, F. Zhao, S. Gao, J. J. Vittal, *Eur. J. Inorg. Chem.* **2005**, 4635–4645.

[10] a) C. Belle, C. Beguin, I. Gautier-Luneau, S. Hamman, C. Philouze, J. L. Pierre, F. Thomas, S. Torelli, E. Saint-Aman, M. Bonin, *Inorg. Chem.* **2002**, *41*, 479–491; b) S. Mukherjee, T. Weyhermuller, E. Bothe, K. Weighardt, P. Chaudhuri, *Dalton Trans.* **2004**, 3842–3853.

[11] a) G. B. Deacon, R. Philips, *Coord. Chem. Rev.* **1980**, *33*, 227–250; b) C. Djordjevic, M. Lee, E. Sinn, *Inorg. Chem.* **1989**, *28*, 719–723; c) J. R. Ferraro, *Low-frequency Vibrations of Inorganic and Coordination compounds*, Plenum Press, New York, **1971**; d) D. A. Edwards, R. N. Hayward, *Can. J. Chem.* **1968**, *46*, 3443–3446.

[12] K. Nakamato, *Infrared and Raman Spectra of Inorganic and Coordination Compounds*, 4th ed., John Wiley & Sons, New York, **1986**, pp. 191–371.

[13] a) L. Sacconi, M. Ciampolini, *J. Chem. Soc.* **1964**, 276–280; b) A. B. P. Lever, *Inorganic Electronic Spectroscopy*, Elsevier, New York, **1968**.

[14] a) A. B. P. Lever, *Inorganic Electronic Spectroscopy*, Elsevier, Amsterdam, **1984**; pp. 553–572; b) C. T. Yang, B. Moubaraki, K. S. Murray, J. D. Ranford, J. J. Vittal, *Inorg. Chem.* **2001**, *40*, 5934–5941; c) W. Mazurek, B. J. Kennedy, K. S. Murray, M. J. O'Connor, J. R. Rodger, M. R. Snow, A. G. Wedd, P. R. Zwak, *Inorg. Chem.* **1985**, *24*, 3258–3264; d) R. C. Holz, J. M. Brink, F. T. Gobena, C. J. O'Connor, *Inorg. Chem.* **1994**, *33*, 6086–6092; e) B. Bleaney, K. D. Bowers, *Proc. R. Soc. A* **1952**, *214*, 451–465; f) O. Kahn, *Molecular Magnetism*, VCH, New York, **1993**.

[15] a) A. W. Addison, T. N. Rao, J. Reedijk, J. V. Rijn, G. C. Verschoor, *J. Chem. Soc., Dalton Trans.* **1984**, 1349–1356; b) G. Murphy, C. O. Sullivan, B. Murphy, B. Hathaway, *Inorg. Chem.* **1998**, *37*, 240–248; c) D. S. Marlin, M. M. Olmstead, P. K. Mascharak, *Inorg. Chem.* **2001**, *40*, 7003–7008; d) C. T. Yang, J. J. Vittal, *Inorg. Chim. Acta* **2003**, *344*, 65–76, and references therein.

[16] a) B. F. Hoskins, R. Robson, *J. Am. Chem. Soc.* **1990**, *112*, 1546–1554; b) R. W. Gable, B. F. Hoskins, R. Robson, *J. Chem. Soc., Chem. Commun.* **1990**, 1677–1678; c) M. J. Zaworotko, *Chem. Commun.* **2001**, 1–9; d) B. Moulton, M. J. Zaworotko, *Chem. Rev.* **2001**, *101*, 1629–1658; e) A. N. Khlobystov, A. J. Blake, N. R. Champness, D. A. Lemenovskii, A. G. Majouga, N. V. Zyk, M. Schröder, *Coord. Chem. Rev.* **2001**, *222*, 155–192; f) B. Kumar, M. Fujita, *J. Chem. Soc., Dalton Trans.* **2000**, 3805–3810; g) L. Carlucci, G. Ciani, D. M. Proserpio, *New J. Chem.* **1998**, *22*, 1319–1321; h) S. R. Bettens, R. Robson, *Angew. Chem. Int. Ed. Engl.* **1998**, *37*, 1460–1494; i) S. R. Bettens, B. F. Hoskins, R. Robson, *Chem. Eur. J.* **2000**, *6*, 156–161; j) S. R. Bettens, *CrystEngComm* **2001**, *3*, 67–73.

[17] a) G. R. Desiraju, *Crystal Engineering: The Design of Organic Solids*, Elsevier, Amsterdam, **1989**; b) G. R. Desiraju, *Acc. Chem. Res.* **2002**, *35*, 565–573; c) C. B. Aakeroy, A. M. Beatty, D. S. Leinen, *Angew. Chem. Int. Ed.* **1999**, *38*, 1815–1819; d) A. M. Beatty, *CrystEngComm* **2001**, *51*, 1–15; e) J. K. Craig, M. S. S. Janet, L. W. James, M. S. V. W. Solange, N. L. John, C. Glidewell, *Acta Crystallogr., Section B* **2002**, *58*, 94–108; f) T. Steiner, *Angew. Chem. Int. Ed.* **2002**, *41*, 48–76.

[18] a) A. B. P. Lever, B. S. Ramaswamy, S. R. Pickens, *Inorg. Chim. Acta* **1980**, *46*, L59–61; b) T. R. Demmin, M. D. Swerdloff, M. M. Rogic, *J. Am. Chem. Soc.* **1981**, *103*, 5795–5804; c) F. Zippel, F. Ahlers, R. Werner, W. Haase, H.-F. Nolting, B. Krebs, *Inorg. Chem.* **1996**, *35*, 3409–3419; d) Y.-H. Chung, H.-H. Wei, Y.-H. Liu, G.-H. Lee, Y. Wang, *J. Chem. Soc., Dalton Trans.* **1997**, 2825–2829; e) R. Wegner, M. Gottschaldt, H. Gorls, E.-G. Jager, D. Klemm, *Angew. Chem. Int. Ed.* **2000**, *39*, 595–599; f) R. Wegner, M. Gottschaldt, H. Gorl, E.-G. Jager, D. Klemm, *Chem. Eur. J.* **2001**, *7*, 2143–2157; g) P. Gentschev, N. Moller, B. Krebs, *Inorg. Chim. Acta* **2000**, *300–302*, 442–452; h) M. Merkel, N. Moller, M. Piacenza, S. Grimme, A. Rompel, B. Krebs, *Chem. Eur. J.* **2005**, *11*, 1201–1209; i) I. A. Koval, D. Pursche, A. F. Stassen, P. Gamez, B. Krebs, J. Reedijk, *Eur. J. Inorg. Chem.* **2003**, 1669–1674.

[19] For mononuclear complexes see: a) N. Oshi, Y. Nishida, K. Ida, S. Kida, *Bull. Chem. Soc. Jpn.* **1980**, *53*, 2847–2850; b) U. Casellato, S. Tamburini, P. A. Vigato, A. de Stefani, M. Vidali, D. E. Fenton, *Inorg. Chim. Acta* **1983**, *69*, 45–51; c) M. R. Malachowski, M. G. Davidson, *Inorg. Chim. Acta* **1989**, *162*, 199–204; d) C.-H. Kao, H.-H. Wie, Y.-H. Liu, G.-H. Lee, Y. Wang, C.-J. Lee, *J. Inorg. Biochem.* **2001**, *84*, 171–178.

[20] For redox potentials of catechols see: a) L. Horner, E. Geyer, *Chem. Ber.* **1965**, *98*, 2016–2045; b) S. Harmalker, S. E. Jones, D. T. Sawyer, *Inorg. Chem.* **1983**, *22*, 2790–2794; c) J. Rall, M. Wanner, M. Albrecht, F. M. Hornung, W. Kaim, *Chem. Eur. J.* **1999**, *5*, 2802–2808.

[21] a) A. Rompel, H. Fischer, D. Meiwes, K. Buldt-Karentzoloulos, R. Dillinger, F. Tuczek, H. Witzel, B. Krebs, *J. Biol. Inorg. Chem.* **1999**, *4*, 56–63; b) T. Klabunde, C. Eicken, J. C. Sacchettini, B. Krebs, *Nat. Struct. Biol.* **1998**, *5*, 1084–1090; c) C. Eicken, B. Krebs, J. C. Sacchettini, *Curr. Opin. Struct. Biol.* **1999**, *9*, 677–683.

[22] a) K. D. Karlin, M. S. Nasin, B. I. Cohen, R. W. Cruse, S. Kaderli, A. D. Zuberbuhler, *J. Am. Chem. Soc.* **1994**, *116*, 1324–1336; b) K. D. Karlin, N. Wei, B. Jung, S. Kaderli, P. Niklaus, A. D. Zuberbuhler, *J. Am. Chem. Soc.* **1993**, *115*, 9506–9514; c) G. Battaini, E. Monzani, L. Casella, L. Santagostini, R. Pagliarin, *J. Biol. Inorg. Chem.* **2000**, *5*, 262–268.

[23] a) M. Thirumavalavan, P. Akilan, M. Kandaswamy, *Supramol. Chem.* **2004**, *16*, 137–146; b) M. R. Malachowski, B. Dorsey, J. G. Sackett, R. S. Kelly, A. L. Ferko, R. N. Hardin, *Inorg. Chim. Acta* **1996**, *249*, 85–92; c) M. R. Malachowski, J. Carden, M. G. Davidson, W. L. Driessen, J. Reedijk, *Inorg. Chim. Acta* **1997**, *257*, 59–67.

[24] a) S. Torelli, C. Belle, I. Gautier-Luneau, J. L. Pierre, E. Saint-Aman, J. M. Latour, L. Le Pape, D. Luneau, *Inorg. Chem.* **2000**, *39*, 3526–3536; b) C. Fernandes, A. Neves, A. J. Bortoluzzi, A. S. Mangrich, E. Rentschler, B. Szpoganicz, E. Schwin-


 © 2006 Wiley-VCH Verlag GmbH & Co. KGaA, Weinheim 

gel, *Inorg. Chim. Acta* **2001**, *320*, 12–21; c) C.-H. Kao, H.-H. Wie, Y.-H. Liu, G.-H. Lee, Y. Wang, C.-J. Lee, *Inorg. Biochem.* **2001**, *84*, 171–178; d) R. Than, A. A. Feldman, B. Krebs, *Coord. Chem. Rev.* **1999**, *182*, 211–241.

[25] a) J. Mukherjee, R. Mukherjee, *Inorg. Chim. Acta* **2002**, *337*, 429–438; b) A. Neves, L. M. Rossi, A. J. Bortoluzzi, B. Szpoganicz, C. Wiezbicki, E. Schwingel, W. Haase, S. Ostrovsky, *Inorg. Chem.* **2002**, *41*, 1788–1794; c) O. Seneque, M. Campion, B. Douziech, M. Giorgi, E. Riviere, Y. Journaux, Y. L. Mest, O. Reinaud, *Eur. J. Inorg. Chem.* **2002**, 2007–2014.

[26] a) K. D. Karlin, S. Kaderli, A. D. Zuberbuhler, *Acc. Chem. Res.* **1997**, *30*, 139–147; b) N. Kitajima, Y. Moro-oka, *Chem. Rev.* **1994**, *94*, 737–757; c) E. I. Solomon, F. Tuczek, D. E. Root, C. A. Brown, *Chem. Rev.* **1994**, *94*, 827–856.

[27] J. Ackermann, F. Meyer, E. Kaifer, H. Pritzkow, *Chem. Eur. J.* **2002**, *8*, 247–258.

[28] J. Reim, B. Krebs, *J. Chem. Soc., Dalton Trans.* **1997**, 3793–3804.

[29] J. McMurray, *Organic Chemistry*, Brooks/Cole, Monterey, California, 3rd ed., **1992**.

[30] a) J. P. Chyn, F. L. Urbach, *Inorg. Chim. Acta* **1991**, *189*, 157–163; b) J. Balla, T. Kiss, R. F. Jameson, *Inorg. Chem.* **1992**, *31*, 58–62; c) K. Selmeczi, M. Reglier, M. Giorgi, G. Speier, *Coord. Chem. Rev.* **2003**, *245*, 191–201.

[31] a) E. Monzani, L. Quinti, A. Perotti, L. Casella, M. Gullotti, L. Randaccio, S. Geremia, G. Nardin, P. Faleschini, G. Tabbi, *Inorg. Chem.* **1998**, *37*, 553–562; b) E. Monzani, G. Battaini, A. Perotti, L. Casella, M. Gullotti, L. Santagostini, G. Nardin, L. Randaccio, S. Geremia, P. Zanello, G. Opromolla, *Inorg. Chem.* **1999**, *38*, 5359–5369.

[32] a) A. Granata, E. Monzani, L. Casella, *J. Biol. Inorg. Chem.* **2004**, *9*, 903–913.

[33] C. Eicken, C. Gerdemann, B. Krebs, in: *Handbook of Metalloproteins* (Ed.: A. Messerschmidt), John Wiley & Sons, Chichester, **2001**, vol. 2, pp. 1319–1329.

[34] a) *SMART* & *SAINT* Software Reference Manuals, Version 6.22, Bruker AXS Analytic X-ray Systems, Inc., Madison, WI, **2000**; b) G. M. Sheldrick, *SADABS*, Software for Empirical Absorption Correction, University of Gottingen, Germany, **2000**; c) *SHELXTL* Reference Manual, Version 5.1, Bruker AXS, Analytic X-ray Systems, Inc., Madison, WI, **1997**.

Received: January 11, 2006
Published Online: April 26, 2006

 © 2006 Wiley-VCH Verlag GmbH & Co. KGaA, Weinheim 

DOI: 10.1002/ejic.200600068

# A Two-Step Spin Transition and Order–Disorder Phenomena in the Mononuclear Compound [Fe(Hpy-DAPP)]$(BF_4)_2$

**Galina S. Matouzenko,*[a] Dominique Luneau,[b] Gábor Molnár,[c] Nawell Ould-Moussa,[c] Samir Zein,[a] Serguei A. Borshch,[a] Azzedine Bousseksou,[c] and Frédéric Averseng[a]**

**Keywords:** Density functional calculations / Iron / Magnetic properties / Mössbauer spectroscopy / N ligands / Spin crossover

This paper reports the synthesis and detailed characterization of the mononuclear complex $[Fe^{II}(Hpy\text{-}DAPP)](BF_4)_2$ (Hpy-DAPP = {bis[*N*-(2-pyridylmethyl)-3-aminopropyl](2-pyridylmethyl)amine}), which manifests a two-step spin crossover accompanied by an ordering and a conformational transition in the ligand. The magnetic susceptibility measurements and Mössbauer spectra reveal that the two steps of the spin transition are separated by an inflexion point at about 130 K at which 50 % of the complex undergoes a spin conversion. The high-temperature step centered at 181 K is gradual, whereas the low-temperature one displays a thermal hysteresis with two transition temperatures ($T_{c\downarrow}$ = 119 and $T_{c\uparrow}$ = 123 K). The single-crystal X-ray structure has been determined for the HS (298 K) and LS (90 K) forms, as well as for the mixed form with an HS:LS ratio of 1:1 (130 K). The structural studies show that the crystal lattice contains a single $Fe^{II}$ crystallographic site over the whole temperature range. At room temperature, the most important peculiarity of the HS complex structure is the disorder of the N3 amino aliphatic atom, which is in the first coordination sphere of $Fe^{II}$, over two positions. The strong involvement of the N3 atoms in H-bonding with two neighboring counterions is considered as a possible origin of this disorder. At 130 K, the disorder is increased by the distribution of the N1 and C9 atoms over two positions, leading to the conformational disorder (*chair* and *twist-boat* conformations with a 1:1 ratio) in the six-membered N2C7C8C9N1Fe chelate cycle. At 90 K, the disorder in the positions of the N1, N3, and C9 atoms disappears and the N2C7C8C9N1Fe metallacycle adopts a unique *twist-boat* conformation. The results of structural studies suggest that the two-step spin-transition behavior of the complex $[Fe(Hpy\text{-}DAPP)](BF_4)_2$ is induced by two different geometries of the $[FeN_6]$ coordination core generated by the disorder in the ligand. The HS → LS transition is also associated with the conformational change in the chelate cycle. Both crystallographic data analysis and electronic structure calculations allow us to relate the disordered geometries of the $[FeN_6]$ coordination core to their HS and LS character.
(© Wiley-VCH Verlag GmbH & Co. KGaA, 69451 Weinheim, Germany, 2006)

## Introduction

The phenomenon of spin transition between low-spin (LS) and high-spin (HS) electronic states[1] is an important area in iron(II) coordination chemistry. Its theoretical and experimental aspects, as well as its potential applications, give rise to a permanent interest in this phenomenon. The bi-stable behavior (HS, $S = 2$, $^5T_2 \leftrightarrow$ LS, $S = 0$, $^1A_1$) underlies the design of new molecular materials for technological applications[1b,1d,2] and can be induced by a variation of temperature, pressure, light irradiation, or by application of a magnetic field. The potential applications of spin-crossover systems for information storage require an abrupt spin transition with a relatively large thermal hysteresis centered near to ambient temperature. Currently, two approaches are employed to design new cooperative spin-crossover compounds, namely supramolecular and polymeric approaches.[3] The use of new polydentate ligands containing nitrogen donor atoms with different chemical functions, which generate an intermediate ligand field that favors spin-state interconversion, is one of the possible synthetic strategies for engineering spin transition systems. However, the ligand-field splitting is not the only factor that determines the existence and character of a spin transition. The interplay of the spin pairing energy and the ligand-field strength is very sensitive to small structural perturbations in the metal environment, which may result from the existence of sterically demanding ligands and/or from minor crystal-packing changes associated with the nature of the counterions, or even the presence of a solvent of crystallization. As has been noted,[1i] even more subtle changes, such as the number of chelate rings and/or the replacement of five- with six-membered cycles, can also affect the spin state of the

[a] Laboratoire de Chimie (UMR CNRS and ENS-Lyon n° 5182), École Normale Supérieure de Lyon,
46, allée d'Italie, 69364 Lyon cedex 07, France
E-mail: Galina.Matouzenko@ens-lyon.fr
[b] Université Claude Bernard Lyon-1, Laboratoire des Multimatériaux et Interfaces (UMR CNRS n° 5615),
69622 Villeurbanne cedex, France
[c] Laboratoire de Chimie de Coordination (UPR CNRS n° 8241),
205, route de Narbonne, 31077 Toulouse cedex, France
Supporting information for this article is available on the WWW under http://www.eurjic.org or from the author.

 © 2006 Wiley-VCH Verlag GmbH & Co. KGaA, Weinheim 

resulting iron(II) complex. In this context, polydentate ligands that are capable of generating one or more flexible six-membered metallocycles upon coordination with $Fe^{II}$ are of special interest. In this case, a high flexibility of the coordination sphere of a complex can manifest itself in different ways, one of which is the yield of several reaction products. For example, the enlargement of just one of three chelate cycles from five-membered in $[Fe(DPEA)(NCS)_2]$[4a] [DPEA = (2-aminoethyl)bis(2-pyridylmethyl)amine] to six-membered in $[Fe(DPPA)(NCS)_2]$[4b] [DPPA = (3-aminopropyl)bis(2-pyridylmethyl)amine] has allowed the isolation of four species with the DPPA ligand (three of them with the spin change), namely three polymorphic modifications and one solvated complex, instead of just one complex with DPEA. Another situation arises due to the conformational freedom of six-membered chelate cycles.[5] Recently, a new cooperative spin-crossover compound $[Fe(DAPP)(abpt)](ClO_4)_2$ [DAPP = bis(3-aminopropyl)(2-pyridylmethyl)-amine; abpt = 4-amino-3,5-bis(pyridin-2-yl)-1,2,4-triazole], which displays simultaneous spin change and two order–disorder transitions (in the DAPP ligand and the counterion), has been reported.[6] At high temperatures, the disorder over two positions was observed for one carbon atom in the six-membered metallacycle, which is in a *half-boat* conformation. This peculiarity, i.e. the thermal ordering of the ligand directly coordinated to the metal, was documented for spin-crossover systems for the first time. The order–disorder phenomena and the spin transition in $[Fe(DAPP)(abpt)](ClO_4)_2$ were found to be interrelated. Both tuning of the ligand-field strength by the DAPP ligand and reinforcement of the cooperative interactions due to the thermal ordering in the perchlorate ions were proposed as initiators of the spin transition.

Following our studies on the role of metallocycle size on the spin-transition process, a new complex $[Fe(Hpy-DAPP)](BF_4)_2$ (Hpy-DAPP = {bis[*N*-(2-pyridylmethyl)-3-aminopropyl](2-pyridylmethyl)amine}) has been synthesized. The hexadentate Hpy-DAPP ligand (Scheme 1) was prepared starting from tetradentate DAPP. The modification of the DAPP ligand was motivated by its ability to form disordered six-membered chelate cycles upon coordination with $Fe^{II}$. The magnetic susceptibility measurements and Mössbauer spectra of the title compound display a two-step spin transition with thermal hysteresis in the low-temperature step. The single-crystal X-ray structure was determined for the HS (298 K) and LS (90 K) forms, as well as for the mixed form with an HS:LS ratio of 1:1 (130 K). The results of our experimental and theoretical studies suggest that $[Fe(Hpy-DAPP)](BF_4)_2$ can be considered as the first mononuclear complex with a unique $Fe^{II}$ crystallographic site for which the two-step spin transition occurs within the same space group and is accompanied by a ligand ordering in conjugation with a conformational transition.

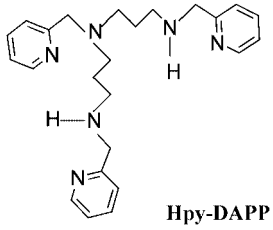


Scheme 1. Representation of the Hpy-DAPP ligand.

## Results

### Magnetic Susceptibility Data

Magnetic susceptibility measurements were carried out on two different batches of freshly prepared samples of $[Fe(Hpy-DAPP)](BF_4)_2$ and also on some thermally cycled samples. Within the experimental precision, the magnetic susceptibility of these samples was the same at each temperature. Variable-temperature magnetic susceptibility data were measured in both cooling and warming modes in the range 15–290 K. The magnetic properties of the complex (Figure 1) display the HS ↔ LS transition. At 290 K, the magnitude of $\chi_M T$, where $\chi_M$ is the molar magnetic susceptibility, is 3.56 $cm^3 mol^{-1} K$ ($\mu_{eff}$ = 5.34 $\mu_B$) and corresponds to a quintet spin state. This value remains fairly constant with decreasing temperature until 230 K and then gradually decreases upon cooling to 1.78 $cm^3 mol^{-1} K$ at 130 K. Below 130 K, the $\chi_M T$ value descends more steeply to reach 0.53 $cm^3 mol^{-1} K$ at 90 K, and then it slowly decreases to 0.40 $cm^3 mol^{-1} K$ at 15 K. This weak paramagnetism may be related to a residual amount (about 10%) of the HS fraction. The presence of a residual paramagnetic HS fraction at low temperature was confirmed by Mössbauer spectroscopy (vide infra). The shape of the susceptibility curve reveals that the spin transition takes place in two steps, which are separated by an inflexion point at about 130 K at which 50% of the complex has undergone a thermal spin conversion. The gradual high-temperature step is centered at 181 K. The low-temperature step displays a thermal hysteresis. The observed transition temperatures are $T_{c\downarrow}$ = 119 and $T_{c\uparrow}$ = 123 K in the cooling and warming modes, respectively.

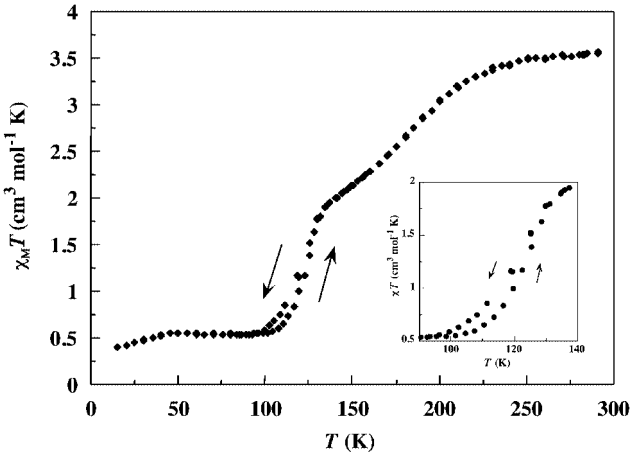


Figure 1. Thermal variation of $\chi_M T$ for $[Fe(Hpy-DAPP)](BF_4)_2$.

 © 2006 Wiley-VCH Verlag GmbH & Co. KGaA, Weinheim 

### Description of the Structure

The crystal structure of [Fe(Hpy-DAPP)]$(BF_4)_2$ was determined at 298, 130, and 90 K for the HS, mixed-spin states, and predominantly LS form, respectively. No change in the space group was observed at these three temperatures. All structures belong to the monoclinic $P2_1/c$ group with $Z = 4$. Selected bond lengths are given in Table 1. Six nitrogen atoms of Hpy-DAPP ligand constitute the first coordination sphere around the $Fe^{II}$ atom (Figure 2). The ligand, upon coordination to iron(II), forms three five-membered and two six-membered chelate cycles. It should be noted that three pyridine rings (or three aliphatic amino groups) of the Hpy-DAPP ligand can have either a facial or a meridional arrangement, which gives rise, in principle, to a number of isomers. An octahedral coordination leads to the possible existence of two stereoisomers (Δ or Λ configuration). In [Fe(Hpy-DAPP)]$(BF_4)_2$, the ligand adopts a *fac* configuration and the unit cell contains two pairs of symmetry-related left-handed and right-handed enantiomers.

Table 1. Selected bond lengths [Å] for [Fe(Hpy-DAPP)]$(BF_4)_2$.[a]

| | $T$ = 298 K | $T$ = 130 K | $T$ = 90 K |
|---|---|---|---|
| Fe(1)–N(1) | 2.208(3) | | 2.009(5) |
| Fe(1)–N(1A) | | 2.140(3) | |
| Fe(1)–N(1B) | | 2.034(10) | |
| Fe(1)–N(2) | 2.238(2) | 2.152(4) | 2.128(4) |
| Fe(1)–N(3) | | | 2.085(6) |
| Fe(1)–N(3A) | 2.151(4) | 2.084(8) | |
| Fe(1)–N(3B) | 2.217(5) | 2.104(10) | |
| Fe(1)–N(4) | 2.181(2) | 2.071(4) | 2.049(4) |
| Fe(1)–N(5) | 2.191(2) | 2.030(5) | 2.033(5) |
| Fe(1)–N(6) | 2.235(2) | 2.079(5) | 2.061(4) |

[a] Estimated standard deviations in the least significant digits are given in parentheses.

#### *High-Spin Complex Structure (T = 298 K)*

The $[FeN_6]$ coordination core is severely distorted at room temperature, and the Fe–N distances fall within the range 2.151(4)–2.238(2) Å (see Table 1). The average Fe–N distance is equal to 2.206 Å, typical for iron(II) in the HS state. The octahedron is axially elongated along the N2–Fe–N6 direction, which can be seen as a pseudo-Jahn–Teller distortion. The secondary N3 amino aliphatic atom is disordered over two positions (Figure 3, a), with an occupancy close to 0.5:0.5. The two Fe–N3(A) and Fe–N3(B) distances are rather different and equal to 2.151(4) and 2.217(5) Å, respectively. The N–Fe–N angles between the adjacent and the opposite nitrogen atoms fall within the range 73.7(2)–111.6(2)° and 160.5(2)–166.5(1)°, respectively. The largest deviation (74–78°) from 90° is observed in three five-membered chelate cycles due to steric strain. In contrast, the N–Fe–N angles in the FeN2C7C8C9N1 and FeN2C16C17C18N3(A/B) six-membered chelate cycles are close to the ideal octahedral value, probably owing to the flexibility of the amino aliphatic chain. The former metallocycle adopts a *chair* conformation (Figure 3, a).

The $BF_4$ counterions were found to be badly disordered at room temperature (Figure 2). This disorder was modeled over two orientations in a 0.5:0.5 occupation ratio. The disordered groups are represented as a superposition of two tetrahedra with a unique position for the B atoms and eight different orientations for the F atoms. However, the large values of the anisotropic displacement parameter for the F atoms indicate that the disorder model with only two positions for the $BF_4$ groups, derived from the SHELXS-97 program, is not fully satisfactory. It is therefore very likely that both counterions are disordered over several rather close orientations at room temperature.

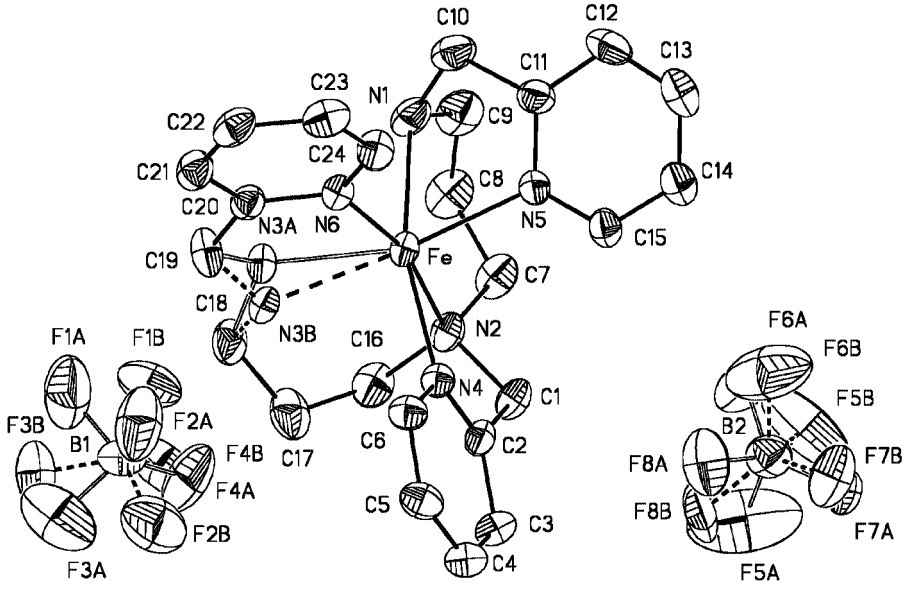


Figure 2. ORTEP view of [Fe(Hpy-DAPP)]$(BF_4)_2$ at 298 K. Ellipsoids enclose 30% probability. The hydrogen atoms have been omitted for clarity.

 © 2006 Wiley-VCH Verlag GmbH & Co. KGaA, Weinheim 

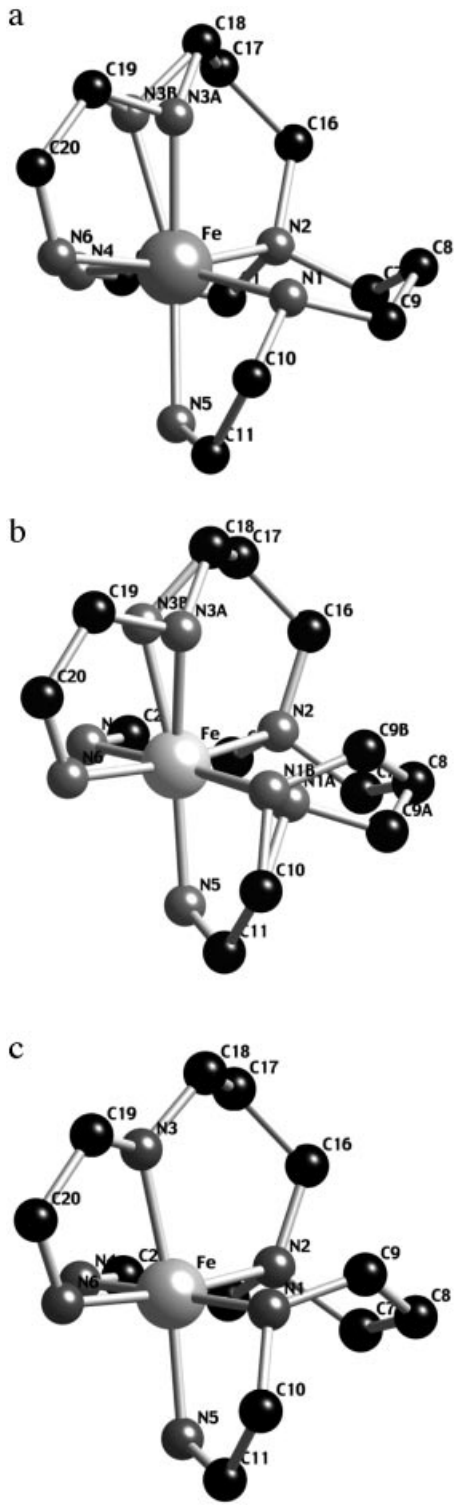


Figure 3. Fragment of the molecular structure of [Fe(Hpy-DAPP)]$(BF_4)_2$ at 298 K (a), 130 K (b), and 90 K (c).

Figure 4 displays a projection of the crystal structure on the *ac* plane. The cohesion between the cation complexes is achieved by numerous indirect hydrogen bonds passing via the fluorine atoms of both counteranions (Table 2). The fluorine atoms of the B1 tetrafluoroborate ion are strongly involved in the formation of sixteen H-bonds, namely four intramolecular bonds with the N1 atom, two intra- and two intermolecular bonds with the disordered N3 atom, and three intra- and five intermolecular bonds with C13 and C19 atoms, respectively. The intermolecular interactions concerning the B1 counterion link the molecules related by the symmetry operation $x$, $0.5 - y$, $0.5 + z$ into infinite chains that propagate in the *c* direction. The fluorine atoms of the B2 tetrafluoroborate anions, much less involved in the hydrogen bonding, take part in only a few H-bonds (Table 2). They link the molecules from neighboring infinite chains into a three-dimensional network. The H-bonds with the B2 counterions spread in the directions corresponding to the two diagonals in the *ab* plane.

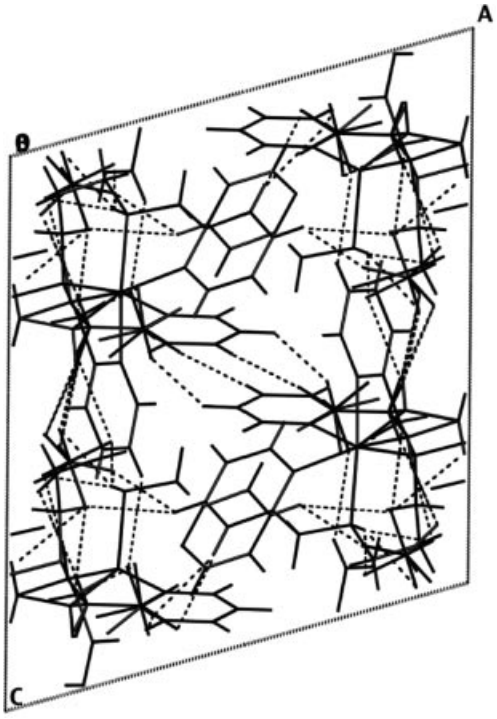


Figure 4. Projection of the molecular structure on the *ac* plane showing the H-bonding network at 298 K.

### *T = 130 K (Cooling Mode)*

The main feature of the structure is the disorder enhancement within the $Fe^{II}$ coordination core despite the lowering of the temperature. The disorder of the N3 amino aliphatic group over two equally occupied sites is retained (Figure 3, b). Moreover, the second amino aliphatic N1 atom, as well as the adjacent C9 methylene group, which are only slightly agitated at room temperature, were resolved to be also disordered over two A and B sites with a 0.5:0.5 occupancy ratio. At 130 K, the FeN2C7C8C9(A)N1(A) and FeN2C7C8C9(B)N1(B) six-membered chelate cycles adopt two different conformations. The former, as at room temperature, has a *chair* conformation, whereas the latter adopts a *twist-boat* conformation (Figure 3, b). At this temperature, the geometry of the $[FeN_6]$ octahedron reflects the changes conforming to a partial HS→LS transition. The distances in the coordination core decrease (Table 1) and the average Fe–N distance decreases to 2.087 Å.

 © 2006 Wiley-VCH Verlag GmbH & Co. KGaA, Weinheim 

Table 2. Interatomic distances [Å] and angles [°] for the hydrogen-bonding interactions in[Fe(Hpy-DAPP)]$(BF_4)_2$.[a,b]

| D–H···A | D–H | H···A | D···A | D–H···A |
|---|---|---|---|---|
| 298 K | | | | |
| N(1)–H(1N)···F(1A)[1] | 0.910 | 2.547 | 3.336(7) | 145.4 |
| N(1)–H(1N)···F(1B)[1] | 0.910 | 2.430 | 3.242(7) | 148.7 |
| N(1)–H(1N)···F(2A)[1] | 0.910 | 2.097 | 2.944(6) | 154.4 |
| N(1)–H(1N)···F(3B)[1] | 0.910 | 2.343 | 3.170(6) | 151.0 |
| N(3A)–H(3NA)···F(3A)[1] | 0.910 | 2.135 | 3.007(9) | 160.2 |
| N(3A)–H(3NA)···F(3B)[1] | 0.910 | 2.229 | 3.134(9) | 172.6 |
| N(3B)–H(3NB)···F(4A)[2] | 0.910 | 2.498 | 3.301(9) | 147.3 |
| N(3B)–H(3NB)···F(4B)[2] | 0.910 | 2.408 | 3.118(9) | 134.9 |
| C(12)–H(12A)···F(7A)[1] | 0.930 | 2.483 | 3.378(9) | 161.6 |
| C(13)–H(13A)···F(2A)[3] | 0.930 | 2.543 | 3.240(6) | 132.0 |
| C(19)–H(19A)···F(1A)[2] | 0.970 | 2.418 | 3.243(9) | 142.7 |
| C(19)–H(19A)···F(1B)[2] | 0.970 | 2.538 | 3.299(7) | 135.4 |
| C(19)–H(19A)···F(4B)[2] | 0.970 | 2.322 | 3.280(8) | 169.2 |
| C(19)–H(19B)···F(2B)[1] | 0.970 | 2.483 | 3.139(8) | 124.8 |
| C(19)–H(19C)···F(1A)[2] | 0.970 | 2.297 | 3.243(9) | 164.9 |
| C(19)–H(19D)···F(3A)[1] | 0.970 | 2.535 | 3.443(8) | 155.7 |
| C(19)–H(19D)···F(2B)[1] | 0.970 | 2.240 | 3.139(8) | 153.8 |
| C(21)–H(21A)···F(7A)[4] | 0.930 | 2.487 | 3.212(5) | 135.0 |
| C(22)–H(22A)···F(7B)[2] | 0.930 | 2.517 | 3.396(5) | 157.7 |
| 130 K | | | | |
| N(1A)–H(1NA)···F(1)[1] | 0.930 | 2.450 | 3.22(3) | 140.7 |
| N(1B)–H(1NB)···F(1)[1] | 0.930 | 2.332 | 3.04(2) | 132.6 |
| N(1A)–H(1NA)···F(3)[1] | 0.930 | 2.493 | 3.39(3) | 163.3 |
| N(1B)–H(1NB)···F(3)[1] | 0.930 | 2.542 | 3.21(1) | 129.6 |
| N(3A)–H(3NA)···F(3)[1] | 0.930 | 2.134 | 3.03(1) | 162.5 |
| N(3B)–H(3NB)···F(4)[2] | 0.930 | 2.394 | 3.17(1) | 141.2 |
| C(9A)–H(9A)···F(5)[5] | 0.990 | 2.210 | 2.82(2) | 118.6 |
| C(9B)–H(9C)···F(3)[1] | 0.990 | 2.456 | 3.00(1) | 113.9 |
| C(12)–H(12A)···F(7)[1] | 0.950 | 2.455 | 3.39(1) | 169.4 |
| C(13)–H(13A)···F(2)[3] | 0.950 | 2.483 | 3.32(1) | 146.3 |
| C(19)–H(19A)···F(4)[2] | 0.990 | 2.328 | 3.30(1) | 166.7 |
| C(19)–H(19B)···F(2)[1] | 0.990 | 2.531 | 3.19(1) | 123.9 |
| C(19)–H(19D)···F(2) [1] | 0.990 | 2.222 | 3.19(1) | 162.8 |
| C(24)–H(24A)···N(5)[1] | 0.950 | 2.600 | 3.130(7) | 115.6 |
| 90 K | | | | |
| N(1)–H(1N)···F(1)[1] | 0.930 | 2.403 | 3.087(8) | 130.3 |
| N(1)–H(1N)···F(3)[1] | 0.930 | 2.497 | 3.209(9) | 133.5 |
| N(3)–H(3N)···F(4)[2] | 0.930 | 2.381 | 3.186(1) | 144.7 |
| C(7)–H(7A)···N(5)[1] | 0.990 | 2.616 | 3.167(8) | 115.2 |
| C(9)–H(9B)···F(3)[1] | 0.990 | 2.562 | 3.05(1) | 110.6 |
| C(12)–H(12A)···F(7)[1] | 0.950 | 2.455 | 3.39(1) | 166.3 |
| C(13)–H(13A)···F(2)[3] | 0.950 | 2.548 | 3.35(1) | 142.3 |
| C(16)–H(16A)···F(5)[6] | 0.990 | 2.539 | 3.27(1) | 130.7 |
| C(19)–H(19B)···F(2)[1] | 0.990 | 2.316 | 3.18(1) | 145.7 |
| C(24)–H(24A)···N(5)[1] | 0.950 | 2.613 | 3.133(7) | 114.9 |

[a] Symmetry operations: (1) $x$, $y$, $z$; (2) $x$, $0.5 - y$, $0.5 + z$; (3) $1 - x$, $0.5 + y$, $0.5 - z$; (4) $1 - x$, $-0.5 + y$, $0.5 - z$; (5) $1 - x$, $1 - y$, $-z$; (6) $-1 + x$, $y$, $z$. [b] Estimated standard deviations in the least significant digits are given in parentheses.

Several models of splitting of the $BF_4$ anions at 130 K were tested. However, the best result was obtained for an ordered model. This suggests that the tetrafluoroborate anions undergo an order–disorder transition above 130 K. The anisotropic thermal parameters for the fluorine atoms are considerably reduced relative to 298 K. Nevertheless, they remain slightly higher than those for the other atoms.

Upon lowering the temperature to 130 K, the shortening of the unit-cell parameters and the bond lengths due to both thermal contraction and partial spin-transition occurs. Relative to 298 K, the unit-cell volume decreases by 5.3% (151 Å$^3$), although the crystal packing is similar to that at room temperature. The number of H-bonds is lower but the topology of their propagation in the crystal is quite similar (Table 2). As above, the B1 tetrafluoroborate anions participate in the formation of intra- and intermolecular interactions that result in infinite chains of H-bound complex cations spreading in the *c* direction. The intermolecular distances connected with H-bonding (Table 2) are slightly reduced, showing a relative strengthening of the intermolecular interactions upon cooling.

### *Low-Spin Complex Structure (T = 90 K)*

At this temperature, according to the magnetic and Mössbauer data (vide infra), the LS sample contains small amounts of the HS isomer (10%). Despite the presence of a residual HS fraction, the structural characteristics found at 90 K are close to those usually observed for LS complexes.

The main result of the structural determination at this temperature is the disappearance of disorder in the positions of both N1 and N3 secondary amino aliphatic nitrogen atoms observed at 130 K (Figure 3, c). Despite a general decrease, the anisotropic displacement parameter values for several atoms (N1, N3, and C9, as well as F2, F3, F5, and F6) remain slightly higher than those for the other atoms. This can be explained by the contribution of disorder introduced by the residual HS fraction. The FeN2C7C8C9N1 six-membered chelate cycle adopts a *twist-boat* conformation (Figure 3, c), whereas the FeN2C16C17C18N3 metallacycle has an intermediate conformation between the *chair* and *half-boat* ones.

Upon cooling, the metal–ligand distances in the $[FeN_6]$ coordination core become shorter (Table 1), in full accordance with the HS→LS transition. The reductions of the Fe–N distances are 0.199 (Fe–N1), 0.110 (Fe–N2), 0.099 (Fe–N3), 0.132 (Fe–N4), 0.158 (Fe–N5), and 0.174 Å (Fe–N6), relative to the room-temperature values. The N–Fe–N angles also vary in the direction of a more regular geometry of the $[FeN_6]$ octahedron.

At 90 K, the unit-cell volume decreases by 5.94% (168 Å$^3$) relative to that at 298 K due to both the lattice thermal contraction and the shortening of the Fe–N distances upon spin transition. The anisotropy of the unit-cell contraction amounts to 3.23, 1.01, and 1.48% for the *a*, *b*, and *c* axes, respectively, and 0.57% for the $\beta$ angle. The network of intermolecular contacts represented by hydrogen bonds is rather similar to that for the HS form (Table 2): the crystal packing consists of chains of molecules spreading in the *c* direction. The cohesion within the chains is provided by H-bonding through the B1 tetrafluoroborate anion, whereas between the chains it mainly occurs via the B2 counterion.

## Mössbauer Data

Mössbauer spectra for [Fe(Hpy-DAPP)]$(BF_4)_2$ were recorded on two different batches of freshly prepared sam-

 © 2006 Wiley-VCH Verlag GmbH & Co. KGaA, Weinheim 

ples. Within the experimental error, the Mössbauer parameters were found to be the same for the two syntheses. Figure 5 shows some representative spectra at different temperatures. The values of the main Mössbauer parameters obtained from a least-square fitting procedure are listed in Table 3 for the whole temperature range. The room-temperature Mössbauer spectrum consists of a unique quadrupole-split doublet with parameters typical for iron(II) in the HS state ($\delta$ = 0.955 mm s$^{-1}$, $\Delta E_q$ = 1.848 mm s$^{-1}$). The Mössbauer spectra at lower temperatures can be best fitted with two doublets corresponding to HS and LS iron(II) species. The Mössbauer area fraction [$A_{HS}/(A_{HS} + A_{LS})$] is plotted as a function of temperature (in the cooling mode) in Figure 6. It reveals the same two-step spin-crossover behavior as the magnetic measurements. The low-temperature residual HS fraction was found to be significantly different in the two series of Mössbauer measurements. We attribute this difference to the somewhat different cooling procedure in the two cases. To check this hypothesis, we carried out a series of thermal quenching experiments down to 80 K at different cooling rates (0.1, 1, 10, and 50 K min$^{-1}$). The HS fractions obtained at different cooling rates are included in Figure 6. At the lowest cooling rate we obtained about 8% HS residue, while at 10 and 50 K min$^{-1}$ the trapped HS fraction reached 31 and 32%, respectively.

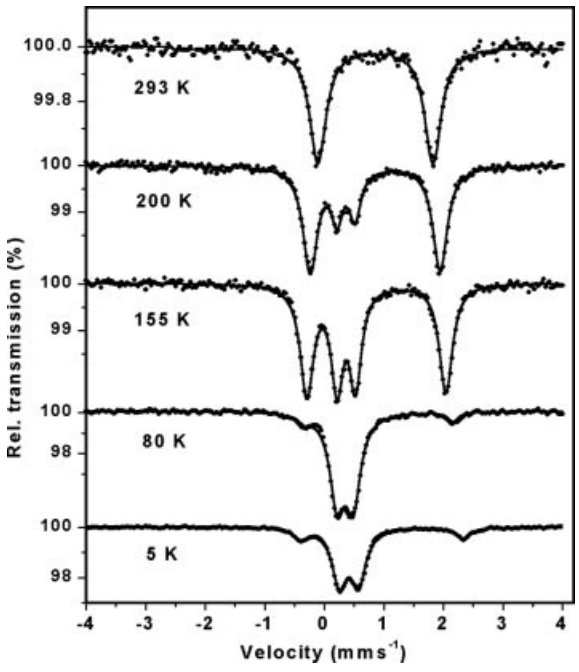


Figure 5. Representative Mössbauer spectra of [Fe(Hpy-DAPP)](BF$_4$)$_2$. The solid lines represent fitted curves.

The thermal variation of the Mössbauer parameters in the vicinity of the inflexion point (80–200 K) was carefully analyzed. Figures showing the evolution of the isomer shift ($\delta$), half-height width ($\Gamma$), quadrupole splitting ($\Delta E_q$) of the HS and LS Mössbauer lines, and the logarithm of the total Mössbauer spectrum area as a function of the temperature in the cooling cycle are provided as Supporting Information. Due to the second-order Doppler effect, both the HS and LS isomer shifts increase almost linearly with decreasing temperature. One can observe a slight deviation from the linear behavior around 125 K, but it hardly exceeds the experimental incertitude. The line widths of the HS and LS Mössbauer lines show an opposing tendency: while the former decreases, the latter increases slightly with decreasing temperatures. The thermal variation of $\Gamma_{LS}$ displays a jump between 125 and 117.5 K. For $\Gamma_{HS}$ the statistical errors become too high around these temperatures due to the small proportion of HS molecules. As a general ten-

Table 3. Least-squares fitted Mössbauer data for [Fe(Hpy-DAPP)](BF$_4$)$_2$.[a]

| | HS | | | LS | | | $A_{HS}/(A_{tot})$ |
|---|---|---|---|---|---|---|---|
| $T$ [K] | $\delta$ [mm s$^{-1}$] | $\Delta E_q$ [mm s$^{-1}$] | $\Gamma/2$ [mm s$^{-1}$] | $\delta$ [mm s$^{-1}$] | $\Delta E_q$ [mm s$^{-1}$] | $\Gamma/2$ [mm s$^{-1}$] | |
| 293* | 0.955(2) | 1.848(4) | 0.159(3) | – | – | – | 1 |
| 250 | 0.997(2) | 2.103(3) | 0.155(3) | 0.49(1) | 0.29(2) | 0.10(1) | 0.91(1) |
| 200* | 1.011(3) | 2.221(5) | 0.149(4) | 0.50(1) | 0.30(1) | 0.13(1) | 0.76(1) |
| 200 | 1.017(1) | 2.265(3) | 0.150(2) | 0.508(3) | 0.317(5) | 0.119(4) | 0.733(5) |
| 185 | 1.026(2) | 2.317(3) | 0.147(2) | 0.507(3) | 0.319(4) | 0.118(3) | 0.680(5) |
| 170 | 1.032(2) | 2.371(3) | 0.143(2) | 0.516(2) | 0.319(3) | 0.121(3) | 0.615(5) |
| 155 | 1.039(1) | 2.425(3) | 0.137(2) | 0.514(2) | 0.321(3) | 0.122(2) | 0.555(4) |
| 150* | 1.033(2) | 2.431(4) | 0.143(3) | 0.524(2) | 0.326(3) | 0.124(3) | 0.508(2) |
| 140 | 1.046(2) | 2.465(4) | 0.138(3) | 0.517(2) | 0.317(3) | 0.125(3) | 0.519(5) |
| 132.5 | 1.053(2) | 2.494(4) | 0.139(3) | 0.514(2) | 0.315(3) | 0.126(2) | 0.496(5) |
| 125 | 1.054(2) | 2.512(4) | 0.139(3) | 0.523(2) | 0.320(3) | 0.129(2) | 0.467(6) |
| 117.5 | 1.070(3) | 2.521(5) | 0.133(4) | 0.504(2) | 0.303(4) | 0.146(3) | 0.389(7) |
| 110 | 1.058(3) | 2.562(6) | 0.142(5) | 0.516(1) | 0.300(2) | 0.144(2) | 0.294(6) |
| 100* | 1.053(4) | 2.594(8) | 0.122(7) | 0.528(1) | 0.300(2) | 0.139(2) | 0.19(1) |
| 95 | 1.043(6) | 2.62(1) | 0.13(1) | 0.523(1) | 0.296(2) | 0.145(2) | 0.14(1) |
| 80 | 1.06(1) | 2.62(2) | 0.11(1) | 0.50(1) | 0.277(2) | 0.150(2) | 0.08(1) |
| 5* | 1.128(4) | 2.806(8) | 0.137(6) | 0.557(1) | 0.326(2) | 0.150(1) | 0.16(1) |

[a] $\delta$: isomer shift (with reference to metallic iron at 293 K); $\Delta E_q$: quadrupole splitting; $\Gamma$: half-height width; $A_{HS}$: area of HS doublet; $A_{tot}$: total Mössbauer spectrum area. The error bars of statistical origin are given in parentheses. Temperature values marked with (*) correspond to measurements on a separate batch of synthesis.

 © 2006 Wiley-VCH Verlag GmbH & Co. KGaA, Weinheim 

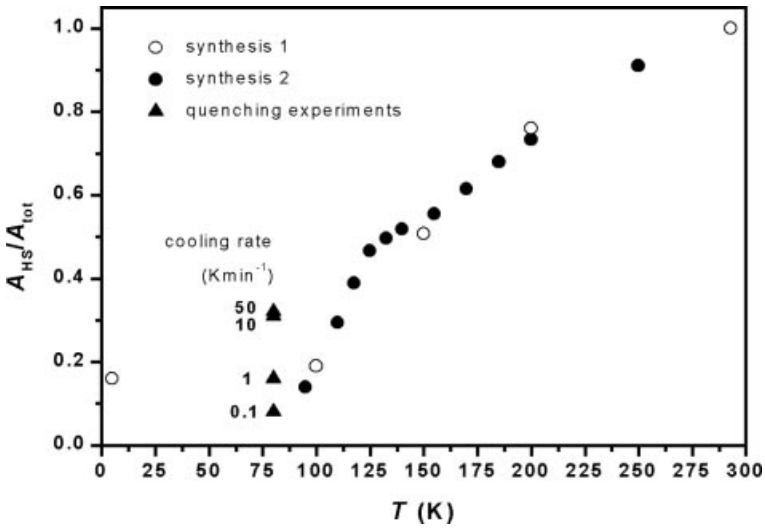


Figure 6. Temperature dependence of the Mössbauer area ratio for [Fe(Hpy-DAPP)](BF$_4$)$_2$ (two batches of synthesis). See the text for explanation of the quenching experiments.

dency, however, the HS quadrupole splitting increases between 200 and 80 K while it remains almost constant in the LS state. This behavior of $\Delta E_q$ is typical for iron(II) ions in the HS and LS spin states.[7] A closer inspection of quadrupole splittings reveals a jump in the $\Delta E_q^{LS}$ values between 125 and 117.5 K and a less monotonous increase of $\Delta E_q^{HS}$ below 132 K. This latter observation may, however, be hampered by increasing experimental errors when the HS fraction decreases. The natural logarithm of the Mössbauer line area as a function of temperature shows the continuous increasing tendency with decreasing temperature without any noticeable discontinuity.

### Electronic Structure Calculations

The molecular geometry of the isolated [Fe(Hpy-DAPP)]$^{2+}$ complex cation was firstly optimized in the HS and LS states. The optimized bond lengths in the LS and HS states reproduce the geometry found from the X-ray study at 90 K and 300 K, respectively, quite reasonably. All attempts to find another equilibrium geometry of the complex by modifying the departure geometry in the optimization procedure were unsuccessful. This means that the disorder in the spin transition complex is not due to the existence of several intrinsic complex conformations that are close in energy. At the next step, the single-point calculations were performed for the molecular structures obtained by X-ray crystallography at different temperatures. The calculations with the structure observed at 90 K correctly reproduce the ground LS state, with an energy gap to the HS state of 33 kJ mol$^{-1}$. If the molecular structures manifest a disorder, as is found at 300 and 130 K, the calculations were done for each observed geometry. Thus, with the 300-K structure the energies of the HS and LS states were calculated separately for the geometries with N3(A) and N3(B). In both cases, the HS state lies lower than the LS state of the same geometry. The energy gap is equal to 115 and 121 kJ mol$^{-1}$ for the N3(A) and N3(B) positions, respectively. These two values are quite similar, which suggests that the geometry with the N3(A) position is slightly closer to the spin transition. Disorder was observed for the two nitrogen atoms, as at 130 K, and as, a priori, we have no grounds to presume a correlation between the N1 and N3 positions, four geometries were considered, corresponding to the combinations N1(A)N3(A), N1(A)N3(B), N1(B)N3(A), and N1(B)N3(B). The ground HS state was obtained for the first two geometries with the energy gaps to the excited LS state equal to 23 and 14 kJ mol$^{-1}$ for N1(A)N3(A) and N1(A)N3(B), respectively. An inverse order of the spin levels was found for the N1(B)N3(A) and N1(B)N3(B) geometries, with the LS state stabilized by 6 and 17 kJ mol$^{-1}$, respectively.

The preference of the N1(B)N3(B) geometry for the formation of the LS state directly follows from comparison of Mulliken atomic charges, which are equal to –0.54 and –0.55 for N1(B) and N3(B), respectively, and to –0.48 for N1(A) and N3(A). These numbers indicate that the N1(B) N3(B) geometry corresponds to a stronger crystal field. This effect is also displayed in the energies of the molecular orbitals. All antibonding orbitals of the d block have about the same energies for N1(A)N3(A) and N1(B)N3(B), besides that originating from $d_{x^2-y^2}$, which is stabilized in N1(A)N3(A) by 55 kJ mol$^{-1}$. The antibonding character of the MO in the N1(A)N3(A) conformation is counterbalanced by a bonding behavior between the 2p atomic orbital of N1 and the $d_{x^2-y^2}$ atomic orbital of the Fe atom (Figure 7).

The results of calculations unambiguously show that the structural disorder revealed at 130 K by X-ray crystallography is accompanied by the coexistence in the crystal of complexes in the HS and LS states. Two statistically possible geometries result in the HS ground state, whereas for two others the order of spin states is the same as at low temperature.

 © 2006 Wiley-VCH Verlag GmbH & Co. KGaA, Weinheim 

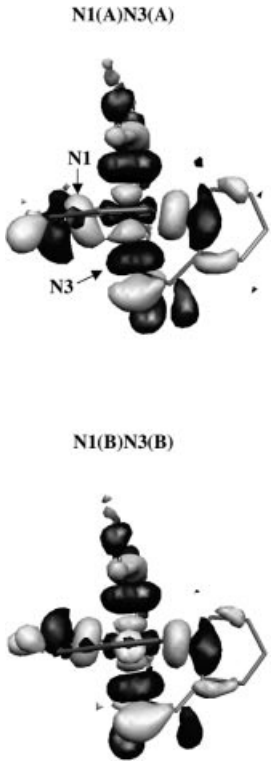


Figure 7. Three-dimensional plot of the $d_{x^2-y^2}$-containing molecular orbital in the $[Fe(Hpy\text{-}DAPP)]^{2+}$ complex cation.

## Discussion

The magnetic measurements of the [Fe(Hpy-DAPP)]$(BF_4)_2$ complex display a two-step spin transition. Such spin transitions have been reported for both binuclear[8] and mononuclear[9,10] $Fe^{II}$ spin-crossover compounds. Until now, the origin of two steps within the family of mononuclear compounds has been associated with the presence of two crystallographically inequivalent iron(II) sites in the unit cell. If two metal sites coexist whatever the temperature,[9] the thermal two-step spin transition can occur without change of the crystallographic symmetry group. The structural distinction between the two lattice sites leads to different transition temperatures. Two inequivalent $Fe^{II}$ sites can also appear upon cooling as a result of a crystallographic phase transition accompanied by a change of the space group.[10] It is interesting to note that the extensively studied mononuclear complex $[Fe(2\text{-pic})_3]Cl_2\cdot EtOH$[11] has been considered during the last 25 years as the only example of an iron(II) compound with a unique metal site[12] for which a two-step spin transition[13] takes place without any crystallographic phase transition. This phenomenon was interpreted in terms of coexisting positive and negative interactions,[8a] respectively, over a long and short range.[14a–14c] However, a recent detailed X-ray reinvestigation of $[Fe(2\text{-pic})_3]Cl_2\cdot EtOH$[10b] has shown that the expected negative correlations exhibit a long-range character in the plateau temperature range. Two steps on the thermal spin-transition curve result from two successive re-entrant structural phase-transitions of the order–disorder type. Nevertheless, the existence of HS-LS pairs with short correlation lengths was found for the photoinduced state.[14d]

The striking feature of the two-step spin-transition compound [Fe(Hpy-DAPP)]$(BF_4)_2$ consists in the absence of two crystallographically inequivalent iron(II) lattice sites, as well as a crystallographic phase transition accompanied by a change of space group. The most important peculiarity of the HS structure of the [Fe(Hpy-DAPP)]$(BF_4)_2$ complex is the disorder of the secondary N3 amino aliphatic atom over two positions (Figures 2 and 3a). A possible origin of the disorder of the N3 atoms, which constitute the first coordination sphere in iron(II), may be looked for in their strong involvement in H-bonding with their own and neighboring B1 counterions (Figure 8). Each B1 counterion is simultaneously attached by hydrogen bonds to the N3 atom belonging to its own complex cation and to the N3 atom of the neighboring complex (symmetry operation $x$, $0.5 - y$, $0.5 + z$), thus forming infinite chains of complexes in the $c$ direction. One can suppose that the strong H-bonding of the same N3 atom with two different counterions might produce appreciable constraint in the position of the N3 atom, thereby favoring a disorder between the A and B positions. This disorder is facilitated by a high flexibility of the N3-containing six-membered chelate cycle. At room temperature, the N1 amino aliphatic atom is also strongly involved in hydrogen bonding but only with its own B1 counterion. At room temperature, in contrast to the N3 atom, the position of the N1 atom is ordered.

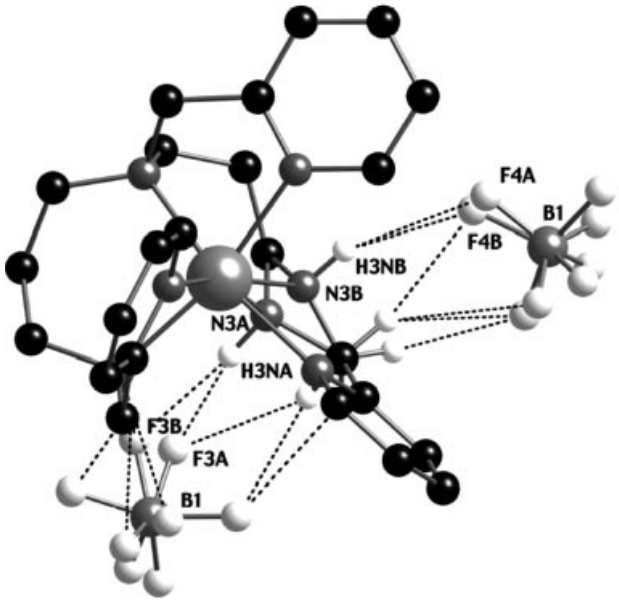


Figure 8. View of the hydrogen bonds of the N3 atom with its own and neighboring (symmetry operation: $x$, $0.5 - y$, $0.5 + z$) B1 counterions at 298 K. The labels for the other atoms have been omitted for clarity.

The structure determination at 130 K, corresponding to the inflexion point on the magnetic curve when the conversion from high to low spin reaches 50%, shows some new features. The disorder of the N3 amino aliphatic atom observed at room temperature is attended by the distribution

 © 2006 Wiley-VCH Verlag GmbH & Co. KGaA, Weinheim 

of the N1 atom between the two A and B positions. Moreover, the C9 methylene atom directly linked to the N1 atom is also equally distributed over C9(A) and C9(B) sites, which are stabilized by two new hydrogen bonds with the B1 and B2 counterions (Table 2). The two N1(A) and N1(B) positions are very close, whereas the C9(A) and C9(B) positions are rather distant one from another. The presence of the two sites for atoms N1 and C9 causes the two conformations of the N2C7C8C9N1Fe six-membered metallacycle (Figure 3, b). The N2C7C8C9(A)N1(A)Fe cycle has a *chair* conformation that is very close to that observed at room temperature (Figure 3, a), whereas the *twist-boat* conformation N2C7C8C9(B)N1(B)Fe appears in the course of spin conversion. This result strongly suggests that the spin conversion above the inflexion point is accompanied by the conformational change in the ligand. The crystallographic data obtained at 170 K confirm the coexistence of the C9(A) and C9(B) sites already at this temperature. However, the conformational motion in the complex is not drastic enough to modify the space group. It is important to underline that the 1:1 ratio of the HS and LS forms at 130 K coincides with the distribution of the N2C7C8C9N1Fe chelate cycle over two conformations.

Upon lowering the temperature to 90 K, the average metal–ligand distance becomes 0.142 Å shorter than at room temperature, which conforms to the occurrence of the HS→LS transition. The disorder found at 130 K for the positions of the N1, N3, and C9 atoms disappears at 90 K. The N2C7C8C9N1Fe metallacycle adopts a unique *twist-boat* conformation at 90 K (Figure 3, c). It should be noted that the geometry of the N2N7N8N9N1Fe chelate cycle in the LS complex is very close to that observed for the N2C7C8C9(B)N1(B)Fe metallacycle at 130 K (Figure 3, b). One may therefore conclude that the HS→LS transition in the complex is accompanied by order–disorder phenomena in conjugation with a conformational change in the ligand.

Let us now consider the relationship between the disorder in the [FeN$_6$] coordination core and the magnetic behavior of the system. A priori, the mononuclear [Fe(Hpy-DAPP)](BF$_4$)$_2$ complex without any crystallographic phase transition should be expected to display a one-step spin transition. Nevertheless, the magnetic measurements show the two steps in the spin transition. The presented X-ray data for [Fe(Hpy-DAPP)](BF$_4$)$_2$ do not contradict the basic assumption of two-step transition models, which involves the competition between positive and negative interactions[8a] possibly giving rise to short-range negative correlations[14a–14c] or to LS-HS sub-lattice ordering.[8a] However, our crystallographic data suggest that the origin of the two-step transition in [Fe(Hpy-DAPP)](BF$_4$)$_2$ can also be looked for in the [FeN$_6$] coordination core ordering. At room temperature, the distribution of the N3 amino aliphatic atom over two lattice positions preforms two geometries of the coordination core around the crystallographically unique Fe$^{II}$ center, with N3(A) and N3(B), respectively (Figure 3, a). Both geometries correspond to the HS state at 298 K. The systematic variation of the Mössbauer line widths for the HS doublet above 160 K (see Supporting Information) might suggest the existence of two different iron(II) environments with very similar Mössbauer parameters. However, these changes are very small and no reliable fit could be obtained with two doublets in the whole high temperature range. The congruency of two doublets corresponding to two different coordination geometries due to the high temperature disorder of counterions, as has been proposed for the compound [Fe(mtz)$_6$](BF$_4$)$_2$,[15] cannot, however, be excluded. Upon lowering the temperature from 298 to 230 K, the $\chi_M T$ value changes slightly, thus showing that the complex remains predominantly in the HS state. A further decrease of temperature leads to a continuous reduction of the $\chi_M T$ value, which indicates the beginning of spin transition. On cooling, both tetrafluoroborate counteranions become less agitated. The reduction of the counteranions' motion leads to their more regular arrangement in the crystal lattice, resulting in some modifications of the H-bonds between the B1 counteranions and the secondary amino aliphatic atoms. These modifications induce subtle perturbations of the N1 and N3 nitrogen atoms directly coordinated to the iron(II) center and affect the ligand field strength, initiating, in turn, the spin transition. The inflexion point on the magnetic curve denotes that at 130 K the spin transition is complete in half the sites whereas the other half remain in the HS state. At this temperature four possible coordination cores can be formally distinguished around the same Fe$^{II}$ atom. These four coordination cores may include, in addition to the N2N4N5N6 atoms, the pairs N1(A)N3(A), N1(A)N3(B), N1(B)N3(A), or N1(B)N3(B). The 0.5:0.5 occupation ratio for both the N1 and N3 atoms suggests that either all four combinations, or only two of them, namely N1(A)N3(A) and N1(B)N3(B), exist. The difference in the average Fe–N distances in the four cores (2.093, 2.096, 2.075, and 2.078 Å) is not significant enough to allow a proper identification of the HS and LS sites.

It has been demonstrated previously that not only metal–ligand distances but also angular distortions can modulate the ground-state spin.[16] As has been noted above, the geometries of the N2C7C8C9(B)N1(B)Fe chelate cycle at 130 K and the N2C7C8C9N1Fe chelate cycle in the LS complex at 90 K are very similar, with both being in the *twist-boat* conformation (see parts b and c in Figure 3). One may suppose that the LS coordination core at 130 K should involve the N1(B) atom. At 130 K, two coordination site geometries, from four formally possible, contain the N1(B) atom. The quantum-chemical calculations show that both the N1(B)N3(A) and N1(B)N3(B) pairs lead to the LS state. However, a very short distance (2.669 Å) between the N1(B) and N3(A) atoms, as well as between the attached hydrogen atoms (1.846 Å), should lead to an important steric strain (note that the van der Waals radii for the nitrogen and hydrogen atoms are 1.55 and 1.20 Å, respectively). Moreover, the presence of H-bonds between the N1(B) and N3(A) atoms must also be rejected due to the rather small N–H···N angles of 95.7° and 104.0°. Thus, it may be concluded that the LS site at 130 K contains the N1(B) and N3(B) atoms, i.e. the N1(B)N3(B) and N1(A)N3(A) pairs conform

 © 2006 Wiley-VCH Verlag GmbH & Co. KGaA, Weinheim 

to the LS and HS isomers, respectively. The spin conversion in the N1(B)N2N3(B)N4N5N6 core is accompanied by a conformational transition in the ligand, whereas the high-spin N1(A)N2N3(A)N4N5N6 core retains a geometry close to that observed at room temperature.

The first step in the spin transition is very gradual but the second one is abrupt, with a hysteresis loop of 4 K. The change in the abruptness in the spin transition may be explained by the strengthening of intermolecular interactions, which leads to a higher cooperativity in the low-temperature step. The second step in the spin conversion is also associated with a conformational change in the ligand similar to that observed for the first step. So, two geometries of the $[FeN_6]$ coordination core, generated by order–disorder phenomena at room temperature, in the course of the spin transition converge to a unique geometry of the $Fe^{II}$ coordination site. The hysteresis in the low-temperature step is not connected either with a crystallographic phase transition or with strong changes of the unit-cell parameters and/or topology of the cooperative interactions.[6] One can suppose that the hysteresis results from a slow conformational transition in the ligand at low temperature. Indeed, the efficient quenching of the HS form indicates that the HS → LS relaxation is very slow at around 80 K. In order to throw more light on this phenomenon, further experiments will be necessary (magnetic measurements at different scan rates, thermal quenching and photoswitching experiments followed by relaxation studies).

In summary, we would like to underline that our studies suggest that $[Fe(Hpy\text{-}DAPP)](BF_4)_2$ is the first example of a spin-transition system that displays a disorder in the first coordination sphere of the metal center. Two different geometries of the $[FeN_6]$ coordination core generated by the disorder in the ligand may be at the origin of the two-step spin-transition behavior of the system. However, keeping in mind that it took 25 years to clarify the origin of the two-step transition in $[Fe(2\text{-}pic)_3]Cl_2{\cdot}EtOH$,[10b,12–14] we consider that further advanced crystallographic studies are needed to verify this hypothesis. The HS → LS transition is conjugated with the conformational change in the chelate cycle, and other examples of conformationally driven electronic transitions are known in the literature.[17] Conformational transformations in the solid state have been observed for thermochromic systems and electron-transfer mixed-valence complexes. However, this phenomenon for spin-transition systems in the solid state has not been described until now.

## Experimental Section

**Chemistry:** All reagents and solvents used in this study are commercially available and were used without further purification. All syntheses involving $Fe^{II}$ species were carried out in deoxygenated solvents under an inert atmosphere of $N_2$ using glovebox techniques. [Bis(3-aminopropyl)(2-pyridylmethyl)amine] (DAPP) was obtained according to the procedure we have recently reported.[6] $FeCl_2{\cdot}2H_2O$ was prepared as described elsewhere.[18] $^1H$ NMR spectra were recorded in $CDCl_3$ on a Bruker AC200 spectrometer operating at 200 MHz.

**Ligand Synthesis (Hpy-DAPP):** A mixture of DAPP (96 μL, 0.5 mmol) and 2-pyridinecarboxaldehyde (107 mg, 1 mmol) in methanol (15 mL) was refluxed under argon for 15 min. Then, an excess of $NaBH_4$ (100 mg) was added in several small portions. The solution was allowed to stand overnight at room temperature and the solvent was evaporated under vacuum. After successive extraction of the crude product with $CHCl_3$ and $Et_2O$, 180 mg of pure HpyDAPP was obtained as a pale-yellow oil. $^1H$ NMR ($CDCl_3$): $\delta$ = 8.53–7.08 (m, 12 H, aromatic H's), 3.84 (s, 4 H, $CH_2$), 3.68 (s, 2 H, $CH_2$), 2.67–2.60 (t, 4 H, $CH_2$), 2.56–2.49 (t, 4 H, $CH_2$), 1.74–1.60 (q, 4 H, $CH_2$) ppm.

**Synthesis of the Iron(II) Complex:** $FeCl_2{\cdot}2H_2O$ (24.4 mg, 0.15 mmol) was dissolved in 2 mL of ethanol/methanol (1:1 mixture), and Hpy-DAPP (60.7 mg, 0.15 mmol) in 2 mL of the same mixture of alcohols was added. A light yellow-green solution was formed. The addition of 116.2 mg (0.30 mmol) of $NBu_4BF_4$ in 4 mL of ethanol/methanol turned the color of this solution to green. The solution was filtered and allowed to stand overnight at room temperature to give green crystals of $[Fe(Hpy\text{-}DAPP)](BF_4)_2$, which were collected by filtration, washed with ethanol, and dried in vacuo. The crystal used in the X-ray structure determination was selected from this sample. $C_{24}H_{32}B_2F_8FeN_6$ (634.01): calcd. C 45.47, H 5.09, Fe 8.81, N 13.26; found C 45.78, H 4.92, Fe 8.52, N 13.01.

**Magnetic Properties:** Magnetic susceptibilities were measured in the temperature range 15–300 K with a fully automated Manics DSM-10 susceptometer equipped with a TBT continuous-flow cryostat and an electromagnet operating at about 1.6 T. Data were corrected for magnetization of the sample holder and for diamagnetic contributions, which were estimated from the Pascal constants.

**Mössbauer Spectra:** The variable-temperature $^{57}Fe$ Mössbauer measurements were carried out on a constant-acceleration spectrometer with a 50 mCi $^{57}Co(Rh)$ source. A powder sample (60 mg) was enclosed in a 12-mm-diameter cylindrical plastic sample holder, the size of which had been determined to optimize the absorption. Spectra were obtained at 5, 100, 150, 200, and 293 K using a custom-designed, liquid helium bath cryostat (DTA, Air Liquid). A second series of measurements was carried out in the 80–250 K range (in the cooling cycle) using a MD306 He exchange gas, liquid nitrogen bath cryostat (Oxford Instruments). A least-squares computer program was used to fit the Mössbauer parameters and to determine the standard deviations of statistical origin (given in parentheses).[19] The isomer shift values are given with respect to metallic iron at room temperature.

**Solution and Refinement of the X-ray Structure:** The data collection was made with a Nonius Kappa CCD diffractometer equipped with a normal monochromatized focus X-ray tube with a molybdenum target. The selected crystals were mounted on a thin glass fiber. The data were collected using the COLLECT software,[20] then were processed with the DENZO reduction software.[21] Three collections were made: the first one at room temperature (298 K), the second one at 130 K after a slow decrease of the temperature with a cool, dry nitrogen gas stream, and the third one at 90 K after cooling the crystal in a cold nitrogen gas flow. From 10 frames with 1° steps, the initial set of cell parameters was obtained for each measurement. A total of 12331 reflections were collected at room temperature, of which 6326 unique reflections were used for the structure determination. The second collection at 130 K is formed from 10356 measured reflections, 5738 of which were independent reflections. The third collection at 90 K concerns 8580 measured reflections, of which 5358 unique reflections were used for the hypothesis and refinement. The structures were solved by

 © 2006 Wiley-VCH Verlag GmbH & Co. KGaA, Weinheim 

direct methods with the SHELXS-97 program.[22] The structures were then refined by the least-squares method using SHELXL-97,[23] with anisotropic temperature factors for all non-H atoms. The hydrogen atoms were introduced at calculated positions and refined as riding on their carrier atoms. The final $R$ factor [with $I > 2\sigma(I)$] was 0.059, 0.091, and 0.091 at 298, 130, and 90 K, respectively. Crystal data and refinement results are summarized in Table 4. The perspective view of the asymmetric unit at three temperatures was calculated with PLATON[24] and is shown in Figure 2.

Table 4. Crystallographic data for $[Fe(Hpy\text{-}DAPP)](BF_4)_2$.

| | $T$ = 298 K | $T$ = 130 K | $T$ = 90 K |
|---|---|---|---|
| Formula | | $C_{24}H_{32}B_2F_8FeN_6$ | |
| $Fw$ | 634.03 | | |
| $a$ [Å] | 13.298(1) | 12.897(1) | 12.868(1) |
| $b$ [Å] | 14.368(1) | 14.251(1) | 14.223(1) |
| $c$ [Å] | 15.409(1) | 15.207(1) | 15.180(1) |
| $\beta$ [°] | 106.09(1) | 106.71(1) | 106.69(1) |
| $V$ [Å$^3$] | 2828.6(1) | 2676.9(2) | 2661.2(3) |
| $Z$ | 4 | 4 | 4 |
| Space group | $P2_1/c$ | $P2_1/c$ | $P2_1/c$ |
| $\lambda$ [Å] | 0.71073 | 0.71073 | 0.71073 |
| $\rho_{calcd.}$ [g cm$^{-3}$] | 1.489 | 1.573 | 1.583 |
| $\mu$ [cm$^{-1}$] | 6.12 | 6.47 | 6.51 |
| $R$[a] [$I > 2\sigma(I)$] | 0.059 | 0.091 | 0.091 |
| $wR_2$[b] [$I > 2\sigma(I)$] | 0.141 | 0.194 | 0.207 |

[a] $R = \sum(||F_o| - |F_c||)/\sum|F_o|$. [b] $wR_2 = \{\sum[w(F_o^2 - F_c^2)^2]/\sum[w(F_o^2)^2]\}^{1/2}$.

CCDC-295576 to -295578 contain the supplementary crystallographic data for this paper. These data can be obtained free of charge from The Cambridge Crystallographic Data Center via www.ccdc.cam.ac.uk/data_request/cif.

**Electronic Structure Calculations:** Calculations of the electronic structure of the isolated $[Fe(Hpy\text{-}DAPP)]^{2+}$ complex cation were performed using the formalism of density functional theory (DFT). Single-point calculations for molecular geometries, extracted from the X-ray crystallographic data for different temperatures, were carried out with the Gaussian 2003 package.[25] In each case, both HS and LS states were considered. The LANL2DZ basis set, including the double-ζ basis with the Los Alamos effective core potential for Fe and the Dunning–Huzinaga all-electron double-ζ basis set with polarization functions for the H, C, and N atoms[26,27] were used. The choice of exchange-correlation functional for calculations of the energy gap between HS and LS states is widely debated in the literature. The hybrid Hartree–Fock/GGA (generalized gradient approximation) B3LYP functional and its re-parameterized version B3LYP* are more often recommended.[28–30] In this work we firstly use the parameter-free density functional model PBE0 obtained by combining the so-called PBE GGA functional with a predefined amount of exact exchange.[31] The calculations with this functional result in a correct order of the HS and LS states for experimental structures obtained at different temperatures.


[1] a) H. A. Goodwin, *Coord. Chem. Rev.* **1976**, *18*, 293; b) J. Zarembowitch, O. Kahn, *New J. Chem.* **1991**, *15*, 181; c) E. König, *Struct. Bond.* **1991**, *76*, 51; d) P. Gütlich, A. Hauser, H. Spiering, *Angew. Chem. Int. Ed. Engl.* **1994**, *33*, 2024; e) O. Kahn, *Molecular Magnetism*; VCH Publishers, New York, **1993**; f) J. A. Real, *Transition Metals in Supramolecular Chemistry* (Ed.: J. P. Sauvage), John Wiley & Sons, **1999**; g) M. Sorai, *Bull. Chem. Soc. Jpn.* **2001**, *74*, 2223; h) *Topics in Current Chemistry*, vol. 233–235, *Spin Crossover in Transition Metal Compounds I–III* (Eds.: P. Gütlich, H. A. Goodwin), Springer, Berlin, **2004**; i) A. Bousseksou, G. Molnár, G. S. Matouzenko, *Eur. J. Inorg. Chem.* **2004**, 4353; j) J. A. Real, A. B. Gaspar, V. Niel, M. C. Muñoz, *Coord. Chem. Rev.* **2003**, *236*, 121; k) J. A. Real, A. B. Gaspar, M. C. Muñoz, *Dalton Trans.* **2005**, 2062.

[2] a) O. Kahn, J. P. Launay, *Chemtronics* **1988**, *3*, 140; b) O. Kahn, J. Kröber, C. Jay, *Adv. Mater.* **1992**, *4*, 718; c) A. Bousseksou, G. Molnár, P. Demont, J. Menegotto, *J. Mater. Chem.* **2003**, *13*, 2069.

[3] a) O. Kahn, E. Codjovi, *Philos. Trans. R. Soc. London, Ser. A* **1996**, *354*, 359; b) O. Kahn, Y. Garcia, J. F. Létard, C. Mathonière, *NATO ASI Ser., Ser. C* **1998**, *518*, 127.

[4] a) G. S. Matouzenko, A. Bousseksou, S. Lecocq, P. J. van Koningsbruggen, M. Perrin, O. Kahn, A. Collet, *Inorg. Chem.* **1997**, *36*, 2975; b) G. S. Matouzenko, A. Bousseksou, S. Lecocq, P. J. van Koningsbruggen, M. Perrin, O. Kahn, A. Collet, *Inorg. Chem.* **1997**, *36*, 5869.

[5] D. Cremer, J. A. Pople, *J. Am. Chem. Soc.* **1975**, *97*, 1354.

[6] G. S. Matouzenko, A. Bousseksou, S. A. Borshch, M. Perrin, S. Zein, L. Salmon, G. Molnár, S. Lecocq, *Inorg. Chem.* **2004**, *43*, 227.

[7] N. N. Greenwood, T. C. Gibb, *Mössbauer Spectroscopy*, Chapman and Hall Ltd., London, UK, **1971**.

[8] a) J. A. Real, H. Bolvin, A. Bousseksou, A. Dworkin, O. Kahn, F. Varret, J. Zarembowitch, *J. Am. Chem. Soc.* **1992**, *114*, 4650; b) J. A. Real, I. Castro, A. Bousseksou, M. Verdaguer, R. Burriel, M. Castro, J. Linares, F. Varret, *Inorg. Chem.* **1997**, *36*, 455.

[9] a) Y. Garcia, O. Kahn, L. Rabardel, B. Chansou, L. Salmon, J.-P. Tuchagues, *Inorg. Chem.* **1999**, *38*, 4663; b) G. S. Matouzenko, J.-F. Létard, A. Bousseksou, S. Lecocq, L. Capes, L. Salmon, M. Perrin, O. Kahn, A. Collet, *Eur. J. Inorg. Chem.* **2001**, *11*, 2935; c) W. Hibbs, P. J. van Koningsbruggen, A. M. Arif, W. W. Shum, J. S. Miller, *Inorg. Chem.* **2003**, *42*, 5645.

[10] a) D. Boinnard, A. Bousseksou, A. Dworkin, J. M. Savariault, F. Varret, J.-P. Tuchagues, *Inorg. Chem.* **1994**, *33*, 271; b) D. Chernyshov, M. Hostettler, K. W. Törnroos, H.-B. Bürgi, *Angew. Chem. Int. Ed.* **2003**, *42*, 3825.

[11] G. A. Renovitch, W. A. Baker Jr., *J. Am. Chem. Soc.* **1967**, *89*, 6377.

[12] a) M. Mikami, M. Konno, Y. Saito, *Chem. Phys. Lett.* **1979**, *63*, 566; b) B. A. Katz, C. E. Strouse, *J. Am. Chem. Soc.* **1979**, *101*, 6214; c) M. Mikami, M. Konno, Y. Saito, *Acta Crystallogr., Sect. B* **1980**, *36*, 275.

[13] a) H. Köppen, E. W. Müller, C. P. Köhler, H. Spiering, E. Meissner, P. Gütlich, *Chem. Phys. Lett.* **1982**, *91*, 348; b) K. Kaji, M. Sorai, *Thermochim. Acta* **1985**, *88*, 185.

[14] a) R. Jakobi, H. Spiering, P. Gütlich, *J. Phys. Chem. Solids* **1992**, *53*, 267; b) H. Romstedt, H. Spiering, P. Gütlich, *J. Phys. Chem. Solids* **1998**, *59*, 1253; c) H. Spiering, T. Kohlhaas, A. Hauser, C. Bruns-Yilmaz, J. Kusz, P. Gütlich, *Coord. Chem. Rev.* **1999**, *190–192*, 629; d) J. Kusz, D. Schollmeyer, H. Spiering, P. Gütlich, *J. Appl. Crystallogr.* **2005**, *38*, 528.

[15] P. Poganiuch, S. Decurtins, P. Gütlich, *J. Am. Chem. Soc.* **1990**, *112*, 3270.

[16] a) S. Alvarez, *J. Am. Chem. Soc.* **2000**, *125*, 6795; b) *Topics in Current Chemistry*, vol. 234, *Spin Crossover in Transition Metal Compounds I–III* (Eds.: P. Gütlich, H. A. Goodwin), Springer, Berlin, **2004**, p. 98; c) M. Marchivie, P. Guionneau, J.-F. Létard, D. Chasseau, *Acta Crystallogr., Sect. B* **2005**, *61*, 25.

[17] a) M. Sorai, *Bull. Chem. Soc. Jpn.* **2001**, *74*, 2223; b) M. Sorai, *J. Chem. Thermodyn.* **2002**, *34*, 1207; c) M. Sorai, *Pure Appl. Chem.* **2005**, *77*, 1331.

[18] H. R. Chang, J. K. McCusker, H. Toftlund, S. R. Wilson, A. X. Trautwein, H. Winkler, D. N. Hendrickson, *J. Am. Chem. Soc.* **1990**, *112*, 6814.

[19] F. Varret, *Proceedings of the International Conference on Mössbauer Effect Applications*, Jaipar, India, **1981**; Indian National Science Academy, New Delhi, **1982**.

[20] Nonius, *COLLECT*, Nonius BV, Delf, The Netherlands, **1997–2000**.


 © 2006 Wiley-VCH Verlag GmbH & Co. KGaA, Weinheim 

[21] Z. Otwinowski, W. Minor, *Methods Enzymol.* **1997**, *276*, 307.
[22] G. M. Sheldrick, *SHELXS-97*, *Program for Crystal Structure Determination*; University of Göttingen, Germany, **1997**.
[23] G. M. Sheldrick, *SHELXL-97*, *Program for Crystal Structure Refinement*; University of Göttingen, Germany, **1997**.
[24] A. L. Spek, *PLATON, A Multipurpose Crystallographic Tool*; Utrecht University, Utrecht, The Netherlands, **1999**.
[25] M. J. Frisch, G. W. Trucks, H. B. Schlegel, G. E. Scuseria, M. A. Robb, J. R. Cheeseman, J. A. Montgomery Jr., T. Vreven, K. N. Kudin, J. C. Burant, J. M. Millam, S. S. Iyengar, J. Tomasi, V. Barone, B. Mennucci, M. Cossi, G. Scalmani, N. Rega, G. A. Petersson, H. Nakatsuji, M. Hada, M. Ehara, K. Toyota, R. Fukuda, J. Hasegawa, M. Ishida, T. Nakajima, Y. Honda, O. Kitao, H. Nakai, M. Klene, X. Li, J. E. Knox, H. P. Hratchian, J. B. Cross, V. Bakken, C. Adamo, J. Jaramillo, R. Gomperts, R. E. Stratmann, O. Yazyev, A. J. Austin, R. Cammi, C. Pomelli, J. W. Ochterski, P. Y. Ayala, K. Morokuma, G. A. Voth, P. Salvador, J. J. Dannenberg, V. G. Zakrzewski, S. Dapprich, A. D. Daniels, M. C. Strain, O. Farkas, D. K. Malick, A. D. Rabuck, K. Raghavachari, J. B. Foresman, J. V. Ortiz, Q. Cui, A. G. Baboul, S. Clifford, J. Cioslowski, B. B. Stefanov, G. Liu, A. Liashenko, P. Piskorz, I. Komaromi, R. L. Martin, D. J. Fox, T. Keith, M. A. Al-Laham, C. Y. Peng, A. Nanayakkara, M. Challacombe, P. M. W. Gill, B. Johnson, W. Chen, M. W. Wong, C. Gonzalez, and J. A. Pople, *Gaussian 03*, Revision C.02, Gaussian, Inc., Wallingford CT, **2004**.
[26] T. H. Dunning Jr., P. J. Hay, *Modern Theoretical Chemistry* (Ed.: H. F. Schaefer III), vol. 3, Plenum, New York, **1976**, p. 1–28.
[27] P. J. Hay, W. R. Wadt, *J. Chem. Phys.* **1985**, *82*, 270.
[28] a) S. Zein, G. S. Matouzenko, S. A. Borshch, *J. Phys. Chem. A* **2005**, *109*, 8568; b) S. Zein, S. A. Borshch, *J. Am. Chem. Soc.* **2005**, *127*, 16197; c) S. Zein, G. S. Matouzenko, S. A. Borshch, *Chem. Phys. Lett.* **2004**, *397*, 475.
[29] G. Brehm, M. Reiher, S. Schneider, *J. Phys. Chem. A* **2002**, *106*, 12024.
[30] M. Reiher, *Inorg. Chem.* **2002**, *41*, 6928.
[31] C. Adamo, V. Barone, *J. Chem. Phys.* **1999**, *110*, 6158.

Received: January 23, 2006
Published Online: April 25, 2006

 © 2006 Wiley-VCH Verlag GmbH & Co. KGaA, Weinheim 

DOI: 10.1002/ejic.200600120

# Synthesis and Structure of Trialkyltantalum Complexes Stabilized by Aminopyridinato Ligands

**Awal Noor,[a] Winfried Kretschmer,[b] and Rhett Kempe*[a,c]**

**Keywords:** Amido ligands / Aminopyridinato ligands / N ligands / Olefin polymerization / Tantalum

(4-Methylpyridin-2-yl)(trimethylsilyl)amine (**1**), (6-methylpyridin-2-yl)(trimethylsilyl)amine (**2**), and (2,6-diisopropylphenyl)(pyridin-2-yl)amine (**3**) were deprotonated and used as ligands to synthesize trialkyltantalum complexes. The reaction of 2 equiv. of **1** or **2** with pentabenzyltantalum afforded tribenzyltantalum(V) complexes by toluene elimination. Analogous reaction using **3** failed. Lithiation of **3** followed by the reaction with tribenzyltantalum dichloride gave rise to the corresponding tribenzyl complex. Other alkyltantalum complexes stabilized by this ligand environment can be prepared by treating tantalum pentachloride with 2 equiv. of lithiated **3** to form a bis(aminopyridinato)tantalum trichloride. The reaction of this trichloride with 3 equiv. of alkyllithium compounds like methyllithium affords the corresponding trialkyltantalum complexes. X-ray diffraction studies of four of the synthesized complexes were carried out. They adopt two different coordination environments, either slightly distorted capped octahedrons (sterically less demanding aminopyridinato ligands) or pentagonal bipyramids (bulkier aminopyridinato ligands). The alkyl species were surprisingly stable at elevated temperatures and no formation of mixed alkyl/alkylidene complexes was observed. Alkyl cation formation and the behaviour of a selection of these compounds in olefin polymerization were explored.
(© Wiley-VCH Verlag GmbH & Co. KGaA, 69451 Weinheim, Germany, 2006)

## Introduction

Aminopyridinato ligands[1] are interesting amido ligands because of the flexibility of their binding mode and the ligand "asymmetry". The dominating binding mode in early transition metal and lanthanide chemistry[2] is the strained $\eta^2$ coordination (Scheme 1, left). The bridging binding mode (Scheme 1, right) is characteristic for late transition metal complexes. Of course, there are exceptions like homoleptic strained $\eta^2$-bound (aminopyridinato)palladium complexes.[3] The ligand "asymmetry" caused by the two different donor functionalities−the pyridine and amido function−might be considered as an additional interesting feature especially in comparison to the closest "relatives", the amidinates.[4]

Group 5 metal complexes stabilized by aminopyridinato ligands (Scheme 2, left) have been investigated to a lesser extent than related amidinate[5] complexes (Scheme 2, right).

The first Ap (Ap = aminopyridinato) group 5 metal complex was published by Gambarotta 15 years ago.[6] A more detailed investigation of some aspects of the coordination chemistry of these ligands was started by Polamo. He applied the "direct synthesis" method to prepare a variety of niobium and tantalum complexes stabilized by aminopyridinato ligands.[7–10] Interesting examples of aminopyridinato low oxidation state group 5 metal complexes have been described by Gambarotta and Cotton.[11] Reactivity studies employing organometallic species are still very rare.[12,13] Because of this lack of information we became interested in alkyltantalum complexes. We also expect an easy access into this chemistry because of the recently published Kol synthesis of $[Ta(CH_2C_6H_5)_5]$.[14,15] We report here on the synthesis and structure of organotantalum complexes stabilized by aminopyridinato ligands. The formation of organ-

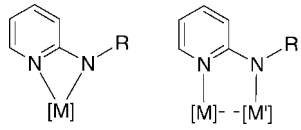


Scheme 1. Important binding modes of deprotonated 2-aminopyridines ([M] and [M′] = transition metal moiety; R = aryl, silyl, or alkyl substituent).

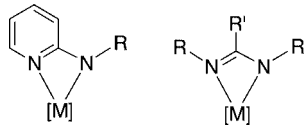


Scheme 2. Aminopyridinato (left) and amidinate (right) ligands ([M] = group 5 metal complex moiety; R, R′ = substituent).

[a] Lehrstuhl Anorganische Chemie II, Universität Bayreuth, 95440 Bayreuth, Germany
E-mail: kempe@uni-bayreuth.de
[b] Stratingh Institut for Chemistry and Chemical Engineering, Center for Catalytic Olefin Polymerization, University of Groningen,
Nijenborgh 4, 9747 AG Groningen, The Netherlands
[c] Leibniz-Institut für Katalyse,
Albert-Einstein-Str. 29a, 18059 Rostock, Germany

 © 2006 Wiley-VCH Verlag GmbH & Co. KGaA, Weinheim 

ocations and the relevance to olefin polymerization of a selection of these species is also discussed.

## Results and Discussion

### Synthesis of Ligands

Compounds **1** and **2** were prepared as reported.[16,17] The aminopyridine **3** can be synthesized by palladium-catalyzed arylamination.[18] The reaction of 2-bromopyridine with 2,6-diisopropylaniline and sodium *tert*-butoxide in the presence of a Pd catalyst in toluene (90 °C, 48 h) leads after workup and purification by crystallization to compound **3** (Scheme 3) in good yield (70%).

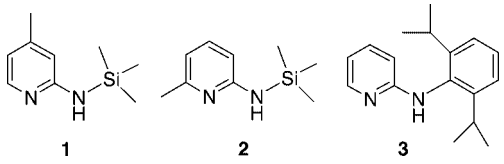


Scheme 3. Applied aminopyridines.

### Synthesis and Structure of Tantalum Complexes

Reaction of 2 equiv. of **1** with $[Ta(CH_2C_6H_5)_5]$ in hexane at 60 °C results in the formation of **4** by toluene elimination (Scheme 4). No formation of benzylidene functionalities is observed by NMR spectroscopy in the course of this reaction. Complex **4** was isolated after workup in hexane in moderate yield as a yellow crystalline material.

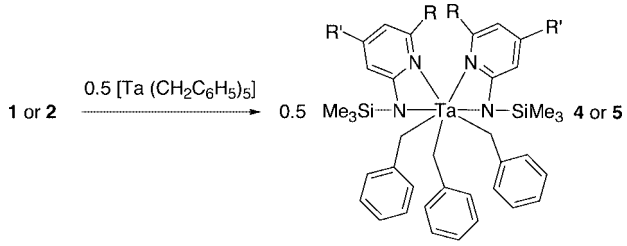


Scheme 4. Synthesis of **4** and **5** (**4**: R = H, R′ = $CH_3$; **5**: R = H, R′ = $CH_3$).

The three benzyl groups show a broad doublet at $\delta$ = 2.96 ppm at room temperature indicative of a fast ligand exchange. Crystals suitable for X-ray analysis were grown from a hexane solution. Details of the X-ray crystal structure analysis are summarized in Table 3. The molecular structure of **4** is shown in Figure 1. The coordination of **4** is best described as a distorted capped octahedron. The methylene carbon atom of one of the benzyl ligands (C15) as well as the two pyridine nitrogen atoms occupy the first triangle and C8 as well as the two amido nitrogen atoms the second triangle. In order to apply a slightly increased steric bulk in close proximity to the metal center 2 equiv. of **2** were treated with $[Ta(CH_2C_6H_5)_5]$ under the same conditions as applied to **4**. The resulting benzyl complex **5** was obtained in moderate yield (Scheme 4). The three benzyl groups give two doublets at $\delta$ = 2.98 and 3.18 ppm. The product was characterized by X-ray analysis (molecular structure is shown in Figure 2) in addition to NMR spectroscopy. Details of the X-ray crystal structure analysis are summarized in Table 3. The coordination of **5** is best described as a capped octahedron (first triangle N1, N2, and N4; second triangle N3, C15, and C22). In both cases, the rigid aminopyridinato ligands induce distortion from the ideal symmetry. The Ta–C bond lengths lay in the ranges of 2.247–2.318 Å and 2.248–2.264 Å, respectively, for **4** and **5**, which clearly indicate $\eta^1$ binding of all benzyl groups in the solid state.

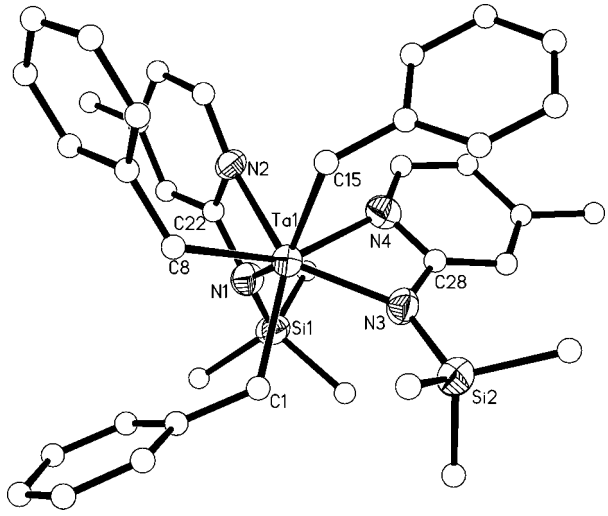


Figure 1. Molecular structure of **4**; selected bond lengths [Å] and angles [°]: Ta–C1 2.248(9), Ta–N4 2.230(8), Ta–N2 2.266(8), Ta–N1 2.123(10), Ta–N3 2.132(8), Ta–C8 2.264(1), Ta–C15 2.257(10), N2–C22 1.332(13), N1–C22 1.400(13), N3–C28 1.376(13); N1–Ta–N2 61.00(3), N1–C22–N2 109.49(8), Ta–N2–C22 92.05(6), Ta–N1–C22 96.31(6), N4–Ta–N3 59.10(3), N3–C28–N4 109.06(8), Ta–N3–C28 96.53(6), Ta–N4–C28 93.21(6), C1–Ta–C8 78.28(4), C15–Ta–C8 78.60(4), C1–Ta–C15 126.83(4).

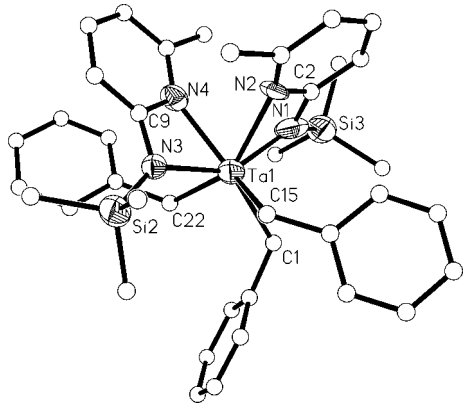


Figure 2. Molecular structure of **5**; selected bond lengths [Å] and angles [°]: Ta–C1 2.250(11), Ta–N2 2.382(10), Ta–N4 2.248(10), Ta–N1 2.069(11), Ta–N3 2.212(9), Ta–C15 2.247(11), Ta–C22 2.318(10), N2–C2 1.379(16), N4–C9 1.355(14), N1–C2 1.375(15), N3–C9 1.391(13); C1–Ta–C15 81.09(5), C1–Ta–C22 76.15(4), C15–Ta–C22 130.18(5), N1–Ta–N2 60.31(4), N1–C2–N2 109.77(12), Ta–N1–C2 101.02(8), Ta–N2–C2 87.22(9), N4–Ta–N3 61.44(3), Ta–N3–C9 93.36(7), Ta–N4–C9 92.80(7), N4–C9–N3 112.12(11).

 © 2006 Wiley-VCH Verlag GmbH & Co. KGaA, Weinheim 

In order to increase the steric bulk of the used aminopyridinato ligands drastically we introduced the 2,6-diisopropylphenyl substituent at the amido nitrogen atom instead of the $SiMe_3$ group. Application of the toluene elimination route starting from $[Ta(CH_2C_6H_5)_5]$ was not successful and salt metathesis was adopted. The reaction of 2 equiv. of the lithium salt of **3** with $[TaCl_2(CH_2C_6H_5)_3]$[14] at room temperature (Scheme 5) resulted in the formation of the tribenzyl complex **6**. The $^1H$ NMR spectra of this compound shows two different sets of signals for benzyl protons. One signal corresponds to four methylene protons of the benzyl substituents and the other to the remaining two. We propose a pentagonal-bipyramidal arrangement in solution with the two amino and one of the benzyl moieties in the equatorial plane. Because of the steric bulk of the deprotonated **3** no exchange on the NMR time scale at room temperature is observed. Two benzyl resonances were found, one at $\delta$ = 3.60 ppm and the second at $\delta$ = 2.79 ppm.

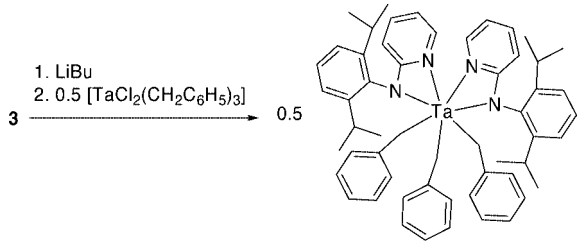


**6**

Scheme 5. Synthesis of **6**.

The first Schrock-type alkylidene complex, $[Ta(CH_2tBu)_3(CHtBu)]$, was prepared in 1974.[19] Various mono- and polydentate ligand systems that support this functionality have been introduced in recent years and several synthetic methodologies are known that lead to the alkylidene complexes like, for instance, an α-elimination reaction sequence from dialkyl precursors.[20] However, the complexes **4**, **5**, and **6** do not form mixed benzyl/benzylidene complexes neither during the synthesis nor by treatment of the trialkyltantalum complexes at elevated temperatures (80 °C). In order to prepare other trialkyltantalum complexes supported by deprotonated **3** — the sterically most demanding of the three ligands described in this publication — we synthesized the corresponding tantalum trichloride species **7** (Scheme 6).

Compound **7** can be synthesized by the reaction of **3** with $TaCl_5$ (Polamo method "direct synthesis"[7]). Because of a relatively low yield using this "direct synthesis" salt metathesis (Scheme 6) was applied and gave rise to **7** in better yield. The success of salt metathesis using lithiated **3** and $TaCl_5$ is in contrast to Polamo's observations. He developed his method due to problems with the salt metathesis approach in similar reactions. The trimethyltantalum complex **8** results when 3 equiv. of LiMe were treated with **7**. The X-ray crystal structures of **7** (Figure 3) and **8** (Figure 4) revealed a distorted pentagonal-bipyramidal coordination. In **7** the two chloro ligands occupy the axial positions of the polyhedra and the two pairs of nitrogen and the third chloride ion form the pentagonal (equatorial) plane. In **8** methyl ligands adopt the same coordination sites as the chloro ligands in **7**. A distortion is caused by the small N–Ta–N angles due to the strained binding mode of the aminopyridinato ligands. In **7** they are 60.1(3) and 60.4(3)° and in **8** 59.25(2)°. Both lead to a situation in which all other angles in the pentagonal plane are over 72°. In **7** N–Ta–Cl(2) *cis* angles are 77.9(2) and 77.3(2)° and in **8** the N–Ta–C(1) *cis* angles are 77.43(10)°. N–Ta–N angles involving the amido bonds of the aminopyridinato ligands are the widest, 84.4(3)° in **7** and 86.65(18)° in **8**. The $Cl_{ax}$-Ta–$Cl_{eq}$ angles for **7** are 99.87(9)° and 99.64(9)° and the $C_{ax}$-Ta–$C_{eq}$ angles for **8** are 94.02(15)° and 93.23(16)°. Details of the X-ray crystal structure analyses of **7** and **8** are summarized in Table 3. The $^1H$ NMR spectrum shows two different sets of signals for methyl protons. The two methyl groups present above and below the pentagonal plane (axial positions) show a resonance at $\delta$ = 1.26 ppm and the in-plane methyl ligand at $\delta$ = 0.63 ppm. Similar observations have been made for **6**. The trimethyl complex **8** was found to be stable

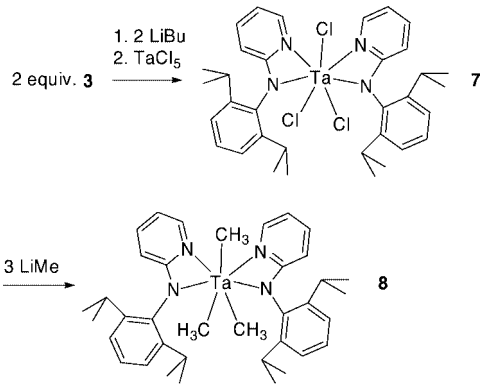


Scheme 6. Synthesis of **7** and **8**.

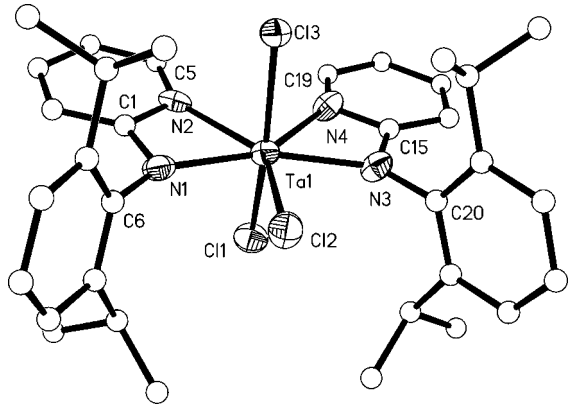


Figure 3. Molecular structure of **7**; selected bond lengths [Å] and angles [°]: C1–N2 1.339(11), C1–N1 1.376(11), C5–N2 1.337(11), C6–N1 1.438(11), C15–N3 1.391(10), C15–N4 1.352(12), C19–N4 1.337(11), C20–N3 1.422(11), N1–Ta1 2.072(8), N2–Ta1 2.264(8), N3–Ta1 2.098(7), N4–Ta1 2.263(7), Cl1–Ta1 2.352(2), Cl2–Ta1 2.349(2), Cl3–Ta1 2.376(2); C1–N1–Ta 100.45(6), C1–N2–Ta 92.92(5), C1–N2–C5 118.55(8), C15–N4–C19 118.13(8), C15–N3–Ta 99.66(6), C15–N4–Ta 93.42(5), N1–Ta–N2 60.05(3), N3–Ta–N4 60.38(3), N2–C1–N1 106.52(8), N4–C15–N3 106.53(8), Cl1–Ta–Cl3 160.49(8), Cl1–Ta–Cl2 99.87(9), Cl2–Ta–Cl3 99.63(9).

 © 2006 Wiley-VCH Verlag GmbH & Co. KGaA, Weinheim 

towards elevated temperatures in terms of the formation of mixed methyl/methylidene species. Heating of **8** in toluene at 80 °C for 40 min did not affect the structure of the compound. When harsher conditions were employed, i.e., heating to 120 °C for 30 min, **8** started to decompose slowly without any signs of methylidene formation.

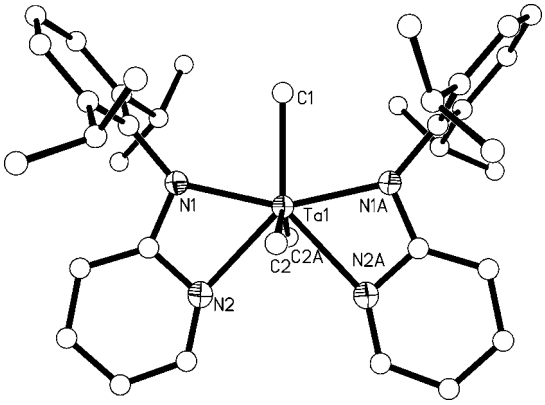


Figure 4. Molecular structure of **8**; selected bond lengths [Å] and angles [°]: C1–Ta1 2.190(6), C2–Ta1 2.203(4), N1–Ta1 2.105(3), N2–Ta1 2.332(4), N1–Ta1–N1A 154.86(19), C1–Ta1–C2 106.89(12), N1–Ta1–C2 93.23(16), C2A–Ta(1)–C2 146.2(2), N1–Ta1–N2 145.88(13), N1–Ta1–N2 59.25(13), C1–Ta1–N2 136.67(9), C2–Ta1–N2 77.25(16), N2–Ta1–N2A 86.65(18).

### Formation of Organocations and Their Application in Ethylene Polymerization

Because of the high ethylene polymerization activity observed for the tantalum complexes **9** and **10**[12] (Scheme 7) we became interested in exploring the polymerization behavior of some of the complexes discussed in this study.

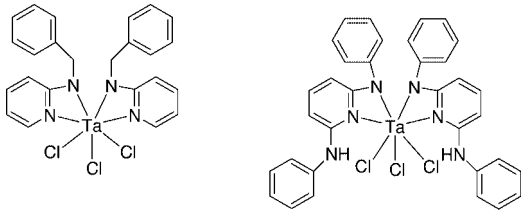


Scheme 7. Structures of **9** and **10**.

Ethylene polymerization studies were performed using **7** (Table 1) and **8** (Table 2) as pre-catalysts.

Table 1. Ethylene polymerization results, activation of **7** using PMAO [PMAO = polymethylaluminoxane $(AlOMe)_x$].[a]

| Pre-cat. [μmol] | PMAO [mmol] | PE [g] | Activity [kg(PE)mol(Ta)$^{-1}$h$^{-1}$bar$^{-1}$] |
|---|---|---|---|
| 10 | 5 | 0.2 | 16 |

[a] 260 mL of toluene as solvent, 5 bar of ethene, 50 °C, 15 min run time, Ta/Al = 1:500 (m/m).

Ethylene polymerization activity of **7** after activation with PMAO is low. This is in contrast to what was observed for **9** and **10**. Thus, we expected to see a significantly better catalyst performance when starting from the methyl complex **8** and activating with trialkylammonium tetrakis(pentafluorophenyl)borate. No significant improvement in terms of activity was found by changing the activation procedure. Because of the low activity no molecular weight analysis of the polymers was accomplished. The generation of cationic complexes was studied in an NMR scale reaction. Reaction of **8** with 1 equiv. of $B(C_6F_5)_3$ in $CD_2Cl_2$ results in the abstraction of one of the axial methyl groups. A new resonance at $\delta$ = 1.86 ppm was observed for this methyl group in the $^1$H NMR spectra. The resulting organocation is not stable in solution and decomposes rapidly into unidentified species.

Table 2. Ethylene polymerization results, activation of **8** using trialkylammonium tetrakis(pentafluorophenyl)borate.[a]

| Run no. | Pre-cat. [μmol] | $B(C_6F_5)_4^-$ [μmol] | TIBAO [mmol] | PE [g] | Activity [kg(PE)mol(Ta)$^{-1}$h$^{-1}$bar$^{-1}$] |
|---|---|---|---|---|---|
| 1 | – | 11 | 0.1 | 0.05 | – |
| 2 | 10 | 11 | 0.1 | 0.06 | 5 |
| 3 | 10 | 22 | 0.1 | 0.16 | 13 |

[a] 260 mL of toluene as solvent, 5 bar of ethene, 80 °C, 15 min run time, Ta/Al = 1:20 (m/m); TIBAO = tetraisobutylaluminoxane ($[iBu_2Al]_2O$).

## Conclusions

Trialkyltantalum complexes stabilized by aminopyridinato ligands can be synthesized by salt metathesis or toluene elimination. They adopt the coordination of either a capped octahedron or a pentagonal bipyramid depending on the steric demand of the aminopyridinato ligand. These trialkyltantalum complexes are thermally unusually stable towards α-H elimination. They form rather unstable organocations and the instability of these cations might be the reason for the low activity in ethylene polymerization.

## Experimental Section

### General Procedures

**Synthesis and Structure Analysis:** All manipulations were performed with rigorous exclusion of oxygen and moisture in Schlenk-type glassware on a dual manifold Schlenk line or in an argon-filled glove box (mBraun 120-G) with a high-capacity recirculator (<0.1 ppm $O_2$). Non-halogenated solvents were dried by distillation from sodium wire/benzophenone. Commercial $TaCl_5$ (Lancaster) was used as received. Deuterated solvents were obtained from Cambridge Isotope Laboratories and were degassed, dried, and distilled prior to use. NMR spectra were recorded with a Bruker ARX at 250 MHz and chemical shifts are reported in ppm relative to the deuterated solvent. Elemental analyses (CHN) were carried out using a Vario EL III instrument. X-ray crystal structure analyses were performed by using a STOE-IPDS II diffractometer equipped with an Oxford Cryostream low-temperature unit. Crystal structure data are presented in Table 3. Structure solution and refinement was accomplished using SIR97,[21] SHELXL97,[22] and WinGX.[23] CCDC-297697 (**4**), -297698 (**5**), -297699 (**7**), and -297700 (**8**) contain the supplementary crystallographic data for

 © 2006 Wiley-VCH Verlag GmbH & Co. KGaA, Weinheim 

Table 3. Details of the X-ray crystal structure analyses.

| Compound | **4** | **5** | **7** | **8** |
|---|---|---|---|---|
| Crystal system | monoclinic | monoclinic | triclinic | monoclinic |
| Space group | *C*2/*c* | $P2_1/n$ | $P\bar{1}$ | *C*2/*c* |
| *a* [Å] | 23.279(3) | 13.955(3) | 10.3627(9) | 14.1240(10) |
| *b* [Å] | 18.761(2) | 14.704(3) | 19.7101(18) | 12.5620(10) |
| *c* [Å] | 20.204(3) | 18.617(3) | 21.343(2) | 22.694(2) |
| *α* [°] | 90 | 90 | 96.120(7) | 90 |
| *β* [°] | 117.557(8) | 91.680(2) | 103.540(7) | 93.375(5) |
| *γ* [°] | 90 | 90 | 90.410(7) | 90 |
| *V* [Å$^3$] | 7823(3) | 3818(2) | 4211.6(7) | 4019.5(6) |
| Crystal size [mm] | 0.12 × 0.1 × 0.08 | 0.12 × 0.11 × 0.06 | 0.16 × 0.1 × 0.05 | 0.99 × 0.34 × 0.44 |
| $\rho_{calcd.}$ [g cm$^{-3}$] | 1.381 | 1.414 | 1.434 | 1.333 |
| $\mu$ [mm$^{-1}$] (Mo-$K_\alpha$) | 0.7107 | 0.7107 | 0.7107 | 0.7107 |
| *T* [K] | 193(2) | 193(2) | 193(2) | 193(2) |
| *θ* range [°] | 1.47–26.19 | 1.77–26.21 | 1.35–25.83 | 1.80–25.68 |
| No. of unique refl. | 7732 | 7506 | 15909 | 3604 |
| No. of obsd. refl. [$I > 2\sigma(I)$] | 4508 | 2470 | 9228 | 3508 |
| No. of parameters | 415 | 409 | 880 | 214 |
| $wR_2$ (all data) | 0.1282 | 0.1033 | 0.1018 | 0.0924 |
| *R* value [$I > 2\sigma(I)$] | 0.0755 | 0.0542 | 0.0632 | 0.0312 |

this paper. These data can be obtained free of charge from The Cambridge Crystallographic Data Centre via www.ccdc.cam.ac.uk/data_request/cif.

**Polymerization:** Toluene (Aldrich, anhydrous, 99.8%) was passed through columns of $Al_2O_3$ (Fluka), BASF R3-11 supported Cu oxygen scavenger, and molecular sieves (4 Å, Aldrich). Ethylene (AGA polymer grade) was passed over BASF R3-11 supported Cu oxygen scavenger and molecular sieves (4 Å, Aldrich). PMAO (4.9 wt.-% Al in toluene, Akzo Nobel), *N*,*N*,*N*-trialkylammonium tetrakis(pentafluorophenyl)borate [6.2 wt.-% $B(C_6F_5)_4^-$ in Isopar, DOW Chemicals], and TIBA (Witco) were used as received. TIBAO was prepared according to published procedures.[24]

**Synthesis of 3:**[25] Toluene (25 mL) was added to a Schlenk vessel charged with tris(dibenzylideneacetone)dipalladium (0.082 g, 0.09 mmol), NaO*t*Bu (0.750 g, 7.8 mmol), and 1,3-bis(diphenylphosphanyl)propane (0.074 g, 0.18 mmol). To the resulting suspension 2-bromopyridine (0.57 mL, 6 mmol) and 2,6-diisopropylaniline (1.47 mL, 7.8 mmol) was added. The solution was stirred and heated to 90 °C for 48 h. On cooling to room temperature, water and diethyl ether were added to the resulting red solution. The organic phase was extracted and the remaining inorganic phase was further washed with diethyl ether (3 × 20 mL). The combined organic phases were washed with a saturated sodium chloride solution and dried with sodium sulfate. The solvent was removed under reduced pressure and the resulting reddish solid was purified using silica gel chromatography (eluent: dichloromethane). The solvent was removed under reduced pressure and the product was recrystallized from pentane as a white crystalline material. Yield 1.07 g (70%). $C_{17}H_{22}N_2$ (254.37): calcd. C 80.27, H 8.72, N 11.01; found C 80.30, H 8.75, N 10.82. $^1$H NMR ($C_6D_6$, 298 K): $\delta$ = 1.10 [d, 12 H, $CH(CH_3)_2$], 3.39 [sept, 2 H, $CH(CH_3)_2$], 5.88 (d, 1 H, Py-3-H), 6.20 (dd, 1 H, Py-5-H), 6.89 (t, 1 H, Py-4-H), 7.17–7.29 (m, 3 H, Ar-CH), 7.99 (dd, 1 H, Py-6-H), 8.34 (br. s, 1 H, NH) ppm. $^{13}$C NMR ($C_6D_6$, 298 K): $\delta$ = 23.98 [4 $CH_3$, $CH(CH_3)_2$], 28.67 [2 CH, $CH(CH_3)_2$], 105.62 (CH, Py-C-5), 112.94 (CH, Py-C-3), 124.22 (2 CH, Ar-C-9,11), 134.69 (CH, Py-C-4), 137.68 (2 CH, Ar-C-8,12), 148.45 (1 C, Ar-C-7), 148.57 (1 CH, Py-C-6), 160.51 (1 CH, Py-C-2) ppm.

**Synthesis of 4:** Compound **1** (0.380 g, 2 mmol, 425 μL) in hexane (5 mL) was added slowly to a stirred solution of $[Ta(CH_2C_6H_5)_5]$ (0.636 g, 1 mmol) in hexane (15 mL) at –33 °C. The mixture was warmed to room temperature and was further heated at 60 °C for 2 h as a color change was observed from brown to deep red. The mixture was filtered and the volume of the solvent was reduced in vacuo. The solution was cooled at –25 °C overnight to afford a yellow crystalline material. Yield 0.365 g (43%). $C_{39}H_{51}N_4Si_2Ta$ (812.97): calcd. C 57.62, H 6.32, N 6.89; found C 57.36, H 6.62, N 6.29. $^1$H NMR ($C_6D_6$, 298 K): $\delta$ = 0.40 [s, 18 H, $Si(CH_3)_3$], 1.61 (s, 6 H, $CH_3$), 2.96 (br. d, 6 H, $CH_2$), 5.76 (d, 2 H, Py-5-H), 5.88 (s, 2 H, Py-3-H), 6.74 (t, 3 H, Ar-4-H), 6.89–7.10 (m, 14 H, Py-6-H, Ar-2, 3, 5, 6 H) ppm. $^{13}$C NMR ($C_6D_6$, 298 K): $\delta$ = 2.45 (6 C, 6 $CH_3$), 21.6 (2 C, 2 $CH_3$), 99.40 (br. and flat s, 3 $CH_2$), 111.87 (2 CH, Py-C-3/5), 114.05 (2 CH, Py-C-3/5), 122.49 (3 CH, Benz-C-4), 126.83 (6 CH, Benz-C-3,5), 128.20 (6 CH, Benz-C-2,6), 141.51 (3 C, Benz-C-1), 151.53 (2 C, Py-C-4), 153.26 (2 CH, Py-C-6), 164.91 (2 C, Py-C-2) ppm.

**Synthesis of 5:** Compound **2** (0.463 g, 2.57 mmol, 546 μL) in hexane (5 mL) was added slowly to a stirred solution of $[Ta(CH_2C_6H_5)_5]$ (0.817 g, 1.28 mmol) in hexane (15 mL) at –33 °C. The mixture was warmed to room temperature and further heated at 60 °C for 2 h. The mixture was filtered and the volume of the solvent was reduced in vacuo. The solution was cooled at –25 °C overnight to afford a yellow crystalline material. Yield 0.460 g (44%). $C_{39}H_{51}N_4Si_2Ta$ (812.97): calcd. C 57.62, H 6.32, N 6.89; found C 56.73, H 6.24, N 6.54. $^1$H NMR ($C_6D_6$, 298 K): $\delta$ = 0.27 [s, 18 H, $Si(CH_3)_3$], 1.92 (s, 6 H, $CH_3$), 3.15–2.96 (2 d, 6 H, $CH_2$), 5.65 (d, 2 H, Py-5-H), 5.83 (d, 2 H, Py-3-H), 6.69 (dd, 6 H, Benz-2,6-H), 7.00 (t, 6 H, Benz-3,5-H), 7.44 (t, 2 H, Py-4-H) ppm. $^{13}$C NMR ($C_6D_6$, 298 K): $\delta$ = 2.57 (6 C, 6 $CH_3$), 21.56 (2 C, 2 $CH_3$), 100.34 (3 $CH_2$), 108.34 (2 CH, Py-C-3/5), 113.95 (2 CH, Py-C-3/5), 122.66 (3 CH, Benz-C-4), 126.67 (6 CH, Benz-C-3,5), 129.42 (6 CH, Benz-C-2,6), 138.32 (3 C, Benz-C-1), 151.97 (2 CH, Py-C-4), 153.17 (2 C, Py-C-6), 161.49 (2 C, Py-C-2) ppm.

**Synthesis of 6:** To a stirred solution of **3** (0.557 g, 2.14 mmol) in diethyl ether (10 mL), *n*BuLi (1.34 mL, 1.6 M, 2.14 mmol) was added at 0 °C. This "ligand solution" was warmed slowly to room temperature and stirred for 2 h. This solution was slowly added to $[TaCl_2(CH_2C_6H_5)_3]$ (0.562 g, 1.07 mmol) in hexane (10 mL) at room temperature. The mixture was stirred overnight and a color change from red to dark brown was observed. LiCl was filtered off

 © 2006 Wiley-VCH Verlag GmbH & Co. KGaA, Weinheim 

and the volume of the solvent was reduced in vacuo. The solution was cooled at –25 °C overnight to afford an orange crystalline material. Yield 0.564 g (55%). $C_{55}H_{63}N_4Ta$ (961.06): calcd. C 68.74, H 6.61, N 5.83; found C 67.44, H 6.64, N 5.51. $^1$H NMR ($C_6D_6$, 298 K): $\delta$ = 1.15–1.27 [dd, 24 H, 2 $CH(CH_3)_2$], 2.79 (s, 2 H, $CH_2$), 3.60 (s, 4 H, 2 $CH_2$), 3.85 [sept, 4 H, 4 $CH(CH_3)_2$], 5.52 (d, 2 H, Py-3-H), 5.81 (t, 2 H, Py-5-H), 6.22 (d, 4 H, Ar-H), 6.27 (d, 2 H, Py-4-H), 6.62 (dd, 2 H, Py-6-H), 6.78–6.67 (m, 5 H, Ar-H), 6.94–6.86 (m, 6 H, Ar-H), 7.19–7.16 (m, 6 H, Ar-CH) ppm. $^{13}$C NMR ($C_6D_6$, 298 K): $\delta$ = 23.22 [8 $CH_3$, $CH(CH_3)_2$], 26.28 [2 CH, $CH(CH_3)_2$], 28.80 [2 CH, $CH(CH_3)_2$], 83.50 (3 C, $CH_2$), 106.53 (2 CH, Py-C-3/5), 112.39 (2 CH, Py-C-3/5), 123.18 (4 CH, Ar-C-9,11), 125.31 (6 CH, Benz-C-3,5), 126.57 (6 CH, Benz-C-2,6), 127.09 (3 CH, Benz-C-4), 129.96 (4 CH, Ar-C-8,12), 139.55 (2 CH, Ar-C-10), 141.87 (2 CH, Py-C-4), 143.08 (2 C, Ar-C-7), 146.36 (3 C, Benz-C-1), 148.46 (2 CH, Py-C-6), 169.21 (2 CH, Py-C-2) ppm.

**Synthesis of 7. Method I:** $TaCl_5$ (1.432 g, 4 mmol) and **3** (2.035 g, 8 mmol) were heated at 110 °C. The melt started to turn dark brown immediately. During the reaction gas formation was observed. After 1 h, toluene (30 mL) was added and the dark-red reaction mixture was further refluxed for 2 h. The solution was filtered while hot and the volume was reduced until red crystals began to appear. The solution was cooled and a red crystalline material was obtained overnight. Yield 1.103 g (35%). $C_{34}H_{42}Cl_3N_4Ta$ + 0.5 $C_7H_8$ (840.10): calcd. C 53.61, H 5.51, N 6.67; found C 53.67, H5.54, N 6.08. $^1$H NMR ($C_6D_6$, 298 K): $\delta$ = 1.13–1.48 [dd, 24 H, $CH(CH_3)_2$], 2.10 (s, 3 H, toluene) 3.86 [sept, 4 H, $CH(CH_3)_2$], 5.74 (d, 2 H, Py-3-H), 6.05 (t, 2 H, Py-5-H), 6.83 (t, 2 H, Py-4-H), 7.28–7.16 (m, 6 H, Ar-H), 8.06 (d, 2 H, Py-6-H) ppm. $^{13}$C NMR ($C_6D_6$, 298 K): $\delta$ = 24.73 [4 $CH_3$, $CH(CH_3)_2$], 24.95 [4 $CH_3$, $CH(CH_3)_2$], 28.22 [4 CH, $CH(CH_3)_2$], 107.56 (2 CH, Py-C-3/5), 113.50 (2 CH, Py-C-3/5), 124.46 (4 CH, Ar-C-9,11), 140.19 (2 CH, Ar-C-10), 140.66 (CH, Py-C-4), 141.15 (2 C, Ar-C-7), 147.37 (4 C, 2 CH, Ar-C-8,12, Py-C-6), 169.86 (2 C, Py-C-2) ppm. **Method II:** Lithiated **3** (1.041 g, 4 mmol) in diethyl ether (20 mL) was added to $TaCl_5$ (0.716 g, 2 mmol) in toluene (5 mL) at room temperature and the reaction mixture was stirred at room temperature overnight. The solution was filtered and the solvent was removed in vacuo. The red residue was washed with hexane (5 mL) and dried under vacuum. Yield 0.92 g (58%).

**Synthesis of 8:** LiMe (1.88 mL, 1.6 M, 3 mmol) was added to a stirred suspension of **7** (0.794 g, 1 mmol) in hexane (20 mL) at –40 °C. The red suspension was warmed to room temperature as the color started changing from red to yellow. The suspension was further stirred for 2 h. The brown solution was filtered and the residue washed with diethyl ether (5 mL). The volume was reduced in vacuo and the solution was cooled at –25 °C overnight to afford a yellow crystalline material. Yield 0.432 g (59%). $C_{37}H_{51}N_4Ta$ (732.78): calcd. C 60.65, H 7.02, N 7.65; found C 60.37, H 7.04, N 7.50. $^1$H NMR ($C_6D_6$, 298 K): $\delta$ = 0.63 (s, 3 H, $CH_3$), 1.13 [d, 12 H, $CH(CH_3)_2$], 1.26 (s, 6 H, 2 $CH_3$),1.34 [d, 12 H, $CH(CH_3)_2$], 3.61 [sept, 4 H, $CH(CH_3)_2$], 5.54 (d, 2 H, Py-3-H), 6.18 (dd, 2 H, Py-5-H), 6.86 (t, 2 H, Py-4-H), 7.24–7.17 (m, 6 H, Ar-8,9,10-H) ppm.$^{13}$C NMR ($C_6D_6$, 298 K): $\delta$ = 24.10 [4 $CH_3$, $CH(CH_3)_2$], 24.18 [4 $CH_3$, $CH(CH_3)_2$], 25.10 (3 $CH_3$), 27.75 [2 CH, $CH(CH_3)_2$], 27.93 [2 CH, $CH(CH_3)_2$], 105.67 (2 CH, Py-C-3/5), 113.36 (1 CH, Py-C-3/5), 113.56 (1 CH, Py-C-5), 124.45 (4 CH, Ar-C-9,11), 127.09 (1 CH, Ar-C-10), 127.14 (1 CH, Ar-C-10), 138.91 (1 CH, Py-C-4), 139.11 (1 CH, Py-C-4), 141.32 (4 CH, Ar-C-8,12), 146.09 (4 CH, Py-C-6, 2 C, Ar-C-7), 168.32 (1 C, Py-C-2) ppm.

**General Description of Polymerization Experiments:** The catalytic ethylene polymerization reactions were performed in a stainless steel 1-L autoclave (Medimex) in semi-batch mode (ethylene was added by replenishing flow to keep the pressure constant). The reactor was temperature- and pressure-controlled and equipped with separated toluene, catalyst, and cocatalyst injection systems and a sample outlet for continuous reaction monitoring. At 5 bar of ethylene pressure multiple injection of the catalyst with a pneumatically operated catalyst-injection system was used. During a polymerization run the pressure, ethylene flow, inner and outer reactor temperature, and the stirrer speed were monitored continuously. In a typical semi-batch experiment, the autoclave was evacuated and heated at 125 °C for 1 h prior to use. The reactor was then brought to the desired temperature with stirring at 600 rpm and charged with 230 mL of toluene together with either the required amount of PMAO [2.76 g, Ta/Al = 1:500 (m/m)] or TIBAO scavenger [1 mL of a 0.1 M stock solution in toluene, Ta/Al = 1:20 (m/m)]. After pressurizing with ethylene to reach 5 bar total pressure the autoclave was equilibrated for 5 min. Subsequently 1 mL of a 0.01 M stock solution of the tantalum complex in toluene was injected together with 30 mL of toluene, to start the reaction. In the case where trialkylammonium tetrakis(pentafluorophenyl)borate was the activator, 1 mL of the tantalum complex stock solution and the appropriate amount of borate [0.12 g, Ta/B = 1:1.1 (m/m)] were premixed before injection. During the run the ethylene pressure was kept constant to within 0.2 bar of the initial pressure by replenishing flow. After the desired reaction time, the reactor was vented and the residual PMAO/TIBAO was destroyed by addition of 20 mL of ethanol. Polymeric product was collected, stirred in acidified ethanol for 30 min, and rinsed with ethanol and acetone on a glass frit. The polymer was initially dried in air and subsequently in vacuo at 80 °C.

## Acknowledgments

Financial support from the Fonds der Chemischen Industrie and Deutsche Forschungsgemeinschaft is gratefully acknowledged.

[1] Review article on aminopyridinato ligands: R. Kempe, *Eur. J. Inorg. Chem.* **2003**, 791–803.
[2] Review article on (aminopyridinato)lanthanide chemistry: R. Kempe, H. Noss, T. Irrgang, *J. Organomet. Chem.* **2002**, *647*, 12–20.
[3] a) A. Spannenberg, M. Oberthür, H. Noss, H. A. Tillack, P. Arndt, R. Kempe, *Angew. Chem.* **1998**, *110*, 2190–2192; *Angew. Chem. Int. Ed. Engl.* **1998**, *37*, 2079–2082; b) S. Deeken, S. Proch, E. Casini, H. F. Braun, C. Mechtler, C. Marschner, G. Motz, R. Kempe, *Inorg. Chem.*, in press.
[4] Selected reviews on amidinate chemistry: a) J. Barker, M. Kilner, *Coord. Chem. Rev.* **1994**, *133*, 219–300; b) F. T. Edelmann, *Coord. Chem. Rev.* **1994**, *137*, 403–481; c) N. Nagashima, H. Kondo, T. Hayashida, Y. Yamaguchi, M. Gondo, S. Masuda, K. Miyazaki, K. Matsubara, K. Kirchner, *Coord. Chem. Rev.* **2003**, *245*, 177–190.
[5] For selected publications on group 5 chemistry please see: a) M. G. B. Drew, J. D. Wilkins, *Acta Crystallogr. Sect. B* **1975**, *31*, 177–182; b) M. G. B. Drew, J. D. Wilkins, *Acta Crystallogr. Sect. B* **1975**, *31*, 2642–2648; c) F. Schrumpf, H. W. Roesky, T. Subrahmanyan, M. Noltemeyer, *Z. Anorg. Allg. Chem.* **1990**, *583*, 124–132; d) M. Vivanco, J. Ruiz, C. Floriani, A. Chiesi-Villa, C. Rizzoli, *Organometallics* **1993**, *12*, 1794–1801; e) S. Hao, P. Berno, R. K. Minhas, S. Gambarotta, *Inorg. Chim. Acta* **1996**, *244*, 37–49; f) P. J. Stewart, A. J. Blake, P. Mountford, *Inorg. Chem.* **1997**, *36*, 1982–1986; g) D. Y. Dawson, J. Arnold, *Organometallics* **1997**, *16*, 1111–1113; h) M. J. R. Brandsma, E. A. C. Brussee, A. Meetsma, B. Hessen, J. H. Teuben, *Eur. J. Inorg. Chem.* **1998**, 1867–1870; i) E. A. C.

 © 2006 Wiley-VCH Verlag GmbH & Co. KGaA, Weinheim 

Brussee, A. Meetsma, B. Hessen, J. H. Teuben, *Organometallics* **1998**, *17*, 4090–4095; j) J. M. Decker, S. J. Geib, T. Y. Meyer, *Organometallics* **1999**, *18*, 4417–4420; k) S. M. Mullins, R. G. Bergman, J. Arnold, *Organometallics* **1999**, *18*, 4465–4467; l) C.-T. Chen, L. H. Doerrer, V. C. Williams, M. L. H. Green, *J. Chem. Soc. Dalton Trans.* **2000**, 967–974; m) E. A. C. Brussee, A. Meetsma, B. Hessen, J. H. Teuben, *Chem. Commun.* **2000**, 497–498; n) C.-T. Chen, L. H. Rees, A. R. Cowley, M. L. H. Green, *J. Chem. Soc. Dalton Trans.* **2001**, 1761–1767; o) D. D. Ellis, A. L. Spek, *Acta Crystallogr. Sect. C* **2001**, *57*, 147–148; p) B. S. Lim, A. Rahtu, J.-S. Park, R. G. Gordon, *Inorg. Chem.* **2003**, *42*, 7951–7958.

[6] J. J. H. Edenma, S. Gambarotta, A. Meetsma, A. L. Spek, N. Veldman, *Inorg. Chem.* **1991**, *30*, 2062–2066.

[7] M. Polamo, M. Leskelä, *J. Chem. Soc. Dalton Trans.* **1996**, 4345–4349.

[8] M. Polamo, *Acta Crystallog., Sect. C* **1996**, *52*, 2977–2980.

[9] M. Polamo, M. Leskelä, *Acta Chem. Scand.* **1997**, *51*, 449–454.

[10] M. Polamo, M. Leskelä, *Acta Chem. Scand.* **1997**, *51*, 709–713.

[11] a) M. Tayebani, S. Gambarotta, G. Yap, *Organometallics* **1998**, *17*, 3639–3641; b) M. Tayebani, K. Feghali, S. Gambarotta, G. Yap, L. K. Thompson, *Angew. Chem.* **1999**, *111*, 3893–3895; *Angew. Chem. Int. Ed.* **1999**, *38*, 3659–3661; c) F. A. Cotton, E. A. Hillard, C. A. Murillo, X. Wang, *Inorg. Chem.* **2003**, *42*, 6063–6070; d) F. A. Cotton, L. M. Daniels, C. A. Murillo, H.-C. Zhou, *Inorg. Chim. Acta* **2000**, *305*, 69–74.

[12] K. Hakala, B. Löfgren, M. Polamo, M. Leskelä, *Macromol. Rapid Commun.* **1997**, *18*, 635–638.

[13] a) G. Hillebrand, A. Spannenberg, P. Arndt, R. Kempe, *Organometallics* **1997**, *16*, 5585–5588; b) A. Spannenberg, H. Fuhrmann, P. Arndt, W. Baumann, R. Kempe, *Angew. Chem.* **1998**, *110*, 3565–3567; *Angew. Chem. Int. Ed. Engl.* **1998**, *37*, 3363–3365.

[14] The compound was first reported by Schrock: R. R. Schrock, *J. Organomet. Chem.* **1976**, *122*, 209–225.

[15] Recently, Kol et al. described a more efficient synthesis allowing the use of this compound as a starting material in larger scale reactions: S. Groysman, I. Goldberg, M. Kol, *Organometallics* **2003**, *22*, 3793–3795.

[16] R. Kempe, P. Arndt, *Inorg. Chem.* **1996**, *35*, 2644–2649.

[17] L. M. Engelhardt, G. E. Jacobsen, P. C. Junk, C. L. Raston, B. W. Skelton, A. H. White, *J. Chem. Soc. Dalton Trans.* **1988**, 1011–1020.

[18] a) S. Wagaw, S. L. Buchwald, *J. Org. Chem.* **1996**, *61*, 7240–7241; b) J. F. Hartwig, *Synlett* **1996**, 329–340; c) J. P. Wolfe, H. Tomori, J. P. Sadihghi, J. Yin, S. L. Buchwald, *J. Org. Chem.* **2000**, *65*, 1158–1174; d) T. Schareina, G. Hillebrand, R. Kempe, *Eur. J. Inorg. Chem.* **2001**, 2421–2426; e) M. R. Buchmeiser, T. Schareina, R. Kempe, K. Wurst, *J. Organomet. Chem.* **2001**, *634*, 39–46; f) J. Silberg, T. Schareina, R. Kempe, K. Wurst, M. R. Buchmeiser, *J. Organomet. Chem.* **2001**, *622*, 6–18; g) N. M. Scott, T. Schareina, O. Tok, R. Kempe, *Eur. J. Inorg. Chem.* **2004**, 3297–3304.

[19] a) R. R. Schrock, *J. Am. Chem. Soc.* **1974**, *96*, 6796–6797; b) R. R. Schrock, J. D. Fellmann, *J. Am. Chem. Soc.* **1978**, *100*, 3359–3370.

[20] R. R. Schrock, *Chem. Rev.* **2002**, *102*, 145–179.

[21] A. Altomare, M. C. Burla, M. Camalli, G. L. Cascarano, C. Giacovazzo, A. Guagliardi, A. G. G. Moliterni, G. Polidori, R. Spagna, *J. Appl. Crystallogr.* **1999**, *32*, 115–119.

[22] G. M. Sheldrick, *SHELX 97, Program for Crystal Structure Analysis*, Release 97-2, University of Göttingen, Germany, **1998**.

[23] L. J. Farrugia, *J. Appl. Crystallogr.* **1999**, *32*, 837–838.

[24] J. F. van Baar, P. A. Schut, A. D. Horton, O. T. Dall, G. M. M. van Kessel, World Pat. Appl. WO 2000035974 A1 to Montell Techn. Co., June 22, **2000**.

[25] The structure of **3** was published by Polamo recently. Crystals of **3** for X-ray analysis were synthesized from 2-chloropyridine and 2,6-diisopropylaniline hydrochloride at 180 °C. This reaction seems to be easier to accomplish than our synthesis and less expensive since no palladium catalyst is needed. The yield was not reported. M. Polamo, M. Talja, A. J. Piironen, *Z. Kristallogr. – New Cryst. Struct.* **2005**, *220*, 41–42.

Received: February 9, 2006
Published Online: April 27, 2006

 © 2006 Wiley-VCH Verlag GmbH & Co. KGaA, Weinheim 

DOI: 10.1002/ejic.200600230

# Oxovanadium(IV) Complexes with Pyrazinecarboxylic Acids: The Coordinating Properties of Ligands with the ($N_{aromatic}$, $COO^-$) Donor Set

**Eugenio Garribba,*[a] Giovanni Micera,*[a] Elzbieta Lodyga-Chruscinska,[b] and Daniele Sanna[c]**

**Keywords:** Vanadium / N,O ligands / Isomers / Magnetic properties / EPR spectroscopy

Complex formation between the $V^{IV}O$ ion and four pyrazine derivatives, 2-pyrazinecarboxylic acid (pzc), 5-methyl-2-pyrazinecarboxylic acid (5-Mepzc), 2,3-pyrazinedicarboxylic acid (3-COOHpzc) and 5-hydroxy-2-pyrazinecarboxylic acid (5-OHpzc), was studied in aqueous solution and in the solid state through the combined application of potentiometric and spectroscopic (EPR and FT-IR) techniques. The results indicate that in acidic and neutral aqueous solution all the ligands form mono(chelated), bis(chelated) and dinuclear species of composition VOL, $VOL_2$ and $(VO)_2L_2H_{-2}$. Hexacoordinated $VOL_2$ complexes are characterised by a *cis*/*trans* isomerism, where *cis* and *trans* are the species with a water molecule bound in the *cis* or *trans* position with respect to the V=O group. The *trans* arrangement is favoured over the *cis* arrangement. Three solid derivatives, $[VO(5\text{-}Mepzc)_2]$ (**1**), *cis*-$[VO(pzc)_2(H_2O)]$ (**2**) and *cis*-$[VO(3\text{-}COOHpzc)_2(H_2O)]$ (**3**), were isolated and characterised. Based on the experimental results and on the data in the literature, the stability of *cis* and *trans* isomers in aqueous solution and in the solid state has been discussed, showing that with ligands of comparable basicity and size of the chelate ring the hydrophilicity favours the *cis* species and determines the relative amount of the two isomers. The analysis of the magnetic properties of the hydroxo-bridged $V^{IV}O$ dimers suggests that for the $(VO)_2L_2H_{-2}$ species the *anti*-coplanar arrangement is realised.

(© Wiley-VCH Verlag GmbH & Co. KGaA, 69451 Weinheim, Germany, 2006)

## Introduction

Vanadium plays a number of roles in biological systems.[1] Among others, a growing interest is devoted to the insulin-mimetic activity of its compounds.[2] Initially, both $V^V$ and $V^{IV}$ inorganic salts were extensively used as insulin mimics, but the introduction of $V^{IV}$ complexes has considerably improved their pharmacological potential by minimising the dose required for effective diabetic control.[2b]

The insulin-mimetic properties of complexes with coordination modes $VO(O_4)$,[3,4] $VO(N_2S_2)$,[3,5] $VO(S_4)$,[6] $VO(S_2O_2)$,[7] $VO(N_4)$[8] and $VO(N_2O_2)$[9,10] have been examined. Generally, N,O ligation is more efficient than O,O or O/N,S coordination, irrespective of the vanadium oxidation state.[11]

$V^{IV}O$ compounds with $N_2O_2$ coordination are very promising in the treatment of insulin-dependent diabetes mellitus.[12] In particular, $V^{IV}O(picolinato)_2(H_2O)$ and $V^{IV}O(6\text{-methylpicolinato})_2$ are strong inhibitors of the mobilisation of fatty acids and effective in the treatment of rats affected by diabetes induced with streptozotocin (STZ).[9,10] In addition, the complex formed by 6-methylpicolinate, with long-acting character and low toxicity, is the most effective in the treatment of insulin-dependent diabetes mellitus (IDDM) as well as non-insulin-dependent diabetes mellitus (NIDDM) when administrated orally.[13]

In the last few years several studies have been devoted to the complexation of the $V^{IV}O$ ion by bidentate ligands provided with an aromatic nitrogen atom and a carboxylate oxygen atom as donors.[14] Usually, VOL and $VOL_2$ species are formed in aqueous solution, with the possibility of *cis*/*trans* isomerism for the hexacoordinate bis(complexes) (Scheme 1).[15] The presence of di-μ-hydroxo EPR-silent species of composition $(VO)_2L_2H_{-2}$ has been proposed in some systems.[14b,14c,14e]

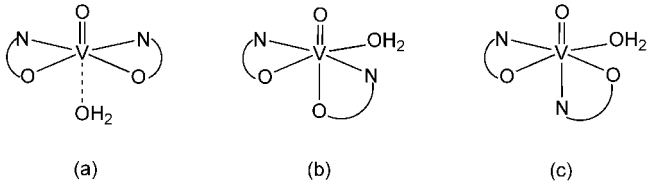


Scheme 1. Possible structures for the isomers of a bis(chelated) $V^{IV}O$ complex: (a) *trans* arrangement; (b) and (c) *cis* arrangements.

[a] Department of Chemistry, University of Sassari, Via Vienna 2, 07100 Sassari, Italy
Fax: +39-079-229559
E-mail: garribba@uniss.it
micera@uniss.it
[b] Institute of General Food Chemistry, Technical University of Lodz, ul. Stefanowskiego 4/10, 90924 Lodz, Poland
[c] Istituto C.N.R. di Chimica Biomolecolare, Trav. La Crucca 3, 07040 Li Punti, Sassari, Italy

 © 2006 Wiley-VCH Verlag GmbH & Co. KGaA, Weinheim 

In this work we investigated the $V^{IV}O$ complex formation with four pyrazine derivatives: 2-pyrazinecarboxylic (pzc), 5-methyl-2-pyrazinecarboxylic (5-Mepzc), 2,3-pyrazinedicarboxylic (3-COOHpzc) and 5-hydroxy-2-pyrazinecarboxylic (5-OHpzc) acids (Scheme 2). Only one potentiometric study, although not supported by spectroscopic measurements, is available on the interaction of the $V^{IV}O$ ion with 2-pyrazinecarboxylic and 2,3-pyrazinedicarboxylic acids in aqueous solution.[16] To the best of our knowledge, no data on the formation of solid complexes have been reported. Here, the behaviour in aqueous solution and in the solid state of the four ligands is presented together with a discussion of the coordinating properties of ligands provided with the ($N_{aromatic}$, $COO^-$) donor set.

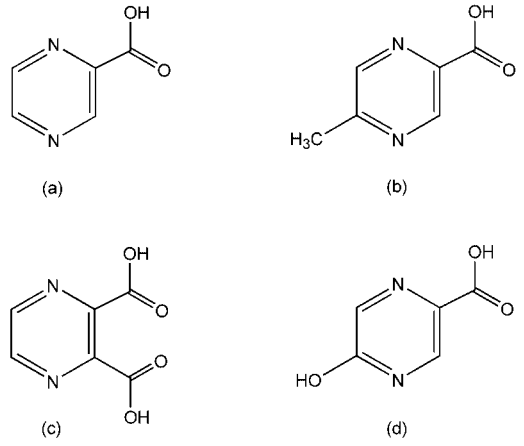


Scheme 2. Ligands: (a) 2-pyrazinecarboxylic acid (pzc), (b) 5-methyl-2-pyrazinecarboxylic acid (5-Mepzc), (c) 2,3-pyrazinedicarboxylic acid (3-COOHpzc) and (d) 5-hydroxy-2-pyrazinecarboxylic acid (5-OHpzc).

## Results

### Studies in Aqueous Solution

Fully protonated forms of 2-pyrazinecarboxylic and 5-methyl-2-pyrazinecarboxylic acids in aqueous solution can be denoted as $H_3L^{2+}$ and those of 2,3-pyrazinedicarboxylic and 5-hydroxy-2-pyrazinecarboxylic acids as $H_4L^{2+}$.

Two deprotonation processes are measurable for pzc, 5-Mepzc and 3-COOHpzc in the titrable pH range with p$K_a$ values of 1.83 and 2.73 for pzc, 2.06 and 3.13 for 5-Mepzc, and 1.50 and 3.25 for 3-COOHpzc (Table 1). The two processes can be assigned to the pyrazine $–NH^+$ and the –COOH groups, respectively. The values measured for pzc and 3-COOHpzc are in very good agreement with those previously reported.[16] Owing to its very high acidity, the deprotonation of the first $–NH^+$ group is not detectable. A comparison with 2-pyridinecarboxylic acid, for which p$K_a$ values of about 1 and 5.19 are reported,[14b] indicates that the presence of a second nitrogen atom in the aromatic ring significantly reduces the basicity of the $–NH^+$ group. On the other hand, the carboxylic group slightly increases the basicity of the second $–NH^+$ group with respect to pyrazine, for which a p$K_a$ of 0.65 is reported.[17] The increase in basicity is due to the formation of a cyclic structure, which stabilises the $–NH^+$ form through an internal hydrogen bond between the protonated pyrazine nitrogen atom and the –COOH group. The value for the deprotonation of the carboxylic group of pzc is comparable with that measured by Toma and Borges (2.82).[18] The electron-releasing effect of the methyl group reduces the acidity of both the $–NH^+$ and –COOH groups in 5-Mepzc (Table 1).

Table 1. Protonation constants of the ligands (log $K$) and stability constants of the $V^{IV}O$ complexes (log $\beta_{pqr}$) at 25.0 ± 0.1 °C and $I$ = 0.1 M ($KNO_3$).

| log $K$/log $\beta_{pqr}$ | pzc | 5-Mepzc | 3-COOHpzc | 5-OHpzc |
|---|---|---|---|---|
| $–N1_{pyr}H^+$ | <1 | <1 | <1 | <1 |
| $–N2_{pyr}H^+$ | 1.83 | 2.06 | 1.50 | <1 |
| –COOH1 | 2.73 | 3.13 | 3.25 | 3.44 |
| –COOH2 | – | – | <1 | – |
| –OH | – | – | – | 7.78 |
| VOL | 3.42(2) | 3.49(2) | 3.99(2) | 7.01(2) |
| $VOL_2$ | 6.09(2) | 6.99(2) | 7.02(3) | 12.97(2) |
| $(VO)_2L_2H_{-2}$ | 0.11(3) | 0.58(2) | 1.79(3) | 5.85(3) |

Only two deprotonation steps, of the four possible ones, can be determined for 2,3-pyrazinedicarboxylic acid. Owing to the strong internal hydrogen bond between COOH and $COO^-$, one of the two carboxylic groups is protonated only at pH < 1. This effect had already been observed for 2,3-pyridinedicarboxylic[19] and 4,5-imidazoledicarboxylic acids.[14a] For the same reason, the deprotonation of the second –COOH group takes place at higher pH values with respect to pzc and 5-Mepzc. Moreover, the electron-withdrawing properties of the carboxylic group increase the acidity of the pyrazine nitrogen atom in comparison with pzc and 5-Mepzc.

The carboxylic group of 5-OHpzc is more basic than in other ligands for the presence of an –OH group in the *para* position according to the Hammett equation;[20] p$K_a$ values of 0.1 and 8.23 are reported for the $–NH^+$ and –OH groups in 2-hydroxypyrazine,[17] and of 6.85 for the –OH group in 2-hydroxy-5-nitropyridine.[21] The presence of –COOH, more efficient in the electron-withdrawing effect than –H and less than $–NO_2$, explains the value of 7.78 measured for 5-OHpzc, intermediate between the other two p$K_a$ values.

According to the potentiometric results, all the ligands form VOL, $VOL_2$ and $(VO)_2L_2H_{-2}$ species, in which five-membered chelate rings are formed by the ($N_{pyr}$, $COO^-$) donor set. The formation constants of the complexes are listed in Table 1 and the order of stability is 5-OHpzc >> 5-Mepzc > pzc ≈ 3-COOHpzc. For example, the higher stability of the bis(chelated) species formed by 5-OHpzc is reflected by the values of the stability constant for the reaction VOL + HL → $VOL_2$ + $H^+$ (2.52 for 5-OHpzc, 0.37 for 5-Mepzc, –0.06 for pzc and –0.22 for 3-COOHpzc). The amount of $(VO)_2L_2H_{-2}$ dimers increases in solution with decreasing stability of VOL and $VOL_2$ species; in equimolar solutions at pH = 6 with a $V^{IV}O$ concentration of $5 \times 10^{-2}$ M, it is 88.5% with 3-COOHpzc, 65.9% with pzc, 63.4% with 5-Mepzc and 38.2% with 5-OHpzc. The

 © 2006 Wiley-VCH Verlag GmbH & Co. KGaA, Weinheim 

strength of the ligands can be explained by the effect of the substituents on the aromatic ring of their fully deprotonated forms, displayed in Scheme 3: $-O^-$ is the most effective electron-releasing group, followed by $-CH_3$, whereas –COOH is an electron-withdrawing group. To reduce the hydrolytic processes, the EPR spectra were recorded with a ligand/metal molar ratio of 2 with 5-OHpzc, 5 with 5-Mepzc and 10 with pzc and 3-COOHpzc.

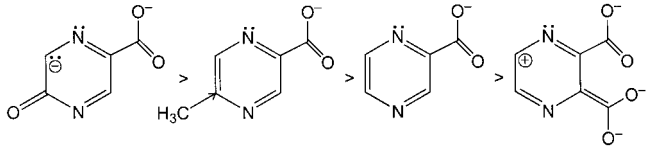

Scheme 3. Resonance forms of the fully deprotonated ligands.

The distribution curves of the species as a function of pH, calculated from the stability constants reported in Table 1, for the weaker (3-COOHpzc) and the stronger ligand (5-OHpzc) are shown in Figures 1 and 2, respectively.

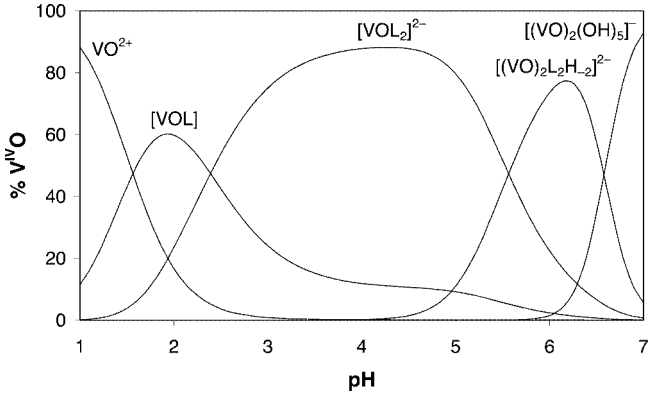


Figure 1. Species distribution for the $V^{IV}O$/3-COOHpzc system with a metal/ligand molar ratio of 1:10 and a $V^{IV}O$ concentration of 1 mM.

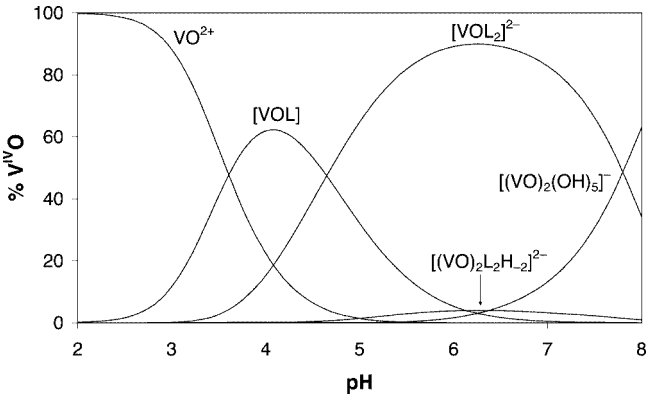


Figure 2. Species distribution for the $V^{IV}O$/5-OHpzc system with a metal/ligand molar ratio of 1:3 and a $V^{IV}O$ concentration of 1 mM.

The $g_\parallel$ and $A_\parallel$ values (Table 2) of the mono(chelated) complexes VOL (**I** in Figure 3) are consistent with the donor set ($N_{pyr}$, $COO^-$).[14b] By applying the additivity rule of Chasteen,[22] corrected for carboxylate by Kiss and Costa Pessoa,[23] a value of about $174 \times 10^{-4}$ $cm^{-1}$ is predicted for $A_\parallel$.

In the range of existence of the bis(chelated) complexes, the EPR spectra show two partly overlapped resonances, indicating the presence of the *cis* and *trans* isomers (**II** and **III** in Figure 3). The $A_\parallel$ value of the *trans* species (Table 2) is similar to that measured with 4-imidazoleacetic acid[14a] and corresponds to an [($N_{pyr}$, $COO^-$); ($N_{pyr}$, $COO^-$); $H_2O^{ax}$] set, with a water molecule weakly coordinated in the axial position (see Scheme 1a).

Two different arrangements of the two ligand molecules are possible for the *cis* species (Scheme 1b and c): one with two aromatic nitrogen atoms and one carboxylate oxygen atom, and another with one aromatic nitrogen atom and two carboxylate oxygen atoms in the equatorial plane of the vanadyl ion. The additivity rule assigns to an aromatic nitrogen atom a lower contribution to the parallel hyperfine coupling constant ($40.7 \times 10^{-4}$ $cm^{-1}$)[22] in comparison with

Table 2. EPR parameters and donor sets for the $V^{IV}O$ complexes in aqueous solution.

| Ligand | Complex | $g_\parallel$ | $A_\parallel$[a] | $D$[b] | Donor set |
|---|---|---|---|---|---|
| pzc | VOL | 1.938 | 174 | | [($N_{pyr}$, $COO^-$); $H_2O$; $H_2O$; $H_2O^{ax}$] |
| | *cis*-$VOL_2$ | 1.943 | 170 | | [($N_{pyr}$, $COO^-$); ($N_{pyr}$, $COO^{-ax}$); $H_2O$] |
| | *trans*-$VOL_2$ | 1.945 | 164 | | [($N_{pyr}$, $COO^-$); ($N_{pyr}$, $COO^-$); $H_2O^{ax}$] |
| | $(VO)_2L_2H_{-2}$ | 1.968 | 85 | 0.0603 | [($N_{pyr}$, $COO^-$); $H_2O$; $OH^-$; $OH^{-ax}$] |
| 5-Mepzc | VOL | 1.938 | 173 | | [($N_{pyr}$, $COO^-$); $H_2O$; $H_2O$; $H_2O^{ax}$] |
| | *cis*-$VOL_2$ | 1.942 | 169 | | [($N_{pyr}$, $COO^-$); ($N_{pyr}$, $COO^{-ax}$); $H_2O$] |
| | *trans*-$VOL_2$ | 1.945 | 163 | | [($N_{pyr}$, $COO^-$); ($N_{pyr}$, $COO^-$); $H_2O^{ax}$] |
| | $(VO)_2L_2H_{-2}$ | 1.967 | 85 | 0.0607 | [($N_{pyr}$, $COO^-$); $H_2O$; $OH^-$; $OH^{-ax}$] |
| 3-COOHpzc | VOL | 1.938 | 174 | | [($N_{pyr}$, $COO^-$); $H_2O$; $H_2O$; $H_2O^{ax}$] |
| | *cis*-$VOL_2$ | 1.943 | 168 | | [($N_{pyr}$, $COO^-$); ($N_{pyr}$, $COO^{-ax}$); $H_2O$] |
| | *trans*-$VOL_2$ | 1.945 | 163 | | [($N_{pyr}$, $COO^-$); ($N_{pyr}$, $COO^-$); $H_2O^{ax}$] |
| | $(VO)_2L_2H_{-2}$ | 1.965 | 86 | 0.0608 | [($N_{pyr}$, $COO^-$); $H_2O$; $OH^-$; $OH^{-ax}$] |
| 5-OHpzc | VOL | 1.937 | 173 | | [($N_{pyr}$, $COO^-$); $H_2O$; $H_2O$; $H_2O^{ax}$] |
| | *cis*-$VOL_2$ | 1.944 | 168 | | [($N_{pyr}$, $COO^-$); ($N_{pyr}$, $COO^{-ax}$); $H_2O$] |
| | *trans*-$VOL_2$ | 1.946 | 163 | | [($N_{pyr}$, $COO^-$); ($N_{pyr}$, $COO^-$); $H_2O^{ax}$] |
| | $(VO)_2L_2H_{-2}$ | 1.965 | 86 | 0.0601 | [($N_{pyr}$, $COO^-$); $H_2O$; $OH^-$; $OH^{-ax}$] |

[a] $A_\parallel$ measured in $10^{-4}$ $cm^{-1}$ units. [b] $D$ measured in $cm^{-1}$ units.

 © 2006 Wiley-VCH Verlag GmbH & Co. KGaA, Weinheim 

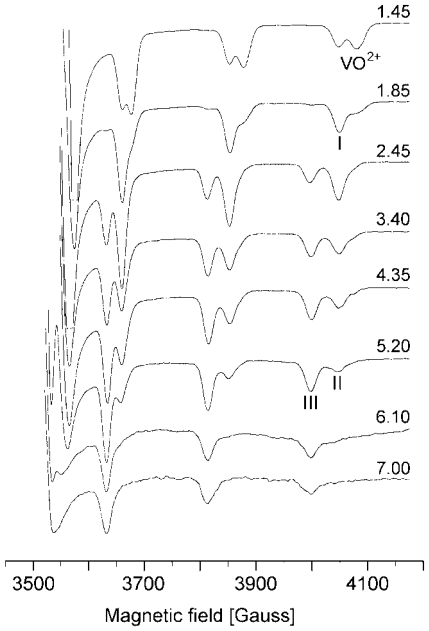


Figure 3. High-field region of the X-band anisotropic EPR spectra recorded at 140 K as a function of pH on an aqueous solution of $V^{IV}O$ and 5-Mepzc with a metal/ligand molar ratio of 1:5 and a $V^{IV}O$ concentration of 4 mM. **I**, **II** and **III** denote VOL, *cis*-$VOL_2$ and *trans*-$VOL_2$ complexes.

a carboxylate oxygen atom ($42.1\times10^{-4}$ $cm^{-1}$).[23] Therefore, a lower value of $A_{\parallel}$ is expected for the set [($N_{pyr}$, $COO^{-}$); ($N_{pyr}$, $COO^{-ax}$); $H_2O$] than for [$N_{pyr}$, $COO^{-}$); ($N_{pyr}^{ax}$, $COO^{-}$); $H_2O$]. The experimental data are in agreement with the first possibility. This is in agreement with the structures in the solid state formed by 5-methoxycarbonylpicolinic acid (5MeOpicH), *cis*-[$V^{IV}O(5MeOpic)_2(H_2O)$],[14e] and by 4,5-dicarboxy-1-methylimidazole ($H_2MDCI$), *cis*-[$V^{IV}O(HMDCI)_2(H_2O)$].[24] They have two aromatic nitrogen atoms in the equatorial plane and $A_{\parallel}$ values of 168 and $171\times10^{-4}$ $cm^{-1}$, comparable with those measured in this study for the *cis* isomers.

As an example, the anisotropic EPR spectra of the system with 5-Mepzc as a function of pH are presented in Figure 3.

At pH ≈ 7, the potentiometric titrations show a deprotonation process. The fitting of the data is improved considerably by the insertion of a $(VO)_2L_2H_{-2}$ species into the model. This suggests that the hydrolytic processes transform $VOL_2$ complexes into the di-μ-hydroxo $(VO)_2L_2H_{-2}$ dimers, according to the principle established by Felcman and Fraústo da Silva.[25] Differently from the usual behaviour of the $V^{IV}O$ systems, a ferromagnetic interaction between the two $S = 1/2$ ions is observed with a distinctive EPR signal superimposed to the resonances of $VOL_2$. A forbidden signal at half field (ca. 1650 G) in the $\Delta M = \pm2$ region is also detected (see Discussion). The spectra recorded on an equimolar solution of $V^{IV}O$ and pzc, in both the $\Delta M = \pm1$ and $\Delta M = \pm2$ regions, are shown in Figures 4 and 5.

The possible configurations of a $[VO(\mu\text{-}OH)_2VO]^{2+}$ core in complexes consisting of two edge-sharing octahedrally coordinated $V^{IV}O$ ions are classified according to the orien-

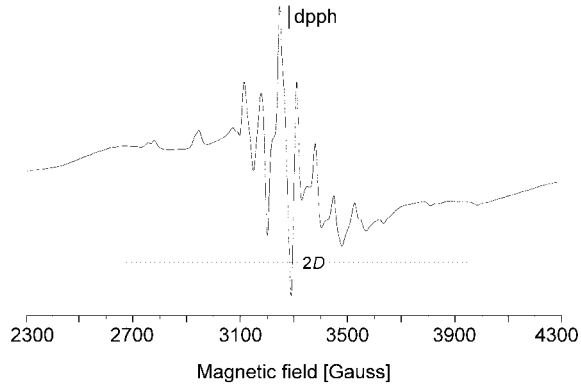


Figure 4. $\Delta M = \pm1$ region of the X-band anisotropic EPR spectrum recorded at 140 K and pH = 5.65 on an equimolar aqueous solution of $V^{IV}O$ and pzc with a concentration of $5\times10^{-2}$ M.

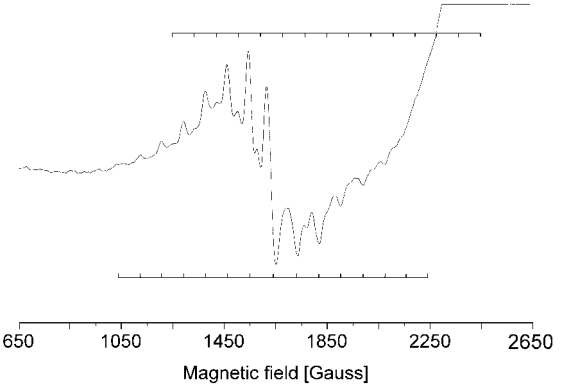


Figure 5. $\Delta M = \pm2$ region of the X-band anisotropic EPR spectrum recorded at 140 K and pH = 5.65 on an equimolar aqueous solution of $V^{IV}O$ and pzc with a concentration of $5\times10^{-2}$ M.

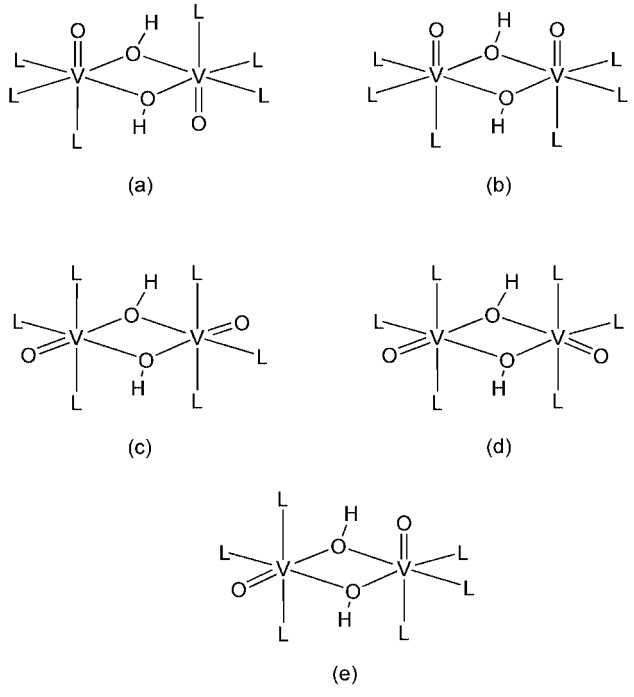


Scheme 4. Possible arrangements of the $[VO(\mu\text{-}OH)_2VO]^{2+}$ core: (a) *anti*-orthogonal, (b) *syn*-orthogonal, (c) *anti*-coplanar, (d) *syn*-coplanar, and (e) twisted.

 © 2006 Wiley-VCH Verlag GmbH & Co. KGaA, Weinheim 

tation of the V=O group with respect to the plane defined by the two vanadium atoms and the two bridging oxygen atoms (orthogonal, coplanar and twisted) and the orientation of the two V=O bonds (*syn* or *anti*) (Scheme 4).[26]

The magnitude of the coupling constant in the $\Delta M = \pm 2$ region is nearly half of that expected for $A_{\parallel}$ in the monomeric species with the same equatorial donors. Values of about $84 \times 10^{-4}$ cm$^{-1}$ for the set [($N_{pyr}$, $COO^-$); $H_2O$; $OH^-$] (*anti*-coplanar arrangement) and of about $80 \times 10^{-4}$ cm$^{-1}$ for [($N_{pyr}$, $COO^-$); $OH^-$; $OH^-$] (*anti*- or *syn*-orthogonal arrangement) are expected. The experimental values, in the range $85–86 \times 10^{-4}$ cm$^{-1}$ (Table 2), are consistent with the structure depicted in Scheme 5, where two $OH^-$ ions bridge two metal ions in one equatorial and one axial position, with the remaining three equatorial sites occupied by the ($N_{pyr}$, $COO^-$) set and a $H_2O$ molecule in an *anti*-coplanar arrangement.

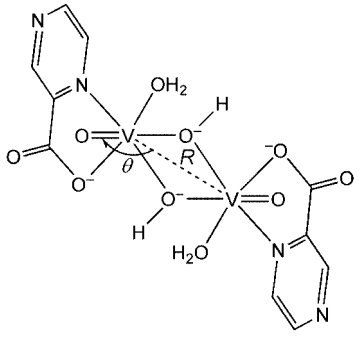


Scheme 5. Structure of the dimeric complex $(VO)_2L_2H_{-2}$ formed by pzc. *R* is the distance between the two $V^{IV}O$ ions and $\theta$ the angle formed by the V=O and V–V directions.

## Studies on the Solid Compounds

The solid compounds **1**, **2** and **3** were characterised by thermogravimetric, elemental, FT-IR and EPR analyses. Attempts to obtain solid compounds with reproducible stoichiometry with 5-OHpzc were unsuccessful.

Thermogravimetric and elemental analyses indicate a [$VOL_2$] composition for 5-Mepzc, and a [$VOL_2(H_2O)$] stoichiometry for pzc and 3-COOHpzc. The presence of a water molecule strongly bound to the metal ion in **2** and **3** is supported by the decomposition step at $> 150$ °C to yield the five-coordinate species [$VO(pzc)_2$] and [$VO(3\text{-}COOHpzc)_2$]. This temperature value is typical of vanadyl complexes containing equatorially coordinated water.[14e] On the contrary, the thermogravimetric analysis of **1** indicates the absence of water and the decomposition of the complex starts above 300 °C.

IR spectroscopy shows the presence of water in **2** and **3** and its absence in **1**. The V=O stretching frequency is normal for $V^{IV}O$ complexes. The separation between the asymmetrical ($\nu_{as}$) and symmetrical ($\nu_s$) stretching vibrations of the carboxylate group, $\Delta(\nu_{as} - \nu_s)$, for complexes **1**, **2** and **3**, in the range 212–243 cm$^{-1}$, suggests a monodentate coordination to the $V^{IV}O$ ion and allows a bridging behaviour to be ruled out.[27] In compound **3** the band at 1729 cm$^{-1}$ indicates that the carboxylic group in position 3 of the aromatic ring is protonated (Table 3).

The solid compounds **1**–**3** were dissolved in an anhydrous weakly coordinating solvent ($CH_3OH$) or in a mixture of non-coordinating solvent ($CHCl_3$/toluene, 60:40, v:v) in order to study the geometry and the coordination mode of the ligands through EPR spectroscopy (Figure 6). Anisotropic spectra exhibit an axial symmetry with two *g* and two *A* values (Table 4). No traces of mono(chelated) or dimeric complexes are observed.

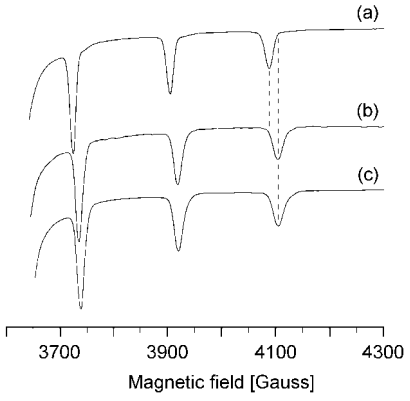


Figure 6. High-field region of the X-band anisotropic EPR spectra recorded at 140 K in $CH_3OH$. (a) [$VO(5\text{-}Mepzc)_2$] (**1**); (b) *cis*-[$VO(pzc)_2(H_2O)$] (**2**); and (c) *cis*-[$VO(3\text{-}COOHpzc)_2(H_2O)$] (**3**).

Table 4. EPR parameters of complexes **1**–**3** in $CH_3OH$.

| Complex | $g_{\parallel}$ | $A_{\parallel}$[a] | $g_{\perp}$ | $A_{\perp}$[a] |
|---|---|---|---|---|
| [$VO(5\text{-}Mepzc)_2$] (**1**) | 1.947 | 163 | 1.982 | 59 |
| *cis*-[$VO(pzc)_2(H_2O)$] (**2**) | 1.944 | 168 | 1.985 | 60 |
| *cis*-[$VO(3\text{-}COOHpzc)_2(H_2O)$] (**3**) | 1.944 | 168 | 1.986 | 60 |

[a] $A_{\parallel}$ and $A_{\perp}$ measured in $10^{-4}$ cm$^{-1}$ units.

Table 3. Selected IR parameters of the ligands and complexes **1**–**3**.[a]

| Ligand/complex | $\nu_{as}$(COOH) | $\nu_{as}$($COO^-$) | $\nu_s$(COOH) | $\nu_s$($COO^-$) | $\Delta(\nu_{as} - \nu_s)$ | $\nu$(V=O) |
|---|---|---|---|---|---|---|
| 5-Mepzc | 1731 vs | | 1654 sh | | | |
| [$VO(5\text{-}Mepzc)_2$] (**1**) | | 1630 vs | | 1418 s | 212 | 986 vs |
| pzc | 1713 vs | | 1670 s | | | |
| *cis*-[$VO(pzc)_2(H_2O)$] (**2**) | | 1629 vs | | 1393 vs | 236 | 984 vs |
| 3-COOHpzc | 1714 vs | | 1689 vs | | | |
| *cis*-[$VO(3\text{-}COOHpzc)_2(H_2O)$] (**3**) | 1729 s | 1632 vs | | 1389 s | 243 | 986 vs |

[a] $\nu$ and $\Delta$ values measured in cm$^{-1}$.

 © 2006 Wiley-VCH Verlag GmbH & Co. KGaA, Weinheim 

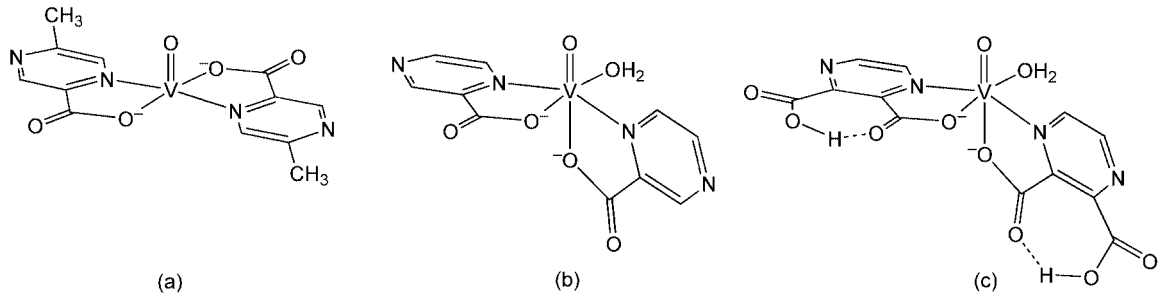


Scheme 6. Structure of the solid complexes **1** (a), **2** (b) and **3** (c).

The $A_{\parallel}$ value measured for the methyl derivative **1** is $163 \times 10^{-4}$ cm$^{-1}$, indicative of an equatorial [($N_{pyr}$, $COO^-$); ($N_{pyr}$, $COO^-$)] coordination mode. The value is comparable with those reported for [$V^{IV}O$(8-quinolinecarboxylato)$_2$] in a $CH_2Cl_2$/toluene mixture ($161 \times 10^{-4}$ cm$^{-1}$)[14d] and for $V^{IV}O$-doped [$Ti^{IV}O$(8-quinolinecarboxylato)$_2$] ($161 \times 10^{-4}$ cm$^{-1}$).[14d] For the analogous complex formed by 2-pyridylacetate a value of $162 \times 10^{-4}$ cm$^{-1}$ was measured.[28] The coincidence of $A_x$ and $A_y$ values allows a distortion of the pentacoordinate square-pyramidal structure towards the trigonal bipyramid to be ruled out.[29]

The spectra of **2** and **3** are characterised by a larger hyperfine coupling constant ($168 \times 10^{-4}$ cm$^{-1}$) than for **1** (Table 4), because of the presence of weaker donors in the equatorial plane of the vanadyl ion. This clearly indicates that water replaces one of the two equatorially bound carboxylate ions, increasing the value of $A_{\parallel}$ by about $4 \times 10^{-4}$ cm$^{-1}$,[22,30] and that one ligand molecule switches its coordination mode from an (equatorial–equatorial) to an (equatorial–axial) arrangement. In the absence of single-crystal X-ray determinations, the three structures shown in Scheme 6 can be proposed.

The carboxylic group in position 3 of the pyrazine aromatic ring in **3** is protonated, similarly to the results obtained with the bis(chelated) complexes of $Co^{II}$[31] and $Ni^{II}$.[32,33] The structure is stabilised by an intramolecular hydrogen bond between the protonated carboxylic group and the coordinating deprotonated carboxylate ion in position 2 of the aromatic ring (Scheme 6). An analogous hydrogen bond is exhibited by *cis*-[$V^{IV}O$(HMDCI)$_2$($H_2O$)],[24] formed by 4,5-dicarboxy-1-methylimidazole ($H_2$MDCI) similar to 3-COOHpzc. A further stabilisation of **2** and **3** could be provided by a network of intermolecular hydrogen bonds between the coordinated water molecules, as happens with the $Co^{II}$ ion.[31]

## Discussion

### Stability of the *cis* and *trans* Isomers of Bis(chelated) $V^{IV}O$ Complexes

Few $V^{IV}O$ compounds with ($N_{aromatic}$, $COO^-$) coordination are known compared to those with ($N_{imino}$, $O^-$) coordination. A search in the Cambridge Structural Database[34] for monomeric vanadyl complexes formed by bidentate ligands with N,O donors yields 22 structures; among them, 18 do not exhibit water molecules coordinated to the $V^{IV}O$ ion and show a square-pyramidal geometry. Six-membered chelate rings characterise all the structures except [$V^{IV}O$(2-methyl-5-methylthio-8-hydroxyquinolato)$_2$],[35] [$V^{IV}O${2-[(–)-(1*S*,2*S*,5*R*)-menthylpyridine}$_2$][36] and [$V^{IV}O$(2-methyl-8-quinolinolato)$_2$].[37]

Rather surprisingly, the only four structures with the ($N_{aromatic}$, $COO^-$) donor set exhibit a water molecule bound to the $V^{IV}O$ ion. Two are characterised by a *cis* arrangement of the $H_2O$ molecule with respect to the V=O bond: *cis*-[$V^{IV}O$(5-methoxycarbonylpicolinato)$_2$($H_2O$)][14e] and *cis*-[$V^{IV}O$(1-methyl-4,5-dicarboxyimidazolato)$_2$($H_2O$)].[24] In the other two, *trans*-[$V^{IV}O$(6-ethylpicolinato)$_2$($H_2O$)][38] and *trans*-[$V^{IV}O$(2-quinolinecarboxylato)$_2$($H_2O$)],[39] $H_2O$ is *trans* to the V=O bond. This indicates that the ($N_{aromatic}$, $COO^-$) set favours the binding of water, probably for the high polarity of the carboxylate group, which makes the solvation of the complexes easier. In addition, other binary structures with the ($N_{aromatic}$, $COO^-$) donor set have been fully characterised in the solid state without single-crystal X-ray determination.[9,10,14c,14d,40–42]

Finally, three mixed complexes, in which one of the two bidentate donor sets is ($N_{aromatic}$, $COO^-$), have been described. One of them is *cis*-[VO(Hhpic-O,O)(Hhpic-O,N)($H_2O$)], with $H_2$hpic = 3-hydroxy-2-pyridinecarboxylic acid,[43] where one of the two $Hhpic^-$ anions coordinates the vanadyl ion through the phenolate and carboxylate groups in the equatorial plane and the other one through the carboxylate group in *trans* position and the pyridine nitrogen atom in *cis* position with respect to the V=O bond, whereas the remaining equatorial site is occupied by a water molecule. The other two complexes are [$V^{IV}O$(dipic)(HDMCI)]$^-$ and *cis*-[$V^{IV}O$(acac)(HDMCI)($H_2O$)], with $H_2$dipic = 2,6-pyridinedicarboxylic acid and Hacac = 2,4-pentanedione.[24] These last three examples highlight the preference of the ($N_{aromatic}$, $COO^-$) donor set to assume an orientation *cis* with respect to the V=O bond, with the aromatic nitrogen atom in the equatorial plane and the carboxylate oxygen atom in the axial position.

It is worth noting that the *cis* complexes are formed with more hydrophilic ligands (5-methoxycarbonylpicolinate,[14e] 4,5-dicarboxy-1-methylimidazolate,[24] picolinate,[9,14b,40] 3-hydroxy-2-pyridinecarboxylate[43]), whereas the *trans* structures are favoured by more hydrophobic ligands (6-methylpicolinate,[10,14c,41] 8-hydroxy-2-methylquinoline,[37] 6-ethylpicolinate[38]) and six-membered chelate rings (8-quinoline-

 © 2006 Wiley-VCH Verlag GmbH & Co. KGaA, Weinheim 

carboxylate,[14d] 2-pyridylacetate[28]). The results are confirmed by this study: the hydrophobic 5-methyl derivative forms the anhydrous pentacoordinate complex **1**, whereas the more hydrophilic pzc and 3-COOHpzc ligands form the *cis* complexes **2** and **3** with a water molecule coordinated in the equatorial plane of the $V^{IV}O$ ion.

The preference of a ligand for the *trans* or *cis* arrangement is not easily predictable. For instance, picolinate forms only the *cis* complex,[14b] 6-methylpicolinate the *trans* and *cis* isomers in comparable amounts,[14c] and 2-pyridylacetate only the *trans* species.[28] Generally, stronger ligands and six-membered chelate rings favour the *trans* isomer, as demonstrated by the comparison of carboxylates, pyrones and catechols,[44,45] and of oxalate and malonate[44] or picolinate[14b] and 2-pyridylacetate.[28]

For the four systems considered in this work, the amount of the *cis* isomer (**I** in Figure 7) increases in the order: 5-Mepzc < pzc < 5-OHpzc < 3-COOHpzc. With ligands yielding the same size and steric hindrance of the chelate ring, the order of stability does not follow the basicity of the donors, but the relative amount of the two isomers depends on the hydrophilicity of the species; in particular, the hydrophilicity of the complexes favours the *cis* isomer. Indeed, the *cis* arrangements are mainly formed by the two more hydrophilic ligands, 3-COOHpzc and 5-OHpzc, whereas the most hydrophobic, 5-Mepzc, gives almost exclusively the *trans* structure (Figure 7). The hydrophobicity of the complex hinders the approach and the coordination of a water molecule to the $V^{IV}O$ ion and, therefore, the formation of the *cis* complex: for instance, picolinate forms only the *cis* isomer,[14b] whereas the less hydrophilic 6-methyl derivative forms both the *trans* and *cis* complexes.[14c]

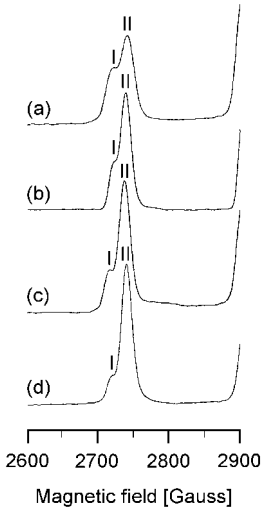


Figure 7. Low-field region of the X-band anisotropic EPR spectra of the bis(chelated) complexes formed by pzc, 5-Mepzc, 3-COOHpzc and 5-OHpzc recorded on aqueous solutions at 140 K with a $V^{IV}O$ concentration of 4 mM. (a) 3-COOHpzc, L/M = 10, pH = 5.05; (b) 5-OHpzc, L/M = 2, pH = 5.25; (c) pzc, L/M = 10, pH = 4.35; (d) 5-Mepzc, L/M = 5, pH = 5.00. **I** and **II** denote *cis*-$VOL_2$ and *trans*-$VOL_2$ complexes.

## Magnetic Properties of the Hydroxo-Bridged $V^{IV}O$ Dimeric Complexes

A qualitative interpretation of the magnetic interactions in transition-metal dimers is given by the Goodenough–Kanamori rules,[46] based on the interactions between pairs of magnetic orbitals (the unpaired electron for $V^{IV}O$ generally resides in the $d_{xy}$ orbital). The magnetic interaction of two ions with spin $S_1$ and $S_2$ is described by the Heisenberg Hamiltonian $\hat{H} = -J\hat{S}_1 \cdot \hat{S}_2$, where $J$ is the exchange coupling constant. If $S = 1/2$, as for $V^{IV}O$ dimers, the energy difference between the triplet ($S = 1$) and the singlet ($S = 0$) spin states is about $J$. Thus, if the $J$ value is positive, the triplet state is more stable than the singlet one, the interaction is ferromagnetic and an EPR spectrum can be detected; in the opposite case, the singlet state is more stable, the interaction is antiferromagnetic and no EPR signal is observed. Plass demonstrated that for the two orthogonal configurations of the $[VO(\mu\text{-}OH)_2VO]^{2+}$ core (Scheme 4) either a direct interaction or a superexchange mechanism between the magnetic orbitals can be expected to be operative, yielding rather strong antiferromagnetic coupling.[26] However, the configuration of the core, the nature of the terminal ligands and the structural distortions can influence the exchange coupling constant.[47,48] It has been found that for certain combinations of the V–O–V angle and V···V distance, the value of $J$ can become positive.[48]

In order to find examples of magnetic coupling between two $V^{IV}O$ ions in the literature, two searches have been performed on the Cambridge Structural Database.[34] The first, on the dimeric $[VO(\mu\text{-}OH)_2VO]^{2+}$ core, yielded six structures, four with an *anti*-orthogonal,[49] one with a *syn*-orthogonal[50] and one with a *syn*-coplanar arrangement.[51] All show antiferromagnetic behaviour with $-J$ values in the range 6–177 $cm^{-1}$. The second search, on the $[VO(\mu_2\text{-}OR)_2VO]^{2+}$ core, yielded 31 structures, 15 with an *anti*-orthogonal,[52] 10 with a *syn*-orthogonal,[53] 5 with an *anti*-coplanar[26,53j,54] and 1 with a twisted configuration.[26] Magnetic measurements are reported for 15 of them. The four structures with an *anti*-orthogonal and the seven with a *syn*-orthogonal arrangement show antiferromagnetic coupling with $-J$ values in the range 6–212 $cm^{-1}$. On the other hand, the six structures with an *anti*-coplanar and a twisted configuration display ferromagnetic coupling with $J$ values in the range 3–56 $cm^{-1}$. This confirms the suggestions of Plass that for edge-shared dinuclear units, only the relative orientation of the vanadyl groups is necessary to qualitatively predict their magnetic behaviour in terms of antiferro- (*anti*- and *syn*-orthogonal and *syn*-coplanar) or ferromagnetic interactions (*anti*-coplanar and twisted) between the metal centres.[26]

A ferromagnetic interaction leads to a detectable EPR signal. For a system with tetragonal symmetry the anisotropic EPR spectrum consists of four bands, whose separation depends on the molecular interactions. The external lines, corresponding to the V=O orientation parallel to the magnetic field direction, are separated by $2D$, whereas the internal lines corresponding to the perpendicular orienta-

 © 2006 Wiley-VCH Verlag GmbH & Co. KGaA, Weinheim 

tion are separated by $D$, where $D$ is the zero-field splitting. In the case of weak paramagnetic interaction the zero-field splitting has contributions of only dipolar origin and can be correlated to the distance between the two vanadium interacting centres ($R$) and to the angle formed by the V=O and V–V directions ($\theta$) through the Stevens equation (1):[55]

$$D = 0.325 g^2 \frac{\left|1 - 3\cos^2\theta\right|}{R^3} \quad (1)$$

with $D$ in $cm^{-1}$ and $R$ in Å. Usually two broad transitions in the $\Delta M = \pm 1$ region centred at $g \approx 2$ and a well-resolved $^{51}V$ hyperfine structure in the $\Delta M = \pm 2$ region at $g \approx 4$ are detectable.[56] If the symmetry of the complex is axial, two sets of 15 lines, partially overlapping, are observed in the forbidden $\Delta M = \pm 2$ region, with the magnitude of the coupling constant nearly half of that expected for $A_{\parallel}$ in the monomeric species with the same equatorial donors (Figure 5).

All four $(VO)_2L_2H_{-2}$ complexes formed by pzc, 5-Mepzc, 3-COOHpzc and 5-OHpzc exhibit a separation of the parallel components ($2D$) in the range 1312–1328 G between the high-field resonance at about 3990 G and the low-field resonance at about 2670 G, corresponding to a $D$ value of about 660 G or 0.06 $cm^{-1}$ (Table 2). In the literature, no agreement exists on the attribution of these transitions to the perpendicular or parallel components of the ***D*** tensor. In Figure 8, the $D$ value derived from the Stevens equation is represented as a function of the $\theta$ angle for five $R$ distances; the $g$ value has been approximated to 2. For five of the six di-μ-hydroxo-bridged $V^{IV}O$ compounds reported in the literature, $R$ is in the range 2.965–3.122 Å;[49,50] only the sixth compound is characterised by a higher value (3.45 Å), but this is due to the presence of a $\mu_2$-squarato-$O,O'$ bridging ligand, which keeps the metal ions distant.[51] Therefore, we believe that an estimate of about 2.9–3.1 Å for $R$ is reasonable also for 2-pyrazinecarboxylic acid and its derivatives. For $R > 2.9$ Å, values higher than 0.11 $cm^{-1}$ should result in $\cos^2\theta > 1$ and are not to be expected for $D$ (Figure 8). This is a very important conclusion because it demonstrates that the separation measured on the experimental EPR spectrum cannot be attributed to the perpendicular components of the ***D*** tensor, to which a value of about 1320 G or 0.12 $cm^{-1}$ would correspond.

From Figure 8 it is worth noting that if $D \approx 0.06$ $cm^{-1}$ and $R$ = 2.9–3.1 Å, only the angles in the range 27.2–32.7 and 147.3–152.8° satisfy the Stevens equation. These values are consistent with an *anti*-coplanar arrangement of the two $V^{IV}O$ ions (angles of 130.7 and 132.8° for the two *anti*-coplanar complexes $[\{V^{IV}O(Hsabhea)\}_2]\cdot 2CH_3OH$ and $[\{V^{IV}O(Hsabhea)\}_2]\cdot CH_3OH$, with $H_3$sabhea = *N*-salicylidene{2-[bis(2-hydroxyethyl)amino]ethyl}amine, were reported[26]), but not with an *anti*- or a *syn*-orthogonal configuration, for which much lower values of $\theta$ are expected ($\theta$ is in the range 101.0–111.4° for the five di-μ-hydroxo structures in the literature[49,50]).

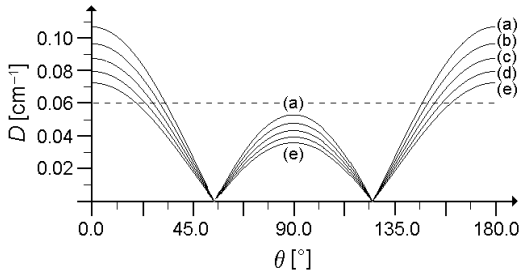


Figure 8. $D$ value derived from the Stevens equation as a function of the $\theta$ angle: (a) $R$ = 2.9 Å; (b) $R$ = 3.0 Å; (c) $R$ = 3.1 Å; (d) $R$ = 3.2 Å; and (e) $R$ = 3.3 Å. The $g$ value has been approximated to 2.

In conclusion, an *anti*-coplanar arrangement with an aromatic nitrogen atom and a carboxylate oxygen atom, one water molecule and an $OH^-$ ion in the equatorial plane and a second $OH^-$ ion of another unit in the axial position of each $V^{IV}O$ ion is realised for the $(VO)_2L_2H_{-2}$ species formed by pzc, 5-Mepzc, 3-COOHpzc and 5-OHpzc (Scheme 5). These findings are supported by recent results[28] with hyphetri-COOH {4-[3,5-bis(2-hydroxyphenyl)-1,2,4-triazol-1-yl]benzoic acid} and hyphetri-$SO_3H$ {4-[3,5-bis(2-hydroxyphenyl)-1,2,4-triazol-1-yl]benzenesulfonic acid}.[57] In weakly acidic aqueous solutions, they give $\Delta M = \pm 1$ (at $g \approx 2$) and $\Delta M = \pm 2$ (at $g \approx 4$) EPR signals analogous to those of pzc and its derivatives. Because they are tridentate chelating ligands, which occupy three equatorial positions of the $V^{IV}O$ ion with the donor set ($O^-_{aromatic}$, $N_{aromatic}$, $O^-_{aromatic}$), they enforce the formation of an *anti*-coplanar arrangement for the corresponding $(VO)_2L_2H_{-2}$ species with the two bridging $OH^-$ ions in *cis* and *trans* positions with respect to the V=O bond.

## Conclusions

2-Pyrazinecarboxylic acid and three of its derivatives (5-methyl-2-pyrazinecarboxylic, 2,3-pyrazinedicarboxylic and 5-hydroxy-2-pyrazinecarboxylic acids) coordinate the $V^{IV}O$ ion forming VOL, $VOL_2$ and $(VO)_2L_2H_{-2}$ species in acidic and neutral solutions. Bis(chelated) species are hexacoordinate and are characterised by a *cis*/*trans* isomerism, with the *trans* arrangement favoured with respect to the *cis* one. The application of the additivity rule[22] allows identification of the donors coordinated in the equatorial plane of the $V^{IV}O$ ion. The relative stability of the two isomers in aqueous solution is influenced by a number of factors, like the ligand bite, the size of the chelate ring, the basicity and the steric requirements of the ligands. Generally, large ligand bites, six-membered chelate rings and strong ligands favour the *trans* isomer.[44,45] However, these rules are only effective if applied to ligands with different bite, basicity and size of the chelate ring. Instead, if ligands of the same series are compared, like those derived from 2-pyrazinecarboxylic acid (same size of the chelate ring, comparable ligand bite and basicity), the hydrophilicity of the complexes becomes determinant. This conclusion is supported by the

 © 2006 Wiley-VCH Verlag GmbH & Co. KGaA, Weinheim 

solid-state structures because the hydrophobic 5-methyl derivative forms the pentacoordinate *trans* complex **1**, whereas the more hydrophilic pzc and 3-COOHpzc form the hexacoordinate *cis* compounds **2** and **3**, with a water molecule in the equatorial plane of the $V^{IV}O$ ion. The hydrophilicity, because of the presence of the polar carboxylate group, explains the reason why the only four monomeric $V^{IV}O$ complexes with a water molecule coordinated, among 22 structures found formed by bidentate ligands with an N,O coordination,[34] are characterised by an ($N_{aromatic}$, $COO^-$) donor set.

In weakly acidic solutions a $(VO)_2L_2H_{-2}$ species is detected by EPR spectroscopy and potentiometry. The rule established by Felcman and Fraústo da Silva suggests that the hydrolysis of a mono(chelated) $V^{IV}O$ complex with two adjacent equatorial sites occupied by water molecules gives a di-μ-hydroxo-bridged dimer,[25] but there are different possibilities for their geometrical arrangement (Scheme 4). Usually, these species are EPR-silent, as proved in several cases, for example with picolinic[14b] and 6-methylpicolinic acids.[14c] Plass demonstrated that an *anti*- and a *syn*-orthogonal configuration results in an antiferromagnetic coupling, whereas an *anti*-coplanar and a twisted arrangement give rise to a ferromagnetic coupling.[26] An *anti*-coplanar configuration for a ferromagnetically coupled $V^{IV}O$ complex can also be predicted through the Stevens equation.[55] Moreover, an analysis of this equation suggests that the signals present in the $\Delta M = \pm 1$ region of the EPR spectrum belong to the parallel components of the ***D*** tensor. These findings are supported by the value of the coupling constant in the $\Delta M = \pm 2$ region, which must be half of that expected for $A_{\parallel}$ in the monomeric species with the same equatorial donors. In this case, it allows the set [($N_{pyr}$, $COO^-$); $H_2O$; $OH^-$], expected for an *anti*-coplanar arrangement, to be distinguished from [($N_{pyr}$, $COO^-$); $OH^-$; $OH^-$], characteristic of an *anti*- or *syn*-orthogonal configuration. In conclusion, the theoretical and experimental results, compared with the data in the literature, suggest an *anti*-coplanar configuration for $(VO)_2L_2H_{-2}$ species, with two bridging $OH^-$ ions in the equatorial and axial positions and the ($N_{pyr}$, $COO^-$) set and an $H_2O$ molecule completing the coordination sphere of the $V^{IV}O$ ion (Scheme 5).

At the moment, the factors that favour the *anti*-coplanar configuration with respect to the *anti*- or *syn*-orthogonal are not clear to us. Although for bidentate ligands the simplest and more common *anti*- or *syn*-orthogonal arrangements of the $[VO(\mu\text{-}OH)_2VO]^{2+}$ core should be expected, this is not the case for 2-pyrazinecarboxylic acid and its derivatives. So, one of the next challenges in the chemistry of the $V^{IV}O$ ion is to try to understand the factors that stabilise each of the five configurations of the $[VO(\mu\text{-}OH)_2VO]^{2+}$ core and determine the ferromagnetic or antiferromagnetic coupling.

## Experimental Section

**Chemicals:** All the ligands were Aldrich or Fluka products of puriss. quality. Their purity and their concentration in solution were determined by the Gran method.[58] $V^{IV}O$ solutions were prepared according to a procedure described in the literature.[59] All operations were performed under purified argon in order to avoid oxidation of the $V^{IV}O$ ion.

**Potentiometric Measurements:** The protonation constants of the ligands ($\log K$) and the stability constants of the $V^{IV}O$ complexes were determined by pH-potentiometric titrations of 2.0-mL samples. The ligand/metal molar ratio was in the range 1:1–10:1. The concentration of $V^{IV}O$ was 0.001 M. Measurements were carried out at 25 ± 0.1 °C and at a constant ionic strength of 0.1 M $KNO_3$ with a MOLSPIN pH-meter equipped with a digitally operated syringe (Molspin DSI 0.250 mL) controlled by a computer. The titrations were performed with a carbonate-free NaOH solution of known concentration (about 0.1 M) using a Russel CMAWL/S7 semimicro combined electrode, calibrated for hydrogen ion concentration by the method of Irving et al.[60] The number of experimental points was 100–150 for each titration curve. The reproducibility of the titration points included in the evaluation was within 0.005 pH units in the whole pH range examined (2–10). The stability constants of the complexes, reported as the logarithm of the overall formation constants $\beta_{pqr} = [VO_pL_qH_r]/[VO]^p[L]^q[H]^r$, where VO is the vanadyl ion, L is the deprotonated form of the ligand and H is the proton, were calculated with the aid of the SUPERQUAD program.[61] Standard deviations were calculated by assuming random errors. The conventional notation has been used. Negative indices for H in the formulas indicate either the dissociation of groups that do not deprotonate in the absence of $V^{IV}O$ coordination, or hydroxo ligands. Hydroxo complexes of $V^{IV}O$ were taken into account in the calculations. The following species were assumed: $[VO(OH)]^+$ ($\log\beta_{10-1} = -5.94$), $[(VO)_2(OH)_2]^{2+}$ ($\log\beta_{20-2} = -6.95$), with stability constants calculated from the data of Henry et al.[62] and corrected for the different ionic strengths by use of the Davies equation,[63] $[VO(OH)_3]^-$ ($\log\beta_{10-3} = -18.0$) and $[(VO)_2(OH)_5]^-$ ($\log\beta_{20-5} = -22.0$).[64]

***trans*-[VO(5-Mepzc)$_2$]:** $VOSO_4 \cdot 5H_2O$ (0.1265 g), dissolved in MeOH (5 mL), was added at room temperature to 5-Mepzc (0.1480 g), dissolved in MeOH (5 mL). The resulting solution was stirred at 50 °C. After 1 h, $CH_3CN$ (20–30 mL) was added and the suspension was stirred at room temperature for 1 h. The dark brown solid was filtered under vacuum, washed with diethyl ether and dried under $N_2$. $C_{12}H_{10}N_4O_5V$ (341.18): calcd. C 42.25, H 2.95, N 16.42, $V_2O_5$ 26.6; found C 41.56, H 3.21, N 16.87, $V_2O_5$ 25.8.

***cis*-[VO(pzc)$_2$(H$_2$O)]:** Pzc (0.1316 g) was dissolved in MeOH (10 mL) by heating at 50 °C. $VOSO_4 \cdot 5H_2O$ (0.1265 g), dissolved in MeOH (5 mL), was added to the ligand. The mixture was stirred at 50 °C for 1 h. Subsequently, acetone (30 mL) was added and the suspension was stirred at room temperature for 1 h. The greenish solid was filtered under vacuum, washed with acetone and diethyl ether and dried under $N_2$. $C_{10}H_8N_4O_6V$ (331.14): calcd. C 36.27, H 2.43, N 16.92, $H_2O$ 5.4, $V_2O_5$ 27.5; found C 36.73, H 2.65, N 17.02, $H_2O$ 6.0, $V_2O_5$ 28.0.

***cis*-[VO(3-COOHpzc)$_2$(H$_2$O)]:** 3-COOHpzc (0.1480 g) was dissolved in MeOH (10 mL) at room temperature. $VOSO_4 \cdot 5H_2O$ (0.1265 g), dissolved in MeOH (5 mL), was added to the ligand. The solution was stirred at 50 °C for 1 h. Subsequently, diethyl ether (30 mL) was added and the suspension was stirred at room temperature for 1 h. The dark green solid was filtered under vacuum, washed with diethyl ether and dried under $N_2$. $C_{12}H_8N_4O_{10}V$ (419.16): calcd. C 34.39, H 1.92, N 13.37, $H_2O$ 4.3, $V_2O_5$ 21.7; found C 34.54, H 1.75, N, 13.07, $H_2O$ 5.0, $V_2O_5$ 21.2.

**Spectroscopic and Analytical Measurements:** Anisotropic EPR spectra were recorded on aqueous solutions with an X-band (9.15 GHz)

 © 2006 Wiley-VCH Verlag GmbH & Co. KGaA, Weinheim 

Varian E-9 spectrometer in the temperatures range 120–140 K. The spectra were simulated with the computer program Bruker WinEPR SimFonia. Infrared spectra (4000–600 $cm^{-1}$) were obtained with a JASCO FT-IR 480 Plus interferometer using KBr disks. Elemental analyses (C, H, N) were performed with a Perkin–Elmer 240 B analyser. The thermogravimetric studies, which allowed the determination of the $H_2O$ and $V_2O_5$ content, were carried out with a Perkin–Elmer TGS-2 instrument under nitrogen.


[1] a) D. Rehder in *Metal Ions in Biological Systems* (Eds.: A. Sigel, H. Sigel), Marcel Dekker, New York, **1995**, vol. 31, pp. 1–43; b) D. C. Crans, J. J. Smee, E. Gaidamauskas, L. Yang, *Chem. Rev.* **2004**, *104*, 849–902.

[2] a) Y. Shechter, I. Goldwaser, M. Mironchik, M. Fridkin, D. Gefel, *Coord. Chem. Rev.* **2003**, *237*, 3–11; b) K. H. Thompson, J. H. McNeill, C. Orvig, *Chem. Rev.* **1999**, *99*, 2561–2571.

[3] H. Sakurai, K. Tsuchiya, M. Nukatsuka, J. Kawada, S. Ishikawa, M. Komatsu, *J. Clin. Biochem. Nutr.* **1990**, *8*, 193–200.

[4] a) B. A. Reul, S. S. Amin, J. P. Buchet, L. N. Ongemba, D. C. Crans, S. M. Brichard, *Br. J. Pharmacol.* **1999**, *126*, 467–477; b) S. S. Amin, K. Cryer, B. Zhang, S. K. Dutta, S. S. Eaton, O. P. Anderson, S. M. Miller, B. A. Reul, S. M. Brichard, D. C. Crans, *Inorg. Chem.* **2000**, *39*, 406–416.

[5] M. C. Cam, G. H. Cros, J. J. Serrano, R. Lazaro, J. H. McNeill, *Diabetes Res. Clin. Pract.* **1993**, *20*, 111–121.

[6] a) H. Watanabe, M. Nakai, K. Komazawa, H. Sakurai, *J. Med. Chem.* **1994**, *37*, 876–877; b) H. Sakurai, H. Watanabe, H. Tamura, H. Yasui, R. Matsushita, J. Takada, *Inorg. Chim. Acta* **1998**, *283*, 175–183.

[7] a) H. Sakurai, H. Sano, T. Takino, H. Yasui, *Chem. Lett.* **1999**, 913–914; b) H. Sakurai, H. Sano, T. Takino, H. Yasui, *J. Inorg. Biochem.* **2000**, *80*, 99–105.

[8] L. C. Woo, V. G. Yuen, K. H. Thompson, J. H. McNeill, C. Orvig, *J. Inorg. Biochem.* **1999**, *76*, 251–257.

[9] H. Sakurai, K. Fujii, H. Watanabe, H. Tamura, *Biochem. Biophys. Res. Commun.* **1995**, *214*, 1095–1101.

[10] Y. Fujisawa, S. Fujimoto, H. Sakurai, *J. Inorg. Biochem.* **1997**, *67*, 396.

[11] D. Rehder, J. Costa Pessoa, C. F. G. C. Geraldes, T. Kabanos, T. Kiss, B. Meier, G. Micera, L. Pettersson, M. Rangel, A. Salifoglou, I. Turel, D. Wang, *J. Biol. Inorg. Chem.* **2002**, *7*, 384–396.

[12] H. Sakurai, K. Fujii, S. Fujimoto, Y. Fujisawa, K. Takechi, H. Yasui in *Vanadium Compounds: Chemistry, Biochemistry and Therapeutic Applications* (Eds.: A. S. Tracey, D. C. Crans), ACS symposium series 711, Washington DC, **1998**, pp. 344–352.

[13] H. Sakurai, Y. Fujisawa, S. Fujimoto, H. Yasui, T. Takino, *J. Trace Elem. Exp. Med.* **1999**, *12*, 393–401.

[14] a) D. Sanna, G. Micera, P. Buglyó, T. Kiss, T. Gajda, P. Surdy, *Inorg. Chim. Acta* **1998**, *268*, 297–305; b) T. Kiss, K. Petrohan, D. Sanna, E. Garribba, G. Micera, T. Kiss, *Polyhedron* **2000**, *19*, 55–61; c) E. Kiss, E. Garribba, G. Micera, T. Kiss, H. Sakurai, *J. Inorg. Biochem.* **2000**, *78*, 97–108; d) E. Garribba, G. Micera, D. Sanna, E. Chruscinska, *Inorg. Chim. Acta* **2003**, *348*, 97–106; e) J. Gätjens, B. Maier, T. Kiss, E. M. Nagy, P. Buglyó, H. Sakurai, K. Kawabe, D. Rehder, *Chem. Eur. J.* **2003**, *9*, 4924–4935.

[15] In this work the *cis* nomenclature refers to the bis(chelated) complexes in which the two ligand molecules adopt an (equatorial–equatorial) and an (equatorial–axial) arrangement with respect to the V=O bond of the vanadyl ion; *cis* isomers are hexacoordinate with one solvent molecule coordinated in the fourth equatorial position; *trans* isomers are bis(chelated) complexes in which both ligand molecules adopt an (equatorial–equatorial) arrangement with respect to the V=O group; *trans* isomers can be pentacoordinate or hexacoordinate according to the absence or presence of a solvent molecule bound in the axial position.

[16] A. Napoli, A. L. Magrì, *Ann. Chim. (Rome)* **1989**, *79*, 93–96.

[17] A. Albert, J. N. Phillips, *J. Chem. Soc.* **1956**, 1294–1304.

[18] H. E. Toma, R. H. U. Borges, *J. Coord. Chem.* **1981**, *11*, 143–152.

[19] M. S. Saleh, K. A. Idriss, M. S. Abu-Bakr, E. Y. Hashem, *Analyst* **1992**, *117*, 1003–1007.

[20] L. P. Hammett, *J. Am. Chem. Soc.* **1937**, *59*, 96–103.

[21] L. Forlani, G. Cristoni, C. Boga, P. E. Todesco, E. Del Vecchio, S. Selva, M. Monari, *ARKIVOC* **2002**, 198–215.

[22] N. D. Chasteen in *Biological Magnetic Resonance* (Eds.: L. J. Berliner, J. Reuben), Plenum Press, New York, **1981**, vol. 3, pp. 53–119.

[23] T. Jakusch, P. Buglyó, A. I. Tomaz, J. Costa Pessoa, T. Kiss, *Inorg. Chim. Acta* **2002**, *339*, 119–128.

[24] T. S. Smith II, C. A. Roof, J. W. Kampf, P. G. Rasmussen, V. L. Pecoraro, *J. Am. Chem. Soc.* **2000**, *122*, 767–775.

[25] J. Felcman, J. J. R. Fraústo da Silva, *Talanta* **1983**, *30*, 565–570.

[26] W. Plass, *Angew. Chem. Int. Ed. Engl.* **1996**, *35*, 627–631.

[27] K. Nakamoto in *Infrared and Raman Spectra of Inorganic and Coordination Compounds*, 3rd ed., John Wiley & Sons, New York, **1978**.

[28] E. Garribba, G. Micera, D. Sanna, K. Hegetschweiler, unpublished results.

[29] a) C. R. Cornman, K. M. Geisre-Bush, S. R. Rowley, P. D. Boyle, *Inorg. Chem.* **1997**, *36*, 6401–6408; b) E. Garribba, G. Micera, A. Panzanelli, D. Sanna, *Inorg. Chem.* **2003**, *42*, 3981–3987.

[30] E. Garribba, E. Lodyga-Chruscinska, G. Micera, A. Panzanelli, D. Sanna, *Eur. J. Inorg. Chem.* **2005**, 1369–1382.

[31] C. J. O'Connor, E. Sinn, *Inorg. Chem.* **1981**, *20*, 545–551.

[32] L. Mao, S. J. Rettig, R. C. Thompson, J. Trotter, S. Xia, *Can. J. Chem.* **1996**, *74*, 433–444.

[33] H. Ptasiewicz-Bak, J. Leciejewicz, *Pol. J. Chem.* **1999**, *73*, 717–726.

[34] F. H. Allen, O. Kennard, *Chem. Des. Autom. News* **1993**, *8*, 31–37.

[35] L. Pech, Y. A. Bankovsky, V. K. Belsky, J. Asaks, A. N. Sobolev, *Latv. Kim. Z.* **1997**, 64–73.

[36] S. Bellemin-Laponnaz, K. S. Coleman, J. A. Osborn, *Polyhedron* **1999**, *18*, 2533–2536.

[37] M. Shiro, Q. Fernando, *Anal. Chem.* **1971**, *43*, 1222–1230.

[38] T. Sasagawa, Y. Yoshikawa, K. Kawabe, H. Sakurai, Y. Kojima, *J. Inorg. Biochem.* **2002**, *88*, 108–112.

[39] N. Okabe, Y. Muranishi, *Acta Crystallogr., Sect. E: Struct. Rep. Online* **2002**, *58*, m287–m289.

[40] M. Melchior, K. H. Thompson, J. M. Jong, S. J. Rettig, E. Shuter, V. G. Yuen, Y. Zhou, J. H. McNeill, C. Orvig, *Inorg. Chem.* **1999**, *38*, 2288–2293.

[41] S. Fujimoto, K. Fujii, H. Yasui, R. Matsushita, J. Takada, H. Sakurai, *J. Clin. Biochem. Nutr.* **1997**, *23*, 113–129.

[42] a) T. Takino, H. Yasui, A. Yoshitake, Y. Hamajima, R. Matsushita, J. Takada, H. Sakurai, *J. Biol. Inorg. Chem.* **2001**, *6*, 133–142; b) H. Sakurai, A. Tamura, T. Takino, K. Ozutsumi, K. Kawabe, Y. Kojima, *Inorg. React. Mech.* **2002**, *2*, 69–77; c) H. Yasui, A. Tamura, T. Takino, H. Sakurai, *J. Inorg. Biochem.* **2002**, *91*, 327–338.

[43] M. Nakai, M. Obata, F. Sekiguchi, M. Kato, M. Shiro, A. Ichimura, I. Kinoshita, M. Mikuriya, T. Inohara, K. Kawabe, H. Sakurai, C. Orvig, S. Yano, *J. Inorg. Biochem.* **2004**, *98*, 105–112.

[44] P. Buglyó, E. Kiss, I. Fabian, T. Kiss, D. Sanna, E. Garribba, G. Micera, *Inorg. Chim. Acta* **2000**, *306*, 174–183.

[45] P. Buglyó, T. Kiss, D. Sanna, E. Garribba, G. Micera, *J. Chem. Soc., Dalton Trans.* **2002**, 2275–2282.

[46] A. P. Ginsberg, *Inorg. Chim. Acta Rev.* **1971**, *5*, *45*–68.

[47] R. Cortés, J. L. Pizarro, L. Lezama, M. I. Arriortua, T. Rojo, *Inorg. Chem.* **1994**, *33*, 2697–2700.

[48] A. Rodríguez-Fortea, P. Alemany, S. Alvarez, E. Ruiz, *Eur. J. Inorg. Chem.* **2004**, 143–153.

[49] a) K. Wieghardt, U. Bossek, K. Volckmar, W. Swiridoff, J. Weiss, *Inorg. Chem.* **1984**, *23*, 1387–1389; b) M. I. Khan, S.


 © 2006 Wiley-VCH Verlag GmbH & Co. KGaA, Weinheim 

Cevik, D. Powell, S. Li, C. J. O'Connor, *Inorg. Chem.* **1998**, *37*, 81–86; c) N. S. Dean, M. R. Bond, C. J. O'Connor, C. J. Carrano, *Inorg. Chem.* **1996**, *35*, 7643–7648; d) G. Paul, A. Choudhury, R. Nagarajan, C. N. R. Rao, *Inorg. Chem.* **2003**, *42*, 2004–2013.

[50] A. Neves, C. Wieghardt, B. Nuber, J. Weiss, *Inorg. Chim. Acta* **1988**, *150*, 183–187.

[51] M. I. Khan, Y.-D. Chang, Q. Chen, J. Salta, Y.-S. Lee, C. J. O'Connor, J. Zubieta, *Inorg. Chem.* **1994**, *33*, 6340–6350.

[52] a) M. M. Musiani, F. Milani, R. Graziani, M. Vidali, U. Casellato, P. A. Vigato, *Inorg. Chim. Acta* **1982**, *61*, 115–120; b) K. Thiele, H. Gorls, W. Imhof, W. Seidel, *Z. Anorg. Allg. Chem.* **1999**, *625*, 1927–1933; c) A. S. Ceccato, A. Neves, M. A. de Brito, S. M. Drechsel, A. S. Mangrich, R. Werner, W. Haase, A. J. Bortoluzzi, *J. Chem. Soc., Dalton Trans.* **2000**, 1573–1577; d) Y. Sun, M. Melchior, D. A. Summers, R. C. Thompson, S. J. Rettig, C. Orvig, *Inorg. Chem.* **1998**, *37*, 3119–3121; e) T. Carofiglio, E. Solari, C. Floriani, A. Chiesi-Villa, C. Rizzoli, *Polyhedron* **1996**, *15*, 4435–4440; f) J. Salta, J. Zubieta, *Inorg. Chim. Acta* **1997**, *257*, 83–88; g) S. Kitagawa, M. Munakata, M. Ueda, T. Yonezawa, *Inorg. Chim. Acta* **1990**, *175*, 3–4; h) S. Bhattacharyya, A. Martinsson, R. J. Batchelor, F. W. B. Einstein, A. S. Tracey, *Can. J. Chem.* **2001**, *79*, 938–948; i) S. Mukherjee, T. Weyhermuller, E. Bothe, P. Chaudhuri, *Eur. J. Inorg. Chem.* **2003**, 1956–1965; j) S. Meicheng, Z. Yongjian, Z. Zeying, T. Youqi, *Sci. Chin., Ser. B (Engl. Ed.)* **1988**, *31*, 781; k) S. L. Castro, M. E. Cass, F. J. Hollander, S. L. Bartley, *Inorg. Chem.* **1995**, *34*, 466–472; l) Z. Zhao-Hui, W. Hui-Lin, H. Sheng-Zhi, T. Khi-Rui, *Jiegou Huaxue* **1995**, *14*, 337.

[53] a) D. del Rio, A. Galindo, R. Vicente, C. Mealli, A. Ienco, D. Masi, *Dalton Trans.* **2003**, 1813–1820; b) G. Foulon, J.-D. Foulon, N. Hovnanian, *Polyhedron* **1993**, *12*, 2507–2511; c) C. J. Carrano, C. M. Nunn, R. Quan, J. A. Bonadies, V. L. Pecoraro, *Inorg. Chem.* **1990**, *29*, 944–951; d) Z. Janas, P. Sobota, M. Kimowicz, S. Szafert, K. Szczegot, L. B. Jerzykiewicz, *J. Chem. Soc., Dalton Trans.* **1997**, 3897–3901; e) S. Duclos, H. Stoeckli-Evans, T. R. Ward, *Helv. Chim. Acta* **2001**, *84*, 3148–3161; f) H. Glas, K. Kohler, E. Herdtweck, P. Maas, M. Spiegler, W. R. Thiel, *Eur. J. Inorg. Chem.* **2001**, 2075–2080; g) S. Burojevic, I. Shweky, A. Bino, D. A. Summers, R. C. Thompson, *Inorg. Chim. Acta* **1996**, *251*, 75–79; h) M. Mikuriya, M. Fukuya, *Bull. Chem. Soc. Jpn.* **1996**, *69*, 679–683; i) R. Das, K. K. Nanda, A. K. Mukherjee, M. Mukherjee, M. Helliwell, K. Nag, *J. Chem. Soc., Dalton Trans.* **1993**, 2241–2246; j) M. Tsaramyrsi, M. Kaliva, A. Salifoglou, C. P. Raptopoulou, A. Terzis, V. Tangoulis, J. Giapintzakis, *Inorg. Chem.* **2001**, *40*, 5772–5779.

[54] M. Velayutham, B. Varghese, S. Subramanian, *Inorg. Chem.* **1998**, *37*, 1336–1340.

[55] K. W. H. Stevens, *Proc. R. Soc. London, Ser. A* **1952**, *214*, 237–244.

[56] a) T. D. Smith, J. F. Boas, J. R. Pilbrow, *Aust. J. Chem.* **1974**, *27*, 2535–2545; b) A. Ozarowski, D. Reinen, *Inorg. Chem.* **1986**, *25*, 1704–1708; c) E. Alberico, G. Micera, D. Sanna, A. Dessì, *Polyhedron* **1994**, *13*, 1763–1771; d) D. Sanna, I. Bódi, S. Boushina, G. Micera, T. Kiss, *J. Chem. Soc., Dalton Trans.* **1999**, 3275–3282; e) M. Kosugi, S. Hikichi, M. Akita, Y. Moro-oka, *Inorg. Chem.* **1999**, *38*, 2567–2578; f) Á. Dörnyei, E. Garribba, T. Jakusch, P. Forgó, G. Micera, T. Kiss, *Dalton Trans.* **2004**, 1882–1891.

[57] a) U. Heinz, K. Hegetschweiler, P. Acklin, B. Faller, R. Lattmann, H. P. Schnebli, *Angew. Chem. Int. Ed.* **1999**, *38*, 2568–2570; b) S. Steinhauser, U. Heinz, J. Sander, K. Hegetschweiler, *Z. Anorg. Allg. Chem.* **2004**, *630*, 1829–1838.

[58] G. Gran, *Acta Chem. Scand.* **1950**, *4*, *559*–577.

[59] I. Nagypál, I. Fábián, *Inorg. Chim. Acta* **1982**, *61*, 109–113.

[60] H. Irving, M. G. Miles, L. D. Pettit, *Anal. Chim. Acta* **1967**, *38*, 475–481.

[61] P. Gans, A. Vacca, A. Sabatini, *J. Chem. Soc., Dalton Trans.* **1985**, 1195–1200.

[62] R. P. Henry, P. C. H. Mitchell, J. E. Prue, *J. Chem. Soc., Dalton Trans.* **1973**, 1156–1159.

[63] C. W. Davies, *J. Chem. Soc.* **1938**, 2093–2098.

[64] a) A. Komura, M. Hayashi, H. Imanaga, *Bull. Chem. Soc. Jpn.* **1977**, *50*, 2927–2931; b) L. F. Vilas Boas, J. Costa Pessoa in *Comprehensive Coordination Chemistry* (Eds.: G. Wilkinson, R. D. Gillard, J. A. McCleverty), Pergamon Press, Oxford, **1987**, vol. 3, pp. 453–583.

Received: March 14, 2006
Published Online: May 2, 2006

 © 2006 Wiley-VCH Verlag GmbH & Co. KGaA, Weinheim 

DOI: 10.1002/ejic.200501092

# New Heterometallic ($Cu^{II}$ and $Cr^{III}$) Complexes – First Crystal Structure of an Oxalate-Bridged Ferromagnetically Coupled [$Cu^{II}Cr^{III}Cu^{II}$] System

**Marijana Jurić,[a] Pavica Planinić,[a] Nevenka Brničević,*[a] Dalibor Milić,[b] Dubravka Matković-Čalogović,[b] Damir Pajić,[c] and Krešo Zadro[c]**

**Keywords:** Crystal structure / Copper complexes / Chromium complexes / Oxalate bridges / Ferromagnetic interaction

Two new heterotemetallic complexes [{Cu(μ-$C_2O_4$)(bpy)$_2$}$_2$-Cr($C_2O_4$)]$NO_3$·$H_2O$ (**1**) and [Cu(bpy)$_3$][Cr($C_2O_4$)$_3$]$NO_3$·$9H_2O$ (**2**) (bpy = 2,2′-bipyridine) have been synthesized. The crystal structures were determined and magnetic and spectroscopic (IR, UV/Vis) characterization accomplished. In **1**, the central [Cr($C_2O_4$)$_3$]$^{3-}$ unit acts as a bridge between two copper(II) ions, each of them having a distorted octahedral geometry. The apical positions are occupied by one oxygen atom belonging to the bridging oxalate anion [Cu–O2 = 2.6439(18) Å] and one nitrogen atom from one of the bpy ligands [Cu–N1 = 2.1079(18) Å]. The $N_3O$ equatorial environment consists of three bpy nitrogen atoms [Cu–N = 1.995 Å (mean value)] and the second oxygen atom from the bridging oxalate anion [Cu–O1 = 2.1168(15) Å]. The chromium(III) atom is in a slightly distorted octahedral environment of four oxygen atoms from two bridging oxalate groups [Cr–O = 1.988 Å (mean value)] and two oxygen atoms from the terminally bonded bidentate oxalate group [Cr–O = 1.9454(16) Å]. Complex **2** consists of two mononuclear [Cu(bpy)$_3$]$^{2+}$ cations, one mononuclear [Cr($C_2O_4$)$_3$]$^{3-}$ anion, one $NO_3^-$ anion and nine molecules of water of crystallisation. The copper(II) ions in two crystallographically independent [Cu(bpy)$_3$]$^{2+}$ cations are in a tetragonally distorted octahedral coordination environment of six N atoms from the bpy ligands. The chromium(III) ion in [Cr($C_2O_4$)$_3$]$^{3-}$ has a slightly distorted octahedral environment of oxygen atoms from three oxalate groups [with the Cr–O bond lengths ranging from 1.964(3) to 1.982(3) Å]. Analysis of the magnetic properties (1.8–290 K) of **1** showed a ferromagnetic exchange interaction between $Cu^{II}$ and $Cr^{III}$ with $J$ = +1.20 $cm^{-1}$ [using $\mathbf{H}_{INT} = -J(S_{Cu1}S_{Cr} + S_{Cu2}S_{Cr})$].

(© Wiley-VCH Verlag GmbH & Co. KGaA, 69451 Weinheim, Germany, 2006)

## Introduction

The design of molecule-based magnetic materials has become one of the most stimulating challenges for chemists nowadays.[1,2] A generally accepted strategy for synthesizing these materials consists of assembling paramagnetic metal centres in such a way that the resulting solid lattices, with their components properly arranged, exhibit desired physical properties such as magnetic exchange interactions. In designing homo- and heteropolynuclear complexes, a very essential role belongs to the oxalate ion, $C_2O_4^{2-}$, because of its ability to adopt a bis(chelating) coordination mode as well as to mediate magnetic interactions between paramagnetic metal centres. On this account, stable mononuclear anionic oxalate complexes are often used as ligands toward the second metal ion, an approach known as "complexes as ligands" or "building-blocks chemistry".

One of the possibilities for the synthesis of molecule-based ferromagnetic materials, developed in the early 1990's, is based on the use of the tris(oxalato)chromate(III) anion, [Cr($C_2O_4$)$_3$]$^{3-}$,[3] as one of the starting components. The advantage of using this anion is its stability towards ligand substitution as well as good control over the reaction products. By using [Cr($C_2O_4$)$_3$]$^{3-}$ as a building block, a series of mixed-metal assemblies {[$NR_4$][$M^{II}Cr^{III}$($C_2O_4$)$_3$]}$_n$ (R = *n*-butyl; $M^{II}$ = Mn, Fe, Co, Ni, Cu, Zn) was obtained, for which the ferromagnetic phase transition was observed up to 14 K;[3a] the crystal structures of these assemblies were not known. Shortly afterwards, determination of the crystal structures of {[$NR_4$][$Mn^{II}Cr^{III}$($C_2O_4$)$_3$]}$_n$ (R = *n*-butyl, *n*-propyl)[4] and {[$PR_4$][$Mn^{II}Cr^{III}$($C_2O_4$)$_3$]}$_n$ (R = phenyl)[5] revealed a 2D structure, and ferromagnetic behaviour was confirmed. The anion [Cr($C_2O_4$)$_3$]$^{3-}$ was also used in the preparation of the cubic 3D coordination polymers [$M^{I}Cr^{III}$($C_2O_4$)$_3$]$_n^{2n-}$ ($M^{I}$ = Li, Na)[6] or [$M^{II}Cr^{III}$-($C_2O_4$)$_3$]$_n^{n-}$ ($M^{II}$ = Mn, Fe, Co, Ni, Cu, Zn)[7] in which the charge was counterbalanced by a tris(chelated) transition-metal (M′) diimine, [M′(bpy)$_3$]$^{m+}$ (bpy = 2,2′-bipyridine; *m* = 2, 3). Other anionic oxalate complexes of chromium(III)

[a] Ruđer Bošković Institute,
Bijenička cesta 54, 10000, Zagreb, Croatia
[b] Department of Chemistry, Faculty of Science, University of Zagreb,
Horvatovac 102a, 10000, Zagreb, Croatia
[c] Department of Physics, Faculty of Science, University of Zagreb,
Bijenička cesta 32, 10000, Zagreb, Croatia

Supporting information for this article is available on the WWW under http://www.eurjic.org or from the author.

 © 2006 Wiley-VCH Verlag GmbH & Co. KGaA, Weinheim 

have also served as building blocks: the mono(oxalato) complexes $[CrL(C_2O_4)]^-$ [L = *N*,*N*′-ethylenebis(salicylideneaminate)][8] and $[CrL_2(C_2O_4)]^-$ (L = acetylacetonate)[9] have been used for the synthesis of heterodinuclear compounds, whereas the bis(oxalato) complexes $[CrL(C_2O_4)_2]^-$ (L = 2,2′-bipyridine,[10] 1,10-phenanthroline,[10d,11] 2,2′-bipyrimidine[12]) produced heterodinuclear as well as heteropolynuclear species of different dimensionalities.

Recently, the $[Cr(C_2O_4)_3]^{3-}$ and $[Fe(C_2O_4)_3]^{3-}$ anions were used in the synthesis of some oxalate-bridged trinuclear complexes such as $[Cu_2M^{III}(C_2O_4)_3(Mephen)_2]ClO_4$ ($M^{III}$ = Cr, Fe; Mephen = 5-methyl-1,10-phenanthroline).[13a] The magnetic susceptibility data revealed an intramolecular ferromagnetic interaction between the copper(II) and chromium(III) ions through the oxalate bridge and an antiferromagnetic interaction between the copper(II) and iron(III) centres with spin-coupling constants of $+14.9\ cm^{-1}$ and $-12.7\ cm^{-1}$ [using $\mathbf{H}_{INT} = -2J(S_{Cu1}S_M + S_{Cu2}S_M)$], respectively. Slightly reduced values were obtained for similar complexes when Mephen was substituted by tmen (*N*,*N*,*N*′,*N*′-tetramethylethylenediamine).[13b] The occurrence of intramolecular ferromagnetic interactions between the copper(II) and chromium(III) ions through the oxalate bridge with spin-coupling constants of $+6.36\ cm^{-1}$ and $+7.02\ cm^{-1}$ [using $\mathbf{H}_{INT} = -2J(S_{Cu1}S_{Cr} + S_{Cu2}S_{Cr} + S_{Cu3}S_{Cr})$], has also been found for the tetranuclear complexes $[Cu_3Cr(C_2O_4)_3L_3](ClO_4)_3$ with L = diaminoethane and 1,3-diaminopropane, respectively.[13c] All of these complexes[13] were prepared as polycrystalline solids. Because of the lack of single crystals suitable for X-ray structural analysis, their structures remain unknown.

In relation to our current magneto-structural studies on the polynuclear transition-metal complexes, we report in this paper on two new heterometallic complexes, $[\{Cu(\mu\text{-}C_2O_4)(bpy)_2\}_2Cr(C_2O_4)]NO_3\cdot H_2O$ (**1**) and $[Cu(bpy)_3]_2[Cr(C_2O_4)_3]NO_3\cdot 9H_2O$ (**2**), which have been obtained by using the $[Cr(C_2O_4)_3]^{3-}$ anion as building block. To the best of our knowledge, the complex $[\{Cu(\mu\text{-}C_2O_4)(bpy)_2\}_2Cr(C_2O_4)]NO_3\cdot H_2O$ is, so far, the first heterotrinuclear oxalate-bridged copper(II)–chromium(III)–copper(II) compound for which the crystal structure has been determined. The structural data of the complexes have been correlated with magnetic and other measurements.

## Results and Discussion

### Preparation

Complex **1** was obtained in the form of dark-green crystals from the reaction of aqueous solutions of $K_3[Cr(C_2O_4)_3]\cdot 3H_2O$ and $Cu(NO_3)_2\cdot 3H_2O$ and an ethanolic solution of 2,2′-bipyridine in the ratio 1:2:4. Single crystals of **2** were formed as the only solid by slow concentration of the aqueous solution containing $K_3[Cr(C_2O_4)_3]\cdot 3H_2O$ and $[Cu(bpy)_3](NO_3)_2\cdot 6H_2O$ in the ratio 1:1. When this reaction was performed with a 1:2 ratio of the precursors, crystals of **1** and **2** formed simultaneously. Both compounds are moderately stable in air and rather insoluble in common organic solvents.

### Description of the Structures

#### *[{Cu(μ-C$_2$O$_4$)(bpy)$_2$}$_2$Cr(C$_2$O$_4$)]NO$_3$·H$_2$O (1)*

The structure of **1** consists of trinuclear $[\{Cu(\mu\text{-}C_2O_4)(bpy)_2\}_2Cr(C_2O_4)]^+$ cations, nitrate anions and uncoordinated water molecules. The trinuclear cation (Figure 1) can be considered as being composed of two $[Cu(bpy)_2]^{2+}$ moieties bridged by the $[Cr(C_2O_4)_3]^{3-}$ complex anion, which acts as a bidentate ligand towards each of the copper atoms.

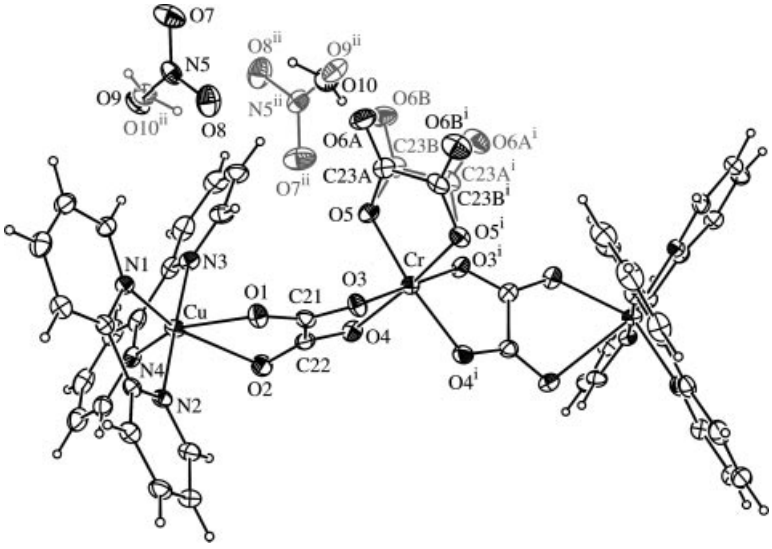


Figure 1. Asymmetric unit of **1** with atom numbering scheme and displacement ellipsoids drawn at the 50% probability level. Two halves of the $[\{Cu(\mu\text{-}C_2O_4)(bpy)_2\}_2Cr(C_2O_4)]^+$ cation are related by the symmetry operator (i) $1-x, y, 1/2-z$. The carboxylate groups of the terminal oxalate ligand are disordered (see text for explanation). The water molecule and nitrate ion are disordered over two sites related by the symmetry operator (ii) $1-x, -y, -z$. Atoms in the alternative sites and their numbering scheme are shown in grey.

 © 2006 Wiley-VCH Verlag GmbH & Co. KGaA, Weinheim 

Although compound **1** crystallises in the space group *C*2/*c* (see Exp. Sect.) with the chromium atom situated on the twofold axis, the trinuclear cation possesses only approximate $C_2$ symmetry: atoms C23 and O6 of the terminal oxalate group (which is intersected by the crystallographic twofold axis) are disordered over two sites (denoted A and B). The distance between C23A and the equivalent atom generated by the twofold symmetry C23A(1 – *x*, *y*, 1/2 – *z*) is 1.657(18) Å, whereas the distance C23A–C23B(1 – *x*, *y*, 1/2 – *z*) is 1.572(18) Å and is closer to the value for a C–C single bond.[14] This suggests that the two atoms from one of the carboxylate groups are in the A site and the corresponding atoms from the other carboxylate group of the terminal oxalate ligand are in the B site (Figure 1). This oxalate group is, therefore, statistically disordered, and the occupancies of the C23A, C23B, O6A and O6B atoms were fixed at 0.50 during refinement. Furthermore, the lattice water molecules and nitrate ions are disordered over two sites related by the inversion centre, so that the occupancy of each site equals exactly one half (Figure 1).

The apical positions in the distorted octahedron around Cu are occupied by the O2 and N1 atoms. The Cu–O2 bond [2.6439(18) Å] is significantly longer than the Cu–O1 bond [2.1168(15) Å]. The Cu–N1 bond [2.1079(18) Å] is the longest one among the four Cu–N bonds (Table 1). The remaining three bpy nitrogen (N2, N3 and N4) atoms having an average Cu–N bond length of 1.995 Å as well as the O1 atom are located in the equatorial plane. The pyridyl rings of the bpy ligands are slightly tilted towards each other. The dihedral angles between the planes of the pyridyl rings are 15.78(10)° (for the bpy ligand including N1 and N2) and 4.52(11)° (for the ligand including N3 and N4).

Table 1. Selected bond lengths [Å] and angles [°] for compound **1**.

| | | | |
|---|---|---|---|
| Cu–O1 | 2.1168(15) | Cu–N1 | 2.1079(18) |
| Cu–O2 | 2.6439(18) | Cu–N2 | 1.9774(19) |
| Cr–O3 | 1.9866(16) | Cu–N3 | 1.9663(19) |
| Cr–O4 | 1.9900(16) | Cu–N4 | 2.0423(19) |
| Cr–O5 | 1.9454(16) | | |
| O3–Cr–O4 | 82.52(7) | O1–Cu–N3 | 92.59(7) |
| O3–Cr–O5 | 90.79(7) | O1–Cu–N4 | 148.62(7) |
| O3–Cr–O3$^{i}$[a] | 179.51(7) | O2–Cu–N1 | 162.09(6) |
| O3–Cr–O4$^{i}$ | 97.14(7) | O2–Cu–N2 | 101.23(7) |
| O3–Cr–O5$^{i}$ | 89.57(7) | O2–Cu–N3 | 78.23(7) |
| O4–Cr–O5 | 93.17(7) | O2–Cu–N4 | 78.32(6) |
| O4–Cr–O4$^{i}$ | 91.14(7) | N1–Cu–N2 | 80.68(7) |
| O4–Cr–O5$^{i}$ | 171.41(7) | N1–Cu–N3 | 99.37(7) |
| O5–Cr–O5$^{i}$ | 83.56(7) | N1–Cu–N4 | 119.13(7) |
| O1–Cu–O2 | 70.30(6) | N2–Cu–N3 | 178.42(7) |
| O1–Cu–N1 | 92.22(6) | N2–Cu–N4 | 99.87(8) |
| O1–Cu–N2 | 85.83(7) | N3–Cu–N4 | 81.49(8) |

[a] Symmetry code: (i) 1 – *x*, *y*, 1/2 – *z*.

The Cr atom in **1** is bonded to six oxygen atoms arranged in a slightly distorted octahedron. As already observed in similar complexes,[10a,15,16] the Cr–O bonds are longer for the bridging oxalate ligands [1.9866(16) Å and 1.9900(16) Å] than for the terminal one [1.9454(16) Å], but they are all shorter than the Cu–O bonds (Table 1). The carboxylate groups of the oxalate ligands are not coplanar; instead, they are rotated around the C–C bond by 14.05(12)° in the bridging ligands and by 6.0(17)° in the terminal one.

The complex cations, mutually related by the twofold axis, are stacked in columns parallel to the *c* axis because of the offset π–π interactions between pyridyl moieties. The columns of the complex cations are further connected with the neighbouring columns by zipper-like offset π–π stacking interactions between the pyridyl moieties: in this way, layers parallel to (010) are formed. These layers consist of pyridyl rings with two different orientations alternating in the *a*-direction: (a) the rings almost parallel to (012) and (b) those almost parallel to (01$\bar{2}$) (Figure 2). The contact distances between atoms involved in the pyridyl π–π stacking interactions range from 3.324(3) Å to 3.594(3) Å, which indicates that these are strong to modest π–π interactions.[17] The two layers of the complex cations are held together by the C–H···O hydrogen bonds and other interactions mediated by the nitrate ions and water molecules: each water molecule bridges the complex cation and the nitrate anion by forming two hydrogen bonds: O10–H101···O6A of 2.92(2) Å and O10–H102···O8 of 2.814(19) Å, (Figure 3; Table 2). Additionally, the carboxylate group of the terminal oxalate ligand occupying the B site and the nitrate ion are in close contact [N5···O6B(1 – *x*, –*y*, –*z*) = 3.201(7) Å; O7···C23B(1 – *x*, –*y*, –*z*) = 3.103(14) Å] and exhibit a π–π stacking interaction [the angle between the plane of the nitrate ion and that of the carboxylate group B equals 18.7(9)°]. In the proposed structural model, the carboxylate group nearest to the nitrate ion always occupies the B site; otherwise, unacceptably short contacts between the nitrate ion and carboxylate group at the A site [N5···O6A(1 – *x*, –*y*, –*z*) = 2.588(8) Å; O7···C23A(1 – *x*, –*y*, –*z*) = 2.775(16) Å] would be present.

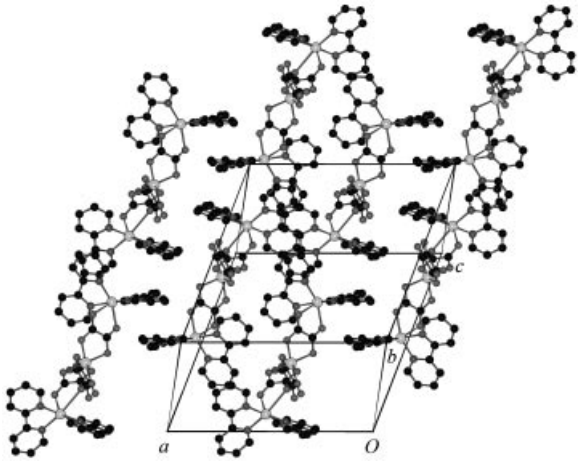


Figure 2. Pyridyl π–π stacking in **1**. The stacking almost parallel to (012) alternates in the *a*-direction with the stacking almost parallel to (01$\bar{2}$). Hydrogen atoms are omitted for clarity.

The Cu···Cr distance across the bridging oxalate group is 5.4605(5) Å. It is similar to the corresponding values found elsewhere: in the dinuclear complex [(bpy)($C_2O_4$)Cr-(μ-$C_2O_4$)Cu(Hfsaaep)($H_2O$)]·2$H_2O$ {$H_2$fsaaep = 3-[*N*-2-(pyridylethyl)formimidoyl]salicylic acid; Cu···Cr =

 © 2006 Wiley-VCH Verlag GmbH & Co. KGaA, Weinheim 

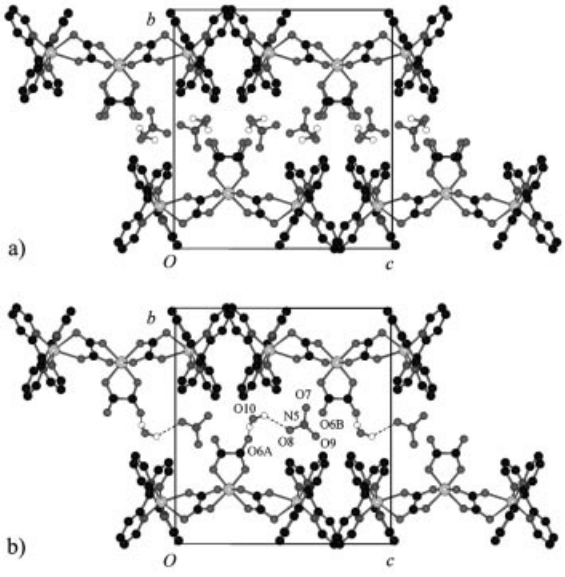


Figure 3. The cavities between two layers of the trinuclear cations in **1** are filled with nitrate ions and water molecules. Hydrogen atoms attached to the carbon atoms are omitted for clarity. (a) Each water–nitrate pair is disordered over two sites related by the inversion centre. (b) One of two possible orientations of the water–nitrate pairs in the cavities in a row, mutually related by the glide plane *c*.

Table 2. O–H···O hydrogen-bonding interactions in compound **1**.

| D–H···A | D–H [Å] | H···A [Å] | D···A [Å] | D–H···A [°] |
|---|---|---|---|---|
| O10–H101···O6A | 0.80 | 2.20 | 2.92(2) | 150 |
| O10–H102···O8 | 0.88 | 2.15 | 2.814(19) | 132 |

5.506 Å},[16] in the trinuclear complex $[CuCr_2(bpy)_2(C_2O_4)_4(H_2O)_2]\cdot 1.5H_2O$ (Cu···Cr = 5.288 Å)[10a] or in the tetranuclear compound $[Cr_2Cu_2(bpy)_4(C_2O_4)_5]\cdot 2H_2O$ [Cu···Cr = 5.4473(17) Å].[15b] The oxalate bridging mode in all of these complexes is the same as that in **1**. The shortest intermolecular Cu···Cu, Cu···Cr and Cr···Cr distances in the structure of **1** are 6.0311(6) Å [Cu···Cu(1 – *x*, *y*, –1/2 – *z*)], 7.6473(8) Å [Cu···Cr(1 – *x*, 1 – *y*, –*z*)] and 9.4527(7) Å [Cr···Cr(3/2 – *x*, 1/2 – *y*, 1 – *z*)], respectively.

### *[Cu(bpy)$_3$]$_2$[Cr(C$_2$O$_4$)$_3$]NO$_3$·9H$_2$O (2)*

The asymmetric unit of **2** is composed of two mononuclear, crystallographically independent $[Cu(bpy)_3]^{2+}$ cations, a mononuclear $[Cr(C_2O_4)_3]^{3-}$ anion, a nitrate anion and nine molecules of water of crystallisation, two of which are disordered over two positions (Figure 4). Each copper atom is coordinated by six nitrogen atoms of the three chelating bpy ligands. The two axial Cu–N bonds in each of the $[Cu(bpy)_3]^{2+}$ cations [Cu1–N2 = 2.247(3) Å and Cu1–N5 = 2.291(3) Å; Cu2–N8 = 2.171(3) Å and Cu2–N11 = 2.200(4) Å] are significantly longer than the other four [ranging from 2.027(3) Å to 2.055(5) Å for Cu1 and from 2.068(5) Å to 2.088(5) Å for Cu2; Table 3]; thus an elongated octahedron is formed (as expected as a result of the Jahn–Teller effect). The dihedral angles between pyridyl moieties are smaller for the ligands coordinated to Cu1 [5.0(3)°, 5.19(18)° and 6.23(19)°] than for those coordinated to Cu2 [10.4(2)°, 9.76(19)° and 6.6(3)°]. The geometrical parameters of $[Cu(bpy)_3]^{2+}$ in **2** are significantly different from those found in some other $[Cu(bpy)_3]^{2+}$ complexes {the apical Cu–N distances in $[Cu(bpy)_3][Ni(tdtdt)_2]_2$ (tdtdt = 2-thioxo-1,3-dithiole-4,5-dithiolate)[18] are longer than the equatorial ones by only 0.02 Å; the octahedral geometry in $[Cu(bpy)_3](ClO_4)_2$[19] is more distorted than in **2**; the coordination polyhedron around Cu in $[Cu(bpy)_3][Hg_2I_6]$[20] is a flattened octahedron}, but they are similar to those found in $[Cu(dmbpy)_3](BF_4)_2\cdot C_2H_5OH$, where the ligand dmbpy indicates 5,5-dimethyl-2,2′-bipyridine.[21] The Cr atom in $[Cr(C_2O_4)_3]^{3-}$ is coordinated by six oxygen atoms of the three bidentate oxalate ligands in a slightly distorted octahedral arrangement. The Cr–O bond lengths range from 1.964(3) Å to 1.982(3) Å, and the structure of the

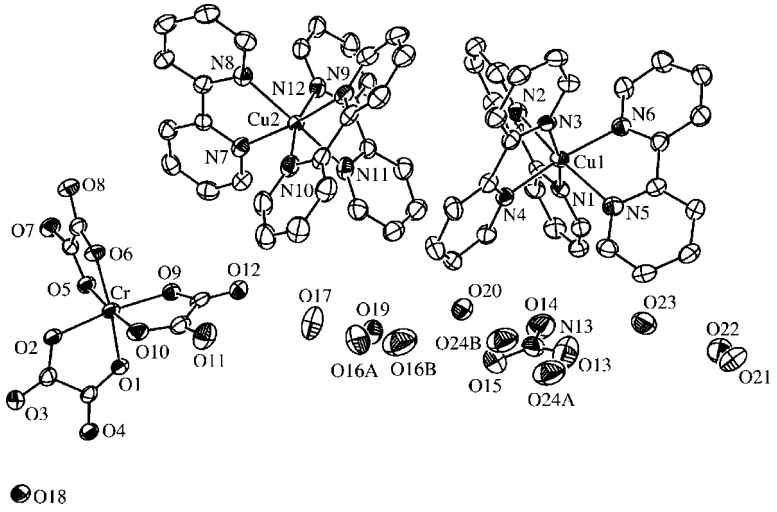


Figure 4. Asymmetric unit of **2** with atom numbering scheme and displacement ellipsoids drawn at the 50% probability level. Two water molecules are disordered over two positions, namely O16A and O16B, O24A and O24B. Occupancies of the oxygen atoms at the A and B sites are 0.84 and 0.16, respectively. Hydrogen atoms are omitted for clarity.

 © 2006 Wiley-VCH Verlag GmbH & Co. KGaA, Weinheim 

$[Cr(C_2O_4)_3]^{3-}$ anion is very similar to that found in $K_3[Cr(C_2O_4)_3]\cdot 3H_2O$.[22]

Table 3. Selected bond lengths [Å] and angles [°] for compound **2**.

| | | | |
|---|---|---|---|
| Cu1–N1 | 2.041(3) | Cu2–N7 | 2.088(5) |
| Cu1–N2 | 2.247(3) | Cu2–N8 | 2.171(3) |
| Cu1–N3 | 2.027(3) | Cu2–N9 | 2.068(5) |
| Cu1–N4 | 2.051(4) | Cu2–N10 | 2.085(3) |
| Cu1–N5 | 2.291(3) | Cu2–N11 | 2.200(4) |
| Cu1–N6 | 2.055(5) | Cu2–N12 | 2.075(3) |
| Cr–O1 | 1.967(3) | Cr–O6 | 1.964(3) |
| Cr–O2 | 1.970(4) | Cr–O9 | 1.966(4) |
| Cr–O5 | 1.982(3) | Cr–O10 | 1.964(3) |
| N1–Cu1–N2 | 77.23(12) | N7–Cu2–N8 | 77.48(15) |
| N1–Cu1–N3 | 169.39(14) | N7–Cu2–N9 | 169.83(11) |
| N1–Cu1–N4 | 95.70(16) | N7–Cu2–N10 | 97.05(17) |
| N1–Cu1–N5 | 97.94(12) | N7–Cu2–N11 | 96.53(15) |
| N1–Cu1–N6 | 92.99(15) | N7–Cu2–N12 | 91.84(15) |
| N2–Cu1–N3 | 93.39(12) | N8–Cu2–N9 | 93.55(15) |
| N2–Cu1–N4 | 95.92(14) | N8–Cu2–N10 | 95.92(12) |
| N2–Cu1–N5 | 171.23(13) | N8–Cu2–N11 | 171.29(14) |
| N2–Cu1–N6 | 96.80(15) | N8–Cu2–N12 | 96.34(12) |
| N3–Cu1–N4 | 80.17(16) | N9–Cu2–N10 | 78.94(17) |
| N3–Cu1–N5 | 91.99(12) | N9–Cu2–N11 | 92.90(15) |
| N3–Cu1–N6 | 93.06(15) | N9–Cu2–N12 | 93.93(16) |
| N4–Cu1–N5 | 91.81(14) | N10–Cu2–N11 | 91.05(13) |
| N4–Cu1–N6 | 165.92(12) | N10–Cu2–N12 | 166.17(14) |
| N5–Cu1–N6 | 75.99(15) | N11–Cu2–N12 | 77.38(14) |
| O1–Cr–O2 | 83.19(14) | O2–Cr–O10 | 91.86(14) |
| O1–Cr–O5 | 92.08(13) | O5–Cr–O6 | 82.27(12) |
| O1–Cr–O6 | 172.95(15) | O5–Cr–O9 | 95.00(13) |
| O1–Cr–O9 | 92.01(14) | O5–Cr–O10 | 174.71(17) |
| O1–Cr–O10 | 92.71(13) | O6–Cr–O9 | 92.68(15) |
| O2–Cr–O5 | 90.94(14) | O6–Cr–O10 | 93.12(13) |
| O2–Cr–O6 | 92.66(14) | O9–Cr–O10 | 82.59(14) |
| O2–Cr–O9 | 172.50(11) | | |

The crystal structure of **2** consists of hydrophobic and hydrophilic regions. The $[Cu(bpy)_3]^{2+}$ cations are arranged in honeycomb-like hydrophobic layers parallel to $(10\bar{1})$ (Figure 5). The cations are interconnected by the aromatic–aromatic interactions with C···C contact distances in the 3.417(9)–3.598(7) Å range. Each hydrophobic layer is sandwiched between two hydrophilic layers composed of $[Cr(C_2O_4)_3]^{3-}$, nitrate anions and water molecules; all of them are involved in an extensive hydrogen-bonding network (Table 4). The water molecule situated in each hexagonal cell of the "hydrophobic honeycomb" (O18) links two hydrophilic layers by forming hydrogen bonds with the oxalate ligands of $[Cr(C_2O_4)_3]^{3-}$ units from different layers (Figure 6). The crystal structure is additionally stabilised by

Table 4. O–H···O hydrogen-bonding interactions in compound **2**.

| D–H···A | D–H [Å] | H···A [Å] | D···A [Å] | D–H···A [°] |
|---|---|---|---|---|
| O16A–H161···O17 | 0.84 | 2.12 | 2.824(7) | 141 |
| O16B–H[a]···O2$^{vi}$[b] | – | – | 2.73(3) | – |
| O16B–H[a]···O24B | – | – | 2.98(5) | – |
| O17–H171···O19 | 0.82 | 2.12 | 2.910(5) | 160 |
| O17–H172···O11 | 0.86 | 2.51 | 3.253(6) | 144 |
| O17–H172···O12 | 0.86 | 2.24 | 2.963(5) | 141 |
| O18–H181···O3 | 0.94 | 2.24 | 2.874(5) | 125 |
| O18–H181···O4 | 0.94 | 2.03 | 2.903(5) | 153 |
| O18–H182···O8$^{i}$ | 0.72 | 2.05 | 2.755(4) | 165 |
| O19–H191···O20 | 0.86 | 2.10 | 2.953(6) | 172 |
| O19–H192···O9$^{ii}$ | 0.84 | 2.07 | 2.893(4) | 171 |
| O20–H201···O14 | 0.76 | 2.19 | 2.948(6) | 172 |
| O20–H202···O5$^{ii}$ | 0.88 | 2.04 | 2.868(4) | 155 |
| O21–H211···O22 | 0.85 | 2.12 | 2.772(4) | 133 |
| O21–H212···O2$^{iii}$ | 0.85 | 2.11 | 2.941(4) | 165 |
| O22–H221···O23 | 0.90 | 1.90 | 2.787(5) | 170 |
| O22–H222···O7$^{iii}$ | 0.90 | 2.05 | 2.910(6) | 160 |
| O23–H231···O14 | 0.86 | 2.26 | 3.044(7) | 151 |
| O23–H[a]···O23$^{v}$ | – | – | 2.793(5) | – |
| O24A–H241···O13 | 0.86 | 2.15 | 2.914(6) | 147 |
| O24A–H242···O21$^{iv}$ | 0.86 | 2.17 | 2.876(6) | 139 |
| O24B–H[a]···O13 | – | – | 2.73(2) | – |
| O24B–H[a]···O15 | – | – | 2.71(2) | – |
| O24B–H[a]···O21$^{iv}$ | – | – | 2.77(2) | – |

[a] The water hydrogen atom was not found and could not be modelled. [b] Symmetry codes: (i) $x$, $1/2 - y$, $-1/2 + z$; (ii) $1 - x$, $-y$, $1 - z$; (iii) $-1 + x$, $y$, $-1 + z$; (iv) $-x$, $1 - y$, $-z$; (v) $-x$, $-y$, $-z$; (vi) $1 - x$, $1 - y$, $1 - z$.

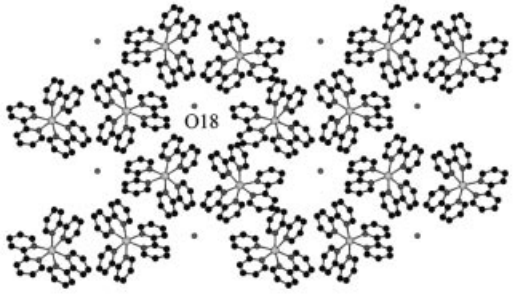


Figure 5. Honeycomb-like layer of $[Cu(bpy)_3]^{2+}$ cations in **2** parallel to $(10\bar{1})$. There is one water molecule (O18) in every hexagonal "honeycomb cell". Hydrogen atoms are omitted for clarity. This view is perpendicular to the layer.

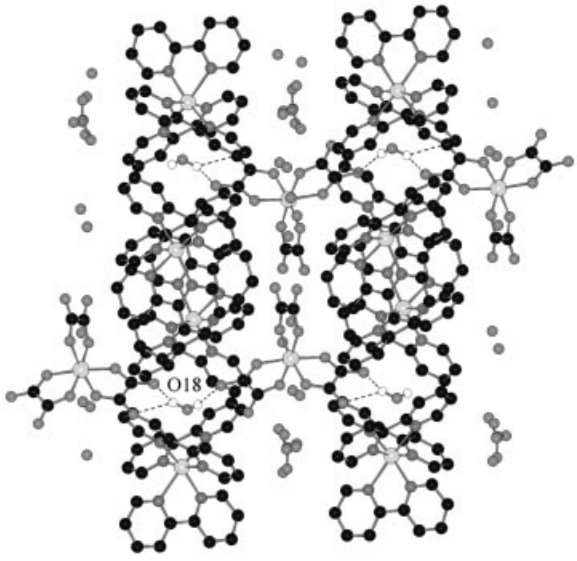


Figure 6. Hydrophobic and hydrophilic layers in **2**. Water molecules bearing the oxygen atoms labelled as O18 link two hydrophilic layers by forming hydrogen bonds (shown by dashed lines) with the oxalate groups of the $[Cr(C_2O_4)_3]^{3-}$ anions. Hydrogen atoms (except those bound to O18) are omitted for clarity. This view is along the *b*-axis.

 © 2006 Wiley-VCH Verlag GmbH & Co. KGaA, Weinheim 

many C–H···O interactions at the interface between two layers.

The shortest Cu···Cu, Cu···Cr and Cr···Cr distances in the structure of **2** are 7.7558(10) Å [Cu2···Cu2(1 – *x*, –1/2 + *y*, 3/2 – *z*)], 8.0770(10) Å [Cu2···Cr(*x*, 1/2 – *y*, 1/2 + *z*)] and 10.7121(15) Å [Cr···Cr(1 – *x*, –*y*, 1 – *z*)], respectively.

## Spectroscopic Properties

### *Infrared Spectra*

Inspection of the IR spectra of **1** and **2** clearly indicates the presence of the absorption bands of the bidentate oxalate group, the bipyridine ligands, the ionic nitrate group and the water molecules in both complexes, in addition to the absorption bands of bis(bidentate) bridging oxalate group in compound **1**. In the spectrum of **1** the absorption bands at: 1717, 1705, 1672, 1663 $cm^{-1}$ [$\nu_{as}$(CO)], 1370, 1251 $cm^{-1}$ [$\nu_s$(CO)] and 801, 795 $cm^{-1}$ [δ(OCO)] are characteristic of bidentate oxalate,[23] whereas those due to the bis(bidentate) bridging oxalate at 1625 $cm^{-1}$ [$\nu_{as}$(CO)], 1338 $cm^{-1}$ [$\nu_s$(CO)] and 817 $cm^{-1}$ [δ(OCO)] agree well with the values reported for dinuclear[8] or tetranuclear[15b] bis(bidentate) bridging oxalate $Cu^{II}Cr^{III}$ complexes. The latter three bands are absent from the spectrum of **2**, and those originating from the bidentate oxalate ligand are found at similar positions as those observed in **1** (see Exp. Sect.).

### *Electronic Spectra*

Electronic spectroscopic data for **1** and **2** were obtained from aqueous solutions and are presented in Table 5. Data for $[Cu(bpy)_3](NO_3)_2{\cdot}6H_2O$ and $K_3[Cr(C_2O_4)_3]{\cdot}3H_2O$ are included for comparison. For the new complexes, the spectra were also recorded as KBr pellets, but this method resulted in essentially the same UV/Vis absorption maxima as those recorded in solution, which indicates that the structures of the complex ions in **1** and **2** are preserved in aqueous media.

The electronic spectra of **1** and **2** exhibit very similar patterns, which confirms the similarity of the local coordination environments around the metal centres in the two complexes. The spectra show the superposition of bands characteristic for both the $Cu^{II}$ and $Cr^{III}$ six-coordinate ions. In the visible region, they are dominated by a broad absorption band with a pronounced shoulder on the lower energy side (of the spectra), which corresponds to the presence of a $Cu^{II}$ ion in a more or less distorted octahedral environment. The unsymmetrical absorption bands for **1** and **2**, having maxima at ca. 715 and ca. 675 nm, respectively, are in good agreement with the spectrum of the starting $[Cu(bpy)_3](NO_3)_2{\cdot}6H_2O$ compound (Table 5), which must have essentially a distorted octahedral geometry. The type of the distortion of the $[Cu(bpy)_3]^{2+}$ ion is significantly dependent on the counteranion present,[18–20] and, in general, does not influence a lot the position of the band maxima. Therefore, the shift of the main absorption maximum in the spectrum of **1** towards the lower energy side relative to the spectrum of **2** could be perceived as a consequence of the different chromophores present in **1** and **2**, namely $[Cu^{I}{}^{I}N_4O_2]$ and $[Cu^{II}N_6]$ (nitrogen ligands exerting higher field strength), rather than as a result of somewhat different geometrical parameters found for $Cu^{II}$ in the two complexes (see Description of the Structures). The presence of an octahedrally coordinated $Cr^{III}$ ion is indicated by the two shoulders, one appearing at the higher energy side of the main visible absorption band (at ca. 565 and 580 nm for **1** and **2**, respectively) and the other observed at the lower energy side of the strong UV band of the spectra (at ca. 415 nm in both cases). The two shoulders in the spectra of **1** and **2** agree well in positions and intensities with the two main absorption bands in the electronic spectrum of $K_3[Cr(C_2O_4)_3]{\cdot}3H_2O$ (maxima appearing at 420 and 570 nm) and can account for the two spin-allowed d–d transitions, $^4A_{2g}(F) \rightarrow {}^4T_{1g}(F)$ and $^4A_{2g}(F) \rightarrow {}^4T_{2g}(F)$, in the octahedral ligand field of a $d^3$ configuration. An extremely narrow and very weak band observed at ca. 700 nm in both spectra could be ascribed to the spin-forbidden $^4A_{2g} \rightarrow {}^2T_{2g}(F) + {}^2E_g$ transition, characteristic of chromium(III) six-coordinate compounds.

Very strong absorptions (with ε of the order of magnitude of several tens of thousands) in the UV region of the spectra (at ca. 240 and ca. 300 nm) originate from ligand-specific and charge-transfer metal-to-ligand transitions.[24,25]

## TG Analysis

As is evidenced from the thermogravimetric analysis, the thermal behaviour of the two compounds is significantly different. Complex **1**, with bridging oxalate groups, is thermally more stable than complex **2**, in both synthetic air and under nitrogen. In synthetic air, the decomposition of **1** starts only after 170 °C by a distinctive step visible in the TG curve and corresponding to the loss of approximately one water molecule (calcd. 1.57%; found 1.75%). The next large step (ca. 58%) in the decomposition curve, in the tem-

Table 5. Electronic spectroscopic data for complexes **1** and **2** and the mononuclear copper(II) and chromium(III) precursor complexes.[a]

| Complex | $\lambda_{max}$ [nm] (ε [$dm^3\,mol^{-1}\,cm^{-1}$]) | | | | |
|---|---|---|---|---|---|
| | Ligand-specific and CT bands | $^4A_{2g}(F) \rightarrow {}^4T_{1g}(F)$ | $^4A_{2g}(F) \rightarrow {}^4T_{2g}(F)$ | $^4A_{2g} \rightarrow {}^2T_{2g}(F) + {}^2E_g$ | $^2E \rightarrow {}^2A_1$ |
| **1** | 243 (50840), 300 (48800) | 413 (sh) | 565 (sh) | 698 (sh) | 715 (120) |
| **2** | 243 (57640), 297 (54100) | 415 (sh) | 580 (sh) | 697 (sh) | 675 (135) |
| $[Cu(bpy)_3](NO_3)_2{\cdot}6H_2O$ | 232 (55000), 297 (52000) | | | | 680 (130) |
| $K_3[Cr(C_2O_4)_3]{\cdot}3H_2O$ | 269 (1500) | 420 (105) | 568 (87) | 697 (8) | |

[a] In aqueous solutions.

 © 2006 Wiley-VCH Verlag GmbH & Co. KGaA, Weinheim 

perature range of ca. 200–300 °C, comprises the removal of bipyridine molecules together with the $NO_3^-$ group. Decomposition of the oxalate groups proceeds in a rather narrow temperature range of 300–400 °C as a strongly exothermic process. Afterwards, the remaining mass stays constant and corresponds to a mixture of copper(II) and chromium(III) oxides.

The elimination of water molecules in **2** proceeds in two well-separated steps taking place in the temperature intervals 40–105 °C and 110–145 °C, both followed by an endothermic peak in the DTA curve. In the first step, six lattice water molecules are expelled (calcd. 6.75%; found 7.05%), the remaining three (calcd. 3.37%; found 3.62%) are lost at higher temperature. The further course of the decomposition process follows that of complex **1**.

## Magnetic Properties

The results of magnetic measurements on **1** and **2** are shown in Figure 7, in terms of the dependence of the product of molar susceptibility and temperature, $\chi_M T$, on temperature. The value of $\chi_M T$ for **1** at temperatures above 50 K is almost constant at an average of 2.84 $cm^3 mol^{-1} K$. This corresponds to the effective magnetic moment per molecule $\mu = 4.77\beta$, where $\beta$ stands for the Bohr magneton. Generally, the spin-only value of the effective magnetic moment for three uncoupled spins is obtained according to the expression:

$$\mu = \beta\sqrt{g_1^2 S_1(S_1 + 1) + g_2^2 S_2(S_2 + 1) + g_3^2 S_3(S_3 + 1)}$$

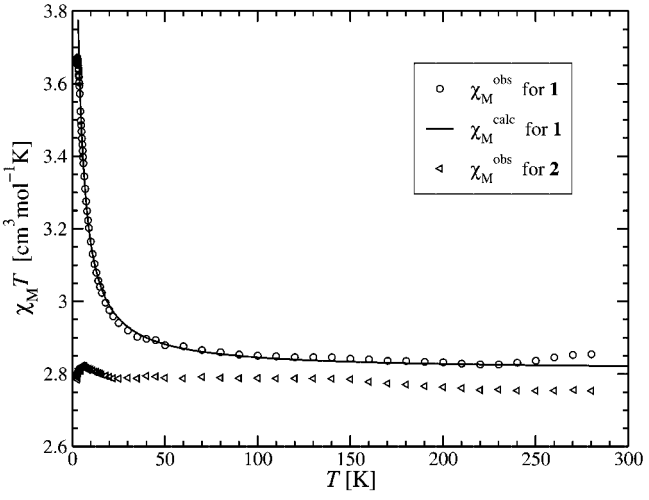


Figure 7. Plots of $\chi_M T$ vs. $T$ for compounds **1** and **2**. The solid line represents the curve of best fit.

For compound **1**, with ($S_{Cu1}$, $S_{Cr}$, $S_{Cu2}$) = (1/2, 3/2, 1/2) and taking $g_{Cu} = g_{Cr} = 2$, the above expression gives a value of $\mu = 4.58\beta$. The measured value is slightly higher and corresponds to $g_{Cu,Cr} = 2.08$. As shown in Figure 7, on cooling the compound below 50 K, the $\chi_M T$ product increases rapidly, and at 2.8 K it attains a value of 3.67 $cm^3 mol^{-1} K$, corresponding to $\mu = 5.42\beta$. This increase of $\chi_M T$ points to the emergence of a ferromagnetic interaction. Below 2.8 K, a very slight decrease of $\chi_M T$ is observed.

The value of the $\chi_M T$ product for **2** at temperatures above 30 K is almost constant and equals 2.77 $cm^3 mol^{-1} K$, which is very close to that of **1**. On cooling the sample below 30 K, first an increase in $\chi_M T$ was observed, but this increase was much smaller than the corresponding increase for **1**. A value of 2.82 $cm^3 mol^{-1} K$ was reached at 5.7 K. With further cooling, the $\chi_M T$ product decreased abruptly to 2.79 $cm^3 mol^{-1} K$ at 3 K. The room temperature effective magnetic moment per molecule for **2** is $\mu = 4.71\beta$. The corresponding $g$ factor which gives this value of $\mu$ for the (1/2, 3/2, 1/2) uncoupled spin system is $g_{Cu,Cr} = 2.06$.

The good linear dependences of the reciprocal magnetic susceptibilities, $\chi_M^{-1}$, on temperature (above 50 K) give the Weiss constants ($\theta = 0.8 \pm 0.1$ K for **1** and $\theta = 0.3 \pm 0.1$ K for **2**) which point to a negligible long-range ordering interaction. The absence of a 3D interaction is also in agreement with the value of the effective molecular magnetic moments at the measured temperatures. Therefore, the observed ferromagnetic interaction should be analyzed on the molecular level.

On the basis of the structure of the compound **1** and the magnetic properties of $Cu^{II}$ and $Cr^{III}$ ions, it is reasonable to write the interaction Hamiltonian as in Equation (1):

$$\mathbf{H}_{INT} = -J(S_{Cu1}S_{Cr} + S_{Cu2}S_{Cr}) \quad (1)$$

where $J$ is the exchange interaction between $Cu^{II}$ and $Cr^{III}$ ions in the same molecule, whereas $S$ is the spin operator for the ions labelled by indices.

In the above Hamiltonian only the isotropic Heisenberg exchange term appears, as the $Cu^{II}$ ion does not have zero-field splitting, and for the $Cr^{III}$ ion it is negligible in a first approximation,[1] as shown by the observed magnetic and structural properties. Therefore, the anisotropic and antisymmetric exchange terms are omitted.

Taking $g_{Cu} = g_{Cr} = g$, the following formula is obtained [Equation (2)]:

$$\chi_M = \frac{N\beta^2}{4k}\cdot\frac{g^2}{T}\cdot\frac{10 + e^{-\frac{5J}{2T}} + 10e^{-\frac{J}{T}} + 35e^{\frac{3J}{2T}}}{2 + e^{-\frac{5J}{2T}} + 2e^{-\frac{J}{T}} + 3e^{\frac{3J}{2T}}} \quad (2)$$

The nonlinear fitting of the susceptibility vs. temperature dependence for **1** in the temperature range 2.8–300 K gave the following results: $J = +1.20$ $cm^{-1}$, $g = 2.07$. The discrepancy factor $R$, defined as $R = \Sigma[(\chi_M T)_{obsd.} - (\chi_M T)_{calcd.}]^2 / \Sigma[(\chi_M T)_{obsd.}]^2$, equals $1.8 \cdot 10^{-5}$. A small decrease of the magnetic moment below ca. 2.5 K may be generally attributed to an intermolecular antiferromagnetic interaction and/or a zero-field splitting on $Cr^{III}$.[8,10a]

In order to describe the mechanism of the spin-exchange interaction in oxalate-bridged transition-metal complexes, several models have been considered.[26–28] According to these models only a strict orbital orthogonality results in a ferromagnetic interaction. In the structure of **1** (Figure 1)

 © 2006 Wiley-VCH Verlag GmbH & Co. KGaA, Weinheim 

the O1 and O1$^{i}$ atoms from the bridging oxalate groups are located in the equatorial planes [consisting of the O1, N2, N3 and N4 atoms for Cu and O1$^{i}$, N2$^{i}$, N3$^{i}$ and N4$^{i}$ for Cu$^{i}$ ($i = 1 - x, y, 1/2 - z$)] of the distorted Cu octahedra, whereas the O2 and O2$^{i}$ atoms from the corresponding bridging oxalate ligands occupy the apical positions. The significantly shorter Cu–O1 bond relative to the Cu–O2 bond (Table 1) indicates a strong orbital interaction in the equatorial planes of the two Cu coordination polyhedra, which are mutually related by the twofold axis through the chromium atom. It is clear that the unpaired electron on each copper(II) ion should be described by the $d_{x^2-y^2}$ as the highest energy orbital[1] that will interact with the σ-type oxygen orbitals, forming one of the magnetic orbitals. Simultaneously, the chromium(III) $t_{2g}$ orbitals, with three unpaired electrons, interact with the π-type oxygen orbitals, also resulting in magnetic orbitals. Consequently, a ferromagnetic spin coupling results from the orthogonality of the magnetic orbitals involved. A similar explanation was given for the appearance of a ferromagnetic interaction in [(bpy)($C_2O_4$)Cr(μ-$C_2O_4$)Cu(Hfsaaep)($H_2O$)]·2$H_2O$.[16] In the absence of necessary symmetry conditions, the magnetic interaction in $Cu^{II}Cr^{III}$ oxalate-bridged complexes is antiferromagnetic.[10a,15] For the ferromagnetic $Cu^{II}Cr^{III}Cu^{II}$ compounds mentioned in the introduction,[13a,13b] the values for $J$ were found to be higher than that for **1**. Because the crystal structures of these complexes are still unknown, it is not possible to comment on their $J$ values. Structurally, the coordination environment of $Cu^{II}$ in **1** is similar to that found in the dinuclear compound [(bpy)($C_2O_4$)Cr(μ-$C_2O_4$)-Cu(Hfsaaep)($H_2O$)]·2$H_2O$, for which the ferromagnetic spin-coupling constant $J = +1.4\ cm^{-1}$ (using $\mathbf{H}_{INT} = -JS_{Cu}S_{Cr}$) has been measured.[16] The ferromagnetic interaction with $J = +2.8\ cm^{-1}$ (using $\mathbf{H}_{INT} = -2JS_{Cu}S_{Cr}$) has also been found for the dinuclear complex [Cr(salen)(μ-$C_2O_4$)Cu(acpy)].[8] The exchange constant ($J = +1.2\ cm^{-1}$) obtained for **1** is comparable to these two values.

Appearance of a slight increase followed by a slight decrease of $\chi_M T$ for the compound **2** when lowering the temperature may come from the zero-field splitting on $Cr^{III}$ and/or from a 3D interaction effect. However, it is not quantitatively well understood at present and is the subject of further investigations.

## Conclusion

We have prepared two new heterometallic ($Cu^{II}$ and $Cr^{III}$) complexes. In **1**, metal atoms are oxalate-bridged in the trinuclear [{Cu(μ-$C_2O_4$)(bpy)$_2$}$_2$Cr($C_2O_4$)]$^+$ cation, whereas **2** consists of two [Cu(bpy)$_3$]$^{2+}$ cations and two {[Cr($C_2O_4$)]$^{3-}$ and $NO_3^-$} anions. Compound **1** is the first trinuclear $Cu^{II}Cr^{III}Cu^{II}$ complex with solved crystal structure. This fact allowed us to explain the pathway of a ferromagnetic exchange interaction between the $Cu^{II}$ and $Cr^{III}$ metal ions mediated through the bridging oxalate groups. We are currently engaged in a more detailed study aiming to understand the magnetic behaviour of **2** at low temperature.

## Experimental Section

**General Remarks:** All the reagents used in the syntheses were purchased from commercial sources and used without further purification. K$_3$[Cr($C_2O_4$)$_3$]·3$H_2O$ and [Cu(bpy)$_3$]($NO_3$)$_2$·6$H_2O$ were prepared according to the literature methods.[29,30]

**Synthesis of [{Cu(μ-$C_2O_4$)(bpy)$_2$}$_2$Cr($C_2O_4$)]$NO_3$·$H_2O$ (1):** To an aqueous solution (15 mL) of K$_3$[Cr($C_2O_4$)$_3$]·3$H_2O$ (146.7 mg, 0.301 mmol) were added an aqueous solution (12 mL) of $Cu(NO_3)_2$·3$H_2O$ (145.8 mg, 0.603 mmol) and an ethanolic solution (10 mL) of bpy (188.4 mg, 1.206 mmol) dropwise with stirring at room temperature. Slow concentration of the resulting solution at ambient conditions led to the formation of dark-green single crystals of **1** as the only solid with a yield of 297.1 mg (86%). $C_{46}H_{34}CrCu_2N_9O_{16}$ (1147.90): calcd. C 48.13, H 2.98, N 10.98; found C 47.74, H 3.14, N 10.93. IR data (KBr): $\tilde{\nu}$ = 3434 (w, br), 3073 (w), 1717 (m), 1705 (m), 1672 (vs), 1663 (vs), 1625 (vs), 1607 (m), 1598 (s), 1493 (m), 1474 (m), 1444 (s), 1415 (s), 1382 (vs), 1370 (sh), 1338 (m), 1314 (m), 1276 (m), 1251 (m), 1226 (m), 1175 (w), 1162 (w), 1105 (w), 1029 (w), 1013 (w), 898 (w), 817 (sh), 801 (m), 795 (m), 773 (vs), 732 (m), 534 (m), 460 (w), 419 (m), 410 (m), 304 (w) $cm^{-1}$.

**Synthesis of [Cu(bpy)$_3$]$_2$[Cr($C_2O_4$)$_3$]$NO_3$·9$H_2O$ (2):** To an aqueous solution (15 mL) of K$_3$[Cr($C_2O_4$)$_3$]·3$H_2O$ (103.3 mg, 0.212 mmol) was added an aqueous solution (10 mL) of [Cu(bpy)$_3$]($NO_3$)$_2$·6$H_2O$ (162.0 mg, 0.212 mmol) dropwise with stirring at room temperature. The green-blue plate-like crystals of **2** were formed in the solution in a period of three days. The yield was 125.8 mg (37%, based on Cr). $C_{66}H_{66}CrCu_2N_{13}O_{24}$ (1604.40): calcd. C 49.41, H 4.15, N 11.35; found C 49.14, H 4.40, N 11.71. IR data (KBr): $\tilde{\nu}$ = 3415 (m, br), 3074 (w), 1708 (m), 1681 (s), 1650 (m), 1594 (m), 1491 (w), 1472 (m), 1441 (s), 1384 (vs), 1372 (m), 1312 (w), 1257 (sh), 1248 (m), 1176 (w), 1158 (w), 1101 (w), 1062 (w), 1043 (w), 1015 (m), 910 (w), 806 (m), 797 (m), 776 (vs), 734 (m), 650 (m), 538 (m), 475 (w), 411 (m), 307 (w) $cm^{-1}$.

When the reaction of K$_3$[Cr($C_2O_4$)$_3$]·3$H_2O$ and [Cu(bpy)$_3$]($NO_3$)$_2$·6$H_2O$ was performed in a molar ratio of 1:2, crystals of both **1** and **2** formed simultaneously.

**Physical Techniques:** Infrared absorption spectra were recorded by using KBr pellets with an ABB Bomem FT model MB 102 spectrometer, in the 4000–200 $cm^{-1}$ region. Thermogravimetric measurements were carried out with a Shimadzu DTG-60 analyzer, with a heating rate of 10 °C $min^{-1}$ in a stream of synthetic air. Electronic spectra were measured with a Cary 50 Probe spectrophotometer. Solution spectra were recorded in $H_2O$ by using 1-cm silica cells. For solid-state spectra, the samples were prepared as KBr pellets which were mounted in the pathway of the radiation beam. A weighed pure-KBr pellet was used as the reference.

Magnetic moments were measured with a commercial SQUID magnetometer (MPMS-5, Quantum Design). Measurements were performed in the temperature range 1.8–290 K at an applied magnetic field of 1 T. The field dependence of the magnetic moment was checked up to 5 T, and both samples showed linearity up to more than 1 T even at 2 K, so the susceptibilities analyzed here are field-independent. The calculated molar magnetic susceptibilities were corrected for the diamagnetic contributions of the constituent atoms, which are $-560 \cdot 10^{-6}\ cm^3\ mol^{-1}$ for **1** and $-874 \cdot 10^{-6}\ cm^3\ mol^{-1}$ for **2** according to Pascal's constants.[31] Also, a correction was made for temperature-independent paramagnetism, which is $110 \cdot 10^{-6}\ cm^3\ mol^{-1}$ for $Cr^{III}$ and $60 \cdot 10^{-6}\ cm^3\ mol^{-1}$ for $Cu^{II}$ ions.[10d]

**X-ray Crystallographic Study:** Each of the selected single crystals of **1** and **2** was glued on the tip of a glass fibre and coated with a

 © 2006 Wiley-VCH Verlag GmbH & Co. KGaA, Weinheim 

thin layer of silicone grease. The X-ray data were collected at 100(1) K by $\omega$ scans with an Oxford Diffraction Xcalibur 3 CCD diffractometer with graphite-monochromated Mo-$K_\alpha$ radiation ($\lambda$ = 0.71073 Å). Data reduction including the absorption correction was performed with the CrysAlis software package.[32] Crystal data, experimental conditions and final refinement parameters are summarized in Table 6. Solution, refinement and analysis of the structures was performed by using the programs integrated in the WinGX system.[33] Both structures were solved by direct methods (SIR92)[34] and refined by the full-matrix least-squares method based on $F^2$ against all reflections (SHELXL-97).[35] All non-hydrogen atoms were refined anisotropically. The anisotropic displacement parameters of the disordered atoms were restrained during refinement, except those of the atoms C23B in **1** and O24B in **2** which were constrained to equal the anisotropic displacement parameters of C23A and O24A, respectively (EADP). Additionally, in **1**, the geometries of the two parts of the disordered non-bridging oxalate ligands were restrained to be equal. Furthermore, the atoms in each of the sets {O5, O6A, C23A, C23B($1-x$, $y$, $1/2-z$)} and {O5, O6B, C23B, C23A($1-x$, $y$, $1/2-z$)} were restrained to be coplanar. In both structures, the hydrogen atoms bound to the carbon atoms were treated as riding in idealized positions, with C–H = 0.95 Å, and displacement parameters were assigned as $U_{iso}(H) = 1.2U_{eq}$ of the attached C atom. Initial positions of the water H atoms in **1** as well as those of some of the H atoms of the water molecules in **2** were found in the difference Fourier map. Other modelled water H atoms of **2** were obtained by combined geometric and force-field calculations on the basis of hydrogen-bonding interactions (CALC-OH).[36] For all water H atoms, the O–H vector directions were kept fixed, while the O–H distances were restrained (DFIX 0.85 0.02) during refinement. Prior to applying the mentioned constraints and restraints to the water molecules, those having the calculated H atoms were additionally refined as rigid bodies by using the O atoms as the pivot ones. Displacement parameters of all water H atoms were assigned as $U_{iso}(H) = 1.5U_{eq}$ of the joined O atom. Geometrical calculations were performed using PLATON[37] and the figures were produced by using ORTEP-3[38] and SCHAKAL99.[39]

Table 6. Crystallographic data for compounds **1** and **2**.

| Compound | **1** | **2** |
|---|---|---|
| Empirical formula | $C_{46}H_{34}CrCu_2N_9O_{16}$ | $C_{66}H_{66}CrCu_2N_{13}O_{24}$ |
| $M_r$ | 1147.90 | 1604.40 |
| Crystal colour, habit | dark green prism | green-blue prism |
| Crystal size [mm] | 0.48×0.21×0.20 | 0.44×0.24×0.15 |
| Crystal system | monoclinic | monoclinic |
| Space group | *C*2/*c* (no. 15) | $P2_1/c$ (no. 14) |
| *a* [Å] | 16.4284(12) | 31.314(3) |
| *b* [Å] | 17.1622(11) | 13.5356(11) |
| *c* [Å] | 16.7494(12) | 22.202(2) |
| $\beta$ [°] | 110.721(7) | 132.012(13) |
| *V* [Å$^3$] | 4417.0(6) | 6992.0(18) |
| *Z* | 4 | 4 |
| *T* [K] | 100(1) | 100(1) |
| $D_{calcd.}$ [g cm$^{-3}$] | 1.726 | 1.524 |
| $\mu$ (Mo-$K_\alpha$) [mm$^{-1}$] | 1.285 | 0.845 |
| Absorption correction | numerical | numerical |
| $T_{min}/T_{max}$ | 0.659/0.816 | 0.710/0.896 |
| *F*(000) | 2332 | 3308 |
| $\theta$ range for collected data [°] | 4.15–30.00 | 3.88–25.00 |
| Limiting indices | $-23 \le h \le 23$ | $-37 \le h \le 37$ |
| | $-24 \le k \le 24$ | $-16 \le k \le 15$ |
| | $-23 \le l \le 23$ | $-26 \le l \le 26$ |
| Data total/unique | 34029/6427 | 85275/12253 |
| $R_{int}/R_\sigma$ | 0.0238/0.0245 | 0.0500/0.0356 |
| Completeness to $\theta_{max}$ | 0.997 | 0.995 |
| Observed data [$I > 2\sigma(I)$] | 5450 | 10113 |
| Data/restraints/parameters | 6427/37/370 | 12253/16/977 |
| *S*/restrained *S* | 1.113/1.111 | 1.156/1.160 |
| $R_1$, $wR_2$ [$I > 2\sigma(I)$] | 0.0357, 0.0896 | 0.0570, 0.1496 |
| $R_1$, $wR_2$ (all data) | 0.0456, 0.0930 | 0.0753, 0.1637 |
| $\Delta\rho_{max}$ [e Å$^{-3}$] | 0.748 | 1.116 |
| $\Delta\rho_{min}$ [e Å$^{-3}$] | –0.413 | –0.647 |

CCDC-279737 (**1**) and CCDC-279738 (**2**) contain the supplementary crystallographic data for this paper. These data can be obtained free of charge from The Cambridge Crystallographic Data Centre via www.ccdc.cam.ac.uk/data_request/cif.

**Supporting Information** (see footnote on the first page of this article): All hydrogen-bonding interactions in the structure of **1** (Table S1) and the structure of **2** (Table S2).

## Acknowledgments

This research was supported by the Ministry of Science, Education and Sports of the Republic of Croatia (Grants No. 0098066, 0119632 and 0119258).

[1] O. Kahn, *Molecular Magnetism*, Wiley-VCH, New York, **1993**.
[2] W. Linert, M. Verdaguer (Eds.), *Molecular Magnets Recent Highlights*, Springer-Verlag, Wien, **2003**.
[3] a) H. Tamaki, Z. J. Zhong, N. Matsumoto, S. Kida, M. Koikawa, N. Achiwa, Y. Hashimoto, H. Ōkawa, *J. Am. Chem. Soc.* **1992**, *114*, 6974–6979; b) Z. J. Zhong, N. Matsumoto, H. Ōkawa, S. Kida, *Chem. Lett.* **1990**, 87–90.
[4] a) L. O. Atovmyan, G. V. Shilov, R. N. Lyubovskaya, E. I. Zhilyaeva, N. S. Ovanesyan, S. I. Pirumova, I. G. Gusakovskaya, Y. G. Morozov, *JETP Lett.* **1993**, *58*, 766–769; b) R. Pellaux, H. W. Schmalle, R. Huber, P. Fischer, T. Hauss, B. Ouladdiaf, S. Decurtins, *Inorg. Chem.* **1997**, *36*, 2301–2308.
[5] S. Decurtins, H. W. Schmalle, H. R. Oswald, A. Linden, J. Ensling, P. Gütlich, A. Hauser, *Inorg. Chim. Acta* **1994**, *216*, 65–73.
[6] a) S. Decurtins, H. W. Schmalle, P. Schneuwly, J. Ensling, P. Gütlich, *J. Am. Chem. Soc.* **1994**, *116*, 9521–9528; b) S. Decurtins, H. W. Schmalle, R. Pellaux, P. Schneuwly, A. Hauser, *Inorg. Chem.* **1996**, *35*, 1451–1460; c) R. Sieber, S. Decurtins, H. Stoeckli-Evans, C. Wilson, D. Yufit, J. A. K. Howard, S. C. Capelli, A. Hauser, *Chem. Eur. J.* **2000**, *6*, 361–368.
[7] a) E. Coronado, J. R. Galán-Mascarós, C. J. Gómez-García, J. M. Martínez-Agudo, *Inorg. Chem.* **2001**, *40*, 113–120; b) R. Andrés, M. Brissard, M. Gruselle, C. Train, J. Vaissermann, B. Malézieux, J.-P. Jamet, M. Verdaguer, *Inorg. Chem.* **2001**, *40*, 4633–4640.
[8] M. Ohba, H. Tamaki, N. Matsumoto, H. Ōkawa, *Inorg. Chem.* **1993**, *32*, 5385–5390.
[9] T. Sanada, T. Suzuki, T. Yoshida, S. Kaizaki, *Inorg. Chem.* **1998**, *37*, 4712–4717.
[10] a) M. Andruh, R. Melanson, C. V. Stager, F. D. Rochon, *Inorg. Chim. Acta* **1996**, *251*, 309–317; b) F. D. Rochon, R. Melanson, M. Andruh, *Inorg. Chem.* **1996**, *35*, 6086–6092; c) M. C. Muñoz, M. Julve, F. Lloret, J. Faus, M. Andruh, *J. Chem. Soc., Dalton Trans.* **1998**, 3125–3131; d) R. Lescouëzec, G. Marinescu, J. Vaissermann, F. Lloret, J. Faus, M. Andruh, M. Julve, *Inorg. Chim. Acta* **2003**, *350*, 131–142.
[11] G. Marinescu, M. Andruh, R. Lescouëzec, M. C. Muñoz, J. Cano, F. Lloret, M. Julve, *New J. Chem.* **2000**, *24*, 527–536.
[12] G. De Munno, D. Armentano, M. Julve, F. Lloret, R. Lescouëzec, J. Faus, *Inorg. Chem.* **1999**, *38*, 2234–2237.
[13] a) Y.-T. Li, C.-W. Yan, H.-S. Guan, *Polyhedron* **2003**, *22*, 3223–3230; b) Y.-T. Li, C.-W. Yan, J.-F. Lou, H.-S. Guan, *J. Magn. Magn. Mater.* **2004**, *281*, 68–76; c) Y.-T. Li, C.-W. Yan, H.-S. Guan, *Transition Met. Chem.* **2004**, *29*, 537–542.

 © 2006 Wiley-VCH Verlag GmbH & Co. KGaA, Weinheim 

[14] F. H. Allen, O. Kennard, D. G. Watson, L. Brammer, A. G. Orpen, R. Taylor, *J. Chem. Soc., Perkin Trans. 2* **1987**, S1–S19.
[15] a) O. Costisor, K. Mereiter, M. Julve, F. Lloret, Y. Journaux, W. Linert, M. Andruh, *Inorg. Chim. Acta* **2001**, *324*, 352–358; b) E. Coronado, M. C. Giménez, C. J. Gómez-García, F. M. Romero, *Polyhedron* **2003**, *22*, 3115–3122.
[16] G. Marinescu, D. Visinescu, A. Cucos, M. Andruh, Y. Journaux, V. Kravtsov, Y. A. Simonov, J. Lipkowski, *Eur. J. Inorg. Chem.* **2004**, 2914–2922.
[17] C. Janiak, *J. Chem. Soc., Dalton Trans.* **2000**, 3885–3896.
[18] C. Faulmann, Y. S. J. Veldhuizen, J. G. Haasnoot, J. Reedijk, P. Cassoux, *Acta Crystallogr., Sect. C* **1998**, *54*, 1827–1830.
[19] P. Majumdar, A. K. Ghosh, L. R. Falvello, S.-M. Peng, S. Goswami, *Inorg. Chem.* **1998**, *37*, 1651–1654.
[20] J.-L. Song, H.-Y. Zeng, B.-P. Yang, Z.-C. Dong, G.-C. Guo, J.-S. Huang, *Jiegou Huaxue* **2003**, *22*, 29.
[21] G. A. van Albada, A. Mohamadou, I. Mutikainen, U. Turpeinen, J. Reedijk, *Eur. J. Inorg. Chem.* **2004**, 3733–3742.
[22] D. Taylor, *Aust. J. Chem.* **1978**, *31*, 1455.
[23] K. Nakamoto, *Infrared and Raman Spectra of Inorganic and Coordination Compounds*, 5th ed., John Wiley, New York, **1997**.
[24] D. Sutton, *Electronic Spectra of Transition Metal Complexes*, McGraw-Hill, London, **1968**.
[25] A. B. P. Lever, *Inorganic Electronic Spectroscopy*, Elsevier, Amsterdam, **1968**.
[26] M. Julve, M. Verdaguer, A. Gleizes, M. Philoche-Levisalles, O. Kahn, *Inorg. Chem.* **1984**, *23*, 3808–3818.
[27] Y. Pei, Y. Journaux, O. Kahn, *Inorg. Chem.* **1989**, *28*, 100–103.
[28] J. Cano, P. Alemany, S. Alvarez, M. Verdaguer, E. Ruiz, *Chem. Eur. J.* **1998**, *4*, 476–484.
[29] G. Brauer (Ed.), *Handbuch der Präparativen Anorganischen Chemie*, Ferdinand Enke Verlag, Stuttgart, **1954**.
[30] F. M. Jaeger, J. A. van Dijk, *Z. Anorg. Allg. Chem.* **1936**, *227*, 273–327.
[31] P. W. Selwood, *Magnetochemistry*, Interscience Publishers, Inc., New York, **1956**.
[32] Oxford Diffraction, Oxford Diffraction Ltd., *Xcalibur CCD System, CrysAlis Software System*, Version 1.170, **2003**.
[33] L. J. Farrugia, *J. Appl. Crystallogr.* **1999**, *32*, 837–838.
[34] A. Altomare, G. Cascarano, C. Giacovazzo, A. Guagliardi, *J. Appl. Crystallogr.* **1993**, *26*, 343–350.
[35] M. Sheldrick, *SHELXL-97, Program for the Refinement of Crystal Structures*, University of Göttingen, Germany, **1997**.
[36] M. Nardelli, *J. Appl. Crystallogr.* **1999**, *32*, 563–571.
[37] a) A. L. Spek, *Acta Crystallogr., Sect. A* **1990**, *46*, C34; b) A. L. Spek, *PLATON – A Multipurpose Crystallographic Tool*, Utrecht University, Utrecht, The Netherlands, **2005**.
[38] L. J. Farrugia, *J. Appl. Crystallogr.* **1997**, *30*, 565.
[39] E. Keller, *J. Appl. Crystallogr.* **1989**, *22*, 19–22.

Received: December 6, 2005
Published Online: April 25, 2006

 © 2006 Wiley-VCH Verlag GmbH & Co. KGaA, Weinheim 

EurJIC
European Journal of Inorganic Chemistry

Issue 14/2006

Pages 2713–2912

*Papers available ahead of print in Early View at www.interscience.wiley.com*

*Earliest available Table of Contents:*
*Automatically, free of charge by e-mail through*
*www.interscience.wiley.com/alerts*

## COVER PICTURE

**The cover picture shows** the two types of complexes formed by the reaction of diethylzinc and tripodal monoanionic amine mono(phenolate) ligand precursors bearing two methoxy sidearm donors. The ligand precursor bearing bulky (*t*Bu) phenolate substituents leads cleanly to a mono(ethyl) mononuclear zinc complex in which the two methoxy sidearm donors are bound to the metal atom as confirmed by spectroscopic data and X-ray structure analysis. The ligand precursors bearing less bulky phenolate substituents lead cleanly to dinuclear pentacoordinate complexes that are bridged by phenolate oxygen atoms, and only one of the two sidearm donors is bound. Details are discussed in the article by M. Kol et al. on p. 2739 ff.

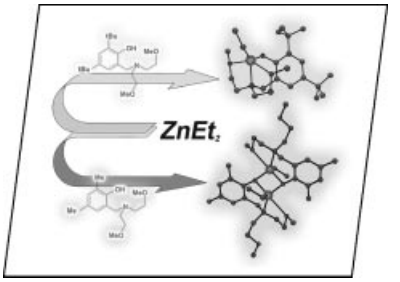


## MICROREVIEW

**Contents**

**2725** **D. Collison, E. J. L. McInnes,* E. K. Brechin***

Tetrahedra, Super-Tetrahedra, Bipyramids, Boxes and More: Polymetallic Clusters of Benzotriazole

**Keywords:** Benzotriazole / Clusters / Transition metals / Large spin ground states / Single-molecule magnets

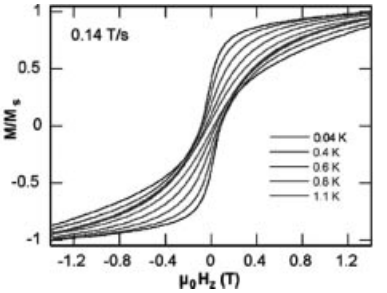


 © 2006 Wiley-VCH Verlag GmbH & Co. KGaA, Weinheim 

# SHORT COMMUNICATIONS


**2735** **R. Le Lagadec, L. Alexandrova, H. Estevez, M. Pfeffer, V. Laurinavičius, J. Razumiene, A. D. Ryabov***

Bis-Ruthena(III)cycles $[Ru(C^{\cap}N)_2(N^{\cap}N)]PF_6$ as Low-Potential Mediators for PQQ Alcohol Dehydrogenase ($C^{\cap}N$ = 2-phenylpyridinato or 4-(2-tolyl)pyridinato, $N^{\cap}N$ = bpy or phen)

**Keywords:** Ruthenium / Metallacycles / X-ray diffraction / Biosensors / PQQ dehydrogenase


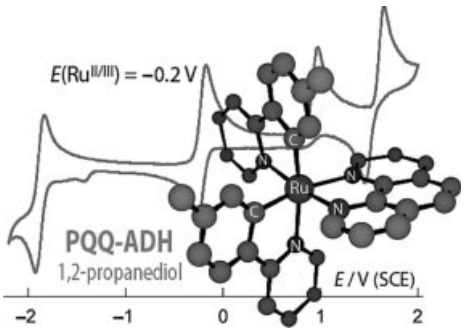


# FULL PAPERS


**2739** **S. Groysman, E. Sergeeva, I. Goldberg, M. Kol***

Zinc Complexes of Amine Mono(phenolate) $[NOO_2]$ Ligands: Controlling Coordination Modes by Bulk of Phenolate Substituents

**Keywords:** Zinc / N,O ligands / Tripodal ligands / Polynuclear complexes


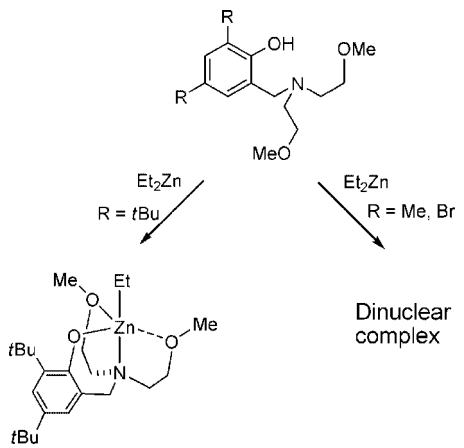



**2746** **S. Delgado,* A. Barrilero, A. Molina-Ontoria, M. E. Medina, C. J. Pastor, R. Jiménez-Aparicio, J. L. Priego**

Novel Coordination Polymers Generated from Angular 2,2′-Dipyridyl Ligands and Bis(hexafluoroacetylacetonate) Copper(II): Crystal Structures and Magnetic Properties

**Keywords:** Coordination polymers / Copper / N ligands


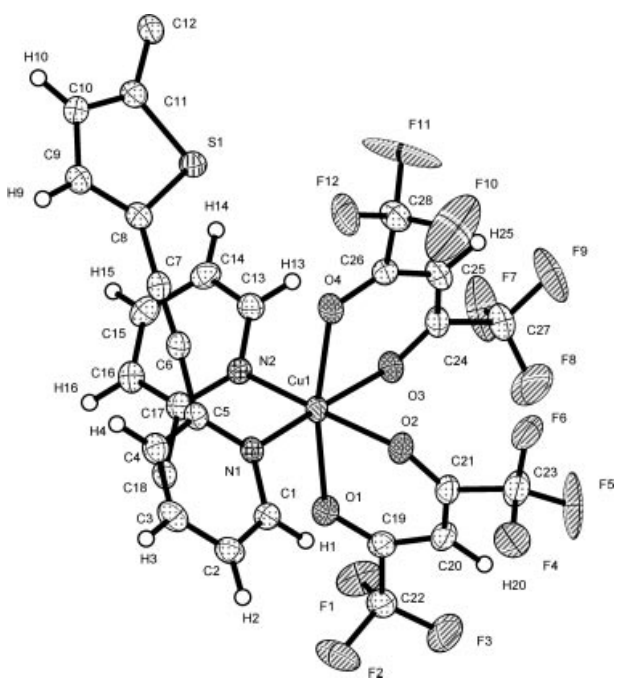

**2760** **D.-X. Jia,* Q.-X. Zhao, Y. Zhang, J. Dai, J. Zhou**

Solvothermal Synthesis, Crystal Structures, and Properties of New Selenidoantimonates $[Ln(en)_4(SbSe_4)]$ (Ln = La, Nd) and $[Sm(en)_4]SbSe_4 \cdot 0.5en$: The First Example of an $SbSe_4^{3-}$ Anion Acting as a Ligand to a Lanthanide Complex

**Keywords:** Selenidoantimonates / Lanthanides / Antimony / Solvothermal synthesis / Crystal structures

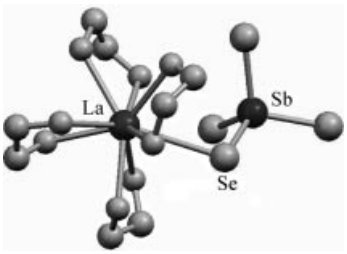


**2766** **T. Doussineau, J.-O. Durand, O. El-Mahdi, C. Maillet, O. Melnyk, C. Olivier, M. Smaïhi***

Semicarbazide-Functionalized Silicate Nanoparticles for Peptide Ligation

**Keywords:** Zeolites / Colloids / Peptides / Fluorescence spectroscopy / Organic−inorganic composites

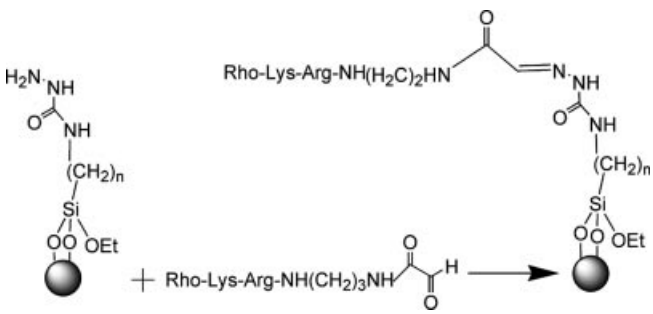


**2773** **M. F. Davis, M. Clarke, W. Levason,* G. Reid, M. Webster**

Tin(IV) Fluoride Complexes with Tertiary Phosphane Ligands − A Comparison of Hard and Soft Donor Ligands

**Keywords:** Tin / Fluoride / Phosphane / Multinuclear NMR / Crystal structures

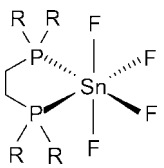

**2783** **J. Notni, S. Schenk, A. Roth, W. Plass, H. Görls, U. Uhlemann, A. Walter, M. Schmitt, J. Popp, S. Chatzipapadopoulos, T. Emmler, H. Breitzke, J. Leppert, G. Buntkowsky, K. Kempe, E. Anders***

Zinc Thiolate Complexes $[ZnL_n(SR)]^+$ with Azamacrocyclic Ligands, Part II: Mechanism of the Reaction with $CS_2$

**Keywords:** Zinc / Macrocyclic ligands / Enzyme models / Heterocumulenes / Density functional calculations

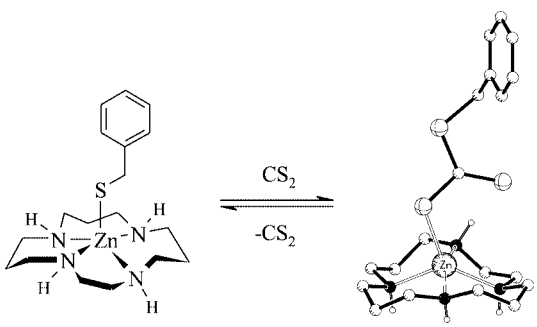


**2792** **D. Kuppert, P. Comba, K. Hegetschweiler***

The Reactivity of Hexa(*N*-methylideneimine)-$Co^{III}$ Complexes towards Nucleophiles: Structure and Mechanism

**Keywords:** Nucleophilic addition / Hydrogen transfer / N ligands / Cobalt / Chelates

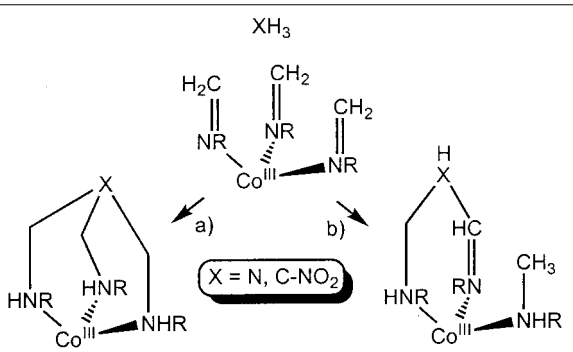


 © 2006 Wiley-VCH Verlag GmbH & Co. KGaA, Weinheim 

**2808** **Z.-Z. Liu, W. Q. Tian,* J.-K. Feng,* G. Zhang, W.-Q. Li, Y.-H. Cui, C.-C. Sun**

A Theoretical Study on Structures, Bonding Energies and Aromaticity of Two New Series of Dinuclear Phosphametallocenes: ($\eta^5$-$P_5$)MM′-($\eta^5$-$P_5$) and ($\eta^5$-$C_5H_5$)MM′($\eta^5$-$P_5$) (M, M′ = Zn, Cd)

**Keywords:** Dinuclear phosphametallocenes / Structures / Bonding energies / Aromaticity / Density functional theory

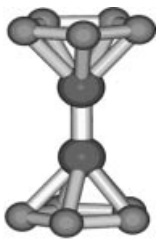

($\eta^5$–$P_5$)$Zn_2$($\eta^5$–$P_5$)

**2819** **I. Correia, A. Dornyei, T. Jakusch, F. Avecilla, T. Kiss,* J. C. Pessoa***

Water-Soluble $Sal_2$en- and Reduced $Sal_2$en-Type Ligands: Study of Their $Cu^{II}$ and $Ni^{II}$ Complexes in the Solid State and in Solution

**Keywords:** Copper(II) / Nickel(II) / Reduced Schiff bases / Speciation / Crystal structure

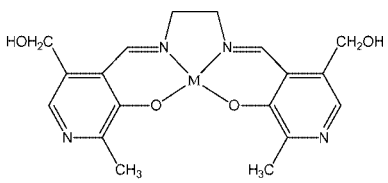

Mpyr$_2$en

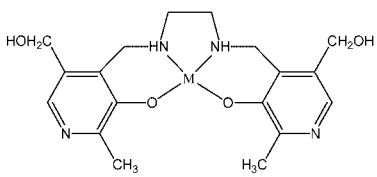

MRpyr$_2$en

**2831** **M. Wei, X. Y. Xu, X. R. Wang, F. Li, H. Zhang, Y. L. Lu, M. Pu, D. G. Evans, X. Duan***

Study on the Photochromism of Ni−Al Layered Double Hydroxides Containing Nitrate Anions

**Keywords:** Layered compounds / Photochromism / Host−guest systems

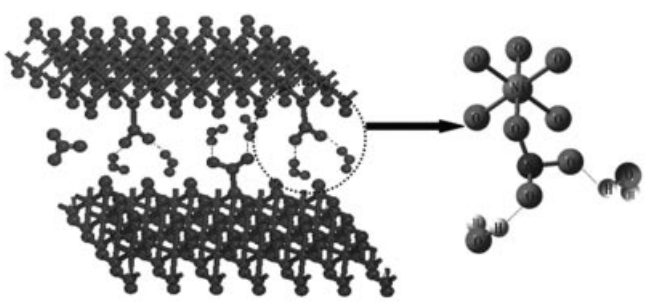

**2839** **R. Gobetto,* G. Caputo, C. Garino, S. Ghiani, C. Nervi, L. Salassa, E. Rosenberg,* J. B. A. Ross, G. Viscardi, G. Martra, I. Miletto, M. Milanesio**

Synthesis, Electrochemical and Electrogenerated Chemiluminescence Studies of Ruthenium(II) Bis(2,2′-bipyridyl){2-(4-methylpyridin-2-yl)-benzo[*d*]-X-azole} Complexes

**Keywords:** Electrochemistry / Luminescence / Ruthenium / ECL / Bioinorganic chemistry

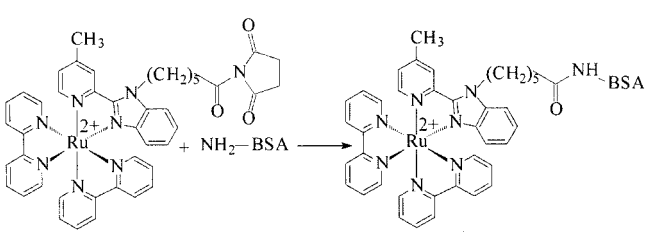


 © 2006 Wiley-VCH Verlag GmbH & Co. KGaA, Weinheim 

**2850** **S.-H. Yang, G.-B. Li,* S.-J. Tian, F.-H. Liao, J.-H. Lin**

Synthesis, Structure, and Magnetic Properties of Hydroxo-Bridged Vanadium Oxalate $V_2O_2(OH)_2(C_2O_4)(H_2O)_2$

**Keywords:** Vanadium / Bridging ligands / Magnetic properties / Dimers / Oxalates

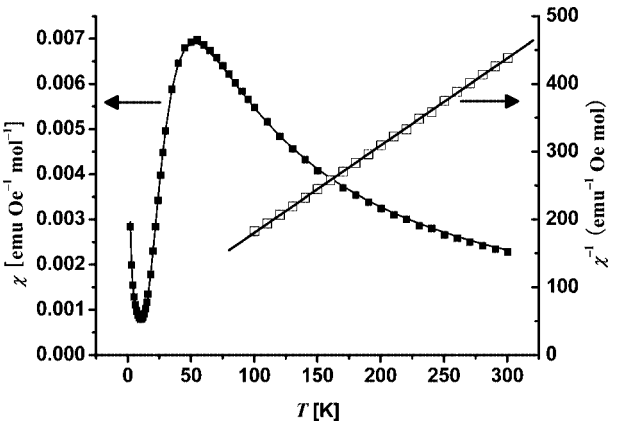


**2855** **J. Díez, M. P. Gamasa, E. Lastra,* A. García-Fernández, M. P. Tarazona**

Transfer Hydrogenation of Ketones Catalysed by New Half-Sandwich Ruthenium(II) Complexes Bearing the Sulfonated Phosphane (*meta*-Sulfonatophenyl)diphenylphosphane Potassium Salt (TPPMS)

**Keywords:** Water-soluble catalysts / Sulfonated phosphanes / Arene complexes / Ruthenium(II) / Hydrogen transfer

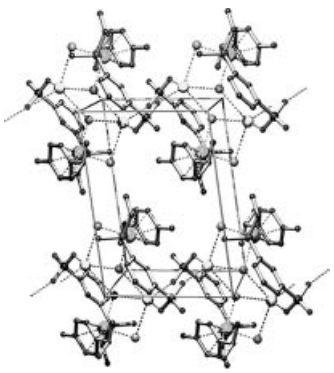

**2865** **P. C. Andrews,* M. Minopoulos, E. G. Roberston**

Coordination and Reduction of HMPA in the Lithiation of (*S*)-*N*-(-α-Methylbenzyl)allylamine: Crystal Structures of $\{(S)$-α-$[PhC(H)CH_3](CH_2CH{=}CH_2)NLi{\cdot}HMPA\}_2$ and $[(Me_2N)_2POLi]_6$

**Keywords:** Lithium / Chiral metal amides

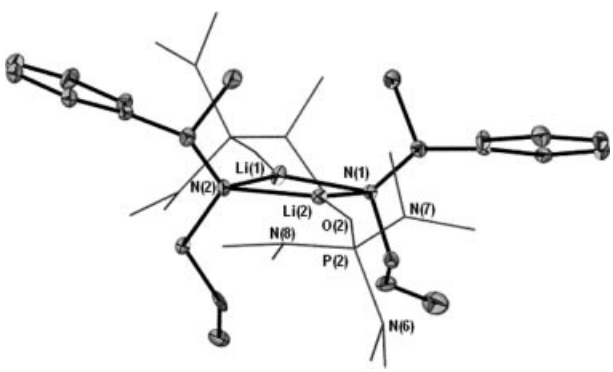


**2871** **V. K. Muppidi, S. Pal***

Dicopper(II) Complexes with the Enantiomers of a Bidentate Chiral Reduced Schiff Base: Inclusion of Chlorinated Solvents and Chiral Recognition of 1,2-Dichloroethane Rotamers in the Crystal Lattice

**Keywords:** Dicopper(II) complexes / Chiral reduced Schiff Bases / Crystal structures / Chlorinated solvents / Enantioselective inclusion

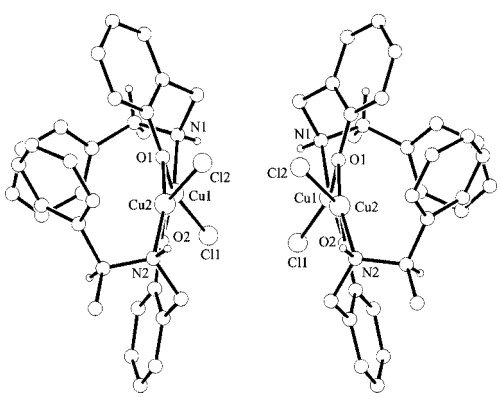


 © 2006 Wiley-VCH Verlag GmbH & Co. KGaA, Weinheim 

**2878** **A. Lehtonen,* R. Sillanpää**

Reactions of Aminobis(phenolate)-Supported Dioxidotungsten(VI) and Dioxidomolybdenum(VI) Complexes

**Keywords:** Molybdenum / Tungsten / Oxido ligands / N,O ligands / Halides

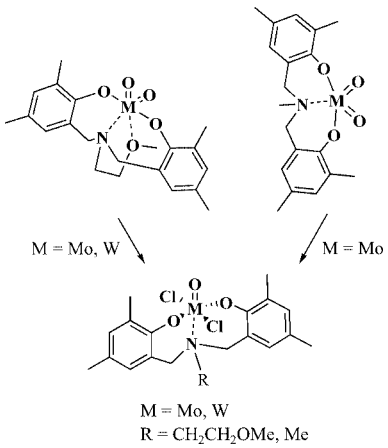


**2885** **C. Garino, S. Ghiani, R. Gobetto, C. Nervi,* L. Salassa, G. Croce, M. Milanesio, E. Rosenberg,* J. B. A. Ross**

Tricarbonylchlororhenium(I) Carboxaldimine Derivatives: Synthesis, Structure, and NMR Characterization of *Z* and *E* Isomers

**Keywords:** *E*/*Z* isomerization / Density functional calculations / N ligands / Rhenium

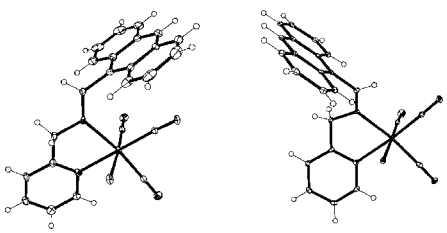

**2894** **M. Kotowski, R. Marcec, V. Butkovic, A. Bakac,* M. Orhanovic**

Preparation, Characterization, and Aquation Kinetics of Pyridine *N*-Oxide Complexes of Chromium(III)

**Keywords:** Pyridine oxide / Chromium / Kinetics / Mechanism / Aquation

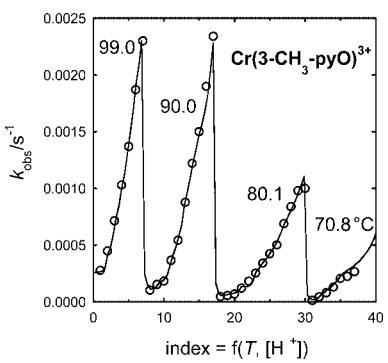


**2900** **S.-L. Li, J.-Y. Wu, Y.-P. Tian,* H. Ming, P. Wang, M.-H. Jiang, H.-K. Fun**

Design, Crystal Growth, Characterization, and Second-Order Nonlinear Optical Properties of Two New Three-Dimensional Coordination Polymers Containing Selenocyanate Ligands

**Keywords:** Self-assembly / Coordination polymer / Crystal growth / Nonlinear optical properties

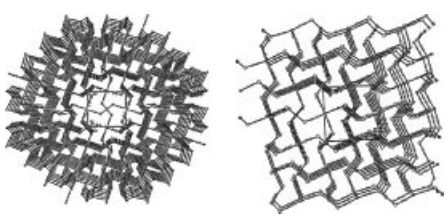

 © 2006 Wiley-VCH Verlag GmbH & Co. KGaA, Weinheim 

DOI: 10.1002/ejic.200600206

# Tetrahedra, Super-Tetrahedra, Bipyramids, Boxes and More: Polymetallic Clusters of Benzotriazole

**David Collison,[a] Eric J. L. McInnes,*[a] and Euan K. Brechin*[b]**

**Keywords:** Benzotriazole / Clusters / Transition metals / Large spin ground states / Single-molecule magnets

The syntheses, structures and magnetic properties of a host of polymetallic 3d transition-metal clusters made with the pro-ligand benzotriazole (BtaH) and its analogues are reported. These range from a family of tetradecametallic clusters with spin ground states as large as $S \approx 25$, to decametallic vanadium "boxes", to iron and manganese tetra- and super-tetrahedra, to hexaicosametallic manganese single-molecule magnets.
(© Wiley-VCH Verlag GmbH & Co. KGaA, 69451 Weinheim, Germany, 2006)

## Introduction

The synthesis and characterization of polynuclear clusters of paramagnetic metal ions has attracted intense study since the discovery that such molecules can display the phenomenon of single-molecule magnetism.[1] In these molecules there exists an energy barrier to the relaxation of the magnetization due to the combination of a large ground-state spin multiplicity and significant negative magnetoanisotropy. This imparts a molecular magnetic memory effect that can be observed as temperature- and sweep-rate-dependent hysteresis loops in $M$ vs. $H$ studies.[2]

Single-Molecule Magnets (SMMs) have many potential applications including high-density information storage in

[a] School of Chemistry, The University of Manchester, Oxford Road, Manchester, M13 9PL, UK
E-mail: eric.mcinnes@manchester.ac.uk
[b] School of Chemistry, The University of Edinburgh, West Mains Road, Edinburgh, EH9 3JJ, UK
E-mail: ebrechin@staffmail.ed.ac.uk

*David Collison graduated (University of Manchester) in 1976 and after a PhD (Manchester, with C. D. Garner and I. H. Hillier), and post-doctoral work (Manchester, F E. Mabbs; Manchester, C. D. Garner; UMIST, N. J. Blackburn), became a SRC Fellow (Manchester) and subsequently a Royal Society University Research Fellow (Manchester). He was appointed Senior Lecturer at the University of Manchester in 1994 and promoted to his current position of Reader in 1998. His research concentrates on the electronic structure of transition metals in chemical, biological and materials sciences.*

*Eric McInnes is a Reader in the School of Chemistry at The University of Manchester. He completed his PhD in 1995 under the supervision of Dr Lesley J. Yellowlees at the University of Edinburgh, where he also obtained his BSc in 1992. He was a post-doctoral researcher in Manchester with Drs. Frank E. Mabbs and David Collison, then at the University of East Anglia with Profs Andrew J. Thomson FRS and Annie K. Powell, before taking a lectureship in Manchester in 2000.*

*Euan Brechin was born in Greenock, Scotland, in 1972. He completed both his BSc (1994) and PhD (1997) degrees at The University of Edinburgh (UK), the latter under the supervision of Dr R. E. P. Winpenny. After postdoctoral work with Professor George Christou at Indiana University (USA) he was awarded a Lloyd's of London Tercentenary Foundation Fellowship at the University of Manchester (UK). In 2003 he was awarded an EPSRC Advanced Fellowship at the same institution, before moving to his present position at The University of Edinburgh in September 2004.*

 © 2006 Wiley-VCH Verlag GmbH & Co. KGaA, Weinheim 

which each bit of information is stored as the magnetization orientation of an individual molecule, and as qubits for quantum computation where the required arbitrary superposition of quantum states with opposite projections of spin are produced by either quantum tunneling of the magnetization (QTM), intermolecular exchange, or multi-frequency EPR pulses.[3]

Single-molecule magnetism spans areas as diverse as physics, theoretical chemistry, spectroscopy, materials chemistry and synthetic coordination chemistry, as demonstrated by the several hundred papers published on the topic over the last ten years. There are now several species displaying such behavior – formed by a multitude of successful synthetic strategies ranging from the self-assembly of 3d-metal carboxylate clusters, to molecular Prussian Blues, to heterometallic 3d–4f complexes and most recently to simple 4f monometallic species.[4] By far the most productive route has been by the self-assembly of 3d transition metals with flexible organic bridging ligands such as carboxylates and alkoxides. Here we describe some of our efforts toward the synthesis of large polymetallic 3d clusters using the ligand benzotriazole (and its analogues), including some of the largest nuclearity and highest-spin ground-state molecules known.

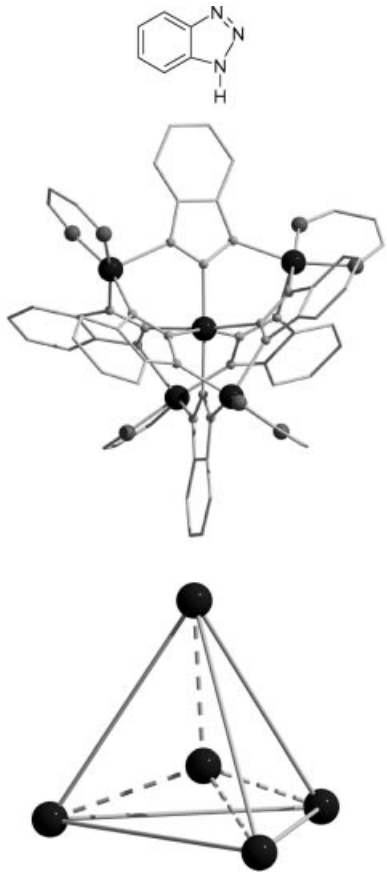

Figure 1. The structure of benzotriazole (BtaH, top); the structure of the complex $[Cu_5(Bta)_6(acac)_4]$ (middle); and its centered tetrahedral $\{Cu_5\}$ core (bottom). The $-CH_3$ groups of the $acac^-$ ligands have been removed for clarity.

Benzotriazole (BtaH, $C_6H_5N_3$; Figure 1) and substituted benzotriazoles are well established corrosion inhibitors for copper and its alloys,[5] and as a result the coordination chemistry of benzotriazoles with various $M^{2+}$ species has been thoroughly investigated, producing many new cluster compounds. Of these the most well-known and thoroughly studied are the family of compounds of general formula $[M_5(OH)_x(R)_{6-x}(L)_4(H_2O)_{4x}]$ [where M = Cu, Zn, Ni; R = $Bta^-$, $Me_2Bta^-$ (5,6-$Me_2$-$bta^-$); L = β-diketonate, $x$ = 0, 1].[6] These pentametallic species consist of a tetrahedral arrangement of four $M^{2+}$ ions centered on a fifth, with each $\mu_3$-benzotriazole spanning an edge of the tetrahedron (Figure 1). Magnetic studies have shown that weak antiferromagnetic exchange between the metals leads to spin ground states equal to that of the *"isolated"* central $M^{2+}$ ion.

Although a number of other $Ni^{2+}$,[7] $Cu^{2+}$,[8] $Hg^{2+}$,[9] $Re^{5+}$,[10] and $Ag^{+}$[11] complexes have been reported, the chemistry of BtaH and its derivatives with $M^{3+}$ species has, until now, not been investigated.

## Our Work

Despite the large numbers of $M^{2+}$ pentamers structurally characterized, only one "related" $M^{3+}$ pentamer has been reported.[12] The complex $[HNEt_3]_x[Fe_5O_2(OMe)_2(Bta)_4(BtaH)_{1-x}(MeOH)_{5-x}Cl_{5+x}]$ (1, $x$ = 1, 0; Figure 2) consists of an elongated tetrahedral array of four $Fe^{3+}$ ions centered on a fifth. The central Fe ion is attached to the apical Fe ions by two $\mu_3$-$O^{2-}$ ions forming a $[Fe_5O_2]^{11+}$ core, with the two $OMe^-$ ligands bridging between the apical Fe ions on each short edge of the elongated tetrahedron and the $Bta^-$ ligands bridging in a $\eta^1$:$\eta^1$:$\mu_2$-fashion between the central Fe ion and the apical Fe ions along the long edges of the elongated tetrahedron. The coordination geometry of the apical Fe ions is completed by a combination of terminal $Cl^-$ and MeOH ligands. The central Fe is antiferromagnetically coupled to the peripheral Fe ions resulting in an $S$ = 15/2 spin ground state (Figure 2), with the best fit obtained for the two independent exchange interactions being $J_1 = -7.3\ cm^{-1}$, $J_2 = 8.6\ cm^{-1}$.[12] As expected, this suggests that the interaction between the central Fe ion and the apical Fe ions by the $\mu_3$-$O^{2-}$ ions is antiferromagnetic and the interaction between the two apical Fe centers mediated by the $\mu_2$-$MeO^-$ is ferromagnetic. A spin ground state of $S$ = 15/2 can thus be rationalized by assuming the central Fe is "spin-up" and the apical Fe ions are "spin-down" (Figure 2).

The only other iron cluster containing benzotriazole is the tetradecametallic complex $[Fe_{14}O_6(OMe)_{18}(Bta)_6Cl_6]$ (**2**, Figure 3) – formed from the reaction between $[Fe_3O(OAc)_6(H_2O)_3]Cl$ and BtaH in MeOH at 100 °C in a Teflon-lined autoclave.[13] The structure comprises a hexa-capped hexagonal bipyramid of $Fe^{3+}$ ions with caps on alternate faces (Figure 4). The $Bta^-$ ligands coordinate in the maximal $\mu_3$-mode to form two $\{Fe_4(Bta)_3\}$ moieties which sandwich a central $\{Fe_6\}$ ring, bridged by eighteen $\mu_2$-$OMe^-$ and six $\mu_4$-$O^{2-}$ ions. The $\{Fe_4(Bta)_3\}$ fragment is reminiscent of the

 © 2006 Wiley-VCH Verlag GmbH & Co. KGaA, Weinheim 

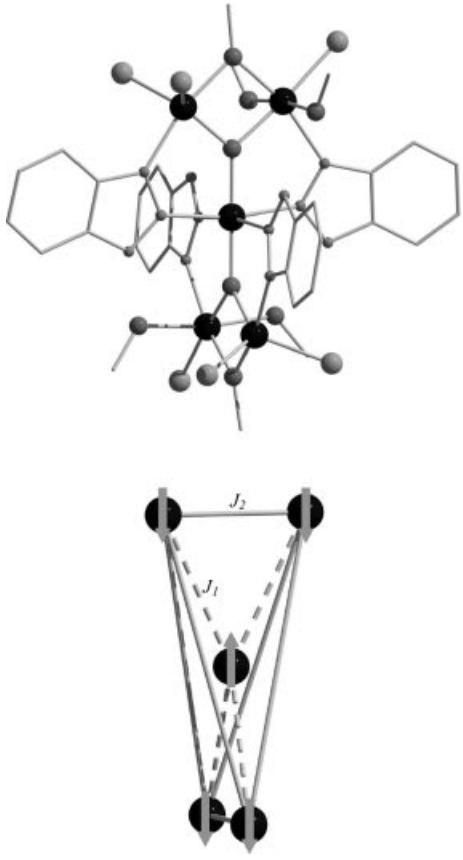


Figure 2. The molecular structure of complex **1** and its elongated, centered tetrahedral $\{Fe_5\}$ core showing the two independent exchange interactions and the resultant spin topology.

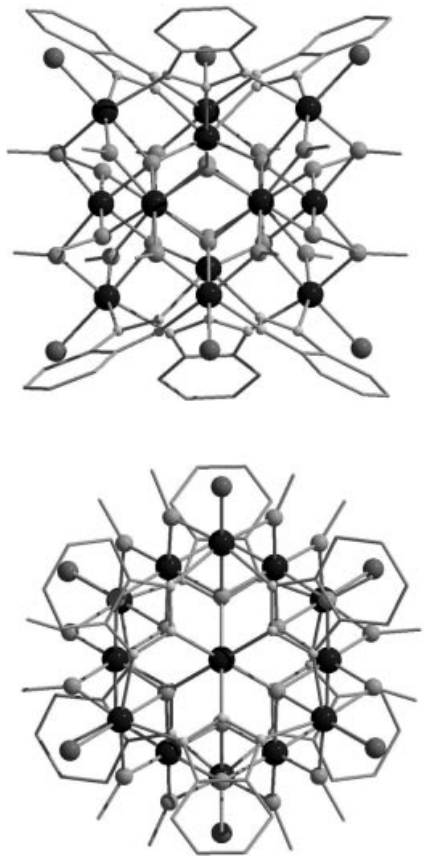

Figure 3. Molecular structure of $[Fe_{14}O_6(OMe)_{18}(Bta)_6Cl_6]$ (**2**) viewed perpendicular (top) and parallel (bottom) to the apical Fe ions.

$M^{2+}$ pentamers above (Figure 1) and here they act to stop the growth of the Fe–oxide–alkoxide cluster. Complex **2** exhibits one of the largest spin ground states yet seen with magnetization data suggesting $S \approx 25$ and $D \approx 0$ cm$^{-1}$ (Figure 5).[13–15] An $S = 25$ ground state can be rationalized from competing antiferromagnetic exchange interactions within the cluster: the relative magnitude of the four chemically distinct, nearest-neighbor exchange pathways via $\mu_4$-$O^{2-}$ ions and/or $\mu^2$-$OMe^-$ ions can be predicted on the basis of the Fe–O–Fe angles (Figure 4). The Fe(apex)–Fe(face cap) [$J_1$] and Fe(apex)–Fe(ring) [$J_3$] interactions are expected to be the most antiferromagnetic because they are defined by the largest angles and therefore dominate over the much weaker antiferromagnetic Fe(face-cap)–Fe(ring) [$J_2$] and Fe(ring)–Fe(ring) [$J_4$] interactions. This would lead to a very simple spin structure in the ground state with the two apical Fe ions of the bipyramid "spin down" and all other Fe ions "spin up". Conventional fitting of the experimental magnetic susceptibility data to a spin Hamiltonian to derive $J_1$–$J_4$ is not possible, but DFT calculations in tandem with Monte Carlo simulations support this model giving: $J_1 = -22$ cm$^{-1}$, $J_2 = -8.7$ cm$^{-1}$, $J_3 = -29.7$ cm$^{-1}$ and $J_4 = -3.7$ cm$^{-1}$.[14]

Despite its huge ground state S, **2** does not behave as an SMM. This is due to the near isotropic nature of this ground state ($D \approx 0$). However, this is interesting in itself as it gives rise to an unusually large magnetocaloric effect (MCE) below 10 K.[15] The 51-fold degeneracy of the (isotropic) ground state gives rise to very large magnetic entropy changes $\Delta S_m$ on magnetization. If isothermal magnetization (at temperature $T_i$) is followed by adiabatic demagnetization then magnetic cooling can be achieved with a characteristic temperature change $\Delta T_{ad}$. The huge spin of **2** (combined with an additional entropy contribution from low-lying excited states) gives rise to $\Delta S_m(T)$ and $\Delta T_{ad}(T)$ values ($\Delta T_{ad} = 5.8$ K for $T_i = 6$ K) that are not only much larger than those displayed by other molecular clusters but more than 30% larger than any other material for $T_i <$ 10 K, including the best intermetallic materials such as $[(Dy_xEr_{1-x})Al_2]$.[16] Thus **2** has potential applications in low temperature magnetic refrigeration.

The analogous clusters $[Cr_{14}O_6(OMe)_{18}(Bta)_6Cl_6]$ (**3**) and $[V_{14}O_6(OMe)_{18}(Bta)_6Cl_6]$ (**4**) can be made in an identical manner,[17] but in both cases magnetic measurements indicate the complexes to have $S = 0$ spin ground states. This (presumably) arises because of small changes in the relative magnitudes of the four exchange interactions such that the order $|J_3| > |J_1| > |J_2| > |J_4|$ seen in $[Fe_{14}]$ is not maintained in either $[Cr_{14}]$ or $[V_{14}]$.[17] If the reaction mixture leading to **4** is exposed to atmospheric $O_2$ then $[(V^{IV}O)_6V^{III}{}_8O_6(OMe)_{18}(Bta)_6]$ (**5**) can be isolated, in which each face cap is oxidized from a $[V^{III}–Cl]^{2+}$ moiety to the isoelectronic

 © 2006 Wiley-VCH Verlag GmbH & Co. KGaA, Weinheim 

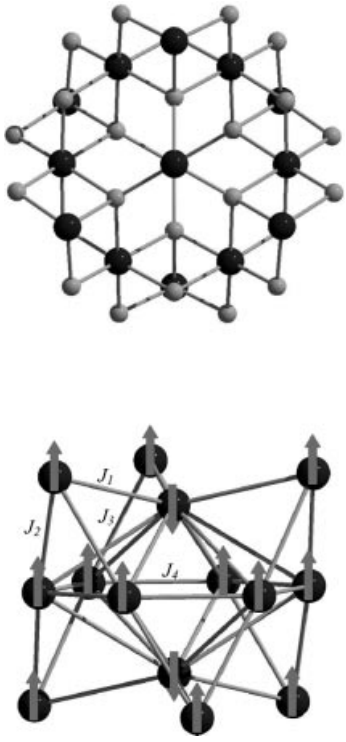


Figure 4. The metal–oxygen core of **2** viewed parallel to the apical Fe ions (top); the hexacapped hexagonal bipyramidal metallic skeleton of **2** (bottom) showing the four independent exchange interactions and the resultant spin topology.

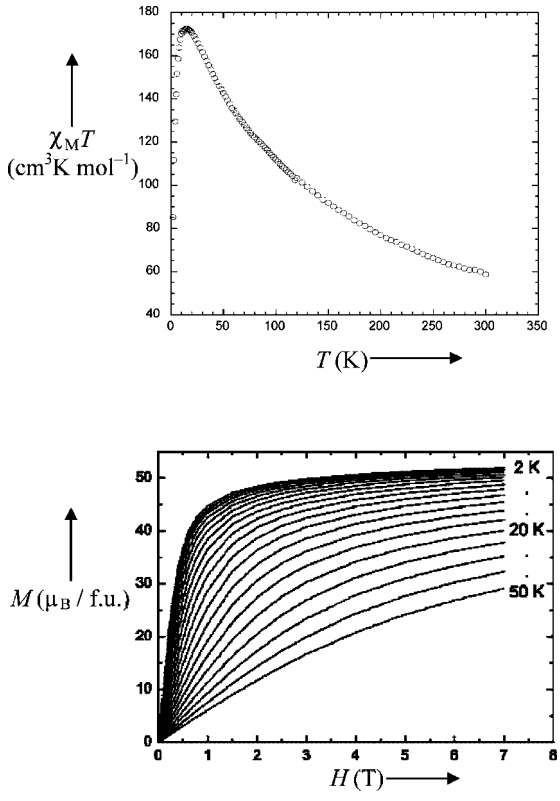


Figure 5. Plot of $\chi_M T$ vs. $T$ for complex **2** in the 300–1.8 K temperature range, and isothermal $M(H)$ curves measured in the temperature range 2–50 K.

vanadyl $[V^{IV}{=}O]^{2+}$ unit. If these reactions are performed under non-solvothermal, lower temperature conditions then the "box-like" complex $[V^{IV}_8V^{III}_2O_8(OH)_4(OMe)_{10}(Bta)_8]$ (**6**) forms (Figure 6).[18] The complex consists of a square-prism of vanadyl ions where the square faces are bridged through the 1,3-bridging mode of the $Bta^-$. The "box" surrounds two $V^{III}$ ions that form a $[V^{III}_2(OMe)_2]$ dimer that bind to the vertices of the square-prism by the four $\mu_3$-hydroxides. The topology, and the highly reduced $[V^{IV}_8V^{III}_2]$ state, of **6** is unique for a polyoxoalkoxovanadate. This chemistry also highlights the importance of exploring a wide temperature range in cluster chemistry – under the higher temperature, solvothermal conditions this reaction gives a less oxidized, higher nuclearity product.

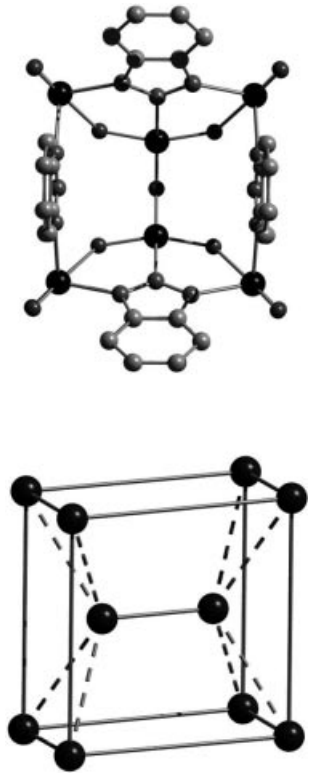

Figure 6. The molecular structure of complex **6** (top); and the $\{V^{IV}_8\}$ box encapsulating the $\{V^{III}_2\}$ fragment (bottom). Some of the $MeO^-$ ions have been removed for clarity.

The magnetic properties of **6** are dominated by strong antiferromagnetic interactions: the room temperature $\chi_M T$ value of 3.3 $cm^3{\cdot}K{\cdot}mol^{-1}$, is well short of the value expected for eight uncoupled $V^{4+}$ and two $V^{3+}$ ions, and is already rapidly decreasing with decreasing temperature. The low temperature value tends towards zero indicating a diamagnetic ground state for the cage. This strong antiferromagnetic coupling is consistent with the structure – very strong coupling is expected for the face-sharing $(VO)_2$ pairs on the short edges of the box.

The majority of Single-Molecule Magnets (SMMs) reported to date have been clusters containing $Mn^{3+}$ ions.[4,19] In each case the clusters have been made, at least initially, via the serendipitous assembly of Mn starting materials

 © 2006 Wiley-VCH Verlag GmbH & Co. KGaA, Weinheim 

with flexible organic bridging ligands such as carboxylates or alkoxides. Manganese clusters often display "*unusually*" large spin ground states with respect to other 3d transition metals, and large and negative magnetoanisotropies resulting from the presence of Jahn–Teller distorted $Mn^{3+}$ ions. However this presents a synthetic problem: there are few *simple* readily available sources of $Mn^{3+}$. This has resulted in the use of two alternative techniques. The first is the use of the basic metal carboxylates of general formula, $[M_3O(RCO_2)_6L_3]^{0/+}$, which can contain either two or three $Mn^{3+}$ ions, and the second is the oxidation of $Mn^{2+}$ salts with permanganate, $MnO_4^-$.[4] Both of these techniques have been successful, particularly the former. An alternative approach is to use $MnF_3$. The main disadvantage of using metal fluorides is their relative insolubility and therefore the apparent need for more "complicated" synthetic procedures – indeed the majority of fluoride-containing clusters have been isolated at elevated temperatures.[20] For $MnF_3$ this insolubility can be easily overcome by using either a "melt" reaction whereby the BtaH acts as the solvent (MPt = 100 °C) in which the $MnF_3$ dissolves as the reaction proceeds,[21] or by the simple reflux of the reaction mixture in a particular solvent. For example the complex $[Mn^{III}{}_{26}O_{17}(OH)_8(OMe)_4F_{10}(Bta)_{22}(MeOH)_{14}(H_2O)_2]$ (**7**, Figure 7) is made by simply mixing $MnF_3$ and BtaH in MeOH at ca. 60 °C. The rather complicated $[Mn^{III}{}_{26}O_{17}(OH)_8(OMe)_4]^{32+}$ core of **7** can be described as a central distorted tetra-face-capped octahedron either side of which are attached vertex-sharing tetrahedra. The $O^{2-}$ ions all bridge in their usual $\mu_3$-fashion, forming $\{Mn_3O\}^{7+}$ triangular units. The $OH^-$ ions are of two types: four are $\mu_3$-bridging and are situated within the tetra-face-capped octahedron, while the remaining ions are $\mu_2$-bridging and are situated both in the tetra-face-capped octahedron and within the two vertex-sharing tetrahedra. The 22 deprotonated $Bta^-$ ligands are of two types: four use all three nitrogens to bond to three $Mn^{3+}$ centers while the remaining 18 use only two nitrogen atoms to bond to two $Mn^{3+}$ centers, the third nitrogen atom H bonds to adjacent MeOH, $H_2O$ or $OH^-$ ligands. The four $MeO^-$ ions are all $\mu_2$-bridging, but rather unusually there are also two MeOH molecules which act as $\mu_2$-bridges, whilst the ten $F^-$ ions are bonded terminally. Fitting the magnetization ($M$ vs. $H$) data for complex **7** gives $S = 4$, $g = 2.0$ and $D = -0.90\ cm^{-1}$. Ac susceptibility measurements performed on **7** in the 1.8–4.00 K range show the presence of out-of-phase ac susceptibility signals, but no peaks. Low-temperature single-crystal studies performed on **7** on an array of micro-SQUIDS[22] show the time and temperature-dependent hysteresis loops indicative of single-molecule magnetism behavior (Figure 8). Below 1.2 K, hysteresis loops are observed in magnetization vs. field studies whose coercivities increase with decreasing temperature, at a sweep rate of 0.14 T/s. The loops do not show the step-like features associated with quantum tunneling of magnetization (QTM), and appear typical for a cluster with a distribution of energy barriers. The steps may be present but broadened out, due to the inherent disorder associated with the crystal of **7**,[21] resulting in a distribution of $Mn^{3+}$ environments. These observations have been reported for other large SMMs.[23] Relaxation data at very low temperatures were determined from dc relaxation decay measurements (Figure 9). The relaxation of crystals of SMMs is often very complicated, leading to non-exponential relaxation laws, and the $M/M_s$-vs-$t$ curves for **7** cannot be fitted by a simple-exponential, stretched-exponential or square-root law. In order to extract the temperature dependence of the mean relaxation time $\tau(T)$, it is necessary to use a single scaling function $f[t/\tau(T)]$.[24] This scaling analysis allows $\tau(T)$ to be determined without making any particular assumption about the relaxation law, and allows the mean relaxation time $\tau(T)$ to be extracted. Fitting of these data to the Arrhenius law (Figure 9) gives an effective mean barrier for the reversal of magnetization of approximately 15 K and a pre-exponential factor of $\tau_0 = 3 \cdot 10^{-9}$ s. Below ca. 0.2 K, the relaxation rates become temperature-independent, strongly suggesting the presence of QTM in the ground state. The experimentally derived $U_{eff}$ value of 15 K is comparable to the theoretical value ($U = S^2|D| \approx 21$ K). Indeed, $U$ is expected to be larger than $U_{eff}$ as the reversal of magnetization has two components: thermally activated relaxation over the barrier and quantum tunneling of magnetization (QTM) through the barrier.

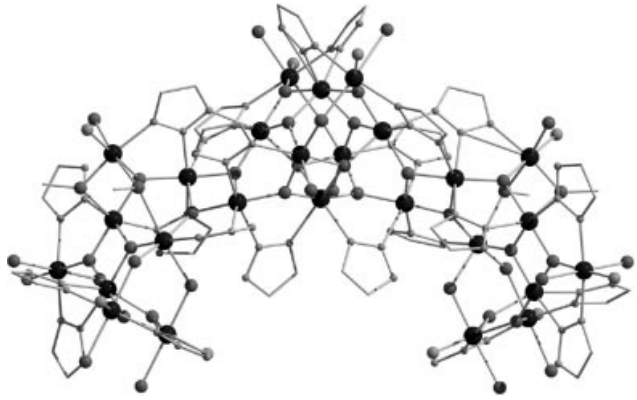

Figure 7. The molecular structure of complex **7**.

Repeating the reaction that produces complex **7** but in the presence of pyridine affords the decametallic complex $[Mn_{10}O_6(OH)_2(Bta)_8(py)_8F_8]$ (**8**), while the same reaction in the presence of triethylamine produces the trimetallic species $[NHEt_3]_2[Mn_3O(Bta)_6F_3]$ (**9**).[21,25] Complex **8** (Figure 10) consists of a "supertetrahedral" $[Mn^{III}{}_{10}]$ core bridged by six $\mu_3$-$O^{2-}$ ions, two $\mu_3$-$OH^-$ ions, four $\mu_2$-$F^-$ ions and eight $\mu_2$-$Bta^-$ ions, while complex **9** (Figure 11) has a structure analogous to that of the basic metal carboxylates of general formula $[M_3O(RCO_2)_6L_3]^{0/+}$, consisting of an oxo-centered metal triangle with $\mu_2$-$Bta^-$ ligands bridging each edge of the triangle and the fluoride ions acting as the terminal "L" ligands. Both complexes display dominant antiferromagnetic exchange interactions resulting in small spin ground states. For complex **9**, the best fit to the experimental $\chi_M T$ vs. $T$ data was obtained for the following pa-

 © 2006 Wiley-VCH Verlag GmbH & Co. KGaA, Weinheim 

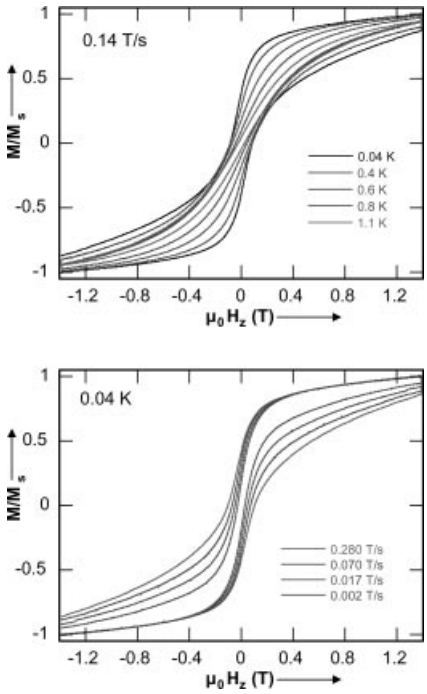


Figure 8. Magnetization ($M$) of **7** vs. applied magnetic field ($\mu_0 H$). The magnetization is normalized to its saturation value. The resulting hysteresis loops are shown at different temperatures and different field sweep.

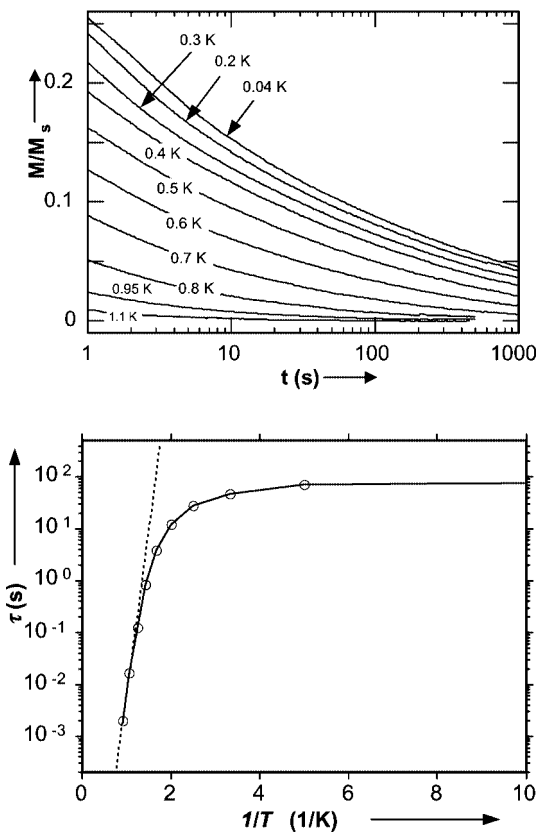


Figure 9. Relaxation data for **7** plotted as $M/M_s$ vs. time, $M$ is normalized to its saturation value (top); Arrhenius plot for **7** using dc decay data on a single crystal. The dashed line is the fit of the data in the thermally activated region.

rameters: $J_a = -5.01$ cm$^{-1}$; $J_b = +9.16$ cm$^{-1}$ and $g = 2.00$, resulting in an $S = 2$ spin ground state. DFT calculations, however, suggest an $S = 0$ ground state with $J_a = -2.95$ cm$^{-1}$ and $J_b = -2.12$ cm$^{-1}$ with two $S = 1$ states at 1.46 cm$^{-1}$ and 5.9 cm$^{-1}$, and an $S = 2$ state at 6.1 cm$^{-1}$ above the ground state.[21] The presence of low-lying excited states leads to obvious problems when trying to satisfactorily fit the experimental data. The ground state of this molecule can be changed from $S = 0$ to $S = 2$ by small changes in the exchange interaction $J_b$. The ratio of $J_a/J_b$ vs. the Eigen values obtained for these exchange parameters is shown in Figure 11. For a value of $J_a/J_b < 1$, the ground state spin value varies from $S = 2$ to $S = 1$; for $J_a/J_b = 1$ the ground state becomes $S = 0$, and for $J_a/J_b > 1$ the ground state varies from $S = 0$ to $S = 2$. For the DFT calculated values, the $J_a/J_b$ ratio is found to be 1.37 and the ground state is $S = 0$. However, it is also clear that for $J_a/J_b > 1$ the energy levels are very closely separated, and the fact that the ground state depends on the ratio of $J_a/J_b$ reveals that a degree of spin frustration exists in the triangle. At lower and higher values of $J_a/J_b$ the degree of spin frustration is minimal, giving rise to an $S = 2$ ground state which can be accounted for by a simple pairwise exchange interaction. At intermediate values of $J_a/J_b$, spin frustration causes a net spin vector alignment, which cannot be accounted for by considering a simple pairwise exchange interaction, and the value of the ground state depends on the degree of spin frustration.[21,25]

By replacing BtaH with its dimethyl derivative ($Me_2$-BtaH; 5,6-dimethylbenzotriazole) in otherwise similar reactions to those above affords completely different clusters: the octametallic complex $[Mn_8O_4(OMe)_2(Me_2Bta)_6F_8$-

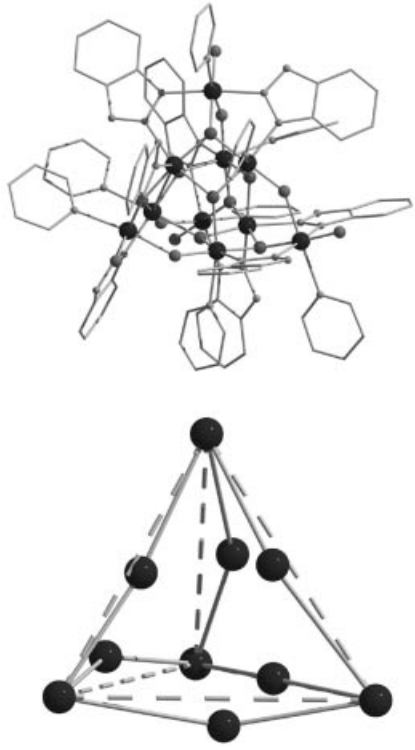

Figure 10. The molecular structure of complex **8** (top) and its supertetrahedral metallic core (bottom).

 © 2006 Wiley-VCH Verlag GmbH & Co. KGaA, Weinheim 

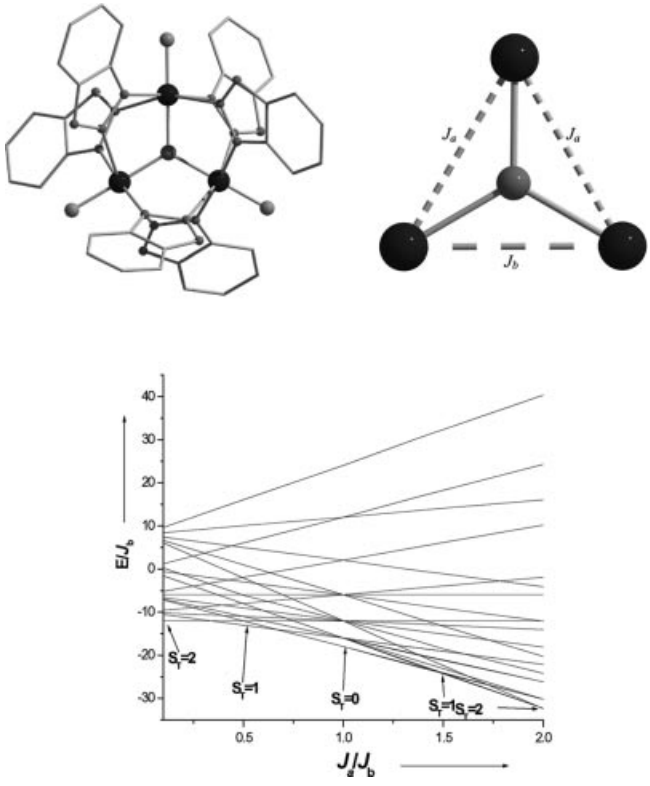


Figure 11. Top: Molecular structure of complex **9** and the two independent exchange interactions; bottom: Plot of calculated Eigen values vs. $J_a/J_b$ for complex **9**. The experimental data was fitted with a two-*J* model that employed the spin Hamiltonian $\hat{H} = -2[J_a(\hat{S}_3\hat{S}_2) + J_a(\hat{S}_3\hat{S}_1) + J_b(\hat{S}_2\hat{S}_1)]$. For more details see ref.[21]

$(Me_2BtaH)(MeOH)_8]$ (**10**), and the tridecametallic complex $[Mn_{13}O_{12}(Me_2Bta)_{12}F_6(MeOH)_{10}(H_2O)_2]$ (**11**).[25] The core of **10** (Figure 12) consists of a central $[Mn_4O_2]^{8+}$ butterfly unit, the body atoms of which are also part of a peripheral $[Mn_3O]^{4+}$ triangular unit. The $[Mn_4O_2]$ butterfly is near planar with the two peripheral $[Mn_3O]$ triangles perpendicular to this plane, attached via an $O^{2-}$ ion forming a $[Mn_8O_4]^{16+}$ core. Two $MeO^-$ and two $F^-$ ions act as $\mu_2$-bridges, the $MeO^-$ bridging one side of the $[Mn_3O]$ unit and the $F^-$ linking the $[Mn_3O]$ unit to the central $[Mn_4O_2]$ butterfly. The $F^-$ bridges are asymmetric as, in each case, one Mn–F bond lies on a Jahn–Teller axis. The six $Me_2Bta^-$ ligands all bond in a $\mu_2$-fashion and the remaining six $F^-$ ions and eight MeOH molecules all are terminal. The core of **11** (Figure 13) consists of a $[Mn^{IV}_3Mn^{III}_4O_{12}]$ centered hexagon. The $Mn^{4+}$ ions form a linear $[Mn_3O_4]$ trimer through the centre of the hexagon with the $Mn^{3+}$ ions attached on either side. The twelve $O^{2-}$ ions are all $\mu_3$-bridging and are of two types: six are bound to the central $Mn^{4+}$ ion and link this ion to the outer six Mn ions of the hexagon. The remaining six $O^{2-}$ ions bridge between the outer Mn ions of the centered-hexagon and the remaining six $Mn^{3+}$ ions that are located, alternately, above and below the plane of the $[Mn^{IV}_3Mn^{III}_4O_{12}]$ core. The $\mu_2$-$Me_2Bta^-$ ligands are all deprotonated and link the Mn ions in the central hexagon to the Mn ions above and below this plane.

The coordination of these six Mn ions is completed by a terminal $F^-$ ion and either two MeOH molecules or one MeOH and one $H_2O$ molecule. The central $[Mn^{IV}_3Mn^{III}_4O_{12}]$ core of **11** is reminiscent of the hexagonal close-packed structure present in $CdI_2$ and is similar to the cores found in several large cluster compounds.[26] Magnetic studies reveal that both **10** and **11** have small spin ground states.

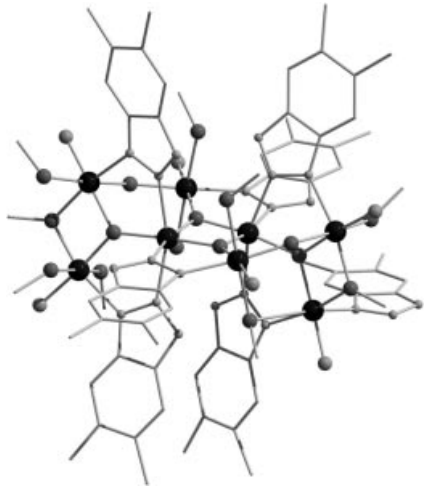

Figure 12. The molecular structure of complex **10**.

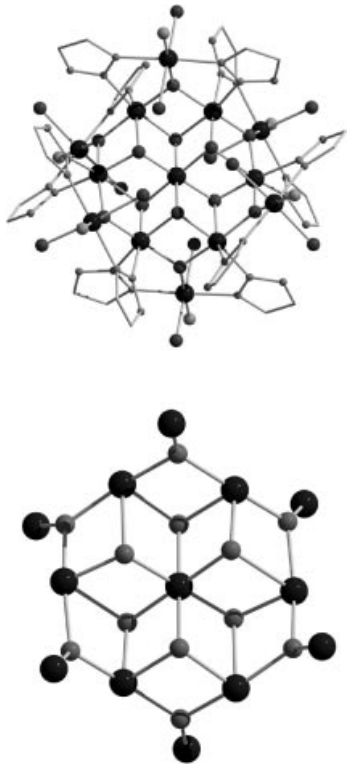

Figure 13. The molecular structure of complex **11** (top) and its metal–oxygen core (bottom).

 © 2006 Wiley-VCH Verlag GmbH & Co. KGaA, Weinheim 

Complexes **7**–**11** can all be described as aggregated $\{Mn_3O\}$ triangular units: compound **7** consists of twenty triangular units; **8** is made from eight edge-sharing units; **9** consists of one triangular unit; **10** contains four edge- and vertex-sharing units; and **11** contains twelve such units. This perhaps suggests that triangular $[Mn_3OF_3]^{4+}$ units may be present in all of the above solutions and that the identity of the isolated crystalline product is then dependent on the nature of the added base. Indeed complex **10** could be thought of as an "intermediate" in the formation of **11**: both clusters are comprised of aggregated $\{Mn_3O\}$ units and the $\{Mn_8O_4\}$ unit present in **10** can be seen three times in the core of **11**.

## Conclusions

The work here clearly illustrates that the use of benzotriazole and its analogues is a successful synthetic strategy for the formation of large polymetallic cluster compounds. The complexes isolated thus far range in nuclearity from three to twenty six and in topologies (amongst others) ranging from simple triangles and tetrahedra, to rectangular boxes, supertetrahedra and hexacapped hexagonal prisms. Some of these complexes have displayed interesting magnetic properties including some of the largest spin ground states ever seen and single-molecule magnetism behavior. The science remains in its infancy, but given our initial results the future promises many more exciting complexes.

## Acknowledgments

We would like to thank the EPSRC, Leverhulme Trust and Lloyd's of London Tercentenary Foundation for financial assistance (UK). The EC (HPRN-CT-1999-00012)/TMR network "Molnanomag", and MRTN-CT-2003-504880 "QuEMolNa". The work described has been done in collaboration with a number of groups. In particular, the authors would like to thank Prof George Christou (University of Florida), Dr Wolfgang Wernsdorfer (Laboratoire Louis Néel), Prof Talal Mallah (Université Paris-Sud), Drs Marco Evangelisti and Marco Affronte (INFM-CNR, Modena), Drs Guillem Aromí and Joan Cano (Universitat de Barcelona). EKB, EJLM and DC would also like to thank Drs Leigh Jones, David Low, Rebecca Laye and Gopalan Rajaraman for their invaluable contribution to this work.

[1] a) R. Sessoli, H.-L. Tsai, A. R. Schake, S. Wang, J. B. Vincent, K. Folting, D. Gatteschi, G. Christou, D. N. Hendrickson, *J. Am. Chem. Soc.* **1993**, *115*, 1804; b) R. Sessoli, D. Gatteschi, A. Caneschi, M. A. Novak, *Nature* **1993**, *365*, 141; c) R. Sessoli, D. Gatteschi, D. N. Hendrickson, G. Christou, *MRS Bull.* **2000**, *25*, 66.

[2] See for example a) D. N. Hendrickson, G. Christou, H. Ishimoto, J. Yoo, E. K. Brechin, A. Yamaguchi, E. M. Rumberger, S. M. J. Aubin, Z. Sun, G. Aromí, *Mol. Cryst. Liq. Cryst.* **2002**, *376*, 301; E. K. Brechin, *Chem. Commun.* **2005**, 5141.

[3] a) M. N. Leuenberger, D. Loss, *Nature* **2001**, *410*, 789; b) W. Wernsdorfer, N. Aliaga-Acalde, D. N. Hendrickson, G. Christou, *Nature* **2002**, *416*, 406; c) S. Hill, R. S. Edwards, N. Aliaga-Alcade, G. Christou, *Science* **2003**, *302*, 1015; d) J. Tejada, E. M. Chudnovsky, E. del Barco, J. M. Hernandez, T. P. Spiller, *Nanotechnology* **2001**, *12*, 181; e) E. J. L. McInnes, *Struct. Bond.* **2006**, *122*, in press.

[4] E. K. Brechin, G. Aromí, *Struct. Bond.*, DOI: 10.1007/430_022.

[5] I. Dugdale, J. B. Cotton, *Corros. Sci.* **1963**, *3*, 69.

[6] a) M. Murrie, D. Collison, C. D. Garner, M. Helliwell, P. A. Tasker, S. S. Turner, *Polyhedron* **1998**, *17*, 3031; b) J. H. Marshall, *Inorg. Chem.* **1978**, *17*, 3711; c) J. Handley, D. Collison, C. D. Garner, M. Helliwell, R. Docherty, J. R. Lawson, P. A. Tasker, *Angew. Chem. Int. Ed. Engl.* **1993**, *32*, 1036; d) E. G. Bakalbassis, E. Diamontopoulou, S. P. Perlepes, C. P. Raptopoulou, V. Tangoulis, A. Terzis, T. F. Zafiropoulos, *J. Chem. Soc., Chem. Commun.* **1995**, 1347; e) V. Tangoulis, C. P. Raptopoulou, A. Terzis, E. G. Bakalbassis, E. Diamontopoulou, S. P. Perlepes, *Inorg. Chem.* **1998**, *37*, 3142.

[7] V. Tangoulis, C. P. Raptopoulou, A. Terzis, E. G. Bakalbassis, E. Diamontopoulou, S. P. Perlepes, *Mol. Cryst. Liq. Cryst.* **1999**, *335*, 463.

[8] I. Sotofte, K. Nielsen, *Acta Chem. Scand.* **1984**, *38*, 253.

[9] A. L. Spek, A. R. Siedle, J. Reedijk, *Inorg. Chim. Acta* **1985**, *100*, L15.

[10] B. Machura, J. O. Dziegielewski, R. Kruszynski, T. J. Batczak, *Polyhedron* **2003**, *22*, 2869.

[11] I. Ino, J. C. Zhong, M. Munakata, T. Kuroda-Sowa, M. Maekawa, Y. Suenaga, Y. Kitamori, *Inorg. Chem.* **2000**, *39*, 4273.

[12] J. Tabernor, L. F. Jones, S. L. Heath, C. Muryn, G. Aromí, J. Ribas, E. K. Brechin, D. Collison, *Dalton Trans.* **2004**, 975.

[13] D. M. Low, L. F. Jones, A. Bell, E. K. Brechin, T. Mallah, E. Rivière, S. J. Teat, E. J. L. McInnes, J. L. Eric, *Angew. Chem. Int. Ed.* **2003**, *42*, 3781.

[14] G. Rajaraman, J. Cano, E. K. Brechin, E. J. L. McInnes, *Chem. Commun.* **2004**, 1476.

[15] M. Evangelisti, A. Candini, A. Ghirri, M. Affronte, E. K. Brechin, E. J. L. McInnes, *Appl. Phys. Lett.* **2005**, *87*, 072504.

[16] A. L. Lima, K. A. Gschneidner Jr, V. K. Pecharsky, A. O. Pecharsky, *Phys. Rev. B* **2003**, *68*, 134409.

[17] D. M. Low, L. F. Jones, R. Laye, T. Mallah, E. Rivière, S. J. Teat, E. K. Brechin, E. J. L. McInnes, manuscript in preparation.

[18] R. H. Laye, Q. Wei, P. Mason, E. Shanmugan, E. K. Brechin, E. J. L. McInnes, *J. Am. Chem. Soc.* **2006**, submitted.

[19] G. Christou, *Polyhedron* **2005**, *24*, 2065.

[20] a) E. J. L. McInnes, S. Piligkos, G. A. Timco, R. E. P. Winpenny, *Coord. Chem. Rev.* **2005**, *249*, 2577; b) N. V. Gerbeleu, Y. T. Struchkov, G. A. Timco, A. S. Batsanov, K. M. Indrichan, G. A. Popovic, *Dokl. Chem.* **1991**, *313*, 232; c) N. V. Gerbeleu, Y. T. Struchkov, G. A. Timco, A. S. Batsanov, K. M. Indrichan, G. A. Popovic, *Dokl. Akad. Nauk SSSR* **1991**, *313*, 1459; d) F. K. Larsen, J. Overgaard, S. Parsons, E. Rentschler, A. A. Smith, G. A. Timco, R. E. P. Winpenny, *Angew. Chem. Int. Ed.* **2003**, *42*, 5978; e) A. Bino, M. Ardon, D. Lee, B. Spingler, S. J. Lippard, *J. Am. Chem. Soc.* **2002**, *124*, 4578; f) E. M. Rumberger, L. N. Zakharov, A. L. Rheingold, D. N. Hendrickson, *Inorg. Chem.* **2004**, *43*, 6531.

[21] L. F. Jones, G. Rajaraman, J. Brockman, M. Murugesu, J. Raftery, S. J. Teat, W. Wernsdorfer, G. Christou, E. K. Brechin, D. Collison, *Chem. Eur. J.* **2004**, *10*, 5180.

[22] W. Wernsdorfer, *Adv. Chem. Phys.* **2001**, *118*, 99.

[23] a) M. Soler, W. Wernsdorfer, K. Folting, M. Pink, G. Christou, *J. Am. Chem. Soc.* **2004**, *126*, 2156; b) A. J. Tasiopolous, A. Vinslava, W. Wernsdorfer, K. A. Abboud, G. Christou, *Angew. Chem. Int. Ed.* **2004**, *43*, 2117.

[24] L. Thomas, A. Caneschi, B. Barbara, *Phys. Rev. Lett.* **1999**, *83*, 2398.

[25] a) L. F. Jones, E. K. Brechin, D. Collison, J. Raftery, S. J. Teat, *Inorg. Chem.* **2003**, *42*, 6971; b) L. F. Jones, J. Raftery, S. J. Teat, D. Collison, E. K. Brechin, *Polyhedron* **2005**, *24*, 2443.

 © 2006 Wiley-VCH Verlag GmbH & Co. KGaA, Weinheim 

[26] See for example a) E. K. Brechin, S. G. Harris, A. Harrison, S. Parsons, A. G. Whittaker, R. E. P. Winpenny, *Chem. Commun.* **1997**, 653; b) A. K. Powell, S. L. Heath, D. Gatteschi, L. Pardi, R. Sessoli, G. Spina, F. Del Giallo, F. Pieralli, *J. Am. Chem. Soc.* **1995**, *117*, 2491; c) D. J. Price, S. R. Batten, B. Moubaraki, K. S. Murray, *Chem. Commun.* **2002**, 762; d) J. T. Brockman, J. C. Huffman, G. Christou, *Angew. Chem. Int. Ed.* **2002**, *41*, 2506.

Received: March 8, 2006
Published Online: June 1, 2006

 © 2006 Wiley-VCH Verlag GmbH & Co. KGaA, Weinheim 

DOI: 10.1002/ejic.200600375

# Bis-Ruthena(III)cycles $[Ru(C^{\frown}N)_2(N^{\frown}N)]PF_6$ as Low-Potential Mediators for PQQ Alcohol Dehydrogenase ($C^{\frown}N$ = 2-phenylpyridinato or 4-(2-tolyl)-pyridinato, $N^{\frown}N$ = bpy or phen)

**Ronan Le Lagadec,[a] Larissa Alexandrova,[b] Hebert Estevez,[a] Michel Pfeffer,[c] Valdas Laurinavičius,[d] Julija Razumiene,[d] and Alexander D. Ryabov*[e]**

**Keywords:** Ruthenium / Metallacycles / X-ray diffraction / Biosensors / PQQ dehydrogenase

Bis-cyclometalated analogs of tris(2,2′-bipyridine)ruthenium(II), namely $[Ru^{III}(C^{\frown}N)_2(N^{\frown}N)]PF_6$ complexes **3**, are prepared in 52–57% yield from the mono-cyclometalated *N*,*N*-dimethylbenzylamine (dmbaH) derivatives $[Ru^{II}(dmba)(N^{\frown}N)(MeCN)_2]PF_6$ ($N^{\frown}N$ = bpy or phen) and mercurated 2-phenylpyridinato- or 4-(2-tolyl)pyridinato ($C^{\frown}N$) species $Hg(C^{\frown}N)Cl$. Two new bis-ruthenacycles studied by X-ray crystallography revealed a $C_1$ symmetry, with the C and N atoms of different $C^{\frown}N$ ligands *trans* to the nitrogen atoms of the $N^{\frown}N$ ligand. The reduction potential of the $Ru^{II/III}$ feature of **3** is as low as ca.–0.2 V (vs. SCE in MeCN). Complexes **3** display a unique mediating ability in moving electrons from the reduced active site of PQQ-dependent alcohol dehydrogenase (PQQ-ADH) to an electrode with 1,2-propanediol as a substrate at a working potential of +0.1 V.

(© Wiley-VCH Verlag GmbH & Co. KGaA, 69451 Weinheim, Germany, 2006)

The $Ru^{II/III}$ reduction potential for $[Ru^{II}(bpy)_3]^{2+}$ is +1.34 V in MeCN (vs. SCE).[1] The structurally similar mono-cyclometalated complex $[Ru^{II}(phpy)(bpy)_2]^+$ (Scheme 1), in which one N donor is replaced by a σ-bound $sp^2$ carbon, has a drastically lower $Ru^{II/III}$ reduction potential (+0.52 V).[2] The new bis-cyclometalated species $[Ru^{III}(phpy)_2(bpy)]^+$ (**3a**), the central atom of which is σ-bound to two $sp^2$ carbon atoms, has the lowest $Ru^{II/III}$ potentials of ca. –0.2 V. The synthesis, X-ray structural study, and electrochemistry of a new family of $Ru^{III}$ bis-cyclometalated complexes **3** and their record mediating ability in moving electrons from the reduced active site of PQQ-dependent alcohol dehydrogenase (PQQ-ADH) to an electrode are described here. Examples of *bis-cyclometalated Ru complexes* are very limited; those known are the $Ru^{II}$ derivatives of benzo[*h*]quinoline,[3] azobenzene,[4] benzylidene aniline,[5] and $P(OPh_3)_3$.[6] SciFinder tracks the term that is italicized[7] but the species listed do not have two Ru–C bonds at one metal center as in **3**.

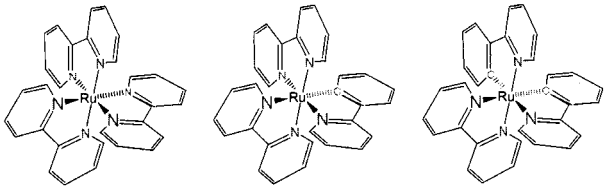


Scheme 1. A family of related cations discussed in this work. Charges in structures are omitted for clarity.

Two approaches were explored for the synthesis of the blackish-green compounds **3** (Scheme 2). The precursor bis(acetonitrile) ruthena(II)cycles are cyclometalated 2-phenyl- or 4-(2-tolyl)pyridine (**1**) and *N*,*N*-dimethylbenzylamine (**2**, dmbaH).[8] Their labile nitrile and dmba ligands are readily substituted in hot methanol by 2-phenylpyridinato or 4-(2-tolyl)pyridinato $C^{\frown}N$ chelates, which are transferred from the corresponding organomercurial compounds **4** or **5**.[9] Complexes **1** have to be treated with the symmetric organomercurial compound **4**, whereas the reactivity of the asymmetric molecule **5** is sufficient to convert **2** into **3** in 52–57% yield. It is worth noting that the formation of **3** by path **B** resembles the exchange of cyclometalated ligands[10] at $Ru^{II}$. Pincer $N^{\frown}C^{\frown}N$ ligands were previously replaced by $P^{\frown}C^{\frown}P$ fragments at $Ru^{II}$.[7c] Path **B** in Scheme 2 illustrates the exchange between bidentate $C^{\frown}N$ chelates.

[a] Instituto de Química, UNAM,Circuito Exterior s/n, Ciudad Universitaria,
04510 Mexico D. F., Mexico
[b] Instituto de Investigaciones en Materiales, UNAM, Circuito Exterior s/n, Ciudad Universitaria,
04510 Mexico D. F., Mexico
[c] Laboratoire de Synthèses Métallo-Induites, UMR CNRS 7513, Université Louis Pasteur,
4 rue Blaise Pascal, 67070 Strasbourg, France
[d] Laboratory of Bioanalysis, Institute of Biochemistry,
Mokslininku 12, Vilnius 2600, Lithuania
[e] Department of Chemistry, Carnegie Mellon University,
4400 Fifth Ave., Pittsburgh, PA 15213, USA
E-mail: ryabov@andrew.cmu.edu
Supporting information for this article is available on the WWW under http://www.eurjic.org or from the author.

 © 2006 Wiley-VCH Verlag GmbH & Co. KGaA, Weinheim 

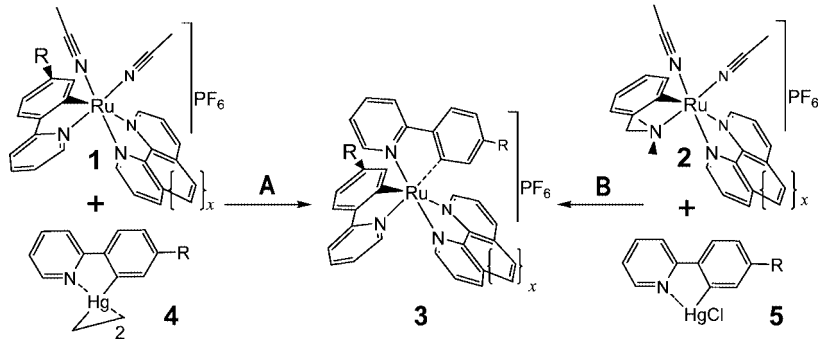


Scheme 2. Syntheses of complexes **3** (**a**: $x$ = 0, R = H; **b**: $x$ = 1, R = H; **c**: $x$ = 0, R = $CH_3$; **d**: $x$ = 1, R = $CH_3$).

Two C^N ligands of charge –1 make the complexes susceptible to oxidation, and hence the isolated compounds **3** are paramagnetic $Ru^{III}$ species. Their study by $^1H$ NMR spectroscopy is complicated, and hence, in addition to the combustion, mass-spectral, and electrochemical analyses, X-ray crystal-structure analysis of **3a** and **3d** was performed. The study on **3a** confirmed its composition (see Supporting Information), but the true stereoisomer (A, B, or C) could not be determined because the three ligands of **3a** are crystallographically identical, and the four nitrogen atoms are indistinguishable from the two carbon atoms.[11]

The X-ray data for **3d** indicates structure B with $C_1$ symmetry, which was established by the long Ru–N bond *trans* to the Ru–C σ-bond and by the $CH_3$ groups at the C^N chelates. There are two different donor atoms, i.e. N and C, *trans* to the nitrogen atoms of the phen ligand in the distorted octahedron. Accordingly, the $sp^2$ C1 atom is located *trans* to N21 of the second C^N ligand. The Ru–N21 and Ru–N38 bonds are longer than the other Ru–N bonds, as expected. This reflects the ground state *trans*-influence of the σ-bound $sp^2$ atoms C1 and C14, respectively (Figure 1).

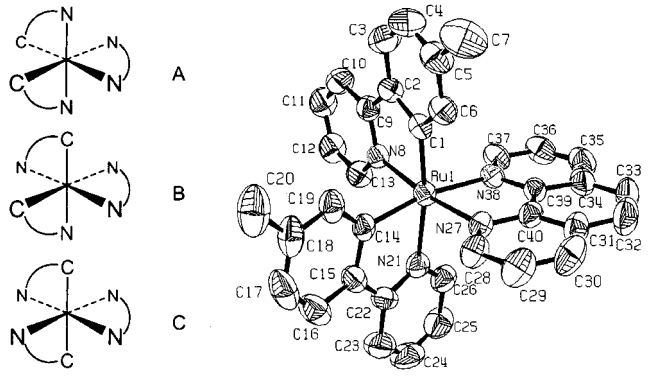


Figure 1. Possible geometric isomers of **3**, A, B, and C, and ORTEP diagram of **3d**. Selected bond lengths: Ru–C1 1.999(3), Ru–N8 2.059(2), Ru–C14 2.0209(3), Ru–N21 2.174(2), Ru–N27 2.067(2), Ru–N38 2.164(2) Å. For X-ray structure of **3a**, see SI.

It is perhaps worth noting that the properties of **3** were previously theoretically investigated.[12] The bis-ruthenacycles were unknown then, and the calculations were performed for arbitrary selected isomers A and C of $C_2$ symmetry. Properties of nonexistent species were thus simulated.

Rich cyclic voltammograms of complexes **3** that consist of three one-electron quasi-reversible and one irreversible features (Figure 2, Table 1) were interpreted by using the previously obtained data for mono-cyclometalated species such as $[Ru(phpy)(bpy)_2]^{+}$[2,13] and $[Ru(bpy)_3]^{2+}$.[1,14] The peaks around –0.2 V represent the $Ru^{II/III}$ couple, since each replacement of bpy by $phpy^-$ causes ca. 0.7 V decrease. The peaks at ca. –1.9 and +1.5 V could be assigned to the $Ru^{I/II}$ (alternatively, to a ligand-centered reduction) and $Ru^{III/IV}$ couples, respectively. Irreversible peaks at 0.9–1.0 V are presumably due to a ligand-centered oxidation. Post-peaks of lower and variable intensity that follow each peak of **3a** might be due to adsorption; they are not observed for complexes other than **3a**.

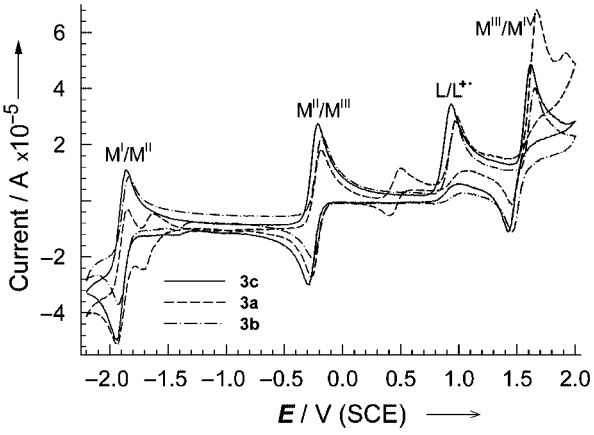


Figure 2. Cyclic voltammograms of ruthena(III)cycles **3** in MeCN (0.1 M $nBu_4NPF_6$, 0.1 V $s^{-1}$, 25 °C, glassy carbon, $N_2$; background subtraction is applied, $E_0$ = –2.2 V).

Table 1. Assignment of reduction potentials for **3** (in V vs. SCE) from the CVA data in Figure 2 in MeCN.

| **3** | $M^I/M^{II}$ | $M^{II}/M^{III}$ | $L/L^{\cdot+}$[a] | $M^{III}/M^{IV}$ |
|---|---|---|---|---|
| **3a** | –1.90 (–1.67)[b] | –0.23 (+0.45)[b] | 0.98 | 1.56 (1.91)[b] |
| **3b** | –1.88 | –0.21 | 0.97 | 1.56 |
| **3c** | –1.90 | –0.25 | 0.93 | 1.52 |

[a] Irreversible. [b] Post-peaks in parenthesis.

The mediating performance of complexes **3**, their precursors **1** and **2**, and related ruthena- and osmacycles in moving electrons from reduced active sites to an electrode[15] was evaluated with PQQ-ADH (Type II ADH IIG) from

 © 2006 Wiley-VCH Verlag GmbH & Co. KGaA, Weinheim 

*Pseudomonas putida* HK5 by using screen-printed carbon paste electrodes.[16] Remarkably, the largest currents (Figure 3) were registered for the new complexes **3** than for mono-metalated Ru and Os[17] species, though the optimal electrode potential for **3** was around 0.35 V vs. Ag/AgCl (see Figure S2 of the Supporting Information). Currents in Figure 3 depend hyperbolically on the alcohol concentration ($I = I_{M,app}[S]/(K_{M,app} + [S])$), and the values of $I_{M,app}$ (in parenthesis in Figure 3) emphasize a superior performance of the bis-cycloruthenated species **3**. The major advantage of complexes **3** as mediators of PQQ-ADH is that they are remarkably efficient at a low working electrode potential, i.e. 0.1 V. A decrease in the current because of the voltage drop is minor, and $I_{M,app}$ equals 2290 and 2110 nA for complexes **3a** and **3b**, respectively (cf. with the data in Figure 3).

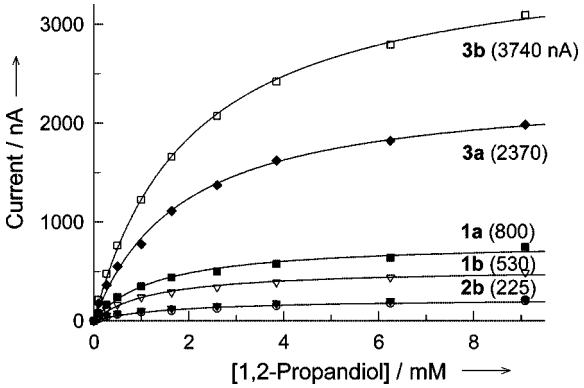


Figure 3. Current as a function of [1,2-propanediol] at 0.5 V for screen-printed electrodes incorporating PQQ-ADH and complexes **1**–**3**; pH 6, 1 mM $Ca^{2+}$, 22 °C. Numbers in parentheses are calculated values of $I_{M,app}$, which for mono-cyclometalated complexes [Ru(phpy)(phen)(MeCN)$_2$]X and [Ru(dmba)(phen)$_2$]X are close to that of **2b** and for [Os(phpy)(phen)$_2$]X is that for **1b** (X = $PF_6$).

In conclusion, the synthesis, full characterization, and numerous properties of previously anticipated but unknown complexes **3** are reported here. The X-ray study of **3d** reveals a structural type B. A "cyclometalation" tool has demonstrated its virtue again by showing how the electronic properties of compositional analogs of $[Ru(bpy)_3]^{2+}$ can further be coarsely altered by replacing N by C donors. An illustrative example of a bioanalytical use of the new complexes **3** highlighted their potential as efficient mediators of enzymatic electron transport which are capable of functioning at low electrode potentials.

## Experimental Section

**General Procedures for Preparation of [Ru(C^N)$_2$(N^N)]PF$_6$ (3) – Path B:** $Ru^{II}$ precursors **1** and **2** were described elsewhere;[8] **5** and **4** were synthesized according to the procedure of Black et al.[18] In a Schlenk tube fitted with a condenser, a solution of complex **2** (0.313 mmol) and organomercurial compound **5** (0.313 mmol) in dry methanol (30 mL) was heated at reflux for 20 h. The solvent was evaporated to dryness under vacuum, and the residue was purified by column chromatography on alumina by using a MeCN/$CH_2Cl_2$ (1:6) mixture as the eluent. The dark green band was collected, and the solvent removed. Blackish crystals were obtained by a slow diffusion of $Et_2O$ into a concentrated solution of the compound in 1:1 MeCN/$CH_2Cl_2$. Crystals were washed with $Et_2O$ (3 × 10 mL) and dried under vacuum. Reaction of **2** with **4** (Path **A**) under the same conditions gave compounds **3a**–**d** in lower yields.

**Complex 3a:** Yield 52% (115 mg) from 193 mg of **2** and 268 mg of **5**. MS: *m*/*z* (%) = 566 (13) $[M+H]^+$, 410 (20) $[M+H-bpy]^+$, 255 (4) $[M+H-bpy-phpy]^+$. IR: 839 (s, $PF_6$) $cm^{-1}$. $C_{32}H_{24}F_6N_4PRu$ (711.07): calcd. C 54.09, H 3.40, N 7.88; found C 53.89, H 3.61, N 7.69%.

**Complex 3b:** Yield 57%. MS: *m*/*z* (%) = 590 (100) $[M+H]^+$, 436 (23) $[M+H-phpy]^+$, 410 (35) $[M+H-phen]^+$, 255 (7) $[M+H-phen-phpy]^+$. IR: 841 (s, $PF_6$) $cm^{-1}$. $C_{34}H_{24}F_6N_4PRu$ (735.07): calcd. C 55.59, H 3.29, N 7.63;. found C 55.10, H 3.29, N 7.51%.

**Complex 3c:** Yield 50%. MS: *m*/*z* (%) = 594 (55) $[M+H]^+$, 438 (20) $[M+H-bpy]^+$, 426 (20) $[M+H-tolpy]^+$. IR: 836 (s, $PF_6$) $cm^{-1}$. $C_{34}H_{28}F_6N_4PRu$ (739.10): calcd. C 55.29, H 3.82, N 7.59; found C 55.20, H 3.91, N 7.69%.

**Complex 3d:** Yield 54%. MS: *m*/*z* (%) = 618 (65) $[M+H]^+$, 450 (10) $[M+H-tolpy]^+$, 438 (13) $[M+H-phen]^+$. IR: 840 (s, $PF_6$) $cm^{-1}$. $C_{36}H_{28}F_6N_4PRu\cdot 1/2(C_2H_5)_2O$ (800.13): calcd. C 57.07, H 4.16, N 7.01; found C 56.71, H 4.78, N 6.69%.

**Preparation of Biosensors:** The screen-printed carbon electrodes (CE) were designed as described.[16] A carbon paste electrode (working area 0.125 $cm^2$) was impregnated with 4 μL of a solution of mediator **1**–**3** (1 mg in 1 mL acetone). The enzyme was immobilized on the electrode surface by adsorption of 3 μL of enzyme solution for 1 h. Soluble PQQ-dependent alcohol dehydrogenase (Type II ADH IIG) from *Pseudomonas putida* HK5 (activity 1.54 U/0.2 mL) was used.

**Electrochemical Measurements:** These were performed with a three-electrode system containing a screen-printed carbon electrode as a working electrode, a Pt wire as a counter electrode, and a saturated KCl Ag/AgCl reference electrode. Steady-state currents were recorded at 0.5 or 0.1 V on a polarographic analyzer PGZ 402 (Radiometer Analytical). Acetate buffer (0.05 M, pH 6.0, 1 mM $Ca^{II}$) was used. Experimentally measured steady-state currents ($I$) as a function of the concentration of the substrate of the enzymatic reaction ([S]) were fitted to: $I = I_{M,app}[S]/(K_{M,app}+[S])$, where $I_{M,app}$ is the apparent maximal current and $K_{M,app}$ is the apparent Michaelis constant.

**Crystallography:** The crystals were mounted on the top of glass fibers and transferred to a Bruker SMART-APEX CCD diffractometer. Crystal data and details of data collection and structure refinement are given in Table S1. Absorption corrections were based on face-indexed measurements (program XPREP in SHELXTL).[19] The structures were refined anisotropically on $F^2$ with SHELXTL.[19] For both complexes, hydrogen atoms were included using a riding model. For more details, see Supporting Information. CCDC-606516 and -606515 contain the supplementary crystallographic data for **3a** and **3d**, respectively. These data can be obtained free of charge from The Cambridge Crystallographic Data Centre via www.ccdc.cam.ac.uk/data_request/cif.

**Supporting Information** (see also the footnote on the first page of this article): Crystal data and structure refinement parameters, details for **3a**, bond lengths and bond angles in Tables S1, S2, and Figure S1; current as a function of applied potential (Figure S2).

 © 2006 Wiley-VCH Verlag GmbH & Co. KGaA, Weinheim 

## Acknowledgments

We thank the University Louis Pasteur for a visiting professorship to A. D. R., Dr. R. A. Toscano for X-ray studies, and CONACyT and the Lithuanian State Science and Studies Foundation (C-02/2005, BIOHEMAS) for support.

[1] N. E. Tokel-Takvoryan, R. E. Hemingway, A. J. Bard, *J. Am. Chem. Soc.* **1973**, *95*, 6582–6589.
[2] E. C. Constable, J. M. Holmes, *J. Organomet. Chem.* **1986**, *301*, 203–208.
[3] J. M. Patrick, A. H. White, M. I. Bruce, M. J. Beatson, D. S. C. Black, G. B. Deacon, N. C. Thomas, *J. Chem. Soc., Dalton Trans.* **1983**, 2121–2123.
[4] M. I. Bruce, O. B. Shawkataly, M. R. Snow, E. R. T. Tiekink, *Acta Crystallogr., Sect. C* **1987**, *43*, 243–245.
[5] K. R. Flower, V. J. Howard, R. G. Pritchard, J. E. Warren, *Organometallics* **2002**, *21*, 1184–1189.
[6] a) M. F. Garbauskas, J. S. Kasper, L. N. Lewis, *J. Organomet. Chem.* **1984**, *276*, 241–248; b) M. I. Bruce, M. R. Snow, E. R. T. Tiekink, *J. Organomet. Chem.* **1986**, *311*, 217–223.
[7] a) M. Beley, S. Chodorowski, J. P. Collin, J. P. Sauvage, *Tetrahedron Lett.* **1993**, *34*, 2933–2936; b) C. Patoux, J. P. Launay, M. Beley, S. Chodorowski-Kimmes, J. P. Collin, S. James, J. P. Sauvage, *J. Am. Chem. Soc.* **1998**, *120*, 3717–3725; c) P. Dani, M. Albrecht, G. P. M. van Klink, G. van Koten, *Organometallics* **2000**, *19*, 4468–4476; d) P. Dani, M. A. M. Toorneman, G. P. M. van Klink, G. van Koten, *Organometallics* **2000**, *19*, 5287–5296; e) P. Dani, B. Richter, G. P. M. van Klink, G. van Koten, *Eur. J. Inorg. Chem.* **2001**, 125–131.
[8] a) R. Le Lagadec, L. Rubio, L. Alexandrova, R. A. Toscano, E. V. Ivanova, R. Meškys, V. Laurinavicius, M. Pfeffer, A. D. Ryabov, *J. Organomet. Chem.* **2004**, *689*, 4820–4832; b) A. D. Ryabov, R. Le Lagadec, H. Estevez, R. A. Toscano, S. Hernandez, L. Alexandrova, V. S. Kurova, A. Fischer, C. Sirlin, M. Pfeffer, *Inorg. Chem.* **2005**, *44*, 1626–1634.
[9] D. S. C. Black, G. B. Deacon, G. L. Edwards, B. M. Gatehouse, *Aust. J. Chem.* **1993**, *46*, 1323–1336.
[10] A. D. Ryabov in *Perspectives in Coordination Chemistry* (Eds.: A. F. Williams, C. Floriani, A. E. Merbach), Verlag NY, **1992**, pp. 271–292.
[11] The same was found for $[Ru(phpy)(bpy)_2]PF_6$: E. V. Ivanova, I. V. Kurnikov, A. Fischer, L. Alexandrova, A. D. Ryabov, *J. Mol. Catal. B: Enzym.*, in press.
[12] E. C. Constable, C. E. Housecroft, *Polyhedron* **1990**, *9*, 1939–1947.
[13] a) A. D. Ryabov, V. S. Sukharev, L. Alexandrova, R. Le Lagadec, M. Pfeffer, *Inorg. Chem.* **2001**, *40*, 6529–6532; b) A. D. Ryabov, V. S. Kurova, E. V. Ivanova, R. Le Lagadec, L. Alexandrova, *Anal. Chem.* **2005**, *77*, 1132–1139.
[14] T.-a. Koizumi, T. Tomon, K. Tanaka, *J. Organomet. Chem.* **2005**, *690*, 1258–1264.
[15] A. D. Ryabov, *Adv. Inorg. Chem.* **2004**, *55*, 201–270.
[16] a) J. Razumiene, M. Niculescu, A. Ramanavicius, V. Laurinavicius, E. Csöregi, *Electroanalysis* **2002**, *14*, 43–49; b) V. Laurinavicius, J. Razumiene, A. Ramanavicius, A. D. Ryabov, *Biosens. Bioelectron.* **2004**, *20*, 1217–1222.
[17] A. D. Ryabov, V. S. Soukharev, L. Alexandrova, R. Le Lagadec, M. Pfeffer, *Inorg. Chem.* **2003**, *42*, 6598–6600.
[18] D. S. C. Black, G. B. Deacon, G. L. Edwards, B. M. Gatehouse, *Aust. J. Chem.* **1993**, *46*, 1323–1336.
[19] G. M. Sheldrick, *SHELXTL* (Version 6.10), Bruker AXS Inc., Madison, Wisconsin, USA, **2000**.

Received: March 10, 2006
Published Online: June 7, 2006

 © 2006 Wiley-VCH Verlag GmbH & Co. KGaA, Weinheim 

DOI: 10.1002/ejic.200600019

# Zinc Complexes of Amine Mono(phenolate) [$NOO_2$] Ligands: Controlling Coordination Modes by Bulk of Phenolate Substituents

**Stanislav Groysman,[a] Ekaterina Sergeeva,[a] Israel Goldberg,[a] and Moshe Kol*[a]**

**Keywords:** Zinc / N,O ligands / Tripodal ligands / Polynuclear complexes

The coordination chemistry of three tripodal monoanionic amine mono(phenolate) ligands bearing two methoxy sidearm donors with ethylzinc(II) is reported. Reacting diethylzinc with the ligand precursor bearing bulky (*t*Bu) phenolate substituents led cleanly to a mono(ethyl) mononuclear $C_s$-symmetric zinc complex according to spectroscopic data. X-ray structure analysis revealed a semi-pentacoordinate complex as one of the methoxy sidearm donors was tightly bound whereas the other one was weakly bound. The ligand precursors bearing less bulky electron-donating (Me) or electron-withdrawing (Br) phenolate substituents led cleanly to dinuclear pentacoordinate complexes, bridged by phenolate oxygens, in which only one of the two sidearm donors was bound, and in a weak manner.
(© Wiley-VCH Verlag GmbH & Co. KGaA, 69451 Weinheim, Germany, 2006)

## Introduction

Zinc plays a major role in bioinorganic chemistry, fulfilling structural and catalytic functions in various enzymes.[1,2] When coordinated by S-based (cysteinate) ligands, or by a mixed set of S- and N-based (histidine) ligands, the role of zinc is mainly structural.[2] On the other hand, a coordination sphere containing O-based ligands is characteristic for a catalytic metal site, as the O-based hard donors ($H_2O$ or $HO^-$) are readily replaced at the zinc metal center, providing a vacant coordination site to be occupied by a substrate.[2] According to these general observations, simple analogues of the zinc biological active sites are sought.

In such research, controlling the nuclearity of metal species is a major goal. For many applications, mononuclear species are desired, as they lead to better-defined catalytic performance in comparison to multinuclear species. The most practical route toward such species is the utilization of chelating multidentate ligands such as the "tripodal" ligands, having three donor arms, which have become very abundant in the last two decades.[3] One particular family of tripodal ligand, that attracts ever-increasing attention, is the family of tripodal ligands possessing a central nitrogen donor atom, in addition to the three donor arms. Several ligand families of this type have been employed in zinc chemistry, including neutral tris(picolyl)amine ([$NN_3$]),[4,5] *N*-bis[2-(methylthio)ethyl]-*N*-[(6-neopentylamino-2-pyridyl)-methyl]amine ([$NS_2N$]),[6] and tris[(*N*-*tert*-butylcarbamoyl)-methyl]amine ([$NN_3$]) ligands,[7] or monoanionic dipicolylglycinate ([$NON_2$]),[8] and 2-mercaptobenzyl-bis(2-pyridylmethyl)amine ([$NN_2S$]) ligands [9] (Figure 1).

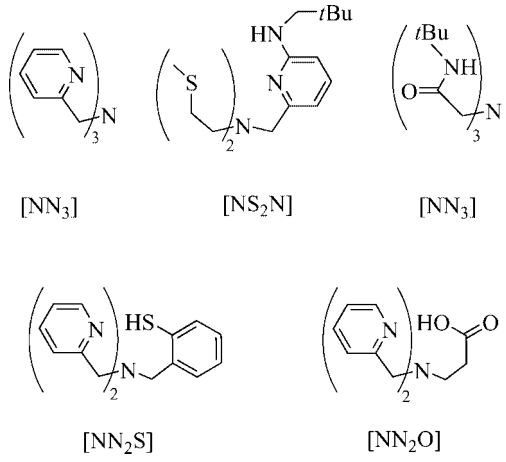


Figure 1. Various tripodal ligands, having a central nitrogen donor employed in zinc chemistry.

The zinc chemistry of monoanionic amine mono(phenolate) ligands, carrying two additional arms, has been investigated in the last decade, mainly by the groups of Fenton and Vahrenkamp.[10–13] The advantages of the amine mono(phenolate) ligands include their straightforward synthesis, and their broad structural diversity.[10–17] Yet, until now, the zinc chemistry of these ligands was limited to ligands having two additional pyridine arms,[10–12] or pyridyl and pyrrolidinyl arms (Figure 2).[13] The [$NON^{py}_2$] ligands, having no substituents, or *t*Bu substituents at the phenolate ring, were shown to bind the metal firmly through all four donors, with the three "tripodal" donors lying in the equatorial plane.[11,12] Both ligands led to neutral mononuclear complexes, possessing an additional, monodentate ligand in

[a] School of Chemistry, Raymond and Beverly Sackler Faculty of Exact Sciences, Tel Aviv University,
Tel Aviv 69978, Israel
E-mail: moshekol@post.tau.ac.il
Supporting information for this article is available on the WWW under http://www.eurjic.org or from the author.

 © 2006 Wiley-VCH Verlag GmbH & Co. KGaA, Weinheim 

the fifth position: Cl, Br, I, OPh, and SPh. In this study, we were aiming at extending the chemistry of tripodal monoanionic [$NOX_2$] ligands. Specifically, we wanted to reveal structural effects on coordination chemistry of [$NOO_2$]-zinc complexes, in which zinc binds to labile oxygen donors.

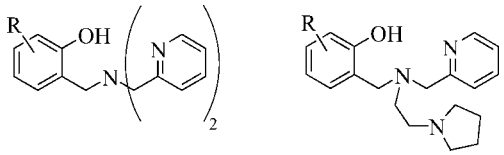

Figure 2. Two tripodal amine mono(phenolate) ligands, employed in zinc chemistry.

## Results and Discussion

We previously reported the preparation of the ligand precursor $Lig^1H$.[17] $Lig^2H$ and $Lig^3H$ ligand precursors were prepared in a similar way, via a single-step Mannich condensation between the respective phenol, secondary amine, and formaldehyde (Scheme 1). The ligand precursors were obtained as yellow oils, and their identity was confirmed by NMR and elemental analyses.

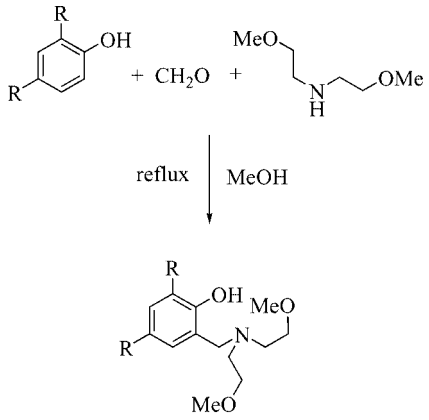

$Lig^1H$: R = *t*Bu; $Lig^2H$: R = Me; $Lig^3H$: R = Br

Scheme 1. Synthesis of ligand precursors $Lig^1H$–$Lig^3H$.

Diethylzinc provides a convenient entry into zinc chemistry with sufficiently acidic ligands.[18,19] An ethereal solution of $Lig^1H$ was added to a hexane solution of diethylzinc at –30 °C, followed by warming to room temperature and stirring for 1 h. Subsequent removal of solvent and recrystallization from pentane led to pure **1** in 80% yield, obtained as colorless crystals. According to its NMR spectra, **1** contains a single type of phenolate ring, and a single type of metal-bound ethyl group. As anticipated, the zinc-bound methylene group gives rise to high-field NMR signals [$\delta(^{13}C)$ –1.8 ppm; $\delta(^1H)$ 0.58 ppm]. The $^1H$ and $^{13}C$ NMR spectra of this compound clearly signify a $C_s$-symmetrical species at room temp. Thus, the $^1H$ spectrum featured a single resonance for the O$CH_3$ groups at $\delta$ = 2.85 ppm [$\delta(^{13}C)$ 58.7 ppm], and a sharp singlet for the two benzyl (Ar$CH_2$N) protons at $\delta$ = 3.31 ppm (these groups are reflected by a mirror plane). The N$CH_2CH_2$OMe protons appear as four distinct signals, of ddd (or dt) multiplicity, whose connectivity pattern was validated by a 2D $^1J_{C,H}$ (HMQC) experiment. This indicates that all four methylene protons of a particular "sidearm" are different; thus, the ligand seems to wrap around the metal in a well-defined fashion, in which the two sidearms are reflected by a mirror plane. However, the possibility of a fast (on the NMR timescale) exchange process, in which only one of the sidearms is bound at a given time, cannot be excluded a priori.

To distinguish between these two possibilities, we carried out a VT NMR experiment for **1** in [$D_8$]toluene. For the latter scenario, two different sidearms should be observed at low temperatures. In contrast, for the compound containing an effective mirror plane, no significant difference between proton spectra at room temp. vs. low temperatures should be anticipated. Upon cooling to as low as 210 K, no splitting in the peak attributed to the O$CH_3$ groups was observed; the N$CH_2CH_2$OMe appeared as four distinct signals as well, though all signals were somewhat broadened. The signals attributed to the ethyl group also underwent no change. This data is consistent with a $C_s$-symmetrical complex in solution, featuring binding of both sidearms (Figure 3). The slight broadening of peaks is attributed to a low-barrier conformational flip of the methylene-phenolate group. A freezing of this flip would result in a $C_1$-symmetrical complex, as revealed from the X-ray structure of **1**. The X-ray structure also reveals different MeO–Zn bond lengths (vide infra).

The complex of the nonbulky [$NOO_2$] electron-donating ligand $Lig^2$ was prepared in a similar way, by a protonolysis reaction between the ligand precursor $Lig^2H$ and $Et_2Zn$ (Figure 3). Complex **2** was obtained as colorless crystals upon recrystallization from ether. Even at room temp. the NMR spectrum of **2** in deuteriobenzene displays different features: the methylene N$CH_2CH_2$OMe protons appear as two broad signals vs. four sharp signals of ddd (dt) multiplicity for **1** (Figure 3). The O$CH_3$ protons appear as a single resonance at $\delta$ = 2.85 ppm at room temp. and the ethyl group gives rise to single triplet and quartet resonances, at $\delta$ = 0.39 and 1.56 ppm, respectively. However, in contrast to **1**, cooling **2** to 210 K causes splitting of the O$CH_3$ resonance into two discrete signals (coalescence at 221 K). The quartet signal attributed to the metal-bound methylene was split into two multiplets at that temperature as well, signifying a different chemical environment for the two methylene protons. Thus, a different binding of the nonbulky [$NOO_2$] ligand to the metal should be anticipated, according to the VT-NMR spectroscopic data (Figure 3).

The X-ray structure determination of these complexes provided a solid evidence for the different coordination modes of these [$NOO_2$] ligands around zinc. According to our expectations for the structure of **1**, the ligand is bound to the metal through all four donors, forming a mononuclear, pentacoordinate species of highly distorted TBP geometry (Figure 4, Table 1). In the previously disclosed zinc complexes featuring the [$NO(N^{py})_2$] ligand,[11,12] the three

 © 2006 Wiley-VCH Verlag GmbH & Co. KGaA, Weinheim 

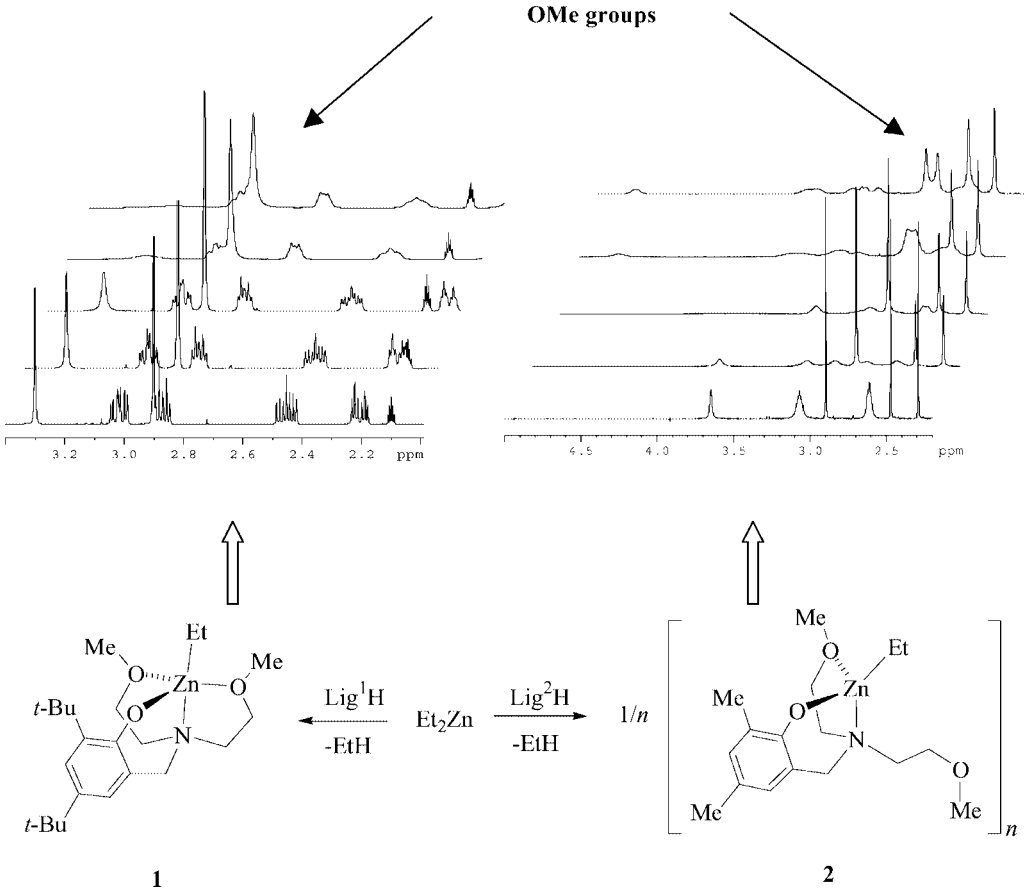


Figure 3. Syntheses of the amine mono(phenolate) complexes **1** and **2**, and their proposed structures; (bottom), based on VT $^1$H NMR spectra (top). See text for details.

arms of the tripodal ligand occupied the equatorial positions, while the central amine and the additional monodentate ligand were located in the axial positions. In the present case, the phenolate oxygen, the central nitrogen, and the ethyl methylene carbon are located in the equatorial plane, whereas the methoxy donors occupy the axial positions. The phenolate oxygen, amine donor, and the ethyl methylene carbon all feature strong bonding to the metal center. In contrast, the two methoxy groups are inequivalent, displaying weak binding to the metal: 2.308 vs. 2.598 Å. The pronounced difference in bond lengths may result from the conformation of the ethyl group, as its methylene carbon points toward the remote methoxy group, or from the conformation of the phenolate ring, as the *t*Bu group points toward that group as well, or by a combination of both. It may also signify an "arrested" dynamic process equilibrating bound and unbound sidearm donors. The Zn–O–C(Ph) angle is narrow (114.9°), as is anticipated for a $d^{10}$ metal complex experiencing no π-donation from the phenolate oxygen to the metal, vs. 128–148° in $d^0$ or $d^2$ ($Ta^V$, $V^{III}$, $V^V$, or $Ti^{IV}$) complexes.[20–22]

In a sharp contrast to the structure of **1**, **2** is a dinuclear complex of $C_i$-symmetry, in which the two nearby zinc atoms (Zn···Zn separation of 3.108 Å) are bridged by the two phenolate oxygen atoms (Figure 5, Table 1). This

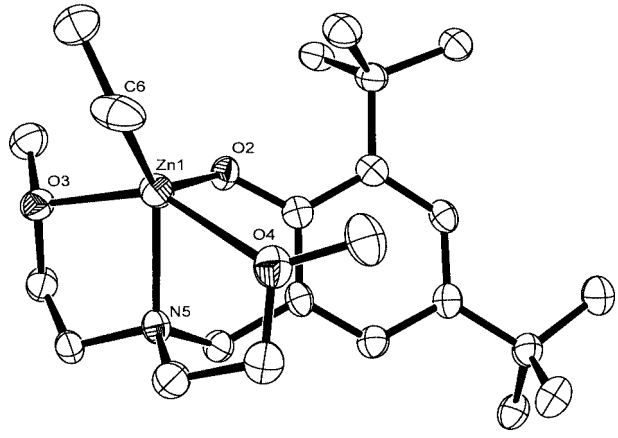


Figure 4. The X-ray structure of **1**. ORTEP representation, 50% probability.

$Zn_2O_2$ core is a common structural motif in zinc coordination chemistry, found frequently in zinc-phenolate species.[23–27] The Zn–O(Ph) bond lengths are not identical, being 2.018 and 2.123 Å, respectively. One of the sidearms is unbound, creating a pentacoordinate, nearly TBP geometry at each metal center. One of the phenolate oxygen atoms and the methoxy donor are in the axial position [O(Ph)-Zn-

 © 2006 Wiley-VCH Verlag GmbH & Co. KGaA, Weinheim 

Table 1. Bond lengths [Å] around Zn in the solid-state structure of **1**, **2**, and **3**.

| | 1 | 2 | 3 |
|---|---|---|---|
| Zn1–O2 | 1.931(2) | 2.018(2) | 2.036(5) |
| Zn1–O2′ | | 2.123(2) | 2.143(4) |
| Zn1–O3 | 2.308(2) | 2.549(3) | 2.451(5) |
| Zn1–O4 | 2.598(2) | | |
| Zn1–N5 | 2.150(2) | 2.169(3) | 2.155(6) |
| Zn1–C6 | 1.962(2) | 1.986(4) | 1.975(7) |

(R)OMe 159.0°], whereas the second phenolate oxygen, the ethyl methylene carbon, and the central nitrogen are in the equatorial positions. Consistently with the previous structure, the central amine is bound tightly (2.169 Å), and the methoxy donor is bound very weakly (2.549 Å).

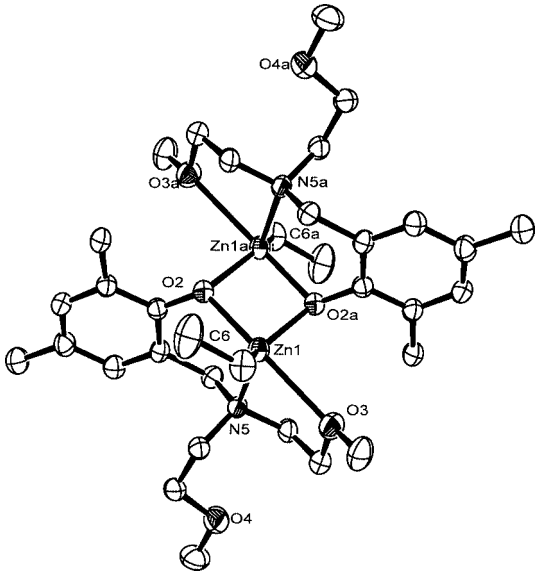


Figure 5. The X-ray structure of **2**. ORTEP representation, 40% probability. The asymmetric unit contains only half of the *Ci*-symmetric dimer, and the second half is generated by a symmetry operation. The structure also contains a disordered solvent molecule, not shown here.

An additional ligand, employed in this research, was Lig[3], carrying *ortho*, *para* bromo substituents, that are comparable in size to the methyl groups, yet are electron-withdrawing and may reduce the tendency of the phenolate oxygen atoms to act as bridging groups. The ligand precursor Lig[3]H was treated with diethylzinc in analogy to Lig[1]H and Lig[2]H; the product **3** was obtained in a good yield after washing out of the impurities with pentane and ether. In general, the room temp. $^1$H NMR spectrum of **3** displays similar features to that of **2**. In both cases, the NC$H_2$C$H_2$O methylene protons give rise to two resonances: For **2**, these are represented by two broad peaks; for **3**, one of these signals is broad, while the second appears as a relatively sharp triplet. The VT NMR behavior of **3** was not identical to the spectrum of **2**: for example, the methylene NC$H_2$C$H_2$O protons were observed in **2** at 278 K as four broad multiplets, while in **3** they gave rise to two broad signals at that temperature. Moreover, in spite of a significant broadening in the OC$H_3$ and Zn-C$H_2$ resonances, no splitting was observed down to 200 K, which may indicate a lower-energy process in **3** than in **2**; it does not exclude, however, the possibility of a mononuclear, nearly $C_s$-symmetrical complex.

The X-ray structure analysis provided a clear evidence for the dinuclear nature of **3** (Figure 6). In the solid state, the *Ci*-symmetric **3** possesses a very similar structure to that of **2**, displaying two pentacoordinate metal centers in close proximity (Zn···Zn separation of 3.163 Å), bridged by the phenolate oxygen atoms. The bond lengths in **3** are reminiscent of those in **2**; the major structural difference between these structures lies in the Zn–O(R)Me bond lengths [2.451(5) in **3** vs. 2.549(3) Å in **2**]. The stronger bonding of the weak donor in **3** may be traced back to the electron deficiency at the metal center, as a result of the electron-poor ligand.

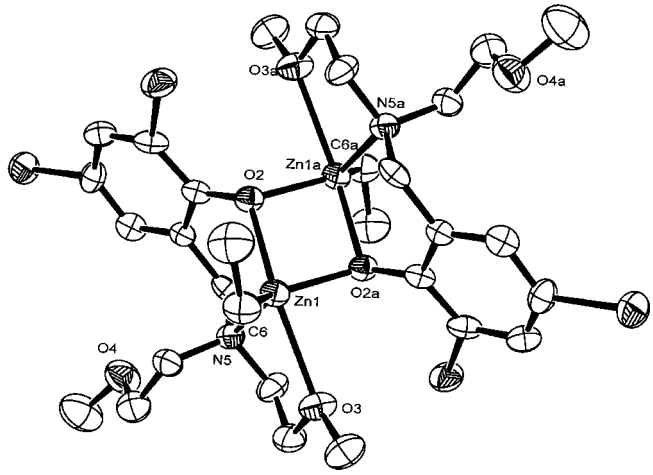


Figure 6. The X-ray structure of **3**. ORTEP representation, 40% probability. The asymmetric unit contains only half of the *Ci*-symmetric dimer, and the second half is generated by a symmetry operation.

On the basis of the above results, we propose that a point of divergence for the different nuclearity in [$NOO_2$]ZnEt species lies in a delicate balance between the weakness (lability) of the dative Zn–O(R)Me bond and the steric bulk imposed by the groups in the *ortho* positions of the phenolate ring. Presumably, formation of a dinuclear phenolate-bridged species in the [$NOO_2$] zinc complexes is favorable due to the weakness of the Zn–O(R)Me dative bond. However, the formation of dinuclear species is precluded by sufficient steric bulk at the *ortho* positions of the phenolate group.[28] As a result, mononuclear species arise, in which the weak, yet nonbulky, second O(R)Me donor is able to bind to the metal center, accomplishing a pentacoordinate geometry.

To summarize, we investigated the coordination chemistry of zinc(II) in the environment of the amine mono(phenolate) ligands, carrying two neutral oxygen-type arms, in addition to the anionic phenolate oxygen. A neutral oxygen donor, known to bind weakly to zinc, was found to display varying coordination modes, influenced by the steric bulk

 © 2006 Wiley-VCH Verlag GmbH & Co. KGaA, Weinheim 

at the phenolate ring. In the case of small groups at the phenolate ring, formation of a dinuclear complex was observed, in which every metal atom was bound to two phenolate oxygen atoms, at the expense of binding of a second weak donor. In contrast, utilization of bulkier, *t*Bu, groups at the phenolate ring prohibited the formation of a dinuclear complex, leading to a mononuclear species instead, in which both neutral oxygen donors were bound.

## Experimental Section

**General:** All manipulations of the metal complexes were performed under dry nitrogen in a nitrogen-filled glovebox. 2,4-Di-*tert*-butylphenol, bis(2-methoxyethyl)amine, formaldehyde (37% in water), and diethylzinc (1.0 M in hexane) were obtained from Aldrich and used without purification. Lig$^1$H was prepared as described previously.[17] Ether was purified by reflux and distillation under dry Ar from Na/benzophenone. Pentane was washed with $HNO_3/H_2SO_4$ prior to distillation from Na/benzophenone. [$D_6$]-Benzene was flushed with Ar and stored on molecular sieves in the glovebox. [$D_8$]Toluene was dried on Na before being used. NMR spectroscopic data for the metal complexes were collected with Bruker AC-200 and AC-400 spectrometers, and referenced to protio impurities in [$D_6$]benzene and [$D_8$]toluene ($\delta$ = 7.15 and 2.1 ppm, respectively) and to the $^{13}$C chemical shift of benzene ($\delta$ = 128.06 ppm). Routine characterization of metal complexes consisted of $^1$H, BB, and DEPT-135 $^{13}$C NMR experiments, performed in [$D_6$]benzene at 298(2) K. VT NMR experiments were performed in [$D_8$]toluene. X-ray diffraction measurements were performed with a Nonius Kappa CCD diffractometer system, using Mo-$K_\alpha$ ($\lambda$ = 0.7107 Å) radiation. The analyzed crystals were embedded within a drop of viscous oil and freeze-cooled to 110 K. The structures were solved by a combination of direct methods and Fourier techniques using SIR-92 software,[29] and were refined by full-matrix least-squares with SHELXL-97.[30] The crystal and experimental data are summarized in Table 2. CCDC-294424 (for **1**), -294425 (for **2**), and -294426 (for **3**) contain the supplementary crystallographic data for this paper. These data can be obtained free of charge from The Cambridge Crystallographic Data Centre via www.ccdc.cam.ac.uk/data_request/cif. Elemental analyses were performed in the microanalytical laboratory in the Hebrew University of Jerusalem.

Table 2. Crystallographic experimental details.

| | **1** | **2** | **3** |
|---|---|---|---|
| Formula | $C_{23}H_{41}NO_3Zn$ | $C_{17}H_{29}NO_3Zn$ | $C_{15}H_{23}Br_2NO_3Zn$ |
| *fw* | 444.94 | 360.78 | 490.53 |
| *a* [Å] | 9.4730(6) | 26.8350(7) | 10.4670(5) |
| *b* [Å] | 9.8160(6) | 26.8350(7) | 9.2700(6) |
| *c* [Å] | 13.890(1) | 10.6420(3) | 18.1480(10) |
| *α* [deg] | 82.162(4) | 90.00 | 90.00 |
| *β* [deg] | 69.988(3) | 90.00 | 93.036(4) |
| *γ* [deg] | 81.258(4) | 90.00 | 90.00 |
| Crystal system | triclinic | tetragonal | monoclinic |
| Space group | $P\bar{1}$ | $I4_1/a$ | $P2_1/c$ |
| *V* [Å$^3$] | 1194.55(14) | 7663.5(4) | 1758.41(17) |
| $D_c$ [g cm$^{-1}$] | 1.237 | 1.251 | 1.853 |
| $\mu$ [cm$^{-1}$] | 1.049 | 1.293 | 5.952 |
| *Z* | 2 | 16 | 4 |
| No. of measd. reflns. | 5559 | 4543 | 3226 |
| No. of reflns. [$I > 2\sigma(I)$] | 3890 | 3307 | 2205 |
| $R_1$ [$I > 2\sigma(I)$] | 0.0524 | 0.0534 | 0.0546 |
| $wR_2$ [$I > 2\sigma(I)$] | 0.1104 | 0.1498 | 0.1163 |
| GOF | 1.003 | 1.042 | 1.010 |

**Synthesis of Lig$^2$H:** 2,4-Dimethylphenol (5.5 mL, 46 mmol), bis(2-methoxyethyl)amine (13 mL, 89 mmol), and formaldehyde (13 mL, 37% in water) were mixed in MeOH (20 mL). The mixture was heated to 110 °C in a pressure flask and stirred for 48 h, yielding a deep orange biphasic solution. The crude reaction mixture was poured into water/$CH_2Cl_2$ (40 mL each), the organic phase was separated, dried with anhydrous $MgSO_4$, and the solvent was removed under reduced pressure. The traces of amine were removed under vacuum (0.5 mbar), while heating to 80 °C, yielding the desired product as orange oil (9.243 g, 35 mmol, 76%). $C_{15}H_{25}NO_3$ (267.36): calcd. C 67.38, H 9.42, N 5.24; found C 67.31, H 9.71, N 5.44. $^1$H NMR (200 MHz, $CDCl_3$): $\delta$ = 10.32 (s, 2 H, O-*H*), 6.74 (br. s, 2 H, Ar-H), 6.52 (br. s, 2 H, Ar-H), 3.69 (s, 2 H, ArC$H_2$N), 3.43 (t, $^3J_{H,H}$ = 5.5 Hz, 4 H, NC$H_2$C$H_2$O), 3.23 (s, 6 H, OC$H_3$), 2.70 (t, $^3J_{H,H}$ = 5.5 Hz, 4 H, NC$H_2$C$H_2$O), 2.11 (s, 6 H, Ar-C$H_3$) ppm. $^{13}$C NMR (50.29 MHz, $CDCl_3$): $\delta$ = 153.7 (*C*O), 130.6 (*C*H), 127.6 (*C*), 126.9 (*C*H), 124.8 (*C*), 121.5 (*C*), 70.5 (*C*H$_2$), 58.8 (O*C*H$_3$), 58.6 (*C*H$_2$), 53.4 (*C*H$_2$), 20.5 (C*H*$_3$), 15.8 (C*H*$_3$) ppm.

**Synthesis of Lig$^3$H:** 2,4-Dibromophenol (1.97 g, 7.8 mmol), bis(2-methoxyethyl)amine (2 mL, 13.6 mmol), and formaldehyde (3.2 mL, 37% solution in water) were mixed in MeOH (20 mL). The mixture was stirred and refluxed for two weeks. The crude reaction mixture was poured into water/$CH_2Cl_2$ (20 mL each), the organic phase was separated, dried with anhydrous $MgSO_4$, and the solvent was removed under reduced pressure. The remaining product was dried (0.5 mbar, 100 °C) for 2 h, yielding the desired product as brown oil (2.86 g, 7.2 mmol, 92%). $^1$H NMR (200 MHz, $C_6D_6$): $\delta$ = 7.57 (d, $^4J_{H,H}$ = 2.4 Hz, 2 H, Ar-*H*), 6.79 (d, $^4J_{H,H}$ = 2.4 Hz, 2 H, Ar-*H*), 3.23 (s, 2 H, ArC$H_2$N), 3.01 (t, $^3J_{H,H}$ = 5.1 Hz, 4 H, NC$H_2$C$H_2$O), 2.94 (s, 6 H, OC$H_3$), 2.34 (t, $^3J_{H,H}$ = 5.4 Hz, 4 H, NC$H_2$C$H_2$O) ppm. $^{13}$C NMR (100.58 MHz, $CDCl_3$, 300 K): $\delta$ = 154.4 (*C*O), 134.1 (*C*H), 130.4 (*C*H), 125.3 (*C*), 111.1 (*C*), 110.5 (*C*), 70.4 (*C*H$_2$), 59.2 (O*C*H$_3$), 58.4 (*C*H$_2$), 53.6 (*C*H$_2$) ppm.

**Synthesis of 1:** Lig$^1$H (86 mg, 0.25 mmol) was dissolved in ether (1 mL) and cooled to –35 °C. While cold, it was added slowly to a pre-cooled solution of $ZnEt_2$ in hexane (1.0 M, 0.25 mL). The resulting bright yellow solution was warmed to room temp. and stirred for 1 h. The solvent was removed under reduced pressure, the resulting bright yellow solid was dissolved in pentane and the solution was left at –35 °C overnight. Colorless crystals of X-ray quality were separated from the solution, washed with cold pentane and dried under reduced pressure to afford **1** (91 mg, 0.20 mmol, 80%). $C_{23}H_{41}NO_3Zn$ (444.97): calcd. C 62.08, H 9.29, N 3.15; found: C 61.85, H 9.31, N 3.25. $^1$H NMR (400 MHz, $C_6D_6$, 298 K): $\delta$ = 7.58 (d, $^4J_{H,H}$ = 2.7 Hz, 2 H, Ar-*H*), 6.88 (d, $^4J_{H,H}$ = 2.7 Hz, 2 H, Ar-*H*), 3.31 (s, 2 H, PhC$H_2$N), 2.96 (ddd, $^2J_{H,H}$ = 10.1, $^3J_{H,H}$ = 9.0, $^3J_{H,H}$ = 3.7 Hz, 2 H, NCH$_2$C$H_2$O), 2.85 (s, 6 H, OC$H_3$), 2.81 (dt, $^2J_{H,H}$ = 10.1, $^3J_{H,H}$ = 4.5 Hz, 2 H, NCH$_2$C$H_2$O), 2.41 (ddd, $^2J_{H,H}$ = 13.3, $^3J_{H,H}$ = 8.9, $^3J_{H,H}$ = 4.5 Hz, 2 H, NC$H_2$CH$_2$O), 2.17 (dt, $^2J_{H,H}$ = 13.3, $^3J_{H,H}$ = 4.0 Hz, 2 H, NC$H_2$CH$_2$O), 1.86 [s, 9 H, C(C$H_3$)$_3$], 1.63 (t, $^3J_{H,H}$ = 8.1 Hz, 3 H, Zn-CH$_2$C$H_3$), 1.46 [s, 9 H, C(C$H_3$)$_3$], 0.59 (q, $^3J_{H,H}$ = 8.1 Hz, 2 H, Zn-C$H_2$CH$_3$) ppm. $^{13}$C NMR (100.58 MHz, $C_6D_6$, 298 K): $\delta$ = 164.4 (*C*O), 138.5 (*C*), 135.1 (*C*), 125.3 (*C*H), 124.1 (*C*H), 122.4 (*C*), 68.5 (C$H_2$), 59.6 (C$H_2$), 58.7 (OC$H_3$), 56.5 (C$H_2$), 35.9 [*C*(CH$_3$)$_3$], 34.2 [*C*(CH$_3$)$_3$], 32.4 [C(*C*H$_3$)$_3$], 30.2 [C(*C*H$_3$)$_3$], 13.5 (Zn-CH$_2$*C*H$_3$), –1.8 (Zn-*C*H$_2$CH$_3$) ppm. $^1$H NMR (400 MHz, $C_7D_8$, 301 K, selected resonances): $\delta$ = 3.30 (s, 2 H, PhC$H_2$N), 3.01 (ddd, $^2J_{H,H}$ = 10.0, $^3J_{H,H}$ = 9.0, $^3J_{H,H}$ = 3.7 Hz, 2 H, NCH$_2$C$H_2$O), 2.90 (s, 6 H, OC$H_3$),

 © 2006 Wiley-VCH Verlag GmbH & Co. KGaA, Weinheim 

2.81 (dt, $^2J_{H,H}$ = 10.1, $^3J_{H,H}$ = 4.5 Hz, 2 H, NCH$_2$C$H_2$O), 2.45 2.41 (ddd, $^2J_{H,H}$ = 13.4, $^3J_{H,H}$ = 9.0, $^3J_{H,H}$ = 4.5 Hz, 2 H, NC$H_2$CH$_2$O), 2.21 (dt, $^2J_{H,H}$ = 13.4, $^3J_{H,H}$ = 4.2 Hz, 2 H, NC$H_2$CH$_2$O), 1.56 (t, $^3J_{H,H}$ = 8.1 Hz, 3 H, Zn-CH$_2$C$H_3$), 0.49 (q, $^3J_{H,H}$ = 8.1 Hz, 2 H, Zn-C$H_2$CH$_3$) ppm. $^1$H NMR (400 MHz, C$_7$D$_8$, 210 K, selected resonances): $\delta$ = ca. 3.1 (br. s, 2 H, PhC$H_2$N), 2.89 (br. s, 2 H, NCH$_2$C$H_2$O), 2.84 (s, 6 H, OC$H_3$), 2.60 (br. s, 2 H, NCH$_2$C$H_2$O), 2.29 (br. s, 2 H, NC$H_2$CH$_2$O), 1.87 (br. s, 2 H, NC$H_2$CH$_2$O), 1.76 (t, $^3J_{H,H}$ = 8.0 Hz, 3 H, Zn-CH$_2$C$H_3$), 0.69 (q, $^3J_{H,H}$ = 8.1 Hz, 2 H, Zn-C$H_2$CH$_3$) ppm.

**Synthesis of 2:** Lig$^2$H (165 mg, 0.62 mmol) was dissolved in ether (2 mL), cooled to –35 °C, and added slowly to a pre-cooled solution of ZnEt$_2$ in hexane (1.0 M, 0.63 mL). The resulting bright yellow solution was warmed to room temp. and stirred for 1 h. The solvent was removed under reduced pressure, the resulting bright yellow solid was dissolved in diethyl ether (ca. 3 mL overall) and the solution was left at –35 °C for 2 days. Colorless crystals of X-ray quality were separated from the solution, washed with cold ether and dried under reduced pressure to afford **2** (157 mg, 0.44 mmol, 71%). $C_{34}H_{58}N_2O_6Zn_2$ (721.61): calcd. C 56.59, H 8.10, N 3.88; found C 56.27, H 8.25, 3.86. $^1$H NMR (400 MHz, C$_6$D$_6$, 300 K): $\delta$ = 7.05 (d, $^4J_{H,H}$ = 1.9 Hz, 2 H, Ar-*H*), 6.66 (d, $^4J_{H,H}$ = 2.1 Hz, 2 H, Ar-*H*), 3.83 (s, 2 H, PhC$H_2$N), 3.13 (br. s, 4 H, NCH$_2$C$H_2$O), 2.86 (s, 6 H, OC$H_3$), 2.85 (br. s, 4 H, NC$H_2$CH$_2$O), 2.51 (s, 3 H, Ar-C$H_3$), 2.29 (s, 3 H, Ar-C$H_3$), 1.11 (t, $^3J_{H,H}$ = 8.1 Hz, 3 H, Zn-CH$_2$C$H_3$), 0.40 (q, $^3J_{H,H}$ = 8.1 Hz, 2 H, Zn-C$H_2$CH$_3$) ppm. $^1$H NMR (400 MHz, C$_7$D$_8$, 301 K, selected resonances): $\delta$ = 3.65 (s, 2 H, PhC$H_2$N), 3.07 (br. s, 4 H, NCH$_2$C$H_2$O), 2.90 (s, 6 H, OC$H_3$), 2.61 (br. s, 4 H, NCH$_2$C$H_2$O), 2.47 (s, 3 H, Ar-C$H_3$), 2.29 (s, 3 H, Ar-C$H_3$), 1.51 (t, $^3J_{H,H}$ = 8.1 Hz, 3 H, Zn-CH$_2$C$H_3$), 0.38 (q, $^3J_{H,H}$ = 8.1 Hz, 2 H, Zn-C$H_2$CH$_3$) ppm. $^1$H NMR (400 MHz, C$_7$D$_8$, 210 K, selected resonances): $\delta$ = 2.85 (s, 3 H, OC$H_3$), 2.77 (s, 3 H, OC$H_3$), 1.79 (t, $^3J_{H,H}$ = 8.0 Hz, 3 H, Zn-CH$_2$C$H_3$), 0.40 (br. s, 1 H, Zn-C*H*HCH$_3$), 0.31(br. s, 1 H, Zn-CH*H*CH$_3$) ppm. $^{13}$C NMR (100.58 MHz, C$_6$D$_6$, 300 K): $\delta$ = 161.4 (*C*O), 132.4 (*C*H), 129.5 (*C*H), 128.4 (*C*), 124.1 (*C*), 123.4 (*C*), 68.9 (C$H_2$), 59.3 (C$H_2$), 58.4 (OC$H_3$), 53.2 (C$H_2$), 20.8 (Ar-*C*H$_3$), 17.8 (Ar-*C*H$_3$), 13.7 (Zn-CH$_2$C$H_3$), –1.7 (Zn-C$H_2$CH$_3$) ppm.

**Synthesis of 3:** Lig$^3$H (51 mg, 0.13 mmol) was dissolved in an ether/THF mixture (5 mL) and added to a solution of ZnEt$_2$ in hexane (1.0 M, 0.13 mL). The resulting dark yellow solution was stirred for 1.5 h. The solvent was removed under reduced pressure, and the resulting yellow solid was washed with pentane (ca. 2 mL) and ether (2 mL) and dried under reduced pressure to afford **3** (47 mg, 74%). X-ray quality crystals were obtained upon recrystallization from ether. $C_{30}H_{46}Br_4N_2O_6Zn_2$ (981.09): calcd. C 66.07, H 10.52, N 7.97; found C 66.11, H 10.77, N 7.88. $^1$H NMR (400 MHz, C$_6$D$_6$, 300 K): $\delta$ = 7.82 (d, $^4J_{H,H}$ = 2.6 Hz, 2 H, Ar-*H*), 6.86 (d, $^4J_{H,H}$ = 2.6 Hz, 2 H, Ar-*H*), 3.06 (s, 2 H, PhC$H_2$N), 2.80 (s, 6 H, OC$H_3$), 2.69 (t, $^3J_{H,H}$ = 5.4 Hz, 4 H, NCH$_2$C$H_2$O), 2.24 (br. s, 2 H, NC$H_2$CH$_2$O), 1.99 (br. s, 2 H, NC$H_2$CH$_2$O), 1.53 (t, $^3J_{H,H}$ = 8.1 Hz, 3 H, Zn-CH$_2$C$H_3$), 0.49 (q, $^3J_{H,H}$ = 8.1 Hz, 2 H, Zn-C$H_2$CH$_3$) ppm. $^1$H NMR (400 MHz, C$_7$D$_8$, 301 K, selected resonances): $\delta$ = 3.10 (s, 2 H, PhC$H_2$N), 2.85 (s, 6 H, OC$H_3$), 2.76 (t, $^3J_{H,H}$ = 5.4 Hz, 4 H, NCH$_2$C$H_2$O), ca. 2.3 (br. s, 2 H, NC$H_2$CH$_2$O), ca. 2.1 (br. s, 2 H, NC$H_2$CH$_2$O), 1.48 (t, $^3J_{H,H}$ = 8.1 Hz, 3 H, Zn-CH$_2$C$H_3$), 0.42 (q, $^3J_{H,H}$ = 8.1 Hz, 2 H, Zn-C$H_2$CH$_3$) ppm. $^1$H NMR (400 MHz, C$_7$D$_8$, 200 K, selected resonances): $\delta$ = around 2.8 (broad and flat resonance, 14 H), 2.26 (br. s, 2 H), 1.78 (t, $^3J_{H,H}$ = 8.0 Hz, 3 H, Zn-CH$_2$C$H_3$), ca. 0.45 (br. s, 2 H, Zn-C$H_2$CH$_3$) ppm. $^{13}$C NMR (50.29 MHz, C$_6$D$_6$, 298 K): $\delta$ = 135.6 (*C*H), 132.1 (*C*H), 128.4 (*C*), 126.2 (*C*), 117.1 (*C*), 67.9 (C$H_2$), 58.5 (OC$H_3$), 57.9 (C$H_2$), 56.1 (C$H_2$), 13.4 (Zn-CH$_2$C$H_3$), –1.8 (Zn-C$H_2$CH$_3$) ppm.

**Supporting Information** (see footnote on the first page of this article) includes VT NMR spectra for complexes **1**–**3**.

## Acknowledgments

We thank the Israel Science Foundation and the United States-Israel Binational Science Foundation for financial support. We thank Adi Yeori for helpful discussions.

[1] G. Parkin, *Chem. Rev.* **2004**, *104*, 699.
[2] S. J. Lippard, J. M. Berg, *Principles of Bioinorganic Chemistry*, University Science Books, Mill Valley, CA, **1994**, p. 354.
[3] G. Parkin, *Chem. Commun.* **2000**, 1971.
[4] N. N. Murthy, K. D. Karlin, *J. Chem. Soc., Chem. Commun.* **1993**, 1236.
[5] H. Adams, N. A. Bailey, D. E. Fenton, Q.-Y. He, *J. Chem. Soc., Dalton Trans.* **1997**, 1533.
[6] L. M. Berreau, R. A. Allred, M. M. Makowska-Grzyska, A. M. Arif, *Chem. Commun.* **2000**, 1423.
[7] M. Ray, B. S. Hammes, G. P. A. Yap, A. L. Rheingold, A. S. Borovik, *Inorg. Chem.* **1998**, *37*, 1527.
[8] A. Abufarag, H. Vahrenkamp, *Inorg. Chem.* **1995**, *34*, 2207.
[9] R. Burth, A. Stange, M. Schäfer, H. Vahrenkamp, *Eur. J. Inorg. Chem.* **1998**, 1759.
[10] H. Adams, N. A. Bailey, D. E. Fenton, Q.-Y. He, *J. Chem. Soc., Dalton Trans.* **1996**, 2857.
[11] A. Trösch, H. Vahrenkamp, *Eur. J. Inorg. Chem.* **1998**, 827.
[12] A. Trösch, H. Vahrenkamp, *Inorg. Chem.* **2001**, *40*, 2305.
[13] A. Abufarag, H. Vahrenkamp, *Inorg. Chem.* **1995**, *34*, 3279.
[14] H. Adams, N. A. Bailey, C. O. Rodriguez de Bazan, D. E. Fenton, Q.-Y. He, *J. Chem. Soc., Dalton Trans.* **1996**, 2233.
[15] Y. Inoue, K. Matyjaszewski, *Macromolecules* **2003**, *36*, 7432.
[16] Y. Inoue, K. Matyjaszewski, *Macromolecules* **2004**, *37*, 4014.
[17] S. Groysman, E. Sergeeva, I. Goldberg, M. Kol, *Inorg. Chem.* **2005**, *44*, 8188.
[18] C. K. Williams, L. E. Breyfogle, S. K. Choi, W. Nam, V. G. Young Jr, M. A. Hillmyer, W. B. Tolman, *J. Am. Chem. Soc.* **2003**, *125*, 11350.
[19] M. H. Chisholm, C.-C. Lin, J. C. Gallucci, B.-T. Ko, *Dalton Trans.* **2003**, 406.
[20] S. Groysman, I. Goldberg, M. Kol, E. Genizi, Z. Goldschmidt, *Organometallics* **2004**, *23*, 1880.
[21] S. Groysman, I. Goldberg, Z. Goldschmidt, M. Kol, *Inorg. Chem.* **2005**, *44*, 5073.
[22] S. Groysman, E. Tshuva, I. Goldberg, M. Kol, Z. Goldschmidt, M. Shuster, *Organometallics* **2004**, *23*, 5291.
[23] E. Bukhaltsev, I. Goldberg, A. Vigalok, *Organometallics* **2005**, *24*, 5732.
[24] K. Matsufuji, H. Shiraishi, Y. Miyasato, T. Shiga, M. Ohba, T. Yokoyama, H. Ōkawa, *Bull. Chem. Soc. Jpn.* **2005**, *78*, 851.
[25] J. S. Matalobos, A. M. García-Deibe, M. Fondo, D. Navarro, M. R. Bermejo, *Inorg. Chem. Commun.* **2004**, *7*, 311.
[26] A. J. Atkins, D. Black, R. L. Finn, A. Marin-Beccera, A. J. Blake, L. Ruiz-Ramirez, W.-S. Li, M. Schröder, *Dalton Trans.* **2003**, 2730.
[27] For a heptadentate monophenolate ligand leading to a dinuclear zinc complex, see: H. Sakiyama, R. Mochizuki, A. Sugawara, M. Sakamoto, Y. Nishida, M. Yamasaki, *J. Chem. Soc., Dalton Trans.* **1999**, 997.
[28] The "heteroscorpionate" ligands studied by Carrano led to complexes of different nuclearity depending on the presence of a *t*Bu group on a phenolate ring. See: T. C. Higgs, K. Spartalian, C. J. O'Connor, B. F. Matzanke, C. J. Carrano, *Inorg.*

 © 2006 Wiley-VCH Verlag GmbH & Co. KGaA, Weinheim 

*Chem.* **1998**, *37*, 2263; B. S. Hammes, C. J. Carrano, *Inorg. Chem.* **1999**, *38*, 4593.
[29] A. Altomare, M. C. Burla, M. Camalli, M. Cascarano, C. Giacovazzo, A. Guarliardi, G. Polidori, *J. Appl. Crystallogr.* **1994**, *27*, 435.
[30] G. M. Sheldrick, *SHELX-97*, University of Göttingen, Germany, **1998**.

Received: January 10, 2006
Published Online: May 24, 2006

 © 2006 Wiley-VCH Verlag GmbH & Co. KGaA, Weinheim 

DOI: 10.1002/ejic.200500960

# Novel Coordination Polymers Generated from Angular 2,2′-Dipyridyl Ligands and Bis(hexafluoroacetylacetonate) Copper(II): Crystal Structures and Magnetic Properties

**Salomé Delgado,*[a] Aitor Barrilero,[a] Agustín Molina-Ontoria,[a] Manuela E. Medina,[b] Cesar J. Pastor,[b] Reyes Jiménez-Aparicio,[c] and José L. Priego[c]**

**Keywords:** Coordination polymers / Copper / N ligands

The synthesis of the ligand 2,5-bis(2-pyridylethynyl)thiophene (**L2**) is described and the coordination chemistry of the 2,2′-long conjugated bidentate ligands 1,2-di(2-pyridyl)-butadiyne (**L1**), 2,5-bis(2-pyridylethynyl)thiophene (**L2**), and 2,2′-dipyridyl disulfide (**L3**) with $Cu(hfac)_2$ (hfac = hexafluoroacetylacetonate) is investigated. Three new coordination polymers $\{[Cu(hfac)_2L]_n$ (**1** for L = **L1**, **2** for L = **L2** and **3** for L = **L3**)} are prepared and fully characterized by infrared spectroscopy, elemental analysis, thermogravimetric analysis, and X-ray diffraction. They are obtained by a combination of **L1**, **L2**, or **L3** with $Cu(hfac)_2{\cdot}H_2O$ in dichloromethane ($CH_2Cl_2$) as the solvent. When $CH_2Cl_2$ solutions of **3** were left standing for longer than one day or were refluxed for two days, rearrangements took place and **3** was transformed into **4** and **5**. Compounds **1**–**3** adopt a one-dimensional chain structure with the copper atom in a six-coordinate 4+2 pseudooctahedral geometry. In **1** and **2**, four equatorial sites Cu–O/N and two axial sites Cu–O are found with an unusual *cis* orientation of two $\mathbf{L_1}$ or $\mathbf{L_2}$ ligands, respectively, while in **3** the four equatorial sites are defined by four oxygen atoms from two hfac chelating ligands and the axial sites by two nitrogen donors from two *trans*-**L3** ligands. Compound **4** contains a (1-hydro-2-pyridinio)thio group that is bound to a hexafluoroacetylacetonate anion through a S–C bond and **5** is a molecular compound where the $Cu^{II}$ ion is pentacoordinate to two oxygen atoms of the hfac anion, two nitrogen atoms of two 2-pyridyl sulfide fragments, and one carbon atom of the $CC(O)CF_3$ fragment, which has been inserted into the S–S bond of the 2,2′-dipyridyl disulfide ligand, giving a new tridentate ligand. The reaction of **L3** with copper acetate leads to the molecular 1:2 adduct $Cu_2(\mu\text{-}OAc)_4(L3)_2$ (**6**), where the $Cu^{II}$ ion is pentacoordinate to four oxygen atoms of four different acetate anions and one nitrogen atom from the pyridine ring of **L3** to form a square-pyramidal geometry.

(© Wiley-VCH Verlag GmbH & Co. KGaA, 69451 Weinheim, Germany, 2006)

## Introduction

The rational design of new coordination polymers is of current interest in the field of supramolecular chemistry and crystal engineering because of their exploitable properties; these include magnetism,[1] catalysis and separation,[2] non-linear optics,[3] and molecular sensing.[4] Coordination polymers with diverse architectures, such as linear or zigzag chains, helices, honey-combs, square grids, ladders, brick walls, and interwoven diamondoids have been extensively developed.[5] In particular, much research has been concentrated on the use of bridging 4,4′-bipyridyne-based rodlike ligands,[6] whereas bent ligands are relatively less frequently used as building blocks because of the difficulty in predicting the structure. Recently, crystalline polymers have been synthesized by using 1,2-di(3-pyridyl)ethyne or 2,5-di(3-pyridyl)-1,3,4-oxadiazole and $Cd^{II}$, $Co^{II}$, $Cu^{II}$ salts.[7] Moreover, unsaturated metal complexes such as bis(hexafluoroacetylacetonate)metal(II) are promising metal building blocks and have proved to be very useful precursors in the synthesis of several types of molecular materials including thin metallic and oxide films and magnetic materials.[8–10]

With this in mind, the aim of this work is to study the effect of the 2,2′-positional orientation of the nitrogen atoms in *N*,*N*′-bidentate ligands on the coordination framework and to affect the polymeric architectures of the crystalline materials. Ligands with nitrogen atoms at the 2-position of the pyridyl ring do not readily form polymeric compounds, as is the case for ligands with nitrogen atoms at the 3- and 4-positions. Therefore, the reaction between 1,2-di(2-

[a] Departamento de Química Inorgánica de la Universidad Autónoma de Madrid,
28049 Madrid, Spain
E-mail: salome.delgado@uam.es
[b] Servicio Interdepartamental de Investigación, Laboratory of Single Crystal X-ray Diffraction, Universidad Autónoma de Madrid,
28049 Madrid, Spain
[c] Departamento de Química Inorgánica. Facultad de Ciencias Químicas, Universidad Complutense de Madrid, Ciudad Universitaria,
28040 Madrid, Spain

 © 2006 Wiley-VCH Verlag GmbH & Co. KGaA, Weinheim 

pyridyl)ethyne and $Cu(hfac)_2$ only formed solutions when a methanol solution of ligand was layered over a dichloromethane solution of copper(II) hexafluoroacetylacetonate.[11]

In this report, we focus on 1,2-di(2-pyridyl)butadiyne (**L1**), 1,2-bis(2-pyridylethynyl)thiophene (**L2**), and 2,2′-dipyridyl disulfide (**L3**), in which the first two are rigid ligands and the last one is a flexible ligand that may assume a twisted conformation because of the flexible –S–S– bridging group. The C–S–S–C torsion angles in aromatic disulfides are known to be generally within a range of 70–90°.[12a] Further, oxidation of 2,2′-dipyridyl disulfide to pyridine-2-sulfinate in the presence of the $Cu^{II}$ ion and water has been reported.[12b] Here we describe the synthesis, structures, and properties of new $Cu^{II}$ coordination polymers. The 1,2-bis(2-pyridylethynyl)thiophene ligand was synthesised and used first as a linker.

## Results and Discussion

When dichloromethane solutions of **L1** and **L2** were allowed to diffuse, at room temperature, into a solution of $Cu(hfac)_2$ in the same solvent (ratio 1:1), the infinite coordination polymers **1** and **2** were afforded as green and yellow crystalline materials, respectively, within 2–3 days. Similar results were obtained when layering the dichloromethane solution of copper(II) hexafluoroacetylacetonate over a solution of **L1** or **L2**.

Treatment of $Cu(hfac)_2$ with 2,2′-dipyridyl disulfide (**L3**), depending on the conditions, leads to the formation of different products. When a methanol solution of **L3** is allowed to diffuse, at room temperature, into a solution of $Cu(hfac)_2$ in the same solvent, the coordination polymer **3** is obtained as a green solid after one day. By contrast, when the reaction is carried out in $CH_2Cl_2$, under similar conditions, **3** is also isolated together with the orange organic compound **4** and the violet mononuclear compound **5** as minor products. The amount of **3** diminished significantly and the yield of **4** and **5** increased up to 50% after prolonged standing in contact with $CH_2Cl_2$. If the same reagents are allowed to react together under reflux in $CH_2Cl_2$ or MeOH for two days, only **4**, as the major product, and **5** are obtained. During this process **3** is converted into 2-[(1-hydro-2-pyridinio)thio]hexafluoroacetylacetonate (**4**) and the mononuclear compound **5**, where a new copper–carbon bond is formed (Scheme 1). Crystals of **3** can be stored unchanged at room temperature. It is also stable in ether or $CCl_4$ solutions but slowly decomposes to **4** and **5** in acetone solutions. In order to explain the formation of complexes **4** and **5** from **3**, we have carried out additional experiments. In order to test whether $H_2O$ or $O_2$ play a role in the formation of the final products, we have repeated the

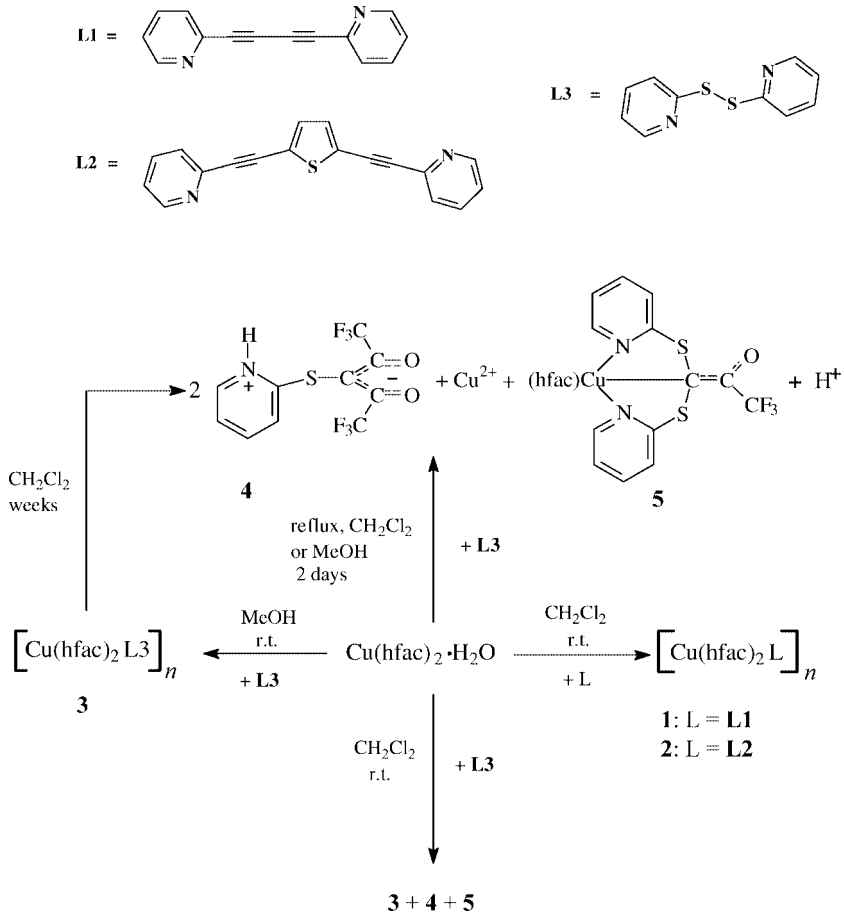


Scheme 1.

 © 2006 Wiley-VCH Verlag GmbH & Co. KGaA, Weinheim 

reactions, in $CH_2Cl_2$ at reflux, under both anaerobic and anhydrous conditions, and monitored the reactions by FT-IR spectroscopy until the strong $\nu_{C\equiv O}$ band at 1641 $cm^{-1}$ assigned to **3** disappeared. However, the results were similar to those previously obtained.

One possible mechanism that could explain the formation of **4** and **5** from **3** involves the homolytic cleavage of the S–S bond in the **L3** ligand, probably promoted by the $Cu^{II}$ ion. It is known that the disulfide bond in R–S–S–R–systems is broken by metal ions.[12b] The attack of the imine carbon atom of the $hfac^-$ anion on the sulfur atom of the pyridyl sulfide radical leads to the formation of **4**. This pathway is predominant because **4** is obtained in higher yield than **5**. Along with this, some $hfac^-$ is broken apart and $C(H)C(O)CF_3$ fragments are bonded to the sulfur atom of pyridyl sulfide to give **5**, probably via the formation of an intermediate with an acid proton, which is easily removed by the stabilization that allows the formation of two five-membered rings. The $CF_3$–C(O) fragments could be recombined to produce the 1,2-diketone $F_3C$–C(O)–C(O)–$CF_3$, which could not be detected because of its high volatility (b.p. = 19 °C). Some of the $CF_3$–C(O) fragments could also lead to $CHF_3$ and CO, but neither of these were detected during the reaction (Scheme 2).

Finally, when $Cu(OAc)_2{\cdot}H_2O$ dissolved in methanol is reacted at room temperature with **L3** in methanol in a 1:1 molar ratio, a green solution is obtained. After workup, green crystals of the molecular 1:2 adduct $Cu_2(\mu\text{-}OAc)_4(L3)_2$ (**6**) were obtained. The polymeric compound was not formed. This complex dissociates to $Cu(OAc)_2{\cdot}H_2O$ and **L3** after prolonged standing in contact with the solution.

All compounds have been characterized by analytical and IR spectroscopic data. Details are given in the Experimental Section. In the IR spectra of **1** and **2**, the $\nu$(CO) stretching bands appear to be split into two bands (1654, 1592 $cm^{-1}$and 1644, 1594 $cm^{-1}$, respectively) while in **3** only one $\nu$(CO) is observed (1641 $cm^{-1}$). This is consistent with a pseudooctahedral geometry around the copper(II) ion (see the description of the structures). In **1** and **2** the former bands are assigned to the stretching of C(4)=O(3),

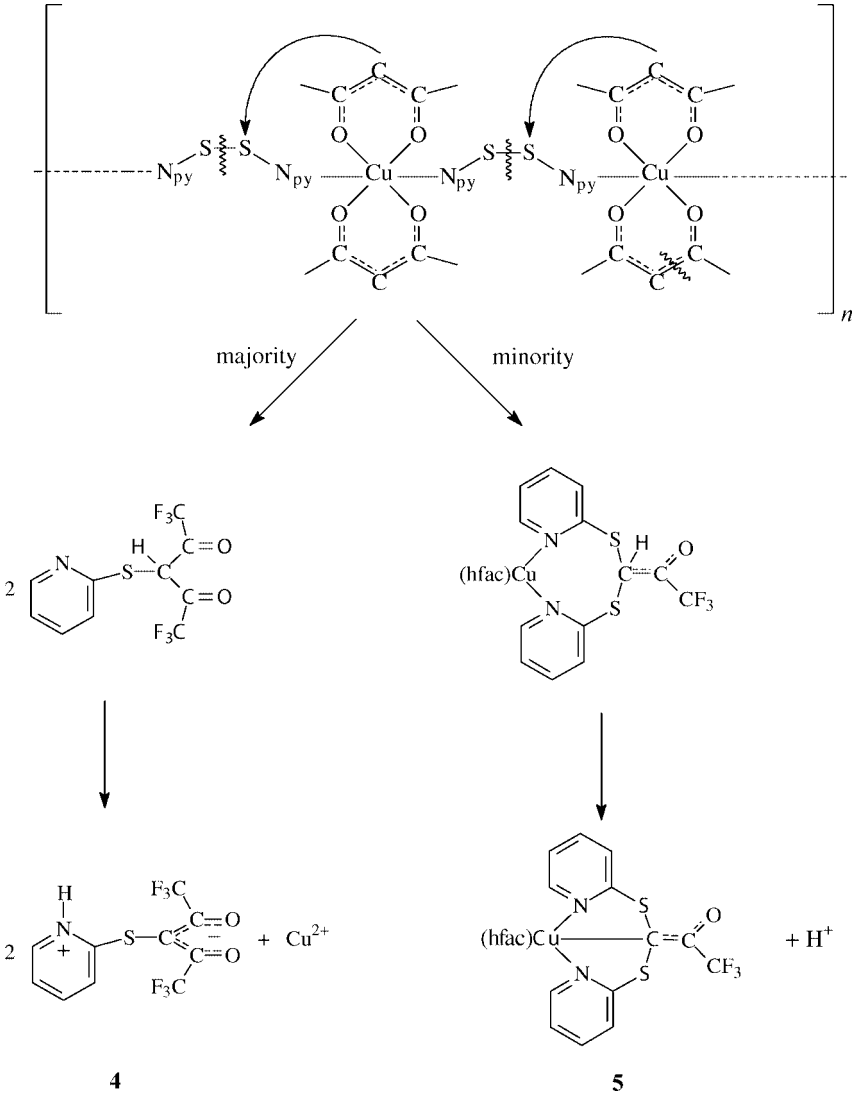


Scheme 2.

 © 2006 Wiley-VCH Verlag GmbH & Co. KGaA, Weinheim 

C(24)=O(3) and C(3)=O(2), C(21)=O(2), respectively; these oxygen atoms are more strongly bonded to the $Cu^{II}$ ion, and the latter to C(1)=O(1), C(19)=O(1) and C(6)=O(4), respectively. In **3**, the four (C=O) distances of the two hfac rings have similar values. In the IR spectrum of **4** a single $\nu$(CO) band is observed at 1679 $cm^{-1}$, at a higher energy than those for polymers **1**–**3**, which is in accordance with the shorter (C–O) bond. Moreover, a $\nu$(N–H) band is located at 3103 $cm^{-1}$, and a $\nu$(C=N) band and three $\nu$(C=C) bands at 1606, 1583, 1452, and 1420 $cm^{-1}$, respectively, are observed. The latter four bands are shifted to a higher energy with respect to the free ligand (1570, 1556, 1443, and 1416 $cm^{-1}$, respectively); the same behavior is observed when pyridine and pyridinium ligands are compared. Finally, at 838 $cm^{-1}$ a new band appears that can be attributed to a (C–S) vibration of the new bond, which has formed. In the IR spectrum of **5**, two types of $\nu$(CO) stretching bands are observed. A single (CO) band at 1673 $cm^{-1}$, attributed to the stretching of C(30)=O(6) from the –C–C(O)–$CF_3$ fragment and a (CO) stretching band with two peaks at 1650 and 1611 $cm^{-1}$ from the chelating hfac ligand. As in **1** and **2**, the first band is assigned to the stretching of C(32)=O(4), which is more strongly bonded to the $Cu^{II}$ ion, and the second to C(34)=O(5).

For **6** the characteristic bands of the acetate anions appear at 1620 $\nu_{as}$(C–O), 1427 $\nu_{sym}$(C–O) and 682 $\delta$(O–C–O) $cm^{-1}$ together with the absorption bands resulting from the aromatic rings in the 1400–1600 $cm^{-1}$ range. The $\Delta$ value ($\nu_{as} - \nu_{sym}$) indicates that the acetate anion coordinates to the $Cu^{II}$ center in a bridging mode.

## Description of the Crystal Structures

### *[Cu(hfac)$_2$L1]$_n$ (1)*

The crystallographic data are given in Table 1 (compounds **1**–**3**). An ORTEP view of a copper center is shown in Figure 1 (a), together with the atom numbering scheme. Selected bond lengths and angles are listed in Table 2. The coordination geometry of the copper(II) ion is pseudooctahedral in which four oxygen atoms from two hfac ligands chelate to the $Cu^{II}$ center, while the other two sites are occupied by two nitrogen atoms from two *cis*-1,2-di(2-pyridyl)-butadiyne ligands. The pyridyl groups of the **L1** ligand are coplanar through the diyne portion. Usually a *trans* orientation of the pyridine rings is adopted in these types of complexes [Cu(hfac)$_2$L$_2$] [L = pyrazine,[13] 1,2-di(2-pyridyl)-ethyne][7] or the analogous 1,2-bis(3-pyridyl)butadiyne ligand.[14] This different behavior suggests that the relative orientation of the pyridyl nitrogen donors can control the coordination framework and influence the polymeric architectures of the crystalline materials. To the best of our knowledge, a *cis* orientation has only been found in [Cu(hfac)$_2$(4-PDS)] (4-PDS = 4,4′-dipyridyl disulfide).[15] As already known, $Cu^{II}$ is Jahn–Teller-active, so it is expected to adopt a 4+2 coordination environment with two long bond lengths and four shorter ones, as is usually observed. As a result of this, the bond angles within the $CuO_4N_2$ octahedra deviate appreciably from 90° and vary from 81.61(5) to 100.57(6)° for O(2)–Cu(1)–O(1) and N(2)–Cu(1)–O(4), respectively. Similar types of distorted coordination geometries are reported for [Cu(hfac)$_2$L]$_n$ complexes.[16,17] In addition to this, the N(2)–Cu(1)–N(1) bond angle, which is 96.37(6)°, deviates from a perfect right angle.

The Cu–N bond length of 2.0438(2) Å in **1** is intermediate between the Cu–N bond length found in the Cu(hfac)$_2$ complexes with 1,2-bis(3-pyridyl)ethyne {2.061(3) Å}[7] and 1,2-bis(3-pyridyl)butadiyne {2.026(2) Å};[15] and significantly longer than that in the polymeric compound [Cu(hfac)$_2${1,2-bis(4-pyridyl)ethane}]$_n$ [Cu–N 2.014 (7) Å].[13]

Two copper centers bond through the N1 and N2 atoms of two $\mathbf{L_1}$ molecules in a *transoid* conformation forming dimers. As a result of this, the extended structure consists of polymeric 1D chains that run parallel to the *b* axis as is shown in Figure 2, where the **L1** ligand links the Cu(hfac)$_2$ moieties together. The intra- and interpolymer Cu···Cu distances are 8.950 Å and 8.221 Å, respectively. Because **L1** affords close contact between neighboring polymeric chains, the interpolymeric Cu···Cu distance is significantly shorter than that in the polymer constructed from the 1,2-bis(3-pyridyl)butadiyne ligand (13.88 Å).[14] Surprisingly, no interpolymer hydrogen-bonding interactions were found.

### *[Cu(hfac)$_2$L2]$_n$ (2)*

The crystallographic data are given in Table 1 (compounds **1**–**3**). Selected bond lengths and angles are listed in Table 3. The structure, emphasizing the coordination environment around the copper atom, is shown in Figure 1 (b). As in **1**, the copper atom has a six-coordinate 4+2 pseudo-octahedral geometry defined by two nitrogen donors from two *cis*-**L2** ligands and four oxygen donors from two hfac chelating ligands. In contrast, the pyridyl groups of the **L2** ligand are not coplanar through the diyne portion and form an angle of 68°. The Cu–N and Cu–O bond lengths are very close to those found in compound **1**. In contrast to **1**, the two Cu(hfac)$_2$ units of compound **2** are joined by the **L2** ligand in a *cisoid* conformation. The structure of **2** consists of one-dimensional chains running parallel to the *a* axis, as is shown in Figure 3. The intra- and interpolymer Cu···Cu distances are 9.421 Å and 10.983 Å, respectively. Interpolymer hydrogen bonding was not observed.

### *[Cu(hfac)$_2$L3]$_n$ (3)*

An ORTEP view of the copper center is shown in Figure 4 (a), together with the atom numbering scheme. Table 1 (compounds **1**–**3**) gives the crystallographic data for **3**, while selected bond lengths and angles are listed in Table 4. In this compound the copper atom has a six-coordinate 4+2 pseudooctahedral geometry, where the four equatorial sites are defined by four oxygen atoms from two hfac chelating ligands (1.9365 Å to 1.9572 Å), but in contrast to compounds **1** and **2**, the axial sites have two nitrogen donors from two *trans*-**L3** ligands. This is unusual because four equatorial sites Cu–O/N and two axial sites Cu–O are

 © 2006 Wiley-VCH Verlag GmbH & Co. KGaA, Weinheim 

Table 1. Crystallographic data for compounds **1** to **3** and compounds **4** to **6**.

| | **1** | **2** | **3** |
|---|---|---|---|
| Empirical formula | $C_{24}H_{10}CuF_{12}N_2O_4$ | $C_{28}H_{12}CuF_{12}N_2O_4S$ | $C_{20}H_{10}CuF_{12}N_2O_4S_2$ |
| Molecular mass [g/mol] | 681.88 | 764.00 | 697.96 |
| Temperature [K] | 100(2) | 100(2) | 100(2) |
| Wavelength [Å] | 1.54178 | 1.54178 | 1.54178 |
| Crystal system | monoclinic | tricilinic | monoclinic |
| Space group | *P*21/*n* | $P\bar{1}$ | *P*21/*n* |
| Unit cell dimensions | *a* = 13.0798(1) | *a* = 9.4206(1) | *a* = 17.2605(8) |
| *a*, *b*, *c* [Å] | *b* = 15.6050(1) | *b* = 10.4051(1) | *b* = 8.1387(7) |
| *α*, *β*, *γ* [°] | *c* = 13.3245(1) | *c* = 15.5323(1) | *c* = 19.1467(1) |
| | *α* = 90 | *α* = 81.8410(1) | *γ* = 90 |
| | *β* = 107.465(1) | *β* = 75.1390(1) | *β* = 115.396(3) |
| | *α* = 90 | *γ* = 80.9270(10) | *γ* = 90 |
| Volume [Å$^3$] | 2594.29(3) | 1444.94(2) | 2429.8(3) |
| *Z* | 4 | 2 | 4 |
| Density (calculated) [mg/m$^3$] | 1.746 | 1.756 | 1.908 |
| Absorption coefficient [mm$^{-1}$] | 2.339 | 2.838 | 4.075 |
| *F*(000) | 1348 | 758 | 1380 |
| Crystal size [mm] | 0.25 × 0.20 × 0.12 | 0.20 × 0.20 × 0.10 | 0.20 × 0.18 × 0.06 |
| Theta range for data collection [°] | 4.15 to 70.62 | 2.96 to 70.52 | 2.89 to 69.15 |
| Index ranges | $-15 \le h \le 15$ | $-11 \le h \le 10$ | $-20 \le h \le 20$ |
| | $-18 \le k \le 19$ | $-12 \le k \le 12$ | $-9 \le k \le 9$ |
| | $-15 \le l \le 16$ | $-18 \le l \le 18$ | $-23 \le l \le 22$ |
| Reflections collected | 16356 | 14930 | 18573 |
| Independent reflections | 4769 | 5225 | 4378 |
| | [*R*(int) = 0.0258] | [*R*(int) = 0.0260] | [*R*(int) = 0.0477] |
| Completeness to *θ* = 70.62°/70.52°/69.15° [%] | 95.9 | 94.2 | 96.6 |
| Absorption correction | | semi-empirical from equivalents | |
| Refinement method | | full-matrix least-squares on $F^2$ | |
| Data/restraints/parameters | 4769/0/428 | 5225/0/535 | 4378/0/413 |
| Goodness-of-fit on $F_2$ | 1.048 | 1.037 | 1.023 |
| Final *R* indices [$I > 2\sigma(I)$] | $R_1$ = 0.0337 | $R_1$ = 0.0346 | $R_1$ = 0.0324 |
| | $wR_2$ = 0.0878 | $wR_2$ = 0.0903 | $wR_2$ = 0.0819 |
| *R* indices (all data) | $R_1$ = 0.0361 | $R_1$ = 0.0381 | $R_1$ = 0.0416 |
| | $wR_2$ = 0.0894 | $wR_2$ = 0.0927 | $wR_2$ = 0.0876 |
| Largest diff. peak and hole [e/Å$^3$] | 0.758 and –0.498 | 0.485 and –0.369 | 0.426 and –0.482 |
| | **4** | **5** | **6** |
| Empirical formula | $C_{10}H_5F_6NO_2S$ | $C_{18}H_9CuF_9N_2O_3S_2$ | $C_{28}H_{28}Cu_2N_4O_8S_4$ |
| Molecular mass [g/mol] | 317.21 | 599.93 | 803.86 |
| Temperature [K] | 100(2) | 100(2) | 100(2) |
| Wavelength [Å] | 1.54178 | 1.54178 | 1.54178 |
| Crystal system | monoclinic | monoclinic | monoclinic |
| Space group | *C*2/*c* | *P*21/*c* | *P*21/*c* |
| Unit cell dimensions | *a* = 17.4388(4) | *a* = 17.3908(3) | *a* = 7.9211(9) |
| *a*, *b*, *c* [Å] | *b* = 11.0843(2) | *b* = 15.5348(2) | *b* = 26.961(3) |
| *α*, *β*, *γ* [°] | *c* = 13.8206(4) | *c* = 17.2529(2) | *c* = 7.6840(10) |
| | *α* = 90 | *α* = 90 | *α* = 90 |
| | *β* = 117.039(2) | *β* = 116.1050(1) | *β* = 93.393(4) |
| | *γ* = 90 | *γ* = 90 | *γ* = 90 |
| Volume [Å$^3$] | 2379.48(1) | 4185.60(1) | 1638.1(3) |
| *Z* | 8 | 8 | 2 |
| Density (calculated) [mg/m$^3$] | 1.771 | 1.904 | 1.630 |
| Absorption coefficient [mm$^{-1}$] | 3.241 | 4.353 | 4.454 |
| *F*(000) | 1264 | 2376 | 820 |
| Crystal size [mm] | 0.20 × 0.08 × 0.03 | 0.20 × 0.18 × 0.09 | 0.16 × 0.10 × 0.08 |
| Theta range for data collection[°] | 4.90 to 69.27 | 2.83 to 68.27 | 3.28 to 68.74 |
| Index ranges | $-21 \le h \le 19$ | $-20 \le h \le 20$ | $-9 \le h \le 8$ |
| | $-13 \le k \le 13$ | $-18 \le k \le 18$ | $-28 \le k \le 32$ |
| | $-14 \le l \le 16$ | $-20 \le l \le 20$ | $-8 \le l \le 9$ |
| Reflections collected | 9377 | 31380 | 9381 |
| Independent reflections | 2175 | 7549 | 2932 |
| | [*R*(int) = 0.0275] | [*R*(int) = 0.0370] | [*R*(int) = 0.0589] |
| Completeness to *θ* = 69.27°/68.27°/68.74° [%] | 97.3 | 98.6 | 96.8 |
| Absorption correction | | semi-empirical from equivalents | |
| Refinement method | | full-matrix least-squares on $F^2$ | |
| Data/restraints/parameters | 2175/0/201 | 7549/0/631 | 2932/0/210 |
| Goodness-of-fit on $F^2$ | 1.033 | 1.035 | 1.036 |
| Final *R* indices [$I > 2\sigma(I)$] | $R_1$ = 0.0277 | $R_1$ = 0.0317 | $R_1$ = 0.0457 |
| | $wR_2$ = 0.0736 | $wR_2$ = 0.0777 | $wR_2$ = 0.1116 |
| *R* indices (all data) | $R_1$ = 0.0305 | $R_1$ = 0.0373 | $R_1$ = 0.0597 |
| | $wR_2$ = 0.0760 | $wR_2$ = 0.0812 | $wR_2$ = 0.1213 |
| Largest diff. peak and hole [e/Å$^3$] | 0.338 and –0.233 | 0.523 and –0.360 | 0.900 and –0.386 |

 © 2006 Wiley-VCH Verlag GmbH & Co. KGaA, Weinheim 

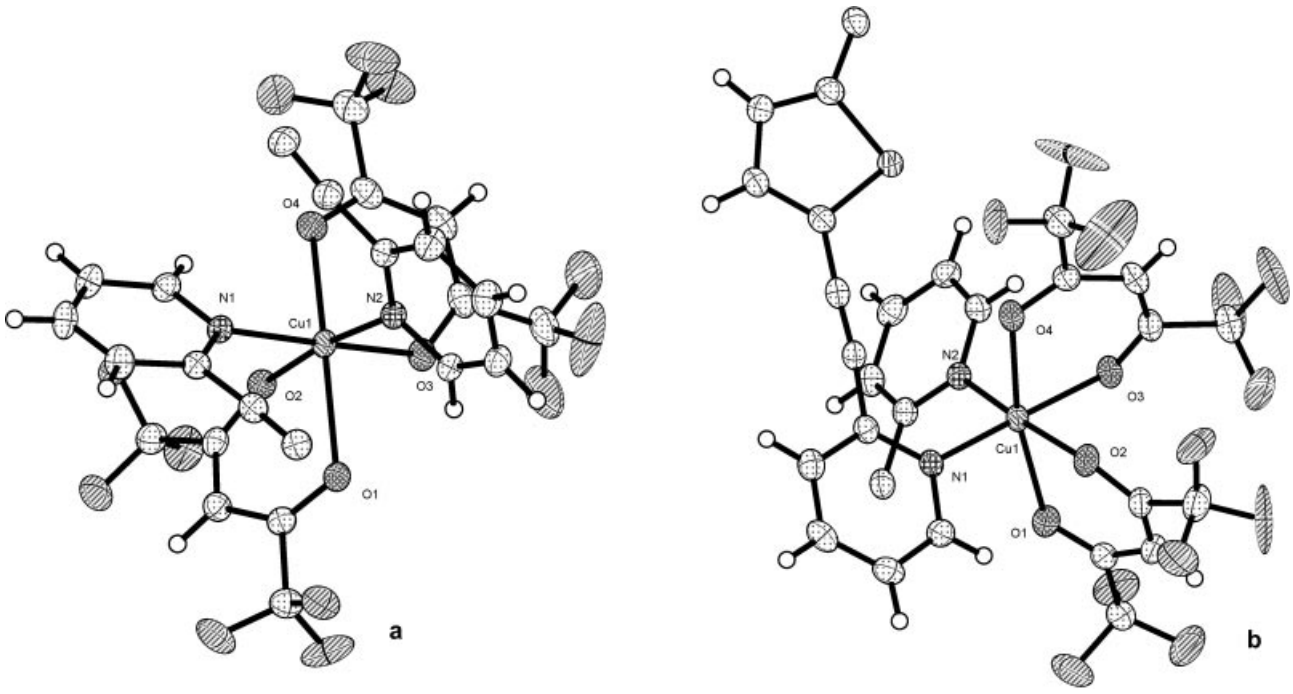


Figure 1. **a**: Molecular structure of **1**, **b**: molecular structure of **2** (displacement ellipsoids are shown at the 50% probability level).

Table 2. Selected bond lengths and angles for compound **1**.

| Selected bond lengths [Å] | Selected angles [°] | |
|---|---|---|
| Cu(1)–O(3) 1.9927(1) | O(3)–Cu(1)–O(2) 89.84(6) | N(2)–Cu(1)–O(4) 100.57(6) |
| Cu(1)–O(2) 2.0133(1) | O(3)–Cu(1)–N(2) 87.31(6) | N(1)–Cu(1)–O(4) 90.97(6) |
| Cu(1)–N(2) 2.0348(2) | O(2)–Cu(1)–N(2) 173.28(6) | O(3)–Cu(1)–O(1) 85.92(5) |
| Cu(1)–N(1) 2.0438(2) | O(3)–Cu(1)–N(1) 175.51(6) | O(2)–Cu(1)–O(1) 81.61(5) |
| Cu(1)–O(4) 2.2408(1) | O(2)–Cu(1)–N(1) 86.77(6) | N(2)–Cu(1)–O(1) 92.12(6) |
| Cu(1)–O(1) 2.3225(1) | N(2)–Cu(1)–N(1) 96.37(6) | N(1)–Cu(1)–O(1) 96.48(6) |
| C(3)–O(2) 1.2690(2) | O(3)–Cu(1)–O(4) 85.82(6) | O(4)–Cu(1)–O(1) 164.50(5) |
| C(4)–O(3) 1.259(3) | O(2)–Cu(1)–O(4) 85.28(5) | |
| C(6)–O(4) 1.232(3) | | |

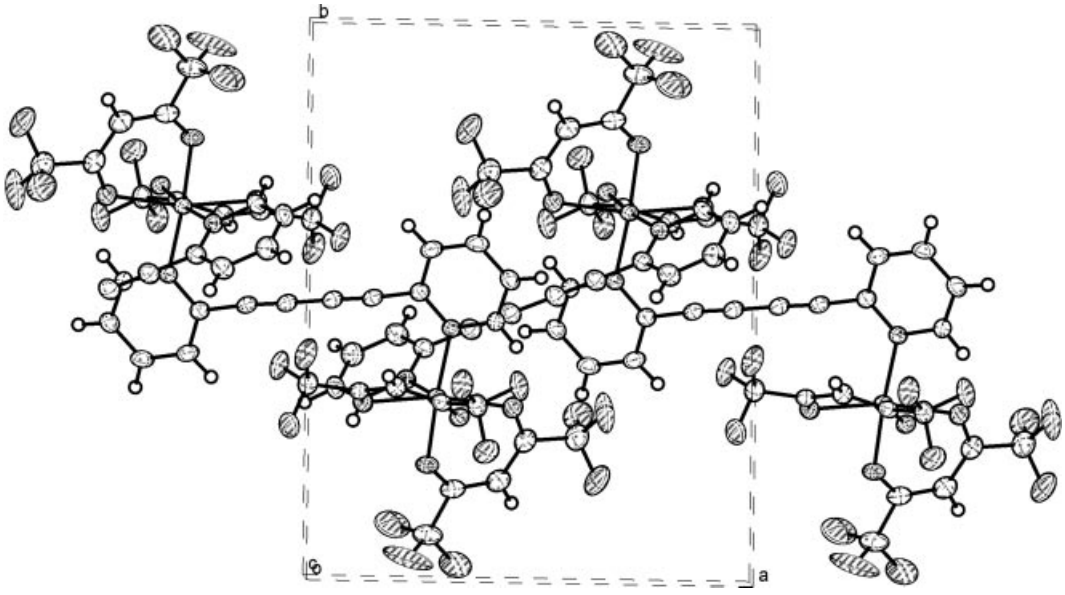


Figure 2. View of the one-dimensional chain formed by compound **1**. The chains are shown along the crystallographic *a* axis.

 © 2006 Wiley-VCH Verlag GmbH & Co. KGaA, Weinheim 

Table 3. Selected bond lengths and angles for compound **2**.

| Selected bond lengths [Å] | Selected angles [°] | |
|---|---|---|
| Cu(1)–O(2) 2.0145(15) | O(2)–Cu(1)–O(3) 84.09(6) | N(1)–Cu(1)–O(4) 90.09(6) |
| Cu(1)–O(3) 2.0155(15) | O(2)–Cu(1)–N(1) 88.85(6) | N(2)–Cu(1)–O(4) 96.82(6) |
| Cu(1)–N(1) 2.0379(16) | O(3)–Cu(1)–N(1) 171.74(6) | O(2)–Cu(1)–O(1) 84.58(6) |
| Cu(1)–N(2) 2.0408(17) | O(2)–Cu(1)–N(2) 172.29(6) | O(3)–Cu(1)–O(1) 87.33(6) |
| Cu(1)–O(4) 2.2739(15) | O(3)–Cu(1)–N(2) 89.29(6) | N(1)–Cu(1)–O(1) 96.29(6) |
| Cu(1)–O(1) 2.2750(15) | N(1)–Cu(1)–N(2) 98.03(6) | N(2)–Cu(1)–O(1) 91.19(6) |
| | O(2)–Cu(1)–O(4) 86.58(6) | O(4)–Cu(1)–O(1) 168.98(5) |
| | O(3)–Cu(1)–O(4) 85.22(6) | |

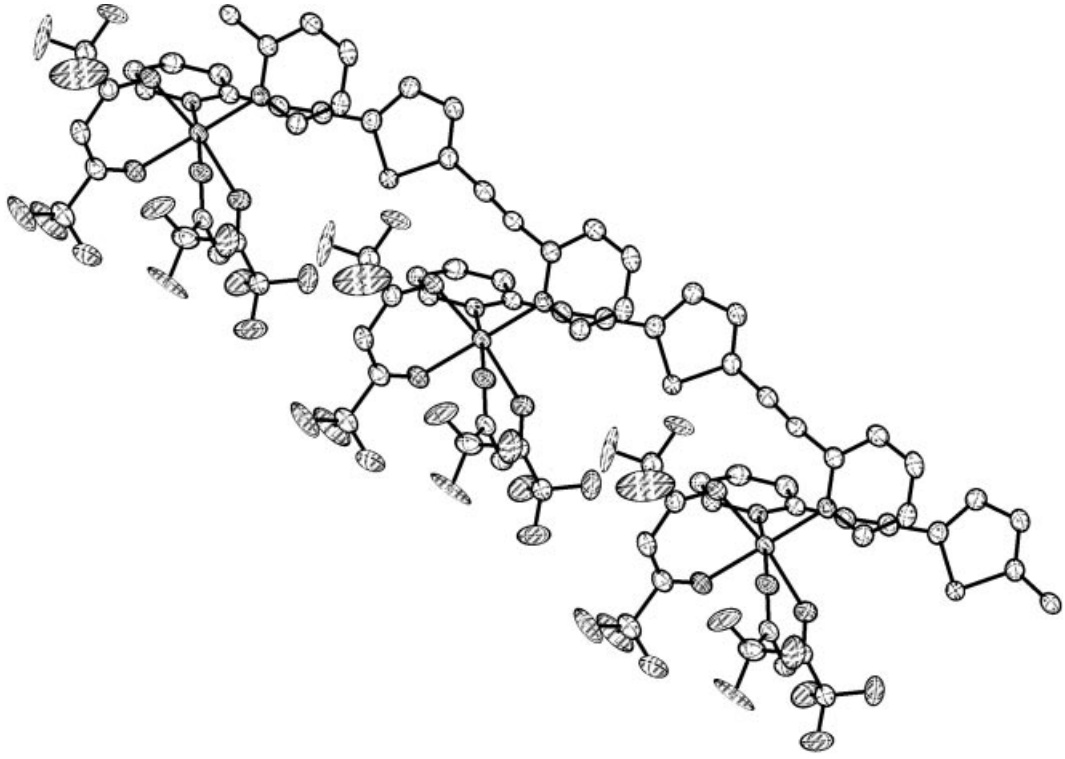

Figure 3. View of the one-dimensional chain architecture of **2**. The chains are shown along the crystallographic *a* axis.

found in $L_2Cu(hfac)_2$ type complexes. The Cu–N bond lengths are 2.4587(19) and 2.5968(19) Å, unexpectedly longer than distances found in copper dipyridyl disulfide compounds[14,15,18] or in N-donor-coordinated $Cu(hfac)_2$ complexes, including **1** and **2**. A similar distance is reported for $[Cu(hfac)_2(pyz)]$ [2.529(9) Å][19a] and $Cu(hfac)_2$(ted) [2.566(7) Å].[19b] One possible explanation for these very long Cu–N bonds is the interaction of the pyridine rings with the hfac ring (see part a in Figure 4). The intramolecular geometry of the **L3** ligand shows a C–S–S–C torsion angle of 79.8(10)°, smaller than that in the free ligand (87.1°) and in the analogous $Cu(hfac)_2$(4,4′-dipyridyl disulfide)[15] [88.1(2)°], which seems to indicate a slight deformation when **L3** is coordinated to the metal ion. The S–S bond length of 2.0369(8) Å is in close agreement with the value found in the free **L3** ligand [2.016(2)].[20] The angle between the two pyridyl rings is 79.83(10)°. Compound **3** assumes a one-monodimensional zigzag chain structure, as shown in part b of Figure 4, where each copper center is bridged by the twisted ligands of 2,2′-dipyridyl disulfide in a *cisoid* conformation. The interchain and intrachain Cu–Cu distances are 8.139 and 9.573 Å, respectively.

### *2-[(1-Hydro-2-pyridinio)thio]hexafluoroacetylacetonate (4)*

The structure is shown in Figure 5 (a) together with the atom numbering scheme. Crystallographic data are given in Table 1 (compounds **4**–**6**), and the selected bond lengths and angles are listed in Table 5. The molecule adopts a nonplanar disposition. The pyridinium ring is oriented almost perpendicular to the hexafluoroacetylacetonate anion (89.75°). The intramolecular geometry of the hexafluoroacetylacetonate anion shows O–C–C, C–C–C, and C–S–C torsion angles of 126.40(13), 118.66(12), and 104.84(7)°, respectively; these values are comparable to those found for compound **3** [128.2(2), 121.1(2), and 104.64(8)°, respectively] and indicates that the $hfac^-$ moiety seems to maintain its characteristic shape. The C–S distances are 1.7573(15) and 1.7601(14) Å, which are similar to those found in other copper dipyridyl disulfide compounds[15,18] and slightly

 © 2006 Wiley-VCH Verlag GmbH & Co. KGaA, Weinheim 

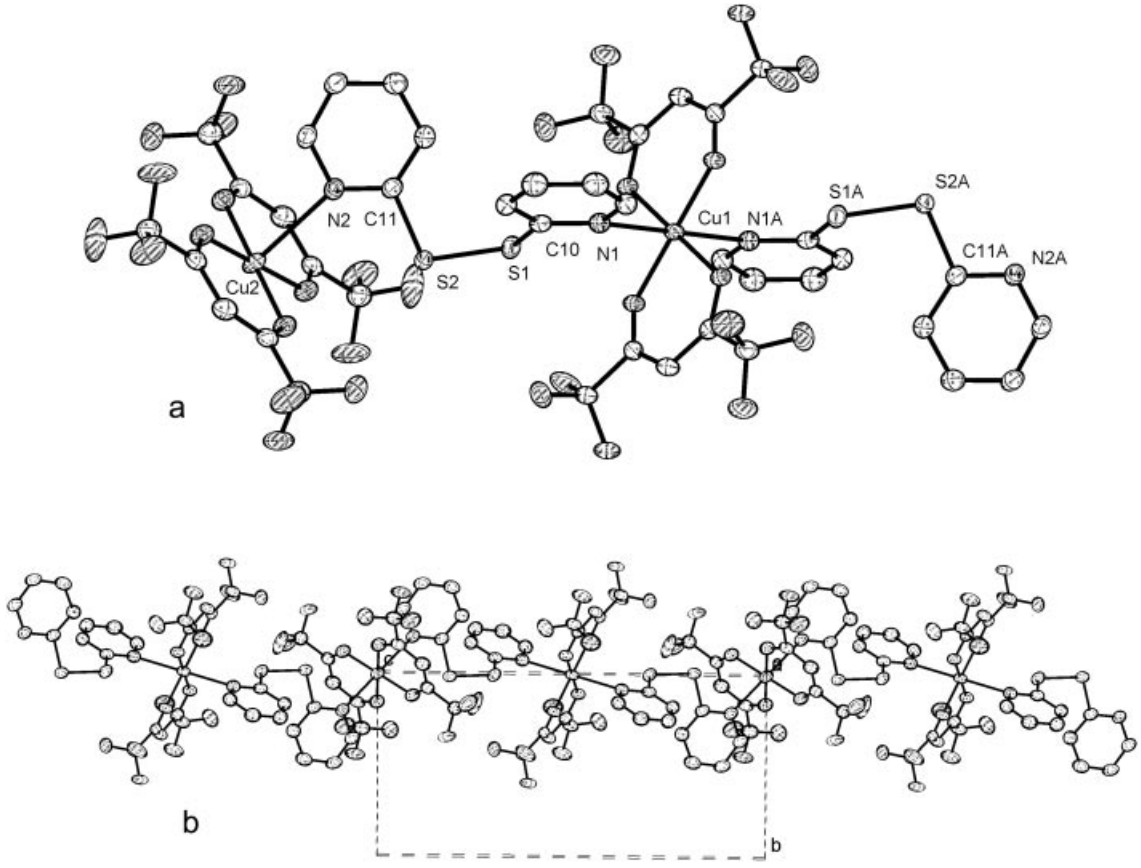


Figure 4. **a**: View of two bonded molecules of **3**, **b**: polymeric chains, shown along the crystallographic *c* axis.

Table 4. Selected bond lengths and angles for compound **3**.

| Selected bond lengths [Å] | Selected angles [°] | |
|---|---|---|
| Cu(1)–O(1) 1.9572(1) | O(1)–Cu(1)–O(1)#1 180.00(1) | O(2)–Cu(1)–N(1) 88.89(6) |
| Cu(1)–O(1)#1 1.9572(1) | O(1)–Cu(1)–O(2) 88.10(6) | O(2)#1–Cu(1)–N(1) 91.11(6) |
| Cu(1)–O(2) 1.9702(1) | O(1)#1–Cu(1)–O(2) 91.90(6) | N(1)#1–Cu(1)–N(1) 180.0 |
| Cu(1)–O(2)#1 1.9702(1) | O(1)–Cu(1)–O(2)#1 91.90(6) | O(4)–Cu(2)–O(4)#2 180.00(1) |
| Cu(1)–N(1)#1 2.4587(2) | O(1)#1–Cu(1)–O(2)# 188.10(6) | O(4)–Cu(2)–O(3) 92.85(7) |
| Cu(1)–N(1) 2.4587(2) | O(2)–Cu(1)–O(2)#1 180.00(8) | O(4)#2–Cu(2)–O(3) 87.15(7) |
| Cu(2)–O(4) 1.9365(1) | O(1)–Cu(1)–N(1)#1 86.79(6) | O(4)–Cu(2)–O(3)#2 87.15(7) |
| Cu(2)–O(4)#2 1.9365(1) | O(1)#1–Cu(1)–N(1)#1 93.21(6) | O(4)#2–Cu(2)–O(3)#2 92.85(7) |
| Cu(2)–O(3) 1.9440(2) | O(2)–Cu(1)–N(1)#1 91.11(6) | O(3)–Cu(2)–O(3)#2 180.00(1) |
| Cu(2)–O(3)#2 1.9440(2) | O(2)#1–Cu(1)–N(1)#1 88.89(6) | O(4)–Cu(2)–N(2) 86.87(6) |
| Cu(2)–N(2) 2.5968(2) | O(1)–Cu(1)–N(1) 93.21(6) | O(4)#2–Cu(2)–N(2) 93.13(6) |
| | O(1)#1–Cu(1)–N(1) 86.79(6) | O(3)–Cu(2)–N(2) 90.23(6) |
| | | O(3)#2–Cu(2)–N(2) 89.77(6) |

shorter than the **L3** ligand [1.785(2) Å]. Two molecules of **4** are linked through hydrogen bonds between the hydrogen atom of the pyridinium ring and oxygen atoms of the hexafluoroacetylacetonate anion resulting in dimers (Figure 5, b).

### *[(hfac)Cu($C_{13}H_8N_2S_2OF_3$)] (5)*

The molecular structure is shown in Figure 6. Table 1 (compounds **4**–**6**) shows the crystallographic data, while selected bond lengths and angles are summarized in Table 6. The $Cu^{II}$ ion is pentacoordinated to two oxygen atoms of the hfac anion, two nitrogen atoms of two 2-pyridyl sulfide fragments and one carbon atom of the $CC(O)CF_3$ fragment that has been inserted into the S–S bond of the **L3** ligand, giving a new tridentate ligand with two five-membered rings and coordination to the copper atom through nitrogen atoms of the pyridine rings and the terminal carbon atom of the $CC(O)CF_3$ fragment. Although the S–S bond in **L3** is reactive and can undergo several transformations,[13,19b] to the best of our knowledge, this is the first example of rearrangement that involves scission and insertion into the disulfide S–S bond. The environment of the copper atom is of particular interest. The geometry may be described as a highly distorted trigonal bipyramidal with N4, N3, and O4 atoms at the equatorial position and O5 and C29 atoms at

 © 2006 Wiley-VCH Verlag GmbH & Co. KGaA, Weinheim 

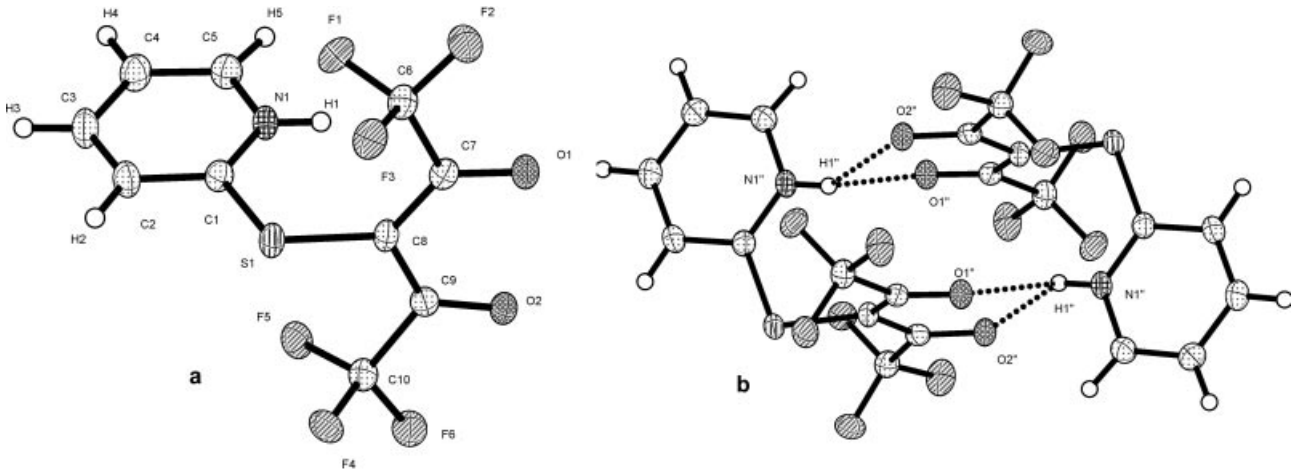


Figure 5. **a**: Molecular structure of **4** (displacement ellipsoids are shown at the 50% probability level), **b**: view of the H bridges between two molecules of this compound.

Table 5. Selected bond lengths and angles for compound **4**.

| Selected bond lengths [Å] | Selected angles [°] |
|---|---|
| S(1)–C(1) 1.7573(1) | C(1)–S(1)–C(8) 104.84(7) |
| C(7)–O(1) 1.2213(2) | O(1)–C(7)–C(8) 126.40(13) |
| S(1)–C(8) 1.7601(1) | O(2)–C(9)–C(8) 126.98(13) |
| C(9)–O(2) 1.2318(2) | |
| N(1)–H(1) 0.84(2) | |

the axial positions. In copper(II) pentacoordinate complexes, trigonal-bipyramidal and square-pyramidal structures are well known; the structures are mostly square pyramidal with various degrees of distortion.[21] Generally, the Cu–$L_{axial}$ bond is longer than the Cu–$L_{equatorial}$ bond in square-pyramidal structures while the opposite is true for the trigonal-bipyramidal geometry. In this compound, all Cu–L distances are similar [2.0034(14) to 2.1461(14) Å]. The Cu–N bond lengths of 2.0074(2) Å and 2.0439(2) Å are very close to the Cu–N bond lengths found in **1** and **2** and are shorter than those in **3**. The ($C_{pyridine\ ring}$–S) and ($C_{29}$–S) distances are 1.7546(19), 1.7502(19) Å and 1.7915(19), 1.8033(19) Å, respectively, and are similar to those found for **3**, **4**, and **L3**. The (C–Cu) distance is 2.0857(19) Å. The C24–S4–C29 and C19–S3–C29 torsion angles of each of the five-membered rings are similar [102.32(9) and 102.22(9)°], respectively, and these rings are not coplanar [C24–S4–C29–S3 and C19–S3–C29–S4 torsion angles are 102.21(11) and 158.59(10)°, respectively]. Both of the five-membered rings form an angle of 54.94(0.04)°.

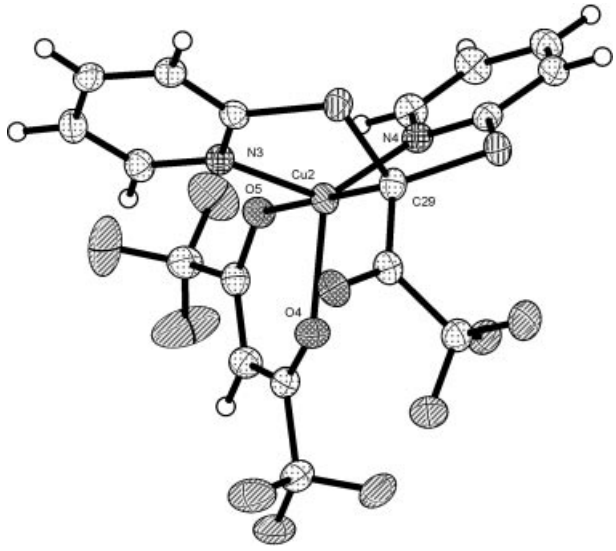


Figure 6. Molecular structure of **5** (displacement ellipsoids are shown at the 50% probability level).

### *[Cu$_2$(μ-OAc)$_4$(L3)$_2$] (6)*

Figure 7 shows the ORTEP drawing of **6**, with the numbering scheme. Table 1 (compounds **4**–**6**) shows the crystal-

Table 6. Selected bond lengths and angles for compound **5**.

| Selected bond lengths [Å] | Selected angles [°] | |
|---|---|---|
| Cu(1)–O(1) 1.9979(1) | O(1)–Cu(1)–N(1) 90.69(6) | O(5)–Cu(2)–N(4) 91.43(6) |
| Cu(1)–N(1) 2.0085(2) | O(1)–Cu(1)–N(2) 92.70(6) | O(5)–Cu(2)–N(3) 92.10(6) |
| Cu(1)–N(2) 2.0226(2) | N(1)–Cu(1)–N(2) 146.57(7) | N(4)–Cu(2)–N(3) 133.57(7) |
| Cu(1)–C(11) 2.0722(2) | O(1)–Cu(1)–C(11) 176.47(7) | O(5)–Cu(2)–C(29) 179.88(9) |
| Cu(1)–O(2) 2.2194(1) | N(1)–Cu(1)–C(11) 88.53(7) | N(4)–Cu(2)–C(29) 88.66(7) |
| Cu(2)–O(5) 2.0033(1) | N(2)–Cu(1)–C(11) 86.07(7) | N(3)–Cu(2)–C(29) 87.89(7) |
| Cu(2)–N(4) 2.0074(2) | O(1)–Cu(1)–O(2) 85.12(6) | O(5)–Cu(2)–O(4) 85.50(5) |
| Cu(2)–N(3) 2.0439(2) | N(1)–Cu(1)–O(2) 120.92(6) | N(4)–Cu(2)–O(4) 125.88(6) |
| Cu(2)–C(29) 2.0857(2) | N(2)–Cu(1)–O(2) 92.51(6) | N(3)–Cu(2)–O(4) 100.55(6) |
| Cu(2)–O(4) 2.1461(1) | C(11)–Cu(1)–O(2) 98.23(7) | C(29)–Cu(2)–O(4) 94.39(7) |

 © 2006 Wiley-VCH Verlag GmbH & Co. KGaA, Weinheim 

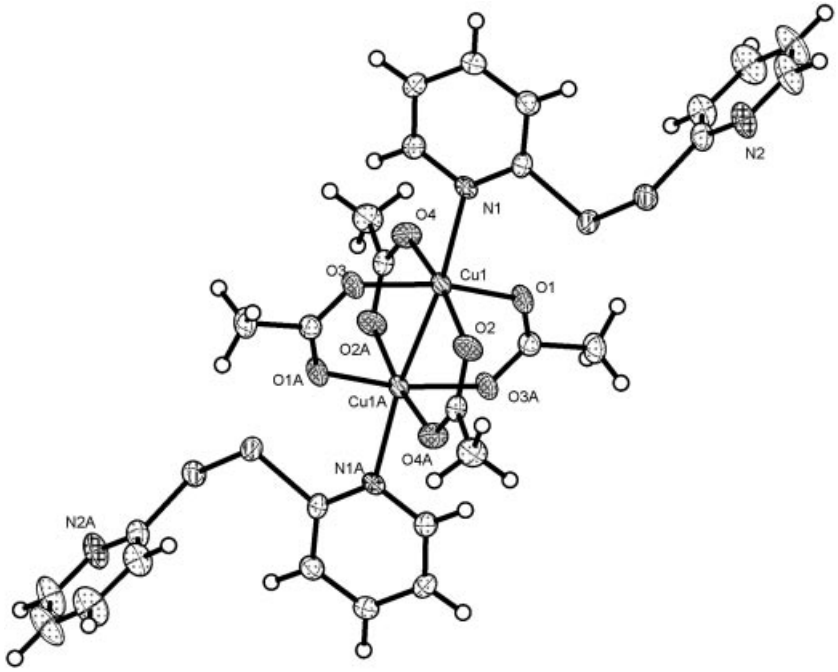


Figure 7. View of two copper centers bonded in compound **6**.

Table 7. Selected bond lengths and angles for compound **6**.

| Selected bond lengths [Å] | Selected angles [°] | |
|---|---|---|
| Cu(1)–O(1) 1.956(2) | O(1)–Cu(1)–O(2) 90.53(11) | O(2)–Cu(1)–N(1) 102.42(1) |
| Cu(1)–O(2) 1.965(3) | O(1)–Cu(1)–O(3) 168.72(1) | O(3)–Cu(1)–N(1) 92.16(1) |
| Cu(1)–O(3) 1.973(2) | O(2)–Cu(1)–O(3) 87.83(1) | O(4)–Cu(1)–N(1) 88.63(1) |
| Cu(1)–O(4) 1.981(3) | O(1)–Cu(1)–O(4) 89.21(1) | O(1)–Cu(1)–Cu(1)#1 84.28(2) |
| Cu(1)–N(1) 2.252(3) | O(2)–Cu(1)–O(4) 168.85(1) | O(2)–Cu(1)–Cu(1)#1 85.55(2) |
| Cu(1)–Cu(1)#1 2.6229(9) | O(3)–Cu(1)–O(4) 90.25(1) | O(3)–Cu(1)–Cu(1)#1 84.47(2) |
| | O(1)–Cu(1)–N(1) 99.09(1) | O(4)–Cu(1)–Cu(1)#1 83.33(2) |

lographic data, and selected bond lengths and angles are summarized in Table 7. The structure consists of the molecular 1:2 adduct $Cu_2(\mu\text{-}OAc)_4(L3)_2$ where the $Cu^{II}$ ion is pentacoordinate to four oxygen atoms of four different acetate anions and one nitrogen atom from the pyridine ring of **L3** to form a square-pyramidal geometry. The Cu(II) center deviates from the mean equatorial plane, defined by four coordinated oxygen atoms, toward the apical nitrogen atom by 0.1536 Å. The Cu–O distances [1.956(2)–1.981(3) Å] are similar to those in its analogous compounds[22] and the Cu–N [2.252(3) Å] distance is shorter than that in **3** but longer than those in **1** and **2** and similar to $[Cu(hfac)_2]_2(pyz)$ [2.25(2) Å].[19a] Four acetate anions bridge two $Cu^{II}$ centers in *syn-syn* fashion to form a $[Cu_2(OAc)_4]$ dinuclear building unit with a Cu–Cu distance of 2.6229(9) Å, which is linked by two **L3** ligands in a *trans* disposition. A similar structure is observed in $[Cu_2(\mu\text{-}OAc)_4(bpt)_2]$bpt [bpt = 1-(2-pyridyl)-2-(2-pyridylsulfanyl)ethane].[23]

Two pyridyl rings within each **L3** ligand are in a *cisoid* arrangement with a C–S–S–C torsion angle of 89.37(17)°, almost similar to that in the free ligand (87.1°). Steric factors produced by the 2,2′-dipyridyl orientation could explain why the molecular compound $[Cu_2(\mu\text{-}OAc)_4(L3)_2]$ (**6**) is formed instead of the polymeric compound $[Cu_2(\mu\text{-}OAc)_4(L3)]_n$. Reactions with dipyridyl ligands with an orientation different from 2,2′ are in progress in order to test how the nature of the ligand affects the structure of the compound.

## Magnetic Properties

The magnetic moment of complex **6** at room temperature is 2.05 $\mu_B$. This magnetic moment is smaller than that expected for two magnetically isolated spin $S = 1/2$ centers per molecule. The representation of the magnetic moment versus temperature shows a pronounced decrease until 100 K and drops more slowly to 0.43 $\mu_B$ at 2 K. The decrease of the magnetic moment could result from a strong antiferromagnetic coupling. The existence of antiferromagnetic interactions in this complex is also supported by the variation of the magnetic susceptibility with the temperature. Thus, a broad maximum from room temperature to 125 K is observed in the plot of $\chi_M$ vs. $T$. This feature is characteristic of antiferromagnetically coupled $Cu^{II}$ pairs.[24] A paramagnetic tail at very low temperatures is

 © 2006 Wiley-VCH Verlag GmbH & Co. KGaA, Weinheim 

also observed, which indicates the presence of a paramagnetic impurity. Similar paramagnetic impurities are usually present in complexes with strong antiferromagnetic coupling. Thus, the magnetic data of complex **6** have been analyzed[25] with the isotropic spin Hamiltonian of Equation (1) with $S_1 = S_2 = 1/2$.

$$H = -JS_1S_2 \quad (1)$$

From this spin Hamiltonian the Bleaney–Bowers formula has been derived in which terms corresponding to a paramagnetic impurity (P) and temperature independent paramagnetism (TIP) have been added [Equation (2)]. $N$, $g$, $\beta$, $k$, and $T$ have the usual meaning and $P$ is the molar fraction of the noncoupled paramagnetic impurity. In this expression it is assumed that the paramagnetic impurity follows the Curie law and has the same molecular weight and the same $g$ value as complex **6**.

$$\chi_M = \{2Ng^2\beta^2/kT[3 + \exp(-J/kT)] + TIP\}(1 - P) + (Ng^2\beta^2/2kT)P \quad (2)$$

A very good agreement between the experimental and calculated curves of the magnetic moment and the molar susceptibility for complex **6** was observed with this model. The magnetic parameters obtained in the best fit are: $g$ = 2.21, $J$ = –352 cm$^{-1}$, $TIP = 2.83 \times 10^{-4}$, and $P$ = 2.53%. The agreement factor is $2.95 \times 10^{-5}$. Figure 8 shows the experimental and calculated curves for complex **6**.

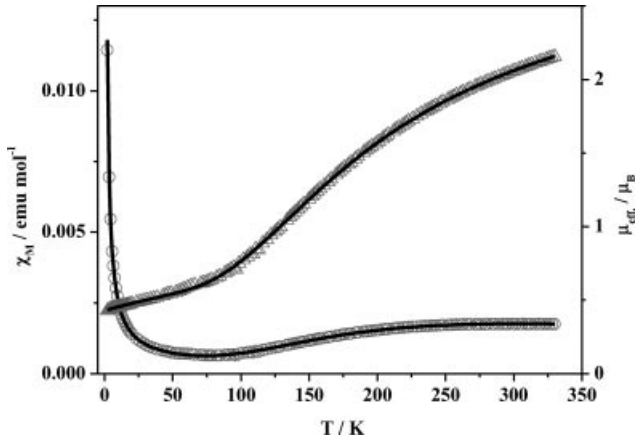


Figure 8. Experimental and calculated curves of $\chi_M$ and $\mu_{eff}$ vs. $T$ for complex **6**.

The $J$ value indicates that the Cu$^{II}$ centers of each molecule are very strongly antiferromagnetically coupled. This coupling constant is in good agreement with those observed in other tetracarboxylatodicopper(II) complexes.[24–26] Because of the large Cu–Cu distance the antiferromagnetic interaction is probably produced through the carboxylate groups. In fact, it has been pointed out[26d] in similar compounds that the $J$ parameter is more related to the O–Cu–Cu–O bond angles and the O–C–O planes than the Cu–Cu distance.

On the other hand, **1**–**3** shows magnetic moments corresponding to the presence of one unpaired electron per mol of copper at room temperature. The magnetic moment remains almost constant with the temperature and decreases sharply only at very low temperatures. This decrease could be explained by Zeeman level depopulation effects in the applied magnetic field. However, as these complexes form monodimensional systems with very long Cu–Cu distances, mediated by the size of the organic ligands, a weak antiferromagnetic coupling between the Cu$^{II}$ centers could also be possible. Thus, to fit these magnetic data we have considered the molecular field approximation applied to a paramagnetic model with $S$ = 1/2 [Equation (3)]. $\chi_{Cu} = Ng^2\beta^2/4kT$, $z$ is the number of neighbors and $J$ is the magnitude of the interaction of the Cu$^{II}$ centers.

$$\chi_M = \frac{\chi_{Cu}}{1 - [2\,zJ/N\,g^2\,\beta^2]\chi_{Cu}} \quad (3)$$

The parameters of the best fits are collected in Table 8. Figure 9 shows the experimental and calculated curves for complex **2**. Similar curves have been obtained for the other complexes. The $zJ$ values (from –0.45 to –0.16 cm$^{-1}$) are very low, in accordance with the presence of a very weak antiferromagnetic interaction between the copper(II) centers.

Table 8. Magnetic parameters for complexes **1**–**3** obtained from the fits of the magnetic moment as a function of temperature.

| Compound | $g$ | $J$ [cm$^{-1}$] | $\sigma^{2}$[a] |
|---|---|---|---|
| **1** | 2.20 | –0.45 | $4.33 \times 10^{-5}$ |
| **2** | 2.20 | –0.24 | $7.55 \times 10^{-5}$ |
| **3** | 2.17 | –0.16 | $9.39 \times 10^{-5}$ |

[a] $\sigma^2 = \Sigma(\mu_{eff.\ calcd.} - \mu_{eff.\ exp.})^2 / \Sigma\mu_{eff.\ exp.}{}^2$, [$\sigma^2 = \Sigma(\chi_{mol\ calcd.} - \chi_{mol\ exp.})^2 / \Sigma\chi_{mol\ exp.}{}^2$].

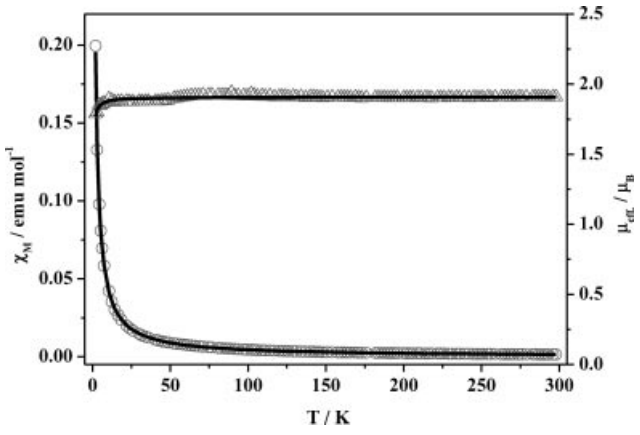


Figure 9. Experimental and calculated curves of $\chi_M$ and $\mu_{eff}$ vs. $T$ for complex **1**.

 © 2006 Wiley-VCH Verlag GmbH & Co. KGaA, Weinheim 

### Thermal Properties

The thermal properties of the compounds were examined by thermal gravimetric analysis (TGA/DTA) and differential scanning calorimetry (DSC). Compounds **1**–**3** and **6** were heated to 600 °C under a nitrogen atmosphere. TGA data suggest that the framework of **1** is stable up to 170° and show a weight loss of 60.80% (calcd. 60.30%) from 170 to 325 °C corresponding to the loss of one 1,2-di(2-pyridyl) butadiyne (**L1**) and one hfac chelating ligand per formula unit. Further weight loss is observed above 325 °C, with CuO remaining as a black powder (observed 11.82%, calcd. 11.67%). Compound **2** is also stable up to 170 °C, and in the temperature range 170–435 °C it undergoes two weight loss steps corresponding to one 1,2-bis(2-pyridylethynyl)-thiophene ligand (**L2**) and one hfac chelating ligand (found 64.42%, calcd. 64.57%). Above 435 °C, weight loss is also observed and the black powdery product once again is CuO (found 10.62%, calcd. 10.40%). Compound **3** is stable up to 80 °C, and up to 415 °C undergoes three weight loss steps; the first two (up to 160 °C and up to 215 °C) produce a loss of 15.60% and 15.45%, respectively, each corresponding to a 2-pyridyl sulfide fragment (calcd. 15.77%). In the range 215–415 °C, the loss of one hfac anion is observed (found 29.50, calcd. 29.67%). Above 415 °C, the weight loss observed is assigned to CuO (obsd. 11.20%, calcd. 11.39%). Compound **6** is stable up to 125 °C; in the 125–260 °C and 260–400 °C ranges, a loss of two 2,2′-dipyridyl disulfide (**L3**) ligands and three acetate anions, respectively, is observed. Above 400 °C, weight loss is also observed (10.35%) and is attributed to CuO (calcd. 10.52%).

This behavior is common for organic–inorganic coordination polymers consisting of $Cu(hfac)_2$ cations and *N*,*N*′-bidentate-type ligands.[13] DSC analyses of hermetically sealed samples of **1** and **2** display sharp endothermic peaks at 126.4 °C and 177.2 °C, respectively, which correspond to the melting point.

## Conclusions

Six new compounds generated from the reactions of 1,2-di(2-pyridyl)-1,3-butadiyne (**L1**), 2,5-bis(2-pyridylethynyl)-thiophene (**L2**), and 2,2′-dipyridyl disulfide (**L3**) with $Cu(hfac)_2$ and copper acetate have been synthesized and structurally characterized by X-ray diffraction.

The **1**–**3** coordination polymers described in this paper are some of the first reported examples of polymers based on dipyridyl ligands in 2,2′-positions and illustrate that the positional orientation of pyridyl nitrogen atoms and the nature of the ligands (**L1** and **L2** are rigid, **L3** is flexible) affects the structure during the self-assembly process. Moreover, new interesting transformations take place from 2,2′-dipyridyl disulfide (**L3**), because of the reactivity of the S–S bond, and the organic and mononuclear copper compounds **4** and **5** are obtained. In **5**, as a result of rearrangement, a copper–carbon bond is formed. The reaction of **L3** with copper acetate does not lead to polymeric compounds but a molecular complex **6** (1:2 adduct). Further studies of these ligands with transition metal salts are in progress in our laboratories.

## Experimental Section

**General:** All the solvents were of reagent grade quality and were used as received. 2,5-Dibromothiophene (Aldrich), 2-ethynylpyridine (Aldrich), tetramethylethylenediamine (Aldrich), $PdCl_2$ (Aldrich), CuI (Aldrich), $Cu(hfac)_2{\cdot}H_2O$ (hfac = hexafluoroacetylacetonate) (Aldrich), and 2,2′-dipyridyl disulfide (**L3**) (Lancaster) were used as received. $Et_3N$ (Fluka) was distilled from KOH immediately before use. $Pd(PPh_3)_4$[27] and the **L1** ligand[28] were prepared according to a literature procedure and **L2** was synthesized by us from a literature method.[29] The $^1H$ and $^{13}C$ NMR spectra were recorded with Bruker AMX-300 or 500 instruments. Solid-state NMR measurements were performed at room temperature with a Bruker AV 400WB (9.4 T) with a 4 mm MAS probehead. Infrared spectra were measured with a Perkin–Elmer 1650 infrared spectrometer. Elemental analyses were performed by the Microanalytical Laboratory of the University Autónoma of Madrid with a Perkin–Elemer 240 B microanalyzer. The Mass spectrum was measured with a VG-Autospec mass spectrometer for FAB by the Mass Laboratory of the University Autónoma of Madrid. Single-crystal diffraction experiments were performed with samples mounted on a glass fiber and transferred to a Bruker SMART 6 K CCD area-detector three-circle diffractometer with a Rigaku Rotating Anode (Cu-$K_\alpha$ radiation, $\lambda$ = 1.54178 Å) generator equipped with Goebel mirrors at settings of 50 kV and 100 mA. X-ray data were collected at 100 K, with a combination of six runs at different $\varphi$ and $2\theta$ angles, 3600 frames. The data were collected using 0.3° wide $\omega$ scans with a crystal-to-detector distance of 4.0 cm.

The substantial redundancy in data allows empirical absorption corrections (SADABS) to be applied using multiple measurements of symmetry-equivalent reflections.

The raw intensity data frames were integrated with the SAINT program, which also applied corrections for Lorentz and polarization effects.

The software package SHELXTL version 6.10 was used for space group determination, structure solution, and refinement. The space group determination was based on a check of the Laue symmetry and systematic absences and was confirmed using the structure solution. The structures were solved by direct methods (SHELXS-97), completed with difference Fourier syntheses, and refined with full-matrix least-squares using SHELXL-97 minimizing $\omega(F_o^2 - F_c^2)^2$. Weighted *R* factors ($R_w$) and all goodness of fits *S* are based on $F^2$; conventional *R* factors (*R*) are based on *F*. All scattering factors and anomalous dispersion factors are contained in the SHELXTL 6.10 program library. Table 1 contains crystal data for complexes **1**–**6**.

CCDC-264487, -264488, -287409, -287410, -287412, and -287878 contain the supplementary crystallographic data for complexes **1**–**6**. These data can be obtained free of charge from The Cambridge Crystallographic Data Centre via www.ccdc.cam.ac.uk/data_request/cif. The variable-temperature magnetic susceptibilities were measured on polycrystalline samples with a Quantum Design MPMSXL SQUID (Superconducting Quantum Interference Device) susceptometer over a temperature range of 2 to 300 K (Complutense University of Madrid). All data were corrected for the diamagnetic contribution of both the sample holder and the compound to the susceptibility. The molar diamagnetic corrections for the complexes were calculated based on Pascal's constants.

 © 2006 Wiley-VCH Verlag GmbH & Co. KGaA, Weinheim 

The thermal properties were examined by thermal gravimetric analysis (TGA) and differential scanning calorimetry (DSC). The gravimetric data were obtained on a Seiko DTA/TG 320 U using an open pan, which was purged with $N_2$ and at a heating rate of 5 °C/min. The calorimetric data were obtained with a Perkin–Elmer Pyris 1DSC instrument using a sealed pan with a heating rate of 5 °C/min. The melting points were also obtained by using a conventional melting point apparatus.

**Synthesis of 1,2-Bis(2-pyridylethynyl)thiophene (L2):** A mixture of 2,5-dibromothiophene (1.75 g, 7.27 mmol), 2-ethynylpyridine (3.00 g, 29 mmol), $Pd(PPh_3)_4$ (1.26 g, 1.09 mmol), and CuI (0.192 g, 1.0 mmol) in triethylamine (40 mL) and THF (40 mL) was stirred under Ar at 70 °C for 20 h. The solution was cooled to room temperature and after evaporation of the solvent a brown solid was obtained. The crude product was extracted with several portions of ether, filtered and evaporated at reduced pressure. The residue was purified by chromatography on silica gel eluting with ether/$CH_2Cl_2$ (1:1). The product 1,2-bis(2-pyridylethynyl)thiophene (**L2**) was isolated as a yellow solid (1.78 g, 85%); m.p. 115–116 °C. (KBr): $\tilde{\nu}$ = 2204 (s, $\nu_{C\equiv C}$), 1576 and 1556 (s, $\nu_{C=C,}$ $\nu_{C=N}$, conj), 987 (vs, py), 774 (m) and 737 (s, py-H) $cm^{-1}$. $^1H$ NMR ([D$_6$]acetone, 300 MHz): $\delta$ = 8.63 (d, $J$ = 4.3 Hz, 2 H), 7.85 (td, $J$ = 2.7and 0.67 Hz, 2 H), 7.64 (dt, $J$ = 2.7 and 0.3 Hz, 2 H), 7.45 (s, 2 H), 7.40 (td, $J$ = 2.0 and 0.3 Hz, 2 H) ppm. $^{13}C$ NMR (500 MHz, $CDCl_3$): $\delta$ = 81.9 (C8), 93.1 (C7), 123.1(C3), 124.6 (C5), 127.1 (C9), 136.2 (C4), 133.2 (C10), 142.8 (C2), 150.2 (C6) ppm. MS (FAB$^+$): $m/z$ (%) = 286 [M$^+$]. $C_{18}H_{10}N_2S$ (287): calcd. C 75.52, H 3.49, N 9.79; found C 75.58, H 3.43, N 9.70.

**Synthesis of $[Cu(hfac)_2L1]_n$ (1):** A solution of $Cu(hfac)_2{\cdot}H_2O$ (110 mg; 0.245 mmol) in $CH_2Cl_2$ (5 mL) was slowly layered onto a solution of **L$_1$** (50 mg; 0.245 mmol) in $CH_2Cl_2$ (5 mL). The solution was allowed to stand at 0 °C for 2 d. Green crystals were obtained (150.3 mg, 90%). M.p. 133 °C. IR (KBr): $\tilde{\nu}$ = 3077 (w), 1654 (s), 1592 (m), 1574 (s), 1561 (s), 1525 (s), 1475 (s), 1459 (vs), 1425 (s), 1258 (vs), 1240 (m), 1197 (vs), 1146 (vs), 798 (m), 774 (vs), 733 (s), 666 (s), 629 (m), 583 (m), 532 (s) $cm^{-1}$. $C_{24}H_{10}CuF_{12}N_2O_4$ (681.88): calcd. C 42.47, H 1.48, N 4.11; found C 42.24, H 1.50, N 4.08.

**Synthesis of $[Cu(hfac)_2L2]_n$ (2):** A solution of **L2** (40 mg, 0.139 mmol) in $CH_2Cl_2$ (2 mL) was slowly added to a $CH_2Cl_2$ solution (2 mL) of $Cu(hfac)_2{\cdot}H_2O$ (66.8 mg, 0.139 mmol). The solution was allowed to stand at room temperature. After 2 d a yellowish solution appeared. The solvent was then slowly evaporated over a period of 1 d to half the initial volume. The solution was allowed to stand at 0 °C for 2 d and yellow crystals were obtained (90.26 mg, 85%). M.p. 175 °C. IR (KBr): $\tilde{\nu}$ = 3100 (w), 2209 (vs), 1644 (vs), 1594 (vs), 1561 (vs), 1546 (vs), 1523 (vs), 1471 (vs), 1433 (s), 1337 (m), 1320 (m), 1250 (vs), 1196 (vs), 1132 (vs), 1084 (vs), 808 (vs), 790 (vs), 771 (vs), 756 (s), 740 (s), 667 (vs), 583 (vs), 521 (s) $cm^{-1}$. $C_{28}H_{12}CuF_{12}N_2O_4S$ (764): calcd. C 44.00, H 1.57, N 3.67; found C 43.98, H 1.54, N 3. 63.

**Synthesis of $[Cu(hfac)_2L3]_n$ (3), Zwitterionic Compound 4 and $[(hfac)Cu(C_{13}H_8N_2S_2OF_3)]$ (5). Method (a):** A solution of **L3** (100 mg, 0.455 mmol) in $CH_2Cl_2$ (3 mL) was added to a $CH_2Cl_2$ solution (8 mL) of $Cu(hfac)_2{\cdot}H_2O$ (217 mg, 0.455 mmol). After the mixture was left for 2 d at room temperature, the solvent was evaporated. After recrystallization in $CH_2Cl_2$/hexane (1:1), **3** was obtained as a green solid (206.2 mg, 65%), **4** as a yellow solid (36.08 mg, 25%), and **5** as a violet solid (13.65 mg, 5%). X-ray quality crystals of **3** and **4** were grown by slow evaporation of $CH_2Cl_2$ solutions at –10 °C and room temperature, respectively. Crystals suitable for X-ray analysis of **5** were obtained by slow evaporation of hexane solutions at room temperature.

**3:** M.p. 88 °C. IR (KBr): $\tilde{\nu}$ = 3055 (w), 1641 (vs), 1611 (w), 1580 (s), 1561 (s), 1535 (m), 1485 (vs), 1472 (vs), 1455 (vs), 1420 (vs), 1255 (vs), 1224 (vs), 1210 (vs), 1147 (vs), 807 (s), 799 (s), 760 (s), 679 (s), 596 (s), 527 (m) $cm^{-1}$. $C_{20}H_{10}CuF_{12}N_2O_4S_2$ (697.96): calcd. C 34.41, H 1.43, N 4.01, S 9.17; found C 34.32, H 1.48, N 3.97, S 9.23.

**4:** M.p. 102 °C. IR (KBr): 3103 (w), 3070 (w), 1679 (vs), 1606 (m), 1583 (s), 1507 (m), 1452 (s), 1420 (s), 1260 (m), 1203 (vs), 1203 (vs), 837 (m), 803 (m), 758 (s), 722 (s), 520 (m) $cm^{-1}$. $^1H$ NMR ($CDCl_3$, 300 MHz): $\delta$ = 8.40 (d, $J$ = 4.3 Hz, 1 H), 7.56 (dd, $J$ = 3.7 and 1.0 Hz, 1 H), 7.33 (dd, $J$ = 2.3 and 1.8 Hz, 1 H) ppm. $^1H$ NMR ($CD_2Cl_2$, 300 MHz): $\delta$ = 8.68 (d, $J$ = 4.2 Hz, 1 H),8.20 (t, $J$ = 2.6 Hz, 1 H), 7.74 (d, $J$ = 1.05 Hz, 1 H), 7.62 (t, $J$ = 2.24 Hz, 1 H) ppm. $C_{10}H_5NO_2SF_6$ (317.21): C 37.82, H 1.58, N 4.42, S 10.10; found C 3.72, H 1.61, N 4.37, S 9.99.

**5:** M.p. 150 °C. IR (KBr): $\tilde{\nu}$ = 3076 (w), 1673 (vs), 1650 (vs), 1611 (w), 1593 (s), 1559 (s), 1522 (m), 1486 (vs), 1457 (vs), 1421 (vs), 1302 (s), 1285 (s), 1260 (vs), 1203 (vs), 1205 (vs), 1147 (vs), 1051 (s), 1013 (s), 879 (m), 807 (m), 797 (m), 789 (s), 770 (vs), 760 (vs), 729 (s), 703 (s), 679 (s), 668 (s), 586 (m), 527 (m), 486 (m), 410 (m) $cm^{-1}$. $^1H$ NMR ($CDCl_3$, 300 MHz): 8.00 (br. s, 2 H), 7.63 (br. s, 2 H) ppm. $C_{18}H_9CuO_3N_2S_2F_9$ (599.93): calcd. C 36.00, H 1.50, N 4.07, S 10.67; found C 36.18, H 1.47, N 4.06, S 10.58.

**Method (b):** A solution of **L3** (100 mg, 0.455 mmol) in MeOH (2 mL) was added to a solution of $Cu(hfac)_2{\cdot}H_2O$ (217 mg, 0.455 mmol, 6 mL) in the same solvent. After the solution was slowly evaporated at room temperature for 2 d, only green crystals of **3** were obtained (285.8 mg, 90%).

**Method (c):** $Cu(hfac)_2{\cdot}H_2O$ (434 mg, 0.91 mmol) in $CH_2Cl_2$ (15 mL) was added to a solution of **L3** (200 mg, 0.91 mmol) in $CH_2Cl_2$ (6 mL). The reaction was monitored by FT-IR spectroscopy. After the mixture was refluxed for 48 h, the pH was checked and an acidic pH was observed. The solvent was removed under vacuum and the residue was extracted with hexane giving a violet solution. Slow evaporation of the solvent gave crystals of **5** (49.13 mg, 18%) suitable for X-ray analysis. The insoluble residue in hexane was redissolved in $CH_2Cl_2$ and stood for about 3 d at –10 °C. Yellow crystals of **4** were obtained (101.0 mg, 70%). Similar results were obtained when the reaction was carried out in MeOH.

**Synthesis of $[Cu_2(\mu\text{-}OAc)_4(L3)_2]$ (6):** A solution of $Cu(OAc)_2{\cdot}H_2O$ (55 mg, 0.28 mmol) in $CH_3OH$ (15 mL) was added to a solution of **L3** (62 mg, 0.28 mmol) in $CH_3OH$ (3 mL). The solution was left for 2 d at room temperature and for about 2 d in the refrigerator (–10 °C). Blue crystals of copper acetate were isolated by filtration; the solution was filtered off, the solvent was removed under vacuum and the residue was washed several times with hexane/$CH_2Cl_2$ (10:2) to isolate **L3**. Extraction of the solid with $CH_2Cl_2$/$CH_3OH$ (1:1), followed by slow solvent evaporation afforded green crystals of **6** (87 mg, 50%). M.p. 205 °C. IR (KBr): $\tilde{\nu}$ = 3055 (w), 1618 (vs), 1573 (vs), 1561 (vs), 1457 (vs), 1427 (vs), 1418 (vs), 1347 (m), 1288 (m), 1163 (s), 1117 (s), 1051 (s), 1000 (s), 774 (vs), 754 (vs), 719 (s), 682 (vs), 627 (vs) $cm^{-1}$. $C_{28}H_{28}Cu_2N_4O_8S_4$ (803.86): calcd. C 41.84, H 3.49, N 6.97, S 15.94; found C 41.40, H 3.48, N 7.08, S 15.66.

## Acknowledgments

We express great appreciation to the Dirección General de Investigación Científica y Tecnológica (Grant n°. BQU 2002-02522, MAT 2004-22102-E Spain). We are grateful to the student J. Toledano for the help in the preparation of the compounds **L2** and **2**

 © 2006 Wiley-VCH Verlag GmbH & Co. KGaA, Weinheim 

and to Dra. R. Rojas (Instituto de Materiales, CSIC, Spain) for the DSC and DTA/TG measurements.

[1] a) S. Kitagawa, S. Noro, *Comprehensive Coord. Chem. II* (Eds.: J. A. McCleverty, T. J. Meyer) Elsevier, Oxford, **2004**, vol. 7, p. 231; b) L. Brammer, *Chem. Soc. Rev.* **2004**, *33*, 476; c) T. Yuen, C. L. Lin, T. W. Mihalisin, M. A. Lawandy, J. Li, *J. Appl. Phys.* **2000**, *87*, 6001; d) J. L. Manson, A. M. Arif, C. D. Incarvito, L. M. Liable-Sands, A. L. Reinghold, J. S. Miller, *J. Solid State Chem.* **1999**,*145*, 369; e) F. Lloret, G. De Munno, M. Julve, J. Cano, R. Ruiz, A. Caneschi, *Angew. Chem. Int. Ed. Engl.* **1998**, *37*, 135.

[2] a) M. E. Kosal, J.-H. Chou, S. R. Wilson, K. S. Suslick, *Nat. Mater.* **2002**, *1*, 118; b) S. Kitagawa, R. Kitaura, S. Noro, *Angew. Chem. Int. Ed.* **2004**, *43*, 2334; c) M. Kondo, T. Okubo, A. Asami, S. Noro, T. Yoshimoti, S. Kitagawa, T. Ishii, H. Matzusaka, K. Seki, *Angew. Chem. Int. Ed.* **1999**, *38*, 140.

[3] a) H. Hou, X. Meng, Y. Song, Y. Fan, Y. Zhu, H. Lu, C. Du, W. Shao, *Inorg. Chem.* **2002**,*41*, 4068; b) W. Lin, Z. Wang, L. Ma, *J. Am. Chem. Soc.* **1999**, *121*, 11249; c) C. Chen, K. S. Suslick, *Coord. Chem. Rev.* **1993**, *128*, 293.

[4] a) M. Albrecht, M. Lutz, A. L. Spek, G. van Koten, *Nature* **2000**, *406*, 970; b) L. G. Beauvais, M. P. Sores, J. R. Long, *J. Am. Chem. Soc.* **2000**, *122*, 2763.

[5] a) M. Munakata, L. P. Wu, T. Kuroda-Sowa, *Adv. Inorg. Chem.* **1999**, *46*, 173; b) A. J. Blake, N.-R. Champness, P. Hubberstey, W. S. Li, M. A. Withersby, M. Schroder, *Coord. Chem. Rev.* **1999**, *183*, 117; c) O. M. Yaghi, H. Li, C. Davis, D. Richardson, T. L. Groy, *Acc. Chem. Res.* **1998**, *31*, 474; d) O. S. Jung, Y. J. Kim, Y. A. Lee, J. K. Park, H. K. Chae, *J. Am. Chem. Soc.* **2000**, *122*, 9921.

[6] a) N. G. Pschirer, D. M. Ciurtin, M. D. Smith, U. H. F. Bunz, H. C. zur Loye, *Angew. Chem. Int. Ed.* **2002**, *41*, 603; b) K. Biradha, Y. Hongo, M. Fujita, *Angew. Chem. Int. Ed.* **2000**, *39*, 3843; c) D. Hargman, R. P. Hammond, R. Haushalter, J. Zubieta, *Chem. Mater.* **1998**, *10*, 2091; d) M. Fujita, Y. J. Kwon, S. Washizu, K. Ogura, *J. Am. Chem. Soc.* **1994**, *116*, 1151.

[7] Z. Huang, H.-B. Song, M. Du, S.-T. Chen, X.-H. Bu, *Inorg. Chem.* **2004**, *43*, 931.

[8] a) A. Jain, T. T. Kodas, T. S. Corbitt, J. M. Hampden-Smith, *Chem. Mater.* **1996**, *8*, 1119; b) R. J. Puddephatt, *Polyhedron* **1994**, *13*, 1233; c) J. Pinkas, J. C. Huffman, D. V. Baxter, M. H. Chisholm, K. G. Caulton, *Chem. Mater.* **1995**, *7*, 1589.

[9] W. Fujita, K. Awaga, *J. Am. Chem. Soc.* **2001**, *123*, 3610.

[10] a) Y. Sano, M. Tanaka, N. Koga, M. Matsuda, H. Iwamura, P. Rabu, M. Drillon, *J. Am. Chem. Soc.* **1997**, *119*, 8246; b) S. Karasawa, Y. Sano, T. Akita, N. Koga, T. Itoh, H. Iwamura, P. Rabu, M. Drillon, *J. Am. Chem. Soc.* **1998**, *120*, 10080; c) Y. Ishimaru, M. Kitano, H. Kumada, N. Koga, H. Iwamura, *Inorg. Chem.* **1998**, *37*, 2273; d) A. Kamiyama, T. Noguchi, T. Kajiwara, T. Ito, *Inorg. Chem.* **2002**, *41*, 507.

[11] M. B. Zaman, M. D. Smith, D. M. Ciurtin, H. C. zur Loye, *Inorg. Chem.* **2002**, *41*, 4895.

[12] a) L. S. Higashi, M. Lundeen, K. Seff, *J. Am. Chem. Soc.* **1978**, *100*, 8101; b) L. S. Higashi, M. Lundeen, E. Hilti, K. Seff, *Inorg. Chem.* **1977**, *16*, 310.

[13] Y. B. Dong, M. D. Smith, R. C. Layland, H. C. zur Loye, *Inorg. Chem.* **1999**, *38*, 5027.

[14] M. B. Zaman, K. A. Udachin, J. A. Ripmeester, *Cryst. Eng. Commun.* **2002**, *4*, 613.

[15] R. Horikoshi, T. Mochida, H. Moriyama, *Inorg. Chem.* **2001**, *40*, 2430.

[16] A. Escuer, T. Comas, J. Ribas, R. Vincent, X. Xolans, C. Zanchini, D. Gatteschi, *Inorg. Chim. Acta* **1989**, *162*, 97.

[17] a) J. L. Manson, *Inorg. Chem.* **2003**, *42*, 2602; b) S. Karasawa, H. Kumada, N. Koga, H. Iwamura, *J. Am. Chem. Soc.* **2001**, *123*, 1387; c) M. J. Plater, M. R. Foreman, A. M. Z. Slawin, *Inorg. Chim. Acta* **2000**, *303*, 132.

[18] a) J. Luo, M. Hong, R. Wang, D. Yuan, R. Cao, L. Han, Y. Xu, Z. Lin, *Eur. J. Inorg. Chem.* **2003**, 3623; b) I. Kinoshita, L. J. Wrigth, S. Kubo, K. Kimura, A. Sakata, T. Yana, R. Miyamoto, T. Nishioka, K. Isobe, *Dalton Trans.* **2003**, 1993.

[19] a) R. C. E. Belford, D. E. Fenton, M. R. Truter, *J. Chem. Soc., Dalton Trans.* **1974**, 17; b) R. C. E. Belford, D. E. Fenton, M. R. Truter, *J. Chem. Soc., Dalton Trans.* **1972**, 2208.

[20] N. V. Raghavan, K. Seff, *Acta Crystallogr., Sect. B* **1977**, *33*, 38.

[21] M. Melnik, M. Kabesova, M. Dunaj-Jurco, C. E. Holloway, *J. Coord. Chem.* **1997**, *41*, 35.

[22] a) M. Du, Z. Huang, S.-t. Chen, Y.-M. Guo, *Inorg. Chem.* **2003**, *42*, 552; b) Z. Huang, H.-B. Song, M. Du, S.-T. Chen, X.-H. Bu, *Inorg. Chem.* **2004**, *43*, 931.

[23] S. C. Davies, M. C. Durrant, D. L. Hughes, K. Leidenberger, C. Stapper, R. L. Richards, *J. Chem. Soc., Dalton Trans.* **1997**, 2409.

[24] J. Mrozinski, *Coord. Chem. Rev.* **2005**, *249*, 2534.

[25] O. Kahn, *Molecular Magnetism*, VCH Publishers, Inc., USA, **1993**, p. 107.

[26] For example, see: a) Z. Huang, H.-B. Song, M. Du, S.-T. Chen, X.-H. Bu, J. Ribas, *Inorg. Chem.* **2004**, *43*, 931; b) P. Stachová, D. Valigura, M. Koman, M. Melník, M. Korabik, J. Mrozinski, T. Glowiak, *Polyhedron* **2004**, *23*, 1303; c) M. Du, X.-H. Bu, Z. Huang, S.-T. Chen, Y.-M. Guo, C. Díaz, J. Ribas, *Inorg. Chem.* **2003**, *42*, 552; d) M. Rusjan, Z. Chaia, O. E. Piro, D. Guillond, F. D. Cukiernik, *Acta Crystallogr., Sect. B* **2000**, *56*, 666.

[27] D. R. Coulson, *Inorg. Synth.* **1990**, *28*, 107.

[28] J. G. Rodríguez, R. Martínez-Villamil, F. H. Cano, I. Fonseca, *J. Chem. Soc., Perkin Trans. 1* **1997**, 709.

[29] K. Sonogashira, Y. Tohda, N. Hagihara, *Tetrahedron Lett.* **1975**, *16*, 4467.

Received: October 28, 2005
Published Online: May 12. 2006

 © 2006 Wiley-VCH Verlag GmbH & Co. KGaA, Weinheim 

DOI: 10.1002/ejic.200600155

# Solvothermal Synthesis, Crystal Structures, and Properties of New Selenidoantimonates $[Ln(en)_4(SbSe_4)]$ (Ln = La, Nd) and $[Sm(en)_4]SbSe_4 \cdot 0.5en$: The First Example of an $SbSe_4^{3-}$ Anion Acting as a Ligand to a Lanthanide Complex

**Ding-Xian Jia,*[a] Qian-Xin Zhao,[a] Yong Zhang,[a] Jie Dai,[a] and Jian Zhou[a]**

**Keywords:** Selenidoantimonates / Lanthanides / Antimony / Solvothermal synthesis / Crystal structures

Three new lanthanide selenidoantimonates $[Ln(en)_4(SbSe_4)]$ [Ln = La (**1**), Nd (**2**)] and $[Sm(en)_4]SbSe_4 \cdot 0.5en$ (**3**) (en = ethylenediamine) were first synthesized by treating $LnCl_3$, Sb, and Se in a stoichiometric ratio with en under mild solvothermal conditions. Compounds **1** and **2** are isostructural. The $Ln^{3+}$ ion has a nine-coordinate environment involving eight N atoms from four en ligands and one Se atom from the $SbSe_4^{3-}$ anion forming a distorted bicapped pentagonal bipyramid. $[La(en)_4(SbSe_4)]$ and $[Nd(en)_4(SbSe_4)]$ are the first examples of solvothermally synthesized selenidoantimonates with an $SbSe_4^{3-}$ anion acting as a ligand in a lanthanide complex. The crystal structure of **3** contains an isolated bicapped trigonal-prismatic coordinated $[Sm(en)_4]^{3+}$ cation, a tetrahedral $SbSe_4^{3-}$ anion, and half a free en molecule in its asymmetric unit. The bandgaps of 2.22 eV for **1**, 2.33 eV for **2**, and 2.54 eV for **3** have been derived from optical absorption spectra. Compound **1** loses the en ligands in one step, whereas compound **2** loses them in two steps.
(© Wiley-VCH Verlag GmbH & Co. KGaA, 69451 Weinheim, Germany, 2006)

## Introduction

The mild solvothermal reaction in amine has proven to be a versatile route for the synthesis of main group chalcogenometalates.[1–3] In the case of chalcogenoantimonates, since the compound $[Co(en)_3]CoSb_4S_8$[4] was prepared, a large number of thioantimonates have been synthesized using amino transition metal (TM) complexes $[TM(amine)_m^{n+}]$ as structural directors under solvothermal conditions, giving $[M(en)_3]Sb_2S_4$ (M = Co, Ni),[5] $[M(en)_3]Sb_4S_7$ (M = Mn, Co, Ni),[5,6] $Mn_2(en)Sb_2S_5$,[7] $[Co(en)_3]Sb_{12}S_{19}$,[8] $[Ni(dien)_2]Sb_4S_8$,[9] $[Fe(dien)_2]Sb_6S_{10} \cdot 0.5H_2O$,[10] $[Ni(dien)_2]Sb_4S_9$,[11] $[Ni(dien)_2]_9Sb_{22}S_{42} \cdot 0.5H_2O$,[12] $[Ni(dien)_2]_3(Sb_3S_6)_2$,[13] $[Fe(dien)_2]Fe_2Sb_4S_{10}$[14] (dien = diethylenediamine), $[M(tren)]Sb_2S_4$ (M = Co, Ni),[15] $[M(tren)]Sb_4S_7$ (M = Mn, Fe, Co, Zn),[16] $[Co(tren)]_2Sb_4S_8$,[17] $[Mn(tren)]_4Mn_2Sb_4S_{12}$,[18] and $[Mn(tren)]_2Sb_2S_5$[19] [tren = tris(2-aminoethyl)amine], for example. The thioantimonates exhibit rich structural diversity because of the variable coordination behaviors of $Sb^{III}$ atoms caused by the stereochemically active lone pair.[20] However, compared with the bewildering thioantimonates, the selenidoantimonates combined with transition metals are less explored under mild solvothermal conditions and only a few examples have been reported.[21–25]

The combination of lanthanide metals with chalcogenometalates should lead to new architectural features with unique properties. However, the chemistry explored involving the synthesis of chalcogenometalates integrating with lanthanide metal ions ($Ln^{3+}$) by the solvothermal methodology is very limited. It is a challenge to combine the $Ln^{3+}$ ion with the so-called soft-base chalcogenometalate anions in solution because of the weak coordination of chalcogenometalate anions and the hydrolysis of lanthanide ions. Very recently, templated by (en)lanthanide(III) complexes, two series of lanthanide thioantimonates(V), $[Ln(en)_3(H_2O)_x(\mu_{3-x}\text{-}SbS_4)]$ ($x$ = 0, 1; Ln = La, Nd, Sm) and $[Ln(en)_4]SbS_4 \cdot 0.5en$ (Ln = Sm, Eu, Dy, Yb),[26,27] were obtained from the synthetic system $Ln^{3+}$/Sb/S/en under solvothermal conditions during our systematic synthesis of chalcogenometalates in superheated en.[28–31] The present contribution reports the synthesis, crystal structures, and properties of new lanthanide selenidoantimonates(V) $[La(en)_4(SbSe_4)]$, $[Nd(en)_4(SbSe_4)]$, and $[Sm(en)_4]SbSe_4 \cdot 0.5en$, which were obtained from a solvothermal route. To the best of our knowledge, the present compounds are the only examples of selenidoantimonates combined with lanthanide(III) complex cations.

## Results and Discussion

The compounds **1** and **2** crystallize in the monoclinic space group $P2_1/n$ with four formula units in the unit cell and are isostructural. The molecular structure of **1** is de-

[a] School of Chemistry and Chemical Engineering, Suzhou University,
Suzhou 215123, P. R. China
Fax: +86-512-65880089
E-mail: jiadingxian@suda.edu.cn

 InterScience © 2006 Wiley-VCH Verlag GmbH & Co. KGaA, Weinheim 

picted in Figure 1. The lanthanide(III) ion is coordinated by four bidentate en ligands and a monodentate $SbSe_4^{3-}$ anion leading to a neutral complex $[Ln(en)_4(SbSe_4)]$ [Ln = La (**1**), Ln = Nd (**2**)]. The central $Ln^{3+}$ ion lies within a nine-coordinate environment forming a distorted monocapped square antiprism $LnN_8Se$. The Ln–N bond lengths are 2.648(4)–2.773(3) Å for La–N and 2.628(3)–2.725(3) Å for Nd–N, and are consistent with those in other compounds containing (en)lanthanide(III) complexes.[27,32] The La–Se [3.3197(5) Å] and Nd–Se [3.2992(6) Å] bond lengths are comparable to those in multinary lanthanum and neodymium selenides [3.1070(12)–3.3625(12) Å for La–Se in $KLaP_2Se_6$[33] and 2.979(1)–3.245(1) Å for Nd–Se in $Nd_4MnOSe_6$[34]]. The Ln–N and Ln–Se bond lengths decrease from La to Nd, as expected from the lanthanide contraction. The $SbSe_4^{3-}$ anion is a distorted tetrahedron, as evidenced by Sb–Se bond lengths ranging from 2.4654(5) to 2.4851(7) Å and Se–Sb–Se angles ranging from 107.715(18) to 111.558(17)°. Both lengths and angles are comparable to those observed in other compounds containing tetrahedral $SbSe_4^{3-}$ anions.[21–24] The Sb–Se(1) bonds [2.4848(5) Å for **1**, 2.4851(7) Å for **2**] are expectedly longer than other Sb–Se bonds (Table 1) because of the coordination of Se(1) with the lanthanide(III) ion.

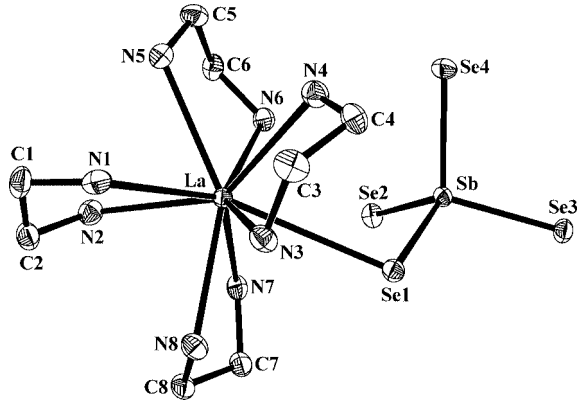


Figure 1. Crystal structure of **1** with labeling scheme; the probability ellipsoids are drawn at the 50% level. Hydrogen atoms are omitted for clarity.

In **1**, the terminal Se atoms of $[La(en)_4(SbSe_4)]$ are involved in intermolecular N–H···Se hydrogen bonding with adjacent molecules resulting in a chainlike arrangement of $[La(en)_4(SbSe_4)]$ moieties parallel to the *a* axis (Figure 2). The chains are further connected through N–H···Se hydrogen bonds leading to a three-dimensional network. The N···Se distances vary from 3.443(4) to 3.755(4) Å and the N–H···Se angles vary from 138.1 to 167.7° (Table 2), and are consistent with the values reported in the literature.[35] Similar intermolecular hydrogen bonding is observed in compound **2** (Table 2).

Compound **3** crystallizes in the space group $P2_1/n$ with four formula units in the unit cell. Its molecular structure is quite different from those of **1** and **2**, but it is isostructural to the thio analog of $[Sm(en)_4]SbS_4 \cdot 0.5en$.[26] The crystal structure of **3** consists of an isolated four-en-coordinated $[Sm(en)_4]^{3+}$ cation, a tetrahedral $SbSe_4^{3-}$ anion, and half a free en molecule in its asymmetric unit (Figure 3). The atom C(2) is disordered and the occupancies of disordered C and C′ are assigned as 55% and 45%, respectively. The $Sm^{3+}$ ion is in an eight-coordinate environment with eight amino N atoms from four bidentate en ligands forming a distorted bicapped trigonal prism. The Sm–N bond lengths [2.532(5)–2.576(6) Å] are comparable with those reported in the literature.[26] The Sb–Se distances and Se–Sb–Se angles are in agreement with those in **1** and **2** (see Tables 1 and 3). The Se atoms of the $SbSe_4^{3-}$ anion are in contact with $-NH_2$ groups with N···Se distances ranging from 3.402(5) to 3.764(5) Å and N–H···Se angles ranging from 142.1 to 171.9°, indicating weak hydrogen bonds. An N(6)–H(6A)···N(9) hydrogen bond is formed with an N(6)···N(9) distance of 3.100(8) Å and an N(6)–H(6A)···N(9) angle of 156.2°. The N–H···Se and N–H···N hydrogen-bonding interactions lead to a three-dimensional network structure. The crystal packing of **3** is illustrated in Figure 4.

In our systematic investigation of lanthanide thioantimonate compounds in superheated en, two types of compounds were obtained across the lanthanide series. The lighter (en)lanthanide(III) complex cations are bridged by $\mu_3$-$SbS_4$ or $\mu_2$-$SbS_4$ ligands to form one-dimensional neutral polymers $[Ln(en)_3(H_2O)_x(\mu_{3-x}\text{-}SbS_4)]$ (Ln = La, Nd, Sm),[26,27] whereas the heavier ones form compounds

Table 1. Selected bond lengths [Å] and angles [°] for **1** and **2**.

| | **1** | **2** | | **1** | **2** |
|---|---|---|---|---|---|
| Sb–Se(1) | 2.4848(5) | 2.4851(7) | Sb–Se(2) | 2.4671(5) | 2.4654(5) |
| Sb–Se(3) | 2.4675(5) | 2.4719(6) | Sb–Se(4) | 2.4701(5) | 2.4665(6) |
| Ln–Se(1) | 3.3197(5) | 3.2992(6) | Ln–N(1) | 2.648(4) | 2.623(3) |
| Ln–N(2) | 2.737(4) | 2.725(3) | Ln–N(3) | 2.702(3) | 2.678(3) |
| Ln–N(4) | 2.700(4) | 2.592(3) | Ln–N(5) | 2.773(3) | 2.646(3) |
| Ln–N(6) | 2.686(3) | 2.646(3) | Ln–N(7) | 2.735(3) | 2.681(3) |
| Ln–N(8) | 2.692(4) | 2.628(3) | | | |
| Se(1)–Sb–Se(2) | 108.852(17) | 111.395(19) | Se(1)–Sb–Se(3) | 111.017(18) | 108.248(16) |
| Se(1)–Sb–Se(4) | 108.424(17) | 108.882(16) | Se(2)–Sb–Se(3) | 109.311(18) | 107.715(18) |
| Se(2)–Sb–Se(4) | 111.521(18) | 109.06(2) | Se(3)–Sb–Se(4) | 107.722(18) | 111.558(17) |
| Se(1)–Ln–N | 69.60(7)–141.18(8) | 68.88(7)–141.04(7) | Sb–Se(1)–Ln | 102.926(15) | 103.837(17) |
| N–Ln–N | 62.77(10)–145.40(11) | 63.72(9)–144.65(9) | | | |

 © 2006 Wiley-VCH Verlag GmbH & Co. KGaA, Weinheim 

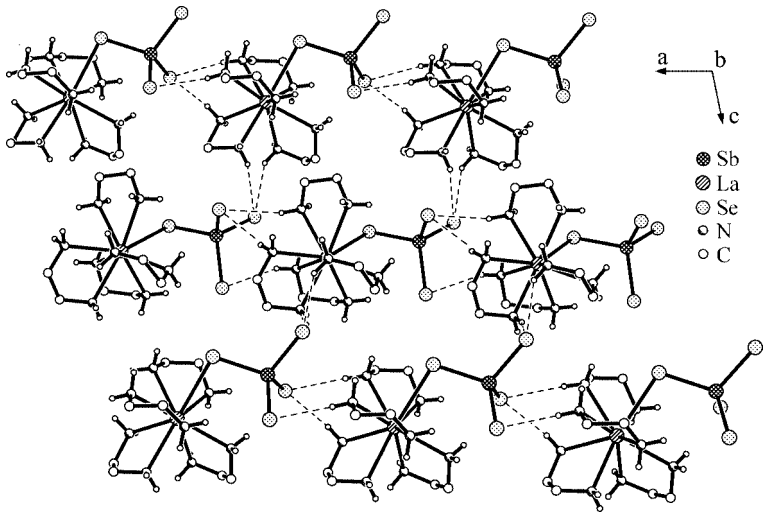


Figure 2. N–H···Se hydrogen bonds between the $[La(en)_4(SbSe_4)]$ molecules viewing along the *b* axis. Hydrogen atoms of C–H are omitted for clarity.

Table 2. Selected N···Se distances [Å] and N–H···Se angles [°] for **1** and **2**.

| N–H | Se | N···Se | N–H···Se |
|---|---|---|---|
| **1** | | | |
| N(1)–H(1A) | Se(4)[a] | 3.443(4) | 149.2 |
| N(1)–H(1B) | Se(3)[b] | 3.508(4) | 161.4 |
| N(2)–H(2A) | Se(3)[c] | 3.651(4) | 160.0 |
| N(3)–H(3A) | Se(4)[a] | 3.755(4) | 156.6 |
| N(5)–H(5A) | Se(3)[c] | 3.650(3) | 147.9 |
| N(6)–H(6A) | Se(4) | 3.589(4) | 164.3 |
| N(6)–H(6B) | Se(2) | 3.477(4) | 138.1 |
| N(7)–H(7B) | Se(2) | 3.597(4) | 167.7 |
| N(8)–H(8B) | Se(2)[a] | 3.546(4) | 149.1 |
| **2** | | | |
| N(1)–H(1A) | Se(4) | 3.476(3) | 139.4 |
| N(1)–H(1B) | Se(3) | 3.590(3) | 166.1 |
| N(2)–H(2A) | Se(2)[d] | 3.768(3) | 139.5 |
| N(2)–H(2B) | Se(2)[c] | 3.627(3) | 147.8 |
| N(4)–H(4A) | Se(2)[d] | 3.493(3) | 160.4 |
| N(4)–H(4B) | Se(3)[a] | 3.432(3) | 148.9 |
| N(5)–H(5B) | Se(3)[a] | 3.784(3) | 154.4 |
| N(6)–H(6B) | Se(3) | 3.616(3) | 173.0 |
| N(7)–H(7A) | Se(4) | 3.596(3) | 166.5 |
| N(8)–H(8A) | Se(4)[a] | 3.550(3) | 147.9 |

[a] Symmetry code: $x + 1, y, z$. [b] Symmetry code: $-x + 3/2, y - 1/2, -z + 3/2$. [c] Symmetry code: $x + 1/2, -y + 3/2, z - 1/2$. [d] Symmetry code: $-x + 3/2, y + 1/2, -z + 1/2$.

$[Ln(en)_4]SbS_4 \cdot 0.5en$ (Ln = Sm, Eu, Dy, Yb)[26,27] that are constructed from isolated $[Ln(en)_4]^{3+}$ and $SbS_4^{3-}$ ions. The two types of thioantimonates are related to the stability of the (en)lanthanide(III) complexes, coordination number, and the radii of the metal ions.[27] A similar situation is observed in the case of selenidoantimonate. The (en)lanthanide(III) complexes also form two kinds of selenidoantimonates with the $SbSe_4^{3-}$ anion in en. In **1** and **2**, $[Ln(en)_4]^{3+}$ (Ln = La, Nd) cations combine with $SbSe_4^{3-}$ through an Ln–Se bond, while $[Sm(en)_4]^{3+}$ does not bond with $SbSe_4^{3-}$ in **3**. Although the lanthanide(III) ions do not exhibit restricted stereochemistry in coordination complexes and are characterized by variable coordination numbers and geometries in the solid state,[36] it is commonly observed that the lighter lanthanide ions prefer coordination numbers of nine and heavier ones prefer coordination numbers of eight in solution.[37] Because en is a bidentate ligand, the $[La(en)_4]^{3+}$ and $[Nd(en)_4]^{3+}$ ions are bonded to the monodentate ligand $SbSe_4^{3-}$ to maintain the coordination number of nine for $La^{3+}$ and $Nd^{3+}$, and $[La(en)_4(SbSe_4)]$ and $[Nd(en)_4(SbSe_4)]$ are formed. It is worth noting

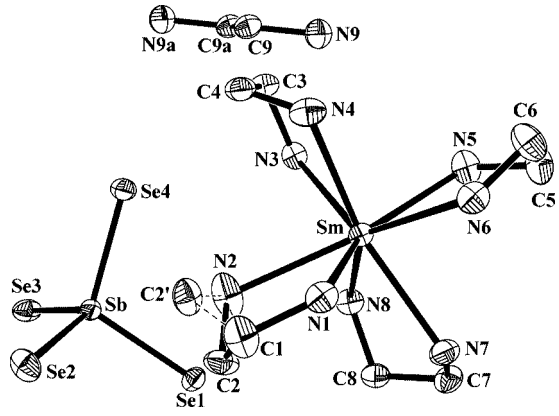


Figure 3. Crystal structure of **3** with labeling scheme. The probability ellipsoids are drawn at the 50% level; hydrogen atoms are omitted for clarity.

Table 3. Selected bond lengths [Å] and angles [°] for **3**.

| | | | |
|---|---|---|---|
| Sb–Se(1) | 2.4793(7) | Sb–Se(2) | 2.4601(8) |
| Sb–Se(3) | 2.4548(8) | Sb–Se(4) | 2.4640(8) |
| Sm–N(1) | 2.580(5) | Sm–N(2) | 2.615(6) |
| Sm–N(3) | 2.559(5) | Sm–N(4) | 2.533(5) |
| Sm–N(5) | 2.569(6) | Sm–N(6) | 2.580(5) |
| Sm–N(7) | 2.560(5) | Sm–N(8) | 2.547(5) |
| Se(1)–Sb–Se(2) | 105.33(3) | Se(1)–Sb–Se(3) | 109.28(3) |
| Se(1)–Sb–Se(4) | 110.06(3) | Se(2)–Sb–Se(3) | 113.74(3) |
| Se(2)–Sb–Se(4) | 108.99(3) | Se(3)–Sb–Se(4) | 109.35(3) |
| N–Sm–N | | 66.08(16)–154.23(17) | |

 © 2006 Wiley-VCH Verlag GmbH & Co. KGaA, Weinheim 

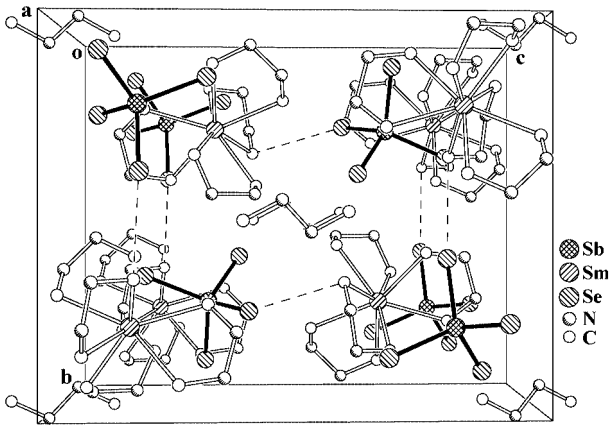


Figure 4. Crystal structure of $[Sm(en)_4]SbSe_4 \cdot 0.5en$ viewed along the *a* axis; hydrogen atoms are omitted for clarity.

that $SbS_4^{3-}$ and $SbSe_4^{3-}$ exhibit different coordination modes when bound to the same lanthanide ions. For example, in $[La(en)_3(\mu_3\text{-}SbS_4)]$, $SbS_4^{3-}$ acts as a $\mu_3$-$SbS_4$ tridentate ligand to interlink $[La(en)_3]^{3+}$ ions, while $SbSe_4^{3-}$ coordinates to the $[La(en)_4]^{3+}$ ion as a monodentate ligand in the compound $[La(en)_4(SbSe_4)]$. This structural difference can be interpreted in terms of the lower coordination ability of the $SbSe_4^{3-}$ anion with respect to $SbS_4^{3-}$. Compared with the $SbS_4^{3-}$ ligand, $SbSe_4^{3-}$is a soft-base ligand for the hard-acid cations of lanthanide(III) because of the larger radius of the selenium atom. Therefore, lanthanum can be coordinated with three sulfur atoms ($\mu_3$-$SbS_4$) and six nitrogen atoms to form the $\mu_3$-$SbS_4$ compound $[La(en)_3(\mu_3\text{-}SbS_4)]$ in a sulfide solution, but with one selenium atom and eight nitrogen atoms to form the mono-$SbSe_4$ compound $[La(en)_4(SbSe_4)]$ in a selenide solution.

## Optical Properties

The optical absorption spectra of compounds **1**–**3** show well-defined abrupt absorption edges from which the bandgaps were estimated as 2.22 eV for **1**, 2.33 eV for **2**, and 2.54 eV for **3** (see Figure 5). These bandgaps are larger than those of the multinary lanthanide polythioantimonates(III), such as $K_2La_2Sb_2S_9$ (2.20 eV)[38] and $La_2SbS_5Br$ (2.08 eV),[39] which are free of organic components.

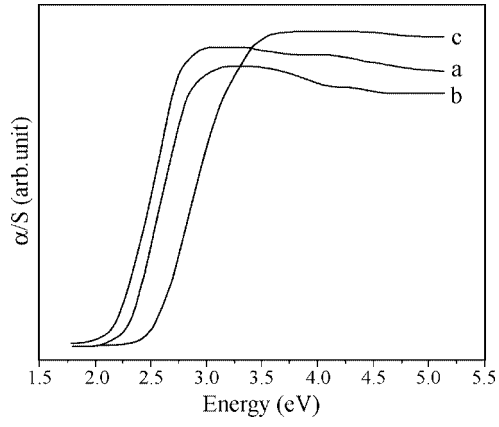


Figure 5. Optical absorption spectra of compounds **1** (a), **2** (b), and **3** (c).

## Thermal Investigations

On heating in a nitrogen stream, compound **1** starts to decompose at $T_{onset}$ = 190 °C with a weight loss of 29.2% (calcd. 29.4% for four en ligands) in one step. The weight loss is in good agreement with the theoretical value of 29.4% involving the complete removal of four en ligands. The decomposition process is accompanied by a strong endothermic signal in the DSC curve with peak temperature $T_p$ = 222 °C (Figure 6a). In the IR spectrum of the residue no H–N, H–C, C–N, and C–C vibrations could be detected. For **3**, thermal decomposition occurs in two steps with a weight loss of 3.0% (calcd. 3.5% for 0.5 en ligands) and 28.0% (calcd. 28.0% for four en ligands), which correspond with the removal of free en and coordinated en ligands, respectively. The two decomposition steps are accompanied by two endothermic signals in the DSC curve with peak temperatures of $T_p$ = 118 °C and $T_p$ = 236 °C (Figure 6b).

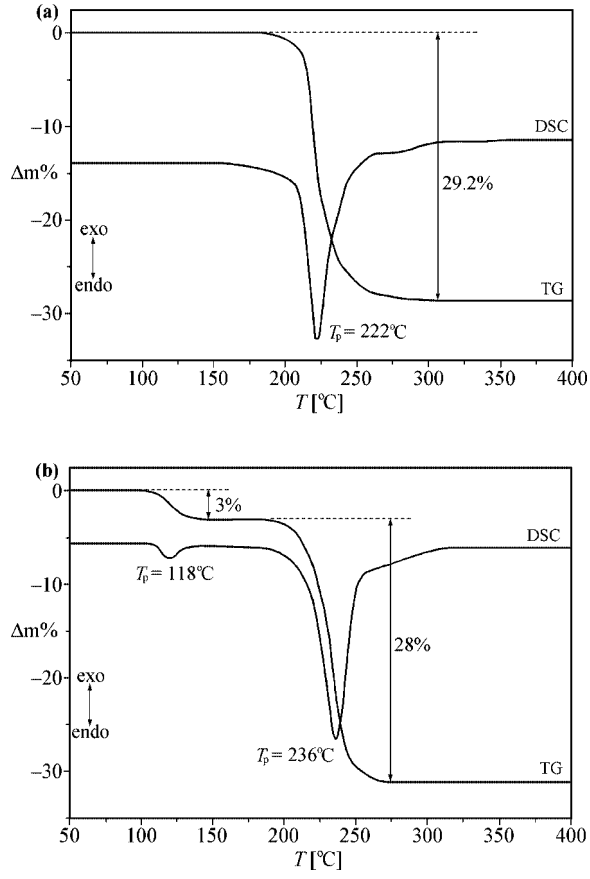


Figure 6. TG-DSC curves of compounds **1** (a) and **3** (b).

 © 2006 Wiley-VCH Verlag GmbH & Co. KGaA, Weinheim 

## Conclusions

The lanthanides(III) typically produce "hard"-acid cations, which preferentially bond to oxygen and nitrogen donor atoms in solution so it is a challenge to combine $Ln^{3+}$ ions with the so-called soft-base chalcogenometalate anions in an amine solvent. We have successfully synthesized novel selenidoantimonates containing lanthanide(III) in an en solvent under solvothermal conditions. $[Ln(en)_4(SbSe_4)]$ (Ln = La, Nd) and $[Sm(en)_4]SbSe_4{\cdot}0.5en$ are the first examples of solvothermally synthesized selenidoantimonates. The solvothermal method is a new route for the synthesis of multinary lanthanide selenides decorated by organic components. The synthesis and solid-state structural studies described in this article show that the soft-base ligand $SbSe_4^{3-}$ can coordinate to lanthanide(III) ions in an amine solution. This will shed light on a more complete understanding of the coordination chemistry of lanthanides(III) and preparation of lanthanide selenidometalates by mild solvothermal methods.

## Experimental Section

**General:** All analytical grade chemicals were obtained commercially and used without further purification. Elemental analysis was conducted with an MOD 1106 elemental analyzer. FT-IR spectra were recorded with a Nicolet Magna-IR 550 spectrometer using dry KBr discs in the 4000–400 $cm^{-1}$ range. Room-temperature optical diffuse reflectance spectra of the powdered samples were obtained with a Shimadzu UV-3150 spectrometer. The absorption ($\alpha$/S) data were calculated from the reflectance using the Kubelka–Munk function $\alpha/S = (1 - R)^2/2R$,[40] where $R$ is the reflectance at a given energy, $\alpha$ is the absorption, and S is the scattering coefficient. Thermoanalytical measurements were performed with a DCS-TGA microanalyzer of SDT 2960, and all the samples were heated under a nitrogen stream of 100 mL $min^{-1}$ with a heating rate of 5 °C $min^{-1}$.

**Synthesis of $[La(en)_4(SbSe_4)]$ (1):** The reactants $LaCl_3$ (122.6 mg, 0.5 mmol), Sb (61 mg, 0.5 mmol), and Se (158 mg, 2 mmol) were mixed in ethylenediamine (3 mL) whilst stirring. The mixture was loaded into a Teflon-lined stainless steel autoclave with an inner volume of 15 mL, and the sealed autoclave was then heated to 140 °C for 7 d. After cooling to ambient temperature, orange block crystals of **1** were obtained. The crystals were washed with ethanol and diethyl ether, dried and stored under vacuum. Yield: 188 mg (46%). $C_8H_{32}LaN_8SbSe_4$ (816.92): calcd. C 11.86, H 3.95, N 13.72; found C 11.81, H 3.92, N 13.66. IR (KBr): $\tilde{\nu}$ = 3383 (s), 3241 (s), 3106 (s), 2924 (s), 2870 (m), 1582 (vs), 1489 (s), 1454 (s), 1385 (m), 1327 (s), 1277 (m), 1146 (w), 1103 (w), 1007 (vs), 860 (w), 822 (w), 633 (m), 494 (m) $cm^{-1}$.

**Synthesis of $[Nd(en)_4(SbSe_4)]$ (2):** Orange-yellow platelet crystals of **2** were obtained by using a similar synthesis procedure to that used in **1** except that reactant $LaCl_3$ was replaced by $NdCl_3$. Yield: 226 mg (55%). $C_8H_{32}N_8NdSbSe_4$ (822.25): calcd. C 11.69, H 3.92, N 13.63; found C 11.54, H 3.88, N 13.60. IR (KBr): $\tilde{\nu}$ = 3335 (s), 3240 (s), 3167 (s), 2940 (s), 2870 (s), 1597 (s), 1578 (s), 1481, 1459 (s), 1385 (m), 1354 (s), 1214 (w), 1157 (w), 1080 (s), 1030 (vs), 822 (w), 779 (w), 640 (s), 513 (w), 440 (m) $cm^{-1}$.

**Synthesis of $[Sm(en)_4]SbSe_4{\cdot}0.5en$ (3):** Yellow prism crystals of **3** were obtained by using a similar synthesis procedure to that used in **1** except that reactant $LaCl_3$ was replaced by $SmCl_3$. Yield: 223 mg (52%). $C_9H_{36}N_9SbSe_4Sm$ (858.41): calcd. C 12.59, H 4.23, N 14.68; found C 12.54, H 4.25, N 14.62. IR (KBr): $\tilde{\nu}$ = 3301 (vs), 3280 (s), 3245 (s), 3132 (s), 2930 (vs), 2880 (s), 1570 (vs), 1515 (s), 1385 (m), 1331 (s), 1157 (w), 1007 (s), 868 (w), 814 (w), 776 (w), 660 (w), 498 (m) $cm^{-1}$.

**X-ray Crystal Structure Determinations:** A summary of crystal data and refinement parameters is given in Table 4. Data were collected with a Rigaku Mercury CCD diffractometer at 193(2) K using graphite-monochromated Mo-$K_\alpha$ radiation ($\lambda$ = 0.71073 Å) by an $\omega$-scan method with a maximum $2\theta$ value of 54.96°. An orange $0.22 \times 0.15 \times 0.10$ mm block crystal of **1**, an orange-yellow $0.46 \times 0.28 \times 0.05$ mm platelet crystal of **2**, and a yellow $0.35 \times 0.06 \times 0.05$ mm prism crystal of **3** were used for data collection. An absorption correction was applied for all the compounds using a multi-scan correction method. The structures were solved by direct methods using the SHELXS-97 program.[41] The refinement was performed against $F^2$ using the SHELXL-97 program.[42]

Table 4. Crystallographic data for **1**, **2**, and **3**.

| | **1** | **2** | **3** |
|---|---|---|---|
| Empirical formula | $C_8H_{32}N_8Se_4LaSb$ | $C_8H_{32}N_8Se_4NdSb$ | $C_9H_{36}N_9Se_4SmSb$ |
| Formula mass [g $mol^{-1}$] | 816.92 | 822.25 | 858.41 |
| Crystal system | monoclinic | monoclinic | monoclinic |
| Space group | $P2_1/n$ | $P2_1/n$ | $P2_1/n$ |
| $a$ [Å] | 9.4711(6) | 9.473(2) | 11.3777(8) |
| $b$ [Å] | 14.6905(9) | 14.625(3) | 13.1107(9) |
| $c$ [Å] | 16.0388(10) | 15.937(3) | 16.3772(11) |
| $\beta$ [°] | 98.920(2) | 98.847(4) | 92.400(2) |
| $V$ [Å$^3$] | 2204.6(2) | 2181.6(8) | 2440.8(3) |
| $Z$ | 4 | 4 | 4 |
| $T$ [K] | 193(2) | 193(2) | 193(2) |
| $D_{calcd.}$ [g $cm^{-3}$] | 2.461 | 2.503 | 2.336 |
| $\mu$(Mo-$K_\alpha$) [$mm^{-1}$] | 9.749 | 10.273 | 9.466 |
| Measured reflections | 24400 | 24034 | 26983 |
| Independent reflections | 5034 | 4996 | 5575 |
| Reflections with $I > 2\sigma(I)$ | 4537 | 4496 | 4659 |
| $R_{int}$ | 0.0396 | 0.0533 | 0.0653 |
| $R(F)$ [$F^2 > 2\sigma(F^2)$][a] | 0.0308 | 0.0276 | 0.0444 |
| $R_w(F^2)$ (all data)[b] | 0.0595 | 0.0609 | 0.0930 |
| Largest difference peak/hole [e Å$^{-3}$] | 0.670/–1.111 | 1.087/–1.762 | 1.207/–1.497 |

[a] $R_1 = \Sigma||F_o| - |F_c||/\Sigma|F_o|$. [b] $wR_2 = \{\Sigma[w(F_o^2 - F_c^2)^2]/\Sigma[w(F_o^2)^2]\}^{1/2}$.

 © 2006 Wiley-VCH Verlag GmbH & Co. KGaA, Weinheim 

All the non-hydrogen atoms were refined anisotropically. The hydrogen atoms were positioned with idealized geometries and refined with fixed isotropic displacement parameters using a riding model. The H atoms of C(1), C(2), and N(2) in **3** were not dealt with because of the disorder of atom C(2). CCDC-299097 (**1**), -299098 (**2**), and -299099 (**3**) contain the supplementary crystallographic data for this paper. These data can be obtained free of charge from the Cambridge Crystallographic Data Centre via www.ccdc.cam.ac.uk/data_request/cif.

## Acknowledgments

This work was supported by the Natural Science Foundation of the Education Committee of Jiangsu Province (No. 05KJB150110) and the National Natural Science Foundation of P. R. China (No. 20071024, 20371033).

[1] W. S. Sheldrick, M. Wachhold, *Coord. Chem. Rev.* **1998**, *176*, 211–322.
[2] J. Li, Z. Chen, R. J. Wang, D. M. Proserpio, *Coord. Chem. Rev.* **1999**, *190–192*, 707–735.
[3] W. S. Sheldrick, *J. Chem. Soc., Dalton Trans.* **2000**, 3041–3052.
[4] H. O. Stephan, M. G. Kanatzidis, *J. Am. Chem. Soc.* **1996**, *118*, 12226–12227.
[5] H. O. Stephan, M. G. Kanatzidis, *Inorg. Chem.* **1997**, *36*, 6050–6057.
[6] W. Bensch, M. Schur, *Z. Naturforsch., Teil B* **1997**, *52*, 405–409.
[7] M. Schur, W. Bensch, *Z. Naturforsch., Teil B* **2002**, *57*, 1–7.
[8] P. Vaqueiro, A. M. Chippindale, A. V. Powell, *Inorg. Chem.* **2004**, *43*, 7963–7965.
[9] W. Bensch, C. Näther, R. Stähler, *Chem. Commun.* **2001**, 477–478.
[10] R. Stähler, C. Näther, W. Bensch, *Eur. J. Inorg. Chem.* **2001**, 1835–1840.
[11] R. Stähler, B.-D. Mosel, H. Eckert, W. Bensch, *Angew. Chem. Int. Ed.* **2002**, *41*, 4487–4489.
[12] R. Stähler, W. Bensch, *Z. Anorg. Allg. Chem.* **2002**, *628*, 1657–1662.
[13] R. Kiebach, F. Studt, C. Näther, W. Bensch, *Eur. J. Inorg. Chem.* **2004**, 2553–2556.
[14] R. Kiebach, W. Bensch, R.-D. Hoffmann, R. Pöttgen, *Z. Anorg. Allg. Chem.* **2003**, *629*, 532–538.
[15] R. Stähler, W. Bensch, *Eur. J. Inorg. Chem.* **2001**, 3073–3078.
[16] M. Schaefer, R. Stähler, W.-R. Kiebach, C. Näther, W. Bensch, *Z. Anorg. Allg. Chem.* **2004**, *630*, 1816–1822.
[17] R. Stähler, W. Bensch, *J. Chem. Soc., Dalton Trans.* **2001**, 2518–2522.
[18] M. Schaefer, C. Näther, W. Bensch, *Solid State Sci.* **2003**, *5*, 1135–1139.
[19] M. Schaefer, C. Näther, N. Lehnert, W. Bensch, *Inorg. Chem.* **2004**, *43*, 2914–2921.
[20] Schur, W. Bensch, *Z. Anorg. Allg. Chem.* **1998**, *624*, 310–314.
[21] M. A. Pell, J. A. Ibers, *Inorg. Chem.* **1996**, *35*, 4559–4562.
[22] W. Bensch, C. Näther, M. Schur, *Chem. Commun.* **1997**, 1773–1774.
[23] F. Wendland, C. Näther, M. Schur, W. Bensch, *Acta Crystallogr. Sect. C* **1998**, *54*, 317–319.
[24] R. Blachnik, A. Fehlker, H. Reuter, *Z. Kristallogr.* **2001**, *216*, 211–212.
[25] Z. Chen, R.-J. Wang, X.-Y. Huang, J. Li, *Acta Crystallogr. Sect. C* **2000**, *56*, 1100–1103.
[26] D. X. Jia, Q. Y. Zhu, J. Dai, W. Lu, W. J. Guo, *Inorg. Chem.* **2005**, *44*, 819–821.
[27] D. X. Jia, Q. X. Zhao, Y. Zhang, J. Dai, J. L. Zou, *Inorg. Chem.* **2005**, *44*, 8861–8867.
[28] D. X. Jia, Y. Zhang, J. Dai, Q. Y. Zhu, X. M. Gu, *Z. Anorg. Allg. Chem.* **2004**, *630*, 313–318.
[29] D. X. Jia, J. Dai, Q. Y. Zhu, Y. Zhang, X. M. Gu, *Polyhedron* **2004**, *23*, 937–942.
[30] D. X. Jia, Y. Zhang, J. Dai, Q. Y. Zhu, X. M. Gu, *J. Solid State Chem.* **2004**, *177*, 2477–2483.
[31] D. X. Jia, J. Dai, Q. Y. Zhu, L. H. Cao, H. H. Lin, *J. Solid State Chem.* **2005**, *178*, 874–881.
[32] J. Li, Z. Chen, F. Chen, D. M. Proserpio, *Inorg. Chim. Acta* **1998**, *273*, 255–258.
[33] J. H. Chen, P. Dorhout, *Inorg. Chem.* **1995**, *34*, 5705–5706.
[34] I. Ijjaali, B. Deng, J. A. Ibers, *J. Solid State Chem.* **2005**, *178*, 1503–1507.
[35] S. Dehnen, C. Zimmermann, *Z. Anorg. Allg. Chem.* **2002**, *628*, 2463–2469.
[36] A. Cassol, P. Di Bernardo, R. Portanova, M. Tolazzi, G. Tomat, P. Zanonato, *J. Chem. Soc., Dalton Trans.* **1992**, 469–474.
[37] C. Cossy, A. C. Barnes, J. E. Enderby, A. E. Merbach, *J. Chem. Phys.* **1989**, *90*, 3254–3259.
[38] K. S. Choi, J. A. Hanko, M. G. Kanatzidis, *J. Solid State Chem.* **1999**, *147*, 309–319.
[39] D. Gout, S. Jobic, M. Evain, R. Brec, *Solid State Sci.* **2001**, *3*, 223–234.
[40] W. W. Wendlandt, H. G. Hecht, *Reflectance Spectroscopy*, Interscience Publishers, New York, **1966**.
[41] G. M. Sheldrick, *SHELXS-97, Program for Crystal Structure Determination*, University of Göttingen, Germany, **1997**.
[42] G. M. Sheldrick, *SHELXL-97, Program for the Refinement of Crystal Structures*, University of Göttingen, Germany, **1997**.

Received: February 22, 2006
Published Online: May 3, 2006

 © 2006 Wiley-VCH Verlag GmbH & Co. KGaA, Weinheim 

DOI: 10.1002/ejic.200600171

# Semicarbazide-Functionalized Silicate Nanoparticles for Peptide Ligation

Tristan Doussineau,[b] Jean-Olivier Durand,[c] Ouafâa El-Mahdi,[a] Céline Maillet,[a] Oleg Melnyk,[a] Christophe Olivier,[a] and Monique Smaïhi*[b]

**Keywords:** Zeolites / Colloids / Peptides / Fluorescence spectroscopy / Organic–inorganic composites

Monodisperse silicate nanoparticles have been used for the development of a site-specific ligation method that enables the control of the biomolecule orientation at the solid–liquid interface. Two types of zeolite nanoparticles were studied: zeolite β, which possesses a Si/Al ratio of 25, and silicalite-1, which is a fully silicic material. Zeolite-type materials are microporous silicate with pores of a well-defined size ranging from 2 to 20 Å. Semicarbazide-functionalized silicate colloids have been prepared for the site-specific ligation of COCHO-modified polypeptides. The obtained colloidal suspensions have been characterized by complementary techniques providing information on the size distribution, morphology, and porosity of the particles and chemical nature of the grafting. The specificity of the particles' surface for the semicarbazide group has been studied by fluorescence spectroscopy with two peptides labeled with rhodamine. A first peptide bares a COCHO functionality, which should bind covalently with the semicarbazide surface. The second peptide bares an amine end-group, which should interact by nonspecific adsorption with the surface. The results demonstrated that the peptide/colloids' reactivity is dramatically influenced by the chemical composition of the particles' surface. Indeed, while zeolite β (aluminosilicate) particles react indifferently with the two peptides, silicalite particles (pure silicate) anchor exclusively the peptide bearing the COCHO functionality. This particular physisorption phenomenon of zeolite β is attributed to the aluminum atoms present at the particles' surface, which have a specific affinity for peptides.
(© Wiley-VCH Verlag GmbH & Co. KGaA, 69451 Weinheim, Germany, 2006)

## Introduction

Nanoparticles (NPs) have great promise in bioanalysis and biotechnological applications because of their unique optical properties, high surface-to-volume ratio, and other size-dependent qualities.[1–3] When combined with surface modifications and composition control, these properties provide probes for highly selective and ultrasensitive bioassays.

The use of silica as a substrate in bioanalysis has a special advantage, as shown by its widespread use in biosensors and biochips. Silica can be synthesized by various preparation techniques to prepare NPs, transparent films, or solid flat materials.[4] Silica synthesis is governed by the chemical properties of the surface, which, in return, are based on the silanols and siloxanes present on the surface.[5] Silanol groups can be functionalized through different procedures.[6,7] Therefore, the versatility of silica in synthesis aspects as well as surface modifications offers a great advantage to the use of the materials in bioanalysis.

Among inorganic materials, the synthesis and studies of nanosized zeolites have attracted considerable attention in the last decade.[8] Zeolite-type materials are microporous silicate crystals with pores of a well-defined size ranging from 2 to 20 Å. This discrete pore system gives molecular sieve properties to these materials, which have found great utility as catalysts and sorption media. Lately, functionalized zeolite nanoparticles were envisaged for the preparation of controlled release capsules, artificial cells, chemical sensors, and adsorbents.

In many cases, covalent attachment of a biomolecule at the NPs' surface is preferred to avoid leaching of the biomolecules. The usual pathways for covalent attachment of biomolecules on silica surfaces consist of their functionalization by epoxides,[9] aldehydes,[10] or thiol groups.[11] However, as biomolecules usually possess more than one nucleophilic group, a random immobilization through multiple points of attachment is often observed.[12] Therefore, site-specific ligation methods are highly desired in order to control the biomolecule orientation at the solid–liquid interface.

Recently, we have described the preparation of α-oxo aldehyde (COCHO)- and semicarbazide-functionalized silica, for the site-specific ligation of hydrazinoacetyl- or COCHO-modified polypeptides.[13] Indeed α-oxo aldehyde peptides were shown to react chemoselectively and readily

[a] Biological Institute of Lille, UMR 8161 CNRS/Université de Lille 2/Institut Pasteur de Lille,
1 rue du Pr Calmette, 59021 Lille Cedex, France
E-mail: oleg.melnyk@ibl.fr
[b] IEM, UMR 5635 CNRS-ENSCM-UM2,
1919 route de Mende, 34193 Montpellier Cedex 5, France
E-mail: monique.smaihi@iemm.univ-montp2.fr
[c] Laboratoire de Chimie Moléculaire et Organisation du Solide, UMR 5637, case 007-Université Montpellier II,
Place Eugène Bataillon, 34095 Montpellier Cedex 5, France
Fax: +33-46714-3852
E-mail: durand@univ-montp2.fr

 © 2006 Wiley-VCH Verlag GmbH & Co. KGaA, Weinheim 

with the surface semicarbazide groups in very mild aqueous conditions. The α-oxohydrazone bond was readily formed and was very stable; no further reduction of the hydrazone bond was needed.

We have extended the α-oxo hydrazone chemistry to monodisperse silicate nanoparticles using α-oxo aldehyde peptides labeled with rhodamine. Two types of zeolite nanoparticles were studied: zeolite β and silicalite-1. Here, we describe the preparation of these nanoparticles, and their reactivity and selectivity for the covalent immobilization of COCHO-modified polypeptides.

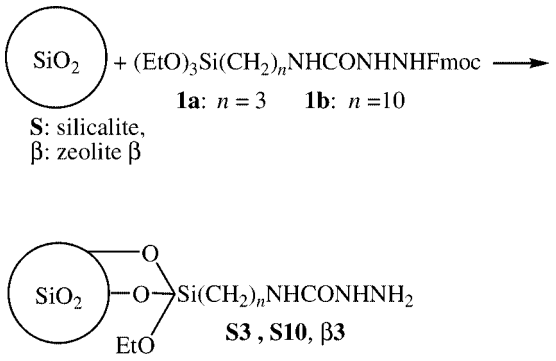


Scheme 1. Semicarbazide grafting chemistry (Fmoc: fluorenylmethoxycarbonyl).

## Results and Discussion

Two types of samples have been used, differing mainly in their chemical composition: while silicalite is an "all-silica" zeolite, zeolite β contains aluminum atoms in its framework, with a Si/Al ratio that can be varied between 10 and 500. The zeolite β samples prepared in this study have a Si/Al ratio equal to 25.

As-synthesized zeolites contain an organic structure-directing agent (SDA) located in the framework channels. The SDA removal of zeolites through calcination is a common method employed to reveal the zeolite micropores, where the organic structure-directing agent is burned away. As-synthesized nanoparticles as well as template-free colloids have been used in this study as substrates for peptide ligation.

The anchoring of the peptides at the surface of these colloidal nanoparticles has been done in two steps. First, a semicarbazide coupling agent (SC) has been anchored at the colloids' surface followed by the grafting of peptides labeled with rhodamine. The specificity of the anchoring has been studied using two different peptides. One peptide molecule bares a COCHO functionality, which reacts covalently with the SC. The other peptide should only interact with the SC surface through physisorption, as it lacks the COCHO functionality.

Regardless of the zeolite framework and peptide used, stable colloidal suspensions were obtained for all samples. The different stages of the preparation procedure are presented in Scheme 1 and Scheme 2.

Subsequently, at each step of the preparation procedure, the size and morphology of the nanoparticles were studied by dynamic light scattering (DLS) and SEM. The influence of the various treatments on the porous characteristics of the samples has been analyzed by nitrogen sorption experiments.

$^{29}Si$ and $^{13}C$ NMR were performed also at each step of the preparation procedure in order to characterize the surface bonding.

Finally, the specificity of the peptide anchoring was investigated by fluorescence spectroscopy.

The zeolite β and silicalite-1 nanoparticles are called **β** and **S**, respectively, in the following text, and the template-free silicalite and zeolite β nanoparticles are named tf-**S** and tf-**β**, respectively.

As indicated in Scheme 1, functionalization of zeolite **β** and silicalite **S** with silane **1a** leads to **β3** and **S3**, respectively. Alternatively, reaction of silanes **1** on template-free zeolite nanoparticles gives tf-**β3**, tf-**S3**, and tf-**S10**.

As indicated in Scheme 2, grafting of peptides **i** on nanoparticles of zeolite **β3** and silicalite **S3** leads to samples **β3-i** and **S3-i**.

### Particle Size and Morphology

The DLS study performed after each step of the preparation procedure shows that the average diameter of the particles increases after the grafting procedure (Table 1, Fig-

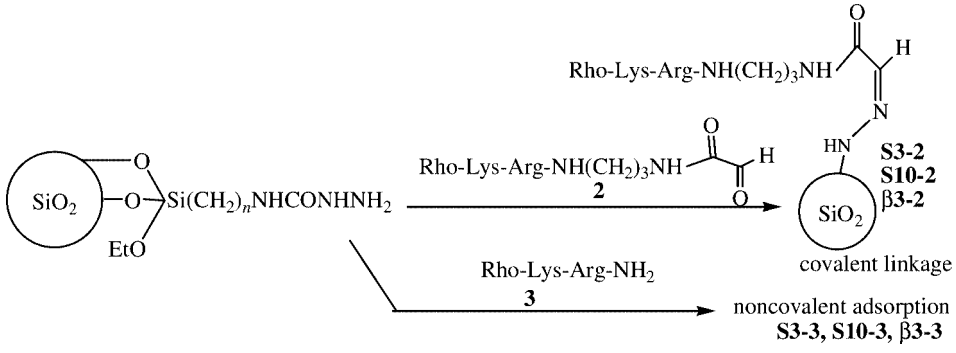


Scheme 2. Peptide grafting chemistry.

 © 2006 Wiley-VCH Verlag GmbH & Co. KGaA, Weinheim 

ure 1). According to the DLS measurements, the average particle sizes of the initial zeolite β and silicalite-1 nanoparticles are about 57 and 64 nm respectively. After functionalization, the **β3**- and **S3**-grafted colloids show average particle sizes around 140 nm (Table 1). The same tendency is observed for template-free colloids. This increase in the average particle size does not only reflect the presence of anchored organic groups at the colloids' surface. Indeed, the maximum particle diameter increase in the case of SC10 functions would be about 4 nm. Therefore the average particle size increase is attributed to a modification of the colloids' surface reactivity after grafting, which leads to the adsorption of solvent molecules, which, in return, increases their hydrodynamic diameter. This effect is well known for silica colloids.[14] The stability of the final colloidal suspensions will enable the use of conventional spectroscopic techniques to study the particles grafted with rhodamine-labeled peptides.

SEM of the samples before and after functionalization (Figure 2) does not show morphological differences between the as-prepared and grafted samples. As these observations are performed on dry particles, sizes derived by this measurement do not take into account any adsorbed solvent crown. Therefore, the particle sizes observed by SEM can be considered as bulk (or core) sizes and are not in contradiction with those measured by DLS.

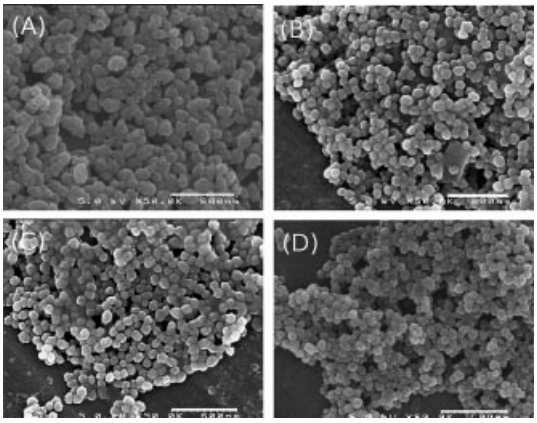


Figure 2. SEM micrographs of silicalite nanoparticles at various steps of the preparation: (A) as-synthesized **S** colloids, (B) **S3** particles, (C) tf-**S3** particles, and (D) tf-**S10** suspensions. Scale bar: 600 nm.

## Microporosity

In order to follow the influence of the various treatments on the porous characteristics of the zeolite samples, nitrogen gas sorption analyses were performed on the as-synthesized nanoparticles and the grafted nanoparticles. The zeolite microporosity is revealed by $N_2$ adsorption on template-free samples (ca. 0.2 $cm^3 \cdot g^{-1}$) and the specific surface area

Table 1. DLS, $N_2$ adsorption/desorption, and elemental analysis data obtained for the as-synthesized, calcined, and grafted particles.

| | Average diameter [nm ± 5%] | Specific area [$m^2 \cdot g^{-1}$] | Micropore volume [$cm^3 \cdot g^{-1}$] | % N | % C | Loading[a] [$\mu mol \cdot g^{-1}$] | Loading[b] [$\mu mol \cdot g^{-1}$] |
|---|---|---|---|---|---|---|---|
| **β** | 57 | 224 | 0.098 | 1.65 | 12.50 | 0 | 0 |
| **β3** | 114 | 168 | 0.044 | 3.65 | 14.55 | 1.2 | 476 |
| tf-**β** | 62 | 439 | 0.142 | 0 | 0 | 0 | 0 |
| tf-**β3** | 163 | 223 | 0.082 | 2.61 | 8.27 | 2 | 621 |
| **S** | 64 | 75 | 0 | 0.76 | 9.85 | 0 | 0 |
| **S3** | 145 | 80 | 0 | 1.6 | 10.74 | 0.6 | 200 |
| tf-**S** | – | 505 | 0.155 | 0 | 0 | 0 | 0 |
| tf-**S3** | 145 | 370 | 0.107 | 1.48 | 4.31 | 2.4 | 352 |
| tf-**S10** | 147 | 217 | 0.056 | 1.17 | 7.98 | 1.5 | 278 |

[a] Theoretical values. [b] Measured from elemental analysis.

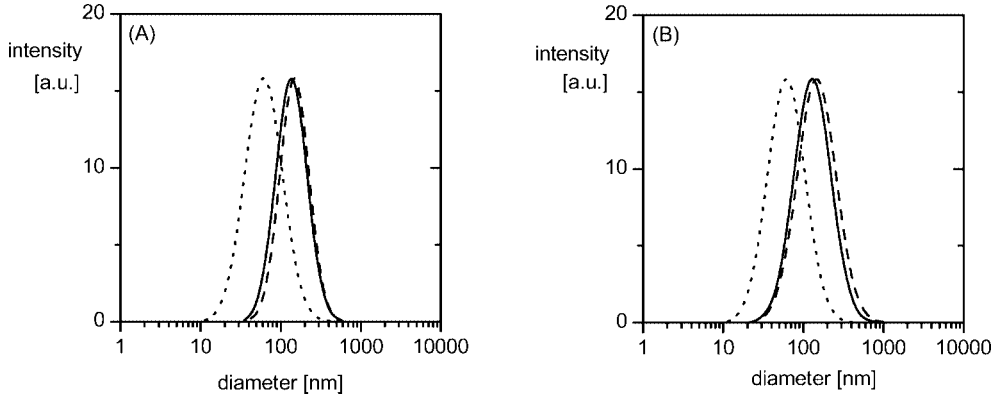


Figure 1. DLS profiles of silicalite nanoparticles at various steps of the preparation: (A) as-synthesized **S** colloids (dotted line), **S3** particles (solid line), and **S10** suspensions (dashed line); (B) as-synthesized **S** colloids (dotted line), tf-**S3** particles (solid line), and tf-**S10** suspensions (dashed line).

 © 2006 Wiley-VCH Verlag GmbH & Co. KGaA, Weinheim 

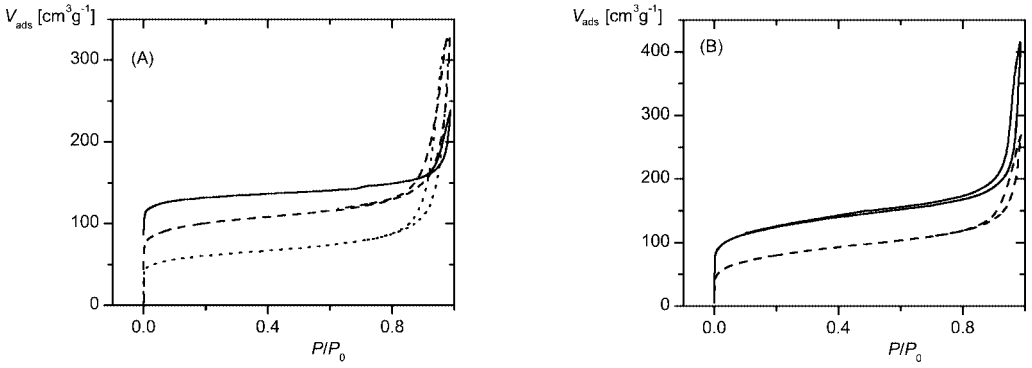


Figure 3. $N_2$ adsorption isotherms of silicalite nanoparticles (A) and zeolite β colloids (B): tf-**S** and tf-**β** (solid line), tf-**S3** and tf-**β3** (dashed line), tf-**S10** (dotted line).

is dramatically increased (ca. 3 times that of the as-synthesized samples) (Table 1). Grafting the zeolite nanoparticles, regardless of the structure used (β or silicalite-1), slightly decreases the specific surface area of the template-free sample (Table 1, Figure 3). This decrease of the micropore volume may indicate that some part of the grafting occurs inside the micropores. However, this decrease of the micropore volume is also observed for silane **1b**-grafted silicalite (tf-**S10** samples), although the size of this molecule forbids its entry through the pores. Therefore, the decrease of the measured micropore volume may be due to a decrease of its accessibility to $N_2$ (because of the presence of functional groups) instead of an actual decrease.

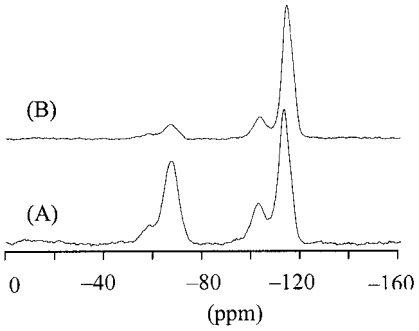


Figure 4. $^{29}$Si CP-MAS NMR spectra recorded for **S3** (A) and **S10** (B) samples.

### Grafting Quantification

Elemental analysis (N and C) allowed determination of the loading of the nanoparticles after the grafting procedure (Table 1). Assuming that each grafted silane molecule occupies 24 Å$^2$, the theoretical loading for a monolayer ranges between 0.55 and 2.4 mmol·g$^{-1}$ depending on the specific surface area of the particles (Table 1).[15–18] As the experimental loading is below a monolayer coverage for each sample, this shows that the microporosity of the nanoparticles is not accessible for silanes **1a** and **1b**.

### Grafting Analysis

CPMAS $^{29}$Si NMR spectra of **S3** and **S10** nanoparticles present signals at $\delta$ = –101 and –110 ppm (Figure 4). Around –110 ppm, the overlapping resonances for both samples are assigned to zeolite framework silicon atoms. Resonances around –113/–115 ppm and –109/–110 ppm are assigned to *Si*(OSi)$_4$, Q4 species with minor resolution of the crystallographic sites. The signal at $\delta$ = –100 ppm is assigned to *Si*(OSi)$_3$OH, Q3 species.[19] The presence of a signal between –60 and –70 ppm indicates that silane **1** is covalently linked to the zeolite framework silicon atoms. Two resonances are observed corresponding to Si attached to the organic chain in two different chemical environments [–67 ppm: C–*Si*–(OSi)$_3$, T3 and –60 ppm: C–*Si*–(OSi)$_2$OH, T2 species].[20]

The presence of T2–T3 species, the absence of T1, C–*Si*(OSi)(OH)$_2$ and Q2, *Si*(OSi)$_2$(OH)$_2$ species and finally the variation in signal intensity for species Q3 and Q4 relative to bare particles demonstrated the efficient grafting of silane **1** on the surface of **S3** and **S10** nanoparticles. Spectra recorded on samples **S3** and **S10** present significant differences in the relative intensity of these characteristic resonances. Although, in the case of CP-MAS spectra, the peak intensity is not directly proportional to the species abundance, this intensity difference may reflect a greater grafting loading for silane **1a** than silane **1b**. This is a further confirmation of the elemental analysis results, which gave a higher coverage for a functionalization with silane **1a** than silane **1b**.

The CPMAS $^{13}$C spectrum of **S3** nanoparticles presents three resonances situated at 9.7, 22.7 and 42.9 ppm corresponding to the propyl chain of silane **1a** (Figure 5). The additional resonance at $\delta$ = 162.1 ppm is attributed to the carbonyl group of the semicarbazide function. Signals corresponding to ethoxy groups or fluorenylmethoxycarbonyl (Fmoc) groups were not detected. This indicates the completion of the grafting reaction and the quality of the centrifugation–redispersion procedure.

$^{29}$Si and $^{13}$C MAS NMR characterization of zeolite β nanoparticles leads to similar spectra presenting the characteristic resonances of T species around –60 ppm for $^{29}$Si spectra and the carbonyl resonance at –162 ppm for $^{13}$C spectra.

 © 2006 Wiley-VCH Verlag GmbH & Co. KGaA, Weinheim 

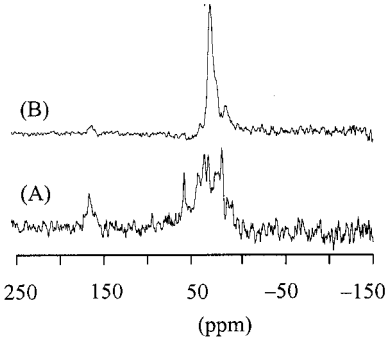


Figure 5. $^{13}C$ CP-MAS NMR spectra recorded for **S3** (A) and **S10** (B) samples.

### Fluorescence Analysis

The nature of the interaction of peptides **2** and **3** with substrates **S**, **β**, **β3**, tf-**β3**, **S3**, and tf-**S10** was analyzed by fluorescence spectroscopy.

First, we checked the eventuality of nonspecific adsorption of peptides **2** and **3** on bare nanoparticles of zeolite **β** and silicalite **S**. After mixing peptides **2** and **3** with zeolite **β** nanoparticles, an intense fluorescence is observed (Figure 6). Meanwhile, very weak fluorescence intensity is obtained for samples based on silicalite **S** (Figure 6). Therefore, this indicates that the zeolite **β** surface is able to immobilize peptides by noncovalent interactions. This physisorption phenomenon is attributed to the presence of aluminum atoms at the zeolite **β** surface, which have been reported to present an affinity for peptides.[21] Fluorescence spectra registered on functionalized samples, **β3** and tf-**β3** treated with peptides **2** and **3**, presented an intense fluorescence for all samples, regardless of the peptide's nature (Figure 7). Therefore, interactions between peptides **2** or **3** and the zeolite **β** surface occurred even after surface modification. Indeed, as the fluorescence intensity observed for samples prepared with peptide **3** is higher than that obtained with peptide **2**, nonspecific adsorption is a highly probable phenomenon for samples based on zeolite **β**.

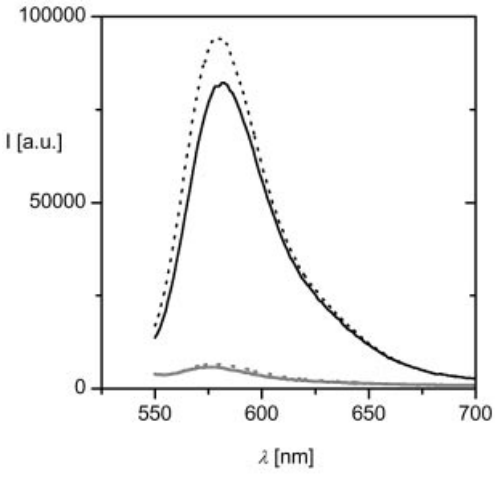


Figure 6. Fluorescence emission spectra of samples obtained after reaction between peptides **2** (dotted line) and **3** (solid line) with nanoparticles of zeolite **β** (black lines) and silicalite **S** (gray lines).

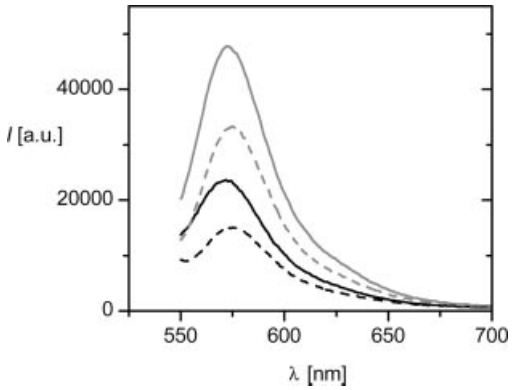


Figure 7. Fluorescence emission spectra of samples obtained after reaction between peptides **2** (dotted line) and **3** (solid line) with nanoparticles of zeolite **β3** (black lines) and tf-**β3** (gray lines).

By contrast, fluorescence spectra obtained with silicalite-based samples indicate a higher level of chemoselectivity. Therefore, for all these silicalite-based samples, the extent of physisorption was low and immobilization occurred mainly through the formation of a covalent bond between the semicarbazide groups on the surface and the α-oxo aldehyde group on the peptide molecule (Figure 8 and Figure 9). Fluorescence intensity ratio between samples **S3** obtained with peptide **3** and **2** (**S3-2/S3-3**) is around 40, showing that noncovalent interactions are rare with silicalite **S** (Figure 9).

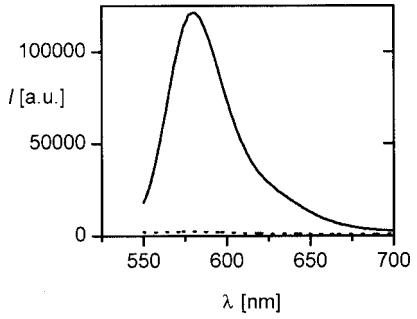


Figure 8. Fluorescence emission spectra of samples obtained after reaction between peptides **2** (dotted line) and **3** (solid line) with nanoparticles **S3**.

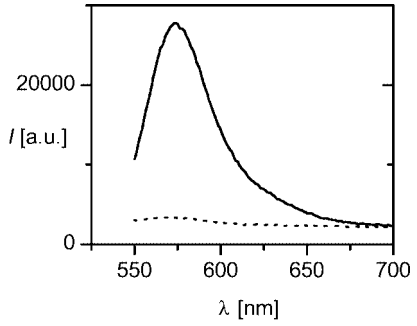


Figure 9. Fluorescence emission spectra of samples obtained after reaction between peptides **2** (dotted line) and **3** (solid line) with tf-**S10** nanoparticles.

 © 2006 Wiley-VCH Verlag GmbH & Co. KGaA, Weinheim 

A similar fluorescence intensity ratio is obtained with tf-**S10** samples reacted with peptide **3** and **2** (Figure 9). Therefore, this demonstrates that whatever the micropore volume or the spacer length of the silicalite substrate, COCHO-modified polypeptides are specifically and covalently immobilized on silicalite surfaces.

Comparison of fluorescence spectra obtained for **S3**, tf-**S3**, and tf-**S10** samples of identical concentrations indicates a lower fluorescence intensity for tf-**S10** samples (Figure 10). This may be attributed to the lower loading obtained for these samples for silane **1b** than silane **1a** (Table 1).

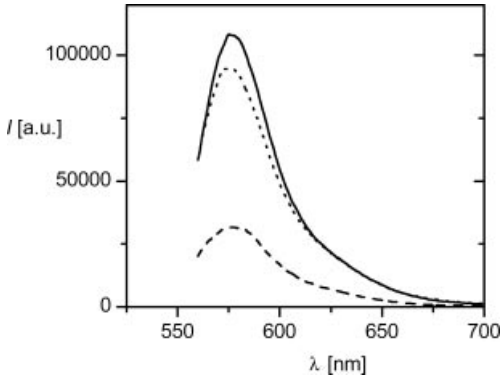


Figure 10. Fluorescence emission spectra of samples obtained after reaction between peptide **3** and **S3** (solid line), tf-**S3** (dotted line), and tf-**S10** nanoparticles (dashed line).

## Conclusions

Monodisperse zeolite nanoparticles have been used to develop colloids bearing polypeptides anchored on the solid surface by a site-specific ligation method, which enables the control of the biomolecule orientation at the solid–liquid interface.

Two types of nanoparticles were studied: zeolite β, which possesses a Si/Al ratio of 25, and silicalite-1, which is a fully silicic material.

Fluorescence spectroscopy results demonstrated that the specificity of the ligation is dramatically influenced by the chemical composition of the particles' surface. Indeed, while zeolite β (aluminosilicate) particles react by nonspecific adsorption with the peptides, silicalite particles (pure silicate) anchor exclusively a peptide bearing the COCHO functionality. This particular physisorption phenomenon of zeolite β is attributed to the aluminum atoms present at the particles' surface, which have a specific affinity for peptides.

These materials could find applications in immunodiagnostics and drug delivery.

## Experimental Section

Chemicals were purchased from commercial sources. They were reagent grade and used as received. Distilled deionized water (18 MΩ) was used for the preparation of all aqueous solutions.

### Nanoparticle Preparation

**Preparation of Colloidal Zeolite Nanoparticles:** Colloidal zeolite β nanoparticles with a Si/Al ratio of 18.5 were synthesized under mild hydrothermal conditions from a clear solution containing $0.28Na_2O/9.0(TEA)_2O/0.5Al_2O_3/25SiO_2/430H_2O$, where TEA is tetraethylammonium hydroxide, the structure directing agent (SDA) (Fluka, 20% in water). The synthesis was performed at 100 °C for 8 days. Colloidal zeolite β crystals were purified by a series of high-speed centrifugation and ultrasonic redispersion in water or ethanol.

Colloidal silicalite-1 nanoparticles were synthesized under mild hydrothermal conditions from a clear solution containing $9.0(TPA)_2O/25SiO_2/295H_2O$, where TPA is tetrapropylammonium hydroxide, the structure directing agent (SDA) (Fluka, 20% in water). The synthesis was performed at 100 °C for 24 h. Colloidal silicalite-1 crystals were purified by a series of high-speed centrifugation and ultrasonic redispersion in water or ethanol.

Template-free colloidal silicalite and zeolite β nanoparticles were obtained by using a procedure described previously.[22] This approach is based on surface-grafted organic ligands, for example (2-aminoethyl)phoshonic acid (APA) $[H_2N(CH_2)_2PO(OH)_2$ from Fluka, or (3-aminopropyl)triethoxysilane (APTS) $[H_2N(CH_2)_3Si(OC_2H_5)_3$, ABCR]. These compounds are used as aggregation inhibitors and crystallinity stabilizers during high-temperature combustion of SDA. The grafting and subsequent calcination processing has no influence on size, morphology, and crystallinity of the zeolite nanoparticles. This procedure provides stable colloidal template-free monodisperse zeolite nanoparticles with particle size distribution similar to the initial colloid.

### Semicarbazide Grafting of the Nanoparticles

We have recently described the preparation of semicarbazide-functionalized monodisperse silica ludox nanoparticles.[23] The same strategy was adopted here for each type of porous nanoparticle (silicalite and zeolite β). (Scheme 1).

First, silanes **1** were synthesized by reacting (3-isocyanatopropyl)- or (10-isocyanatodecyl)triethoxysilane[13] with $FmocNHNH_2$.[24] Then, silanes **1** were reacted as shown in Scheme 1, on the nanoparticles. The grafting of semicarbazide functionality was performed in DMF using silane **1** (3 mmol·g$^{-1}$) in the presence of piperidine, which permitted the in situ removal of the Fmoc-protecting group and improved the silanization process.[26] The nanoparticles were washed with DMF by centrifugation and stored at 4 °C, 1% (w/v) in DMF. The suspensions were found to be stable for months.

### Peptide Grafting of the Nanoparticles

The nanoparticles were then reacted with peptides **2** and **3** labeled with (5)-6-carboxymethylrhodamine. Detailed synthesis of the peptides has been reported elsewhere.[25] The peptide grafting (1 mL, 0.5–1 mM) was performed in acetate buffer (100 mM, pH = 5.51) at 37 °C. The excess of peptide was eliminated by five cycles of centrifugation (11000 rpm, 20 min). The final water suspension [1% (w/v)] was stored at 4 °C.

As peptide **2** bares a COCHO functionality, it should react with the semicarbazide surface, whereas immobilization of peptide **3**, which lacks the COCHO, should occur only through physisorption (Scheme 2).

### Sample Characterization

**Nanoparticle Size:** The mean particle size was determined by dynamic light scattering (DLS) using an argon laser (Spectra Physics Series 2000) operating at 632.8 nm. Light-scattering measurements

 © 2006 Wiley-VCH Verlag GmbH & Co. KGaA, Weinheim 

were made at 25 ± 0.1 °C. Hydrodynamic measurements were performed at a 90° angle, after dilution of the sample to 10 μg·mL$^{-1}$ in water. The data were analyzed according to the method of cumulants for apparent mean diameter and polydispersity index.[26]

**Nanoparticle Morphology:** The morphology of the nanoparticles was investigated by scanning electron micrography (SEM, Hitachi S-4500) and transmission electron microscopy (TEM, JEOL 1200 EX with 120 keV accelerating voltage). SEM samples were prepared by depositing colloidal suspension on platinum-coated (2–3 nm) aluminum mounts fixed with carbon conducting tape. TEM samples were prepared by depositing 5 μL of silica nanoparticles water suspension (diluted 1:20) on 300 mesh copper grid with carbon film backing.

**Nanoparticle Microstructure:** The microstructure was studied by gas sorption experiments (Micromeretics ASAP 2010). Nitrogen was used as the adsorbate at 77 K. Samples were outgassed at 80 °C in dynamic vacuum ($3\times10^{-6}$ bar) before the adsorption. Determination of the specific surface was done by the BET method and total micropore volume was obtained by t-plot method based on the Harkins-Jura equation.

**Nanoparticle Grafting:** The nature of the functionalization was studied with $^{29}$Si and $^{13}$C CP-MAS NMR performed on the samples after each step of the preparation procedure. $^{29}$Si solid-state NMR spectroscopy gave useful information on the silanization step, as the chemical shift of $^{29}$Si was highly sensitive to number and nature of groups attached to it. $^{29}$Si CP-MAS NMR spectra of the solid samples were recorded with a Bruker spectrometer at 79.49 MHz using 5-μs single pulses (60° flip angle) with 10-s repetition rate and 15-ms contact time employing magic angle spinning at 3.5 kHz; 10000 scans were accumulated. All $^{29}$Si chemical shifts were referenced to tetramethylsilane (TMS). $^{13}$C CP-MAS NMR spectra were recorded with a Bruker spectrometer at 100.62 MHz using 10-μs single pulses (π/6) with 5-s repetition rate and 3-ms contact time employing magic-angle spinning at 3.5 kHz; 50000 scans were accumulated.

The powder samples were filled into 4-mm diameter zirconia rotors.

**Elemental Analysis:** Elemental analysis by the "Laboratoire Central d'Analyses du CNRS", Vernaison (France) enabled the evaluation of the grafting loading after functionalization.

**Photophysical Properties:** The optical properties of the particles were evaluated by recording static fluorescence spectra using a Spex Fluorolog 1681 spectrofluorimeter (scanning rate of 2 nm·s$^{-1}$). Spectra were recorded on 0.05% w/w particle suspensions.

## Acknowledgments

Funding of this work by the Ministère Délégué à la Recherche (ACI Nanosciences 045 270 and 042 130) is gratefully acknowledged. The authors thank Grace-Davidson for generously providing Ludox silica samples for the zeolite synthesis.

[1] C. M. Niemeyer, *Angew. Chem. Int. Ed.* **2001**, *40*, 4128–4158.
[2] N. L. Rosi, C. A. Mirkin, *Chem. Rev.* **2005**, *105*, 1547.
[3] T. Pellegrino, S. Kudera, T. Liedl, A. Muñoz Javier, L. Manna, W. J. Parak, *Small* **2005**, *1*, 48–63.
[4] *Chem. Mater.*, special issue on organic–inorganic nanocomposite materials, **2001**, *13*, 3059–3809.
[5] S. Onclin, B. J. Ravoo, D. N. Reinhoudt, *Angew. Chem. Int. Ed.* **2005**, *44*, 6282–6304.
[6] I. Lukěs, M. Borbaruah, L. D. Quin, *J. Am. Chem. Soc.* **1994**, *116*, 1737.
[7] R. D. Badley, W. T. Ford, F. J. McEnroe, R. A. Assink, *Langmuir* **1990**, *6*, 792.
[8] L. Tosheva, V. Valtchev, *Chem. Mater.* **2005**, *17*, 2494–2513.
[9] B. Wheatley, D. E. Schmidt Jr, *J. Chromatogr. A* **1999**, *849*, 1–12.
[10] W. Clarke, J. D. Beckwith, A. Jackson, B. Reynolds, E. M. Karle, D. S. Hage, *J. Chromatogr. A* **2000**, *888*, 13–22.
[11] B. Lu, J. Xie, C. Lu, C. Wu, Y. Wie, *Anal. Chem.* **1995**, *67*, 83–87.
[12] A. Vijayendran, D. E. Leckband, *Anal. Chem.* **2001**, *73*, 471–480.
[13] P. Joly, N. Ardès-Guisot, S. Kar, M. Granier, J.-O. Durand, O. Melnyk, *Eur. J. Org. Chem.* **2005**, *12*, 2473–2480.
[14] R. K. Iler, *The Chemistry of Silica*, Wiley, New York, NY, **1979**.
[15] A. Y. Fadeev, T. J. McCarthy, *Langmuir* **1999**, *15*, 3759–3766.
[16] A. Y. Fadeev, T. J. McCarthy, *Langmuir* **2000**, *16*, 7268.
[17] M. J. Stevens, *Langmuir* **1999**, *15*, 2773–2778.
[18] S. Pawsey, K. Yach, L. Reven, *Langmuir* **2002**, *18*, 5205–5212.
[19] G. Engelhardt, D. Michel, *High Resolution Solid-State NMR of Silicates and Zeolites*, Wiley, New York, NY, **1987**.
[20] G. S. Caravajal, D. E. Leyden, G. R. Quinting, G. E. Macial, *Anal. Chem.* **1988**, *60*, 1776.
[21] M. V. Graf, B. Saegesser, G. A. Schoenenberger, *Anal. Biochem.* **1986**, *157*, 295.
[22] M. Smaïhi, E. Gavilan, J.-O. Durand, V. Valtchev, *J. Mater. Chem.* **2004**, *14*, 1347–1351.
[23] O. El-Mahdi, X. Duburcq, C. Maillet, C. Olivier, J. M. Garcia, J. O. Durand, O. Melnyk, *Anal. Chem.*, manuscript submitted.
[24] E. Zhang, Y. L. Cao, M. W. Hearn, *Anal. Biochem.* **1991**, *195*, 160–167.
[25] C. Olivier, D. Hot, L. Huot, N. Ollivier, O. El-Mahdi, C. Gouyette, T. Huynh-Dinh, H. Gras-Masse, Y. Lemoine, O. Melnyk, *Bioconjugate Chem.* **2003**, *14*, 430–439.
[26] D. E. Koppel, *J. Chem. Phys.* **1972**, *57*, 4814.

Received: February 27, 2006
Published Online: May 18, 2006

 © 2006 Wiley-VCH Verlag GmbH & Co. KGaA, Weinheim 

DOI: 10.1002/ejic.200600202

# Tin(IV) Fluoride Complexes with Tertiary Phosphane Ligands – A Comparison of Hard and Soft Donor Ligands

**Martin F. Davis,[a] Maria Clarke,[a] William Levason,*[a] Gillian Reid,[a] and Michael Webster[a]**

**Keywords:** Tin / Fluoride / Phosphane / Multinuclear NMR / Crystal structures

The first phosphane complexes of the hard Lewis acid $SnF_4$ have been synthesised including *trans*-$[SnF_4(PR_3)_2]$ (R = Me or Cy) and *cis*-$[SnF_4$(diphosphane)] [diphosphane = $R_2P(CH_2)_2PR_2$, R = Me, Et, Ph or Cy; *o*-$C_6H_4(PR_2)_2$, R = Me or Ph] and characterised by IR and multinuclear NMR ($^1H$, $^{19}F$, $^{31}P$, $^{119}Sn$) spectroscopy. The crystal structures of *trans*-$[SnF_4(PCy_3)_2]$ and *cis*-$[SnF_4\{Et_2P(CH_2)_2PEt_2\}]$ are reported. Tin(IV) fluoride complexes of 2,2′-bipyridyl, 1,10-phenanthroline, $MeO(CH_2)_2OMe$, $Me_2N(CH_2)_2NMe_2$, pyridine and THF have been characterised by multinuclear NMR spectroscopy, the structures of *cis*-$[SnF_4$(L–L)] (L–L = 1,10-phenanthroline and $MeO(CH_2)_2OMe$) determined, and the properties were compared with those of the phosphane complexes. Complexes of *o*-$C_6H_4(PMe_2)_2$, $Et_2P(CH_2)_2PEt_2$, and $MeC(CH_2AsMe_2)_3$ with $SnCl_4$ and $SnBr_4$ are also reported and the structures of *cis*-$[SnCl_4\{Et_2P(CH_2)_2PEt_2\}]$ and *cis*-$[SnBr_4\{\kappa^2$-$MeC(CH_2AsMe_2)_3\}]$ described. Attempts to prepare tertiary arsane complexes of $SnF_4$ have been unsuccessful.

(© Wiley-VCH Verlag GmbH & Co. KGaA, 69451 Weinheim, Germany, 2006)

## Introduction

Tin(IV) chloride is widely used in synthesis both as a source of tin(IV) and as a strong Lewis acid.[1,2] A very wide range of adducts of $SnCl_4$ with neutral ligands (L) are known, mostly six-coordinate $[SnCl_4L_2]$, and similar complexes are formed by $SnBr_4$ and $SnI_4$, although Lewis acidity decreases $SnCl_4 > SnBr_4 >> SnI_4$. The majority of these ligands have hard O or N donor atoms, but examples with softer P, As, S, Se or Te donors have also been characterised.[3–10] In marked contrast little is known about adducts of $SnF_4$ with neutral ligands. Some examples were reported in the period 1950–1975, often as part of larger surveys including the heavier tin(IV) halides, but little data were provided and only a single complex, $[SnF_4$(2,2′-bipy)], was structurally characterised.[11–16] There appear to be no reports of $SnF_4$ complexes with softer donor ligands. This neglect in part is similar to that of other p-block fluorides, whose Lewis acidity, except towards $F^-$ or in superacid media (for $MF_5$, M = As or Sb), is little explored, but also reflects the more difficult synthetic entry into the complexes. The $SnX_4$ (X = Cl, Br or I) are tetrahedral molecules readily soluble in weak or non-coordinating solvents such as chlorocarbons, hydrocarbons or arenes, and synthesis of $[SnX_4(L)_2]$ usually involves simply mixing the constituents in a solvent with precautions to avoid hydrolysis. In contrast, $SnF_4$ has a polymeric structure based upon vertex sharing $SnF_6$ octahedra,[17] and although readily hydrolysed, is otherwise rather unreactive and insoluble in weak donor solvents. Tudela and co-workers have reported[18] the preparation of $[SnF_4(MeCN)_2]$ from $SnF_2$ and $I_2$ in MeCN. We have found that this provides a convenient entry into the chemistry of $SnF_4$, and recently reported the synthesis and detailed spectroscopic and structural studies of a series of tin(IV) fluoride complexes of phosphane- or arsane oxides, including $[SnF_4(R_3EO)_2]$ ($R_3EO$ = $Ph_3PO$, $Ph_3AsO$, $Me_3PO$ or $Me_3AsO$) and $[SnF_4$(L–L)] {L–L = *o*-$C_6H_4[P(O)Ph_2]_2$, *o*-$C_6H_4[P(O)Me_2]_2$ or $Ph_2P(O)CH_2P(O)Ph_2$}.[19] These studies showed that toward pnictogen oxide ligands, $SnF_4$ was the strongest Lewis acid of the four tin(IV) halides, evidenced by shorter Sn–O and longer P–O bonds and larger $^{31}P$ NMR coordination shifts in the fluorides, compared to corresponding data in complexes with the heavier halides. Here we report the first investigations of the synthesis, structures and spectroscopy of tin(IV) fluoride adducts with tertiary phosphanes and arsanes. Comparisons of these complexes with $SnF_4$ species containing N- or O donor ligands and with the heavier $Sn^{IV}$ halides are described.

## Results and Discussion

**Phosphane Complexes:** The reactions of $[SnF_4(MeCN)_2]$ with $PMe_3$ or $PCy_3$ (L), in anhydrous dichloromethane under a dinitrogen atmosphere yielded $[SnF_4L_2]$ complexes in moderate to good yields. However we were unable to obtain a pure sample of $[SnF_4(PPh_3)_2]$ by this route. Since neither the $[SnF_4(MeCN)_2]$ nor the resulting complexes are easily soluble in this solvent, some care is needed to obtain pure

[a] School of Chemistry, University of Southampton, Southampton SO17 1BJ, UK

 © 2006 Wiley-VCH Verlag GmbH & Co. KGaA, Weinheim 

products. The complexes are both moisture and dioxygen sensitive in solution, although the dry solids only slowly decomposed in air (see below). They are much less soluble in chlorocarbons than corresponding complexes of the heavier tin halides, and prone to retain lattice solvent as evidenced in their $^1$H NMR spectra and in some of the X-ray structures.[19] $[SnF_4(THF)_2]$[18] was also explored as a synthon, but appeared to have no advantages over the acetonitrile complex. We also reacted $[SnF_4(MeCN)_2]$ with molten $PPh_3$, but the $^{31}P\{^1H\}$ and $^{19}F\{^1H\}$ NMR spectra showed a complex mixture of products, and it appears that some fluorination of the phosphane occurs under these conditions. The $[SnF_4L_2]$ complexes were identified as *trans* isomers from their $^{19}F\{^1H\}$ and $^{31}P\{^1H\}$ NMR spectra which are respectively triplets and quintets [in each case with weak satellites due to $^{119}$Sn and $^{117}$Sn ($^{117}$Sn: $I$ = 1/2, 7.7%, $\Xi$ = 35.63 MHz; $^{119}$Sn: $I$ = 1/2, 8.6%, $\Xi$ = 37.27 MHz)] (Table 1). The $^{119}$Sn NMR spectra are 15-line patterns (triplet of quintets) with the coupling constants shown in Table 1. The structure of $[SnF_4(PCy_3)_2]$ was determined and shows (Table 2, Figure 1) a centrosymmetric molecule with Sn–P = 2.654(1) Å and Sn–F = 1.959(2), 1.980(2) Å. The Sn–P is longer than that in *trans*-$[SnCl_4(PEt_3)_2]$ [2.615(5) Å],[20] and marginally longer than in *trans*-$[SnCl_4\{\kappa^1$-$Ph_2PCH_2PPh_2\}_2]$ [2.649(1) Å],[21] but shorter than found in *trans*-$[SnI_4(P\textit{i}Pr_3)_2]$ [2.69(1) Å],[22] although the differing steric requirements of the three phosphanes preclude a more detailed discussion.

Table 2. Selected bond lengths [Å] and angles [°] for *trans*-$[SnF_4(PCy_3)_2]$.[a]

| | | | |
|---|---|---|---|
| Sn1–F1 | 1.959(2) | Sn1–F2 | 1.980(2) |
| Sn1–P1 | 2.6538(11) | P1–C1 | 1.860(4) |
| P1–C7 | 1.845(4) | P1–C13 | 1.851(4) |
| F1–Sn1–F2 | 91.21(10) | F1–Sn1–F2a | 88.79(10) |
| F1–Sn1–P1 | 89.86(7) | F2–Sn1–P1 | 88.24(7) |
| C1–P1–C7 | 108.09(17) | C7–P1–C13 | 104.81(16) |
| C1–P1–C13 | 107.96(17) | Sn1–P1–C1 | 112.95(12) |
| Sn1–P1–C7 | 113.77(12) | Sn1–P1–C13 | 108.81(12) |
| F1–Sn1–P1–C1 | –60.0(2) | F1–Sn1–P1–C7 | 63.7(2) |
| F1–Sn1–P1–C13 | –179.9(2) | | |

[a] Symmetry operation, a: $-x$, $-y$, $2-z$.

The corresponding reactions of $[SnF_4(MeCN)_2]$ with the diphosphanes $Me_2P(CH_2)_2PMe_2$, $Et_2P(CH_2)_2PEt_2$, $Cy_2P(CH_2)_2PCy_2$, *o*-$C_6H_4(PPh_2)_2$, $Ph_2P(CH_2)_2PPh_2$ and *o*-$C_6H_4(PMe_2)_2$ (L–L) gave $[SnF_4(L–L)]$. The $[SnF_4\{Me_2P(CH_2)_2PMe_2\}]$ was essentially insoluble in chlorocarbons or nitromethane and decomposed by DMSO, and although it appeared to be similar to the other examples, we were unable to obtain any solution spectroscopic data and it will not be discussed further. The other examples are as expected *cis* isomers showing doublet of doublets of triplets in their $^{31}P\{^1H\}$ NMR spectra and two $^{19}F\{^1H\}$ resonances, a triplet of triplets for the $F_{trans\text{-}F}$ and a doublet of doublet of triplets for the $F_{trans\text{-}P}$, with the coupling constants shown in Table 1 (again all resonances have tin satellites). The $^{119}$Sn NMR resonances of the diphosphane com-

Table 1. Selected NMR spectroscopic data for $SnF_4$ complexes.[a]

| Compound | $\delta(^{31}P\{^1H\})$[b] | $\Delta P$[c] | $\delta(^{119}Sn)$[d] | $\delta(^{19}F\{^1H\})$ | $^1J(^{19}F\text{-}^{119}Sn)$ | $^nJ(^{31}P\text{-}^{19}F)$ | $^2J(^{19}F\text{-}^{19}F)$ | $^nJ(^{31}P\text{-}^{119}Sn)$ |
|---|---|---|---|---|---|---|---|---|
| $[SnF_4\{o\text{-}C_6H_4(PMe_2)_2\}]$ | –37.8 (t,d,d) | 17 | –657.6 (t,t,t) | –131.7 (t,t) | 2470 | 117, 98, 54 | 42 | 1520 |
| | | | | –161.1 (d,d,t) | 2160 | | | |
| $[SnF_4\{o\text{-}C_6H_4(PPh_2)_2\}]$ | –18.9 (t,d,d) | –6 | –665.9 (t,t,t) | –123.8 (t,t) | 2627 | 93, 73, 48 | 52 | 1512 |
| | | | | –155.5 (d,d,t) | 2207 | | | |
| *trans*-$[SnF_4(Me_3P)_2]$ | –19.1 (q) | 43 | –628.0 (t,q) | –132.8 (t) | 2745 | 155 | | 2975 |
| *trans*-$[SnF_4(Cy_3P)_2]$ | +22.2 (q) | 11 | –628.5 (t,q) | –98.9 (t) | 2993 | 124 | | 2530 |
| $[SnF_4\{Et_2P(CH_2)_2PEt_2\}]$ | –11.6 (t,d,d) | 6 | –649.4 (t,t,t) | –123.8 (t,t) | 2552 | 110, 95, 46 | 40 | 1628 |
| | | | | –150.2 (d,d,t) | 2183 | | | |
| $[SnF_4\{Cy_2P(CH_2)_2PCy_2\}]$ | –9.9 (t,d,d) | –12 | –639.1 (t,t,t) | –113.7 (t,t) | 2644 | 98, 88, 46 | 46 | 1528 |
| | | | | –139.5 (d,d,t) | 2205 | | | |
| $[SnF_4\{Ph_2P(CH_2)_2PPh_2\}]$ | –17.8 (t,d,d) | –4 | –668.1 (t,t,t) | –112.4 (t,t) | 2650 | 118, 87, 44 | 46 | 1630 |
| | | | | –147.1 (d,d,t) | 2212 | | | |
| $[SnF_4(2,2'\text{-bipyridyl})]$ | | | –708.2 (t,t) | –149.8 (t) | 1964 | | 48 | |
| | | | | –179.8 (t) | 1978 | | | |
| $[SnF_4(1,10\text{-phen})]$ | | | –715.1 (t,t) | –149.5 (t) | 1987 | | 50 | |
| | | | | –180.8 (t) | 1982 | | | |
| $[SnF_4(THF)_2]$ (220 K) | | | | | | | | |
| *trans* isomer | | | –775.4 (q) | –166.7 (s) | 1910 | | | |
| *cis* isomer | | | –775.3 (t,t) | –166.2 (t) | 1918 | | 54 | |
| | | | | –178.8 (t) | 2074 | | | |
| *trans*-$[SnF_4(pyridine)_2]$ | | | –670.8 (q) | –163.8 (s) | 1983 | | | |
| $[SnF_4\{Me_2N(CH_2)_2NMe_2\}]$ | | | [e] | –167.8 (t) | 2266 | | 50 | |
| | | | | –184.4 (t) | 2096 | | | |
| $[SnF_4(MeCN)_2]$ | | | n.o.[f] | –181.0 (s) | n.o. | | | |
| $[SnF_4\{MeO(CH_2)_2OMe\}]$ | | | –753.8 (t,t) | –167.1 | 2233 | | 61 | |
| (190 K) | | | | –183.3 | 2189 | | | |

[a] In $CH_2Cl_2$/10% $CDCl_3$. [b] Ligand chemical shifts are: *o*-$C_6H_4(PMe_2)_2$ –55 ppm; *o*-$C_6H_4(PPh_2)_2$ –13 ppm; $Ph_2P(CH_2)_2PPh_2$ –13 ppm; $Et_2P(CH_2)_2PEt_2$ –18 ppm; $Me_2P(CH_2)_2PMe_2$ –48 ppm; $Cy_2P(CH_2)_2PCy_2$ +2 ppm; $PMe_3$ –62 ppm; $PCy_3$ +11.5 ppm. [c] Coordination shift ($\delta_{complex}-\delta_{ligand}$). [d] $^{119}$Sn NMR spectra were typically recorded at 250 K. [e] Insufficently soluble to record spectrum. [f] n.o. = not observed in temperature range 295–180 K.

 © 2006 Wiley-VCH Verlag GmbH & Co. KGaA, Weinheim 

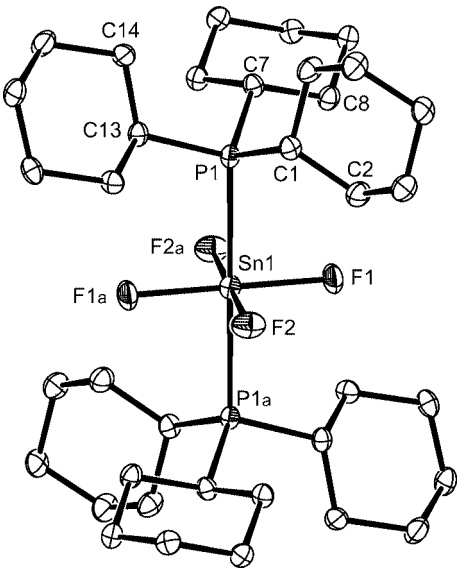


Figure 1. Structure of *trans*-[$SnF_4(PCy_3)_2$] showing a partial atom numbering scheme. Cyclohexyl groups are numbered cyclically starting at the P-bonded C atom. Ellipsoids are drawn at the 50% probability level and H atoms omitted for clarity. Sn1 is positioned on a centre of symmetry. Symmetry operation, a: $-x$, $-y$, $2-z$.

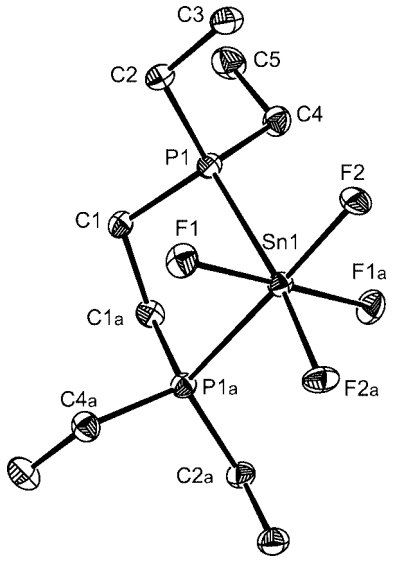


Figure 2. Structure of [$SnF_4\{Et_2P(CH_2)_2PEt_2\}$] showing the atom numbering scheme. Ellipsoids are drawn at the 50% probability level and H atoms omitted for clarity. A twofold axis passes through Sn1 and the centre of the C1–C1a bond. Symmetry operation, a: $-x$, $y$, $1/2-z$.

plexes are 27-line patterns (triplet of triplets of triplets), the spectra typically being recorded at 250 K to reduce any line broadening due to the onset of reversible ligand dissociation. The modest solubility necessitated long accumulations, and in some cases the weakest outer lines of the multiplets were rather unclear, although the various couplings were readily extracted (Table 1). The trends in the various NMR parameters will be discussed in a later section in comparison with those of related complexes (see below). The structure of [$SnF_4\{Et_2P(CH_2)_2PEt_2\}$] was determined and confirms the *cis* geometry deduced from the NMR studies (Table 3, Figure 2). The Sn–P distance is 2.606(1) Å, shorter than in the *trans*-[$SnF_4(PCy_3)_2$] [2.654(1) Å], and also shorter than the value in *cis*-[$SnCl_4\{Et_2P(CH_2)_2PEt_2\}$] [2.648(2) Å] described below. The Sn–$F_{trans\text{-}F}$ 1.986(2) Å is significantly longer than Sn–$F_{trans\text{-}P}$ 1.953(2) Å, a pattern which is found in most adducts of $SnX_4$ (X = Cl, Br or I) with soft donor ligands.[6–10]

Table 3. Selected bond lengths [Å] and angles [°] for [$SnF_4\{Et_2P(CH_2)_2PEt_2\}$].[a]

| | | | |
|---|---|---|---|
| Sn1–F1 | 1.9863(17) | P1–C1 | 1.821(3) |
| Sn1–F2 | 1.9532(16) | P1–C2 | 1.815(3) |
| Sn1–P1 | 2.6058(9) | P1–C4 | 1.814(3) |
| P1···P1a | 3.409(2) | | |
| F1–Sn1–F2 | 92.60(7) | P1–Sn1–F1 | 84.66(5) |
| F1–Sn1–F2a | 91.36(7) | P1–Sn1–F2 | 93.14(6) |
| F1–Sn1–F1a | 174.29(10) | P1–Sn1–F1a | 91.02(5) |
| F2–Sn1–F2a | 92.29(10) | P1–Sn1–F2a | 173.40(5) |
| P1–Sn1–P1a | 81.70(4) | Sn1–P1–C1 | 102.52(9) |
| Sn1–P1–C2 | 114.54(10) | Sn1–P1–C4 | 116.34(10) |

[a] Symmetry operation, a: $-x$, $y$, $\frac{1}{2}-z$.

**Other $SnF_4$ Complexes:** A small number of complexes of hard N- or O-donor ligands, previously obtained directly from $SnF_4$, were re-prepared in this study for comparison purposes from [$SnF_4(MeCN)_2$], viz [$SnF_4$(L–L)] (L–L = 2,2′-bipyridyl, 1,10-phenanthroline, *N*,*N*,*N*′*N*′-tetramethylethanediamine and 1,2-dimethoxyethane) and [$SnF_4$(pyridine)$_2$]. The complexes with N donor ligands are unaffected by exposure to air for several hours, although moisture-sensitive in solution. They are much less readily decomposed than the phosphane complexes. The solid [$SnF_4(L)_2$] [L = THF or $L_2$ = $MeO(CH_2)_2OMe$] are very deliquescent. The $^{19}F\{^1H\}$ and $^{119}Sn$ NMR spectroscopic data are shown in Table 1. Although the ranges overlap, there is a general shift to lower frequency in the $^{119}Sn$ NMR shifts with donor, P → N → O. The complexes with L–L = 2,2′-bipyridyl, 1,10-phenanthroline, $Me_2N(CH_2)_2NMe_2$ have the expected *cis* geometry, whilst the [$SnF_4$(pyridine)$_2$] is the *trans* isomer. In contrast to the N donor complexes, the ether adducts, [$SnF_4\{MeO(CH_2)_2OMe\}$] and [$SnF_4(THF)_2$], are undergoing rapid neutral ligand exchange in solution at ambient temperatures, and only at low temperatures was it possible to record $^{19}F\{^1H\}$ and $^{119}Sn$ NMR spectroscopic data. These revealed that in $CH_2Cl_2$ solution at 220 K the THF complex was a mixture of *cis* and *trans* isomers in approximately equal amounts. On the basis of IR and Mössbauer data Tudela[18] concluded that the [$SnF_4L'_2$] (L′ = pyridine or THF) were *trans* isomers in the solid state. Crystals of [$SnF_4\{MeO(CH_2)_2OMe\}$] and [$SnF_4$(1,10-phenanthroline)] were grown from $CH_2Cl_2$/*n*-hexane. The structure of the former shows (Table 4, Figure 3) the expected *cis* geometry with Sn–O = 2.156(2), 2.144(2) Å, which are shorter than those in *trans*-[$SnCl_4(THF)_2$][23] but significantly longer than the Sn–O distances in phosphane oxide adducts of

 © 2006 Wiley-VCH Verlag GmbH & Co. KGaA, Weinheim 

$SnF_4$, which lie in the range of ca. 2.045(3)–2.088(5) Å.[18] The latter complexes show no dissociation in solution, which is indicative of stronger binding of the phosphane oxide ligands compared to the ethers. The differences in the distances Sn–$F_{trans\text{-}F}$ [1.926(2), 1.927(2) Å] and Sn–$F_{trans\text{-}O}$ [1.921(2), 1.923(2) Å] are much less than in the phosphane complex described previously. The structure of [$SnF_4$(1,10-phenanthroline)] [Sn–N = 2.157(7) Å] (Table 5, Figure 4) may be compared with that of [$SnCl_4$(1,10-phenanthroline)],[24] which possess Sn–N = 2.234(7)–2.251(8) Å. One can also compare the literature data on [$SnX_4$(2,2′-bipyridyl)] for which Sn–N are X = F [2.181(3), 2.183(3) Å], X = Cl [2.247(4), 2.226(4) Å], X = Br [2.23(1), 2.23(1) Å], X = I [2.28(2) Å].[16,25,26] The 2,2′-bipyridyl series shows the longest Sn–N bonds in the iodide and the shortest in the fluoride, with the chloride and bromide less clearly discriminated, support for the fluoride being the strongest Lewis acid of the four halides.

Table 4. Selected bond lengths [Å] and angles [°] for [$SnF_4${$MeO(CH_2)_2OMe$}].

| | | | |
|---|---|---|---|
| Sn1–F1 | 1.9263(17) | Sn1–F3 | 1.9274(17) |
| Sn1–F2 | 1.9210(18) | Sn1–F4 | 1.9234(18) |
| Sn1–O1 | 2.1559(19) | Sn1–O2 | 2.144(2) |
| O1–C1 | 1.463(3) | O2–C3 | 1.454(3) |
| O1–C2 | 1.456(3) | O2–C4 | 1.463(3) |
| C2–C3 | 1.502(4) | O1···O2 | 2.673(3) |
| F2–Sn1–F4 | 99.27(8) | F1–Sn1–F3 | 170.07(7) |
| F–Sn1–F (the rest) | 92.09(8)–93.93(8) | O2–Sn1–O1 | 76.88(8) |
| F2–Sn1–O2 | 169.84(8) | F4–Sn1–O1 | 167.62(8) |
| F–Sn1–O (the rest) | 84.27(8)–93.07(8) | | |
| Sn1–O1–C1 | 117.34(18) | Sn1–O2–C3 | 112.38(17) |
| Sn1–O1–C2 | 111.60(15) | Sn1–O2–C4 | 121.09(17) |
| O1–C2–C3 | 107.0(2) | O2–C3–C2 | 106.5(2) |

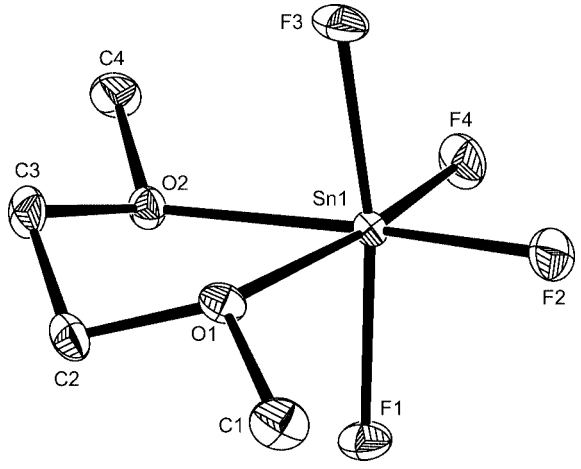


Figure 3. Structure of [$SnF_4${$MeO(CH_2)_2OMe$}] showing the atom numbering scheme. Ellipsoids are drawn at the 50% probability level and H atoms omitted for clarity.

Table 5. Selected bond lengths [Å] and angles [°] for [$SnF_4$(1,10-phenanthroline)]·MeOH.[a]

| | | | |
|---|---|---|---|
| Sn1–F1 | 1.887(5) | Sn1–N1 | 2.157(7) |
| Sn1–F2 | 1.860(6) | N1–C1 | 1.339(11) |
| N1···N1a | 2.670(13) | N1–C6 | 1.349(10) |
| F1–Sn1–F2 | 93.3(3) | F1–Sn1–F2a | 91.9(3) |
| F2–Sn1–F2a | 99.2(4) | F1–Sn1–F1a | 172.0(3) |
| F1–Sn1–N1 | 88.0(3) | F2–Sn1–N1 | 168.4(3) |
| N1–Sn1–N1a | 76.5(3) | | |
| Sn1–N1–C1 | 126.4(5) | Sn1–N1–C6 | 115.1(5) |

[a] Symmetry operation, a: $1-x$, $1/2-y$, $z$.

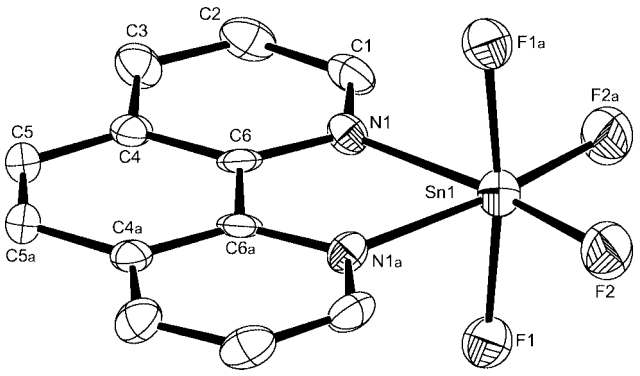


Figure 4. Structure of [$SnF_4$(1,10-phenanthroline)]·MeOH showing the atom numbering scheme. Ellipsoids are drawn at the 40% probability level and H atoms omitted for clarity. The tin atom is on a twofold axis. Symmetry operation, a: $1-x$, $1/2-y$, $z$.

**Other Tin(IV) Halide Adducts:** For comparison several new complexes of $SnX_4$ (X = Cl, Br or I) with phosphane or arsane ligands were also prepared, in these cases by direct reaction of $SnX_4$ with the appropriate ligand in anhydrous

Table 6. Selected NMR spectroscopic data for $SnX_4$ (X = Cl, Br or I) complexes.[a]

| Compound | $\delta(^{31}P\{^1H\})$[b] | $\Delta P$[c] | $\delta(^{119}Sn)$[d] | $^1J(^{31}P\text{-}^{119}Sn)$ | Ref. |
|---|---|---|---|---|---|
| [$SnCl_4${$o$-$C_6H_4(PMe_2)_2$}] | –28.1 | 27 | –616 (t) | 945 | this work |
| [$SnBr_4${$o$-$C_6H_4(PMe_2)_2$}] | –31.9 | 23 | –1188 (t) | 581 | this work |
| [$SnI_4${$o$-$C_6H_4(PMe_2)_2$}] | –59.5 (243 K) | –5 | n.o.[e] | 240 | this work |
| [$SnCl_4${$Et_2P(CH_2)_2PEt_2$}] | –4.9 | 13 | –615 (t) | 1049 | this work |
| [$SnCl_4${$Me_2P(CH_2)_2PMe_2$}] | –20.9 | 27 | –617 (t) | 1005 | [9] |
| [$SnCl_4${$Ph_2P(CH_2)_2PPh_2$}] | –18.8 | –5.5 | –626 (t) | 890 | [9] |
| [$SnCl_4${$o$-$C_6H_4(PPh_2)_2$}] | –13.9 | –1 | –607.5 (t) | 890 | [9] |
| [$SnCl_4${$o$-$C_6H_4(AsMe_2)_2$}] | – | – | –675 (s) | – | [9] |
| [$SnBr_4${$o$-$C_6H_4(AsMe_2)_2$}] | – | – | –1354 (s) | – | [9] |
| [$SnCl_4${$MeC(CH_2AsMe_2)_3$}] | – | – | –696 (s) | – | this work |
| [$SnBr_4${$MeC(CH_2AsMe_2)_3$}] | – | – | –1290 (s) | – | this work |

[a] In $CH_2Cl_2$/10% $CDCl_3$. [b] Ligand chemical shifts are: $o$-$C_6H_4(PMe_2)_2$ –55 ppm; $o$-$C_6H_4(PPh_2)_2$ –13 ppm; $Ph_2P(CH_2)_2PPh_2$ –13 ppm; $Et_2P(CH_2)_2PEt_2$ –18 ppm; $Me_2P(CH_2)_2PMe_2$ –48 ppm; $Cy_2P(CH_2)_2PCy_2$ +2 ppm; $PMe_3$ –62 ppm; $PCy_3$ +11.5 ppm. [c] Coordination shift ($\delta_{complex}-\delta_{ligand}$). [d] $^{119}Sn$ NMR spectra were typically recorded at 250 K. [e] n.o. = not observed in temperature range 295–180 K.

 © 2006 Wiley-VCH Verlag GmbH & Co. KGaA, Weinheim 

dichloromethane, and the NMR spectra were recorded (Table 6). Like other complexes of this type, they are very moisture sensitive and also dioxygen sensitive to varying degrees in solution,[9,27] but also much more soluble in chlorocarbons than their tin(IV) fluoride analogues. The $^{119}Sn$ chemical shifts are surprisingly similar for corresponding complexes of $SnF_4$ and $SnCl_4$, but those of $SnBr_4$ and $SnI_4$ show much more deshielded resonances (Table 6). The $^1J(^{119}Sn\text{-}^{31}P)$ coupling constants fall with halogen F > Cl > Br > I. The structure of *cis*-$[SnCl_4\{Et_2P(CH_2)_2PEt_2\}]$ was determined (Table 7, Figure 5) and provides a direct comparison with the fluoride structure discussed above. Again there is a marked difference between $Sn–Cl_{trans\text{-}Cl}$ [2.453(1) Å] and $Sn–Cl_{trans\text{-}P}$ [2.408(1) Å] with Sn–P = 2.648(2) Å. Other structurally characterised phosphane complexes of $SnCl_4$ are *trans*-$[SnCl_4(PEt_3)_2]$ [Sn–P = 2.615(5) Å],[20] *trans*-$[SnCl_4(\kappa^1\text{-}Ph_2PCH_2PPh_2)_2]$ [Sn–P = 2.649(1) Å],[21] and *cis*-$[SnCl_4\{Ph_2P(CH_2)_2PPh_2\}]$ [Sn–P = 2.679(2), 2.653(2) Å, Sn–Cl = 2.402(2), 2.406(2), 2.408(2), 2.447(2) Å].[28]

Table 7. Selected bond lengths [Å] and angles [°] for $[SnCl_4\{Et_2P(CH_2)_2PEt_2\}]$.[a]

| | | | |
|---|---|---|---|
| Sn1–Cl1 | 2.4529(14) | Sn1–P1 | 2.6481(17) |
| Sn1–Cl2 | 2.4084(14) | P1–C2 | 1.821(6) |
| P1–C4 | 1.824(6) | P1–C5 | 1.825(5) |
| P1···P1a | 3.422(3) | | |
| Cl1–Sn1–Cl2 | 90.16(5) | Cl1–Sn1–Cl2a | 93.97(5) |
| Cl1–Sn1–Cl1a | 174.00(7) | Cl2–Sn1–Cl2a | 92.99(7) |
| Cl1–Sn1–P1 | 84.19(5) | Cl2–Sn1–P1 | 171.65(5) |
| P1–Sn1–P1a | 80.49(7) | Sn1–P1–C2 | 117.0(2) |
| Sn1–P1–C4 | 114.0(2) | Sn1–P1–C5 | 102.09(18) |
| P1–C5–C5a–P1a | 67.7(6) | | |

[a] Symmetry operation, a: $1-x$, $y$, $1/2-z$.

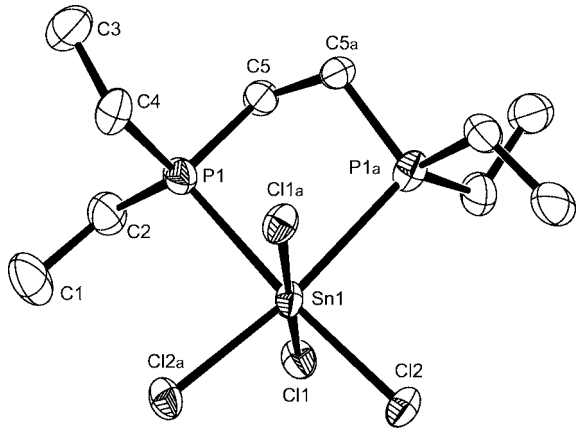


Figure 5. Structure of $[SnCl_4\{Et_2P(CH_2)_2PEt_2\}]$ showing the atom numbering scheme. Ellipsoids are drawn at the 40% probability level and H atoms omitted for clarity. The tin atom is on a twofold axis. Symmetry operation, a: $1-x$, $y$, $1/2-z$.

**Reactions with Dioxygen:** We have reported elsewhere[9] that mixtures of phosphanes or diphosphanes and $SnX_4$ (X = Cl, Br or I) in chlorocarbon solution air-oxidise readily to the corresponding phosphane oxides. Catalytic amounts of $SnI_4$ can be used to cleanly generate phosphane oxides from the corresponding phosphanes using dry air or dioxygen, and whilst the mechanism remains obscure, the use of $^{18}O_2$ in these reactions showed that the source of the oxygen is $O_2$, not water as in a halogenation/hydrolysis mechanism.[27] The phosphane complexes of tin(IV) fluoride made in the present study also show varying degrees of oxygen sensitivity, especially in solution. The $[SnF_4(PCy_3)_2]$ is particularly sensitive and even brief exposure to air of a $CH_2Cl_2$ solution produced substantial oxidation. The $[SnF_4(PMe_3)_2]$ and the diphosphane complexes are less rapidly air-oxidised, but modest amounts of phosphane oxides can be detected by $^{31}P$ NMR in solutions exposed to air for some hours. In these systems the phosphane oxide binds strongly to the $SnF_4$ (cf. ref.[19]), and thus in contrast to the extensively dissociated $SnI_4$ systems[27] the formation of phosphane oxide is stoichiometric, because the phosphane oxides remove the $SnF_4$ by complexation preventing further reaction. Crystals of $[SnF_4(OPPh_3)_2]$ were obtained over several days from a $CH_2Cl_2$ solution of the products of melting $[SnF_4(MeCN)_2]$ with excess $PPh_3$. The structure (Figure 6, Table 8) shows it to be the *trans* isomer, and the bond lengths are entirely in keeping with our previous conclusions[19] that $SnF_4$ is the strongest Lewis acid of the four tin(IV) halides towards O donor phosphane oxide ligands.

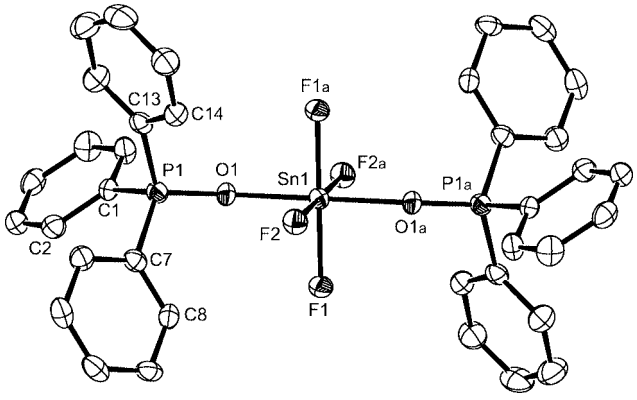


Figure 6. Structure of *trans*-$[SnF_4(Ph_3PO)_2]$ showing a partial atom numbering scheme. Phenyl groups are numbered cyclically starting at the *ipso* C atom. Ellipsoids are drawn at the 50% probability level and H atoms omitted for clarity. Sn1 is positioned on a centre of symmetry. Symmetry operation, a: $-x$, $1-y$, $1-z$.

Table 8. Selected bond lengths [Å] and angles [°] for *trans*-$[SnF_4(Ph_3PO)_2]\cdot 2CH_2Cl_2$.

| | | | |
|---|---|---|---|
| Sn1–F1 | 1.928(3) | Sn1–O1 | 2.050(3) |
| Sn1–F2 | 1.934(3) | O1–P1 | 1.523(3) |
| P1–C1 | 1.792(5) | P1–C7 | 1.795(5) |
| P1–C13 | 1.797(6) | | |
| F1–Sn1–F2 | 90.56(12) | F1–Sn1–O1 | 89.06(13) |
| F2–Sn1–O1 | 91.79(13) | Sn1–O1–P1 | 146.3(2) |
| O1–P1–C1 | 108.0(2) | O1–P1–C7 | 112.5(2) |
| O1–P1–C13 | 111.4(2) | | |

**Attempted Preparation of Tertiary Arsane Complexes:** In contrast to the results with phosphane ligands, repeated attempts to isolate complexes of $SnF_4$ with tertiary arsanes including $AsMe_3$, *o*-$C_6H_4(AsMe_2)_2$ and $MeC(CH_2AsMe_2)_3$ were unsuccessful. The reaction of $[SnF_4(MeCN)_2]$ or $[SnF_4(THF)_2]$ in $CH_2Cl_2$ or toluene with *o*-$C_6H_4(AsMe_2)_2$,

 © 2006 Wiley-VCH Verlag GmbH & Co. KGaA, Weinheim 

Table 9. Selected bond lengths [Å] and angles [°] for $[SnBr_4\{MeC(CH_2AsMe_2)_3\}]$.

| | | | |
|---|---|---|---|
| Sn1–Br1 | 2.5708(6) | Sn1–Br3 | 2.6340(5) |
| Sn1–Br2 | 2.5479(5) | Sn1–Br4 | 2.5807(5) |
| Sn1–As1 | 2.6932(5) | Sn1–As2 | 2.7095(6) |
| As1–C6 | 1.930(4) | As2–C8 | 1.935(3) |
| As1–C7 | 1.932(3) | As2–C9 | 1.928(3) |
| As3–C10 | 1.966(3) | As3–C11 | 1.972(3) |
| As1–C3 | 1.953(4) | As2–C4 | 1.954(3) |
| As3–C5 | 1.987(3) | As1···As2 | 3.712(1) |
| Br–Sn1–Br (ca. 90°) | 91.979(17)–94.850(17) | Br3–Sn1–Br4 | 170.563(15) |
| Br–Sn1–As (ca. 90°) | 82.905(16)–90.337(16) | Br1–Sn1–As2 | 173.739(14) |
| Br2–Sn1–As1 | 174.623(16) | As1–Sn1–As2 | 86.791(16) |
| C–As1–C | 101.08(16)–108.21(15) | C–As2–C | 99.62(13)–107.75(14) |
| C–As3–C | 93.50(15)–98.69(16) | | |

which is a very strongly coordinating ligand towards many d-block metals,[29] resulted in white solids of variable composition which appeared to be mixtures of the starting complex, possibly $[SnF_4\{o\text{-}C_6H_4(AsMe_2)_2\}]$ and $SnF_4$. The IR spectra showed the presence of the diarsane, a broad υ(SnF) at ca. 570 $cm^{-1}$, and usually some MeCN or THF. The $^1H$ NMR spectra of these products in $CD_2Cl_2$ solution showed only MeCN or THF and "free" $o\text{-}C_6H_4(AsMe_2)_2$ [as $o\text{-}C_6H_4(AsMe_2)_2$ is a liquid, this is evidence for coordination of the diarsane to tin in the solids]. The $^{19}F\{^1H\}$ NMR spectra showed no resonances at room temperature, but below ca. 210 K, two new broad resonances at $\delta$ = –138 and –152 were observed, which seem reasonable for $[SnF_4\{o\text{-}C_6H_4(AsMe_2)_2\}]$, but no F–F coupling was resolved even at 190 K. The data suggest that $[SnF_4\{o\text{-}C_6H_4(AsMe_2)_2\}]$ forms in the reaction, but that it is extensively dissociated in solution and even use of a substantial excess of diarsane does not produce a pure product. In the cases of $AsMe_3$ or $MeC(CH_2AsMe_2)_3$ there was little evidence for coordination to $SnF_4$. In contrast, arsane complexes of $SnX_4$ (X = Cl, Br or I) form readily,[9] and indeed $[SnI_4\{o\text{-}C_6H_4(AsMe_2)_2\}]$ is one of the very small number of structurally characterised neutral ligand adducts of $SnI_4$. The explanation of this marked difference to phosphanes probably arises from the fact the $SnF_4$ is a very hard Lewis acid with contracted tin acceptor orbitals, and correspondingly has less ability to bind the large soft arsenic centre. For many transition-metal systems the differences between binding corresponding phosphanes and arsanes is small, but becomes very significant with high oxidation state and/or harder metal centres of the 3d series such as $Fe^{IV}$, $Ni^{IV}$ or $Mn^{II}$, where the phosphanes result in significantly more stable complexes.[29] Our results suggest similar discrimination by $SnF_4$.

In the course of this work the $[SnX_4\{MeC(CH_2AsMe_2)_3\}]$ (X = Cl or Br) were prepared from the appropriate $SnX_4$ and triarsane in $CH_2Cl_2$ and their $^1H$ NMR spectra show the triarsane bound as a bidentate to a six-coordinate tin centre. The $^{119}Sn$ NMR chemical shifts of $\delta$ = –696 and –1290 ppm (Table 6) are typical of $SnX_4As_2$ donor sets.[9] The structures were confirmed by a X-ray study of $[SnBr_4\{MeC(CH_2AsMe_2)_3\}]$ (Table 9, Figure 7), which showed a distorted octahedral tin centre with $Sn–Br_{trans\text{-}Br}$ [2.5807(5), 2.6340(5) Å] longer than $Sn–Br_{trans\text{-}As}$ [2.5708(6), 2.5479(5) Å], and with the axial Br–Sn–Br unit bent towards the neutral ligand (Br3–Sn1–Br4 = 170.6°), as found in tin(IV) halide structures with a variety of soft donors.[6–9] The Sn–As [2.6932(5), 2.7095(6) Å] are slightly shorter than those in the only other structurally characterised tin–arsane complexes $[SnI_4\{o\text{-}C_6H_4(AsMe_2)_2\}]$ [2.716(2), 2.752(2) Å],[9] and *trans*-$[SnCl_4(AsPh_3)_2]$ [2.762(1) Å].[30] The wide As–Sn–As angle [86.79(2)°] in the present complex reflects the six-membered chelate ring present and compares with 78.43(7)° in $[SnI_4\{o\text{-}C_6H_4(AsMe_2)_2\}]$ which contains a five-membered ring.

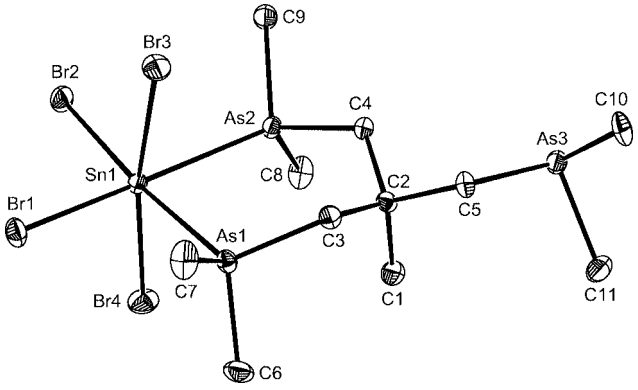


Figure 7. Structure of $[SnBr_4\{MeC(CH_2AsMe_2)_3\}]$ showing the atom numbering scheme. Ellipsoids are drawn at the 50% probability level and H atoms omitted for clarity.

## Comparisons and Conclusions

This work has provided the first examples of $SnF_4$ adducts with soft phosphane ligands and also a considerable amount of spectroscopic and structural data on comparable complexes with hard N- or O-donor ligands and with the heavier tin(IV) halides. The structural data discussed in preceding sections clearly show that for a fixed hard neutral ligand the Sn–ligand bond lengths are shortest in the fluoride complexes, consistent with $SnF_4$ being the strongest Lewis acid. The corresponding data for *cis*-$[SnX_4\{Et_2P(CH_2)_2PEt_2\}]$ (X = F or Cl), which are exact analogues (isostructural), also show the shortest Sn–P bond in the fluoride, indicating that similar trends hold with the soft (but strong σ-donor) phosphorus. The longer Sn–P

 © 2006 Wiley-VCH Verlag GmbH & Co. KGaA, Weinheim 

bond in *trans*-$[SnF_4(PCy_3)_2]$ is almost certainly due to steric effects caused by the bulky cyclohexyl substituents ($PCy_3$ has a cone angle of ca. 170°). However, the instability of $SnF_4$ adducts of arsanes suggests that towards even softer ligands, $SnCl_4$ will be more strongly coordinated.

These studies have also produced a wealth of NMR spectroscopic data (Table 1 and Table 6), but although several empirical trends in the chemical shifts and coupling constants with change in halide or neutral ligand can be discerned, the patterns are complicated, indicating several competing factors are present. Thus, the $^{119}Sn$ chemical shifts show consistent low frequency shifts with X: Cl → F → Br → I, the same as observed in halostannates(IV),[31,32] evidence that electronegativity is not the dominant factor.[33] Low frequency shifts also occur with neutral donor atoms P → N → O. The $^{31}P$ chemical shifts and the coordination shifts ($\delta_{complex}-\delta_{ligand}$) for the phosphane complexes are not systematic with changes in halide co-ligand. Although phosphanes mostly show high frequency coordination shifts when bound to transition metals, both high and low frequency shifts have been observed in p-block element complexes, and the reasons remain obscure.[33,34] The $^1J(^{31}P\text{-}^{119}Sn)$ coupling constants are largest for the fluorides and much larger for *trans*-P–Sn–P than for *cis*-P–Sn–P arrangements (Table 1), whilst the $^1J(^{19}F\text{-}^{119}Sn)$ couplings are larger in the phosphane complexes than in the N- or O-donor ligand cases. The $^1J(^{19}F\text{-}^{119}Sn)_{F-trans-F}$ are markedly larger than $^1J(^{19}F\text{-}^{119}Sn)_{F-cis-F}$ in the phosphane complexes, but this difference is small or absent in the complexes with harder donor co-ligands. A more detailed understanding of the factors responsible for these trends must await further work on related systems.

Given that stable complexes of soft phosphane donor ligands have now been prepared for the hard Lewis acid $SnF_4$, similar complexes should be obtainable for other main-group fluorides. Studies to explore this are underway.

## Experimental Section

All compounds were made under dinitrogen using dry solvents and standard Schlenk and glove box techniques. $SnF_2$, $SnCl_4$, $SnBr_4$ and $SnI_4$ were obtained from Aldrich and used as received. $[SnF_4(MeCN)_2]$ was made as described.[18] Ligands were obtained from Aldrich: $PMe_3$, $PPh_3$, $PCy_3$, $AsMe_3$, $Me_2P(CH_2)_2PMe_2$, $Et_2P(CH_2)_2PEt_2$, $Cy_2P(CH_2)_2PCy_2$, or were made by literature methods: *o*-$C_6H_4(PPh_2)_2$, $Ph_2P(CH_2)_2PPh_2$, *o*-$C_6H_4(PMe_2)_2$, *o*-$C_6H_4(AsMe_2)_2$, $MeC(CH_2AsMe_2)_3$.[35–38] 2,2′-Bipyridyl and 1,10-phenanthroline were dried by heating in vacuo, 1,2-dimethoxyethane was dried with sodium and freshly distilled. Pyridine and $Me_2N(CH_2)_2NMe_2$ were dried by distillation from BaO, tetrahydrofuran was dried by distillation from Na-benzophenone ketyl, MeCN and $CH_2Cl_2$ from $CaH_2$. IR spectra were recorded as Nujol mulls on a Perkin–Elmer PE 983G spectrometer, $^1H$ NMR spectra in $CDCl_3$, $CD_2Cl_2$ or $CD_3NO_2$ solutions on a Bruker AV300, $^{31}P\{^1H\}$, $^{19}F\{^1H\}$ and $^{119}Sn$ NMR spectra on a Bruker DPX400 and referenced to 85% $H_3PO_4$, $CFCl_3$ and neat $SnMe_4$ respectively. The $^{119}Sn$ NMR spectra were recorded from solutions containing $[Cr(acac)_3]$ as a relaxation agent and without proton decoupling to avoid NOE diminution of the signal due to the negative magnetogyric ratio of the isotope. Microanalytical measurements on new complexes were performed by the microanalytical service at Strathclyde University.

**$[SnF_4\{o\text{-}C_6H_4(PMe_2)_2\}]$:** $[SnF_4(MeCN)_2]$ (0.276 g, 1.0 mmol) was dissolved in $CH_2Cl_2$ (20 mL) and *o*-$C_6H_4(PMe_2)_2$ (0.198 g, 1.0 mmol) added and the mixture stirred overnight at ambient temperatures. The white precipitate was filtered off and dried in vacuo. Yield 0.205 g, 52%. $C_{10}H_{16}F_4P_2Sn\cdot CH_2Cl_2$ (477.8): calcd. C 27.6, H 3.8; found C 26.9, H 3.8. $^1H$ NMR (300 MHz, $CDCl_3$, 25 °C): $\delta$ = 1.87 (t, $^2J+^5J_{P-H}$ = 4 Hz, 12 H, Me), 5.4 ($CH_2Cl_2$), 7.75–7.81 (m, 4 H, $C_6H_4$) ppm. IR (Nujol): $\tilde{\nu}$ = 564 (s), 534 (s) $\upsilon$(SnF) $cm^{-1}$.

**$[SnCl_4\{o\text{-}C_6H_4(PMe_2)_2\}]$:** A solution of $SnCl_4$ (0.12 mL, 1.0 mmol) in $CH_2Cl_2$ (5 mL) was added to *o*-$C_6H_4(PMe_2)_2$ (0.198 g, 1.0 mmol) in $CH_2Cl_2$ (20 mL) producing an immediate white precipitate. After 30 min the solid was filtered off and dried in vacuo. Yield 0.427 g, 93%. $C_{10}H_{16}Cl_4P_2Sn$ (458.7): calcd. C 26.2, H 3.5; found C 25.9, H 3.2. $^1H$ NMR (300 MHz, $CDCl_3$, 25 °C): $\delta$ = 1.97 (t, $^2J+^5J_{P-H}$ = 4.4 Hz, 12 H, Me), 7.75–7.81 (m, 4 H, $C_6H_4$) ppm. IR (Nujol): $\tilde{\nu}$ = 307 (s), 296 (s) $\upsilon$(SnCl) $cm^{-1}$.

**$[SnBr_4\{o\text{-}C_6H_4(PMe_2)_2\}]$:** Prepared similarly to the chloride as a yellow solid. Yield 93%. $C_{10}H_{16}Br_4P_2Sn$ (636.5): calcd. C 18.9, H 2.5; found C 18.7, H 2.4. $^1H$ NMR (300 MHz, $CDCl_3$, 25 °C): $\delta$ = 1.95 (t, $^2J+^5J_{P-H}$ = 4.5 Hz, 12 H, Me), 7.75–7.81 (m, 4 H, $C_6H_4$) ppm. IR (Nujol): $\tilde{\nu}$ = 205 (sh), 202 (s), 199 (sh), 196 (s) $\upsilon$(SnBr) $cm^{-1}$.

**$[SnI_4\{o\text{-}C_6H_4(PMe_2)_2\}]$:** Prepared similarly to the chloride as a brown powder. Yield 80%. $C_{10}H_{16}I_4P_2Sn$ (824.5): calcd. C 14.6, H 2.0; found C 14.6, H 1.9. $^1H$ NMR (300 MHz, $CDCl_3$, 25 °C): $\delta$ = 1.83 (t, $^2J+^5J_{P-H}$ = 4.8 Hz, 12 H, Me), 7.75–7.81 (m, 4 H, $C_6H_4$) ppm.

**$[SnF_4\{o\text{-}C_6H_4(PPh_2)_2\}]$:** $[SnF_4(MeCN)_2]$ (0.276 g, 1.00 mmol) was suspended in $CH_2Cl_2$ (20 mL) and a solution of *o*-$C_6H_4(PPh_2)_2$ (0.446 g, 1.00 mmol) in $CH_2Cl_2$ (5 mL) added and the mixture stirred for 8 h at ambient temperatures. The white precipitate was filtered off and dried in vacuo. Yield 0.17 g, 27%. $C_{30}H_{24}F_4P_2Sn$ (641.2): calcd. C 56.2, H 3.8; found C 56.9, H 4.1. $^1H$ NMR (300 MHz, $CDCl_3$, 25 °C): $\delta$ = 7.30–7.68 (m, Ph) ppm. IR (Nujol): $\tilde{\nu}$ = 574 (s), 557 (s), 526 (s) $\upsilon$(SnF) $cm^{-1}$.

**$[SnF_4(PMe_3)_2]$:** $[SnF_4(MeCN)_2]$ (0.277 g, 1.00 mmol) was suspended in $CH_2Cl_2$ (10 mL), trimethylphosphane (0.167 g, 2.20 mmol) was added and stirred at room temperature for 1 h. Some of the $CH_2Cl_2$ was removed in vacuo and then dry hexane (20 mL) was added. A white solid precipitated out which was filtered off under nitrogen and dried in vacuo. Yield 0.250 g, 68%. $C_6H_{18}F_4P_2Sn\cdot 2CH_2Cl_2$ (516.7): calcd. C 18.6, H 4.3; found C 18.3, H 4.5. $^1H$ NMR (300 MHz, $CDCl_3$, 25 °C): $\delta$ = 1.68 (m, Me), 5.4 ($CH_2Cl_2$) ppm. IR (Nujol): $\tilde{\nu}$ = 546 (br) $\upsilon$(SnF) $cm^{-1}$.

**$[SnF_4(PCy_3)_2]$:** $[SnF_4(MeCN)_2]$ (0.277 g, 1.00 mmol) was suspended in $CH_2Cl_2$ (10 mL), tricyclohexylphosphane (0.588 g, 2.10 mmol) was added and stirred at room temperature for 3 h. No precipitation had occurred so the solution was reduced to ca. 5 mL in vacuo and then dry hexane (5 mL) was added. A white solid precipitated out which was filtered off under nitrogen and dried in vacuo. Yield 0.45 g, 60%. $C_{32}H_{66}F_4P_2Sn\cdot 1/2CH_2Cl_2$ (750.0): calcd. C 54.9, H 8.5; found C 54.4, H 8.8. $^1H$ NMR (300 MHz, $CDCl_3$, 25 °C): $\delta$ = 1.29–2.34 (m, Cy), 5.4 ($CH_2Cl_2$) ppm. IR (Nujol): $\tilde{\nu}$ = 557 (s), 535 (s) $\upsilon$(SnF) $cm^{-1}$.

**$[SnF_4\{Et_2P(CH_2)_2PEt_2\}]$:** $[SnF_4(MeCN)_2]$ (0.278 g, 1.00 mmol) was suspended in $CH_2Cl_2$ (20 mL), 1,2-bis(diethylphosphanyl)ethane (0.28 mL, 1.20 mmol) was added dropwise and stirred for 1.5 h.

 © 2006 Wiley-VCH Verlag GmbH & Co. KGaA, Weinheim 

Table 10. Crystal data and structure refinement details.[a]

| Compound | $[SnF_4(Ph_3PO)_2]\cdot 2CH_2Cl_2$ | $[SnF_4\{Et_2P(CH_2)_2PEt_2\}]$ | $[SnF_4\{MeO(CH_2)_2OMe\}]$ |
|---|---|---|---|
| Formula | $C_{38}H_{34}Cl_4F_4O_2P_2Sn$ | $C_{10}H_{24}F_4P_2Sn$ | $C_4H_{10}F_4O_2Sn$ |
| $M$ | 921.08 | 400.92 | 284.81 |
| Crystal system | monoclinic | monoclinic | monoclinic |
| Space group | $P2_1/n$ (no. 14) | $C2/c$ (no. 15) | $P2_1/n$ (no. 14) |
| $a$ [Å] | 8.8697(16) | 8.8994(12) | 6.2957(15) |
| $b$ [Å] | 14.771(4) | 11.663(3) | 20.987(6) |
| $c$ [Å] | 14.446(4) | 14.774(4) | 6.693(2) |
| $\alpha$ [°] | 90 | 90 | 90 |
| $\beta$ [°] | 95.236(16) | 104.257(12) | 111.941(15) |
| $\gamma$ [°] | 90 | 90 | 90 |
| $U$ [Å$^3$] | 1884.7(8) | 1486.2(5) | 820.2(4) |
| Z | 2 | 4 | 4 |
| $\mu$ [mm$^{-1}$] | 1.101 | 1.956 | 3.137 |
| $F(000)$ | 924 | 800 | 544 |
| Total no. of observations ($R_{int}$) | 21329 (0.138) | 9486 (0.053) | 6388 (0.037) |
| Unique observations | 4312 | 1708 | 1867 |
| Min., max. transmission | 0.681, 1.000 | 0.726, 1.000 | 0.651, 1.000 |
| No. of parameters, restraints | 232, 0 | 78, 0 | 100, 0 |
| Goodness-of-fit on $F^2$ | 0.98 | 1.07 | 1.14 |
| Resid. electron density [e·Å$^{-3}$] | –0.83 to +0.74 | –0.64 to +0.69 | –0.76 to +0.48 |
| $R_1$, $wR_2$ [$I > 2\sigma(I)$][b] | 0.058, 0.106 | 0.030, 0.053 | 0.023, 0.054 |
| $R_1$, $wR_2$ (all data) | 0.135, 0.131 | 0.042, 0.056 | 0.027, 0.056 |

| Compound | [SnF$_4$(1,10-phenanthroline)]·MeOH | $[SnF_4(PCy_3)_2]$ | $[SnCl_4\{Et_2P(CH_2)_2PEt_2\}]$ |
|---|---|---|---|
| Formula | $C_{13}H_{12}F_4N_2OSn$ | $C_{36}H_{66}F_4P_2Sn$ | $C_{10}H_{24}Cl_4P_2Sn$ |
| $M$ | 406.94 | 755.52 | 466.72 |
| Crystal system | tetragonal | triclinic | monoclinic |
| Space group | $I4_1/a$ (no. 88) | $P\bar{1}$ (no. 2) | $C2/c$ (no. 15) |
| $a$ [Å] | 9.471(3) | 8.251(2) | 9.708(3) |
| $b$ [Å] | 9.471(3) | 9.868(3) | 12.177(2) |
| $c$ [Å] | 29.964(8) | 11.832(4) | 16.301(5) |
| $\alpha$ [°] | 90 | 77.192(15) | 90 |
| $\beta$ [°] | 90 | 85.601(10) | 107.108(12) |
| $\gamma$ [°] | 90 | 69.240(15) | 90 |
| $U$ [Å$^3$] | 2687.8(15) | 878.3(4) | 1841.7(9) |
| Z | 8 | 1 | 4 |
| $\mu$ [mm$^{-1}$] | 1.948 | 0.864 | 2.122 |
| $F(000)$ | 1584 | 398 | 928 |
| Total no. of observations ($R_{int}$) | 9075 (0.097) | 18769 (0.088) | 8628 (0.049) |
| Unique observations | 1539 | 4030 | 2100 |
| Min., max. transmission | 0.569, 1.000 | 0.778, 1.000 | 0.722, 1.000 |
| No. of parameters, restraints | 96, 1 | 196, 0 | 80, 0 |
| Goodness-of-fit on $F^2$ | 1.04 | 1.05 | 1.05 |
| Resid electron density [e·Å$^{-3}$] | –1.12 to +1.17 | –0.69 to +0.97 | –0.88 to +1.65 |
| $R_1$, $wR_2$ [$I > 2\sigma(I)$][b] | 0.072, 0.180 | 0.051, 0.101 | 0.054, 0.112 |
| $R_1$, $wR_2$ (all data) | 0.128, 0.207 | 0.070, 0.108 | 0.092, 0.126 |

| Compound | $[SnBr_4\{MeC(CH_2AsMe_2)_3\}]$ |
|---|---|
| Formula | $C_{11}H_{27}As_3Br_4Sn$ |
| $M$ | 822.42 |
| Crystal system | monoclinic |
| Space group | $P2_1/c$ (no. 14) |
| $a$ [Å] | 11.371(2) |
| $b$ [Å] | 12.839(2) |
| $c$ [Å] | 15.227(2) |
| $\alpha$ [°] | 90 |
| $\beta$ [°] | 91.731(10) |
| $\gamma$ [°] | 90 |
| $U$ [Å$^3$] | 2221.9(6) |
| Z | 4 |
| $\mu$ [mm$^{-1}$] | 12.766 |
| $F(000)$ | 1528 |
| Total no. of observations ($R_{int}$) | 22702 (0.064) |
| Unique observations | 5084 |
| Min., max. transmission | 0.767, 1.000 |
| No. of parameters, restraints | 179, 0 |
| Goodness-of-fit on $F^2$ | 1.03 |
| Resid electron density [e·Å$^{-3}$] | –0.91 to +0.84 |
| $R_1$, $wR_2$ [$I > 2\sigma(I)$][b] | 0.026, 0.050 |
| $R_1$, $wR_2$ (all data) | 0.045, 0.053 |

[a] Common items: temperature = 120 K; wavelength (Mo-$K_\alpha$) = 0.71073 Å; $\theta_{max.}$ = 27.5°. [b] $R_1 = \Sigma||F_o|-|F_c||/\Sigma|F_o|$. $wR_2 = [\Sigma w(F_o^2-F_c^2)^2/\Sigma wF_o^4]^{1/2}$.

 © 2006 Wiley-VCH Verlag GmbH & Co. KGaA, Weinheim 

The white precipitate was filtered off and dried in vacuo. Yield 0.32 g, 80%. $C_{10}H_{24}F_4P_2Sn$ (400.95): calcd. C 29.9, H 6.0; found C 29.0, H 6.0. $^1H$ NMR (300 MHz, $CDCl_3$, 25 °C): $\delta$ = 2.13–2.07 (m, 2 H, $CH_2$), 1.37–1.26 (m, 6 H, Me) ppm. IR (Nujol): $\tilde{\nu}$ = 553 (m), 526 (s) $\upsilon$(SnF) $cm^{-1}$.

**[$SnF_4${$Cy_2P(CH_2)_2PCy_2$}]:** [$SnF_4(MeCN)_2$] (0.278 g, 1.00 mmol) was suspended in $CH_2Cl_2$ (10 mL), 1,2-bis(dicyclohexylphosphanyl)ethane (0.444 g, 1.05 mmol) in $CH_2Cl_2$ (5 mL) was added. This was stirred under nitrogen for 3 h. No precipitation had occurred so the solution was reduced to ca. 5 mL in vacuo and then dry hexane (5 mL) was added. Again no significant precipitate was observed so the solvent was removed in vacuo to give a white solid. Yield 0.51 g, 83%. $C_{26}H_{48}F_4P_2Sn{\cdot}1/2CH_2Cl_2$ (826.1): calcd. C 48.2, H 7.5; found C 49.2, H 8.3. $^1H$ NMR (300 MHz, $CDCl_3$, 25 °C): $\delta$ = 2.21–1.255 (m, $CH_2$, Cy), 5.4 ($CH_2Cl_2$) ppm. IR (Nujol): $\tilde{\nu}$ = 560 (s), 530 (s) $\upsilon$(SnF) $cm^{-1}$.

**[$SnF_4${$Ph_2P(CH_2)_2PPh_2$}]:** [$SnF_4(MeCN)_2$] (0.28 g, 1.0 mmol) was suspended in $CH_2Cl_2$ (15 mL), 1,2-bis(diphenylphosphanyl)ethane (0.42 g, 1.05 mmol) in $CH_2Cl_2$ (10 mL) was added and the mixture stirred for 3 h. Most of the solvent was removed in vacuo and the white precipitate was filtered off and dried in vacuo. Yield 0.46 g, 78%. $C_{26}H_{24}F_4P_2Sn{\cdot}1/2CH_2Cl_2$ (635.6): calcd. C 50.0, H 4.0; found C 49.6, H 3.7. $^1H$ NMR (300 MHz, $CDCl_3$, 25 °C): $\delta$ = 7.89–7.45 (m, 5 H, Ph), 5.4 ($CH_2Cl_2$). 2.81 (br, 1 H, $CH_2$) ppm. IR (Nujol): $\tilde{\nu}$ = 566 (br) $\upsilon$(SnF) $cm^{-1}$.

**[$SnCl_4${$Et_2P(CH_2)_2PEt_2$}]:** $SnCl_4$ (0.260 g, 1.00 mmol) was dissolved in $CH_2Cl_2$ (15 mL), 1,2-bis(diethylphosphanyl)ethane (0.245 mL, 1.05 mmol) was added and stirred for 2 h. Immediate precipitation occurred, and the solid was filtered off and dried in vacuo to give a white crystalline solid. Yield 0.45 g, 96%. $C_{10}H_{24}Cl_4P_2Sn{\cdot}CH_2Cl_2$ (551.7): calcd. C 23.95, H 4.8; found C 23.5, H 5.0. $^1H$ NMR (300 MHz, $CDCl_3$, 25 °C): $\delta$ = 2.12–2.11 (m, 6 H, $CH_2$), 1.39–1.21 (m, 6 H, Me), 5.4 ($CH_2Cl_2$) ppm. IR (Nujol): $\tilde{\nu}$ = 318 (sh), 307 (sh), 282 (br) $\upsilon$(SnCl) $cm^{-1}$.

**[$SnF_4$(2,2′-bipyridyl)]:** [$SnF_4(MeCN)_2$] (0.276 g, 1.00 mmol) was suspended in $CH_2Cl_2$ (10 mL) and a solution of 2,2′-bipy (0.156 g, 1.00 mmol) in $CH_2Cl_2$ (5 mL) added and the mixture refluxed for 2 h. The white precipitate was filtered off and dried in vacuo. Yield 0.365 g, 97%. $^1H$ NMR (300 MHz, $CD_3NO_2$, 25 °C): $\delta$ = 9.41 (s, 1 H), 9.15 (s, 1 H), 8.99 (s, 1 H), 8.49 (s, 1 H) ppm. IR (Nujol): $\tilde{\nu}$ = 580 (s), 560, 520 (sh) $\upsilon$(SnF) $cm^{-1}$.

**[$SnF_4$(1,10-phenanthroline)]:** Prepared similarly to the above. Yield 60%. $^1H$ NMR (300 MHz, $CDCl_3$, 25 °C): $\delta$ = 9.35 (m, 2 H), 9.16 (m, 2 H), 8.45 (m, 4 H) ppm. IR (Nujol): $\tilde{\nu}$ = 587 (s), 566 (s) $\upsilon$(SnF) $cm^{-1}$.

**[$SnF_4${$MeO(CH_2)_2OMe$}]:** 1,2-Dimethoxyethane (0.1 mL, 1.0 mmol) was added to a solution of [$SnF_4(MeCN)_2$] (0.276 g, 1.0 mmol) in $CH_2Cl_2$ (10 mL), and the mixture stirred at reflux for 2 h. The white precipitate was filtered off and dried in vacuo. Yield 77%. $^1H$ NMR (300 MHz, $CDCl_3$, 200 K): $\delta$ = 3.98 (s, 3 H, Me), 4.25 (s, 2 H, $CH_2$) ppm. IR (Nujol): $\tilde{\nu}$ = 609 (s), 584 (s), 540 (m) $\upsilon$(SnF) $cm^{-1}$.

**[$SnF_4$(pyridine)$_2$]:** Pyridine (0.16 g, 2.0 mmol) was added to a solution of [$SnF_4(MeCN)_2$] (0.186 g, 0.67 mmol) in $CH_2Cl_2$ (10 mL). This was stirred at reflux under nitrogen for 2 h. The white precipitate was filtered off and dried in vacuo. Yield 80%. $^1H$ NMR (300 MHz, $CDCl_3$, 25 °C): $\delta$ = 9.00 (m, 2 H), 8.2 (m, 1 H), 7.7 (m, 2 H) ppm. IR (Nujol): $\tilde{\nu}$ = 568 (s) $\upsilon$(SnF) $cm^{-1}$.

**[$SnF_4${$Me_2N(CH_2)_2NMe_2$}]:** [$SnF_4(MeCN)_2$] (0.276 g, 1.0 mmol) was suspended in $CH_2Cl_2$ (10 mL), *N*,*N*,*N*′*N*′-tetramethylethylenediamine (0.15 g, 1.00 mmol) was added and the mixture stirred for 12 h. The white precipitate was filtered off and dried in vacuo. Yield 0.14 g, 54%. $C_6H_{16}F_4N_2Sn{\cdot}1/2CH_2Cl_2$ (277.4): calcd. C 22.1, H 4.9, N 7.9; found C 22.3, H 5.1, N 8.1. $^1H$ NMR (300 MHz, $CDCl_3$, 25 °C): $\delta$ = 2.89 (s, 12 H, Me), 3.02 (s, 4 H, $CH_2$) ppm. IR (Nujol): $\tilde{\nu}$ = 570 (s), 547 (s) $\upsilon$(SnF) $cm^{-1}$.

**[$SnF_4$(THF)$_2$]:** Was made as described.[18] $^1H$ NMR (300 MHz, $CDCl_3$, 25 °C): $\delta$ = 2.1 (br., 2 H, $CH_2$), 4.4(br., 2 H, $CH_2$) ppm. IR (Nujol): $\tilde{\nu}$ = 600 (vbr) $\upsilon$(SnF), 1013 (br), 845 (m) $\upsilon$(COC) $cm^{-1}$.

**[$SnCl_4${$MeC(CH_2AsMe_2)_3$}]:** $MeC(CH_2AsMe_2)_3$ (0.384 g, 1.0 mmol) was dissolved in $CH_2Cl_2$ (10 mL) under nitrogen. To this solution $SnCl_4$ (0.26 g, 1.0 mmol) was added and an immediate white precipitate formed. This was filtered off and dried in vacuo to give a white powder. Yield 0.21 g, 33%. $^1H$ NMR (300 MHz, $CDCl_3$, 25 °C): $\delta$ = 1.03 (s, 6 H, AsMe), 1.35 (s, 3 H, CMe), 1.73 (s, 12 H, AsMe), 1.77 (s, 2 H, $CH_2$), 2.39 (d, $^2J$ = 12 Hz, 2 H, $CH_2$) 2.54 (d, $^2J$ = 12 Hz, 2 H, $CH_2$) ppm. IR (Nujol): $\tilde{\nu}$ = 310 (sh), 302 (s), 280 (sh) $\upsilon$(SnCl) $cm^{-1}$.

**[$SnBr_4${$MeC(CH_2AsMe_2)_3$}]:** $MeC(CH_2AsMe_2)_3$ (0.384 g, 1.0 mmol) was dissolved in $CH_2Cl_2$ (10 mL) under nitrogen. To this solution $SnBr_4$ (0.438 g, 1.0 mmol) was added and an immediate yellow precipitate formed in a yellow solution. This was filtered and the filtrate was left to stand to give yellow crystals. Yield 0.18 g, 22%. $C_{11}H_{27}As_3Br_4Sn$ (822.4): calcd. C 16.1, H 3.3; found C 15.3, H 3.1. $^1H$ NMR (300 MHz, $CDCl_3$, 25 °C): $\delta$ = 1.04 (s, 6 H, AsMe), 1.37 (s, 3 H, CMe), 1.70 (br., 12 H, AsMe), 1.78 (br., 2 H, $CH_2$), 2.32 (br., 2 H, $CH_2$) 2.55 (br., 2 H, $CH_2$) ppm. IR (Nujol): $\tilde{\nu}$ = 215 (sh), 207 (s), 199 (s) $\upsilon$(SnBr) $cm^{-1}$.

**X-ray Experimental:** Crystals were grown from anhydrous $CH_2Cl_2$ solutions of the complexes by vapour diffusion of *n*-hexane under dinitrogen. Brief details of the crystal data and refinement are given in Table 10. Data collections were carried out with a Bruker-Nonius Kappa CCD diffractometer with graphite-monochromated Mo-$K_\alpha$ radiation ($\lambda$ = 0.71073 Å) and with the crystals held at 120 K in a nitrogen gas stream. Structure solution and refinement were routine[39–41] except as discussed below, with in all cases H atoms added in calculated positions. The [$SnF_4$(1,10-phenanthroline)]·MeOH complex showed, after identifying the tin residue, two peaks in the difference electron-density map associated with a solvent molecule. The larger of the peaks positioned on a twofold axis (proposed as an O atom) with the second peak and its symmetry related peak being a disordered C atom of an adventitious MeOH solvate molecule. No attempt was made to position H atoms on this residue.

CCDC-299706 [for F/O(P)], -299707 [for F/P($Et_2$)], -299708 [for F/O(Me)], -299709 (for F/N), -299710 [for F/P($R_3$)], -299711 (for Cl/P), -299712 (for Br/As) contain the supplementary crystallographic data for this paper (the atoms in parentheses indicate the atoms bonded to Sn). These data can be obtained free of charge from The Cambridge Crystallographic Data Centre via www.ccdc.cam.ac.uk/data_request/cif.

## Acknowledgments

We thank EPSRC for support (GR/T09613/01).

[1] P. G. Harrison (Ed.), *The Chemistry of Tin*, Blackie, London, **1984**.
[2] P. G. Harrison, in *Comprehensive Coordination Chemistry* (Eds.: G. Wilkinson, R. D. Gillard, J. A. McCleverty), Pergamon Press, Oxford, **1987**, vol. 3., chap. 26.

 © 2006 Wiley-VCH Verlag GmbH & Co. KGaA, Weinheim 

[3] P. G. Harrison, B. C. Lane, J. J. Zuckerman, *Inorg. Chem.* **1972**, *11*, 1537–1543.
[4] E. W. Abel, S. K. Bhargava, K. G. Kite, V. Sik, *Inorg. Chim. Acta* **1981**, *49*, 25–30.
[5] a) S. J. Ruzicka, A. E. Merbach, *Inorg. Chim. Acta* **1976**, *20*, 221–229; b) S. J. Ruzicka, C. M. P. Favez, A. E. Merbach, *Inorg. Chim. Acta* **1977**, *23*, 239–247.
[6] S. E. Dann, A. R. J. Genge, W. Levason, G. Reid, *J. Chem. Soc., Dalton Trans.* **1996**, 4471–4478.
[7] S. E. Dann, A. R. J. Genge, W. Levason, G. Reid, *J. Chem. Soc., Dalton Trans.* **1997**, 2207–2213.
[8] A. R. J. Genge, W. Levason, G. Reid, *J. Chem. Soc., Dalton Trans.* **1997**, 4549–4554.
[9] A. R. J. Genge, W. Levason, G. Reid, *Inorg. Chim. Acta* **1999**, *288*, 142–149.
[10] W. Levason, M. L. Matthews, R. Patel, G. Reid, M. Webster, *New J. Chem.* **2003**, *27*, 1784–1788.
[11] A. A. Woolf, *J. Inorg. Nucl. Chem.* **1956**, *3*, 285–288.
[12] J. P. Clark, V. M. Langford, C. J. Wilkins, *J. Chem. Soc. A* **1967**, 792–794.
[13] C. E. Michelson, D. S. Dyer, R. O. Ragsdale, *J. Inorg. Nucl. Chem.* **1970**, *32*, 833–838.
[14] C. J. Wilkins, H. M. Haendler, *J. Chem. Soc.* **1965**, 3174–3178.
[15] S. H. Hunter, V. M. Langford, G. A. Rodley, C. J. Wilkins, *J. Chem. Soc. A* **1968**, 305–308.
[16] A. D. Adley, P. H. Bird, A. R. Fraser, M. Onyszchuk, *Inorg. Chem.* **1972**, *11*, 1402–1409.
[17] M. Bork, R. Hoppe, *Z. Anorg. Allg. Chem.* **1996**, *622*, 1557–1563.
[18] a) D. Tudela, F. Rey, *Z. Anorg. Allg. Chem.* **1989**, *575*, 202–208; b) D. Tudela, F. Patron, *Inorg. Synth.* **1997**, *31*, 92–93.
[19] M. F. Davis, W. Levason, G. Reid, M. Webster, *Polyhedron* **2006**, *25*, 930–936.
[20] G. G. Mather, G. M. McLaughlin, A. Pidcock, *J. Chem. Soc., Dalton Trans.* **1973**, 1823–1827.
[21] D. Dakternieks, H. Zhu, E. R. T. Tiekink, *Main Group Met. Chem.* **1994**, *17*, 519–535.
[22] N. Bricklebank, S. M. Godfrey, C. A. McAuliffe, R. G. Pritchard, *J. Chem. Soc., Chem. Commun.* **1994**, 695–696.
[23] G. R. Willey, T. J. Woodman, R. J. Deeth, W. Errington, *Main Group Met. Chem.* **1998**, *21*, 583–591.
[24] V. J. Hall, E. R. T. Tiekink, *Z. Kristallogr.* **1996**, *211*, 247–250.
[25] V. N. Zakharov, A. V. Yatsenko, A. L. Kamyshnyi, L. A. Aslanov, *Koord. Khim.* **1991**, *17*, 789–794; (*Chem. Abstr.* **1991**, *115*, 291749v).
[26] K. A. Paseshnichenko, L. A. Aslanov, A. V. Yatsenko, S. V. Medvedev, *Koord. Khim.* **1984**, *10*, 1279–1284; (*Chem. Abstr.* **1984**, *101*, 220263 g).
[27] W. Levason, R. Patel, G. Reid, *J. Organomet. Chem.* **2003**, *688*, 280–282.
[28] F. Kunnkel, K. Dehnicke, *Z. Naturforsch., Teil B* **1995**, *50*, 848–850.
[29] a) L. F. Warren, M. A. Bennett, *Inorg. Chem.* **1976**, *15*, 3126–3140; b) W. Levason, *Comments Inorg. Chem.* **1990**, *9*, 331–361.
[30] M. F. Mahon, N. L. Moldovan, K. C. Molloy, A. Muresan, I. Silaghi-Dumitrescu, L. Silaghi-Dumitrescu, *Dalton Trans.* **2004**, 4017–4021.
[31] P. A. W. Dean, D. F. Evans, *J. Chem. Soc. A* **1968**, 1154–1166.
[32] K. B. Dillon, A. Marshall, *J. Chem. Soc., Dalton Trans.* **1984**, 1245–1247.
[33] J. Mason (Ed.), *Multinuclear NMR*, Plenum, NY, **1987**.
[34] M. Sigl, A. Schier, H. Schmidbauer, *Eur. J. Inorg. Chem.* **1998**, 203–210.
[35] R. D. Feltham, R. S. Nyholm, A. Kasenally, *J. Organomet. Chem.* **1967**, *7*, 285–288.
[36] H. C. E. McFarlane, W. McFarlane, *Polyhedron* **1983**, *2*, 303–304.
[37] A. M. Aguiar, J. Beisler, *J. Org. Chem.* **1964**, *29*, 1660–1662.
[38] E. P. Kyba, S. T. Liu, R. L. Harris, *Organometallics* **1983**, *2*, 1877–1879.
[39] G. M. Sheldrick, SHELXS-97, *Program for crystal structure solution*, University of Göttingen, Germany, **1997**.
[40] G. M. Sheldrick, SHELXL-97, *Program for crystal structure refinement*, University of Göttingen, Germany, **1997**.
[41] G. M. Sheldrick, SADABS, *Bruker-Nonius area detector scaling and absorption correction* (V2.10), University of Göttingen, Germany, **2003**.

Received: March 6, 2006
Published Online: May 2, 2006

 © 2006 Wiley-VCH Verlag GmbH & Co. KGaA, Weinheim 

DOI: 10.1002/ejic.200500948

# Zinc Thiolate Complexes $[ZnL_n(SR)]^+$ with Azamacrocyclic Ligands, Part II: Mechanism of the Reaction with $CS_2$[‡]

**Johannes Notni,[a] Stephan Schenk,[a] Arne Roth,[b] Winfried Plass,[b] Helmar Görls,[c] Ute Uhlemann,[d] Angela Walter,[d] Michael Schmitt,[d] Jürgen Popp,[d] Susana Chatzipapadopoulos,[d] Thomas Emmler,[e] Hergen Breitzke,[d] Jörg Leppert,[f] Gerd Buntkowsky,[d] Kristian Kempe,[a] and Ernst Anders*[a]**

**Keywords:** Zinc / Macrocyclic ligands / Enzyme models / Heterocumulenes / Density functional calculations

The thiolate complexes $[Zn([15]aneN_4)(S–CH_2–C_6H_5)]ClO_4$ (**1**) ([15]aneN$_4$ = 1,4,8,12-tetraazacyclopentadecane) and $[Zn(i\text{-}[14]aneN_4)(S–CH_2–C_6H_5)]ClO_4$ (**2**) (*i*-[14]aneN$_4$ = 1,4,7,11-tetraazacyclotetradecane) have been reacted with carbon disulfide. The trithiocarbonate complexes $[Zn([15]aneN_4)\{S–C(S)–S–CH_2–C_6H_5\}]ClO_4$ {**1a**, monoclinic, space group $P2_1/n$, $Z = 8$, $a = 13.2338(1)$ Å, $b = 12.9251(2)$ Å, $c = 30.1669(4)$ Å, $\beta = 101.463(1)°$, $V = 5057.1(1)$ Å$^3$} and $[Zn(i\text{-}[14]aneN_4)\{S–C(S)–S–CH_2–C_6H_5\}]ClO_4$ {**2a**, orthorhombic, space group $P2_12_12_1$, $Z = 8$, $a = 9.9936(1)$ Å, $b = 22.1261(4)$ Å, $c = 22.3192(4)$ Å, $V = 4935.2(1)$ Å$^3$} were obtained. The reaction of **1** with $CS_2$ is second order with a rate constant of $k = (57.6 \pm 2.4) \times 10^{-3}$ M$^{-1}$·s$^{-1}$ at 25 °C. The experimentally determined Eyring activation barrier is $\Delta H_{exp}^{‡} = 65.3 \pm 0.7$ kJ·mol$^{-1}$ ($\Delta S_{exp}^{‡} = -49.9 \pm 2.5$ J·mol$^{-1}$·K$^{-1}$) and a free energy of activation of $\Delta G^{‡} = 80.2 \pm 1.5$ kJ·mol$^{-1}$ at 25 °C. To discriminate between an associative and a dissociative mechanism the barriers for both processes were calculated using density functional theory at the C-PCM(B98/G3MP2Large)//B3LYP/6-311+G(d) level. The associative mechanism is clearly favored with a difference in free energies of activation of $\delta\Delta G^{‡} \approx 80$ kJ·mol$^{-1}$. Its calculated barrier $\Delta G_{theor}^{‡} = 114.3$ kJ·mol$^{-1}$ is in reasonable agreement with the experimental value.

(© Wiley-VCH Verlag GmbH & Co. KGaA, 69451 Weinheim, Germany, 2006)

## Introduction

Carbonic anhydrase (CA) is a ubiquitous zinc enzyme that accelerates the reversible hydration of $CO_2$ by a factor of up to $10^7$ when compared with the uncatalyzed reaction.[2–4] This enzymatic process is very important in all living organisms for the exchange of $CO_2$ with the atmosphere. (Detailed references to the numerous studies concerning the catalytic mechanism are given elsewhere.[2,5]) The rate-determining step of the reaction is the nucleophilic attack of a zinc-bound hydroxide ligand on carbon dioxide. From quantum mechanical calculations it has been concluded that the reaction proceeds via a four-center transition structure (see Scheme 1).[6,7]

Recent studies of Kesselmeier et al. have shown that CA is also implicated in the fixation of COS, a sulfur-containing heterocumulene that occurs as a trace gas in the atmosphere.[8] This process is performed by many organisms, such as higher plants,[9] algae,[10] lichens,[11] and even by components of the soil.[12] This interconversion has been reproduced experimentally by reacting an established CA model, $[Tp^{Ph,Me}ZnOH]$, with COS.[13] In the course of the reaction, $CO_2$ is released and the sulfur-analog complex $Tp^{Ph,Me}ZnSH$ is obtained. In addition, this complex is also formed by reacting $Tp^{Ph,Me}ZnOH$ with $CS_2$. In this case, COS is produced instead of $CO_2$, which in turn is capable of reacting with the zinc hydroxide complex to yield $CO_2$. This type of reaction, the fixation of sulfur-containing heterocumulenes by CA model compounds, has also been studied by us using computational methods.[5,14] In analogy to the fixation of $CO_2$, it has been found for all the studied systems that the insertion of the heterocumulene into the Zn–O bond via a four-center transition structure is the rate-determining step of the reaction.[5,6,14]

These studies show that the reaction of natural carbonic anhydrase is likely to result in the formation of a sulfur-analog enzyme with a hydrosulfide instead of a hydroxide

[‡] For further reference see: Zinc Thiolate Complexes $[ZnL_n(SR)]^+$ with Azamacrocyclic Ligands, Part I: Synthesis and Structural Properties[1]

[a] FSU Jena, Institut für Organische Chemie und Makromolekulare Chemie,
Humboldtstr. 10, 07743 Jena, Germany
E-mail: ernst.anders@uni-jena.de
[b] FSU Jena, Institut für Anorganische und Analytische Chemie, Carl-Zeiss-Promenade 10, 07745 Jena, Germany
[c] FSU Jena, Institut für Anorganische und Analytische Chemie, Lessingstr. 8, 07743 Jena, Germany
[d] FSU Jena, Institut für Physikalische Chemie, Helmholtzweg 4, 07743 Jena
[e] FU Berlin, Institut für Chemie und Biochemie, Takustr. 3, 14195 Berlin
[f] Leibniz Institut für Altersforschung, Beutenbergstr. 11, 07745 Jena

Supporting information for this article is available on the WWW under http://www.eurjic.org or from the author.

 © 2006 Wiley-VCH Verlag GmbH & Co. KGaA, Weinheim 

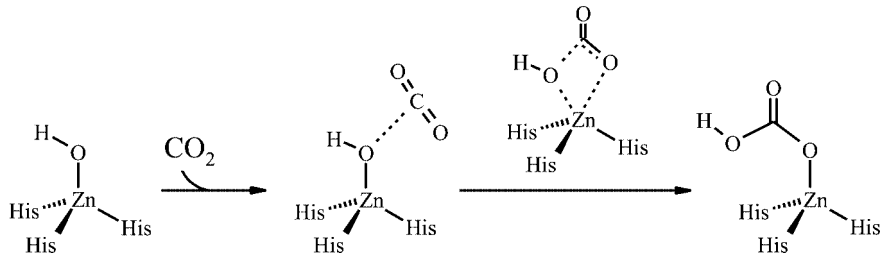


Scheme 1. Insertion of carbon dioxide into the Zn–S bond of CA.

ligand. Since this reaction is exothermic, natural CA would become inactivated in this 'sulfurated state'.[5] Kesselmeier et al. have pointed out, though, that in the case of lichens, atmospheric sulfur compounds are the only available source of sulfur.[11] Apparently, the fixation of sulfur-containing compounds by CA is not a side reaction but rather essential for some organisms. This gives rise to the question of how CA can dispose of the sulfur in order to be reactivated. In a preceding theoretical study of a CA model system, a nucleophilic reaction of the Zn–SH moiety with $CO_2$ has been proposed for regeneration of the active catalyst.[5] However, until now this theory has not been supported by any experimental investigations.

In this work, we report on a reaction of the $CS_2$ with a zinc thiolate complex. We are fully aware that this may seem to be a large stretch of the subject. Nevertheless, the results are of value for the understanding of the reaction principles of a zinc-bound sulfur nucleophile with heterocumulenes in general. It is worth noting that a similar reaction has not previously been reported in the literature; even the available structural models for the sulfur-analog CA, e.g. $Tp^{Ph,Me}ZnSH$,[15] do not react with heterocumulenes. In the past, numerous computational studies have examined the fixation of heterocumulenes by zinc hydroxide complexes, but only one addresses zinc hydrosulfides and the mechanism of their heterocumulene reactions.[5] The results presented in this work are the first steps in elucidating the mode of heterocumulene fixation by sulfur-analog CA models. Investigations concerning the reactions of COS and $CO_2$ will be published soon.

## Results

### Heterocumulene Insertions

The starting materials, thiolate complexes **1** and **2** (see Scheme 2), are examples of a series of 24 novel zinc thiolate complexes.[1] The progress of the $CS_2$ insertion reaction can easily be monitored by the appearance of a yellow color from the formation of the trithiocarbonates. When reacting the neat substances with $CS_2$, only a very slow reaction was observed. This is not surprising, since the thiolates are virtually insoluble in $CS_2$. The reaction is obviously not possible while the complex cations are fixed in the crystal lattice. In contrast to this, the reaction proceeds quite fast when the starting materials are dissolved.

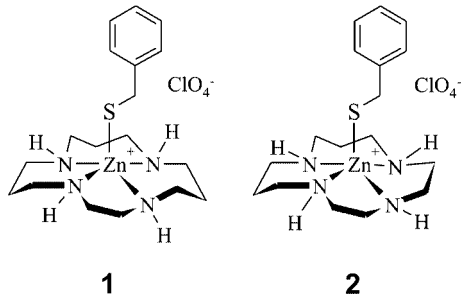


Scheme 2. Thiolate complexes **1** and **2**.

### *Structures*

Compounds **1a** (Figure 1) and **2a** (Figure 2) precipitated from concentrated dichloromethane solutions upon addition of a large excess of $CS_2$. Yellow crystals were obtained that were subjected to an X-ray crystallographic structure determination. The configuration of the four N atoms in the trithiocarbonates is the same as that found for the corresponding thiolates.[1] One of the N-bound hydrogens is found on the thiolate side of the ligand and three are located on the opposite side [the so-called (+ – – –)-configuration[16,17]]. For both compounds, the crystal lattices comprise two independent molecules with differences in conformation and bond lengths. In the case of **1a**, these

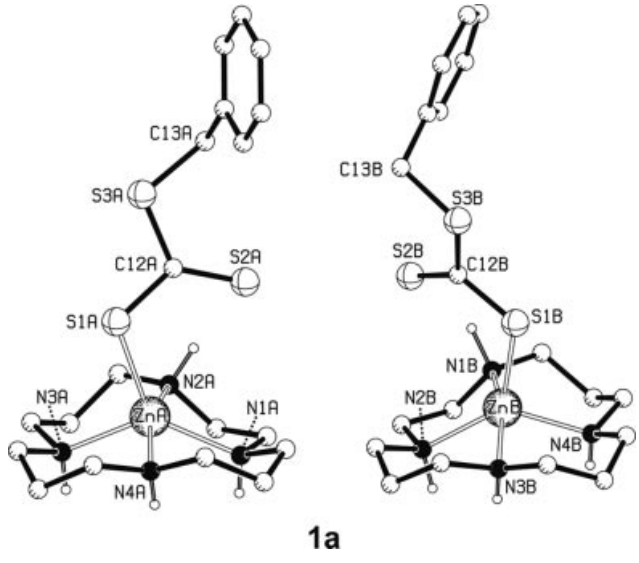


Figure 1. Molecular structures of the trithiocarbonate complex cation of **1a**.

 © 2006 Wiley-VCH Verlag GmbH & Co. KGaA, Weinheim 

two molecules are enantiomers because of the configuration of the nitrogen donors, which does not match the symmetry of the ligand, as was found for **2a**. However, the structural parameters of all trithiocarbonate moieties show very little variation and the Zn–S distances of both **1a** and **2a** are almost identical (Table 1).

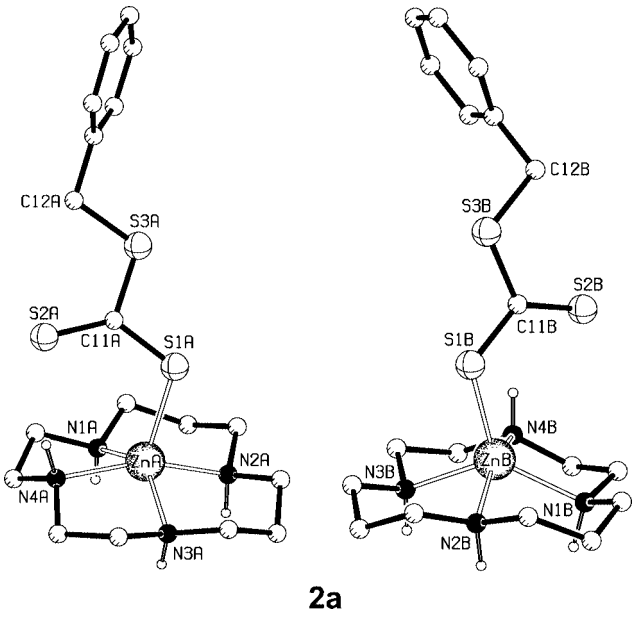


Figure 2. Molecular structures of the trithiocarbonate complex cation of **2a**.

Table 1. Selected bond lengths [Å] and angles [°] for **1a** and **2a** (atom numbers of **2a** are given in parentheses where they are different from **1a**).

| Value | **1a** (A) | **1a** (B) | **2a** (A) | **2a** (B) |
|---|---|---|---|---|
| Zn–S1 | 2.373(1) | 2.363(1) | 2.373(1) | 2.353(1) |
| Zn–N1 | 2.153(4) | 2.187(4) | 2.101(4) | 2.110(4) |
| Zn–N2 | 2.188(3) | 2.117(4) | 2.144(3) | 2.176(4) |
| Zn–N3 | 2.117(3) | 2.209(3) | 2.106(4) | 2.149(4) |
| Zn–N4 | 2.169(3) | 2.110(3) | 2.149(4) | 2.185(4) |
| C12(C11)–S1 | 1.723(3) | 1.720(4) | 1.722(4) | 1.708(4) |
| C12(C11)–S2 | 1.639(4) | 1.640(4) | 1.658(4) | 1.652(5) |
| C12(C11)–S3 | 1.750(3) | 1.756(3) | 1.739(4) | 1.755(5) |
| S3–C13(C12) | 1.806(4) | 1.816(4) | 1.813(5) | 1.823(6) |
| Zn–S1–C12(C11) | 107.3(1) | 108.6(1) | 112.5(2) | 109.9(2) |
| S1–C12(C11)–S2 | 126.8(2) | 128.0(2) | 130.3(3) | 128.1(3) |
| S1–C12(C11)–S3 | 108.4(2) | 108.2(2) | 108.2(2) | 108.9(3) |
| S2–C12(C11)–S2 | 124.8(2) | 134.8(2) | 121.4(2) | 123.0(3) |
| C12(C13)–S3–C13(C12) | 105.6(2) | 105.7(2) | 105.3(2) | 106.1(3) |

### *NMR Spectra*

For the NMR spectroscopic investigations, chloroform solutions of **1** and **2** containing an equimolar amount and a 10-fold excess of $CS_2$ were analyzed. In these solutions, complexes **1a** and **2a** exist in a dynamic equilibrium with **1** and **2**, respectively (see Scheme 4). This causes all carbon atoms, particularly the trithiocarbonate carbons, to exhibit an increased line width in the $^{13}C$ spectra. Thus, their detection requires a large number of scans (>10.000) in order to reduce the signal-to-noise ratio.

Table 2 shows that upon addition of a 10-fold molar excess of $CS_2$ compound **1** is converted nearly completely to the trithiocarbonate **1a**, whereas the turnover is only two thirds for **2a** under the same conditions. This renders the reaction of **1** to **1a** suitable for the investigation of subsequent reactions and for determination of the thermal parameters of the insertion. Furthermore, it is worth noting that small changes of the macrocyclic ligand can have a dramatic effect on the reactivity of the thiolate, even though the structural parameters of the substrates and the products are nearly identical.

Table 2. Turnover of thiolates to trithiocarbonates in chloroform solutions containing different amounts of $CS_2$ (derived from $^1H$ NMR spectroscopic data).

| Mol. equiv. of $CS_2$ | **1a** [%] | **2a** [%] |
|---|---|---|
| 1 | 50 | 19 |
| 10 | >98 | 67 |

The $^{13}C$ NMR spectrum of **1a** shows 12 methylene signals. This indicates that the molecule has an asymmetric structure in a chloroform solution. It is most probable that the (+ – – –)-configuration is adopted, analogous with the solid-state structure. In contrast to the thiolate complex **1**,[1] the NMR spectra of **1a** do not provide any evidence for the presence of a second configurational isomer. As mentioned above, the zinc(II) ion of **1a** is chiral in nature due to the asymmetric configuration of the macrocyclic ligand. Thus, the benzyl protons of **1a** are in a diastereotopic environment. Nevertheless, the increased multiplicity of the corresponding NMR signals found for **1**[1] was not observed in the $^1H$ NMR spectrum of **1a**. This is a result of the spacer function of the trithiocarbonate moiety. The benzyl protons of **1a** are located at a much larger distance from the zinc atom than in complex **1**. The influence of the center of chirality is thus reduced to a minimum.

### *Solid-State NMR Spectroscopy*

While the thiolate complexes **1** and **2** do not have any spectral intensity in the range 230–240 ppm, the $^{13}C$ NMR spectra of the insertion products show strong signals in this spectral region. These lines show the formation of a thiocarbonyl group and thus corroborate the proposed structure of the trithiocarbonate moiety. Interestingly, both the thiocarbonyl line of **1a** and the line of the quaternary aromatic carbon C14 exhibit a splitting into an asymmetric doublet. These splittings reflect the conformational polymorphism of **1a**, which obviously is not as pronounced in **2a**. A splitting of the corresponding lines could not be observed in this case. (For graphical representations of all spectra and peak assignments see the Supporting Information.)

### *Raman Spectroscopy*

Complexes **1** and **1a** have also been investigated using Raman spectroscopy. Two strong signals at 507 and 1032 $cm^{-1}$ appear in the spectra of the reaction product **1a**. These are because of the symmetric (SCS) and the (C=S)

 © 2006 Wiley-VCH Verlag GmbH & Co. KGaA, Weinheim 

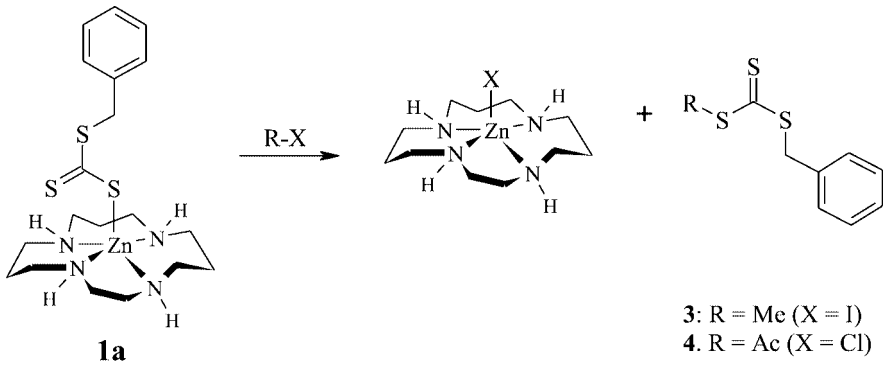


Scheme 3. Reaction of the trithiocarbonate complex **1a** with electrophiles (only cations shown).

vibration, respectively, which correspond to the trithiocarbonate moiety of **1a**. At the same time, a signal at 1223 $cm^{-1}$ decreases in intensity. Raman monitoring of the reaction has shown that the formation of **1a** occurs in a clean reaction. Currently, we have no evidence for the formation of any intermediates or side products. (For a graphical representation of the spectra and a more detailed discussion see Supporting Information.)

### *Reactions of Complex 1a*

Similar to the thiolates, the trithiocarbonate complexes possess nucleophilic properties, as was found when reacting compound **1a** with electrophiles (see Scheme 3). Methyl iodide was added to a concentrated solution of **1** with a 10-fold excess of $CS_2$. As mentioned above, under these conditions the equilibrium is almost completely shifted to the insertion product **1a**. However, the reaction product of **1** with methyl iodide, which is benzyl methyl sulfide, was isolated in approx. 20% yield. Obviously, the thiolate **1** reacts several times faster than the trithiocarbonate **1a**, most likely because of the higher nucleophilicity of the thiolate sulfur in **1**. The quenching reaction with acetyl chloride results in the formation of the corresponding acetyl-substituted benzyltrithiocarbonate. The products were isolated and identified by their NMR spectra, which were known from authentic samples prepared for this purpose (see Exp. Sect.).

## Mechanism of $CS_2$ Insertion

The possible reaction mechanisms for the insertion of $CS_2$ into the Zn–S bond are outlined in Scheme 4. An attack of the zinc-bound thiolate on the carbon disulfide should result in clean second-order kinetic behavior of the reaction (path A). We assume that this is the preferred mechanism in a nonpolar solvent. An attack of the free thiolate (path B) should be much faster than the preliminary dissociation of the complex and result in clean first-order kinetics. Nevertheless, one could possibly observe second-order kinetics because of the perturbation effects or in the case where the dissociation step is unexpectedly not much slower than the $CS_2$ reaction. Thus, both mechanisms cannot be distinguished simply by comparing the order of their reaction kinetics. It is highly improbable, though, that the actual rate constants and activation barriers of both reaction modes are identical. Hence, we determined the activation barrier of this reaction and compared it with the calculated value for both of the possible pathways.

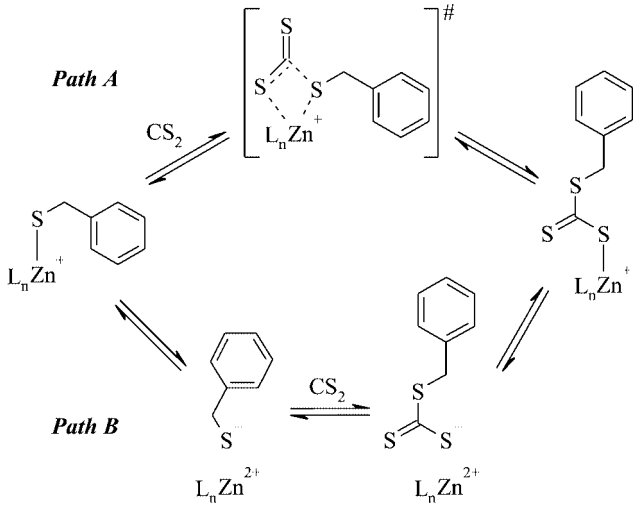


Scheme 4. Possible mechanisms for the formation of the trithiocarbonate complexes **1a** and **2a**.

### *Kinetic Study*

Since the insertion product **1a** absorbs at 434 nm the reaction progress could be monitored using electronic spectroscopy. At room temperature, the reaction proceeds on a time scale of minutes. Thus it was convenient to measure the rate constants at temperatures between 10 and 35 °C.

Because the reaction is an equilibrium reaction, the obtained data are a superposition of forward and backward reactions. In order to determine only the kinetic parameters of the insertion reaction, the perturbation effect of the back reaction must be eliminated. This was achieved by reacting **1** with $CS_2$ under pseudo first-order conditions. Only the data collected immediately after the start of the reaction were employed for the calculation of the rate constants.

A solution of **1** (0.05 M) was treated with a 20-fold excess of carbon disulfide. Under these conditions, the equilibrium is virtually completely shifted to the side of the insertion product. This was verified by NMR spectroscopy. The loga-

 © 2006 Wiley-VCH Verlag GmbH & Co. KGaA, Weinheim 

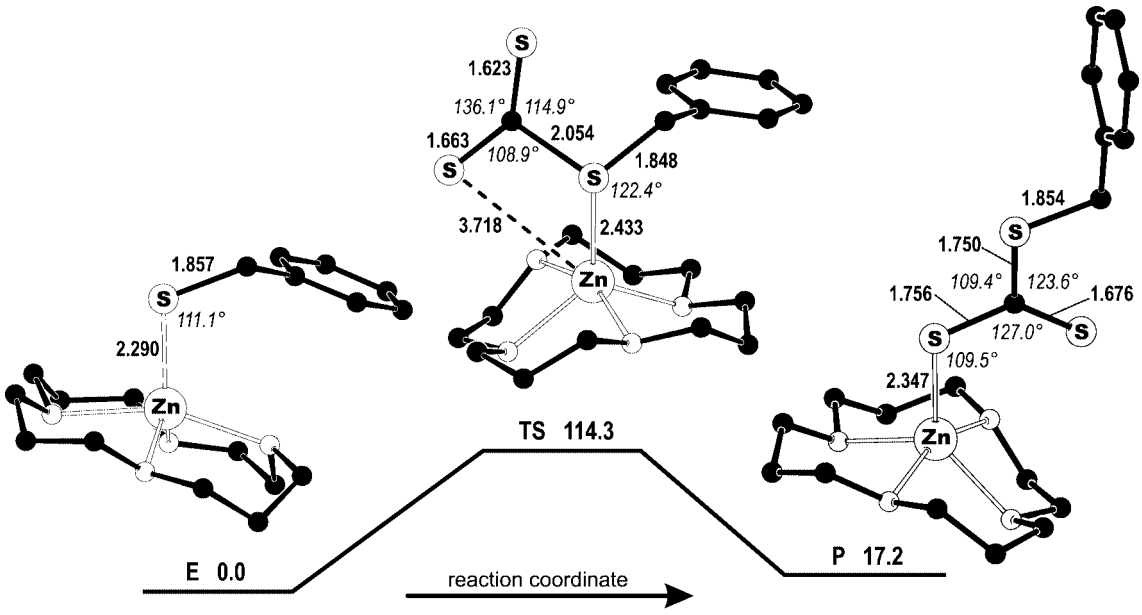


Figure 3. Structures and energy profile of the fixation of $CS_2$ by **1**, calculated at the C-PCM(B98/G3MP2Large)//B3LYP/6-311+G(d) level of theory. $\Delta G$ values are given in kJ·mol$^{-1}$.

rithmic plots employed for the calculation of the rate constants show only a very small variation from linearity with standard deviations of less than 1%. This emphasizes the clean pseudo first-order kinetic behavior of the observed reaction and proves that the perturbation effect of the back reaction is insignificant. Thus, the obtained kinetic and thermal parameters reliably represent the second-order insertion reaction. Analysis of a data set of 21 rate constants according to the Eyring theory resulted in $\Delta H^{\ddagger}$ = 65.3 ± 0.7 kJ·mol$^{-1}$ and $\Delta S^{\ddagger}$ = –49.9 ± 2.5 J·mol$^{-1}$·K$^{-1}$. The resulting free energy of activation at 25 °C is $\Delta G^{\ddagger}$ = 80.2 ± 1.5 kJ·mol$^{-1}$.

### *Quantum Mechanical Calculations*

The geometries of the starting material (**E**), the transition structure (**TS**), and the product (**P**) of the associative mechanism were optimized at the B3LYP/6-311+G(d) level of theory (Figure 3). For both **E** and **P** the X-ray structures of **1** and **1a**, respectively, served as starting points. The effect of the solvent chloroform on the reaction has been incorporated through the C-PCM model by B98/G3MP2Large single point calculations using the previously optimized B3LYP gas phase geometries. (For more detailed information see Computational Details.)

For the associative mechanism, the free energy of activation was calculated to be $\Delta G^{\ddagger}$ = 114.3 kJ·mol$^{-1}$. For comparison with the experimental results, the enthalpy of activation was computed to be $\Delta H^{\ddagger}$ = 60.7 kJ·mol$^{-1}$. The overall reaction is slightly endergonic ($\Delta_R G$ = 17.2 kJ·mol$^{-1}$).

For the dissociative mechanism a lower limit for the activation energy was estimated by calculating the energy required for the dissociation of **1** according to Equation (1) at the same level of theory. The initial dissociation of **E** requires $\Delta G$ = 191.8 kJ·mol$^{-1}$ and the barrier is thus quite substantial. Upon reaction with $CS_2$ the energy decreases slightly to $\Delta G$ = 165.4 kJ·mol$^{-1}$.

$$[Zn([15]aneN_4)(C_7H_7)]^+ \rightleftharpoons [Zn([15]aneN_4)]^{2+} + (C_7H_7)^- \quad (1)$$

## Discussion

The main issue we want to address in this work is the question of whether insertion of $CS_2$ proceeds via an associative mechanism or via a dissociative mechanism involving free thiolate. Preceding work has shown that the insertion of heterocumulenes into Zn–X (X = O, S) bonds usually involves a four-center transition structure.[5–7,13,14,18] For this type of reaction, this structure generally represents the rate-determining step. For the reaction we investigated, we thus proposed a mechanism that features a similar four-center transition structure, **TS**. In addition, it is highly improbable that the missing reaction step, the rearrangement (i.e. bond rotation) that leads to the reaction product **P**, involves an intermediate with a higher energy than the insertion step. No such example has been reported in the literature. Hence, we conclude that the free energy of the transition structure **TS** constitutes the actual reaction barrier and is thus comparable to the experimental value. Therefore, the different mechanisms can be distinguished by directly comparing the barriers and by comparison with the experimentally determined value.

From the calculations it is evident that the associative mechanism is favored by approximately 80 kJ·mol$^{-1}$ ($\Delta G^{\ddagger}$ = 114.3 kJ·mol$^{-1}$ for path A compared with $\Delta G^{\ddagger}$ > 190 kJ·mol$^{-1}$ for path B). Obviously, the entropy gain accompanying dissociation is not large enough to counterbal-

 © 2006 Wiley-VCH Verlag GmbH & Co. KGaA, Weinheim 

ance the unfavorable reaction enthalpy. Furthermore, the calculated barrier of path A ($\Delta G^{\ddagger}$ = 114.3 kJ·mol$^{-1}$) is in reasonable agreement, although somewhat larger, with the experimental value ($\Delta G^{\ddagger}$ = 80.2 kJ. mol$^{-1}$).

In addition, we would like to emphasize the good agreement of the values for the enthalpy of activation ($\Delta H^{\ddagger}$) obtained experimentally and theoretically. The correlation ($\Delta H_{exp}{}^{\ddagger}$ = 65.3 ± 0.7 kJ·mol$^{-1}$ versus $\Delta H_{theor}{}^{\ddagger}$ = 60.7 kJ·mol$^{-1}$) is striking, with a difference of only 5 kJ·mol$^{-1}$. Naturally, a very good agreement is therefore also obtained for the activation energy ($E_a$) according to the Arrhenius equation. The experimentally determined value is $E_{a(exp)}$ = 67.8 ± 0.8 kJ·mol$^{-1}$ compared to a computed value of $E_{a(theor)}$ = 63.2 kJ·mol$^{-1}$. (Admittedly, it is also possible that we benefit from some kind of fortuitous error cancellation here. However, with respect to the error margins of the computation this is not of significance concerning the overall conclusions of this work.)

The data presented above provides strong evidence that the insertion of $CS_2$ proceeds via an associative mechanism and that a dissociative mechanism is very unlikely under the chosen experimental conditions. Moreover, the applied technique of using gas-phase geometries and deriving energies from single-point C-PCM calculations can only yield results of restricted accuracy. We thus assume that the deviations of the calculated energies from experimental data are mainly caused by these deficiencies in the treatment of solvent effects.

## Conclusions

The chemistry of the $L_nZn$–XR motif (X = O, S; R = H, alkyl, aryl; $L_n$: 3 or 4 nitrogen donors) is highly relevant to biosystems. The heterocumulene reactions of these systems follow two basic principles: First, the nucleophilic attack of the zinc-bound heteroatom is facilitated by the polarizing effect of the Zn–X linkage on the heterocumulene. Second, the zinc(II) ion is able to accept a variety of coordination numbers and geometries and thus even severely distorted transition structures are possible. For these reasons, nucleophilic anions in zinc complexes can attack the heterocumulene in a zinc-bound state rather than acting as free (dissociated) anions. We would like to point out that in several studies an associative (zinc-bound) mechanism was invariantly found for heterocumulene reactions of widely different examples of $L_nZn$–XR complexes: for sterically unsaturated species such as $[(py)_nZn–OH]^+$ and $[(im)_nZn–OH]^+$ ($n$ = 1–3) with $CO_2$;[18] for several species resembling the 'classic' CA motif $[N_3Zn–OH]^+$ with $CO_2$,[6,7,19] COS,[5] and $CS_2$;[13,14] and for sterically demanding zinc thiolates with $CS_2$ (this work). Thus, we conclude that the principle of heterocumulene fixation involving a four-center transition structure is generally applicable and largely independent of the nature of the heterocumulene and the nucleophilic ligand (XR).

Currently, these investigations are being extended to other heterocumulene substrates, namely COS and $CO_2$. In this case, the elucidation of molecular structures of the products is much more difficult due to the fact that it is apparently not possible to obtain a standard NMR spectroscopic or an X-ray structural analysis. Thus, additional spectroscopic investigations are required, namely solid-state NMR and Raman spectroscopy. In the present work, these methods were applied for calibration purposes and appear to be of great value for determining structural details. A report on this continued study will be available soon.

## Experimental Section

**General:** All reagents used were of analytical purity. NMR spectra were recorded using a Bruker AC 250 or AC 400 spectrometer, respectively, at a temperature of 30 °C. IR data was collected from the neat substances using a Nicolet Avatar 320 FT-IR spectrometer. Elemental analysis was performed using a Heraeus Vario EL III system. Melting points were determined with a Büchi Melting Point B545 apparatus and are uncorrected. Raman measurements were performed on a LabRam HR inverse spectrometer (Jobin Yvon) with an excitation wavelength of 532 nm (Nd:YAG laser). A 100× objective was used to focus the laser beam on the sample. With a 300 lines/mm grating and a CCD detector, a spectral resolution of 5 cm$^{-1}$ was reached. The accumulation time was between 30 and 120 s.

**[Zn([15]aneN$_4$){S–C(S)–SCH$_2$C$_6$H$_5$}]ClO$_4$ (1a):** Complex **1** (250 mg) was dissolved in a minimal amount (ca. 0.5 mL) of dichloromethane. $CS_2$ (2 mL) was then added to this soulution. The mixture immediately turned yellow. After a short time, yellow crystals formed, which were separated and washed with a small amount of $CS_2$. Yield: 85%. M.p. = 112–113 °C. $C_{19}H_{33}N_4S_3ClO_4Zn$ (578.49): calcd. C 39.45, H 5.75, Cl 6.13, N 9.68, S 16.63; found C 39.27, H 5.92, Cl 6.27, N 9.69, S 16.63. IR: $\tilde{\nu}$ = 3252 (m), 2925 (m), 2864 (m), 1071 (vs), 1024 (vs), 821 (s), 706 (s), 620 (s) cm$^{-1}$. NMR: 25 mg of **1** in 0.4 mL chloroform with a 10-fold molar excess of $CS_2$, contains virtually exclusively complex **1a** and only traces of **1**. $^1$H NMR (400 MHz, $CDCl_3$): $\delta$ = 1.75–1.95 (range of multiplets, 7 H), 2.63–3.83 (range of multiplets, 21 H), 4.44 (s, 2 H, Ar-C*H*$_2$), 7.21–7.30 (multiplet, 5 H, Ar-*H*) ppm. $^{13}$C NMR (100 MHz, $CDCl_3$, 13911 scans): $\delta$ = 24.8, 27.9, 28.1, 46.2, 47.1, 48.3, 49.8, 51.4, 52.3, 52.4, 53.8, 54.0, 127.3, 128.5, 129.2, 135.8, 239.0 ppm.

**[Zn(*i*-[14]aneN$_4$){S–C(S)–SCH$_2$C$_6$H$_5$}]ClO$_4$ (2a):** The preparation was carried out similarly to that for **1a**. Yield: 81%. No melting point detectable; decomposition at 115–120 °C yields the thiolate complex **2**. $C_{18}H_{31}N_4S_3ClO_4Zn$ (564.47): calcd. C 38.30, H 5.54, Cl 6.28, N 9.96, S 17.04; found C 38.19, H 5.43, Cl 6.27, N 9.96, S 16.89. IR: $\tilde{\nu}$ = 3260 (m), 3165 (w), 2919 (m), 2866 (m), 1080 (s), 1076 (vs), 1033 (vs), 975 (s), 930 (s), 812 (s), 716 (m), 621 (vs) cm$^{-1}$. NMR: 25 mg of **2** in 0.4 mL chloroform with a 10-fold molar excess of $CS_2$, contains approx. 67% of complex **2a** and 33% of **2**. $^1$H NMR (400 MHz, $CDCl_3$): $\delta$ = 1.8–3.4 (range of multiplets), 4.48 (s, Ar-C*H*$_2$), 7.25–7.36 (multiplet, Ar-*H*) ppm. $^{13}$C NMR (100 MHz, $CDCl_3$): $\delta$ = 27.9, 45.8, 47.7, 49.1, 50.2, 51.9, 128.0, 128.5, 129.1, 135.8, 238.9 ppm.

### Crystal Structure Determination

The intensity data was collected on a Nonius Kappa CCD diffractometer, using graphite-monochromated Mo-$K_\alpha$ radiation. Data was corrected for Lorentz and polarization effects, but not for absorption effects.[20,21] The structures were solved by direct methods (SHELXS[22]) and refined by full-matrix least-squares

 © 2006 Wiley-VCH Verlag GmbH & Co. KGaA, Weinheim 

techniques against $F_o^2$ (SHELXL-97[23]). The hydrogen atoms of the amine groups were located by difference Fourier synthesis and refined isotropically. All other hydrogen atoms were included at calculated positions with fixed thermal parameters. All non-hydrogen atoms were refined anisotropically.[23] XP (SIEMENS Analytical X-ray Instruments, Inc.) was used for structure representations. The drawings in the paper were generated using the program PLATON.[24]

**Crystal Data for 1a:**[25] $C_{19}H_{33}N_4S_3Zn{\cdot}ClO_4$, $M_r$ = 578.49 g·mol$^{-1}$, yellow prism, size 0.03 × 0.03 × 0.02 mm, monoclinic, space group $P2_1/n$, $a$ = 13.2338(1), $b$ = 12.9251(2), $c$ = 30.1669(4) Å, $\beta$ = 101.463(1)°, $V$ = 5057.1(1) Å$^3$, $T$ = –90 °C, $Z$ = 8, $\rho$(calcd.) = 1.520 g·cm$^{-3}$, $\mu$(Mo-$K_\alpha$) = 13.58 cm$^{-1}$, $F$(000) = 2416, 20403 reflections in $h$(–17/17), $k$(–16/15), $l$(–39/39), measured in the range 1.84° ≤ $\Theta$ ≤ 27.49°, completeness $\Theta_{max}$ = 98.5%, 11426 independent reflections, $R_{int}$ = 0.049, 6885 reflections with $F_o > 4(F_o)$, 608 parameters, $R1_{obs}$ = 0.049, $wR2_{obs}$ = 0.103, $R1_{all}$ = 0.1065, $wR2_{all}$ = 0.119, GOOF = 1.014, largest difference peak and hole: 0.676/–0.583 e·Å$^{-3}$.

**Crystal Data for 2a:**[25] $C_{18}H_{31}N_4S_3Zn{\cdot}ClO_4$, $M_r$ = 564.47 g·mol$^{-1}$, yellow prism, size 0.06 × 0.05 × 0.05 mm$^{-3}$, orthorhombic, space group $P2_12_12_1$, $a$ = 9.9936(1), $b$ = 22.1261(4), $c$ = 22.3192(4) Å, $V$ = 4935.2(1) Å$^3$, $T$ = –90 °C, $Z$ = 8, $\rho$(calcd.) = 1.519 g·cm$^{-3}$, $\mu$(Mo-$K_\alpha$) = 13.89 cm$^{-1}$, $F$(000) = 2352, 11275 reflections in $h$(–12/12), $k$(–28/28), $l$(–28/28), measured in the range 1.84° ≤ $\Theta$ ≤ 27.49°, completeness $\Theta_{max}$ = 99.7%, 11275 independent reflections, 9902 reflections with $F_o > 4(F_o)$, 591 parameters, $R1_{obs}$ = 0.045, $wR2_{obs}$ = 0.106, $R1_{all}$ = 0.057, $wR2_{all}$ = 0.113, GOOF = 1.047, Flack-parameter 0.08(1), largest difference peak and hole: 0.652/–0.534 e·Å$^{-3}$.

**Solid State NMR Spectroscopy:** The $^{13}C$ solid state NMR spectra were measured with three different solid state NMR spectrometers, namely a Bruker AMX 400, a Varian Unity 500, and a Varian CMX Infinity 600 plus at fields of 9.4, 11.7, and 14 T, respectively. All spectra were recorded under high power proton decoupling at ambient temperature. The spectra of **1**, **2**, and **1a** were measured employing a variable amplitude cross polarization with a contact time of 1.2 ms. For the insertion product **2a** we were not able to obtain a signal from the suspected thiocarbonyl group with this technique. We therefore did additional measurements employing $^{13}C$ 90° pulse excitation on this sample, using a recycle time of 100 s. In this experiment, we were able to reveal the thiocarbonyl signal (see Supporting Information). While the spectral assignment of the thiocarbonyl groups is obvious from the prominent chemical shift, the assignment of the aromatic and aliphatic carbons was done employing simulations with the NMR predictor program of ACDlabs.

### Reactions of 1a

**Methyl Iodide:** $CS_2$ (300 μL, 5 mmol) was added to a solution of **1a** (251 mg, 0.5 mmol) in chloroform (1 mL). After 30 min. methyl iodide (310 μL, 5 mmol) was added and the mixture was stirred overnight. The solvents were removed and the residue was washed several times with pentane. The combined pentane extracts were concentrated and chromatographed on 20 cm$^3$ of silica (eluent: pentane). After the elution of benzyl methyl sulfide (12 mg, 0.087 mmol), which was collected separately, benzyl methyl trithiocarbonate (**3**) (82 mg, 0.38 mmol, 76%) was obtained as a yellow oil. The substance was identified by NMR analyses and compared with data from the literature.[26] $^1H$ NMR (250 MHz, $CDCl_3$): $\delta$ = 2.78 (s, 3 H, $CH_3$), 4.66 (s, 2 H, $CH_2$), 7.26–7.41 (m, 5 H, $C_6H_5$) ppm. $^{13}C$ NMR (62.5 MHz, $CDCl_3$): $\delta$ = 20.2, 41.6, 127.8, 128.7, 129.3, 135.1, 224.2 ppm.

**Acetyl Chloride:** $CS_2$ (300 μL, 5 mmol) was added to a solution of **1** (251 mg, 0.5 mmol) in chloroform (1 mL). After 30 min. acetyl chloride (36 μL, 0.5 mmol) was added while stirring. After 20 min the mixture was subjected to chromatography on 20 cm$^3$ of silica (eluent: $CHCl_3$). **4** (88 mg, 72%) was isolated and identified by $^1H$ and $^{13}C$ NMR spectra.

**Synthesis of 4 (Reference Sample):** Benzyl mercaptan (205 mg, 1.65 mmol) was added to a solution of KOH (92.7 mg, 1.65 mmol) in methanol (10 mL),. After stirring for 30 min at room temp., the solvent was removed under reduced pressure. The residue was carefully dried in a desiccator. The salt was dissolved in dried THF (5 mL) and an excess of $CS_2$ (0.84 mL, 14 mmol) was added at 0 °C. The temperature was raised to 25 °C after stirring for 60 min. The reaction mixture was then cooled to –78 °C. Acetyl chloride (0.178 mL, 2.5 mmol) was added dropwise, whereupon the yellow solution turned red. After stirring for 20 min the solvent was evaporated. The residue was purified by chromatography on silica (eluent: $CHCl_3$), yielding 107 mg (27%) of a red oil that decomposed at room temp. within a few weeks. $C_6H_5$–$CH_2$–S–C(S)–S–C(O)–$CH_3$ ($C_{10}H_{10}OS_3$) (242.39): calcd. C 49.55, H 4.16, S 39.20; found C 50.28, H 4.10, S 39.20. $^1H$ NMR (250 MHz, $CDCl_3$): $\delta$ = 2.41 (s, 3 H, $CH_3$), 4.49 (s, 2 H, $CH_2$), 7.28–7.36 (m, 5 H, $C_6H_5$) ppm. $^{13}C$ NMR (62.5 MHz, $CDCl_3$): $\delta$ = 29.8, 42.9, 128.0, 128.8, 129.4, 133.8, 189.9, 212.4 ppm.

### Kinetics

**Experimental Setup:** The insertion of $CS_2$ was monitored by UV/Vis spectroscopy. Complex **1a** shows an absorption maximum at 434 nm, whereas the starting complex **1** does not show any absorption in the visible range at all. Measurements were performed using a Cary 5000 UV/Vis spectrometer from Varian. For keeping the temperature constant, a Cary dual cell peltier accessory from Varian was used. 1 cm quartz cuvettes were obtained from Hellma. During the reaction the mixture was stirred with a magnetic stirrer. The reaction temperature was determined with a sensor that was placed directly in the reaction medium.

**Measurements:** An amount of 2 mL was placed into a cuvette from a 20 mM stock solution (502.4 mg of **1** in 50 mL of chloroform). After the desired temperature was reached, 48 μL (61 mg, 800 μmol) of $CS_2$ was added and data collection was started. For the first 60 s, data were collected every second and later every 10 s. The reactions were monitored until no further alteration of the absorbance could be detected. For details on the data analysis see Supporting Information.

### Computational Details

Full geometry optimizations, i.e. without constraints, as well as frequency calculations on the stationary points thus obtained were carried out using the Gaussian03[27] program package. Depending on the number of imaginary modes all points on the hypersurface were rigorously characterized as true minima (no imaginary mode) or transition structures (exactly one).

All optimizations were performed using the hybrid B3LYP[28] density functional method, which includes the use of a term that accounts for the effect of dynamic electron correlation (Coulomb hole).[29] Geometries were optimized in the gas phase using the standard 6-311+G(d) basis set.

To estimate solvent effects, single point calculations in the presence of a dielectric field, as described by the C-PCM model,[30–32] were carried out on the gas phase geometries. In this model, the species of interest are embedded in a cavity of molecular shape surrounded by a polarizable continuum whose field is described by polarization

 © 2006 Wiley-VCH Verlag GmbH & Co. KGaA, Weinheim 

charges distributed on the cavity surface. This procedure is known to be very good at reproducing experimental hydration energies.[30] In the framework of the C-PCM model the default UA0 cavities (based on the united atom topological model) and the dielectric constant of chloroform ($\varepsilon$ = 4.9) were used.

For all single point calculations the B98[33] functional was used. The G3MP2Large basis set[34] was employed on all atoms except zinc where the 6-311+G(3df) basis set as implemented in Gaussian03 was applied. The B98 density functional was chosen for the calculation of the energies because it has recently been shown that it outperforms the more popular B3LYP functional, both for absolute energies and barrier heights, especially for larger molecules.[35–37] In all these studies the assessment was performed using single point calculations on some reference geometry, basically the same approach that we used in this work. We therefore believe that the use of the well-established B3LYP density functional for the geometry optimizations has only a minor effect on the calculated energies. This is even more plausible with respect to the fact that geometry relaxation effects from the dielectric field of the solvent are completely neglected. The absolute error of B98 on the G3/05 set is approximately 14 kJ·mol$^{-1}$,[35] but the relative errors are generally smaller.

All energies were calculated by adding the appropriate thermodynamic corrections [gas phase, B3LYP/6-311+G(d)] to the total free energy in solution (including electrostatic and nonelectrostatic terms) obtained from the single point calculations (B98/G3MP2Large). The gas phase correction values were calculated with the standard thermodynamic routines in Gaussian03 (with $T$ = 298.15 K and $p$ = 1 atm) using the frequencies computed at the B3LYP/6-311+G(d) optimal gas phase geometries.

**Supporting Information** (see footnote on the first page of this article): Details are given on the Raman spectroscopy (including two spectra), the solid-state NMR spectroscopy (including four spectra), and the analysis of the kinetic data (including two kinetic plots). The Cartesian coordinates and absolute energies of all calculated structures are provided.

## Acknowledgments

Financial support of this work by the Deutsche Forschungsgemeinschaft, SFB 436 "Metal Mediated Reactions Modeled After Nature" is gratefully acknowledged.

[1] J. Notni, H. Görls, E. Anders, *Eur. J. Inorg. Chem.* **2006**, 1444–1455.
[2] G. Parkin, *Chem. Rev. (Washington, DC, U. S.)* **2004**, *104*, 699–767.
[3] F. Botre, G. Gros, B. T. Storey, *Carbonic Anhydrase*, VCH, New York, **1991**.
[4] I. Bertini, C. Luchinat, W. Maret, M. Zeppezauer, *Zinc Enzymes*, Birkhäuser, Boston, **1986**.
[5] S. Schenk, J. Kesselmeier, E. Anders, *Chem. Eur. J.* **2004**, *10*, 3091–3105.
[6] M. Mauksch, M. Bräuer, J. Weston, E. Anders, *ChemBioChem* **2001**, *2*, 190–198.
[7] M. Bräuer, J. L. Pérez-Lustres, J. Weston, E. Anders, *Inorg. Chem.* **2002**, *41*, 1454–1463.
[8] U. Kuhn, C. Ammann, A. Wolf, F. X. Meixner, M. O. Andreae, J. Kesselmeier, *Atmos. Environ.* **1999**, *33*, 995–1008.
[9] G. Protoschill-Krebs, C. Wilhelm, J. Kesselmeier, *Atmos. Environ.* **1996**, *30*, 3151–3156.
[10] S. Blezinger, C. Wilhelm, J. Kesselmeier, *Biogeochemistry* **2000**, *48*, 185–197.
[11] U. Kuhn, A. Wolf, C. Gries, T. H. Nash, J. Kesselmeier, *Atmos. Environ.* **2000**, *34*, 4867–4878.
[12] J. Kesselmeier, A. Hubert, *Atmos. Environ.* **2002**, *36*, 4679–4686.
[13] M. Bräuer, E. Anders, S. Sinnecker, W. Koch, M. Rombach, H. Brombacher, H. Vahrenkamp, *Chem. Commun.* **2000**, 647–648.
[14] S. Sinnecker, M. Bräuer, W. Koch, E. Anders, *Inorg. Chem.* **2001**, *40*, 1006–1013.
[15] M. Rombach, H. Vahrenkamp, *Inorg. Chem.* **2001**, *40*, 6144–6150.
[16] R. Luckay, T. E. Chantson, J. H. Reibenspies, R. D. Hancock, *J. Chem. Soc., Dalton Trans.* **1995**, 1363–1367.
[17] F. Wagner, M. T. Mocella, M. J. D'Aniello Jr, A. H.-J. Wang, E. K. Barefield, *J. Am. Chem. Soc.* **1974**, *96*, 2625–2627.
[18] D. Schröder, H. Schwarz, S. Schenk, E. Anders, *Angew. Chem. Int. Ed.* **2003**, *42*, 5087–5090; *Angew. Chem.* **2003**, *115*, 5241–5244.
[19] A. Bottoni, C. Z. Lanza, G. P. Miscione, D. Spinelli, *J. Am. Chem. Soc.* **2004**, *126*, 1542–1550.
[20] *Molen, an interactive structure solution procedure*, **1999**, Enraf–Nonius, Delft, The Netherlands.
[21] *Collect*, *data collection software*, **1998**, Nonius, The Netherlands.
[22] G. M. Sheldrick, *Acta Crystallogr., Sect. A: Found. Crystallogr.* **1990**, *46*, 467–473.
[23] G. M. Sheldrick, *Shelxl-97, release 97-2*, **1997**, University of Göttingen, Germany, http://shelx.uni-ac.gwdg.de/SHELX/.
[24] A. L. Spek, *Platon, a multipurpose crystallographic tool*, **2004**, Utrecht University, Utrecht, The Netherlands, http://www.cryst.chem.uu.nl/platon.
[25] CCDC-258933 (for **1a**) and -286778 (for **2a**) contain the supplementary crystallographic data for this paper. These data can be obtained free of charge from The Cambridge Crystallographic Data Centre via http://www.ccdc.cam.ac.uk/data_request/cif.
[26] S. Tanimoto, T. Oida, H. Ikehira, M. Okano, *Bull. Chem. Soc. Jpn.* **1982**, *55*, 1977–1978.
[27] M. J. Frisch, G. W. Trucks, H. B. Schlegel, G. E. Scuseria, M. A. Robb, J. R. Cheeseman, J. A. J. A. Montgomery Jr, T. Vreven, K. N. Kudin, J. C. Burant, J. M. Millam, S. S. Iyengar, J. Tomasi, V. Barone, B. Mennucci, M. Cossi, G. Scalmani, N. Rega, G. A. Petersson, H. Nakatsuji, M. Hada, M. Ehara, K. Toyota, R. Fukuda, J. Hasegawa, M. Ishida, T. Nakajima, Y. Honda, O. Kitao, H. Nakai, M. Klene, X. Li, J. E. Knox, H. P. Hratchian, J. B. Cross, C. Adamo, J. Jaramillo, R. Gomperts, R. E. Stratmann, O. Yazyev, A. J. Austin, R. Cammi, C. Pomelli, J. W. Ochterski, P. Y. Ayala, K. Morokuma, G. A. Voth, P. Salvador, J. J. Dannenberg, V. G. Zakrzewski, S. Dapprich, A. D. Daniels, M. C. Strain, O. Farkas, D. K. Malick, A. D. Rabuck, K. Raghavachari, J. B. Foresman, J. V. Ortiz, Q. Cui, A. G. Baboul, S. Clifford, J. Cioslowski, B. B. Stefanov, G. Liu, A. Liashenko, P. Piskorz, I. Komaromi, R. L. Martin, D. J. Fox, T. Keith, M. A. Al-Laham, C. Y. Peng, A. Nanayakkara, M. Challacombe, P. M. W. Gill, B. Johnson, W. Chen, M. W. Wong, C. Gonzalez, J. A. Pople, *Gaussian03, revision C.02*, **2004**, Gaussian, Inc., Wallingford, CT, http://www.gaussian.com.
[28] A. D. Becke, *J. Chem. Phys.* **1993**, *98*, 5648–5652.
[29] C. Lee, W. Yang, R. G. Parr, *Phys. Rev. B: Condens. Matter Mater. Phys.* **1988**, *37*, 785–789.
[30] V. Barone, M. Cossi, *J. Phys. Chem. A* **1998**, *102*, 1995–2001.
[31] M. Cossi, N. Rega, G. Scalmani, V. Barone, *J. Comput. Chem.* **2003**, *24*, 669–681.
[32] A. Klamt, G. Schüürmann, *J. Chem. Soc., Perkin Trans. 2* **1993**, 799–805.
[33] H. L. Schmider, A. D. Becke, *J. Chem. Phys.* **1998**, *108*, 9624–9631.

 © 2006 Wiley-VCH Verlag GmbH & Co. KGaA, Weinheim 

[34] L. A. Curtiss, P. C. Redfern, K. Raghavachari, V. Rassolov, J. A. Pople, *J. Chem. Phys.* **1999**, *110*, 4703–4709.
[35] L. A. Curtiss, P. C. Redfern, K. Raghavachari, *J. Chem. Phys.* **2005**, *123*, 124107–124119.
[36] S. Andersson, M. Grüning, *J. Phys. Chem. A* **2004**, *108*, 7621–7636.
[37] Y. Zhao, J. Pu, B. J. Lynch, D. G. Truhlar, *Phys. Chem. Chem. Phys.* **2004**, *6*, 673–676.

Received: October 26, 2005
Published Online: May 3, 2006

 © 2006 Wiley-VCH Verlag GmbH & Co. KGaA, Weinheim 

DOI: 10.1002/ejic.200501120

# The Reactivity of Hexa(*N*-methylideneimine)Co$^{III}$ Complexes towards Nucleophiles: Structure and Mechanism[‡]

**Dirk Kuppert,[a] Peter Comba,[b] and Kaspar Hegetschweiler*[a]**

**Keywords:** Nucleophilic addition / Hydrogen transfer / N ligands / Cobalt / Chelates.

The reactivity of the ***h***exa(*N*-***m***ethylidene***i***mine)Co$^{III}$ complex [Co-hmi-(taci)$_2$]$^{3+}$ (taci = 1,3,5-triamino-1,3,5-trideoxy-*cis*-inositol) towards the nucleophiles ammonia, aniline and cyanide was investigated and the main products were identified by spectroscopic methods and by a crystal structure analysis. The relative energies of the complexes formed and those of possible stereo isomers were analysed by means of molecular mechanics calculations. In the reaction with $NH_3$, two condensation products, [Co(L$^a$)]$^{3+}$ and [Co(L$^b$)]$^{3+}$, were identified with the two taci moieties linked by one or two N=CH–N(H)-CH$_2$–NH bridges, respectively. The reaction with aniline yielded the complex [Co(L$^c$)(L$^d$)]$^{3+}$ (where L$^c$ is a mono-*N*-methylated and L$^d$ a phenylformamidine-substituted taci), whereas the reaction with cyanide resulted in the formation of [Co(L$^e$)]$^{3+}$ having an NH–CH$_2$–C(NH$_2$)=N bridge between the two taci subunits. A mechanism that accounts for the different types of products can be suggested as follows: In [Co(L$^a$)]$^{3+}$, [Co(L$^b$)]$^{3+}$ and [Co(L$^c$)(L$^d$)]$^{3+}$, *N*-methylation was observed and this can be interpreted in terms of an intramolecular Cannizzaro type hydride shift. For [Co(L$^a$)]$^{3+}$ and [Co(L$^b$)]$^{3+}$ two subsequent addition steps of the nucleophile to adjacent imino groups must take place prior to the hydride shift, whereas for [Co(L$^c$)(L$^d$)]$^{3+}$ the hydride shift appears to have already occurred after the first addition step of aniline to an imino group. Formation of [Co(L$^e$)]$^{3+}$ can be explained in terms of a nucleophilic attack of CN$^-$ to an imino group and a subsequent attack of a deprotonated amino group (which must have previously been formed by hydrolysis of a methylideneimino group) to the nitrile C-atom.
(© Wiley-VCH Verlag GmbH & Co. KGaA, 69451 Weinheim, Germany, 2006)

## Introduction

Polyaza macrocycles and polyaza macrobicycles are interesting classes of chelators for transition metal cations, since the complexes formed thereof are often of exceptionally high stability and inertness.[1] A variety of synthetic procedures have been established for the preparation of such ligands and among them the template method, in which a set of subunits is precoordinated to a metal centre, is particularly effective.[2] Sargeson discovered that the condensation of an (amine)Co$^{III}$ complex with formaldehyde under basic conditions, followed by a capping step, resulted in the formation of the corresponding cage complexes.[3] The capping reagent is usually a weakly acidic, tribasic component $H_3X$ such as ammonia or nitromethane[4] and the entire reaction may be performed either in an aqueous or a nonaqueous medium. The procedure was found to be particularly effective for the capping of [Co$^{III}$(en)$_3$]$^{3+}$ (en = ethane-1,2-diamine) where the two cages sepulchrate (sep, X = N) and sarcophagine (sar, X = C-NO$_2$) could be isolated in high yields. It is generally believed that the reaction proceeds via intermediate methylideneimine formation with the capping agent being finally added with subsequent deprotonation to the coordinated imines (Scheme 1).[5] Although the entire procedure is usually performed as a one-pot reaction without isolation of intermediates, some of the imines are of sufficient stability to allow their characterisation[6] and some of them could even be crystallised.[7,8] We reported the crystal structure of the ***h***exa(*N*-***m***ethylidene-***i***mine) (hmi) complex [Co-hmi-(taci)$_2$]$^{3+}$ (Scheme 2a, R = OH; taci = 1,3,5-***t***ri***a***mino-1,3,5-trideoxy-***c***is-***i***nositol) some years ago.[9]

Sargeson has already found that in complexes with sterically demanding diamine ligands such as *trans*-cyclohexane-1,2-diamine (*trans*-chxn), the capping reaction proceeds at a comparatively low rate.[10] Moreover, formation of a variety of by-products was noted. In particular, it was observed that some of the coordinated amino groups underwent methylation. It is thus apparent that, in general, the bridging process may be more complex than it appears at first glance.[11] After formation of the first two X–C bonds, additional deprotonation of XH can occur and the resultant anion could attack the electrophilic carbon atom of a third

[‡] 1,3,5-Triamino-1,3,5-trideoxy-*cis*-inositol, a Ligand with Remarkable Versatility for Metal Ions, 15. Part 14: K. Hegetschweiler, P. J. Hagrman, J. Zubieta in *Advances in Coordination, Bioinorganic and Inorganic Chemistry* (Eds: M. Melník, J. Šima, M. Tatarko), Slovak Technical University Press, Bratislava, **2005**.

[a] Universität des Saarlandes, Anorganische Chemie, Postfach 151150, 66041 Saarbrücken, Germany
Fax: +49-681-302-2663
E-mail: hegetschweiler@mx.uni-saarland.de.
[b] Universität Heidelberg, Anorganisch-chemisches Institut, Im Neuenheimer Feld 270, 69120 Heidelberg, Germany

Supporting information for this article is available on the WWW under http://www.eurjic.org or from the author.

 © 2006 Wiley-VCH Verlag GmbH & Co. KGaA, Weinheim 

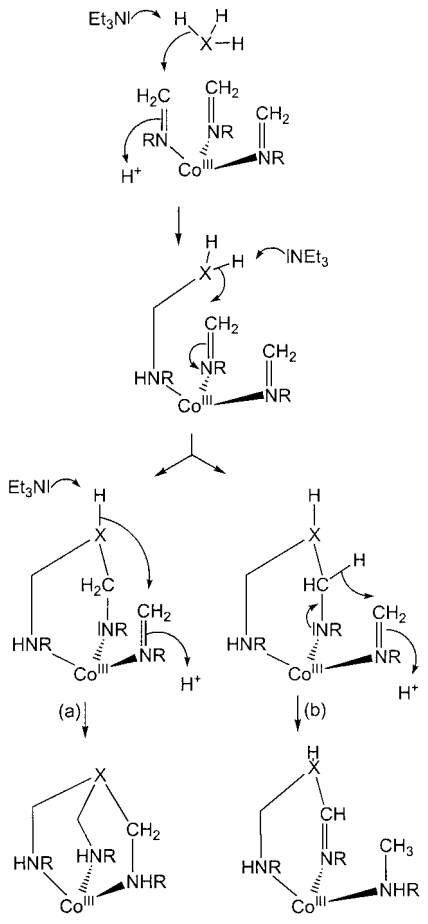

Scheme 1. Reaction of (hexaimine)$Co^{III}$ complexes with a capping reagent $H_3X$; mechanistic details for the formation of a cap (a) or a strap (b, Cannizzaro type hydride shift). Some of the charges are omitted for clarity.

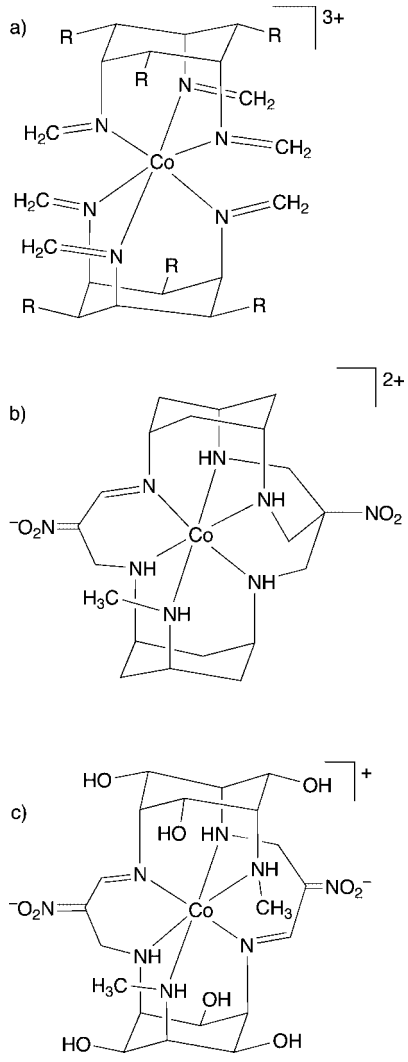

Scheme 2. a) Structures of [Co-hmi-(*cis*-tach)$_2$]$^{3+}$ (R = H) and [Co-hmi-(taci)$_2$]$^{3+}$ (R = OH).[9] b) and c): Major products isolated from the condensation reaction of the two (hmi)$Co^{III}$ complexes with nitromethane. The reaction was carried out either in an alkaline aqueous medium (b)[12] or in acetonitrile using triethylamine as base (c)[9] (taci = 1,3,5-triamino-1,3,5-trideoxy-*cis*-inositol, *cis*-tach = all-*cis*-cyclohexane-1,3,5-triamine).

imino group (Scheme 1a). It is also possible at this stage, however, that an N=C double bond could reform within the NH–$CH_2$–XH–$CH_2$–$N^-$ bridge in conjunction with hydride transfer from the methylene carbon to an adjacent imino group (Scheme 1b). Such an intramolecular, Cannizzaro type hydride shift would explain formation of the *N*-methylated by-products observed in the capping reaction of [$Co^{III}$-(*trans*-chxn)$_3$]$^{3+}$. In the corresponding reaction of [$Co^{III}$(*cis*-tach)$_2$]$^{3+}$ with formaldehyde and two equiv. of nitromethane, both types of reaction were observed within the same molecule (Scheme 2b).[12] The addition of one of the nitromethane molecules yielded an $O_2N$–C($CH_2$–NH)$_3$ cap whereas addition of the other resulted in the formation of an HN–$CH_2$–CH($NO_2$)–CH=N strap. The hydrogen atom of the CH($NO_2$) moiety was found to be strongly acidic and the complex was thus isolated as a dication with a carbanionic ligand having a delocalised $O_2N$=C–C=N π-system. Moreover, in the reaction of [$Co^{III}$-hmi-(taci)$_2$]$^{3+}$ with two equiv. of nitromethane, the resultant product was devoid of any $O_2N$–C($CH_2$–NH)$_3$ cap (Scheme 2c). Both nitromethane entities were incorporated as HN–$CH_2$–C($NO_2$)$^-$–CH=N straps.[9]

It is noteworthy that the rigidity of the ligand backbones increases in the order en < *trans*-chxn < *cis*-tach < taci. It appears, thus, that increasing the rigidity of the coordinated amine ligands tends to disfavour the capping reaction. Formation of such HN–$CH_2$–XH–CH=N straps has previously only been observed in the capping reaction with nitromethane.[9,12] It would be interesting to investigate the products formed when other types of nucleophiles are used. Such an investigation would not only shed light on the mechanism of this type of condensation processes but it could potentially open synthetic pathways to novel and interesting macrocyclic ligand systems. We therefore decided to extend our investigation of the capping of [$Co^{III}$-hmi-(taci)$_2$]$^{3+}$ using ammonia, aniline and cyanide as possible nucleophiles. In this paper, we describe the molecular structures of the products obtained and discuss the mechanism of the corresponding coupling reaction. We also carried out a series of molecular mechanics calculations to look for low-energy structures of the different possible stereoisomers.

 © 2006 Wiley-VCH Verlag GmbH & Co. KGaA, Weinheim 

## Results

### Reaction of [Co-hmi-(taci)$_2$]$^{3+}$ with Ammonia

Formation of the well known (sepulchrate)Co$^{III}$ complex has been reported to occur readily upon mixing [Co$^{III}$-(en)$_3$]$^{3+}$ with formaldehyde and ammonia in an alkaline aqueous solution.[5] Consequently, initial attempts to carry out an analogous reaction of [Co$^{III}$-hmi-(taci)$_2$]$^{3+}$ (Scheme 2a, R = OH) with ammonia were performed in aqueous media. However, these experiments resulted in the complete hydrolysis of the imino groups, together with reduction of Co$^{III}$ to Co$^{II}$. The protonated H$_3$taci$^{3+}$ was the only product which could be isolated after acidification. Further experiments were therefore performed in acetonitrile. To achieve the required solubility, the chloride salt of [Co$^{III}$-hmi-(taci)$_2$]$^{3+}$ was converted into the corresponding triflate salt.[13] Reaction of [Co$^{III}$-hmi-(taci)$_2$](CF$_3$SO$_3$)$_3$ in acetonitrile with concentrated aqueous ammonia resulted in formation of a deep red solution containing a variety of different Co$^{III}$ complexes. After hydrolysis of the remaining imines, two main products were isolated by chromatographic techniques. The major red component, [Co(HL$^a$)]Cl$_4$ (L$^a$ = C$_{15}$H$_{33}$N$_7$O$_6$),[14] consisted of a complex in which the two taci-ligands are interlinked by an N=CH–NH–CH$_2$–NH bridge and where one of the coordinated amino group was methylated (Scheme 3). In a minor pink component, composed of [Co(H$_2$L$^b$)]Cl$_5$ (L$^b$ = C$_{18}$H$_{36}$N$_8$O$_6$),[14] the taci moieties were connected by two such N=CH–NH–CH$_2$–NH bridges and two methylated amino groups were formed. Both compounds were characterised by FAB$^+$ mass spectrometry in which the pseudo-molecular ions [Co$^{II}$-(H$_{-1}$L$^a$)]$^+$ (*m*/*z* = 465) and [Co$^{II}$(H$_{-1}$L$^b$)]$^+$ (*m*/*z* = 518)[15,16] could be observed with high intensities.

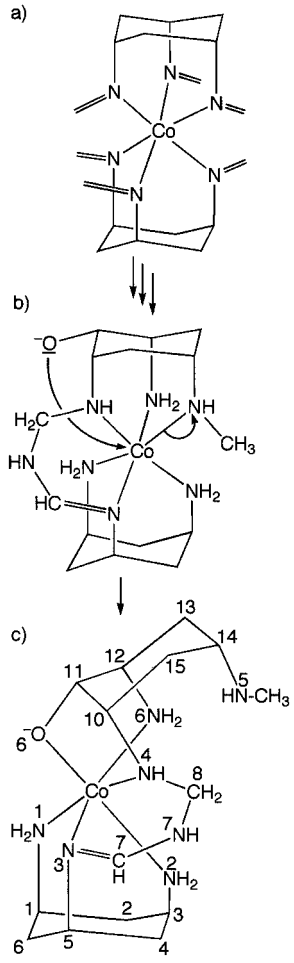


Scheme 3. Formation of [Co(H$_{-1}$L$^a$)]$^{2+}$.[14] A part of the numbering scheme of this complex is shown in c). The non-coordinating OH-groups are omitted for clarity.

### Characterisation of [Co(L$^a$)]$^{3+}$[14]

A $^1$H-$^1$H COSY NMR spectrum exhibited two independent spin systems each with six resonances for the H(-C) ring protons of the two taci frameworks. Clearly no element of symmetry of the $D_{3d}$ [Co$^{III}$-hmi-(taci)$_2$]$^{3+}$ precursor is retained in this complex. Four additional signals were indicative of one HC=N imino group, one N-CH$_3$ methyl group and one N–CH$_2$–N group. The $^{13}$C{$^1$H} NMR spectrum was consistent with this analysis exhibiting fifteen signals which, on the basis of a DEPT experiment, could be assigned to one CH$_3$, one CH$_2$ and 13 CH-carbon resonances.[17] One of the CH signals was strongly deshielded (170–173 ppm, depending on pD) and clearly originated from the imino group.[6] The remaining 12 CH signals were assigned to the two taci backbones. They appeared in the range of 52–80 ppm. Eleven of them were located in a comparatively narrow range of 52–68 ppm, whereas one single CH-resonance was displaced to a particularly high frequency ($\delta$ = 80.0 ppm at pD 8). Such a significant low-field shift of a single cyclohexane carbon atom is indicative of asymmetric $\kappa^3$-*O*,*N*,*O* or $\kappa^3$-*N*,*O*,*N* coordination (formation of two five-membered chelate rings).[18–20] The additional $^{13}$C-$^1$H HMQC and $^{13}$C-$^1$H HMBC experiments[17] provided evidence that the imine portion of the N=CH–NH–CH$_2$–NH bridge and the N-CH$_3$ group are not bound to the same taci-unit. These structural assignments were subsequently confirmed by a single-crystal X-ray analysis of a hydrated [Co(HL$^a$)][ZnBr$_4$]$_2$ salt (Table 1, Figure 1). Although serious disorder was observed for one of the [ZnBr$_4$]$^{2-}$ anions (see experimental section), the structure proved to be of sufficient quality to establish unambiguously the formation of the novel ligand L$^a$. Significant structural properties are: (i) Different coordination modes[21] of the two taci fragments with a $\kappa^3$-*N*,*N*,*N* coordination for the moiety with the imino group and a $\kappa^3$-*N*,*O*,*N* coordination for the moiety with the N–CH$_3$ group (the N–CH$_3$ group itself is detached from Co); (ii) Different conformations for the two cyclohexane rings: the $\kappa^3$-*N*,*N*,*N*-coordinating fragment forms a regular chair, whereas the $\kappa^3$-*N*,*O*,*N*-coordinating unit has a twisted boat conformation.[22] (iii) A planar geometry around the atoms N3, C7 and N7 (the sums of bond angles are 360.0 ± 0.1°), indicative of sp$^2$ hybridisation for all the atoms of the amidine fragment.

 © 2006 Wiley-VCH Verlag GmbH & Co. KGaA, Weinheim 

Table 1. Comparison between experimental[a] and calculated[b] bond lengths [Å] and bond angles [°] for $[Co(HL^a)]^{4+}$.

| | Experimental | Calculated |
|---|---|---|
| Co–O(6) | 1.931(6) | 1.93 |
| Co–N(3) | 1.921(8) | 1.93 |
| Co–N(2) | 1.944(7) | 1.94 |
| Co–N(1) | 1.956(8) | 1.96 |
| Co–N(4) | 1.974(8) | 1.97 |
| Co–N(6) | 2.023(7) | 1.97 |
| C(7)–N(3) | 1.299(12) | 1.32 |
| | | |
| N(1)–Co–N(2) | 91.4(3) | 93 |
| N(1)–Co–N(3) | 90.4(4) | 92 |
| N(2)–Co–N(3) | 90.2(3) | 92 |
| N(4)–Co–O(6) | 82.4(3) | 81 |
| N(4)–Co–N(6) | 84.1(3) | 86 |
| N(6)–Co–O(6) | 83.4(3) | 88 |
| N(3)–C(7)–N(7) | 122.8(10) | 122 |

[a] Single-crystal X-ray structure analysis of $[Co(HL^a)][ZnBr_4]_2 \cdot 5H_2O$. [b] Molecular mechanics calculations using the MOMEC force field[46,47] together with the extension listed in Table 4.

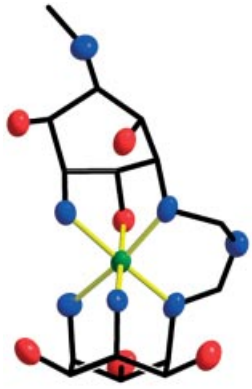

Figure 1. Molecular structure of $[Co(HL^a)]^{4+}$.[14] The carbon skeleton is shown as a stick model, other non-hydrogen atoms are shown as vibrational ellipsoids at the 30% probability level. Hydrogen atoms are omitted for clarity. Colour code: Co green, O red, N blue. The numbering scheme is shown in Scheme 3c.

$[Co(HL^a)][ZnBr_4]_2 \cdot 5H_2O$ was isolated from an acidic medium and, consequently, both the coordinated oxygen and the non-coordinating methylamino group are protonated as supported by charge balance considerations. In aqueous solution, however, the two sites could be deprotonated reversibly. Corresponding p$K_a$ values of 2.0(1) and 5.28(1) were determined by potentiometric titration (25 °C, 0.1 M KCl). The first value (deprotonation of the coordinated hydroxy group) agrees nicely with the value of 2.0(2) observed for the model complex [Co(*cis*-tach)(Htaci-κ$^3$-*O*$^1$,*N*$^2$,*O*$^3$)]$^{4+}$ (Supporting Information, Scheme S1b, structure O7).[20] However, the p$K_a$ of the methylammonium group is surprisingly low (the corresponding values for [Co(*cis*-tach)(Htaci)]$^{4+}$ are 7.23 and 8.84). An NMR titration experiment of $[Co(HL^a)]^{4+}$ (306 K, $D_2O$, no inert electrolyte) in the range 0.5 < pH < 8.5 (Figure 2) revealed a characteristic pD-dependence of the individual $^1$H resonances of the complex. The two protonation constants could be assigned as p$K_1$ = 1.16 and p$K_2$ = 5.60 which is in good agreement with the values determined by potentiometric measurements. In accord with a protonation of a nearby basic site, H(-C) resonances can be expected to shift to higher frequency upon protonation of this site and this effect should decrease with an increasing number of bonds between this site and the H(-C) group under consideration.[23] For the deprotonation of the coordinated hydroxy group, the resonances most affected (H10–H12) in the range 0.5 < pD < 2 are all in close proximity to O6; and H11, which is located in the α position, did indeed exhibit the most significant shift (see Scheme 3c for the numbering scheme). However, for the deprotonation of the methylammonium group the most significant shift can be observed for the hydrogen atoms in the β positions (H13 and H15). The shift observed for the α hydrogen atom (H14) is almost negligible. Moreover, in the range 4.5 < pD < 6.5, this signal is shifted to a higher frequency with increasing pD. This behaviour becomes understandable if a conformational change of the κ$^3$-*O*,*N*,*O*-coordinated cyclohexane residue takes place upon deprotonation of the methylammonium group. Below pD 4 the conformation of this ring corresponds to a twisted boat (Figure 1).[22] In terms of torsional strain, a corresponding chair conformation is expected to be of lower energy. However, as long as the non-coordinated nitrogen is protonated, such a geometry would give rise to dramatic repulsion between the three axial substituents (Scheme 4). This strain is released upon deprotonation because the methylamino group can act as a proton acceptor in an intramolecular hydrogen bond. A similar change in conformation has recently been described for a related complex with κ$^3$-*N*,*O*,*N*

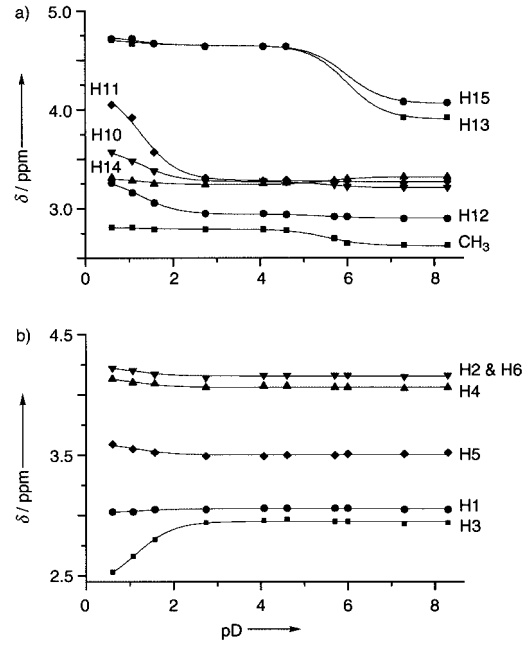


Figure 2. pD dependence of the $^1$H NMR resonances of $[Co(HL^a)]^{4+}$ ($D_2O$, 33 °C, TSP = 0 ppm).[14] a) κ$^3$-*O*,*N*,*O*-coordinated taci ring b) κ$^3$-*N*,*N*,*N*-coordinated taci ring. Squares, triangles and circles correspond to the experimental values, the lines are calculated (minimisation of $\Sigma[\delta_{obs} - \delta_{calcd}]^2$. The numbering scheme shown in Scheme 3c has been used.

 © 2006 Wiley-VCH Verlag GmbH & Co. KGaA, Weinheim 

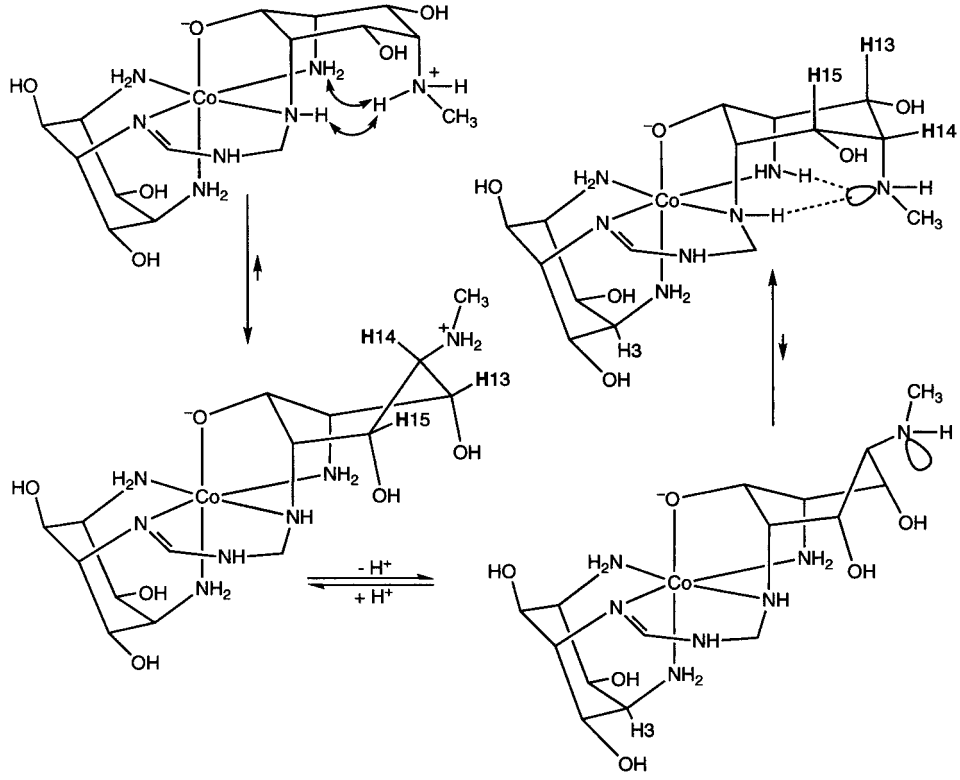


Scheme 4. The pH-dependent conformational equilibrium for the monobridged complex with a twisted boat conformation in acidic media ($[Co(HL^a)]^{4+}$ and $[Co(L^a)]^{3+}$) and a chair conformation at high pH ($[Co(H_{-1}L^a)]^{2+}$) as major species.[14] H–H Repulsion interactions are marked with arrows, possible hydrogen bonds are shown by dashed lines.

coordination in which hydrogen bonding to the non-coordinating amino group is suppressed by its conversion to an amide.[24] Molecular mechanics calculations support this interpretation, namely, for the fully deprotonated $[Co(H_{-1}L^a)]^{2+}$, the twisted boat conformer has a strain energy which is 17 kJ mol$^{-1}$ higher than for the corresponding chair conformation. The change from the twisted boat to the chair conformation brings H14 into an equatorial and H13/H15 into an axial position. It is well known that equatorial hydrogens in a cyclohexane moiety generally appear at higher frequencies. Clearly the two effects (change from an axial to an equatorial position and shielding by deprotonation) tend to the same direction for the hydrogens in the β position but to opposite directions for the hydrogen in the α position of the methylamino group. Consequently, the resultant shift is almost zero for H14 and twice as much as expected for H13 and H15. The release of strain which is caused by this conformational change represents an additional driving force for the deprotonation of the methylammonium group and helps to explain the above-mentioned rather low value of 5.3 for this p$K_a$. A conformational change is further supported by the observation that the resonances of H13, H15 and of the methyl group exhibited strong line broadening in the range $4.5 \leq pD \leq 6$, indicative of some dynamic behaviour within the molecule.

The pD-dependence of most of the resonances of the κ$^3$-*N*,*N*,*N*-bonded moiety is relatively minor as expected (Figure 2b). There is one remarkable exception, however. H3, which is *trans* to the coordinated oxygen donor, exhibits a strong shift in the range $0.5 < pD < 2$ and even more interestingly, this signal is shifted to *higher* frequency with increasing pD. The observed pD behaviour clearly implies that this effect must be due to the deprotonation of the coordinated hydroxy group. We recently demonstrated that such a specific *trans* effect is very characteristic for the deprotonation of a coordinated oxygen in Co$^{III}$ complexes with polyamino-polyalcohol ligands.[25]

The $^1A_{1g}$–$^1T_{1g}$ transition of the $CoN_5O$ chromophore of $[Co(H_{-1}L^a)]^{2+}$ and $[Co(HL^a)]^{4+}$ can be observed at 508 nm (pH 12) and 513 nm (10 M HCl), respectively. These values are slightly higher than the corresponding values in the nonbridged [Co(*cis*-tach)(taci-κ$^3$-*N*,*O*,*N*)]$^{4+}$ ($\lambda_{max}$ = 484 nm).[20] Cyclic voltammetry (Hg-electrode) revealed quasi-reversible redox behaviour with a reduction potential $E_{1/2}$ (Co$^{III}$/Co$^{II}$) of –0.12 V (vs. NHE).

### Characterisation of $[Co(L^b)]^{3+}$[14]

The second pink coloured fraction was identified as a doubly bridged and dimethylated species.[15] The $^{13}C\{^1H\}$ NMR spectrum exhibited a total of nine signals for the 18 carbon atoms. They were assigned to one $CH_3$ resonance, one $CH_2$ resonance and seven CH resonances on the basis of DEPT experiments.[17] In the $^1H$ NMR spectrum two singlets, one of them at the low end and the other at the

 © 2006 Wiley-VCH Verlag GmbH & Co. KGaA, Weinheim 

high end of the range observed for the chemical shifts, were assigned to the N–$CH_3$ methyl groups (6 H) and to the N=CH imine protons (2 H), respectively. The remaining eight resonances (each representing two hydrogen atoms) corresponded to the twelve cyclohexane ring protons and to the $CH_2$ groups of the bridges. Their mutual coupling pattern was established by a series of $^1$H-$^1$H and $^1$H-$^{13}$C correlation experiments (Scheme 5). The reduced number of signals is indicative of some symmetry. However, the $C_s$-symmetric forms **C** and **D** with the two imino groups attached to the same taci ring can be excluded from further consideration since a total of twelve rather than nine signals would be expected for such isomers in the $^{13}$C NMR spectrum. The $C_i$ and $C_2$ symmetric isomers **A** and **B** on the other hand are both consistent with the NMR characteristics. Further information about the structure of this complex can be obtained from the pD-dependence of the $^1$H NMR resonances (Figure 3). The $\delta$ vs. pD curves could be modelled successfully using the four p$K$ values p$K_1$ = 0.1, p$K_2$ = 2.4, p$K_3$ = 4.9 and p$K_4$ = 5.9. The exclusive and significant shift of H1 in the range $0 \leq$ pD $\leq 2$ is again indicative of a deprotonation of the α hydroxy groups and the low values for the two corresponding p$K_a$ values must be interpreted in terms of a coordination of these oxygen donors. p$K_3$ and p$K_4$ belong to the deprotonation of the non-coordinating methylammonium groups. Clearly, an asymmetric κ$^3$-*N*,*O*,*N*-binding mode, as already observed for $[Co(HL^a)]^{4+}$, has to be considered in the doubly bridged derivative and, based on symmetry arguments, both taci fragments must adopt such a coordination mode. As seen in the previous section, this type of coordination implies formation of five membered chelate rings and this is again clearly shown by the significant offset of C1 in the $^{13}$C NMR spectrum.[18–20] Similar to $[Co(L^a)]^{3+}$, the resultant $CoN_4O_2$ chromophore exhibits a $\lambda_{max}$ (525 nm in 12 M HCl, 517 nm at pH = 12) for the $^1A_{1g}$–$^1T_{2g}$ transition which is slightly higher than those of nonbridged analogues such as $[Co(cis\text{-tach})(taci\text{-}\kappa^3\text{-}O^1,N^2,O^3)]^{3+}$ ($\lambda_{max}$ = 498) and $[Co(taci\text{-}\kappa^3\text{-}N^1,N^3,N^5)(taci\text{-}\kappa^3\text{-}O^1,N^2,O^3)]^{3+}$ ($\lambda_{max}$ = 494).[20] The minor blue shift observed for this band upon an increase in pH is well established as an indicator for deprotonation of the coordinated ROH groups. The rearrange-

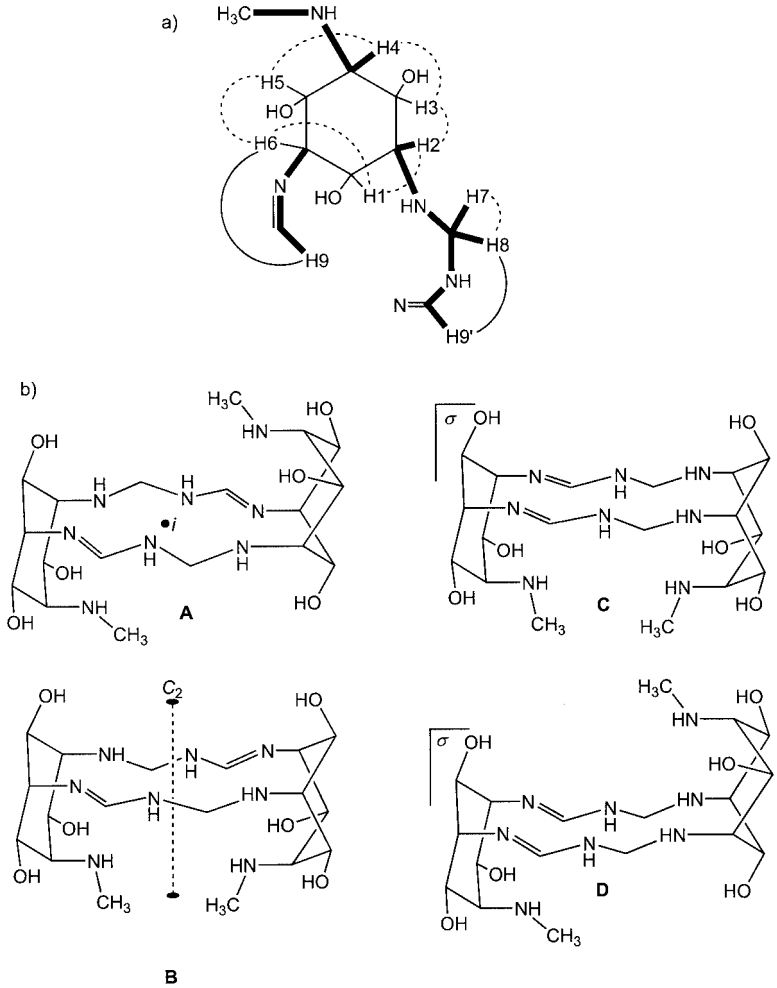


Scheme 5. a) The structural fragment of $L^b$ established by NMR spectroscopic measurements.[14] Selected $^1$H $^{13}$C long range couplings are depicted in bold, geminal and vicinal $^1$H $^1$H coupling interactions and long range $^1$H $^1$H coupling interactions are marked with dashed and full lines, respectively. The carbon atoms are labelled with the same numbering scheme as shown for the corresponding hydrogen atoms. b) Representations for **A** ($C_i$), **B** ($C_2$), **C** ($C_s$), and **D** ($C_s$) showing possible structures of $L^b$ as discussed in the text.

 © 2006 Wiley-VCH Verlag GmbH & Co. KGaA, Weinheim 

ment from a $\kappa^3$-*N*,*N*,*N* to a $\kappa^3$-*N*,*O*,*N* coordination mode appears to proceed in an analogous way to that of $[Co(L^a)]^{3+}$. However, it is worthy to note that in the mono-bridged complex only the moiety with three $sp^3$ nitrogen donors switches to a $\kappa^3$-*N*,*O*,*N*-mode (the moiety with the N=C group retains the adamantane-like triamine coordination), whereas in $[Co(L^b)]^{3+}$ both rings, although attached to an imine nitrogen, adopt a $\kappa^3$-*N*,*O*,*N* coordination.

For a further discussion of the stereochemistry of this complex, it should be kept in mind that the two NH bridge heads become stereogenic when coordinated to the $Co^{III}$ centre and, consequently, different diastereomers must be taken into account. Based on symmetry arguments, the two nitrogen atoms must have related configurations (*R*,*S* in the $C_i$ isomer **1** and *R*,*R* or *S*,*S* in the $C_2$ isomers **2** and **3** shown in Scheme 6). For the $C_i$ symmetric ligand **A** (Scheme 5), only structure **1** (Scheme 6) is compatible with these considerations. However, the $C_2$ symmetric macrocycle **B** can be wrapped around the $Co^{III}$ centre in two different ways resulting in distinct structures (**2** and **3**) where either the two $sp^2$ or the two $sp^3$ nitrogen donors have a *trans* orientation within the coordination sphere (for **B** the two oxygen donors of the $C_2$ symmetric ligand are always oriented *cis*). The observation that the deprotonation of the two coordinated hydroxy groups did not result in any reverse shift of any of the H(–C–N) ring protons (low-field shift upon in-

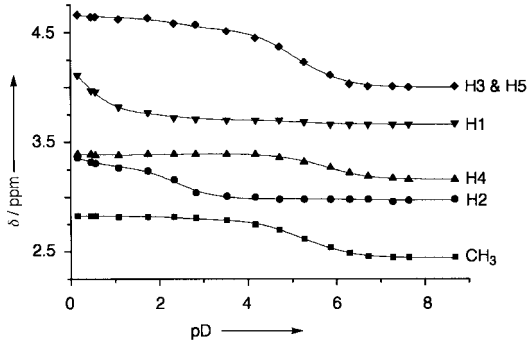


Figure 3. pD dependence of the $^1H$ NMR resonances of $[Co(H_2L^b)]^{5+}$ ($D_2O$, 33 °C, TSP = 0 ppm).[14] Squares, triangles and circles represent experimental values, the lines are calculated (minimisation of $\Sigma[\delta_{obs} - \delta_{calcd}]^2$. The numbering scheme of Scheme 5a has been used. The signal corresponding to H6 has been omitted due to pronounced line broadening around pD 5 (see text).

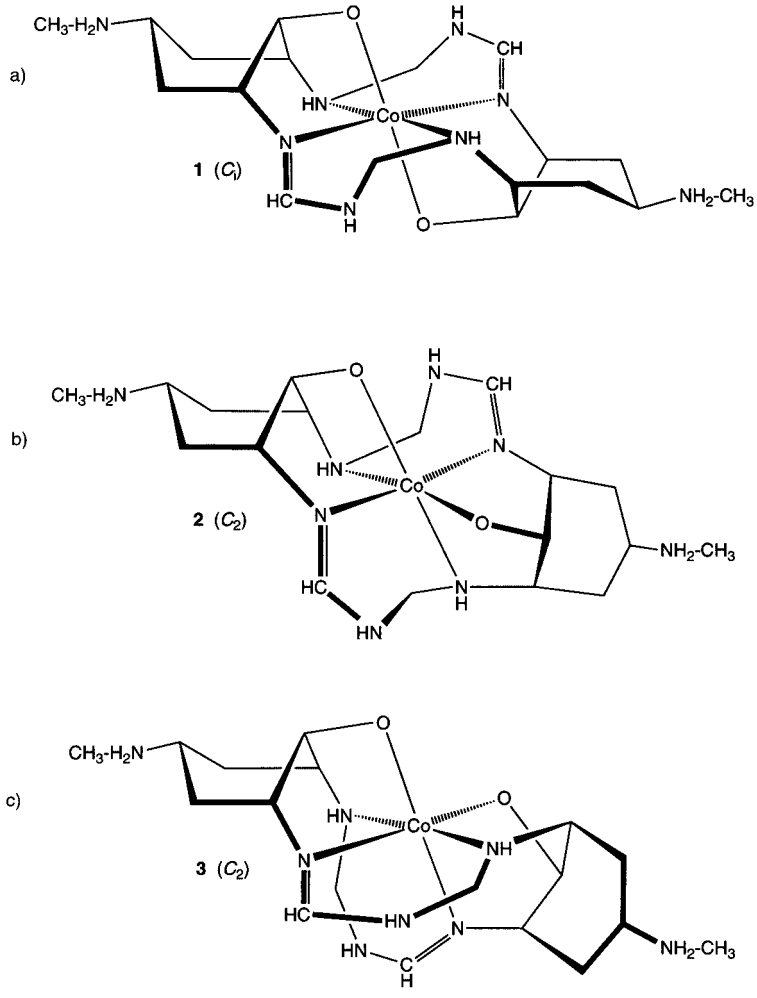


Scheme 6. Possible structures of $[Co(L^b)]^{3+}$ with $C_i$ (a) or $C_2$ symmetry (b and c).[14] Non-coordinating hydroxy groups and charges are omitted for clarity.

 © 2006 Wiley-VCH Verlag GmbH & Co. KGaA, Weinheim 

creasing pD in the range $0 < pH < 2$, see the corresponding feature for H3 of $[Co(HL^a)]^{4+}$ in Figure 2) would exclude the presence of an O–Co–N–CH substructure with a *trans* O–Co–N orientation.[25] Consequently, the $C_i$ symmetric structure **1** remains as the only stereoisomer which is compatible with all the NMR spectroscopic characteristics.

Further inspection of the pH dependence of the $^1H$ NMR signals in the range $2.5 \leq pD \leq 7.5$ revealed considerable line broadening. Similar behaviour has already been noted for the monobridged species $[Co(HL^a)]^{4+}$, although the line broadening observed for the doubly bridged complex is much more pronounced and some of the signals such as H5 and H6 disappear completely around pH 5. We interpret this line broadening again in terms of a changeover from a twisted boat to a chair conformation of the two cyclohexane back bones. These structural changes are a consequence of the deprotonation of the two non-coordinated methylammonium groups, allowing N–H···N hydrogen bonding in the deprotonated form. Molecular mechanics calculations for the fully deprotonated $[Co(H_{-2}L^b)]^+$ predict that among the various possible isomers the $C_2$ symmetric form **2** (Scheme 6) is of the lowest energy (Table S2, supporting information). The $C_i$ symmetric isomer **1** has a slightly higher, and the $C_2$-symmetric isomer **3** a considerably higher strain energy. At first glance this result is in disagreement with the assignment of the centrosymmetric structure **1** for $[Co(L^b)]^{3+}$ as follows from the NMR spectroscopic data. However, it should be kept in mind that in analogy to the monobridged ion $[Co(L^a)]^{3+}$, the primary product of the condensation reaction is an $N_6$-coordinated complex and the $N_4O_2$-coordinated product is formed in a subsequent rearrangement (Scheme 3). Our calculations indeed revealed that the $N_6$-coordinated forms are all considerably more strained than the $N_4O_2$-coordinated species **1** and **2**. Furthermore, the $N_6$-coordinated complex with the $C_i$ symmetric ligand **A** (Scheme 5) is about 9 kJ mol$^{-1}$ less strained than the corresponding complex with ligand **B**. The calculations would thus be in full agreement with the experimental findings, if we assume formation of the $N_6$-coordinated species as the rate-limiting step in the entire reaction sequence.

### Coupling with Aniline

Aniline was used as an alternative nitrogen nucleophile to study the influence of an aromatic substituent on the coupling reaction with $[Co^{III}\text{-hmi-(taci)}_2]^{3+}$. However, a noticeable conversion was only observed if an additional base such as triethylamine was added to the reaction mixture. Workup under acidic conditions yielded a very complex mixture with a $^{13}C\{^1H\}$ NMR spectrum exhibiting more than forty resonances. After further treatment of this product with aqueous NaOH (pH 11), a single red $Co^{III}$ complex could be isolated as the major component by chromatographic methods. The $FAB^+$ mass spectrum showed an *m*/*z* value of 529 for the molecular ion which is consistent with the composition $[Co(C_{20}H_{36}N_7O_6)]^+$. The structure of this complex was again elucidated by NMR spectroscopy (Figure 4). Two independent spin systems were observed for the two cyclohexane rings. Additionally, one of the coordinated nitrogen donors bears a methyl group, another a $C_7H_7N$ substituent. The latter clearly contains the aniline component in the form of a coordinated formamidine moiety. The monosubstituted phenyl ring of this substituent could be readily recognised by its $^1H$ and $^{13}C$ NMR spectroscopic characteristics and the amidine functionality was identified by a strong C=N stretch vibration at 1658 cm$^{-1}$ and corresponding NMR resonances at $\delta$ = 8.74 ppm and 162.6 ppm in the $^1H$ and $^{13}C$ spectra.[6,26] Bridging of the two taci moieties was, however, not observed. The $^4J$ coupling between the H(–C)–imine proton and the cyclohexane proton H7 together with the $^3J_{C,H}$ coupling between H7 and the imine carbon atom enabled an unambiguous localisation of the amidine fragment. An additional long range coupling between H2 and the methyl group established that the amidine substituent and the methyl group are not attached to the same taci moiety. None of the $^1H$ resonances showed any pH dependence and we can therefore exclude a changeover from the $CoN_6$ to a $CoN_5O$ coordination. This contention is also supported by the $^{13}C$ NMR characteristics whereby a resonance above 70 ppm, indicative of five-membered chelate rings,[18] was not observed. The relative orientation of the methyl group and the $C_7H_7N$ substituent could not be deduced from experimental data. However, mechanistic considerations (hydride shift, see above) would clearly point to a *cis* arrangement of these two non-hydrogen substituents. Two different tautomers **I** and **II** are possible for the amidine moiety (Figure 4b) and, for each of them, a *Z* or *E* configuration of the C=N double bond and an *R* or *S* configuration of the stereogenic coordinated $sp^3$ amine donors must be taken into consideration. For the tautomers **I** with a coordinated imine, the methyl group of the NH–$CH_3$ donor can adopt a *syn* or *anti* orientation with respect to the amidine moiety. The reverse tautomers **II**, in which the C=N double bond is in conjugation with the phenyl ring, have two stereogenic nitrogen donors with either an *S*,*R*-, *R*,*S*-, *R*,*R*-, or *S*,*S* configuration. Once again, it was not possible to establish from experimental data which of the various isomers is predominantly formed. We therefore analysed the steric strain by means of molecular mechanics methods and these calculations established clearly that the tautomers with a coordinated imine (form **I**) are more stable (i.e. less strained) than the corresponding tautomers of the type **II** (Table 2). Moreover, form **I** enables the possibility for an extended π delocalisation within the N=C–NH–phenyl fragment which would not be possible in type **II**. A type **I** form is also in agreement with the structure observed for the organic analogue in which the Co centre and the taci subunit are replaced by two methyl groups.[27] Our calculations further revealed that the type **I** isomer with an *E* orientation for Co and NH-phenyl and a *syn* configuration of the amidine moiety and the methyl group is of lowest energy.[28] For this particular geometry, the calculations predicted $Co^{III}$–N bond lengths in the range of 1.95–1.99 Å (mean value 1.98 Å) with the 1.95 Å

 © 2006 Wiley-VCH Verlag GmbH & Co. KGaA, Weinheim 

and the 1.99 Å distances corresponding to the bonds to the imine and methylamine nitrogen donor, respectively. For all possible isomers of $[Co(L^c)(L^d)]^{3+}$,[14] the increased strain is mainly caused by additional nonbonding interactions between the non-hydrogen substituents at the nitrogen donors and this is partially compensated for by an elongation of some of the Co–N bonds. As a matter of fact, it seems likely that these bonds are even somewhat longer than stated, since the calculations tend to slightly underestimate long $Co^{III}$–N distances.[29–31] The increased strain results in some weakening of the ligand field and this effect together with a possible conjugation between the 3d orbitals of Co and the extended π system of the amidine fragment supposedly contributes to the rather high $\lambda_{max}$ value of 510 nm observed for the $^1A_{1g}$–$^1T_{2g}$ transition.[32,33]

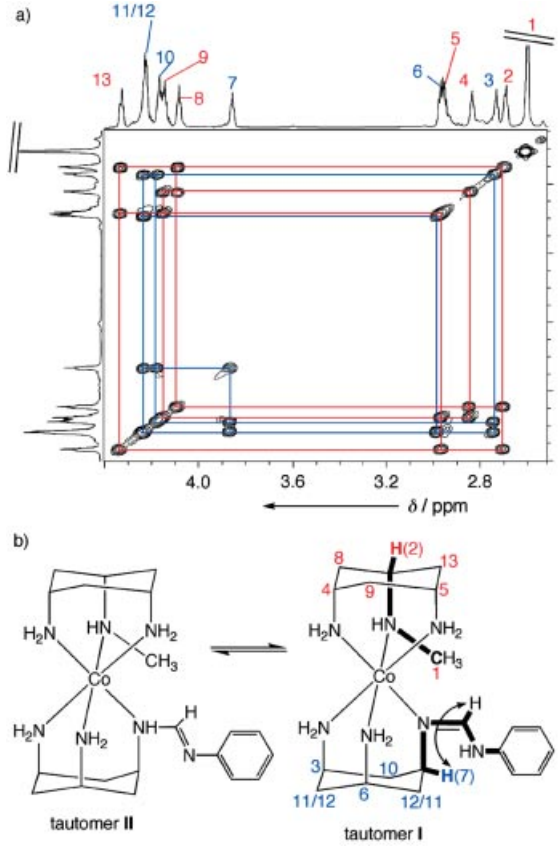


Figure 4. a) Section of the $^1$H-$^1$H COSY NMR spectrum of $[Co(L^c)(L^d)]^{3+}$ with the two independent spin systems shown in blue and red.[14] b) Structural representation of the two possible types of tautomers of $[Co(L^c)(L^d)]^{3+}$ (OH groups omitted) with numbering scheme. C–H long-range and H–H long-range coupling interactions are shown by bold bonds and by an arrow, respectively.

Hydrogenation of $[Co(L^c)(L^d)]^{3+}$ in an aqueous acidic medium on Pd/C (5 atm) resulted in decomposition of the complex and complete hydrolysis of the amidine moiety. As a consequence, the reaction product consisted of a 1:1 mixture of taci and its monomethylated derivative.

Table 2. Calculated strain energies and Co–N bond lengths of possible isomers for $[Co(taci)_2]^{3+}$ and $[Co(L^c)(L^d)]^{3+}$.[a]

| Complex | Relative strain energy [kJ mol$^{-1}$] | Co–N bond lengths [Å] range, mean |
|---|---|---|
| $[Co(taci)_2]^{3+}$ | | 1.969 |
| $[Co(L^c)(L^d)]^{3+}$, Tautomer **I** | | |
| *E*/*syn* [b] | 0 | 1.95–1.99, 1.975 |
| *E*/*anti* [b] | 6 | 1.96–1.99, 1.977 |
| *Z*/*syn* [b] | 25 | 1.96–2.00, 1.979 |
| *Z*/*anti* [b] | 20 | 1.97–1.99, 1.981 |
| $[Co(L^c)(L^d)]^{3+}$, Tautomer **II** | | |
| *E*/*S*,*S* [c] | 25 | 1.97–2.00, 1.984 |
| *E*/*S*,*R* [c] | 34 | 1.97–2.00, 1.985 |
| *E*/*R*,*S* [c] | 24 | 1.98–1.99, 1.984 |
| *E*/*R*,*R* [c] | 25 | 1.97–2.00, 1.984 |
| *Z*/*S*,*S* [c] | 39 | 1.97–2.01, 1.985 |
| *Z*/*S*,*R* [c] | 51 | 1.97–2.01, 1.987 |
| *Z*/*R*,*S* [c] | 37 | 1.98–1.99, 1.984 |
| *Z*/*R*,*R* [c] | 38 | 1.97–2.00, 1.985 |

[a] Molecular mechanics calculations using the MOMEC force field[46,47] together with the extensions listed in Table 4. [b] *E* and *Z* refer to the NH and Co substituents at the C=N double bond. Note that the free ligand $L^d$ and the complex $[Co(L^c)(L^d)]^{3+}$ have opposite stereo-descriptors: the *Z*-ligand[14] forms a complex with an *E* configuration and vice versa (Figure 4b). The descriptors *syn* and *anti* refer to the orientation of the methyl group with reference to the amidine moiety. [c] *E* and *Z* refer to the NH and $C_6H_5$ substituents at the C=N double bond, the two stereo-descriptors *R* and *S* refer to the configuration at the chiral amidine and methylamine nitrogen atoms, respectively, as shown in Figure 4b.

## Coupling with Cyanide

The reaction of $CN^-$ with $[Co^{III}$-hmi-$(taci)_2]^{3+}$ in aqueous solution again yielded a complex reaction mixture. Several different fractions could be separated on a Sephadex column but only the major red component could be identified unequivocally by means of MS and NMR spectroscopic measurements as a monobridged derivative $[Co^{III}(L^e)]^{3+}$ (Figure 5).[14] The $FAB^+$ spectrum exhibited signals of the pseudo-molecular ions $[Co^{II}(H_{-1}L^e)]^+$ and $[Co^{II}(L^e)Cl]^+$ ($L^e = C_{14}H_{31}N_7O_6$) with intensities of 100% and 13%, respectively. $[Co(L^e)]^{3+}$ is completely asymmetric as indicated by the $^1$H and $^{13}$C NMR spectra which contained a total of 10 and 11 signals for the two taci rings, respectively (one signal in the $^{13}$C NMR and two signals in the $^1$H NMR spectrum with double intensity corresponded to the resonances of two atoms). The $^1$H-$^1$H correlated 2D spectrum showed two independent spin system each consisting of six hydrogen atoms. The corresponding carbon atoms, which were identified as CH groups from a DEPT experiment,[17] were assigned by a $^1$H-$^{13}$C correlated spectrum. An additional $CH_2$ group with two diastereotopic hydrogen atoms was located and the $^{13}$C spectrum also exhibited a strongly deshielded signal at $\delta$ = 176 ppm, indicative of the formation of an imino group. Formation of a C=N double bond was further confirmed by a strong, sharp band at 1647 cm$^{-1}$ in the IR spectrum.[26] However, the DEPT experiment together with the $^1$H characteristics clearly show that, in contrast to the products obtained in the reaction with ammonia or aniline, the amidine-C is not bonded to any hydrogen atoms. Furthermore, the NMR spectroscopic

 © 2006 Wiley-VCH Verlag GmbH & Co. KGaA, Weinheim 

data gave no indication of the presence of an N–$CH_3$ group. The bridging position of the N=C($NH_2$)–$CH_2$–NH moiety was finally established from a long-range 2D C-H correlated experiment in which long range interactions from the bridging moiety to both cyclohexane entities could be observed. In analogy to $[Co(L^c)(L^d)]^{3+}$, it was not possible to conclude from the experimental data as to which of the two possible tautomers is formed. However, as outlined in the previous section it seems highly probable that the form with the imine nitrogen donor bonded to Co$^{III}$ is more stable. Indications for a $\kappa^3$-*N*,*O*,*N* coordination mode as described above for $[Co(HL^a)]^{4+}$ and $[Co(H_2L^b)]^{5+}$ have not been detected.

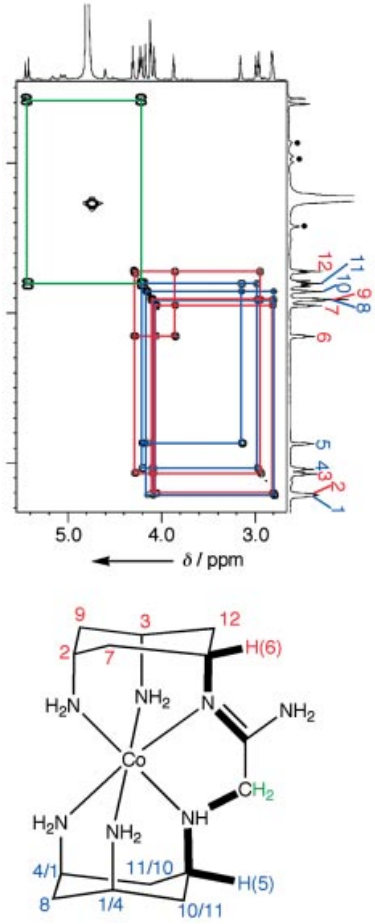


Figure 5. a) Section of the $^1$H-$^1$H COSY NMR spectrum of $[Co(L^e)]^{3+}$;[14] H(–N) protons of the coordinated amino groups are marked with black circles. b) structural representation of $[Co(L^e)]^{3+}$ with numbering scheme.[14] C–H long-range coupling interactions are shown in bold. The hydroxy groups in positions 7,9,12 and 8,10,11 are omitted for clarity.

The two doublets of the methylene group exhibited a rather large $^2J_{H,H}$ coupling constant of 18 Hz. Such unusually large coupling constants are known for spin systems with a π electron system attached to the $CH_2$ group as observed in cyclopentene-1,4-dione and it has been proposed that this enhancement is particularly large if the vector between the two protons is oriented parallel to the π orbitals[34] which is clearly the case for the N=C($NH_2$)–$CH_2$–NH bridge of $[Co^{III}(L^e)]^{3+}$. The $CH_2$-groups are weakly acidic and, if a solution of $[Co^{III}(L^e)]^{3+}$ in $D_2O$ is brought to a pD of about 11, the signals of the methylene group disappear in the $^1$H NMR spectrum and they do not reappear after addition of DCl. However, the DEPT spectrum still showed the presence of a methylene group indicative of H/D exchange. It is clear that the corresponding carbanion which is formed above pD 10 is stabilised by significant electron delocalisation.

The entire structure of $[Co^{III}(L^e)]^{3+}$ was again modelled by molecular mechanics calculations. In this model, the Co$^{III}$–$N_{imine}$ bond length proved to be relatively short (1.92 Å), whereas the remaining Co$^{III}$–$N_{amine}$ bonds lengths (1.96–1.97 Å) are consistent with the values reported in the literature for X-ray structures of a range of (hexaamine)-Co$^{III}$ complexes.[33] The high rigidity of the amidine-bridge resulted in some distortion of the octahedral coordination geometry with N–Co–N angles between 84° and 99°. The $^1A_{1g}$–$^1T_{2g}$ transition appeared at 497 nm which again indicates some weakening of the ligand field. Cyclic voltammetry showed a quasi-reversible redox process with a redox potential of –0.35 V (vs. NHE). A similar value has been observed for the parent system $[Co^{II/III}(taci)_2]^{2+/3+}$.[20,35]

## Discussion

The reaction of $[Co^{III}\text{-hmi-}(taci)_2]^{3+}$ with the three nucleophiles $NH_3$, aniline and $CN^-$ yielded three considerably different types of products. The reaction with $NH_3$ resembles the previously reported reaction with nitromethane insofar as formation of NH–$CH_2$–XH–CH=N bridges [XH = NH, C(H)-$NO_2$], connecting the two taci frames, coincides with methylation of an adjacent primary amino group.[9] The mechanism of this reaction has been discussed in terms of an intramolecular Cannizzaro reaction (Scheme 1, b) whereby a hydride is transferred from the methylene group of the initially formed NH–$CH_2$–XH–$CH_2$–$N^-$ bridge to an imino group. However, some characteristic differences are evident: (i) In the reaction with nitromethane (X = C-$NO_2$), the XH proton is finally abstracted by $NEt_3$ and the ligand appears in a carbanionic form, whereas in the reaction with $NH_3$, the nitrogen atom in the bridge (X = N) retains its proton. (ii) In the reaction with nitromethane, the doubly bridged complex was isolated as the main product while in the reaction with ammonia, the monobridged species was formed as the major product and the doubly bridged complex was only obtained as a very minor component. (iii) The bridging process with $NH_3$ was generally followed by a rearrangement of the coordination sphere of the Co$^{III}$ centre, i.e. the taci-moiety which becomes methylated switches from a $\kappa^3$-*N*,*N*,*N* to a $\kappa^3$-*N*,*O*,*N* coordination mode (Scheme 3). Consequently, an alkoxo-pentaamine coordination was observed for the monobridged complex and the doubly bridged derivative exhibits a dialkoxo-tetraamine coordination mode (Scheme 6). In the reaction with nitromethane, such a rearrangement of the coordination sphere was not observed. The isolated product

 © 2006 Wiley-VCH Verlag GmbH & Co. KGaA, Weinheim 

retains its hexaamine coordination. It has, however, been noted that the nitromethane adduct undergoes a characteristic structural rearrangement in strongly alkaline solutions and re-acidification leads to a species which was not identical with the initial condensation product. It is particularly interesting to note that in the initial product a total of 30 signals were observed in the $^{13}C$ NMR spectrum and that this number was reduced to a total of 10 at high pH. Moreover, in the initial reaction product, no resonance was observed above 70 ppm for the cyclohexane carbon atoms, whereas at high pH one of these signals shifted to 76 ppm. Based on the results presented in this paper, it thus appears highly probable that the previously observed[9] "low-energy isomer" has a doubly bridged structure with an analogous $CoN_4O_2$-coordination mode as reported here for $[CoL^b]^{3+}$.

For $[Co^{III}(cis\text{-tach})(H_{-1}ino)]^{2+}$ (ino = *cis*-inositol, Structure O6 in Scheme S1b), an equilibrium between two different stereoisomers has been observed in aqueous solution.[36] In the first isomer, the metal is bound to the three axial hydroxy groups of *cis*-inositol whereas in the second isomer the binding occurred by means of three hydroxy groups having a subsequent axial-equatorial-axial orientation. The kinetics of the isomerisation reaction have been investigated in detail and it has been found that (i) this reaction occurs at a considerably higher rate than complete dissociation of the inositol ligand, (ii) the isomerisation reaction becomes dramatically accelerated at high pH and (iii) the equilibrium between the triaxial and the axial-equatorial-axial coordination mode is influenced by the possibility of intramolecular O···H–O hydrogen bond formation. The higher rate of isomerisation compared with ligand dissociation was interpreted in terms of a mechanism in which the inositol ligand remains partially coordinated. For $[Co(L^a)]^{3+}$ and $[Co(L^b)]^{3+}$ with a hypothetical hexaamine coordination, the presence of an N–$CH_3$ group would generate significant strain due to nonbonding interactions between the methyl group and a hydrogen atom of a primary amino group of the neighbouring taci frame.[9] This strain is clearly responsible for the change to the $\kappa^3$-*N*,*O*,*N* axial-equatorial-axial coordination mode. By analogy with $[Co^{III}(cis\text{-tach})(ino)]^{3+}$, the rearrangement can occur without dissociation of the ligand (Scheme 3) and it is particularly fast in an alkaline medium. Similar to $[Co^{III}(cis\text{-tach})(ino)]^{3+}$, the pH has a significant influence on the possibility of intramolecular hydrogen bond formation: As long as the methylamino group remains deprotonated, it can act as a proton acceptor and can thus stabilise the corresponding cyclohexane chair. However, after protonation, significant nonbonding N–H···H–N repulsive interactions would arise. In contrast to $[Co^{III}(cis\text{-tach})(ino)]^{3+}$, this conflict cannot be resolved by a return to the double-adamantane-type structure and the only way for strain to be minimised is by the adoption of a twisted boat conformation (Scheme 4).

The reaction of $[Co^{III}\text{-hmi-}(taci)_2]^{3+}$ with aniline is remarkable because the resultant structure is devoid of any bridge between the two taci-frames. Formation of an amidine moiety together with *N*-methylation must again be interpreted in terms of a Cannizzaro type hydride shift. The lack of observation of a bridge is, however, a clear sign that the hydride shift already occurs after the first condensation step (bridge formation would require a double attack of the nucleophile to two adjacent imino groups, see Scheme 1). At present, it is still not clear why the hydride shift already occurs here at an earlier stage. Either electronic properties (reduced nucleophilicity of the aniline nitrogen) or steric reasons (increased repulsion due to the larger aromatic substituent) may account for this behaviour.

The reaction of the hexaimine complex with cyanide is special because $CN^-$ cannot undergo multiple binding to adjacent $H_2C{=}N(R)$–Co groups. In a nonaqueous medium, the reaction of $CN^-$ with an imine would simply generate a Co–$N(R)^-$–$CH_2$–CN moiety. Such a product could then become protonated to give Co–N(R)H–$CH_2$–CN. It would, however, remain in equilibrium with the initial components.[37] In an aqueous environment, $CN^-$ binding and hydrolysis may occur simultaneously as competing processes. It is possible to control the reaction in such a way that one imino group reacts with $OH^-$ reforming the deprotonated, coordinated amine, whereas at the same time, an adjacent imino group reacts with $CN^-$ (Scheme 7). The nitrile-carbon atom can now react as an electrophilic centre,[26,38] being able to accept the adjacent, negative nitrogen donor. In organic chemistry, the reaction of a nitrile RCN with an amine to give a corresponding amidine is only known for nitriles which are activated either by a strongly electron-withdrawing substituent R or by coordination of a Lewis acid.[39] The situation is different in coordination chemistry in which the generation of a metal-bound amidine by an intramolecular reaction between a deprotonated, coordinated amine and a nitrilo group has been documented with a few examples.[37,40]

Owing to the reversible addition of $CN^-$ to the imine, successful formation of $[Co(L^e)]^{3+}$ requires a well balanced ratio of the two reaction rates. This ratio can be influenced by varying either the $CN^-$ or the $OH^-$ concentration. We obtained reasonable yields of the mono-bridged species in aqueous solution around pH 10–12. Even at this relatively moderate $OH^-$ concentration, complete hydrolysis of the hexaimine represents a significant side reaction as indicated by the isolation of considerable amounts of $[Co(taci)_2]^{3+}$ from the reaction mixture. Further lowering of the pH should, however, be avoided, due to possible HCN formation. We have not yet succeeded in the isolation of any doubly bridged product and it appears that the formation of a second bridge would occur at a significantly lower rate. Since the reaction of a coordinated imine with $CN^-$ is reversible, all of the remaining imino groups are hydrolysed and the final product was found to be devoid of any *N*-methylidene-imino groups. The reaction of $[Co\text{-hmi-}(taci)_2]^{3+}$ with $CN^-$ in aqueous media thus represents a promising route for connecting two taci-rings by one N–C–C–N bridge. However, we have not yet established whether reduction of the amidine to the amine and de-metallation can be readily achieved. Similar to the reaction of $[Co^{III}\text{-hmi-}(taci)_2]^{3+}$ with aniline and with nitromethane, the hexaamine coordination appears to be retained in $[Co(L^e)]^{3+}$,

 © 2006 Wiley-VCH Verlag GmbH & Co. KGaA, Weinheim 

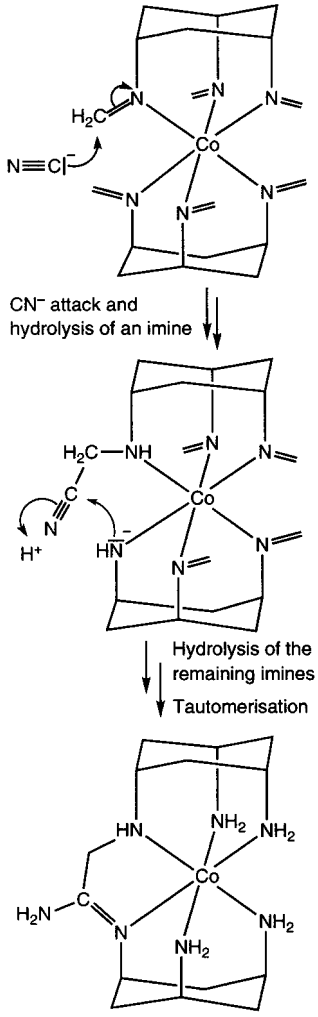


Scheme 7. Proposed mechanism for the formation of $[Co(L^e)]^{3+}$.[14] The non-coordinating OH-groups are omitted for clarity.

although molecular mechanics calculation indicated some distortion from regular octahedral geometry. $[Co(L^e)]^{3+}$ is the only example in this study in which the coupling reaction does not result in formation of a methylamino group. Clearly a hydride shift from the Co–N(R)$^-$–$CH_2$–CN methylene group to an adjacent imino group is not possible.

In conclusion, our study has fully confirmed that the successful capping reaction observed for $[Co(en)_3]^{3+}$ cannot be applied to (hexaamine)Co$^{III}$ complexes with rigid cyclic amine ligands. Sargeson proposed that the lack of observation of the capping process in such systems is a consequence of the slow exchange rate of the amine protons.[10] Such an assumption is plausible because condensation with the aldehyde and addition of the capping reagent can be performed in a single reaction with N–H deprotonation as the first step. In our investigation, we have used the hexamethylideneimine derivative as a starting material and it has thus become evident that other factors must be responsible for the different behaviour of the cyclic ligands. We attribute the slow rate or indeed the failure to observe bridge formation to be mainly due to steric constraints. The molecular mechanics calculations provided unambiguous evidence that in general, bridging of two taci moieties by means of two nitrogen donors of the hexaamine coordination implies a significant increase of strain and that this strain increases with an increasing number of bridges.

## Experimental Section

**Physical Measurements and Analyses:** $^1H$ and $^{13}C$ NMR spectra were recorded in $D_2O$ at 306 K with a Bruker Avance DRX 500 spectrometer at frequencies of 500.13 MHz and 125.9 MHz, respectively. Chemical shifts (in ppm) are given relative to [$D_4$]sodium (trimethylsilyl)propionate (0 ppm) as the internal standard. The pD values of the NMR samples were adjusted with NaOD and DCl and were determined as described previously.[41] Multiplicities are abbreviated as follows: s = singlet, d = doublet, t = triplet, q = quartet, m = multiplet. The gradient-selected (gs) $^1H$-$^1H$ COSY, gs $^1H$-$^{13}C$ COSY and gs $^1H$-$^{13}C$ HMBQ experiments were performed as described in the literature.[42] $CH_3$, $CH_2$ and CH carbon atoms were assigned using $^{13}C$ DEPT experiments.[17] IR spectra were recorded on a Perkin-Elmer 883 IR spectrometer (KBr wafer) and UV/Vis spectra were measured on a Uvikon 940 spectrometer at 25 ± 1 °C. FAB$^+$ mass spectra were recorded on a VG ZAB VSEQ instrument. The samples were measured as aqueous solutions using a glycerol matrix. Cyclic voltammetry was performed at ambient temperature (23 ± 2 °C) on a BAS C2 cell equipped with an Hg or Au electrode, a platinum counter electrode and an Ag/AgCl reference electrode with a BAS 100B/W potentiostat. The measurements were performed in an aqueous borax buffer (pH 9) with 1-mM sample concentrations and NaCl (1 M) as a supporting electrolyte. p$K_a$ values were determined by potentiometric titrations as described previously[41] (25.0 °C, 0.10 M KCl) and evaluated using a fixed value of 13.78 for p$K_w$. C, H and N analyses were performed by H. Feuerhake (Universität des Saarlandes).

**Materials:** $Et_3N$, $CH_3CN$, aniline, aqueous $NH_3$ (≈ 25%), KCN and trisodium citrate dihydrate were commercially available products from Fluka. $CH_3CN$ was dried with $P_4O_{10}$. Aniline was freshly distilled prior to use. $CF_3SO_3H$ (>98%) was purchased from Lancaster Synthesis and stored under $N_2$. $[Co(taci)_2](NO_3)_3{\cdot}2H_2O$[31] and its hexamethylideneimino (hmi) derivative [Co-hmi-(taci)$_2$]-$Cl_3{\cdot}6H_2O$[9] were prepared according to published procedures. Dowex 50 W-X2 cation-exchange resin (100–200 mesh, $H^+$ form) was obtained from Fluka. SP-Sephadex C-25 cation exchange resin (200 mesh, from Pharmacia Biotech) was converted into the $Na^+$ form by elution with NaCl (2 M) prior to use and sufficient rinsing with $H_2O$ until the eluent was free of chloride (checked with $AgNO_3$).

**[Co-hmi-(taci)$_2$](CF$_3$SO$_3$)$_3$·2H$_2$O:** [Co-hmi-(taci)$_2$]$Cl_3{\cdot}6H_2O$ (500 mg, 0.71 mmol) was dissolved in $CF_3SO_3H$ (20 mL). The clear yellow solution was heated to 80 °C and a stream of dry $N_2$ was passed through the mixture for 3 h. The clear, dark yellow solution was cooled to room temperature and was then cautiously poured into $Et_2O$ (750 mL). A solid precipitated which was removed by filtration, washed six times carefully with $Et_2O$ (portions of 100 mL) and dried in air. Yield: 636 mg (92%) of a pale yellow solid. $C_{21}H_{34}CoF_9N_6O_{17}S_3$ (968.6): calcd. C 26.04, H 3.54, N 8.68; found C 26.22, H 3.34, N 8.71. IR (KBr): $\tilde{\nu}$ = 1618 (s) cm$^{-1}$. $^1H$ NMR ($D_2O$, pD < 1): $\delta$ = 4.07 (t, $J$ = 3.0 Hz, 6 H), 4.62 (t, $J$ = 3.0 Hz, 6 H), 7.91 (d, $J$ = 7.5 Hz, 6 H), 8.13 (d, $J$ = 7.5 Hz, 6 H) ppm. $^{13}C\{^1H\}$ NMR ($D_2O$, pD < 1): $\delta$ = 68.5 (CH), 76.7 (CH), 122.6 (q, $J_{C,F}$ = 317 Hz), 187.2 (C) ppm.

**Reaction of [Co-hmi-(taci)$_2$](CF$_3$SO$_3$)$_3$·2H$_2$O with NH$_3$:** [Co-hmi-(taci)$_2$](CF$_3$SO$_3$)$_3$·2H$_2$O (1.0 g, 1.03 mmol) was dissolved in dry

 © 2006 Wiley-VCH Verlag GmbH & Co. KGaA, Weinheim 

$CH_3CN$ (100 mL). To the yellow solution was rapidly added concentrated aqueous $NH_3$ (10 mL). An immediate colour change to dark green was noted and the reaction mixture turned to a reddish brown within a few minutes. A brownish solid finally precipitated. The suspension was stirred for 24 h at room temperature giving a bright red solution together with a yellow solid. The entire mixture was poured into a solution of aqueous $H_2SO_4$ (30 g of conc. $H_2SO_4$ dissolved in 600 mL of $H_2O$). The solution was further diluted with $H_2O$ to a total volume of 1 L (pH ≈ 1) and adsorbed on Dowex 50. The column was washed with $H_2O$ until the eluent was neutral and then elution with aqueous HCl (0.5 M) was carried out. Further elution with HCl (3 M) yielded a red fraction which was evaporated to dryness and redissolved in $H_2O$ (100 mL). Traces of acid were neutralised by adding small portions of NaOH (1 M). The solution was then adsorbed on Sephadex. Elution with trisodium citrate (0.2 M) resulted in the separation of three bands: A pink fast moving minor fraction (F1) followed by a major red fraction (F2) and a slower moving badly resolved third fraction (F3). The yellow front part of F3 was identified as $[Co(taci)_2]^{3+}$ by $^1H$ and $^{13}C$ NMR spectroscopy. According to NMR and MS measurements, the purple coloured tailing part of F3 was a mixture of several components which could be neither separated nor identified. Each fraction was desalted on Dowex 50, (elution with 0.5 M HCl and 3 M HCl). The products which were obtained in the 3-M HCl fractions were evaporated under reduced pressure and dried in air.

**Analytical Data of Fraction F1 {$[Co(H_2L^b)]Cl_5$}:**[14] Yield: 5 mg of pink brittle flakes. $^1H$ NMR ($D_2O$, pD = 0.2): $\delta$ = 2.83 (s, 6 H), 3.36 (m, 2 H), 3.39 (t, $J$ = 5 Hz, 2 H), 3.71 and 3.98 (AB-system, $J$ = 12 Hz, 4 H), 4.11 (t, $J$ = 4 Hz, 2 H), 4.33 (m, 2 H), 4.66 (m,4 H), 8.53 (s, 2 H) ppm. $^{13}C\{^1H\}$ NMR ($D_2O$, pD = 1): $\delta$ = 35.7 ($CH_3$), 60.0 (CH), 61.0 ($CH_2$), 62.2 (CH), 62.9 (CH), 63.2 (CH), 64.9 (CH), 76.4 (CH), 174.1 (CH) ppm. MS-FAB$^+$ $m/z$ (%) = 518 (36) $[Co(H_{-1}L^b)]^+$,[15] 554 (6) $[Co(L^b)Cl]^+$. UV/Vis: $\lambda_{max}$ = 525 nm (12 M HCl), $\lambda_{max}$ = 517 nm (pH = 12).

**Analytical Data of Fraction F2 {$[Co(HL^a)]Cl_4\cdot H_2O$}:**[14] Yield: 283 mg (0.45 mmol, 44%) of a deep red solid. $C_{15}H_{36}CoCl_4N_7O_7$ (627.2): calcd. C 28.72, H 5.79, N 15.63; found C 28.84, H 5.83, N 15.70. IR (KBr): $\tilde{\nu}$ = 1628 (s) cm$^{-1}$. $^1H$ NMR ($D_2O$, pD = 1): $\delta$ = 2.55 (t, $J$ = 3.5 Hz, 1 H), 2.82 (s, 3 H), 3.04 (t, $J$ = 3.5 Hz, 1 H), 3.28 (m, 1 H), 3.32 (m,1 H), 3.58 (m, 1 H), 3.60 (t, $J$ = 3.5 Hz, 1 H), 3.84 and 3.96 (AB-system, $J$ = 11.5 Hz, 2 H), 4.04 (m, 1 H), 4.13 (t, $J$ = 3.5 Hz, 1 H), 4.22 (t, $J$ = 3.5 Hz, 1 H), 4.23 (t, $J$ = 3.5 Hz, 1 H), 4.71 (m, obscured by HDO, $\delta$ taken from $^1H$ $^1H$-COSY, 1 H) 4.75 (m, obscured by HDO, $\delta$ taken from $^1H$ $^1H$-COSY, 1 H), 8.15 (s, 1 H) ppm. $^{13}C\{^1H\}$ NMR ($D_2O$, pD = 1): $\delta$ = 33.2 ($CH_3$), 52.0 (CH), 52.1 (CH), 54.8 (CH), 57.9 (CH), 59.7 (CH), 61.4 ($CH_2$), 62.2 (CH), 62.7 (CH), 64.1 (CH), 65.8 (CH), 65.9 (CH), 66.7 (CH), 75.7 (CH), 172.8 (CH); (pD = 8): 40.2, 52.5, 53.2, 60.5, 61.7, 65.1, 65.5, 66.0, 66.85, 66.94, 67.3, 68.1, 68.3, 80.0, 170 ppm. MS-FAB$^+$ $m/z$ (%): 465 (100) $[Co(H_{-1}L^a)]^+$, 501 (13) $[Co(L^a)Cl]^+$. UV/Vis (12 M HCl): $\lambda_{max}$ = 383 nm ($\varepsilon$ = 289 M$^{-1}$cm$^{-1}$), $\lambda_{max}$ = 513 nm ($\varepsilon$ = 120 M$^{-1}$cm$^{-1}$); (NaOH, pH = 12) $\lambda_{max}$ = 386 nm ($\varepsilon$ = 170 M$^{-1}$cm$^{-1}$), $\lambda_{max}$ = 508 nm ($\varepsilon$ = 90 M$^{-1}$cm$^{-1}$). Crystals of composition $[Co(HL^a)][ZnBr_4]_2\cdot 5H_2O$ suitable for X-ray analysis were grown by slow diffusion of EtOH into an acidified (HBr) aqueous solution of $[Co(HL^a)]Cl_4$ saturated with $ZnBr_2$ at 4 °C.

**Reaction of [Co-hmi-(taci)$_2$](CF$_3$SO$_3$)$_3\cdot 2H_2O$ with Aniline:** Aniline (3.3 mL, 36 mmol) and [Co-hmi-(taci)$_2$](CF$_3$SO$_3$)$_3\cdot 2H_2O$ (520 mg, 0.54 mmol) were dissolved in dry $CH_3CN$ (150 mL). $NEt_3$ (6.6 mL, 47 mmol) was added to the resultant light yellow solution which caused an immediate colour change to dark green. The mixture was stirred for 30 min at room temperature and then poured into aqueous $H_2SO_4$ (18 g of $H_2SO_4$ in 400 mL of $H_2O$). The reddish orange solution was further diluted with $H_2O$ to a total volume of 1 L and sorbed on Dowex 50. The column was eluted with aqueous HCl (0.5 M and 4 M). The 4-M HCl fraction was evaporated to dryness and the residue redissolved in $H_2O$ (50 mL). NaOH (1.5 M) was added carefully in small portions until the pH reached a value of 11 (checked using a glass electrode). During this addition, the colour changed to violet and precipitation of a solid was observed. The suspension was stirred at room temperature for 24 h, acidified with dilute HCl to pH 7 and sorbed onto Sephadex. Elution with $Na_2SO_4$ (0.28 M) resulted in the separation of three bands: a very small fast moving light red band which was discarded, a yellow band of $[Co(taci)_2]^{3+}$, and a strong red band of $[Co(L^c)(L^d)]^{3+}$. The last red fraction was desalted on Dowex 50, evaporated to dryness and dried in vacuo. Yield: 177 mg (0.26 mmol, 49%) of red $[Co(L^c)(L^d)]Cl_3\cdot 2H_2O$.[14] $C_{20}H_{41}CoCl_3N_7O_8$ (672.9): calcd. C 35.70, H 6.14, N 14.57; found C 35.94; H 5.77; N 14.54. IR (KBr): $\tilde{\nu}$ = 1658 (s) cm$^{-1}$. $^1H$ NMR ($D_2O$): $\delta$ = 2.60 (s, 3 H), 2.69 (t, $J$ = 3.5 Hz, 1 H), 2.72 (t, $J$ = 3.5 Hz, 1 H), 2.83 (t, $J$ = 3.5 Hz, 1 H), 2.95 (t, $J$ = 3.5 Hz, 1 H), 2.96 (t, $J$ = 3.5 Hz, 1 H), 3.84 (t, $J$ = 3.5 Hz, 1 H), 4.07 (t, $J$ = 3.5 Hz, 1 H), 4.13 (t, $J$ = 3.5 Hz, 1 H), 4.16 (t, $J$ = 3.5 Hz, 1 H), 4.21 (m, 2 H), 4.32 (t, $J$ = 3.5 Hz, 1 H), 7.29 (m, 3 H), 7.47 (m, 2 H), 8.74 (s, 1 H) ppm. $^{13}C\{^1H\}$ NMR ($D_2O$): $\delta$ = 44.3 ($CH_3$), 52.3 (CH), 52.4 (CH), 52.8 (CH), 53.5 (CH), 55.5 (CH), 61.6 (CH), 65.3 (CH), 65.6 (CH), 65.8 (CH), 66.7 (CH), 67.6 (CH), 68.9 (CH), 120.7 ($CH_{arom}$), 128.1 ($CH_{arom}$), 132.5 ($CH_{arom}$), 141.0 ($C_{arom}$), 162.6 (CH) ppm. MS-FAB$^+$ $m/z$ (%): 529 (97) $[H_{-1}\{Co(L^c)(L^d)\}]^+$, 565 (9) $[Co(L^c)(L^d)]Cl^+$. UV/Vis ($H_2O$): $\lambda_{max}$ = 368 nm ($\varepsilon$ = 147 M$^{-1}$cm$^{-1}$), $\lambda_{max}$ = 510 nm ($\varepsilon$ = 44 M$^{-1}$cm$^{-1}$).

**Reaction of [Co-hmi-(taci)$_2$]Cl$_3\cdot 6H_2O$ with KCN: Caution!** KCN and HCN are strong poisons. All manipulations must be performed in a well ventilated fume hood. HCN must be destroyed by passing any evolving gas through an NaOCl solution. A solution of KCN (250 mg, 3.84 mmol) in $H_2O$ (250 mL) was added to a solution of [Co-hmi-(taci)$_2$]Cl$_3\cdot 6H_2O$ (1.05 g, 1.50 mmol) in $H_2O$ (250 mL). The first 50 mL of the KCN solution were added dropwise whereas the remaining 200 mL were added in one portion. The solution, which by this time showed a red colour, was stirred at room temperature for 30 min and then poured into aqueous sulfuric acid (15 g of conc. $H_2SO_4$ in 500 mL of $H_2O$). **Caution!** Formation of HCN. The solution was further diluted with $H_2O$ until a pH of 2 was reached and was then sorbed on Dowex 50. The resin was eluted with $H_2O$ and with aqueous HCl (0.5 M). Further elution with HCl (3 M) gave a major broad band with a yellow front ($[Co(taci)_2]^{3+}$) and a red tail. The red portion was collected. However, complete separation from the yellow part was not possible. The resultant solution was evaporated to dryness, redissolved in 250 mL of $H_2O$ and sorbed on Sephadex. Elution with trisodium citrate (0.2 M) gave four bands: a fast moving, very weak pink band which was discarded, a yellow band of $[Co(taci)_2]^{3+}$, a major red band and a violet band. NMR measurements showed that the violet band consisted of several unidentified $Co^{III}$ complexes. The red and the yellow bands again showed some overlap and could not be separated completely. The entire red fraction was collected, desalted on Dowex 50 and the solvents evaporated to dryness. Remaining traces of $[Co(taci)_2]^{3+}$ could be removed by crystallisation: The solid was dissolved in $H_2O$ (5 mL). $ZnBr_2$ (500 mg, dissolved in 4 mL of $H_2O$) and HBr (5 mL 48% in $H_2O$) were added and the solution was allowed to stand at 4 °C for 12 h. $[Co(taci)_2]^{3+}$ precipitated quantitatively as the $[ZnBr_4]^{2-}$ salt which was removed by filtration. The remaining red solution was then sorbed again on Dowex 50. The column was washed with $H_2O$ and eluted with aqueous HCl (0.5 M and 1.0 M). Further elution with HCl (3 M) gave a red solu-

 © 2006 Wiley-VCH Verlag GmbH & Co. KGaA, Weinheim 

tion of the pure $[Co(L^e)]^{3+}$. This solution was evaporated to dryness and dried in vacuo. Yield: 261 mg (28%) of red $[Co(L^e)]Cl_3 \cdot 3.5H_2O$.[14] $C_{14}H_{38}CoCl_3N_7O_{9.5}$ (621.8): calcd. C 27.04, H 6.16, N 15.77; found C 26.89, H 6.22, N 15.99. IR (KBr): $\tilde{\nu}$ = 1647 (s) cm$^{-1}$. $^1$H NMR ($D_2O$): $\delta$ = 2.78 (m, 2 H), 2.93 (t, $J$ = 4.0 Hz, 1 H), 2.96 (t, $J$ = 4.0 Hz, 1 H), 3.13 (t, $J$ = 3.0 Hz, 1 H), 3.84 (t, $J$ = 4.0 Hz, 1 H), 4.05 (t, $J$ = 4.0 Hz, 1 H), 4.09 (m, 2 H), 4.14 (t, $J$ = 3.0 Hz, 1 H), 4.19 (t, $J$ = 4.0 Hz, 1 H), 4.19 (d, $J$ = 18.0 Hz, 1 H), 4.27 (t, $J$ = 4.0 Hz, 1 H), 5.41 (d, $J$ = 18.0 Hz, 1 H) ppm. $^{13}$C{$^1$H} NMR ($D_2O$): $\delta$ = 51.3 (CH), 51.6 (CH), 53.3 (CH), 54.3 (CH), 57.5 (2 CH), 58.2 ($CH_2$), 65.6 (CH), 65.9 (CH), 67.0 (CH), 67.2 (CH), 68.3 (CH), 68.6 (CH), 175.9 (C) ppm. MS-FAB$^+$ *m*/*z* (%): 451 (100) $[Co(H_{-1}L^e)]^+$, 487 (13) $[Co(L^e)Cl]^+$. UV/Vis ($H_2O$): $\lambda_{max}$ = 345 nm ($\varepsilon$ = 343 M$^{-1}$ cm$^{-1}$), $\lambda_{max}$ = 497 nm ($\varepsilon$ = 198 M$^{-1}$ cm$^{-1}$).

**X-ray Diffraction Analysis:**[43] Diffraction data of $[Co(HL^a)][ZnBr_4]_2 \cdot 5H_2O$ were collected at room temperature on a Siemens CCD Platform using monochromated Mo-$K_\alpha$ radiation and a crystal of dimensions 0.24 × 0.16 × 0.14 mm (Table 3). 21887 reflections were collected in the range 1.49° < $\theta$ < 23.24°. An empirical absorption correction was performed (SADABS). Of a total of 5572 unique reflections 3217 were observed with 2σ($I$). The structure was solved by direct methods and refined using full-matrix least-squares calculations on $F^2$.[44] One of the two counter-anions (Zn2) proved to be disordered and was modelled using a superposition of three discrete positions with occupancies of 50%, 38% and 12%. The Zn2 centre was located on two split positions (Zn2a and Zn2b) with a Zn2a–Zn2b separation of 0.753 Å. Both of these positions had an occupancy of 50%. The four Br$^-$ ligands (Br21–Br24) which are bound to Zn2a could be unambiguously located. They were also refined with occupancies of 50%. The Zn2a–Br distances and Br–Zn2a–Br angles are as expected. For each of the four Br$^-$ ligands bound to Zn2b, a major (Br31–Br34, 38%) and a minor (Br41–Br44, 12%) position was assigned. The major component refined well again but the minor component, which corresponds to a relatively small amount of electron density, was rather poorly defined (Zn2b–Br distances: 2.12–2.64 Å, mean value: 2.37 Å, and Br–Zn2b–Br angles of 89–133°, mean value: 108.5 °). Five additional peaks (O1S–O5S) were interpreted as $H_2O$ molecules. The distances O1···O3S···O4S···O5S and O4···O2S fall between 2.7–2.8 Å which is the range expected for normal O–H···O hydrogen bonds. The O4S···O6 distance of 2.50 Å is rather short and indicative of a strong hydrogen bond. This is consistent with the high acidity of the coordinated hydroxy group (see Characterisation of $[Co(L^a)]^{3+}$ in the Results section above). O2S was found to be distributed over two positions with an O2Sa···O2Sb separation of 0.98 Å and occupancy factors of 60 and 40%. O1S and O5S were located in proximity to the disordered $[Zn2Br_4]^{2-}$ counterion and some of the corresponding O···Br separations were considerably shorter than the sum of the van der Waals radii. A split model was again used for O5S with occupancies of 20% for O5Sa (which is in conflict with Br24) and 80% for O5Sb. O1S was found to be in conflict with Br43. Since Br43 itself has an occupancy of only 12%, the occupancy of O1S was set to 88%. Although the remaining 12% of this $H_2O$ molecule could not be located, a search for free voids[45] clearly indicated that sufficient empty space would be available for accommodation of this $H_2O$ molecule within the Zn2bBr41–Br44 variant of the structure. Anisotropic displacement parameters were refined for all nonhydrogen atomic positions except for the two split positions of the disordered $H_2O$ oxygen O5S. Hydrogen atoms of the complex cation were placed in calculated sites (riding model) and isotropic displacement parameters were used which were fixed at 1.5 × $U_{eq}$ of the pivot atom of hydroxy, amino, and methyl groups and 1.2 × $U_{eq}$ for all other C atoms. Owing to the isolation from an acidic medium (HBr), the meaningful hydrogen bonding scheme and based on charge balance considerations, N5 and O6 were both considered as being protonated. A total of 495 parameters were used in the final refinement, yielding a residual electron density with a minimum and a maximum of –0.58 and +1.07 e Å$^{-3}$. Puckering parameters of the two cyclohexane rings were calculated using the computer program PLATON.[45]

Table 3. Crystallographic data for $[Co(HL^a)][ZnBr_4]_2 \cdot 5H_2O$ and $[Co(taci)_2][NO_3]_3 \cdot 2H_2O$.

| Empirical formula | $C_{15}H_{44}Br_8CoN_7O_{11}Zn_2$ | $C_{12}H_{34}CoN_9O_{17}$ |
|---|---|---|
| Formula mass [g mol$^{-1}$] | 1327.52 | 635.41 |
| Crystal size [mm] | 0.24 × 0.16 × 0.14 | 0.20 × 0.15 × 0.15 |
| Crystal system | monoclinic | monoclinic |
| Space group | $P2_1/c$ (No. 14) | $I2/a$ (No. 15) |
| $a$ [Å] | 9.0419(2) | 14.696(3) |
| $b$ [Å] | 27.1800(6) | 8.9090(18) |
| $c$ [Å] | 16.0600(4) | 17.875(4) |
| $\beta$ [°] | 98.8170(10) | 91.27(3) |
| $V$ [Å$^3$] | 3900.25(16) | 2339.7(8) |
| $Z$ | 4 | 4 |
| $T$ [K] | 298(2) | 298(2) |
| $\lambda$ [Å] | 0.71073 (Mo-$K_\alpha$) | 0.71073 (Mo-$K_\alpha$) |
| $\rho_{calcd.}$ [g cm$^{-3}$] | 2.261 | 1.804 |
| $\mu$ [mm$^{-1}$] | 9.889 | 0.837 |
| $R$ [$I > 2\sigma(I)$] | 0.0500 | 0.0282 |
| $wR_2$ (all data) | 0.1438 | 0.0692 |

Diffraction data of $[Co(taci)_2](NO_3)_3 \cdot 2H_2O$ were collected at 25(2) °C on a Stoe Stadi 4 diffractometer using monochromated Mo-$K_\alpha$ radiation and a crystal of dimensions 0.20 × 0.15 × 0.15 mm. Of a total of 3975 reflections which were collected in the range 2.28° < $\theta$ < 25.00°, 2066 were unique and 1742 were observed with $I > 2\sigma(I)$. An empirical absorption correction was applied to the data. The structure was solved by direct methods and was refined using full-matrix least-squares calculations on $F^2$ (259 parameters).[44] All non-hydrogen atoms were refined in the anisotropic mode. The hydrogen atoms (including $H_2O$) were all located in a difference Fourier map and were refined using variable isotropic displacement parameters. One of the $NO_3^-$ counterions was found to be slightly disordered. Its nitrogen atomic position (N5) was located on a two fold rotational axis and each of the oxygen atoms were equally distributed over two positions. The minimum and maximum in the final residual electron density map were –0.21 and +0.29 e Å$^{-3}$.

**Molecular Modelling:** The commercially available program MOMEC97 was used for the calculations.[46,47] Since the structures of the complexes investigated in this paper contain a variety of fragments which were not considered in MOMEC97, additional parameters had to be added to the force field. These parameters were derived from a total of 30 related structures with their geometries obtained from the Cambridge Structural Data Base (see Scheme S1, and Table S1 in the Supporting Information). The required parameters were estimated and systematically varied until the calculated bond lengths could reproduce the experimental values within ± 0.02 Å and the bond angles within ± 5°. This additional data set is listed in Table 4. In the course of geometry optimisation, it became obvious that three of the already supplied parameters (CI–NI bond-stretch, CI–NI–CT valence angle and **–NI–CT–** torsion angle) also had to be adjusted slightly in order to get better consistency during the parametrisation procedure. In all calculations, the N=C–N portion of the amidine moieties was modelled

 © 2006 Wiley-VCH Verlag GmbH & Co. KGaA, Weinheim 

using the atom types NI–CI–NT. The structures were refined using the geometry optimization procedure with the full-matrix Newton Rapson algorithm. Convergence was reached in all calculations. As exemplified in Table 1 for $[Co(HL^a)]^{4+}$, the new parameter set allowed accurate reproduction of the structural parameters.

Table 4. New MOMEC force-field parameters.[a]

Bond-stretch parameters

| Atom 1 | Atom 2 | $k_b$ [mdyn Å$^{-1}$][b] | $r_o$ [Å] |
|---|---|---|---|
| CO3 | NI | 1.750 | 1.870 |
| CO3 | OW | 3.000 | 1.900 |
| CI | NT | 6.700 | 1.317 |
| CI | CT | 5.000 | 1.500 |
| CI | NI | 7.200 | 1.290 |
| CT | NI | 6.000 | 1.480 |
| CA | NI | 5.940 | 1.399 |
| NI | H | 6.030 | 0.910 |

Torsional angle parameters[c]

| Atom | Atom | Atom | Atom | $k_\varphi$ [mdyn Å] | $m$ | $\varphi_{offset}$ [rad] |
|---|---|---|---|---|---|---|
| ** | CA | NI | ** | 0.0100 | 6 | 1.571 |
| ** | CI | NT | ** | 0.0005 | 6 | 0.524 |
| ** | CI | CT | ** | 0.0005 | 6 | 0.524 |
| ** | OR | CT | ** | 0.0080 | 3 | 0.000 |
| ** | NI | CI | ** | 0.0250 | 2 | 1.571 |
| ** | NI | CT | ** | 0.0001 | 2 | 1.571 |

Valence-angle parameters

| Atom 1 | Atom 2 | Atom 3 | $k_\theta$ [mdyn Å rad$^{-2}$] | $\theta_0$ [rad] |
|---|---|---|---|---|
| CO3 | NI | CT | 0.200 | 1.920 |
| CO3 | NI | CI | 0.400 | 2.150 |
| CO3 | NT | CI | 0.200 | 1.920 |
| CO3 | OW | CT | 0.050 | 1.915 |
| CO3 | OW | H | 0.100 | 1.915 |
| OW | CO3 | OW | 0.040 | 1.571 |
| OW | CO3 | NI | 0.150 | 1.650 |
| NI | CO3 | NI | 0.050 | 1.571 |
| NI | CI | NT | 0.015 | 2.094 |
| CT | CI | H | 0.450 | 2.094 |
| CT | OW | H | 0.360 | 1.909 |
| CT | CI | NI | 0.450 | 2.094 |
| CT | CT | OR | 0.450 | 1.909 |
| CA | CA | NI | 0.970 | 2.094 |
| CA | NI | CI | 0.490 | 2.030 |
| CA | NI | H | 0.490 | 2.059 |
| OR | CT | H | 0.360 | 1.909 |
| H | CI | H | 0.450 | 2.094 |
| NI | CI | CT | 0.450 | 2.094 |
| NI | CT | CT | 0.450 | 1.911 |
| NI | CT | H | 0.450 | 1.911 |
| NT | CO3 | OW | 0.040 | 1.571 |
| NT | CO3 | NI | 0.050 | 1.571 |
| NT | CI | CT | 0.450 | 2.094 |
| NT | CT | CI | 0.450 | 1.911 |
| NT | CI | H | 0.450 | 2.094 |
| NT | CT | OR | 0.450 | 1.911 |
| NT | CT | NI | 0.450 | 1.911 |
| CI | NT | CT | 0.450 | 1.911 |
| CI | NT | CA | 0.450 | 1.911 |
| CI | CT | CT | 0.450 | 1.911 |
| CI | NI | CT | 0.970 | 2.094 |
| CI | NI | H | 0.490 | 2.059 |
| CI | NT | H | 0.450 | 2.050 |
| CI | CT | H | 0.360 | 1.909 |

[a] For atom-type labels, see ref.[46] [b] 1 dyn = $10^{-5}$ N. [c] ** = any atom.

**Supporting Information** (see footnote on the first page of this article): Comments on the parametrisation procedure. Table S1 and Scheme S1: Structures (CCDC) considered for parametrisation. Table S2: Strain energies for the isomers **1**–**3** of $[Co(H_{-2}L^b)]^+$ and $[Co(\kappa^6\text{-}N_6\text{-}L^b)]^{3+}$.

## Acknowledgments

We thank Dr. Irmgard Buder, Prof. Dr. Frank Endres and Prof. Dr. G. Schwitzgebel (Saarbrücken) for the cyclovoltammetric measurements, Dr. Norbert Okon and Dr. Gilber Lauer (both Heidelberg) for help with the parametrisation of the force field and Dr. Walter Amrein (ETH Zürich) for the measurements of the FAB-mass spectra. Single crystals of $[Co(taci)_2](NO_3)_3{\cdot}2H_2O$ were prepared by Jochen Huppert (Saarbrücken). The crystal structure analyses of $[Co(HL^a)][ZnBr_4]_2{\cdot}5H_2O$ and $[Co(taci)_2](NO_3)_3{\cdot}2H_2O$ were performed by Dr. Fabio Zürcher (ETH Zürich), Stefan Steinhauser and Dr. Volker Huch (both from Saarbrücken). We thank Dr. Peter Osvath (Melbourne) and Prof. Johann Jauch (Saarbrücken) for valuable advice. Financial support by the Studienstiftung des deutschen Volkes for D. K. is gratefully acknowledged.

[1] a) J.-M. Lehn, *Acc. Chem. Res.* **1978**, *11*, 49; b) J. Nelson, V. McKee, G. Morgan, *Prog. Inorg. Chem.* **1998**, *47*, 167.
[2] a) G. A. Lawrance, M. Maeder, E. N. Wilkes, *Rev. Inorg. Chem.* **1993**, *13*, 199; b) O. Costisor, W. Linert, *Rev. Inorg. Chem.* **2000**, *20*, 63.
[3] A. M. Sargeson, *Pure Appl. Chem.* **1986**, *58*, 1511.
[4] a) I. I. Creaser, J. M. Harrowfield, A. J. Herlt, A. M. Sargeson, J. Springborg, R. J. Geue, M. R. Snow, *J. Am. Chem. Soc.* **1977**, *99*, 3181; b) R. J. Geue, T. W. Hambley, J. M. Harrowfield, A. M. Sargeson, M. R. Snow, *J. Am. Chem. Soc.* **1984**, *106*, 5478.
[5] I. I. Creaser, R. J. Geue, J. M. Harrowfield, A. J. Herlt, A. M. Sargeson, M. R. Snow, J. Springborg, *J. Am. Chem. Soc.* **1982**, *104*, 6016.
[6] a) A. Höhn, R. J. Geue, A. M. Sargeson, A. C. Willis, *J. Chem. Soc. Chem. Commun.* **1989**, 1648; b) A. P. Arnold, R. Bhula, X. Chen, R. J. Geue, W. G. Jackson, *Inorg. Chem.* **1999**, *38*, 1966.
[7] a) E. Larsen, S. Larsen, G. Lunding, *Inorg. Chem.* **1988**, *27*, 3051; b) P. V. Bernhardt, L. A. Jones, *J. Chem. Soc. Dalton Trans.* **1998**, 1757.
[8] J. W. Pauly, J. Sander, D. Kuppert, M. Winter, G. J. Reiss, F. Zürcher, R. Hoffmann, T. F. Fässler, K. Hegetschweiler, *Chem. Eur. J.* **2000**, *6*, 2830.
[9] K. Hegetschweiler, M. Weber, V. Huch, R. J. Geue, A. D. Rae, A. C. Willis, A. M. Sargeson, *Inorg. Chem.* **1998**, *37*, 6136.
[10] R. J. Geue, M. G. McCarthy, A. M. Sargeson, *J. Am. Chem. Soc.* **1984**, *106*, 8282.
[11] R. J. Geue, M. G. McCarthy, A. M. Sargeson, B. W. Skelton, A. H. White, *Inorg. Chem.* **1985**, *24*, 1607.
[12] R. J. Geue, M. G. McCarthy, A. M. Sargeson, E. Horn, M. R. Snow, *J. Chem. Soc. Chem. Commun.* **1986**, 848.
[13] N. E. Dixon, G. A. Lawrance, P. A. Lay, A. M. Sargeson, H. Taube, *Inorg. Synth.* **1986**, *24*, 243.
[14] Systematic names $L^a$ = (1*E*)-*N*-({[*all-cis*-3-amino-2,4,6-trihydroxy-5-(methylamino)cyclohexyl]amino}methyl)-*N*′-(*all-cis*-3,5-diamino-2,4,6-trihydroxycyclohexyl)imidoformamide, $L^b$ = *all-cis*-(2*E*,12*E*)-9,19-bis(methylamino)-2,4,6,12,14,16-hexaazatricyclo[15.3.1.1$^{7,11}$]docosa-2,12-diene-8,10,18,20,21,22-hexol, $L^c$ = 1,3-diamino-1,3,5-trideoxy-5-(methylamino)-*cis*-inositol, $L^d$ = (1*Z*)-*N*′-(3,5-diamino-2,4,6-trihydroxycyclohexyl)-*N*-phenylimidoformamide, $L^e$ = (1*Z*)-*N*′-(*all-cis*-3,5-diamino-2,4,6-trihydroxycyclohexyl)-2-[*all-cis*-

 © 2006 Wiley-VCH Verlag GmbH & Co. KGaA, Weinheim 

(3,5-diamino-2,4,6-trihydroxycyclohexyl)amino]ethanimidamide.

[15] The multi-peak signal in the range of $515 \leq m/z \leq 520$ was interpreted in terms of a superposition of $[Co^{III}(H_{-4}L^b)]^+$ (5%), $[Co^{II}(H_{-3}L^b)]^+$ (8%), $[Co^{III}(H_{-2}L^b)]^+$ (19%), $[Co^{II}(H_{-1}L^b)]^+$ (55%) and $[Co^{I}(L^b)]^+$ (13%). This assignment was established by least-squares calculations $R^2$ = min, with $R = \Sigma|I_{calc}-I_{obs}|/\Sigma I_{obs} = 0.016$ for all possible isotopomers. The different types of ions postulated for the interpretation of this signal are in line with well established processes observed in a glycerol matrix under FAB conditions, where the bombarding of the matrix with fast atoms results in the generation of organic radicals which can either abstract $H_2$ from the NH–$CH_3$ single bond (generation of a corresponding imine) or reduce the central metal cation (generation of $Co^{II}$ and $Co^{I}$).[16]

[16] K. Hegetschweiler, T. Kradolfer, V. Gramlich, R. D. Hancock, *Chem. Eur. J.* **1995**, *1*, 74.

[17] a) D. M. Doddrell, D. T. Pegg, M. R. Bendall, *J. Magn. Reson.* **1982**, *48*, 323; b) A. Bax, S. Subramanian, *J. Magn. Reson.* **1986**, *67*, 565; c) A. Bax, M. F. Summers, *J. Am. Chem. Soc.* **1986**, *108*, 2093.

[18] M. D. Meienberger, K. Hegetschweiler, H. Rüegger, V. Gramlich, *Inorg. Chim. Acta* **1993**, *213*, 157.

[19] In the reference complex $[Co^{III}(cis\text{-tach})(H_{-1}taci\text{-}\kappa^3\text{-}N^1,O^2,N^3)]^{2+}$ (Supporting Information, Scheme S1b, structure O8), the resonance of the carbon atom attached to the coordinated oxygen donor was observed at $\delta$ = 87 ppm.[20] For $[Co(L^a)]^{3+}$ and $[Co(L^b)]^{3+}$, this value is somewhat lower apparently due to a $\gamma$ effect caused by the non-hydrogen substituents attached to the neighbouring nitrogen donors. The 2D NMR experiments confirmed our proposition that it is the high-frequency cyclohexane-carbon atom at $\delta$ = 76–80 ppm which is directly bonded to the coordinated oxygen donor.

[20] M. Ghisletta, L. Hausherr-Primo, K. Gajda-Schrantz, G. Machula, L. Nagy, H. W. Schmalle, G. Rihs, F. Endres, K. Hegetschweiler, *Inorg. Chem.* **1998**, *37*, 997.

[21] K. Hegetschweiler, *Chem. Soc. Rev.* **1999**, *28*, 239.

[22] Puckering parameters (according to D. Cremer, J. A. Pople, *J. Am. Chem. Soc.* **1975**, *97*, 1354): $Q$ = 0.57 Å, $\theta$ = 178°, $\varphi$ = 5.0° ($\kappa^3$-*N,N,N*-coordinated ring) and $Q$ = 0.72 Å, $\theta$ = 87.4°, $\varphi$ = 81.0° ($\kappa^3$-*N,O,N*-coordinated ring).

[23] J. L. Sudmeier, C. N. Reilley, *Anal. Chem.* **1964**, *36*, 1698.

[24] A. Kramer, R. Alberto, A. Egli, I. Novak-Hofer, K. Hegetschweiler, U. Abram, P. V. Bernhardt, P. A. Schubiger, *Bioconjugate Chem.* **1998**, *9*, 691.

[25] K. Hegetschweiler, D. Kuppert, J. Huppert, M. Straka, M. Kaupp, *J. Am. Chem. Soc.* **2004**, *126*, 6728.

[26] P. M. Angus, A. J. Elliott, A. M. Sargeson, A. C. Willis, *J. Chem. Soc. Dalton Trans.* **2000**, 2933.

[27] a) M. Yogavel, P. G. Aravindan, D. Velmurugan, P. T. Perumal, S. Shanmuga Sundara Raj, H.-K. Fun, *Acta Crystallogr. Sect. E* **2003**, *59*, o662; b) R. W. Taft, E. D. Raczynska, P.-C. Maria, I. Leito, J.-F. Gal, M. Decouzon, T. Drapala, F. Anvia, *Pol. J. Chem.* **1995**, *69*, 41.

[28] A. F. Hegarty, A. Chandler, *J. Chem. Soc. Chem. Commun.* **1980**, 130.

[29] For $[Co(taci)_2]^{3+}$, the calculated Co–N bond length is 1.97 Å, whereas the value obtained from X-ray diffraction analysis is 1.99 Å.[30] Similarly, the Co–N6 distance in $[Co(HL^a)]^{4+}$ was calculated as 1.97 Å instead of 2.02 Å as observed in the crystal structure (Table 1). The slight underestimation of long Co–N distances might be due to the use of a harmonic potential for the $Co^{III}$–N bond, see: P. Comba, A. F. Sickmüller, *Angew. Chem. Int. Ed. Engl.* **1997**, *36*, 2006.

[30] The crystal structure of $[Co(taci)_2](NO_3)_3{\cdot}2H_2O$ was determined several years ago.[31] Because of the moderate quality of the data, we decided to determine this structure again. Consequently we now possess a data set of significantly higher accuracy. The Co–N bond lengths changed from 1.991(6) Å–2.009(5) Å (mean value: 2.000 Å)[31] to 1.9854(18) Å–2.0057(18) Å (mean value 1.994 Å).

[31] M. Ghisletta, H.-P. Jalett, T. Gerfin, V. Gramlich, K. Hegetschweiler, *Helv. Chim. Acta* **1992**, *75*, 2233.

[32] The corresponding $\lambda_{max}$ of the parent $[Co(taci)_2]^{3+}$ is 470 nm[31] which falls in the usual range observed for (hexaamine)Co$^{III}$ complexes.[33]

[33] P. Hendry, A. Ludi, *Adv. Inorg. Chem.* **1990**, *35*, 117.

[34] H. Friebolin, *Ein- und zweidimensionale NMR-Spektroskopie*, VCH, Weinheim, **1992**.

[35] a) K. Hegetschweiler, M. Weber, V. Huch, M. Veith, H. W. Schmalle, A. Linden, R. J. Geue, P. Osvath, A. M. Sargeson, A. C. Willis, W. Angst, *Inorg. Chem.* **1997**, *36*, 4121; b) J. Romba, D. Kuppert, B. Morgenstern, C. Neis, S. Steinhauser, T. Weyhermüller, K. Hegetschweiler, *Eur. J. Inorg. Chem.* **2006**, 314.

[36] L. Hausherr-Primo, K. Hegetschweiler, H. Rüegger, L. Odier, R. D. Hancock, H. W. Schmalle, V. Gramlich, *J. Chem. Soc. Dalton Trans.* **1994**, 1689.

[37] J. Springborg, R. J. Geue, A. M. Sargeson, D. Taylor, M. R. Snow, *J. Chem. Soc. Chem. Commun.* **1978**, 647.

[38] D. A. Buckingham, C. R. Clark, B. M. Foxman, G. J. Gainsford, A. M. Sargeson, M. Wein, A. Zanella, *Inorg. Chem.* **1982**, *21*, 1986.

[39] G. Rousselet, P. Capdevielle, M. Maumy, *Tetrahedron Lett.* **1993**, *34*, 6395.

[40] J. M. Harrowfield, A. M. Sargeson, *J. Am. Chem. Soc.* **1979**, *101*, 1514.

[41] K. Hegetschweiler, O. Maas, A. Zimmer, R. J. Geue, A. M. Sargeson, J. Harmer, A. Schweiger, I. Buder, G. Schwitzgebel, V. Reiland, W. Frank, *Eur. J. Inorg. Chem.* **2003**, 1340.

[42] a) R. E. Hurd, *J. Magn. Reson.* **1990**, *87*, 422; b) M. von Kienlin, C. T. W. Moonen, A. van der Toorn, P. C. M. van Zijl, *J. Magn. Reson.* **1991**, *93*, 423; c) R. E. Hurd, B. K. John, *J. Magn. Reson.* **1991**, *91*, 648; d) J. Ruiz-Cabello, G. W. Vuister, C. T. W. Moonen, P. van Gelderen, J. S. Cohen, P. C. M. van Zijl, *J. Magn. Reson.* **1992**, *100*, 282; e) W. Wilker, D. Leibfritz, R. Kerssebaum, W. Bermel, *Magn. Reson. Chem.* **1993**, *31*, 287.

[43] Crystallographic data (excluding structure factors) for $[Co(HL^a)][ZnBr_4]_2{\cdot}5H_2O$ and $[Co(taci)_2](NO_3)_3{\cdot}2H_2O$ have been deposited with The Cambridge Crystallographic Data Centre as supplementary publication nos. CCDC-293087 and -293088. These data can be obtained free of charge from The Cambridge Crystallographic Data Centre via www.ccdc.cam.ac.uk/data_request/cif.

[44] a) G. M. Sheldrick, SHELXS-97, *Program for Crystal Structure Solution*, Göttingen, **1990**; b) G. M. Sheldrick, SHELXL-97, *Program for Crystal Structure Refinement*, Göttingen, **1997**.

[45] A. L. Spek PLATON, *A Multipurpose Crystallographic Tool*, Utrecht University, Utrecht, The Netherlands, **2005**; see also: A. L. Spek, *J. Appl. Crystallogr.* **2003**, *36*, 7.

[46] a) P. Comba, T. W. Hambley, G. Lauer, N. Okon, *MOMEC97, a molecular modeling package for inorganic compounds*, University of Heidelberg, www.comba-group.uni-hd.de, **1997**; b) J. E. Bol, C. Buning, P. Comba, J. Reedijk, M. Ströhle, *J. Comput. Chem.* **1998**, *19*, 512.

[47] P. Comba, T. W. Hambley, *Molecular Modelling of Inorganic Compounds*. VCH, Weinheim, Germany, **1995**.

Received: December 16, 2005
Published Online: May 10, 2006

 © 2006 Wiley-VCH Verlag GmbH & Co. KGaA, Weinheim 

DOI: 10.1002/ejic.200501148

# A Theoretical Study on Structures, Bonding Energies and Aromaticity of Two New Series of Dinuclear Phosphametallocenes: ($\eta^5$-$P_5$)MM′($\eta^5$-$P_5$) and ($\eta^5$-$C_5H_5$)MM′($\eta^5$-$P_5$) (M, M′ = Zn, Cd)

**Zi-Zhong Liu,[a,b,c] Wei Quan Tian,*[a] Ji-Kang Feng,*[a,c] Gang Zhang,[a] Wei-Qi Li,[a] Yan-Hong Cui,[a] and Chia-Chung Sun[a]**

**Keywords:** Dinuclear phosphametallocenes / Structures / Bonding energies / Aromaticity / Density functional theory

The equilibrium geometries, the energies, the harmonic vibrational frequencies, and the nucleus independent chemical shifts (NICSs) of the ground state of ($\eta^5$-$P_5$)MM′($\eta^5$-$P_5$) and ($\eta^5$-$C_5H_5$)MM′($\eta^5$-$P_5$) (M, M′ = Zn, Cd) are calculated by the hybrid density functional method B3LYP with LANL2DZ basis sets. The analysis of energy and harmonic frequencies on the equilibrium geometries of both series dinuclear deca- and pentaphosphametallocenes shows that all the minima with singlet electronic state have an staggered ($9° \leq D_{(E-M-M-E')} \leq 36°$) conformation except for the eclipsed $CpCd_2(P_5)$ ($C_{5v}$), and all the $D_{5h}$ and the $D_{5d}$ symmetric conformations are transition states while the energy differences between the most stable minimum and the transition states are very small ($\leq$ 0.1 kcal/mol), thus, the rotation of the $P_5$ ring about M–M bond in all complexes is almost free. The analysis of the NBO, the Laplacian of the electron density, the electrostatic interaction energy, the bonding energy decomposition, and the molecular orbital correlation diagrams for the two series complexes reveals that the properties of all the dinuclear phosphametallocenes investigated are similar to that of the dizinc metallocenes. The M–M (or M–M′) bond in the dinuclear phosphametallocenes is a weak σ covalent bond, and the magnitude of bonding energy of the M–M (or M–M′) bond correlates with the energy difference between the energy of HOMO in M($\eta^5$-$P_5$) (or MCp) ($^2A$, $C_{5v}$) fragment and the energy of HOMO-2 in [MM′($\eta^5$-$P_5$)$_2$] ($^1A$, $D_5$, or $D_{5h}$) [or ($\eta^5$-$P_5$)MM′Cp ($^1A$, $C_5$, or $C_{5v}$)] (M, M′ = Zn, Cd). The strength of the M–M (or M–M′) bond plays a decisive role on the stability of the dinuclear phosphametallocenes. However, the M–($\eta^5$-$P_5$) (or M–Cp) bonding mainly is ionic. Among the different dinuclear phosphametallocenes with the same ligands, the bonding energies of the M–M (or M–M′) bond and of the M–($\eta^5$-$P_5$) (or M–Cp) bond decrease as M varying from Zn to Cd. Among the different phosphametallocenes with the same metals, the bonding energies of the M–M (or M–M′) bond and the M–ligand bond increase with ligand varying from the ($\eta^5$-$P_5$) to the Cp. The negative NICSs indicate that all dinuclear phosphametallocenes have aromaticity. The various dissected bond NICS contributions reveal that the NICS contributions of the metal–ligand bond, the metal–metal bond, and the metal lone pair electrons to the overall aromaticity in the Zn-containing dinuclear phosphametallocenes are different from their counterpart contributions in the Cd-containing dinuclear phosphametallocenes, such difference causes that the overall NICSs of the Zn-containing dinuclear phosphametallocenes are more negative than that of the Cd-containing dinuclear phosphametallocenes.

(© Wiley-VCH Verlag GmbH & Co. KGaA, 69451 Weinheim, Germany, 2006)

## 1. Introduction

The successful synthesis of the linear organometallic molecule, decamethyldizincocene, [$Zn_2$($\eta^5$-Cp*)$_2$] (Cp* = $C_5Me_5$) by Resa and co-workers recently,[1,2] has provided inorganic chemists with their first example of a stable organometallic compound with a homonuclear metal Zn–Zn bond, and has been considered as a new frontier of the dinuclear metallocenes study.[3] One motivation of the present study is stimulated by the new synthesis routes[4,5] and theoretical studies on the structures, the bond interactions,[2] and the vibrational signatures of the Zn–Zn stretching mode in the novel molecule.[6] The analogous dinuclear metallocenes, such as $CpCu_2Cp$ and $CpNi_2Cp$,[7] [$M_2$($\eta^5$-$Cp^X$)$_2$] (M = Zn and Cd, $Cp^X$ = $C_5Me_5$ and $C_5H_5$),[8] and the dinuclear cyclopentadienylcobalt carbonyls[9] were investigated. The homodinuclear metallocenes, [$M_2$-($\eta^5$-Cp)$_2$] (M = Be, Mg, and Ca),[10] and the heterodinuclear metallocenes, CpE–MCp (E = B, Al, Ga; M = Li, Na, K),[11] and Cp–Zn–Cd–Cp[12] were studied as well. These studies are fascinating and encourage our further explorations of analogous homodinuclear and heterodinuclear phosphametallocenes.

Since the first synthesis of pentamethylpentaphosphaferrocene by Scherer et al.[13] and pentaphosphacyclopentadi-

[a] State Key Laboratory of Theoretical and Computational Chemistry, Institute of Theoretical Chemistry, Jilin University, Changchun 130023, China
[b] Chemistry and Environment Science College of Inner Mongolia Normal University, Huhhot, 010022 China
[c] The College of Chemistry, Jilin University, Changchun 130023, China

 © 2006 Wiley-VCH Verlag GmbH & Co. KGaA, Weinheim 

enide anion ($P_5^-$) by Baudler and co-workers,[14,15] the structure of pentaphosphametallocene and the aromaticity of polyphosphaphospholes and $P_5^-$ have attracted much attention from the chemistry community by the fact that metallocene and analogous organometallic compounds have been found in many applications, e.g. synthetic reagents, catalysts of polymerization and hydrogenation of olefin, and building blocks for new materials.[16–32] Experimental and computational studies suggested that the pentaphospholyl anion, $P_5^-$, is aromatic, as cyclopentadienyl anion, $Cp^-$.[16–21,33,35] Recent synthesis and X-ray structural analysis of the homoleptic sandwich complex with pentaphospholyl anion ligands, $[Ti(\eta^5\text{-}P_5)_2]^{2-}$,[34] gave a new impetus to the versatile chemistry of phosphametallocenes. The structure, bonding and aromaticity of the decaphosphametallocenes $[Ti(\eta^5\text{-}P_5)_2]^{2-}$ were theoretically reported by Lein et al.[35] and our group,[33] respectively. $[Ti(\eta^5\text{-}P_5)_2]^{2-}$ is aromatic with stronger aromaticity.[33] However, it has not been investigated, to the best of our knowledge, on the stabilities, electronic structures and aromaticity of the homodinuclear phosphametallocenes: $[M_2(\eta^5\text{-}P_5)_2]$ and $(\eta^5\text{-}C_5H_5)\text{-}M_2(\eta^5\text{-}P_5)$, (M = Zn, Cd), and the heterodinuclear phosphametallocenes: $(\eta^5\text{-}P_5)MM'(\eta^5\text{-}P_5)$ and $(\eta^5\text{-}C_5H_5)\text{-}MM'(\eta^5\text{-}P_5)$ (M, M′ = Zn, Cd).

To better understand the bonding nature of the M–M (or M–M′) and of the M–$(\eta^5\text{-}P_5)$ in titled molecules, it is necessary to investigate the geometric and electronic structures and binding energies of a series of complexes. The purpose of this paper is to exhibit the features of structures, the bonding energies and the aromaticity of the homodinuclear and the heterodinuclear phosphametallocenes within density functional theory (DFT). Meanwhile, the qualitative analysis of the molecular orbital correlation diagram and the Laplacian of the electron density $[\nabla^2\rho(r)]$ of the atom in molecule (AIM)[36–38] are performed to characterize the bonding features of the interaction and to provide insights into the influences of metals and ligands on the bonding character and aromaticity in both series of complexes.

## 2. Computational Methods

The DFT geometry optimizations at B3LYP/gen [P: 6-311+G(2d), C, H: 6-311+G(d,p), Zn, Cd: LANL2DZ] level of theory are carried out on several symmetrical conformations [eclipsed ($D_{5h}$ or $C_{5v}$), staggered ($D_{5d}$, $D_5$ and $C_5$)] of the homodinuclear with homo-ligands, the heterodinuclear with homo-ligands, the homodinuclear with hetero-ligands and the heterodinuclear with hetero-ligands sandwich-like complexes with pentaphospholyl ligands and Cp ligand: $(\eta^5\text{-}P_5)M_2(\eta^5\text{-}P_5)$, $(\eta^5\text{-}P_5)MM'(\eta^5\text{-}P_5)$, $(\eta^5\text{-}C_5H_5)\text{-}M_2(\eta^5\text{-}P_5)$ and $(\eta^5\text{-}C_5H_5)MM'(\eta^5\text{-}P_5)$ (M, M′ = Zn, Cd), respectively (as shown in Figure 1). In order to check our computational reliability and to compare the differences between $[M_2(\eta^5\text{-}P_5)_2]$ and $[M_2(\eta^5\text{-}Cp)_2]$ (M = Zn, Cd), we optimized the dinuclear metallocene $[M_2(\eta^5\text{-}Cp)_2]$ ($D_{5h}$, $D_{5d}$, $D_5$) reported by Xie et al.[8] The vibrational frequencies were calculated and the DFT wavefunction instabilities were checked at the same level of theory. The nature of all the stationary points on the potential energy surface (PES) are verified with the vibrational frequency calculations in which Hessian (the second order derivatives of total energy with respect to nuclear coordinates on PES) are calculated. If all eigenvalues in Hessian are positive for a stationary point, this stationary point is a minimum on the PES. One or more negative eigenvalues of a stationary point indicates a saddle point on PES. The natural bond orbital (NBO)[39] analyses are performed to gain insight into the bonding pattern of these complexes. The bond lengths, the natural atomic charges, the vibrational frequencies, the Wiberg bond index (WBI) in Natural Atomic Orbital (NAO), and the Laplacian of the electron density $\nabla^2\rho(r)$ of the constituent atoms of the complexes under investigation are calculated. The nucleus-independent chemical shift (NICS), as an index of aromaticity, at different positions in every structure are predicted with GIAO-B3LYP//B3LYP/gen [P: 6-311+G(2d), C, H: 6-311+G(d,p), Zn,Cd: LANL2DZ]. The NICS(0) is computed at the ring center, the NICS(1) is computed at 1 Å above the ring center, and the NICS(–1) is computed at 1 Å beneath the ring center. All of the NICS dissections of various bonds and cores are computed by NBO3.1.[39,40] All the calculations were carried out with the Gaussian03 program package.[39] The molecular orbitals (MOs) of the complexes are plotted with MOLDEN 4.0.[40]

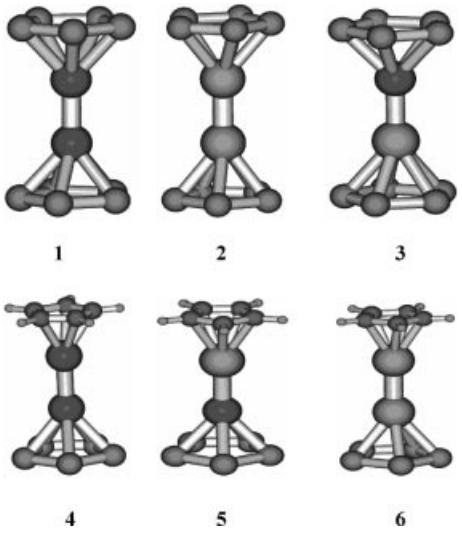


Figure 1. Molecular structures. 1 $(\eta^5\text{-}P_5)Zn_2(\eta^5\text{-}P_5)$, 2 $(\eta^5\text{-}P_5)\text{-}Cd_2(\eta^5\text{-}P_5)$, 3 $(\eta^5\text{-}P_5)ZnCd(\eta^5\text{-}P_5)$, 4 $CpZn_2(\eta^5\text{-}P_5)$, 5 $CpCd_2(\eta^5\text{-}P_5)$, 6 $CpCdZn(\eta^5\text{-}P_5)$.

## 3. Results and Discussions

### 3.1 Geometric Structures

Table 1 and Table 2 list the bond lengths, the WBI in NAO, the natural atomic charge (NAC) $q|e|$, the staggered angle ($D_{(E\text{–}M\text{–}M\text{–}E')}$) between the two $P_5$ (or Cp) rings, and the Laplacian of the electron density $\nabla^2\rho(r)$ between the M

 © 2006 Wiley-VCH Verlag GmbH & Co. KGaA, Weinheim 

atoms and between the M atom and the ligand ring for the homodinuclear phosphametallocenes, $[M_2(\eta^5\text{-}P_5)_2]$ and $(\eta^5\text{-}C_5H_5)M_2(\eta^5\text{-}P_5)$ (M = Zn and Cd) and the heterodinuclear phosphametallocenes, $(\eta^5\text{-}P_5)MM'(\eta^5\text{-}P_5)$ and $(\eta^5\text{-}C_5H_5)MM'(\eta^5\text{-}P_5)$ (M, M′ = Zn, Cd).

All the minima of the dinuclear phosphametallocenes with singlet electronic state, including the homodinuclear phosphametallocenes, $[M_2(\eta^5\text{-}P_5)_2]$ and $(\eta^5\text{-}C_5H_5)M_2(\eta^5\text{-}P_5)$ (M = Zn and Cd) and the heterodinuclear phosphametallocenes, $(\eta^5\text{-}P_5)MM'(\eta^5\text{-}P_5)$ and $(\eta^5\text{-}C_5H_5)MM'(\eta^5\text{-}P_5)$ (M, M′ = Zn, Cd), have an staggered ($9° \leq D_{(E\text{–}M\text{–}M\text{–}E')} \leq 36°$) conformation except for the eclipsed $CpCd_2(P_5)$ ($C_{5v}$, $D_{(E\text{–}M\text{–}M\text{–}E')} = 0°$). All the $D_{5h}$ and $D_{5d}$ symmetric conformations are transition states while the energy differences between the minima and the transition states are very small ($\leq 0.1$ kcal/mol). This is in agreement with the energy differences (0.01 kcal/mol) between the minima in $D_{5d}$ symmetry and the transition states in $D_{5h}$ symmetry in CpZnZnCp,[8] CpNiNiCp,[8] and $[M_2(\eta^5\text{-}Cp)_2]$ (M = Be, Mg, Ca).[10] These results indicate that the rotation of $P_5$ ring about the M–M bond in all complexes is almost free. It suggests that the $[M_2(\eta^5\text{-}P_5)_2]$ (M = Zn, Cd) may be similar to CpMMCp (M = Zn, Cd).

As shown in the Table 1, the Zn–Zn bond lengths in our predictions, 2.487, 2.476, and 2.466 Å in $[Zn_2(\eta^5\text{-}P_5)_2]$, $[CpZn_2(\eta^5\text{-}P_5)]$, and $CpZn_2Cp$, respectively, are close to

Table 1. Bond lengths, natural atomic charge, WBI in NAO, staggered angle, electrostatic interaction energies ($V_{Ep\text{–}M_2^{2+}(M)}$) and the Laplacian of the electron density $\nabla^2\rho(r)$ between M atoms and between M atom and ligand ring for the local minima of $(\eta^5\text{-}P_5)M_2(\eta^5\text{-}P_5)$, $CpM_2(\eta^5\text{-}P_5)$ and $CpM_2Cp$ (M = Zn and Cd) predicted at B3LYP/Gen [P: 6-311+G(2d), C, H: 6-311+G(d,p), Zn,Cd: LANL2DZ] level.

| | $[M_2(P_5)_2]$ | | | $CpM_2(P_5)$ | | | | $CpM_2Cp$ | | |
|---|---|---|---|---|---|---|---|---|---|---|
| | $P_5^-$ | $Zn(P_5)$ | $Cd(P_5)$ | $Zn(P_5)$ | ZnCp | $Cd(P_5)$ | CdCp | Cp | ZnCp | CdCp |
| $r_{E\text{–}E}$[a] | 2.119 | 2.137 | 2.139 | 2.135 | 1.423 | 2.137 | 1.424 | 1.415 | 1.422 | 1.423 |
| $r_{Ep\text{–}M}$ | | 2.126 | 2.370 | 2.157 | 2.050 | 2.392 | 2.162 | | 2.067 | 2.309 |
| $r_{M\text{–}M}$ | | 2.487 | 2.764 | 2.476 | | 2.747 | | | 2.466 | 2.729 |
| $q_{Ep}$ | –1.00 | –0.79 | –0.80 | –0.80 | –0.87 | –0.81 | –0.85 | –1.00 | –0.87 | –0.86 |
| $q_{M_2^{2+}}$ | | 1.58 | 1.59 | 1.67 | | 1.70 | | | 1.74 | 1.72 |
| $WBI_{E\text{–}E}$ | 1.406 | 1.360 | 1.361 | 1.365 | 1.383 | 1.368 | 1.382 | 1.405 | 1.385 | 1.384 |
| $WBI_{M\text{–}M}$ | | 0.765 | 0.765 | 0.809 | | 0.801 | | | 0.864 | 0.852 |
| $WBI_{M\text{–}E}$ | | 0.063 | 0.050 | 0.058 | 0.048 | 0.052 | 0.052 | | 0.048 | 0.048 |
| $D_{(E\text{–}M\text{–}M\text{–}E')}$ [°] | | 18.0 | 22.1 | 27.0 | | 0.0 | | | 18.0 | 0 |
| Group | $D_{5h}$ | $D_5$ | $D_5$ | $C_5$ | | $C_{5v}$ | | $D_{5h}$ | $D_5$ | $D_{5h}$ |
| $\nabla^2\rho(r_{E\rho}\text{–}M)$ | | 0.054 | 0.061 | 0.046 | 0.139 | 0.059 | 0.130 | | 0.114 | 0.126 |
| $\nabla^2\rho(r_{M\text{–}M})$ | | 0.020 | 0.061 | 0.031 | | 0.066 | | | 0.021 | 0.072 |
| $V_{E\rho\text{–}M}$[b] | | 0.29 | 0.27 | 0.26 | 0.41 | 0.25 | 0.37 | | 0.37 | 0.32 |

[a] E = P or CH, Ep = $\eta^5$-$P_5$ or Cp. [b] $V_{Ep\text{–}M^+}$ is the electrostatic interaction energies between Ep and M, $V_{Ep\text{–}M_2^{2+}} = k\frac{q_{M_2^{2+}}q_{Ep}}{r_{M_2^{2+}\text{–}Ep}}$, or $V_{Ep\text{–}M^{2+}} = k\frac{q_{M^{2+}}q_{Ep}}{r_{M^{2+}\text{–}Ep}}$, the $k$ unit is $-\frac{1}{4\pi\varepsilon_0}$. The $r_{M_2^{2+}\text{–}Ep}$ (or $r_{M^{2+}\text{–}Ep}$) is distance between the center of Ep ring and $M_2^{2+}$(or $M^{2+}$).

Table 2. Bond lengths, natural atomic charge, WBI in NAO, staggered angle, electrostatic interaction energies ($V_{Ep\text{–}M_2^{2+}(M)}$) and the Laplacian of the electron density $\nabla^2\rho(r)$ between M atoms and between M atom and ligand ring for the local minima of $(\eta^5\text{-}P_5)ZnCd(\eta^5\text{-}P_5)$, $CpCdZn(\eta^5\text{-}P_5)$ and CpZnCdCp predicted at B3LYP/Gen level.

| | $(P_5)ZnCd(P_5)$ | | $CpCdZn(P_5)$ | | CpZnCdCp | |
|---|---|---|---|---|---|---|
| | $(P_5)Zn$ | $Cd(P_5)$ | $Zn(P_5)$ | CdCp | CpZn | CdCp |
| $r_{E\text{–}E}$[a] | 2.138 | 2.138 | 2.137 | 1.424 | 1.423 | 1.423 |
| $r_{Ep\text{–}M}$ | 2.127 | 2.377 | 2.154 | 2.295 | 2.027 | 2.275 |
| $r_{M\text{–}M}$ | 2.625 | | 2.612 | | 2.597 | |
| $q_{Ep}$ | – 0.79 | – 0.80 | –0.80 | –0.85 | –0.87 | –0.86 |
| $q_{M_2^{2+}}$ | 0.74 | 0.85 | 0.68 | 0.97 | 0.85 | 0.88 |
| $WBI_{E\text{–}E}$ | 1.360 | 1.365 | 1.364 | 1.382 | 1.384 | 1.384 |
| $WBI_{M\text{–}M'}$ | 0.760 | | 0.793 | | 0.856 | |
| $WBI_{M\text{–}E}$ | 0.059 | 0.060 | 0.028 | 0.050 | 0.047 | 0.047 |
| $D_{(E\text{–}M\text{–}M'\text{–}E')}$ | 9.0 | | 36.0 | | 36.0 | |
| Group | $C_5$ | | $C_{5v}$ | | $C_5$ | |
| $\nabla^2\rho(r_{Ep\text{–}M})$ | 0.053 | 0.061 | 0.053 | 0.130 | 0.114 | 0.127 |
| $\nabla^2\rho(r_{M\text{–}M})$ | 0.040 | | 0.043 | | 0.045 | |
| $V_{Ep\text{–}M^+}$[b] | 0.28 | 0.29 | 0.25 | 0.36 | 0.37 | 0.33 |

[a] E = P or CH, Ep = $\eta^5$-$P_5$ or Cp. [b] $V_{Ep\text{–}M^+}$ is the electrostatic interaction energies between Ep and $M^+$ in $MM'^{2+}$, $V_{Ep\text{–}M^{2+}} = k\frac{q_{M^{2+}}q_{Ep}}{r_{M^+\text{–}Ep}}$, the $k$ unit is $-\frac{1}{4\pi\varepsilon_0}$. The $r_{M^+\text{–}Ep}$ is distance between the center of Ep ring and $M^+$(or $M^{2+}$) in $MM'^{2+}$(M, M′ = Zn, Cd).

 © 2006 Wiley-VCH Verlag GmbH & Co. KGaA, Weinheim 

each other, and decrease with the ligand varying from $P_5$ to Cp. The change of the Cd–Cd bond length in $[Cd_2(\eta^5\text{-}P_5)_2]$, $CpCd_2(\eta^5\text{-}P_5)$, and $CpCd_2Cp$ is analogous to that of the Zn–Zn bond length in three Zn-containing complexes, while the Cd–Cd bond length is longer than Zn–Zn in their counterparts. The Zn–($\eta^5$-$P_5$) (2.126 Å) distance in $[Zn_2(\eta^5\text{-}P_5)_2]$ is longer than the Zn–Cp (2.067 Å) distance in $CpZn_2Cp$, and the Cd ligand distance is analogous to the Zn ligand distance. The M–($\eta^5$-$P_5$) distance in $[M_2(\eta^5\text{-}P_5)_2]$ is shorter than the M–Cp distance in $[CpM_2(\eta^5\text{-}P_5)]$ (M = Zn and Cd). However, the Zn ligand distance is shorter than the Cd ligand distance. This indicates that the interaction between the M atom and the $\eta^5$-$P_5$ rings is similar to that between the M atom and the Cp rings, while the interaction in the former is slightly smaller than that in the latter, and the interaction between the Zn atoms and the ligand rings is stronger than that between the Cd atoms and the ligand rings. The interaction trends between the M atom and the ligand rings is completely in the same trends as the electrostatic interaction energies between Ep and $M^+$ as $V_{Ep-M^+}$ listed in Table 1, in which the electrostatic interaction between the M atom and the $\eta^5$-$P_5$ rings is similar to that between the M atom and the Cp rings, but the electrostatic interaction in the former is slightly smaller than that in the latter, and the electrostatic interaction between the Zn atoms and the ligand rings is stronger than that between the Cd atom and the ligand rings. The analyses of the WBI and the $\nabla^2\rho(r)$[36–39,42] between M atoms, and between M atoms and the ligand rings, indicate that the M–M bond is predominantly weakly covalent, and the M–($\eta^5$-$P_5$) bonding is mainly of ionic, and the bond strengths of the M–M bond in the two series complexes are very close.

As shown in Table 2, in the heterodinuclear phosphametallocenes, the magnitudes of bond length, the WBI and the$\nabla^2\rho(r)$ between Zn and Cd, and between M and Ligands, reveal that the Zn–Cd bond is a weak covalent, and the M–Ligand bond is main ionic, too. The electrostatic interaction between the M atom and the $\eta^5$-$P_5$ rings is slightly weaker than the interaction between the M atom and Cp ring, while the covalent interaction in the former is stronger than that in the latter.

Comparing the $r_{P-P}$ in the homodinuclear or the heterodinuclear phosphametallocenes with that in the $\eta^5$-$P_5^-$($D_{5h}$) ion, in which all P–P bonds are equal, we can find that the $r_{P-P}$ in the former is longer than that in the latter. According to the fact that the bond lengths of $r_{P-P}$ lie between the single P–P (≥ 2.21 Å) and the double P=P (≤ 2.02 Å) bonds,[21,34] and the calculated adjacent P–P WBI in all molecules from the NBO analyses is in the range of 1.3–1.4, which is between the standard values of single-bond (1.0) and double-bond (2.0), we can infer that the building block $P_5$ in all $[M_2(\eta^5\text{-}P_5)_2]$ complexes has conjugated P–P bonds, and all molecules have aromaticity according to the P–P bond lengths.

### 3.2 Dissociation Energies

On the basis of the NBO charge and the sign of the $\nabla^2\rho(r)$ in the complexes, in which the $M_2$ unit (or M) and the ($\eta^5$-$P_5$) building block have nearly +2 |e| (or +1 |e|) and –1 |e| charges, respectively, and the $\nabla^2\rho(r) > 0$, the interaction between M and the ($\eta^5$-$P_5$) is mainly ionic. In order to compare their stabilities, eight dissociation pathways are proposed, and their dissociation energies are calculated for each pathway as shown in Table 3 and Table 4.

The pathways (1) and (4) involve breaking of the M–M and the M–M′ (M,M′ = Zn, Cd) bond. From Table 3 and Table 4, according to the magnitude of the dissociation energies of the M–M (M = Zn, Cd) bond, except for that of the Cd–Cd bond in $[Cd_2(\eta^5\text{-}P_5)_2]$, the dissociation energies of the M–M (or M–M′) (M = Zn, Cd) bond in the complexes and in the $CpM_2Cp$ ($D_5$ or $D_{5h}$) are very close, especially, that of the Zn–Zn bond. These results indicate that the stability of three complexes is analogous to $CpZn_2Cp$ which was successfully synthesized by Resa et al.,[1] that

Table 3. Dissociation energies for ($\eta^5$-$P_5$)$M_2$($\eta^5$-$P_5$), $CpM_2$($\eta^5$-$P_5$) and $CpM_2Cp$ (M = Zn, Cd) at 3LYP/Gen level of theory.[a]

| Dissociation pathway | $[(Ep)_2M_2]$ | | $C_pM_2(P_5)$ | | $C_pM_2C_p$ | |
|---|---|---|---|---|---|---|
| | Zn | Cd | Zn | Cd | Zn | Cd |
| (1) $[(Ep)_2M_2] \xrightarrow{\Delta E_1} Ep\,M + MEp$ | 51.4 | 44.6 | 53.8 | 47.1 | 55.4 | 49.1 |
| (2) $[(Ep)_2M_2] \xrightarrow{\Delta E_{21}} EpM_2^{\prime} + Ep^-$ | 121.3 | 104.9 | 154.9[b] (124.9)[c] | 143.8[b] (115.0)[c] | 164.8 | 142.5 |
| $EpM_2^+ \xrightarrow{\Delta E_{22}} M_2^{2+} + Ep^-$ | 278.8 | 251.9 | 315.6[b] (278.8)[c] | 251.9[b] (280.9)[c] | 315.6 | 280.9 |
| (3) $[(Ep)_2M_2] \xrightarrow{\Delta E_3} M_2^{2+} + 2\,Ep^-$ | 400.1 | 367.7 | 440.6 | 395.7 | 480.5 | 423.2 |

[a] All $EpM_2^+$ have $C_{5v}$ symmetry and $^2A_1$ electronic state, all EpM have $C_{5v}$ symmetry and $^2A_1$, electronic state, all Ep and Cp have $D_{5h}$ symmetry and $^1A_{1g}$ electronic state; $M_2^{2+}$ have $^1S_{gg}$ electronic state. [b] The dissection energy of $P_5M_2$–Cp as the equation $CpM_2P_5 \rightarrow P_5M_2^+ + Cp^-$. [c] The dissection energy of $CpM_2$–$P_5$ as the equation $CpM_2P_5 \rightarrow CpM_2^+ + P_5^-$.

 © 2006 Wiley-VCH Verlag GmbH & Co. KGaA, Weinheim 

Table 4. Dissection energies for ($\eta^5$-$P_5$)ZnCd($\eta^5$-$P_5$), CpZnCd($\eta^5$-$P_5$) and CpZnCdCp at B3LYP/6-311+G(d,p) level of theory.[a]

| Dissociation pathway | $(P_5)ZnCd(P_5)$ | | $C_pCdZn(P_5)$ | | $C_pZnCdC_p$ | |
|---|---|---|---|---|---|---|
| | Zn—$P_5$ Cd—$P_5$ | Cd—$P_5$ Zn—$P_5$ | Cd—$C_p$ Zn—$C_p$ | Cd—$C_p$ Zn—$C_p$ | Zn—$P_5$ Cd—$C_p$ | Cd—$C_p$ Zn—$P_5$ |
| (4) $[(Ep)_2ZnCd] \xrightarrow{\Delta E_4}$ Ep Zn + CdEp | 47.8 | | 50.15 | | 64.3 | |
| (5) $[(Ep)_2ZnCd] \xrightarrow{\Delta E_{51}} EpZnCd^+ + Ep^-$ | 122.6 | 114.1 | 203.3 | 203.3 | 115.3 | 142.02 |
| $EpZnCd^+ \xrightarrow{\Delta E_{52}} ZnCd^{2-} + Ep^-$ | 260.4 | 268.8 | 302.6 | 302.6 | 302.6 | 268.84 |
| (6) $[(Ep)_2ZnCd] \xrightarrow{\Delta E_6} ZnCd^{2+} + 2\ Ep^-$ | 329.0 | | 410.9 | | 469.9 | |

[a] All $EpZnCd^+$ have $C_{5v}$ symmetry and $^2A$ electronic state, all EpM (M = Zn and Cd) have $C_{5v}$ symmetry and $^2A_1$ electronic state; all Ep and Cp have $D_{5h}$ symmetry and $^1A_{1g}$ electronic state; $ZnCd^{2+}$ has $^1S_g$ electronic state.

they can be synthesized. However, the dissociation energy of the M–M (M = Zn, Cd) bond in the homodinuclear phosphametallocenes or of the M–M′ (M, M′ = Zn, Cd) bond in heterodinuclear phosphametallocenes increases with the number of Cp ligands, i.e. $[M_2(P_5)_2] < CpM_2(P_5) < CpM_2Cp$, and $(P_5)ZnCd(P_5) < CpCdZn(P_5) < CpZnCdCp$, though their energy differences are very small, only about 1.6–2.5kcal/mol in homodinuclear phosphametallocenes, and bout 1.6–14.1 kcal/mol in heterodinuclear phosphametallocenes. Comparison the dissociation energy of the dinuclear phosphametallocenes with that of the counterpart metallocenes indicates that the M–M (M = Zn, Cd) bond and the M–M′ (M, M′ = Zn, Cd) bond in phosphametallocenes are slightly weaker than that in the counterpart metallocenes. Comparison of the dissociation energy of the Zn–Zn bond in the dizinc phosphametallocenes with that of the Cd–Cd bond in the dicadmium phosphametallocenes reveals that the Zn–Zn bond is stronger than the Cd–Cd bond. Thus the dizinc phosphametallocenes are more stable than the dicadmium phosphametallocenes. These results are consistent with the $WBI_{M-M}$ analysis that the M–M (M = Zn, Cd) bond in phosphametallocenes is less stable than that in metallocenes which is a weak covalent bond.

Pathway (2) or (5) in Table 3 and Table 4 involves the breaking of the metal–ligand bonds in two-step dissection, while pathway (3) or (6) involves the breaking of the two metal–ligand bonds in one-step dissection. As shown in Table 3 and Table 4, the first and the second dissociation energies of the metal–ligand bonds in pathway (2) [or pathway (5)] are not equal. The first dissociation energy ($E_{21}$) is much smaller than the second one ($E_{22}$). This indicates that the first group metal–ligand bonds are easier to break while the second group metal–ligand bonds are more stable after the first step dissection. $\Delta E_{21}$, $\Delta E_{22}$, and 1/2 $\Delta E_3$ in Table 3 (or $\Delta E_{51}$, $\Delta E_{52}$ and 1/2 $\Delta E_6$ in Table 4) giving the first, the second and the average dissociation energy of the $M_2^{2+}$ ($^1S_{gg}$) with $P_5^-$ ($^1A_1$, $D_{5h}$) in the dinuclear phosphametallocenes are very large, thus indicating that the bonding of $M_2^{2+}$ with $P_5^-$ is very strong in those systems.

Comparing the first, the second and the average dissociation energy of the metal–$P_5$ bonds in the dinuclear phosphametallocenes with those of the metal–Cp bonds in the dinuclear metallocenes, it can be inferred that the interaction between $M_2^{2+}$ and $P_5^-$ is close to (and slightly weaker than) that between $M_2^{2+}$ and $Cp^-$. Furthermore, this interaction is consistent with the electrostatic interaction, in which the $V_{Ep-M^+}$ between the M cation and the $P_5$ anion in the dinuclear phosphametallocenes is close to that between the M cation and the Cp anion in the dinuclear metallocenes, though the magnitude in the former is slightly smaller. However, this is opposite to the conclusion of the WBI analysis between the metal and the ligand ($P_5$ or Cp), in which the WBI between the M cation and the $P_5$ anion in the dinuclear phosphametallocenes is larger than that between the M cation and the Cp anion in the dinuclear metallocenes. It further illustrates that the electrostatic interaction between the metal and the ligand ($P_5$ or Cp) in the dinuclear phosphametallocenes dominates the overall interactions.

Comparison of the dissociation energy of the Zn–$P_5$ bonds in $[Zn_2(\eta^5\text{-}P_5)_2]$ ($D_5$) with that of the Cd–$P_5$ bonds in $[Cd_2(\eta^5\text{-}P_5)_2]$ ($D_5$), and comparison of the dissociation energy of the Zn–$P_5$ bonds with that of Cd–$P_5$ bonds in $[ZnCd(\eta^5\text{-}P_5)_2]$ ($C_5$) show that the dissociation energy of the Zn–$P_5$ bonds is larger than that of the Cd–$P_5$ bonds. The analysis of electrostatic interactions (the $V_{Ep-M^+}$ listed in Table 3 and Table 4) also supports this observation.

Comparison of the dissociation energy of the M–M (or M–M′; M, M′ = Zn, Cd) bond with that of the M–($\eta^5$-$P_5$) bonds in the dinuclear phosphametallocenes, in which the magnitude of the former from 45 to 64 kcal/mol is much smaller than that of the latter from 105 to 316 kcal/mol, reveals that the strength of the M–M bond is much weaker than that of the M–($\eta^5$-$P_5$) bond. Therefore, the stability of the dinuclear phosphametallocenes mainly depend on the

 © 2006 Wiley-VCH Verlag GmbH & Co. KGaA, Weinheim 

magnitude of the M–M bond strength, i.e. the strength of the M–M bonding plays a more dominant role to the stability of the dinuclear phosphametallocenes.

### 3.3 Electronic Structures

Analyses of the WBI, the $\nabla^2\rho(r)$ and the dissociation energy of the M–M (or M–M′) and the M–($\eta^5$-$P_5$) in the dinuclear phosphametallocenes reveal that the M–M (or M–M′) bond is covalent and the interaction between M and ligands is mainly ionic. In order to gain insight into the covalent nature of the M–M (or M–M′) bond and to explore the reason for the stabilities of the dinuclear phosphametallocenes, a correlation diagram between the M($\eta^5$-$P_5$) fragments is depicted in Figure 2, in which several most relevant MOs in M($\eta^5$-$P_5$) and [$M_2$($\eta^5$-$P_5$)$_2$] (M = Zn, Cd) are plotted.

As shown in Figure 2, the frontier MOs for the M($\eta^5$-$P_5$) fragment are singly occupied HOMO [5a, an antibonding combination of the π-($\eta^5$-$P_5$) orbital in $P_5^-$($D_{5h}$) and the *n*s orbital in the M atom] and a pair of degenerate MOs. However, the frontier MOs for the [$M_2$($\eta^5$-$P_5$)$_2$] (M = Zn, Cd) are two degenerate nonbonding doubly occupied HOMO and HOMO-1 and a doubly occupied HOMO-2 ($5a_1$, a M–M bonding MO). The bonding MO of the M–M bond with σ symmetry mostly forms from the weak interaction of the singly occupied HOMOs of two M($\eta^5$-$P_5$) fragments [partly

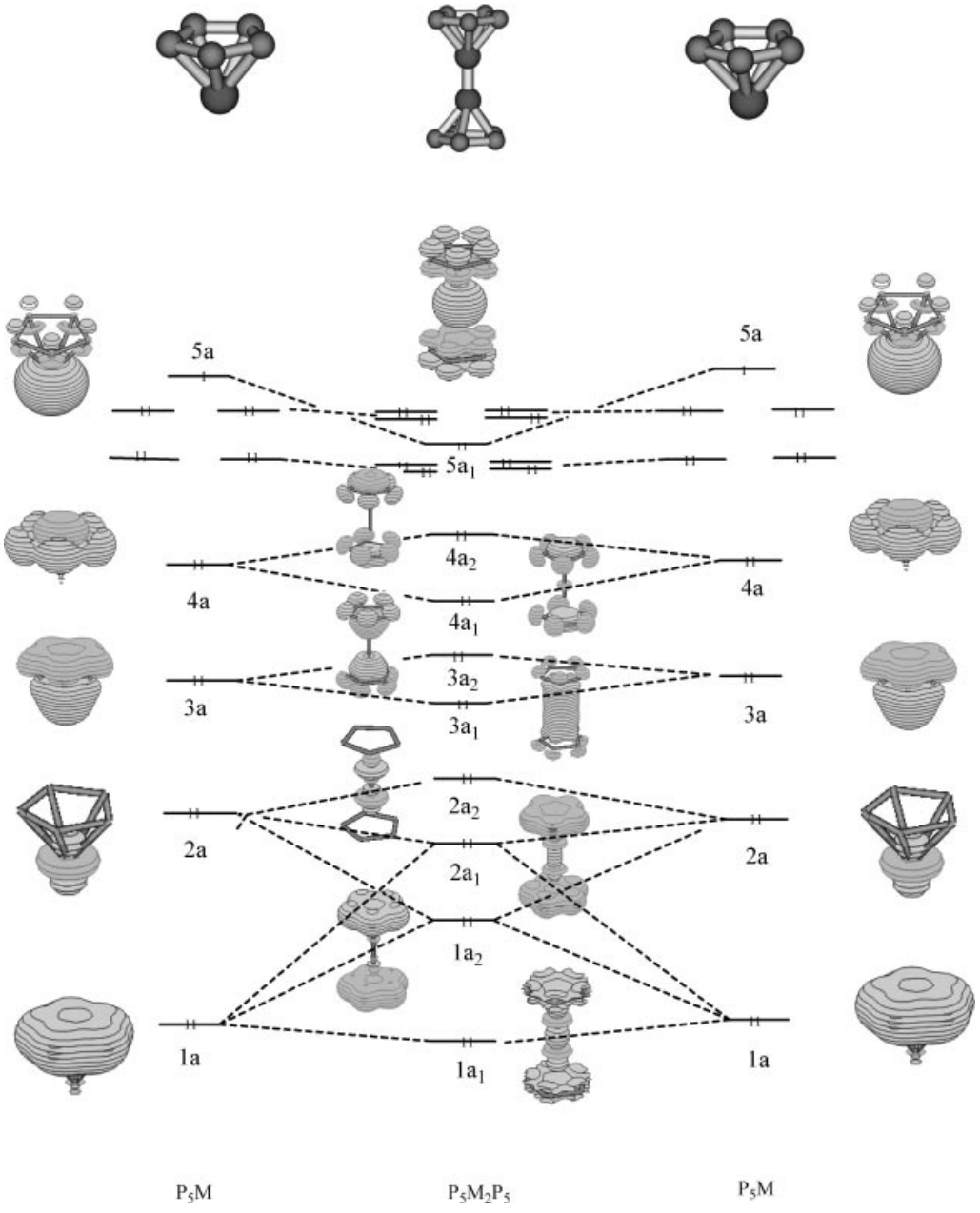


Figure 2. Orbital correlation diagram between the fragments M($\eta^5$-$P_5$) in ($\eta^5$-$P_5$)$M_2$($\eta^5$-$P_5$) and showing the most relevant orbital plots of the fragments M($\eta^5$-$P_5$) and the correlative molecular orbital plots of ($\eta^5$-$P_5$)$M_2$($\eta^5$-$P_5$) (M = Zn, Cd).

 © 2006 Wiley-VCH Verlag GmbH & Co. KGaA, Weinheim 

Table 5. Correlative occupied orbital energy differences between the HOMO (5a) in *Ep*M Fragments and the HOMO–2 ($5a_1$) in [$M_2(\eta^5$-$P_5)_2$] {or $CpM_2Cp$, [$MM'(\eta^5$-$P_5)_2$], Cp $MM'(\eta^5$-$P_5)$ and CpMM′Cp (M, M′ = Zn, Cd)}.

| Energy difference | $[Zn_2(P_5)_2]$ | $P_5Cd_2P_5$ | $P_5ZnCdP_5$ | $CpZn_2P_5$ | $CpCd_2P_5$ | $CpCdZnP_5$ | $CpZn_2Cp$ | $CpCd_2Cp$ |
|---|---|---|---|---|---|---|---|---|
| $\Delta E_{5a-5a_1}$ (cal/mol) | 55.3 | 52.4 | 53.8 | 59.4 | 55.0 | 55.9 | 59.1 | 54.9 |

coming from the interactions of the double occupied 3a, 2a and 1a of the two M($\eta^5$-$P_5$) fragments and resulting in $3a_1$, $2a_1$, and $1a_1$ MOs as shown in Figure 2, but these weak bonding interactions are counteracted by their antibonding interactions]. Meanwhile, Figure 2 shows that the stabilities of the dinuclear phosphametallocenes correlates with the M–M bond strength, i.e. the magnitude of the MO energy difference ($\Delta E_{5a-5a_1}$) between the singly occupied HOMOs of M($\eta^5$-$P_5$) fragments and the HOMO–2($5a_1$) representing the M–M bonding orbital in the dinuclear phosphametallocenes correlates with stability of the dinuclear phosphametallocenes. The orbital energy differences ($\Delta E_{5a-5a_1}$) of the phosphametallocenes are listed in Table 5. For comparison, the results of the similar calculations for the $CpM_2Cp$ ($D_5$ or $D_{5h}$) (M = Zn, Cd) are listed in Table 3 as well.

As shown in Figure 2 and Table 5, the magnitudes of the orbital energy differences ($\Delta E_{5a-5a_1}$) for the dinuclear phosphametallocenes are very close, and they are slightly smaller than that of the $CpM_2Cp$ ($D_5$ or $D_{5h}$). The energy differences among them are small, for example, the $\Delta E_{5a-5a_1}$ difference between [$Zn_2(\eta^5$-$P_5)_2$] ($D_5$) and $CpZn_2Cp$ ($D_5$) is about 3.8 kcal/mol, and that between [$Cd_2(\eta^5$-$P_5)_2$] ($D_5$) and $CpCd_2Cp$ ($D_{5h}$) is only about 2.5 kcal/mol. The magnitude of the orbital energy difference in [$Zn_2(\eta^5$-$P_5)_2$] ($D_5$) is bigger than that in [$Cd_2(\eta^5$-$P_5)_2$] ($D_5$), and such energy difference in $P_5ZnCdP_5$ ($C_5$)lies between those of [$Zn_2(\eta^5$-$P_5)_2$] ($D_5$) and [$Cd_2(\eta^5$-$P_5)_2$] ($D_5$). On the basis of the magnitude of the $\Delta E_{5a-5a_1}$, the order of the stabilities of the dinuclear phosphametallocenes and the dinuclear $CpM_2Cp$ ($D_5$ or $D_{5h}$) is that: $CpZn_2P_5$ ($C_5$) ≈ $CpZn_2Cp$ ($D_5$) > $CpCdZnP_5$ ($C_5$) ≈ [$Zn_2(P_5)_2$]($D_5$) ≈ $CpCd_2P_5$ ($C_{5v}$) ≈ $CpCd_2Cp$ ($D_{5h}$) > $P_5ZnCdP_5$ ($C_5$) ≈ $P_5Cd_2P_5$ ($D_5$).

Comparison of the $\Delta E_{5a-5a_1}$ ($52.4 \le \Delta E_{5a-5a_1} \le 59.4$ kcal/mol) and the change trends with those of the dissociation energy of the M–M (or M–M′, M, M′ = Zn, Cd) bond ($44.6 \le \Delta E \le 55.4$ kcal/mol) as calculated from equations (1) and (5) (listed in Table 3 and Table 4) reveals that the magnitudes and the change trends of the $\Delta E_{5a-5a_1}$ and the dissociation energy of the M–M are very similar. Therefore, the stability of the dinuclear phosphametallocenes correlates with the magnitude of the $\Delta E_{5a-5a_1}$.

The plots of the $3a_1$ and $3a_2$ MO electron density distribution in [$M_2(\eta^5$-$P_5)_2$], derived from the interaction of the unoccupied antibonding $e_u$ of the $M_2^{2+}$ with the doubly occupied 3a, the π bond of $(\eta^5$-$P_5)^-$, shows that there is small amount of orbital overlap between the $M_2^{2+}$ and the $(\eta^5$-$P_5)^-$, thus the covalent interaction between the $M_2^{2+}$ and the ($\eta^5$-$P_5$) plays a secondary role in the stability of [$M_2(\eta^5$-$P_5)_2$], while the electrostatic interaction plays the dominant role. This conclusion is consistent with that the interaction between the $M_2^{2+}$ and the ($\eta^5$-$P_5$) is ionic basing on the analysis of the Laplacian of the electron density.

In addition, the ring currents of the electrons of $4a_1$, $4a_2$, $3a_1$, $3a_2$, $2a_1$, $1a_1$, and $1a_2$ in [$M_2(\eta^5$-$P_5)_2$] as shown in Figure 2 indicate that the dinuclear phosphametallocenes have aromaticity.

## 4. Aromaticity

The dinuclear phosphametallocenes have equivalent P–P bonds and the charge of the $P_5$ ring is close to –1 |e| as listed in Tables 1 and 2, which satisfy the geometric criterion of aromaticity and the $(4n+2)\pi$ Hückel's rule.[43] As shown in Figure 2, there are $\sigma$ ring current[44,45] in the $1a_2$, $1a_1$, $2a_1$, $4a_1$, and $4a_2$ MOs and π ring current in the $3a_1$ and $3a_2$ MOs in $P_5M_2P_5$ ($D_5$)(M = Zn, Cd). These results indicate that the $P_5$ rings in the dinuclear phosphametallocenes have aromaticity, and is worthy of further studying on the degree of aromaticity of the complexes.

The NICSs of the optimized structures of the dinuclear phosphametallocenes at the ring center [NICS(0)], at 1 Å above [NICS(1)] and beneath [NICS(–1)] the ring center are computed with GIAO–B3LYP/Gen method. All of the NICSs are listed in Table 6 and Table 7.

NICS has the negative value of the magnetic shielding. It is a simple and efficient aromaticity probe proposed by Schleyer et al.,[46–48] and one of the effective measures of aromaticity recommended by Katritzky et al.[45] This concept has been applied to both organic[46,48] and inorganic compounds,[17,47] transition metal complexes.[49,50] Aromaticity, antiaromaticity, and multiple fold aromaticity,[51] presented in molecules that possess more than one independent

Table 6. Total NICSs (in ppm) for ($\eta^5$-$P_5$)$M_2$($\eta^5$-$P_5$), $CpM_2$($\eta^5$-$P_5$) and $CpM_2Cp$ (M = Zn, Cd) at GIAO–B3LYP/Gen level of theory.

| | $[M_2(P_5)_2]$ | | | $CpM_2(P_5)$ | | | | $CpM_2Cp$ | | |
|---|---|---|---|---|---|---|---|---|---|---|
| | $P_5^-$ | $(P_5)Zn$ | $(P_5)Cd$ | $Zn(P_5)$ | CpZn | $(P_5)Cd$ | CpCd | Cp | CpZn | CpCd |
| NICS(0) | –15.4 | –15.1 | –11.2 | –15.4 | –14.6 | –10.5 | –11.1 | –12.5 | –14.9 | –11.5 |
| NICS(1) | –14.8 | –15.2 | –13.7 | –15.0 | –11.5 | –13.2 | –11.0 | –9.52 | –11.4 | –11.9 |
| NICS(–1) | –14.8 | –24.4 | –11.4 | –23.8 | –22.4 | –10.2 | –8.0 | –9.52 | –23.1 | –10.3 |

 © 2006 Wiley-VCH Verlag GmbH & Co. KGaA, Weinheim 

Table 7. Total NICS for ($\eta^5$-$P_5$)ZnCd($\eta^5$-$P_5$), CpCdZn($\eta^5$-$P_5$), and CpZnCdCp at GIAO–B3LYP/Gen level of theory.

| | $(P_5)ZnCd(P_5)_2$ | | CpCdZn ($P_5$) | | CpZnCdCp | |
|---|---|---|---|---|---|---|
| | $(P_5)Zn$ | $Cd(P_5)$ | $(P_5)Zn$ | CdCp | CpZn | CpCd |
| NICS(0) | –15.5 | –13.2 | –15. 9 | –10.9 | –15.8 | –10.4 |
| NICS(1) | –15.4 | –14.3 | –15.4 | –11.2 | –11.5 | –11.9 |
| NICS(–1) | –25.6 | –14.5 | –25.2 | –11.1 | –24.0 | –9.5 |

delocalized bonding system, either σ-type or π-type, have also been found in the all–metal systems[52,53] and the sandwich–like complexes.[33,38,43,54–57] Recently, we extended NICS to $P_5^-$ and $[Ti(P_5)_2]^{2-}$,[33] and dinuclear metallocene $[CpZn_2Cp]$.[58] Negative NICSs denote aromaticity, positive NICSs denote antiaromaticity, and zero NICS means non-aromaticity. The magnitude of NICSs indicates the degree of aromaticitiy or antiaromaticity.[46,47] According to the dissected NICS analysis on π-aromaticity and antiaromaticity, NICS(1) values (i.e. at 1 Å above) was recommended as better measures of π aromaticity than NICS(0) for benzene (i.e. at the ring centers).[59]

As shown in Table 6 and Table 7, NICS(0), NICS(1) and NICS(–1) in all the dinuclear phosphametallocenes and $CpM_2Cp$ ($D_5$ or $D_{5h}$) (M = Zn, Cd) being negative indicates that they are aromatic. However, the differences of NICSs at the same position in different systems reveal that their magnitude of local aromaticity is different. First, the magnitude of NICS(0) in $[M_2(\eta^5\text{-}P_5)_2](D_5)$ is less negative than that in the building block $P_5^-$ ($D_{5h}$) ion, while NICS(1) and NICS(–1) in $[Zn_2(\eta^5\text{-}P_5)_2](D_5)$ are more negative than those of counterpart in the building block $P_5^-$ ($D_{5h}$) ion. These are consistent with elongation of the calculated P–P bond lengths. The present calculation predict that the mono-facially coordinated cyclo-$P_5$ in dinuclear phosphametallocenes undergoes significant ring expansion leading to "loosening of P–P bond " as observed experimentally and calculated theoretically by Malar.[19,32] The consequent loss of local aromaticity in the central cyclo-$P_5$ indicates that a significant π-electron density can be further transferred from the ring towards the $M_2^{2+}$ unit, such that the positive charge of the $M_2^{2+}$ unit becomes small and the negative charge of cyclo-$P_5^-$ decreases as listed in Table 1 and Table 2. Second, in both the dinuclear phosphametallocenes and $CpM_2Cp$ ($D_5$ or $D_{5h}$) (M = Zn, Cd), the magnitude of NICSs in all Zn–($\eta^5$-$P_5$) (or Zn–Cp) ring plane is more negative than that in all Cd($\eta^5$-$P_5$) (or Cd–Cp) ring plane, and the magnitude of NICSs in the former (Zn) is more negative than that in the $P_5^-$ ($D_{5h}$)[or $C_5H_5^-$ ($D_{5h}$)] ion. Finally, the magnitude of NICSs in $[M_2(\eta^5\text{-}P_5)_2](D_5)$ is more negative than those in counterpart $CpM_2Cp$ ($D_5$ or $D_{5h}$). This may be because that the NICSs in the building block $P_5^-$ ($D_{5h}$) ion are more negative than those in the building block $C_5H_5^-$ ($D_{5h}$) ion as listed in Table 6 so that the magnitude of NICSs in $[M_2(\eta^5\text{-}P_5)_2]$ ($D_5$) is more negative than those in counterpart $CpM_2Cp$ ($D_5$ or $D_{5h}$).

We dissected the total NICS values of $P_5^-$ ring in $P_5^-$ ($D_{5h}$), $[Zn_2(\eta^5\text{-}P_5)_2]$ ($D_5$) and $[Cd_2(\eta^5\text{-}P_5)_2]$ ($D_5$) into different P–P bond contributions (σ and π), the M–M bond contribution, the lone pair electrons contributions of P atom and M atom, and the M–($\eta^5$-$P_5$) bonding contribution are shown in Figures 3, 4 and 5.

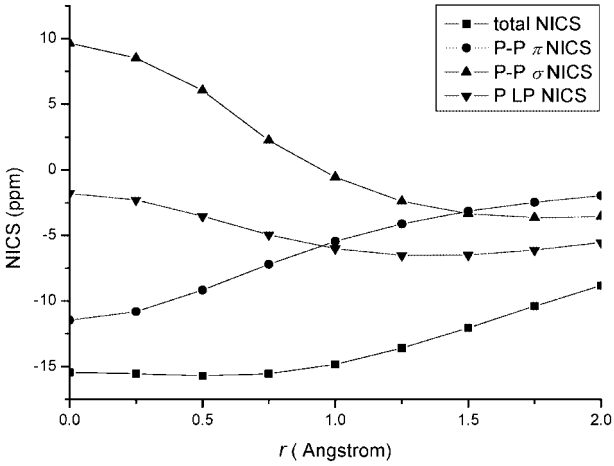


Figure 3. Plot of the NICS contributions of various bonds and total NICS distribution at the center of $P_5^-$($D_{5h}$) ring up to 2.0 Å above at GIAO-B3LYP/+G(2d).

As shown in Figures 3, 4 and 5, although there is a minimum in curves of total NICS distributions of the outer of cyclo- $P_5$ plane for $P_5^-$ ($D_{5h}$), $[Zn_2(\eta^5\text{-}P_5)_2]$ ($D_5$), and $[Cd_2(\eta^5\text{-}P_5)_2]$ ($C_5$), the magnitude of NICS and the position got the minimum is not complete same, NICS(0.5) = –15.7 ppm for $P_5^-$ ($D_{5h}$), NICS(0.75) = –15.9 ppm for $[Zn_2(\eta^5\text{-}P_5)_2]$ ($D_5$), NICS(0.75) = –13.9 ppm for $[Cd_2(\eta^5\text{-}P_5)_2]$ ($C_5$). This result reveals that the maximal π-electron ring current of the cyclo- $P_5$ plane in $[M_2(\eta^5\text{-}P_5)_2]$ is shifted from ring center to outer of plane corresponding to $P_5^-$ ($D_{5h}$). It confirms that there is indeed the expansion of the π-electron density in dinuclear phosphametallocenes again. Therefore, we suggest that the most negative NICS($r$) ($r$ may be not equal to 1 Å) should be one of criterion of π aromaticity, too.[33,57]

Comparison of the NICS contributions of various bonds and total NICS distribution in the out-of $P_5^-$ ($D_{5h}$) plane (as shown in Figure 3) with that in out-of $P_5$ ring plane of $[Zn_2(\eta^5\text{-}P_5)_2]$ ($D_5$) [as shown in Figure 4 (a)] indicates that both magnitudes and distributions of total NICS are very similar. Although the NICS contribution of the Zn–Zn bond in $[Zn_2(\eta^5\text{-}P_5)_2]$ ($D_5$) is positive, and that of Zn–($\eta^5$-$P_5$) bonding contribution is negative, and the negative contribution slight preponderates the positive contribution, both magnitude and distribution of total NICS in two contributions are very close while the other bond contributions are very close in two contributions. However, the analogous

 © 2006 Wiley-VCH Verlag GmbH & Co. KGaA, Weinheim 

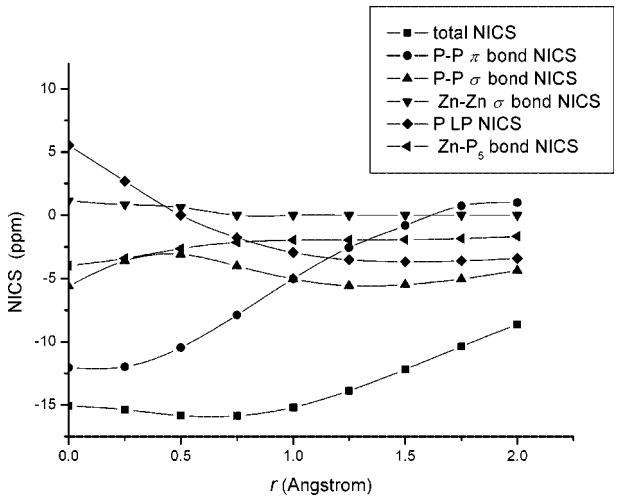


(a)

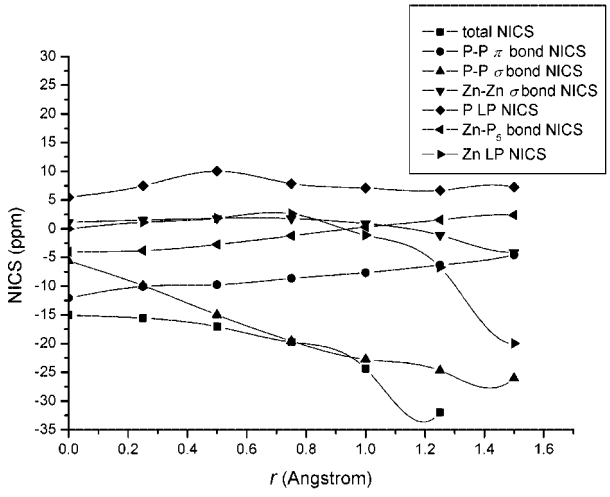


(b)

Figure 4. Plot of the NICS contributions of various bonds and total NICS distribution at the center of $P_5^-$ ring up to 2.0 Å above in $P_5Zn_2P_5$ ($D_5$) at GIAO-B3LYP/Gen (a) out-of-plane (b) in-plane.

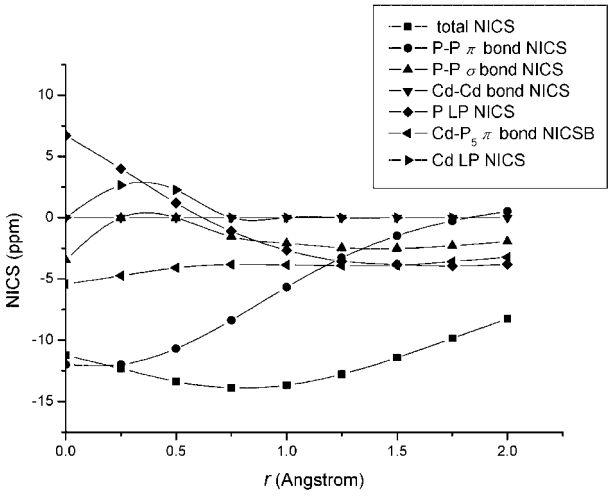


(a)

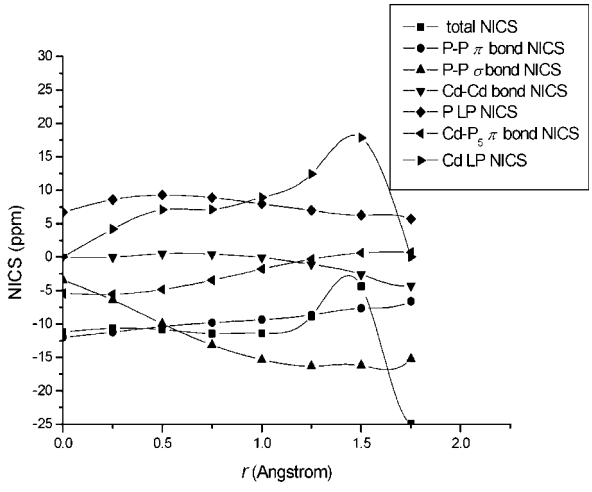


(b)

Figure 5. Plot of the NICS contributions of various bonds and total NICS distribution at the center of $P_5^-$ ring up to 2.0 Å above in $P_5Cd_2P_5$ ($D_5$) at GIAO-B3LYP/Gen (a) out-of-plane (b) in-plane.

comparison of NICS of out-of $P_5^-$ ($D_{5h}$) ion plane (as shown in Figure 3) with that of out-of $P_5$ ring plane of $[Cd_2(\eta^5\text{-}P_5)_2]$ ($D_5$) [as shown in Figure 5 (a)] reveals that the sum of the positive NICS contribution of the lone pair (LP) electron of Cd atom and of the P–P σ bond preponderates the negative NICS contribution of Cd–($\eta^5$-$P_5$) bonding while the other bonding NICS contributions are very close. So that the magnitude of total NICS of the out-of $P_5$ ring plane in $[Cd_2(\eta^5\text{-}P_5)_2]$ ($D_5$) is not as negative as that of $P_5^-$ ($D_{5h}$) ion. As for the NICSs of the other dinuclear phosphametallocenes, the magnitude and distribution of total NICS is analogous to that in $[Zn_2(\eta^5\text{-}P_5)_2]$ ($D_5$) and $[Cd_2(\eta^5\text{-}P_5)_2]$ ($D_5$). Therefore, the NICSs of the dizinc phosphametallocenes is slightly more negative than that of $P_5^-$ ($D_{5h}$) ion except for NICS(0), but the NICSs of the dicadmium phosphametallocenes is less negative than that of $P_5^-$ ($D_{5h}$) ion.

As for the reason that NICS(–1) of the dizinc phosphametallocenes is much more negative than that of the dicadmium phosphametallocenes, as shown in Figure 4 (b) and Figure 5 (b), the curve of total NICS distribution of inner side of the $P_5$ ring plane in $[M_2(\eta^5\text{-}P_5)_2]$ ($D_5$) [M = Zn, Cd] drops off with the distance to the $M_2^{2+}$ unit, but the curve of total NICS distribution in $[Zn_2(\eta^5\text{-}P_5)_2]$ ($D_5$) is much steeper than that in $[Cd_2(\eta^5\text{-}P_5)_2]$ ($D_5$), so that the distribution curves of NICS contributions of in-$P_5$-ring

 © 2006 Wiley-VCH Verlag GmbH & Co. KGaA, Weinheim 

plane for the Zn–Zn bond, the LP of Zn, and the P–P σ bond in $[Zn_2(\eta^5\text{-}P_5)_2]$ ($D_5$) is much steeper than that of the Cd–Cd bond, the LP of Cd, and the P–P σ bond in $[Cd_2(\eta^5\text{-}P_5)_2]$ ($D_5$). Therefore, the magnitude of total NICS of inner side of the $P_5$ ring plane in $[Zn_2(\eta^5\text{-}P_5)_2]$ ($D_5$) is much more negative than that in $[Cd_2(\eta^5\text{-}P_5)_2]$ ($D_5$) at the same position, the NICS(–1) of $[Zn_2(\eta^5\text{-}P_5)_2]$ ($D_5$) is much more negative than that of $[Cd_2(\eta^5\text{-}P_5)_2]$ ($D_5$). The NICS(–1) of other dinuclear phosphametallocenes has similar phenomena.

## 5. Conclusions

The analysis of energy and the harmonic frequencies on the equilibrium geometries of both series of dinuclear phosphametallocenes, $[MM'(\eta^5\text{-}P_5)_2]$ and $(\eta^5\text{-}P_5)MM'Cp$ (M, M′ = Zn, Cd), shows that all the minima of the dinuclear phosphametallocenes with singlet electronic state have an staggered ($9° \leq D_{(E\text{–}M\text{–}M\text{–}E')} \leq 36°$) conformation except for the eclipsed $CpCd_2(P_5)$ ($C_{5v}$, $D_{(E\text{–}M\text{–}M\text{–}E')} = 0°$), and all the $D_{5h}$ and the $D_{5d}$ symmetric conformations are transition states while the energy differences between the most stable minimum and the transition states are very small ($\leq 0.1$ kcal/mol). The rotation of $P_5$ ring about the M–M bond in all complexes is almost free.

The analyses of the NBO, the Laplacian of the electron density, the electrostatic interaction energy, the bonding energy decomposition, and the MO correlation diagrams for the two series complexes reveal that the properties of all the dinuclear phosphametallocenes are similar to that of the dizinc metallocenes. The M–M (or M–M′) bond in the dinuclear phosphametallocenes is a weak σ covalent bond, and the magnitude of bonding energy of the M–M (or M–M′) bond correlates with the energy difference between the energy of HOMO in $M(\eta^5\text{-}P_5)$ [or MCp] ($^2A$, $C_{5v}$) fragment and the energy of HOMO–2 in $[MM'(\eta^5\text{-}P_5)_2]$ ($^1A$, $D_5$, or $D_{5h}$) [or $(\eta^5\text{-}P_5)MM'Cp$ ($^1A$, $C_5$ or $C_{5v}$)] (M, M′ = Zn, Cd). The M–M (or M–M′) bond strength plays a dominant role in the stability of the dinuclear phosphametallocenes. On the other hand, the M–($\eta^5$-$P_5$) [or M–Cp] bonding is mainly ionic. Among the different dinuclear phosphametallocenes with the same ligands, the bonding energies of the M–M (or M–M′) bond and the M–($\eta^5$-$P_5$) (or M–Cp) bonds decrease as M varying from Zn to Cd. However, among the different dinuclear phosphametallocenes with the same metal, the bonding energies of the M–M (or M–M′) bond and the M–ligand bonds increase as ligand varying from ($\eta^5$-$P_5$) to Cp.

The negative NICSs indicate that all dinuclear phosphametallocenes have aromaticity. The various dissected bond NICS contributions reveal that the NICS contributions of the metal–ligand bond, the metal–metal bond and the metal lone pair electrons to the overall aromaticity in the Zn-containing dinuclear phosphametallocenes are different from their counterpart contributions in the Cd-containing dinuclear phosphametallocenes, such difference causes that the overall NICSs of the Zn-containing dinuclear phosphametallocenes are more negative than that of the Cd-containing dinuclear phosphametallocenes.

## Acknowledgments

This research was supported by the National Nature Science Foundation of China (no. 20473031) and the Key Laboratory for Supramolecular Structure and Material of Jilin University. W. Q. T. thanks Japan Society for the Promotion of Science for financial support and is grateful to Professor Yuriko Aoki for her hospitality.

[1] I. Resa, E. Carmona, E. Gutierrez-Puebla, A. Monge, *Science* **2004**, *305*, 1136–1138.
[2] D. d. Río, A. Galindo, I. Resa, E. Carmona, *Angew. Chem. Int. Ed.* **2005**, *44*, 1244–1247.
[3] G. Parkin, *Science* **2004**, *305*, 1117–1118.
[4] A. Schnepf, H.-J. Himmel, *Angew. Chem. Int. Ed.* **2005**, *44*, 3006–3008.
[5] A. Schnepf, H.-J. Himmel, *Angew. Chem.* **2005**, *117*, 3066–3068.
[6] S. L. Richardson, T. Baruah, M. R. Pederson, *Chem. Phys. Lett.* **2005**, *404*, 141 –145.
[7] Y.-M. Xie, H. F. Schaefer III, R. B. King, *J. Am. Chem. Soc.* **2005**, *127*, 2818–2819.
[8] Z.-Z. Xie, W. H. Fang, *Chem. Phys. Lett.* **2005**, *404*, 212–216.
[9] H. Wang, Y.-M. Xie, R. B. King, H. F. Schaefer III, *J. Am. Chem. Soc.* **2005**, *127*, 11646–11651.
[10] Y.-M. Xie, H. F. Schaefer III, E. D. Jemmis, *Chem. Phys. Lett.* **2005**, *402*, 414–421.
[11] A. Y. Timoshkin, H. F. Schaefer, *Organometallics* **2005**, *24*, 3343–3345.
[12] H. S. Kang, *J. Phys. Chem. A* **2005**, *109*, 4342–4351.
[13] O. J. Scherer, T. Brück, *Angew. Chem. Int. Ed. Engl.* **1987**, *26*, 59–59.
[14] M. Baudler, S. Akpapoglou, H. Budzikiewicz, H. Münster, *Angew. Chem. Int. Ed. Engl.* **1988**, *27*, 280–281.
[15] P. H. Tracy, H. F. Schaefer III, *Angew. Chem. Int. Ed. Engl.* **1989**, *28*, 485–486.
[16] E. J. P. Malar, *J. Org. Chem.* **1992**, *57*, 3694–3698.
[17] A. Dransfeld, L. Nyulászi, P. v. R. Schleyer, *Inorg. Chem.* **1998**, *37*, 5600–5606.
[18] H.-J. Zhai, L.-S. Wang, A. E. Kuznetsov, A. I. Boldyrev, *J. Phys. Chem. A* **2002**, *106*, 5600–5606.
[19] E. J. P. Malar, *Eur. J. Inorg. Chem.* **2004**, 2723–2732.
[20] F. D. Proft, P. W. Fowler, R. W. A. Havenith, P. v. R. Schleyer, G. V. Lier, P. Geerlings, *Chem. Eur. J.* **2004**, *10*, 940–950.
[21] Q. Jin, B. Jin, G. W. Xu, W. Zhu, *J. Mol. Struct. (THEOCHEM.)* **2005**, *713*, 113–117.
[22] E. J. P. Malar, *Inorg. Chem.* **2003**, *42*, 3873–3883.
[23] Ê. D. V. Bruce, R. R. Willian, *Organometallics* **2004**, *23*, 5308–5313.
[24] J. A. Chamizo, M. R. Mazőn, R. Salcedo, R. A. Tosano, *Inorg. Chem.* **1990**, *29*, 879–880.
[25] R. F. Winter, W. E. Geiger, *Organometallics* **1999**, *18*, 1827–1833.
[26] F. G. N. Cloke, J. C. Green, J. R. Hanks, J. F. Nixon, J. L. Suter, *J. Chem. Soc., Dalton Trans.* **2000**, 3534–3536.
[27] M. Lein, J. Frunzke, A. Timoshkin, G. Frenking, *Chem. Eur. J.* **2001**, *7*, 4155–4163.
[28] J. Frunzke, M. Lein, G. Frenking, *Organometallics* **2002**, *21*, 3351–3359.
[29] V. M. Rayón, G. Frenking, *Chem. Eur. J.* **2002**, *8*, 4693–4707.
[30] A. R. Kudinov, D. A. Loginov, Z. A. Starikova, P. V. Petrovskii, M. Corsini, P. Zanello, *Eur. J. Inorg. Chem.* **2002**, 3018–3027.
[31] M. Lein, J. Frunzke, G. Frenking, *Angew. Chem. Int. Ed.* **2003**, *42*, 1303–1306.
[32] E. J. P. Malar, *Theor. Chem. Acc.* **2005**, *114*, 213–221.
[33] Z.-Z. Liu, W. Q. Tian, J.-K. Feng, G. Zhang, W.-Q. Li, *J. Phys. Chem. A* **2005**, *109*, 5645–5655.
[34] E. Urnėžius, W. W. Brennessel, C. J. Cremer, J. E. Ellis, P. v. R. Schleyer, *Science* **2002**, *295*, 832–834.

 © 2006 Wiley-VCH Verlag GmbH & Co. KGaA, Weinheim 

[35] M. Lein, J. Frunzke, G. Frenking, *Inorg. Chem.* **2003**, *42*, 2504–2511.
[36] U. Koch, P. L. A. Popelier, *J. Phys. Chem.* **1995**, *99*, 9747–9757.
[37] P. L. A. Popelier, *J. Phys. Chem. A* **1998**, *102*, 1873–1878.
[38] W. Chen, Z.-R. Li, D. Wu, Y. Li, C.-C. Sun, *J. Chem. Phys.* **2005**, *123*, 164306–164311.
[39] Gaussian NBO version 3.1: E. D. Glendening, A. E. Reed, J. E. Carpenter, F. Weinhold, Theoretical Chemistry Institute and Department of Chemistry, University of Wisconsin, **1990**.
[40] M. J. Frisch, G. W. Trucks, H. B. Schlegel, G. E. Scuseria, M. A. Robb, J. R. Cheeseman, J. A.Montgomery Jr, T. Vreven, K. N. Kudin, J. C. Burant, J. M. Millam, S. S. Iyengar, J. Tomasi, V. Barone, G. Cossi; Scalmani, N. Rega, G. A. Petersson, H. Nakatsuji, M. Hada, M. Ehara, K. Toyota, R. Fukuda, J. Hasegawa, M. Ishida, T. Nakajima, Y. Honda, O. Kitao, H. Nakai, M. Klene, X. Li, J. E. Knox, H. P. Hratchian, J. B. Cross, C. Adamo, J. Jaramillo, R. Gomperts, R. E. Stratmann, O. Yazyev, A. J. Austin, R. Cammi, C. Pomelli, J. W. Ochterski, P. Y. Ayala, K. Morokuma, G. A. Voth, P. Salvador, J. J. annenberg, V. G. Zakrzewski, S. Dapprich, A. D. Daniels, M. C. Strain, O. Farkas, D. K. Malick, A. D. Rabuck, K. Raghavachari, J. B. Foresman, J. V. Ortiz, Q. Cui, A. G. Baboul, S. Clifford, J. Cioslowski, B. B. Stefanov, G. Liu, A. Liashenko, P. Piskorz, I. Komaromi, R. L. Martin, D. J. Fox, T. Keith, M. A. Al-Laham, C. Y. Peng, A. Nanayakkara, M. Challacombe, P. M. W. Gill, B. Johnson, W. Chen, M. W. Wong, C. Gonzalez, J. A. Pople, *Gaussian 03*, Revision B.03, Gaussian, Inc., Pittsburgh PA, **2003**.
[41] G. Schaftenaar, J. H. J. Noordik, *J. Comput. Aided Mol. Des.* **2000**,*14*, 123.
[42] At present, some scientists differentiate the type of chemical bonds using the Laplacian of the electron density of the bond critical points (BCPs). For ionic bonds, hydrogen bonds, and van der Waals interactions, the Laplacian of the electron density $\nabla^2\rho(r)$ is positive, while the $\nabla^2\rho(r_{Ep-M})$ is negative for covalent bond. We think that the $\nabla^2\rho(r_{Ep-M})$ near to zero indicates both ionic bond and covalent bond.
[43] E. D. Jemmis, P. v. R. Schleyer, *J. Am. Chem. Soc.* **1982**, *104*, 4781.
[44] K. Jug, *J. Org. Chem.* **1983**, *48*, 1344–1348.
[45] A. R. Katritzky, K. Jug, D. C. Oniciu, *Chem. Rev.* **2001**, *101*, 1421–1449.
[46] P. v. R. Schleyer, C. Maerker, A. Dransfeld, H. Jiao, N. J. R. V. E. Hommes, *J. Am. Chem. Soc.* **1996**, *118*, 6317–6318.
[47] P. v. R. Schleyer, H.-J. Jiao, N. J. R. v. E. Hommes, V. G. Malkin, O. L. Malkina, *J. Am. Chem. Soc.* **1997**, *119*, 12669–12670.
[48] T. Heine, P. v. R. Schleyer, C. Corminboeuf, G. Seifert, R. Reviakine, J. Weber, *J. Phys. Chem. A* **2003**, *107*, 6470–6475.
[49] A. C. Tsipis, C. A. Tsipis, *J. Am. Chem. Soc.* **2003**, *125*, 1136–1137.
[50] P. v. R. Schleyer, B. Kiran, D. V. Simion, T. S. Sorensen, *J. Am. Chem. Soc.* **2000**, *122*, 510–513.
[51] E. D. Jemmis, P. v. R. Schleyer, *J. Am. Chem. Soc.* **1982**, *104*, 4781–4788.
[52] J. M. Mercero, J. M. Ugalde, *J. Am. Chem. Soc.* **2004**, *126*, 3380–3381.
[53] Z.-F. Chen, C. Corminboerf, T. Heine, J. Bohmann, P. v. R. Schleyer, *J. Am. Chem. Soc.* **2003**, *125*, 13930–13931.
[54] J. M. Mercero, J. M. Matxain, J. M. Ugalde, *Angew. Chem. Int. Ed.* **2004**, *43*, 5485–5488.
[55] S.-D. Li, J.-C. Guo, C.-Q. Miao, G.-M. Ren, *Angew. Chem.* **2005**, *117*, 2–5.
[56] S.-D. Li, J.-C. Guo, C.-Q. Miao, G.-M. Ren, *Angew. Chem. Int. Ed.* **2005**, *44*, 2158–2161.
[57] Ê. D. V. Bruce, W. Rocha, *Organometallics* **2004**, *23*, 5308–5313.
[58] Z.-Z. Liu, W. Q. Tian, J.-K. Feng, G. Zhang, W.-Q. Li, *J. Mol. Struct. (THEOCHEM)* **2006**, *758*, 127–138.
[59] P. v. R. Schleyer, M. Manoharan, Z.-X. Wang, B. Kiran, H. Jiao, R. Puchta, N. J. R. van Eikema Hommes, *Org. Lett.* **2001**, *3*, 2465–2468.

Received: December 26, 2005
Published Online: May 3, 2006

 © 2006 Wiley-VCH Verlag GmbH & Co. KGaA, Weinheim 

DOI: 10.1002/ejic.200600030

# Water-Soluble $Sal_2en$- and Reduced $Sal_2en$-Type Ligands: Study of Their $Cu^{II}$ and $Ni^{II}$ Complexes in the Solid State and in Solution

**Isabel Correia,[a] Agnes Dornyei,[b] Tamás Jakusch,[c] Fernando Avecilla,[d] Tamás Kiss,*[b,c] and João Costa Pessoa*[a]**

**Keywords:** Copper(II) / Nickel(II) / Reduced Schiff bases / Speciation / Crystal structure

The $Cu^{II}$ and $Ni^{II}$ complexes of the Schiff base $pyr_2en$ [*N*,*N*′-ethylenebis(pyridoxyliminato)] and reduced Schiff bases $Rpyr_2en$ [*N*,*N*′-ethylenebis(pyridoxylaminato)] and $R(SO_3$–sal$)_2en$ ($SO_3$–sal = salicylaldehyde-5-sulfonate) were prepared and characterized by elemental analysis, IR, UV/Vis, and EPR spectroscopy. The structure of $Ni(pyr_2en)\cdot 3H_2O$ was determined by single-crystal X-ray diffraction. The $pyr_2en^{2-}$ ligand is coordinated through two phenolate-O and imine-N atoms, in a distorted square-planar geometry. The complexation of $Cu^{II}$ and $Ni^{II}$ with $Rpyr_2en$ in aqueous solution is studied by pH-potentiometry, UV/Vis spectroscopy, as well as by EPR spectroscopy for the $Cu^{II}$ system, and $^1H$ NMR spectroscopy for the $Ni^{II}$ system. Complex formation constants were determined and binding modes proposed. While for the $Cu^{II}$ system all complexes present a 1:1 stoichiometry with different protonation states, for the $Ni^{II}$ system the 2:1 (L/M) complexes become important in the basic pH range at a higher ligand excess.
(© Wiley-VCH Verlag GmbH & Co. KGaA, 69451 Weinheim, Germany, 2006)

## Introduction

The application of Green Chemistry principles in organic transformations has attracted increased attention in the development of transition metal catalysts. $Sal_2en$-type ligands derived from *o*-hydroxyaldehydes and diamines are one of the most important ligand systems in asymmetric, homogeneous, and heterogeneous catalysis and in stereoselective synthesis.[1–5] Their transition metal complexes can be used in a large variety of applications, namely asymmetric ring opening of epoxides,[4] cyclopropanation,[6] and enantioselective epoxidation of olefins.[7] Their versatility and selectivity in chemical reactions is partly due to the ability of $sal_2en$-type ligands to complex a variety of transition metals in several oxidation states. They normally form square-pyramidal or octahedral complexes in which the four donor atoms coordinate in an almost planar fashion. Numerous $sal_2en$-type ligands have been synthesized and investigated, but most of them show low solubility in aqueous solution, which can be overcome by changing the diamine precursor and/or the ring substituents on the aldehyde.

In solution, Schiff base (SB) ligands have the disadvantage of the hydrolysis of the C=N bond, particularly in water-containing solvents. Reduction of the SB to give an amine may present interesting advantages. The reduced SBs (hereafter designated by $sal_2an$) are not so prone to hydrolysis and are more flexible and unrestrained to remain planar when coordinated to a metal center. Several $sal_2an$ complexes have been synthesized and characterized, namely with $Cu^{II}$,[8–10] $Co^{II}$,[8] $Ni^{II}$,[11] $VO^{IV}$,[12,13] $Fe^{III}$,[14] and $Zn^{II}$.[15] In the $Ni^{II}$ and $Co^{II}$ complexes the ligand coordinates in a slightly distorted square-planar geometry, and these complexes have shown the ability to interact with oxygen:[9,11] when dissolved in organic solvents these complexes can undergo oxidative dehydrogenation,[9,11] i.e. in the presence of $O_2$ one of the C–N bonds may be oxidized to an imine-type bond. This process has not been observed in most of the $Cu^{II}$ complexes, which are stable in organic solutions exposed to air.

One of the guidelines in Green Chemistry research is the elimination of hazardous solvents in reaction media. As mentioned above, $sal_2en$ complexes are frequently used as catalysts for several applications. As most $sal_2en$ complexes are not water soluble one of our objectives is the synthesis of water-soluble ligands and complexes.

In a previous work[12] we reported the preparation and characterization of the Schiff base *N*,*N*′-ethylenebis(pyridoxyliminato) ($pyr_2en$) and its reduced derivative *N*,*N*′-ethylenebis(pyridoxylaminato) ($Rpyr_2en$). Their $V^{IV}O$ and $V^{V}O_2$ complexes were characterized in the solid state and in

[a] Centro Química Estrutural, Instituto Superior Técnico, Av. Rovisco Pais, 1049-001 Lisboa, Portugal
[b] Department of Inorganic and Analytical Chemistry, University of Szeged, P. O. Box 440, 6701 Szeged, Hungary
[c] Bioinorganic Chemistry Research Group of the Hungarian Academy of Sciences, Department of Inorganic and Analytical Chemistry, University of Szeged, P. O. Box 440, 6701 Szeged, Hungary
[d] Departamento de Química Fundamental, Universidade da Coruña, Campus de A Zapateira, 15071 A Coruña, Spain
Supporting information for this article is available on the WWW under http://www.eurjic.org or from the author.

 © 2006 Wiley-VCH Verlag GmbH & Co. KGaA, Weinheim 

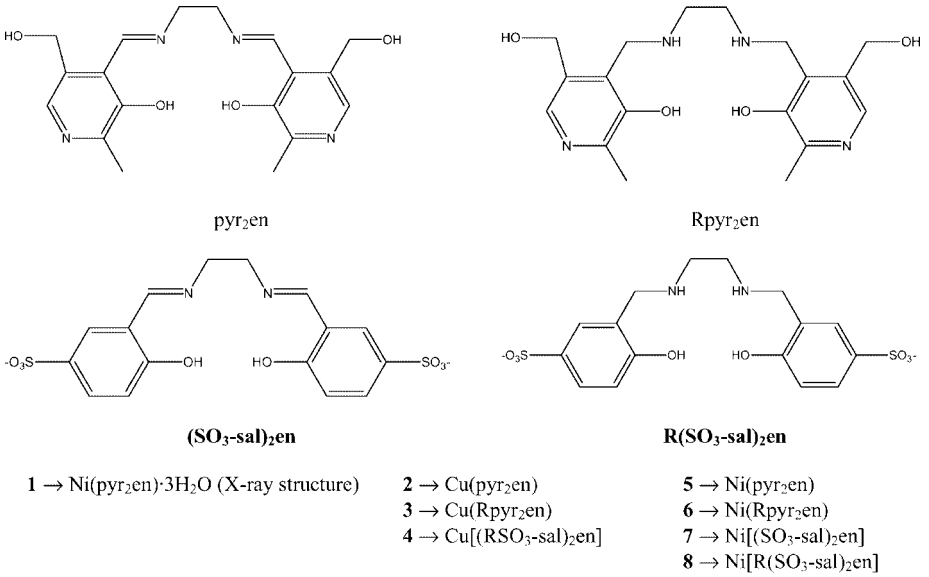


**1** → Ni(pyr$_2$en)·3H$_2$O (X-ray structure)
**2** → Cu(pyr$_2$en)
**3** → Cu(Rpyr$_2$en)
**4** → Cu[(RSO$_3$-sal)$_2$en]
**5** → Ni(pyr$_2$en)
**6** → Ni(Rpyr$_2$en)
**7** → Ni[(SO$_3$-sal)$_2$en]
**8** → Ni[R(SO$_3$-sal)$_2$en]

Scheme 1. Structural formulae of the prepared complexes. The complex characterized by single-crystal X-ray diffraction is indictaed.

solution. The molecular structure of two dioxovanadium(V) complexes with this reduced SB evidenced the tetradentate binding mode and the flexibility of the Rpyr$_2$en when coordinated to the metal ion. The solution studies showed that Rpyr$_2$en forms much more stable complexes with $V^{IV}$ and $V^{V}$ than the corresponding Schiff base pyr$_2$en, and that the SB has a much higher tendency to hydrolyze in aqueous solution. This is reflected in the proton displacement constants ($K$*), characteristic for the formation equilibrium: $H_6L + V^{IV}O^{2+} \leftrightarrows [V^{IV}OLH_2]^{2+} + 4H^+$; the log$K$* values are –14.1 and –5.63 for pyr$_2$en and Rpyr$_2$en, respectively.[12] Similar results were obtained for (SO$_3$–sal)$_2$en and R(SO$_3$–sal)$_2$en with their vanadium complexes.[16]

In this work we report on the preparation of several new moderately water-soluble $Cu^{II}$ and $Ni^{II}$ complexes (the ligands and formula names are shown in Scheme 1), one of them characterized by single-crystal X-ray diffraction. We also report on the solution study of the reduced SB Rpyr$_2$en with $Cu^{II}$ and $Ni^{II}$ by pH-potentiometry, visible absorption (Vis), EPR ($Cu^{II}$), and $^1$H NMR ($Ni^{II}$) spectroscopy.

## Results and Discussion

### Synthesis and Characterization of the Solid Compounds

Sal$_2$en-type ligands were prepared by the condensation of ethylenediamine with the aldehyde derivative. Reduction with NaBH$_4$ yielded the reduced SB.[12,16] From solutions containing $Ni^{II}$ and Rpyr$_2$en, orange crystals of the SB complex Ni(pyr$_2$en)·3H$_2$O were obtained. This implies that the two amine bonds underwent dehydrogenation. The solid-state characterization of all complexes was done by taking into account that this process might also have occurred with the other metal complexes. For the Rpyr$_2$en complexes the characterization (elemental analysis, IR, and UV/Vis spectroscopy) is consistent with a formulation of M(Rpyr$_2$en) (M = $Ni^{II}$ or $Cu^{II}$). Complex K$_2${Ni[R(SO$_3$–sal)$_2$en]}, although it was characterized and is included here, is not stable; its color changes from grey, immediately after the synthesis, to soft pink, and after a week to brown. The ESI mass spectrum, measured for solutions of the pink solid, confirms the presence of the reduced Schiff base showing important peaks that can be assigned to [NiL + 2K + 1]$^+$ ($m/z$ = 565) and [NiL + 3K]$^+$ ($m/z$ = 603).

### X-ray Diffraction Studies

#### *Ni(pyr$_2$en)·3H$_2$O (1)*

Figure 1 includes an ORTEP representation of the molecular structure of Ni(pyr$_2$en)·3H$_2$O (**1**), and Table 1 shows selected bond lengths and angles. The molecule is neutral with both pyridinic nitrogens deprotonated, and the ligand coordinates the Ni atom through two phenolate oxygen ($O_{phenolate}$) and two imine nitrogen ($N_{imine}$) atoms. The geometry around the metal ion is distorted square planar, and there are three water molecules in the asymmetric unit (not shown). The planar arrangement Ni(ONNO) is slightly distorted due to the *cis*/*trans* angles, which are not 90° and 180°. The *cis* and *trans* angles are 84.2 and 94.8°, and 178.4 and 178.5°, respectively. The ligand forms a set of chelate rings of (6+5+6)-members, and the highest deviation from planarity is found in the ring defined by Ni(1)–N(1)–C(2)–C(1)–N(2), which has an rms value of 0.1074(75) Å (the others are less than 0.05 Å). It is noteworthy that the torsion angle between the N(1)–C(2)–C(1)–N(2) atoms is only 29.24(1.71)°, lower than those previously observed in this type of complexes.[17] The pyridoxal rings are planar, with rms values of 0.0172(63) and 0.0127(58) Å.

The Ni–O and Ni–N bond lengths are similar and in the usual range found for $Ni^{II}$–sal$_2$en-type complexes.[11,18–21] The C–O distances are also typical for this type of ligands,[9,11,19–21] and the C=N bonds show double bond character with distances of ca. 1.3 Å. After coordination to

 © 2006 Wiley-VCH Verlag GmbH & Co. KGaA, Weinheim 

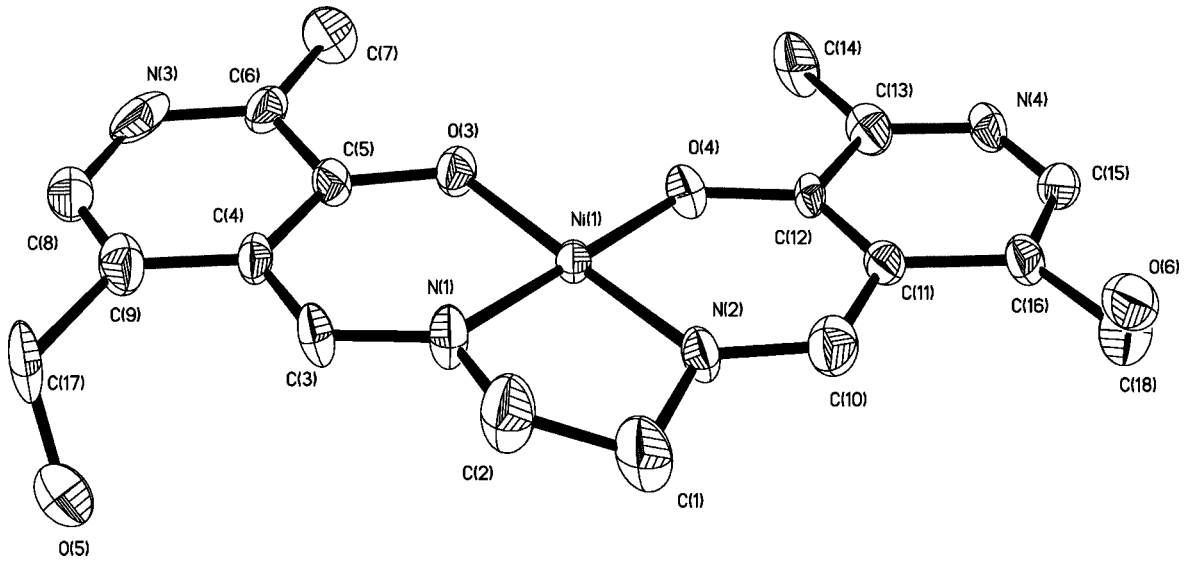


Figure 1. ORTEP diagram of $Ni(pyr_2en)\cdot 3H_2O$ (**1**) showing the atom labeling scheme. The thermal ellipsoids were drawn at the 30% probability level. The water molecules were omitted for clarity.

Table 1. Selected bond lengths [Å] and angles [°] for complex $Ni(pyr_2en)\cdot 3H_2O$ (**1**).

| Bond lengths [Å] | | Bond angles [°] | |
|---|---|---|---|
| Ni(1)–O(3) | 1.838(5) | O(3)–Ni(1)–O(4) | 84.2(3) |
| Ni(1)–O(4) | 1.842(5) | O(3)–Ni(1)–N(1) | 94.4(3) |
| Ni(1)–N(1) | 1.849(7) | O(4)–Ni(1)–N(1) | 178.5(3) |
| Ni(1)–N(2) | 1.821(7) | O(3)–Ni(1)–N(2) | 178.4(3) |
| O(3)–C(5) | 1.310(10) | O(4)–Ni(1)–N(2) | 94.8(3) |
| O(4)–C(12) | 1.328(9) | N(1)–Ni(1)–N(2) | 86.7(3) |
| N(2)–C(1) | 1.455(12) | | |
| N(2)–C(10) | 1.308(11) | | |
| N(1)–C(2) | 1.451(12) | | |
| N(1)–C(3) | 1.262(10) | | |

the metal ion the ligand does not undergo a significant change in the $C–O_{phenolic}$ and $C–N_{imine}$ bond lengths: the C–O bonds decrease by 0.034 Å and the C=N bonds increase by 0.035 Å.[12] In the complex the $HO–(CH_2)–$ groups of the pyridoxal rings are perpendicular to the apparent molecular plane, in an *anti* position to each other. This results in a three-dimensional crystalline structure connected by H bonds. ESI-1 shows the crystalline packing and emphasizes the intermolecular bonds. The molecular planes are approximately parallel, but overlaid in an alternate manner; this is probably because of the *anti* position of the hydroxy groups. The distance between neighboring Ni atoms is between 6.381 and 8.268 Å.

### Infrared Spectroscopy

Table 2 contains selected IR bands of the complexes. The assignment was based on data from refs.[22–25] and by comparison with the spectra of the ligands.[12] All complexes present broad bands in the 2400–3600 $cm^{-1}$ range, which correspond to the stretching vibration (symmetric and antisymmetric) of the $CH_2O–H$ groups of the pyridoxal rings (for the $Rpyr_2en$ complexes) and to the water molecules. The weak $\nu$(N–H) band that emerged from the broad band at 3286 $cm^{-1}$ in $Rpyr_2en$[12] appears in the complexes at lower wavenumbers, in agreement with the coordination through the $N_{amine}$ groups. The $\nu(C–O)_{phenolate}$ band appears in the normal range for these types of complexes.[23,26] The strong $\nu$(C=N) band of complex $Cu(pyr_2en)$ is assigned to the band at 1635 $cm^{-1}$, at a higher wavenumber than the ligand (1626 $cm^{-1}$),[12] and no such band is seen in the IR spectrum of $Cu(Rpyr_2en)$. Similarly, while the $\nu$(C=N) band of $Ni(pyr_2en)$ appears at ca. 1620 $cm^{-1}$, no band is seen in the IR spectrum of $Ni(Rpyr_2en)$, which might be assigned to this vibration. Complex $Ni[(SO_3–sal)_2en]$ presents a very

Table 2. Selected IR [$cm^{-1}$] and UV/Vis absorption bands of the prepared complexes.

| | FT-IR $\nu(N–H)_{stretch}$ | $\nu$(C=N) | $\nu(C–O)_{phenolate}$ | $\nu$(O–H) | UV/Vis Solvent | $\lambda_{max}$ [nm] ($\varepsilon$ [$M^{-1}\,cm^{-1}$]) |
|---|---|---|---|---|---|---|
| **1** | – | 1618 (s) | 1197 (m) | broad band at 3600–2900 | DMSO | 360 (8000), 426 (5000) |
| **2** | – | 1635 (s) | 1207 (m) | broad band centered at 3400 | DMSO | 260 sh (9100), 280 (11800), 380 (10000), 580 (345) |
| **3** | 3285 (w) | – | 1244 (m) | broad band at 3600–2900 | DMSO | 260 (10000), 310 (11000), 355 sh (1660), 625 (318) |
| **4** | several bands | – | 1182 (s) | broad band at 3600–2900 | $H_2O$ | 420 sh (260), 635 (83) |
| **5** | – | 1620 (s) | 1204 (s) | broad band at 3600–2800 | DMSO | 265 (24000), 275 sh (21750), 360 (8500), 427 (5300) |
| **6** | 3385 (w) | – | 1250 (m) | broad band at 3600–2800 | DMSO | 263 (27300), 315 (10500), 495 (542) |
| **7** | – | 1609 (s) | 1204 (s) | broad band centered at 3350 | $H_2O$ | 296 sh (7500), 384 (4600), 416 sh (2500) 508 sh (150) |
| **8** | 3271 (w, br) | – | 1185 (s) | broad band at 3600–2900 | $H_2O$ | 254 (18700), 328 sh (557), 378 sh (325), 450 sh (77) |

 © 2006 Wiley-VCH Verlag GmbH & Co. KGaA, Weinheim 

strong band at 1609 $cm^{-1}$ assigned to $\nu$(C=N). This band is absent in the corresponding reduced SB complex Ni[R($SO_3$–sal)$_2$en], which presents bands at 1593 and 1639 $cm^{-1}$, assigned to aromatic =C–H and C=C stretching vibrations.

### UV/Vis Absorption Spectroscopy

The UV/Vis spectra were recorded over the 250–900 nm range in DMSO or water. The results are summarized in Table 2. Some of the intense bands at low wavelengths ($\lambda <$ 400 nm) are assigned to charge transfer (CT), imine π-π* (when appropriate), and intramolecular transitions in the aromatic rings. In the visible range ($\lambda >$ 420 nm) the bands are predominantly due to d-d transitions. The copper complexes **2**–**4** have one well-defined broad d-d band at $\lambda_{max}$ = 550–650 nm, and stronger bands at ca. $\lambda$ = 380–420 nm from the $Cu^{II} \rightarrow$ phenolate (π*) transitions [and also imine π-π* in the case of Cu(pyr$_2$en)], which is in agreement with that expected for tetrahedrally distorted square-planar complexes of the $CuO_2N_2$ type.[27,28] The $Ni^{II}$ complexes **5**–**8** have low intensity broad bands in the 400–550 nm range, assigned to transitions from the four low-lying d orbitals to the σ antibonding $d_{x^2-y^2}$ orbital. At higher energies ($\lambda <$ 400 nm) a group of high intensity bands appears, and in the case of Ni(pyr$_2$en) and Ni[($SO_3$–sal)$_2$en] relatively intense bands from the imine π-π* transition also show up. The UV/Vis data of the complexes in DMSO are in agreement with that expected for $Ni^{II}$ and $Cu^{II}$ complexes with square-planar geometries.[9,10,27] The relatively high $\varepsilon$ values of the d-d bands of the Ni complexes suggest some borrowing of intensity from CT bands and/or a significant distortion of the coordination geometry.

### EPR Spectroscopy

The EPR spectra of the $Cu^{II}$ complexes were measured in "frozen" ($T \approx$ 77 K) solutions of an adequate solvent. The spectrum of Cu(pyr$_2$en) in DMSO showed a broad band centered at $g$ = 1.995 without hyperfine structure. This is probably because of molecular aggregation during the freezing process. No signal was detected at $g$ = 4.

The EPR spectrum of Cu(Rpyr$_2$en) was measured in water and DMSO at 77 K. Both show well-resolved hyperfine structure and suggest axial symmetry. The spin Hamiltonian parameters were obtained by computer simulation of the experimental spectra using a program from Rockenbauer and Korecz.[29] Among other factors, the $g_\parallel$ and $A_\parallel$ values depend on the nature of the donor atoms and can be used to confirm the binding mode. The parameters (DMSO: $g_\perp$ = 2.047, $A_\perp = 22.2\times10^{-4}$ $cm^{-1}$, $g_\parallel$ = 2.233, $A_\parallel = 197.3\times10^{-4}$ $cm^{-1}$; $H_2O$: $g_\perp$ = 2.052, $A_\perp = 38.4\times10^{-4}$ $cm^{-1}$, $g_\parallel$ = 2.237, $A_\parallel = 193.5\times10^{-4}$ $cm^{-1}$) fit well with that expected for a $N_2O_2$ binding mode.[30] On the other hand, the $g_\parallel/A_\parallel$ ratio of 113 in DMSO and 116 in $H_2O$ indicates a square-planar coordination environment.[30] In the spectrum of Cu(Rpyr$_2$en), dissolved in water, superhyperfine structure is observed in the perpendicular region of the spectrum, arising from the interaction of the $Cu^{II}$ unpaired electron with the two nitrogen donor atoms of the ligand, which results in a five line splitting ($A_N = 10.5\times10^{-4}$ $cm^{-1}$).

In the EPR spectrum of Cu[R($SO_3$–sal)$_2$en], dissolved in $H_2O$, more than one species is present. Observation of the low-field range and comparison with the EPR spectrum of $[Cu(OH_2)_6]^{2+}$ in the same solvent, shows that part of the ligand was removed from the coordination sphere of the metal ion upon dissolution and that some free $Cu^{2+}$ is present in solution (see ESI-2). Since the simulation of such $Cu^{II}$ spectra with more than one species is difficult, only an estimate of the parameters for the complex was obtained: $g_\parallel$ = 2.25 and $A_\parallel = 189\times10^{-4}$ $cm^{-1}$. The $g_\parallel/A_\parallel$ ratio (119) also indicates a square-planar geometry for this complex.[30] These parameters are similar to those obtained for other $Cu^{II}$–sal$_2$an complexes, which present square-planar geometry and a $N_2O_2$ coordination mode.[8]

### Study of the Oxidative Dehydrogenation Process of Ni(Rpyr$_2$en)

Some $Ni^{II}$ complexes with the sal$_2$an-type ligands are able to react with dissolved $O_2$.[9,11] In solutions of organic solvents the complexes undergo oxidative dehydrogenation, and one of the two C–N bonds dehydrogenates yielding a C=N bond. Further dehydrogenation of the second C–N bond has not been previously observed.[9,11] Since crystals of Ni(pyr$_2$en) (**1**) were obtained from the filtrate solution of the Ni(Rpyr$_2$en) synthesis, we might expect that in the present system the dehydrogenation is complete. To further investigate the process, complex Ni(Rpyr$_2$en) was dissolved in DMSO and air was bubbled through the stirred solution over a period of three days; the initial pink solution slowly became orange. Another identical solution was saturated with $N_2$; it also became progressively orange but at a much slower rate. The process was monitored by UV/Vis spectroscopy and Figure 2 shows the spectra recorded for both solutions. Initially there is an isosbestic point at ca. 510 nm, indicating the transformation of the reduced SB complex into another species, but it is quite clear that the final product is not Ni(pyr$_2$en) (its spectrum is included in the figure for comparison). The spectrum of the final product obtained in solution has similar features to those reported for $Ni^{II}$ complexes of half dehydrogenated complexes:[9,11] two new bands develop at 390 and 460 nm.

$^1$H NMR spectra of complexes Ni(Rpyr$_2$en) and Ni(pyr$_2$en) were measured in $(CD_3)_2SO$. The spectrum of Ni(pyr$_2$en) did not change over 24 hours, and all peaks could be easily assigned (see Experimental Section), while after 24 hours the spectrum of Ni(Rpyr$_2$en) showed features corresponding to two compounds [half dehydrogenated complex and Ni(Rpyr$_2$en)], indicating that the complex suffered partial dehydrogenation at only one of its amine bonds.

 © 2006 Wiley-VCH Verlag GmbH & Co. KGaA, Weinheim 

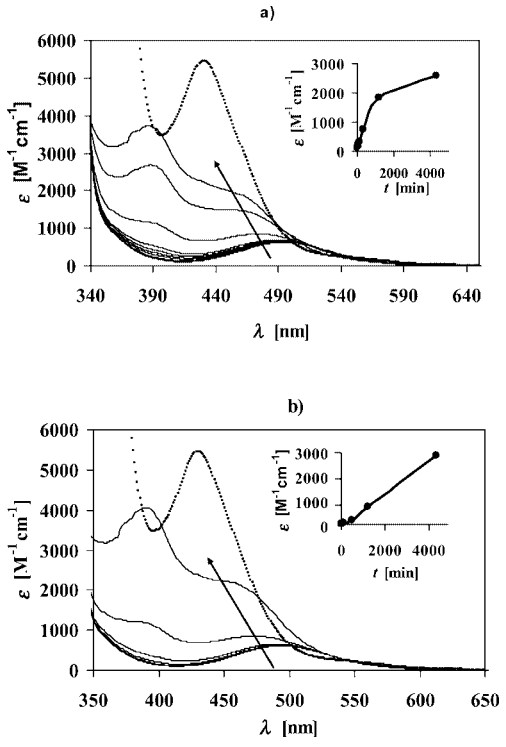


Figure 2. Time-dependence of the UV/Vis spectra of solutions containing Ni(R$pyr_2$en) in DMSO: (a) Bubbling air through the solution; (b) Under $N_2$ atmosphere. Insets: variation of the molar absorptivity at 412 nm. The arrows indicate increasing time (from 0 to 3 d). The spectrum of Ni($pyr_2$en) in DMSO (dotted) is included in both figures for comparison.

## Speciation Studies

The acid-base behavior of $pyr_2$en, R$pyr_2$en, and R($SO_3$–sal)$_2$en and their complexation with $V^{IV}$ and $V^{V}$ were previously reported.[12,16] The study of the $Cu^{II}$– and $Ni^{II}$–R$pyr_2$en systems by pH-potentiometry, Vis, EPR (for the $Cu^{II}$ system), and $^1$H NMR (for the $Ni^{II}$ system) spectroscopy is now presented.

### *$Cu^{II}$–R$pyr_2$en*

The pH-metric titration curves were measured between pH 2 and 11.3, and the best equilibrium model that fitted the experimental data corresponds to a model similar to that obtained for the $V^{IV}O$ system.[12] The stability constants are listed in Table 3 and a species distribution diagram is depicted in Figure 3 (a).

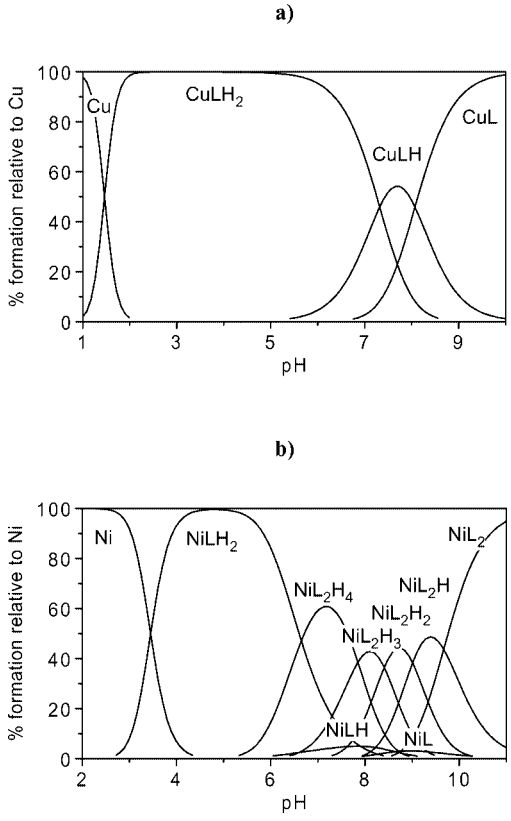


Figure 3. Species distribution diagram for the complexes formed in the (a) $Cu^{II}$–R$pyr_2$en system for solutions containing $C_{Cu}$ = 2.0 mmol dm$^{-3}$ and a L/M ratio of 2; (b) $Ni^{II}$–R$pyr_2$en system for solutions containing $C_{Ni}$ = 3.0 mmol dm$^{-3}$ and a L/M ratio of 4.

Analysis of the potentiometric data with the PSEQUAD program[31] shows the presence of only 1:1 complexes in solution over the whole pH range, in various protonation states. In the pH range 1–10 stoichiometries $[CuLH_2]^{2+}$, $[CuLH]^{+}$, and [CuL] are formed, with the deprotonations taking place at the N-pyridine atoms of the pyridoxal rings.

Table 3. Protonation and formation constants for the $M_pL_qH_r$ species formed in the $Cu^{II}$- and $Ni^{II}$-R$pyr_2$en systems, calculated from the pH-potentiometric and spectrophotometric data (EPR and UV/Vis) with the PSEQUAD program.[31]

| | $\log\beta_H$ (L = R$pyr_2en^{2-}$)[a] [12] | $\log\beta_H$[d] (L = pyrN$^-$) | | $\log\beta$ ($Cu^{II}$)[c] (L = R$pyr_2en^{2-}$) | $\log\beta$ ($Cu^{II}$)[d] (L = pyrN$^-$) | $\log\beta$ ($Ni^{II}$)[a] (L = R$pyr_2en^{2-}$) | $\log\beta$ ($Ni^{II}$)[d] (L = pyrN$^-$) |
|---|---|---|---|---|---|---|---|
| HL | 10.50 ± 0.01 | 10.41 | $MLH_2$ | 35.3 ± 0.3[c] | 21.34 | 28.52 ± 0.01 | – |
| $H_2L$ | 19.65 ± 0.01 | 18.56 | MLH | 28.04 ± 0.02 | 17.22 | 20.62 ± 0.02 | 14.20 |
| $H_3L$ | 27.33 ± 0.01 | 22.06 | ML | 19.98 ± 0.02 | 10.80 | 11.98 ± 0.02 | 6.46 |
| $H_4L$ | 33.30 ± 0.01 | | $ML_2H_4$ | – | – | 51.44 ± 0.03 | – |
| $H_5L$ | 36.31 ± 0.02 | | $ML_2H_3$ | – | 38.91 | 43.59 ± 0.04 | – |
| $H_6L$ | 38.60 ± 0.02 | | $ML_2H_2$ | – | 32.53 | 35.18 ± 0.04 | 28.14 |
| | | | $ML_2H$ | – | 25.46 | 26.17 ± 0.03 | – |
| | | | $ML_2$ | – | 17.47 | 16.50 ± 0.03 | 10.52 |
| | | | fitting[b] | $3.9 \times 10^{-3}$ [c] | | $3.0 \times 10^{-3}$ | |
| | | | no. of points | 244 | | 651 | |

[a] Three times the standard deviations (3×S.D.) of the calculations are included. [b] The average difference between the calculated and the experimental titration curves expressed in mL of titrant. The total initial volumes were 25 mL. [c] The S.D. values reflect the different calculated values from the pH-potentiometric and the spectroscopic data. [d] From ref.[32] ($I$ = 0.15 M $NaNO_3$; 37 °C).

 © 2006 Wiley-VCH Verlag GmbH & Co. KGaA, Weinheim 

The stability of the complexes is high, and even at pH 2 the amount of $[Cu(OH_2)_6]^{2+}$ is very small.

The Vis spectra for this system as the pH is varied (Figure 4) consists of a broad band (of d-d origin) with a maximum around 625 nm ($\varepsilon \approx 200$ mol dm$^{-3}$ cm$^{-1}$ at pH = 6.0). Deprotonation of the pyridine nitrogen atoms causes significant changes in the UV/Vis spectra: the d-d transition shifts to a higher energy as the pH is increased and the shoulder at ca. 420 nm (ascribed to phenolate → $Cu^{II}$ CT transition) shows a bathochromic effect with increasing pH. These shifts demonstrate that the pyridoxal ring forms a connected electron system and thus deprotonation of the pyridine-NH groups will influence the donor properties of the phenolate oxygen atoms.

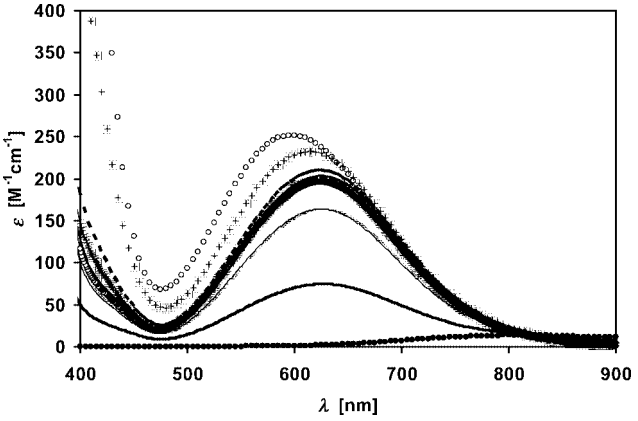


Figure 4. Visible spectra of aqueous solutions containing $Cu^{II}$ and $Rpyr_2en$, with $C_{Cu}$ = 5 mmol dm$^{-3}$ and a L/M ratio of 1 at several pH values. Below pH 2 the solutions were individually prepared and the $[H^+]$ was determined from a calibration curve (see Exp. Sect.). $[Cu(OH_2)_6]^{2+}$ (···), pH = 1.29 (——), 1.60 (——), 6.64 (---), 7.71 (+++), 10.56 (○). The superimposed spectra correspond to pH values in the pH range 2.2–6.0.

EPR spectra of samples containing $C_{Cu}$ = 5 mM and a L/M ratio of 1.1 at several pH values were measured at room temperature and 77 K. The parameters are collected in Table 4, and Figure 5 shows a few of the spectra obtained at room temperature. The frozen solution spectra (data not shown) show axial symmetry with resolved hyperfine structure, supporting the tetradentate binding of the ligand. For pH > 3 the spin Hamiltonian parameters do not show significant variation, confirming that the coordination mode for complexes $CuLH_2$, CuLH, and CuL is the same ($N_2O_2$),[30] that the deprotonation processes $[CuLH_2]^{2+} \rightarrow [CuLH]^+ \rightarrow [CuL]$ involve only the $NH^+_{pyridinic}$ groups of the ligand (these are not involved in the coordination), and that the coordination geometry is square planar.

It is clear from the speciation (Figure 3, a) and spectroscopic data (Figures 4 and 5) that for pH < 2 a significant amount of $Cu^{II}$ is already complexed by the ligand, and that the relevant data for calculation of the $\log\beta_{112}$ value occurs at pH ≤ 2. The visible absorption and room temperature EPR spectra were used to confirm the calculated stability constant obtained for $[CuLH_2]^{2+}$ and the proposed speciation model. The molar fraction of each species, obtained from both the EPR and visible absorption data for

Table 4. Spin Hamiltonian parameters for the $Cu^{II}$–$Rpyr_2en$ system obtained by computer simulation of the experimental spectra.[29]

| | $g_o$[a] | $A_o$ [×10$^4$cm$^{-1}$][a] | | |
|---|---|---|---|---|
| $[Cu(H_2O)_6]^{2+}$ | 2.196 | 32.7 | | |
| $CuLH_x$ [c] | 2.112 | 77.4 | | |
| | $g_\perp$[b] | $A_\perp$ [×10$^4$ cm$^{-1}$][b] | $g_\parallel$[b] | $A_\parallel$ [×10$^4$ cm$^{-1}$][b] |
| $[Cu(H_2O)_6]^{2+}$ | 2.082 | 1.8 | 2.417 | 133.1 |
| $CuLH_x$ [c] | 2.050 | 24.9 | 2.238 | 191.7 |

[a] Parameters obtained from spectra measured at room temperature. [b] Parameters obtained from spectra measured at 77 K (liquid nitrogen temperature). [c] $x$ = 0, 1, 2.

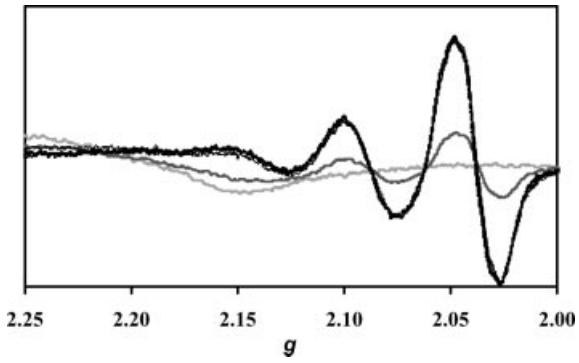


Figure 5. EPR X-band spectra (room temperature) of solutions containing $Cu^{II}$ and $Rpyr_2en$ with $C_{Cu}$ = 5 mmol dm$^{-3}$ and a L/M ratio of 1.1 at several pH values. $[Cu(OH_2)_6]^{2+}$ (light gray) and pH = 1.3 (dark gray). The superimposed black lines correspond to spectra measured at pH 1.6, 2.19 and 6.0.

pH ≤ 2 were introduced into the PSEQUAD program,[31] and a $\log\beta_{112}$ value of 35.64 ± 0.12 was refined for $CuLH_2$. On the other hand, from the pH-potentiometry data a $\log\beta_{112}$ = 35.01 ± 0.01 was obtained from data in the pH range 1.7–11, but varying the $\log\beta_{112}$ in the range 35.0–35.7 hardly affects the fitting parameter of the PSEQUAD program when using only the pH-metric data. The difference may be due to (i) the ionic strength, which was not exactly constant in the spectroscopic experiments at pH ≤ 2 and (ii) the higher error associated with the pH-metric data used in the pH range 1.7–2.0. The $\log\beta_{112}$ presented in Table 3 is the average of both values and the corresponding S.D. value reflects the different calculated values.

It should be emphasized that in complexes with the $sal_2an$ ligands, once each of the $N_{amine}$ atoms coordinates they become a stereogenic centers and *R* and *S* configurations become possible. Therefore, for each of the stoichiometries $MLH_2$, MLH, and ML at least three diastereoisomers are possible. These diastereoisomers are schematically represented by the configuration of the coordinated amine i.e. (*R*,*R*), (*S*,*S*), (*S*,*R*), or (*R*,*S*). Only for the MLH stoichiometry does the complex represented by (*S*,*R*) differ from (*R*,*S*). As found by DFT calculations for the $V^{IV}O$– and $V^{V}O_2$–$Rpyr_2en$ complexes,[12] the energies of the (*S*,*R*) and (*R*,*S*) diastereoisomers do not differ much from (*R*,*R*) or (*S*,*S*) (for this pair they are the same), and we predict that in solution all of them should form. With the techniques used

 © 2006 Wiley-VCH Verlag GmbH & Co. KGaA, Weinheim 

in this work it is not possible to distinguish between these different diastereoisomers.

Pyridoxamine (pyrN) is a vitamin $B_6$ analog and $Rpyr_2en$ can be seen as two pyridoxamine molecules linked by an ethylene bridge. The acid-base behavior and complexation of pyrN with $Cu^{II}$ and $Ni^{II}$ has been reported[32] and the data ($I$ = 0.15 M $NaNO_3$, 37 °C) is included in Table 3 for comparison. PyrN forms complexes with $Cu^{II}$ with the stoichiometry 1:1 and 2:1 (L/M) in various protonation states. The stability of the complexes formed in both ligand systems can be compared based on the constants ($\log K^*$) for the displacement of four protons: $H_6L + Cu^{2+} \leftrightarrows CuLH_2 + 4H^+$ (for $Rpyr_2en$), and $2H_3L + Cu^{2+} \leftrightarrows CuL_2H_2 + 4H^+$ (for pyrN). The $\log K^*$ values are –3.3 and –11.6, respectively. As expected, because of the chelate effect, the stability of the $Rpyr_2en$-$Cu^{II}$ complexes is much higher than that of the corresponding pyridoxamine complexes.

### *$Ni^{II}$–$Rpyr_2en$*

In equimolar solutions slow processes take place at pH > 8, and precipitation of a pink complex occurs. However, for solutions with L/M ratios greater than 1 the pH-metric titration curves could be measured up to 11.7. The model that best fitted the experimental data was obtained considering the formation of 1:1 and 2:1 complexes. Without bis complexes the fitting parameter of PSEQUAD was ca. five times higher. The stability constants obtained are listed in Table 3, and Figure 3b depicts a species distribution diagram.

As is usually the case for $Ni^{II}$ complexes the large zero-field splitting precluded the observation of any X-band resonances.[33] Although samples were measured by EPR spectroscopy, we were not able to obtain any EPR spectra. Moreover, $^1H$ NMR titrations carried out in $D_2O$ with L/M ratios of 1 and 4 confirmed that the $Ni^{II}$ complexes are paramagnetic. In fact, in solutions with a L/M ratio of 1, no $^1H$ NMR peaks were observed for pH > 3, where only metal bound ligand is present, while for pH < 3 only the peaks from the noncomplexed ligand are seen. In solutions with a L/M ratio of 4 only the free ligand peaks were observed, and for pH > 3 their areas decrease (when compared with the peak of the internal reference).

Spectroscopic data for solutions of complexes Cu($Rpyr_2en$) or Ni($Rpyr_2en$) in DMSO are consistent with a square-planar coordination of the $Rpyr_2en$ ligand. In water the spectroscopic data of Ni($Rpyr_2en$) is consistent with an octahedral geometry involving the donor set: $O_{phen}$, $N_{amine}$,$N_{amine}$,$O_{phen}$,$O_w$,$O_w$ ($O_{phen}$ = phenolate-$O^-$ donor atom, $N_{amine}$ = amine-N donor atom, $O_w$ = water-O atom).

In aqueous solutions containing $Ni^{II}$ and $Rpyr_2en$ the situation is more complex. To confirm the pH-metric results and the presence of the bis complexes, spectrophotometric measurements were carried out with L/M ratios of 1 and 4. Upon changing the pH the spectra show a continuous change, indicating that the speciation is much more complex than that for the $Cu^{II}$ system. Below pH 3 (Figure 6, a) the spectra present two d-d bands in the wavelength range shown, with maxima at ca. 725 and 395 nm, which can be assigned to the $[Ni(H_2O)_6]^{2+}$ transitions $^3T_{1g}(F) \leftarrow {}^3A_{2g}$ and $^3T_{1g}(P) \leftarrow {}^3A_{2g}$, respectively.[34] As the pH is increased stronger bands progressively build up. At pH 5.0, where species $NiLH_2$ is ca. 100% formed, the $\lambda_{max}$ are at 620 and 430 nm, and the latter transition [$^3T_{1g}(P) \leftarrow {}^3A_{2g}$, using the notation for an octahedral symmetry] overlapping the $O_{phen}$–Ni CT band tailing in from the UV region. Spectra were also measured for pH > 3 in the near IR range (see Supporting Information, Figure SI-7 in ESI-3), which show the presence of a broad band at ca. 995 nm ($\varepsilon$ = 18 mol dm$^{-3}$ cm$^{-1}$ at pH = 6.7), confirming the octahedral geometry of the complexes. This band, assigned to $^3T_{2g} \leftarrow {}^3A_{2g}$, gives a measure of the ligand field and shifts to higher energies between pH 3 and 6, confirming the increase in the field strength as the ligand replaces water in the $Ni^{II}$ coordination sphere. For solutions with a L/M ratio of 4 (Figure 6, b), the spectral features are the same as for L/M = 1 up to pH ca. 6, but above this pH the changes in the Vis spectra, upon increasing the pH, differ. With solutions containing L/M ratios of 4 no precipitation is observed below pH ca. 9.5, but at higher pH values a slight increase in the baseline suggests the presence of a small amount of precipitate. In the pH range 7.0–8.7, and for solutions with L/M = 4 (Figure 6, b), the spectra roughly intersect at 425 and 475 nm (not exactly isosbestic points) indicating the presence of two main types of species in equilibrium (between 1:1 and 2:1 complexes). Overall the Vis spectra confirm the species distribution diagram shown in Figure 3 (b).

ESI mass spectra were also measured to confirm the presence of the 2:1 (L/M) species. For aqueous solutions containing L/M = 1, $C_{Ni} \approx 1$ mM and pH = 5.3 several species were found in solution: $m/z$ = 363.5 $[L + 1]^+$, 419.3 $[NiL + 1]^+$, 455.0 $[NiL + 2H_2O]^+$, 781.0 $[NiL_2 + 1]^+$. For solutions containing L/M = 4, $C_{Ni} \approx 1$ mM and pH = 7.1: $m/z$ = 363.1 $[L + 1]^+$, 385.1 $[L + Na]^+$, 419.1 $[NiL + 1]^+$, 780.9 $[NiL_2 + 1]^+$. Although $NiL_2$ is found in both solutions, the intensity ratio of the MS peaks $NiL/NiL_2$ is 10:5 in the L/M = 1 solutions and 3.5:10 in the L/M = 4 solutions, showing the much higher importance of the bis complexes in solutions containing an excess of ligand.

$NiLH_2$ is the dominant species in the pH range 4–6 (see Figure 3). Its coordination geometry corresponds to a $O_{phen}$,$N_{amine}$,$N_{amine}$,$O_{phen}$,$O_w$,$O_w$ donor set, where the pyridine-N atoms are protonated. For pH > 5.5 the species $NiL_2H_4$, $NiL_2H_3$, $NiL_2H_2$, $NiL_2H$, and $NiL_2$ successively form up to a pH ca. 10.

For 2:1 complexes with tridentate ligands containing an $O_{phen}$, $N_{imine}$ or $N_{hydrazone}$, and $N_{amine}$ donor set binding modes corresponding to what is shown schematically as **I** have been characterized in the solid state by X-ray diffraction.[35–37] While in these compounds a significant part of each of the two ligands [($O_{phen}$ and $N_{imine}$ or $N_{hydrazone}$)] is constrained to be planar, the $Rpyr_2en$ ligand is much more flexible, and to the best of our knowledge this study is the first example of Ni–$sal_2en$- or Ni–$sal_2an$-type complexes reported showing the formation of bis complexes.

The intensity of the phenolate–$Ni^{II}$ CT band increases over the pH range ca. 5.3 to ca. 8.5. This suggests an in-

 © 2006 Wiley-VCH Verlag GmbH & Co. KGaA, Weinheim 

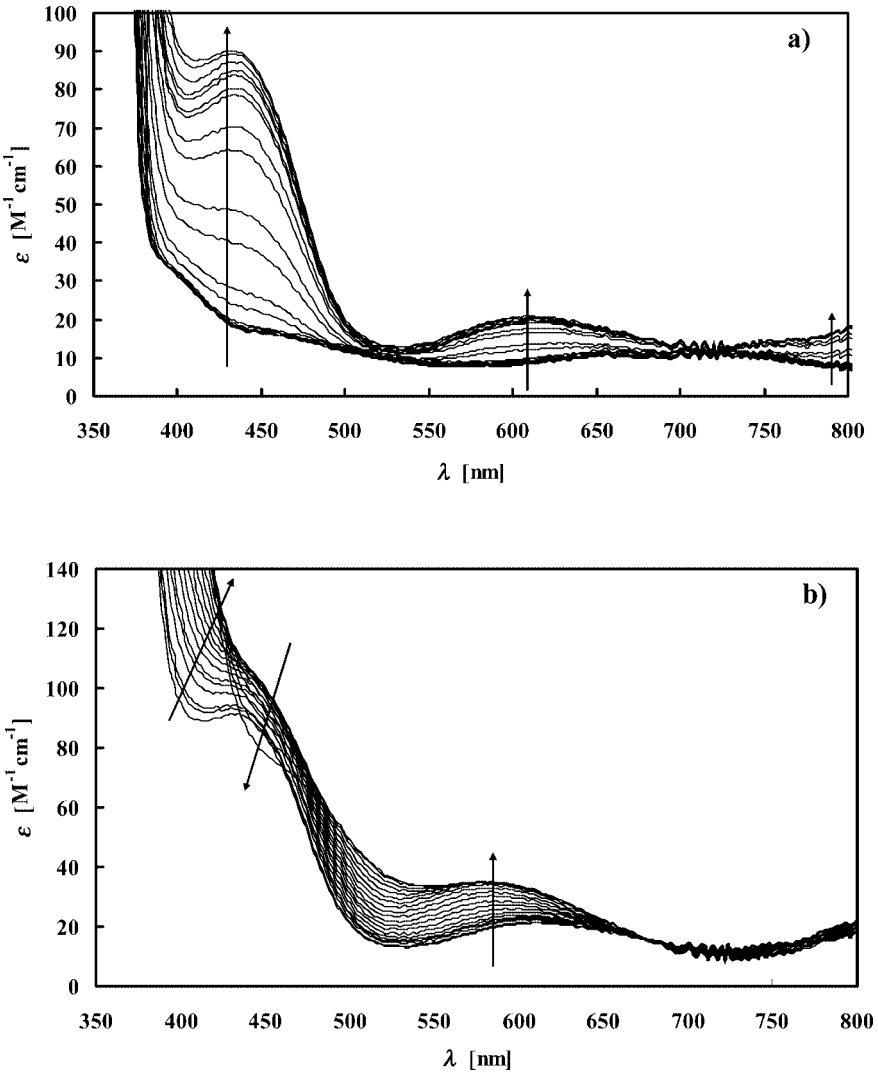


Figure 6. Visible spectra of aqueous solutions containing $Ni^{II}$ and $Rpyr_2en$, with $C_{Ni}$ = 2 mmol dm$^{-3}$ and L/M = 4 between (a) pH 2.10–5.02 and (b) pH 5.02–9.11. Arrows indicate increasing pH. Signal perturbations in the range 690–750 nm are due to instrumental noise.

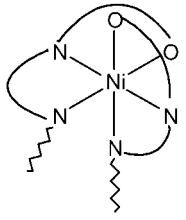


**I**

crease in the number of phenolate donor atoms in the $Ni^{II}$ coordination sphere upon the successive formation of $NiLH_2 \rightarrow NiL_2H_4 \rightarrow NiL_2H_3$. For pH > 8.7 the CT band remains approximately unchanged up to ca. 11.7, while the absorption over the wavelength range 450–800 nm increases until pH 10.3, and then decreases up to 11.7 (see Supporting Information, Figure SI-5 in ESI-3). However, the structure of the 2:1 Ni–$Rpyr_2en$ complexes in water is not easily anticipated. Formation of 2:1 complexes possibly involves displacement of one donor atom of the first ligand and the tridentate coordination of the second ligand. Binding modes such as **I** are a reasonable hypothesis, but the increase in intensity of the $O_{phen}$–Ni CT band may be indicative of the coordination of at least a third $O_{phen}$-donor atom.

The ratio $\log(K_{MLH_2}/K_{ML_2H_4}) = 0.55$ indicates a favorable interaction between the side chains in the bis complexes. These may be stabilized by intramolecular H bonds formed between groups of the coordinated ligands. In fact, the $Rpyr_2en$ ligand is quite flexible and contains several groups that may be involved in H bond formation: e.g. the pyridine-N atom (either as $N_{pyridine}$ or $NH^+_{pyridine}$), the –$(CH_2)$–OH groups of pyridoxal, or the phenolic-O atoms ($O_{phen}$ or $OH_{phen}$). Many possible binding modes and types of H bonds can be envisaged but discussing these further would be mainly speculation, as the techniques used do not help in this regard.

A comparison with pyridoxamine, which forms complexes of 1:1 and 2:1 L/M stoichiometry with $Ni^{II}$, can be

 © 2006 Wiley-VCH Verlag GmbH & Co. KGaA, Weinheim 

done based on the $\log K^*$ for the same equilibrium, as in the case of $Cu^{II}$ (see above); the $\log K^* = -10.08$ for $Rpyr_2en$ and –15.99 for pyrN[32] shows the higher stability of the $Rpyr_2en$ complexes, and also the lower stability of the $Ni^{II}$–$Rpyr_2en$ complexes when compared with those of $Cu^{II}$–$Rpyr_2en$.

## Conclusions

The coordination of the $sal_2en$- and $sal_2an$-type ligands $pyr_2en$, $Rpyr_2en$, and $R(SO_3–sal)_2en$ to $Cu^{II}$ and $Ni^{II}$ was investigated. These ligands form stable and moderately water-soluble complexes with $Cu^{II}$ and $Ni^{II}$. From solutions containing $Ni^{II}$ and $Rpyr_2en$, crystals of the SB complex $Ni(pyr_2en)$ were obtained, resulting from oxidative dehydrogenation of the two amine bonds, probably by molecular oxygen. The solution and solid-state characterization of the metal complexes showed that this process did not occur with the other complexes. Time-dependent visible absorption spectroscopic studies in aqueous solution with $Ni(Rpyr_2en)$ indicated that the dehydrogenation process, facilitated by molecular $O_2$, stops after oxidation of one amine bond. On standing for longer periods $Ni(pyr_2en)$ was obtained but only in the solid state.

The complexation of $Rpyr_2en$ with $Cu^{II}$ and $Ni^{II}$ could be studied by pH-potentiometry and spectroscopic techniques in aqueous solutions. In the $Cu^{II}$–$Rpyr_2en$ system very stable 1:1 complexes form, and at pH ca. 2 these correspond to ca. 95% of the total $Cu^{II}$. Characterization of the solid complex obtained indicates a square-planar coordination geometry involving the two $O_{phenolate}$ and two $N_{amine}$ as donor atoms. In the $Ni^{II}$–$Rpyr_2en$ system, when an excess of ligand is used bis complexes are formed in aqueous solution at pH > 6, avoiding the precipitation of the neutral NiL complex. The proton displacement constants ($K^*$) of the process $H_6L + M^{2+} \leftrightarrows ML{H_2}^{2+} + 4H^+$ are as follows: $K^*(CuLH_2^{2+}) = -3.27$; $K^*(V^{IV}OLH_2^{2+}) = -5.63$,[12] $K^*(NiLH_2^{2+}) = -10.08$, $K^*(ZnLH_2^{2+}) = -11.38$,[38] i.e. the stability order is $Cu^{II} > V^{IV}O > Ni^{II} > Zn^{II}$.

We should emphasize several aspects of the ligands studied in this work (or ligands obtained using the same aldehyde precursors and other diamines), which may have considerable advantages for e.g. catalytic applications using less toxic solvents, namely their higher solubility in aqueous and alcoholic solutions, when compared with most $sal_2en$-type ligands reported so far, because of the presence of hydrophilic groups in the aromatic rings. Moreover, the lower susceptibility to hydrolysis of the reduced $sal_2an$ derivatives, when compared with the corresponding SB, and the higher stability of $V^{IV}O$, $V^V$,[12] $Cu^{II}$, and $Ni^{II}$ complexes formed with the $sal_2an$-type ligands, may be important for both improving reaction yields and catalyst recovery. Finally, the higher flexibility of the $sal_2an$-type ligands and the fact that the coordinated $N_{amine}$ atoms are stereogenic centers may also prove useful for asymmetric synthesis if suitable diamine and/or aldehyde precursors are chosen. In the particular case of $Rpyr_2en$, with ligands containing $N_{pyridinic}$ atoms, the possibility of the various protonation states for the pyridinic nitrogens, which do not participate in coordination to the metal ions, allowing the formation of neutral and cationic complexes with the same coordination mode, may also help in tuning the redox characteristics of the complexes formed.

## Experimental Section

The synthesis of $pyr_2en$, $Rpyr_2en$, and $R(SO_3–sal)_2en$ was previously reported.[12,16]

### Synthesis of Complexes

**Crystals of $Ni(pyr_2en)\cdot 3H_2O$ (1):** From the filtrate solution of the reaction mixture used in the preparation of complex **6** orange crystals suitable for X-ray diffraction studies were obtained after six weeks.

**$Cu(pyr_2en)$ (2):** The Schiff base $pyr_2en$ (0.05 g, 0.2 mmol) was dissolved in water (25 mL) and the pH was adjusted to 7 by addition of KOH (3 M). Cupric acetate (0.03 g, 0.1 mmol) was added and the mixture was heated to 50 °C for an hour. A dark pink solid precipitated, which was collected by filtration and washed with water, ethanol, and diethyl ether, and dried under vacuum. Yield: 0.063 g, 68%. $C_{18}H_{20}N_4O_4Cu\cdot 2.3H_2O$ (461.36) {$[Cu(pyr_2en)]\cdot 2.3H_2O$}: calcd. C 46.86, H 5.37, N 12.14; found C 46.9, H 5.5, N 12.0.

**$Cu(Rpyr_2en)$ (3):** The procedure was similar to the one used for **2**. A blue solid was obtained. Yield: 0.043 g, 45%. $C_{18}H_{24}N_4O_4Cu\cdot 2.7H_2O$ (472.60) {$[Cu(Rpyr_2en)]\cdot 2.7H_2O$}: calcd. C 45.75, H 6.27, N 11.86; found C 45.8, H 6.3, N 11.7.

**$Cu\{R(SO_3–sal)_2en\}$ (4):** The procedure was similar to the one used for complex **2**. A green solid was obtained. Yield: 0.053 g, 50.0%. $C_{16}H_{18}N_2O_8S_2Cu\cdot 2H_2O$ (531.03), {$[Cu\{R(SO_3–sal)_2en\}]\cdot 2H_2O$}: calcd. C 36.26, H 4.18, N 5.29, S 12.10; found C 36.2, H 4.5, N 5.1, S 12.5.

**$Ni(pyr_2en)$ (5):** $Pyr_2en$ (0.5 g, 1.4 mmol) was dissolved in methanol (25 mL) containing a few drops of a KOH solution. $Ni(CH_3COO)_2\cdot 4H_2O$ (0.35 g, 1.4 mmol) dissolved in methanol/water (1:1, 25 mL) was slowly added and the mixture became orange. The pH was adjusted to 7 by the addition of methanolic HCl. An orange solid precipitated and was collected by filtration and washed with water, methanol, and diethyl ether, and dried under vacuum. Yield: 0.53 g, 85%. $C_{18}H_{20}N_4O_4Ni\cdot 1.7H_2O$ (445.70) {$[Ni(pyr_2en)]\cdot 1.7H_2O$}: calcd. C 48.51, H 5.29, N 12.57; found C 48.5, H 5.6, N 12.3. $^1H$ NMR [300 MHz, $(CD_3)_2SO$, 297 K]: $\delta$ = 8.23 (s, 2 H, CH=N), 7.47 (s, 2 H, $CH_{arom}$), 4.50 (s, 4 H, $CH_2CH_2$), 3.56 (s, 4 H, $CH_2OH$) and 2.51 (s, 6 H, $CH_3$) ppm. ESI-MS ($H_2O$): $m/z$ = 415.2 $[M + 1]^+$.

**$Ni(Rpyr_2en)$ (6):** The procedure was similar to the one used for **5**. A pink complex was obtained. Yield: 0.47 g, 72%. $C_{18}H_{24}N_4O_4Ni\cdot 2.4H_2O$ (462.34), {$[Ni(Rpyr_2en)]\cdot 2.4H_2O$}: calcd. C 46.76, H 6.28, N 12.12; found C 47.0, H 6.8, N 11.8. $^1H$ NMR [300 MHz, $(CD_3)_2SO$, 297 K]: $\delta$ = 6.97 (s, 2 H, $CH_{arom}$), 4.92 (s, 4 H, $CH_2OH$), 4.24 (s, 4 H, $CH_2NH$), 3.40 (s, 4 H, $CH_2$ $CH_2$), 2.75 (s, 6 H, $CH_3$) ppm. ESI-MS ($H_2O$): $m/z$ = 419.2 $[M + 1]^+$.

**$Ni[(SO_3–sal)_2en]$ (7):** The procedure was similar to the one used for the preparation of **5**. An orange solid was obtained. Yield: 0.35 g, 82%. $C_{16}H_{12}N_2O_8S_2NiK_2\cdot 3.8H_2O$ (629.75) {$K_2\{Ni[(SO_3–sal)_2en]\cdot 3.8H_2O$} calcd. C 30.52, H 3.14, N 4.45, S 10.18; found C 30.7, H 2.5, N 5.2, S 8.7. $^1H$ NMR [300 MHz, $D_2O$, 297 K]: $\delta$ = 7.97 (s, 2

 © 2006 Wiley-VCH Verlag GmbH & Co. KGaA, Weinheim 

H, CH=N), 7.74 (s, 2 H, $CH_{arom}$), 7.55 (d, 2 H, $CH_{arom}$), 6.87 (d, 2 H, $CH_{arom}$), 3.45 (s, 4 H, $CH_2CH_2$).

**Ni[R(SO$_3$–sal)$_2$en] (8):** The procedure was similar to the one used for the preparation of **5**. Since there was no precipitation at pH 7 the solution was evaporated to dryness. Methanol was added to the residue, which did not dissolve everything. The solid was filtered, washed with methanol and diethyl ether, and dried under vacuum. After a few hours the grey solid obtained turned soft pink and after a week brown. Yield: 0.52 g, 62.0%. $C_{16}H_{16}N_2O_8S_2NiK_2{\cdot}8.5H_2O$ (718.45) {$K_2${Ni[R(SO$_3$–sal)$_2$en]·8.5H$_2$O} calcd. C 26.75, H 4.63, N 3.90, S 8.92; found C 27.1, H 4.0, N 4.0, S 7.2. ESI-MS ($H_2O$): $m/z$ = 565.0 $[M + 2K + 1]^+$ and 603.0 $[M + 3K]^+$.

**Physical and Spectroscopic Studies:** Infrared spectra were recorded with a BioRad FTS 3000 MX FTIR spectrometer. UV/Visible spectra were recorded either with a Hitachi U-2000, a Perkin–Elmer Lambda 9 UV/Vis/NIR, or an HP 8452A diode array spectrophotometer. The EPR spectra were recorded with a Bruker ESP 300E X-band spectrometer. $^1$H NMR spectra were recorded with a Varian Unity 300 spectrometer at probe temperature.

**X-ray Crystal Structure Determination:** Three-dimensional X-ray data were collected with a Bruker SMART 1000 CCD diffractometer by the $\varphi$-$\omega$ scan method. Data was collected at room temperature. Reflections were measured from a hemisphere of data collected from frames each covering 0.3° in $\omega$. Of the 12502 reflections measured, all of which were corrected for Lorentz and polarization effects, and for absorption by semi-empirical methods based on symmetry-equivalent and repeated reflections, 1941 independent reflections exceeded the significance level $|F|/\sigma(|F|) > 4.0$. Because of the crystal nature (possibly pseudo-merohedrally twined emulating a metrically orthorhombic cell) and diffraction capabilities, some discrepant reflections were suppressed. Complex scattering factors were taken from the program package SHELXTL.[39] The structures were solved by direct methods and refined by full-matrix least-squares methods on $F^2$. The hydrogen atoms were included in calculated positions and refined by using a riding model, except the hydrogen atoms from the water molecules. Hydrogen atoms H(11W) and H(21W) of one water molecule were located from a difference electron density map and fixed to 0.97 Å from the corresponding heteroatom. Hydrogen atoms of the other two water molecules were left to refine freely. Refinement converged with allowance for thermal anisotropy of all non-hydrogen atoms. Minimum and maximum final electron densities are: –0.586 and 0.758 e Å$^{-3}$. Crystal data and details on data collection and refinement are summarized in Table 5.

Table 5. Crystal data collection and refinement.

| | **1** |
|---|---|
| Formula | $C_{18}H_{26}N_4O_7Ni$ |
| $M_r$ [g mol$^{-1}$] | 469.14 |
| Crystal system | monoclinic |
| Space group | $P2_1/c$ |
| $T$ [K] | 298(2) |
| $a$ [Å] | 8.268(2) |
| $b$ [Å] | 12.637(3) |
| $c$ [Å] | 19.634(5) |
| $\alpha$ [°] | 90 |
| $\beta$ [°] | 90.492(5) |
| $\gamma$ [°] | 90 |
| $V$ [Å] | 2051.3(9) |
| $F$(000) | 984 |
| $Z$ | 4 |
| $D_{calcd.}$ [g cm$^{-3}$] | 1.519 |
| $\mu$ [mm$^{-1}$] | 0.994 |
| $R_{int}$ | 0.1304 |
| No. of measured reflections | 12052 |
| No. of observed reflections | 1941 |
| Data / restraints / parameters | 4705 / 5 / 292 |
| Goodness-of-fit on $F^2$ | 0.938 |
| $R_1$[a] | 0.0953 |
| $wR_2$[b] (all data) | 0.2813 |

[a] $R_1 = \Sigma||F_o| - |F_c|| / \Sigma|F_o|$. [b] $wR_2 = \{\Sigma[w(|F_o|^2 - |F_c|^2)^2]| / \Sigma[w(F_o^4)]\}^{1/2}$.

CCDC-287242 contains the supplementary crystallographic data for this paper. These data can be obtained free of charge from The Cambridge Crystallographic Data Centre via www.ccdc.cam.ac.uk/data_request/cif.

**Solution Studies:** All solutions were manipulated in an inert atmosphere (high purity nitrogen or purified argon). The stock solution of $Cu^{II}$ was prepared and standardized as described earlier.[40] The $Ni^{II}$ stock solution was prepared by dissolving $NiCl_2$ of puriss quality in HCl solution. The $Ni^{II}$ content was determined by complexometry with EDTA, and the free acid content was measured pH-metrically. The ionic strength was adjusted to 0.2 mol dm$^{-3}$ with KCl. For pH-potentiometric measurements the temperature was 25.0 ± 0.1 °C, and for Vis spectra 25.0 ± 0.3 °C with circulating water.

**pH Measurements**

**Spectroscopic Measurements:** For the preparation of the solutions and pH calibrations we used a special glass vessel with a double wall, with entries for the combined electrode (Radiometer "Red Rod" pHC2015–8), thermometer, nitrogen, and reagents (e.g. base). A computerized system developed locally was used to control the titration conditions for pH calibrations. The emf measurements were performed with a Denver Model 15 pH meter.

**pH-Potentiometric Titrations:** Stability constants were determined from pH-metric titrations of 25 mL samples. The ligand concentrations were in the range 0.001–0.004 mol dm$^{-3}$ and the metal ion to ligand molar ratio was varied from 1 to 4 (up to 10 for the Ni–Rpyr$_2$en system). Titrations were normally made from pH 2.0 up to 11.7, but some titration curves started at 1.7, with a KOH solution of known concentration (ca. 0.2 mol dm$^{-3}$) under a purified argon atmosphere. The reproducibility of titration points included in the evaluation was within 0.005 pH units over the whole pH range. For the $Cu^{II}$– and $Ni^{II}$–Rpyr$_2$en systems 5 and 7 titration curves were measured, respectively.

The pH was measured with an Orion 710A precision digital pH meter equipped with an Orion Ross 8103BN type combined glass electrode, calibrated for hydrogen ion concentration as described earlier.[41] The ionic product of water was p$K_w$ = 13.76. The concentration stability constants $\beta_{pqr} = [M_pL_qH_r]/[M]^p[L]^q[H]^r$ were calculated with the aid of the PSEQUAD computer program.[31] When referring to stoichiometries of complexes present in solution the normal $M_pL_qH_r$ notation is used, where L = Rpyr$_2$en$^{2-}$.

**Spectroscopic Measurements:** Visible absorption spectra were measured using cells with 0.1, 1, or 3 cm path lengths. The spectral range covered was normally 300–900 nm, and in some cases 350–1100 nm. For the $Cu^{II}$–Rpyr$_2$en system the EPR (at 77 K) and Vis spectra were recorded varying the pH and using a ligand to metal ratio of approximately 1 and $C_{Cu} \approx 5$ mmol dm$^{-3}$. To obtain data for the low pH range individual samples containing the same metal ion concentration and L/M ratio were also prepared by adding different amounts of HCl. A calibration curve ($E_{measured}$ versus p[H$^+$]) was measured to determine the system response to the [H$^+$] of the samples. The standards were prepared by mixing various accurately

 © 2006 Wiley-VCH Verlag GmbH & Co. KGaA, Weinheim 

known volumes of HCl of known concentration (ca. 0.1 mol dm$^{-3}$) with water. The Vis ($300 < \lambda < 900$ nm) and room temperature EPR spectra of these samples were recorded and used for the determination of the speciation model at low pH, namely the $\log\beta$ of $CuLH_2$ with the PSEQUAD program.[31]

For the $Ni^{2+}$–$Rpyr_2en$ system the spectral range covered was 190–820 nm (for the quantitative evaluation only the 390–820 nm range was used). The absorption spectra were recorded at L/M ratios of 1 and 4 (the total concentrations of the $Ni^{II}$ [$C_M$] were 0.004 and 0.002 mol dm$^{-3}$, respectively). All other experimental conditions were as described for the pH-potentiometric titrations. For the solutions with a L/M ratio of 1 ($C_{Ni}$ = 0.004 mol dm$^{-3}$) precipitation of a pink compound occurred at pH ca. 8.3; this was not observed for solutions with L/M ratios of 4. With the latter solutions, the increasing absorbance of the baseline above pH ca. 9.2 suggested the presence of small amounts of precipitate. In order to confirm the octahedral geometry of the complexes Vis spectra with a L/M ratio of 1 and $C_{Ni}$ = 0.003 mol dm$^{-3}$ were measured at several pH values (3.0–7.7) in the 350–1100 nm range.

In the absence of ethylene glycol a relatively broad background was present in most of the frozen solution EPR spectra; therefore most spectra were run with solutions containing 5% of ethylene glycol.

For the $^1$H NMR measurements, solutions containing $Ni^{II}$ and $Rpyr_2en$ with a L/M ratio of 1 (5 mmol dm$^{-3}$) and 4 (16:4 mmol dm$^{-3}$) were prepared in $D_2O$ (DSS, sodium 3-trimethylsilyl-[$D_4$]propionate, as internal reference), and the pD was adjusted with DCl or $CO_2$ free KOD, using a Crison micropH 2002 instrument fitted with a combined Mettler Toledo U402-M3 S7/200 microelectrode. The microelectrode was previously calibrated with standard buffered aqueous solutions and –log[$D^+$] was measured directly in the NMR tubes. The final values of pD were determined from pD = pH* + 0.40, where pH* corresponds to the reading from the pH meter previously calibrated with two aqueous buffers at pH 4 and 7.

Mass spectrometer experiments were performed with a LCQ Duo (Finnigan, San Jose, CA, USA) ion trap mass spectrometer equipped with an electrospray ion source, operated in the positive mode and maintained at 4.5 kV. The temperature of the heated capillary was set to 200 °C. The flow rate of the electrospray solution was 5 μL min$^{-1}$. Other parameters, including capillary voltage, lens, and octapole voltages and sheath gas flow rate were optimized for maximum abundance of the ions of interest.

The ESI mass spectra measurements were done with solutions of nickel complexes **5**–**8** ($1 \times 10^{-4}$ mol dm$^{-3}$) and of solutions containing $Ni^{II}$ and $Rpyr_2en$ with a L/M ratio of 1 (1 mmol dm$^{-3}$) and 4 (4:1 mmol dm$^{-3}$). All solutions were prepared with deionized water.

**Supporting Information** (see also the footnote on the first page of this article): **ESI-1** Crystalline packing in complex Ni(pyr$_2$en)·3H$_2$O (**1**). **ESI-2** EPR spectra of complex Cu[R-(SO$_3$–sal)$_2$en] (**4**) and $[Cu(OH_2)_6]^{2+}$ in $H_2O$. **ESI-3** Visible spectra for the $Ni^{II}$–$Rpyr_2en$ system with L/M = 1 and 4.

## Acknowledgments

The authors thank Dr Maria da Conceição Oliveira for her help with the ESI mass spectra, Fundação para a Ciência e a Tecnologia (FCT), POCTI (POCTI/QUI/56949/2004 and POCTI/QUI/55985/2004), the Hungarian National Research Fund (OTKA T31896/2000), the Hungarian Academy of Sciences, the bilateral Portugal–Hungary Cooperation Program, the bilateral Acção Integrada Luso-Espanhola E-56/05, and COST D29 Action (D29/0016/04: "Novel sustainable metal-catalysed oxidations with $H_2O_2$ and $O_2$") for financial support.

[1] P. G. Cozzi, *Chem. Soc. Rev.* **2004**, *33*, 410–421.
[2] J. F. Larrow, E. N. Jacobsen, *Top. Organomet. Chem.* **2004**, *6*, 123–152.
[3] T. Achard, Y. N. Belokon, J. A. Fuentes, M. North, T. Parsons, *Tetrahedron* **2004**, *60*, 5919–5930.
[4] E. N. Jacobsen, *Acc. Chem. Res.* **2000**, *33*, 421–431.
[5] T. Katsuki, *Chem. Soc. Rev.* **2004**, *33*, 437–444.
[6] T. Fukuda, T. Katsuki, *Tetrahedron* **1997**, *53*, 7201–7208.
[7] B. D. Brandes, E. N. Jacobsen, *Tetrahedron Lett.* **1995**, *36*, 5123–5126.
[8] M. Valko, R. Klement, P. Pelikan, R. Boca, L. Dlhán, A. Boettcher, H. Elias, A. Muller, *J. Phys. Chem.* **1995**, *99*, 137–143.
[9] A. Boettcher, H. Elias, E. G. Jaeger, H. Langfelderova, M. Mazur, A. Muller, H. Paulus, P. Pelikan, M. Rudolph, M. Valko, *Inorg. Chem.* **1993**, *32*, 4131–4138.
[10] R. Klement, F. Stock, H. Elias, H. Paulus, P. Pelikan, M. Valko, M. Mazúr, *Polyhedron* **1999**, *18*, 3617–3628.
[11] A. Bottcher, H. Elias, L. Muller, H. Paulus, *Angew. Chem. Int. Ed. Engl.* **1992**, *31*, 623–625.
[12] I. Correia, J. Costa Pessoa, M. T. Duarte, R. T. Henriques, M. F. M. Piedade, L. F. Veiros, T. Jackusch, A. Dornyei, T. Kiss, M. M. C. A. Castro, C. F. G. C. Geraldes, F. Avecilla, *Chem. Eur. J.* **2004**, *10*, 2301–2317.
[13] P. Román, A. Aranzabe, A. Luque, M. Gutierrez-Zorrila, M. Martínez-Ripoll, *J. Chem. Soc., Dalton Trans.* **1995**, 2225–2231.
[14] A. Jancsó, I. Torok, L. Korecz, A. Rockenbauer, T. Gajda, *J. Chem. Soc., Dalton Trans.* **2002**, 2601–2607.
[15] E. M. Case, *Biochem. J.* **1932**, *26*, 753.
[16] I. Correia, J. C. Costa Pessoa, M. T. Duarte, M. F. M. Piedade, T. Jackusch, T. Kiss, M. M. C. A. Castro, C. F. G. C. Geraldes, F. Avecilla, *Eur. J. Inorg. Chem.* **2005**, 732–744.
[17] M. Nakai, M. Obata, F. Sekigushi, M. Kato, M. Shiro, A. Ichimura, I. Kinoshita, M. Mikuriya, T. Inohara, K. Kawabe, H. Sakurai, C. Orvig, S. Yano, *J. Inorg. Biochem.* **2004**, *98*, 105–112.
[18] M. Valko, R. Boca, R. Klement, J. Kozísek, M. Mazur, P. Pelikan, H. Morris, H. Elias, L. Muller, *Polyhedron* **1997**, *16*, 903–908.
[19] D. F. Evans, *J. Chem. Soc.* **1959**, 2003–2005.
[20] E. Sinn, A. B. Blake, W. Haussain, R. Paschke, J. R. Chipperfield, *Inorg. Chem.* **1995**, *34*, 1125–1129.
[21] I. C. Santos, M. Vilas-Boas, M. F. M. Piedade, C. Freire, M. T. Duarte, B. de Castro, *Polyhedron* **2000**, *19*, 655–664.
[22] D. H. Williams, I. Fleming, in: *Spectroscopic Methods in Organic Chemistry*, McGraw-Hill, London **1995**, pp. 42–49.
[23] K. Nakamoto, in: *Infrared and Raman Spectra of Inorganic Compounds* **1997**, pp. 73–271.
[24] R. M. Silverstein, G. C. Bassler, T. C. Morril, in: *Spectrometric Identification of Organic Compounds*, John Wiley & Sons, New York, **1991**, pp. 122–125.
[25] G. Socrates, in: *Infrared and Raman Characteristic Group Frequencies. Tables and Charts*, John Wiley & Sons, Chichester, **2001**, pp. 108–113.
[26] A. K. Rappé, C. J. Casewit, K. S. Colwell, W. A. Goddard III, W. M. Skiff, *J. Am. Chem. Soc.* **1992**, *114*, 10024.
[27] A. R. Amundsen, B. Bosnich, *J. Am. Chem. Soc.* **1977**, *99*, 6730–6739.
[28] P. S. Subramanian, E. Suresh, D. Srinivas, *Inorg. Chem.* **2000**, *39*, 2053–2060.
[29] A. Rockenbauer, L. Korecz, *Appl. Magn. Reson.* **1996**, *10*, 29.
[30] U. Sakaguchi, A. W. Addison, *J. Chem. Soc., Dalton Trans.* **1979**, 600–608.
[31] L. Zekany, I. Nagypal, in: *Computational Methods for the Determination of Stability Constants* (Ed.: D. Leggett), Plenum, New York, **1985**.

 © 2006 Wiley-VCH Verlag GmbH & Co. KGaA, Weinheim 

[32] M. S. El-Ezabi, F. M. Al-Sogais, *Polyhedron* **1982**, *1*, 791–798.
[33] B. N. Figgis, M. A. Hitchman, in: *Ligand Field Theory and its Applications*, Wiley-VCH, New York, **2000**, pp. 294–303.
[34] N. N. Greenwood, A. Earnshaw, in: *Chemistry of the elements*, Pergamon Press, London, **1984**, pp. 1144–1172.
[35] S. V. Zublov, I. I. Seifullina, Z. A. Starikova, A. I. Yanovsky, *Zh. Neorg. Khim.* **1999**, *44*, 35–40.
[36] M. N. Tahir, D. Uelkue, H. Nazir, O. Atakol, *Acta Crystallogr. Sect. C* **1997**, *53*, 181–183.
[37] M. Di Vaira, P. Orioli, *Inorg. Chem.* **1967**, *6*, 490–494.
[38] I. Correia, A. Dornyei, F. Avecilla, T. Kiss, J. C. Costa Pessoa, *Eur. J. Inorg. Chem.* **2006**, 656–662.
[39] G. M. Sheldrick, *SHELXT-97, A program for refining crystal structures* (release 5.1), **1997**.
[40] J. Costa Pessoa, L. F. Vilas Boas, R. D. Gillard, R. Lancashire, *Polyhedron* **1988**, *7*, 1245–1262.
[41] R. D. Gillard, J. Costa Pessoa, T. Gajda, T. Kiss, S. M. Luz, J. J. G. Moura, I. Tomaz, J. P. Telo, I. Török, *J. Chem. Soc., Dalton Trans.* **1998**, 3587–3600.

Received: January 12, 2006
Published Online: May 8, 2006

 © 2006 Wiley-VCH Verlag GmbH & Co. KGaA, Weinheim 

DOI: 10.1002/ejic.200600058

# Study on the Photochromism of Ni–Al Layered Double Hydroxides Containing Nitrate Anions

**Min Wei,[a] Xiangyu Xu,[a] Xinrui Wang,[a] Feng Li,[a] Hui Zhang,[a] Yanluo Lu,[a] Min Pu,[a] David G. Evans,[a] and Xue Duan*[a]**

**Keywords:** Layered compounds / Photochromism / Host–guest systems

The photochromism of nitrate-containing nickel–aluminum layered double hydroxides (NiAl-$NO_3$-LDHs) has been studied. Powder X-ray diffraction (PXRD), FTIR, UV/Vis, XPS, ESR, EXAFS, and elemental analysis were used to investigate the structure, composition, and photochromic behavior of NiAl-$NO_3$-LDHs. A possible photochromic mechanism in NiAl-$NO_3$-LDHs has been proposed.

(© Wiley-VCH Verlag GmbH & Co. KGaA, 69451 Weinheim, Germany, 2006)

## Introduction

Layered double hydroxides (LDHs) consist of metal brucite type layers – $Mg(OH)_2$ sheets where octahedra of $Mg^{2+}$ ions, sixfold coordinated to $OH^-$, share edges to form two-dimensional infinite sheets. LDHs constitute a vast family of compounds of general formula $[M^{II}_{1-x}M^{III}_x(OH)_2]A^{y-}_{x/y}\cdot nH_2O$, where $x$ typically varies between 0.20 and 0.33. They are stacks of positively charged, partially substituted brucite-like layers that are spaced by exchangeable $A^{y-}$ anions and water molecules.[1,2] LDHs are attractive materials for various fields of application such as catalysis,[3] optical materials,[4,5] biomimetic catalysis,[6,7] separation science,[8,9] medical science,[10,11] and electrochemistry.[12,13]

Recently, research on photochromic materials has received much attention because of the potential use of these materials in photonic applications. Practical applications are also well established, for example, in optical transmission.[14] Photochromism is also widely utilized from the molecular level up to complete devices; representative examples are molecular switching of host–guest aggregates,[15,16] sol–gel thin films,[17] and pigment–protein complexes involved in proton pumping.[18] However, there are very few reports of LDHs being used as candidates for photochromic materials. It has been reported that a sulfonated spiropyran dye (SP-$SO_3^-$) intercalated in Mg–Al, Zn–Al, and Li–Al LDHs exhibited photochromism due to interlayer reversible photoisomerization between SP-$SO_3^-$ and photoinduced merocyanine.[19,20]

Although photochromism resulting from the properties of the interlayer organic guest has been observed in LDH composites, the mechanism related to the host–guest interaction has not been reported. In this paper, we report for the first time photochromism in a NiAl-$NO_3$-LDH. PXRD, FTIR, UV/Vis, ESR, XPS, EXAFS, and elemental analysis were used to investigate the photochromic behavior, and its possible mechanism has also been proposed.

[a] State Key Laboratory of Chemical Resource Engineering, Beijing University of Chemical Technology,
Beijing 100029, P. R. China
E-mail: duanx@mail.buct.edu.cn

## Results and Discussion

### The Crystalline Structure and Chemical Composition of NiAl-$NO_3$-LDHs

Figure 1 shows the PXRD pattern for NiAl-$NO_3$-LDHs. A typical PXRD pattern was found for NiAl-$NO_3$-LDHs prepared by a hydrothermal method (a profile similar to those observed in hydrotalcite-like compounds): sharp and symmetric peaks related to 00$l$ reflections and broad and less symmetric peaks related to 0$kl$ reflections (Figure 1). The peaks were indexed in a hexagonal cell with rhombohedral symmetry, where $c$ = 26.79 Å and $a$ = 3.00 Å. The $d_{003}$ parameter, which corresponds to an interlayer distance of 8.93 Å, is typical for hydrotalcite-like materials containing nitrate anions.[2]

On the basis of elemental analysis, the chemical composition of this particular NiAl-$NO_3$-LDH (Ni/Al = 2) was found to be $[Ni_{0.643}Al_{0.357}(OH)_2](NO_3^-)_{0.357}\cdot 0.7H_2O$ (calcd. H 2.92, Al 8.29, N 4.30, Ni 32.62; found H 3.01, Al 8.15, N 4.23, Ni 33.49).

Figure 2A shows the Ni $K$-edge $k^1\chi(k)$ spectrum and Fourier transform magnitude of the powdered NiAl-$NO_3$-LDH, while Figure 2B displays the experimental (solid) and fitted (dotted) EXAFS curves with $k^1$-weight for Ni–O coordination in the powdered NiAl-$NO_3$-LDH. The fitting parameters are listed in Table 1 [$Ni(OH)_2$ was used as a reference sample]. Data analysis suggests a Ni–O distance of 2.04 Å and a Ni–O coordination number ($CN_{Ni-O}$) of six

 © 2006 Wiley-VCH Verlag GmbH & Co. KGaA, Weinheim InterScience 

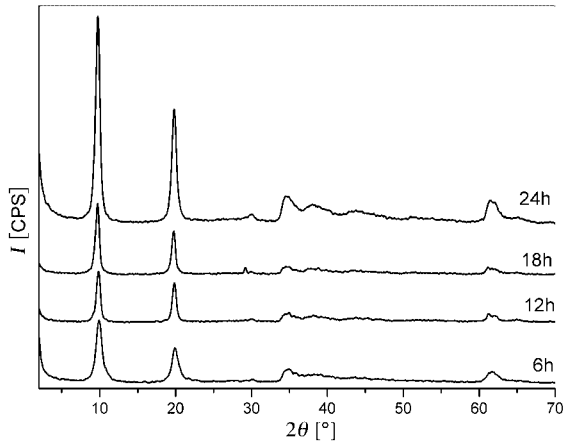


Figure 1. Powder XRD patterns of NiAl-$NO_3$-LDHs with different aging times at 180 °C.

for the NiAl-$NO_3$-LDH, which corresponds well to the data reported by Scheidegger et al.[21] This reveals that the first coordination shell of Ni comprises six oxygen atoms at 2.04 Å, indicating that $Ni^{II}$ is coordinated in an octahedral environment.

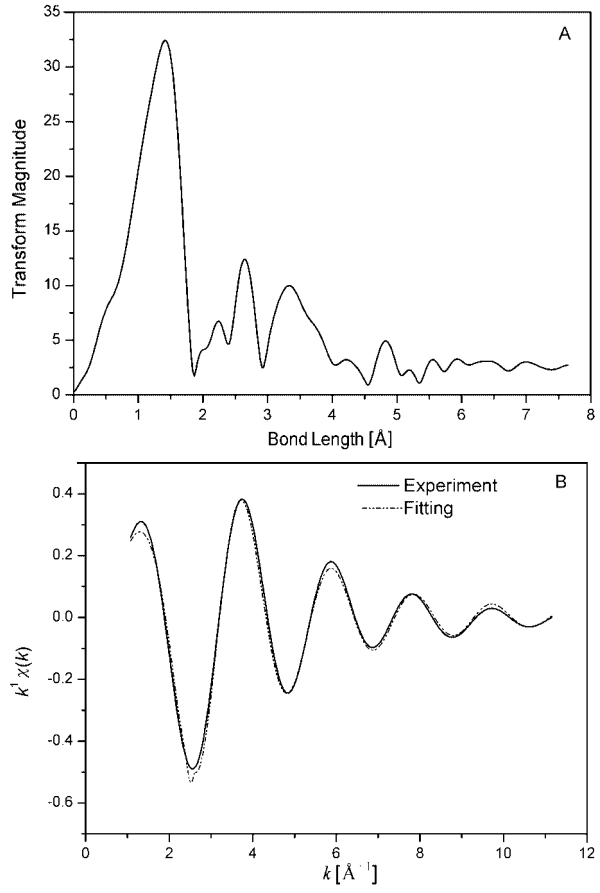


Figure 2. (A) Ni *K*-edge $k^1\chi(k)$ spectrum and Fourier transform magnitude of powdered NiAl-$NO_3$-LDH. (B) Experimental (solid line) and fitted (dotted line) EXAFS curves with $k^1$-weight for Ni–O coordination in powdered NiAl-$NO_3$-LDH.

Table 1. Local coordination parameters around Ni in powdered NiAl-$NO_3$-LDH.

| Sample | $CN_{Ni-O}$ | $R_{Ni-O}$ [Å] | $\sigma^2_{Ni-O}$ [Å]$^2$ |
|---|---|---|---|
| $Ni(OH)_2$ | 6.0 | 2.05 | 0.002 |
| NiAl-$NO_3$-LDH | 6.0 | 2.04 | 0.003 |

### Photochromism in NiAl-$NO_3$-LDHs

Photochromism in NiAl-$NO_3$-LDHs has been observed for the first time in this work. Figure 3c shows the UV/Vis absorption spectra of NiAl-$NO_3$-LDH both before and after UV irradiation. For the as-synthesized NiAl-$NO_3$-LDH sample before UV irradiation, two absorption peaks (at ca. 376 and 652 nm) were observed, which were assigned to the (d–d) spin-allowed electronic transitions expected for a $Ni^{2+}$ ion in an octahedral crystal field.[22] Upon irradiation of NiAl-$NO_3$-LDH with UV light, the green samples rapidly turned black. Furthermore, there was a remarkable enhancement of absorption in the wavelength range 300–650 nm (Figure 3c). No change in color could be observed, even when the black-colored NiAl-$NO_3$-LDH was kept at room temperature for a week. However, upon heating to 70 °C for 2 h, the color returned to green. The UV/Vis absorption spectrum also recovered its original profile (dotted line shown in Figure 3c, almost coincident with the initial spectrum), demonstrating the reversibility of the photochromism. Moreover, both the reversibility and reproducibility of the photochromism were investigated. The inset in Figure 3 displays the UV absorbance of this material at 500 nm, before and after ten irradiation cycles, indicating a rather high reversibility and reproducibility.

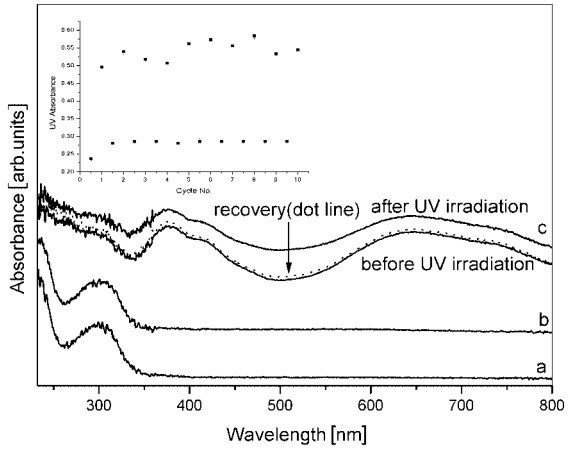


Figure 3. UV/Vis absorption spectra of (a) MgAl-$NO_3$-LDH, (b) ZnAl-$NO_3$-LDH and (c) NiAl-$NO_3$-LDH, before and after UV irradiation [absorption curves of before and after UV irradiation for (a) and (b) are coincident]. Inset: the relationship between the UV absorbance of NiAl-$NO_3$-LDH at 500 nm (before and after irradiation) and cycle number.

### The Photochromic Mechanism in NiAl-$NO_3$-LDHs

#### *Influence of Nickel Ions*

In order to study the effect of the nickel ions of the host layers on photochromic behavior, MgAl-$NO_3$-LDH and

 © 2006 Wiley-VCH Verlag GmbH & Co. KGaA, Weinheim 

ZnAl-$NO_3$-LDH were prepared as samples for comparison. All three samples exhibit a PXRD pattern characteristic of LDH-like materials, and the interlayer distance of the three intercalates is about 0.88 nm, indicating well-defined LDHs containing nitrate anions.

Figure 3 displays the UV/Vis absorption spectra of the three samples, both before and after UV irradiation. No obvious change could be observed in the spectra of MgAl- and ZnAl-$NO_3$-LDHs after UV-light irradiation (Figure 3a and Figure 3b, respectively). This observation is in agreement with their invariable white color, and in contrast with the photochromic behavior that was observed in the case of NiAl-$NO_3$-LDH, as described above. This indicates that the nickel ions in the host layer play an important role in the photochromic behavior. This is possibly related to the octahedral coordination environment of the nickel ion.

### *Influence of Aging Conditions*

Figure 1 and Figure 4 display the PXRD patterns of NiAl-$NO_3$-LDHs with different aging times and aging temperatures, respectively. All nine samples exhibit a PXRD pattern characteristic of LDH-like materials, with an interlayer distance of approximately 0.89 nm. It can be seen from Figure 1 and Figure 4 that the reflection intensity of the LDHs becomes stronger with an increase in the aging time or aging temperature. The indexing parameters are listed in Table 2. It should be noted that there is a decrease in the half-peak-width parameter, and an increase in the crystallite size in the *c* direction, upon increasing aging time or temperature. This is an indication that the stacking sequences of the LDHs become more ordered and higher crystallinity is obtained with increasing aging time or temperature.

Figure 5A and Figure 6A show the UV/Vis absorption spectra of powdered NiAl-$NO_3$-LDHs with different aging times and temperatures, respectively, both before and after UV irradiation. On irradiation the samples prepared with a 6 h aging time, or at 70 °C aging temperature, show the most remarkable enhancement of absorption in the wavelength range 300–650 nm. They are also accompanied by

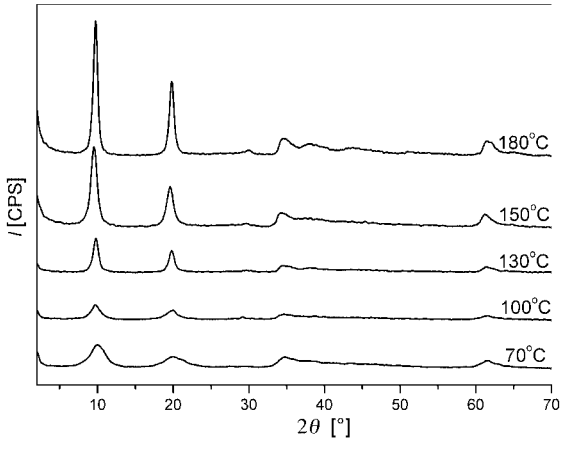


Figure 4. Powder XRD patterns of NiAl-$NO_3$-LDH aged for 24 h at different aging temperatures.

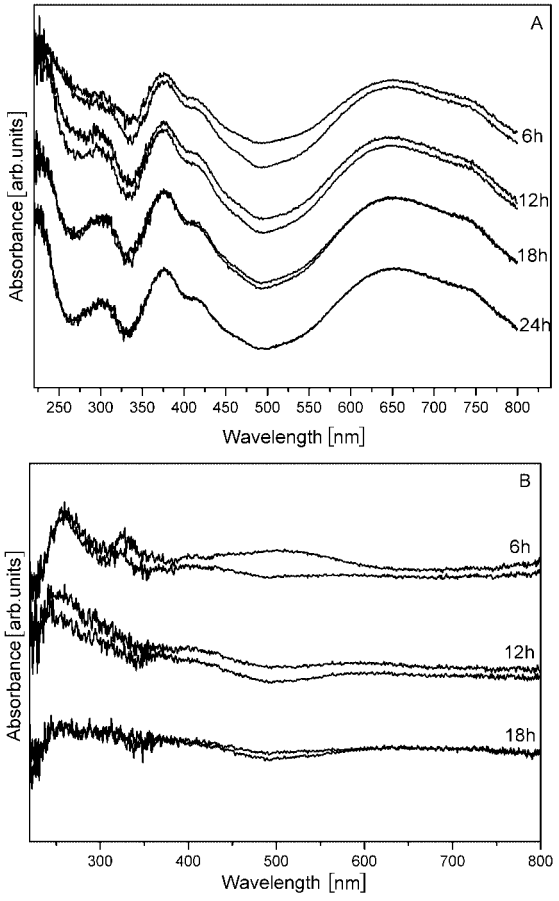


Figure 5. (A) UV/Vis absorption spectra of NiAl-$NO_3$-LDHs with different aging times at 180 °C, before and after UV irradiation. (B) Background correction for the absorption spectra of the NiAl-$NO_3$-LDHs from (A) before and after UV irradiation.

Table 2. Lattice parameters of NiAl-$NO_3$-LDHs prepared under different conditions.

| Parameters | Samples with different aging temperatures | | | | | Samples with different aging times | | | |
|---|---|---|---|---|---|---|---|---|---|
| | 70 °C | 100 °C | 130 °C | 150 °C | 180 °C | 6 h | 12 h | 18 h | 24 h |
| $d_{003}$ [nm] | 0.879 | 0.904 | 0.927 | 0.903 | 0.906 | 0.893 | 0.900 | 0.912 | 0.906 |
| half-peak width of the 003 reflection [°] | 1.810 | 1.270 | 0.933 | 0.808 | 0.515 | 0.866 | 0.613 | 0.583 | 0.515 |
| $d_{110}$ [nm] | 0.151 | 0.151 | 0.151 | 0.151 | 0.151 | 0.150 | 0.151 | 0.152 | 0.151 |
| lattice parameter *a* [nm][a] | 0.302 | 0.302 | 0.302 | 0.302 | 0.302 | 0.300 | 0.302 | 0.304 | 0.302 |
| lattice parameter *c* [nm][b] | 2.637 | 2.712 | 2.781 | 2.709 | 2.718 | 2.679 | 2.700 | 2.736 | 2.718 |
| crystallite size in *c* direction [nm][c] | 4.361 | 6.215 | 8.458 | 9.768 | 15.32 | 9.115 | 12.88 | 13.54 | 15.32 |

[a] $a = 2d_{110}$. [b] $c = 3d_{003}$. [c] Value calculated from the Scherrer equation.

 © 2006 Wiley-VCH Verlag GmbH & Co. KGaA, Weinheim 

the most obvious change in sample color, which indicates the most significant photochromism. Moreover, the enhancement of the absorption in the range 300–650 nm decreased upon increasing aging time or temperature. As the aging time was increased to 24 h, or the aging temperature was increased to 180 °C, no change could be observed in either the absorption spectra or the sample color following UV-light irradiation, which implied the absence of photochromic behavior. On the basis of the PXRD characterization above, it can be concluded that the ordered stacking sequences and the crystallinity of NiAl-$NO_3$-LDH have a marked influence on its photochromism. Moreover, the effect of the wavelength of the excitation light has been studied, and it was found that UV light with a wavelength below 376 nm could cause photochromism in the material.

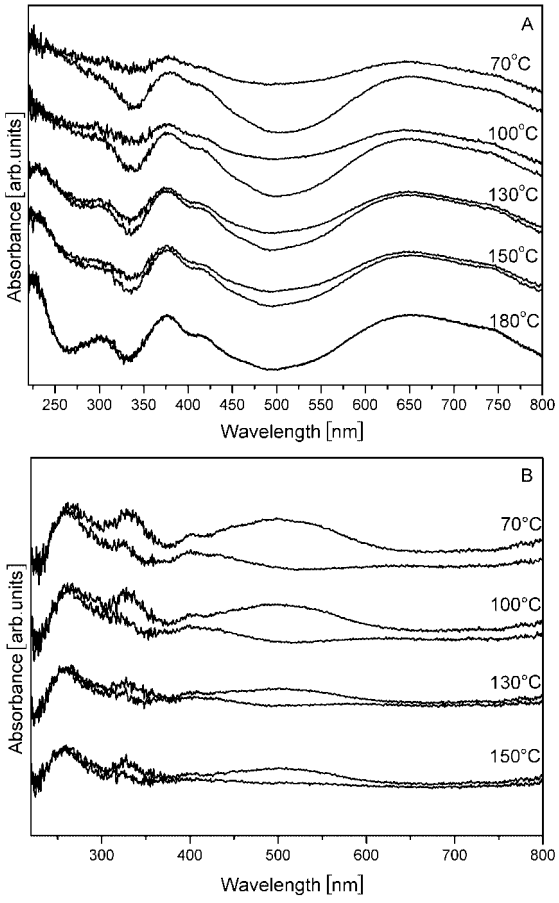


Figure 6. (A) UV/Vis absorption spectra of NiAl-$NO_3$-LDHs with different aging temperatures and aged for 24 h, before and after UV irradiation. (B) Background correction for the absorption spectra of the NiAl-$NO_3$-LDHs from (A) before and after UV irradiation.

In order to gain direct insight into photochromism in NiAl-$NO_3$-LDH, the NiAl-$NO_3$-LDH samples which were nonphotochromic (aging time 24 h and aging temperature 180 °C) were used as the baseline reference for further analysis of the UV/Vis spectra. Background correction was performed by subtracting the absorption spectrum of the nonphotochromic sample from the photochromic NiAl-$NO_3$-LDH samples, both before and after UV irradiation. The results are shown in Figure 5B and Figure 6B. Comparing the UV/Vis absorption spectra before and after UV irradiation, it can be seen that there is an obvious peak at approximately 500 nm. This indicates that there might be some specific structural unit, with Ni in an octahedrally coordinated environment, which results in photochromism in NiAl-$NO_3$-LDH. As the aging time or temperature increases, the stacking sequences of the LDHs become more ordered, leading to the loss of the specific structural unit and thus to the loss of photochromic behavior.

### *Influence of Host–Guest Interactions*

In order to study the influence of host–guest interactions, two samples of NiAl-$CO_3$-LDH were prepared: one by the ion-exchange method from a NiAl-$NO_3$-LDH precursor and the other by direct coprecipitation. Both samples exhibit a PXRD pattern characteristic of LDH-like materials, with an interlayer distance of approximately 0.76 nm, indicating well-defined LDHs containing carbonate anions. Figure 7 displays a comparison of the FTIR spectra of the two NiAl-$CO_3$-LDH samples. Both show the strong, sharp band at approximately 1363 $cm^{-1}$ due to the absorption of interlayer carbonate anions. However, it can be seen that a peak at approximately 1384 $cm^{-1}$ was observed in the sample prepared by ion-exchange (Figure 7a), which indicates the presence of a small amount of nitrate anions.

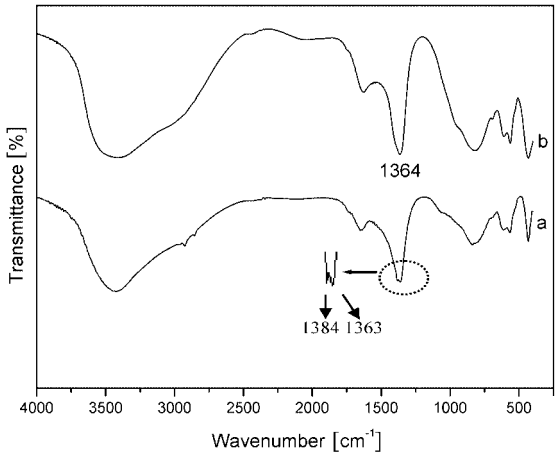


Figure 7. FTIR spectra of NiAl-$CO_3$-LDHs prepared by (a) ion exchange and (b) coprecipitation.

On the basis of elemental analysis, the chemical composition of the NiAl-$CO_3$-LDH that was prepared by coprecipitation was found to be $[Ni_{0.656}Al_{0.344}(OH)_2](CO_3^{2-})_{0.172}\cdot 0.8H_2O$ (calcd. C 2.06, H 3.37, Al 8.70, Ni 36.27; found C 2.12, H 3.31, Al 8.73, Ni 36.19). However, the chemical composition of the NiAl-$CO_3$-LDH that was prepared by the ion-exchange method from a NiAl-$NO_3$-LDH precursor was found to be $[Ni_{0.647}Al_{0.353}(OH)_2](CO_3^{2-})_{0.151}(NO_3^{-})_{0.051}\cdot 0.7H_2O$ (calcd. C 1.70, H 3.19, Al 8.95, N 0.67, Ni 35.83; found C 1.62, H 3.13, Al 8.86, N 0.71, Ni 35.76). It can be seen that the sample prepared by coprecipitation was a pure $CO_3^{2-}$ LDH, while the other one, prepared by ion-exchange from a NiAl-$NO_3$-LDH precursor, contained both $CO_3^{2-}$ and a little unexchangeable $NO_3^{-}$.

 © 2006 Wiley-VCH Verlag GmbH & Co. KGaA, Weinheim 

Figure 8a and b show the UV/Vis absorption spectra of the two powdered NiAl-$CO_3$-LDH samples before and after UV irradiation. It was found that almost no change in the absorption spectrum, after UV-light irradiation, could be observed for the NiAl-$CO_3$-LDH prepared by coprecipitation (Figure 8b), which means that photochromism is not an intrinsic property of NiAl-$CO_3$-LDHs. However, in the case of the sample prepared by ion exchange, a considerable enhancement in the 300–650 nm range (Figure 8a) was observed after UV irradiation. This is an indication that the interaction between $Ni^{2+}$ and co-intercalated nitrate anions is indispensable for the photochromism in NiAl-$CO_3$-LDHs prepared by ion exchange. This is possibly related to the remaining nitrate anions that interact strongly with $Ni^{2+}$ ions in NiAl-$NO_3$-LDHs through chemical bonding and thus cannot be exchanged by $CO_3^{2-}$.

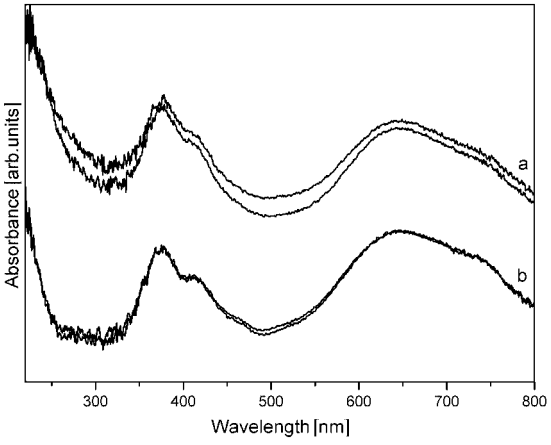


Figure 8. UV/Vis absorption spectra of powdered NiAl-$CO_3$-LDHs, both before and after UV irradiation, prepared by (a) ion exchange and (b) coprecipitation.

### *XPS Data*

In order to confirm whether the photochromic behavior of NiAl-$NO_3$-LDHs is related to the redox of $Ni^{2+}$, XPS was used to determine the chemical environment of Ni, N, and O before and after UV irradiation. The XPS Ni2$p_{3/2}$, N1s, and O1s core level spectra of NiAl-$NO_3$-LDHs, before and after UV irradiation, are shown in Figure 9. The binding energy (BE) value of the main Ni2$p_{3/2}$ peak, at around 856.4/856.5 eV, is assigned to the $Ni^{2+}$ ion by comparison with the known BE value for Ni2$p_{3/2}$ photoelectrons in $Ni(OH)_2$ (855.6–856.6 eV).[23] The XPS N1s peak at around 406.6/406.7 eV is attributed to $N^{5+}$ from the nitrate anions, and the XPS O1s peak at around 531.9/531.8 eV is due to $O^{2-}$ from the nitrate anions. As no remarkable change in the values of the BE can be observed after UV irradiation, it is reasonable to deduce that the oxidation states of Ni, N, and O in NiAl-$NO_3$-LDHs do not change, and hence a mechanism based on the redox of $Ni^{2+}$ can be excluded.

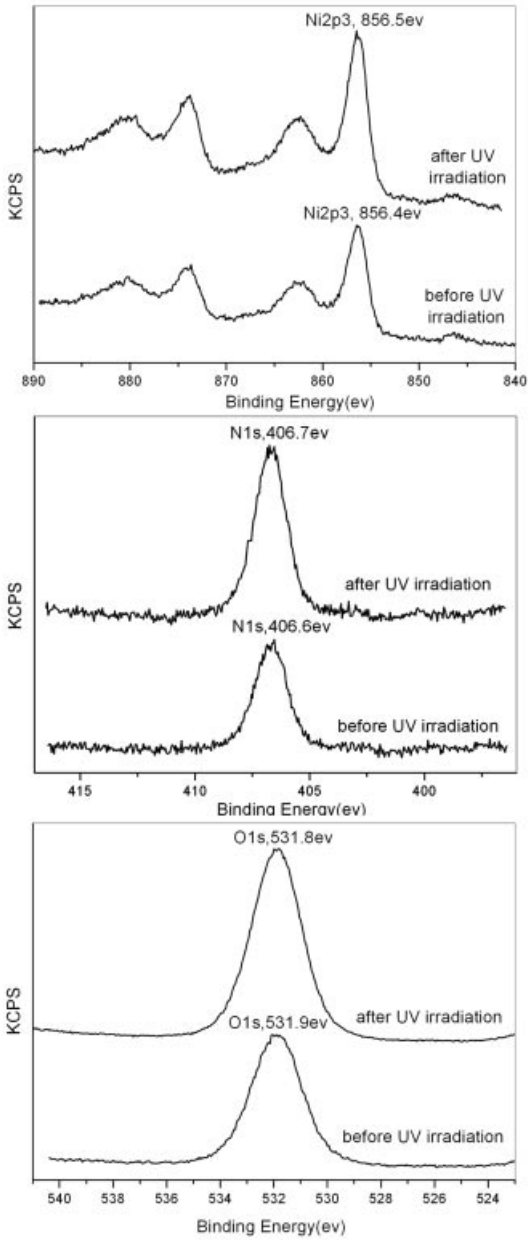


Figure 9. XPS spectra of Ni2$p_{3/2}$, N1s, and O1s for NiAl-$NO_3$-LDHs before and after UV irradiation.

### *ESR Data*

ESR was used to study the coordination environment of $Ni^{2+}$ in NiAl-$NO_3$-LDHs to obtain a further understanding of the photochromic mechanism. It has been reported that $Ni^{2+}$ ions in $Ni(OH)_2$ are ESR silent at room temperature, most probably because of the regular octahedral crystal field.[22] Figure 10 displays the ESR spectra of powdered NiAl-$NO_3$-LDH before and after UV irradiation, as well as that of NiAl-$CO_3$-LDH prepared by coprecipitation, as a reference sample. It can be seen from Figure 10a that NiAl-$CO_3$-LDH is ESR silent at room temperature and at liquid nitrogen temperature, because of its Ni–OH regular octahedral crystal field. However, in the case of NiAl-$NO_3$-LDH, distinct signals with $g$ = 2.163 (Figure 10b) and $g$ = 2.643

 © 2006 Wiley-VCH Verlag GmbH & Co. KGaA, Weinheim 

(Figure 10c) were observed for the sample before and after UV irradiation, respectively. These can be attributed to $Ni^{2+}$ ions ($3d^8$ electronic configuration) in a strongly distorted octahedral crystal field.[22] The difference in the *g* values indicates that the distortion in the octahedral crystal field for NiAl-$NO_3$-LDH is not completely the same before and after UV irradiation.

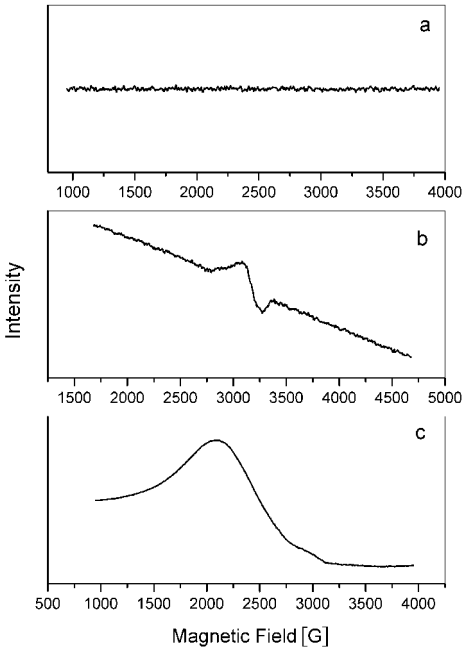


Figure 10. ESR spectra of powdered NiAl-$CO_3$-LDH prepared by coprecipitation (a), and NiAl-$NO_3$-LDHs before irradiation (b) and after irradiation (c).

On the basis of the discussion above, it can be concluded that the host–guest interaction between $Ni^{2+}$ and the nitrate anions, and thus the presence of the specific octahedral crystal field of the $Ni^{2+}$, leads to photochromism in NiAl-$NO_3$-LDHs. Single-crystal structure analysis of CaAl-$NO_3$/$CO_3$/$SO_4$/Cl-LDHs has revealed that $Ca^{2+}$ ions are sevenfold coordinated by O atoms. A water molecule, a carbonate anion, or a nitrate anion occupies the seventh coordination site of three of the four $Ca^{2+}$ ions contained in the main layer.[24–27] Moreover, Steven et al. reported that, in the layered material $Ni_2(OH)_3NO_3$, the nitrate anion was located in the interlayer region and was coordinated through one oxygen atom directly to the matrix $Ni^{2+}$ cation.[28] In the current study, taking into account the confirmation by EXAFS data that $Ni^{2+}$ ions are sixfold coordinated (Table 1), the evidence from ESR data that $Ni^{2+}$ ions exist in a distorted octahedral crystal field, and the presence of unexchangeable $NO_3^-$, it can be concluded that there are specific units of octahedral structure in which $Ni^{2+}$ is coordinated by five hydroxy groups and one nitrate anion through the O atom in NiAl-$NO_3$-LDH, as shown in Figure 11. The influence of water cannot be excluded completely, and there is the possibility that a hydrogen-bonding system exists between the host hydroxy and nitrate anions, and water molecules, and thus water has a secondary influence on the photochromism of NiAl-$NO_3$-LDH (as shown in Figure 11). Further studies on the effects of water, as well as theoretical calculations, are under investigation at our laboratory.

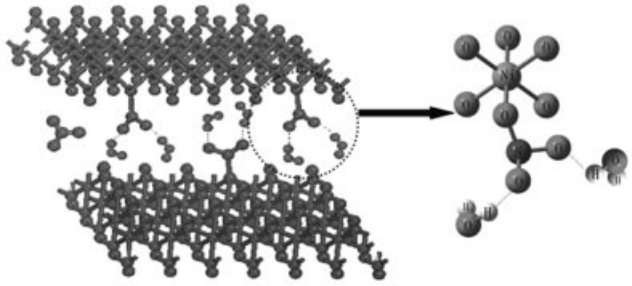

Figure 11. Schematic representation of the structure of NiAl-$NO_3$-LDH.

The electronic configuration of $Ni^{2+}$ ions in the ground state is $3d^8$ ($t_{2g}^6e_g^2$). As shown in Figure 12a, the octahedral crystal field of the $Ni^{2+}$ ions is generated by the coordinated O atom of the nitrate anion, and is somewhat distorted with a *g* value of 2.163, derived from ESR spectroscopy data. Under UV-light irradiation, the electronic configuration of the $Ni^{2+}$ ions in the excited state is $3d^8$ ($t_{2g}^5e_g^3$), which speaks in favor of the Jahn–Teller effect, and thus leads to a more strongly distorted octahedral crystal field (Figure 12b). The latter structure is quite stable at room temperature and cannot revert spontaneously. In comparison with the sample before UV irradiation, it demonstrates changes in the UV/Vis absorption spectrum (especially the strong absorption enhancement in at a wavelength of 500 nm) and in the *g* value determined by ESR spectroscopy (from 2.163 to 2.634). Upon heating, the radiation-induced structure recovers its original state, and the color changes from black to green. Because the distorted octahedral structure [$Ni(OH)_5NO_3$] was a metastable state thermodynamically, it reverted to the stable regular octahedral unit [$Ni(OH)_6$] by substitution of the $NO_3^-$ by an $OH^-$ group upon increasing aging time or temperature during the preparation process. As a result, the specific octahedral crystal field of the $Ni^{2+}$ ion, coordinated by a nitrate anion, leads to photochromism in NiAl-$NO_3$-LDHs.

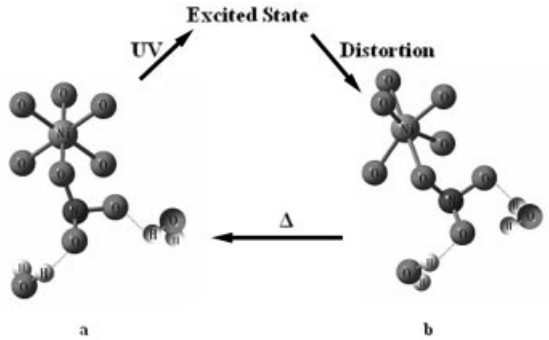


Figure 12. Photochromic mechanism in NiAl-$NO_3$-LDH: (a) structure before UV irradiation and (b) structure after UV irradiation.

 © 2006 Wiley-VCH Verlag GmbH & Co. KGaA, Weinheim 

## Conclusions

Photochromism in NiAl-$NO_3$-LDHs has been studied in this work. The crystalline structure and chemical composition of NiAl-$NO_3$-LDHs have been characterized on the basis of the results of PXRD, FTIR, EXAFS, and elemental analysis. The studies on the influence of aging conditions indicate that the host–guest interaction between the nickel ion in the host layer and the interlayer $NO_3^-$ plays an important role in its photochromic behavior. Taking into account the confirmation by EXAFS data that the $Ni^{2+}$ ions are sixfold coordinated, the ESR spectroscopy data that indicates that $Ni^{2+}$ is ESR active in NiAl-$NO_3$-LDHs, the confirmation of the presence of some unexchangeable $NO_3^-$, and the exclusion of the redox of $Ni^{2+}$, it can be concluded that there is a specific unit of distorted octahedral structure. This unit consists of a $Ni^{2+}$ ion, which is coordinated by O atoms from five hydroxy groups and one nitrate anion, and results in photochromism in NiAl-$NO_3$-LDHs.

## Experimental Section

**Preparation of NiAl-$NO_3$-LDH:** NiAl-$NO_3$-LDH was synthesized by a hydrothermal method.[29] Typically, an aqueous solution of NaOH (24 g, 0.6 mol) in deionized water (40 mL) was added dropwise to a vigorously stirred, freshly prepared solution containing $Ni(NO_3)_2{\cdot}6H_2O$ (58.156 g, 0.2 mol) and $Al(NO_3)_3{\cdot}9H_2O$ (37.513 g, 0.1 mol) ($Ni^{2+}/Al^{3+}$ = 2) in deionized water (100 mL) under a nitrogen atmosphere at room temperature. The final pH was approximately 6. The suspension was transferred to a Teflon-lined autoclave and heated at 70, 100, 130, 150, or 180 °C for a specific time. The solid precipitate was collected by filtration through a membrane filter under suction, washed thoroughly with water, and dried at 70 °C for 18 h.

**Preparation of MgAl-$NO_3$-LDH and ZnAl-$NO_3$-LDH:** MgAl-$NO_3$-LDH and ZnAl-$NO_3$-LDH, which were used as comparison samples, were synthesized by a hydrothermal method. MgAl-$NO_3$-LDH was synthesized by a procedure similar to that described previously.[30] A solution of $Mg(NO_3)_2{\cdot}6H_2O$ (32.0 g, 0.125 mol) and $Al(NO_3)_3{\cdot}9H_2O$ (11.7 g, 0.062 mol) in deionized water (200 mL) was added dropwise over 2 h to a solution of NaOH (12.5 g, 0.310 mol) and $NaNO_3$ (18.2 g, 0.210 mol) in water (250 mL). The mixture was transferred to a Teflon-lined autoclave and heated at 70 °C for 24 h. The precipitate was separated by centrifugation, washed with water, and dried at 70 °C for 18 h. ZnAl-$NO_3$-LDH was obtained by a similar method.

**Preparation of NiAl-$CO_3$-LDH:** NiAl-$CO_3$-LDH was prepared by both coprecipitation and ion exchange. The sample prepared by the coprecipitation method was synthesized according to a literature procedure.[31] In the case of the NiAl-$CO_3$-LDH sample obtained by ion exchange, the precursor NiAl-$NO_3$-LDH was synthesized first by the procedure described above. Subsequently, a solution of $Na_2CO_3$ in deionized water (50 mL) was added to a suspension of NiAl-$NO_3$-LDH in water (50 mL), and the mixture was then heated to 70 °C for 24 h. The product was washed extensively with deionized water, centrifuged, and dried at 70 °C for 18 h.

### Characterization Techniques

PXRD patterns were obtained by using a Shimadzu XRD-6000 diffractometer under the following conditions: Cu-$K_\alpha$ radiation ($\lambda$ = 1.542 Å, $2\theta$ = 2–70°), 40 kV, 30 mA. Infrared spectra of samples were recorded by using a Bruker Vector 22 FTIR spectrometer. Specimens were prepared as KBr pellets. Elemental analysis of the metal content was performed with an ICPS-7500 inductively coupled plasma optical-emission spectrometer. C, H, and N elemental analysis was carried out with an Elementar Vario elemental analyzer. The ESR spectra were recorded at room temperature with a Bruker ESP300 spectrometer. A standard 100 MHz field modulation and a 5–10 G modulation width were used. XPS was recorded with a VG Scientific ESCALab220i-XL (VG Scientific Ltd., UK) spectrometer.

The EXAFS spectrum around the Ni *K*-adsorption edge was obtained by using the beamline 4W1B of the Beijing Synchrotron Radiation Facility (BSRF). The NiAl-$NO_3$-LDH nanoparticles were homogeneously smeared on Scotch adhesive tape. More than eight layers were folded to reach the optimum absorption thickness. The X-ray absorption spectrum of the Ni *K*-edge of NiAl-$NO_3$-LDH was collected at ambient temperature in the transmission mode. The storage ring was operated at 2.2 GeV with a typical current of 50 mA. Fixed-exit Si(111) flat double crystals were used as a monochromator. The incident and transmission X-ray intensities were detected by using ion chambers installed in front of and behind the sample. The X-ray energy was calibrated by using the Ni *K*-absorption edge (8348 eV). The absorption spectrum was collected from 200 eV below the absorption threshold to over 700 eV above the threshold.

EXAFS data reduction was performed by using WinXAS 97 1.1 and following standard procedures. The first maximum of the first derivative of the absorption edge was chosen as the energy threshold. The pre-edge absorption background was fitted and subtracted by using a linear function. A derivative method was used to derive the EXAFS signal and remove the post-edge absorption background. EXAFS functions were normalized by using the absorption-edge jump and were Fourier-transformed to *R* space with $k^1$-weight in the range 1.1–11.3 Å. Fourier filters were used in the range 0.3–1.8 Å. Theoretical scattering paths for the fit were calculated by using the structures of α-$Ni(OH)_2$. To reduce the number of adjustable parameters, the amplitude reduction factor, $S_0^2$, was fixed at 1.1. The $R_{Ni–O}$ values are estimated to be accurate to 0.02 Å, and the $\Delta E_0$ and $CN_{Ni–O}$ values are estimated to be accurate to 20%. The accuracy estimates are based on the results of theoretical fits to the spectra of the reference compounds of known structure.

**Study of the Photochromic Properties of LDHs:** UV irradiation was carried out by using a 500-W xenon lamp. Absorption spectra were recorded by using a UV/Vis spectrophotometer (Shimadzu UV-2501 PC).

## Acknowledgments

This project was supported by the National Natural Science Foundation Key Project of China (Project No.: 90306012), the National Basic Research Program (973 Program) (Project No.: 2004CB720602), the Ministry of Education Science and Technology Research Project of China (Project No.: Key 104239), the Beijing Nova Program (No.: 2004A13), and the Program for Changjiang Scholars and Innovative Research Team in University (PCSIRT). We also acknowledge the Beijing Synchrotron Radiation Facility (BSRF) for provision of synchrotron radiation facilities and thank Dr. Yaning Xie and Tao Liu for assistance in using beamline 4W1B.

 © 2006 Wiley-VCH Verlag GmbH & Co. KGaA, Weinheim 

[1] M. Meyn, K. Beneke, G. Lagaly, *Inorg. Chem.* **1990**, *29*, 5201–5207.
[2] G. A. Caravaggio, C. Detellier, Z. Wronski, *J. Mater. Chem.* **2001**, *11*, 912–921.
[3] A. Corma, V. Fornes, F. Rey, A. Cervilla, E. Llopis, A. Ribera, *J. Catal.* **1995**, *152*, 237–242.
[4] M. Ogawa, K. Kuroda, *Chem. Rev.* **1995**, *95*, 399–438.
[5] H. Tagaya, A. Ogata, T. Kuwahara, S. Ogata, M. Karasu, J. I. Kadokawa, J. Chiba, *Microporous Mater.* **1996**, *7*, 151–158.
[6] B. Sels, D. De Vos, M. Buntinx, F. Pierard, A. Kirsch-De Mesmaeker, P. Jacobs, *Nature* **1999**, *400*, 855–857.
[7] L. Ukrainczyk, M. Chibwe, T. J. Pinnavaia, S. A. Boyd, *Environ. Sci. Technol.* **1995**, *29*, 439–445.
[8] A. M. Fogg, V. M. Green, H. G. Harvey, D. O'Hare, *Adv. Mater.* **1999**, *11*, 1466–1469.
[9] A. M. Fogg, J. S. Dunn, S. G. Shyu, D. R. Cary, D. O'Hare, *Chem. Mater.* **1998**, *10*, 351–355.
[10] A. I. Khan, L. Lei, A. J. Norquist, D. O'Hare, *Chem. Commun.* **2001**, 2342–2343.
[11] V. Ambrogi, G. Fardella, G. Grandolini, L. Perioli, *Int. J. Pharm.* **2001**, *220*, 23–32.
[12] P. V. Kamath, M. Dixit, L. Indira, A. K. Shukla, V. G. Kumar, N. Munichandraiah, *J. Electrochem. Soc.* **1994**, *141*, 2956–2959.
[13] A. Sugimoto, S. Ishida, K. Hanawa, *J. Electrochem. Soc.* **1999**, *146*, 1251–1255.
[14] J. C. Crano, T. Flood, D. Knowles, A. Kumar, B. Van Gemert, *Pure Appl. Chem.* **1996**, *68*, 1395–1398.
[15] J. M. Lehn, *Supramolecular Chemistry*, VCH, Weinheim, **1995**, p. 105.
[16] F. Vogtle, *Supramolekulare Chemie*, Teubner, Stuttgart, **1992**, ch. 7.
[17] J. Peretti, J. Biteau, J. P. Boilot, F. Chaput, V. I. Safarov, J. M. Lehn, A. Fernandez-Acebes, *Appl. Phys. Lett.* **1999**, *74*, 1657–1659.
[18] K. Schaffner, S. E. Braslavsky, A. R. Holzwarth, *Adv. Photochem.* **1990**, *15*, 229–277.
[19] H. Tagaya, T. Kuwahara, S. Sato, J. I. Kadokawa, M. Karasu, K. Masa, K. Chiba, *J. Mater. Chem.* **1993**, *3*, 317–318.
[20] H. Tagaya, S. Sato, T. Kuwahara, J. I. Kadokawa, K. Masa, K. Chiba, *J. Mater. Chem.* **1994**, *4*, 1907–1912.
[21] A. M. Scheidegger, E. Wieland, A. C. Scheinost, R. Dahn, P. Spieler, *Environ. Sci. Technol.* **2000**, *34*, 4545–4548.
[22] A. Davidson, J. F. Tempere, M. Che, *J. Phys. Chem.* **1996**, *100*, 4919–4929.
[23] P. Dufresne, E. Grimblot, J. P. Bonnelle, *J. Phys. Chem.* **1981**, *85*, 2344–2351.
[24] A. Tersis, S. Filippakis, H. J. Kuzel, H. Burzlaff, *Z. Kristallogr.* **1987**, *181*, 29–34.
[25] R. Allmann, J. Neues, *Neues Jahrb. Mineral. Monatsh.* **1977**, *3*, 136–144.
[26] M. Francois, G. Renaudin, O. Evrard, *Acta Crystallogr. Sect. A* **1998**, *54*, 1214–1217.
[27] G. Renaudin, M. Francois, *Acta Crystallogr. Sect. A* **1999**, *55*, 835–838.
[28] P. N. Steven, J. William, *J. Solid State Chem.* **1999**, *148*, 26–40.
[29] F. Prinetto, D. Tichit, R. Teissier, B. Coq, *Catal. Today* **2000**, *55*, 103–116.
[30] J. H. Lee, S. W. Rhee, D. Y. Jung, *Chem. Mater.* **2004**, *16*, 3774–3779.
[31] F. Kooli, K. Kosuge, A. Tsunashima, *J. Solid State Chem.* **1995**, *118*, 285–291.

Received: January 20, 2006
Published Online: May 9, 2006

 © 2006 Wiley-VCH Verlag GmbH & Co. KGaA, Weinheim 

DOI: 10.1002/ejic.200600099

# Synthesis, Electrochemical and Electrogenerated Chemiluminescence Studies of Ruthenium(II) Bis(2,2′-bipyridyl){2-(4-methylpyridin-2-yl)benzo[*d*]-X-azole} Complexes

**Roberto Gobetto,*[a] Giuseppe Caputo,[b] Claudio Garino,[a] Simona Ghiani,[a] Carlo Nervi,[a] Luca Salassa,[a,c] Edward Rosenberg,*[c] J. B. Alexander Ross,[c] Guido Viscardi,[d] Gianmario Martra,[b] Ivana Miletto,[d] and Marco Milanesio[e]**

**Keywords:** Electrochemistry / Luminescence / Ruthenium / ECL / Bioinorganic chemistry

A series of photoactive complexes of [$Ru^{II}$bis(bipyridyl){2-(4-methylpyridin-2-yl)benzo[*d*]-X-azole}]$(PF_6)_2$ (X = N–$CH_3$, **1**; S, **2**; or O, **3**) have been synthesized and fully characterized by proton and $^{13}C$ NMR spectroscopy and UV/Vis spectroscopy. The X-ray structure of **1** is also reported. The electrochemical behavior and the photophysical properties of **1**–**3** have been investigated. Cyclic voltammetry (CV) reveals the presence of three consecutive one-electron reduction processes and a single one-electron oxidation process that are chemically and electrochemically reversible. In all cases, electrogenerated chemiluminescence (ECL) has been observed in the presence of the co-reactant tri-*n*-propylamine (TPA). An analogue of **1** has been synthesized, [$Ru^{II}$bis(bipyridyl){2-(4-methylpyridin-2-yl)benzo[*d*]-X-azole}]$(PF_6)_2$ [X = $N(CH_2)_5CO_2H$, **4**], it has been coupled with bovine serum albumin (BSA), and its photophysical properties investigated.
(© Wiley-VCH Verlag GmbH & Co. KGaA, 69451 Weinheim, Germany, 2006)

## Introduction

Luminescent techniques are among the fastest-growing analytical tools in life science and analytical chemistry.[1] These techniques are useful because they couple high sensitivity and selectivity with automated monitoring. Furthermore, many parameters can be detected: luminescence intensity, quantum yield, lifetime, luminescence polarization, quenching efficiency, and radiative and nonradiative energy transfer.

In recent years, metal–ligand complexes (MLCs) have gained paramount importance in luminescence spectroscopy because of their wide range of absorption and emission wavelengths and their long decay times, which range from 100 ns to 10 μs.[1] Careful selection of metal and ligand can result in properties that are helpful for specific applications; for example, absorption wavelengths between 460 and 700 nm can be obtained using osmium and ruthenium in MLCs. Also, ruthenium complexes have been used as lifetime-based optical sensors for pH,[2,3] potassium,[4] chloride,[5] and carbon dioxide detection.[6] In addition, ruthenium complexes have been developed as luminescent probes for immunoassays.[7–10] Furthermore, the rotation of proteins and other macromolecules can be studied by a combination of polarized emission and time-resolved measurements in the microsecond range. Lastly, the use of ruthenium complexes in place of ethidium bromide in DNA analysis has also been reported.[11] In this application, the probe's luminescence increases when it intercalates into double-stranded DNA. Thus, the spectral and temporal resolution of MLC-based excited-state microscopy can result in increased resolution and probe selectivity for biological applications.

Our focus is the development of novel electrogenerated chemiluminescence (ECL) devices suitable for the detection of different biological analytes of clinical and environmental interest. To this end, we report the synthesis, characterization, redox behavior, and photophysical properties of the series of complexes [$Ru^{II}$bis(bipyridyl){2-(4-methylpyridin-2-yl)benzo[*d*]-X-azole}]$(PF_6)_2$ (X = N–$CH_3$, **1**; S, **2**; or O, **3**). The use of [2-(4-methylpyridin-2-yl)-1*H*-benzoimidazole] (X = NH) as a free ligand offers the opportunity to introduce a substituent in the 1*H* position suitable for bioconjugation using standard synthetic organic techniques. As an example of a biological application, we also

[a] Dipartimento di Chimica IFM, MI Center of Excellence, Università di Torino,
Via P. Giuria 7, 10125 Torino, Italy
[b] Dipartimento di Chimica IFM, NIS Center of Excellence, Università di Torino,
Via P. Giuria 7, 10125 Torino, Italy
[c] Department of Chemistry, University of Montana,
Missoula, MT 59812, USA
[d] Dipartimento di Chimica Generale ed Organica Applicata and NIS Centre of Excellence, Università di Torino,
Corso M. D'Azeglio 48, 10125 Torino, Italy
[e] Dipartimento di Scienze e Tecnologie Avanzate, Università del Piemonte Orientale,
"A. Avogadro", Via Bellini 25/G, 15100 Alessandria, Italy
E-mail: roberto.gobetto@unito.it
Supporting information for this article is available on the WWW under http://www.eurjic.org or from the author.

 © 2006 Wiley-VCH Verlag GmbH & Co. KGaA, Weinheim 

report the synthesis of an analogue of **1** in which the methyl group is substituted by 1-hexanoic acid and the resulting complex, **4**, is bioconjugated to bovine serum albumin (BSA) through an amidic bond. Photophysical investigations show efficient luminescence and ECL properties for all the derivatives. The synthesis of **2** and **3** also allows us to evaluate how the electronic and photophysical properties of the metal complex are affected by subtle alterations in the bidentate heterocyclic ligand.

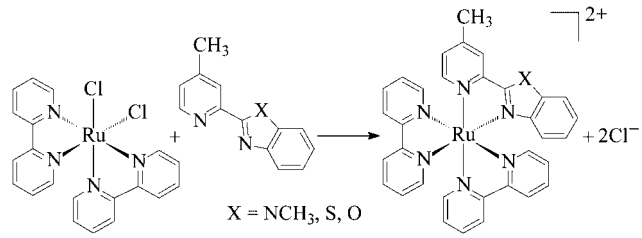


Scheme 1.

## Results and Discussion

Following our synthesis of novel metal complexes of ruthenium and osmium with potentially useful fluorescence properties,[12,13] we investigated the reactivity of $Ru(bpy)_2Cl_2$ with bidentate ligands of formula 2-(4-methylpyridin-2-yl)benzo[*d*]-X-azole (X = N–$CH_3$, S, or O). The choice of this unsymmetrical bidentate ligand, which has a single, easily modifiable site in the case of the benzimidazole ligand, avoids the formation of unwanted isomeric species, which are often difficult to separate from the desired product.

The reaction of $Ru(bpy)_2Cl_2$ with 2-(4-methylpyridin-2-yl)benzo[*d*]-X-azole (X = N–$CH_3$, S, or O) in refluxing ethylene glycol gives a single orange crystalline product in good yield for all the ligands that have been identified as **1**, **2**, and **3** respectively (Scheme 1). The products have been recrystallized as $PF_6^-$ salts and in the case of **1**, analyzed by single-crystal X-ray diffraction.

### Crystal Structure of [$Ru^{II}$bis(bipyridyl){2-(4-methylpyridin-2-yl)benzo[*d*]-X-azole}]$(PF_6)_2$ (X = N–$CH_3$, 1)

The crystal structure of **1** is illustrated in Figure 1, crystallographic data are given in Table 5, and selected distances and angles are given in Table 1. The asymmetric unit of the complex is arranged in the $P2_1/c$ space group. Two $PF_6^-$ anions assure the electrical neutrality of the structure. As already observed in related structures,[13,14] the $PF_6^-$ moieties are rather mobile, as evidenced by their large equivalent atomic displacement parameters (ADP), ranging from 0.090(1) for F(2) to 0.149(2) for F(5). Also the atoms belonging to the bpy and 2-pyridyl-benzimidazole ligands show large ADP values. The magnitudes of the ADP increase with increasing distance from the ruthenium atom, as expected. For example, the 6 N atoms, N(1)–N(6), bonded to Ru show ADP values in the range 0.044(1)–0.048(1), whereas C(33), the atom furthest away from the Ru atom, has an ADP value of 0.114(3).

The geometry around the Ru atom is a fairly regular octahedron with five-membered chelate rings having bite

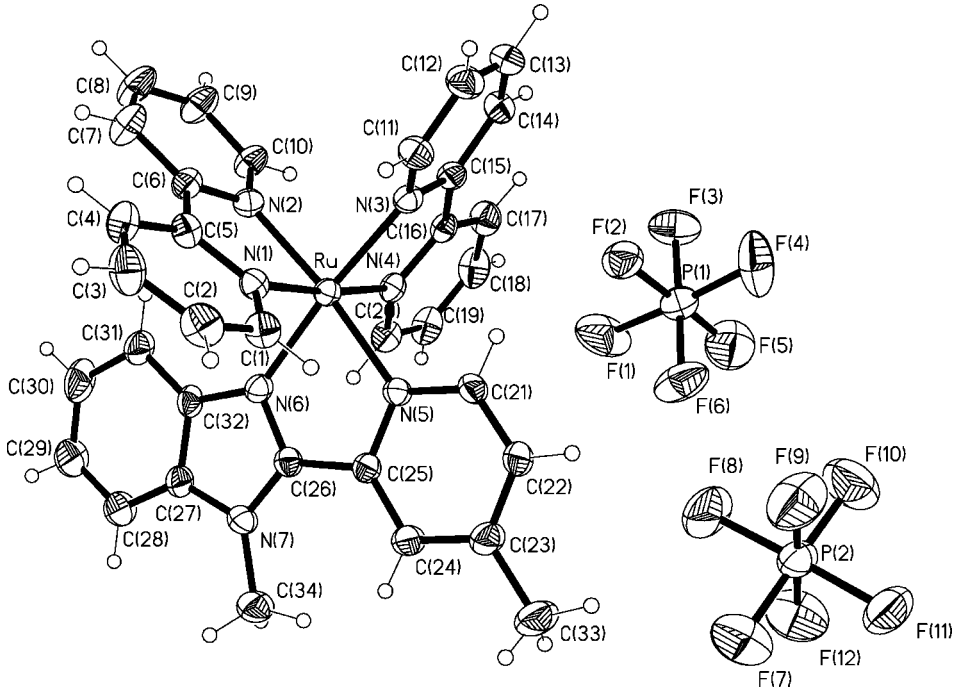


Figure 1. Molecular structure of compound **1** showing the adopted labeling scheme, with displacement ellipsoids drawn at 20% probability. A half-populated $CH_3CN$ moiety, located in the electron density, is not shown for the sake of clarity.

 © 2006 Wiley-VCH Verlag GmbH & Co. KGaA, Weinheim 

Table 1. Selected distances and bond angles for **1**.[a]

| Distances [Å] | | | | | |
|---|---|---|---|---|---|
| Ru–N(1) | 2.051(4) | N(6)–C(32) | 1.399(6) | N(1)–C(5) | 1.357(6) |
| Ru–N(2) | 2.050(4) | N(6)–C(26) | 1.335(5) | N(2)–C(6) | 1.349(6) |
| Ru–N(3) | 2.066(4) | C(25)–C(26) | 1.469(6) | N(2)–C(10) | 1.353(6) |
| Ru–N(4) | 2.064(4) | N(5)–C(25) | 1.364(6) | N(7)–C(26) | 1.356(6) |
| Ru–N(5) | 2.078(4) | N(5)–C(21) | 1.343(6) | N(7)–C(27) | 1.395(6) |
| Ru–N(6) | 2.060(4) | N(1)–C(1) | 1.324(6) | | |
| **Angles [°]** | | | | | |
| N(1)–Ru–N(2) | 78.9(2) | N(1)–Ru–N(4) | 174.3(1) | N(1)–Ru–N(3) | 97.6(2) |
| N(3)–Ru–N(4) | 78.9(2) | N(2)–Ru–N(5) | 173.0(1) | N(1)–Ru–N(5) | 95.6(2) |
| N(5)–Ru–N(6) | 77.4(1) | N(3)–Ru–N(6) | 173.3(2) | N(2)–Ru–N(4) | 96.3(2) |
| N(1)–Ru–N(6) | 88.5(2) | C(26)–N(6)–C(32) | 105.4(4) | N(3)–Ru–N(5) | 99.1(1) |
| N(2)–Ru–N(3) | 85.9(2) | C(21)–N(5)–C(25) | 116.9(4) | N(4)–Ru–N(6) | 95.3(2) |
| N(4)–Ru–N(5) | 89.4(1) | C(6)–N(2)–C(10) | 116.8(4) | | |

[a] Numbers in parentheses are estimated standard deviations.

angles of 78.8(2)°, and the angles between the chelate rings are divided into the usual two groups of 85.9–88.5(2)° and 95.6–99.1(2)° (Table 1). This geometry is very similar to the closely related complex $[Ru(bpy)_2(bbbpyH_2)](ClO_4)_2$ [$bbbpyH_2$ = 2,2′-bis(benzimidazol-2-yl)-4,4′-bipyridine][15] and to bis(bipyridyl) complexes in general.[16,17] Similarly, the Ru–N bipyridyl bond lengths [2.050–2.078(4) Å] and the benzimidazole bond length [Ru–N(6) = 2.060(4) Å] are very similar to Ru–N bonds in the related complexes.[16,17] The N(6)–C(32) and N(6)–C(26) bond lengths of 1.399(6) and 1.335(5) Å are also similar to the previously reported Ru-benzimidazole complex [1.39(1) and 1.35(1) Å] as are the other N–C bonds within the bipyridyl rings.[15] Although it is dangerous to draw conclusions about relative bond strengths from metal–ligand bond lengths alone, it would seem from these data that the benzimidazole ring has donor properties similar to those of the pyridinyl ligands and that these properties are relatively insensitive to substitution of a methyl group in the 3-position of the ring.

In the solid state, the cationic and anionic moieties are vertically stacked in layers (Figure 2), and are stabilized by ionic interactions between anions and cations and by weak C–H···F interactions (dotted lines in Figure 2). The layers are connected by $PF_6^-$ ions to form a low-density structure – 1.570 $Mg/m^3$ is small for a Ru-containing compound – with channels containing two acetonitrile molecules in half-occupancy. The acetonitrile positions are represented in Figure 2 by circles located in the acetonitrile centers of mass. The acetonitrile molecules are only weakly bound to the cation–anion couple by weak CH···F and CH···N interactions, depicted by broken lines in Figure 3. The geometric features of the C(36)–H···F and C–H···N(8) interactions that are shorter than 3.0 Å are reported in Table 2. The contact distances are large, being just within twice the standard deviation of the sum of the van der Waals radii ($vdW_N + vdW_H$ = 2.75 Å, $vdW_F + vdW_H$ = 2.64 Å) except in the case of the C(36)–H(36B)···F8 contact. Because of the long contact distances, the acetonitrile moiety can be accommodated by optimizing the contact angles, which range from 124(1)° to 154(1)°. The acetonitrile moieties thus have considerable freedom of movement and, in fact, they are disordered in the crystal structure and can be successfully refined only by imposing a 1/2 population of the N(8), C(1), and C(2) atoms.

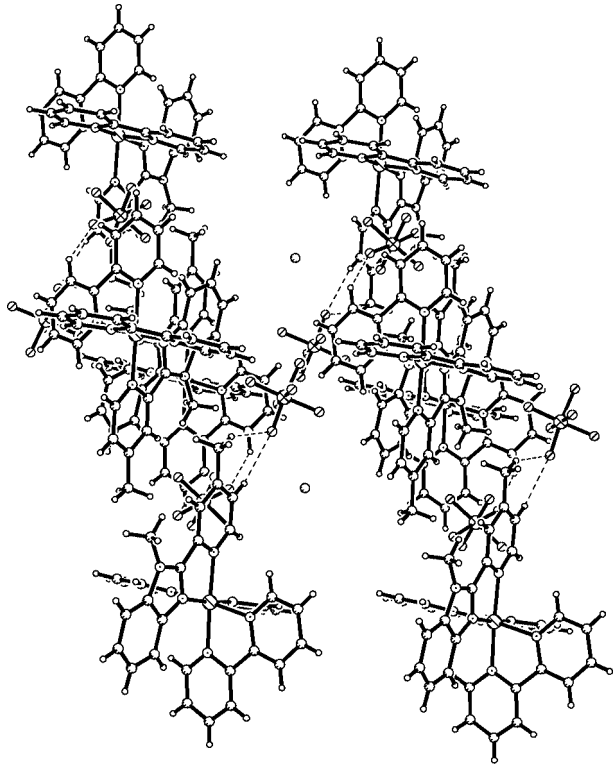

Figure 2. Crystal packing of compound **1**, showing the channels between the layers formed by the $[Ru(bpy)_2(LegN)](PF_6)_2$ ionic couples. Acetonitrile positions are indicated by their center of mass.

## NMR Spectroscopy

The $^1H$ NMR spectrum (Figure 4, top) of **1** recorded in acetone is entirely consistent with the structure found in the solid state, showing 22 proton resonances in the aromatic region from 7.10 to 8.82 ppm and one at $\delta$ = 5.94 ppm. Sixteen signals belong to protons of the two-bpy moieties and the other seven are assigned to the 2-(4-methylpyridin-

 © 2006 Wiley-VCH Verlag GmbH & Co. KGaA, Weinheim 

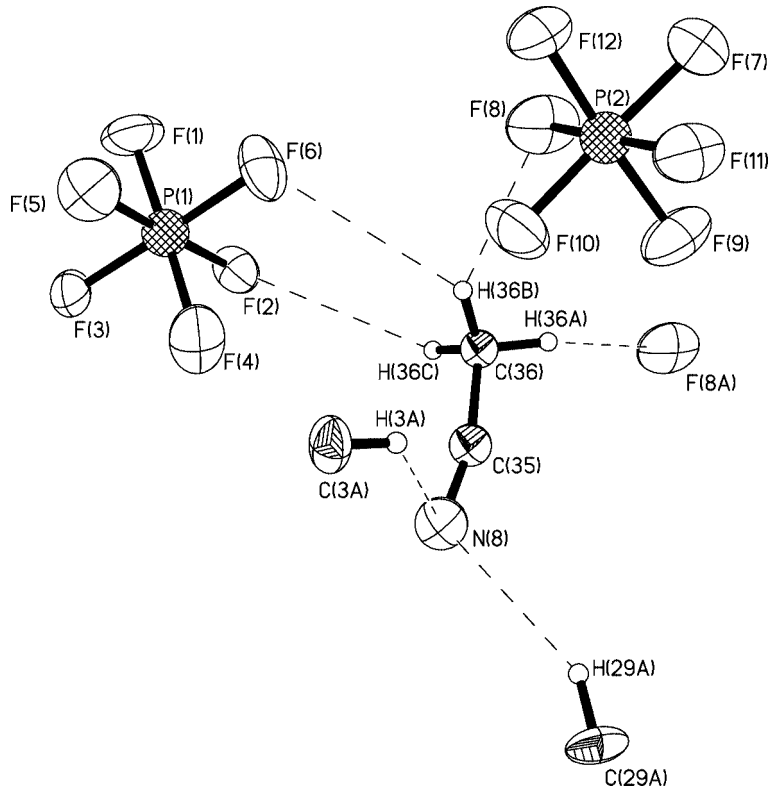


Figure 3. The weak interactions, observed in the solid state, between the acetonitrile moiety and the ions of **1**.

Table 2. Geometric features of the weak hydrogen bonds connecting the acetonitrile moiety and **1** (distances in Å and angles in °).[a]

| Compound | **1** |
|---|---|
| N(8)···H(3A) | 2.89(2) |
| N(8)···H(3A)–C(3A) | 135(1) |
| N(8)···H(29A) | 2.72(2) |
| N(8)···H(29A)–C(29A) | 154(1) |
| H(36A)···F(8A) | 2.84(2) |
| C(36–36A)···F(8A) | 147(1) |
| H(36B)···F(8) | 2.54(2) |
| C(36)–H(36B)···F(8) | 144(1) |
| H(36B)···F(6) | 2.98(2) |
| C(36)–H(36B)···F(6) | 133(1) |
| C(36)–H(36C)···F(2) | 2.82(2) |
| C(36)–H(36C)···F(2) | 124(1) |

[a] Numbers in parentheses are estimated standard deviations.

2-yl)-benzimidazole ligand. Furthermore, two other signals are observed at $\delta$ = 4.5 and 2.5 ppm, assigned to methyl groups of the benzimidazole and pyridine rings, respectively.

As for **1**, the spectra of **2** and **3** also show 23 proton resonances in the aromatic range and a signal at 2.6 ppm because of the 4-pyridine methyl group. The $^{13}C$ spectra of complexes **1**–**3** are also consistent with the proposed structures (see Figure 4, bottom for **1**).

### Electrochemistry

The cyclic voltammetric (CV) response in acetonitrile at a glassy carbon (GC) electrode for each of the Ru derivatives shows three sequential ligand-centered one-electron reductions (Figure 5, top) and a single metal-centered one-electron oxidation (Figure 5, bottom). The electrochemical behavior described is similar to that of the well-known $Ru(bpy)_3Cl_2$ and related complexes.[18] In the particular case of $Ru(bpy)_3Cl_2$, however, the chlorine ions undergo an additional irreversible oxidation in acetonitrile solutions.[19] We do not observe this particular oxidation process in the CV of complexes **1**–**3**, as the counterion is $PF_6^-$. The redox processes are chemically and electrochemically reversible, with $i_p^a/i_p^c \approx 1$ and $|E_p^c - E_p^a| \approx 60$–70 mV at scan rates ranging from 0.050 to 1.000 V/s. The half-wave redox potentials evaluated as a mean of the cyclic voltammetric anodic and cathodic peaks, as well as the peak-to-peak separations, are reported in Table 3. In the case of **1**, the processes centered at $E_{1/2}(+2/+3)$ = +0.732, $E_{1/2}(+2/+1)$ = –1.782, $E_{1/2}(+1/0)$ = –1.982, and $E_{1/2}(0/-1)$ = –2.215 V versus $Fc/Fc^+$ are shifted towards more negative values of about 0.2 V when compared with the corresponding values of **2** and **3**. This is in line with the better σ-donor electronic properties of the ligand containing nitrogen. In addition, the closely related mononuclear and dinuclear $Ru(bpy)_2$ complexes of the free ligand 2,2′-bis(benzimidazol-2yl)-4,4′-bipyridine have similar oxidation and reduction potentials.[15,20] The oxidation of $[Ru(bpy)_3]^{2+}$ is at the somewhat more positive potential [$E_{1/2}(+2/+3)$ = +0.881 vs. $Fc/Fc^+$] in acetonitrile, indicating that the benzimidazole ring is a slightly better donor than bipyridyl. On the contrary, reductions of compounds **2** and **3** occur at less negative potentials. The diffusion coefficient of **1** ($D_1$) relative to that

 © 2006 Wiley-VCH Verlag GmbH & Co. KGaA, Weinheim 

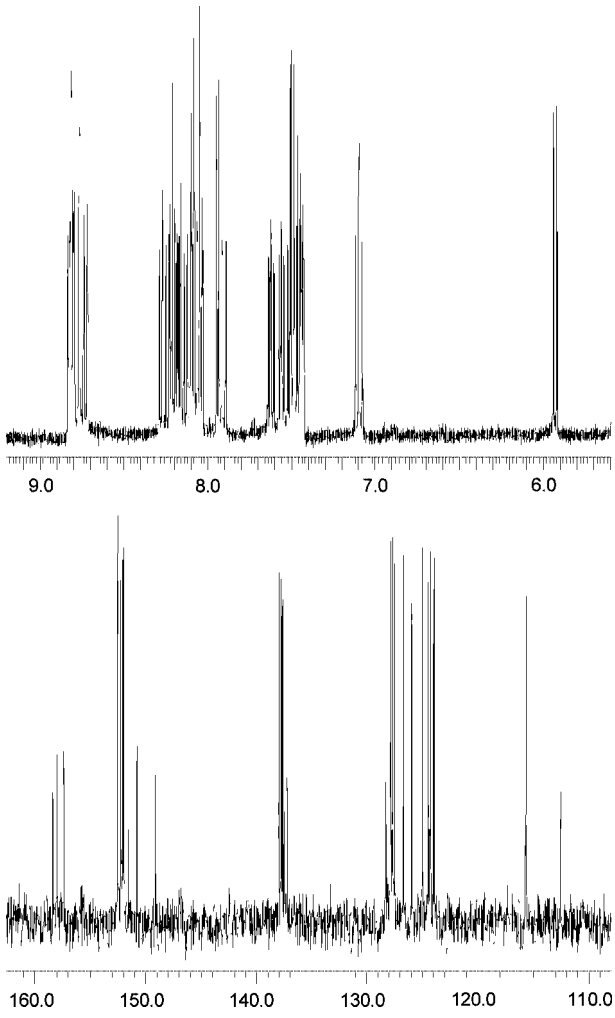


Figure 4. $^{1}H$ NMR expansion of the aromatic region and $^{13}C$ NMR of **1** at 400 MHz in acetone.

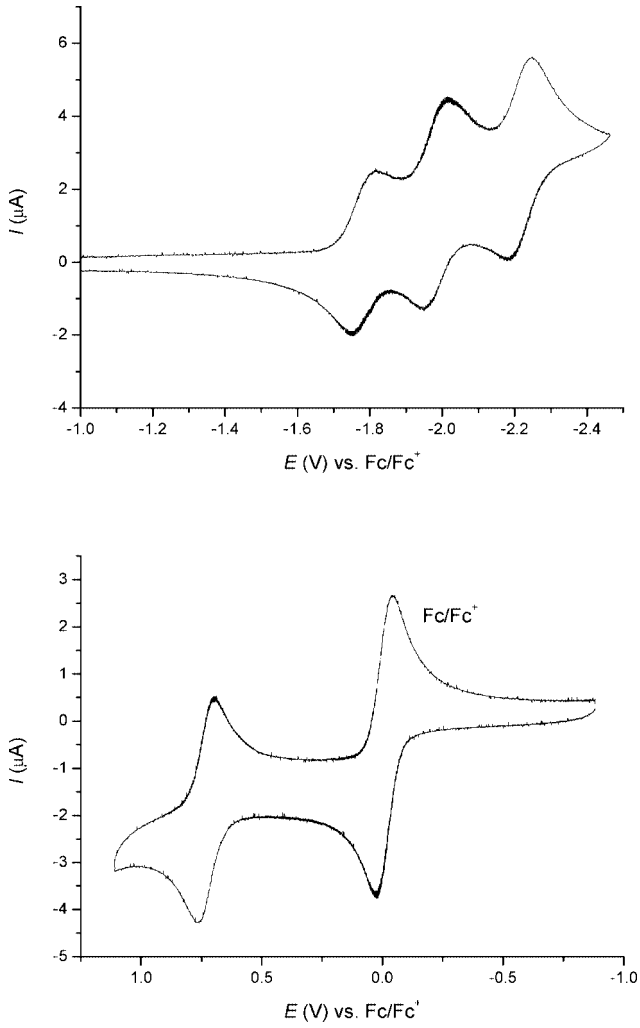


Figure 5. Top: cyclic voltammogram (reduction only) of a 1 mM solution of **1** in MeCN at a GC electrode, scan rate of 0.100 V/s. Bottom: cyclic voltammogram (oxidation only) of an equimolar (1 mM) solution of **1** and ferrocene in MeCN at a GC electrode, scan rate of 0.100 V/s.

of ferrocene ($D_{Fc}$) can be evaluated to be $D_{\mathbf{1}}/D_{Fc} = 0.588$ through the Nicholson–Shain equation[21] by means of the ratio between the anodic peak current of ferrocene and that of **1** (Figure 5, bottom) because the one-electron oxidation processes are Nernstian. Exactly the same value is obtained[22] by the Stoke–Einstein equation[23] using the crystallographic molecular volumes of **1** and ferrocene:[24]

$D_{\mathbf{1}}/D_{Fc} = (V_{Fc}/V_{\mathbf{1}})^{1/3} = (203.08\ Å^3/1001.5\ Å^3) \approx 0.587$

### Absorption Spectra and Photoluminescence

UV/Vis absorption spectra of **1**–**3** are characterized by several ligand-based transitions in the UV with metal-to-ligand charge transfer (MLCT) bands in the visible region. In $CH_3CN$ solution, the complexes display four absorption bands, three in the range of 250–400 nm attributable to the π-to-π* transitions of the bipyridine and heterocyclic rings and one in the 450–460 nm range assigned to a MLCT transition. The MLCT absorption bands display a maximum at 460 nm for **1** and at 450 nm for **2** and **3**. Their luminescent behavior has been investigated by acquiring emission spectra and by evaluating the molar extinction coefficient for absorption and the quantum yields of the emission after irradiation at $\lambda_{max}$ for the MLCT transition (Table 4).

Table 3. Redox potentials (V vs. $Fc/Fc^+$) and peak-to-peak separation in parenthesis (mV) at a scan rate of 0.1 V/s in acetonitrile for the reference $Ru(bpy)_3Cl_2$ and complexes **1**–**3**.

| $E_{1/2}$ | $Ru(bpy)_3Cl_2$ | **1** | **2** | **3** |
|---|---|---|---|---|
| +2/+3 | +0.881 (70) | +0.732 (65) | +0.920 (86) | +0.944 (77) |
| +2/+1 | –1.738 (66) | –1.782 (66) | –1.506 (75) | –1.579 (70) |
| +1/0 | –1.923 (69) | –1.982 (71) | –1.886 (77) | –1.898 (73) |
| 0/–1 | –2.165 (75) | –2.215 (66) | –2.138 (82) | –2.145 (85) |
| –1/–2 | –2.77 (irr) | –2.72 (irr) | –2.560 (72) | –2.63 (irr) |
| –2/–3 | | –2.91 (irr) | –2.98 (irr) | –2.89 (irr) |

The systems display broad emission spectra with maximums in energy at 634, 684, and 666 nm with Stoke's shifts of 174, 234, and 216 nm for **1**–**3**, respectively. Quantum efficiencies were found to be 0.021, 0.008, and 0.008 for **1**–**3**, respectively. These values were determined using $Ru(bpy_3)^{2+}$ ($\Phi_{em} = 0.062$)[25] as a standard (Table 4). The lumi-

 © 2006 Wiley-VCH Verlag GmbH & Co. KGaA, Weinheim 

Table 4. MLCT absorptions, extinction coefficient, emission properties, and ECL efficiencies for **1**–**3**.

| | $\lambda_{ex}$ (nm) | $\varepsilon$ | $\lambda_{em}$ (nm) | $\Phi_{em}$ | $\delta$ (nm) | $\tau$ (ns) | $\Phi_{ECL}$ |
|---|---|---|---|---|---|---|---|
| $Ru(bpy)_3^{2+}$ | 450 | 13300 | 614 | 0.062 | 164 | 890 | 1 |
| **1** | 460 | 12200 | 634 | 0.021 | 174 | 139 | 0.35 |
| **2** | 450 | 10700 | 684 | 0.008 | 234 | 184 | 0.04 |
| **3** | 450 | 10700 | 666 | 0.008 | 216 | 138 | 0.03 |

nescence lifetimes of the metal complexes, determined by time-correlated single-photon counting as described in Methods, were single exponential decays (see Table 4).

### Electrogenerated Chemiluminescence

Electrochemiluminescence (ECL) involves the production of reactive intermediates at the electrode surface from stable precursors. These intermediates can react in various ways to form excited states that emit light at or near the electrode surfaces. ECL has useful commercial applications in clinical analyses (e.g. immunoassays, DNA probes) using $Ru(bpy)_3^{2+}$ and a co-reactant to generate the signal. The co-reactant is generally defined as a species that, after electrochemical oxidation or reduction, produces intermediates that can react with other compounds in the solution and that are able to produce excited states. We used the well-known tri-*n*-propylamine (TPA) as co-reactant. Details of the mechanism by which TPA acts[26] are found in the excellent ECL review by Richter.[27] Compounds **1**–**3** show stable reversible electrochemistry, and therefore are promising ECL luminophores.

Solutions containing only the Ru complex or only the co-reactant do not give an ECL signal. The intense ECL signals resulting from the oxidation of TPA in aqueous solutions of all three complexes were acquired simultaneously with the CV in the potential range between 0 and +1.5 V, at a scan rate of 50 mV/s. The ECL efficiencies, $\Phi_{ECL}$, in water were estimated using the following equation:[28,29]

$$\Phi_{ECL} = \Phi°_{ECL}(IQ°/I°Q)$$

where $\Phi°_{ECL}$ is the ECL efficiency of the standard $Ru(bpy)_3Cl_2$ under the same conditions, $I$ and $I°$ are the integrated ECL intensities of the luminophore under investigation, and the standard, and $Q$ and $Q°$ are the charges passed (in coulombs) for the luminophore and the standard, respectively. In experiments performed with the co-reactant, the absolute ECL quantum efficiency for the reference system $Ru(bpy)_3Cl_2$/TPA is unknown, so relative efficiencies are reported taking its $\Phi°_{ECL} = 1$. The $\Phi_{ECL}$ values in Table 4 are a mean of the first three sequential measurements and are subject to an error of about ±10%. It has been reported that adsorption phenomena could influence the ECL emission.[30,31] Moreover, the MLCT states, and hence the luminescence properties, are sensitive to the nature of the environment and to the solvation shell.[32] Typical ECL responses are sketched in Figure 6.

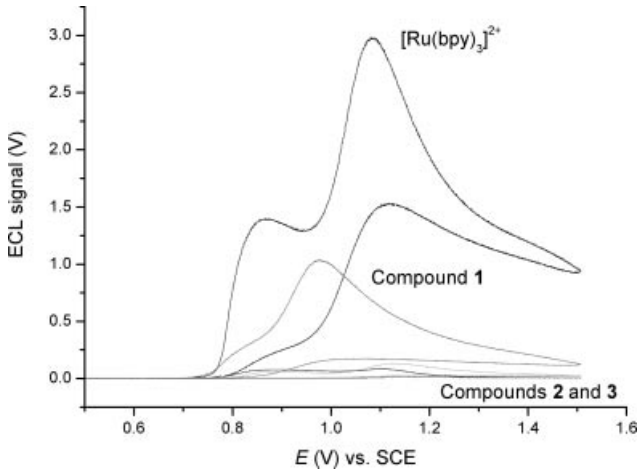


Figure 6. Electrochemiluminescence (ECL) of complexes **1**–**3** in the presence of tri-*n*-propylamine (TPA) in water borate buffer at pH = 8.5.

The presence of dissolved oxygen in water (acquired primarily from ambient air) is undesirable, as this often results in quenching of the luminophore. However, at the high TPA concentrations used in this work (20 mM), the influence of dissolved oxygen on the emission of the $Ru(bpy)_3^{2+}$/TPA system is negligible, provided the source of oxygen is air only.[33] For these reasons we performed all measurements in air.

Despite the limitations described above, it is worth noting that the $\Phi_{ECL}$ for **1** is almost an order of magnitude greater than either **2** or **3**. This is undoubtedly due to the lower oxidation potential of **1** relative to **2** and **3**. It is generally accepted that the primary mechanisms for producing ECL with $Ru(bpy)_3^{2+}$ in the presence of the co-reactant TPA are: (1) oxidation of $Ru(bpy)_3^{1+}$, produced by reduction of $Ru(bpy)_3^{2+}$ by $TPA^{\cdot}$ (this species results from ejection of a proton from the relatively long-lived $TPA^{\cdot+}$), which gives rise to an excited state $Ru(bpy)_3^{2+}$; and (2) reduction of electrochemically generated $Ru(bpy)_3^{3+}$ by $TPA^{\cdot}$ to give the same excited state $Ru(bpy)_3^{2+}$.[26] In the ECL spectrum reported in Figure 6, the first peak is due to the effect of the oxidation of TPA at the electrode, whereas the latter is relative to the oxidation of $Ru(bpy)_3^{2+}$.[26] In the case of **1**, its lower oxidation potential relative to **2** and **3** would contribute to both of these mechanisms. The better donor properties of the benzimidazole ligand are not only due to electronegativity considerations, but also to the expected greater contribution of the resonance structure (shown in Scheme 2) as a result of more efficient π overlap.

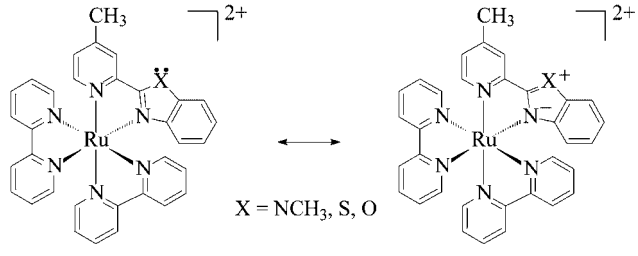


Scheme 2.

 © 2006 Wiley-VCH Verlag GmbH & Co. KGaA, Weinheim 

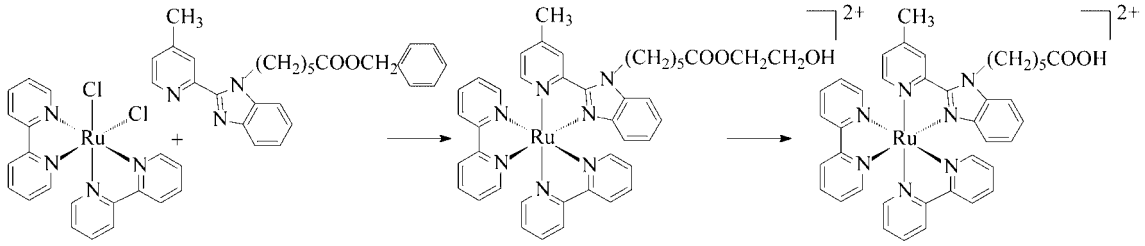

Scheme 3.

## Bioconjugation

Although the ECL efficiency of **1** is only about one-third that of $Ru(bpy)_3^{2+}$, its luminescent properties are sufficient to take advantage of the fact that the 2-(4-methylpyridin-2-yl)-benzo-X-azole (X = NH) ligand can be readily and regioselectively modified at the NH group with a linker suitable for bioconjugation. Thus, by reacting $Ru(bpy)_2Cl_2$ with the benzyl ester in ethylene glycol, an intermediate 1-hexanoic acid glycol ester analogue of **1** is obtained, which on acid hydrolysis yields the corresponding hexanoic acid complex **4** in good yield (Scheme 3).

This complex was characterized by one- and two-dimensional $^1H$ NMR and $^{13}C$ NMR spectroscopy. Complex **4** has virtually the same absorption spectrum as **1**, showing absorption maxima at 250, 290, 330, and 458 nm and emission band at 630 nm.

The reaction of **4** with *N*-hydroxysuccinimide (NHS) in the presence of dicyclohexylcarbodiimide (DCC) in anhydrous DMF gives the activated succinimide ester **4-NHS** (Scheme 4),[34] suitable for bioconjugation with BSA. The primary structures of BSA, a 67-kDa acidic protein with prolate ellipsoidal shape, and its human homologue, HSA,[35] are well established.[36] Among the 582 amino acids that form BSA, 59 lysines and one N-terminal residue are potentially available for the coupling. In nondenaturing conditions (i.e. low temperature, physiological pH, and low concentration of organic co-solvent), 30–40 lysines are believed to be accessible to coupling reagents.[37] The reaction was monitored by HPLC, and the unstable activated ester **4-NHS** was immediately incubated with BSA in borate buffer (pH = 8.5, ratio dye:protein = 10:1). The resulting **4**-BSA conjugate was purified by gel exclusion chromatography on a Sephadex G-25 M prepacked column with detection at 460 nm. The **4**-BSA conjugate showed an absorption spectrum virtually identical to that of **4** except for increased absorbance at 280 nm because of the protein (Figure 7). Irradiation of the **4**-BSA conjugate at 460 nm gave an emission at 630 nm, identical to that of **4** and very similar to that of **1** (Figure 8). It must be noted that, besides the similarity in shape, the photoluminescent signal of the solution of **4** alone and **4-BSA** equimolar in fluorophore (determined on the basis of the dye-to-protein ratio reported below) exhibited almost the same intensity, indicating that **4** maintains its $\Phi_{em}$ when linked to the protein. The dye-to-protein ratio of the **4**-BSA conjugate and the whole protein concentration were estimated by measuring the absorbance of **4-BSA** at 460 nm ($\varepsilon_{460}$ = 12200 $M^{-1}$/cm)[38,39] and by the Bradford method,[40] respectively. The molar dye-to-protein conjugation ratio of **4-BSA** was 1.2.

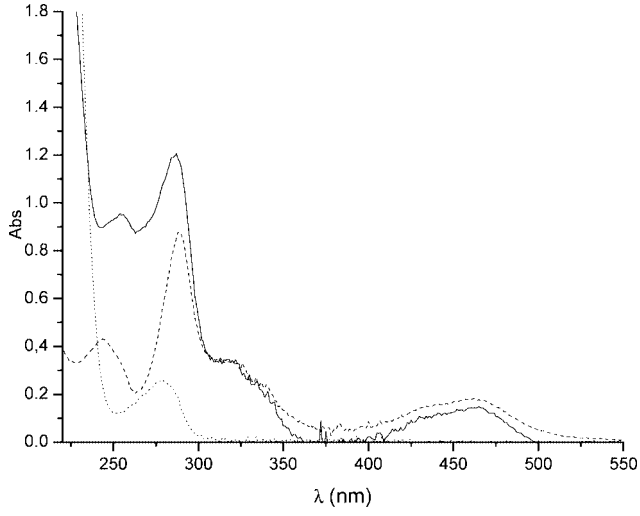


Figure 7. UV/Vis absorption spectra of BSA (···), **4** (----), and **4-BSA** (—) in water borate buffer at pH = 8.5.

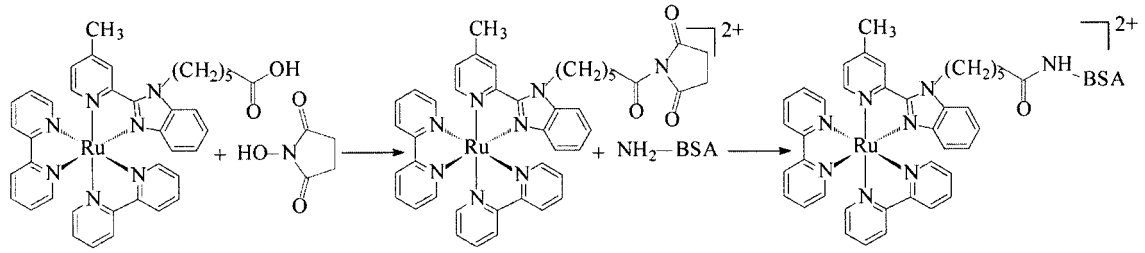

Scheme 4.

 © 2006 Wiley-VCH Verlag GmbH & Co. KGaA, Weinheim 

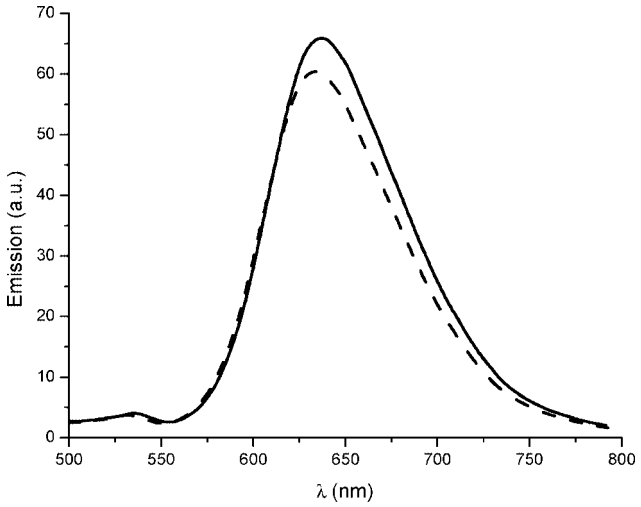


Figure 8. Emission spectra, obtained under irradiation at 460 nm, of **4** (---) and **4-BSA** (—) in water borate buffer at pH = 8.5.

## Conclusions

We report a new series of ruthenium complexes based on the ligand system 2-(4-methylpyridin-2-yl)benzo[*d*]-X-azole (X = N–$CH_3$, S, or O). The benzimidazole complex **1** exhibits the highest quantum yield for luminescence and also the highest ECL efficiency based on its superior donor properties. The X-ray crystal structure of **1** is reported. The photophysical and ECL properties of the series correlate well with their electrochemical properties, and this observation for a homologous series such as **1**–**3** lends support to the idea that such correlations should be general. This study shows also that the ECL emission of **1** in aqueous solutions with the co-reactant TPA is 0.35 times that of the reference compound $Ru(bpy)_3Cl_2$, still reasonably efficient for use as a biological marker. Furthermore, the protocol presented here for bioconjugation is particularly valuable because it provides a simple pathway that can be generalized for linking **4** to small peptides for selective conjugation to proteins and protein receptor sites. The carboxylic acid group in **4** can also be easily modified to target other functionalities besides primary amines.

Further studies are currently in progress for the synthesis of ruthenium derivatives bioconjugated to monoclonal antibodies to serve as novel photoluminescent and electrochemiluminescent probes for diagnostics at very low concentration.

## Experimental Section

**Materials:** Ruthenium(III) chloride hydrate was purchased from Lancaster and used as received. 2,2′-Bipyridine, obtained from Aldrich, was purified by crystallization from hexane and dried under vacuum over $P_2O_5$.[41] *cis*-$[Ru(bpy)_2Cl_2]\cdot 2H_2O$ was prepared according to the literature methods.[42] The intermediate 6-bromohexanoic acid benzyl ester[43] and the ligands 2-(4-methylpyridin-2-yl)benzo[*d*]-X-azole (X = N–$CH_3$, S, or O) and 2-(4-methylpyridin-2-yl)-1*H*-benzoimidazole[44,45] were prepared according to published procedures. Tetrabutylammonium hexafluorophosphate ($TBAPF_6$) was obtained as previously reported.[12] Acetonitrile was distilled from calcium hydride just before use. Triple-distilled water was used routinely. BSA was purchased from Fluka and used as received. Prepacked PD-10 columns Sephadex™ G-25 M were purchased from Amersham Biosciences. All other reagents and solvents, obtained from commercial suppliers, were of reagent grade and were used as received without any further purification. All the reactions involving the metal complexes were carried out in argon by standard Schlenk techniques.

**Physical Methods:** NMR spectra were recorded with a JEOL EX 400 spectrometer ($B_0$ = 9.8 T, $^1H$ operating frequency 399.78 MHz) with chemical shifts referenced to residual protons in the solvent ([$D_6$]acetone). Absorption spectra were measured at room temperature, using a DR LANGE CADAS 200 spectrophotometer, and emission spectra were measured with a Perkin Elmer LS 55 spectrofluorimeter.

Luminescence lifetimes were performed under magic angle polarization conditions by time-correlated single-photon counting[1] using excitation with picosecond pulses of 455-nm light at a repetition rate of 500 kHz generated by a Ti:Sapphire laser system (Verdi V10, Mira 900, and pulse picker from Coherent, Inc., Santa Clara, CA. Second harmonic generation was provided by a 5-050 system from Inrad, Northvale, NJ). The sample was maintained at 20 °C in an automated sample chamber (FLASC 1000 from Quantum Northwest, Spokane, WA). The emission was collected using a bandpass of 20 nm. The data were collected into 2048 channels (1 ns/channel) to 40000 counts in the peak channel. Because the excitation pulse is essentially a delta function at this time resolution, the decays were fit directly without reconvolution as sums of exponentials using Origin 7 (Northampton, MA 01060, USA). IR spectra were recorded with a V22 Bruker FTIR spectrophotometer with a resolution of 2 $cm^{-1}$ and an accumulation of 64 scans.

**Electrochemistry:** Electrochemistry was performed either with an EG&G PAR 273 electrochemical analyzer or with an AMEL potentiostat model 7050 connected to a PC. All experiments employed a standard three-electrode cell; the reference electrode was a 3 M KCl calomel electrode, the auxiliary electrode a platinum wire, and the working electrode a glassy carbon (GC) with a diameter of 1 mm (CV in acetonitrile) or 2 mm (ECL experiments in water). Positive feedback *iR* compensation was applied routinely. Measurements were carried out either in water or acetonitrile. The supporting electrolytes were 0.1 M phosphate buffer and tetrabutylammonium hexafluorophosphate ($TBAPF_6$), in water and acetonitrile, respectively.

Experiments in acetonitrile were carried out in argon. We used ferrocene (Fc) as an internal standard, and potentials are reported relative to the Fc(0/+1) redox couple [measured $E_{1/2}$(0/+1) = 0.384 V in MeCN, with a peak-to-peak separation of 65 mV]. The aqueous measurements were carried out in air, and the potentials reported relative to the 3 M KCl Calomel Electrode. The ECL along with the cyclic voltammetric (CV) signals (scan rate of 50 mV/s) were measured simultaneously with the AMEL 7050 combined with a photomultiplier tube (PMT, Hamamatsu H9306-03) installed under the electrochemical cell. A home-built power supply (±15 V) regulates the amplification of the PMT, which is directly proportional to the logarithm of the output (between 0 and 10 V). A dark cage, equipped with electrical connection for WE, RE, CE, stirring and inert gas inlet, was built around the electrochemical cell and the PMT, resulting in a background current at the maximum PMT amplification of about 18 ± 12 mV. The measurements were made at half-amplification, where the signal output is attenuated about 200 times with respect to the maximum of the amplifi-

 © 2006 Wiley-VCH Verlag GmbH & Co. KGaA, Weinheim 

cation. The concentration of the solutions employed were: TPA 20 mM, $Ru(bpy)_2LX$ $1.0\times10^{-6}$ M, supporting electrolyte 0.1 M.

**X-ray Structure Determination:** The crystal structure of **1** was solved by single-crystal X-ray diffraction analysis. Suitable crystals were obtained by slow evaporation of an acetonitrile–ethanol solution. Diffraction data were collected at room temperature on a Bruker SMART-APEX CCD[46] area detector diffractometer, using graphite monochromated Mo-$K_\alpha$ = 0.71073 Å radiation. Absorption correction was performed using SADABS.[47] The structure was solved by direct methods (SIR97)[48] and refined by full-matrix least-squares (SHELX97).[49] All hydrogen atoms were generated in their calculated positions with the XP[50] software and refined as riding atoms. All non-hydrogen atoms, except C1, C2, and N8 belonging to the acetonitrile molecule, were refined employing anisotropic ADP parameters. Two restraints on the C1–C2 and on the C2–N8 distances were used because of the disorder of the acetonitrile moiety. Crystallographic data and details of data collections and refinements are given in Table 5.

Table 5. Crystal data for **1**.

| | **1** |
|---|---|
| Empirical formula | $C_{35}H_{30.5}F_{12}N_{7.5}P_2Ru$[a] |
| Formula weight | 947.18 |
| Temperature [K] | 293(2) |
| Wavelength [Å] | 0.71069 |
| Crystal system | monoclinic |
| Space group | $P2_1/c$ |
| $a$ [Å] | 13.254(2) |
| $b$ [Å] | 12.129(2) |
| $c$ [Å] | 25.034(5) |
| $\alpha$ [°] | 95.49(3) |
| $V$ [Å$^3$] | 4005.9(2) |
| $Z$ | 4 |
| Density (calculated) [Mg/m$^3$] | 1.570 |
| Absorption coefficient [mm$^{-1}$] | 0.564 |
| $F$(000) | 1900 |
| Crystal size [mm] | $0.26\times0.24\times0.22$ |
| $\theta$ range for data collection [°] | 1.54–24.71 |
| Index range | $-15 \le h \le 15$<br>$-14 \le k \le 14$<br>$-29 \le l \le 29$ |
| Reflections collected | 46984 |
| Independent reflections | 6833 [$R_{int}$ = 0.0387] |
| Completeness to $\theta$ = 24.71° | 100.0% |
| Refinement method | full-matrix least-squares on $F^2$ |
| Data/restraints/parameters | 6833/2/512 |
| Goodness-of-fit on $F_2$ | 1.007 |
| Final $R$ indices [$I > 2\sigma(I)$] | $R_1$ = 0.0525, $wR_2$ = 0.1529 |
| $R$ indices (all data) | $R_1$ = 0.0681, $wR_2$ = 0.1587 |
| Largest diff. peak and hole [Å$^{-3}$] | 1.274 and –0.776 |

[a] The empirical formula has nonintegral values because of the half-populated $CH_3CN$ moiety.

CCDC-288567 contains the supplementary crystallographic data for this paper. These data can be obtained free of charge at www.ccdc.cam.ac.uk/data_request/cif.

**Synthesis of Complexes**

**[Ru(bpy)$_2${1-methyl-2-(4-methylpyridin-2-yl)-1*H*-benzo[*d*]imidazole}](PF$_6$)$_2$ (X = N–CH$_3$, 1):** $[Ru(bpy)_2Cl_2]\cdot2H_2O$ (0.200 g, $3.84\times10^{-4}$ mol) and 1-methyl-2-(4-methylpyridin-2-yl)-1*H*-benzo[*d*]imidazole (0.128 g, $5.73\times10^{-4}$ mol) were refluxed in ethylene glycol (50 mL) for 4 h. After cooling to room temperature, water (20 mL) and an aqueous $NH_4PF_6$ solution (1.0 g/10 mL) were added and the resulting precipitate was collected. The crude product was recrystallized from acetonitrile/ethanol. The sample was dried under vacuum for several hours before elemental analysis. Yield: 0.286 g (80.4%).

$C_{34}H_{29}F_{12}N_7P_2Ru$ (926.65): calcd. (from **1** without crystallization solvent) C 44.07, H 3.15, N 10.58; found C 43.80, H 3.65, N 9.59. $^1$H NMR (400 MHz, [D$_6$]acetone): $\delta$ = 8.82 (m, 3 H), 8.77 (s, 1 H), 8.73 (d, 1 H, $J$ = 8.05 Hz), 8.28 (t of d, 1 H, $J_1$ = 7.87, $J_2$ = 1.46 Hz), 8.16 (m, 5 H), 8.05 (t, 2 H, $J_1$ = 6.04 Hz), 7.95 (d, 1 H, $J$ = 8.86 Hz), 7.91 (d, 1 H, $J$ = 8.54 Hz), 7.63 (m, 1 H), 7.57 (m, 1 H), 7.48 (m, 4 H), 7.10 (t, 1 H, $J$ = 7.81 Hz), 5.94 (d, 1 H, $J$ = 8.42 Hz), 4.59 (s, 3 H), 2.63 (s, 3 H) ppm. $^{13}$C NMR (100 MHz, [D$_6$]acetone): $\delta$ = 159.92, 159.54, 158.96, 158.92, 154.06, 154.03, 153.77, 153.61, 153.53, 153.09, 152.30, 150.65, 142.24, 139.50, 139.32, 139.18, 139.00, 138.78, 129.85, 129.43, 129.36, 129.22, 129.04, 128.22, 127.50, 126.53, 126.01, 125.85, 125.78, 125.48, 117.19, 114.02, 34.62, 22.00 ppm.

**[Ru(bpy)$_2${2-(4-methylpyridin-2-yl)benzo[*d*]thiazole}](PF$_6$)$_2$ (X = S, 2):** $[Ru(bpy)_2Cl_2]\cdot2H_2O$ (0.200 g, $3.84\times10^{-4}$ mol) and 2-(4-methylpyridin-2-yl)benzo[*d*]thiazole (0.130 g, $5.74\times10^{-4}$ mol) were refluxed in ethylene glycol (50 mL) for 4 h. After cooling to room temperature, water (20 mL) and an aqueous $NH_4PF_6$ solution (1.0 g/10 mL) were added and the resulting precipitate was collected. The crude product was washed with water and dried with diethyl ether. Yield: 0.298 g (83.5%). $C_{33}H_{26}F_{12}N_6P_2RuS$ (929.67): calcd. C 42.63, H 2.82, N 9.04; found C 43.47, H 2.93, N 8.77. Deviation of the C% value from the calculated one indicates the presence of some impurity, probably because of the presence of reaction solvent. $^1$H NMR (400 MHz, [D$_6$]acetone): $\delta$ = 8.86 (m, 3 H), 8.76 (d, 1 H, $J$ = 8.05 Hz), 8.67 (s, 1 H), 8.36 (d, 1 H, $J$ = 7.81 Hz), 8.26 (m, 5 H), 8.15 (t of d, 1 H, $J_1$ = 8.05, $J_2$ = 1.46 Hz), 8.06 (d, 1 H, $J$ = 4.88 Hz), 8.01 (d, 1 H, $J$ = 5.61 Hz), 7.91 (d, 1 H, $J$ = 5.74 Hz), 7.68 (m, 1 H), 7.63 (m, 1 H), 7.55 (m, 4 H), 7.34 (m, 1 H), 6.48 (d, 1 H, $J$ = 8.54 Hz), 2.62 (s, 3 H) ppm. $^{13}$C NMR (100 MHz, [D$_6$]acetone): $\delta$ = 168.85, 159.69, 159.34, 158.89, 158.82, 154.68, 154.59, 153.97, 153.68, 153.58, 153.18, 152.91, 140.06, 139.94, 139.72, 139.64, 135.86, 131.16, 130.28, 129.85, 129.68, 129.64, 129.62, 129.55, 129.13, 126.19, 126.14, 126.00, 125.79, 121.40, 21.70 ppm.

**[Ru(bpy)$_2${2-(4-methylpyridin-2-yl)benzo[*d*]oxazole}](PF$_6$)$_2$ (X = O, 3):** $[Ru(bpy)_2Cl_2]\cdot2H_2O$ (0.200 g, $3.84\times10^{-4}$ mol) and 2-(4-methylpyridin-2-yl)benzo[*d*]oxazole (0.120 g, $5.71\times10^{-4}$ mol) were refluxed in ethylene glycol (50 mL) for 4 h. After cooling to room temperature, water (20 mL) and an aqueous $NH_4PF_6$ solution (1.0 g/10 mL) were added and the resulting precipitate was collected. The crude product was washed with water and dried with diethyl ether. Yield: 0.275 g (78.4%). $C_{33}H_{26}F_{12}N_6OP_2Ru$ (913.61): calcd. C 43.38, H 2.87, N 9.20; found C 43.84, H 3.04, N 9.04. $^1$H NMR (400 MHz, [D$_6$]acetone): $\delta$ = 8.84 (m, 3 H), 8.76 (d, 1 H, $J$ = 8.18 Hz), 8.53 (s, 1 H), 8.46 (d, 1 H, $J$ = 5.61 Hz), 8.30 (m, 2 H), 8.20 (m, 4 H), 8.08 (d, 1 H, $J$ = 5.61 Hz), 7.98 (s, 1 H), 7.96 (d, 1 H, $J$ = 3.17 Hz), 7.60 (m, 6 H), 7.34 (t, 1 H, $J$ = 7.87 Hz), 6.12 (d, 1 H, $J$ = 8.18 Hz), 2.66 (s, 1 H) ppm. $^{13}$C NMR (100 MHz, [D$_6$]-acetone): $\delta$ = 165.62, 160.03, 159.62, 158.84, 154.80, 154.49, 154.32, 154.17, 153.86, 153.21, 153.08, 146.94, 140.46, 140.06, 139.66, 132.06, 130.44, 129.75, 129.51, 129.43, 129.16, 128.90, 128.55, 126.11, 125.94, 125.85, 125.63, 118.36, 114.54, 21.82 ppm.

**Benzyl 6-[2-(4-Methylpyridin-2-yl)benzoimidazol-1-yl]hexanoate:** Freshly sublimated potassium *tert*-butoxide (0.63 g, $5.6\times10^{-3}$ mol) was added to a 50-mL three-neck round-bottom flask containing a solution of 2-(4-methylpyridin-2-yl)-1*H*-benzoimidazole (1 g, $4.80\times10^{-3}$ mol) in anhydrous dimethylformamide (10 mL) at room temperature in argon. After 15 min of mechanical stirring a solu-

 © 2006 Wiley-VCH Verlag GmbH & Co. KGaA, Weinheim 

tion of 6-bromohexanoic acid benzyl ester (4.6 g, 0.016 mol) in dimethylformamide (2.5 mL) was added drop by drop. After 15 h of heating at 45 °C, the mixture was cooled and deionized water (20 mL) added. The mixture was extracted with ethyl acetate, and the organic layers were dried with anhydrous sodium sulfate, evaporated under vacuum, and purified chromatographically over silica gel with linear gradients using hexane/ethyl acetate mixture as eluent, 95:5 to 70:30. A slightly yellow oil was obtained with a yield of 75% (1.49 g). $^1$H NMR (400 MHz, $CD_2Cl_2$): $\delta$ = 8.82 (m, 3 H), 8.77 (s, 1 H), 8.50 (d, 1 H, $J$ = 5.00 Hz), 8.23 (s, 1 H), 7.73 (d, 1 H, $J$ = 7.20 Hz), 7.43 (d, 1 H, $J$ = 7.20 Hz), 7.32 (m, 7 H), 7.15 (d, 1 H, $J$ = 5.00 Hz), 5.06 (s, 2 H), 4.80 (t, 2 H, $J$ = 7.57 Hz), 2.43 (s, 3 H), 2.31 (t, 2 H, $J$ = 7.57 Hz), 1.89 (m, 2 H, $J$ = 7.57 Hz), 1.68 (m, 2 H, $J$ = 7.57 Hz), 1.38 (m, 2 H, $J$ = 7.57 Hz) ppm. $^{13}$C NMR (100 MHz, $CD_2Cl_2$): $\delta$ = 173.31, 150.82, 150.23, 148.63, 148.30, 143.00, 136.97, 136.64, 128.68, 128.28, 125.45, 124.90, 123.17, 122.40, 120.02, 110.39, 66.14, 45.38, 34.20, 29.83, 26.43, 24.65, 21.08 ppm.

**[Ru(bpy)$_2${6-[2-(4-methylpyridin-2-yl)benzo[*d*]imidazol-1-yl]hexanoic acid}](PF$_6$)$_2$ (4):** [Ru(bpy)$_2$Cl$_2$]·2H$_2$O (0.200 g, $3.84\times10^{-4}$ mol) and benzyl 6-{2-(4-methylpyridin-2-yl)benzo[*d*]imidazol-1-yl}hexanoate (0.185 g, $5.74\times10^{-4}$ mol) were dissolved in ethylene glycol (50 mL). The mixture was degassed with argon for 15 min and then refluxed for 4 h. After cooling at room temperature, water (20 mL) and an aqueous solution of $NH_4PF_6$ (1.0 g/10 mL) were added. The precipitate was then collected, washed with water (10 mL) and dried with $Et_2O$. 0.304 g of [Ru(bpy)$_2${2-(4-methylpyridin-2-yl)-benzo-X-azole}](PF$_6$)$_2$ [X = N(CH$_2$)$_5$CO$_2$CH$_2$CH$_2$OH] was obtained (yield 74%). The complex was dissolved in methanol (80 mL) containing 10% KOH and then stirred for 15 h at room temperature. After acidification at pH ≈ 2–3 with $H_2SO_4$, the methanol was removed at reduced pressure, and the acidic solution was extracted with dichloromethane. All the organic fractions were collected, dehydrated with $Na_2SO_4$, and the solvent was removed at reduced pressure. Yield: 0.250 g (86%). $^1$H NMR (400 MHz, [D$_6$]-acetone): $\delta$ = 8.82 (m, 3 H), 8.72 (d, 1 H, $J$ = 8.05 Hz), 8.58 (s, 1 H), 8.27 (t, 1 H, $J$ = 8.05 Hz), 8.19 (m, 3 H), 8.09 (m, 3 H), 8.04 (d, 1 H, $J$ = 5.37 Hz), 7.96 (m, 2 H), 7.63 (t, 1 H, $J$ = 6.35 Hz), 7.52 (m, 4 H), 7.44 (d, 1 H, $J$ = 5.61 Hz), 7.11 (t, 1 H, $J$ = 7.81 Hz), 5.96 (d, 1 H, $J$ = 8.42 Hz), 5.08 (t, 1 H, $J$ = 7.14 Hz), 2.63 (s, 3 H) 2.26 (d, 2 H, $J$ = 7.20 Hz), 2.13 (m, 2 H), 1.65 (m, 2 H), 1.52 (m, 2 H) ppm. $^{13}$C NMR (400 MHz, [D$_6$]acetone): $\delta$ = 175.21, 159.86, 159.44, 158.94, 158.91, 153.92, 153.88, 153.49, 153.42, 152.52, 152.22, 150.24, 142.27, 139.54, 139.36, 139.25, 139.06, 138.48, 129.92, 129.46, 129.41, 129.31, 129.04, 127.90, 127.72, 126.73, 126.05, 125.93, 125.81, 125.52, 117.34, 114.25, 47.14, 34.55, 31.39, 27.35, 25.84, 22.11 ppm.

**Conjugation of 6-{2-(4-Methylpyridin-2-yl)-1*H*-benzo[*d*]imidazol-1-yl}hexanoic Acid with BSA:** Complex **4** ($1.34\times10^{-5}$ mol), dicyclohexylcarbodiimide (DCC) ($2.68\times10^{-5}$ mol) and *N*-hydroxy succinimide (NHS) ($2.68\times10^{-5}$ mol) were added to anhydrous DMF (5 mL). The mixture was stirred for 5 h at 70 °C over a silicon oil bath. The total conversion to **4-NHS** was assessed by HPLC using an RP $C_{18}$ column with an acetonitrile/water gradient and UV/Vis detection, and the **4-NHS** was used immediately. *N*-Hydroxysuccinimide ester of **4** (56 μL, $1.50\times10^{-7}$ mol) was added to BSA ($1.50\times10^{-8}$ mol) in sodium borate buffer (1 mL, pH 8.5) giving a 10-fold molar excess. After stirring for 2 h at room temperature, *N*-hydroxysuccinimide ester of **4** (56 μL) was added, and the reaction continued for another 2 h. The reaction mixture was then passed over a PD10-type prepacked chromatographic column containing Sephadex G-25 M and was eluted with sodium borate (pH 8.5). One-milliliter fractions were collected and detection was performed at 460 nm. The absorbance and fluorescence spectra of the fractions collected (1–8 mL) showed absorption maxima at 250, 290, 330, and 460 nm with an emission at 630 nm upon irradiation at 460 nm.

**Supporting Information Available** (see also the footnote on the first page of this article): IR spectra of complexes **1**–**4**.

## Acknowledgments

We acknowledge financial support of this work by Regione Piemonte and European Commission DG-XII (IFCA Project, contract number G5RD-CT2002-00723). G.V. and I.M. were supported by the University of Torino and are particularly grateful to Compagnia di San Paolo (Torino) and Fondazione della Cassa di Risparmio di Torino (Italy), for the supply of laboratory equipment. We are indebted to Prof. G. Civera (Politecnico di Torino, Italy) for building a power supply that regulates the amplification of the PMT, and to Prof. D. Viterbo and Dr. G. Croce (Università del Piemonte Orientale, Italy) for useful discussions and assistance during X-ray diffraction analysis. J.B.A.R. gratefully acknowledges support by NSF MCB-0517644 and by NIH COBRE RR-15583.

[1] J. R. Lakowicz, *Principles of Fluorescence Spectroscopy*, Kluwer Academic/Plenum Publishers, New York, **1999**.
[2] U. Kosch, I. Klimant, T. Werner, O. S. Wolfbeis, *Anal. Chem.* **1998**, *70*, 3892–3897.
[3] Z. Murtaza, Q. Chang, G. V. Rao, H. Lin, J. R. Lakowicz, *Anal. Biochem.* **1997**, *247*, 216–222.
[4] C. Krause, T. Werner, C. Huber, I. Klimant, O. S. Wolfbeis, *Anal. Chem.* **1998**, *70*, 3983–3985.
[5] C. Huber, T. Werner, C. Krause, I. Klimant, O. S. Wolfbeis, *Anal. Chim. Acta* **1998**, *364*, 143–151.
[6] G. Neurauter, I. Klimant, O. S. Wolfbeis, *Anal. Chim. Acta* **1999**, *382*, 67–75.
[7] E. Terpetschnig, H. Szmacinski, H. Malak, J. R. Lakowicz, *Biophys. J.* **1995**, *68*, 342–350.
[8] E. Terpetschnig, J. D. Dattelbaum, H. Szmacinski, J. R. Lakowicz, *Anal. Biochem.* **1997**, *251*, 241–245.
[9] H. Szmacinski, E. Terpetschnig, J. R. Lakowicz, *Biophys. Chem.* **1996**, *62*, 109–120.
[10] F. N. Castellano, J. D. Dattelbaum, J. R. Lakowicz, *Anal. Biochem.* **1998**, *255*, 165–170.
[11] A. E. Friedman, J. C. Chambron, J. P. Sauvage, N. J. Turro, J. K. Barton, *J. Am. Chem. Soc.* **1990**, *112*, 4960–4962.
[12] C. Garino, S. Ghiani, R. Gobetto, C. Nervi, L. Salassa, V. Ancarani, P. Neyroz, L. Franklin, J. B. A. Ross, E. Seibert, *Inorg. Chem.* **2005**, *44*, 3875–3879.
[13] C. Garino, R. Gobetto, C. Nervi, L. Salassa, G. Croce, M. Milanesio, E. Rosenberg, J. B. A. Ross, *Eur. J. Inorg. Chem.* **2005**, 606–614.
[14] R. Gobetto, C. Nervi, B. Romanin, L. Salassa, M. Milanesio, G. Croce, *Organometallics* **2003**, *22*, 4012–4019.
[15] M. A. Haga, M. M. Ali, S. Koseki, K. Fujimoto, A. Yoshimura, K. Nozaki, T. Ohno, K. Nakajima, D. J. Stufkens, *Inorg. Chem.* **1996**, *35*, 3335–3347.
[16] D. P. Rillema, D. S. Jones, C. Woods, H. A. Levy, *Inorg. Chem.* **1992**, *31*, 2935–2938.
[17] B. D. J. R. Fennema, R. A. G. Degraaff, R. Hage, J. G. Haasnoot, J. Reedijk, J. G. Vos, *J. Chem. Soc., Dalton Trans.* **1991**, 1043–1049.
[18] N. E. Tokel-Takvoryan, R. E. Hemingway, A. J. Bard, *J. Am. Chem. Soc.* **1973**, *95*, 6582–6589.
[19] N. E. Tokel, A. J. Bard, *J. Am. Chem. Soc.* **1972**, *94*, 2862–2863.
[20] A. Juris, V. Balzani, F. Barigelletti, S. Campagna, P. Belser, A. Von Zelewsky, *Coord. Chem. Rev.* **1988**, *84*, 85–277.
[21] R. S. Nicholson, I. Shain, *Anal. Chem.* **1964**, *36*, 706–723.

 © 2006 Wiley-VCH Verlag GmbH & Co. KGaA, Weinheim 

[22] In the Stoke–Einstein equation, the diffusion coefficient *D* is inversely proportional to the molecular radius. Assuming a spherical shape, *D* is also inversely proportional to the cubic root of the crystallographic volume of the molecule.
[23] J. O. Bockris, A. K. M. Reddy, *Modern Electrochemistry*, Plenum, New York, **1970**, Chapter IV, p. 380.
[24] C. P. Brock, Y. G. Fu, *Acta Crystallogr., Sect. B: Struct. Sci.* **1997**, *53*, 928–938.
[25] J. V. Casper, J. T. Meyer, *Inorg. Chem.* **1983**, *22*, 2444–2453.
[26] W. J. Miao, J. P. Choi, A. J. Bard, *J. Am. Chem. Soc.* **2002**, *124*, 14478–14485.
[27] M. M. Richter, *Chem. Rev.* **2004**, *104*, 3003–3036.
[28] J. V. Caspar, T. J. Meyer, *J. Am. Chem. Soc.* **1983**, *105*, 5583–5590.
[29] J. Van Houten, R. J. Watts, *J. Am. Chem. Soc.* **1976**, *98*, 4853–4858.
[30] P. McCord, A. J. Bard, *J. Electroanal. Chem.* **1991**, *318*, 91–99.
[31] T. C. Richards, A. J. Bard, *Anal. Chem.* **1995**, *67*, 3140–3147.
[32] F. Barigelletti, L. Decola, V. Balzani, R. Hage, J. G. Haasnoot, J. Reedijk, J. G. Vos, *Inorg. Chem.* **1991**, *30*, 641–645.
[33] H. Z. Zheng, Y. B. Zu, *J. Phys. Chem. B* **2005**, *109*, 12049–12053.
[34] G. T. Hermanson, *Bioconjugate Techniques*, Academic Press, San Diego, CA, **1996**.
[35] X. M. He, D. C. Carter, *Nature* **1992**, *358*, 209–215.
[36] T. Peters Jr, *Adv. Protein Chem.* **1985**, *37*, 161–245.
[37] B. F. Erlanger, *Methods Enzymol.* **1980**, *70*, 85–104.
[38] H. J. Youn, E. Terpetschnig, H. Szmacinski, J. R. Lakowicz, *Anal. Biochem.* **1995**, *232*, 24–30.
[39] E. Terpetschnig, H. Szmacinski, J. R. Lakowicz, *Anal. Biochem.* **1995**, *227*, 140–147.
[40] M. M. Bradford, *Anal. Biochem.* **1976**, *72*, 248–254.
[41] L. F. Amarengo, D. D. Perrin, *Purification of Laboratory Chemicals*, Butterworth-Heinemann, Oxford, **1998**.
[42] B. P. Sullivan, D. J. Salmon, J. T. Meyer, *Inorg. Chem.* **1978**, *17*, 3334–3341.
[43] S. Hiiromitsu, K. Takeo, H. Takeru, *J. Pharm. Sci.* **1988**, *77*, 855–860.
[44] E. Barni, P. Savarino, *J. Heterocycl. Chem.* **1977**, *14*, 937–940.
[45] E. Barni, C. Barolo, P. Quagliotto, P. Savarino, G. Viscardi, D. Marabello, *J. Heterocycl. Chem.* **2003**, *40*, 649–654.
[46] SMART© 1998, Madison, WI 53719, USA, Bruker AXS, Inc., **1998**.
[47] G. M. Sheldrick, *SADABS*, Germany, University of Göttingen, **1996**.
[48] A. Altomare, M. C. Burla, M. Camalli, G. L. Cascarano, C. Giacovazzo, A. Guagliardi, A. G. Moliterni, G. Polidori, R. Spagna, *J. Appl. Crystallogr.* **1999**, *32*, 115–119.
[49] G. M. Sheldrick, *SHELXL-97*, University of Göttingen, Germany, **1997**.
[50] *SHELXTL*, Bruker AXS, Inc., Madison, WI 53719, USA, **1998**.

Received: February 3, 2006
Published Online: May 29, 2006

 © 2006 Wiley-VCH Verlag GmbH & Co. KGaA, Weinheim 

DOI: 10.1002/ejic.200600103

# Synthesis, Structure, and Magnetic Properties of Hydroxo-Bridged Vanadium Oxalate $V_2O_2(OH)_2(C_2O_4)(H_2O)_2$

Sihai Yang,[a] Guobao Li,*[a] Shujian Tian,[a] Fuhui Liao,[a] and Jianhua Lin[a]

**Keywords:** Vanadium / Bridging ligands / Magnetic properties / Dimers / Oxalates

The reaction of $V_2O_5$ with $H_2C_2O_4{\cdot}2H_2O$ in the presence of $H_3BO_3$ under hydrothermal conditions has afforded $V_2O_2(OH)_2(C_2O_4)(H_2O)_2$ (**1**), which crystallizes in the triclinic system, space group $P\bar{1}$ with $a$ = 5.2405(10) Å, $b$ = 5.7340(11) Å, $c$ = 7.1778(14) Å, $\alpha$ = 76.44(3)°, $\beta$ = 69.37(3)°, $\gamma$ = 75.37(3)°. The vanadium atoms in **1** form dimers by sharing edges consisting of μ-OH groups, and these dimers are connected further by oxalate ligands to form chains. The magnetic susceptibility data of **1** fit excellently with the Heisenberg dimer model in the temperature interval 2–300 K. Compound **1** is antiferromagnetic with a $J$ value of –29.6 $cm^{-1}$.

(© Wiley-VCH Verlag GmbH & Co. KGaA, 69451 Weinheim, Germany, 2006)

## Introduction

The oxalate ion $C_2O_4^{2-}$ shows a large variety of structural characteristics. It can act as a monodentate,[1] bidentate,[2] tridentate,[3] or tetradentate[4] donor ligand and can form chains,[5] layers,[6] or three-dimensional networks with metal centers.[7] In the presence of water molecules directly linked to the metal ions or weakly bonded to the framework,[5,8] abundant structural architectures in one-, two-, or three dimensions can be formed.[9] Moreover, the oxalate ion can mediate strong spin coupling between paramagnetic centers separated by more than 5 Å.[10] Thus, homo- and heterometallic systems involving oxalate ions (ox) as bridging ligands have been studied intensively in the search for new molecular-based magnets.[11–13] Because of the variable oxidation states of vanadium ($V^{III}$, $V^{IV}$, and $V^{V}$) and the coordination geometries of vanadium oxide polyhedra (tetrahedral, square pyramidal, trigonal bipyramidal, and octahedral),[14] many compounds containing both vanadium atoms and oxalate ions have been reported,[10,15–17] with different linkages between the vanadium atoms and the oxalate ions as shown in Figure 1, which result in different magnetic properties.[10,16,18–21] Recently, a new bonding mode for vanadium atoms and oxalate ions (Figure 1i) has been found in the compound $V_2O_2(OH)_2(C_2O_4)(H_2O)_2$ (**1**). The synthesis, structure and magnetic properties of **1** are reported below.

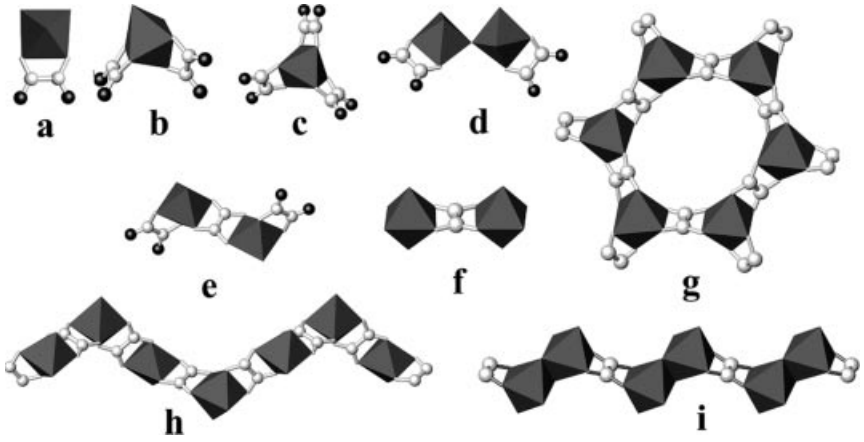


Figure 1. Different linkages between vanadium atoms and oxalate ions found in the literature. a) from ref.[19]; b) ref.[20]; c) ref.[10]; d) ref.[16]; e) ref.[21]; f) ref.[18]; g) inferred by ref.[10]; h) from ref.[21]; i) this work. C, white ball; O, black ball; $VO_6$, gray octahedron.

[a] Beijing National Laboratory for Molecular Sciences (BNLMS), State Key Laboratory of Rare Earth Materials Chemistry and Applications, College of Chemistry and Molecular Engineering, Peking University,
Beijing 100871, P. R. China
E-mail: liguobao@pku.edu.cn
Fax: +8610-62753541

 © 2006 Wiley-VCH Verlag GmbH & Co. KGaA, Weinheim 

## Results and Discussion

### Synthesis

The synthesis of compound **1** was performed in an aqueous solution of $H_3BO_3$ under hydrothermal conditions. Some experimental parameters, including the $V_2O_5/H_2C_2O_4$ molar ratio, were varied, but the resulting products remained the same. Finally, a $V_2O_5/H_2C_2O_4$ ratio of 1:14 was used. The formation of **1** was found to be sensitive to the presence of $H_3BO_3$. Compound **1** did not form when no $H_3BO_3$ was added to the mixture of $V_2O_5$, $H_2C_2O_4{\cdot}2H_2O$, and water. Although crystals of **1** formed from an aqueous solution, their solubility in pure water was low.

### Crystal Structure

$V_2O_2(OH)_2(C_2O_4)(H_2O)_2$ is centrosymmetric in the triclinic system with the space group $P\bar{1}$, the center of inversion lies along the C–C bond of the bridging oxalato moiety, or on the common edge of two adjacent $VO_6$ octahedra. The asymmetric unit of **1** corresponds to half of the molecular formula, including one vanadium(IV) atom, half an oxalate ligand, one water molecule, one oxygen atom, and two half μ-OH groups. As shown in Figure 2, the vanadium(IV) atom binds to two oxygen atoms from one oxalate ligand, one oxygen atom from a water molecule, two oxygen atoms from the μ-OH groups, and one terminal oxo oxygen atom to form a distorted octahedron, a very common geometry in vanadium(IV) compounds.[10,16,18–21]

The $VO_6$ octahedra of **1** link together by sharing a common edge consisting of two μ-OH groups to form $V_2O_{10}$ dimers; this type of link is rare in vanadium oxalate compounds. The typical ways to link oxalate ligands with $VX_6$ (X = O, Cl, F, and/or N) octahedra are shown in Figure 1.

The $V_2O_{10}$ dimers are further linked by oxalate ligands to form chains (Figure 1i). The oxygen atoms of the μ-OH groups (O4) in one chain form hydrogen bonds with the oxygen atoms (O3) from the oxalate ions in the neighboring chain, which connects the chains into layers (Figure 3a). The water molecules coordinated to the vanadium atoms in one layer form two hydrogen bonds with the oxygen atoms

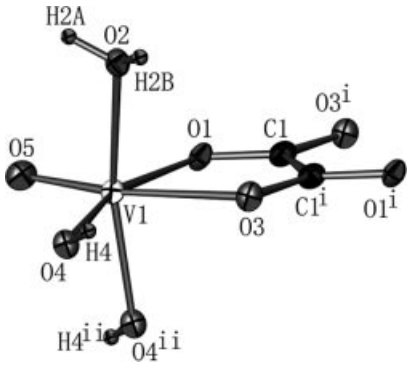


Figure 2. ORTEP drawing (at 30% probability) of the coordination environment of the vanadium atoms in $V_2O_2(OH)_2(C_2O_4)(H_2O)_2$. Symmetry codes: i) $1 - x, 1 - y, -z$; ii) $-x, 1 - y, 1 - z$.

of the μ-OH groups (O4) and the terminal oxo oxygen atoms (O5) in neighboring layers (Figure 3b). This results in the formation of a three dimensional net structure for **1**.

### Vibrational Spectroscopy

The Fourier transform infrared (FTIR) spectrum of **1** exhibits two broad peaks centered at 3272 and 3041 $cm^{-1}$, mainly attributed to the symmetric and asymmetric stretching modes of water molecules and hydroxy groups. The signal for the bending mode of water expected at around 1600 $cm^{-1}$ is overlapped by the intense oxalate band. The antisymmetric stretching mode of the oxalate ion appears at 1650 $cm^{-1}$. The peaks at 1355 $cm^{-1}$ and 1311 $cm^{-1}$ correspond to the symmetric stretching modes of the oxalate ion. The peak at around 979 $cm^{-1}$ is assigned to the bending mode of the μ-OH group. The strong bands observed at around 771 and 731 $cm^{-1}$ correspond to the in-plane deformation mode of the oxalate ion.

### Thermal Stability

Thermogravimetric analysis shows that compound **1** is stable up to 200 °C and then undergoes decomposition to form a mixture of products with a maximum weight loss of

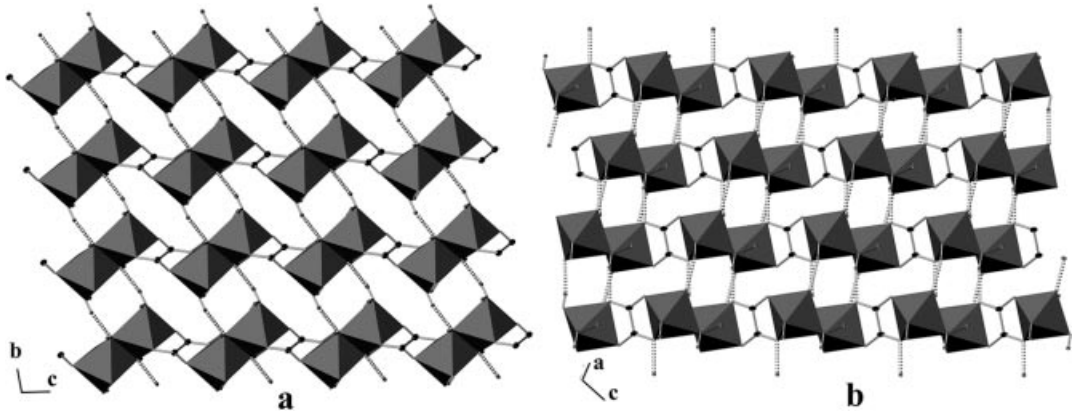


Figure 3. Packed structure of $V_2O_2(OH)_2(C_2O_4)(H_2O)_2$, showing hydrogen bonding.

 © 2006 Wiley-VCH Verlag GmbH & Co. KGaA, Weinheim 

40.0%. The mixture is then slowly oxidized to $V_2O_5$ with a total weight loss of 37.8% (calcd. 37.7%), as confirmed by X-ray diffraction data.

### Magnetochemical Investigations

The magnetic properties of $V_2O_2(OH)_2(C_2O_4)(H_2O)_2$ are depicted in Figure 4. A near-perfect fit with the Heisenberg dimer model is attainable with the parameters listed in Table 3. A susceptibility maximum occurs near 50 K, and the compound exhibits Curie–Weiss paramagnetism at high temperatures. The compound is thus strongly antiferromagnetic with a $J$ value of about –30 $cm^{-1}$, which is comparable to values for copper hydroxo-bridged dimers with antiferromagnetic coupling[22,23] and is larger than those for the (oxo)vanadium(IV) ($d^1$) oxalate-bridged dimers listed in Table 3. In fact, when oxalate bridging is considered, $V_2O_2(OH)_2(C_2O_4)(H_2O)_2$ can be seen to consist of alternating-exchange Heisenberg chains with $S = 1/2$.[24–26] In this case, two exchange constants $J$ and $\alpha J$ should be considered in order to understand the magnetic properties. However, the value of $\alpha$ is so small that the interaction represented by $\alpha J$ may be neglected (see Table 3). Therefore, the magnetic data fit very well with the dimeric model.

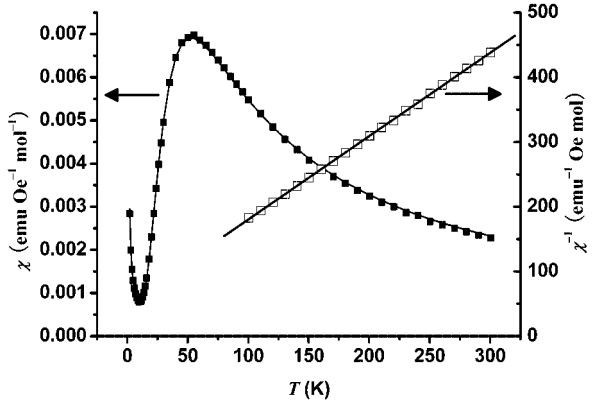


Figure 4. Thermal variation of the molar magnetic susceptibility and the reciprocal magnetic susceptibility for $V_2O_2(OH)_2(C_2O_4)(H_2O)_2$; the solid line represents the best fit obtained with the parameters reported in the text.

## Conclusions

The use of oxalate, with the help of $H_3BO_3$, has led to the preparation of $V_2O_2(OH)_2(C_2O_4)(H_2O)_2$ from $V_2O_5$. The $V_2O_{10}$ dimer connected by a common edge found in this compound induces a stronger antiferromagnetic coupling than the oxalato-bridged (oxo)vanadium(IV) dimer.[27]

## Experimental Section

**Materials and Analyses:** All reagents were of analytical grade and were used as obtained from commercial sources without further purification. IR spectra were recorded in the 400–4000 $cm^{-1}$ range with a Magna-IR 750 FTIR spectrometer. Elemental analyses were carried out on an Elementar Vario EL III microanalyzer. TG analysis was performed with a heating rate of 10 °C $min^{-1}$ using a Dupont 1090 instrument.

**Preparation of $V_2O_2(OH)_2(C_2O_4)(H_2O)_2$ (1):** A mixture of $V_2O_5$ (1.00 g, 5.50 mmol), $H_2C_2O_4{\cdot}2H_2O$ (10.0 g, 79.4 mmol), $H_3BO_3$ (10.0 g, 162 mmol), and deionized $H_2O$ (15 mL, 0.83 mol) with a mol ratio of about 1.0:14:29:151 was placed in a 50-mL Teflon-lined stainless steel autoclave, and the autoclave was sealed, heated to 155 °C under autogenous pressure for 20 d, and then cooled to room temperature at a rate of 5 °C/h. The pH values of the system before and after synthesis are about 2 and 1, respectively. The blue crystalline product was filtered, washed with hot distilled water, and dried at ambient temperature to give about 1.44 g of complex

Table 1. Single-crystal data and structure refinement details of the compound $V_2O_2(OH)_2(C_2O_4)(H_2O)_2$ (**1**).

| | |
|---|---|
| Empirical formula | $C_2H_6O_{10}V_2$ |
| Formula mass | 291.94 |
| Crystal system | triclinic |
| Space group | $P\bar{1}$(No.2) |
| $a$ [Å] | 5.2405(10) |
| $b$ [Å] | 5.7340(11) |
| $c$ [Å] | 7.1778(14) |
| $\alpha$ [°] | 76.44(3) |
| $\beta$ [°] | 69.37(3) |
| $\gamma$ [°] | 75.37(3) |
| $V$ [Å] | 192.77(8) |
| $Z$ | 1 |
| $\rho_{calcd.}$ [g $cm^{-3}$] | 2.515 |
| $\mu$ [$mm^{-1}$] | 2.465 |
| Reflections collected | 797 |
| Unique data/parameters | 719/61 |
| $R_{int}$ | 0.0218 |
| Reflections with $I \geq 2\sigma$ | 695 |
| Goodness of fit ($S$) | 1.000 |
| $R_1/wR_2$ ($I \geq 2\sigma$) | 0.0472/0.1372 |
| $R_1/wR_2$ [all data] | 0.0483/0.1400 |

$R_1 = \Sigma(|F_o| - |F_c|)/\Sigma|F_o|$; $wR_2 = [\Sigma w(F_o^2 - F_c^2)^2/\Sigma w(F_o^2)^2]^{1/2}$; $w = 1/[\sigma^2(F_o^2) + (0.1343P)^2 + 0.1200P]$ with $P = (|F_o|^2 + 2|F_c|^2)/3$.

Table 2. Selected bond lengths [Å] and angles [°] for $V_2O_2(OH)_2(C_2O_4)(H_2O)_2$ (**1**).

| | | | |
|---|---|---|---|
| V1–O5 | 1.598(3) | O4–V1–O4 | 79.6(1) |
| V1–O4 | 1.993(3) | O4–V1–O3 | 86.0(1) |
| V1–O4 | 2.014(2) | O4–V1–O3 | 84.8(1) |
| V1–O1 | 2.049(3) | O4–V1–O1 | 160.5(1) |
| V1–O2 | 2.059(3) | O4–V1–O1 | 91.3(1) |
| V1–O3 | 2.246(3) | O4–V1–O2 | 93.6(1) |
| O1– C1 | 1.244(5) | O4–V1–O2 | 164.5(1) |
| O3– C1 | 1.250(4) | O2–V1–O3 | 80.8(1) |
| C1– C1 | 1.539(6) | O1–V1–O2 | 90.8(1) |
| O5–V1–O4 | 101.25(1) | O1–V1–O3 | 75.9(1) |
| O5–V1–O4 | 100.70(1) | O3–C1–C1 | 115.8(4) |
| O5–V1–O3 | 171.5(1) | C1–O1–V1 | 118.8(2) |
| O5–V1–O1 | 97.4(1) | O1–C1–O3 | 127.3(3) |
| O5–V1–O2 | 94.2(1) | O1–C1–C1 | 116.9(4) |
| V1–O4–V1 | 100.4(1) | C1–O3–V1 | 112.5(2) |

| D–H···A | D···A [Å] | H···A [Å] | D–H···A [Å] |
|---|---|---|---|
| O2–H2A···O4[a] | 0.82 | 1.91 | 2.714(4) |
| O2–H2B···O5[b] | 0.82 | 1.93 | 2.747(4) |
| O4–H4···O3[c] | 0.82 | 2.00 | 2.806(3) |

[a] Symmetry transformations used to generate equivalent atoms: $-x, -y+2, -z+1$. [b] $x+1, y, z$. [c] $-x+1, -y+1, -z+1$.

 © 2006 Wiley-VCH Verlag GmbH & Co. KGaA, Weinheim 

Table 3. Best-fit magnetic parameters.

| Compound[a] | *g* | *J* [cm$^{-1}$] | *ρ* | *tip* | *α* |
|---|---|---|---|---|---|
| **1** | 1.95 ± 0.01 | –29.60 ± 0.05 | 0.008 ± 0.001 | 0.00012 ± 0.00001 | |
| **1**[b] | 1.95 ± 0.01 | –29.28 ± 0.05 | 0.002 ± 0.001 | 0.00004 ± 0.00001 | 0.025(2) |
| **2**[27] | 1.93 ± 0.01 | –6.50 ± 0.05 | 0.01 ± 0.002 | 0.0018 ± 0.00005 | |
| **3**[27] | 1.95 ± 0.01 | –6.25 ± 0.05 | 0.02 ± 0.002 | –0.0004 ± 0.00005 | |
| **4**[18] | 1.91 | –3.85 | 0.008 | | |
| **5**[16] | 1.927 | –4.35 | | 0.00064 | |

[a] **1**, $V_2O_2(OH)_2(C_2O_4)(H_2O)_2$ (this work); **2**, $[Et_4N]_2[(VO)_2(C_2O_4)_3(H_2O)_2]\cdot 4H_2O$; **3**, $[Et_4N]_2[(VO)_2(C_2O_4)(C_3H_2O_4)_2(H_2O)_2]\cdot 2H_2O$; **4**, $[V_2O_2(C_2O_4)(H_2O)_6]Cl_2\cdot 4Bu_4NCl\cdot H_2O$; **5**, $[Ph_4P]_2[(VO)_2(C_2O_4)_3(H_2O)_2]\cdot 4H_2O$. [b] These values were obtained by fitting the data using Heisenberg alternating chain model with Equation (2) and all others are for the Heisenberg dimer model with Equation (1).

**1** (yield 90% based on $V_2O_5$). Complex **1** is stable and insoluble in water and most organic solvents. $V_2O_2(OH)_2(C_2O_4)(H_2O)_2$ (291.94): calcd. C 8.22, H 2.05; found: C 8.32, H 2.13.

**Crystallographic Studies:** Intensity data were collected on a Rigaku AFC6S diffractometer with graphite-monochromated Mo-$K_\alpha$ ($\lambda$ = 0.71073 Å) radiation by using the $\omega$-$2\theta$ scan method at room temperature. The structure was solved with direct methods and refined on $F^2$ with full-matrix least-squares methods using SHELXS-97 and SHELXL-97 programs, respectively.[28] All non-hydrogen atoms were refined anisotropically. The hydrogen atoms were added in the riding model and refined isotropically with O–H = 0.82 Å. The crystallographic data are summarized in Table 1, and the selected bond lengths are listed in Table 2. CCDC-294737 contains the supplementary crystallographic data for this paper. These data can be obtained free of charge from The Cambridge Crystallographic Data Centre via www.ccdc.cam.ac.uk/data_request/cif.

**Magnetic Measurements:** Magnetic data of polycrystalline samples ($H$ = 5000 Oe) were recorded on 47.90 mg of **1** in the 2–300 K temperature range with a Quantum Design MPMS-5S SQUID Spectrometer. Correction for the sample holder was applied. The data were fitted to the Heisenberg dimer model for two $S$ = 1/2 spins [Equation (1)] whilst taking into account the presence of monomeric paramagnetic impurities (second term) and temperature-independent magnetism (third term) [where $\chi$ is the magnetic susceptibility, $N_A$ the Avogadro constant, $k_B$ the Boltzmann constant, $\mu_B$ the Bohr magneton, $T$ the temperature, $g$ the $g$ factor, $J$ the exchange constant, $\rho$ the ratio of the paramagnetic impurities, *tip* is the temperature-independent contribution]. The best-fit parameters are given in Table 3.

$$\chi = (1-\rho)\frac{N_A g^2 \mu_B^2}{k_B T}\frac{2\exp\left(\frac{2J}{k_B T}\right)}{1+3\exp\left(\frac{2J}{k_B T}\right)} + \rho\frac{N_A g^2 \mu_B^2}{2k_B T} + tip \qquad (1)$$

The data were also fitted to the Heisenberg alternating chain model with $S$ = 1/2 using the following Equation (2), where the first term describes the Heisenberg alternating chain model, $x = |J|/k_B T$, $J$ is the exchange integral between a spin and its right neighbor, $\alpha J$ the exchange integral between a spin and its left neighbor, the values for $A(\alpha)$, $B(\alpha)$, $C(\alpha)$, $D(\alpha)$, $E(\alpha)$, and $F(\alpha)$ can be found in ref.[25] The fit was good, and the best-fit parameters are listed in Table 3.

$$\chi = (1-\rho)\frac{N_A g^2 \mu_B^2}{k_B T}\frac{A(\alpha)+[B(\alpha)]x+[C(\alpha)]x^2}{1+[D(\alpha)x+[E(\alpha)]x^2+[F(\alpha)]x^3]} + \rho\frac{N_A g^2 \mu_B^2}{2k_B T} + tip \qquad (2)$$

## Acknowledgments

This work was supported by the National Natural Science Foundation of China (Grant 20471003).

[1] G. M. Miskelly, C. R. Clark, J. Simpson, D. A. Buckingham, *Inorg. Chem.* **1983**, *22*, 3237–3241.
[2] J. Carranza, H. Grove, J. Sletten, F. Lloret, M. Julve, P. E. Kruger, C. Eller, D. P. Rillema, *Eur. J. Inorg. Chem.* **2004**, 4836–4848.
[3] H. Oshio, U. Nagashima, *Inorg. Chem.* **1992**, *31*, 3295–3301.
[4] O. R. Evans, W. B. Lin, *Cryst. Growth Des.* **2001**, *1*, 9–11.
[5] U. García-Couceiro, O. Castillo, A. Luque, J. P. García-Terán, G. Beobide, P. Román, *Eur. J. Inorg. Chem.* **2005**, 4280–4290.
[6] E. Coronado, J. R. Galán-Mascarós, C. J. Gómez-García, P. Gütlich, *Chem. Eur. J.* **2000**, *6*, 552.
[7] E. Coronado, J. R. Galán-Mascarós, C. J. Gómez-García, E. Martínez-Ferrero, M. Almeida, J. C. Waerenborgh, *Eur. J. Inorg. Chem.* **2005**, 2064–2070.
[8] S.-H. Yang, G.-B. Li, S.-J. Tian, F.-H. Liao, J.-H. Lin, *J. Solid State Chem.* **2005**, *178*, 3703–3707.
[9] C. N. R. Rao, S. Natarajan, R. Vaidhyanathan, *Angew. Chem. Int. Ed.* **2004**, *43*, 1466.
[10] K. S. Min, A. L. Rhinegold, J. S. Miller, *Inorg. Chem.* **2005**, *44*, 8433–8441.
[11] E. Coronado, J. R. Galán-Mascarós, C. J. Gómez-García, C. Martí-Gastaldo, *Inorg. Chem.* **2005**, *44*, 6197–6202.
[12] H. Tamaki, Z. J. Zhong, N. Matsumoto, S. Kida, M. Koikawa, N. Achiwa, Y. Hashimoto, H. Okawa, *J. Am. Chem. Soc.* **1992**, *114*, 6974–6979.
[13] E. Coronado, J. R. Galán-Mascarós, C. J. Gómez-García, V. Laukhin, *Nature* **2000**, *408*, 447–449.
[14] M. Schindler, F. C. Hawthorne, W. H. Baur, *Chem. Mater.* **2000**, *12*, 1248.
[15] R. Cortes, M. K. Urtiaga, L. Lezama, M. I. Arriortua, T. Rojo, *Inorg. Chem.* **1994**, *33*, 829–832.
[16] O. Costisor, M. Brezeanu, Y. Journaux, K. Mereiter, P. Weinberger, W. Linert, *Eur. J. Inorg. Chem.* **2001**, 2061–2066.
[17] W. M. Chang, S. L. Wang, *Chem. Mater.* **2005**, *17*, 74–80.
[18] S. Triki, F. Bérézovsky, J. S. Pala, M. T. Garland, *Inorg. Chim. Acta* **2000**, *308*, 31–36.
[19] Y. M. Tsai, S. L. Wang, C. H. Huang, K. H. Lii, *Inorg. Chem.* **1999**, *38*, 4183–4187.

 © 2006 Wiley-VCH Verlag GmbH & Co. KGaA, Weinheim 

[20] W. R. Scheidt, C. Tsai, J. L. Hoard, *J. Am. Chem. SOC.* **1971**, *93*, 3867–3872.
[21] J. Salta, C. J. O'Connor, L. Sichu, J. Zubieta, *Inorg. Chim. Acta* **1996**, *250*, 303–310.
[22] D. B. Leznoff, N. D. Draper, R. J. Batchelor, *Polyhedron* **2003**, *22*, 1735–1743.
[23] M. J. Katz, C. J. Shorrock, R. J. Batchelor, D. B. Leznoff, *Inorg. Chem.* **2006**, *45*, 1757–1765.
[24] J. W. Hall, W. E. Marsh, R. R. Weller, W. E. Hatfield, *Inorg. Chem.* **1981**, *20*, 1033–1037.
[25] W. E. Hatfield, L. W. ter Haar, M. M. Olmstead, W. K. Musker, *Inorg. Chem.* **1986**, *25*, 558–563.
[26] E. Herrling, G. Fischer, S. Matejcek, B. Pilawa, H. Henke, I. Odenwald, W. Wendl, *Phys. Rev. B* **2003**, *67*, 014407.
[27] B. Baruah, V. O. Golub, C. J. O'Connor, A. Chakravorty, *Eur. J. Inorg. Chem.* **2003**, 2299–2303.
[28] a) G. M. Sheldrick, *SHELXS97 Program for Crystal Structure Solution*, University of Göttingen, Göttingen, Germany, **1997**; b) G. M. Sheldrick, *SHELXL97 Program for Crystal Structure Refinement*, University of Göttingen, Göttingen, Germany, **1997**.

Received: February 6, 2006
Published Online: May 18, 2006

 © 2006 Wiley-VCH Verlag GmbH & Co. KGaA, Weinheim 

DOI: 10.1002/ejic.200600115

# Transfer Hydrogenation of Ketones Catalysed by New Half-Sandwich Ruthenium(II) Complexes Bearing the Sulfonated Phosphane (*meta*-Sulfonatophenyl)diphenylphosphane Potassium Salt (TPPMS)

**Josefina Díez,[a] M. Pilar Gamasa,[a] Elena Lastra,*[a] Almudena García-Fernández,[a] and M. Pilar Tarazona[b]**

*Dedicated to Professor Victor Riera on the occasion of his 70th birthday*

**Keywords:** Water-soluble catalysts / Sulfonated phosphanes / Arene complexes / Ruthenium(II) / Hydrogen transfer

New half-sandwich ruthenium(II) complexes [$RuCl_2$($\eta^6$-arene)(TPPMS)] [$\eta^6$-arene = *p*-cymene (**1a**), benzene (**1b**)] and [RuCl($\eta^6$-arene)$(TPPMS)_2$][Cl] [$\eta^6$-arene = *p*-cymene (**2a**), benzene (**2b**)] containing the water-soluble (*meta*-sulfonatophenyl)diphenylphosphane potassium salt (TPPMS) have been synthesised. The X-ray analysis for complex **1a** revealed that, in the solid state, complex anions are held together in the crystal lattice by weak electrostatic interactions with potassium cations leading to a linear chain structure. The extent of the association in solution depends on the solvent and the determination of the size of the particles in THF can be accomplished using Multiangle Light Scattering (MALS). The new complexes proved to be excellent catalysts for transfer hydrogenation of ketones and the hydrophilic properties of the TPPMS ligand allow the catalyst recovery. The hydride derivative [RuClH($\eta^6$-*p*-cymene)(TPPMS)] (**4**) has also been shown to be an efficient catalyst for these processes. Moreover, when **1a** was used as catalyst, complex **4** was observed as the main product after the catalysis, supporting the implication of hydride species in transfer hydrogenation catalysis.

(© Wiley-VCH Verlag GmbH & Co. KGaA, 69451 Weinheim, Germany, 2006)

## Introduction

Over the last decades, aqueous organometallic chemistry has become a priority research area. This interest has arisen from the advantages of replacing organic solvents with water and from the attention directed to the aqueous-biphasic technology in catalysis which allows the separation of the products from the catalyst and subsequent catalyst recovery and recycling.[1]

One of the most common approaches to obtain water-soluble organometallic compounds is the use of ligands with hydrophilic properties. The phosphane ligands containing sulfonated groups are among the most widely used ligands for this purpose.

In particular, complexes containing the sodium or potassium salt of (*meta*-sulfonatophenyl)diphenylphosphane (TPPMS) have been used as catalysts in a number of processes.[2] Thus, palladium complexes with TPPMS act as catalysts in cross coupling reactions[3] and cationic iridium(I) complexes show a moderate catalytic activity in hydrogenation reactions.[4] Ruthenium complexes containing the TPPMS ligand[5] have been widely used in two phase and aqueous hydrogenation reactions.[6] Thus the preformed complexes [RuClH(CO)$(TPPMS)_3$],[7] [$Ru(CO)_3$-$(TPPMS)_2$],[8] [$RuH_2(CO)(TPPMS)_3$][8] and [RuH(CO)-(NCMe)$(TPPMS)_3$][9] have shown catalytic activity for the hydrogenation of olefins. Furthermore, ruthenium complexes with *N*-donor ligands [$RuHCl(L)_2(TPPMS)_2$] (L = 1,2,3,4-tetrahydroquinoline, aniline) catalyse the hydrogenation of quinoline and benzothiophene[10] and the complexes [$RuCl_3(TPPMS)_2(NO)$][11] and [$RuCl_2(TPPMS)_2]_2$[12] show catalytic activity in the hydrogenation of carbon dioxide and hydrogencarbonate.

Aqueous transfer hydrogenation has been less developed and, in spite of the recent studies in aqueous transfer hydrogenation,[13] the only ruthenium-TPPMS complex reported as a catalyst for these reactions[14] has been [$RuCl_2$-$(TPPMS)_2$].[15] In addition, to the best of our knowledge, the only isolated half-sandwich ruthenium(II) complexes

[a] Departamento de Química Orgánica e Inorgánica, Instituto de Química Organometálica "Enrique Moles" (Unidad Asociada al C.S.I.C.), Universidad de Oviedo,
33006 Oviedo, Principado de Asturias, Spain
Fax: +34-985103446
E-mail: elb@uniovi.es
[b] Departamento de Química Física, Universidad de Alcalá, 28871 Alcalá de Henares, Spain

 © 2006 Wiley-VCH Verlag GmbH & Co. KGaA, Weinheim 

bearing the TPPMS ligand[16] are the complexes [RuCl($\eta^5$-$C_5H_5$)(TPPMS)$_2$][17] and [RuCl($\eta^5$-$C_5H_5$)(TPPMS)$_2$]-[$SnCl_3$][18] and no catalytic studies have been carried out.

Due to the lack of half-sandwich ruthenium(II) complexes containing the water-soluble ligand TPPMS and our interest in the catalytic activity of new half-sandwich ruthenium(II) complexes[19] and their reactivity in coupling-coupling reactions,[20] we have considered the synthesis of $\eta^6$-arene complexes and in this paper we report the synthesis and catalytic activity of new water-soluble half-sandwich ruthenium(II) complexes with the ligand TPPMS on the transfer hydrogenation of ketones.

## Results and Discussion

### Synthesis of Half-Sandwich Ruthenium(II) Complexes Containing the TPPMS Ligand

#### *a) Synthesis of [$RuCl_2$($\eta^6$-arene)(TPPMS)] [$\eta^6$-arene = p-cymene (1a), benzene (1b)]*

The reaction of two equiv. of the potassium salt of (*meta*-sulfonatophenyl)diphenylphosphane (TPPMS) with the dinuclear complex [RuCl(μ-Cl)($\eta^6$-arene)]$_2$ ($\eta^6$-arene = *p*-cymene, benzene) in methanol at room temperature gives the complexes [$RuCl_2$($\eta^6$-arene)(TPPMS)] [$\eta^6$-arene = *p*-cymene (**1a**), benzene (**1b**)] which can be isolated as air-stable orange solids in yields of 95% (**1a**) and 68%[21] (**1b**) (Scheme 1).

Complexes **1a** and **b** are soluble in water and in common organic solvents such as alcohols, acetone, chloroform, dichloromethane, acetonitrile and dimethylsulfoxide but insoluble in diethyl ether and hexane. The complexes have an ionic character due to the potassium sulfonate group of the TPPMS ligand as shown in the conductivity measurements (see Exp. Sect.).

Spectroscopic data (IR as well as $^1$H, $^{13}$C{$^1$H} and $^{31}$P{$^1$H} NMR) support the proposed formulation (see Exp. Sect. for details). In particular, the following must be noted: i) The IR spectra (KBr) show the characteristic strong $\nu(SO_3)$ absorption for the TPPMS ligand at 1200 (**1a**) and 1198 (**1b**) cm$^{-1}$; ii) a singlet resonance can be observed at 26.1 (**1a**) and 29.6 (**1b**) ppm in the $^{31}$P{$^1$H} NMR spectra; iii) the $^1$H NMR spectra show a high field doublet at 8.37 ($^3J_{H,P}$ = 10.2 Hz) (**1a**) and 8.28 ($^3J_{H,P}$ = 11.1 Hz) (**1b**) corresponding to the hydrogen atom in an *ortho* position with respect to the phosphorus atom and to the sulfonato group ($H_o$).

Slow diffusion of diethyl ether into a solution of **1a** in methanol resulted in crystals suitable for X-ray diffraction studies. In this ruthenium derivative, the asymmetric unit consists of two anionic complexes which are held together in the crystal lattice by electrostatic interactions with potassium cations. An ORTEP type representation is shown in Figure 1. Selected bonding data are collected in the caption.

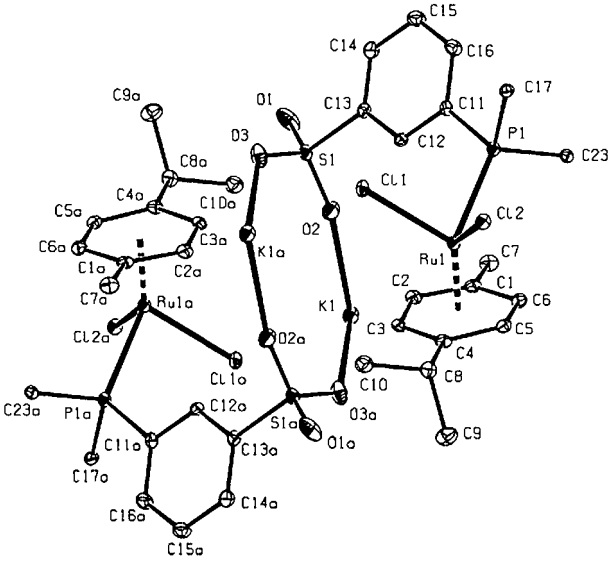


Figure 1. Molecular structure and atom labelling scheme for complex **1a**. Nonhydrogen atoms are represented by their 20% probability ellipsoids. Hydrogen atoms and phenyl rings ($Ph_2P$) have been omitted for clarity. Selected bond lengths [Å]: Ru(1)–C* 1.7061(3), Ru(1)–P(1) 2.3656(11), Ru(1)–Cl(1) 2.4046(10), Ru(1)–Cl(2) 2.4227(10), O(2)–K(1) 2.573(4). Selected bond angles [°]: C*–Ru(1)–P(1) 132.38 (3), C*–Ru(1)–Cl(1) 125.49(3), C*–Ru(1)–Cl(2) 123.46(3), Cl(1)–Ru(1)–P(1) 84.64(4), Cl(2)–Ru(1)–P(1) 88.54(4), Cl(1)–Ru(1)–Cl(2) 88.81 (4). C* means the centroid of C(1), C(2), C(3), C(4), C(5) and C(6) atoms.

The ruthenium atom, which exhibits a pseudo-octahedral three-legged piano stool geometry, is bonded to the phosphorus atom of the TPPMS ligand, to two chlorine atoms and $\eta^6$- to the *p*-cymene ring. An important feature of this crystal structure is that the complex in the solid state consists of linear chains (Figure 2) generated by the crystal periodicity along the *a* axis. These chains are generated by

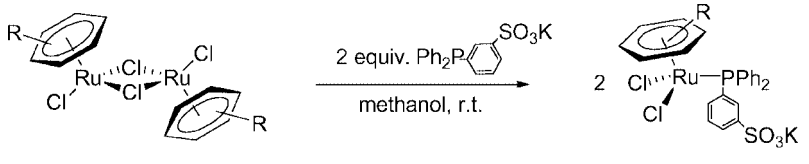


Scheme 1.

 © 2006 Wiley-VCH Verlag GmbH & Co. KGaA, Weinheim 

electrostatic interactions between the anionic complexes and the potassium atoms. Thus, three ruthenium complexes surround each potassium atom leading to a pentacoordinate environment provided by two chlorine atoms of one anionic moiety, a chlorine and an oxygen from a second and an oxygen atom from a third unit (Figure 3).

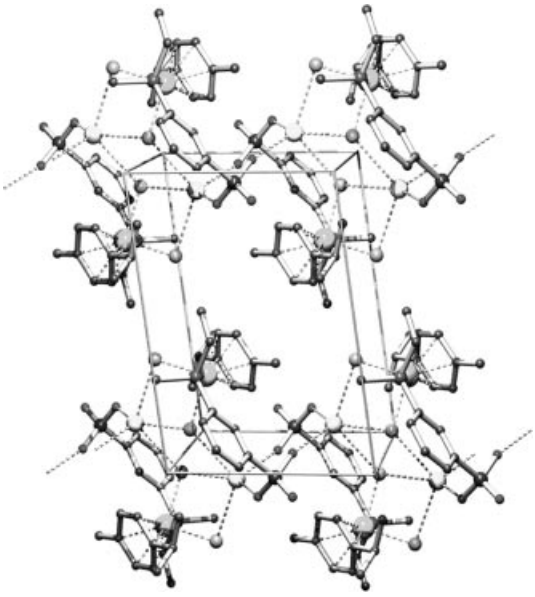

Figure 2. Layer structure for complex **1a**. Hydrogen atoms and phenyl rings have been omitted for clarity.

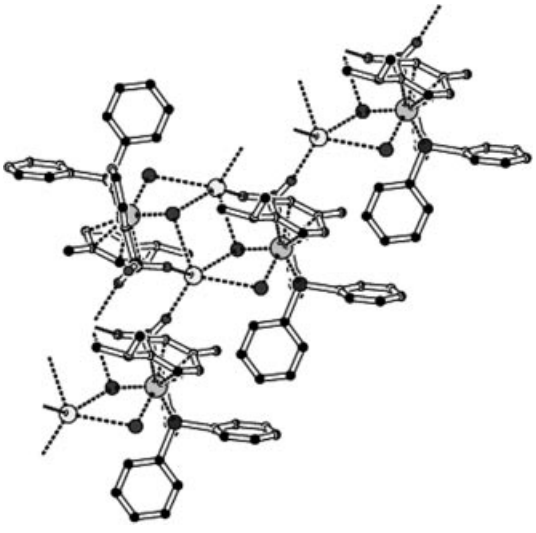

Figure 3. Potassium environment in the chain structure of **1a**. Hydrogen atoms have been omitted for clarity.

In addition, this complex shows different NMR spectroscopic behaviour depending on the solvent. In polar solvents such as $CD_3OD$ or $D_2O$ the NMR spectra show sharp signals while in $CD_2Cl_2$, $CDCl_3$ or $[D_8]$THF very broad signals may be observed. This prompted us to explore whether the chains are retained in solution leading to aggregates, the size of which being dependent on the solvent. In order to find the particle size in solution, the radius of gyration of the complex in THF solution has been measured using a detector of multiangle light scattering (MALS) coupled to size exclusion chromatographic equipment. The MALS spectrophotometer measures the excess Rayleigh ratio of the light scattered by the solute molecules in solution at different scattering angles. Thus, it enables the determination of the molecular dimensions, in terms of the radius of gyration, from the angular dependence of the scattered light (see Exp. Sect.). The mean square of the radius of gyration, $<s^2>$, is a very convenient quantity for expressing the molecular dimensions because it can be directly obtained from light scattering data and its definition is applicable to macromolecules of any shape.

When MALS is used as a second detector in size exclusion chromatography (SEC), together with a concentration dependent detector such as a differential refractive index interferometer (RI), the radius of gyration for each individual slice across the whole chromatogram of the sample can be determined. Thus, the SEC-MALS technique allows the analysis of the distribution of the radius of gyration with elution volume.[22]

The chromatograms obtained from different injections are reproducible and there were no adsorption problems in the columns. Figure 4 depicts the signal of the differential refractive index detector (RI) (which is sensitive to the sample concentration) and the light scattering signals, determined with the MALS spectrophotometer, at different values of the scattering angle $\theta$. The dependence of the intensity of the signal on the angle is evident and the scattering is therefore anisotropic. Thus the size of the molecules, i.e. the radius of gyration, can be determined for each slice of the chromatogram.[22] These values of the radii of gyration for the different slices are shown in Figure 5. The signal of the light scattering detector at 90° is superimposed. As can be seen in this figure, if we do not take into account the values determined for the head and tail of the chromatogram, the precision of which is lower, the monodispersity of the radius of gyration values is impressive. Both the appearance of the chromatogram, a very neat and defined peak, and the uniformity of the radius of gyration obtained through the slices of the chromatogram support the stability of the aggregates in THF. This stability is enough to bear the high pressures used in the chromatography. The average value for the root mean squared radius of gyration calculated for the sample is $<s^2>^{1/2} = 25 \pm 5$ nm. A water-soluble organometallic polymer which retains the polymeric structure in solution has been recently reported.[23]

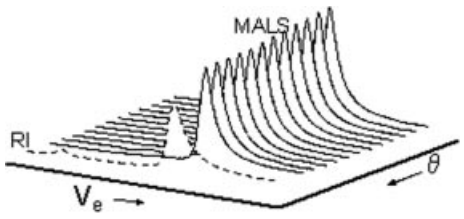


Figure 4. Refractive index, RI, signal (dashed line) and light scattering signals (solid lines) at different scattering angles, vs. elution volume.

 © 2006 Wiley-VCH Verlag GmbH & Co. KGaA, Weinheim 

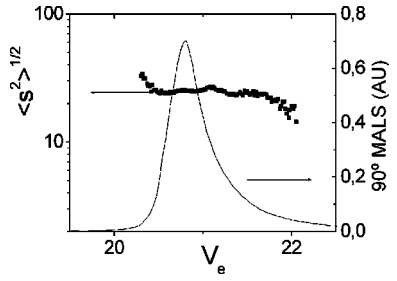


Figure 5. Root mean squared radius of gyration, $<s^2>^{1/2}$, in nm and 90° light scattering signal vs. elution volume.

### *b) Synthesis of [RuCl(η⁶-arene)(TPPMS)₂][Cl] [η⁶-arene = p-cymene (2a), benzene (2b)]*

Addition of an aqueous solution of TPPMS to a solution of [RuCl(μ-Cl)(η⁶-arene)]$_2$ (η⁶-arene = *p*-cymene, benzene) in toluene affords, after five minutes at room temperature, the disubstituted complexes [RuCl(η⁶-arene)(TPPMS)$_2$][Cl] [η⁶-arene = *p*-cymene (**2a**), benzene (**2b**)] isolated from the aqueous phase as yellow solids in yields of 94% (**2a**) and 90% (**2b**) (Scheme 2).

Complexes **2a** and **b** are soluble in water, alcohols and dichloromethane but insoluble in diethyl ether. Elemental analyses agree with the proposed stoichiometry for each.[24] Conductivity measurements for these complexes were not very useful since the observed values are strongly dependent on the solvent (112–166 $\Omega^{-1}cm^2mol^{-1}$ in water, 66–80 $\Omega^{-1}cm^2mol^{-1}$ in acetone). The reason can be found in ionic associations between the ions which are important for these types of electrolytes and which increase when the dielectric constant of the solvent decreases.[25]

The most remarkable features of complexes **2a** and **2b** are: i) the ν(SO$_3$) absorption for the TPPMS ligand at 1197 cm$^{-1}$ (**2a**) and 1198 cm$^{-1}$ (**2b**) in the IR spectra (KBr); ii) the $^{31}P\{^1H\}$ NMR spectra show a singlet signal at $\delta$ = 22.5 (**2a**) and 22.8 ppm (**2b**) and iii) the high field signal at 8.39 (**2a**) and 8.24 ppm (**2b**) corresponding to the two H$_o$ hydrogen atoms of the TPPMS ligand which appears as a broad unresolved signal for these complexes.

Metathesis of the halide with $KPF_6$ in complex **2a** allows the synthesis of [RuCl(η⁶-*p*-cymene)(TPPMS)$_2$][PF$_6$] (**2a′**) which shows almost the same spectroscopic data as the former complex **2a**, except for the signals due to the $PF_6^-$ group in the IR and in the $^{31}P\{^1H\}$ NMR spectra.

It is worth noting that **1a** and **b** as well as **2a** and **b** have been synthesised under very mild conditions in comparison with the recently reported analogous complexes with the tris(*meta*-sulfonatophenyl)phosphane trisodium salt (TPPTS) ligand, namely [RuCl$_2$(η⁶-*p*-cymene)(TPPTS)][26] and [RuCl(η⁶-benzene)(TPPTS)$_2$][Cl][27] which require reflux temperatures (methanol and water, respectively).

## Reactivity of the Complex [RuCl$_2$(η⁶-*p*-cymene)(TPPMS)] (1a)

### *a) Synthesis of the Complex [RuCl(η⁶-p-cymene)(NCMe)-(TPPMS)][SbF₆] (3)*

Treatment of complex **1a** with an appropriate chloride abstractor easily generates the non-isolated unsaturated species [RuCl(η⁶-*p*-cymene)(TPPMS)]$^+$ which can be identified by means of its reactivity. Thus, the reaction of complex **1a** with $AgSbF_6$ in the presence of acetonitrile gives rise to the adduct [RuCl(η⁶-*p*-cymene)(NCMe)-(TPPMS)][SbF$_6$] (**3**) in a moderate yield (58%) (Scheme 3).

Complex **3** can be isolated as an air-stable yellow solid which is soluble in water, methanol, acetonitrile and acetone but insoluble in diethyl ether and hexane. It has been analytically and spectroscopically characterised. The spectroscopic data agree with the proposed stoichiometry (see the Exp. Sect. for details). Thus, the IR spectrum shows a strong band at 1199 cm$^{-1}$ for the sulfonato group and one at 660 cm$^{-1}$ for the $SbF_6^-$ anion. The $^{31}P\{^1H\}$ NMR spectrum shows a singlet resonance at $\delta$ = 35.1 ppm. The expected signals for the methyl group of the acetonitrile ligand appear at $\delta$ = 2.12 ppm in the $^1H$ NMR spectrum and at $\delta$ = 3.4 ppm in the $^{13}C\{^1H\}$ NMR spectrum.

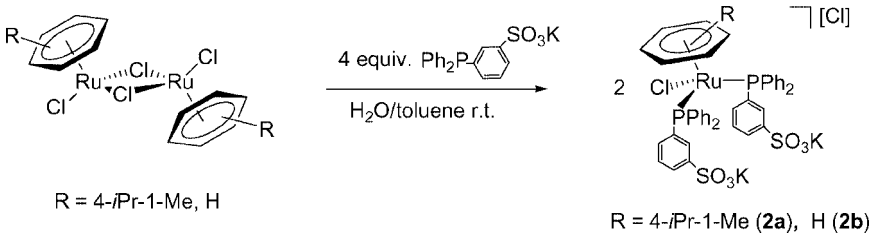


Scheme 2.

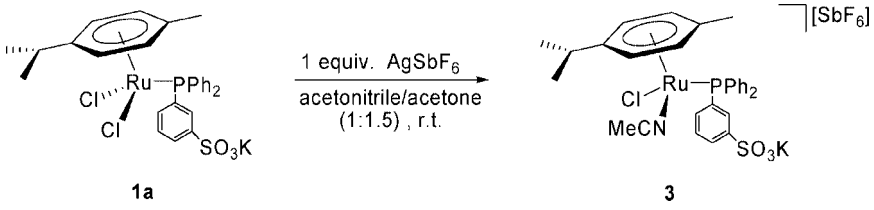


Scheme 3.

 © 2006 Wiley-VCH Verlag GmbH & Co. KGaA, Weinheim 

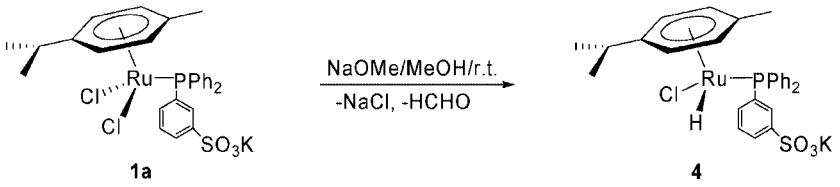


Scheme 4.

### *b) Synthesis of [RuClH(η⁶-p-cymene)(TPPMS)] (4)*

One of the most efficient synthetic methods for transition metal hydrides is that using sodium alkoxides bearing β hydrogen atoms as hydrogen transfer agents.[28] Thus, the reaction of [$RuCl_2$(η⁶-*p*-cymene)(TPPMS)] (**1a**) with NaOMe in methanol yields the hydride derivative [RuClH(η⁶-*p*-cymene)(TPPMS)] (**4**) which can be isolated as a yellow solid in 63% yield after work-up (Scheme 4).

IR and NMR spectroscopic data of **4** are in accordance with the proposed formulation (see Exp. Sect. for details). Significantly, i) the IR spectrum of **4** shows the ν(RuH) absorption at 1954 $cm^{-1}$ and the ν($SO_3$) absorption at 1196 $cm^{-1}$; ii) the $^{31}P\{^1H\}$ spectrum displays a singlet resonances at $\delta$ = 55.0 ppm and iii) the $^1H$ NMR spectrum shows a high-field doublet resonance ($\delta$ = –7.45 ppm, $^2J_{H,P}$ = 53.0 Hz) due to the hydride ligand. This value is in agreement with that reported by Bennett for the analogous complex [RuClH($C_6Me_6$)($PPh_3$)].[29]

## Catalytic Transfer Hydrogenation of Ketones

In recent years, transition metal catalysed transfer hydrogenation reactions between alcohols and ketones have become an efficient and clean alternative to the hydrogenation of carbonyl groups as illustrated by useful applications recently reported.[30] Also, ruthenium(II) complexes have been widely applied as efficient catalysts in these processes.[31] However, as in most of the homogeneous processes, the main problem stems from the difficulty in separating the products from the catalysts and in the recycling of expensive noble metals. The use of catalysts with hydrophilic properties can be a clean alternative for these processes since a simple extraction with water easily enables catalyst recovery.

This prompted us to explore the catalytic activity of the water-soluble complexes **1a** and **b** and **2a** and **b** in the reaction of transfer hydrogenation. The transfer hydrogenation of cyclohexanone by propan-2-ol was used as a model reaction. For comparative purposes, the activity of the derivative [RuCl(η⁵-$C_9H_7$)($TPPMS)_2$] is also reported.[32] Thus, in a typical experiment, KOH was added to an *i*PrOH solution of the ruthenium catalyst precursor (0.2 mol-%) and the ketone at 82 °C and the reaction was monitored by gas chromatography. In order to optimise the reaction, the following parameters were investigated: i) concentration: the best results were obtained with concentrated solutions (0.5 or 1 M). This result allows the reduction of the volume of *i*PrOH used in the catalysis in contrast with the conditions reported for other catalysts, where the best conditions are 0.1 or 0.2 M.[31] ii) base: KOH was the preferred option. Again, in our system, the amount of base could be drastically reduced (1.2 mol-%) compared with the usual conditions reported for this reaction (2–4 mol-%); iii) temperature: the activity of the catalyst decreases with temperature and almost no reactivity was observed at room temperature.

On the basis of our results, we conclude that the best conditions for the catalysis with these systems are as follow: 0.5 M cyclohexanone, 0.2 mol-% catalyst and 1.2 mol-% KOH in a total volume of 10 mL of *i*PrOH

Table 1 shows the results obtained with the different complexes in the reduction of cyclohexanone under the optimised reaction conditions. Although all the complexes studied have been shown to be active catalysts for the reduction of cyclohexanone to cyclohexanol, the arene complexes **1a** and **b**, and **2a** and **b** are much more efficient than the indenyl complex [RuCl(η⁵-$C_9H_7$)($TPPMS)_2$].

Table 1. Transfer hydrogenation of cyclohexanone.[a]

| Complex | *t* (min) | Conv. (%) | *TOF* ($h^{-1}$) |
|---|---|---|---|
| [$RuCl_2$(η⁶-*p*-cymene)(TPPMS)] (**1a**) | 15 | > 99 | 1994 |
| [$RuCl_2$(η⁶-benzene)(TPPMS)] (**1b**) | 10 | > 99 | 2982 |
| [RuCl(η⁶-*p*-cymene)($TPPMS)_2$][Cl] (**2a**) | 45 | > 99 | 663 |
| [RuCl(η⁶-benzene)($TPPMS)_2$][Cl] (**2b**) | 30 | > 99 | 1000 |
| [RuCl(η⁵-$C_9H_7$)($TPPMS)_2$] | 270 | 63 | 70 |

[a] 0.2 mol-% catalyst, 0.5 M cyclohexanone, 10 mL *i*PrOH and 0.06 mmol KOH.

Complexes **1a** and **b** are very efficient catalysts leading to quantitative conversions in very short times. Therefore, the activity of complex **1a** as catalyst in the reduction of a variety of ketones to the corresponding alcohols was explored. Table 2 summarises the results obtained.

For all ketones, quantitative conversions were obtained. The observed TOF decrease appreciably when open-chain ketones with bulkier substituents were used (entries 5 and 7 vs. 4 and 6) indicating that steric requirements are important. Finally, aliphatic ketones are easier to reduce than aromatic ketones as shown for phenyl methyl ketone (entry 3).

Unfortunately, the activity of the catalyst decreases drastically when using water as a solvent or in biphasic conditions. The possibility of chloride dissociation in aqueous solutions, which would explain this behaviour, can be ruled out since the NMR spectra of complexes **1a** and **1b** were recorded in both $D_2O$ and $CD_3OD$ and no significance differences were detected. In addition, the conductivity measurements do not indicate chloride dissociation.

Although the diminished catalytic activity of **1a** in the presence of water prevents further studies on transfer hy-

 © 2006 Wiley-VCH Verlag GmbH & Co. KGaA, Weinheim 

Table 2. Transfer hydrogenation of ketones[a] by the complex [$RuCl_2$(η⁶-*p*-cymene)(TPPMS)] (**1a**).

| Entry | Ketone | *t* [min] | Conv. [%] | *TOF* [$h^{-1}$] |
|---|---|---|---|---|
| **1** | | 15 | > 99 | 1994 |
| **2** | | 75 | 99 | 394 |
| **3** | 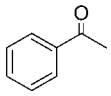 | 285 | 97 | 102 |
| **4** | | 70 | > 99 | 425 |
| **5** | | 120 | 98 | 245 |
| **6** | 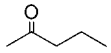 | 90 | 98 | 328 |
| **7** | 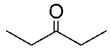 | 210 | > 99 | 142 |

[a] 0.2 mol-% catalyst, 0.5 M ketone, 10 mL of *i*PrOH and 0.06 mmol of KOH.

drogenation with these complexes, the hydrophilic character of the complexes allows catalyst recovery. Thus, once the catalytic process has finished, the solvents can be evaporated under vacuum and diethyl ether and water added. The catalyst can be then easily recovered by extracting the mixture with water while the alcohol remains in the organic phase. Evaporation of the water under vacuum leads to a brown solid which can be reused for a further catalytic cycle. Figure 6 shows the results for three consecutive catalytic cycles.

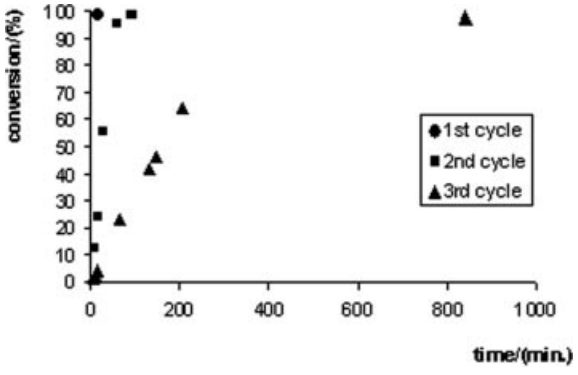


Figure 6. Transfer hydrogenation of cyclohexanone in three consecutive catalytic cycles.

The $^{31}P\{^1H\}$ and $^1H$ NMR spectra of the sample recovered after the catalysis show the presence of the hydride complex **4**, along with some other species. This observation agrees with the proposed hydride active species as a catalysts in the transfer hydrogenations reactions.[33] We have also tested the isolated hydride **4** as a catalyst. The reaction was complete within 40 minutes when a 1:1 ratio of KOH to catalyst was added. When the reaction was carried out without base, the catalytic activity decreased with time showing that a minimum amount of base is required, probably to promote the hydrogen transfer and/or the regeneration of the catalyst during the catalytic cycle.

## Conclusions

In summary, we have reported the mild synthetic conditions of new water-soluble half-sandwich ruthenium(II) complexes and a preliminary study of their reactivity. The structure of complex **1a** has been determined X-ray diffraction studies showing a linear chain structure which is retained in nonpolar solvents. The radius of gyration calculated for the sample in a THF solution of $<s^2>^{1/2}$ = 25 ± 5 nm supports this assertion.

The derivatives **1a** and **b** as well as **2a**, **2b** and **4** allow fast transfer hydrogenation of ketones at low catalyst and base loading with TOF values of up to 3000 $h^{-1}$. Furthermore, the catalyst can be recycled due to the hydrophilic properties of the TPPMS ligand. The implication of hydride species in transfer hydrogenation catalysis can be assessed by the presence of the hydride derivative [RuClH(η⁶-*p*-cymene)(TPPMS)] (**4**) in the reaction mixture after the catalytic reactions.

## Experimental Section

**General Procedures:** All manipulations were performed under an atmosphere of dry nitrogen using vacuum-line and standard Schlenk techniques. All reagents were obtained from commercial suppliers and used without further purification. Solvents were dried by standard methods and distilled under nitrogen before use. The compounds [RuCl(μ-Cl)(η⁶-*p*-cymene)]$_2$,[34] [RuCl(μ-Cl)(η⁶-benzene)]$_2$[34] and (*meta*-sulfonatophenyl)diphenylphosphane potassium salt (TPPMS)[35] were prepared by previously reported methods. Infrared spectra were recorded on a Perkin–Elmer FTIR Paragon 1000 spectrometer. The conductivities were measured at room temperature in ca. $5 \times 10^{-4}$ mol $dm^{-3}$ solutions with a Jenway PCM3 conductimeter. The C, H and N analyses were carried out with a Perkin–Elmer 240-B microanalyser. NMR spectra were recorded on Bruker AC300 and 300DPX instruments at 300 MHz ($^1H$), 121.5 MHz ($^{31}P$) or 75.4 MHz ($^{13}C$) using $SiMe_4$ or 85% $H_3PO_4$ as standards. DEPT experiments were carried out for all the compounds. Coupling constants *J* are given in Hertz. Abbreviations used: br, broad signal; d, doublet; dd, double doublet; m, multiplet; sept, septuplet; s, singlet. Gas chromatographic measurements were made on Hewlett–Packard HP6890 instrument using a Supelco Beta-Dex 120 (30 m, 0.25 mm) column. The instability of complex **4** prevented us from obtaining any satisfactory analyses.

**Synthesis of [$RuCl_2$(η⁶-*p*-cymene)(TPPMS)] (1a):** To a solution of the dimer [RuCl(μ-Cl)(η⁶-*p*-cymene)]$_2$ (100 mg, 0.16 mmol) in methanol (15 mL) was added the (*m*-sulfonatophenyl)diphenylphosphane potassium salt (TPPMS) (103 mg, 0.32 mmol) and the reaction mixture was stirred for 30 min at room temperature. The solvents were removed under vacuum and the residue was washed with diethyl ether (2 × 10 mL) and dried under vacuum to afford

 © 2006 Wiley-VCH Verlag GmbH & Co. KGaA, Weinheim 

complex **1a** as an orange solid. Yield: 201 mg (95%). IR (KBr): $\tilde{\nu}$ ($SO_3$) = 1200 $cm^{-1}$. Conductivity (water): 159 $\Omega^{-1}cm^2mol^{-1}$. $^1H$ NMR (300 MHz, $CD_3OD$, 20 °C): $\delta$ = 8.37 (d, $^3J_{H,P}$ = 10.2 Hz, 1 H, $H_o$), 7.78 (m, 5 H, TPPMS), 7.40 (m, 8 H, TPPMS), 5.33 (d, $^3J_{H,H}$ = 6.0 Hz, 2 H, CH of *p*-cymene), 5.20 (d, $^3J_{H,H}$ = 6.0 Hz, 2 H, CH of *p*-cymene), 2.63 [sept, $^3J_{H,H}$ = 6.8 Hz, 1 H, C*H*($CH_3$)$_2$], 1.87 (s, 3 H, $CH_3$), 1.06 [d, $^3J_{H,H}$ = 6.8 Hz, 6 H, CH(C*H*$_3$)$_2$] ppm. $^{13}C\{^1H\}$ NMR (75.4 MHz, $CD_3OD$, 20 °C): $\delta$ = 143.3–126.0 (TPPMS), 108.5 (d, $^2J_{C,P}$ = 2.4 Hz, C of *p*-cymene), 95.4 (s, C of *p*-cymene), 87.7 (d, $^2J_{C,P}$ = 3.8 Hz, CH of *p*-cymene), 85.8 (d, $^2J_{C,P}$ = 4.9 Hz, CH of *p*-cymene), 28.8 [s, *C*H($CH_3$)$_2$], 19.4 [s, CH(*C*H$_3$)$_2$], 15.2 (s, $CH_3$) ppm. $^{31}P\{^1H\}$ NMR (121.5 MHz, $CD_3OD$, 25 °C): $\delta$ = 26.1 (s) ppm. $C_{28}H_{28}Cl_2KO_3PRuS$ (686.60): calcd. C 48.98, H 4.11; found C 48.90, H 4.13.

**Synthesis of [$RuCl_2$(η⁶-benzene)(TPPMS)] (1b):** To a solution of TPPMS (160 mg, 0.40 mmol) in methanol (100 mL) was added the dimer [RuCl(μ-Cl)(η⁶-benzene)]$_2$ (100 mg, 0.20 mmol) and the reaction mixture was stirred for 2 h at room temperature. The solution was then filtered through kieselguhr and concentrated under vacuum to a volume of approx. 1 mL. Addition of diethyl ether afforded an orange precipitate. The solvents were decanted and the solid residue was washed with diethyl ether (2 × 10 mL) and dried under vacuum to afford complex **1b** as an orange solid. Yield: 170 mg (68%). Conductivity (water): 160 $\Omega^{-1}$ $cm^2mol^{-1}$. IR (KBr): $\tilde{\nu}$ ($SO_3$) = 1198 $cm^{-1}$. $^1H$ NMR (300 MHz, $CD_3OD$, 20 °C): $\delta$ = 8.28 (d, $^3J_{H,P}$ = 11.1 Hz, 1 H, $H_o$), 7.90 (br. s, 1 H, TPPMS), 7.72–7.65 (m, 4 H, TPPMS), 7.50–7.30 (m, 8 H, TPPMS), 5.52 (s, 6 H, CH of $C_6H_6$) ppm. $^{13}C\{^1H\}$ NMR (75.4 MHz, $CD_3OD$, 20 °C): $\delta$ = 137.3–126.7 (m, TPPMS), 90.6 (d, $^2J_{C,P}$ = 3.7 Hz, CH of $C_6H_6$) ppm. $^{31}P\{^1H\}$ NMR (121.5 MHz, $CD_3OD$, 20 °C): $\delta$ = 29.6 (s) ppm.

**Syntheses of [RuCl(η⁶-arene)(TPPMS)$_2$][Cl]·2$H_2O$ (2a) and (2b):** A solution of TPPMS (206 mg, 0.64 mmol) in water (20 mL) was added dropwise to a solution of the respective dimer [RuCl(μ-Cl)(η⁶-*p*-cymene)]$_2$ (100 mg, 0.16 mmol) or [RuCl(μ-Cl)(η⁶-benzene)]$_2$ (80 mg, 0.16 mmol) in toluene (5 mL) and the reaction mixture was stirred for 5 min at room temperature. Then the aqueous layer was separated, filtered through kieselguhr and the solvent was removed under vacuum. The residue was washed with diethyl ether (2 × 10 mL) and dried under vacuum to afford the complexes **2a** or **2b** as yellow solids. **2a**: Yield: 330 mg (94%). IR (KBr): $\tilde{\nu}$ ($SO_3$) = 1197 $cm^{-1}$. Conductivity (water): 176 $\Omega^{-1}$ $cm^2$ $mol^{-1}$. $^1H$ NMR (300 MHz, $CD_3OD$, 20 °C): $\delta$ = 8.39 (br. s, 2 H, $H_o$), 7.87 (d, $J_{H,H}$ = 7.7 Hz, 2 H,TPPMS), 7.49–7.17 (m, 24 H, TPPMS), 5.76 (d, $^3J_{H,H}$ = 6.4 Hz, 2 H, CH of *p*-cymene), 5.51 (d, $^3J_{H,H}$ = 6.4 Hz, 2 H, CH of *p*-cymene), 2.87 [sept, $^3J_{H,H}$ = 6.9 Hz, 1 H, C*H*($CH_3$)$_2$], 1.21 [d, $^3J_{H,H}$ = 6.9 Hz, 6 H, CH(C*H*$_3$)$_2$], 1.00 (s, 3 H, $CH_3$) ppm. $^{13}C\{^1H\}$ NMR (75.4 MHz, $CD_3OD$, 20 °C): $\delta$ = 144.5–125.5 (TPPMS), 109.4 (s, C of *p*-cymene), 99.8 (s, C of *p*-cymene), 97.0 (s, CH of *p*-cymene), 88.7 (d, $J_{C,P}$ = 4.5 Hz, CH of *p*-cymene), 30.4 [s, *C*H($CH_3$)$_2$], 20.0 [s, CH(*C*H$_3$)$_2$], 13.6 (s, $CH_3$) ppm. $^{31}P\{^1H\}$ NMR (121.5 MHz, $CD_3OD$, 20 °C): $\delta$ = 22.5 (s) ppm. $C_{46}H_{46}Cl_2K_2O_8P_2RuS_2$ (1067.08): calcd. C 50.09, H, 4.20; found C 49.03, H 4.20. **2b**: Yield: 340 mg (90%). IR (KBr): $\tilde{\nu}$ ($SO_3$) = 1198 $cm^{-1}$. Conductivity (water): 200 $\Omega^{-1}cm^2mol^{-1}$. $^1H$ NMR (300 MHz, $CD_3OD$, 20 °C): $\delta$ = 8.24 (br. s, 1 H, TPPMS), 7.91 (br. s, 1 H, TPPMS), 7.16 (m, 26 H, TPPMS), 5.67 (s, 6 H, CH of $C_6H_6$) ppm. $^{13}C\{^1H\}$ NMR (75.4 MHz, $CD_3OD$, 20 °C): $\delta$ = 143.9–128.4 (TPPMS), 96.6 (s, CH of $C_6H_6$) ppm. $^{31}P\{^1H\}$ NMR (121.5 MHz, $CD_3OD$, 20 °C): $\delta$ = 22.8 (s) ppm. $C_{42}H_{38}Cl_2K_2O_8P_2RuS_2$ (1010.97): calcd. C 48.18, H 3.66; found C 48.20, H 3.03.

**Synthesis of [RuCl(η⁶-*p*-cymene)(NCMe)(TPPMS)][$SbF_6$] (3):** To a solution of [$RuCl_2$(η⁶-*p*-cymene)(TPPMS)] (**1a**) (100 mg, 0.15 mmol) in a mixture acetonitrile (20 mL) and acetone (50 mL) was added $AgSbF_6$ (50 mg, 0.15 mmol) and the reaction mixture was stirred for 14 h at room temperature in the absence of light. The solution was then filtered through kieselguhr and concentrated under vacuum to a volume of approx. 1 mL. Addition of diethyl ether afforded a yellow precipitate. The solvents were decanted and the solid residue was washed with diethyl ether (2 × 10 mL) and dried under reduced pressure to afford complex **3**. Yield: 80 mg (58%). IR (KBr): $\tilde{\nu}$ ($SO_3$) = 1199, $\tilde{\nu}$ ($SbF_6$) = 660 $cm^{-1}$. Conductivity (acetonitrile): 92 $\Omega^{-1}cm^2mol^{-1}$. $^1H$ NMR (300 MHz, $CD_3OD$, 20 °C): $\delta$ = 8.19 (d, $^3J_{H,P}$ = 12.2 Hz, 1 H, $H_o$), 7.95 (m, 1 H, TPPMS), 7.62–7.46 (m, 12 H, TPPMS), 6.05 (d, $^3J_{H,H}$ = 6.2 Hz, 1 H, CH of *p*-cymene), 5.56 (d, $^3J_{H,H}$ = 6.2 Hz, 1 H, CH of *p*-cymene), 5.53 (d, $^3J_{H,H}$ = 6.3 Hz, 1 H, CH of *p*-cymene), 5.21 (d, $^3J_{H,H}$ = 6.0 Hz, 1 H, CH of *p*-cymene), 2.72 [sept, $^3J_{H,H}$ = 6.8 Hz, 1 H, C*H*($CH_3$)$_2$], 2.12 (m, 3 H, NCC*H*$_3$), 1.87 (s, 3 H, $CH_3$), 1.23 [d, $^3J_{H,H}$ = 6.8 Hz, 3 H, CH(C*H*$_3$)$_2$], 1.19 [d, $^3J_{H,H}$ = 7.1 Hz, 3 H, CH(C*H*$_3$)$_2$] ppm. $^{13}C\{^1H\}$ NMR (75.4 MHz, $CD_2Cl_2$, 20 °C): $\delta$ = 135.3–128.4 (TPPMS and N*C*$CH_3$), 114.6 (s, C of *p*-cymene), 103.1 (s, C of *p*-cymene), 93.7 (s, CH of *p*-cymene), 89.0 (s, CH of *p*-cymene), 88.7 (s, CH of *p*-cymene), 31.3 [s, CH(*C*H$_3$)$_2$], 22.8 [s, CH(*C*H$_3$)$_2$], 21.0 [s, *C*H($CH_3$)$_2$], 18.0 (s, $CH_3$), 3.4 (s, NC*C*H$_3$) ppm. $^{31}P\{^1H\}$ NMR (121.5 MHz, $CD_3OD$, 20 °C): $\delta$ = 35.1 (s) ppm. $C_{30}H_{31}ClF_6KNO_3PRuSSb$ (927.98): calcd. C 38.83, H 3.37, N 1.51; found C 38.39, H 3.63, N 1.36. MS (FAB+): *m*/*z* = 614 [$M^+$–K–NCMe], 576 [$M^+$–Cl –K–$NCCH_3$], 271 [$M^+$+2–NCMe –TPPMS].

**Synthesis of [RuClH(η⁶-*p*-cymene)(TPPMS)] (4):** A solution of complex **1a** (100 mg, 0.15 mmol) in methanol (5 mL) was added dropwise to a solution of NaOMe (4 mg, 0.17 mmol) in methanol (5 mL) and the reaction mixture was stirred at room temperature for 1 h. The solvent was removed and the solid residue was extracted with dichloromethane and the resultant solution filtered through kieselguhr and concentrated under vacuum to a volume of approx. 1 mL. Addition of diethyl ether afforded a yellow precipitate. The solvents were decanted and the solid residue was washed with diethyl ether (4 × 10 mL) and dried under reduced pressure to afford complex **4**. Yield: 45 mg (46%). IR (KBr): $\tilde{\nu}$ (Ru–H) = 1954, $\tilde{\nu}$ ($SO_3$) = 1199 $cm^{-1}$. Conductivity (methanol): 87 $\Omega^{-1}cm^2mol^{-1}$. $^1H$ NMR (300 MHz, $CD_3OD$, 20 °C): $\delta$ = 8.34–7.36 (m, 14 H, TPPMS), 5.68 (d, $^3J_{H,H}$ = 6.4 Hz, 1 H, CH of *p*-cymene), 5.20 (d, $^3J_{H,H}$ = 6.4 Hz, 1 H, CH of *p*-cymene), 4.97 (dd, $^3J_{H,H}$ = 6.4 and 5.6 Hz, 1 H, CH of *p*-cymene), 4.25 (d, $^3J_{H,H}$ = 5.6 Hz, 1 H, CH of *p*-cymene), 2.16 [m, 1 H, C*H*($CH_3$)$_2$], 1.99 (s, 3 H, $CH_3$), 1.12 [d, $^3J_{H,H}$ = 6.8 Hz, 3 H, CH(C*H*$_3$)$_2$], 1.06 [d, $^3J_{H,H}$ = 6.8 Hz, 3 H, CH(C*H*$_3$)$_2$], –7.45 (d, $^2J_{H,P}$ = 53.0 Hz, 1 H, Ru–H) ppm. $^{13}C\{^1H\}$ NMR (75.4 MHz, $CD_3OD$, 20 °C): $\delta$ = 144.0–125.2 (m, TPPMS), 104.6 (s, 2 × C of *p*-cymene), 91.4 (s, CH of *p*-cymene), 91.3 (s, CH of *p*-cymene), 79.3 (s, CH of *p*-cymene), 79.2 (s, CH of *p*-cymene), 30.5 [s, *C*H($CH_3$)$_2$], 22.6 [s, CH(*C*H$_3$)$_2$], 21.3 [s, CH(*C*H$_3$)$_2$], 17.0 (s, $CH_3$) ppm. $^{31}P\{^1H\}$ NMR (121.5 MHz, $CD_3OD$, 20 °C): $\delta$ = 55.0 (s) ppm.

**Synthesis of [RuCl(η⁶-*p*-cymene)(TPPMS)$_2$][$PF_6$]·2$H_2O$ (2a′):** To a solution of complex **2a** (50 mg, 0.05 mmol) in methanol (5 mL) was added $KPF_6$ (11 mg, 0.06 mmol). The mixture was stirred for 30 min at room temperature and was then evaporated to dryness. The residue was extracted with dichloromethane and concentrated under vacuum to a volume of approx. 1 mL. Addition of diethyl ether afforded a yellow precipitate. The solvents were decanted and the solid residue was washed with diethyl ether (2 × 10 mL) and

 © 2006 Wiley-VCH Verlag GmbH & Co. KGaA, Weinheim 

dried under vacuum to afford complex **2a′**. IR (KBr): $\tilde{\nu}$ ($PF_6^-$) = 844 $cm^{-1}$.

**Transfer Hydrogenation of Ketones – General Procedure:** The samples were typically prepared as follows: the ketone (5 mmol), ruthenium catalyst precursor (0.01 mmol, 0.2 mol-% of Ru) and propan-2-ol (9.25 mL) were introduced into a Schlenk tube fitted with a condenser and heated at 82 °C for 15 min in an inert atmosphere. KOH was then added (0.75 mL of a 0.08 M solution in propan-2-ol, 1.2 mol-%) and the reaction monitored by gas chromatography. The corresponding alcohol and acetone were the only products detected in all cases. The identity of the alcohols was assessed by comparison with commercially available (Aldrich Chemical Co. or Acros Organics) pure samples.

**X-ray Crystal Structure Determination of Complex 1a:** Crystals suitable for X-ray diffraction analysis were obtained by slow diffusion of diethyl ether into a saturated solution of the complex in methanol. The most relevant crystal and refinement data are collected in Table 3. A light-orange prismatic single crystal was mounted on a glass fibre and transferred to a Bruker SMART 6 K CCD area-detector three-circle diffractometer (Cu-$K_\alpha$ radiation, $\lambda$ = 1.5418 Å).[36] X-ray data were collected at 100(2) K with a combination of three runs at different $\varphi$ and $2\theta$ angles. The data were collected using 0.3° wide $\omega$ scans with a crystal-to-detector distance of 4.0 cm. The substantial redundancy in data allowed empirical absorption corrections (SADABS)[37] to be applied using multiple measurements of symmetry-equivalent reflections (ratio of minimum to maximum apparent transmission = 0.602305). A total number of 8520 reflections were collected, with 4401 independent reflections ($R_{int}$ = 0.0316). The raw intensity data frames were integrated with the SAINT program[38] which also applied corrections for Lorentz and polarisation effects.

Table 3. Crystal data and structure refinement for **1a**.

| | **1a** |
|---|---|
| Chemical formula | $C_{28}H_{28}Cl_2KO_3PRuS$ |
| *F*w | 686.60 |
| *T* [K] | 100(2) |
| Wavelength [Å] | 1.5418 |
| Crystal system | triclinic |
| Space group | $P\bar{1}$ |
| *a* [Å] | 9.1813(2) |
| *b* [Å] | 12.1763(2) |
| *c* [Å] | 12.5166(2) |
| *α* [°] | 94.1940(10) |
| *β* [°] | 96.1750(10) |
| *γ* [°] | 94.8240(10) |
| *V* [Å$^3$] | 1381.46(4) |
| *Z* | 2 |
| $\rho_{calcd.}$ [g $cm^{-3}$] | 1.651 |
| $\mu$ [$mm^{-1}$] | 9.219 |
| *F*(000) | 696 |
| Crystal size [mm] | 0.12 × 0.09 × 0.104 |
| $\theta$ range [°] | 3.56 to 66.73 |
| Index ranges | $-9 \le h \le 10$; $-14 \le k \le 13$; $-13 \le l \le 14$ |
| No. of reflections collected | 8520 |
| No. of unique reflections | 4401 [$R_{int}$ = 0.0316] |
| Completeness to $\theta_{max.}$ | 90.1% |
| No. of parameters/restraints | 337/0 |
| Goodness-of-fit on $F^2$ | 1.034 |
| $R_1$[a] [$I > 2\sigma(I)$]; $wR_2$[a] [$I > 2\sigma(I)$] | 0.0400; 0.1011 |
| $R_1$(all data); $wR_2$(all data) | 0.0497; 0.1078 |
| Largest diff peak and hole [e Å$^{-3}$] | 1.295 and –0.510 |

[a] $R_1 = \Sigma(||F_o| - |F_c||)/\Sigma|F_o|$; $wR_2 = \{\Sigma[w(F_o^2 - F_c^2)^2]/\Sigma[w(F_o^2)^2]\}^{1/2}$.

CCDC-290177 (for **1a**) contains the supplementary crystallographic data for this paper. These data can be obtained free of charge from the Cambridge Crystallographic Data Centre via www.ccdc.cam.ac.uk/data_request/cif.

The software package WINGX was used for space group determination, structure solution and refinement.[39] The space group determination was based on a check of the Laue symmetry and systematic absences and ascertained from the structure solution. The structure was solved by Patterson interpretation and phase expansion using DIRDIF,[40] completed with difference Fourier syntheses and refined with full-matrix least-squares using SHELXL-97.[41] Weighted *R* factors ($R_w$) and all goodness of fit *S* are based on $F^2$. Conventional *R* factors (*R*) are based on *F*. All nonhydrogen atoms were refined with anisotropic displacement parameters. All hydrogen atoms were geometrically located and their coordinates were refined as riding on their parent atoms. The function minimised was $[\Sigma w(F_o^2 - F_c^2)/\Sigma w(F_o^2)]^{1/2}$ where $w = 1/[\sigma^2(F_o^2) + (0.0921P)^2 + 0.0000P]$ with $\sigma^2(F_o^2)$ from counting statistics and $P = [\max(F_o^2, 0) + 2F_c^2]/3$. Atomic scattering factors were taken from the International Tables for X-ray Crystallography.[42] Geometrical calculations were made with PARST.[43] Plots were made with PLATON.[44]

**Radius of Gyration Measurements:** Size exclusion chromatography (SEC) measurements were carried out using a Waters Associates instrument coupled with an Optilab interferometric differential refractive index detector (RI) and a multiangle light scattering (MALS) DAWN DSP-F laser photometer detector both from the Wyatt Technology Corp. The photometer was calibrated with spectrometric grade toluene (Scharlau) and the normalisation of its detectors in THF was performed with low molecular weight standard samples of polystyrene. The same polystyrene standard was used to determine the interdetector volume. Two columns PLgel mixed B (Polymer Laboratories) in series completed the setup and THF freshly distilled from sodium and benzophenone, filtered through a 0.2 μm Fluoropore membrane (Millipore) and degassed, was used as eluent. The flow rate was 1.0 mL $min^{-1}$ and the temperature 25 °C.

The basic light-scattering equation at the small concentrations used in the size exclusion chromatography is[45] given by Equation (1).

$$\frac{K_c}{\Delta R_\theta} = \frac{1}{M}\left(1 + \frac{16\pi^2}{3\lambda^2} < s^2 > \sin^2\left(\frac{\theta}{2}\right) + \cdots\right) \quad (1)$$

where $R_\theta$ is the excess Rayleigh ratio of the light scattered by the solute molecules in a solution, *c* is the concentration of the solution, $\lambda$ is the wavelength of the incident light in the medium, $\theta$ is the scattering angle, $<s^2>$ the mean squared radius of gyration and *K* is an optical constant.

The parentheses of Equation (1) contain the terms of the particle form factor which takes into account the interferences among light scattered at different angles for large molecules. At $\theta = 0$ the interferences vanish and the following expression can be written (Equation 2).

$$\frac{\Delta R_{\theta=0}}{\Delta R_\theta} = 1 + \frac{16\pi^2}{3\lambda^2} < s^2 > \sin^2\left(\frac{\theta}{2}\right) + \cdots \quad (2)$$

Thus the angular dependence of the scattered light enables the measurement of radius of gyration provided that the size of the par-

 © 2006 Wiley-VCH Verlag GmbH & Co. KGaA, Weinheim 

ticles is large enough compare with the wavelength and that the normalisation constants for the different detectors have been determined.[22,45]

## Acknowledgments

This work was supported by the Spanish M.C.T. (BQU2003-00255). MALS equipment was supported by CAM (GR/MAT/0810/2004) and CTQ2005-04710. A. G.-F. thanks the Spanish Ministerio de Educación, Cultura y Deporte for a scholarship.

[1] a) F. Joó, *Aqueous Organometallic Catalysis*, Kluwer, Dordrecht, **2001**; b) *Aqueous Phase Organometallic Catalysis – Concepts and Applications*, 2nd ed. (Eds.: B. Cornils, W. A. Herrmann), Wiley-VCH, Weinheim, **2004**.
[2] N. Pinault, D. W. Bruce, *Coord. Chem. Rev.* **2003**, *241*, 1–25.
[3] a) A. L. Casalnuovo, J. C. Calabrese, *J. Am. Chem. Soc.* **1990**, *112*, 4324–4330; b) A. I. Roschin, N. A. Bumagin, I. P. Beletskaya, *Tetrahedron Lett.* **1995**, *36*, 125 –128.
[4] a) D. P. Paterniti, L. W. Francisco, J. D. Atwood, *Organometallics* **1999**, *18*, 123–127; b) J. Kovács, T. Decuir, J. H. Reibenspies, F. Joó, D. J. Darensbourg, *Organometallics* **2000**, *19*, 3963–3969.
[5] In 1974 the ligand TPPMS was used in situ for hydrogenation reactions: F. Joó, M. T. Beck, *Reaction Kinetics Catal. Lett.* **1975**, *2*, 257–263.
[6] Z. Tóth, F. Joó, M. T. Beck, *Inorg. Chim. Acta* **1980**, *42*, 153–161.
[7] a) A. Andriollo, A. Bolivar, F. A. López, D. E. Páez, *Inorg. Chim. Acta* **1995**, *238*, 187–192; b) A. Andriollo, J. Carrasquel, J. Mariño, F. A. López, D. E. Páez, I. Rojas, N. Valencia, *J. Mol. Catal. A: Chem.* **1997**, *116*, 157–165.
[8] a) P. J. Baricelli, G. Rodríguez, M. Rodríguez, E. Lujano, F. López-Linares, *Appl. Catal., A* **2003**, *239*, 25–34; b) P. J. Baricelli, E. Lujano, M. Rodríguez, A. Fuentes, R. A. Sánchez Delgado, *Appl. Catal., A* **2004**, *263*, 187–191.
[9] P. J. Baricelli, L. Izaguirre, J. López, E. Lujano, F. López-Linares, *J. Mol. Catal. A: Chem.* **2004**, *208*, 67–72.
[10] M. A. Busolo, F. López-Linares, A. Andriollo, D. E. Páez, *J. Mol. Catal. A: Chem.* **2002**, *189*, 211–217.
[11] A. Kathó, Z. Opre, G. Laurenczy, F. Joó, *J. Mol. Catal. A: Chem.* **2003**, *204–205*, 143–148.
[12] J. Elek, L. Nádasdi, G. Papp, G. Laurenczy, F. Joó, *Appl. Catal., A* **2003**, *255*, 59–67.
[13] For recent examples of aqueous transfer hydrogenation reactions catalysed by ruthenium(II) complexes see: a) J. Canivet, G. Labat, H. Stoeckli-Evans, G. Süss-Fink, *Eur. J. Inorg. Chem.* **2005**, 4493–4500; b) J. Canivet, L. Karmazin-Brelot, G. Süss-Fink, *J. Organomet. Chem.* **2005**, *690*, 3202–3211; P. N. Liu, J. G. Deng, Y. Q. Tu, S. H. Wang, *Chem. Commun.* **2004**, 2070–2071; Y. Ma, H. Liu, L. Chen, X. Cui, J. Zhu, J. Deng, *Org. Lett.* **2003**, *5*, 2103–2106.
[14] a) F. Joó, A. Bényei, *J. Organomet. Chem.* **1989**, *363*, C19–C21; b) A. Bényei, F. Joó, *J. Mol. Catal.* **1990**, *58*, 151–163.
[15] In 1997 this complex was reformulated as a dimer $[RuCl_2(TPPMS)_2]_2$: R. A. Sánchez Delgado, M. Medina, F. López-Linares, A. Fuentes, *J. Mol. Catal. A: Chem.* **1997**, *116*, 167–177.
[16] Catalytic activity of $[RuCl_2(\eta^6\text{-}p\text{-cymene})(TPPMS)]$ for the hydrogenation of hydrogencarbonate has been reported but no synthetic or spectroscopic data for that complex have been published to date. H. Horváth, G. Laurenczy, A. Kathó, *J. Organomet. Chem.* **2004**, *689*, 1036–1045.
[17] T. Suárez, B. Fontal, M. Reyes, F. Bellandi, R. Contreras, G. Leon, P. Cancines, *Reaction Kinetics Catal. Lett.* **2002**, *76*, 161–169.
[18] C. R. Anthony, L. McElwee-White, *J. Mol. Catal. A: Chem.* **2005**, *227*, 113 –117.
[19] a) P. Álvarez, J. Gimeno, E. Lastra, S. García-Granda, J. F. Van der Maelen, M. Bassetti, *Organometallics* **2001**, *20*, 3762–3771; b) P. Álvarez, J. Gimeno, E. Lastra, *Organometallics* **2002**, *21*, 5678–5680.
[20] a) P. Álvarez, E. Lastra, J. Gimeno, M. Bassetti, L. R. Falvello, *J. Am. Chem. Soc.* **2003**, *125*, 2386–2387; b) J. Díez, M. P. Gamasa, J. Gimeno, E. Lastra, A. Villar, *Organometallics* **2005**, *24*, 1410–1418.
[21] No analytical data for **1b** can be reported since this complex is obtained contaminated with 3% of the complex $[RuCl(\eta^6\text{-benzene})(TPPMS)_2][Cl]$ (**2b**) detected by NMR spectroscopy.
[22] M. P. Tarazona, E. Saiz, *J. Biochem. Biophys. Methods* **2003**, *56*, 95–116.
[23] C. Lidrissi, A. Romerosa, M. Saoud, M. Serrano-Ruiz, L. Gonsalvi, M. Peruzzini, *Angew. Chem. Int. Ed.* **2005**, *44*, 2568–2572.
[24] Recently, ruthenium(II) complexes with the sulfonated diphosphane 1,2-bis(di-*p*-sulfonatophenylphosphanyl)benzene (dppbts) were formulated as anionic complexes $[RuCl(\eta^6\text{-arene})(dppbts)_2][Na]_3$. C. Daguenet, R. Scopelliti, P. J. Dyson, *Organometallics* **2004**, *23*, 4849–4857.
[25] I. N. Levine, *Physical Chemistry*, 5th ed., McGraw-Hill, New York, **2001**.
[26] P. J. Dyson, D. J. Ellis, G. Laurenczy, *Adv. Synth. Catal.* **2003**, *345*, 211–215.
[27] M. Tokunaga, T. Suzuki, N. Koga, T. Fukushima, A. Horiuchi, Y. Wakatsuki, *J. Am. Chem. Soc.* **2001**, *123*, 11917–11924.
[28] M. I. Bruce, H. G. Humphrey, A. G. Swincer, R. C. Wallis, *Aust. J. Chem.* **1984**, *37*, 1747.
[29] a) M. A. Bennett, T. N. Huang, A. K. Smith, T. W. Turney, *J. Chem. Soc. Chem. Commun.* **1978**, 582–583; b) M. A. Bennett, T. N. Huang, J. L. Latten, *J. Organomet. Chem.* **1984**, *272*, 189–205.
[30] a) D. Matharu, D. J. Morris, A. M. Kawamoto, G. J. Clarkson, M. Wills, *Org. Lett.* **2005**, *7*, 1523–7060; b) F. Wang, H. Liu, L. Cun, J. Zhu, J. Deng, Y. Jiang, *J. Org. Chem.* **2005**, *70*, 9424–9429; c) X. Wu, D. Vinci, T. Ikariya, J. Xiao, *Chem. Commun.* **2005**, 4447–4449; d) K. Ohno, Y. Kataoka, K. Mashima, *Org. Lett.* **2004**, *6*, 4695–4697; e) X. Li, X. Wu, W. Chen, F. E. Hancock, F. King, J. Xiao, *Org. Lett.* **2004**, *6*, 3321–3324; f) J. Q. Yu, H. C. Wu, C. Ramarao, J. B. Spencer, S. V. Ley, *Chem. Commun.* **2003**, 678–679; g) G. Zassinovich, G. Mestroni, S. Gladiali, *Chem. Rev.* **1992**, *92*, 1051–1069.
[31] a) A. M. Hayes, D. J. Morris, G. J. Clarkson, M. Wills, *J. Am. Chem. Soc.* **2005**, *127*, 7318–7319; b) W. Baratta, E. Herdtweck, K. Siega, M. Toniutti, P. Rigo, *Organometallics* **2005**, *24*, 1660–1669; c) W. Baratta, G. Chelucci, S. Gladiali, K. Siega, M. Toniutti, M. Zanette, E. Sangrando, P. Rigo, *Angew. Chem. Int. Ed.* **2005**, *44*, 6214–6219; d) N. Shan, H. Adams, J. A. Thomas, *Inorg. Chim. Acta* **2005**, *358*, 3377–3383; e) J. Hannedouche, G. J. Clarkson, M. Wills, *J. Am. Chem. Soc.* **2004**, *126*, 986–987; f) D. Cuervo, M. P. Gamasa, J. Gimeno, *Chem. Eur. J.* **2004**, *10*, 425–432; g) M. Albrecht, R. H. Crabtree, J. Mata, E. Peris, *Chem. Commun.* **2002**, 32–33; h) R. Noyori, M. Yamakawa, S. Hashiguchi, *J. Org. Chem.* **2001**, *66*, 7931–7944; i) R. Noyori, S. Hashiguchi, *Acc. Chem. Res.* **1997**, *30*, 97–102.
[32] The synthesis and reactivity of the complex $[RuCl(\eta^5\text{-}C_9H_7)(TPPMS)_2]$ will be reported elsewhere.
[33] a) J. E. Bäckvall, *J. Organomet. Chem.* **2002**, *652*, 105–111; b) O. Pàmies, J. E. Bäckvall, *Chem. Eur. J.* **2001**, *7*, 5052–5058; c) Y. R. S. Laxmi, J. E. Bäckvall, *Chem. Commun.* **2000**, 611–612; d) A. Aranyos, G. Csjernyik, K. J. Szabó, J. E. Bäckvall, *Chem. Commun.* **1999**, 351–352.
[34] M. A. Bennett, A. K. Smith, *J. Chem. Soc. Dalton Trans.* **1974**, 233–241.
[35] F. Joó, J. Kovács, A. Kathó, A. C. Bényei, T. Decuir, D. J. Darensbourg, *Inorg. Synth.* **1998**, *32*, 8–25.

 © 2006 Wiley-VCH Verlag GmbH & Co. KGaA, Weinheim 

[36] *SMART* version 5.625, Area-Detector Software Package, Bruker AXS **1997**–**2001**, Madison, WI.
[37] G. M. Sheldrick, *SADABS* version 2.03: *Program for Empirical Absorption Correction*, University of Göttingen, Göttingen, Germany, **1997**–**2001**.
[38] *SAINT+NT* version 6.04, SAX Area-Detector Integration Program, Bruker AXS **1997–2001**, Madison, WI.
[39] L. J. Farrugia, *J. Appl. Crystallogr.* **1999**, *32*, 837.
[40] P. T. Beurskens, G. Admiraal, G. Beurskens, W. P. Bosman, S. García-Granda, R. O. Gould, J. M. M. Smits, C. Smykalla, *The DIRDIF Program System*, Technical Report of the Crystallographic Laboratory, University of Nijmegen: Nijmegen, The Netherlands, **1999**.
[41] G. M. Sheldrick, *SHELXL-97: Program for the Refinement of Crystal Structures*, University of Göttingen, Göttingen, Germany, **1997**.
[42] *International Tables for X-ray Crystallography*, Kynoch Press, Birminghan, U. K., **1974**, vol. IV (present distributor: Kluwer Academic Publishers, Dordrecht, The Netherlands).
[43] M. Nardelli, *Comput. Chem.* **1983**, *7*, 95–98.
[44] A. L. Spek, *PLATON: A Multipurpose Crystallographic Tool*, University of Utrecht, The Netherlands, **2005**.
[45] P. J. Wyatt, *Anal. Chim. Acta* **1993**, *272*, 1–40.

Received: February 8, 2006
Published Online: May 24, 2006

 © 2006 Wiley-VCH Verlag GmbH & Co. KGaA, Weinheim 

DOI: 10.1002/ejic.200600191

# Coordination and Reduction of HMPA in the Lithiation of (*S*)-*N*-(α-Methylbenzyl)allylamine: Crystal Structures of {(*S*)-α-[PhC(H)$CH_3$](C$H_2$CH=C$H_2$)NLi·HMPA}$_2$ and [(Me$_2$N)$_2$POLi]$_6$

**Philip C. Andrews,*[a] Magdaline Minopoulos,[a] and Evan G. Roberston[a]**

**Keywords:** Lithium / Chiral metal amides

Monolithiation of the chiral amine (*S*)-*N*-(α-methylbenzyl)allylamine, in the presence of the strong Lewis donor solvent hexamethylphoshoramide (HMPA), results in pale yellow crystals which have been crystallographically analysed revealing the structure of the complex to be an asymmetric *cisoid* dimer {(*S*)-α-[PhC(H)$CH_3$](C$H_2$CH=C$H_2$)NLi·HMPA}$_2$. Variable-temperature NMR studies show this complex can undergo a thermally induced rearrangement to a 1-azaallyl complex at ca. 90 °C. Attempted dilithiation of the chiral amine at the N and vinylic C centres with *n*BuLi and HMPA results in competitive reduction of HMPA to give crystals of the lithium dimethylamidophosphite, structurally authenticated as the hexamer [(Me$_2$N)$_2$POLi]$_6$, in which the Li cation is bonded preferentially to the O centre and not P. The effect is a reduction in the oxidation state of the P centre from (V) to (III), which is supported by ab initio calculations showing the crystal structure to represent the most thermodynamically stable of the possible isomers.
(© Wiley-VCH Verlag GmbH & Co. KGaA, 69451 Weinheim, Germany, 2006)

## Introduction

Chiral lithium amides derived from α-methylbenzylamine are invaluable reagents in the formation of β-amino acids and β-lactams from their selective conjugate addition reaction with unsaturated β-amino esters and amides.[1] In particular, the use of lithium (*S*)-*N*-(α-methylbenzyl)allylamide, as developed by Davies and co-workers, has proved highly effective because of the ease by which deprotection of the conjugate addition product can be achieved by simple application of Wilkinson's catalyst in removing the allyl group.[1,2] Our recent endeavours in probing the causes of high selectivity have focused on establishing the structural chemistry and unexpected anion transformations which occur when the common chiral amines derived from α-methylbenzylamine are treated with *n*BuM (M = Li, Na, K) in the presence of Lewis bases. A variance in the metal, solvents and/or Lewis donors can promote dramatic and unexpected structural changes such as azaallyl and enamide formation.[3,4] In this regard, we have previously shown that the complex formed on reaction of (*S*)-*N*-(α-methylbenzyl)allylamine (= *S*-*N*-α-mba) with *n*BuNa in the presence of tmeda undergoes a 1,3-sigmatropic shift, converting from the expected allylamide to the 1-azaallylic complex, {[(*S*)-α-(PhC(H)$CH_3$N⁻⁻C(H)⁻⁻$CHCH_3$)]Na·tmeda}$_2$,[5] Figure 1, and because our numerous attempts at crystallising analogous lithium complexes with a variety of Lewis donors resulted only in a series of impure oils, we were unable to confirm definitively whether a similar transformation was, or could be, occurring with lithium (*S*)-*N*-(α-methylbenzyl)-allylamide.

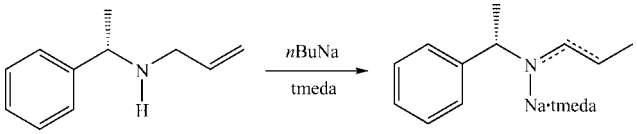


Figure 1. The 1-azaallyl structure of {[(*S*)-α-(PhC(H)$CH_3$N⁻⁻C(H)⁻⁻$CHCH_3$)]Na·tmeda}$_2$ derived from sodiation of (*S*)-*N*-(α-methylbenzyl)allylamine.

This lack of success in obtaining definitive structural information from the monolithiation reactions led us to subsequently examine and describe the cyclic structures of the homo- and hetero-bimetallic complexes, which result from a second deprotonation of lithium (*S*)-*N*-(α-methylbenzyl)-allylamide at the terminal vinylic site by Li, Na and K organyls.[6] The synthesis and reactions of the dilithiated complex have been described previously by Yus who used *t*BuLi to force metallation at the terminal vinylic proton,[7] though we have since noted that despite the proximity of the relative p$K_a$ values of the terminal vinylic protons (44) and Bu*H* (50) that the dilithiated product will also form using only *n*BuLi in toluene, albeit slowly and in low yield.[6] Recent detailed structural and ab initio studies by Williard and co-workers on related *N*-silylallylamines have highlighted the importance of using ethereal solvents to increase the kinetic reactivity of the terminal vinylic protons towards *n*BuLi, and their influence in determining a *cis* stereochemi-

[a] School of Chemistry, Monash University,
P. O. Box 23, Clayton, Melbourne, Vic. 3800, Australia
Fax: +61-3-9905-4597
E-mail: phil.andrews@sci.monash.edu.au

 © 2006 Wiley-VCH Verlag GmbH & Co. KGaA, Weinheim 

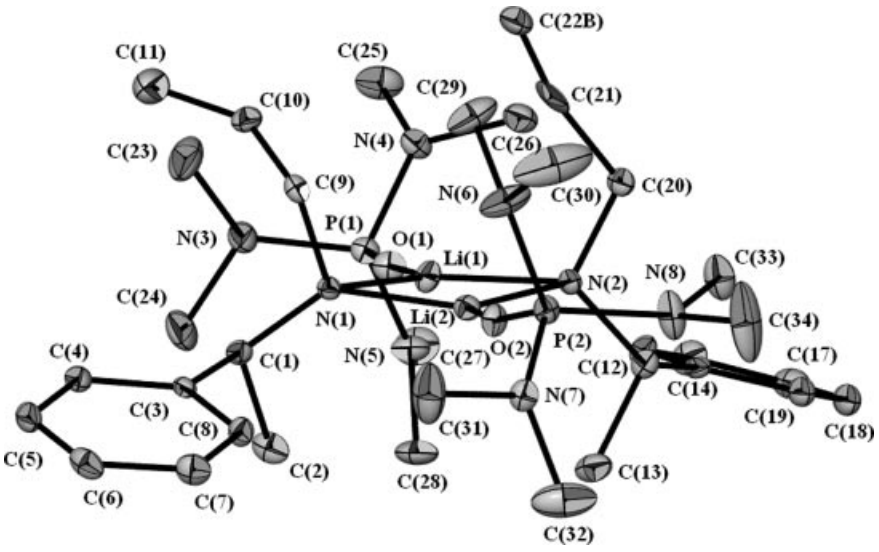


Figure 2. Structure of $\{(S)$-α-$(PhC(H)CH_3)(CH_2CH{=}CH_2)NLi{\cdot}HMPA\}_2$ (**1**). Thermal ellipsoids shown at 30% probability and all H atoms omitted for clarity. Important bond lengths [Å] and angles [°]: N(1)–Li(1) 1.994(6), N(1)–Li(2) 1.994(6), N(2)–Li(1) 2.023(7), N(2)–Li(2) 2.061(6), N(1)–C(1) 1.448(4), N(1)–C(9) 1.466(4), C(9)–C(10) 1.494(5), C(10)–C(11) 1.311(5), O(1)–Li(1) 1.858(7), O(2)–Li(2) 1.845(6); C(1)–N(1)–C(9) 109.4(3), C(1)–N(1)–Li(2) 135.7(3), C(9)–N(1)–Li(2) 101.9(3), C(1)–N(1)–Li(1) 115.9(3), C(9)–N(1)–Li(1) 114.3(3) Li(2)–N(1)–Li(1) 76.1(3), C(12)–N(2)–C(20) 109.6(3), C(12)–N(2)–Li(1) 125.8(3), C(20)–N(2)–Li(1) 110.1(3), C(12)–N(2)–Li(2) 114.0(2), C(20)–N(2)–Li(2) 120.3(3), Li(1)–N(2)–Li(2) 74.0(3), N(1)–Li(1)–N(2) 105.4(3), O(1)–Li(1)–N(1) 124.4(3), O(1)–Li(1)–N(2) 130.1(3), O(2)–Li(2)–N(1) 126.6(3), O(2)–Li(2)–N(2) 128.3(3), N(1)–Li(2)–N(2) 104.1(3).

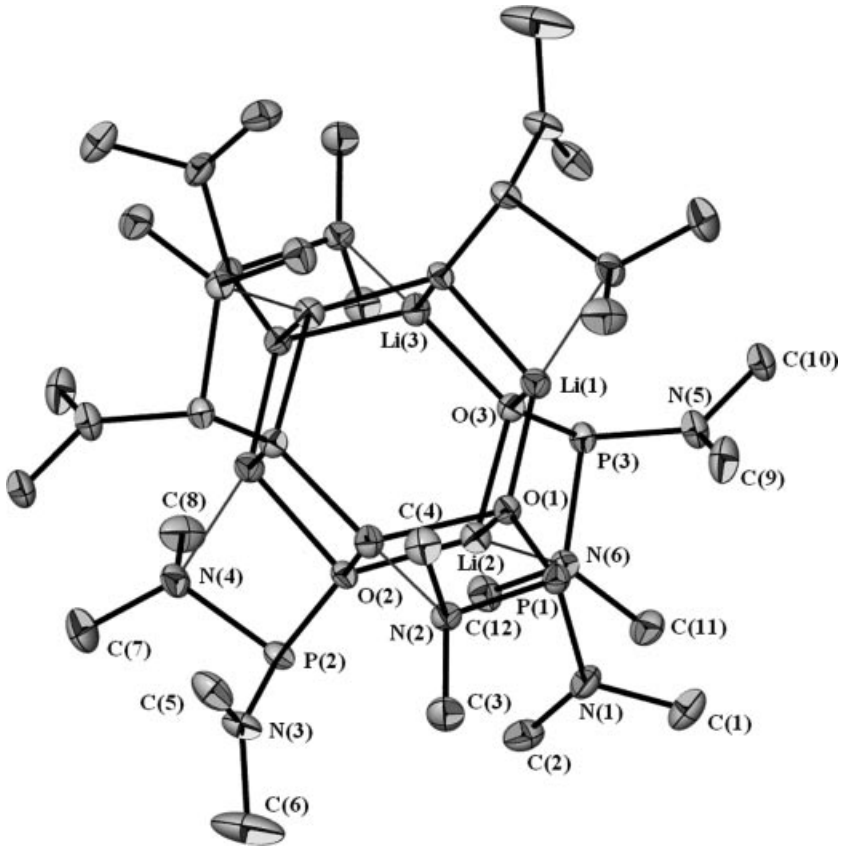


Figure 3. Structure of $\{(Me_2N)_2POLi\}_6$ (**2**). Thermal ellipsoids shown at 50% probability and all H atoms omitted for clarity. Selected bond lengths [Å] and angles [°]: O(2)–Li(2) 1.909(3), O(2)–Li(3′) 1.983(3), O(2)–Li(1′) 1.994(4), O(3)–Li(3) 1.906(4), O(3)–Li(1) 1.970(3), O(3)–Li(2) 1.996(3), O(1)–Li(1) 1.911(3), O(1)–Li(2) 1.953(3), O(1)–Li(3′) 1.982(3): O(1)–P(1)–N(1) 107.2(1), O(1)–P(1)–N(2) 95.9(1), N(1)–P(1)–N(2) 99.9(1), P(1)–O(1)–Li(1) 134.0(1), P(1)–O(1)–Li(2) 128.1 (1), Li(1)–O(1)–Li(2) 84.2(1), P(1)–O(1)–Li(3′) 100.9(1), Li(1)–O(1)–Li(3′) 116.8(2), C(2)–N(1)–P(1) 126.0(2), C(1)–N(1)–P(1) 118.2(2), C(3)–N(2)–P(1) 116.5(2), C(4)–N(2)–P(1) 108.4(1).

 © 2006 Wiley-VCH Verlag GmbH & Co. KGaA, Weinheim 

cal outcome for the dilithiated complex, even when the solvents are used in catalytic amounts.[8,9]

Because structural information is crucial in establishing and understanding the causes of stereo- and regioselectivies, and observed enantioselectivities, we have re-examined both the mono- and dilithiation reactions of *n*BuLi with *S*-*N*-α-mba in the presence of HMPA, and now report the crystal structure of the formerly elusive $[(S)$-α-$(PhC(H)CH_3)$-$(CH_2CH{=}CH_2)NLi{\cdot}HMPA]_2$ complex (**1**), Figure 2, and the unexpected reduction of HMPA in the attempted dilithiation reaction to give the hexameric lithium dimethylamidophosphite, $[(Me_2N)_2POLi]_6$ (**2**), Figure 3, as the only isolated crystalline product.

## Results and Discussion

The synthesis of **1** and **2** are shown in Scheme 1. While all other standard aprotic Lewis bases produced only oils on their addition to lithium (*S*)-*N*-(α-methylbenzyl)allylamide we found that with HMPA a yellow powder could be forced to precipitate by rapid cooling. This precipitate, which is often accompanied by an orange oil, can be readily redissolved and, with slow cooling and storage at 4 °C, produces fine yellow needles. These crystals were analysed by single-crystal X-ray diffraction and revealed the solid-state structure to be unusual on two counts: the dimer itself is asymmetric, comprised of two independent lithium amide monomers, and adopts an atypical *cisoid* arrangement of the allyl and benzyl groups relative to the planar $(NLi)_2$ ring, in what is generally considered an energetically less favourable arrangement for such dimers.[10] The few other crystallographically characterised lithium amide dimers complexed by HMPA all display a symmetrical *trans* arrangement of the amido moieties relative to the central $(NLi)_2$ ring.[11–15] The structure of **1** is shown in Figure 2.

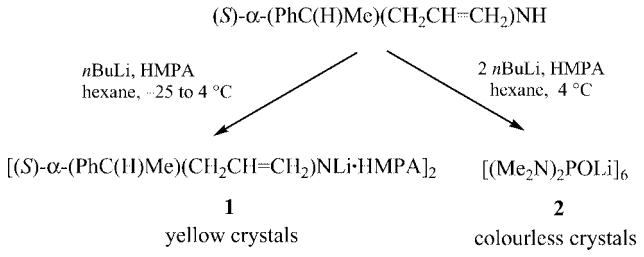


Scheme 1. Synthesis of compounds **1** and **2**.

Importantly, and in contrast to the sodium analogue, the allylic nature of the chiral amide is retained [N(1)–C(9) 1.466(4), C(9)–C(10) 1.494(5), C(10)–C(11) 1.311(5) Å] supporting the structural assumptions made in its application in conjugate addition reactions. Though one of the allyl groups is slightly disordered, mainly at the terminal vinylic carbon, they are clearly oriented differently relative to the Li centres, and both appear on the same side of the $Li_2N_2$ plane. This inequivalency is evident from an analysis of the bonding environment of the Li centres with the closest Li to allylic C($H_2$) distances being 2.707 Å for Li(2)–C(9) and 2.871 Å for Li(1)–C(20), both of which are within the range for agostic bonding.

NMR studies in $C_6D_6$ indicate that the solution-state structure is consistent with that observed for the monomeric unit in the solid state. In comparison to the free amine, the NC$H_2$CH protons are diastereotopic ($\delta$ = 3.91 and 3.66 ppm) and because these are the same protons that are involved in the agostic interactions observed in the solid-state structure of **1**, it suggests that these interactions with the lithium centre are retained in solution. Variable-temperature studies in $C_7D_8$, in the range –60 °C to 90 °C, revealed an interesting transformation. At lower temperatures only a broadening of the peaks occurs. However, upon heating to 80 °C, followed by sustained heating at 90 °C for 10 min, the complex undergoes significant rearrangement to the 1-azaallyl isomer, as observed in $\{[(S)$-α-$(PhC(H)CH_3N{\cdots}C(H){\cdots}CHCH_3)]Na{\cdot}tmeda\}_2$. This is most clearly indicated by a decrease in the multiplet for –C$H$=C$H_2$ at $\delta$ = 6.23 ppm, which is mirrored by the emergence of a new multiplet for this proton at $\delta$ = 3.81 ppm. The two dd of dd for NC$H_2$ at $\delta$ = 3.77 and 3.54 ppm decrease with the concomitant emergence of a doublet (N···C$H$···C) at $\delta$ = 6.77 ppm. The new Me group appears as a doublet at $\delta$ = 1.83 ppm with a coincident diminution of signals for the =C$H_2$ protons at $\delta$ = 5.09 and 4.96 ppm. The overall transformation at this temperature was ca. 75% complete. As we observed for related 2-azaallyl formation in group-1 (α-methylbenzyl)benzylamides, the effect of using sodium is to induce anion changes which require thermal promotion for Li.[4]

HMPA, despite its acknowledged carcinogenicity, is still a ubiquitous, highly useful and remarkably versatile ligand in organolithium chemistry. In the vast majority of cases it behaves simply as a highly polar solvent and/or a strongly coordinating Lewis base; however, it has been observed, through chemical trapping reactions, to undergo decomposition on addition of *n*BuLi, MeLi or with NaH at elevated temperatures.[16,17] We now present unequivocal structural evidence of this decomposition and the nature of the lithiated species.

The addition of one equiv. of HMPA to promote the second lithiation of (*S*)-*N*-(α-methylbenzyl)allylamine at the terminal vinylic proton resulted only in isolation of large colourless crystals, which were identified by single-crystal X-ray diffraction to be $[(Me_2N)_2POLi]_6$ (**2**). The structure is shown in Figure 3 and indicates that the asymmetric unit comprises three Li atoms and three dimethylamidophospite units with the hexameric inner core resembling two stacked trimers. While analogous stacked trimer-type structures have been previously reported for lithium imides,[18] enolates[19] and alkoxides (e.g. $[PhOLi{\cdot}thf]_6$),[20,21] the structure of the monomeric unit of **2**, $(Me_2N)_2POLi$, is unique.

The loss of $Me_2N^-$, believed to occur through electron transfer from RLi to HMPA with elimination of RH,[16] is accompanied by reduction of the P centre from oxidation state (V) to (III). This stands in contrast to previous assumptions that the lithium dimethylphosphite could still be viewed as a $P^V$ compound and formulated as $(Me_2N)_2P$-

 © 2006 Wiley-VCH Verlag GmbH & Co. KGaA, Weinheim 

(=O)Li, assuming a covalent P–Li bond. The preference for the $Li^+$ cation to bond with the O atom has previously been observed in related lithiated $P^V$ phosphane oxide complexes derived from deprotonation of alkyl[22] and amino substituents,[23,24] and though these may be functionally related to **2** there is no $P^{III}$ centre formed and the P–O bonds retain most of their double bond character. A close analysis of the structure adopted by **2** reveals an interesting bonding arrangement within the unique lithiated dimethylamidophosphite moiety, and a comparison is given with the datively bound intact HMPA molecule in **1** in Figure 4.

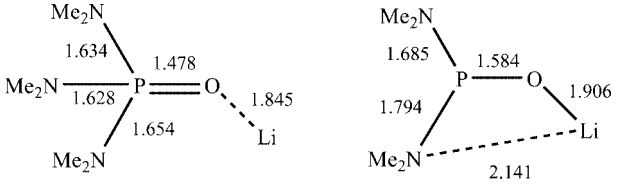


Figure 4. Comparison of the bonding arrangements for coordinated HMPA and the structurally determined dimethylamidophosphite anion in **1** and **2**, respectively. Bond lengths in Å.

There are two differing N–P bond lengths, with the longest found for the N, which datively bonds with a nearby Li cation [range 2.14(4) to 2.16(9) Å]; elongation presumably resulting from removal of the lone-pair electrons from any contribution to the N–P bond itself. This affects the bonding angles around the two N centres which differ substantially, with the longer datively bound N displaying the more acute C–*N*–P angles. Each O is bound to three Li atoms and, as is typical of stacked trimers, show a range of short, medium and longer bonds [e.g. O(3)–Li(1), 1.906(4); O(3)–Li(2), 1.970(3); O(3)–Li(3), 1.996(3) Å].

To further probe the nature of the amidophosphite intermediate ab initio calculations were performed using the Gaussian03 suite of programs.[25] Figure 5 shows structures obtained at the MP2/6-311G(d,p) level, while relative energies are reported in Table 1. Structure **2a** shows the tetrahedral complex previously proposed as the reaction intermediate.[16,17] This structure is not a potential energy minimum – it can be obtained only by constraining the angle Li–P–O. When this angle is allowed to optimize, **2a** undergoes a rearrangement to the form **2a′** which is 100 kJ·mol$^{-1}$ more stable. It is clear that **2a** is not a viable structure. Structures **2b** and **2c** are a further 50 kJ·mol$^{-1}$ more stable than **2a′**. Structures **2b** and **2c** both show pyramidal bonding at the phosphorus, with the Li atom preferring to be associated with the oxygen (and nitrogen) atoms. The structure **2c** consistent with the X-ray data is preferred over **2b** by just 1.6 kJ·mol$^{-1}$ at the MP2/6-311G(d,p) level and by a larger margin of 14.6 kJ·mol$^{-1}$ at the B3LYP/6-311+G(d,p) level. The N atom interacting with the Li also has its N–P bond lengthened relative to the other N atom in **2c**, as is evident in the crystal structure.

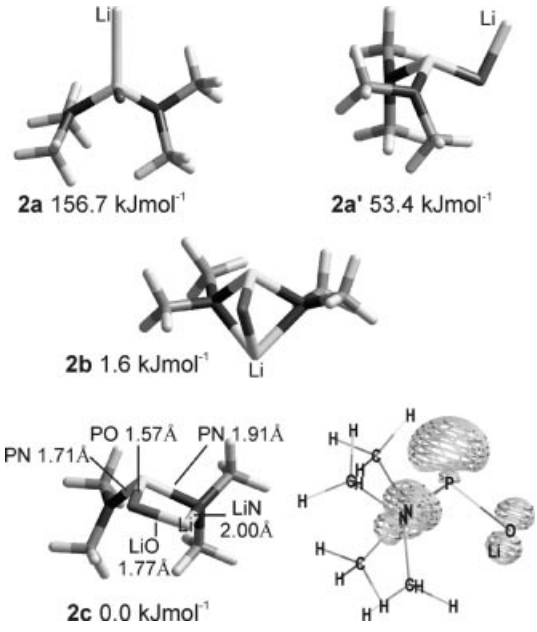


Figure 5. Li···OP[N(CH$_3$)$_2$]$_2$ structures computed at MP2/6-311G(d,p) level, together with their relative energies and HOMO of **2c**.

Calculated Mulliken charges on the P atom, at the MP2 level are given in Table 1. There is a large and significant difference between the charge of 1.8 e found in $Li^+$[OP[N(CH$_3$)$_2$]$_3$], and the charges of around 1.0 e found in structures **2a**–**2c**. This strongly suggests that the phosphorus atom in these forms has been reduced to $P^{III}$. The HOMO orbital for **2c** plotted in Figure 5 has the character of a "lone pair" on the phosphorus, consistent with this conclusion.

The first step in aggregation has also been investigated by computing dimeric structures based on **2b** and **2c**. These are shown in Figure 6. In the dimer structures, the energetic preference for **2c** is further increased: 7.6 kJ·mol$^{-1}$ at the MP2/6-311G(d,p)//MP2/6-31G(d,p) level and 45 kJ·mol$^{-1}$ at the B3LYP/6-311+G(d,p) level (Table 2). This is presumably due to the formation of slightly stronger, shorter LiO bonds – see Figure 6. In regard to larger aggregates, the lithium and oxygen atoms of **2c** are more accessible steri-

Table 1. Calculated Mulliken charges on the P atom, and relative energies of alternative LiOP[N(CH$_3$)$_2$]$_2$ structures at the MP2/6-311G(d,p) level.

| Structure | $Li^+$[OP[N(CH$_3$)$_2$]$_3$] | **2a** | **2a′** | **2b** | **2c** |
|---|---|---|---|---|---|
| Mulliken charge on P (MP2) | 1.77 | 1.06 | 0.88 | 0.96 | 1.00 |
| $E_{rel}$ (B3LYP)[a] [kJ·mol$^{-1}$] | | 148.9 | 49.1 | 12.4 | 0.0 |
| $E_{rel}$ (B3LYP+z.p.)[a],[b] [kJ·mol$^{-1}$] | | – | 47.8 | 14.6 | 0.0 |
| $E_{rel}$ (MP2)[c] [kJ·mol$^{-1}$] | | 156.7 | 53.4 | 1.6 | 0.0 |
| $E_{rel}$ (MP2+z.p.)[b,c] [kJ·mol$^{-1}$] | | – | 52.1 | 3.8 | 0.0 |

[a] B3LYP/6-311+G(d,p) level. [b] Including B3LYP/6-311+G(d,p) zero point correction. [c] MP2/6-311G(d,p) level.

 © 2006 Wiley-VCH Verlag GmbH & Co. KGaA, Weinheim 

cally so that it is able to form the hexamer found in the crystal structure with each lithium atom coordinated to three oxygen atoms. This arrangement is precluded in **2b** due to the increased steric crowding.

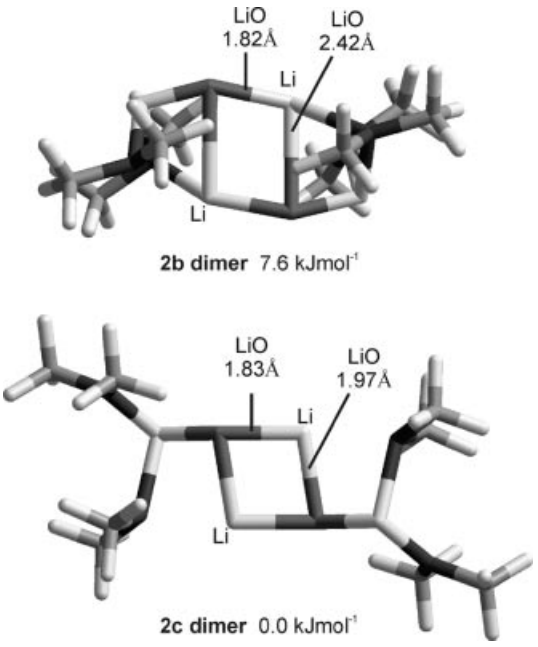


Figure 6. Dimeric structures, together with their relative energies computed at MP2/6-311G(d,p)//MP2/6-31G(d,p) level.

Table 2. Calculated relative energies of dimers formed from **2b** and **2c**.

| Dimer | $(\mathbf{2b})_2$ | $(\mathbf{2c})_2$ |
|---|---|---|
| $E_{rel}$ (B3LYP + z.p.)[a] [kJ·mol$^{-1}$] | 44.7 | 0.0 |
| $E_{rel}$ (MP2)[b] [kJ·mol$^{-1}$] | 7.6 | 0.0 |
| $E_{rel}$ (MP2 + z.p.)[a,b] [kJ·mol$^{-1}$] | 10.0 | 0.0 |

[a] Including B3LYP/6-311+G(d,p) zero point correction. [b] MP2/6-311G(d,p)//MP2/6-31G(d,p) level.

Thus, while the results of Williard[9] indicate that the presence of thf produces a particular structural dimer, which facilitates deprotonation of the terminal vinylic group, it seems from our results that HMPA is preferentially cleaved, and that this most likely occurs at a greater rate than deprotonation can occur. One reason for this, which may support Williard's findings, is that the HMPA molecule is just too bulky to promote close interaction of the vinylic group and lithium base in the particular mixed aggregate structure required for deprotonation.

## Experimental Section

Compound manipulations were carried out under strict inert atmosphere and dry conditions using a vacuum/argon line Schlenk techniques and a high purity argon gas recirculating dry box. Prior to use, solvents were dried by reflux over Na/K alloy and stored over molecular sieves (4 Å). (*S*)-*N*-(α-methylbenzyl)allylamine was prepared by a literature procedure.[7] *n*BuLi was purchased from Aldrich (2.5 M solution in heptane). NMR spectra were obtained on Bruker DRX-400 spectrometer with chemical shifts referenced to the appropriate deuterated solvent. Elemental analyses were carried out by CMAS, Australia.

**Synthesis of $[(S)$-α-$(PhC(H)CH_3)(CH_2CH{=}CH_2)NLi{\cdot}HMPA]_2$ (1):** A solution of *n*BuLi (2 mL, 2.5 M in heptane, 5 mmol) was added dropwise to a stirring solution of *S*-*N*-α-mba (0.81 g, 5 mmol) in hexane (≈ 25 mL) at room temperature. The solution was stirred for 30 min, during which time the colour changed from clear to pale yellow. The solution was then cooled to 0 °C. HMPA (0.87 mL, 5 mmol) was then added dropwise. The resulting cloudy solution was stirred and warmed to room temperature, changing to a clear yellow colour. The solution was cooled rapidly to –25 °C resulting in the precipitation of a yellow solid. The mixture was gently heated in order to dissolve the precipitate and cooled slowly to room temperature before being stored at 4 °C. This resulted in the formation of needle-like crystals. The pale yellow crystals of **1** were filtered, washed with cold hexane and dried under vacuum. Yield 1.28 g, 74%. M.p. 84–86 °C. $^1$H NMR (300 MHz, $C_6D_6$, 30 °C): $\delta$ = 7.86 (d, $^1J$ = 6.9 Hz, 2 H, *ortho*-H), 7.38 (t, $^1J$ = 7.2 Hz, 2 H, *meta*-H), 7.24 (t, $^1J$ = 7.2 Hz, 1 H, *para*-H), 6.43 (m, 1 H, $CH_2CH{=}CH_2$), 5.28 (dd, $^1J$ = 3.0 Hz, $^2J$ = 17.1 Hz, 1 H, $CH_2CH{=}CH_2^a$), 5.14 (dd, $^1J$ = 3.0 Hz, $^2J$ = 9.9 Hz, 1 H, $CH_2CH{=}CH_2^b$), 4.44 [q, $^1J$ = 6.7 Hz, $^2J$ = 13.2 Hz, 1 H, PhC(*H*)-$CH_3$], 3.90 (dd, $^1J$ = 5.7 Hz, $^2J$ = 13.3 Hz, 1 H, $CH_2^aCH{=}CH_2$), 3.66 (dd, $^1J$ = 7.5 Hz, $^2J$ = 13.2 Hz, 1 H, $CH_2^bCH{=}CH_2$), 2.38 (d, $^1J$ = 3.03 Hz, 18 H, $PO[N(CH_3)_2]_3$), 1.81 [d, $^1J$ = 6.0 Hz, 3 H, $PhC(H)CH_3$] ppm. $^{13}$C NMR (300 MHz, $C_6D_6$, 30 °C): $\delta$ = 156.4 ($CH_2CH{=}CH_2$), 146.3 ($CH_2CH{=}CH_2$), 129.3 (*o*-C), 128.7 (*m*-C), 125.8 (*p*-C), 111.8 (*ipso*-C), 65.7 [$PhCH)CH_3$], 59.4 ($CH_2CH{=}CH_2$) 37.6 ($PO[N(CH_3)_2]_3$), 29.2 [$PhC(H)CH_3$] ppm. $C_{34}H_{64}LiN_4OP$ (582.8): calcd. C 59.0, H 9.3, N 16.2; found C 58.9, H 9.4, N 16.0.

**Synthesis of $\{(Me_2N)_2P{=}OLi\}_6$ (2):** A solution of *n*BuLi (4 mL, 2.5 M in heptane, 10 mmol) was added dropwise to a stirred solution of S-*N*-α-mba (0.81 g, 5 mmol) in hexane (≈ 25 mL) at room temperature. The solution changed to a yellow colour and was further stirred for 1 hour. It was then cooled to 0 °C and HMPA (0.87 mL, 5 mmol) was added slowly. The solution became cloudy and dark yellow in colour, and warming to room temperature resulted in a dark orange oil falling out of solution. The emulsion was homogenised and filtered, and the mother liquor subsequently reduced by 50%. The solution was stored at 4 °C overnight resulting in the precipitation of colourless block crystals of **2**. Yield (0.23 g, 32%). M.p. 187–189 °C (dec.) $^1$H NMR (300 MHz, $C_6D_6$, 30 °C): $\delta$ = 2.60 (d, $^1J$ = 8.8 Hz, 12 H, $PO[N(CH_3)_2]_2$) ppm. $^{13}$C NMR (300 MHz, $C_6D_6$, 30 °C): $\delta$ = 38.5 (d, $^1J$ = 19.8 Hz, 4 C, $PO[N(CH_3)_2]_2$) ppm. $C_4H_9LiN_2OP$ (142): calcd: C 33.8, H 8.5, N 19.7; found C 33.9, H 8.4, N 19.6.

**Crystallography:** Single crystals of **1** and **2** were coated in oil under argon in a dry box, mounted on a fibre and data collected with an Enraf Nonius KappaCCD at 123 K with Mo-$K_a$ radiation ($\lambda$ = 0.71073 Å). The structure was solved by direct methods (SHELXS 97)[26] and refined by full-matrix least-squares on $F^2$. All H were placed in calculated positions (C–H 0.95 Å) and included in the final least-squares refinement. All other atoms were located and refined anisotropically.

CCDC-297298 and -297299 contain the supplementary crystallographic data for this paper. These data can be obtained free of charge from The Cambridge Crystallographic Data Centre via www.ccdc.cam.ac.uk/data_request/cif.

**Crystallographic Data for 1:** $C_{34}H_{64}LiN_4OP$, $M$ = 582.8, $T$ = 123 K, orthorhombic $P2_12_12_1$, $a$ = 8.5429(17), $b$ = 15.629(3), $c$ = 31.008(6) Å $\beta$ = 90°, $V$ = 4140.0(14) Å$^3$, $D_{calcd.}$ = 1.403 g/cm$^3$, $Z$ =

 © 2006 Wiley-VCH Verlag GmbH & Co. KGaA, Weinheim 

6, $F(000)$ = 1932, $\mu_{mo\text{-}K}$ = 0.138 mm$^{-1}$, $2\theta_{max}$ = 56.6°, final $R$, $R_w$ = 0.0669, 0.1113 $N_o$ = 5041 "observed" [$I > 2\sigma(I)$] reflections out of $N$ = 9946, $R_{int}$ = 0.1368, GooF = 0.990. Disorder in the terminal vinylic carbon C22 which was modelled at 50% occupancy at each site.

**Crystallographic Data for 2**: $C_{12}H_{36}Li_3N_6O_3P_3$, $M$ = 426.2, $T$ = 123 K, orthorhombic *Pbca*, $a$ = 14.648(3), $b$ = 16.236(3), $c$ = 20.038(4) Å, $\beta$ = 90°, $V$ = 4765.5(16) Å$^3$, $D_{calcd.}$ = 1.188 g/cm$^3$, $Z$ = 8, $F(000)$ = 1824, $\mu_{Mo\text{-}K}$ = 0.271 mm$^{-1}$, $2\theta_{max}$ = 56.6°, final $R$, $R_w$ = 0.024, 0.0840, $N_o$ = 3975 "observed" [$I > 2\sigma(I)$] reflections out of $N$ = 5886, $R_{int}$ = 0.086. GooF = 1.021.

## Acknowledgments

We thank the Australian Research Council and Monash University for financial support. Quantum chemistry calculations were carried out using the Australian Partnership for Advanced Computing (APAC) National Facility.

[1] S. G. Davies, A. D. Smith, P. D. Price, *Tetrahedron: Asymmetry* **2005**, *16*, 2833.
[2] S. G. Davies, C. P. Smethurst, A. D. Smith, G. D. Smyth, *Tetrahedron: Asymmetry* **2000**, *11*, 2437.
[3] P. C. Andrews, P. J. Duggan, G. D. Fallon, T. D. McCarthy, A. C. Peatt, *J. Chem. Soc., Dalton Trans.* **2000**, 2505.
[4] P. C. Andrews, P. J. Duggan, G. D. Fallon, T. D. McCarthy, A. C. Peatt, *J. Chem. Soc., Dalton Trans.* **2000**, 1937.
[5] P. C. Andrews, S. M. Calleja, M. Maguire, P. J. Nichols, *Eur. J. Inorg. Chem.* **2002**, 1583.
[6] P. C. Andrews, S. M. Calleja, M. Maguire, *J. Chem. Soc., Dalton Trans.* **2002**, 3640.
[7] M. F. Yus, M. Foubelo, L. R. Falvello, *Tetrahedron: Asymmetry* **1995**, *6*, 2081.
[8] F. Haeffner, M. A. Jacobson, I. Keresztes, P. G. Williard, *J. Am. Chem. Soc.* **2004**, *126*, 17032.
[9] P. G. Williard, M. A. Jacobson, *Org. Lett.* **2000**, *2*, 2753.
[10] W. Clegg, L. Horsburgh, S. T. Liddle, F. M. Mackenzie, R. E. Mulvey, A. Robertson, *J. Chem. Soc., Dalton Trans.* **2000**, 1225.
[11] P. C. Andrews, M. Maguire, E. Pombo-Villar, *Helv. Chim. Acta* **2002**, *85*, 3516.
[12] J. Barker, D. Barr, N. D. R. Barnett, W. Clegg, I. Cragg-Hine, M. G. Davidson, R. P. Davies, S. M. Hodgson, J. A. K. Howard, M. Kilner, C. W. Lehmann, I. Lopez-Solera, R. E. Mulvey, P. R. Raithby, R. Snaith, *J. Chem. Soc., Dalton Trans.* **1997**, 951.
[13] D. R. Armstrong, D. R. Baker, F. J. Craig, R. E. Mulvey, W. Clegg, L. Horsburgh, *Polyhedron* **1996**, *15*, 3533.
[14] D. Barr, W. Clegg, R. E. Mulvey, R. Snaith, *J. Chem. Soc., Chem. Commun.* **1984**, 700.
[15] D. Barr, W. Clegg, R. E. Mulvey, R. Snaith, *J. Chem. Soc., Chem. Commun.* **1984**, 285.
[16] E. B. Nadler, E. S. Zipory, Z. Rappoport, *J. Org. Chem.* **1991**, *56*, 4241.
[17] E. M. Kaiser, J. D. Petty, L. E. Solter, *J. Organomet. Chem.* **1973**, *61*, C1.
[18] K. Gregory, P. v. R. Schleyer, R. Snaith, *Adv. Inorg. Chem.* **1991**, *37*, 47.
[19] P. G. Williard, G. B. Carpenter, *J. Am. Chem. Soc.* **1985**, *107*, 3345.
[20] B. Goldfuss, P. v. R. Schleyer, F. Hampel, *J. Am. Chem. Soc.* **1996**, *118*, 12183.
[21] L. M. Jackman, D. Cizmeciyan, P. G. Williard, M. A. Nichols, *J. Am. Chem. Soc.* **1993**, *115*, 6262.
[22] A. Armstrong, T. Chivers, M. Krahn, M. Parvez, G. Schatte, *Chem. Commun.* **2002**, 2332.
[23] C. J. Cramer, S. E. Denmark, P. C. Miller, R. L. Dorow, K. A. Swiss, S. R. Wilson, *J. Am. Chem. Soc.* **1994**, *116*, 2437.
[24] S. E. Denmark, P. C. Miller, S. R. Wilson, *J. Am. Chem. Soc.* **1991**, *113*, 1468.
[25] M. J. Frisch, G. W. Trucks, H. B. Schlegel, G. E. Scuseria, M. A. Robb, J. R. Cheeseman, J. A. Montgomery Jr, T. Vreven, K. N. Kudin, J. C. Burant, J. M. Millam, S. S. Iyengar, J. Tomasi, V. Barone, B. Mennucci, M. Cossi, G. Scalmani, N. Rega, G. A. Petersson, H. Nakatsuji, M. Hada, M. Ehara, K. Toyota, R. Fukuda, J. Hasegawa, M. Ishida, T. Nakajima, Y. Honda, O. Kitao, H. Nakai, M. Klene, X. Li, J. E. Knox, H. P. Hratchian, J. B. Cross, V. Bakken, C. Adamo, J. Jaramillo, R. Gomperts, R. E. Stratmann, O. Yazyev, A. J. Austin, R. Cammi, C. Pomelli, J. W. Ochterski, P. Y. Ayala, K. Morokuma, G. A. Voth, P. Salvador, J. J. Dannenberg, V. G. Zakrzewski, S. Dapprich, A. D. Daniels, M. C. Strain, O. Farkas, D. K. Malick, A. D. Rabuck, K. Raghavachari, J. B. Foresman, J. V. Ortiz, Q. Cui, A. G. Baboul, S. Clifford, J. Cioslowski, B. B. Stefanov, G. Liu, A. Liashenko, P. Piskorz, I. Komaromi, R. L. Martin, D. J. Fox, T. Keith, M. A. Al-Laham, C. Y. Peng, A. Nanayakkara, M. Challacombe, P. M. W. Gill, B. Johnson, W. Chen, M. W. Wong, C. Gonzalez, J. A. Pople, *Gaussian 03*, Revision C.02, Gaussian, Inc. Wallingford, CT, **2004**.
[26] G. M. Sheldrick, *SHELXS97, Program for the Solution of Crystal Structures*, Göttingen, Germany, **1997**.

Received: March 3, 2006
Published Online: May 29, 2006

 © 2006 Wiley-VCH Verlag GmbH & Co. KGaA, Weinheim 

DOI: 10.1002/ejic.200600248

# Dicopper(II) Complexes with the Enantiomers of a Bidentate Chiral Reduced Schiff Base: Inclusion of Chlorinated Solvents and Chiral Recognition of 1,2-Dichloroethane Rotamers in the Crystal Lattice

**Vamsee Krishna Muppidi[a] and Samudranil Pal*[a]**

**Keywords:** Dicopper(II) complexes / Chiral reduced Schiff Bases / Crystal structures / Chlorinated solvents / Enantioselective inclusion

Bisphenoxo-bridged dicopper(II) complexes $[Cu_2L^n{}_2Cl_2]$ {**1** ($n$ = 1) and **2** ($n$ = 2)} with the N,O-donor reduced Schiff bases *N*-(2-hydroxybenzyl)-(*R*)-α-methylbenzylamine ($HL^1$) and *N*-(2-hydroxybenzyl)-(*S*)-α-methylbenzylamine ($HL^2$) have been synthesised and characterised. In both **1** and **2**, the bidentate chiral ligands coordinate the metal centres through the secondary amine N atom and the bridging phenolate O atom. The chloride ion occupies the fourth coordination site and completes a slightly distorted square-planar $NO_2Cl$ environment around each copper(II) centre. Magnetic susceptibility measurements in the solid state suggest a strong antiferromagnetic interaction between the metal centres in both complexes. Both **1** and **2** readily form 1:1 host-guest compounds with chlorinated solvents such as $CH_2Cl_2$, $CHCl_3$ and $Cl(CH_2)_2Cl$. All the host-guest compounds crystallise in noncentrosymmetric space groups. **1**·$CH_2Cl_2$ and **2**·$CH_2Cl_2$ crystallise in the $P2_1$ space group while **1**·$CHCl_3$, **2**·$CHCl_3$, **1**·$Cl(CH_2)_2Cl$ and **2**·$Cl(CH_2)_2Cl$ crystallise in the $P2_12_12_1$ space group. In these inclusion crystals, the C–H···Cl interactions between the guest and the host molecules are primarily responsible for enclatheration of the chloroalkane molecules. In the case of $CH_2Cl_2$, one of its Cl atoms acts as the acceptor. On the other hand, for $CHCl_3$ and $Cl(CH_2)_2Cl$, the metal coordinated Cl atom of the host complex acts as the acceptor. The structures of **1**·(*P*)-$Cl(CH_2)_2Cl$ and **2**·(*M*)-$Cl(CH_2)_2Cl$ provide rare examples for chiral recognition of the right handed (*P*) and the left handed (*M*) gauche forms of $Cl(CH_2)_2Cl$ in molecular assemblies.

(© Wiley-VCH Verlag GmbH & Co. KGaA, 69451 Weinheim, Germany, 2006)

## Introduction

Materials generated by noncentrosymmetric organisation of molecules in the crystalline state are of current interest because of their potential applications in a variety of research areas such as enantioselective separation, asymmetric catalysis, drug delivery, non-linear optical effects and ferro-, pyro- and piezoelectricity.[1,2] The general strategy for noncentrosymmetric organisation in the crystal lattice is insertion of chirality in the molecule.[3] Synthesis and structures of some coordination complexes with chiral Schiff bases and their nonlinear optical properties have been reported recently.[4] Compared to the Schiff bases the reduced Schiff bases with the $–CH_2–NH–$ backbone are considered to be conformationally more flexible. In coordination complexes with reduced Schiff bases, the increased acidity of the N–H fragment resulting from metal coordination is also expected to facilitate its participation in intermolecular hydrogen bonding interactions.[5] Introduction of chirality to such metal coordinated reduced Schiff bases often leads to novel metal–organic frameworks through intermolecular noncovalent interactions.[5,6] Complexes of this type have shown the potential for applications in DNA cleavage activity and asymmetric catalysis.[6e,f] Recently we have reported two mononuclear square-pyramidal copper(II) complexes of the general formula $[Cu(L^nNO_2)_2(H_2O)]$ with the N,O-donor chiral reduced Schiff bases *N*-(2-hydroxy-5-nitrobenzyl)-(*R*)-α-methylbenzylamine {(*R*)-2(OH)-5-$(NO_2)$-$C_6H_3CH_2NHCH(CH_3)C_6H_5$, $HL^1NO_2$} and *N*-(2-hydroxy-5-nitrobenzyl)-(*S*)-α-methylbenzylamine {(*S*)-2(OH)-5-$(NO_2)$-$C_6H_3CH_2NHCH(CH_3)C_6H_5$, $HL^2NO_2$}. The complexes crystallise in the noncentrosymmetric space group *C*2 with $Cl(CH_2)_2Cl$ molecules as the guests. The crystal packing of these 1:1 inclusion compounds revealed intermolecular hydrogen-bonding-assisted, perfectly polar alignment of both host and guest molecules as well as enantioselective confinement of the chiral rotamers of $Cl(CH_2)_2Cl$.[7] In the present work, we report the synthesis and characterisation of the enantiomeric pair of bisphenoxo-bridged dicopper(II) complexes $[Cu_2L^1{}_2Cl_2]$ (**1**) and $[Cu_2L^2{}_2Cl_2]$ (**2**) with $HL^n$, the unsubstituted analogues of $HL^nNO_2$. Both **1** and **2** are found to be very good hosts to confine chloroalkanes [$CH_2Cl_2$, $CHCl_3$ and $Cl(CH_2)_2Cl$] and to isolate the enantiopure chiral rotamers of $Cl(CH_2)_2Cl$ in the noncentrosymmetric crystal lattice through intermolecular C–H···Cl interactions.

[a] School of Chemistry, University of Hyderabad, Hyderabad 500046, India
Fax: +91-40-2301-2460
E-mail: spsc@uohyd.ernet.in

 © 2006 Wiley-VCH Verlag GmbH & Co. KGaA, Weinheim 

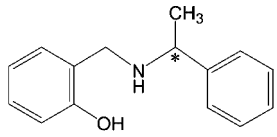


(HL$^n$)

## Results and Discussion

### Synthesis and Some Properties

The chiral reduced Schiff bases *N*-(2-hydroxybenzyl)-(*R*)-α-methylbenzylamine (HL$^1$) and *N*-(2-hydroxybenzyl)-(*S*)-α-methylbenzylamine (HL$^2$) were synthesised in about 75% yield by condensation of salicylaldehyde with the corresponding α-methylbenzylamine (*R* or *S*) in methanol followed by reduction with $NaBH_4$.[5,7] The elemental analysis and the spectroscopic data (IR and $^1$H NMR) for HL$^1$ and HL$^2$ are very similar and consistent with the expected molecular formula and structure. The reactions of these reduced Schiff bases (HL$^n$) with $CuCl_2{\cdot}2H_2O$ (1:1 mol ratio) in methanol provided the dark brown complexes **1** ($n$ = 1) and **2** ($n$ = 2) in about 60% yield. The elemental analysis data for **1** and **2** are consistent with the empirical formula CuL$^n$Cl. In solutions, the complexes are electrically nonconducting in nature. Thus in each complex the metal ions are in the +2 oxidation state and the chloride ions are coordinated to the metal centres.

The IR spectra of **1** and **2** are very similar. A sharp band observed at 3245 cm$^{-1}$ is assigned to the secondary amine N–H group of the ligands. Several weak bands are observed in the range 2800–3050 cm$^{-1}$. These are possibly due to the aromatic and aliphatic C–H stretches. The absence of any band near 3400 cm$^{-1}$ indicates the deprotonation of the phenolic OH of the bidentate ligands in both complexes. Thus, it is very likely that in each complex the metal ions are coordinated to the bridging phenoxo groups and the secondary amine N atoms of the two ligands. The remaining fourth coordination site of each metal ion is occupied by the chloride ion. X-ray structures (vide infra) confirm this type of coordination of the metal ions by the deprotonated reduced Schiff bases and the chloride ions in **1** and **2**.

The electronic spectral features of both complexes in chloroform solutions are essentially identical. A weak absorption observed near 650 nm is followed by three strong absorptions in the range 430–268 nm. The absorption at 650 nm is assigned to the d-d transition. The occurrence of this weak absorption in this region is consistent with square-based coordination geometry around the metal centre.[8] The intense absorptions at higher energy are most likely from the ligand-to-metal charge transfer and intraligand transitions.

### Magnetic Properties

Room temperature (300 K) magnetic moments of **1** and **2** in the powder phase are 1.10 and 1.11 $\mu_B$, respectively. These values suggest a strong antiferromagnetic spin coupling between the metal centres in each of the two complexes. In similar bisphenoxo-bridged dicopper(II) complexes, strong to very strong antiferromagnetic spin coupling is very common. The magnitude of the coupling constant $J$ varies from –145 to –429 cm$^{-1}$ in this type of species.[9,10] To quantify the extent of antiferromagnetic spin coupling in the present complexes we have collected the magnetic susceptibility data of **1** in the temperature range 300–18 K at a fixed magnetic field of 5 kG. On cooling the magnetic moment gradually decreases and reaches a value of 0.20 $\mu_B$ at 18 K. The nature of the curve obtained by plotting the $\mu_{eff}$ against $T$ is typical for two antiferromagnetically coupled copper(II) centres (Figure 1). The data were analysed using the Bleany–Bowers expression[11] for $\chi_M$ versus $T$ derived from the isotropic spin-exchange Hamiltonian $H = -2JS_1{\cdot}S_2$, where $S_1 = S_2 = 1/2$. The best least-squares fit[12] was obtained with $g$ = 1.93(2), $J$ = –307(2) cm$^{-1}$, $p$ (paramagnetic impurity with $S$ = 1/2) = 0.5% and TIP (temperature independent paramagnetism) = $1.2\times10^{-4}$ emu mol$^{-1}$ (Figure 1).

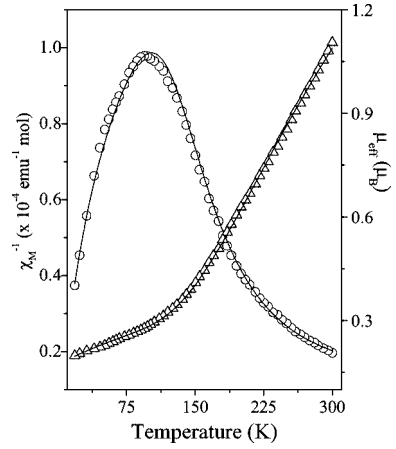


Figure 1. Temperature dependence of the inverse molar magnetic susceptibilities (O) and the effective magnetic moments (Δ) of $[Cu_2L^1{}_2Cl_2]$ (**1**); the solid lines were generated from the best least-squares fit parameters given in the text.

### Molecular Structures of 1 and 2

X-ray structures of very few bisphenoxo-bridged dicopper(II) complexes of formula $[Cu_2L_2X_2]$ (L = monoanionic bridging N,O-donor ligand and X = halide) are known.[10] All these complexes are with achiral Schiff bases and they crystallise in centrosymmetric space groups with the monomeric unit in the asymmetric unit. The $Cu_2O_2$ core is perfectly planar as the crystallographic inversion centre sits at the centre of the dimeric structure. For the same reason the X–Cu···Cu–X torsion angles are exactly 180° indicating a perfect trans orientation of the metal coordinated halides. In contrast, the host-guest compounds of both **1** and **2** crystallise in noncentrosymmetric space groups as they contain chiral ligands. In each case, the asymmetric unit contains a

 © 2006 Wiley-VCH Verlag GmbH & Co. KGaA, Weinheim 

complete dimeric complex molecule. Representative molecular structures of **1** and **2** are depicted in Figure 2 and the bond parameters associated with the metal ions for all the structures are listed in Table 1. The $NO_2Cl$ coordination sphere around each metal centre is constituted by the secondary amine N atom, two bridging phenoxo groups and the chloride ion. The metal to coordinating atom bond lengths are essentially identical in all the structures and they are comparable with the values reported for copper(II) species having the same coordinating atoms.[7,9,10] In the N,O-donor reduced Schiff bases, $HL^1$ and $HL^2$, the chiral C centre has the absolute configuration *R* or rectus and *S* or sinister, respectively. After complexation with the metal ion the N atom of the deprotonated monoanionic ligand becomes chiral. In **1**, the absolute configuration of the N centre is found to be *S* while in **2**, it is found to be *R*. Thus the generation of the new chiral centre is heterogeneous in both cases. As expected, the structures of **1** and **2** are mirror images of each other (Figure 2). In all the structures, the geometrical parameters for the $Cu_2N_2O_2Cl_2$ fragment are very similar. The $NO_2Cl$ coordination sphere around each metal centre is not exactly square planar. The Cl atoms deviate significantly from the $NO_2$ plane. The deviation of Cl2 [1.198(8)–1.385(5) Å] is noticeably larger than that of Cl1 [0.674(9)–0.876(7) Å] (Figure 2). There is a relatively marginal deviation of the metal centre (0.05–0.09 Å for Cu1 and 0.15–0.21 Å for Cu2) from the $NO_2$ plane. The $Cu_2O_2$ core is also not planar in any of the structures; it is folded along the O···O line. The fold angles are in the range 18.61(9)–21.02(13)°. However, the solid angles (358.34–359.99°) indicate that the bridging phenoxide O atoms have essentially no pyramidal character. The Cu–O–Cu bridge angles and the Cu···Cu distances are in the ranges 100.01(12)–103.17(12)° and 3.0198(8)–3.0280(8) Å, respectively. Unlike the previously known structures of analogous dicopper(II) complexes,[10] the metal coordinated chlorides are not trans orientated in the present structures (Figure 2). Here the Cl1–Cu1···Cu2–Cl2 torsion angles are in the range 105–112°. Although the $Cu_2N_2O_2Cl_2$ fragments are very similar in all the structures, the overall molecular conformations of the dicopper(II) complexes differ to some extent in the adducts of $CH_2Cl_2$ compared to the very similar conformations in the adducts of $CHCl_3$ and $Cl(CH_2)_2Cl$. The difference arises primarily from the variation in the orientation of the phenyl ring of the α-methylbenzylamine fragment of the chiral bidentate ligands. The overlay diagrams of the dicopper(II) complex molecules **1** and **2** in all the inclusion compounds are shown in Figure 3.

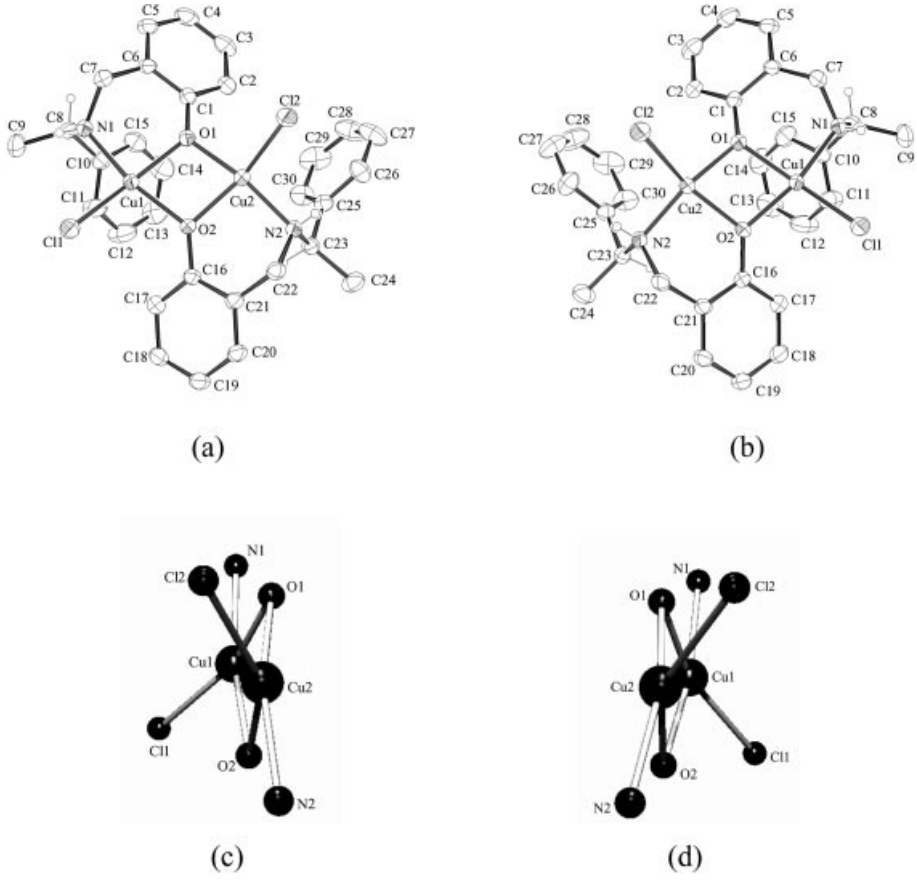


Figure 2. Molecular structures of (a) $[Cu_2L^1{}_2Cl_2]$ (**1**) and (b) $[Cu_2L^2{}_2Cl_2]$ (**2**) with the atom-labelling scheme; all non-hydrogen atoms are represented by their 30% probability thermal ellipsoids; except the hydrogen atoms on the chiral centres all other hydrogen atoms are omitted for clarity; the ball-stick representations of the $Cu_2N_2O_2Cl_2$ units in (c) **1** and (d) **2**.

 © 2006 Wiley-VCH Verlag GmbH & Co. KGaA, Weinheim 

Table 1. Selected bond lengths [Å] and angles [°] for **1**·$CH_2Cl_2$, **1**·$CHCl_3$, **1**·$Cl(CH_2)_2Cl$, **2**·$CH_2Cl_2$, **2**·$CHCl_3$ and **2**·$Cl(CH_2)_2Cl$.

| Compound | **1**·$CH_2Cl_2$ | **1**·$CHCl_3$ | **1**·$Cl(CH_2)_2Cl$ | **2**·$CH_2Cl_2$ | **2**·$CHCl_3$ | **2**·$Cl(CH_2)_2Cl$ |
|---|---|---|---|---|---|---|
| Cu(1)–O(1) | 1.944(2) | 1.944(3) | 1.938(3) | 1.941(3) | 1.942(3) | 1.939(3) |
| Cu(1)–O(2) | 1.965(2) | 1.985(3) | 1.975(3) | 1.964(2) | 1.980(3) | 1.979(3) |
| Cu(1)–N(1) | 1.993(3) | 2.011(4) | 2.004(4) | 1.991(3) | 2.010(4) | 2.000(4) |
| Cu(1)–Cl(1) | 2.2108(11) | 2.2176(13) | 2.2129(14) | 2.2090(12) | 2.2164(13) | 2.2126(13) |
| Cu(1)–Cu(2) | 3.0238(5) | 3.0280(8) | 3.0252(9) | 3.0240(6) | 3.0266(7) | 3.0198(8) |
| Cu(2)–O(1) | 1.920(2) | 1.922(3) | 1.926(3) | 1.920(3) | 1.921(3) | 1.924(3) |
| Cu(2)–O(2) | 1.963(2) | 1.954(3) | 1.961(3) | 1.959(3) | 1.951(3) | 1.962(3) |
| Cu(2)–N(2) | 1.967(3) | 1.970(4) | 1.979(4) | 1.966(3) | 1.971(4) | 1.971(3) |
| Cu(2)–Cl(2) | 2.2102(10) | 2.2189(14) | 2.2190(14) | 2.2105(11) | 2.2172(14) | 2.2141(13) |
| O(1)–Cu(1)–O(2) | 76.65(10) | 76.07(12) | 76.44(14) | 76.50(10) | 75.95(12) | 76.65(12) |
| O(1)–Cu(1)–N(1) | 91.53(11) | 91.00(16) | 91.22(16) | 91.56(13) | 91.05(15) | 91.42(15) |
| O(2)–Cu(1)–N(1) | 167.41(11) | 166.79(16) | 166.95(16) | 167.19(13) | 166.66(16) | 167.28(15) |
| O(1)–Cu(1)–Cl(1) | 161.45(9) | 164.92(12) | 165.03(13) | 161.51(10) | 164.82(12) | 164.96(13) |
| O(2)–Cu(1)–Cl(1) | 100.40(8) | 100.47(10) | 100.46(11) | 100.59(9) | 100.62(10) | 100.48(10) |
| N(1)–Cu(1)–Cl(1) | 92.19(9) | 92.72(14) | 92.55(13) | 92.20(11) | 92.72(14) | 92.18(12) |
| O(1)–Cu(2)–O(2) | 77.24(10) | 77.30(13) | 77.06(14) | 77.08(10) | 77.11(12) | 77.41(12) |
| O(1)–Cu(2)–N(2) | 165.17(12) | 167.55(17) | 166.33(18) | 165.14(12) | 167.27(17) | 166.49(17) |
| O(2)–Cu(2)–N(2) | 93.25(11) | 93.15(15) | 92.89(15) | 93.28(11) | 93.26(15) | 92.60(14) |
| O(1)–Cu(2)–Cl(2) | 98.70(8) | 97.85(11) | 98.30(12) | 98.75(9) | 97.92(10) | 98.05(11) |
| O(2)–Cu(2)–Cl(2) | 153.36(9) | 155.40(12) | 156.12(12) | 153.55(10) | 155.59(12) | 156.46(12) |
| N(2)–Cu(2)–Cl(2) | 94.84(9) | 94.12(13) | 94.59(12) | 94.85(10) | 94.25(13) | 94.69(12) |
| Cu(1)–O(1)–Cu(2) | 102.98(11) | 103.09(13) | 103.02(17) | 103.09(11) | 103.17(12) | 102.84(13) |
| Cu(1)–O(2)–Cu(2) | 100.69(11) | 100.50(14) | 100.44(15) | 100.85(11) | 100.67(13) | 100.01(12) |

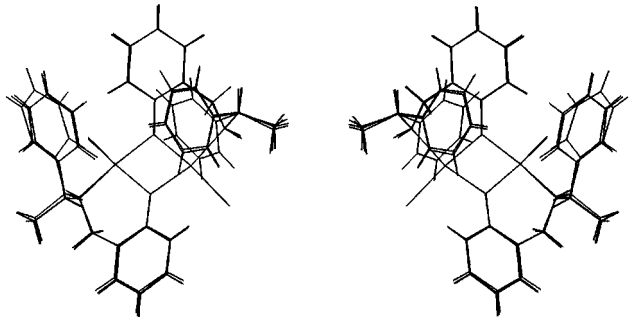


Figure 3. Overlay diagrams of (a) the molecules of $[Cu_2L^1{}_2Cl_2]$ (**1**) and (b) the molecules of $[Cu_2L^2{}_2Cl_2]$ (**2**) in the host-guest crystals with $CH_2Cl_2$, $CHCl_3$ and $Cl(CH_2)_2Cl$.

## Host-Guest Interactions

Attempts to grow single crystals of both **1** and **2** revealed that the host lattices formed by these enantiomeric complexes have considerable structural adaptability to accommodate a range of chlorinated solvents such as $CH_2Cl_2$, $CHCl_3$ and $Cl(CH_2)_2Cl$. In all the cases, 1:1 host-guest crystals have been isolated. The host-guest crystals involving $CH_2Cl_2$ crystallise in the monoclinic $P2_1$ space group while the other host-guest crystals involving $CHCl_3$ and $Cl(CH_2)_2Cl$ crystallise in the orthorhombic $P2_12_12_1$ space group. Both space groups are noncentrosymmetric. In each case, the asymmetric unit contains one dicopper(II) complex molecule and one chloroalkane molecule. Recently, there have been several reports on the propensity of the Cl atom of C–Cl and M–Cl moieties to act as an acceptor in intermolecular hydrogen bonding interactions.[13] The crystal structures described here provide examples for both C–H···Cl–C and C–H···Cl–Cu hydrogen bonding interactions involving the host and guest molecules. The geometrical parameters associated with the observed C–H···Cl interactions are listed in Table 2.

Table 2. Geometrical parameters for intermolecular hydrogen bonds.

| Compound | D···A | $d_{(D\cdots A)}$ [Å] | D–H···A [°] |
|---|---|---|---|
| **1**·$CH_2Cl_2$ | C(11)···Cl(3) | 3.444(7) | 132 |
| | C(22)···Cl(4) | 3.726(4) | 161 |
| **2**·$CH_2Cl_2$ | C(11)···Cl(3) | 3.451(8) | 134 |
| | C(22)···Cl(4) | 3.724(4) | 161 |
| **1**·$CHCl_3$ | C(31)···Cl(2) | 3.450(11) | 153 |
| **2**·$CHCl_3$ | C(31)···Cl(2) | 3.446(10) | 152 |
| **1**·(*P*)-$Cl(CH_2)_2Cl$ | C(31)···Cl(2) | 3.695(13) | 137 |
| **2**·(*M*)-$Cl(CH_2)_2Cl$ | C(31)···Cl(2) | 3.678(14) | 134 |

In both **1**·$CH_2Cl_2$ and **2**·$CH_2Cl_2$, the C–H groups from the phenyl ring of the α-methylbenzylamine fragment (C11–H) of one ligand and the methylene group (C22–H) of the other ligand participate in the C–H···Cl interactions with the Cl atoms (Cl3 and Cl4) of the two adjacent $CH_2Cl_2$ molecules. As a result a one-dimensional arrangement of hydrogen bonded alternating dicopper(II) complexes and $CH_2Cl_2$ molecules is formed. These chains propagate along the *b* axis and there is a mirror-image relationship between the chains formed by **1**·$CH_2Cl_2$ and **2**·$CH_2Cl_2$ (Figure 4).

In the case of **1**·$CHCl_3$ and **2**·$CHCl_3$, one of the metal coordinated Cl atoms acts as the acceptor in the C–H···Cl interaction involving the C–H group of the $CHCl_3$ molecule. These C–H···Cl connected host-guest units, **1**·$CHCl_3$ and **2**·$CHCl_3$, are mirror images of each other (Figure 5). There is no other noncovalent interaction between these discrete host-guest units to form extended networks in the crystal lattice.

The same type of C–H···Cl interaction as observed in **1**·$CHCl_3$ and **2**·$CHCl_3$ is present in the cases of **1**·Cl-

 © 2006 Wiley-VCH Verlag GmbH & Co. KGaA, Weinheim 

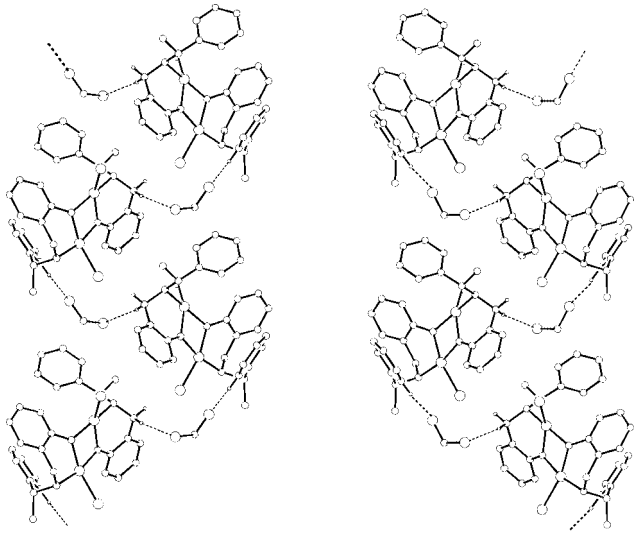


Figure 4. One-dimensional assemblies of (a) $[Cu_2L^1{}_2Cl_2]\cdot CH_2Cl_2$ (**1**·$CH_2Cl_2$) and (b) $[Cu_2L^2{}_2Cl_2]\cdot CH_2Cl_2$ (**2**·$CH_2Cl_2$) in the crystal lattice along the *b* axis through C–H···Cl–C interactions; except for the hydrogen atoms of the methylene groups that are involved in intermolecular interactions, all other hydrogen atoms are omitted for clarity.

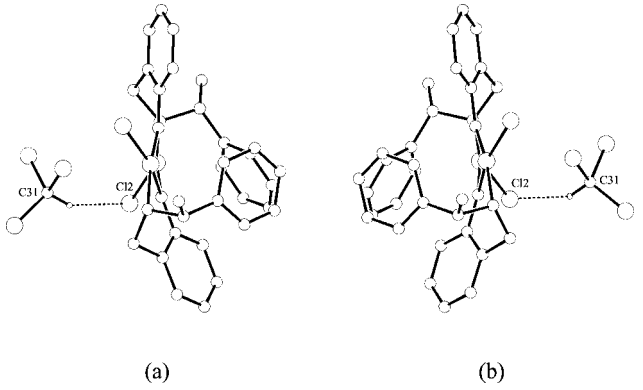


Figure 5. The discrete C–H···Cl–Cu connected (a) $[Cu_2L^1{}_2Cl_2]\cdot CHCl_3$ (**1**·$CHCl_3$) and (b) $[Cu_2L^2{}_2Cl_2]\cdot CHCl_3$ (**2**·$CHCl_3$) units; hydrogen atoms of **1** and **2** are omitted for clarity.

$(CH_2)_2Cl$ and **2**·$Cl(CH_2)_2Cl$. One of the metal coordinated Cl atoms and the C–H group of one of the two methylene groups of $Cl(CH_2)_2Cl$ participate in the C–H···Cl interaction. Here as well, no other noncovalent interactions are observed and the crystal lattice contains the discrete C–H···Cl connected host-guest units. Reports on the isolation of the gauche form of $Cl(CH_2)_2Cl$ are very rare.[7,14] In each of the two present structures, the guest $Cl(CH_2)_2Cl$ molecule is in the chiral gauche form. The Cl–C–C–Cl torsion angles are 58(6)° and 50(7)° in **1**·$Cl(CH_2)_2Cl$ and **2**·$Cl(CH_2)_2Cl$, respectively. The right-handed or *P* form of the enantiomer is stabilised in the host lattice formed by **1** while the left-handed or *M* form of the enantiomer exists in the host lattice formed by **2** (Figure 6). Thus the chiral host complexes **1** and **2** produce the appropriate crystal lattices for enantioselective confinement of the chiral *P* and *M* forms of the $Cl(CH_2)_2Cl$ rotamers, respectively.

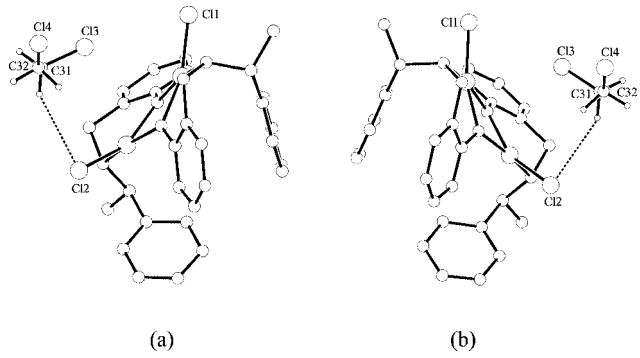


Figure 6. The discrete C–H···Cl–Cu connected (a) $[Cu_2L^1{}_2Cl_2]\cdot(P)$-$Cl(CH_2)_2Cl$ {**1**·(*P*)- $Cl(CH_2)_2Cl$} and (b) $[Cu_2L^2{}_2Cl_2]\cdot(M)$-$Cl(CH_2)_2$-Cl {**2**·(*M*)-$Cl(CH_2)_2Cl$} units; hydrogen atoms of only the $Cl(CH_2)_2Cl$ molecules are shown.

## Conclusions

An enantiomeric pair of bisphenoxo-bridged dicopper(II) complexes, $[Cu_2L^1{}_2Cl_2]$ (**1**) and $[Cu_2L^2{}_2Cl_2]$ (**2**), with the N,O-donor reduced Schiff bases *N*-(2-hydroxybenzyl)-(*R*)-α-methylbenzylamine ($HL^1$) and *N*-(2-hydroxybenzyl)-(*S*)-α-methylbenzylamine ($HL^2$) have been synthesised and characterised. In each complex, a strong antiferromagnetic spin coupling is operative between the metal centres. Crystallisation efforts revealed that both complexes are excellent hosts for small chloroalkane molecules such as $CH_2Cl_2$, $CHCl_3$ and $Cl(CH_2)_2Cl$. In all the cases, 1:1 host-guest compounds are formed which crystallise in the noncentrosymmetric space groups. The asymmetric unit of each structure contains a dicopper(II) complex molecule and a guest molecule. The molecular structures of **1** and **2** are mirror images of each other. The $NO_2Cl$ coordination sphere around each metal centre is distorted from square-planar geometry mainly because of the deviation of the Cl atom from the $NO_2$ plane. The previously known analogous dicopper(II) complexes are all centrosymmetric and the metal coordinated Cl atoms are trans oriented. In contrast, **1** and **2** are noncentrosymmetric and the Cl atoms are in between the trans and cis orientations. The guest molecules are held in the crystal lattice by intermolecular C–H···Cl interactions. In these interactions, the Cl atom of $CH_2Cl_2$ acts as the acceptor while for both $CHCl_3$ and $Cl(CH_2)_2Cl$ the metal coordinated Cl atom acts as the acceptor. Self-assembly of **1**·$CH_2Cl_2$ and **2**·$CH_2Cl_2$ leads to one-dimensional ordering in the crystal lattice. On the other hand, the crystal lattice contains discrete host-guest units when $CHCl_3$ or $Cl(CH_2)_2Cl$ is the guest. Finally, the rare enantioselective trapping of the chiral rotamers (*P*)-$Cl(CH_2)_2Cl$ and (*M*)-$Cl(CH_2)_2Cl$ has been realised in the host lattices formed by **1** and **2**, respectively.

 © 2006 Wiley-VCH Verlag GmbH & Co. KGaA, Weinheim 

## Experimental Section

**Materials:** The chiral reduced Schiff bases ($HL^1$ and $HL^2$) have been synthesised from salicylaldehyde, *R*- or *S*-α-methylbenzylamine and $NaBH_4$ by following the procedure reported previously.[5,7] All other chemicals and solvents were of analytical grade available commercially and were used as received.

**Physical Measurements:** Microanalytical (C, H, N) data were obtained with a Thermo Finnigon Flash EA1112 series elemental analyser. Infrared spectra were collected by using KBr pellets with a Jasco-5300 FT-IR spectrophotometer. A Shimadzu 3101-PC UV/Vis/NIR spectrophotometer was used to record the electronic spectra. Solution electrical conductivities were measured with a Digisun DI-909 conductivity meter. The variable temperature (18–300 K) magnetic susceptibility measurements on powdered samples of **1** were performed using the Faraday technique with a setup comprising a George Associates Lewis coil force magnetometer, a CAHN microbalance and an Air Products closed-cycle helium cryostat. $Hg[Co(NCS)_4]$ was used as the standard. Diamagnetic corrections calculated from Pascal's constants[15] were used to obtain the molar paramagnetic susceptibilities.

**Synthesis of the Complexes**

**$[Cu_2L^1{}_2Cl_2]$ (1):** A methanol solution (10 mL) of $CuCl_2{\cdot}2H_2O$ (170 mg, 1.0 mmol) was added to a methanol solution (20 mL) of $HL^1$ (227 mg, 1.0 mmol). The mixture was stirred at room temperature in air for 1 h. The brown solid that separated was collected by filtration, washed with cold methanol (10 mL) and finally dried in air. Yield obtained was 390 mg (60%). $C_{30}H_{32}Cl_2Cu_2N_2O_2$ (650.6): calcd. C 55.38, H 4.96, N 4.31; found C 55.45, H 5.02, N 4.20. Electronic spectroscopic data in $CHCl_3$: $\lambda_{max}$ (ε) = 650 sh (345), 430 (3670), 336 sh (2520), 268 nm (12140).

**$[Cu_2L^2{}_2Cl_2]$ (2):** This complex was synthesised in 62% yield from $HL^2$ and $CuCl_2{\cdot}2H_2O$ (1:1 mol ratio) by following the same procedure as described for **1**. It was isolated as a brown solid. $C_{30}H_{32}Cl_2Cu_2N_2O_2$ (650.6): calcd. C 55.38, H 4.96, N 4.31; found C 55.24, H 4.92, N 4.26. Electronic spectroscopic data in $CHCl_3$: 650 sh (353), 430 (3800), 336 sh (2790), 268 (12530).

**X-ray Crystallography:** X-ray quality crystals of the host-guest species **1**·$CH_2Cl_2$, **2**·$CH_2Cl_2$, **1**·$CHCl_3$, **2**·$CHCl_3$, **1**·$Cl(CH_2)_2Cl$ and **2**·$Cl(CH_2)_2Cl$ were grown by slow evaporation of the solutions of **1** and **2** in the corresponding solvents in air at room temperature (298 K). Unit cell parameters and the intensity data for all the crystals were collected with a Bruker-Nonius SMART APEX CCD single crystal diffractometer, equipped with a graphite monochromator and a Mo-*K*a fine-focus sealed tube ($\lambda$ = 0.71073 Å) operated at 2.0 kW. The detector was placed at a distance of 6.0 cm from the crystal. Data were collected at 298 K with a scan width of 0.3° in $\omega$ and an exposure time of 15 s/frame. The SMART software was used for data acquisition and the SAINT-Plus software was used for data extraction.[16] The absorption corrections were performed with the help of the SADABS programme.[17] The structures were solved by direct methods and refined on $F^2$ by full-matrix least-squares procedures. In each structure, all the non-hydrogen atoms were refined using anisotropic thermal parameters. For all the structures, the hydrogen atoms of the metal coordinated secondary amine N atoms were located in the difference Fourier maps and refined isotropically. The rest of the hydrogen atoms in each structure were included in the structure factor calculation at idealised positions by using a riding model, but not refined. The SHELX-97 programmes[18] of the WinGX package[19] were used for structure solution and refinement. The ORTEX6a[20] and Platon packages[21] were used for molecular graphics. Selected crystal and refinement data are listed in Table 3.

CCDC-600238 to -600243 contain the supplementary crystallographic data for this paper. These data can be obtained free of charge from The Cambridge Crystallographic Data Centre via www.ccdc.cam.ac.uk/data_request/cif.

## Acknowledgments

Financial support for this work was provided by the Council of Scientific and Industrial Research (CSIR), New Delhi [Grant No. 01(1880)/03/EMR-II]. V. K. M. thanks the CSIR for a research fellowship. Our sincere thanks go to Prof. A. R. Chakravarty for providing the cryomagnetic data. X-ray crystallographic studies were performed at the National Single Crystal Diffractometer Facility, School of Chemistry, University of Hyderabad (funded by the Department of Science and Technology, New Delhi). We thank the University Grants Commission, New Delhi for the facilities provided under the UPE and CAS programmes.

Table 3. Selected crystallographic data for **1**·$CH_2Cl_2$, **2**·$CH_2Cl_2$, **1**·$CHCl_3$, **2**·$CHCl_3$, **1**·$Cl(CH_2)_2Cl$ and **2**·$Cl(CH_2)_2Cl$.

| Compound | **1**·$CH_2Cl_2$ | **2**·$CH_2Cl_2$ | **1**·$CHCl_3$ | **2**·$CHCl_3$ | **1**·$Cl(CH_2)_2Cl$ | **2**·$Cl(CH_2)_2Cl$ |
|---|---|---|---|---|---|---|
| Empirical formula | $C_{31}H_{34}Cl_4Cu_2N_2O_2$ | $C_{31}H_{34}Cl_4Cu_2N_2O_2$ | $C_{31}H_{33}Cl_5Cu_2N_2O_2$ | $C_{31}H_{33}Cl_5Cu_2N_2O_2$ | $C_{32}H_{36}Cl_4Cu_2N_2O_2$ | $C_{32}H_{36}Cl_4Cu_2N_2O_2$ |
| Formula mass [g mol$^{-1}$] | 735.5 | 735.5 | 769.9 | 769.9 | 749.5 | 749.5 |
| Crystal system | monoclinic | monoclinic | orthorhombic | orthorhombic | orthorhombic | orthorhombic |
| Space group | $P2_1$ | $P2_1$ | $P2_12_12_1$ | $P2_12_12_1$ | $P2_12_12_1$ | $P2_12_12_1$ |
| *a* [Å] | 8.5479(6) | 8.5359(6) | 12.7319(6) | 12.7250(7) | 12.822(3) | 12.7982(13) |
| *b* [Å] | 13.0697(9) | 13.0565(10) | 13.7805(7) | 13.7785(8) | 14.046(3) | 14.0366(14) |
| *c* [Å] | 14.1650(9) | 14.1597(10) | 19.4266(10) | 19.4192(11) | 18.744(4) | 18.7009(19) |
| $\beta$ [°] | 90.941(1) | 90.954(1) | 90 | 90 | 90 | 90 |
| *V* [Å$^{-3}$] | 1582.28(19) | 1577.9(2) | 3408.4(3) | 3404.8(3) | 3375.9(12) | 3359.5(6) |
| *Z* | 2 | 2 | 4 | 4 | 4 | 4 |
| $\mu$ [mm$^{-1}$] | 1.713 | 1.718 | 1.670 | 1.672 | 1.607 | 1.615 |
| Reflections unique | 7370 | 7305 | 7958 | 6928 | 6517 | 7860 |
| Reflections [$I > 2\sigma(I)$] | 6813 | 6744 | 5909 | 5521 | 4934 | 5870 |
| Parameters | 378 | 378 | 387 | 387 | 387 | 387 |
| *R*1, *wR*2 [$I > 2\sigma(I)$] | 0.0393, 0.1128 | 0.0403, 0.1162 | 0.0516, 0.1327 | 0.0488, 0.1258 | 0.0475, 0.1151 | 0.0493, 0.1229 |
| *R*1, *wR*2 (all data) | 0.0424, 0.1154 | 0.0432, 0.1187 | 0.0769, 0.1489 | 0.0607, 0.1316 | 0.0727, 0.1242 | 0.0810, 0.1439 |
| Flack parameter | 0.007(12) | 0.022(12) | –0.014(17) | –0.029(16) | 0.029(17) | –0.001(17) |
| GOF on $F^2$ | 1.061 | 1.056 | 1.018 | 0.986 | 1.047 | 1.057 |

 © 2006 Wiley-VCH Verlag GmbH & Co. KGaA, Weinheim 

[1] a) X. X. Zhang, J. S. Bradshaw, R. M. Izatt, *Chem. Rev.* **1997**, *97*, 3313; b) M. Munakata, L. P. Wu, T. Kuroda-Sowa, *Adv. Inorg. Chem.* **1999**, *46*, 173; c) K. T. Holman, A. M. Pivovar, M. D. Ward, *Science* **2001**, *294*, 1907; d) F. Toda, *Pure Appl. Chem.* **2001**, *73*, 1137; e) B. Moulton, M. J. Zaworotko, *Chem. Rev.* **2001**, *101*, 1629; f) M. Eddaoudi, D. B. Moler, H. Li, B. Chen, T. M. Reineke, M. O'Keeffe, O. M. Yaghi, *Acc. Chem. Res.* **2001**, *34*, 319; g) O. R. Evans, W. Lin, *Acc. Chem. Res.* **2002**, *35*, 511; h) E. Brunet, *Chirality* **2002**, *14*, 135; i) L. Pérez-García, D. B. Amabilino, *Chem. Soc. Rev.* **2002**, *31*, 342; j) B. Kesanli, W. Lin, *Coord. Chem. Rev.* **2003**, *246*, 305; k) L. Brammer, *Chem. Soc. Rev.* **2004**, *33*, 476; l) L. Yeo, K. D. M. Harris, *Mendeleev Commun.* **2004**, 263; m) W. Lin, *J. Solid State Chem.* **2005**, *178*, 2486.

[2] a) *Molecular Nonlinear Optics: Materials, Physics and Devices* (Ed.: J. Zyss), Academic Press, London, **1994**; b) *Handbook of Laser Science and Technology* (Ed.: J. M. Webber), CRC Press, Boca Ralton, FL, **1995**.

[3] a) J. Zyss, J.-F. Nicoud, M. Coquillary, *J. Chem. Phys.* **1984**, *81*, 4160; b) D. E. Eaton, *Science* **1991**, *253*, 281.

[4] a) F. Averseng, P. G. Lacroix, I. Malfant, F. Dahan, K. Nakatani, *J. Mater. Chem.* **2000**, *10*, 1013; b) S. R. Korupoju, N. Mangayakarasi, S. Ameerunisha, E. J. Valente, P. S. Zacharias, *J. Chem. Soc., Dalton Trans.* **2000**, 2845; c) C. Evans, D. Luneau, *J. Chem. Soc., Dalton Trans.* **2002**, 83.

[5] V. K. Muppidi, P. S. Zacharias, S. Pal, *Inorg. Chem. Commun.* **2005**, *8*, 543.

[6] a) J. D. Ranford, J. J. Vittal, D. Wu, *Angew. Chem. Int. Ed.* **1998**, *37*, 1114; b) J. D. Ranford, J. J. Vittal, D. Wu, X. Yang, *Angew. Chem. Int. Ed.* **1999**, *38*, 3498; c) C. T. Yang, B. Moubaraki, K. S. Murray, J. D. Ranford, J. J. Vittal, *Inorg. Chem.* **2001**, *40*, 5934; d) J. J. Vittal, X. Yang, *Cryst. Growth Des.* **2002**, *2*, 259; e) S. R. Korupoju, N. Mangayakarasi, P. S. Zacharias, J. Mijuthani, H. Nishihara, *Inorg. Chem.* **2002**, *41*, 4099; f) J. Gao, J. H. Ribenspies, A. E. Martell, *Angew. Chem. Int. Ed.* **2003**, *42*, 6008; g) C. T. Yang, B. Moubaraki, K. S. Murray, J. J. Vittal, *Dalton Trans.* **2003**, 880; h) B. Sreenivasulu, J. J. Vittal, *Cryst. Growth Des.* **2003**, *3*, 635; i) M. A. Alam, M. Nethaji, M. Ray, *Angew. Chem. Int. Ed.* **2003**, *42*, 1940; j) C. T. Yang, M. Vetrichelvan, X. Yang, B. Moubaraki, K. S. Murray, J. J. Vittal, *Dalton Trans.* **2004**, 113; k) B. Sreenivasulu, J. J. Vittal, *Angew. Chem. Int. Ed.* **2004**, *43*, 5769.

[7] V. K. Muppidi, P. S. Zacharias, S. Pal, *Chem. Commun.* **2005**, 2515.

[8] a) H. S. Maslen, T. N. Waters, *Coord. Chem. Rev.* **1975**, *17*, 137; b) S. Das, G. P. Muthukumaragopal, S. N. Pal, S. Pal, *New J. Chem.* **2003**, *27*, 1102; c) S. Das, S. Pal, *J. Mol. Struct.* **2005**, *753*, 68.

[9] a) S. K. Mandal, L. K. Thompson, M. J. Newlands, E. J. Gabe, K. Nag, *Inorg. Chem.* **1990**, *29*, 1324; b) K. Nag, *Proc. Indian Acad. Sci. (Chem. Sci.)* **1990**, *102*, 269; c) N. R. Sangeetha, K. Baradi, R. Gupta, C. K. Pal, V. Manivannan, S. Pal, *Polyhedron* **1999**, *18*, 1425.

[10] a) C. M. Harris, E. Sinn, *J. Inorg. Nucl. Chem.* **1968**, *30*, 2723; b) E. Sinn, W. T. Robinson, *J. Chem. Soc., Chem. Commun.* **1972**, 359; c) R. M. Countryman, W. T. Robinson, E. Sinn, *Inorg. Chem.* **1974**, *13*, 2013; d) P. Gluvchinsky, G. M. Mockler, P. C. Healy, E. Sinn, *J. Chem. Soc., Dalton Trans.* **1974**, 1156; e) R. J. Butcher, E. Sinn, *Inorg. Chem.* **1976**, *15*, 1604; f) B. Chiari, O. Piovesana, T. Tarantelli, P. F. Zanazzi, *Inorg. Chem.* **1987**, *26*, 952; g) R. Paschke, S. Liebsch, C. Tschierske, M. A. Oakley, E. Sinn, *Inorg. Chem.* **2003**, *42*, 8230.

[11] B. Bleany, K. D. Bowers, *Proc. R. Soc. London Ser. A* **1952**, *214*, 451.

[12] G. V. R. Chandramouli, C. Balagopalakrishna, M. V. Rajasekharan, P. T. Manoharan, *Comput. Chem.* **1996**, *20*, 353.

[13] a) G. Aullón, D. Bellamy, L. Brammer, E. A. Bruton, A. G. Orpen, *Chem. Commun.* **1998**, 653; b) L. Brammer, E. A. Bruton, P. Sherwood, *Cryst. Growth Des.* **2001**, *1*, 277; c) V. Balamurugan, M. S. Hundal, R. Mukherjee, *Chem. Eur. J.* **2004**, *10*, 1683; d) L. Brammer, *Chem. Soc. Rev.* **2004**, *33*, 476; e) M. Prbhakar, P. S. Zacharias, S. K. Das, *Inorg. Chem.* **2005**, *44*, 2585.

[14] F. Toda, K. Tanaka, R. Kuroda, *Chem. Commun.* **1997**, 1227.

[15] W. E. Hatfield, *Theory and Applications of Molecular Paramagnetism* (Eds.: E. A. Boudreaux, L. N. Mulay), Wiley, New York, **1976**, p. 491.

[16] *SMART V5.630 and SAINT-plus V6.45*, Bruker-Nonius Analytical X-ray Systems Inc., Madison, WI, USA, **2003**.

[17] G. M. Sheldrick, *SADABS Program for area detector absorption correction*, University of Göttingen, Göttingen, Germany, **1997**.

[18] G. M. Sheldrick, *SHELX-97 Structure Determination Software*, University of Göttingen, Göttingen, Germany, **1997**.

[19] L. J. Farrugia, *J. Appl. Crystallogr.* **1999**, *32*, 837.

[20] P. McArdle, *J. Appl. Crystallogr.* **1995**, *28*, 65.

[21] A. L. Spek, *PLATON A Multipurpose Crystallographic Tool*, Utrecht University, Utrecht, The Netherlands, **2002**.


Received: March 20, 2006
Published Online: May 12, 2006

 © 2006 Wiley-VCH Verlag GmbH & Co. KGaA, Weinheim 

DOI: 10.1002/ejic.200600249

# Reactions of Aminobis(phenolate)-Supported Dioxidotungsten(VI) and Dioxidomolybdenum(VI) Complexes

**Ari Lehtonen*[a] and Reijo Sillanpää[b]**

**Keywords:** Molybdenum / Tungsten / Oxido ligands / N,O ligands / Halides

The dioxidotungsten(VI) and -molybdenum(VI) complexes $[WO_2(O_2NO^{Me})]$ (**1**), $[MoO_2(O_2NO^{Me})]$ (**2**) and $[\{MoO_2(O_2N^{Me})\}_2]$ (**3**) [$O_2NO^{Me}$ methoxyethylamino-*N*,*N*-bis(2-methylene-4,6-dimethylphenolate) dianion, $O_2N^{Me}$ = methylamino-*N*,*N*-bis(2-methylene-4,6-dimethylphenolate) dianion] can react with chloride sources ($Me_3SiCl$, $SOCl_2$) to form resultant monooxido dichloro compounds $[WOCl_2(O_2NO^{Me})]$ (**4**), $[MoOCl_2(O_2NO^{Me})]$ (**5**) and $[MoOCl_2(O_2N^{Me})]$ (**6**), respectively. The reaction of tungsten complex yields of the mixture of *cis*-**4** and *trans*-**4**, which can be separated and characterized. The reactions of analogous molybdenum complexes with $Me_3SiCl$ yield *trans* isomers of **5** and **6** as individual products. Reaction of dioxidotungsten complex **1** with isopropyl isocyanate was found to produce a tungsten(VI) complex $[W(O_2NO^{Me})(N\text{-}i\text{Pr})(L)]$ (**7**) (L = *N*,*N*′-diisopropylureate) with a terminal imido group and a bidentate ureate ligand.

(© Wiley-VCH Verlag GmbH & Co. KGaA, 69451 Weinheim, Germany, 2006)

## Introduction

The research on early transition metal complexes with chelating aryloxide ligands is mostly motivated by their relevance in organometallic and catalytic chemistry.[1,2] For example, various oxidomolybdenum and oxidotungsten compounds with diverse aryloxide ligands have attracted considerable attention as they can catalyze scientifically and industrially interesting olefin metathesis reactions.[3] In particular, oxidotungsten complexes with various numbers of aryloxide and chloride ligands can form active catalysts when treated with alkylating aluminium or tin cocatalysts.[4] The chloride ligands seems to enhance the activity of these catalyst systems, as they allow the alkylation and formation of catalytically active carbene complexes.[3] The standard procedure for these oxidotungsten(VI) phenoxides comprises a straightforward reaction of $WOCl_4$ with a stoichiometric amount of phenolic ligand precursor in an appropriate solvent. On the other hand, reports on molybdenum complexes $[MoO(OAr)_{4-n}Cl_n]$ are very scarce in comparison with their tungsten congeners, which is most probably due to the poor stability of the starting material $MoOCl_4$. Some monooxidomolybdenum aryloxides, e.g. $[MoOCl_2(OAr)_2]$ (Ar = 2,6-*i*Pr$_2$C$_6$H$_3$) have been prepared from a commercially available precursor, $MoO_2Cl_2$ and parent phenols ArOH.[5] However, these preparations are rather delicate and they require sophisticated inert atmosphere techniques, while moisture and acidic impurities have to be rigorously excluded from the reaction medium.

Various cyclopentadienyl derivatives of dioxidotungsten(VI) and -molybdenum(VI) can be converted into the corresponding monooxido dichloro species using HCl as a chloride source.[6] This reaction proceeds probably via a stepwise addition of two HCl molecules across one of the M=O bonds, which yields one molecule of water as a by-product. Other efficient chlorination reagents are $Me_3SiCl$ and $PCl_5$, which can initially react with proton sources, e.g. traces of water or alcohols, to generate the necessary amount of HCl for the reaction. Group 6 metallocenes $Cp_2MO$ (M = Cr, Mo, W) were reported to undergo a direct silylation of M=O group with $Me_3SiCl$ to yield $Cp_2MCl_2$ complexes.[7] Silylation of benzene-1,2-dithiolate (bdt) complex $[WO_2(bdt)_2]^{2-}$ leads to the formation of anionic chloro monooxido complex $[WO(bdt)_2Cl]^-$.[8] Molybdenum(VI) complex $[MoO_2(Sap)(EtOH)]$ (Sap = *N*-salicylidene-2-aminophenolate dianion) has been reported to react with $SOCl_2$ to yield the dichloro complex *trans*- $[MoO(Sap)Cl_2]$.[9] In this reaction, the active species are proposed to be $SOCl^+$ or $Cl^-$. Previously, we have prepared series of new dioxidomolybdenum(VI) and -tungsten(VI) complexes with dianionic aminobis(phenolato) ligands and studied their use as catalysts in oxotransfer reactions and ROMP of norbornene.[10] For example, $[WO_2(O_2NO^{Me})]$ (**1**), $[MoO_2(O_2NO^{Me})]$ (**2**) and $[\{MoO_2(O_2N^{Me})\}_2]$ (**3**) [$O_2NO^{Me}$-methoxyethylamino-*N*,*N*-bis(2-methylene-4,6-dimethylphenolate) dianion, $O_2N^{Me}$ = methylamino-*N*,*N*-bis(2-methyl-

[a] Department of Chemistry, University of Turku, 20014, Turku, Finland
Fax: + 358-2-333-6700
E-mail: Ari.Lehtonen@utu.fi
[b] Department of Chemistry, University of Jyväskylä, 40351 Jyväskylä, Finland

Supporting information for this article is available on the WWW under http://www.eurjic.org or from the author.

 © 2006 Wiley-VCH Verlag GmbH & Co. KGaA, Weinheim 

ene-4,6-dimethylphenolate) dianion] have been synthesized and structurally characterized.[10b,10c] We supposed that these air-stable dioxido compounds may also provide useful entries to the new monooxido-dichloro-tungsten(VI) and -molybdenum(VI) complexes, which would resemble well-known metathesis catalyst precursors. In present study we demonstrate a chloride-for-oxide substitution as a simple route to prepare dichloro oxidotungsten(VI) and oxidomolybdenum(VI) complexes with aminobis(phenolate) ligands. In addition, the reaction of tungsten complex **1** with isopropyl isocyanate is studied.

## Results and Discussions

### Chloride-for-Oxide Substitution of Dioxidotungsten(VI) Complex 1

In order to prepare aminobis(phenolate)-supported dichloro monooxido complex of tungsten(VI), we treated dioxidotungsten complex **1** with various potential chloride sources, i.e. HCl, $SOCl_2$, $Me_3Cl$ and $PCl_5$. The stirred mixtures in various solvents ($CHCl_3$, THF, PhMe) were allowed to react with an excess of chlorinating reagents to obtain intense red solutions.[11] The reaction mixtures that formed were then heated to the reflux temperature while the reactions were monitored by TLC. As a result, complex **1** reacted smoothly to produce the mixtures of three distinct products (Scheme 1).

Dark red mixtures were separated by column chromatography to get two intense red solids and one yellow product as a minor component. The IR spectra of red solids presented strong absorption bands at ca. 950 $cm^{-1}$ instead of characteristic doublet (939 and 899 $cm^{-1}$) for $WO_2^{2+}$ moiety in complex **1**.[10c] NMR spectra of red solids were closely similar to those found for isomers of a related compound $[WOCl_2(O_2N^{Me})]$,[12] thus they were identified as *cis* and *trans* isomers of expected dichloro monooxido complex **4**. The third component in the reaction mixtures was a bright yellow complex **4′**, which was formed as trace amounts in all separate experiments. Spectroscopic studies of **4′** suggested some changes in the original aminobis(phenolate) ligand. Compound **4′** was finally identified by X-ray crystallography (see below) to be a mononuclear, monooxido chloro complex, in which the degraded aminobis(phenolato) ligand has coordinated as a tetradentate trianion. When the reaction parameters were optimized, it was found that the highest total conversion could be obtained when the starting compound **1** is dissolved in commercial chloroform with 1% of EtOH stabilizer and subsequently treated with excess of $SOCl_2$. Under these conditions, the reaction yielded a *trans* isomer of **4** as a major component. Although various amounts of both isomers were formed in all of these experiments, any selective reaction conditions for the preparation of *cis*-**4** could not be found.[13] As $SOCl_2$ reacts readily with EtOH to produce HCl, we can assume that the actual reaction is an addition of two HCl molecules across one of the W=O bonds, like reported by Legzdins[6a] and Schrock.[6b] Formation of the *trans* isomer as an eventual result of studied chloride-for-oxide substitution appears reasonable, seeing that two newly introduced chloride ligands replace one terminal oxido group and one neutral oxygen donor, which are at *trans* positions. Conversely, the development of the *cis* isomer is not so obvious, as it results in the substantial rearrangement of the aminobis(phenolate) ligand. Besides, the *cis* isomer appears to be thermodynamically less favourable, as it tends to isomerize in solutions. However, our attempts to isomerize quantitatively *cis*-**4** to *trans*-**4** by heating a sample in a xylene solution at reflux temperature failed, leading mainly to the decomposition of initial complex. Interestingly, the only isolable de-

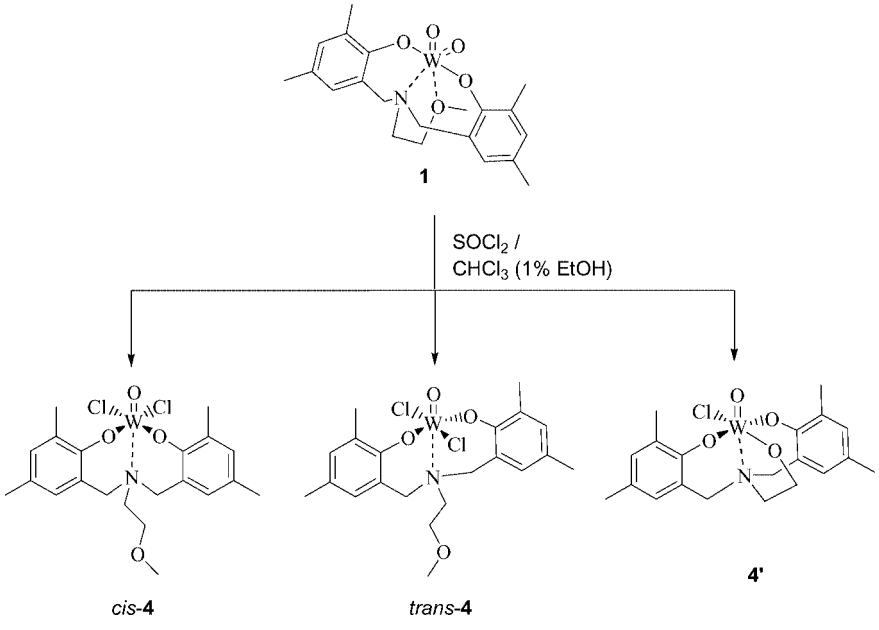


Scheme 1. Reaction of $[WO_2(O_2NO^{Me})]$ with $SOCl_2$.

 © 2006 Wiley-VCH Verlag GmbH & Co. KGaA, Weinheim 

composition product was abovementioned **4′**. The formation of this complex is appealing, as the emergence of the atrane-type ligand[14] requires a breaking of the ether C–O bond upon formation of the metal alkoxide bond. Such an ether cleavage as this is a well-known transformation in organic synthesis, and it can be catalyzed by various Lewis and Brönstedt acids.[15] For example; $WCl_6$ can catalyze acylative cleavage of ether C–O bonds, while the reaction is supposed to proceed via a metal alkoxide intermediate.[16] Similar demethylation of the methoxy group upon coordination is earlier observed in the reaction of $TaCl_5$ with *p-tert*-butylcalix[4]arene dimethyl ether.[17] Correspondingly, we can assume that in present experiments, the ether functionality of the ligand side-arm reacts with the metal centre leading to the formation of W–O bond associated with evolution of $CH_3Cl$.

### Chloride-for-Oxide Substitution of Dioxidomolybdenum(VI) Complexes 2 and 3

The reactions of the monomeric molybdenum complex **2** and the dimeric complex **3** with selected chlorinating agents in various solvents were conducted identically as described for tungsten complex **1** (see above). To our discontent, when chloride sources $SOCl_2$ or $PCl_5$ were added to the stirred solutions of dioxidomolybdenum(VI) complexes in $CHCl_3$, the vigorous reactions yielded predominantly to the swift decomposition of starting complexes, whereas only minor amounts of chlorinated products **5** or **6** could be isolated. However, the silylation of Mo=O moiety with $Me_3SiCl$ in toluene proved a convenient procedure for the chloride-for-oxide substitution of these reactive molybdenum complexes. The reaction of complex **2** with $Me_3SiCl$ in a toluene suspension at room temperature led to the formation of dark blue solution, from which the dichloro monooxido complex **5** was obtained in a high yield (Scheme 2).

The IR spectrum of dark purple solid indicated the absence of initial $MoO_2^{2+}$ moiety, whereas the NMR spectra of complex were practically identical to those of *trans*-**4**. Consequently, this isolable reaction product was identified as the *trans* isomer of the expected dichloro derivative. The reaction of **2** appeared to yield also a minor amount of *cis* isomer (according to TLC and $^1H$ NMR analyses), but it could not be isolated, probably due to its tendency to isomerize during processing. The reaction of practically insoluble **3** in a toluene suspension led correspondingly to the intense blue solution, from which the complex **6** was obtained in practically quantitative yield as a dark blue solid. This solid has closely analogous IR and NMR spectra to **2** and tungsten complexes *trans*-[$WOCl_2(O_2N^{Me})$],[12] therefore it was identified as *trans*-[$MoOCl_2(O_2N^{Me})$]. The suspected structure was also verified by X-ray crystallography (see below).

### Reaction of Dioxidotungsten(VI) Complex with Isopropyl Isocyanate

Some transition metal oxido compounds are known to react with alkyl and aryl isocyanates to produce corresponding metal imido complexes.[18,19] In our experiment, dioxidotungsten complex **1** was treated with an excess of isopropyl isocyanate in toluene and the reaction mixture was heated for 120 min at 100 °C in a screw cap vial. As a result, the reaction mixture turned red while complex **1** dissolved. This red solution was subsequently cooled to the room temperature to obtain complex **7** as orange-red crystals. Somehow, identical reaction involving molybdenum complex **2** did not yield any isolable products. IR spectrum of complex **7** presented a strong absorption band at 1634 $cm^{-1}$, which can be assigned as a C=O stretch. X-ray crystal structure analysis verified that the product contains one imido group and one diisopropylureate ligand. The ureate ligand is supposedly formed via bis-imido intermediate, which reacts further with the additional molecule of isocyanate (Scheme 3).[18,20]

Legzdins et al. have studied analogous reactivity of dioxidotungsten complex $Cp^*WO_2(CH_2SiMe_3)$ with *p*-tolyl isocyanate, and reported that the use of hexanes as a reaction medium yields mono- and bis(imido) complexes, whereas the reaction in toluene solution affords an imido ureate complex.[18a] In our experiments, the reaction was conducted in a toluene solution, while the tungsten precursor dissolved slowly upon reaction. Thus, the stoichiometry of starting materials was unfeasible to control and the reaction yielded the ultimate ureate complex without any isolable intermediates. Complex **7** is stable in air as crystalline solid, but it decomposes in organic solvents, therefore adequate NMR spectroscopic data were not obtained.

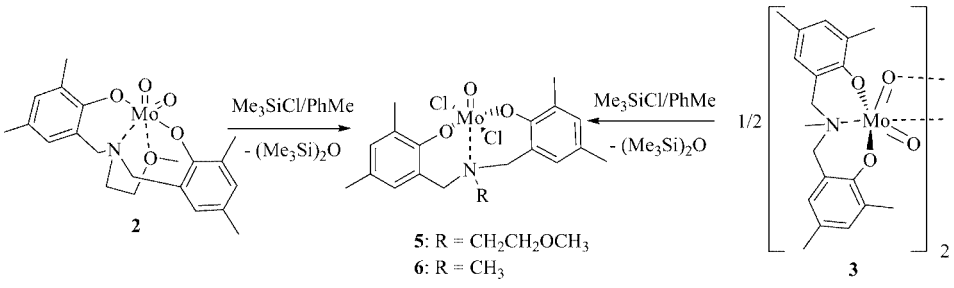


Scheme 2. Reactions of [$MoO_2(O_2NO^{Me})$] and [{$MoO_2(O_2N^{Me})$}$_2$] with $Me_3SiCl$.

 © 2006 Wiley-VCH Verlag GmbH & Co. KGaA, Weinheim 

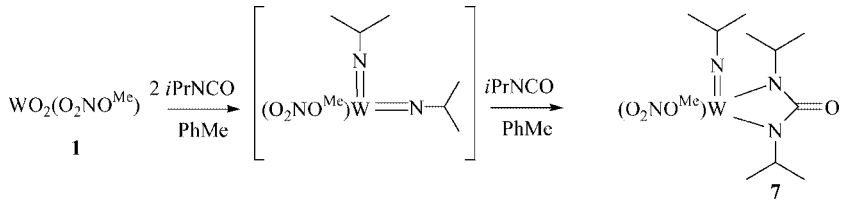


Scheme 3. Reaction of $[WO_2(O_2NO^{Me})]$ with isopropyl isocyanate.

## Structural Studies

X-ray structure determinations were carried out for complexes *trans*-**4**, **4′**, **6** and **7**. In t*rans*-**4** the tungsten(VI) cation has adopted a distorted octahedral coordination geometry, whereas the aminobis(phenolate) ligand is coordinated as a tridentate $O_2N$ donor (Figure 1). Two chloro ligands are in *trans* orientation. General structural parameters, e. g. W–O and W–Cl distances along with O–W–O and Cl–W–Cl angles, are of the same magnitude as usually found in $[WOCl_2(OAr)_2]$ complexes.[4,21] Consequently, the overall structure of *trans*-**4** is essentially similar to that found in related complexes with methylamino-*N*,*N*-bis(2-methylene-4,6-dialkylphenolate) ligands.[12] Complex **4′** forms monomeric molecules in which the aminobis(phenolate)ethanolate group has coordinated as a tetradentate trianionic ligand through three oxygen donors and one nitrogen donor (Figure 2). The nitrogen donor is located t*rans* to the terminal oxido group, while the chloro ligand is sited *trans* to the alkoxide oxygen. In the solid-state structure of **4′**, the $W–O_{aryloxide}$ bond lengths are 1.896(5) and 1.918(5) Å, whereas the $W–O_{alkoxide}$ bond is 1.909(4) Å. The bonding parameters between the metal centre and the aminobis(phenolato)ethanolato ligand is rather expected, although the W–O bond lengths are slightly longer and W–N distances are slightly shorter than in comparable oxidotungsten(VI) complexes with tridentate aminobis(phenolates). In general, the solid-state structure of **4′** resembles those found in oxidotungsten(VI) complexes with tripodal aminotris(phenolate)s.[22]

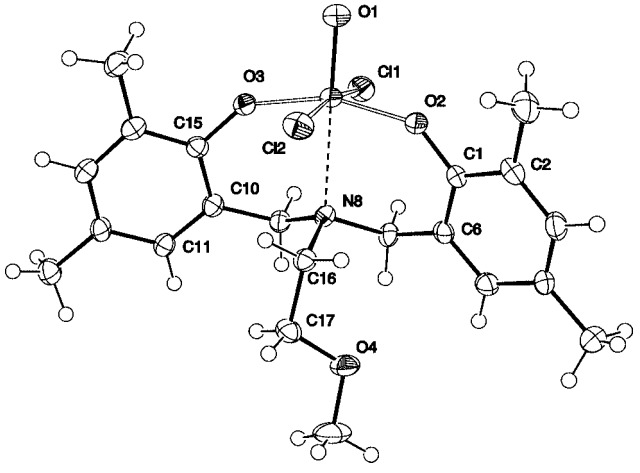


Figure 1. Molecular structure of *trans*-**4**. Thermal ellipsoids have been drawn at 30% probability level.

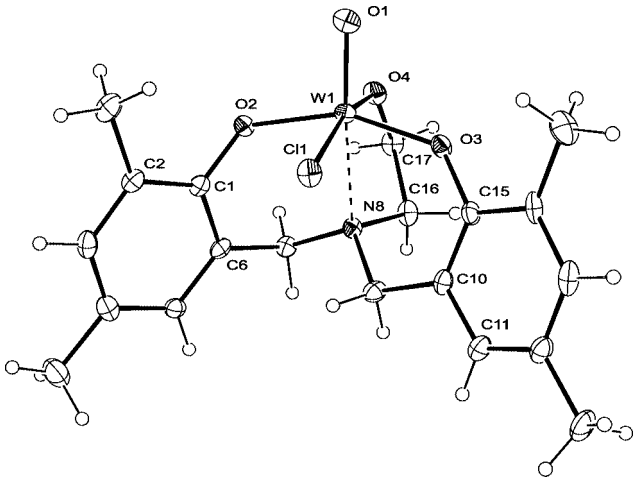


Figure 2. Molecular structure of **4′**. Thermal ellipsoids have been drawn at 30% probability level.

The coordination sphere around the metal centre in the molybdenum complex **6** (Figure 3.) is very similar to that in *trans*-**4** and other related tungsten complexes. Essentially, complex **6** is isostructural with the equivalent tungsten compound $[WOCl_2(O_2N^{Me})]$.[12] Only small structural differences are found between these two complexes, e.g. the M=O and M–N bond lengths are 1.672(4) and 2.536(4) for the Mo complex, whereas corresponding distances for the tungsten analogue are 1.696(5) Å and 2.512(5) Å, respectively.

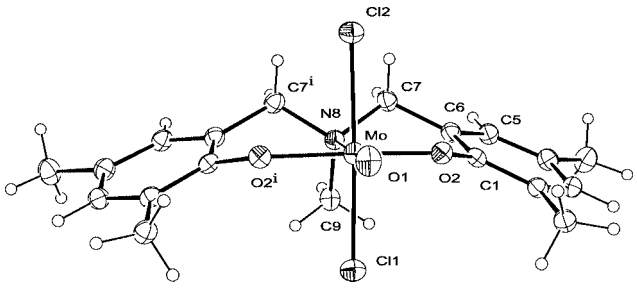


Figure 3. Molecular structure of **6**. Thermal ellipsoids have been drawn at 30% probability level.

In complex **7** the metal centre is surrounded by two phenoxides oxygen atoms, one neutral nitrogen donor, one imido group and two amido nitrogen donors (Figure 4.). The phenoxides oxygen atoms of aminobis(phenolato) ligand have arranged in a *cis* fashion [the O–W–O angle is 107.51(19)°], while the neutral amino nitrogen has located

 © 2006 Wiley-VCH Verlag GmbH & Co. KGaA, Weinheim 

*trans* to the imido nitrogen atom. Amido nitrogen atoms of the ureate group are in *cis* positions by necessity [the N–W–N angle is 63.4(2) °]. The $W{=}N_{imido}$ and two $W{-}N_{ureate}$ distances [1.723(6), 1.926(4) and 1.939(5) Å, respectively] are slightly shorter than found in related high-valent metal complexes derived from aromatic isocyanates.[18]

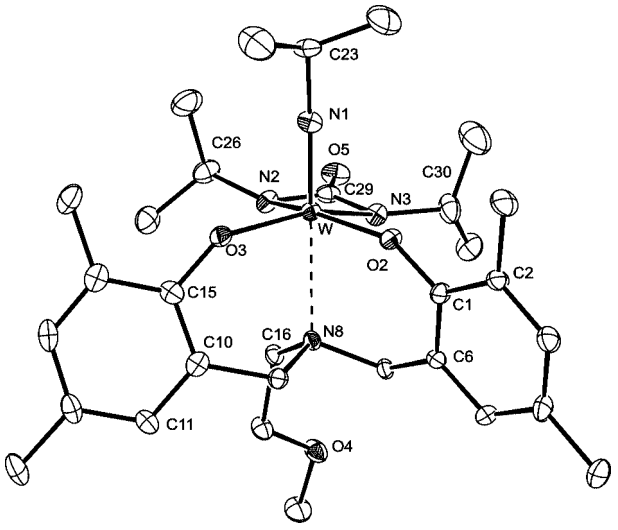


Figure 4. Molecular structure of **7**. Hydrogen atoms are omitted for clarity. Thermal ellipsoids have been drawn at 30% probability level. Selected bond lengths [Å] and angles [°]: W–N1, 1.723(6); W–N2, 2.062(5); W–N3, 2.063(5); W–O2, 1.926(4); W–O3, 1.939(5); W–N(3), 2.064(5); W–N8, 2.458(5); W–N1–C23, 172.0(5); N2–W–N3, 63.4(2); O2–W–O3, 107.51(19); N1–W–N8, 170.2(2).

## Conclusions

In summary, we have shown that aminobis(phenolate)-supported dioxidotungsten(VI) and -molybdenum(VI) complex can be used as starting materials for new dichloro monooxido complexes. The chloride-for-oxide substitution can be easily carried out using $SOCl_2$ or $Me_3SiCl$ as chloride sources. Particularly, the chlorination of molybdenum complexes can be easily carried out in synthetically useful yields. Resulting oxidometal(VI) complexes carry primarily a *trans* dichloro functionality. These complexes resemble potential metathesis catalyst precursors; therefore their use in catalytic applications will be probed in future. The aminobis(phenolate)-supported dioxidotungsten(VI) can also react with isopropyl isocyanate to generate corresponding imido ureate complex.

## Experimental Section

Starting complexes **1**, **2** and **3** were prepared according published procedures.[10b,10c] Other chemicals were from commercial sources and were used as purchased. Solvents were of HPLC grade. All syntheses and manipulations were performed under ambient laboratory atmosphere if not otherwise stated. $^1H$ and $^{13}C$ NMR spectra (500 MHz) were recorded at 20 °C using Bruker AV 500 spectrometer in $CDCl_3$ solutions and were referenced internally to $SiMe_4$. IR spectra were recorded as Nujol mulls using a Mattson Galaxy FTIR spectrometer. Elemental analyses were obtained using a Perkin–Elmer CHNS Analyzer 2400. Crystalline samples were dried in vacuo at 40 °C for 4 h prior to elemental analyses.

**Chloride-for-Oxide Substitutions of 1:** Complex **1** (110 mg, 0.20 mmol) was mixed with $CHCl_3$ (10 mL, stabilized with 1% of EtOH) and subsequently treated with $SOCl_2$ (0.10 mL, 1.4 mmol). The reaction mixture was then heated at reflux temperature under dynamic $N_2$ atmosphere for two hours while the reaction was monitored by TLC (toluene as an eluent). As a result, complex **1** reacted completely to produce a mixture of two red products and one yellow product. The dark red mixture was separated by silica column chromatography using toluene as an eluent to get *trans* and *cis* isomers, in that order, of dichloro complex **4** as intense red solids. The third component in the reaction mixture was a bright yellow complex **4′**.

***cis*-4:** Yield: 8 mg (7%). $C_{21}H_{27}Cl_2NO_4W$ ($M$ = 612.19 g mol$^{-1}$): calcd. C 41.20, H 4.45, N 2.29; found C 40.80, H 4.27, N 2.11. $^1H$ NMR ($CDCl_3$): $\delta$ = 7.13 (s, 2 H, Ar), 6.91 (s, 2 H, Ar), 3.75–3.78 (overlapping d + s, 6 H, $CH_2$), 3.36 (s, 3 H, $OCH_3$), 2.95 (s, 2 H, $CH_2$), 2.50 (s, 6 H, $ArCH_3$), 2.47 (s, 6 H, $ArCH_3$) ppm. $^{13}C$ NMR ($CDCl_3$): $\delta$ = 155.91, 135.83, 131.16, 129.46, 128.24, 127.42, 68.23, 58.81, 57.90, 56.98, 20.80, 16.00 ppm. IR (Nujol): $\tilde{\nu}$ = 1304 (w), 1236 (s), 1220 (s), 1156 (s), 1144 (m), 1082 (w), 1038 (w), 976 (s), 966 (vs), 941 (s), 880 (s), 862 (vs), 835 (m), 745 (w), 665 (w), 604 (m), 560 (m) cm$^{-1}$.

***trans*-4:** Yield: 79 mg (65%) $C_{21}H_{27}Cl_2NO_4W$ ($M$ = 612.19 g mol$^{-1}$): calcd. C 41.20, H 4.45, N 2.29; found C 40.88, H, 4.22, N 2.02. $^1H$ NMR ($CDCl_3$): $\delta$ = 7.15 (s, 2 H, Ar), 6.92 (s, 2 H, Ar), 4.83 (d, $J$ = 13.4 Hz,2 H, Ar-$CH_2$), 3.90 (d, $J$ = 13.4 Hz,2 H, Ar-$CH_2$), 3.50 (t, $J$ = 5.2 Hz,2 H, $CH_2$), 3.28 (s, 3 H, $OCH_3$), 2.57 (t, $J$ = 5.2 Hz,2 H, $CH_2$), 2.55 (s, 6 H, $ArCH_3$), 2.48 (s, 6 H, $ArCH_3$) ppm. $^{13}C$ NMR ($CDCl_3$): $\delta$ = 155.20, 136.38, 131.15, 128.97, 128.68, 127.17, 66.87, 58.95, 56.12, 50.71, 20.87, 15.93 ppm. IR (Nujol): $\tilde{\nu}$ = 1312 (w), 1240 (s), 1227 (s), 1157 (s), 1140 (w), 1090 (w), 964 (vs), 951 (s), 876 (vs), 843 (m), 745 (s), 728 (m), 667 (w), 600 (m), 571 (m) cm$^{-1}$.

**4′:** Yield: 8 mg (7%). $C_{20}H_{24}ClNO_4W$ ($M$ = 561.70 g mol$^{-1}$): calcd. C 42.77, H 4.31, N 2.49; found C 42.40, H 4.07, N 2.47. $^1H$ NMR ([D$_6$]DMSO): $\delta$ = 7.07 (s, 2 H, Ar), 6.78 (s, 2 H, Ar), 4.99 (t, $J$ = 5.8 Hz, 2 H, $CH_2$), 4.11 (d, $J$ = 14.6 Hz, 2 H, Ar-$CH_2$), 3.91 (d, $J$ = 14.1 Hz, 2 H, Ar-$CH_2$), 2.98 (d, $J$ = 7.4 Hz, 2 H,$CH_2$), 2.30 (s, 6 H, $ArCH_3$), 2.20 (s, 6 H,$ArCH_3$) ppm. IR (Nujol): $\tilde{\nu}$ = 1300 (m), 1240 (s), 1223 (s), 1159 (s), 1092 (m), 1038 (w), 956 (vs), 945 (s), 860 (vs), 842 (s), 748 (m), 734 (m), 696 (w), 665 (m), 599 (m), 572 (m) cm$^{-1}$.

**Chloride-for-Oxide Substitutions of 2 and 3:** Stirred suspensions of **2** (1.410 g, 3.00 mmol) and **3** (1.284 g, 1.50 mmol) in toluene (50 mL) were treated with $Me_3SiCl$ (2.0 mL, 12 mmol). The intense blue reaction mixtures were stirred at room temperature for 18 h. The resulting dark blue solutions were filtered through a short pad of silica. The volatiles were then removed in a vacuum and remaining dark purple solids were washed with cold hexane (20 mL) and dried in air.

**5:** Yield: 1.330 g (85%). $C_{21}H_{27}Cl_2MoNO_4$ ($M$ = 524.30 g mol$^{-1}$): calcd. C 48.11, H 5.19, N 2.67; found C 48.41, H 5.07, N 2.48. $^1H$ NMR ($CDCl_3$): $\delta$ = 7.10 (s,2 H, Ar), 6.97 (s,2 H, Ar), 4.69 (d, $J$ = 13.3 Hz,2 H, Ar-$CH_2$), 3.89 (d, $J$ = 13.3 Hz, 2 H, Ar-$CH_2$), 3.49 (t, $J$ = 5.1 Hz, 2 H,$CH_2$), 3.28 (s, 3 H, $OCH_3$), 2.56 (s, 6 H,$ArCH_3$), 2.48 (s, 6 H, $ArCH_3$) 2.38 (t, $J$ = 5.1 Hz, 2 H,$CH_2$) ppm. $^{13}C$ NMR ($CDCl_3$): $\delta$ = 161.21, 138.86, 130.83, 129.83, 129.68, 128.03, 66.82,

 © 2006 Wiley-VCH Verlag GmbH & Co. KGaA, Weinheim 

Table 1. Summary of Crystallographic data for *trans*-**4**, **4′**, **6** and **7** at 173(2) K.

| | *trans*-**4** | **4′** | **6** | **7** |
|---|---|---|---|---|
| Formula | $C_{21}H_{27}Cl_2NO_4W$ | $C_{20}H_{24}ClNO_4W$ | $C_{19}H_{23}Cl_2MoNO_3$ | $C_{31}H_{48}N_4O_4W$ |
| $M_r$ | 612.19 | 561.70 | 480.22 | 724.58 |
| Crystal system | monoclinic | monoclinic | monoclinic | monoclinic |
| Space group (no.) | *C*2/*c* (15) | $P2_1/c$ (14) | $P2_1/m$ (11) | $P2_1/n$ (14) |
| *a* [Å] | 35.7507(12) | 8.1556(2) | 7.6901(13) | 9.1641(3) |
| *b* [Å] | 8.0281(4) | 34.1160(10) | 16.014(3) | 17.1466(6) |
| *c* [Å] | 15.7217(7) | 14.8612(4) | 8.0501(8) | 20.5434(7) |
| *α* [°] | 90 | 90 | 90 | 90 |
| *β* [°] | 93.821(2) | 104.5020(10) | 93.171(9) | 102.645(2) |
| *δ* [°] | 90 | 90 | 90 | 90 |
| *V* [Å$^3$] | 4502.3(3) | 4003.18(19) | 989.8(3) | 3149.75(19) |
| *Z* | 8 | 8 | 2 | 4 |
| $D_c$ [g cm$^{-1}$] | 1.806 | 1.864 | 1.611 | 1.528 |
| $\mu$(Mo-$K_\alpha$) [cm$^{-1}$] | 53.95 | 59.30 | 9.51 | 37.08 |
| Observed reflections | 5600 | 9233 | 2015 | 7701 |
| $R_{int}$ | 0.0320 | 0.0483 | 0.0331 | 0.0447 |
| Parameters | 268 | 495 | 127 | 372 |
| $R_1$[a] | 0.0421 (0.0307) | 0.0635 (0.0449) | 0.058 (0.048) | 0.0713 (0.0524) |
| $wR_2$[a] | 0.0613 (0.0572) | 0.0836 (0.0769) | 0.100 (0.095) | 0.1132 (0.1025) |

[a] Values in parentheses for reflections with $I > 2.0\sigma(I)$: $R_1 = \Sigma||F_o|-|F_c||/\Sigma|F_o|$. $wR_2 = \{\Sigma[w(F_o^2-F_c^2)^2]/\Sigma[w(F_o^2)^2]\}^{1/2}$ and $w = 1/[\sigma^2(F_o^2)+(aP)^2+bP]$, where $P = (2F_c^2+F_o^2)/3$.

58.92, 56.45, 50.53, 21.33, 16.43 ppm. IR (Nujol): ṽ = 1306 (w), 1239 (s), 1219 (s), 1171 (vs), 1117 (s), 1090 (m), 959 (vs), 882 (vs), 873 (m), 746 (s), 731 (m), 681 (w), 661 (m), 598 (m), 574 (m) cm$^{-1}$.

**6:** Yield: 1.325 g (92%). $C_{19}H_{23}Cl_2MoNO_3$ ($M$ = 480.22 g mol$^{-1}$): calcd. C 47.52, H 4.83, N 2.92; found C 47.81, H 5.05, N 2.78. $^1$H NMR ($CDCl_3$): $\delta$ = 7.11 (s, 2 H, Ar), 6.94 (s, 2 H, Ar), 4.86 (d, $J$ = 13.0 Hz, 2 H,Ar-$CH_2$), 3.08 (d, $J$ = 13.0 Hz, 2 H,Ar-$CH_2$), 2.56 (s, Ar$CH_3$, 6 H), 2.48 (s, 6 H,Ar$CH_3$) 1.86 (s, 3 H,N–$CH_3$) ppm. $^{13}$C NMR ($CDCl_3$): $\delta$ = 160.78, 138.95, 131.03, 129.56, 129.20, 128.25, 62.80, 46.83, 21.23, 16.43 ppm. IR (Nujol): ṽ = 1300 (m), 1240 (s), 1223 (s), 1157 (s), 1132 (m), 1082 (vs, br), 955 (vs), 937 (m), 866 (vs), 844 (m), 748 (w), 696 (w), 666 (w), 600 (m), 573 (w) cm$^{-1}$.

**Reaction of 1 with Isopropyl Isocyanate:** Complex **1** (110 mg, 0.20 mmol) was mixed with toluene (3.0 mL) in a screw cap vial and subsequently treated with isopropyl isocyanate (0.10 mL, 1.0 mmol). The reaction mixture was then heated at 110 °C for 16 hours. The red solution formed was cooled to the room temperature and hexane (3.0 mL) was added to enhance the crystallization. The solution was then kept at –18 °C overnight, after that the orange-red crystals (85 mg, 60%) were separated by decantation and washed by hexane. Crystals were stable in air for several days, but they decompose quickly upon dissolution.

Table 2. Selected bond lengths [Å] and angles [°] for *trans*-**4**, **4′** and **6**.

| | *trans*-**4** | **4′**[a] | **6** |
|---|---|---|---|
| M–O1 | 1.693(3) | 1.714(5) | 1.672(4) |
| M–O2 | 1.868(3) | 1.918(5) | 1.862(3) |
| M–O3 | 1.869(3) | 1.896(5) | 1.862(3)[b] |
| M–Cl1 | 2.3699(11) | 2.3701(16) | 2.3692(17) |
| M–Cl2/O4 | 2.3713(11) | 1.909(4) | 2.3822(18) |
| M–N8 | 2.534(3) | 2.407(5) | 2.536(4) |
| O1–M–N8 | 177.67(13) | 168.2(2) | 178.4(2) |
| O2–M–O3 | 159.21(11) | 154.46(18) | 158.76(16)[b] |
| Cl1–M–Cl2/O2 | 170.96(4) | 165.60(14) | 167.88(6) |

[a] Parameters for the W1-centered molecule. [b] O3 corresponds to O2$^i$, where $i = x, -y+1/2, z$.

**7**: Yield: 54 mg (37%). $C_{31}H_{48}N_4O_4W$ ($M$ = 724.58 g mol$^{-1}$): C 51.39, H 6.68, N 7.73; found C 50.99, H 6.35, N 7.59. IR: ṽ = 1634 (vs, br), 1283 (vs), 1245 (vs), 1221 (vs), 1159 (s), 1113 (s), 1094 (m), 1055 (m), 1038 (w), 988 (m), 961 (m), 932 (m), 860 (s), 855 (vs), 783 (m), 750 (m), 733 (m), 690 (w), 598 (m), 556 (m), 422 (w) cm$^{-1}$.

**X-ray Crystallography:** Crystals of *trans*-**4** and **4′**, suitable for X-ray measurements were grown at 4 °C from acetonitrile. Crystals of **6** were obtained from concentrated toluene solution at room temperature. Crystals of **7** precipitated from the reaction mixture at –18 °C. Crystal data for the compounds *trans*-**4**, **4′**, **6** and **7** along with other experimental details are summarized in Table 1. Single-crystal data collections, reduction, and subsequent calculations were performed essentially as described in our earlier papers.[12,22] Figures were drawn with *Ortep-3 for Windows*[23] (Table 2).

CCDC-601925, -601926, -601927 and -601928 contain the supplementary crystallographic data for this paper. These data can be obtained free of charge from The Cambridge Crystallographic Data Centre via www.ccdc.cam.ac.uk/data_request/cif.


[1] For recent reviews see: a) Y. Suzuki, H. Terao, T. Fujita, *Bull. Chem. Soc. Jpn.* **2003**, *76*, 1493–1517; b) Y. Chen, S. Yekta, A. K. Yudin, *Chem. Rev.* **2003**, *103*, 3155–3211; c) R. R. Schrock, A. H. Hoveyda, *Angew. Chem. Int. Ed.* **2003**, *42*, 4592–4633.

[2] For example, see a) F. Wolff, C. Lorber, R. Choukroun, B. Donnadieu, *Inorg. Chem.* **2003**, *42*, 7839–7845; b) S. Groysman, E. Y. Tsuva, I. Goldberg, M. Kol, Z. Goldschmidt, M. Shuster, *Organometallics* **2004**, *23*, 5291–5299; c) Y.-L. Wong, J.-F. Ma, W.-F. Law, Y. Yan, W.-T. Wong, Z.-Y. Zhang, T. C. W. Mak, D. K. P. Ng, *Eur. J. Inorg. Chem.* **1999**, 313–321.

[3] K. J. Ivin, J. C. Mol, *Olefin Metathesis and Metathesis Polymerisation*, Academic Press, London, **1997**.

[4] a) S. Hayano, H. Kurakata, Y. Tsunogae, Y. Nakayama, Y. Sato, H. Yasuda, *Macromolecules* **2003**, *36*, 7422–7431; b) D. L. Barnes, N. W. Eilerts, J. A. Heppert, W. H. Huang, M. M. Morton, *Polyhedron* **1994**, *13*, 1267–1275; c) W. A. Nugent, J. Feldman, J. C. Calabrese, *J. Am. Chem. Soc.* **1995**, *117*, 8992–8998; d) F. J. Gómez, K. A. Abboud, K. B. Wagener, *J. Mol. Catal. A* **1998**, *133*, 159–166; e) F. J. Gómez, M. S. Manak, K. A. Abboud, K. B. Wagener, *J. Mol. Catal. A* **2000**, *160*, 145–


 © 2006 Wiley-VCH Verlag GmbH & Co. KGaA, Weinheim 

156; f) D. R. Kelsey, D. L. Handlin, M. Narayana, B. M. Scardino, *J. Polym. Sci., Part A: Polym. Chem.* **1997**, *35*, 3027–3047.
[5] T. A. Hanna, A. K. Ghosh, C. Ibarra, L. N. Zakharov, A. L. Rheingold, W. H. Watson, *Inorg. Chem.* **2004**, *43*, 7567–7569.
[6] a) P. Legzdins, E. C. Phillips, L. Sánchez, *Organometallics* **1989**, *8*, 940–949; b) J. F. Buzinkai, R. R. Schrock, *Organometallics* **1987**, *6*, 1447–1452.
[7] L. Lubin, G. Lanza, I. L. Fragalà, C. L. Stern, T. J. Marks, *J. Am. Chem. Soc.* **1998**, *120*, 3111–3122.
[8] C. Lorber, J. P. Donahue, C. A. Goddard, E. Norlander, R. H. Holm, *J. Am. Chem. Soc.* **1998**, *120*, 8102–8112.
[9] W.-S. Jung, H.-Y. Moon, Y.-Y. Park, *Polyhedron* **1997**, *16*, 2169–2173.
[10] a) A. Lehtonen, *Inorg. Chem. Commun.* **2005**, *8*, 122–124; b) A. Lehtonen, R. Sillanpää, *Polyhedron* **2005**, *24*, 257–265; c) A. Lehtonen, M. Wasberg, R. Sillanpää, *Polyhedron* **2006**, *25*, 767–775.
[11] Chloride-for-oxide substitution of the dioxidotungsten(VI) complex **1** was carried out using HCl, $SOCl_2$, $Me_3Cl$ and $PCl_5$ as chloride sources in various solvents ($CHCl_3$, THF, PhMe). Isolated yields of *cis*-**4**, *trans*-**4** and **4′** from each experiment are reported in the Supporting Information.
[12] A. Lehtonen, R. Sillanpää, *Inorg. Chem.* **2004**, *43*, 6501–6506.
[13] Dichloro complex **4** was prepared also by a direct reaction of $WOCl_4$ with ligand precursor $H_2O_2NO^{Me}$. This reaction was repeated in toluene and THF solutions at reflux temperature. Consequently, it was appreciated, that the use of THF afforded *cis*-**4** as an only isolable product, although the yield was moderate low (35%), whereas the reaction in toluene lead to the isomeric mixture. Again, these reactions produced also small amounts of yellow **4′**.
[14] Y. Kim, J. G. Verkade, *Organometallics* **2002**, *21*, 2395–2399.
[15] R. C. Larock, *Comprehensive organic transformations: a guide to functional group preparations*; Wiley-VCH, New York, **1989**.
[16] Q. Guo, T. Miyaji, R. Hara, B. Shen, T. Takahashi, *Tetrahedron* **2002**, *58*, 7327–7334.
[17] B. Castellano, A. Zanotti-Gerosa, E. Solari, C. Floriani, *Organometallics* **1996**, *15*, 4894–4896.
[18] For example, see a) P. Legzdins, E. C. Phillips, S. J. Rettig, J. Trotter, J. E. Veltheer, V. C. Yee, *Organometallics* **1992**, *11*, 3104–3110; b) J. C. Bryan, A. K. Burrell, M. M. Miller, W. H. Smith, C. J. Burns, A. P. Sattelberger, *Polyhedron* **1993**, *12*, 1769–1777; c) R. I. Michelman, R. A. Andersen, R. G. Bergman, *J. Am. Chem. Soc.* **1991**, *113*, 5100–5102; d) S. R. Dubberley, A. Friedrich, D. A. Willman, P. Mountford, U. Radius, *Chem. Eur. J.* **2003**, *9*, 3634–3654; e) D. C. Bradley, M. B. Hursthouse, K. M. A. Malik, R. L. Short, *J. Chem. Soc., Dalton Trans.* **1983**, 2651–2656.
[19] a) W. A. Nugent, B. L. Haymore, *Coord. Chem. Rev.* **1980**, *31*, 123–175; b) R. A. Eikey, M. M. Abu-Omar, *Coord. Chem. Rev.* **2003**, *243*, 83–124.
[20] a) M. Jolly, J. P. Mitchell, V. V. Gibson, *J. Chem. Soc., Dalton Trans.* **1992**, 1329–1330; b) H.-W. Lam, G. Wilkinson, B. Hussain-Bates, M. B. Hursthouse, *J. Chem. Soc., Dalton Trans.* **1993**, 781–788.
[21] A. Lehtonen, R. Sillanpää, *Polyhedron* **2002**, *21*, 349–352.
[22] A. Lehtonen, R. Sillanpää, *Organometallics* **2005**, *24*, 2795–2800.
[23] L. J. Farrugia, *J. Appl. Crystallogr.* **1999**, *32*, 837–838.

Received: March 20, 2006
Published Online: May 18, 2006

 © 2006 Wiley-VCH Verlag GmbH & Co. KGaA, Weinheim 

DOI: 10.1002/ejic.200600252

# Tricarbonylchlororhenium(I) Carboxaldimine Derivatives: Synthesis, Structure, and NMR Characterization of *Z* and *E* Isomers

**Claudio Garino,[a] Simona Ghiani,[a] Roberto Gobetto,[a] Carlo Nervi,*[a] Luca Salassa,[a] Gianluca Croce,[b] Marco Milanesio,[b] Edward Rosenberg,*[c] and J. B. Alexander Ross[c]**

**Keywords:** *E*/*Z* isomerization / Density functional calculations / N ligands / Rhenium

The ligand *N*-(2-pyridylmethyl)anthracene-9-carboxaldimine (**1**) has been synthesized and characterized by NMR spectroscopic techniques. The experimental procedure leads selectively to the *E* isomer, which has been studied by a combined theoretical (Density Functional Theory) and 2D NOESY NMR spectroscopic approach. The trifluoroacetic acid promotes the *E* to Z isomerization of **1**. The process has been investigated by NMR spectroscopy and computationally for the neutral ligand **1**. DFT methods calculate that the *E* isomer is 2.2 kcal/mol more stable than the *Z* isomer, whereas the reverse situation is observed for the protonated species, where the *Z* isomer is 4.5 kcal/mol more stable than the *E* isomer. Transition state calculations for the interconversion of the neutral and protonated *E* species into their corresponding *Z* isomers show that the energy barriers are 27.6 and 20.3 kcal/mol for the neutral and protonated species, respectively. The reaction with pentacarbonylchlororhenium leads, in the absence and in the presence of trifluoroacetic acid, to the synthesis of the corresponding tricarbonylchlororhenium isomer complexes **Re-*E*-1** and **Re-*Z*-1**, respectively. Compounds **Re-*E*-1** and **Re-*Z*-1** were characterized by 1D and 2D NMR spectroscopy in solution, and their crystal structures were determined. Their photophysical and electrochemical properties are also reported.
(© Wiley-VCH Verlag GmbH & Co. KGaA, 69451 Weinheim, Germany, 2006)

## Introduction

The electrochemical, photophysical, and photochemical properties of α,α′-diimino ligands have made their coordination chemistry with transition metals, in particular with ruthenium, one of the most relevant in recent decades.[1–4] $Re(CO)_3X$ (where X = halogen) derivatives bearing α,α′-diimine ligands have been studied for their effectiveness in the electrocatalytic reduction of $CO_2$[5,6] and for their photo-induced electron and energy transfer properties.[7,8] The nitrogen atoms contained in these ligands are most commonly part of heterocyclic rings like pyridine, pyrimidine, and pyrazine. In comparison, less attention has been devoted to the investigation of similar Schiff base ligands, such as carboxaldimines, in which at least one nitrogen atom is not part of an aromatic ring. Rhenium derivatives with 2,2′-azobispyridine,[9–11] pyridinylmethylene amino derivatives,[8,12] and the $Re(CO)_3$ mediated Schiff base formation from the in situ reaction between pyridinecarbaldehyde and $NH_2$-containing biomolecules[13] have been studied. This class of compounds is of great interest because of their close relationship with their better-known counterparts, mentioned above. Furthermore, the imine functional group has become important in the synthesis of therapeutic agents, for example the third generation of the class of antibiotics known as cephalosporins,[14] and in the modeling of metal biosites in proteins and enzymes.[15] They have also attracted interest in asymmetric homogeneous and heterogeneous catalysis,[16] and in the synthesis of chiral heterocycles.[17] Their photophysical properties have also been studied theoretically by means of DFT calculations.[18,19] Because of the lower energy of the π* states, in metal complexes containing Schiff base ligands, their adsorption and emission MLCT bands show a red shift when compared with the MLCT transitions of the corresponding bipyridyl derivatives. This red shift can be explained in terms of a distortion of the excited states (π-π* and n-π*) that are localized on the C=N double bond and that contribute significantly to the composition of the LUMO,[20–22] especially in the case of carboxaldimines.[12] In general, imine–metal complexes are relatively unstable towards hydrolysis, particularly in the case of ruthenium and osmium.[23] Bulky ligands could be employed in the synthesis of more stable metal complexes with the aim of limiting or blocking such hydrolysis. Also, the acid-catalyzed *E*/*Z* isomerization is well known and several attempts towards understanding its mechanism have been made.[14] Yet, in some cases the de-

[a] Dipartimento di Chimica IFM, Università di Torino, via P. Giuria 7, 10125, Torino, Italy
Fax: +39-011-6707855
E-mail: carlo.nervi@unito.it
[b] Dipartimento di Scienze e Tecnologie Avanzate, Università del Piemonte Orientale "A. Avogadro", via Bellini 25/G, 15100 Alessandria, Italy
[c] Department of Chemistry, University of Montana, Missoula, MT 59812, USA
Supporting information for this article is available on the WWW under http://www.eurjic.org or from the author.

 © 2006 Wiley-VCH Verlag GmbH & Co. KGaA, Weinheim 

tails of the isomerization mechanism itself remain unclear. In this contribution we report the coordination of tricarbonylchlororhenium to the new organic ligand *N*-(2-pyridylmethyl)anthracene-9-carboxaldimine (**1**) in its *Z* and *E* isomeric forms, which leads to the synthesis of rather stable complexes.

## Results and Discussion

### *Z* and *E* Isomers of the Ligand 1

The ligand *N*-(2-pyridylmethyl)anthracene-9-carboxaldimine (**1**), was synthesized in refluxing ethanol by the condensation of 2-(aminomethyl)pyridine with anthracene-9-carboxaldehyde (Scheme 1).

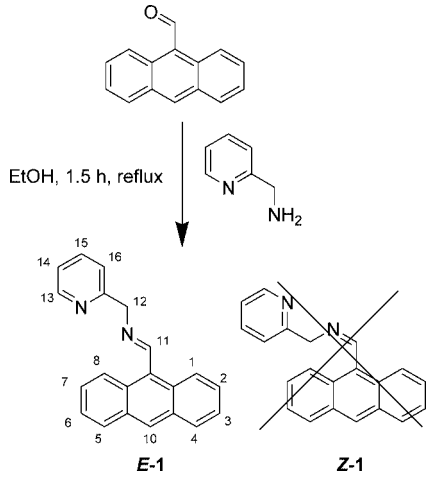


Scheme 1.

The imine **1** can exist in the *E* or *Z* isomeric forms. The presence/absence of bulky groups is generally accepted as the main reason for the preferential formation of one isomer over the other. However, to the best of our knowledge, a complete understanding of the process is not available to date. It is interesting to note that the procedure shown in Scheme 1 yields the isomer ***E*-1**, exclusively (see below). In the DFT-optimized structures of *E* and *Z* isomers, obtained using Jaguar[24] at the B3LYP/6-311++G** level, the two planes defined by the C=N imine and the anthracene moieties are perpendicular to each other. This situation is commonly found whenever an imine carries bulky groups.[25,26] From the DFT calculations it turns out that these geometries have a plane of symmetry, and that the *Z* isomer is only 0.8 kcal/mol more stable than the *E* form. The difference in energy is very small and much lower than the expected accuracy of the DFT method (about 2 kcal/mol).[27] The DFT calculations were repeated by using Gaussian 03[28] for the conformations resulting from 10° rotations around the imine bond. The highest energy conformation was noted at 90°, and the calculated value of 53 kcal/mol for the C=N rotational barrier appears to be fairly high. A similar value (56 kcal/mol) has been obtained for the rotational pathway of the *E*/*Z* isomerization in methyleneimine.[29] Attempts to gain thermal corrections based on harmonic frequencies from these symmetric structures of ***E*-1** and ***Z*-1** failed because of the oscillations of the computed energies. The difficulty in getting stable frequency calculations, and the fact that we get more than one imaginary frequency, suggested that these symmetric forms are only at a local rather than a global energy minimum (saddle point). In order to overcome these local minima of energies, we started from slightly distorted structures and excluded the use of symmetry during the optimization process. The geometries of *E* and *Z* isomers corresponding to the global minima, found by DFT optimizations with Jaguar at the same level, namely B3LYP/6-311++G**, are shown in Figure 1. The frequency calculations performed on these optimized asymmetric structures reveal that the *E* form is more stable than the *Z* form by 2.2 kcal/mol. Thus, better thermodynamic agreement with the experimental observations is obtained, although the difference in energy is still comparable with the accuracy of the DFT method. The calculated structures of *E* and *Z* have very different intramolecular H–H distances (see Table 1), which are doubled in the case of the asymmetric ones because the two geminal H(12) and the two H(1) and H(8) hydrogen atoms are not equivalent. However, whatever the real dynamic structures are, both the symmetrical (local minimum) and nonsymmetrical (global minimum) structures of *Z* have H(11)–H(12) distances that are larger than those of the *E* isomers. This peculiarity is revealed experimentally by the phase-sensitive NOESY spectrum, in which an evident cross-peak system from the dipolar interaction between the lone H(11) and the two H(12) hydrogen atoms is clear evidence of the presence of the ***E*-1** isomer. Proton NMR resonances have been assigned by conventional 1D, 2D COSY, and NOESY spectra (see Supporting Information), and are summarized in Table 2. Moreover, variable temperature experiments performed on ***E*-1** in the range 220–300 K do not produce any changes in the NMR spectra, revealing that *Z* and *E* isomers are not easily interconverted. Having obtained both the optimized structures, we have performed a search for the transition state (TS) associated with the isomerization of neutral ***E*-1** to ***Z*-1**. The optimized TS structure is provided in Figure 2 (a). The calculated structure of the TS shows that the bond angle C=N–C is linear, clearly indicating that the isomerization of the neutral species proceeds via an in-plane lateral shift process. The calculated free energy of the TS relative to the reactant, i.e. the energetic barrier for isomerization of neutral ***E*-1** to ***Z*-1** is moderately high (27.6 kcal/mol), but much lower than the energetic barrier associated with the pure C=N rotation. Similar values were calculated for the in-plane lateral shift process of methyleneimine (32.5 kcal/mol) and dicyandiamide (29 kcal/mol).[29,30]

However, when a slight molar excess of $CF_3COOH$ is added to a $CD_2Cl_2$ solution of ***E*-1**, the resonances of H(11) and H(12) shift from 9.63 and 5.23 to 10.34 and 5.94 ppm, and then rapidly convert into two new resonances at 11.40 and 4.80 ppm, respectively. The conversion does not occur significantly when only a catalytic amount of acid is used, at least not over short periods. This new species does not

 © 2006 Wiley-VCH Verlag GmbH & Co. KGaA, Weinheim 

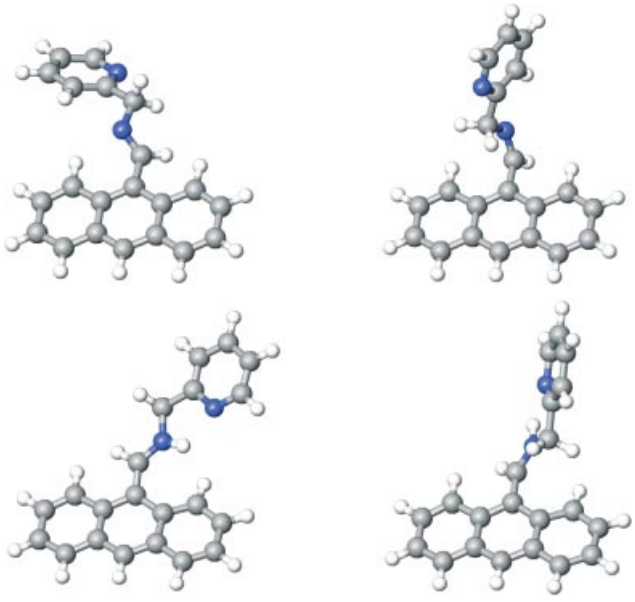

Figure 1. DFT optimized geometries of the ligand **1**. Neutral (up) and protonated (down) forms, and isomers *E* (left) and *Z* (right), at the B3LYP/6-311G++** level.

Table 1. Selected H–H distances [Å] of the optimized DFT geometries for the two isomers of **1** (local minimums, $C_s$ symmetry, and global minimums, no symmetry).

| Distances | *Z* | *E* | *Z* asymmetric | *E* asymmetric |
|---|---|---|---|---|
| H(11)–H(12) | 3.686 | 2.558 | 3.645 | 3.136 |
| | | | 3.848 | 2.166 |
| H(11)–H(1),H(8) | 2.855 | 2.893 | 2.557, 3.133 | 2.065, 3.579 |
| H(12)–H(1),H(8) | 2.958 | 3.343 | 3.727, 3.334 | 4.232, 4.172 |
| | | | 4.879, 2.537 | 3.767, 4.047 |

Table 2. Experimental and calculated $^1$H NMR resonances for ***E*-1** and ***Z*-1**.

| H | Experimental | | Symmetric, calculated by Gaussian 03<br>Asymmetric, calculated by Jaguar 6.5 (mean) | |
|---|---|---|---|---|
| | ***E*-1** | **[*Z*-1H]$^+$** | ***E*-1** | ***Z*-1** |
| 1 | 8.61 | 9.02 | 8.22 | 8.44 |
| | | | 9.82 (9.31) | 8.25 (8.33) |
| 8 | 8.61 | 9.02 | 8.22 | 8.44 |
| | | | 8.80 (9.31) | 8.40 (8.33) |
| 2 | 7.52 | 7.75 | 7.61 | 7.84 |
| | | | 7.81 (7.86) | 7.89 (7.82) |
| 7 | 7.52 | 7.75 | 7.61 | 7.84 |
| | | | 7.91 (7.86) | 7.76 (7.82) |
| 3 | 7.52 | 7.60 | 7.65 | 7.82 |
| | | | 7.75 (7.78) | 7.83 (7.79) |
| 6 | 7.52 | 7.60 | 7.65 | 7.82 |
| | | | 7.81 (7.78) | 7.76 (7.79) |
| 4 | 8.06 | 8.12 | 8.31 | 8.31 |
| | | | 8.30 (8.33) | 8.42 (8.40) |
| 5 | 8.06 | 8.12 | 8.31 | 8.31 |
| | | | 8.37 (8.33) | 8.38 (8.40) |
| 10 | 8.53 | 8.82 | 8.90 | 8.70 |
| | | | 8.83 | 8.86 |
| 11 | 9.63 | 11.40 | 10.18 | 9.74 |
| | | | 10.27 | 9.94 |
| 12 | 5.23 | 4.80 | 5.51 | 4.53 |
| | | | 6.01, 5.12 (5.56) | 4.98, 4.44 (4.71) |
| 13 | 8.59 | 8.80 | 8.99 | 9.04 |
| | | | 8.94 | 8.66 |
| 14 | 7.23 | 8.58 or 8.06 | 7.27 | 7.21 |
| | | | 7.33 | 7.08 |
| 15 | 7.72 | 8.06 or 8.58 | 7.73 | 7.54 |
| | | | 8.00 | 7.86 |
| 16 | 7.52 | 8.19 | 7.35 | 6.55 |
| | | | 8.59 | 8.39 |

show the above-mentioned NOESY cross peak signal (see Supporting Information). The overall process is therefore explained as (a) instantaneous protonation of ***E*-1**, (***E*-1H$^+$**) and (b) relatively fast conversion into the protonated ***Z*-1** form (***Z*-1H$^+$**). Thus ***E*-1** is easily converted into ***Z*-1** by adding trifluoroacetic acid. The trend in the proton resonance sequences on going from ***E*-1** to ***E*-1H$^+$**, and finally to the ***Z*-1H$^+$** form is more difficult to interpret. As mentioned, for H(11) and H(12) the experimental sequences are 9.63 to 10.34 to 11.40 ppm and 5.23 to 5.94 to 4.80 ppm, respectively. We optimized the geometries of ***E*-1**, ***E*-1H$^+$** and ***Z*-1H$^+$**, and the corresponding calculated $^1$H NMR chemical shift sequences of H(11) and H(12) are 10.18 to 10.45 to 10.51 ppm and 5.51 to 5.59 to 4.81 ppm, respectively. Although quantum mechanical calculations of $^1$H NMR chemical shifts are subject to significant errors,[31–33] especially whenever hydrogen bonds are involved, the same experimental trend is reproduced. More importantly, a frequency calculation gives a Gibbs free energy value for ***Z*-1H$^+$** that is 4.5 kcal/mol lower than that of the corresponding ***E*-1H$^+$**. This small but significant inversion of energy gives further support to the outlined interpretation, and it is in agreement with the experimental observation, which

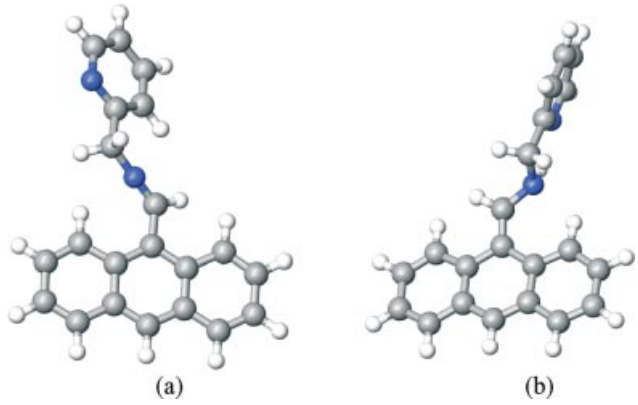


Figure 2. Transition State (TS) optimized structures for the isomerization processes ***E*-1** to ***Z*-1** (a) and ***E*-1H$^+$** to ***Z*-1H$^+$** (b).

shows that the ratio between the integrated $^1$H NMR resonances H(12) of ***E*-1H$^+$** and ***Z*-1H$^+$**, namely the signals centered at $\delta$ = 5.94 and 4.80 ppm, respectively, are 1:16 (see Supporting Information). This corresponds to a Gibbs free energy difference of 1.6 kcal/mol between the two isomers at 298 K, in reasonable agreement with the calculated value. Computational searches for the TS for the isomerization process ***E*-1H$^+$** to ***Z*-1H$^+$** leads to the structure shown in

 © 2006 Wiley-VCH Verlag GmbH & Co. KGaA, Weinheim 

Figure 2 (b). The calculated free energy of the TS relative to the reactant ***E*-1H$^+$** is evaluated to be 20.3 kcal/mol. As one could expect, in both the neutral and protonated TSs, the dihedral angle that defines the rotation around the C=N double bond, $D_{C=N}$, is roughly midway between the values observed for the *Z* and *E* isomers. However, it is interesting to note that the protonated TS has a $D_{C=N}$ value closer to that of the *Z* isomer. The $D_{C=N}$ values for ***E*-1H$^+$**, ***Z*-1H$^+$**, and for the corresponding TS are 178.3, 12.0, and 111.5°, respectively, whereas the $D_{C=N}$ values for ***E*-1**, ***Z*-1**, and for the corresponding neutral TS are 179.3, 0.8, and 89.4°, respectively. The neutral and protonated TSs have a HC=N–$CH_2$ bond angle of 177.7 and 114.9°, and only one imaginary frequency of 274i and 325i cm$^{-1}$, respectively. Therefore, these first-order saddle points are real transition states. The vibrational mode of the neutral TS is associated with the reaction coordinate that involves major motion of the nitrogen atom (in-plane lateral shift), whereas the vibrational mode of the protonated TS is associated with the reaction coordinate that involves major motion of the hydrogen atoms HC=N and NH. Therefore, the protonation has two effects: the first is evident and it is to alter the geometry of the transition state and to significantly decrease its energy for the isomerization process, whereas the second effect is less certain, but most likely makes the *Z* isomer thermodynamically more stable than the *E* isomer. This could also explain why the isomerization is not observed with only a small, catalytic amount of acid. Finally, it should be pointed out that whereas the DFT calculations apparently reproduce the ground-state structures very well, the energies of the transition states are presumably overemphasized.

**Rhenium Complexes of 1**

The reaction of $Re(CO)_5Cl$ with ***E*-1** in refluxing toluene, under an Ar atmosphere, produces the corresponding complex (***E*-1**)$Re(CO)_3Cl$ (**Re-*E*-1**). When carrying out the same reaction in the presence of an approximately half molar quantity of $CF_3COOH$, we obtained a mixture of **Re-*E*-1** and (***Z*-1**)$Re(CO)_3Cl$, hereafter called **Re-*Z*-1**. The latter compound was obtained only in small amounts. Remarkably, **Re-*E*-1** and **Re-*Z*-1** have different solubilities in benzene, and can be separated by a simple extraction. The two rhenium-imino derivatives **Re-*E*-1** and **Re-*Z*-1** have been fully characterized with several spectroscopic techniques. In particular, the $^1$H NMR spectrum of **Re-*E*-1** in $CD_2Cl_2$ shows three resonances at $\delta$ = 9.63, 6.23, and 5.60 ppm, assigned to H(11) and to the two diastereotopic $CH_2$ protons H(12a) and H(12b), respectively, whereas in the case of **Re-*Z*-1** the corresponding signals are observed at $\delta$ = 9.99, 5.12, and 4.76 ppm.

More interestingly, the NOESY experiment on **Re-*E*-1** reveals the presence of a dipolar interaction between H(11) and the two H(12) protons, which is absent in the case of **Re-*Z*-1** (see Supporting Information). Determination of the X-ray structures of the two isomers **Re-*E*-1** and **Re-*Z*-1** confirms the retention of the ligand conformation on coordination to the metal center (Figure 3). The isomerization does not take place after the metal complex formation, since the NMR spectra of **Re-*E*-1** and **Re-*Z*-1** in $CD_2Cl_2$ solutions before and after the addition of a molar amount of $CF_3COOH$ are identical, most likely because the coordination of the metal does not allow the protonation of the ligand, which then freezes the isomerization process.

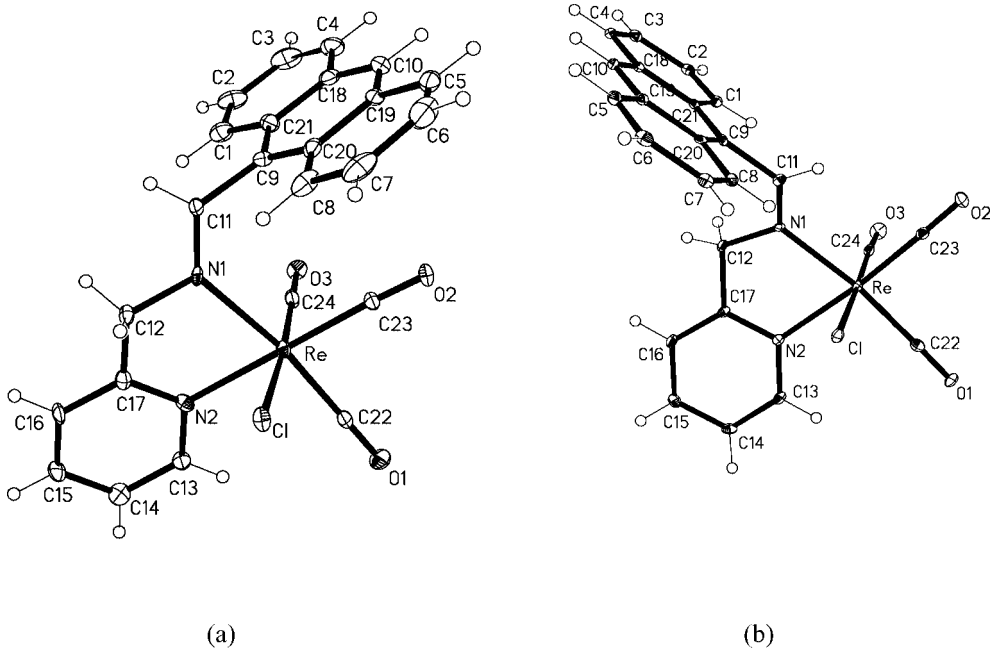


Figure 3. Molecular structures of **Re-*E*-1** (a) and **Re-*Z*-1** (b), showing the adopted labeling scheme, with displacement ellipsoids drawn at the 20% probability. A solvated benzene molecule in **Re-*Z*-1** is not shown for the sake of clarity.

 © 2006 Wiley-VCH Verlag GmbH & Co. KGaA, Weinheim 

### Crystal Structure Analysis

The structures of **Re-*E*-1** and **Re-*Z*-1** isomers are illustrated in Figure 3 and the crystallographic data are given in Table 5. **Re-*E*-1** is arranged in the $P2_1$ chiral space group, while **Re-*Z*-1** is arranged in the centrosymmetric $P\bar{1}$ space group. The *E* isomer was therefore obtained chirally pure, while the *Z* isomer is a racemate of the two possible enantiomers. Compound **Re-*Z*-1** crystallizes with one benzene molecule of solvation.

The *E*/*Z* isomerization of the N(1)–C(11) double bond causes significant rearrangements of the overall shape and of the crystal packing of the two complexes. The selected geometric parameters for the two isomers, and the differences and significances with respect to esd's, are reported in Table 3. The larger differences between the two isomers (Δ values larger than 8) are due to the location and the orientation of the anthracene moiety with respect to the metal core of the complex. Also the pyridine group orientation, defined by the Cl–Re–N(2)–C(17) torsion angle, with Δ = 16.5, is rather different in the two isomers. Conversely, the planarity of the anthracene and of the pyridine groups are similar in the two isomers: 0.035(6) and 0.003(5) Å in **Re-*E*-1** and 0,020(3) and 0.003(2) Å in the **Re-*Z*-1** isomer, respectively. As a result of the above mentioned differences, the anthracene group in **Re-*E*-1** is bent towards the C(23)–O(2) and C(23)–O(4) carbonyl groups, the resulting contact distances being rather short (reported with respect to anthracene center of mass, $A_{CM}$ in Table 3), while in **Re-*Z*-1** the anthracene group is located in the external part of the complex, far away from the metal core and the carbonyl groups. The C(11)–H(11) bond shows an opposite behavior, pointing towards carbonyl groups in **Re-*Z*-1** and towards the anthracene moiety of the adjacent molecule in **Re-*E*-1**. This opposite behavior has a dramatic effect on the crystal packing features of the two isomers. In fact, in **Re-*Z*-1** the crystal packing (see Figure 4, b) is clearly driven by the π-π stacking between parallel anthracene moieties, as indicated by the similar distances observed between the anthracene centers of mass (3.694 Å) and between planes containing adjacent anthracene moieties (3.743 Å). On the contrary, in **Re-*E*-1** the anthracene groups once again lie on parallel planes, with a distances between planes of 3.422 Å, much smaller than the distances between the centers of mass (7.823 Å), thus avoiding the π-π stacking.

In **Re-*E*-1** the anthracene moiety is too close to the metal center to allow the π-π stacking observed in **Re-*Z*-1** and the molecules are helicoidally packed, obeying to the $2_1$ screw axis. Finally, CH···OC and CH···Cl interactions are also present.

The *E*/*Z* isomerization also affects the coordination geometry of the Re atom, as indicated by the Δ values highlighted in bold character in Table 3. The differences mostly occur with the Cl ligand (Δ values larger than 2 esd.). Smaller differences, close to the detection limit ($1 < \Delta < 2$ in Table 3) involve the C(24)–O(3) distance and the N(2) atom of the pyridine ligand.

Table 3. Selected geometric parameters for **Re-*E*-1** and **Re-*Z*-1** (distances in Å and angles in °) and relevance of difference with respect to esd's (Δ), calculated as Δ = {esd.[value(**Re-*E*-1**), value(**Re-*Z*-1**)]}/{esd.[value(**Re-*E*-1**)] + esd.[value(**Re-*Z*-1**)]}. Values differing by a significant value (Δ > 1) are highlighted in **bold**.

| | **Re-*E*-1** | **Re-*Z*-1** | Δ |
|---|---|---|---|
| Distances | | | |
| Re(1)–Cl(1) | 2.474(2) | 2.483(1) | **2.1** |
| Re(1)–N(1) | 2.203(8) | 2.173(3) | **1.9** |
| Re(1)–N(2) | 2.178(8) | 2.184(3) | 0.4 |
| Re(1)–C(22) | 1.914(10) | 1.925(4) | 0.6 |
| Re(1)–C(23) | 1.945(9) | 1.926(4) | 1.0 |
| Re(1)–C(24) | 1.898(11) | 1.912(5) | 0.6 |
| O(1)–C(22) | 1.149(12) | 1.155(5) | 0.2 |
| O(2)–C(23) | 1.136(11) | 1.152(5) | 0.7 |
| O(3)–C(24) | 1.173(13) | 1.146(5) | **1.1** |
| N(1)–C(15) | 1.262(12) | 1.287(5) | 1.0 |
| N(1)–C(16) | 1.472(11) | 1.472(5) | 0.0 |
| N(2)–C(17) | 1.341(12) | 1.351(5) | 0.4 |
| N(2)–C(21) | 1.372(12) | 1.352(5) | 0.8 |
| C(1)–C(15) | 1.494(14) | 1.478(5) | 0.6 |
| C(16)–C(17) | 1.493(13) | 1.505(5) | 0.5 |
| H(15)–O(2) | 5.24(2) | 3.15(1) | **49.3** |
| $A_{CM}^{(*)}$–Re | 4.39(1) | 5.932(3) | **83.9** |
| $A_{CM}^{(*)}$–O(2) | 3.59(1) | 6.522(5) | **138.2** |
| $A_{CM}^{(*)}$–O(3) | 4.36(1) | 7.164(5) | **132.2** |
| $A_{CM}^{(*)}$–C(23) | 3.58(1) | 6.149(5) | **121.1** |
| $A_{CM}^{(*)}$–C(24) | 4.11(1) | 6.531(5) | **114.1** |
| Angles | | | |
| C(22)–Re–Cl | 95.2(3) | 94.9(1) | 0.5 |
| C(23)–Re–Cl | 93.6(3) | 91.7(1) | **3.4** |
| C(24)–Re–Cl | 176.1(3) | 178.2(1) | **3.7** |
| N(1)–Re–Cl | 83.7(2) | 83.4(1) | 0.7 |
| N(2)–Re–Cl | 80.9(2) | 82.8(1) | **4.4** |
| C(24)–Re–N(2) | 96.4(4) | 96.6(1) | 0.3 |
| C(22)–Re–N(2) | 96.0(3) | 96.9(1) | **1.6** |
| C(23)–Re–N(2) | 174.1(3) | 171.6(1) | 0.7 |
| C(24)–Re–N(1) | 92.9(4) | 94.8(1) | **2.7** |
| C(22)–Re–N(1) | 171.7(3) | 172.9(1) | 0.4 |
| C(23)–Re–N(1) | 101.6(4) | 97.2(1) | **2.1** |
| N(2)–Re(1)–N(1) | 75.6(3) | 76.0(1) | 0.7 |
| C(24)–Re–C(22) | 87.9(4) | 86.9(2) | **1.2** |
| C(24)–Re–C(23) | 88.9(4) | 88.7(2) | 0.2 |
| C(22)–Re–C(23) | 86.7(4) | 89.8(2) | **3.7** |
| C(15)–N(1)–Re | 131.4(7) | 125.9(3) | **1.3** |
| C(16)–N(1)–Re | 111.9(6) | 114.7(2) | 0.7 |
| C(17)–N(2)–Re | 116.5(6) | 116.9(3) | 0.1 |
| C(21)–N(2)–Re | 125.0(7) | 125.1(3) | 0.0 |
| O(1)–C(22)–Re | 177.9(10) | 176.1(4) | 0.5 |
| O(2)–C(23)–Re | 177.1(8) | 178.1(4) | 0.2 |
| O(3)–C(24)–Re | 179.9(11) | 176.7(4) | 0.9 |
| N(1)–C(15)–C(1) | 124.2(9) | 126.5(4) | 0.5 |
| N(2)–C(17)–C(16) | 117.7(8) | 117.4(3) | 0.1 |
| N(1)–C(16)–C(17) | 111.5(8) | 110.9(3) | 0.1 |
| C(11)–H(11)–O(2) | 16(1) | 137(1) | **24.4** |
| C(23)–O(2)–$A_{CM}^{(*)}$ | 80.1(8) | 66.2(4) | **8.2** |
| C(24)–O(3)–$A_{CM}^{(*)}$ | 70.0(8) | 52.6(4) | **10.3** |
| Torsion angles | | | |
| Cl–Re–N(2)–C(17) | 71.2(6) | 92.2(3) | **16.5** |
| Cl–Re–N(1)–C(11) | 123(1) | 74.3(5) | **23.2** |
| Re–N(1)–C(11)–C(9) | –6(2) | –175(1) | **39.8** |
| C(20)–C(9)–C(11)–N(1) | –84(1) | 115.7(5) | **94.1** |

$A_{CM}^{(*)}$ = center of mass of anthracene moiety

 © 2006 Wiley-VCH Verlag GmbH & Co. KGaA, Weinheim 

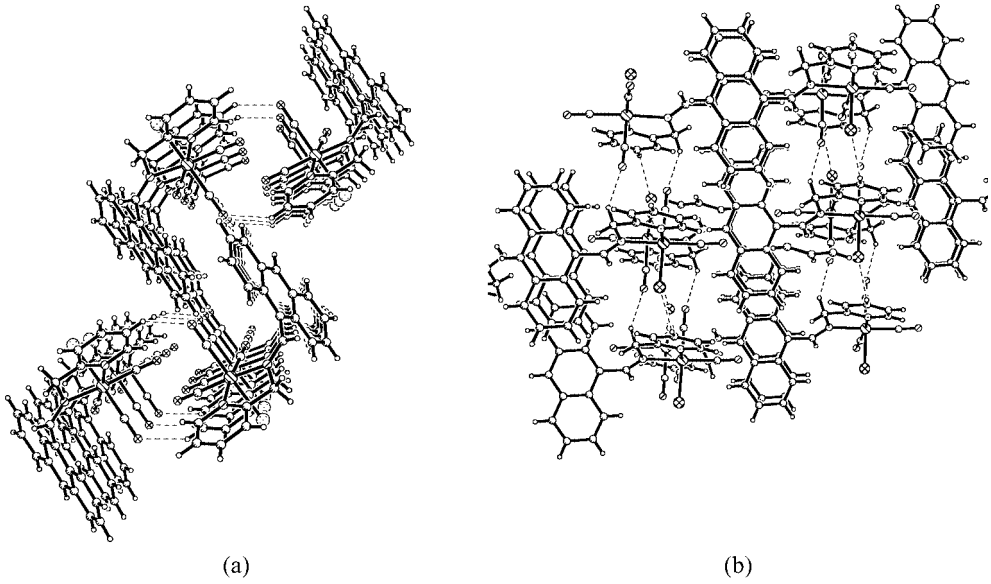


Figure 4. The crystal packing of **Re-*E*-1** (a) and **Re-*Z*-1** (b).

### Electronic Absorption and Emission Spectra

The electronic absorption spectrum of ***E*-1** in $CH_3CN$ solution shows an intense absorption peak at 251 nm ($\varepsilon$ = 64800 $M^{-1}$) and three bands at 351, 369, and 387 nm, which probably correspond to the $\pi\rightarrow\pi^*$ and $n\rightarrow\pi^*$ transitions. Excitation at 370 nm in $CH_3CN$ produces an intense emission peak at 440 nm. These absorption and emission peaks are very similar to those of pure anthracene.[34] Rhenium complexes **Re-*E*-1** and **Re-*Z*-1** have identical absorption (bands at 354, 371, and 389 nm) and emission spectra, which in turn are very similar to that of the free ligand ***E*-1**. However, **Re-*E*-1** and **Re-*Z*-1** show a weaker emission centered at 441 nm (Figure 5). We did not observe a metal-centered MLCT emission band. $Re(bpy)(CO)_3Cl$ and analogous imino derivatives[8,12,35] usually have MLCT absorptions in the range 340–430 nm. Time-Dependent DFT calculations (TDDFT) help to understand these data. The geometries of ***E*-1**, **Re-*E*-1**, and **Re-*Z*-1** were optimized in the singlet ground state in the gas phase. The HOMO and LUMO of ***E*-1** are mostly localized on the anthracene unit, only slightly involving the C=N double bond. The spectroscopic properties were calculated employing the combined TDDFT/CPCM computational approach, which is currently considered to be the most appropriate method for the treatment of the solvent effects on the excited-state energies of transition-metal complexes.[36,37] A number of singlet excited states of ***E*-1**, **Re-*E*-1**, and **Re-*Z*-1** in acetonitrile were calculated and are reported in Table 4. The absorption of ***E*-1** with the highest oscillator strength (393 nm) is mainly from a HOMO→LUMO transition. In the case of **Re-*E*-1** and **Re-*Z*-1**, the absorptions calculated at 420 and 424 nm are still largely HOMO→LUMO transitions, and therefore labeled as ligand-centered transitions, with a modest contribution from the metal ion. This supports the absence of charge transfer states observed in the absorption and emission spectra of the free ligands and metal complexes. Furthermore, there is a very small effect of the rhenium atom on the fluorescence lifetime. In fact, the average lifetime is 11.5 ns for the ligand and 11.3 ns for the complexes.

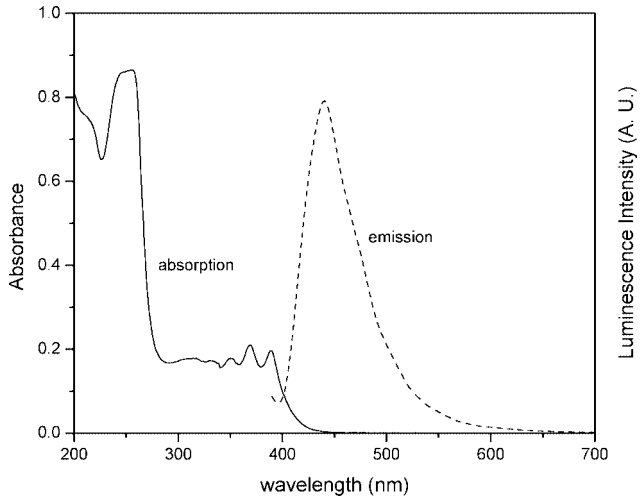


Figure 5. Absorption and emission spectra (excitation at 370 nm) of **Re-*E*-1** in $CH_3CN$.

Table 4. Energies (in nm) and oscillator strengths (*f*) of the first calculated singlet excited states for ***E*-1**, **Re-*E*-1**, and **Re-*Z*-1** in acetonitrile.

| ***E*-1** | | **Re-*E*-1** | | **Re-*Z*-1** | |
|---|---|---|---|---|---|
| *f* | *E* [nm] | *f* | *E* [nm] | *f* | *E* [nm] |
| | | 0.14 | 420 | 0.21 | 424 |
| 0.089 | 393 | 0.03 | 374 | 0.002 | 374 |
| 0.001 | 335 | 0.04 | 368 | 0.02 | 366 |
| 0.003 | 319 | 0.02 | 354 | 0.001 | 357 |
| 0.001 | 298 | 0.03 | 343 | 0.001 | 334 |
| 0.001 | 293 | 0.001 | 336 | 0.001 | 333 |

 © 2006 Wiley-VCH Verlag GmbH & Co. KGaA, Weinheim 

### Electrochemistry

The electrochemical behavior of the rhenium complexes **Re-*E*-1** and **Re-*Z*-1** has been investigated by cyclic voltammetry (CV) and square wave voltammetry (SWV) in $CH_2Cl_2$ solutions using glassy carbon as a working electrode, under an Ar atmosphere. The CV response of **Re-*E*-1**, identical to that of **Re-*Z*-1**, exhibits a 1e chemically irreversible reduction at $E_p$ = –1.89 V vs. $Fc/Fc^+$, and a multi-electron chemically irreversible oxidation at $E_p$ = +1.11 V vs. $Fc/Fc^+$. Our attempts to slow down the chemical complications by lowering the temperature were unsuccessful. CV performed as low as –80 °C and at a scan rate between 0.05 and 5 V/s did not freeze the homogeneous chemical reactions and the redox processes remained chemically irreversible.

## Experimental Section

**(*E*)-*N*-(Methyl-2-pyridyl)antracen-9-carboxaldimine (*E*-1):** Anthracene-9-carboxaldehyde (1.00 g, 4.85 mmol) was dissolved in absolute ethanol (250 mL) and the solution was degassed for 10 min under argon. 2-(Aminomethyl)pyridine (0.524 g, 4.85 mmol) was added and the solution was refluxed for 1.5 h. After evaporation of the solvent, the yellow solid was washed with hexane (20–25 mL) and recrystallized from ethanol (yield 75%, 1.078 g). $^1$H NMR [400 MHz, $(CD_3)_2CO$, 25 °C]: $\delta$ = 9.75 (s, 1 H), 8.75 [d, $^3J_{H,H}$ = 7.7 Hz, 2 H], 8.65 (s, 1 H), 8.61 (d, $^3J_{H,H}$ = 4.2 Hz, 1 H), 8.11 (d, $^3J_{H,H}$ = 8.4 Hz, 2 H), 7.78 (t, $^3J_{H,H}$ = 7.7 Hz, 1 H), 7.60 (d, $^3J_{H,H}$ = 7.9 Hz, 1 H), 7.53 (m, 4 H), 7.28 (t, $^3J_{H,H}$ = 6.4 Hz, 1 H), 5.25 (s, 2 H) ppm. $^1$H NMR (400 MHz, $CD_2Cl_2$, 25 °C): $\delta$ = 9.63 (t, $^3J_{H,H}$ = 1.3 Hz, 1 H, 11-H), 8.61 (m, 2 H, 1-H and 8-H), 8.59 (m, 1 H, 13-H), 8.53 (s, 1 H, 10-H), 8.06 (dd, $^3J_{H,H}$ = 7.9 and 1.9 Hz, 2 H, 4-H and 5-H), 7.72 (t, $^3J_{H,H}$ = 7.7 and 1.9 Hz, 1 H, 15-H), 7.52 (m, 5 H, 16-H, 2-H, 3-H, 6-H, 7-H), 7.23 (dd, $^3J_{H,H}$ = 5.0 and 1.1 Hz, 1 H, 14-H), 5.23 (d, $^3J_{H,H}$ = 1.3 Hz, 2 H, 12-H) ppm. $^{13}$C NMR [100 MHz, $(CD_3)_2CO$, 25 °C]: $\delta$ = 162.34, 159.69, 149.51, 136.72, 131.60, 130.27, 129.59, 128.99, 128.56, 126.80, 125.54, 125.40, 122.54, 122.24, 68.15 ppm. $^{13}$C NMR (100 MHz, $CD_2Cl_2$, 25 °C): $\delta$ = 162.46, 159.54, 149.70, 136.92, 131.63, 130.37, 129.77, 129.11, 128.52, 126.98, 125.62, 125.27, 122.75, 122.39, 68.68 ppm. Electronic spectrum in $CH_3CN$: absorption, $\lambda_{max}$ = 251, 351, 369, 387 nm, emission, $\lambda_{max}$ = 440 nm.

**(*Z*)-*N*-(2-Pyridylmethyl)antracen-9-carboxaldimine (*Z*-1):** The *Z* isomer was obtained from the irradiation for 3 h at 365 nm, 50 W, of a $CH_2Cl_2$ solution of the *E* isomer containing an equimolar amount of $CF_3COOH$. The conversion occured without any side reaction. $^1$H NMR (400 MHz, $CD_2Cl_2$, 25 °C) of the protonated species: $\delta$ = 11.40 (s, 1 H), 9.02 (dd, $^3J_{H,H}$ = 9.0 and 0.8 Hz, 2 H), 8.82 (s, 1 H), 8.80 (dd, $^3J_{H,H}$ = 5.9 and 1.3 Hz, 1 H), 8.58 (t, $^3J_{H,H}$ = 7.9 Hz, 1 H), 8.19 (d, $^3J_{H,H}$ = 7.9 Hz, 1 H) 8.12 (d, $^3J_{H,H}$ = 8.4 Hz, 2 H), 8.06 (t, $^3J_{H,H}$ = 5.9 Hz, 1 H), 7.75 (dd, $^3J_{H,H}$ = 9.0 and 1.5 Hz, 2 H), 7.60 (dd, $^3J_{H,H}$ = 8.6 and 1.0 Hz, 2 H), 4.80 (s, 2 H) ppm. $^{13}$C NMR (100 MHz, $CD_2Cl_2$, 25 °C): $\delta$ = 195.24, 147.77, 146.13, 143.11, 137.68, 133.15, 131.10, 130.15, 129.85, 129.68, 128.13, 126.02, 123.29, 40.94 ppm.

**Re(*E*-1)(CO)$_3$Cl (Re-*E*-1):** $Re(CO)_5Cl$ (300 mg) was refluxed in toluene (50 mL) for 2 h with a 10% excess of ***E*-1** (270 mg) under argon. The solution was then cooled before the yellow product was filtered and washed with toluene and hexane. Finally, the solid was dried in vacuo (yield 78%, 390 mg). $^1$H NMR [400 MHz, $(CD_3)_2CO$, 25 °C]: $\delta$ = 9.96 (s, 1 H), 8.87 (d, $^3J_{H,H}$ = 5.4 Hz, 1 H), 8.77 (s, 1 H), 8.15 (m, 4 H), 98.04 (d, $^3J_{H,H}$ = 8.5 Hz, 1 H), 7.91 (d, $^3J_{H,H}$ = 7.8 Hz, 1 H), 7.53 (m, 5 H), 6.29 (d, $^3J_{H,H}$ = 18.3 Hz, 1 H), 6.06 (d, $^3J_{H,H}$ = 18.6 Hz, 1 H) ppm. $^1$H NMR (400 MHz, $CD_2Cl_2$, 25 °C): $\delta$ = 9.63 (s, 1 H), 8.82 (d, $^3J_{H,H}$ = 5.3 Hz, 1 H), 8.70 (s, 1 H), 8.13 (m, 2 H), 8.06 (d, $^3J_{H,H}$ = 8.5 Hz, 1 H), 8.00 (t, $^3J_{H,H}$ = 7.9 Hz, 1 H), 7.81 (m, 1 H), 7.65 (m, 2 H), 7.56 (m, 3 H), 7.38 (t, $^3J_{H,H}$ = 6.5 Hz, 1 H), 6.23 (d, $^3J_{H,H}$ = 18.2 Hz, 1 H), 5.60 (d, $^3J_{H,H}$ = 18.2 Hz, 1 H) ppm. $^{13}$C NMR [100 MHz, $(CD_3)_2CO$, 25 °C]: $\delta$ = 198.11, 194.40, 191.62, 175.53, 160.38, 152.34, 139.66, 131.43, 131.21, 129.87, 128.84, 128.75, 128.24, 126.74, 126.60, 125.90, 125.78, 125.34, 124.57, 122.14, 69.12 ppm. IR (powder-ATR): $\tilde{\nu}$ = 2025, 1922, 1897 cm$^{-1}$. $^{13}$C NMR (100 MHz, $CD_2Cl_2$, 25 °C): $\delta$ = 198.11, 194.40, 191.62, 174.71, 163.26, 159.13, 152.95, 139.57, 131.50, 131.29, 130.48, 129.41, 129.16, 128.31, 127.54, 127.29, 126.38, 125.55, 124.88, 124.75, 121.89, 69.78 ppm. Electronic spectrum in $CH_3CN$: absorption, $\lambda_{max}$ = 255, 317, 335, 354, 372, 391 nm, emission, $\lambda_{max}$ = 440 nm.

**Re(*Z*-1)(CO)$_3$Cl (Re-*Z*-1):** The complex was obtained as a side product during a modified synthesis of **Re-*E*-1**. $Re(CO)_5Cl$ (200 mg) was stirred in toluene (50 mL) with a 10% excess of ***E*-1** (180 mg) under argon. $CF_3COOH$ (30 μL) was added, and the solution was refluxed for 4 h. After cooling at room temperature, a yellow precipitate of **Re-*E*-1** and a red solution containing a mixture of **Re-*E*-1** and **Re-*Z*-1** were obtained. The solution was filtered, and the solvent evaporated. The solid was treated with benzene, which only dissolved **Re-*Z*-1**. Finally, the solvent was evaporated and the solid dried in vacuo (yield 15%, 50 mg). $^1$H NMR (400 MHz, $CD_2Cl_2$, 25 °C): $\delta$ = 9.99 (t, $^3J_{H,H}$ = 2.3 Hz, 1 H), 8.89 (d, $^3J_{H,H}$ = 5.3 Hz, 1 H), 8.72 (s, 1 H), 8.22 (d, $^3J_{H,H}$ = 8.4 Hz, 1 H), 8.16 (m, 2 H), 7.83 (d, $^3J_{H,H}$ = 8.4 Hz, 1 H), 7.75 (t, $^3J_{H,H}$ = 7.9 and 1.6 Hz, 1 H), 7.61 (m, 4 H), 7.33 (t, $^3J_{H,H}$ = 6.7 Hz, 1 H), 7.01 (d, $^3J_{H,H}$ = 7.9 Hz, 1 H), 5.12 (dd, $^3J_{H,H}$ = 19.0 and 2.5 Hz, 1 H), 4.76 (dd, $^3J_{H,H}$ = 19.0 and 2.5 Hz, 1 H) ppm. IR (powder-ATR): $\tilde{\nu}$ = 2024, 1921, 1896 cm$^{-1}$. Electronic spectrum in $CH_3CN$: absorption, $\lambda_{max}$ = 255, 303, 335, 354, 372, 391 nm, emission, $\lambda_{max}$ = 440 nm.

**Physical Methods:** The NMR spectra were recorded with a JEOL EX 400 spectrometer ($B_0$ = 9.8 T) with chemical shifts referenced to residual protons in the solvent ($CD_2Cl_2$). COSY and NOESY experiments were acquired using standard procedures. IR spectra were recorded as powder-ATR using a Thermo-Nicolet 670 FT-IR spectrophotometer with a resolution of 1 cm$^{-1}$ and an accumulation of 64 scans. Absorption spectra were measured at room temperature, in $CH_2Cl_2$, using a Hitachi U-3210 double-beam spectrophotometer, and emission spectra were measured with a SLM 4800 spectrofluorimeter. Luminescence lifetimes were performed under magic-angle polarization conditions by time-correlated single-photon counting using excitation with picosecond pulses of 370 nm light at a repetition rate of 500 kHz generated by a Ti:Sapphire laser system (Verdi V10, Mira 900, and pulse picker from Coherent, Inc., Santa Clara, CA. Second harmonic generation was provided by a 5–050 system from Inrad, Northvale, NJ). The sample was maintained at 20 °C in an automated sample chamber (FLASC 1000 from Quantum Northwest, Spokane, WA). The emission was collected using a bandpass of 20 nm. The data were collected into 2048 channels (0.25 ns/channel) to 40,000 counts in the peak channel. Because the excitation pulse is essentially a delta function at this time resolution, the decays were fitted directly without reconvolution as sums of exponentials using Origin 7 (Northampton, MA 01060, USA).

**X-ray Structure Determinations:** Single crystal diffraction data were collected at 100 K, using an Oxford Cryostream low temperature

 © 2006 Wiley-VCH Verlag GmbH & Co. KGaA, Weinheim 

device, on an Oxford Xcalibur CCD area detector diffractometer, using graphite monochromatic Mo-$K_\alpha$ ($\lambda$ = 0.71069 Å) radiation. Data reduction and absorption corrections were performed using CrysAlis RED 1.171.26 (Oxford Diffraction). The structure was solved by direct methods using SIR2004[38] and refined by full-matrix least-squares using SHELX-97.[39] All hydrogen atoms were located in the electron density map and then refined using isotropic displacement parameters.

The Crystallographic Information File (CIF) has been deposited with deposition number CCDC-298650 for the **Re-*E*-1** structure and CCDC-298651 for the **Re-*Z*-1** structure. These data can be obtained free of charge from The Cambridge Crystallographic Data Centre via www.ccdc.cam.ac.uk/data_request/cif. Details of data collections and refinements are given in Table 5.

Table 5. Crystallographic data for **Re-*E*-1** and **Re-*Z*-1** isomers.

| | **Re-*E*-1** | **Re-*Z*-1** |
|---|---|---|
| Empirical formula | $C_{24}H_{16}ClN_2O_3Re$ | $C_{24}H_{16}ClN_2O_3Re$ |
| Formula mass [g/mol] | 602.04 | 602.04 |
| Temperature [K] | 123 (2) | 100 (2) |
| Wavelength [Å] | 0.71073 | 0.71073 |
| Crystal system | $P2_1$ | $P\bar{1}$ |
| Space group | monoclinic | triclinic |
| Unit cell dimensions | $a$ = 11.222(1) | $a$ = 8.834(1) |
| (edges in Å and angles in °) | $b$ = 7.712(1) | $b$ = 11.494(1) |
| | $c$ = 12.761(1) | $c$ = 12.327(1) |
| | $\beta$ = 96.564(5)° | $\alpha$ = 80.55(1) |
| | | $\beta$ = 80.32(1) |
| | | $\gamma$ = 74.42(1) |
| Volume [Å$^3$] | 1097.1(1) | 1179.0(2) |
| $Z$ | 2 | 2 |
| Density (calculated) [mg/m$^3$] | 1.822 | 1.693 |
| Absorption coefficient [mm$^{-1}$] | 5.688 | 5.292 |
| $F$(000) | 580 | 578 |
| Crystal size [mm] | 0.35×0.15×0.09 | 0.11×0.25×0.20 |
| Theta range for data collection [°] | 1.61 to 27.50 | 4.40 to 20.81 |
| Index ranges | $-14 \le h \le 14$ | $-8 \le h \le 8$ |
| | $-10 \le k \le 10$ | $-11 \le k \le 11$ |
| | $-16 \le l \le 16$ | $-12 \le l \le 12$ |
| Reflections collected | 15981 | 5316 |
| Independent reflections | 5023 | 2452 |
| | [$R$(int) = 0.0851] | [$R$(int) = 0.0181] |
| Completeness to $\theta$ = 20.81° | 99.9% | 99.0% |
| Refinement method | Full-matrix least-squares on $F^2$ | Full-matrix least-squares on $F^2$ |
| Data/restraints/parameters | 5023/1/280 | 2452/0/307 |
| Goodness-of-fit on $F^2$ | 1.005 | 1.066 |
| Final $R$ indices [$I > 2\sigma(I)$] | $R_1$ = 0.0488, | $R_1$ = 0.0194, |
| | $wR_2$ = 0.1135 | $wR_2$ = 0.0396 |
| $R$ indices (all data) | $R_1$ = 0.0637, | $R_1$ = 0.0225, |
| | $wR_2$ = 0.1215 | $wR_2$ = 0.0407 |
| Largest diff. peak and hole [e/Å$^3$] | 2.836 and –1.748 | 1.021 and –0.365 |

**Electrochemistry:** Dichloromethane was distilled over calcium hydride just before use. Tetrabutylammonium hexafluorophosphate ($Bu_4NPF_6$) was obtained from a metathesis reaction between $KPF_6$ (Fluka) and tetrabutylammonium iodide (Aldrich), recrystallized three times from 95% ethanol and dried in a vacuum oven at 110 °C overnight. The electrochemistry was performed in a three-electrode cell using a potentiostat AMEL 7050 and an EG&G PAR 273 electrochemical analyzer, both connected to a PC. The reference electrode was a 3 M KCl Calomel Electrode, the auxiliary electrode a platinum wire, and the working electrode a glassy carbon (GC). Positive feedback *iR* compensation was applied routinely. All measurements were carried out under Ar in anhydrous deoxygenated solvents. We used ferrocene (Fc) as the internal standard, and potentials are reported against the Fc(0/+1) redox couple, which under our conditions is $E°$(0/+1) = 0.595 V.

**DFT Calculations:** The DFT method with Becke's[40] three-parameter hybrid functional and Lee–Yang–Parr's[41] gradient corrected correlation functional was used. The calculations have been made with the Gaussian 03 (G03)[28] and Jaguar[24] programs. The Stuttgart–Dresden (SDD) ECP[42] was used for the Re atom and the 6-311++G** basis set for all other atoms. Calculations of the absolute magnetic shielding $\sigma$ were performed at the B3LYP/6-311++G** level using either G03 or Jaguar. The $\sigma$ absolute values were converted into proton chemical shifts $\delta$, relative to the magnetic shielding of tetramethylsilane computed with the same basis set (31.9793, H and 184.1441, C for G03; 31.9821, H and 184.0820, C for Jaguar). The nature of transition states was confirmed by performing a harmonic vibrational frequencies calculation and a normal-mode analysis. Vibrational frequencies and Gibbs free energy calculations were performed at 298.15 K and 1 atm. Time-dependent density functional theory[43,44] (TDDFT) combined with the conductor-like polarizable continuum model[45–47] (CPCM) method with acetonitrile as solvent has been used to calculate the excited-state energies by means of G03.

**Supporting Information** (see also the footnote on the first page of this article): $^1$H, $^1$H-$^1$H COSY and $^1$H-$^1$H NOESY NMR spectra of ***E*-1**, **Re-*E*-1**, and **Re-*Z*-1** in $CD_2Cl_2$, and the $^1$H NMR spectra of **1** before, after, and during its *E* to *Z* isomerization by means of $CF_3COOH$ in $CD_2Cl_2$.

## Acknowledgments

We gratefully acknowledge the Italian MURST (PRIN 2005), Regione Piemonte, and the Department of Energy (E.R., grant # DE-FG02-01ER45869). J.B.A.R. gratefully acknowledges support by NSF MCB-0517644 and by NIH COBRE RR-15583. We thank Centre of Excellence for Molecular Imaging (Torino), and Ayesha Sharmin, University of Montana for IR powder-ATR measurements.

[1] W. P. Griffith, in: *Comprehensive Coordination Chemistry* (Eds.: G. Wilkinson, J. A. McCleverty), Pergamon, Oxford, **1987**, p. 519.
[2] M. Schröder, T. A. Stephenson, in: *Comprehensive Coordination Chemistry* (Eds.: G. Wilkinson, J. A. McCleverty), Pergamon, Oxford, **1987**, p. 277.
[3] V. Balzani, F. Scandola, *Supramolecular Photochemistry*, Ellis-Horwood, Chichester, UK, **1991**.
[4] K. Kalyansundaram, *Photochemistry of Polypyridine and Porphyrin Complexes*, Academic Press, New York, **1992**.
[5] J. Hawecker, J. M. Lehn, R. Ziessel, *J. Chem. Soc., Chem. Commun.* **1984**, 328.
[6] B. P. Sullivan, T. J. Meyer, *J. Chem. Soc., Chem. Commun.* **1984**, 1244.
[7] D. M. Dattelbaum, K. M. Omberg, P. J. Hay, N. L. Gebhart, R. L. Martin, J. R. Schoonover, T. J. Meyer, *J. Phys. Chem. A* **2004**, *108*, 3527–3536.
[8] N. M. Shavaleev, Z. R. Bell, G. Accorsi, M. D. Ward, *Inorg. Chim. Acta* **2003**, *351*, 159–166.
[9] H. Hartmann, T. Scheiring, J. Fiedler, W. Kaim, *J. Organomet. Chem.* **2000**, *604*, 267–272.
[10] S. Frantz, J. Fiedler, I. Hartenbach, T. Schleid, W. Kaim, *J. Organomet. Chem.* **2004**, *689*, 3031–3039.
[11] S. Frantz, M. Weber, T. Scheiring, J. Fiedler, C. Duboc, W. Kaim, *Inorg. Chim. Acta* **2004**, *357*, 2905–2914.
[12] R. N. Dominey, B. Hauser, J. Hubbard, J. Dunham, *Inorg. Chem.* **1991**, *30*, 4754–4758.

 © 2006 Wiley-VCH Verlag GmbH & Co. KGaA, Weinheim 

[13] W. W. Wang, B. Spingler, R. Alberto, *Inorg. Chim. Acta* **2003**, *355*, 386–393.
[14] J. E. Johnson, N. M. Morales, A. M. Gorczyca, D. D. Dolliver, M. A. McAllister, *J. Org. Chem.* **2001**, *66*, 7979.
[15] K. D. Karlin, Z. Tyeklar, *Bioinorganic Chemistry of Copper*, Chapman and Hall, New York, **1993**.
[16] F. Fache, E. Schulz, M. L. Tommasino, M. Lemaire, *Chem. Rev.* **2000**, *100*, 2159–2231.
[17] J. Royer, M. Bonin, L. Micouin, *Chem. Rev.* **2004**, *104*, 2311–2352.
[18] J. M. Villegas, S. R. Stoyanov, D. P. Rillema, *Inorg. Chem.* **2002**, *41*, 6688–6694.
[19] S. R. Stoyanov, J. M. Villegas, D. P. Rillema, *Inorg. Chem.* **2002**, *41*, 2941–2945.
[20] F. Fischer, Y. Frei, *J. Chem. Phys.* **1957**, *27*, 808.
[21] G. Wettermark, L. Dogliotti, *J. Chem. Phys.* **1964**, *40*, 1486.
[22] M. Maruyama, Y. Kaizu, *Inorg. Chim. Acta* **1996**, *247*, 155.
[23] A. K. Ghosh, K. K. Kamar, P. Paul, S. M. Peng, G. H. Lee, S. Goswami, *Inorg. Chem.* **2002**, *41*, 6343–6350.
[24] Jaguar, Version 6.5, Schrodinger, LLC, New York, NY, **2005**.
[25] J. Bjørgo, D. R. Boyd, C. G. Watson, W. B. Jennings, *J. Chem. Soc., Perkin Trans. 2* **1974**, 757–762.
[26] H. B. Bürgi, J. D. Dunitz, *J. Chem. Soc. C* **1969**, 472–473.
[27] D. G. Musaev, K. Hirao, *J. Phys. Chem. A* **2003**, *107*, 1563–1573.
[28] M. J. Frisch, G. W. Trucks, H. B. Schlegel, G. E. Scuseria, M. A. Robb, J. R. Cheeseman, J. A. Montgomery Jr, T. Vreven, K. N. Kudin, J. C. Burant, J. M. Millam, S. S. Iyengar, J. Tomasi, V. Barone, B. Mennucci, M. Cossi, G. Scalmani, N. Rega, G. A. Petersson, H. Nakatsuji, M. Hada, M. Ehara, K. Toyota, R. Fukuda, J. Hasegawa, M. Ishida, T. Nakajima, Y. Honda, O. Kitao, H. Nakai, M. Klene, X. Li, J. E. Knox, H. P. Hratchian, J. B. Cross, C. Adamo, J. Jaramillo, R. Gomperts, R. E. Stratmann, O. Yazyev, A. J. Austin, R. Cammi, C. Pomelli, J. Ochterski, P. Y. Ayala, K. Morokuma, G. A. Voth, P. Salvador, J. J. Dannenberg, V. G. Zakrzewski, S. Dapprich, A. D. Daniels, M. C. Strain, O. Farkas, D. K. Malick, A. D. Rabuck, K. Raghavachari, J. B. Forestman, J. V. Ortiz, Q. Cui, A. G. Baboul, S. Clifford, J. Cioslowski, B. B. Stefanov, G. Liu, A. Liashenko, P. Piskorz, I. Komaromi, R. L. Martin, D. J. Fox, T. Keith, M. A. Al-Laham, C. Y. Peng, A. Nanayakkara, M. Challacombe, P. M. W. Gill, B. Johnson, W. Chen, M. W. Wong, C. Gonzales, J. A. Pople, *Gaussian 03*, Version revision C.02, Gaussian Inc., Wallingford CT, **2004**.
[29] T. J. Lang, G. J. Wolber, R. D. Bach, *J. Am. Chem. Soc.* **1981**, *103*, 3275–3282.
[30] R. D. Bach, J. J. W. McDouall, A. L. Owensby, H. B. Schlegel, J. W. Holubka, J. C. Ball, *J. Phys. Org. Chem.* **1991**, *4*, 125–134.
[31] T. Helgaker, M. Jaszunski, K. Ruud, *Chem. Rev.* **1999**, *99*, 293–352.
[32] R. Gobetto, C. Nervi, B. Romanin, L. Salassa, M. Milanesio, G. Croce, *Organometallics* **2003**, *22*, 4012–4019.
[33] M. Kaupp, M. Bühl, V. G. Malkin, *Calculation of NMR and EPR Parameters - Theory and Applications*, Wiley-VCH, Weinheim, **2004**.
[34] B. Valeur, *Molecular Fluorescence: Principles and Applications*, Wiley-VCH, Weinheim, **2002**.
[35] J. V. Caspar, T. J. Meyer, *J. Phys. Chem. A* **1983**, *87*, 952–957.
[36] S. R. Stoyanov, J. M. Villegas, D. P. Rillema, *Inorg. Chem. Commun.* **2004**, *7*, 838–841.
[37] J. M. Villegas, S. R. Stoyanov, W. Huang, D. P. Rillema, *Inorg. Chem.* **2005**, *44*, 2297–2309.
[38] A. Altomare, M. C. Burla, M. Camalli, G. L. Cascarano, C. Giacovazzo, A. Guagliardi, A. G. Moliterni, G. Polidori, R. Spagna, *J. Appl. Crystallogr.* **1999**, *32*, 115–119.
[39] G. M. Sheldrick, *SHELXL-97*, University of Göttingen, Germany, **1997**.
[40] A. D. Becke, *J. Chem. Phys.* **1993**, *98*, 5648–5652.
[41] C. Lee, W. Yang, R. G. Parr, *Phys. Rev. B: Condens. Matter* **1988**, *37*, 785.
[42] D. Andrae, U. Haussermann, M. Dolg, H. Stoll, H. Preuss, *Theor. Chim. Acta* **1990**, *77*, 123–141.
[43] R. E. Stratmann, G. E. Scuseria, M. J. Frisch, *J. Chem. Phys.* **1998**, *109*, 8218–8224.
[44] M. E. Casida, C. Jamorski, K. C. Casida, D. R. Salahub, *J. Chem. Phys.* **1998**, *108*, 4439–4449.
[45] V. Barone, M. Cossi, *J. Phys. Chem. A* **1998**, *102*, 1995–2001.
[46] M. Cossi, V. Barone, *J. Chem. Phys.* **2001**, *115*, 4708–4717.
[47] M. Cossi, N. Rega, G. Scalmani, V. Barone, *J. Comput. Chem.* **2003**, *24*, 669–681.

Received: March 21, 2006
Published Online: May 29, 2006

 © 2006 Wiley-VCH Verlag GmbH & Co. KGaA, Weinheim 

DOI: 10.1002/ejic.200600260

# Preparation, Characterization, and Aquation Kinetics of Pyridine *N*-Oxide Complexes of Chromium(III)

**Mirjana Kotowski,[a][‡] Radovan Marcec,[a][†] Vjera Butkovic,[a] Andreja Bakac,*[b] and Matko Orhanovic[a]**

**Keywords:** Pyridine oxide / Chromium / Kinetics / Mechanism / Aquation

A series of $(H_2O)_5Cr(X\text{-}pyO)^{3+}$ ions (pyO = pyridine *N*-oxide, X = H, 3-$CH_3$, 4-$CH_3$, 4-$OCH_3$, 4-$NO_2$) were prepared by the reduction of the corresponding pyridine *N*-oxide adducts of diperoxochromium(VI) species with acidic ferrous perchlorate. The $(H_2O)_5Cr(X\text{-}pyO)^{3+}$ complexes undergo aquation to yield $Cr(H_2O)_6^{3+}$ and X-pyO according to the rate law $k_{obs} = k_o + k_{-1}[H^+]^{-1}$. The values of the rate constants extrapolated to 298 K at 1.0 M ionic strength are: $k_0 = 2.80\times10^{-6}\,s^{-1}$, $k_{-1} = 1.86\times10^{-8}\,M\,s^{-1}$ (X = 4-$NO_2$); $7.80\times10^{-8}$, $6.27\times10^{-10}$ (H); $4.80\times10^{-8}$, $3.20\times10^{-10}$ (3-$CH_3$); $3.05\times10^{-8}$, $1.60\times10^{-10}$ (4-$CH_3$); and $2.37\times10^{-9}$, $4.76\times10^{-11}$ (4-$OCH_3$). The reaction of the 4-$OCH_3$ complex exhibits two additional terms in the rate law, $k_1[H^+] + k_{-2}[H^+]^{-2}$. The binding of 4-$OCH_3$–pyO to chromium is suggested to take place through the methoxy group. (© Wiley-VCH Verlag GmbH & Co. KGaA, 69451 Weinheim, Germany, 2006)

## Introduction

Pyridine *N*-oxides (X-pyO) are important reagents in thermal[1,2] and photochemical[3–5] oxidations. Often, although not always,[6] such reactions involve oxygen-atom transfer[7–9] with pyridine *N*-oxide playing a role of either oxygen-atom donor[2,7–12] or a promoter of oxygen transfer from active donors to the substrate.[13–16] Metal catalysis is frequently involved[17] in such processes, which makes mechanistic studies of transition-metal complexes of pyridine *N*-oxides an important area of investigation.

A large number of complexes with an array of metal ions have been prepared and characterized structurally, spectroscopically, electrochemically, and chemically. There are, however, few reports available on the kinetics and mechanisms of the reactions of such complexes,[18–20] especially in aqueous solutions.[21,22] Several pentaamminecobalt(III) ions, $(NH_3)_5Co(X\text{-}pyO)^{3+}$ have been prepared[21,22] and found to be reasonably stable at room temperature, provided there are no cyano substituents on the pyridine ring, in which case facile hydrolysis to a bound amide takes place.[21] The reduction of the parent $(H_2O)_5Co(pyO)^{3+}$ by chromium(II) is believed to take place by an inner-sphere mechanism whereby $Cr_{aq}^{2+}$ attacks at the coordinated pyO oxygen,[21] although the expected product, $(H_2O)_5Cr(pyO)^{3+}$, was not observed, possibly because of its decomposition on ion-exchange resin. In the reduction of $(NH_3)_5Co(X\text{-}pyO)^{3+}$ by 2-hydroxy-2-propyl radicals, $^{\cdot}C(CH_3)_2OH$, the initial site of attack was shown to be at the aromatic ring of the coordinated X-pyO.[23]

These studies have now been extended to a series of chromium complexes, $(H_2O)_5Cr(X\text{-}pyO)^{3+}$ (X = H, 3-$CH_3$, 4-$CH_3$, 4-$OCH_3$, 4-$NO_2$). In this first report, we focus on the preparation and spectral and kinetic characterization of these complexes. Prior to this work, only the parent ion, $(H_2O)_5Cr(pyO)^{3+}$, was known.[24] It was generated by thermal equilibration of $Cr(H_2O)_6^{3+}$ with an excess of pyO in slightly acidic aqueous solutions at elevated temperatures, followed by ion exchange. In the present work, our previously published procedure for the preparation of pyridine chromium complexes[22] was applied to pyridine *N*-oxide analogues. This method represents a great advantage over the thermal equilibration method because it yields exclusively the mono-substituted products.

## Results

The method used to prepare the complexes in Table 1 is based on the chemistry that we have developed earlier for the pyridine complexes.[22] By analogy to that work, the blue paste-like material generated from $CrO_3$, X-pyO and $H_2O_2$ is assigned the formula $CrO(O_2)_2(X\text{-}pyO)$. Reduction with $Fe_{aq}^{2+}$ produces the desired $(H_2O)_5Cr(X\text{-}pyO)^{3+}$, Equation (1).

The chemical composition of the complexes was confirmed by chromium and ligand analysis after the complex had been allowed to aquate. In every case, the [Cr]/[X-pyO]

[a] Rugjer Boskovic Institute,
Bijenicka 54, 10000 Zagreb, Croatia
[b] Iowa State University, Chemistry Department,
Ames, IA 50011, Iowa, USA
[‡] Current address: Max Planck Institute for Chemistry,
55128 Mainz, Germany
[†] Deceased.
Supporting information for this article is available on the WWW under http://www.eurjic.org or from the author.

 InterScience © 2006 Wiley-VCH Verlag GmbH & Co. KGaA, Weinheim 

Table 1. UV/Vis spectral data for $(H_2O)_5Cr(X\text{-}pyO)^{3+}$ and X-pyO.

| X | $(H_2O)_5Cr(X\text{-}pyO)^{3+}$ $\lambda_{max}$ [nm] ($\varepsilon$, $M^{-1}\,cm^{-1}$)[a][b] | | | X-pyO $\lambda_{max}$, [nm] ($\varepsilon$, $M^{-1}\,cm^{-1}$)[c] | $XpyOH^+$ |
|---|---|---|---|---|---|
| H | 588 (25.7) | 417 (30.5) | 240 ($1.15\times10^4$) | 254 ($1.15\times10^4$) | 257 ($2.9\times10^3$) |
| | 586 (26.0)[d] | 414 (30.8)[d] | | | 217 ($4.9\times10^3$) |
| 3-$CH_3$ | 590 (25.9) | 418 (31.7) | 242 ($1.08\times10^4$) | 254 ($1.17\times10^4$) | 263 ($3.5\times10^3$) |
| | | | | 209 ($1.98\times10^4$) | 220 ($4.2\times10^3$) |
| 4-$CH_3$ | 588 (29.8) | 417 (40.9) | 246 ($1.35\times10^4$) | 256 ($1.40\times10^4$) | 254 ($2.7\times10^3$) |
| | | | | 206 ($1.87\times10^4$) | 226 ($8.3\times10^3$) |
| 4-$OCH_3$ | 582 (27.9) | 417 (37.9) | 262 ($1.50\times10^4$) | 261 ($1.60\times10^4$)[b] | 243 ($1.20\times10^4$)[a][b] |
| 4-$NO_2$ | 585 (33.6) | sh | 266 ($1.28\times10^4$) | 313 ($1.25\times10^4$) | 280 ($3.8\times10^3$) |
| | | | | 226 ($8.0\times10^3$) | 244 ($8.2\times10^3$) |

[a] In 1.0 M aqueous $HClO_4$. [b] This work. [c] Ref. [25]. [d] Ref. [24].

$$CrO(O_2)_2(X\text{-}pyO) + 7Fe_{aq}^{2+} + 10H^+ \rightarrow (H_2O)_5Cr(X\text{-}pyO)^{3+} + 7Fe_{aq}^{3+} \quad (1)$$

ratio was found to be $1.00 \pm 0.02$. As expected, the behavior of the complexes on the cation-exchange resin was consistent with a 3+ charge.

The UV/Visible spectroscopic data are summarized in Table 1. The spectrum of the unsubstituted material (X = H) agrees well with the literature data for a complex obtained by anation of $Cr(H_2O)_6^{3+}$ with pyO followed by ion-exchange to remove $Cr(H_2O)_6^{3+}$ and *cis*- and *trans*-$(H_2O)_4Cr(pyO)_2^{3+}$.[24]

The kinetics of aquation of $(H_2O)_5Cr(X\text{-}pyO)^{3+}$ complexes were studied as a function of acidity and temperature at 1.0 M ionic strength. As illustrated in Figure 1 for $(H_2O)_5Cr(pyO)^{3+}$, the spectra exhibit clean isosbestic points as expected if the stoichiometry remains unchanged throughout the reaction, and no long-lived intermediates are involved.

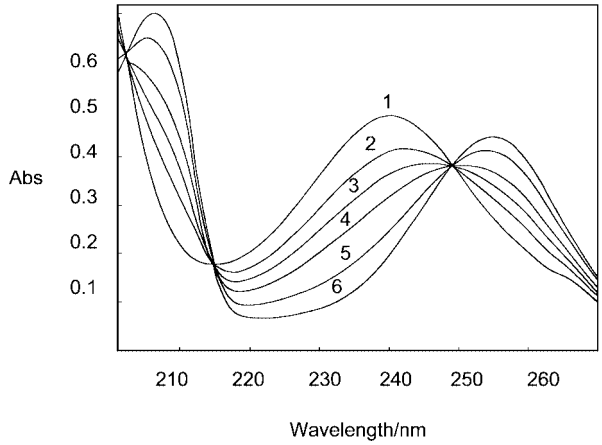


Figure 1. Spectral changes accompanying the aquation of $4.16\cdot10^{-5}$ M $(H_2O)_5Cr(pyO)^{3+}$ in 0.020 M $HClO_4$ at 1.0 M ionic strength and 90 °C. Spectrum **1** was obtained on a fresh sample at 25 °C before the onset of the reaction. Spectra **2** through **6** were measured at time 0 (arbitrary), 8, 18, 45.5, and 1250 minutes.

The standard treatment of the exponential kinetic traces yielded first-order rate constants $k_{obs}$ which decreased with an increase in $[H^+]$ according to the expression in Equation (2) for all the complexes except for $(H_2O)_5Cr(4\text{-}OCH_3\text{–}pyO)^{3+}$, which exhibited a more complex behavior, see below.

$$k_{obs} = k_o + k_{-1}\,[H^+]^{-1};\ X = H,\ 3\text{-}CH_3,\ 4\text{-}CH_3,\ 4\text{-}NO_2 \quad (2)$$

The adherence to Equation (2) is shown for X = 3-$CH_3$ in Figure 2. The plot of $k_{obs}$ against $1/[H^+]$ at several temperatures is linear yielding $k_0$ as an intercept and $k_{-1}$ as a slope. Data for the remaining complexes (X = H, 4-$CH_3$, and 4-$NO_2$) are presented in the supporting information (Figures S1–S3; for supporting information see also the footnote on the first page of this article). The kinetic data are summarized in Table 2.

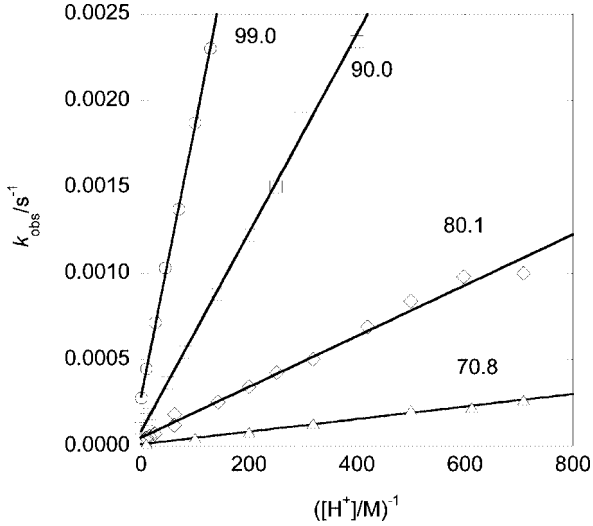


Figure 2. Plot of $k_{obs}$ vs. $1/[H^+]$ for the aquation of $(H_2O)_5Cr(3\text{-}CH_3\text{–}pyO)^{3+}$ at 99.0 °C (circles), 90.0° (squares), 80.1° (diamonds), and 70.8° (triangles).

The activation parameters, also shown in Table 2, were obtained by fitting simultaneously all the individual acid-dependent rate constants $k_{obs}$ for a given complex to the Eyring expression, Equation (3), where $k_B$ and $h$ are the Boltzman and Planck constants, respectively, $T$ is the absolute temperature, and $i = 0$ and $-1$. The fit of the data to Equation (3) for $(H_2O)_5Cr(3\text{-}CH_3\text{–}pyO)^{3+}$ is shown in Figure 3, and for the rest of the complexes in Figures S4–S7 in the supporting information.

The plots of $k_{obs}$ vs. $1/[H^+]$ for the 4-methoxy complex, Figure 4, exhibited deviations from Equation (2) at both the

 © 2006 Wiley-VCH Verlag GmbH & Co. KGaA, Weinheim 

Table 2. Summary of kinetic data for the aquation of $(H_2O)_5Cr(X\text{-}pyO)^{3+}$ complexes.[a]

| X | $T$ [°C] | $k_0$ [$s^{-1}$][b] | $k_{-1}$ [M $s^{-1}$][c] |
|---|---|---|---|
| 4-$NO_2$[d] | 70.2 | $4.47(\pm0.27)\times10^{-4}$ | $2.58(\pm0.14)\times10^{-5}$ |
| | 65 | $2.92(\pm0.05)\times10^{-4}$ | $1.15(\pm0.01)\times10^{-5}$ |
| | 60.2 | $1.79(\pm0.13)\times10^{-4}$ | $5.20(\pm0.09)\times10^{-6}$ |
| | 50.2 | $5.64(\pm0.15)\times10^{-5}$ | $1.31(\pm0.01)\times10^{-6}$ |
| | 40.1 | $1.68(\pm0.17)\times10^{-5}$ | $2.76(\pm0.10)\times10^{-7}$ |
| | 25.0 | $2.80\times10^{-6}$ [e] | $1.86\times10^{-8}$ [e] |
| | | $\Delta H_0^{\ddagger} = 93.9\pm2.2$ | $\Delta H_{-1}^{\ddagger} = 129\pm3$ |
| | | $\Delta S_0^{\ddagger} = -36\pm6$ | $\Delta S_{-1}^{\ddagger} = 40\pm8$ |
| H | 99.0 | $3.7(\pm1.8)\times10^{-4}$ | $1.95(\pm0.22)\times10^{-5}$ |
| | 90.0 | $6.6(\pm4.8)\times10^{-5}$ | $8.98(\pm0.21)\times10^{-6}$ |
| | 80.0 | $1.2(\pm4.1)\times10^{-5}$ | $2.20(\pm0.07)\times10^{-6}$ |
| | 70.0 | $1.05(\pm0.14)\times10^{-5}$ | $5.50(\pm0.05)\times10^{-7}$ |
| | 25.0 | $7.80\times10^{-8}$ [e] | $6.27\times10^{-10}$ [e] |
| | | $\Delta H_0^{\ddagger} = 104\pm47$ | $\Delta H_{-1}^{\ddagger} = 125\pm4$ |
| | | $\Delta S_0^{\ddagger} = -32\pm127$ | $\Delta S_{-1}^{\ddagger} = -1.6\pm10$ |
| 4-$CH_3$ | 98.6 | $1.80(\pm0.29)\times10^{-4}$ | $1.26(\pm0.04)\times10^{-5}$ |
| | 90.0 | $9.96(\pm0.81)\times10^{-5}$ | $3.82(\pm0.04)\times10^{-6}$ |
| | 80.1 | $2.70(\pm0.54)\times10^{-5}$ | $1.17(\pm0.02)\times10^{-6}$ |
| | 70.0 | $6.6(\pm2.8)\times10^{-6}$ | $3.00(\pm0.07)\times10^{-7}$ |
| | 25.0 | $3.05\times10^{-8}$ [e] | $1.60\times10^{-10}$ [e] |
| | | $\Delta H_0^{\ddagger} = 109\pm24$ | $\Delta H_{-1}^{\ddagger} = 139\pm3$ |
| | | $\Delta S_0^{\ddagger} = -23\pm64$ | $\Delta S_{-1}^{\ddagger} = 34\pm8$ |
| 3-$CH_3$ | 99.0 | $2.87(\pm0.13)\times10^{-4}$ | $1.57(\pm0.02)\times10^{-5}$ |
| | 90.0 | $8.6(\pm2.2)\times10^{-5}$ | $5.75(\pm0.11)\times10^{-6}$ |
| | 80.1 | $4.8(\pm1.7)\times10^{-5}$ | $1.47(\pm0.05)\times10^{-6}$ |
| | 70.8 | $1.09(\pm0.50)\times10^{-5}$ | $3.63(\pm0.11)\times10^{-7}$ |
| | 25.0 | $4.80\times10^{-8}$ [e] | $3.20\times10^{-10}$ [e] |
| | | $\Delta H_0^{\ddagger} = 104\pm21$ | $\Delta H_{-1}^{\ddagger} = 134\pm2$ |
| | | $\Delta S_0^{\ddagger} = -36\pm56$ | $\Delta S_{-1}^{\ddagger} = 23\pm6$ |
| 4-$OCH_3$[f] | 99.3 | $1.52(\pm0.10)\times10^{-4}$ | $6.20(\pm0.08)\times10^{-6}$ |
| | 90.4 | $5.03(\pm0.39)\times10^{-5}$ | $1.98(\pm0.04)\times10^{-6}$ |
| | 80.0 | $2.10(\pm0.37)\times10^{-5}$ | $3.08(\pm0.29)\times10^{-7}$ |
| | 70.2 | $3.95(\pm0.63)\times10^{-6}$ | $8.75(\pm0.61)\times10^{-8}$ |
| | 25.0 | $2.37\times10^{-9}$ [f] | $4.76(\pm0.39)\times10^{-11}$ [f] |
| | | $\Delta H_0^{\ddagger} = 135\pm11$ | $\Delta H_{-1}^{\ddagger} = 142\pm2$ |
| | | $\Delta S_0^{\ddagger} = 43\pm29$ | $\Delta S_{-1}^{\ddagger} = 34\pm7$ |

[a] Ionic strength: 1.0 M ($HClO_4 + NaClO_4$). Units: $\Delta H^{\ddagger}$ in kJ $mol^{-1}$, $\Delta S^{\ddagger}$ in J $mol^{-1}$ $K^{-1}$. [b] Obtained as intercept of $k_{obs}$ vs. 1/[$H^+$] plots, as in Figure 2. [c] Obtained as a slope of $k_{obs}$ vs. 1/[$H^+$] plots, as in Figure 2. [d] Additional data in 1.0 M $HClO_4$: $1.36\times10^{-3}$ $s^{-1}$ (80 °C), $8.43\times10^{-4}$ (75 °C), $9.10\times10^{-5}$ (55 °C). [e] Calculated from the activation parameters. [f] At >5 mM [$H^+$], a term directly proportional to [$H^+$] also contributes, $\Delta H_1^{\ddagger} = 104\pm43$ kJ $mol^{-1}$, $\Delta S_1^{\ddagger} = -48\pm115$ J $mol^{-1}$ $K^{-1}$.

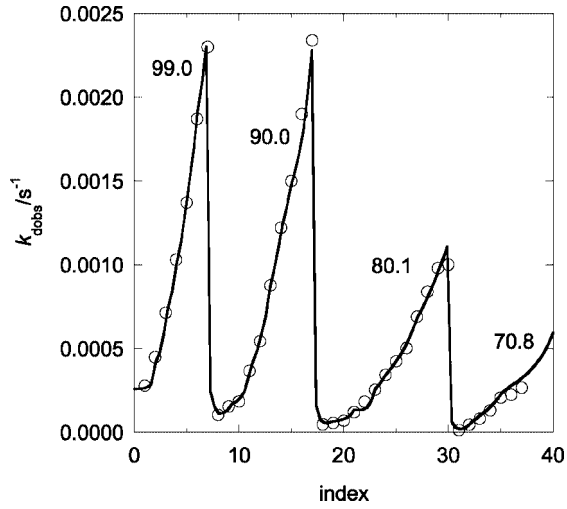


Figure 3. Fit of the data for the aquation of $(H_2O)_5Cr(3\text{-}CH_3\text{–}pyO)^{3+}$ to Equation 3 with use of the program Kaleidagraph 3.6. Index numbers on the $x$ axis identify each unique point at a given acidity and temperature. Temperature (in °C) for each data set is indicated.

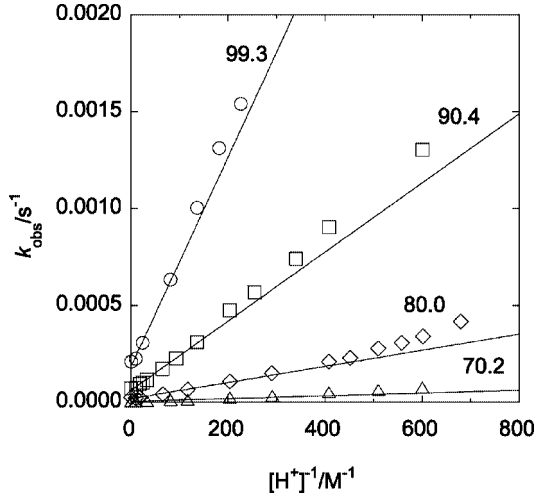


Figure 4. Plot of $k_{obs}$ vs. 1/[$H^+$] for the aquation of $(H_2O)_5Cr(4\text{-}OCH_3\text{–}pyO)^{3+}$ at 1.0 M ionic strength.

$$k_{obs} = \frac{k_B T}{h}\sum_i [H^+]^i (e^{-\Delta H_i^{\ddagger}/RT} e^{\Delta S_i^{\ddagger}/R}) \quad (3)$$

high and low ends of [$H^+$], and required two additional terms in the rate law, Equation (4), which is analogous to that reported for the azido complex, $(H_2O)_5CrN_3^{2+}$.[26]

The attempted fit of all the data to the multi-term Eyring expression of Equation (3) with $i$ = 1, 0, –1, and –2 failed to converge, presumably because the contribution from the $k_{-2}$ term was small and thus subject to large error under all of the conditions. The activation parameters in Table 2 were obtained by fitting only the data at >5 mM [$H^+$] to a 3-term variant of Equation (3), i.e., $i$ = 1, 0, and –1. The rather

$$k_{obs} = k_1[H^+] + k_o + k_{-1}[H^+]^{-1} + k_{-2}[H^+]^{-2};\ X = 4\text{-}OCH_3 \quad (4)$$

large errors, especially for the less prominent terms, were to be expected for a complex fit and a large number of parameters.

To ascertain that the $k_1$ term is real and not a result of misinterpreted deviations from a simpler rate law, several experiments were conducted at higher acid concentrations at 4.0 M ionic strength where $k_1$ and $k_0$ terms should dominate. The results are shown in Figure 5, which clearly confirms the expectations. The rate constants at 99.0 °C are $k_0$ = $2.20(\pm0.14)\times10^{-4}$ $s^{-1}$ and $k_1$ = $1.16(\pm0.07)\times10^{-4}$ $M^{-1}$ $s^{-1}$. The corresponding values extracted from the more complex

 © 2006 Wiley-VCH Verlag GmbH & Co. KGaA, Weinheim 

set of data at 1.0 M ionic strength are $k_0 = 1.52(\pm 0.11) \times 10^{-4}$ $s^{-1}$ and $k_1 = 5.6(\pm 1.9) \times 10^{-5}$ $M^{-1}$ $s^{-1}$.

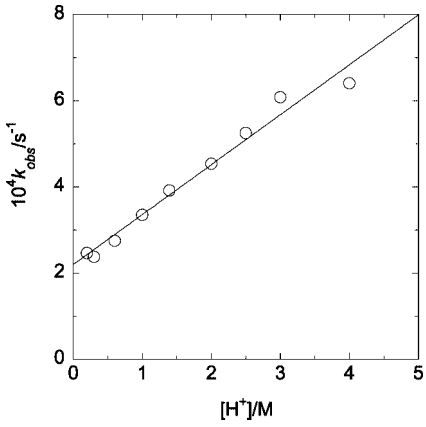


Figure 5. Plot of $k_{obs}$ vs. $[H^+]$ for the aquation of $(H_2O)_5Cr(4\text{-}OCH_3\text{–}pyO)^{3+}$ at 4.0 M ionic strength and 99 °C.

## Discussion

**UV/Vis Spectra:** The ligand-field transitions for all the pyridine *N*-oxide complexes studied (Table 1) are red-shifted relative to the corresponding pyridine complexes,[22] consistent with the greater ligand-field strength of the pyridines.

With the exception of the 4-$OCH_3$ derivative, the positions of the UV bands for $(H_2O)_5Cr(X\text{-}pyO)^{3+}$ ions are considerably different from those of the free ligands. As an example, $(H_2O)_5Cr(4\text{-}CH_3\text{–}pyO)^{3+}$ in 1 M $H^+$ exhibits a maximum at 246 nm ($\varepsilon = 1.35 \times 10^4$ $M^{-1}$ $cm^{-1}$). Under the same conditions, the free ligand has maxima at 254 nm ($\varepsilon = 2.7 \times 10^3$) and 226 nm ($\varepsilon = 8.3 \times 10^3$). In neutral solutions, these maxima shift to 256 nm ($\varepsilon = 1.40 \times 10^4$) and 206 nm ($1.9 \times 10^4$). Similar spectral differences between the free and Cr-bound pyridine *N*-oxides are observed for the rest of the materials in Table 1. Only the spectrum of $(H_2O)_5Cr(4\text{-}OCH_3\text{–}pyO)^{3+}$ ($\lambda_{max} = 262$ nm, $\varepsilon = 1.50 \times 10^4$ $M^{-1}$ $cm^{-1}$) is almost identical to that of the free ligand in $H_2O$. This observation suggests that the binding of 4-$OCH_3$–pyO to chromium perhaps takes place at the methoxy oxygen, whereas the rest of the complexes utilize the pyridine oxide oxygen. We rationalize this assignment by noting that coordination via the methoxy group should affect the intraligand charge-transfer transitions to a lesser extent than coordination via the *N*-oxo group, or the protonation of the *N*-oxo group. Additional arguments in favor of the unique binding mode in $(H_2O)_5Cr(4\text{-}OCH_3\text{–}pyO)^{3+}$ will be presented shortly.

**Kinetics of Aquation of $(H_2O)_5Cr(X\text{-}pyO)^{3+}$ (X = H, 3-$CH_3$, 4-$CH_3$, 4-$NO_2$):** The two-term rate law of Equation (2) is common to all the complexes with the exception of the 4-methoxy derivative which exhibits two additional terms, $k_1[H^+]$ and $k_{-2}[H^+]^{-2}$, Equation (4). The rate law of Equation (2) is typical for the aquation of pentaaquachromium(III) complexes, including those of the closely related $(H_2O)_5Cr(X\text{-}py)^{3+}$ ions. A reasonable mechanism features parallel reactions of the pentaaqua complex and its conjugate base, Equations (5), (6) and (7) leading to the rate law in Equation (8). In the limit $K_a << [H^+]$, Equation (8) reduces to the observed form, Equation (2), where $k_{-1} = k_{-1}'K_a$.

$$(H_2O)_5Cr(4\text{-}X\text{-}pyO)^{3+} \rightleftharpoons (H_2O)_4(OH)Cr(4\text{-}X\text{-}pyO)^{2+} + H^+ \; K_a \quad (5)$$

$$(H_2O)_5Cr(4\text{-}X\text{-}pyO)^{3+} \xrightarrow{H_2O} Cr(H_2O)_6^{3+} + 4\text{-}X\text{-}pyO \; k_0 \quad (6)$$

$$(H_2O)_4(OH)Cr(4\text{-}X\text{-}pyO)^{2-} \xrightarrow{H_2O} (H_2O)_5CrOH^{2+} + 4\text{-}X\text{-}pyO \; k_{-1}' \quad (7)$$

$$k_{obs} = \frac{k_0[H^+] + k_{-1}'K_a}{K_a + [H^+]} \quad (8)$$

The acidity constants for the pyridine oxide complexes have not been determined, but the excellent fit of the data to Equation (2) throughout the acid range studied places a limit $K_a << 10^{-3}$ M for all the complexes in the temperature range examined.

The activation enthalpies are large for both pathways for all the complexes. Activation entropies are moderately negative for the $k_0$ path, and moderately positive for the $k_{-1}$ path. The only exception seems to be the parent pyO complex, for which $\Delta S_{-1}^{\ddagger}$ is close to zero ($-1.6 \pm 10$ $J\,mol^{-1}\,K^{-1}$). These results are consistent with a strong associative component in the $k_0$ path, as is often the case with aqua $Cr^{III}$ complexes, including the water substitution in $Cr(H_2O)_6^{3+}$.[27] The $k_{-1}$ path is a composite, which makes the mechanistic assignment of the kinetic step more difficult to make. Still, given that the $\Delta S^0$ component (associated with the $K_a$) will be positive, and the overall $\Delta S_{-1}^{\ddagger}$ is only on the order of 20–40 $J\,mol^{-1}\,K^{-1}$, one can all but rule out a strong dissociative contribution to $k_{-1}$. The data are consistent with an interchange mechanism in either dissociative or associative regime.

**The Case of $(H_2O)_5Cr(4\text{-}OCH_3\text{-}pyO)^{3+}$:** As already mentioned, the aquation of aqua and amine complexes of chromium(III) often follows the general rate law of Equation (2). The direct dependence on $[H^+]$, on the other hand, has been observed only for those complexes that have a ligand with an open basic site, i.e. anions such as $F^-$, $N_3^-$, $SO_4^{2-}$, $CN^-$, or $CH_3COO^-$.[28–32] This path is not expected to operate for $(H_2O)_5Cr(X\text{-}pyO)^{3+}$ complexes; the basicity of X-pyO oxygen is greatly reduced upon coordination to Cr, and the probability of protonation is minimal. The complexes having X = H, 3-$CH_3$, 4-$CH_3$, and 4-$NO_2$ follow this prediction and do not feature a $k_1[H^+]$ term. The 4-$OCH_3$ de-

 © 2006 Wiley-VCH Verlag GmbH & Co. KGaA, Weinheim 

rivative, on the other hand, has a pronounced $k_1[H^+]$ term which would be difficult to explain for a complex having a Cr–oxopyridine bond, Cr–Opy(4-$OCH_3$). If, however, the ligand is coordinated through the methoxy group, as in Cr–$O(CH_3)$pyO, then the protonation at the exposed pyO oxygen becomes more likely. We suggest that bonding through the methoxy group indeed takes place and is responsible for the unique behavior of the 4-$OCH_3$–py complex. The UV spectrum discussed earlier supports this assignment. Even though the basicity of the methoxy oxygen should be greatly diminished in the chromium complex as compared to the free base, the protonation can still take place at the high end of $[H^+]$ used in this work. The proposed isomer, $(H_2O)_5Cr–O(CH_3)pyO^{3+}$, should not be considered an unusual species in that related alcohol complexes of $Cr^{III}$, such as $(H_2O)_{6-n}Cr[O(H)CH_3]_n^{3+}$, are well known and quite stable.[33]

The positive $\Delta S_0^{\ddagger}$ value for $(H_2O)_5Cr(4\text{-}OCH_3\text{–}pyO)^{3+}$, $43 \pm 29\ J\,mol^{-1}\,K^{-1}$, seems outstanding, and may suggest a mechanistic deviation from the associative interchange assigned to the rest of the complexes in Table 2. The large error bars for all the entropy values in Table 2, however, make such a conclusion uncertain. We also note that an unexplained positive $\Delta S_0^{\ddagger}$ term was observed in the aquation of $(H_2O)_5Cr(3\text{-}CH_3\text{–}py)^{3+}$,[22] which does not appear outstanding in any other respect.

The $k_{-2}$ path was observed only for $(H_2O)_5Cr(4\text{-}CH_3O\text{–}pyO)^{3+}$, implying a greater acidity of the coordinated waters for this complex. This is a surprising observation and contrary to what one might expect on the basis of the strong electron donation from the 4-methoxy group and the greater basicity of 4-$CH_3O$–pyO[34] compared to other pyridine oxides in this work. It is not clear whether the different binding mode to $Cr^{III}$ would cause the observed shift in the $pK_a$.

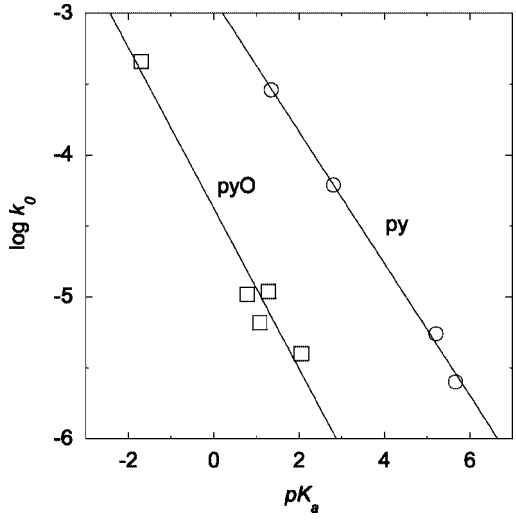


Figure 6. Plot of $\log k_0$ vs. $pK_a$ of the free ligands for the aquation of $Cr(H_2O)_5^{3+}$ complexes of pyridines (py, circles) and pyridine *N*-oxides (pyO, squares) at 70 °C. The substituents on pyO, in the order of increasing $pK_a$, are 4-$NO_2$, H, 3-$CH_3$, 4-$CH_3$, and 4-$OCH_3$. In the pyridine series, the order is 3-CN, 3-Cl, H, 3-$CH_3$. Data are from Table 2 and references [22], [23] and [34].

**Comparison with Pyridine Complexes:** Figure 6 shows a plot of the logarithms of the first-order rate constants $k_0$ against the $pK_a$ of the protonated ligands for complexes of $Cr^{III}$ with pyridines and pyridine *N*-oxides at 70 °C. The correlation was not sought for $k_{-1}$, which is a composite of rate and acid dissociation constants.

Both sets of rate constants in Figure 6 are linearly related to the ligand $pK_a$, a measure of σ electron donation. In both cases, the greater thermodynamic affinity for the proton results in a kinetically more inert chromium complex, i.e. the greater the $pK_a$ the slower the aquation. When the two series are compared to each other, however, then the $pK_a$ argument breaks down; the less basic pyridine *N*-oxides bind to the chromium more strongly, at least in the kinetic sense. One obvious source of the apparent anomalous inertness of pyridine *N*-oxide complexes is the greater ability of pyridine *N*-oxides to engage in π-bonding with the metal.

## Experimental Section

**Preparation of Complexes. $(H_2O)_5Cr(pyO)^{3+}$:** To a stirred, ice-cold aqueous solution (2 mL) of 1 M pyridine oxide (PyO) and 1 M $CrO_3$ was added dropwise cold 30% $H_2O_2$ (2 mol-equiv.). The resulting blue paste was immediately treated with a solution containing 7.5 mol-equiv. of ferrous perchlorate and 11 mol-equiv. of $HClO_4$. The green product solution was loaded onto a column of Dowex 50W-X8 cation-exchange resin. Iron(III) ions were eluted with 0.1 M NaSCN in 1 M $HClO_4$. The column was rinsed with 1 M $HClO_4$ to remove the remaining NaSCN. Chromium(III) species were eluted with 3 M $HClO_4$ and collected in several fractions. The blue $Cr(H_2O)_6^{3+}$ was eluted first, followed by the green $(H_2O)_5Cr(pyO)^{3+}$. The middle fraction of this complex was used for all the kinetics and spectral measurements. The same procedure was used to prepare the ring-substituted complexes $(H_2O)_5Cr(X\text{-}pyO)^{3+}$ (X = 3-$CH_3$, 4-$CH_3$, 4-$CH_3O$ and 4-$NO_2$), except that in the case of $(H_2O)_5Cr(4\text{-}NO_2\text{–}pyO)^{3+}$, the solvent water in the initial step was replaced by a 1:1 $H_2O$/dioxane mixture to increase the solubility of the ligand.

**Materials:** Pyridine *N*-oxides (pyO, 3-$CH_3$–pyO, 4-$CH_3$–pyO, and 4-$NO_2$–pyO) were purchased from Fluka and recrystallized twice from ethanol. 4-$CH_3O$–pyO was prepared by refluxing 28 g 4-$NO_2$–pyO (Fluka) and 28 g $K_2CO_3$ in 200 mL of methanol for 8 hours.[35] The product was recrystallized twice from heptane. Solutions of iron(II) perchlorate were prepared by zinc amalgam reduction of the $Fe^{III}$ salt. Sodium perchlorate was prepared from perchloric acid and sodium carbonate. The solid was recrystallized three times from doubly distilled water. Other chemicals were purchased at the highest purity available and used as received.

**Analyses:** The chromium content of $(H_2O)_5Cr(X\text{-}pyO)^{3+}$ was determined spectrophotometrically after oxidizing the chromium to chromate ($\varepsilon_{372} = 4.82 \cdot 10^3\ M^{-1}\,cm^{-1}$)[36] with alkaline hydrogen peroxide. The concentration of the appropriate pyridine *N*-oxides generated by hydrolysis of the complex in 0.10 M $HClO_4$ for ≥ 10 half-lives was determined spectrophotometrically.

**Kinetic Measurements:** The aquation of all the complexes was monitored spectrophotometrically at a wavelength, typically close to $\lambda_{max}$ for the free ligand, where the difference in molar absorptivities for reactants and products was at a maximum. The initial concentration of all the complexes was in the range 3–30 μM. In most cases, the change in absorbance was monitored continuously inside

 © 2006 Wiley-VCH Verlag GmbH & Co. KGaA, Weinheim 

a thermostatted cell compartment of a Cary 17 spectrophotometer. In some experiments, especially those at ≥ 90 °C, the samples were sealed in glass ampoules and immersed into thermostatted (±0.05 °C) oil. At the desired times, an ampoule was removed, and the reaction quenched in either ice-cold water or liquid nitrogen. The sample was brought to room temperature to record the absorbance. The rate constants and activation parameters were obtained by fitting the data to appropriate equations with the program Kaleidagraph 3.6.

**Supporting Information** (see also the footnote on the first page of this article): Figures S1–S7, kinetic data.

## Acknowledgments

This work was supported by grants from the National Science Foundation, CHE 0240409 and CHE 0602183. Some of the work was conducted with the use of facilities at the Ames Laboratory. We are also thankful to the Croatian Ministry of Science for a continuous support of the research at RBI.

[1] S. N. Brown, J. M. Mayer, *J. Am. Chem. Soc.* **1996**, *118*, 12119–12133.
[2] S. M. Mullins, R. G. Bergman, J. Arnold, *Organometallics* **1999**, *18*, 4465–4467.
[3] M. N. Akhtar, D. R. Boyd, J. D. Neill, D. M. Jerina, *J. Chem. Soc., Perkin Trans.1* **1980**, 1693–1699.
[4] M. M. Alam, A. Watanabe, O. Ito, *Photochem. Photobiol.* **1996**, *63*, 53–59.
[5] G. Bucher, J. C. Scaiano, *J. Phys. Chem.* **1994**, *98*, 12471–12473.
[6] G. A. Vaughan, G. L. Hillhouse, R. T. Lum, S. L. Buchwald, A. L. Rheingold, *J. Am. Chem. Soc.* **1988**, *110*, 7215–7217.
[7] H. Ohtake, T. Higuchi, M. Hirobe, *J. Am. Chem. Soc.* **1992**, *114*, 10660–10662.
[8] D. Chatterjee, *J. Mol. Catal. A* **1999**, *150*, 49–52.
[9] D. M. Baird, C. Aburri, L. S. Barron, S. A. Rodriguez, *Inorg. Chim. Acta* **1995**, *237*, 117–122.
[10] R. R. Conry, J. M. Mayer, *Inorg. Chem.* **1990**, *29*, 4862–4867.
[11] K.-M. Sung, R. H. Holm, *J. Am. Chem. Soc.* **2001**, *123*, 1931–1943.
[12] J. P. Caradonna, P. R. Reddy, R. H. Holm, *J. Am. Chem. Soc.* **1988**, *110*, 2139–2144.
[13] E. G. Samsel, K. Srinivasan, J. K. Kochi, *J. Am. Chem. Soc.* **1985**, *107*, 7606–7617.
[14] C. R. J. Lepage, L. Mihichuk, D. G. Lee, *Can. J. Chem.* **2003**, *81*, 75–80.
[15] S. Premsingh, N. S. Venkataramanan, S. Rajagopal, S. P. Mirza, M. Vairamani, P. S. Rao, K. Velavan, *Inorg. Chem.* **2004**, *43*, 5744–5753.
[16] D. L. Hughes, G. B. Smith, J. Liu, G. C. Dezeny, C. H. Senanayake, R. D. Larsen, T. R. Verhoeven, P. J. Reider, *J. Org. Chem.* **1997**, *62*, 2222–2229.
[17] J. H. Espenson, *Adv. Inorg. Chem.* **2003**, *54*, 157–202.
[18] P. S. Hall, G. E. Jackson, J. R. Moss, D. A. Thornton, *J. Coord. Chem.* **1993**, *30*, 63–69.
[19] S. Toyota, M. Oki, *Bull. Chem. Soc. Jpn.* **1988**, *61*, 699–705.
[20] J. C. Ronfard-Haret, C. Chachaty, *J. Phys. Chem.* **1978**, *82*, 1541–1547.
[21] W. L. Purcell, *Inorg. Chem.* **1989**, *28*, 2312–2315.
[22] A. Bakac, R. Marcec, M. Orhanovic, *Inorg. Chem.* **1974**, *13*, 57–60.
[23] A. Bakac, V. Butkovic, J. H. Espenson, J. Lovric, M. Orhanovic, *Inorg. Chem.* **1996**, *35*, 5168–5172.
[24] T. J. Weeks Jr, E. L. King, *J. Am. Chem. Soc.* **1968**, *90*, 2545–2550.
[25] H. H. Jaffe, *J. Am. Chem. Soc.* **1954**, *77*, 4451–4453.
[26] T. W. Swaddle, E. L. King, *Inorg. Chem.* **1964**, *3*, 234–236.
[27] R. G. Wilkins, *Kinetics and Mechanisms of Reactions of Transition Metal Complexes*, 2nd thoroughly revised edition, chapter 4, VCH, Weinheim, **1991**.
[28] J. P. Birk, J. H. Espenson, *Inorg. Chem.* **1968**, *7*, 991–998.
[29] E. Deutsch, H. Taube, *Inorg. Chem.* **1968**, *7*, 1532–1544.
[30] J. E. Finholt, S. N. Deming, *Inorg. Chem.* **1967**, *6*, 1533–1536.
[31] T. W. Swaddle, E. L. King, *Inorg. Chem.* **1964**, *3*, 234–236.
[32] T. W. Swaddle, E. L. King, *Inorg. Chem.* **1965**, *4*, 532–538.
[33] J. C. Jayne, E. L. King, *J. Am. Chem. Soc.* **1964**, *86*, 3989–3994.
[34] L. Chmurzynski, *Anal. Chim. Acta* **1996**, *321*, 237–244.
[35] E. Profft, W. Krueger, P. Kuhn, W. Lietz, *Chem. Abstracts* **1970**, *72*, 90309w.
[36] G. W. Haupt, *J. Res. Natl. Bur. Stand. (U.S.)* **1952**, *48*, 2331.

Received: March 24, 2006
Published Online: May 29, 2006

 © 2006 Wiley-VCH Verlag GmbH & Co. KGaA, Weinheim 

DOI: 10.1002/ejic.200500906

# Design, Crystal Growth, Characterization, and Second-Order Nonlinear Optical Properties of Two New Three-Dimensional Coordination Polymers Containing Selenocyanate Ligands

**Sheng-Li Li,[a,b] Jie-Ying Wu,[a] Yu-Peng Tian,*[a,c,d] Hai Ming,[b] Pei Wang,[b] Min-Hua Jiang,[c] and Hoong-Kun Fun[e]**

**Keywords:** Self-assembly / Coordination polymer / Crystal growth / Nonlinear optical properties

Two new second-order nonlinear optical coordination polymers, zinc cadmium tetraselenocyanate ($[ZnCd(SeCN)_4]_n$, **1**) and cadmium mercury tetraselenocyanate ($[CdHg(SeCN)_4]_n$, **2**), have been synthesized by reactions of self-assembly. Their structural, optical, and physicochemical properties were characterized by X-ray diffraction, infrared and Raman spectroscopy, electronic spectra, and thermal analyses. Structure analyses reveal that they belong to the tetragonal system $I\bar{4}$ space group. The cell dimensions for **1**: $a$ = 11.3420(1), $b$ = 11.3420(1), $c$ = 4.6326(1) Å, $V$ = 595.94(1) Å$^3$, $Z$ = 2, $D_c$ = 3.331 g·cm$^{-3}$, $R_1$ = 0.0411, $wR_2$ = 0.1058; for **2**: $a$ = 11.6579(7), $b$ = 11.6579(7), $c$ = 4.5109(4) Å, $V$ = 613.06(8) Å$^3$, $Z$ = 2, $D_c$ = 3.970 g·cm$^{-3}$, $R_1$ = 0.0432, $wR_2$ = 0.1031. The structural features of **1** and **2** are Cd–Se=C=N–Zn and Hg–Se=C=N–Cd bridges, respectively, which lead to the formation of an infinite three-dimensional (3D) network. Consistent with their polar structures, compounds **1** and **2** exhibit powder second harmonic generation (SHG) responses much stronger than urea, indicating quite a promising application potential as useful nonlinear optical (NLO) materials.
(© Wiley-VCH Verlag GmbH & Co. KGaA, 69451 Weinheim, Germany, 2006)

## Introduction

It is well known that the rapidly developing area of research on supramolecular architectures has provided implications for the rational design of functional materials[1,2] and a number of the assemblies are predominantly controlled by the coordination preferences of the transition metal and the ligand building blocks.[3,4] Recent developments in the specific, efficient syntheses by self-assembly processes of coordination complexes have afforded a variety of unusual topologies such as molecular helicates, grids, ladders, rings, and boxes.[5,6] Self-assembly of polynuclear structure has received considerable attention from researchers in areas ranging from chemistry to solid-state physics and biology.[7] Some complexes are of interest not only for their unusual structures and the simple synthetic methods used to prepare them, but also because they allow the preparation of polynuclear complexes in which several potentially interesting metal centers are designed to link in a well-defined spatial array. The use of metal complexes to function as molecular devices is one of the major interests in coordination chemistry.

There has been considerable interest in the synthesis of new materials with optical nonlinearities because of their potential use in device applications in telecommunications, optical computing, optical storage, and optical information processing. However, organic systems can suffer from problems such as volatility, low thermal stability, and mechanical weakness. The low-energy d–d transitions present in nearly all organometallic compounds, normally observed in the visible light region, will limit the usefulness of these materials. On the other hand, the inorganic ligands such as the ambidentate thiocyanate ($SCN^-$) and the selenocyanate ($SeCN^-$) ligand, can govern the nonlinearities for the metal complexes from the viewpoint of molecular design.[8] In particular, the group IIB divalent $d^{10}$ ions, $Zn^{2+}$, $Cd^{2+}$, and $Hg^{2+}$ complexes, have attracted our interest for their unique characteristics of pale color and high thermal stability.[9]

As a result of the unsymmetrical nature of complexes, optical activity can occur as specific physical effects such as nonlinear optical (NLO) response.[10] The incorporation of the strong conjugation ligands, such as the asymmetric selenocyanate (SeCN) groups in the title polymers with a three-dimensional (3D) network, can introduce strong electronic asymmetry and electron delocalization in the whole unsym-

[a] Department of Chemistry, Anhui University,
Hefei 230039, P. R. China
Fax: +86-551-5107342
E-mail: lsl1968@ahu.edu.cn
yptian@ahu.edu.cn
[b] Department of Physics, University of Science and Technology of China,
Hefei 230026, P. R. China
[c] State Key Laboratory of Crystal Materials, Shandong University,
Jinan 250100, P. R. China
[d] State Key Laboratory of Coordination Chemistry, Nanjing University,
Nanjing 210093, P. R. China
[e] X-ray Crystallography Unit, School of Physics, University Sains Malaysia,
11800 USM, Penang, Malaysia

 © 2006 Wiley-VCH Verlag GmbH & Co. KGaA, Weinheim 

metrical structure, resulting in large second-order microscopic and macroscopic nonlinearity. Considering this, attention has been paid to the following facts: (1) The large nonlinear optical response comes with a big conjugation system, which is able to provide sufficient electronic channels for the photoelectric process. (2) The electronic nature of the metal center has an influential effect on the nonlinear optical interactions. In particular, the d orbital of the transition metal can become a component of the π conjugation system, thus extending the electronic interactions; (3) Reducing the molecular symmetry can help the formation of a noncentrosymmetric space group. Then, specific crystallization techniques are taken into account to form a proper crystal lattice, in which the good microscopic NLO response can be collected rather than eliminated; (4) Making use of the coordination bond or forming the polymeric complex to connect molecules and sequentially control the alignment of molecules in the crystal, the interaction for the bulk NLO response could be accumulated.

As far as we know, the preparation of selenocyanate-containing metal–inorganic compounds along with their characterization have been reported, but the NLO properties of the selenocyanate-containing polymers have scarcely been described hitherto. Referring to the title NLO polymers, we have systemically carried out research[11] not only on the preparation, crystal growth, physicochemical, and nonlinear optical properties of the complexes, but also on the design and structure–property relationship, which is original and different from other related reports.[12] In the crystal growth process, we used a one-step building-block approach capable of forming a chemically stable system, which enabled us to grow the high-quality and transparent polymeric single crystals, in contrast to the complicated approach used before resulting in mixtures of small molecular compounds or perhaps even monomers. In this context, the building-block approach of self-assembly for the synthesis of coordination polymers illustrates both the importance of metal-ion geometry and the effect that the ligand backbone can have on network construction. This article deals with two novel 3D coordination polymers, $[ZnCd(SeCN)_4]_n$ (**1**) and $[CdHg(SeCN)_4]_n$ (**2**), and their preparation, crystal growth, structures, and NLO properties are described.

## Results and Discussion

### Single-Crystal Growth

The chalcogenocyanate ion, $SeCN^-$, is a linear triatomic pseudohalide and a highly versatile ambidentate ligand with a polarizable π system. It can coordinate to transition-metal ions through either the hard nitrogen or the soft selenium atom, or both, giving rise to linkage isomers or polymers.

The crystal growth processes of **1** and **2** were carried out in one step by self-assembling in aqueous solutions containing cadmium chloride, potassium selenocyanate, and zinc chloride (for **1**) or mercury chloride (for **2**). Preparations were accomplished by two continuous reactions, where M = Zn or Hg:

$$4\ KSeCN + MCl_2 = K_2M(SeCN)_4 + 2\ KCl$$

$$K_2M(SeCN)_4 + CdCl_2 = MCd(SeCN)_4 + 2\ KCl$$

We have obtained good single crystals from RMS and the experiments showed that the success of growing large and high-quality single crystals with low defect density was highly dependent on the purity of the starting materials. Several foreign metallic cations, such as $Al^{3+}$, $Fe^{3+}$, $Co^{2+}$, $Ni^{2+}$, $Cu^{2+}$ and so forth, would badly influence the quality of the crystals, especially their transparency. Meanwhile, the crystal growth processes of the two polymers were affected by the pH value of RMS. We optimized the pH values of **1** and **2** solutions at 3.5–5.0 to get well-developed and transparent single crystals. As potassium selenocyanate (KSeCN) easily decomposes in air, the entire crystallization process was performed in a desiccator in vacuo. Moreover, the experiments indicated that the colors of **1** and **2** solutions easily turn slightly red or gray when the precipitates form as byproducts at a relatively high temperature, although the crystals show no decomposition and hygroscopic effect at atmospheric pressure and room temperature.

### IR and Raman Spectra

Figure 1 and Figure 2 show the IR transmission spectra of **1** and **2** crystals. The assignments of the main characteristic IR band frequencies observed for KSeCN,[13] $Cd(SeCN)_4Zn$,[12a] **1**, and **2** are listed in Table 1. It is known that in IR spectra of the metal (M) complexes containing monodentate SeCN ligands, $\nu_{CN}$ often lies higher than 2085 $cm^{-1}$, $\nu_{CSe}$ lies at about 700–620 $cm^{-1}$ (N–M bonding) or 550–500 $cm^{-1}$ (Se–M bonding), and $\delta_{SeCN}$ lies near 425 $cm^{-1}$ (N–M bonding) or 370 $cm^{-1}$ (Se–M bonding).[14] From Table 1, one can see the sharp increase in frequencies of $\nu_{CN}$ stretching and $\nu_{CSe}$ stretching and the decrease in frequencies of $\delta_{SeCN}$ bending in **1** and **2** compared with the corresponding bands in the free selenocyanate radical of KSeCN. This can be explained by the electron transport model.[15] In **1** and **2** crystals, the SeCN group is a good

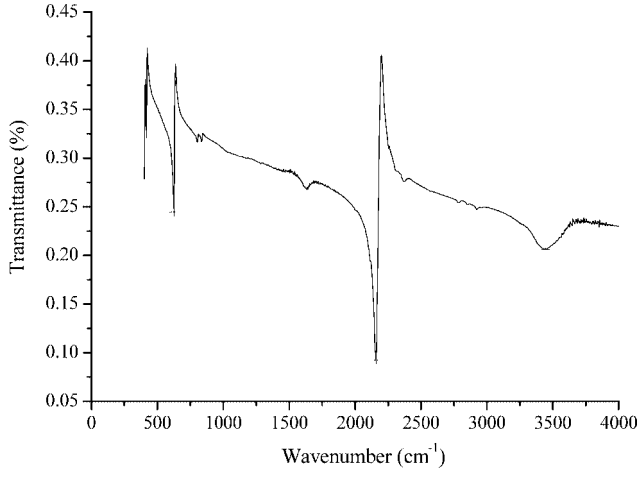


Figure 1. IR transmission spectra of **1** crystal.

 © 2006 Wiley-VCH Verlag GmbH & Co. KGaA, Weinheim 

electron supplier, whereas $Zn^{2+}$, $Cd^{2+}$, and $Hg^{2+}$ are all strong electron acceptors. The electron transformation from $SeCN^-$ to $Zn^{2+}$, $Cd^{2+}$, and $Hg^{2+}$ ions makes the wavenumbers of CN and CSe stretching vibrations increase significantly and that of SeCN bending vibrations decrease. This confirms the presence of M–N and M–Se bands in their structures.

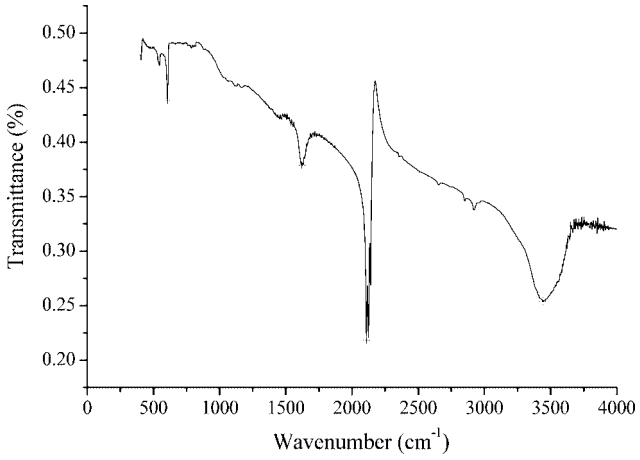


Figure 2. IR transmission spectra of **2** crystal.

Table 1. Assignments of the main characteristic IR band frequencies [$cm^{-1}$] observed for KSeCN,[13] $Cd(SeCN)_4Zn$,[12a] **1**, and **2**.

| | KSeCN | $Cd(SeCN)_4Zn$ | **1**, $[ZnCd(SeCN)_4]_n$ | **2**, $[CdHg(SeCN)_4]_n$ |
|---|---|---|---|---|
| $\nu_{CN}$ | 2070 | 2154 | 2158 | 2140 |
| $\nu_{CSe}$ | 558 | 628 | 625 | 606 |
| $\delta_{NCSe}$ | 424, 416 | 420, 406 | 417, 403 | 407, 393 |

The Raman spectra (Figure 3 and Figure 4) of $AB(SeCN)_4$ (A = Zn, B = Cd for **1**; A = Cd, B = Hg for **2**), recorded at room temperature in the frequency range from 50 to 2500 $cm^{-1}$, consist of four frequency regions (below 100 $cm^{-1}$, lattice vibration modes; 100–300 $cm^{-1}$, vibration bands of A and B centers; 300–1200 $cm^{-1}$, NCSe internal vibration modes; and 2100–2200 $cm^{-1}$, CN stretching vibration modes). According to the vibrational spectra,[16] the Raman peaks can be assigned as $\nu_1$ [a doubly degenerate $B(SeCN)_4$ bending vibration mode], $\nu_2$ [a doubly degenerate $A(NCSe)_4$ bending vibration mode], $\nu_3$ (a SeCN bending vibration mode), $\nu_4$ (a doubly degenerate SeCN bending vibration mode), $\nu_5$ (a CSe stretching vibration mode), and $\nu_6$ (a CN stretching vibration mode). The Raman peaks ($\nu_1$ and $\nu_2$) are split on the low-wavenumber side owing to the distortion of the $B(SeCN)_4$ and $A(NCSe)_4$ tetrahedra in $AB(SeCN)_4$ crystals. The observed bands along with their vibrational assignments are summarized in Table 2.

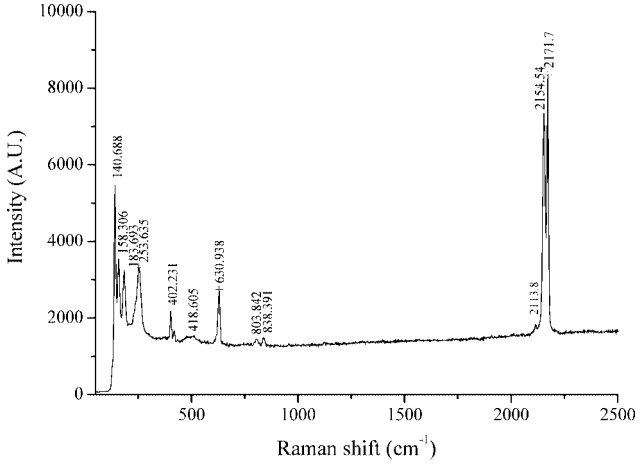


Figure 3. Raman spectra of **1** crystal.

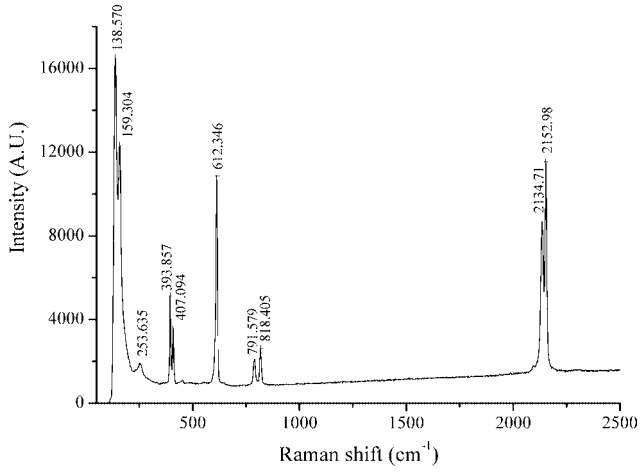


Figure 4. Raman spectra of **2** crystal.

Table 2. Assignments of the main characteristic Raman vibrational spectra data [$cm^{-1}$] observed for **1** and **2**.

| Assignment[a] | **1**, $[ZnCd(SeCN)_4]_n$ | **2**, $[CdHg(SeCN)_4]_n$ |
|---|---|---|
| $\delta_{SeBSe}$ | 141, 158, 184 | 138, 159 |
| $\delta_{NAN}$ | 254 | 253 |
| $\delta_{SeCN}$ | 402, 418 | 394, 407 |
| $\nu_{CSe}$ | 631 | 612 |
| $2\delta_{SeCN}$ | 804, 838 | 792, 818 |
| $\nu_{CN}$ | 2114, 2155, 2172 | 2135, 2153 |

[a] A stands for Zn in **1** and for Cd in **2**; B stands for Cd in **1** and for Hg in **2**.

## UV/Vis Spectra

Linear absorption spectra of **1** and **2** powders, resolved in dimethyl formamide (DMF), were determined with a 1-cm path and a concentration of $1\times10^{-5}$ mol·$dm^{-3}$. The spectra show a distinctly strong absorption band at about 270 nm for **1** and 266 nm for **2**. Additionally, the solid-state electronic spectra show an intense band at approximately 263 nm for **1**, and 268 and 311 nm for **2**. These bands may be assigned to the metal-mediated ligand $\pi\rightarrow\pi^*$ charge transition of the polymeric metal–selenocyanate system. Such a transition is believed to be the origin of the NLO response.[8a]

 © 2006 Wiley-VCH Verlag GmbH & Co. KGaA, Weinheim 

### Thermal Stability and Solubility

Thermogravimetric analyses (TGA) of **1** and **2** were performed on the single-crystal samples. The TGA curves of the two complexes exhibited that **1** was stable up to its decomposition temperature of 345.5 °C without showing any melting process and **2** did not melt until the decomposition temperature of 278.2 °C, indicating the high stability of each polymeric structure. Furthermore, in water, **1** is stable at atmospheric pressure and 65 °C for several days without decomposition and hydrolysis, while **2** decomposes and hydrolyzes if it is kept at over 45 °C for several hours.

Because of the poor solubility of **1** and **2** in common solvents, no considerably large single crystal can be grown. The experiments show that the crystals exhibit relatively high solubilities in a mixture of water and acetone (v/v = 1:3); while acetone is very volatile, they can be easily recrystallized and purified by this mixed solvent.

### Description of the Structures

Some valuable experiences have been accumulated that enhance the possibility of obtaining the optimal crystallization. Single crystals obtained have low $R$ values: polymer **1**, $R_1 = 0.0411$ and $wR_2 = 0.1058$; and polymer **2**, $R_1 = 0.0432$ and $wR_2 = 0.1031$. The latter final $R$ indices [$I > 2\sigma(I)$] and the crystal size $0.26 \times 0.22 \times 0.14$ mm of **2** are superior to those in the related article.[12b] The crystal structures of **1** and **2** are shown in Figure 5 and Figure 6 and their molecule stackings are shown in Figure 7 and Figure 8, respectively. Crystallographic data and structure refinements for **1** and **2** are summarized in Table 3 and selected bond lengths [Å] and angles [°] are shown in Table 4.

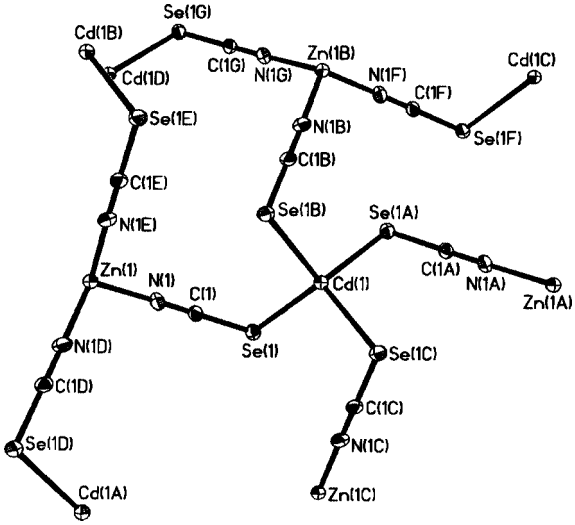


Figure 5. Crystal structure with the atom-numbering scheme of **1**.

Crystals **1** and **2** consist of two kinds of slightly flattened coordinate tetrahedrons with a local symmetry of $D_{2d}$: for **1** one is $ZnN_4$ and the other is $CdSe_4$ and for **2** one is $CdN_4$ and the other is $HgSe_4$. The central atoms, Zn and Cd in **1**

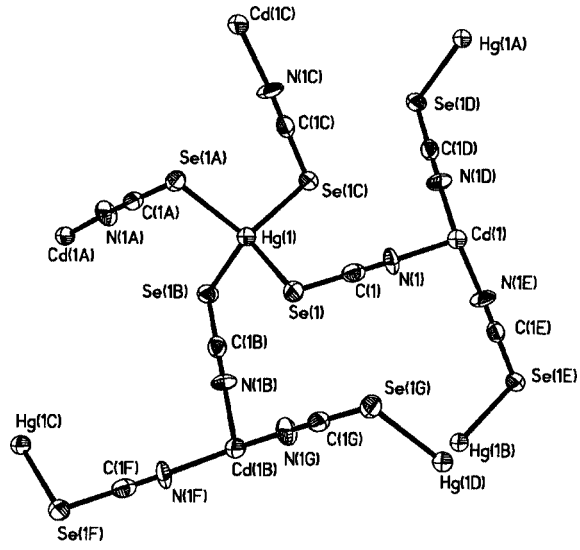


Figure 6. Crystal structure with the atom-numbering scheme of **2**.

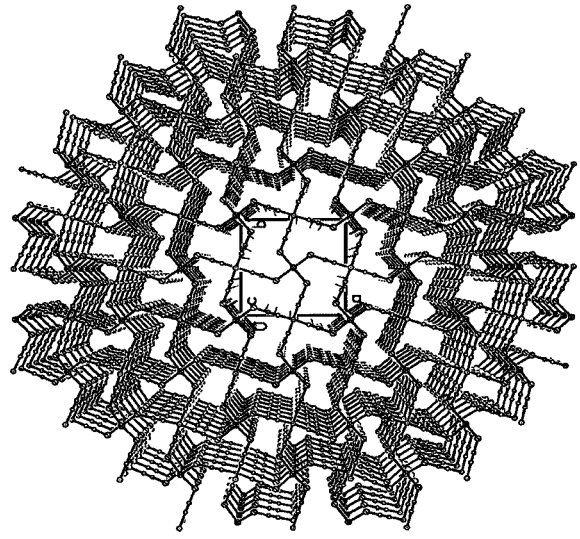

Figure 7. Molecular packing of polymer **1**.

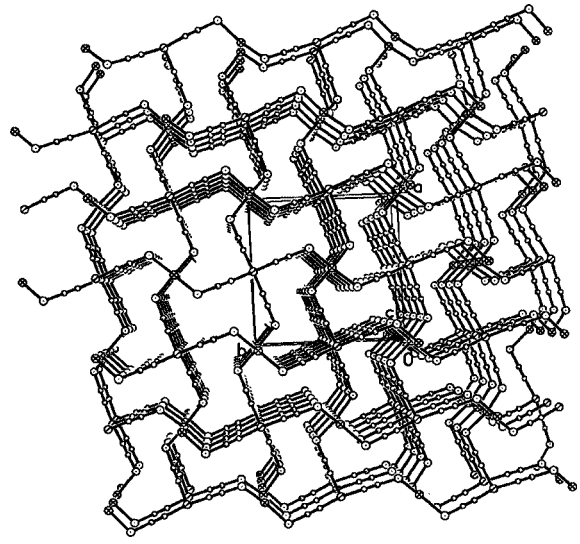

Figure 8. Molecular packing of polymer **2**.

 © 2006 Wiley-VCH Verlag GmbH & Co. KGaA, Weinheim 

Table 3. Crystallographic data and refinements for **1** and **2**.

| Compound | **1** | **2** |
|---|---|---|
| Empirical formula | $C_4CdN_4Se_4Zn$ | $C_4CdHgN_4Se_4$ |
| Formula mass | 597.69 | 732.91 |
| Temperature [K] | 293(2) | 293(2) |
| Wavelength [Å] | 0.71073 | 0.71073 |
| Crystal system, space group | tetragonal, $I\bar{4}$ | tetragonal, $I\bar{4}$ |
| Unit cell dimensions [Å] | $a$ = 11.3420(1) | $a$ = 11.6579(7) |
| | $c$ = 4.6326(1) | $c$ = 4.5109(4) |
| Volume [Å$^3$] | 595.942(15) | 613.06(8) |
| $Z$, calculated density [g·cm$^{-3}$] | 2, 3.331 | 2, 3.970 |
| Absorption coefficient [mm$^{-1}$] | 15.976 | 26.080 |
| $F$(000) | 532 | 632 |
| Crystal size [mm] | 0.22×0.18×0.16 | 0.26×0.22×0.14 |
| Theta range for data collection [°] | $2.54 < \theta < 29.30$ | $2.47 < \theta < 28.21$ |
| Reflections collected/unique | 2130/745 [$R$(int) = 0.0628] | 2180/740 [$R$(int) = 0.1012] |
| Data/restraints/parameters | 745/0/32 | 740/0/33 |
| Goodness-of-fit on $F^2$ | 1.049 | 1.103 |
| Final $R$ indices [$I > 2\sigma(I)$] | $R_1$ = 0.0411, $wR_2$ = 0.1058 | $R_1$ = 0.0432, $wR_2$ = 0.1031 |
| $R$ indices (all data) | $R_1$ = 0.0428, $wR_2$ = 0.1070 | $R_1$ = 0.0533, $wR_2$ = 0.1054 |
| Largest diff. peak and hole [e·Å$^{-3}$] | 0.809 and –1.779 | 1.236 and –1.972 |

Table 4. Selected bond lengths [Å] and angles [°] for **1** and **2**.

| **1** | | | |
|---|---|---|---|
| Cd(1)–Se(1)#1 | 2.6651(8) | Zn(1)–N(1)#5 | 1.964(8) |
| Cd(1)–Se(1)#2 | 2.6651(8) | Zn(1)–N(1) | 1.964(8) |
| Cd(1)–Se(1) | 2.6651(8) | Zn(1)–N(1)#6 | 1.964(8) |
| Cd(1)–Se(1)#3 | 2.6651(8) | Se(1)–C(1) | 1.798(8) |
| Zn(1)–N(1)#4 | 1.964(8) | N(1)–C(1) | 1.163(12) |
| Se(1)#1–Cd(1)–Se(1)#2 | 113.10(4) | N(1)#5–Zn(1)–N(1) | 107.9(3) |
| Se(1)#1–Cd(1)–Se(1) | 107.688(18) | N(1)#4–Zn(1)–N(1)#6 | 107.9(2) |
| Se(1)#2–Cd(1)–Se(1) | 107.688(18) | N(1)#5–Zn(1)–N(1)#6 | 112.7(5) |
| Se(1)#1–Cd(1)–Se(1)#3 | 107.689(18) | N(1)–Zn(1)–N(1)#6 | 107.9(2) |
| Se(1)#2–Cd(1)–Se(1)#3 | 107.688(18) | C(1)–Se(1)–Cd(1) | 95.1(3) |
| Se(1)–Cd(1)–Se(1)#3 | 113.10(4) | C(1)–N(1)–Zn(1) | 177.6(8) |
| N(1)#4–Zn(1)–N(1)#5 | 107.9(2) | N(1)–C(1)–Se(1) | 179.6(8) |
| N(1)#4–Zn(1)–N(1) | 112.7(5) | | |
| **2** | | | |
| Hg(1)–Se(1) | 2.6680(13) | Cd(1)–N(1) | 2.169(12) |
| Hg(1)–Se(1)#1 | 2.6680(13) | Cd(1)–N(1)#5 | 2.169(12) |
| Hg(1)–Se(1)#2 | 2.6680(13) | Cd(1)–N(1)#6 | 2.169(12) |
| Hg(1)–Se(1)#3 | 2.6680(13) | Se(1)–C(1) | 1.811(15) |
| Cd(1)–N(1)#4 | 2.169(12) | N(1)–C(1) | 1.140(19) |
| Se(1)–Hg(1)–Se(1)#1 | 106.91(3) | N(1)–Cd(1)–N(1)#5 | 112.9(9) |
| Se(1)–Hg(1)–Se(1)#2 | 114.73(6) | N(1)#4–Cd(1)–N(1)#6 | 112.9(9) |
| Se(1)#1–Hg(1)–Se(1)#2 | 106.91(3) | N(1)–Cd(1)–N(1)#6 | 107.8(5) |
| Se(1)–Hg(1)–Se(1)#3 | 106.91(3) | N(1)#5–Cd(1)–N(1)#6 | 107.8(4) |
| Se(1)#1–Hg(1)–Se(1)#3 | 114.73(6) | C(1)–Se(1)–Hg(1) | 95.6(4) |
| Se(1)#2–Hg(1)–Se(1)#3 | 106.91(3) | C(1)–N(1)–Cd(1) | 172.2(16) |
| N(1)#4–Cd(1)–N(1) | 107.8(4) | N(1)–C(1)–Se(1) | 177.1(15) |
| N(1)#4–Cd(1)–N(1)#5 | 107.8(5) | | |

or Hg and Cd in **2**, are located at the center of the fourfold inversion axis. From Table 4, one can see that all the Se–C–N bond angles in the two crystals are very close to 180°, that is, the SeCN group is almost perfectly linear. Therefore, the bond parameters of **1** and **2** are quite similar and it is not strange that both of them belong to the tetragonal system $I\bar{4}$ space group. Furthermore, the most striking features of the structures are the Cd–Se=C=N–Zn bridges and Hg–Se=C=N–Cd bridges, which effectively lead to the formation of an infinite three-dimensional (3D) network in a zigzag way. The coordination modes in the structures can be rationalized in terms of the hard–soft acid–base (HSAB) concept.[17]

The structural characteristics of **1** and **2** account for quite high physicochemical stability. They both possess high thermal stability and do not show hygroscopic or decomposition effects at room temperature to a great extent because of the presence of this strong polymeric structure. The asymmetric arrangements of Se and N atoms around the metal atom give rise to asymmetrical metal coordination and highly asymmetric electronic distribution about the metal atom. The extended π conjugation system within the

 © 2006 Wiley-VCH Verlag GmbH & Co. KGaA, Weinheim 

3D network structure, with the high polarizabilities of both the metal and the ligand, can induce desirable physical properties such as NLO effects.[8a,18]

### X-ray Powder Diffraction

The X-ray powder diffraction (XRPD) patterns and diffraction indices of **1** and **2** are shown in Figure 9 and Figure 10, respectively. The tetragonal unit-cell parameters calculated by the TREOR program[19] according to the values of $2\theta$ in the XRPD patterns are $a$ = 11.3352, $c$ = 4.5709 Å, $V$ = 587.30 Å$^3$ for **1**, and $a$ = 11.6450, $c$ = 4.2155 Å, $V$ = 571.65 Å$^3$ for **2**, which agree well with the results determined by the Siemens SMART CCD area detector diffractometer mentioned above.

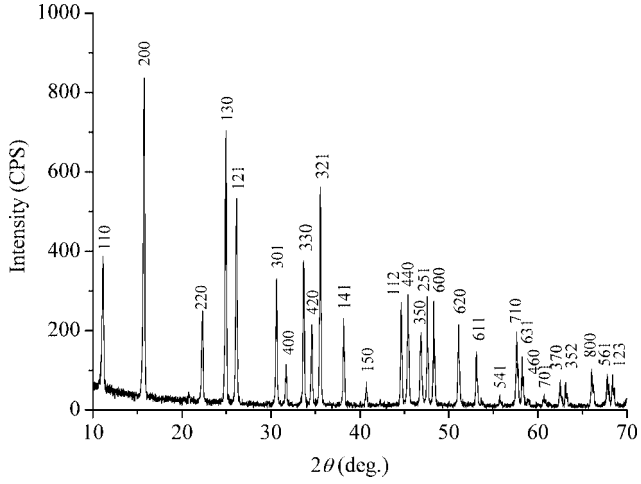


Figure 9. XRPD pattern and diffraction indices of **1** crystal.

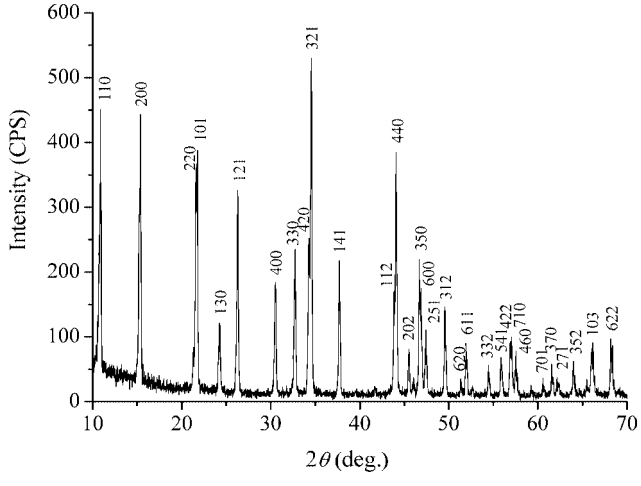


Figure 10. XRPD pattern and diffraction indices of **2** crystal.

### Optical Properties

As for the feature of unsymmetrical structure, NLO activity can occur as specific physical effects. Complexes **1** and **2**, with the noncentrosymmetric space group $I\bar{4}$, were expected to give rise to efficient SHG effects for NLO application. Preliminary experimental results confirmed this and showed they both displayed strong powder SHG efficiencies. The SHG intensity was determined by the powder technique of Kurtz and Perry,[20] in which the second harmonic output was generated by irradiating powder samples of randomly oriented crystallites. The incident radiation came from a Q-switched and mode-locked Nd:YAG laser, and the results indicate that the power SHG efficiency of **1** is superior to that of **2**. The 532 nm second harmonic intensities of **1** and **2** powders were estimated as about 45 and 25 times that of NLO urea powders by direct frequency doubling of a laser diode at 1064 nm at room temperature. We assume that the high nonlinearity of the two crystals is attributed to two structural factors. One is the conjugated charge-moving bridges (Cd–Se=C=N–Zn for **1** and Hg–Se=C=N–Cd for **2**) that connect all the distorted tetrahedrons together, and the other is the effective sum of the microscopic hyperpolarizabilities originating from the parallel molecular stacking in the direction of the fourfold inversion axis. The second harmonic responses of **1** and **2** evidently resulted from the polar arrangement of all the bridging $SeCN^-$ groups, as the utilization of the asymmetric ligands can introduce electronic asymmetry, which is essential for a SHG response.[21] Considering their high thermal stability and tolerance to hydrolysis, both **1** and **2** are considered as quite promising SHG materials. Now we are managing to improving the SHG output efficiency along with exploring better crystal growth conditions.

## Conclusions

The present study shows that a rational design utilizing suitable ligands and metal ions has prepared new supramolecular polymers with nonlinear optical property. The synthetic approach is based on self-assembly of the functional components into well-defined crystalline materials, which allows important structure–property relationships to be established. The title crystals possess better stability and do not show any decomposition and hygroscopic effects at room temperature, but the pH value sensitivity in solution and the physicochemical change at high temperature show the difficulties of single-crystal growth. X-ray diffraction investigations reveal that they crystallize in the same noncentrosymmetric space group, $I\bar{4}$. The high degree of polarizability of the chosen metal and the ambidentate ligand $SeCN^-$, together with the three-dimensional (3D) network structures, provide the crystals with a large interaction force between molecules, which in turn induces large macroscopic NLO properties. The SHG intensities of **1** and **2** were observed to be much stronger than that of urea powders because of the presence of distorted $AN_4$ (A = Zn or Cd) and $BSe_4$ (B = Cd or Hg) tetrahedra in the 3D structure. In summary, being 3D coordination polymers, **1** and **2** have emerged as two promising candidate materials for generation of blue-violet light using a diode laser and this, their high SHG efficiency, excellent optical transparency, and

 © 2006 Wiley-VCH Verlag GmbH & Co. KGaA, Weinheim 

high thermal stability make them attractive for device applications. Further studies on related properties are currently under way.

## Experimental Section

**General:** Potassium selenocyanate (KSeCN) was prepared by the method given in the literature.[22] All other starting materials were analytical reagent grade (Purity ≥ 98.0%) and used as purchased, and all the synthetic and growth processes were carried out in aqueous solutions. Elemental analyses were performed with a Perkin–Elmer 240 instrument. IR spectra were recorded with a Nicolet FTIR 170SX instrument (KBr discs) in the 4000–400 $cm^{-1}$ region. The far-IR spectra (500–100 $cm^{-1}$) were recorded in Nujol mulls between polyethylene sheets. UV/Vis spectra were recorded with a UV-265 spectrophotometer. TGA analyses were recorded with a Perkin–Elmer Pris-1 DMDA-V1 analyzer in nitrogen at a heating rate of 5 °C $min^{-1}$. The second-order nonlinear optical tests were carried out by the powder second harmonic generation (SHG) method.[20]

Room-temperature Raman spectra of the two crystal powders were measured on a LABRAM microscopic Raman spectrometer with a slit width of 100 nm, using a 100 mW argon ion laser at 514.53 nm with a power density of 5 mW·μ$m^{-2}$ at the sample. The Raman spectra with a resolution of 0.15 $cm^{-1}$ and a wavelength precision of 0.5 $cm^{-1}$ in a wavenumber range from 50 to 2500 $cm^{-1}$ were collected.

The XRPD patterns of the **1** and **2** crystals were registered with a Rigaku D/Max-γA diffractometer, operated at 40 KV and 40 mA, using a Cu target tube and a graphite monochromator. Fixed scatter and divergence slits of 1° and a 0.15-mm receiving slit were used. The intensity data were recorded by continuous scan in a $2\theta/\theta$ mode from 10° to 70° with a step size of 0.02° and a scan speed of 4°$min^{-1}$.

**Syntheses**

**$[ZnCd(SeCN)_4]_n$ (1):** Cadmium chloride ($CdCl_2$) (0.03 mol, 5.50 g) was dissolved in deionized water (30 mL) at room temperature. This solution was added slowly to a colorless solution (50 mL) containing zinc chloride ($ZnCl_2$) (0.03 mol, 4.09 g) and potassium selenocyanate (KSeCN) (0.12 mol, 17.29 g). The stoichiometric mixture was stirred for 1 h and then filtered. The resulting filtrate was kept standing and evaporated slowly in a desiccator in vacuo over calcium chloride. Two weeks later, the colorless and transparent tetrahedral-shaped single crystals were obtained. Yield 12.98 g (72.4%). $ZnCd(SeCN)_4$ (597.69): calcd. C 8.03, N 9.36; found C 8.07, N 9.39.

**$[CdHg(SeCN)_4]_n$ (2):** This complex was prepared in an analogous way to that of **1**. Cadmium chloride ($CdCl_2$) (0.03 mol, 5.50 g) was dissolved in solution and then added slowly into a colorless solution containing mercury chloride ($HgCl_2$) (0.03 mol, 8.14 g) and potassium selenocyanate (KSeCN) (0.12 mol, 17.29 g) with stirring. After 1 h the stoichiometric mixture was filtered and evaporated slowly in a desiccator in vacuo. Twenty days later, the silvery gray and transparent tetrahedral-shaped single crystals were obtained. Yield 14.85 g (67.5%). $CdHg(SeCN)_4$ (732.91): calcd. C 6.55, N 7.64; found C 6.59, N 7.67.

**Crystallographic Structure Determination:** High optical quality **1** and **2** single crystals suitable for X-ray diffraction analyses were grown from their reaction mother solutions (RMS) by the solvent-evaporation method and then separated and dried, respectively. A single crystal of polymer **1** or **2** with suitable dimensions was mounted on a glass fiber and data collections were performed using a Siemens SMART CCD area detector diffractometer with Mo-$K_\alpha$ radiation with $\omega$-scan mode ($\lambda$ = 0.71073 Å). The structures were solved with direct methods using the program SHELXTL[23] and refined anisotropically with SHELXTL using the full-matrix least-squares procedure.

CCDC-207921 (for **1**) and -207922 (for **2**) contain the supplementary crystallographic data for this paper. These data can be obtained free of charge from The Cambridge Crystallographic Data Centre via www.ccdc.cam.ac.uk/data_request/cif.

## Acknowledgments

This work was supported by the National Nature Science Foundation of China (50532030, 50335050), Doctoral Program Foundation of the Education Ministry of China, the Education Office Foundation of Anhui Province (2005KJ101), and the Malaysian Government and Universiti Sains Malaysia for the Scientific Advancement Grant Allocation (SAGA) grant No. 304/PFIZIK/653003/A118.

[1] I. Manners, *J. Polym. Sci., Part A: Polym. Chem.* **2002**, *40*, 179–191.
[2] E. Coronado, J. R. Galan-Mascaros, C. J. Gomez-Garcia, V. Laukhin, *Nature* **2000**, *408*, 447–449.
[3] A. J. Blake, N. R. Champness, P. Hubberstey, W. S. Li, M. Schröder, M. A. Withersby, *Coord. Chem. Rev.* **1999**, *183*, 117–138.
[4] P. H. Dinolfo, J. T. Hupp, *Chem. Mater.* **2001**, *13*, 3113–3125.
[5] M. Munakata, L. P. Wu, T. Kuroda-Sowa, *Adv. Inorg. Chem.* **1999**, *46*, 173–303.
[6] a) R. Kramer, I. O. Fritsky, H. Pritzkow, L. A. Kovbasyuk, *J. Chem. Soc., Dalton Trans.* **2002**, 1307–1314; b) S. Sain, T. K. Maji, G. Mostafa, T. H. Lu, M. Y. Chiang, N. R. Chaudhuri, *Polyhedron* **2002**, *21*, 2293–2299; c) K. M. Park, S. Y. Kim, J. Heo, D. Whang, S. Sakamoto, K. Yamaguchi, K. Kim, *J. Am. Chem. Soc.* **2002**, *124*, 2140–2147; d) W. J. He, F. Liu, C. Y. Duan, Z. J. Guo, S. Z. Zhou, Y. J. Liu, L. G. Zhu, *Inorg. Chem.* **2001**, *40*, 7065–7071.
[7] a) T. Bark, M. Duggeli, H. Stoeckli-Evans, A. V. Zelewsky, *Angew. Chem. Int. Ed.* **2001**, *40*, 2848–2851; b) T. W. Bell, H. Jonsselin, *Nature* **1994**, *367*, 441–444; c) W. Yeung, W. Wong, J. Zuo, T. Lau, *J. Chem. Soc., Dalton Trans.* **2000**, 629–631; d) Z. P. Zheng, *Chem. Commun.* **2001**, 2521–2529.
[8] a) H. Zhang, X. M. Wang, K. C. Zhang, B. K. Teo, *Coord. Chem. Rev.* **1999**, *183*, 157–195; b) H. Zhang, D. E. Zelmon, G. E. Price, B. K. Teo, *Inorg. Chem.* **2000**, *39*, 1868–1873; c) X. Q. Wang, D. Xu, M. K. Lu, D. R. Yuan, G. H. Zhang, F. Q. Meng, S. Y. Guo, M. Zhou, J. R. Liu, X. R. Li, *Cryst. Res. Technol.* **2001**, *36*, 73–84; d) X. Q. Wang, D. Xu, M. K. Lu, D. R. Yuan, G. H. Zhang, S. X. Xu, S. Y. Guo, X. N. Jiang, J. R. Liu, C. F. Song, Q. Ren, J. Huang, Y. P. Tian, *Mater. Res. Bull.* **2001**, *36*, 1287–1299.
[9] a) N. Zhang, M. H. Jiang, D. R. Yuan, D. Xu, X. T. Tao, Z. S. Shao, *J. Cryst. Growth* **1990**, *102*, 581–584; b) W. B. Hou, D. R. Yuan, D. Xu, N. Zhang, W. T. Yu, M. G. Liu, X. T. Tao, S. S. Ying, M. H. Jiang, *Mater. Res. Bull.* **1993**, *28*, 645–653.
[10] T. Hahn, H. Klapper, *International Tables for Crystallography*, Reidel, Dordrecht, The Netherlands, **1993**, vol. A., ch. 10.5, pp. 780–782.
[11] Y. P. Tian, S. L. Li, J. Y. Wu, S. Y. Zhang, J. X. Yang, W. Ma, "Process for the preparation of blue-violet light frequency-doubling selenocyanate complexes", CN 1440974A, September 9, **2003**; *Invention Patent Bulletin of China* (ISSN 1008-4274) **2003**, *19*, 37.

 © 2006 Wiley-VCH Verlag GmbH & Co. KGaA, Weinheim 

[12] a) M. Nagao, H. Inoue, S. Yanagisawa, *J. Coord. Chem.* **1980**, *10*, 29–32; b) H. Q. Sun, W. T. Yu, D. R. Yuan, X. Q. Wang, G. Xue, *Acta Crystallogr. Sect. E: Struct. Rep. Online* **2005**, *61*, i111–i112; c) Y. Y. Kharitonov, V. V. Skopenko, *Zh. Neorg. Khim.* **1965**, *10*, 1803–1805; d) G. V. Tsintsadze, V. V. Skopenko, A. E. Shvelashvili, *Soobshcheniya Akademii Nauk Gruzinskoi SSR.* **1966**, *41*, 337–340.
[13] H. W. Morgan, *J. Inorg. Nucl. Chem.* **1961**, *16*, 367–368.
[14] a) J. Chatt, L. A. Duncanson, *Nature* **1956**, *178*, 997–998; b) A. Turco, C. Pecile, M. Niccolini, *Proc. Chem. Soc. London* **1961**, 213–214; c) A. Turco, C. Pecile, M. Niccolini, *J. Chem. Soc.* **1962**, 3008–3015; d) J. L. Burmeister, Y. Al-Janabi, *Inorg. Chem.* **1965**, *4*, 962–965.
[15] K. Nakamoto, Translated by D. R. Huang, R. Q. Wang, *Infrared and Raman Spectra of Inorganic and Coordination Compounds*, 3rd ed., Chemical Industry Press, Beijing, **1986** (in Chinese).
[16] a) J. Lewis, R. S. Nyholm, P. W. Smith, *J. Chem. Soc.* **1960**, *83*, 1992–1996; b) A. Muller, K. H. Schmidt, K. H. Tytko, J. Bouwma, F. Jellinek, *Spectrochim. Acta, Part A* **1972**, *28*, 381–391; c) G. J. Kubas, L. H. Jones, *Inorg. Chem.* **1974**, *13*, 2816–2819.
[17] a) R. G. Pearson, *J. Am. Chem. Soc.* **1963**, *85*, 3533–3539; b) R. G. Pearson, *J. Am. Chem. Soc.* **1967**, *89*, 1827–1836; c) R. G. Pearson, *Science* **1966**, *151*, 172–177.
[18] J. Zyss, *Nonlinear Opt.* **1991**, *1*, 3–18.
[19] P. E. Werner, L. Eriksson, M. Westdahl, *J. Appl. Crystallogr.* **1985**, *18*, 367–370.
[20] S. K. Kurtz, T. T. Perry, *J. Appl. Phys.* **1968**, *39*, 3798–3813.
[21] a) O. R. Evans, R. G. Xiong, Z. Wang, G. K. Wong, W. Lin, *Angew. Chem. Int. Ed.* **1999**, *38*, 536–538; b) S. R. Batten, R. Robson, *Angew. Chem. Int. Ed. Engl.* **1998**, *37*, 1461–1494.
[22] G. R. Waitkins, R. Shutt, *Inorganic Synthesis*, McGraw-Hill, New York, NY, **1946**, vol. II, pp. 186–187.
[23] G. M. Sheldrick, *SHELXTL V5.1 Software Reference Manual*, Bruker AXS, Inc., Madison, WI, USA, **1997**.

Received: October 12, 2005
Published Online: May 8, 2006

 © 2006 Wiley-VCH Verlag GmbH & Co. KGaA, Weinheim 

EurJIC
European Journal of Inorganic Chemistry

Issue 15/2006

Pages 2913–3120

*Papers available ahead of print in Early View at www.interscience.wiley.com*

*Earliest available Table of Contents:*
*Automatically, free of charge by e-mail through*
*www.interscience.wiley.com/alerts*

## COVER PICTURE

**The cover picture shows** a chiral catalyst heterogenized into confined nanospaces of porous materials. The site-isolation of catalytic sites easily prevents the formation of inactive multinuclear species, consequently increasing the stability and turnover numbers of catalysts. In addition to this enhanced stability, increased enantioselectivity was also found upon immobilization in the confined spaces, due to the confinement effect originating from the interaction of catalyst/substrate with pore surfaces. Details of this chemistry are described in the Microreview by C. E. Song et al. on p. 2927 ff.

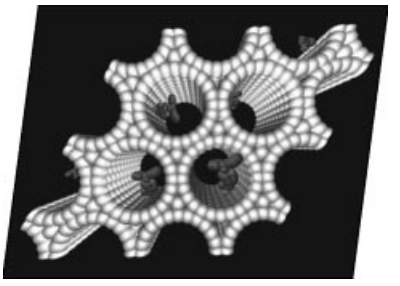

## MICROREVIEW

**Contents**

**2927** **C. E. Song,* D. H. Kim, D. S. Choi**

Chiral Organometallic Catalysts in Confined Nanospaces: Significantly Enhanced Enantioselectivity and Stability

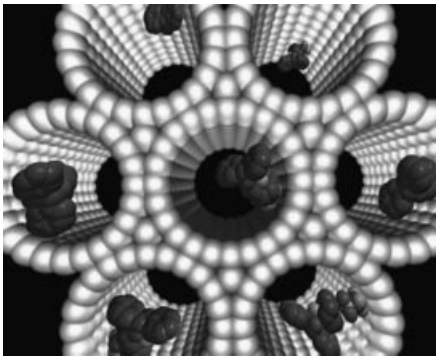

**Keywords:** Asymmetric catalysis / Supported catalysts / Mesoporous materials / Zeolite analogs / Nanostructures

 © 2006 Wiley-VCH Verlag GmbH & Co. KGaA, Weinheim 

# SHORT COMMUNICATIONS


**2937** **T. M. Klapötke, B. Krumm,* K. Polborn, M. Scherr**

Formation of Unexpected Selenium-Rich Compounds by Selenation of the Very Bulky $(PhMe_2Si)_3CLi$: *s*-Tetraselenane, a Novel Polyseleno Heterocycle

**Keywords:** Bulky substituents / DFT calculations / Selenium / Structure elucidation

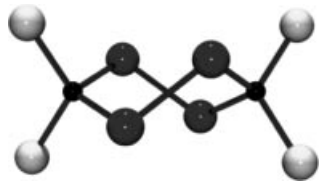

**2942** **N. Barooah, R. J. Sarma, J. B. Baruah***

Metal Directed Assemblies of a Dipeptide: Formation of β-Pleated Sheets

**Keywords:** Hydrogen bonding / Self-assembly / Dipeptide / β-Sheets / Coordination polymer

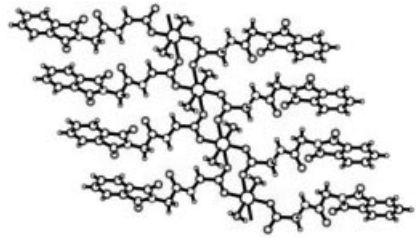

**2947** **Y. Liu, J. Peng, S. Zhai, J. Li, J. Mao, M. Li, H. Qiu, G. Lai***

Synthesis of Ionic Liquid Functionalized SBA-15 Mesoporous Materials as Heterogeneous Catalyst toward Knoevenagel Condensation under Solvent-Free Conditions

**Keywords:** Mesoporous materials / Heterogeneous catalysis / Ionic liquids

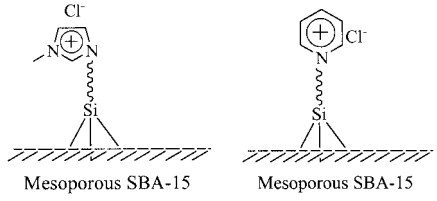



# FULL PAPERS


**2951** **J. Konu, T. Bajorek, R. S. Laitinen,* T. Chivers, R. J. Suontamo, M. Ahlgrén**

Bonding Trends in Lewis Acid Adducts of $S_4N_4$ − X-ray Structure of $TeCl_4 \cdot S_4N_4$

**Keywords:** Lewis acid adducts of $S_4N_4$ / Tellurium tetrachloride / DFT calculations / Vibrational spectroscopy / X-ray crystallography

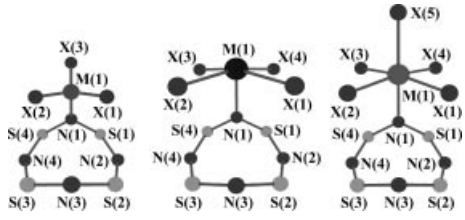


**2959** **H. Xue, H. Gao, B. Twamley, J. M. Shreeve***

Energetic Nitrate, Perchlorate, Azide and Azolate Salts of Hexamethylenetetramine

**Keywords:** Hexamethylenetetrammonium salts / Energetic materials / Quaternization / Heats of formation

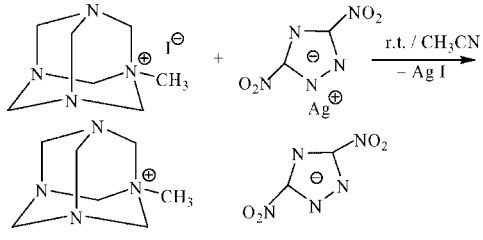



 © 2006 Wiley-VCH Verlag GmbH & Co. KGaA, Weinheim 

**2966** **P. Kurz, B. Probst, B. Spingler, R. Alberto***

Ligand Variations in [ReX(diimine)$(CO)_3$] Complexes: Effects on Photocatalytic $CO_2$ Reduction

**Keywords:** Photocatalysis / $CO_2$ reduction / Rhenium / Technetium / Diimine ligands

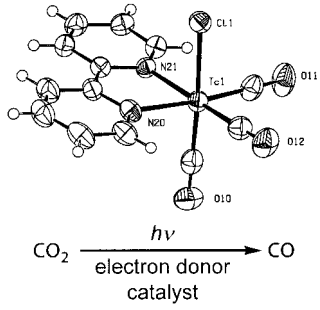


**2975** **M. K. Samantaray, V. Katiyar, D. Roy, K. Pang, H. Nanavati, R. Stephen, R. B. Sunoj,* P. Ghosh***

A Cationic (N-Heterocyclic carbene)silver Complex as Catalyst for Bulk Ring-Opening Polymerization of L-Lactides

**Keywords:** Carbenes / DFT studies / Functionalized NHC / Ring-opening polymerization (ROP) / Organometallic catalysis / Silver

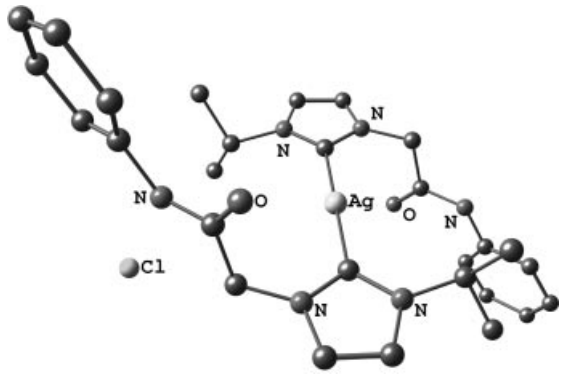


**2985** **M. M. Khusniyarov, K. Harms, O. Burghaus, J. Sundermeyer***

Molecular and Electronic Structures of Homoleptic Nickel and Cobalt Complexes with Non-Innocent Bulky Diimine Ligands Derived from Fluorinated 1,4-Diaza-1,3-butadiene (DAD) and Bis(arylimino)acenaphthene (BIAN)

**Keywords:** EPR spectroscopy / Magnetochemistry / Non-innocent ligands / Nickel / Cobalt / X-ray diffraction

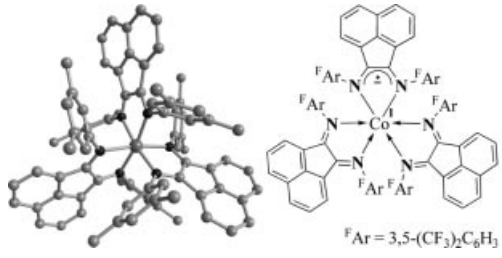


**2997** **A. Tamayo, L. Escriche,* J. Casabó, B. Covelo, C. Lodeiro***

Synthesis, Complexation and Spectrofluorometric Studies of a New $NS_3$ Anthracene-Containing Macrocyclic Ligand

**Keywords:** PET Systems / N,S ligands / Macrocycles / Fluorescence / Palladium

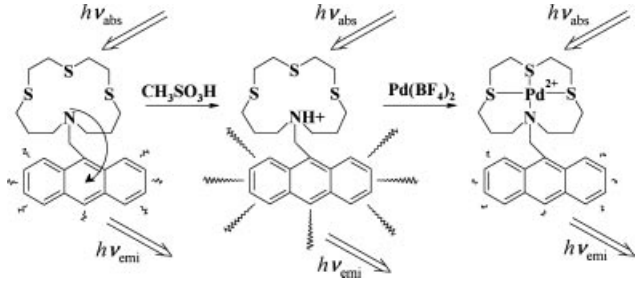


 © 2006 Wiley-VCH Verlag GmbH & Co. KGaA, Weinheim 

**3005** **S. Chikkali, D. Gudat***

Hydrophosphanation of Phenolic Aldehydes as Facile Synthetic Approach to Catechol-Functionalized Phosphane Oxides and Phosphanes

**Keywords:** Phosphanes / Phosphane oxides / P,O ligands / Hydrophosphanation / Rearrangement

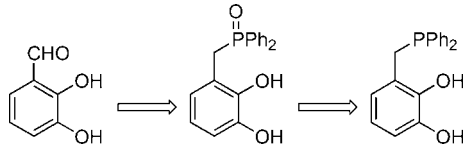


**3010** **P. Antoniotti, S. Borocci, N. Bronzolino, M. Giordani, F. Grandinetti***

Fluoromethyl Cations and Group XIV Congeners $AH_nF_{3-n}^+$ (A = Si, Ge, Sn, Pb; $n = 0-2$): From Covalent Structures to Ion-Molecule Complexes

**Keywords:** Ab initio calculations / Fluorinated cations / Group XIV elements / Ion-molecule complexes / Structure and stability

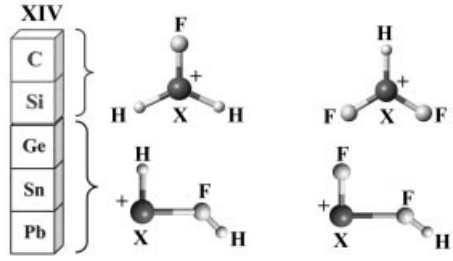


**3016** **A. Amoedo, L. A. Adrio, J. M. Antelo, J. Martínez, M. T. Pereira, A. Fernández, J. M. Vila***

Synthesis, Characterization, and Crystal Structure Analysis of the First Terdentate [C,N,S] Thiosemicarbazone Complex with a Six-Membered Palladacycle: Influence of Steric Effects on Ring Size

**Keywords:** Thiosemicarbazones / Cyclometalation / Palladium / Indole / Crystal structure

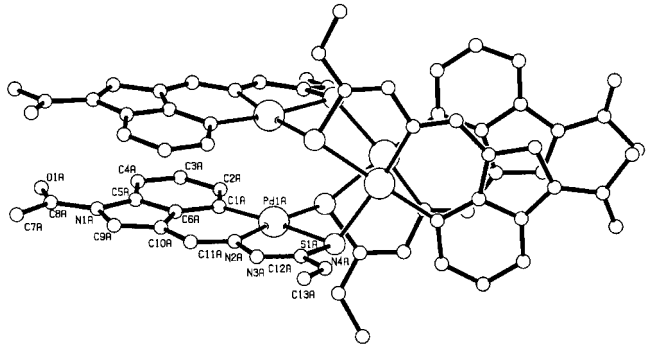


**3022** **J. Nishijo, N. Nishi***

Synthesis, Structure and Magnetic Properties of a New Low-Spin Iron(III) Complex [$FeL_3$] {L = $[HNC(CH_3)]_2C(CN)$}

**Keywords:** Iron / Magnetic properties / N ligands

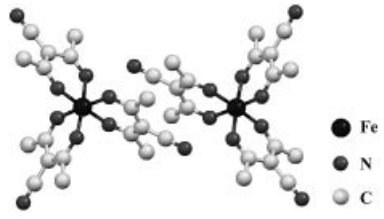


**3028** **J. Bravo,* J. Castro, S. García-Fontán,* M. C. Rodríguez-Martínez, P. Rodríguez-Seoane**

New Dinuclear Face- and Edge-Sharing Bioctahedral Ruthenium Compounds Containing 1,2-Bis(diphenylphosphanyloxy)ethane

**Keywords:** Ruthenium / P ligands / Chelates / Bimetallic complexes

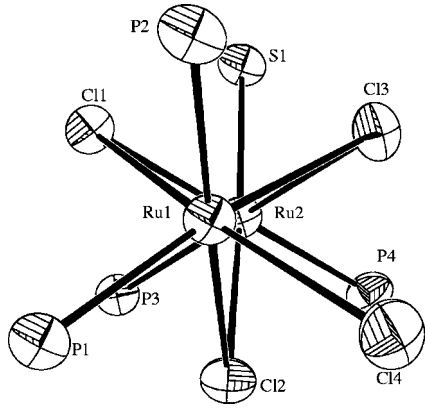



 © 2006 Wiley-VCH Verlag GmbH & Co. KGaA, Weinheim 

**3041** **S. Wang, H. Xing, Y. Li, J. Bai,* Y. Pan, M. Scheer,* X. You**

2D and 3D Cadmium(II) Coordination Polymers from a Flexible Tripodal Ligand of 1,3,5-Tris(carboxymethoxy)benzene and Bidentate Pyridyl-Containing Ligands with Three-, Eight- and Ten-Connected Topologies

**Keywords:** Metal-organic frameworks / Tripodal ligands / Topology / Metal carboxylates

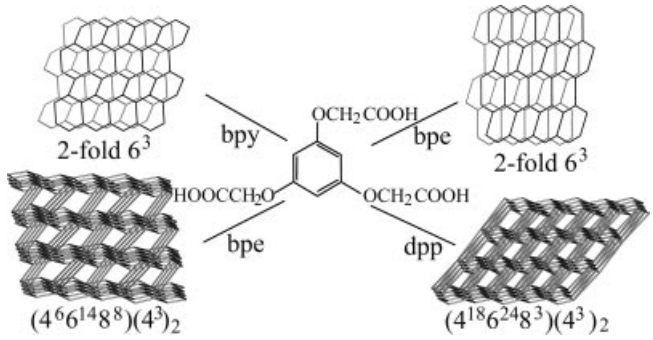


**3054** **C. Shi, R. Wang,* G. Zhu, S. Qiu,* J. Long**

In Situ Synthesis, Characterization of SiPMo-X, and Different Catalytic Properties of SiPMo-X and SiPW-X

**Keywords:** In situ synthesis / Heteropolyacids / Mesoporous materials / Encapsulation / Bulky molecule reactions / Zeolites

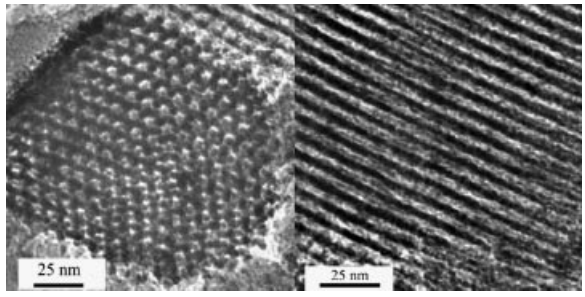


**3061** **V. N. Ikorskii, I. G. Irtegova, E. Lork, A. Y. Makarov, R. Mews,* V. I. Ovcharenko,* A. V. Zibarev***

Early Alkali Metal (Li, Na, K) and Tris(dimethylamino)sulfonium (TAS) Salts of [1,2,5]Thiadiazolo[3,4-*c*][1,2,5]thiadiazolidyl Radical Anion: Rational Syntheses, Structures and Magnetic Properties

**Keywords:** Magnetic properties / Nitrogen heterocycles / Radical anions / Sulfur heterocycles

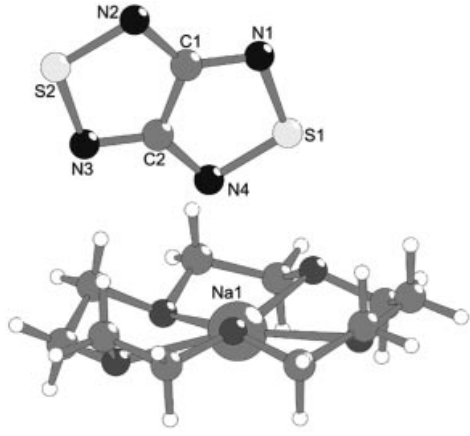


**3068** **J. D. E. T. Wilton-Ely,* M. Wang, D. M. Benoit, D. A. Tocher**

Spectroscopic, Structural and Theoretical Investigation of Alkenyl Ruthenium Complexes Supported by Sulfur−Nitrogen Mixed-Donor Ligands

**Keywords:** Mixed-donor ligands / Ruthenium / Alkenyl / Thiolate / Ab initio / Density functional theory

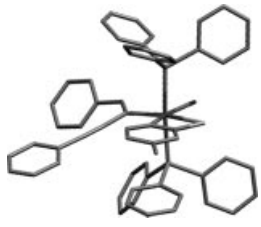

 © 2006 Wiley-VCH Verlag GmbH & Co. KGaA, Weinheim 

**3079** **U. Abram, A. Castiñeiras,* I. García-Santos, R. Rodríguez-Riobó**

Symmetrisation in the Interaction of Chloro-[2-(dimethylaminomethyl)phenyl-C$^1$]mercury(II) with Thiosemicarbazone Derivatives of Pyridine-2-carboxamide and Pyrazin-2-carboxamide

**Keywords:** Mercury complexes / Symmetrisation / Thiosemicarbazones / Crystal structures / Weak hydrogen bonds / C−H···π interactions

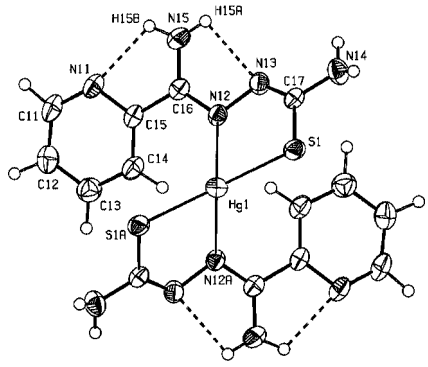


**3088** **A. L. Johnson,* M. G. Davidson,* M. D. Lunn, M. F. Mahon**

Synthesis, Isolation and Structural Investigation of Schiff-Base Alkoxytitanium Complexes: Steric Limitations of Ligand Coordination

**Keywords:** Titanium / Alkoxide / Steric effects / Schiff-base ligands / Coordination

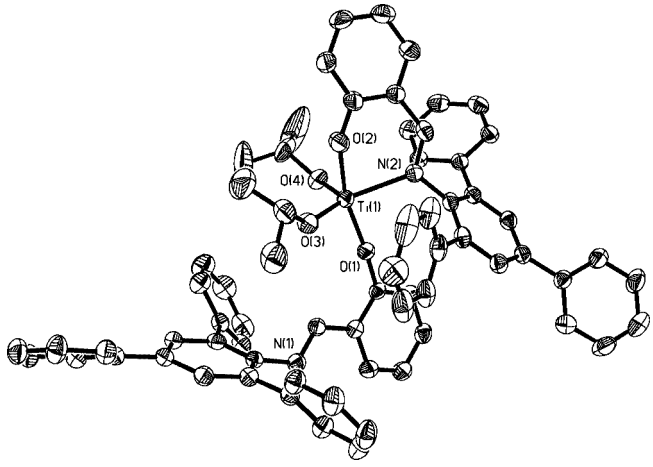


**3099** **B. M. Petersen, J. K. Bjernemose, J. O. Jeppesen***

Characterization of a Byproduct in the Alkylation of DMIT: Alkylation on the Least Nucleophilic Sulfur Atom

**Keywords:** Alkylation / DMIT / Nucleophilic substitution / Sulfur heterocycles

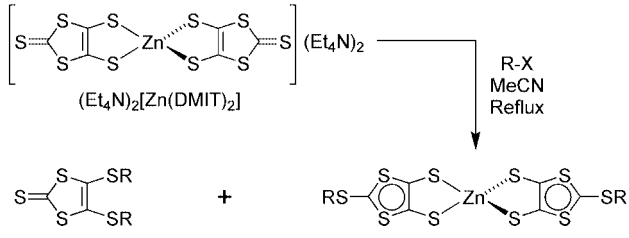


**3105** **L. Labat, J.-F. Lamère, I. Sasaki, P. G. Lacroix,* L. Vendier, I. Asselberghs, J. Pérez-Moreno, K. Clays**

Synthesis, Crystal Structure, and Second-Order Nonlinear Optical Properties of Ruthenium(II) Complexes with Substituted Bipyridine and Phenylpyridine Ligands

**Keywords:** Ligand design / Donor−acceptor systems / Ruthenium / Nonlinear optics / Density functional calculations

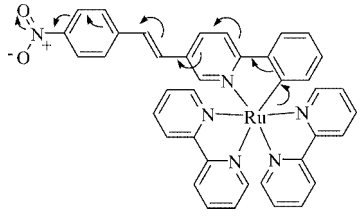


 © 2006 Wiley-VCH Verlag GmbH & Co. KGaA, Weinheim 

# CORRECTION

**3115** **E. Annoni, M. Pizzotti,* R. Ugo, S. Quici, T. Morotti, M. Bruschi, P. Mussini**

Synthesis, Electronic Characterisation and Significant Second-Order Non-Linear Optical Responses of *meso*-Tetraphenylporphyrins and Their $Zn^{II}$ Complexes Carrying a Push or Pull Group in the β Pyrrolic Position

**Keywords:** Cyclic voltammetry / Nonlinear optics / Porphyrins / UV/Vis spectroscopy / Zinc

 © 2006 Wiley-VCH Verlag GmbH & Co. KGaA, Weinheim 

DOI: 10.1002/ejic.200600344

# Chiral Organometallic Catalysts in Confined Nanospaces: Significantly Enhanced Enantioselectivity and Stability

**Choong Eui Song,*[a] Dong Hyun Kim,[a] and Doo Seoung Choi[a]**

**Keywords:** Asymmetric catalysis / Supported catalysts / Mesoporous materials / Zeolite analogs / Nanostructures

This microreview presents some selected representative examples which demonstrate that significant improvement in the catalytic performance (increase in catalytic activity, stability and chemo- and enantioselectivity) of organometallic chiral catalysts as well as their recycling ability can be achieved by heterogenizing them in the confined spaces of porous or layered support materials. The positive effects of immobilization on the catalytic efficiencies are discussed in terms of the confinement effect and site-isolation effect, etc., with the aim of understanding the extent to which such effects lead to positive changes in the catalytic properties.

(© Wiley-VCH Verlag GmbH & Co. KGaA, 69451 Weinheim, Germany, 2006)

## Introduction

For economic, environmental and social reasons, the trend towards the application of optically pure compounds is undoubtedly increasing. Among the various methods which can be used to selectively produce single enantiomer, asymmetric catalysis is the most attractive method from the atom-economic point of view.[1,2] Over the last thirty years, numerous catalytic reactions allowing the enantioselective formation of C–H, C–C, C–O, C–N and other bonds have been discovered. A number of homogeneous organometallic chiral catalysts have gained wide acceptance in terms of their efficiency and selectivity, and some of them are even

[a] Institute of Basic Science, Department of Chemistry, Sungkyunkwan University,
300 Cheoncheon-dong, Jangan-gu, Suwon City, Gyeonggi-do, 440-746, Korea
Fax: +82-31-290-7075
E-mail: s1673@skku.edu

*Choong Eui Song has been a Professor at Sungkyunkwan University since 2004. He received his B.S. in 1980 from Chungang University and obtained a Diploma (1985) and a Ph.D. (1988) at RWTH Aachen in Germany. After completing his Ph.D. he worked as a Principal Research Scientist at the Korea Institute of Science and Technology (KIST). In 2001 he was appointed as head of the national research laboratory for Green Chirotechnology in Korea. In 2004 he moved to his current position and in 2006 he was appointed as a director at the Research Institute of Advanced Nanomaterials and Institute of Basic Science in Sungkyunkwan University. His research interests focus on asymmetric catalysis, ionic liquid chemistry and nanochemistry. He received an academic award from the KIST (2000) and the Scientist of the Month Award from the Ministry of Science and Technology in Korea.*

*Dong Hyun Kim was born in 1978 in Seoul, Korea. He received his B.S. degree in 2005 from Korea University. He is currently a MS student with Professor Song at the same university, focusing on heterogeneous asymmetric catalysis and chiral sensors.*

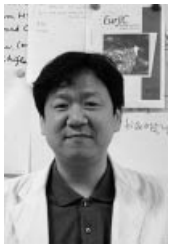

*Doo Seoung Choi was born in 1965 in Seoul, Korea. He worked in the field of process development for Chong-Kun Dang pharmaceutical company in Korea from 1993 to 2001 and then he moved to C-TRI Co. Ltd. in Korea, where he worked in the R&D team investigating ionic liquids as a team manager for three years. He is currently a PhD student with Professor Song at the same university, focusing on heterogeneous asymmetric catalysis. During summer 2005, as a visiting fellow, he worked at the laboratory of Professor Benjamin List in the Max Planck-Institute (Muellheim), Germany.*

 © 2006 Wiley-VCH Verlag GmbH & Co. KGaA, Weinheim 

used on an industrial scale.[3–5] However, in spite of the huge amount of work devoted to this subject in both the academic and industrial fields, the contribution of asymmetric catalysis to the overall production of chiral chemicals is much lower than originally expected. One of the major drawbacks of homogeneous catalysis is the need to separate the relatively expensive chiral catalysts from the reaction mixture at the end of the process. The possible contamination of the product with metal catalysts also severely restricts their use in industry. In order to overcome these drawbacks, a great deal of effort has been made to develop effective heterogenized catalyst systems, mainly, by immobilizing homogeneous chiral catalyst on solid supports by: (i) covalent bonding, (ii) adsorption or ion-pair formation, (iii) encapsulation, or (iv) entrapment, etc.[6–8] In any case of heterogenization method, the support materials need to be thermally, chemically, and mechanically stable during the reaction process. Moreover, the structure of the support needs to be such that the active sites are well dispersed on its surface and easily accessible. Generally, this requires the support to have a reasonably high surface area (typically $>100\ m^2\,g^{-1}$) and an appropriate pore size (i.e. >20 Å), in order to allow for the easy diffusion of the reactants to the active sites.[9] Thus, inorganic supports[10] such as mesoporous silica and clay, have been extensively used for the immobilization of catalysts because of their large surface area, chemical and physical stability, and tunable pore or layer structure. One obvious benefit of supported catalysts is the easy separation of the relatively expensive chiral catalysts from the reaction mixture at the end of the process. In addition, catalysts immobilized on porous or layered materials have sometimes been found to exhibit much better catalytic performances than their homogeneous analogues due to geometrical constraints imposed by the pores or layers.[11–13]

The instability of homogeneous catalysts is often due to the formation of inactive multinuclear species. However, the colocalization of the catalytic sites can easily be prevented by immobilizing the catalysts in confined spaces, i.e., by the site-isolation of the catalytic sites,[14–16] consequently increasing the stability and turnover numbers of the catalyst. In this respect, mesoporous-type materials appear to be more attractive, due to their regular structures and tunable pore diameters. In addition to this enhanced stability, increased activity and selectivity were also observed upon immobilization in the confined space, due to the confinement effect originating from the weak interactions (hydrogen bond, van der Waals force, adsorption, etc.) between catalyst/substrate and pore surfaces. The polar or acidic pore surface can participate in the catalysis cooperatively, e.g., by stabilizing a charged transition state and thereby increasing the reaction rate.[17–19] In addition, because this weak interactions between catalyst/substrate and pore surfaces is about the same level as the energy difference between the two transition states corresponding to the (*R*) product and the (*S*) product, the enantioselectivity can also be very sensitively (positively or negatively) altered.[11] Enantioselectivity can be, thus, increased or decreased, or even reversed. Therefore, the enantioselectivity could be improved by careful tuning the confinement effect based on the molecular designing of the pore/surface and the immobilized catalysts according to the requirements of chiral reactions.[11–13] In this microreview, some selected examples will be given which can nicely demonstrate that a significant improvement in the stereoselectivity of the organometallic catalyst may be achieved by heterogenizing it into the confined nanospaces of porous or layered materials. Also, the effects positively influencing the catalytic efficiencies of the supported catalysts are discussed in terms of the confinement effect and site-isolation effect, etc., with the aim of understanding how such effects lead to positive changes in the catalytic properties.

## Selected Examples

### Asymmetric Hydrogenation

Several striking examples of the positive control effected by nanopores have been provided by the research group of Thomas and Johnson.[20–24] The Pd catalyst **1** supported on the mesoporous channels of MCM-41 affected the hydrogenation of ethyl 1,4,5,6-tetrahydronicotinate (**3**) to afford nipecotic acid ethyl ester (**4**) in 17% *ee*, whereas the use of the soluble version **2** resulted in a racemic mixture (Scheme 1). This enhanced chiral induction was explained in terms of the confinement effect of the ordered mesopore of MCM-41, which confine the substrate and ligand of the catalysts.[21]

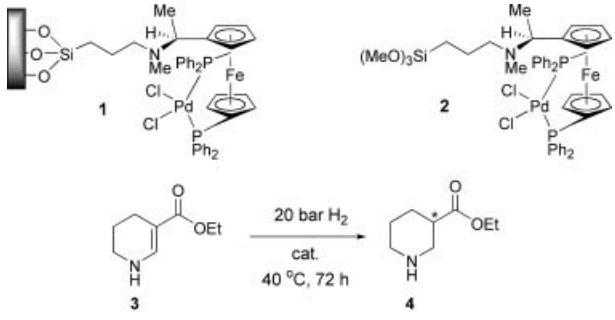


Using homogeneous catalyst **2**: racemic, TON = 98
Using heterogeneous catalyst **1**: 17% *ee*, TON = 291

Scheme 1.

The same research group[23] incorporated (*S*)-2-aminomethyl-1-ethylpyrrolidine (AEP) or (1*R*,2*R*)-1,2-diphenylethylenediamine (DED) into the concave surface of MCM-41 (pore diameter 30 Å) and to the convex surface of nonporous silica (Carbosil). Catalytic reactions were carried out using heterogeneous Rh and Pd catalysts for the asymmetric hydrogenation of (*E*)-α-phenylcinnamic acid and methyl benzoyl formate. Compared to the corresponding homogeneous catalyst or silica-supported catalyst, a significant enhancement of the *ee* value was observed for the MCM-41-supported catalyst (with the concave surface). For example, surprisingly, the Rh(COD)- and Pd(allyl)

 © 2006 Wiley-VCH Verlag GmbH & Co. KGaA, Weinheim 

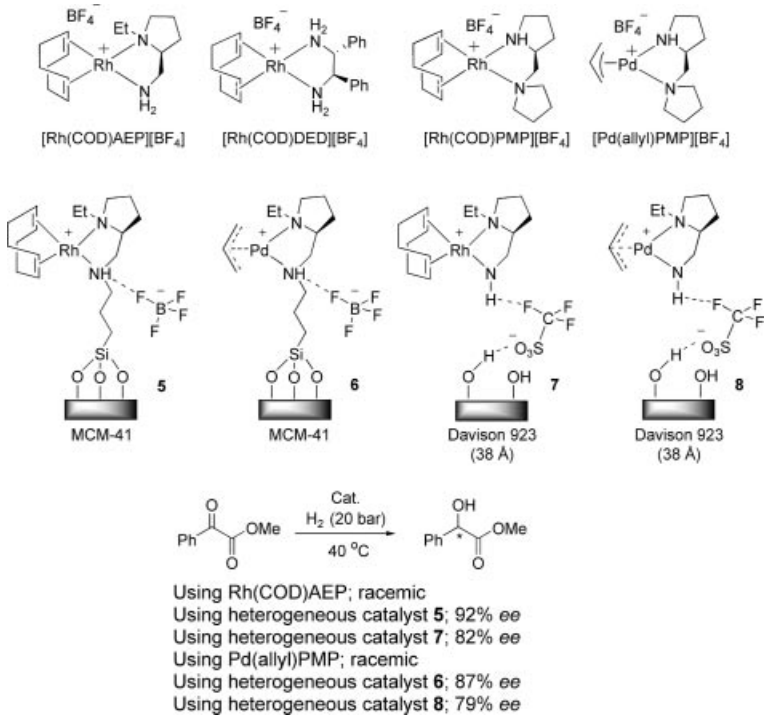


Scheme 2.

complex of AEP anchored on MCM-41, **5** and **6**, gave 92 and 87% *ee*, respectively, in the hydrogenation of methyl benzoyl formate, while the homogeneous catalysts gave a racemic product (Scheme 2). This increase in the *ee* values was attributed to the restricted access of the reactant to the active site generated by the concavity of the pore. Soon after, the same group[24] also anchored [Rh(COD)(*S*)-PMP][$CF_3SO_3$], [Pd(allyl)(*S*)-1-(2-PMP)] [$CF_3SO_3$], [Rh(COD)(*S*)-AEP] [$CF_3SO_3$] and [Rh(COD) (1*R*,2*R*)-DED][$CF_3SO_3$] noncovalently through N–H···F hydrogen bonding with the triflate ion, $CF_3SO_3^-$ to the inner surface of a set of silicas with narrowed pore-size distributions (38, 60, and 250 Å). The catalytic performances of the heterogeneous catalysts were tested in the asymmetric hydrogenation of methyl benzoyl formate to produce methyl mandelate. The supported catalysts generally exhibited remarkably higher *ee* values than their homogeneous counterparts. Notably, the heterogeneous catalysts **7** and **8** gave up to 82 and 79% *ee*, respectively, while their two homogeneous counterparts, $[Rh(COD)AEP]^+$ and $[Rh(COD)DED]^+$, did not display any significant *ee* (Scheme 2). The increase of the *ee* values of the supported catalysts was observed in a manner that logically reflects the declining influence of spatial constraint in proceeding from the 38-Å- to the 60-Å- to the 250-Å-pore-diameter silica. A similar enhancement of enantioselectivity in the hydrogenation of (*E*)-α-phenylcinnamic acid affording 2,3-diphenylpropanoic acid was also observed by heterogenizing [Rh(COD)(*S*)-AEP][$CF_3SO_3$] and [Rh(COD)(1*R*,2*R*)-DED][$CF_3SO_3$] noncovalently through H bonding of the triflate ion, $CF_3SO_3^-$ to the silanol groups of inner surface of MCM-41.[25]

The above examples provided by the research group of Thomas and Johnson strongly suggest that the conventional heterogenization approach, i.e., heterogenizing those catalysts designed for homogeneous processes, may not necessarily be the best solution for the development of efficient heterogenized chiral catalyst systems when it comes to immobilizing catalysts in the confined spaces of porous or layered support materials. Moreover, the above-mentioned results also suggest that the heterogenization of catalysts in confined spaces may provide a new paradigm for the development of highly efficient chiral catalysts.

## Other Examples

Augustine et al.[26] immobilized various Rh complexes of well-known chiral bis(phosphane) ligands, such as DiPamp (**9**), Prophos (**10**), Me-DuPhos (**11**), and BPPM (**12**) onto heteropolyacid-modified inorganic supports, e.g., montmorillonite K, alumina. Somewhat surprisingly, both reaction rates and enantioselectivities significantly increased upon subsequent reuse of the recovered immobilized catalysts. After 9$^{th}$ reuse, DiPamp-rhodium supported on a PTA-alumina gave rise to a 97% *ee* vs. 76% *ee* for the homogeneous complex during the hydrogenation of methyl 2-acetamidoacrylate (**13**) (Scheme 3). Rege et al. also observed that the noncovalent immobilization of [(*R*,*R*)-Me-(DuPHOS)Rh(COD)]OTf afforded by interaction of triflate counterion with surface silanol groups of MCM-41 resulted in 99% *ee* in the hydrogenation of **13**, compared to 87% *ee* with the homogeneous Rh complex of **11** (Scheme 3).[27]

 © 2006 Wiley-VCH Verlag GmbH & Co. KGaA, Weinheim 

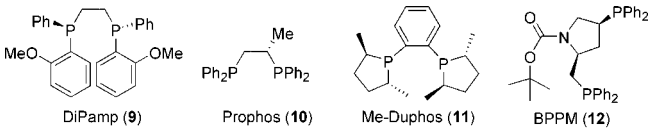


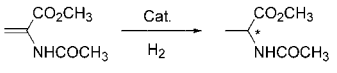


13

Using homogeneous catalyst **9**; 76% *ee*, TOF($min^{-1}$) = 0.25
Using PTA-alumina supported **9**; 97% *ee*, TOF($min^{-1}$) = 1.29
Using homogeneous catalyst **11**; 87% *ee* (in hexane)
Using MCM-41 supported **11**; 99% *ee* (in hexane)

Scheme 3.

Corma et al.[28–31] immobilized a number of proline derivatives on silica and modified USY zeolite (pore diameter 12–30 Å) (e.g. **15a** and **15b** in Scheme 4), and used them for the hydrogenation of various (*Z*)-*N*-acylcinnamic acid derivatives such as **16a** and **16b**. For all of the substrates tested using these catalysts, the enantioselectivity was higher with the zeolite-supported complex **15a** than with either the silica-supported **15b** or unsupported complex **14**, suggesting that the steric constraints of the support play an important role, especially in the case of zeolite where the reaction must take place in the confined spaces of the supermicropores. This is the first example in which the steric constraints of support (in this case, zeolite) was found to have positive effect on enantioselectivity.[28,29]

Pérez et al. also reported that the enantioselectivity of the supported complex was significantly increased compared with that obtained with the homogeneous one.[32] (*S*)-MAB-Ru anchored onto MCM-41 (**19**-Ru) catalyze the asymmetric hydrogenation of itaconic acid and α-acetamidocinnamic acid to yield the (*R*) product with 100% yield and 97% *ee*, while the homogeneous one, (*S*)-MAB-Ru (**18**-Ru), gave only moderate *ee* values (80 and 69.8%, respectively) (Scheme 5). The authors hypothesized that the interaction of the ligands with the pendant hydroxy groups present on the pores of MCM-41 may increase the rigidity of the overall catalytic structure. This, in turn, would restrict the rotation of the transition state and favor formation of nearly pure stereoisomers. In addition, the reaction yield remained at 100% while the enantioselectivity decreased only slightly, from 97 to 94%, after three runs.

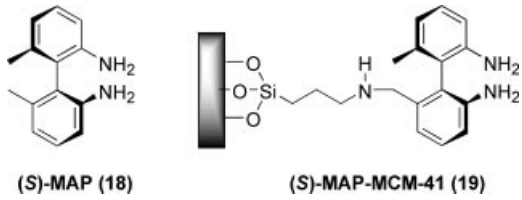

**(*S*)-MAP (18)** **(*S*)-MAP-MCM-41 (19)**

Scheme 5.

In an effort to rationally design functional hybrid solids based on organic linkers and metal nodes, Hu et al.[33] designed and synthesized novel chiral porous zirconium phosphonates containing Ru-BINAP-DPEN moieties **20**. The synthesized chiral porous hybrid solid catalyzed the asymmetric hydrogenation of unfunctionalized aromatic ketones with remarkably higher activity and enantioselectivity (up to 99.2% *ee*) than the parent homogeneous counterpart Ru-BINAP-DPEN system **19**. For example, acetophenone was hydrogenated to 1-phenylethanol with complete conversion and 96.3% *ee* in 2-propanol with 0.1 mol% loading of the solid catalyst **20**. This level of enantioselectivity is significantly higher than that observed for the parent homogeneous catalyst **19** which typically gives ca. 80% *ee* for the

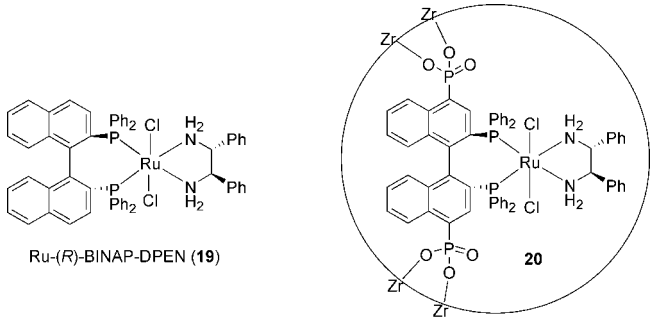

Ru-(*R*)-BINAP-DPEN (**19**) **20**

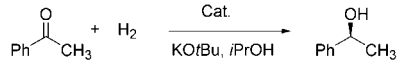


Using the homogeneous catalyst **19**: ~80% *ee*
Using the solid catalyst **20**: 96.3% *ee*

Scheme 6.

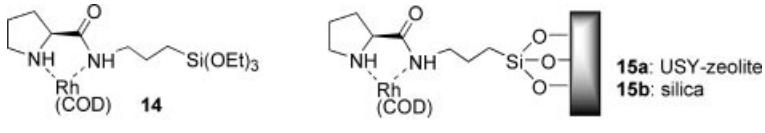

**14** **15a**: USY-zeolite **15b**: silica

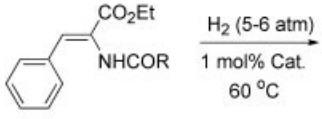


**16a:** R = $CH_3$
**16b**: R = Ph

**17a:** R = $CH_3$
homogeneous 84.1% ee
silica: 88.0% ee
USY zeolite: 97.9% ee
**17b**: R = Ph
homogeneous 90.3% *ee*
silica:93.5% ee
USY zeolite: 96.8% *ee*

Scheme 4.

 © 2006 Wiley-VCH Verlag GmbH & Co. KGaA, Weinheim 

same reaction (Scheme 6). A similar method has also been used to synthesize other chiral, porous hybrid ruthenium solids.[34] In the heterogeneous asymmetric hydrogenation of β-keto esters, an *ee* value of up to 95% was achieved.

### Asymmetric Oxidation

An extremely exciting example was very recently provided by Caps et al.,[35] which demonstrates that the heterogenization of catalysts in confined spaces can be used not only to improve the stereoselectivity but also to generate a new chiral species in situ from achiral catalyst precursors. The heterogenization of the achiral cluster, $Os_3(CO)_{12}$, on the internal space of MCM-41 using simple chemical vapor deposition (CVD) gave a superior enantioselectivity towards the (*S*,*S*) configuration of the 1,2-diphenyl-1,2-ethanediol in the dihydroxylation of *trans*-stilbene using *N*-methylmorpholine *N*-oxide (NMO) as an oxidant without adding any chiral ligand. This surprising effect was even more pronounced when surface Al sites were introduced into the silicate [90% *ee* for (*S*,*S*)-isomer] (Scheme 7). This 90% *ee* towards the (*S*,*S*) configuration is much higher than that reported using a homogeneous $OsO_4$/NMO/acetone/water system containing a chiral ligand (78%).[36] One possible reason for this chiral induction might be the "spontaneous symmetry breaking"[37–39] of achiral $Os_3(CO)_{12}$ during CVD on the MCM-41 or related surfaces, resulting in a new surface-chiral catalytic species. However, unfortunately, many attempts by us to reproduce this highly interesting result have been failed yet.

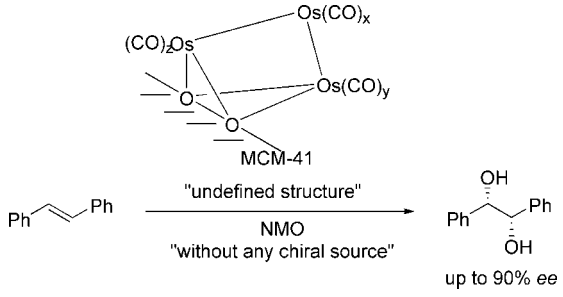


Scheme 7.

A significant enhancement of the enantioselectivity as a result of the confinement effect was also observed in the epoxidation of α-methylstyrene with hypochlorite.[40] Jacobsen's Mn(salen) complex encapsulated in the spacious supercages of MCM-22 (**22**) showed significantly better enantioselectivity than the homogeneous catalyst **21** under the same conditions, i.e., 91.3% *ee* vs. 51% *ee* (Scheme 8). Moreover, the encapsulated complex was three times more active than the homogeneous counterpart **21**, which is also attributed to site-isolation, i.e., to the suppressed formation of dimeric and other oligomeric Mn oxo complexes due to geometric constraints.

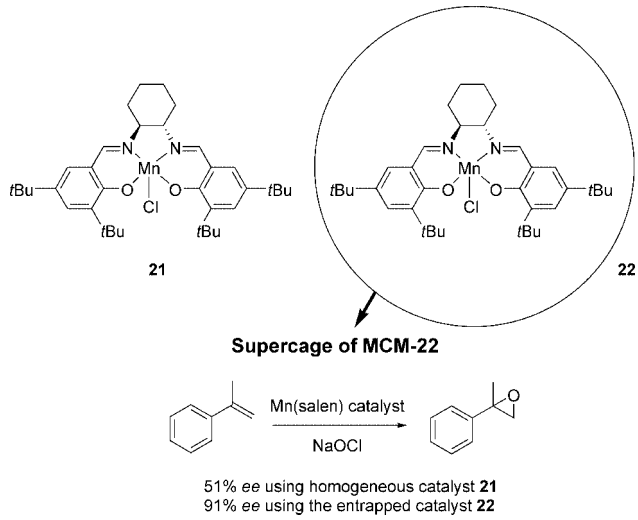


Scheme 8.

Li et al. also observed that the immobilization of the chiral Mn(salen) complex through the complexation of manganese by the oxygen atoms of the phenoxyl groups grafted on the surface of MCM-41 leads to a markedly higher *ee* value than that observed for the free complex in the asymmetric epoxidation of simple olefins.[41] For example, in the epoxidation of α-methylstyrene in $CH_2Cl_2$ with NaOCl as the oxidant, the enantiomeric excess is notably increased from 56% for the homogeneous catalyst to 72% for the heterogeneous Mn(salen)/MCM-41 catalyst (**23**). Soon after, the same group also reported that chiral manganese(salen) catalysts axially immobilized in nanopores by Ph sulfonic groups (**24**) also resulted in remarkably higher *ee* values (up to 95%) for the asymmetric epoxidation of unfunctionalized olefins (Scheme 9).[42,43]

Similar results were observed with other salen-M complexes anchored on porous supports.[44–46] Kim et al.[44] reported that, for the asymmetric epoxidation of α-methylstyrene, the *ee* value increased from 51% to 59% after the immobilization of Mn(salen) on the siliceous MCM-41 by multi-step grafting. Kureshy et al.[45] also reported that montmorillonite clay supported dicationic Mn(salen) exhibited similar or even higher *ee* values for the epoxidation of 2,2-dimethyl-6-nitrochromene, indene, and styrene than the corresponding homogeneous catalysts. It has also been reported that, for the enantioselective epoxidation of β-methylstyrene, the *ee* value increased from 54% to 73% after the immobilization of Cr(salen) through axial $NH_2$ complexation.[46]

Another good example of the confinement effect in heterogenized catalysts on porous supports was provided by Corma et al. The use of $Mo^{VI}$ complexes of chiral ligands derived from (2*S*,4*R*)-4-hydroxyproline, heterogenized onto a modified USY zeolite by covalent bonding,[47] in the epoxidation of geraniol and nerol with TBHP as the oxygen source resulted in much higher enantioselectivities (47% *ee* for geraniol and 64% *ee* for nerol) than those (up to 27.6% *ee* for geraniol and up to 10.4% *ee* for nerol) obtained with the homogeneous counterpart **25**. This enhanced enantio-

 © 2006 Wiley-VCH Verlag GmbH & Co. KGaA, Weinheim 

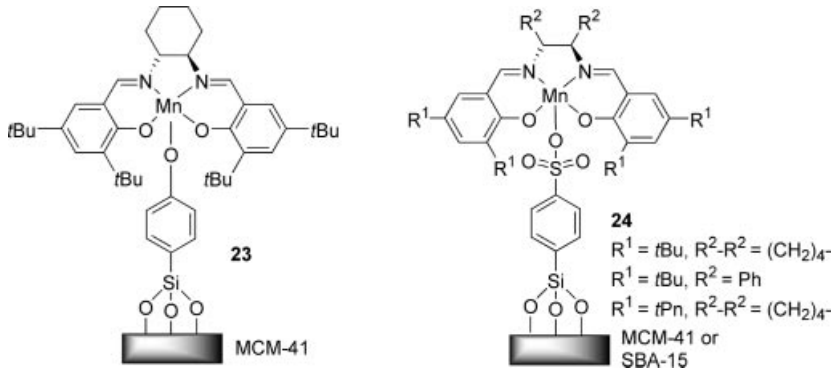


Scheme 9.

selectivity can also be ascribed to the additional steric constraints imposed by the zeolite pores. The lifetime of the heterogenized catalyst was also examined by the repeated use of the catalyst **26** which showed similar rates and yields of epoxide, even after five runs (Scheme 10). The enhanced stability of the heterogenized complex was ascribed to the stronger coordination of the dihydroxy ligand to Mo than that of the acetylacetonate or hydroxy group present on the substrate, *tert*-butyl alcohol or hydroperoxide. The site-isolated catalyst molecules on the mesopores could also avoid being deactivated by dimerization and oligomerization of the Mo species.

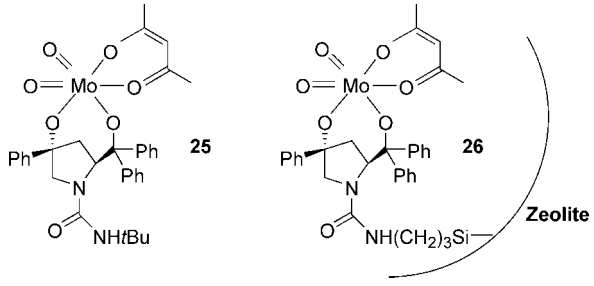


Scheme 10.

## Asymmetric C–X and C–C Bond-Forming Reactions

A good example of the confinement effect dramatically improving the performance of chiral catalysts for C–X bond-forming reactions was described by Thomas et al.[48] In the case of the allylic amination of cinnamyl acetate, catalyst **29**, immobilized on the inner walls of mesoporous MCM-41, exhibited superior catalytic properties than catalyst **28** anchored on Carbosil (a nonporous, high-area silica) and than homogeneous catalyst **27**. The MCM-41-immobilized catalyst **29** showed a degree of regioselectivity for the desirable branched product (51%) and extremely high enantioselectivity (>99% *ee*), whereas the Carbosil-immo-

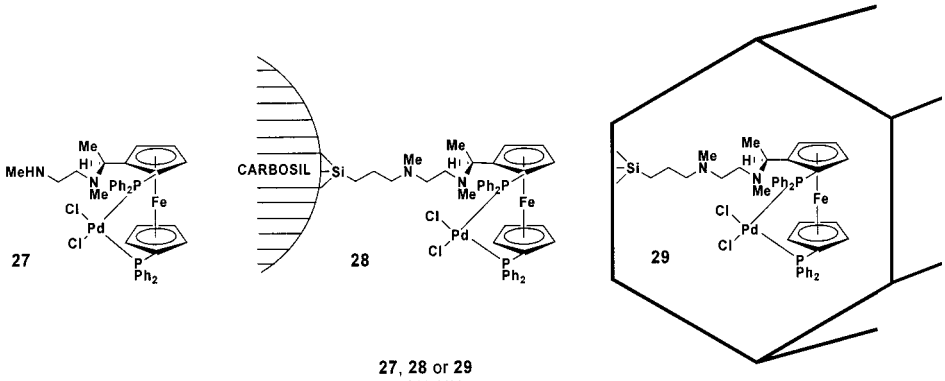


| Catalyst | Conversion (%) | Straight chain (%) | Branched (%) | %*ee* |
|---|---|---|---|---|
| **27** | 76 | >99 | - | - |
| **28** | 98 | 98 | 2 | 43 |
| **29** | >99 | 49 | 51 | >99 |

Scheme 11.

 © 2006 Wiley-VCH Verlag GmbH & Co. KGaA, Weinheim 

bilized catalysts **28** afforded the branched product in only 2% yield and with 43% *ee*. In the case of the homogeneous catalyst **27**, the reaction produced solely the straight chain product (Scheme 11). Although the regioselectivity of **29** is still not very high, the careful design of active centers and the control of pore size of supports will probably lead to more unexpected selectivities.

Also in the Si–H insertion reactions of dimethylphenylsilane with methylphenyldiazoacetate, a significant improvement in enantioselectivity was observed by immobilizing the chiral dirhodium complexes on Aerosil 200.[49,50] This immobilized catalyst, $SiO_2$–$(CH_2)_2COO$–$Rh_2[(4S)\text{-BNOX}]_3$ (**31**), showed a more than 10-fold increase in enantioselectivity (up to 28% *ee*), while the homogeneous analogue $Rh_2[(4R)\text{-BNOX}]_4$ (**30**) gave nearly racemic product (Scheme 12). In contrast to the catalysts immobilized on Aerosil 200 having an average pore size of 50 nm, none of the catalysts immobilized inside the pores of MCM-41 showed any activity. It is possible that there is not enough space inside the pores of MCM-41 for the reaction to take place. This result is reasonable, considering that the average pore diameter (19 Å) of MCM-41 is only slightly larger than the catalyst size (between 19 and 13 Å). A transition state requiring a space-demanding conformation of the catalyst might, therefore, be impossible under these circumstances.

Sanchez and co-workers[51] anchored the Ni complex of the L-proline amide **32b** on USY zeolites or silica by covalent bonding. Although the use of the insoluble catalysts **33** and **34** caused the conjugate addition of $ZnEt_2$ to the enones **35** to take place more slowly, the *ee* values of the resulting saturated ketones **36** were much higher for the zeolite-supported Ni complex **33** (91 and 95% *ee*, for R = Ph and Me, respectively) than its homogeneous counterpart **32a** (77 and 75% *ee*, for R = Ph and Me, respectively) or the silica-supported analogue **34** (34% *ee*, R = Ph) (Scheme 13). The steric constraint imposed by the zeolite pore was thought to contribute to the enhanced enantioselectivities that were observed. Sanchez et al. also attached a series of chiral amines covalently to modified USY zeolite and MCM-41 zeolite supports, and evaluated the ability of the obtained chiral base catalysts confined in porous hosts to improve stereoselectivity in conjugate additions of nucleophiles to enones.[52] It was found that the reaction rate was enhanced, and the catalysts showed higher selectivity than the free amines.

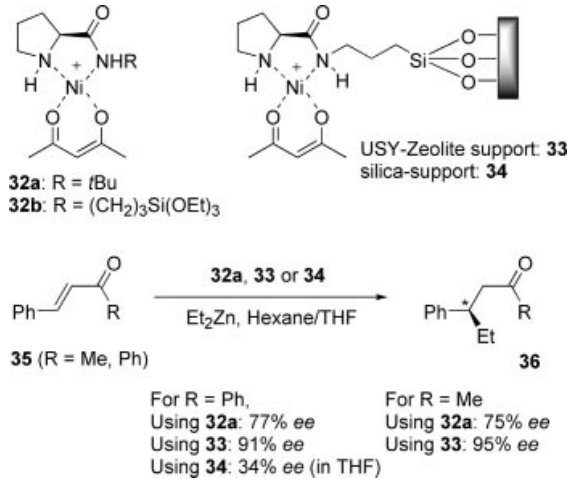


Scheme 13.

Chiral bis(oxazoline)copper complexes are known to be highly effective enantioselective, homogeneous catalysts for many C–C and C–X bond -forming reactions, such as Diels–Alder, aldol, Michael, ene, amination and aziridination reactions. It has also been reported that chiral bis(oxazoline)copper complexes constrained within the confined spaces of porous materials exhibited substantially higher enantioselectivity than the homogeneous catalyst.[53–56] For example, Wan et al. immobilized the Ph-substituted bis(oxazoline)copper(II) complex in zeolite Y for the hetero-Diels–Alder reaction of (ethyl *E*)-pentenoate (**39**) with ethyl vinyl ether, affording the dihydropyran **40** (Scheme 14).[53] The enantioselectivity (41%) of the solid catalyst **38** was significantly higher than that obtained with

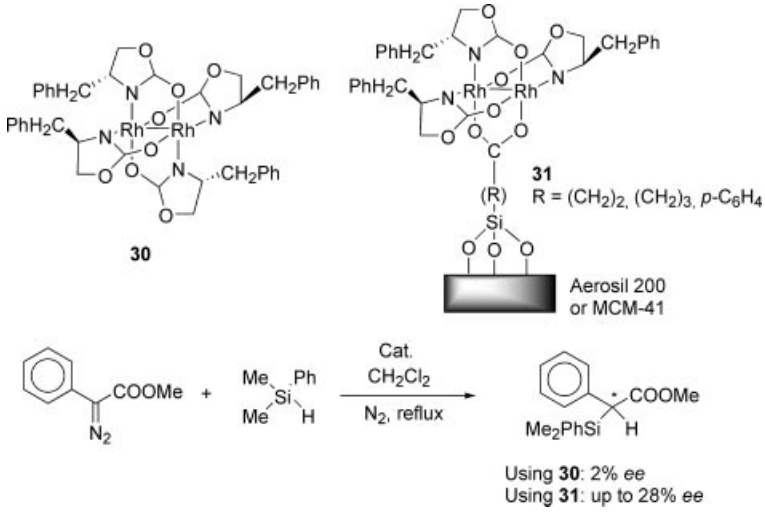


Scheme 12.

 © 2006 Wiley-VCH Verlag GmbH & Co. KGaA, Weinheim 

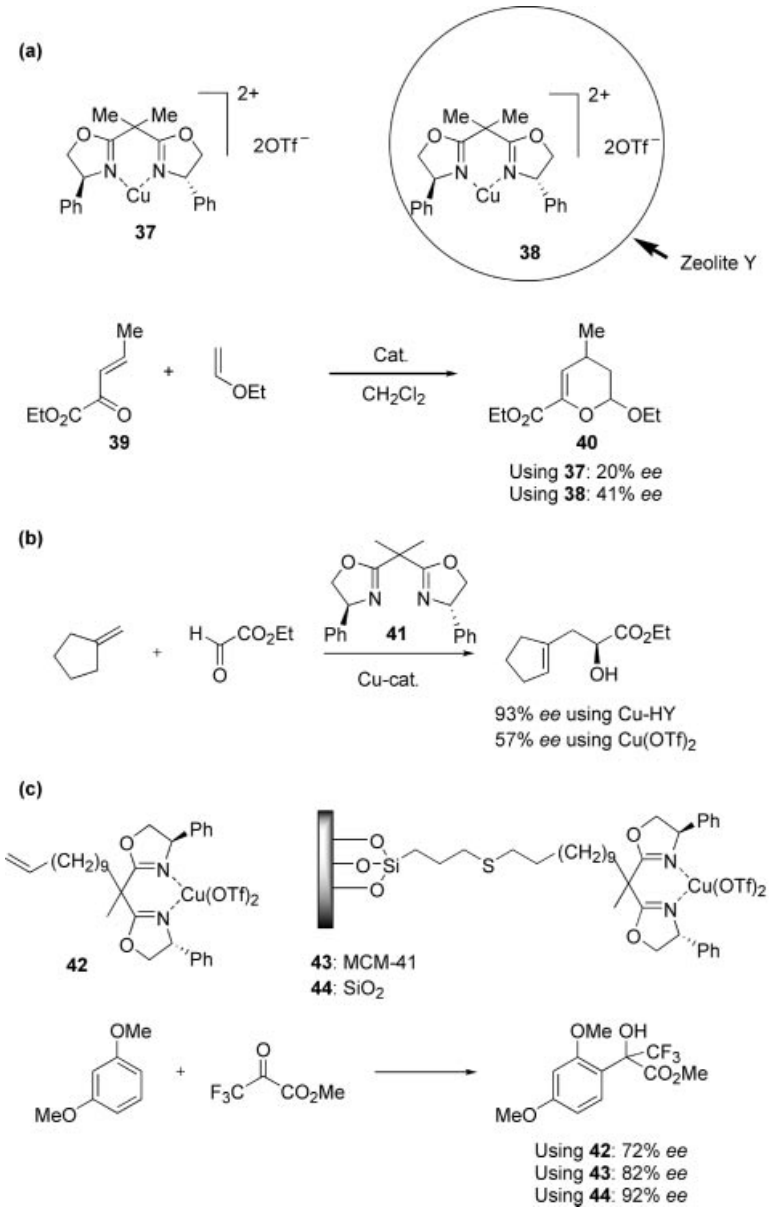


Scheme 14. Selected examples of chiral bis(oxazoline)copper complexes constrained within confined spaces and their use in catalytic reactions.

the homogeneous catalyst **37** (20% *ee*) (Scheme 14a). Very interestingly, the configuration of the (2*S*,4*R*) product obtained from the heterogeneous reaction is opposite to the (2*R*,4*S*) product obtained from the homogeneous reaction. As described in the introduction section, this reversed enantioselectivity could also be attributed to the confinement effect of the porous supports.

The heterogeneous catalyst obtained by impregnating $Cu^{II}$ ion in zeolite Y and subsequent modification with the bisoxazoline ligand **41**[54] also exhibited the superior enantioselectivity (93% *ee*) compared to the homogeneous catalyst (57% *ee*) for the reaction of methylenecyclopentane with ethyl glyoxylate (Scheme 14, b). The same authors observed a similar enhancement of the *ee* value in the aziridination reaction which result from the confinement effect of the zeolite pores.[55]

Corma et al. covalently anchored the chiral bis(oxazoline)copper(II) onto silica and MCM-41 and tested its catalytic ability in the Friedel–Crafts hydroxyalkylation of 1,3-dimethoxybenzene with 3,3,3-trifluoropyruvate.[56] The activity and enantioselectivity of the two heterogeneous catalysts were higher than those of the homogeneous analogue (Scheme 14, c).

## Conclusions

This microreview presents some selected representative examples which demonstrate that not only facile catalyst recycling but also a significant improvement in the catalytic performances (activity, stability and enantioselectivity) of the organometallic chiral catalysts can be achieved by hetero-

 © 2006 Wiley-VCH Verlag GmbH & Co. KGaA, Weinheim 

genizing them in the confined spaces of porous or layered support materials. Surprisingly, in some cases, even non-enantioselective catalysts showed significant asymmetric induction when they were anchored into confined nanospaces.[21,23,24,35,48] These results suggest that the conventional approaches, i.e. (i) designing chiral catalysts for homogeneous conditions and (ii) heterogenizing those catalysts well-designed for homogeneous processes, may not necessarily be the best solution for the development of efficient chiral catalyst systems. In conclusion, the heterogenization of catalysts in confined spaces will provide a new paradigm for the development of a highly efficient chiral catalyst in future.

## Acknowledgments

This work was supported by a Korea Research Foundation Grant (KRF-2005-005-J11901) funded by MOEHRD, and by the grants, R01-2006-000-10426-0 (KOSEF) and R11-2005-008-00000-0 (SRC program of MOST/KOSEF).

[1] E. N. Jacobsen, A. Pfaltz, H. Yamamoto (Eds.), *Comprehensive Asymmetric Catalysis*, Springer, Berlin, **1999**.
[2] I. Ojima (Ed.), *Catalytic Asymmetric Synthesis*, VCH, New York, 2nd ed., **2000**.
[3] H. U. Blaser, E. Schmidt (Eds.), *Asymmetric Catalysis on Industrial Scale*, Wiley-VCH, Weinheim, **2004**.
[4] A. N. Collins, G. N. Sheldrake, J. Crosby (Eds.), *Chirality in Industry*, John Wiley & Sons, Chichester, **1992**.
[5] A. N. Collins, G. N. Sheldrake, J. Crosby (Eds.), *Chirality in Industry II*, John Wiley & Sons, Chichester, **1996**.
[6] D. E. de Vos, I. F. J. Vankelecom, P. A. Jacobs (Eds.), *Chiral Catalyst Immobilization and Recycling*, Wiley-VCH, New York, **2000**.
[7] C. E. Song, S.-g. Lee, *Chem. Rev.* **2002**, *102*, 3495–3524.
[8] Q.-H. Fan, Y.-M. Li, A. C. S. Chan, *Chem. Rev.* **2002**, *102*, 3385–3465.
[9] P. M. Price, J. H. Clark, D. J. Macquarrie, *J. Chem. Soc., Dalton Trans.* **2000**, 101–110.
[10] I. F. J. Vankelecom, P. A. Jacobs in *Catalyst Immobilization on Inorganic Supports* (Eds.: D. E. de Vos, I. F. J. Vankelecom, P. A. Jacobs), Wiley-VCH, Weinheim, **2000**, pp. 19–42.
[11] C. Li, *Catal. Rev.* **2004**, *46*, 419–492.
[12] C. E. Song, I. S. Park in *Advances in Organic Synthesis*, ch. 8, Bentham Publishers, **2005**, pp. 233–260.
[13] C. E. Song, *Annu. Rep. Prog. Chem. Sect. C: Phys. Chem* **2005**, *101*, 143–173.
[14] R. S. Drago, D. C. Pribich, *Inorg. Chem.* **1985**, *24*, 1983–1985.
[15] B. Pugin, *J. Mol. Catal. A* **1996**, *107*, 273–279.
[16] D. Meunier, A. Piechaczyk, A. de Mallmann, J.-M. Basset, *Angew. Chem. Int. Ed.* **1999**, *38*, 3540–3542.
[17] E. Angeletti, C. Canepa, G. Martinetti, P. Venturello, *J. Chem. Soc., Perkin Trans. 1* **1989**, 105–107.
[18] V. Ayala, A. Corma, M. Iglesias, J. A. Rincon, F. Sanchez, *J. Catal.* **2004**, *224*, 170–177.
[19] A. Cormas-Vives, C. Gonzalez-Arellano, A. Corma, M. Iglesias, F. Sanchez, G. Ujaque, *J. Am. Chem. Soc.* **2006**, *128*, 4756–4765.
[20] J. M. Thomas, T. Maschmeyer, B. F. G. Johnson, D. S. Shephard, *J. Mol. Catal. A* **1999**, *141*, 139–144.
[21] S. A. Raynor, J. M. Thomas, R. Raja, B. F. G. Johnson, R. G. Bell, M. D. Mantle, *Chem. Commun.* **2000**, 1925–1926.
[22] J. M. Thomas, B. F. G. Johnson, R. Raja, G. Sankar, P. A. Midgley, *Acc. Chem. Res.* **2003**, *36*, 20–30.
[23] M. D. Jones, R. Raja, J. M. Thomas, B. F. G. Johnson, D. W. Lewis, J. Rouzaud, K. D. M. Harris, *Angew. Chem. Int. Ed.* **2003**, *42*, 4326–4331.
[24] R. Raja, J. M. Thomas, M. D. Jones, B. F. G. Johnson, D. E. W. Vaughan, *J. Am. Chem. Soc.* **2003**, *125*, 14982–14983.
[25] J. Rouzaud, M. D. Jones, R. Raja, B. F. G. Johnson, J. M. Thomas, M. J. Duer, *Helv. Chim. Acta* **2003**, *86*, 1753–1759.
[26] R. Augustine, S. Tanielyan, S. Anderson, H. Yang, *Chem. Commun.* **1999**, 1257–1258.
[27] F. M. deRege, D. K. Morita, K. C. Ott, W. Tumas, R. D. Broene, *Chem. Commun.* **2000**, 1797–1798.
[28] A. Corma, M. Iglesias, C. del Pino, F. Sa′nchez, *J. Chem. Soc., Chem. Commun.* **1991**, 1253–1255.
[29] A. Corma, M. Iglesias, C. del Pino, F. Sa′nchez, *J. Organomet. Chem.* **1992**, *431*, 233–246.
[30] A. Carmona, A. Corma, M. Iglesias, A. S. Jose′, F. Sa′nchez, *J. Organomet. Chem.* **1995**, *492*, 11–21.
[31] A. Corma, M. Iglesias, F. Mohino, F. Sa′nchez, *J. Organomet. Chem.* **1997**, *544*, 147–156.
[32] C. Pérez, S. Pérez, G. A. Fuentes, A. Cormac, *J. Mol. Catal. A* **2003**, *197*, 275–281.
[33] A. Hu, H. L. Ngo, W. Lin, *J. Am. Chem. Soc.* **2003**, *125*, 11490–11491.
[34] A. Hu, H. L. Ngo, W. Lin, *Angew. Chem. Int. Ed.* **2003**, *42*, 6000–6003.
[35] V. Caps, I. Paraskevas, S. C. Tsang, *Chem. Commun.* **2005**, 1781–1783.
[36] H.-L. Kwong, C. Sorato, Y. Ogino, H. Chen, K. B. Sharpless, *Tetrahedron Lett.* **1990**, *31*, 2999–3002.
[37] I. D. Gridnev, *Chem. Lett.* **2006**, *35*, 148–153.
[38] K. Mikami, M. Yamanaka, *Chem. Rev.* **2003**, *103*, 3369–3400.
[39] D. K. Konepudi, K. Asakura, *Acc. Chem. Res.* **2001**, *34*, 946–954.
[40] G. Gbery, A. Zsigmond, K. J. J. Balkus, *Catal. Lett.* **2001**, *74*, 77–80.
[41] S. Xiang, Y. Zhang, Q. Xin, C. Li, *Chem. Commun.* **2002**, 2696–2697.
[42] H. Zhang, S. Xiang, C. Li, *Chem. Commun.* **2005**, 1209–1211.
[43] H. Zhang, Y. Zhang, C. Li, *J. Catal.* **2006**, *238*, 369–381.
[44] G.-J. Kim, J.-H. Shin, *Tetrahedron Lett.* **1999**, *40*, 6827–6830.
[45] R. I. Kureshy, N. H. Khan, S. H. R. Abdi, I. Ahmad, S. Singh, R. V. Jasra, *J. Catal.* **2004**, *221*, 234–240.
[46] X. Zhou, X. Yu, J. Huang, S. Li, L. Li, C. Che, *Chem. Commun.* **1999**, 1789–1790.
[47] A. Corma, A. Fuerte, M. Iglesias, F. Sanchez, *J. Mol. Catal. A* **1996**, *107*, 225–234.
[48] B. F. G. Johnson, S. A. Raynor, D. S. Shephard, T. Mashmeyer, J. M. Thomas, G. Sankar, S. Bromley, R. Oldroyd, L. Gladden, M. D. Mantle, *Chem. Commun.* **1999**, 1167–1168.
[49] H. M. Hultman, M. de Lang, I. W. C. E. Arends, U. Hanefeld, R. A. Sheldon, T. Maschmeyer, *J. Catal.* **2003**, *217*, 275–283.
[50] H. M. Hultman, M. de Lang, M. Nowotny, I. W. C. E. Arends, U. Hanefeld, R. A. Sheldon, T. Maschmeyer, *J. Catal.* **2003**, *217*, 264–274.
[51] A. Corma, M. Iglesias, M. V. Martin, J. Rubio, F. Sanchez, *Tetrahedron: Asymmetry* **1992**, *3*, 845–848.
[52] M. Iglesias, F. Sanchez, *Stud. Surf. Sci. Catal.* **2000**, *130D*, 3393–3398.
[53] Y. Wan, P. McMorn, F. E. Hancock, G. J. Hutchings, *Catal. Lett.* **2003**, *91*, 145–148.
[54] N. A. Caplan, F. E. Hancock, P. P. C. Bulman, G. J. Hutchings, *Angew. Chem. Int. Ed.* **2004**, *43*, 1685–1688.
[55] S. Taylor, J. Gullick, P. McMorn, D. Bethell, P. C. Bulman Page, F. E. Hancock, F. King, G. J. Hutchings, *J. Chem. Soc., Perkin Trans. 2* **2001**, 1714–1723.
[56] A. Corma, H. Garcia, A. Moussaif, M. J. Sabater, R. Zzniber, A. Redouane, *Chem. Commun.* **2002**, 1058–1059.

Received: April 18, 2006
Published Online: June 23, 2006

 © 2006 Wiley-VCH Verlag GmbH & Co. KGaA, Weinheim 

DOI: 10.1002/ejic.200600497

# Formation of Unexpected Selenium-Rich Compounds by Selenation of the Very Bulky $(PhMe_2Si)_3CLi$: *s*-Tetraselenane, a Novel Polyseleno Heterocycle

**Thomas M. Klapötke,[a] Burkhard Krumm,*[a] Kurt Polborn,[a][‡] and Matthias Scherr[a][‡]**

**Keywords:** Bulky substituents / DFT calculations / Selenium / Structure elucidation

The reaction of the highly crowded trisilylmethyllithium compound $(PhMe_2Si)_3CLi$ with elemental selenium resulted in a variety of products, among them the triselane $[(PhMe_2Si)_3CSe]_2Se$, the unexpected diselane $[(PhMe_2Si)_2HCSe]_2$ and the novel heterocycle $[(PhMe_2Si)_2CSeSe]_2$. The constitution of the latter could be elucidated from the NMR spectroscopic data and was confirmed by the crystal structure which displays the $C_2Se_4$ cycle in the twist form. Calculations were performed for the chair and twist conformers of the heterocycles $[(H_3Si)_2CXX]_2$ (X = O, S, Se, Te, Po).

## Introduction

The stabilization of low-coordinated main-group compounds is possible with extremely bulky substituents and has been reviewed recently in detail.[1] Chalcogen compounds containing the tris(trimethylsilyl)methyl group, $(Me_3Si)_3C$, have been prepared (sulfur,[2] selenium,[3–5] and tellurium[3,6]). The introduction of such sterically demanding substituents at the heavier chalcogen elements has been a part of our research for the recent time, because they have been useful to stabilize or detect rather reactive species or intermediates in tellurium(II),[7] and selenium(II) azide chemistry.[8] The tris[dimethyl(phenyl)silyl]methyl group, $(PhMe_2Si)_3C$, is expected to have some increased shielding properties compared to the permethylated substituent. The tellurolate $(PhMe_2Si)_3CTeLi$ and the corresponding ditellane, tellurenyl iodide and azide were isolated and characterized by us very recently. In this communication we would like to present our study of the reactivity of $(PhMe_2Si)_3CLi$ towards selenium.

## Results and Discussion

The alkyllithium reagent $(PhMe_2Si)_3CLi$, generated as described,[7] was treated with elemental selenium to give the selenolate $(PhMe_2Si)_3CSeLi$ in a straightforward manner according to $^{77}Se$ NMR spectroscopy (in THF: $\delta$ = –63.3 ppm). The product mixture, which was obtained after hydrolysis and oxidation (exposure to air) of the selenolate, was surprisingly complex and, according to $^{77}Se$ NMR spectroscopy, consisted of several selenium-containing species. From this mixture the four main components could be separated, isolated and identified [Equation (1)].

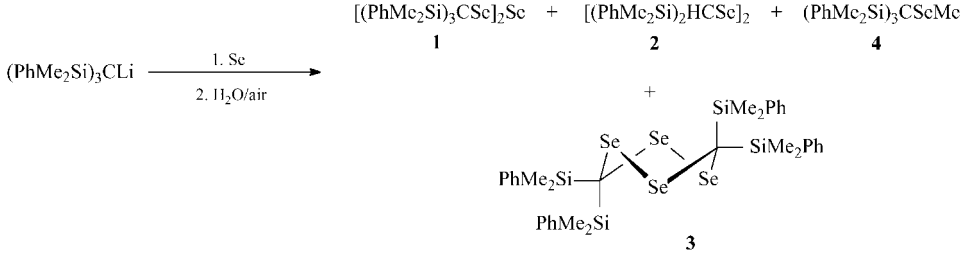


(1)

No evidence was found for the formation of the diselane $(PhMe_2Si)_3CSeSeC(SiMe_2Ph)_3$, which is usually formed as the main product by oxidation of selenolates RSeLi or selenols RSeH; the corresponding ditellane is also the main product in the oxidation of $(PhMe_2Si)_3CTeLi$.[7] Here, the triselane $(PhMe_2Si)_3CSeSeSeC(SiMe_2Ph)_3$ (**1**) is the main

[a] Department of Chemistry and Biochemistry, Ludwig-Maximilian University of Munich,
Butenandtstr. 5–13(D), 81377 Munich, Germany
Fax: +49-89-2180-77492
E-mail: bkr@cup.uni-muenchen.de
[‡] X-ray crystallography
Supporting information for this article is available on the WWW under http://www.eurjic.org or from the author.

 © 2006 Wiley-VCH Verlag GmbH & Co. KGaA, Weinheim 

product, which can be explained by the bulkiness of the substituent, to stabilize selanes with increased chain lengths in the case of smaller chalcogens. The triselane **1** was separated from the mixture because of its lower solubility in diethyl ether. The remaining mixture was subjected to column chromatography and resulted finally in the isolation and identification of two further selanes, the diselane $(PhMe_2Si)_2HCSeSeCH(SiMe_2Ph)_2$ (**2**) and the heterocycle $[(PhMe_2Si)_2CSeSe]_2$ (**3**). The formation and existence of **2** demonstrates that three dimethyl(phenyl)silyl groups attached to the carbon atom are too bulky for a corresponding diselane, but two dimethyl(phenyl)silyl groups, in the bis[dimethyl(phenyl)silyl]methyl group which is slightly less bulky, form a stable diselane **2**. The formation of the novel heterocycle **3**, a tetrasilyl-substituted *s*-tetraselenane, cannot be explained with certainty. Probably due to similar reasons as observed with **2**, one silyl group was eliminated and maybe a radical $(PhMe_2Si)_2CSeSe$, for which we have no evidence, dimerized to give the stable six-membered $C_2Se_4$ heterocycle **3**. The fourth main component of this reaction

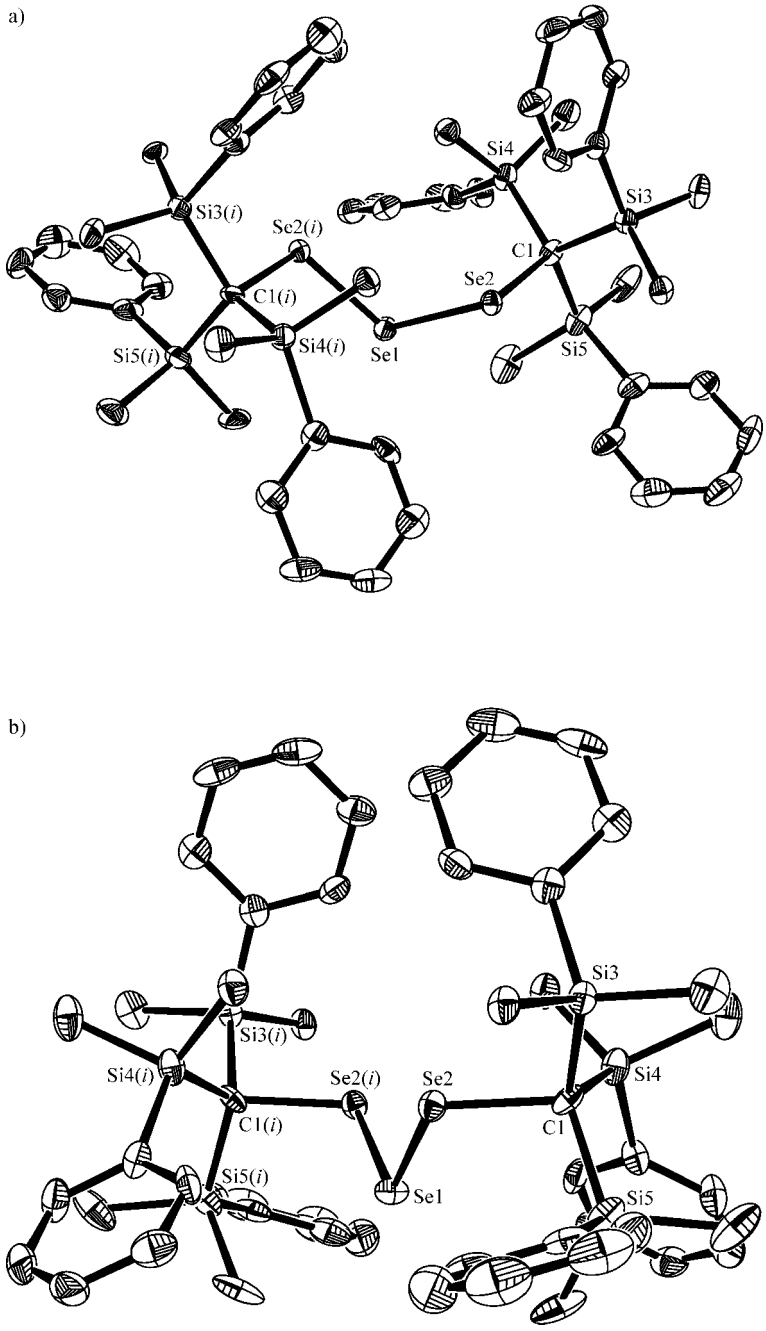


Figure 1. Different views (a) and (b) of the molecular structure of **1** with thermal ellipsoids of 50% probability. Selected bond lengths [Å] and angles [°]: Se1–Se2 2.340(1), Se2–C1 2.013(9); Se2–Se1–Se2(*i*) 109.90(7), C1–Se2–Se1 110.6(2), Si3–C1–Se2 98.7(4), Si4–C1–Se2 112.2(4), Si5–C1–Se2 104.5(4), Se2(*i*)–Se1–Se2–C1 –101.6(3); $i = 11/2-x, 11/2-y, z$.

 © 2006 Wiley-VCH Verlag GmbH & Co. KGaA, Weinheim 

was identified as the mixed monoselane $(PhMe_2Si)_3CSeMe$ (**4**). The formation of **4** can be explained by the always incomplete lithiation of $(PhMe_2Si)_2CH$ with methyllithium. Upon addition of selenium, immediate formation of MeSeLi occurs which can combine with tris[dimethyl(phenyl)silyl]methyl groups to give **4**. The monoselane **4** is already detected by $^{77}Se$ NMR in the THF solution of $(PhMe_2Si)_3CSeLi$ in amounts of ca 3–5% as the only other selenium-containing product.

The triselane **1** displays two resonances in the $^{77}Se$ NMR spectrum at $\delta$ = 666 ppm for the central selenium atom, and 552 ppm for the two terminal selenium atoms. The coupling constant $^1J(^{77}Se\text{-}^{77}Se)$ = 20.7 Hz is in the typical range found for other dialkyltriselanes.[9] The diselane **2**, as well as the symmetric *s*-tetraselenane **3**, exhibit single resonances at $\delta$ = 391 ppm and $\delta$ = 456 ppm, respectively. The resonance of the monoselane **4** is found at relatively high field at $\delta$ = 135 ppm, displaying a quartet due to coupling with methyl hydrogen atoms.

The crystal structure of the triselane **1** is shown in Figure 1 and gives an impression of the rather extreme bulkiness of the tris[dimethyl(phenyl)silyl]methyl substituent which allows the stabilization of this triselane (Figure 1a). In general, triselanes show a high propensity to eliminate red selenium at higher temperatures or already in solution at lower temperatures to form the corresponding diselanes.[10,11] The characteristic features of the triselane chain consist of the typical V-shaped unit (Figure 1b) with an angle of 109.90(7)° and an Se–Se bond length of 2.340(1) Å, forming a torsion angle Se2(*i*)–Se1–Se2–C1 of –101.6(3)°, parameters which are comparable to the structures of other undisturbed dialkyl triselanes.[10,12]

The structure of the novel *s*-tetraselenane **3**, shown in Figure 2 also can be regarded a cyclic bis(diselane), adopting a twist-boat conformation. The analoguous sulfur heterocycle, an *s*-tetrathiane, is fairly well known and also crystal structures exist. Whereas the bis(pentamethylene) derivative displays a chair configuration of the heterocycle,[13] the tetramethyl derivative, "duplodithioacetone", adopts the twist-boat conformation.[14] The Se–Se [2.3120(6)/2.3085(6) Å] and C–Se bond lengths [1.993(4)–2.001(4) Å] of **3** are in the same range as found in the structures of

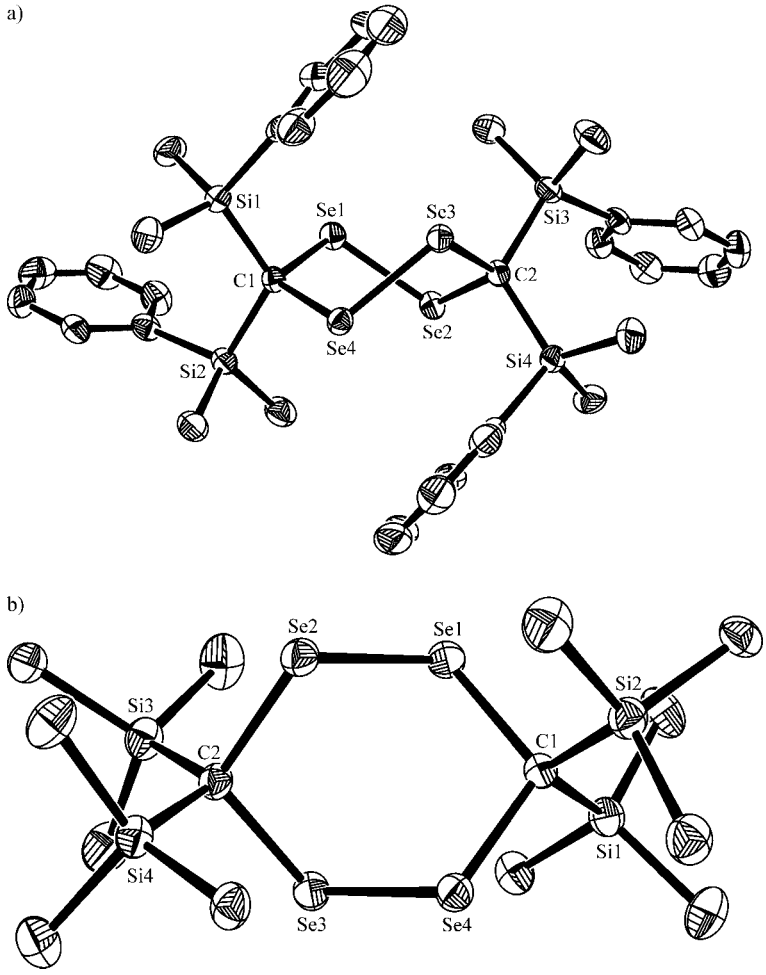


Figure 2. Different views (a) and (b) of the molecular structure of **3** with thermal ellipsoids of 30% probability. Selected bond lengths [Å] and angles [°]: Se1–Se2 2.3120(6), Se3–Se4 2.3085(6), Se1–C1 1.993(4), Se4–C1 2.001(4), Se2–C2 2.000(4), Se3–C2 1.999(3), Si1–C1 1.907(4), Si2–C1 1.905(4), Si3–C2 1.910(4), Si4–C2 1.903(4), C1–Se1–Se2 104.7(1), C1–Se4–Se3 104.0(1), C2–Se2–Se1 104.7(1), C2–Se3–Se4 103.2(1), Se1–C1–Se4 109.8(2), Se3–C2–Se2 110.3(2), Si2–C1–Si1 119.4(2), Si4–C2–Si3 119.2(2), C1–Se1–Se2–C2 –78.7(2), C2–Se3–Se4–C1 –81.9(2).

 © 2006 Wiley-VCH Verlag GmbH & Co. KGaA, Weinheim 

acyclic aliphatic and aromatic diselanes.[4,15] Figure 2a nicely shows the twisted six-membered heterocycle encumbered by two bis[dimethyl(phenyl)silyl]methylene moieties. In Figure 2b a view onto the heterocycle is given with all phenyl groups omitted for clarity.

The NMR spectra of **3** indicate a restricted rotation of the methyl groups, visible for the corresponding resonances in the $^{1}H$ and $^{13}C$ NMR spectra. At 25 °C two broadened resonances are observed for the methyl groups in the $^{1}H$ and $^{13}C$ NMR spectra, respectively. In the $^{1}H$ NMR spectrum coalescence is observed at 32 °C, whereas in the $^{13}C$ NMR spectrum at 47 °C both resonances coalesce. The resonance of the $CSi_2Se_2$ carbon atom remains unaffected. The variable-temperature $^{77}Se$ NMR spectrum of **3** shows only the temperature dependency of the resonance, i.e. spanning from $\delta$ = 462 ppm at 60 °C over $\delta$ = 456 ppm at 25 °C to $\delta$ = 443 ppm at –60 °C (all in $CDCl_3$). No additional resonances were detected within this temperature range, which then could indicate a change of the conformation of the heterocycle.

The experimentally observed twist conformation of **3** was subject of calculations for the sulfur analogue *s*-tetrathiane, where a molecular mechanics (MM) and an NMR study already predicted the twist conformer to be favored over the chair conformer by 0.7 kcal mol$^{-1}$.[16] In order to confirm the early MM study we now decided to compute the full series of O, S, Se, Te and Po heterocycles using hybrid density functional theory (DFT) at the B3LYP level. The model compounds, which were included in the computation were the chair and twist conformers of the heterocycles $[(H_3Si)_2CXX]_2$ (X = O, S, Se, Te, Po) (Table S1, Figure S1 in Supporting Information). The structures of all ten species were fully optimized and the vibrational frequencies calculated at the B3LYP/SDD level of theory. All ten entities represent stable minima on their potential energy surface. Whereas according to our calculations for the oxygen and sulfur compounds the chair conformers are favored by 5.8 and 0.4 kcal mol$^{-1}$ (nicely in agreement with our X-ray structure for the selenium heterocycle), the twist conformers of the Se, Te and Po heterocycles represent the lower energy species, although the energy differences are again relatively small: $\Delta E$(chair–twist) = +1.9 (Se), +3.1 (Te), +3.3 (Po) kcal mol$^{-1}$. It seems that the relative stability of the twist over the chair conformer increases with the heteroatoms (O → Po) descending within group 16 (Figure 3). For oxygen the chair is favored, for sulfur the chair and twist conformer are essentially identical in their energy, whereas for the heavier congeners Se, Te and Po the twist structure is favored over the chair conformer.

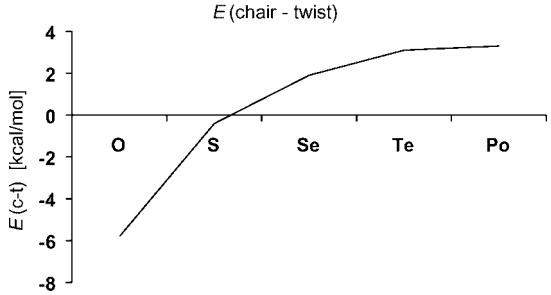


Figure 3. Relative stabilities of the chair and twist conformers of $[(H_3Si)_2CXX]_2$ (X = O, S, Se, Te, Po).

The existence of a claimed tetratellurium analogue, *s*-tetratellurane $(CH_2Te_2)_2$,[17] remains highly questionable in our opinion, due to the poor spectroscopic data. Substituted *s*-tetratellurane derivatives may possibly be prepared in the future, if one considers the relatively high stability of the corresponding sulfur and selenium heterocycles, and as well taking the calculations into account.

## Experimental Section

**General:** All manipulations of air- and moisture-sensitive materials were performed under dry argon using flame-dried glass vessels and Schlenk techniques. The compounds $PhMe_2SiCl$,[18] and $(PhMe_2Si)_3CH$[19] were prepared according the literature, elemental selenium and methyllithium (1.6 M in $Et_2O$) (Aldrich) was used as received. Solvents were dried by standard methods and freshly distilled prior to use. NMR spectra were recorded with a JEOL Eclipse 400 instrument in $CDCl_3$ at 25 °C, and chemical shifts are with respect to $Me_4Si$ ($^{1}H$: 400.2 MHz; $^{13}C$: 100.6 MHz; $^{29}Si$: 79.5 MHz) and $Me_2Se$ ($^{77}Se$: 76.3 MHz). Raman spectra were recorded with a Perkin–Elmer 2000 NIR FT spectrometer fitted with an Nd-YAG laser (1064 nm, 100 mW, 25 °C), and only 100% peak and Se–Se stretching frequency listed. Mass spectrometric data were obtained with a JEOL MStation JMS spectrometer. Elemental analyses: Analytical service LMU. Melting points were determined in capillaries using a Büchi B540 instrument.

**Lithiation and Selenation of $(PhMe_2Si)_3CH$:** Into a solution of $(PhMe_2Si)_3CH$ (6.0 g, 14.3 mmol, sublimed at 90 °C/10$^{-3}$ mbar) in 75 mL of THF was added methyllithium (10 mL, 16 mmol) in diethyl ether (1.6 M) at 25 °C within 1 h. This mixture was stirred at ambient temperature for an additional 1 h and then heated to 60 °C for 3 h. After cooling to ambient temperature, selenium (1.2 g, 15.2 mmol) was added in one portion and the mixture stirred for 1 h. The selenium reacted immediately and darkening of the solution occurred. This mixture was stirred at ambient temperature, now upon contact with air, for 3 d. All volatile materials were removed in vacuo, and the resulting dark orange residue was treated with 50 mL $Et_2O$, and 30 mL water was slowly added at 25 °C. Additionally, 20 mL of 10% HCl was added carefully at 0 °C and the mixture stirred for 2 h. The extracted dark red diethyl ether phases were separated and dried. The solvent was removed in vacuo, and the brown-red solid residue was treated again with small amounts of cold diethyl ether. The insoluble solid was washed repeatedly. This material was only poorly soluble in $Et_2O$ and was shown to be pure triselane $(PhMe_2Si)_3CSeSeSeC(SiMe_2Ph)_3$ (**1**) (600 mg, ca. 8% yield). The remaining diethyl ether soluble fraction, a highly viscous red-brown oil, still containing considerable amounts of the triselane **1**, was subjected to column chromatography. The eluent was an *n*-hexane/chloroform mixture (10:1). The first fraction was the monoselane **4**, the second fraction contained a mixture of the diselane **2** and the *s*-tetraselenane **3**. The last fraction, containing a mixture of further other selenium-containing species that could not be separated, was discarded. The mixture consisting of **2** and **3**, could be separated by their different solubilities in diethyl ether. By repeated extraction of the mixture, the diselane **2** could be separated because of its slightly higher solubility in diethyl ether than that of the *s*-tetraselenane **3**.

 © 2006 Wiley-VCH Verlag GmbH & Co. KGaA, Weinheim 

**$(PhMe_2Si)_3CSeSeSeC(SiMe_2Ph)_3$ (1):** M.p. 176–178 °C. $^1H$ NMR: $\delta$ = 7.70 (2 H)/7.35 (1 H)/7.28 (2 H) (m, Ar-H), 0.37 [$^2J(^1H\text{-}^{29}Si)$ = 6.0 Hz, 6 H, $CH_3$] ppm. $^{13}C$ NMR: $\delta$ = 139.5 [$^1J(^{13}C\text{-}^{29}Si)$ = 66.5 Hz, C-1], 136.1 (C-3), 129.1 (C-4), 127.3 (C-2), 19.9 [$^1J(^{13}C\text{-}^{29}Si)$ = 32.6 Hz, $^1J(^{13}C\text{-}^{77}Se)$ = 84.2 Hz, $CSi_3$], 2.1 [$^1J(^{13}C\text{-}^{29}Si)$ = 42.0 Hz, $CH_3$] ppm. $^{29}Si$ NMR: $\delta$ = –3.45 [$^2J(^{29}Si\text{-}^{77}Se)$ = 8.7 Hz] ppm. $^{77}Se$ NMR: $\delta$ = 666 [$^1J(^{77}Se\text{-}^{77}Se)$ = 20.7 Hz, 1 Se], 552 (2 Se) ppm. Raman: $\tilde{\nu}$ (%) = 1001 (100) [δ(Ph-H)], 272 (32) [ν(SeSe)] $cm^{-1}$. DEI-MS: *m*/*z* (%) = 1072 (0.1) [$M^+$], 994 (0.1) [$M^+$ – Se], 936 (0.1) [$M^+$ – $PhMe_2Si$], 860 (0.9) [$M^+$ – Se – $PhMe_2Si$], 726 (3) [$M^+$ – Se – 2 $PhMe_2Si$], 576 (8) [$M^+$ – Se – $(PhMe_2Si)_3C$], 495 (6) [$M^+$ – 2 Se – $(PhMe_2Si)_3C$], 135 (100) [$PhMe_2Si^+$]. $C_{50}H_{66}Se_3Si_6$ (1072.45): calcd. C 56.0, H 6.2; found C 54.6, H 6.1.

**$(PhMe_2Si)_2HCSeSeCH(SiMe_2Ph)_2$ (2):** M.p. 60–63 °C. $^1H$ NMR: $\delta$ = 7.44–7.32 (m, 10 H, Ar-H), 1.21 [$^2J(^1H\text{-}^{29}Si)$ = 8.0 Hz, $^2J(^1H\text{-}^{77}Se)$ = 10.5 Hz, 1 H, CH], 0.162/0.157 (12 H, $CH_3$) ppm. $^{13}C$ NMR: $\delta$ = 138.9 [$^1J(^{13}C\text{-}^{29}Si)$ = 69.2 Hz, C-1], 134.1 (C-3), 129.0 (C-4), 127.5 [$^2J(^{13}C\text{-}^{29}Si)$ = 23.4 Hz, C-2], 19.8 [$^1J(^{13}C\text{-}^{29}Si)$ = 43.8 Hz, $^1J(^{13}C\text{-}^{77}Se)$ = 75.3 Hz, $CHSi_2$], –1.6/–2.2 [$^1J(^{13}C\text{-}^{29}Si)$ = 53.8/54.6 Hz, $CH_3$] ppm. $^{29}Si$ NMR: $\delta$ = –3.35 ppm [$^2J(^{29}Si\text{-}^{77}Se)$ = 9.7 Hz]. $^{77}Se$ NMR: $\delta$ = 391 ppm. Raman: $\tilde{\nu}$ (%) = 1000 (100) [δ(Ph-H)], 293 (30) [ν(SeSe)] $cm^{-1}$. DEI-MS: *m*/*z* (%) = 726 (30) [$M^+$], 646 (0.5) [$M^+$ – Se], 442 (0.6) [$M^+$ – $(PhMe_2Si)_2CH$ – H], 363 (10) [$M^+$ – $SeCH(SiMe_2Ph)_2$], 135 (100) [$PhMe_2Si^+$]. $C_{34}H_{46}Se_2Si_4$ (725.08): calcd. C 56.3, H 6.4; found C 54.6, H 6.3.

**$[(PhMe_2Si)_2CSeSe]_2$ (3):** M.p. 181–183 °C. $^1H$ NMR: $\delta$ = 7.56 (2 H)/7.40 (1 H)/7.31 (2 H) (m, Ar-H), 0.32/0.29 (6 H, $CH_3$) ppm. $^{13}C$ NMR: $\delta$ = 137.1 [$^1J(^{13}C\text{-}^{29}Si)$ = 67.6 Hz, C-1], 135.4 (C-3), 129.3 (C-4), 127.4 (C-2), 9.7 [$^1J(^{13}C\text{-}^{29}Si)$ = 12.3 Hz, $^1J(^{13}C\text{-}^{77}Se)$ = 91.9 Hz, $CSi_2Se_2$], –1.7/–2.2 (br., $CH_3$) ppm. $^{29}Si$ NMR: $\delta$ = –0.56 [$^2J(^{29}Si\text{-}^{77}Se)$ = 5.8 Hz] ppm. $^{77}Se$ NMR: $\delta$ = 456 ppm. Raman: $\tilde{\nu}$ (%) = 1000 (100) [δ(Ph-H)], 292 (48) [ν(SeSe)] $cm^{-1}$. DEI-MS: *m*/*z* (%) = 882 (3) [$M^+$], 667 (6) [$M^+$ – Se – $PhMe_2Si$], 520 (1) [$M^+$ – Se – $(PhMe_2Si)_2C$], 442 (16) [$(PhMe_2Si)_2CSe_2^+$], 362 (12) [$(PhMe_2Si)_2CSe^+$], 135 (100) [$PhMe_2Si^+$]. $C_{34}H_{44}Se_4Si_4$ (880.89): calcd. C 46.4, H 5.0; found C 45.2, H 5.0.

**$(PhMe_2Si)_3CSeMe$ (4):** $^1H$ NMR: $\delta$ = 7.52–7.35 (m, 15 H, Ar-H), 0.59 [$^2J(^1H\text{-}^{77}Se)$ = 9.8 Hz, 3 H, $CH_3Se$], 0.35 [$^2J(^1H\text{-}^{29}Si)$ = 6.4 Hz, 18 H, $CH_3Si$] ppm. $^{13}C$ NMR: $\delta$ = 141.8 [$^1J(^{13}C\text{-}^{29}Si)$ = 66.0 Hz, C-1], 133.2 (C-3), 128.3 (C-4), 127.5 (C-2), 2.0 [$^1J(^{13}C\text{-}^{29}Si)$ = 5.8 Hz, $^1J(^{13}C\text{-}^{77}Se)$ = 53.8 Hz, $CSi_3$], 1.6 [$^1J(^{13}C\text{-}^{29}Si)$ = 52.7 Hz, $CH_3Si$], 0.1 [$^1J(^{13}C\text{-}^{77}Se)$ = 38.1 Hz, $CH_3Se$] ppm. $^{29}Si$ NMR: $\delta$ = –3.65 [$^2J(^{29}Si\text{-}^{77}Se)$ = 3.9 Hz] ppm. $^{77}Se$ NMR: $\delta$ = 135 (q) ppm.

**Crystal Data for 1:** $C_{50}H_{66}Se_3Si_6$ (1072.45), orange platelet, 0.58 × 0.11 × 0.52 mm, orthorhombic, space group *Pccn*, *a* = 13.8952(7), *b* = 17.1669(9), *c* = 21.759(1) Å, *V* = 5190.3(5) $Å^3$, *Z* = 4, $\rho_{calcd.}$ = 1.372 $g/cm^{-3}$, $\mu$ = 2.297 $mm^{-1}$, *F*(000) = 2208, Oxford XCalibur CCD, Mo-$K_\alpha$, $\lambda$ = 0.71073 Å, *T* = 200 K; $\theta$ range = 3.8–22.0°, $-9 \le h \le 14$, $-18 \le k \le 17$, $-22 \le l \le 22$, 17116 reflections collected, 3172 independent reflections ($R_{int}$ = 0.1395), 2749 observed reflections [$I > 2\sigma(I)$], structure solution: SHELX-97,[20] direct methods, data/parameters ratio: 11.9:1 {10.3:1 [$I > 2\sigma(I)$]}, final *R* indices [$I > 2\sigma(I)$]: $R_1$ = 0.0824, $wR_2$ = 0.1293, $R_1$ = 0.0982, $wR_2$ = 0.1371 (all data), GOF on $F^2$ = 1.184.

**Crystal Data for 3:** $C_{34}H_{44}Se_4Si_4$ (880.89), orange platelet, 0.57 × 0.33 × 0.43 mm, monoclinic, space group $P2_1/c$, *a* = 11.846(1), *b* = 14.641(2), *c* = 22.313(2) Å, $\beta$ = 97.56(1)°, *V* = 3836.3(7) $Å^3$, *Z* = 4, $\rho_{calcd.}$ = 1.525 $g/cm^{-3}$, $\mu$ = 3.972 $mm^{-1}$, *F*(000) = 1760, Nonius Kappa CCD, Mo-$K_\alpha$, $\lambda$ = 0.71073 Å, *T* = 295 K; $\theta$ range = 2.7–25.6°, $-14 \le h \le 0$, $-17 \le k \le 0$, $-26 \le l \le 27$, 7534 reflections collected, 7010 independent reflections ($R_{int}$ = 0.0161), 4864 observed reflections [$I > 2\sigma(I)$], structure solution: SHELX-97,[20] direct methods, data/parameters ratio: 18.2:1 {12.6:1 [$I > 2\sigma(I)$]}, final *R* indices [$I > 2\sigma(I)$]: $R_1$ = 0.0312, $wR_2$ = 0.0683, $R_1$ = 0.0659, $wR_2$ = 0.0822 (all data), GOF on $F^2$ = 1.020.

CCDC-600115 (**1**) and -282655 (**3**) contain the supplementary crystallographic data for this paper. These data can be obtained free of charge from The Cambridge Crystallographic Data Centre via www.ccdc.cam.ac.uk/data_request/cif.

**Supporting Information** (see footnote on the first page of this article): Detailed description of the chair-twist calculations.

## Acknowledgments

Financial support by the University of Munich and the Fonds der Chemischen Industrie is gratefully acknowledged. We also would like to thank cand. chem. T. Kerscher for his engagement with column chromatography.

[1] a) C. Eaborn, J. D. Smith, *J. Chem. Soc. Dalton Trans.* **2001**, 1541–1552; b) P. P. Power, *J. Organomet. Chem.* **2004**, *689*, 3904–3919.
[2] M. Ostrowski, J. Jeske, P. G. Jones, W.-W. Du Mont, *Chem. Ber.* **1993**, *126*, 1355–1359.
[3] F. Sladky, B. Bildstein, C. Rieker, A. Gieren, H. Betz, T. Hübner, *J. Chem. Soc. Chem. Commun.* **1985**, 1800–1801.
[4] I. Wagner, W.-W. Du Mont, S. Pohl, W. Saak, *Chem. Ber.* **1990**, *123*, 2325–2327.
[5] M. Ostrowski, I. Wagner, W.-W. Du Mont, P. G. Jones, J. Jeske, *Z. Anorg. Allg. Chem.* **1993**, *619*, 1693–1698.
[6] a) K. Giselbrecht, B. Bildstein, F. Sladky, *Chem. Ber.* **1989**, *122*, 1255–1256; b) W. Fimml, F. Sladky, *Chem. Ber.* **1991**, *124*, 1131–1133.
[7] T. M. Klapötke, B. Krumm, H. Nöth, J. C. Galvez-Ruiz, K. Polborn, I. Schwab, M. Suter, *Inorg. Chem.* **2005**, *44*, 5254–5265.
[8] T. M. Klapötke, B. Krumm, K. Polborn, *J. Am. Chem. Soc.* **2004**, *126*, 710–711.
[9] H. Eggert, O. Nielsen, L. Henriksen, *J. Am. Chem. Soc.* **1986**, *108*, 1725–1730.
[10] F. Hansen, L. Henriksen, S. Larsen, L. Teuber, *Acta Chem. Scand.* **1989**, *43*, 450–457.
[11] T. M. Klapötke, B. Krumm, P. Mayer, *Z. Naturforsch. Teil B* **2004**, *59*, 547–553.
[12] B. J. McKinnon, P. De Mayo, N. C. Payne, B. Ruge, *New J. Chem.* **1978**, *2*, 91–94.
[13] C. H. Bushweller, G. Bhat, L. J. Letendre, J. A. Brunelle, H. W. Bilofsky, H. Ruben, D. H. Templeton, A. Zalkin, *J. Am. Chem. Soc.* **1975**, *97*, 65–73.
[14] J. D. Korp, I. Bernal, S. F. Watkins, F. R. Fronczek, *Tetrahedron Lett.* **1981**, *22*, 4767–4770.
[15] a) T. G. Back, P. W. Codding, *Can. J. Chem.* **1983**, *61*, 2749–2752; b) J. Jeske, A. Martens-Von Salzen, W.-W. Du Mont, P. G. Jones, *Acta Crystallogr. Sect. C* **1998**, *54*, 1873–1875; c) T. M. Klapötke, B. Krumm, P. Mayer, H. Piotrowski, K. Polborn, *J. Fluorine Chem.* **2003**, *123*, 133–138.
[16] a) N. L. Allinger, M. J. Hickey, J. Kao, *J. Am. Chem. Soc.* **1976**, *98*, 2741–2745; b) R. Susilo, R. Gmelin, K. Roth, H. Bauer, *Z. Naturforsch. Teil B* **1982**, *37*, 234–235.
[17] F. J. Berry, B. C. Smith, C. H. W. Jones, *J. Organomet. Chem.* **1976**, *110*, 201–203.
[18] R. Lehnert, A. Porzel, K. Rühlmann, *Z. Chem.* **1988**, *5*, 190–192.
[19] S. S. Al-Juaid, C. Eaborn, A. Habtemariam, P. B. Hitchcock, J. D. Smith, K. Tavakkoli, A. D. Webb, *J. Organomet. Chem.* **1993**, *462*, 45–55.
[20] G. M. Sheldrick, University of Göttingen, Germany, **1997**.

Received: May 29, 2006
Published Online: July 3, 2006

 © 2006 Wiley-VCH Verlag GmbH & Co. KGaA, Weinheim 

DOI: 10.1002/ejic.200600219

# Metal Directed Assemblies of a Dipeptide: Formation of β-Pleated Sheets

Nilotpal Barooah,[a] Rupam J. Sarma,[a] and Jubaraj B. Baruah*[a]

**Keywords:** Hydrogen bonding / Self-assembly / Dipeptide / β-Sheets / Coordination polymer

The crystal structure of *N*-phthaloylglycylglycine and its complexes with copper(II) and zinc(II) are studied. The *N*-phthaloylglycylglycinato copper(II) complex has a polymeric structure formed by bridging carboxylates. The corresponding *N*-phthaloylglycylglycinato zinc(II) complex is monomeric. Both the metal complexes have self-assembled hydrogen-bonded structures in which dipeptide ligand adopt β-pleated conformations.
(© Wiley-VCH Verlag GmbH & Co. KGaA, 69451 Weinheim, Germany, 2006)

Directed assembly of molecules through noncovalent interactions and metal coordination is a fundamental process in nature.[1] Self-organization and molecular recognition of biomolecules[1e] using peptides are rationalized by taking into account a host of weak interactions[2] that include hydrogen bonding, aromatic π interactions, and hydrophobic interactions. The ability of peptides to adopt various secondary structures has been a subject of extensive study,[3] and in this regard the effects of metal ions in stabilizing particular conformations of peptides have immense importance.[4] The β-sheet assembly of peptide chains is particularly important in case of globular proteins and various template-directed strategies to assemble natural or non-natural peptides and synthetic peptide analogs into similar assemblies have been investigated.[5] Coordination of the peptide to a particular metal ion predominantly governs the local structure of the active site in metalloenzymes.[6] Even though attempts have been made to rationalize the interaction of metal ions with peptides,[7] the structural elucidation of such assemblies with regard to tuning the secondary interactions in the peptide[5b,8] is scarce. Given this background, we report the solid-state structures of the *N*-protected dipeptide derived from glycylglycine, and subsequently rationalize the effect of metal-ion templating on the self-assembly of this dipeptide.

Condensation of glycylglycine with phthalic anhydride under hydrothermal conditions and subsequent recrystallization from aqueous ethanol afforded the *N*-protected dipeptide, *N*-phthaloylglycylglycine (**L**) as colorless needles. The introduction of the phthaloyl group was expected to stabilize the two-dimensional assembly of the molecules in the solid state through intermolecular aromatic interactions.[9] These π interactions can be complementary in nature to the intermolecular N–H···O interactions observed in case of amides, which have a dominating effect on the self-assembly process.[10] Crystal structure shows that the self-assembly of the dipeptide **L** in the solid state is governed by intermolecular hydrogen-bonding interactions; the molecule adopts a puckered conformation as shown in Figure 1. The amide N–H is involved in the formation of hydrogen bonds with the carbonyl oxygen atom of the phthalimide unit ($d_{N2\cdots O4}$ 3.04 Å; ∠ D–H···A 156.0°), which extends along crystallographic *a* axis. Moreover, the amide carbonyl is strongly hydrogen-bonded to the oxygen atom of the carboxylic acid group ($d_{O1\cdots O3}$ 2.59 Å; ∠ D–H···A 165.1°) as shown in Figure 1. Thus, intermolecular hydrogen-bonding interactions in **L** leads to the formation of two-dimensional sheets, wherein the individual molecules adopt folded conformations; however, the structure does not correspond to β-pleated sheet structure. The torsion angle for rotation about the C–N bond ($\varphi$) is 70.9° while the corresponding angle for the C–C bond rotation ($\psi$) is 19.9°. The important hydrogen bond angles and bond lengths of **L** in the hydrogen-bonded assembly are listed in Table 1. It is important to note that the interplanar distance between the phthalimide groups of **L** is ca. 3.34 Å, which could indicate the presence of weak aromatic π interactions.

The templating effect of $Cu^{II}$ and $Zn^{II}$ ions, two of the biologically important metal ions, on the self-assembly of the dipeptide **L** has been studied by preparing the corresponding $Cu_2L_4(H_2O)_4{\cdot}2H_2O$ and $ZnL_2(H_2O)_4$ complexes. Reaction of **L** with copper acetate mono hydrate results in the formation of the complex **1** which possess the molecular formula $CuL_2(H_2O)_2{\cdot}2H_2O$. The crystal structure of **1** shows that each of the copper center is coordinated to **L** through the oxygen atoms of the carboxylate group; the coordinated water molecules are *trans* to each other in a nearly square-planar geometry with Cu1···O1 and Cu1···O6 bond lengths of 1.9471(10) and 1.9445(13) Å, respectively. The carbonyl oxygen of another adjacent glycinato unit leads to a weak Cu1···O2 ($d_{Cu1\cdots O2}$ 2.650 Å) coordination,

[a] Department of Chemistry, Indian Institute of Technology, Guwahati, 781 039, India
E-mail: juba@iitg.ernet.in
Supporting information for this article is available on the WWW under http://www.eurjic.org or from the author.

 © 2006 Wiley-VCH Verlag GmbH & Co. KGaA, Weinheim 

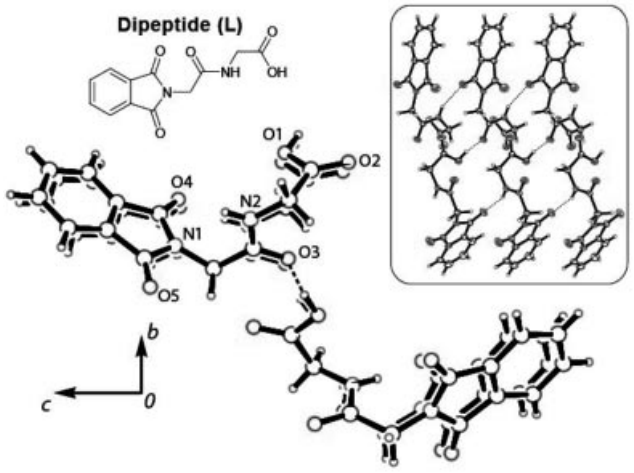


Figure 1. 2D Molecular sheets arising from intermolecular hydrogen bonding in **L**; (Inset) The hydrogen-bonded molecular sheets viewed parallel to *bc* plane.

Table 1. Hydrogen-bonding geometry (distances and angles) in *N*-phthaloylglycylglycine (**L**).

| D–H···A | $d_{D–H}$ [Å] | $d_{H···A}$ [Å] | $d_{D···A}$ [Å] | ∠ D–H···A[°] |
|---|---|---|---|---|
| N2–H···O4$^{\#[a]}$ | 0.85 | 2.24 | 3.044 | 157.03 |
| O1–H···O3$^{\#\#}$ | 0.89 | 1.71 | 2.593 | 164.82 |

[a] Symmetry transformations used to generate atoms: $^{\#}$ $x-1$, $y$, $z$, $^{\#\#}$ $-x+3/2$, $y+1/2$, $-z+1/2$.

which gives the $Cu^{II}$ center axially distorted octahedral geometry as shown in Figure 2 (a). The unusual bridging mode of the carboxylate group in this coordination motif leads to a one-dimensional coordination network of $Cu^{II}$ ions along crystallographic *b* axis with $Cu^{II}\cdots Cu^{II}$ distance of 4.71 Å. The two O1···Cu1···O6 and O1···Cu1···O2 bond angles are 93.40° and 86.85°, respectively. The distorted octahedral geometry (Figure 2, b) of the $Cu^{II}$ center in complex **1** is also obvious from its ESR spectra. At room temperature, the ESR spectrum of the solid complex **1** shows a strong signal with center field at 3177.6 G ($g$ = 2.124), which is an indication for the axially distorted octahedral geometry around the $Cu^{II}$ center. It may be pointed out here that metal-directed self-assembled systems also give rise to porous metal-organic frameworks as well as coordination polymers.[11]

In the case of complex **1**, the water molecules included inside the lattice probably underlines the importance of water in stabilizing the β-sheets,[2] formed by the dipeptide units connected to the $Cu^{II}$ center. We have found that the ligand organization in this complex is governed by weak hydrogen-bonding interactions between the amide groups of the dipeptide and the interstitial water molecules. In this complex, intermolecular hydrogen bonding between the amide N–H groups and the amide carbonyl groups ($d_{N1···O3}$ 2.94 Å; ∠ D–H···A 157.8°) is complemented by weak C–H···O interaction involving C4–H as donor and O3 as acceptor ($d_{C4···O3}$ 3.05 Å). This weak C–H···O interaction is well within the range reported elsewhere.[2b] These two weak interactions assemble the *N*-phthaloylglycylglycinato ligands leading to a parallel β-pleated sheet conformation as shown in the Figure 2 (a). The torsion angle for rotation about the C–N bond ($\varphi$) is –135.3°, while the corresponding angle for the C–C bond rotation ($\psi$) is 169.2° which is within the limit of β-sheet structure.[3a–3b] This corresponds to a *trans* conformation about the C–C bond.[3b] The hydrogen-bond donor···acceptor distances and angles of complex **1** are listed in Table 2.

Table 2. Hydrogen bonding geometry (distances and angles) in complex **1**[a].

| D–H···A | $d_{D–H}$ [Å] | $d_{H···A}$ [Å] | $d_{D···A}$ [Å] | ∠ D–H···A[°] |
|---|---|---|---|---|
| N1–H···O3$^{\#[b]}$ | 0.79 | 2.18 | 2.944 | 162.3 |
| O6–H···O7$^{\#\#}$ | 0.81 | 1.89 | 2.668 | 158.5 |
| O6–H···O2 | 0.81 | 1.88 | 2.650 | 157.7 |
| O7–H···O2+$^{\#\#\#}$ | 0.74 | 2.11 | 2.851 | 170.5 |

[a] O6 is from coordinated water; O7 is from interstitial water. [b] Symmetry transformations used to generate atoms: $^{\#}$ $x$, $y+1$, $z$; $^{\#\#}$ $x-1$, $y+1$, $z+1$, $^{\#\#\#}$ $-x+1$, $y$, $-z+3/2$.

In a similar way, the $Zn^{II}$ complex $ZnL_2(H_2O)_4$ (**2**) was synthesized and structurally characterized. Each $Zn^{II}$ ion is coordinated to two monodentate carboxylic groups of **L** and four water molecules; which results in an octahedral

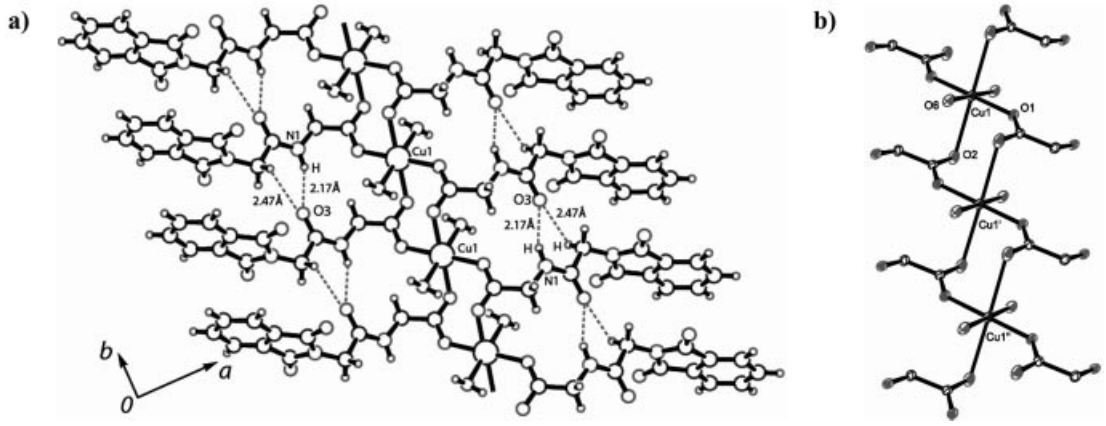


Figure 2. (a) Structure of the hydrogen-bonded sheets in complex **1** (interstitial water molecules are excluded for clarity); (b) Coordination environment of $Cu^{II}$ centers in the complex (thermal ellipsoids drawn to 30% probability).

 © 2006 Wiley-VCH Verlag GmbH & Co. KGaA, Weinheim 

coordination environment around each $Zn^{II}$ center as shown in Figure 3. The Zn1···O1, Zn1···O6 and Zn1···O7 bond lengths are 2.0921(15), 2.0586(16), 2.1429(16) Å, respectively. The crystal structure of **2** also reveals that the *N*-phthaloyl-protected dipeptide residues assemble through intermolecular N1–H···O3 hydrogen bonds ($d_{N1\cdots O3}$ 3.04 Å; ∠ D–H···A 157.8°) along with weak C4–H···O3 interactions ($d_{C4\cdots O3}$ 3.11 Å). These two weak interactions lead to the formation of parallel β-pleated sheets as shown in Figure 3.

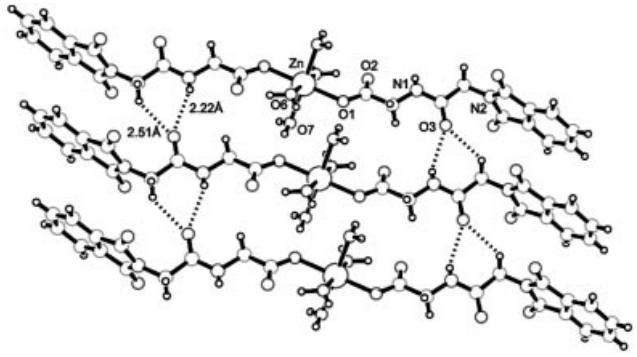


Figure 3. Ligand organization around the $Zn^{II}$ centers of the complex **2**.

It is noteworthy that in both the structures of complexes **1** and **2**, the presence of coordinated water as well as the interstitial water molecules (in case of **1**) is crucial in stabilizing the self-assembled β-pleated sheets. The hydrogen bond lengths and bond angles that are involved in the formation in complex **2** are listed in Table 3. The torsion angle for rotation about the C–N bond ($\varphi$) in this case is –153.6° and for the C–C bond rotation ($\psi$) is 165.7°, which are similar to those in the complex **1** and is indicative of β-pleated sheets.[2b]

Table 3. Hydrogen bonding geometry (distances and angles) in complex **2**.

| D–H···A | $d_{D-H}$ [Å] | $d_{H\cdots A}$ [Å] | $d_{D\cdots A}$ [Å] | ∠ D–H···A[°] |
|---|---|---|---|---|
| N1–H···O3 [$x$, $y+1$, $z$] | 0.86 | 2.23 | 3.044 | 157.8 |
| O6–H···O2 | 1.03 | 1.65 | 2.652 | 159.7 |
| O7–H···O1 [$x$, $y+1$, $z$] | 0.80 | 1.88 | 2.672 | 170.4 |

The presence of two interstitial water molecules per formula unit in complex **1** has a structural role to play, as they hold the hydrogen-bonded dipeptide β-sheets (Figure 4, a) through intermolecular O7–H···O2 ($d_{O7\cdots O2}$ 2.85 Å; ∠ D–H···A 170.5°) and O7–H···O5 ($d_{O7\cdots O5}$ 2.99 Å; ∠ D–H···A 165.7°) interactions. Furthermore, each interstitial water molecule is bound to a coordinated water molecule through intermolecular O6–H···O7 ($d_{O6\cdots O7}$ 2.66 Å; ∠ D–H···A 158.5°) hydrogen bonds. The presence two interstitial water molecules in the lattice is reflected in the thermogram of the compound, which shows 8.9% weight loss in the temperature range 75–120 °C corresponding to loss of three water molecules (theoretical weight loss 8.2%) corresponding to interstitial and coordinated water molecules. In the case of **2**, the coordinated water molecules are involved in intramolecular O6–H···O7 ($d_{O6\cdots O7}$ 2.91 Å; ∠ D–H···A 149.9°) and intermolecular O7–H···O4 ($d_{O7\cdots O4}$ 3.02 Å; ∠ D–H···A 150.2°) hydrogen-bonding interactions. These interactions stabilize the formation of individual β-pleated sheets in **1** and **2** as shown in Figure 4, parts a and b, respectively. Thermogravimetric analysis of complex **2** (please refer to supporting information, for supporting information see also the footnote on the first page of this article) shows that the four-coordinated water molecules are lost between 70–135 °C, which corresponding to about 9.3% weight loss (theoretically calculated weight loss for such process corresponds to 10.9%).

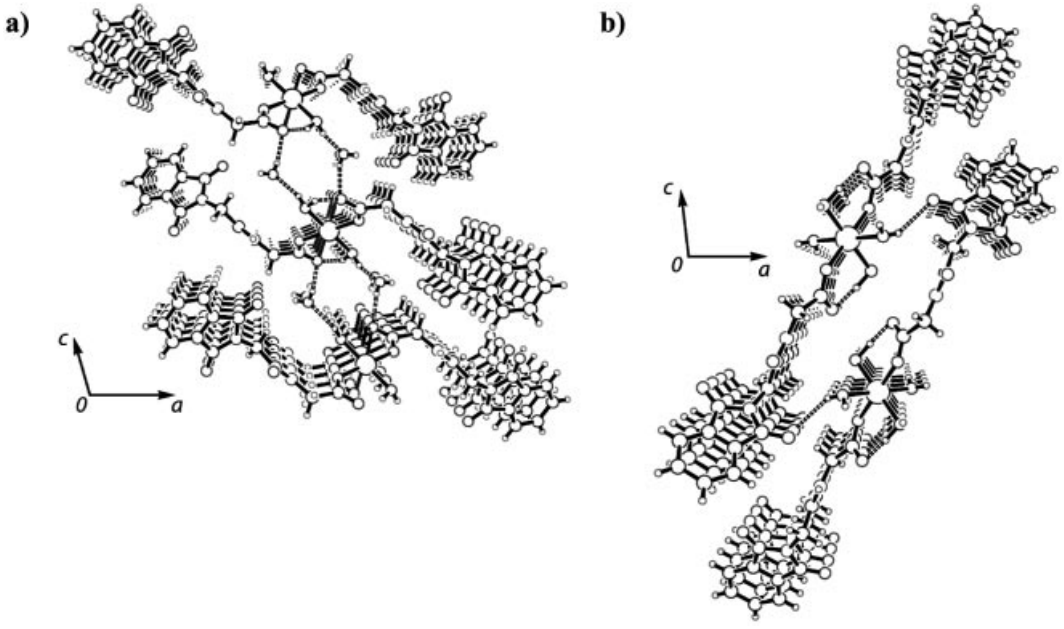


Figure 4. (a) Packing pattern of **1** (viewed along *b* axis); (b) packing pattern of **2** (viewed along *b* axis).

 © 2006 Wiley-VCH Verlag GmbH & Co. KGaA, Weinheim 

Thus, we have structurally characterized the solid-state assemblies of *N*-phthaloylglycylglycine that are formed through intermolecular hydrogen bonding, and shown that the self-assembly of this molecule can be tuned to adopt a β-sheet conformation by introduction of metal ions, in this case $Cu^{II}$ and $Zn^{II}$. It is found that the parallel β-pleated sheet assembly of the dipeptide leads to a one-dimensional $Cu^{II}$ carboxylate coordination polymer through carboxylate bridging in a different manner over conventional paddle-wheel-type of structures.[12] Currently, we are studying the different motifs that are crucial in the metal template assembly of similar dipeptides and higher analogs.

## Experimental Section

The X-ray diffraction data were collected at room temperature with a Bruker 3-circle diffractometer (Bruker Nonius SMART APEX 2) equipped with CCD area detectors, and using graphite-monochromated Mo-$K_\alpha$ radiation ($\lambda$ = 0.71073 Å) from 60W microfocus Siemens Microsource with glass polycapillary optics. X-ray diffraction data for all the crystals were collected with Bruker SMART software. This software was also used for indexing and determining the unit cell parameters. The structures were solved by direct methods and refined by full-matrix least-squares against $F^2$ for all data using SHELXTL software.[14] All non-H atoms were refined by full-matrix least-squares in the anisotropic approximation and the hydrogen atoms attached to these atoms were treated as "riding" in calculated positions in the case of complex **2**; with **L** and complex **1** the hydrogen atoms were located on the difference Fourier maps. In all cases, the hydrogen atoms attached to polar atoms such as O and N were located on the difference Fourier maps and refined in the final structure in isotropic approximation.

CCDC-297186 (for **1**), -297187 (for **2**) and -299730 (for **L**) contain the supplementary crystallographic data for this paper. These data can be obtained free of charge from The Cambridge Crystallographic Data Centre via www.ccdc.cam.ac.uk/data_request/cif.

Glycylglycine, phthalic anhydride, copper(II) acetate dihydrate and zinc(II) acetate dihydrate were procured from Fluka and used as received. The NMR spectra were recorded with a Varian 400 MHz spectrophotometer at room temperature while the FT-IR spectra were recorded with Nicolet Impact–410 spectrometer using OMNIC software.

**Synthesis of *N*-Phthaloylglycylglycine (L):** A finely ground mixture of phthalic anhydride (0.444 g, 3 mmol) and glycylglycine (0.396 g, 3 mmol) was heated to approximately 175 °C in a 50-mL round-bottomed flask. The molten mixture was cooled to room temperature, and the resulting solid was purified by recrystallization from ethanol/water (1:9, v/v) mixture to obtain the product. Yield: 0.30 g (39%). IR (KBr): $\tilde{\nu}$ = 3363 (s), 2935 (br. s), 2873 (br. s), 2597 (s), 1737 (s), 1701 (s), 1621 (s), 1543 (s), 1419 (s), 1393 (s), 1332 (w), 1230 (s), 1107 (w), 953 (s), 728 (w) $cm^{-1}$. $^1H$ NMR ([$D_6$]DMSO): $\delta$ = 12.8 (br. s, 1 $H_{-COOH}$), 8.5 (s, 1 $H_{-NH}$), 7.8 (m, 4 H), 4.2 (s, 2 H), 3.7 (d, $J$ = 5.6 Hz, 2 H) ppm. $^{13}C$ NMR ([$D_6$]DMSO): $\delta$ = 176.1,172.7, 171.7, 139.9, 137.1, 128.5, 46.2, 45.7 ppm.

**Synthesis of Complex 1:** A solution of copper(II) acetate dihydrate (0.100 g, 0.5 mmol) in ethanol (20 mL) was added dropwise to a homogeneous stirred solution of **L** (0.263 g, 1 mmol) in ethanol/water (20 mL, 1:9, v/v) at room temperature. Light blue precipitate had started appearing within 15 minutes of addition of the ligand. The solution was stirred for another two hours, and the resulting precipitate was filtered and washed with ethanol. The precipitate was redissolved in 20 mL of distilled water, concentrated to 10 mL, and left undisturbed. After three days light blue needle-like crystals of the product were collected by filtration and dried in air. Yield for the crystalline product: 0.067 g (20% based on Cu). IR (KBr): $\tilde{\nu}$ = 3590 (s), 3309 (s) 3094 (br. s), 1772 (w), 1726 (s), 1658 (s), 1562 (s), 1409 (s), 1322 (w), 1265 (w), 1122 (w), 958 (s), 758 (s), 723 (s) $cm^{-1}$.

**Synthesis of Complex 2:** A solution of zinc(II) acetate dihydrate (0.110 g, 0.5 mmol) in 20 mL ethanol was added dropwise to a homogeneous stirred solution of **L** (0.263 g, 1 mmol) in ethanol/water (20 mL, 1:1, v/v) at room temperature. Off-white precipitate had started appearing within 15 minutes of addition. The solution was stirred for another two hours, and the resulting precipitate was filtered and washed with ethanol. The precipitate was redissolved in 20 mL of distilled water, concentrated to 10 mL and left undisturbed. After five days light colorless plate-like crystals of the product were collected by filtration and dried in air. Yield for the crystalline product: 0.078 g (23% based on Zn). IR (KBr): $\tilde{\nu}$ = 3534 (s), 3319 (s) 3075 (br. s), 1770 (w), 1722 (s), 1650 (s), 1551 (s), 1411 (s), 1311 (w), 1246 (w), 1116 (w), 955 (s), 755 (s), 715 (s) $cm^{-1}$. $^1H$ NMR ([$D_6$]DMSO): $\delta$ = 8.3 (s, 1 $H_{-NH}$), 7.8 (m, 4 H), 4.2 (s, 2 H), 3.6 (d, $J$ = 4.4 Hz, 2 H) ppm.

**Supporting Information** (see also the footnote on the first page of this article) is available for selected crystallographic data, FT-IR spectra of the dipeptide and complex **1**, the ESR spectrum of **1** and $^1H$ HOMOCOSY spectra of complex **2**.

## Acknowledgments

The authors thank DST (India) for financial support.

[1] a) J. M. Lehn, *Science* **2002**, *295*, 2400–2403; b) G. M. Whitesides, B. Grzybowsi, *Science* **2002**, *295*, 2418–2421; c) C. Piguet, G. Bernardinelli, G. Hopfgartner, *Chem. Rev.* **1997**, *97*, 2005–2062; d) A. Nurit, W. S. Horne, R. M. Ghadiri, *Small* **2006**, *2*, 99–102; e) S. M. Butterfield, M. L. Waters, *J. Am. Chem. Soc.* **2003**, *125*, 9580–9581.

[2] a) E. A. Meyer, R. K. Castellano, F. Diederich, *Angew. Chem. Int. Ed.* **2003**, *42*, 1210–1250; b) G. R. Desiraju, T. Steiner, *The Weak Hydrogen Bonds in Structural Chemistry and Biology*, Oxford University Press, **1999**, Oxford; c) T. Steiner, *Angew. Chem. Int. Ed.* **2002**, *41*, 48–76.

[3] a) D. Seebach, D. F. Hook, A. Glattli, *Biopolymers* **2006**, *84*, 23–37; b) R. P. Cheng, S. H. Gellman, W. F. DeGrado, *Chem. Rev.* **2001**, *101*, 3219–3232; c) J. T. Pelton, L. R. McLean, *Anal. Biochem.* **2000**, *277*, 167–176.

[4] a) D. L. Minor Jr, P. S. Kim, *Nature* **1994**, *367*, 360–363; b) C. A. Kim, J. M. Berg, *Nature* **1993**, *362*, 267–270; c) D. L. Minor Jr, P. S. Kim, *Nature* **1994**, *371*, 264–267; d) L. Regan, W. F. DeGrado, *Science* **1988**, *241*, 976–978; e) Z.-Q. Tian, P. A. Bartlett, *J. Am. Chem. Soc.* **1996**, *118*, 943–949; f) A. Pessi, E. Bianchi, A. Crameri, S. Venturini, A. Tramontano, M. Sollazzo, *Nature* **1993**, *362*, 367–369.

[5] a) M. D. Struthers, R. P. Cheng, B. Imperiali, *J. Am. Chem. Soc.* **1996**, *118*, 3073–3081; b) J. P. Snyder, A. S. Lakdawala, M. J. Kelso, *J. Am. Chem. Soc.* **2003**, *125*, 632–633; c) E. L. Baker, R. E. Hubbard, *Prog. Biophys. Mol. Biol.* **1984**, *44*, 97–179; d) V. Venkatraman, S. V. Shankaramma, P. Balaram, *Chem. Rev.* **2001**, *101*, 3131–3152; e) J. S. Nowick, S. Mahrus, E. M. Smith, J. W. Ziller, *J. Am. Chem. Soc.* **1996**, *118*, 1066–1072; f) J. F. Espinosa, S. H. Gellman, *Angew. Chem. Int. Ed.* **2000**, *39*, 2330–2333.

 © 2006 Wiley-VCH Verlag GmbH & Co. KGaA, Weinheim 

[6] a) S. J. Lippard, J. M. Berg, *Principles of Bioinorganic Chemistry*, University Science Books, **1994**; b) J. J. R. Frausto Da Silva, R. J. P. Williams, *The Biological Chemistry of The Elements: The Inorganic Chemistry of Life*, Oxford University Press, Oxford, **2001**; c) M. A. Halcrow, *Angew. Chem. Int. Ed.* **2001**, *40*, 346–349.
[7] a) K. Suzuki, H. Hiroaki, D. Kohda, H. Nakamura, T. Tanaka, *J. Am. Chem. Soc.* **1998**, *120*, 13008–13015; b) M. R. Ghadiri, C. Soares, C. Choi, *J. Am. Chem. Soc.* **1992**, *114*, 4000–4002; c) M. R. Ghadiri, C. Soares, C. Choi, *J. Am. Chem. Soc.* **1992**, *114*, 825–831; d) W. S. Horne, D. C. Stout, M. R. Ghadiri, *J. Am. Chem. Soc.* **2003**, *125*, 9372–9376; e) D. T. Bong, M. R. Ghadiri, *Angew. Chem. Int. Ed.* **2001**, *40*, 2163–2166; f) M. R. Ghadiri, C. Choi, *J. Am. Chem. Soc.* **1990**, *112*, 1630–1632.
[8] a) K. Haas, W. Ponikwar, H. Nöth, W. Beck, *Angew. Chem. Int. Ed.* **1998**, *37*, 1086–1089; b) C. S. Burns, E. Aronoff-Spencer, C. M. Dunham, P. Lario, N. I. Avdievich, W. E. Antholine, M. M. Olmstead, A. Vrielink, G. J. Gerfen, J. Peisach, W. G. Scott, G. L. Millhauser, *Biochemistry* **2002**, *41*, 3991–4001.
[9] a) N. Barooah, R. J. Sarma, A. S. Batsanov, J. B. Baruah, *Polyhedron* **2006**, *25*, 17–24; b) N. Barooah, R. J. Sarma, J. B. Baruah, *Cryst. Growth Des.* **2003**, *3*, 639–641.
[10] R. J. Sarma, J. B. Baruah, *CrystEngComm* **2005**, *7*, 706–771; M. A. Halcrow, *Dalton Trans.* **2003**, *23*, 4375–4384.
[11] a) O. M. Yaghi, M. O'Keeffe, N. W. Ockwig, H. K. Chae, M. Eddaoudi, J. Kim, *Nature* **2003**, *423*, 705–714; b) O. M. Yaghi, H. Li, C. Davis, D. Richardson, T. L. Groy, *Acc. Chem. Res.* **1998**, *31*, 474–484; c) H. Y. An, E.-B. Wang, D. R. Xiao, Y. G. Li, Z. M. Su, L. Xu, *Angew. Chem. Int. Ed.* **2006**, *45*, 904–908; d) X.-J. Luan, Y.-Y. Wang, D.-S. Li, P. Lie, H.-M. Hu, Q.-Z. Shi, S.-M. Peng, *Angew. Chem. Int. Ed.* **2005**, *44*, 3864–3867; e) F. M. Tabellion, S. R. Seidel, A. M. Arif, P. J. Stang, *Angew. Chem. Int. Ed.* **2001**, *40*, 1529–1532; f) R. Matsuda, R. Kitaura, S. Kitagawa, Y. Kubota, T. C. Kobayashi, S. Horika, M. Takata, *J. Am. Chem. Soc.* **2004**, *126*, 14063–14070; g) J. V. Barth, G. Costantini, K. Kern, *Nature* **2005**, *437*, 671–679.
[12] a) G. M. Brown, M. George, R. Chidambaram, *Acta Crystallogr., Sect. B* **1973**, *29*, 2393–2403; b) K. Seki, *Chem. Commun.* **2001**, 1496–1497.
[13] a) G. M. Sheldrick, *SHELXS97, Program for the solution of crystal structures*, Univ. of Göttingen, Germany, **1997**; b) G. M. Sheldrick, *SHELXS97, Program for the refinement of crystal structures*, Univ. of Göttingen, Germany, **1997**.
[14] G. M. Sheldrick, *SHELXTL, The complete software package for single crystal structure determination*, release 5.10, Bruker AXS, Inc., Madison, **1997**.

Received: March 10, 2006
Published Online: June 14, 2006

 © 2006 Wiley-VCH Verlag GmbH & Co. KGaA, Weinheim 

DOI: 10.1002/ejic.200600289

# Synthesis of Ionic Liquid Functionalized SBA-15 Mesoporous Materials as Heterogeneous Catalyst toward Knoevenagel Condensation under Solvent-Free Conditions

**Yong Liu,[a] Jiajian Peng,[a] Shangru Zhai,[b] Jiayun Li,[a] Jianjiang Mao,[a] Meijiang Li,[a] Huayu Qiu,*[a] and Guoqiao Lai*[a]**

**Keywords:** Mesoporous materials / Heterogeneous catalysis / Ionic liquids

1-Methyl-3-propylimidazolium chloride (MPImCl) and 1-propylpyridinium chloride (PPyCl) ionic liquid functionalized SBA-15 mesoporous materials were synthesized and used as heterogeneous catalysts in Knoevenagel reactions with excellent yields and reusability.

(© Wiley-VCH Verlag GmbH & Co. KGaA, 69451 Weinheim, Germany, 2006)

## Introduction

The Knoevenagel condensation, one of the most important preparation methods of substituted alkenes, is widely employed to synthesize intermediates of fine chemicals (Scheme 1). Compared to traditional homogeneous catalysts including organic bases (primary, secondary, tertiary amines), $ZnCl_2$, LiCl, and cetyltrimethylammonium bromide (CTAB),[1] solid-based heterogeneous catalysts are more desirable for their advantages in separation and reusability. In recent years, resins, zeolites, hydrotalcites etc. have been applied to this reaction as heterogeneous catalysts,[2] among which organo-functionalized mesoporous silicas are specially studied due to their unique properties such as high surface area, uniform pore structure and controllable surface properties.[3] Recently, synthesis and catalysis activities of different structured mesoporous materials functionalized by amino/diamino groups have been reported.[4]

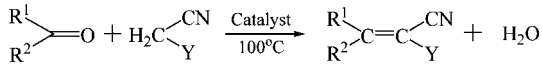


Scheme 1.

Ionic liquids, known as novel environmental benign media, have attracted great interest in the last two decades[5] since they can serve not only as favorable solvents for catalysis but also as green catalysts themselves in many reactions such as cycloaddition, Biginelli reaction, nitration, Beckmann rearrangement[6] and Knoevenagel condensation as well.[7] However, in some cases ionic liquids are miscible with some products or reactants, leaving separation and reuse of catalyst still a problem. Thus, immobilization of ionic liquids on solid-based materials is of particular interest. Recently, several groups reported the successful synthesis of silica-based ionic liquids,[8] while reports on ordered ionic liquids functionalized mesoporous materials are still quite rare.[9] Herein, we report the synthesis of MPImCl and ionic liquid functionalized SBA-15 mesoporous material and its catalytic activity toward Knoevenagel condensation under solvent-free conditions. The resulting hetergeneous catalyst could be easily recovered with high catalytic activity remaining after 10 cycles.

## Results and Discussion

1-Methyl-3-[(triethoxysilyl)propyl]imidazolium chloride (MTESPImCl) and 1-[(triethoxysilyl)propyl]pyridinium chloride (TESPPyCl) were prepared by the reaction of 1-methylimidazole or pyridine with (3-chloropropyl)triethoxysilane, different from the literature[8a] not only because the reactants were cheaper but also the corresponding pyridine species could be obatined. The XRD patterns of the MPImCl-SBA materials obtained with different MTESPImCl amounts are given in Figure 1. When the MTESPImCl content in the initial mixture was 5%, one intense diffraction peak together with two weak ones could been seen (Figure 1, b), corresponding to the (100), (110), and (200) planes of highly ordered SBA-15 structured mesoporous materials, respectively. As the MTESPImCl content increased to 10%, the (110) and (200) peaks disappeared (Fig-

[a] Key Laboratory of Organosilicon Chemistry and Material Technology of the Ministry of Education, Hangzhou Teachers College,
Hangzhou 310012, China
Fax: +86-571-28865135
E-mail: yjg@hztc.edu.cn
[b] Department of Chemical Engineering and Materials, Dalian Institute of Light Industry,
Dalian 116034, China

 © 2006 Wiley-VCH Verlag GmbH & Co. KGaA, Weinheim 

ure 1, c), indicating the decrease of pore regularity. With a further increase of the MTESPImCl content to 15%, no characteristic peaks of SBA-15 mesoporous materials could be seen. It is noteworthy that when the pre-hydrolysis time of tetraethyl orthosilicate (TEOS) was prolonged to 4 h, the order of pore structure (MTESPImCl content 10%) was greatly improved (Figure 1, a). Similar phenomena have been reported in the synthesis of sulfonic acid and aminopropyl functionalized SBA-15 mesoporous materials under acid conditions[4c,10] and could be explained by the following reasons: On one hand, MTESPImCl can perturb the self-assembly of surfactant micelles and silica precursors; on the other hand, the cationic part of MTESPImCl probably interacts with ethoxy groups of TEOS, thus inhibiting its hydrolysis and condensation. Therefore, prolonging the pre-hydrolysis time of TEOS can prevent MTESPImCl from disturbing the mesophase. XRD results of PPy-SBA materials also proved that orderd structures could be obtained with TEOS pre-hydrolyzed for 4 h (Figure 2).

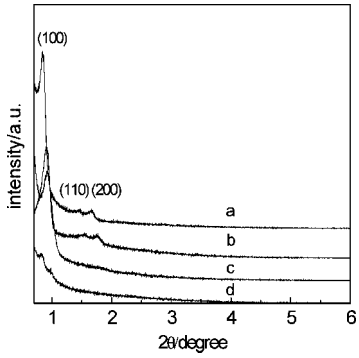


Figure 1. XRD patterns of MPImCl-SBA materials with different MTESPImCl contents and different TEOS pre-hydrolyze times.

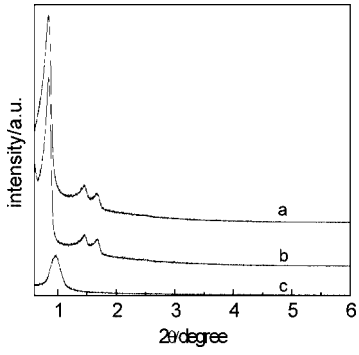


Figure 2. XRD patterns of PPyCl-SBA materials with different TESPPyCl contents with TEOS prehydrolyzed for 4 h; a: 5%, b: 10%, c: 15%.

$N_2$ adsorption-desorption was carried out to supply further information about the physical properties of the ionic liquid functionalized SBA-15 materials. As shown in Table 1, surface areas, pore volumes and pore diameters of the products all decreased as the ionic liquid content increased from 0 to 15%, which could be attributed to the increasing distribution of ionic liquid moieties in the interior mesopore surfaces. PPy-SBA materials were found to display higher surface areas and larger pore diameters compared with MPImCl counterparts, and longer pre-hydrolysis time was found helpful to improve the structures of products, which was in agreement with XRD results. Elemental analysis was used to obtain accurate amounts of the ionic liquid attached to the mesopores. As summarized in Table 1, loading amounts of PPy-SBA and MPImCl-SBA were comparable and increased with the increase of the ionic liquid contents in the initial mixture. The effect of pre-hydrolysis time on the loading amounts was negligible. Solid-state $^{29}Si$ NMR spectroscopy and thermogravimetric analysis (TGA) were also used to characterize the ionic liquid functionalized mesoporous materials and the results well agree with that of the elemental analysis.

Table 1. $N_2$ adsorption-desorption and elemental analysis results of ionic liquid functionalized SBA-15 materials.

| Ionic liquid, amount [%] | $S_{BET}$ [$m^2$/g] | $V_p$ [$cm^3$/g] | Pore diameter [nm] | Loading amount [mmol/g] |
|---|---|---|---|---|
| –, 0[a] | 688 | 0.937 | 5.51 | 0 |
| MTESPImCl, 5[a] | 482 | 0.849 | 5.33 | 0.512 |
| MTESPImCl, 10[a] | 400 | 0.564 | 5.13 | 0.943 |
| MTESPImCl, 15[a] | 143 | 0.221 | 4.12 | 1.322 |
| MTESPImCl, 10[b] | 529 | 0.653 | 5.89 | 0.966 |
| TESPPyCl, 5[b] | 558 | 0.997 | 8.04 | 0.569 |
| TESPPyCl, 10[b] | 504 | 0.901 | 8.03 | 0.986 |
| TESPPyCl, 15[b] | 368 | 0.775 | 5.74 | 1.409 |

[a] TEOS pre-hydrolysis time 40 min. [b] TEOS pre-hydrolysis time 4 h.

In view of the increasing emphasis on the adoption of clean manufacturing processes and environmentally benign technologies, clean, solvent-free and highly efficient catalytic technologies for the chemical production are highly desirable, so we carried out the Koevenagel condensation of various aldehydes with malononitrile/ethyl cyanoacetate at 100 °C under solvent-free conditions. 10% MPImCl-SBA and 10% PPy-SBA were used as catalysts, respectively, and the optimal amount of catalyst was determined to be 0.8 mol-% based on the reaction of benzaldehyde with malononitrile (Table 2, Entries 1–3). As illustrated in Table 2 (Entries 4, 6, 13, 15), the catalytic activities of PPy-SBA were slightly lower than those of MPImCl-SBA; thus, MPImCl-SBA was slected as catalyst for the other reactions. As shown in Entries 7–10, reactions of malononitrile with all tested aldehydes were complete in 3.5 h with excellent yields (not lower than 87%), which was not lower (if not higher) compared with those in traditional homogeneous systems.[1,2] The influence of substituents in the aromatic ring was negligible, indicating the high catalysis activity of the MPImCl-SBA materials. In the case of ethyl cyanoacetate, however, the yields decreased even if the reaction time was prolonged to 6 h (Entries 9–15). Besides, aldehydes with electron-donating groups (Entries 11, 14, 15) showed lower yields compared with the others. The reusability of the MPImCl-SBA materials was examined by the reaction of benzaldehyde with malononitrile. As shown in Entry 20, a yield as high as 86.1% was obtained in the 10th cycle.

 © 2006 Wiley-VCH Verlag GmbH & Co. KGaA, Weinheim 

Table 2. Knoevenagel condensation of aldehydes with malononitrile/ethyl cyanoacetate.

| Entry | $R^1$ | $R^2$ | Y | Ionic liquid amount [mol-%] | Time [h] | Isolated yield [%] |
|---|---|---|---|---|---|---|
| 1 | Ph[a] | H | CN | 0.2 | 3.5 | 63.5 |
| 2 | Ph[a] | H | CN | 0.4 | 3.5 | 89.6 |
| 3 | Ph[a] | H | CN | 0.8 | 3.5 | 93.5 |
| 4 | Ph[b] | H | CN | 0.8 | 3.5 | 92.8 |
| 5 | 2-$ClC_6H_4$[a] | H | CN | 0.8 | 3.5 | 92.4 |
| 6 | 2-$ClC_6H_4$[b] | H | CN | 0.8 | 3.5 | 89.6 |
| 7 | 4-$MeOC_6H_4$[a] | H | CN | 0.8 | 3.5 | 89.6 |
| 8 | 4-$ClC_6H_4$[a] | H | CN | 0.8 | 3.5 | 91.5 |
| 9 | 4-$HOC_6H_4$[a] | H | CN | 0.8 | 3.5 | 87.7 |
| 10 | 4-$MeC_6H_4$[a] | H | CN | 0.8 | 3.5 | 93.2 |
| 11 | Ph[a] | H | $CO_2Et$ | 0.8 | 3.5 | 69.6 |
| 12 | Ph[a] | H | $CO_2Et$ | 0.8 | 6.0 | 85.6 |
| 13 | Ph[b] | H | $CO_2Et$ | 0.8 | 6.0 | 84.0 |
| 14 | 2-$ClC_6H_4$[a] | H | $CO_2Et$ | 0.8 | 6.0 | 90.5 |
| 15 | 2-$ClC_6H_4$[b] | H | $CO_2Et$ | 0.8 | 6.0 | 82.9 |
| 16 | 4-$MeOC_6H_4$[a] | H | $CO_2Et$ | 0.8 | 6.0 | 79.1 |
| 17 | 4-$ClC_6H_4$[a] | H | $CO_2Et$ | 0.8 | 6.0 | 86.9 |
| 18 | 4-$HOC_6H_4$[a] | H | $CO_2Et$ | 0.8 | 6.0 | 81.4 |
| 19 | 4-$MeC_6H_4$[a] | H | $CO_2Et$ | 0.8 | 6.0 | 75.0 |
| 20 | Ph[a,c] | H | CN | 0.8 | 3.5 | 86.1 |

[a] MPImCl-SBA as catalyst. [b] PpyCl-SBA as catalyst. [c] MPImCl-SBA in the 10th cycle.

In summary, ionic liquid functionalized SBA-15 mesoporous materials were synthesized and gave high yields and good reusability in Koevenagel condensations. These materials might be used not only as heterogeneous catalysts in reactions such as cycloaddition and Biginelli reactions but also as support for transition metals (work in this direction is in progress and will be reported soon).

## Experimental Section

In a typical procedure to synthesize MPImCl-SBA materials, 4.378 g of P123 ($EO_{20}PO_{70}EO_{20}$) was dissolved in 115 g of $H_2O$ to which 25 g of HCl was added. After 10.17 mL (0.045 mol) of TEOS was added and pre-hydrolyzed for 40 min, 1.535 g (0.005) of MTESPImCl was added. The mixture was stirred at 40 °C for 24 h and then transferred into a Teflon-lined stainless steel autoclave and kept at 100 °C for 24 h. The precipitate was filtered, subsequently washed with distilled water and EtOH, and dried at 60 °C in air. The template was removed by refluxing the as-synthesized material in EtOH for 24 h. The Knoevenagel condensation was carried out at 100 °C under solvent-free conditions. In a typical procedure, 1.82 g (0.025 mol) of malononitrile, 2.41 g (0.023 mol) of benzaldehyde and 0.22 g (0.2 mmol MPImCl) of 10% MPImCl-SBA were mixed and allowed to react for an appropriate time. The products were purified by column chromatography and the catalyst was filtered, washed with $CH_2Cl_2$, and collected for reusability test.

X-ray powder diffraction (XRD) data were acquired with a Rigaku D/max 2500V/PC diffractometer with Cu-$K_\alpha$ radiation. $N_2$ adsorption and desorption isotherms were measured with a Quantacrome Autosorb-1 system at 77 K. Surface areas were calculated according to the BET method with relative pressures in the range 0.2–0.3, and pore volumes were taken at the $P/P_0$ = 0.9923 single point. Pore diameters were determined from absorption branches according to the Barrett–Joyner–Halenda (BJH) method. Loading amounts of ionic liquids were caculated from the nitrogen contents performed with an Elementar Vario EC III CHNOS element analyzer.


[1] a) G. Jones, *Org. React.* **1967**, *15*, 204–599; b) R. P. Shanthan, R. V. Venkataratnam, *Tetrahedron Lett.* **1991**, *32*, 5821–5823; c) G. Gowravaram, B. V. S. Reddy, R. S. Babu, J. S. Yadav, *Chem. Lett.* **1998**, 773–774; d) S. Wang, Z. Ren, W. Cao, W. Tong, *Synth. Commun.* **2001**, *31*, 673.

[2] a) Y. Goa, P. Wu, T. Tatsumi, *J. Catal.* **2004**, *224*, 107–114; b) J. Simpson, D. L. Rathbone, D. C. Billington, *Tetrahedron Lett.* **1999**, *40*, 7031–7033; c) F. A. Khan, J. Dash, R. Satapathy, S. K. Upadhyay, *Tetrahedron Lett.* **2004**, *45*, 3055–3058; d) M. L. Kantam, B. M. Choudary, C. K. Venkat Reddy, K. K. Rao, F. Figueras, *Chem. Commun.* **1998**, 1033–1034.

[3] a) A. Corma, *Chem. Rev.* **1997**, *97*, 2373–2419; b) A. Sayari, S. Hamoudi, *Chem. Mater.* **2001**, *13*, 3151–3168; c) C. Li, *Catal. Rev.* **2004**, *46*, 419–492; d) R. Corriu, A. Mehdi, C. Reye, *J. Organomet. Chem.* **2004**, *689*, 4437–4450.

[4] a) S. G. Wang, *Catal. Commun.* **2003**, *4*, 469–470; b) Y. Kubota, Y. Nishizaki, H. Ikeya, M. Saeki, T. Hida, S. Kawazu, M. Yoshida, H. Fujii, Y. Sugi, *Microporous Mesoporous Mater.* **2004**, *70*, 135–149; c) X. G. Wang, K. S. K. Lin, J. C. C. Chan, S. Cheng, *J. Phys. Chem. B* **2005**, *109*, 1763–1769; d) D. Brunel, *Microporous Mesoporous Mater.* **1999**, *27*, 329–344.

[5] a) T. Welton, *Chem. Rev.* **1999**, *99*, 2071–2083; b) J. Dupont, R. F. Souza, P. A. Z. Suarez, *Chem. Rev.* **2002**, *102*, 3667–3692; c) A. Ouadi, B. Gadenne, P. Hesemann, J. J. E. Moreau, I. Billard, C. Gaillard, S. Mekki, G. Moutiers, *Chem. Eur. J.* **2006**, *12*, 3074–3081; d) M. Antonietti, D. Kuang, B. Smarsly, Y. Zhou, *Angew. Chem. Int. Ed.* **2004**, *43*, 4988–4992; e) J. Dupont, *J. Braz. Chem. Soc.* **2004**, *15*, 341–350.

[6] a) J. J. Peng, Y. Q. Deng, *New J. Chem.* **2001**, *25*, 639–641; b) J. M. Sun, S. I. Fujita, M. Arai, *J. Organomet. Chem.* **2005**, *690*, 3490–3497; c) J. J. Peng, Y. Q. Deng, *Tetrahedron Lett.* **2001**, *42*, 5917–5919; d) K. Qiao, C. Yokoyama, *Chem. Lett.* **2004**, *33*, 808–809; e) J. J. Peng, Y. Q. Deng, *Tetrahedron Lett.* **2001**, *42*, 403–405.

[7] a) J. R. Harjani, S. J. Nara, M. M. Salunkhe, *Tetrahedron Lett.* **2002**, *43*, 1127–1130; b) D. C. Forbe, A. M. Law, D. W. Morrison, *Tetrahedron Lett.* **2006**, *47*, 1669–1703; c) P. Formentin, H. Garcia, A. Leyva, *J. Mol. Catal. A* **2004**, *214*, 137–142.

[8] a) C. P. Mehnert, R. A. Cook, N. C. Dispenziere, M. Afeworki, *J. Am. Chem. Soc.* **2002**, *124*, 12932–12933; b) C. P. Mehnert, E. J. Mozeleski, R. A. Cook, *Chem. Commun.* **2002**, 3010–3011; c) K. Qiao, H. Hagiwara, C. Yokoyama, *J. Mol. Catal. A* **2006**, *246*, 65–69.

[9] a) B. Gadenne, P. Hesemann, J. J. E. Moreau, *Chem. Commun.* **2004**, 1768–1769; b) M. H. Valkenberg, C. Castro, W. F. Hölderich, *Green Chem.* **2002**, *4*, 88–93.

[10] D. Margolese, J. A. Melero, S. C. Christiansen, B. F. Chmelka, G. D. Stucky, *Chem. Mater.* **2000**, *12*, 2448–2459.


Received: April 1, 2006
Published Online: June 12, 2006

 © 2006 Wiley-VCH Verlag GmbH & Co. KGaA, Weinheim 

DOI: 10.1002/ejic.200600138

# Bonding Trends in Lewis Acid Adducts of $S_4N_4$ – X-ray Structure of $TeCl_4 \cdot S_4N_4$

**Jari Konu,[a] Tom Bajorek,[a] Risto S. Laitinen,*[a] Tristram Chivers,[b] Reijo J. Suontamo,[c] and Markku Ahlgrén[d]**

**Keywords:** Lewis acid adducts of $S_4N_4$ / Tellurium tetrachloride / DFT calculations / Vibrational spectroscopy / X-ray crystallography

Tetrasulfur tetranitride and tellurium tetrachloride react in dichloromethane to form a 1:1 adduct $TeCl_4 \cdot S_4N_4$ (**1**). The crystal structure of **1** shows that $TeCl_4$ is bonded to the $S_4N_4$ ring through a Te–N linkage. As a consequence, the transannular S···S bonds in $S_4N_4$ are broken and the molecule assumes an open, monocyclic conformation. The Te–N bond of 2.16(1) Å is slightly longer than the single bond. The S–N bonds span a range of 1.55(1)–1.67(1) Å. The adduct **1** was also characterized by mass spectrometry and Raman spectroscopy. The bonding and spectroscopic properties of **1** are compared by DFT calculations at the B3PW91/(RLC ECP) level of theory with those of $BF_3 \cdot S_4N_4$ (**2**), $SO_3 \cdot S_4N_4$ (**3**), $AsF_5 \cdot S_4N_4$ (**4**), $SbCl_5 \cdot S_4N_4$ (**5**) for which experimental structural information is available. The structural and bonding trends in $TeF_4 \cdot S_4N_4$ (**6**), $TeBr_4 \cdot S_4N_4$ (**7**), and $SeX_4 \cdot S_4N_4$ [X = F (**8**), Cl (**9**), Br (**10**)] are also discussed.
(© Wiley-VCH Verlag GmbH & Co. KGaA, 69451 Weinheim, Germany, 2006)

## Introduction

Tetrasulfur tetranitride is known to react in inert solvents with a wide variety of Lewis acids and a number of 1:1 adducts have been structurally characterized. The crystal structures are known for $BF_3 \cdot S_4N_4$,[1] $SO_3 \cdot S_4N_4$,[2] $AsF_5 \cdot S_4N_4$,[3] $SbCl_5 \cdot S_4N_4$,[4–6] $FeCl_3 \cdot S_4N_4$,[7,8] $TaCl_5 \cdot S_4N_4$,[9] and $TiCl_4 \cdot S_4N_4$.[10] The complexes $SnCl_4 \cdot 2S_4N_4$[11] and $TiCl_4 \cdot 2S_4N_4$[10] exemplify structurally characterized adducts with a 1:2 stoichiometry. However, the number of other known tellurium tetrahalide adducts containing a Te–N bond is sparse. Gieren et al.[12] have reported the crystal structure of $TeF_4(NNCHCHCH)_2$ and Massa et al.[13] have determined that of $[Te_6N_8(TeCl_4)_4] \cdot 4THF$.

The preparation of $TeCl_4 \cdot S_4N_4$ (**1**) by the reactions of $S_4N_4$ with $TeCl_4$ in various solvents,[14–16] or $S(NSO)_2$ with $TeCl_4$ in $CH_2Cl_2$[17] has been reported. The compound, however, was identified only by elemental analysis and IR spectroscopy. While Paul et al.[14] concluded on the basis of conductance measurements that in the solid state **1** has an ionic structure, Alange et al.[15] inferred $TeCl_4 \cdot S_4N_4$ to be a covalent coordination complex by comparing the IR spectrum of the adduct with those of the structurally characterized analogues $BF_3 \cdot S_4N_4$ and $SbCl_5 \cdot S_4N_4$. Ginn et al.[16] used **1** to produce a platinum complex containing the $^{15}N$-labelled $TeSN_2$ ligand, but they did not provide structural details of $TeCl_4 \cdot S_4N_4$.

In this paper, we describe the structural and vibrational characterization of **1** and demonstrate that the compound represents one further example of a tellurium tetrahalide bonded to nitrogen. DFT MO calculations have been utilized to compare the trends in the molecular structures, bonding, stabilities, and spectroscopic properties of **1**, $BF_3 \cdot S_4N_4$ (**2**), $SO_3 \cdot S_4N_4$ (**3**), $AsF_5 \cdot S_4N_4$ (**4**), and $SbCl_5 \cdot S_4N_4$ (**5**) for which there is experimental information available, and to evaluate the corresponding properties in $TeF_4 \cdot S_4N_4$ (**6**), $TeBr_4 \cdot S_4N_4$ (**7**), and $SeX_4 \cdot S_4N_4$ [X = F (**8**), Cl (**9**), Br (**10**)]. $S_4N_4H^+$ (**11**) is included in this study for comparison.[18]

## Results and Discussion

### Synthesis and Spectroscopic Characterization of $TeCl_4 \cdot S_4N_4$ (1)

$TeCl_4 \cdot S_4N_4$ was produced by the reaction of $S_4N_4$ with $TeCl_4$ in $CH_2Cl_2$ as orange powder in ca. 76% yield. The EI mass spectrum of the product shows $TeS_4N_4^+$ ($m/z$ = 314) as the fragment with highest mass. Although the mass spectrum shows no evidence of the molecular ion, the fragmentation pattern indicates the correct composition for $TeCl_4 \cdot S_4N_4$. The observed and calculated isotopic distributions were in good agreement for all fragments.

The $^{14}N$ NMR spectrum of the reaction solution from which the orange precipitate was removed by filtration

[a] Department of Chemistry, University of Oulu, P. O. Box 3000, 90014 Oulu, Finland
Fax: +358-8-553-1608
E-mail: risto.laitinen@oulu.fi
[b] Department of Chemistry, University of Calgary, Calgary, Alberta T2N 1N4, Canada
[c] Department of Chemistry, University of Jyväskylä, P. O. Box 35, 40014 Jyväskylä, Finland
[d] Department of Chemistry, University of Joensuu, P. O. Box 111, 80101 Joensuu, Finland
Supporting information for this article is available on the WWW under http://www.eurjic.org or from the author.

 © 2006 Wiley-VCH Verlag GmbH & Co. KGaA, Weinheim 

shows one resonance at $\delta$ = –256 ppm, but we did not observe the $^{125}$Te resonance. The single resonance in the $^{14}$N NMR spectrum is assigned to $S_4N_4$.[20] The compound **1** is expected to give rise to one resonance in the $^{125}$Te NMR spectrum and three resonances with the intensity ratio of 1:2:1 in the $^{14}$N NMR spectrum. Conductance measurements[14] imply that **1** has a different structure in solution than that observed in the solid state. The NMR spectroscopic data and the insolubility of the product give further support for this conclusion.

Raman spectra were recorded for both the orange powder and the red crystals that were used for the X-ray structure determination. The adduct $TeCl_4{\cdot}S_4N_4$ belongs to the point group $C_s$ and, therefore, all 33 fundamental vibrations are Raman active. The observed and calculated B3PW91/(RLC ECP) fundamental vibrations together with the main contributions to their potential energy distributions are given in Table 1, and the observed and calculated spectra are shown in Figure 1. The calculated values yield a good agreement with the observed wavenumbers and Raman activities (the DFT calculations are discussed in more detail below).[21] The four observed Raman lines in the region 672–1045 cm$^{-1}$ are mainly due to $\nu_{S-N}$ stretching modes. The $\nu_{Te-Cl}$ stretching is the main contributor to the line at 265 cm$^{-1}$ and also appears to be the major vibrational mode of the strongest Raman line at 296 cm$^{-1}$ together with a torsion mode. The remainder of the Raman lines are predominantly torsional vibrations with the exception of the lines at 138 and 149 cm$^{-1}$ for which the $\delta_{ClTeCl}$ bending mode is also a significant contributor.

## Crystal Structure of $TeCl_4{\cdot}S_4N_4$ (1)

The crystal structure of $TeCl_4{\cdot}S_4N_4$ (**1**) with the atomic numbering scheme is shown in Figure 2(d), and the selected bond parameters are compared with those for related $S_4N_4$ adducts in Table 2. The molecule consists of an opened mo-

Table 1. Observed Raman and IR spectra, and calculated B3PW91/(RLC ECP) Fundamental vibrations [cm$^{-1}$], Raman intensities, and IR intensities of $TeCl_4{\cdot}S_4N_4$ ($C_s$).

| Calcd.[a] | | Raman obsd. | $I_{obsd.}$ | $I_{calcd.}$[c] | IR[b] | $I_{obsd.}$ | $I_{calcd.}$[c] | Potential energy distribution [%][d] |
|---|---|---|---|---|---|---|---|---|
| | | | | | 1156 | vw | | |
| 1072 | a′′ | | | 6 | 1048 | vs | 90 | 78 $\nu_{NS}$ |
| 1043 | a′ | 1045 | 10 | 38 | | | 2 | 64 $\nu_{NS}$, 18 $\tau$, 10 $\delta_{NSN}$ |
| 973 | a′′ | | | 5 | 966 | vs | 30 | 75 $\nu_{NS}$, 12 $\delta_{NSN}$ |
| 833 | a′′ | 807 | 1 | 6 | 807 | s | 36 | 50 $\nu_{NS}$, 20 $\tau$, 14 $\delta_{TeNS}$, 12 $\delta_{ClTeN}$ |
| 758 | a′ | 761 | 42 | 79 | 760 | vs | 35 | 34 $\nu_{NS}$, 21 $\tau$, 14 $\nu_{TeN}$, 13 $\delta_{SNS}$ |
| | | | | | 727 | w | | |
| 681 | a′ | 672 | 2 | 2 | 671 | m | 8 | 44 $\nu_{NS}$, 23 $\tau$, 16 $\delta_{SNS}$ |
| 634 | a′′ | | | 4 | 635 | m | 22 | 46 $\nu_{NS}$, 41 $\tau$, 10 $\delta_{SNS}$ |
| 616 | a′ | 611 | 19 | 45 | 613 | m, sh | <1 | 52 $\tau$, 17 $\nu_{NS}$, 16 $\delta_{NSN}$ |
| 559 | a′ | 566 | 9 | 23 | 563 | w | 6 | 27 $\tau$, 25 $\nu_{NS}$, 18 $\delta_{SNS}$, 17 $\delta_{NSN}$ |
| | | | | | 549 | w | | |
| 521 | a′′ | | | 2 | 500 | s, br | 44 | 30 $\delta_{NSN}$, 29 $\tau$, 24 $\delta_{SNS}$, 12 $\nu_{NS}$ |
| 411 | a′ | 415 | 11 | 25 | | | 27 | 57 $\tau$, 15 $\delta_{NSN}$ |
| 364 | a′′ | | | <1 | 360 | vs, br | 19 | 81 $\tau$ |
| 342 | a′ | 350 | 30 | 45 | | | 18 | 79 $\tau$ |
| 296 | a′ | 296 | 100 | 100 | | | 13 | 40 $\tau$, 39 $\nu_{TeCl}$ |
| 282 | a′′ | | | 7 | 251 | s, br | 100 | 47 $\nu_{TeCl}$, 38 $\tau$ |
| 281 | a′ | | | 8 | | | 96 | 54 $\nu_{TeCl}$, 30 $\tau$ |
| 257 | a′′ | 265 | 61 | 45 | | | 1 | 76 $\nu_{TeCl}$ |
| 250 | a′ | | | 7 | | | 11 | 76 $\tau$ |
| 247 | a′′ | 248 | 39 | 6 | | | <1 | 43 $\tau$, 17 $\delta_{NSN}$, 11 $\delta_{TeNS}$, 10 $\delta_{ClTeN}$ |
| 231 | a′ | | | 12 | | | <1 | 69 $\tau$ |
| 211 | a′ | 212 | 33 | 10 | 225 | w | 1 | 70 $\tau$, 11 $\delta_{SNS}$ |
| 173 | a′′ | 175 | 39 | 20 | | | 1 | 48 $\tau$, 15 $\delta_{NSN}$, 11 $\delta_{TeNS}$ |
| 155 | a′ | 169 | 54 | 12 | | | 8 | 25 $\tau$, 13 $\delta_{SNS}$, 12 $\delta_{ClTeCl}$, 12 $\nu_{TeN}$, 10 $\delta_{ClTeN}$ |
| 143 | a′ | 149 | 54 | 9 | | | 20 | 37 $\tau$, 29 $\delta_{ClTeCl}$, 19 $\delta_{ClTeN}$ |
| 132 | a′ | 138 | 61 | 10 | | | <1 | 43 $\tau$, 41 $\delta_{ClTeCl}$ |
| 118 | a′′ | | | 1 | | | <1 | 63 $\tau$, 17 $\delta_{ClTeC}$ |
| 112 | a′ | 109 | 22 | 2 | | | 1 | 64 $\tau$, 14 $\delta_{ClTeCl}$ |
| 99 | a′′ | 102 | 21 | 1 | | | <1 | 43 $\tau$, 23 $\delta_{ClTeCl}$, 22 $\delta_{ClTeN}$ |
| 87 | a′′ | 91 | 30 | 2 | | | <1 | 43 $\tau$, 15 $\delta_{ClTeN}$, 13 $\nu_{TeCl}$, 11 $\delta_{ClTeCl}$ |
| 86 | a′ | | | 6 | | | 1 | 43 $\tau$, 14 $\delta_{ClTeN}$, 11 $\delta_{ClTeCl}$, 11 $\nu_{TeCl}$, 10 $\delta_{SNS}$ |
| 79 | a′′ | 76 | 7 | 3 | | | <1 | 77 $\tau$ |
| 67 | a′ | | | | | | <1 | 79 $\tau$ |
| 26 | a′′ | | | | | | <1 | 90 $\tau$ |

[a] The calculated wavenumbers have been scaled by the factor of 0.993 to eliminate systematic errors.[55] [b] Ref.[15] [c] B3PW91/(RLC ECP) Raman activities. [d] The assignment is based on the most significant contributions (>10%) in the potential energy distribution.

 © 2006 Wiley-VCH Verlag GmbH & Co. KGaA, Weinheim 

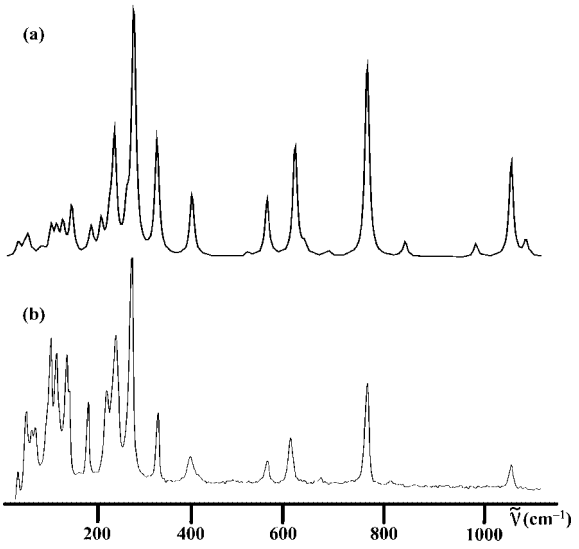


Figure 1. (a) Calculated B3PW91/(RLC ECP) fundamental vibrations and Raman activities of $TeCl_4{\cdot}S_4N_4$ (**1**). (b) Observed Raman spectrum of $TeCl_4{\cdot}S_4N_4$ (**1**).

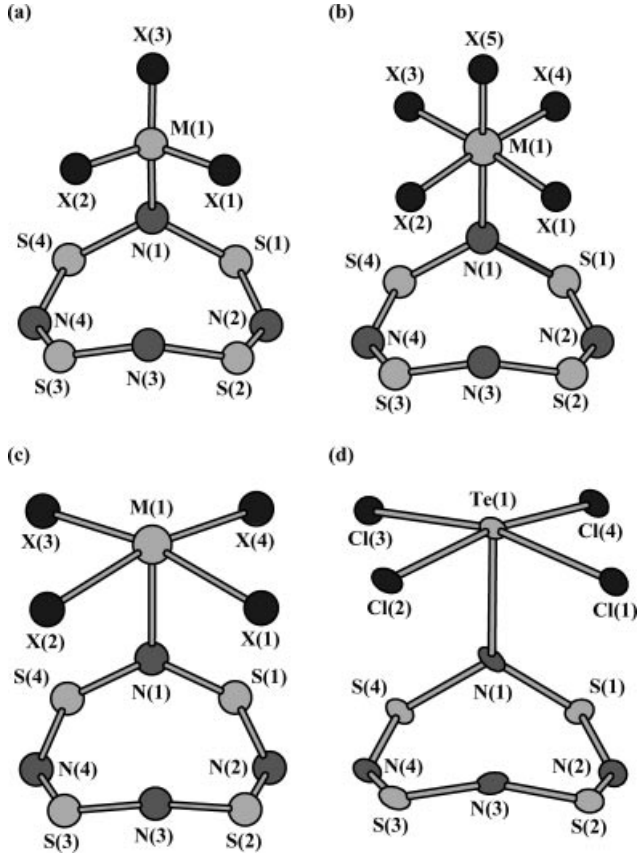


Figure 2. The B3PW91/(RLC ECP)-optimized geometries of (a) $BF_3{\cdot}S_4N_4$ (**2**) and $SO_3{\cdot}S_4N_4$ (**4**), (b) $AsF_5{\cdot}S_4N_4$ (**4**) and $SbCl_5{\cdot}S_4N_4$ (**6**), (c) $TeX_4{\cdot}S_4N_4$ [X = F (**6**), Cl (**1**), Br (**7**)] and $SeX_4{\cdot}S_4N_4$ [X = F (**8**), Cl (**9**), Br (**10**)]. (d) The X-ray structure of $TeCl_4{\cdot}S_4N_4$ (**1**). The thermal ellipsoids have been drawn at 50% probability level. The numbering of the atoms in all adducts is indicated in the figures.

nocyclic $S_4N_4$ ring in boat conformation that is bonded to $TeCl_4$ through one nitrogen atom. The S–N bond lengths [range 1.55(1)–1.67(1) Å] and the S–N–S bond angles (range 110.2–140.7°) in **1** are in good agreement with those reported for other adducts of $S_4N_4$ (Table 2).[1–9] The S(2)–S(4) and S(1)–S(3) distances [4.09(1) and 4.125(1) Å] across the ring are significantly longer than the corresponding distances in $S_4N_4$ [2.595(1) and 2.590(1) Å][26] indicating the expected loss of transannular S···S interaction.

The Te–N bond length of 2.16(1) Å in $TeCl_4{\cdot}S_4N_4$ is significantly longer than the single bond length[27] and ca. 0.12 Å longer than the $Cl_4Te$–N bond length in $[Te_6N_8(TeCl_4)_4]{\cdot}4THF$.[12] The Te–Cl bonds [2.464(3)–2.504(4) Å] are similar to the bond length of 2.516(4) Å in $[Te_6N_8(TeCl_4)_4]{\cdot}4THF$.[13] The shortest intermolecular Te···Cl contacts in $TeCl_4{\cdot}S_4N_4$ are 3.37(1) and 3.44(2) Å and are typical for secondary bonding interactions involving tellurium {for instance, the shortest intermolecular Te···Cl contact in $[Cl_2Te(\mu\text{-}NtBu)_2TeCl_2]_3$ is 3.107(1) Å[30]}. These contacts and a weak intermolecular S···N interaction link the molecules into a three-dimensional network (see Figure 3).

### A DFT Study of Selected Lewis Acid Adducts of $S_4N_4$

The B3PW91/(RLC ECP)-optimized geometries of $TeCl_4{\cdot}S_4N_4$, $BF_3{\cdot}S_4N_4$, $SO_3{\cdot}S_4N_4$, $AsF_5{\cdot}S_4N_4$, $SbCl_5{\cdot}S_4N_4$, and $S_4N_4H^+$ are shown in Table 2 and compared to experimental information from crystal structure determinations. Whereas the optimized bond lengths show a slight overestimation, it can be seen that the calculated bond angles are close to the experimental values. The RMS deviation between the calculated and observed bond lengths is only 0.034 Å and that of the bond angles is 2°. The optimized geometries of all adducts exhibit local minima with molecular symmetry $C_s$. The geometries are slightly distorted from the ideal in the crystal structures due to packing effects in the lattices. The optimized bond parameters of $TeF_4{\cdot}S_4N_4$, $TeBr_4{\cdot}S_4N_4$, and $SeX_4{\cdot}S_4N_4$ (X = F, Cl, Br) are shown in Table 3 and exhibit features similar to those species for which experimental information is available (c.f. Table 2).

The $S_4N_4$ ring in all adducts shows similar structural features irrespective of the identity of the Lewis acid (see Figure 2). The transannular S···S interactions of the free $S_4N_4$ cage are absent and, in each adduct, the molecule exhibits a monocyclic ring in the boat conformation.[31]

The B3PW91/(RLC ECP) natural atomic charges and Mayer–Mulliken bond orders of the adducts **1**–**10** are shown in Table 4. With the exception of values involving N(1), the atomic charges and bond orders within the $S_4N_4$ ring are virtually independent of the Lewis acid. While the bond orders of N(1)–S(1) and N(1)–S(4) bonds are close to unity, those of other S–N bonds are significantly higher. This might indicate delocalization of π-electron density, but the high bond orders and consequently short S–N bond lengths have also been discussed in terms of electrostatic reinforcement of the bonds.[32–36]

The bond orders of the M(1)–N(1) bond and the natural atomic charges of M(1) and N(1) expectedly show variation

 © 2006 Wiley-VCH Verlag GmbH & Co. KGaA, Weinheim 

Table 2. Selected bond lengths [Å] and angles [°] of $TeCl_4{\cdot}S_4N_4$, $BF_3{\cdot}S_4N_4$, $SO_3{\cdot}S_4N_4$, $AsF_5{\cdot}S_4N_4$, $SbCl_5{\cdot}S_4N_4$, and $S_4N_4H^+$.

| | $TeCl_4{\cdot}S_4N_4$ | | $BF_3{\cdot}S_4N_4$ | | $SO_3{\cdot}S_4N_4$ | | $AsF_5{\cdot}S_4N_4$ | | $SbCl_5{\cdot}S_4N_4$ | | $S_4N_4H^+$ | |
|---|---|---|---|---|---|---|---|---|---|---|---|---|
| | Expt.[a] | DFT[b] | Expt.[c] | DFT[b] | Expt.[d] | DFT[b] | Expt.[e] | DFT[b] | Expt.[f] | DFT[b] | Expt.[g] | DFT[b] |
| S(1)–N(1) | 1.63(1) | 1.672 | 1.666(5) | 1.667 | 1.668(4) | 1.669 | 1.64(1) | 1.668 | 1.662(9) | 1.667 | 1.656(3) | 1.688 |
| S(1)–N(2) | 1.59(1) | 1.608 | 1.595(5) | 1.615 | 1.575(6) | 1.613 | 1.60(2) | 1.612 | 1.581(9) | 1.610 | 1.582(2) | 1.607 |
| S(2)–N(2) | 1.55(1) | 1.570 | 1.542(6) | 1.569 | 1.555(6) | 1.566 | 1.56(2) | 1.567 | 1.53(1) | 1.570 | 1.573(2) | 1.561 |
| S(2)–N(3) | 1.60(1) | 1.599 | 1.580(6) | 1.604 | 1.585(6) | 1.602 | 1.59(2) | 1.601 | 1.59(1) | 1.602 | 1.555(2) | 1.603 |
| S(3)–N(3) | 1.57(1) | 1.599 | 1.588(6) | 1.604 | 1.593(5) | 1.602 | 1.57(2) | 1.601 | 1.58(1) | 1.602 | 1.569(2) | 1.603 |
| S(3)–N(4) | 1.56(1) | 1.570 | 1.550(6) | 1.569 | 1.511(7) | 1.566 | 1.55(2) | 1.567 | 1.54(1) | 1.570 | 1.539(3) | 1.561 |
| S(4)–N(4) | 1.59(1) | 1.608 | 1.591(6) | 1.615 | 1.616(6) | 1.613 | 1.58(2) | 1.612 | 1.57(1) | 1.610 | 1.595(3) | 1.607 |
| S(4)–N(1) | 1.67(1) | 1.672 | 1.651(5) | 1.667 | 1.688(4) | 1.699 | 1.70(1) | 1.668 | 1.651(9) | 1.667 | 1.643(3) | 1.688 |
| M(1)–N(1) | 2.16(1) | 2.174 | 1.577(8) | 1.632 | 1.749(4) | 1.935 | 1.90(1) | 1.992 | 2.134(7) | 2.249 | 0.72(3) | 1.019 |
| M(1)–X(1) | 2.448(3) | 2.503 | 1.371(8) | 1.381 | 1.429(6) | 1.463 | 1.71(1) | 1.752 | 2.352(4) | 2.416 | | |
| M(1)–X(2) | 2.504(4) | 2.503 | 1.371(7) | 1.381 | 1.428(5) | 1.463 | 1.72(1) | 1.752 | 2.360(3) | 2.416 | | |
| M(1)–X(3) | 2.501(3) | 2.500 | 1.377(8) | 1.365 | 1.442(5) | 1.453 | 1.72(1) | 1.737 | 2.342(3) | 2.408 | | |
| M(1)–X(4) | 2.464(3) | 2.500 | | | | | 1.73(1) | 1.737 | 2.359(3) | 2.408 | | |
| M(1)–X(5) | | | | | | | 1.70(1) | 1.709 | 2.334(3) | 2.363 | | |
| N(1)–S(1)–N(2) | 110.2(6) | 109.7 | 110.3(3) | 110.9 | 108.6(3) | 111.4 | 110.5(8) | 111.0 | 110.1(5) | 110.3 | 109.7(1) | 110.9 |
| S(1)–N(2)–S(2) | 141(1) | 137.4 | 137.6(4) | 136.4 | 139.0(4) | 137.2 | 137(1) | 137.8 | 138.4(8) | 137.2 | 138.9(2) | 141.4 |
| N(2)–S(2)–N(3) | 119.2(7) | 121.4 | 120.2(3) | 121.5 | 119.7(3) | 121.4 | 119.1(8) | 121.6 | 120.8(6) | 121.6 | 119.3(1) | 119.7 |
| S(2)–N(3)–S(3) | 139.0(9) | 139.2 | 137.9(4) | 136.9 | 140.0(4) | 137.9 | 139(1) | 138.4 | 138.4(8) | 138.0 | 138.1(1) | 137.1 |
| N(3)–S(3)–N(4) | 118.9(7) | 121.4 | 121.3(3) | 121.5 | 121.2(3) | 121.4 | 118.4(9) | 121.6 | 119.6(6) | 121.6 | 118.8(1) | 119.7 |
| S(3)–N(4)–S(4) | 140.5(9) | 137.4 | 137.3(4) | 136.4 | 137.7(3) | 137.2 | 140(1) | 137.8 | 139.7(8) | 137.2 | 138.0(2) | 141.4 |
| N(4)–S(4)–N(1) | 110.7(6) | 109.7 | 110.2(3) | 110.9 | 107.6(3) | 111.4 | 109.1(8) | 111.0 | 109.8(5) | 110.3 | 111.1(1) | 110.9 |
| S(4)–N(1)–S(1) | 112.6(6) | 112.7 | 112.7(3) | 111.7 | 116.3(3) | 114.7 | 112.3(8) | 113.6 | 112.6(5) | 112.0 | 118.4(1) | 119.5 |
| S(1)–N(1)–M(1) | 123.9(6) | 122.3 | 121.1(4) | 123.1 | 124.5(3) | 121.5 | 124.7(8) | 123.1 | 123.3(5) | 123.2 | 113(2) | 118.8 |
| S(4)–N(1)–M(1) | 123.0(7) | 122.3 | 126.0(4) | 123.1 | 119.2(3) | 121.5 | 123.1(7) | 123.1 | 123.4(5) | 123.2 | 121(2) | 118.8 |
| N(1)–M(1)–X(1) | 84.6(3) | 84.5 | 107.1(5) | 104.7 | 101.1(3) | 98.0 | 88.2(6) | 87.0 | 89.2(2) | 86.1 | | |
| N(1)–M(1)–X(2) | 82.1(3) | 84.5 | 109.2(5) | 104.7 | 103.8(2) | 98.0 | 89.8(6) | 87.0 | 88.1(3) | 86.2 | | |
| N(1)–M(1)–X(3) | 81.7(3) | 82.7 | 108.9(5) | 107.4 | 104.4(3) | 101.4 | 90.3(6) | 86.6 | 88.0(2) | 85.3 | | |
| N(1)–M(1)–X(4) | 86.7(3) | 82.7 | | | | | 89.1(6) | 86.6 | 88.5(3) | 85.3 | | |
| N(1)–M(1)–X(5) | | | | | | | 178.5(6) | 179.7 | 179.8(2) | 180.0 | | |
| X(1)–M(1)–X(2) | 91.5(1) | 90.2 | 111.1(5) | 113.0 | 115.0(3) | 117.4 | 90.2(6) | 89.4 | 90.6(1) | 90.1 | | |
| X(1)–M(1)–X(3) | 166.3(1) | 167.2 | 112.2(5) | 113.0 | 116.9(4) | 117.6 | 178.5(6) | 173.6 | 177.2(1) | 171.5 | | |
| X(1)–M(1)–X(4) | 89.9(1) | 88.6 | | | | | 89.9(6) | 89.4 | 88.8(1) | 89.3 | | |
| X(1)–M(1)–X(5) | | | | | | | 91.3(6) | 92.7 | 90.9(1) | 93.8 | | |
| X(2)–M(1)–X(3) | 87.3(1) | 88.6 | 108.3(5) | 113.1 | 113.2(3) | 117.6 | 89.8(6) | 89.3 | 89.8(1) | 89.3 | | |
| X(2)–M(1)–X(4) | 168.5(1) | 167.2 | | | | | 178.9(6) | 173.6 | 176.5(1) | 171.5 | | |
| X(2)–M(1)–X(5) | | | | | | | 91.5(6) | 92.7 | 91.7(1) | 93.9 | | |
| X(3)–M(1)–X(4) | 88.7(1) | 89.7 | | | | | 90.1(6) | 91.2 | 90.7(1) | 89.9 | | |
| X(3)–M(1)–X(5) | | | | | | | 90.2(6) | 93.6 | 91.9(1) | 94.7 | | |
| X(4)–M(1)–X(5) | | | | | | | 89.6(6) | 93.6 | 91.7(1) | 94.7 | | |

[a] This work. [b] The calculations have been carried out at the B3PW91/(RLC ECP) level of theory. [c] Ref.[1] [d] Ref.[2] [e] Ref.[3] [f] Ref.[6] [g] Ref.[19]

with respect to the identity of $MX_n$, and therefore play a role in the stabilities of the adducts.

The calculated energies of formation of the different Lewis acid adducts of $S_4N_4$ are listed in Table 5 (see Supporting Information for zero-point energy-corrected total energies of the relevant molecular species). While the formation of each adduct is an energetically favorable process, the energy changes span a wide range of values from almost energy-neutral formation of $SeBr_4{\cdot}S_4N_4$ to a very strongly exothermic reaction yielding $AsF_5{\cdot}S_4N_4$. There are two qualitative trends that affect the energy of formation, as shown in Figure 4. On one hand, the energy of formation becomes less negative with increasing M(1)–N(1) bond order. On the other hand, the energy of formation becomes more negative with increasing difference of charges between the M(1) and N(1) atoms. It can be concluded that the most stable adducts have the largest ionic contribution and the smallest covalent contribution in their M(1)–N(1) bonds.

## Vibrational Spectroscopy

As discussed above, the calculated fundamental vibrations and Raman activities of $TeCl_4{\cdot}S_4N_4$ yield a good agreement with the observed Raman spectrum and provide the definite identification of the orange bulk powder that is obtained from the direct reaction of $S_4N_4$ and $TeCl_4$ (see Table 1). The Raman spectrum of the red crystals that were obtained as a side product in the reaction of $(Me_3SiNSN)_2S$ and $TeCl_4$ was virtually identical with that recorded for the orange powder.

The observed IR spectra of $BF_3{\cdot}S_4N_4$,[37] $SO_3{\cdot}S_4N_4$,[2] $AsF_5{\cdot}S_4N_4$,[38] $SbCl_5{\cdot}S_4N_4$,[15] $SeCl_4{\cdot}S_4N_4$,[15] and $TeF_4{\cdot}S_4N_4$[15] are also in good agreement with the calculated B3PW91/(RLC ECP) wavenumbers and intensities, as shown in the Supporting Information. This good agreement between the calculated and observed parameters also enables the prediction of both IR and Raman spectra of

 © 2006 Wiley-VCH Verlag GmbH & Co. KGaA, Weinheim 

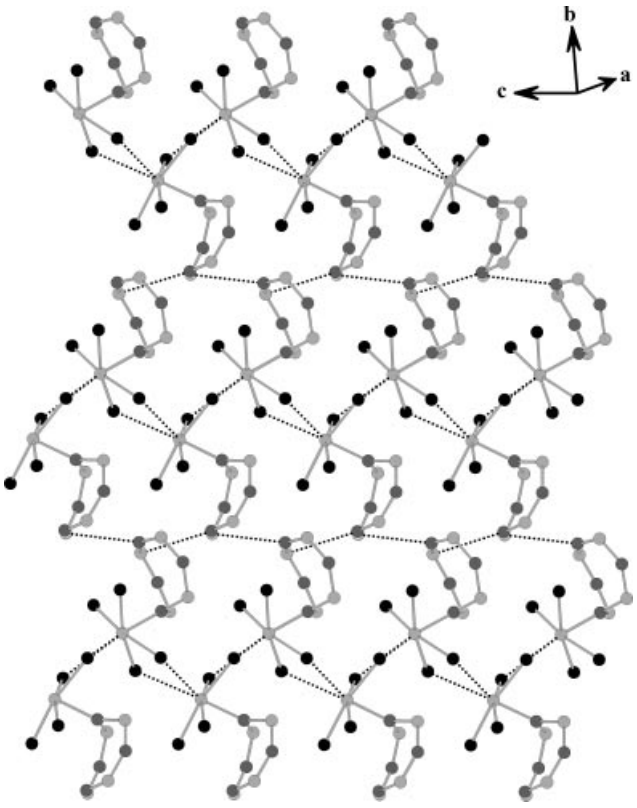


Figure 3. The closest Te···Cl contacts of 3.37(1) and 3.44(2) Å and the closest S···N contact of 3.31(1) Å link the $TeCl_4{\cdot}S_4N_4$ molcules into a continuous network.

Table 3. The B3PW91/(RLC ECP)-optimized bond lengths [Å] and angles [°] of $TeF_4{\cdot}S_4N_4$ (**6**), $TeBr_4{\cdot}S_4N_4$ (**7**), and $SeX_4{\cdot}S_4N_4$ [X = F (**8**), Cl (**9**), Br (**10**)].

| | $TeF_4{\cdot}S_4N_4$ | $TeBr_4{\cdot}S_4N_4$ | $SeF_4{\cdot}S_4N_4$ | $SeCl_4{\cdot}S_4N_4$ | $SeBr_4{\cdot}S_4N_4$ |
|---|---|---|---|---|---|
| S(1)–N(1) | 1.665 | 1.672 | 1.659 | 1.663 | 1.670 |
| S(1)–N(2) | 1.612 | 1.610 | 1.611 | 1.609 | 1.610 |
| S(2)–N(2) | 1.568 | 1.571 | 1.567 | 1.570 | 1.571 |
| S(2)–N(3) | 1.601 | 1.599 | 1.598 | 1.597 | 1.597 |
| S(3)–N(3) | 1.601 | 1.599 | 1.598 | 1.597 | 1.597 |
| S(3)–N(4) | 1.568 | 1.571 | 1.567 | 1.570 | 1.571 |
| S(4)–N(4) | 1.612 | 1.610 | 1.611 | 1.609 | 1.610 |
| S(4)–N(1) | 1.665 | 1.672 | 1.659 | 1.663 | 1.670 |
| M(1)–N(1) | 2.156 | 2.205 | 1.993 | 2.022 | 2.018 |
| M(1)–X(1) | 1.978 | 2.672 | 1.869 | 2.375 | 2.547 |
| M(1)–X(2) | 1.978 | 2.672 | 1.869 | 2.375 | 2.547 |
| M(1)–X(3) | 1.960 | 2.675 | 1.841 | 2.375 | 2.557 |
| M(1)–X(4) | 1.960 | 2.675 | 1.841 | 2.375 | 2.557 |
| N(1)–S(1)–N(2) | 110.6 | 109.8 | 110.9 | 109.7 | 109.5 |
| S(1)–N(2)–S(2) | 137.1 | 137.2 | 137.2 | 137.1 | 137.2 |
| N(2)–S(2)–N(3) | 121.7 | 121.6 | 121.8 | 121.7 | 121.5 |
| S(2)–N(3)–S(3) | 138.5 | 139.3 | 139.7 | 140.5 | 140.6 |
| N(3)–S(3)–N(4) | 121.7 | 121.6 | 121.8 | 121.7 | 121.5 |
| S(3)–N(4)–S(4) | 137.1 | 137.2 | 137.2 | 137.1 | 137.2 |
| N(4)–S(4)–N(1) | 110.6 | 109.8 | 110.9 | 109.7 | 109.5 |
| S(4)–N(1)–S(1) | 113.5 | 112.5 | 116.0 | 115.4 | 114.4 |
| S(1)–N(1)–M(1) | 123.2 | 122.2 | 122.0 | 121.2 | 121.3 |
| S(4)–N(1)–M(1) | 123.2 | 122.2 | 122.0 | 121.2 | 121.3 |
| N(1)–M(1)–X(1) | 78.6 | 86.0 | 81.9 | 88.2 | 90.4 |
| N(1)–M(1)–X(2) | 78.6 | 86.0 | 81.9 | 88.2 | 90.4 |
| N(1)–M(1)–X(3) | 77.8 | 83.5 | 81.0 | 85.5 | 87.2 |
| N(1)–M(1)–X(4) | 77.8 | 83.5 | 81.0 | 85.5 | 87.2 |
| X(1)–M(1)–X(2) | 87.8 | 90.4 | 89.1 | 90.5 | 90.7 |
| X(1)–M(1)–X(3) | 156.4 | 169.5 | 163.0 | 173.7 | 177.6 |
| X(1)–M(1)–X(4) | 86.5 | 89.9 | 87.8 | 89.3 | 89.6 |
| X(2)–M(1)–X(3) | 86.5 | 89.9 | 87.8 | 89.3 | 89.6 |
| X(2)–M(1)–X(4) | 156.4 | 169.5 | 163.0 | 173.7 | 177.6 |
| X(3)–M(1)–X(4) | 89.6 | 89.7 | 90.3 | 90.5 | 90.0 |

$SeF_4{\cdot}S_4N_4$, $SeBr_4{\cdot}S_4N_4$, and $TeBr_4{\cdot}S_4N_4$ for which no experimental information is available (see Supporting Information).

## Conclusions

The X-ray structure of $TeCl_4{\cdot}S_4N_4$ reveals features similar to those reported for other 1:1 adducts of $S_4N_4$ with Lewis acids. The coordination of a nitrogen centre to the acid results in loss of the transannular S···S interactions in $S_4N_4$ ring, which adopts a boat conformation. DFT calculations for a series of 1:1 adducts reveal that the π electron density in the ring is delocalized. Consequently, all S–N bond lengths lie between those of single and double bonds. The B3PW91/(RLC ECP) Mayer–Mulliken bond orders support this conclusion. The bond parameters, natural atomic charges, and bond orders within the $S_4N_4$ ring are rather insensitive to the chemical identity of the Lewis acid, the most notable exceptions being the charge on the nitrogen atom that is bonded to the acid molecule.

The B3PW91/(RLC ECP) energies of formation of the adducts from their component molecules vary significantly. The formation of $AsF_5{\cdot}S_4N_4$ is most exothermic and that of $SeBr_4{\cdot}S_4N_4$ is almost thermoneutral. The DFT calculations qualitatively show that the relative stabilities of the adducts with respect to their components depend on the ionic character of the M–N bond.

The fundamental vibrations calculated at the B3PW91/(RLC ECP) level of theory show good agreement with the experimental IR and Raman vibrations and their intensities. The calculations indicate that vibrational spectroscopy can be used to identify the species formed upon adduct formation and that this level of theory is sufficient to predict the vibrational spectra of the adducts that are still unknown.

## Experimental Section

**General Procedures:** All reactions and manipulations of air- and moisture-sensitive reagents were carried out under argon passed through $P_4O_{10}$. The reagents $SCl_2$, $SO_2Cl_2$ and $TeCl_4$ (Aldrich) were used without further purification. $[(Me_3Si)_2N]_2S$ was prepared from $(Me_3Si)_2NH$ by utilizing the method of Wolmershäuser et al.[39] and purified by distillation. $S_4N_4$ was produced by the reaction of $[(Me_3Si)_2N]_2S$ with a mixture of $SCl_2$ and $SO_2Cl_2$.[40] Dichloromethane was dried by distillation over $P_4O_{10}$ under nitrogen prior to use.

**Spectroscopic Methods and Vibrational Analysis:** The $^{14}N$ and $^{125}Te$ NMR spectra were recorded in dichloromethane with a Bruker DPX 400 spectrometer operating at 28.909 and 126.240 MHz, respectively. The spectral widths were 14.49 and 95.24 kHz, yielding

 © 2006 Wiley-VCH Verlag GmbH & Co. KGaA, Weinheim 

Table 4. B3PW91/(RLC ECP) natural atomic charges and Mayer–Mulliken bond orders in **1**–**10**.

| | $MX_3{\cdot}S_4N_4$[a] | | $MX_5{\cdot}S_4N_4$[b] | | | $MX_4{\cdot}S_4N_4$[c] | | | | | $S_4N_4H^+$ |
|---|---|---|---|---|---|---|---|---|---|---|---|
| | **2** | **3** | **4** | **5** | **6** | **1** | **7** | **8** | **9** | **10** | **11** |
| Natural atomic charges | | | | | | | | | | | |
| S(1) | 1.02 | 1.03 | 1.05 | 1.06 | 1.05 | 1.06 | 1.05 | 1.06 | 1.08 | 1.08 | 1.03 |
| N(1) | –1.17 | –1.20 | –1.26 | –1.20 | –1.26 | –1.24 | –1.23 | –1.20 | –1.18 | –1.17 | –1.11 |
| S(2) | 1.21 | 1.23 | 1.23 | 1.22 | 1.23 | 1.23 | 1.22 | 1.25 | 1.24 | 1.23 | 1.30 |
| N(2) | –0.96 | –0.96 | –0.96 | –0.97 | –0.96 | –0.98 | –0.98 | –0.97 | –0.98 | –0.99 | –0.95 |
| S(3) | 1.21 | 1.23 | 1.23 | 1.22 | 1.23 | 1.23 | 1.22 | 1.25 | 1.24 | 1.23 | 1.30 |
| N(3) | –1.09 | –1.10 | –1.10 | –1.09 | –1.09 | –1.08 | –1.07 | –1.07 | –1.07 | –1.07 | –1.12 |
| S(4) | 1.02 | 1.03 | 1.06 | 1.06 | 1.05 | 1.06 | 1.05 | 1.06 | 1.08 | 1.08 | 1.30 |
| N(4) | –0.96 | –0.96 | –0.96 | –0.97 | –0.96 | –0.98 | –0.98 | –0.97 | –0.98 | –0.99 | –0.95 |
| M(1) | 1.41 | 2.60 | 2.83 | 1.74 | 2.50 | 1.48 | 1.27 | 2.11 | 1.04 | 0.83 | 0.47 |
| X(1) | –0.58 | –0.99 | –0.64 | –0.42 | –0.70 | –0.47 | –0.41 | –0.65 | –0.38 | –0.33 | |
| X(2) | –0.58 | –0.99 | –0.64 | –0.42 | –0.70 | –0.47 | –0.41 | –0.65 | –0.38 | –0.33 | |
| X(3) | –0.56 | –0.94 | –0.62 | –0.40 | –0.68 | –0.43 | –0.38 | –0.62 | –0.35 | –0.30 | |
| X(4) | | | –0.62 | –0.40 | –0.68 | –0.43 | –0.38 | –0.62 | –0.35 | –0.30 | |
| X(5) | | | –0.60 | –0.36 | | | | | | | |
| Mayer–Mulliken bond orders | | | | | | | | | | | |
| S(1)–N(1) | 1.15 | 1.12 | 1.14 | 1.12 | 1.12 | 1.08 | 1.08 | 1.13 | 1.09 | 1.08 | 1.08 |
| S(1)–N(2) | 1.31 | 1.31 | 1.32 | 1.33 | 1.32 | 1.32 | 1.32 | 1.31 | 1.32 | 1.31 | 1.32 |
| S(2)–N(2) | 1.53 | 1.53 | 1.52 | 1.50 | 1.52 | 1.50 | 1.49 | 1.52 | 1.49 | 1.48 | 1.55 |
| S(2)–N(3) | 1.33 | 1.33 | 1.34 | 1.34 | 1.34 | 1.35 | 1.35 | 1.35 | 1.35 | 1.35 | 1.33 |
| S(3)–N(3) | 1.33 | 1.33 | 1.34 | 1.34 | 1.34 | 1.35 | 1.35 | 1.35 | 1.35 | 1.35 | 1.33 |
| S(3)–N(4) | 1.53 | 1.53 | 1.52 | 1.50 | 1.52 | 1.50 | 1.49 | 1.52 | 1.49 | 1.48 | 1.55 |
| S(4)–N(4) | 1.31 | 1.31 | 1.32 | 1.33 | 1.32 | 1.32 | 1.32 | 1.31 | 1.32 | 1.31 | 1.32 |
| S(4)–N(1) | 1.15 | 1.12 | 1.14 | 1.12 | 1.12 | 1.08 | 1.08 | 1.13 | 1.09 | 1.08 | 1.08 |
| M(1)–N(1) | 0.58 | 0.48 | 0.34 | 0.35 | 0.42 | 0.46 | 0.48 | 0.47 | 0.53 | 0.54 | 0.72 |
| M(1)–X(1) | 0.91 | 1.70 | 0.73 | 0.85 | 0.57 | 0.83 | 0.77 | 0.66 | 0.86 | 0.94 | |
| M(1)–X(2) | 0.91 | 1.70 | 0.73 | 0.85 | 0.57 | 0.83 | 0.77 | 0.66 | 0.86 | 0.94 | |
| M(1)–X(3) | 0.98 | 1.81 | 0.75 | 0.87 | 0.61 | 0.84 | 0.78 | 0.70 | 0.86 | 0.93 | |
| M(1)–X(4) | | | 0.75 | 0.87 | 0.61 | 0.84 | 0.78 | 0.70 | 0.86 | 0.93 | |
| M(1)–X(5) | | | 0.80 | 0.98 | | | | | | | |

[a] M = B, S; X = F, O. [b] M = As, Sb; X = F, Cl. [c] M = Te, Se; X = F, Cl, Br.

Table 5. B3PW91/(RLC ECP) energies of formation of $MX_n{\cdot}S_4N_4$.

| Reaction | | | $\Delta E$ [kJ·mol$^{-1}$][a] |
|---|---|---|---|
| $BF_3 + S_4N_4$ | → | $BF_3{\cdot}S_4N_4$ | –81.4 |
| $SO_3 + S_4N_4$ | → | $SO_3{\cdot}S_4N_4$ | –58.6 |
| $SeF_4 + S_4N_4$ | → | $SeF_4{\cdot}S_4N_4$ | –42.2 |
| $SeCl_4 + S_4N_4$ | → | $SeCl_4{\cdot}S_4N_4$ | –23.4 |
| $SeBr_4 + S_4N_4$ | → | $SeBr_4{\cdot}S_4N_4$ | –8.2 |
| $TeF_4 + S_4N_4$ | → | $TeF_4{\cdot}S_4N_4$ | –69.5 |
| $TeCl_4 + S_4N_4$ | → | $TeCl_4{\cdot}S_4N_4$ | –43.0 |
| $TeBr_4 + S_4N_4$ | → | $TeBr_4{\cdot}S_4N_4$ | –30.5 |
| $AsF_5 + S_4N_4$ | → | $AsF_5{\cdot}S_4N_4$ | –116.3 |
| $SbCl_5 + S_4N_4$ | → | $SbCl_5{\cdot}S_4N_4$ | –66.7 |

[a] The energy changes are based on total energies of the molecular species incorporating the zero-point-energy corrections.

the respective resolutions of 7.08 and 1.45 Hz/data point. The pulse widths were 12.0 μs for $^{14}N$ and 6.67 μs for $^{125}Te$, corresponding to nuclear tip angles of 44 and 30°, respectively. All spectra were recorded unlocked. The $^{14}N$ NMR chemical shifts are reported relative to $CH_3NO_2$ and $^{125}Te$ NMR spectra were referenced externally to a saturated solution of $H_6TeO_6$. The MS-EI mass spectrum was recorded with a Micromass Quattro II spectrometer at 70 eV of electron energy. Raman spectra were recorded for solid samples at room temperature with a Bruker IFS-66 spectrometer equipped with a FRA-16 Raman unit and Nd:YAG laser (power 110 mW; 8–64 scans; spectral resolution ±1 cm$^{-1}$; Blackmann–Harris four-term apodization, no white light correction, 180 ° scattering geometry).

**Preparation of $TeCl_4{\cdot}S_4N_4$ (1):** $S_4N_4$ (0.092 g, 0.5 mmol) was dissolved in dichloromethane (10 mL) and added to a suspension of $TeCl_4$ (0.135 g, 0.5 mmol) in dichloromethane (10 mL) at –80 °C. The reaction mixture was stirred overnight and warmed slowly to room temperature to give a yellow solution and an orange, insoluble precipitate of **1** (0.174 g, 76%). This precipitate was used for vibrational and mass spectroscopic characterization of the product. The NMR spectrum was recorded from the yellow solution obtained after filtration. $^{14}N$ NMR ($CH_2Cl_2$, 25 °C): $\delta$ = –256 ($S_4N_4$) ppm. MS: *m*/*z* (%) = 46 (100) [$SN^+$], 78 (18) [$S_2N^+$], 92 (26) [$S_2N_2^+$], 130 (77) [$Te^+$], 138 (18) [$S_3N_3^+$], 144 (7) [$TeN^+$], 165 (72) [$TeCl^+$], 176 (25) [$TeSN^+$], 184 (5) [$S_4N_4^+$], 200 (52) [$TeCl_2^+$], 211 (22) [$TeClSN^+$], 235 (38) [$TeCl_3^+$], 246 (28) [$TeCl_2SN^+$], 257 (67) [$TeClS_2N_2^+$], 292 (19) [$TeCl_2S_2N_2^+$], 314 (5) [$TeS_4N_4^+$]. All fragments show expected isotopic distributions. The *m*/*z* and intensities in the list above refer to the fragments containing the $^{130}Te$ isotope.

**X-ray Crystallography:** A small number of red, moisture-sensitive crystals of $TeCl_4{\cdot}S_4N_4$ (**1**) were obtained by the reaction of $(Me_3SiNSN)_2S$ with $TeCl_4$ in $CH_2Cl_2$.[41] *FW* = 453.68 g/mol, monoclinic, space group *Cc*, *a* = 12.998(2), *b* = 11.914(2), *c* = 7.214(1) Å, $\beta$ = 101.65(1)°; *V* = 1080.5(3) Å$^3$; *Z* = 4, $D_c$ = 2.789 g cm$^{-3}$; *F*(000) = 848; $\mu$(Mo-$K_\alpha$) = 4.471 mm$^{-1}$, *T* = 120 K, crystal dimensions 0.2 × 0.1 × 0.1 mm$^3$. Reflections (2890 total, 1610 unique, $\theta$ range 3.42–26.00°, $R_{int}$ = 0.0369) were collected on Nonius Kappa CCD diffractometer using graphite-monochromated Mo-$K_\alpha$ radiation ($\lambda$ = 0.71073 Å). The intensity data were corrected for Lorentz and polarization effects, and an empirical absorption correction was applied to the net intensities. The structure was solved by direct meth-

 © 2006 Wiley-VCH Verlag GmbH & Co. KGaA, Weinheim 

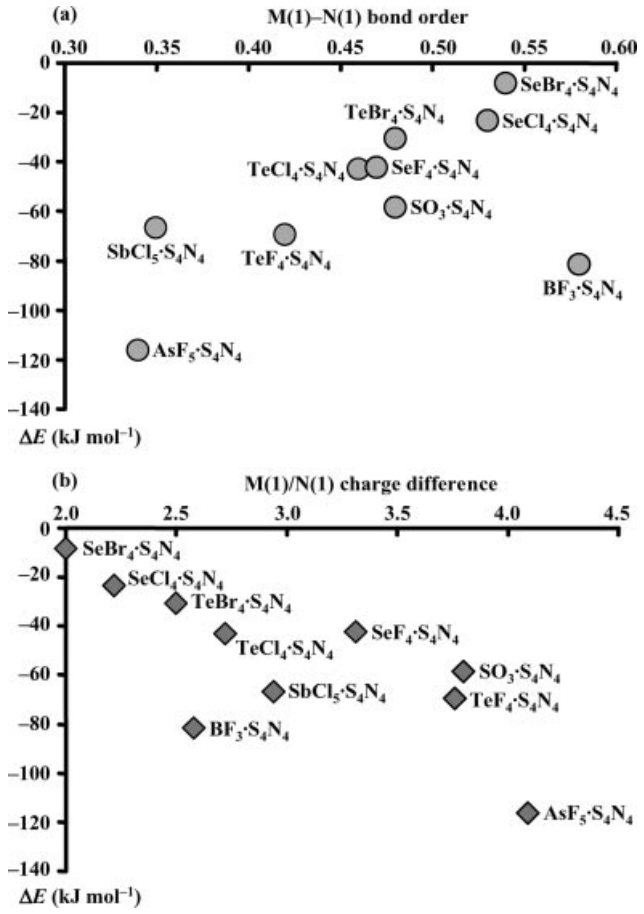


Figure 4. The dependence of the B3PW91/(RLC ECP) energy of formation of adducts **1**–**10** on (a) M(1)–N(1) bond order and (b) difference of atomic charges of M(1) and N(1) (see Table 4).

ods using SHELXS-97[43] and refined using SHELXL-97.[44] The scattering factors for the neutral atoms were those incorporated with the programs. The final $R_1 = 0.0515$ [$I > 2\sigma(I)$] and $wR_2 = 0.1242$ (all data) [$R_1 = \Sigma||F_o| - |F_c||/\Sigma|F_o|$, $wR_2 = [\Sigma w(F_o^2 - F_c^2)^2/\Sigma wF_o^4]1/2$, $w = [\sigma^2(F_o^2) + (0.0700P)^2 + 10.00P]^{-1}$ where $P = \{\max(F_o^2,0) + 2F_c^2\}/3$]. Maximum and minimum values in the final difference Fourier synthesis are 2.342 and –1.629 e·Å$^{-3}$.

Further details of the crystal-structure investigation of **1** can be obtained free of charge from the Fachinformationszentrum Karlsruhe, 76344 Eggenstein-Leopoldshafen, Germany, Fax: +49-7247-808-666, E-mail: crysdata@fiz-karlsruhe.de, http://www.fiz-karlsruhe.de (under "Products and Services") on quoting the depository number CSD-416253.

**Computational Details:** The molecular orbital calculations of $TeCl_4{\cdot}S_4N_4$ (**1**), $BF_3{\cdot}S_4N_4$ (**2**), $SO_3{\cdot}S_4N_4$ (**3**), $AsF_5{\cdot}S_4N_4$ (**4**), $SbCl_5{\cdot}S_4N_4$ (**5**), $TeF_4{\cdot}S_4N_4$ (**6**), $TeBr_4{\cdot}S_4N_4$ (**7**), and $SeX_4{\cdot}S_4N_4$ [X = F (**8**), Cl (**9**), Br (**10**)] were carried out at the DFT level of theory involving Becke's three parameter hybrid functionals with the Perdew/Wang 91 correlation (B3PW91)[45–51] and using the Stuttgart relativistic large core effective core potential approximation (RLC ECP)[52–54] by augmenting the double-zeta quality basis sets of the valence orbitals by two polarization functions for all atoms except for hydrogen for which a standard Pople-type 6-31G* basis was used, as implemented in Gaussian 98 and Gaussian 03. Complete geometry optimizations were performed for each adduct. Fundamental vibrations were calculated to establish the nature of the stationary points and to enable the assignment of the Raman spectra. The calculated wavenumbers and zero-point-energy corrections (ZPE) were scaled by 0.993 to eliminate the systematic errors.[55] The calculations were mainly performed with the GAUSSIAN 03 (Rev. B.04) program package.[56] The wavefunction files for NBO 5.0,[57] however, were calculated with the GAUSSIAN 98 (Rev. A.9) package.[58]

**Supporting Information** (see also the footnote on the first page of this article): Table S1. B3PW91/(RLC ECP) total and formation energies, and ZPE scaled by 0.993 of $MX_3(S_4N_4)$ (M = B, S; X = F, O), $MX_4(S_4N_4)$ (M = Se, Te; X = F, Cl, Br), $MX_5(S_4N_4)$ (M = As, Sb; X = F, Cl) and $S_4N_4H^+$. Table S2. Scaled B3PW91/(RLC ECP) fundamental vibrations of $MX_4(S_4N_4)$ (M = Se, Te; X = F, Cl, Br). Table S3. Scaled B3PW91/(RLC ECP) fundamental vibrations of $MX_3(S_4N_4)$ (M = B, S; X = F, O), $MX_5(S_4N_4)$ (M = As, Sb; X = F, Cl) and $S_4N_4H^+$.

## Acknowledgments

Financial support from the Academy of Finland, the Emil Aaltonen Foundation, Finnish Cultural Foundation, and the Natural Sciences and Engineering Research Council (Canada) is gratefully acknowledged.

[1] M. G. B. Drew, D. H. Templeton, A. Zalkin, *Inorg. Chem.* **1967**, *6*, 1906.
[2] A. Gieren, B. Diederer, H. W. Roesky, N. Amin, O. Petersen, *Z. Anorg. Allg. Chem.* **1978**, *440*, 119.
[3] W. Isenberg, R. Mews, G. Sheldrick, *Z. Anorg. Allg. Chem.* **1985**, *525*, 54.
[4] D. Neubauer, J. Weiss, M. Becke-Goehring, *Z. Naturforsch. Teil B* **1959**, *14*, 284.
[5] D. Neubauer, J. Weiss, *Z. Anorg. Allg. Chem.* **1960**, *303*, 28.
[6] R. J. Gillespie, J. F. Sawyer, D. R. Slim, J. D. Tyrer, *Inorg. Chem.* **1982**, *21*, 1296.
[7] U. Thewalt, *Z. Anorg. Allg. Chem.* **1981**, *476*, 105.
[8] U. Thewalt, *Z. Naturforsch. Teil B* **1980**, *35*, 855.
[9] U. Thewalt, G. Albrecht, *Z. Naturforsch. Teil B* **1982**, *37*, 1098.
[10] U. Thewalt, K. Holl, *Z. Naturforsch. Teil B* **1988**, *43*, 467.
[11] H. Martan, J. Weiss, *Z. Anorg. Allg. Chem.* **1984**, *514*, 107.
[12] A. Gieren, K. Hofer, T. Hubner, *Z. Kristallogr.* **1987**, *178*, 68.
[13] W. Massa, C. Lau, M. Möhlen, B. Neumuller, K. Dehnicke, *Angew. Chem. Int. Ed. Engl.* **1998**, *37*, 2840.
[14] R. C. Paul, C. L. Arora, J. Kishore, K. C. Malhotra, *Aust. J. Chem.* **1971**, *24*, 1637.
[15] G. G. Alange, A. J. Banister, *J. Inorg. Nucl. Chem.* **1978**, *40*, 203.
[16] V. C. Ginn, P. F. Kelly, J. D. Woollins, *Polyhedron* **1994**, *13*, 1501.
[17] A. Haas, M. Pryka, *Chem. Ber.* **1995**, *128*, 11.
[18] A MNDO comparison of $S_4N_4H^+$ and some Lewis acid adducts of $S_4N_4$ has been presented by Cordes et al.[19]
[19] A. W. Cordes, C. G. Marcellus, M. C. Noble, R. T. Oakley, W. T. Pennington, *J. Am. Chem. Soc.* **1983**, *105*, 6008.
[20] T. Chivers, R. T. Oakley, O. J. Scherer, G. Wolmershäuser, *Inorg. Chem.* **1981**, *20*, 914.
[21] The assignment of the Raman spectra is also consistent with that which have recently been carried out for some related chalcogen-nitrogen systems.[22–25].
[22] A. Maaninen, J. Siivari, R. J. Suontamo, J. Konu, R. S. Laitinen, T. Chivers, *Inorg. Chem.* **1997**, *36*, 2170.
[23] A. Maaninen, R. S. Laitinen, T. Chivers, T. A. Pakkanen, *Inorg. Chem.* **1999**, *38*, 3450.
[24] A. Maaninen, J. Konu, R. S. Laitinen, T. Chivers, G. Schatte, J. Pietikäinen, M. Ahlgrén, *Inorg. Chem.* **2001**, *40*, 3559.
[25] R. Fleischer, B. Walfort, A. Gbureck, P. Scholz, W. Kiefer, D. Stalke, *Chem. Eur. J.* **1998**, *4*, 2266.

 © 2006 Wiley-VCH Verlag GmbH & Co. KGaA, Weinheim 

[26] M. L. DeLucia, P. Coppens, *Inorg. Chem.* **1978**, *17*, 2336.
[27] The sum of the covalent radii for tellurium and nitrogen is 2.07 Å.[28] The $Te^{II}$–N single bond lengths in $[(Me_3Si)_2N–Te–N(SiMe_3)_2]$ are 2.053(2) and 2.045(2) Å.[29]
[28] J. Emsley, *The Elements*, 3rd ed., Clarendon Press, Oxford **1998**.
[29] M. Björgvinsson, H. W. Roesky, F. Pauer, D. Stalke, G. M. Sheldrick, *Inorg. Chem.* **1990**, *29*, 5140.
[30] T. Chivers, N. Enright, N. Sandblom, G. Schatte, M. Parvez, *Inorg. Chem.* **1999**, *38*, 5431.
[31] The MNDO calculations of some Lewis acid adducts of $S_4N_4$ by Cordes et al.[19] lead to similar geometric and bonding features in the $S_4N_4$ ring as our present higher level DFT calculations.
[32] T.-H. Tang, R. F. W. Bader, P. J. MacDougall, *Inorg. Chem.* **1985**, *24*, 2047.
[33] W. Scherer, M. Spiegler, B. Pedersen, M. Tafipolsky, W. Hieringer, B. Reinhard, A. J. Downs, G. S. McGrady, *Chem. Commun.* **2000**, 635.
[34] D. Leusser, B. Walfort, D. Stalke, *Angew. Chem. Int. Ed.* **2002**, *41*, 2079.
[35] J. Henn, D. Hge, D. Leusser, D. Stalke, B. Engels, *J. Phys. Chem. B* **2004**, *108*, 9442.
[36] D. Leusser, J. Henn, N. Kocher, B. Engels, D. Stalke, *J. Am. Chem. Soc.* **2004**, *126*, 1781.
[37] K. J. Wynne, W. L. Jolly, *Inorg. Chem.* **1967**, *6*, 107.
[38] R. Mews, D.-L. Wagner, O. Glemser, *Z. Anorg. Allg. Chem.* **1975**, *412*, 148.
[39] G. Wolmershäuser, C. R. Brulet, G. B. Street, *Inorg. Chem.* **1978**, *17*, 3586.
[40] A. Maaninen, J. Siivari, R. S. Laitinen, T. Chivers, *Inorg. Synth.* **2003**, *3*, 196.
[41] We have recently observed that $S_4N_4$ is one product in the reaction of $(Me_3SiNSN)_2S$ with $TeCl_4$.[42] It reacts with unreacted $TeCl_4$ and forms a small amount of well-formed red crystals of $TeCl_4{\cdot}S_4N_4$ that were suitable for the X-ray structure determination. While the direct reaction between $S_4N_4$ and $TeCl_4$ yields an orange powder that could be shown by vibrational analysis and mass spectroscopy to be $TeCl_4{\cdot}S_4N_4$, we were unable to obtain single crystals from this direct reaction.
[42] J. Konu, M. Ahlgrén, S. M. Aucott, T. Chivers, S. H. Dale, M. R. J. Elsegood, K. E. Holmes, S. L. M. James, P. F. Kelly, R. S. Laitinen, *Inorg. Chem.* **2005**, *44*, 4992.
[43] G. M. Sheldrick, SHELXS-97, *Program for Crystal Structure Determination*, University of Göttingen, Göttingen, Germany, **1997**.
[44] G. M. Sheldrick, SHELXL-97, *Program for Crystal Structure Refinement*, University of Göttingen, Göttingen, Germany, **1997**.
[45] A. D. Becke, *J. Phys. Chem.* **1993**, *98*, 5648.
[46] K. Burke, J. P. Perdew, Y. Wang, *Electron Density Functional Theory: Recent Progress and New Directions* (Eds.: J. F. Dobson, G. Vignale, M. P. Das), Plenum, New York, **1998**.
[47] J. P. Perdew, *Electronic Structure of Solids* (Eds.: P. Ziesche, H. Eschrig), Akademie Verlag, Berlin, **1991**.
[48] J. P. Perdew, Y. Wang, *Phys. Rev. B* **1992**, *45*, 13244.
[49] J. P. Perdew, J. A. Chevary, S. H. Vosko, K. A. Jackson, M. R. Pederson, D. J. Singh, C. Fiolhais, *Phys. Rev. B* **1992**, *46*, 6671.
[50] J. P. Perdew, J. A. Chevary, S. H. Vosko, K. A. Jackson, M. R. Pederson, D. J. Singh, C. Fiolhais, *Phys. Rev. B* **1993**, *48*, 4978.
[51] J. P. Perdew, K. Burke, Y. Wang, *Phys. Rev. B* **1996**, *54*, 16553.
[52] W. Kuechle, M. Dolg, H. Stoll, H. Preuss, *Mol. Phys.* **1991**, *74*, 1245.
[53] A. Bergner, M. Dolg, W. Kuechle, H. Stoll, H. Preuss, *Mol. Phys.* **1993**, *80*, 1431.
[54] M. Buhl, W. Thiel, U. Fleischer, W. Kutzelnigg, *J. Phys. Chem.* **1995**, *99*, 4000.
[55] A. P. Scott, L. Radom, *J. Phys. Chem.* **1996**, *100*, 16502.
[56] M. J. Frisch, G. W. Trucks, H. B. Schlegel, G. E. Scuseria, M. A. Robb, J. R. Cheeseman, J. A. Montgomery Jr, T. Vreven, K. N. Kudin, J. C. Burant, J. M. Millam, S. S. Iyengar, J. Tomasi, V. Barone, B. Mennucci, M. Cossi, G. Scalmani, N. Rega, H. G. Petersson, A. Nakatsuji, M. Hada, M. Ehara, K. Toyota, R. Fukuda, J. Hasegawa, M. Ishida, T. Nakajima, Y. Honda, O. Kitao, H. Nakai, M.Klene, X. Li, J. E. Knox, H. P. B. Hratchian, J. Cross, C. Adamo, J. Jaramillo, R. Gomperts, R. E. Stratmann, O. Yazyev, A. J. Austin, R. Cammi, C. Pomelli, J. W. Ochterski, P. Y. Ayala, K. Morokuma, G. A. Voth, P. Salvador, J. J. Dannenberg, V. G. Zakrzewski, S. Dapprich, A. D. Daniels, M. C. Strain, O. Farkas, D. K. Malick, A. D. Rabuck, K. Raghavachari, J. B. Foresman, J. V. Ortiz, Q. Cui, A. G. Baboul, S. Clifford, J. Cioslowski, B. B. Stefanov, G. Liu, A. Liashenko, P. Piskorz, I. Komaromi, R. L. Martin, D. J. Fox, T. Keith, M. A. Al-Laham, C. Y. Peng, A. Nanayakkara, M. Challacombe, P. M. W. Gill, B. Johnson, W. Chen, M. W. Wong, C. Gonzalez, J. A. Pople, *Gaussian 03*, revision B.04, Inc., Pittsburgh PA, **2003**.
[57] E. D. Glendening, J. K. Badenhoop, A. E. Reed, J. E. Carpenter, J. A. Bohmann, C. M. Morales, F. Weinhold, *NBO 5.0*, Theoretical Chemistry Institute, University of Wisconsin, Madison, WI, **2001**.
[58] M. J. Frisch, G. W. Trucks, H. B. Schlegel, G. E. Scuseria, M. A. Robb, J. R. Cheeseman, V. G. Zakrzewski, J. A. Montgomery Jr, R. E. Stratmann, J. C. Burant, S. Dapprich, J. M. Millam, A. D. Daniels, K. N. Kudin, M. C. Strain, O. Farkas, J. Tomasi, V. Barone, M. Cossi, R. Cammi, B. Mennucci, C. Pomelli, C. Adamo, S. Clifford, J. Ochterski, G. A. Petersson, P. Y. Ayala, Q. Cui, K. Morokuma, D. K. Malick, A. D. Rabuck, K. Raghavachari, J. B. Foresman, J. Cioslowski, J. V. Ortiz, A. G. Baboul, B. B. Stefanov, G. Liu, A. Liashenko, P. Piskorz, I. Komaromi, R. Gomperts, R. L. Martin, D. J. Fox, T. Keith, M. A. Al-Laham, C. Y. Peng, A.Nanayakkara, M. Challacombe, P. M. W. Gill, B. Johnson, W. Chen, M. W. Wong, J. L. Andres, C. Gonzalez, M. Head-Gordon, E. S. Replogle, J. A. Pople, *Gaussian 98*, revision A.9, Inc., Pittsburgh PA, **1998**.

Received: February 17, 2006
Published Online: June 6, 2006

 © 2006 Wiley-VCH Verlag GmbH & Co. KGaA, Weinheim 

DOI: 10.1002/ejic.200600148

# Energetic Nitrate, Perchlorate, Azide and Azolate Salts of Hexamethylenetetramine

**Hong Xue,[a] Haixiang Gao,[a] Brendan Twamley,[a] and Jean'ne M. Shreeve*[a]**

**Keywords:** Hexamethylenetetrammonium salts / Energetic materials / Quaternization / Heats of formation

Hexamethylenetetrammonium salts, composed of energetic anions 3,5-dinitropyrazolate, 4,5-dinitroimidazolate, 3,5-dinitro-1,2,4-triazolate, 5-nitrotetrazolate, perchlorate, nitrate and azide, were synthesized and characterized. The structure of *N*-methyl-hexamethylenetetrammonium 3,5-dinitro-1,2,4-triazolate (**6**) was confirmed by X-ray analysis. The standard enthalpies of formation for the new salts were calculated by using the computationally feasible DFT(B3LYP) and MP2 methods in conjunction with an empirical approach based on the densities of the salts. The calculated values range from $\Delta H_f^\circ$ = –30.6 (**7**) to +468.8 kJ·mol$^{-1}$ (**10**) where the experimental densities > 1.35 g cm$^{-3}$.
(© Wiley-VCH Verlag GmbH & Co. KGaA, 69451 Weinheim, Germany, 2006)

## Introduction

In recent years, the synthesis of energetic heterocyclic compounds has attracted considerable interest,[1–7] especially the syntheses of new members of heterocyclic-based energetic, low-melting salts.[8,9] Energetic materials that are salt-based often possess advantages over non-ionic molecules because these salts tend to exhibit lower vapor pressure and higher densities than their atomically similar non-ionic analogues. The cation is generally a bulky organic species with low symmetry. Nitrogen-containing heterocyclic-based salts predominate. The anion most frequently is inorganic, such as nitrate,[8,9,10g] perchlorate,[8,9,10e] dinitramide,[8,9c,10] azide[10g] and tetraazidoborate anion.[11] However, reports are already available that describe analogous salts with organic anions, such as α-cyano-4-hydroxycinnamate, anthraquinone-2-sulfonate,[12] salicylate and lactate,[13] imidazolate and triazolate and tetrazolate.[9e,14,15] Some metal salts composed of organic anions, such as lithium 4,5-dicyano-1,2,3-triazolate, were reported as electrolytes.[16] Alkali metal salts of 5,5′-azotetrazolate[17] and transition-metal salts of 5-nitro-2,4-dihydro-3*H*-1,2,4-triazol-3-one[18] were also synthesized as energetic compounds.

Hexamethylenetetramine is an interesting raw material which is useful in the production of antibacterial agents, adhesives, coatings, dye fixatives, anticorrosive agents as well as powerful explosives, e.g., 1,3,5,7-tetranitro-1,3,5,7-tetraazacyclooctane (HMX), 1,3,5-trinitro-1,3,5-triazacyclohexane (RDX) and pentaerythrol tetranitrate (PETN).[19] The mechanisms of nitration of hexamethylenetetramine were also studied in detail.[20] The preparation of certain salts of hexamethylenetetramine has long been known, including both inorganic salts, such as chloride, sulfate, phosphate, and organic salts, such as formate, methanesulfonate, *p*-toluenesulfonate and many others.[21] The literature data of energetic hexamethylenetetramine dinitrate (HEXADI) and related compounds were given recently.[22] The syntheses and crystal structures of various energetic urotropinium salts with azide, nitrate, dinitramide and azotetrazolate counterions are also reported,[23] but no energetic characterization was cited. Our main interest in this work is to investigate the syntheses and thermal properties of hexamethylenetetrammonium salts containing both energetic inorganic and organic anions, such as nitrate, perchlorate, and azide, and 3,5-dinitropyrazolate, 4,5-dinitroimidazolate, 3,5-dinitro-1,2,4-triazolate, and 5-nitrotetrazolate, respectively. The calculated heats of formation of these compounds based on DFT(B3LYP) and MP2 methods in conjunction with an empirical approach based on densities of salts are also presented.[10h]

## Results and Discussion

Hexamethylenetetrammonium salts with nitrate, azide, dinitramide and azotetrazolate counterions have been prepared either from hexamethylenetetramine and nitric acid or the metathesis reaction from the corresponding iodide (or sulfate) with $AgN_3$, $[AgNCCH_3][N(NO_2)_2]$, or barium azotetrazolate.[23] It was found that 4,5-dinitroimidazole and 5-nitrotetrazole, which are strong NH acids ($pK_a$ = –0.8 for 5-nitrotetrazole)[24] with electron-withdrawing nitro substituents on the ring, can be readily quaternized with azoles to form energetic azolium-azolate salts.[9e] Here we synthesized several new hexamethylenetetrammonium salts

[a] Department of Chemistry, University of Idaho, Moscow, Idaho 83843-2343, USA
E-mail: jshreeve@uidaho.edu
Supporting information for this article is available on the WWW under http://www.eurjic.org or from the author.

 © 2006 Wiley-VCH Verlag GmbH & Co. KGaA, Weinheim 

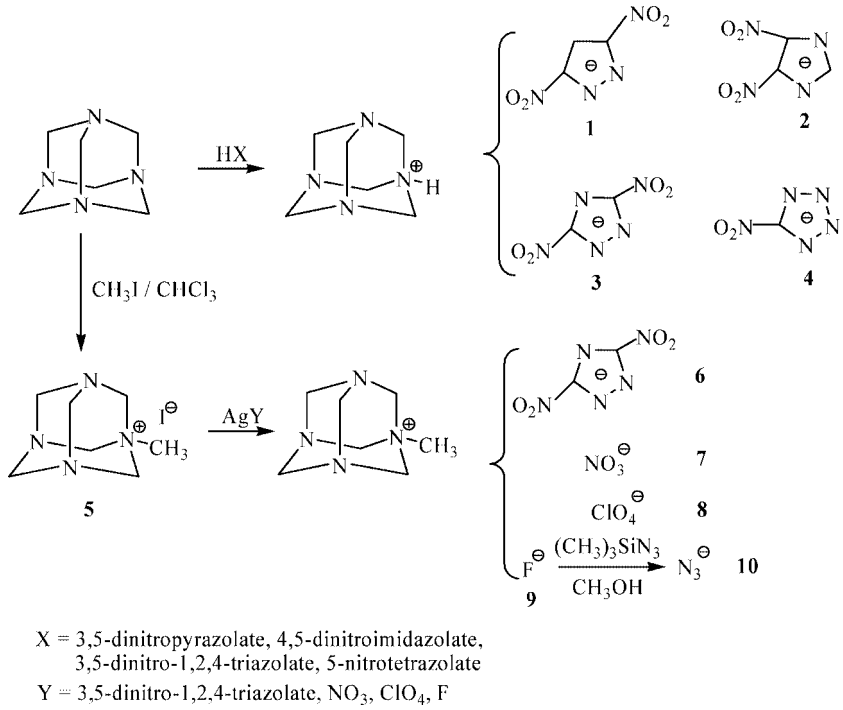


X = 3,5-dinitropyrazolate, 4,5-dinitroimidazolate, 3,5-dinitro-1,2,4-triazolate, 5-nitrotetrazolate
Y = 3,5-dinitro-1,2,4-triazolate, $NO_3$, $ClO_4$, F

Scheme 1. Syntheses of energetic hexamethylenetetrammonium salts.

based on energetic azolate anions (3,5-dinitropyrazolate, 4,5-dinitroimidazolate, 3,5-dinitro-1,2,4-triazolate and 5-nitrotetrazolate) and inorganic anions (nitrate, perchlorate and azide). Typical examples for preparation of such salts are given in Scheme 1. It was found that 3,5-dinitropyrazole, 4,5-dinitroimidazole, 3,5-dinitro-1,2,4-triazole and 5-nitrotetrazole can readily quaternize hexamethylenetetramine in methanol. The salts were formed in nearly quantitative yields and in high purity (**1**–**4**). However, although excess 4,5-dinitroimidazole (or 5-nitrotetrazole) was heated with hexamethylenetetramine, it was not possible to react more than one mol of either azole. This is in contrast with the diammonium salt which resulted when excess nitric acid was employed.[22]

*N*-(Methyl)hexamethylenetetrammonium iodide (**5**) was prepared in quantitative yield from hexamethylenetetramine and $CH_3I$ with chloroform as solvent based on a modified literature method.[23] Initially, the synthesis of *N*-(methyl)-hexamethylenetetrammonium 3,5-dinitro-1,2,4-triazolate was attempted by metathesis reactions of the corresponding iodide salt with sodium 3,5-dinitro-1,2,4-triazolate.[25] However, the reaction did not work well. Although silver 3,5-dinitro-1,2,4-triazolate[26] was water-insoluble, it had good solubility in acetonitrile. Therefore, metathesis of the quaternary iodide **5** with silver 3,5-dinitro-1,2,4-triazolate with $CH_3CN$ as solvent led to the formation of the new quaternary salt **6** in nearly quantitative yield and in high purity. The quaternary salts **7**–**9** were also obtained in high yield using a similar method as **6**, from compound **5** and $AgNO_3$, $AgClO_4$ and AgF with water as solvent. *N*-(Methyl)hexamethylenetetrammonium azide (**10**) was obtained from compound **9** and $Si(CH_3)_3N_3$ in methanol as solvent in high purity and in quantitative yield.[27]

The structure of compound **6** was determined by single-crystal X-ray diffraction, and the asymmetric unit is shown in Figure 1. This consists of two independent ion pairs.

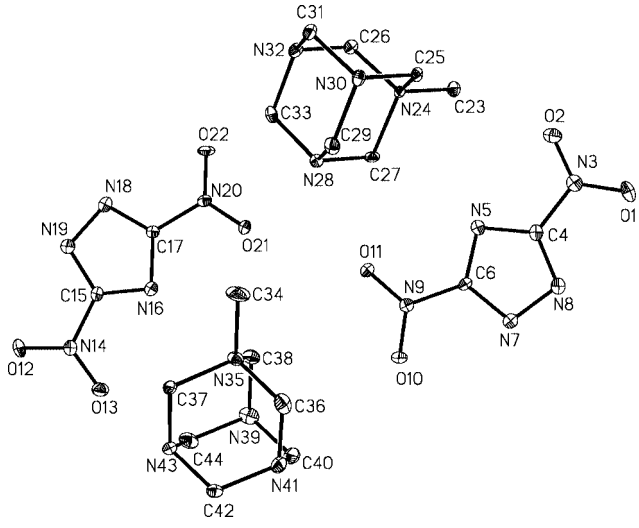


Figure 1. Thermal ellipsoid plot (30%) of the asymmetric unit of compound **6**. Hydrogen atoms omitted for clarity.

The most distinctive feature of this structure is the angle of the $NO_2$ groups to the triazolate anion which vary widely (O1–N3–O2, 2.7°; O10–N9–O11, 7.8°; O12–N14–O13, 7.5°; O21–N20–O22, 14°). These dinitrotriazolate anions pack in offset stacks parallel to the *b* axis, with an inter anion spacing of 3.11 Å (see supporting information). A summary of the crystal data for compound **6** is given in Table 1.

 © 2006 Wiley-VCH Verlag GmbH & Co. KGaA, Weinheim 

Table 1. Crystallographic data for compound **6**.

| Compound | **6** |
|---|---|
| Formula | $C_9H_{15}N_9O_4$ |
| Formula weight | 313.30 |
| Crystal system | monoclinic |
| Space group | *P*21/*n* |
| *a* [Å] | 20.499(6) |
| *b* [Å] | 6.2209(18) |
| *c* [Å] | 20.890(6) |
| *β* [°] | 102.924(6) |
| *V* [Å$^3$] | 2596.4(13) |
| *Z* | 8 |
| *T* [K] | 87(2) |
| *λ* [Å] | 0.71073 |
| $\rho_{calcd.}$ [Mg m$^3$] | 1.603 |
| *μ* [mm$^{-1}$] | 0.129 |
| *F*(000) | 1312 |
| Crystal size [mm] | 0.30 × 0.07 × 0.04 |
| *θ* range [°] | 1.00 to 25.25 |
| Index ranges | $-24 \le h \le 24$, $-7 \le k \le 7$, $-25 \le l \le 25$ |
| No. reflections collected | 37831 |
| No. indepentent reflections | 4691 [*R*(int) = 0.0624] |
| Data/restraints/parameters | 4691/0/400 |
| GOF | 1.083 |
| $R_1$ [$I > 2\sigma(I)$][a] | 0.0549 |
| $wR_2$ [$I > 2\sigma(I)$][a] | 0.1276 |
| Largest diff. peak, hole [e·Å$^{-3}$] | 0.419, –0.250 |

[a] $R_1 = \Sigma||F_o| - |F_c||/\Sigma|F_o|$; $wR_2 = \{\Sigma[w(F_o^2 - F_c^2)^2]/\Sigma[w(F_o^2)^2]\}^{1/2}$.

Comparison of the melting points of compounds **1**–**4**, and **6**, **7**, **8**, **10** (Table 2), clearly illustrates the influence of different anions, e.g., the melting point for compound **4** (m.p. 166 °C), which has 5-nitrotetrazolate as anion, is considerably lower than that of 3,5-dinitropyrazolate, 4,5-dinitroimidazolate and 3,5-dinitro-1,2,4-triazolate as anions in **1** (m.p. 180 °C), **2** (m.p. 183 °C) and **3** (m.p. 177 °C), respectively. The melting point for compound **6** (m.p. 170 °C), which has 3,5-dinitro-1,2,4-triazolate as anion, is lower or higher than that of nitrate, perchlorate or azide as anions, which melts at 194 °C, 200 °C, and 165 °C, respectively. It is also can be seen that compounds **3** and **6** have the same anion (3,5-dinitro-1,2,4-triazolate), for **6**, which has a *N*-methyl group on the cation ring, its melting point and decomposition temperature (**6**, $T_d$ = 202 °C) are lower and higher than that of compound **3** ($T_d$ = 182 °C), respectively.

Density, oxygen coefficient, and enthalpy of formation are important characteristics of energetic compounds, and are governed by their molecular structures. Increasing the number of nitrogen atoms in a heterocycle results in a considerable gain in the heat of formation.[5] Density, oxygen coefficients, nitrogen content and the calculated heats of formation for the energetic salts are listed in Table 2. Densities for all of the compounds exceed 1.35 g cm$^{-3}$, and compound **3** has the highest density (1.72 g cm$^{-3}$). The oxygen coefficient (*α*), which is defined as $\alpha = c/(2a + b/2)$ for the molecular formula $C_aH_bO_cN_d$, is calculated by a literature method.[28a] Incorporation of a nitro group can substantially improve the oxygen balance of the corresponding compounds, and eventually results in higher exothermicities

Table 2. Phase transition, decomposition temperatures, densities, oxygen coefficient (*α*), nitrogen content (N), and thermochemical results for synthesized salts.

| Compd. | $T_m$[a] [°C] | $T_d$[b] [°C] | *d*[c] [g cm$^{-3}$] | N [%] | *α*[d] [%] | $-\Delta H_L$[e] [kJ·mol$^{-1}$] | $\Delta_f H_m°$[f] [kJ·mol$^{-1}$] |
|---|---|---|---|---|---|---|---|
| **1** | 180 | 184 | 1.56 | 37.6 | 16 | 452.7 | – |
| **2** | 183 | 183 | 1.41 | 37.6 | 16 | 441.3 | – |
| **3** | 177 | 182 | 1.72 | 42.1 | 18 | 463.7 | 268.7 |
| **4** | 166 | 169 | 1.48 | 49.4 | 10 | 464.7 | 435.3 |
| **6** | 170 | 202 | 1.45 | 40.2 | 16 | 438.9 | 250.7 |
| **7** | 194 | 196 | 1.42 | 32.2 | 14 | 479.2 | –30.6 |
| **8** | 200 | 205 | 1.47 | 22.0 | – | 464.2 | 14.5 |
| **10** | 165 | 176 | 1.35 | 49.7 | 0 | 484.9 | 468.8 |
| **11**[g] | 160 | – | 1.57 | – | – | – | –388.3 |

[a] Melting point ($T_m$). [b] Thermal degradation ($T_d$). [c] Measured density using gas pycnometer at 25 °C. [d] For $C_aH_bO_cN_d$: $\alpha = 100c/(2a + b/2)$. [e] Lattice energy. [f] Calculated molar enthalpy of formation. [g] Hexamethylenetetrammonium dinitrate, ref.[22].

of the combustion and detonation processes. The oxygen coefficient values of C,H,O,N-containing energetic compounds belong to the classes of fuels ($\alpha < 0.4$), explosives ($0.4 \le \alpha \le 1.0$), and oxidants ($\alpha > 1.0$).[28b] The oxygen coefficients for the new salts are between 0.10–0.18 (Table 2), which fall at < 0.4 among the majority of the known energetic compounds.[28b] The calculated nitrogen contents for the new salts are between 22–50% (Table 2).

The standard molar enthalpy of formation ($\Delta_f H_m°$) for the salts **3**, **4**, **6**–**8**, **10** were calculated by the following Born–Haber energy cycles (Scheme 2). Calculations were made with the Gaussian03 (Revision D.01) suite of programs.[29] The geometric optimization of the structures and frequency calculations were performed at (DFT)[30,31]/B3LYP[32] level of theory using the 6-31+G** basis set. Single-point energies were calculated at the MP2/6-311++G** level.[33,34] According to the previous studies, the computed harmonic vibrational frequencies were scaled uniformly by a factor of 0.96 to take into account the systematic overestimation of these frequencies in the B3LYP/6-31+G** calculations.[35] Based on this data, the heats of formation of the anions and cations were calculated and combined with the lattice energy of the salts to give the heats of formation of the salts. Because the most efficient computational procedure for finding accurate heats of formation is based on isodesmic (bond type conserving) reactions,[36] in the present case, the reactions used to calculate the heat of formation of both cations and anions are given in Scheme 3.

The heat of formation of 3,5-dinitrotriazole was calculated by averaging its actual resonance hybrids shown in Equations (5) and (6) in Scheme 3. The lattice potential energy $\Delta H_L$ for $M_pX_q$ was calculated using the relationship provided by Jenkins (equation **A**),[37] where $n_M$ and $n_X$ depend on the nature of the ions $M_p^+$ and $Xq^-$, respectively, and is equal to

$$\Delta H_L = U_{POT} + [p(n_M/2 - 2) + q(n_X/2 - 2)]RT \quad \textbf{(A)}$$

with $n$ = 3 for monatomic ions, 5 for linear polyatomic ions, and 6 for nonlinear polyatomic ions.

 © 2006 Wiley-VCH Verlag GmbH & Co. KGaA, Weinheim 

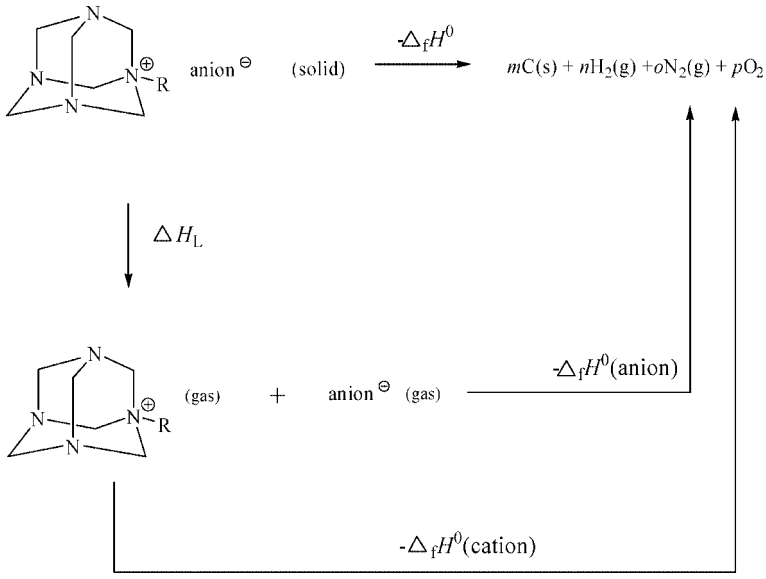


Scheme 2. General Born–Haber cycle for the formation of hexamethylenetetrammonium salts. For **3:** R = H, anion = 3,5-dinitrotriazolate, $m$ = 8, $n$ = 6.5, $o$ = 4.5, $p$ = 2, $q$ = 0; **4:** R = H, anion = 5-nitrotetrazolate, $m$ = 7, $n$ = 6.5, $o$ = 4.5, $p$ = 1, $q$ = 0; **6:** R = $CH_3$, anion = 3,5-dinitrotriazolate, $m$ = 9, $n$ = 7.5, $o$ = 4.5, $p$ = 2, $q$ = 0; **7:** R = $CH_3$, anion = $NO_3^-$, $m$ = 7, $n$ = 7.5, $o$ = 2.5, $p$ = 1.5, $q$ = 0; **8:** R = $CH_3$, anion = $ClO_4^-$, $m$ = 7, $n$ = 7.5, $o$ = 2, $p$ = 2, $q$ = 0.5; **10:** R = $CH_3$, anion = $N_3^-$, $m$ = 7, $n$ = 7.5, $o$ = 3.5, $p$ = 0, $q$ = 0.

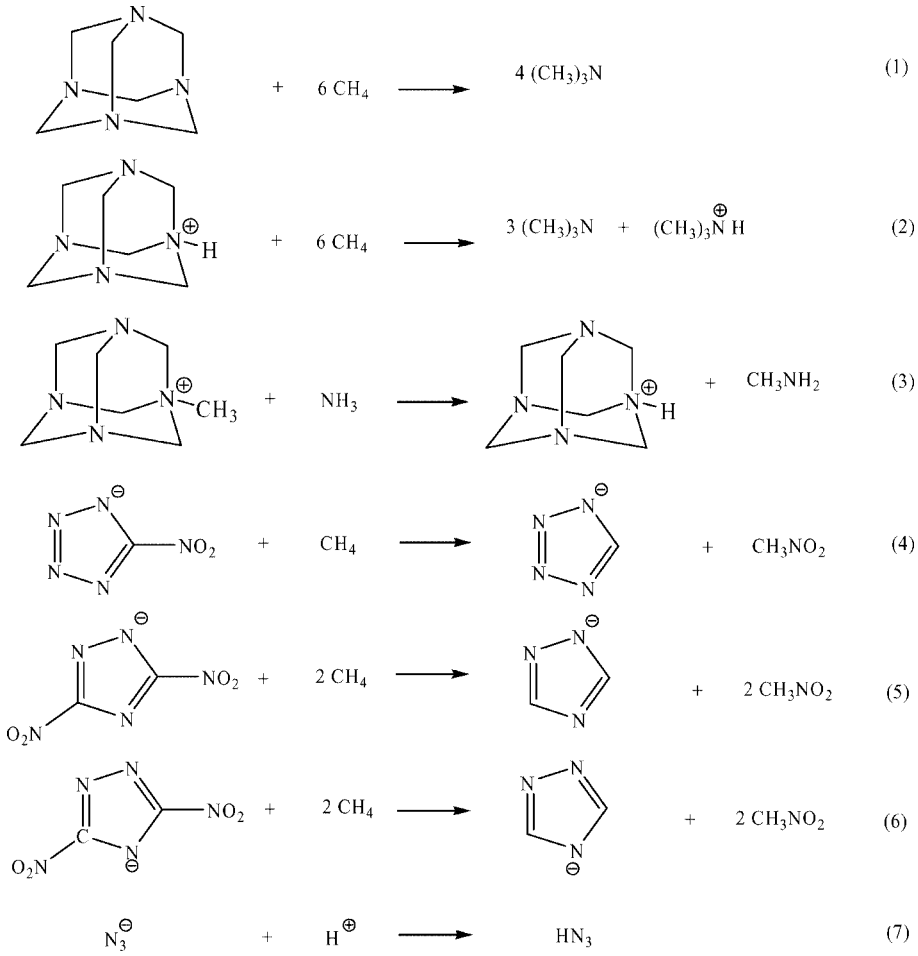


Scheme 3. Isodesmic reactions for calculating the heats of formation of both cations and anions.

 © 2006 Wiley-VCH Verlag GmbH & Co. KGaA, Weinheim 

The equation for lattice potential energy $U_{POT}$ (equation **B**) has the form

$$U_{POT}\ [kJ{\cdot}mol^{-1}] = \gamma\ (\rho_m/M_m)^{1/3} + \delta \qquad (\mathbf{B})$$

where $\rho_m$ [g cm$^{-3}$] is the density, $M_m$ is the chemical formula mass of the ionic material [g or Mg]; the coefficients $\gamma$ [kJ·mol$^{-1}$ cm] and $\delta$ [kJ·mol$^{-1}$] are equal to 8375.6 and –178.8, respectively. Comparison of the data for compounds **3** and **4** reveals that $\Delta_f H_m°$ for **4** (+435.3 kJ·mol$^{-1}$), which has 5-nitrotetrazolate as the anion, is considerably higher than that for the 3,5-dinitro-1,2,4-triazolate anion and **3** (+268.7 kJ·mol$^{-1}$). From the $\Delta_f H_m°$ values for **6**, **7**, **8**, **10** it can be seen that for the same cation, the heat of formation of the compound with azide as anion, is considerably higher than those of corresponding compounds with 3,5-dinitro-1,2,4-triazolate, perchlorate or nitrate as anions, which varies as **10** (azide) > **6** (3,5-dinitro-1,2,4-triazolate) > **8** (perchlorate) > **7** (nitrate) (+468.8, +250.7, +14.5, –30.6 kJ·mol$^{-1}$), respectively.

In conclusion, we have synthesized new hexamethylenetetrammonium salts composed of the energetic anions 3,5-dinitropyrazolate, 4,5-dinitroimidazolate, 3,5-dinitro-1,2,4-triazolate, 5-nitrotetrazolate, perchlorate, nitrate and azide. Most of the new salts exhibit valuable physical properties, including relatively high densities (>1.35 g cm$^{-3}$) and high positive heats of formation.

## Experimental Section

**Caution:** Although we have not experienced any problems in handling these compounds, based on the high positive heats of formation, all materials should be handled with extreme care.

**General Methods:** $^1$H and $^{13}$C NMR spectra were recorded with a 300-MHz nuclear magnetic resonance spectrometer operating at 300.13, and 75.48 MHz, respectively. Chemical shifts were reported relative to $Me_4Si$. The melting and decomposition points were recorded with a differential scanning calorimeter and a thermogravimetric analyzer at a scan rate of 10 °C min$^{-1}$, respectively. IR spectra were recorded using KBr pellets for solids. Densities of solid salts were measured at room temperature using a Micromeritics Accupyc 1330 gas pycnometer. Elemental analyses were measured with a CE-440 elemental analyzer.

3,5-Dinitropyrazole,[42] 4,5-dinitroimidazole,[43] 3,5-dinitro-1,2,4-triazolate[25] 5-nitrotetrazole[44] and silver 3,5-dinitro-1,2,4-triazolate[26] were synthesized according to literature procedures.

**X-ray Crystallographic Studies:** Crystals of compound **6** were removed from the flask and covered with a layer of hydrocarbon oil. A suitable crystal was selected, attached to a glass fiber and placed in the low-temperature nitrogen stream.[38] Data for **6** were collected at 87(2) K with a Bruker/Siemens SMART APEX instrument (Mo-$K_\alpha$ radiation, $\lambda$ = 0.71073 Å) equipped with a Cryocool NeverIce low-temperature device. Data were measured using $\omega$ scans of 0.3° per frame for 60 s, and a full sphere of data was collected. A total of 2400 frames were collected with a final resolution of 0.83 Å. The first 50 frames were recollected at the end of data collection to monitor for decay. Cell parameters were retrieved using SMART[39] software and refined using SAINTPlus[40] on all observed reflections. Data reduction and correction for Lp and decay were performed using the SAINTPlus software. Absorption corrections were applied using SADABS.[41a] The structure was solved by direct methods and refined by least-squares method on $F^2$ using the SHELXTL program package.[41b] The structure was solved in the space group $P21/n$ (#14) by analysis of systematic absences. All non-hydrogen atoms were refined anisotropically. No decomposition was observed during data collection.

CCDC-294742 (for **6**) contains the complete set of crystallographic data for this paper. These data can be obtained free of charge from The Cambridge Crystallographic Data Centre via www.ccdc.cam.ac.uk/data_request/cif.

**Supporting Information** (see footnote on the first page of this article): Ball and stick packing diagrams of **6** and a table with hydrogen bonds for **6**.

**Hexamethylenetetrammonium 3,5-Dinitropyrazolate (1):** A dry, nitrogen-filled Schlenk glass tube was charged with hexamethylenetetramine (0.140 g, 1.0 mmol), dry methanol (5 mL), and 3,5-dinitropyrazole (0.158 g, 1.0 mmol). The mixture was stirred 10 h at room temperature. The solvent was removed under vacuum overnight to leave a white solid **1**: 97% yield (0.29 g), m.p. 180 °C. IR (KBr): $\tilde{\nu}$ = 3151, 2949, 2899, 2253, 1540, 1487, 1438, 1346, 1315, 1262, 1224, 1161, 1066, 1016, 982, 871, 823, 748, 686, 662 cm$^{-1}$. $^1$H NMR ([D$_6$]DMSO): $\delta$ = 4.82 (s, 12 H), 7.29 (s, 1 H) ppm. $^{13}$C NMR ([D$_6$]DMSO): $\delta$ = 157.24, 99.16, 72.17 ppm. $C_9H_{14}N_8O_4{\cdot}0.5H_2O$ (307.11): calcd. C 35.18, H 4.88, N 36.48; found C 35.52, H 4.52, N 36.89.

**Hexamethylenetetrammonium 4,5-Dinitroimidazolate (2):** A dry, nitrogen-filled Schlenk glass tube was charged with hexamethylenetetramine (0.140 g, 1.0 mmol), dry methanol (5 mL), and 4,5-dinitroimidazole (0.158 g, 1.0 mmol). The mixture was stirred for 10 h at room temperature. The solvent was taken off under vacuum overnight to give a yellow solid **2**: 97% yield (0.29 g), m.p. 183 °C. IR (KBr): $\tilde{\nu}$ = 3106, 2937, 2777, 2555, 2485, 1760, 1535, 1506, 1462, 1351, 1311, 1261, 1219, 1184, 1098, 1063, 985, 817, 751, 659 cm$^{-1}$. $^1$H NMR ([D$_6$]DMSO): $\delta$ = 4.83 (s, 12 H), 6.96 (s, 1 H) ppm. $^{13}$C NMR ([D$_6$]DMSO): $\delta$ = 141.69, 140.77, 72.70 ppm. $C_9H_{14}N_8O_4$ (298.11): calcd. C 36.24, H 4.73, N 37.57; found C 35.88, H 4.56, N 37.11.

**Hexamethylenetetrammonium 3,5-Dinitro-1,2,4-triazolate (3):** Compound **3** was prepared by a similar procedure as above, from hexamethylenetetramine (0.140 g, 1.0 mmol) and 3,5-dinitro-1,2,4-triazole (0.159 g, 1.0 mmol) to form a white solid in 98% yield, m.p. 177 °C. IR (KBr): $\tilde{\nu}$ = 3092, 2967, 2679, 2390, 1549, 1489, 1384, 1350, 1285, 1265, 1206, 1101, 1010, 977, 840, 815, 748, 650 cm$^{-1}$. $^1$H NMR ([D$_6$]DMSO): $\delta$ = 4.84 (s, 12 H) ppm. $^{13}$C NMR ([D$_6$]-DMSO): $\delta$ = 163.75, 72.07 ppm. $C_8H_{13}N_9O_4$ (299.11): calcd. C 32.11, H 4.38, N 42.13; found C 31.79, H 4.17, N 41.88.

**Hexamethylenetetrammonium 5-Nitrotetrazolate (4):** Compound **4** was prepared by a similar procedure as above, from hexamethylenetetramine (0.140 g, 1.0 mmol) and 5-nitrotetrazole (0.115 g, 1.0 mmol) to form a white solid in 98% yield, m.p. 166 °C. IR (KBr): $\tilde{\nu}$ = 2953, 2813, 2771, 2548, 2410, 2133, 1541, 1466, 1413, 1364, 1314, 1267, 1216, 1143, 1011, 818, 745, 654 cm$^{-1}$. $^1$H NMR ([D$_6$]DMSO): $\delta$ = 4.84 (s, 12 H) ppm. $^{13}$C NMR ([D$_6$]DMSO): $\delta$ = 170.27, 72.57 ppm. $C_7H_{13}N_9O_2{\cdot}H_2O$ (273.12): calcd. C 30.77, H 5.49, N 46.15; found C 30.99, H 4.66, N 46.68.

***N*-Methylhexamethylenetetrammonium Iodide (5):** Compound **5** was prepared by a minor modification of the previous synthesis,[23] from hexamethylenetetramine and $CH_3I$ at room temperature, using chloroform as solvent to give a white solid **5** in quantitative yield: m.p. 202 °C. IR (KBr): $\tilde{\nu}$ = 2955, 1736, 1462, 1431, 1382, 1312, 1253, 1150, 1043, 1018, 993, 958, 816, 712, 648 cm$^{-1}$. $^1$H NMR

 © 2006 Wiley-VCH Verlag GmbH & Co. KGaA, Weinheim 

([$D_6$]DMSO): $\delta$ = 2.49 (s, 3 H), 4.41–4.62 (q, $^2J$ = 12.0 Hz, 6 H), 5.09 (s, 6 H) ppm. $^{13}$C NMR ([$D_6$]DMSO): $\delta$ = 80.81, 71.22, 43.70 ppm.

**General Procedure for the Preparation of Salts from 5**

***N*-Methylhexamethylenetetrammonium 3,5-Dinitro-1,2,4-triazolate (6):** To a magnetically stirred solution of **5** (0.282 g, 1.0 mmol) in $CH_3CN$ (5 mL) was added silver 3,5-dinitro-1,2,4-triazolate (0.266 g, 1.0 mmol). After 2 h at room temperature, silver iodide was removed by filtration. The filtrate was dried in vacuo to give a yellow solid (0.30 g, 96% yield), m.p. 170 °C. IR (KBr): $\tilde{\nu}$ = 2960, 2713, 2434, 2139, 1535, 1483, 1463, 1375, 1335, 1244, 1150, 1097, 1039, 1015, 990, 956, 823, 648 cm$^{-1}$. $^1$H NMR ([$D_6$]DMSO): $\delta$ = 2.47 (s, 3 H), 4.40–4.64 (q, $^2J$ = 12.0 Hz, 6 H), 5.04 (s, 6 H) ppm. $^{13}$C NMR ([$D_6$]DMSO): $\delta$ = 164.43, 80.93, 71.27, 43.76 ppm. $C_9H_{15}N_9O_4$ (313.12): calcd. C 34.51, H 4.83, N 40.24; found C 34.53, H 4.58, N 40.14.

***N*-Methylhexamethylenetetrammonium Nitrate (7):** Compound **7** was prepared by a similar procedure as compound **6**, from **5** (0.282 g, 1.0 mmol) and silver nitrate (0.170 g, 1.0 mmol) using $H_2O$ as solvent to form a white solid in 98% yield, m.p. 194 °C. IR (KBr): $\tilde{\nu}$ = 2959, 2712, 2152, 2059, 1742, 1634, 1470, 1376, 1246, 1145,1043, 993, 957, 817, 785, 713, 650 cm$^{-1}$. $^1$H NMR ([$D_6$]-DMSO): $\delta$ = 2.47 (s, 3 H), 4.40–4.64 (q, $^2J$ = 12.0 Hz, 6 H), 5.05 (s, 6 H) ppm. $^{13}$C NMR ([$D_6$]DMSO): $\delta$ = 80.88, 71.24, 43.70 ppm. $C_7H_{15}N_5O_3$ (217.12): calcd. C 38.70, H 6.96, N 32.24; found C 38.22, H 6.85, N 32.10.

***N*-Methylhexamethylenetetrammonium Perchlorate (8):** Compound **8** was prepared by a similar procedure as compound **6**, from **5** (0.282 g, 1.0 mmol) and silver perchlorate (0.208 g, 1.0 mmol) using $H_2O$ as solvent to give a white solid in 98% yield, m.p. 200 °C. IR (KBr): $\tilde{\nu}$ = 3012, 2972, 2453, 2178, 1634, 1469, 1381, 1267, 1247, 1147, 1086, 992, 952, 821, 785, 650, 619 cm$^{-1}$. $^1$H NMR ($D_2O$): $\delta$ = 2.65 (s, 3 H), 4.55–4.75 (q, $^2J$ = 12.0 Hz, 6 H), 5.09 (s, 6 H) ppm. $^{13}$C NMR ($D_2O$): $\delta$ = 81.00, 70.95, 44.11 ppm. $C_7H_{15}N_4ClO_4$ (254.08): calcd. C 33.01, H 5.94, N 22.00; found C 33.10, H 5.98, N 21.88.

***N*-Methylhexamethylenetetrammonium Fluoride (9):** Compound **9** was prepared by a similar procedure as compound **6**, from **5** (0.282 g, 1.0 mmol) and silver fluoride (0.127 g, 1.0 mmol) using $H_2O$ as solvent to form a white solid in 98% yield, m.p. 68 °C. IR (KBr): $\tilde{\nu}$ = 3397, 2958, 1666, 1457, 1389, 1246, 1148, 1011, 959, 933, 816, 648 cm$^{-1}$. $^1$H NMR ($D_2O$): $\delta$ = 2.65 (s, 3 H), 4.55–4.75 (q, $^2J$ = 12.0 Hz, 6 H), 5.08 (s, 6 H) ppm. $^{13}$C NMR ($D_2O$): $\delta$ = 80.98, 70.93, 44.08 ppm. $^{19}$F NMR ($D_2O$): $\delta$ = –122.35 (s, 1F) ppm. $C_7H_{15}N_4F{\cdot}0.8H_2O$ (188.53): calcd. C 44.58, H 8.82, N 29.72; found C 44.60, H 8.88, N 30.03.

***N*-Methylhexamethylenetetrammonium Azide (10):** Compound **10** was prepared by a modified literature method,[23,27] from **9** (0.174 g, 1.0 mmol) and $(CH_3)_3SiN_3$ (0.173 g, 1.5 mmol) using dry methanol as solvent, stirred at room temperature for 5 h to leave a white solid in quantitative yield, m.p. 165 °C. IR (KBr): $\tilde{\nu}$ = 3443, 3282, 2956, 2890, 2446, 2293, 2030, 1627, 1460, 1386, 1315, 1248, 1147, 1043, 993, 956, 817, 713, 648 cm$^{-1}$. $^1$H NMR ($D_2O$): $\delta$ = 2.66 (s, 3 H), 4.56–4.76 (q, $^2J$ = 12.0 Hz, 6 H), 5.10 (s, 6 H) ppm. $^{13}$C NMR ($D_2O$): $\delta$ = 81.00, 70.95, 44.09 ppm.

## Acknowledgments

The authors gratefully acknowledge the support of AFOSR (F49620-03-1-0209), NSF (CHE0315275), and ONR (N00014-02-1-0600). We appreciate the high quality assistance of Drs. Gary Knerr and Alex Blumenfeld for mass spectra and NMR analyses, respectively. We are grateful to Drs. Jerry A. Boatz and Gregory W. Drake for many helpful discussions. The Bruker (Siemens) SMART APEX diffraction facility was established at the University of Idaho with the assistance of the NSF-EPSCoR program and the M. J. Murdock Charitable Trust, Vancouver, WA.

[1] M. X. Zhang, P. E. Eaton, R. D. Gilardi, *Angew. Chem. Int. Ed.* **2000**, *39*, 401–404.
[2] a) D. E. Chavez, M. A. Hiskey, R. D. Gilardi, *Angew. Chem. Int. Ed.* **2000**, *39*, 1791–1793; b) D. E. Chavez, M. A. Hiskey, R. D. Gilardi, *Org. Lett.* **2004**, *6*, 2889–2891.
[3] a) A. Hammerl, T. M. Klapötke, M. Warchhold, *Inorg. Chem.* **2001**, *40*, 3570–3575; b) J. Geith, T. M. Klapötke, J. Weigand, G. Holl, *Propellants Explos. Pyrotech.* **2004**, *29*, 3–8; c) A. Hammerl, G. Holl, M. Kaiser, T. M. Klapötke, P. Mayer, H. Nöth, H. Piotrowski, M. Warchhold, *Eur. J. Inorg. Chem.* **2002**, 834–845; d) T. M. Klapötke, P. Mayer, A. Schulz, J. J. Weigand, *Propellants Explos. Pyrotech.* **2004**, *29*, 325–332.
[4] a) Y. Ou, B. Chen, J. Li, H. Jia, *Heterocycles* **1994**, *38*, 1651–1664; b) K. Y. Lee, J. E. Kennedy, B. W. Asay, S. F. Son, E. S. Martin, AIP Conference Proceedings, Springer-Verlag: New York, **2004**, *706* (Shock Compression of Condensed Matter, 2003, Part 2), 855–858; c) J. C. Bottaro, R. J. Schmitt, M. A. Petrie, P. E. Penwell, US Patent 6,255,512, Jul. 3, **2001**; d) M. S. Pevzner, *Russ. Chem. J.* **1997**, *41*, 73–81; e) O. P. Shitov, V. L. Korolev, V. S. Bogdanov, V. A. Tartakovsky, *Russ. Chem. Bull.* **2003**, *52*, 695–699.
[5] V. A. Ostrovskii, M. S. Pevzner, T. P. Kofman, I. V. Tselinskii, *Targets in Heterocycl. Systems* **1999**, *3*, 467–526.
[6] J. Köhler, R. Meyer, *Explosivstoffe*, 9th ed., Wiley-VCH, Weinheim, **1998**.
[7] a) A. Hammerl, T. M. Klapötke, M. Warchhold, *Propellants Explos. Pyrotech.* **2003**, *28*, 163–173; b) A. Hammerl, T. M. Klapötke, P. Mayer, J. J. Weigand, G. Holl, *Propellants Explos. Pyrotech.* **2005**, *30*, 17–26.
[8] a) G. Drake, T. Hawkins, A. Brand, L. Hall, M. Mckay, A. Vij, I. Ismail, *Propellants Explos. Pyrotech.* **2003**, *28*, 174–180; b) G. Drake, US Patent 6,509,473, Jan. 21, **2003**; c) G. Drake, T. Hawkins, AFOSR Ionic Liquids Workshop, Dulles, VA. October **2002**; d) G. Drake, AFOSR Ionic Liquids Workshop, Aberdeen, MD. September **2003**; e) G. Kaplan, G. Drake, K. Tollison, L. Hall, T. Hawkins, *J. Heterocycl. Chem.* **2005**, *42*, 19–27; f) G. W. Drake, T. M. Hawkins, J. Boatz, L. Hall, A. Vij, *Propellants Explos. Pyrotech.* **2005**, *30*, 156–163; g) R. D. Rogers, *Ionic Liquids IIIA: Fundamentals, Progress, Challenges, and Opportunities: Properties and Structure*, ACS Symposium Series, American Chemical Society: Washington, DC, **2005**.
[9] a) H. Xue, Y. Gao, B. Twamley, J. M. Shreeve, *Chem. Mater.* **2005**, *17*, 191–198; b) H. Xue, S. W. Arritt, B. Twamley, J. M. Shreeve, *Inorg. Chem.* **2004**, *43*, 7972–7977; c) Y. Gao, S. W. Arritt, B. Twamley, J. M. Shreeve, *Inorg. Chem.* **2005**, *44*, 1704–1712; d) C. F. Ye, J. M. Shreeve, *Chem. Commun.* **2005**, 2570–2572; e) H. Xue, Y. Gao, B. Twamley, J. M. Shreeve, *Inorg. Chem.* **2005**, *44*, 5068–5072; f) H. Xue, B. Twamley, J. M. Shreeve, *J. Mater. Chem.* **2005**, *15*, 3459–3465; g) H. Xue, B. Twamley, J. M. Shreeve, *Adv. Mater.* **2005**, *17*, 2142–2146; h) H. Xue, B. Twamley, J. M. Shreeve, *Inorg. Chem.* **2005**, *44*, 7009–7013; i) C.-M. Jin, C. F. Ye, C. Piekarski, B. Twamley, J. M. Shreeve, *Eur. J. Inorg. Chem.* **2005**, *18*, 3760–3767; j) K. Muralidharan, B. A. Omotowa, B. Twamley, C. Piekarski, J. M. Shreeve, *Chem. Commun.* **2005**, 5193–5195; k) E. P. Kirpichev, Yu. I. Rubtsov, *Zh. Fiz. Khim.* **1969**, *43*, 2025–2028.
[10] a) K. O. Christe, W. W. Wilson, M. A. Petrie, H. H. Michels, J. C. Bottaro, R. Gilardi, *Inorg. Chem.* **1996**, *35*, 5068–5071; b) M. A. Petrie, J. A. Sheehy, J. A. Boatz, G. Rasul, G. K. Surya Prakash, G. A. Olah, K. O. Christe, *J. Am. Chem. Soc.* **1997**, *119*, 8802–8808; c) J. C. Bottaro, P. E. Penwell, R. J. Schmitt, *J. Am. Chem. Soc.* **1997**, *119*, 9405–9410; d) R. Gil-

 © 2006 Wiley-VCH Verlag GmbH & Co. KGaA, Weinheim 

ardi, J. Flippen-Anderson, C. George, R. J. Butcher, *J. Am. Chem. Soc.* **1997**, *119*, 9411–9416; e) T. M. Klapötke, P. Mayer, A. Schulz, J. J. Weigand, *J. Am. Chem. Soc.* **2005**, *127*, 2032–2033; f) D. E. G. Jones, Q. S. M. Kwok, M. Vachon, C. Badeen, W. Ridley, *Propellants Explos. Pyrotech.* **2005**, *30*, 140–147; g) J. C. Gálvez-Ruiz, G. Holl, K. Karaghiosoff, T. M. Klapötke, K. Löhnwitz, P. Mayer, H. Nöth, K. Polborn, C. J. Rohbogner, M. Suter, J. J. Weigand, *Inorg. Chem.* **2005**, *44*, 4237–4253; h) M. W. Schmidt, M. S. Gordon, J. A. Boatz, *J. Phys. Chem. A* **2005**, *109*, 7285–7295.

[11] W. Fraenk, T. Habereder, A. Hammerl, T. M. Klapötke, B. Krumm, P. Mayer, H. Nöth, M. Warchhold, *Inorg. Chem.* **2001**, *40*, 1334–1340.

[12] D. W. Armstrong, L. K. Zhang, L. F. He, M. L. Gross, *Anal. Chem.* **2001**, *73*, 3679–3686.

[13] J. Pernak, I. Goc, *Pol. J. Chem.* **2003**, *77*, 975–984.

[14] W. Ogihara, M. Yoshizawa, H. Ohno, *Chem. Lett.* **2004**, *33*, 1022–1023.

[15] a) A. R. Katritzky, S. Singh, K. Kirichenko, J. D. Holbrey, M. Smiglak, W. M. Reichert, R. D. Rogers, *Chem. Commun.* **2005**, 868–870; b) A. Hammerl, M. A. Hiskey, G. Holl, T. M. Klapötke, K. Polborn, J. Stierstorfer, J. J. Weigand, *Chem. Mater.* **2005**, *17*, 3784–3793.

[16] M. Egashira, B. Scrosati, M. Armand, S. Béranger, C. Michot, *Electrochem. Solid-State Lett.* **2003**, *6*, A71–A73.

[17] A. Hammerl, G. Holl, T. M. Klapötke, P. Mayer, H. Nöth, H. Piotrowski, M. Warchhold, *Eur. J. Inorg. Chem.* **2002**, 834–845.

[18] G. Singh, I. P. S. Kapoor, S. P. Felix, *Propellants Explos. Pyrotech.* **2002**, *27*, 16–22.

[19] a) W. E. Bachmann, J. C. Sheehan, *J. Am. Chem. Soc.* **1949**, *71*, 1812; b) W. E. Bachmann, W. J. Horton, E. L. Jenner, L. B. Scott, *J. Am. Chem. Soc.* **1951**, *73*, 2769; c) W. E. Bachmann, E. L. Jenner, *J. Am. Chem. Soc.* **1951**, *73*, 2773.

[20] a) A. P. Cooney, M. R. Crampton, M. Jones, *J. Heterocycl. Chem.* **1987**, *24*, 1163; b) M. R. Crampton, M. Jones, J. K. Scranage, P. Golding, *Tetrahedron* **1988**, *44*, 1679.

[21] H. P. Orem, D. R. Hart, J. E. Hill, US Patent 3,936,451, Feb. 3, **1976**.

[22] J. Vágenknecht, S. Zeman, *J. Hazard. Mater.* **2005**, *A119*, 1–11.

[23] H. G. Ang, W. Fraenk, K. Karaghiosoff, T. M. Klapötke, H. Nöth, J. Sprott, M. Suter, M. Vogt, M. Warchhold, *Z. Anorg. Allg. Chem.* **2002**, *628*, 2901–2906.

[24] V. A. Ostrovskii, G. I. Koldobskii, N. P. Shirokova, V. S. Poplavskii, *Khim. Geterotsikl. Soedin.* **1981**, *4*, 559–562.

[25] T. P. Kofman, E. A. Paketina, *Russ. J. Org. Chem.* **1997**, *33*, 1125–1132.

[26] H. P. Burchfield, D. K. Gullstrom, U. S. Pat. 3,054,800, Sept. 18, **1962**.

[27] K. O. Christe, W. W. Wilson, R. Bau, S. W. Bunte, *J. Am. Chem. Soc.* **1992**, *114*, 3411–3414.

[28] a) A. R. Martin, H. J. Yallop, *Trans. Faraday Soc.* **1958**, *54*, 257–267; b) I. M. Krukovskii, M. S. Molchanova, A. V. Evtushenko, V. A. Shlyapochnikov, *Russ. Chem. Bull.* **1998**, *47*, 1266–1273.

[29] M. J. Frisch, G. W. Trucks, H. B. Schlegel, G. E. Scuseria, M. A. Robb, J. R. Cheeseman, J. A. Montgomery Jr, T. Vreven, K. N. Kudin, J. C. Burant, J. M. Millam, S. S. Iyengar, J. Tomasi, V. Barone, B. Mennucci, M. Cossi, G. Scalmani, N. Rega, G. A. Petersson, H. Nakatsuji, M. Hada, M. Ehara, K. Toyota, R. Fukuda, J. Hasegawa, M. Ishida, T. Nakajima, Y. Honda, O. Kitao, H. Nakai, M. Klene, X. Li, J. E. Knox, H. P. Hratchian, J. B. Cross, V. Bakken, C. Adamo, J. Jaramillo, R. Gomperts, R. E. Stratmann, O. Yazyev, A. J. Austin, R. Cammi, C. Pomelli, J. W. Ochterski, P. Y. Ayala, K. Morokuma, G. A. Voth, P. Salvador, J. J. Dannenberg, V. G. Zakrzewski, S. Dapprich, A. D. Daniels, M. C. Strain, O. Farkas, D. K. Malick, A. D. Rabuck, K. Raghavachari, J. B. Foresman, J. V. Ortiz, Q. Cui, A. G. Baboul, S. Clifford, J. Cioslowski, B. B. Stefanov, G. Liu, A. Liashenko, P. Piskorz, I. Komaromi, R. L. Martin, D. J. Fox, T. Keith, M. A. Al-Laham, C. Y. Peng, A. Nanayakkara, M. Challacombe, P. M. W. Gill, B. Johnson, W. Chen, M. W. Wong, C. Gonzalez, and J. A. Pople, Gaussian, Inc., Wallingford CT, **2004**.

[30] R. G. Parr, W. Yang, *Density Functional Theory of Atoms and Molecules*; Oxford University Press: New York, **1989**.

[31] W. Koch, M. C. Holthausen, *A Chemist's View of Density Functional Theory*; Wiley-VCH: Weinheim, Germany, **2000**.

[32] A. D. Becke, *J. Chem. Phys.* **1993**, *98*, 5648–5652.

[33] C. M. Møller, M. S. Plesset, *Phys. Rev.* **1934**, *46*, 618–622.

[34] J. A. Pople, J. S. Binkely, R. Seeger, *Int. J. Quantum Chem.* **1976**, *10*, 1–19.

[35] A. P. Scott, L. Radom, *J. Phys. Chem.* **1996**, *100*, 16502–16513.

[36] W. J. Hehre, R. Ditchfield, L. Radom, J. A. Pople, *J. Am. Chem. Soc.* **1970**, *92*, 4796–4801.

[37] H. D. B. Jenkins, D. Tudeal, L. Glasser, *Inorg. Chem.* **2002**, *41*, 2364–2367.

[38] H. Hope, *Prog. Inorg. Chem.* **1994**, *41*, 1–3.

[39] *SMART*: *version 5.625, Bruker Molecular Analysis Research Tool*, Bruker AXS: Madison, WI, **2001**.

[40] *SAINTPlus: version 6.22, Data Reduction and Correction Program*, Bruker AXS: Madison, WI, **2001**.

[41] a) G. M. Sheldrick, *SADABS: version 2.01, An Empirical Absorption Correction Program*, Bruker AXS: Madison, WI, **2001**; b) *SHELXTL: version 6.10, Structure Determination Software Suite*, Bruker AXS: Madison, WI, **2001**.

[42] J. W. A. M. Janssen, H. J. Koeners, C. G. Kruse, C. L. Habraken, *J. Org. Chem.* **1973**, *38*, 1777–1782.

[43] S. S. Novikov, L. I. Khmel'nitskii, O. V. Lebedev, V. V. Sevast'yanova, L. V. Epishina, *Chem. Heterocycl. Compd.* **1970**, *6*, 503–507.

[44] G. I. Koldobskii, D. S. Soldatenko, E. S. Gerasimova, N. R. Khokhryakova, M. B. Shcherbinin, V. P. Lebedev, V. A. Ostrovskii, *Russ. J. Org. Chem.* **1997**, *33*, 1771–1783.

Received: February 20, 2006
Published Online: June 6, 2006

 © 2006 Wiley-VCH Verlag GmbH & Co. KGaA, Weinheim 

DOI: 10.1002/ejic.200600166

# Ligand Variations in [ReX(diimine)(CO)$_3$] Complexes: Effects on Photocatalytic $CO_2$ Reduction

**Philipp Kurz,[a][‡] Benjamin Probst,[a] Bernhard Spingler,[a] and Roger Alberto*[a]**

**Keywords:** Photocatalysis / $CO_2$ reduction / Rhenium / Technetium / Diimine ligands

Two series of complexes [MX(diimine)(CO)$_3$] (M = Tc, Re) have been prepared, fully characterised and investigated for their ability to act as photocatalysts for the reduction of $CO_2$ to CO. One series consists of complexes with different aromatic diimine ligands while keeping X = Br$^-$ constant. The second series describes complexes with diimine = 2,2-bipyridine and variations in the anionic ligand X$^-$. Although numerous complexes of this type have been prepared and investigated before, a systematic study of their photocatalytic activity has not yet been carried out. Electrochemical and spectroscopic characterisation of these complexes has been performed with the objective of better understanding their respective activity in the photocatalytic $CO_2$ reduction. Despite various modifications, catalytic activity is retained for all compounds exhibiting fluorescence, including [$^{99}$TcCl(bipy)(CO)$_3$], whereas nonfluorescing compounds did not convert $CO_2$ to CO. The correlation of catalytic activity and spectroscopic or electrochemical properties such as absorption or emission wavelengths, redox potentials or Stern–Volmer constants for the reductive quenching of the excited complexes is difficult. Nevertheless, the study emphasises the possibility to obtain [ReX(CO)$_3$(diimine)] complexes with a wide range of physicochemical properties by ligand variations and the great potential of compounds of this class of complexes as inorganic photosensitisers.

(© Wiley-VCH Verlag GmbH & Co. KGaA, 69451 Weinheim, Germany, 2006)

## Introduction

The development of a system for the conversion of solar energy into a chemical fuel is one of the most demanding challenges chemists face today. The choice of the photosensitiser performing the initial step of light absorption is of key importance. Complexes of the type [Ru(diimine)$_3$]$^{2+}$ have been most thoroughly studied in this respect.[1–4] Among further possible candidates, rhenium tricarbonyl diimine complexes [ReX(diimine)(CO)$_3$] have also attracted broad interest.[5–14] The complex [ReCl(phen)(CO)$_3$] was one of the first rhenium(I) carbonyl compounds ever synthesised.[15] Detailed studies have unveiled the remarkable photochemical properties of [ReCl(phen)(CO)$_3$] and related compounds such as [ReX(bipy)(CO)$_3$] (X = Cl$^-$ **1**, X = Br$^-$ **2**).[5,9,16,17] The excited state generated by visible light absorption at 450 to 500 nm has been identified as a metal to ligand charge transfer (MLCT) state, with the photoelectron ejected from a metal-centred π-d into a vacant ligand-centred π* orbital with up to μsec lifetimes. On the basis of the Rehm-Weller approximation[18] the photoexcited molecules are powerful oxidising agents with potentials of +500 to +1200 mV (vs. Ag/AgCl).[6] Thermodynamically, [ReX(diimine)(CO)$_3$] complexes can therefore oxidise very poor electron donors, even $H_2O$, in their excited states, which makes them very interesting compounds for light-energy conversion.

In a marked contrast to the large number of physicochemical investigations, there are only a few examples of light-driven reactions with these complexes as photosensitisers. Most prominent is a system for the photochemical reduction of $CO_2$ developed in Strasbourg over 20 years ago. Hawecker et al. found that **1** and **2** are both able to act as photosensitiser and reduction catalysts for the two-electron conversion of $CO_2$ to CO transferring reduction equivalents from poor reducing agents like triethanolamine (TEOA, $\Delta E°_{1/2}$ = +0.8 V) (Scheme 1).[10,19] In this "Strasbourg system", the energetically uphill, two-electron reduction process is achieved using the energy of absorbed

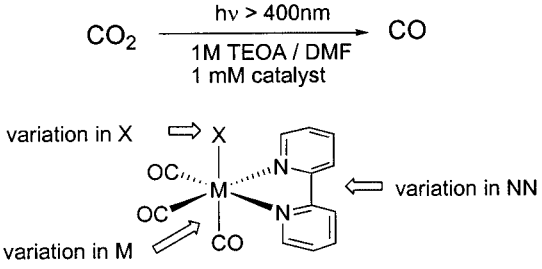


Scheme 1. Photocatalytic conversion of $CO_2$ to CO and variation of the catalyst.

[a] Institute of Inorganic Chemistry, University of Zürich, Winterthurerstrasse 190, 8057 Zürich, Switzerland
E-mail: ariel@aci.unizh.ch
[‡] Present address: Department of Photochemistry and Molecular Science, Uppsala University, Box 523, 751 20 Uppsala, Sweden

 © 2006 Wiley-VCH Verlag GmbH & Co. KGaA, Weinheim 

visible light. From the initial experiments on, the mechanism of this unprecedented reaction has been of great interest.[8,10,20,21] Many experiments have been carried out with the original catalysts **1** or **2**, but studies of the catalytic performance with variations in the anion $X^-$ or the diimine ligand N∩N are rare.[13,20]

We present in this study the synthesis and characterisation of two series of [ReX(diimine)(CO)$_3$] complexes and an investigation of the respective ligand effects on the photocatalytic activities. In a first series of complexes [ReX(bipy)(CO)$_3$] (**4**–**7**), also including the Tc(I) analogue [TcCl(bipy)(CO)$_3$] **3**, the bipy ligand is kept constant and X is varied. In a second series of [ReBr(diimine)(CO)$_3$] (**8**–**15**), the $Br^-$ ligand is kept constant but the diimine ligand is altered. The selected diimine ligands are depicted in Scheme 2. The detailed study of these series of complexes showed that the influence of both diimine and terminal $X^-$ ligands on physicochemical and catalytic properties is large. Nevertheless, catalytic activity is retained in most cases.

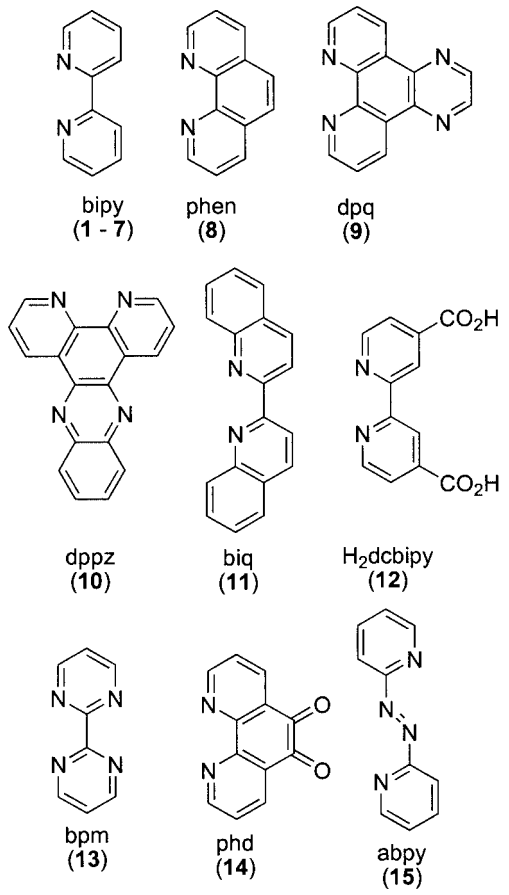


Scheme 2. Diimine ligands used for the synthesis of [ReBr(diimine)(CO)$_3$] complexes with the numbering of the corresponding complexes in brackets: 2,2′-bipyridine (bipy) (**1**–**7**); 1,10-phenanthroline (phen) (**8**); dipyrido[3,2-*f*:2′,3′-*h*]quinoxaline (dpq) (**9**); dipyrido[3,2-*a*:2′,3′-*c*]phenazine (dppz) (**10**); 2,2′-biquinoline (biq) (**11**); 2,2′-bipyridine-4,4′-dicarboxylic acid ($H_2$dcbipy) (**12**); 2,2′-bipyrimidine (bpm) (**13**); 1,10-phenanthroline-5,6-dione (phd) (**14**); 2,2′-azobispyridine (abpy) (**15**).

## Results and Discussion

**Synthesis and Characterisation:** The complexes [ReBr(CO)$_5$] and $(NEt_4)_2$[ReBr$_3$(CO)$_3$] are convenient starting materials from which [ReBr(diimine)(CO)$_3$] complexes are directly afforded with the diimine ligands shown in Scheme 2. The Tc(I) complex **3** was prepared similarly from $(NEt_4)_2$[TcCl$_3$(CO)$_3$]. For the synthesis of the [ReX(bipy)(CO)$_3$] series, [Re(bipy)(CO)$_3$(sol)]$^+$ was prepared as an intermediate by halide precipitation and in a consecutive step the ligands X = $OH_2$ (**4**), $SCN^-$ (**5**) or $CN^-$ (**6**) were introduced. Treatment of **4** with only half an equivalent of cyanide gave the dinuclear complex **7** in which two Re centres are linked by a cyanide bridge with a Re–Re distance of 5.4 Å.[22]

**Structures:** All complexes depict an octahedral ligand arrangement with a facial tricarbonyl moiety, a bidentate diimine ligand and an anion X. The structure of the Tc surro-

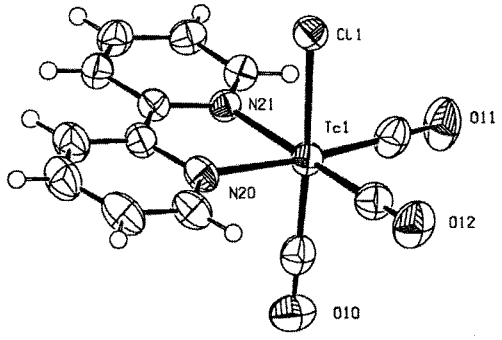


Figure 1. ORTEP drawing of one of the two independent molecules of [TcCl(bipy)(CO)$_3$] (**3**).

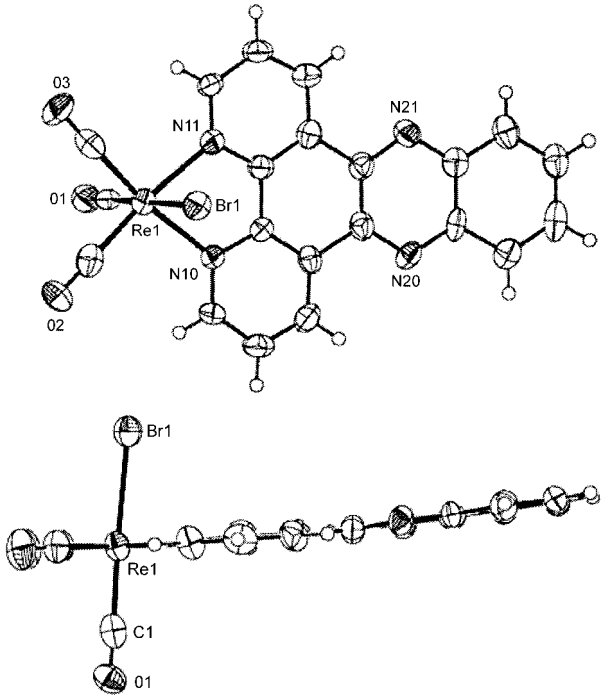


Figure 2. ORTEP representation of **10**, showing a view of the molecule from above and from the side.

 © 2006 Wiley-VCH Verlag GmbH & Co. KGaA, Weinheim 

gate **3** of the original photocatalyst **1** is shown in Figure 1 and complex **10** with the most extended ligand dppz in Figure 2. In all cases the two equatorial carbonyl ligands, the rhenium centre and aromatic rings of the diimine ligand are in a nearly ideal planar arrangement. Bond lengths and angles around the metal centres (see data deposited in The Cambridge Crystallographic Centre) are similar for all structures and comparable to those in closely related compounds.[23–25]

For the biquinoline (biq) complex **11** the usual planar arrangement of metal centre, diimine ligand and equatorial CO's was not observed. The aromatic rings of biq are displaced from the otherwise favoured $Re(CO)_2$- plane by 23 and 12°, respectively, due to steric strain between the hydrogen atoms of the outer aromatic rings and the equatorial carbonyl ligands (Figure 3). Similar biq complexes show comparable structural features.[26] The different twist angles for the two quinoline rings seem to be an effect of crystal packing since only six $^1H$ NMR signals are observed, indicating equivalence for the biq rings on the NMR timescale in solution.

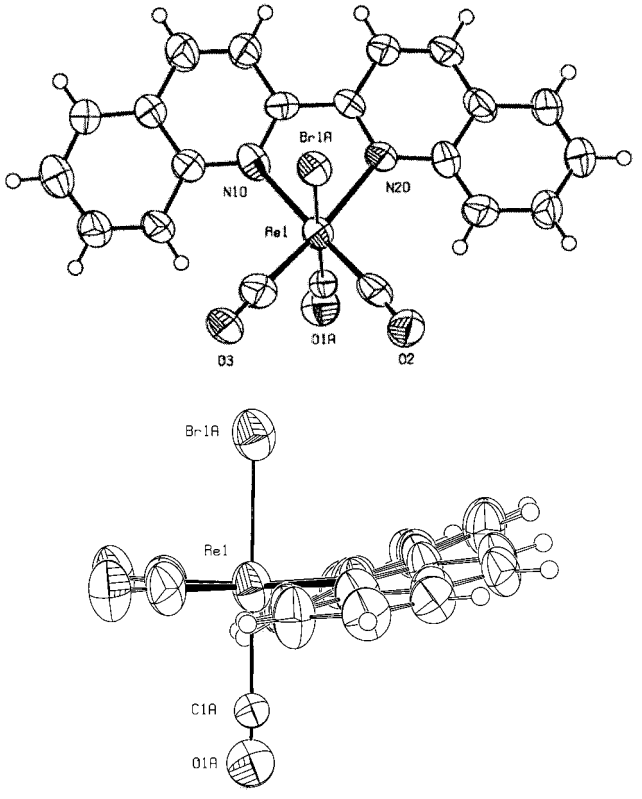


Figure 3. ORTEP drawings of a top and side view of **11**.

**Spectroscopic Properties:** Table 1 summarises analytical data obtained for the [ReX(bipy)$(CO)_3$] series of complexes. Variation of ligand $X^{(-)}$ causes clear effects, but a correlation between $X^{(-)}$ and the spectroscopic or electronic data of the corresponding complexes is not readily obvious. The exchange of $Br^-$ for water results in the formation of the cationic complex **4**. As a consequence of its charge, complex **4** has the series' lowest reduction potential and its light absorption shifts towards higher energy, as it is more difficult to excite an electron. The π- backbonding is reduced in **4** and the IR vibrations $\nu_{CO}$ shift to higher wavenumbers. The mono-cation **7** fits in this series with respect to the $\nu_{CO}$ frequencies, however, $E_{1/2}$ is larger than for example **5**. Considering $\nu_{CO}$, the thiocyanate complex **5** appears to be about as low in electron density as **4**, yet its visible absorption is shifted the most towards lower energies. The lowest carbonyl vibration frequency of the series is observed for the cyano complex **6**. This indicates high electron density on $Re^I$, but is in contrast to the low wavelength of visible light absorption found for **6**.

Table 1. Spectroscopic and electrochemical properties of [ReX(bipy)$(CO)_3$] complexes.

| Ligand X | $\lambda_{max}$ [nm][a] | $\lambda_{em}$ [nm][a] | $\tilde{\nu}_{CO}$ [$cm^{-1}$][b] | $E_{1/2,red}$ [mV][c] |
|---|---|---|---|---|
| Cl (**1**) | 370 | 580 | 2019, 1883 | –1130 |
| Br (**2**) | 370 | 575 | 2019, 1905 | –1190 |
| $H_2O$ (**4**) | 350 | 540 | 2036, 1918 | –1000 |
| SCN (**5**) | 375 | 580 | 2020, 1928 | –1015 |
| CN (**6**) | 355 | 540 | 2006, 1878 | –1125 |
| M–CN–Re (**7**) | 365 | 535 | 2025, 1910 | –1050 |

[a] In DMF solution. [b] KBr pellets. [c] In DMF solution containing 0.1 M $NBu_4PF_6$.

Much larger differences in spectroscopic properties are observed when the diimine ligand is altered (Table 2). The carbonyl stretching frequencies vary by only about ±5 $cm^{-1}$ for all the complexes, thus, the electron density on $Re^I$ does not seem to be as greatly affected as in the case of the [ReX(bipy)$(CO)_3$] series. The differences in the spectroscopic properties stem from the decreased energy of the diimine's LUMO when going to larger aromatic systems or heteroatom substitution.[1,16] The shift in $\lambda_{max}$ towards smaller energies causes a larger part of the absorption to be in the visible spectrum for complexes like **10**, **11** or **15** (Figure 4). While all other compounds are orange yellow solids, **11** and **15** are deep red and dark blue-green, respectively. For **11**, this might be explained by the effect of the unusual coordination geometry on the electronics of the molecule. In the case of **15**, the exceptionally low-lying, par-

Table 2. Spectroscopic and electrochemical properties of [ReBr(diimine)$(CO)_3$] complexes.

| Diimine ligand | $\lambda_{max}$ [nm][a] | $\lambda_{em}$ [nm][a] | $\tilde{\nu}_{CO}$ [$cm^{-1}$][b] | $E_{1/2,red}$ [mV][c] |
|---|---|---|---|---|
| bipy (**2**) | 370 | 575 | 2019, 1905 | –1190 |
| phen (**8**) | 370 | 570 | 2018, 1933 | –1090 |
| dpq (**9**) | ≈ 375[d] | 585 | 2025, 1948 | –975 |
| dppz (**10**) | ≈ 425[d] | 520 | 2018, 1918 | –705 |
| biq (**11**) | 435 | [e] | 2014, 1895 | –735 |
| Hdcbipy (**12**) | 360 | 540 | 2024, 1896 | –1250[f] |
| bpm (**13**) | 385 | [e] | 2030, 1931 | –860 |
| phd (**14**) | 375[d] | [e] | 2033, 1943 | –15, –755 |
| abpy (**15**) | 550, 360[d] | [e] | 2020, 1924 | +50 |

[a] In DMF solution. [b] KBr pellets. [c] In DMF solution containing 0.1 M $NBu_4PF_6$. [d] Absorption shoulder. [e] No fluorescence observed at room temperature in DMF solution. [f] Irreversible reduction.

 © 2006 Wiley-VCH Verlag GmbH & Co. KGaA, Weinheim 

ticularly stabilised LUMO of this ligand has already been reported to cause the unusual absorption properties of abpy- complexes.[27]

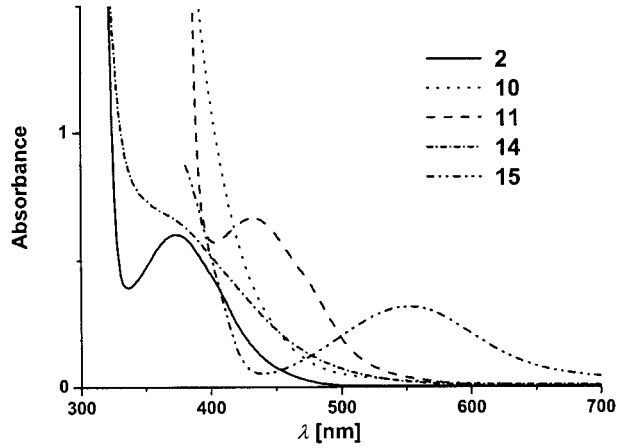


Figure 4. Absorption spectra for different [ReBr(diimine)(CO)$_3$] complexes in DMF (all solutions 0.2 mM).

According to Table 2, not all of the complexes exhibit room temperature fluorescence in DMF when irradiated with light between 350 and 450 nm (Figure 5). The emission maxima are between 520 and 585 nm for **2**, **8**, **9**, **10** and **12**, but **11**, **13**, **14** and **15** do not fluoresce. This behaviour is rationalised in **11** and **15** by the small energy gap between ground and excited states as indicated by the high values of $\lambda_{max}$. Accordingly, radiationless decay to the ground state will be fast in accordance with the energy gap law.[18] Other reasons must account for the absence of fluorescence in **13** and **14** as the energy gap is similar to the structurally related complexes **2** and **8**, respectively. The emission of the dppz complex **10** is observed at much lower wavelengths (520 nm) than that of all other fluorescing complexes of this study. Because of the special nature of the dppz ligand, both diimine and phenazine centred excited states are theoretically possible,[28] resulting in the observation of MLCT or LC emissions, respectively. It was found in a recent study of closely related complexes of [Re(CO)$_3$Cl] with 11-substituted dppz that the ligand-centred emission dominates for two 11-X-dppz complexes of rhenium tricarbonyl,[25] thus explaining the unusual emission behaviour observed for **10**.

**Electrochemistry:** Reversible, one-electron reduction is observed for all complexes except **12**. This process has been assigned to a ligand-centred reduction resulting in the formation of what is best described as a rhenium(I) organic radical anion species [ReX(CO)$_3$(diimine$^{-}$)].[11] In agreement with the spectroscopic properties, the exchange of the ligand X influences the reduction potential $E_{1/2,red}$ of the complexes far less than the variation of the diimine ligand (Table 1 and Table 2).

Factors changing $E_{1/2,red}$ are the overall charge of the complex and the size of the aromatic system of the diimine. In the [ReX(CO)$_3$bipy] series, cationic **4** is the one most easily reduced. Similarly, the reduction of the cationic dinuclear cyano complex **7** is more facile compared to, for example, the neutral complex **6**. It is furthermore easier to place an additional electron into the LUMO of a large aromatic ligand, as seen for the [ReBr(CO)$_3$(diimine)] series for which the reduction potential of the complexes increases with the size of the diimine ligand.

Remarkable redox behaviour was found for **14** and **15**. Complex **15** shows a very high reduction potential of $E_{1/2,red}$ = +50 mV as the additional electron is localised in its unusual LUMO at the azo-bridge.[29] The electrochemistry of **14**, its molecular structure shown in Figure 6, is special since the phd ligand is formally an *ortho*-benzoquinone system. The first reduction already occurs at –15 mV and generates a strongly stabilised semiquinone radical. The diolate is formed at –755 mV in a second reversible step. Increasing concentrations of $H_2O$ shift the second reduction to higher potentials, as direct two-electron reduction to the diol is known to occur in the presence of protons (Figure 7).[30] The phd complex **15** thus offers the possibility of a reversible storage of two electrons within a range of accessible potentials, which is unique within this series of rhenium diimine complexes.

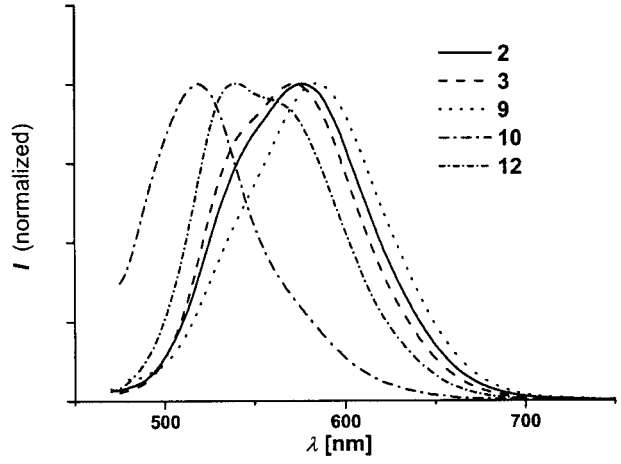


Figure 5. Emission spectra for different [ReBr(CO)$_3$(diimine)] complexes in DMF (all solutions 0.2 mM).

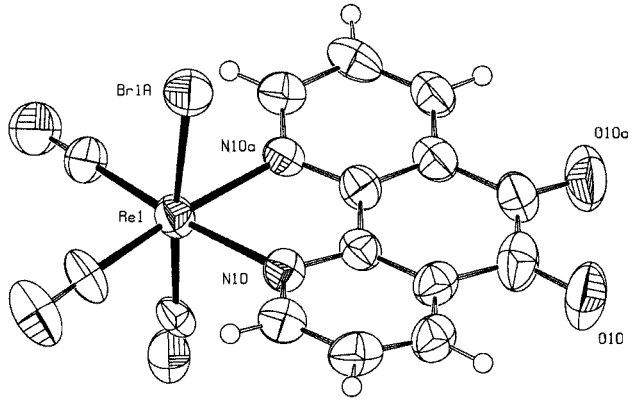


Figure 6. ORTEP drawing of **14**, which contains a mirror plane going through Re1, Br1A and the ligand between the nitrogen atoms.

 © 2006 Wiley-VCH Verlag GmbH & Co. KGaA, Weinheim 

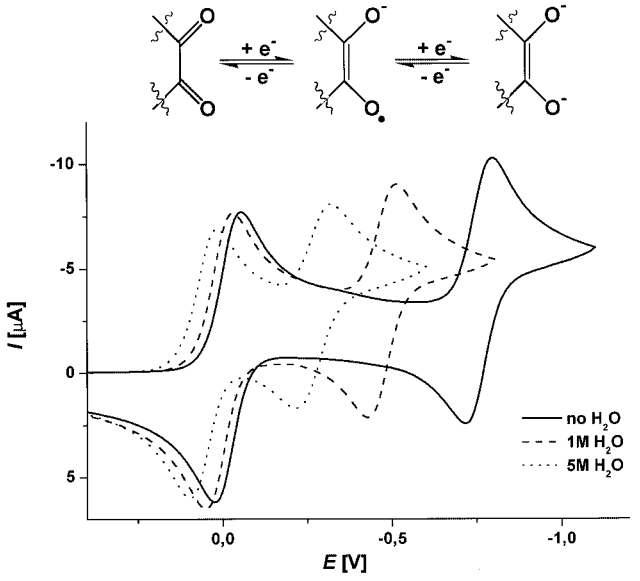


Figure 7. Cyclic voltammograms of the two reversible reduction steps observed for **14** in DMF containing increasing concentrations of water. A Scheme illustrating the successive reduction of the phd dione to form a semiquinone and then a diolate is shown above.

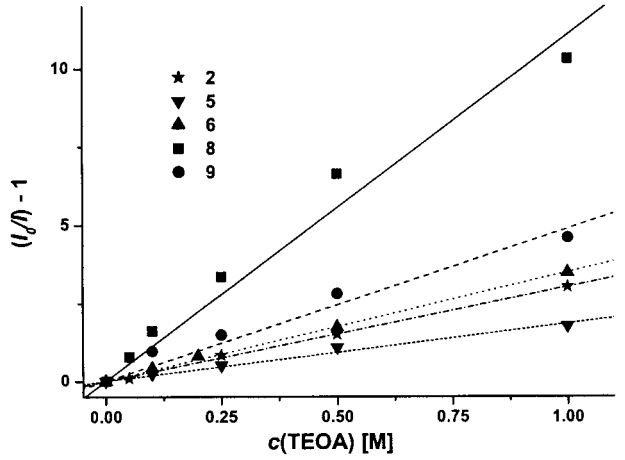


Figure 8. Stern–Volmer plots for the fluorescence quenching of the excited states of different [ReX(diimine)(CO)$_3$] complexes by TEOA.

Table 3. Stern–Volmer constants determined by linear fits of the data forced through zero together with the corresponding values of $E_{1/2,red}$ and $\lambda_{em}$.

| Complex | $K_{SV}$ | $E_{1/2,red}$ [mV] | $\lambda_{em}$ [nm] |
|---|---|---|---|
| **1** | 0.6 | –1130 | 580 |
| **2** | 3.0 | –1190 | 575 |
| **5** | 1.9 | –1015 | 580 |
| **6** | 3.5 | –1125 | 540 |
| **8** | 11.1 | –1090 | 570 |
| **9** | 4.9 | –975 | 585 |
| **10** | 13.5 | –705 | 520 |
| **12** | 20.5 | –1250 | 540 |

**Reductive Fluorescence Quenching:** The original work on the "Strasbourg system" suggested that the primary events of reaction are photoexitation of the complex followed by the reaction of the thexi- state with the electron donor.[8,10,21] It was therefore of interest how the synthetic modifications of the catalyst influence the ability of the excited complexes to react with the standard electron donor TEOA.

$$I_0/I = 1 + k_{q\ \tau}\,[Q] = 1 + K_{SV}\,[Q]$$

Fluorescence quenching is a good way to probe the reactions of the excited state with electron donors. For all fluorescing complexes, Stern–Volmer kinetics are observed for the reductive quenching by TEOA in DMF solutions. According to the Stern–Volmer equation, constants $K_{SV}$ can be determined from plots of $(I_0/I) - 1$ versus quencher concentration (Figure 8).[18]

Table 3 summarises the determined $K_{SV}$ values, which are indicators for the "success rate" of forming the reduced complex after photoexcitation in the presence of a quencher. The variations of diimine or $X^-$ cause $K_{SV}$ to vary by a factor of up to five. To explain this result, measurements of the excited state lifetimes $\tau$ would be necessary to estimate differences in the bimolecular quenching reaction rate $k_q$. It is known that the $k_q$ of this reaction can vary by at least up to a factor of 2.5 for a series of much more closely related [ReX(CO)$_3$bipy] compounds.[13] Unfortunately, we did not have access to an instrument for fluorescence decay measurements.

A number of experiments were carried out to probe the possibility of finding a different solvent/donor combination for which reductive fluorescence quenching is observed. Fluorescence quenching of **2** by either TEOA or TEA is also found in acetonitrile or acetonitrile/water solutions, but the $K_{SV}$ values found in these systems are smaller than in DMF by a factor of 2 and 5, respectively. The use of ternary amines as sacrificial electron donors restricts the reactions to alkaline conditions. This is a particular disadvantage for the goal of shifting the reactivity from $CO_2$ to $H_2O$ reduction, as $H_2O$ reduction is thermodynamically more difficult under basic or neutral conditions. Therefore other, nonbasic electron donors with irreversible oxidation between +0.5 and +1 V and solubility in DMF, MeCN or $H_2O$ were studied. Well-suited candidates are oxalic acid, vitamin C, cystamine or EDTA.[31] None of these donors caused any quenching of [ReX(diimine)(CO)$_3$] fluorescence in solution, although all meet the requirements of a thermodynamically accessible, irreversible oxidation.[31]

**Photochemical $CO_2$ Reductions:** Experiments to study the photocatalytic activity of these complexes in the Strasbourg system were carried out under conditions similar to the reported set-up.[10] Only CO with no detectable quantities of $H_2$ was found in the headspace of the reaction solutions.

The time course of produced CO per mol of catalyst for the [ReX(bipy)(CO)$_3$] series and the technetium homologue **3** are shown in Figure 9. All complexes of this series are active catalysts, though at very different rates (Table 4). It is most interesting to note that after a significant change of the metal centre — from rhenium to technetium — catalytic

 © 2006 Wiley-VCH Verlag GmbH & Co. KGaA, Weinheim 

activity was retained. The thiocyanato complex **5** is a better catalyst than the original complexes **1** and **2** as it combines a rate as fast as **1**, but with improved long-term stability, as the turnover rate for **5** does not change over the first 2 h. The reason for this enhanced stability might be the suppression of the formation of the catalytically inefficient formato complex [Re(HCOO)(bipy)(CO)$_3$][10] as an undesired side product in reactions catalysed by **1** or **2**. The complexes of the larger diimines (**8**, **9** and **10**) are all active photocatalysts but at smaller rates than **2** (Table 4). No CO or any other gaseous products were detected for reactions using **11**, **13**, **14** or **15**. Thus, there is a strict correlation between the detection of room temperature fluorescence and catalytic activity: all fluorescing complexes are active catalysts for photocatalytic $CO_2$ reduction while the others are not.

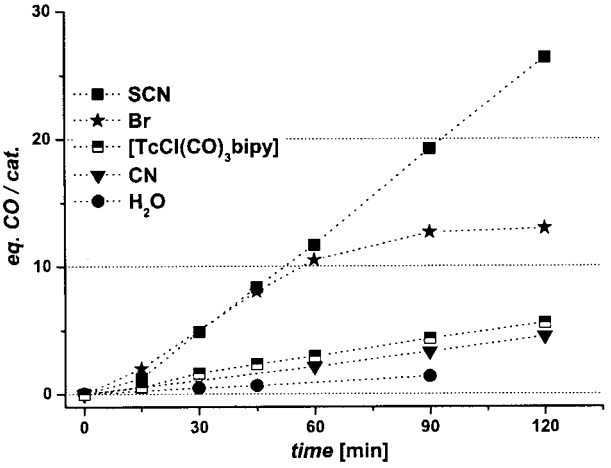


Figure 9. Formation of CO. Reactions with different [ReX(bipy)(CO)$_3$] and [TcCl(bipy)(CO)$_3$(bipy)] complexes.

Table 4. Formation of CO for reactions of photocatalysts of the [ReX(CO)$_3$(bipy)] series and [TcCl(bipy)(CO)$_3$].

| Catalyst | CO after 30 min. [equiv./cat.] | CO after 120 min. [equiv./cat.] |
|---|---|---|
| **1** | 4.6 | 8.2 |
| **2** | 4.0 | 13.0 |
| **3** | 1.6 | 5.5 |
| **4** | 0.5 | 1.8 |
| **5** | 4.9 | 26.4 |
| **6** | 1.1[a] | 4.5 |
| **7** | 0.6[a] | 2.6 |
| **8** | 4.8 | 11.5 |
| **9** | 0.5 | 1.1 |
| **12** | 2.2 | 7.7 |

[a] Extrapolated values.

In agreement with the fluorescence quenching experiments described earlier, the same experiments with different donors such as cystamine or vitamin C in DMF gave no CO. Furthermore, it has been claimed in the literature that the system would switch from $CO_2$ to $H_2O$ reduction if the reaction was carried out in a THF/water mixture instead of DMF.[32] We tried to reproduce this result multiple times with our catalysts but no product at all, neither $H_2$ nor CO, was detected in a THF/water (4:1) mixture. On the other hand, about half the rate of CO production was observed with **2** in DMF/10% water.

These results support the original catalytic mechanism proposed by the Strasbourg group.[10] The well-established initial step is the absorption of a visible-light photon by the catalyst [Re$^{I}$X(diimine)(CO)$_3$] and subsequent MLCT to form the excited state [Re$^{II}$X(diimine$^{-}$)(CO)$_3$]. This step occurs for all complexes discussed here but for **11**, **13**, **14** and **15** nonradiative relaxation pathways to the ground state are most probably so fast that no consecutive reactions can occur, as the absence of fluorescence for these compounds indicates. Hence, they are inactive as Strasbourg catalysts regardless of their electro- or photochemical properties.

According to our results, there is no evidence to support a carboxylate-bridged rhenium dimer as a key intermediate, as proposed in a recent study,[14] as this is in disagreement with the pronounced influence observed for the terminal ligands in the [ReX(bipy)(CO)$_3$] series. Also, the different compounds act both as photoactive and catalytic centres for the reduction of $CO_2$, but none show any reactivity to reduce water, as has been claimed before.[32]

## Conclusions

We were able to show in this study that the [ReX(bipy)(CO)$_3$] catalysts could easily be modified for the Strasbourg system. The catalytic activity for photocatalytic reduction of $CO_2$ is retained in most cases or even enhanced, even though spectroscopic and electrochemical properties of the complexes are substantially altered. There are, however, limitations to the degree to which the diimine ligand can be varied. For a group of [ReBr(CO)$_3$(diimine)] compounds, catalytic activity is lost together with the ability of these complexes to fluoresce, indicating that a sufficiently long excited state life-time is of course a key prerequisite for photoreactivity. While many of the rhenium complexes are able to catalyse the two-electron photoreduction of $CO_2$, none show any reactivity for the reduction of the much more important substrate $H_2O$. Nevertheless, the unusual reactivity of [ReX(CO)$_3$(diimine)] compounds, observed once more in this study, justifies the idea that they should be considered as promising alternatives to the [Ru(diimine)$_3$]$^{2+}$ class of compounds.

## Experimental Section

**General:** All chemicals were of reagent grade and used without further purification. Water was doubly distilled before use. Synthetic reactions were carried out under $N_2$ using standard Schlenk techniques. Abbreviations of the diimine ligands are according to Scheme 2. The complexes [ReBr(CO)$_5$],[33] (NEt$_4$)$_2$[ReBr$_3$(CO)$_3$][34] and (NEt$_4$)$_2$[TcCl$_3$(CO)$_3$],[35] [ReCl(bipy)(CO)$_3$][36] (**1**), [ReBr(bipy)(CO)$_3$][36] (**2**), [ReBr(phen)(CO)$_3$][37] (**8**), [ReBr(biq)(CO)$_3$][38] (**11**) as well as the ligands abpy,[39] dpq,[40] dppz[41] and phd[42] were synthesised according to published procedures. Preparations of the complexes **4**,[43] **5**,[44] **6**,[45] **7**,[45] **13**[37] and **15**[46] have been reported before in the literature but for this study these compounds were ob-

 © 2006 Wiley-VCH Verlag GmbH & Co. KGaA, Weinheim 

tained via the different, in most cases more facile, routes described below.

***Caution!*** $^{99}$Tc is a weak $\beta$-emitter with a half-life of $2.12 \cdot 10^5$ years. Although radiation from small amounts of material is absorbed completely by the walls of the glassware, reactions should only be carried out in specially equipped laboratories and under well-ventilated hoods.

**[$^{99}$TcCl(bipy)(CO)$_3$] (3):** $(NEt_4)_2[^{99}TcCl_3(CO)_3]$ (33 mg, 0.06 mmol) was stirred in $H_2O$ (5 mL) for 2 h, bipy (15.5 mg, 0.1 mmol) was added, dissolved in a mixture of EtOH (1 mL) and $H_2O$ (2 mL). After 30 min a yellow precipitate started to form, which was filtered off after a reaction time of 12 h, washed with diethyl ether and dried in vacuo. Yield: 18 mg (80%). IR (KBr): $\tilde{\nu}_{CO}$ = 2031 (s), 1944 (s), 1920(s); $\tilde{\nu}_{bipy}$ = 1601 (m), 1469(m), 1441 (m), 771 (m) cm$^{-1}$. $^1$H NMR ([D$_4$]MeOH): $\delta$ = 9.03 (br., 2 H), 8.63 (d, 2 H), 8.28 (m, 2 H), 7.75 (m, 2 H) ppm. $^{99}$Tc NMR ([D$_4$]MeOH): $\delta$ = –1094.0 (s) ppm.

**[Re(H$_2$O)(bipy)(CO)$_3$](OTf) (4):** Complex **2** (150 mg, 0.3 mmol) was dissolved in acetone (15 mL) and AgOTf (76.1 mg, 1 equiv.) in acetone (5 mL) was added. The mixture was heated to 70 °C for 2 h. AgBr was filtered off and the solvent was removed in vacuo. The yellow residue was suspended in water (20 mL) and stirred at room temperature for 3 h. Insoluble parts were filtered off and the yellow solution was lyophilised to obtain the yellow, slightly hygroscopic product. Yield: 105 mg (60%). $\lambda_{max}$ (DMF): 350 nm (sh, $\varepsilon$ = 4000), 553 nm ($\varepsilon$ = 1500). IR (KBr): $\tilde{\nu}_{CO}$ = 2036 (s), 1918 (s); $\tilde{\nu}_{bipy}$ = 1604 (m), 1475 (m), 1447 (m), 771 (m); $\tilde{\nu}_{OTf}$ = 1291 (m), 1230 (m), 1179 (m) cm$^{-1}$. ESI-MS (MeOH): *m*/*z* (%) = 426.87 [(M – H$_2$O)$^+$]. $^1$H NMR ([D$_4$]MeOH): $\delta$ = 9.17 (m, 2 H), 8.70 (m, 2 H), 8.39 (m, 2 H), 7.82 (m, 2 H) ppm. $^{13}$C NMR ([D$_4$]MeOH): $\delta$ = 155.3, 142.9, 129.7, 125.8 ppm. $C_{14}H_{10}F_3N_2O_7ReS_1$ (593.51): calcd. C 28.33, H 1.70, N 4.72; found C 28.99, H 1.79, N 5.08.

**[Re(SCN)(bipy)(CO)$_3$] (5):** **2** (50.6 mg, 0.1 mmol) was dissolved in acetone (5 mL) and AgOTf (17.1 mg, 1 equiv.) in acetone (2 mL) was added. The mixture was heated to 70 °C for 2 h. AgBr was filtered off and the solvent removed in vacuo. The residue was stirred MeOH (10 mL) for 1 h. KSCN (20 mg, 2 equiv.), dissolved in $H_2O$ (2 mL), was added and the mixture heated to 70 °C for 4 h to obtain a clear yellow solution. The product precipitated after 1 d at 4 °C. The yellow compound was filtered off, washed with cold $H_2O$, MeOH and ether and dried in vacuo. Yield: 30 mg (60%). $\lambda_{max}$ (DMF): 376 nm ($\varepsilon$ = 2500). $\lambda_{em}$ (DMF): 580 nm. IR (KBr): $\tilde{\nu}_{SCN}$ = 2093 (s); $\tilde{\nu}_{CO}$ = 2020 (s), 1928 (s), 1914 (s); $\tilde{\nu}_{bipy}$ = 1602 (m), 1471(m), 1444 (m), 765 (m) cm$^{-1}$. ESI-MS (acetone): *m*/*z* (%) = 426.87 [(M – SCN)$^+$]. $^1$H NMR ([D$_6$]acetone): $\delta$ = 9.15 (m, 2 H), 8.77 (m, 2 H), 8.42 (m, 2 H), 7.86 (m, 2 H) ppm. $^{13}$C NMR ([D$_6$]acetone): $\delta$ = 154.4, 141.6, 129.1, 125.3 ppm.

**[Re(CN)(bipy)(CO)$_3$] (6):** $(NEt_4)_2[ReBr_3(CO)_3]$ (100 mg, 0.13 mmol) was dissolved in $H_2O$ (5 mL) and $AgNO_3$ (66.2 mg, 3 equiv.) in $H_2O$ (3 mL) was added. The solution was stirred at room temperature for 30 min before AgBr was removed by filtration. Bipy (20.3 mg, 1 equiv.), dissolved in EtOH (2 mL) was added. HPLC analysis confirmed the quantitative formation of $[Re(H_2O)(bipy)(CO)_3]^+$ after 12 h. The addition of KCN (25.4 mg, 3 equiv.) and 20 h of stirring at 100 °C, resulted in the quantitative conversion to **6**, as detected by HPLC. The solvent was removed in vacuo and the product was obtained by extraction of the residue with three 5-mL portions of THF. Yield: 45 mg (75%). $\lambda_{max}$ (DMF): 354 nm ($\varepsilon$ = 2300). $\lambda_{em}$ (DMF): 540 nm. IR (KBr): $\tilde{\nu}_{CN}$ = 2117 (w); $\tilde{\nu}_{CO}$ = 2006 (s), 1878 (s); $\tilde{\nu}_{bipy}$ = 1603 (m), 1473 (m), 1445 (m), 775 (m) cm$^{-1}$. ESI-MS (MeOH): *m*/*z* (%) = 453.60 [M$^+$]. $^1$H NMR ([D$_6$]acetone): $\delta$ = 9.07 (d, 2 H), 8.21 (d, 2 H), 8.07 (m, 2 H), 7.54 (m, 2 H) ppm. $^{13}$C NMR ([D$_6$]acetone): $\delta$ = 154.4, 140.8, 128.8, 125.1 ppm.

**[{Re(bipy)(CO)$_3$}$_2$(μ-CN)](ClO$_4$) (7):** $(NEt_4)_2[ReBr_3(CO)_3]$ (100 mg, 0.13 mmol) was dissolved in $H_2O$ (10 mL) and $AgClO_4$ (80.8 mg, 3 equiv.) was added. AgBr was removed after 30 min by filtration. Bipy (20.3 mg, 1 equiv.), dissolved in EtOH (5 mL) was added. After 20 h at room temperature $[Re(bipy)(CO)_3(H_2O)]^+$ formed quantitatively, and KCN (4.2 mg, 0.5 equiv.) in $H_2O$ (2 mL) was added. After 2 h at 100 °C, a yellow precipitate started to form which was filtered off after 20 h, washed with $H_2O$ and diethyl ether and dried in vacuo. Yield: 28 mg (45%). $\lambda_{max}$ (DMF): 363 nm ($\varepsilon$ = 2000). $\lambda_{em}$ (DMF): 535 nm. IR (KBr): $\tilde{\nu}_{CN}$ = 2151 (w); $\tilde{\nu}_{CO}$ = 2025 (s), 1910 (s), 1896 (s); $\tilde{\nu}_{bipy}$ = 1605 (m), 1473 (m), 1446 (m), 771 (m); $\tilde{\nu}_{ClO4}$ = 1121 (m) cm$^{-1}$. ESI-MS (MeOH): *m*/*z* (%) = 879.53 [M$^+$]. $^1$H NMR ([D$_6$]acetone): $\delta$ = 8.83 (br., 4 H), 8.00 (br., 4 H), 7.60 (br., 4 H), 7.41 (br., 4 H) ppm. $^{13}$C NMR ([D$_6$]acetone): $\delta$ = 154.3, 154.1, 142.2, 141.8, 129.0 (2C), 125.9, 125.7 ppm.

**[ReBr(dpq)(CO)$_3$] (9):** A procedure similar to the published method for the preparation of [ReBr(phen)(CO)$_3$] was applied.[37] A suspension was prepared consisting of $[ReBr(CO)_5]$ (50 mg, 0.12 mmol) and dpq (28.5 mg, 1 equiv.) in petroleum ether (10 mL, boiling range 100–130 °C). The suspension was heated to 100 °C for 2 h to obtain the product as a yellow precipitate. The powder was filtered off, washed with portions of petroleum ether and diethyl ether and then dried in vacuo to obtain the product as a yellow powder. Yield: 70 mg (quantitative). $\lambda_{max}$ (DMF): 400 nm (sh, $\varepsilon$ = 2500). $\lambda_{em}$ (DMF): 585 nm. IR (KBr): $\tilde{\nu}_{CO}$ = 2025 (s), 1948 (s), 1902 (s); $\tilde{\nu}_{dpq}$ = 1402 (m), 1384 (m), 820 (w), 729(w), 631 (w) cm$^{-1}$. ESI-MS (MeOH): *m*/*z* (%) = 530.40 [M – Br + CO]$^+$, 502.80 [M – Br]$^+$. $^1$H NMR ([D$_6$]acetone): $\delta$ = 9.96 (m, 2 H), 9.82 (m, 2 H), 9.38 (s, 2 H), 8.45 (m, 2 H) ppm. $^{13}$C NMR ([D$_6$]acetone): $\delta$ = 155.8, 147.8, 136.5, 128.3 ppm. $C_{17}H_8BrN_4O_3Re$ (582.39): calcd. C 35.06, H 1.38, N 9.62; found C 35.38, H 1.53, N 9.69.

**[ReBr(dppz)(CO)$_3$] (10):** The same procedure as for $[ReBr(dpq)(CO)_3]$ was applied, using $[ReBr(CO)_5]$ (50 mg, 0.12 mmol) and dppz (33.8 mg, 1 equiv.), to obtain the complex as an orange powder. Yield: 50 mg (65%). $\lambda_{max}$ (DMF): 400 nm (sh, $\varepsilon$ = 5000). $\lambda_{em}$ (DMF): 520 nm. IR (KBr): $\tilde{\nu}_{CO}$ = 2018 (s), 1918 (s), 1890 (s); $\tilde{\nu}_{dppz}$ = 1493 (m), 1418 (m), 1384 (m), 1360 (m), 822 (w), 773 (w), 729 (w) cm$^{-1}$. ESI-MS (MeOH): *m*/*z* (%) = 580.53 [M – Br + CO]$^+$, 553.00 [M – Br]$^+$. $^1$H NMR ($CDCl_3$): $\delta$ = 10.04 (m, 2 H), 9.88 (m, 2 H), 8.47 (m, 2 H), 8.08 (m, 2 H), 7.26 (m, 2 H) ppm. $C_{21}H_{10}BrN_4O_3Re$ (632.45): calcd. C 39.88, H 1.59, N 8.86; found C 39.53, H 1.77, N 8.58.

**(NEt$_4$)[ReBr(Hdcbipy)(CO)$_3$] (12):** $(NEt_4)_2[ReBr_3(CO)_3]$ (154 mg, 0.2 mmol) was dissolved in $H_2O$ (15 mL) and $H_2$dcbipy (53.7 mg, 1.1 equiv.) was added as a solid. The pH of the solution was raised to pH ca. 6–7 by the careful addition of 10 mM NaOH. The mixture was stirred for 2 d at room temperature and some yellow precipitate formed, which was filtered off. The filtrate was lyophilised, triturated three times with $CH_2Cl_2$ (5 mL) to remove $NEt_4Br$ and then dried in vacuo. Yield: 75 mg (50%). $\lambda_{max}$ (DMF): 360 nm (sh, $\varepsilon$ = 3000). $\lambda_{em}$ (DMF): 540 nm. IR (KBr): $\tilde{\nu}_{CO}$ = 2024 (s), 1896 (s); $\tilde{\nu}_{dcbipy}$ = 1719 (w), 1619 (m), 1551 (w), 1366 (m), 1289 (m), 1071 (w), 766 (m), 682 (m) cm$^{-1}$. ESI-MS (MeOH): *m*/*z* (%) = 468.40 [(M – Br – COOH – H)$^-$]. $^1$H NMR ($D_2O$/NaOH): $\delta$ = 9.02 (m, 2 H), 8.65 (s, 2 H), 7.81 (m, 2 H) ppm. $^{13}$C NMR ($D_2O$/NaOH): $\delta$ = 151.6, 124.2, 120.7 ppm.

**[ReBr(bpm)(CO)$_3$] (13):** $(NEt_4)_2[ReBr_3(CO)_3]$ (385 mg, 0.5 mmol) was dissolved in $H_2O$ (20 mL) and bpm (87 mg, 1.1 equiv.), dissolved in EtOH (2 mL) was added. The mixture was stirred for 2 d at room temperature, after which a fine orange precipitate had

 © 2006 Wiley-VCH Verlag GmbH & Co. KGaA, Weinheim 

formed. The solid was filtered off, washed with $H_2O$, cold EtOH and ether, and dried in vacuo. Yield: 210 mg (80%). $\lambda_{max}$ (DMF): 383 nm ($\varepsilon$ = 2500). IR (KBr): $\tilde{\nu}_{CO}$ = 2030 (s), 1931 (s), 1906 (s); $\tilde{\nu}_{bpm}$ = 1575 (m), 1547 (w), 1407 (s), 834 (w), 755 (w) cm$^{-1}$. ESI-MS ([D$_6$]acetone/MeOH): *m*/*z* (%) = 508.00 [M$^+$]. $^1$H NMR ([D$_6$]-acetone): $\delta$ = 9.41 (dd, 2 H), 9.35 (dd, 2 H), 7.98 (dd, 2 H). $^{13}$C NMR ([D$_6$]acetone): $\delta$ = 162.0, 161.4, 125.6 ppm. $C_{11}H_6BrN_4O_3Re$ (508.30): calcd. C 25.99, H 1.19, N 11.02; found C 26.24, H 1.05, N 10.87.

**[ReBr(phd)(CO)$_3$] (14):** The same procedure as for [ReBr(bpm)-(CO)$_3$] was applied, using $(NEt_4)_2[ReBr_3(CO)_3]$ (500 mg, 0.65 mmol) and phd (163 mg, 1.2 equiv.) to isolate the orange complex. Yield: 350 mg (95%). $\lambda_{max}$ (DMF): 375 nm (sh, $\varepsilon$ = 3000). IR (KBr): $\tilde{\nu}_{CO}$ = 2033 (s), 1943 (s), 1885 (s); $\tilde{\nu}_{phd}$ = 1703 (m), 1573 (w), 1427 (m), 1298 (w), 1026 (w), 828 (w), 727 (w) cm$^{-1}$. ESI-MS (MeOH): *m*/*z* (%) = 512.73 [(M – Br + MeOH)$^+$], 480.73 [(M – Br)$^+$]. $^1$H NMR ([D$_6$]acetone): $\delta$ = 9.34 (dd, 2 H), 8.81 (dd, 2 H), 8.05 (dd, 2 H) ppm. $^{13}$C NMR ([D$_6$]acetone): $\delta$ = 158.0, 139.0, 129.8 ppm. $C_{15}H_6BrN_2O_5Re$ (560.33): calcd. C 32.15, H 1.08, N 5.00; found C 32.37, H 1.12, N 5.08.

**[ReBr(abpy)(CO)$_3$] (15):** The same procedure as for [ReBr(bpm)(CO)$_3$] was applied, using $(NEt_4)_2[ReBr_3(CO)_3]$ (76 mg, 0.1 mmol) and abpy (27 mg, 1.5 equiv.) to isolate the violet-blue compound. Yield: 50 mg (95%). $\lambda_{max}$ (DMF): 361 nm ($\varepsilon$ = 5000), 553 nm ($\varepsilon$ = 1500). IR (KBr): $\tilde{\nu}_{CO}$ = 2020 (s), 1924 (s), 1900 (s); $\tilde{\nu}_{abpy}$ = 1465 (w), 1433 (m), 1370 (w), 797 (m) cm$^{-1}$. ESI-MS (MeOH): *m*/*z* (%) = 454.67 [M – Br]$^+$. $^1$H NMR ([D$_6$]acetone): $\delta$ = 9.33 (m, 1 H), 8.96 (m, 1 H), 8.87 (m, 1 H), 8.57 (td 1 H), 8.20 (br., 2 H), 8.00 (br., 1 H), 7.85 (br., 1 H) ppm. $^{13}$C NMR ([D$_6$]-acetone): $\delta$ = 152.7, 149.7, 142.7, 140.3, 131.4, 130.9, 129.5, 115.7 ppm. $C_{13}H_8BrN_4O_3Re$ (534.34): calcd. C 29.22, H 1.51, N 10.49; found C 29.61, H 1.43, N 10.56.

**Physical Measurements:** UV/Vis spectra were measured with a Cary 50 spectrometer with solution samples in 1-cm quartz cells. If necessary, cells with silicon septa lids were used to keep samples under an inert gas atmosphere during measurements. Fluorescence measurements were performed with a Perkin–Elmer LS50B fluorescence spectrometer with argon purged solution samples in 1-cm cells. IR spectra were recorded with a Bio-Rad FTS-45 spectrometer with samples in compressed KBr pellets. $^1$H NMR spectra were recorded with Varian Mercury and Varian Gemini-2000 spectrometers ($^1$H at 199.97 MHz and 300.08 MHz, respectively) and $^{13}$C NMR spectra were recorded with Varian Gemini-2000 and Bruker DRX500 spectrometers ($^{13}$C at 75.47 MHz and 125.81 MHz, respectively). The chemical shifts are reported relative to residual solvent protons as a reference. $^{99}$Tc NMR spectra were recorded with a Varian Gemini-2000 spectrometer ($^{99}$Tc resonance 67.40 MHz), referenced to $[^{99}TcO_4]^-$. Electrospray ionisation mass spectra (ESI-MS) were recorded with a Merck–Hitachi M-8000 spectrometer, reported are the values of the $^{187}$Re isotope. Elemental analyses were performed with a Leco CHNS-932 elemental analyser. It was found that cyano- and thiocyanato compounds analysed by this instrument often show elemental analyses differing greatly from the expected calculated percentages. This analytical problem was also observed for commercial, analytical grade chemicals like NaCN, $K_3[Fe(CN)_6]$ or CuSCN. Electrochemical measurements were carried out in DMF containing 0.1 M TBA $PF_6$ as conducting electrolyte. A Metrohm 757 VA Computrace electrochemical analyser was used with a standard three-electrode setup of glassy carbon working and auxiliary electrodes and a Ag/AgCl reference electrode. All potentials are given vs. Ag/AgCl (NHE: +221 mV). Gas chromatograms were recorded with a Varian CP-3800 gas chromatograph with helium as the carrier gas. The permanent gases CO, $N_2$, $O_2$ and $H_2$ were separated by a 3 m × 2 mm column packed with Varian molecular sieves 13X. The gases were detected using a thermal conductivity detector (Varian). Calibrations were performed by the injection of known quantities of pure gases.

**Photochemical Carbon Dioxide Reductions:** Reactions catalysed by [Re(CO)$_3$(diimine)X] complexes were tested in 50 mL septum capped Schlenk tubes. Exact volumes were determined gravimetrically. 10 mL of a solution containing TEOA (1 M) and the catalyst (1 mM) in DMF were prepared, wrapped in black foil and degassed using a $CO_2$-purged Schlenk-line. The mixture was equilibrated under 1.5 bar $CO_2$ pressure for 15 min and then transferred to a dark room for illumination. The light source was a Leica Pradovit S AF slide projector equipped with a 250-W Osram Xenophot HLX lamp. The light was filtered by a 400-nm cut-off filter (Schott GG 400) before reaching the sample at 40 cm distance from the projector. Light intensities illuminating the sample were determined by a TES 1332A luxmeter to be 46.000 lux. 100-μL gas samples were

Table 5. Crystal and structure refinement data for **1**, **3**, **10**, **11** and **14**.

| Compound No. | **1** | **3** | **10** | **11** | **14** |
|---|---|---|---|---|---|
| Formula | $C_{13}H_8ClN_2O_3Re$ | $C_{13}H_8ClN_2O_3Tc$ | $C_{21}H_{10}BrN_4O_3Re$ | $C_{21}H_{12}BrN_2O_3Re$ | $C_{15}H_6BrN_2O_5Re$ |
| $M_r$ | 461.86 | 373.67 | 632.44 | 606.44 | 560.33 |
| Crystal system | monoclinic | triclinic | triclinic | triclinic | orthorhombic |
| Space group | $P2_1/n$ | $P\bar{1}$ | $P\bar{1}$ | $P\bar{1}$ | *Pnma* |
| *a* [Å] | 6.8740(5) | 10.9879(8) | 6.9955(7) | 7.5081(10) | 7.2858(5) |
| *b* [Å] | 15.0038(9) | 11.5003(9) | 12.9547(11) | 9.7573(10) | 12.7348(6) |
| *c* [Å] | 13.5114(11) | 11.1203(9) | 13.2653(12) | 12.9934(18) | 16.7641(9) |
| $\alpha$ [°] | | 93.703(10) | 111.200(10) | 94.697(15) | |
| $\beta$ [°] | 96.494(10) | 103.282(9) | 98.272(11) | 94.288(16) | |
| $\gamma$ [°] | | 86.214(9) | 95.110(11) | 106.434(14) | |
| *V* [Å$^3$] | 1384.57(17) | 1362.87(18) | 1096.10(17) | 905.1(2) | 1555.43(15) |
| *Z* | 4 | 4 | 2 | 2 | 4 |
| $D_c$ [g cm$^{-3}$] | 2.216 | 1.821 | 1.916 | 2.225 | 2.393 |
| $\mu$(Mo-$K_\alpha$) [mm$^{-1}$] | 8.976 | 1.259 | 7.394 | 8.946 | 10.409 |
| Goodness-of-fit on $F^2$ | 0.882 | 0.867 | 0.926 | 1.042 | 1.047 |
| R[a,b] | 0.0464 | 0.0426 | 0.0593 | 0.0749 | 0.0701 |
| $wR_2$[a,c] | 0.0702 | 0.0990 | 0.1685 | 0.1893 | 0.1835 |
| Max., min. peaks [e·Å$^{-3}$] | 3.433, –1.822 | 0.661, –0.970 | 3.063, –1.710 | 2.066, –2.314 | 2.002, –1.804 |

[a] Observation criterion: $I > 2\sigma(I)$. [b] $R = \Sigma||F_o| - |F_c||/\Sigma|F_o|$. [c] $wR_2 = \{\Sigma[w(F_o^2 - F_c^2)^2]/\Sigma[w(F_o^2)^2]\}^{1/2}$.

 © 2006 Wiley-VCH Verlag GmbH & Co. KGaA, Weinheim 

drawn from the headspace above the solution and injected into the GC-TCD gas analyser.

**X-ray Diffraction Studies:** Suitable crystals were covered with Paratone N oil, mounted on top of a glass fibre and immediately transferred to a Stoe IPDS diffractometer. Data was collected at 183(2) K using graphite-monochromated Mo radiation (0.71073 Å). Data was corrected for Lorentz and polarisation effects as well as for absorption. Structures were solved with direct methods using SHELXS-97[47] or SIR97[48] and were refined by full-matrix least-squares methods on $F^2$ with SHELXL-97.[49] ORTEP plots were generated by the PLATON software package[50] and are drawn at 50% probability. The crystal data and refinement parameters of the presented structures are summarised in Table 5.

CCDC-299061 to -299065 contain the supplementary crystallographic data for this paper. These data can be obtained free of charge from The Cambridge Crystallographic Centre via www.ccdc.cam.ac.uk/datarequest/cif.

## Acknowledgments

We would like to thank Prof. Jon Dilworth and his group for the possibility to carry out initial $CO_2$ reduction experiments at the Inorganic Chemistry Laboratory of the University of Oxford, Great Britain. H. C. Starck, Berlin, Germany, generously donated rhenium metal to support our research.

[1] K. Kalyanasundaram, *Photochemistry of Polypyridine and Porphyrin Complexes*, Academic Press, London, **1992**.
[2] V. Balzani, A. Juris, M. Venturi, S. Campagna, S. Serroni, *Chem. Rev.* **1996**, *96*, 759–833.
[3] M. Grätzel, *Nature* **2001**, *414*, 338–344.
[4] P. Wang, C. Klein, R. Humphry-Baker, S. M. Zakeeruddin, M. Grätzel, *J. Am. Chem. Soc.* **2005**, *127*, 808–809.
[5] M. Wrighton, D. L. Morse, *J. Am. Chem. Soc.* **1974**, *96*, 998–1003.
[6] J. C. Luong, L. Nadjo, M. S. Wrighton, *J. Am. Chem. Soc.* **1978**, *100*, 5790–5795.
[7] J. V. Caspar, T. J. Meyer, *J. Phys. Chem.* **1983**, *87*, 952–957.
[8] C. Kutal, M. A. Weber, G. Ferraudi, D. Geiger, *Organometallics* **1985**, *4*, 2161–2166.
[9] K. Kalyanasundaram, *J. Chem. Soc., Faraday Trans. 2* **1986**, *82*, 2401–2415.
[10] J. Hawecker, J. M. Lehn, R. Ziessel, *Helv. Chim. Acta* **1986**, *69*, 1990–2012.
[11] W. Kaim, S. Kohlmann, *Chem. Phys. Lett.* **1987**, *139*, 365–369.
[12] D. J. Stufkens, *Comments Inorg. Chem.* **1992**, *13*, 359–385.
[13] H. Hori, J. Ishihara, K. Koike, K. Takeuchi, T. Ibusuki, O. Ishitani, *J. Photochem. Photobiol. A* **1999**, *120*, 119–124.
[14] Y. Hayashi, S. Kita, B. S. Brunschwig, E. Fujita, *J. Am. Chem. Soc.* **2003**, *125*, 11976–11987.
[15] W. Hieber, H. Fuchs, *Z. Anorg. Allg. Chem.* **1941**, *248*, 269–275.
[16] A. Juris, S. Campagna, I. Bidd, J. M. Lehn, R. Ziessel, *Inorg. Chem.* **1988**, *27*, 4007–4011.
[17] L. Wallace, D. P. Rillema, *Inorg. Chem.* **1993**, *32*, 3836–3843.
[18] G. J. Kavarnos, *Fundamentals of Photoinduced Electron Transfer*, VCH, Weinheim, **1993**.
[19] J. Hawecker, J. M. Lehn, R. Ziessel, *J. Chem. Soc., Chem. Commun.* **1983**, 536–538.
[20] G. Calzaferri, K. Haedener, J. Li, *J. Photochem. Photobiol. A* **1992**, *64*, 259–262.
[21] C. Kutal, A. J. Corbin, G. Ferraudi, *Organometallics* **1987**, *6*, 553–557.
[22] H. Hartmann, W. Kaim, M. Wanner, A. Klein, S. Frantz, C. Duboc-Toia, J. Fiedler, S. Zalis, *Inorg. Chem.* **2003**, *42*, 7018–7025.
[23] S. F. Haddad, J. A. Marshall, A. Crosby, B. Twamley, *Acta Crystallogr., Sect. E* **2002**, *58*, m559–m561.
[24] Y. D. Chen, L. Y. Zhang, Z. N. Chen, *Acta Crystallogr., Sect. E* **2005**, *61*, m121–m122.
[25] N. J. Lundin, P. J. Walsh, S. L. Howell, J. J. Mcgarvey, A. G. Blackman, K. C. Gordon, *Inorg. Chem.* **2005**, *44*, 3551–3560.
[26] J. Guerrero, S. A. Moya, M. T. Garland, R. F. Baggio, *Acta Crystallogr., Sect. C* **1999**, *55*, 932–934.
[27] W. Kaim, *Coord. Chem. Rev.* **2001**, *219–221*, 463–488.
[28] J. Fees, W. Kaim, M. Moscherosch, W. Matheis, J. Klima, M. Krejcik, S. Zalis, *Inorg. Chem.* **1993**, *32*, 166–174.
[29] H. Hartmann, T. Scheiring, J. Fiedler, W. Kaim, *J. Organomet. Chem.* **2000**, *604*, 267–272.
[30] T. S. Eckert, T. C. Bruice, J. A. Gainor, S. M. Weinreb, *Proc. Natl. Acad. Sci. USA* **1982**, *79*, 2533–2536.
[31] A. I. Krasna, *Photochem. Photobiol.* **1979**, *29*, 267–276.
[32] C. Pac, K. Ishii, S. Yanagida, *Chem. Lett.* **1989**, 765–768.
[33] S. P. Schmidt, W. C. Trogler, F. Basolo, *Inorg. Synth.* **1990**, *28*, 160–165.
[34] R. Alberto, A. Egli, U. Abram, K. Hegetschweiler, V. Gramlich, P. A. Schubiger, *J. Chem. Soc., Dalton Trans.* **1994**, 2815–2820.
[35] R. Alberto, R. Schibli, P. A. Schubiger, U. Abram, T. A. Kaden, *Polyhedron* **1996**, *15*, 1079–1089.
[36] D. Vitali, F. Calderazzo, *Gazz. Chim. Ital.* **1972**, *102*, 587–596.
[37] E. W. Abel, P. J. Heard, K. G. Orrell, *Inorg. Chim. Acta* **1997**, *255*, 65–71.
[38] S. A. Moya, J. Guerrero, R. Pastene, R. Sartori, R. Schmidt, R. Sariego, J. Sanz-Aparicio, I. Fonseca, M. Martinez-Ripoll, *Inorg. Chem.* **1994**, *33*, 2341–2346.
[39] A. Kirpal, E. Reiter, *Ber. Dtsch. Chem. Ges.* **1927**, *60*, 664–666.
[40] R. Van Belzen, R. A. Klein, W. J. J. Smeets, A. L. Spek, R. Benedix, C. J. Elsevier, *Recl. Trav. Chim. Pays.Bas* **1996**, *115*, 275–285.
[41] J. E. Dickeson, L. A. Summers, *Aust. J. Chem.* **1970**, *23*, 1023–1027.
[42] C. Hiort, P. Lincoln, B. Norden, *J. Am. Chem. Soc.* **1993**, *115*, 3448–3454.
[43] B. Salignac, P. V. Grundler, S. Cayemittes, U. Frey, R. Scopelliti, A. E. Merbach, R. Hedinger, K. Hegetschweiler, R. Alberto, U. Prinz, G. Raabe, U. Kolle, S. Hall, *Inorg. Chem.* **2003**, *42*, 3516–3526.
[44] A. M. B. Rodriguez, A. Gabrielsson, M. Motevalli, P. Matousek, M. Towrie, J. Sebera, S. Zalis, A. Vlcek, *J. Phys. Chem. A* **2005**, *109*, 5016–5025.
[45] K. Kalyanasundaram, M. Grätzel, M. K. Nazeeruddin, *Inorg. Chem.* **1992**, *31*, 5243–5253.
[46] S. Frantz, M. Weber, T. Scheiring, J. Fiedler, C. Duboc, W. Kaim, *Inorg. Chim. Acta* **2004**, *357*, 2905–2914.
[47] G. M. Sheldrick, *Acta Crystallogr., Sect. A* **1990**, *46*, 467–473.
[48] A. Altomare, M. C. Burla, M. Camalli, G. L. Cascarano, C. Giacovazzo, A. Guagliardi, A. G. G. Moliterni, G. Polidori, R. Spagna, *J. Appl. Crystallogr.* **1999**, *32*, 115–119.
[49] G. M. Sheldrick, T. R. Schneider, *Macromolecular Crystallography, Part B* **1997**, *277*, 319–343.
[50] A. L. Spek, *J. Appl. Crystallogr.* **2003**, *36*, 7–13.

Received: February 23, 2006
Published Online: June 23, 2006

 © 2006 Wiley-VCH Verlag GmbH & Co. KGaA, Weinheim 

DOI: 10.1002/ejic.200600209

# A Cationic (N-Heterocyclic carbene)silver Complex as Catalyst for Bulk Ring-Opening Polymerization of L-Lactides

**Manoja K. Samantaray,[a] Vimal Katiyar,[b] Dipankar Roy,[a] Keliang Pang,[c] Hemant Nanavati,[b] Raji Stephen,[a] Raghavan B. Sunoj,*[a] and Prasenjit Ghosh*[a]**

**Keywords:** Carbenes / DFT studies / Functionalized NHC / Ring-opening polymerization (ROP) / Organometallic catalysis / Silver

Synthetic, theoretical, and catalysis studies of a cationic functionalized N-heterocyclic carbene complex of silver, namely [{1-isopropyl-3-(*N*-phenylacetamido)imidazol-2-ylidene}$_2$-Ag]$^+$Cl$^-$ (**1b**), is reported. Specifically, **1b** was synthesized by the reaction of 1-isopropyl-3-(*N*-phenylacetamido)imidazolium chloride (**1a**) with $Ag_2O$ in 64 % yield; **1a** was synthesized by the alkylation reaction of 1-isopropylimidazole with *N*-phenyl chloroacetamide in 90 % yield. The molecular structure of **1b** was determined by X-ray diffraction studies and was found to be active for polymerization of L-lactide at elevated temperatures under solvent-free melt conditions to give polylactide of moderate molecular weight with narrow molecular weight distribution. Density functional theory studies of the cationic species **2b**, derived from NHC silver complex **1b**, were employed to obtain an understanding of the structure, bonding, and electronic features of the molecule. Bonding in complex **2b** has been probed with the help of charge decomposition analysis (CDA), the atoms in molecules (AIM) approach as well as natural bond orbital (NBO) methods. The Ag–NHC bond has been found to be more covalent with NHC acting as an effective σ-donor. The π-back-bonding from the metal atom to the ligand was found to be negligible. It has been noticed that the imidazole rings remain nearly orthogonal with respect to each other, in contrast to the experimental geometry. Intramolecular hydrogen bonds as well as Ag···O interaction involving the carbonyl oxygen atoms have been identified as additional stabilizing factors contributing towards the lower energy conformer of **2b** compared to the corresponding planar geometry.

(© Wiley-VCH Verlag GmbH & Co. KGaA, 69451 Weinheim, Germany, 2006)

## Introduction

Ever since the first successful isolation of a stable singlet carbene by Arduengo,[1] there has been phenomenal growth in the field of N-heterocyclic carbene (NHC) chemistry.[2] As a consequence, the N-heterocyclic carbenes have found wide-spread application in chemical catalysis with new catalysts being discovered recently.[3] The growth in NHC chemistry has made a profound impact, particularly in the field of organometallic catalysis, with the NHC-based catalysts exhibiting superior performance over the traditional catalysts in many important transformations. For example, it is now a well-established fact that Grubbs' second-generation ROMP catalyst bearing NHC exhibits better efficiency over the original phosphane-based ruthenium catalyst, $(PCy_3)_2(Cl)_2Ru{=}CHPh$.[4–6] Not surprisingly, the trendy NHCs are fast replacing the phosphanes and are gradually emerging as the designer's choice of ligand in organometallic catalysis. Remarkably, the NHC transition metal complexes have exhibited catalytic activities for a truly impressive range of reactions covering the C–C coupling reaction,[7,8] olefin metathesis,[9] hydrogenation,[10,11] hydroformylation,[12] hydrosilylation,[13] CO/ethylene copolymerization,[14] and hydroboration[15] reactions to name a few. In addition to the newly found successes in organometallic catalysis, the NHCs have shown promise in organocatalysis as potent nucleophilic organic catalysts and are increasingly gaining popularity and acceptance in such roles. Recently, there have been several reports of organocatalysis by NHCs particularly in transesterification reactions[16] and in ring-opening lactide polymerization reactions.[17–19] Both the in-situ generated carbenes as well as the isolable stable singlet N-heterocyclic carbenes have been directly employed in these organocatalysis reactions.

The mainstay of N-heterocyclic carbene chemistry has been its silver complexes, which played an important role in the development of the field of NHCs.[20] The interest in NHC silver complexes is primarily due to it being an effec-

[a] Department of Chemistry, Indian Institute of Technology Bombay,
Powai, Mumbai 400076, India
Fax: +91-22-2572-3480
E-mail: pghosh@chem.iitb.ac.in
sunoj@chem.iitb.ac.in
[b] Department of Chemical Engineering, Indian Institute of Technology Bombay,
Powai, Mumbai 400076, India
[c] Department of Chemistry, Columbia University,
3000 Broadway, New York, NY 10027, USA

Supporting information for this article is available on the WWW under http://www.eurjic.org/ or from the author.

 © 2006 Wiley-VCH Verlag GmbH & Co. KGaA, Weinheim 

tive transmetallating agent, a property which is being extensively used for synthesizing other desired transition metal complexes. Lin[21] provided a commonly employed methodology for synthesizing the NHC silver complexes using $Ag_2O$, which represents by far the most popular route to these complexes. As an outcome of all the efforts toward designing new N-heterocyclic carbene systems, many silver complexes were synthesized and structurally characterized.[22–25] A notable feature of the silver complexes is their structural diversity in the solid state. For example, an NHC ligand with a sterically demanding mesityl substituent gave a neutral (NHC)AgCl-type complex with a 1:1 ligand/metal ratio, whereas the less bulky variant of the same ligand bearing a methyl substituent gave a cationic $(NHC)_2$-$Ag^+$-type complex with a 2:1 ligand/metal ratio.[26]

Interestingly, apart from its exclusive use in transmetallation reactions, a few reports of the utility of NHC silver complexes in chemical catalysis have appeared lately. For instance, there have been reports of the NHC silver complexes exhibiting catalytic activity in ethyl diazoacetate (EDA) assisted carbene transfer reactions,[27] in transesterification reactions, and in ring-opening lactide polymerization reactions.[28] Thus, for the NHC silver complexes, the focus of research is gradually shifting from being solely used in transmetallation reactions to its applications in chemical catalysis, which has opened up a new frontier of research. As the catalytic applications of NHC silver complexes are relatively less explored, we became interested in investigating the catalytic properties of these complexes.

NHCs are often compared with the tertiary phosphane ligands because of their good σ-donating ability.[29] However, a closer scrutiny based on both theoretical[30–34] and experimental[35,36] results revealed that the NHCs are more strongly σ-donating than the phosphanes.[37] Another notable difference between the two is that the NHCs are generally easier to synthesize but harder to metallate while the reverse is true for phosphanes. In general, the success of NHCs can be attributed partly to their ease of synthetic accessibility and partly to the observed improved air, moisture,[38] and thermal stabilities[39] of the so-called NHC catalysts. The issue of improved stabilities of NHC metal complexes may be related to the nature of the metal–carbene (NHC) bond in these complexes and this requires a detailed theoretical study to gain a better understanding of these complexes. Alongside our main aim of designing new NHC silver complexes for applications in chemical catalysis, we became interested in carrying out a detailed theoretical analysis of our NHC silver complexes in order to gain insight into their reactivity pattern and catalytic potential. In this regard, we have recently communicated a detailed synthetic and theoretical study of a newly designed neutral monomeric NHC silver complex, [1-isopropyl-3-(2-*tert*-butyl-2-oxoethyl)imidazol-2-ylidene]AgCl.[40] In addition to the theoretical understanding, our interest is in the testing of these new NHC silver complexes for catalysis, particularly with regard to ring-opening polymerization (ROP) of L-lactides. Because of ecological reasons, the ROP of L-lactides is of current research interest. The polylactide polymers (PLAs), not only are biodegradable but they can also be generated from renewable resources (i.e. the L- and D-lactide monomers) by a corn fermentation process or from agricultural starch wastes.[41] Because of their good mechanical properties and biocompatibility, the PLAs have found wide utility in medical and pharmaceutical applications.[42,43] As the sequence of stereocenters in the polymer chain has a direct bearing on its mechanical properties, the ring-opening polymerization of cyclic lactides thus enjoys inherent advantage over α-olefin polymerizations that need intricate ligand design for control of polymer tacticity.

Herein, we report the synthesis and structural characterization of a silver complex, namely [{1-isopropyl-3-(*N*-phenylacetamido)imidazol-2-ylidene}$_2$Ag]$^+$Cl$^-$ (**1b**), of a new functionalized N-heterocyclic carbene ligand along with a theoretical study. Furthermore, in this contribution we disclose that **1b** effectively catalyzes ring-opening polymerization of L-lactides (Scheme 1) at elevated temperatures under solvent-free melt conditions to give a polylactide polymer of moderate molecular weight with narrow molecular weight distribution.

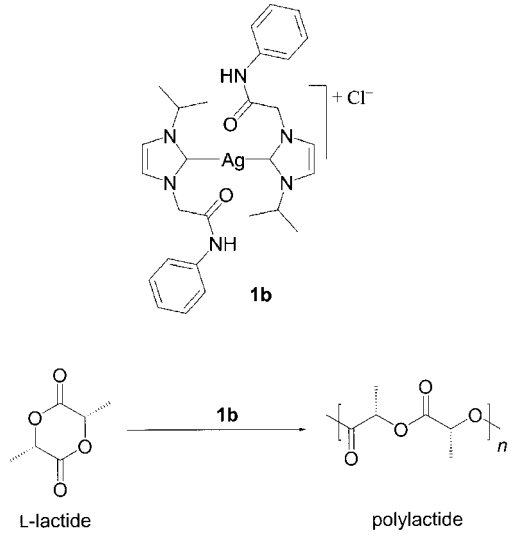


Scheme 1.

## Results and Discussion

Despite the phenomenal successes of NHCs and NHC metal complexes in chemical catalysis, the NHC silver complexes have so far shown only limited utility as catalysts. Recently, there was a report of NHC silver complexes catalyzing a carbene transfer reaction from ethyl diazoacetate to cyclohexane.[27] On another occasion, Waymouth and Hedrick reported NHC silver complexes as novel carbene delivery agents for ring-opening polymerization of L-lactides and for transesterification reactions.[28] These promising applications of NHC silver complexes in chemical catalysis have opened up a new frontier of research. As this area still remains largely unexplored, we became interested in designing novel N-heterocyclic carbene silver complexes

 © 2006 Wiley-VCH Verlag GmbH & Co. KGaA, Weinheim 

and testing their catalytic utility in ring-opening polymerization of L-lactides.

### Synthesis of [{1-Isopropyl-3-(*N*-phenylacetamido)imidazol-2-ylidene}$_2$Ag]$^+$Cl$^-$ (1b)

The N-heterocyclic carbene ligand precursor, 1-isopropyl-3-(*N*-phenylacetamido)imidazolium chloride (**1a**), was synthesized by the alkylation reaction of 1-isopropylimidazole with *N*-phenyl chloroacetamide in refluxing toluene in 90% yield (Scheme 2). Recently, Burgess[44] synthesized similar *N*-acetamidoimidazolium chloride derivatives, synthesized by analogous alkylation procedures, for preparing theNHC silver and palladium complexes. The NMR analysis of 1-isopropyl-3-(*N*-phenylacetamido)imidazolium chloride (**1a**) showed that the diagnostic imidazolium (NC*H*N) resonance appeared downfield-shifted at $\delta$ = 9.97 ppm in the $^1$H NMR spectrum and at $\delta$ = 137.7 ppm in the $^{13}$C NMR spectrum. As expected, the amide proton (CON*H*) resonance appeared downfield-shifted at $\delta$ = 11.37 ppm in the $^1$H NMR spectrum, while the amide carbon (*C*ONH) resonance appeared at $\delta$ = 163.0 ppm in the $^{13}$C NMR spectrum. The C–O stretching frequency of the amide group (CONH) appeared at 1697 cm$^{-1}$ in the IR spectrum.

The silver complex, [{1-isopropyl-3-(*N*-phenylacetamido)-imidazol-2-ylidene}$_2$Ag]$^+$Cl$^-$ (**1b**), was prepared by the reaction of 1-isopropyl-3-(*N*-phenylacetamido)imidazolium chloride (**1a**) with $Ag_2O$ in $CH_2Cl_2$ at room temperature in 64% yield (Scheme 2). Consistent with the formation of the silver complex, the (NC*H*N) resonance of the starting material was conspicuously absent at $\delta$ = 9.97 ppm in the $^1$H NMR spectrum, while a new peak at $\delta$ = 179.5 ppm, corresponding to the silver-bound carbene (N*C*N) resonance, was observed in the $^{13}$C NMR spectrum. The (*C*ONH) resonance appeared at $\delta$ = 165.0 ppm in the $^{13}$C NMR spectrum. The carbonyl peak ($\nu_{CO}$) of the amide moiety (CONH) appeared at 1694 cm$^{-1}$ in the IR spectrum. The electrospray mass analysis gave a 100% abundance peak at *m*/*z* = 593 corresponding to the cationic [{1-isopropyl-3-(*N*-phenylacetamido)imidazol-2-ylidene}$_2$Ag]$^+$ fragment.

The molecular structure of [{1-isopropyl-3-(*N*-phenylacetamido)imidazol-2-ylidene}$_2$Ag]$^+$Cl$^-$ (**1b**) was determined by X-ray diffraction (Figure 1). In the complex, two [{1-isopropyl-3-(*N*-phenylacetamido)imidazol-2-ylidene}] ligands are found to be bound to the metal center. It is noteworthy that for a related NHC ligand, 1-isopropyl-3-(2-*tert*-butyl-2-oxoethyl)imidazolin-2-ylidene, a neutral monomeric complex [1-isopropyl-3-(2-*tert*-butyl-2-oxoethyl)-imidazolin-2-ylidene]AgCl[40] bearing a 1:1 ligand/metal ratio was obtained under analogous reaction conditions unlike the cationic 2:1 ligand/metal ratio observed in the present case. Köhler et al.[45] have recently demonstrated that for the same ligand both the cationic 2:1 NHC/metal complex and the neutral 1:1 NHC/metal complex could be isolated upon changing the polarity of the reaction medium. For example, the reaction in THF gave a neutral 1:1 NHC/metal complex of the type [(saturated NHC)AgCl] while the same in highly polar water gave a 2:1 NHC/metal complex of the type [(saturated NHC)$_2$Ag]$^+$BF$_4^-$.

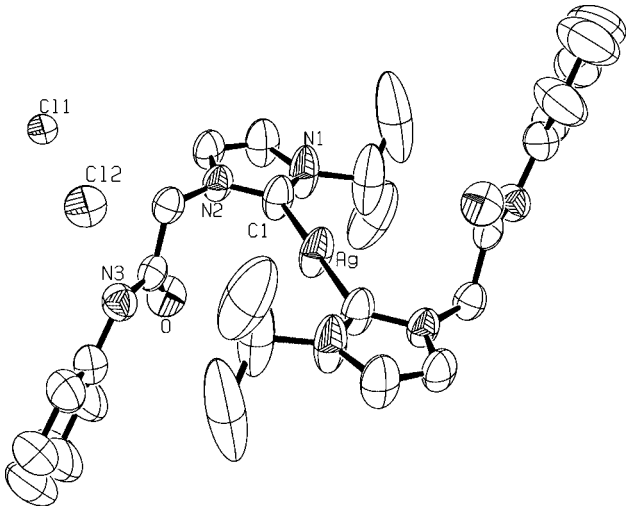


Figure 1. ORTEP of **1b**. The Cl$^-$ ion is disordered with Cl1 having 1/3 occupancy and Cl2 having 2/3 occupancy. Selected bond lengths [Å] and angles [°]: Ag–C(1) 2.085(3), N(1)–C(1) 1.350(4), N(1)–C(2) 1.379(4), C(1)–Ag–C(1) 180.000(1), N(2)–C(1)–N(1) 104.0(2), N(2)–C(1)–Ag 124.7(2), N(1)–C(1)–Ag 131.3(2).

Another notable feature of the **1b** structure is that the two imidazolyl rings surrounding the silver atom are coplanar. The isopropyl and the *N*-phenylacetamide substituents on the imidazole rings are at a *trans* disposition to each other presumably for steric reasons. The coordination geometry around the silver atom is linear [$\angle C_{carb}$–Ag–$C_{carb}$ angle is 180.0(1)°] and is consistent with the preferred linear

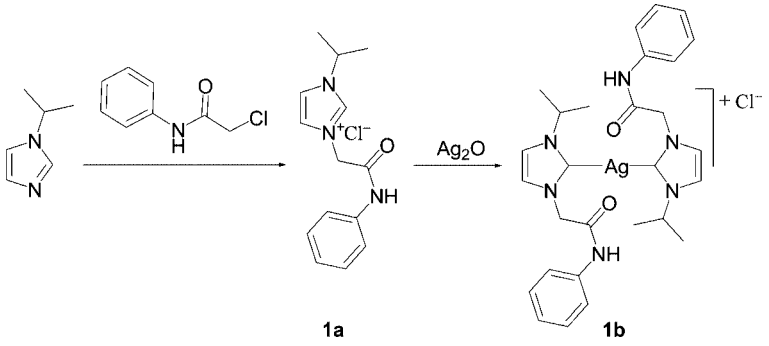


Scheme 2.

 © 2006 Wiley-VCH Verlag GmbH & Co. KGaA, Weinheim 

geometry exhibited by two-coordinate $Ag^I$ complexes having $d^{10}$ configuration.[46] The chloride anion is disordered in the structure with Cl2 having 2/3 occupancy while Cl1 has 1/3 occupancy. The Ag–$C_{carb}$ bond length of 2.085(3) Å more closely resembles a single bond, being slightly shorter than the sum of the covalent radii of silver and carbon (2.111 Å)[47] and also falls well within the observed range of Ag–$C_{carb}$ bond lengths of other analogous complexes (Table 1). Furthermore, the ∠(N–$C_{carb}$–N) angle of 104.0(2)° in **1b** is consistent with that observed for other analogous complexes (Table 1).

Table 1. Selected metrical data for some [(*N*-$R^1$-*N*′-$R^2$-imidazol-2-ylidene)$_2$Ag]$^+$-type complexes.

| Complexes | *d*($C_{carb}$–Ag)/ [Å] | ∠(N–$C_{carb}$–N)/ [°] | ∠($C_{carb}$–Ag–$C_{carb}$)/ [°] | Ref. |
|---|---|---|---|---|
| 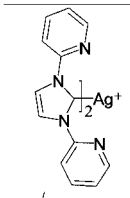 | 2.117(5)<br>2.106(6) | 103.6(5)<br>103.5(5) | 176.8(2) | [24] |
| 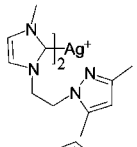 | 2.092(10)<br>2.088(11) | 103.9(9)<br>105.0(9) | 179.5(4) | [26] |
| 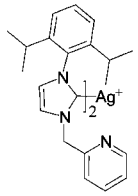 | 2.069(5)<br>2.074(5) | 102.7(4) | 175.90(19) | [77] |
| 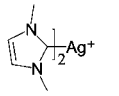 | 2.096(6)[a]<br>2.084(5)[b] | 105.3(6)[a]<br>104.6(5)[b] | 180.0(4)[a]<br>180.0[b] | [78] |
| 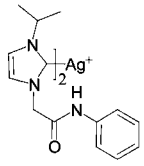 | 2.085(3) | 104.0(2) | 180.0(1) | this work |

[a] Counter anion is $AgCl_2^-$. [b] Counter anion is $AgBr_2^-$.

Important is the comparison of the structure of **1b** with a related [(saturated NHC)$_2$Ag]$^+$ counterpart. For example, in an analogous saturated NHC silver complex, bis[(4*R*,5*S*)-4,5-diallyl-1,3-bis(2,4,6-trimethylphenyl)-4,5-dihydro-3*H*-imidazolin-2-ylidene]silver(I) tetrafluoroborate,[45] the ∠(N–$C_{carb}$–N) angle of 109.0(4)° is larger than the corresponding value of 104.0(2)° observed in the case of **1b** and this is presumably due to the differences in their respective N-heterocyclic ring geometries. The Ag–$C_{carb}$ bond lengths [2.082(4) and 2.087(4) Å] in bis[(4*R*,5*S*)-4,5-diallyl-1,3-bis(2,4,6-trimethylphenyl)-4,5-dihydro-3*H*-imidazolin-2-ylidene]silver(I) tetrafluoroborate, however, compare well with the corresponding values of 2.085(3) Å observed in complex **1b**.

## Density Funtional Theory Studies

Electronic structure calculations using the density functional theory were performed on the [{1-isopropyl-3-(*N*-phenylacetamido)imidazol-2-ylidene}$_2$Ag]$^+$ cationic complex (**2b**) in order to gain further insights into structure and bonding. We used the B3LYP/SDD,6-31G* level of theory. Two major conformers differing in energy by about 2.66 kcal/mol were identified.[48] In the lower energy conformer the imidazole rings were found to remain nearly orthogonal to each other. In an earlier study by Frenking and co-workers on a series of unfunctionalized (NHC)$_2$Ag$^+$ complexes, the energy difference between such conformers was reported to be of the order of 5 kcal/mol with only a negligible barrier to interconversion.[33] A close inspection of the optimized structure with that obtained through X-ray crystallography revealed interesting facts. In the experimental structure, where the imidazole rings are coplanar, it appears that there is an obvious intermolecular hydrogen bonding interaction involving olefinic hydrogen atoms (C8–C10) from the imidazole unit with that of the carbonyl O atom from the functional side-arm of the neighboring NHC silver molecule.[49] Furthermore, additional intramolecular stabilization interactions were noticed in the nonplanar conformer rather than in the planar one (vide infra).

In general, agreement between computed and experimental geometrical parameters was found to be quite good (Table 2). Calculated structural parameters for the unbound carbene, in its singlet ground state, are indicated in Figure 2. It can be seen that the bond lengths in the imidazole ring do not undergo any major change, except for the ∠(N–$C_{carb}$–N) angle, which shows a modest widening by about 1.8°. Since NHCs are known to act as efficient σ-donors through the carbenic carbon atom, one can expect only a minimal geometric distortion as predicted by the computed geometries in Figure 2.

The σ-donation increases the electron deficiency on the $C_{carb}$ atom and thus facilitates a better N→$C_{carb}$ π-donation. We have found an effective delocalization of the nitrogen lone pair electrons into the adjacent C–N bond with the help of natural bond orbital (NBO) analysis. Such delocalizations are responsible for shorter C–N distances in complex **2b** compared to that of the unbound carbene.[50] The computed natural population on C7 (and C42) revealed that the pπ atomic orbital is substantially more populated (1.14 e) in the complex **2b** than in the unbound singlet ground state (0.83 e).[51] The NPA charges on the imidazole nitrogen atoms were found to be increasingly positive upon complexation while the charges on the $C_{carb}$ atoms remain unchanged. Similar observations on related systems have been made earlier and independently by Frenking[31] and Scherer.[32]

In order to gain better insight into the nature of the chemical bonding we carried out charge decomposition analysis (CDA) using the B3LYP wave function. CDA has been known to be a useful tool in analyzing the extent of back-bonding in organometallic systems.[52] The CDA results in **2b** show a significant $C_{carb}$→Ag σ-donation (*d* =

 © 2006 Wiley-VCH Verlag GmbH & Co. KGaA, Weinheim 

Table 2. Comparison between selected distances [Å] and angles [°] in **1b** (X-ray structure) and **2b** (computed structure).

| Parameter[a] | Exp. | Calcd. | Parameter | Exp. | Calcd. |
|---|---|---|---|---|---|
| Ag–C1 | 2.085(3) | 2.109 | C2–C3 | 1.328(5) | 1.357 |
| Ag–C1 | 2.085(3) | 2.109 | C4–C5 | 1.507(4) | 1.546 |
| N1–C1 | 1.350(4) | 1.356 | C11–C12 | 1.473(10) | 1.532 |
| N1–C2 | 1.379(4) | 1.388 | C11–C13 | 1.526(12) | 1.532 |
| N1–C11 | 1.502(5) | 1.484 | C21–C22 | 1.378(6) | 1.401 |
| N2–C1 | 1.350(4) | 1.363 | C21–C26 | 1.388(6) | 1.402 |
| N2–C3 | 1.384(4) | 1.388 | C22–C23 | 1.390(7) | 1.396 |
| N2–C4 | 1.445(4) | 1.453 | C23–C24 | 1.369(12) | 1.395 |
| N3–C5 | 1.365(4) | 1.361 | C24–C25 | 1.326(11) | 1.396 |
| N3–C21 | 1.427(4) | 1.422 | C25–C26 | 1.383(7) | 1.392 |
| C5–O | 1.206(3) | 1.227 | Ag–O | 3.980 | 3.262 |
| | | | Ag–O | 3.980 | 3.220 |
| C1–Ag–C1 | 180.0(1) | 172.5 | O–C5–N3 | 125.1(3) | 125.6 |
| C1–N1–C2 | 110.9(3) | 111.1 | O–C5–C4 | 122.7(3) | 120.8 |
| C1–N1–C11 | 124.5(3) | 124.3 | N3–C5–C4 | 112.2(3) | 113.6 |
| C2–N1–C11 | 124.4(3) | 124.6 | C12–C11–N1 | 111.5(5) | 110.7 |
| C1–N2–C3 | 111.5(2) | 111.1 | C12–C11–C13 | 113.6(6) | 113.3 |
| C1–N2–C4 | 123.3(2) | 124.3 | N1–C11–C13 | 106.8(6) | 110.4 |
| C3–N2–C4 | 125.1(2) | 124.5 | C22–C21–C26 | 120.9(4) | 120.0 |
| C5–N3–C21 | 127.5(3) | 129.2 | C22–C21–N3 | 122.9(4) | 123.1 |
| N2–C1–N1 | 104.0(2) | 104.6 | C26–C21–N3 | 116.1(4) | 116.8 |
| N2–C1–Ag | 124.7(2) | 125.5 | C21–C22–C23 | 117.6(6) | 119.1 |
| N1–C1–Ag | 131.3(2) | 128.4 | C24–C23–C22 | 120.7(7) | 121.2 |
| C3–C2–N1 | 107.5(3) | 106.9 | C25–C24–C23 | 121.3(6) | 119.4 |
| C2–C3–N2 | 106.2(3) | 106.4 | C24–C25–C26 | 120.4(7) | 120.2 |
| N2–C4–C5 | 112.3(2) | 112.4 | C25–C26–C21 | 119.0(5) | 120.2 |
| N3–C7–C42–N38 | 0.85 | 77.94 | | | |

[a] The calculated structure does not include chloride ions and thus refers to the cationic complex **2b**. The atom numbering is therefore different from that in the cif file. For optimized coordinates, please refer to the Supporting Information.

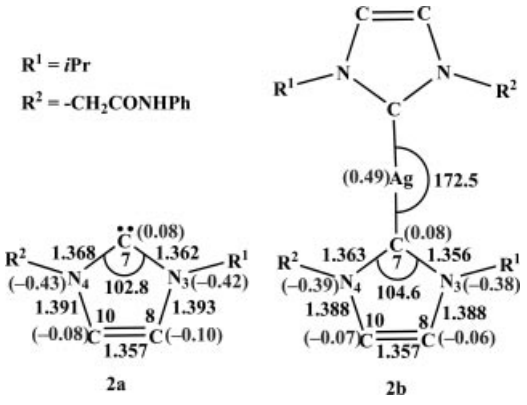


Figure 2. Calculated key structural parameters of free carbene **2a** and the complex **2b**. NPA charges are given in parentheses.

0.656) and a very negligible $C_{carb}$←Ag back-donation ($b$ = 0.053). A $d/b$ ratio of 11.4 and 12.4 between Ag and the two NHC ligands evidently underscores the ability of NHC to function as an effective σ-donor ligand (see Table S3, Supporting Information). The structural parameters as well as population analysis presented in the previous sections are in concurrence with the CDA result that the back-bonding in **2b** is not very significant.

Analysis of the topological features of electron density offers valuable information pertaining to the nature of chemical bonding in molecules. Bader's theory of "Atoms In Molecules" (AIM) has widely been applied to examine interesting bonding situations.[53] Topological properties such as the density at the bond critical point ($\rho_{bc}$), Laplacian of electron density ($\nabla^2\rho_{bc}$) as well as the total energy density ($H$) are analyzed. A covalent interaction is characterized by a negative value for $\nabla^2\rho_{bc}$ as well as $H < 0$. The value of $H$ is widely accepted as a better descriptor in determining the nature of interaction than the $\nabla^2\rho_{bc}$ value.[54] Inspection of computed topological features in the present system, as given in Table 3, reveals that the $C_{carb}$–Ag bond is covalent. For **2b**, values of Laplacian $\nabla^2\rho_{bc}$ as well as total energy density $H_{bc}$ for the $C_{carb}$–Ag bonds were found to be –0.07 and –4.5 au, respectively. These values suggest that the $C_{carb}$–Ag bond is more covalent than ionic. Further, the computed NPA charges on Ag (+0.49) and $C_{carb}$ (+0.08) are consistent with this observation (Figure 2). All other bonds such as C–N and C=C of the imidazole ring were found to be more covalent, as expected. Another noticeable feature emerging from the AIM analysis pertains to the π-bonds in the imidazole rings. The characteristic ellipticity associated with π-bonds is clearly reflected in the computed $\varepsilon$ values that are found to be as high as 0.4 for the C=C bonds. The $C_{carb}$–Ag bond exhibits the lowest value for ellipticity, again indicating lack of π-bonding interactions. Interestingly, the $\varepsilon$ values for the N3–C8 and N4–C10 (also N38–C43 and N39–C45) bonds suggest a moderate π-character, presumably arising due to an N→$C_{carb}$ π-donation into the carbene π-type orbital.

Table 3. Summary of the AIM analysis performed on **2b** at the AIM//B3LYP/SDD,6-31G* level of theory.[a]

| Bond | $\rho_{bc}$ [e·Å$^{-3}$] | $\nabla^2\rho_{bc}$ [e·Å$^{-5}$] | $\varepsilon$ | $H_{bc}$ |
|---|---|---|---|---|
| Ag1–C7 | 0.102 | –0.071 | 0.04 | –4.49 |
| C7–N3 | 0.320 | 0.158 | 0.09 | –14.68 |
| C7–N4 | 0.314 | 0.150 | 0.06 | –14.41 |
| N3–C8 | 0.301 | 0.187 | 0.16 | –12.52 |
| N4–C10 | 0.299 | 0.173 | 0.17 | –12.47 |
| C8–C10 | 0.337 | 0.243 | 0.39 | –13.19 |
| Ag1–C42 | 0.102 | –0.071 | 0.04 | –4.50 |
| C42–N38 | 0.320 | 0.158 | 0.08 | –14.53 |
| C42–N39 | 0.315 | 0.154 | 0.04 | –14.56 |
| N38–C43 | 0.301 | 0.186 | 0.17 | –12.28 |
| N39–C45 | 0.300 | 0.177 | 0.17 | –12.61 |
| C45–C43 | 0.337 | 0.243 | 0.39 | –13.09 |
| O2···H49 | 0.008 | –0.007 | 0.13 | –0.30 |
| O37···H21 | 0.003 | –0.003 | 0.13 | –0.12 |
| Ag1···O2 | 0.009 | –0.006 | 0.50 | –0.38 |
| Ag1···O37 | 0.010 | –0.007 | 0.61 | –0.40 |

[a] See Figure 3 for atom numbers.

As mentioned earlier, the geometry of the lowest energy conformer has a nearly orthogonal disposition of the imidazole rings. In the optimized geometry, there are two interesting intramolecular hydrogen bonds, rendering additional stabilization as shown in Figure 3. The first one is between the hydrogen atom of the tethered isopropyl group of one imidazole ring with the carbonyl group of the other imidazole ring (2.91 Å, $\rho$ = 0.003). The second hydrogen bond-

 © 2006 Wiley-VCH Verlag GmbH & Co. KGaA, Weinheim 

ing interaction is between the methylene hydrogen atom and the carbonyl group attached to another imidazole ring (2.49 Å, $\rho$ = 0.008). These intramolecular interactions were identified correctly by the AIM calculations, where the densities at the bond critical points ($\rho_{bc}$) were found to fall within the hydrogen bonding range.[55] There are also additional interactions between the carbonyl oxygen atoms from both imidazole rings and the silver atom (3.26 Å, $\rho$ = 0.01). These interactions together could be responsible for the near orthogonal orientations of the imidazole rings in the gas-phase-optimized geometry.

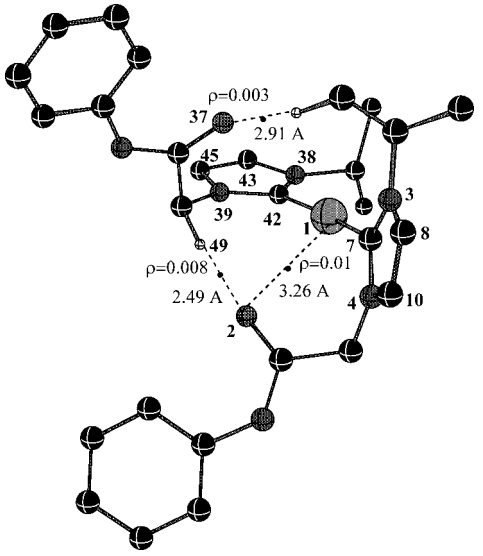


Figure 3. The B3LYP/SDD,6-31G* optimized geometry of **2b** showing weak intramolecular interactions and the corresponding densities at the bond critical points ($\rho_{bc}$) computed using the AIM theory (only selected hydrogen atoms are shown for clarity).

## Polymerization Studies

The silver complex [{1-isopropyl-3-(*N*-phenylacetamido)-imidazol-2-ylidene}$_2$Ag]$^+$Cl$^-$ (**1b**) was found to be an active catalyst for ring-opening polymerization of L-lactides carried out at elevated temperatures under melt conditions in the absence of any solvent.[56] For example, a typical run involved heating of L-lactide and [{1-isopropyl-3-(*N*-phenylacetamido)imidazol-2-ylidene}$_2$Ag]$^+$Cl$^-$ (**1b**) in a sealed vessel under vacuum at designated temperatures for stipulated periods of time. Under these conditions the reaction mixture would form a monomer melt in which the polymerization would occur. The variation of the [M]/[C] ratio (M = monomer, C = catalyst) at 160 °C showed that the maximum molecular weight ($M_w$ = 12.2·10$^3$, Entry 2, Table 4) was obtained at a 100:1 monomer/catalyst ratio. The observed polydispersity index (PDI) was in the range 1.22–1.47. Consistent with the observed molecular weight distributions, the time dependence studies (Entries 2 and 7–9, Table 4) showed no correlation of the observed molecular weight with time thereby ruling out the possibility of a true living polymerization process. The temperature dependence study carried out in the range 100–180 °C[57] (Entries 2 and 10–13, Table 4) showed that the molecular weight of the polymer decreased with an increase in temperature, with the highest molecular weight observed at 100 °C (13.5·10$^3$, Entry 10, Table 4). The decrease in molecular weight with the increase in temperature may be caused by thermal depolymerization as well as an enhanced transesterification reaction occurring at elevated temperatures. In this regard, Liao et al.[56a] and Albertsson and Varma[42] have recently reported a similar decrease in polymer molecular weight with temperature, arising from thermal depolymerization and accelerated transesterification reactions.

Table 4. Melt polymerization of L-lactide by **1b**.

| Entry | L-Lactide/**1b** | Temp. [°C] | Time [h] | $M_w$ | $M_w/M_n$ | Conv. [%] |
|---|---|---|---|---|---|---|
| 1 | 50 | 160 | 4 | 8.1·10$^3$ | 1.37 | 90 |
| 2 | 100 | 160 | 4 | 12.2·10$^3$ | 1.40 | 98 |
| 3 | 250 | 160 | 4 | 9.2·10$^3$ | 1.41 | 78 |
| 4 | 500 | 160 | 4 | 6.6·10$^3$ | 1.28 | 46 |
| 5 | 750 | 160 | 4 | 5.3·10$^3$ | 1.23 | 35 |
| 6 | 1000 | 160 | 4 | 4.9·10$^3$ | 1.22 | 36 |
| 7 | 100 | 160 | 3 | 11.0·10$^3$ | 1.41 | 79 |
| 8 | 100 | 160 | 1.5 | 11.4·10$^3$ | 1.47 | 78 |
| 9 | 100 | 160 | 0.5 | 10.6·10$^3$ | 1.29 | 65 |
| 10 | 100 | 100 | 4 | 13.5·10$^3$ | 1.27 | 84 |
| 11 | 100 | 120 | 4 | 11.9·10$^3$ | 1.46 | 81 |
| 12 | 100 | 140 | 4 | 11.2·10$^3$ | 1.36 | 91 |
| 13 | 100 | 180 | 4 | 8.3·10$^3$ | 1.35 | 94 |

In order to gain insight into the nature of the active species in the catalytic cycle, the thermal stability of [{1-isopropyl-3-(*N*-phenylacetamido)imidazol-2-ylidene}$_2$Ag]$^+$Cl$^-$ (**1b**) was studied by a thermogravimetric analysis (TGA) experiment (Figure 4). Compound **1b** was found to be stable up to 180 °C above which drastic mass loss started to occur presumably caused by the generation of the carbene. Consistent with the TGA results, the attempts to trap the in-situ generated carbene from the thermal decomposition of **1b** with $CS_2$, carried out at a much lower temperature (60 °C), proved to be unsuccessful.[58]

In this regard, it is worth mentioning that Waymouth and Hedrick[28] have recently proposed a mechanism invoking in-situ generation of carbene from similar NHC silver complexes for the ring-opening polymerization of L-lactides. However, for sterically demanding NHC silver precatalysts that were thermally sufficiently stable and did not dissociate to generate carbenes at the polymerization temperature, the possibility of the silver complexes directly mediating the polymerization was also suggested to exist. A similar possibility of silver directly participating in the polymerization also exists in the case of **1b** and is in agreement with the TGA experiment that showed the complex did not undergo significant mass loss below 180 °C while the polymerizations were carried out at a lower temperature range (100–180 °C). Such direct metal-mediated polymerization would lead to the capping of polymer chain ends with NHC fragments (Scheme 3) and indeed, the characteristic resonances of the NHC moieties could be seen in both the $^1$H NMR and $^{13}$C NMR spectra of the polymer.[59] The MALDI spectrometric analysis of the polymer also confirms the presence of NHC chain end groups.[60] In this re-

 © 2006 Wiley-VCH Verlag GmbH & Co. KGaA, Weinheim 

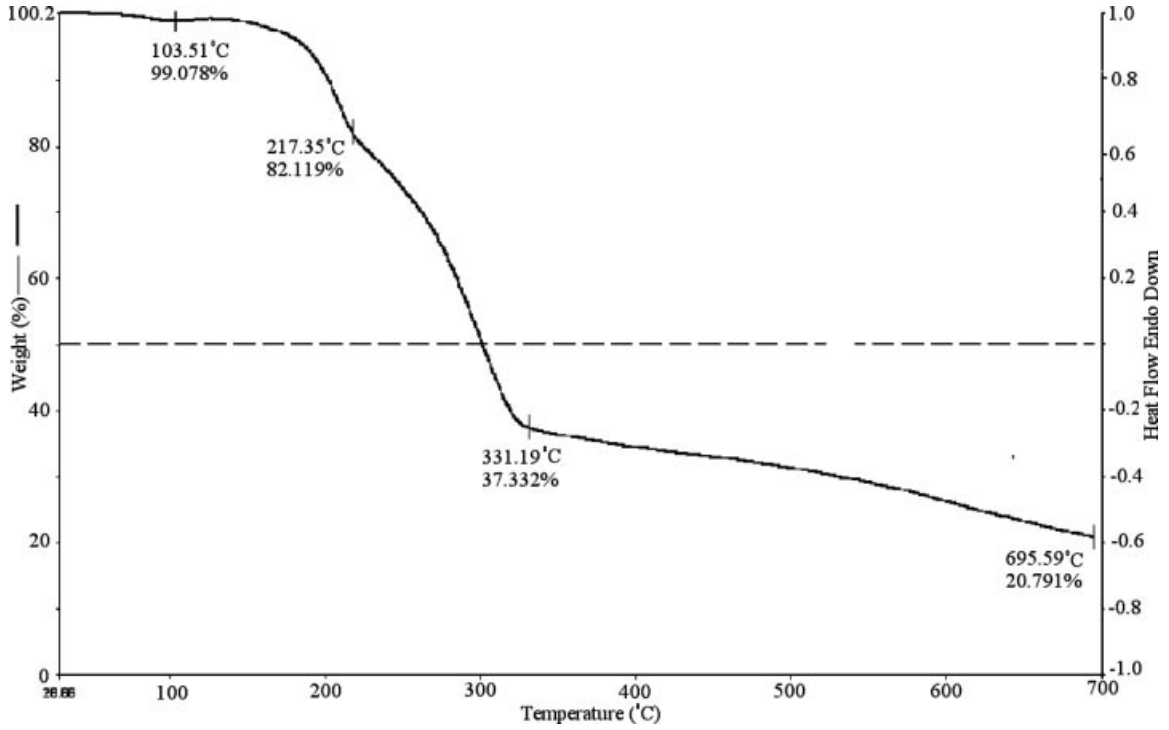


Figure 4. Thermogravimetric analysis of **1b** as a function of temperature.

gard it is worth mentioning that a $(NHC)Y^{III}$ complex has been recently reported to exhibit metal-mediated coordination insertion polymerization of lactides.[61] However, the other possibility that minute amounts of carbene, generated during the thermal decomposition of **1b**, are responsible for the polymerization also cannot be ruled out completely. Currently, detailed mechanistic studies are underway to establish the identity of the active species responsible for the catalysis.

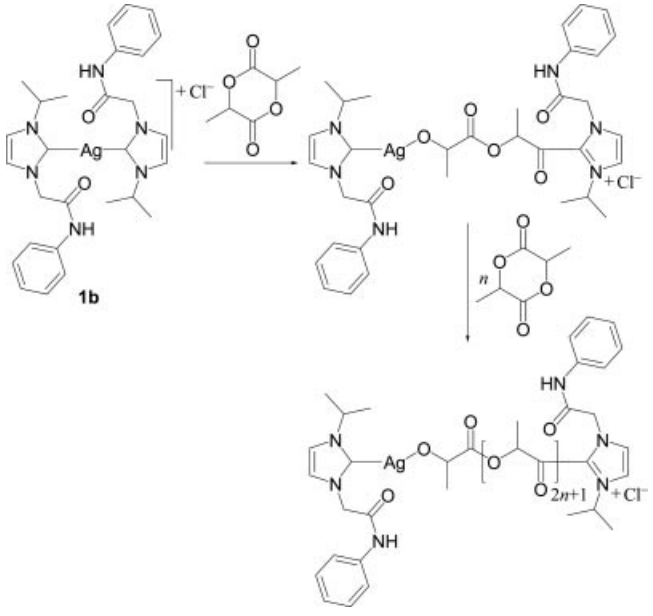


Scheme 3.

## Conclusions

In summary, a new functionalized N-heterocyclic carbene ligand precursor, 1-isopropyl-3-(*N*-phenylacetamido)-imidazolium chloride (**1a**), was synthesized by the alkylation of 1-iso-proplyimidazole with *N*-phenyl chloroacetamide. The silver complex, $[\{1\text{-isopropyl-3-(}N\text{-phenylacetamido)imidazol-2-ylidene}\}_2Ag]^+Cl^-$ (**1b**), was synthesized by treatment of **1a** with $Ag_2O$. Complex **1b** has been structurally characterized by X-ray diffraction studies and was found to effectively initiate polymerization of L-lactide at higher temperatures under solvent-free melt conditions producing polylactide polymers with a narrow molecular weight distribution. Density functional theory studies and post-wave function analysis were able to establish that the functionalized NHC was acting as an effective σ-donor. Weak intramolecular stabilizing interactions were identified as responsible factors in contributing to the perpendicular dispositions of the imidazole rings, compared to the coplanar arrangement as revealed by the X-ray crystallographic study.

## Experimental Section

**General Procedures:** All manipulations were carried out using a combination of a glovebox and standard Schlenk techniques. Solvents were purified and degassed by standard procedures. $Ag_2O$ was purchased from SD-Fine Chemicals (India) and used without any further purification. L-Lactide was purchased from Sigma Aldrich (Germany) and was subjected to polymerization without further purification. L-Lactide was stored at 4 °C as supplied, to avoid the formation of lactyl lactate. *N*-Phenyl chloroacetamide[62] and 1-

 © 2006 Wiley-VCH Verlag GmbH & Co. KGaA, Weinheim 

isopropylimidazole[63] were synthesized according to literature procedures. $^1H$ and $^{13}C\{^1H\}$ NMR spectra were recorded with a Varian 400 MHz NMR spectrometer. $^1H$ NMR peaks were labeled as singlet (s), doublet (d), triplet (t), and septet (sept). Infrared spectra were recorded with a Perkin–Elmer Spectrum One FT-IR spectrometer. Mass spectrometry measurements were carried out with a Micromass Q-Tof spectrometer. The thermal analysis was performed in $N_2$ (flow rate: 10 mL/min) with a heating rate of 10 °C/min using a Perkin–Elmer Pyris thermal analyzer. X-ray diffraction data were collected with a Bruker P4 diffractometer equipped with a SMART CCD detector, and crystal data collection and refinement parameters are summarized in Table 5. The structures were solved by direct methods and standard difference map techniques, and were refined by full-matrix least-squares procedures on $F^2$ with SHELXTL (Version 6.10). CCDC-297479 (for compound **1b**) contains the supplementary crystallographic data for this paper. These data can be obtained free of charge from The Cambridge Crystallographic Data Centre via www.ccdc.cam.ac.uk/data_request/cif. The polymer molecular weights were determined using a Waters GPC (Waters 2414 RI Detector) with PL-gel, a 5 μ-mixed-D (2×300 mm) column, with polystyrene standards in chloroform, and a covered molecular weight range of 140 to $4{\cdot}10^5$. The MALDI-TOF MS measurements were performed with a Voyager-DE STR Biospectrometry Workstation mass spectrometer. A 19 kV accelerating voltage was used with pulsed ion extraction (PIE). The positive ions were detected using the reflection mode (20 kV). A nitrogen laser (337 nm, 1 ns pulse width operating at 4 Hz) was used to produce laser desorption and 50 shots were scanned per spectra. The instrument was calibrated with four standards [Des-Arg 1, Bradykinn and Angiotensin-1, and ACTH (1-17)] by means of linear calibration. The sample was prepared with an α-cyanohydroxy cinnamic acid (CHC) matrix (10 mg /mL). A 1 μL analyte solution (10 mg/mL) was deposited onto the sample plate (stainless steel) and allowed to air-dry. Subsequently, a 1 μL matrix solution (50:50 v/v, CHC/acetonitrile) was added to the analyte.

Table 5. X-ray crystallographic data for **1b**.

| | |
|---|---|
| Lattice | rhombohedral |
| Empirical formula | $C_{28}H_{34}AgClN_6O_2$ |
| Formula mass | 629.93 |
| Space group | $R\bar{3}$ |
| $a$ [Å] | 18.2066(8) |
| $b$ [Å] | 18.2066(8) |
| $c$ [Å] | 28.102(2) |
| $\alpha$ [°] | 90 |
| $\beta$ [°] | 90 |
| $\gamma$ [°] | 120 |
| $V$ [Å$^3$] | 8067.3(8) |
| $Z$ | 9 |
| Temperature [K] | 243(2) |
| Radiation, $\lambda$ [Å] | 0.71073 |
| $\rho$(calcd.) [g·cm$^{-3}$] | 1.167 |
| $\mu$(Mo-$K_\alpha$) [mm$^{-1}$] | 0.665 |
| $\theta_{max}$ [°] | 28.30 |
| No. of data | 4167 |
| No. of parameters | 175 |
| $R_1$ | 0.0461 |
| $wR_2$ | 0.1326 |
| GOF | 1.030 |

**Synthesis of 1-Isopropyl-3-(*N*-phenylacetamido)imidazolium Chloride (1a):** *N*-Phenyl chloroacetamide (2.01 g, 11.8 mmol) and 1-isopropylimidazole (1.30 g, 11.8 mmol) were added to toluene (ca. 10 mL) and heated at 140 °C for 12 h during which a brown precipitate was formed. The precipitate was collected by filtration and washed with hot hexane (ca. 8 mL) and dried under vacuum to give the product as a brown crystalline solid (2.98 g, 90%). $^1H$ NMR (400 MHz, $CDCl_3$, 25 °C, TMS): $\delta$ = 11.37 (s, 1 H, N*H*), 9.97 (s, 1 H, NC*H*N), 7.71 (d, $^3J_{H,H}$ = 7 Hz, 2 H, *o*-$C_6H_5$), 7.59 (s, 1 H, NC*H*CHN), 7.28 (s, 1 H, NCHC*H*N), 7.22 (t, $^3J_{H,H}$ = 7 Hz, 2 H, *m*-$C_6H_5$), 7.03 (t, $^3J_{H,H}$ = 7 Hz, 1 H, *p*-$C_6H_5$), 5.60 (s, 2 H, C$H_2$), 4.63 [sept, $^3J_{H,H}$ = 6 Hz, 1 H, C*H*$(CH_3)_2$], 1.52 [d, $^3J_{H,H}$ = 7 Hz, 6 H, CH(C$H_3$)$_2$] ppm. $^{13}C\{^1H\}$ NMR ($CDCl_3$, 100 MHz, 25 °C): $\delta$ = 163.0 (*C*O), 137.7 (N*C*N), 135.8 (*ipso*-$C_6H_5$), 128.4 (*o*-$C_6H_5$), 124.0 (N*C*HCHN), 123.7 (NCH*C*HN), 119.8 (*p*-$C_6H_5$), 118.9 (*m*-$C_6H_5$), 52.9 (*C*$H_2$), 51.9 [*C*$(CH_3)_2$], 22.6 [C(*C*$H_3$)$_2$] ppm. IR (KBr pellet): $\tilde{\nu}$ = 1697 (s) ($\nu_{CO}$) cm$^{-1}$. LRMS (ES): *m*/*z* (%) = 244 (100) [NHC ligand]$^+$. HRMS (ES): calcd. for [NHC ligand]$^+$ 244.1450, found 244.1455.

**Synthesis of [{1-Isopropyl-3-(*N*-phenylacetamido)imidazol-2-ylidene}$_2$Ag]$^+$Cl$^-$ (1b):** The reaction was carried out under exclusion of light. A mixture of **1a** (1.81 g, 6.47 mmol) and $Ag_2O$ (0.748 g, 3.23 mmol) in dichloromethane (ca. 25 mL) was stirred at room temperature for 4 h. The reaction mixture was filtered and the solvent was removed under vacuum to give the product as a light yellow solid (1.30 g, 64%). $^1H$ NMR (400 MHz, $CDCl_3$, 25 °C, TMS): $\delta$ = 11 (br., 1 H, N*H*), 7.78 (d, $^3J_{H,H}$ = 8 Hz, 2 H, *o*-$C_6H_5$), 7.29 (s, 1 H, NC*H*CHN), 7.20 (t, $^3J_{H,H}$ = 8 Hz, 2 H, *m*-$C_6H_5$), 7.02 (t, $^3J_{H,H}$ = 8 Hz, 1 H, *p*-$C_6H_5$), 6.99 (s, 1 H, NCHC*H*N), 5.27 (s, 2 H, C$H_2$), 4.60 [sept, $^3J_{H,H}$ = 7 Hz, 1 H, C*H*$(CH_3)_2$], 1.42 [d, $^3J_{H,H}$ = 7 Hz, 6 H, CH(C$H_3$)$_2$] ppm. $^{13}C\{^1H\}$ NMR ($CDCl_3$, 100 MHz, 25 °C): $\delta$ = 179.5 (N*C*N), 165.0 (*C*O), 138.0 (*ipso*-$C_6H_5$), 128.1 (*o*-$C_6H_5$), 123.5 (N*C*HCHN), 122.6 (NCH*C*HN), 119.5 (*p*-$C_6H_5$), 116.4 (*m*-$C_6H_5$), 54.4 [*C*$(CH_3)_2$], 53.5 (*C*$H_2$), 23.2 [C(*C*$H_3$)$_2$] ppm. IR (KBr pellet): $\tilde{\nu}$ = 1694 (s) ($\nu_{CO}$) cm$^{-1}$. LRMS (ES): *m*/*z* (%) = 593 (100) [(NHC ligand)$_2$Ag]$^+$.

**Computational Methods:** The density functional theory calculations were performed on the [{1-isopropyl-3-(*N*-phenylacetamido)imidazol-2-ylidene}$_2$Ag]$^+$ cationic complex (**2b**) using the Gaussian98 suite of quantum chemical programs.[64] The Becke three-parameter exchange functional in conjunction with the Lee–Yang–Parr correlation functional (B3LYP) was employed in this study.[65,66] The Stuttgart-Dresden effective core potential (ECP), representing 19 core electrons, along with valence basis sets (SDD) was used for the silver atom.[67] All other atoms were treated with the 6-31G(d) basis set.[68] We will be designating the level of theory hereafter as B3LYP/SDD,6-31G*. Inspection of the metal–ligand donor–acceptor interactions was carried out using charge decomposition analysis (CDA).[69] CDA is a valuable tool for analyzing the interactions between molecular fragments in a quantitative fashion, with an emphasis on the electron donation.[70] The CDA calculations were performed with the program AOMIX using the B3LYP/SDD,6-31G* wave function.[71] Natural bond orbital analysis was performed using the NBO3.1 program as implemented in the Gaussian98 package.[72] Second-order perturbation energy analysis, natural charges,[73] and bond orders[74] for **2b** were calculated using the B3LYP wave function. The nature of the chemical bonding was further explored with Bader's "Atoms in Molecules" approach[75] using the AIM2000 program.[76]

**Polymerization Experiments:** Typical polymerization experiment: L-Lactide (1.01 g, 7.01 mmol) and **1b** (0.044 g, 0.070 mmol) were charged in an ampoule inside a glove box. The ampoule was taken out and put under vacuum at 50 °C for 15 min, after which the ampoule was sealed under vacuum and heated at 160 °C for 4 h. Under these conditions, the reaction mixture turned into a monomer melt in which polymerization occurred. Subsequently, the molten reactive polymer mixture was cooled by submerging the se-

 © 2006 Wiley-VCH Verlag GmbH & Co. KGaA, Weinheim 

aled ampoule into liquid nitrogen to stop the polymerization. The conversion of L-lactide monomer was determined using the size exclusion chromatography method. The analyses were performed on the crude reaction mixture, no precipitation was executed to avoid fractionation of the sample so as not to influence the results.

**Supporting Information** (see footnote on the first page of this article): Polymer characterization data, B3LYP-optimized coordinates for NPA data, and list of NBO delocalizations for **2b**.

## Acknowledgments

We thank the Department of Science and Technology (Grant No. SR/S1/IC-25/2003) for financial support of this research. M. K. S. and D. R. thank CSIR, New Delhi for research fellowships. Computational facilities from the IIT Bombay computer center are gratefully acknowledged.

[1] A. J. Arduengo III, R. L. Harlow, M. A. Kline, *J. Am. Chem. Soc.* **1991**, *113*, 361–363.
[2] For recent developments, see the following reviews and the references therein: a) C. M. Crudden, D. P. Allen, *Coord. Chem. Rev.* **2004**, *248*, 2247–2273; b) M. C. Perry, K. Burgess, *Tetrahedron: Asymmetry* **2003**, *14*, 951–961; c) P. L. Arnold, *Heteroat. Chem.* **2002**, *13*, 534–539.
[3] a) E. Peris, R. H. Crabtree, *Coord. Chem. Rev.* **2004**, *248*, 2239–2246; b) K. J. Cavell, D. S. McGuinness, *Coord. Chem. Rev.* **2004**, *248*, 671–681; c) W. A. Hermann, *Angew. Chem. Int. Ed.* **2002**, *41*, 1290–1309.
[4] a) T. Weskamp, F. J. Kohl, W. Hieringer, D. Gleich, W. A. Herrmann, *Angew. Chem. Int. Ed.* **1999**, *38*, 2416–2419; b) T. Weskamp, W. C. Schattenmann, M. Spiegler, W. A. Herrmann, *Angew. Chem. Int. Ed. Engl.* **1998**, *37*, 2490–2493.
[5] a) M. S. Stanford, M. Ulman, R. H. Grubbs, *J. Am. Chem. Soc.* **2001**, *123*, 749–750; b) W. A. Herrmann, L. J. Goossen, M. Spiegler, *Organometallics* **1998**, *17*, 2162–2168; c) T.-L. Choi, R. H. Grubbs, *Chem. Commun.* **2001**, 2648–2649; d) J. Huang, H.-J. Schanz, E. D. Stevens, S. P. Nolan, *Organometallics* **1999**, *18*, 2370–2375.
[6] For the elaborate development of the topic, see the following reviews and the references therein: a) U. Frenzel, O. Nuyken, *J. Polym. Sci., Part A: Polym. Chem.* **2002**, *40*, 2895–2916; b) T. M. Trnka, R. H. Grubbs, *Acc. Chem. Res.* **2001**, *34*, 18–29.
[7] D. S. McGuinness, K. J. Cavell, *Organometallics* **2000**, *19*, 741–748.
[8] L. Xu, W. Chen, J. F. Bickley, A. Steiner, J. Xiao, *J. Organomet. Chem.* **2000**, *598*, 409–416.
[9] J. Huang, E. D. Stevens, S. P. Nolan, *Organometallics* **2000**, *19*, 1194–1197.
[10] For representative examples, see: a) J. R. Miecznikowski, R. H. Crabtree, *Organometallics* **2004**, *23*, 629–631; b) S. Kuhl, R. Schneider, Y. Fort, *Organometallics* **2003**, *22*, 4184–4186; c) V. K. Dioumaev, D. J. Szalda, J. Hanson, J. A. Franz, R. M. Bullock, *Chem. Commun.* **2003**, 1670–1671; d) L. D. Vázquesz-Serrano, B. T. Owens, J. M. Buriak, *Chem. Commun.* **2002**, 2518–2519; e) H. M. Lee, T. Jiang, E. D. Stevens, S. P. Nolan, *Organometallics* **2001**, *20*, 1255–1258; f) M. T. Powell, D.-R. Hou, M. C. Perry, X. Cui, K. Burgess, *J. Am. Chem. Soc.* **2001**, *123*, 8878–8879.
[11] M. Albrecht, J. R. Miecznikowski, A. Samuel, J. W. Faller, R. H. Crabtree, *Organometallics* **2002**, *21*, 3596–3604.
[12] H. van Rosenburg, R. P. Tooze, D. F. Foster, A. M. Z. Slawin, *Inorg. Chem.* **2004**, *43*, 2468–2470.
[13] For representative examples, see: a) E. Mas-Marźa, M. Poyatos, M. Sanaú, E. Peris, *Inorg. Chem.* **2004**, *43*, 2213–2219; b) H. Kaur, F. K. Zinn, E. D. Stevens, S. P. Nolan, *Organometallics* **2004**, *23*, 1157–1160; c) K. H. Park, S. Y. Kim, S. U. Son, Y. K. Chung, *Eur. J. Org. Chem.* **2003**, *22*, 4341–4345; d) W.-L. Duan, M. Shi, G.-B. Rong, *Chem. Commun.* **2003**, 2916–2917; e) I. E. Marko, S. Stérin, O. Buisine, G. Mignani, P. Branlard, B. Tinanti, J.-P. Declercq, *Science* **2002**, *298*, 204–206; f) V. K. Dioumaev, R. M. Bullock, *Nature* **2000**, *424*, 530–532.
[14] M. G. Gardiner, W. A. Herrmann, C. P. Reisinger, M. Spiegler, *J. Organomet. Chem.* **1999**, *572*, 239–247.
[15] G. Grasa, Z. Moore, K. L. Martin, E. D. Stevens, S. P. Nolan, V. Paquet, H. Lebel, *J. Organomet. Chem.* **2002**, *658*, 126–131.
[16] G. A. Garsa, R. M. Kissling, S. P. Nolan, *Org. Lett.* **2002**, *4*, 3583–3586.
[17] E. F. Connor, G. W. Nyce, M. Myers, A. Mőck, J. L. Hedrick, *J. Am. Chem. Soc.* **2002**, *124*, 914–915.
[18] G. W. Nyce, T. Glauser, E. F. Connor, A. Mőck, R. M. Waymouth, J. L. Hedrick, *J. Am. Chem. Soc.* **2003**, *125*, 3046–3056.
[19] G. W. Nyce, S. Csihony, R. M. Waymouth, J. L. Hedrick, *Chem. Eur. J.* **2004**, *10*, 4073–4079.
[20] J. C. Garrison, W. J. Youngs, *Chem. Rev.* **2005**, *105*, 3978–4008.
[21] H. M. J. Wang, I. J. B. Lin, *Organometallics* **1998**, *17*, 972–975.
[22] a) J. J. V. Veldhuizen, J. E. Campbell, R. E. Giudici, A. H. Hoveyda, *J. Am. Chem. Soc.* **2005**, *127*, 6877–6882; b) Y. A. Wanniarachchi, M. A. Khan, L. M. Slaughter, *Organometallics* **2004**, *23*, 5881–5884.
[23] C. Y. Legault, C. Kendall, A. B. Charette, *Chem. Commun.* **2005**, 3826–3827.
[24] V. J. Catalano, M. A. Malwitz, A. O. Etogo, *Inorg. Chem.* **2004**, *43*, 5714–5724.
[25] A. Kascatan-Nebioglu, M. J. Panzner, J. C. Garrison, C. A. Tessier, W. J. Youngs, *Organometallics* **2004**, *23*, 1928–1931.
[26] H. M. Lee, P. L. Chiu, C.-H. Hu, C.-L. Lai, Y.-C. Chou, *J. Organomet. Chem.* **2005**, *690*, 403–414.
[27] M. M. Díaz-Requejo, P. J. Pérez, *J. Organomet. Chem.* **2005**, *690*, 5441–5450.
[28] A. C. Sentman, S. Csihony, R. M. Waymouth, J. L. Hedrick, *J. Org. Chem.* **2005**, *70*, 2391–2393.
[29] W. A. Herrmann, C. Kőcher, *Angew. Chem. Int. Ed. Engl.* **1997**, *36*, 2162–2187.
[30] M.-T. Lee, C.-H. Hu, *Organometallics* **2004**, *23*, 976–983.
[31] C. Boehme, G. Frenking, *Organometallics* **1998**, *17*, 5801–5809.
[32] M. Tafipolsky, W. Scherer, K. Öfele, G. Artus, B. Pederson, W. A. Herrmann, G. S. McGardy, *J. Am. Chem. Soc.* **2002**, *124*, 5865–5880.
[33] D. Nemcsok, K. Wichmann, G. Frenking, *Organometallics* **2004**, *23*, 3640–3646.
[34] E. Baba, T. R. Cundari, I. Firkin, *Inorg. Chim. Acta* **2005**, *358*, 2867–2875.
[35] R. Dorta, E. D. Stevens, N. M. Scott, C. Costabile, L. Cavallo, C. D. Hoff, S. P. Nolan, *J. Am. Chem. Soc.* **2005**, *127*, 2485–2495.
[36] A. R. Chianese, X. Li, M. C. Janzen, J. W. Faller, R. H. Crabtree, *Organometallics* **2003**, *22*, 1663–1667.
[37] X. Hu, I. Castro-Rodriguez, K. Olsen, K. Meyer, *Organometallics* **2004**, *23*, 755–764.
[38] Charette recently reported an air- and moisture-stable (NHC) $Ag^{I}$ complex that could be stored on a bench without any precautions for over 4 months, see ref.[23]
[39] For example, Faller and Crabtree recently reported two such remarkable catalysts namely (i) an air- and thermally stable Pd catalyst (see ref.[39a]) for the Heck olefination reaction with activated aryl chlorides and (ii) an air- and moisture-stable Ir catalyst for an efficient transfer hydrogenation reaction involving ketones. The Ir catalysts could even survive column chromatography, with which they were purified (see ref.[11]): a) S. Gründemann, M. Albrecht, J. A. Loch, J. W. Faller, R. H. Crabtree, *Organometallics* **2001**, *20*, 5485–5488.
[40] M. K. Samantaray, D. Roy; A. Patra, R. Stephen, M. Saikh, R. B. Sunoj, P. Ghosh, *J. Organomet. Chem.*, in press.
[41] a) K. A. M. Thakur, R. T. Kean, E. S. Hall, J. J. Kolstad, E. J. Munson, *Macromolecules* **1998**, *31*, 1487–1494; b) K. A. M. Thakur, R. T. Kean, E. S. Hall, J. J. Kolstad, T. A. Lindgren,

 © 2006 Wiley-VCH Verlag GmbH & Co. KGaA, Weinheim 

M. A. Doscotch, J. I. Siepmann, E. J. Munson, *Macromolecules* **1997**, *30*, 2422–2428.

[42] A. C. Albertsson, I. K. Varma, *Biomacromolecules* **2003**, *4*, 1466–1486.

[43] a) M. Okada, *Prog. Polym. Sci.* **2002**, *27*, 87–133; b) H. R. Kriecheldorf, *Chemosphere* **2001**, *43*, 49–54.

[44] M. C. Perry, X. Cui, K. Burgess, *Tetrahedron: Asymmetry* **2002**, *13*, 1969–1972.

[45] K. Weigl, K. Köhler, S. Dechert, F. Meyer, *Organometallics* **2005**, *24*, 4049–4056.

[46] F. A. Cotton, G. Wilkinson, C. A. Murillo, M. Bochmann, *Advanced Inorganic Chemistry*, 6th ed., Wiley, New York, **1999**, pp. 1085–1094.

[47] L. Pauling, *The Nature of the Chemical Bond*, 3rd ed., Cornell University Press, Ithaca, NY, **1960**, pp. 224–225, 256.

[48] It was noticed that during geometry optimization, the initial guess geometry with coplanar imidazole rings goes out of plane and ends up with the nonplanar structure. The coplanar structure is obtained as a result of a constrained optimization with the N3–C7–C42–N38 angle fixed.

[49] See Figure S1 in the Supporting Information.

[50] Details of various delocalizations and the corresponding second-order perturbation energies obtained with NBO analysis are summarized in Table S1 in the Supporting Information.

[51] Details of the natural populations obtained at the NPA/B3LYP//B3LYP/SDD,6-31(d) level are provided in Table S2 in the Supporting Information.

[52] a) S. Bi, A. Ariafard, G. Jia, Z. Lin, *Organometallics* **2005**, *24*, 680–686; b) T. J. M. de Bruin, A. Milet, A. E. Greene, Y. Gimbert, *J. Org. Chem.* **2004**, *69*, 1075–1080.

[53] R. F. W. Bader, C. F. Matta, *Organometallics* **2004**, *23*, 6253–6263.

[54] a) W. Koch, G. Frenking, J. Gauss, D. Cremer, J. R. Collins, *J. Am. Chem. Soc.* **1987**, *109*, 5917–5934; b) I. Rozas, I. Alkorta, J. Elguero, *J. Am. Chem. Soc.* **2000**, *122*, 11154–11161.

[55] a) U. Koch, P. L. A. Popelier, *J. Phys. Chem.* **1995**, *99*, 9747–9754; b) E. Cubero, M. Orozco, P. Hobza, F. J. Luque, *J. Phys. Chem. A* **1999**, *103*, 6394–6401.

[56] For ring-opening polymerization of L-lactides under similar solvent-free monomer melt conditions, see: a) X. Wang, K. Liao, D. Quan, Q. Wu, *Macromolecules* **2005**, *38*, 4611–4617; b) A. J. Nijenhuis, D. W. Grijpma, A. J. Pennings, *Macromolecules* **1992**, *25*, 6419–6424.

[57] The bulk polymerization temperatures were chosen to be higher than the melting point of the lactide monomer (96 °C).

[58] Because of the low boiling point of $CS_2$ (46 °C) these carbene trapping experiments could not be carried out at a high temperature (> 180 °C) where the carbene generation was supposed to take place according to the thermal gravimetric analysis results.

[59] It is noteworthy that the NHC end-groups were seen in the $^1H$ NMR and $^{13}C\{^1H\}$ NMR spectra of the polymer when analyzed directly from the melt as well as after dissolving in a minimum of dichloromethane and precipitating with hexane whereas no NHC resonances were observed when the precipitation of the polymer was done with methanol. See Figures S2 and S3 in the Supporting Information.

[60] A series of sodium (23 Da) cationized peaks of the polymers bearing NHC end groups can be recognized in the MALDI spectrum. See Figure S4 in Supporting Information. The mass ($M_C$) of the sodium cationized peak of the polymer bearing the (NHC)Ag (350 Da) and NHC (243 Da) end groups is given by $M_C = 72x + 350 + 243 + 23$ where $x$ = number of repeat unit (72Da).

[61] D. Patel, S. T. Liddle, S. A. Mungur, M. Rodden, A. J. Blake, P. L. Arnold, *Chem. Commun.* **2006**, 1124–1126.

[62] M. P. Dave, J. M. Patel, N. A. Langalia, S. R. Shah, K. A. Thaker, *J. Indian Chem. Soc.* **1985**, *62*, 386–387.

[63] E. Mas-Marzá, E. Peris, I. Castro-Rodríguez, K. Meyer, *Organometallics* **2005**, *24*, 3158–3162.

[64] M. J. Frisch, G. W. Trucks, H. B. Schlegel, G. E. Scuseria, M. A. Robb, J. R. Cheeseman, V. G. Zakrzewski, J. A. Montgomery, Jr., R. E. Stratmann, J. C. Burant, S. Dapprich, J. M. Millam, A. D. Daniels, K. N. Kudin, M. C. Strain, O. Farkas, J. Tomasi, V. Barone, M. Cossi, R. Cammi, B. Mennucci, C. Pomelli, C. Adamo, S. Clifford, J. Ochterski, G. A. Petersson, P. Y. Ayala, Q. Cui, K. Morokuma, D. K. Malick, A. D. Rabuck, K. Raghavachari, J. B. Foresman, J. Cioslowski, J. V. Ortiz, B. B. Stefanov, G. Liu, A. Liashenko, P. Piskorz, I. Komaromi, R. Gomperts, R. L. Martin, D. J. Fox, T. Keith, M. A. Al-Laham, C. Y. Peng, A. Nanayakkara, C. Gonzalez, M. Challacombe, P. M. W. Gill, B. Johnson, W. Chen, M. W. Wong, J. L. Andres, C. Gonzalez, M. Head-Gordon, E. S. Replogle, J. A. Pople, *Gaussian 98*, revision A.6, Gaussian, Inc., Pittsburgh, PA, **1998**.

[65] A. D. Becke, *Phys. Rev. A* **1988**, *38*, 3098–3100.

[66] C. Lee, W. Yang, R. G. Parr, *Phys. Rev. B* **1988**, *37*, 785–789.

[67] a) M. Dolg, U. Wedig, H. Stoll, H. Preuss, *J. Chem. Phys.* **1987**, *86*, 866–872; b) D. Andrae, U. Haussermann, M. Dolg, H. Stoll, H. Preuss, *Theor. Chim. Acta* **1990**, *77*, 123–141; c) A. Alkauskas, A. Baratoff, C. Bruder, *J. Phys. Chem. A* **2004**, *108*, 6863–6868.

[68] W. J. Hehre, R. Ditchfield, J. A. Pople, *J. Chem. Phys.* **1972**, *56*, 2257–2261.

[69] S. Dapprich, G. Frenking, *J. Phys. Chem.* **1995**, *99*, 9352–9362.

[70] a) S. F. Vyboishchikov, G. Frenking, *Chem. Eur. J.* **1998**, *4*, 1439–1448; b) G. Frenking, U. Pidun, *J. Chem. Soc., Dalton Trans.* **1997**, 1653–1662.

[71] S. I. Gorelsky, *AOMix, program for molecular orbital analysis*,, York University, Toronto, Canada, **1997**, http://www.sg-chem.net/

[72] A. E. Reed, L. A. Curtiss, F. Weinhold, *Chem. Rev.* **1988**, *88*, 899–926.

[73] A. E. Reed, R. B. Weinstock, F. Weinhold, *J. Chem. Phys.* **1985**, *83*, 735–746.

[74] K. B. Wiberg, *Tetrahedron* **1968**, *24*, 1083–1096.

[75] R. F. W. Bader, *Atoms in Molecules – A Quantum Theory*, Oxford University Press, Oxford, U. K., **1990**.

[76] F. Biegler-Konig, J. Schonbohm, D. Bayles, *J. Comput. Chem.* **2001**, *22*, 545–559.

[77] A. A. D. Tulloch, A. A. Danopoulos, S. Winston, S. Kleinhenz, G. Eastham, *J. Chem. Soc., Dalton Trans.* **2000**, 4499–4506.

[78] K. M. Lee, H. M. J. Wang, I. J. B. Lin, *J. Chem. Soc., Dalton Trans.* **2002**, 2852–2856.

Received: March 9, 2006
Published Online: June 12, 2006

 © 2006 Wiley-VCH Verlag GmbH & Co. KGaA, Weinheim 

DOI: 10.1002/ejic.200600236

# Molecular and Electronic Structures of Homoleptic Nickel and Cobalt Complexes with Non-Innocent Bulky Diimine Ligands Derived from Fluorinated 1,4-Diaza-1,3-butadiene (DAD) and Bis(arylimino)acenaphthene (BIAN)

**Marat M. Khusniyarov,[a] Klaus Harms,[a] Olaf Burghaus,[a] and Jörg Sundermeyer*[a]**

*Dedicated to Professor Hansgeorg Schnöckel on the occasion of his 65th birthday*

**Keywords:** EPR spectroscopy / Magnetochemistry / Non-innocent ligands / Nickel / Cobalt / X-ray diffraction

The diimine complexes with bulky fluorinated *N*-substituents $[Ni^{II}(^{F}DAD)_2]$ **1** and $[Co^{II}(^{F}DAD)_2]$ **2** [$^{F}$DAD = *N*,*N*′-bis-(pentafluorophenyl)-2,3-dimethyl-1,4-diaza-1,3-butadiene] as well as diimine complexes with extended π system $[Ni^{II}(^{F}BIAN)_2]$ **3** and $[Co^{I}(^{F}BIAN)_3]$ **4** ($^{F}$BIAN = bis[*N*-{3,5-bis(trifluoromethyl)phenyl}imino]acenaphthene) were synthesized. Compound **4** represents the first complex with three bis(imino)acenaphthene ligands synthesized so far. The molecular structures of the complexes **1**–**4** were determined by X-ray crystallography at 193 K. Complexes **1**, **2** and **3** comprise the divalent metal ions with pairs of radical monoanionic ligands, whereas **4** is best described as a cobalt(I) complex with two neutral $(^{F}BIAN)^0$ and one $(^{F}BIAN)^{1-}$ ligand in the radical monoanionic form. The electronic structures of the paramagnetic cobalt complexes **2** and **4** were investigated by SQUID measurements and X-band EPR spectroscopy. Both complexes possess a doublet ground state, with electron density located mostly in the metal d-orbitals. The doublet–quartet energy gap for **4** was established to be 159 $cm^{-1}$.

(© Wiley-VCH Verlag GmbH & Co. KGaA, 69451 Weinheim, Germany, 2006)

## Introduction

Homoleptic complexes of substituted 1,4-**di**aza-1,3-buta-**d**iene (DAD) with late transition metals $[M(DAD)_2]$ are well know since the first publication of Balch and Holm in early 1966.[1] They synthesized the extremely oxygen-sensitive complex $[Ni\{Ph\text{-}DAD(Me)\}_2]$ and proposed the electronic structure as a $Ni^{II}$ center with two radical monoanionic $(DAD)^{1-}$ ligands.

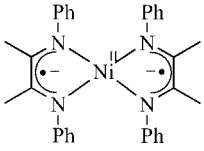

Nowadays, it is clearly established that the $(DAD)^0$ ligand possessing a low-lying antibonding π* orbital is able to accept one or two electrons giving open-shell monoanion $(DAD)^{1-}$ or closed-shell dianion $(DAD)^{2-}$, respectively. Thus, DAD along with related *o*-phenylenediamido ligands belong to the classical *N*,*N*′-coordinating non-innocent ligands.[2]

R'-DAD(R) :

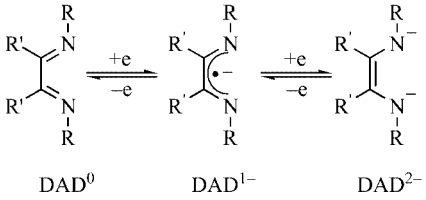

$DAD^0$ $DAD^{1-}$ $DAD^{2-}$

The class of $[M(DAD)_2]$ complexes was expanded by the groups of tom Dieck (M = Fe,[3] Ni[4]) and von Walther (M = Fe,[5] Co,[5,6] Ni[7]). Later, several $[Ni(DAD)_2]$ complexes were characterized by single-crystal X-ray analysis.[8,9] In contradiction to the electronic model given by Balch and Holm all these complexes were formulated as zero-valent metal species with pairs of closed-shell $(DAD)^0$ ligands. At the same time closely related complexes derived from *o*-phenylenediamine $[Ni^{II}(sbqdi)_2]$[10] [sbqdi – **s**emi**b**enzo-**q**uinone**di**iminato(1–)] and diaminomaleonitrile $[Ni^{II}(sdisn)_2]$[11] [sdisn – **s**emi**di**imino**s**ucci**n**o**n**itrilo(1–)] are well known to consist of a divalent metal and a pair of monoanionic radical ligands.

[a] Fachbereich Chemie, Philipps-Universität Marburg, Hans-Meerwein-Straße, 35032 Marburg, Germany
Fax: +49-6421-28-28917
E-mail: jsu@chemie.uni-marburg.de

Supporting information for this article is available on the WWW under http://www.eurjic.org or from the author.

 © 2006 Wiley-VCH Verlag GmbH & Co. KGaA, Weinheim 

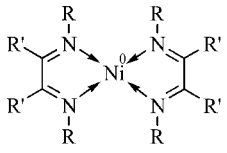

$[Ni(DAD)_2]$

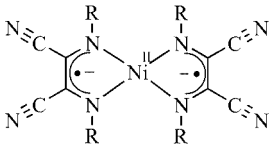

$[Ni(sdisn)_2]$

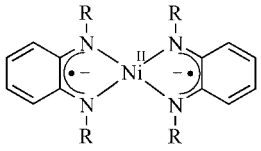

$[Ni(sbqdi)_2]$

Throughout this paper we carefully distinguish between formal[12] and spectroscopic (or physical)[13] oxidation states. The formal oxidation state of a metal ion in a given coordination compound is a non-measurable, physically meaningless, usually integral number that is derived by heterolytic removal of all ligands in their closed-shell electron configuration, whereas the spectroscopic oxidation state is derived from the actual electron configuration of the metal ion in a given ligand regime.

Complexes of late transition metals with redox active non-innocent ligands[2] are of particular interest with regard to their electronic structures. Since late transition metals can exist in several oxidation states, ambiguity of oxidation state determination may arise with transition metals coordinated to non-innocent ligands. Often spectroscopic (or physical) oxidation state of the non-innocent ligand can be elegantly determined using a high-quality single-crystal X-ray analysis, as different oxidation states of the ligand reveal different characteristic bond lengths.[14]

Following our studies on complexes of late transition metals containing non-innocent ligands[15] we report here the first structurally characterized $[Co(DAD)_2]$ complex along with its Ni analogue. Both molecular and electronic structures of them are being investigated by X-ray analysis, EPR spectroscopy, and variable-temperature magnetic susceptibility measurements.

Similar to DAD **b**is(aryl**i**mino)**ac**e**n**aphthene (BIAN)[16] owing to its non-innocent nature is known to form complexes in different ligand oxidation states.

Ar-BIAN:

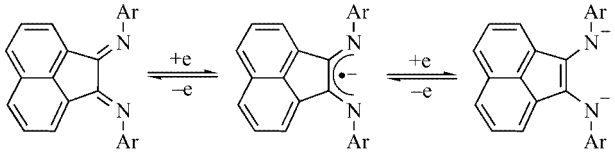

$BIAN^0$ $BIAN^{1-}$ $BIAN^{2-}$

Very recently, Fedushkin et al.[17] reported the first homoleptic complexes of the type $[M^{II}(BIAN)_2]$ (M = Mg, Ca). The molecular structure of $[Ca^{II}(dip\text{-}BIAN)_2]$ (dip = 2,6-diisopropylphenyl) was established and monoanionic nature of both ligands along with conventional oxidation state for calcium were established. To the best of our knowledge homoleptic complexes of the type $[M(BIAN)_2]$ with transition metals have been not isolated and structurally characterized so far. Therefore, the class of homoleptic DAD complexes has been further expanded by us to corresponding BIAN complexes. Molecular structures of BIAN complexes of nickel and cobalt are reported. The electronic structure of the paramagnetic cobalt complex is investigated in detail by means of EPR spectroscopy and variable-temperature magnetic susceptibility measurements.

## Results and Discussion

### Synthesis and Characterization of DAD Complexes

In order to synthesize complexes **1** and **2** we employed a variation of the well-known in situ reduction method.[7,8] Complexes **1** and **2** were obtained in moderate to high yields by complexation of anhydrous metal salts with two equivalents of the ligand in the presence of two equivalents of $C_8K$ as a reducing agent. The target complexes are oxygen and moisture sensitive and should be handled and stored under strictly anaerobic conditions.

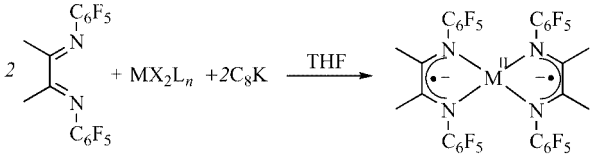

M = Ni, X = Br, L = DME, $n$ = 1 $[Ni^{II}(^{F}DAD)_2]$ **1**

M = Co, X = Cl, $n$ = 0 $[Co^{II}(^{F}DAD)_2]$ **2**

At room temperature complex **1** is diamagnetic in solution and shows three sharp multiplets in the $^{19}F$ NMR spectrum in the expected region –150 to –164 ppm vs. $CFCl_3$. It is interesting to note significant changes in the $^1H$ NMR spectrum accompanying the complexation. While in the free ligand the methyl group is observed at $\delta$ = 2.24 ppm, it is slightly broadened ($W_{1/2}$ = 6 Hz) and strongly high-field shifted in the complex and observed at $\delta$ = –1.98 ppm. The same observation was made by tom Dieck et al. for a series of $[Ni(DAD)_2]$ complexes.[8] We ascribe this unusual shift to residual paramagnetism of **1** derived from a low-lying triplet state populated at room temperature. The signal at $\delta$ = –1.98 ppm in the $^1H$ NMR spectrum of **1** is virtually temperature-independent, it is only slightly low-field shifted to –1.79 ppm by cooling the sample from 300 to 243 K.

Although a distorted tetrahedral environment of $Ni^{II}$ (vide infra) results in high-spin complex ($S_{Ni}$ = 1), the two radical ligands seem to couple antiferromagnetically with the metal giving ultimately a diamagnetic complex. Quenching of inherent paramagnetism of $Ni^{II}$ in a distorted tetrahedral arrangement of two chelating radical ligands has recently been reported by Wieghardt et al.[18] EPR spectroscopy applied to **1** gave evidence for its diamagnetism. Complex **1** was X-band EPR silent in solution/frozen solution at temperatures 4–300 K.

 © 2006 Wiley-VCH Verlag GmbH & Co. KGaA, Weinheim 

Complex **2** is paramagnetic both in solid state and in solution, the effective magnetic moment, $\mu_{eff}$ = 3.26 ($\mu_B$), was measured for the solid at room temperature. This value is close to the spin state $S$ = 3/2, further investigation of the electronic structure of **2** is given below.

### Crystal Structures of DAD Complexes

The molecular structure of **1** consists of two *N*,*N*′-chelating $^F$DAD ligands coordinated to the metal center (Figure 1). Two $^F$DAD ligands form a dihedral angle 55.28(9)° reflecting a twisted tetrahedral geometry at the metal center. The complex shows $C_2$ symmetry having twofold symmetry axis defined by Ni atom and the centroids of the diimine C–C bonds. Two metallacycles NiNCCN do not show any bend along NN′ axis, which would be the characteristic feature for doubly reduced DAD ligands.[19] In contrast they are essentially planar with maximum deviation of 0.031(2) Å from the best-fit planes defined by $E_1$ (Ni1N1C1C1′N1′) and $E_2$ (Ni1N2C3C3′N2′). The sum of angles at each nitrogen atom is close to 360° typical for planar $sp^2$-hybridized N-centers. Since the bond lengths in two diimines are the same within ±0.012 Å (3σ), two ligands have an identical oxidation state.

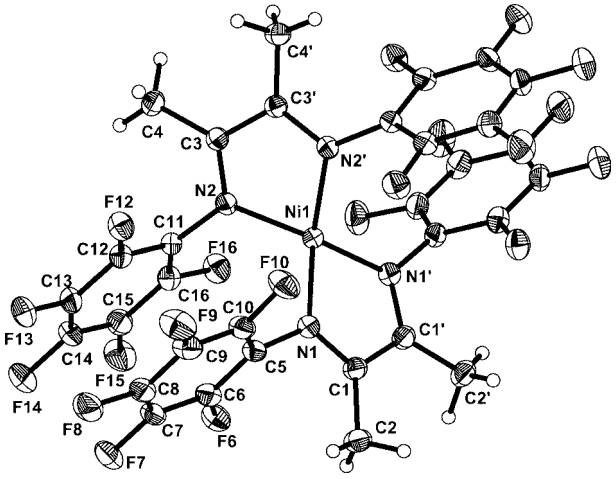


Figure 1. Molecular structure of **1**, thermal ellipsoids are drawn at 30% probability level.

The oxidation state of the ligands and consequently of the metal can be unambiguously assigned on the basis of the bond lengths analysis. In comparison of C–C and C–N bond lengths of diimine moieties in **1** (Table 1) with corresponding bond lengths in complexes, whose structures were determined accurately (Scheme 1), it is evident that both ligands in **1** are radical monoanions ($^F$DAD)$^{1-}$. The C–N bond length, on average 1.344(3) Å, along with the C–C bond of NCCN backbone, on average 1.413(5) Å, are in good agreement with the presence of an open-shell ($^F$DAD)$^{1-}$.[20] Since the complex possesses no extra charge, the physical (or spectroscopic)[13] oxidation state of Ni is +II ($d^8$ electronic configuration).

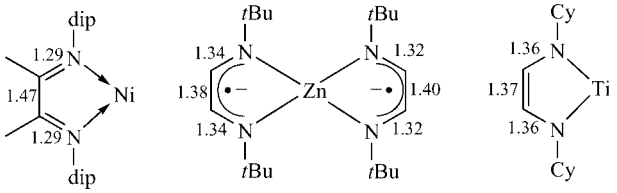


Scheme 1. Characteristic bond lengths for DAD ligand in different oxidation states: $(DAD)^0$ in $[Ni^{II}\{dip\text{-}DAD(Me)\}(CH_2SiMe_3)_2]$[38] (left), $(DAD)^{1-}$ in $[Zn^{II}\{t\text{Bu-}DAD(H)\}_2]$[20] (middle), and $(DAD)^{2-}$ in $[Ti^{IV}\{Cy\text{-}DAD(H)\}Cl_2(THF)_2]$[39] (right).

The molecular structures of several homoleptic complexes $[Ni(DAD)_2]$ were reported previously.[8,9] All of them were formulated as $Ni^0$ complexes containing a pair of closed-shell $(DAD)^0$ ligands. Taking into account the bond lengths of diimine moieties found in these complexes we suggest reformulation of their electronic structures. For example, the structure of $[Ni\{dmp\text{-}DAD(H)\}_2]$[8b] (dmp = 2,6-dimethylphenyl) reveals C–N bonds on av. 1.341(2) Å and C–C bonds of NCCN backbone on av. 1.374(2) Å. The bond length pattern observed in the former is in better agreement with the presence of the open-shell $(DAD)^{1-}$ rather than the closed-shell $(DAD)^0$. Having analyzed molecular structures of a series of reported $[Ni(DAD)_2]$ complexes we suggest new electronic structures for the following complexes: $[Ni^{II}\{Cy\text{-}DAD(H)\}^{1-}_2]$,[8a] $[Ni^{II}\{dmp\text{-}DAD(H)\}^{1-}_2]$,[8b] $[Ni^{II}\{t\text{Bu-}DAD(H)\}^{1-}_2]$,[9a] $[Ni^{II}\{dip\text{-}DAD(H)\}^{1-}_2]$.[9b]

Almost all related homoleptic *o*-phenylenediamine-derived complexes $[Ni^{II}(sbqdi)_2]$[10a,21] and the diaminomaleonitrile-derived $[Ni^{II}(sdisn)_2]$[11a] show strictly square-planar geometry, whereas **1** as well as $[Ni(DAD)_2]$ structurally characterized previously reveal twisted tetrahedral geometry. The dihedral angle formed by two diimine moieties varies from 44.5° in $[Ni\{dmp\text{-}DAD(H)\}_2]$[8b] to 88.95° in $[Ni\{t\text{Bu-}DAD(H)\}_2]$.[9a] The large deviation from a square-planar geometry observed in $[Ni(DAD)_2]$ complexes can be rationalized by steric repulsion of bulky *N*-substituents. In

Table 1. Selected bond lengths [Å] of complexes **1**–**4**.

| $[Ni^{II}(^FDAD)_2]$ (**1**) | | $[Co^{II}(^FDAD)_2]$ (**2**) | | $[Ni^{II}(^FBIAN)_2]$ (**3**) | | $[Co^{I}(^FBIAN)_3]$ (**4**) | | | |
|---|---|---|---|---|---|---|---|---|---|
| | | | | | | **I** | | **II** | |
| Ni1–N1 | 1.9173(18) | Co1–N1 | 1.932(3) | Ni1–N1 | 1.9399(15) | Co1–N1 | 2.144(2) | Co1–N3 | 2.125(2) |
| Ni1–N2 | 1.9165(17) | Co1–N2 | 1.931(3) | Ni1–N2 | 1.9370(15) | Co1–N2 | 2.119(2) | | |
| C1–N1 | 1.340(3) | C7–N1 | 1.352(5) | C1–N1 | 1.333(2) | C1–N1 | 1.302(4) | C29–N3 | 1.331(3) |
| C3–N2 | 1.348(3) | C15–N2 | 1.357(5) | C2–N2 | 1.344(2) | C2–N2 | 1.304(3) | | |
| C1–C1# | 1.414(5) | C7–C7# | 1.408(8) | C1–C2 | 1.427(3) | C1–C2 | 1.474(4) | C29–C29# | 1.442(5) |
| C3–C3# | 1.411(4) | C15–C15# | 1.412(8) | | | | | | |

 © 2006 Wiley-VCH Verlag GmbH & Co. KGaA, Weinheim 

contrast, a series of $[Ni^{II}(sbqdi)_2]$ and $[Ni^{II}(sdisn)_2]$ complexes with small N–H substituents do not show any deviation from square-planar geometry, whereas $[Ni^{II}(sbqdi)_2]$ having bulky $C_6F_5$ groups attached to four nitrogen atoms does show tetrahedral distortion: the two planar ligands form dihedral angle of 53.7(1)°.[22]

The strong distortion from planarity in **1** is caused by interaction between the bulky $C_6F_5$ groups engaged in intramolecular $C_6F_5$–$C_6F_5$ stacking. The phenyl rings form dihedral angles in the range of 65.7(1)–67.3(1)° with corresponding diimine NCCN planes and are pairwise close to coplanar with an interplanar angle of 2.9(1)°. The smaller distance between $C_6F_5$ centroid and the least-squares plane of adjacent $C_6F_5$ ring is 3.23 Å. If we assume that complex **1** adopts a square-planar geometry without significant changes in bond lengths and angles, a simple geometrical consideration predicts that the coplanar $C_6F_5$ rings would be forced to a face-to-face distance of approximately 2.9 Å. Recently, by DFT calculations Lorenzo et al.[23] have shown that energy minimum for the gas-phase dimer $(C_6F_6)_2$ in face-to-face configuration is reached when the interplanar distance $C_6F_6$–$C_6F_6$ is 3.31–3.37 Å. Assuming that the energy minima for the pair $C_6F_5$–$C_6F_5$ in **1** and the calculated pair $C_6F_6$–$C_6F_6$ are reached at the close distances we expect strong repulsion between two pairs of $C_6F_5$ rings in the hypothetical square-planar complex **1**.

A tetrahedral distortion of the complex and synchronous rotation of the phenyl rings provide a relaxation of repulsive interaction and sufficient increase of the $C_6F_5$–$C_6F_5$ distances. The molecular structure of **1** reveals a slipped arrangement of two pairs of $C_6F_5$ rings. The interplanar $C_6F_5$–$C_6F_5$ distance found at 3.23 Å is in good agreement with distances 3.23 and 3.32 Å between $C_6F_5$ rings engaged in intramolecular stacking in the sandwich complex bis[$\eta^5$-1,2,4-tris(pentafluorophenyl)cyclopentadienyl]iron(II)[24] and with distances 3.20–3.28 Å in the series of complexes $[M(^{F}sbqdi)_2]$ [M = Co, Ni, Pd, Cu, $^{F}$sbqdi – radical anion derived from doubly deprotonated *N*,*N*′-bis(pentafluorophenyl)-*o*-phenylenediamine].[22]

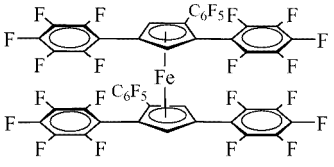

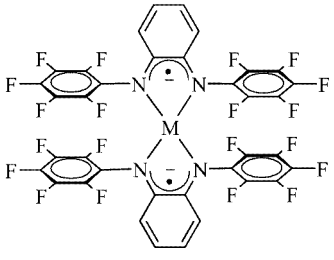

In conclusion, the twisted tetrahedral geometry of **1** is determined by repulsion forces between the two pairs of perfluorinated rings, which is a typical feature of four-coordinate $Ni^{II}$ complexes with bulky ligands.

Although the synthesis of one homoleptic cobalt complex [Co{Ph-DAD(Ph)}$_2$] was reported earlier[5,6] up to now no structural information about $[Co(DAD)_2]$ complexes is available. The molecular structure of $[Co^{II}(^{F}DAD)_2]$ (**2**), which is isomorphous with **1**, is shown in Figure 2. The cobalt atom is located in a twisted tetrahedral environment of two chelating $^{F}$DAD ligands, nearly planar diimine moieties form a dihedral angle of 58.0(2)°. The molecule is symmetrical having a $C_2$-axis defined by the cobalt atom and the centroids of the diimine C–C bonds. The five-membered metallacycles formed are essentially planar: the maximum deviation from the best-fit plane is 0.027(4) Å for both rings. The bond lengths and angles within the two $^{F}$DAD moieties are the same within 3σ.

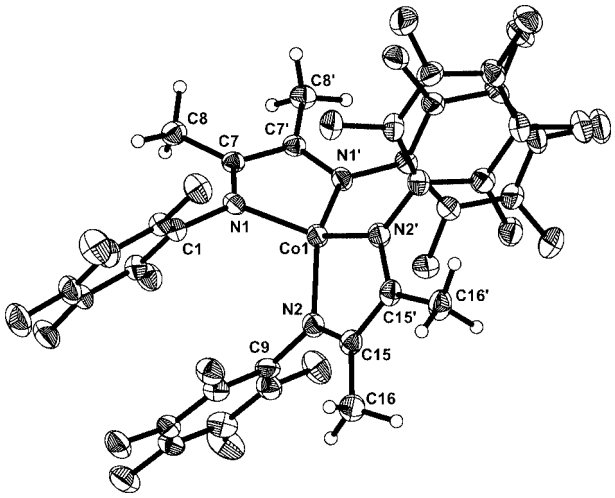


Figure 2. Molecular structure of **2** showing distorted tetrahedral geometry around the metal center; thermal ellipsoids are drawn at 30% probability level.

By comparison of the bond length pattern of the NCCN moieties in **2** with that of **1** it is found that $^{F}$DAD ligands in both complexes are nearly similar. In complex **2** the C–N bond lengths on av. 1.355(5) Å along with the C–C bonds of the NCCN backbone on av. 1.410(8) Å are in good agreement with the presence of two radical monoanions $(^{F}DAD)^{1-}$. Taking into account that the complex is not charged we assign the cobalt oxidation state to be +II ($d^7$ electronic configuration).

Slight C–N bond lengthening of 0.011 Å along with negligibly small C–C bond shortening of 0.003 Å in NCCN backbone of **2** compared to **1** are ascribed to slightly higher population of π* orbitals of the ligands in **2**. Nearly coplanar $C_6F_5$ rings with a dihedral angle of 3.9(2)° display an interplanar distance close to that observed in **1**: the smaller distance between $C_6F_5$-centroid and the least-squares plane of adjacent $C_6F_5$ ring is 3.27 Å. Close interplanar distances $C_6F_5$–$C_6F_5$ observed for **1** and **2** confirm that the geometry of both complexes is governed by intramolecular $C_6F_5$–$C_6F_5$ interactions.

 © 2006 Wiley-VCH Verlag GmbH & Co. KGaA, Weinheim 

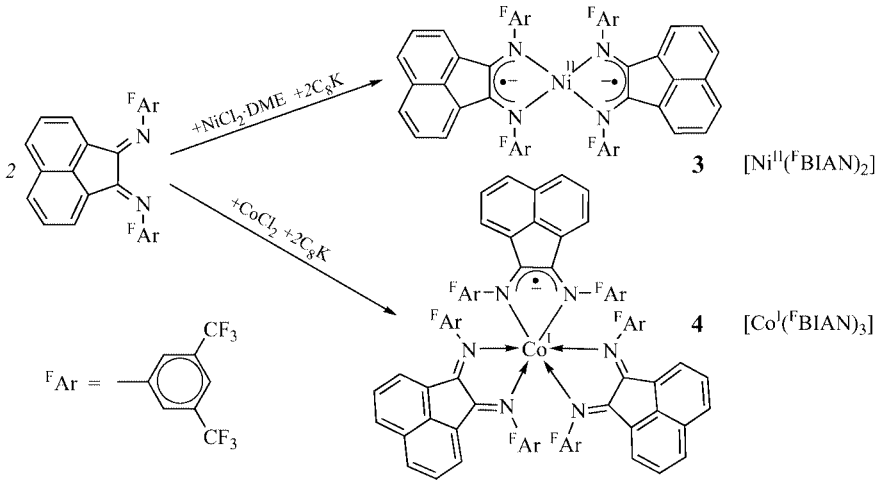


## Synthesis and Characterization of BIAN Complexes

Complexes **3** and **4** were prepared by ligand reduction with $C_8K$ in the presence of the metal salts as described before for $^F$DAD complexes. Surprisingly, the reaction of 2 equiv. of the ligand with 1 equiv. of $CoCl_2$ gave neutral [Co($^F$BIAN)$_3$] but not the expected [Co($^F$BIAN)$_2$]. Subsequent reaction of $CoCl_2$ with 3 equiv. of $^F$BIAN led to the formation of the same [Co($^F$BIAN)$_3$] with improved yield. Both complexes are sensitive towards oxygen and water. Strict anaerobic conditions should be applied during working with the extremely sensitive [Co($^F$BIAN)$_3$].

[Ni$^{II}$($^F$BIAN)$_2$] shows sharp signals in $^1$H and $^{19}$F NMR spectra demonstrating its diamagnetism, whereas **4** is clearly paramagnetic. The $\mu_{eff}$ measured for solid **4** at room temperature is found to be 3.80 $\mu_B$, which is consistent with three unpaired electrons per molecular unit and spin state $S = 3/2$. By means of NMR and X-band EPR spectroscopy we did not detect any equilibrium between **3** and free $^F$BIAN with a hypothetical octahedral nickel analogue of **4**. Complex **3** was EPR silent in solution/frozen solution in the temperature range 4–300 K.

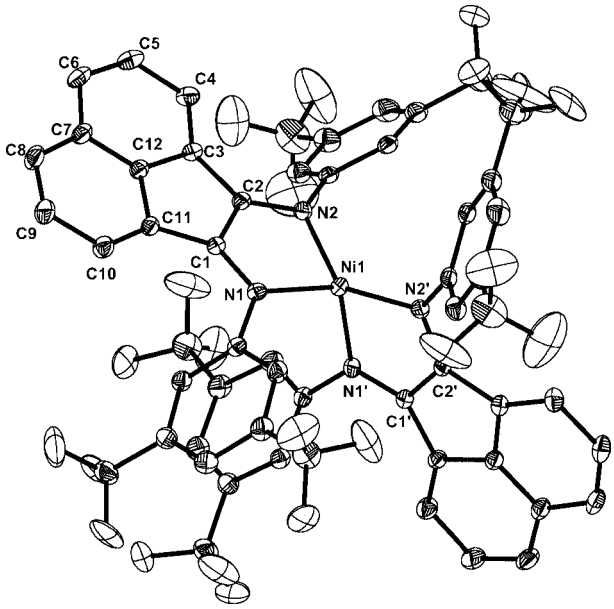


Figure 3. Molecular structure of **3**: disordered fluorine atoms are shown as semitransparent ellipsoids, hydrogen atoms are omitted for clarity, thermal ellipsoids are drawn at 30% probability level.

## Crystal Structures of BIAN Complexes

The molecular structure of **3** consists of two planar chelating $^F$BIAN ligands attached to the nickel atom (Figure 3). Similar to **1** and **2** the two $^F$BIAN ligands in **3** form a distorted tetrahedral $NiN_4$ ligand environment. The dihedral angle formed by two diimine chelates is found to be 83.66(8)°.

It is interesting to note that the two almost orthogonal diimine ligands do not form a regular tetrahedron. Instead, one ligand seems to be turned around the axis through Ni, perpendicular to the plane of the other diimine. For visualization of this unusual geometry the first coordination sphere of **3** is depicted in Figure 4. Consequently, local symmetry is missing completely in **3**. In contrast, complexes **1**, **2**, and all structurally characterized [Ni(DAD)$_2$] complexes with diverse sterically demanding *N*-substituents,[8,9] as well as [Ca(dip-BIAN)$_2$] with bulky *N*-dip groups[17] all form distorted tetrahedra with pseudo $C_2/D_2$ symmetry. The distorted tetrahedral geometry of **3** can be ascribed to intermolecular arene–arene interactions observed in the crystal structure. The acenaphthene rings involved in π stacking are parallel with respect to each other and show an interplanar distance of 3.533 Å (see Figure S1 in the supporting information).

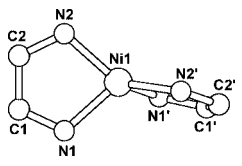


Figure 4. Ligands arrangement in **3**: a view exactly perpendicular to the plane defined by Ni1N1C1C2N2 (paper plane).

 © 2006 Wiley-VCH Verlag GmbH & Co. KGaA, Weinheim 

Oxidation state of the ligands can be unambiguously assigned by a bond lengths analysis. Typical bond lengths of bis(arylimino)acenaphthene ligand in different oxidation states are represented in Scheme 2. As the naphthalene system does not show distinct changes in bond lengths only C–N and C–C bond lengths of diimine moieties are given for the ligand in different oxidation states. In complex **3** the diimine C–N bond length is found to be on average 1.339(2) Å and the diimine bridging C–C bond is 1.427(3) Å long. After having compared the bond length pattern observed in **3** with those of known structures we assign both diimines in **3** to be in monoanionic radical form (Scheme 2). This implies that the oxidation state of Ni is +II and the electronic configuration of the metal is $d^8$.

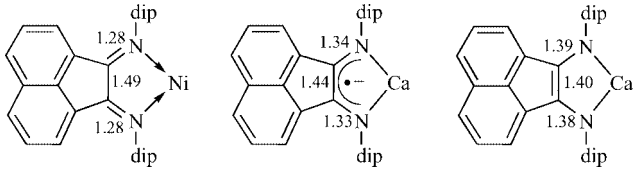


Scheme 2. Characteristic bond lengths for BIAN ligand in different oxidation states: $(BIAN)^0$ in $[Ni^{II}(dip\text{-}BIAN)Br_2]_2$[40] (left), $(BIAN)^{1-}$ in $[Ca^{II}(dip\text{-}BIAN)_2]$[17] (middle), and $(BIAN)^{2-}$ in $[Ca^{II}(dip\text{-}BIAN)(THF)_3]$[41] (right).

The *N*-phenyl rings in **3** form dihedral angles 57.9(1) and 49.9(1)° with the corresponding diimine moieties, hence the influence of these rings on the π system of $^F$BIAN is negligible. The observed dihedral angles along with deviation of N–C(phenyl) bonds from the diimine planes can be readily ascribed to intramolecular interactions between sterically demanding substituted phenyl rings. The only structurally characterized complex of the type $[M(BIAN)_2]$ was reported very recently by Fedushkin et al.[17] The crystal structure of paramagnetic $[Ca^{II}(dip\text{-}BIAN)_2]$ reveals a dihedral angle of 28° between the diimine moieties and does not show any π stacking between the diimine moieties in the crystal lattice.

The molecular structure of cobalt complex **4** is represented in Figure 5. It consists of three(!) sterically demanding $^F$BIAN ligands attached to the metal center. While complexes containing three less demanding DAD ligands are known,[25] to the best of our knowledge complexes containing three BIAN ligands are unknown so far.

The cobalt ion in **4** has a slightly distorted octahedral environment. Three diimine ligands show considerable planarity and planes of them are almost perpendicular to each other, as expected for a perfect octahedron. Taking into account that synthesis of complex **4** is performed under strong reducing conditions we disagree with its description as $Co^{III}$ with three $(^FBIAN)^{1-}$ ligands. The oxidation state of the metal is assumed to be +II or lower. Analysis of bond lengths of diimines shows non-equivalence of the three ligands. Two $^F$BIAN ligands are crystallographically identical (Table 1, form **I**), whereas the third one (form **II**) reveals a distinctly differing bond pattern. The bond length pattern observed in **II** closely resembles that in complex **3**. The diimine C–N bond on av. 1.331(3) Å and diimine C–C bond of 1.442(5) Å in **II** [1.339(2) and 1.427(3) Å, respectively, in complex **3**] are in agreement with the formulation of **II** as a radical monoanion. On the other hand, C–N bonds in **I** are significantly shorter, on av. 1.303(4) Å, the diimine C–C bond is significantly longer [1.474(4) Å] compared to **II** indicating neutral diimine character. Comparison of bond lengths in **I** with those of previously characterized complexes confirms that **I** is best described as neutral ligand. Hence complex **4** contains one diimine in form of the radical monoanion and two neutral diimine ligands. This implies that the oxidation state of the cobalt atom in **4** is best described as +I with $d^8$ electronic configuration and correct description of **4** is $[Co^I(^FBIAN)^0{}_2(^FBIAN)^{1-}]$.

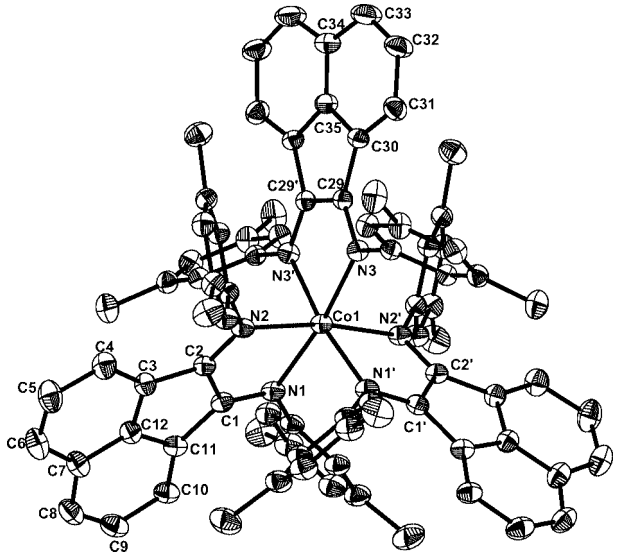


Figure 5. Molecular structure of **4**: hydrogen and disordered fluorine atoms are omitted for clarity, thermal ellipsoids are drawn at 30% probability level.

As expected the Co–N distances were found to be much longer in **4** compared to **2**. This is due to the increase of effective ionic radius $Co^{II}\rightarrow Co^I$ and to a change of coordination number from four in complex **2** to six in complex **4**. It can be noted that in complex **4** the distances Co–N in monoanionic $(^FBIAN)^{1-}$ at 2.125(2) Å are slightly shorter then those in closed-shell $(^FBIAN)^0$ at av. 2.132(2) Å. We refer this difference to the additional attraction between monoanionic $(^FBIAN)^{1-}$ and positive charged metal, which is lacking in the case of the neutral $(^FBIAN)^0$. The observed Co–N bond lengths are close to that reported for $[Co(bpy)_3]Cl$ at av. 2.11(2) Å.[26]

## Magnetochemistry and EPR Spectroscopy

The electronic structures of the paramagnetic complexes **2** and **4** were further investigated by variable-temperature magnetic susceptibility measurements and X-band EPR spectroscopy.

The temperature dependence of the effective magnetic moment ($\mu_{eff}$) of **2** is shown in Figure 6. The magnetic mo-

 © 2006 Wiley-VCH Verlag GmbH & Co. KGaA, Weinheim 

ment decreases gradually from 3.26 $\mu_B$ at 300 K to 2.36 $\mu_B$ at 5 K. From the crystal structure we have established that **2** contains $Co^{II}$ ion ($d^7$) and two radical anionic ligands. Therefore **2** represents a three-center odd-electron system. The value of $\mu_{eff}$ at low temperatures is in agreement with a doublet ground state ($S$ = 1/2). The first excited quartet state ($S$ = 3/2) becomes populated with increasing temperature.

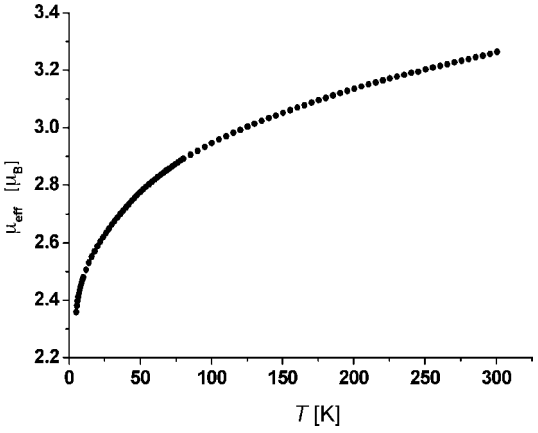


Figure 6. Temperature dependence of the effective magnetic moment of **2**.

The spin state of cobalt is not inherently clear because of the twisted coordination geometry around the metal center of **2**. Most cobalt(II) complexes are high-spin compounds ($S_{Co}$ = 3/2) in tetrahedral, but low-spin ($S_{Co}$ = 1/2) in planar environment. The molecular structure of **2** showing the dihedral angle of 58.0(2)° between the two diimines moieties takes an intermediate position between the tetrahedral and the planar geometries. The doublet ground state can be achieved by combination of the high-spin cobalt ion with the two radical ligands both coupled antiferromagnetically with the metal (Scheme 3, **A**). Another possibility to achieve the ground state doublet is to let the low-spin cobalt ion couple with two organic radicals, where two more types of electronic structures are to be considered. Two organic radicals couple in ferromagnetic fashion with each other but in antiferromagnetic fashion with the metal (**B**) yielding required $S$ = 1/2. Or the two ligand spins couple antiferromagnetically with each other so that the metal spin is aligned ferromagnetically to one of the ligand spin but antiferromagnetically to the other one resulting in the doublet ground state (**C**).

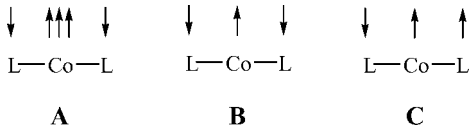


Scheme 3. Ground state spin models for **2**.

In recent publications by Wieghardt et al.[10] it was shown that related planar complexes $[M^{II}(sbqdi)_2]$ (M = Ni, Pd, Pt) containing radical ligands reveal strong antiferromagnetic coupling between two remote ligands. The ligands interact strongly with each other via an efficient superexchange mechanism that is mediated by a back-bonding interaction to the central metal. Such a superexchange interaction between two remote radicals is efficient only for certain geometries of the complexes. Very recently Ye et al.[27] showed, that if the geometry of such complexes deviates significantly from planarity, the interaction between two remote radical ligands becomes significantly weaker. Therefore, the spin state of **2** is likely to be of type **A** or **B**, with dominating antiferromagnetic interactions between the cobalt and radical ligand, but unlikely **C**, with dominating antiferromagnetic coupling between two radical ligands.

For fitting the experimental data we tentatively used the following Hamiltonian, see Equation (1).

$$\mathbf{H} = -J_{ab}(\mathbf{S_{Co}}\cdot\mathbf{S_1} + \mathbf{S_{Co}}\cdot\mathbf{S_2}) - J_{aa}(\mathbf{S_1}\cdot\mathbf{S_2}) + \beta[(\mathbf{S_1} + \mathbf{S_2})\cdot\mathbf{g_R} + \mathbf{S_{Co}}\cdot\mathbf{g_{Co}}]\cdot H \quad (1)$$

Here the first term is the Heisenberg term accounting for the isotropic exchange interaction between the metal and the radical ligands with $J_{ab}$, the second term relates to the isotropic exchange between two radical ligands with $J_{aa}$, and the third one is the Zeeman perturbation term. For the spin model **A** $S_{Co}$ = 3/2 and for the model **B** $S_{Co}$ = 1/2. The $\mathbf{g_{Co}}$ and $\mathbf{g_R}$ were assumed to be isotropic with $g_{Co}$ and $g_R$ principal values, for radical ligands $S_1 = S_2$ = 1/2. Unfortunately, we were not able to obtain a reasonable fit to the experimental data for both low- and high-spin cobalt complex models. The introduction of the intermolecular interactions and paramagnetic impurities did not improve the fit significantly. A more accurate model considering the local anisotropy and/or anisotropic interactions is therefore needed.

In spite of the unsuccessful simulations of magnetic susceptibility data, the ground state of **2** can be determined by EPR spectroscopy at cryogenic temperatures. Indeed, if we reject **C** because of geometrical reasons, then **A** and **B** would give apparently different EPR spectra at low temperatures. Model **A** would give the EPR signal typical for cobalt(II) complexes, whereas **B** would give a spectrum of an organic radical.

The X-band EPR spectrum of **2** measured in a frozen solution at 20 K is shown in Figure 7. The large anisotropy of the $g$ tensor and the hyperfine splitting of $^{59}Co$ ($I$ = 7/2) indicate that the unpaired electron is located mostly on the metal d-orbitals and not on the ligands. Therefore the model **A** with high-spin $Co^{II}$ is the most plausible description of this system. The EPR spectrum of **2** has been successfully simulated by using the orthorhombic $g$ tensor: $g_1$ = 4.296, $g_2$ = 1.676, $g_3$ = 1.625, with $^{59}Co$ hyperfine coupling constants: $A_1$ = 197, $A_2$ = 52, $A_3$ = 56 G. Furthermore, the line width dependence was introduced as shown in Equation (2), where $m_I$ is the nuclear spin ($m_I$ = –7/2, ..., +7/2 for $^{59}Co$ nucleus); $\alpha_i$, $\beta_i$, $\gamma_i$ are orientation-dependent ($i = x, y, z$) line width parameters.

$$\Delta B(m_I) = \sum_{i=1}^{3} \alpha_i + \beta_i m_I + \gamma_i m_I^2 \quad (2)$$

 © 2006 Wiley-VCH Verlag GmbH & Co. KGaA, Weinheim 

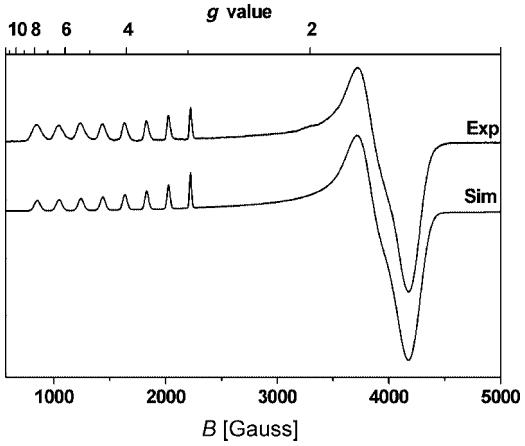


Figure 7. X-band EPR spectrum of **2**. Conditions: THF/toluene ca. 1:1 at 20 K; frequency 9.2265 GHz; power 5.0 μW; modulation amplitude 10 G. The fit parameters are given in the text.

The temperature dependence of $\mu_{eff}$ of **4** is shown in Figure 8. The magnetic moment measured at 300 K is 3.80 $\mu_B$ indicates the presence of three unpaired electrons ($S$ = 3/2). With decreasing temperature $\mu_{eff}$ gradually decreases to the value of 2.07 $\mu_B$ at 10 K followed by a steep descent to 1.79 $\mu_B$ at 1.8 K. This behavior is explainable by the presence of the high-spin $Co^I$ ($d^8$, $S_{Co}$ = 1, pseudooctahedral environment) and a radical ligand ($S_R$ = 1/2) coupled in antiferromagnetic fashion. Thus, the ground state of **4** is a doublet with an excited quartet populated at higher temperatures. The abrupt decreasing of the magnetic moment at temperatures below 10 K can be ascribed to the intermolecular antiferromagnetic interactions in the solid.

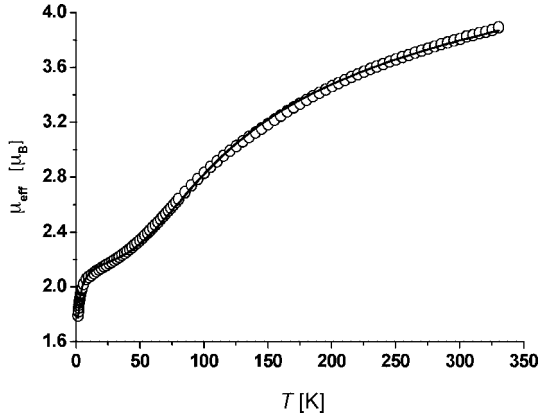


Figure 8. Temperature dependence of the effective magnetic moment of **4**, the fit parameters are given in the text.

To fit the experimental data we used the following Hamiltonian, see Equation (3), where the first term is the Heisenberg term related to the isotropic exchange interaction ($J$) between two magnetic centers and the second term is the Zeeman perturbation, nonequivalence of **g** tensors is supposed.

$$\mathbf{H} = -J\mathbf{S_{Co}}\cdot\mathbf{S_R} + \beta(\mathbf{S_{Co}}\cdot\mathbf{g_{Co}} + \mathbf{S_R}\cdot\mathbf{g_R})\cdot H \quad (3)$$

Assuming tensors $\mathbf{g_{Co}}$ and $\mathbf{g_R}$ to be isotropic with $g_{Co}$ and $g_R$ principal values and taking $S_{Co}$ = 1, $S_R$ = 1/2 the equation for magnetic susceptibility can then be derived, Equation (4).[28]

$$\chi = \frac{N\beta^2}{4kT}\frac{g_{1/2}^2 + 10g_{3/2}^2\exp(3J/2kT)}{1+2\exp(3J/2kT)} \quad (4)$$

Here $g_{1/2}$ and $g_{3/2}$ factors correspond to each of the spin states, they are related to the local $g$ factors through Equation (5).

$$g_{1/2} = (4g_{Co} - g_R)/3 \qquad g_{3/2} = (2g_{Co} + g_R)/3 \quad (5)$$

By adding temperature-independent paramagnetism (*TIP*) into Equation (4) it was possible to obtain a good fit for magnetic susceptibility for the temperature range 10–330 K. To fit the data on the whole temperature range we modified Equation (4) according to the molecular field approximation for weak intermolecular interactions, Equation (6).[29] Here $z$ is the number of the nearest neighbors around a given magnetic molecule in the crystal lattice and $J'$ is the interaction parameter, the $g$ factor in Equation (6) was taken as equal to 2.

$$\chi' = \frac{\chi}{1-(2zJ'/Ng^2\beta^2)\chi} + TIP \quad (6)$$

The best fit using Equation (6) was obtained with the following parameters: $g_R$ = 2.00 (fixed), $g_{Co}$ = 2.37, $J$ = –106.0 $cm^{-1}$, $zJ'$ = –0.78 $cm^{-1}$, $TIP = 1.23\times10^{-3}$ $cm^3\,mol^{-1}$. The accuracy of the fit used is very good showing $R^2$ = 0.99924. Hence, the ground state doublet is separated from the excited quartet by $-3J/2$ = 159 $cm^{-1}$. Week intermolecular antiferromagnetic interactions are present in the polycrystalline sample of **4**, as indicated by negative value of $zJ'$ = –0.78 $cm^{-1}$. Abrupt decreasing of $\mu_{eff}$ of **4** at low temperatures may be governed by zero-field splitting effect as well, this supposition was not examined.

The X-band EPR spectrum of **4** measured in frozen solution at 4 K is shown in Figure 9. It is evident that more than one paramagnetic species is present. We propose two compounds to exist in the frozen solution. The first one is a cobalt complex with a large anisotropy of the $g$ tensor (**Tet**): a well resolved octet centered at $g \approx 3.8$ and a less resolved signal at $g \approx 1.9$. The second species is a cobalt complex as well, but with a higher symmetric arrangement at the metal (**Oct**), its signal is partly hidden by those of **Tet** and centered at $g \approx 2.3$. Because **4** is extremely sensitive towards both oxygen and moisture, the EPR experiment was repeated several times with freshly prepared solutions. All samples measured gave nearly identical spectra. It was concluded that the two cobalt species observed originate not from decomposition of **4**, but from partially dissociation.

 © 2006 Wiley-VCH Verlag GmbH & Co. KGaA, Weinheim 

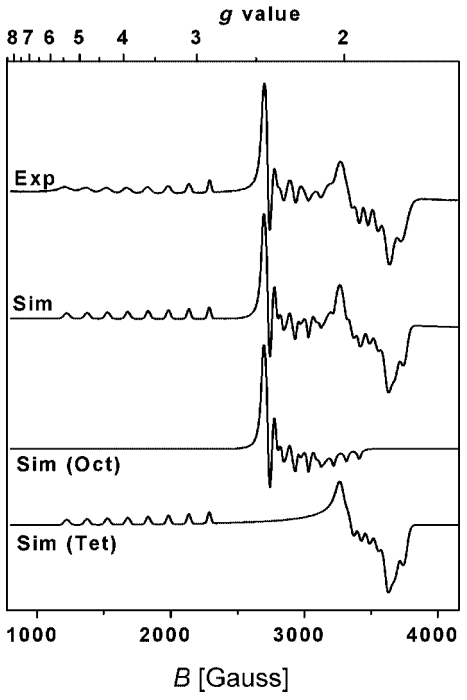


Figure 9. X-band EPR spectrum of **4**. Conditions: THF/toluene ca. 1:1 at 4 K; frequency 9.2278 GHz; power 1.3 μW; modulation amplitude 10 G. The fit parameters are given in the text.

Thus the distorted octahedral complex **4** partially dissociates in solution (toluene/THF ≈ 1:1) into the neutral species [Co($^{F}$BIAN)$_2$], which has very likely distorted tetrahedral geometry, and the free ligand $^{F}$BIAN. Assuming that this dissociation takes place we can readily assign the signals in the EPR spectrum. Species **Tet** is expected to be [Co($^{F}$BIAN)$_2$], whereas **Oct** is apparently **4**. The EPR spectrum is therefore best explained by the superposition of two orthorhombic signals. The spectrum has been successfully simulated by using the following parameters: for **Oct** $g_1$ = 2.363, $g_2$ = 2.243, $g_3$ = 2.143, hyperfine coupling constants ($^{59}$Co) $A_1$ = 17, $A_2$ = 58, $A_3$ = 96 G; for **Tet** $g_1$ = 3.756, $g_2$ = 1.874, $g_3$ = 1.895, hyperfine structure ($^{59}$Co) $A_1$ = 153, $A_2$ = 65, $A_3$ = 38 G. For **Tet** showing the large anisotropy the line width dependence was included in the simulation. On warming, the signal of **Oct** disappears much faster than that of **Tet**. At 100 K only the poorly resolved signal of **Tet** is observed. This indicates that the relaxation time for **Oct** compared to **Tet** is small.

### Electronic Spectra

Electronic spectra of the complexes **1**–**4** in chloroform and in *n*-hexane solutions were recorded at room temperature in the range 200–1100 nm. Spectra of DAD complexes **1** and **2** consist of a strong band in the ultra-violet ($\varepsilon > 10^4$ dm$^3$·mol$^{-1}$·cm$^{-1}$) and weaker two (**1**) or four bands (**2**) in the visible region. The UV absorption can be assigned to intra-ligand (IL) transition, since the free ligand absorbs in the similar region. The long-wavelength bands in visible, determining the intensive color of the complexes presumably are charge-transfer (CT) transitions. Solvent dependence and high intensity renders them easily distinguishable from solvent-independent and low-intensity d–d transitions. The two bands in the visible region are characteristic of [Ni(DAD)$_2$] complexes, as was observed by tom Dieck for a series of such complexes.[8]

UV/Vis spectra of BIAN complexes **3**–**4** are dominated by intense IL electronic transitions (329–332 nm, $\varepsilon > 10^4$ dm$^3$·mol$^{-1}$·cm$^{-1}$), and three transitions in visible/NIR. The latter are supposed to be CT transitions relying on their relative high intensities ($\varepsilon$ = 8–10·10$^3$ and 5–12·10$^3$ dm$^3$·mol$^{-1}$·cm$^{-1}$ for **3** and **4**, respectively) and solvatochromism. High-energy absorption maxima in visible at 512 and 519 nm for **3** and **4**, respectively, are indicative of the presence of a radical anion (BIAN)$^{1-}$. Several complexes reported recently by Fedushkin[30] containing the radical (BIAN)$^{1-}$ all show absorption maximum/maxima in the region 420–530 nm.

We refrain from discussing the more specific assignment of electronic absorptions of **1**–**4** in visible/NIR as sufficient confidence may only be achieved in combination with high-quality excited-state TD-DFT calculations.

## Conclusions

We have synthesized new complexes of nickel and cobalt containing the non-innocent highly π acidic diimine ligands $^{F}$DAD and $^{F}$BIAN with bulky fluorinated *N*-substituents. The oxidation states of the ligands and subsequently of the metals were determined by single-crystal X-ray analysis at low temperatures. The electronic structure of [Ni$^{II}$($^{F}$DAD)$_2$] as well as electronic structures of [Ni(DAD)$_2$] complexes previously characterized by X-ray analysis were shown to be consistent with a divalent nickel d$^8$ ion and a pair of radical monoanionic ligands. The unique [Co$^{I}$($^{F}$BIAN)$_3$] comprises a cobalt(I) ion, two neutral ($^{F}$BIAN)$^0$ ligands and one radical monoanion ($^{F}$BIAN)$^{1-}$. Both [Co$^{II}$($^{F}$DAD)$_2$] and [Co$^{I}$($^{F}$BIAN)$_3$] possess a doublet ground state with electron density located mostly in the metal d-orbitals as was concluded from magnetic susceptibility measurements and the X-band EPR spectroscopy.

## Experimental Section

The ligand $C_6F_5$-DAD(Me) (= $^{F}$DAD) can be prepared by a known procedure in low yield.[31] Here we describe an alternative method of its preparation with much higher yield (vide infra). Anhydrous metal salts $NiCl_2$·DME,[32] $NiBr_2$·DME[32] as well as [3,5-$(CF_3)_2$-$C_6H_3$]-BIAN[33] (= $^{F}$BIAN) and $C_8K$[34] were prepared according to the known procedures. Anhydrous $CoCl_2$ was obtained by refluxing of $CoCl_2$·$n$H$_2$O with $SOCl_2$ for several hours followed by removing the volatiles under reduced pressure at 90 °C. Syntheses of all complexes were performed under a dry argon atmosphere using standard Schlenk techniques and dried solvents.

**Physical Measurements:** Mass spectra were obtained on a Finnigan MAT 95S mass spectrometer (70 eV, EI). IR spectra were obtained in Nujol mull using a Nicolet 510 FT-IR. UV/Vis spectra were measured on a Shimadzu UV-1601PC instrument in absolute

 © 2006 Wiley-VCH Verlag GmbH & Co. KGaA, Weinheim 

$CHCl_3$ and *n*-hexane at concentrations $10^{-4}$ to $10^{-5}$ M. NMR spectra were recorded at room temperature on a Bruker ARX 200 spectrometer at 200.13 MHz for $^1H$ and 188.29 MHz for $^{19}F$. $^1H$ NMR spectra are referenced (in ppm) to residual proton signals of $CDCl_3$ ($\delta$ = 7.26 ppm) and $C_6D_6$ ($\delta$ = 7.15 ppm). $^{19}F$ NMR spectra were referenced to external standard $CFCl_3$. Abbreviations used are the following: s = singlet, d = doublet, t = triplet, pst = pseudo-triplet, m = multiplet. EPR spectra were recorded in the X-band on a Bruker System ESP 300. The magnetic susceptibility measurements were performed on a powder samples using a Quantum Design MPMS2 SQUID magnetometer with an applied field of 1 T. Experimental susceptibility data were corrected for the underlying diamagnetism using Pascal's constants.

**X-ray Crystallographic Data Collection and Refinement of the Structures:** Single crystals of **1**–**4** were coated with inert oil, picked up with a glass fiber and mounted in the nitrogen cold stream of the STOE IPDS2 (**1**, **3**, **4**) or STOE IPDS diffractometer (**2**). Intensity data were collected at 193 K using graphite-monochromated Mo-$K_\alpha$ radiation ($\lambda$ = 0.17073 Å). Data collection was performed by hemisphere runs taking frames at 1.0° in $\omega$. Final cell constants were obtained from a least-squares fit of a subset of several thousand strong reflections. Intensity data of **1** and **3** were corrected using indexed crystal faces, the data of **4** using the semiempirical correction routine MulScanAbs.[35] For **2** an absorption correction did not improve the quality of the data and was not applied. There was disordered solvent (toluene) present in the crystal structures of **1**, **2**, and **4**. In the crystal structures of **3** and **4** the $CF_3$ groups are disordered: two positions for each fluorine atom with different occupancies were found. All structures have been solved by the direct methods in SHELXS-97[36] (**1**, **3**, **4**) or SIR92[37] (**2**) and refined using the full-matrix least-squares refinement procedure of SHELXL97,[36] all non-hydrogen atoms anisotropically; H atoms have been located and isotropically refined (**1**, **3**) or have been placed at calculated positions and have been refined using a riding model with $U_{iso}(H) = 1.2U_{eq}(C)$ (**2**, **4**). Crystallographic data of the compounds are listed in Table 2.

CCDC-290299 to -290302 contain the complete crystallographic data for this paper. These data can be obtained free of charge from The Cambridge Crystallographic Data Centre via www.ccdc.cam.ac.uk/data_request/cif.

**Synthesis of $C_6F_5$-DAD(Me) (1a):** To 2,3,4,5,6-pentafluoroaniline (9.15 g, 0.050 mol) dissolved in dry MeOH (15 mL), 2,3-butanedione (3.2 mL, 0.038 mol), *p*-toluenesulfonic acid (ca. 0.2 g), and trimethyl orthoformate (10.0 mL, 0.097 mol) were added. After stirring for 1 day at room temperature the pale yellow precipitate was filtered, washed with cold MeOH and dried in vacuo. Yield: 5.19 g (50%). $^1H$ NMR (200.13 MHz, $CDCl_3$, 300 K): $\delta$ = 2.24 (t, $J$ = 1.2 Hz, 6H, $CH_3$) ppm. $^{19}F$ NMR (188.29 MHz, $CDCl_3$, 300 K): $\delta$ = –151.3 (d, $^3J_{F,F}$ = 20 Hz, 4F, $Ar_{ortho}$), –161.3 (t, $^3J_{F,F}$ = 21 Hz, 2F, $Ar_{para}$), –162.9 (pst, $^3J_{F,F}$ = 20 Hz, 4F, $Ar_{meta}$) ppm.

**Syntheses of Complexes. [$Ni^{II}${$C_6F_5$-DAD(Me)}$_2$] (1):** $NiBr_2$·DME (371 mg, 1.20 mmol), $C_8K$ (341 mg, 2.52 mmol) and **1a** (1000 mg, 2.40 mmol) were placed in a Schlenk flask and THF (50 mL) was added. The reaction mixture was stirred overnight at room temperature. The mixture was filtered via Celite and THF was removed in vacuo giving a purple powder. The raw product was repeatedly extracted with boiling toluene (50 mL) from a glass frit until almost colorless solution. After the toluene extract was stored for a night at –30 °C, dark-purple crystals were collected by decantation of the solvent. The crystals were washed with cold *n*-hexane (2 × 5 mL) and dried in vacuo. Yield: 660 mg (62%). Single crystals of **1** suitable for X-ray crystallography were obtained from a THF/toluene mixture (1:2) by cooling. M.p. 200–203 °C. $C_{32}H_{12}F_{20}N_4Ni$ (891.13): calcd. C 43.13, H 1.36, N 6.29; found C 43.66, H 1.85, N 5.96. MS (EI): *m/z* = 889 [M–H$^+$], 474 [M–(DAD)$^+$], 416 [(DAD)$^+$]. $^1H$ NMR (200.13 MHz, $CDCl_3$, 300 K): $\delta$ = –1.98 ppm (s, 12H, $CH_3$) ppm. $^{19}F$ NMR (188.29 MHz, $CDCl_3$, 300 K): $\delta$ = –150.2 (m, 8F, $Ar_{ortho}$), –160.1 (t, $^3J_{F,F}$ = 21 Hz, 4F, $Ar_{para}$), –164.0 (m, 8F, $Ar_{meta}$) ppm. IR (Nujol): $\tilde{\nu}$ = 1630 (w), 1508 (s), 1408 (s), 1308 (w), 1260 (w), 1196 (m), 1146 (w), 1117 (m), 1033 (s), 987 (s), 928 (m), 798 (w), 732 (m), 696 (w), 644 (w), 598 (w), 558 (w), 466

Table 2. Crystallographic data for **1**·($C_7H_8$), **2**·($C_7H_8$), **3**, and **4**·2($C_7H_8$).

| | **1**·($C_7H_8$) | **2**·($C_7H_8$) | **3** | **4**·2($C_7H_8$) |
|---|---|---|---|---|
| Empirical formula | $C_{39}H_{20}F_{20}N_4Ni$ | $C_{39}H_{20}CoF_{20}N_4$ | $C_{56}H_{24}F_{24}N_4Ni$ | $C_{98}H_{52}CoF_{36}N_6$ |
| Formula mass [g/mol] | 983.30 | 983.52 | 1267.50 | 2056.39 |
| Crystal size [mm] | 0.45 × 0.12 × 0.06 | 0.28 × 0.06 × 0.04 | 0.28 × 0.27 × 0.05 | 0.40 × 0.14 × 0.04 |
| Crystal shape | plate | needle | plate | prism |
| Crystal system | orthorhombic | orthorhombic | monoclinic | monoclinic |
| Space group | *Pbcn* | *Pbcn* | *C*2/*c* | *C*2/*c* |
| *a* [Å] | *a* = 20.0534(10) | 20.077(2) | 18.3645(19) | 28.843(2) |
| *b* [Å] | *b* = 12.9233(7) | 12.9232(14) | 18.1763(14) | 13.3691(9) |
| *c* [Å] | *c* = 14.2875(10) | 14.3559(12) | 16.7383(18) | 23.2949(19) |
| $\beta$ [°] | | | 113.662(12) | 101.695(6) |
| *V* [Å$^3$] | 3702.7(4) | 3724.8(6) | 5119.1(9) | 8796.3(11) |
| *Z* | 4 | 4 | 4 | 4 |
| $D_{calcd.}$ [g/cm$^3$] | 1.764 | 1.754 | 1.645 | 1.553 |
| $\mu$ [mm$^{-1}$] | 0.663 | 0.599 | 0.511 | 0.325 |
| $\theta_{min.}/\theta_{max.}$ [°] | 1.87/26.24 | 1.87/26.26 | 1.65/26.01 | 1.44/26.20 |
| $T_{max.}/T_{min.}$ | 0.95/0.80 | | 0.97/0.87 | 0.95/0.91 |
| Reflections collected | 33387 | 28558 | 25039 | 62074 |
| Reflections unique | 3719 | 3744 | 4890 | 8806 |
| Reflections observed | 2536 | 1825 | 3355 | 4840 |
| No. of parameters | 328 | 312 | 544 | 790 |
| *R*(*F*) | 0.0315 | 0.0527 | 0.0330 | 0.0507 |
| *Rw* ($F^2$) | 0.0810 | 0.0916 | 0.0714 | 0.1139 |
| *S* (GOF) on $F^2$ | 0.896 | 0.910 | 0.876 | 0.908 |
| $\Delta\rho_{max}$ [e Å$^3$]/$\Delta\rho_{min}$ [e Å$^3$] | 0.30/–0.19 | 0.27/–0.35 | 0.26/–0.25 | 0.52/–0.38 |

 © 2006 Wiley-VCH Verlag GmbH & Co. KGaA, Weinheim 

(w) $cm^{-1}$. UV/Vis ($CHCl_3$): $\lambda_{max}$ ($\varepsilon_{max}$/$dm^3 \cdot mol^{-1} \cdot cm^{-1}$) = 756 sh (3200), 524 (8000), ≈ 292 (15200) nm.

**[$Co^{II}${$C_6F_5$-DAD(Me)}$_2$] (2):** $CoCl_2$ (156 mg, 1.20 mmol), $C_8K$ (341 mg, 2.52 mmol) and **1a** (1000 mg, 2.40 mmol) were placed in a Schlenk flask and THF (40 mL) was added. The reaction mixture was stirred overnight at room temperature. The mixture was filtered and THF was removed in vacuo giving a brown powder. The raw product was extracted with *n*-hexane (65 mL), concentrated in vacuo and washed with cold benzene (5 mL). Yield: 431 mg (40%). Brown single crystals of **2** suitable for X-ray crystallography were obtained from a THF/toluene mixture (3:1) by cooling. M.p. 194–196 °C. $C_{32}H_{12}CoF_{20}N_4$ (891.38): calcd. C 43.12, H 1.36, N 6.29; found C 42.92, H 1.69, N 5.91. MS (EI): *m*/*z* = 890 [M–$H^+$], 475 [M–(DAD)$^+$], 416 [(DAD)$^+$]. IR (Nujol): $\tilde{\nu}$ = 1632 (w), 1514 (s), 1504 (s), 1402 (m), 1308 (w), 1197 (m), 1142 (w), 1119 (m), 1030 (s), 987 (s), 929 (m), 797 (w), 683 (m), 640 (w), 597 (w) $cm^{-1}$. UV/Vis ($CHCl_3$): $\lambda_{max}$ ($\varepsilon_{max}$/$dm^3 \cdot mol^{-1} \cdot cm^{-1}$) = 697 (1200), 529 (3100), 470 (5400), 429 (5200), 335 (11600) nm.

**[$Ni^{II}$({3,5-$(CF_3)_2C_6H_3$}-BIAN)$_2$] (3):** $NiCl_2$·DME (610 mg, 1.00 mmol), $C_8K$ (143 mg, 1.06 mmol) and $^F$BIAN (111 mg, 0.51 mmol) were placed in a Schlenk flask and THF (30 mL) was added. The reaction mixture was stirred overnight at room temperature. The resulting dark-blue suspension was concentrated under reduced pressure. The raw product was extracted with toluene (40 mL). After toluene was removed, a dark-blue fine crystalline material was obtained, which was washed with MeCN and dried in vacuo. Yield: 518 mg (81%). Single crystals of **3** suitable for X-ray crystallography were obtained from a saturated *n*-hexane solution by cooling. M.p. 321–323 °C. $C_{56}H_{24}F_{24}N_4Ni$ (1267.47): calcd. C 53.07, H 1.91, N 4.42; found C 52.53, H 2.01, N 4.41. MS (EI): *m*/*z* = 1266 [$M^+$], 1247 [M–$F^+$], 662 [M–(BIAN)$^+$]. $^1$H NMR (200.13 MHz, $C_6D_6$, 300 K): $\delta$ = 8.98 (s, 4H, $H_{Ph}$), 7.97 (m, 4H, $H_{Ph}$, $H_{naph}$), 7.10 (d, $^3J_{H,H}$ = 7.2 Hz, 2H, $H_{naph}$), 6.41 (pst, $^3J_{H,H}$ = 7.7 Hz, 2H, $H_{naph}$) ppm. $^{19}$F NMR (188.29 MHz, $C_6D_6$, 300 K): $\delta$ = –63.0 (s, 12F, $CF_3$) ppm. IR (Nujol): $\tilde{\nu}$ = 1776 (w), 1600 (m), 1510 (w), 1418 (w), 1275 (s), 1243 (w), 1127 (s), 1091 (s), 1014 (s), 974 (m), 884 (m), 850 (m), 812 (m), 761 (m), 700 (m), 678 (m), 544 (w), 496 (w) $cm^{-1}$. UV/Vis ($CHCl_3$): $\lambda_{max}$ ($\varepsilon_{max}$/$dm^3 \cdot mol^{-1} \cdot cm^{-1}$) = 874 (8300), 600 (12200), 512 (10300), ≈ 332 (32700) nm.

**[$Co^{I}$({[3,5-$(CF_3)_2C_6H_3$]-BIAN}$_3$] (4):** $CoCl_2$ (43 mg, 0.33 mmol), $C_8K$ (95 mg, 0.70 mmol) and $^F$BIAN (604 mg, 1.00 mmol) were placed in a Schlenk flask and THF (15 mL) was added. The reaction mixture was stirred overnight at room temperature. THF was removed in vacuo and the raw product was extracted with toluene (50 mL). Toluene solution was concentrated to 25 mL, *n*-hexane (25 mL) was added and the resulting solution was stored for a night at –30 °C. Solution was decanted, dark-purple crystals were washed with *n*-hexane and dried in vacuo. Yield: 283 mg (46%). Single crystals of **4** suitable for X-ray crystallography were obtained from a toluene/*n*-hexane mixture by cooling. M.p. 275–278 °C. $C_{84}H_{36}CoF_{36}N_6$ (1872.13): calcd. C 53.89, H 1.94, N 4.49; found C 53.44, H 1.96, N 4.47. MS (EI): *m*/*z* = 1267 [M–(BIAN)$^+$], 1248 [M–(BIAN)–$F^+$], 663 [M–2(BIAN)$^+$]. IR (Nujol): $\tilde{\nu}$ = 1600 (w), 1278 (s), 1261 (m), 1242 (m), 1175 (s), 1140 (s), 1102 (m), 1035 (m), 1019 (m), 972 (m), 892 (m), 856 (m), 846 (m), 822 (w), 795 (w), 770 (m), 723 (m), 705 (w), 683 (m), 668 (m), 616 (w), 576 (w), 533 (m), 513 (m), 481 (m) $cm^{-1}$. UV/Vis ($CHCl_3$): $\lambda_{max}$ ($\varepsilon_{max}$/$dm^3 \cdot mol^{-1} \cdot cm^{-1}$) = 735 (5000), 519 sh (12100), ≈ 329 (41300) nm.

**Supporting Information** (see also the footnote on the first page of this article): Intermolecular π stacking in the crystal structure of **3** (Figure S1).


[1] A. L. Balch, R. H. Holm, *J. Am. Chem. Soc.* **1966**, *88*, 5201–5209.

[2] a) M. D. Ward, J. A. McCleverty, *J. Chem. Soc., Dalton Trans.* **2002**, 275–288; b) A. Vlček, Jr., *Coord. Chem. Rev.* **2002**, *230*, 225–242; c) P. Chaudhuri, K. Wieghardt, *Prog. Inorg. Chem.* **2001**, *50*, 151–216.

[3] H. tom Dieck, H. Bruder, *J. Chem. Soc., Chem. Commun.* **1977**, 24–25.

[4] H. tom Dieck, M. Svoboda, J. Kopf, *Z. Naturforsch. B: Chem. Sci.* **1978**, *33*, 1381–1385.

[5] D. von Walther, G. Kreisel, R. Kirmse, *Z. Anorg. Allg. Chem.* **1982**, *487*, 149–160.

[6] R. Kirmse, J. Stach, D. von Walther, R. Boettcher, *Z. Chem.* **1980**, *29*, 224–225.

[7] D. von Walther, *Z. Anorg. Allg. Chem.* **1974**, *405*, 8–18.

[8] a) M. Svoboda, H. tom Dieck, *Z. Naturforsch. B: Chem. Sci.* **1981**, *36*, 814–822; b) H. tom Dieck, M. Svoboda, T. Greiser, *Z. Naturforsch. B: Chem. Sci.* **1981**, *36*, 823–832.

[9] a) H. Görls, D. Walther, J. Sieler, *Cryst. Res. and Technol.* **1987**, *22*, 1145–1151; b) W. Bonrath, K. R. Pörschke, R. Mynott, C. Krüger, *Z. Naturforsch. B: Chem. Sci.* **1990**, *45*, 1647–1650.

[10] a) D. Herebian, E. Bothe, F. Neese, T. Weyhermüller, K. Wieghardt, *J. Am. Chem. Soc.* **2003**, *125*, 9116–9128; b) D. Herebian, K. E. Wieghardt, F. Neese, *J. Am. Chem. Soc.* **2003**, *125*, 10997–11005; c) V. Bachler, G. Olbrich, F. Neese, K. Wieghardt, *Inorg. Chem.* **2002**, *41*, 4179–4193.

[11] a) S.-M. Peng, Y. Wang, C.-K. Chiang, *Acta Crystallogr., Sect. C: Cryst. Struct. Commun.* **1984**, *40*, 1541–1542; b) C.-S. Lee, T.-S. Hwang, Y. Wang, S.-M. Peng, C.-S. Hwang, *J. Phys. Chem.* **1996**, *100*, 2934–2941.

[12] L. S. Hegedus, *Transition Metals in the Synthesis of Complex Organic Molecules*; University Science Books: Mill Valley, CA, **1994**, p. 3.

[13] C. K. Jörgensen, *Oxidation Numbers and Oxidation States*, Springer: Heidelberg, Germany, **1969**.

[14] P. Chaudhuri, C. N. Verani, E. Bill, E. Bothe, T. Weyhermüller, K. Wieghardt, *J. Am. Chem. Soc.* **2001**, *123*, 2213–2223.

[15] M. M. Khusniyarov, K. Harms, J. Sundermeyer, *J. Fluorine Chem.* **2006**, *127*, 200–204.

[16] a) R. van Asselt, C. J. Elsevier, W. J. J. Smeets, A. L. Spek, R. Benedix, *Recl. Trav. Chim. Pays-Bas* **1994**, *113*, 88–98; b) R. van Asselt, C. J. Elsevier, C. Amatore, A. Jutand, *Organometallics* **1997**, *16*, 317–328; c) L. K. Johnson, C. M. Killian, M. Brookhart, *J. Am. Chem. Soc.* **1995**, *117*, 6414–6415; d) C. M. Killian, D. J. Tempel, L. K. Johnson, M. Brookhart, *J. Am. Chem. Soc.* **1996**, *118*, 11664–11665.

[17] I. L. Fedushkin, A. A. Skatova, V. A. Chudakova, V. K. Cherkasov, S. Dechert, H. Schumann, *Russ. Chem. Bull. Int. Ed.* **2004**, *53*, 2142–2147.

[18] S. Blanchard, F. Neese, E. Bothe, E. Bill, T. Weyhermüller, K. Wieghardt, *Inorg. Chem.* **2005**, *44*, 3636–3656.

[19] a) L. R. Chamberlain, L. D. Durfee, P. E. Fanwick, L. M. Kobriger, S. L. Latesky, A. K. McMullen, B. D. Steffey, I. P. Rothwell, K. Folting, J. C. Huffman, *J. Am. Chem. Soc.* **1987**, *109*, 6068–6076; b) S. L. Latesky, A. K. McMullen, G. P. Niccolai, I. P. Rothwell, J. C. Huffman, *Organometallics* **1985**, *4*, 1896–1898; c) W. A. Herrmann, M. Denk, W. Scherer, F.-R. Klingan, *J. Organomet. Chem.* **1993**, *444*, C21–C24; d) K. Mashima, Y. Matsuo, K. Tani, *Organometallics* **1999**, *18*, 1471–1481; e) R. L. Huff, S.-Y. S. Wang, K. A. Abboud, J. M. Boncella, *Organometallics* **1997**, *16*, 1779–1785; f) K. Mashima, Y. Matsuo, K. Tani, *Chem. Lett.* **1997**, 767–768; g) T.-G. Ong, D. Wood, G. P. A. Yap, D. S. Richeson, *Organometallics* **2002**, *21*, 1–3; h) Y. Matsuo, K. Mashima, K. Tani, *Angew. Chem. Int. Ed.* **2001**, *40*, 960–962; i) J. Scholz, M. Dlikan, D. Strohl, A. Dietrich, H. Schumann, K.-H. Thiele, *Chem. Ber.* **1990**, *123*, 2279–2285; j) J. Wunderle, J. Scholz, U. Baumeister, H. Hartung, *Z. Kristallogr.* **1996**, *211*, 423–424; k) G. A. Hadi, J. Wunderle, K.-H. Thiele, R. Froehlich, *Z. Kristallogr.* **1994**, *209*, 372;


 © 2006 Wiley-VCH Verlag GmbH & Co. KGaA, Weinheim 

l) B. Richter, J. Scholz, J. Sieler, K.-H. Thiele, *Angew. Chem. Int. Ed. Engl.* **1995**, *34*, 2649–2651; m) A. Merkoulov, K. Harms, J. Sundermeyer, *Z. Anorg. Allg. Chem.* **2005**, *631*, 2877–2880.
[20] M. G. Gardiner, G. R. Hanson, M. J. Henderson, F. C. Lee, C. L. Raston, *Inorg. Chem.* **1994**, *33*, 2456–2461.
[21] a) G. S. Hall, R. H. Soderberg, *Inorg. Chem.* **1968**, *7*, 2300–2303; b) A. V. Reshetnikov, A. A. Sidorov, S. S. Talismanov, G. G. Aleksandrov, Y. A. Ustynyuk, S. E. Nefedov, I. L. Eremenko, I. I. Moiseev, *Russ. Chem. Bull. (Translation Izv. Akad. Nauk SSSR, Ser. Khim.)* **2000**, *49*, 1771–1774; c) H.-Y. Cheng, C.-C. Lin, B.-C. Tzeng, S.-M. Peng, *J. Chin. Chem. Soc. (Taipei)* **1994**, *41*, 775–781.
[22] M. M. Khusniyarov, K. Harms, J. Sundermeyer, B. Sarkar, W. Kaim, J. van Slageren, J. Fiedler, manuscript in preparation.
[23] S. Lorenzo, G. R. Lewis, I. Dance, *New J. Chem.* **2000**, *24*, 295–304.
[24] M. P. Thornberry, C. Slebodnick, P. A. Deck, F. R. Fronczek, *Organometallics* **2000**, *19*, 5352–5369.
[25] a) M. J. Blandamer, J. Burgess, J. Fawcett, P. Guardado, C. D. Hubbard, S. Nuttall, L. J. S. Prouse, S. Radulovic, D. R. Russell, *Inorg. Chem.* **1992**, *31*, 1383–1389; b) P. J. Daff, M. Etienne, B. Donnadieu, S. Z. Knottenbelt, J. E. McGrady, *J. Am. Chem. Soc.* **2002**, *124*, 3818–3819; c) K.-H. Thiele, B. Richter, B. Neumuller, *Z. Anorg. Allg. Chem.* **1994**, *620*, 1627–1630; d) M. N. Bochkarev, A. A. Trifonov, F. G. N. Cloke, C. I. Dalby, P. T. Matsunaga, R. A. Anderson, H. Schumann, J. Loebel, H. Hemling, *J. Organomet. Chem.* **1995**, *486*, 177–182; e) B. Chaudret, H. Koster, R. Poilblanc, *J. Chem. Soc., Chem. Commun.* **1981**, 266–268; f) B. Chaudret, C. Cayret, H. Koster, R. Poilblanc, *J. Chem. Soc., Dalton Trans.* **1983**, 941–945; g) B. Richter, J. Scholz, B. Neumuller, R. Weimann, H. Schumann, *Z. Anorg. Allg. Chem.* **1995**, *621*, 365–372.
[26] D. J. Szalda, C. Creutz, D. Mahajan, N. Sutin, *Inorg. Chem.* **1983**, *22*, 2372–2379.
[27] S. Ye, B. Sarkar, F. Lissner, T. Schleid, J. van Slageren, J. Fiedler, W. Kaim, *Angew. Chem. Int. Ed.* **2005**, *44*, 2103–2106.
[28] O. Kahn, *Molecular Magnetism*, VCH Publishers, New York, **1993**.
[29] C. J. O'Connor, *Prog. Inorg. Chem.* **1982**, *29*, 203–283.
[30] a) I. L. Fedushkin, A. A. Skatova, V. K. Cherkasov, V. A. Chudakova, S. Dechert, M. Hummert, H. Schumann, *Chem. Eur. J.* **2003**, *9*, 5778–5783; b) I. L. Fedushkin, A. A. Skatova, V. A. Chudakova, V. K. Cherkasov, G. K. Fukin, M. A. Lopatin, *Eur. J. Inorg. Chem.* **2004**, 388–393; c) I. L. Fedushkin, N. M. Khvoinova, A. Y. Baurin, G. K. Fukin, V. K. Cherkasov, M. P. Bubnov, *Inorg. Chem.* **2004**, *43*, 7807–7815; d) I. L. Fedushkin, A. A. Skatova, M. Hummert, H. Schumann, *Eur. J. Inorg. Chem.* **2005**, 1601–1608.
[31] J. C. Gordon, P. Shukla, A. H. Cowley, J. N. Jones, D. W. Keogh, B. L. Scott, *Chem. Commun.* **2002**, 2710–2711.
[32] L. G. L. Ward, D. M. Paul, *Inorg. Synth.* **1971**, *13*, 154–164.
[33] M. Gasperini, F. Ragaini, S. Cenini, *Organometallics* **2002**, *21*, 2950–2957.
[34] F. A. Cotton, E. A. Hillard, C. A. Murillo, X. Wang, *Inorg. Chem.* **2003**, *42*, 6063–6070.
[35] PLATON, A Multipurpose Crystallographic Tool, Utrecht University, Utrecht, The Netherlands, A. L. Spek, **2005**.
[36] SHELX97 – Programs for Crystal Structure Analysis (Release 97–2). G. M. Sheldrick, Institute of Inorganic Chemistry, University of Göttingen, Göttingen, Germany, **1998**.
[37] A. Altomare, G. Cascarano, C. Giacovazzo, A. Guagliardi, *J. Appl. Crystallogr.* **1993**, *26*, 343–350.
[38] T. Schleis, T. P. Spaniol, J. Okuda, J. Heinemann, R. Mülhaupt, *J. Organomet. Chem.* **1998**, *569*, 159–167.
[39] T. Spaniel, H. Görls, J. Scholz, *Angew. Chem. Int. Ed.* **1998**, *37*, 1862–1865.
[40] J. O. Liimatta, B. Lofgren, M. Miettinen, M. Ahlgren, M. Haukka, T. T. Pakkanen, *J. Polym. Sci., Part A: Polym. Chem.* **2001**, *39*, 1426–1434.
[41] I. L. Fedushkin, A. A. Skatova, V. A. Chudakova, G. K. Fukin, S. Dechert, H. Schumann, *Eur. J. Inorg. Chem.* **2003**, 3336–3346.

Received: March 15, 2006
Published Online: June 7, 2006

 © 2006 Wiley-VCH Verlag GmbH & Co. KGaA, Weinheim 

DOI: 10.1002/ejic.200600288

# Synthesis, Complexation and Spectrofluorometric Studies of a New $NS_3$ Anthracene-Containing Macrocyclic Ligand

**Abel Tamayo,[a] Lluis Escriche,*[a] Jaume Casabó,[a] Berta Covelo,[b] and Carlos Lodeiro*[b]**

**Keywords:** PET Systems / N,S ligands / Macrocycles / Fluorescence / Palladium

A new fluorescent device for detecting protons and metal ions, 11-(9-anthracenylmethyl)-1,4,7-trithia-11-azacyclotetradecane (**L**), has been synthesised. In addition, the photophysical properties of both the free and protonated species have been examined by absorption and fluorescence titrations of dichloromethane solutions of **L** with methanesulfonic acid. The coordinating properties of **L** toward $Pd^{II}$, $Zn^{II}$, $Ni^{II}$ and $Co^{II}$ have been studied both in solution and in the solid state. Different behaviours have been observed in the absorption and fluorescence titrations of **L** with the above-mentioned transition-metal ions. To evaluate whether these differences were due to the existence of equilibria between protonated and complexed species, such titrations have been repeated in the presence of an equivalent amount of acid. The structure of the $[Pd(\mathbf{L})](BF_4)_2$ complex has been solved by X-ray crystallography.
(© Wiley-VCH Verlag GmbH & Co. KGaA, 69451 Weinheim, Germany, 2006)

## Introduction

The design of new fluorescence chemosensors capable of signalling the presence of metal ions is a subject of particular interest for chemists.[1] These systems usually consist of a fluorescent moiety (signalling unit), covalently connected to a binding site (receptor unit).[2] The more specific the interaction between the receptor unit and the analyte, the greater the selectivity of the chemosensor. Many fluorescence chemosensors have macrocycles as receptor units, as the coordinating properties of macrocycles have been shown to be more effective than those of the analogous acyclic ligands. Most of these chemosensors are made up of polyoxa,[3] polyaza[4] and oxa-azamacrocycles,[5] which have been used for the detection of alkali and *hard* metal ions. However, less attention has been paid to the study of thiamacrocycle-containing chemosensors, which could be useful for detecting *soft* transition-metal ions.[6] On the other hand, the stronger the effects of the ion on the properties of the fluorophore, the greater the sensitivity of the chemosensor. Aliphatic amines closely bonded to anthracene moieties are known to be involved in electron transfer quenching, which facilitates the signalling of the presence of metal ions in amine-containing systems.[7] Taking these considerations into account, we here report the synthesis of a new fluorescence device 11-(9-anthracenylmethyl)-1,4,7-trithia-11-azacyclotetradecane (**L**), which consists of an azathiamacrocycle connected by its aliphatic amine to an anthracene moiety. Protonation and coordination properties towards $Pd^{II}$, $Zn^{II}$, $Ni^{II}$ and $Co^{II}$ have also been studied, with the crystallographic data of the $[Pd(\mathbf{L})](BF_4)_2$ complex analysed as well.

[a] Departament de Química, Universitat Autònoma de Barcelona, 08193 Bellaterra, Barcelona, Spain
Fax: +34-93-581-2497
E-mail: lluis.escriche@uab.es
[b] REQUIMTE-CQFB, Departamento de Química, Faculdade de Ciências e Tecnologia, Universidade Nova de Lisboa, 2829-516 Monte de Caparica, Portugal
Fax: +351-21-2948385
E-mail: lodeiro@dq.fct.unl.pt

## Results and Discussion

### Synthesis of Ligands

Scheme 1 shows the two methods used to synthesise the anthracene-containing macrocycle **L**. The first method (pathway A in Scheme 1) is based on using macrocycle **2** as a precursor of **L**. Compound **2** was obtained by cyclisation of 2,2′-thiobis(ethanethiol) with the dichloride precursor **1**, following a procedure similar to that described by Buter and Kellogg for the synthesis of sulfur-containing macrocycles. This method is based on the simultaneous reaction between aliphatic α,ω-dithiols and α,ω-dihalides, using DMF as a solvent and $Cs_2CO_3$ as a base.[8] In our case, CsOH was used instead of $Cs_2CO_3$, as the carbonate ions react with **1** to produce 3-(3-chloropropyl)-[1,3]oxazin-2-one.[9] This modification allowed us to obtain **2** in 62% of the yield. The preparation of **2** was previously reported in the literature using other methods.[10] Those methods avoid the reaction between the carbonate ions and the dihalide **1** by using protection–deprotection strategies, which increase the number of synthetic steps and decrease the final yields. The last step in synthetic procedure A is the functionalisation of **2** with an anthracene derivative. This was performed by a reaction of **2** with 9-(chloromethyl)anthracene in the presence of KI, as we have recently shown that iodide

 © 2006 Wiley-VCH Verlag GmbH & Co. KGaA, Weinheim 

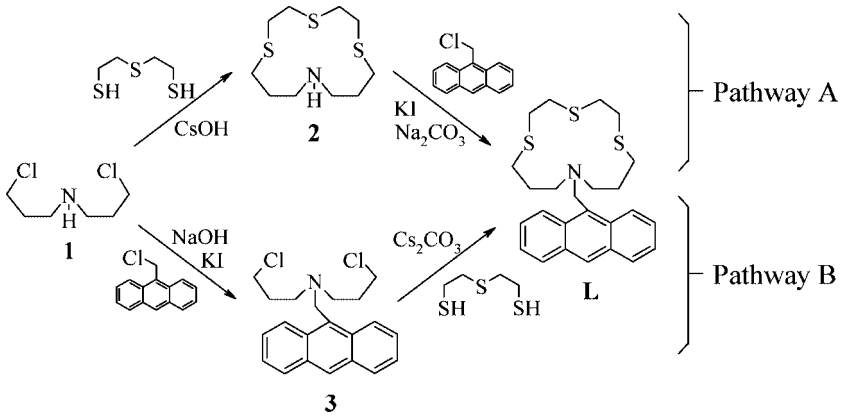


Scheme 1.

ions can be used as catalysts for the nucleophilic substitution reactions of 9-(chloromethyl)anthracene and secondary aliphatic amines.[11] The overall yield of pathway A was 45%.

The second method for the synthesis of **L** (pathway B in Scheme 1) is based on the functionalisation of the dichloride precursor **1**, prior its use in the cyclisation reaction with 2,2′-thiobis(ethanethiol). Although the cyclisation conditions of pathway B are very close to those optimised for the synthesis of sulfur-containing macrocycles,[8] as $Cs_2CO_3$ could be used as a base,[12] the overall yield of this second pathway (38%) was not significantly different from that found in pathway A.

### Complexation of L

The reaction of equimolar amounts of **L** and $Pd(BF_4)_2 \cdot 4CH_3CN$ in acetonitrile yielded a light brown solution. The addition of diethyl ether to this solution led to the precipitation of a crystalline product, whose elemental analysis is consistent with the formula $Pd(\mathbf{L})(H_2O)_2(BF_4)_2$. Its IR spectrum confirmed the presence of **L**, tetrafluoroborate ions and water molecules, as well as the absence of acetonitrile, as no signal was observed between 2250 and 2350 $cm^{-1}$. This compound behaves as a 2:1 electrolyte in acetonitrile solution, which indicates that the tetrafluoroborate anions are not coordinated with the metal ions. The $^1H$ NMR spectrum of this complex in acetonitrile solution shows a complex pattern in the aliphatic region, as most of the signals become multiplets because of the nonequivalence of the hydrogen atoms. However, its $^{13}C\{^1H\}$NMR spectrum shows the same number of signals as that of the free ligand, which indicates that although the two protons bonded to each carbon atom are magnetically nonequivalent, each pair of carbon atoms is chemically equivalent. On the other hand, those carbons directly bonded to a donor atom of **L** show downfield displacement compared with those of the free ligand, which suggests that the $Pd^{II}$ ion is coordinated to all four donor atoms of **L**. This fact, together with the ESI-MS and electronic spectra of this complex, points to the presence of the $[Pd(\mathbf{L})]^{2+}$ unit, which was confirmed by X-ray analysis of the pale brown crystals obtained by slow diffusion of hexane into a dichloromethane solution of $[Pd(\mathbf{L})](BF_4)_2 \cdot 2H_2O$. It is important to note that although the elemental analysis, as well as the IR spectrum of this complex, indicates the presence of water molecules, these are not present in the crystal lattice of the complex. Therefore, they were probably lost during the crystallisation process.

The crystal structure of this complex consists of discrete $[Pd(\mathbf{L})]^{2+}$ cations and tetrafluoroborate anions. A displacement ellipsoid representation of the cation complex and a list of selected bond lengths and angles are given in Figure 1. The metal coordination geometry is square-planar with the N2, S6, S9, S12 and Pd atoms on a plane. The largest deviation from this plane is 0.0941 Å for the S9 atom. The Pd–N distance [2.133(2) Å] is slightly larger than that of the analogous $Pd^{II}$ complex without the pendant arm.[10b] The Pd–S bond lengths [2.2718(9), 2.306(3) and

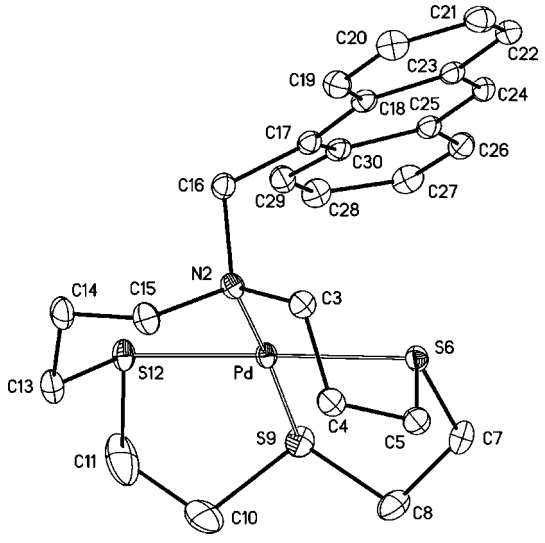


Figure 1. Displacement ellipsoid representation of the $[Pd(\mathbf{L})]^{2+}$ cation with the atom-numbering scheme adopted. Tetrafluoroborate counterions and hydrogen atoms have been omitted for clarity. Selected bond lengths [Å] and angles [°]: Pd–N2 2.133(2), Pd–S9 2.2718(9), Pd–S12 2.306(3), Pd–S6 2.3221(9), N2–Pd–S9 174.34(6), N2–Pd–S12 94.45(9), S9–Pd–S12 85.56(7), N2–Pd–S6 93.10(6), S9–Pd–S6 87.21(3), S12–Pd–S6 171.92(8). Ellipsoids are shown at the 30% probability level.

 © 2006 Wiley-VCH Verlag GmbH & Co. KGaA, Weinheim 

2.3221(9) Å] are similar to those found for other $Pd^{II}$ complexes of thioether-containing macrocycles.[10b,13] In this structure, **L** adopts a conformation in which all carbon atoms of the macrocyclic unit lie below the plane defined by the four heteroatoms, whereas the whole anthracene moiety lies over this plane. As expected, the anthracene unit is essentially planar. In fact, the largest deviation from the least-squares plane calculated using all 14 aromatic atoms is 0.126 Å for the C29 atom. A ring of the anthracene moiety is located over the $Pd^{II}$ ion. The distance between the centroid of such a ring [Cg(1): C25–C26–C27–C28–C29–C30] and the metal ion is 3.635 Å, whereas the angle between the normal of the ring and the Cg(1)···Pd vector is 41.26°. These considerations may suggest a weak intramolecular cation···π interaction.[14] On the other hand, nonclassical C–H···F hydrogen bonds lead to the formation of a 2D supramolecular network along the crystallographic *ab* plane (Figure 2).

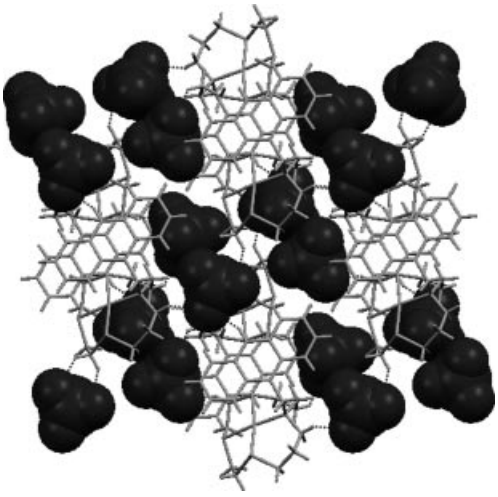

Figure 2. A fragment of an infinite 2D network through C–H···F hydrogen bonds of $[Pd(\mathbf{L})](BF_4)_2$ showing the close packing in the plane *ab*. Tetrafluoroborate counterions in space-filling mode.

All attempts to obtain solid complexes with $Ni^{II}$, $Co^{II}$ and $Zn^{II}$ were unsuccessful, as no homogeneous products were isolated. This fact could be attributed to the protonation of **L**, as was also observed in the titrations of other tertiary amine-containing ligands with these metal ions.[11]

## Spectrophotometric and Spectrofluorometric Studies

### *Ligand Protonation*

The absorption spectrum of a dichloromethane solution of **L** shows the characteristic band of the anthracene derivatives above 330 nm. The absorption band of **L** has a vibrational fine structure with maxima at 333, 350, 368 and 388 nm. The effect of the protonation on the absorption spectrum of this ligand was determined by titration with methanesulfonic acid (Figure 3, A). This absorption titration revealed seven isosbestic points at 335, 342, 352, 361, 371, 380 and 391 nm, which suggests the presence of two species in equilibrium. The protonation induced a red shift of the absorption maxima, as well as a decrease in the absorption coefficient of this band. As can be seen in the inset of Figure 3 (A), an equivalent amount of acid is required to complete the protonation of **L**.

The fluorescence emission and excitation spectra of **L** show the characteristic bands of the anthracene systems (Figure 3, B). An "off–on" behaviour is observed when a dichloromethane solution of **L** is titrated with acid, as the nonprotonated ligand is slightly emissive in dichloromethane, whereas the protonated form is at least 30 times more

Table 1. Quantum yields in dichloromethane at 298 K.

| | $\Phi$ |
|---|---|
| **L** | 0.010 |
| **L** + $H^+$ | 0.341 |
| **L** + $Pd^{2+}$ | 0.005 |
| **L** + $Zn^{2+}$ | 0.254 |
| **L** + $Ni^{2+}$ | 0.203 |
| **L** + $Co^{2+}$ | 0.208 |

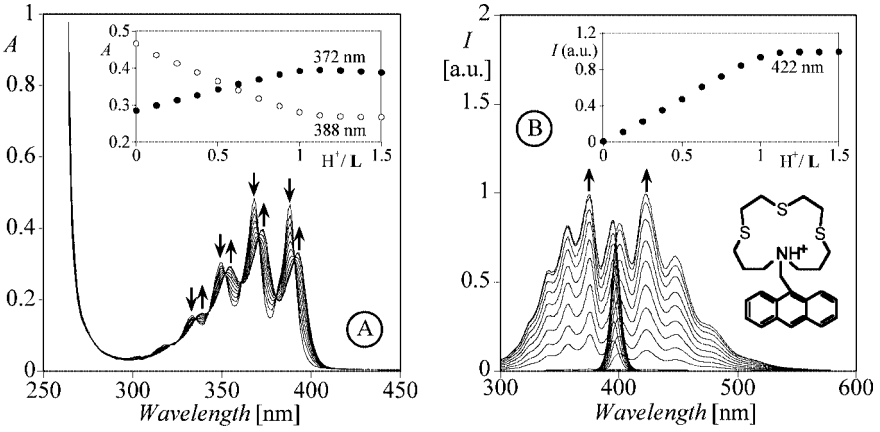


Figure 3. (A) Absorption spectra of a dichloromethane solution of **L** as a function of added $CH_3SO_3H$. The inset shows the absorbances at 372 and 388 nm. (B) Excitation and emission spectra of a dichloromethane solution of **L** as a function of added $CH_3SO_3H$. The inset shows the normalised fluorescence intensity at 422 nm ($[\mathbf{L}] = 5.14 \times 10^{-5}$ M, $T$ = 298 K, $\lambda_{exc}$ = 368 nm; $\lambda_{em}$ = 423 nm).

 © 2006 Wiley-VCH Verlag GmbH & Co. KGaA, Weinheim 

emissive than the free ligand. This increase in the fluorescence intensity is also reflected by comparing the quantum yield of the nonprotonated and protonated ligands (see Table 1), and is due to the fact that protonation prevents photoinduced electron transfer (PET) from the lone pair of electrons of the nitrogen atom to the anthracene moiety.

### *Metal Ion Titrations*

To explore the utility of **L** as a fluorescence device, titrations with several transition-metal ions were performed. Two different behaviours were observed as a function of the used metal ion.

### *$Pd^{II}$ Titrations*

To identify the absorption bands that exclusively resulted from the interactions between the $Pd^{II}$ cations and the macrocyclic moiety of **L**, we first performed a titration of the nonfunctionalised macrocycle **2** with this metal ion. The addition of $Pd(BF_4)_2 \cdot 4CH_3CN$ to a dichloromethane solution of **2** led to the formation of two absorption bands at 258 and 330 nm, assigned to MLCT and *d*–*d* bands respectively.[15] The inset of Figure 4 shows that the titration was completed after the addition of 1 equiv. of metal ion, which is in agreement with the formation of mononuclear species.

Figure 5 (A) shows the absorption spectra of the titration of **L** with $Pd(BF_4)_2$. The addition of the metal ion causes a

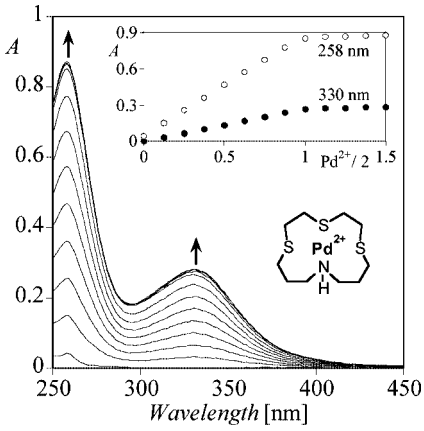


Figure 4. Absorption spectra of a dichloromethane solution of **2** as a function of added $Pd(BF_4)_2$. The inset shows the absorbances at 258 and 330 nm ([**2**] = $5.50 \times 10^{-5}$ M, $T$ = 298 K).

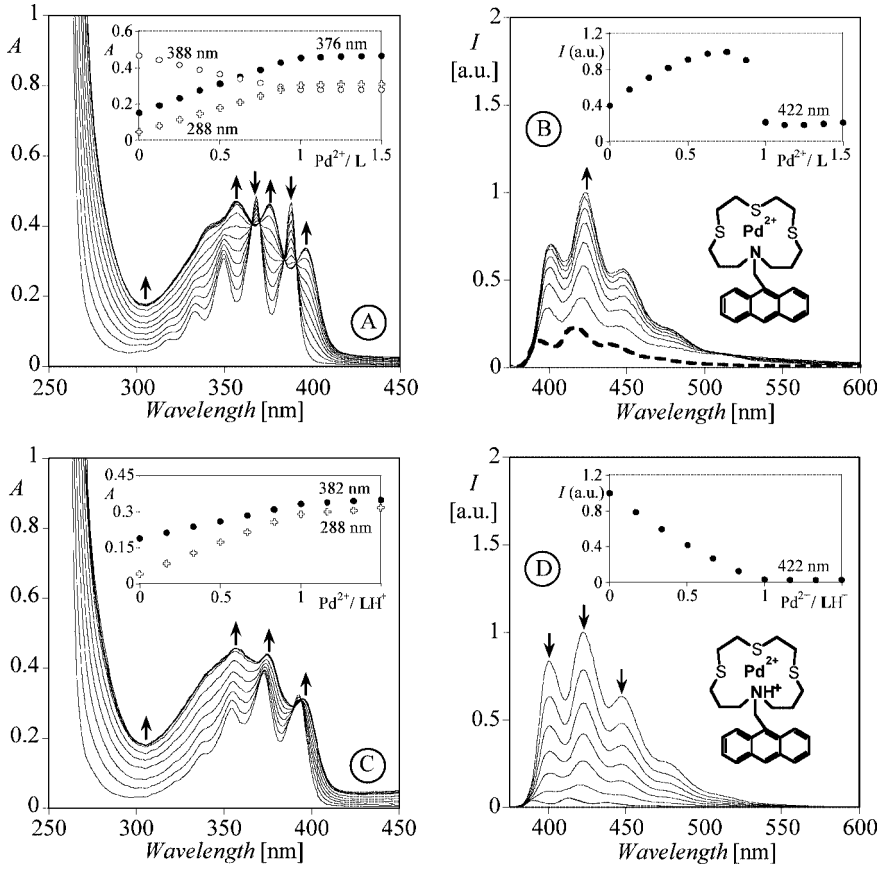


Figure 5. (A) Absorption spectra of **L** as a function of increasing amounts of $Pd(BF_4)_2$. The inset shows the absorbances at 288, 376 and 388 nm. (B) Emission spectra of **L** as a function of added $Pd(BF_4)_2$. Those spectra between the maximum and the end of the titration have been omitted for clarity. The last spectrum of each titration is shown as a dotted line. The inset shows the normalised fluorescence intensity at 422 nm. (C) Absorption spectra of $\mathbf{LH}^+$ as a function of increasing amounts of $Pd(BF_4)_2$. The inset shows the absorbances at 288 and 382 nm. (D) Emission spectra of $\mathbf{LH}^+$ as a function of added $Pd(BF_4)_2$. The inset shows the normalised fluorescence intensity at 422 nm (dichloromethane solution, [**L**] = [$\mathbf{LH}^+$] = $5.14 \times 10^{-5}$ M, $T$ = 298 K, $\lambda_{exc}$ = 368 nm).

 © 2006 Wiley-VCH Verlag GmbH & Co. KGaA, Weinheim 

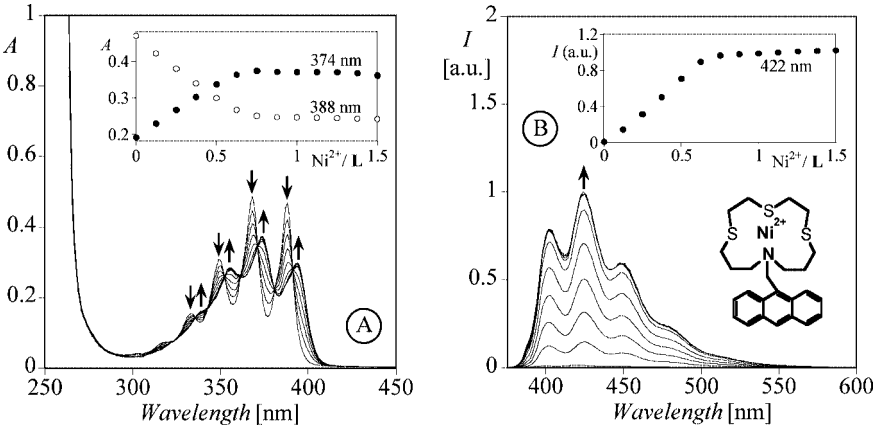


Figure 6. (A) Absorption spectra of a dichloromethane solution of **L** as a function of increasing amounts of $Ni(BF_4)_2$. The inset shows the absorbances at 374 and 388 nm. (B) Emission spectra of a dichloromethane solution of **L** as a function of added $Ni(BF_4)_2$. The inset shows the normalised fluorescence intensity at 422 nm. ([**L**] = $5.14 \times 10^{-5}$ M, $T$ = 298 K, $\lambda_{exc}$ = 368 nm).

red shift of the anthracene band, as well as an incremental increase in the molar absorption coefficient in the region around 300 nm. This increment is attributed to the formation of the absorption bands analogous to those observed in the titration of **2**. As can be seen in the inset of Figure 5 (A), a plateau is reached after the addition of an equivalent amount of metal ion, which suggests that each macrocyclic unit is coordinated to one metal ion. Figure 5 (B) shows the fluorescence titration of **L** with $Pd(BF_4)_2$. Although initial additions of the metal ion increase the fluorescence of the ligand, supplementary additions cause a strong quenching of the fluorescence, as well as a blue shift of about 6 nm. The *chelation enhancement of the quenching* (CHEQ) effect can be explained by assuming that $Pd^{II}$, as well as other transition-metal ions with partially filled d orbitals, is known to induce fluorescence quenching through photoinduced electron transfer or energy transfer mechanisms.[16] The initial increase of the fluorescence could be explained by the protonation of the amine, which prevents PET from its nitrogen atom to the anthracene moiety. This protonation is probably due to the presence of water in the metal ion solutions, which acts as an acid.

To verify this hypothesis, both absorption and fluorescence titrations of **L** were repeated in the presence of 1 equiv. of methanesulfonic acid (see parts C and D in Figure 5). The absorption titration of $\mathbf{LH}^+$ with $Pd(BF_4)_2$ followed the same pattern as that observed for **L**. On the other hand, the fluorescence titration of $\mathbf{LH}^+$ was significantly different from that of **L**, as the intensity of fluorescence decreased after each addition of metal ion. These results are in agreement with the simultaneous presence of protonated and complexed species in the early stages of the titration of **L** with $Pd(BF_4)_2$, and with the presence of only complexed species in the last stages of this titration. The insets of Figure 5 (parts C and D) show that 1 equiv. of $Pd^{II}$ is required to complete the complexation of $\mathbf{LH}^+$, which indicates that the $Pd^{II}$ ions can efficiently replace the protons of the $\mathbf{LH}^+$ moieties.

### *$Zn^{II}$, $Ni^{II}$ and $Co^{II}$ Titrations*

No significant differences were found in the absorption or in the fluorescence titrations of **L** when this ligand was titrated with $Zn(CF_3SO_3)_2$, $Ni(BF_4)_2$ or $Co(BF_4)_2$. As a representative example, Figure 6 shows both the absorption and fluorescence titrations of **L** with $Ni^{II}$. The addition of any of these salts causes a red shift in the anthracene absorption maximum of **L**, as well as a decrease in its molar absorption coefficient. These changes occur until the addition of 0.6 equiv. of $Zn^{II}$ or $Ni^{II}$ or 0.7 equiv. of $Co^{II}$.

As in the case of the fluorescence titration of **L** with $Pd^{II}$, initial additions of $Zn^{II}$, $Ni^{II}$ or $Co^{II}$ increase the fluorescence of **L**. However, further additions cause neither the shift nor the quenching of the emission band. These observations suggest that the addition of $Zn^{II}$, $Ni^{II}$ or $Co^{II}$ also leads to the initial protonation of **L**, after which no interaction between **L** and these metal ions can occur. This hypothesis was confirmed when the titrations were repeated in the presence of an equivalent amount of acid, as the addition of these ions to dichloromethane solutions of $\mathbf{LH}^+$ did not cause significant changes either in the absorption or in the emission spectrum of the ligand, which indicates that these metal ions cannot efficiently replace the protons in the protonated macrocycles.

The different behaviour observed between the titrations with $Pd^{II}$ and those with $Zn^{II}$, $Ni^{II}$ or $Co^{II}$ is probably due to the different affinity between the metal ion and the donor atoms of **L**. This is in agreement with the fact that the *soft* nature of the $NS_3$ set of **L** leads to the formation of complexes with only the *softest* of these metal ions, that of $Pd^{II}$.

## Conclusions

The azathiamacrocycle **2** can be synthesised by reacting *N*,*N*-bis(3-chloropropyl)amine with 2,2′-thiobis(ethanethiol) in the presence of CsOH. This new method allowed

 © 2006 Wiley-VCH Verlag GmbH & Co. KGaA, Weinheim 

us to obtain **2** without using any amine-protecting group, which decreases the number of synthetic steps and improves the final yield. The anthracene-containing macrocycle **L** can be obtained either by functionalisation of **2** with 9-(chloromethyl)anthracene or by cyclisation of *N*,*N*-bis(3-chloropropyl)-9-anthracenemethanamine with 2,2′-thiobis-(ethanethiol). Both methods allow the synthesis of **L** in moderately high yields.

As observed in the spectra of the fluorescence titration of **L** with methanesulfonic acid, the protonation of this ligand greatly increase its fluorescence. This protonation also occurs when **L** is titrated with $Pd^{II}$, $Zn^{II}$, $Ni^{II}$ or $Co^{II}$ solutions, as the water molecules present in such solutions are acidic enough to produce the protonation of the ligand, which reflects the basic nature of its tertiary amine group.

Only the $Pd^{II}$ ions can efficiently remove the protons from the protonated $\mathbf{LH}^+$ molecules to yield complexed species, which indicates that the interactions between **L** and the $Pd^{II}$ ions are stronger than those between **L** and protons, whereas the interactions between **L** and the $Zn^{II}$, $Ni^{II}$ or $Co^{II}$ ions are weaker than those between **L** and the proton ions. These differences explain why only characterisable species with $Pd^{II}$ could be isolated. The high affinity of **L** towards $Pd^{II}$ could be potentially useful in the development of new molecular devices.

## Experimental Section

**General Remarks:** Elemental analyses were performed with a Carlo–Erba EA-1108 instrument by the Chemical Analysis Service at the Universitat Autònoma de Barcelona. Mass spectra were recorded with a HP298S GC–MS system. NMR spectra were recorded with a Bruker 250 MHz AC instrument. Conductivity measurements were carried out with a Cyberscan 500 conductimeter. IR spectra were recorded with a Perkin–Elmer FT-1710 instrument. Organic reagents and transition-metal salts were purchased from Aldrich and used as received. All syntheses were carried out using standard Schlenk techniques. *N*,*N*-Bis(3-chloropropyl)amine (**1**) was prepared from 3-amino-1-propanol and 3-chloro-1-propanol according to the published method but using chloroform instead of benzene as solvent.[17] *N*,*N*-Bis(3-chloropropyl)-9-anthracenemethanamine (**3**) was prepared from **1** and 9-(chloromethyl)anthracene as previously reported in the literature.[11]

**X-ray Crystal Structure Determinations:** A single crystal of $[Pd(\mathbf{L})](BF_4)_2$ was mounted on a glass fibre and used for data collection. A summary of the crystallographic data is reported in Table 2. Crystallographic measurements were performed with a Bruker Smart CCD apparatus at 293 K, using graphite-monochromated Mo-$K_\alpha$ radiation ($\lambda$ = 0.71073 Å) in RIAIDT (University of Santiago de Compostela, Spain). Crystallographic data were corrected for Lorentz and polarisation effects. The frames were integrated with the Bruker SAINT Software package,[18] and the data were corrected for absorption using the SADABS program.[19] The structure was determined by direct methods using the SIR-97 program.[20] All non-hydrogen atoms were refined with anisotropic thermal parameters by full-matrix least-squares calculations on $F^2$ using the SHELXL97 program.[21] Hydrogen atoms were inserted at calculated positions and constrained with isotropic thermal parameters. Tetrafluoroborate anions and the S12 sulfur atom of the macrocyclic ligand were modelled with disorder. Special computations for the crystal structure discussions were carried out with PLATON.[22]

Table 2. Crystallographic data for $[Pd(\mathbf{L})](BF_4)_2$.

| | |
|---|---|
| Empirical formula | $C_{25}H_{31}B_2F_8NPdS_3$ |
| Formula mass | 721.71 |
| Crystal system | monoclinic |
| Space group | *C*2/*c* |
| *a* [Å] | 17.614(5) |
| *b* [Å] | 14.495(5) |
| *c* [Å] | 21.754(5) |
| $\beta$ [°] | 97.310(5) |
| *V* [Å$^3$] | 5509(3) |
| *Z*, $\rho_{calcd}$ [g/cm$^3$] | 8, 1.740 |
| *F*(000) | 2912 |
| Crystal size [mm] | 0.34 × 0.31 × 0.14 |
| Absorption coefficient [mm$^{-1}$] | 0.974 |
| $\theta$ range [°] | 1.83–28.32 |
| Max./min. transmission | 0.873–0.748 |
| Reflections collected | 25542 |
| Independent reflections ($R_{int}$) | 6677 (0.0331) |
| Final *R* indices [$I > 2\sigma(I)$] | $R_1$ = 0.0330, $wR_2$ = 0.0768 |
| Final *R* indices (all data) | $R_1$ = 0.0468, $wR_2$ = 0.0840 |

CCDC-266369 contains the supplementary crystallographic data for this paper. The data can be obtained free of charge from The Cambridge Crystallographic Data Centre via www.ccdc.cam.uk/data_request/cif.

**Spectrophotometric and Spectrofluorometric Measurements:** Absorption spectra were recorded with a Shimadzu UV-2501PC spectrophotometer and fluorescence emissions on a Horiba–Jobin–Yvon SPEX Fluorolog 3.22 spectrofluorimeter at the Universidade Nova de Lisboa. The linearity of the fluorescence emission versus concentration was verified for the concentration range used ($10^{-4}$ to $10^{-6}$ M). A correction for the absorbed light was performed when necessary. The absorption and fluorescence titrations were performed by adding microlitre amounts of acetonitrile, or ethanol solutions of the corresponding titrating agent, to dichloromethane solutions of the ligand. [**2**] = $5.50 \times 10^{-5}$ M. [**L**] = $5.14 \times 10^{-5}$ M, $\lambda_{exc}$ = 368 nm; $\lambda_{em}$ = 423 nm. Luminescence quantum yields were measured using a solution of sublimated anthracene in cyclohexane as a standard [$\Phi_F$ = 0.36].[23]

**1,4,7-Trithia-11-azacyclotetradecane (2):** A solution of **1** (3.32 g, 15.54 mmol) in deoxygenated DMF (50 mL) and a solution of 2,2′-thiobis(ethanethiol) (3.02 g, 15.54 mmol) in deoxygenated DMF (50 mL) were added simultaneously (at 2 mL/h using a perfusor) to a round-bottomed flask equipped with a magnetic stirrer and charged with CsOH (6.45 g, 39.06 mmol) and deoxygenated DMF (700 mL). Subsequently, the solvent was removed and the residue was dissolved in $CHCl_3$ (200 mL). The solution was filtered off and the solvent was removed to obtain a pale brown oil. This residue was purified by column chromatography on silica gel using a mixture of $CHCl_3$/$CH_3OH$ (10:1 v/v ratio) as eluent. Yield 3.07 g, 62%. $C_{10}H_{21}NS_3$ (251.48): calcd. C 47.76, H 8.42, N 5.57, S 38.25; found C 47.55, H 8.30, N 5.55, S 37.80. $^1$H NMR (250 MHz, $CDCl_3$, 25 °C): $\delta$ = 1.18 (s, 1 H, -$CH_2$-N*H*-$CH_2$-), 1.72 (m, $^3J_{H,H}$ = 6.23 Hz, 4 H, -S-$CH_2$-C*H*$_2$-$CH_2$-NH-), 2.63–2.74 (m, 8 H, -S-C*H*$_2$-$CH_2$-C*H*$_2$-NH-), 2.74 (m, 8 H, -S-C*H*$_2$-C*H*$_2$-S-) ppm. $^{13}$C{$^1$H} NMR ($CDCl_3$, 25 °C): $\delta$ = 28.9 (-S-$CH_2$-*C*H$_2$-$CH_2$-NH-), 30.4 (-S-*C*H$_2$-$CH_2$-$CH_2$-NH-), 31.9 (-S-$CH_2$-*C*H$_2$-S-*C*H$_2$-$CH_2$-S-), 32.5 (-S-*C*H$_2$-$CH_2$-S-$CH_2$-*C*H$_2$-S-), 46.9 (-S-$CH_2$-$CH_2$-*C*H$_2$-NH-) ppm. UV/Vis ($CH_2Cl_2$): $\lambda$ = 258 nm ($\varepsilon$ = 769 M$^{-1}$/cm). ESI-MS: *m*/*z* (%) = 252.4 [**2** + H]$^+$. IR (KBr pellet): $\tilde{\nu}$ = 3316, 2925, 2819, 1675, 1424, 1265, 1191, 1122, 693 cm$^{-1}$.

 © 2006 Wiley-VCH Verlag GmbH & Co. KGaA, Weinheim 

**11-(9-Anthracenylmethyl)-1,4,7-trithia-11-azacyclotetradecane (L). Preparation from 2:** A mixture of anhydrous $Na_2CO_3$ (0.31 g, 2.94 mmol), KI (0.20 g, 1.20 mmol), 9-(chloromethyl)anthracene (0.49 g, 2.15 mmol) and **2** (0.65 g, 1.47 mmol) in $CH_3CN$ (100 mL) was refluxed for 4 h. The mixture was filtered off and the solvent was removed with a rotary evaporator. The resultant yellow residue was purified by column chromatography on silica gel using $CHCl_3$ as eluent. Yield 1.14 g, 73%.

**Preparation from 3:** A solution of 2,2′-thiobis(ethanethiol) (0.77 g, 4.98 mmol) in deoxygenated DMF (50 mL) and a solution of **3** (1.79 g, 4.98 mmol) in deoxygenated DMF (50 mL) were added simultaneously at 2 mL/h using a perfusor to a round-bottomed flask equipped with magnetic stirrer and charged with a solution of $Cs_2CO_3$ (1.78 g, 5.50 mmol) in deoxygenated DMF (700 mL). The solvent was removed and the residue was dissolved in $CHCl_3$. This solution was filtered off and the solvent was removed to yield a yellow oil that was purified by column chromatography on silica gel using $CHCl_3$ as eluent to afford 0.90 g (40% yield) of yellow solid. $C_{25}H_{31}NS_3$ (441.72): calcd. C 67.98, H 7.07, N 3.17, S 21.78; found C 67.55, H 7.10, N 3.10, S 21.40. $^1$H NMR (250 MHz, $CDCl_3$, 25 °C): $\delta$ = 1.73 (m, 4 H, -S-$CH_2$-C$H_2$-$CH_2$-N-), 2.26 (t, $^3J_{H,H}$ = 7.93 Hz, 4 H, -S-C$H_2$-$CH_2$-$CH_2$-N-), 2.59 (t, $^3J_{H,H}$ = 6.19 Hz, 4 H, -S-$CH_2$-$CH_2$-C$H_2$-N-), 2.69 (s, 8 H, -S-C$H_2$-C$H_2$-S-), 4.51 (s, 2 H, An-C$H_2$-N-), 7.50 (m, 4 H, *An*-$CH_2$-N-), 8.00 (m, 2 H, *An*-$CH_2$-N-), 8.44 (m, 3 H, *An*-$CH_2$-N-) ppm. $^{13}$C{$^1$H} NMR ($CDCl_3$, 25 °C): $\delta$ = 28.5 (-S-$CH_2$-C$H_2$-$CH_2$-N-), 29.8 (-S-C$H_2$-$CH_2$-$CH_2$-N-), 31.1 (-S-$CH_2$-C$H_2$-S-C$H_2$-$CH_2$-S-), 31.8 (-S-C$H_2$-$CH_2$-S-$CH_2$-C$H_2$-S-), 52.0 (An-C$H_2$-N-), 53.7 (-S-$CH_2$-$CH_2$-C$H_2$-NH-), 124.8, 125.6, 127.6, 129.1, 130.1, 131.2, 131.4 (*An*-$CH_2$-N-) ppm. UV/Vis ($CH_2Cl_2$): $\lambda$ = 333 ($\varepsilon$ = 3024), 350 (5902), 368 (9418), 388 nm (9096 $M^{-1}$/cm). ESI-MS: *m*/*z* (%) = 442.7 [**L** + H]$^+$. IR (KBr pellet): $\tilde{\nu}$ = 3048, 2949, 2922, 2810, 1677, 1622, 1444, 1436, 1426, 1336, 1279, 1190, 1023, 893, 735, 541 $cm^{-1}$.

**[Pd(L)](BF$_4$)$_2$·2H$_2$O:** A dichloromethane solution of **L** (90 mg, 0.20 mmol, 4 mL) was added dropwise to an acetonitrile solution of $Pd(BF_4)_2$·4$CH_3CN$ (91 mg, 0.20 mmol, 4 mL). The resulting solution was stirred at room temperature for 2 h, and the solvent was partially removed to about 3 mL. Diethyl ether was slowly infused into the solution producing a powdery precipitate, which was filtered off and washed with diethyl ether. This complex was recrystallised by diffusion of diethyl ether into acetonitrile solutions. The yield was 130 mg (88%). Crystals suitable for X-ray diffraction were obtained by diffusion of hexane into a dichloromethane solution. $C_{25}H_{31}B_2F_8NPdS_3$·2$H_2O$ (757.72): calcd. C 39.63, H 4.66, N 1.85, S 12.69; found C 39.40, H 4.85, N 1.80, S 12.25. Conductivity ($CH_3CN$, $1 \times 10^{-3}$ M): 231 μS/cm. $^1$H NMR (250 MHz, $CD_3NO_2$, 25 °C): $\delta$ = 2.29 (m, 2 H, -S-$CH_2$-C$H_2$-$CH_2$-N-), 2.47 (m, 2 H, -S-$CH_2$-C$H_2$-$CH_2$-N-), 2.70 (m, 2 H, -S-$CH_2$-$CH_2$-C$H_2$-N-), 3.03 (m, 2 H, -S-C$H_2$-$CH_2$-$CH_2$-N-), 3.11 (m, 4 H, -S-C$H_2$-$CH_2$-C$H_2$-N-), 3.32 (m, 4 H, -S-$CH_2$-C$H_2$-S-C$H_2$-$CH_2$-S-), 3.35 (m, 2 H, -S-C$H_2$-$CH_2$-S-$CH_2$-C$H_2$-S-), 3.84 (m, 2 H, -S-C$H_2$-$CH_2$-S-$CH_2$-C$H_2$-S-), 5.02 (s, 2 H, An-C$H_2$-N-), 7.46 (m, 2 H, *An*-$CH_2$-N-), 7.63 (m, 2 H, *An*-$CH_2$-N-), 8.04 (d, $^3J_{H,H}$ = 8.40 Hz, 2 H, *An*-$CH_2$-N-), 8.56 (d, $^3J_{H,H}$ = 8.95 Hz, 2 H, *An*-$CH_2$-N-), 8.61 (s, 1 H, *An*-$CH_2$-N-) ppm. $^{13}$C{$^1$H} NMR ($CD_3NO_2$, 25 °C): $\delta$ = 24.6 (-S-$CH_2$-C$H_2$-$CH_2$-N-), 32.6 (-S-C$H_2$-$CH_2$-$CH_2$-N-), 39.8 (-S-$CH_2$-C$H_2$-S-C$H_2$-$CH_2$-S-), 41.1 (-S-C$H_2$-$CH_2$-S-$CH_2$-C$H_2$-S-), 57.5 (An-C$H_2$-N-), 61.0 (-S-$CH_2$-$CH_2$-C$H_2$-NH-), 123.3, 123.4, 125.9, 128.4, 130.1, 131.1, 131.7, 132.5 (*An*-$CH_2$-N-) ppm. UV/Vis ($CH_2Cl_2$): $\lambda$ = 357 ($\varepsilon$ = 9154), 376 (9019), 397 nm (6542 $M^{-1}$/cm). ESI-MS: *m*/*z* (%) = 634.9 [Pd(BF$_4$)(**L**)]$^+$. IR (KBr pellet): $\tilde{\nu}$ = 3424, 2923, 1623, 1446, 1295, 1084, 1063, 1038, 739, 534, 521 $cm^{-1}$.

## Acknowledgments

This work was supported by the Spanish Government (CYCIT) under project CTQ2004-04134, and by the Fundação para a Ciência e Tecnologia (Portugal) and FEDER under projects POCI/QUI/55519/2004 and POCTI/QUI/47357/2002. Financial support by the Departament d'Universitats Recerca i Societat de la Informació of the Catalan Government for Grant FI2002-00320 (A.T.) and Caixanova (Spain) for a postdoctoral grant (B.C.) are also acknowledged.

[1] a) F. Mancin, E. Rampazzo, P. Tecilla, U. Tonellato, *Chem. Eur. J.* **2006**, *12*, 1844–1854; b) V. Amendola, L. Fabbrizzi, F. Foti, M. Licchelli, C. Mangano, P. Pallavincini, A. Poggi, D. Sacchi, A. Taglietti, *Coord. Chem. Rev.* **2006**, 273–299.

[2] a) A. W. Czarnik, *Acc. Chem. Res.* **1994**, *27*, 302–308; b) R. A. Bissell, A. P. de Silva, H. Q. N. Gunaratne, P. L. M. Lynch, G. E. M. Maguire, K. R. A. S. Sandanayake, *Chem. Soc. Rev.* **1992**, *21*, 187–195.

[3] a) J.-H. Bu, Q.-Y. Zheng, C.-F. Chen, Z.-T. Huang, *Org. Lett.* **2004**, *6*, 3301–3303; b) S. A. McFarland, N. S. Finney, *J. Am. Chem. Soc.* **2002**, *124*, 1178–1179; c) S. A. de Silva, B. Amorelli, D. C. Isidor, K. C. Loo, K. E. Crooker, Y. E. Pena, *Chem. Commun.* **2002**, 1360–1361; d) C. Lodeiro, J. L. Capelo, *J. Inclusion Phenom. Macrocyclic Chem.* **2004**, 249–258.

[4] a) C. Bazzicalupi, A. Bencini, E. Berni, A. Bianchi, A. Danesi, C. Giorgi, B. Valtancoli, C. Lodeiro, J. C. Lima, F. Pina, M. A. Bernardo, *Inorg. Chem.* **2004**, *43*, 5134–5146; b) M. P. Clares, J. Aguilar, R. Aucejo, C. Lodeiro, M. T. Albelda, F. Pina, J. C. Lima, A. J. Parola, F. Pina, J. Seixas de Melo, C. Soriano, E. García-España, *Inorg. Chem.* **2004**, *43*, 6114–6122; c) C. Lodeiro, F. Pina, A. J. Parola, A. Bencini, A. Bianchi, C. Bazzicalupi, S. Ciattini, C. Giorgi, A. Masotti, B. Valtancoli, J. Seixas de Melo, *Inorg. Chem.* **2001**, *40*, 6813–6819.

[5] a) E. S. Meadows, S. L. De Wall, L. J. Barbour, G. W. Gokel, *J. Am. Chem. Soc.* **2001**, *123*, 3092–3107; b) M. Vicente, M. R. Bastida, C. Lodeiro, A. Macías, A. J. Parola, L. Valencia, S. E. Spey, *Inorg. Chem.* **2003**, *42*, 6768–6779.

[6] a) A. J. Blake, A. Bencini, C. Caltagirone, G. De Filippo, L. S. Dolci, A. Garau, F. Isaia, V. Lippolis, P. Mariani, L. Prodi, M. Montalti, N. Zaccheroni, C. Wilson, *Dalton Trans.* **2004**, 2771–2779; b) M. C. Aragoni, M. Arca, A. Bencini, A. J. Blake, C. Caltagirone, A. Decortes, F. Demartin, F. A. Devillanova, E. Faggi, L. S. Dolci, A. Garau, F. Isaia, V. Lippolis, L. Prodi, C. Wilson, B. Valtancoli, N. Zaccheroni, *Dalton Trans.* **2005**, 2994–3004.

[7] a) M. T. Albelda, P. Díaz, E. García-España, J. C. Lima, C. Lodeiro, J. S. de Melo, A. J. Parola, F. Pina, C. Soriano, *Chem. Phys. Lett.* **2002**, *353*, 63–68; b) G.-Q. Zhang, G.-Q. Yang, L.-Y. Yang, Q.-Q. Chen, J.-S. Ma, *Eur. J. Inorg. Chem.* **2005**, 1919–1926.

[8] J. Buter, R. M. Kellogg, *J. Org. Chem.* **1981**, *46*, 4481–4485.

[9] A. Tamayo, J. Casabo, L. Escriche, C. Lodeiro, B. Covelo, C. D. Brondino, R. Kivekäs, R. Sillampää, *Inorg. Chem.* **2006**, *45*, 1140–1149.

[10] a) N. Li, M. Struttman, C. Higginbotham, A. J. Grall, J. F. Skerlj, J. F. Vollano, S. A. Bridger, L. A. Ochrymowycz, A. R. Ketring, M. J. Abrams, W. A. Volkert, *J. Nucl. Med.* **1997**, *38*, 85–92; b) B. Chak, A. McAuley, T. W. Whitcombe, *Inorg. Chim. Acta* **1996**, 349–360.

[11] A. Tamayo, C. Lodeiro, L. Escriche, J. Casabó, B. Covelo, P. González, *Inorg. Chem.* **2005**, *44*, 8105–8115.

[12] The functionalisation of the dihalide precursor avoids the reaction between its amine nitrogen and the carbonate ions.

[13] a) M. Vetrichelvan, Y.-H. Lai, K. F. Mok, *Dalton Trans.* **2003**, 295–303; b) M. Arca, A. J. Blake, J. Casabó, F. Demartin, F. A. Devillanova, A. Garau, F. Isaia, V. Lippolis, R. Kivekas, V. Muns, M. Schröder, G. Verani, *J. Chem. Soc., Dalton Trans.* **2001**, 1180–1188; c) I. M. Atkinson, J. D. Chartres, A. M.

 © 2006 Wiley-VCH Verlag GmbH & Co. KGaA, Weinheim 

Groth, L. F. Lindoy, M. P. Lowe, G. V. Meehan, B. W. Skelton, A. H. White, *J. Chem. Soc., Dalton Trans.* **2001**, 2801–2806.
[14] a) S. D. Zarić, D. M. Popović, E.-W. Knapp, *Chem. Eur. J.* **2000**, *6*, 3935–3942; b) J. C. Ma, D. A. Dougherty, *Chem. Rev.* **1997**, *97*, 1303–1324.
[15] a) A. B. P. Lever, *Inorganic Electronic Spectroscopy*, 2nd ed., Elsevier Science Publishers, The Netherlands, **1986**; b) W. R. Mason, H. B. Gray, *J. Am. Chem. Soc.* **1968**, *90*, 5721–5729.
[16] a) A. W. Czarnik, *Fluorescent Chemosensors for Ion and Molecule Recognition*, American Chemical Society, Washington, DC, **1993**; b) L. Fabbrizzi, M. Licchelli, P. Pallavicini, A. Perotti, A. Taglietti, D. Sacchi, *Chem. Eur. J.* **1996**, *2*, 75–82.
[17] C. Granier, R. Guilard, *Tetrahedron* **1995**, *51*, 1197–1208.
[18] *SMART (control) and SAINT (integration) software*, Bruker Analytical X-ray Systems, Madison, WI, **1994**.
[19] G. M. Sheldrick, *SADABS, A Program for Absorption Corrections*, University of Göttingen, Germany, **1996**.
[20] A. Altomare, M. C. Burla, M. Camalli, G. L. Cascarazo, C. Giacovazzo, A. Guagliardi, A. G. Moliterni, G. Polidori, R. Spagna, *J. Appl. Crystallogr.* **1999**, *32*, 115–119.
[21] G. M. Sheldrick, *SHELXL97, A Program for the Refinement of Crystal Structures from X-ray Data*, University of Göttingen, Germany, **1997**.
[22] A. L. Spek, *PLATON, A Multipurpose Crystallographic Tool*, Utrecht University, The Netherlands, **2004**.
[23] I. B. Berlan, *Handbook of Fluorescence Spectra of Aromatic Molecules*, 2nd ed., Academic Press, New York, **1971**.

Received: March 31, 2006
Published Online: June 12, 2006

 © 2006 Wiley-VCH Verlag GmbH & Co. KGaA, Weinheim 

DOI: 10.1002/ejic.200600330

# Hydrophosphanation of Phenolic Aldehydes as Facile Synthetic Approach to Catechol-Functionalized Phosphane Oxides and Phosphanes

**Samir Chikkali[a] and Dietrich Gudat*[a]**

**Keywords:** Phosphanes / Phosphane oxides / P,O ligands / Hydrophosphanation / Rearrangement

Reactions of diphenylphosphane with mono- and dihydroxybenzaldehydes yield as initial products α-phosphanyl-carbinols that exist according to NMR studies in dynamic equilibrium with the starting materials in solution but are stable in the solid state. The facile rearrangement of the initial products yields isomeric phosphane oxides which react with MeI and excess $LiAlH_4$ via deoxygenation to give the corresponding phosphanes. Phosphane oxides and phosphanes were isolated and characterized by analytical and spectroscopic data. The reactions described represent an improved synthesis for phosphanes with phenol and catechol functionalities that are useful for applications as ligands or supramolecular building blocks.

(© Wiley-VCH Verlag GmbH & Co. KGaA, 69451 Weinheim, Germany, 2006)

## Introduction

The addition of a P–H bond to a carbonyl group is a fundamental and synthetically useful reaction of phosphorus-hydrogen substituted phosphanes $PH_nR_{3-n}$. These transformations proceed normally strictly regioselective via P–C bond formation to give α-phosphanyl-carbinols (Scheme 1, a) and are used for the synthesis of functional tertiary phosphanes.[1] We have recently found that N-heterocyclic phosphanes **1** react with aldehydes and ketones via reduction rather than alkylation of the carbonyl moiety (Scheme 1, b).[2] The reversed regioselectivity ("umpolung") has been related to the unique hydride-like polarization of the P–H bond in **1** which owes to the special bonding situation in the heterocycle.[2]

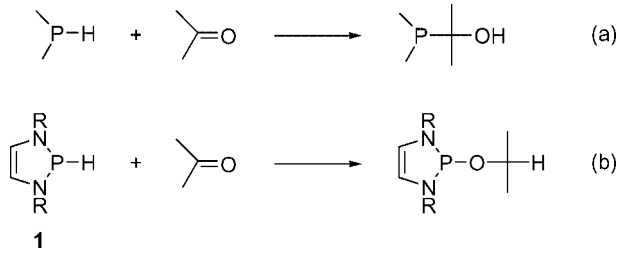


Scheme 1. Possible reaction modes of phosphanes with carbonyl groups.

During a study on hydrophosphanation of carbonyl compounds we noticed that the reaction of diphenylphosphane with salicylic aldehyde affords a benzylphosphane oxide. Similar reactions were observed earlier and explained by a two-step sequence involving a "normal" hydrophosphanation followed by isomerization of the transient α-phosphanyl-carbinol [pathway (i), Scheme 2].[3] In the context of our studies on controlling the regioselectivity in hydrophosphanations[2] it was of interest to elucidate mechanistic aspects of this reaction in more detail. In particular, we wanted to exclude that the product was formed via "inverse" addition of the P–H bond of the phosphane and subsequent Michaelis–Arbuzov rearrangement of a transient phosphinite [pathway (ii) in Scheme 2] which might, in view of the reactivity of **1** and earlier observations of Michaelis–Arbuzov rearrangements under conditions similar to the ones applied here,[4] provide a conceivable alternative to the standard mechanism. We present here the results of studies of the transformations of diphenylphosphane and phenolic aldehydes into phenol-functionalized phosphane oxides, and demonstrate that these species can easily be converted into phosphanes. The products thus accessible belong to a class of multifunctional ligands that have recently attracted increasing attention as supramolecular building blocks[5]

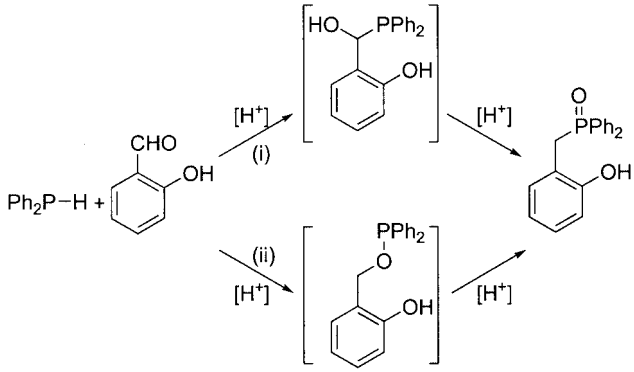


Scheme 2.

[a] Institut für Anorganische Chemie, Universität Stuttgart, Pfaffenwaldring 55, 70550 Stuttgart, Germany
E-mail: gudat@iac.uni-stuttgart.de

 © 2006 Wiley-VCH Verlag GmbH & Co. KGaA, Weinheim 

and anchoring groups that are capable of immobilizing metal complexes on the surface of a metal oxide support.[6]

## Results and Discussion

The reaction of equimolar amounts of diphenylphosphane (**2**) and salicylic aldehyde (**3a**) in methanol or ethers ($Et_2O$, DME) in the presence of catalytic amounts of hydrochloric or *p*-toluenesulfonic acid affords directly the phosphane oxide **5a**[7] which has been isolated in good yield after work-up (Scheme 3).

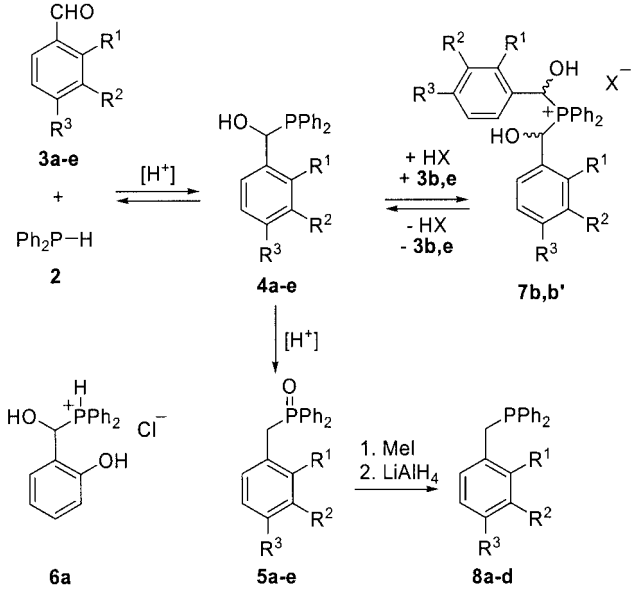


| | 3a–9a | 3b–8b | 3c–8c | 3d–8d | 3e–7e |
|---|---|---|---|---|---|
| $R^1$ | OH | OH | H | H | H |
| $R^2$ | H | OH | H | OH | OH |
| $R^3$ | H | H | OH | OH | H |

X = 4-$CH_3$–$C_6H_4SO_3^-$

Scheme 3.

$^{31}P$ NMR studies revealed that **5a** remained the only spectroscopically detectable species beside unreacted **2** and minor side products. The latter were not further characterized but their chemical shifts precluded assignment as an α-phosphanyl-carbinol. In order to elucidate mechanistic details we set out to find reaction conditions that facilitated the detection of a precursor to **5a**. In these studies it was established that treatment of an ethereal solution of **2** and **3a** with excess concd. hydrochloric acid lead to immediate precipitation of a colorless solid which was isolated by filtration. A solid-state $^{31}P$ CP/MAS NMR spectrum disclosed an isotropic shift ($\delta^{31}P_{iso}$ = –0.8) which differs clearly from that of **5a** ($\delta^{31}P_{iso}$ = 39.3) but resembles that of the α-phosphanyl-carbinol obtained from reaction of **2** and benzaldehyde. A spectrum recorded under conditions that allow to detect scalar couplings to protons revealed a doublet splitting attributable to a one-bond *J*-coupling (Figure 1, $J_{PH}$ = 501 Hz). Consequently, we assume that α-phosphanyl-carbinol hydrochloride **6a** is formed which is deemed to represent the initial product formed by attack of the phosphane on the protonated aldehyde. This structural assignment was further corroborated by satisfactory analytical data. Attempts to characterize **6a** by solution NMR spectroscopy revealed that the product decomposes upon dissolution in methanol to give a mixture of the starting materials and the phosphane oxide **5a**, an observation that emphasizes the character of a reaction intermediate for **6a**.

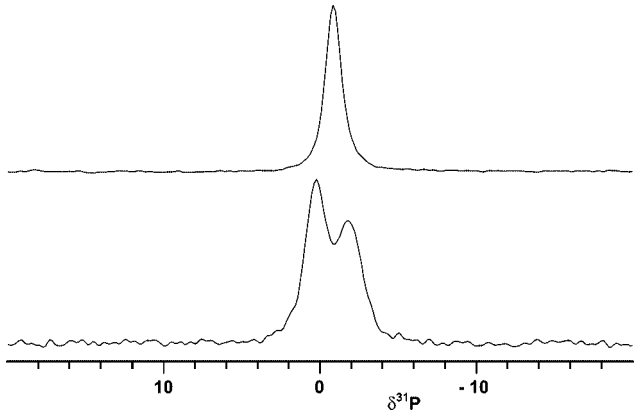


Figure 1. Isotropic line of the solid state CP/MAS $^{31}P$ NMR spectrum of **6a** at a spinning speed of 13.2 kHz recorded with high-power proton decoupling (top trace) and frequency-shifted Lee–Goldburg decoupling[9] (bottom trace) to suppress homonuclear dipolar coupling between protons. As the decoupling sequence scales the heteronuclear coupling by a factor of 0.577, the observed splitting of 289 Hz corresponds to a value of $^1J_{PH}$ = 501 Hz.

The above results allow to conclude that the reaction of **2** with salicylic aldehyde involves a "normal" hydrophosphanation as the key step. The same regioselectivity was observed in the acid-catalyzed reaction of **2** with 2,3-dihydroxybenzaldehyde (**3b**). NMR studies allowed in this case the direct detection of a small amount of the α-phosphanyl-carbinol **4b** and two further intermediates. The constitution of the latter was assigned as diastereomeric phosphonium salts **7b**, **7′b** by 2D NMR studies, and dynamic exchange between all four species was established by a 2D $^{31}P$ EXSY NMR spectrum. All products were eventually converted into the phosphane oxide **5b** which was isolated after work-up and characterized by analytical and spectroscopic data. Species similar to **7b**, **7′b** have previously been obtained by reaction of diphenylphosphane (**2**) with formaldehyde in the presence of strong acids.[1,8]

The reaction of **2** with 4-hydroxybenzaldehyde (**3c**) affords as primary product the α-phosphanyl-carbinol **4c** which was isolated by precipitation from methanol and characterized by $^{31}P$ CP/MAS NMR and analytical data. Key to the structural assignment was the observation of a single resonance ($\delta^{31}P$ = –7.2) which appears at somewhat higher field than that of **6a** and shows no splitting due to $^1J_{PH}$ coupling. In contrast to the elusive 2-hydroxy-substituted carbinol **4a**, the signal of **4c** is also observable in solution $^{31}P$ NMR spectra although in these solutions, even in the absence of additional acid, partial decomposition to **2** and **3c** occurs (obviously the acidity of the phenolic OH moiety is sufficient to promote an auto-catalytic reaction). Acidic catalysts promote the complete conversion to phos-

 © 2006 Wiley-VCH Verlag GmbH & Co. KGaA, Weinheim 

phane oxide **5c**. The same behavior can be observed in the reaction of **2** with 3,4-dihydroxybenzaldehyde (**3d**) which affords **5d** as final product. Both **5c** and **5d** were isolated after work-up and characterized by analytical and spectroscopic data.

Finally, the acid-catalyzed reaction of **2** with 3-hydroxybenzaldehyde (**3e**) gives a mixture of dynamically exchanging products the structures of which were assigned to the phosphanyl-carbinol **4e** and the diastereomeric phosphonium salts **7e/7e′** on the basis of a comparison of the observed $^{31}P$ chemical shifts with those of the products of the previously described reactions. A 1:1 mixture of **7e/7e′** precipitated from the reaction solution and was isolated by filtration. The constitution was confirmed by analytical data; a slow-spinning technique $^{31}P$ CP/MAS NMR spectrum shows the presence of two isotropic signals of equal intensity with negligible chemical shielding anisotropy. The precipitate dissolved again when the mixture was stirred for prolonged reaction times, and $^{31}P$ NMR studies allowed to detect the formation of the phosphane oxide **5e** as final product which eventually precipitated from the solution and was characterized by spectroscopic data.

In summary it can be stated that the reactions of the phosphane **2** with hydroxybenzaldehydes **3a**–**e** proceed via hydrophosphanation to yield α-phosphanyl-carbinols **4a**–**e** as initial products. These species are in dynamic equilibrium with the starting materials and phosphonium salts **7** resulting from acid-promoted reaction with further aldehyde. The composition of the equilibrium mixtures depends on the substitution pattern of the aldehydes and lies for **3a**–**d** which feature at least one OH substituent in 2- or 4-position largely on the side of the starting materials, whereas for **3e** the formation of the phosphonium salts **7e**,**e′** appears to be favored. As a consequence, the equilibrium concentration of the adducts **4a**–**e** is rather low, or these species may not be detectable at all. The reduced stability of the adducts with respect to the starting materials is attributable to the electron-releasing nature of the additional hydroxy-substituents which should render the aldehydes weaker electrophiles and the attack by the nucleophilic phosphane energetically less favorable. Aldehydes with 2-hydroxy substituents such as **3a**,**b** may further benefit from additional stabilization by strong intramolecular hydrogen bonding. The observation that all primary adducts may eventually rearrange quantitatively to the corresoponding phosphane oxides **5a**–**e** suggests that the latter are thermodynamically much more stable so that the isomerization is practically irreversible. The easy occurrence of this rearrangement is presumably also facilitated by the stabilization of the resulting transient intermediates by the electron-releasing phenolic OH substituents.

Deoxygenation of the phosphane oxides **4a**–**e** is readily achieved by adaptation of an established procedure[10] involving quaternization of the phosphane oxide moiety with methyl iodide and subsequent reduction with $LiAlH_4$ (Scheme 3). No special protection of the phenol groups is necessary, however, the use of a sufficient excess of the hydride to achieve complete deprotonation of the acidic OH groups is mandatory to obtain reasonable yields of products. Aqueous work-up of the reaction mixture and purification of the crude products by column chromatography affords the phosphanes **8a**–**d** as colorless, moderately oxygen-sensitive solids that were characterized by analytical and spectroscopic data.

## Conclusions

It has been confirmed that the reaction of diphenylphosphane with phenolic aldehydes is initiated by reversible formation of α-phosphanyl-carbinols. The presence of OH groups in *p*- or *o*-position appears to destabilize the adducts relative to the starting materials, thus keeping their concentration in the equilibrium mixtures low. The initial adducts rearrange easily to afford isomeric phosphane oxides which may further be reduced to the corresponding phosphanes. The overall reaction sequence permits to access the first alkylphosphane derivatives with tethered catechol and phenol moieties from readily available starting materials and without the necessity of additional efforts for the protection and deprotection of the reactive OH groups. This procedure constitutes a substantial improvement over previously known synthetic protocols which required often more complicated approaches.[4,11] The utilization of this procedure should prove useful for the preparation of functional phosphanes in applications as chelating ligands or supramolecular building blocks.

## Experimental Section

**General Remarks:** Manipulations were carried out under dry argon and solvents were dried by standard procedures if required. Solution NMR spectra were recorded at 30 °C on Bruker Avance 400 ($^1H$: 400.1 MHz, $^{13}C$: 100.5 MHz, $^{31}P$: 161.9 MHz) or AC 250 spectrometers ($^1H$: 250 MHz, $^{13}C$: 62.8 MHz, $^{31}P$: 101.2 MHz) at 303 K; chemical shifts are referenced to ext. TMS ($^1H$, $^{13}C$) or 85% $H_3PO_4$ ($\Xi$ = 40.480747 MHz, $^{31}P$). Solid state MAS NMR spectra were recorded on a Bruker Avance 400 instrument with spinning rates between 3 and 14 kHz. Cross polarization with a ramp-shaped contact pulse and mixing times between 3 and 5 ms was used for signal enhancement. MAS NMR spectra aiming at the determination of $^1J_{P,H}$ couplings were recorded under frequency-shifted Lee–Goldburg decoupling of homonuclear proton–proton interactions[9] which scales the visible splitting by a factor of 0.577. All coupling constants are given as absolute values; prefixes *i*, *o*, *m*, *p* denote phenyl ring positions of *P*-$C_6H_5$ substituents. The resonances of OH protons were not always detectable, presumably as a consequence of chemical exchange, and data are not listed when unequivocal assignment was unfeasible. MS: Varian MAT 711, EI, 70 eV. Elemental analyses: Perkin–Elmer 2400CHSN/O Analyser. Melting points were determined in sealed capillaries.

**General Procedure for the Synthesis of Phenol-Functionalized Phosphane Oxides:** Diphenylphosphane **2** (12 mmol) was added to a solution of the appropriate aldehyde **3a**–**e** (12 mmol) in DME (10 mL). The solution was stirred for five minutes at room temperature. A catalytic amount of *p*-toluenesulfonic acid (approx. 3–6 mmol) was added and the stirring continued for 48 h. The color-

 © 2006 Wiley-VCH Verlag GmbH & Co. KGaA, Weinheim 

less precipitate formed was isolated by filtration, washed twice with 5 mL of DME, and dried in vacuo for 4 h.

**2-[(Diphenylphosphinoyl)methyl]phenol (5a):** Yield 2.59 g (70%); m.p. 177 °C; elemental analysis: $C_{19}H_{17}O_2P$ (308.32): calcd. C 74.02 H 5.56, found C 73.90 H 5.37. Spectroscopic data are identical with the values reported in the literature.[7]

**3-[(Diphenylphosphinoyl)methyl]benzene-1,2-diol (5b):** Yield 3.31 g (85%); m.p. 194 °C; elemental analysis: $C_{19}H_{17}O_3P$ (324.32): calcd. C 70.37 H 5.28; found C 70.44 H 5.35. $^1$H NMR (400 MHz, $CDCl_3$): $\delta$ = 8.2 (br., 2 H, OH), 7.74 (m, 4 H, *o*-H), 7.58 (m, 2 H, *p*-H), 7.50 (m, 4 H, *m*-H), 6.81 (ddd, $^3J_{HH}$ = 8.0 Hz, $^4J_{HH}$ = 1.7 Hz, $^6J_{PH}$ = 1.7 Hz, 1 H, H-6), 6.63 (dt, $^3J_{HH}$ = 8.0 Hz, $^5J_{PH}$ = 0.9 Hz, 1 H, H-5), 6.34 (dddm, $^3J_{HH}$ = 7.7 Hz, $^4J_{HH}$ = 1.7 Hz, $^4J_{PH}$ = 1.7 Hz, 1 H, H-4), 3.73 (d, $^2J_{PH}$ = 12.8 Hz, 2 H, $CH_2$) ppm. $^{13}$C{$^1$H} NMR (100 MHz, $CDCl_3$): $\delta$ = 148.2 (d, $J_{PC}$ = 2.7 Hz), 143.9 (d, $J_{PC}$ = 4.2 Hz), 133.2 (d, $J_{PC}$ = 2.7 Hz, *p*-C), 131.6 (d, $J_{PC}$ = 9.6 Hz, *o*-C), 130.9 (d, $J_{PC}$ = 100.4 Hz, *i*-C), 129.4 (d, $J_{PC}$ = 12.1 Hz, *m*-C), 122.9 (d, $J_{PC}$ = 6.3 Hz), 121.7 (d, $J_{PC}$ = 1.9 Hz), 119.9 (d, $J_{PC}$ = 8.4 Hz), 114.6 (d, $J_{PC}$ = 2.5 Hz), 35.6 (d, $J_{PC}$ = 67.1 Hz, $CH_2$) ppm. $^{31}$P NMR (101 MHz, $CDCl_3$): $\delta$ = 40.4 (s) ppm. MS (EI = 70 eV): *m*/*z* (%) = 324.1 (100) [$M^+$]; 202.1 (38) [$Ph_2POH^+$], 201 (54) [$Ph_2PO^+$].

**4-[(Diphenylphosphinoyl)methyl]phenol (5c):** Yield 2.22 g (60%); m.p. 223 °C; elemental analysis: $C_{19}H_{17}O_2P$ (308.32): calcd. C 74.02 H 5.56; found 74.19 H 5.82. $^1$H NMR (400 MHz, $CDCl_3$): $\delta$ = 8.2 (br., 1 H, OH), 7.76 (m, 4 H, *o*-H), 7.57 (m, 2 H, *p*-H), 7.49 (m, 4 H, *m*-H), 6.82 (m, 2 H, $C_6H_4$), 6.56 (m, 2 H, $C_6H_4$), 3.62 (d, $^2J_{PH}$ = 12.2 Hz, 2 H, $CH_2$) ppm. $^{13}$C{$^1$H} NMR (100 MHz, $CDCl_3$): $\delta$ = 156.9 (d, $J_{PC}$ = 1.7 Hz), 132.7 (s), 131.8 (d, $^2J_{PC}$ = 9.2 Hz, *o*-C), 131.6 (d, $J_{PC}$ = 4.8 Hz), 129.3 (d, $^3J_{PC}$ = 11.7 Hz, *m*-C), 128.6 (d, $J_{PC}$ = 99.6 Hz), 120.7 (d, $J_{PC}$ = 7.5 Hz), 117.0 (d, $J_{PC}$ = 2.1 Hz), 37.4 (d, $J_{PC}$ = 72.1 Hz, $CH_2$) ppm. $^{31}$P NMR (162 MHz, $CDCl_3$): $\delta$ = 32.2 (s) ppm.

**4-[(Diphenylphosphinoyl)methyl]benzene-1,2-diol (5d):** Yield 3.50 g (90%); m.p. 192 °C; elemental analysis: $C_{19}H_{17}O_3P$ (324.32): calcd. C 70.37 H 5.28; found C 69.98 H 5.17. $^1$H NMR (250 MHz, $CDCl_3$): $\delta$ = 7.47 to 7.23 (m, 10 H, $C_6H_5$), 6.53 (s, 1 H, $C_6H_3$), 6.31 (d, $^3J_{HH}$ = 8.1 Hz, 1 H, $C_6H_3$), 6.12 (d, $^3J_{HH}$ = 8.1, 1 H, $C_6H_3$), 3.42 (d, $^2J_{PH}$ = 12.9 Hz, 2 H, $CH_2$) ppm. $^{13}$C{$^1$H} NMR (62 MHz, $CD_3CN/CDCl_3$): $\delta$ = 143.8 (d, $J_{PC}$ = 2.3 Hz), 143.2 (d, $J_{PC}$ = 3.1 Hz), 131.7 (d, $J_{PC}$ = 1.8 Hz, *p*-C), 130.3 (d, $J_{PC}$ = 9.4 Hz, *o*-C), 128.1 (d, $J_{PC}$ = 11.7 Hz, *m*-C), 126.9 (d, $J_{PC}$ = 101.8 Hz, *i*-C), 121.2 (d, $J_{PC}$ = 6.1 Hz), 120.9 (d, $J_{PC}$ = 8.4 Hz), 116.6 (d, $J_{PC}$ = 4.8 Hz), 114.4 (d, $J_{PC}$ = 2.3 Hz), 35.1 (d, $J_{PC}$ = 68.2 Hz) ppm. $^{31}$P NMR (101 MHz, $CDCl_3$): $\delta$ = 40.4 (s) ppm.

**3-[(Diphenylphosphinoyl)methyl]phenol (5e):** Yield 2.22 g (60%); m.p. 198 °C; elemental analysis: $C_{19}H_{17}O_2P$ (308.32): calcd. C 74.02 H 5.56; found C 74.10 H 5.60. $^1$H NMR (250 MHz, $CD_3CN/CDCl_3$): $\delta$ = 7.55 (m, 4 H, *o*-H), 7.40 to 7.25 (m, 6 H, *m*/*p*-H), 6.80 (t, $^3J_{HH}$ = 8.0 Hz, 1 H, H-5), 6.59 (s, 1 H, H-2), 6.44 (d, $^3J_{HH}$ = 8.0 Hz, 1 H, H-4/6), 6.41 (d, $^3J_{HH}$ = 8.0 Hz, 1 H, H-4/6), 3.50 (d, $^2J_{PH}$ = 13.4 Hz, 2 H, $CH_2$) ppm. $^{13}$C{$^1$H} NMR (62 MHz, $CD_3CN/CDCl_3$): $\delta$ = 157.1 (d, $J_{PC}$ = 2.6 Hz), 132.4 (d, $J_{PC}$ = 2.9 Hz, *p*-C), 131.2 (d, $J_{PC}$ = 9.5 Hz, *o*-C), 131.0 (s), 130.9 (d, $J_{PC}$ = 102.3 Hz, *i*-C), 129.5 (d, $J_{PC}$ = 2.1 Hz), 128.9 (d, $J_{PC}$ = 11.8 Hz, *m*-C), 121.8 (d, $J_{PC}$ = 5.8 Hz), 117.5 (d, $J_{PC}$ = 5.0 Hz), 114.2 (d, $J_{PC}$ = 2.9 Hz), 37.1 (d, $J_{PC}$ = 67.1 Hz) ppm. $^{31}$P{$^1$H}NMR (101 MHz, $CDCl_3$): $\delta$ = 31.4 ppm.

**2-[(Diphenylphosphanyl)hydroxymethyl]phenol Hydrochloride (6a):** 2-Hydroxybenzaldehyde (**3a**) (0.64 mL, 6 mmol) was added to a solution of diphenylphosphane **2** (1.05 mL, 6 mmol) in diethyl ether (10 mL). This mixture was stirred for five minutes at room temperature and an excess of conc. hydrochloric acid (2 mL, 24 mmol) was added. A colorless precipitate formed immediately. The reaction mixture was then stirred for further 60 min, the precipitate filtered off, washed twice with diethyl ether (5 mL), and dried for 1 h in vacuo. Yield: 1.86 g (90%); m.p. 104 °C; elemental analysis: $C_{19}H_{18}ClO_2P$ (344.78): calcd. C 66.19 H 5.26 Cl 10.28; found C 66.76 H 5.38 Cl 8.54. $^{31}$P{$^1$H}NMR (solid, 162 MHz, CP/MAS): $\delta_{iso}$ = –0.8.

**4-[(Diphenylphosphanyl)hydroxymethyl]phenol (4c):** A solution of diphenylphosphane (**2**) (1.43 mL, 8.2 mmol) and 4-hydroxybenzaldehyde (**3c**) (1.00 g, 8.2 mmol) in methanol (10 mL) was stirred for 5 min at room temperature and conc. hydrochloric acid (0.25 mL, 3 mmol) was added. A colorless precipitate formed immediately. The reaction mixture was stirred for further 60 min, the precipitate filtered off and dried for 1 h in vacuo. Yield: 2.27 g (90%); m.p. 168 °C; elemental analysis: $C_{19}H_{17}O_2P$ (308.32): calcd. C 74.02 H 5.92; found 74.29 H 5.92. $^{31}$P NMR (101 MHz, THF): $\delta$ = –2.3 (s) ppm. $^{31}$P{$^1$H}NMR (solid, 162 MHz, CP/MAS): $\delta_{iso}$ = –7.2 ppm.

**Bis[hydroxy(3-hydroxyphenyl)methyl]diphenylphosphonium Toluenesulfonate (7e/7e′):** A solution of diphenylphosphane (**2**) (1.43 mL, 8.2 mmol) and 3-hydroxy benzaldehyde (**3e**) (1.00 g, 8.2 mmol) in DME (5 mL) was stirred for 5 min at room temperature and *p*-toluenesulfonic acid (0.60 g, 3.2 mmol) was added. A colorless precipitate began to form after 10 min. The reaction mixture was stirred for 12 h, the precipitate filtered off, washed twice with DME, and dried for 4 h in vacuo. Yield: 1.73 g (90%); m.p. 121 °C; elemental analysis: $C_{33}H_{31}O_7PS$ (602.64): calcd. C 65.77 H 5.19; found 65.39 H 5.30. $^{31}$P{$^1$H}NMR (solid, 162 MHz, CP/MAS): $\delta_{iso}$ = 30.5, 29.9 ppm.

**General Procedure for the Synthesis of Phenol-Functionalized Phosphanes:** The appropriate phosphane oxide **5a**–**d** (10 mmol) was dissolved in dry THF (100 mL). Methyl iodide (0.69 mL, 11 mmol) was added via a syringe and the solution stirred for 2 h at room temperature. The mixture was then cooled to 0 °C and solid $LiAlH_4$ (1.7 g, 45 mmol) added in several small portions. The reaction mixture was warmed to ambient temperature, and stirring was continued for another 5–6 h. The progress of the reaction was monitored by TLC. The reaction flask was again cooled to 0 °C, and 50 mL of 1 M hydrochloric acid were added in several portions (the first few drops had to be added very carefully until the exothermic reaction became less violent). The organic layer was separated and the aqueous layer washed with ethyl acetate (3 × 50 mL). The combined organic phases were dried overnight with $Na_2SO_4$ and all volatiles evaporated in vacuo. The crude products were purified by column chromatography (silica, petroleum ether:ethyl acetate = 7:3).

**2-[(Diphenylphosphanyl)methyl]phenol (8a):** Yield 1.81 g (62%); colorless oil, elemental analysis: $C_{19}H_{17}OP$ (292.32): calcd. C 78.07 H 5.86; found C 74.33 H 5.91. $^1$H NMR (250 MHz, [$D_8$]toluene): $\delta$ = 6.8 to 7.5 (m, 10 H, $C_6H_5$), 6.80 (t, 1 H, $^3J_{HH}$ = 7.7 Hz), 6.74 (d, 1 H, $^3J_{HH}$ = 7.7 Hz), 6.61 (d, 1 H, $^3J_{HH}$ = 7.8 Hz), 6.50 (t, 1 H, $^3J_{HH}$ = 7.5 Hz), 3.32 (s, 2 H, $CH_2$) ppm. $^{31}$P{$^1$H} NMR (101 MHz, [$D_8$]toluene): $\delta$ = –15.0 ppm. The $^1$H NMR spectroscopic data match those published earlier.[11]

**3-[(Diphenylphosphanyl)methyl]benzene-1,2-diol (8b):** Yield 1.85 g (60%); m.p. 82 °C; elemental analysis: $C_{19}H_{17}O_2P$ (308.32): calcd. C 74.02 H 5.56; found C 73.91 H 5.73. $^1$H NMR (400 MHz, $CDCl_3$): $\delta$ = 7.52 to 7.30 (m, 10 H, $C_6H_5$), 6.78 (dm, $^3J_{HH}$ = 7.9 Hz, 1 H, $C_6H_3$), 6.64 (tm, $^3J_{HH}$ = 7.9 Hz, 1 H, $C_6H_3$), 6.43 (dm, $^3J_{HH}$ = 7.9 Hz, 1 H, $C_6H_3$), 6.02 (br., 1 H, OH), 5.86 (br., 1 H, OH), 3.52 (d, $^2J_{PH}$ = 1.7 Hz, 2 H, $CH_2$) ppm. $^{13}$C{$^1$H} NMR (100 MHz, $CDCl_3$): $\delta$ = 145.0 (d, $J_{PC}$ = 1.6 Hz), 141.7 (d, $J_{PC}$ = 3.7 Hz), 132.8

 © 2006 Wiley-VCH Verlag GmbH & Co. KGaA, Weinheim 

(d, $^3J_{PC}$ = 17.4 Hz, *m*-C), 130.9 (d, $^2J_{PC}$ = 9.5 Hz), 129.3 (s, *p*-C), 128.9 (d, $^3J_{PC}$ = 12.1), 128.6 (d, $J_{PC}$ = 7.4 Hz, *o*-C), 122.4 (d, $J_{PC}$ = 6.3 Hz), 121.0 (d, $J_{PC}$ = 1.6 Hz), 113.6 (d, $J_{PC}$ = 2.6 Hz), 30.7 (d, $^1J_{PC}$ = 10.5 Hz, $CH_2$) ppm. $^{31}$P NMR (101 MHz, $CDCl_3$): $\delta$ = –13.1 (s) ppm. MS (EI = 70 eV): *m*/*z* (%) = 308.1 (100) [$M^+$], 186.1 (45) [$Ph_2PH^+$], 185.1 (44) [$Ph_2P^+$], 183.0 (54) [$Ph_2P^+$–$H_2$], 123.1 (45) [$M^+$–$PPh_2$], 108.1 (54).

**4-[(Diphenylphosphanyl)methyl]benzene-1,2-diol (8d):** Yield 2.16 g (70%); m.p. 144 °C; elemental analysis: $C_{19}H_{17}O_2P$ (308.32): calcd. C 74.02 H 5.56; found C 74.06 H 5.59. $^1$H NMR (400 MHz, [$D_8$]-THF): $\delta$ = 7.68 (s, 1 H, OH), 7.53 (s, 1 H, OH), 7.41 (m, 4 H, *o*-H), 7.33 to 7.25 (m, 6 H, *m*/*p*-H), 6.58 (dd, $^4J_{HH}$ = 1.7 Hz, $^4J_{PH}$ = 1.7 Hz, 1 H, $C_6H_3$), 6.52 (d, $^3J_{HH}$ = 8.1 Hz, 1 H, $C_6H_3$), 6.38 (dm, $^3J_{HH}$ = 8.0 Hz, 1 H, $C_6H_3$), 3.31 (s, 2 H, $CH_2$) ppm. $^{13}$C{$^1$H} NMR (100 MHz, [$D_8$]THF): $\delta$ = 145.6 (d, $J_{PC}$ = 1.5 Hz), 144.2 (d, $J_{PC}$ = 2.9 Hz), 139.9 (d, $J_{PC}$ = 16.8 Hz, *i*-C), 133.3 (d, $J_{PC}$ = 18.7 Hz, *m*-C), 129.1 (d, $J_{PC}$ = 8.8 Hz), 128.7 (s, *p*-C), 128.6 (d, $J_{PC}$ = 6.3 Hz, *o*-C), 120.9 (d, $J_{PC}$ = 7.1 Hz), 116.7 (d, $J_{PC}$ = 7.6 Hz), 115.3 (d, $J_{PC}$ = 1.5 Hz), 35.6 (d, $J_{PC}$ = 15.1 Hz) ppm. $^{31}$P{$^1$H} NMR (162 MHz, $CDCl_3$): $\delta$ = –10.4 ppm. MS (EI = 70 eV): *m*/*z* (%) = 308.1 (48) [$M^+$], 186.1 (38) [$Ph_2PH^+$], 183.0 (27) [$Ph_2P^+$–$H_2$], 123.1 (100) [$M^+$–$PPh_2$], 108.1 (27).


[1] K. V. Katti, H. Gali, C. J. Smith, D. E. Berning, *Acc. Chem. Res.* **1999**, *32*, 9–17.

[2] D. Gudat, A. Haghverdi, M. Nieger, *Angew. Chem.* **2000**, *112*, 3211–3214; *Angew. Chem. Int. Ed.* **2000**, *39*, 3084–3086; S. Burck, D. Gudat, M. Nieger, W. W. Du Mont, *J. Am. Chem. Soc.* **2006**, *128*, 3946–3955.

[3] S. Trippett, *J. Chem. Soc.* **1961**, 1813–1816.

[4] P.-Y. Renard, P. Vayron, C. Mioskowski, *Org. Lett.* **2003**, *5*, 1661–1664; A. N. Bovin, A. N. Yarkevich, A. N. Kharitonov, E. N. Tsvetkov, *J. Chem. Soc., Chem. Commun.* **1994**, 973–974.

[5] X. Sun, D. W. Johnson, D. L. Caulder, R. E. Powers, K. N. Raymond, E. H. Wong, *Angew. Chem. Int. Ed.* **1999**, *38*, 1303–1307; X. Sun, D. W. Johnson, K. N. Raymond, E. H. Wong, *Inorg. Chem.* **2001**, *40*, 4504–4506; X. Sun, D. W. Johnson, D. L. Caulder, K. N. Raymond, E. H. Wong, *J. Am. Chem. Soc.* **2001**, *123*, 2752–2763.

[6] N. T. Lucas, J. M. Hook, A. M. McDonagh, S. B. Colbran, *Eur. J. Inorg. Chem.* **2005**, 496–503; N. T. Lucas, A. M. McDonagh, I. G. Dance, S. B. Colbran, D. C. Craig, *Dalton Trans.* **2006**, 680–685.

[7] N. A. Bondarenko, E. N. Tsvetkov, E. I. Matrosov, M. I. Kabachnik, *Izv. Akad. Nauk SSSR, Ser. Khim.* **1979**, 432–435; V. I. Evreinov, V. E. Baulin, Z. N. Vostroknutova, N. A. Bondarenko, T. Kh. Syundyukova, E. N. Tsvetkov, *Izv. Akad. Nauk SSSR, Ser. Khim.* **1989**, 1990–1997.

[8] J. Fawcett, P. A. T. Hoye, R. D. W. Kemmitt, D. J. Law, D. R. Russell, *J. Chem. Soc., Dalton Trans.* **1993**, 2563–2568.

[9] A. Bielecki, A. C. Kolbert, M. H. Levitt, *Chem. Phys. Lett.* **1989**, *155*, 341–346; M. H. Levitt, A. C. Kolbert, A. Bielecki, D. J. Ruben, *Solid State Nucl. Magn. Reson.* **1993**, *2*, 151–163.

[10] T. Imamoto, S. Kikuchi, T. Miura, Y. Wada, *Org. Lett.* **2001**, *3*, 87–90.

[11] K. Kellner, S. Rothe, E.-M. Steyer, A. Tzschach, *Phosphorus, Sulfur Relat. Elem.* **1980**, *9*, 269–274.


Received: April 11, 2006
Published Online: June 1, 2006

 © 2006 Wiley-VCH Verlag GmbH & Co. KGaA, Weinheim 

DOI: 10.1002/ejic.200600388

# Fluoromethyl Cations and Group XIV Congeners $AH_nF_{3-n}^+$ (A = Si, Ge, Sn, Pb; $n$ = 0–2): From Covalent Structures to Ion-Molecule Complexes

**Paola Antoniotti,[a] Stefano Borocci,[b] Nicoletta Bronzolino,[b] Maria Giordani,[b] and Felice Grandinetti*[b]**

**Keywords:** Ab initio calculations / Fluorinated cations / Group XIV elements / Ion-molecule complexes / Structure and stability

Ab initio calculations at the MP2 and CCSD(T) level of theory (triple-zeta quality basis sets for Si and Ge and effective core potentials plus DZ valence basis sets for tin and lead) have been performed to investigate the geometries, harmonic frequencies and relative stabilities of the $(Si,H,F)^+$, $(Ge,H,F)^+$, $(Si,F_3)^+$, $(Ge,F_3)^+$ and $(A,H_n,F_{3-n})^+$ (A = Si, Ge, Sn, Pb; $n$ = 1 and 2) isomeric ions. While the H–Si–F$^+$, F–$SiH_2^+$, H–$SiF_2^+$ and $SiF_3^+$ covalent structures are invariably predicted as the most stable isomers, the Ge$^+$–(HF), FA$^+$–($H_2$) and FA$^+$–(HF) complexes (A = Ge, Sn, Pb) are the global minima on the potential energy surfaces, more stable than the corresponding covalent structures by up to some tens of kilocalories per mole. For tin and lead, the HA$^+$–(HF) isomeric ions are also significantly more stable than F–$AH_2^+$ (A = Sn and Pb). Compared with the parent group XIV hydrides $(A,H_3)^+$, investigated so far by Schleyer and co-workers (*J. Am. Chem. Soc.* **1996**, *118*, 12154–12158) and found to possess, for A = Sn and Pb, energetically favoured HA$^+$–($H_2$) connectivities, the structural switch from covalent structures to ion-dipole complexes occurs, therefore, even earlier. This suggests that the "regular" covalent connectivity of even the simplest $AH_2X^+$ or $AHX_2^+$ cations of group XIV cannot be taken for granted, and, especially for germanium, tin and lead, the role of ion-molecule complexes must be carefully investigated.
(© Wiley-VCH Verlag GmbH & Co. KGaA, 69451 Weinheim, Germany, 2006)

## Introduction

In 1996, Schleyer and co-workers performed a benchmark theoretical study[1] on the structure and stability of the heavier group XIV congeners of the methyl cation. Before that investigation, the $D_{3h}$ geometries of all the $AH_3^+$ ions (X = C, Si, Ge, Sn, Pb) had been taken for granted, as such species are expected to obey the Walsh rules for six valence electron compounds.[2] As a matter of fact, for $CH_3^+$ the $D_{3h}$ structure is the only energy minimum located at the highest levels of theory.[3] However, for the heaviest, Sn and Pb, the calculations show[1] that the HSn$^+$–($H_2$) and HPb$^+$–($H_2$) ion-molecule complexes are more stable than the $SnH_3^+$ and $PbH_3^+$ $D_{3h}$ covalent structures by about 5 and 23 kcal mol$^{-1}$, respectively. In addition, although $SiH_3^+$ and $GeH_3^+$ are more stable than HSi$^+$–($H_2$) and HGe$^+$–($H_2$), the energy difference between the covalent structure and the ion-molecule complex substantially reduces from about 28 to about 10 kcal mol$^{-1}$ passing from silicon to germanium.[1] The order of stability of the $GeH_3^+$ and HGe$^+$–($H_2$) isomers has been more recently confirmed by Schwarz and co-workers,[4] who have also found that the Ge$^+$–($H_2$) complex is nearly degenerate with the H–Ge–H$^+$ covalent structure ($C_{2v}$ symmetry) and plays an active role in the gas-phase ion chemistry of $GeH_2^+$. The order of stability of Si$^+$–($H_2$) and H–Si–H$^+$ is, however, opposite, and the latter species is more stable by about 12 kcal mol$^{-1}$.[5] From a general point of view, these theoretical and experimental findings are in line with the increased tendency, down group XIV, toward lower oxidation numbers, clearly evident, for example, in the thermodynamic instability of various Pb(IV) compounds.[6,7] Concerning the structure of cations such as $AHX^+$, $AX_2^+$, $AH_2X^+$, $AHX_2^+$ and $AX_3^+$ (A = C, Si, Ge, Sn, Pb; X = monovalent group), they are usually assumed to be "regular" covalent structures and the conceivable role of ion-molecule complexes such as A$^+$–(HX), AH$^+$–(HX) or AX$^+$–($H_2$) is still essentially unexplored. As a first step in this direction, stimulated by our continuing interest in the chemistry of fluorinated cations,[8] we report here an ab initio study on the heavier congeners of the fluoromethyl cations $CH_2F^+$, $CHF_2^+$ and $CF_3^+$, which are known to possess covalent structures of $C_{2v}$ or $D_{3h}$ symmetry,[9–12] as well as on the additional exemplary species $SiHF^+$ and $GeHF^+$. While the $(Si,H,F)^+$ and $(Si,H_n,F_{3-n})^+$ ($n$ = 0–3) isomeric ions are structurally similar to their carbon congeners, the global minima on the $(Ge,H,F)^+$,

[a] Dipartimento di Chimica Generale ed Organica Applicata, Università degli Studi di Torino,
C.so M. D'Azeglio 48, 10125 Torino, Italy
[b] Dipartimento di Scienze Ambientali, Università della Tuscia,
L.go dell' Università, s.n.c., 01100 Viterbo, Italy
Fax: +39-0761-357179
E-mail: fgrandi@unitus.it
Supporting information for this article is available on the WWW under http://www.eurjic.org or from the author.

 © 2006 Wiley-VCH Verlag GmbH & Co. KGaA, Weinheim 

$(A,H_2,F)^+$ and $(A,H,F_2)^+$ potential energy surfaces (A = Ge, Sn, Pb) are invariably ion-molecule complexes such as $Ge^+$–(HF), $HA^+$–(HF) or $FA^+$–($H_2$). Therefore, our calculations provide additional examples of only "seemingly familiar"[1] compounds of group XIV and confirm the crucial role of noncovalent isomers in the gas-phase ion chemistry of the heaviest elements: germanium, tin and lead.

## Results and Discussion

All the $(Si,H,F)^+$, $(Ge,H,F)^+$, $(Si,F_3)^+$, $(Ge,F_3)^+$ and $(A,H_n,F_{3-n})^+$ (A = Si, Ge, Sn, Pb; $n$ = 1 and 2) isomeric ions shown in Figure 1, Figure 2, Figure 3 and Figure 4 have been characterised as minimum points on the MP2(full)/6-311G(d,p) (Si and Ge) or MP2(full)/6-311G(d,p)/LANL2DZ (Sn and Pb) potential energy surfaces. Their harmonic frequencies are listed in Tables 1S–4S of the supporting information. The geometries of the silicon- and germanium-containing ions were also refined at the CCSD(T,full)/cc-pVTZ level of theory, finding however only minor differences with the MP2(full)/6-311G(d,p) bond lengths and bond angles. The CCSD(T,full)/cc-pVTZ-optimised structures were finally used to perform CCSD(T,full)/aug-cc-pVTZ single-point calculations, so as to obtain accurate estimates of the relative stability of the various isomers and to evaluate the accuracy of the corresponding values obtained by MP2 calculations. The obtained data, reported in Table 1 and Table 2, reveal that the MP2(full)/6-311G(d,p) level of theory invariably predicts the correct order of stability of the various isomers but in general overestimates the stability of the ion-molecule com-

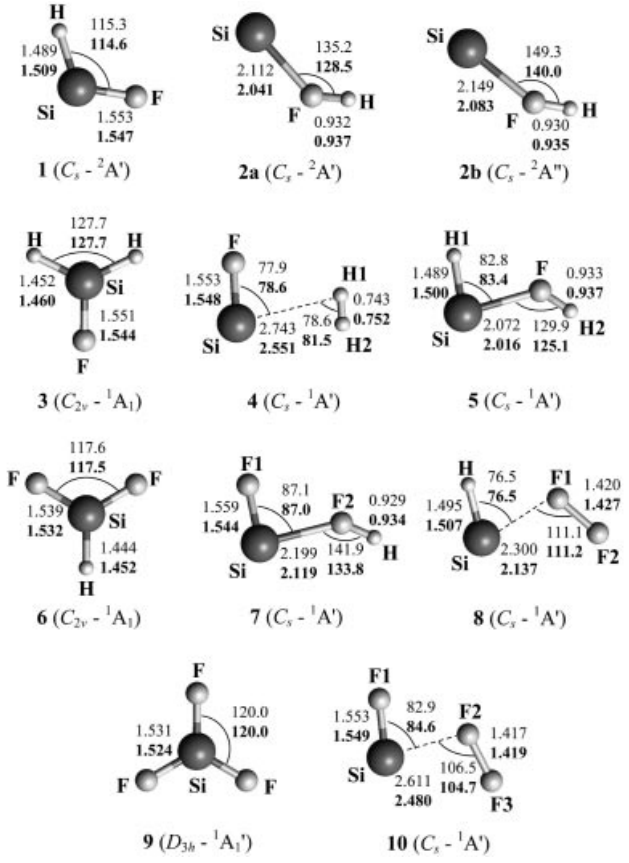


Figure 1. MP2(full)/6-311G(d,p) and CCSD(T,full)/cc-pVTZ-optimised (bold) geometries [Å and °] of the $(Si,H,F)^+$ and $(Si,H_n,F_{3-n})^+$ isomeric ions ($n$ = 0–3).

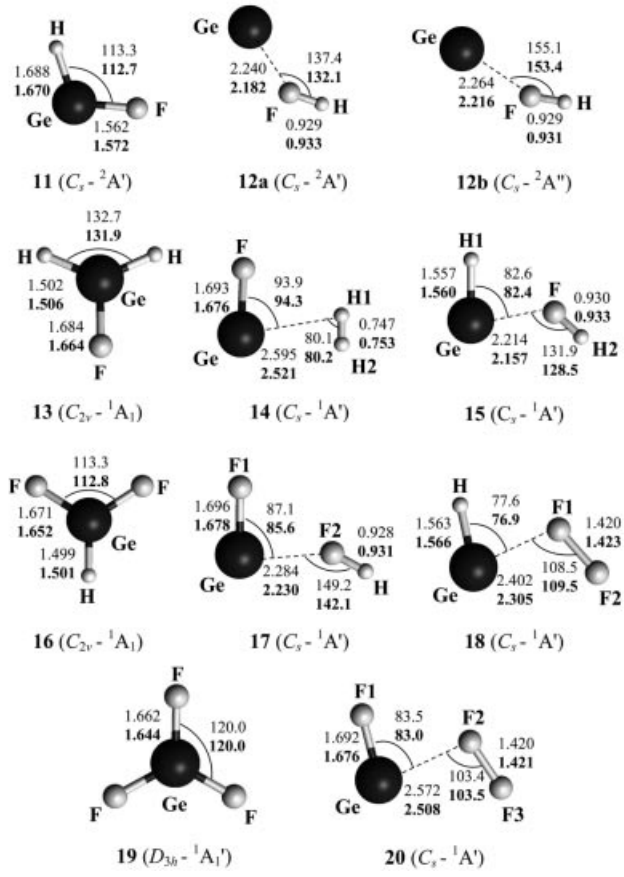


Figure 2. MP2(full)/6-311G(d,p) and CCSD(T,full)/cc-pVTZ-optimised (bold) geometries [Å and °] of the $(Ge,H,F)^+$ and $(Ge,H_n,F_{3-n})^+$ isomeric ions ($n$ = 0–3).

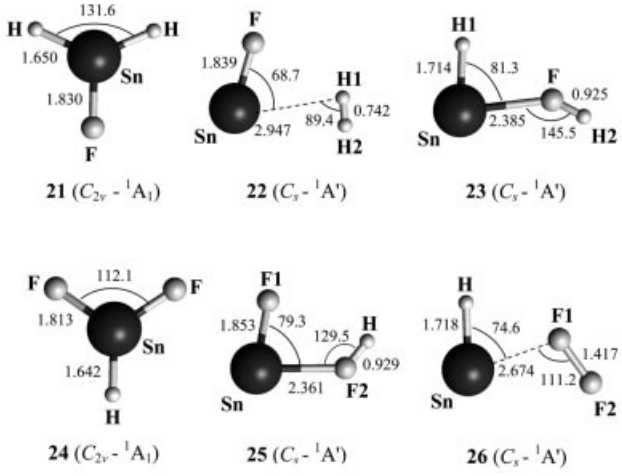


Figure 3. MP2(full)/6-311G(d,p)/LANL2DZ-optimised geometries [Å and °] of the $(Sn,H_2,F)^+$ and $(Sn,H,F_2)^+$ isomeric ions.

 © 2006 Wiley-VCH Verlag GmbH & Co. KGaA, Weinheim 

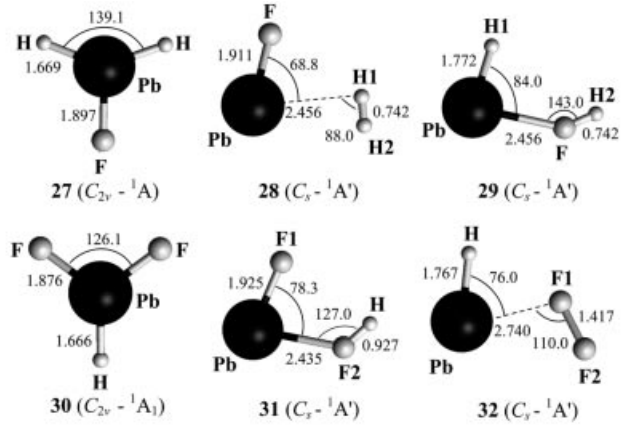


Figure 4. MP2(full)/6-311G(d,p)/LANL2DZ-optimised geometries [Å and °] of the $(Pb,H_2,F)^+$ and $(Pb,H,F_2)^+$ isomeric ions.

plexes by about 4–6 kcal mol$^{-1}$ for the silicon-containing ions and by about 10–12 kcal mol$^{-1}$ for the germanium-containing ions. On the other hand, from Table 3, the large energy differences of up to some tens of kilocalories per mole predicted at the MP2(full)/6-311G(d,p)/LANL2DZ level of theory between the various $(A,H_2,F)^+$ and-$(A,H,F_2)^+$ (A = Sn and Pb) isomeric structures are confirmed, within a few kilocalories per mole, by CCSD(T) single-point calculations.

## Structure and Stability of the $(Si,H,F)^+$ and $(Si,H_n,F_{3-n})^+$ Isomeric Ions ($n$ = 0–3)

The optimised parameters and the harmonic frequencies of the bent H–Si–F$^+$ isomer **1**[13] are in very good agreement with previous HF/6-31G(d) data[14,15] and identify the cat-

Table 1. Total energies (atomic units), zero-point energies (ZPE, atomic units), thermal corrections (TC, atomic units) and total entropies ($S$, cal·mol$^{-1}$ K$^{-1}$) of the $(Si,H,F)^+$ and $(Si,H_n,F_{3-n})^+$ ($n$ = 0–3) isomeric ions (see Figure 1).

| Species | CCSD(T,full)/aug-cc-pVTZ[a] | ZPE[b] | TC (298.15 K)[b] | $S$ (298.15 K)[c] | $\Delta E$ (0 K)[d] | $\Delta G$ (298.15 K)[d] |
|---|---|---|---|---|---|---|
| | | | $(Si,H,F)^+$ | | | |
| **1** | –389.12644 | 0.00890 | 0.00297 | 58.1 | 0.0 (0.0) | 0.0 (0.0) |
| **2a** | –389.09152 | 0.01073 | 0.00353 | 59.8 | +23.1 (+17.2) | +22.9 (+17.0) |
| **2b** | –389.08922 | 0.01036 | 0.00373 | 60.0 | +24.3 (+18.0) | +24.2 (+17.9) |
| | | | $(Si,H_2,F)^+$ | | | |
| **3** | –389.78084 | 0.01917 | 0.00310 | 56.6 | 0.0 (0.0) | 0.0 (0.0) |
| **4** | –389.76142 | 0.01463 | 0.00497 | 67.0 | +9.3 (+8.9) | +7.4 (+7.0) |
| **5** | –389.71984 | 0.01868 | 0.00388 | 61.3 | +38.0 (+34.2) | +37.1 (+33.3) |
| | | | $(Si,H,F_2)^+$ | | | |
| **6** | –489.00399 | 0.01445 | 0.00352 | 61.9 | 0.0 (0.0) | 0.0 (0.0) |
| **7** | –488.97642 | 0.01373 | 0.00484 | 69.6 | +16.9 (+10.8) | +15.4 (+9.3) |
| **8** | –488.67361 | 0.00967 | 0.00490 | 70.4 | +204.3 (+203.5) | +202.7 (+201.9) |
| | | | $(Si,F_3)^+$ | | | |
| **9** | –588.21217 | 0.00959 | 0.00412 | 64.7 | 0.0 (0.0) | 0.0 (0.0) |
| **10** | –587.93165 | 0.00521 | 0.00596 | 81.1 | +173.3 (+169.1) | +169.5 (+165.3) |

[a] At the CCSD(T,full)/cc-pVTZ-optimised geometries. [b] Based on MP2(full)/6-311G(d,p) harmonic frequencies. [c] Based on MP2(full)/6-311G(d,p) harmonic frequencies and moments of inertia. [d] At the CCSD(T,full)/aug-cc-pVTZ//CCSD(T)/cc-pVTZ level of theory. The MP2(full)/6-311G(d,p) values are given in parentheses.

Table 2. Total energies (atomic units), zero-point energies (ZPE, atomic units), thermal corrections (TC, atomic units) and total entropies ($S$, cal·mol$^{-1}$ K$^{-1}$) of the $(Ge,H,F)^+$ and $(Ge,H_n,F_{3-n})^+$ ($n$ = 0–3) isomeric ions (see Figure 2).

| Species | CCSD(T,full)/aug-cc-pVTZ[a] | ZPE[b] | TC (298.15 K)[b] | $S$ (298.15 K)[c] | $\Delta E$ (0 K)[d] | $\Delta G$ (298.15 K)[d] |
|---|---|---|---|---|---|---|
| | | | $(Ge,H,F)^+$ | | | |
| **11** | –2175.66017 | 0.00740 | 0.00308 | 61.5 | 0.0 (0.0) | 0.0 (0.0) |
| **12a** | –2175.66498 | 0.01057 | 0.00365 | 63.1 | –1.0 (–13.9) | –1.2 (–14.1) |
| **12b** | –2175.66326 | 0.01018 | 0.00389 | 63.2 | –0.2 (–13.4) | –0.2 (–13.4) |
| | | | $(Ge,H_2,F)^+$ | | | |
| **13** | –2176.30594 | 0.01731 | 0.00325 | 59.9 | 0.0 (0.0) | 0.0 (0.0) |
| **14** | –2176.30696 | 0.01459 | 0.00469 | 68.2 | –2.4 (–8.7) | –4.0 (–10.3) |
| **15** | –2176.28782 | 0.01765 | 0.00414 | 65.2 | +11.6 (+0.6) | +10.6 (–0.4) |
| | | | $(Ge,H,F_2)^+$ | | | |
| **16** | –2275.49306 | 0.01225 | 0.00383 | 65.5 | 0.0 (0.0) | 0.0 (0.0) |
| **17** | –2275.52119 | 0.01266 | 0.00525 | 74.2 | –17.4 (–29.6) | –19.1 (–31.3) |
| **18** | –2275.24304 | 0.00893 | 0.00507 | 74.0 | +154.8 (+145.9) | +153.1 (+144.2) |
| | | | $(Ge,F_3)^+$ | | | |
| **19** | –2374.66216 | 0.00722 | 0.00464 | 68.7 | 0.0 (0.0) | 0.0 (0.0) |
| **20** | –2374.47694 | 0.00463 | 0.00602 | 83.4 | +114.6 (+104.6) | +111.1 (+101.1) |

[a] At the CCSD(T,full)/cc-pVTZ-optimised geometries. [b] Based on MP2(full)/6-311G(d,p) harmonic frequencies. [c] Based on MP2(full)/6-311G(d,p) harmonic frequencies and moments of inertia. [d] At the CCSD(T,full)/aug-cc-pVTZ//CCSD(T)/cc-pVTZ level of theory. The MP2(full)/6-311G(d,p) values are given in parentheses.

 © 2006 Wiley-VCH Verlag GmbH & Co. KGaA, Weinheim 

Table 3. MP2(full)/6-311G(d,p)/LANL2DZ total energies ($E$, atomic units), zero-point energies (ZPE, atomic units), thermal corrections (TC, atomic units) and total entropies ($S$, cal·mol$^{-1}$K$^{-1}$) of the $(M,H_2,F)^+$ and $(M,H,F_2)^+$ isomeric ions (M = Sn and Pb) (see Figures 3 and 4).

| Species | $E$ | ZPE | TC (298.15 K) | $S$ (298.15 K) | $\Delta E$ (0 K)[a] | $\Delta G$ (298.15 K)[a] |
|---|---|---|---|---|---|---|
| | | | $(Sn,H_2,F)^+$ | | | |
| **21** | –103.87133 | 0.01560 | 0.00340 | 62.1 | 0.0 (0.0) | 0.0 (0.0) |
| **22** | –103.91097 | 0.01373 | 0.00512 | 72.2 | –26.0 (–27.2) | –28.0 (–29.2) |
| **23** | –103.89916 | 0.01649 | 0.00450 | 68.4 | –16.9 (–19.6) | –18.1 (–20.8) |
| | | | $(Sn,H,F_2)^+$ | | | |
| **24** | –202.98699 | 0.01079 | 0.00406 | 68.0 | 0.0 (0.0) | 0.0 (0.0) |
| **25** | –203.06645 | 0.01323 | 0.00480 | 73.5 | –48.3 (–50.6) | –49.5 (–51.8) |
| **26** | –202.78237 | 0.00797 | 0.00538 | 77.6 | +126.6 (+113.6) | +124.6 (+111.6) |
| | | | $(Pb,H_2,F)^+$ | | | |
| **27** | –103.93178 | 0.01498 | 0.00347 | 64.1 | 0.0 (0.0) | 0.0 (0.0) |
| **28** | –104.01583 | 0.01379 | 0.00504 | 73.5 | –53.5 (–52.8) | –55.3 (–54.6) |
| **29** | –104.00859 | 0.01634 | 0.00445 | 70.0 | –47.3 (–48.6) | –48.5 (–49.8) |
| | | | $(Pb,H,F_2)^+$ | | | |
| **30** | –203.03090 | 0.00987 | 0.00426 | 70.4 | 0.0 (0.0) | 0.0 (0.0) |
| **31** | –203.16985 | 0.01303 | 0.00492 | 76.0 | –85.2 (–86.0) | –86.5 (–87.3) |
| **32** | –202.89244 | 0.00757 | 0.00551 | 80.3 | +85.4 (+73.7) | +83.3 (+71.6) |

[a] The values in parentheses are based on CCSD(T,full)/6-311G(d,p)/LANL2DZ single-point calculations.

ion as a typical covalent structure, with Si–H and Si–F bond lengths of about 1.5 Å and corresponding stretching frequencies around 2150 and 1050 cm$^{-1}$, respectively. On the other hand, the geometries and harmonic frequencies of the nearly degenerate $Si^+$–(HF) isomers **2a** and **2b**, located as distinct minima on the A′ and A″ doublet potential energy surface, point to ion-dipole complexes between $Si^+$ and HF. The Si–F bond lengths are longer than 2.0 Å, the corresponding stretching frequencies range around 250 cm$^{-1}$ and the CCSD(T,full)/aug-cc-pVTZ//CCSD(T,full)/cc-pVTZ dissociation energies into $Si^+(^2P)$ and HF amount to 22.3 kcal mol$^{-1}$ for isomer **2a** and 21.1 kcal mol$^{-1}$ for isomer **2b**. At the same computational level, the two ions are less stable than **1** by 23.1 and 24.3 kcal mol$^{-1}$, respectively. This difference is larger than the energy gap between $SiH_2^+$ ($C_{2v}$) and $Si^+$–($H_2$), obtained so far as 11.5 kcal mol$^{-1}$ at the complete active space SCF level of theory followed by second-order CI (CASSCF–SOCI)[5] and presently confirmed as 11.4 kcal mol$^{-1}$ at the CCSD(T,full)/aug-cc-pVTZ//CCSD(T,full)/cc-pVTZ level of theory.

The geometries and harmonic frequencies of the F–$SiH_2^+$ isomer **3** and of the H–$SiF_2^+$ isomer **6** of $C_{2v}$ symmetry are also in good agreement with previous HF,[14–16] MP2[10,17] and CASSCF[18] ab initio studies and are again typical of covalent structures. On the other hand, the bond lengths, harmonic frequencies and dissociation energies of the $(Si,H_2,F)^+$ isomers **4** and **5**, and of the $(Si,H,F_2)^+$ isomers **7** and **8**, point to ion-molecule complexes between ground-state $SiF^+(^1\Sigma^+)$[19] and $H_2$ (**4**) or HF (**7**), and ground-state $SiH^+(^1\Sigma^+)$[20] and HF (**5**) or $F_2$ (**8**). The bond lengths between the constituting moieties range from about 2.0 Å (isomer **5**) to about 2.6 Å (isomer **4**), and their CCSD(T,full)/aug-cc-pVTZ//CCSD(T,full)/cc-pVTZ interaction energies, computed as 3.3 kcal mol$^{-1}$ for isomer **4**, 8.4 kcal mol$^{-1}$ for isomer **8**, and 22.1 and 18.6 kcal mol$^{-1}$, respectively, for isomers **5** and **7**, parallel the increasing solvation ability of $H_2$, $F_2$ and HF. From Table 1, these ions are less stable than the corresponding covalent structures **3** or **6** by 9.3 kcal mol$^{-1}$ (isomer **4**), 38.0 kcal mol$^{-1}$ (isomer **5**), 16.9 kcal mol$^{-1}$ (isomer **7**) and 204.3 kcal mol$^{-1}$ (isomer **8**) (in the context of the protonation of $SiF_2$, the energy difference between isomers **6** and **7** has been obtained[21] as 15.9 kcal mol$^{-1}$ at the G2 level of theory). These energy differences and orders of stabilities, namely $FSi^+$–($H_2$) > $HSi^+$–(HF) and $FSi^+$–(HF) >> $HSi^+$–($F_2$), reflect a balance of several factors, including the different strength of the Si–$H^+$ and Si–$F^+$ covalent bonds[22] (75 vs. 151 kcal mol$^{-1}$), the different thermodynamic stability of $H_2$, HF and $F_2$, and the different solvation ability of these ligands. Consistently, the ion-molecule complex **10**, arising from the weak interaction [5.5 kcal mol$^{-1}$ at the CCSD(T,full)/aug-cc-pVTZ//CCSD(T,full)/cc-pVTZ level of theory] between $SiF^+$ and the highly unstable, poorly solvating $F_2$, is less stable than $SiF_3^+$ ($D_{3h}$) by more than 170 kcal mol$^{-1}$.

### Structure and Stability of the $(Ge,H,F)^+$ and $(Ge,H_n,F_{3-n})^+$ Isomeric Ions ($n$ = 0–3)

As already pointed out in the Introduction, the energy difference of about 28 kcal mol$^{-1}$ between $SiH_3^+$ ($D_{3h}$) and $HSi^+$–($H_2$)[1] is reduced to about 10 kcal mol$^{-1}$ for $GeH_3^+$ and $HGe^+$–($H_2$).[4] Similarly, H–Si–$H^+$ ($C_{2v}$) is more stable than $Si^+$–($H_2$) by about 11 kcal mol$^{-1}$,[5] but, according to highly accurate ab initio calculations,[4] H–Ge–$H^+$ and $Ge^+$–($H_2$) are nearly degenerate. Therefore, passing from $(Si,H,F)^+$ and $(Si,H_n,F_{3-n})^+$ ($n$ = 0–3) to $(Ge,H,F)^+$ and $(Ge,H_n,F_{3-n})^+$ ($n$ = 0–3), one expects an overall stabilisation of the ion-molecule complexes with respect to the corresponding covalent structures. From Table 2, the clearest confirmation of this qualitative expectation is the high stability of the $FGe^+$–(HF) isomer **17**, which is more stable than the covalent H–$GeF_2^+$ (**16**) by more than 17 kcal mol$^{-1}$ at the CCSD(T,full)/aug-cc-pVTZ//CCSD(T,full)/cc-pVTZ

 © 2006 Wiley-VCH Verlag GmbH & Co. KGaA, Weinheim 

level of theory. The $FGe^+$–($H_2$) isomer **14** is also more stable than F–$GeH_2^+$ (**13**) by about 2 kcal mol$^{-1}$, while the two $Ge^+$–(HF) isomers **12a** and **12b**, located as distinct energy minima on the A′ and A′′ doublet potential energy surfaces, are nearly degenerate with the H–Ge–$F^+$ cation **11**. Ions **12a**, **12b**, **14** and **17**, as well as the $HGe^+$–(HF) isomer **15** and the $HGe^+$–($F_2$) isomer **18** feature bond lengths, bond angles and harmonic frequencies that point to ion-molecule complexes between ground state $Ge^+(^2P)$, $GeH^+(^1\Sigma^+)$[23] and $GeF^+(^1\Sigma^+)$,[24] and $H_2$, HF or $F_2$. Similar to their silicon congeners, the distances between the constituting moieties range in fact from about 2.0 Å to more than 2.5 Å and the CCSD(T,full)/aug-cc-pVTZ//CCSD(T,full)/cc-pVTZ interaction energies regularly increase from the $H_2$ complex **14** (4.6 kcal mol$^{-1}$) to the $F_2$ complex **18** (8.6 kcal mol$^{-1}$), and arrive at about 20–22 kcal mol$^{-1}$ for the HF complexes **12**, **15** and **17**. In addition, the orders of stability of these isomers, namely $FGe^+$–($H_2$) > $HGe^+$–(HF) and $FGe^+$–(HF) >> $HGe^+$–($F_2$), parallel that of their silicon congeners and again reflect the increasing strength of Ge–$H^+$ and Ge–$F^+$ covalent bonds (68 vs. 125 kcal mol$^{-1}$), and the different thermodynamic stability and solvation ability of $H_2$, HF and $F_2$. It is therefore not surprising that the $FGe^+$–($F_2$) loosely bound complex **20** (the interaction between $GeF^+$ and $F_2$ amounts to 7.0 kcal mol$^{-1}$) is less stable than $GeF_3^+$ ($D_{3h}$) by 114.6 kcal mol$^{-1}$.

### Structure and Stability of the $(A,H_2,F)^+$ and $(A,H,F_2)^+$ Isomeric Ions (A = Sn and Pb)

Passing to the tin- and lead-containing ions $(A,H_2,F)^+$ and $(A,H,F_2)^+$ (A = Sn and Pb), with the only exception of the $HSn^+$–($F_2$) isomer **26** and the $HPb^+$–($F_2$) isomer **32**, all the $FA^+$–($H_2$), $HA^+$–(HF) and $FA^+$–(HF) isomers, **22**, **23**, **25**, **28**, **29** and **31** (A = Sn and Pb), become appreciably more stable than the corresponding covalent structures **21** (F–$SnH_2^+$), **24** (H–$SnF_2^+$), **27** (F–$PbH_2^+$) and **30** (H–$PbF_2^+$). The MP2(full)/6-311G(d,p)/LANL2D energy differences amount to about 17 kcal mol$^{-1}$ for $HSn^+$–(HF) and 26.0 kcal mol$^{-1}$ for $FSn^+$–($H_2$), range around 50 kcal mol$^{-1}$ for $FSn^+$–(HF), $FPb^+$–($H_2$) and $HPb^+$–(HF), and become as large as about 85 kcal mol$^{-1}$ for the $FPb^+$–(HF) isomer. The values obtained by CCSD(T) single-point calculations are essentially similar, but these estimates could be in principle appreciably affected by geometry optimisations. We note in fact from Figure 1 and Figure 2 that, for the Si and Ge analogues, the MP2 distances of the ion-neutral complexes are considerably larger than the CCSD(T) values.

From Figure 3 and Figure 4, any $FA^+$–($H_2$), $HA^+$–(HF), $HA^+$–($F_2$) and $FA^+$–(HF) isomeric structure (A = Sn and Pb) features bond lengths between the constituting moieties that are typical of ion-molecule complexes. In addition, similar to their silicon and germanium congeners, their stabilisation energies with respect to the separated ions and neutrals, computed as about 0.5 kcal mol$^{-1}$ for isomers **22** and **28**, about 3 kcal mol$^{-1}$ for isomers **26** and **32**, and about 17–24 kcal mol$^{-1}$ for isomers **23**, **25**, **29** and **31**, are again related to the increasing solvation ability of their constituting $H_2$, $F_2$ or HF neutral moieties. They also follow the orders of stability already noted for Si and Ge, namely $FA^+$–($H_2$) > $HA^+$–(HF) and $FA^+$–(HF) >> $HA^+$–($F_2$) (A = Sn and Pb).

## Concluding Remarks

The benchmark theoretical study by Schleyer and coworkers[1] on cationic hydrides of group XIV first disclosed a periodic structural switch from covalent structures to ion-molecule complexes, which results in particular in the higher stability of $HSn^+$–($H_2$) and $HPb^+$–($H_2$) with respect to $SnH_3^+$ and $PbH_3^+$. The results of our calculations indicate that, for the fluorine-substituted cations, this structural switch occurs even earlier and ion-molecule complexes such as $FGe^+$–($H_2$) and $FGe^+$–(HF), as well as $Ge^+$–(HF), are already more stable than their corresponding covalent structures. In addition, for the tin- and lead-containing analogues, the energy differences become as large as some tens of kilocalories per mole. From a general point of view, these findings suggest that the covalent structure of even the simplest $AH_2X^+$- or $AHX_2^+$-substituted cations of group XIV cannot be taken for granted, and, especially for the ions containing germanium, tin and lead, the role of ion-molecule complexes such as $A^+$–(HX), $AH^+$–(HX) or $AX^+$–($H_2$) must be carefully investigated.

## Computational Details

The quantum chemical calculations were performed using Unix versions of the Gaussian03[25] and MOLPRO 2000.1[26] sets of programs installed on an Alphaserver 1200 and an HP Proliant DL585 machine. The geometries of all the silicon- and germanium-containing ions were first optimised, using the 6-311G(d,p) basis set,[27] at the second-order Møller-Plesset level of theory with inclusion of the inner electrons, MP2(full),[28] and subsequently refined, using the Dunning's correlation consistent triple-zeta basis set (cc-pVTZ)[29] at the coupled cluster level of theory (full electrons), including the contribution from single and double substitutions and an estimate of connected triples, CCSD(T,full).[30,31] To evaluate the influence of diffuse functions, single-point calculations were finally performed at the CCSD(T,full) level of theory with the aug-cc-pVTZ basis set. For the doublet state species, we used the spin-restricted coupled cluster theory as implemented in MOLPRO.[32,33] The MP2(full)/6-311G(d,p) unscaled frequencies were used to calculate the zero-point vibrational energies (ZPE) and the vibrational contribution to the thermal correction (TC), obtained at 298.15 K by standard statistical mechanics formulas.[34] The overall TC term was finally obtained by adding the translational (3/2 RT) and rotational (RT) contributions at this temperature. The structure and harmonic frequencies of the tin- and lead-containing species were computed at the MP2(full) level of theory using the 6-311G(d,p) basis set for H and F and the Los Alamos ECP plus DZ (LANL2DZ) for Sn and Pb.[35]

**Supporting Information** (see footnote on the first page of this article): Tables 1S–4S containing the MP2(full)/6-311G(d,p) and

 © 2006 Wiley-VCH Verlag GmbH & Co. KGaA, Weinheim 

MP2(full)/6-311G(d,p)/LANL2DZ harmonic frequencies of the presently investigated ions.

## Acknowledgments

We thank the Italian Ministero dell' Istruzione, dell' Università e della Ricerca (MIUR) and the Consiglio Nazionale delle Ricerche (CNR) for financial support.

[1] J. Kapp, P. R. Schreiner, P. v. R. Schleyer, *J. Am. Chem. Soc.* **1996**, *118*, 12154–12158.
[2] A. H. Pakiari, F. Nazari, *J. Mol. Struct. (Theochem)* **2005**, *717*, 189–197, and references therein.
[3] K. Raghavachari, R. A. Whiteside, J. A. Pople, P. v. R. Schleyer, *J. Am. Chem. Soc.* **1981**, *103*, 5649–5657.
[4] P. Jackson, N. Sändig, M. Diefenbach, D. Schröder, H. Schwarz, R. Srinivas, *Chem. Eur. J.* **2001**, *7*, 151–160.
[5] S. P. Mort, N. A. Jennings, G. G. Balint-Kurti, D. M. Hirst, *J. Chem. Phys.* **1994**, *101*, 10576–10601, and references therein.
[6] F. A. Cotton, G. Wilkinson, C. A. Murillo, M. Bochmann, *Advanced Inorganic Chemistry*, 6th ed., Wiley, New York, **1999**.
[7] X. Wang, L. Andrews, *J. Am. Chem. Soc.* **2003**, *125*, 6581–6587.
[8] a) F. Grandinetti, *Recent Res. Devel. Mol. Struct.* **2002**, *1*, 23–40, and references cited therein; b) P. Antoniotti, P. Facchini, F. Grandinetti, *Chem. Phys. Lett.* **2003**, *372*, 455–463; c) N. Bronzolino, F. Grandinetti, *J. Mol. Struct. (Theochem)* **2003**, *635*, 221–227; d) S. Borocci, N. Bronzolino, F. Grandinetti, *Helv. Chim. Acta* **2004**, *87*, 1467–1482; e) S. Borocci, N. Bronzolino, M. Giordani, F. Grandinetti, *Int. J. Mass Spectrom.* **2006**, in press.
[9] L. Andrews, F. T. Prochaska, *J. Chem. Phys.* **1979**, *70*, 4714–4723.
[10] G. Frenking, S. Fau, C. M. Marchand, H. Grützmacher, *J. Am. Chem. Soc.* **1997**, *119*, 6648–6655.
[11] G. Rasul, G. K. S. Prakash, G. A. Olah, *J. Mol. Struct. (Theochem)* **1999**, *466*, 245–255.
[12] C. W. Bauschlicher Jr, A. Ricca, *J. Phys. Chem. A* **2000**, *104*, 4581–4585.
[13] At the CCSD(T,full)/aug-cc-pVTZ//CCSD(T,full)/cc-pVTZ level of theory we have also located on the doublet surface a linear isomer (Si–H: 1.473 Å, Si–F: 1.550 Å), which was, however, less stable than **1** by about 55 kcal mol$^{-1}$.
[14] A. C. Hopkinson, M. H. Lien, *Can. J. Chem.* **1989**, *67*, 991–997.
[15] E. W. Ignacio, H. B. Schlegel, *J. Phys. Chem.* **1990**, *94*, 7439–7445.
[16] a) Y. Apeloig, *Tetrahedron Lett.* **1977**, *18*, 4647–4650; b) Y. Apeloig, S. A. Godleski, D. J. Heacock, J. M. McKelvey, *Tetrahedron Lett.* **1981**, *22*, 3297–3300.
[17] M. Sana, M. Decrem, G. Leroy, M. T. Nguyen, L. G. Vanquickenborne, *J. Chem. Soc. Faraday Trans.* **1994**, *90*, 3505–3511.
[18] H. Basch, T. Hoz, S. Hoz, *J. Phys. Chem. A* **1999**, *103*, 6458–6467.
[19] K. A. Peterson, R. C. Woods, P. Rosmus, H.-J. Werner, *J. Chem. Phys.* **1990**, *93*, 1889–1894.
[20] C. J. Reid, *J. Phys. B* **1993**, *26*, 2359–2375.
[21] I. Rozas, I. Alkorta, J. Elguero, *J. Phys. Chem. A* **1999**, *103*, 8861–8869.
[22] M. W. J. Chase, J. Phys. Chem. Ref. Data **1998**, Monograph 9, 1.
[23] K. K. Das, K. Balasubramanian, *J. Chem. Phys.* **1990**, *93*, 5883–5889.
[24] P. Antoniotti, S. Borocci, N. Bronzolino, M. Giordani, F. Grandinetti, *J. Phys. Chem. A* **2006**, *110*, 4900–4905.
[25] M. J. Frisch, G. W. Trucks, H. B. Schlegel, G. E. Scuseria, M. A. Robb, J. R. Cheeseman, J. A. Montgomery Jr, T. Vreven, K. N. Kudin, J. C. Burant, J. M. Millam, S. S. Iyengar, J. Tomasi, V. Barone, B. Mennucci, M. Cossi, G. Scalmani, N. Rega, G. A. Petersson, H. Nakatsuji, M. Hada, M. Ehara, K. Toyota, R. Fukuda, J. Hasegawa, M. Ishida, T. Nakajima,Y. Honda, O. Kitao, H. Nakai, M. Klene, X. Li, J. E. Knox, H. P. Hratchian, J. B. Cross, C. Adamo, J. Jaramillo, R. Gomperts, R. E. Stratmann, O. Yazyev, A. J. Austin, R. Cammi, C. Pomelli, J. W. Ochterski, P. Y. Ayala, K. Morokuma, G. A. Voth, P. Salvador, J. J. Dannenberg, V. G. Zakrzewski, S. Dapprich, A. D. Daniels, M. C. Strain, O. Farkas, D. K. Malick, A. D. Rabuck, K. Raghavachari, J. B. Foresman, J. V. Ortiz, Q. Cui, A. G. Baboul, S. Clifford, J. Cioslowski, B. B. Stefanov, G. Liu, A. Liashenko, P. Piskorz, I. Komaromi, R. L. Martin, D. J. Fox, T. Keith, M. A. Al-Laham, C. Y. Peng, A. Nanayakkara, M. Challacombe, P. M. W. Gill, B. Johnson, W. Chen, M. W. Wong, C. Gonzalez, J. A. Pople, *Gaussian 03*, Revision C.02, Gaussian, Inc., Wallingford, CT, **2004**.
[26] MOLPRO is a package of ab initio programs written by H.-J. Werner and P. J. Knowles, with contributions from R. D. Amos, A. Bernhadsson, A. Berning, P. Celani, D. L. Cooper, M. J. O. Deegan, A. J. Dobbyn, F. Eckert, C. Hampel, G. Hetzer, T. Korona, R. Lindh, A. W. Lloyd, S. J. McNicholas, F. R. Manby, W. Meyer, M. E. Mura, A. Nicklass, P. Palmieri, R. Pitzer, G. Rauhut, M. Schatz, H. Stoll, A. J. Stone, R. Tarroni, T. Thorsteinsson.
[27] W. J. Hehre, L. Radom, P. v. R. Schleyer, J. A. Pople, *Ab Initio Molecular Orbital Theory*, Wiley, New York, **1986**.
[28] C. Møller, M. S. Plesset, *Phys. Rev.* **1934**, *46*, 618–622.
[29] a) D. E. Woon, T. H. Dunning, *J. Chem. Phys.* **1993**, *98*, 1358–1371; b) R. A. Kendall, T. H. Dunning Jr, R. J. Harrison, *J. Chem. Phys.* **1992**, *96*, 6796–6806; c) T. H. Dunning Jr, *J. Chem. Phys.* **1989**, *90*, 1007–1023; d) K. A. Peterson, D. E. Woon, T. H. Dunning Jr, *J. Chem. Phys.* **1994**, *100*, 7410–7415; e) A. Wilson, T. van Mourik, T. H. Dunning Jr, *J. Mol. Struct. (Theochem)* **1997**, *388*, 339–349.
[30] K. Raghavachari, G. W. Trucks, J. A. Pople, M. Head-Gordon, *Chem. Phys. Lett.* **1989**, *157*, 479–483.
[31] C. Hampel, K. Peterson, H.-J. Werner, *Chem. Phys. Lett.* **1992**, *190*, 1–12.
[32] P. J. Knowles, C. Hampel, H.-J. Werner, *J. Chem. Phys.* **1993**, *99*, 5219–5227.
[33] J. D. Watts, J. Gauss, R. J. Bartlett, *J. Chem. Phys.* **1993**, *98*, 8718–8733.
[34] D. McQuarrie, *Statistical Mechanics*, Harper & Row, New York, **1976**.
[35] a) P. J. Hay, W. R. Wadt, *J. Chem. Phys.* **1985**, *82*, 270–283; b) W. R. Wadt, P. J. Hay, *J. Chem. Phys.* **1985**, *82*, 284–298; c) P. J. Hay, W. R. Wadt, *J. Chem. Phys.* **1985**, *82*, 299–310.

Received: April 4, 2006
Published Online: June 19, 2006

 © 2006 Wiley-VCH Verlag GmbH & Co. KGaA, Weinheim 

DOI: 10.1002/ejic.200501100

# Synthesis, Characterization, and Crystal Structure Analysis of the First Terdentate [C,N,S] Thiosemicarbazone Complex with a Six-Membered Palladacycle: Influence of Steric Effects on Ring Size

**Adriana Amoedo,[a] Luis A. Adrio,[a] José M. Antelo,[a] Javier Martínez,[a] M. Teresa Pereira,[a] Alberto Fernández,[b] and José M. Vila*[a]**

*Dedicated to Professor Victor Riera on the occasion of his 70th birthday*

**Keywords:** Thiosemicarbazones / Cyclometalation / Palladium / Indole / Crystal structure

The reaction of the thiosemicarbazone ligands 1-(COMe)-3-[C(H)=NN(H)C(=S)NHR]$C_8H_5N$, (R = H **a**, Me **b**, Et **c**) with potassium tetrachloropalladate in an ethanol/water mixture led to the new tetranuclear palladium(II) compounds [Pd{1-(COMe)-3-[C(H)=NN=C(S)NHR]$C_8H_4N$-$k^3C5,N,S$}]$_4$ (R = H **1a**, Me **1b**, Et **1c**) which contain six-membered metallacycles. The thiosemicarbazone ligands in these complexes are terdentate through the C, N, and S atoms and are deprotonated at the NH group. The Pd–S bond formed is sufficiently strong to undergo reactions with nucleophiles without bond cleavage. Reaction of **1a** and **1b** with 1,2-bis(diphenylphosphanyl)ethane (dppe) gave the dinuclear species [{Pd[1-(COMe)-3-{C(H)=NN=C(S)NHR}$C_8H_4N$]}$_2$(μ-$Ph_2P(CH_2)_2PPh_2$)] (R = H **2a**, Me **2b**). The molecular structure of complex **1b** has been determined by X-ray diffraction analysis.

(© Wiley-VCH Verlag GmbH & Co. KGaA, 69451 Weinheim, Germany, 2006)

## Introduction

Cyclometalated compounds, which make up a fair portion of species pertaining to the organometallic family, are quite numerous and have been studied to a great degree, among other reasons owing to the great number of organic substrates that can undergo a cyclometalation reaction to form a stable five-membered ring.[1–7] In particular, thiosemicarbazone ligands are prominent in this process in view of the donor atoms they display, which is not only limited to the nitrogen and sulfur atoms of the thiosemicarbazide chain, or to additional donors set on the parent aldehyde or ketone, but also because metal–carbon bonding makes them appropriate terdentate [C,N,S] ligands. This makes them reminiscent of the related terdentate [C,N,N] Schiff bases[8–10] and [C,N,O] semicarbazones[11] in that compounds with two fused rings at the metal center are formed; recently, a further example of [C,N,N] pincer complexes has been reported.[12]

That thiosemicarbazone derivatives exhibit an altogether different chemical behavior is due to the strength of the Pd–$S_{chelate}$ bond, which hinders opening of the metalated and coordination rings at the metal center, thus making the ligands excellent pincer species that powerfully occupy three of the four coordination positions of the metal, thereby allowing only the fourth coordination site to undergo further reaction with nucleophiles.

Another interesting issue related to these ligands is that upon treatment with the corresponding palladium or platinum salt, tetrameric compounds bearing a central $Pd_4S_4$ or $Pt_4S_4$ central core are obtained, an outcome which, in the majority of cases, seems to be an inevitable consequence of their chemistry. In view of our previous results, and in efforts to progress further into the chemistry of cyclometalated thiosemicarbazones, we were interested in establishing if tetrameric compounds could also be obtained in the case of six-membered palladacycles, for which purpose we chose ligands derived from condensed systems where five- or six-membered metalated rings may be formed. It has been reported that in ligands with condensed rings, the site and/or the electronic properties of the substituents may force the formation of six-membered metalated rings as opposed to the more stable five-membered ones.[13,14] Furthermore, previous studies have also shown that bulky groups close to the potential metalation site impede metal–carbon bond formation by hindering approach of the metal to the carbon atom.[15] With this in mind we chose the thiosemicarbazones derived from the condensation of 1-acetyl-3-in-

[a] Departamento de Química Inorgánica, Universidad de Santiago de Compostela,
15782 Santiago de Compostela, Spain
Fax: +34-981-595-012
E-mail: qideport@usc.es
[b] Departamento de Química Fundamental, Universidad de A Coruña,
15071 A Coruña, Spain

 © 2006 Wiley-VCH Verlag GmbH & Co. KGaA, Weinheim 

dolecarboxaldehyde and the corresponding thiosemicarbazide, where, although metalation could, in principle, be achieved through the pyrrole (C2) or the phenyl (C5) carbon atoms to give a five- or a six-membered metalated ring, respectively, the acetyl group on the pyrrole nitrogen atom should sufficiently hinder approach of the palladium atom to the C(2) carbon, in which case metalation of the ligand should occur at the C(5) carbon. This paper describes the results of this endeavor.

## Results and Discussion

The ligands **a**–**c** were prepared by reaction of 1-acetyl-3-indolecarboxaldehyde with thiosemicarbazide, 4-methylthiosemicarbazide, or 4-ethylthiosemicarbazide, respectively (see Exp. Sect.). The bands at around 3380 and 3140 $cm^{-1}$ in the IR spectra of these compounds are due to ν(N–H) absorption of the $NH_2$ and NH groups, respectively; the latter is not present in the spectra of the complexes.[15] The ligands also show characteristic ν(C=N) and ν(C=S) stretches in their IR spectra at around 1615 and 830 $cm^{-1}$, respectively. In the $^1H$ NMR spectra the resonances at around $\delta$ = 11.5 and 8.30 ppm were assigned to the NH and HC=N protons, respectively (see Exp. Sect.). New cyclometalated compounds were obtained from the ligands, as shown in Scheme 1. In a typical experiment, a suspension of $K_2PdCl_4$ in ethanol/water was treated with the corresponding thiosemicarbazone ligand to give complexes [Pd{1-(COMe)-3-[C(H)=NN=C(S)NHR]$C_8H_4$N-$k^3C5,N,S$}]$_4$ (R = H **1a**, Me **1b**, Et **1c**) as air-stable solids, which were fully characterized, with the ligand in the (*E*,*Z*) configuration. The mass spectrum (FAB) shows peaks at *m*/*z* 1458 (**1a**), 1515 (**1b**), and 1571 (**1c**) for the molecular ion, and the isotopic composition suggests a tetranuclear complex of formula $C_{48}H_{40}N_{16}O_4Pd_4S_4$ (**1a**), $C_{52}H_{48}N_{16}O_4Pd_4S_4$ (**1b**), and $C_{56}H_{56}N_{16}O_4Pd_4S_4$ (**1c**).

The IR data are in agreement with deprotonation of the ligand at the hydrazine nitrogen upon complex formation[16–19] (vide supra). The ν(C=N) band is shifted to lower wavenumbers,[20] contrary to the trend observed for other thiosemicarbazone complexes, which show a shift to higher wavenumbers.[15] The ν(C=S) band disappears, in agreement with loss of double-bond character upon deprotonation of the NH group. Although these data are in good accordance with metalation of the thiosemicarbazone, they give little insight as to the metalated carbon atom, for which definite proof was obtained from the $^1H$ NMR spectra, whose data are fully consistent with metalation of the C(1)

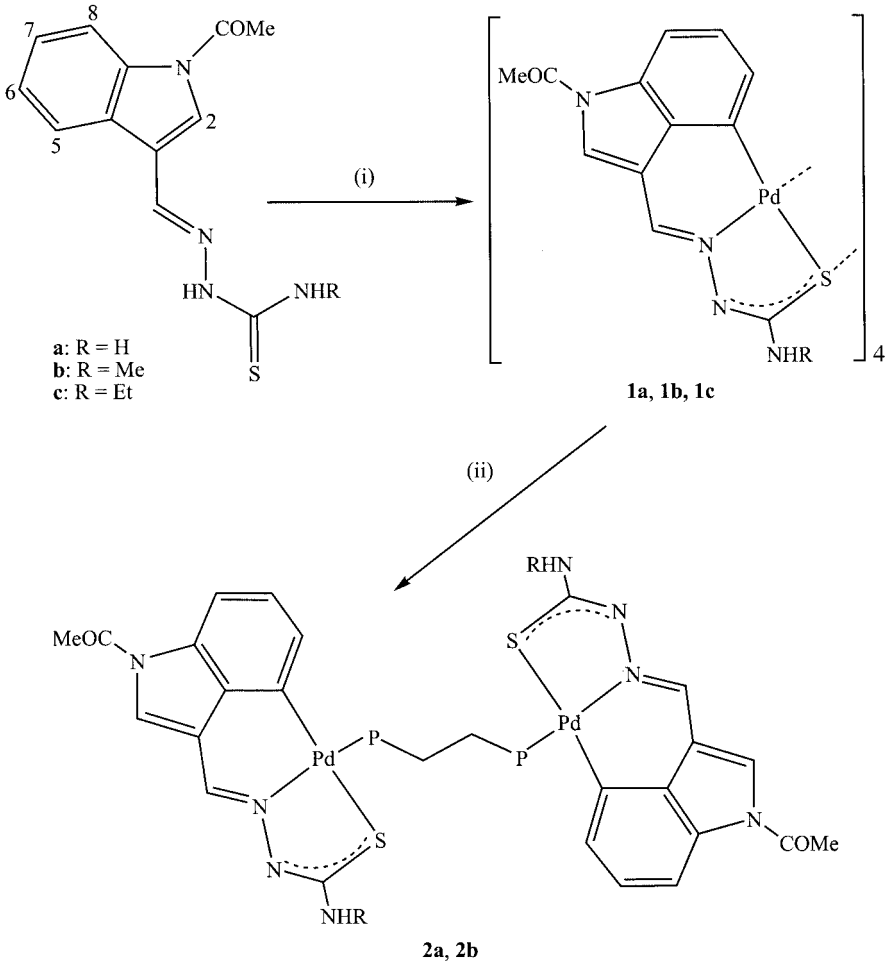


Scheme 1. (i) $K_2PdCl_4$/EtOH; (ii) $Ph_2P(CH_2)_2PPh_2$/$Me_2CO$, 1:2.

 © 2006 Wiley-VCH Verlag GmbH & Co. KGaA, Weinheim 

carbon atom. Thus, a singlet at $\delta$ = 7.41 (**1a**), 7.41 (**1b**) and 7.68 ppm (**1c**) was assigned to the pyrrole C(2)*H* proton resonance, which is shifted to lower frequency with respect to its position in the spectra of the free ligands ($\delta \approx$ 8.3 ppm). The complex ABCD spin system due to the H(5)–H(8) protons that is seen for the ligands is absent in the spectra of the complexes, where it gives way to a simple three-proton first-order spectrum that can be unambiguously assigned and clearly indicates loss of the H5 proton upon metalation. Thus, two doublets at around $\delta$ = 8.6 and 8.4–8.0 ppm were ascribed to the H6 and H8 protons, respectively, whereas a triplet at around $\delta$ = 7.1 ppm was assigned to the H7 resonance (see Exp. Sect.). Also relevant is the absence of the signal for the NH group and the high-field shift of the HC=N resonance by about 0.4–0.9 ppm.[21,22] Only one set of signals was detected in the $^1$H NMR spectra, thereby precluding mixtures of compounds bearing different metalated carbons and confirming the strong steric hindrance exerted by the C(O)Me group, which selectively directs the palladium atom towards the phenyl C5 atom.

### Crystal and Molecular Structure of 1b

Suitable crystals of complex **1b** were grown by slowly evaporating a DMSO solution. Crystal data are given in the Exp. Sect. An ORTEP illustration of the structure, with selected interatomic distances and angles, is shown in Figure 1.

The asymmetric unit of **1b** consists of two molecules of compound **1b** and eight DMSO solvent molecules. Although the overall structure for each molecule is only approximately $S_4$-symmetric, the four cyclometalated moieties are not symmetry-related. Nevertheless, discussion shall be limited to the data pertaining to one fourth of the molecule, i.e., the one involving Pd(1A); the structural data for the other three molecular units are very similar. The palladium atom exhibits a slightly distorted square-planar geometry with a central nucleus comprised of an eight-membered ring of alternating palladium and sulfur atoms, which adopts a boat conformation. Each palladium atom is bonded to four different donor atoms: three pertaining to a terdentate thiosemicarbazone, namely the aryl C(1) carbon, the imine N(2) nitrogen, and the thioamide S(1) sulfur atom, with a fourth donor being a sulfur atom S(1B) from a neighboring ligand. The plane formed by the ligating atoms at palladium [C(1A), N(2A), S(1A), S(1B): plane 1] is essentially planar (rms = 0.0132), with slight displacement of the metal atom by ±0.0395 Å. The remaining planes at palladium: the metallacycle [Pd(1A), C(1A), C(6A), C(10A), C(11A), N(2A): plane 2], the coordination ring [Pd(1A), N(2A), N(3A), C(12A), S(1A): plane 3], and the metalated phenyl ring [C(1A), C(2A), C(3A), C(4A), C(5A), C(6A): plane 4] are nearly coplanar [angles between planes 1 and 2 = 1.60(0.08)°, 1 and 3 = 1.13(0.08)°, 1 and 4 = 1.35(0.10)°, 2 and 3 = 2.70(0.08)°, 2 and 4 = 2.80(0.12)°, and 3 and 4 = 1.23(0.11)°]. All bond lengths are in their typical ranges, and the S(1A)–C(12A) [1.765(8) Å] and N(3A)–C(12A) bond lengths [1.299(7) Å] are consistent with increased single- and double-bond character, respectively. The Pd(1A)–S(1A) bond [2.3380(14) Å] is longer than the Pd(1A)–S(1B) bond [2.3208(13) Å], thus confirming the greater *trans* influence of the phenyl carbon as compared to the imine nitrogen atom. The Pd(1A)–C(1A) bond [2.021(5) Å] is shorter than the expected value of 2.081 Å,[23] probably due to partial multiple-bond character.[11,24] The Pd(1)–N(1) bond [2.064(4) Å] is longer than previous values found in related complexes (sum of the covalent radii for palladium and nitrogen: 2.01 Å[10]), due not only to the *trans* influence of the sulfur atom but also to the greater size of the met-

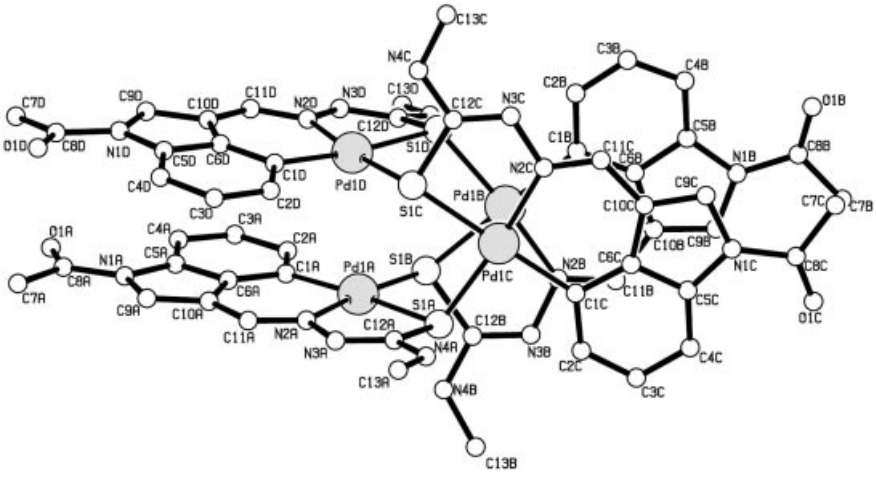


Figure 1. Molecular structure of **1b**, with labelling scheme. Hydrogen atoms have been omitted for clarity. Selected bond lengths and angles: Pd(1A)–C(1A) 2.021(5), Pd(1A)–N(2A) 2.064(4), Pd(1A)–S(1B) 2.3208(13), Pd(1A)–S(1A) 2.3380(14), S(1A)–C(12A) 1.749(6), N(3A)–C(12A) 1.299(7), N(3A)–N(2A) 1.439(5), N(2A)–C(11A) 1.292(6), C(1A)–C(6A) 1.390(6), C(11A)–C(10A) 1.410(7), C(10A)–C(6A) 1.457(6); C(1A)–Pd(1A)–N(2A) 94.27(18), C(1A)–Pd(1A)–N(2A) 94.27(18), N(2A)–Pd(1A)–S(1B) 173.23(12), C(1A)–Pd(1A)–S(1A) 176.29(14), N(2A)–Pd(1A)–S(1A) 83.45(12), S(1B)–Pd(1A)–S(1A) 89.92(5), C(6A)–C(1A)–Pd(1A) 118.7(4), C(1A)–C(6A)–C(10A) 130.4(5), C(11A)–C(10A)–C(6A) 125.2(4), N(2A)–C(11A)–C(10A) 123.5(5), C(11A)–N(2A)–N(3A) 112.1(4), C(11A)–N(2A)–Pd(1A) 128.0(4), N(3A)–N(2A)–Pd(1A) 119.9(3), C(12A)–N(3A)–N(2A) 113.6(4), N(3A)–C(12A)–S(1A) 127.2(4), C(12A)–S(1A)–Pd(1A) 95.4(2).

 © 2006 Wiley-VCH Verlag GmbH & Co. KGaA, Weinheim 

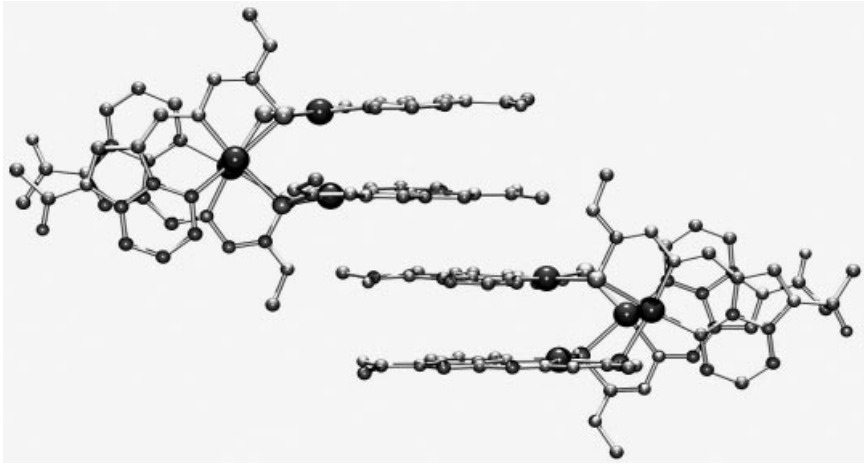

Figure 2. Packing diagram of compound **1b** showing the parallel arrangement of the cyclometalated units.

alated ring in the present compound. The angles between adjacent atoms in the coordination sphere are close to the expected value of 90°. However, as opposed to previous results where the C–Pd–N bite angle was less than 90°, due to formation of a five-membered metallacycle,[25,26] the six-membered ring in the present case allows a larger bite of the *C*,*N* chelate, thereby relieving strain on the angle at the metal; consequently, the C(1A)–Pd(1A)–N(1A) angle is 94.27°. On the other hand, inspection of the N(2A)–Pd(1A)–S(1A) bite angle of the five-membered Pd–N–N–C–S ring shows a similar value to that observed earlier in related complexes, with a value of 83.45°. The Pd–Pd bond lengths across parallel sets of cyclometalated moieties, which are in the range 3.8–4.1 Å, preclude any interaction between the metal atoms.

Two noteworthy observations regarding the structure are that pairs of metalated units are fixed in a nearly co-planar parallel mode (angle between planes of about 3.2°, with groups of parallel units separated by about 3.6 Å), and at an angle of 43° to the *a* axis (see Figure 2), thus indicating a possible weak π-stacking with the pyrrole rings set in an alternating disposition (see Figure 2).

### Reactivity of the Complexes

Reactions of **1a** and **1b** with $Ph_2P(CH_2)_2PPh_2$ (dppe) were tested in order to corroborate the behavior observed by us in related compounds. Thus, treatment of **1a** and **1b** with $Ph_2P(CH_2)_2PPh_2$ in a 1:2 molar ratio gave compounds [{Pd[1-(COMe)-3-[C(H)=NN=C(S)NHR]$C_8H_4N$]}$_2$(μ-$Ph_2P(CH_2)_2PPh_2$)] (R = H **2a**, Me **2b**) as pure, air-stable solids, which were fully characterized (Scheme 1). The $^1$H NMR spectra show a signal at $\delta$ = 8.79 (**2a**) and 8.32 ppm (**2b**), shifted to higher frequency with respect to the corresponding tetramers, which was assigned to the HC=N resonance. It appears as a doublet owing to coupling to the phosphorus nucleus. The H6 resonance [$\delta$ = 6.11 (**2a**) and 6.11 ppm (**2b**)] is shifted to lower frequency by about 1.5 ppm with respect to the parent complexes owing to shielding by the phosphane phenyl rings, in accordance with a phosphorus *trans* to nitrogen. The $^{31}$P NMR resonance is a singlet at $\delta$ = 70.41 (**2a**) and 70.34 ppm (**2b**), thus showing the equivalence of the two $^{31}$P nuclei. The $^{31}$P chemical shift values are also consistent with a phosphorus *trans* to nitrogen.[27–30]

## Conclusions

We have shown that thiosemicarbazones derived from condensed systems, such as indole, may behave as terdentate [C,N,S] pincer ligands in a cyclometalation reaction with palladium salts to give new tetranuclear species, which have been fully characterized in solution, as has one compound in the solid state. From a structural point of view they are closely related to similar systems reported by us previously, although in the present case the condensed rings seem to favor π stacking of the molecules in the unit cell. An added novelty to these compounds is the formation of a six-membered metallacycle, the first example with thiosemicarbazones, which is induced by the presence of bulky groups that hinder formation of the more common, and stable, five-membered metalated ring.

## Experimental Section

**General Remarks:** Solvents were purified by standard methods.[31] All chemicals were reagent grade. $K_2PdCl_4$ was purchased from Alfa Products and 1,2-bis(diphenylphosphanyl)ethane (dppe) from Aldrich-Chemie. Microanalyses were carried out at the Servicio de Análisis Elemental at the Universidad de Santiago using a Carlo Erba Elemental Analyzer (model 1108). IR spectra were recorded as Nujol mulls or KBr discs with a Perkin–Elmer 1330 or a Mattson spectrophotometer. NMR spectra were obtained for solutions in [$D_6$]DMSO with Bruker WM-250 and AMX-300 spectrometers and are referenced to $SiMe_4$ ($^1$H) or 85% $H_3PO_4$ ($^{31}$P{$^1$H}). All chemical shifts are reported downfield from standards. The FAB mass spectra were recorded with a Fisons Quatro mass spectrometer with a Cs ion gun; 3-nitrobenzyl alcohol was used as the matrix.

**Synthesis of 1-(COMe)-3-[C(H)=NN(H)C(=S)$NH_2$]$C_8H_5N$ (a):** 1-Acetyl-3-indolecarboxaldehyde (411 mg, 0.002 mol) and hydrochlo-

 © 2006 Wiley-VCH Verlag GmbH & Co. KGaA, Weinheim 

ric acid (35%, 0.6 mL) were added to a suspension of thiosemicarbazide (200 mg, 0.002 mol) in water (25 mL) to give a clear solution, which was stirred at room temperature for 4 h. The white solid that precipitated was filtered off, washed with cold water, and dried in vacuo. Yield: 497 mg (87%). $C_{12}H_{12}N_4OS$ (260.32): calcd. C 55.4, H 4.7, N 21.5, S 12.3; found C 55.5, H 4.7, N 21.6, S 12.4. IR: ν(N–H) 3388 m, 3132 m $cm^{-1}$; ν(C=O) 1709 s; ν(C=N) 1617 s; ν(C=S) 838 m. $^1H$ NMR ([D$_6$]DMSO): δ = 11.48 (s, 1 H, NH), 8.35 (s, 1 H, H2), 8.34 (m, 2 H, H5,H8), 8.30 (s, 1 H, *H*C=N), 8.24, 7.61 (br., 2 H, N$H_2$), 7.36 (m, 2 H, H6, H7), 2.68 ppm (s, 3 H, COMe).

Thiosemicarbazones **b** and **c** were prepared following a similar procedure.

**1-(COMe)-3-[C(H)=NN(H)C(=S)NHMe]$C_8H_5N$ (b):** Yield: 480 mg (92%). $C_{13}H_{14}N_4OS$ (274.35): calcd. C 56.9, H 5.1, N 20.4, S 11.7; found C 56.7, H 5.0, N 20.6, S 11.8. IR: ν(N–H) 3289 m, 3129 m $cm^{-1}$; ν(C=O) 1715 s; ν(C=N) 1612 s; ν(C=S) 823 m. $^1H$ NMR ([D$_6$]DMSO): δ = 11.50 (s, 1 H, NH), 8.37 (m, 2 H, H5,H8), 8.33 (s, 1 H, H2), 8.30 (s, 1 H, *H*C=N), 8.06 (br., 1 H, N*H*Me), 7.39 (m, 2 H, H6, H7), 3.08 (d, $^3J_{H,H}$ = 4.4 Hz, 3 H, NH*Me*), 2.68 ppm (s, 3 H, COMe).

**1-(COMe)-3-[C(H)=NN(H)C(=S)NHEt]$C_8H_5N$ (c):** Yield: 431 mg (89%). $C_{14}H_{16}N_4OS$ (288.37): calcd. C 55.8, H 5.6, N 19.4, S 11.1; found C 55.6, H 5.5, N 19.3, S 11.0. IR: ν(N–H) 3372 m, 3140 m $cm^{-1}$; ν(C=O) 1719 s; ν(C=N) 1615 s; ν(C=S) 831 m. $^1H$ NMR ([D$_6$]DMSO): δ = 11.45 (s, 1 H, NH), 8.36 (m, 2 H, H5, H8), 8.33 (s, 1 H, H2), 8.30 (s, 1 H, *H*C=N), 8.10 (br., 1 H, N*H*Et), 7.40 (m, 2 H, H6, H7), 3.65 (m, 2 H, NH*CH$_2$*CH$_3$), 2.67 (s, 3 H, COMe), 1.19 ppm (t, $^3J_{H,H}$ = 7.1 Hz, 3 H, NH CH$_2$*CH$_3$*).

**Preparation of 1a:** Ethanol (40 mL) was added to a stirred solution of $K_2PdCl_4$ (100 mg, 0.306 mmol) in water (6 mL) and the fine yellow suspension obtained was treated with **a** (80 mg, 0.306 mmol). The mixture was stirred for 24 h at room temperature. The brown precipitate was filtered off, washed with ethanol, and dried in vacuo. Yield: 264 mg (59%). $C_{48}H_{40}N_{16}O_4Pd_4S_4$ (1458.9): calcd. C 39.5, H 2.8, N 15.4, S 8.8; found C 39.8, H 2.8, N 15.2, S 8.7. IR: ν(N–H) 3331 m $cm^{-1}$; ν(C=O) 1709 s; ν(C=N) 1604 m. $^1H$ NMR ([D$_6$]DMSO): δ = 8.66 (br., 1 H, H6), 8.41 (s, 1 H, H2), 8.24 and 7.61 (br., 2 H, N$H_2$), 7.98 (br., 1 H, H8), 7.44 (s, 1 H, *H*C=N), 7.13 (t, $^3J_{H7,H6}$ = $^3J_{H7,H8}$ = 7.8 Hz, 1 H, H7), 2.72 ppm (s, 3 H, COMe). FAB-MS: *m*/*z* 1458 $[M]^+$.

Compounds **1b** and **1c** were synthesized following a similar procedure.

**1b:** Yield: 342 mg (62%). $C_{52}H_{48}N_{16}O_4Pd_4S_4$ (1515.0): calcd. C 41.2, H 3.2, N 15.0, S 8.5; found C 40.9, H 3.2, N 15.2, S 8.6. IR: ν(N–H) 3394 m $cm^{-1}$; ν(C=O) 1710 s; ν(C=N) 1600 m. $^1H$ NMR ([D$_6$]DMSO): δ = 8.58 (d, $^3J_{H7,H6}$ = 8.0 Hz, 1 H, H6), 7.98 (d, $^3J_{H7,H8}$ = 8.0 Hz, 1 H, H8), 7.86 (s, 1 H, *H*C=N); 7.41 (s, 1 H, H2), 7.05 (t, $^3J_{H7,H6}$ = $^3J_{H7,H8}$ = 8.0 Hz, 1 H, H7), 6.20 (br., 2 H, N*H*Me), 2.85 (d, $^3J_{H,H}$ = 4.4 Hz, 3 H, NH*Me*), 2.55 ppm (s, 3 H, COMe). FAB-MS: *m*/*z* 1515 $[M]^+$.

**1c:** Yield: 300 mg (55%). $C_{56}H_{56}N_{16}O_4Pd_4S_4$ (1571.10): calcd. C 42.8, H 3.6, N 14.3, S 8.2; found C 43.0, H 3.6, N 14.2, S 8.1. IR: ν(N–H) 3359 m $cm^{-1}$; ν(C=O) 1716 s; ν(C=N) 1603 m. $^1H$ NMR ($CDCl_3$): δ = 8.63 (d, $^3J_{H7,H6}$ = 8.1 Hz, 1 H, H6), 8.41 (d, $^3J_{H7,H8}$ = 8.1 Hz, 1 H, H8), 7.68 (s, 1 H, H2), 6.79 (t, $^3J_{H7,H6}$ = $^3J_{H7,H8}$ = 8.1 Hz, 1 H, H7), 6.33 (s, 1 H, *H*C=N), 4.83 (br., 2 H, N*H*Et), 3.39 (m, 2 H, NH*CH$_2$*CH$_3$), 2.76 (s, 3 H, COMe), 0.88 ppm (t, $^3J_{H,H}$ = 6.7 Hz, 3 H, NH CH$_2$*CH$_3$*). FAB-MS: *m*/*z* 1571 $[M]^+$.

**Complex 2a:** 1,2-Bis(diphenylphosphanyl)ethane (11 mg, 0.028 mmol) was added to a suspension of complex **1a** (20 mg, 0.014 mmol) in acetone (15 mL). The mixture was stirred for 3 h and the resulting orange solid filtered off and dried. Yield: 23.5 mg (76%). $C_{50}H_{44}N_8O_2P_2Pd_2S_2$ (1127.9): calcd. C 53.3, H 3.9, N 9.9, S 5.7; found C 53.1, H 4.0, N 9.8, S 5.8. IR: ν(N–H) 3344 m $cm^{-1}$; ν(C=O) 1714 s; ν(C=N) 1607 m. $^1H$ NMR ([D$_6$]DMSO): δ = 8.96 (s, 1 H, H2), 8.79 (d, $J_{H,P}$ = 2.7 Hz, 1 H, *H*C=N), 8.25 (d, $^3J_{H7,H8}$ = 8.4 Hz, 1 H, H8), 7.09 (t, 1 H, H7), 6.11 (d, $^3J_{H7,H6}$ = 8.4 Hz, 1 H, H6), 2.66 ppm (s, 3 H, COMe). $^{31}P\{^1H\}$ NMR ([D$_6$]DMSO): δ = 70.41 ppm (s). FAB-MS: *m*/*z* 1128 $[M]^+$.

Compound **2b** was synthesized following a similar procedure.

**2b:** Yield: 23.8 mg (78%). $C_{52}H_{48}N_8O_2P_2Pd_2S_2$ (1155.9): calcd. C 54.0, H 4.2, N 9.7, S 5.6; found C 53.8, H 4.1, N 9.8, S 5.5. IR: ν(N–H) 3375 m $cm^{-1}$; ν(C=O) 1710 s; ν(C=N) 1599 m. $^1H$ NMR ([D$_6$]DMSO): δ = 8.90 (s, 1 H, H2), 8.32 (d, $J_{H,P}$ = 2.7 Hz, 1 H, *H*C=N), 8.25 (d, $^3J_{H7,H8}$ = 8.8 Hz, 1 H, H8), 6.83 (t, 1 H, H7), 6.21 (br., 2 H, N*H*Me), 6.11 (d, $^3J_{H7,H6}$ = 8.8 Hz, 1 H, H6), 2.74 (s, 3 H, COMe), 2.50 ppm (d, $^3J_{H,H}$ = 4.4 Hz, 3 H, NH*Me*). $^{31}P\{^1H\}$ NMR ([D$_6$]DMSO): δ = 70.34 ppm (s). FAB-MS: *m*/*z* 1156 $[M]^+$.

**X-ray Crystallographic Study:** A single crystal of complex **1b** was mounted on a glass fiber and transferred to the diffractometer. Three-dimensional, room temperature X-ray data were collected on a Bruker SMART CCD diffractometer by the ω-scan method using graphite-monochromated Mo-$K_\alpha$ radiation (see Table 1 for details). All the measured reflections were corrected for Lorentz and polarization effects and for absorption by semi-empirical methods based on symmetry-equivalent and repeated reflections ($T_{max.}/T_{min.}$ = 0.816/0.587). The structure was solved by direct methods and refined by full-matrix least-squares on $F^2$. Hydrogen atoms were included in calculated positions and refined in a riding mode. The structure contains eight symmetry-related voids of 37 $Å^3$ containing unresolvable solven; this was treated using the squeeze method, which lowered the $R_1$ value by about 25%.[32] Refinement converged at a final $R$ = 0.0827 (observed data, $F$) and $wR_2$ = 0.1128

Table 1. Crystal data and structure refinement for compound **1b**.

| | |
|---|---|
| Empirical formula | $C_{208}H_{176}N_{64}O_{16}Pd_{16}S_{16}$ |
| Formula weight | 6043.49 |
| Temperature | 293(2) K |
| Wavelength | 0.71073 Å |
| Crystal system | triclinic |
| Space group | $P\bar{1}$ |
| Unit cell dimensions | $a$ = 13.018(3) Å, α = 86.517(4)° |
| | $b$ = 21.501(5) Å, β = 88.051(4)° |
| | $c$ = 26.225(6) Å, γ = 86.305(4)° |
| Volume | 7308(3) $Å^3$ |
| $Z$ | 1 |
| Calculated density | 1.373 $Mg\,m^{-3}$ |
| Absorption coefficient | 1.130 $mm^{-1}$ |
| $F$(000) | 2992 |
| Crystal size | 0.65 × 0.40 × 0.18 $mm^3$ |
| Theta range for data collection | 0.95 to 26.43° |
| Limiting indices | $-16 \le h \le 16$, |
| | $-26 \le k \le 26$, |
| | $0 \le l \le 32$ |
| Reflections collected/unique | 83071/29736 [$R$(int) = 0.0447] |
| Completeness to θ | 98.9% (26.43°) |
| Absorption correction | Multi-scan |
| Refinement method | Full-matrix least-squares on $F^2$ |
| Data/restraints/parameters | 29736/0/1457 |
| Goodness-of-fit on $F^2$ | 1.016 |
| Final $R$ indices [$I > 2\sigma(I)$] | $R_1$ = 0.0404, $wR_2$ = 0.1005 |
| $R$ indices (all data) | $R_1$ = 0.0827, $wR_2$ = 0.1128 |
| Largest diff. peak and hole | 0.900 and –0.681 e $Å^{-3}$ |

 © 2006 Wiley-VCH Verlag GmbH & Co. KGaA, Weinheim 

(all unique data, $F^2$), with allowance for thermal anisotropy of all non-hydrogen atoms. Minimum and maximum final electron density –0.681 and 0.900 e Å$^{-3}$. The structure solution and refinement were carried out using the program package SHELX-97.[33]

CCDC-291523 contains the supplementary crystallographic data for this paper. These data can be obtained free of charge from The Cambridge Crystallographic Data Center via www.ccdc.cam.ac.uk/data_request/cif.

## Acknowledgments

We thank the Xunta de Galicia, Spain (project PGIDT99PXI20907B) and the DGES (grant no. PB98-0638-C02-01/02) for financial support.

[1] S. Trofimenko, *Inorg. Chem.* **1973**, *12*, 1215–1221.
[2] M. I. Bruce, *Angew. Chem. Int. Ed. Engl.* **1977**, *16*, 73–86.
[3] a) I. Omae, *Chem. Rev.* **1979**, *79*, 287–321; b) I. Omae, *Coord. Chem. Rev.* **1988**, *83*, 137–167.
[4] I. Omae, *Organometallic Intramolecular-Coordination Compounds*, Elsevier, Amsterdam, **1986**.
[5] V. V. Dunina, O. A. Zalevskaya, V. M. Potapov, *Russ. Chem. Rev.* **1988**, *57*, 434–473.
[6] G. R. Newkome, W. E. Puckett, W. K. Gupta, G. E. Kiefer, *Chem. Rev.* **1986**, *86*, 451–489.
[7] a) J. Dupont, M. Pfeffer, J. Spencer, *Eur. J. Inorg. Chem.* **2001**, 1917–1927; b) J. Dupont, C. S. Consorti, J. Spencer, *Chem. Rev.* **2005**, *105*, 2527–2571.
[8] J. M. Vila, M. Gayoso, M. T. Pereira, A. Suárez, J. J. Fernández, J. M. Ortigueira, A. Fernández, M. López-Torres, *Trends Organomet. Chem.* **1997**, *2*, 21–37.
[9] J. M. Vila, M. Gayoso, M. T. Pereira, M. López-Torres, J. J. Fernández, J. M. Ortigueira, *J. Organomet. Chem.* **1997**, *532*, 171–180.
[10] J. M. Vila, M. T. Pereira, J. M. Ortigueira, D. Lata, M. López-Torres, J. J. Fernández, A. Fernández, H. Adams, *J. Organomet. Chem.* **1998**, *566*, 93–101.
[11] J. M. Vila, M. T. Pereira, J. M. Ortigueira, M. López-Torres, A. Castiñeiras, J. J. Fernández, A. Fernández, D. Lata, *J. Organomet. Chem.* **1998**, *556*, 21–30.
[12] C. Bianchini, G. Lenoble, W. Overhauser, S. Parisel, F. Zanobini, *Eur. J. Inorg. Chem.* **2005**, 4794–4800.
[13] a) I. Aiello, A. Crispini, M. Ghedini, M. La Deda, F. Barigelletti, *Inorg. Chim. Acta* **2000**, *308*, 121–128; b) M. Hugentobler, A. J. Klaus, H. Mettler, P. Rys, G. Wehrle, *Helv. Chim. Acta* **1982**, *65*, 1202–1211.
[14] J. M. Vila, A. Suárez, M. T. Pereira, E. Gayoso, M. Gayoso, *Polyhedron* **1987**, *6*, 1003–1007.
[15] T. S. Lobana, A. Sánchez, J. S. Casas, A. Castiñeiras, J. Sordo, M. S. García-Tasende, E. M. Vázquez-López, *J. Chem. Soc., Dalton Trans.* **1997**, 4289–4299.
[16] T. Kawamoto, Y. Kushi, *Chem. Lett.* **1992**, 1057–1058.
[17] T. Kawamoto, Y. Nagasawa, H. Kuma, Y. Kushi, *Inorg. Chem.* **1996**, *35*, 2427–2432.
[18] F. Hueso-Ureña, N. A. Illán-Cabeza, M. Moreno-Carretero, A. L. Peñas-Chamorro, R. Faure, *Inorg. Chem. Commun.* **1999**, *2*, 323–326.
[19] D. Kovala-Demertzi, A. Domopoulou, M. A. Demertzis, C. P. Raptopoulou, A. Terzis, *Polyhedron* **1994**, *13*, 1917–1925.
[20] D. X. West, J. S. Ives, G. A. Bain, A. E. Liberta, J. Valdés-Martínez, K. H. Ebert, S. Hernández-Ortega, *Polyhedron* **1997**, *16*, 1895–1905.
[21] H. Onoue, Y. Moritani, *J. Organomet. Chem.* **1972**, *43*, 431–436.
[22] Y. Ustynyuk, V. A. Chertov, J. V. Barinov, *J. Organomet. Chem.* **1971**, *29*, C53–C54.
[23] L. Pauling, *The Nature of the Chemical Bond*, 3rd ed., Cornell University Press, New York, **1960**.
[24] J. M. Vila, T. Pereira, J. M. Ortigueira, A. Amoedo, M. Graña, G. Alberdi, M. López-Torres, A. Fernandez, *J. Organomet. Chem.* **2002**, *663*, 239–248.
[25] J. M. Vila, M. T. Pereira, J. M. Ortigueira, M. Graña, D. Lata, A. Suárez, J. J. Fernández, A. Fernández, M. López-Torres, H. Adams, *J. Chem. Soc., Dalton Trans.* **1999**, 4193–4201.
[26] J. Martinez, M. T. Pereira, I. Buceta, G. Alberdi, A. Amoedo, J. J. Fernandez, M. Lopez-Torres, J. M. Vila, *Organometallics* **2003**, *22*, 5581–5584.
[27] P. S. Pregosin, R. W. Kuntz, *$^{31}$P and $^{13}$C NMR of Transition Metal Phosphine Complexes* (Eds.: P. Diehl, E. Fluck, R. Kosfeld), Springer, Berlin, **1979**.
[28] J. Albert, M. Gómez, J. Granell, J. Sales, *Organometallics* **1990**, *9*, 1405–1413.
[29] R. Bosque, J. Granell, J. Sales, M. Font-Bardía, X. Soláns, *J. Organomet. Chem.* **1993**, *453*, 147–154.
[30] J. Albert, J. Granell, J. Sales, M. Font-Bardía, X. Soláns, *Organometallics* **1995**, *14*, 1393–1404.
[31] D. D. Perrin, W. L. F. Armarego, D. L. Perrin, *Purification of Laboratory Chemicals*, 3rd ed., Pergamon, London, **1998**.
[32] P. van der Slius, A. L. Spek, *Acta Crystallogr., Sect. A* **1990**, *46*, 194–197.
[33] G. M Sheldrick, *SHELX-97*, *An Integrated System for Solving and Refining Crystal Structures from Diffraction Data*, University of Göttingen, Germany, **1997**.

Received: December 7, 2005
Published Online: June 6, 2006

 © 2006 Wiley-VCH Verlag GmbH & Co. KGaA, Weinheim 

DOI: 10.1002/ejic.200600070

# Synthesis, Structure and Magnetic Properties of a New Low-Spin Iron(III) Complex [$FeL_3$] {L = [$HNC(CH_3)]_2C(CN)$}

**Junichi Nishijo[a] and Nobuyuki Nishi*[a]**

**Keywords:** Iron / Magnetic properties / N ligands

High-temperature treatment of acetonitrile with $CaC_2$ and $FeCl_2$ afforded crystals of the new iron(III) $S = 1/2$ low-spin complexes [$FeL_3$]ROH (R = $CH_3$ or $C_2H_5$), whose crystal structures were determined by single-crystal X-ray structural analysis. The methanol complex consists of a one-dimensional arrangement of the iron moieties, while each methanol molecule is separated from each other by the complexes. On the other hand, the ethanol complex contains a two dimensional arrangement of the iron moieties and one dimensionally aligned ethanol molecules elongated perpendicular to the sheet. Because of the large difference in the inter-complex overlap patterns between the ligands, the two materials show quite different magnetic properties. The magnetism of the crystal containing ethanol is well described by the singlet–triplet model with the antiferromagnetic interaction $2J/k_B = -7.5$ K, while that containing methanol obeys the Curie law with a negligibly small Weiss temperature.

(© Wiley-VCH Verlag GmbH & Co. KGaA, 69451 Weinheim, Germany, 2006)

## Introduction

Transition-metal complexes of π-conjugated N-ligands have attracted much attention over the years. In these complexes, the strong coordination bonds with the lone pair of the nitrogen atoms bring the d-electrons of the transition metal and the π-electrons of the ligands close to each other, and the interaction between d- and π-electrons leads to several important properties, such as a modified reactivity of the center metal, high photon absorbance and efficient charge transfer. Previous studies with such complexes have revealed their usefulness as catalysts[1–7] and dye-sensitized solar cells.[8–10] From the viewpoint of molecule-based magnets, this kind of complex would offer a strong spin–spin interaction as the strong metal–nitrogen interaction brings about a high spin density at the nitrogen atom. On the other hand, it is known that the π-electrons can convey spin polarization from one side of the molecule to the other side through the π-conjugated system.[11–13] Because a π-conjugated N-ligand has both of these features, it is expected that transition-metal complexes based on these ligands would enable a strong, long-range spin–spin interaction.[14–18] Furthermore, the flat π-conjugated molecules tend to stack their molecular planes, which results in a large intermolecular orbital overlap and thus a strong intermolecular spin–spin interaction.[19,20]

The strong coordination bond is also essential to investigate the effect of the intermolecular arrangement on the magnetism. It is well known that the magnetism of molecule-based magnets largely depends on the intermolecular overlap patterns, and that some of them can be controlled by the absorption/desorption of solvent.[21–23] By using π-conjugated N ligands, the complex approximately keep its intra-complex structure thanks to the rigidness of the ligand and the strong coordination bonds, while the inter-complex arrangement is considerably rearranged upon changing the solvent molecules;[24,25] that is, we can investigate only the effect of the inter-complex arrangement.

Because of the features mentioned above, it is important to synthesize new transition-metal complexes of π-conjugated N-ligands. We decided to use the bidentate ligand 2-amino-3-cyanopent-2-en-4-imine (HL, Figure 1) for the following two reasons. First, its bidentate nature is promising to create magnetic complexes because they are likely to form stable coordination bonds like bipyridine. Secondly, the planer shape of the ligand and the protruding cyano group seem to ease the intermolecular orbital overlaps which causes inter-complex spin–spin interaction. However, although the structure of this ligand is attractive, its instability prevents the easy synthesis of complexes. Thus, although it was first synthesized more than 40 years ago,[26,27]

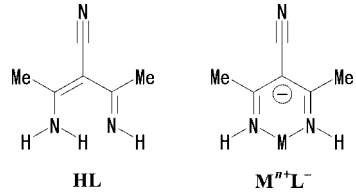


Figure 1. The molecular structure of 2-amino-3-cyanopent-2-en-4-imine (HL). The deprotonated form of the molecule behaves as a bidentate ligand ($M^{n+}L^-$).

[a] Institute for Molecular Science,
Nishigo-naka 38, Myodaiji, Okazaki 444-8585, Japan
E-mail: nishi@ims.ac.jp

 © 2006 Wiley-VCH Verlag GmbH & Co. KGaA, Weinheim 

up to the present time only one complex of Co and a few complexes of Ga, Al, and In with the deprotonated ligand ($L^-$) have been synthesized.[28–30] In this paper, we report new transition-metal complexes based on this ligand synthesized by an unconventional method, and report the remarkable solvent dependency of their structure and magnetism.

## Results and Discussion

### Synthesis

To obtain the transition-metal complex based on the ligand, we tried to develop a new synthesis method by using a strong base under water-free conditions. It is known that the ligand can be synthesized by the trimerization of acetonitrile molecules in the presence of a strong base, as shown in Scheme 1.[28–30] Furthermore, the strong base stabilizes the deprotonated form of the ligand and enables complex formation. Because the ligand is easily decomposed in the presence of water molecules,[27] the synthesis should be done under strictly water-free conditions. In light of these two conditions, calcium carbide is one of the most suitable reagents as a strong base because it is an easily acquired water-free base that is strong enough to deprotonate acetonitrile molecules. A stainless-steel airtight vessel is appropriate for the synthesis as this not only allows exclusion of water from the air but also enables the synthesis to be performed at high temperature, where the trimerization of acetonitrile is accelerated. Despite the water-sensitivity of the free ligand molecule, the complex [$FeL_3$] is stable even in air. It should be noted that vigorous stirring, a longer reaction time, or a higher reaction temperature lead only to carbon-encapsulated iron nanoparticles due to the reductive nature of $C_2^{2-}$.[31] This one-pot synthesis method gives the complex [$FeL_3$].

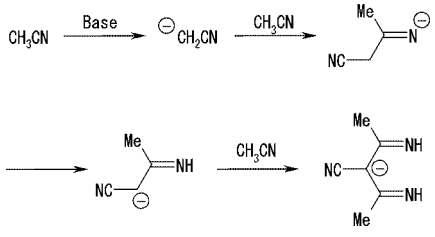


Scheme 1.

### Crystal Structures

The complex was obtained as a racemic crystal regardless of the solvent molecules. The unit cells of [$FeL_3$]$CH_3OH$ and [$FeL_3$]$C_2H_5OH$ contain two crystallographically equivalent Δ- and Λ-[$FeL_3$] and one Δ- and one Λ-[$FeL_3$] moieties, respectively. Selected bond lengths and angles, and the molecular structures of [$FeL_3$]ROH can be found in Tables 1 and 2, and Figures 2 and 3, respectively. The intra-complex structures are nearly identical regardless of the solvent molecules. Each complex consists of an iron atom and three chelating ligand molecules such that the iron atom is surrounded by the six nitrogen atoms of the ligands to form an octahedral $FeN_6$ chromophore. The six Fe–N bonds have similar lengths, and no Jahn–Teller distortion was observed at room temperature despite the low-spin $d^5$ configuration of iron(III), as evidenced by the small Curie constant (discussed later). The Fe–N bond lengths of [$FeL_3$]ROH range from 1.916(4) to 1.957(3) Å and are in reasonable agreement with the values for other iron complexes with Schiff-base-type ligands.[32,33] The intra-ligand bond lengths are close to those of other complexes of the $L^-$ ligand reported previously.[28–30] The C–N bond lengths, which range from 1.292(6) to 1.316(5) Å, and the π-conjugated C–C bond lengths, which range from 1.406(7) to 1.433(6) Å, indicate that the negative charges are delocalized over the π-conjugated system of the ligand. Because of this aromaticity, the six-membered chelate rings tend to be planar except for a small inflection at the coordinated nitrogen atoms. For example, the torsion angles of Fe1–N1–N2–C3, Fe1–N4–N5–C9, and Fe1–N8–N7–C15 in the [$FeL_3$]$CH_3OH$ crystal have values [172.74(13)°, 155.84(13)°, and 166.69(13)°, respectively] that are slightly smaller than 180°, while the ligand molecules keep its almost flat structure.

Table 1. Selected bond lengths [pm] and angles [°] for [$FeL_3$]-$CH_3OH$.

| | | | |
|---|---|---|---|
| Fe1–N1 | 192.3(3) | N8–C16 | 130.5(4) |
| Fe1–N2 | 192.4(3) | C2–C3 | 142.4(4) |
| Fe1–N4 | 192.6(3) | C3–C4 | 142.4(5) |
| Fe1–N5 | 193.8(3) | C3–C6 | 141.7(5) |
| Fe1–N7 | 195.7(3) | C8–C9 | 142.1(4) |
| Fe1–N8 | 193.0(3) | C9–C10 | 142.5(4) |
| N1–C2 | 130.0(4) | C9–C12 | 141.6(4) |
| N2–C4 | 130.1(4) | C14–C15 | 142.2(5) |
| N4–C8 | 130.5(4) | C15–C16 | 142.1(5) |
| N5–C10 | 130.6(4) | C15–C18 | 142.7(5) |
| N7–C14 | 129.8(4) | | |
| N1–Fe1–N7 | 177.82(11) | N1–Fe1–N2 | 90.80(12) |
| N2–Fe1–N5 | 178.81(12) | N4–Fe1–N5 | 88.17(12) |
| N4–Fe1–N8 | 177.67(12) | N7–Fe1–N8 | 87.96(13) |

Table 2. Selected bond lengths [pm] and angles [°] for [$FeL_3$]-$C_2H_5OH$.

| | | | |
|---|---|---|---|
| Fe1–N1 | 192.6(4) | N8–C15 | 131.4(6) |
| Fe1–N2 | 191.6(4) | C1–C2 | 142.4(6) |
| Fe1–N4 | 193.2(4) | C2–C3 | 142.8(6) |
| Fe1–N5 | 195.4(4) | C2–C6 | 142.4(6) |
| Fe1–N7 | 195.3(4) | C7–C8 | 142.2(6) |
| Fe1–N8 | 195.3(4) | C8–C9 | 141.8(7) |
| N1–C1 | 129.6(6) | C8–C12 | 142.3(6) |
| N2–C3 | 130.8(6) | C13–C14 | 143.5(7) |
| N4–C7 | 131.6(5) | C14–C15 | 140.6(7) |
| N5–C9 | 130.5(6) | C14–C18 | 143.3(6) |
| N7–C13 | 129.2(6) | | |
| N1–Fe1–N5 | 177.57(16) | N1–Fe1–N2 | 90.39(16) |
| N2–Fe1–N7 | 176.22(16) | N4–Fe1–N5 | 88.43(17) |
| N4–Fe1–N8 | 176.83(16) | N7–Fe1–N8 | 87.05(17) |

 © 2006 Wiley-VCH Verlag GmbH & Co. KGaA, Weinheim 

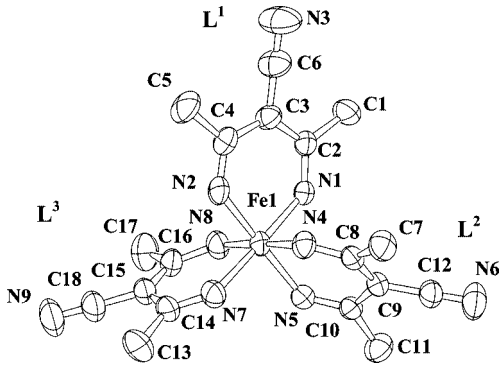


Figure 2. Thermal ellipsoid plot (50% probability) of $[FeL_3]$-$CH_3OH$. The labels $L^i$ identify the three crystallographically independent ligand molecules. A methanol molecule and hydrogen atoms have been omitted for clarity.

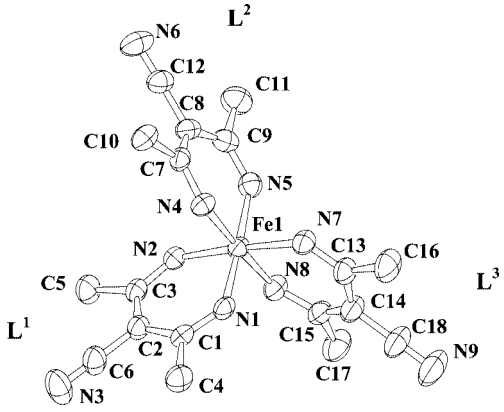


Figure 3. Thermal ellipsoid plot (50% probability) of $[FeL_3]$-$C_2H_5OH$. The labels $L^i$ identify the three ligand molecules. An ethanol molecule and hydrogen atoms have been omitted for clarity.

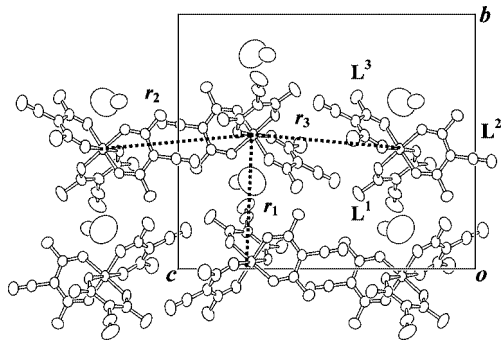


Figure 4. The crystal structure of $[FeL_3]CH_3OH$ viewed along the *a* axis. Hydrogen atoms have been omitted for clarity. The dotted lines indicate the short iron–iron distances (see text).

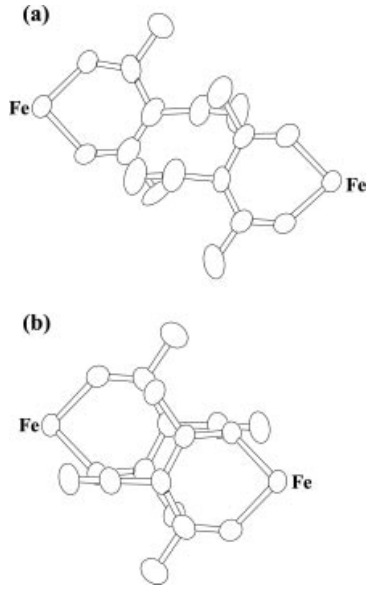


Figure 5. The two kinds of stacking modes between adjacent ligands viewed perpendicular to the six-membered chelate rings: a) Type A, b) Type B (see text). Hydrogen atoms have been omitted for clarify.

In contrast to the intra-complex structure, the inter-complex arrangement depends greatly on the solvent. In the crystal of $[FeL_3]CH_3OH$, each $[FeL_3]$ moiety has two short contacts with two adjacent complexes, as shown in Figure 4, and the ligands $L^2$ and $L^3$ face their counterparts in adjacent complexes. The complexes are connected to each other by these short ligand–ligand contacts and are arranged one-dimensionally parallel to the *c* axis. The cyano group of ligand $L^1$ is directed towards the hydroxy group of a neighboring methanol molecule. The stacking structures of $L^2$–$L^2$ and $L^3$–$L^3$ resemble each other. This stacking mode (type A) is shown in Figure 5 (a), where the cyano groups of the ligands are placed at the midpoints of the C–C bonds between the imine groups and methyl groups. In these contacts, the interatomic distance between the nitrogen atom of the cyano group and the carbon atom of the imine group is about 3.5 Å. In type-A stacking, the overlap between π-orbitals of the ligands is expected to be small due to the displacement of the two six-membered chelate rings, thus suggesting a weak spin–spin interaction between the complexes. The short iron–iron distances in the *bc* plane (Figure 4) are $r_1$ = 8.495(5), $r_2$ = 9.359(5), and $r_3$ = 9.337(5) Å, while that in the *a* direction is 8.099(5) Å.

The crystal structure of $[FeL_3]C_2H_5OH$ is characterized by a two-dimensional cage-like arrangement of the complexes and one-dimensionally aligned ethanol molecules. In the crystal, four complexes form a cage that encloses an ethanol molecule, as shown in Figure 6, and this cage-like structure spreads as a sheet in the *bc* plane. Each ligand in a sheet is close to a neighboring crystallographically equivalent ligand, and the stacking mode of the ligand pairs $L^1$–$L^1$ and $L^3$–$L^3$ is also classified as type A (see Figure 5), with an N–C interatomic contact of about 3.5 Å, while that of $L^2$–$L^2$ is of type B, with an interatomic distance of around 3.8 Å between the carbon atom of the cyano group and the carbon or nitrogen atom of the imine group. Although the interatomic distance of type B stacking is longer than that of type A, it is expected that the larger π-orbital overlap of type B stacking brings about a stronger spin–spin interaction than that of type A. The sheets of the cage-like structures are stacked along the *a* axis, where the adjacent sheets are weakly bonded by the inter-plane type A stacking of $L^2$

 © 2006 Wiley-VCH Verlag GmbH & Co. KGaA, Weinheim 

ligands. In short, one complex has two small intra-sheet overlaps (type A, $L^1$–$L^1$ and $L^3$–$L^3$), one small inter-sheet overlap (type A, $L^2$–$L^2$), and one large intra-sheet overlap (type B, $L^2$–$L^2$). The cavities of the cages are connected and form one-dimensional tunnel structures that are elongated parallel to the *a* axis; these are filled with ethanol molecules. The short iron–iron distances in the *bc* plane shown in Figure 6 are $r_1$ = 8.142(4), $r_2$ = 10.881(4), and $r_3$ = 9.337(4) Å, while that in the *a* direction is 8.195(3) Å. The shortest iron–iron distance in the crystal of $[FeL_3]C_2H_5OH$ is therefore slightly longer than that of $[FeL_3]CH_3OH$.

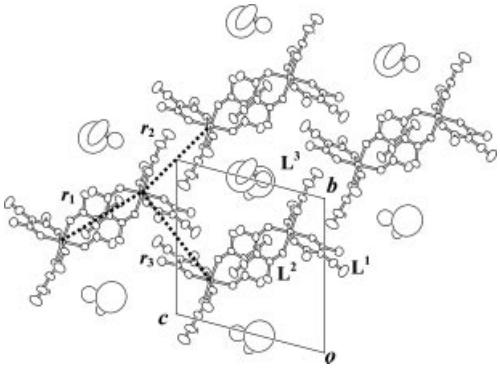


Figure 6. The crystal structure of $[FeL_3]C_2H_5OH$ viewed along the *a* axis. Hydrogen atoms have been omitted for clarify. The dotted lines indicate the short iron–iron distances (see text).

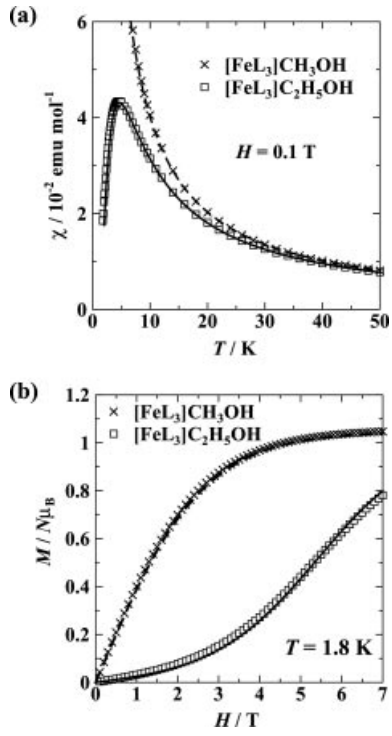


Figure 7. a) The magnetic susceptibilities and b) the reduced magnetization curves of $[FeL_3]ROH$. The dashed lines are the theoretical curves for the free $S$ = 1/2 spins having $g$ = 2.08, and the solid lines are the theoretical curves based on the singlet–triplet model with the values of $2J/k_B$ = –7.5 K and $g$ = 2.08 (see text).

## Magnetic Properties

The temperature dependencies of the magnetic susceptibilities, $\chi$, of $[FeL_3]ROH$ and the magnetization curves at 1.8 K are shown in Figure 7 (parts a and b), respectively. The magnetic susceptibility of $[FeL_3]CH_3OH$ follows the Curie–Weiss law in the whole temperature range, with a Curie constant, $C$, of 0.406 emu K mol$^{-1}$ and a negligibly small Weiss temperature, $\Theta$. The fact that $\Theta$ is almost zero indicates that the type A overlap of the ligands does not contribute to the spin–spin interaction due to the poor overlap of the π-orbitals. The observed value of $C$ roughly agrees with the spin-only value for a $S$ = 1/2 species (0.375), thereby indicating the low-spin nature of the iron(III). The small enhancement of $C$ from that of a free $S$ = 1/2 spin can be attributed to the slightly larger $g$ value predicted from the magnetization curve. The magnetization curve of $[FeL_3]CH_3OH$ is very close to the Brillouin curve of $S$ = 1/2 spins with a $g$ value of 2.08, which indicates that the inter-complex spin–spin interaction is negligible.

The magnetic susceptibility of $[FeL_3]C_2H_5OH$ can also be described by the Curie–Weiss law in the high-temperature region above 10 K ($C$ = 0.403 emu K mol$^{-1}$, $\Theta$ = –3.3 K). Below 10 K, $\chi$ reaches a peak at 4.6 K and then decreases rapidly with decreasing temperature. A linear extrapolation of $\chi$ to lower temperature gives $\chi$ = 0 at a finite temperature of 0.7 K, thus suggesting that the ground state of the spin system is a singlet. Despite the longer iron–iron distance and smaller spin density of $[FeL_3]C_2H_5OH$ relative to those of $[FeL_3]CH_3OH$, the inter-complex spin–spin interaction of $[FeL_3]C_2H_5OH$ is stronger than that of $[FeL_3]$-$CH_3OH$. This fact confirms that the spin–spin interaction is strongly dependent on the inter-ligand overlap of the π-orbitals, as predicted from the crystal structures, as in some previously reported materials, where ligand–ligand contacts play important roles.[34,35] Based on the crystal structure, where only one strong inter-complex interaction is expected, a singlet–triplet model is the appropriate for the spin system of $[FeL_3]C_2H_5OH$. In this model, the spin Hamiltonian, $H$, is described as shown in Equation (1), where $J$, $S_i$, $g$, $\mu_B$, and $H_{ex}$ are the interaction between spins, the spin values, the $g$ value, the Bohr magneton, and the external magnetic field, respectively.

$$H = -2JS_1 \cdot S_2 + g\mu_B \sum_i S_i \cdot H_{ex} \quad (1)$$

By using this spin Hamiltonian, the partition function $Z$ [Equation (2)], the free energy $F$ [Equation (3)], the magnetization, $M$, and $\chi$ can be calculated, as shown in Equations (4) and (5), where $N$ and $k_B$ are the Avogadro number and the Boltzmann constant, respectively. The best fit, shown as solid lines in parts a and b of Figures 7 is nearly indistinguishable from the observed values with the adjustable parameters of $2J/k_B$ = –7.5 K and $g$ = 2.08. This consistency offers evidence that only the type B overlap can bring about a strong spin–spin interaction.

 © 2006 Wiley-VCH Verlag GmbH & Co. KGaA, Weinheim 

$$Z = T_r \exp(-H/k_B T) \quad (2)$$

$$F = -k_B T \cdot \ln Z \quad (3)$$

$$M(H_{ex},T) = -\frac{\partial F}{\partial H_{ex}} = \frac{Ng\mu_B \exp(2J/k_B T)\sinh(g\mu_B H_{ex}/k_B T)}{1+\exp(2J/k_B T)[1+2\cosh(g\mu_B H_{ex}/k_B T)]} \quad (4)$$

$$\chi(T) = \left(\frac{\partial M}{\partial H_{ex}}\right)_{H_{ex}=0} = \frac{Ng^2\mu_B{}^2}{k_B T}\frac{1}{3+\exp(-2J/k_B T)} \quad (5)$$

## Conclusions

Crystals of the new iron(III) complex $[FeL_3]$ containing ROH (R = $CH_3$ and $C_2H_5$) have been obtained. The crystal structure of $[FeL_3]CH_3OH$ is characterized by a one-dimensional arrangement of the $[FeL_3]$ moieties where the cyano groups are placed above the methyl groups of adjacent moieties. Because of the small overlap between the π-orbitals of the ligands, the inter-complex spin–spin interaction of $[FeL_3]CH_3OH$ is weak, as evidenced by the almost zero value of the Weiss temperature and the absence of a magnetic transition. On the other hand, the crystal of $[FeL_3]$-$C_2H_5OH$ consists of a two-dimensional sheet-like arrangement of $[FeL_3]$ moieties and one-dimensionally aligned ethanol molecules elongated perpendicular to the sheets. In this structure, $[FeL_3]$ moieties are dimerized by the large inter-ligand overlap and a cyano group is placed above an imine group of the neighboring complex. Owing to the dimerization of the complexes, the magnetic properties of $[FeL_3]C_2H_5OH$ are consistent with a singlet–triplet model with the inter-complex spin–spin interaction $2J/k_B$ = –7.5 K.

## Experimental Section

**Materials and Measurements:** $CaC_2$ (Kojundo Chemical Lab. Co.) was used after ball-milling under argon for 12 h, while $FeCl_2$ and anhydrous acetonitrile were used as supplied. IR spectra were recorded with a Shimadzu FTIR-8600PC for KBr disks. Elemental analysis was performed with a Yanaco MT-6. Single-crystal X-ray diffraction data were collected with a Rigaku AFC7R MERCURY CCD diffractometer with graphite-monochromated Mo-$K_\alpha$ radiation ($\lambda$ = 0.71069 Å) and a rotating anode generator (50 kV, 100 mA). The structures were solved by direct methods (SHELXS-97), then refined with full-matrix least-squares (SHELXL-97).[36] Graphics were produced with ORTEP-III.[37] The positions of hydrogen atoms, except N-H groups, were refined with a "riding" model with $U_{iso}$ = 1.2 $U_{eq}$ of the connected non-hydrogen atom or as ideal $CH_3$ groups with $U_{iso}$ = 1.5 $U_{eq}$. The crystal data of $[FeL_3]$-ROH are shown in Table 3.

Table 3. Crystallographic data for $[FeL_3]$ROH.

| | $[FeL_3]CH_3OH$ | $[FeL_3]C_2H_5OH$ |
|---|---|---|
| Crystal system | monoclinic | triclinic |
| Space group | $P2_1/n$ | $P\bar{1}$ |
| $a$ [Å] | 8.099(5) | 8.195(2) |
| $b$ [Å] | 15.576(5) | 12.736(3) |
| $c$ [Å] | 18.563(5) | 13.404(2) |
| $\alpha$ [°] | 90 | 73.149(2) |
| $\beta$ [°] | 79.690(5) | 68.550(2) |
| $\gamma$ [°] | 90 | 81.190(3) |
| $V$ [Å$^3$] | 2303.9(17) | 1244.4(5) |
| Z | 4 | 2 |
| $\rho$ | 1.310 | 1.127 |
| $F$(000) | 956 | 442 |
| Crystal size [mm] | 0.53×0.44×0.38 | 0.08×0.07×0.05 |
| Temperature [K] | 296.15 | 296.16 |
| Absorption correction | numerical | numerical |
| Index range ($h$,$k$,$l$) | $-9 \le h \le 10$ | $-9 \le h \le 10$ |
| | $-16 \le k \le 20$ | $-15 \le k \le 16$ |
| | $-23 \le l \le 21$ | $-17 \le l \le 15$ |
| No. of reflections | 21966 | 6034 |
| No. of unique reflections | 5144 | 4384 |
| No. of reflections [$F > 2\sigma(F)$] | 4791 | 3820 |
| Residuals [$I > 2\sigma(I)$] | $R_1$ = 0.0696 | $R_1$ = 0.0715 |
| | $wR_2$ = 0.1678 | $wR_2$ = 0.2090 |
| Residuals (all data) | $R_1$ = 0.0742 | $R_1$ = 0.0823 |
| | $wR_2$ = 0.1710 | $wR_2$ = 0.2183 |

CCDC-295169 and -295168 contain the supplementary crystallographic data for this paper. These data can be obtained free of charge from The Cambridge Crystallographic Data Centre via www.ccdc.cam.ac.uk/data_request/cif.

A Quantum Design MPMS-XL SQUID magnetometer was used to measure DC magnetic susceptibilities of $[FeL_3]$ROH between 300 and 1.8 K in a 0.1-T static magnetic field. The core temperature independent diamagnetic susceptibility was subtracted from the experimental values based on Pascal's constants for all constituent atoms.

**Reaction:** In a water- and oxygen-free glove box, $CaC_2$ (449 mg, 7 mmol) and $FeCl_2$ (634 mg, 5 mmol) were suspended in anhydrous acetonitrile (300 mL). The suspension was sealed in a SUS-316 stainless-steel high-temperature, high-pressure reactor (TPR-1, Taiatsu techno, Tokyo, Japan), then the solution was heated to 240 °C at around 3 MPa for 12 h with gentle stirring. After cooling to room temperature, the solution was exposed to air and absolute methanol (100 mL) was added. Vigorous stirring of the solution for 20 min under air resulted in a deep-blue solution, which was then filtered. The residue was extracted with methanol, and the extract was added to the filtrate. The solution was dried in vacuo, then the precipitate was washed with toluene (200 mL) and extracted with dichloromethane (300 mL). The solution was dried in vacuo again. The blue powder was dissolved in hot methanol (20 mL), then cooled to –10 °C. The purple crystalline product was collected by filtration. Recrystallization from hot methanol gave 85 mg of $[FeL_3]CH_3OH$ (4%) as reddish-purple block crystals. $C_{19}H_{28}FeN_9O$ (454.34): calcd. C 50.23, H 6.21, N 27.75; found C 50.18, H 6.40 N 27.61. IR (KBr): ν(N–H) = 3280 cm$^{-1}$; $\nu_2$(C≡N) = 2177; ν(C=N) = 1582 cm$^{-1}$. A single crystal of $[FeL_3]C_2H_5OH$ was obtained as follows. Pure $[FeL_3]CH_3OH$ crystals were dissolved in a mixture of THF (30 mL) and ethanol (10 mL). The solution was slowly evaporated at ambient pressure, and subsequent filtration gave small, deep-purple crystals. $C_{20}H_{30}FeN_9O$ (468.37): calcd. C 51.29, H 6.46, N 26.92; found C 51.23, H 6.25 N 26.99. IR (KBr): ν(N–H) = 3284 cm$^{-1}$; ν(C≡N) = 2182; ν(C=N) = 1579 cm$^{-1}$.

 © 2006 Wiley-VCH Verlag GmbH & Co. KGaA, Weinheim 

## Acknowledgments

This work was supported by a program entitled "Research for the Future of Japan Society of the Promotion of Science" (RFTF: 99P01201). Part of this work was also supported by a Grant-in-Aid for Scientific Research (13NP0201) and the "Nanotechnology Support Project" of the Ministry of Education, Culture, Sports, Science and Technology (MEXT), Japan.

[1] D. E. De Vos, M. Dams, B. F. Sels, P. A. Jacobs, *Chem. Rev.* **2002**, *102*, 3615–3640 and references cited therein.
[2] R. Belzen, R. A. Klein, H. Kooijman, N. Veldman, A. L. Spek, C. J. Elsevier, *Organometallics* **1998**, *17*, 1812–1825.
[3] T. E. Patten, C. Troeltzsch, M. M. Olmstead, *Inorg. Chem.* **2005**, *44*, 9197–9206.
[4] T. Okada, N. Arimura, C. Ono, M. Yuasa, *Electrochim. Acta* **2005**, *51*, 1130–1139.
[5] S.-I. Murahashi, S. Noji, T. Hirabayashi, N. Komiya, *Tetrahedron: Asymmetry* **2005**, *16*, 3527–3535.
[6] I. Luobeznova, M. Raizman, I. Goldberg, Z. Gross, *Inorg. Chem.* **2006**, *45*, 386–394.
[7] Y. N. Belokon′, S. Caveda-Cepas, B. Green, N. S. Ikonnikov, V. N. Khrustalev, V. S. Larichev, M. A. Moscalenko, M. North, C. Orizu, V. I. Tararov, M. Tasinazzo, G. I. Timofeeva, L. V. Yashkina, *J. Am. Chem. Soc.* **1999**, *121*, 3968–3973.
[8] M. K. Nazeeruddin, A. Kay, I. Rodicio, R. Humphry-Baker, E. Müller, P. Liska, N. Vlachopoulos, M. Grätzel, *J. Am. Chem. Soc.* **1993**, *115*, 6382–6390.
[9] U. Bach, D. Lupo, P. Comte, J. E. Moser, F. Weissörtel, J. Salbeck, H. Spreitzer, M. Grätzel, *Nature* **1998**, *395*, 583–585.
[10] A. S. Polo, M. K. Itokazu, N. Y. M. Iha, *Coord. Chem. Rev.* **2004**, *248*, 1343–1361 and references cited therein.
[11] H. Iwamura, *Pure Appl. Chem.* **1993**, *65*, 57–64.
[12] H. Oshio, H. Ichida, *J. Phys. Chem.* **1995**, *99*, 3294–3302.
[13] I. Seggern, F. Tuczek, W. Bensch, *Inorg. Chem.* **1995**, *34*, 5530–5547.
[14] M. Ferbinteanu, H. Miyasaka, W. Wernsdorfer, K. Nakata, K. Sugiura, M. Yamashita, C. Coulon, R. Clérac, *J. Am. Chem. Soc.* **2005**, *127*, 3090–3099.
[15] J.-P. Costes, F. Dahan, A. Dupuis, *Inorg. Chem.* **2000**, *39*, 165–168.
[16] E. Colacio, M. Ghazi, R. Kivekäs, J. M. Moreno, *Inorg. Chem.* **2000**, *39*, 2882–2890.
[17] C.-M. Liu, S. Gao, D.-Q. Zhang, Y.-H. Huang, R.-G. Xiong, Z.-L. Liu, F.-C. Jiang, D.-B. Zhu, *Angew. Chem. Int. Ed.* **2004**, *43*, 990–994.
[18] H. Oshio, N. Hoshino, T. Ito, M. Nakano, *J. Am. Chem. Soc.* **2004**, *126*, 8805–8812.
[19] S. S. Turner, D. L. Pevelen, P. Day, K. Prout, *J. Chem. Soc., Dalton Trans.* **2000**, 2739–2744.
[20] S. S. Turner, C. Michaut, S. Durot, P. Day, T. Gelbrich, M. B. Hursthouse, *J. Chem. Soc., Dalton Trans.* **2000**, 905–909.
[21] W. Fujita, K. Awaga, *J. Am. Chem. Soc.* **1997**, *119*, 4563–4564.
[22] O. Kahn, J. Larionova, J. V. Yakuhmi, *Chem. Eur. J.* **1999**, *5*, 3443–3449.
[23] D. Maspoch, D. Ruiz-Molina, K. Wurst, N. Domingo, M. Cavallini, F. Biscarini, J. Tejada, C. Rovira, J. Veciana, *Nat. Mater.* **2003**, *2*, 190–195.
[24] M. Hostettler, K. W. Törnroos, D. Chernyshov, B. Vangdal, H.-B. Bürgi, *Angew. Chem. Int. Ed.* **2004**, *43*, 4589–4594.
[25] M. C. Giménez-López, M. Clemente-León, E. Coronado, F. M. Romero, S. Shova, J.-P. Tuchagues, *Eur. J. Inorg. Chem.* **2005**, 2783–2787.
[26] K. L. Wierzchiwski, D. Shugar, A. R. Kataritzky, *J. Am. Chem. Soc.* **1963**, *85*, 827–828.
[27] K. L. Wierzchiwski, D. Shugar, *Photochem. Photobiol.* **1963**, *2*, 377–391.
[28] M. R. Kopp, B. Neumüller, *Z. Anorg. Allg. Chem.* **1999**, *625*, 739–745; M. R. Kopp, B. Neumüller, *Z. Anorg. Allg. Chem.* **1999**, *625*, 1246–1248.
[29] M. R. Kopp, T. Kräuter, A. Dashti-Mommertz, B. Neumüller, *Organometallics* **1998**, *17*, 4226–4231.
[30] M. L. Durán, J. A. García-Vázquez, C. Gómez, A. Sousa-Pedrares, J. Romero, A. Sousa, *Eur. J. Inorg. Chem.* **2002**, 2348–2354.
[31] K. Kosugi, M. J. Bushiri, N. Nishi, *Appl. Phys. Lett.* **2004**, *84*, 1753–1755.
[32] B. Weber, I. Käpplinger, H. Görls, E.-G. Jäger, *Eur. J. Inorg. Chem.* **2005**, 2794–2811.
[33] M. Weitzer, S. Brooker, *Dalton Trans.* **2005**, 2448–2454.
[34] F. Setifi, S. Golhen, L. Ouahab, A. Miyazaki, K. Okabe, T. Enoki, T. Toita, J. Yamada, *Inorg. Chem.* **2002**, *41*, 3786–3790.
[35] J. Nishijo, A. Miyazaki, T. Enoki, *Bull. Chem. Soc. Jpn.* **2004**, *77*, 715–727.
[36] G. M. Sheldrick, *SHELXS-97*, program for crystal structure determination, and SHELXL-97, program for crystal structure refinement, Institut für Anorganische Chemie der Universität, Tammanstrasse 4, Göttingen, Germany, **1997**.
[37] ORTEP3 for Windows: L. J. Farrugia, *J. Appl. Crystallogr.* **1997**, *30*, 565.

Received: January 24, 2006
Published Online: June 7, 2006

 © 2006 Wiley-VCH Verlag GmbH & Co. KGaA, Weinheim 

DOI: 10.1002/ejic.200600183

# New Dinuclear Face- and Edge-Sharing Bioctahedral Ruthenium Compounds Containing 1,2-Bis(diphenylphosphanyloxy)ethane

**Jorge Bravo,*[a] Jesús Castro,[a] Soledad García-Fontán,*[a] M. Carmen Rodríguez-Martínez,[a] and Pilar Rodríguez-Seoane[a]**

**Keywords:** Ruthenium / P ligands / Chelates / Bimetallic complexes

The bidentate diphosphinite ligand 1,2-bis(diphenylphosphanyloxy)ethane (L), $Ph_2P–O–(CH_2)_2–O–PPh_2$, can be sequentially incorporated into a series of dinuclear chloro-bridged ruthenium compounds using $[RuCl_2(DMSO)_4]$ as a precursor to give the new bioctahedral compounds $[Ru_2(\mu\text{-}Cl)_3(DMSO)_3Cl(\eta^2\text{-}L)]$ (**1**), $[Ru_2(\mu\text{-}Cl)_3(DMSO)Cl(\eta^2\text{-}L)_2]$ (**2**) and $[Ru_2Cl_2(\eta^2\text{-}L)_2\{\eta^1\text{-}L(O)\}_2(\mu\text{-}Cl)_2]$ (**3**). Compound **3** contains two partially oxidised diphosphinite ligands that act in a monodentate manner. These compounds can also be obtained by direct reaction of $[RuCl_2(DMSO)_4]$ with the appropriate stoichiometric amount of L but in the case of **3** (in which prolonged heating is necessary) the reaction affords two mononuclear compounds $[RuCl_2(\eta^2\text{-}L)(Ph_2POPPh_2)]$ (**7**) and $[RuCl(CO)(\eta^2\text{-}L)(Ph_2POCH_2)]$ (**8**), with ligand fragments coordinated to the metal probably originating in metal-mediated disruptions of L. Reaction of **2** with the monodentate ligands $PPh_{3-n}(OEt)_n$ ($n$ = 1–3) (L′) affords the dinuclear doubly chloro-bridged compound $[Ru_2(\mu\text{-}Cl)_2Cl_2(\eta^2\text{-}L)_2(L')_2]$ (**4**), the dinuclear triply chloro-bridged compound $[\{Ru(\eta^2\text{-}L)(L')\}_2(\mu\text{-}Cl)_3]Cl$ (**5**) and the mononuclear compound $[RuCl_2(\eta^2\text{-}L)(L')_2]$ (**6**). The solid-state structures of **2** (*transoid* isomer), **5** (*transoid* isomer), **6**, **7** and **8** are reported.
(© Wiley-VCH Verlag GmbH & Co. KGaA, 69451 Weinheim, Germany, 2006)

## Introduction

Ruthenium complexes continue to attract attention because they can be used in a range of applications in many different fields including catalytic processes[1] and bioinorganic processes.[2] Moreover, the discovery of the anticancer activity of $[RuCl_2(DMSO)_4]$ has increased interest in the properties of new Ru–DMSO complexes.[3] A number of chelating diphosphines have been used to stabilise transition-metal complexes but, surprisingly, studies on analogous diphosphinites are rare, although some such compounds have proved to be efficient catalysts.[4] Furthermore, the presence of halogeno bridges between the metal centres provides higher reactivity, thus enhancing their possibilities for successful use as new catalysts.[5]

We report here the results obtained in the reaction between $[RuCl_2(DMSO)_4]$ and 1,2-bis(diphenylphosphanyloxy)ethane (L) to yield a range of new mono- and dinuclear ruthenium complexes (Scheme 1). It is worth mentioning that, in contrast with the behaviour observed for other diphosphinite ligands,[6] it was possible to obtain different products when the stoichiometric relationship between the metal-containing precursor and the ligand was varied.

[a] Departamento de Química Inorgánica, Facultade de Química, Universidade de Vigo,
36310 Vigo, Spain
Fax: +34-986-813798
E-mail: jbravo@uvigo.es
sgarcia@uvigo.es

Supporting information for this article is available on the WWW under http://www.eurjic.org or from the author.

## Results and Discussion

### Reaction of $[RuCl_2(DMSO)_4]$ with L – Preparation of $[Ru_2(\mu\text{-}Cl)_3(DMSO)_3Cl(L)]$ (1)

Reaction of $[RuCl_2(DMSO)_4]$ with 1,2-bis(diphenylphosphanyloxy)ethane (L) in a 2:1 molar ratio in refluxing toluene for 1/2 h gave a yellow solid. The analytical data for this compound are consistent with the empirical formula $Ru_2LCl_4(DMSO)_3$. The IR spectrum shows a strong band at 1093 $cm^{-1}$, which is consistent with the presence of the $\eta^1$-*S* (DMSO) ligands.[7] The $^{31}P\{^1H\}$ NMR spectrum in $CDCl_3$ shows a singlet at $\delta$ = 158.2 ppm, indicating the magnetic equivalence of the two phosphorus atoms of the bidentate ligand L. The $^1H$ NMR spectrum shows, in the same solvent, three singlets at $\delta$ = 3.04, 3.12 and 3.43 ppm (integrating to 6 protons each), which can be assigned to the three DMSO ligands, and two multiplets at $\delta$ = 3.72 and 4.26 ppm (integrating to 2 protons each) corresponding to the methylene groups of L. Further evidence for the dinuclear nature of **1** comes from the FAB-MS spectrum, which shows signals corresponding to the molecular ion $[M^+]$ and to the fragments $[M^+ – Cl]$, $[M^+ – (DMSO)]$, $[M^+ – 3(DMSO)]$, $[M^+ – 3(DMSO) – Cl]$ and $[M^+ – Ru – 3(DMSO) – 2Cl]$. Two of the three isomers shown in Scheme 2 are compatible with this structural information.

 © 2006 Wiley-VCH Verlag GmbH & Co. KGaA, Weinheim 

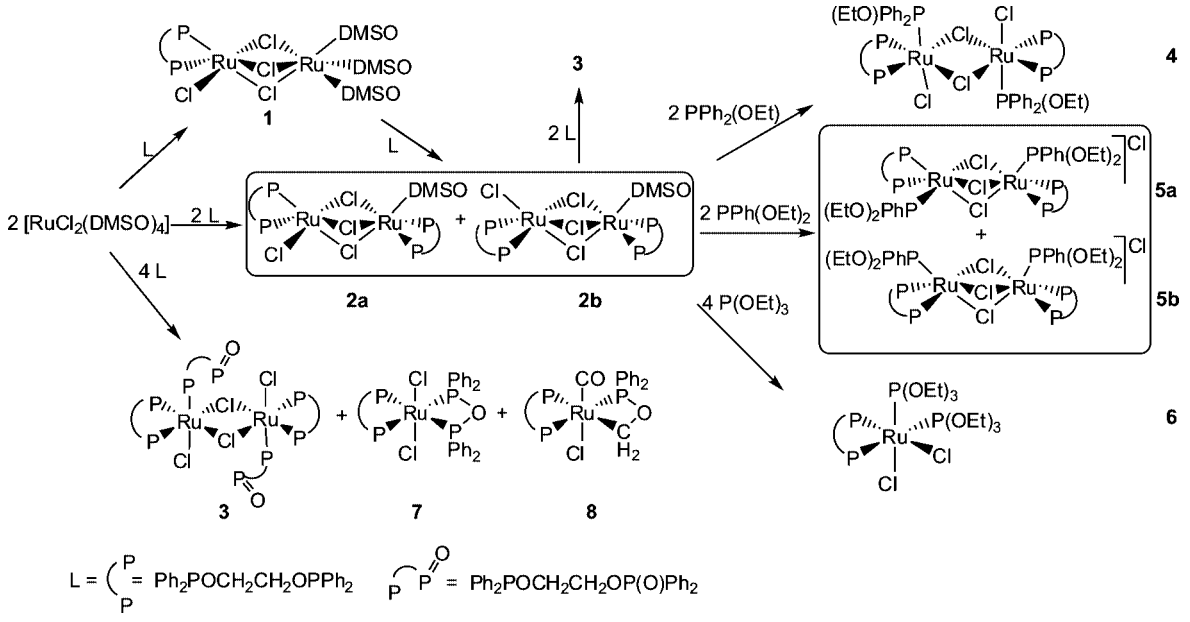


Scheme 1.

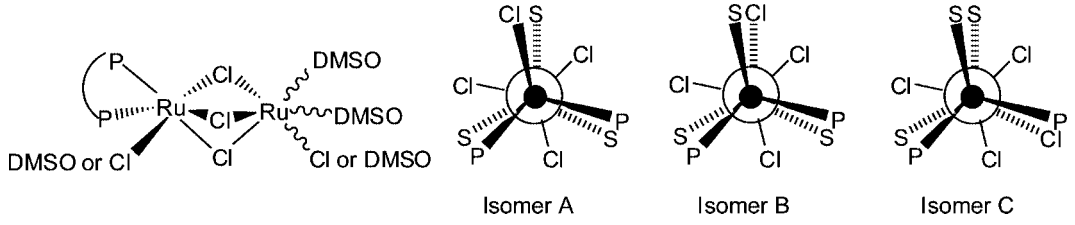


Scheme 2.

Isomer C can be ruled out because the two P nuclei are not equivalent. Isomer A is our preferred choice between isomers A and B because the chemical shift of P is similar to that observed for compounds with the same environment[8] and the methyl groups of each DMSO do not appear as two diastereotopic singlets (we carried out a 2D $^{1}H$, $^{13}C$ HSQC experiment to confirm this, see Supporting Information) as one would expect them to if they were in proximity to a bidentate ligand. Moreover, the 2D $^{1}H$, $^{31}P$ NMR HMBC experiments do not show any evidence of an interaction between the P atoms and the $CH_3$ protons of the DMSO ligands (although such negative evidence is not conclusive).

### Reaction of Compound 1 with L – Preparation of $[Ru_2(\mu\text{-}Cl)_3(DMSO)Cl(L)_2]$ (2)

Reaction of **1** with L in a 1:1 molar ratio in refluxing toluene for 1/2 h gave a yellow solid. The analytical data for this product are consistent with the formulation $[Ru_2(\mu\text{-}Cl)_3(\eta^2\text{-}L)_2Cl(DMSO)]$ (**2**).[9] The IR spectrum shows a strong band at 1093 $cm^{-1}$, which is consistent with the presence of a $\eta^1$-*S* sulfoxide ligand.[7]

The $^{31}P\{^{1}H\}$ NMR spectrum in $CDCl_3$ shows two sets of signals. The first set (indicated in Figure 1 by an asterisk) consists of a pair of doublets and a quartet [consistent with an AX spin system ($\delta$ = 160.7, 151.9 ppm, $J_{AX}$ = 54 Hz) and an AB spin system ($\delta$ = 148.3 ppm, $J_{AB}$ = 44 Hz), respectively]. This is a characteristic pattern of compounds of the type $[RuCl(PP)(\mu\text{-}Cl)_3Ru(PP)L]$[10] and can be assigned to the *transoid* form of **2** in which the four P atoms are not equivalent (see Scheme 3).

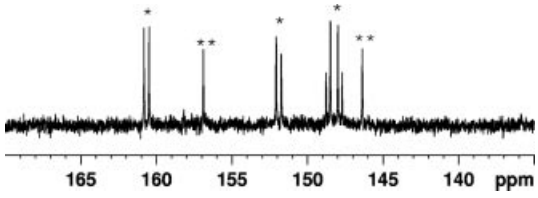


Figure 1. $^{31}P\{^{1}H\}$ NMR spectrum in $CDCl_3$ for compound **2**.

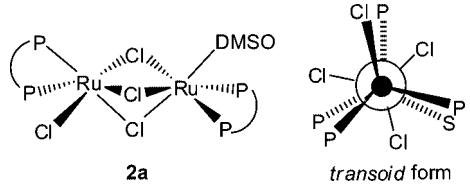


Scheme 3.

The second set of signals consists of two singlets [$\delta$ = 156.9, 146.4 ppm] (indicated by a double asterisk in Figure 1) and corresponds to the *cisoid* structure **2b** (see

 © 2006 Wiley-VCH Verlag GmbH & Co. KGaA, Weinheim 

Scheme 4) in which both phosphorus nuclei, belonging to each bidentate ligand, are magnetically equivalent.

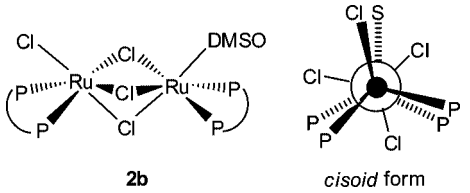


Scheme 4.

The $^1H$ NMR spectrum in $CDCl_3$ also presents signals that correspond to both structures. For example, two singlets at $\delta$ = 2.54 and 2.87 ppm can be assigned to the two diastereotopic methyl groups of DMSO corresponding to the *transoid* structure. At 3.22 ppm a singlet with a lower intensity can be assigned to the methyl groups of the DMSO ligand corresponding to the *cisoid* structure (there are no diastereotopic signals in this case because of its higher symmetry). A similar situation occurs with the signals corresponding to the methylene groups of the bidentate ligand. As observed in other halide compounds bearing this ligand,[11] these groups usually display one multiplet for each proton. In our case different multiplets were observed that integrate as one proton each and these coexist with other signals of lower intensity that may correspond to the *cisoid* structure.

An HMBC $^1H,^{31}P\{^1H\}$ NMR study (see Supporting Information) shows that there is a correlation between the signal at $\delta$ = 148.3 ppm (in $CDCl_3$) and that at $\delta$ = 2.54 ppm attributed to one of the DMSO methyl groups. This indicates that – in agreement with the assignment made by Bianchini for a similar complex – this resonance corresponds to the bidentate ligand coordinated to the Ru atom that bears the DMSO molecule.[8a] The relative intensities of the signals of the two isomers change significantly when benzene is used as the solvent, with the signals of the *cisoid* structure almost residual in this case. This must be due to the different solubility of the two isomers, because a VT NMR study carried out in $CDCl_3$ from 25 °C to –50 °C and in $C_6D_6$ from 25 °C to 45 °C did not provide any evidence for interconversion between them.

Finally, the $^{13}C\{^1H\}$ spectrum in $CD_2Cl_2$ shows two singlets at $\delta$ = 50.5 and 51.0 ppm, which can be assigned to the two inequivalent methyl groups of the DMSO ligand corresponding to the *transoid* structure. A signal with a lower intensity was also observed at $\delta$ = 51.3 ppm and this can be assigned to the two equivalent methyl groups of the *cisoid* structure.

We were able to obtain single crystals of the *transoid* isomer of compound **2** (**2a**) to carry out an X-ray diffraction analysis. Selected bond lengths and angles are reported in Table 1 and an ORTEP view is shown in Figure 2.

Table 1. Bond lengths [Å] and angles [°] for **2a**.

| Bond lengths | | | |
|---|---|---|---|
| Ru(1)–P(2) | 2.203(5) | Ru(1)–P(1) | 2.228(5) |
| Ru(1)–Cl(4) | 2.377(5) | Ru(1)–Cl(1) | 2.422(4) |
| Ru(1)–Cl(2) | 2.502(5) | Ru(1)–Cl(3) | 2.551(5) |
| Ru(2)–P(3) | 2.267(5) | Ru(2)–P(4) | 2.258(5) |
| Ru(2)–S(1) | 2.260(5) | Ru(2)–Cl(3) | 2.515(5) |
| Ru(2)–Cl(1) | 2.495(4) | Ru(2)–Cl(2) | 2.395(5) |
| **Bond angles** | | | |
| P(2)–Ru(1)–P(1) | 91.21(19) | P(2)–Ru(1)–Cl(4) | 91.86(19) |
| P(1)–Ru(1)–Cl(4) | 90.28(18) | P(2)–Ru(1)–Cl(1) | 96.88(17) |
| P(1)–Ru(1)–Cl(1) | 100.39(17) | Cl(4)–Ru(1)–Cl(1) | 166.02(18) |
| P(2)–Ru(1)–Cl(2) | 174.95(18) | P(1)–Ru(1)–Cl(2) | 92.70(17) |
| Cl(4)–Ru(1)–Cl(2) | 91.30(17) | Cl(1)–Ru(1)–Cl(2) | 79.28(15) |
| P(2)–Ru(1)–Cl(3) | 98.52(18) | P(1)–Ru(1)–Cl(3) | 170.27(17) |
| Cl(4)–Ru(1)–Cl(3) | 89.63(17) | Cl(1)–Ru(1)–Cl(3) | 78.32(15) |
| Cl(2)–Ru(1)–Cl(3) | 77.57(15) | P(4)–Ru(2)–S(1) | 93.51(19) |
| P(4)–Ru(2)–P(3) | 90.14(19) | S(1)–Ru(2)–P(3) | 93.99(18) |
| P(4)–Ru(2)–Cl(2) | 9515(18) | S(1)–Ru(2)–Cl(2) | 169.72(17) |
| P(3)–Ru(2)–Cl(2) | 91.52(17) | P(4)–Ru(2)–Cl(1) | 172.99(18) |
| S(1)–Ru(2)–Cl(1) | 90.95(17) | P(3)–Ru(2)–Cl(1) | 94.94(16) |
| Cl(2)–Ru(2)–Cl(1) | 79.93(15) | P(4)–Ru(2)–Cl(3) | 96.65(18) |
| S(1)–Ru(2)–Cl(3) | 93.26(17) | P(3)–Ru(2)–Cl(3) | 169.73(18) |
| Cl(2)–Ru(2)–Cl(3) | 80.25(16) | Cl(1)–Ru(2)–Cl(3) | 77.68(15) |
| Ru(1)–Cl(1)–Ru(2) | 86.56(14) | Ru(2)–Cl(2)–Ru(1) | 86.97(15) |
| Ru(2)–Cl(3)–Ru(1) | 83.43(15) | | |

Complex **2** adopts a triply chloride-bridged diruthenium *transoid* structure (**2a**) in which the coordination geometry

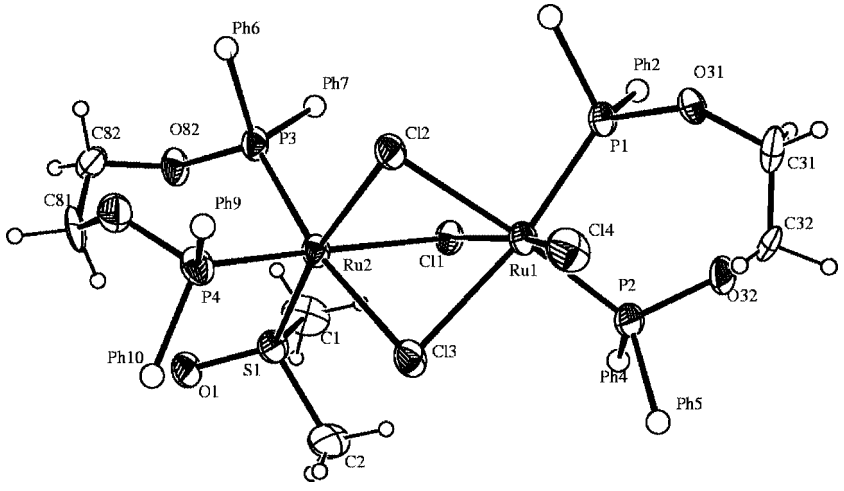


Figure 2. ORTEP view of $[Ru_2(\mu\text{-}Cl)_3(DMSO)Cl(L)_2]$ (**2a**). The phenyl groups are omitted for clarity.

 © 2006 Wiley-VCH Verlag GmbH & Co. KGaA, Weinheim 

at each metal centre is a distorted octahedron. The structure is unsymmetrical, with Ru(2) bearing a DMSO and Ru(1) a chloride ligand. The structural features are similar to those found in previously reported face-sharing bioctahedral $Ru^{II}$–$Ru^{II}$ complexes.[7b,12] The Ru–$Cl_{terminal}$ distance is shorter than the Ru–$Cl_{bridge}$ distances. Of all the Ru–$Cl_{bridge}$ distances, those that are *trans* to a phosphorus atom are the longest. The shortest Ru–$Cl_{bridge}$ distance is that with the DMSO ligand in the *trans* position. It is worth noting that the Ru(1)–P distances (with Ru bound to a terminal chloro ligand) are significantly shorter than the Ru(2)–P distances (with Ru bound to the DMSO ligand).

The seven-membered chelate rings allow P–Ru–P angles of 91.21(19) and 90.14(19)°. The $Cl_{bridge}$–Ru–$Cl_{bridge}$ angles have values between 77.57(15) and 80.25(16)°, with this being the main source of distortion of the octahedron. As shown in Figure 3, the environment of the metal atoms corresponds with the $C_1$-symmetric *transoid* isomer, with the dihedral torsion angle Cl(4)–Ru(1)–Ru(2)–S(1) having a value of 122.4(2)°. The Ru–Ru distance of 3.371(2) Å lies in the range expected for this type of dinuclear $Ru^{II}$ complex (3.28–3.44 Å).[12a]

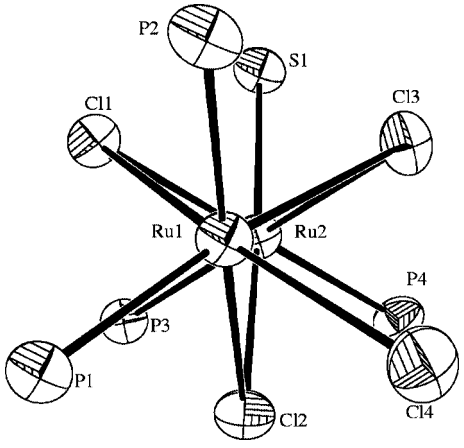


Figure 3. Environment of the Ru atoms in **2a**.

### Reaction of Compound 2 with L – Preparation of $[\{RuCl(\eta^2\text{-}L)[\eta^1\text{-}L(O)]\}_2(\mu\text{-}Cl)_2]$ (3)

The reaction of **2** with L (1:2 molar ratio) in refluxing toluene for 1 h gave the new compound **3**. The $^{31}P\{^1H\}$ NMR spectrum in $CDCl_3$ displays a doublet at $\delta$ = 159.0 ppm ($J$ = 46 Hz), a triplet at $\delta$ = 138.3 ppm and a singlet at $\delta$ = 32.5 ppm with an intensity ratio of 2:1:1, respectively. The singlet at higher field is consistent with the existence of a P=O group (corresponding to a partially oxidised molecule of L) that is not coordinated to the metal. The other two signals can be assigned to the P atoms of $\eta^2$-L and $\eta^1$-L(O), respectively. The $^1H$ NMR spectrum in $CDCl_3$ displays four multiplets at 3.68, 3.73, 4.17 and 4.49 ppm with an integral ratio 1:1:1:1. These signals correspond to the $CH_2$ groups of the two ligands. The 2D $^1H$, $^1H$ COSY and the 2D $^1H$, $^{31}P$ HMQC spectra allow full assignment of those signals (see Exp. Sect.). The FAB mass spectrum contains peaks at mass values for fragments of dinuclear species [$M^+$ – Cl – L(O)], [$M^+$ – 2Cl – L(O)], [$M^+$ – 2Cl – 2L(O)] and, interestingly, the strongest fragment was found at 1013, which corresponds exactly to the monomeric unit [RuClLL(O)]. Finally, treatment of a sample of **3** with excess $NaBPh_4$ in ethanol resulted in the precipitation of a new product, **3′**. The $^{31}P\{^1H\}$ NMR spectrum of this compound contains two sets of signals: three pseudotriplets integrating in a 1:1:1 ratio, and a triplet and a doublet integrating in a 1:2 ratio (the first set integrates to three times the second one) coexisting with traces of the original compound (very small signals at 159 and 138 ppm). When the sample in the NMR tube was stored for five days, evidence was observed that the reaction had gone backwards and the small signals had increased in intensity to levels similar to those observed at the beginning of the experiment.

All these data suggest the formation of neutral edge-sharing bioctahedra with two chloro bridges [{RuCl($\eta^2$-L)[$\eta^1$-L(O)]}$_2$($\mu$-Cl)$_2$] for compound **3** and this converts into the cationic face-sharing bioctahedral compound **3′** by reaction with $NaBPh_4$ – as depicted in Scheme 5.

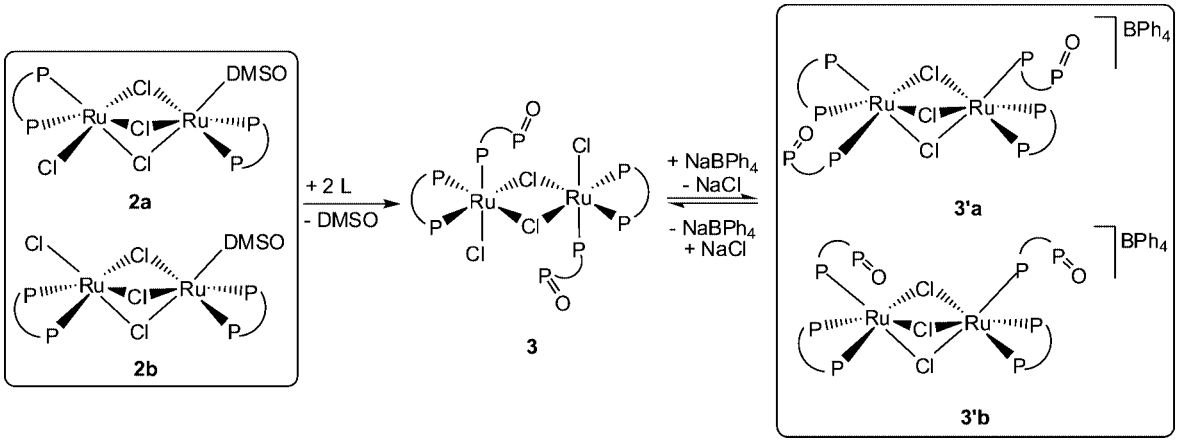


Scheme 5.

 © 2006 Wiley-VCH Verlag GmbH & Co. KGaA, Weinheim 

**Reaction of 2 with L′ [L′ = $PPh_{3-n}(OEt)_n$; *n* = 1–3]**

In an effort to complement the results described above and to gather more information about the reactivity of complex **2**, we investigated the reaction of **2** with the monodentate phosphinite, phosphonite and phosphite ligands of formulae $PPh_{3-n}(OEt)_n$ (*n* = 1–3) (L′). Unexpectedly, different results were obtained when L′ was changed from a phosphinite (*n* = 1) to a phosphite (*n* = 3).

***L′ = $PPh_2(OEt)$ – Preparation of [{RuCl(η²-L)[$PPh_2(OEt)$]}₂(μ-Cl)₂] (4)***

When a mixture of **2** and $PPh_2(OEt)$ in a 1:2 molar ratio was heated under reflux in toluene for 1 h, the new compound [{RuCl(η²-L)[$PPh_2(OEt)$]}₂(μ-Cl)₂] (**4**) was obtained. Compound **4** shows spectral features that are very similar to those of compound **3**. The $^{31}P\{^1H\}$ NMR spectrum shows a doublet at $\delta$ = 159.7 ppm and a triplet at $\delta$ = 136.3 ppm (integrating to 2:1, $J$ = 46 Hz), which are very similar to the signals of **3**. The $^1H$ NMR spectrum also contains a set of signals that is consistent with this formulation. The signals at 4.31 (m, 4 H) and 3.86 (m, 4 H) ppm can be assigned to the –$CH_2$– groups of the bidentate ligand L, and those at 3.50 (m, 4 H) and 1.22 (t, 6 H) can be assigned to the ethoxy group of L′. The FAB mass spectrum of **4** displays (as observed for compound **3**) peaks that indicate the dinuclear nature of the compound: 1630 ($M^+$ – Cl), 1435 ($M^+$ – L′), 1400 ($M^+$ – L′ – Cl), 830 $[RuCl_2LL']^+$, 797 $[RuClLL']^+$.

Treatment of a sample of **4** with excess $NaBPh_4$ in ethanol gave similar results to those obtained in the case of complex **3**, with a new dinuclear face-shared bioctahedral complex, **4′**, formed as a mixture of both *cisoid* and *transoid* isomers.[13] However, in this case the proportion of the *transoid* isomer for the face-shared bioctahedra is significantly greater than in the case of compound **3**. In agreement with this situation, the $^{31}P\{^1H\}$ NMR spectrum of **4′** in $CDCl_3$ displays three pseudotriplets at 134.1, 141.9 and 145.7 ppm (corresponding to a *transoid* isomer) along with a doublet at $\delta$ = 143.3 ppm (the triplet is probably obscured by the signal at $\delta$ = 134.1 ppm) that corresponds to the *cisoid* form.

***L′ = $PPh(OEt)_2$ – Preparation of [{Ru(η²-L)[$PPh(OEt)_2$]}₂(μ-Cl)₃]Cl (5)***

When a mixture of **2** and $PPh(OEt)_2$ in a 1:2 molar ratio was heated under reflux in toluene for 1.5 h, we obtained a solid with $^{31}P\{^1H\}$ and $^1H$ NMR spectra consistent with a mixture (approx. 1:3) of both *cisoid* and *transoid* isomers of the cationic trichloro-bridged dinuclear compound [{Ru(η²-L)[$PPh(OEt)_2$]}₂(μ-Cl)₃]Cl (**5**) (see Scheme 1). The $^{31}P\{^1H\}$ NMR spectrum displays a doublet at $\delta$ = 151.7 ppm and a triplet at $\delta$ = 158.2 ppm ($J$ = 53 Hz) (*cisoid* isomer) and three pseudotriplets at 149.7, 153.0 and 156.1 ppm (*transoid* isomer). Careful inspection of the $^1H$ NMR spectrum also enables the signals of both isomers to be assigned (see Exp. Sect.). The mass spectrum shows the $[M^+]$ peak at $m/z$ = 1567, which is consistent with a dinuclear formulation. Moreover, treatment of a solution of this complex with excess $NaBPh_4$ in ethanol gave a tan solid with spectral features identical to those of the original product, thus confirming its ionic nature. We were also able to obtain suitable crystals for an X-ray diffraction study. The structure of the complex cation and the most relevant distances and angles are shown in Figure 4 and in Tables 2 and 3, respectively.

It can be seen that the cation complex **5a** adopts a *transoid* [dihedral torsion angle P(1)–Ru(1)–Ru(2)–P(2) of 115.5(2)°] triply chloride-bridged diruthenium structure similar to **2a** (Figure 5). The coordination geometry around each metal centre is a distorted octahedron, with the same coordination sphere at each ruthenium atom (three bridging chlorine atoms and three phosphorus atoms). The two met-

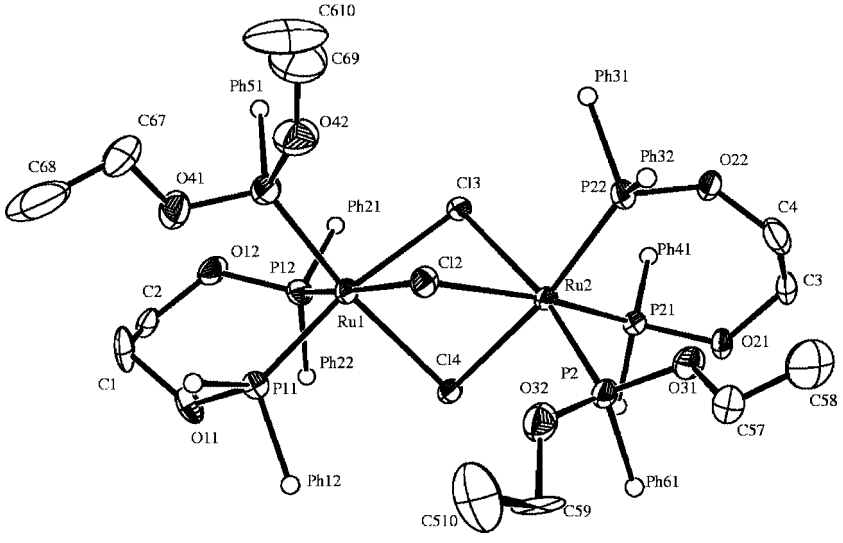


Figure 4. The cation of [{Ru(η²-L)[$PPh(OEt)_2$]}₂(μ-Cl)₃]Cl (**5a**) drawn at 20% probability level. The phenyl rings were replaced by spheres of arbitrary radius.

 © 2006 Wiley-VCH Verlag GmbH & Co. KGaA, Weinheim 

Table 2. Selected bond lengths [Å] and angles [°] for complex cation **5a**.

| Bond lengths | | | |
|---|---|---|---|
| Ru(1)–Cl(3) | 2.478(3) | Ru(1)–Cl(4) | 2.482(2) |
| Ru(1)–Cl(2) | 2.535(3) | Ru(1)–P(1) | 2.241(3) |
| Ru(1)–P(12) | 2.261(3) | Ru(1)–P(11) | 2.274(3) |
| Ru(2)–Cl(3) | 2.495(3) | Ru(2)–Cl(2) | 2.511(3) |
| Ru(2)–Cl(4) | 2.473(2) | Ru(2)–P(2) | 2.253(3) |
| Ru(2)–P(21) | 2.284(3) | Ru(2)–P(22) | 2.265(3) |
| Ru(2)–Ru(1) | 3.4417(12) | | |
| **Bond angles** | | | |
| P(1)–Ru(1)–P(12) | 89.78(12) | P(1)–Ru(1)–P(11) | 93.54(11) |
| P(12)–Ru(1)–P(11) | 89.89(11) | P(1)–Ru(1)–Cl(3) | 95.13(11) |
| P(12)–Ru(1)–Cl(3) | 94.82(11) | P(11)–Ru(1)–Cl(3) | 170.14(10) |
| P(1)–Ru(1)–Cl(4) | 169.52(10) | P(12)–Ru(1)–Cl(4) | 99.34(10) |
| P(11)–Ru(1)–Cl(4) | 91.65(10) | P(1)–Ru(1)–Cl(2) | 93.28(11) |
| P(12)–Ru(1)–Cl(2) | 171.16(11) | P(11)–Ru(1)–Cl(2) | 98.19(11) |
| Cl(3)–Ru(1)–Cl(2) | 76.66(9) | Cl(4)–Ru(1)–Cl(2) | 76.95(8) |
| Cl(3)–Ru(1)–Cl(4) | 79.05(8) | P(2)–Ru(2)–P(22) | 94.45(11) |
| P(2)–Ru(2)–P(21) | 90.66(11) | P(22)–Ru(2)–P(21) | 90.05(10) |
| P(2)–Ru(2)–Cl(4) | 94.10(10) | P(22)–Ru(2)–Cl(4) | 170.80(10) |
| P(21)–Ru(2)–Cl(4) | 93.22(9) | P(2)–Ru(2)–Cl(3) | 168.04(11) |
| P(22)–Ru(2)–Cl(3) | 92.09(10) | P(21)–Ru(2)–Cl(3) | 99.34(10) |
| P(2)–Ru(2)–Cl(2) | 92.30(11) | P(22)–Ru(2)–Cl(2) | 98.72(10) |
| P(21)–Ru(2)–Cl(2) | 170.49(9) | Cl(4)–Ru(2)–Cl(2) | 77.56(8) |
| Cl(3)–Ru(2)–Cl(2) | 76.80(9) | Cl(4)–Ru(2)–Cl(3) | 78.90(8) |
| Ru(2)–Cl(2)–Ru(1) | 86.02(8) | Ru(1)–Cl(3)–Ru(2) | 87.59(9) |
| Ru(2)–Cl(4)–Ru(1) | 87.99(8) | | |

Table 3. Hydrogen bonding parameters for complex cation **5a** [Å and °].

| D–H···A | *d*(D–H) | *d*(H···A) | *d*(D···A) | blabla(DHA) |
|---|---|---|---|---|
| C(3)–H(3B)···Cl(1A) | 0.97 | 2.79 | 3.500(9) | 131.1 |
| C(1)–H(1A)···Cl(1) | 0.97 | 2.93 | 3.586(10) | 125.7 |
| C(2)–H(2A)···Cl(1) | 0.97 | 2.89 | 3.610(10) | 131.3 |

als maintain the same oxidation state (+II) as a disordered chloride ion is acting as a counterion. Two of the phosphorus atoms coordinated to each metal atom come from the bidentate phosphinite ligand L, and the third one comes from the monodentate ligand L′. In contrast to complex **2a**, the environment around each ruthenium atom is quite similar, with similar values for bond lengths and angles. The Ru–P bonds are slightly shorter, by 0.01 Å, when the ligand is the monodentate phosphonite ligand. The Ru–Cl bond lengths range from 2.473(2) to 2.535(3) Å, with the longer ones corresponding to those including the labelled Cl(2) atom, the only one that is simultaneously *trans* to two phosphinite phosphorus atoms. The Ru(1)–Cl(2)–Ru(2) angle, 86.02(8)°, is also the most acute of the three Ru–Cl–Ru angles.

The seven-membered chelate rings allows P–Ru–P angles of 89.89(11) and 90.05(10)°, which are virtually identical to one another and similar to those found in **2a**. The Cl–Ru–Cl angles involving the triple bridge have values between 76.66(9) and 79.05(8)° and once again this is the main source of distortion of the octahedron. The Ru–Ru separation of 3.4417(12) Å is in the upper limit of the range expected for this type of dinuclear $Ru^{II}$ complex, 3.28–3.44 Å.[12a]

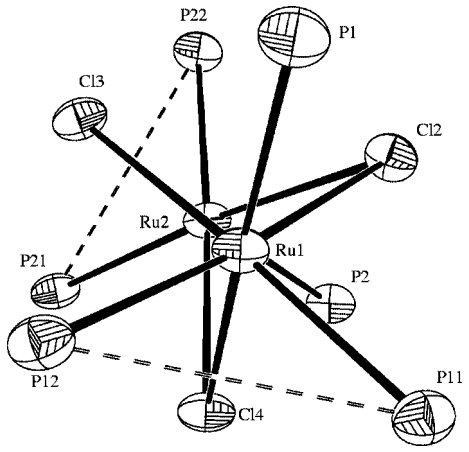


Figure 5. Environment of the Ru atoms in the complex cation **5a**.

### *L′ = P(OEt)$_3$ – Preparation of [RuCl$_2$(η$^2$-L){P(OEt)$_3$}$_2$] (6)*

When a mixture of **2** and $P(OEt)_3$ in a 1:2 molar ratio was heated under reflux in toluene for 1 h, we obtained a solid that has NMR features consistent with a mononuclear species of formula $[RuCl_2(\eta^2\text{-}L)\{P(OEt)_3\}_2]$ (**6**), in which one bidentate ligand and two phosphite ligands (mutually *cis*) are present. The $^{31}P\{^1H\}$ NMR spectrum consists of four double doublets of doublets at 97.8 ($P_1$), 122.0 ($P_4$), 129.8 ($P_2$) and 150.7 ($P_3$) ppm ($J_{12}$ = 48, $J_{13}$ = 24, $J_{14}$ = 544, $J_{23}$ = 47, $J_{24}$ = 64 and $J_{34}$ = 46 Hz). The $^1H$ NMR spectrum displays two triplets at $\delta$ = 0.90 and 1.22 ppm ($J$ = 7 Hz), which integrate to 9 protons each, and these signals can be assigned to the methyl groups of L′. These signals demonstrate the nonequivalence of the two ligands. The signals corresponding to the methylene protons of both L and L′ appear as seven multiplets of different intensity. These signals were fully characterised by 2D $^1H$, $^{13}C\{^1H\}$ HSQC correlation (see Figure 6). The methylene protons of the bidentate ligand L appear as four multiplets at 3.43, 3.98, 4.40 and 5.67 ppm, integrating to one proton each. On the other hand, the methylene protons of both L′ ligands appear as four multiplets centred at 3.26, 3.43, 4.23 and 4.46 and these signals integrate to three protons each because of the nonequivalence of the two L′ ligands and the diastereotopic nature of each pair of geminal $CH_2$ protons.

Crystals suitable for X-ray analysis were obtained. The structure of the complex is shown in Figure 7 and the most relevant distances and angles are given in Table 4. The compound consists of discrete units in which the ruthenium atom is in a slightly distorted octahedral environment, coordinated to two mutually *cis* chlorine atoms, two phosphorus atoms of a diphosphinite ligand and two phosphorus atoms of two monodentate phosphite ligands, which are also mutually *cis*. The *cis* angles range from 84.78(5) to 97.28(6)°, with the latter value corresponding to the chelate angle allowed by the seven-membered chelate ring. The *trans* angles range from 170.42(6) to 177.02(6)° and these show the regu-

 © 2006 Wiley-VCH Verlag GmbH & Co. KGaA, Weinheim 

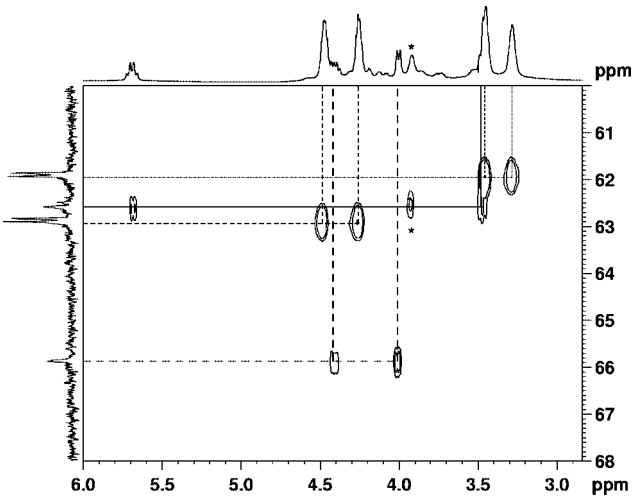


Figure 6. 2D $^{1}H,^{13}C\{^{1}H\}$ HSQC experiment in $CDCl_3$ for compound **6**. Signals in the $^{13}C$ spectrum can be assigned as follows: $\delta$ = 65.9, 62.6 (br. s, $CH_2$, L), 62.9, 61.9 (d, $J_{CP}$ = 10 Hz, $CH_2$, L′). Signals marked with an asterisk correspond to an impurity.

larity of the octahedron, which is probably only distorted due the steric hindrance of the diphosphinite ligand. The *cis* Cl–Ru–Cl angle, 86.81(5)°, is similar to those found in *cis* complexes $RuCl_2P_4$.[14] The Ru–Cl distances are similar to one another but the Ru–P distances show small differences in the order Ru–P4 < Ru–P1 < Ru–P3 < Ru–P2. This order is consistent with the greater *trans* influence of phosphorus ligands than Cl and the higher π-acceptor character of phosphite ligands as compared with phosphinites.

Table 4. Selected bond lengths [Å] and angles [°] for complex **6**.

| Bond lengths | | | |
|---|---|---|---|
| Ru–P(4) | 2.2333(17) | Ru–P(1) | 2.2777(15) |
| Ru–P(3) | 2.3040(17) | Ru–P(2) | 2.4406(16) |
| Ru–Cl(2) | 2.4633(15) | Ru–Cl(1) | 2.4675(15) |
| **Bond angles** | | | |
| P(4)–Ru–P(1) | 93.48(6) | P(4)–Ru–P(3) | 91.09(6) |
| P(1)–Ru–P(3) | 92.24(6) | P(4)–Ru–P(2) | 89.36(6) |
| P(1)–Ru–P(2) | 97.28(6) | P(3)–Ru–P(2) | 170.42(6) |
| P(4)–Ru–Cl(2) | 177.02(6) | P(1)–Ru–Cl(2) | 85.91(5) |
| P(3)–Ru–Cl(2) | 91.85(6) | P(2)–Ru–Cl(2) | 87.82(5) |
| P(4)–Ru–Cl(1) | 93.95(5) | P(1)–Ru–Cl(1) | 172.04(6) |
| P(3)–Ru–Cl(1) | 84.78(5) | P(2)–Ru–Cl(1) | 85.65(5) |
| Cl(2)–Ru–Cl(1) | 86.81(5) | | |

### Reaction of $[RuCl_2(DMSO)_4]$ with L in a 1:2 Molar Ratio

A mixture of $[RuCl_2(DMSO)_4]$ and L in a 1:2 molar ratio was heated under reflux in toluene for 2 h and the progression of the reaction was followed by $^{31}P$ NMR spectroscopy. A complicated spectrum was observed with different sets of signals, suggesting the presence of a mixture of several new compounds. The solution was evaporated to dryness and the residue was treated with $Et_2O$. An orange solid and a yellow solution were obtained. The solid was filtered off, washed with $Et_2O$ and dried to afford the same compound, $[\{RuCl(\eta^2\text{-}L)[\eta^1\text{-}Ph_2PO(CH_2)_2OP(O)Ph_2]\}_2(\mu\text{-}Cl)_2]$ (**3**), as was already obtained in the reaction of complex **2** with L.[15] The yellow solution was purified by column chromatography to yield the two new compounds $[RuCl_2(L)(Ph_2POPPh_2)]$ (**7**) and $[RuCl(CO)(L)(Ph_2PO-$

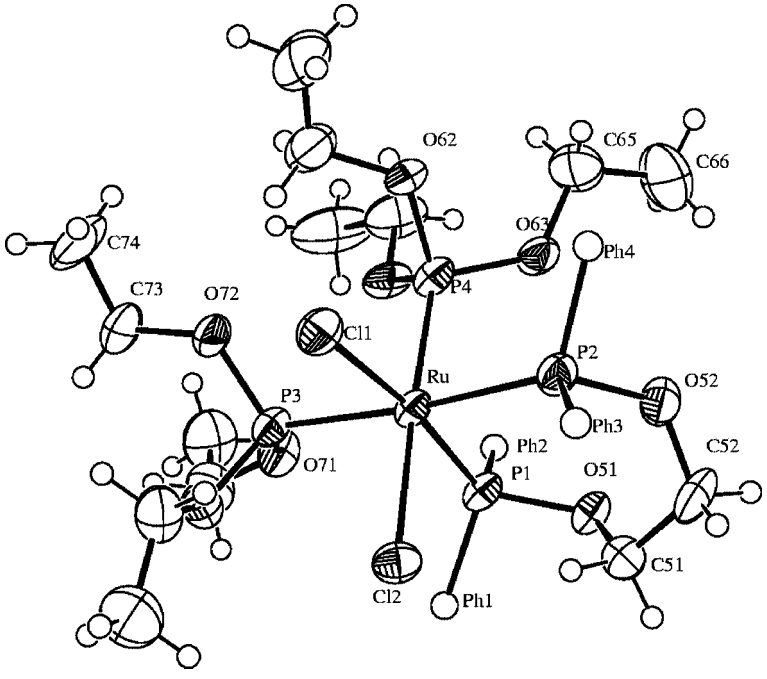


Figure 7. ORTEP representation of complex $[RuCl_2(\eta^2\text{-}L)\{P(OEt)_3\}_2]$ (**6**) drawn at the 30% probability level. The phenyl rings were replaced by spheres of arbitrary radius.

 © 2006 Wiley-VCH Verlag GmbH & Co. KGaA, Weinheim 

$CH_2$)] (**8**) (see Exp. Sect. for details). We were able to obtain single crystals of both compounds that were suitable for X-ray analysis.

### *[RuCl$_2$(L)(Ph$_2$POPPh$_2$)] (7)*

The reaction probably involves a metal-promoted disruption of the bidentate ligand to tetraphenyldiphosphoxane,[16] although in a somewhat similar reaction between $[Rh(COE)_2Cl]_2$ (COE = cyclooctene) and $P(NMe_2)_3$ in toluene, the generation of a diphosphoxane complex was attributed to a hydrolysis impurity present in the commercial $P(NMe_2)_3$.[17] This is probably not the situation in our case because we did not observe such a process in reactions between the same ligand and other metals such as Re and Mn.[18] Other authors have observed the same product (POP) and suggested a P–P(O) to P–O–P thermal rearrangement prior to metal coordination,[19] a process that is favoured when R groups bonded to P are inductively electron-withdrawing groups like OR groups (as in our case). A likely mechanism involves partial hydrolysis of the ligand due to the prolonged heating and the presence of adventitious moisture, followed by a tautomeric rearrangement from the P–P(O) to the P–O–P form.

The $^1$H NMR spectrum of **7** in $CDCl_3$ shows a multiplet centred at $\delta$ = 4.30 ppm, which is assigned to the methylene protons of the bidentate diphosphinite ligand, and signals between 6.90 and 7.50 ppm corresponding to the phenyl groups of the two chelating ligands. The $^{31}P\{^1H\}$ NMR spectrum in $CDCl_3$ shows two doublets of multiplets centred at $\delta$ = 106.8 and 133.0 ppm, corresponding to the two phosphorus nuclei of each bidentate ligand. The signal at lower field can be assigned to the bisphosphinite ligand L (as shown in the 2D $^1$H, $^{31}P\{^1H\}$ HMBC correlation experiment by the cross-peak present with the methylene signal of L at $\delta$ = 4.30 ppm, see Supporting Information) and the multiplet at $\delta$ = 106.8 ppm can be assigned to the phosphorus nuclei of the tetraphenyldiphosphoxane ligand. The IR spectrum contains a strong band at 791 cm$^{-1}$ and this is assigned to the P–O–P asymmetric stretching mode in accordance with its chelating nature (reported values of 775–800 cm$^{-1}$).[16,20]

An ORTEP view of compound **7** is shown in Figure 8 along with the labelling scheme. Selected distances and angles are given in Table 5. The compound consists of discrete units, although some intermolecular nonclassical Cl···HC hydrogen bonds can be found (Table 6). The ruthenium atom is in a distorted octahedral environment and is coordinated to two chlorine atoms that are mutually *trans*, two phosphorus atoms of a tetraphenyldiphosphoxane ligand and two phosphorus atoms of a diphosphinite ligand.

Table 5. Bond lengths [Å] and angles [°] for compound **7**.

| Bond lengths | | | |
|---|---|---|---|
| Ru(1)–P(2) | 2.3271(7) | Ru(1)–P(1) | 2.3423(7) |
| Ru(1)–P(3) | 2.3783(7) | Ru(1)–P(4) | 2.4119(7) |
| Ru(1)–Cl(1) | 2.4237(7) | Ru(1)–Cl(2) | 2.4280(7) |
| O(1)–P(4) | 1.6593(17) | O(1)–P(3) | 1.6652(17) |
| **Bond angles** | | | |
| P(1)–Ru(1)–P(2) | 92.43(3) | P(3)–Ru(1)–P(4) | 66.37(2) |
| P(2)–Ru(1)–P(3) | 98.56(2) | P(1)–Ru(1)–P(4) | 102.76(3) |
| P(1)–Ru(1)–P(3) | 168.91(2) | P(2)–Ru(1)–P(4) | 164.42(3) |
| P(2)–Ru(1)–Cl(1) | 98.32(3) | P(1)–Ru(1)–Cl(1) | 92.53(3) |
| P(3)–Ru(1)–Cl(1) | 84.41(2) | P(4)–Ru(1)–Cl(1) | 84.58(2) |
| P(2)–Ru(1)–Cl(2) | 90.25(3) | P(1)–Ru(1)–Cl(2) | 87.69(3) |
| P(3)–Ru(1)–Cl(2) | 93.75(3) | P(4)–Ru(1)–Cl(2) | 86.99(2) |
| Cl(1)–Ru(1)–Cl(2) | 171.40(2) | P(4)–O(1)–P(3) | 104.14(9) |

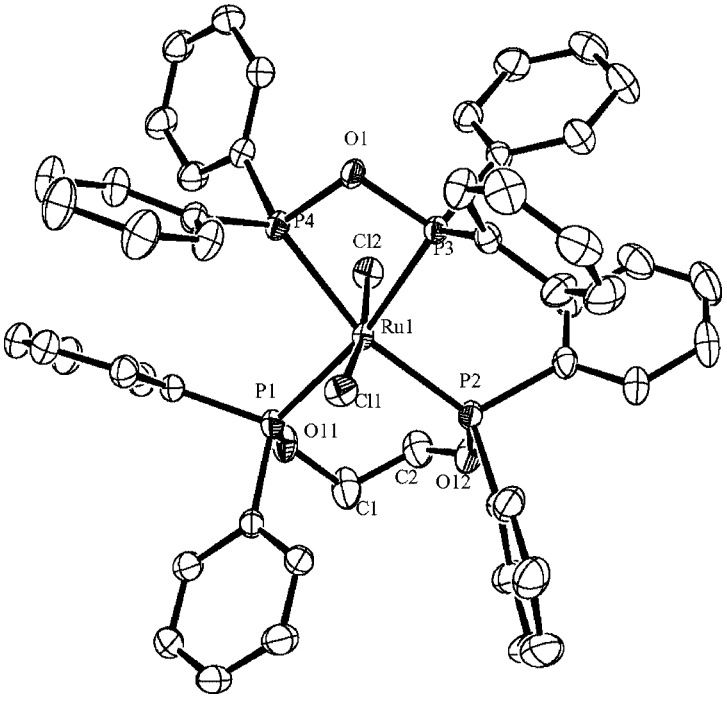


Figure 8. ORTEP drawing of the complex [RuCl$_2$(L)(Ph$_2$POPPh$_2$)] (**7**).

 © 2006 Wiley-VCH Verlag GmbH & Co. KGaA, Weinheim 

The four phosphorus atoms are located in the equatorial plane (rms = 0.057). The chelate ring angle of the tetraphenyldiphosphoxane ligand is only 66.37(2)° and is the main source of distortion. To the best of our knowledge, this is the first example of a ruthenium complex with this type of chelating ligand, but the chelate angle is similar to that found in the chromium, molybdenum and rhodium complexes.[17,21] The chelate angle allowed by the seven-membered chelate ring is close to the theoretical value of 90° [92.43(3)°] and, consequently, the other two angles in the equatorial plane increase to 98.56(2) and 102.76(3)°. The *trans* Cl–Ru–Cl angle is also slightly different than the expected value of 180° [171.40(2)°] and this is due to a small deviation of the chlorine atom labelled as Cl(1), as shown by the P–Ru–Cl angles. The four-membered chelate ring is almost planar, with the O(1) atom only 0.103(2) Å out of the P(3)–Ru–P(4) plane.

Table 6. Hydrogen bond parameters for **7** [Å and °].[a]

| D–H···A | *d*(D–H) | *d*(H···A) | *d*(D···A) | blabla(DHA) |
|---|---|---|---|---|
| C(2)–H(2B)···Cl(2) | 0.97 | 2.61 | 3.397(3) | 138.8 |
| C(12)–H(12)···Cl(1) | 0.93 | 2.61 | 3.234(3) | 124.8 |
| C(32)–H(32)···Cl(2) | 0.93 | 2.69 | 3.506(3) | 147.2 |
| C(56)–H(56)···Cl(1) | 0.93 | 2.69 | 3.302(3) | 124.3 |
| C(86)–H(86)···Cl(2) | 0.93 | 2.82 | 3.423(3) | 123.8 |
| C(85)–H(85)···Cl(2)#1 | 0.93 | 2.87 | 3.738(3) | 156.5 |

[a] Symmetry transformations used to generate equivalent atoms: $1 - x, y + 1/2, 1/2 - z$.

The angle P(4)–O(1)–P(3) has a value of 104.14(9)°, which is slightly less acute than those reported for the aforementioned complexes.[17,21] The ruthenium atom is only 0.0184(4) Å out of the equatorial plane defined by the four phosphorus atoms (rms = 0.057). The plane defined by the two phosphorus atoms and the two oxygen atoms of the diphosphinite ligand (rms = 0.088) forms a dihedral angle with the equatorial plane of 41.73(6)°. However, the plane P(3)–Ru–P(4) forms a dihedral angle of only 6.00(7)° with the equatorial plane and can essentially be considered as coplanar [the oxygen atom O(1) is only 0.096(2) Å out of the equatorial plane].

### *[RuCl(CO)(L)(Ph$_2$POCH$_2$)] (8)*

Compound **8** has a surprising structure in which the ruthenium centre is coordinated by an intact ligand L, Cl and CO ligands, and an anionic fragment $Ph_2POCH_2^-$ of this ligand. This arrangement stabilises, in spite of the strain, a ruthena-phospha-oxa-cyclobutane ring. As the only source of CO is the bis(phosphinite) L ligand, and we did not observe similar behaviour for L with other metals,[18] these fragments must come from a metal-promoted disruption of the bidentate ligand. Moreover, although the yields are low, the reaction is perfectly reproducible. The complex was characterised in solution by multinuclear NMR spectroscopy. The $^{31}P\{^1H\}$ NMR spectrum of **8** in $CDCl_3$ shows three doublet of doublets, which is consistent with a structure presenting two mutually *trans* phosphorus atoms [one on the $Ph_2POCH_2^-$ fragment ($\delta$ = 76.0 ppm) and one on the L ligand ($\delta$ = 133.3 ppm), $J_{trans}$ = 341 Hz] and the other in a *cis* disposition ($\delta$ = 131.5 ppm), $J_{cis}$ = 14 and 31 Hz. The $^1H$ NMR spectrum of **8** in $CDCl_3$ shows two groups of multiplets, one in the range 3.80–4.80 ppm that integrates to six protons and corresponds to the methylene groups of the two ligands, and other between 7.20–7.80 (30 H) that corresponds to the phenyl groups. An HMBC $^{31}P\{^1H\}$–$^1H$ correlation enabled identification of the dif-

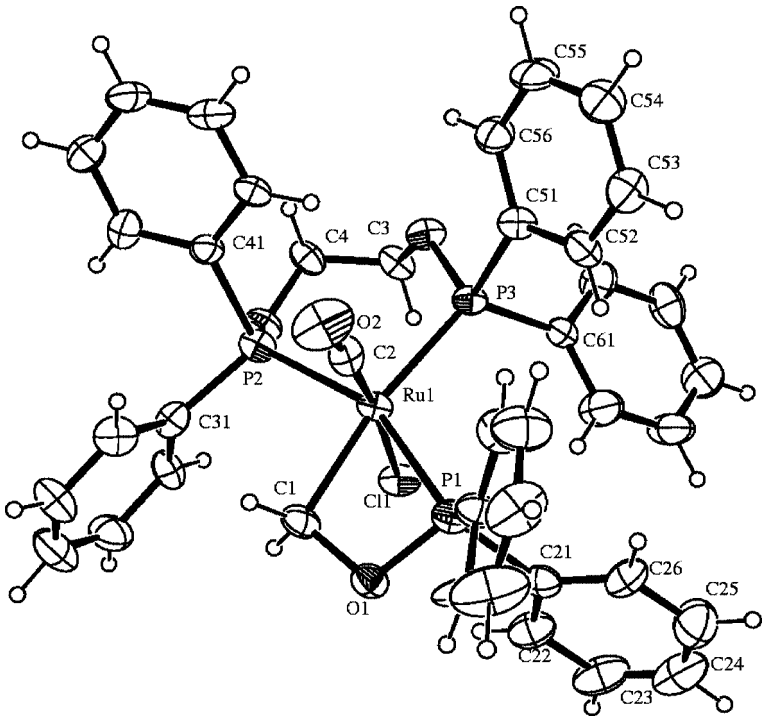


Figure 9. ORTEP drawing of complex **8**.

 © 2006 Wiley-VCH Verlag GmbH & Co. KGaA, Weinheim 

ferent proton signals, showing that the multiplets at $\delta$ = 3.97 and 4.77 ppm (integrating to 2 protons each) can be assigned to the methylene groups of L, and the multiplets at $\delta$ = 4.52 and 4.68 ppm (integrating to one proton each) correspond to the $CH_2$ group bonded to the ruthenium. This observation shows that these two protons are diastereotopic.

An ORTEP view of compound **8** is shown in Figure 9 along with the labelling scheme. Selected distances and angles are given in Table 7. The compound consists of discrete units, although some intermolecular nonclassical Cl···HC hydrogen bonds can be found (see Table 8). The ruthenium atom is in a distorted octahedral environment, coordinated to one chlorine atom, two phosphorus atoms of a diphosphinite ligand, one phosphorus atom, a carbon atom of the diphenyl(oxymethyl-κ*C*)phosphinite-κ*P* ligand and a carbon atom of a carbonyl ligand. Two of the ligands act as bidentate systems (diphosphinite and phosphinite ligand) and these can be considered to be in the equatorial plane. The four-membered chelate ring is one of the main sources of distortion in the octahedron, with an angle of 62.9(3)°. The opposite seven-membered chelate angle in the equatorial plane is slightly larger than one would expect for this ligand, 93.59(9)°, but the two adjacent angles in the equatorial plane do not increase to the same extent [P(1)–Ru(1)–P(3) = 110.85(9)°, C(1)–Ru(1)–P(2) = 92.4(3)°]. The differences found in these angles are due to the steric effects of the phenyl rings on the phosphorus atoms. For the same reason, all the axial angles in the octahedron are close to the expected 180°, except for the P(2)–Ru(1)–P(1) angle [155.26(9)°]. The plane formed by the four atoms in the chelate ring (rms = 0.069) forms a dihedral angle of only 7.2(2)° with the equatorial plane of the donor atoms (rms = 0.047). The ruthenium atom is only 0.096(3) Å out of this plane.

Table 7. Selected bond lengths [Å] and angles [°] for complex **8**.

| Bond lengths | | | |
|---|---|---|---|
| Ru(1)–C(2) | 1.835(11) | Ru(1)–C(1) | 2.181(10) |
| Ru(1)–P(2) | 2.336(3) | Ru(1)–P(1) | 2.346(3) |
| Ru(1)–P(3) | 2.378(3) | Ru(1)–Cl(1) | 2.467(2) |
| P(1)–O(1) | 1.582(6) | O(1)–C(1) | 1.465(11) |
| **Bond angles** | | | |
| C(2)–Ru(1)–C(1) | 89.8(4) | C(2)–Ru(1)–P(2) | 91.9(3) |
| C(1)–Ru(1)–P(2) | 92.4(3) | C(2)–Ru(1)–P(1) | 88.8(3) |
| C(1)–Ru(1)–P(1) | 62.9(3) | P(2)–Ru(1)–P(1) | 155.26(9) |
| C(2)–Ru(1)–P(3) | 97.3(3) | C(1)–Ru(1)–P(3) | 170.5(3) |
| P(2)–Ru(1)–P(3) | 93.59(9) | P(1)–Ru(1)–P(3) | 110.85(9) |
| C(2)–Ru(1)–Cl(1) | 174.0(3) | C(1)–Ru(1)–Cl(1) | 84.3(3) |
| P(2)–Ru(1)–Cl(1) | 87.09(8) | P(1)–Ru(1)–Cl(1) | 89.60(8) |
| P(3)–Ru(1)–Cl(1) | 88.64(8) | O(2)–C(2)–Ru(1) | 176.2(9) |

To the best of our knowledge, the diphenyl(oxymethyl-κ*C*)phosphinite-κ*P* ligand has only previously been found to show this behaviour in the manganese complex tetracarbonyl-2,2-diphenyl-1-oxa-2-phospha-3-manganacyclobutane.[22]

Table 8. Hydrogen-bonding parameters for complex **8** [Å and °].[a]

| D–H···A | *d*(D–H) | *d*(H···A) | *d*(D···A) | blabla(DHA) |
|---|---|---|---|---|
| C(43)–H(43)···Cl(1′) | 0.93 | 2.95 | 3.743(10) | 143.8 |
| C(36)–H(36)···O(4) | 0.93 | 2.48 | 2.854(11) | 104.1 |
| C(56)–H(56)···O(3) | 0.93 | 2.46 | 2.871(11) | 107.2 |

[a] Symmetry transformations used to generate equivalent atoms: ′ *x* – 1, *y*, *z*.

## Conclusions

New dinuclear ruthenium complexes bearing the 1,2-bis(diphenylphosphinite)ethane ligand in different proportions were prepared and characterised. The compounds $[Ru_2(\mu\text{-}Cl)_3(DMSO)_3Cl(\eta^2\text{-}L)]$ (**1**) and $[Ru_2(\mu\text{-}Cl)_3(DMSO)\text{-}Cl(\eta^2\text{-}L)_2]$ (**2**) present a face-sharing bioctahedral structure while compound $[Ru_2Cl_2(\eta^2\text{-}L)_2\{\eta^1\text{-}L(O)\}_2(\mu\text{-}Cl)_2]$ (**3**) has an edge-sharing bioctahedral structure with two chelating L units and two monodentate ligands in which a phosphorus atom is oxidised and remains uncoordinated. Reaction of compound **2** [a mixture of both *cisoid* (**2a**, minor component) and *transoid* (**2b**, major component) isomers] with the monodentate ligands $PPh_{3-n}(OEt)_n$ ($n$ = 1–3) (L′) affords different compounds depending on the structure of L′. When L′ is structurally similar to L (both phosphinites), the resulting compound is the dinuclear doubly chloro-bridged complex $[\{RuCl(\eta^2\text{-}L)(L')\}(\mu\text{-}Cl)_2]$ (**4**), which is very similar to compound **3** – obtained by reacting compound **2** with L. Reaction of compound **2** with the phosphonite L′ ($n$ = 2) gave the face-sharing octahedral compound $[\{Ru(\eta^2\text{-}L)(L')\}_2(\mu\text{-}Cl)_3]Cl$ (**5**) as a mixture of both *cisoid* (**5a**) and *transoid* (**5b**) isomers. On the other hand, when L′ is a phosphite ($n$ = 3) the reaction with compound **2** yields the mononuclear compound $[RuCl_2(\eta^2\text{-}L)(L')_2]$ (**6**). Finally, compound **3** can also be obtained by reaction of $[RuCl_2(DMSO)_4]$ with L, but in this case two more products with formulae $[RuCl_2(L)(Ph_2POPPh_2)]$ (**7**) and $[RuCl(CO)(L)(Ph_2POCH_2)]$ (**8**) were also obtained. In these products a chelating diphosphinite L coexists with new phosphorus ligands formed in situ by metal-mediated disruptions of L.

## Experimental Section

**General:** All experimental manipulations were carried out under argon using Schlenk techniques. All solvents were purified by conventional procedures[23] and distilled prior to use. $[RuCl_2(DMSO)_4]$[24] and 1,2-bis(diphenylphosphanyloxy)ethane[18c] were prepared using published methods. All the other chemicals were commercial products and were used as received without further purification. 1D and 2D NMR spectra ($\delta$, ppm) were recorded in $CDCl_3$, $CD_2Cl_2$ or $C_6D_6$ (as indicated) with a Bruker ARX-400 spectrometer (161 MHz for $^{31}P\{^1H\}$, 100 MHz for $^{13}C\{^1H\}$, 400 MHz for $^1H$) using the solvent as the internal lock. $^{31}P\{^1H\}$ chemical shifts are referred to 85% $H_3PO_4$ with downfield values reported as positive. $^1H$ and $^{13}C\{^1H\}$ signals are referred to residual protonated solvents as internal standards. IR spectra of samples in KBr pellets were obtained with a Bruker Vector IFS28 FT spectrophotometer. Mass spectra were recorded with a Micromass Au-

 © 2006 Wiley-VCH Verlag GmbH & Co. KGaA, Weinheim 

tospec M LSIMS ($FAB^+$) system with 3-nitrobenzyl alcohol as matrix. Microanalyses were carried out with a Fisons EA-1108 apparatus. Merck silica gel 60 (0.040–0.063 mm) was used for column chromatography.

**Synthesis of $[Ru_2(\mu\text{-}Cl)_3(DMSO)_3Cl(L)]$ (1):** A solution of L (2.0 mL, 0.56 mmol) in toluene was added to a solution of $[RuCl_2(DMSO)_4]$ (0.5 g, 1.03 mmol) in toluene (20 mL). The solution was heated under reflux for 1/2 h, cooled to room temperature and concentrated under vacuum. The residue was treated with EtOH to give a yellow solid, which was washed with EtOH and dried under vacuum. Yield: 0.40 g (77%). $C_{32}H_{42}Cl_4O_5P_2Ru_2S_3$ (108.77): calcd. C 38.10, H 4.20, S 9.54; found C 37.97, H 4.19, S 9.50. $^1H$ NMR ($CDCl_3$): $\delta$ = 3.04 (s, 6 H, DMSO), 3.12 (s, 6 H, DMSO), 3.43 (s, 6 H, DMSO), 3.72 (m, 2 H, $CH_2$), 4.26 (m, 2 H, $CH_2$), 7.29 (m, 12 H, Ph), 7.49 (m, 4 H, Ph), 7.78 (m, 4 H, Ph). $^{31}P\{^1H\}$ NMR ($CDCl_3$): $\delta$ = 158.2 (s). IR (KBr): $\nu$(SO) 1093 (s) $cm^{-1}$. $FAB^+$/MS: *m/z* (calculated for the most abundant isotopes) = 1010, ($M^+$), 975 ($M^+$ – Cl), 932 ($M^+$ – DMSO), 776 ($M^+$ – 3 DMSO), 741 ($M^+$ – 3 DMSO – Cl), 602 $[RuCl_2L]^+$.

**Synthesis of $[Ru_2(\mu\text{-}Cl)_3(DMSO)Cl(L)_2]$ (2):** Method (a): A solution of L (1.8 mL, 0.50 mmol) in toluene was added to a solution of **1** (0.50 g, 0.49 mmol) in toluene (20 mL). The solution was heated under reflux for 1/2 h and then cooled to room temperature. The solvent was removed under vacuum and EtOH was added to the oily residue. The resulting yellow precipitate was filtered off, washed with EtOH and dried under vacuum. Yield: 0.43 g (68%). Method (b): A solution of L (4.0 mL, 1.14 mmol) in toluene was added to a solution of $[RuCl_2(DMSO)_4]$ (0.5 g, 1.03 mmol) in toluene (20 mL). The reaction mixture was heated under reflux for 1 h and then cooled to room temperature. The solvent was removed under vacuum and EtOH was added to the oily residue. The resulting yellow precipitate was filtered off, washed with EtOH and dried under vacuum. Yield: 0.39 g (59%). $C_{54}H_{54}Cl_4O_5P_4Ru_2S$ (1282.92): calcd. C 50.55, H 4.24, S 2.50; found C 50.32, H 4.26, S 2.55. $^1H$ NMR ($CDCl_3$) (intensity ratio 1:4 *cisoid*/*transoid* isomers): $\delta$ = 2.54 (s, 3 H, $CH_3'SO$, *transoid*), 2.87 (s, 3 H, $CH_3''SO$, *transoid*), 3.22 (s, 6 H, DMSO, *cisoid*), 3.57–4.13 [m, (5 H, $CH_2$, *transoid* + 5 H, $CH_2$, *cisoid*)], 4.33 [m, (1 H, $CH_2$, *transoid* + 1 H, $CH_2$, *cisoid*)], 4.50 (m, 1 H, $CH_2$, *cisoid*), 4.59 (m, 1 H, $CH_2$, *cisoid*), 4.76 (m, 1 H, $CH_2$, *transoid*), 4.90 (m, 1 H, $CH_2$, *transoid*), 6.80–8.30 [m, (40 H, Ph, *cisoid* + 40 H, Ph, *transoid*)] ppm. $^{31}P\{^1H\}$ NMR ($CDCl_3$): $\delta$ = 146.4 (s, *cisoid*), 148.3 (q, $J_{AB}$ = 44 Hz, *transoid*), 151.9 (d, $J_{AX}$ = 55 Hz), 156.9 (s, *cisoid*), 160.7 (d, $J$ = 55 Hz, *transoid*) ppm. $C_{54}H_{54}Cl_4O_5P_4Ru_2S$: calcd. C 50.55, H 4.24, S 2.50; found C 49.82, H 4.28, S 2.67. $FAB^+$/MS: *m/z* (calculated for the most abundant isotopes) 1284 ($M^+$), 1249 ($M^+$ – Cl), 1206 ($M^+$ – DMSO). X-ray quality crystals were obtained by slow evaporation of a $CH_2Cl_2/Et_2O$ (1:10 v/v) solution.

**Synthesis of $[Ru_2(\mu\text{-}Cl)_2Cl_2(L)_2\{L(O)\}_2]$ (3):** Method (a): A solution of compound **2** (0.150 g, 0.12 mmol) in toluene (20 mL) was added to a solution of L (0.75 mL, 0.26 mmol) in toluene and the mixture was heated under reflux for 1 h, cooled to room temperature and the solvent removed under vacuum. $Et_2O$ was added to the residue and the resulting yellow solid was filtered off, washed with $Et_2O$ and dried under vacuum. Yield: 0.18 g (92%). Method (b): A mixture of $[RuCl_2(DMSO)_4]$ (0.5 g, 1.03 mmol) and a solution of L (7.5 mL, 2.14 mmol) in toluene (20 mL) was heated under reflux for 2 h with stirring. The solution was cooled to room temperature and the solvent was removed under vacuum to give an oily residue. $Et_2O$ (5 mL) was added and the resulting yellow solid was filtered off. Compounds **7** and **8** were obtained from the filtrate (see below). The solid was washed with $Et_2O$ and dried under vacuum. Yield: 0.72 g (42%). $C_{104}H_{96}Cl_4O_{10}P_8Ru_2$ (2097.61): calcd. C 59.55, H 4.61; found C 59.20, H 4.63. $^1H$ NMR ($CDCl_3$): $\delta$ = 3.68 (m, 4 H, $CH_2$, L), 3.73 [m, 4 H, $CH_2$, L(O)], 4.17 [m, 4 H, $CH_2$, L(O)], 4.49 (m, 4 H, $CH_2$, L), 6.80–8.00 (m, 80 H, Ph) ppm. $^{31}P\{^1H\}$ NMR ($CDCl_3$): $\delta$ = 32.5 [s, (P=O), L(O)], 138.3 [t, $J$ = 46 Hz, P, L(O)], 159.0 (d, $J$ = 46 Hz, 2P, L) ppm. $FAB^+$/MS: *m/z* (calculated for the most abundant isotopes) 1617 [$M^+$ – Cl – L(O)], 1580 [$M^+$ – 2 Cl – L(O)], 1013 $[RuClLL(O)]^+$.

**Synthesis of $[Ru_2(\mu\text{-}Cl)_2Cl_2(L)_2\{PPh_2(OEt)\}_2]$ (4):** $PPh_2(OEt)$ (0.05 mL, 0.24 mmol) was added to a solution of compound **2** (0.150 g, 0.12 mmol) in toluene (20 mL). The mixture was heated under reflux for 1 h and the solvent was removed under vacuum. Addition of $Et_2O$ gave an orange-yellow precipitate and this was filtered off, washed with $Et_2O$ and dried under vacuum. Yield: 0.15 g (75%). $C_{80}H_{78}Cl_4O_6P_6Ru_2$ (1665.27): calcd. C 57.70, H 4.72; found C 57.53, H 4.71. $^1H$ NMR ($CDCl_3$): $\delta$ = 1.22 (t, $J$ = 7 Hz, 6 H, $CH_3$), 3.50 (m, 4 H, $OCH_2$), 3.86 (m, 4 H, $CH_2$), 4.31 (m, 4 H, $CH_2$), 6.50–7.90 (m, 60 H, Ph) ppm. $^{31}P\{^1H\}$ NMR ($CDCl_3$): $\delta$ = 136.3 (t, $J$ = 46 Hz, P, L′), 159.7 (d, $J$ = 46 Hz, 2P, L) ppm. $FAB^+$/MS: *m/z* (calculated for the most abundant isotopes) 1631 ($M^+$ – Cl), 1436 ($M^+$ – L′), 1401 ($M^+$ – L′ – Cl), 832 $[RuCl_2LL']^+$, 797 $[RuClLL']^+$.

**Synthesis of $[Ru_2(\mu\text{-}Cl)_3(L)_2\{PPh(OEt)_2\}_2]Cl$ (5):** $PPh(OEt)_2$ (0.07 mL, 0.24 mmol) was added to a solution of compound **2** (0.150 g, 0.12 mmol) in toluene (20 mL). The mixture was heated under reflux for 1.5 h and the solvent was removed under vacuum. Addition of $Et_2O$ gave a yellow precipitate and this was filtered off, washed with $Et_2O$ and dried under vacuum. Yield: 0.13 g (67%). $C_{72}H_{78}Cl_4O_8P_6Ru_2$ (1601.18): calcd. C 54.01, H 4.91; found C 53.81, H 4.88. $^1H$ NMR ($CDCl_3$): $\delta$ = 0.83 (t, 6 H, $J$ = 7 Hz, $CH_3$, *transoid*), 0.97 (t, 6 H, $J$ = 7 Hz, $CH_3$, *transoid*), 1.25 (m, 12 H, $CH_3$, *cisoid*), 3.50–3.90 [m, 16 H, $CH_2$ (L + L′), *transoid*], 4.01 [m, 8 H, $CH_2$ (L′), *cisoid*], 4.26 [m, 4 H, $CH_2$, (L)], 4.51 [m, 4 H, $CH_2$, (L)], 6.40–8.00 [m, (50 H, Ph, *cisoid*) + (50 H, Ph, *transoid*)] ppm. $^{31}P\{^1H\}$ NMR ($CDCl_3$): $\delta$ = 149.6 [$t_{apparent}$, $J_{app}$ = 48 Hz, 2P (L), *transoid*], 151.7 [d, $J$ = 53 Hz, 4P (L), *cisoid*], 153.0 [$t_{apparent}$, $J_{app}$ = 48 Hz, 2P (L), *transoid*], 156.1 [$t_{apparent}$, $J_{app}$ = 53 Hz, 2P (L′), *transoid*], 158.2 [t, $J$ = 53 Hz, 2P (L′), *cisoid*] ppm. $FAB^+$/MS *m/z* (calculated for the most abundant isotopes) 1567 ($M^+$), 1530 ($M^+$ – Cl), 765 $[RuClLL']^+$. X-ray quality crystals were obtained by slow evaporation of a $CH_2Cl_2/Et_2O$ (1:10 v/v) solution.

**Synthesis of $[RuCl_2L\{P(OEt)_3\}_2]$ (6):** $P(OEt)_3$ (0.08 mL, 0.48 mmol) was added to a solution of compound **2** (0.150 g, 0.12 mmol) in toluene (20 mL). The mixture was heated under reflux for 1 h and the solvent was removed under vacuum. Addition of $Et_2O$ gave a pale yellow precipitate and this was filtered off, washed with $Et_2O$ and dried under vacuum. Yield: 0.14 g (62%). $C_{38}H_{54}Cl_2O_8P_4Ru$ (934.71): calcd. C 48.83, H 5.82; found C 49.05, H 5.85. $^1H$ NMR ($CDCl_3$): $\delta$ = 0.90 (t, $J$ = 7 Hz, 9 H, $CH_3$), 1.22 (t, $J$ = 7 Hz, 9 H, $CH_3$), 3.26 [m, 3 H, $CH_2$ (L′)], 3.43 [m, 3 H, $CH_2$ (L′) + 1 H, $CH_2$ (L)], 3.98 [m, 1 H, $CH_2$ (L)], 4.23 [m, 3 H, $CH_2$ (L′)], 4.40 [m, 1 H, $CH_2$ (L)], 4.46 [m, 3 H, $CH_2$ (L′)], 5.67 [m, 1 H, $CH_2$ (L)] ppm. $^{31}P\{^1H\}$NMR ($CDCl_3$): $\delta$ = 97.8 (ddd, $J_{cis}$ = 24, 48 Hz, $J_{trans}$ = 544 Hz, $P_1$), 122.0 (ddd, $J_{cis}$ = 46, 64 Hz, $J_{trans}$ = 544 Hz, $P_4$), 129.8 (ddd, $J_{cis}$ = 47, 48, 64 Hz, $P_2$), 150.7 (ddd, $J_{cis}$ = 24, 46, 47 Hz, $P_3$) ppm. $FAB^+$/MS: *m/z* (calculated for the most abundant isotopes) 899 ($M^+$ – Cl), 733 [$M^+$ – Cl – $P(OEt)_3$]. X-ray quality crystals were obtained by slow evaporation of a $CH_2Cl_2/Et_2O$ (1:10 v/v) solution.

**Synthesis of $[RuCl_2(L)(Ph_2POPPh_2)]$ (7) and $[RuCl(CO)(L)(PPh_2OCH_2)]$ (8):** From the ether solution obtained during the synthesis of compound **3** [Method (b), see above], the solvent was re-

 © 2006 Wiley-VCH Verlag GmbH & Co. KGaA, Weinheim 

moved under vacuum, and the residue was treated with MeOH to give a yellow solid, which was washed with MeOH and dried under vacuum. This solid was a mixture of compounds **7** and **8** and these were separated by column chromatography using silica gel as the stationary phase. Complex **7** was eluted first using a mixture of $CH_2Cl_2/Et_2O$ (10:1, v:v). The eluent was removed under vacuum and the residue was treated with EtOH to give a yellow solid, which was filtered off, washed with EtOH and dried under vacuum. Yield: 0.012 g (12%). $^1H$ NMR ($CDCl_3$): $\delta$ = 4.30 (m, 4 H, $CH_2$), 6.90–7.50 (m, 40 H, Ph) ppm. $^{31}P\{^1H\}$ NMR ($CDCl_3$): $\delta$ = 106.8 (m, $P_{3,4}$), 133.0 (m, $P_{1,2}$) ppm. $C_{50}H_{44}Cl_2O_3P_4Ru$ (988.75): calcd. C 60.74, H 4.49; found C 60.60, H 4.50. $FAB^+$/MS: *m*/*z* (calculated for the most abundant isotopes) 988 ($M^+$), 953 ($M^+$ – Cl), 602 $[RuCl_2L]^+$. X-ray quality crystals were obtained by slow evaporation of a $CH_2Cl_2$/EtOH (1:10 v/v) solution. Complex **8** was eluted using $CH_2Cl_2$ as eluent. The solvent was removed under vacuum and the residue was treated with EtOH. The resulting white solid was filtered off, washed with EtOH and dried under vacuum. Yield: 0.013 g (1.5%). IR (KBr disc): 1953 (s) ($\nu_{co}$) $cm^{-1}$. $^1H$ NMR ($CDCl_3$): $\delta$ = 3.80–4.80 (m, 6 H, $CH_2$), 7.20–7.80 (m, 30 H, Ph) ppm. $^{31}P\{^1H\}$ NMR ($CDCl_3$): $\delta$ = 76.0 (dd, $J_{12}$ = 341, $J_{13}$ = 14 Hz, $P_1$), 131.5 (dd, $J_{23}$ = 31 Hz, $P_3$), 133.3 (dd, $P_2$) ppm. $C_{40}H_{36}ClO_4P_3Ru$ (810.15): calcd. C 59.30, H 4.48; found C 59.46, H 4.46. $FAB^+$/MS: *m*/*z* (calculated for the most abundant isotopes) 782 ($M^+$ – CO), 775 ($M^+$ – Cl), 747 ($M^+$ – CO – Cl), 595 $[RuCl(CO)L]^+$. X-ray quality crystals were obtained by slow evaporation of a $CH_2Cl_2$/EtOH (1:10 v/v) solution.

CCDC-297717 to -297721 contain the supplementary crystallographic data for this paper. These data can be obtained free of charge from The Cambridge Crystallographic Data Centre via www.ccdc.cam.ac.uk/data_request/cif.

Details of crystal data and structural refinement are given in Table 9. The data were collected with a SIEMENS Smart CCD area-detector diffractometer with graphite-monochromated Mo-$K_\alpha$ radiation. Absorption correction was carried out using SADABS.[25]

The structures of **5a** and **8** were solved by Patterson methods and the structures of **2a**, **6** and **7** were solved by direct methods. All of the structures were refined by a full-matrix least-squares based on $F^2$.[26] In the case of **5a** and **7** the compounds crystallised with a solvent molecule and the Squeeze program was used to correct the reflection data for the diffuse scattering due to disordered solvent.[27] Non-hydrogen atoms were refined with anisotropic displacement parameters. Hydrogen atoms were included in idealised positions and refined with isotropic displacement parameters. Atomic scattering factors and anomalous dispersion corrections for all atoms were taken from International Tables for X-ray Crystallography.[28]

Table 9. Crystallographic data for **2a**, **5a**, **6**, **7** and **8**.

| Compound | **2a** | **5a** | **6** | **7** | **8** |
|---|---|---|---|---|---|
| Empirical formula | $C_{54}H_{54}Cl_4O_5P_4Ru_2S$ | $C_{72}H_{78}Cl_4O_8P_6Ru_2$ | $C_{38}H_{54}Cl_2O_8P_4Ru$ | $C_{50}H_{44}Cl_2O_3P_4Ru$ | $C_{40}H_{36}ClO_4P_3Ru$ |
| Formula mass | 1282.85 | 1601.10 | 934.66 | 988.70 | 810.12 |
| Temperature [K] | 293(2) | 293(2) | 293(2) | 293(2) | 293(2) |
| Wavelength [Å] | 0.71073 | 0.71073 | 0.71073 | 0.71073 | 0.71073 |
| Crystal system | triclinic | triclinic | monoclinic | monoclinic | monoclinic |
| Space group | $P\bar{1}$ | $P\bar{1}$ | $P2_1/c$ | $P2_1/c$ | $P2_1/c$ |
| *a* [Å] | 13.089(2) | 12.312(4) | 19.068(4) | 18.2857(15) | 10.3989(19) |
| *b* [Å] | 14.520(3) | 16.121(5) | 13.511(3) | 10.9637(9) | 30.417(5) |
| *c* [Å] | 19.143(3) | 24.310(7) | 17.006(4) | 23.896(2) | 14.4224(19) |
| $\alpha$ [°] | 110.211(4) | 73.483(8) | 90 | 90 | 90 |
| $\beta$ [°] | 93.650(4) | 81.195(6) | 102.146(5) | 94.062(2) | 125.777(9) |
| $\gamma$ [°] | 99.004(4) | 83.280(7) | 90 | 90 | 90 |
| Volume [Å$^3$] | 3344.8(10) | 4558(2) | 4283.4(17) | 4778.6(7) | 3701.0(10) |
| *Z* | 2 | 2 | 4 | 4 | 4 |
| $D_{calcd}$ [Mg/m$^3$] | 1.274 | 1.167 | 1.449 | 1.374 | 1.454 |
| Absorption coefficient [mm$^{-1}$] | 0.776 | 0.596 | 0.688 | 0.614 | 0.666 |
| *F*(000) | 1300 | 1640 | 1936 | 2024 | 1656 |
| Crystal size [mm] | 0.24 × 0.14 × 0.09 | 0.29 × 0.214 × 0.23 | 0.34 × 0.21 × 0.20 | 0.50 × 0.33 × 0.26 | 0.25 × 0.27 × 0.15 |
| $\theta$ range for data collection [°] | 1.52–28.11 | 1.68–28.19 | 1.86–28.07 | 1.71–28.03 | 1.34–28.08 |
| Index ranges | $-17 \le h \le 17$ | $-16 \le h \le 15$ | $-25 \le h \le 20$ | $-16 \le h \le 23$ | $-13 \le h \le 13$ |
| | $-19 \le k \le 19$ | $-21 \le k \le 13$ | $-16 \le k \le 17$ | $-13 \le k \le 14$ | $-40 \le k \le 25$ |
| | $-16 \le l \le 25$ | $-31 \le l \le 30$ | $-17 \le l \le 22$ | $-31 \le l \le 31$ | $-18 \le l \le 18$ |
| Reflections collected | 17668 | 30329 | 27353 | 27535 | 19695 |
| Independent reflections | 12503 [*R*(int) = 0.0740] | 21088 [*R*(int) = 0.1186] | 10210 [*R*(int) = 0.1652] | 10879 [*R*(int) = 0.0441] | 8278 [*R*(int) = 0.1512] |
| Reflections observed ($>2\sigma$) | 3658 | 3904 | 3373 | 6882 | 2658 |
| Data completeness | 0.765 | 0.939 | 0.981 | 0.940 | 0.918 |
| Max. and min. transmission | 1.00000 and 0.81992 | 1.0000 and 0.7838 | 1.0000 and 0.711 | 1.00000 and 0.817076 | 1.0000 and 0.36612 |
| Data/restraints/parameters | 12503/0/598 | 21088/0/833 | 10210/0/484 | 10879/0/541 | 8278/0/450 |
| Goodness-of-fit on $F^2$ | 0.969 | 0.608 | 0.700 | 0.849 | 0.811 |
| Final *R* indices [$I > 2\sigma(I)$] | $R_1$ = 0.0987 | $R_1$ = 0.0724 | $R_1$ = 0.0553 | $R_1$ = 0.0386 | $R_1$ = 0.0732 |
| | $wR_2$ = 0.2866 | $wR_2$ = 0.1638 | $wR_2$ = 0.0699 | $wR_2$ = 0.0673 | $wR_2$ = 0.1231 |
| *R* indices (all data) | $R_1$ = 0.2550 | $R_1$ = 0.2650 | $R_1$ = 0.1974 | $R_1$ = 0.0748 | $R_1$ = 0.2516 |
| | $wR_2$ = 0.3317 | $wR_2$ = 0.1992 | $wR_2$ = 0.0915 | $wR_2$ = 0.0728 | $wR_2$ = 0.1652 |
| Largest diff. peak/hole [e/Å$^3$] | 2.637/–0.637 | 0.632/–0.451 | 0.695/–1.054 | 0.509/–0.371 | 1.088/–0.617 |

 © 2006 Wiley-VCH Verlag GmbH & Co. KGaA, Weinheim 

**Supporting Information** (see also the footnote on the first page of this article): 2D $^{1}H,^{13}C\{^{1}H\}$ HSQC experiment for $[Ru_2(\mu\text{-}Cl)_3(DMSO)_3Cl(L)]$ (**1**); 2D $^{1}H,^{31}P\{^{1}H\}$ HMBC experiments for $[Ru_2(\mu\text{-}Cl)_3(DMSO)Cl(L)_2]$ (**2**) and $[RuCl_2(L)(Ph_2POPPh_2)]$ (**7**); synthesis and crystal structure of $[Ru_2(\mu\text{-}Cl)_3(L)_2\{PPh_2(OEt)\}_2]Cl$.

## Acknowledgments

Financial support from the Xunta de Galicia (Project PGIDT04PXIC31401PN) and from the Spanish Ministry of Education and Science (Project BQU2003-06783) is gratefully acknowledged. We thank the University of Vigo CACTI services for collecting X-ray data and recording NMR spectra.

[1] a) B. M. Trost, M. U. Frederiksen, M. T. Rudd, *Angew. Chem. Int. Ed.* **2005**, *44*, 6630–6666; b) J. Gimeno, *Curr. Org. Chem.* **2006**, *10*, 113.

[2] a) S. C. Weatherly, I. V. Yang, H. H. Thorp, *J. Am. Chem. Soc.* **2001**, *123*, 1236–1237; b) C. J. Burrows, J. G. Muller, *Chem. Rev.* **1998**, *98*, 1109–1151.

[3] a) J. Malina, O. Novakova, B. K. Keppler, E. Alessio, V. Bravec, *J. Biol. Inorg. Chem.* **2001**, *6*, 435–445; b) M. J. Clark, F. Zhu, D. R. Frasca, *Chem. Rev.* **1999**, *99*, 2511–2533.

[4] a) V. Alezra, G. Bernardinelli, C. Corminboeuf, U. Frey, E. P. Kündig, A. E. Merbach, C. M. Saudan, F. Viton, J. Weber, *J. Am. Chem. Soc.* **2004**, *126*, 4843–4853; b) Y.-G. Zhou, X. Zhang, *Chem. Commun.* **2002**, *10*, 1124–1125; c) Y.-G. Zhou, W. Tang, W.-B. Wang, W. Li, X. Zhang, *J. Am. Chem. Soc.* **2002**, *124*, 4952–4953; d) Z. Csok, G. Szalontai, G. Czira, L. Kollar, *J. Organomet. Chem.* **1998**, *570*, 23–29.

[5] a) L. Quebatte, R. Scopelliti, K. Severin, *Angew. Chem. Int. Ed.* **2004**, *43*, 1520–1524; b) B. De Clerq, F. Verpoort, *Tetrahedron Lett.* **2002**, *43*, 4687–4690; c) A. C. da Silve, H. Piotrowski, P. Mayer, K. Polborn, K. Severin, *Eur. J. Inorg. Chem.* **2001**, 685–691; d) M. T. Reetz, M. H. Becker, M. Liebl, A. Fürstner, *Angew. Chem. Int. Ed.* **2000**, *39*, 1236–1239.

[6] T. J. Geldbach, A. B. Chaplin, K. D. Hänni, R. Scopelliti, P. J. Dyson, *Organometallics* **2005**, *24*, 4974–4980.

[7] a) E. Iengo, E. Zangrando, E. Baiutti, F. Munini, E. Alessio, *Eur. J. Inorg. Chem.* **2005**, 1019–1031; b) A. M. Joshi, I. S. Thorburn, S. J. Rettig, B. R. James, *Inorg. Chim. Acta* **1992**, *198–200*, 283–296; c) J. S. Jaswal, S. J. Rettig, B. R. James, *Can. J. Chem.* **1990**, *68*, 1808–1817.

[8] a) C. Bianchini, P. Barbaro, G. Scapacci, F. Zanobini, *Organometallics* **2000**, *19*, 2450–2461; b) see compound **2** in next paragraph.

[9] Compound **2** can also be obtained by reaction of $[RuCl_2(DMSO)_4]$ with L in a 1:1 molar ratio in refluxing toluene for 1 h.

[10] S. D. Drouin, S. Monfette, D. Amoroso, G. P. A. Yap, D. E. Fogg, *Organometallics* **2005**, *24*, 4721–4728.

[11] a) J. Bravo, J. Castro, S. García-Fontán, E. M. Lamas, P. Rodríguez-Seoane, *Z. Anorg. Allg. Chem.* **2003**, *629*, 297–302; b) F. Fernández-García, S. Bolaño, R. Carballo, S. García-Fontán, J. Bravo, *Polyhedron* **2001**, *20*, 2675–2681.

[12] a) F. A. Cotton, R. C. Torralba, *Inorg. Chem.* **1991**, *30*, 2196–2207; b) S. Gauthier, L. Quebatte, R. Scopelliti, K. Severin, *Chem. Eur. J.* **2004**, *10*, 2811–2821.

[13] The structure of **4′** has been accidentally confirmed by the serendipitous preparation and X-ray structure analysis of $[\{Ru(\eta^2\text{-}L)[PPh_2(OEt)]\}_2(\mu\text{-}Cl)_3]Cl$ (see Supporting Information) that presents spectral features identical to those of the *transoid* isomer of **4′**.

[14] a) D. J. Darensbourg, F. Joó, M. Kannisto, A. Katho, J. H. Reibenspies, D. J. Daigle, *Inorg. Chem.* **1994**, *33*, 200–208; b) A. R. Chakravarty, F. A. Cotton, W. Schwotzer, *Inorg. Chim. Acta* **1984**, *84*, 179–185; c) R. F. Winter, B. M. Brunner, T. Scheiring, *Inorg. Chim. Acta* **2000**, *310*, 21–26; d) A. Keller, B. Jasionka, T. Glowiak, A. Ershov, R. Matusiak, *Inorg. Chim. Acta* **2003**, *344*, 49–60.

[15] This compound can be obtained in two other ways using $[RuCl_2(COD)]_n$ or $[RuCl_2(PPh_3)_4]$ as metallic precursors.

[16] D. J. Irvine, C. Glidewell, D. J. Cole-Hamilton, J. C. Barnes, A. Howie, *J. Chem. Soc., Dalton Trans.* **1991**, 1765–1772.

[17] K. Wang, T. J. Emge, A. S. Goldman, *Organometallics* **1994**, *13*, 2135–2137.

[18] a) J. Bravo, J. A. Castro, E. Freijanes, S. García-Fontán, E. M. Lamas, P. Rodríguez-Seoane, *Z. Anorg. Allg. Chem.* **2005**, *631*, 2067–2074; b) S. Bolaño, J. Bravo, S. García-Fontán, *Inorg. Chim. Acta* **2001**, *315*, 81–87; c) S. Bolaño, J. Bravo, R. Carballo, S. García-Fontán, U. Abram, E. M. Vázquez-López, *Polyhedron* **1999**, *18*, 1431–1436.

[19] M. M. Turnbull, E. H. Wong, E. J. Gabe, F. L. Lee, *Inorg. Chem.* **1986**, *25*, 3189–3194.

[20] a) C. S. Kraihanzel, C. M. Bartish, *J. Am. Chem. Soc.* **1972**, *94*, 3572–3575; b) D. E. C. Corbridge, *Phosphorus. An Outline of its Chemistry, Biochemistry and Technology*, 5th ed., Elsevier, **1995**, chapter 10.

[21] a) E. H. Wong, L. Prasad, E. J. Gabe, F. C. Bradley, *J. Organomet. Chem.* **1982**, *236*, 321–331; b) F. C. Bradley, E. H. Wong, E. J. Gabe, F. L. Lee, Y. Lepage, *Polyhedron* **1987**, *6*, 1103–1110; c) D. J. Irvine, D. J. Cole-Hamilton, J. Barnes, P. K. G. Hodgson, *Polyhedron* **1989**, *8*, 1575–1577.

[22] E. Lindner, H.-J. Eberle, S. Hoehne, *Chem. Ber.* **1981**, *114*, 413–422.

[23] D. D. Perrin, W. L. F. Armarego, *Purification of Laboratory Chemicals*, 3rd ed., Butterworth and Heinemann, Oxford, **1988**.

[24] I. P. Evans, A. Spencer, G. Wilkinson, *J. Chem. Soc., Dalton Trans.* **1973**, *2*, 204–209.

[25] G. M. Sheldrick, *SADABS. An empirical absorption correction program for area detector data*, University of Göttingen, Germany, **1996**.

[26] G. M. Sheldrick, *SHELX-97. Program for the solution and refinement of crystal structures.* University of Göttingen, Germany, **1997**.

[27] A. L. Spek, *Acta Crystallogr., Sect. A: Found. Cystallogr.* **1990**, *46*, C34.

[28] International Tables for X-ray Crystallography, vol. C, Kluwer, Dordrecht, **1992**.

Received: March 1, 2006
Published Online: June 6, 2006

 © 2006 Wiley-VCH Verlag GmbH & Co. KGaA, Weinheim 

DOI: 10.1002/ejic.200600189

# 2D and 3D Cadmium(II) Coordination Polymers from a Flexible Tripodal Ligand of 1,3,5-Tris(carboxymethoxy)benzene and Bidentate Pyridyl-Containing Ligands with Three-, Eight- and Ten-Connected Topologies

**Suna Wang,[a] Hang Xing,[a] Yizhi Li,[a] Junfeng Bai,*[a] Yi Pan,[a] Manfred Scheer,*[b] and Xiaozeng You[a]**

**Keywords:** Metal-organic frameworks / Tripodal ligands / Topology / Metal carboxylates

Four novel cadmium(II) coordination polymers, $[Cd_3(TCMB)_2(4,4'\text{-bipy})(H_2O)_{16}]_n$ (**1**), $[Cd_3(TCMB)_2(bpe)(H_2O)_{13}]_n$ (**2**), $[Cd_3(TCMB)_2(bpe)_2(H_2O)_4]_n$ (**3**), and $[Cd_3(TCMB)_2(dpp)_2(H_2O)_3]_n$ (**4**), [TCMB = 1,3,5-tris(carboxymethoxy)benzene, 4,4-bipy = (4,4-bipyridine), bpe = 1,2-bis(4-pyridyl)ethane, dpp = 1,3-bis(4-pyridyl)propane] have been hydrothermally synthesized by the self-assembly of the flexible tripodal acid TCMB and $Cd(OAc)_2{\cdot}2H_2O$ with pyridyl-containing ligands possessing different flexibilities. Single-crystal X-ray diffraction analysis reveals that the four polymers exhibit novel frameworks due to diverse coordination modes and different conformations of the flexible TCMB as well as pyridyl-containing ligands. Complex **1** shows a unique twofold parallel interpenetrating 2D honeycomb network structure with an unusual $6^3$ topology, in which two different large hexagonal rings are arranged alternately, with extraordinary dimensions of ca. 22.172(6) × 12.947(2) Å (A) and 17.233(2) × 12.947(2) Å (B) based on the distances of the atoms at the opposite positions of the rings. Complex **2** is almost isostructural to complex **1**, except that the bidentate bpe ligands bridge the cadmium centers in an *anti* conformation, rendering the network more flexible. Complex **3** features a 3D network with one of the scarce eight-connected $(4^6, 6^{14}, 8^8)(4^3)_2$ topologies based on the rare $CdI_2$-type layer constructed from secondary building units (SBUs) of rare $[Cd_3(CO_2)_4]^{2-}$ isosceles triangle cadmium clusters. Complex **4** possesses distorted $CdI_2$-type layers constructed from unprecedented ten-connected $Cd_3$ clusters which are linked by more flexible dpp ligands in a *trans-gauche* (TG) conformation in (4,4) networks, leading to another 3D framework of the unusual $(4^{18}, 6^{24}, 8^3)(4^3)_2$ topology. Such an arrangement represents the highest connected topology presently known for the frameworks. Among them, complex **1** displays photoluminescent properties at 460 nm due to the ligand-to-metal charge transfer (LMCT).

(© Wiley-VCH Verlag GmbH & Co. KGaA, 69451 Weinheim, Germany, 2006)

## Introduction

In recent years, self-assembly of metal-organic frameworks (MOFs) has attracted much attention not only for the potential discovery of novel functional materials, which may have applications in the areas including gas storage, molecular sieves, ion-exchange, catalysis, magnetism, and optoelectronics, but also for their intriguing variety of architectures and topologies, such as molecular grids, bricks, herringbones, ladders, rings, boxes, diamondoids, and honeycombs.[1–4] In particular, exploring highly symmetrical multi-topic ligands and suitable metal salts in order to construct supramolecular architectures is of great interest.[5,6] On the basis of $[Cp^*Fe(\eta^5\text{-}P_5)]$, we have synthesized the inorganic fullerene-like molecules and 1D or 2D coordination polymers.[7] Generally, rigid symmetrical multi-topic ligands which have been intensively investigated can lead to more predictable supramolecular structures, but the diversity of them has been limited to some extent due to the fact that little or even no conformational changes can be observed for these kinds of ligands when treated with metal ions. By contrast, flexible ligands can adopt different conformations and coordination modes according to the geometric requirements of different metal ions and may afford unpredictable and interesting supramolecular networks. Their reactivities and coordination chemistry have been less explored and the investigation of metal-organic frameworks is still a great challenge.[6]

In order to extend our work in this field, we have turned our attention to an unexplored tripodal ligand, 1,3,5-tris(carboxymethoxy)benzene (TCMB). In comparison with the more intensively investigated rigid ligand, 1,3,5-benzenetricarboxylic acid (BTC),[8] it exhibits additional interesting characteristics, such as more flexibility because of the

[a] The State Key Laboratory of Coordination Chemistry & School of Chemistry and Chemical Engineering, Nanjing University, Nanjing 210093, P. R. China
E-mail: bjunfeng@nju.edu.cn
[b] Institut für Anorganische Chemie der University of Regensburg, 93040 Regensburg, Germany
E-mail: manfred.scheer@chemie.uni-regensburg.de

Supporting information for this article is available on the WWW under http://www.eurjic.org or from the author.

 © 2006 Wiley-VCH Verlag GmbH & Co. KGaA, Weinheim 

presence of a $–OCH_2–$ spacer between the benzene ring and carboxylate moiety, which may bend to enable it to coordinate metal centers, and the existence of the ether oxygen atom may function as an electron-donor forming hydrogen bonds to stabilize the entire structure. Thus, rich topologies, including coordination modes, packing fashions, and dimensionalities of supramolecular coordination solids, may result from this interesting ligand. Herein, we report four novel 2D and 3D cadmium(II) compounds with unusual topologies and different pyridyl-containing coligands, among which $[Cd_3(TCMB)_2(4,4'\text{-bipy})(H_2O)_{16}]_n$ (**1**) and $[Cd_3(TCMB)_3(bpe)(H_2O)_{13}]_n$ (**2**) exhibit a novel kind of 2D-twofold interpenetrating $6^3$ network with two types of large hexagonal rings arranged alternately, whereas $[Cd_3(TCMB)_2(bpe)_2(H_2O)_4]_n$ (**3**) shows a 3D compact network composed of rare 2D $CdI_2$-type layers linked by the bpe ligand, with a topology of $(4^6, 6^{14}, 8^8)(4^3)_2$ where the novel isosceles triangle $Cd_3$ SBUs are taken as eight-connected nodes and TCMB ligands as three-connected nodes. $[Cd_3(TCMB)_2(dpp)_2(H_2O)_3]_n$ (**4**) has ten-connected nodes similar to $Cd_3$ SBUs connected by more flexible dpp ligands with a different topology of $(4^{18}, 6^{24}, 8^3)(4^3)_2$. Moreover, the effects of the coligand, different pyridyl-containing coligands on the structures, and luminescent properties of the metal-organic frameworks have been investigated in detail.

## Results and Discussion

### Syntheses of the Complexes

Because of the low solubility of the TCMB ligand, the hydrothermal method was employed in our syntheses. The crystals cannot be obtained through general hydrothermal conditions above 100 °C and only comparably low temperatures such as 80 °C are appropriate for the isolation of good-quality crystals. Additionally, the polarity of the solvent may also influence the process of assembly and it has been proven that the addition of cosolvent $CH_3OH$ or $C_2H_5OH$ helps with the formation of the complexes.[9] For the rigid 4,4-bipy ligand the ratio of bases/acids is in the range 1:1 to 3:1 and seems to have no effect on the product. However, increasing the ratio of bpe ligand/acids from 1:1 to 3:1 extends the two-dimensional structure to the three-dimensional network, and dpp crystals can only be formed from reactions where this coligand is in excess. Other cadmium salts such as $Cd(NO_3)_2{\cdot}6H_2O$ were used instead of $Cd(OAc)_2{\cdot}2H_2O$, but only precipitates were afforded, indicating that the $OAc^-$ anion may play an important role in the formation of the crystals.

### Structural Description

#### *$[Cd_3(TCMB)_2(4,4'\text{-bipy})(H_2O)_{16}]_n$ (1)*

Single-crystal X-ray studies reveal that the fundamental building unit of complex **1** consists of two repeating crystallographically independent $Cd^{II}$ centers (Cd1 and Cd2) [Figure 1(a)]. Two chelating carboxylate groups (O4, O5, $O6^i$, $O7^i$: symmetry code i: $1+x, -1+y, z$) from different TCMB ligands as well as one nitrogen atom from the 4,4-bipy ligand occupy the equatorial positions around the Cd1 center, and two aqua molecules occur at the apical positions, leading to the heptacoordinated pentagonal-bipyramidal coordination geometry. The average Cd–O and Cd–N distances are ca. 2.376(4) Å and 2.338(5) Å, respectively. The coordinated carboxylate groups are statistically different in that for the O6 and O7 carboxylate group, the Cd–O distances are 2.350(4) Å and 2.507(4) Å, respectively, suggesting that the pentagonal bipyramid is significantly distorted. On the other hand, the Cd2 center exhibits an octahedral geometry, with two oxygen atoms from aqua molecules (O3w, $O3w^{ii}$) (symmetry code ii: $-x, -y, 2-z$) and two monodentate carboxylate groups of separated TCMB ligands (O9, $O9^{ii}$) in *trans* positions composing the equatorial plane, and two other aqua molecules (O4w, $O4w^{ii}$) in apical sites completing the coordination sphere. All the Cd–O and Cd–N distances are listed in Table 1; they are slightly larger than the results for other Cd–OFs.[10]

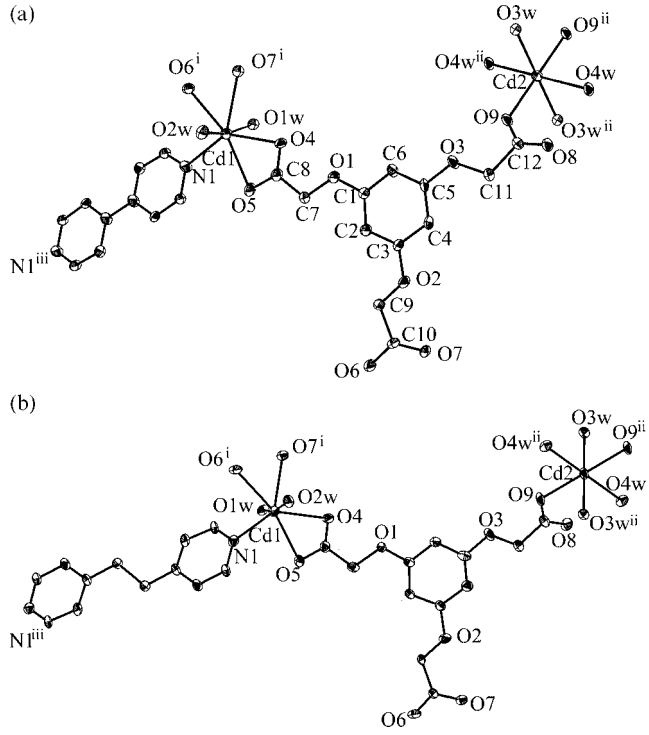


Figure 1. Coordination environments for the $Cd^{2+}$ centers in **1** (a) and **2** (b). Hydrogen atoms and solvent molecules have been omitted for clarity, and thermal ellipsoids are drawn at the 30% probability level. Selected bond information is listed in Table 1. Symmetry codes for **1**: (i) $1+x, -1+y, z$; (ii) $-x, -y, 2-z$; (iii) $3-x, 1-y, -z$: for **2**: (i) $1+x, -1+y, z$; (ii) $2-x, 1-y, 3-z$; (iii) $1-x, 3-y, -1-z$.

The TCMB ligand is completely deprotonated and acts as a $\mu^3$-bridge linking three cadmium centers, and ether oxygen atoms are not involved in the coordination spheres [Scheme 1(a)]. Two kinds of coordination fashions exist for the three carboxylate groups, in which two of them adopt bidentate chelating modes to connect Cd1 centers while the third bridges one Cd2 center through one carboxylate oxy-

 © 2006 Wiley-VCH Verlag GmbH & Co. KGaA, Weinheim 

Table 1. Selected bond lengths [Å] and angles [°] from the four complexes.[a]

| | | | |
|---|---|---|---|
| Complex **1** | | | |
| Cd(1)–O(1w) | 2.300(4) | O(5)–Cd(1)–O(4) | 53.97(13) |
| Cd(1)–O(2w) | 2.295(5) | O(4)–Cd(1)–O(7)$^{i}$ | 85.23(12) |
| Cd(1)–O(4) | 2.344(4) | O(7)$^{i}$–Cd(1)–O(6)$^{i}$ | 53.68(13) |
| Cd(1)–O(5) | 2.463(4) | O(6)$^{i}$–Cd(1)–N(1) | 85.04(16) |
| Cd(1)–N(1) | 2.338(5) | N(1)–Cd(1)–O(5) | 83.96(16) |
| Cd(1)–O(6)$^{i}$ | 2.350(4) | O(2w)–Cd(1)–O(1w) | 167.36(14) |
| Cd(1)–O(7)$^{i}$ | 2.507(4) | O(2w)–Cd(1)–N(1) | 99.31(18) |
| Cd(2)–O(9) | 2.275(4) | O(2w)–Cd(1)–O(5) | 83.94(16) |
| Cd(2)–O(3w) | 2.232(4) | O(1w)–Cd(1)–O(4) | 87.33(15) |
| Cd(2)–O(4w) | 2.396(4) | O(1w)–Cd(1)–O(7)$^{i}$ | 83.16(14) |
| | | O(3w)–Cd(2)–O(4w)$^{ii}$ | 84.78(16) |
| | | O(9)–Cd(2)–O(9)$^{ii}$ | 180.0(2) |
| | | O(9)–Cd(2)–O(4w)$^{ii}$ | 96.35(13) |
| | | O(9)–Cd(2)–O(3w) | 94.25(16) |
| Complex **2** | | | |
| Cd(1)–O(1w) | 2.287(3) | O(5)–Cd(1)–O(4) | 54.31(10) |
| Cd(1)–O(2w) | 2.319(3) | O(4)–Cd(1)–O(7)$^{i}$ | 86.93(10) |
| Cd(1)–O(4) | 2.342(3) | O(7)$^{i}$–Cd(1)–O(6)$^{i}$ | 52.90(10) |
| Cd(1)–O(5) | 2.421(3) | O(6)$^{i}$–Cd(1)–N(1) | 82.47(11) |
| Cd(1)–N(1) | 2.308(4) | N(1)–Cd(1)–O(5) | 87.26(11) |
| Cd(1)–O(6)$^{i}$ | 2.395(3) | O(2w)–Cd(1)–O(1w) | 167.75(11) |
| Cd(1)–O(7)$^{i}$ | 2.399(3) | O(2w)–Cd(1)–N(1) | 85.40(12) |
| Cd(2)–O(9) | 2.317(3) | O(2w)–Cd(1)–O(5) | 105.95(12) |
| Cd(2)–O(3w) | 2.279(3) | O(1w)–Cd(1)–O(4) | 90.68(12) |
| Cd(2)–O(4w) | 2.300(3) | O(1w)–Cd(1)–O(7)$^{i}$ | 82.24(11) |
| | | O(3w)–Cd(2)–O(4w)$^{ii}$ | 91.98(11) |
| | | O(9)–Cd(2)–O(9)$^{ii}$ | 180.000(1) |
| | | O(9)–Cd(2)–O(4w)$^{ii}$ | 96.43(11) |
| | | O(9)–Cd(2)–O(3w) | 95.49(11) |
| Complex **3** | | | |
| Cd(1)–O(4) | 2.346(3) | O(5)–Cd(1)–O(4) | 55.35(9) |
| Cd(1)–O(5) | 2.368(3) | O(4)–Cd(1)–O(9)$^{ii}$ | 100.57(10) |
| Cd(1)–O(1w) | 2.299(2) | O(9)$^{ii}$–Cd(1)–O(1w) | 108.36(11) |
| Cd(1)–O(6)$^{i}$ | 2.255(3) | O(1w)–Cd(1)–O(5) | 95.65(10) |
| Cd(1)–O(9)$^{ii}$ | 2.245(3) | N(1)–Cd(1)–O(5) | 93.62(12) |
| Cd(1)–N(1) | 2.305(3) | N(1)–Cd(1)–O(9)$^{ii}$ | 90.12(12) |
| Cd(2)–O(4) | 2.310(2) | N(1)–Cd(1)–O(1w) | 85.73(11) |
| Cd(2)–O(8) | 2.268(3) | N(1)–Cd(1)–O(6)$^{i}$ | 168.82(12) |
| Cd(2)–N(2) | 2.325(3) | O(6)$^{i}$–Cd(1)–O(9)$^{ii}$ | 84.18(11) |
| | | O(6)$^{i}$–Cd(1)–O(5) | 95.50(11) |
| | | O(8)$^{v}$–Cd(2)–N(2) | 95.28(11) |
| | | N(2)–Cd(2)–O(8)$^{ii}$ | 89.98(11) |
| | | O(8)$^{v}$–Cd(2)–O(4)$^{iv}$ | 89.17(10) |
| | | O(4)$^{iv}$–Cd(2)–O(8)$^{ii}$ | 85.68(10) |
| | | O(4)–Cd(2)–N(2) | 87.97(11) |
| | | N(2)$^{iv}$–Cd(2)–O(4) | 178.52(11) |
| Complex **4** | | | |
| Cd(1)–O(5) | 2.412(3) | O(5)–Cd(1)–O(4) | 54.74(11) |
| Cd(1)–(4) | 2.354(3) | O(4)–Cd(1)–O(9)$^{ii}$ | 91.93(11) |
| Cd(1)–O(1w) | 2.311(3) | O(9)$^{ii}$–Cd(1)–O(1w) | 88.23(11) |
| Cd(1)–O(6)$^{i}$ | 2.242(3) | O(1w)–Cd(1)–O(4) | 147.15(12) |
| Cd(1)–O(9)$^{ii}$ | 2.232(3) | N(1)–Cd(1)–O(4) | 95.52(13) |
| Cd(1)–N(1) | 2.305(4) | N(1)–Cd(1)–O(9)$^{ii}$ | 172.38(12) |
| Cd(2)–O(4) | 2.287(4) | N(1)–Cd(1)–O(1w) | 84.65(13) |
| Cd(2)–O(7)$^{i}$ | 2.291(3) | N(1)–Cd(1)–O(6)$^{i}$ | 92.51(14) |
| Cd(2)–N(2) | 2.307(4) | O(6)$^{i}$–Cd(1)–O(9)$^{ii}$ | 87.07(14) |
| | | O(6)$^{i}$–Cd(1)–O(4) | 104.97(12) |
| | | O(7)$^{i}$–Cd(2)–N(2) | 91.95(13) |
| | | N(2)–Cd(2)–O(7)$^{iv}$ | 91.84(13) |
| | | O(7)$^{iv}$–Cd(2)–O(4)$^{iii}$ | 90.18(12) |
| | | O(4)–Cd(2)–O(7)$^{iv}$ | 86.00(12) |
| | | O(4)–Cd(2)–N(2) | 87.55(13) |
| | | N(2)–Cd(2)–O(4)$^{iii}$ | 177.92(13) |

[a] Symmetry codes for **1**: (i) 1 + *x*, –1 + *y*, *z*; (ii) –*x*, –*y*, 2 – *z*; for **2**: (i) 1 + *x*, –1 + *y*, *z*; (ii) 2 – *x*, 1 – *y*, 2 – *z*; for **3**: (i) *x*, 1 – *y*, –1/2 + *z*; (ii) *x*, 2 – *y*, –1/2 + *z*; (iii) 3/2 – *x*, 5/2 – *y*, 2 – *z*; (iv) 1 – *x*, *y*, 3/2 – *z*; for **4**: (i) *x*, 2 – *y*, –1/2 + *z*; (ii) *x*, 1 – *y*, –1/2 + *z*; (iii) 2 – *x*, *y*, 1/2 – *z*; (iv) 2 – *x*, 2 – *y*, 1 – *z*.

gen atom. One chelating carboxylate group is approximately coplanar with the aromatic ring, while the other chelating and monodentate groups form small dihedral angles of ca. 14.4° and 30.9°, respectively.

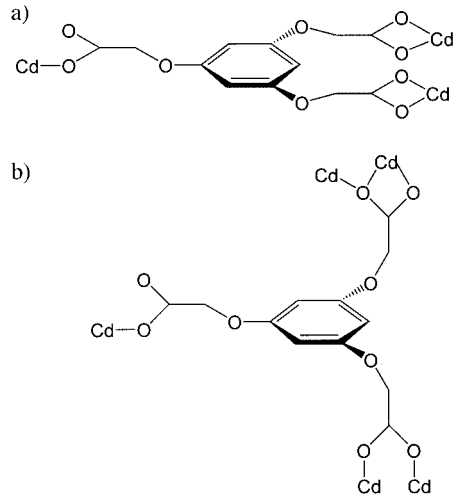


Scheme 1. Coordination modes of the TCMB ligand in the four complexes.

Furthermore, two-dimensional frameworks containing compact triple-metallic layers are afforded by two sheets of Cd1 centers bridged through 4,4′-bipy ligands and one of the Cd2 centers connected through TCMB ligands, in which all the same kinds of metal centers are arranged in straight lines as depicted in Figure 2(a). In this way, large hexagonal rings are formed and adjacent rings have extremely different environments, i.e. ring A and ring B. Four TCMB ligands are linked together by two Cd1 centers and two Cd2 centers alternately to form a 48-membered macrocycle (ring A). The distances between two opposite pairs of $Cd^{2+}$ centers on the macrocycle are Cd1···Cd1$^{ii}$ with a distance of 22.172(6) Å and Cd2···Cd2$^{i}$ with a distance of 12.947(2) Å (symmetry code i: 1 + *x*, –1 + *y*, *z*; ii: –*x*, –*y*, 2 – *z*). The second type of ring (B) is involved in Cd1 centers of adjacent layers bridged by the bidentate 4,4′-bipy ligand, which is also a macrocycle with 44 atoms, four Cd1 centers, and benzene rings of two TCMB ligands located at the vertexes of this hexagon as well as two 4,4-bipy ligands at the opposite edges. The distance between the opposite carbon atoms of the TCMB ligands at the vertexes is 17.233(2) Å, whilst the edges are separated by 12.947(2) Å based on the Cd2···Cd2$^{i}$ distance (symmetry code i: 1 + *x*, –1 + *y*, *z*). If only the Cd1 ions and the geometrical centers of the benzene ring of the TCMB ligands are considered as three-connected nodes, the structure can be best described as an infinite two-dimensional network with a $6^3$ topology in which two types of large hexagonal rings are arranged alternately. To the best of our knowledge, in most of the reported complexes with such topologies[11] only two examples with different cavities have been found,[12] whereas the others only contain haploid cavities.

 © 2006 Wiley-VCH Verlag GmbH & Co. KGaA, Weinheim 

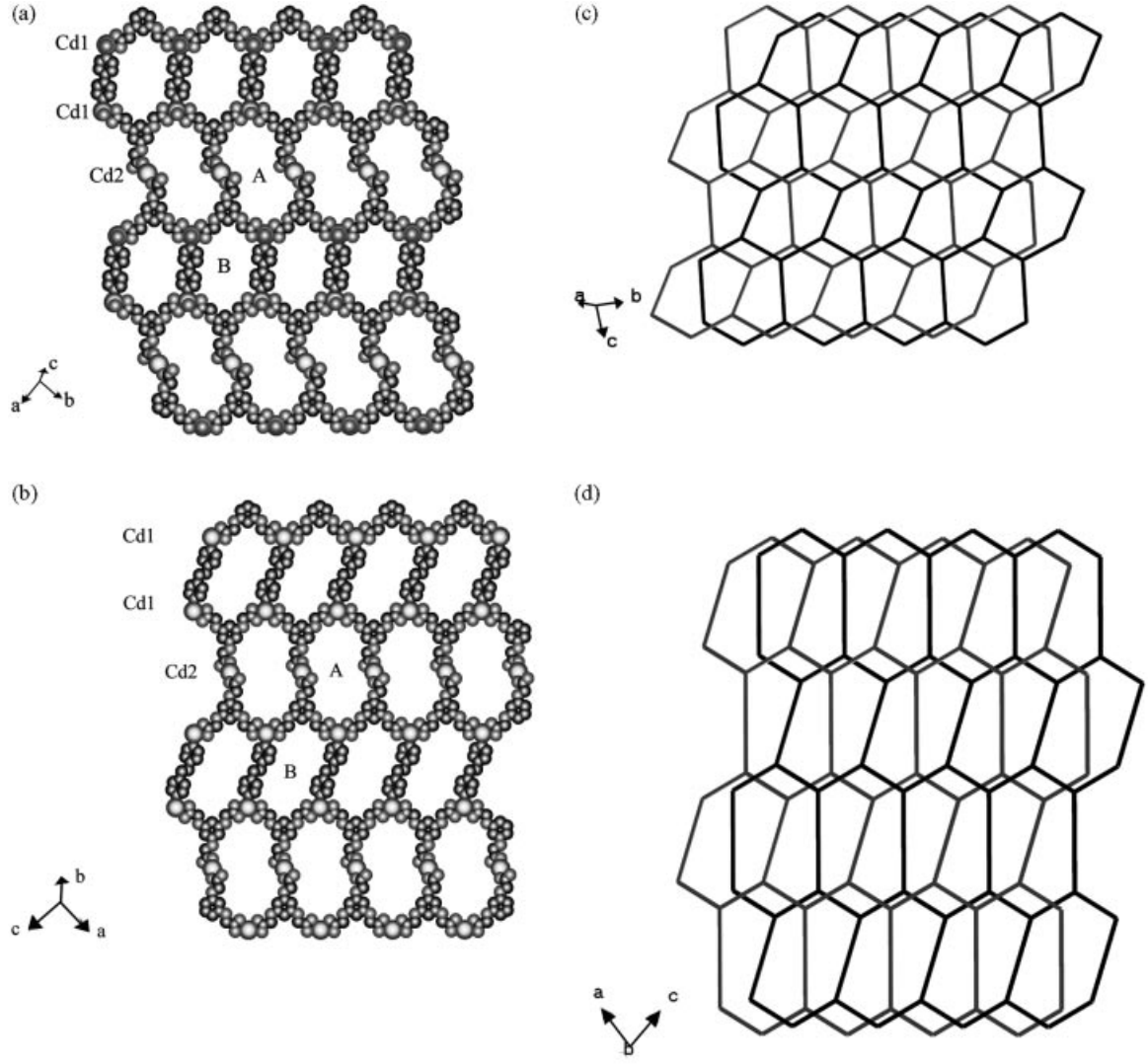


Figure 2. Space-filling representation of the 2D layer with a cross-section of the two different rings A and B for **1** (a) and **2** (b). Topological representation of the twofold interpenetration of the adjacent layers in **1** (c) and **2** (d). Cd1 centers and the geometrical centers of the benzene ring of the TCMB ligands are considered as three-connected nodes. Hydrogen atoms and the coordinated water molecules are omitted for clarity.

Because of the flexibility of the TCMB ligand, the metal atoms in one layer of the network do not lie in the same plane. All the atoms in ring B are almost coplanar while the Cd2 centers are located "above" and "below" alternately, with a dihedral angle between the monodentate carboxylate group and the plane of the aromatic ring of ca. 30.9°, leading to chair conformations for ring A. Such a bonding arrangement gives rise to a corrugated sheet topology and two undulating sheets pass through each other, forming the twofold interpenetrating 2D networks parallel to the *ac* plane with a layer thickness of ca. 3.50 Å [Figure 2(c)]. Furthermore, weak π···π interactions between the aromatic rings of adjacent layers lead to the 3D metal-organic framework, in which the composite 2D sheets are stacked in an ...ABC... fashion, with a mean distance between the double sheets of ca. 4.08 Å (Figure 3). Such an uncommon stacking mode for doubly interpenetrated sheets reduces the voids to a large extent, even though the single network contains large windows as described above. It is noteworthy that one-dimensional channels still exist along the *a* axis, and crystallographically unique uncoordinated water molecules are distributed freely in the network, which are involved in strong hydrogen bonds with the ether and carboxylate oxygen atoms between neighboring layers (see Supporting Information). Details of hydrogen bond parameters are summarized in Table 2. Interestingly, the hydrogen bonds influence the coordination environment of the Cd1 atom significantly. Because of the presence of the strong interaction between O7 and O1w with an O(1w)···O(7)$^{iii}$ (symmetry code iii: $-x+1, -y+1, -z+1$) distance of 2.689(6) Å and an O(1w)–H1(wB)···O(7)$^{iii}$ angle of 169.9°, which is a relatively strong hydrogen bond, the corresponding Cd1–O7$^{i}$ (symmetry code i: $1+x, -1+y, z$) bond is weakened and is rather long.

 © 2006 Wiley-VCH Verlag GmbH & Co. KGaA, Weinheim

Figure 3. Topological representation of the side view of the crystal packing for **1** in the ...ABC... model.

Table 2. Hydrogen bond geometries for complex **1** [Å and °].[a]

| D–H···A | *d*(D···A) | <(D–H···A) |
|---|---|---|
| O(8w)–H(8WA)···O(6)$^{i}$ | 2.725(6) | 127.8 |
| O(3w)–H(3WB)···O(5w)$^{ii}$ | 2.643(6) | 145.2 |
| O(2w)–H(2WC)···O(7w)$^{iii}$ | 2.735(6) | 125.4 |
| O(1w)–H(1WC)···O(8)$^{iv}$ | 2.732(6) | 140.8 |
| O(8w)–H(8WB)···O(4w)$^{iv}$ | 2.795(6) | 131.9 |
| O(5w)–H(5WB)···O(1w)$^{v}$ | 2.892(5) | 140.2 |
| O(2w)–H(2WA)···O(8w)$^{vi}$ | 2.753(6) | 123.4 |
| O(3w)–H(3WC)···O(7w)$^{vii}$ | 3.209(6) | 151.3 |
| O(1w)–H1(WB)···O(7)$^{viii}$ | 2.689(6) | 169.9 |
| O(6w)–H(6WB)···O(9)$^{viii}$ | 3.212(6) | 156.9 |
| O(5w)–H(5WD)···O(1)$^{viii}$ | 3.193(6) | 139.2 |

[a] Symmetry codes for **1**: (i) $x$, $y-1$, $z$; (ii) $x$, $y-1$, $z+1$; (iii) $x+1$, $y$, $z$; (iv) $x+1$, $y$, $z-1$; (v) $x-1$, $y+1$, $z$; (vi) $-x+2$, $-y$, $-z+1$; (vii) $-x$, $-y$, $-z+2$; (viii) $-x+1$, $-y+1$, $-z+1$.

### *[$Cd_3$(TCMB)$_2$(bpe)($H_2O$)$_{13}$]$_n$ (2)*

Complex **2** is isostructural to complex **1**, which also consists of a 2D $6^3$ network with two types of hexagonal rings as described in Figure 2(b). In general, increased flexibility of the ligand may probably lead to the corresponding change of the dimensionality, void space, degree of interpenetration, or topology.[13] However, in this case, the introduction of two $CH_2$ groups into the bipy molecule results in a slightly changed framework, which may be attributed to the flexible TCMB ligand with the ability to bend in order to satisfy coordination to the metal centers. The bidentate bpe ligand in an *anti* conformation bridges two Cd1 centers with a Cd1···Cd1$^{iv}$ (symmetry code iv: $1-x$, $3-y$, $-1-z$) distance of 13.624(6) Å, which is slightly shorter than that of similar bridges.[14] Apparently, the orientations of the ligands adjust themselves to the requirements of the particular networks.

Comparing these two complexes, the distances of Cd–O and Cd–N have changed after the substitution of the flexible bpe for the rigid 4,4′-bipy ligand. The carboxylate groups in the TCMB ligand coordinate to the Cd1 centers with an average Cd–O distance of 2.378(3) Å, similar to that in complex **1**. The bond lengths of Cd1–O6$^{i}$ and Cd1–O7$^{i}$ (symmetry code i: $1+x$, $-1+y$, $z$) are 2.395(3) Å and 2.399(3) Å, respectively, showing approximately symmetrical chelating conformation of the O6 and O7 carboxylate group [Figure 1(b)]. Consequently, because of the flexibility of the bpe ligands and interpenetration of the sheets, the two types of hexagonal rings become distorted with a slightly expanded ring A and a seriously compressed ring B. The dimensions corresponding to those in complex **1** are changed to 22.905(0)×12.902(3) Å, and 18.887(4)×12.902(3) Å, respectively. Obviously, the comparable dimensions of the two different kinds of rings enable the two adjacent layers to interpenetrate more easily than those in complex **1** [Figure 2(d)].

In addition, hydrogen bonds are involved in the neighboring layers, which may play a crucial role in constructing the whole three-dimensional network (Table 3). The ether oxygen atom (O1) can form a weak hydrogen bond with the free water molecule O6w, where the O6w···O1$^{v}$ (symmetry code v: $1-x$, $1-y$, $1-z$) distance is 3.130(5) Å and the O6w–H6w···O1$^{v}$ angle is 146.9°. Three water molecules O5w, O6w, and O7w are bonded to each other through hydrogen bonds (Figure 4). The O5w atom acts as a double donor, while O6w and O7w act as single acceptors, and O5w can still form hydrogen bonds with another O5w$^{vi}$ water molecule (symmetry code vi: $-x$, $1-y$, $1-z$). Thus, hexameric water clusters are formed between the adjacent layers. Interestingly, the six O atoms of the hexameric unit assume a rather uncommon centrosymmetrical planar conformation, different from those in other reported hexameric water clusters.[15] Nonbonding Ow···Ow distances and neighboring Ow···Ow···Ow angles are listed in Table 4, and show wide variations commensurate with the MOF structure. The average Ow···Ow distance [2.883(5) Å] is slightly longer than that of liquid water with a value of 2.85 Å, determined from the X-ray diffraction radial distribution curve, and that of the gas phase value of 2.86 Å.[16]

Table 3. Hydrogen bond geometries for complex **2** [Å and °].[a]

| D–H···A | *d*(D···A) | <(D–H···A) |
|---|---|---|
| O(6w)–H(6wB)···O(1)$^{i}$ | 3.130(4) | 146.9 |
| O(6w)–H(6wA)···O(2w)$^{ii}$ | 2.869(5) | 130.5 |
| O(5w)–H(5wA)···O(5w)$^{iii}$ | 2.889(8) | 115.4 |
| O(4w)–H(4wA)···O(8)$^{iv}$ | 2.833(5) | 139.1 |
| O(3w)–H(3wB)···O(7)$^{v}$ | 3.319(4) | 147.5 |
| O(2w)–H(2wA)···O(7)$^{vi}$ | 2.638(4) | 173.8 |
| O(2w)–H(2wB)···(8)$^{vii}$ | 2.777(5) | 152.1 |
| O(1w)–H(1wA)···O(5)$^{viii}$ | 2.695(4) | 166.7 |
| O(1w)–H(1wB)···O(3w)$^{ix}$ | 3.143(4) | 161.5 |
| O(5w)–H(5wB)···O(6w) | 2.781(4) | 112.4 |

[a] Symmetry codes for **2**: (i) $-x+1$, $-y+1$, $-z+1$; (ii) $x-1$, $y-1$, $z+1$; (iii) $-x$, $-y+1$, $-z+1$; (iv) $-x+2$, $-y+1$, $-z+2$; (v) $-x+1$, $-y+1$, $-z+2$; (vi) $-x+1$, $-y+2$, $-z+1$; (vii) $x$, $y+1$, $z-1$; (viii) $-x+1$, $-y+2$, $-z$; (ix) $-x+2$, $-y+1$, $-z+1$.

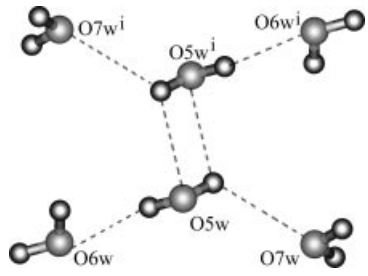


Figure 4. A perspective view of the centrosymmetrical planar hexameric water cluster in **2**, showing the hydrogen bonds between them.

Except for the hydrogen bonds mentioned above, no classical weak hydrogen-bond C–H···O interactions between a carbon atom (C4) of the aromatic ring and the carboxylate

 © 2006 Wiley-VCH Verlag GmbH & Co. KGaA, Weinheim 

Table 4. Geometrical parameters of the hydrogen bonds of the hexameric water clusters in complex **2** [Å and °].[a]

| | |
|---|---|
| O5w···O6w | 2.781(5) |
| O5w···O7w | 2.829(8) |
| O6w···O7w | 5.237(5) |
| O5w···O5w$^{i}$ | 2.889(5) |
| O5w···O5w$^{i}$···O7w$^{i}$ | 103.5 |
| O5w$^{i}$···O5w···O6w | 118.3 |
| O6w···O5w···O7w | 138.0 |

[a] Symmetry code: (i) $-x$, $1-y$, $1-z$.

oxygen atom (O8) of the TCMB ligand exist in this complex. The C(4)···O(8)$^{vii}$ interaction (symmetry code vii: $1-x$, $1-y$, $2-z$) with a distance of 3.310(6) Å and a C(4)–H(4A)···O(8)$^{vii}$ angle of 152.8°, together with the other hydrogen bonds mentioned above, extend the 2D layers into a 3D network.

### *[Cd$_3$(TCMB)$_2$(bpe)$_2$(H$_2$O)$_4$]$_n$ (3)*

The fundamental unit of complex **3** contains two crystallographically independent hexacoordinate Cd$^{II}$ centers (Figure 5). The Cd1 center adopts a distorted octahedral geometry {CdO$_5$N}, and is bonded to four carboxylate oxygen atoms from three separate TCMB ligands in the basal plane, one oxygen atom from the aqua molecule, and one nitrogen atom from the bpe ligand ligating the metal atoms in the two apical positions. The average Cd–O and Cd–N distances are 2.303(3) Å and 2.305(3) Å, respectively. Comparably, the Cd2 center {CdO$_4$N$_2$} is coordinated by four different monodentate carboxylate oxygen atoms from four distinct TCMB ligands and two nitrogen atoms from different bpe ligands, displaying a slightly distorted octahedral geometry. All the values are in good agreement with the reported Cd–OFs.[9]

Unlike that in complex **1** and **2**, the TCMB ligand exhibits essentially different coordination modes and the three carboxylate groups show large deviations from the plane of the central aromatic ring [Scheme 1(b)] due to the rotation of the OCH$_2$ groups; significantly more flexible than the corresponding coordination ability of the BTC ligand.[8] Among the three arms, only one is still almost coplanar with the aromatic ring, whereas the other two are arranged "above" and "below" the plane. Meanwhile, the three carboxylate groups show different coordination fashions: in the plane, the carboxylate group functions in a monodentate fashion with one oxygen atom bonding the Cd1 center; above the plane, the carboxylate group chelates to the Cd1 center and one oxygen atom also bridges the Cd1 and Cd2 centers, exhibiting the chelating-bridging mode, and the third one below the plane behaves in a bidentate bridging fashion, linking the Cd1 and Cd2 atoms. Thus, the TCMB ligand serves as a $\mu_5$-bridge, linking five Cd centers through its three arms in different fashions and losing the original planarity and $C_3$ symmetry observed in the free state.

As an effective intermetallic bridge, the bpe ligand always connects the same type of metal centers; however, in this case, it bridges two crystallographically independent centers

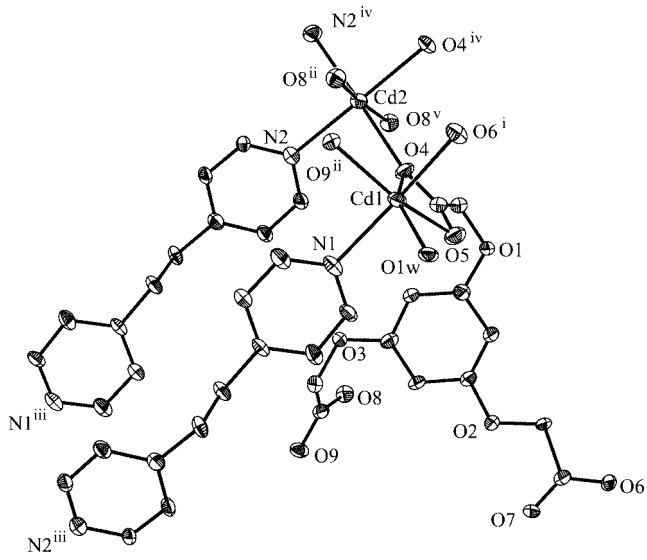


Figure 5. Schematic representation of the distorted octahedral coordination environments for the two crystallographically unique $Cd^{2+}$ metal centers in **3**. Thermal ellipsoids are drawn at the 30% probability level. Hydrogen atoms and other solvent molecules have been omitted for clarity. For bond lengths and angles see Table 1. Symmetry codes used to generate equivalent atoms: (i) $x$, $1-y$, $-1/2+z$; (ii) $x$, $2-y$, $-1/2+z$; (iii) $3/2-x$, $5/2-y$, $2-z$; (iv) $1-x$, $y$, $3/2-z$; (v) $1-x$, $2-y$, $2-z$.

of Cd1 and Cd2 from different $[Cd_3(CO_2)_4]^{2-}$ cores where the metal–metal separation for Cd1···Cd2$^{viii}$ (symmetry code viii: $3/2-x$, $5/2-y$, $2-z$) is ca. 13.883(6) Å. The interplanar angle between the pyridyl rings in bpe is ca. 9.9° and the C–CH$_2$–CH$_2$–C torsion angle is ca. 70.5°, suggesting a deviation from the normal *anti* conformation, which can be viewed as intermediate between the *anti* and the *gauche* conformations. Notably, the dihedral angles between the planes of the 4-pyridyl rings are obviously larger than those in complex **2**, which is probably one of the main causes of the dimensions of these two complexes.

The most interesting feature of the complex is the presence of the unreported isosceles triangle $[Cd_3(CO_2)_4]^{2-}$ cores [Figure 6(a)] in which the Cd2 atom is located at the vertex and doubly bridged to adjacent Cd1 metal atoms by bidentate carboxylate groups in a *syn-syn* conformation as well as one oxygen atom from the chelating-bridging group. The metal–metal separation of Cd1···Cd2 is 4.025(6) Å, significantly longer than those in some discrete dimeric cadmium tetracarboxylate complexes (3.278–3.452 Å),[17] but slightly larger than that in a similar bridge reported recently.[18] The two symmetrical Cd1 centers are separated by the long distance of Cd1···Cd1$^{ix}$ (symmetry code ix: $-x$, $1+y$, $3/2-z$) of ca. 6.731(1) Å. As far as we know, in the few reported Cd–OFs composed of Cd$_3$ SBUs,[19] the metal centers are mostly located in linear arrangements. The arrangement of six TCMB ligands around a $[Cd_3(CO_2)_4]^{2-}$ cluster is shown in Figure 6(b).

Thus, the assembly of these trinuclear SBUs leads to a 3D compact and neutral framework through the bridging of the *exo*-bidentate bpe and the TCMB ligands. On the one hand, each Cd$_3$ SBU is interlinked to other two SBUs

 © 2006 Wiley-VCH Verlag GmbH & Co. KGaA, Weinheim 

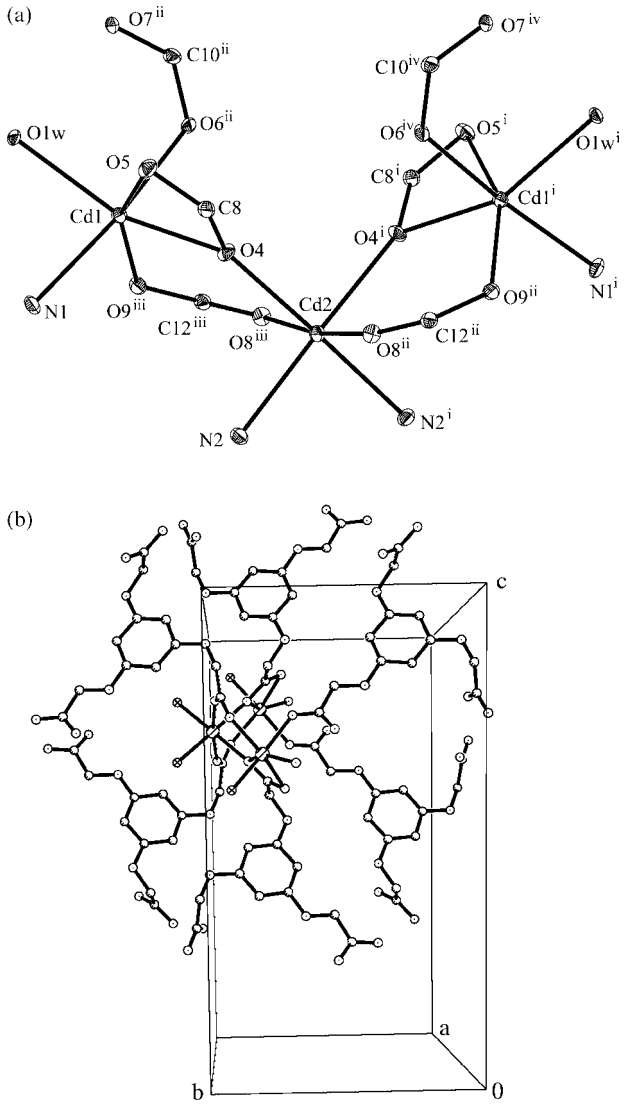


Figure 6. (a) Trinuclear secondary building unit (SBU) in **3**. All of the carboxylate groups are from different TCMB ligands and other parts of the ligand have been omitted for clarity. Nitrogen atoms are from the bpe ligand. Symmetry codes: (i) $1-x$, $+y$, $3/2-z$; (ii) $x$, $1-y$, $-1/2+z$; (iii) $x$, $2-y$, $-1/2+z$; (iv) $1-x$, $1-y$, $2-z$. (b) Perspective view showing the arrangement of six TCMB ligands around one $Cd_3$ cluster in the unit cell of **3**. Large and small open circles represent cadmium and carbon atoms, respectively. Oxygen and nitrogen atoms are shown as dotted and crossed circles, respectively. Solvent molecules, other parts of the bpe ligands and hydrogen atoms are omitted for clarity.

through four bpe ligands, resulting in the formation of one-dimensional doubly interlaced zigzag chains in the *ac* plane (Figure 7). On the other hand, two carboxylate groups "above" and "below" the plane of the aromatic ring from the TCMB ligand connect adjacent $Cd_3$ cores, which results in the helix structure along the *a* axis with a mean core distance of ca. 5 Å, and the third carboxylate groups link the neighboring helices to form the 2D networks in the *bc* plane. Accordingly, the 3D network can be interpreted as the result of inclination of 1D into 2D layers (Figure 8).

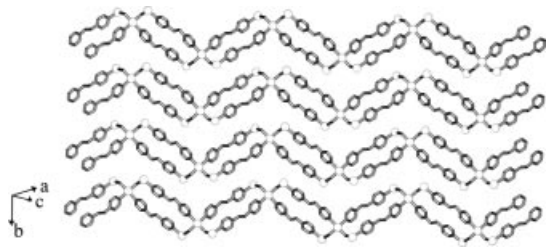


Figure 7. Doubly interlinked chains constructed from $Cd_3$ SBUs and bidentate bpe ligands in **3**.

In addition, C–H···O hydrogen bonds exist in the 3D networks. Carbon atoms with hydrogen atoms (C7–H7, C21–H21) from the $OCH_2$ groups of the TCMB ligand and aromatic rings of the bpe ligand can form C–H···O hydrogen bonds with the carboxylate oxygen atoms (O6, O7) from neighboring motifs. The C···O distance [3.280(5)–3.364(5) Å] and C–H···O angles (156.0–173.0°) of C–H···O hydrogen bonds are both within the ranges of those reported.[20] In spite of the close packing of the whole framework, small one-dimensional channels are still present and are viewed along the *c* axis (see Supporting Information).

In order to classify the network, suitable nodes should be confirmed. In this complex, every $Cd_3$ core is connected through six carboxylate groups and four bpe ligands, but two of the bpe ligands are parallel and can be considered as one linker from a topological view. Thus, the $Cd_3$ core can be viewed as an irregular eight-connected node. Additionally, taking the geometrical center of the benzene ring of the TCMB ligand as a three-connected node, the 3D framework can be represented simply by connecting these nodes according to the connectivity defined by the bpe ligand (Figure 8). When viewed along the *bc* plane, a 2D layer composed of tetragons sharing edges or vertexes can be formed, corresponding to the well-known $CdI_2$-type layer structure, which is quite common for inorganic compounds. To the best of our knowledge, except for several examples of metal alkoxides and hydroxides, few organic-inorganic hybrid materials have been reported with such a net topology.[21] Moreover, such 2D layers are linked by the linear bpe ligands. Thus, tetragons and hexagons as well as octagons can be identified in the projection, which represent the shortest circuit of the three essential rings that define the topology of the whole structure. Because the two kinds of nodes are arranged in a ratio of $Cd_3$/TCMB = 1:2, the short Schläfli symbol of the topology can be expressed as the unusual $(4^6, 6^{14}, 8^8)(4^3)_2$.[22] As far as we know, for the majority of 3D metal-organic framework structures, the connectivity of the building block does not exceed six and, in general, coordination networks with a local connectivity higher than six is very rare. Only some examples involving high coordination number lanthanide metal centers and polynuclear metal-cluster building blocks with eight-connected nodes have been reported.[23] Thus, the complex we report represents a scarce eight-connected topology, known for self-penetrating systems so far.

 © 2006 Wiley-VCH Verlag GmbH & Co. KGaA, Weinheim 

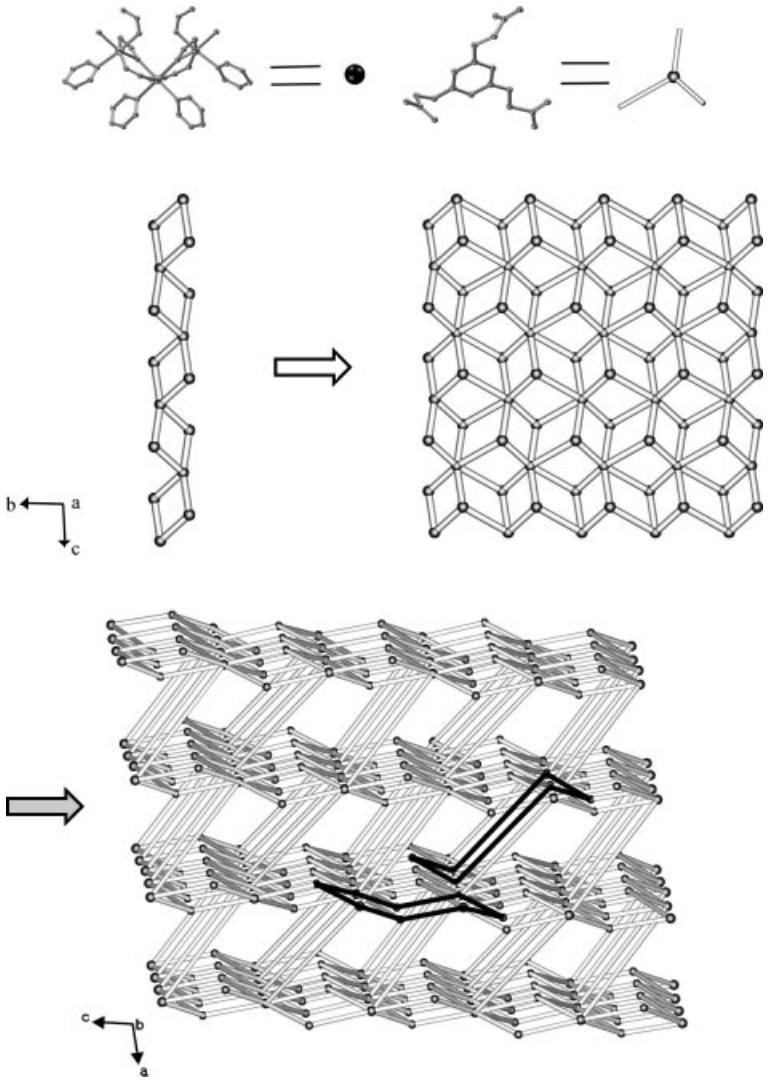


Figure 8. Topological representation of the formation of the whole structure of **3** from a 1D helical chain to a 3D network, showing the self-penetrating shortest circuits (black circles). By this notation, two parallel bpe ligands linking adjacent $Cd_3$ SBUs are viewed as one stick.

### *[Cd$_3$(TCMB)$_2$(dpp)$_2$(H$_2$O)$_3$]$_n$ (4)*

X-ray analysis reveals that in complex **4**, similar $Cd_3$ SBUs are also formed with metal–metal distances for Cd1···Cd2 and Cd1···Cd1$^{x}$ (symmetry code x: $1-x$, $+y$, $3/2-z$) of 3.967(5) Å and 6.459(8) Å, respectively, which are shorter than those in complex **3** (Figure 9). The largest difference lies in the connectivity of the more flexible dpp ligand. In general, the dpp ligand could assume a TT, TG, GG′, or GG conformation with relative orientations of the $CH_2$ groups.[24] In this case, the high flexibility of the dpp molecules enables them to join metal cores in different directions and one dpp ligand connects the Cd1 and Cd2 centers from adjacent cores with a metal–metal separation Cd1···Cd2$^{xi}$ (symmetry code xi: $3/2-x$, $-1/2+y$, $1/2-z$.) of ca. 12.368(7) Å, exhibiting significant dihedral angles of 70.5° between the two phenyl rings, which can be viewed as a *trans-gauche* (TG) conformation. Additionally, the C25 atom of the methylene group is disordered in this conformation. In this way, the dpp ligands establish a physical bridge between the separated $Cd_3$ cores and each $Cd_3$ core is linked to another four adjacent clusters, resulting in the (4,4) network (Figure 10).

Similarly, in this compound, the dpp ligands and the TCMB ligands also interact with each other through C–H···O hydrogen bonds that originate from the C atoms, with hydrogen atoms, (C17–H17, C19–H19, C24–H24) of the dpp ligands and the carboxylate oxygen atoms (O5, O8$^{xii}$, O5$^{xiii}$) (symmetry code xii: $x$, $2-y$, $-1/2+z$; xiii: $3/2-x$, $1/2+y$, $1/2-z$), where the C···O distances are in the range 3.209(7)–3.384(7) Å and the C–H···O angles in the range 132.0–172.0°.

Figure 11 illustrates the simplified self-assembly from 1D helical chains to the 3D network of complex **4**. Similar 2D layers composed of $Cd_3$ SBUs bridged by carboxylate groups can be formed, with significant distortion that is closer to that for the $HgBr_2$-type layer, which is another type of inorganic structure that is very similar to the $CdI_2$ type.[22] Interestingly, the $Cd_3$ cores are bridged to one an-

 © 2006 Wiley-VCH Verlag GmbH & Co. KGaA, Weinheim 

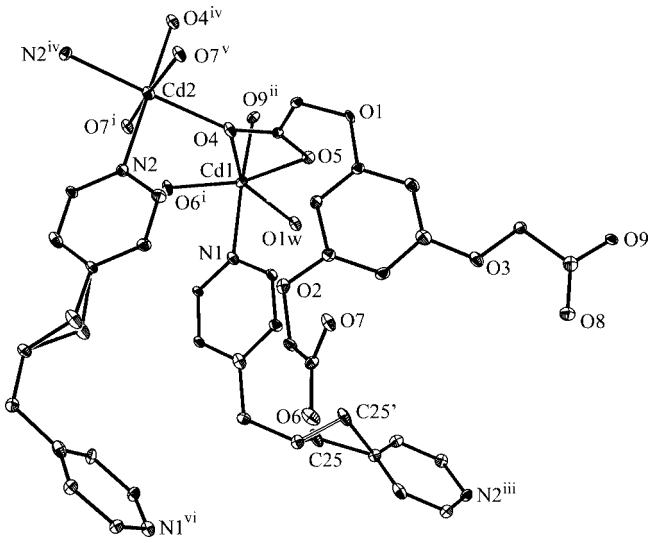


Figure 9. Schematic representation of the distorted octahedral coordination environments for the Cd metal centers in **4**. Hydrogen atoms have been omitted for clarity, and thermal ellipsoids are drawn at the 10% probability level. The disordered dpp ligand is represented in terms of C25 and C25′. For bond lengths and angles see Table 1. Symmetry codes used to generate equivalent atoms: (i) $x, 2-y, -1/2+z$; (ii) $x, 1-y, -1/2+z$; (iii) $-1/2+x, -1/2+y, +z$, (iv) $2-x, y, 1/2-z$; (v) $2-x, 2-y, 1-z$; (vi) $3/2-x, 1/2+y, 1/2-z$.

other by four nonparallel dpp ligands because of the flexibility of such ligands, and thus become a more irregular ten-connected node. The final 3D network of complex **4** can be viewed as the conversion of the parallel (4,4) sheets into the 2D sheet, and the topology defined by the dpp linking of ten-connected and three-connected nodes is rare $(4^{18}, 6^{24}, 8^3)(4^3)_2$.[22] To the best of our knowledge, the complex we report represents the highest connected topology of any known entangled species.

In summary, coligands in the reactions have a great influence on the final products. Firstly, the flexibility of the pyridyl-containing ligands can induce the structures and the acids to adopt diverse coordination modes and facilitate more complicated MOFs. Secondly, different amounts of the bases in the assembly process lead to different dimensions of the final network. Though the amounts of bases in the reactions are equal, for example, complexes **3** and **4**, different frameworks of the products may result from the adjustable conformations of the ligands to enable themselves to satisfy the coordination assemblies. Furthermore, more bases can coordinate to the metal centers competing with the aqua molecules, extending the networks from low-dimensional to high-dimensional structures, such as complex **3** in comparison with complex **2**.

### FT-IR Spectra and Thermogravimetric Analyses

The IR spectra show features attributable to the carboxylate stretching vibrations of the complexes. The absence of signals in the range 1760–1680 cm$^{-1}$ indicates complete deprotonation of the TCMB ligand. The characteristic bands of the carboxylate groups appear in the range 1560–1620 cm$^{-1}$ for the asymmetric stretching and 1370–1490 cm$^{-1}$ for the symmetric stretching. Weak absorptions observed over the range 2900–2950 cm$^{-1}$ can be attributed to the $\nu_{CH2}$ of the TCMB ligand. The broad bands at ca. 3300 cm$^{-1}$ correspond to the vibration of the water ligands in the complexes. The TGA curves of complex **1** and **2** have almost the same thermal characteristics: an obvious weight loss between 40 °C and 150 °C was attributed to the loss of all the solvent water molecules (8 $H_2O$ per unit for **1**: calcd. 10.47, found 10.49; 5 $H_2O$ for **2**: calcd. 6.67, found 7.54) and a rapid weight loss was observed from ca. 320 °C, indicating the decomposition of the whole structure. Complexes **3** and **4** also exhibit similar curves and the gradual decrease occurs from about 100 °C, which is involved in the release of guest water molecules. The complexes begin to decompose from this temperature and the obvious weight loss was observed at ca. 330 °C (see Supporting Information).

### Photoluminescent Properties

The emission spectra of all the complexes in the solid state were measured at room temperature (Figure 12). Complex **1** shows fluorescent emissions at 470 nm with a shoulder peak at about 530 nm, and no enhancement in the fluorescence intensity is realized compared with the free ligand.

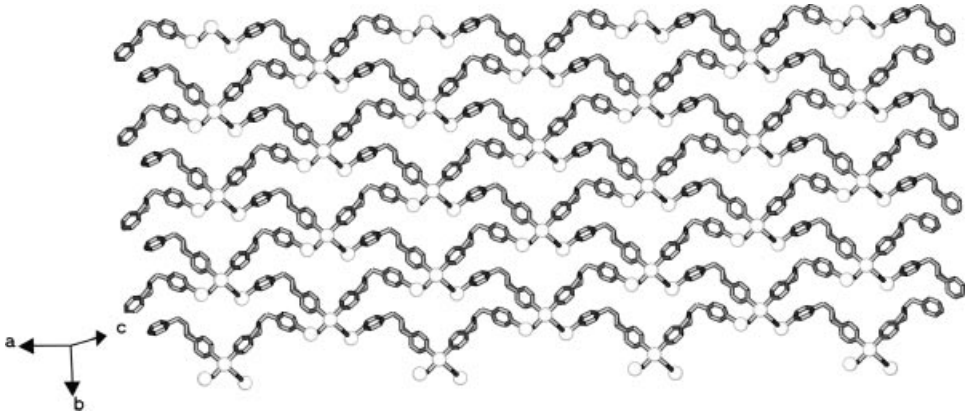


Figure 10. View of the two-dimensional (4,4) layer formed through bidentate dpp-bridging $Cd_3$ SBUs in **4**.

 © 2006 Wiley-VCH Verlag GmbH & Co. KGaA, Weinheim 

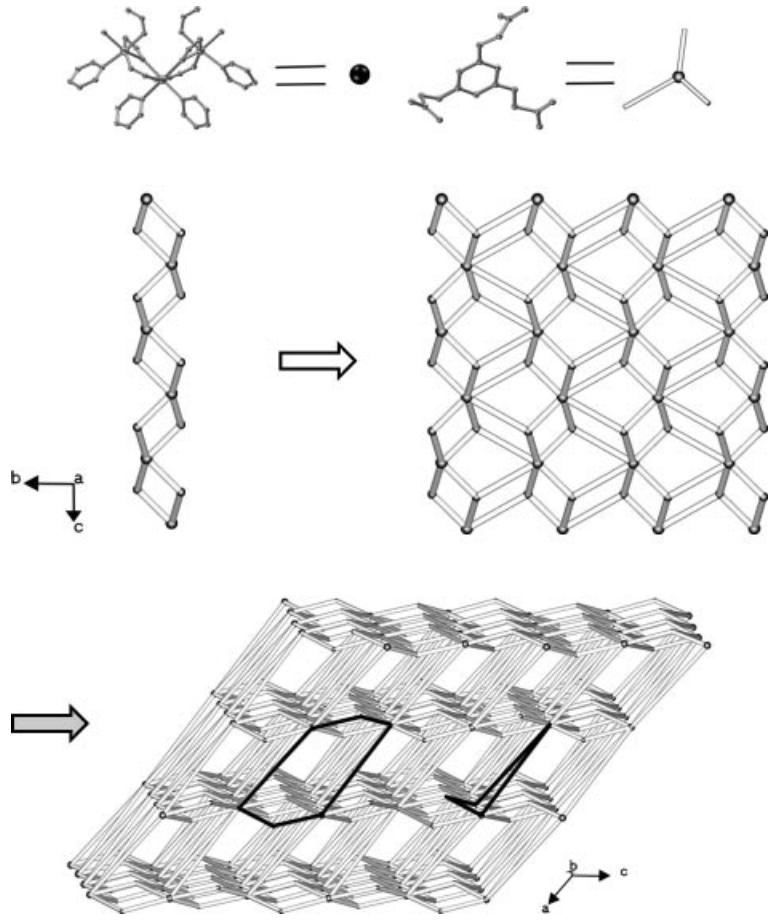


Figure 11. Topological representation of complex **4** from a 1D helical chain to a 3D network, showing the self-penetrating shortest circuits (black circles).

Since the free 4,4′-bipy ligand does not show any luminescence in the range 400–800 nm,[25] the main peak at 470 nm may be interpreted as a ligand-to-metal charge transfer (LMCT).[26] On the other hand, the shoulder peak is neither metal-to-ligand charge transfer (MLCT) nor ligand-to-metal charge transfer (LMCT) in nature, and can probably be attributed to the intraligand fluorescent emission because of the similar emission for the free ligand with the intraligand π-π* transition at 530 nm. Thus, this complex may be an excellent candidate for blue-fluorescent materials. For complexes **2** and **3**, the fluorescence is significantly decreased, and only weak absorptions were observed at 530 nm for the intraligand transition, while complex **4** shows no photoluminescent properties at room temperature. Apparently, this phenomenon is associated with the structure of this complex. In complex **1**, strong π···π interactions exist between the adjacent 2D layers, which is favorable for the reduction of the energy of the π-π* transition to some extent, while for complexes **2**–**4**, the gradually increasing flexibility of the coligands from bpe to dpp largely weakens such interactions, which is disadvantageous to the luminescence. In complex **4**, the interactions are reduced in such a way that even the luminescence was not observed.

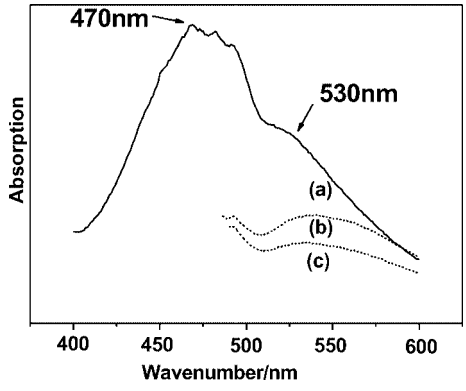


Figure 12. Photoluminescence spectra of (a) complex **1**, (b) complex **2**, and (c) complex **3** at room temperature.

## Conclusions

Four novel cadmium(II) coordination polymers based on an unexplored and flexible tripodal ligand, 1,3,5-tris(carboxymethoxy)benzene (TCMB) and bipyridyl ligands (rigid 4,4-bipy, flexible bpe, dpp) have been hydrothermally synthesized and structurally characterized, and all of them

 © 2006 Wiley-VCH Verlag GmbH & Co. KGaA, Weinheim 

show interesting topologies resulting from the different comformations and coordination modes of the flexible ligands. Complex **1** and **2** have similar unusual twofold parallel interpenetrating 2D $6^3$ networks with two types of hexagonal rings of large dimensions arranged alternately. An excess of the pyridyl-containing ligands leads to the formation of 3D frameworks of complexes **3** and **4** with scarce eight- and ten-connected topologies of $(4^6, 6^{14}, 8^8)(4^3)_2$ and $(4^{18}, 6^{24}, 8^3)(4^3)_2$, respectively, both of which contain rare 2D $CdI_2$ layers consisting of isosceles triangle $[Cd_3(CO_2)_4]^{2-}$ SBUs. They represent one of the few eight-connected and the highest connected topologies, respectively. Complex **1** exhibits luminescent properties resulting from an LMCT and may be a potential candidate for blue luminescent materials. In summary, our research demonstrates for the first time that 1,3,5-tris(carboxymethoxy)benzene (TCMB) could be a potential building block to construct novel cadmium supramolecular architectures with unusual topologies and luminescent properties. Further investigation is ongoing.

## Experimental Section

**General Methods:** TCMB was prepared according to the literature.[27] 4,4-Bipyridine (4,4-bipy), 1,2-bis(4-pyridyl)ethane (bpe), and 1,3-bis(4-pyridyl)propane (dpp) were purchased from Aldrich and used as received without further purification. All of the other reagents were commercially available and used as purchased. The elemental analysis was carried out with a Perkin–Elmer 240C elemental analyzer, at the Center of Materials Analysis, Nanjing University. The FT-IR spectra were recorded from KBr pellets over the range 4000–400 $cm^{-1}$ with a Vector 22 spectrometer. Thermal analyses were performed with a TGA V5.1A Dupont 2100 instrument from room temperature to 700 °C with a heating rate of 10 °C/min under a flow of nitrogen, and the data are consistent with the structures. The emission/excitation spectra were recorded with a Hitachi 850 fluorescence spectrophotometer.

**$[Cd_3(TCMB)_2(4,4'\text{-bipy})(H_2O)_{16}]_n$ (1):** In a general synthesis, an equimolar mixture of TCMB (0.030 g, 0.1 mmol), 4,4′-bipy (0.016 g, 0.1 mmol), and $Cd(OAc)_2{\cdot}2H_2O$ (0.026 g, 0.1 mmol) in $H_2O/C_2H_5OH$ (1:1, v/v) (10 mL) was placed in a Parr Teflon-lined stainless steel vessel and heated to 80 °C for 50 h. The reaction system was then slowly cooled to room temperature and colorless block crystals of **1** were obtained. After filtration, the crystals were washed with water and dried in air; yield 0.026 g [56%, based on $Cd(OAc)_2{\cdot}2H_2O$]. $C_{34}H_{58}Cd_3N_2O_{34}$ (1376.02): calcd. C 29.67, H 4.25, N 2.04; found C 29.98, H 4.36, N 1.98. IR (KBr pellet): $\tilde{\nu}$ = 3446 (s, br), 2924 (w), 1605 (s), 1418 (m), 1336 (w), 1262 (vw), 1165 (m), 1121 (w), 1075 (w), 807 (w), 726 (w), 629 (vw) $cm^{-1}$.

**$[Cd_3(TCMB)_2(bpe)(H_2O)_{13}]_n$ (2):** Similar procedures were performed to obtain colorless crystals of complex **2**, except that ligand bpe was used instead of 4,4′-bipy; yield 0.020 g [45%, based on $Cd(OAc)_2{\cdot}2H_2O$]. $C_{36}H_{56}Cd_3N_2O_{31}$ (1350.03): calcd. C 32.02, H 4.18, N 2.07; found C 32.06, H 4.38, N 2.04. IR (KBr pellet): $\tilde{\nu}$ = 3449 (s,br), 2924 (w), 1611 (s), 1509 (vw), 1422 (m), 1340 (w), 1264 (vw), 1165 (m), 1121 (w), 1075 (w), 807 (w), 726 (w), 671 (w), 629 (w) $cm^{-1}$.

**$[Cd_3(TCMB)_2(bpe)_2(H_2O)_4]_n$ (3):** A mixture of TCMB (0.030 g, 0.1 mmol), bpe (0.036 g, 0.2 mmol), and $Cd(OAc)_2{\cdot}2H_2O$ (0.026 g, 0.1 mmol) with a molar ratio of about 1:3:1 in $H_2O$ (10 mL) with several drops of $CH_3OH$ was placed in a Parr Teflon-lined stainless steel vessel and heated to 80 °C for 50 h. The reaction system was cooled to room temperature to give colorless block crystals of **3** that were filtered, washed with water and dried in air; yield 0.027 g [59%, based on $Cd(OAc)_2{\cdot}2H_2O$]. $C_{48}H_{50}Cd_3N_4O_{22}$ (1372.12): calcd. C 42.01, H 3.67, N 4.08; found C 41.72, H 3.92, N 3.89. IR (KBr pellet): $\tilde{\nu}$ = 3430 (m, br), 2923 (w), 1612 (s), 1474 (w), 1424 (m), 1320 (m), 1267 (vw), 1171 (s), 1157 (s), 1075 (w), 830 (w), 818 (w),712 (w) $cm^{-1}$.

**$[Cd_3(TCMB)_2(dpp)_2(H_2O)_3]_n$ (4):** Complex **4** was obtained in a similar manner to that of complex **3**, except that more flexible dpp (0.057 g, 0.3 mmol) was used instead of the bpe ligand; yield 0.033 g [72%, based on $Cd(OAc)_2{\cdot}2H_2O$]. $C_{100}H_{104}Cd_6N_8O_{42}$ (2764.31): calcd. C 43.44, H 3.79, N 4.05; found C 42.72, H 3.92, N 3.99. IR (KBr pellet): $\tilde{\nu}$ = 3447 (m), 2919 (w), 1615 (s), 1423

Table 5. Crystal data and structure refinement information for the complexes.

| Complex | **1** | **2** | **3** | **4** |
|---|---|---|---|---|
| Emprical formula | $C_{34}H_{58}Cd_3N_2O_{34}$ | $C_{36}H_{56}Cd_3N_2O_{31}$ | $C_{48}H_{50}Cd_3N_4O_{22}$ | $C_{100}H_{104}Cd_6N_8O_{42}$ |
| Formula mass [g mol$^{-1}$] | 1376.02 | 1350.03 | 1372.12 | 2764.31 |
| Space group | $P\bar{1}$ | $P\bar{1}$ | $C2/c$ | $C2/c$ |
| $a$ [Å] | 9.824(3) | 10.906(3) | 22.408(3) | 29.188(3) |
| $b$ [Å] | 11.936(3) | 11.677(3) | 11.382(3) | 11.674(2) |
| $c$ [Å] | 12.680(3) | 11.741(3) | 20.863(3) | 20.848(3) |
| $\alpha$ [°] | 64.57 (1) | 73.56(1) | 90 | 90 |
| $\beta$ [°] | 75.95(1) | 69.35(2) | 99.57(4) | 129.62(2) |
| $\gamma$ [°] | 72.30(1) | 71.18(2) | 90 | 90 |
| $V$ [Å$^3$] | 1268.1(15) | 1299.9(6) | 5247(2) | 5471.8(17) |
| $Z$ | 1 | 1 | 4 | 2 |
| $D_{calcd.}$ [g cm$^{-3}$] | 1.802 | 1.725 | 1.737 | 1.678 |
| $\mu$ [mm$^{-1}$] | 1.349 | 1.311 | 1.290 | 1.236 |
| $\theta$ range [°] | 1.8–26.0 | 1.9–27.0 | 2.0–26.0 | 2.0–26.0 |
| Index ranges | $-12 \le h \le 12$ | $-13 \le h \le 13$ | $-27 \le h \le 15$ | $-35 \le h \le 17$ |
| | $-14 \le k \le 12$ | $-14 \le k \le 14$ | $-14 \le k \le 13$ | $-14 \le k \le 14$ |
| | $-15 \le l \le 12$ | $-14 \le l \le 14$ | $-24 \le l \le 25$ | $-23 \le l \le 24$ |
| $R_1$, $wR_2$[a] [$I > 2\sigma(I)$] | 0.0485; 0.1132 | 0.0514; 0.1124 | 0.0412; 0.0984 | 0.0512; 0.1257 |
| $R_1$, $wR_2$[a] [all data] | 0.0782; 0.1192 | 0.0660; 0.1165 | 0.0503; 0.1004 | 0.0601; 0.1284 |
| Largest difference Fourier peak/hole [e Å$^{-3}$] | 0.75/–0.76 | 0.40/–1.74 | 0.95/–1.58 | 0.42/–1.35 |

[a] $R_1 = \Sigma||F_o| - |F_c||/|F_o|$; $wR_2 = [\Sigma w(\Sigma F_o^2 - F_c^2)^2/\Sigma w(F_o^2)^2]^{1/2}$.

 © 2006 Wiley-VCH Verlag GmbH & Co. KGaA, Weinheim 

(m), 1317 (w), 1266 (vw), 1226 (vw), 1172 (m), 1157 (m), 1079 (w), 1020 (vw), 819 (vw), 725 (vw), 657 (vw) $cm^{-1}$.

**X-ray Crystallographic Study:** Suitable single crystals were selected for indexing and intensity data were measured with a Siemens Smart CCD diffractometer with graphite-monochromated Mo-$K_\alpha$ radiation ($\lambda$ = 0.71073 Å) at 293 K. The raw data frames were integrated into SHELX-format reflection files and corrected using the SAINT program. Absorption corrections based on multiscans were obtained from the SADABS program. The structures were solved with direct methods and refined with full-matrix least-squares techniques using the SHELXS-97 and SHELXL-97 programs, respectively.[28] The coordinates of the non-hydrogen atoms were refined anisotropically, and the positions of the H atoms were generated geometrically, assigned isotropic thermal parameters, and allowed to ride on their parent carbon atoms before the final cycle of refinement. Basic information pertaining to crystal parameters and structure refinement is summarized in Table 5, and selected bond lengths and angles are listed in Table 1. The figures were obtained by using the SHELXP-97[28] and Olex program packages.[29] CCDC-294480 to -294483 for complexes **1**–**4** contain the supplementary crystallographic data for this paper. These data can be obtained free of charge from The Cambridge Crystallographic Data Centre via www.ccdc.cam.ac.uk/data_request/cif.

**Supporting Information** (see footnote on the first page of this article): Additional figures, and TGA and luminescent curves of complexes **1**–**4**.

## Acknowledgments

This work was supported by Talent Development Foundation of Nanjing University, Twenty-one Century Talent Foundation of the Ministry of Education, Foundation for the Returnee of the Ministry of Education, Measurement Foundation of Nanjing University, and National Natural Science Foundation of China (No. 20301010).

[1] a) J. M. Lehn, *Supramolecular Chemistry: Concepts and Perspectives*, VCH, Weinheim, **1995**; b) *Comprehensive Supramolecular Chemistry*, vol. 1–11 (Eds.: J. M. Lehn, J. L. Atwood, E. D. J. Davis, D. D. MacNicol, F. Vögtle), Pergamon, Oxford, **1990–1996**.

[2] Review articles: a) P. J. Stang, B. Olenyuk, *Acc. Chem. Res.* **1997**, *30*, 502–518; b) C. Janiak, *Angew. Chem. Int. Ed. Engl.* **1997**, *36*, 1431–1434; c) O. M. Yaghi, H. Li, C. Davis, D. Richardson, T. L. Groy, *Acc. Chem. Res.* **1998**, *31*, 474–484; d) D. Braga, F. Grepioni, G. R. Desiraju, *Chem. Rev.* **1998**, *98*, 1375–1405; e) A. K. Cheetham, G. Ferey, T. Loiseau, *Angew. Chem. Int. Ed.* **1999**, *38*, 3268–3292; f) B. Moulton, M. J. Zaworotko, *Chem. Rev.* **2001**, *101*, 1629–1658; g) C. Janiak, *Dalton Trans.* **2003**, 2781–2804; h) G, S. Papaefstathiou, L. R. MacGillivray, *Coord. Chem. Rev.* **2003**, *246*, 169–184; i) S. Kitagawa, R. Kitaura, S. Noro, *Angew. Chem. Int. Ed.* **2004**, *43*, 2334–2375; j) D. Bradshaw, J. B. Claridge, E. J. Cussen, T. J. Prior, M. J. Rosseinsky, *Acc. Chem. Res.* **2005**, *38*, 273–282.

[3] a) A. Corma, *Chem. Rev.* **1997**, *97*, 2373–2420; b) S. Noro, S. Kitagawa, M. Kondo, K. Seki, *Angew. Chem. Int. Ed.* **2000**, *39*, 2081–2084; c) J. S. Seo, D. Whang, H. Lee, S. I. Jun, J. Oh, Y. J. Jeon, K. Kim, *Nature* **2000**, *404*, 982–986; d) M. Eddaoudi, D. B. Moler, H. Li, B. Chen, T. M. Reineke, M. O'Keeffe, O. M. Yaghi, *Acc. Chem. Res.* **2001**, *34*, 319–330; e) M. Eddaoudi, J. Kim, N. Rosi, D. Vodak, J. Wachter, M. O'Keeffe, O. M. Yaghi, *Science* **2002**, *295*, 469–472; f) L. Pan, K. M. Adams, H. E. Hernandez, X. T. Wang, C. Zheng, Y. Hattori, K. Kaneko, *J. Am. Chem. Soc.* **2003**, *125*, 3062–3067; g) C. N. R. Rao, S. Natarajan, R. Vaidhyanathan, *Angew. Chem. Int. Ed.* **2004**, *43*, 1466–1496; h) B. B. Ding, Y. Q. Weng, Z. W. Mao, C. K. Lam, X. M. Chen, B. H. Ye, *Inorg. Chem.* **2005**, *44*, 8836–8845; i) E. Y. Lee, S. Y. Jang, M. P. Suh, *J. Am. Chem. Soc.* **2005**, *127*, 6374–6381 and references cited therein; j) J. L. C. Rowsell, O. M. Yaghi, *Angew. Chem. Int. Ed.* **2005**, *44*, 4670–4679.

[4] a) G. S. Hanan, D. Volkmer, U. S. Schubert, J. M. Lehn, G. Baum, D. Fenske, *Angew. Chem. Int. Ed. Engl.* **1997**, *36*, 1842–1844; b) H. Li, C. E. Davis, T. L. Groy, D. G. Kelley, O. M. Yaghi, *J. Am. Chem. Soc.* **1998**, *120*, 2186–2187; c) V. Tangoulis, C. P. Raptopoulou, V. Psycharis, A. Terzis, K. Skorda, S. P. Perlepes, O. Cador, O. Kahn, E. G. Bakalbassis, *Inorg. Chem.* **2000**, *39*, 2522–2529; d) K. Biradha, Y. Hongo, M. Fujita, *Angew. Chem. Int. Ed.* **2002**, *41*, 3395–3398; e) D. L. Liang, R. J. Hill, A. J. Blake, N. R. Champness, P. Hubberstey, C. Wilson, M. Schroder, *Chem. Eur. J.* **2003**, *11*, 1384–1391; f) K. E. Holmes, P. F. Kelly, M. R. J. Elsegood, *Dalton Trans.* **2004**, 3488–3494; g) C. W. Liu, B. J. Liaw, L. S. Liou, J. C. Wang, *Chem. Commun.* **2005**, 1983–1985; h) D. F. Sun, S. Q. Ma, Y. X. Ke, T. M. Petersen, H. C. Zhou, *Chem. Commun.* **2005**, 2663–2665; i) J. J. M. Amoore, C. A. Black, L. R. Hanton, M. D. Spicer, *Cryst. Growth Des.* **2005**, *5*, 1255–1261; j) Z. He, E. Q. Gao, Z. M. Wang, C. H. Yan, M. Kurmoo, *Inorg. Chem.* **2005**, *44*, 862–874.

[5] a) G. B. Gardner, D. Ventakaraman, J. S. Moore, S. Lee, *Nature* **1995**, *374*, 792–795; b) G. B. Gardner, Y.-H. Kiang, S. Lee, A. Asgaonkar, D. Venkataraman, *J. Am. Chem. Soc.* **1996**, *118*, 6946–6953; c) B. F. Abrahams, S. J. Egan, R. Robson, *J. Am. Chem. Soc.* **1999**, *121*, 3535–3536; d) A. Markus, *Angew. Chem. Int. Ed.* **1999**, *38*, 3463–3465; e) B. L. Chen, M. Eddaoudi, S. T. Hyde, M. O'Keeffe, O. M. Yaghi, *Science* **2001**, *291*, 1021–1023; f) S. R. Seidel, P. J. Stang, *Acc. Chem. Res.* **2002**, *35*, 972–983.

[6] a) M. Fujita, S. Nagao, K. Ogura, *J. Am. Chem. Soc.* **1995**, *117*, 1649–1650; b) B. F. Abrahams, S. R. Batten, M. J. Grannas, H. Hamit, B. F. Hoskins, R. Robson, *Angew. Chem. Int. Ed.* **1999**, *38*, 1475–1477; c) M. C. Hong, Y. J. Zhao, W. P. Su, R. Cao, M. Fujita, Z. Y. Zhou, A. S. C. Chan, *Angew. Chem. Int. Ed.* **2000**, *39*, 2468–2470; d) C. Y. Su, Y. P. Cai, C. L. Chen, F. Lissner, B. S. Kang, W. Kaim, *Angew. Chem. Int. Ed.* **2002**, *41*, 3371–3375; e) J.-P. Costes, F. Dahan, F. Nicodeme, *Inorg. Chem.* **2003**, *42*, 6556–6563; f) S. Y. Wan, Y. Z. Li, T. Okamura, J. Fan, W. Y. Sun, N. Uevama, *Eur. J. Inorg. Chem.* **2003**, 3183–3189; g) C. Y. Su, Y. P. Cai, C. L. Chen, M. D. Smith, W. Kaim, H. C. zur Loye, *J. Am. Chem. Soc.* **2003**, *125*, 8595–8613; h) W. Zhao, Y. Song, T. A. Okamura, J. Fan, W. Y. Sun, N. Ueyama, *Inorg. Chem.* **2005**, *44*, 3330–3336.

[7] a) J. F. Bai, A. V. Virovets, M. Scheer, *Angew. Chem. Int. Ed.* **2002**, *41*, 1737–1740; b) J. F. Bai, A. V. Virovets, M. Scheer, *Science* **2003**, *300*, 781–783; c) M. Scheer, J. F. Bai, B. P. Johnson, R. Merkle, A. V. Virovets, C. E. Anson, *Eur. J. Inorg. Chem.* **2005**, 4023–4026.

[8] a) O. M. Yaghi, H. Li, T. L. Groy, *J. Am. Chem. Soc.* **1996**, *118*, 9096–9101; b) S. S. Y. Chui, S. M. F. Lo, J. P. H. Charmant, A. G. Orpen, I. D. Williams, *Science* **1999**, *283*, 1148–1150; c) M. Eddaoudi, H. L. Li, O. M. Yaghi, *J. Am. Chem. Soc.* **2000**, *122*, 1391–1397; d) J. W. Ko, K. S. Min, M. P. Suh, *Inorg. Chem.* **2002**, *41*, 2151–2157; e) T. J. Prior, M. J. Rosseinsky, *Inorg. Chem.* **2003**, *42*, 1564–1575; f) D. Cheng, M. A. Khan, R. P. Houser, *Cryst. Growth Des.* **2004**, *4*, 599–604; g) H. J. Choi, M. P. Suh, *J. Am. Chem. Soc.* **2004**, *126*, 15844–15851; h) L. H. Xie, S. X. Liu, B. Gao, C. D. Zhang, C. Y. Sun, D. H. Li, Z. M. Su, *Chem. Commun.* **2005**, 2402–2404.

[9] a) C.-B. Ma, C.-N. Chen, Q. T. Liu, F. Chen, D.-Z. Liao, L.-C. Li, L.-C. Sun, *Eur. J. Inorg. Chem.* **2004**, 3316–3325; b) J. Kim, B. Chen, T. M. Reineke, H. Li, M. Eddaoudi, D. B. Moler, M. O'Keeffe, O. M. Yaghi, *J. Am. Chem. Soc.* **2001**, *123*, 8239–8247.

[10] a) O. R. Evans, W. Lin, *Inorg. Chem.* **2000**, *39*, 2189–2198; b) E. G. Bakalbassis, M. Korabik, A. Michailides, J. Mrozinski,

 © 2006 Wiley-VCH Verlag GmbH & Co. KGaA, Weinheim 

C. Raptopoulou, S. Skoulika, A. Terzis, D. Tsaousis, *J. Chem. Soc., Dalton Trans.* **2001**, 850–857; c) F. A. A. Paz, J. Klinowski, *Chem. Commun.* **2003**, 1484–1485; d) F. A. A. Paz, J. Klinowski, *Inorg. Chem.* **2004**, *43*, 3948–3954; e) F. A. A. Paz, J. Klinowski, *Inorg. Chem.* **2004**, *43*, 3882–3893.

[11] a) D. A. McMorran, P. J. Steel, *J. Chem. Soc., Dalton Trans.* **2002**, 3321–3326; b) S. Mukhopadhyay, P. B. Chatterjee, D. Mandal, G. Mostafa, A. Caneschi, J. van Slageren, T. J. R. Weakley, M. Chaudhury, *Inorg. Chem.* **2004**, *43*, 3413–3420; c) X. Liu, G. C. Guo, B. Liu, W. T. Chen, J. S. Huang, *Cryst. Growth Des.* **2005**, *5*, 841–843; d) J. P. Lang, C. M. Jiao, S. B. Qiao, W. H. Zhang, B. F. Abrahams, *Inorg. Chem.* **2005**, *44*, 3664–3668.

[12] a) E. Lee, J. Kim, J. Heo, D. Whang, K. Kim, *Angew. Chem. Int. Ed.* **2001**, *40*, 399–402; b) S. A. Bourne, J. J. Lu, B. Moulton, M. J. Zaworotko, *Chem. Commun.* **2001**, 861–862.

[13] a) T. L. Hennigar, D. C. MacQuarrie, P. Losier, R. D. Rogers, M. J. Zaworotko, *Angew. Chem. Int. Ed. Engl.* **1997**, *36*, 972–973; b) S. R. Batten, J. C. Jeffery, M. D. Ward, *Inorg. Chim. Acta* **1999**, *292*, 231–237; c) M. L. Hernandez, M. G. Barandika, M. K. Urtiaga, R. Cortes, L. Lezama, M. I. Arriortua, *J. Chem. Soc., Dalton Trans.* **2000**, 79–84; d) L. Pan, E. B. Woodlock, X. T. Wang, K. C. Lam, A. L. Rheingold, *Chem. Commun.* **2001**, 1762–1763; e) T. P. Vaid, O. L. Sydora, R. E. Douthwaite, P. T. Wolczanski, E. B. Lobkovsky, *Chem. Commun.* **2001**, 1300–1301; f) M. T. Ng, T. C. Deivaraj, W. T. Klooster, G. J. McIntyre, J. J. Vittal, *Chem. Eur. J.* **2004**, *10*, 5853–5859.

[14] a) Z. Y. Fu, X. T. Wu, J. T. Dai, L. M. Wu, C. P. Cui, S. M. Hu, *Chem. Commun.* **2001**, 1856–1857; b) M. J. Plater, M. R. S. J. Foreman, J. M. S. Skakle, *Cryst. Eng.* **2001**, *4*, 293–308; c) F. A. A. Paz, Y. Z. Khimyak, A. D. Bond, J. Rocha, J. Klinowski, *Eur. J. Inorg. Chem.* **2002**, 2823–2828.

[15] a) S. K. Ghosh, P. K. Bharadwaj, *Inorg. Chem.* **2003**, *42*, 8250–8254; b) Y.-P. Ren, L.-S. Long, B.-W. Mao, Y.-Z. Yuan, R.-B. Huang, L.-S. Zheng, *Angew. Chem. Int. Ed.* **2003**, *42*, 532–535; c) J. N. Moorthy, R. Natarajan, P. Venugopalan, *Angew. Chem. Int. Ed.* **2002**, *41*, 3417–3420; d) R. Custecean, C. Afloroaei, M. Vlassa, M. Polverejan, *Angew. Chem. Int. Ed.* **2000**, *39*, 3094–3096.

[16] a) N. H. Fletcher, *The Chemical Physics of Ice*, Cambridge University Press, Cambridge, **1970**; b) D. Eisenberg, W. Kauzmann, *The Structure and Properties of Water*, Oxford University Press, Oxford, **1969**.

[17] a) R. H. Wang, L. Han, F. L. Jiang, Y. F. Zhou, D. Q. Yuan, M. C. Hong, *Cryst. Growth Des.* **2005**, *1*, 129–135; b) . S. L. Li, T. C. W. Mak, *J. Chem. Soc., Dalton Trans.* **1995**, 1519–1524.

[18] a) W. B. Lin, O. R. Evans, Y. Cui, *Cryst. Growth Des.* **2004**, *4*, 409–411; b) R. H. Wang, M. C. Hong, J. H. Luo, R. Cao, J. B. Weng, *Chem. Commun.* **2003**, 1018–1019.

[19] a) W. B. Lin, Z. Y. Wang, L. Ma, *J. Am. Chem. Soc.* **1999**, *121*, 11249–11250; b) Y. H. Liu, Y. L. Lu, H. C. Wu, J. C. Wang, K. L. Lu, *Inorg. Chem.* **2002**, *41*, 2592–2597; c) J. X. Chen, S. X. Liu, E. Q. Gao, *Polyhedron* **2004**, *23*, 1877–1888; d) L. Yi, B. Ding, B. Zhao, P. Cheng, D. Z. Liao, S. P. Yan, Z. H. Jiang, *Inorg. Chem.* **2004**, *43*, 33–43; e) S. L. Zheng, J. H. Yang, X. L. Yu, X. M. Chen, W. T. Wong, *Inorg. Chem.* **2004**, *43*, 830–838.

[20] C. R. Desiraju, *Acc. Chem. Res.* **1996**, *29*, 411–419.

[21] a) C. G. Subhash, A. M. Michael, Y. C. Michael, E. B. William, *J. Am. Chem. Soc.* **1991**, *113*, 1844–1845; b) I. A. M. Pohl, L. G. Westin, M. Kritikos, *Chem. Eur. J.* **2001**, *7*, 3438–3445; c) T. Devic, M. Evain, Y. Moelo, E. Canadell, P. Auban-Senzier, M. Fourmigue, P. Batail, *J. Am. Chem. Soc.* **2003**, *125*, 3295–3301.

[22] A. F. Wells, *Structural Inorganic Chemistry*, 4th ed., Clarendon Oxford University Press, New York, **1975**.

[23] a) X. L. Wang, C. Qin, E. B. Wang, Z. M. Su, L. Xu, S. R. Batten, *Chem. Commun.* **2005**, 4789–4791; b) H. Chun, D. Kim, D. N. Dybtsev, K. Kim, *Angew. Chem. Int. Ed.* **2004**, *43*, 971–974; c) L. Pan, H. M. Liu, X. Y. Huang, D. H. Olson, N. J. Turro, J. Li, *Angew. Chem. Int. Ed.* **2003**, *42*, 542–546; d) D. L. Long, A. J. Blake, N. R. Champness, C. Wilson, M. Schröder, *Angew. Chem. Int. Ed.* **2001**, *40*, 2443–2447.

[24] a) L. Carlucci, G. Ciani, D. W. V. Gudenberg, D. M. Proserpio, *Inorg. Chem.* **1997**, *36*, 3812–3813; b) M. J. Plater, M. R. St. J. Foreman, T. Gelbrich, S. J. Coles, M. B. Hursthouse, *J. Chem. Soc., Dalton Trans.* **2000**, 3065–3073; c) F. M. Tabellion, S. R. Seidel, A. M. Arif, P. J. Stang, *J. Am. Chem. Soc.* **2001**, *123*, 11982–11990; d) E. Q. Gao, Z. M. Wang, C. S. Liao, C. H. Yan, *New J. Chem.* **2002**, *26*, 1096–1098.

[25] J. Tao, J. X. Shi, M. L. Tong, X. X. Zhang, X. M. Chen, *Inorg. Chem.* **2001**, *40*, 6328–6330.

[26] a) J. Tao, M. L. Tong, J. X. Shi, X. M. Chen, S. W. Ng, *Chem. Commun.* **2000**, 2043–2044; b) J. C. Dai, X. T. Wu, Z. Y. Fu, S. M. Hu, W. X. Du, C. P. Cui, L. M. Wu, H. H. Zhang, R. Q. Sun, *Chem. Commun.* **2002**, 12–13; c) Y. X. Li, Y. H. Li, X. R. Zeng, R. G. Xiong, X. Z. You, H. K. Fun, *Inorg. Chem. Commun.* **2003**, *6*, 1144–1147; d) C. Jiang, Z. P. Yu, C. Jiao, S. J. Wang, J. M. Li, Z. Y. Wang, Y. Cui, *Eur. J. Inorg. Chem.* **2004**, *23*, 4669–4674; e) X. J. Liu, Q. R. Fang, G. S. Zhu, M. Xue, X. Shi, G. Wu, G. Tian, S. L. Qiu, L. Fang, *Inorg. Chem. Commun.* **2004**, *7*, 31–34.

[27] J. F. Zhang, Y. H. Hu, D. Z. Wang, *J. Cent. South Univ. Technol. (Chin. Ed.)* **2001**, *32*, 146–169.

[28] G. M. Sheldrick, *SHELXS-97, Program for Crystal Structure Solution*, University of Göttingen, Germany, **1997**; G. M. Sheldrick, *SHELXL-97, Program for Crystal Structure Refinement*, University of Göttingen, Germany, **1997**; G. M. Sheldrick, *SHELXP-97, Program for Crystal Structure Refinement*, University of Göttingen, Germany, **1997**.

[29] O. Dolomanov, *Olex* (updated), University of Nottingham, UK, **2005**.

Received: March 2, 2006
Published Online: June 1, 2006

 © 2006 Wiley-VCH Verlag GmbH & Co. KGaA, Weinheim 

DOI: 10.1002/ejic.200600192

# In Situ Synthesis, Characterization of SiPMo-X, and Different Catalytic Properties of SiPMo-X and SiPW-X

**Chunfeng Shi,[a,b] Runwei Wang,*[a] Guangshan Zhu,[a] Shilun Qiu,*[a] and Jun Long[b]**

**Keywords:** In situ synthesis / Heteropolyacids / Mesoporous materials / Encapsulation / Bulky molecule reactions / Zeolites

SBA-15 frameworks with encapsulated Keggin type heteropolyacids (HPAs) were synthesized in situ under strongly acidic conditions (pH < 0). During the hydrolysis of tetraethyl orthosilicate (TEOS), a P- and a Mo source were added into the initial sol–gel system to form Keggin type HPAs. The texture of the final products was studied by the $N_2$ adsorption–desorption isotherms and transmission electron microscopy (TEM), and their structure was systematically characterized by X-ray diffraction (XRD), UV/Vis diffuse reflectance- (DRS), infrared- (IR), and $^{31}P$ magic angle spinning nuclear magnetic resonance (MAS NMR) spectroscopy. Characterization results suggest that the samples show very ordered hexagonal mesostructure, and the HPAs that are incorporated into the framework of meso-silica are insoluble during catalysis. Results of catalytic tests indicate that the materials demonstrated catalytic activity comparable with or even surpassing those of the bulk HPAs in catalytic tests implementing chemical reactions of bulky molecules (1,3,5-triisopropylbenzene cracking, esterification of benzoic acid with *tert*-butyl alcohol, and 2,3,6-trimethylphenol hydroxylation with $H_2O_2$). Additionally, some other properties, such as easy separation and stability when recycled, ensure their potential applications in the chemical industries. Here, we report not only the in situ synthesis and characterization of SiPMo-X, but also the difference in the catalytic properties of SiPMo-X and SiPW-X.
(© Wiley-VCH Verlag GmbH & Co. KGaA, 69451 Weinheim, Germany, 2006)

## Introduction

In recent years, environmental and economic considerations have raised strong interest in the redesign of commercially important processes so that the use of harmful substances and the generation of toxic wastes could be avoided. In this respect, there is no doubt that heterogeneous catalysis, as an alternative to homogeneous catalysis, can play a key role in the development of environmentally benign processes both in petroleum chemistry and in the production of chemicals, for example, by substitution of liquid acid catalysts by solid materials.[1]

Most notably, zeolites and heteropoly compounds have attracted much attention not only as such acidic catalysts, but also as oxidation catalysts. First of all, zeolites, owing to their uniform intracrystalline microporosity that provides access to a very large and well-defined surface, the molecular sieve effect, and the strong electrostatic field centered at zeolite cations, promised unique opportunities from the start for important improvements in efficiency and economy in gas and liquid sorption and separation technologies. The unique catalytic sites can catalyze many reactions, but zeolites also have some restrictions in general applications, such as weaker acidity, lack of variability in pore size, and the limited number of the constituent elements.[2–12] For heteropoly compounds, peculiarly for HPAs, because their unique acidic and redox properties can be controlled at the atomic/molecular level, their catalytic function in the solid state as well as in solution has attracted much attention: the strong acidity or oxidizing properties of heteropoly compounds, the soft basicity of the polyanions, the high solubility in water and organic solvents, a moderately high thermal stability in the solid state, the relatively simple synthetic procedure, the ability to form pseudoliquid phases, and the possibility of the introduction of several different elements into polyanions and counter-cations. All the above-mentioned advantages of HPAs have led to a large body of work on their applications in homogeneous and heterogeneous catalysis.[3–19] Soluble heteropoly compound catalysts (HPAs are typically strong Brønsted acids and are very soluble in oxygen-containing polar solvents such as water, alcohols, ethers, and ketones.) can catalyze a large variety of reaction types but suffer from their inability to be recycled.[5–25] Much effort has been put into developing stable, water-tolerant solid acid catalysts, as such catalysts do not require a catalyst separation process after usage and are therefore much easier to use when compared with homo-

[a] State Key Laboratory of Inorganic Synthesis and Preparative Chemistry, Department of Chemistry, Jilin University, Changchun 130012, P. R. China
Fax: +86-431-5168589
E-mail: rwwang@mail.jlu.edu.cn
sqiu@mail.jlu.edu.cn
[b] Research Institute of Petroleum Processing, China Petroleum & Chemical Corporation (SINOPEC), Beijing 100083, P. R. China
Fax: +86-10-62311290
E-mail: shicf@ripp-sinopec.com

 © 2006 Wiley-VCH Verlag GmbH & Co. KGaA, Weinheim 

geneous acid catalysts. One approach to obtaining such a catalyst is to immobilize an active acidic species onto a solid support and to practically use this as a solid acidic catalyst. Moreover, the specific surface areas of solid HPAs are low (usually less than 10 $m^2/g$), leading to very few active sites on their surfaces. Thus, immobilization of HPAs onto stable solid supports to create hybrid catalysts is absolutely necessary for using HPAs as solid catalysts. At the same time, their catalytic activities are expected to be improved by this procedure.[10–28]

Mesoporous materials have attracted much attention because of their wide potential industrial applications as catalysts or catalyst supports and hosts since their discovery in the last decade, and it has been widely reported that mesoporous silica SBA-15 has been extensively used as a support and host because of its large pore size, thick walls, and high hydrothermal stability, which make it an excellent candidate for use as a stable solid support as mentioned above.[29–40]

In our previous work, we prepared a series of insoluble HPA-containing hybrid catalysts by incorporation of HPAs into mesoporous supports during the formation of a mesostructure through acid-base interactions or covalent bond formation.[23,25] We also investigated the heterogeneous catalytic behavior of these supported HPA catalysts in polar solvents. It was found that the catalytic activity of HPAs in the hybrid catalyst was significantly improved by the fascinating physical and chemical properties and the unusual internal surface topology of the mesoporous materials. Moreover, the separation and recovery of the HPAs from the reaction environment became easy.[10,21,23,25] We also presented an in situ synthetic method for incorporating HPAs directly into the framework of mesoporous materials without destruction of the mesostructure. For example, we introduced $Na_2HPO_4$ and $Na_2WO_4$ (a P and a W source) or $H_3PO_4$ and $Na_2MoO_4$ (a P and an Mo source) into the initial sol–gel during the preparation of SBA-15 and successfully synthesized in situ new mesoporous silica encapsulated with Keggin type HPAs. Here we report not only the in situ synthesis and characterization of SiPMo-X, but also the different catalytic properties of SiPMo-X and SiPW-X.

## Results and Discussion

### Spectroscopy

#### *X-ray Diffraction*

Low-angle powder XRD patterns of SiPMo-8, HPMo/SBA, and SBA-15 samples are shown in Figure 1. Obviously, the sample of SiPMo-8 (Figure 1b and Table 1) exhibits three clearly well-resolved peaks indexed as (100), (110), and (200), which may be associated with the *p6mm* hexagonal symmetry similar to that of pure silica SBA-15 (Figure 1a).[32] The three clearly well-resolved peaks may also indicate that SiPMo-8 is characterized by the presence of long-range ordering and that the ordering of SiPMo-8 may also be comparable to that of SBA-15. These results indicate that the formation and presence of HPMo in the framework of SBA-15, by the addition of $H_3PO_4$ and $Na_2MoO_4$ into the sol–gel during the hydrolysis of TEOS, does not affect the formation of the mesoporous structure of SBA-15. However, the ordering of conventionally supported HPMo (SBA-15 as the support) (Figure 1c) decreases significantly compared with that of SBA-15, which may be attributed to the fact that the conventional preparation method affects the ordering of the support. Moreover, from Figure 2, we can see that the wide-angle powder XRD

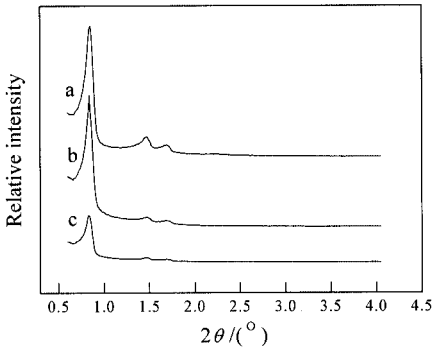


Figure 1. Small-angle XRD patterns of samples: (a) SBA-15, (b) SiPMo-8, and (c) HPMo/SBA.

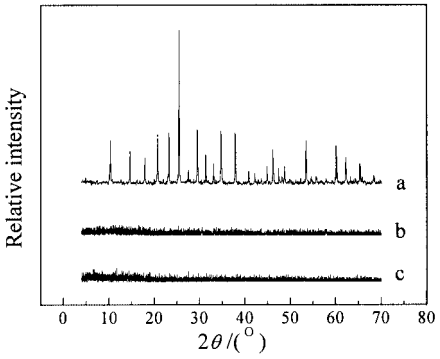


Figure 2. Wide-angle XRD patterns of samples: (a) HPMo, (b) SiPMo-8, and (c) HPMo/SBA.

Table 1. HPMo content and parameters of the pore structure of SiPMo-8, SBA-15, HPMo, and HPMo/SBA.

| Samples | HPW content (wt.-%) | | $d_{(100)}$ | $a$ | Pore size | Wall thickness | Surface area | Pore volume | Carbon residue[b] |
|---|---|---|---|---|---|---|---|---|---|
| | Sol–gel | Product | [nm] | [nm] | [nm] | [nm][a] | [$m^2/g$] | [$cm^3/g$] | |
| SiPMo-8 | 33.3 | 19.6 | 10.4 | 12.0 | 7.6 | 4.4 | 807 | 1.04 | 10.9 |
| SBA-15 | 0.0 | 0.0 | 10.3 | 11.9 | 7.9 | 4.0 | 860 | 1.15 | 8.8 |
| HPMo/SBA | 20.0 | 20.0 | 10.3 | 11.9 | 7.8 | 4.1 | 473 | 0.85 | 8.2 |
| HPMo | 100 | 100 | – | – | – | – | 5 | – | – |

[a] Pore size distributions were determined from $N_2$ adsorption isotherms and the wall thickness was calculated as: thickness = $a$ – pore size ($a = 2 \times d_{(100)}/3^{1/2}$). [b] The units for the carbon residue of samples are $\times 10^{-6}$ mmol/g.

 © 2006 Wiley-VCH Verlag GmbH & Co. KGaA, Weinheim 

patterns of SiPMo-8 (Figure 2b) do not show any obvious characteristic signals for pure HPMo, indicating the very high dispersion of HPMo in the meso-silica matrix.[17,23,25,35]

### *Transmission Electron Microscopy*

Figure 3 shows the TEM images of SiPMo-8 and SBA-15; we can see that the pores of the modified sample SiPMo-8 (Figure 3a, b) represent a hexagonal analogue to that of pure silica SBA-15 (Figure 3c, d).[32] Compared with Figure 3c, d, the images shown in Figure 3a, b suggest that the ordering of the sample SiPMo-8 is only slightly less than that of the SBA-15 sample; these results are consistent with those from XRD.

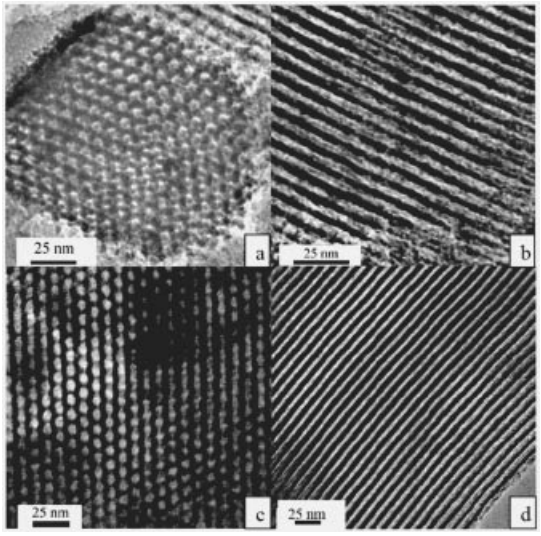


Figure 3. TEM images of samples: (a) SiPMo-8 in the [100] direction, (b) SiPMo-8 in the [110] direction, (c) SBA-15 in the [100] direction, and (d) SBA-15 in the [110] direction.

### *$N_2$ Adsorption Isotherms*

The $N_2$ adsorption isotherms of the SiPMo-8 and HPMo/SBA samples together with that of pure silica SBA-15 are shown in Figure 4, and the porosity parameters, such as the BET specific area, cumulative pore volume, and average pore diameter, are listed in Table 1. Evidently, SiPMo-8 shows a typical adsorption curve of type IV (according to the IUPAC classification) with an obvious hysteresis loop at a relative pressure of $0.70 < P/P_0 < 0.85$ (Figure 4b) that is very similar to that of pure silica SBA-15 (Figure 4a).[32] The hysteresis loop for the material starting at about 0.70 relative pressure suggests the presence of framework mesoporosity. In situ incorporation of HPMo into the framework of SBA-15 only leads to a very slight decrease in the values of surface area and pore volume. For example, the BET surface area and pore volume of SiPMo-8 are given as 807 $m^2/g$ and 1.04 $cm^3/g$, and the corresponding values for SBA-15 are 860 $m^2/g$ and 1.15 $cm^3/g$, so there is no clear difference between the porosity parameters of pure silica SBA-15 and the SiPMo-8 sample, implying the formation and presence of HPMo in the initial gel does not affect the formation of a mesostructure, which is also in agreement with the XRD results. However, the BET surface area and pore volume of HPMo/SBA (Figure 4c) are 473 $m^2/g$ and 0.85 $cm^3/g$, respectively, and comparing these results with the corresponding values for pure silica SBA-15, the BET surface area and pore volume of HPMo/SBA are significantly lower; these results also provide evidence that the conventional preparation method affects the ordering of the support.

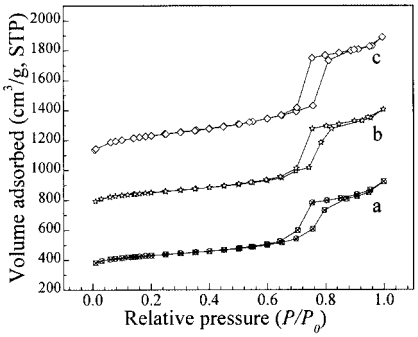


Figure 4. $N_2$ adsorption/desorption isotherms of samples at STP: (a) HPMo/SBA, (b) SiPW-8, and (c) SBA-15.

### *IR Spectra*

The infrared spectra of the samples are shown in Figure 5. It is well known that the Keggin structure of HPMo is composed of one $PO_4$ tetrahedron surrounded by four tri-metal groups of three edge-sharing $MoO_6$ octahedra and that HPMo gives several strong typical IR bands at ca. 1062 $cm^{-1}$ (stretching frequency of P–O in the central tetrahedron $PO_4$), 963 $cm^{-1}$ (terminal bands of Mo=O in the exterior octahedron $MoO_6$), 871, and 793 $cm^{-1}$ (Mo–$O_b$–Mo and Mo–$O_c$–Mo bridge band, respectively) (Figure 5a).[14] It has been widely reported that pure mesoporous silica of SBA-15 shows the framework bands at about 800 $cm^{-1}$ (symmetric stretching of Si–O–Si), 960 $cm^{-1}$ (stretching of Si–O–H), and 1030–1250 $cm^{-1}$ (*anti*-symmetric stretching of Si–O–Si) (Figure 5c).[23,25] In our case, SiPMo-8 gives three intense bands at 1098, 961, 803 $cm^{-1}$, and one shoulder band at 896 $cm^{-1}$ over 600–1400 $cm^{-1}$ regions (Figure 5b). It should be noted that some bands of HPMo in the region partially or fully overlapped with the bands of SBA-15, because of the strong contrast between the weak signals of HPMo in the framework of SiPMo-8 and the very strong signals of SBA-15. Three strong bands in the IR spectrum of SiPMo-8 appeared at 803, 961, and 1098 $cm^{-1}$, from the overlapping of the IR absorption bands of SBA-15 around 800, 960, and 1100 $cm^{-1}$, and those of HPMo at 793, 963, and 1062 $cm^{-1}$, respectively. Consequently, the Keggin unit could only be characterized by the stretching modes assigned to bridging bonds: a very low-intensity peak at about 896 $cm^{-1}$, with slightly shifted shoulder signals, may confirm that the Keggin structure of HPMo encapsulated into the framework of SBA-15 was slightly influenced during the synthesis procedure, in other words, this may indirectly prove that there are interactions

 © 2006 Wiley-VCH Verlag GmbH & Co. KGaA, Weinheim 

between the silicon species and the heteropolyanion in the framework of SiPMo-8, it can thus be deemed that the Keggin structure of HPMo is preserved in the framework of SiPMo-8.[14]

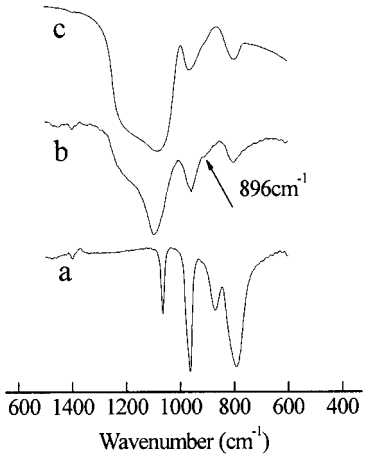


Figure 5. IR spectra of samples: (a) HPMo, (b) SiPMo-8, and (c) SBA-15.

### *UV/Visible Diffuse Reflectance Spectra*

The incorporation of HPMo into the framework of SBA-15 was further indirectly verified by UV/Visible spectra. The UV/Visible spectra of the samples are shown in Figure 6. Bulk HPMo (Figure 6a) shows a broad and strong UV absorption in the range of 200–300 nm, with a maximum centered at about 260 nm, which is a characteristic peak attributed to the oxygen–molybdenum charge-transfer absorption band for Keggin anions. The UV irradiation of the polyoxomolybdate cluster results in charge-transfer from an $O^{2-}$ ion to a $Mo^{6+}$ ion, and this occurs at Mo–O–Mo bonds corresponding to the formation of a pair consisting of a hole center ($O^{-}$) and a trapped electron center ($Mo^{5+}$). The process can be described as follows:[14]

$$[Mo^{6+}–O^{2-}–Mo^{6+}] \xrightarrow{h\nu} [Mo^{5+}–O^{-}–Mo^{6+}]^*$$

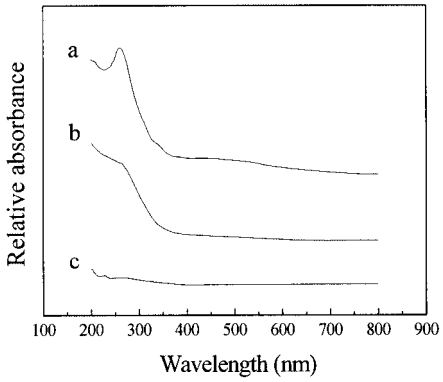


Figure 6. UV/Visible spectra of samples: (a) HPMo, (b) SiPMo-8, and (c) SBA-15.

SBA-15 did not show any signals in the wavelength region studied (Figure 6c). In our case, the SiPMo-8 (Figure 6b) sample has a broad UV absorption in the range 200–300 nm, with a characteristic peak centered at about 260 nm in the spectrum, similar to that of the $[PMo_{12}O_{40}]^{3-}$ species. These results indicate that the primary Keggin structure of HPMo has been introduced into the framework of the mesostructure and is very stable even after the extraction of surfactants and washing with deionized water, which is in agreement with IR results. Similar results can also be observed with $^{31}P$ MAS NMR measurements.

### *$^{31}P$ MAS NMR Spectra*

The $^{31}P$ MAS NMR spectra of bulk HPMo and SiPMo-8 are shown in Figure 7. It is well known that the $^{31}P$ MAS NMR chemical shift of bulk HPMo is strongly dependent on the number of crystallized water molecules, in our case bulk HPMo exhibits an intense and sharp line at a chemical shift of around –4.5 ppm in the $^{31}P$ MAS NMR spectrum (Figure 7b) pointing to a uniform phosphorus environment in the structure of HPMo. The $^{31}P$ MAS NMR spectrum of SiPMo-8 also shows an intense and sharp line at around –4.5 ppm and two low intense down-field and up-field chemical shifts (–5.1 and –3.8 ppm, respectively) are observed (Figure 7a). These could be deemed to represent very strong interactions between the molybdophosphoric anions and the framework of SBA-15, which is made up of a network of $SiO_2$, and could also be attributed to a significant distortion of the heteropoly anion symmetry, whereby the long-range order created by water molecules in the hydrated state of HPMo is lost because of strong chemical interactions between molybdophosphoric anions and the framework of SBA-15. It can be concluded that the Keggin unit (primary structure) is preserved after being incorporated into the framework of SBA-15, because HPMo microcrystallites deposited on the silica surface and heteropoly anions interacting with Si–OH groups have been observed when HPMo was supported on silica.[14]

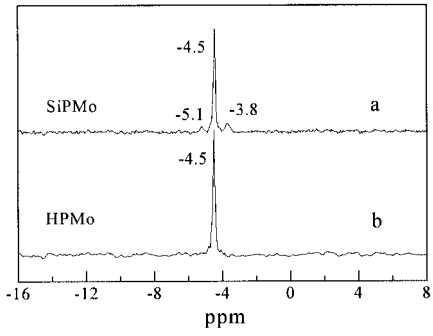


Figure 7. $^{31}P$ MAS NMR spectra of samples: (a) SiPMo-8 and (b) HPMo.

## Catalytic Results

### *1,3,5-Triisopropylbenzene (TIPB) Cracking*

In the reaction of TIPB cracking (see Scheme 1), as shown in Table 2, SBA-15 shows very low catalytic activity (conversion at 2.2%), and HPMo supported on the surface

 © 2006 Wiley-VCH Verlag GmbH & Co. KGaA, Weinheim 

Table 2. Catalytic activity of SBA-15, HPMo, SiPMo-X, HPMo/SBA, and HPW, SiPW-X, HPW/SBA.

| Samples | Conversion of TIPB [wt.-%] | Conversion of esterification[a] [wt.-%] | | TOF of esterification[d] [$h^{-1}$] | Conversion of hydroxylation[b] [wt.-%] | | TOF of hydroxylation[e] [$h^{-1}$] | Selectivity of hydroxylation[f] [wt.-%] | | |
|---|---|---|---|---|---|---|---|---|---|---|
| | | Fresh | Reused[c] | | Fresh | Reused[c] | | C1 | C2 | C3 |
| SiPMo-8 | 50.6 | 10.2 | 9.9 | 3.1 | 26.5 | 26.2 | 251.3 | 83.4 | 11.7 | 4.9 |
| HPMo/SBA | 17.4 | 4.8 | 0.5 | 1.5 | 21.2 | 4.9 | 206.6 | 64.5 | 28.3 | 7.2 |
| HPMo | 34.3 | 8.6 | – | – | 28.7 | – | – | 41.1 | 45.5 | 13.4 |
| SBA-15 | 2.2 | – | – | – | – | – | – | – | – | – |
| SiPW-8 | 61.3 | 12.4 | 12.2 | 4.0 | 17.9 | 17.6 | 180.2 | 89.2 | 9.5 | 1.3 |
| HPW/SBA | 18.8 | 6.9 | 0.7 | 2.2 | 15.8 | 3.0 | 113.0 | 72.3 | 19.3 | 8.4 |
| HPW | 42.6 | 18.1 | – | – | 16.6 | – | – | 50.7 | 38.8 | 10.5 |

[a] Esterification reactions of benzoic acid with *tert*-butyl alcohol. [b] 2,3,6-Trimethylphenol hydroxylation with $H_2O_2$, acetonitrile as the solvent (polar solvent), 2,3,6-trimethylphenol/$H_2O_2$ = 3 (molar ratio); catalyst/2,3,6-trimethylphenol ≈0.05 (weight ratio), temperature: 353 K, reaction time: 2 h. The products are trimethylhydroquinone (C1, TMHQ), trimethylbenzoquinone (C2, TMBQ), others (C3). Conversion = 2,3,6-trimethylphenol converted to TMHQ, TMBQ and other products/2,3,6-trimethylphenol added in the system. [c] The catalysts were reused five times. [d] Turnover frequency of esterification is moles of *tert*-butyl benzoate yield per mol active site on the surface of the catalyst per hour, using the fresh catalysts. [e] Turnover frequency of hydroxylation is moles of 2,3,6-trimethylphenol converted per mol active site on the surface of the catalyst per hour, using the fresh catalysts. The active site numbers on the surface of SiPMo-8, SiPW-8, HPMo/SBA, and HPW/SBA were estimated on the basis of the amount of HPAs (moles) estimated by ICP analysis, and the surface areas were determined by $N_2$ adsorption methods. [f] The selectivity of hydroxylation is that of 2,3,6-trimethylphenol hydroxylation with $H_2O_2$ using the fresh catalysts.

of SBA-15 with impregnation methods gives reaction conversion at 17.4%. In our case, SiPMo-8 shows high catalytic activity and gives reaction conversion at 50.6%, which is higher than that of HPMo/SBA, and the results suggest the potential use of SiPMo-8 as a catalyst for bulky molecule catalytic reactions. Similar phenomena have also been observed when using SiPW-8 and HPW/SBA samples as the catalyst, giving conversion at 61.3 and 18.8%, respectively. We can see that the activity of SiPW-8 in TIPB cracking is higher than that of SiPMo-8, the activity of HPW/SBA is higher than that of HPMo/SBA, and the activity of HPW is also higher than that of HPMo. It is well known that HPW is a stronger acid than HPMo, and TIPB cracking is a typical acidic catalytic reaction, so it is easy to understand the above results.[17]

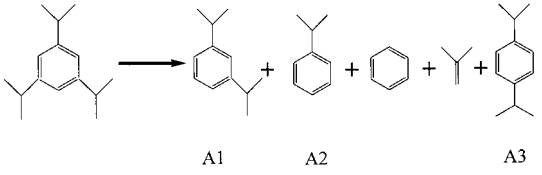


Scheme 1. Catalytic cracking of 1,3,5-triisopropylbenzene (TIPB): [A1] 1,3-diisopropylbenzene; [A2] cumene; [A3] 1,4-diisopropylbenzene.

### *Esterification of Benzoic Acid with tert-Butyl Alcohol*

In esterification (see Scheme 2), as shown in Table 2, the SiPMo-8 sample gives conversion at 10.2% (TOF at 3.1 $h^{-1}$), HPMo/SBA prepared by the impregnation method shows very low catalytic activity (conversion at 4.8%, TOF at 1.5 $h^{-1}$) compared with the SiPMo-8 sample; the SiPW-8 sample gives conversion at 12.4% (TOF at 4.0 $h^{-1}$) and HPW/SBA prepared by the impregnation method shows conversion at 6.9% (TOF at 2.2 $h^{-1}$). Moreover, the SiPMo-8 and SiPW-8 samples still showed similar catalytic activity compared with the corresponding fresh catalysts after the catalysts were reused five times (Table 2), whereas the conversions with HPMo/SBA and HPW/SBA were reduced remarkably after the catalysts were used five times, to only 0.5 and 0.7%, respectively, which may be attributed to the leaching of the HPAs supported on the surface of SBA-15 during the reactions.[23,25] The above results suggest that SiPMo-8 and SiPW-8 are very stable in liquid reactions even when they are reused many times, and the leaching of HPAs is hardly observed, as compared with samples prepared by the impregnation method.[18] Similar phenomena can also be observed in the hydroxylation of 2,3,6-trimethylphenol with $H_2O_2$.

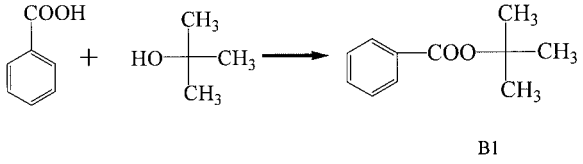


Scheme 2. Esterification of benzoic acid with *tert*-butyl alcohol: [B1] *tert*-butyl benzoate.

### *Hydroxylation of 2,3,6-Trimethylphenol with $H_2O_2$*

In hydroxylation (see Scheme 3),[41] also as shown in Table 2, SiPMo-8 gives conversion at 26.5% (TOF at 251.3 $h^{-1}$), and HPMo/SBA prepared by the impregnation method shows similar catalytic activity (conversion at 21.2%, TOF at 206.6 $h^{-1}$). SiPW-8 gives conversion at 17.9% (TOF at 180.2 $h^{-1}$), HPW/SBA shows similar catalytic activity (conversion at 15.8%, TOF at 113.0 $h^{-1}$). Moreover, after the catalysts were reused five times (Table 2), SiPMo-8 and SiPW-8 still showed similar catalytic activities (26.2 and 17.6%, respectively) compared with the corresponding fresh catalysts (26.5 and 17.9%, respectively), whereas the conversions with HPMo/SBA and HPW/SBA were reduced remarkably, to only 4.9 and 3.0%, respectively, after the catalysts were recycled five times.

 © 2006 Wiley-VCH Verlag GmbH & Co. KGaA, Weinheim 

Other properties of the SiPMo-8 and SiPW-8 samples, such as easy separation and stability when recycled, ensure their potential application in the chemical industries. This phenomenon is very similar to that in esterification and all of these could be attributed to the stability of the HPAs encapsulated into the framework of mesoporous materials and the preservation of the catalytic abilities of the HPAs when encapsulated. The XRD pattern of impregnated samples (Figure 1) reveals the effect of the conventional preparation method on the ordering of the support. For impregnated samples, some heteropolyacid clusters may block the channels of the SBA-15 substrate, which on the one hand reduce the BET surface area and pore volume (Table 1) and on the other hand prohibit bulky reactant molecules from entering the channels of the SBA-15 substrate, so that the heteropolyacids in the channels will not be able to perform their catalytic activity. The number of catalytically active heteropolyacids is reduced, and this leads to a reduction of their apparent total catalytic activity, which in turn gives the apparent result that the activity of impregnated samples is not as high as that of the in situ synthesized sample (SiPMo-8, SiPW-8). We also noticed that the catalytic properties of SiPMo-8 in the esterification and hydroxylation reactions are different from those of SiPW-8. Although both SiPMo-8 and SiPW-8 are very active, SiPMo-8 is more active in hydroxylation and SiPW-8 is more active in esterification; this is because esterification is an acidic catalytic reaction and hydroxylation is an oxidative catalytic reaction, and as HPW is a stronger acid than HPMo and the oxidation ability of HPW is less than that of HPMo. From Table 2, we may notice that, although the specific surface areas of solid HPAs are very low (usually less than 10 $m^2/g$), leading to very few active sites on their surfaces, HPAs are all active in the reactions of TIPB cracking, esterification, and hydroxylation. Properties of HPAs, such as the ability to form pseudo-liquid phases, the soft basicity of the polyanions, and the high solubility in water and organic polar solvents, make them active in reactions of some bulky molecules.[5–10]

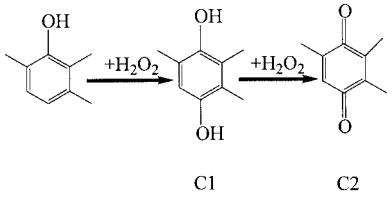


Scheme 3. Hydroxylation of 2,3,6-trimethylphenol with $H_2O_2$: [C1] trimethylhydroquinone (TMHQ); [C2] trimethylbenzoquinone (TMBQ).

## Conclusions

SBA-15 frameworks with encapsulated Keggin type HPAs were synthesized in situ by adding P- and Mo sources into the initial sol–gel system during hydrolysis of TEOS under strongly acidic conditions. Characterization results suggest that samples synthesized in this manner show a very ordered hexagonal mesostructure, and HPAs that are incorporated in the meso-silica are insoluble during catalysis. The results of catalytic reactions suggest that these samples are very active in reactions of bulky molecules (1,3,5-triisopropylbenzene cracking, esterification of benzoic acid with *tert*-butyl alcohol, and 2,3,6-trimethylphenol hydroxylation with $H_2O_2$). We can prepare samples with different types of catalytic activity (such as acid, redox) by incorporating different types of HPA. Additionally, recycling results of the liquid reactions of esterification (polar solvent) and hydroxylation (polar solvent) indicate that these materials are easily separated and recycled as catalysts, which make them interesting for potential industrial applications.

## Experimental Section

**Materials:** Tetraethyl orthosilicate (TEOS), hydrochloric acid (HCl), $H_3PO_4$, benzoic acid, tertiary butyl alcohol, and $H_2O_2$ (30 wt.-%) were of analytical grade and purchased from Tianjin Chemical Co. (China). 12-Molybdophosphoric acid (HPMo) and sodium molybdate ($Na_2MoO_4$) were of analytical grade and supplied by Beijing Chemical Co. (China). $EO_{20}PO_{70}EO_{20}$ (Pluronic P123), 2,3,6-trimethylphenol, and 1,3,5-triisopropylbenzene are Aldrich products.

**Synthesis:** The typical in situ synthesis process of SiPMo-X was as follows: (1) Pluronic P123 (2.0 g) was dissolved in a solution of hydrochloric acid (10 mL, 36 wt.-%) in deionized water (50 mL) followed by the addition of TEOS (4.4 mL), and then the mixture was stirred at 40 °C for 3 h. (2) The requisite amount of $Na_2MoO_4$ and $H_3PO_4$ was added to the above mixture simultaneously to form a yellow precipitate. (3) The mixture was further stirred at 40 °C for 20 h and then transferred into a stainless steel autoclave for crystallization at 100 °C for 48 h. The obtained products were dried in vacuo ($<10^{-2}$ Pa) at 120 °C for 6 h and washed three times with an ethanol solution containing HCl and distilled water, and finally treated in vacuo ($<10^{-2}$ Pa) at 300 °C for 5 h again. The final products were designated as SiPMo-X, where X stands for the Si/Mo molar ratio in the initial gel, in this paper X is equal to 8.

For comparison, pure silica SBA-15 was synthesized according to literature procedures.[32] Conventional supported HPMo (SBA-15 as the support) was made by immersing SBA-15 powder into an HPMo solution under stirring for 3 h, drying at 120 °C for 24 h, and then calcination at 300 °C for 5 h. This product was denoted as HPMo/SBA. The methods of synthesis of HPW, SiPW-8, and HPW/SBA are the same as those in the literature.[23]

**Characterization:** The HPMo contents in solid samples and the carbon residue of the SBA 15 substrate and encaged HPAs were determined by the results of inductively coupled plasma analysis (ICP, Perkin–Elmer 3300DV). Powder X-ray diffraction (XRD) data were recorded with a Siemens D5005 instrument (30 kV, 30 mA) using nickel-filtered Cu-$K_a$ radiation with a wavelength of $\lambda$ = 0.15418 nm, diffraction patterns were collected under ambient conditions in the $2\theta$ range 0.6–4° at a scanning rate of 0.6°/min and in the $2\theta$ range 4–70° at a scanning rate of 6°/min. Transmission electron microscopy (TEM) experiments were performed with a JEM-3010F electron microscope (JEOL, Japan) with an acceleration voltage of 300 kV. The nitrogen isotherms at the temperature of liquid nitrogen were measured using a Micromeritics ASAP 2010M system. The samples were outgassed for 10 h at 300 °C before the

 © 2006 Wiley-VCH Verlag GmbH & Co. KGaA, Weinheim 

measurements, the volume of adsorbed $N_2$ was normalized to standard temperature and pressure, specific surface areas were determined from the linear part of the BET equation, the average pore diameter was calculated by using the adsorption branches of the $N_2$ isotherms. Infrared (IR) spectroscopy was performed with a Bruker IFS 66v/S infrared spectrometer in the range 400–4000 $cm^{-1}$ by using KBr pellets in vacuo (<0.4 Pa) at ambient temperature. The diffuse reflectance UV/Visible spectra for powder samples were obtained with a Perkin–Elmer Lambda 20 UV/Visible spectrometer equipped with an integrating sphere, and $BaSO_4$ was used as the internal standard. Solid-state $^{31}P$ magic angle spinning nuclear magnetic resonance (MAS NMR) spectroscopy was performed with an Infinity Plus-400 spectrometer equipped with MAS at a frequency of 104.26 MHz, chemical shifts were referenced to 85% $H_3PO_4$ as an external standard.

**Catalytic Test**

**Catalytic Cracking of 1,3,5-Triisopropylbenzene**

Catalytic cracking of 1,3,5-triisopropylbenzene was carried out by using the pulse technique in a microreactor, and the analyses of the catalytic products were performed by a gas chromatograph (GC-17A, Shimadzu Co.) equipped with a flame ionization detector (FID) with a flexible, 30-m OV-17 quartz capillary column. The catalytic cracking was performed under the following standard conditions: the reaction temperature was 250 °C (no thermal cracking); the reaction pressure was atmospheric pressure; the mass of the catalyst was 0.050 g; 0.2 μL of TIPB was injected for each test; nitrogen was used as the carrier gas at a flow rate of 45 mL/min.

**Esterification of Benzoic Acid with *tert*-Butyl alcohol**

The esterification of benzoic acid with *tert*-butyl alcohol was performed under nitrogen at 80 °C in a flask (30 mL) containing suspended catalyst powder (60 mesh pass), benzoic acid (5 mmol), and *tert*-butyl alcohol (10 mmol). The amount of catalyst used was 0.150 g. After vigorous agitation for 4 h, the products were analyzed with a gas chromatograph (6890N, Agilent Co.) equipped with a flame ionization detector (FID) with a flexible, 30-m HP-5 quartz capillary column.

**Hydroxylation of 2,3,6-Trimethylphenol with $H_2O_2$**

The hydroxylation reaction of 2,3,6-trimethylphenol with $H_2O_2$ was performed at 80 °C in a flask (50 mL) containing suspended catalyst powder (0.150 g, 60 mesh pass), acetonitrile (5 mL) as the solvent, 2,3,6-trimethylphenol (0.156 mol), and $H_2O_2$ (0.052 mol), all added at the same time followed by vigorous agitation for 2 h. The products were analyzed with a gas chromatograph (6890N, Agilent Co.) equipped with a flame ionization detector (FID) with a flexible, 30-m INNOWAX quartz capillary column.

## Acknowledgments

We are grateful for the financial support of the State Basic Research Project (G2000077507) and the National Natural Science Foundation of China (Grant No. 20101004).

[1] A. Taguchi, F. Schüth, *Microporous Mesoporous Mater.* **2005**, *77*, 1–45.
[2] J. A. Rabo, *Appl. Catal., A* **2002**, *229*, 7–10.
[3] S. Damyanova, L. Dimitrov, R. Mariscal, J. Fierro, L. Petrov, I. Sobrados, *Appl. Catal., A* **2003**, *256*, 183–197.
[4] J. Haber, K. Pamin, L. Matachowski, D. Mucha, *Appl. Catal., A* **2003**, *256*, 141–151.
[5] I. V. Kozhevnikov, *Appl. Catal., A* **2003**, *256*, 3–18.
[6] I. V. Kozhevnikov, *Catal. Rev. - Sci. Eng.* **1995**, *29*, 311–352.
[7] M. N. Timofeeva, *Appl. Catal., A* **2003**, *256*, 19–35.
[8] T. Okuhara, *Appl. Catal., A* **2003**, *256*, 213–224.
[9] M. Misono, *Chem. Commun.* **2001**, 1141–1152.
[10] Y. Guo, C. Hu, C. Jiang, Y. Yang, S. Jiang, X. Li, E. Wang, *J. Catal.* **2003**, *217*, 141–151.
[11] P. A. Jalil, M. A. Al-Daous, A. A. Al-Arfaj, A. M. Al-Amer, J. Beltramini, S. A. I. Barri, *Appl. Catal., A* **2001**, *207*, 159–171.
[12] L. R. Pizzio, P. G. Vázquez, C. V. Cáceres, M. N. Blanco, *Appl. Catal., A* **2003**, *256*, 125–139.
[13] S. Mukai, T. Sugiyama, H. Tamon, *Appl. Catal., A* **2003**, *256*, 99–105.
[14] S. Damyanova, L. Dimitrov, R. Mariscal, J. Fierro, L. Petrov, I. Sobrados, *Appl. Catal., A* **2003**, *256*, 183–197.
[15] A. Bielánski, A. Lubanska, J. Pozniczek, A. Micek-Ilnicka, *Appl. Catal., A* **2003**, *256*, 153–171.
[16] H. Kosslick, G. Lischike, B. Parlitz, W. Storek, R. Fricke, *Appl. Catal., A* **1999**, *184*, 49–60.
[17] A. Ghanbari-Siahkali, A. Philippou, J. Dwyer, M. Anderson, *Appl. Catal., A* **2000**, *192*, 57–69.
[18] Y. Izumi, K. Hisano, T. Hida, *Appl. Catal., A* **1999**, *181*, 277–282.
[19] R. L. Augustine, S. K. Tanielyan, N. Mahata, Y. Gao, A. Zsigmond, H. Yang, *Appl. Catal., A* **2003**, *256*, 69–76.
[20] H. Li, N. Perkas, Q. Li, Y. Gofer, Y. Koltypin, A. Gedanken, *Langmuir* **2003**, *19*, 10409–10413.
[21] Y. Guo, Y. Wang, C. Hu, Y. Wang, E. Wang, *Chem. Mater.* **2000**, *12*, 3501–3508.
[22] K. Nowińska, R. Fórmaniak, W. Kaleta, A. Wacław, *Appl. Catal., A* **2003**, *256*, 115–123.
[23] C. Shi, R. Wang, G. Zhu, S. Qiu, J. Long, *Eur. J. Inorg. Chem.* **2005**, 4801–4807.
[24] Q. Liu, W. Wu, J. Wang, X. Ren, Y. Wang, *Microporous Mesoporous Mater.* **2004**, *76*, 51–60.
[25] C. Shi, M. Xin, R. Wang, Y. Xie, L. Hu, L. Xu, R. Zhang, G. Zhu, S. Qiu, *Chem. J. Chin. Univ.* **2005**, *26*, 1198–1201.
[26] L. Yang, Y. Qi, X. Yuan, J. Shen, J. Kim, *J. Mol. Catal. A* **2005**, *229*, 199–205.
[27] H. Yun, M. Kuwabara, H. Zhou, I. Honma, *J. Mater. Sci.* **2004**, *39*, 2341–2347.
[28] P. M. Rao, A. Wolfson, S. Kababya, S. Vega, M. V. Landau, *J. Catal.* **2005**, *232*, 210–225.
[29] C. T. Kresge, M. E. Leonowicz, W. J. Roth, J. C. Vartuli, J. S. Beck, *Nature* **1992**, *359*, 710–712.
[30] S. S. Kim, W. Zhang, T. J. Pinnavaia, *Science* **1998**, *282*, 1302–1305.
[31] D. Zhao, J. Feng, Q. Huo, N. Melosh, G. H. Fredrickson, B. F. Chmelka, G. D. Stucky, *Science* **1998**, *279*, 548–552.
[32] A. Corma, *Chem. Rev.* **1997**, *97*, 2373–2419.
[33] Y. Liu, Y. Cao, N. Yi, W. Feng, W. Dai, S. Yan, H. He, K. Fan, *J. Catal.* **2004**, *224*, 417–428.
[34] A. Corma, A. Martinez, V. Martinez-Soria, *J. Catal.* **1997**, *169*, 480–494.
[35] T. Blasco, A. Corma, A. Martinez, P. Martinez-Escolano, *J. Catal.* **1998**, *177*, 306–313.
[36] Q.-H. Xia, K. Hidajat, S. Kawi, *J. Catal.* **2002**, *209*, 433–444.
[37] Q.-H. Xia, K. Hidajat, S. Kawi, *J. Catal.* **2002**, *205*, 318–331.
[38] B. Bachiller-Baeza, J. A. Anderson, *J. Catal.* **2002**, *212*, 231–239.
[39] Q.-H. Xia, K. Hidajat, S. Kawi, *Catal. Today* **2001**, *68*, 255–262.
[40] P. M. Rao, M. V. Landau, A. Wolfson, A. M. S.-T. M. Herskowitz, *Microporous Mesoporous Mater.* **2005**, *80*, 43–55.
[41] X. Meng, Z. Sun, S. Lin, M. Yang, X. Yang, J. Sun, D. Jiang, F. Xiao, *Appl. Catal., A* **2002**, *236*, 17–22.

Received: March 3, 2006
Published Online: June 19, 2006

 © 2006 Wiley-VCH Verlag GmbH & Co. KGaA, Weinheim 

DOI: 10.1002/ejic.200600220

# Early Alkali Metal (Li, Na, K) and Tris(dimethylamino)sulfonium (TAS) Salts of [1,2,5]Thiadiazolo[3,4-*c*][1,2,5]thiadiazolidyl Radical Anion: Rational Syntheses, Structures and Magnetic Properties

**Vladimir N. Ikorskii,[c] Irina G. Irtegova,[a] Enno Lork,[b] Alexander Yu. Makarov,[a] Ruediger Mews,*[b] Victor I. Ovcharenko,*[c] and Andrey V. Zibarev*[a,d]**

**Keywords:** Magnetic properties / Nitrogen heterocycles / Radical anions / Sulfur heterocycles

Salts of the [1,2,5]thiadiazolo[3,4-*c*][1,2,5]thiadiazolidyl radical anion (**1**) and the early alkali metals, [Li(12-crown-4)$_2$][**1**] (**3**), [Na(15-crown-5)][**1**] (**4**), and [K(18-crown-6)][**1**] (**5**) as well as the salt [(Me$_2$N)$_3$S][**1**] (**6**) can be prepared by reduction of [1,2,5]thiadiazolo[3,4-*c*][1,2,5]thiadiazole (**2**) with PhS$^-$ anion followed by XRD and ESR characterization. These salts are thermally stable and soluble in MeCN. Low-temperature crystallization of salt **5** from MeCN or storage of **5** under MeCN for a few days at ambient temperature gives the solvate **5**·MeCN (**7**). The radical anion **1** acts as bridging ligand in salts **4** and **5** and as chelating ligand in salt **7**. In salt **3**, the radical anion **1** is not coordinated to the cation and can be considered as "naked" anion. In salt **6**, one of the two crystallographically independent **1** acts as bridging ligand, whilst the other is not coordinated to the cation. Magnetic susceptibility data obtained for salts **4** and **5** in the temperature range of 2–300 K revealed antiferromagnetic exchange interactions between paramagnetic centers: **4**, $J$ = –3.42, $\alpha J$ = –1.12 cm$^{-1}$; **5**, $J$ = –1.22 cm$^{-1}$.

(© Wiley-VCH Verlag GmbH & Co. KGaA, 69451 Weinheim, Germany, 2006)

## Introduction

The design, synthesis and investigation of new molecular materials, especially of conducting, superconducting, and magnetic materials, belong to the topical fields of current scientific and technological progress. Over the past two decades, there has been considerable interest in the syntheses, molecular and electronic structures, and physical properties of heterocyclic thiazyl radicals, neutral and charged, recognized as promising building blocks for new molecular magnets and/or molecular conductors.[1] Numerous neutral and positively charged heterocyclic thiazyl radicals (radical cations) have been carefully explored, while rather rare negatively charged systems (radical anions) have been less studied.[1] In this context, new preparative approaches to heterocyclic thiazyl radical anions are of obvious interest.

Recently, we have described the [K(18-crown-6)]$^+$ salt of the [1,2,5]thiadiazolo[3,4-*c*][1,2,5]thiadiazolidyl radical anion (**1**, Scheme 1) and its solvate with MeCN that was unexpectedly isolated in low yield as a result of spontaneous decomposition of the [K(18-crown-6)] [PhXNSN] (X = S, Se) salts in MeCN solution.[2] Since the radical anion **1** might be of interest to material science as a building block for molecular ion-based conductors and/or magnets,[1] in this work we report on the rational preparation of the early alkali metal (Li, Na, K) and tris(dimethylamino)sulfonium (TAS) salts of the radical ion **1** based on the reduction of [1,2,5]thiadiazolo[3,4-*c*][1,2,5]thiadiazole (**2**) with the PhS$^-$ anion. The salts were isolated in high yields, in the case of the alkali metals as complexes with the corresponding crown ethers (12-crown-4, 15-crown-5, and 18-crown-6), followed by XRD and ESR characterization as well as measurements of magnetic susceptibility in the temperature range of 2–300 K.

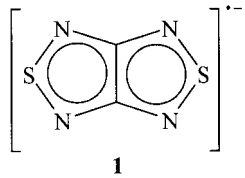


**1**

Scheme 1.

[a] Institute of Organic Chemistry, Russian Academy of Sciences, 630090 Novosibirsk, Russia
Fax: +7-383-330-9752
E-mail: zibarev@nioch.nsc.ru
[b] Institute for Inorganic and Physical Chemistry, University of Bremen,
28334 Bremen, Germany
Fax: +49-421-218-4267
E-mail: mews@chemie.uni-bremen.de
[c] International Tomography Center, Russian Academy of Sciences,
630090 Novosibirsk, Russia
Fax: +7-383-333-1399
E-mail: Victor.Ovcharenko@tomo.nsc.ru
[d] Department of Physics, Novosibirsk State University,
630090 Novosibirsk, Russia

 © 2006 Wiley-VCH Verlag GmbH & Co. KGaA, Weinheim 

## Results and Discussion

In this work, salts of the radical anion **1** and the early alkali metals, [Li(12-crown-4)$_2$][**1**] (**3**), [Na(15-crown-5)][**1**] (**4**), and [K(18-crown-6)][**1**] (**5**), were prepared in a rational way by reduction of compound **2** with the PhS$^-$ anion in MeCN solution (Scheme 2). The corresponding PhSM thiolates (M = Li, Na, K) were used as a source of the PhS$^-$ anion.

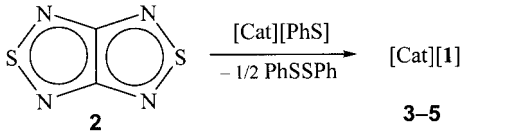


Scheme 2.

For the in situ generation of the PhS$^-$ anion the desilylation of the Ph–S–SiMe$_3$ precursor was employed (Scheme 3). This approach allows to prepare salts of **1** not only with alkali metal cations, for example [K(18-crown-6)], but also with other cations including organic ones, for example the tris(dimethylamino)sulfonium (TAS) salt **6**.

The salts obtained were characterized by XRD (Table 3, Figure 1) and ESR (Figure 2) (for **5** XRD and ESR data were published before).[2] In MeCN solution for all salts the hfc constant $a(^{14}N \times 4)$ = 0.314 mT, and $g$ = 2.0045, are in accordance with previous measurements.[2]

Low-temperature crystallization of salt **5** from MeCN, or storage of **5** under MeCN for a few days at ambient temperature, gives the solvate **5**·MeCN (**7**, XRD and ESR data were published earlier).[2] In the case of **3** and **4**, under the same conditions only the initial salts are recovered, no inclusion of the MeCN solvent into the crystal lattices is observed. Transformation of **5** into **7** is reversible, and crystallization of **7** from boiling MeCN leads to **5**. The procedure can be repeated at least 3 times.

The salts **3**–**7** are thermally stable and soluble in MeCN. When protected from air, the salts **3**–**7** are stable in the crystalline state for several months, and in MeCN solution for several weeks, at least (under electrochemical conditions, a half-life time of **1** in MeCN solution was estimated as 74.5 s on the basis of the ESR data).[2] Upon contact with air,

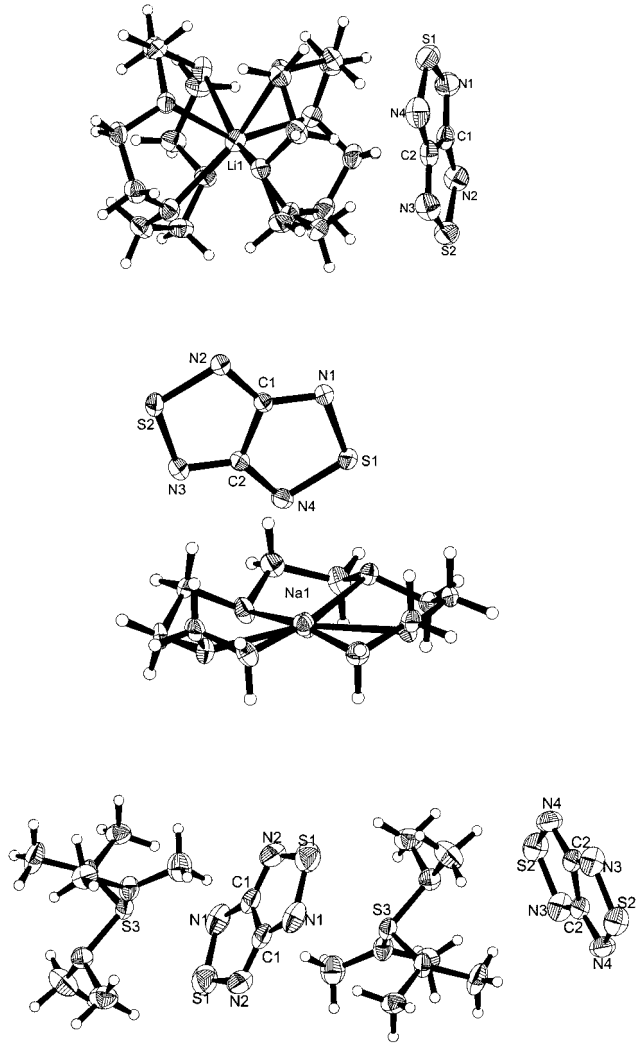


Figure 1. Structure of salts **3** (top), **4** (middle), and **6** (bottom). Crystallographic atom numbering is used; for selected bond lengths and bond angles, see Table 1.

salts **3**–**7** decompose in both solid state and in solution. Among **3**–**7**, salt **3** is the most sensitive towards atmosphere.

It is known that the crystal packing of neutral thiazyl radicals (revealed general tendency to polymorphism)[1b,3] is crucial for their macroscopic magnetic properties.[1b] The crystal packing of salts **3**–**7** is different. The radical anion **1** acts as bridging ligand in salts **4** (Figure 3) and **5**,[2] and

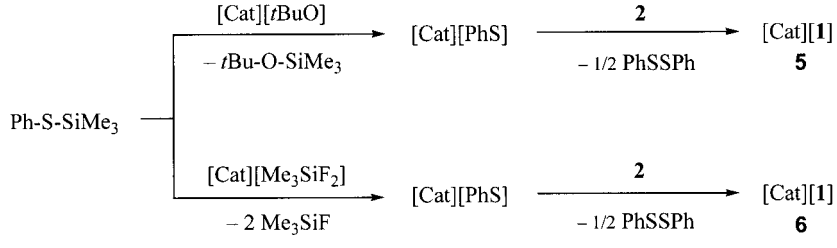


Scheme 3.

 © 2006 Wiley-VCH Verlag GmbH & Co. KGaA, Weinheim 

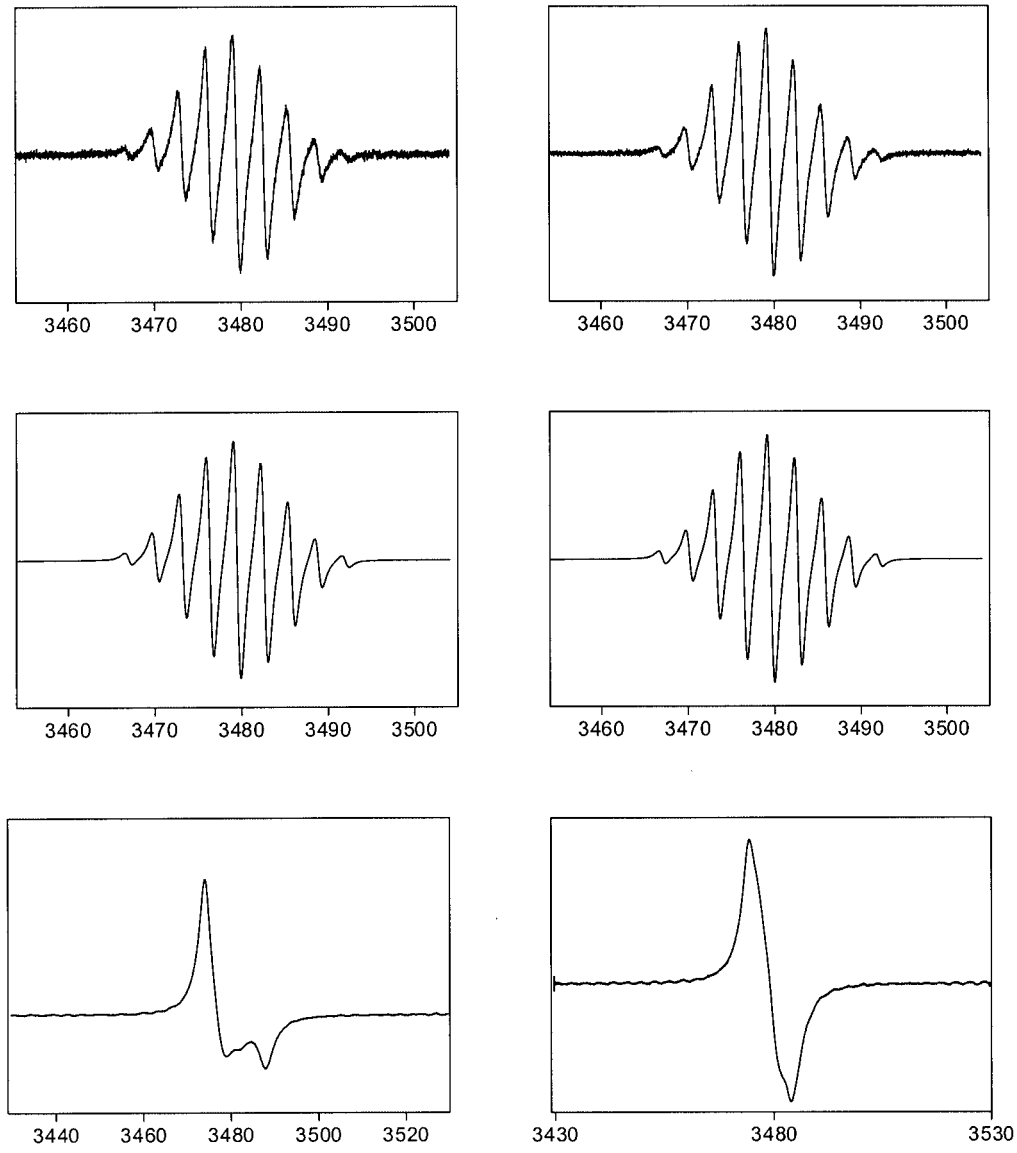


Figure 2. ESR spectra ($|H|\,10^4\,T^{-1}$). Salt **4** (left column): experimental in MeCN solution (top), simulated for solution (middle), and experimental in crystalline state (bottom). Salt **6** (right column): experimental in MeCN solution (top), simulated for solution (middle), and experimental in crystalline state (bottom).

as chelating ligand in salt **7**.[2] In contrast to salt **5** where **1** coordinates two cations symmetrically with N···K contacts of 288.5 pm, in salt **4** the bridging anion **1** coordinates the cations non-symmetrically via N···Na contacts of 251.1 and 283.7 pm, respectively. By these alternating contacts chains are formed along the crystallographic axis *b* (Figure 3).

In salt **3** the radical anion **1** is not coordinated to the Li cation (encapsulated in 2 crown ether molecules, Figure 4) and can be considered as "naked" anion. In salt **6** one of the two crystallographycally independent radical anions **1** acts as bridging ligand via S···S contacts of 361.2 pm, whilst the other is not coordinated to the cation (Figure 5).

Probably, the lack of stabilizing anion-cation interaction leads to the enhanced instability of salt **3** towards atmo-

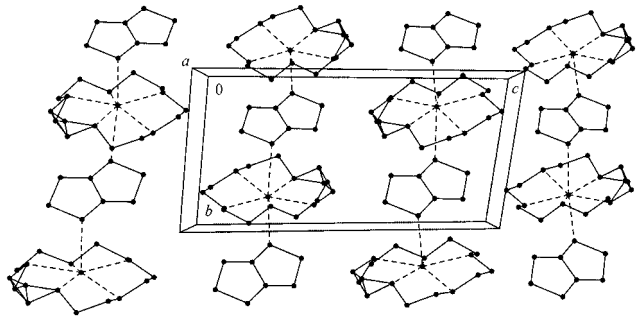


Figure 3. Crystal packing of salt **4** (dashed lines indicate shortened contacts).

 © 2006 Wiley-VCH Verlag GmbH & Co. KGaA, Weinheim 

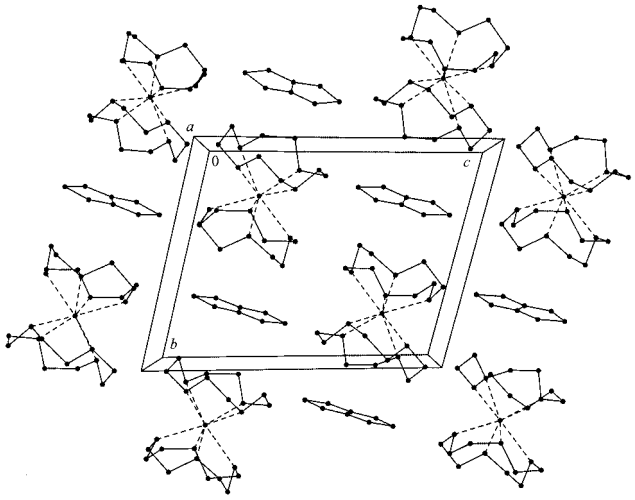


Figure 4. Crystal packing of salt **3** (dashed lines indicate shortened contacts).

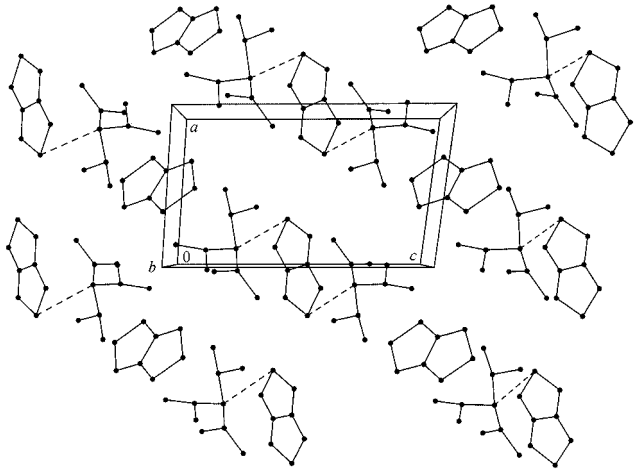


Figure 5. Crystal packing of salt **6** (dashed lines indicate shortened contacts).

sphere as compared with the other alkali metal salts **4**, **5**, and **7**. It should be noted, that the coordination chemistry of thiazyl radicals, both neutral and charged, is still in its infancy.[4]

Molecular geometry data of the radical anion **1** in salts **3**, **4**, and **6** are presented in Table 1 (data for salts **5** and **7** were published earlier).[2] Effects of the coordination of the radical anion **1** to the different cations on its geometry are rather minor.

Attempts to prepare salts with enlarged spin (negative charge) delocalization, for instance [Na(15-crown-5)][**1**][**2**] and [K(18-crown-6)][**1**][**2**], by low-temperature 1:1 co-crystallizations of salts **4** and **5** with the neutral precursor **2** were unsuccessful. The initial compounds were recovered.

The data of magnetic measurements for **4** and **5** are presented in Figure 6. For **4**, temperature dependence of magnetic susceptibility $\chi$ shows the maximum at 8 K. This is indicative of exchange coupling of radical anion clusters with even number of paramagnetic centers. For **5**, $\chi$ increases steadily with temperature lowering.

Table 1. Molecular geometry of **1** in salts **3**, **4**, and **6**.[a]

| Bond [pm]/angle [°] | **3** | **4** | **6**[b] |
|---|---|---|---|
| N1–S2 | 165.95(16) | 165.99(2) | 164.6(10), 166.1(9) |
| S2–N3 | 166.35(15) | 166.5(2) | 166.0(10), 166.3(9) |
| N3–C3a | 133.61(19) | 134.3(2) | 132.6(12), 133.7(11) |
| C3a–N4 | 133.8(2) | 134.2(2) | 130.7(13), 134.8(11) |
| N4–S5 | 165.97(14) | 166.1(2) | 164.6(10), 166.1(9) |
| S5–N6 | 166.30(16) | 166.73(19) | 166.0(10), 166.3(9) |
| N6–C6a | 133.8(2) | 134.4(3) | 132.6(12), 133.7(11) |
| C6a–N1 | 133.5(2) | 134.4(3) | 130.7(13), 134.8(11) |
| C3a–C6a | 145.39(18) | 145.6(3) | 145.5(18), 144.2(17) |
| C6a–N1–S2 | 104.84(10) | 104.96(14) | 106.3(7), 103.8(6) |
| N1–S2–N3 | 101.27(7) | 101.43(9) | 99.8(5), 102.1(4) |
| S2–N3–C3a | 104.54(10) | 104.47(14) | 105.6(7), 103.3(6) |
| C3a–N4–S5 | 104.72(9) | 104.98(15) | 106.3(7), 103.8(6) |
| N4–S5–N6 | 101.30(7) | 101.28(10) | 99.8(5), 102.1(4) |
| S5–N6–C6a | 104.70(10) | 104.56(14) | 105.6(7), 103.6(6) |
| N1–C6a–C3a | 114.55(14) | 114.23(18) | 114.5(12), 114.7(10) |
| C6a–C3a–N3 | 114.81(13) | 114.91(18) | 113.7(14), 115.6(10) |
| N4–C3a–C6a | 114.67(13) | 114.47(18) | 114.5(12), 114.7(10) |
| N6–C6a–C3a | 114.60(14) | 114.70(18) | 113.7(12), 115.6(10) |

[a] Systematic atom numbering is used. [b] Two crystallographically independent molecules.

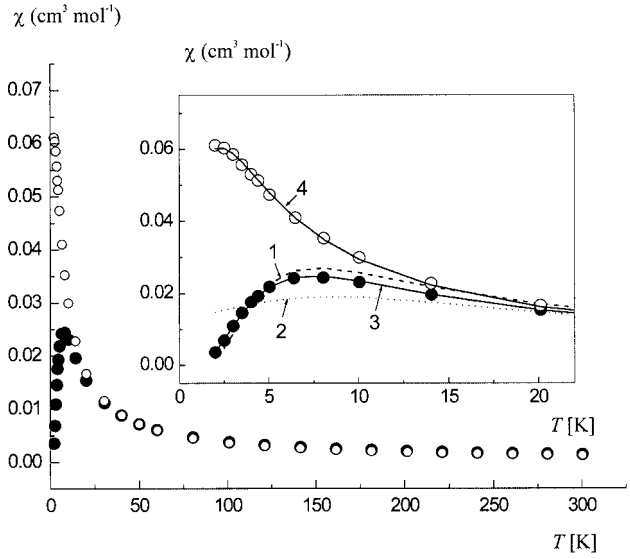


Figure 6. Dependence $\chi$(T) in the temperature ranges of 2–300 K and 2–20 K (insert) for **4** (black circles) and **5** (white circles). Theoretical curves (models) 1 (i), 2 (ii), 3 (iii) and 4 (ii) described in the text.

As mentioned above, crystal packing of **4** and **5** reveals linear chains formed by the N···M (**4**, M = Na; **5**, M = K) contacts, alternating for **4** (251.1 and 283.7 pm) and non-alternating for **5** (288.5 pm). To estimate the energy of exchange interaction $J$ between paramagnetic centers, analytical and numerical expressions of three different models were used, namely: i) the model of dimers,[5] $H = -2JS_1S_2$; ii) the Bonner–Fisher uniform chain model[6] with exchange parameters $J$ equal along the chain, $H = -2J\Sigma S_iS_{i+1}$; and iii) the alternating chain model[6] with exchange parameters $J$ and $aJ$ alternated along the chain, $H = -2J\Sigma(S_{2i}S_{2i-1} + a{\cdot}S_{2i}S_{2i+1})$. The optimized model parameters are given in Table 2. It is seen that the experimental data (Figure 6, in-

 © 2006 Wiley-VCH Verlag GmbH & Co. KGaA, Weinheim 

sert) are best fitted by the alternating chain model (iii) in the case of **4**, and by the Bonner–Fisher model (ii) in the case of **5** (Table 2), in both cases in accordance with the discussed features of the crystal packing. Corresponding theoretical curves are shown in Figure 6 (insert). Thus, despite long distances between radical anions **1** in the crystal lattices of salts **4** and **5**, weak antiferromagnetic exchange interactions are observed.

Table 2. Optimal parameters in modeling exchange interactions.

| Compound | Model | *g* factor | $J$ [cm$^{-1}$] | $-\alpha J$ [cm$^{-1}$] | $R^2$ |
|---|---|---|---|---|---|
| | i | 2.0(1) | 4.06(3) | | 0.9929 |
| **4** | ii | 2.2(2) | 4.9(8) | | 0.8159 |
| | iii | 2.003(7) | 3.46(2) | 1.12(2) | 0.9991 |
| **5** | ii | 1.98(1) | 1.22(2) | | 0.9997 |

One can conclude that even minor changes in the packing observed in going from **4** (this work) to **5**[2] affect the macroscopic magnetic properties of these salts. Overall, the crystal packing of the salts of the radical anion **1** seems to be important for their magnetic behavior.

## Conclusions

Early alkali metal (Li, Na, K) and tris(dimethylamino)-sulfonium (TAS) salts of the [1,2,5]thiadiazolo[3,4-*c*][1,2,5]-thiadiazolidyl radical anion are prepared in a rational way by chemical reduction of [1,2,5]thiadiazolo[3,4-*c*][1,2,5]thiadiazole with the $PhS^-$ anion. The salts, in the case of the alkali metals isolated in the form of complexes with the corresponding crown ethers (12-crown-4, 15-crown-5, and 18-crown-6), are characterized by XRD and ESR. Magnetic measurements confirmed the presence of unpaired electrons in the solids. The temperature dependence of the magnetic susceptibility $\chi$ indicates antiferromagnetic interactions in the solid state.

The salts prepared, which are thermally stable and soluble in MeCN, might be suitable starting materials (sources of the [1,2,5]thiadiazolo[3,4-*c*][1,2,5]thiadiazolidyl radical anion) in the synthesis of new molecular magnets and/or molecular conductors. The synthetic route based on Ph–S–$SiMe_3$ can obviously be generalized to preparation of salts of **1** with transition metal cations (including paramagnetic ones) since the chemistry of metal alkoxides (especially *tert*-butoxides) is well-developed.[7] On the other hand this approach can be expanded to many other π-heterocycles, especially nitrogen ones, possessing high electron affinity and forming stable radical anions.[1g]

## Experimental Section

**General:** Compound **2** was prepared as described earlier.[2] The syntheses described below were performed with exclusion of oxygen in absolutely dry solvents by using a glove box and standard vacuum line techniques. The pressure was normalized with argon where necessary. The GC-MS measurements were performed with a Hewlett–Packard G1800A GCD device for solutions in $CH_2Cl_2$. The ESR measurements were carried out with a Bruker ESP-300 spectrometer (MW power 265 mW, modulation frequency 100 kHz, modulation amplitude 0.005 mT), under anaerobic conditions. The spectral integration and simulation were performed with the Winsim 32 program. The *g* factors were measured using an MnO standard with an accuracy of ±0.0002. Magnetic measurements were carried out on an MPMS-5S Quantum Design SQUID magnetometer in the temperature range of 2–300 K in a magnetic field of 5000 Oe. The molar magnetic susceptibility $\chi$ was calculated using corrections for the diamagnetism equal to $-207 \cdot 10^{-6}$ cm$^3$ mol$^{-1}$ (for **4**) and $-243 \cdot 10^{-6}$ cm$^3$ mol$^{-1}$ (for **5**).

**Crystallographic Analysis:** The data collection for the single-crystal structure determinations (Table 3) were carried out on a Bruker P4 diffractometer with graphite-monochromated Mo-$K_\alpha$ (71.073 pm) radiation. The structures were solved by direct methods by use of the SHELXS-97 program[8] and refined by the least-squares method in the full-matrix anisotropic (isotropic for H atoms) approximation by use of the SHELXL-97 program.[8]

CCDC-293646 (for **3**), -293645 (for **4**), and -293647 (for **6**) contain the supplementary crystallographic data for this paper. These data can be obtained free of charge from The Cambridge Crystallographic Data Centre via www.ccdc.cam.ac.uk/data_request/cif. For **5** and **7**, the data obtained in this work are in full agreement with those published previously.[2]

**Syntheses of Salts 3–5:** At –30 °C, a mixture of 0.144 g (0.001 mol) of **2**, 0.001 mol of PhSM (M = Li, Na, or K) and 0.001 mol (0.002 mol in the case of Li) of the corresponding crown ether was dissolved in 10 mL of MeCN. The wine-red solutions were warmed to 20 °C, stirred for 1 h, and filtered. The solvent was distilled off under reduced pressure, the residue washed with 10 mL of $Et_2O$, and dissolved in 5 mL of boiling MeCN under normal pressure. The solution was filtered and cooled to 20 °C in the case of salt **5**, or to –10 °C in the case of salt **4**. In the case of salt **3**, 10 mL of $Et_2O$ were recondensed onto the filtrate at –196 °C and the two-layered system was placed into cryostat at –40 °C. The solvent was removed with a syringe, and the crystals were washed with 10 mL of $Et_2O$ and dried in vacuo.

Salt **3** forms transparent red plates, yield 0.327 g (65%), m.p. (sealed capillary) 98 °C (dec.).

Salt **4** forms transparent red plates, yield 0.310 g (80%), m.p. (sealed capillary) 100 °C (dec.). $C_{12}H_{20}N_4NaO_5S_2$ (387.44): calcd. C 37.20, H 5.20, N 14.46, S 16.55; found C 37.37, H 5.12, N 14.38, S 16.36.

Salt **5** forms transparent ruby plates, yield 0.335 g (75%), m.p. (sealed capillary) 135 °C (dec.). $C_{14}H_{24}KN_4O_6S_2$ (447.64): calcd. C 37.57, H 5.40, N 12.52, S 14.33; found C 37.42, H 5.28, N 12.61, S 14.22.

In each case evaporation of the initially obtained $Et_2O$ solutions gave PhSSPh (95–98%) identified by GC-MS technique via comparison with an authentic sample.

At –30 °C, a solution of 0.182 g (0.001 mol) of Ph–S–$SiMe_3$[9] in 2 mL of THF was added to a solution of 0.376 g (0.001 mol) of [K(18-crown-6)][*t*BuO][10] in 5 mL of the same solvent. The solution was warmed to 20 °C, stirred for 1 h, and the solvent was distilled off under vacuum to give a white crystalline residue. Compound **2** (0.144 g; 0.001 mol) and 10 mL of MeCN were added at –30 °C, and the wine-red solution obtained was warmed to 20 °C, stirred for 1 h, filtered and the solvents evaporated under vacuum. The residue was washed with 10 mL of $Et_2O$, dissolved in 5 mL of boiling MeCN under normal pressure, and the solution was cooled to 20 °C. The solvent was removed with a syringe, and the crystals were washed with 10 mL of $Et_2O$ and dried in vacuo.

 © 2006 Wiley-VCH Verlag GmbH & Co. KGaA, Weinheim 

Table 3. Crystal data and structure refinement for salts **3**, **4**, and **6**.

| Compound | **3** | **4** | **6** |
|---|---|---|---|
| Empirical formula | $C_{18}H_{32}LiN_4O_8S_2$ | $C_{12}H_{20}N_4NaO_5S_2$ | $C_8H_{18}N_7S_3$ |
| Formula weight | 503.54 | 387.43 | 308.47 |
| Temperature [K] | 173(2) | 173(2) | 173(2) |
| Wavelength [pm] | 71.073 | 71.073 | 71.073 |
| Crystal system | triclinic | triclinic | triclinic |
| Space group | $P\bar{1}$ | $P\bar{1}$ | $P\bar{1}$ |
| Unit cell dimensions *a* [pm] | 837.20(10) | 750.7(2) | 785.6(12) |
| *b* [pm] | 1088.7(2) | 808.6(2) | 804.2(9) |
| *c* [pm] | 1370.2(2) | 1536.2(6) | 1253.3(12) |
| *α* [°] | 102.370(10) | 92.17(2) | 87.51(5) |
| *β* [°] | 96.120(10) | 101.13(3) | 83.68(8) |
| *γ* [°] | 102.370(10) | 112.05(2) | 67.52(10) |
| Volume [nm$^3$] | 1.1762(3) | 0.8418(4) | 0.7272(15) |
| *Z* | 2 | 2 | 2 |
| Density (calcd.) [Mg·m$^{-3}$] | 1.422 | 1.529 | 1.409 |
| Abs. coefficient [mm$^{-1}$] | 0.277 | 0.373 | 0.505 |
| *F*(000) | 534 | 406 | 326 |
| Crystal size [mm$^3$] | 0.90×0.70×0.40 | 0.80×0.30×0.15 | 0.50×0.20×0.10 |
| θ range for data collection [°] | 2.52 to 27.50 | 2.72 to 27.50 | 2.82 to 22.51 |
| Index range | $-10 \le h \le 1$,<br>$-13 \le k \le 13$,<br>$-17 \le l \le 17$ | $-1 \le h \le 9$,<br>$-10 \le k \le 10$,<br>$-19 \le l \le 19$ | $-1 \le h \le 8$,<br>$-8 \le k \le 8$,<br>$-13 \le l \le 13$ |
| Reflections collected | 6527 | 4829 | 2417 |
| Independent reflections | 5336 [*R*(int) = 0.0370] | 3870 [*R*(int) = 0.0281] | 1880 [*R*(int) = 0.0399] |
| Completeness to θ° [%] | 98.9 | 99.9 | 98.4 |
| Absorption correction | nNone | none | none |
| Max. and min. transmission | 0.8971 and 0.7883 | 0.9461 and 0.7544 | 0.9512 and 0.7863 |
| Refinement method | full-matrix least-squares on $F^2$ | full-matrix least-squares on $F^2$ | full-matrix least-squares on $F^2$ |
| Data/restraints/parameters | 5336/0/300 | 3870/7/227 | 1880/0/170 |
| Goodness-of-fit on $F^2$ | 1.043 | 1.032 | 1.168 |
| Final *R* indices [$I>2\sigma(I)$] | *R*1 = 0.0383, *wR*2 = 0.1010 | *R*1 = 0.0423, *wR*2 = 0.0979 | *R*1 = 0.0776, *wR*2 = 0.2067 |
| *R* indices (all data) | *R*1 = 0.0432, *wR*2 = 0.1051 | *R*1 = 0.0619, *wR*2 = 0.1070 | *R*1 = 0.1240, *wR*2 = 0.2303 |
| Largest diff. peak/hole [e Å$^3$] | 0.396/–0.426 | 0.421/–0.471 | 0.483/–0.448 |

Salt **5** forms transparent ruby plates, yield 0.402 g (90%), m.p. (sealed capillary) 135 °C (dec.).

Evaporation of the initially obtained $Et_2O$ solution gave PhSSPh (97%) identified by GC-MS technique via comparison with an authentic sample.

**Synthesis of Salt 6:** At –30 °C, a solution of 0.182 g (0.001 mol) of Ph–S–$SiMe_3$[9] in 1 mL of MeCN was added to a solution of 0.275 g (0.001 mol) of $[(Me_2N)_3S][Me_3SiF_2]$ (TASF)[11] in 5 mL of the same solvent. The solution was warmed to 20 °C, stirred for 1 h, and the solvent was distilled off under vacuum to give a white crystalline residue. A solution of 0.144 g (0.001 mol) of **2** in 10 mL of MeCN was added at –30 °C, the wine-red reaction mixture was warmed to 20 °C, stirred for 1 h, filtered and the solvents evaporated under vacuum. The residue was washed with 10 mL of $Et_2O$ and dissolved in 5 mL of MeCN. Then 10 mL of $Et_2O$ were recondensed onto the solution at –196 °C and the two-layered system was placed into cryostat at –40 °C. The solvent was removed with a syringe, and the crystals were washed with 10 mL of $Et_2O$ and dried in vacuo.

Salt **6** forms transparent red needles, yield 0.230 g (75%), m.p. (sealed capillary) 92 °C (dec.). $C_8H_{18}N_7S_3$ (308.48): calcd. C 31.15, H 5.88, N 31.78, S 31.18; found C 31.30, H 5.74, N 31.85, S 31.06.

The PhSSPh by-product (95%) was identified as described above.

**Preparation of Salt 7:** Upon storage under mother liquor for a few days at ambient temperature, salt **5**, crystallized as described above, transformed slowly into salt **6** (ruby crystals turned to dark-brown). The solvent was removed with a syringe, and the crystals were washed with 10 mL of $Et_2O$ and dried under vacuum for a short time.

Salt **7** forms dark-brown prisms (orange in transmitting light), yield 0.333 g (65%), m.p. (sealed capillary) 125 °C (dec.).

At –196 °C, 10 mL of $Et_2O$ were recondensed onto a solution of 0.224 g (0.5 mmol) of salt **5** into 5 mL of MeCN and the system was placed into a cryostat at –40 °C. The solvent was removed with a syringe, and the crystals of salt **7** (0.243 g, 95%) were washed with 10 mL of $Et_2O$ and dried under vacuum for a short time.

## Acknowledgments

The authors are grateful to Prof. Yuri V. Gatilov for valuable discussions, to Mr. Peter Brackmann for his assistance in the XRD experiments, and to the Deutsche Forschungsgemeinschaft, Germany (grant 436 RUS 113/486/0-3 R), the Russian Foundation for Basic Research, Russia (grants 02-03-04001 and 06-03-32742), and the Siberian Division of the Russian Academy of Sciences (interdisciplinary project N 25) for financial support of this work. A. M. and A. Z. thank the Council for the President of Russian Federation's Grants for Young Scientists and Their Supervisors (grant MK-3178.2005.3), and A. M. thanks the National Science Support Foundation, Russia, for a postdoctoral scholarship.

[1] a) T. Chivers, *A Guide to Chalcogen-Nitrogen Chemistry*, World Scientific: New Jersey e. a., **2005**, pp. 318; b) J. M. Rawson, J. Luzon, F. Palacio, *Coord. Chem. Rev.* **2005**, *249*, 2631–2641; c)

 © 2006 Wiley-VCH Verlag GmbH & Co. KGaA, Weinheim 

L. Beer, J. L. Brusso, R. C. Haddon, M. E. Itkis, R. T. Oakley, R. W. Reed, J. F. Richardson, R. A. Secco, X. Yu, *Chem. Commun.* **2005**, 5745–5747; d) T. S. Cameron, M. L. Lemaire, J. Passmore, J. M. Rawson, K. V. Shuvaev, L. T. Thompson, *Inorg. Chem.* **2005**, *44*, 2576–2578; e) L. Beer, J. L. Brusso, A. W. Cordes, R. C. Haddon, M. E. Itkis, R. T. Oakley, R. W. Reed, *Chem. Commun.* **2002**, 2562–2563; f) J. M. Rawson, F. Palacio, *Struct. Bonding (Berlin)* **2001**, *100*, 93–128; g) R. T. Boere, T. L. Roemmele, *Coord. Chem. Rev.* **2000**, *210*, 369–445; h) J. M. Rawson, G. D. McManus, *Coord. Chem. Rev.* **1999**, *189*, 135–168.

[2] A. Yu. Makarov, I. G. Irtegova, N. V. Vasilieva, I. Yu. Bagryanskaya, T. Borrmann, Yu. V. Gatilov, E. Lork, R. Mews, W.-D. Stohrer, A. V. Zibarev, *Inorg. Chem.* **2005**, *44*, 7194–7199.

[3] a) C. Knapp, E. Lork, K. Gupta, R. Mews, *Z. Anorg. Allg. Chem.* **2005**, *631*, 1640–1644; b) A. Alberola, C. S. Clarke, D. A. Haynes, S. I. Pascu, J. M. Rawson, *Chem. Commun.* **2005**, 4726–4728.

[4] a) M. Jennings, K. E. Preuss, J. Wu, *Chem. Commun.* **2006**, 341–342; b) A. J. Banister, I. May, J. M. Rawson, J. N. B. Smith, *J. Organomet. Chem.* **1998**, *550*, 241–253; c) H. Bock, P. Haenel, R. Neidlein, *Phosphorus Sulfur* **1988**, *39*, 235–252.

[5] O. Kahn, *Molecular Magnetism*, VCH Publishers, New York, **1993**.

[6] W. E. Hatfield, *J. Appl. Phys.* **1981**, *52*, 1985–1990.

[7] D. C. Bradley, *Chem. Rev.* **1989**, *89*, 1317–1322.

[8] G. M. Sheldrick, *SHELX-97 – Programs for Crystal Structure Analysis (Release 97-2)*, Institute for Inorganic Chemistry, University of Göttingen, Göttingen, Germany.

[9] I. Ojima, M. Nihonyangi, T. Nagai, *J. Organomet. Chem.* **1973**, *50*, C26–28.

[10] T. Borrmann, E. Lork, R. Mews, M. M. Shakirov, A. V. Zibarev, *Eur. J. Inorg. Chem.* **2004**, 2452–2458.

[11] W. J. Middleton, *Org. Synth.* **1985**, *64*, 221–224.

Received: March 10, 2006
Published Online: May 30, 2006

 © 2006 Wiley-VCH Verlag GmbH & Co. KGaA, Weinheim 

DOI: 10.1002/ejic.200600241

# Spectroscopic, Structural and Theoretical Investigation of Alkenyl Ruthenium Complexes Supported by Sulfur–Nitrogen Mixed-Donor Ligands

**James D. E. T. Wilton-Ely,*[a] Ming Wang,[b] David M. Benoit,[c] and Derek A. Tocher[b]**

**Keywords:** Mixed-donor ligands / Ruthenium / Alkenyl / Thiolate / Ab initio / Density functional theory

A series of molecules bearing both sulfur and nitrogen donors has been investigated as ligands for σ-alkenyl ruthenium complexes. On deprotonation, the ligands, 4-amino-2-mercaptopyrimidine ($HL_1$), 2-amino-5-mercapto-1,3,4-thiadiazole ($HL_2$), 2-mercaptothiazoline ($HL_3$), 4-hydroxy-2-mercaptopyrimidine ($HL_4$) and 2-mercaptoquinoline ($HL_5$) all react with alkenyl complexes of the form [RuRCl(CO)(BTD)-$(PPh_3)_2$] [R = $CH{=}CHC_6H_5$, $CH{=}CHC_6H_4Me$-4, $C(C{\equiv}CPh){=}CHPh$; BTD = 2,1,3-benzothiadiazole] through loss of chloride and BTD ligands to yield [RuR(L)(CO)$(PPh_3)_2$]. Four of these ligands have alternative potential coordination modes and donor groups. In all cases complexation occurs to form four-membered nitrogen–sulfur chelates with the pendant amino or hydroxy functionality playing no role in coordination. In the case of the 4-aminopyrimidine-2-thiolate ($L_1$) ligand, this was confirmed by a single-crystal X-ray study. 2-Mercaptothiazoline ($L_3$) has the ability to coordinate through two sulfur donors, however, chelation to nitrogen and sulfur donors is preferred as demonstrated by a structural study. This observation is supported by theoretical calculations, which show that a complex displaying the nitrogen–sulfur chelate is of significantly lower energy than one bonded to the ligand through two sulfur donors, despite lone pairs being available in both cases.
(© Wiley-VCH Verlag GmbH & Co. KGaA, 69451 Weinheim, Germany, 2006)

## Introduction

The alkenyl ligand is an important member of the σ-organyl ligand family due to its presence as an intermediate in many catalytic reactions, and has attracted substantial interest over the last 40 years. Alkenyl complexes are known for many metals. This is largely due to well-established synthetic routes such as hydrometallation and the reaction of coordinated alkynes with electrophiles or nucleophiles (Scheme 1).[1]

Since the discovery of hydrometallation of alkynes by the compounds [RuHCl(CO)$L_{2/3}$] (L = P*i*$Pr_3$,[2] $PPh_3$[3]), the resulting alkenyl complexes have been the subject of much pioneering work by the groups of Werner,[10] Esteruelas[11] Santos,[12] and Caulton and Eisenstein[13] covering functional-group transformation, ligand exchange and theoretical calculations. The hydride complexes themselves are known for their ability to catalyse hydrogenation,[14,15] hydrocarbonylation[16] and hydrosilylation[15,17] reactions as well as the formation of diynes.[18]

Previous work from members of this group has concentrated on alkenyl complexes supported by bidentate and tridentate nitrogen and sulfur donor ligands and the reactions of these complexes.[19] This complemented work by other groups exploring the effect of polydentate donors on the structure and reactivity of alkenyl complexes. The majority of this research has concentrated on the use of symmetrical, bidentate phosphorus,[20] nitrogen[21] or chalcogen donors.[22] The investigation of mixed-donor ligands has been largely confined to simple, often homoleptic, coordination compounds. In particular, very few organometallic compounds bearing these ligands have been reported. The work reported here is part of a programme[23] to synthesise σ-

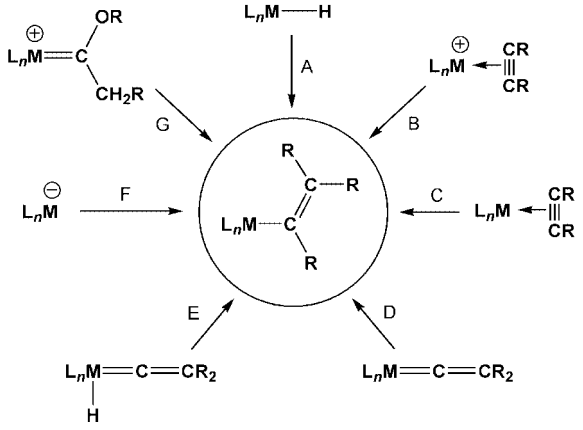


Scheme 1. Common routes to alkenyl complexes: (A) RC≡CR;[2,3] (B) $Nu^-$, nucleophile is β to metal;[4] (C) $E^+$, electrophile is β to metal;[5] (D) $Nu^-$, nucleophile is α to metal;[6] (E) rearrangement yields alkenyl;[7] (F) $H_2C{=}C(X)R$, X = halide;[8] (G) loss of $H^+$ to produce α-alkoxyalkenyls.[9]

[a] Chemistry Research Laboratory, University of Oxford, Mansfield Road, Oxford OX1 3TA, UK
E-mail: james.wilton-ely@chem.ox.ac.uk
[b] Department of Chemistry, University College London, 20 Gordon Street, London WC1H 0AJ, UK
[c] Nachwuchsgruppe Theorie – SFB 569, Universität Ulm, Albert-Einstein-Allee 11, 89081 Ulm, Germany

 © 2006 Wiley-VCH Verlag GmbH & Co. KGaA, Weinheim 

alkenyl complexes bearing mixed-donor bidentate ligands and to investigate their effect on migratory insertion reactions and hemilabile behaviour in these complexes.

Although the coordination chemistry of sulfur derivatives of nucleic bases has received sporadic attention due to the interest in metal-based drugs,[24] the potential of thionucleobases and related molecules as sulfur–nitrogen mixed-donor ligands for organotransition-metal compounds has been overlooked. The reactions of five such molecules with coordinatively-saturated σ-alkenyl ruthenium complexes bearing the labile 2,1,3-benzothiadiazole ligand are discussed below. Four of the ligands have alternative possible coordination modes to those adopted and this aspect is explored in one case using a combination of structural and computational methods.

## Results and Discussion

The organometallic starting materials used in this work are the 2,1,3-benzothiadiazole (BTD) complexes [Ru(alkenyl)Cl(CO)(BTD)($PPh_3$)$_2$],[25] which provide a useful alternative to the 16-electron starting materials, [Ru(alkenyl)Cl(CO)($PPh_3$)$_2$]. The BTD compounds do not suffer contamination by free triphenylphosphane and yield microcrystalline starting complexes of excellent purity, which can be easily (re)crystallized from dichloromethane/ethanol mixtures.

4-Amino-2-mercaptopyrimidine (2-thiocytosine) has been shown to play a role in *E. coli* transfer-RNA,[26] and its coordination chemistry has been explored with a number of metals.[27] Of the coinage metals, copper[28] and silver[29] coordination complexes have been reported, and work by members of our group has investigated its use in supramolecular networks of gold(I) based on hydrogen and aurophilic bonding.[30] In all these reports, the thionucleobase is bonded through sulfur, in many cases as a monodentate ligand. In one study,[31] the cisplatin analogue, [$PtCl_2(L_1)_2$], was prepared, in which 2-thiocytosine is bonded through the amino group, demonstrating the range of coordination options available. Only one organometallic complex (of tin) has been reported very recently.[32]

Treatment of a suspension of [Ru(CH=CHC$_6$H$_4$Me-4)Cl(CO)(BTD)($PPh_3$)$_2$] and 4-amino-2-mercaptopyrimidine in dichloromethane with an ethanolic solution of sodium methoxide led to an immediate colour change from red to yellow. A yellow microcrystalline solid was isolated. This gave rise to a singlet resonance in the $^{31}P\{^1H\}$ NMR spectrum at $\delta$ = 42.1 ppm, indicating a *trans* disposition of the two phosphane ligands; a feature common to all the complexes reported here. The retention of the alkenyl ligand was confirmed by a doublet at 5.84 ($J_{HH}$ = 16.4 Hz) for the β proton and a doublet of triplets to lower field for the α proton at $\delta$ = 7.77 ppm ($J_{HH}$ = 16.4 Hz, $J_{HP}$ = 4.3 Hz) in the $^1$H NMR spectrum. The tolyl substituent was observed as an $(AB)_2$ system at 6.46, 6.87 ppm ($J_{AB}$ = 7.9 Hz) and a methyl resonance at $\delta$ = 2.22 ppm. The mixed-donor ligand itself was identified by a singlet at 4.37 ($NH_2$) and doublet resonances at 4.98 and 6.65 ppm, showing a coupling of 6.3 Hz between the pyrimidine protons. These values are shifted to higher field compared to those at $\delta$ = 5.96 and 7.47 ppm ($J_{HH}$ = 7.15 Hz) in the free ligand.[33] A molecular ion at *m*/*z* = 897 in the Fast Atom Bombardment (FAB) mass spectrum and elemental analysis of the dichloromethane solvate confirmed the overall composition as [Ru(CH=CHC$_6$H$_4$Me-4)($L_1$)(CO)($PPh_3$)$_2$] (**1**) (Scheme 2).

Reaction of [Ru{C(C≡CPh)=CHPh}Cl(CO)(BTD)($PPh_3$)$_2$] with $HL_1$ in a similar manner yielded the disubstituted alkynyl derivative [Ru{C(C≡CPh)=CHPh}($L_1$)-

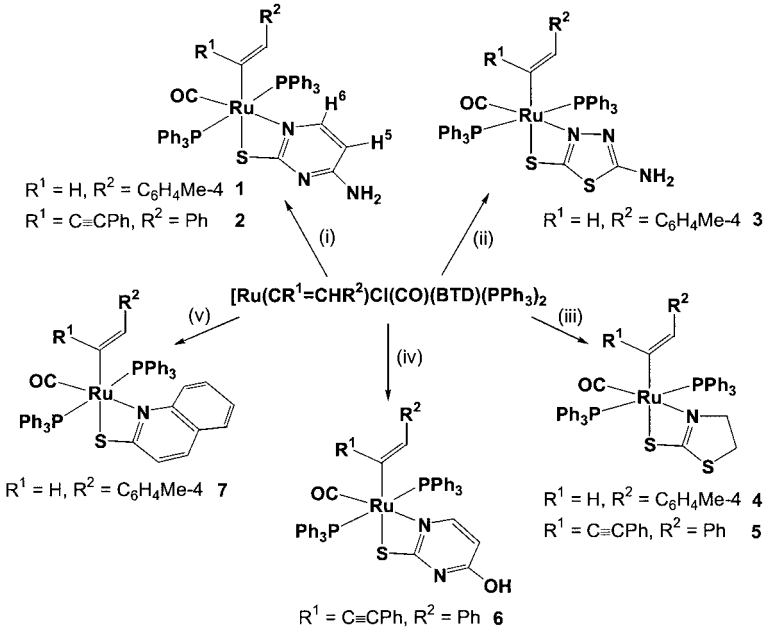


Scheme 2. Alkenyl complexes bearing the mixed-donor ligands, $L_1$–$L_5$. (i) $C_4H_5N_3S$ ($HL_1$), NaOMe; (ii) $C_2H_3N_3S_2$ ($HL_2$), NaOMe; (iii) $C_3H_5NS_2$ ($HL_3$), NaOMe; (iv) $C_4H_4N_2OS$ ($HL_4$), NaOMe; (v) $C_9H_7NS$ ($HL_5$), NaOMe.

 © 2006 Wiley-VCH Verlag GmbH & Co. KGaA, Weinheim 

$(CO)(PPh_3)_2]$ (**2**), which gave rise to a ν(C≡C) absorption of low intensity at 2147 $cm^{-1}$ for the enynyl ligand. A broadened singlet at 4.5 ppm was observed in the $^1H$ NMR spectrum for the $NH_2$ group. In addition to a singlet for the vinylic proton ($\delta$ = 6.13 ppm) and resonances due to the aromatic protons of the alkenyl substituents, two doublets were observed at $\delta$ = 5.12 and 7.69 ppm ($J_{HH}$ = 6.3 Hz) in the $^1H$ NMR spectrum of **2**. The chemical shift of the latter resonance was shifted by approximately 1 ppm downfield with respect to the same feature in complex **1**. A possible explanation for this observation is provided by the crystal structure obtained from single crystals of **2**, grown by slow diffusion of ethanol into a dichloromethane solution of the complex (Figure 1).

An interaction of around 2.6 Å was observed between the triple bond of the enynyl ligand (C10–C11) and the closest proton of the pyrimidine ring (C19–H). The presence of this interaction in solution could explain the apparent deshielding of the proton and hence its shift to lower field. Such CH–π interactions are often found in terminal alkynes,[34] such as in (±)-3-phenylbut-l-ynol, where the distance to the midpoint of the triple bond is 2.62 Å.[34c] On the basis of this evidence, the proton resonances at $\delta$ = 5.12 and 7.69 ppm were assigned to the $H^5$ and $H^6$ protons, respectively.

Recent reports have shown 2-amino-5-mercapto-1,3,4-thiadiazole ($HL_2$) to be an effective corrosion inhibitor for copper[35] and bronze.[36] The properties of its metal complexes have been examined in the inhibition of carbonic anhydrase.[37] $[Ru(CH=CHPh)Cl(CO)(BTD)(PPh_3)_2]$ reacts with $HL_2$ in the presence of base to provide $[Ru(CH=CHPh)(L_2)(CO)(PPh_3)_2]$ (**3**) in good yield. The presence of the mixed-donor ligand was indicated in the $^1H$ NMR spectrum by a singlet at $\delta$ = 5.22 ppm for the $NH_2$ group, along with typical spectroscopic features for the alkenyl ligand. The formulation of the structure (Scheme 2) was based on these data, a molecular ion at $m/z$ = 889 and elemental analysis.

Thiazoline-2-thiolate ($L_3$) has been used as a bridging ligand for palladium centres[38] and to generate polymeric clusters of $Cu^I$ and $Ag^I$.[39] It has also been employed as a ligand in precursor complexes for the deposition of cadmium selenide.[40] However, the potential of the ligand as a bidentate donor has not been widely explored.[41]

The yellow compound $[Ru(CH=CHC_6H_4Me\text{-}4)(L_3)(CO)(PPh_3)_2]$ (**4**) was isolated from the reaction of $HL_3$ with $[Ru(CH=CHC_6H_4Me\text{-}4)Cl(CO)(BTD)(PPh_3)_2]$ and base (Scheme 2). Similar spectroscopic features for the alkenyl ligand were observed in the $^1H$ NMR spectrum as for **1**. Two triplets were also present in the spectrum at $\delta$ = 2.13 and 2.36 ppm, and these were assigned to the thiazoline ring protons showing mutual coupling of 8.2 Hz. The corresponding enynyl derivative, $[Ru\{C(C\equiv CPh)=CHPh\}(L_3)(CO)(PPh_3)_2]$ (**5**), was prepared in an identical manner. Co-

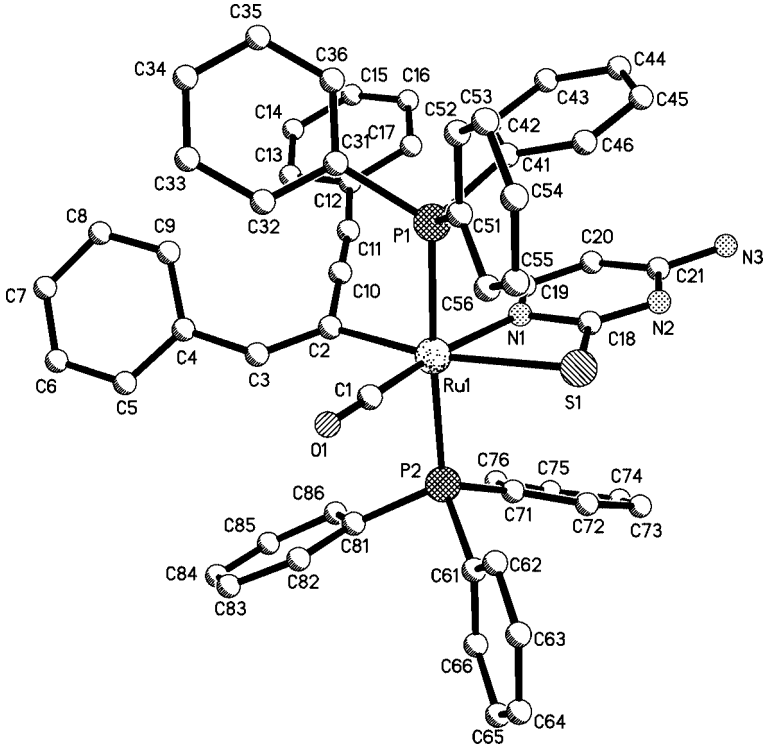


Figure 1. Structure of $[Ru\{C(C\equiv CPh)=CHPh\}(L_1)(CO)(PPh_3)_2]$ (**2**). Selected bond lengths [Å] and angles [°]: Ru1–C1 1.827(4), Ru1–C2 2.111(4), Ru1–N1 2.176(3), Ru1–P2 2.3755(11), Ru1–P1 2.3918(11), Ru1–S1 2.5131(11), S1–C18 1.730(4), N1–C18 1.346(5), C2–C3 1.340(5), C10–C11 1.205(6), C1–Ru1–C2 89.55(16), C2–Ru1–N1 99.97(13), C1–Ru1–P2 89.98(13), C2–Ru1–P2 94.28(11), N1–Ru1–P2 89.80(9), C1–Ru1–P1 89.93(13), C2–Ru1–P1 90.23(11), N1–Ru1–P1 89.55(9), P2–Ru1–P1 175.48(3), C1–Ru1–S1 104.98(13), N1–Ru1–S1 65.49(9), P2–Ru1–S1 89.14(4), P1–Ru1–S1 86.52(4), C18–S1–Ru1 80.18(13), C18–N1–Ru1 102.6(2), C3–C2–Ru1 126.1(3), N1–C18–S1 111.5(3).

 © 2006 Wiley-VCH Verlag GmbH & Co. KGaA, Weinheim 

ordination of the ligand through a thiolate linkage was expected in view of the basic conditions employed and this assumption was reinforced by the observation of NaCl precipitation during the reactions. However, it was not clear whether a bidentate chelate would be achieved through the sulfur or the nitrogen donor on the thiazoline ring. A theoretical study was undertaken in order to examine the mode of coordination of $L_3$. This showed that the chelate should form through sulfur and nitrogen donors rather than both sulfur donors and revealed that there is a significant energy difference between the S,S and S,N coordination modes, favouring the latter (Computational Section). These calculations were found to be in good agreement with a later structural determination using single crystals of the enynyl derivative, [Ru{C(C≡CPh)=CHPh}($L_3$)(CO)($PPh_3$)$_2$] (**5**), which were grown by slow diffusion of ethanol into a dichloromethane solution of the complex (Figure 2).

The thionucleobase, 4-hydroxy-2-mercaptopyrimidine ($HL_4$), also known as 2-thiouracil, has been used to prepare coordination compounds with a number of metals.[42,27a,27k,31] Recent work has investigated the redox properties of complexes using 2-thiouracil as a bridging ligand between ruthenium centres.[27m] However, no organoruthenium species stabilized by this ligand have been reported as far as we are aware.

[Ru{C(C≡CPh)=CHPh}Cl(CO)(BTD)($PPh_3$)$_2$] reacted readily with $HL_4$ and base to yield [Ru{C(C≡CPh)=CHPh}($L_4$)(CO)($PPh_3$)$_2$] (**6**), the hydroxy analogue of the 4-aminopyrimidine-2-thiolate complex, **2**, in excellent yield (Scheme 2). The coordination of the ligand was assumed to be through the N1 and sulfur donors in order to minimize steric interaction between the hydroxy group and the carbonyl and enynyl ligands. Coordination of $L_4$ is also possible as an oxygen–nitrogen mixed-donor. This seemed unlikely, given the thiophilicity of ruthenium(II) and was ruled out by the observation of a broadened singlet at $\delta$ = 1.75 ppm for the hydroxy proton. A doublet for one of the pyrimidine protons was noted at $\delta$ = 5.22 ppm ($J_{HH}$ = 7.3 Hz) which was assigned to $H^5$ on the basis of HMQC and HMBC experiments. The $H^6$ resonance ($\delta$ = 7.43 ppm, $J_{HH}$ = 7.7 Hz in the free ligand[33]) was obscured by the aromatic resonances.

Walton and co-workers have investigated the coordination properties of quinoline-2-thiolate ($L_5$) with rhenium complexes[43] and a few examples have been isolated for molybdenum,[44] cobalt[45] and gold.[46] $HL_5$ has also been used as an analytical reagent for the determination of nickel, copper and palladium.[47] Reaction of a suspension of [Ru(CH=CH$C_6H_4$Me-4)Cl(CO)(BTD)($PPh_3$)$_2$] with $HL_5$ and sodium methoxide resulted in the formation of the yellow complex [Ru(CH=CH$C_6H_4$Me-4)($L_5$)(CO)($PPh_3$)$_2$] (**7**). The peaks observed in the $^1$H NMR spectrum for the alkenyl ligand are similar to those seen in the spectra of **1**, **3** and **4**. The protons of the quinoline rings are all obscured

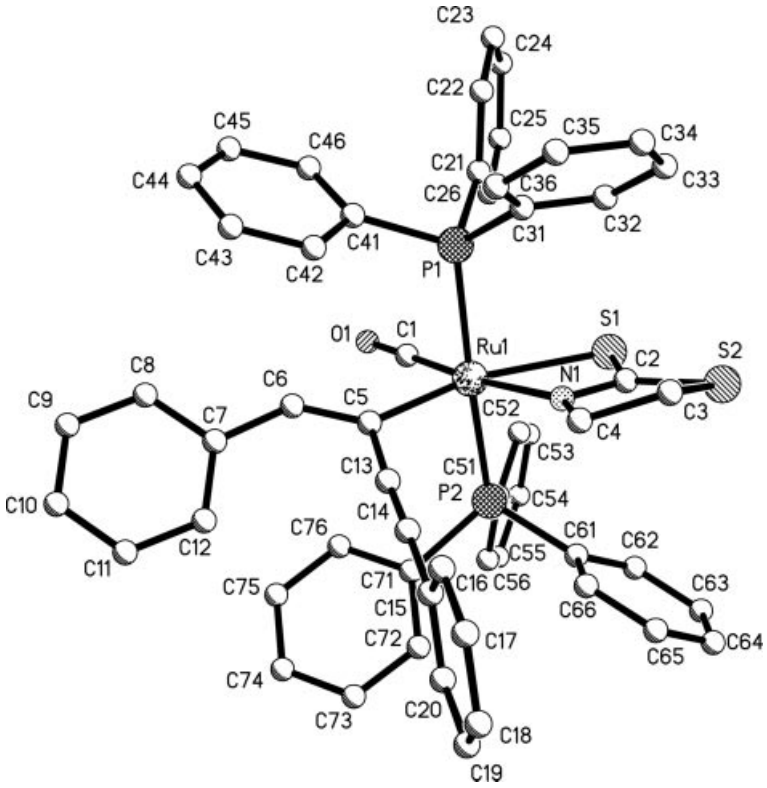


Figure 2. Structure of [Ru{C(C≡CPh)=CHPh}($L_3$)(CO)($PPh_3$)$_2$] (**5**). Selected bond lengths [Å] and angles [°]: Ru1–C1 1.827(2), Ru1–C5 2.102(2), Ru1–N1 2.1766(19), Ru1–P1 2.3667(6), Ru1–P2 2.3746(6), Ru1–S1 2.5521(6), S1–C2 1.720(2), N1–C2 1.283(3), C5–C6 1.361(3), C13–C14 1.205(3), C1–Ru1–C5 88.28(9), C5–Ru1–N1 98.55(8), C1–Ru1–P1 88.62(7), C5–Ru1–P1 94.82(6), N1–Ru1–P1 88.95(5), C1–Ru1–P2 87.87(7), C5–Ru1–P2 90.58(6), N1–Ru1–P2 93.88(5), P1–Ru1–P2 173.46(2), C1–Ru1–S1 108.27(7), N1–Ru1–S1 65.13(5), P1–Ru1–S1 91.26(2), P2–Ru1–S1 84.61(2), C2–S1–Ru1 76.93(8), C2–N1–Ru1 101.39(15), N1–C2–S1 116.55(17), C6–C5–Ru1 126.48(17).

 © 2006 Wiley-VCH Verlag GmbH & Co. KGaA, Weinheim 

by the resonances of the $PPh_3$ ligands with the exception of one proton, which gives rise to a doublet at $\delta$ = 7.92 ppm ($J_{HH}$ = 8.3 Hz). The overall formulation is based on these data, a molecular ion in the FAB mass spectrum at $m/z$ = 931 and elemental analysis.

## Structural Discussion

The structure of [Ru{C(C≡CPh)=CHPh}($L_1$)(CO)($PPh_3$)$_2$] (**2**) (Figure 1) has a distorted octahedral geometry with *cis*-interligand angles in the range 65.49(9)–104.98(13)°. The smallest of these angles corresponds to the bite angle, N1–Ru1–S1, of the 4-aminopyrimidine-2-thiolate ligand ($L_1$). The structure of 4-amino-5-methylmercaptopyrimidine has been determined[48] and can be assumed to be a direct analogue of the free ligand, $HL_1$. This report revealed that the molecule exists essentially in the thione form, however, on coordination to divalent ruthenium in our system, the bond lengths of $L_1$ were observed to be shifted towards the thiolate form. This is seen in the lengthening of the C–S distance from 1.710(4) to 1.730(4) Å in **2**, while the N1–C18 distance shortens from 1.371(5) to 1.346(5) Å on coordination. A complex with the related ligand, 4-methylpyrimidine-2-thiolate (mpymt), [Ru(mpymt)(bpy)$_2$]$^+$ (bpy = 2,2′-bipyridine) has been reported,[42e] in which the C–S distance [1.711(8) Å] is shorter, and the bond length corresponding to N1–C18 [1.367(9) Å] is approximately the same as that found in **2**. This indicates that complexation of $L_1$ in **2** represents a greater shift from the thione to thiolate form than observed in the literature complex. The Ru–S and Ru–N distances for the chelate in [Ru(mpymt)(bpy)$_2$]$^+$ [2.408(2) and 2.103(6) Å, respectively] are considerably shorter than the corresponding distances in **2** of 2.513(11) and 2.176(3) Å. This is likely to be due to the stronger *trans*-influence of the carbonyl and alkenyl donors in [Ru{C(C≡CPh)=CHPh}($L_1$)(CO)($PPh_3$)$_2$] (**2**) compared to 2,2′-bipyridine in the literature complex. The bite angle of $L_1$ in **2** [65.49(9)°] is also smaller than that of 68.2(2)° found in [Ru(mpymt)(bpy)$_2$]$^+$. The bond lengths associated with the alkenyl ligand were found to be unremarkable and fall within the typical range for these ligands.[49] As mentioned above (Results and Discussion), the close proximity of the $H^6$ proton of $L_1$ and the triple bond C10–C11 of the enynyl ligand appears to indicate an interaction that is also present in solution, as suggested by $^1$H NMR evidence.

The structure of 2-mercaptothiazoline ($HL_3$) was only reported very recently and revealed that the molecule adopts the expected thione form in the solid state with the C–S bond [1.6745(16) Å] displaying clear double bond character.[50] As was found for $HL_1$, coordination in the deprotonated form results in a shift of double bond character from the C–S bond to the N–C bond involved in the chelate. The C2–S1 distance of 1.720(2) Å found in the structure of [Ru{C(C≡CPh)=CHPh}($L_3$)(CO)($PPh_3$)$_2$] (**5**) (Figure 2) is considerably longer than that in the free ligand and the N1–C2 distance of 1.283(3) Å is shorter than the corresponding bond length in $HL_3$, 1.319(2) Å. These variations between bonding in the ligand in free and coordinated states are greater than those discussed for $HL_1$ above. The bond lengths between the donors and the ruthenium centre are essentially the same in both **2** and **5** with the exception of the Ru1–S1 bond length, which is around 0.03 Å longer in complex **5**. Unlike the 4-aminopyrimidine-2-thiolate ($L_1$) ligand, the thiazoline-2-thiolate ($L_3$) moiety is not planar due to the saturated C3–C4 linkage. The overall geometry of the structure of **5** is distorted octahedral with *cis*-interligand angles in the range 65.13(5) – 108.27(7)°, the smallest being due to the bite angle of the bidentate ligand. The bond lengths and distances of the enynyl ligand are similar to those found in [Ru{C(C≡CPh)=CHPh}($L_1$)(CO)($PPh_3$)$_2$] (**2**).

## Computational Study

In order to assess the relative stability of the S,N- and S,S-bonding modes available to the complex, [Ru{C(C≡CPh)=CHPh}($L_3$)(CO)($PPh_3$)$_2$] (**5**), it was decided to use ab initio and density functional theory calculations to compute the optimized geometry of two model complexes derived from structure **5**. The calculations were performed using the NWChem4.6 ab initio package[51] running on a dual processor Apple Xserve. Each optimization was performed using analytic gradients and the default convergence criteria of NWChem.

The simplest model for our computational study is obtained by substituting all phenyl groups and $R^2$ by hydrogen atoms, thus reducing the enynyl ligand to the parent alkenyl (Scheme 3).

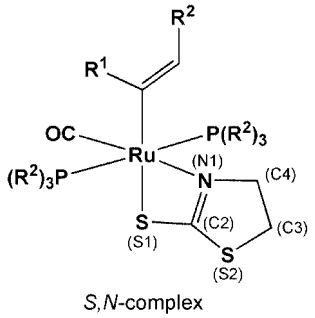


*S,N*-complex

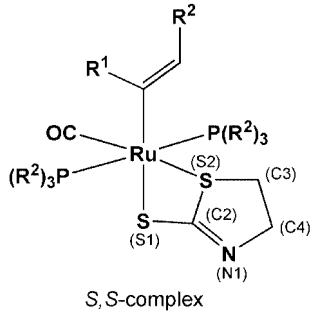


*S,S*-complex

Scheme 3. Computational model. Model A corresponds to $R^1$ = $R^2$ = H. Model B is for $R^1$ = C≡C$CH_3$ and $R^2$ = $CH_3$. Numbering scheme is the same as that used in the structural study.

 © 2006 Wiley-VCH Verlag GmbH & Co. KGaA, Weinheim 

The modest size of model A, along with the use of relativistic pseudo-potentials for each atom developed by Stevens, Basch and Krauss,[52] allowed us to perform fast exploratory calculations using both the Hartree–Fock (HF) method and the local density approximation (LDA) of density functional theory.

The results of our calculations are shown in Table 1, where we report a selection of metal–ligand distances. We observe that the HF distances are much larger than those measured in the experimental X-ray structure, in particular for the two phosphanes and the Ru–S bond. This is to be expected since this method does not take electronic correlation into account. The LDA results for the *S,N*-bonded structure on the other hand are in good agreement with the X-ray values, showing the importance of correlation in describing the electronic structure of transition metal complexes. Moreover, the good agreement with experiment suggests that the computed values for the S,S complex, which was not isolated experimentally, are a plausible representation of the geometrical environment around the ruthenium atom in the S,S system.

In particular, we note that for both levels of theory the S,S complex exhibits a strong degree of ring bending which is absent in the S,N complex. Indeed, Table 1 shows that, while the out-of-plane angle Ru1–S1–C2–C4 remains very low for the S,N complex (about 3° to 5°), the S,S complex has out-of-plane angles between –128° and –110° which indicate that the hybridization of the second sulfur atom (S2) is close to tetrahedral. This, in turn, forces the rest of the thiazoline ring to bend out of the equatorial plane to accommodate the bonding mode of both sulfur donors. The out-of-plane angle computed for the S,N complex on the other hand is in good agreement with that measured in the X-ray structure of –4.5°.

In Table 2, we observe that, for model A, the computed difference of total energy is in favour of the S,N complex in both types of calculations (HF and LDA), which is in line with the experimental observation. The HF method predicts a relatively large energy difference of about 92 kJ·mol$^{-1}$ which is likely to be an overestimation compared to the true value owing to the lack of an appropriate treatment of the electronic correlation. The correlated result computed using LDA brings the energy difference down to about 66 kJ·mol$^{-1}$ which still indicates a very strong preference of the ruthenium for S,N coordination over S,S complex formation.

Table 2. Total energy differences for the *S,N*- and *S,S*-bonded ruthenium structures computed at various levels of ab initio theory.

| | Level of theory | E(S,N complex) – E(S,S complex) |
|---|---|---|
| Model A | HF | – 92.35 kJ·mol$^{-1}$ |
| | LDA | – 65.93 kJ·mol$^{-1}$ |
| Model B | LDA | – 65.41 kJ·mol$^{-1}$ |
| | BP86 | – 64.91 kJ·mol$^{-1}$ |

It has been shown that steric effects can have a great influence on the energetics of ruthenium complexes[53] and, to assess the influence of bulkier phosphane and alkenyl ligands, we replaced the hydrogen atoms of our simple model by methyl and propynyl groups to generate Model B (Scheme 3). The influence of these groups on the stability of the bent ring in the S,S complex can result in an increase of the total energy difference between the S,N and S,S complexes. While these groups cannot account for the overall steric bulk of the phenyl groups used experimentally, we expect that any important steric effects would become apparent with this more limited substitution.

The model B compounds were optimized using local density functional theory and then further refined using a gradient-corrected exchange and correlation functional BP86, which has been developed by Becke and Perdew.[54] It has been shown that this exchange and correlation functional gives good results for transition-metal complexes[55] and ruthenium complexes containing carbonyl ligands in particular.[56]

Our results for these calculations are shown in Table 1 and Table 2. First, we see that the change from model A to model B has a small influence on the computed bond lengths and improves their agreement with the X-ray measurements. We note a slight elongation of the Ru–P bonds for both S,N and S,S complexes and a small contraction of the Ru–S distance for the structure with the S,N coordina-

Table 1. Selected metal–ligand distances for the *S,N*- and *S,S*-bonded ruthenium complex computed at various levels of ab initio theory. The atomic numbering scheme is identical to that in Figure 2.

| | | **S,N Complex** | | | | **S,S Complex** | | | |
|---|---|---|---|---|---|---|---|---|---|
| | | Model A | | Model B | | Model A | | Model B | |
| Distance [Å] | X-ray | HF | LDA | LDA | BP86 | HF | LDA | LDA | BP86 |
| Ru1–C1 | 1.827(2) | 1.997 | 1.854 | 1.842 | 1.856 | 1.983 | 1.843 | 1.830 | 1.847 |
| Ru1–C5 | 2.102(2) | 2.116 | 2.035 | 2.074 | 2.121 | 2.120 | 2.060 | 2.078 | 2.134 |
| Ru1–N1 | 2.1766(19) | 2.203 | 2.107 | 2.132 | 2.208 | 4.165 | 3.859 | 3.823 | 4.122 |
| Ru1–P1 | 2.3667(6) | 2.529 | 2.351 | 2.378 | 2.445 | 2.534 | 2.366 | 2.409 | 2.466 |
| Ru1–P2 | 2.3746(6) | 2.525 | 2.355 | 2.379 | 2.446 | 2.534 | 2.361 | 2.384 | 2.457 |
| Ru1–S1 | 2.5521(6) | 2.730 | 2.638 | 2.613 | 2.681 | 2.663 | 2.579 | 2.581 | 2.644 |
| Ru1–C2 | 2.736 | 2.803 | 2.744 | 2.744 | 2.804 | 3.063 | 2.830 | 2.804 | 3.010 |
| Ru1–S2 | 4.471 | 4.597 | 4.547 | 4.560 | 4.641 | 2.727 | 2.528 | 2.542 | 2.627 |
| Out-of-plane angle | | | | | | | | | |
| Ru1–S1–C2–C4 | –4.50° | 3.3° | 5.0° | 2.5° | 2.8° | –127.9° | –108.6° | –114.8° | –123.5° |

 © 2006 Wiley-VCH Verlag GmbH & Co. KGaA, Weinheim 

tion mode. The values for the out-of-plane angle are also mildly affected and we see both types of complexes becoming slightly flatter. These observations suggest that the steric effects are small and indicate that our initial model (Model A) already provided a good description of both complexes. Second, we note that the energetics of both complexes are not perturbed by the increase in steric bulk of the substituents since the total energy differences between the S,N and S,S complexes remains at about 65 kJ·mol$^{-1}$, again in favour of the S,N complex.

To further investigate the effects of electron correlation on the structure and energetics of both types of complexes, the structures obtained from the LDA calculations on model B were re-optimized using BP86. The resulting geometries for both complexes are shown in Figure 3. As expected, since gradient-corrected functionals such as BP86 tends to elongate bonds in transition metal complexes,[55] we observe a lengthening of most bonds in both complexes. In the S,N complex, BP86 overestimates the Ru–P and the Ru–S distances compared with the experimental values, while the other distances and the out-of-plane angle are relatively unaffected (see Table 1). In the case of the S,S complex, the out-of-plane angle increases and the Ru–P, Ru–S bonds are longer than calculated previously using LDA.

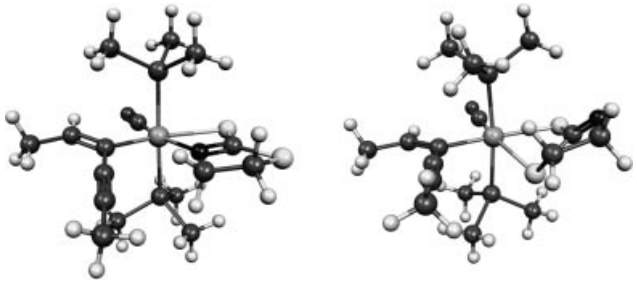

Figure 3. Optimised structures of the S,N complex (left) and S,S complex (right) for model B computed at the BP86/SBK level of theory. Note the large out-of-plane angle in the S,S structure.

Gradient-corrected functionals, such as BP86, provide a more reliable estimation of the binding energy of transition-metal complexes than the local density approximation.[55] Therefore, despite the lengthening of the metal–ligand bonds with BP86, it is interesting to note that the total energy difference between the S,N and the S,S complexes computed with this method remains similar to the value computed using LDA (about 65 kJ·mol$^{-1}$, see Table 2), again pointing to a marked preference for S,N coordination.

Both models and all levels of theory used in this study indicate that the S,N complex is thermodynamically favoured over the S,S complex. There are several possible reasons for the greater stability of a sulfur–nitrogen combination. First, the S,N configuration of the 2-mercaptothiazoline ligand is able to approach the metal centre more closely than the ligand in the S,S arrangement. Indeed, approach of an S,S donor combination is unfavourable due to the constraining bonding mode of the second sulfur atom (S2), which causes out-of-plane ring bending of the rest of the ligand. Second, the HOMO of the 2-mercaptothiazoline ligand is composed mainly of the $p_x$ orbital of the terminal sulfur atom but has a non-negligible contribution from the nitrogen atom, which allows a degree of π bonding with the ruthenium centre. The presence of π ligands in the complex already (e.g., the carbonyl group) means that an additional ligand that can act as a π donor will participate more efficiently in the bonding at the metal centre. Analysis of the molecular orbitals of the S,S complex shows that such π bonding is not possible when the metal centre is bonded to the ligand using the S,S-configuration.

In order to shed some light on a possible kinetic preference at the ligand-binding stage for the formation of the S,N complex over the S,S complex, we computed the charge distribution of the 2-mercaptothiazoline anionic ligand. This calculation was performed using the GAMESS-US suite of programs[57] at the Møllet-Plesset (MP2) level of theory with a TZV(d,p)++ basis set,[58] since it has been recognized that DFT can have problems describing anions.[59] It should be noted that there is a large negative region around the sulfur atom that protrudes out of the thiazoline ring (S1) and around the N atom (N1), while the sulfur atom within the thiazoline ring (S2) is mainly positively charged. This charge distribution could be responsible for a preferential formation of a S,N complex since the orientation of this anionic ligand with respect to a positively charged centre such as $Ru^{II}$ will naturally lead to a closer contact between the metal centre and the atoms S1 and N1.

## Conclusions

This report details the investigation of the coordination properties of five nitrogen–sulfur mixed-donor ligands with alkenyl complexes of ruthenium. We believe that these are the first organoruthenium examples to be reported. Although a number of alternative coordination modes are possible, all ligands adopt a four-membered nitrogen–sulfur chelate, a fact confirmed crystallographically for two examples. In the case of the thiazoline-2-thiolate ligand, the alternative sulfur–sulfur coordination mode was investigated computationally and found to be of much higher energy than the observed S,N coordination, which was confirmed by a structural determination. The excellent correlation of structural and computational data indicates the utility of this theoretical approach in the rationalization of such complexation behaviour.

## Experimental Section

All manipulations were carried out under aerobic conditions with commercially available solvents and reagents, which were used as received. Infrared and NMR spectroscopy was carried out at 25 °C using Shimadzu FTIR 8700 (KBr plates and nujol mulls) and Bruker AMX-300 ($^1$H: 299.87 MHz, $^{31}$P: 121.39 MHz) spectrometers respectively. Infrared spectroscopic features due to the triphenylphosphane ligands have been omitted to aid clarity. FAB-MS spectra (nitrobenzyl alcohol matrices) were measured using a VG 70-SB magnetic sector mass spectrometer. Elemental analysis

 © 2006 Wiley-VCH Verlag GmbH & Co. KGaA, Weinheim 

was performed at University College, London. Solvates were determined by integration of the $^1$H NMR spectra. The complexes [Ru(CH=CHC$_6$H$_4$CH$_3$-4)Cl(CO)(BTD)(PPh$_3$)$_2$],[25] [Ru(CH=CHPh)Cl(CO)(BTD)(PPh$_3$)$_2$],[25] [Ru{C(C≡CPh)=CHPh}Cl(CO)(PPh$_3$)$_2$],[60] were prepared according to published procedures. All other regents were obtained commercially.

**Preparation of [Ru(CH=CHC$_6$H$_4$Me-4)(L$_1$)(CO)(PPh$_3$)$_2$] (1):** [Ru(CH=CHC$_6$H$_4$Me-4)Cl(CO)(BTD)(PPh$_3$)$_2$] (100 mg, 0.106 mmol) and 4-amino-2-mercaptopyrimidine (HL$_1$) (15 mg, 0.118 mmol) were suspended in dichloromethane (20 mL) and ethanol (10 mL) and treated with sodium methoxide (11 mg, 0.204 mmol) in ethanol (10 mL). The reaction was stirred for 1 h, after which the solvent volume was concentrated under reduced pressure until precipitation of a pale yellow product was complete. This was washed with water (5 mL), ethanol (5 mL) and hexane (10 mL). Yield: 68 mg (72%). IR (KBr/nujol): $\tilde{\nu}$ = 1923 [ν(CO)], 1614, 1572, 1545, 1313, 1256, 1186 cm$^{-1}$. $^{31}$P{$^1$H} NMR (CDCl$_3$): $\delta$ = 42.1 ppm. $^1$H NMR (CDCl$_3$): $\delta$ = 2.22 (s, 3 H, CH$_3$), 4.37 (s, 2 H, NH$_2$), 4.98, 6.65 [d×2, $J_{HH}$ = 6.3 Hz, 2×1 H, C$_4$*H*$_2$(NH$_2$)N$_2$S], 5.84 (d, $J_{HH}$ = 16.4 Hz, 1 H, Hβ), 6.46, 6.87 [(AB)$_2$, $J_{AB}$ = 7.9 Hz, 4 H, C$_6$H$_4$], 7.25, 7.58 (m×2, 30 H, C$_6$H$_5$), 7.77 (dt, $J_{HH}$ = 16.4 Hz, $J_{HP}$ = 4.3 Hz, 1 H, Hα) ppm. FAB-MS: *m*/*z* (%) = 897 (1) [M]$^+$, 780 (1) [M – alkenyl]$^+$, 635 (2) [M – PPh$_3$]$^+$. C$_{50}$H$_{43}$N$_3$OP$_2$RuS·CH$_2$Cl$_2$ (981.93): calcd. C 62.4, H 4.6, N 4.3; found C 62.8, H 4.8, N 4.3.

**Preparation of [Ru{C(C≡CPh)=CHPh}(L$_1$)(CO)(PPh$_3$)$_2$] (2):** Synthesis as for **1** using [Ru{C(C≡CPh)=CHPh}Cl(CO)(BTD)(PPh$_3$)$_2$] (100 mg, 0.097 mmol) and 4-amino-2-mercaptopyrimidine (HL$_1$) (14 mg, 0.110 mmol) to provide a yellow product. Yield: 72 mg (76%). IR (KBr/nujol): $\tilde{\nu}$ = 2147 [ν(C≡C)], 1913 [ν(CO)], 1611, 1580, 1537, 1312, 1186, 972, 914 cm$^{-1}$. $^{31}$P{$^1$H} NMR (CDCl$_3$): $\delta$ = 40.1 ppm. $^1$H NMR (CDCl$_3$): $\delta$ = 4.5 (br. s, 2 H, NH$_2$), 5.12, 7.69 [d×2, $J_{HH}$ = 6.3 Hz, 2×1 H, C$_4$*H*$_2$(NH$_2$)N$_2$S], 6.13 (s, 1 H, RuC=CH), 6.78 (d, $J_{HH}$ = 7.4 Hz, 2 H, *ortho*-C$_6$H$_5$), 6.95 (t, $J_{HH}$ = 7.4 Hz, 1 H, *para*-C$_6$H$_5$), 7.27, 7.61 (m×2, 30 H + 7 H, PC$_6$H$_5$ + C$_6$H$_5$) ppm. FAB-MS: *m*/*z* (%) = 982 (9) [M]$^+$, 856 (3) [M – L$_1$]$^+$, 779 (3) [M – alkenyl]$^+$, 720 (5) [M – PPh$_3$]$^+$, 692 (16) [M–CO–PPh$_3$]$^+$. C$_{57}$H$_{45}$N$_3$OP$_2$RuS (983.09): calcd. C 69.6, H 4.6, N 4.3; found C 69.6, H 4.5, N 4.3.

**Preparation of [Ru(CH=CHPh)(L$_2$)(CO)(PPh$_3$)$_2$] (3):** Synthesis as for **1** using [Ru(CH=CHPh)Cl(CO)(BTD)(PPh$_3$)$_2$] (100 mg, 0.108 mmol) and 2-amino-5-mercapto-1,3,4-thiadiazole (HL$_2$) (16 mg, 0.121 mmol) to provide a pale yellow-green product. Yield: 79 mg (82%). IR (KBr/nujol): $\tilde{\nu}$ = 1921 [ν(CO)], 1595, 1580, 1553, 1310, 1184, 972, 847 cm$^{-1}$. $^{31}$P{$^1$H} NMR (CDCl$_3$): $\delta$ = 43.7 ppm. $^1$H NMR (CDCl$_3$): $\delta$ = 5.22 (s, 2 H, NH$_2$), 5.89 (d, $J_{HH}$ = 15.7 Hz, 1 H, Hβ), 6.34 (d, $J_{HH}$ = 7.5 Hz, 2 H, *ortho*-C$_6$H$_5$), 6.82 (t, $J_{HH}$ = 7.5 Hz, 1 H, *para*-C$_6$H$_5$), 6.90 (t, $J_{HH}$ = 7.4 Hz, 2 H, *meta*-C$_6$H$_5$), 7.30–7.53 (m, 30 H, PC$_6$H$_5$), 7.94 (dt, $J_{HH}$ = 15.7 Hz, $J_{HP}$ = 3.2 Hz, 1 H, Hα) ppm. FAB-MS: *m*/*z* (%) = 889 (45) [M]$^+$, 786 (20) [M – alkenyl]$^+$, 627 (12) [M – PPh$_3$]$^+$. C$_{48}$H$_{41}$N$_3$OP$_2$RuS$_2$·1.5CH$_2$Cl$_2$ (1030.42): calcd. C 57.7, H 4.3, N 4.1; found C 57.5, H 4.0, N 4.3.

**Preparation of [Ru(CH=CHC$_6$H$_4$Me-4)(L$_3$)(CO)(PPh$_3$)$_2$] (4):** Synthesis as for **1** using [Ru(CH=CHC$_6$H$_4$Me-4)Cl(CO)(BTD)(PPh$_3$)$_2$] (100 mg, 0.106 mmol) and 2-mercaptothiazoline (HL$_3$) (14 mg, 0.117 mmol) to provide a yellow product. Yield: 77 mg (82%). IR (KBr/nujol): $\tilde{\nu}$ = 1906 [ν(CO)], 1573, 1304, 1188, 1045, 941, 831 cm$^{-1}$. $^{31}$P{$^1$H} NMR (CDCl$_3$): $\delta$ = 40.4 ppm. $^1$H NMR (CDCl$_3$): $\delta$ = 2.13, 2.36 (t×2, $J_{HH}$ = 8.2 Hz, 2×2 H, C$_3$H$_4$NS$_2$), 2.26 (s, 3 H, CH$_3$), 5.84 (d, $J_{HH}$ = 16.5 Hz, 1 H, Hβ), 6.60, 6.92 [(AB)$_2$, $J_{AB}$ = 7.93 Hz, 4 H, C$_6$H$_4$], 7.33, 7.69 (m×2, 30 H, C$_6$H$_5$), 7.84 (dt, $J_{HH}$ = 16.5 Hz, $J_{HP}$ = 3.5 Hz, 1 H, Hα) ppm. FAB-MS: *m*/*z* (%) = 906 (3) [M + H$_2$O]$^+$, 888 (3) [M]$^+$, 771 (1) [M – L$_3$]$^+$, 626 (6) [M – PPh$_3$]$^+$, 598 (2) [M–CO–PPh$_3$]$^+$. C$_{49}$H$_{43}$NOP$_2$RuS$_2$·CH$_2$Cl$_2$ (973.97): calcd. C 61.7, H 4.7, N 1.4; found C 61.3, H 4.6, N 1.5.

**Preparation of [Ru{C(C≡CPh)=CHPh}(L$_3$)(CO)(PPh$_3$)$_2$] (5):** Synthesis as for **1** using [Ru{C(C≡CPh)=CHPh}Cl(CO)(BTD)(PPh$_3$)$_2$] (100 mg, 0.097 mmol) and 2-mercaptothiazoline (HL$_3$) (13 mg, 0.109 mmol) to provide a yellow microcrystalline product. Yield: 72 mg (76%). IR (KBr/nujol): $\tilde{\nu}$ = 2152 [ν(C≡C)], 1917 [ν(CO)], 1591, 1574, 1302, 1049, 941, 914 cm$^{-1}$. $^{31}$P{$^1$H} NMR (CDCl$_3$): $\delta$ = 39.6 ppm. $^1$H NMR (CDCl$_3$): $\delta$ = 2.08, 2.88 (t×2, $J_{HH}$ = 8.0 Hz, 2×2 H, C$_3$H$_4$NS$_2$), 6.08 (s, 1 H, RuC=CH), 6.98–7.81 (m, 30 H + 10 H, PC$_6$H$_5$ + C$_6$H$_5$) ppm. FAB-MS: *m*/*z* (%) = 973 (2) [M]$^+$, 856 (3) [M – L$_3$]$^+$, 771 (2) [M – alkenyl]$^+$, 711 (1) [M – PPh$_3$]$^+$, 684 (8) [M–CO–PPh$_3$]$^+$. C$_{56}$H$_{45}$NOP$_2$RuS$_2$ (975.13): calcd. C 69.0, H 4.7, N 1.4; found C 69.0, H 4.6, N 1.2.

**Preparation of [Ru{C(C≡CPh)=CHPh}(L$_4$)(CO)(PPh$_3$)$_2$] (6):** [Ru{C(C≡CPh)=CHPh}Cl(CO)(BTD)(PPh$_3$)$_2$] (100 mg, 0.097 mmol) and 4-hydroxy-2-mercaptopyrimidine (HL$_4$) (14 mg, 0.109 mmol) were suspended in dichloromethane (20 mL) and ethanol (10 mL) and treated with sodium methoxide (10 mg, 0.185 mmol) in ethanol (10 mL). The reaction was stirred for 1 h, after which all solvent was removed. The residue was dissolved in dichloromethane (10 mL) and filtered through diatomaceous earth to remove NaCl. Diethyl ether (40 mL) was slowly added to precipitate the pale yellow product. This was washed with diethyl ether (10 mL) and hexane (10 mL). Yield: 85 mg (89%). IR (KBr/nujol): $\tilde{\nu}$ = 2151 [ν(C≡C)], 1927 [ν(CO)], 1650, 1595, 1275, 1184, 976, 914 cm$^{-1}$. $^{31}$P{$^1$H} NMR (CDCl$_3$): $\delta$ = 40.3 ppm. $^1$H NMR (CDCl$_3$): $\delta$ = 1.75 (br. s, 1 H, OH), 5.22 [d, $J_{HH}$ = 7.3 Hz, 1 H, C$_5$*H*$_2$(OH)N$_2$S], 6.08 (s, 1 H, RuC=CH), 6.76 (d, $J_{HH}$ = 7.7 Hz, 2 H, *ortho*-C$_6$H$_5$), 6.98–7.72 [m, 30 H + 8 H + 1 H, PC$_6$H$_5$ + C$_6$H$_5$ + C$_5$*H*$_2$(OH)N$_2$S] ppm. FAB-MS: *m*/*z* (%) = 984 (1) [M]$^+$, 857 (0.2) [M – L$_4$]$^+$, 781 (0.6) [M – alkenyl]$^+$, 722 (0.2) [M – PPh$_3$]$^+$, 694 (1.5) [M–CO–PPh$_3$]$^+$, 491 (0.6) [M – alkenyl–CO–PPh$_3$]$^+$. C$_{57}$H$_{44}$N$_2$O$_2$P$_2$RuS·0.75CH$_2$Cl$_2$ (1047.77): calcd. C 66.2, H 4.4, N 2.7; found C 66.2, H 4.4, N 3.0.

**Preparation of [Ru(CH=CHC$_6$H$_4$Me-4)(L$_5$)(CO)(PPh$_3$)$_2$] (7):** [Ru(CH=CHC$_6$H$_4$Me-4)Cl(CO)(BTD)(PPh$_3$)$_2$] (100 mg, 0.106 mmol) and 2-mercaptoquinoline (HL$_5$) (19 mg, 0.118 mmol) were suspended in dichloromethane (20 mL) and ethanol (10 mL) and treated with sodium methoxide (11 mg, 0.204 mmol) in ethanol (10 mL). The reaction was stirred for 1 h, after which the solvent was concentrated under reduced pressure until precipitation of a yellow product had begun. The flask was then kept at –20 °C for 4 hours. The resulting precipitate was washed with water (5 mL), cold ethanol (5 mL) and hexane (10 mL). Yield: 76 mg (77%). Although the product is partially soluble in ethanol, it can be recrystallised from dichloromethane/ethanol mixtures. IR (NaCl/nujol): $\tilde{\nu}$ = 1913 [ν(CO)], 1591, 1545, 1504, 1296, 1184, 1163, 1109, 974, 874, 845, 814 cm$^{-1}$. $^{31}$P{$^1$H} NMR (C$_6$D$_6$): $\delta$ = 35.6 ppm. $^1$H NMR (C$_6$D$_6$): $\delta$ = 2.16 (s, 3 H, CH$_3$), 6.09, 6.59 [(AB)$_2$, $J_{AB}$ = 8.7 Hz, 4 H, C$_6$H$_4$], 6.64 (dt, $J_{HH}$ = 16.7 Hz, $J_{HP}$ = 2.0 Hz, 1 H, Hβ), 6.81–7.16, 7.36–7.78 (m×2, 30 H + 5 H, C$_6$H$_5$ + C$_9$H$_6$NS), 7.92 (d, $J_{HH}$ = 8.3 Hz, 1 H, C$_9$H$_6$NS), 8.65 (dt, $J_{HH}$ = 16.7 Hz, $J_{HP}$ = 3.5 Hz, 1 H, Hα) ppm. FAB-MS: *m*/*z* (%) = 931 (4) [M]$^+$, 669 (7) [M – PPh$_3$]$^+$, 641 (8) [M–CO–PPh$_3$]$^+$, 524 (7) [M – alkenyl–CO–PPh$_3$]$^+$. C$_{55}$H$_{45}$NOP$_2$RuS·0.25CH$_2$Cl$_2$ (952.28): calcd. C 69.7, H 4.8, N 1.5; found C 69.9, H 4.8, N 1.5.

**X-ray Crystallography:** Crystals of complexes **2** and **5** were grown by slow diffusion of ethanol into dichloromethane solutions of the complexes. A single crystal of each compound was mounted on a

 © 2006 Wiley-VCH Verlag GmbH & Co. KGaA, Weinheim 

glass fibre and all geometric and intensity data were taken from this sample with a Bruker SMART APEX CCD diffractometer using graphite-monochromated Mo-$K_\alpha$ radiation ($\lambda$ = 0.71073 Å). Data reduction and integration was carried out with SAINT+ and absorption corrections applied using the program SADABS. The structures were solved by direct methods and developed using alternating cycles of least-squares refinement and difference-Fourier synthesis. All non-hydrogen atoms were refined anisotropically. Hydrogen atoms were placed in calculated positions and their thermal parameters linked to those of the atoms to which they were attached (riding model). Structure solution and refinement used the SHELXTL PLUS V6.10 program package.[61] See Table 3 for selected crystal data.

Table 3. Crystal data for compounds **2** and **5**.

| | **2** | **5**·1.5($CH_2Cl_2$) |
|---|---|---|
| Chemical formula | $C_{57}H_{45}N_3OP_2RuS$ | $C_{57.5}H_{48}Cl_3NOP_2RuS_2$ |
| Fw | 983.03 | 1102.45 |
| Crystal system | monoclinic | monoclinic |
| Crystal colour | yellow | yellow |
| Crystal size [mm] | 0.48×0.12×0.10 | 0.24×0.22×0.12 |
| Space group | *C*2/*c* | $P2_1/n$ |
| *a* [Å] | 28.321(3) | 13.0473(8) |
| *b* [Å] | 19.249(2) | 22.7831(14) |
| *c* [Å] | 21.145(3) | 17.5285(11) |
| *α* [°] | 90 | 90 |
| *β* [°] | 119.139(2) | 104.5250(10) |
| *γ* [°] | 90 | 90 |
| *V* [Å$^3$] | 10068(2) | 5043.9(5) |
| *Z* | 8 | 4 |
| Calculated density [g/cm$^3$] | 1.297 | 1.452 |
| *T* [K] | 293(2) | 150(2) |
| $\mu$(Mo-$K_\alpha$) [mm$^{-1}$] | 0.458 | 0.658 |
| *F*(000) | 4048 | 2260 |
| Reflections collected | 43639 | 44202 |
| Unique reflections ($R_{int}$) | 12004 (0.0563) | 12093 (0.0304) |
| $R_1$ [$I>2\sigma(I)$] | 0.0617 | 0.0405 |
| $wR'_2$ (all data) | 0.1832 | 0.0952 |
| Residual e·Å$^{-3}$ (max., min.) | 1.540, –1.20 | 1.084, –1.214 |

CCDC-263406 and -263407 contain the supplementary crystallographic data for this paper. These data can be obtained free of charge from The Cambridge Crystallographic Data Centre via www.ccdc.cam.ac.uk/data_request/cif.

## Acknowledgments

J. D. E. T. W.-E. gratefully acknowledges the Ramsay Memorial Trust for provision of a Fellowship and Merton College, Oxford, for a Fitzjames Fellowship. We thank the Department of Chemistry at UCL, the University of London Central Research Fund and the UCL Graduate School for funding and Johnson Matthey Ltd. for a generous loan of ruthenium salts.

[1] For an overview of alkenyl chemistry of ruthenium(II), see: A. F. Hill, in: *Comprehensive Organometallic Chemistry II* (Eds.: E. W. Abel, F. G. A. Stone, G. Wilkinson); Pergamon Press: Oxford, U. K., **1995**; vol. 7.

[2] H. Werner, M. A. Esteruelas, H. Otto, *Organometallics* **1986**, *5*, 2295–2299.

[3] M. R. Torres, A. Vegas, A. Santos, J. Ros, *J. Organomet. Chem.* **1986**, *309*, 169–177.

[4] a) S. G. Feng, J. L. Templeton, *Organometallics* **1992**, *11*, 2168–2175; b) D. L. Reger, K. A. Belmore, E. Mintz, N. G. Charles, E. A. H. Griffith, E. L. Amma, *Organometallics* **1983**, *2*, 101–105.

[5] G. P. Elliott, W. R. Roper, *J. Organomet. Chem.* **1983**, *250*, C5–C8.

[6] a) B. Guilbert, B. Demerseman, P. H. Dixneuf, C. Mealli, *J. Chem. Soc., Chem. Commun.* **1989**, 1035–1037; b) B. Demerseman, B. Guilbert, C. Renovard, M. Gonzalez, P. H. Dixneuf, D. Masi, C. Mealli, *Organometallics* **1993**, *12*, 3906–3917; c) C. Bianchini, P. Innocenti, M. Peruzzini, A. Romerosa, F. Zanobini, *Organometallics* **1996**, *15*, 272–285.

[7] A. van Asselt, B. J. Burger, V. C. Gibson, J. E. Bercaw, *J. Am. Chem. Soc.* **1986**, *108*, 5347–5349.

[8] J. Rajaram, R. G. Pearson, J. A. Ibers, *J. Am. Chem. Soc.* **1974**, *96*, 2103–2108.

[9] M. I. Bruce, D. N. Duffy, M. G. Humphrey, A. G. Swincer, *J. Organomet. Chem.* **1985**, *282*, 383–397.

[10] a) S. Jung, K. Ilg, C. D. Brandt, J. Wolf, H. Werner, *Eur. J. Inorg. Chem.* **2004**, 469–480; b) S. Jung, C. D. Brandt, J. Wolf, H. Werner, *Dalton Trans.* **2004**, 375–383; c) H. Werner, S. Jung, P. Gonzalez-Herrero, K. Ilg, J. Wolf, *Eur. J. Inorg. Chem.* **2001**, 1957–1961; d) S. Jung, K. Ilg, J. Wolf, H. Werner, *Organometallics* **2001**, *20*, 2121–2123; e) H. Werner, W. Stüer, S. Jung, B. Weberndörfer, J. Wolf, *Eur. J. Inorg. Chem.* **2002**, 1076–1080; f) H. Werner, A. Stark, P. Steinert, C. Grunwald, J. Wolf, *Chem. Ber.* **1995**, *128*, 49–62.

[11] a) R. Castarlenas, M. A. Esteruelas, E. Oñate, *Organometallics* **2001**, *20*, 2294–2302; b) M. A. Esteruelas, C. García-Yebra, M. Oliván, E. Oñate, M. Tajada, *Organometallics* **2000**, *19*, 5098–5106; c) R. Castarlenas, M. A. Esteruelas, E. Oñate, *Organometallics* **2000**, *19*, 5454–5463; d) M. L. Buil, M. A. Esteruelas, C. García-Yebra, E. Gutiérrez-Puebla, M. Oliván, *Organometallics* **2000**, *19*, 2184–2193; e) C. Bohanna, M. L. Buil, M. A. Esteruelas, E. Oñate, C. Valero, *Organometallics* **1999**, *18*, 5176–5179; f) C. Bohanna, B. Callejas, A. Edwards, M. A. Esteruelas, F. J. Lahoz, L. A. Oro, N. Ruiz, C. Valero, *Organometallics* **1998**, *17*, 373–381; g) M. A. Esteruelas, A. V. Gómez, A. M. López, E. Oñate, *Organometallics* **1998**, *17*, 3567–3573; h) M. A. Esteruelas, F. Liu, E. Oñate, E. Sola, B. Zeier, *Organometallics* **1997**, *16*, 2919–2928; i) M. L. Buil, S. Elipe, M. A. Esteruelas, E. Oñate, E. Peinado, N. Ruiz, *Organometallics* **1997**, *16*, 5748–5755; j) M. A. Esteruelas, F. J. Lahoz, E. Oñate, L. A. Oro, E. Sola, *J. Am. Chem. Soc.* **1996**, *118*, 89–99; k) C. Bohanna, M. A. Esteruelas, J. Herrero, A. M. López, L. A. Oro, *J. Organomet. Chem.* **1995**, *498*, 199–206; l) C. Bohanna, M. A. Esteruelas, F. J. Lahoz, E. Oñate, L. A. Oro, E. Sola, *Organometallics* **1995**, *14*, 4825–4831; m) C. Bohanna, M. A. Esteruelas, F. J. Lahoz, E. Oñate, L. A. Oro, *Organometallics* **1995**, *14*, 4685–4696.

[12] a) B. Gómez-Lor, A. Santos, M. Ruiz, A. M. Echavarren, *Eur. J. Inorg. Chem.* **2001**, 2305–2310; b) A. M. Castaño, A. M. Echavarren, J. López, A. Santos, *J. Organomet. Chem.* **1989**, *379*, 171–175; c) J. Montoya, A. Santos, A. M. Echavarren, J. Ros, *J. Organomet. Chem.* **1990**, *390*, C57–C60; d) H. Loumrhari, J. Ros, M. R. Torres, A. Santos, A. M. Echavarren, *J. Organomet. Chem.* **1991**, *411*, 255–261; e) J. Montoya, A. Santos, J. López, A. M. Echavarren, J. Ros, A. Romero, *J. Organomet. Chem.* **1992**, *426*, 383–398; f) J. López, A. Romero, A. Santos, A. Vegas, A. M. Echavarren, P. Noheda, *J. Organomet. Chem.* **1989**, *373*, 249–258.

[13] a) A. Pedersen, M. Tilset, K. Folting, K. G. Caulton, *Organometallics* **1995**, *14*, 875–888; b) A. V. Marchenko, H. Gérard, O. Eisenstein, K. G. Caulton, *New J. Chem.* **2001**, *25*, 1244–1255; c) A. V. Marchenko, H. Gérard, O. Eisenstein, K. G. Caulton, *New J. Chem.* **2001**, *25*, 1382–1388.

[14] R. A. Sánchez-Delgado, A. Andriollo, O. L. De Ochoa, T. Suarez, N. Valencia, *J. Organomet. Chem.* **1981**, *209*, 77–83.

[15] M. A. Esteruelas, J. Herrero, L. A. Oro, *Organometallics* **1993**, *12*, 2377–2379.

[16] R. A. Sánchez-Delgado, M. Rosales, A. Andriollo, *Inorg. Chem.* **1991**, *30*, 1170–1173.

 © 2006 Wiley-VCH Verlag GmbH & Co. KGaA, Weinheim 

[17] H. Katayma, M. Nagao, R. Moriguchi, F. Ozawa, *J. Organomet. Chem.* **2003**, *676*, 49–54.

[18] a) A. M. Echavarren, J. López, A. Santos, J. Montoya, *J. Organomet. Chem.* **1991**, *414*, 393–400; b) R. B. Bedford, A. F. Hill, A. R. Thompsett, A. J. P. White, D. J. Williams, *Chem. Commun.* **1996**, 1059–1060.

[19] a) A. F. Hill, A. J. P. White, D. J. Williams, J. D. E. T. Wilton-Ely, *Organometallics* **1998**, *17*, 4249–4258; b) J. C. Cannadine, A. F. Hill, A. J. P. White, D. J. Williams, J. D. E. T. Wilton-Ely, *Organometallics* **1996**, *15*, 5409–5415; c) A. F. Hill, A. J. P. White, D. J. Williams, J. D. E. T. Wilton-Ely, manuscript in preparation; d) A. F. Hill, C. T. Ho, J. D. E. T. Wilton-Ely, *Chem. Commun.* **1997**, 2207–2208; e) A. F. Hill, J. D. E. T. Wilton-Ely, *J. Chem. Soc., Dalton Trans.* **1999**, 3501–3510.

[20] a) A. Santos, J. López, A. Galán, J. J. González, P. Tinoco, A. M. Echavarren, *Organometallics* **1997**, *16*, 3482–3488; b) A. Santos, J. López, J. Montoya, P. Noheda, A. Romero, A. M. Echavarren, *Organometallics* **1994**, *13*, 3605–3615.

[21] a) A. Romero, A. Vegas, A. Santos, M. Martinez-Ripoll, *J. Organomet. Chem.* **1987**, *319*, 103–111; b) J. López, A. Santos, A. Romero, A. M. Echavarren, *J. Organomet. Chem.* **1993**, *443*, 221–228.

[22] a) H. Loumrhari, L. Matas, J. Ros, M. R. Torres, A. Perales, *J. Organomet. Chem.* **1991**, *403*, 373–381; b) M. R. Torres, A. Perales, H. Loumrhari, J. Ros, *J. Organomet. Chem.* **1990**, *384*, C61–C64; c) H. Loumrhari, J. Ros, R. Yáñez, M. R. Torres, *J. Organomet. Chem.* **1991**, *408*, 233–239; d) M. R. Torres, A. Perales, H. Loumrhari, J. Ros, *J. Organomet. Chem.* **1990**, *385*, 379–386; e) H. Loumrhari, J. Ros, M. R. Torres, *Polyhedron* **1991**, *10*, 421–427; f) A. L. Hector, A. F. Hill, *J. Organomet. Chem.* **1993**, *447*, C7–C9; g) R. B. Bedford, C. S. J. Cazin, *J. Organomet. Chem.* **2000**, *598*, 20–23; h) H. Adams, P. E. McHugh, M. J. Morris, S. E. Spey, P. J. Wright, *J. Organomet. Chem.* **2001**, *619*, 209–217.

[23] a) P. J. Pogorzelec, D. H. Reid, D. A. Tocher, J. D. E. T. Wilton-Ely, *Z. Naturforsch., Teil B* **2004**, *59*, 1372–1378; b) J. D. E. T. Wilton-Ely, M. Wang, S. Honarkhah, D. A. Tocher, *Inorg. Chim. Acta* **2005**, *358*, 3218–3226; c) J. D. E. T. Wilton-Ely, P. J. Pogorzelec, S. Honarkhah, D. H. Reid, D. A. Tocher, *Organometallics* **2005**, *24*, 2862–2874; d) J. D. E. T. Wilton-Ely, S. Honarkhah, M. Wang, D. A. Tocher, A. M. Z. Slawin, *Dalton Trans.* **2005**, 1930–1939.

[24] N. Farrell, *Transition Metal Complexes as Drugs and Chemotherapeutic Agents*, Kluwer, Dortrecht, **1989**, and references therein.

[25] M. C. J. Harris, A. F. Hill, *Organometallics* **1991**, *10*, 3903–3906.

[26] J. Carbon, H. David, M. H. Studier, *Science* **1968**, *161*, 1146–1147.

[27] a) B. T. Khan, K. Annapoorna, *Inorg. Chim. Acta* **1990**, *171*, 157–163; b) B. T. Khan, A. M. Zakeeruddin, *Transition Met. Chem.* **1991**, *16*, 119–121; c) B. T. Khan, K. Annapoorna, S. Shamsuddin, K. Najmuddin, *Polyhedron* **1992**, *11*, 2109–2114; d) K. Yamanari, M. Yarnarnoto, M. Kida, T. Fujihara, A. Fuyuhiro, S. Kaizaki, *J. Chem. Soc., Dalton Trans.* **1993**, 1651–1655; e) K. Yamanari, S. Dogi, K. Okusako, T. Fujihara, A. Fuyuhiro, S. Kaizaki, *Bull. Chem. Soc. Jpn.* **1994**, *67*, 3004–3008; f) A. Barbieri, A. M. Giuliani, G. Ruisi, A. Silvestri, R. Z. Barbieri, *Z. Anorg. Allg. Chem.* **1995**, *621*, 89–96; g) B. T. Khan, S. R. A. Khan, K. Annapoorna, *Indian J. Chem., Sect. A* **1995**, *34*, 878–882; h) K. Yamanari, T. Nozaki, A. Fuyuhiro, Y. Kushi, S. Kaizaki, *J. Chem. Soc., Dalton Trans.* **1996**, 2851–2856; i) K. Yamanari, T. Nozaki, A. Fuyuhiro, S. Kaizaki, *Chem. Lett.* **1996**, 35–36; j) K. Yamanari, I. Fukuda, S. Yamamoto, Y. Kushi, A. Fuyuhiro, N. Kubota, T. Fukuo, R. Arakawa, *J. Chem. Soc., Dalton Trans.* **2000**, 2131–2136; k) E. Melendez, M. Marrero, C. Rivera, E. Hernandez, A. Segal, *Inorg. Chim. Acta* **2000**, *298*, 178–186; l) C. L. Ma, Y. Shi, Q. Jiang, *Heteroat. Chem.* **2005**, *16*, 69–75; m) S. Chakraborty, R. H. Laye, P. Munshi, R. L. Paul, M. D. Ward, G. K. Lahiri, *J. Chem. Soc., Dalton Trans.* **2002**, 2348–2353.

[28] H. C. Nelson, J. F. Villa, *Inorg. Chim. Acta* **1979**, *34*, L235–L237.

[29] W. McFarlane, P. D. Akrivos, P. Aslanidis, P. Karagiannidis, C. Hatzisymeon, M. Numan, S. Kokkou, *Inorg. Chim. Acta* **1998**, *281*, 121–125.

[30] J. D. E. T. Wilton-Ely, A. Schier, N. W. Mitzel, S. Nogai, H. Schmidbaur, *J. Organomet. Chem.* **2002**, *643*, 313–323.

[31] J. Jolley, W. I. Cross, R. G. Pritchard, C. A. McAuliffe, K. B. Nolan, *Inorg. Chim. Acta* **2001**, *315*, 36–43.

[32] C.-L. Ma, Y. Shi, Q.-F. Zhang, Q. Jiang, *Polyhedron* **2005**, *24*, 1109–1116.

[33] SDBS Spectral database for organic compounds, National Institute for Advanced Industrial Science and Technology, Japan. http://www.aist.go.jp/RIODB/SDBS/cgi-bin/cre_index.cgi.

[34] a) M. Nishio, *CrystEngComm* **2004**, *6*, 130–158; b) D. Philp, J. M. A. Robinson, *J. Chem. Soc., Perkin Trans. 2* **1998**, 1643–1650; c) T. Steiner, E. B. Starikov, A. M. Amado, J. J. C. Teixeira-Dias, *J. Chem. Soc., Perkin Trans. 2* **1995**, 1321–1326; d) T. Steiner, E. B. Starikov, M. Tamm, *J. Chem. Soc., Perkin Trans. 2* **1996**, 67–71.

[35] O. Blajiev, A. Hubin, *Electrochim. Acta* **2004**, *49*, 2761–2770.

[36] Y. Li, F. Zhu, W. J. Wei, *J. Mater. Sci.* **2003**, *38*, 407–411.

[37] a) R. Olar, D. Marinescu, C. Popescu, C. T. Supuran, *Rev. Roum. Chim.* **1997**, *42*, 111–114; b) M. Brezeanu, R. Olar, C. T. Supuran, N. Stanica, M. Stoicescu, *Rev. Roum. Chim.* **1996**, *41*, 681–685; c) M. Brezeanu, R. Olar, A. Meghea, N. Stanica, C. T. Supuran, *Rev. Roum. Chim.* **1996**, *41*, 103–107; d) C. T. Supuran, C. L. Lepadatu, R. Olar, A. Meghea, M. Brezeanu, *Rev. Roum. Chim.* **1993**, *38*, 1509–1517.

[38] M. E. Lizarraga, R. Navarro, E. P. Urriolabeitia, *J. Organomet. Chem.* **1997**, *542*, 51–60.

[39] a) J. P. Fackler, R. J. Staples, C. W. Liu, R. T. Stubbs, C. Lopez, J. T. Pitts, *Pure Appl. Chem.* **1998**, *70*, 839–844; b) J. P. Fackler, C. Lopez, R. J. Staples, S. N. Wang, R. E. P. Winpenny, R. P. Lattimer, *J. Chem. Soc., Chem. Commun.* **1992**, 146–148.

[40] O. F. Z. Khan, P. O'Brien, *Polyhedron* **1991**, *10*, 325–332.

[41] W. S. Sheldrick, C. Landgrafe, *Inorg. Chim. Acta* **1993**, *208*, 145–151.

[42] a) D. A. Stuart, L. R. Nassimbeni, A. T. Hutton, K. R. Koch, *Acta Crystallogr., Sect. B* **1980**, *36*, 2227–2230; b) C. S. W. Harker, E. R. T. Tiekink, M. W. Whitehouse, *Inorg. Chim. Acta* **1991**, *181*, 23–30; c) K. Yamanari, K. Okusako, Y. Kushi, S. Kaizaki, *J. Chem. Soc., Dalton Trans.* **1992**, 1621–1626; d) A. R. Dias, M. T. Duarte, A. M. Galvao, M. H. Garcia, M. M. Marques, M. S. Salema, *Polyhedron* **1995**, *14*, 675–685; e) J. S. Casas, E. Castellano, E. M. S. García-Tasende, A. Sánchez, J. Sordo, E. M. Vázquez-López, J. Zukerman-Schpector, *J. Chem. Soc., Dalton Trans.* **1996**, 1973–1978; f) D. J. Darensbourg, B. J. Frost, A. Derecskei-Kovacs, J. H. Reibenspies, *Inorg. Chem.* **1999**, *38*, 4715–4723; g) D. J. Darensbourg, B. J. Frost, A. Derecskei-Kovacs, J. H. Reibenspeis, *Inorg. Chem.* **1999**, *38*, 4715–4723; h) K. Nomiya, R. Noguchi, T. Shigeta, Y. Kondoh, K. Tsuda, K. Ohsawa, N. Chikaraishi-Kasuga, M. Oda, *Bull. Chem. Soc. Jpn.* **2000**, *73*, 1143–1152; i) S. Patra, B. Mondal, B. Sarkar, M. Niemeyer, G. K. Lahiri, *Inorg. Chem.* **2003**, *42*, 1322–1327.

[43] a) A. L. Ondracek, W. G. Wu, P. E. Fanwick, R. A. Walton, *Inorg. Chem.* **1996**, *35*, 5249–5253; b) T. A. Harris, T. M. McKinney, W. G. Wu, P. E. Fanwick, R. A. Walton, *Polyhedron* **1996**, *15*, 3289–3298; c) M. Leeaphon, A. L. Ondracek, R. J. Thomas, P. E. Fanwick, R. A. Walton, *J. Am. Chem. Soc.* **1995**, *117*, 9715–9724; d) M. Leeaphon, K. Rohl, R. J. Thomas, P. E. Fanwick, R. A. Walton, *Inorg. Chem.* **1993**, *32*, 5562–5568.

[44] P. E. Fanwick, J. S. Qi, Y. P. Wu, R. A. Walton, *Inorg. Chim. Acta* **1990**, *168*, 159–161.

[45] F. E. Hong, S. C. Chen, Y. T. Tsai, Y. C. Chang, *J. Organomet. Chem.* **2002**, *655*, 172–181.

 © 2006 Wiley-VCH Verlag GmbH & Co. KGaA, Weinheim 

[46] J. D. E. T. Wilton-Ely, S. Hofreiter, N. W. Mitzel, H. Schmidbaur, *Z. Naturforsch., Teil B* **2001**, *56*, 1257–1263.
[47] a) M. G. Paneli, A. Voulgaropoulos, *Fresenius J. Anal. Chem.* **1991**, *341*, 716–719; b) J. Xavier, *Fresenius J. Anal. Chem.* **1958**, *163*, 182–187.
[48] V. Ravichandran, K. K. Chacko, M. N. Ponnuswamy, J. Trotter, *Acta Crystallogr., Sect. C* **1985**, *41*, 1470–1473.
[49] A. G. Orpen, L. Brammer, F. H. Allen, O. Kennard, D. G. Watson, R. Taylor, *J. Chem. Soc., Dalton Trans.* **1989**, S1–S83.
[50] H. T. Flakus, A. Miros, P. G. Jones, *Spectrochim. Acta, Part A* **2002**, *58*, 225–237.
[51] a) E. Aprà, T. L. Windus, T. P. Straatsma, E. J. Bylaska, W. de Jong, S. Hirata, M. Valiev, M. Hackler, L. Pollack, K. Kowalski, R. Harrison, M. Dupuis, D. M. A. Smith, J. Nieplocha, V. Tipparaju, M. Krishnan, A. A. Auer, E. Brown, G. Cisneros, G. Fann, H. Früchtl, J. Garza, K. Hirao, R. Kendall, J. Nichols, K. Tsemekhman, K. Wolinski, J. Anchell, D. Bernholdt, P. Borowski, T. Clark, D. Clerc, H. Dachsel, M. Deegan, K. Dyall, D. Elwood, E. Glendening, M. Gutowski, A. Hess, J. Jaffe, B. Johnson, J. Ju, R. Kobayashi, R. Kutteh, Z. Lin, R. Littlefield, X. Long, B. Meng, T. Nakajima, S. Niu, M. Rosing, G. Sandrone, M. Stave, H. Taylor, G. Thomas, J. van Lenthe, A. Wong, Z. Zhang, *NWChem, A Computational Chemistry Package for Parallel Computers*, Version 4.6 (**2004**), Pacific Northwest National Laboratory, Richland, Washington 99352–0999, USA; b) R. A. Kendall, E. Aprà, D. E. Bernholdt, E. J. Bylaska, M. Dupuis, G. I. Fann, R. J. Harrison, J. L. Ju, J. A. Nichols, J. Nieplocha, T. P. Straatsma, T. L. Windus, A. T. Wong, *Comput. Phys. Commun.* **2000**, *128*, 260–283.
[52] a) J. S. Binkley, J. A. Pople, W. J. Hehre, *J. Am. Chem. Soc.* **1980**, *102*, 939–947; b) W. J. Stevens, H. Basch, M. Krauss, *J. Chem. Phys.* **1984**, *81*, 6026–6033; c) W. J. Stevens, M. Krauss, H. Basch, P. G. Jasien, *Can. J. Chem.* **1992**, *70*, 612–630.
[53] S. Z. Knottenbelt, J. E. McGrady, G. A. Heath, *Dalton Trans.* **2003**, 227–232.
[54] a) A. D. Becke, *Phys. Rev. A* **1988**, *38*, 3098–3100; b) J. P. Perdew, *Phys. Rev. B* **1986**, *33*, 8822–8824.
[55] M. R. Bray, R. J. Deeth, V. J. Paget, P. D. Sheen, *Int. J. Quantum Chem.* **1996**, *61*, 85–91.
[56] V. Jonas, W. Thiel, *J. Chem. Phys.* **1995**, *102*, 8474–8484.
[57] M. W. Schmidt, K. K. Baldridge, J. A. Boatz, S. T. Elbert, M. S. Gordon, J. H. Jensen, S. Koseki, N. Matsunaga, K. A. Nguyen, S. J. Su, T. L. Windus, M. Dupuis, J. A. Montgomery, *J. Comput. Chem.* **1993**, *14*, 1347–1363.
[58] a) T. H. Dunning, *J. Chem. Phys.* **1971**, *55*, 716–723; b) A. D. McLean, G. S. Chandler, *J. Chem. Phys.* **1980**, *72*, 5639–5648.
[59] N. Rösch, S. B. Trickey, *J. Chem. Phys.* **1997**, *106*, 8940–8941.
[60] A. F. Hill, M. C. J. Harris, R. P. Melling, *Polyhedron* **1992**, *11*, 781–787.
[61] *SHELTXTL*, V 6.10, Bruker AXS, **2000**.

Received: March 17, 2006
Published Online: June 6, 2006

 © 2006 Wiley-VCH Verlag GmbH & Co. KGaA, Weinheim 

DOI: 10.1002/ejic.200600282

# Symmetrisation in the Interaction of Chloro[2-(dimethylaminomethyl)phenyl-$C^1$]mercury(II) with Thiosemicarbazone Derivatives of Pyridine-2-carboxamide and Pyrazin-2-carboxamide

**Ulrich Abram,[b] Alfonso Castiñeiras,*[a] Isabel García-Santos,[a] and Raul Rodríguez-Riobó[a]**

**Keywords:** Mercury complexes / Symmetrisation / Thiosemicarbazones / Crystal structures / Weak hydrogen bonds / C–H···π interactions

Pyridine- and pyrazine-2-carboxamide thiosemicarbazones (HAm4DH and HAmpz4DH) or their $N^4$,$N^4$-dimethyl derivatives (HAm4DM and HAmpz4DM) react with chloro[2-(dimethylaminomethyl)phenyl-$C^1$]mercury(II), [Hg(damp)Cl], to give the tetrahedral [Hg(TSC)$_2$] complexes [TSC = Am4DH (**1**), Am4DM (**2**), Ampz4DH (**3**) or Ampz4DM (**4**)]. Spectroscopic studies and a X-ray structural analysis show that the potentially tridentate thiosemicarbazones adopt S,N coordination modes, with each deprotonated thiosemicarbazone binding to the $Hg^{II}$ centre through the azomethine nitrogen and the thiolate sulfur atoms, whereas the heterocyclic nitrogen atoms are free of coordination. Intra- and intermolecular hydrogen bonding in all complexes and specific C–H···π interactions with the chelate or pyridyl rings of the complexes **1** and **2** were found in the crystal structures. Furthermore, [Hg(damp)Cl] undergoes symmetrisation to give the symmetric unit [Hg(Hdamp)$_2$]$^{2+}$ in which the Hdamp is protonated at the nitrogen.
(© Wiley-VCH Verlag GmbH & Co. KGaA, 69451 Weinheim, Germany, 2006)

## Introduction

Thiosemicarbazones have been extensively studied due to their pharmacological properties and their coordinative behaviour towards transition-metal ions.[1] However, very few mercury(II) complexes with thiosemicarbazones are known.

The reaction of potentially tridentate thiosemicarbazones, such as 2-acetylpyridine thiosemicarbazone or pyridine-2-carboxamide thiosemicarbazone, with $Hg^{II}$ salts gives rise to five-coordinate compounds [Hg(HL)X$_2$] (X = Cl, Br or I) in which coordination to the metal centre occurs through the pyridine and azomethine nitrogen atoms and the thiocarbonyl sulfur atom (Scheme 1, a).[2–6] Furthermore, compounds such as 2-acetylpyridine *N*-oxide $N^4$,$N^4$-dimethylthiosemicarbazone can act as N,S-bidentate ligands for mercury halides in which the metal atom has a coordination number four with the same formula [Hg(HL)X$_2$] for the complexes (Scheme 1, b).[7] These thiosemicarbazones can also form dimeric or polymeric complexes in which the sulfur or the halogen acts as a bridge between metal centres and, in some cases, they also behave as S-monodentate ligands (Scheme 1, c) to form complexes of the formula [Hg(HL)$_2$X$_2$], where the mercury atom has a tetrahedral coordination geometry.[5,6,8,9]

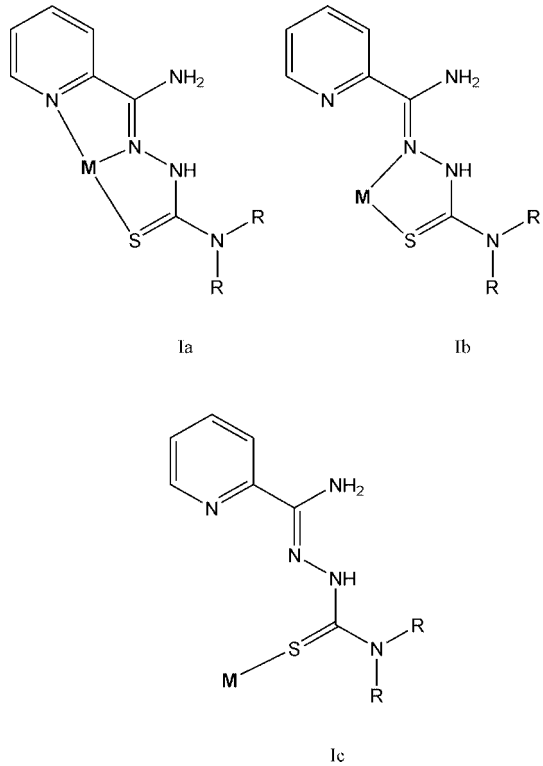


Scheme 1.

[a] Departamento de Química Inorgánica, Facultad de Farmacia, Universidad de Santiago de Compostela, 15782 Santiago de Compostela, Spain
Fax: +34-981547-163
E-mail: qiac01@usc.es
[b] Freie Universität Berlin, Chemisches Institut, Fabeckstr. 34–36, 14195 Berlin, Germany

 © 2006 Wiley-VCH Verlag GmbH & Co. KGaA, Weinheim 

Pyridine-2-carboxamide and pyrazine-2-carboxamide thiosemicarbazone derivatives (Figure 1) are almost always N,N,S-tridentate ligands[2–6] but are sometimes unidentate ligands that coordinate through the sulfur atom.[6] Only in two rhenium complexes does the 2-cyanopyridine thiosemicarbazone act as an N,N-bidentate ligand through the pyridine and azomethine nitrogen atoms (Scheme 2, a)[10] or through the amide and imine nitrogen atoms (Scheme 2, b).[11]

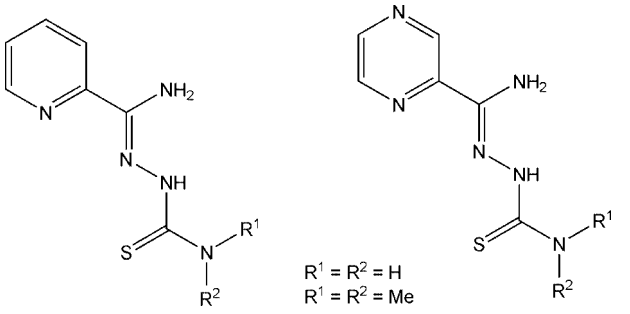


Figure 1. Pyridine-2-carboxamide and pyrazine-2-carboxamide thiosemicarbazone derivatives (left and right, respectively).

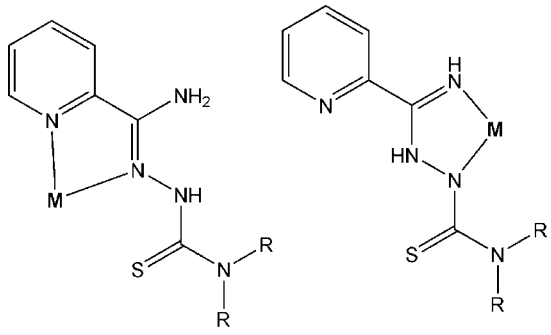


Scheme 2.

The coordination chemistry of organomercury(II) is not as extensive as that of mercury(II) salts such as halides or pseudohalides, probably because organomercury(II) derivatives have a lower tendency to increase their coordination by interaction with donor molecules. Organomercury(II) substrates, RHgX, are known to undergo symmetrisation to form symmetric diorganomercury $HgR_2$ and $Hg^{II}$ complexes.[12–15] Bidentate thiosemicarbazones react with organomercury(II) (RHgX) to form three-coordinate complexes [HgR(TSC)] (R = Ph or Me, TSC = thiosemicarbazone).[16–18]

When "TSC" is benzaldehyde or 4-methoxybenzaldehyde, the $^{199}$Hg NMR spectrum shows two signals, one corresponding to the formation of the aforementioned complex and another corresponding to the formation of $HgPh_2$, indicating that a symmetrisation reaction has occurred. However, when the "TSC" is cyclopentanone, cyclohexanone, 2-hydroxybenzaldehyde, *N*-phenyl pyrrole-2-carbaldehyde, *N*-phenyl thiophene-2-carbaldehyde, or furan-2-carbaldehyde thiosemicarbazonate, the $^{199}$Hg spectra show only one signal, indicating the presence of a single type of chemical environment around the mercury(II) atom. The reaction between acetophenone thiosemicarbazone (Hatsc) and PhHgCl gives compounds of formula $[HgCl_2(Hatsc)_2]$, where the proposed structure is a four-coordinate complex in which the "Hatsc" is bonded to the metal through the thiocarbonyl sulfur atom, and $Ph_2Hg$ as the products of the symmetrisation reaction.[19]

In this paper we report the first examples of the reactions between pyridine-2-carboxamide or pyrazine-2-carboxamide thiosemicarbazone (HAm4DH and HAmpz4DH) and their $N^4$,$N^4$-dimethyl derivatives (HAm4DM and HAmpz4DM), which are usually N,N,S-tridentate ligands, with chloro[2-(dimethylaminomethyl)phenyl-$C^1$]mercury(II) (Figure 2). These reactions give complexes $[Hg(Am4DH)_2]$ (**1**), $[Hg(Am4DM)_2]$ (**2**), $[Hg(Ampz4DH)_2]$ (**3**) and $[Hg(Ampz4DM)_2]$ (**4**), which contain two deprotonated ligands in a bidentate mode chelating to the $Hg^{II}$ through the azomethine nitrogen and thiolate sulfur atoms, a very unusual coordination mode for these potentially tridentate ligands. Furthermore, the $^{199}$Hg NMR spectroscopic data suggest a symmetrisation phenomenon, which is also supported by $^1$H NMR and IR data. In contrast to this behaviour, it was recently reported that thiosemicarbazonate complexes of gold(III) are formed in reactions of [Au(damp-$^1$C,N)$Cl_2$] with pyridine-2-carboxamide thiosemicarbazones, where the organometallic damp$^-$ ligand is protonated during the reactions and the Au–N bond is cleaved.[20]

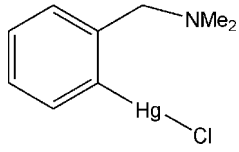


Figure 2. Chloro[2-(dimethylaminomethyl)phenyl-$C^1$]mercury(II).

## Results and Discussion

The reaction of chloro[2-(dimethylaminomethyl)phenyl-$C^1$]mercury(II), [Hg(damp)Cl], with pyridine-2-carboxamide or pyrazine-2-carboxamide thiosemicarbazone (HAm4DH and HAmpz4DH) and their $N^4$,$N^4$-dimethyl derivatives (HAm4DM and HAmpz4DM) give solids of formula $[Hg(TSC)_2]$ (TSC = deprotonated thiosemicarbazone). The products are consistent with the elemental analysis data and are colourless or yellow and quite soluble in common organic solvents.

The FAB$^+$ spectra of all complexes show peaks corresponding to $\{H_2L\}^+$, but only the $N^4$,$N^4$-dimethyl-substituted complexes show fragments that contain mercury. The spectra of **2** and **4** show peaks at *m*/*z* = 646 and *m*/*z* = 648, which can be assigned to a molecular ion of composition $\{HgHL_2\}^+$. Peaks at *m*/*z* = 423 can be assigned to the complex with a loss of a ligand, $\{HgL\}^+$. In the mass spectra of **1** and **3** only the signals due to the protonated ligand can be seen (at *m*/*z* 196 and 197, respectively).

 © 2006 Wiley-VCH Verlag GmbH & Co. KGaA, Weinheim 

### X-ray Crystal Structures

In the molecular structures of the complexes the geometry is essentially similar and contains four coordinate neutral $Hg(TSC)_2$ molcules. However, in the compounds **1**, **3** and **4** the mercury atom lies on a twofold axis and the asymmetric unit consists of half a molecule of complex and, as a consequence, a tetrahedral complex is formed with two chelating anionic ligands around the central metal (Figure 3). Complex **2** crystallises in the orthorhombic space group $Pna2_1$ and the Hg metal ion is tetrahedrally coordinated with two symmetrically independent thiosemicarbazone ligands as monoanionic bidentate N,S-chelators (Figure 4). Selected bond lengths and angles are listed in Table 1 and Table 2, respectively.

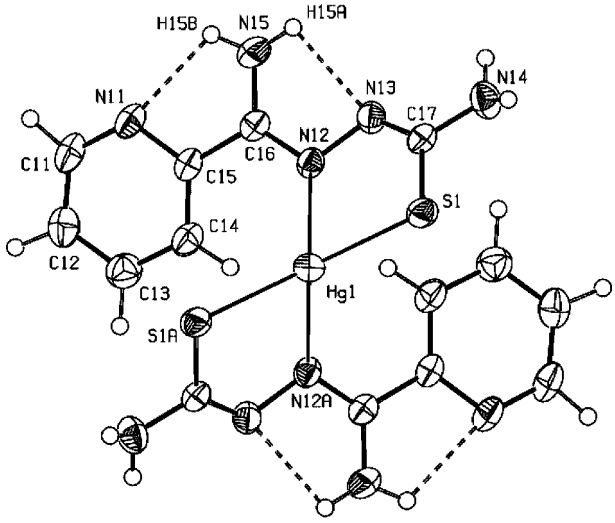


Figure 3. Structure of **1** showing the intramolecular hydrogen bonding. Symmetry codes are as given in Table 2.

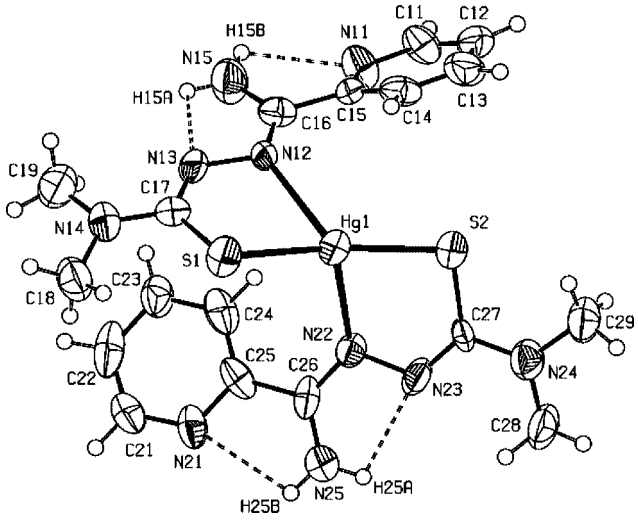


Figure 4. Asymmetric unit of **2** showing the intramolecular hydrogen bonding.

In the complexes **1**, **3** and **4** the tetrahedra are highly deformed with Hg–S bond lengths in the range 2.354(2)–2.362(1) Å, averaging 2.358(1) Å, which is a little shorter than the sum of the single-bond covalent radii (2.52 Å).[21] However, there is a significant difference between the two Hg–S distances in **2** [2.416(5) and 2.313(5) Å]. The Hg–N bond lengths [range 2.484(15)–2.540(3) Å] are somewhat longer than the Hg–N(hydrazinic) distances in tetracoordinate mercury(II) complexes, but in **1** this distance is 2.290(3) Å, which is significantly shorter. Thus, in **1** the thiolate sulfur and hydrazine nitrogen atoms are strongly bound to Hg.

Table 1. Selected bond lengths [Å] for complexes **1**–**4**.

| Bond | **1** | **2**[a] | | **3** | **4** |
|---|---|---|---|---|---|
| Hg1–N12 | 2.490(3) | 2.513(2) | 2.488(4) | 2.540(3) | 2.492(5) |
| Hg1–S1 | 2.363(1) | 2.417(1) | 2.312(1) | 2.356(1) | 2.354(2) |
| C17–S1 | 1.764(3) | 1.759(6) | 1.747(6) | 1.757(4) | 1.768(7) |
| C16–N12 | 1.311(4) | 1.35(2) | 1.302(7) | 1.304(4) | 1.305(8) |
| N12–N13 | 1.402(4) | 1.377(19) | 1.410(6) | 1.400(4) | 1.391(8) |
| N13–C17 | 1.290(4) | 1.332(7) | 1.307(7) | 1.295(4) | 1.308(9) |
| C17–N14 | 1.367(4) | 1.346(7) | 1.336(7) | 1.351(4) | 1.361(8) |
| C16–N15 | 1.340(5) | 1.342(7) | 1.334(7) | 1.347(5) | 1.340(9) |

[a] The second column corresponds to molecule II.

Table 2. Selected bond angles [°] for complexes **1**–**4**.

| Angle | **1** | **2**[b] | | **3** | **4** |
|---|---|---|---|---|---|
| S1–Hg1–S1[a] | 153.80(5) | 159.70(5) | | 152.23(5) | 157.46(9) |
| S1–Hg1–N12[a] | 118.65(7) | 108.05(9) | | 125.52(7) | 120.24(13) |
| S1[a]–Hg1–N12[a] | 79.13(7) | 77.67(9) | | 77.03(7) | 77.51(13) |
| S1–Hg1–N12 | 79.13(7) | 74.5(5) | | 77.03(7) | 77.51(13) |
| S1[a]–Hg1–N12 | 118.65(7) | 121.8(5) | | 125.52(7) | 120.24(13) |
| N12[a]–Hg1–N12 | 100.13(13) | 113.9(5) | | 84.05(13) | 85.4(3) |
| N15–C16–N12 | 123.5(3) | 121.6(10) | 124.0(5) | 124.7(3) | 124.1(6) |
| C15–C16–N12 | 119.9(3) | 121.3(10) | 119.1(5) | 119.7(3) | 117.8(6) |
| C16–N12–N13 | 110.9(3) | 111.2(15) | 112.5(4) | 111.2(3) | 111.6(5) |
| N12–N13–C17 | 118.5(3) | 114.4(10) | 118.5(5) | 117.0(3) | 117.4(5) |
| N13–C17–N14 | 117.5(3) | 115.0(15) | 116.8(5) | 117.2(3) | 117.0(6) |
| N13–C17–S1 | 129.6(2) | 128.2(4) | 126.0(5) | 129.5(3) | 127.6(5) |
| N14–C17–S1 | 112.9(2) | 116.8(4) | 116.9(4) | 113.3(3) | 115.4(5) |

[a] The second column corresponds to molecule II. [b] Symmetry transformations used to generate equivalent atoms: $-x$, $y$, $-z+1/2$ (**1**, **3**); $-x+1$, $y$, $-z+3/2$ (**4**).

The bond angles around the Hg centre vary over a wide range, and in any case the geometry is not clearly tetrahedral. The S–Hg–S bond angles [range 152.23(5)–159.8(2)°] deviate significantly from the ideal tetrahedral angle, but the main differences are in the N–Hg–N angles, which have values of 100.1(1) and 114.(5)° for compounds **1** and **2**, respectively, and 84.1(1) and 85.4(3)° for compounds **3** and **4**, respectively. These values seem to indicate that the pyrazine rings of the thiosemicarbazones have a significant influence on the packing.

The coordination polyhedra in the four complexes are to some extent reminiscent of those adopted by [Hg(H4DMLO)$X_2$] (X = Cl or Br, H4DMLO = 2-acetylpyridine *N*-oxide $N^4$,$N^4$-dimethyl thiosemicarbazone).[7] This can be described as a distorted trigonal pyramid with the mercury atom in the same mean plane as the nitrogen and sulfur atoms of the first thiosemicarbazone, and the sulfur atom of the symmetrical one (**1**, **3** and **4**) or of the

 © 2006 Wiley-VCH Verlag GmbH & Co. KGaA, Weinheim 

second thiosemicarbazone (**2**) [av. 0.2874(2) Å] (Figure 5). These coordination planes form angles in the range 5.5(1)–12.0(2)° (**1**, **3** and **4**) and 16.2(4)–36.2(2)° (**2**) with the mean plane of the thiosemicarbazone moiety.

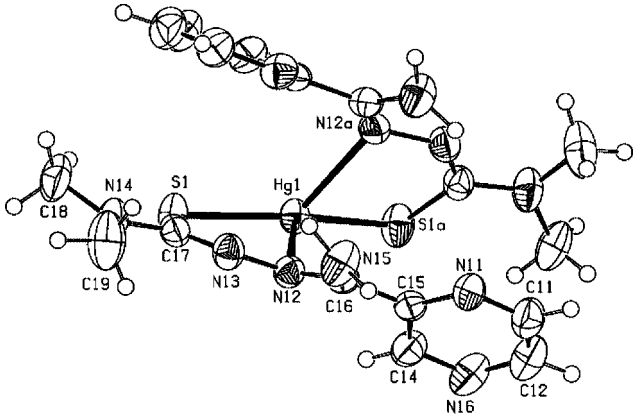


Figure 5. Perspective drawing of **4** oriented as a distorted trigonal pyramid. Symmetry codes are as given in Table 2.

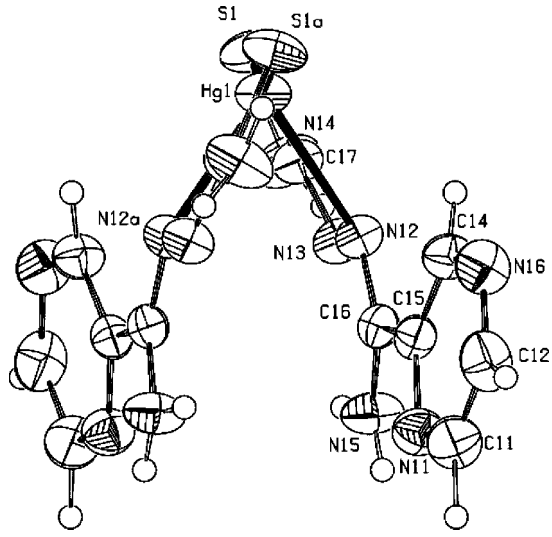


Figure 6. Parallel projection along the [101] direction showing the angle of the thiosemicarbazone moieties in the molecule of **3**. Symmetry codes are as given in Table 2.

The least-squares plane data and deviations from these planes for the complexes are listed in Table 3. In all four complexes the pyridyl and pyrazinyl rings are almost planar. In complex **1** the pyridine ring and the thiosemicarbazone moiety form a dihedral angle of 44.8(1)°, and the two thiosemicarbazonates bonded to the $Hg^{II}$ are nearly orthogonal, forming an angle of 85.3(1)°. However, in complex **2** the deviations are smaller and the angles between the pyridine and the thiosemicarbazone moieties are 25.6(8) and 29.6(7)° for the two non-symmetric ligands and the angle between the thiosemicarbazone main least-squares planes is 64.2(4)°. In complexes **3** and **4** the angles between the pyrazine ring and the thiosemicarbazone moieties are 33.3(1) and 42.7(2)°, respectively, whereas the angles between each thiosemicarbazone moiety and its symmetrical one are 46.8(1) and 45.8(2)°, respectively (Figure 6).

The bond lengths in the noncoordinating pyridine and pyrazine units remain unchanged upon metal-complex formation. These units therefore appear not to participate in the complexation process. The bond lengths for the thiosemicarbazone moieties are as one would expect and the bond lengths in the five-membered chelate rings are intermediate between the usual values for single and double bonds, thus demonstrating metalloaromaticity.[22]

A number of intra- and intermolecular hydrogen bonds are formed in the crystal packing arrangement (Table 4), and it is not only the amine and imine groups that take part but also the pyridine and pyrazine nitrogen atoms of the ligands (Figure 7). The most significant intramolecular interactions occur between the amino donor groups and the imine or pyrazine nitrogen atoms of neighbouring chains, which act as acceptors. These interactions give rise to a three-dimensional supramolecular network (Figure 8).

Table 3. Best least-squares planes for complexes **1**–**4**.

| Compound | Plane | Rms deviation [Å] | Largest deviation [Å] | Angle with previous plane [°] |
|---|---|---|---|---|
| **1** | S1–N12–S1[a] | 0 | Hg1, 0.335(1) | |
| | C16–N12–N13–C17–S1–N14 | 0.1292 | N12, 0.246(2) | 9.8(1) |
| | N11–C11–C12–C13–C14–C15 | 0.0071 | C14, 0.012(3) | 44.8(1) |
| **2** | S1–N12–S2 | 0 | Hg1, 0.215(4) | |
| | C16–N12–N13–C17–S1–N14 | 0.0080 | C17, 0.02(2) | 16.2(4) |
| | N11–C11–C12–C13–C14–C15 | 0.0109 | C13, 0.02(2) | 25.6(8) |
| | N21–C21–C22–C23–C24–C25 | 0.0139 | N21, 0.02(1) | 55.7(7) |
| | C26–N22–N23–C27–S2–N24 | 0.0535 | N24, 0.02(1) | 29.6(7) |
| | S2–N22–S1 | 0 | Hg1, 0.334(4) | 36.2(3) |
| **3** | S1–N12–S1[a] | 0 | Hg1, 0.270(1) | |
| | C16–N12–N13–C17–S1–N14 | 0.0851 | N12, 0.160(3) | 5.5(1) |
| | N11–C11–C12–C13–C14–C15 | 0.0057 | C14, 0.010(3) | 33.3(1) |
| **4** | S1–N12–S1[a] | 0 | Hg1, 0.242(1) | |
| | C16–N12–N13–C17–S1–N14 | 0.0789 | N12, 0.156(4) | 12.0(2) |
| | N11–C11–C12–N16–C14–C15 | 0.0126 | C15, 0.021(6) | 42.7(2) |

[a] Symmetry transformations used to generate equivalent atoms: $-x$, $y$, $-z+1/2$ (**1**, **3**); $-x+1$, $y$, $-z+3/2$ (**4**).

 © 2006 Wiley-VCH Verlag GmbH & Co. KGaA, Weinheim 

Table 4. Hydrogen bonding interactions [Å, °] for complexes **1**–**4**.

| | D–H···A | *d*(D–H) | *d*(H···A) | *d*(D···A) | ∠D–H···A |
|---|---|---|---|---|---|
| **1**[a] | N14–H14B···N13[1] | 0.76 | 2.33 | 3.035(4) | 154.5 |
| | N15–H15A···N13 | 0.90 | 2.22 | 2.565(4) | 101.8 |
| | N15–H15B···N11 | 0.89 | 2.19 | 2.660(4) | 112.0 |
| **2** | N15–H15B···N11 | 0.86 | 2.35 | 2.69(3) | 104.0 |
| | N15–H15A···N13 | 0.86 | 2.22 | 2.53(2) | 101.0 |
| | N25–H25B···N21 | 0.86 | 2.33 | 2.67(2) | 103.5 |
| | N25–H25A···N23 | 0.86 | 2.28 | 2.59(2) | 101.7 |
| **3**[b] | N14–H14A···N13[1] | 0.91 | 2.24 | 3.142(5) | 172.5 |
| | N14–H14B···N16[2] | 0.83 | 2.24 | 3.060(5) | 169.3 |
| | N15–H15A···N13 | 0.95 | 2.22 | 2.586(4) | 102.2 |
| | N15–H15B···N11 | 0.88 | 2.24 | 2.660(5) | 109.0 |
| **4**[c] | N15–H15A···N13 | 0.97 | 2.27 | 2.579(9) | 100.9 |
| | N15–H15B···N11 | 0.97 | 2.46 | 2.772(9) | 102.3 |
| | N15–H15B···N16[1] | 0.92 | 2.56 | 3.251(10) | 132.2 |

[a] Symmetry transformations used to generate equivalent atoms: a) 1: $-x+1/2$, $y+1/2$, $-z+1/2$. [b] 1: $-x$, $-y+1$, $-z$; 2: $x-1/2$, $-y+3/2$, $z-1/2$. [c] 1: $-x+1/2$, $y-1/2$, $-z+1/2$..

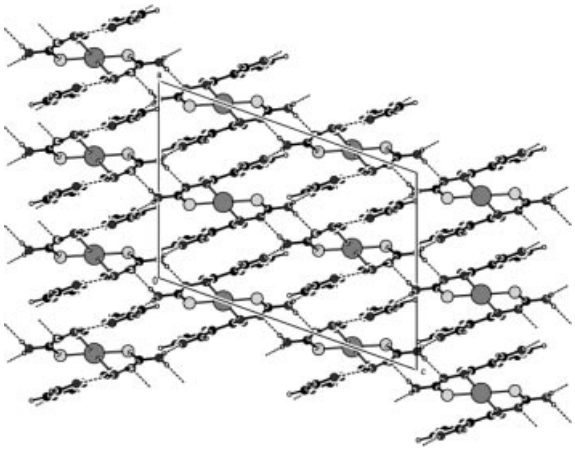

Figure 7. Drawing of the packing diagram of **3** in the *ac* plane showing the intermolecular hydrogen bonding and the patterns of repeating infinite array of layers along the [010] direction.

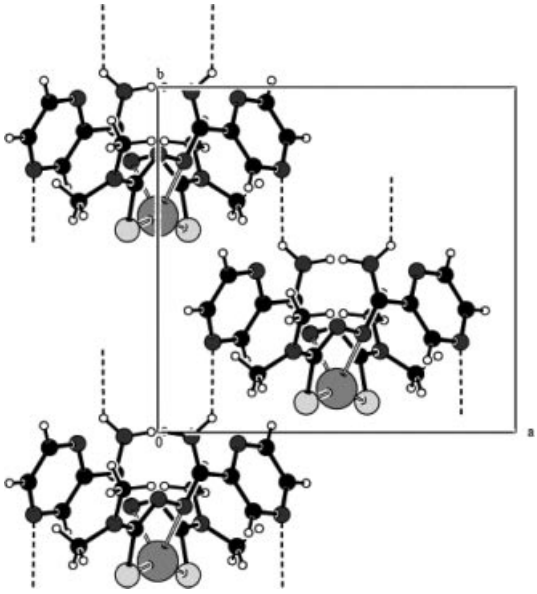

Figure 8. Partial representation of the unit cell of **4** showing the intermolecular hydrogen bonding.

Intermolecular CH···π(chelate ring) interactions between C–H bonds of the pyridyl ligand and the metal chelate ring are observed in complex **1** (Table 5). The H···ring centroid (H···*Ω*) distances are in the range 2.66–2.89 Å, and the *α* and *β* angles have values of 120° and 12.5–19.0°, respectively (Figure 9). These data are comparable with those found in crystal structures with weak C–H···π interactions between an organic moiety and a chelate ring in transition-metal complexes ($\alpha > 110°$, $\beta < 16°$ and $H\cdots\Omega < 3.0$ Å; α, *β*, and *Ω* are defined in Table 5).[23] The crystal structure of complex **2** also displays a weak C–H···π interaction between a methyl group and the pyridyl ring of neighbouring molecules.[24]

Table 5. Intermolecular CH···π ring interaction parameters for complexes **1** and **2**.[a]

| | CH···Ω | H···*Ω* [Å] | *α* [°] | *β* [°] |
|---|---|---|---|---|
| **1** | C11–H11···(Hg1/S1)[1] | 2.89 | 120.4 | 12.7 |
| | C14–H14···(Hg1/S1)[2] | 2.66 | 120.9 | 18.9 |
| **2** | C29–H29B···(N11/C15)[3] | 2.97 | 123.6 | 9.5 |

[a] *Ω* is the ring plane, *α* the angle C–H···centroid of *Ω* and *β* the angle defined by the H···centroid line and the perpendicular to this plane. Symmetry transformations used to generate equivalent atoms: 1: $-x$, $1-y$, $-z$; 2: $-x$, $y$, $½-z$; 3: $-x$, $1-y$, $-1/2+z$.

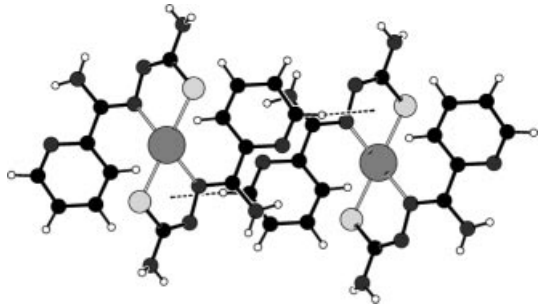

Figure 9. Perspective view of **1** showing an intermolecular C–H···π interaction with the π-system of the chelate ring.

## Spectral Data

The complexes exhibit bands due to ν(NH) vibrations in the range 3500–3146 $cm^{-1}$. The bands associated with ν(C=N) and ν(C=C) appear in the range 1609–1444 $cm^{-1}$ and are shifted to lower and higher frequencies, respectively, compared to those of the ligands. The ν(NH) band is shifted to slightly higher frequencies in the complexes with respect to the ligands, indicating the coordination of the azomethine nitrogen. The ν(CS) band appears at ca. 755 $cm^{-1}$ for the complexes with pyridine and ca. 850 $cm^{-1}$ for the pyrazine derivatives, which is in agreement with observed values for this series of compounds with the sulfur atom coordinated to the metal centre. Furthermore, coordination by the N azomethine and the S thiolate is supported by the localisation of the ν(Hg–N) modes around 405–418 $cm^{-1}$ and the ν(Hg–S) modes around 289–326 $cm^{-1}$, respectively.

In the $^1$H NMR spectra of the complexes, the absence of the $N^3$–H signal is consistent with the thiosemicarbazone

 © 2006 Wiley-VCH Verlag GmbH & Co. KGaA, Weinheim 

in its deprotonated form. The pyridine proton signals appear at around 8.44–7.36 ppm and the pyrazine protons are in the range 9.67–8.48 ppm, which is normal for these aromatic protons. The $N^5H_2$ proton in both **1** and **2** appear as a singlet at $\delta$ = 6.60 ppm in each case and at $\delta$ = 7.06 and 6.51 ppm for **3** and **4**, respectively. The $N^4H_2$ protons appear at $\delta$ = 6.03 ppm in **1** and at 8.33, 8.22 ppm in **3**. The presence of two signals for the $N^4H_2$ protons in **3** must be due to the restriction of free-rotation around the $C^7$–$N^4H_2$ bond.[19,25] The variation in the shielding between the complexes must be related to a different arrangement of the complex in DMSO solution or to a different interaction between the $N^4H_2$ protons and DMSO.

The $^{199}$Hg NMR spectrum of **1** shows two peaks at –577 and –806 ppm (Figure 10). The peak at $\delta$ = –806 ppm is due to our four-coordinate complex, whereas the signal at $\delta$ = –577 ppm may be due to the coordination of the nitrogen atom of the pyridine ring in DMSO solution, a situation that increases the coordination number of the Hg atom and moves the $\delta(^{199}Hg)$ signal to higher frequencies. This observation is in agreement with literature data.[25,26] Furthermore, the $^1$H NMR spectra of the reaction between [Hg(damp)Cl] and HAm4DH in a [$D_6$]DMSO solution shows two peaks for the protons of the pyridine ring, which is also consistent with the suggested coordination of the heterocyclic nitrogen atom in solution.

The behaviour of the complexes in solution was followed by NMR spectroscopy of the reaction between two of the thiosemicarbazones and [Hg(damp)Cl]. The $^{199}$Hg NMR spectra were recorded for the reactions between [Hg(damp)Cl] and HAm4DM or HAmpz4DH in a MeOH/[$D_4$]MeOH mixture in 10-mm NMR tubes. The spectra for these two reactions each show two signals (Figure 11). The first signal is observed at –650 and –655 ppm for the two reactions, respectively, and this may indicate that, in solution, the heterocyclic nitrogen atom is also coordinated to the mercury centre in the complex $HgL_2$.[25,26] The second peak, which appears at –1162 and –1167 ppm, respectively, could correspond to the presence of $[Hg(Hdamp)_2]^{2+}$ as a secondary product formed by symmetrisation.[13,15] These signals are shifted to higher field with respect to that of [Hg(damp)Cl],

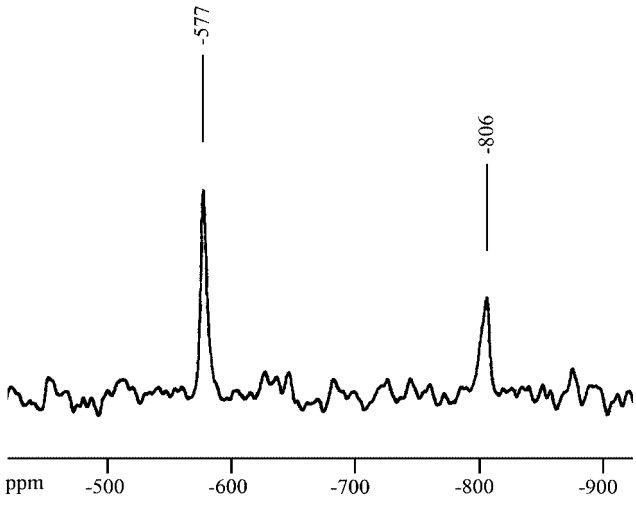


Figure 10. $^{199}$Hg NMR spectrum at room temperature of a solution of complex **1** in DMSO.

which appears at $\delta$ = –1109 ppm. Symmetrisation is a well known reaction in organometallic mercury compounds[27–29] and the occurrence of such a process would be consistent with the tendency for organomercury compounds to maintain linearity in $R_2Hg$ or RHgX systems. The overall reaction can be represented as follows:

It seems likely that the most stable form of the complex in solution is $Hg(TSC)_2^{(NNS)}$, that this is the form first produced when the reaction is carried out in methanol (Scheme 3, reaction **I**), and that its conversion to $Hg(TSC)_2^{(NS)}$ via equilibrium **II** (Scheme 3) is driven by the precipitation of $Hg(TSC)_2^{(NS)}$ as crystals. When $Hg(TSC)_2^{(NS)}$ is dissolved in DMSO, equilibrium **II** (Scheme 3) leads rapidly to the presence of both species.

The molar conductivity values for the solutions discussed above indicate that they are 2:1 electrolytes in MeOH,[30] a finding that is consistent with the presence of the species $[Hg(Hdamp)_2]^{2+}$ and 2 $Cl^-$, and consequently, the formation of a zwitterionic charge distribution in this ligand is not possible. The pH values of the solutions were also measured and significant variations were not found with respect

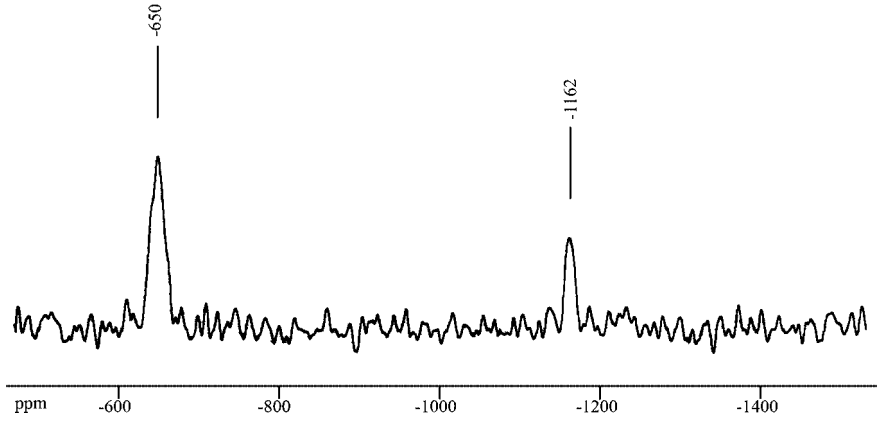


Figure 11. $^{199}$Hg NMR spectrum at room temperature of the reaction between [Hg(damp)Cl] and HA4DM in MeOH/[$D_4$]MeOH. The signal for $[Hg(Am4DM)_2]$ is on the left and that for $[Hg(Hdamp)_2]^{2+}$ on the right.

 © 2006 Wiley-VCH Verlag GmbH & Co. KGaA, Weinheim 

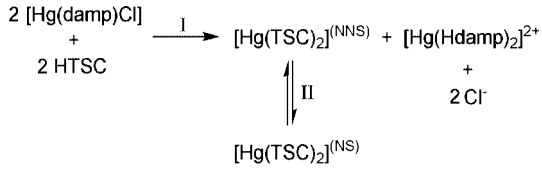


Scheme 3.

to the typical value for MeOH. This observation is consistent with the presence of the species $[Hg(Hdamp)_2]Cl_2$, which would retain the protons lost by the ligand upon coordination to mercury.

The reaction between [Hg(damp)Cl] and HAmpz4DH in DMSO was carried out and $^1H$ NMR spectra were acquired. It was found that, in addition to the signals corresponding to species **3** (as discussed above), a new set of signals appeared due to the presence of organometallic rings (in the range 7.17–7.48 ppm), $CH_2$ ($\delta$ =3.47 ppm) and the methyl groups of $[Hg(Hdamp)_2]Cl_2$ ($\delta$ = 2.23 ppm). Furthermore, the presence of a singlet at $\delta$ = 10.26 ppm in the reaction between [Hg(damp)Cl] and HAmpz4DH provides further evidence for protonation of the Hdamp nitrogen. Similarly, in the reaction between [Hg(damp)Cl] and HAm4DM in $CDCl_3$, as well as the signals described above, a signal was observed at $\delta$ = 11.60 ppm and this is probably due to protonation of the species $[Hg(Hdamp)_2]^{2+}$. Protonation of the ligand Hdamp is supported by IR spectra of damp, which show a band corresponding to ν(N–H) vibrations at around 2670 $cm^{-1}$, a value consistent with those found for other Hdamp complexes,[20,31,32] and with the N–H absorption of free tertiary ammonium salts (ca. 2700 $cm^{-1}$).

## Experimental Section

Elemental analyses were performed with a Carlo Erba 1108 microanalyser. The mass spectra were obtained using the FAB method with a Hewlett–Packard HP5988A mass spectrometer. IR spectra were recorded as KBr disks (4000–400 $cm^{-1}$) or polyethylene-sandwiched Nujol mulls (500–100 $cm^{-1}$) with a Bruker IFS-66v spectrometer. NMR spectra were obtained with a Bruker AMX 300 and AMX 500 spectrometers; chemical shifts are reported in ppm downfield from $Me_4Si$ or $Hg(CH_3)_2$. With the exception of $[Hg(Am4DH)_2]$, the $^{199}Hg$ NMR spectra of the other mercury complexes could not be registered due to their low solubility.

[Hg(damp)Cl] was synthesised according to the reported procedure.[33] The thiosemicarbazones were prepared by reduction of pyridine-2-carboxamide and pyrazine-2-carboxamide with sodium and subsequent reaction with the corresponding thiosemicarbazide as described previously.[6,34,35]

**Synthesis of $[Hg(Am4DH)_2]$ (1):** A mixture of HAm4DH (0.03 g, 0.15 mmol) and [Hg(damp)Cl] (0.06 g, 0.15 mmol) in methanol (25 mL) was heated under reflux for 1 h. The clear pale-yellow solution was left to crystallise and, after several days, colourless crystals suitable for crystal determination were obtained. Yield: 4.86 mg. $C_{14}H_{16}HgN_{10}S_2$ (589.06): calcd. C 28.5, H 2.7, N 23.8, S 10.9; found C 28.6, H 2.6, N 23.2, S 10.1. IR: $\tilde{\nu}_{max}$= 3479–3148 ν(NH), 1606–1552 ν(C=N and C=C), 1003 ν(NN), 795 ν(CS), 415 ν(Hg–N), 322 ν(Hg–S) $cm^{-1}$. $FAB^+$ MS, *m*/*z* (%), assignment: 196.09 (1.47), $[H_2Am4DH]$. $^1H$ NMR ([D$_6$]DMSO, ppm): $\delta$ = 8.44 (d, 1 H, 1-H), 7.83 (d, 1 H, 4-H), 7.67 (td, 1 H, 3-H), 7.36 (m, 1 H, 2-H), 6.60 (s, 2 H, $N5H_2$), 6.03 (s, 2 H, $N4H_2$).

**Synthesis of $[Hg(Am4DM)_2]$ (2):** HAm4DM (0.02 g, 0.1 mmol) in methanol was added to a stirred solution of [Hg(damp)Cl] (0.02 g, 0.1 mmol) in methanol (20 mL). The mixture was stirred for several hours and the resulting yellow solution was left to crystallise. A yellow crystalline solid formed after several days and crystals suitable for X-ray diffraction were obtained from the same solvent. Yield: 15.48 mg. $C_{18}H_{24}HgN_{10}S_2$ (645.17): calcd. C 33.5, H 3.7, N 21.7, S 9.9; found C 33.4, H 3.8, N 21.7, S 9.1. IR: $\tilde{\nu}_{max}$ = 3489–3358 ν(NH), 1609–1544 ν(C=N and C=C), 995 ν(NN), 797 ν(CS), 418 ν(Hg–N), 305 ν(Hg–S) $cm^{-1}$. $FAB^+$ MS, *m*/*z* (%), assignment: 646.27 (1.70), [Hg(HAmDM)(Am4DM)]; 559.26 (17.0), $[Hg(AmDM)(C_6H_8N_4)]$; 423.14 (0.73), [Hg(AmDM)]; 224.12 (3.12), $[H_2Am4DM]$. $^1H$ NMR ([D$_6$]DMSO, ppm): $\delta$ = 8.44 (d, 1 H, 1-H), 7.74 (d, 1 H, 4-H), 7.63 (td, 1 H, 3-H), 7.37 (m, 1 H, 2-H), 6.60 (s, 2 H, $N5H_2$), 3.08 (s, 6 H, 2Me).

**Synthesis of $[Hg(Ampz4DH)_2]$ (3):** A mixture of HAmpz4DH (0.02 g, 0.1 mmol) and [Hg(damp)Cl] (0.04 g, 0.1 mmol) in methanol (25 mL) was heated under reflux for 1 h. The resulting yellow-green precipitate was filtered off and dried under vacuum. Yellow crystals suitable for X-ray structural analysis were obtained from the liquors. Yield: 13.29 mg. Elemental analysis: $C_{12}H_{14}HgN_{12}S_2$ (591.04): calcd. C 24.4, H 2.4, N 28.4, S 10.8; found C 24.5, H 2.3, N 28.3, S 10.7. IR: $\tilde{\nu}_{max}$ = 3500–3146 ν(NH), 1608–1553 ν(C=N and C=C), 1017 ν(NN), 855 ν(CS), 417 ν(Hg–N), 326 ν(Hg–S). $FAB^+$ MS, *m*/*z* (%), assignment: 197.09 (1.64), $[H_2Ampz4DH]$. $^1H$ NMR ([D$_6$]DMSO, ppm): $\delta$ = 9.58 (s, 1 H, 4-H), 8.67 (s, 1 H, 1-H), 8.56 (d, 1 H, 2-H), 6.61 (s, 2 H, $N5H_2$), 6.37, 6.06 (1 H, 1 H, s, s, $N4H_2$).

**Synthesis of $[Hg(Ampz4DM)_2]$ (4):** HAmpz4DM (0.02 g, 0.09 mmol) in methanol was added to a stirred solution of [Hg(damp)Cl] (0.02 g, 0.09 mmol) in methanol (20 mL). The mixture was stirred for several hours and the resulting yellow solution was left to crystallise. A yellow crystalline formed after several days and was filtered off and dried under vacuum. Yellow crystals suitable for X-ray diffraction were obtained from the same solvent. Yield: 8.74 mg. $C_{16}H_{22}HgN_{12}S_2$ (647.14): calcd. C 29.7, H 3.4, N 26.0, S 9.9; found C 29.4, H 3.4, N 25.5, S 10.1. IR: $\tilde{\nu}_{max}$ = 3420–3312 ν(NH), 1607–1573 ν(C=N and C=C), 1019 ν(NN), 861 ν(CS), 405 ν(Hg–N), 289 ν(Hg–S). $FAB^+$ MS, *m*/*z* (%), assignment: 648.20 (34.03), [Hg(HAmpzDM)(Ampz4DM)]; 423.08 (2.01), [Hg(Ampz4DM)]; 225.10 (5.07), $[H_2Ampz4DM]$; 191.12 (55.29), $(C_8H_{11}N_6S)$. $^1H$ NMR ([D$_6$]DMSO, ppm): $\delta$ = 8.84 (s, 1 H, 4-H), 8.58 (s, 1 H, 1-H), 8.48 (s, 1 H, 2-H), 6.51 (s, 2 H, $N5H_2$), 3.14 (s, 6 H, 2Me).

**X-ray Crystallography:** Crystals of all complexes were mounted on glass fibres and used for data collection. Crystal data were obtained with a Bruker SMART CCD-1000 diffractometer at room temperature. X-ray data were processed using the SAINT program[36] and corrected for absorption using SADABS.[37] Structural solution and refinement was carried out using the SHELX suite of programs.[38,39] The hydrogen atoms were located unambiguously from difference Fourier maps (N–H hydrogen atoms) and included as fixed contributions riding on attached atoms or included in geometrically idealized positions employing appropriate riding models, all with isotropic displacement parameters constrained to 1.2 times those of their carrier atoms. Atom scattering factors were taken from the International Tables for Crystallography[40] and molecular graphics were obtained from PLATON[41] (see also Table 6).

 © 2006 Wiley-VCH Verlag GmbH & Co. KGaA, Weinheim 

Table 6. Crystallographic data for complexes **1**–**4**.

| | [Hg(Am4DH)$_2$] | [Hg(Am4DM)$_2$] | [Hg(Ampz4DH)$_2$] | [Hg(Ampz4DM)$_2$] |
|---|---|---|---|---|
| Empirical formula | $C_{14}H_{16}HgN_{10}S_2$ | $C_{18}H_{24}HgN_{10}S_2$ | $C_{12}H_{14}HgN_{12}S_2$ | $C_{16}H_{22}HgN_{12}S_2$ |
| Colour, habit | prism, colourless | yellow, plate | yellow, prism | yellow, prism |
| Formula weight | 589.08 | 645.18 | 591.06 | 647.17 |
| Crystal size [mm] | 0.57×0.26×0.18 | 0.14×0.11×0.06 | 0.16×0.14×0.11 | 0.18×0.17×0.06 |
| Crystal system | monoclinic | orthorhombic | monoclinic | orthorhombic |
| Space group | *C*2/*c* (No. 15) | *Pna*2$_1$ (No. 33) | *C*2/*c* (No.15) | *C*222$_1$ (No. 20) |
| Unit cell dimensions | | | | |
| *a* [Å] | 16.907(4) | 17.892(3) | 13.316(3) | 11.898(4) |
| *b* [Å] | 7.194(2) | 9.070(2) | 7.805(2) | 11.513(4) |
| *c* [Å] | 15.535(3) | 13.915(3) | 18.517(4) | 16.605(5) |
| *α* [°] | 90 | 90 | 90 | 90 |
| *β* [°] | 94.781(4) | 90 | 109.648(3) | 90 |
| *γ* [°] | 90 | 90 | 90 | 90 |
| *V* [Å$^3$] | 1883.0(7) | 2258.2(7) | 1812.4(7) | 2274.6(13) |
| *Z* | 4 | 4 | 4 | 4 |
| $D_{calcd.}$ (g·cm$^{-3}$) | 2.078 | 1.898 | 2.166 | 1.890 |
| *μ* [mm$^{-1}$] | 8.419 | 7.029 | 8.750 | 6.981 |
| *θ* Range for data coll. [°] | 2.42–26.35 | 2.28–26.37 | 2.34–28.28 | 2.45–28.28 |
| Index ranges | $-20 \le h \le 20$ | $-22 \le h \le 0$ | $-16 \le h \le 17$ | $0 \le h \le 15$ |
| | $-8 \le k \le 8$ | $-11 \le k \le 0$ | $0 \le k \le 10$ | $-15 \le k \le 15$ |
| | $-19 \le l \le 19$ | $0 \le l \le 17$ | $-24 \le l \le 0$ | $0 \le l \le 22$ |
| Reflections collected | 7619 | 19433 | 11513 | 10875 |
| Unique reflects., $R_{int}$ | 1914, 0.0341 | 2415, 0.0672 | 2221, 0.0334 | 2756, 0.0307 |
| Data/parameters | 1914/131 | 2415/280 | 2221/123 | 2756/141 |
| Final *R* indices | $R_1$ = 0.0205 | $R_1$ = 0.0430 | $R_1$ = 0.0244 | $R_1$ = 0.0311 |
| [$I > 2\sigma(I)$] | $wR_2$ = 0.0503 | $wR_2$ = 0.0867 | $wR_2$ = 0.0427 | $wR_2$ = 0.0815 |
| *R* indices (all data) | $R_1$ = 0.0220 | $R_1$ = 0.0994 | $R_1$ = 0.0380 | $R_1$ = 0.0379 |
| | $wR_2$ = 0.0510 | $wR_2$ = 0.1107 | $wR_2$ = 0.0466 | $wR_2$ = 0.0878 |
| Goodness-of-fit | 1.101 | 1.097 | 1.082 | 1.058 |
| Flack parameter | – | 0.09(2) | – | 0.00(1) |

CCDC-600478 (for [Hg(Am4DH)$_2$]), -600479 (for [Hg(Am4DM)$_2$]), -600480 (for [Hg(Ampz4DH)$_2$]) and -600481 (for [Hg(Ampz4DM)$_2$]) contain the supplementary crystallographic data for this paper. These data can be obtained free of charge from The Cambridge Crystallographic Data Centre via www.ccdc.cam.ac.uk/data_request/cif.

## Acknowledgments

We thank the Xunta de Galicia (Project PGIDIT03PXIC20302PN) for continued financial support.

[1] D. X. West, S. B. Padhye, P. B. Sonawane, *Struct. Bonding (Berlin)* **1991**, *76*, 1–50.
[2] E. Bermejo, R. Carballo, A. Castiñeiras, R. Domínguez, C. Maichle-Mössmer, J. Strahle, D. X. West, *Polyhedron* **1999**, *18*, 3695–3702.
[3] E. Bermejo, R. Carballo, A. Castiñeiras, R. Domínguez, A. E. Liberta, C. Maichle-Mössmer, M. M. Salberg, D. X. West, *Eur. J. Inorg. Chem.* **1999**, 965–973.
[4] A. Castiñeiras, I. García, E. Bermejo, K. A. Ketcham, D. X. West, A. K. El-Sawaf, *Z. Anorg. Allg. Chem.* **2002**, *628*, 492–504.
[5] E. Bermejo, A. Castiñeiras, I. García, D. X. West, *Polyhedron* **2003**, *22*, 1147–1154.
[6] I. García Santos, PhD Thesis, University of Santiago de Compostela, Spain, **2001**.
[7] E. Bermejo, R. Carballo, A. Castiñeiras, R. Domínguez, A. E. Liberta, C. Maichle-Mössmer, D. X. West, *Z. Naturforsch. Teil A* **1999**, *54*, 777–787.
[8] E. Bermejo, A. Castiñeiras, R. Domínguez, R. Carballo, C. Maichle-Mössmer, J. Strahle, D. X. West, *Z. Anorg. Allg. Chem.* **1999**, *625*, 961–968.
[9] R. Carballo, A. Castiñeiras, T. Pérez, *Z. Naturforsch. Teil A* **2001**, *56*, 881–888.
[10] I. Garcia Santos, U. Abram, R. Alberto, E. Vázquez López, A. Sánchez, *Inorg. Chem.* **2004**, *43*, 1834–1836.
[11] I. García Santos, A. Castiñeiras, U. Abram, unpublished results.
[12] J. L. Wardell, in *Comprehensive Organometallic Chemistry* (Ed.: G. Wilkinson), vol. 2, Pergamon, Oxford, **1982**.
[13] T. S. Lobana, *Coord. Chem. Rev.* **1985**, *63*, 161–215.
[14] T. S. Lobana, M. K. Sandhu, D. C. Povey, G. W. Smith, *J. Chem. Soc., Dalton Trans.* **1988**, 2913–2914.
[15] T. S. Lobana, M. K. Sandhu, *Indian J. Chem. Sect. A* **1990**, *29*, 394–396.
[16] T. S. Lobana, A. Sánchez, J. S. Casas, A. Castiñeiras, J. Sordo, M. S. García-Tasende, E. M. Vázquez-López, *J. Chem. Soc., Dalton Trans.* **1997**, 4289–4300.
[17] T. S. Lobana, A. Sánchez, J. S. Casas, A. Castiñeiras, J. Sordo, M. S. García-Tasende, *Main Group Met. Chem.* **2001**, *24*, 61–62.
[18] J. Zukerman-Schhpector, M. C. Rodríguez-Arguelles, M. I. Suárez, A. Sánchez, J. S. Casas, J. Sordo, *J. Coord. Chem.* **1991**, *24*, 177–182.
[19] T. S. Lobana, A. Sánchez, J. S. Casas, M. S. García-Tasende, J. Sordo, *Inorg. Chim. Acta* **1998**, *267*, 169–172.
[20] I. García Santos, A. Hagenbach, U. Abram, *Dalton Trans.* **2004**, 677–682.
[21] L. Pauling, *The Nature of the Chemical Bond*, 3rd ed., Cornell University Press, New York, **1960**.
[22] M. Calvin, K. Wilson, *J. Am. Chem. Soc.* **1945**, *67*, 2003–2007.
[23] G. A. Bogdanović, A. Spasojević-de Bire, S. D. Zarić, *Eur. J. Inorg. Chem.* **2002**, 1599–1609.
[24] a) M. Nishio, M. Hirota, Y. Umezawa, *The CH/π Interactions*, Wiley-VCH, New York, **1998**; b) T. Steiner, *Angew. Chem. Int. Ed.* **2002**, *41*, 48–76.

 © 2006 Wiley-VCH Verlag GmbH & Co. KGaA, Weinheim 

[25] T. S. Lobana, A. Sánchez, J. S. Casas, A. Castiñeiras, J. Sordo, M. S. García-Tasende, *Polyhedron* **1998**, *17*, 3701–3709.
[26] J. S. Casas, E. E. Castellano, M. S. García-Tasende, A. Sánchez, J. Sordo, E. M. Vázquez-López, J. Zukerman-Schepector, *J. Chem. Soc., Dalton Trans.* **1996**, 1973–1978.
[27] L. G. Makarova, A. N. Nesmeyanov, *The Organic Compounds of Mercury*, North-Holland, Amsterdam, **1967**.
[28] C. A. McAuliffe, *The Chemistry of Mercury*, Macmillan, London, **1977**.
[29] R. C. Larock, Organomercury Compounds, in *Organic Synthesis*, Springer, Berlin, **1985**.
[30] W. J. Geary, *Coord. Chem. Rev.* **1971**, *7*, 81–122.
[31] U. Abram, K. Ortner, R. Gust, K. Sommer, *J. Chem. Soc., Dalton Trans.* **2000**, 735–744.
[32] J. S. Casas, M. V. Castaño, M. C. Cifuentes, J. C. García-Monteagudo, A. Sánchez, J. Sordo, U. Abram, *J. Inorg. Biochem.* **2004**, *98*, 1009–1016.
[33] J. Mack, K. Ortner, U. Abram, R. V. Parish, *Z. Anorg. Allg. Chem.* **1997**, *268*, 191.
[34] A. Castiñeiras, I. García, E. Bermejo, D. X. West, *Polyhedron* **2000**, *19*, 1873–1880.
[35] L. M. Fostiak, I. García, J. K. Swearingen, E. Bermejo, A. Castiñeiras, D. X. West, *Polyhedron* **2003**, *22*, 83–92.
[36] Bruker, SMART and SAINT. *Area Detector Control Integration Software*, Bruker Analytical X-ray Instruments, Inc., Madison, Wisconsin, USA, **1999**.
[37] G. M. Sheldrick, SADABS. *Program for Empirical Absorption Correction of Area Detector Data*, University of Göttingen, Germany, **1997**.
[38] G. M. Sheldrick, *Acta Crystallogr., Sect. A* **1990**, *46*, 467–473.
[39] G. M. Sheldrick, SHELX-97. *Program for the Refinement of Crystal Structures*, University of Göttingen, Germany, **1997**.
[40] A. J. C. Wilson, *International Tables for Crystallography*, vol. C, Kluwer Academic Publishers, Dordrecht, The Netherlands, **1995**.
[41] A. L. Spek, PLATON. *A Multipurpose Crystallographic Tool*, Utrecht University, Utrecht, The Netherlands, **2003**.

Received: March 30, 2006
Published Online: June 6, 2006

 © 2006 Wiley-VCH Verlag GmbH & Co. KGaA, Weinheim 

DOI: 10.1002/ejic.200600113

# Synthesis, Isolation and Structural Investigation of Schiff-Base Alkoxytitanium Complexes: Steric Limitations of Ligand Coordination

**Andrew L. Johnson,*[a] Matthew G. Davidson,*[a] Matthew D. Lunn,[b] and Mary F. Mahon[c]**

**Keywords:** Titanium / Alkoxide / Steric effects / Schiff-base ligands / Coordination

This paper reports the reaction of Ti(O*i*Pr)$_4$ with a series of Schiff-base ligands. The Schiff-base proligands **1a–l** are synthesised by the condensation of salicylaldehyde with a range of primary alkylamine and aniline derivatives. The treatment of **1a–f** with Ti(O*i*Pr)$_4$ yields the octahedral bis(aryloxy–imine)Ti(O*i*Pr)$_2$ complexes **2a–f**. X-ray crystal structure analysis of **2c**, **2d** and **2e** reveals complexes with a *trans*-aldiminato oxygen atom and *cis*-N,*cis*-alkoxide ligand arrangement about the central metal atom. The reactions of Ti(O*i*Pr)$_4$ with the ligands **1g** and **1h** result in a sterically induced ligand rearrangement to form the octahedral complexes **2g** and **2h**, also characterised by X-ray diffraction experiments, in which the nitrogen atoms of the O,N-chelate are now *trans*-orientated at the titanium centre. $^1$H NMR analysis reveals significant deshielding of the isopropoxide methine proton, induced by this coordination mode. In contrast, reactions of **1i** and **1j** with Ti(O*i*Pr)$_4$ result in the formation and isolation of the complexes **2i** and **2j**. X-ray crystal structure analysis shows complex **2j** to have a previously unobserved ligand orientation, in which both ligands are *trans*-orientated, with respect to the aldiminato oxygen atoms, about the titanium centre, but steric bulk of the ligand inhibits the bidentate coordination of both O,N-ligands. Further increase in the steric bulk of the imine substituent results in a reduced reactivity for ligands **1k** and **1l**, such that Ti(O*i*Pr)$_4$ reacts with **1k** to form the dimeric mono(Schiff-base) complex **2k** (characterised by X-ray analysis). No reaction is observed for **1l**.

(© Wiley-VCH Verlag GmbH & Co. KGaA, 69451 Weinheim, Germany, 2006)

## Introduction

In recent years the development of new and increasingly active homogeneous catalysts for polymerisations has been one of the driving forces behind the advances in organometallic chemistry, the most significant progress having been made in the area of metallocene chemistry.[1–5] Much of this chemistry has focused on the development of new non-Cp ligands for alkyl d$^0$ metal compounds, which enhance α-olefin polymerisation, in the presence of co-catalysts, such as methylaluminoxane (MAO). A variety of ligands have been explored in recent years, including, for example, alkoxides and chelating alkoxides such as hydroxybenzaldehydes,[6–9,10] $N_2O_2$ Schiff-base ligands,[11–18] and bidentate N,O ligands such as 8-quinolinolato and pyridine–alkoxides.[19–22] Much of this work has focused on the formation of complexes that incorporate bidentate ligands to afford metal complexes possessing *cis*-located "active" sites, a prerequisite for effective olefin polymerisation. Recently, a family of group 4 transition-metal complexes, possessing just such a *cisoid* arrangement of two aryloxy–imine ligands, have been shown to be highly active catalysts for olefin polymerisation.[23–30] Considerable attention has also focused on the use of group 4 metal alkoxide complexes in the ring-opening polymerisations of cyclic esters such as lactic acid and ε-caprolactone.[31–35]

As part of a more general study of the chemistry of titanium alkoxides, we and others have been interested in the use of similar complexes for a range of Lewis acid mediated reactions and polymerisations.[31,32,36,37] Herein we report the results of a synthetic and structural investigation of the stereochemical control possible by steric variation of ligands, specifically at the imine substituent.

It has been shown previously that *ortho* substitution of the aryloxy–imine ligands (R position) can have a marked effect upon the structure and fluxional properties as well as the activity of the Schiff-base metal complexes as olefin polymerisation catalysts.[38,39]

Previous X-ray crystallographic studies have established that of the five possible isomeric structures of (bidentate)$_2$-$MX_2$ complexes (bidentate = aryloxy–imine ligand, X = unidentate ligand) (Figure 1) the preferred structure is a distorted octahedron with *trans*-O,*cis*-N,*cis*-X ligand arrangement [Figure 1(i)],[14,23–30,40,41] a feature that has also

[a] Department of Chemistry, University of Bath, Claverton Down, Bath BA2 7AY, UK
Fax: +44-1225-8262312
E-mail: a.l.johnson@bath.ac.uk
m.g.davidson@bath.ac.uk
[b] Johnson Matthey Catalysts Ltd., P. O. Box 1, Belasis Avenue, Billingham, Cleveland TS23 1LB, UK
[c] Bath Chemical Crystallography Unit, Department of Chemistry, University of Bath, Claverton Down, Bath BA2 7AY, UK

 © 2006 Wiley-VCH Verlag GmbH & Co. KGaA, Weinheim 

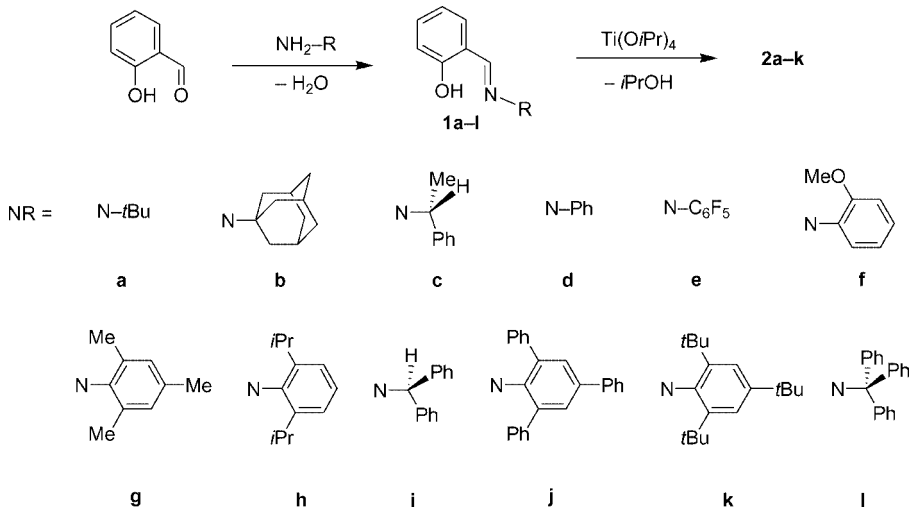


Scheme 1. Synthesis of ligands **1a**–**l** and Ti complexes **2a**–**k**.

been rationalised in terms of simple VSEPR concepts.[42] DFT calculations have also shown this conformation to be favoured in the gas phase.[23] Complexes with a *trans*-N,*cis*-O,*cis*-X ligand arrangement have also been reported.[29]

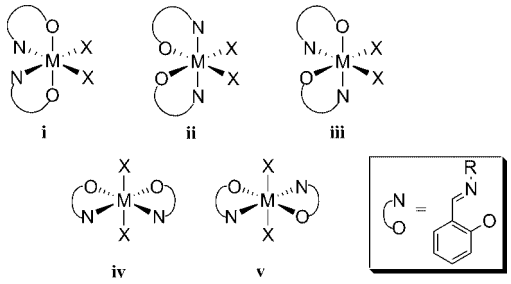


Figure 1. Depiction of the conformational isomers possible for (bidentate)$_2$MX$_2$ complexes.

## Results and Discussion

The aryloxy–imine ligands **1a**–**l** were readily prepared by the condensation of salicylaldehyde with commercially available primary amines or aniline derivatives in methanol using standard procedures (Scheme 1)[43] and isolated as sharp-melting white to yellow crystalline solids following recrystallisation in 70–98% yields. The range of amine and aniline derivatives used in this study were chosen because of their potential to impart different steric demands at metal centres.

### Synthesis and Structural Characterisation of Schiff Base Complexes

During the course of this study clear differences in the stereochemistry of metal complexes isolated, facilitate the

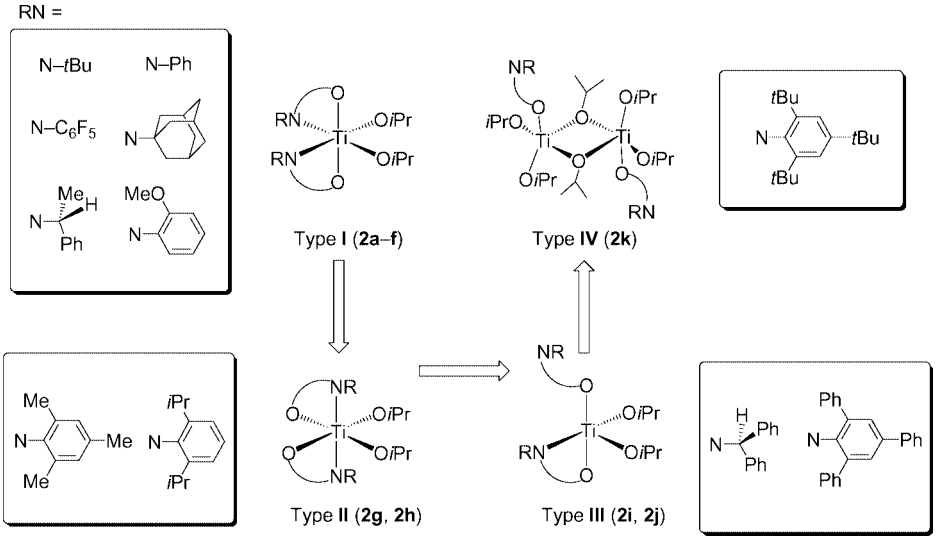


Figure 2. Structural classes of Schiff-base complexes **I**–**IV**.

 © 2006 Wiley-VCH Verlag GmbH & Co. KGaA, Weinheim 

division of their discussion into four distinct categories: bis($\eta^2$-*trans*-O,O) complexes, type **I**; bis($\eta^2$-*trans*-N,N) complexes, type **II**; bis($\eta^2$,$\eta^1$-*trans*-O,O) complexes, type **III**; and mono($\eta^1$) complexes, type **IV** (Figure 2). $^1$H NMR spectroscopic data and X-ray data are discussed below. $^{13}$C NMR spectroscopic data and elemental analyses are reported in the Experimental Section and are consistent with the structures proposed.

### Type I Complexes, Bis($\eta^2$-*trans*-O,O) Coordination

The reactions of Ti(O*i*Pr)$_4$ with 2 equiv. of **1a**–**f** proceed rapidly at room temperature in toluene to afford HO*i*Pr and the bis(ligand) complexes [{RN=C(C$_6$H$_4$O)}$_2$Ti(O*i*Pr)$_2$] (**2a**–**f**) in high yield (Scheme 1). The complexes **2** were isolated as analytically pure crystalline solids by recrystallisation from concentrated toluene solutions.

$^1$H NMR spectra of **2a**–**f** at room temperature contain one single set of sharp resonances, for both Schiff-base ligands and isopropoxide groups. Despite the variation in imine substituents in the complexes **2a**–**f**, signals due to the isopropoxide ligands do not vary significantly (i.e., $\delta$ = 4.6–4.9 ppm for the isopropoxide methine proton). It is well documented that six-cordinate bis(chelate) complexes of the structure types **I** and **II** (Figure 2) can undergo inversion of configuration at the metal centre, exhibiting rapid $\Delta \rightleftharpoons \Lambda$ isomerisation and isopropoxide rotation and/or exchange at ambient temperatures.[44–47] The observation of only one set of resonances for each ligand type in the $^1$H and $^{13}$C NMR spectra of **2a**–**f** is consistent with a $C_2$-symmetric structure. In the specific case of the complexes **2c**–**e**, single-crystal X-ray diffraction studies confirm the complexes to be type **I** (Figure 2) $C_2$-symmetric complexes in the solid state.

In order to probe this fluxional behaviour further, low-temperature $^1$H NMR spectra of **2c**, which incorporates an enantiomerically pure chiral ligand, are particularly informative, because the presence of chiral ligands leads to the formation of diastereoisomers.[20] Variable-temperature $^1$H NMR spectra for the imine CH region are shown in Figure 3. At room temperature (23 °C) the $^1$H NMR spectrum of **2c** shows one broad resonance each for the imine CH, the methine proton of the isopropoxide ligand, and the methine proton of the chiral imine substituent. Cooling of the sample to –20 °C results in resolution of each of these resonances into two peaks of intensity ratio 1:2.1, corresponding to the two diastereoisomers possible for complexes of type **I** shown in Figure 2. {It is likely that the two major isomers observed in solution correspond to the two diastereoisomers of the (*trans*,*cis*,*cis*) isomer [Figure 1(i)] as non-bulky ligands prefer a *trans*-O,*cis*-N conformation.} Cooling of the sample to –30 °C results in further changes in the relative intensities of these signals until at –80 °C the relative intensities are found in a 1:3.6 ratio. Although the absolute stereochemistry of the major diastereoisomer observed in the solution state cannot be determined unequivocally, it may be inferred from the molecular structure determination of **2c**. Compound **2c** crystallises in a chiral space group as only one diastereoisomer (see below), It is therefore likely that this is also the thermodynamically more stable isomer observed in solution.

The fluctional behaviour observed for **2c** at low temperatures is fully reversible, and warming of the sample to 60 °C shows a slight sharpening of the signals in the $^1$H NMR spectrum relative to the room-temperature spectrum, but no evidence for metal-based isomerisation is observed.

The molecular structures of **2c**, **2d**, and **2e** are shown in Figures 4, 5 and 6, respectively, and key parameters are summarised in Tables 1 and 5. All three complexes adopt a distorted octahedral structure of type **I**, with a *trans*-aldiminato,*cis*-alkoxide,*cis*-imine ligand arrangement.

The asymmetric unit of **2c** contains crystallographically independent molecules, both of which possess the same chirality but which differ marginally in the relative orientations of the isopropoxide groups. The coordination geometry

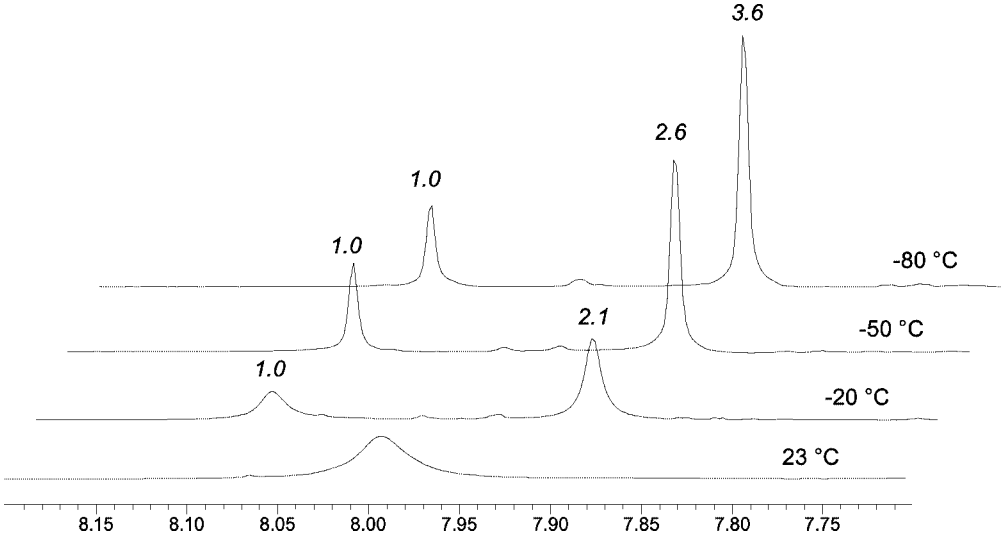


Figure 3. Variable-temperature $^1$H NMR spectra of **2c** showing the imine CH region of the ligand (relative integrals shown in italics above peaks).

 © 2006 Wiley-VCH Verlag GmbH & Co. KGaA, Weinheim 

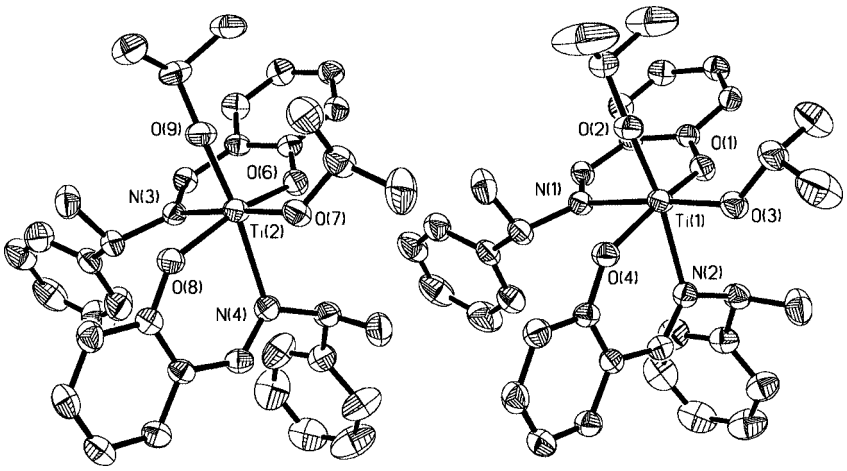


Figure 4. Molecular structures of the two independent molecules, **A** and **B**, in complex **2c**. Structures are shown with 50% displacement ellipsoids; hydrogen atoms have been omitted for clarity.

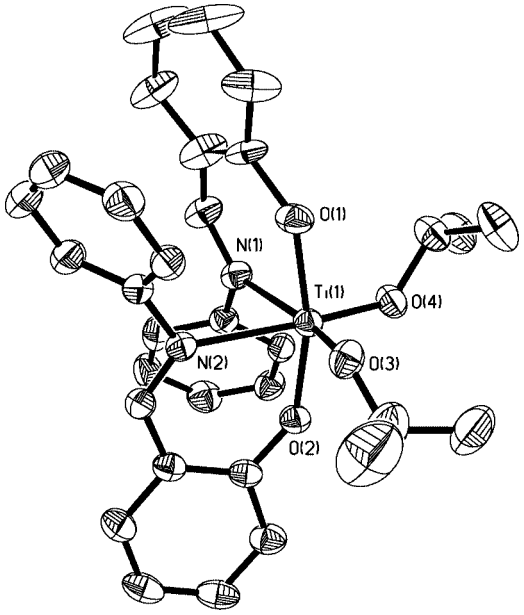


Figure 5. Molecular structure of complex **2d**. The structure is shown with 50% displacement ellipsoids. Hydrogen atoms have been omitted for clarity. Disorder in the aryloxy unit (O1–N1) is not shown.

around the central titanium atom is close to octahedral. The axial O–Ti–O bond angle is distorted away from linearity [O(1)–Ti(1)–O(4), 161.65(8)°; O(6)–Ti(2)–O(8), 161.95(8)°] such that there is a displacement of the aldiminato ring away from the isopropoxide ligands. The Ti–O*i*Pr moieties exhibit bond lengths of 1.777(2) Å [Ti(1)–O(2)], 1.817(2) Å [Ti(1)–O(3)], 1.826(2) Å [Ti(2)–O(7)], and 1.778(2) Å [Ti(2)–O(9)], with O–Ti–O angles of 99.85(9)° and 101.04(8)° about Ti(1) and Ti(2), respectively. As expected, the Ti–N(imine) bonds are considerably longer: Ti(1)–N(1) 2.347(2), Ti(1)–N(2) 2.299(2), Ti(2)–N(3) 2.321(2), Ti(2)–N(4) 2.300(2) Å. The coordination geometries in complexes **2d** and **2e** are similar to that observed in **2c**, although subtle differences between the complexes are apparent (Table 1).

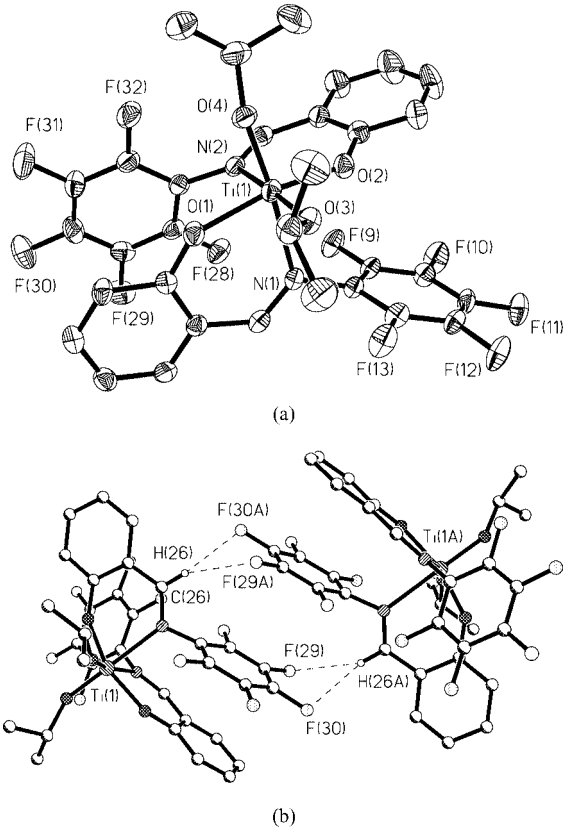


Figure 6. (a) Molecular structure of complex **2e**, shown with 50% displacement ellipsoids. Hydrogen atoms have been omitted for clarity. (b) Supramolecular structure of **2e** highlighting the intermolecular C–H···F interactions C(26)···F(29A) 3.550(4) Å, C(26)···F(30A) 3.406(4) Å, C(26)–H(26)···F(29A) 154.6°, C(26)–H(26)···F(30A) 140.1°.

Previous work has highlighted the role of the imine C–H group in promoting weak intermolecular interactions in the solid-state structures of Schiff-base complexes.[11] Of the titanium compounds described in this work, only **2e** exhibits significant intermolecular interactions involving this hydrogen-bond donor group: pairs of monomers are associ-

 © 2006 Wiley-VCH Verlag GmbH & Co. KGaA, Weinheim 

Table 1. Selected bond lengths [Å] and angles [°] for complexes **2c** (molecules A and B), **2d** and **2e**.

| | 2c | | 2d | 2e |
|---|---|---|---|---|
| | A | B | | |
| Ti–OAr | 1.9262(18) | 1.9417(18) | 1.8945(14) | 1.9190(16) |
| | 1.9312(18) | 1.9181(18) | 1.9042(13) | 1.9327(18) |
| Ti–N | 2.299(2) | 2.300(2) | 2.350(16) | 2.328(2) |
| | 2.347(2) | 2.321(2) | 2.3278(16) | 2.340(2) |
| Ti–OR | 1.7767(19) | 1.7778(18) | 1.8126(14) | 1.7791(19) |
| | 1.8170(18) | 1.8257(18) | 1.8186(14) | 1.7979(17) |
| ArO–Ti–OAr | 161.65(8) | 161.95(8) | 165.35(7) | 156.71(9) |
| N–Ti–N | 83.72(8) | 84.55(8) | 75.98(5) | 82.81(7) |
| O–Ti–N | 81.02(7) | 81.14(7) | 81.06(6) | 79.95(7) |
| RO–Ti–OR | 99.85(9) | 101.04(8) | 104.26(7) | 101.96(9) |

ated through mutual C–H···F interactions as shown in Figure 6(b). In related complexes, in which the imine group is an *ortho*-F-substituted phenyl ring, C–H···F interactions between the imine substituent and the β-H atoms of the growing polymer chain have been cited as the reason for the remarkable stability and catalytic behaviour of such complexes.[48,49]

### Type II Complexes, Bis($\eta^2$-*trans*-N,N) Coordination

Upon increasing the steric bulk of the imine substituent, beyond that of *o*-methoxyaniline, significant changes in the $^1$H NMR spectra are observed, such that the isopropoxide methine resonances shift from $\delta$ = 4.6–4.9 ppm in **2a**–**f** to $\delta$ = 3.4 and 3.7 ppm in **2g** and **2h**, respectively. We believe this change is indicative of a transformation from a type **I** to a type **II** structure. As with complexes **2a**–**f**, NMR spectra of **2g** and **2h** are consistent with $C_2$-symmetric complexes. A single-crystal X-ray structure of **2h** confirms the type **II** structure, in which the bidentate ligands adopt a mutually *trans*-N,*cis*-O(Ar),*cis*-O(R) arrangement, as shown in Figure 7; although there are no significant differences in Ti–N and Ti–O(Ar) bond lengths in **2h** relative to type **I** complexes **2c**–**e** (Tables 1 and 2), there is movement of the axial nitrogen atoms away from the isopropoxide ligands such that the N–Ti–N angle in **2h** is 164.61(8)°. As in the case of **2c**–**e**, the geometry of the aryloxy–imine ligands forces the chelate angles around the Ti atom to deviate from the ideal octahedral geometry, with a "bite" angle [N(1)–Ti(1)–O(1)] of 82.33(10)°, which is comparable to the average "bite" angles found in **2c**–**e** [81.02(7)° (**2cA**), 81.14(7)° (**2cB**), 81.06(6)° (**2d**) and 79.95(7)° (**2e**)]. Erker et al. have previously observed this unusual configuration in Schiff-base Ti and Zr chloride complexes of the ligand **1h**.[29]

The significant shift observed in the $^1$H NMR spectra of the isopropoxide ligands on changing from type **I** to type **II** complexes is not reflected in the Ti–O(isopropoxide) bond lengths, which remain similar in both type **I** and **II** complexes (see Tables 1 and 2). This suggests that the deshielding observed for type **II** complexes (**2g** and **2h**) is due to the proximity of the methine proton to an *N*-aryl group of the Schiff-base ligand rather than due to a differing *trans* effect

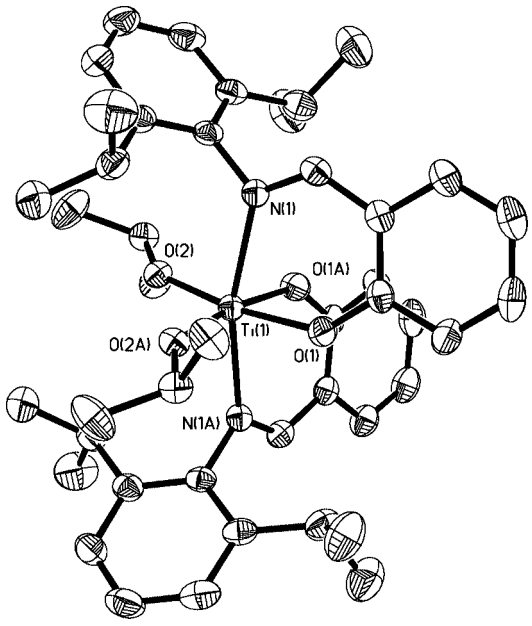


Figure 7. Molecular structure of **2h**. Ellipsoids are shown with 50% displacement probability. Hydrogen atoms have been omitted for clarity. Equivalent atoms (*A) are generated by the symmetry transformations $-x+1$, $y$, $-z+1/2$, and $-x+1/2$, $-y+1/2$, $-z+1$.

Table 2. Selected bond lengths [Å] and angles [°] for complex **2h**.

| | | | |
|---|---|---|---|
| Ti(1)–O(1) | 1.975(1) | O(1)–Ti(1)–O(1*) | 85.30(8) |
| Ti(1)–O(2) | 1.805(1) | O(1)–Ti(1)–O(2) | 171.27(6) |
| Ti(1)–N(1) | 2.228(1) | O(2)–Ti(1)–O(2*) | 95.87(8) |
| N(1)–Ti(1)–N(1*) | 164.61(8) | O(1)–Ti(1)–N(1) | 82.33(6) |

caused by reorientation of the ligands. This inference is supported by the solid-state structures of type **I** and type **II** complexes, in which the isopropoxide methine proton is directed towards an aryl ring in type **II** complexes but not in type **I**. These orientations are apparent from Figures 5 and 7, type **I** and **II** complexes, respectively. Overall, the steric environment surrounding the metal centre is altered significantly because of the reorientation of the Schiff-base ligands as highlighted by the space-filling diagrams shown in Figure 8. It would be surprising if these changes did not influence the reactivity of the metal complexes, and it is interesting to note that a recent report by Matsui et al. suggests that very bulky imine substituents inhibit the activity of Schiff-base Zr complexes as polyolefin precatalysts.[23]

### Type III Complexes, Bis($\eta^2\eta^1$-*trans*-O,O) Coordination

An additional increase in the steric bulk of the imine substituents (ligands **1i** and **1j**) leads to the formation of complexes **2i** and **2j** (Scheme 1). Characterisation of **2i** and **2j** by $^1$H NMR spectroscopy indicates the presence of the same ligand set as for **2a**–**h**. However, for both complexes, the isopropoxide methine proton is only slightly deshielded in comparison to the type **I** complexes **2a**–**f** implying that the isopropoxide group no longer experiences the deshield-

 © 2006 Wiley-VCH Verlag GmbH & Co. KGaA, Weinheim 

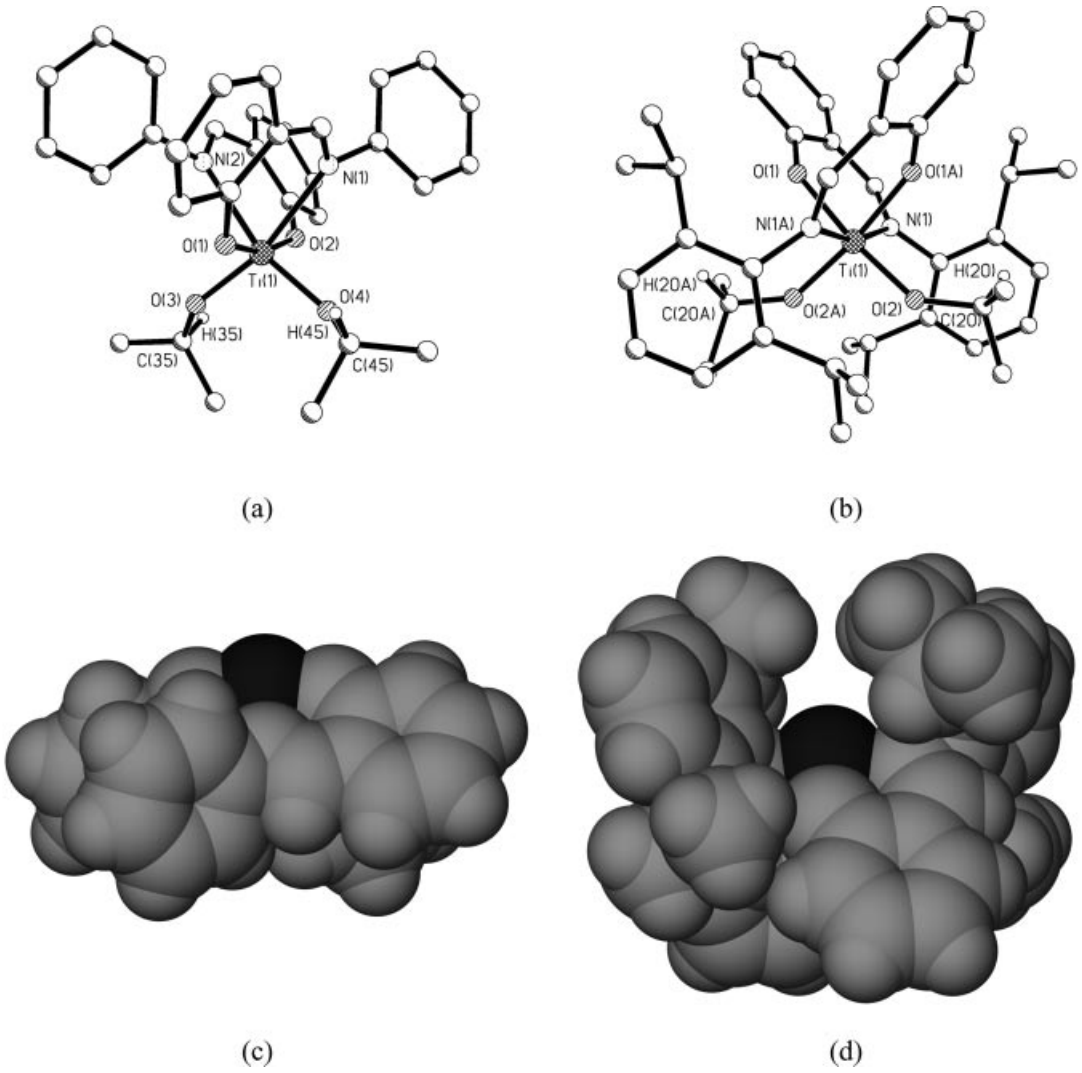


Figure 8. Complexes **2d** [(a) and (c)] and **2h** [(b) and (d)] highlighting orientation of the chelating ligands relative to the isopropoxide methine protons [(a) and (b)] and the difference in the steric environment of the active site in type **I** and type **II** complexes [isopropoxide groups have been omitted in (c) and (d) for clarity].

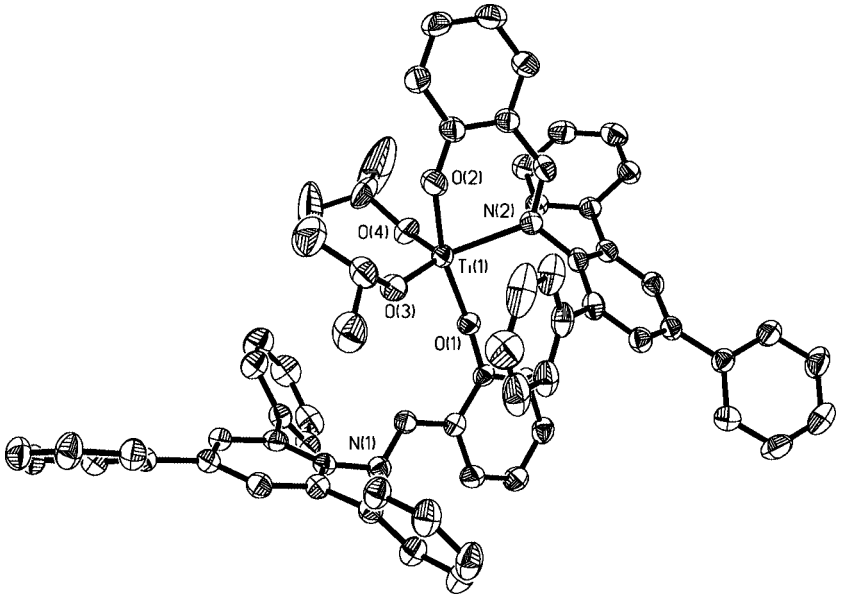


Figure 9. Molecular structure of complex **2j**, shown with 50% displacement ellipsoids; hydrogen atoms have been omitted for clarity.

 © 2006 Wiley-VCH Verlag GmbH & Co. KGaA, Weinheim 

ing effects observed in **2g** and **2h**, and that a further structural change has taken place.

X-ray structural analysis of complex **2j** (Figure 9) reveals the nature of this change and represents a previously uncharacterised structure for disubstituted Schiff-base titanium or zirconium complexes. Complex **2j** exhibits a five-coordinate titanium centre, with a distorted square-pyramidal geometry, supporting two alkoxide ligands and two aryloxide ligands, each exhibiting different bonding modes. One ligand forms a chelate to the metal centre in the expected $\eta^2$ fashion, while the second binds in $\eta^1$ mode solely through the aryloxide group. The 2,4,6-triphenylphenyl group of this monodentate ligand is orientated such that it is remote from the metal centre, thus relieving steric congestion. Selected bond lengths and angles for **2j** are given in Table 3. Complex **2j** may be viewed as a structural model for the proposed intermediate in the $\Delta \rightleftharpoons \Lambda$ enantiomerisation process of octahedral $(AB)_2MX_2$ complexes. The enantiomerisation process is reasoned to proceed via a five-coordinate intermediate formed by the rupture of a metal–ligand bond as shown in Figure 10.[19–21,44–47]

Table 3. Selected bond lengths [Å] and angles [°] for complex **2j**.

| | | | |
|---|---|---|---|
| Ti–O(1) | 1.862(2) | O(2)–Ti–O(1) | 164.72(8) |
| Ti–O(2) | 1.942(2) | O(3)–Ti–O(4) | 112.11(9) |
| Ti–O(3) | 1.791(2) | O(3)–Ti–N(2) | 140.21(8) |
| Ti–O(4) | 1.774(2) | O(4)–Ti–N(2) | 106.25(8) |
| Ti–N(2) | 2.215(2) | O(2)–Ti–N(2) | 80.27(7) |
| C(7)–N(1) | 1.276(3) | | |
| C(46)–N(2) | 1.441(3) | | |

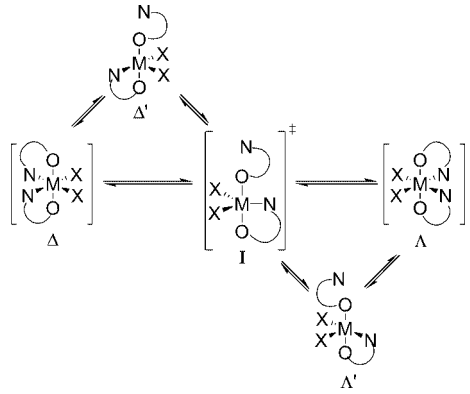

Figure 10. Proposed mechanism of racemisation for interchange of Δ and Λ forms of the bis(aryloxy–imine)titanium complexes. Complexes Δ′ and Λ′ represent the stable five-coordinate species, such as **2j**.[44–47]

### Type IV Complexes, Mono($\eta^1$) Coordination

Further increases in the steric bulk of the imine substituent (ligand **1k**, Scheme 1) inhibits formation of disubstituted complexes analogous to **2a**–**j**, and results in only monosubstitution of Ti(O*i*Pr)$_4$ to yield **2k**, even in the presence of excess **1k** and in refluxing toluene. Under similar reaction conditions, **1l** is recovered intact and no evidence for even monosubstitution is observed.

In the solid state, **2k** has a dimeric structure (Figure 11, Table 4) consisting of two terminal alkoxide and two bridging μ-O*i*Pr groups, as well as one monodentate aryloxide ligand coordinated to each Ti atom. This is structurally similar to the previously reported (alkoxide)(phenoxide)-titanium complex [$Ti_2$(O-2,4,6-$Me_3C_6H_2$)$_2$(O*i*Pr)$_4$(μ-O*i*Pr)$_2$].[18,50] Each titanium centre in **2k** possesses a trigonal-bipyramidal geometry, with one $\mu^2$-O*i*Pr group in an axial and one in an equatorial site (Figure 12). The terminal alkoxy–imine ligand occupies an equatorial site, and within

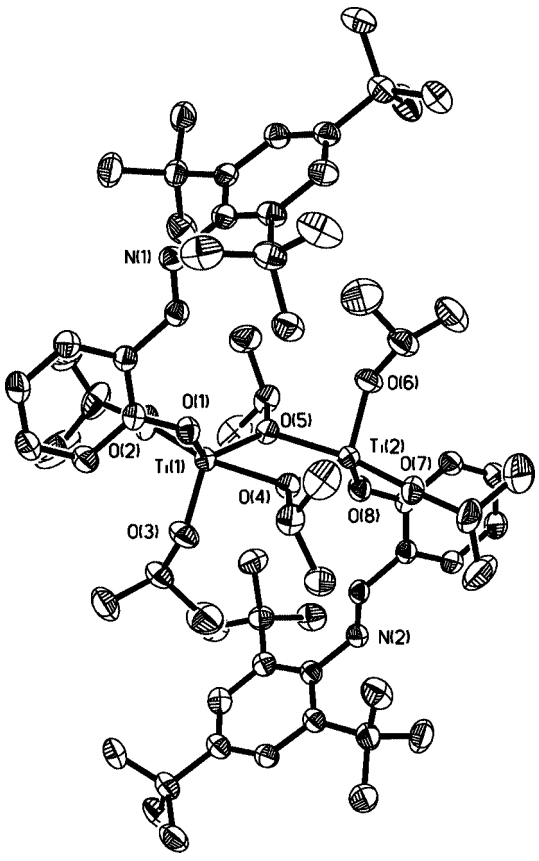


Figure 11. Molecular structure of complex **2k**, shown with 50% displacement ellipsoids; hydrogen atoms have been omitted for clarity.

Table 4. Selected bond lengths [Å] and angles [°] for complex **2k**.

| | | | |
|---|---|---|---|
| Ti(1)–Ti(2) | 3.263(2) | Ti(1)–O(4)–Ti(2) | 107.05(9) |
| | | Ti(1)–O(5)–Ti(2) | 107.63(9) |
| Ti(1)–O(1) | 1.882(2) | O(4)–Ti(1)–O(5) | 72.30(8) |
| Ti(1)–O(2) | 1.762(2) | O(4)–Ti(2)–O(5) | 72.56(8) |
| Ti(1)–O(3) | 1.778(2) | | |
| Ti(1)–O(4) | 2.120(2) | O(2)–Ti(1)–O(4) | 167.09(10) |
| Ti(1)–O(5) | 1.929(2) | O(1)–Ti(1)–O(5) | 125.83(9) |
| C(7)–N(1) | 1.270(4) | O(1)–Ti(1)–O(3) | 111.71(10) |
| | | O(1)–Ti(1)–O(5) | 125.83(9) |
| Ti(2)–O(8) | 1.883(2) | | |
| Ti(2)–O(6) | 1.788(2) | O(5)–Ti(2)–O(7) | 170.29(9) |
| Ti(2)–O(7) | 1.766(2) | O(4)–Ti(2)–O(6) | 115.90(10) |
| Ti(2)–O(4) | 1.924(2) | O(4)–Ti(2)–O(8) | 122.29(9) |
| Ti(2)–O(5) | 2.112(2) | O(6)–Ti(2)–O(8) | 174.69(10) |
| C(87)–N(2) | 1.272(4) | | |

 © 2006 Wiley-VCH Verlag GmbH & Co. KGaA, Weinheim 

the dimer both ligands are arranged *trans* to each other such that the molecule has crystallographic $C_i$ symmetry. The bridging alkoxide ligands do so unsymmetrically, with the equatorial Ti–O bonds [Ti(1)–O(5) 1.929(2) Å, Ti(2)–O(4) 1.924(2) Å] being shorter than the axial [Ti(1)–O(4) 2.120(2) Å, Ti(2)–O(5) 2.112(2) Å] ones. Other bond lengths and angles found in the structure of **2k** are as expected.

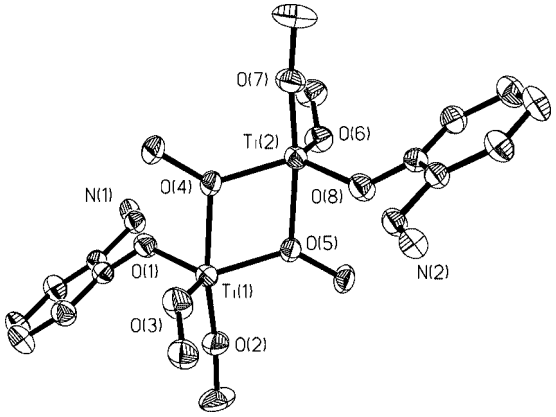


Figure 12. Structure of **2k**, showing the distorted trigonal-bipyramidal geometry about the two titanium centres, with 50% displacement ellipsoids; hydrogen atoms, methyl groups and the imine substituents have been omitted for clarity.

## Conclusions

We have synthesised, isolated and structurally characterised Schiff-base complexes of titanium with the previously observed $C_2$-symmetric type **I** (**2a**–**f**) and type **II** (**2g** and **2h**) structures. Type **II** complexes are characterised in their $^1$H NMR spectra by deshielding of the isopropoxide methine protons which highlights a significant change in the steric characteristics of the metal centre. A further increase in the steric demands of the imine substituent results in the isolation of complexes with the hitherto unknown five-coordinate type **III** structure (**2i** and **2j**), which can be viewed as a structural model for the proposed intermediate in $\Delta \rightleftharpoons \Lambda$ racemisation of $C_2$-symmetric complexes of this type. Increasing the steric bulk of the ligand still further induces a decrease in reactivity of the ligands towards Ti(O*i*Pr)$_4$. Thus, ligand **1k** substitutes only one alkoxide to form the bridged alkoxide complex **2k**, and **1l** is unreactive towards Ti(O*i*Pr)$_4$.

The ability to control molecular structure and particularly the environment about Lewis acidic metal centres, by steric variation at a ligands periphery, described here, clearly shows that, although somewhat distant from the metal centre, the choice of imine substituent is critical to the ligand coordination geometry about the central metal, and points to possible the rational design of metallo-organic complexes for use in catalysis.

## Experimental Section

**General Remarks:** All manipulations were carried out under dry argon using standard Schlenk and glove-box techniques. Solvents were purified by conventional procedures and distilled prior to use. Ti(O*i*Pr)$_4$ was purchased from Aldrich and used as received, without further purification. The ligands **1a**–**m** were prepared using the appropriate amine and salicylaldehyde, all purchased from Aldrich, using standard literature techniques.[51] Solution $^1$H, and $^{13}$C NMR experiments were performed at ambient temperature with a Bruker Avance-300. $^1$H NMR spectroscopic data are referenced to residual non-deuterated solvent.

**Syntheses of Complexes**

**[Ti(O*i*Pr)$_2${η$^2$-OC$_6$H$_4$C(H)N*t*Bu}$_2$] (2a):** To a stirred solution of **1a** (0.36 g, 2 mmol) in 20 mL of toluene was added Ti(O*i*Pr)$_4$ (0.3 mL, 1 mmol) dropwise by syringe, at 0 °C. The mixture was heated at reflux for 2 h. The solution was cooled to room temperature before removal of solvent under reduced pressure. The yellow residue was dissolved in a minimum of fresh toluene (6 mL), warmed to ca. 40 °C, and filtered through a Celite pad into a Schlenk flask. The filtrate was layered with 5 mL of dry pentane and allowed to stand at 4 °C for 2 days after which the solid microcrystalline product was collected by filtration, washed with 5 mL of cold hexane and dried in vacuo. Yield: 0.36 g (70%). $C_{28}H_{42}N_2O_4Ti$ (518.3): calcd. C 64.86, H 8.10, N 5.40; found C 65.1, H 8.17, N 5.41. $^1$H NMR (300 MHz, 23 °C, $CDCl_3$): $\delta$ = 1.17 [br. s, 12 H, OCH(C$H_3$)$_2$], 1.36 [s, 18 H, NC(C$H_3$)$_3$], 4.62 [sept, $^3J_{HH}$ = 6 Hz, OC$H$(CH$_3$)$_2$, 2 H], 6.6–6.85 (br. m, 4 H, CH$_{arom}$), 7.18–7.26 (br. m, 2 H, CH$_{arom}$), 7.27–7.45 (br. m, 2 H, CH$_{arom}$), 8.34 [s, 2 H, C($H$)=N] ppm. $^{13}$C NMR (75.5 MHz, 23 °C, $CDCl_3$): $\delta$ = 25.8, 30.9, 61.4, 77.6, 118.5, 119.3, 123.8, 132.5, 133.2, 160.1, 166.5 ppm.

Complexes **2b**–**2k** were prepared in a manner analogous to that of **2a**.

**[Ti(O*i*Pr)$_2${η$^2$-OC$_6$H$_4$C(H)N(C$_{10}$H$_{15}$)}$_2$] (2b):** Yield: 0.38 g (57%). $C_{40}H_{54}N_2O_4Ti$ (674.4): calcd. C 71.20, H 8.07, N 4.15; found C 71.60, H 8.01, N 4.09. $^1$H NMR (300 MHz, 23 °C, $CDCl_3$): $\delta$ = 1.22 [br . s, 12 H, OCH(C$H_3$)$_2$], 1.53–2.09 (br. m, 30 H, NC$_{10}H_{15}$), 4.69 [br. m, 2 H, OC$H$(CH$_3$)$_2$], 6.67–6.82 (br. m, 4 H, CH$_{arom}$), 7.14–7.28 (br. m, 2 H, CH$_{arom}$), 7.32–7.47 (br. m, 2 H, CH$_{arom}$), 8.32 [s, 2 H, C($H$)=N] ppm. $^{13}$C NMR (75.5 MHz, 23 °C, $CDCl_3$): $\delta$ = 25.9, 30.2, 36.7, 43.3, 78.4, 117.8, 118.7, 119.4, 131.7, 132.5, 160.4, 164.9 ppm.

**[Ti(O*i*Pr)$_2${η$^2$-OC$_6$H$_4$C(H)N[(*R*)-CHMePh]}$_2$] (2c):** Yield: 0.44 g (72%). $C_{36}H_{42}N_2O_4Ti$ (614.3): calcd. C 70.36, H 6.84, N 4.56; found C 69.60, H 6.84, N 4.42. $^1$H NMR (300 MHz, 23 °C, $CDCl_3$): $\delta$ = 1.02 [br. s, 12 H, OCH(C$H_3$)$_2$], 1.45 [br. s, 6 H, CH(C$H_3$)Ph], 4.67 [sept, OC$H$(CH$_3$)$_2$, $^3J_{HH}$ = 6 Hz, 2 H], 5.29 (br. m, 2 H, C$H$MePh) 6.58–6.66 (br. m, 2 H, CH$_{arom}$), 6.76–6.82 (br. m, 2 H, CH$_{arom}$), 6.97 (dd, $^3J_{HH}$ = 7.5 Hz, $^4J_{HH}$ = 1.5 Hz, 2 H, CH$_{arom}$), 7.06–7.15 (br. m, 10 H, CH$_{arom}$), 7.23 (ddd, $^3J_{HH}$ = 8 Hz, $^3J_{HH}$ = 7.2 Hz, $^4J_{HH}$ = 2.1 Hz, 2 H, CH$_{arom}$), 7.88 [s, 2 H, C($H$)=N] ppm. $^{13}$C NMR (75.5 MHz, 23 °C, $CDCl_3$): $\delta$ = 21.6, 25.7, 62.5, 78.6, 117.5, 119.4, 123.0, 126.9, 127.6, 128.8, 128.9, 134.18, 134.52, 163.7, 164.7 ppm.

**[Ti(O*i*Pr)$_2${η$^2$-OC$_6$H$_4$C(H)NC$_6$H$_5$}$_2$] (2d):** Yield: 0.38 g (68%). $C_{32}H_{34}N_2O_4Ti$ (558.2): calcd. C 68.80, H 6.09, N 5.01; found C 68.50, H 6.13, N 4.98. $^1$H NMR (300 MHz, 23 °C, $CDCl_3$): $\delta$ = 1.23 [br. s, 12 H, OCH(C$H_3$)$_2$], 4.9 [sept, $^3J_{HH}$ = 6 Hz, 2 H, OC$H$(CH$_3$)$_2$], 6.11–6.17 (m, 2 H, CH$_{arom}$), 6.49 (ddd, $^3J_{HH}$ = 9 Hz, $^3J_{HH}$ = 7.5 Hz, $^4J_{HH}$ = 1.2 Hz, 2 H, CH$_{arom}$), 6.78–7.04 (m, 14 H, CH$_{arom}$), 7.87 [s, 2 H, C($H$)=N] ppm. $^{13}$C NMR (75.5 MHz, 23 °C, $CDCl_3$): $\delta$ = 25.9, 79.0, 117.8, 119.8, 123.1, 126.2, 128.4, 134.3, 135.2, 154.3, 163.7, 166.3 ppm.

**[Ti(O*i*Pr)$_2${η$^2$-OC$_6$H$_4$C(H)NC$_6$F$_5$}$_2$] (2e):** Yield: 0.6 g (81%). $C_{32}H_{24}F_{10}N_2O_4Ti$ (738.1): calcd. C 52.03, H 3.25, N 3.79; found C

 © 2006 Wiley-VCH Verlag GmbH & Co. KGaA, Weinheim 

51.8, H 3.28, N 3.78. $^1$H NMR (400 MHz, 23 °C, $CDCl_3$): $\delta$ = 1.11 [br. s, 12 H, OCH($CH_3$)$_2$], 4.77 [sept, $^3J_{HH}$ = 5.8 Hz, 2 H, OC$H$(CH$_3$)$_2$], 6.45–6.47 (m, 2 H, CH$_{arom}$), 6.74–6.78 (m, 2 H, CH$_{arom}$), 7.20 (dd, $^3J_{HH}$ = 8 Hz, $^4J_{HH}$ = 1.6 Hz, 2 H, CH$_{arom}$), 7.34 (ddd, $^3J_{HH}$ = 8.4 Hz, $^3J_{HH}$ = 6.8 Hz, $^4J_{HH}$ = 2 Hz, 2 H, CH$_{arom}$), 8.07 [s, 2 H, C($H$)=N] ppm. $^{13}$C NMR (100 MHz, 23 °C, $CDCl_3$): $\delta$ = 25.5, 80.7, 118.0, 118.9, 121.2, 135.0, 136.5, 156.5, 164.9, 171.8 ppm. $^{19}$F NMR (376 MHz, 23 °C, $CDCl_3$): $\delta$ = –148.3 (m), –160.1 (t, $J$ = 21 Hz), –164.0 (m) ppm.

**[Ti(O*i*Pr)$_2${η$^2$-OC$_6$H$_4$C(H)NC$_6$H$_4$-*o*-OCH$_3$}$_2$] (2f):** Yield: 0.46 g (74%). $C_{34}H_{38}N_2O_6Ti$ (618.2): calcd. C 66.02, H 6.15, N 4.53; found C 66.50, H 6.09, N 4.45. $^1$H NMR (300 MHz, 23 °C, $CDCl_3$): $\delta$ = 1.19 [br. s, 12 H, OCH($CH_3$)$_2$], 3.38 (s, 6 H, O$CH_3$), 4.88 [sept, $^3J_{HH}$ = 6 Hz, 2 H, OC$H$(CH$_3$)$_2$], 5.99–6.08 (m, 2 H, CH$_{arom}$), 6.20–6.28 (m, 2 H, CH$_{arom}$), 6.36–6.47 (m, 2 H, CH$_{arom}$), 6.62–6.97 (m, 8 H, CH$_{arom}$), 7.43–7.56 (m, 2 H, CH$_{arom}$), 7.89 [s, 2 H, C($H$)=N] ppm. $^{13}$C NMR (75.5 MHz, 23 °C, $CDCl_3$): $\delta$ = 26.8, 56.0, 79.5, 111.7, 117.7, 119.8, 120.6, 123.8, 126.9, 127.8, 134.5, 135.2, 143.6, 151.6, 136.9, 169.7 ppm.

**[Ti(O*i*Pr)$_2${η$^2$-OC$_6$H$_4$C(H)NC$_6$(CH$_3$)$_3$H$_2$}$_2$] (2g):** Yield: 0.37 g (58%). $C_{38}H_{46}N_2O_4Ti$ (642.3): calcd. C 71.03, H 7.17, N 4.36; found C 71.30, H 7.15, N 4.32. $^1$H NMR (300 MHz, 23 °C,

Table 5. Crystal data and structure refinement for compounds **2c**, **2d**, **2e**, **2h**, **2j** and **2k**.

| Compound | **2c** | **2d** | **2e** |
|---|---|---|---|
| Empirical formula | $C_{36}H_{42}N_2O_4Ti$ | $C_{32}H_{34}N_2O_4Ti$ | $C_{32}H_{24}F_{10}N_2O_4Ti$ |
| Formula mass | 614.62 | 558.51 | 738.43 |
| $T$ [K] | 150(2) | 150(2) | 396(2) |
| Crystal system | monoclinic | monoclinic | monoclinic |
| Space group | $P2_1$ | $P2_1/a$ | $P2_1/c$ |
| $a$ [Å] | 18.1430(3) | 16.7770(1) | 14.3970(2) |
| $b$ [Å] | 10.1730(2) | 9.9880(2) | 20.1450(4) |
| $c$ [Å] | 18.3320(4) | 17.2620(3) | 21.5010(4) |
| $\beta$ [°] | 106.635(1) | 90.143(1) | 149.477(1) |
| $V$ [Å$^3$] | 3241.91(11) | 2892.56(8) | 3167.10(10) |
| $Z$ | 4 | 4 | 4 |
| $D_c$ [g cm$^{-3}$] | 1.259 | 1.283 | 1.549 |
| $\mu$ [mm$^{-1}$] | 0.305 | 0.334 | 0.370 |
| $F$(000) | 1304 | 1176 | 1496 |
| Crystal size [mm] | 0.28 × 0.08 × 0.08 | 0.22 × 0.15 × 0.10 | 0.25 × 0.17 × 0.15 |
| $\theta$ range [°] | 3.52–26.38 | 3.54–27.48 | 3.60–27.49 |
| Reflections collected | 57745 | 41742 | 10943 |
| Independent reflections [$R$(int)] | 13136 [0.0516] | 6582 [0.0380] | 6613 [0.0326] |
| Reflections [$I > 2\sigma(I)$] | 10091 | 5305 | 4509 |
| Data/restraints/parameters | 13136/1/788 | 6582/24/411 | 6613/0/446 |
| Goodness-of-fit on $F^2$ | 0.994 | 1.030 | 1.011 |
| Final $R_1$, $wR_2$ [$I > 2\sigma(I)$] | 0.0423, 0.1024 | 0.0470, 0.1218 | 0.0466, 0.1121 |
| Final $R_1$, $wR_2$ (all data) | 0.0670, 0.1161 | 0.0615, 0.1304 | 0.0814, 0.1304 |
| Max/min difference [e·Å$^{-3}$] | 0.523/–0.308 | 1.236/–0.756 | 0.602/–0.525 |
| Absolute structure parameter | –0.017(16) | – | – |
| Compound | **2h** | **2j** | **2k** |
| Empirical formula | $C_{51}H_{65}N_2O_4Ti$ | $C_{75}H_{66}N_2O_4Ti$ | $C_{75}H_{118}N_2O_8Ti_2$ |
| Formula mass | 817.95 | 1107.20 | 1271.51 |
| $T$ [K] | 150(2) | 150(2) | 150(2) K |
| Crystal system | monoclinic | orthorhombic | triclinic |
| Space group | $C_2/c$ | $Pbca$ | $P\bar{1}$ |
| $a$ [Å] | 23.1450(4) | 18.2330(2) | 15.3200(3) |
| $b$ [Å] | 17.0660(4) | 24.8400(2) | 15.6480(3) |
| $c$ [Å] | 14.5820(4) | 26.3420(3) | 18.1500(4) |
| $\alpha$ [°] | | | 75.569(1) |
| $\beta$ [°] | 126.617(1) | | 65.055(1) |
| $\gamma$ [°] | | | 85.119(1) |
| $V$ [Å$^3$] | 4623.03(18) | 11930.5(2) | 3819.69(13) |
| $Z$ | 4 | 8 | 2 |
| $D_c$ [g cm$^{-3}$] | 1.175 | 1.233 | 1.106 |
| $\mu$ [mm$^{-1}$] | 0.230 | 0.197 | 0.259 |
| $F$(000) | 1756 | 4672 | 1380 |
| Crystal size [mm] | 0.25 × 0.17 × 0.15 | 0.25 × 0.15 × 0.08 | 0.175 × 0.175 × 0.075 |
| $\theta$ range [°] | 3.63–27.46 | 3.54–27.49. | 3.91–24.98 |
| Reflections collected | 39356 | 26279 | 37007 |
| Independent reflections [$R$(int)] | 5270 [0.1181] | 13649 [0.0620] | 13339 [0.0752] |
| Reflections [$I > 2\sigma(I)$] | 3287 | 7735 | 8557 |
| Data/restraints/parameters | 5270/0/275 | 13649/0/768 | 13339/24/868 |
| Goodness-of-fit on $F^2$ | 1.027 | 0.969 | 0.996 |
| Final $R_1$, $wR_2$ [$I > 2\sigma(I)$] | 0.0511, 0.1131 | 0.0552, 0.1351 | 0.0556, 0.1355 |
| Final $R_1$, $wR_2$ (all data) | 0.1035, 0.1332 | 0.1209, 0.1651 | 0.1004, 0.1637 |
| Max/min difference [e·Å$^{-3}$] | 0.346/–0.356 | 0.648/–0.482 | 0.746/–0.373 |

 © 2006 Wiley-VCH Verlag GmbH & Co. KGaA, Weinheim 

$CDCl_3$): $\delta$ = 0.38 [d, $^3J_{HH}$ = 12 Hz, 12 H, OCH($CH_3$)$_2$], 2.21 (s, 3 H, *p*-$CH_3$) 2.38 (s, 6 H, *o*-$CH_3$), 3.45 [sept, $^3J_{HH}$ = 9 Hz, 2 H, OC*H*($CH_3$)$_2$], 6.52 (ddd, $^3J_{HH}$ = 7.6 Hz, $^3J_{HH}$ = 6.8 Hz, $^4J_{HH}$ = 0.9 Hz, 2 H, $CH_{arom}$) 6.59–6.62 (m, 2 H, $CH_{arom}$), 6.83 (s, 4 H, $CH_{arom}$), 7.08 (dd, $^3J_{HH}$ = 7.8 Hz, $^4J_{HH}$ = 1.8 Hz, 2 H, $CH_{arom}$) 7.22 (ddd, $^3J_{HH}$ = 8.4 Hz, $^3J_{HH}$ = 7.2 Hz, $^4J_{HH}$ = 1.8 Hz, 2 H, $CH_{arom}$), 7.88 [s, 2 H, C(*H*)=N] ppm. $^{13}$C NMR (75.5 MHz, 23 °C, $CDCl_3$): $\delta$ = 19.8, 21.1, 24.9, 77.7, 115.7, 119.9, 121.7, 129.0, 131.5, 134.6, 135.4, 135.7, 151.7, 167.8, 169.2 ppm.

**[Ti(O*i*Pr)$_2${$\eta^2$-OC$_6$H$_4$C(H)NC$_6$[CH(CH$_3$)$_2$]$_2$H$_3$}$_2$] (2h):** Yield: 0.6 g (83%). $C_{44}H_{58}N_2O_4Ti$ (726.4): calcd. C 72.73, H 7.99, N 3.86; found C 72.30, H 8.01, N 3.76. $^1$H NMR (300 MHz, 23 °C, $CDCl_3$): $\delta$ = 0.51 [br. s, 12 H, OCH($CH_3$)$_2$], 1.25 [br. s, 24 H, CCCH($CH_3$)$_2$], 3.77 [sept, $^3J_{HH}$ = 7 Hz, 2 H, OC*H*($CH_3$)$_2$], 3.87 [sept, $^3J_{HH}$ = 9.2 Hz, 2 H, CC*H*($CH_3$)$_2$], 6.62–6.65 (m, 4 H, $CH_{arom}$), 7.19–7.27 (m, 8 H, $CH_{arom}$), 7.35–7.39 (m, 2 H, $CH_{arom}$), 8.05 [s, 2 H, C(*H*)=N] ppm. $^{13}$C NMR (75.5 MHz, 23 °C, $CDCl_3$): $\delta$ = 25.29, 27.46, 27.48, 77.8, 115.61, 120.0, 124.17, 124.17, 126.92, 134.9, 136.1, 142.2, 152.2, 167.5, 169 ppm.

**[Ti(O*i*Pr)$_2${$\eta^2$-OC$_6$H$_4$C(H)NCH(Ph)$_2$}$_2$] (2i):** Yield: 0.49 g (66%). $C_{46}H_{46}N_2O_4Ti$ (738.3): calcd. C 74.79, H 6.23, N 3.79; found C 74.70, H 6.20, N 3.78. $^1$H NMR (300 MHz, 23 °C, $CDCl_3$): $\delta$ = 0.92 [d, $^3J_{HH}$ = 6.4 Hz, 12 H, OCH($CH_3$)$_2$], 4.5 [sept, $^3J_{HH}$ = 8.9 Hz, 2 H, OC*H*($CH_3$)$_2$], 6.57–6.60 (m, 2 H, $CH_{arom}$), 6.72–6.73 (m, 2 H, $CH_{arom}$), 6.82–6.84 (m, 4 H, $CH_{arom}$), 7.02–7.27 (m, 20 H, $CH_{arom}$), 7.79 [s, 2 H, C(*H*)=N] ppm. $^{13}$C NMR (75.5 MHz, 23 °C, $CDCl_3$): $\delta$ = 24.3, 70.2, 77.8, 115.9, 118.2, 121.3, 125.8, 126.9, 127.7, 128.1, 133.1, 139.9, 162.6, 166.3 ppm.

**[Ti(O*i*Pr)$_2${$\eta^2$-OC$_6$H$_4$C(H)N[C$_6$H$_2$(Ph)$_3$]}{$\eta^1$-OC$_6$H$_4$C(H)NC$_6$H$_2$-(Ph)$_3$}] (2j):** Yield: 0.59 g (58%). $C_{68}H_{58}N_2O_4Ti$ (1014.4): calcd. C 80.47, H 5.71, N 2.76; found C 80.40, H 5.73, N 2.73. $^1$H NMR (300 MHz, 23 °C, $CDCl_3$): $\delta$ = 0.69 [d, $^3J_{HH}$ = 6.4 Hz, 12 H, OCH($CH_3$)$_2$], 4.14 [sept, $^3J_{HH}$ = 9 Hz, 2 H, OC*H*($CH_3$)$_2$], 6.37–7.50 (m, 42 H, $CH_{arom}$), 8.29 [s, 2 H, C(*H*)=N] ppm. $^{13}$C NMR (75.5 MHz, 23 °C, $CDCl_3$): $\delta$ = 25.6 80.6, 119.1, 120.2, 125.7, 127.2, 127.4, 127.5, 127.7, 128.3, 128.5, 129.3, 130.3, 130.5, 135.3, 138.3, 140.1, 141.1, 150.2, 164.3, 165.9 ppm.

**[Ti(O*i*Pr)$_3$$\eta^1$-OC$_6$H$_4$C(H)N{C$_6$H$_2$(*t*Bu)$_3$}]$_2$ (2k):** Yield: 0.48 g (82%, based on Ti). $C_{68}H_{110}N_2O_8Ti_2$ (1178.7): calcd. C 69.27, H 9.34, N 2.38; found C 69.02, H 9.18, N 2.39. $^1$H NMR (300 MHz, 23 °C, $CDCl_3$): $\delta$ = 0.99 [d, $^3J_{HH}$ = 9 Hz, 36 H, OCH($CH_3$)$_2$], 1.24 [s, 18 H, C($CH_3$)$_3$], 1.27 [s, 36 H, C($CH_3$)$_3$], 4.43 [sept, $^3J_{HH}$ = 6.3 Hz, 6 H, OC*H*($CH_3$)$_2$], 6.8–6.94 (m, 4 H, $CH_{arom}$), 7.11–7.38 (m, 4 H, $CH_{arom}$), 7.96–8.14 (m, 4 H, $CH_{arom}$), 8.56 [s, 2 H, C(*H*)=N] ppm. $^{13}$C NMR (75.5 MHz, 23 °C, $CDCl_3$): $\delta$ = 26.6, 31.9, 32.5, 35.0, 36.4, 77.6, 120.9, 121.9, 122.5, 127.8, 132.6, 138.9, 141.2, 151.9, 158.4, 165.1, 168.2 ppm.

**X-ray Crystallographic Study:** Crystallographic data for compounds **2c**, **2d**, **2e**, **2h**, **2j** and **2k** are summarised in Table 5. All data collections were carried out with a Nonius KappaCCD diffractometer. Structure solution and refinement were performed using SHELX86[52] and SHELX97[53] software, respectively. Experimental data relating to all structure determinations are summarised in Table 5. Full-matrix anisotropic refinement was implemented in the final least-squares cycles throughout. All data were corrected for Lorentz and polarisation and, with the exceptions of **2d**, **2e** and **2j**, for extinction effects. Hydrogen atoms were included at calculated positions throughout. In **2d**, one of the phenyl groups was seen to exhibit positional disorder. In particular, C(1)–C(6) were found to be disordered in a 1:1 ratio with C(1A)–C(6A). All carbon–carbon distances therein were refined subject to rigid-bond restraints. In complex **2h**, the asymmetric unit consisted of one half of a molecule with the central titanium atom residing on a twofold rotation axis, in addition to half of a toluene molecule proximate to a crystallographic inversion centre. The methyl group in the solvent was disordered in a 1:1 ratio by virtue of straddling this inversion centre. One full toluene molecule was also seen to be present in the structure of **2j**. In addition, one of the isopropyl groups exhibited disorder whereby C(90)–(92) were disordered in a 1:1 ratio with C(90′)–(92′). Similarly, the asymmetric unit in **2k** was also observed to contain a solvent molecule (toluene) evenly disordered over two sites. In particular, C(101)–(106) exhibited 1:1 disorder with C(201)–C(206). Both partial rings were refined as rigid hexagons. Disordered toluene methyl groups were not included in the model. Moreover, one *tert*-butyl substituent was also found to be disordered in a 70:30 ratio, whereby C(95A)–(96C) were refined at 70% occupancy and C(95D)–(95F) were refined at 30% occupancy. CCDC-239547 to -239552 contain the supplementary crystallographic data for this paper. These data can be obtained free of charge from The Cambridge Crystallographic Data Centre via www.ccdc.cam.ac.uk/data_request/cif.

## Acknowledgments

We thank Johnson Matthey Catalysts Ltd. (A. L. J., M. G. D., M. D. L.) and the the EPSRC (M. G. D.) for support.

[1] H. G. Alt, E. H. Licht, A. I. Licht, K. J. Schneider, *Coord. Chem. Rev.* **2005**, *250*, 2.
[2] G. Erker, G. Kehr, R. Frohlich, *Coord. Chem. Rev.* **2006**, *250*, 36.
[3] C. Janiak, *Coord. Chem. Rev.* **2006**, *250*, 66.
[4] M. Bochmann, *J. Organomet. Chem.* **2004**, *689*, 3982.
[5] W. Kaminsky, *Adv. Catal.* **2001**, *46*, 89.
[6] A. Vanderlinden, C. J. Schaverien, N. Meijnoom, C. Ganter, A. G. Orpen, *J. Am. Chem. Soc.* **1995**, *117*, 3008.
[7] R. D. J. Froese, D. Musaev, G. T. Matsubara, K. Morokuma, *J. Am. Chem. Soc.* **1997**, *119*, 7190.
[8] R. D. J. Froese, D. Musaev, G. K. Morokuma, *Organometallics* **1999**, *18*, 373.
[9] Y. Nakayama, K. Watanabe, N. Ueyama, A. Nakamura, A. Harada, J. Okuda, *Organometallics* **2000**, *19*, 2498.
[10] L. Matilainen, M. Klinga, M. Leskelä, *J. Chem. Soc., Dalton Trans.* **1996**, 219.
[11] E. B. Tjaden, D. C. Swenson, R. F. Jordan, *Organometallics* **1995**, *14*, 371.
[12] E. Solari, C. Floriani, A. Chiesi-Villa, C. Rizzoli, *J. Chem. Soc., Dalton Trans.* **1992**, 367.
[13] C. Floriani, *Polyhedron* **1989**, *8*, 1717.
[14] R. Fleischer, H. Wunderlich, M. Braun, *Eur. J. Org. Chem.* **1998**, 1063.
[15] H. Chen, P. S. White, R. M. Gagné, *Organometallics* **1998**, *17*, 5358.
[16] P. R. Woodman, I. J. Munslow, P. B. Hitchcock, P. J. Scott, *J. Chem. Soc., Dalton Trans.* **1999**, 4069.
[17] P. R. Woodman, N. W. Alcock, I. J. Munslow, C. J. Sanders, P. J. Scott, *J. Chem. Soc., Dalton Trans.* **2000**, 3340.
[18] J. P. Corden, W. Errington, P. Moore, M. G. H. Wallbridge, *Chem. Commun.* **1999**, 323.
[19] X. Bei, D. C. Swenson, R. F. Jordan, *Organometallics* **1997**, *16*, 3282.
[20] T. Tsukahara, D. C. Swenson, R. F. Jordan, *Organometallics* **1997**, *16*, 3303.
[21] I. Kim, Y. Mishihara, R. F. Jordan, R. D. Rogers, A. L. Rheingold, G. P. Yap, *Organometallics* **1997**, *16*, 3314.
[22] M. C. W. Chan, S. C. F. Kui, J. M. Cole, G. J. McIntyre, S. Matsui, N. Zhu, K.-H. Tam, *Chem. Eur. J.* **2006**, *12*, 2607.
[23] S. Matsui, M. Mitani, J. Saito, Y. Tohi, M. Makio, N. Matsukawa, Y. Takagi, K. Tsuru, M. Nitabaru, T. Nakano, H.

 © 2006 Wiley-VCH Verlag GmbH & Co. KGaA, Weinheim 

Tanaka, N. Kashiwa, T. Fujita, *J. Am. Chem. Soc.* **2001**, *123*, 6847.
[24] J. Tian, G. W. Coates, *Angew. Chem.* **2000**, *112*, 3772; *Angew. Chem. Int. Ed.* **2000**, *39*, 3626.
[25] S. Matsui, Y. Tohi, M. Mitani, J. Saito, M. Makio, H. Tanaka, M. Nitabaru, T. Nakano, T. Fujita, *Chem. Lett.* **1999**, 1065.
[26] S. Matsui, M. Mitani, J. Saito, N. Matsukawa, H. Tanaka, T. Nakano, T. Fujita, *Chem. Lett.* **2000**, 554.
[27] J. Tian, P. D. Hustad, G. W. Coates, *J. Am. Chem. Soc.* **2001**, *123*, 5134.
[28] J. Saito, M. Mitani, J. Mohri, Y. Yoshida, S. Matsui, S. Ishii, S. Kojoh, N. Kashiwa, T. Fujita, *Angew. Chem.* **2001**, *113*, 3002; *Angew. Chem. Int. Ed.* **2001**, *40*, 2918.
[29] J. Strauch, T. H. Warren, G. Erker, R. Fröhlich, P. Saarenketo, *Inorg. Chim. Acta* **2000**, *300*, 810.
[30] M. Mitani, J. Mohri, Y. Yoshida, J. Saito, S. Ishii, K. Tsuru, S. Matsui, R. Furuyama, T. Nakano, H. Tanaka, S. Kojoh, T. Matsugi, N. Kashiwa, T. Fujita, *J. Am. Chem. Soc.* **2002**, *124*, 3327.
[31] A. J. Chmura, M. G. Davidson, M. D. Jones, M. D. Lunn, M. F. Mahon, *Dalton Trans.* **2006**, 887.
[32] M. G. Davidson, M. D. Jones, M. D. Lunn, M. F. Mahon, *Inorg. Chem.* **2006**, *45*, 2282.
[33] Y. Sarazin, R. H. Howard, D. L. Hughes, S. M. Humphrey, M. Bochmann, *Dalton Trans.* **2006**, 340.
[34] S. K. Russel, C. L. Gamble, K. J. Gibbins, K. C. S. Juhl, W. S. Mitchell III, A. J. Tumas, G. E. Hofmeister, *Macromolecules* **2005**, *38*, 10336.
[35] Y. Kim, G. K. Jnaneshwara, J. G. Verkade, *Inorg. Chem.* **2003**, *42*, 1437.
[36] D. C. Bradley, R. C. Mehrotra, I. P. Rothwell, A. Singh, *Alkoxo and Aryloxo Derivatives of Metals*, Academic Press, San Diago, CA, **2001**.
[37] S. D. Bull, M. G. Davidson, A. L. Johnson, D. E. J. E. Robinson, M. F. Mahon, *Chem. Commun.* **2003**, 1750.
[38] M. Mitani, R. Furuyama, J. Mohri, J. Saito, S. Ishii, H. Terao, T. Nakano, H. Tanaka, T. Fujita, *J. Am. Chem. Soc.* **2003**, *125*, 4293.
[39] A. F. Mason, G. W. Coates, *J. Am. Chem. Soc.* **2004**, *126*, 16326.
[40] S. J. Coles, M. B. Hursthouse, D. G. Kelly, A. J. Toner, *Polyhedron* **2000**, *19*, 177.
[41] L. Z. Flores-Lopéz, M. Parra-Hake, R. Somanathan, P. J. Walsh, *Organometallics* **2000**, *19*, 2153.
[42] D. L. Keppert, in *Progress in Inorganic Chemistry*, vol. 23 (Ed.: S. L. Lippard), John Wiley & Sons, Inc., New York, **1997**, chapter 1.
[43] C. Wang, S. Fredrich, T. R. Younkin, R. T. Li, R. H. Grubbs, D. A. Bansleben, M. W. Day, *Organometallics* **1998**, *17*, 3149.
[44] R. C. Fay, *Coord. Chem. Rev.* **1996**, *154*, 99.
[45] H. Gau, R. C. Fay, *Inorg. Chem.* **1990**, *29*, 4974.
[46] R. H. Holm, in *Dynamic Nuclear Magnetic Resonance Spectroscopy* (Eds.: L. M. Jackman, F. A. Cotton), Academic Press, New York, **1975**, chapter 9.
[47] D. G. Bickley, N. Serpone, *Inorg. Chem.* **1979**, *18*, 2200.
[48] G. Talarico, V. Busico, L. Cavallo, *Organometallics* **2004**, *23*, 5989.
[49] R. Furuyama, M. Mitani, J. Mohri, R. Mori, H. Tanaka, T. Fujita, *Macromolecules* **2005**, *38*, 1546.
[50] S. C. James, N. C. Norman, A. G. Orpen, *Acta Crystallogr., Sect. C* **1998**, *54*, 1216.
[51] R. K. J. Bott, D. L. Hughes, M. Schormann, M. Bochmann, S. J. Lancaster, *J. Organomet. Chem.* **2003**, *665*, 135.
[52] G. M. Sheldrick, *SHELX-86, Computer Program for Crystal Structure Determination*, University of Göttingen, Germany, **1986**.
[53] G. M. Sheldrick, *SHELX-97, Computer Program for Crystal Structure Refinement*, Univerity of Göttingen, Germany, **1997**.

Received: February 8, 2006
Published Online: June 7, 2006

 © 2006 Wiley-VCH Verlag GmbH & Co. KGaA, Weinheim 

DOI: 10.1002/ejic.200600213

# Characterization of a Byproduct in the Alkylation of DMIT: Alkylation on the Least Nucleophilic Sulfur Atom

**Bo M. Petersen,[a] Jens K. Bjernemose,[a] and Jan O. Jeppesen*[a]**

**Keywords:** Alkylation / DMIT / Nucleophilic substitution / Sulfur heterocycles

It is generally accepted that the alkylation of $(Et_4N)_2$-$[Zn(DMIT)_2]$ (**1**) is a very clean reaction that produces 4,5-bis(alkylthio)-1,3-dithiole-2-thiones **4** in very high yields. Although this procedure has been widely used, we have found that, in addition to the 4,5-bis(alkylthio)-1,3-dithiole-2-thione products **4**, highly unexpected byproducts are formed during the alkylation reaction in which the thione functionalities of DMIT in $(Et_4N)_2[Zn(DMIT)_2]$ (**1**) are alkylated instead of the more reactive thiolate groups. These byproducts were identified as a novel type of compounds, namely bis(2-alkylthio-1,3-dithiol-1-ium-4,5-dithiolato)zinc compounds **3**, being composed of two identical 2-alkylthio-1,3-dithiol-1-ium-4,5-dithiolate moieties coordinated to a single zinc(II) atom and were characterized by elemental analyses and different spectroscopic techniques as well as single-crystal X-ray structure analyses. A comparison of the physical properties of compounds **3** and $(Et_4N)_2[Zn(DMIT)_2]$ (**1**) has been carried out. The outcome of these investigations revealed significant differences in the physical properties of these two systems.

(© Wiley-VCH Verlag GmbH & Co. KGaA, 69451 Weinheim, Germany, 2006)

## Introduction

Among sulfur-containing heterocycles, derivatives of 2-thioxo-1,3-dithiole-4,5-dithiolate[1] (DMIT), have received a central position in organic and materials chemistry on account of the discovery of superconductivity in some of the metal complexes[2,3] of DMIT and its chalcogene analogs.[4] In addition, derivatives of DMIT are important building blocks for the synthesis[5] of tetrathiafulvalene[6–9] (TTF) systems, such as bis(ethylenedithio)tetrathiafulvalene (BEDT-TTF) which has been employed for the preparation of an extensive range of conducting[10] and superconducting materials.[11,12] DMIT is commonly isolated as its zinc chelate[13] in the form of bis(tetraethylammonium) bis(2-thioxo-1,3-dithiole-4,5-dithiolato)zincate $(Et_4N)_2[Zn(DMIT)_2]$ (**1**) and subsequent alkylation of the chelated thiolate groups can be accomplished with a variety of alkylating agents producing[14] in most cases 4,5-bis(alkylthio)-1,3-dithiole-2-thiones.

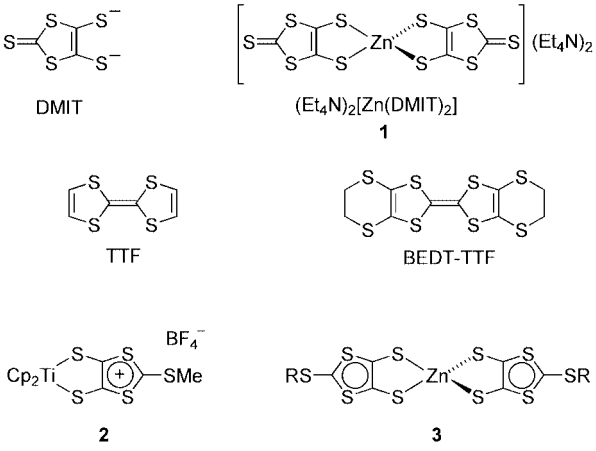


Although alkylation of the thione functionality of 1,3-dithiole-2-thione derivatives are favored by a gain in energy caused by aromatization of the 1,3-dithiole ring to a 1,3-dithiolium system simple alkylating agents, such as alkyl halides, are not sufficiently strong alkylating agents to accomplish this type of reaction for 4,5-bis(alkylthio)-1,3-dithiole-2-thiones. Instead, stronger alkylating agents, such as methyl fluorosulfate, methyl trifluorosulfonate, triethyloxonium tetrafluoroborate, triethyl orthoformate, boron trifluoride–diethyl ether, and dimethyl sulfate must be employed to produce[15] 2,4,5-tris(alkylthio)-1,3-dithiolium salts. Despite several reports on 2,4,5-tris(alkylthio)-1,3-dithiolium salts only one example[16] of a 2-alkylthio-1,3-dithiolium-4,5-dithiolate system – in the form of bis(cyclopentandienyl)(2-methylthio-1,3-dithiolium-4,5-dithiolato)-titanium(IV) (**2**) – has, to the best of our knowledge, been reported so far. In this paper, we present the synthesis and characterization of four systems **3** each containing two 2-alkylthio-1,3-dithiolium-4,5-dithiolate moieties coordinated to a single zinc(II) atom.

[a] Department of Chemistry, University of Southern Denmark, Odense University,
Campusvej 55, 5230 Odense M, Denmark
Fax: +45-66-15-87-80
E-mail: joj@chem.sdu.dk

 © 2006 Wiley-VCH Verlag GmbH & Co. KGaA, Weinheim 

## Results and Discussion

In most cases, the reaction between $(Et_4N)_2[Zn(DMIT)_2]$ (**1**) and an appropriate alkyl halide proceeds smoothly producing (Scheme 1) the corresponding 4,5-bis(alkylthio)-1,3-dithiole-2-thiones **4** in yields ranging from 79% to 94%.[14] In the present investigations, we have observed that, in addition to the desired 4,5-bis(alkylthio)-1,3-dithiole-2-thione products **4**, highly unexpected byproducts are formed during the reaction as a result of alkylation of the thione functionalities instead of the more reactive thiolate groups.

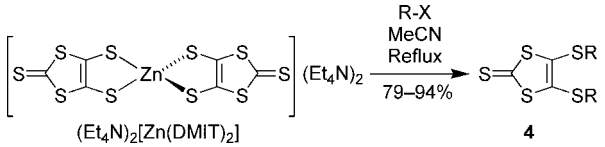


Scheme 1. Synthesis of 4,5-bis(alkylthio)-1,3-dithiole-2-thione products **4**.

In a typically alkylation experiment (Scheme 2), the zincate $(Et_4N)_2[Zn(DMIT)_2]$ (**1**) and the alkyl halide were heated under reflux in MeCN followed by an aqueous workup. Subsequent purification by means of column chromatographic purification afforded a broad yellow fraction together with a weaker blue fraction. The first yellow fraction contained 4,5-bis(alkylthio)-1,3-dithiole-2-thione **4**, whereas it was identified (vide infra) that the second blue band contained the unexpected bis(2-alkylthio-1,3-dithiol-1-ium-4,5-dithiolato)zinc compound **3** as byproduct.

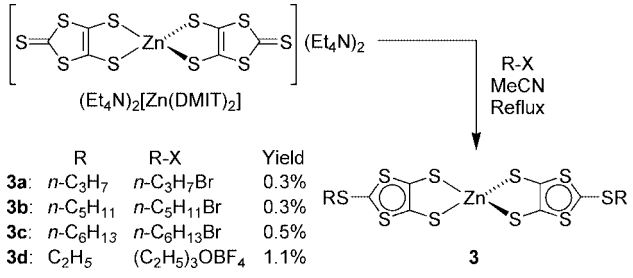


Scheme 2. Synthesis of bis(2-alkylthio-1,3-dithiol-1-ium-4,5-dithiolato)zinc compounds **3**.

As illustrated in Scheme 2, the isolated yields for **3a**–**c** are less than 0.5% when simple alkyl bromides are used as the alkylating agent. However, the yield can be improved by using the stronger alkylating agent triethyloxonium tetrafluoroborate. In this case, **3d** was isolated in a yield just above 1%. The fact that the yields of **3a**–**d** are very low can most likely be accounted for by the presence of the more nucleophilic thiolate groups in $(Et_4N)_2[Zn(DMIT)_2]$ (**1**) which prevents the formation of any larger amounts of **3**. Although **3a**–**d** were isolated in very low yields, the alkylation reactions can be carried out on a large scale allowing substantial amounts (50–150 mg) of **3a**–**d** to be isolated.

The unexpected byproducts **3a**–**d** were all isolated as purple solids. $^1H$ and $^{13}C$ NMR spectroscopy, high-resolution mass spectrometry, and elemental analyses all support the proposed structures of **3a**–**d**. Furthermore, the structures of **3a** and **3b** were unequivocally determined by single-crystal X-ray structure analyses.

### X-ray Crystallographic Studies

Crystals of **3a** and **3b** were grown by letting cyclohexane diffuse into $CHCl_3$ solutions of **3a** and **3b**, respectively. Both compounds show very strong pleochroism with colors changing between bright blue and dark red under polarized light. Crystallographic data were collected with a Nonius KappaCCD diffractometer with Mo-$K_\alpha$ radiation ($\lambda$ = 0.71073 Å) and the structures were solved by direct methods using SIR97[17] followed by refinement with SHELXL97.[18] Table 1 summarizes the crystallographic data obtained for compound **3a** and **3b**.

The two chelating planes form angles of 85.1(4)° in **3a** and 89.58(13)° in **3b** as compared to 83–85° between the chelating planes in $(Et_4N)_2[Zn(DMIT)_2]$ (**1**). The molecular structure of **3b** with a partial labeling scheme is shown in Figure 1a. In both structures Zn is tetrahedrally coordinated with distortions on account of the limited bite angle of the bis(thiolato) ligand. The coordination geometry closely resembles that of $(Et_4N)_2[Zn(DMIT)_2]$ (**1**). However, in the case of **3b**, there is no crystallographically imposed symmetry contrasting with the twofold axial symmetry observed in about half of the known structures related to $(Et_4N)_2[Zn(DMIT)_2]$ (**1**).[19] This lack of restraint makes DOQXOW[20] the best candidate for comparison as it too is unrestrained and its data collected at 150 K (see Table 2 for a comparison of average bond lengths).

There is no apparent change in Zn–S distances despite the reduced charge of the ligand. The only significant geometric difference between the new ligand and $(Et_4N)_2[Zn(DMIT)_2]$ (**1**) is the obvious lengthening of the C(3)–S(5) bond to a value somewhere between a double (DMIT) and single bond [S(5)–C(7)]. An accompanying shortening of S(3)–C(3) cannot be considered significant.

The packing of **3a** and **3b** is almost identical and the packing diagram of **3b** is depicted in Figure 1b. Both have an ordered alkyl chain in perfect staggered conformation in the plane of its attached dithiole ring. These ordered alkyl chains pack together with symmetry-equivalent copies to form layers parallel to the *ab* plane. The other alkyl chain is twisted and has bonds which are orthogonal to its attached dithiole ring. This twist results in a disorder that cannot readily be modeled wherefore large ADPs have been accepted instead. The disordered alkyl chains pack in a mixed layer in which one of the dithiole rings is sandwiched between the simple alkyl layers. The mixed layer is dominated by C–H···S interactions (minima are 2.9 Å and 2.7 Å in **3a** and **3b**, respectively) and S···S interactions (3.5 Å and 3.7 Å); **3b** shows an interaction between the C=C bond and a dithiole S atom (3.3 Å). The fact that the two dithiole rings are orthogonal in **3a** and **3b** precludes more than one alkyl chain from adopting the favorable all-staggered conformation. Thus, if both alkyl chains were supposed to

 © 2006 Wiley-VCH Verlag GmbH & Co. KGaA, Weinheim 

Table 1. Crystallograhpic data for **3a** and **3b**.

| | **3a** | **3b** |
|---|---|---|
| Empirical formula | $C_{12}H_{14}S_{10}Zn$ | $C_{16}H_{22}S_{10}Zn$ |
| $M$ [g·mol$^{-1}$] | 544.20 | 600.31 |
| $T$ [K] | 150(2) K | 150(2) |
| Crystal system | triclinic | triclinic |
| Space group | $P\bar{1}$ | $P\bar{1}$ |
| $a$ [Å] | 7.5896(5) | 7.70290(10) |
| $b$ [Å] | 8.0138(6) | 9.3494(2) |
| $c$ [Å] | 17.1292(15) | 18.1802(4) |
| $\alpha$ [°] | 87.400(3) | 83.9880(10) |
| $\beta$ [°] | 80.111(3) | 89.8730(10) |
| $\gamma$ [°] | 76.148(3) | 65.7950(10) |
| $V$ [Å$^3$] | 996.49(13) | 1186.42(4) |
| $Z$ | 2 | 2 |
| $D_x$ [g cm$^{-3}$] | 1.814 | 1.680 |
| $\mu$ [mm$^{-1}$] | 2.273 | 1.918 |
| $F$(000) | 552 | 616 |
| Crystal size [mm] | 0.21×0.10×0.02 | 0.26×0.20×0.17 |
| $\theta_{min}$ to $\theta_{max}$ [°] | 3.55 to 25.49 | 3.76 to 27.48 |
| Reflections collected/independent [$R$(int)] | 17153/3694 [0.1847] | 16596/5378 [0.0476] |
| $T_{max}/T_{min}$ | 0.952 and 0.652 | 0.721 and 0.611 |
| Data/restraints/parameters | 3694/ 6/208 | 5378/7/245 |
| GoF on $F^2$ | 1.169 | 1.052 |
| $R_1$ [$I>2\sigma(I)$] | 0.0983 | 0.057 |
| $wR_2$ (all data) | 0.2448 | 0.1562 |
| $\Delta\rho_{max/min}$ [e·Å$^{-3}$] | 1.109/–0.723 | 1.508/–1.472 |

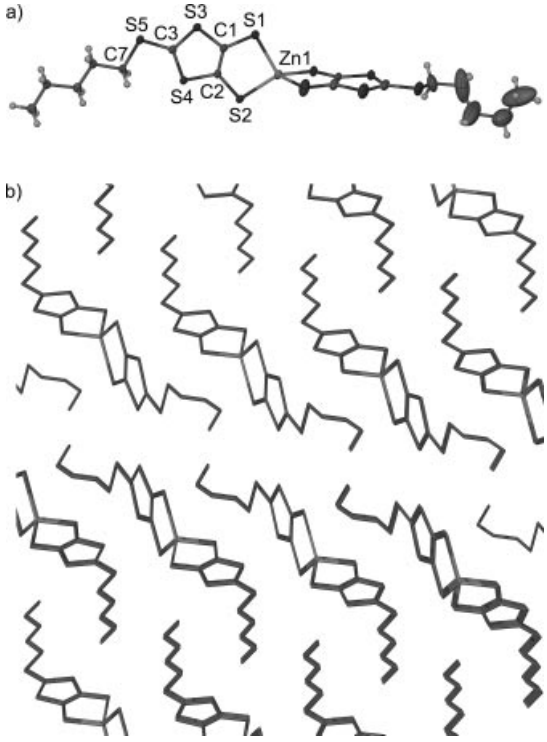


Figure 1. (a) Molecular structure of **3b** with the crystallographic numbering shown. (b) Packing of **3b** viewed along the *a* axis of the unit cell. Hydrogen atoms omitted for clarity.

adopt a staggered conformation in the plane of their attached dithiole rings, one of them would penetrate into the next layer of molecules. Consequently, one of the alkyl chains is forced to twist to avoid such an unfavorable penetration. The molecule essentially makes the best of a bad lot. Only one alkyl chain can adopt the favorable all-staggered conformation and at the same time remain close packed. The other alkyl chain must then fend for itself without packing too loosely. This can apparently be done in a number of only slightly differing ways resulting in extensive disorder.

Table 2. Average bond lengths [Å] for selected chemically equivalent bonds (a few chemically equivalent bonds do deviate more than 3 e.s.d.s). Data for $(Et_4N)_2[Zn(DMIT)_2]$ was taken from the literature.[20]

| | **3a** | **3b** | $(Et_4N)_2[Zn(DMIT)_2]$ (**1**) |
|---|---|---|---|
| Zn(1)–S(1) | 2.342(5) | 2.3410(12) | 2.345 |
| S(1)–C(1) | 1.724(16) | 1.728(4) | 1.735 |
| C(1)–C(2) | 1.42(2) | 1.372(7) | 1.362 |
| C(1)–S(3) | 1.722(16) | 1.739(4) | 1.753 |
| S(3)–C(3) | 1.707(16) | 1.688(5) | 1.721 |
| C(3)–S(5) | 1.701(16) | 1.721(5) | 1.661 |
| S(5)–C(7) | 1.811(17) | 1.818(7) | |

The absence of good hydrogen-bond donors (and hence of strong X–H···S hydrogen bond interactions) may account for the very different appearance of these compounds in the solid state (dark red) and in solution (dark blue).

## NMR Investigations

A comparison of the $^{13}C$ NMR spectra recorded of compound **3c** with those recorded of $(Et_4N)_2[Zn(DMIT)_2]$ and 4,5-bis(hexylthio)-1,3-dithiole-2-thione (**4c**) reveal significant chemical shift differences for the resonances associated with the carbon atoms in the 1,3-dithiole moiety. The chemical shift values summarized in Table 3, suggest that the 1,3-

 © 2006 Wiley-VCH Verlag GmbH & Co. KGaA, Weinheim 

dithiole moiety gains some aromatic character upon alkylation of the thione functionality. This observation is also supported by the bond lengths listed in Table 2.

Table 3. Selected $^{13}C$ NMR spectroscopic data ($\delta$ values in ppm) for $(Et_4N)_2[Zn(DMIT)_2]$ (**1**), 4,5-bis(hexylthio)-1,3-dithiole-2-thione (**4c**), and **3c** at 298 K.

| Compound | Solvent | C=C | S–C–S |
|---|---|---|---|
| $(Et_4N)_2[Zn(DMIT)_2]$ (**1**) | $CD_3CN$ | 136.4 | 210.2 |
| **4c** | $CDCl_3$ | 136.5 | 211.6 |
| **3c** | $CDCl_3$ | 158.5 | 168.5 |

### Photophysical Investigations

The photophysical properties have been studied in $CHCl_3$ solutions at room temperature using absorption spectroscopy. The UV/Vis spectroscopic data of **3a**–**d** are listed in Table 4, together with those of $(Et_4N)_2[Zn(DMIT)_2]$ (**1**) and 4,5-bis(pentylthio)-1,3-dithiole-2-thione (**4b**). A comparison of the absorption spectra of **3b**, $(Et_4N)_2[Zn(DMIT)_2]$ (**1**), and 4,5-bis(pentylthio)-1,3-dithiole-2-thione (**4b**) is displayed in Figure 2.

Table 4. UV/Vis absorption band maxima ($\lambda_{max}$) and molar extinction coefficients ($\varepsilon$) for compounds **1**, **3a**–**d**, and 4,5-bis(pentylthio)-1,3-dithiole-2-thione (**4b**) in $CHCl_3$ at room temperature.

| Compound | $\lambda_{max}$ [nm] ($\varepsilon$ [$M^{-1}$ $cm^{-1}$]) |
|---|---|
| $(Et_4N)_2[Zn(DMIT_2)]$ (**1**) | 315 ($26\cdot10^3$), 494 ($21\cdot10^3$) |
| **3a** | 308 ($20\cdot10^3$), 597 ($19\cdot10^3$) |
| **3b** | 308 ($20\cdot10^3$), 598 ($19\cdot10^3$) |
| **3c** | 308 ($21\cdot10^3$), 598 ($20\cdot10^3$) |
| **3d** | 308 ($19\cdot10^3$), 598 ($19\cdot10^3$) |
| **4b** | 278 ($6.4\cdot10^3$) 386 ($11\cdot10^3$) |

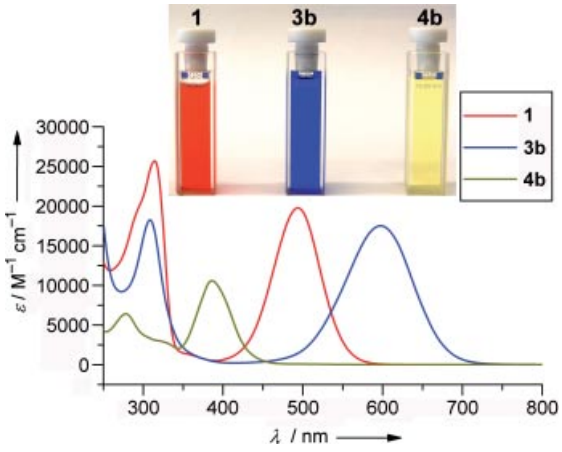


Figure 2. Absorption spectra recorded of $(Et_4N)_2[Zn(DMIT)_2]$ (**1**), **3b**, and 4,5-bis(pentylthio)-1,3-dithiole-2-thione (**4b**). The inset shows the actual color of the solutions of **1**, **3b**, and 4,5-bis(pentylthio)-1,3-dithiole-2-thione (**4b**).

The absorption spectrum of compound 4,5-bis(pentylthio)-1,3-dithiole-2-thione (**4b**) exhibits relative weak absorptions in the 250–450 nm region and no absorptions at $\lambda \geq 500$ nm, consistent with the observed pale yellow color (Figure 2, inset) of 4,5-bis(pentylthio)-1,3-dithiole-2-thione (**4b**) in $CHCl_3$. Dissolving $(Et_4N)_2[Zn(DMIT)_2]$ (**1**) in $CHCl_3$ produced a red solution (Figure 2, inset) with a concomitant strong absorption band being observed at $\lambda_{max}$ = 494 nm ($\varepsilon = 21\cdot10^3$ $M^{-1}$ $cm^{-1}$) in the absorption spectrum, whereas a blue solution (Figure 2, inset) was obtained upon dissolving **3b** in $CHCl_3$. The absorption spectrum recorded of this blue solution of **3b** shows a strong absorption band centered at $\lambda_{max} \approx 598$ nm ($\varepsilon = 20\cdot10^3$ $M^{-1}$ $cm^{-1}$). This band can most likely be assigned to an intramolecular charge transfer (CT) taking place between the relative electron-rich thiolate groups and the 1,3-dithiolium moieties present in **3b**. To support this hypothesis, we carried out some molecular modeling calculations.[21] For simplicity, these investigations were conducted on **3a** which indicate that the two degenerated HOMO and HOMO–1 orbitals (Figure 3) mainly are located on the thiolate groups and the C=C bond, whereas the degenerated LUMO and LUMO+1 orbitals are located on the 1,3-dithiolium moieties. This led us to conclude that the Zn atom has only a minor contribution to the 598 nm absorption band. Instead, this absorption band can most likely be ascribed to an intramolecular electron transfer occurring between the thiolate groups and the 1,3-dithiolium moieties.

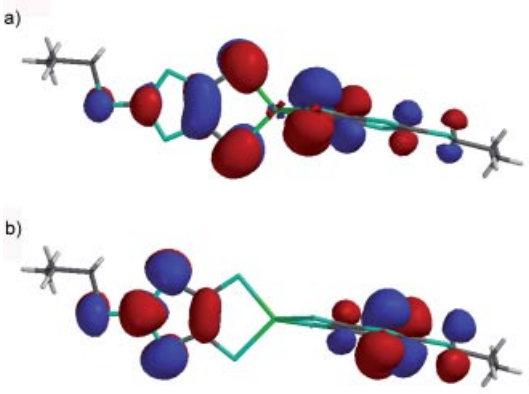


Figure 3. HOMO and LUMO orbitals of **3a**. (a) The degenerated HOMO and HOMO–1 orbitals are mainly located on the thiolate groups and the C=C bond, whereas (b) the degenerated LUMO and LUMO+1 orbitals are located on the 1,3-dithiolium moieties.

## Conclusions

In conclusion, we have shown that alkylation of $(Et_4N)_2[Zn(DMIT)_2]$ (**1**) not only affords 4,5-bis(alkylthio)-1,3-dithiole-2-thiones **4**, but also takes place at the less nucleophilic thione functionalities producing a novel class of compounds **3** in which a Zn atom is coordinated to two aromatic 2-alkylthio-1,3-dithiolium-4,5-dithiolate moieties. Formation of **3** can be detected by the naked eye since solutions of $(Et_4N)_2[Zn(DMIT)_2]$ (**1**) and **3** display different colors, red and blue, respectively. Although the isolated yields of **3** generally were low, it seems that the formation of **3** is a common feature upon alkylation of $(Et_4N)_2[Zn(DMIT)_2]$

 © 2006 Wiley-VCH Verlag GmbH & Co. KGaA, Weinheim 

(**1**). Consequently, it can be expected that the method can be extended to produce more elaborate derivatives of **3**. The findings reported herein are undoubtedly not unimportant given the amount of research devoted to DMIT and its corresponding metal complexes.

## Experimental Section

**General Procedures:** Chemicals and solvents were purchased from Aldrich and were used as received. Bis(tetraethylammonium) bis(2-thioxo-1,3-dithiole-4,5-dithiolato)zincate (**1**) was prepared according to a literature procedure.[13] Thin-layer chromatography (TLC) was carried out using aluminium sheets pre-coated with silica gel 60F (Merck 5554). The plates were inspected under UV light and, if required, developed in $I_2$ vapor. Column chromatography was carried out using silica gel 60F (Merck 9385, 0.040–0.063 mm). Melting points were determined with a Büchi melting point apparatus and are uncorrected. $^1$H (300 MHz) and $^{13}$C NMR (75 MHz) spectra were recorded at 298 K with a Gemini-300BB instrument, using tetramethylsilane (TMS) or the residual solvent as the internal standard. All chemical shifts are quoted on the $\delta$ scale, and all coupling constants (*J*) are expressed in Hertz (Hz). Samples were prepared using $CDCl_3$ or $CD_3CN$ purchased from Cambridge Isotope Labs. High-resolution Fourier transform matrix-assisted laser-desorption/ionization mass spectrometry (HiRes-FT-MALDI-MS) was performed with an IonSpec 4.7 Tesla Ultima Fourier Transform mass spectrometer, utilizing a 2,5-dihydroxybenzoic acid (DHB) matrix. Infrared (IR) spectra were recorded with a Perkin–Elmer 580 spectrophotometer, while absorption spectra (UV/Vis) were recorded with a Shimadazu 1601 spectrophotometer. Elemental analyses were performed by the Atlantic Microlab, Inc., Atlanta, Georgia.

**General Method for the Preparation of the Bis(2-alkylthio-1,3-dithiol-1-ium-4,5-dithiolato)zinc Compounds 3:** Bis(tetraethylammonium) bis(2-thioxo-1,3-dithiole-4,5-dithiolato)zincate (**1**) (21.5 g, 30 mmol) was suspended in anhydrous MeCN (200 mL), whereupon the appropriate alkyl bromide (120 mmol) was added. The dark red reaction mixture was heated under reflux for 1 h until no more starting material could be detected by TLC analysis ($R_f$ = 0.70; eluent: EtOAc/MeCN, 3:2). After being cooled to room temperature, the reaction mixture was concentrated in vacuo, and the resulting dark green oil was dissolved in $CH_2Cl_2$ and purified by column chromatography (750 mL of silica; diameter: 13.5 cm; eluent: $CH_2Cl_2$/petroleum ether, 1:9). The broad yellow band was collected, and the solvent evaporated to afford the 4,5-bis(alkylthio)-1,3-dithiole-2-thiones **4**. Thereafter, the eluent was changed to $CH_2Cl_2$ and a blue band was collected and concentrated to provide the title compounds **3a**–**c** as purple powders. Crystals suitable for X-ray analysis were prepared by diffusion of cyclohexane into $CHCl_3$ solutions of **3a** and **3b**, providing **3a** and **3b** as fine purple plates.

**Bis(2-propylthio-1,3-dithiol-1-ium-4,5-dithiolato)zinc (3a):** Yield: 46 mg (0.28%); $R_f$ = 0.45 (eluent: $CH_2Cl_2$); m.p.183–184 °C (dec.). $^1$H NMR (300 MHz, $CDCl_3$): $\delta$ = 1.09 (t, *J* = 7.2 Hz, 6 H), 1.84 (sext, *J* = 7.2 Hz, 4 H), 3.18 (t, *J* = 7.2 Hz, 4 H). UV/Vis ($CHCl_3$): $\lambda_{max}$ ($\varepsilon$) = 308 ($20{\cdot}10^3$ M$^{-1}$ cm$^{-1}$), 597 nm ($19{\cdot}10^3$ M$^{-1}$ cm$^{-1}$). IR (KBr): $\tilde{\nu}$ = 2960, 2923, 2866, 2013, 1363, 1285, 1013, 979, 906, 469 cm$^{-1}$. $C_{12}H_{14}S_{10}Zn$ (544.3): calcd. C 26.48, H 2.59, S 58.91; found C 26.15, H 2.55, S 58.39.

**Bis(2-pentylthio-1,3-dithiol-1-ium-4,5-dithiolato)zinc (3b):** Yield: 60 mg (0.33%); $R_f$ = 0.46 (eluent: $CH_2Cl_2$); m.p. 148.5–149.5 °C (dec.). $^1$H NMR (300 MHz, $CDCl_3$): $\delta$ = 0.93 (t, *J* = 7.1 Hz, 6 H), 1.34–1.46 (m, 8 H), 1.80 (q, *J* = 7.4 Hz, 4 H), 3.20 (t, *J* = 7.4 Hz, 4 H). $^{13}$C NMR (75 MHz, $CDCl_3$): $\delta$ = 14.0, 22.2, 28.2, 30.8, 40.4, 158.8 (one line for the trithiocarbonate carbon atom is missing). UV/Vis ($CHCl_3$): $\lambda_{max}$ ($\varepsilon$) = 308 ($20{\cdot}10^3$ M$^{-1}$ cm$^{-1}$), 598 nm ($19{\cdot}10^3$ M$^{-1}$ cm$^{-1}$). IR (KBr): $\tilde{\nu}$ = 2946, 2925, 2854, 2008, 1453, 1424, 1349, 1022, 903, 730, 467 cm$^{-1}$. HiRes-FT-MALDI-MS: calcd. for $C_{16}H_{22}S_{10}Zn$ [$M^{+\cdot}$] 597.8215; found: 597.8209. $C_{16}H_{22}S_{10}Zn$ (600.4): calcd. C 32.01, H 3.69, S 53.41; found C 32.01, H 3.60, S 53.60.

**Bis(2-hexylthio-1,3-dithiol-1-ium-4,5-dithiolato)zinc (3c):** Yield: 75 mg (0.49%); $R_f$ = 0.45 (eluent: $CH_2Cl_2$); m.p. 161.5–163.0 °C (dec.). $^1$H NMR (300 MHz, $CDCl_3$): $\delta$ = 0.91 (t, *J* = 6.7 Hz, 6 H), 1.25–1.50 (m, 12 H), 1.79 (q, *J* = 7.4 Hz, 4 H), 3.20 (t, *J* = 7.4 Hz, 4 H). $^{13}$C NMR (75 MHz, $CDCl_3$): $\delta$ = 14.1, 22.6, 28.3, 28.5, 31.2, 40.4, 158.5, 168.5 cm$^{-1}$. UV/Vis ($CHCl_3$): $\lambda_{max}$ ($\varepsilon$) = 308 ($21{\cdot}10^3$ M$^{-1}$ cm$^{-1}$), 598 nm ($20{\cdot}10^3$ M$^{-1}$ cm$^{-1}$). IR (KBr): $\tilde{\nu}$ = 2946, 2922, 2851, 2006, 1462, 1421, 1357, 1009, 904, 725, 465 cm$^{-1}$. HiRes-FT-MALDI-MS: calcd. for $C_{18}H_{26}S_{10}Zn$ [$M^{+\cdot}$] 625.8528; found 625.8522. $C_{18}H_{26}S_{10}Zn$ (628.4): calcd. C 34.40, H 4.17, S 51.02; found C 34.38 H 4.29, S 51.31.

**Bis(2-ethylthio-1,3-dithiol-1-ium-4,5-dithiolato)zinc (3d):** Bis(tetraethylammonium) bis(2-thioxo-1,3-dithiol-1-ylium-4,5-dithiolato)-zincat (**1**) (21.5 g, 30 mmol) was suspended in MeCN (200 mL), whereupon triethyloxonium tetraflouroborate (25.0 g, 120 mmol) was added. The dark red reaction mixture was heated under reflux for 5 min until no more starting material could be detected by TLC analysis ($R_f$ = 0.70; eluent: EtOAc/MeCN, 3:2). The reaction mixture was cooled to room temperature and concentrated in vacuo. The resulting dark red oil was dissolved in $CH_2Cl_2$. Column chromatography (800 mL of silica; diameter: 13.5 cm; eluent: $CH_2Cl_2$/petroleum ether, 1:4) gave a yellow band and a red band which was discarded. The bis(2-ethylthio-1,3-dithiol-1-ium-4,5-dithiolato)zinc (**3d**) was then eluted as a blue band with $CH_2Cl_2$. Removal of the solvent provided the title compound **3d** as a purple microcrystalline powder. Yield: 169 mg (1.1%); $R_f$ = 0.20 (eluent: $CH_2Cl_2$); m.p. 164.0–165.0 °C (dec.). $^1$H NMR (300 MHz, $CDCl_3$): $\delta$ = 1.49 (t, *J* = 7.4 Hz, 6 H), 3.22 (q, *J* = 7.4 Hz, 4 H). UV/Vis ($CHCl_3$): $\lambda_{max}$ ($\varepsilon$) = 308 ($19{\cdot}10^3$ M$^{-1}$ cm$^{-1}$), 598 nm ($19{\cdot}10^3$ M$^{-1}$ cm$^{-1}$). IR (KBr): $\tilde{\nu}$ = 2923, 2011, 1445, 1348, 1288, 1262, 1061, 1016, 905, 787, 466 cm$^{-1}$. HiRes-FT-MALDI-MS: $C_{10}H_{10}S_{10}Zn$ [$M^{+\cdot}$]: calcd. 513.7276; found 513.7265. $C_{10}H_{10}S_{10}Zn$ (516.23): calcd. C 23.27, H 1.95, S 62.11; found C 23.36, H 1.89, S 62.30.

**X-ray Crystallography:** Details are listed in Table 1. CCDC-601004 (**3a**) and -601005 (**3b**) contain the supplementary crystallographic data for this paper. These data can be obtained free of charge from The Cambridge Crystallographic Data Centre via www.ccdc.cam.ac.uk/data_request/cif.

## Acknowledgments

We are grateful to Professor Paul R. Raithby and Hazel Sparks, Department of Chemistry, University of Bath, for the use of diffractometers and help with some of the data collections. We gratefully acknowledge financial support provided by the Danish Natural Science Research Council through the SONS Programme of the European Science Foundation, which is also funded by the European Commission, Sixth Framwork Programme, the Danish Strategic Research Council through the Young Researchers Programme (#2117-05-0115), and the Danish Technical Research Council (#2058-03-0036).

 © 2006 Wiley-VCH Verlag GmbH & Co. KGaA, Weinheim 

[1] N. Svenstrup, J. Becher, *Synthesis* **1995**, 215–235.
[2] P. Cassoux, *Coord. Chem. Rev.* **1999**, *185–186*, 213–232.
[3] A. E. Pullen, R. Olk, *Coord. Chem. Rev.* **1999**, *188*, 211–262.
[4] R. Kato, *Chem. Rev.* **2004**, *104*, 5319–5346.
[5] N. Svenstrup, K. M. Rasmussen, T. K. Hansen, J. Becher, *Synthesis* **1994**, 809–812.
[6] M. R. Bryce, *J. Mater. Chem.* **2000**, *10*, 589–598.
[7] J. L. Segura, N. Martín, *Angew. Chem. Int. Ed.* **2001**, *40*, 1372–1409.
[8] J. O. Jeppesen, J. Becher, *Eur. J. Org. Chem.* **2003**, 3245–3266.
[9] J. O. Jeppesen, M. B. Nielsen, J. Becher, *Chem. Rev.* **2004**, *104*, 5115–5131.
[10] T. Otsubo, K. Takimiya, *Bull. Chem. Soc. Jpn.* **2004**, *77*, 43–58.
[11] R. P. Shibaeva, E. D. Yagubski, *Chem. Rev.* **2004**, *104*, 5347–5378.
[12] K. Miyagawa, K. Kanoda, A. Kawamoto, *Chem. Rev.* **2004**, *104*, 5635–5653.
[13] C. S. Wang, A. S. Batsanov, M. R. Bryce, J. A. K. Howard, *Synthesis* **1998**, 1615–1618.
[14] K. B. Simonsen, N. Svenstrup, J. Lau, O. Simonsen, P. Mørk, G. J. Kristensen, J. Becher, *Synthesis* **1996**, 407–418.
[15] See ref.[1] and references cited herein.
[16] K. Hartke, F. Rauschen, *Z. Naturforsch., Teil B* **1996**, *51*, 1611–1617.
[17] A. Altomare, M. C. Burla, M. Camalli, G. L. Cascarano, C. Giacovazzo, A. Guagliardi, A. G. G. Moliterni, G. Polidori, R. Spagna, *J. Appl. Crystallogr.* **1999**, *32*, 115–119.
[18] G. M. Sheldrick, *SHELX97 – Programs for Crystal Structure Analysis*, release 97-2, Institut für Anorganische Chemie der Universität Göttingen, Germany, **1998**.
[19] N. M. Comerlato, W. T. A. Harrison, R. A. Howie, J. Nicolson Low, A. C. Silvino, J. L. Wardell, S. M. S. V. Wardell, *Acta Crystallogr., Sect. C* **2002**, *58*, m105–m108.
[20] W. T. A. Harrison, R. A. Howie, J. L. Wardell, S. M. S. V. Wardell, N. M. Comerlato, L. A. S. Costa, A. C. Silvino, A. I. de Oliveira, R. M. Silva, *Polyhedron* **2000**, *19*, 821–827.
[21] Single-point energies for **3a** were calculated with B3LYP density functional theory, using the 6-31G* basis set.

Received: March 9, 2006
Published Online: June 6, 2006

 © 2006 Wiley-VCH Verlag GmbH & Co. KGaA, Weinheim 

DOI: 10.1002/ejic.200600258

# Synthesis, Crystal Structure, and Second-Order Nonlinear Optical Properties of Ruthenium(II) Complexes with Substituted Bipyridine and Phenylpyridine Ligands

**Laurence Labat,[a] Jean-François Lamère,[a] Isabelle Sasaki,[a] Pascal G. Lacroix,*[a] Laure Vendier,[a] Inge Asselberghs,[b] Javier Pérez-Moreno,[b] and Koen Clays[b]**

**Keywords:** Ligand design / Donor–acceptor systems / Ruthenium / Nonlinear optics / Density functional calculations

Two new ruthenium(II) complexes of formula $[Ru(bpy)_2(L^1)][PF_6]$ and $[Ru(bpy)_2(L^2)][PF_6]_2$ are reported. $HL^1$ is a (nitrophenyl)ethenyl-substituted phenylpyridine ligand, and $L^2$ is the bipyridine analogue of $HL^1$. The X-ray crystal structure of $[Ru(bpy)_2(L^1)][PF_6]$ has been solved, and the compound is found to crystallize in the monoclinic *C*2/*c* space group. The electronic spectrum of the cyclometalated derivative $[Ru(bpy)_2(L^1)][PF_6]$ exhibits a low-lying transition that is red-shifted from 454 to 546 nm relative to that of the parent bipyridine-based complex, which reveals an important charge-transfer character. To support this assumption, the nonlinear optical properties were investigated by the hyper-Rayleigh scattering technique and indicate a molecular static hyperpolarizability ($\beta_0$) equal to $230 \times 10^{-30}$ cm$^5$ esu$^{-1}$.
(© Wiley-VCH Verlag GmbH & Co. KGaA, 69451 Weinheim, Germany, 2006)

## Introduction

Molecules with π-conjugated electronic structures have been attracting considerable interest due to their potential nonlinear optical (NLO) properties and applications in optoelectronic and photonic devices.[1,2] While the first investigations were initially focused on purely organic systems,[3] the search for alternative organometallic and inorganic derivatives has gradually intensified in the last fifteen years.[4–6] Incorporation of metal atoms into π-conjugated systems introduces many new variables, such as diversity of oxidation states, intensely colored charge-transfers, additional magnetic capabilities, and a diversity of new topologies, which leads to NLO chromophores of much greater complexity than that of the first generation of "push-pull" organic molecules.[6]

For instance, ruthenium complexes have provided intriguing molecular materials with unusual electronic capabilities since the 1960s, in particular as mixed-valence $Ru^{II}Ru^{III}$ complexes.[7] In (pyridine)ruthenium(II) complexes, for example, the metal center is engaged in π-bonding with the organic ligating groups and can be involved in strongly allowed metal-to-ligand charge-transfer (MLCT), and hence provides various candidates for NLO applications. Indeed, ruthenium has led to the most investigated family of (pyridine)metal complexes in nonlinear optics.[8] The reasons for this interest are the possibility of designing various promising octupolar topologies,[9,10] and the observation of switchable NLO responses upon metal oxidation in some cases,[11] a possibility which could attract great interest in relation with the concept of molecular switches.[12,13]

In the last few years several cyclometalated counterparts of (polypyridine)ruthenium complexes have been prepared and their physical properties reported.[14–17] In fact, cyclometalated complexes have found widespread interest as species with promising properties in various research fields[15c] owing to the strong σ-donor ability of the cyclometalating ligand. Basically, replacement of a nitrogen donor by a formal carbanion donor drastically increases the electron density around the metal atom and the crystal-field strength.[14,15a] As a consequence, the d→π* back-donation is reinforced, which leads to a potential enhancement of the overall intramolecular charge transfer, a property which is highly desirable for the design of NLO chromophores. The enhancement of the donating capabilities of the ruthenium(II) center has been evidenced experimentally by the observation of intense charge-transfer properties in $Ru^{II}/Ru^{III}$ complexes with bis(cyclometalating) ligands,[15b,18] and by a shift of the value of the $Ru^{II}/Ru^{III}$ oxidation potential of about 900 mV upon replacement of one nitrogen atom by one carbon atom in tris(bipyridine)ruthenium(II)-like complexes.[14]

Recently, we have developed a new synthetic strategy aimed at providing an access to numerous phenylpyridine ligands substituted in *para* ($R^1$) and *meta* ($R^2$) positions with respect to the nitrogen atom (Scheme 1).[19] In the perspective of nonlinear optics, the presence of an acceptor (A) in the *meta* position is the most desirable to favor an intense

[a] Laboratoire de Chimie de Coordination du CNRS, 205 route de Narbonne, 31077 Toulouse, France
[b] Department of Chemistry, University of Leuven, Celestijnenlaan 200D, 3001 Leuven, Belgium

 © 2006 Wiley-VCH Verlag GmbH & Co. KGaA, Weinheim 

charge-transfer process from electron-rich metal–carbon moieties, as indicated in this scheme, and finally to provide a sizeable NLO response.

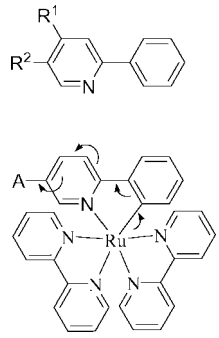

Scheme 1.

Following this idea, we report here our attempt to design a set of two (phenylpyridine and bipyridine)ruthenium complexes with potential MLCT capabilities. In the first section, their synthesis and characterizations will be presented. Then, the crystal structure of the cyclometalated complex will be discussed. Finally, the optical and nonlinear optical properties of both derivatives will be compared in relation to the enhanced "push-pull" character induced by the Ru–C linkage. The investigated molecules of formula $[Ru(bpy)_2(L^1)][PF_6]$ and $[Ru(bpy)_2(L^2)][PF_6]_2$ are shown in Scheme 2.

## Results and Discussion

### Synthesis and Characterization

Two methods for the synthesis of $HL^1$ and $L^2$, which contain the electron-withdrawing substituent $NO_2$, were envisioned: by condensing formylbipyridine or formyl(phenyl)pyridine with the appropriate phosphonate (method A) or by condensing the phosphonate **3a**,**b** derived from the bipyridine or the phenylpyridine with *p*-nitrobenzaldehyde (method B). Method B was chosen as the synthesis of 5-(bromomethyl)-2,2′-bipyridine (**2b**) from **1b**[20] has already been described[21] and was extended here to 5-methyl-2-phenylpyridine (**1a**). The first step involves the conversion of the methyl group to the corresponding bromomethyl group by treatment with *N*-bromosuccinimide (NBS) and azoisobutyronitrile (AIBN). The bromomethyl derivatives **2a**,**b** were then converted into the phosphonate derivatives **3a**,**b**.[22] The final step was the Wadsworth–Emmons reaction of compounds **3a**,**b** with the commercially available *p*-nitrobenzaldehyde, which leads to the styryl derivatives $HL^1$ and $L^2$ in 29% and 37% yields, respectively.[22] The double-bond linkages were confirmed to be (*E*) by $^1H$ NMR analysis based on the value of the $J_{CH=CH}$ coupling constant (ca. 16 Hz).

The syntheses of the two complexes are not similar. The tris(bipyridine) complex was obtained by the classical method, i.e., heating of 1 equiv. of $[Ru(bpy)_2]Cl_2$ with

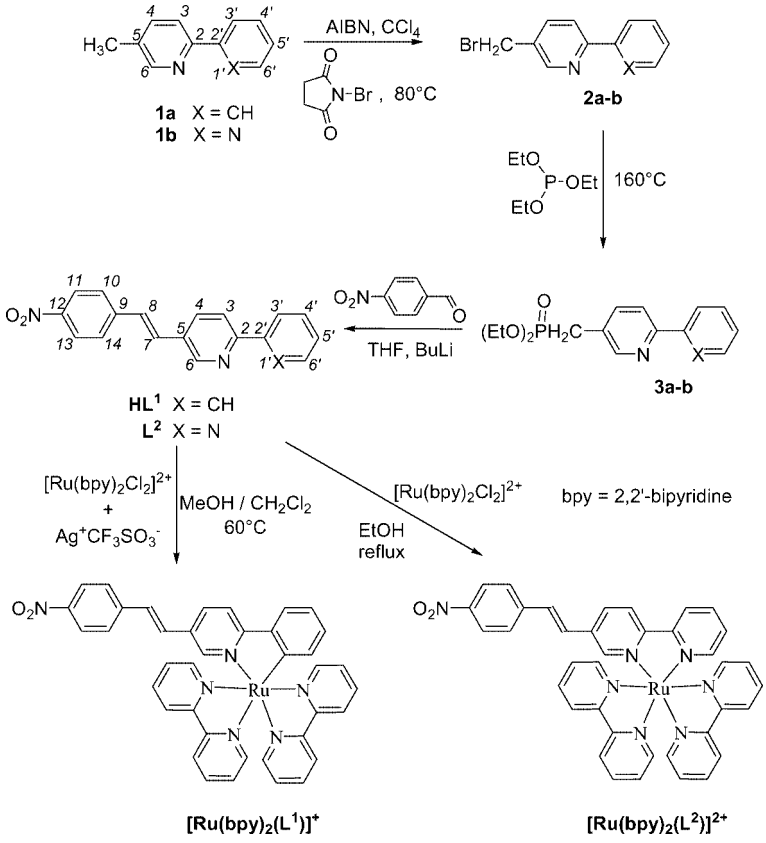


Scheme 2.

 © 2006 Wiley-VCH Verlag GmbH & Co. KGaA, Weinheim 

1 equiv. of $L^2$ in ethanol, whereas for the cyclometalated complex 1 equiv. of $[Ru(bpy)_2]Cl_2$ was treated with 5 equiv. of the phenylpyridine $HL^1$ in the presence of silver triflate.[19] The complexes were characterized by the usual methods. The labelling of the atoms is the one used for the X-ray structure. Characteristic peaks of cyclometalated compounds were observed in the NMR spectra of $[Ru(bpy)_2(L^1)][PF_6]$ and the peaks of the spectra were fully assigned.[14,23,24] Nevertheless, for complex $[Ru(bpy)_2(L^2)][PF_6]_2$, the unambiguous assignment of all the signals was not possible: since the electronic environments of numerous pyridine hydrogen atoms are nearly similar, their signals occur in a very narrow chemical-shift range.

## Structural Data

The crystallographic data are summarized in the Experimental Section, and the X-ray molecular structure of $[Ru(bpy)_2(L^1)][PF_6]$ is presented in Figures 1 and 2. The compound crystallizes in the monoclinic *C*2/*c* space group ($Z = 8$). The asymmetric unit cell (Figure 1) is built up from one ruthenium complex, one $PF_6^-$ anion, and one molecule of diethyl ether. In the crystal, $[Ru(bpy)_2(L^1)][PF_6]$ is organized in extended layers of complexes in the *bc* plane (Figure 2). The π-conjugated skeleton of the substituted phenylpyridine ligands lies parallel to the layers, the direction of highest polarizability (phenyl → $NO_2$) being roughly [001].

The ruthenium atom lies in a distorted octahedral environment. Metal–ligand bond lengths are presented in Table 1. Interestingly, and in contrast with previously reported X-ray data,[16] the Ru–C(1) distance of 2.033(4) Å is not significantly shortened with respect to the average Ru–N distance 2.036(4) Å observed for the bipyridine N(3), N(4) atoms. Nevertheless, a tendency for increased ruthenium–nitrogen bond lengths in the *trans* position with respect to the Ru–C bond is unambiguously seen [Ru–N(6) = 2.133(4) Å]. Along this line, the increase of this latter bond length is indeed the most noticeable geometrical change introduced in the coordination sphere of the metal atom by the presence of a carbon atom, in agreement with the

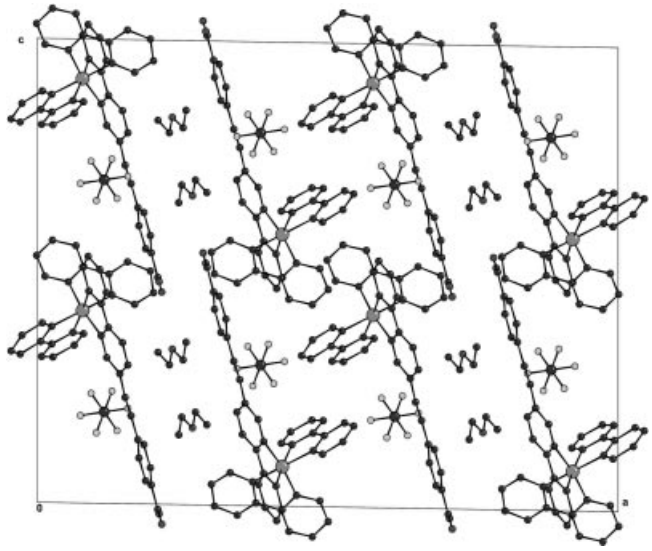

Figure 2. View of the crystal cell of $[Ru(bpy)_2(L^1)][PF_6]$ in the *ac* plane.

$[Ru(bpy)_2(nitrophenpy)]^+$ structure reported in the literature.[16] Another, more surprising, structural feature is the angle of 37.0(3)° observed between the phenyl group carrying the nitro substituent and the pyridine ring of the phenylpyridine ligand. This rotation suggests that the nitrophenyl group is not significantly involved in the charge-transfer process in the solid state. In order to verify whether the torsion arises from crystal packing or from intrinsic electronic effects, the gas-phase geometries of $[Ru(bpy)_2(L^1)][PF_6]$ and $[Ru(bpy)_2(L^2)][PF_6]_2$ were investigated within the framework of density functional theory (DFT).

The calculated coordination spheres are compared in Table 1. The tendency for slightly increases bond lengths obtained by DFT is observed here, as is the case in model Ru(phenpy) complexes (see Experimental Section). In the case of the bipyridine-based derivative, the six bond lengths are very similar, with an average value of 2.1175 Å. By contrast, the coordination sphere of the cyclometalated derivative exhibits the usual structural features of $[Ru(bpy)_2$-

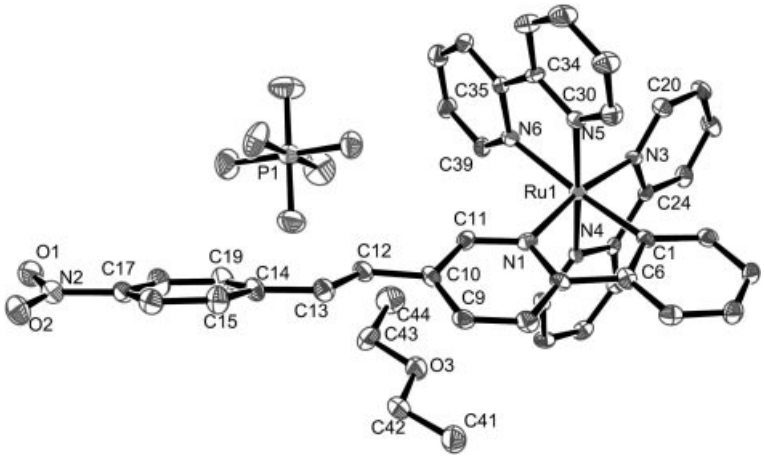


Figure 1. Asymmetric unit cell of $[Ru(bpy)_2(L^1)][PF_6]$. Hydrogen atoms are omitted for clarity.

 © 2006 Wiley-VCH Verlag GmbH & Co. KGaA, Weinheim 

Table 1. Ruthenium–ligand bond lengths [Å] in $[Ru(bpy)_2(L^1)][PF_6]$ and $[Ru(bpy)_2(L^2)][PF_6]_2$.

| | $[Ru(bpy)_2(L^1)][PF_6]$ | | $[Ru(bpy)_2(L^2)][PF_6]_2$ | |
|---|---|---|---|---|
| | X-ray | DFT | X-ray | DFT |
| Ru–C(1) | 2.033(4) | 2.049 | n.a. | 2.117 |
| Ru–N(1) | 2.072(3) | 2.131 | n.a. | 2.120 |
| Ru–N(3) | 2.033(3) | 2.088 | n.a. | 2.118 |
| Ru–N(4) | 2.039(4) | 2.096 | n.a. | 2.116 |
| Ru–N(5) | 2.068(4) | 2.124 | n.a. | 2.116 |
| Ru–N(6) | 2.133(4) | 2.233 | n.a. | 2.118 |

$(phenpy)]^+$ complexes, namely a shortening of the Ru–C bond (2.049 Å) and elongation of the Ru–N bond (2.233 Å) *trans* to the Ru–C bond. Importantly, the angles between the nitrophenyl and pyridine rings are 4.4° and 3.1° for $[Ru(bpy)_2(L^1)]^+$ and $[Ru(bpy)_2(L^2)]^{2+}$, respectively. This result suggests that, to a large extent, the torsion angle of 37° observed in the crystal structure arises from a solid-state effect and is not an intrinsic electronic behavior of the chromophores.

## Optical Properties

The UV/Vis spectra of $[Ru(bpy)_2(L^1)][PF_6]$ and $[Ru(bpy)_2(L^2)][PF_6]_2$ are shown in Figure 3. At first glance, both spectra are grossly similar and reveal three intense transitions located at 296 (65150), 370 (51850), and 546 (14500 $mol^{-1}\,L\,cm^{-1}$) nm for the cyclometalated complex, and at 288 (64850), 365 (44900), and 454 (12250 $mol^{-1}\,L\,cm^{-1}$) nm for the parent bipyridine-based derivative. It is interesting to note that the only significant difference in both spectra is a redshift of 92 nm (3711 $cm^{-1}$) observed for the low-lying transition depending on the presence of an Ru–N or Ru–C linkage. This considerable shift suggests that the low-energy transition is the main signature of the charge transfer arising between the ruthenium atom and the substituted bipyridine or phenylpyridine ligand.

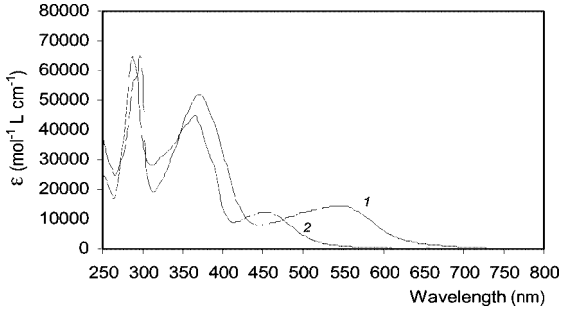


Figure 3. UV/Vis spectra of $[Ru(bpy)_2(L^1)][PF_6]$ (**1**) and $[Ru(bpy)_2(L^2)][PF_6]_2$ (**2**) recorded in acetonitrile.

In order to further analyze the nature of the electronic transitions of ruthenium complexes, the solvatochromic properties have been investigated. Solvatochromism is usually associated with a large dipole moment change upon electronic excitation, and is therefore an interesting probe of large charge-transfer capabilities. The absorption maxima recorded in solvents of different polarities are gathered in Table 2 and presented in Figure 4, where the energy transitions are drawn vs. the Reichardt solvent parameter $E_T^N$.[25] A first comparison conducted on the two transitions of the cyclometalated complex, located at 370 and 546 nm, confirms that the low-lying transition exhibits the largest solvatochromic shift (slope equal to 499 in Figure 4b, vs. 414 in Figure 4a). This is consistent with the anticipation of an intense charge-transfer effect associated with the low-lying transition of these ruthenium complexes. In a second comparison, the low-energy transitions are compared for $[Ru(bpy)_2(L^1)][PF_6]$ (Figure 4b) and the bipyridine-based $[Ru(bpy)_2(L^2)][PF_6]_2$ (Figure 4c). A reduction of the slope to 369 in Figure 4c clearly shows that the solvatochromic shift (and hence the charge transfer properties) are limited in $[Ru(bpy)_2(L^2)][PF_6]_2$. All together, these experimental data confirm the initial intuition that cyclometalated derivatives are promising candidates for the design of molecules with enhanced charge-transfer capabilities.

Table 2.Absorption maxima ($\lambda_{max}$ [nm]) of the lowest-energy optical transitions for $[Ru(bpy)_2(L^1)][PF_6]$ and $[Ru(bpy)_2(L^2)][PF_6]_2$ in solvents of different polarities.

| Solvent | $E_T^{N[a]}$ | $[Ru(bpy)_2(L^1)][PF_6]$ | | $[Ru(bpy)_2(L^2)][PF_6]_2$ | |
|---|---|---|---|---|---|
| MeOH | 0.765 | 369 | 547.0 | 361.5 | 453.0 |
| EtOH | 0.654 | 370.5 | 549.0 | 362.0 | 453.5 |
| 1-PrOH | 0.617 | 370.5 | 550.0 | 362.0 | 453.5 |
| 2-PrOH | 0.552 | 370 | 548.5 | 362.5 | 453.0 |
| MeCN | 0.472 | 372 | 550.0 | 365.0 | 454.0 |
| $CH_2Cl$ | 0.321 | 371.5 | 553.5 | 362.0 | 456.0 |
| CHCl3 | 0.259 | 372.5 | 555.5 | 365.5 | 456.5 |

[a] Reichardt parameter.

A theoretical support is provided from the calculated electronic spectra. Functionals specifically designed for TD-DFT calculations of electronic spectra (LB94, SOAP, GRAC) are not implemented in our version of Gaussian, therefore the spectra were calculated with ZINDO on the basis of the gas-phase DFT structures. The data are gathered in Table 3, where they are compared to the experimental values. There is an important blueshift in the computed wavelengths for both complexes. However, this seems to be a general tendency frequently observed in the calculated spectra of inorganic chromophores.[26] The fact that the magnitude of this shift is especially pronounced in the case of the low-energy transition of $[Ru(bpy)_2(L^1)][PF_6]$, which is assumed to arise from an intense metal–phenyl charge transfer, may be additionally related to an enhancement of the ruthenium–ligand distance within the DFT computation. Apart from these energy differences, a qualitative agreement between experiment and calculation is observed on two important points: (i) both complexes exhibit a very intense high-energy transition and a less intense one located at lower energy; (ii) while the high-energy transitions are grossly located at the same energy range in both derivatives, the low-lying transition is considerably red-shifted in the case of the cyclometalated compound.

To further understand the nature of the charge-transfer behavior, the low-lying transitions can be analyzed at the

 © 2006 Wiley-VCH Verlag GmbH & Co. KGaA, Weinheim 

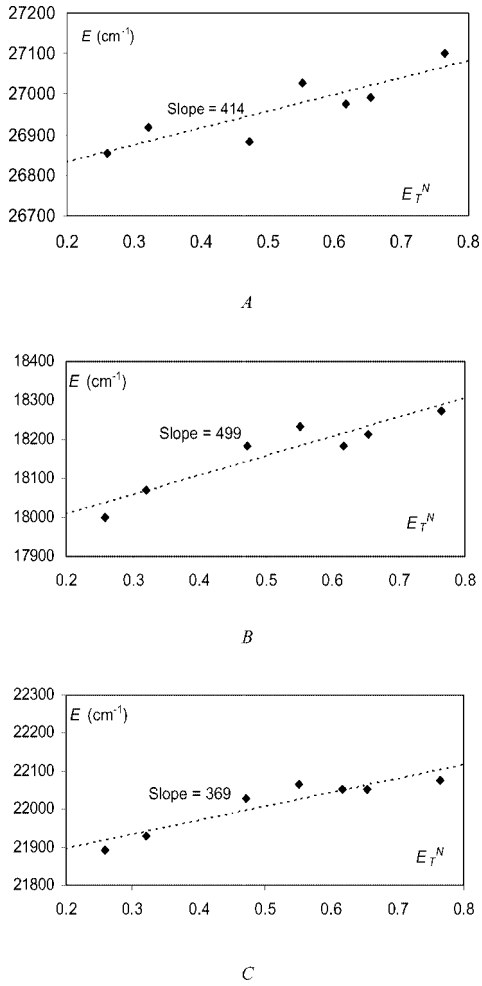


Figure 4. Absorption maxima [$cm^{-1}$] in solvents of different polarity (Reichardt constant $E_T^N$) for $[Ru(bpy)_2(L^1)][PF_6]$ [band at 370 (A) and 546 nm (B)] and for $[Ru(bpy)_2(L^2)][PF_6]_2$ [band at 454 nm (C)].

orbital level. In the case of $[Ru(bpy)_2(L^2)][PF_6]_2$, three dominant excitations contribute to the $1 \rightarrow 2$ transition (Table 3), which leads to 47% of the ground-state electron density in orbital 117. However, this orbital is located on the $L^2$ fragment only (98.1% of the electron density), which results in a ligand-to-ligand charge-transfer process. The contribution of the metal atom to $1 \rightarrow 2$ is weak and is provided by orbital 114 (70.0% centered on the ruthenium atom). In the case of $[Ru(bpy)_2(L^1)][PF_6]$, the dominant excitations involved in the $1 \rightarrow 7$ transition lead to the same 47% of ground-state electron density in orbital 117. However, and in striking contrast with $[Ru(bpy)_2(L^2)][PF_6]_2$, the electron density in orbital 117 is shared between $L^1$ (61.5%) and the ruthenium atom (31.8%). An additional donating contribution of the ruthenium atom is provided by orbital 115 (70.0% ruthenium-based). These differences lead to a significant enhancement of the donating character of the ruthenium atom in $[Ru(bpy)_2(L^1)][PF_6]$. The overall charge-transfer behavior associated with the $1 \rightarrow 7$ transition is shown in Figure 5, which clearly indicates that the ruthenium–phenyl fragment is deeply involved as the donating moiety of the chromophore.

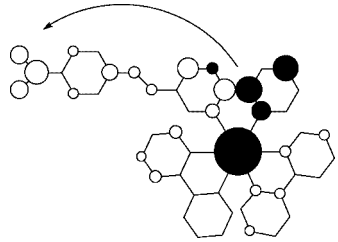

Figure 5. Charge transfer associated with the low-lying electronic transition of $[Ru(bpy)_2(L^1)][PF_6]$. White (black) contributions are indicative of increase (decrease) of electron density occurring upon electron transition.

Additional experimental evidence revealing the enhancement of the electron density around the metal center is provided by the electrochemical studies of the $Ru^{II}/Ru^{III}$ oxidation process. Single-electron waves are observed in both complexes, leading to $E^{1/2}$ values equal to 0.49 and 1.30 V for $[Ru(bpy)_2(L^1)][PF_6]$ and $[Ru(bpy)_2(L^2)][PF_6]_2$, respectively. The effect of cyclometalation on the stability of the $Ru^{III}$ state is illustrated by a cathodic shift of about 810 mV. This behavior demonstrates the strong σ-donating character of the anionic ligand, and the enhancement of the donating ability upon replacement of a nitrogen atom by a carbon atom, in the coordination sphere of the ruthenium atom.[19]

## Nonlinear Optical Properties

Before describing the NLO response of $[Ru(bpy)_2(L^1)][PF_6]$ and $[Ru(bpy)_2(L^2)][PF_6]_2$, it is important to emphasize that the values are not overestimated by multiphoton fluorescence. This is experimentally verified by performing femtosecond hyper-Rayleigh scattering (HRS) ex-

Table 3. Experimental and ZINDO calculated spectra for $[Ru(bpy)_2(L^1)][PF_6]$ and $[Ru(bpy)_2(L^2)][PF_6]_2$.

| Compound | UV/Vis spectra | | ZINDO data | | Assignment | Composition of CI expansion of the low-lying transitions[a] | Orbitals (% electron density on $Ru^{II}$) |
|---|---|---|---|---|---|---|---|
| | λ [nm] | ε [$mol^{-1}Lcm^{-1}$] | λ [nm] | *f* | | | |
| $[Ru(bpy)_2(L^1)][PF_6]$ | 546 | 14500 | 412 | 0.43 | $1 \rightarrow 7$ | 0.529 $\chi_{117\rightarrow123}$ – 0.436 $\chi_{117\rightarrow120}$ + 0.371 $\chi_{115\rightarrow119}$ | 119 (6.1%), 120 (0.3%), 123 (0.9%), 115 (70.0%), 117 (31.8%) |
| | 370 | 51900 | 344 | 0.72 | $1 \rightarrow 11$ | | |
| $[Ru(bpy)_2(L^2)][PF_6]_2$ | 454 | 12300 | 397 | 0.42 | $1 \rightarrow 2$ | 0.529 $\chi_{117\rightarrow118}$ – 0.454 $\chi_{114\rightarrow118}$ – 0.434 $\chi_{117\rightarrow119}$ | 118 (0.2%), 119 (4.2%), 114 (70.0%), 117 (1.6%) |
| | 364 | 44900 | 358 | 0.87 | $1 \rightarrow 10$ | | |

[a] Orbital 117 is the HOMO and orbital 118 the LUMO in both compounds.

 © 2006 Wiley-VCH Verlag GmbH & Co. KGaA, Weinheim 

periments as a function of modulation frequency.[27] The finite lifetime associated with any fluorescence results in a demodulation (reduction of amplitude) for higher frequencies.[28] As exemplified in Figure 6, no such demodulation is observed in the case of $[Ru(bpy)_2(L^1)][PF_6]$, thus implying that the HRS signal is not comprised of any multiphoton fluorescence contribution.[29]

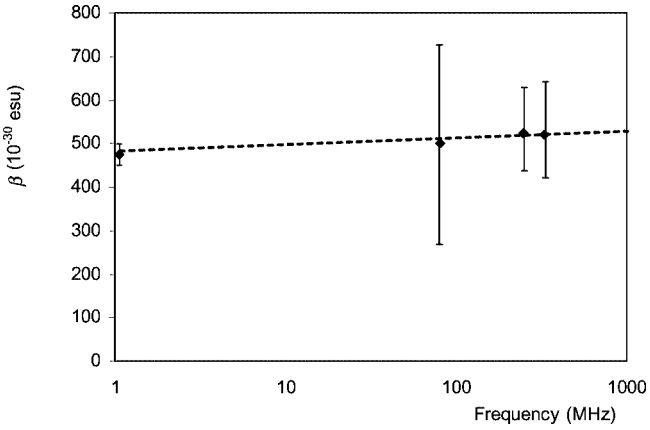


Figure 6. Experimental $\beta$ values as a function of modulation frequency for $[Ru(bpy)_2(L^1)][PF_6]$, showing the frequency-independent response of the multiphoton-fluorescence-free HRS signal.

The HRS data are gathered in Table 4 for both derivatives. In the case of $[Ru(bpy)_2(L^2)][PF_6]_2$, the detected signal falls within the limit of the uncertainty of the present HRS setup; therefore the hyperpolarizability was not determined with full accuracy and the reported data are the upper $\beta$ limit only. It must be pointed out that, as the second harmonic (400 nm) is close to the charge-transfer band located at 546 and 454 nm for $[Ru(bpy)_2(L^1)][PF_6]$ and $[Ru(bpy)_2(L^2)][PF_6]_2$, respectively, the experimental $\beta$ values are necessarily overestimated by resonance. Therefore, the parameter to take into account as the intrinsic hyperpolarizability (independent of the laser frequency) is $\beta_0$ (vide infra). An examination of Table 4 reveals a significant enhancement of the NLO response in the cyclometalated derivative, with an intrinsic hyperpolarizability equal to $230 \times 10^{-30}$ cm$^5$ esu$^{-1}$.

Table 4. Experimental hyperpolarizabilities [$10^{-30}$ cm$^5$ esu$^{-1}$] for the ruthenium complexes, recorded using the hyper-Rayleigh scattering method at 800 nm ($\beta$) and at zero frequency ($\beta_0$).

| | $\beta$ | $\beta_0$ |
|---|---|---|
| $[Ru(bpy)_2(L^1)][PF_6]$ | 500 | 230 (±50) |
| $[Ru(bpy)_2(L^2)][PF_6]_2$ | < 200 | < 40 |

## Conclusions

Two related ruthenium(II) complexes have been investigated to compare their MLCT capabilities and hence the hyperpolarizabilities of metal–phenylpyridine- vs. metal–bipyridine-based chromophores. We have reported on a set of computational, spectroscopic, electrochemical, and nonlinear optical measurements which all prove that a strongly enhanced MLCT behavior takes place in a cyclometalated derivative with respect to the parent metal–bipyridine molecule. The last few years have witnessed a growing interest in (pyridine)ruthenium(II) complexes in relation with the concept of NLO switching obtained by a redox effect.[11] It therefore seems promising to design such cyclometalated ruthenium chromophores that exhibit large NLO responses in addition to reversible and accessible redox properties. Along these lines, these complexes could undoubtedly attract potential interest from the perspective of materials science.

## Experimental Section

**Starting Materials and Equipment:** Reagents and solvents are commercially available and were used as received. **1a**,[19] **1b**,[20] and $[Ru(bpy)_2Cl_2]$[30] were prepared according to literature procedures. $^1$H and $^{13}$C NMR spectra were recorded at 298 K with a Bruker AM 250 spectrometer (250 MHz for $^1$H NMR and 62.9 MHz for $^{13}$C) or a Bruker Avance 500 spectrometer for 2D NMR. The atom labelling used for the assignment is given in Scheme 2. DCI and EI mass spectra were obtained with a Thermo Finnigan TSQ 7000 and FAB mass spectra were recorded with a quadrupolar Nermag R 10-10 instrument using an NBA matrix. UV/Vis spectra were recorded with a Hewlett Packard 8452A spectrophotometer. Elemental analyses were performed by the "Service de Microanalyses du Laboratoire de Chimie de Coordination" (Toulouse) with a Perkin–Elmer 2400 Serie II instrument. Cyclic voltammetry data were recorded with an Autolab PGSTAT 100 potentiostat, in acetonitrile using a Pt disk (1 mm diameter) as the working electrode, a Pt gauze as the auxiliary electrode, and SCE as the reference electrode. $n$Bu$_4$NPF$_6$ (0.1 M) was used as the supporting electrolyte (purum electrochemical grade Fluka, purified by sublimation). All voltammetric experiments were performed at ambient temperature in a home-made, airtight three-electrode cell connected to a vacuum/argon line. The solutions used for the electrochemical studies were typically $10^{-3}$ M in ruthenium complex. Prior to measurements, the solutions were deoxygenated by bubbling with argon gas for 15 min and the working electrode was polished with a polishing machine (Presi P230); during experiments, a stream of argon was passed over the solution.

**5-(Bromomethyl)-2-phenylpyridine (2a):** 5-Methyl-2-phenylpyridine (**1a**; 2.11 g, 12.5 mmol), NBS (2.22 g, 12.9 mmol), and AIBN (36 mg) were refluxed in dry $CCl_4$ (58 mL) for 2 h. After cooling, the suspension was filtered. The solvent was removed in vacuo and $n$-hexane (30 mL) was added to the remaining paste. The mixture was stirred in an ice bath for 1 h, whereupon a white fleecy precipitate appeared. This was filtered off to yield the pure product (837 mg, 27%). $^1$H NMR ($CDCl_3$): $\delta$ = 8.68 (s, 1 H), 7.97 (m, 2 H), 7.75 (m, 2 H), 7.45 (m, 3 H), 4.52 (s, 2 H) ppm. $C_{12}H_{10}BrN$ (248.1) + 0.25 $H_2O$: calcd. C 57.05, H 4.19, N 5.54; found C 56.81, H 3.95, N 5.57. DCI MS ($NH_3$): $m/z$ (%) = 248.1 (33), 250.1 (34) $[MH]^+$.

**5-(Bromomethyl)-2,2′-bipyridine (2b):** Same procedure as for the synthesis of **2a**, starting from 5-methyl-2,2′-bipyridine (**1b**). Yield: 68%. The $^1$H NMR spectrum is identical to those of previous reports.[31,32]

**Diethyl (2-Phenylpyridin-5-yl)methylphosphonate (3a):** Under nitrogen, **2a** (1.01 g, 4 mmol) was dissolved in triethyl phosphite (7 mL) and the mixture was refluxed for 1 d. After cooling, the brown oil was purified by two successive chromatographic separations on alumina (99% $CH_2Cl_2$/1% $CH_3OH$). Yellow oil (1.31 g, 87%). The

 © 2006 Wiley-VCH Verlag GmbH & Co. KGaA, Weinheim 

compound was used in the next step without further purification (triethyl phosphite could not be totally eliminated). $^1$H NMR ($CDCl_3$): $\delta$ = 8.55 (s, 1 H), 7.95 (m, 2 H), 7.70 (m, 2 H), 7.42 (m, 3 H), 4.05 (m, 4 H), 3.14 (d, $J_{H,P}$ = 21.6 Hz, 2 H), 1.26 (t, $J$ = 7.2 Hz, 6 H) ppm.

**Diethyl (2,2′-Bipyridin-5-yl)methylphosphonate (3b):** Same procedure as for the synthesis of **3a**, starting from **2b** and using 98% $CH_2Cl_2$/2% $CH_3OH$ as eluent for the two chromatographic separations. Some traces of triethyl phosphite remained and the compound was used without any further purification (Yield: 76%). $^1$H NMR ($CDCl_3$): $\delta$ = 8.66 (d, $J$ = 4.2 Hz, 1 H), 8.56 (s, 1 H), 8.36 (d, $J$ = 3.6 Hz, 1 H), 8.33 (d, $J$ = 3.8 Hz, 1 H), 7.80 (m, 2 H), 7.28 (m, 1 H), 4.08 (q, $J$ = 7 Hz, 4 H), 3.18 (d, $J_{H,P}$ = 22 Hz, 2 H), 1.35 (t, $J$ = 6.8 Hz, 6 H) ppm.

**5-(*p*-Nitrostyryl)-2-phenylpyridine ($HL^1$):** In a Schlenk flask, **3a** (348 mg, 1.14 mmol) was dissolved in THF (21 mL) and cooled in an ice bath. *n*-Butyllithium (1.6 M in hexane; 0.72 mL, 1.15 mmol) was added dropwise and the solution was stirred at room temperature for 1 h. A THF solution (6 mL) of *p*-nitrobenzaldehyde (174 mg, 1.15 mmol) was then added slowly and the color changed from yellow to brown. The mixture was refluxed for 3 h. After cooling to room temperature, the mixture was hydrolyzed with water (10 mL). The precipitate was filtered off, washed with diethyl ether, and purified by column chromatography on alumina (80% $CH_2Cl_2$/20% *n*-pentane). The product was recovered as a lemon-yellow powder (200 mg, 37% yield). $^1$H NMR ($CDCl_3$): $\delta$ = 8.86 (d, $J$ = 2.1 Hz, 1 H, H6), 8.27 (d, $J$ = 8.8 Hz, 2 H, H11, H13), 8.07 (dd, $J$ = 8.7 and 1.4 Hz, 2 H, H2′, H6′), 7.98 (dd, $J$ = 8.3 and 2.3 Hz, 1 H, H4), 7.81 (d, $J$ = 8.3 Hz, 1 H, H3), 7.70 (d, $J$ = 8.8 Hz, 2 H, H10, H14), 7.53 (dd, $J$ = 7.6 and 7.1 Hz, 2 H, H3′, H5′), 7.47 (t, $J$ = 7.3 Hz, 1 H, H4′), 7.31 (d, $J$ = 16.3 Hz, 1 H, H7), 7.26 (d, $J$ = 16.3 Hz, 1 H, H8) ppm. $^{13}$C NMR ($CDCl_3$): $\delta$ = 155.22 (C2), 148.96 (C6), 147.08 (C12), 143.18 (C9), 138.59 (C1′), 133.87 (C4), 130.36 (C5), 129.41 (C4′), 129.35 (C7), 128.91 (C5′), 127.89 (C8), 127.10 (C10, C14), 126.89 (C6′), 124.27 (C11, C13), 120.48 (C3) ppm. $C_{19}H_{14}N_2O_2$ (302.3): calcd. C 75.48, H 4.67, N 9.27; found C 75.14, H 4.59, N 9.12. DCI MS ($NH_3$): $m/z$ = 303 $[MH]^+$.

**5-(*p*-Nitrostyryl)-2,2′-bipyridine ($L^2$):** According to the procedure described above for the synthesis of $HL^1$, **3b** yielded compound $L^2$ (29% yield) after purification by chromatography on alumina with 0.5% MeOH in $CH_2Cl_2$. $^1$H NMR ($CDCl_3$): $\delta$ = 8.84 (d, $J$ = 1.9 Hz, 1 H, H6), 8.73 (ddd, $J$ = 4.7, 1.6 and 0.8 Hz, 1 H, H6′), 8.51 (d, $J$ = 8.3 Hz, 1 H, H3), 8.47 (d, $J$ = 8 Hz, 1 H, H3′), 8.29 (d, $J$ = 8.9 Hz, 2 H, H11, H13), 8.06 (dd, $J$ = 8.3 and 2.3 Hz, 1 H, H4), 7.88 (td, $J$ = 7.8 and 1.6 Hz, 1 H, H4′), 7.71 (d, $J$ = 8.8 Hz, 2 H, H10, H14), 7.37 (ddd, $J$ = 5.9; 4.9 and 1 Hz, 1 H, H5′), 7.34 (d, $J$ = 16.5 Hz, 1 H, H7), 7.30 (d, $J$ = 15.5 Hz, 1 H, H8) ppm. $^{13}$C NMR ($CDCl_3$): $\delta$ = 155.70 (C2), 155.32 (C2′), 149.15 (C6′), 148.56 (C6), 147.16 (C12), 143.07 (C9), 137.25 (C4′), 133.99 (C4), 131.99(C5) 129.27 (C7), 128.50 (C8), 127.18 (C10, C14), 124.28 (C11, C13), 124.05 (C5′), 121.36 (C3′), 121.22 (C3) ppm. $C_{18}H_{13}N_3O_2$ (303.3): calcd. C 71.28, H 4.32, N 13.85; found C 70.78, H 3.94, N 13.53. EI-MS: $m/z$ = 303 $[M]^+$.

**$[Ru(bpy)_2(L^1)][PF_6]$:** $[Ru(bpy)_2Cl_2]$ (40 mg, 0.073 mmol) and AgOTf (41 mg, 0.16 mmol) were added to a hot solution of $HL^1$ (110 mg, 0.36 mmol) in MeOH/$CH_2Cl_2$ (1:1, 10 mL) and the mixture was heated at 60 °C for 1 h. After cooling, the AgCl precipitate was filtered through glass fiber. The filtrate was concentrated and the crude product was purified by chromatography on alumina using two eluents: 0.5% MeOH in $CH_2Cl_2$ to recover the unreacted excess of ligand, then 3% MeOH in $CH_2Cl_2$ to isolate a dark-violet complex. A second chromatographic purification of this complex was carried out on alumina (3% MeOH in $CH_2Cl_2$) to yield the pure complex (15 mg, 24%). $^1$H NMR ($CD_3COCD_3$): $\delta$ = 8.78 (td, $J$ = 8.2 and 1.1 Hz, 1 H, H36), 8.68 (ddd, $J$ = 8.1, 1.1 and 0.6 Hz, 1 H, H33), 8.62 (ddd, $J$ = 8.2, 1.3 and 0.8 Hz, 1 H, H23), 8.60 (ddd, $J$ = 8.3, 1.2 and 0.8 Hz, 1 H, H26), 8.21 (d, $J$ = 8.8 Hz, 2 H, H16, H18), 8.24–8.17 (m, 3 H, H11, H37, H9), 8.16 (ddd, $J$ = 5.7, 1.5 and 0.7 Hz, 1 H, H30), 8.10 (ddd, $J$ = 5.4, 1.5 and 0.8 Hz, 1 H, H39), 8.06 (ddd, $J$ = 5.8, 1.4 and 0.8 Hz, 1 H, H29), 8.00–7.90 (m, 6 H, H22, H32, H8, H5, H27, H20), 7.71 (d, $J$ = 8.9 Hz, 2 H, H15, H19), 7.64 (ddd, $J$ = 7.6, 5.4 and 1.2 Hz, 1 H, H38), 7.42–7.38 (m, 3 H, H21, H31, H28), 7.29 (d, $J$ = 16.4 Hz, 1 H, H13), 7.21 (d, $J$ = 16.4 Hz, 1 H, H12), 6.92 (dt, $J$ = 7.2 and 1.2 Hz, 1 H, H4), 6.85 (dt, $J$ = 7.2 and 1.3 Hz, 1 H, H3), 6.52 (dd, $J$ = 7.4 and 1 Hz, 1 H, H2) ppm. $^{13}$C NMR ($CD_3COCD_3$): $\delta$ = 194.27 (C1), 167.39 (C7), 157.90 (C34), 157.09 (C24), 156.80 (C25), 155.34 (C35), 154.27 (C30), 150.56 (C29), 150.04 (C20) 149.95 (C8), 149.23 (C39), 147.10 (C17), 145.26 (C6), 143.34 (C14), 136.59 (C37), 135.37 (C2), 135.19 (C32), 134.04 (C22), 133.77 (C27), 132.22 (C9), 131.17 (C10), 128.62 (C3), 128.46 (C12), 127.98 (C13), 127.37 (C38), 127.27 (C15, C19), 126.57 (C21), 126.40 (C31), 126.27 (C28), 124.85 (C5), 123.97 (C16, C18), 123.63 (C33), 123.41 (C36), 123.09 (C26), 123.08 (C23), 120.95 (C4), 118.39 (C11) ppm. The metathesis was carried out as follows: the complex with the triflate counterion was dissolved in the minimum amount of methanol then a saturated aqueous solution of $NH_4PF_6$ was added until no more precipitation occurred. The precipitate was filtered off, rinsed with distilled water and dried under vacuum. $C_{39}H_{29}F_6N_6O_2PRu$ (859.7) + $H_2O$: calcd. C 52.41, H 3.50, N 9.40; found C 52.38, H 3.30, N 9.12. FAB-MS: $m/z$ = 715 $[M-PF_6]^+$.

**$[Ru(bpy)_2(L^2)][PF_6]_2$:** $L^2$ (48 mg, 0.158 mmol) was dissolved in EtOH (25 mL) under $N_2$ and the mixture heated to reflux. $[Ru(bpy)_2Cl_2]$ (85 mg, 0.158 mmol) was then added and the mixture refluxed for 3 h. After cooling in an ice bath, addition of $NH_4PF_6$ (saturated solution in water) led to the precipitation of the complex. The orange precipitate was filtered off, rinsed with water and diethyl ether, and dried in vacuo (115 mg). The compound was obtained by two successive chromatographic purifications on alumina ($CH_3CN$) and finally crystallization from acetone, which yielded the pure, brick-red complex (80 mg, 50%).$^1$H NMR ($CD_3COCD_3$): $\delta$ = 8.88–8.82 (m, 6 H, H8, H5, H26, H23, H33, H36), 8.60 (dd, $J$ = 8.5, 1.9 Hz, 1 H, H9), 8.30–8.06 (m, 7 H, H11, H4, H27, H25, H32, H37, H39), 8.24 (d, $J$ = 9 Hz, 2 H, H16, H18), 8.11 (dd, $J$ = 5.6, 7 Hz, 1 H, H2), 8.09–8.06 (m, 3 H, H29, H20, H30), 7.76 (d, $J$ = 8.8 Hz, 2 H, H15, H19), 7.64–7.58 (m, 5 H, H3, H31, H38, H21, H28), 7.57 (d, $J$ = 16.4 Hz, 1 H, H12), 7.21 (d, $J$ = 16.5 Hz, 1 H, H13) ppm. $^{13}$C NMR ($CD_3COCD_3$): $\delta$ = 157.33, 157.24, 157.21, 157.04, 156.30, 152.07 (C11), 151.92 and 151.83 and 151.75 (C2, C29, C20, C30), 151.05, 147.62, 142.51, 138.09, and 138.00 (C37, C32, C25, C27), 136.53, 133.84 (C9), 132.01 (C12), 127.93, 127.88, 127.86, 127.84 (C15, C19), 127.75, 127.04 (C13), 124.60, 124.50, 124.48, 124.44, 124.35, 124.04, 114.38 ppm. $C_{38}H_{29}F_{12}N_7O_2P_2Ru$ (1006.7): calcd. C 45.34, H 2.90, N 9.74; found C 45.19, H 2.77, N 9.49. FAB-MS: $m/z$ = 862 $[M-PF_6]^+$, 717 $[M-2PF_6]^+$.

**Crystallographic Studies:** Single crystals of $[Ru(bpy)_2(L^1)][PF_6]$ suitable for X-ray structure determination were grown by slow diffusion of diethyl ether into a concentrated solution of the complex in acetonitrile. Data were collected at 180 K with a Stoe Imaging Diffraction System (IPDS) equipped with a graphite-monochromated Mo-$K_\alpha$ radiation source ($\lambda$ = 0.71073 Å) and an Oxford Cryosystems Cryostream Cooler Device. Empirical absorption corrections were applied ($T_{min}$ = 0.811, $T_{max}$ = 0.963).[33] The structure was solved by direct methods using SIR92,[34] and refined by means of least-squares procedures on $F^2$ with the aid of the program

 © 2006 Wiley-VCH Verlag GmbH & Co. KGaA, Weinheim 

SHELXL97[35] included in the software package WinGX version 1.63.[36] Final unit-cell parameters were obtained by means of a least-squares refinement of a set of well-measured reflections. The atomic scattering factors were taken from the International Tables for X-ray Crystallography.[37] All non-hydrogen atoms were refined anisotropically, and in the last cycles of refinement a weighting scheme was used, where weights are calculated with the following formula: $w = 1/[\sigma^2(F_o^2) + (aP)^2 + bP]$ where $P = (F_o^2 + 2F_c^2)/3$. Further details are listed in Table 5. The drawing of the molecule was produced with the program ORTEP32[38] with 50% probability displacement ellipsoids for non-hydrogen atoms. CCDC-602439 contains the supplementary crystallographic data for this paper. These data can be obtained free of charge from The Cambridge Crystallographic Data Centre via www.ccdc.cam.ac.uk/data_request/cif.

Table 5. Crystal data for $[Ru(bpy)_2(L^1)][PF_6]$ (**1**).

| | |
|---|---|
| Empirical formula | $C_{29}H_{29}N_6O_2Ru{\cdot}C_4H_{10}O{\cdot}PF_6$ |
| Formula mass | 933.84 |
| Crystal size [mm] | $0.425 \times 0.125 \times 0.0625$ |
| Crystal system | monoclinic |
| Space group | *C*2/*c* |
| *a* [Å] | 32.661(7) |
| *b* [Å] | 9.5543(19) |
| *c* [Å] | 26.044(5) |
| $\beta$ [°] | 90.92(2) |
| *V* [Å$^3$] | 8126(3) |
| $\rho_{calcd.}$ [g cm$^{-3}$] | 1.527 |
| *T* [K] | 180 |
| $\mu$ (Mo-$K_\alpha$) [mm$^{-1}$] | 0.501 |
| Scan mode | φ |
| $\theta$ range [°] | $2.22 < \theta < 26.10$ |
| Measured reflections | 37036 |
| Independent reflections | 7614 |
| Observed reflections | 7614 |
| No of parameters | 543 |
| H atoms | calculated |
| $R_1$ | 0.0403 |
| $wR_2$ | 0.0491 |
| $\Delta\rho_{max}$ [e Å$^{-3}$] | 0.518 |
| $\Delta\rho_{min}$ [e Å$^{-3}$] | –1.143 |

**Theoretical Methods:** Gas-phase geometries for cations $[Ru(bpy)_2(L^1)]^+$ and $[Ru(bpy)_2(L^2)]^{2+}$ were fully optimized using the Gaussian-03 program package[39] within the framework of DFT at the B3LYP/6-31G*/LANL2DZ(Ru) level.[40,41] The starting metrical parameters for the calculations were taken from the present crystal structure of $[Ru(bpy)_2(L^1)]^+$. In the absence of a crystal structure for $[Ru(bpy)_2(L^2)][PF_6]_2$, the starting model was built up from the previously reported structures of $[Ru(bpy)_3][PF_6]_2$,[42] and 4-hydroxy-4′-nitrobiphenyl.[43] Due to the large size of the molecule, time-consuming vibrational analyses were not performed on the ruthenium complexes. Nevertheless, we checked that the DFT approach provides an accurate description of the molecular geometry in the case of the few previously reported $[Ru(bpy)(phenpy)]^+$ complexes,[16,19] although with a tendency for slightly inflated coordination spheres in the DFT-computed structures. The all-valence INDO (intermediate neglect of differential overlap) method[44] was employed to calculate the electronic transitions in order to analyze the origin of the charge transfer at the atomic level. Calculations were performed using the INDO/1 Hamiltonian incorporated in the commercially available MSI software package ZINDO.[45] The monoexcited configuration interaction (MECI) approximation was employed to describe the excited states. The 100 lowest-energy transitions between the 10 highest occupied molecular orbitals and the 10 lowest unoccupied ones were chosen to undergo CI mixing.

**NLO Measurements:** The experimental $\beta$ measurements were performed with the frequency-resolved femtosecond hyper-Rayleigh scattering (HRS)[46] technique at 800 nm. This setup was used as described before.[27] The samples were dissolved in acetonitrile and crystal violet (CV) dissolved in methanol was used as the reference ($\beta_{xxx} = 338 \times 10^{-30}$ cm$^5$ esu$^{-1}$).[27] A concentration series ws measured and the slopes of the linear fitting compared. The internal field-correction factor $[(n^2+2)/3]^3$, where *n* is the refractive index at the $Na_D$ line, was applied to correct for the difference in solvent ($n_{MeOH} = 1.328$ and $n_{MeCN} = 1.343$). The compounds were analyzed as dipolar structures with $C_{\infty v}$ symmetry. To correct for the difference in symmetry between the dipolar compound and octupolar reference, the following appropriate correction factors were used:[46b,47]

$$\beta^2_{zzz,dipole} = \frac{slope_{dipole}}{slope_{octupole}} \times \frac{28}{9} \times \frac{\left[\left(n^2_{MeOH}+2\right)/3\right]^6}{\left[\left(n^2_{MeCN}+2\right)/3\right]^6} \times \beta^2_{xxx,octupole} \quad (1)$$

The determined apparent hyperpolarizability was found to be independent of the modulation frequency, and the fluorescence-free hyperpolarizability was calculated by averaging the obtained hyperpolarizabilities at different modulation frequencies. Due to the weakness of the $2\omega$ light intensity in the HRS phenomenon, measurements have to be performed close to the resonance, which leads to an artificial enhancement of the NLO signal. In this case, the parameter of interest is the intrinsic hyperpolarizability $\beta_{(0)}$, which is independent of the laser frequency and can be estimated within a two-level model according to the following expressions:[48]

$$\beta_\omega = \frac{3e^2\hbar^2 f_{ge}(\Delta\mu)_{ge}}{2mE_{ge}^3} \times \frac{E_{ge}^4}{\left(E_{ge}^2 - (2\hbar\omega)^2\right)\left(E_{ge}^2 - (\hbar\omega)^2\right)} \quad (2)$$

$$\beta_{(0)} = \frac{3e^2\hbar^2 f_{ge}(\Delta\mu)_{ge}}{2mE_{ge}^3} \quad (3)$$

## Acknowledgments

The authors thank Dr. A. Sournia-Saquet for electrochemical measurements, CALMIP (Calcul en Midi Pyrénées, Toulouse) for parallel computation facilities, and a Programme d'Action Intégrée (PAI-Tournesol) for financial support.

[1] H. S. Nalwa, S. Miyata, *Nonlinear Optics of Organic Molecules and Polymers*, CRC Press, Boca Raton, FL, **1997**.
[2] M. G. Papadopoulos, J. Leszczynski, A. J. Sadlej, *Nonlinear Optical Properties of Matter: From Molecules to Condensed Phases*, Kluwer, Dordrecht, **2005**.
[3] D. S. Chema, J. Zyss, *Nonlinear Optical Properties of Organic Molecules and Crystals*, Academic Press, Orlando, FL, **1987**.
[4] a) S. Di Bella, *Chem. Soc. Rev.* **2001**, *30*, 355; b) P. G. Lacroix, *Eur. J. Inorg. Chem.* **2001**, 339.
[5] B. J. Coe, in *Comprehensive Coordination Chemistry II* (Eds.: J. A. McCleverty, T. J. Meyer), Elsevier Pergamon, Oxford, UK, **2004**, vol. 9, pp. 621.
[6] N. J. Long, *Angew. Chem. Int. Ed. Engl.* **1995**, *34*, 21.

 © 2006 Wiley-VCH Verlag GmbH & Co. KGaA, Weinheim 

[7] a) H. Taube, *Angew. Chem. Int. Ed. Engl.* **1984**, *23*, 329; b) C. Creutz, *Prog. Inorg. Chem.* **1983**, *30*, 1.
[8] H. Le Bozec, T. Renouard, *Eur. J. Inorg. Chem.* **2000**, 229.
[9] For an introduction of octupolar topologies, see: J. Zyss, I. Ledoux, *Chem. Rev.* **1994**, *94*, 77.
[10] For a recent review of ruthenium in octupolar geometry, see: H. Le Bozec, *Acc. Chem. Res.* **2005**, *38*, 691.
[11] a) B. J. Coe, S. Houbrechts, I. Asselberghs, A. Persoons, *Angew. Chem. Int. Ed.* **1999**, *38*, 366; b) B. J. Coe, *Chem. Eur. J.* **1999**, *5*, 2464.
[12] J. M. Lehn, *Supramolecular Chemistry – Concepts and Perspectives*, VCH, Weinheim, **1995**.
[13] M. D. Ward, *Chem. Soc. Rev.* **1995**, *24*, 121.
[14] E. C. Constable, J. M. Holmes, *J. Organomet. Chem.* **1986**, *301*, 203.
[15] a) J. P. Collin, M. Beley, J. P. Sauvage, F. Barigeletti, *Inorg. Chim. Acta* **1991**, *186*, 91; b) S. Chodorowski-Kimmes, M. Beley, J. P. Collin, J. P. Sauvage, *Tetrahedron Lett.* **1996**, *37*, 2963; c) F. Barigelletti, B. Ventura, J. P. Collin, R. Kayhanian, P. Gavina, J. P. Sauvage, *Eur. J. Inorg. Chem.* **2000**, 113.
[16] P. Reveco, R. H. Schmehl, W. R. Cherry, F. R. Fronczek, J. Selbin, *Inorg. Chem.* **1985**, *24*, 4078.
[17] A. J. Lees, *Chem. Rev.* **1987**, *87*, 711.
[18] S. Fraysse, C. Coudret, J. P. Launay, *J. Am. Chem. Soc.* **2003**, *125*, 5880.
[19] I. Sasaki, L. Vendier, A. Sournia-Saquet, P. G. Lacroix, *Eur. J. Inorg. Chem.*, DOI: 10.1002/ejic.200600359.
[20] T. L. J. Huang, D. G. Brewer, *Can. J. Chem.* **1981**, *59*, 1689.
[21] M. Heller, U. S. Schubert, *J. Org. Chem.* **2002**, *67*, 8269.
[22] O. Maury, J. P. Guégan, T. Renouard, A. Hilton, P. Dupau, N. Sandon, L. Toupet, H. Le Bozec, *New J. Chem.* **2001**, *25*, 1553.
[23] E. C. Constable, A. M. W. Cargill Thompson, S. Greulich, *J. Chem. Soc., Chem. Commun.* **1993**, 1444.
[24] P. Reveco, J. H. Medley, A. R. Garber, N. S. Bhacca, J. Selbin, *Inorg. Chem.* **1985**, *24*, 1096.
[25] C. Reichardt, E. Harbush-Görnet, *Liebigs Ann. Chem.* **1983**, *5*, 721.
[26] See for example: a) J. P. Costes, J. F. Lamère, C. Lepetit, P. G. Lacroix, F. Dahan, K. Nakatani, *Inorg. Chem.* **2005**, *44*, 1973; b) F. Averseng, P. G. Lacroix, I. Malfant, G. Lenoble, P. Cassoux, K. Nakatani, I. Maltey-Fanton, J. A. Delaire, A. Aukauloo, *Chem. Mater.* **1999**, *11*, 995; c) P. G. Lacroix, S. Di Bella, I. Ledoux, *Chem. Mater.* **1996**, *8*, 541.
[27] G. Olbrechts, R. Strobbe, K. Clays, A. Persoons, *Rev. Sci. Instrum.* **1998**, *69*, 2233.
[28] G. Olbrechts, K. Wostyn, K. Clays, A. Persoons, S. H. Kang, K. Kim, *Chem. Phys. Lett.* **1999**, *308*, 173.
[29] H. T. Uyeda, Y. Zhao, K. Wotsyn, I. Asselbergs, K. Clays, A. Persoons, M. J. Therien, *J. Am. Chem. Soc.* **2002**, *124*, 13806.
[30] G. Sprintschnik, H. W. Sprintschnik, P. P. Kirsch, D. G. Whitten, *J. Am. Chem. Soc.* **1977**, *99*, 4947.
[31] B. Imperiali, T. J. Prins, S. L. Fisher, *J. Org. Chem.* **1993**, *58*, 1613.
[32] J. Uenishi, T. Tanaka, K. Nishiwaki, S. Wakabayashi, S. Oae, H. Tsukube, *J. Org. Chem.* **1993**, *58*, 4382–4388.
[33] N. Walker, D. Stuart, *Acta Crystallogr. Sect. A* **1983**, *39*, 158.
[34] *SIR92 – A program for crystal structure solution*: A. Altomare, G. Cascarano, C. Giacovazzo, A. Guagliardi, *J. Appl. Crystallogr.* **1993**, *26*, 343.
[35] G. M. Sheldrick, *SHELX97 – Programs for Crystal Structure Analysis*, release 97-2, Institut für Anorganische Chemie der Universität, Göttingen, Germany, **1998**.
[36] *WINGX – Integrated System of Windows Programs for the Solution, Refinement and Analysis of Single Crystal X-ray Diffraction Data*, version 1.63: L. J. Farrugia, *J. Appl. Crystallogr.* **1999**, *32*, 837.
[37] *International Tables for X-ray Crystallography*, Kynoch Press, Birmingham, England, **1974**, vol. IV.
[38] *ORTEP3 for Windows*: L. J. Farrugia, *J. Appl. Crystallogr.* **1997**, *30*, 565.
[39] M. J. Frisch, G. W. Trucks, H. B. Schlegel, G. E. Scuseria, M. A. Robb, J. R. Cheeseman, J. A. Montgomery Jr, T. Vreven, K. N. Kudin, J. C. Burant, J. M. Millam, S. S. Iyengar, J. Tomasi, V. Barone, B. Mennucci, M. Cossi, G. Scalmani, N. Rega, G. A. Petersson, H. Nakatsuji, M. Hada, M. Ehara, K. Toyota, R. Fukuda, J. Hasegawa, M. Ishida, T. Nakajima, Y. Honda, O. Kitao, H. Nakai, M. Klene, X. Li, J. E. Knox, H. P. Hratchian, J. B. Cross, C. Adamo, J. Jaramillo, R. Gomperts, R. E. Stratmann, O. Yazyev, A. J. Austin, R. Cammi, C. Pomelli, J. W. Ochterski, P. Y. Ayala, K. Morokuma, G. A. Voth, P. Salvador, J. J. Dannenberg, V. G. Zakrzewski, S. Dapprich, A. D. Daniels, M. C. Strain, O. Farkas, D. K. Malick, A. D. Rabuck, K. Raghavachari, J. B. Foresman, J. V. Ortiz, Q. Cui, A. G. Baboul, S. Clifford, J. Cioslowski, B. B. Stefanov, G. Liu, A. Liashenko, P. Piskorz, I. Komaromi, R. L. Martin, D. J. Fox, T. Keith, M. A. Al-Laham, C. Y. Peng, A. Nanayakkara, M. Challacombe, P. M. W. Gill, B. Johnson, W. Chen, M. W. Wong, C. Gonzalez, J. A. Pople, *Gaussian 03*, revision B.05, Gaussian, Inc., Pittsburgh, PA, **2003**.
[40] a) A. D. Becke, *J. Chem. Phys.* **1993**, *98*, 564; b) C. Lee, W. Yang, R. G. Parr, *Phys. Rev. B* **1988**, *37*, 785.
[41] a) P. J. Hay, W. R. Wadt, *J. Chem. Phys.* **1985**, *82*, 270; b) P. J. Hay, W. R. Wadt, *J. Chem. Phys.* **1985**, *82*, 284; c) P. J. Hay, W. R. Wadt, *J. Chem. Phys.* **1985**, *82*, 299.
[42] D. P. Rillema, D. S. Jones, H. A. Levy, *J. Chem. Soc., Chem. Commun.* **1979**, 849.
[43] M. Muthuraman, R. Masse, J. F. Nicoud, G. R. Desiraju, *Chem. Mater.* **2001**, *13*, 1473.
[44] a) M. C. Zerner, G. Loew, R. Kirchner, U. Mueller-Westerhoff, *J. Am. Chem. Soc.* **1980**, *102*, 589; b) W. P. Anderson, D. Edwards, M. C. Zerner, *Inorg. Chem.* **1986**, *25*, 2728.
[45] *ZINDO*, release 96.0, Molecular Simulations Inc., Cambridge, U. K., **1996**.
[46] a) K. Clays, A. Persoons, *Phys. Rev. Lett.* **1991**, *66*, 2980; b) E. Hendrickx, K. Clays, A. Persoons, *Acc. Chem. Res.* **1998**, *31*, 675.
[47] S. J. Cyvin, J. E. Rauch, J. C. Decius, *J. Chem. Phys.* **1965**, *43*, 4083.
[48] a) J. L. Oudar, J. Chemla, *J. Chem. Phys.* **1977**, *66*, 2664; b) J. L. Oudar, *J. Chem. Phys.* **1977**, *67*, 446.

Received: March 24, 2006
Published Online: July 5, 2006

 © 2006 Wiley-VCH Verlag GmbH & Co. KGaA, Weinheim 

DOI: 10.1002/ejic.200600401

# Synthesis, Electronic Characterisation and Significant Second-Order Non-Linear Optical Responses of *meso*-Tetraphenylporphyrins and Their $Zn^{II}$ Complexes Carrying a Push or Pull Group in the β Pyrrolic Position

**Elisabetta Annoni,[a] Maddalena Pizzotti,*[a] Renato Ugo,[a] Silvio Quici,[b] Tamara Morotti,[b] Maurizio Bruschi,[c] and Patrizia Mussini[d]**

**Keywords:** Cyclic voltammetry / Nonlinear optics / Porphyrins / UV/Vis spectroscopy / Zinc

*On page 3860 of the original article*[1] *we reported:*

"The preparation of the phosphonium salt **16** was carried out, starting from the aldehyde **13**, according to the synthetic scheme reported in a preliminary communication by Bonfantini and Officer in 1993.[24] However the detailed experimental procedure was never published, hence a careful description of the synthesis and characterisation of intermediate porphyrins **14**, **15** and **16** is given in the Experimental Section."

*Recently, Prof. D. L. Officer informed us that the detailed experimental procedure for the synthesis of compound* ***16*** *was published in his article "Efficient synthesis of free-base 2-formyl-5,10,15,20-tetraarylporphyrins, their reduction and conversion to [(porphyrin-2-yl)methyl]phosphonium salts".*[2] *We apologize for any inconvenience this omission might have caused.*

*The Authors*

[1] E. Annoni, M. Pizzotti, R. Ugo, S. Quici, T. Morotti, M. Bruschi, P. Mussini, *Eur. J. Inorg. Chem.* **2005**, 3857–3874.
[2] E. E. Bonfantini, A. K. Burrell, W. M. Campbell, M. J. Crossley, J. J. Gosper, M. M. Harding, D. L. Officer, D. C. W. Reid, *J. Porphyrins Phthalocyanines* **2002**, *6*, 708–719.

Received: May 3, 2006
Published Online: May 24, 2006

[a] Dipartimento di Chimica Inorganica Metallorganica e Analitica dell'Università di Milano, Unità di Ricerca dell' INSTM, Centro di eccellenza CIMAINA dell'Università di Milano, e Istituto di Scienze e Tecnologie Molecolari del CNR (ISTM), Via G.Venezian 21, 20133 Milano, Italy
Fax: +39-02-50314405
E-mail: maddalena.pizzotti@unimi.it
[b] Istituto di Scienze e Tecnologie Molecolari del CNR (ISTM), Via Golgi 19, 20133 Milano, Italy
[c] Dipartimento di Biotecnologie e Bioscienze, Università di Milano Bicocca, Piazza della Scienza 2, 20126 Milano, Italy
[d] Dipartimento di Chimica Fisica ed Elettrochimica dell'Università di Milano, Via Golgi 19, 20133 Milano, Italy

 © 2006 Wiley-VCH Verlag GmbH & Co. KGaA, Weinheim 

EurJIC
European Journal of Inorganic Chemistry

Issue 16/2006

Pages 3121–3304

*Papers available ahead of print in Early View at www.interscience.wiley.com*

*Earliest available Table of Contents:*
*Automatically, free of charge by e-mail through*
*www.interscience.wiley.com/alerts*

## COVER PICTURE

**The cover picture shows** the structure of a chiral half-sandwich ruthenium(II) complex with the (4*S*)-2-[2-(diphenylphosphanyl)phenyl]-4-isopropyl-1,3-oxazoline ligand that catalyzes the asymmetric 1,3-dipolar cycloaddition reaction of nitrones with methacrolein. Catalyst precursors as well as dipolarophile or nitrone-containing intermediates have been isolated and spectroscopically and/or crystallographically characterized. Details are discussed in the article by D. Carmona, M. P. Lamata, L. A. Oro et al. on p. 3155 ff.

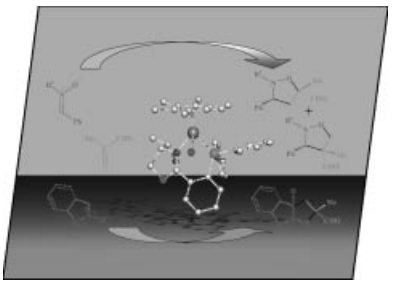

## MICROREVIEW

**Contents**

**3135** **D. J. Mindiola,* B. C. Bailey, F. Basuli**

What a Difference One Electron Makes! Generating Low-Coordinate Ti–C and V–C Multiply Bonded Frameworks Through One Electron Oxidatively Induced α-Hydrogen Abstractions

CHR CR CHR CR
‖ ||| ‖ |||
[Ti] [Ti] [V] [V]

**Keywords:** Alkylidenes / Alkylidynes / Titanium / Vanadium / Hydrogen abstraction / Oxidation

 © 2006 Wiley-VCH Verlag GmbH & Co. KGaA, Weinheim 

# SHORT COMMUNICATIONS


**3147** **L. Huerta, F. Romero-Sarria, O. Marie, C. Guillem, A. Beltrán, J. Latorre, D. Beltrán, P. Amorós***

One-Pot Synthesis of a New High-Aluminium-Content Super-Microporous Aluminosilicate

**Keywords:** Super-microporous / Aluminosilicates / Surfactants

**3152** **F. Mohr,* L. R. Falvello, M. Laguna***

A Silver(I) Coordination Polymer Containing Tridentate *N*- and *P*-Coordinating 1,3,5-Triaza-7-phosphaadamantane (PTA) Ligands

**Keywords:** Silver / Coordination polymer / Phosphane / Self-assembly


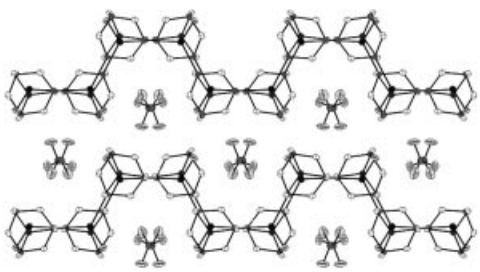

# FULL PAPERS


**3155** **D. Carmona*, M. P. Lamata,* F. Viguri, J. Ferrer, N. García, F. J. Lahoz, M. L. Martín, L. A. Oro***

Chiral Half-Sandwich Ruthenium(II) Complexes as Catalysts in 1,3-Dipolar Cycloaddition Reactions of Nitrones with Methacrolein

**Keywords:** Asymmetric catalysis / Cycloadditions / Ruthenium / Phosphanyloxazolines / Half-sandwich complexes


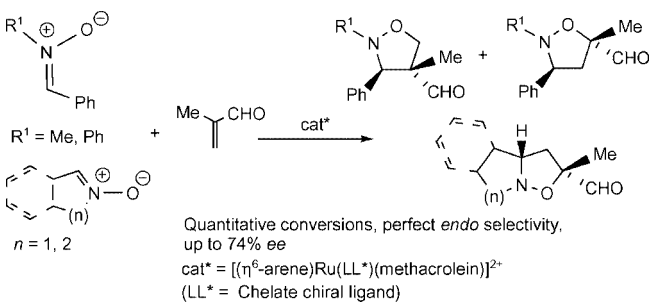



**3167** **P. Biscarini,* M. Benedetti, R. Kuroda, F. Ferranti***

Transfer of Chirality in Complexes with $D_3$ Symmetry: Kinetics of the Formation Reaction of Chiral Tris[*O*,*O*′-bis(2-methylbutyl)dithiophosphato]chromium(III) Complexes (Λ,Δ)-[Cr{(±)-Mebdtp}$_3$], Δ-(+)$_{589}$- and Λ-(−)$_{589}$-[Cr{(+)-(*S*)(*S*)-Mebdtp}$_3$]

**Keywords:** Chirality / Circular dichroism kinetics / UV-Vis spectroscopy / Dithiophosphate / Chromium complexes


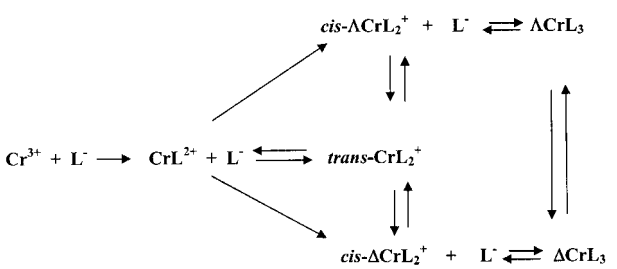

**3177** **M. A. M. Abu-Youssef,* A. Escuer, V. Langer**

Synthesis, Structure, and Magnetic Behavior of Two New 1D Polymeric Manganese Azido Complexes

**Keywords:** Manganese / Coordination polymers / Azido complexes / Aqua complexes / Magnetic properties

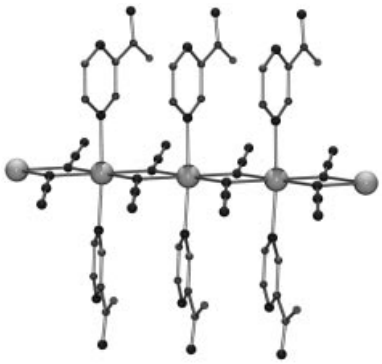

**3185** **G. Q. Wu, L. Y. Wang, D. G. Evans, X. Duan***

Layered Double Hydroxides Containing Intercalated Zinc Sulfide Nanoparticles: Synthesis and Characterization

**Keywords:** Layered compounds / Intercalations / Zinc complex / Organic–inorganic hybrid composites / ZnS nanoparticles

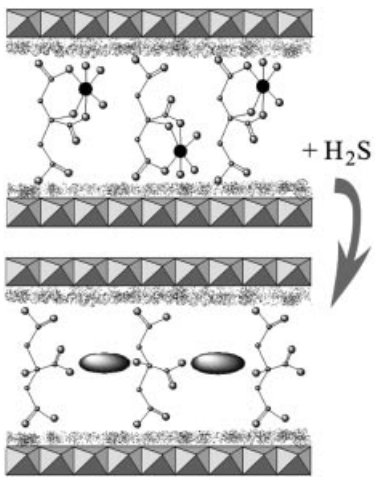


**3197** **L. Cerasino,* G. Natile**

Platinum Complexes with One Monodentate Ligand (1-Methylbenzimidazole or Antiviral Ribavirin) Flanked by Two *cis*-$NMe_2$ Groups: Informative Models for Assessing Interligand Interactions

**Keywords:** Platinum / Pentamethyldiethylenetriamine / 1-Methylbenzimidazole / Ribavirin / Interligand interactions

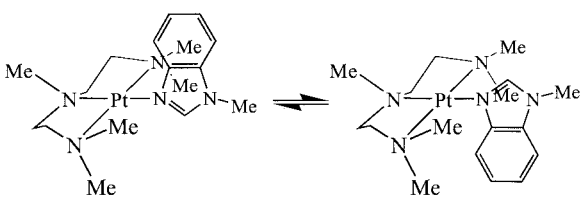

*endo* *exo*

**3204** **L.-C. Song,* J.-H. Ge, X.-G. Zhang, Y. Liu, Q.-M. Hu**

Methoxyphenyl-Functionalized Diiron Azadithiolates as Models for the Active Site of Fe-Only Hydrogenases: Synthesis, Structures, and Biomimetic $H_2$ Evolution

**Keywords:** Biomimetic chemistry / Diiron azadithiolate / Iron-only hydrogenases / Structural elucidation / Catalytic $H_2$ evolution

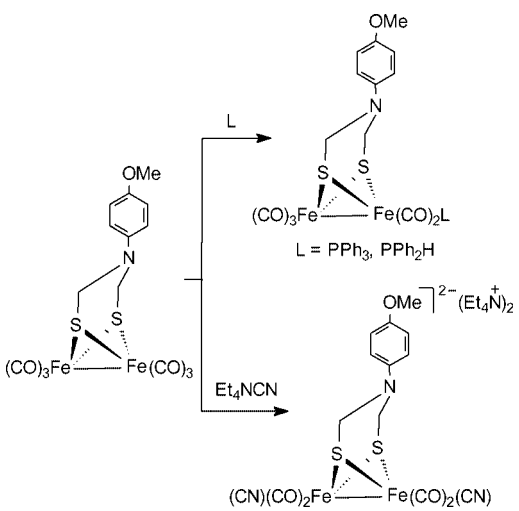


 © 2006 Wiley-VCH Verlag GmbH & Co. KGaA, Weinheim 

**3211** **Y. Sarazin, S. J. Coles, D. L. Hughes, M. B. Hursthouse, M. Bochmann***

Cationic Brønsted Acids for the Preparation of $Sn^{IV}$ Salts: Synthesis and Characterisation of $[Ph_3Sn(OEt_2)][H_2N\{B(C_6F_5)_3\}_2]$, $[Sn(NMe_2)_3(HNMe_2)_2][B(C_6F_5)_4]$ and $[Me_3Sn(HNMe_2)_2][B(C_6F_5)_4]$

**Keywords:** Tin / Cations / N ligands / Anions

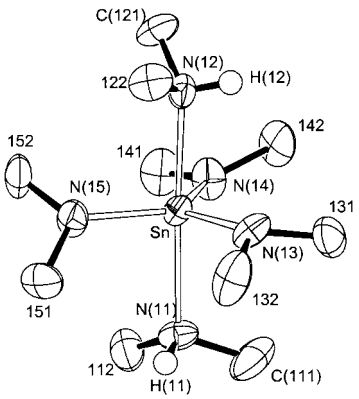


**3221** **H. Gao, C. Ye, R. W. Winter, G. L. Gard, M. E. Sitzmann, J. M. Shreeve***

Pentafluorosulfanyl ($SF_5$) Containing Energetic Salts

**Keywords:** Ionic liquids / Pentafluorosulfanylnitramide / Quaternization / Salts / Heats of formation / Energetic materials

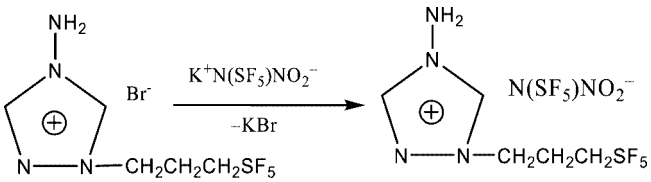


**3227** **A. Peña, J. Gutiérrez,* I. G. de Muro, J. Campo, J. M. Barandiarán, T. Rojo**

Correlation Between Structure and Magnetic and Magnetotransport Properties of $La_{0.7}Pb_{0.3}(Mn_{1-x}Co_x)O_3$ ($0.1 \leq x \leq 0.3$) CMR Manganites

**Keywords:** Manganites / Crystal structure / Magnetic properties / Magnetoresistance / Metal–insulator transition / Perovskite phases

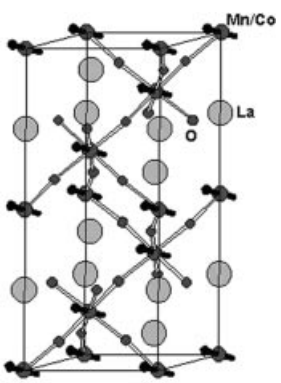


**3236** **T. Yamaguchi, K. Harada, Y. Sunatsuki, M. Kojima,* K. Nakajima, N. Matsumoto**

A Ruthenium(II) Complex with a Tripodal Ligand Containing Three Imidazole Groups

**Keywords:** Ruthenium / Redox chemistry / Chirality / Schiff bases / N ligands / Tripodal ligands

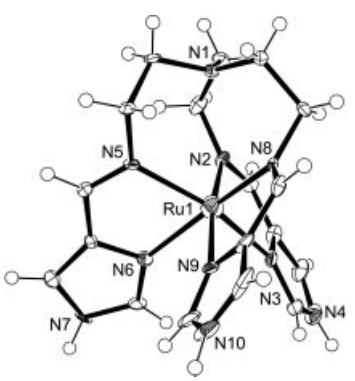


 © 2006 Wiley-VCH Verlag GmbH & Co. KGaA, Weinheim 

**3244** **C. Ma,* Q. Zhang**

A Supramolecular Assembly of Organotin Complexes: Syntheses, Characterization and Crystal Structures of Organotin Complexes with *meso*-2,3-Dimercaptosuccinic Acid

**Keywords:** S ligands / Self-assembly / Supramolecular chemistry / Tin

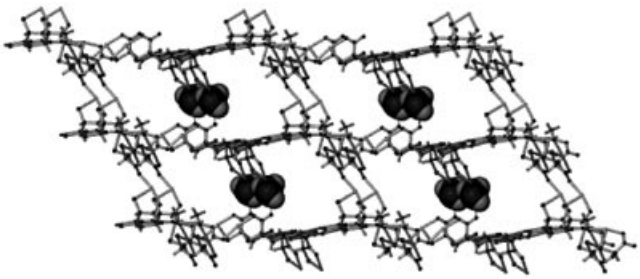

**3255** **R. H. Herber,* I. Nowik, V. Kahlenberg, H. Kopacka, H. Schottenberger**

Metal Atom Vibrational Amplitudes in Decamethylferrocene and Related Organometallics

**Keywords:** Sandwich complexes / Iron / Vibrational amplitudes / Mössbauer spectroscopy / Isotopic enrichment

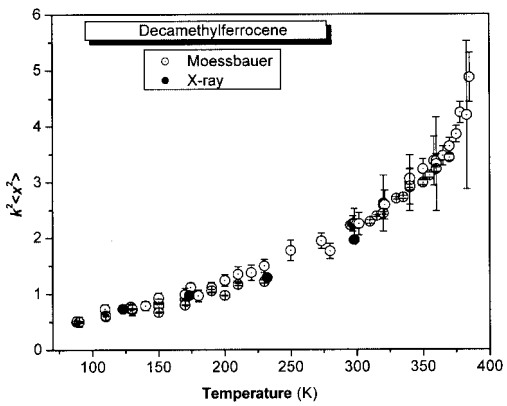


**3261** **P. Gao, Y. Xie,* Z. Li**

Controlling the Size of $BaF_2$ Nanocubes from 1000 to 10 nm

**Keywords:** $BaF_2$ Nanocubes / Nanostructures / Electron diffraction / X-ray diffraction

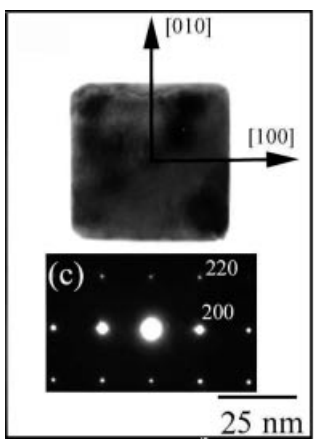


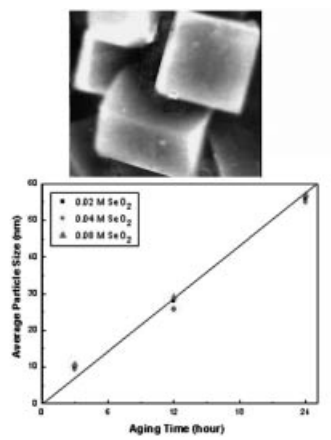


**3266** **I. L. Fedushkin,* M. Hummert, H. Schumann**

Molecular Structures and NMR Studies of Lithium and Germanium(II) Complexes of a New Chelating Amido−Imino Ligand Obtained by Addition of *n*BuLi to 1,2-Bis(arylimino)acenaphthene

**Keywords:** Lithium / N ligands / Germanium / Structure elucidation

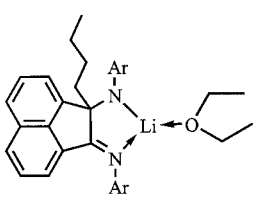


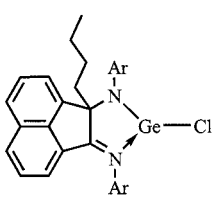


 © 2006 Wiley-VCH Verlag GmbH & Co. KGaA, Weinheim 

**3274** **J.-Q. Wang, C.-X. Ren, G.-X. Jin***

A Route to Multi-Clusters Containing Half-Sandwich Rh and Ir Complexes of Chelating 1,2-Dicarba-*closo*-dodecaborane(12)-1,2-dithiolate Ligands

**Keywords:** Iridium / Rhodium / Carboranes / N ligands / Cluster compounds

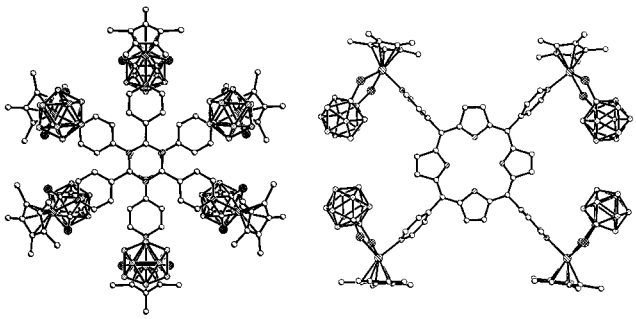

**3283** **M. Puchberger, F. R. Kogler, M. Jupa, S. Gross, H. Fric, G. Kickelbick, U. Schubert***

Can the Clusters $Zr_6O_4(OH)_4(OOCR)_{12}$ and $[Zr_6O_4(OH)_4(OOCR)_{12}]_2$ Be Converted into Each Other?

**Keywords:** Zirconium / Zirconium oxo cluster / Hafnium oxo cluster / Metal carboxylate / Ligand exchange

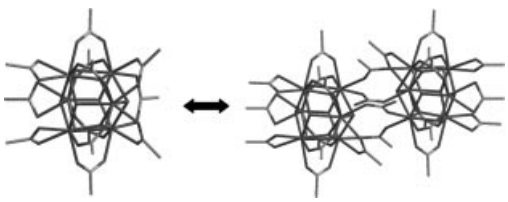

**3294** **I. Sasaki,* L. Vendier, A. Sournia-Saquet, P. G. Lacroix**

Facile Synthesis of Cyclometalated Ruthenium Complexes with Substituted Phenylpyridines

**Keywords:** Metallacycles / N ligands / Ruthenium

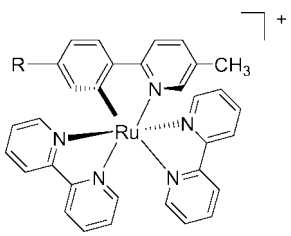

 © 2006 Wiley-VCH Verlag GmbH & Co. KGaA, Weinheim 

DOI: 10.1002/ejic.200600316

# What a Difference One Electron Makes! Generating Low-Coordinate Ti–C and V–C Multiply Bonded Frameworks through One Electron Oxidatively Induced α-Hydrogen Abstractions

**Daniel J. Mindiola,*[a] Brad C. Bailey,[a] and Falguni Basuli[a]**

**Keywords:** Alkylidenes / Alkylidynes / Titanium / Vanadium / Hydrogen abstraction / Oxidation

Low-coordinate, high oxidation state titanium and vanadium complexes containing terminal metal–carbon multiply bonded functionalities have been prepared directly or indirectly through one electron oxidatively induced α-hydrogen abstraction reactions. This synthetic approach offers a mild entry to reactive M=C and M≡C motifs, and does not depend on external stimulants such as heat, light or base to promote the α-hydrogen-abstraction step. In addition, this strategic protocol avoids the use of powerful electrophiles, thus generating terminal and nucleophilic M–C multiple bonds in low-coordination environments. In some cases terminal alkylidenes containing β-hydrogen atoms can also be introduced through this route. This microreview surveys the synthesis and chemistry surrounding isolable titanium and vanadium complexes bearing terminal alkylidene and alkylidyne ligands. Particular emphasis will be placed on the synthesis of the high oxidation state M–C multiple bond.

(© Wiley-VCH Verlag GmbH & Co. KGaA, 69451 Weinheim, Germany, 2006)

## Introduction

Metal–carbon multiple bonds are an important functionality given their utilization in important industrial processes such as metathesis, in particular cross-metathesis, ring-closing metathesis, ring-opening metathesis, ring-opening metathesis polymerization, acyclic diene metathesis polymerization, acetylene polymerization, and Wittig-type (alternatively referred to as group-transfer) reactions.[1] Seminal papers and reviews by Chauvin,[2] Grubbs,[3] and Schrock[4] exemplify both the fundamental and practical use of the M–C multiple bond. The combination of their efforts clearly portray how critical fundamental research addressing the bonding and structure of the M–C linkage can rapidly evolve into a more applied area of chemistry such as catalysis.[1,3,4] Consequently, a cascade of applications such as the synthesis of pharmaceutical fine chemicals, natural products, and the formation of polymers have evolved from a fundamental study involving the M–C multiple bond.[1,3,4] Not surprisingly, the contribution by Chauvin, Grubbs, and Schrock resulted in their winning of the 2005 Nobel Prize in Chemistry.[5]

Extensive reviews covering advances in the field of metal–carbon multiple bonds have been published,[3,4,6] with one of the most comprehensive reviews for high oxidation state transition-metal alkylidenes and alkylidynes being published in 2002 by R. R. Schrock.[4c] For this reason, we will limit our attention to the synthesis and chemistry of high oxidation state alkylidenes and alkylidynes of group 4 and 5 transition metals, since in recent years there has been a dramatic advancement in this group of elements.[4c] More specifically, we will discuss only compounds which have been fully characterized, and that invoke a nucleophilic or "Schrock-like" M–C multiply bonded linkage. We refer the reader to comprehensive reviews discussing the "in situ" preparation of alkylidenes.[1f,6] This microreview will focus on the synthesis, structure, and small-molecule chemistry invoking alkylidene and alkylidyne ligands of group 4 and 5 transition metals, in particular the lighter 3d congeners for each group. Catalytic reactions will not be covered in this review, nor the synthesis and chemistry of bridging alkylidenes or alkylidynes. Given the extensive literature covering this popular field, we apologize in advance for any omission of relevant work pertaining to the subject we are discussing.

[a] Department of Chemistry, Indiana University, Bloomington, Indiana 47405
E-mail: mindiola@indiana.edu

**MICROREVIEWS:** This feature introduces the readers to the authors' research through a concise overview of the selected topic. Reference to important work from others in the field is included.

 © 2006 Wiley-VCH Verlag GmbH & Co. KGaA, Weinheim 

### Synthesis of Group 4 and 5 High Oxidation State Alkylidenes

High oxidation state transition-metal alkylidenes are commonly prepared through an α-hydrogen-abstraction route with the first prototypical examples $(t\mathrm{BuCH_2})_3$-Ta=CH*t*Bu[7] and $(\eta^5\text{-}C_5H_5)_2$Ta=$CHCH_3$[8] being reported by Schrock. For instance, $d^0$ metal complexes containing an alkyl group can often be subjected to heat or light [Equation (1)], sterically imposing Lewis bases [Equation (2)], or Brønsted bases [Equation (3)] to assist in the α-hydrogen abstraction or deprotonation of the alkyl α-hydrogen.[4]

$$L_mM^n(CH_2R)_2 \xrightarrow{\Delta \text{ or } h\nu} L_mM^n{=}CHR + CH_3R \quad (1)$$

$$L_mM^n(CH_2R)_2 \xrightarrow{x\ PR_3} L_mM^n{=}CHR(PR_3)_x + CH_3R \quad (2)$$

$$L_mM^n(CH_2R)X \xrightarrow{2\ Base} L_mM^n{=}CHR(Base) + HX(Base) \quad (3)$$

In most cases, the Lewis base is often restricted to non-nucleophilic reagents such as bulky amides, neutral amines, phospha-ylides, in order to avoid displacement of the alkyl and subsequent redox chemistry from taking place.[4] In addition, the metal–alkyl ligand must lack β-hydrogen atoms, albeit with some exceptions, in order to avoid β-hydrogen-elimination or -abstraction pathways.[4] Alternate routes to the M=C linkage involve the in situ $2e^-$ reduction reactions of diazoalkanes, "$CH_2$" group-transfer reactions using phosphoranes such as $Ph_3P{=}CH_2$ [Equation (4)],[9] or two-electron reduction reactions to promote α-hydrogen elimination [Equation (5)].[10]

$$LM^n(LG) \xrightarrow{\text{"CHR"}} L_mM^{n+2}(CHR) + LG \quad (4)$$
LG = leaving group

$$LM^n(CH_2R)X_2 \xrightarrow[-2X^-]{x\ PR_3,\ +2e^-} L_mM^n(CHR)(H)(PR_3)_x \quad (5)$$
$X^-$ = halide or pseudohalide

Another elegant and rare transformation leading to alkylidene formation is the isomerization of terminal and 1,2-disubstituted olefins using low-valent metal centers [Equation (6)].[4c,11] The microscopic reverse, rearrangement of an alkylidene to an olefin, is not surprising given the intrinsic instability of β-hydrogen atoms with respect to the bound olefin. The latter rearrangement has been recognized as a potentially damaging side-reaction within the alkene metathesis cycle, but quite possibly, an important step in processes such as "alkane metathesis".[12] Recently, two new protocols to assemble low-coordinate metal–carbon multiple bonds have been reported. One applies a one-electron oxidation to promote the α-hydrogen abstraction [Equation

*Daniel Mindiola was born in San Cristóbal, Venezuela, in 1974. In 1996 he received a B.S. degree in chemistry with honors from Michigan State University (East Lansing, Michigan, USA), and then completed a Ph.D. in chemistry from the Massachusetts Institute of Technology under the tutelage of Prof. C. C. Cummins (2000). Following an NIH and Ford postdoctoral fellowship under the direction of Prof. G. L. Hillhouse at the University of Chicago, he then began his independent work in 2002 as an Assistant Professor at Indiana University in Bloomington, Indiana (USA). His research interests include synthesis, reactivity, and mechanistic studies involving low-coordinate early transition metal complexes containing metal–ligand multiple bonds, in particular their development as synthons or catalysts for unusual organometallic transformations.*

*Brad Bailey was born in Clarkston, Michigan, USA on June 10th 1980. In 2002, he received his B.S. from the University of Michigan while working under Dr. David Curtis on the synthesis of polythiophenes for their use as conducting polymers. Brad is currently working under the supervision of Dr. Daniel Mindiola on the preparation of highly reactive terminal titanium alkylidenes and alkylidynes, and exploring the reactivity of these unusual motifs.*

*Falguni Basuli was born in Panskura a small town of Midnapore district of west Bengal, India, in 1972. After completing her Master's (M.Sc.) in chemistry from Vidyasagar University, she received her Ph.D. degree in 2001 from Jadavpur University, Kolkata, in synthetic inorganic chemistry under the supervision of Prof. Samaresh Bhattacharyya. In 2002 she joined Prof. Daniel J. Mindiola's group as a post-doctoral researcher at Indiana University, Bloomington, USA. She continues to work on the syntheses of early transition metal complexes containing metal–ligand multiple bonds (e.g. alkylidenes, alkylidynes, imides, and phosphanylidenes), as well as their reactivity towards different substrates.*

 © 2006 Wiley-VCH Verlag GmbH & Co. KGaA, Weinheim 

(7)],[13] while the second method utilizes a highly reducing metal center to promote P–C bond rupture of a bound trimethylphosphane [Equation (8)].[14]

$$L_mM^n(\eta^2\text{-HRC=CHR'}) \rightleftharpoons L_mM^{n+2}(CRCH_2R') \quad (6)$$

$$L_mM^n(CH_2R)_2 \xrightarrow[-A^0]{[A][X]} L_mM^{n+1}(CHR)(X) + CH_3R \quad (7)$$

$$L_mM^n[P(CH_3)_3] \longrightarrow L_mM^{n+2}(CH_2) + HP(CH_3)_2 \quad (8)$$

The former synthetic strategy has been referred to as an oxidatively induced α-hydrogen abstraction.[13] One advantage to this process is that bis(alkyl) complexes composed of 3d elements such as Ti and V can be readily transformed to the high-valent alkylidene by a single-electron oxidation. Most notably, this protocol can generate low-coordinate complexes bearing terminal M=C linkages with substitutionally labile ligands or counter anions such as $OTf^-$, $I^-$, $Br^-$, $Cl^-$, and $BPh_4^-$. As a result, $d^0$ transition-metal alkylidenes prepared by this route are poised for a subsequent α-hydrogen abstraction or α-hydrogen deprotonation to generate the alkylidyne ligand. Another rare, but known method to generate the terminal alkylidene ligand involves the breaking of dimers (composed of bridging alkylidenes) with donor ligands such as phosphanes [Equation (9)].[15a]

$$[L_mM^n]_2(\mu_2\text{-CHR})_2 \xrightarrow{2\ PR_3} 2\ L_mM^n(CHR)(PR_3) \quad (9)$$

This same strategy can be used for Lewis acid decomplexation of heterobimetallic $\mu_2$-alkylidene systems using strong donors such as HMPA.[15b]

### Alkylidenevanadium and -titanium Complexes

Despite the extensive number of alkylidenetantalum complexes,[4] fewer examples exist for the lighter congener, Nb, while even less cases have been reported for V.[4,6] Table 1 lists high oxidation state alkylidene complexes for V (isolated) along with some diagnostic features. The lower number of V and Nb alkylidenes vs. those for tantalum, can arguably be correlated to the propensity of the former metals to generate low-valent oxidation states.

Theoretical studies by Nugent and co-workers have uncovered that the charge on the atom multiply bonded to the metal (e.g. imides, alkylidenes, oxo groups) decreases as we go up and to the right within the periodic table.[16] Consequently, high-valent $Nb^V$ and $V^V$ are more likely to be reduced by Grignard compounds or alkyllithium compounds as opposed to $Ta^V$. Hence, if one plans to incorporate the M=C linkage onto a lighter congener in a high oxidation state, then perhaps one should work retrosynthetically from the low-valent state by subsequent oxidation reactions. Gratifyingly, two examples for the later hypothesis have been reported (Scheme 1).[17,18] In 1995, McCamley and co-workers trapped a transient niobium alkylidene by a redox route.[17] Their studies described the one-electron oxidation of $Nb^{IV}(\eta^5\text{-}C_5H_4t\text{Bu})_2(CH_2Ph)_2$ with $AgBPh_4$ to generate a $Ag^0$ mirror along with the kinetically unstable benzylidene salt $[Nb^V(\eta^5\text{-}C_5H_4t\text{Bu})_2(CHPh)][BPh_4]$ (Scheme 1, a).[17] The latter intermediate underwent facile C–H activation reactions in toluene to afford the cyclometallated product (Scheme 1, a), but the mechanism of the C–H activation reaction was not discussed in this work. The second example involving one-electron oxidation to generate M=C linkages was reported by Otero and co-workers.[18] In their studies, one-electron oxidation of the $Nb^{IV}$ alkyne $Cp'_2Nb[\eta^2\text{-MeOC(O)C}\equiv\text{CMe}]$ ($Cp' = C_5H_4SiMe_3$) with $[FeCp_2][BPh_4]$ generated a binuclear vinylidene complex (Scheme 1, b).[18] Albeit a fascinating transformation, the mechanism of the latter reaction remains unclear.

Schwartz and co-workers are likely the first group to report the synthesis and characterization (NMR spectroscopic data) of group 4 alkylidenes $Cp_2M=CHR(PR_3)$ (M = Ti and Zr).[9d,15b] Their seminal work was followed-up by Bickelhaupt and co-workers in 1986.[15a] However, it was not until 1992 that Krüger and co-workers structurally characterized the $d^0$ Ti=C bonded complex $(PMe_3)$-

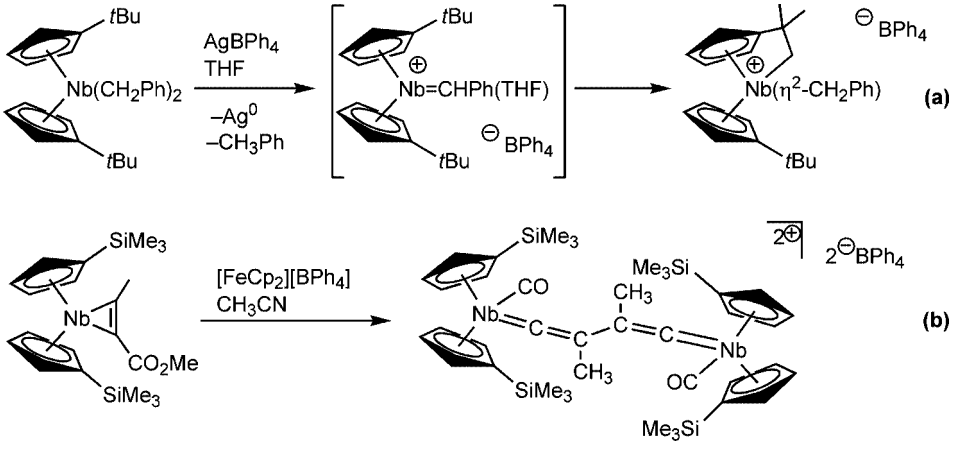


Scheme 1.

 © 2006 Wiley-VCH Verlag GmbH & Co. KGaA, Weinheim 

Table 1. Terminal alkylidenevanadium and -titanium complexes (see also ref.[13,15,32,36–41]).

| Complex | $^{13}$C NMR $\delta$ (ppm); $J_{C-H}$ (Hz) | M=C Bond length (Å) | Ref. |
|---|---|---|---|
| **Vanadium** | | | |
| 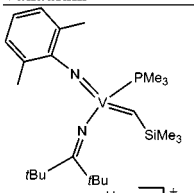 | 302 | 1.860(2) | [32c] |
| 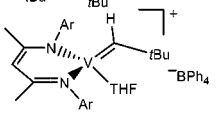 | | 1.795(3) | [13e] |
| Ar = 2,6-(CHMe$_2$)$_2$C$_6$H$_3$ 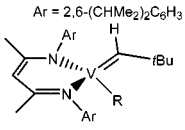 | | R = I, 1.787(3); R = CH$_2$SiMe$_3$, 1.791(6) | [13e,13f] |
| Ar = 2,6-(CHMe$_2$)$_2$C$_6$H$_3$ R = I, CH$_2$SiMe$_3$ 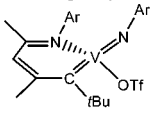 | 320 | 1.899(7) | [13f] |
| Ar = 2,6-(CHMe$_2$)$_2$C$_6$H$_3$ 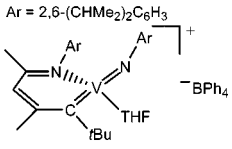 | 323 | | [13f] |
| Ar = 2,6-(CHMe$_2$)$_2$C$_6$H$_3$ 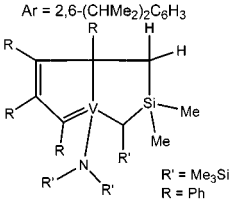 R' = Me$_3$Si R = Ph | 319 | 1.876(7) | [32f] |
| 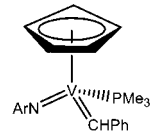 | 304 | 1.922(6) | [32e] |
| Ar = 2,6-(CHMe$_2$)$_2$C$_6$H$_3$ 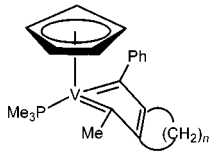 $n$ = 3, 4 | 259.6 ($n$ = 3), 263.4 ($n$ = 4) | | [32b] |
| 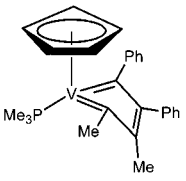 | 273 and 257 | 1.891(3) [V–C(Ph)] 1.884(3) [V–C(Me)] | [32b,32g] |
| 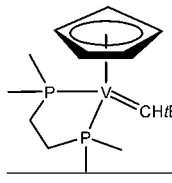 | 260 | 1.809(3) | [32a] |

Table 1. *(Continued)*

| Complex | $^{13}$C NMR $\delta$ (ppm); $J_{C-H}$ (Hz) | M=C Bond length (Å) | Ref. |
|---|---|---|---|
| **Titanium** | | | |
| 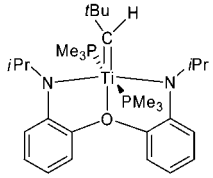 | 229; 80 | 1.884(4) | [36] |
| 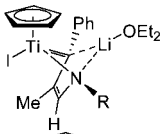 | 245 | 1.958(3) | [37] |
| 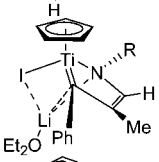 | 245 | 1.979(3) | [37] |
| 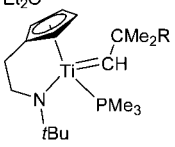 | 251; 83 | | [38] |
| R = Me or Ph 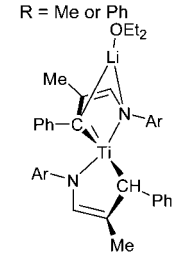 | 236 | 1.978(3) | [39] |
| Ar = 2,6-(CHMe$_2$)$_2$C$_6$H$_3$ 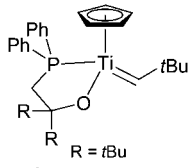 R = *t*Bu | 287; 92 | 1.911(3) | [40] |
| 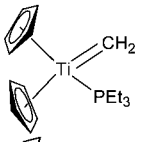 | 287 | | [15b] |
| 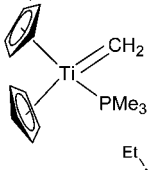 | 285 | | [15a] |
| 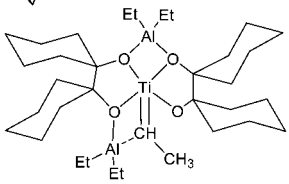 | | 1.933(6) | [41] |
| 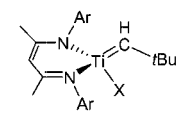 X = OTf, BH$_4$, Cl, Br, I, CH$_2$TMS Ar = 2,6-(CHMe$_2$)$_2$C$_6$H$_3$ | 267–274; 85–95 | 1.826–1.855 | [13a–c] |

 © 2006 Wiley-VCH Verlag GmbH & Co. KGaA, Weinheim 

Table 1. *(Continued)*

| Complex | $^{13}$C NMR $\delta$ (ppm); $J_{C-H}$ (Hz) | M=C Bond length (Å) | Ref. |
|---|---|---|---|
| 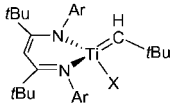 X = OTf, I, $CH_2SiMe_3$, $CH_2Ph$ | 254–260; 88–92 | 1.822–1.852 | [13b–c] |
| Ar = 2,6-$(CHMe_2)_2C_6H_3$ 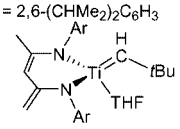 | 254; 93 | 1.86(1) | [13c] |
| Ar = 2,6-$(CHMe_2)_2C_6H_3$ 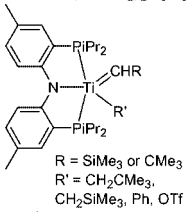 R = $SiMe_3$ or $CMe_3$ R' = $CH_2CMe_3$, $CH_2SiMe_3$, Ph, OTf | 260–311; 86–99 | 1.790(5)–1.883(4) | [13d, 27] |
| 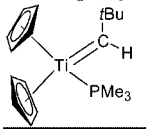 | 313; 110 | | [42] |

$Cp_2Ti{=}C{=}C{=}TiCp_2(PMe_3)$ [Ti=C, 2.051(2) Å].[19] In 1993, Fryzuk and co-workers[20] reported the synthesis and structural elucidation of the first mononuclear and terminal alkylidene $[\eta^5\text{-}C_5H_3\text{-}1,3\text{-}(SiMe_2CH_2P\textit{i}Pr_2)_2]Zr{=}CHPh(Cl)$. Not surprisingly, alkylidene complexes of group 4 are often represented as $^{+}M\text{–}CR_2^{-} \leftrightarrow M{=}CR_2$, much like ylides resonate. This feature explains why common reagents such as Tebbe's complex[21] are much more stable than Lewis acid free and terminal alkylidenes. Table 1 depicts isolable titanium complexes bearing a terminal alkylidene ligand along with diagnostic features.

## Synthesis of Group 4 and 5 High Oxidation State Alkylidynes

High oxidation state alkylidyne transition-metal complexes are far more rare than the corresponding alkylidenes, in particular for the early transition metals prior to group 6.[4c] This fact is not surprising because most $d^0$ alkylidynes are commonly prepared from alkylidenes by an α-hydrogen abstraction or deprotonation reaction [Equation (10)].

$$L_mM^n(CHR)(LG) \longrightarrow LM^n(CR) + H(LG) \quad (10)$$

Some elegant but rare entries to the terminal alkylidyne functionality invoke two-electron reduction of an alkyl group to promote α,α′-dehydrogenation and elimination of $H_2$ [Equation (11)],[11f] or α-hydrogen elimination of a reduced alkylidene–metal complex to generate the alkylidyne–hydride product [Equation (12)].[10,11f]

$$L_mM^n(CH_2R) \longrightarrow L_mM^{n+2}(CR) + H_2 \quad (11)$$

$$L_mM^n(CHR)(X)_2 \xrightarrow[-2X^-]{x\ PR_3} L_mM^n(CR)(H)(PR_3)_x \quad (12)$$

If one includes group 6 alkylidynes, other elegant entries would be methine (CH) group transfer to a low-valent metal center [Equation (13)],[22] trimethylsilyl migration of $\eta^2$-vinyl groups [Equation (14)],[23] and alkyne or nitrile metathesis with $W_2^{(III,III)}$ dimers [Equation (15)].[24]

$$L_mM^n + \text{"CH"} \longrightarrow L_mM^{n+3}(CH) \quad (13)$$

$$L_mM^n(\eta^2\text{-}H_2CCSiMe_3) \xrightarrow{\Delta} L_mM^n(CCH_2SiMe_3) \quad (14)$$

$$L_mM^n{\equiv}M^nL_m + XCR \longrightarrow L_mM^{n+3}(X) + L_mM^{n+3}(CR) \quad X = N \text{ or } CR \quad (15)$$

An extensive description of protocols to achieve group 6 M≡C linkages have been reported, and we refer the reader to this work.[6h] However, prior to group 6 transition metals, M≡CR linkages are far more scarce.[4c] As mentioned previously, our group has developed a novel technique applying one-electron oxidation to promote α-hydrogen abstraction. This strategy can also be applied to alkylidene(alkyl) species of vanadium(IV) thus giving rise to the first example of an alkylidynevanadium complex [Equation (16)].[13f]

$$L_mM^n(CHR)(R') \xrightarrow[-A^0]{[A][X]} L_mM^{n+1}(CR)(X) + HR' \quad (16)$$

Schrock and co-workers reported the first examples of group 5 alkylidynes, which were composed of tantalum(V),[10b,25] but it was not until 2004 that Mindiola and co-workers[13f] reported the only examples of alkylidynevanadium(V) complexes (both in neutral and cationic forms). The latter complexes are derived from two subsequent one-electron oxidation and α-H abstraction steps commencing from a bis(alkyl)vanadium(III) precursor (vide infra). Table 2 compiles a list of terminal alkylidynevanadium complexes.

Not surprisingly, isolable and terminal group 4 alkylidynes are unknown.[4c] Mena and co-workers have reported $\mu_3$-bridging alkylidynes of titanium where the hybridization at the α-C is best described as $sp^3$.[26] Very recently however, transient titanium(IV) complexes bearing terminal alkylidynes can be smoothly generated, mechanistically studied, and also trapped with various substrates (vide infra).[27] Interestingly, the latter alkylidyne precursors have been indirectly derived from a one electron oxidatively induced α-hydrogen abstraction. Table 2 compiles a list of well-defined alkylidynetitanium complexes.

 © 2006 Wiley-VCH Verlag GmbH & Co. KGaA, Weinheim 

Table 2. Terminal alkylidynevanadium and -titanium complexes.[13,26,27]

| Complex | $^{13}$C NMR $\delta$ (ppm); $J_{C-H}$ (Hz) | M≡C Bond length (Å) | Ref. |
|---|---|---|---|
| **Vanadium** | | | |
| 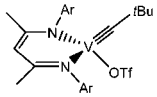 Ar = 2,6-(CHMe$_2$)$_2$C$_6$H$_3$ | 375 | 1.674(2) | [13f] |
| 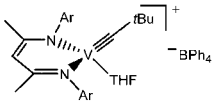 Ar = 2,6-(CHMe$_2$)$_2$C$_6$H$_3$ | 374 | 1.696(3) | [13f] |
| **Titanium** | | | |
| 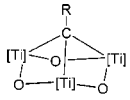 R = Me, H [Ti] = TiCp* | 383 (R = H) and 402 (R = Me) | For R = Me: C–Ti1 = 2.117(4), C–Ti' = 2.127(5) | [26a] |
| 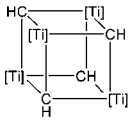 [Ti] = TiCp* | 491 | 2.052(7) | [26b] |
| 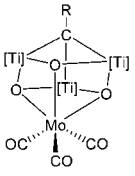 R = Me, H [Ti] = TiCp* | 410 (R = H) and 434 (R = Me) | R = CH$_3$: C–Ti1 = 2.13(5), C–Ti2 = 2.12(2), C–Ti3 = 2.10(2) | [26c] |
| 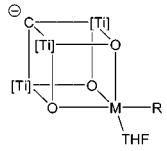 [Ti] = TiCp* M = Li, Na, K, Rb, Cs, Mg, Ca, Sr, Ba R = THF for group I and N(TMS)$_2$ or Cp* for Group II | 577–598 | For M = Ca: C–Ti1 = 1.959(5), C–Ti2 = 1.966(4), C–Ti3 = 1.965(4) | [26d] |
| 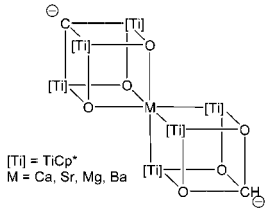 [Ti] = TiCp* M = Ca, Sr, Mg, Ba | | For M = Ca: C–Ti1 = 1.923(6), C–Ti' = 2.123(9) For M = Sr: C–Ti1 = 1.966(2), C–Ti2 = 1.971(2), C–Ti3 = 1.972(3) For M = Mg: C–Ti = 2.06(4), C–Ti' = 2.00(1) | [26d] |
| 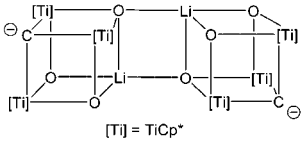 [Ti] = TiCp* | | C–Ti1 = 2.067(6), C–Ti2 = 2.050(6), C–Ti3 = 2.047(6) | [26e] |
| 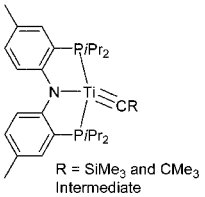 R = SiMe$_3$ and CMe$_3$ Intermediate | | 1.749 (computed) for R = CMe$_3$ | [27] |

### Oxidatively Induced α-Hydrogen Abstraction to Prepare M–C Multiple Bonds of Ti and V.

#### *a. Synthesis of Alkylidenetitanium Complexes*

An attractive entry towards the assembly of low-coordinate systems possessing metal–ligand multiple bonds can be derived from a redox reaction where the low-valent metal is alkylated, then oxidized. Accordingly, the protocol to prepare low-coordinate and terminal alkylidenetitanium complexes involved the use of a $d^1$ precursor complex (nacnac)-$TiCl_2$ (**1**) {nacnac$^-$ = [ArNC(Me)]$_2$CH, Ar = 2,6-(CHMe$_2$)$_2$-C$_6$H$_3$}, reported previously by Budzelaar.[28] The β-diketiminate ancillary ligand, nacnac$^-$, was chosen given its precedence to generate low-coordination environments in both early- and late metal complexes.[29] Hence, the THF base adduct of **1** can be readily alkylated with 2 equiv. of $LiCH_2tBu$ to afford the bis(alkyl)titanium(III) complex (nacnac)Ti($CH_2tBu$)$_2$ (**2**) in excellent yield.[13a] This compound is remarkably stable to heat, but when treated with oxidants such as AgOTf or $I_2$, the four-coordinate alkylidene complexes (nacnac)Ti=CH*t*Bu(X) [X$^-$ = OTf, (**3**)–OTf; X$^-$ = I, (**3**)–I] are readily obtained (Scheme 2).[13a,13b] Complex **3** displays $^1$H and $^{13}$C NMR spectroscopic signatures consistent with $C_s$ symmetry in solution. The alkylidene $C_\alpha$ resonance is centered at $\delta$ ca. 271–272 ppm with a $J_{CH}$ coupling constant of 95–85 Hz. The latter parameters are consistent with these molecules having a terminal alkylidene functionality in which there is a significant α-hydrogen agostic interaction with the metal center.[4c] The low-coordination number of **3** was confirmed by single-crystal X-ray crystallographic studies.[13a,13b] Conveniently, anion exchange or transmetallation in compounds such as **3**-OTf is facile (Scheme 2), thus giving rise to a family of alkylidenes where X$^-$ can be varied from halides (Cl and Br), to alkyl groups ($CH_2SiMe_3$), to a borohydride ($\eta^3$-$BH_4$). These alkylidenes have been thoroughly characterized, but all these compounds are kinetic products inasmuch as they can undergo intramolecular C–H activation transformations[13a] or intramolecular Wittig-like rearrangements to afford compounds such as **4**-OTf and **4**-I (Scheme 2 shows only the Wittig-like conversion of **3**-X to **4**-X, where X$^-$ = OTf or I).[13a,13b] However, the intramolecular Wittig-like rearrangement can be readily blocked by replacing the β-methyl groups on the β-diketiminate NCCCN framework with *t*Bu.[28] As a result, kinetically stable alkylidenetitanium complexes such as ($^{t\text{Bu}}$nacnac)Ti=CH*t*Bu(X) (X$^-$ = OTf, **5**–OTf; X$^-$ = I, **5**–I; $^{t\text{Bu}}$nacnac$^-$ = [Ar]NC(*t*Bu)]$_2$CH) can also be prepared from the corresponding bis(alkyl) precursor ($^{t\text{Bu}}$nacnac)Ti($CH_2tBu$)$_2$ (**6**) (Scheme 3).[13b] Structural and spectroscopic features for **5** are similar to those observed for **3**. With the bulkier $^{t\text{Bu}}$nacnac$^-$ framework, one can also incorporate the isobutylidene ligand onto titanium by oxidizing precursors such as ($^{t\text{Bu}}$nacnac)Ti($CH_2i$Pr)$_2$ (**7**) with AgOTf (Scheme 3).[30] This implies that oxidatively induced α-hydrogen abstraction is the preferred pathway as opposed to the more common β-hydrogen elimination and α-hydrogen abstraction themes. Although isolable, complex ($^{t\text{Bu}}$nacnac)Ti=CH*i*Pr(OTf) (**8**) is a kinetic product since

 © 2006 Wiley-VCH Verlag GmbH & Co. KGaA, Weinheim 

solutions decompose gradually over 24 h at 25 °C to afford the product ($\eta^2$-H*i*PrC=C(*t*Bu)CHC(*t*Bu)N[Ar])Ti=NAr-(OTf) (**9**): a complex resulting from an intramolecular Wittig-like rearrangement.[30] Despite complex **8** having *t*Bu groups to block the intramolecular [2+2]cycloaddition, the alkylidene functionality is apparently far less crowded and therefore more prone to group-transfer processes (Scheme 3).

Oxidatively induced α-hydrogen abstraction is a versatile process because terminal titanium alkylidene ligands can be readily assembled utilizing another ancillary ligand framework such as PNP (PNP = N[2-P(CHMe$_2$)$_2$-4-methylphenyl]$_2^-$).[31] PNP as an ancillary support provides a "hybrid type" coordination environment where both a hard amide and two soft phosphane donors are oriented in a meridional geometry. In addition, this ancillary support is impervious to intramolecular Wittig-like rearrangements often observed with sterically imposing β-diketiminate ligands.[13] Consequently, both (trimethylsilylmethylidene)- and (neopentylidene)titanium (PNP)Ti=CHR(OTf) (**10**: R = SiMe$_3$, **11**: R = *t*Bu),[13d] as well as isobutylidene (PNP)-Ti=CH*i*Pr(OTf) (**12**)[30] complexes can be constructed with this robust and rigid pincer system (Figure 1 shows their synthesis along with their corresponding X-ray structures). Unlike **3**, **5**, and **8**, compounds **10**–**12** display weaker α-hydrogen agostic interactions ($J_{C-H}$ = 85–99 Hz), presumably due to the greater coordination number at titanium. Distinct from **8**, complex **12** is remarkably stable despite having a less hindered and terminal alkylidene with a β-hydrogen.[30] This demonstrates that alkyl reagents that commonly reduce, such as *i*Bu$^-$, can be easily transformed into never-before seen isobutylidene "M=CH*i*Pr" functionalities on titanium. Compounds like **12** might offer an excellent opportunity to study the reverse: alkylidene to olefin conversion (vide supra).

### *b. Synthesis of Alkylidenevanadium Complexes*

Our success in preparing the first four-coordinate neopentylidenetitanium by an oxidatively induced α-abstraction reaction[13] motivated us to pursue other 3d transition metals, which lack such a motif. Unlike titanium, vanadium displays more diverse redox chemistry, which could result in more redox couples as opposed to the more general one-electron oxidation observed with $Ti^{3+}$. Terminal alkylidene

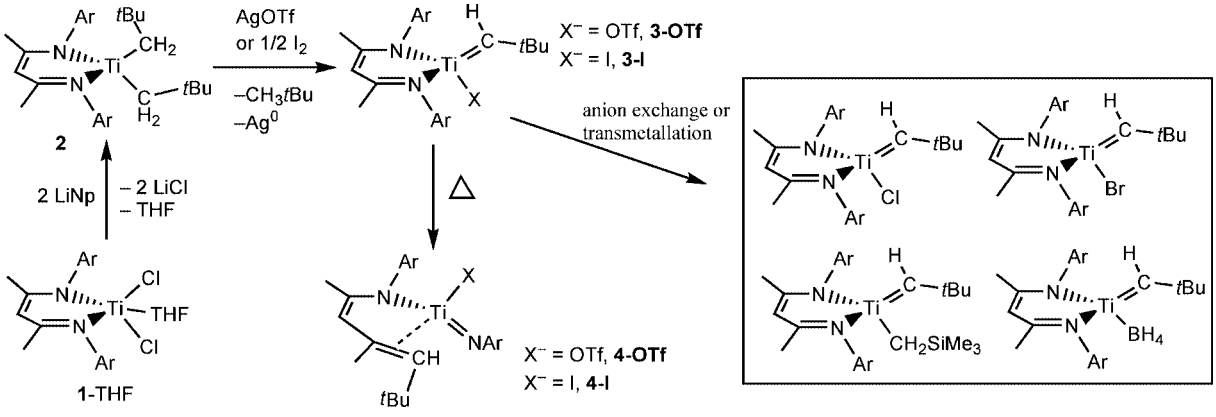


Scheme 2.

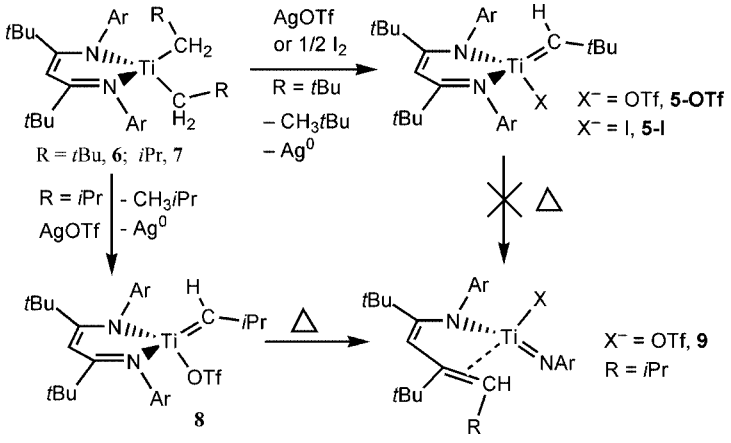


Scheme 3.

 © 2006 Wiley-VCH Verlag GmbH & Co. KGaA, Weinheim 

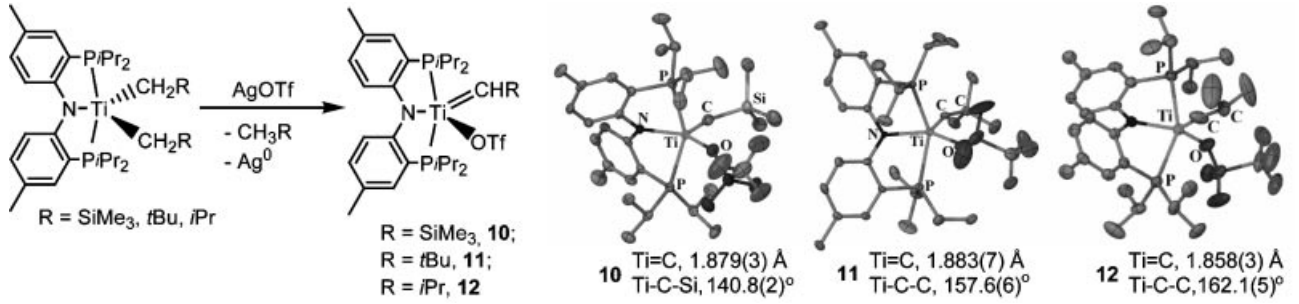


Figure 1. Synthesis of the terminal alkylidenetitanium(IV) complexes **10**–**12**. Single-crystal X-ray structures are displayed to the right with H atoms omitted for clarity. Selected metrical parameters are displayed under each structure.

complexes of vanadium are rare,[32] with the first example being reported by Teuben and co-workers, namely CpV=CH*t*Bu(dmpe) [dmpe = bis(dimethylphosphanyl)ethane].[32a] For us, alkylating Budzelaar's precursor (nacnac)-$VCl_2$[28] with 2 equiv. of $LiCH_2tBu$ afforded the bis-neopentyl complex (nacnac)V($CH_2tBu$)$_2$ (**13**) as dark brown needles. Subsequent one-electron oxidation with $AgBPh_4$ generated a $Ag^0$ mirror along with the alkylidenevanadium(IV) complex [(nacnac)V=CH*t*Bu(THF)][$BPh_4$] (**14**) (Scheme 4).[13e] Complex **14** can readily disproportionate, but anion exchange using $MgI_2$ (or $I_2$) yielded the much more stable alkylidenevanadium(IV) (nacnac)V=CH*t*Bu(I) (**15**).[13e] Not only is the neutral complex **15** far more stable than the corresponding cation, but the $I^-$ ligand can also be readily substituted (vide infra). Compounds **14** and **15** are $d^1$ paramagnets as well as EPR active. More specifically, these compounds display an 8-line hyperfine coupling pattern resulting from coupling of the unpaired electron to the vanadium center ($I$ = 7/2, 99.6%, Figure 2).[13e] Single-crystal X-ray diffraction analysis for each system reveal four-coordinate vanadium complexes bearing a terminal neopentylidene ligand with short V=C distances [**14**, 1.795(3) Å; **15**, 1.787(3) Å], obtuse V=C–C angles [**14**, 159.8(4)°; **15**, 158.7(3)°], and in each case an α-H agostic interaction with the $d^1$-metal center.

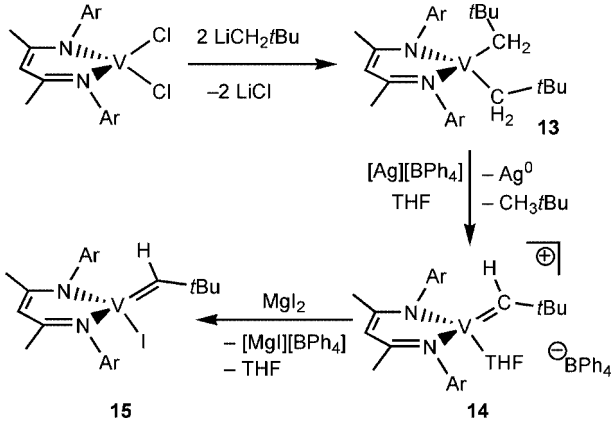


Scheme 4.

### *c. Synthesis of Alkylidynetitanium Complexes*

Terminal alkylidynetitanium complexes are unknown, and the only isolable examples reported in the literature are $\mu^3$-alkylidynes restricted to cubane $Ti^{IV}_4$ clusters.[26] In 2004, Ozerov and co-workers reported remarkably stable alkylidene(alkyl)zirconium complexes of the type (PNP)-Zr=CHR($CH_2$R) (R = Ph or *p*-tolyl), which were prepared by α-hydrogen abstraction through thermolysis of the corresponding tris(alkyl) species.[33] However, α-hydrogen abstraction for the latter complex was not reported. Inspired by their work, we reasoned whether analogous $Ti^{IV}$ derivatives could undergo not one, but two α-hydrogen abstractions given the more congested environment for the $Ti^{4+}$ center. Our hypothesis proved fruitful inasmuch as four-co-

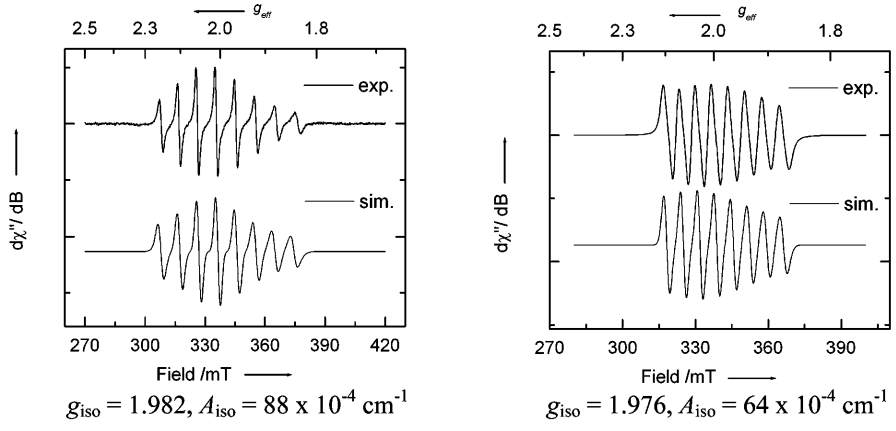


Figure 2. X-Band isotropic EPR spectra of complexes **14** (left) and **15** (right) in a 0.1 mM toluene solution.

 © 2006 Wiley-VCH Verlag GmbH & Co. KGaA, Weinheim 

ordinate alkylidynetitanium complexes can be readily generated by α-hydrogen abstraction reactions utilizing precursors such as **10** and **11**.[27] Accordingly, when complex **11** is treated with $LiCH_2tBu$ in pentane at low temperatures, the neopentylidene–neopentyltitanium complex (PNP)Ti=CH-*t*Bu($CH_2tBu$) (**16**) can be obtained upon rapid work-up of the reaction mixture (Scheme 5). Complex **16** reacts rapidly with benzene at 27 °C within 11.9 hours (4.5 half lives) to afford (PNP)Ti=CH*t*Bu($C_6H_5$) (**17**) quantitatively.[27] The combination of high-level density functional theory (DFT), labeling, and kinetic studies have demonstrated that complex **16** first undergoes α-H abstraction concomitant with elimination of $CH_3tBu$, to afford a transient alkylidynetitanium intermediate (PNP)Ti≡C*t*Bu (**A**), which experiences 1,2 addition of the benzene C–H bond across the reactive Ti≡C*t*Bu linkage to provide **17** (Scheme 5). The reaction energy profile for the C–H activation of benzene has been probed using high-level DFT calculations and is depicted in Figure 3.[27] The post rate-determining step suggests that the reverse process (liberation of benzene to generate alkylidyne, **17** → **A**), is associated with a barrier of 32.8 kcal/mol. In fact, this theoretical prediction can be experimentally proven under elevated temperature conditions. For example, complex **17**-$d_6$ can undergo clean conversion to **17** in $C_6H_6$ (95 °C, 48 hours), and vice-versa, thus linking intermediate **A** to complex **17** in the reaction profile.[27] This paradigm is particularly interesting because complex **17** can potentially be a synthon of **A** (albeit slow), in benzene, at ca. 95–120 °C. We have also found another alkylidyne source. Compound **10** can also be alkylated with $LiCH_2SiMe_3$ to afford (PNP)Ti=CHSiMe$_3$($CH_2SiMe_3$) (**18**). Compound **18** has been shown to generate the transient alkylidyne (PNP)Ti≡CSiMe$_3$ (**B**) in $C_6H_6$, albeit at higher temperatures, to afford the phenyl derivative (PNP)-Ti=CHSiMe$_3$($C_6H_5$) (**19**) (Scheme 6). As observed with **17**, thermolysis of **19** in $C_6D_6$ also leads to complete conversion to **19**-$d_6$, thus consistent with **19** being in equilibrium (at higher temperatures) with the alkylidyne intermediate **B**.[27]

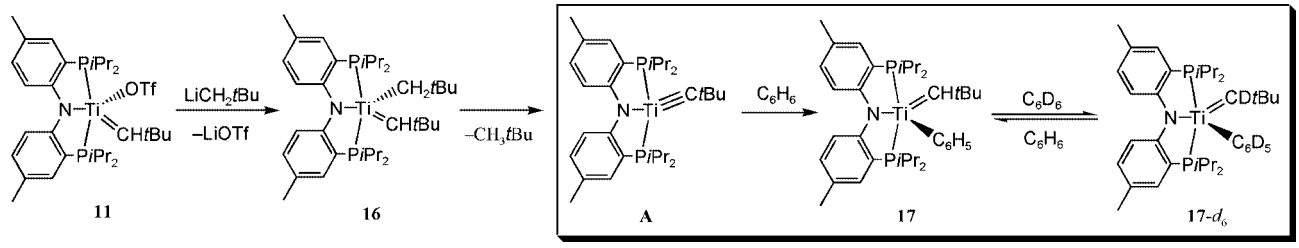


Scheme 5.

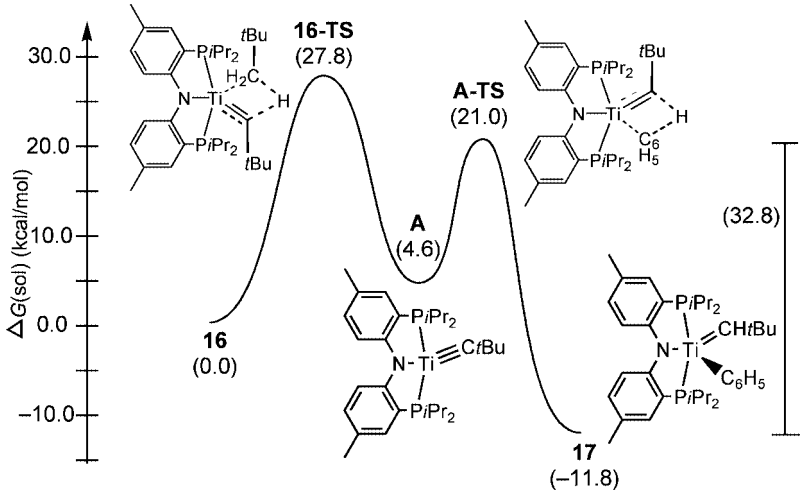


Figure 3. Reaction profile for the **15** → **16** conversion, whereby intermediate **A** is generated. The two transition-state geometries (**TS**) are depicted below.

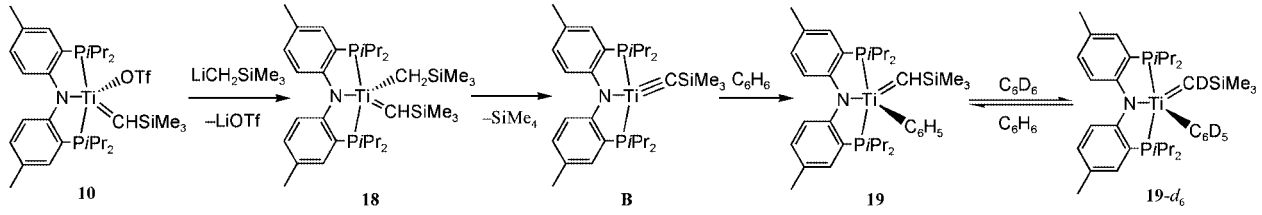


Scheme 6.

 © 2006 Wiley-VCH Verlag GmbH & Co. KGaA, Weinheim 

### *d. Synthesis of Vanadium Alkylidynes*

In 1991, Lippard and Protasiewicz reported the only example of a terminal V≡C linkage, namely the Fischer carbyne $(CO)(dmpe)_2V{\equiv}COSiPh_3$ [V≡C, 1.754(8) Å].[34] However, it was not until recently that the first examples of alkylidynes $d^0$, 3d transition metal complexes of group 5 were reported.[13f] This achievement was in part possible given our access to low-coordinate alkylidenevanadium complexes having labile ligands, namely compounds **14** and **15**.[13e] Accordingly, the four-coordinate neopentylidene complex **15** can be readily alkylated with $LiCH_2SiMe_3$ to afford the neopentylidene(alkyl) species (nacnac)-V=CH*t*Bu($CH_2SiMe_3$) (**20**) (Scheme 7). Complex **20** exhibits an EPR spectrum and a solution magnetic moment in accordance with a $V^{IV}$ radical center,[13f] and when oxidized with AgOTf or $AgBPh_4$, the neutral (nacnac)V≡C*t*Bu(OTf) (**21**) or cationic [(nacnac)V≡C*t*Bu(THF)][$BPh_4$] (**22**) neopentylidynes can be readily obtained, respectively (Scheme 7).[13f] $^1$H NMR spectra are consistent with **21** and **22** retaining $C_s$ symmetry in solution, while the combination of $^{13}$C ($\delta$: **21**, 375 ppm; **22**, 374 ppm)[7] and $^{51}$V (**21**: δ = –882 ppm, **22**: δ = –956 ppm) NMR spectra unambiguously confirms the presence of a terminal neopentylidynevanadium(V) functionality.[13f] In contrast to Schrock's two-electron reduction reactions of high-valent 5d metals to form Ta≡C linkages (vide supra),[10] our work involves two, one electron oxidatively induced α-hydrogen abstraction steps to prepare vanadium alkylidynes. While compounds **21** and **22** are remarkably stable at room temperature, they remain kinetic products from the reaction, since extensive thermolysis at ca. 80 °C results in quantitative conversion to the imidovanadium complex supported by the chelating amido–vinyl ligand, (*t*BuC=C(Me)CHC(Me)N[Ar])V=N-Ar(OTf) (**23**) and [(*t*BuC=C(Me)CHC(Me)N[Ar])-V=NAr(THF)][$BPh_4$] (**24**). Compounds **23** and **24** are best described as azametalacyclohexatriene systems resulting from an intramolecular cross-metathesis transformation involving an azametalacyclobutene transition state **21-TS** (Figure 4).[13f] The conversion **21** → **23** in $C_7D_8$ was determined to be first-order in vanadium with activation parameters $\Delta S^{\ddagger}$ = –6(3) cal/mol·K, $\Delta H^{\ddagger}$ = 25.4(3) kcal/mol. Formation of **23** was also found to be independent of solvent ($C_7D_8$ vs. [$D_8$]THF), which rules out dissociative or associative mechanisms from playing a role in this transformation.[13f] A similar transformation was observed for the analogous alkylidenetitanium systems bearing the same β-diketiminate ligand framework (vide supra).[13a,13b]

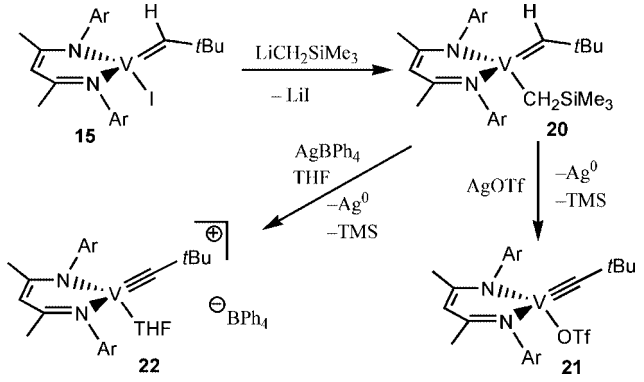


Scheme 7.

## Conclusions and Future Outlook

In this microreview we have compiled a series of synthetic strategies that incorporate the terminal alkylidene and alkylidyne ligands onto the early transition metal series. One particular method which we have focused our attention to has been a reaction denoted "oxidatively induced α-hydrogen abstraction". This protocol combines a one-electron oxidation step with Schrock's seminal α-hydrogen abstraction method. One-electron oxidation does not only promote α-hydrogen abstraction, but also generates metal–carbon multiple bonds in low-coordination environments while in-

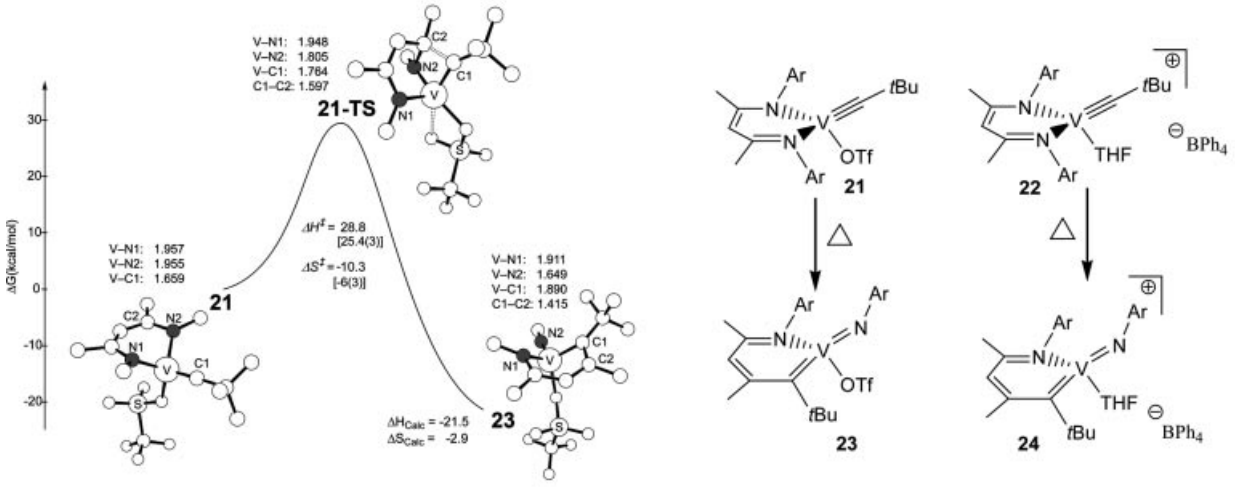


Figure 4. Transformation of the alkylidynevanadium complexes. The reaction coordinate for **21** → **23** is shown to the left with computed enthalpic values for the transition state (**21-TS**) and **23**. Calculated structural features for the cores of **21**, **21-TS**, and **23** are also displayed.

 © 2006 Wiley-VCH Verlag GmbH & Co. KGaA, Weinheim 

corporating labile ligands such as $OTf^-$, $I^-$, or $BPh_4^-$. This feature unavoidably places these compounds along a cascade of other reactions which will ultimately lead to other novel functionalities. For example, terminal alkylidyne ligands can be incorporated onto titanium by an α-hydrogen abstraction pathway, while alkylidynevanadium complexes can be generated by a subsequent one-electron α-hydrogen abstraction reaction stemming from the alkylidene(alkyl) $V^{IV}$ precursor. In addition, the polarized nature of the M=C bond renders alkylidenetitanium and -vanadium functionalities exceedingly nucleophilic thus readily engaging in α-hydrogen migration or deprotonation reactions of primary phosphides to generate novel functionalities such as terminal phosphanylidenetitanium and -vanadium complexes.[13d,35] Fine tuning of the ancillary support has created kinetically robust systems capable of undergoing interesting intermolecular reactions such as C–H activation. The chemistry surrounding high-oxidation M=C and M≡C linkages for group 4 and 5 metals is an immature, yet emerging field in organotransition metal chemistry despite the first alkylidenetantalum being reported by Schrock in the early 70's.[7,8]

With these synthetic strategies now available to generate a library of M=C and M≡C linkages, we are now in position to probe these reactive functionalities and hopefully, pull alongside with the prototypical group 6 alkylidene/alkylidyne reagents commonly used today in catalysis.

## Acknowledgments

This work is dedicated to my former mentors Prof. C. C. Cummins and Prof. G. L. Hillhouse. Their dedication, originality, and level of expertise in fundamental chemistry have been a true inspiration throughout my scientific career. D.J.M. thanks Indiana University-Bloomington, the Camille and Henry Dreyfus Foundation, the Ford Foundation, the Alfred P. Sloan Foundation, and the U.S. National Science Foundation (CHE-0348941, PECASE award) for financial support of this research. D.J.M is also indebted to Dr. Falguni Basuli and Brad C. Bailey for achieving most of the results discussed in this microreview. Other contributors to the science which merit mentioning are Guangyu Zhao, Uriah J. Kilgore, Ingrid Castro-Rodriguez, Xile Hu, and Rodney Clark. Prof. Mu-Hyun Baik, Prof. Kenneth G. Caulton, Prof. Gang Wu, Prof. Karsten Meyer, and Prof. Oleg V. Ozerov are also acknowledged for insightful discussions and fruitful collaborations. The authors thanks Mrs. Jeannette E. Silvers for editing and Dr. John C. Huffman, Dr. John Bollinger, and Dr. Maren Pink for their contribution to X-ray analysis over the last 3.5 years.

[1] For some recent highlights: a) A. M. Rouhi, *Chem. Eng. News* **2002**, *80*, 29–33; b) A. M. Rouhi, *Chem. Eng. News* **2002**, *80*, 34–38; c) R. R. Schrock, *Adv. Synth. Catal.* **2002**, *344*, 571–572; d) R. H. Grubbs, *Adv. Synth. Catal.* **2002**, *344*, 569; e) A. Fürstner, *Adv. Synth. Catal.* **2002**, *344*, 567; f) J. W. Herndon, *Coord. Chem. Rev.* **2005**, *249*, 999–1083; g) J. W. Herndon, *Coord. Chem. Rev.* **2006**, published online.

[2] a) J. L. Herisson, Y. Chauvin, *Makromol. Chem.* **1971**, *141*, 161–176; b) T. J. Katz, J. McGinnis, *J. Am. Chem. Soc.* **1975**, *97*, 1592–1594.

[3] a) R. H. Grubbs, P. L. Burk, D. D. Carr, *J. Am. Chem. Soc.* **1975**, *97*, 3265–3267; b) F. N. Tebbe, G. W. Parshall, G. S. Reddy, *J. Am. Chem. Soc.* **1978**, *100*, 3611–3613; c) T. R. Howard, J. B. Lee, R. H. Grubbs, *J. Am. Chem. Soc.* **1980**, *102*, 6876–6878; d) T. M. Trnka, R. H. Grubbs, *Acc. Chem. Res.* **2001**, *34*, 18–29; e) R. H. Grubbs, S. J. Miller, G. C. Fu, *Acc. Chem. Res.* **1995**, *28*, 446–452.

[4] a) R. R. Schrock, *Acc. Chem. Res.* **1979**, *12*, 98–104; b) R. R. Schrock, *Acc. Chem. Res.* **1990**, *23*, 158–165; c) R. R. Schrock, *Chem. Rev.* **2002**, *102*, 145–179; d) R. R. Schrock, in: *Reactions of Coordinated Ligands* (Eds.: P. R. Braterman); Plenum: N. Y. **1986**; e) J. Feldman, R. R. Schrock, *Prog. Inorg. Chem.* **1991**, *39*, 1–74.

[5] http://nobelprize.org/chemistry/laureates/2005/index.html.

[6] a) J. W. Herndon, *Coord. Chem. Rev.* **1999**, *181*, 177–242; b) J. W. Herndon, *Coord. Chem. Rev.* **2000**, *206–207*, 237–262; c) J. W. Herndon, *Coord. Chem. Rev.* **2000**, *209*, 387–451; d) J. W. Herndon, *Coord. Chem. Rev.* **2001**, *214*, 215–285; e) J. W. Herndon, *Coord. Chem. Rev.* **2002**, *227*, 1–58; f) J. W. Herndon, *Coord. Chem. Rev.* **2003**, *243*, 3–81; g) J. W. Herndon, *Coord. Chem. Rev.* **2004**, *248*, 3–79; h) A. Mayr, H. Hoffmeister, *Adv. Organomet. Chem.* **1991**, *32*, 227–324; i) P. F. Engel, M. Pfeffer, *Chem. Rev.* **1995**, *95*, 2281–2309.

[7] R. R. Schrock, *J. Am. Chem. Soc.* **1974**, *96*, 6796–6797.

[8] R. R. Schrock, *J. Am. Chem. Soc.* **1975**, *97*, 6577–6578.

[9] a) For some examples see: J. L. Polse, A. W. Kaplan, R. A. Andersen, R. G. Bergman, *J. Am. Chem. Soc.* **1998**, *120*, 6316–6328; b) A. W. Kaplan, J. L. Polse, G. E. Ball, R. A. Andersen, R. G. Bergman, *J. Am. Chem. Soc.* **1998**, *120*, 11649–11662; c) T. E. Hanna, I. Keresztes, E. Lobkovsky, W. H. Bernskoetter, P. J. Chirik, *Organometallics* **2004**, *23*, 3448–3458; d) J. Schwartz, K. I. Gell, *J. Organomet. Chem.* **1980**, *184*, C1–C2.

[10] a) J. D. Fellmann, H. W. Turner, R. R. Schrock, *J. Am. Chem. Soc.* **1980**, *102*, 6608–6609; b) M. R. Churchill, H. J. Wasserman, H. W. Turner, R. R. Schrock, *J. Am. Chem. Soc.* **1982**, *104*, 1710–1716.

[11] a) K. F. Hirsekorn, A. S. Veige, M. P. Marshak, Y. Koldobskaya, P. T. Wolczanski, T. R. Cundari, E. B. Lobkovsky, *J. Am. Chem. Soc.* **2005**, *127*, 4809–4830; b) J. S. Freundlich, R. R. Schrock, W. M. Davis, *J. Am. Chem. Soc.* **1996**, *118*, 3643–3655; c) G. A. Miller, N. J. Cooper, *J. Am. Chem. Soc.* **1985**, *107*, 709–711; d) R. P. Hughes, S. M. Maddock, A. L. Rheingold, I. A. Guzei, *Polyhedron* **1998**, *17*, 1037–1043; e) L. Giannini, G. Guillemot, E. Solari, C. Floriani, N. Re, A. Chiesi-Villa, C. Rizzoli, *J. Am. Chem. Soc.* **1999**, *121*, 2797–2807; f) R. R. Schrock, S. W. Seidel, N. C. Mosch-Zanetti, K.-Y. Shih, M. B. O'Donoghue, W. M. Davis, W. M. Reiff, *J. Am. Chem. Soc.* **1997**, *119*, 11876–11893; g) R. R. Schrock, S. W. Seidel, N. C. Mosch-Zanetti, D. A. Dobbs, K.-Y. Shih, W. M. Davis, *Organometallics* **1997**, *16*, 5195–5208.

[12] a) J.-M. Basset, C. Copéret, L. Lefort, B. M. Maunders, O. Maury, E. Le Roux, G. Saggio, S. Soignier, D. Soulivong, G. J. Sunley, M. Taoufik, J. Thivolle-Cazat, *J. Am. Chem. Soc.* **2005**, *127*, 8604–8605; b) D. Soulivong, C. Copéret, J. Thivolle-Cazat, J.-M. Basset, B. M. Maunders, R. B. A. Pardy, G. J. Sunley, *Angew. Chem. Int. Ed.* **2004**, *43*, 5366–5369.

[13] a) F. Basuli, B. C. Bailey, J. Tomaszewski, J. C. Huffman, D. J. Mindiola, *J. Am. Chem. Soc.* **2003**, *125*, 6052–6053; b) F. Basuli, B. C. Bailey, L. A. Watson, J. Tomaszewski, J. C. Huffman, D. J. Mindiola, *Organometallics* **2005**, *24*, 1886–1906; c) F. Basuli, B. C. Bailey, J. C. Huffman, D. J. Mindiola, *Organometallics* **2005**, *24*, 3321–3334; d) B. C. Bailey, J. C. Huffman, D. J. Mindiola, W. Weng, O. V. Ozerov, *Organometallics* **2005**, *24*, 1390–1393; e) F. Basuli, U. J. Kilgore, X. Hu, K. Meyer, M. Pink, J. C. Huffman, D. J. Mindiola, *Angew. Chem. Int. Ed.* **2004**, *43*, 3156–3159; f) F. Basuli, B. C. Bailey, D. Brown, J. Tomaszewski, J. C. Huffman, M.-H. Baik, D. J. Mindiola, *J. Am. Chem. Soc.* **2004**, *126*, 10506–10507; g) F. Basuli, B. C. Bailey, J. C. Huffman, D. J. Mindiola, *Chem. Commun.* **2003**, 1554–1555.

[14] K. F. Hirsekorn, A. S. Veige, P. T. Wolczanski, *J. Am. Chem. Soc.* **2006**, *128*, 2192–2193.

 © 2006 Wiley-VCH Verlag GmbH & Co. KGaA, Weinheim 

[15] a) B. J. J. van de Heisteeg, G. Schat, O. S. Akkerman, F. Bickelhaupt, *J. Organomet. Chem.* **1986**, *310*, C25–C28; b) F. W. Hartner Jr, J. Schwartz, S. M. Clift, *J. Am. Chem. Soc.* **1983**, *105*, 640–641.
[16] a) W. A. Nugent, R. J. McKinney, R. V. Kasowski, F. A. Van-Catledge, *Inorg. Chim. Acta* **1982**, *65*, L91–L93; b) D. E. Wigley, *Prog. Inorg. Chem.* **1994**, *42*, 239–482.
[17] D. J. Duncalf, R. J. Harrison, A. McCamley, B. W. Royan, *J. Chem. Soc., Chem. Commun.* **1995**, 2421–2422.
[18] A. Antinolo, A. Otero, M. Fajardo, C. Garcia-Yebra, R. Gil-Sanz, C. Lopez-Mardomingo, A. Martin, P. Gomez-Sal, *Organometallics* **1994**, *13*, 4679–4682.
[19] P. Binger, P. Müller, P. Phillips, B. Gabor, R. Mynott, A. T. Herrmann, F. Langhauser, C. Krüger, *Chem. Ber.* **1992**, *125*, 2209–2212.
[20] M. D. Fryzuk, S. S. H. Mao, M. J. Zaworotko, L. R. MacGillivray, *J. Am. Chem. Soc.* **1993**, *115*, 5336–5337.
[21] a) R. H. Crabtree, *The Organometallic Chemistry of the Transition Metals*; Wiley: N. Y. **2001**; b) F. N. Tebbe, G. W. Parshall, G. S. Reddy, *J. Am. Chem. Soc.* **1978**, *100*, 3611–3613.
[22] T. Agapie, P. L. Diaconescu, C. C. Cummins, *J. Am. Chem. Soc.* **2002**, *124*, 2412–2413.
[23] Y.-C. Tsai, P. L. Diaconescu, C. C. Cummins, *Organometallics* **2000**, *19*, 5260–5262.
[24] a) R. R. Schrock, M. L. Listemann, L. G. Sturgeoff, *J. Am. Chem. Soc.* **1982**, *104*, 4291–4293; b) M. L. Listemann, R. R. Schrock, *Organometallics* **1985**, *4*, 74–83; c) M. H. Chisholm, D. M. Hoffman, J. C. Huffman, *Inorg. Chem.* **1983**, *22*, 2903–2906; d) M. H. Chisholm, B. K. Conroy, J. C. Huffman, *Organometallics* **1986**, *5*, 2384–2386.
[25] a) M. R. Churchill, W. J. Youngs, *Inorg. Chem.* **1979**, *18*, 171–176; b) S. J. McLain, C. D. Wood, L. W. Messerle, R. R. Schrock, F. J. Hollander, W. J. Youngs, M. R. Churchill, *J. Am. Chem. Soc.* **1978**, *100*, 5962–5964; c) L. J. Guggenberger, R. R. Schrock, *J. Am. Chem. Soc.* **1975**, *97*, 2935.
[26] a) R. Andrés, M. V. Galakhov, A. Martín, M. Mena, C. Santamaría, *Organometallics* **1994**, *13*, 2159–2163; b) R. Andrés, P. Gomez-Sal, E. de Jesus, A. Martín, M. Mena, C. Yelamos, *Angew. Chem. Int. Ed. Engl.* **1997**, *36*, 115–117; c) A. Abarca, M. Galakhov, P. Gómez-Sal, A. Martín, M. Mena, J.-M. Poblet, C. Santamaría, J. P. Sarasha, *Angew. Chem. Int. Ed.* **2000**, *39*, 534–537; d) A. Martín, M. Mena, M. Morales-Varela, C. Santamaria, *Eur. J. Inorg. Chem.* **2004**, *9*, 1914–1921; e) J. Gracia, A. Martín, M. Mena, M. Morales-Varela, J. Poblet, C. Santamaria, *Angew. Chem. Int. Ed.* **2003**, *42*, 927–930.
[27] B. C. Bailey, H. Fan, E. W. Baum, J. C. Huffman, M.-H. Baik, D. J. Mindiola, *J. Am. Chem. Soc.* **2005**, *127*, 16016–16017.
[28] P. H. M. Budzelaar, A. B. Van Oort, A. G. Orpen, *Eur. J. Inorg. Chem.* **1998**, 1485–1494.
[29] L. Bourget-Merle, M. F. Lappert, J. R. Severn, *Chem. Rev.* **2002**, *102*, 3031–3066.
[30] B. C. Bailey, F. Basuli, J. C. Huffman, D. J. Mindiola, *Manuscript accepted to, Organometallics.*
[31] a) L. Fan, B. M. Foxman, O. V. Ozerov, *Organometallics* **2004**, *23*, 326–328; b) O. V. Ozerov, C. Guo, L. Fan, B. M. Foxman, *Organometallics* **2004**, *23*, 5573–5580; c) O. V. Ozerov, C. Guo, V. A. Papkov, B. M. Foxman, *J. Am. Chem. Soc.* **2004**, *126*, 4792–4793; d) L. Fan, L. Yang, C. Guo, B. M. Foxman, O. V. Ozerov, *Organometallics* **2004**, *23*, 4778–4787.
[32] a) B. Hessen, A. Meetsma, J. H. Teuben, *J. Am. Chem. Soc.* **1989**, *111*, 5977–5978; b) B. Hessen, A. Meetsma, F. Van Bolhuis, J. H. Teuben, G. Helgesson, S. Jagner, *Organometallics* **1990**, *9*, 1925–1936; c) J. Yamada, M. Fujiki, K. A. Nomura, *Organometallics* **2005**, *24*, 2248–2250; d) B. Hessen, J.-K. F. Buijink, A. Meetsma, J. H. Teuben, G. Helgesson, M. Hakansson, S. Jagner, A. L. Spek, *Organometallics* **1993**, *12*, 2268–2276; e) J.-K. F. Buijink, J. H. Teuben, H. Kooijman, A. L. Spek, *Organometallics* **1994**, *13*, 2922–2924; f) M. Moore, S. Gambarotta, G. Yap, L. M. Liable-Sands, A. L. Rheingold, *Chem. Commun.* **1997**, 643–644; g) B. Hessen, J. H. Teuben, *J. Organomet. Chem.* **1989**, *367*, C18–C20.
[33] W. Weng, L. Yang, B. M. Foxman, O. V. Ozerov, *Organometallics* **2004**, *23*, 4700–4705.
[34] J. D. Protasiewicz, S. J. Lippard, *J. Am. Chem. Soc.* **1991**, *113*, 6564–6570.
[35] a) F. Basuli, J. Tomaszewski, J. C. Huffman, D. J. Mindiola, *J. Am. Chem. Soc.* **2003**, *125*, 10170–10171; b) F. Basuli, B. C. Bailey, J. C. Huffman, M.-H. Baik, D. J. Mindiola, *J. Am. Chem. Soc.* **2004**, *126*, 1924–1925.
[36] R. Baumann, R. Stumpf, W. M. Davis, L. Liang, R. R. Schrock, *J. Am. Chem. Soc.* **1999**, *121*, 7822–7836.
[37] S. Kahlert, H. Gorls, J. Scholz, *Angew. Chem. Int. Ed.* **1998**, *37*, 1857–1861.
[38] P. Sinnema, L. van der Veen, A. L. Spek, N. Veldman, J. H. Teuben, *Organometallics* **1997**, *16*, 4245–4247.
[39] J. Scholz, H. Gorls, *Organometallics* **2004**, *23*, 320–322.
[40] a) J. A. van Doorn, H. van der Heijden, A. G. Orpen, *Organometallics* **1995**, *14*, 1278–1283; b) J. A. van Doorn, H. van der Heijden, A. G. Orpen, *Organometallics* **1994**, *13*, 4271–4277.
[41] C. Krueger, R. Mynott, C. Siedenbiedel, L. Stehling, G. Wilke, *Angew. Chem. Int. Ed. Engl.* **1991**, *30*, 1668–1670.
[42] H. van der Heijden, B. Hessen, *J. Chem. Soc., Chem. Commun.* **1995**, 145–146.

Received: April 6, 2006
Published Online: July 13, 2006

 © 2006 Wiley-VCH Verlag GmbH & Co. KGaA, Weinheim 

DOI: 10.1002/ejic.200600253

# One-Pot Synthesis of a New High-Aluminium-Content Super-Microporous Aluminosilicate

**Lenin Huerta,[a,b] Francisca Romero-Sarria,[c] Olivier Marie,[c] Carmen Guillem,[a] Aurelio Beltrán,[a] Julio Latorre,[a] Daniel Beltrán,[a] and Pedro Amorós*[a]**

**Keywords:** Super-microporous / Aluminosilicates / Surfactants

A new super-microporous aluminosilicate having a high aluminium content (Si/Al ca. 1) has been prepared through a surfactant-assisted procedure with the use of a commercially available binary precursor (di-*sec*-butoxyaluminooxytriethoxysilane) as a single source of both Al and Si. The formation of super-micropores is a result of a significant network shrinkage associated with the thermal elimination of the surfactant. This solid has been studied by X-ray powder diffraction, electron microscopy, nuclear magnetic resonance spectroscopy and porosimetry. A preliminary analysis of the acidity and the catalytic activity of the super-microporous solid for the selective catalytic reduction of $NO_x$ is also presented. (© Wiley-VCH Verlag GmbH & Co. KGaA, 69451 Weinheim, Germany, 2006)

## Introduction

The discovery of the M41S family of mesoporous silicas by Mobil's researchers was a major step towards the expansion of the typical sizes of uniform micropores in zeotypes.[1] Since then, considerable effort has been devoted to the systematization of processing routes for the manufacture of silica-based mesoporous derivatives that contain pore sizes in the 2–10 nm range. The use of surfactants with alkyl chains of different lengths is the typical procedure employed for this endeavour.[2] While many investigations have been aimed at establishing the most suitable strategies to achieve large mesopores, the number of publications dealing with porous solids in which the pore sizes range between micropores and small-mesopores is limited.[3] The scarcity of results, however, is not an indication of the lack of interest in super-microporous solids since they are in high demand for their potential use in a large variety of applications, such as molecular recognition, adsorption, drug delivery and catalysis.[4] In fact, materials with uniform pore sizes in the 1–2 nm range (i.e. super-microporous) are expected to exhibit interesting shape- and size selectivity in the conversion of large organic substrates.

As mentioned above, there are few reports on super-microporous materials. Sung et al.[5] described the synthesis of porous niobium oxide with pore diameters below 2 nm. Shpeizer et al.[6] have recently reported on a general non-surfactant-assisted procedure to prepare super-microporous mixed oxides. With the exception of these two contributions, all of the remaining publications on super-microporous materials are centred on silica-based compositions. Super-microporous pure silicas have been prepared by different one-pot procedures, which implies the use of "structure-directing agents" or "templates". These templates vary greatly and range from micellar aggregates of surfactants (e.g. ω-hydroxy-bolaform[7] or long chain alkyl amines[8]) to simple, but bulky, organic molecules (e.g. adamantanamine[9]). Besides surfactant-assistance strategies, some strategies are based on the use of a single Si source (α-sodium disilicate[4]) or on a more complex multistep process (pore-entrance size decreases after post-synthetic treatment[10]). In some cases, mesoporous materials can be progressively altered to microporous materials through the incorporation of heteroelements such as Al or Zr.

Porous aluminosilicate compositions have traditionally attracted great interest owing to their capability to act as acid catalysts for bulky hydrocarbon conversion.[11] In practice, a solid acid material in the super-microporous domain could bridge the gap between zeolites and mesoporous aluminosilicates. Incorporation of Al centres in the framework of mesoporous silicas usually leads to a certain pore size decrease. Hence, aluminosilicates with pore sizes at the lower end of the mesoporous range have been obtained with high Al content materials.[12] However, pores in the super-microporous range usually cannot be achieved even with Si/Al ratios as low as 7.[13] In this case, the preparation of super-microporous aluminosilicates requires the combined effects of short-tail surfactants and high Al content in the starting solution[14] or, alternatively, the use of post-syn-

[a] Institut de Ciència dels Materials (ICMUV), Universitat de València,
P. O. Box 2085, 46071-València, Spain
Fax: +34-96-3543633
E-mail: pedro.amoros@uv.es
[b] Departamento de Química, Facultad de Ciencias, Universidad del Zulia,
P. O. Box 526, Maracaibo, Venezuela
[c] Laboratoire Catalyse et Spectrochimie – UMR 6506 – ENSI Caen,
6 Bd Mal Juin, 14050, Caen cedex, France

 © 2006 Wiley-VCH Verlag GmbH & Co. KGaA, Weinheim 

thetic strategies of Al-grafting.[15] Following these synthetic procedures, super-microporous silicas with a maximum Al content in the Si/Al = 2.5–7 range have been described.[16]

We report here on a new, direct and reproducible procedure that has allowed us to prepare a new porous silica with a very high Al content and with pore sizes in the super-microporous range.

## Results and Discussion

### Synthesis Strategy

Our surfactant-assisted strategy is based on the use of a "single-source molecular precursor" (i.e. a molecular precursor that simultaneously contains all the required oxide forming elements, Al and Si in this case). Under the synthetic conditions selected, and working in a water/triethanolamine medium, the use of such a precursor leads to poorly condensed mesostructured solids. Subsequently, the thermal treatment required to eliminate the surfactant also induces a significant network shrinkage, which leads to the formation of the super-micropores. The final material shows a high proportion of tetrahedral Al, and consequently a high acidity, and reasonable catalytic properties in the selective catalytic reduction (SCR) of nitrogen oxides ($NO_x$).

The use of bimetallic complexes, employed extensively by the Tilley group,[17,18] as inorganic precursors constitutes a polished approach towards the synthesis of a variety of mesoporous oxides. Although the composition of the final mixed oxide depends on that of the precursor, this approach is advantageous as it ensures an intimate mixture of the reactive elements from the initial preparative steps. In our case, we have additionally benefited from the complexing ability of triethanolamine (leading to atrane complexes), which in turn plays an essential role as the cosolvent.[19] The first step in our strategy involves the transesterification of commercially-available alkoxy derivatives (primary source of the oxide forming elements) through their treatment with dried triethanolamine at moderate temperatures (130–170 °C). This reaction leads to the formation of atrane complexes (real hydrolytic precursors). In fact, the use of atranes as precursors has allowed us to successfully prepare a diverse range of mesoporous single- and mixed oxides.[19–25] The additional use of triethanolamine as the cosolvent[19] is also supported by its use in the preparation of mesoporous materials in water/alcohol media;[26] however, atrane complex formation does not occur in water-rich media. The atrane alkoxy complexes are, in general, unstable but they are relatively inert towards hydrolysis. In many cases, this resistance towards hydrolysis (induced by the triethanolamine-like ligands) aids in the orchestration of the self-assembling processes (between the inorganic moieties and the surfactant aggregates) that lead to stable mesostructured phases.[19] In fact, the nucleophilic displacement of triethanolamine-related ligands, which occurs as a result of the attack of water on the silicon or aluminium centres, becomes more difficult than for monodentate alkoxo groups. In short, the combined effects of: (1) the use of a rigid binary "single-source molecular precursor", (2) the intrinsic "hydrolysis retarding effect" associated with the formation of atrane complexes, and (3) the buffered water/alcohol medium generated by the triethanolamine favours the formation of a low-condensed mesostructured material. The subsequent thermal evolution of the surfactant (to open the pore system) occurs together with a significant network shrinkage because of the completion of the condensation reactions, which leads to pores in the super-micropore domain.

### Characterization

As expected, the Si/Al molar ratio in the final material [$1.2 \pm 0.2$ from electron probe microanalysis (EPMA)] is very close to that present in the mother liquor. This fact indicates that there is no degradation of the bimetallic precursor under the working conditions. EPMA shows that the samples are chemically homogeneous at the micrometer level (spot area ca. 1 μm) with a regular distribution of Al and Si atoms throughout the inorganic walls. We can conclude that there is no preferential incorporation of Al or Si into the final net.

The mesophasic nature of both the as-synthesized and the super-microporous materials is illustrated by their X-ray powder diffraction (XRD) patterns and TEM images (Figure 1 and Figure 2). Both solids show low-angle XRD patterns with only one strong and relatively broad diffraction peak, which is typical of mesostructured/mesoporous materials prepared through surfactant-assisted procedures (Figure 1). This signal is usually associated with the (100) reflection if a MCM-41-like lattice is assumed. The observation of only one broad signal is characteristic of highly disordered pore systems. The absence of additional signals in the XRD pattern of the as-synthesized material could be due to the incorporation of Al into the walls. In fact, similar XRD patterns were recorded for Al-containing silica materials prepared from independent Si and Al molecular precursors under similar conditions.[12] In general, the incorporation of heteroelements into silica-based hexagonal porous frameworks implies a progressive lowering of the order in the pore array. After calcination, the intensity of the signal decreases, while it also appears significantly broadened. Moreover, calcination also results in a significant shift in the maximum towards high $2\theta$ values.

Hence, the value of the $a_0$ parameter (cell parameter assuming an MCM-41-like hexagonal array; $a_0 = 2 \cdot d_{100}/3^{1/2}$) pronouncedly decreases after calcination (from 5.77 to 5.05 nm). This behaviour indicates that surfactant elimination results in a significant reorganization of the porous walls. A relative loss of order together with a significant network shrinkage occur as a consequence of the calcination process.

While the TEM images (Figure 2) fully correlate to the XRD observations, the $N_2$ adsorption–desorption isotherms confirm the shrinkage of the framework (Figure 3).

 © 2006 Wiley-VCH Verlag GmbH & Co. KGaA, Weinheim 

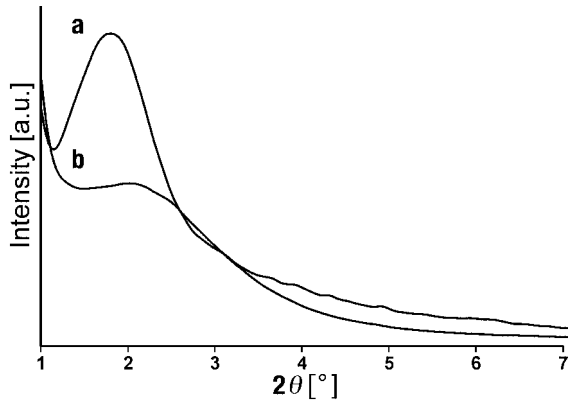


Figure 1. XRD patterns of (a) as-synthesized and (b) super-microporous materials.

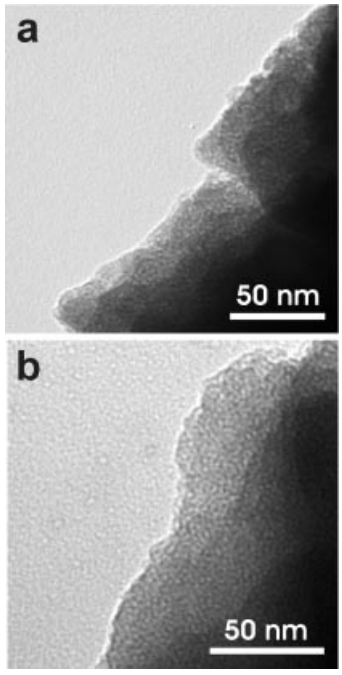


Figure 2. Representative TEM images of (a) as-synthesized and (b) super-microporous materials.

Thus, although the surfactant used (CTMABr) usually leads to the formation of mesopores (i.e. pores usually in the 2–3 nm range), the pore size estimated in this case falls in the microporous domain. In fact, the mean pore size resulting from the $D = 4V/S$ equation (which maintains a certain validity for super-micropores)[16] indicates a pore dimension of 1.3 nm, i.e. in the super-micropore range [pore volume ($V$) = 0.18 $cm^3 g^{-1}$, BET surface area ($S$) = 519 $m^2 g^{-1}$]. Application of the BJH method also indicates pore sizes in the super-micropore range, although these are slightly out of the optimum working range of the instrument. Indeed, we can observe a small maximum in the BJH pore size distribution at ca. 1.45 nm (see Figure 4). Also, the high value of the thickness of the average pore wall (3.8 nm, defined as wall thickness = $a_0$ – pore size) suggests a certain tendency to increase the wall condensation by calcination.

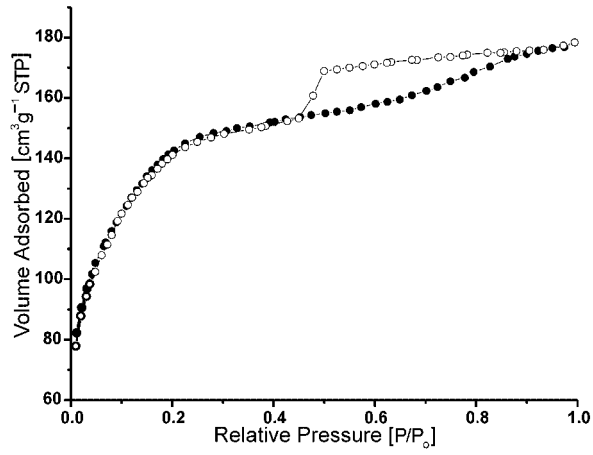


Figure 3. $N_2$ adsorption–desorption isotherms of the super-microporous aluminosilicate.

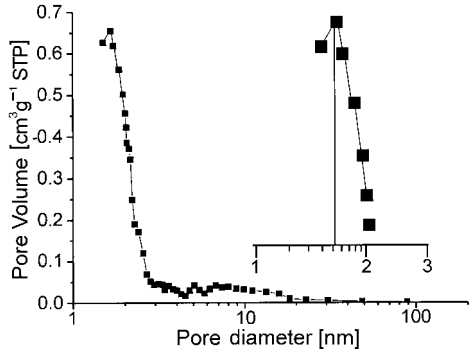


Figure 4. BJH pore size distribution on the adsorption branch of the isotherm.

Besides the above observations, the NMR results provide further evidence and confirm the theory that the condensation occurs in the inorganic walls as a consequence of the thermal treatment. Thus, in the case of the as-synthesized solid, the $^{27}Al$ MAS NMR spectrum shows essentially only one resonance signal at ca. $\delta$ = 57.0 ppm (Figure 5a), which is characteristic of tetrahedral Al sites. On the other hand, its $^{29}Si$ MAS NMR spectrum shows a very strong and broad signal whose centre appears to be shifted downfield ($\delta$ = –80.9 ppm, Figure 5c) when compared to that of a pure siliceous MCM-41. This signal displacement is in accordance with the resonance of $Q^4$ (4Al) environments. The broadness of the signal might be a consequence of other resonances that result from additional minority Si environments [such as $Q^4$ (3Al) and other $Q^3$ sites]. Thus, the MAS NMR results are consistent with the Si/Al = 1.2 ± 0.2 molar ratio determined from EPMA. The evolution of the NMR spectra indicates the occurrence of a significant conversion from a tetrahedral Al to an octahedral Al, which is a consequence of the surfactant removal (Figure 5b). This process also affects the Si sites. In fact, the $^{29}Si$ MAS NMR signal shifts from $\delta$ = –80.9 ppm to $\delta$ = –89.4 ppm (Figure 5d). This is consistent with an increase in $Q^4$ (3Al) centres. In short, the thermal surfactant removal also induces a reorganization, by way of a condensation reaction, of the inor-

 © 2006 Wiley-VCH Verlag GmbH & Co. KGaA, Weinheim 

ganic walls, and this shrinkage is responsible for the formation of the super-micropores. A similar behaviour (evolution from meso to micropores through calcination) has been recently reported in the preparation of pure porous silicas from hydrated α-sodium disilicate as a Si source.[4] In our case, we propose that the geometrical constraints imposed by the use of a single Si–Al molecular source lead to the framework in the as-synthesized material. In fact, when independent Si and Al precursors were used under similar working conditions, the final pore contraction was significantly lower, which resulted in solids with pore sizes that fall within the low limit of the mesoporous range.[12]

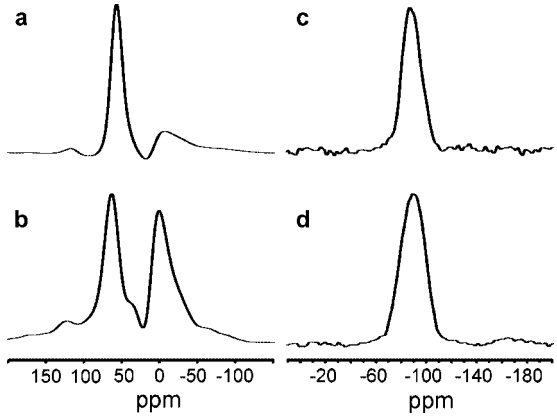


Figure 5. $^{27}$Al MAS NMR spectra of (a) as-synthesized and (b) super-microporous sample. $^{29}$Si MAS NMR spectra of (c) as-synthesized and (d) super-microporous sample.

Although ca. 50% of the Al centres have evolved from tetrahedral to octahedral sites after calcination, the final super-microporous material shows significant acidity, with a total number of acid sites of 800 mmol g$^{-1}$ (determined by nonselective $NH_3$ adsorption), – 375 mmol g$^{-1}$ corresponding to Lewis acid sites (estimated from Lewis selective acetonitrile adsorption) and the remaining 425 mmol g$^{-1}$ to Brønsted acid sites. This result is consistent with the $^{27}$Al MAS NMR spectrum, which shows both tetrahedral Al (responsible for Brønsted acidity) and octahedral Al (responsible for Lewis acidity) after calcination. A preliminary study on the use of this super-microporous aluminosilicate as a catalyst for the low-temperature (433 K) SCR of $NO_x$ with $NH_3$ gives a reasonable conversion level (ca. 72%) with little ammonia leakage. Comparatively, under the same temperature and flow conditions, the use of $NH_4Y$ (Si/Al = 5.7), whose Brønsted acidic strength is higher than that of our super micro-porous aluminosilicate, leads to 100% $NO_x$ conversion without $NH_3$ leakage; this result is in accordance with the acidity values.

## Conclusions

We report here on a simple and reproducible one-pot surfactant-assisted procedure for obtaining a new high-Al-content super-microporous aluminosilicate with well-dispersed Al and Si centres throughout the inorganic walls. Our strategy to diminish the pore size is based on the intermediate formation of a low-condensed framework starting from a binary (Al and Si) rigid precursor. Super-micropores are then formed as a consequence of the structure shrinkage induced by calcination. The final material presents with a high acidity and a reasonable catalytic activity in the SCR of $NO_x$. This strategy can be extended to the preparation of other bimetallic super-microporous oxides.

## Experimental Section

**Chemicals:** All the synthetic reagents were analytically pure and were used as received from Aldrich and Gelest. The Si and Al primary source used was di-*sec*-butoxyaluminooxytriethoxysilane (from Gelest). 2,2′,2′′-Nitrilotriethanol or triethanolamine [$N(CH_2–CH_2–OH)_3$] was used for obtaining the binary (Si and Al) atrane precursor. The templating agent used was cetyltrimethylammonium bromide (CTMABr).

**Synthesis:** The method was a modification of the so-called "atrane route", a simple preparative technique whose main points have been described previously in detail.[19] In a typical synthesis di-*sec*-butoxyaluminooxytriethoxysilane (13.20 g, 0.0375 mol) was slowly added to liquid triethanolamine (33.5 mL, 0.255 mol), and heated at 150 °C for 5 min. After the solution was cooled to 90 °C, CTMABr surfactant (6.84 g, 0.0187 mol) was added. The solution containing the binary (Si and Al) atrane complex (with the triethanolamine-related species as ligands) and the templating agent (CTMABr) was cooled to 60 °C and mixed with water (120 mL, 6.66 mol). After a few seconds, a white powder appeared. The resulting suspension was kept at room temperature for 12 h. The final (mesostructured) powder was filtered off, washed with water and ethanol, and air dried. In order to open the pore system (by surfactant removal), both calcination and chemical extraction procedures were tested. Typical extraction protocols, such as the suspension of the mesostructured solid in an HCl/ethanol solution (about 1 g of powder, 15 mL of 35% HCl and 150 mL of 96% ethanol), were unsuccessful. In practice, this process results in a significant mesostructure degradation or collapse that is provoked by the leaching of a large proportion of the Al atoms in the form of chloride complexes. This result indicates a high accessibility of the Al centres in the mesostructure, which provides evidence for a relatively low condensation in its inorganic walls. Removal of the surfactant was carried out by calcination. The as-synthesized solid was heated at 50 °C under static air for 5 h, thus yielding the final super-microporous material.

**Physical Measurements:** Both the as-synthesized and the super-microporous solids were analyzed for Si and Al content by electron probe microanalysis (EPMA, Philips SEM-515 instrument). X-ray powder diffraction (XRD) data were recorded with a Seifert 3000TT θ-θ diffractometer with Cu-$K_\alpha$ radiation. TEM images were obtained with a Philips CM10 microscope operated at 120 kV. $N_2$ adsorption–desorption isotherms were recorded with a Micromeritics ASAP2010 automated sorption analyzer. $^{29}$Si- and $^{27}$Al MAS NMR spectra were recorded with a Varian Unity 300 spectrometer operating at 79.5 MHz, and with a magic angle spinning speed of at least 4.0 KHz. Acidity was estimated from in situ FTIR experiments with a Nicolet Nexus FTIR instrument equipped with a quartz cell for the $NH_3$ or acetonitrile adsorption. Activity for the SCR of $NO_x$ with $NH_3$ was determined from operando FTIR experiments with a homemade infrared reactor cell.[27] More procedural details about both in situ and operando experiments are given in ref.[28]

 © 2006 Wiley-VCH Verlag GmbH & Co. KGaA, Weinheim 

## Acknowledgments

This research was supported by the Ministerio de Educación y Ciencia (under grant MAT2003–08568-C03–01) and the Generalitat Valenciana (grant GRUPOS03/099). L.H. thanks the Universidad del Zulia for a doctoral grant.

[1] C. T. Kresge, M. E. Leonowicz, W. J. Roth, J. C. Vartuli, J. S. Beck, *Nature* **1992**, *359*, 710–712.
[2] G. J. A. A. Soler-Illia, C. Sanchez, B. Lebeau, J. Patarin, *Chem. Rev.* **2002**, *102*, 4093–4138, and references therein.
[3] S. A. Bagshaw, A. R. Hayman, *Adv. Mater.* **2001**, *13*, 1011–1013.
[4] M. Kato, T. Shigeno, T. Kimura, K. Kuroda, *Chem. Mater.* **2005**, *17*, 6416–6421.
[5] T. Sun, J. Y. Ying, *Angew. Chem. Int. Ed.* **1998**, *37*, 664–667.
[6] B. G. Shpeizer, A. Clearfield, J. M. Heising, *Chem. Commun.* **2005**, 2396–2398.
[7] S. A. Bagshaw, A. R. Hayman, *Chem. Commun.* **2000**, 533–534.
[8] Z. Zhang, X. Yan, B. Tian, C. Yu, B. Tu, G. Zhu, S. Qiu, D. Zhao, *Microporous Mesoporous Mater.* **2006**, *90*, 23–31.
[9] T. Sun, M. S. Wong, J. Y. Ying, *Chem. Commun.* **2000**, 2057–2058.
[10] X. S. Zhao, G. Q. Lu, X. Hu, *Chem. Commun.* **1999**, 1391–1392.
[11] A. Corma, A. Martínez, V. Martínez-Soria, J. B. Montón, *J. Catal.* **1995**, *153*, 25–31.
[12] S. Cabrera, J. El Haskouri, S. Mendioroz, C. Guillem, J. Latorre, A. Beltrán, D. Beltrán, M. D. Marcos, P. Amorós, *Chem. Commun.* **1999**, 1679–1680.
[13] R. Mokaya, W. Jones, *J. Mater. Chem.* **1998**, *8*, 2819–2826.
[14] D. P. Serrano, J. Aguado, J. M. Escola, E. Garagorri, *Chem. Commun.* **2000**, 2041–2042.
[15] E. Bastardo-Gonzalez, R. Mokaya, W. Jones, *Chem. Commun.* **2001**, 1016–1017.
[16] B. Bonelli, B. Onida, J. D. Chen, A. Galarneau, F. Di Renzo, F. Fajula, E. Garrone, *Microporous Mesoporous Mater.* **2004**, *67*, 95–106.
[17] J. W. Kriesel, M. S. Sander, T. D. Tilley, *Chem. Mater.* **2001**, *13*, 3554–3563.
[18] R. L. Brutchey, J. E. Goldberger, T. S. Koffas, T. D. Tilley, *Chem. Mater.* **2003**, *15*, 1040–1046.
[19] S. Cabrera, J. El Haskouri, C. Guillem, J. Latorre, A. Beltrán, D. Beltrán, M. D. Marcos, P. Amorós, *Solid State Sci.* **2000**, *2*, 405–420.
[20] S. Cabrera, J. El Haskouri, S. Mendioroz, C. Guillem, J. Latorre, A. Beltrán, D. Beltrán, M. D. Marcos, P. Amorós, *Chem. Commun.* **1999**, 1679–1680.
[21] S. Cabrera, J. El Haskouri, J. Alamo, A. Beltrán, D. Beltrán, S. Mendioroz, M. D. Marcos, P. Amorós, *Adv. Mater.* **1999**, *11*, 379–381.
[22] S. Cabrera, J. El Haskouri, A. Beltrán, D. Beltrán, M. D. Marcos, P. Amorós, *Solid State Sci.* **2000**, *2*, 513–518.
[23] J. El Haskouri, S. Cabrera, M. Gutierrez, A. Beltrán, D. Beltrán, M. D. Marcos, P. Amorós, *Chem. Commun.* **2001**, 309–310.
[24] J. El Haskouri, D. Ortiz de Zárate, C. Guillem, J. Latorre, M. Caldés, A. Beltrán, D. Beltrán, A. B. Descalzo, G. Rodríguez, R. Martínez, M. D. Marcos, P. Amorós, *Chem. Commun.* **2002**, 330–331.
[25] J. El Haskouri, S. Cabrera, C. J. Gómez-García, C. Guillem, J. Latorre, A. Beltrán, D. Beltrán, M. D. Marcos, P. Amorós, *Chem. Mater.* **2004**, *16*, 2805–2813.
[26] J. Sun, Z. Shan, T. Maschmeyer, J. A. Moulijn, M.-O. Coppens, *Chem. Commun.* **2001**, 2670–2671.
[27] T. Lesage, C. Verrier, P. Bazin, J. Saussey, M. Daturi, *Phys. Chem. Chem. Phys.* **2003**, *5*, 4435–4440.
[28] F. Romero Sarria, J. Saussey, J. P. Gallas, O. Marie, M. Daturi, *Stud. Surf. Sci. Catal.* **2005**, *158*, 821–828.

Received: March 23, 2006
Published Online: July 13, 2006

 © 2006 Wiley-VCH Verlag GmbH & Co. KGaA, Weinheim 

DOI: 10.1002/ejic.200600455

# A Silver(I) Coordination Polymer Containing Tridentate *N*- and *P*-Coordinating 1,3,5-Triaza-7-phosphaadamantane (PTA) Ligands

**Fabian Mohr,*[a][‡] Larry R. Falvello[a] and Mariano Laguna*[a]**

*Dedicated to Prof. Victor Riera on the occasion of his retirement for his contribution to inorganic chemistry*

**Keywords:** Silver / Coordination polymer / Phosphane / Self-assembly

A silver(I) coordination polymer containing 1,3,5-triaza-7-phosphaadamantane (PTA) in an unprecedented bridging, tridentate *P,N,N′*-coordination mode is formed by the reaction of PTA with $AgNO_3$ in water.

(© Wiley-VCH Verlag GmbH & Co. KGaA, 69451 Weinheim, Germany, 2006)

The synthesis of the air-stable, water-soluble phosphane ligand 1,3,5-triaza-7-phosphaadamantane (PTA) was first reported in 1974[1] but only recently has this phosphane been used as a ligand in a variety of inorganic and organometallic compounds.[2] An important driving force for the sudden interest in this ligand has been due to further developments in "green chemistry" and the need for inorganic/organometallic compounds that are soluble and stable in aqueous media.[3,4] One strategy to solubilise metal compounds is by the coordination of water-soluble ligands to a metal centre, which then may impart water solubility to the entire complex. In almost all of the known PTA metal complexes, the phosphane acts as a *P*-donor ligand (Figure 1, **A**). Very recently, the first examples of transition metal compounds that contain *N*-coordinated PTA (Figure 1, **B**) have been observed in manganese complexes $[MnX_2(PTA)_2(H_2O)_2]$ (X = Cl, Br).[5] In 2005, the organometallic Ru/Ag coordination polymers $[CpRu(L)(\mu\text{-}P,N\text{-}PTA)_2AgCl_2]_n$ (L = dmso, $H_2O$) were reported, which constitute the first, and so far only, examples of a PTA complex in which the ligand adopts a bridging *N,P*-coordination mode (Figure 1, **C**).[6]

In the past, we have utilised silver(I) phosphane salts of the type [AgX(P)] (P = tertiary phosphane; X = OTf, $ClO_4$, $NO_3$) as phosphane transfer reagents in the preparation of gold(II) complexes by metathesis reactions.[7] Recently, we reported the synthesis and characterisation of a series of water-soluble and water-stable gold complexes, which includes a gold(II) PTA derivative that was prepared with [Ag(OTf)(PTA)].[8,9] During our studies of various [AgX(PTA)] derivatives, we isolated and structurally characterised the nitrate derivative $[Ag(PTA)(H_2O)]NO_3$. X-ray quality crystals of $[Ag(PTA)(H_2O)]NO_3$[10] were formed when aqueous solutions containing equimolar amounts of PTA and $AgNO_3$ were mixed. This compound is the first example of a complex that contains PTA in a triply bridging *P,N,N′*-coordination mode (Figure 1, **D**). The basic unit of this complex consists of a molecule of *P*-coordinated PTA and water coordinated to the silver atom (Figure 2).

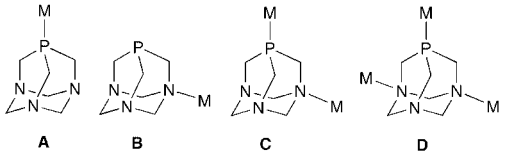


Figure 1. Observed coordination modes of PTA.

These monomers are then arranged such that two of the PTA nitrogen atoms, N-2 and N-3, coordinate to other silver atoms, i.e. each silver atom is connected to one phosphorus atom, P-1, and two nitrogen atoms, N-2 and N-3, from three different PTA molecules in a T-shaped arrangement. The coordinated water molecule completes the distorted tetrahedral coordination geometry about the silver atom. The network structure of the complex can be described as a polymeric net that contains hexagonal units (Figure 3).

In the crystal, these polymeric nets are stacked above each other, and the resulting channels are occupied by the nitrate anions (Figure 4).

In this complex, the PTA ligand behaves very similarly to its all-nitrogen analogue hexamethylenetetramine

[a] Departamento de Química Inorgánica, Instituto de Ciencia de Materiales de Aragón, Universidad de Zaragoza – C.S.I.C., 50009 Zaragoza, Spain
E-mail: fmohr@unizar.es
mlaguna@unizar.es
[‡] Present address: Departamento de Química, Universidad de Burgos, 09001 Burgos, Spain

 InterScience © 2006 Wiley-VCH Verlag GmbH & Co. KGaA, Weinheim 

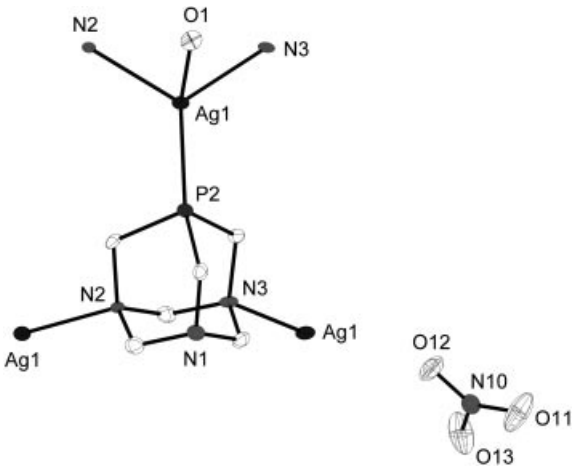


Figure 2. Structure of $[Ag(PTA)(H_2O)]NO_3$ which shows the atom-labelling scheme. Displacement ellipsoids are drawn at 50% probability and hydrogen atoms are omitted for clarity.

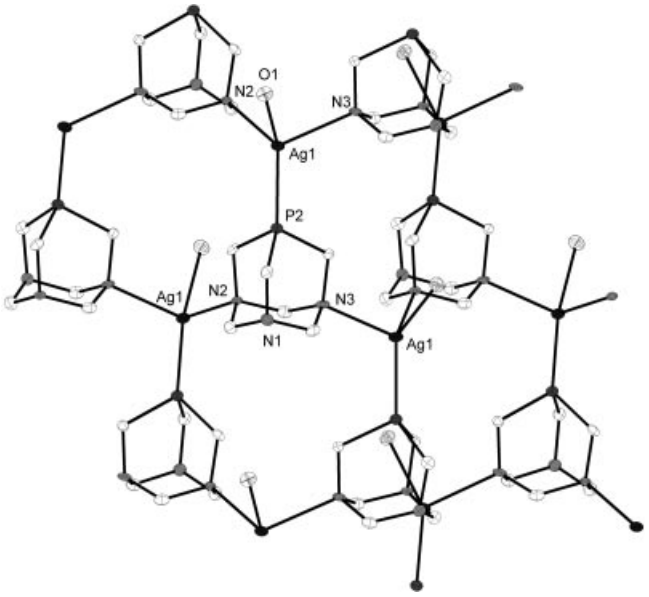


Figure 3. Polymeric net structure of $[Ag(PTA)(H_2O)]NO_3$ which illustrates the *P*,*N*,*N*′-coordination mode of the PTA ligand. Hydrogen atoms, as well as the nitrate anions, are omitted for clarity.

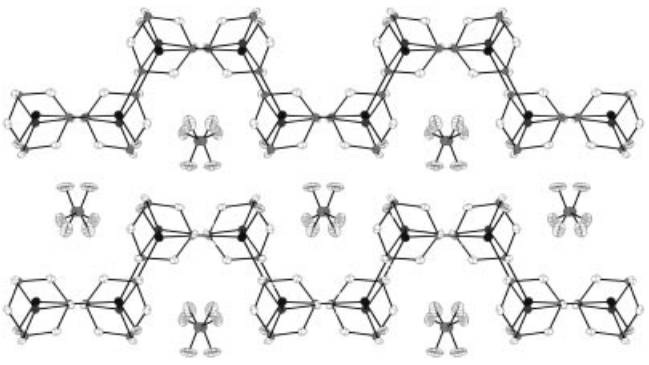

Figure 4. View of $[Ag(PTA)(H_2O)]NO_3$ along the *c*-axis which shows three polymer nets and the nitrate anions located in the channels. Hydrogen atoms are omitted for clarity.

(HMT). A variety of [AgX(HMT)] complexes have been prepared and structurally characterised and, depending on the metal/HMT ratios, the solution pH and the type of counterions, many different two- and three-dimensional network polymers have been observed.[11–13] In particular, the polymeric net structure of $[Ag(NO_3)(HMT)]$[14] is almost identical to that of $[Ag(PTA)(H_2O)]NO_3$, with the exception that a nitrato ligand is *O*-coordinated to the silver atom instead of a water molecule, hence the channels in the 3D network of $[Ag(NO_3)(HMT)]$ are vacant. The Ag–P bond length in $[Ag(PTA)(H_2O)]NO_3$ [2.3822(12) Å] is shorter than the Ag–P distances in other silver(I) nitrate complexes that contain bulky phosphane ligands such as $[Ag(NO_3)(PPh_3)_2]$ and $[Ag(NO_3)\{P(m\text{-}MeC_6H_4)_3\}]$ [2.443(1) and 2.4128(8) Å, respectively].[15] However, if the bulkiness of the phosphane group is decreased, the Ag–P bond length becomes shorter as is evident in $[Ag\{P(CH_2CH_2CN)_3\}_2]NO_3$, whose Ag–P bond length is 2.3832(9) Å.[15] This bond length is very similar to that observed in $[Ag(PTA)(H_2O)]NO_3$ in this work, which illustrates the small steric bulk of PTA. The two Ag–N distances [2.441(4) and 2.468(4) Å] are slightly longer than those observed in $[Ag(NO_3)(HMT)]$ [2.406(5) and 2.335(6) Å] and $[CpRu(H_2O)(\mu\text{-}P,N\text{-}PTA)_2AgCl_2]_n$ [2.423(6) Å].[6]

In summary we present here the first example of a PTA ligand that adopts a tridentate, bridging *P*,*N*,*N*′-coordination mode, which results in a polymeric net structure that contains hexagonal cavities occupied by nitrate anions.

## Acknowledgments

This work was supported by the Ministerio de Ciencia y Tecnología Spain (Grant CTQ2005-08099-C03-01) and F. M. wishes to thank the University of Burgos for a visiting fellowship.

[1] D. J. Daigle, A. B. Pepperman Jr., S. L. Vail, *J. Heterocycl. Chem.* **1974**, *11*, 407.
[2] A. D. Phillips, L. Gonsalvi, A. Romerosa, F. Vizza, M. Peruzzini, *Coord. Chem. Rev.* **2004**, *248*, 955–993.
[3] B. Cornils and W. A. Herrmann (Eds.), *Aqueous-phase Organometallic Catalysis Concepts and Applications*, 1st ed., Wiley-VCH, Weinheim, **1998**.
[4] F. Joó, *Aqueous Organometallic Catalysis*, Kluwer Academic Publishers, Dordrecht, **2001**.
[5] B. J. Frost, C. M. Bautista, R. Huang, J. Shearer, *Inorg. Chem.* **2006**, *45*, 3481–3483.
[6] C. Lidrissi, A. Romerosa, M. Saoud, M. Serrano-Ruiz, L. Gonsalvi, M. Peruzzini, *Angew. Chem. Int. Ed.* **2005**, *44*, 2568–2572.
[7] R. Usón, A. Laguna, M. Laguna, J. Jiménez, P. G. Jones, *J. Chem. Soc., Dalton Trans.* **1991**, 1361–1365.
[8] F. Mohr, S. Sanz, E. Cerrada, M. Laguna, *Organometallics* **2006**, *25*, 3084–3087.
[9] F. Mohr, E. Cerrada, M. Laguna, *Organometallics* **2006**, *25*, 644–648.
[10] Experimental details: A solution of $AgNO_3$ (0.108 g, 0.636 mmol) in water (10 mL) was treated with an aqueous solution of PTA (0.100 g, 0.636 mmol). The solution was left to stand in an open vessel for ca. 48 h, and colourless X-ray quality crystals of the complex were formed, which were isolated by filtration. Yield 0.085 g (41%). $^{31}P\{^1H\}$ NMR (162 MHz, $D_2O$): $\delta$ = –77.81 (broad, unresolved P–Ag coup-

 © 2006 Wiley-VCH Verlag GmbH & Co. KGaA, Weinheim 

ling) ppm. $^1$H NMR (400 MHz, $D_2O$): $\delta$ = 4.29 (d, $J$ = 2.5 Hz, 6 H, C$H_2$N), 4.61 (AB quartet, 6 H, C$H_2$P) ppm. $C_6H_{14}N_4O_4PAg$ (345.05): calcd. C 20.89, H 4.09, N 16.24; found C 20.73, H 3.87, N 16.30. Crystal data: Formula = $C_6H_{14}N_4O_4PAg$. $M$ = 345.05. Colourless plates, 0.08 × 0.22 × 0.22 mm, orthorhombic. Space group = *Pbca*, $a$ = 11.1798(4) Å, $b$ = 11.3646(3) Å, $c$ = 16.9315(6) Å. $\alpha$, $\beta$, $\gamma$ = 90.0°. $V$ = 2151.21(12) Å$^3$. $Z$ = 8. $D_{calcd.}$ = 2.131 mg/m$^3$. $\mu$ = 2.029 mm$^{-1}$. Temperature = 123(2) K. $\lambda$ (Mo-$K_\alpha$) = 0.71073 Å. $T$(SADABS)$_{min/max}$ = 0.7591/1.000. $F$(000) = 1376. $2\theta_{min/max}$ = 9.44/50.00. *hkl* range = –13 to 9, –13 to 13, –20 to 20. No. of reflections = 11401. No. of independent reflections = 1875 ($R_{int}$ = 0.0326). $R_1$ = 0.0428, $wR_2$ = 0.0866, $R_1$ (all data) = 0.0518, $wR_2$ (all data) = 0.0911. GOF (all data) = 1.154. $\Delta\rho_{max/min}$ = 0.923/–0.661. Data were collected with an Oxford Diffraction XCalibur2 CCD diffractometer. The structure was solved by direct methods and refined by the full-matrix least-squares method with SHELXTL-NT 6.1. CCDC-603984 contains the supplementary crystallographic data for this paper. These data can be obtained free of charge from The Cambridge Crystallographic Data Centre via www.ccdc.cam.ac.uk/data_request/cif.

[11] M. L. Tong, S. L. Zheng, X. M. Chen, *Chem. Eur. J.* **2000**, *6*, 3729–3738.
[12] S. L. Zheng, M. L. Tong, X. M. Chen, S. W. Ng, *J. Chem. Soc., Dalton Trans.* **2002**, 360–364.
[13] S. Lu, S. Qin, Y. Ke, J. Li, H. Pei, S. Zhou, X. Wu, W. Du, *Cryst. Res. Technol.* **2004**, *39*, 89–93.
[14] P. A. Michelet, B. Viossat, P. Khodadad, N. Rodier, *Acta Crystallogr. Acta Crystallogr. Sect. B* **1981**, *37*, 2171–2175.
[15] C. W. Liu, H. Pan, J. P. Fackler Jr., G. Wu, R. E. Wasylishen, M. Shang, *J. Chem. Soc., Dalton Trans.* **1995**, 3691–3697.

Received: May 16, 2006
Published Online: July 13, 2006

 © 2006 Wiley-VCH Verlag GmbH & Co. KGaA, Weinheim 

DOI: 10.1002/ejic.200600408

# Chiral Half-Sandwich Ruthenium(II) Complexes as Catalysts in 1,3-Dipolar Cycloaddition Reactions of Nitrones with Methacrolein

**Daniel Carmona,*[a] M. Pilar Lamata,*[b] Fernando Viguri,[b] Joaquina Ferrer,[a] Néstor García,[a] Fernando J. Lahoz,[a] M. Luisa Martín,[a] and Luis A. Oro*[a]**

*Dedicated to Prof. Dr. Víctor Riera on the occasion of his 70th birthday*

**Keywords:** Asymmetric catalysis / Cycloadditions / Ruthenium / Phosphanyloxazolines / Half-sandwich complexes

Ruthenium complexes of formula $[(\eta^6\text{-arene})Ru(LL^*)(H_2O)][SbF_6]_2$ (arene = $C_6H_6$, *p*-$MeC_6H_4iPr$, $C_6Me_6$; $LL^*$ = bidentate chelate chiral ligand with PN, PP or NN donor atoms) have been tested as catalyst precursors for the asymmetric 1,3-dipolar cycloaddition of nitrones to methacrolein. The reaction occurs quantitatively with perfect *endo* selectivity and moderate enantioselectivity (up to 74 % *ee*). The ruthenium aqua complexes can be prepared from the corresponding chlorides, $[(\eta^6\text{-arene})RuCl(LL^*)][SbF_6]$. Dipolarophile intermediates $[(\eta^6\text{-arene})Ru(PNiPr)(methacrolein)][SbF_6]_2$ {PN*i*Pr = (4*S*)-2-(2-diphenylphosphanylphenyl)-4-isopropyl-1,3-oxazoline} as well as nitrone-containing complexes $[(p\text{-}MeC_6H_4iPr)Ru(PNiPr)(nitrone)][SbF_6]_2$ (nitrone = *N*-benzylidenephenylamine *N*-oxide, *N*-benzylidenemethylamine *N*-oxide, 3,4-dihydroisoquinoline *N*-oxide) have been also isolated and characterised. The crystal structures of the chlorides $(R_{Ru})$-$[(\eta^6\text{-}C_6Me_6)RuCl(PNiPr)][SbF_6]$, $(R_{Ru})$-$[(\eta^6\text{-}C_6H_6)RuCl(PNInd)][SbF_6]$ {PNInd = (3a*R*,8a*S*)-2-[2-(diphenylphosphanyl)phenyl]-3a,8a-dihydroindane[1,2-*d*]oxazole} and those of the aqua solvates $(R_{Ru})$-$[(\eta^6\text{-arene})Ru(PNiPr)(H_2O)][SbF_6]_2$ (arene = $C_6H_6$, $C_6Me_6$) were determined by X-ray diffraction methods.

(© Wiley-VCH Verlag GmbH & Co. KGaA, 69451 Weinheim, Germany, 2006)

## Introduction

Asymmetric catalysis has achieved a position as one of the most important areas of modern organic chemistry.[1] Among the wide variety of organic reactions that are used in asymmetric synthesis, cycloaddition processes are one of the most attractive synthetic methodologies because they allow the construction of new molecular skeletons with several stereogenic centres in a single step.[2] 1,3-Dipolar cycloaddition reactions represent a highly atom-efficient and elegant method for the synthesis of five-membered ring systems and, depending on the choice of dipolar reagent and dipolarophile, a large variety of heterocycles can be prepared.[3] Nitrones, in particular, have attracted much attention since they are readily available and easy to handle and their reactions with olefins give convenient access to isoxazolidine derivatives (Scheme 1).[4] Because its N–O bond is readily cleaved to form 3-amino alcohol equivalents under mild reducing conditions, these cyclic compounds have been applied as synthetic intermediates for the synthesis of useful compounds such as alkaloids, β-lactams, amino acids or amino sugars.[3a,5] However, asymmetric versions of this reaction are scarce. Furthermore, alkenoyloxazolidinones are usually employed as bidentate dipolarophiles[3b,4a] and only a few studies on monodentate α,β-unsaturated aldehydes have been reported so far.[6]

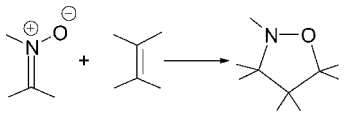

Scheme 1. Reaction of nitrones with alkenes.

On the other hand, it has been shown that chiral pseudo-tetrahedral metal half-sandwich complexes[7] are efficient catalysts for the asymmetric Diels–Alder[8] and hydrogen-transfer reactions.[9] In this context, we have reported that the single-coordination-site transition-metal chiral Lewis acids $[(\eta^5\text{-}C_5Me_5)M(R\text{-Prophos})(H_2O)][SbF_6]_2$ [M = Rh, Ir;

[a] Departamento de Química Inorgánica, Instituto de Ciencia de Materiales de Aragón, Instituto Universitario de Catálisis Homogénea, Universidad de Zaragoza – Consejo Superior de Investigaciones Científicas,
50009 Zaragoza, Spain
Fax: +34-976-761187
E-mail: dcarmona@unizar.es
[b] Departamento de Química Inorgánica, Escuela Universitaria de Ingeniería Técnica Industrial, Instituto de Ciencia de Materiales de Aragón, Instituto Universitario de Catálisis Homogénea, Universidad de Zaragoza – Consejo Superior de Investigaciones Científicas,
María de Luna 3, 50018 Zaragoza, Spain

 © 2006 Wiley-VCH Verlag GmbH & Co. KGaA, Weinheim 

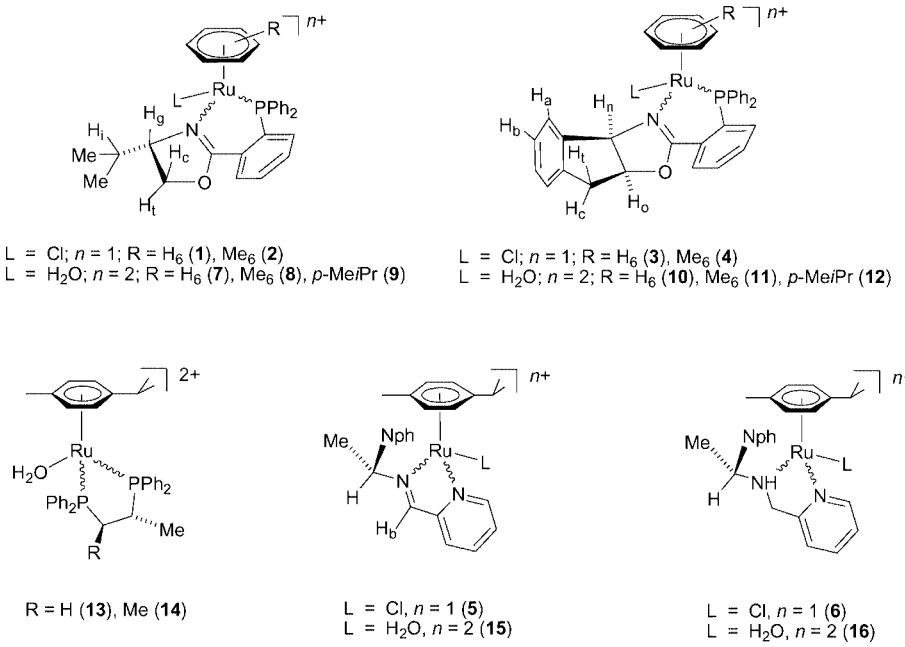


Scheme 2. Half-sandwich hexafluoroantimonate complexes.

*R*-Prophos = 1,2-bis(diphenylphosphanyl)propane] efficiently promote enantioselective 1,3-dipolar cycloaddition reactions (DCR) of nitrones with methacrolein.[10]

Taking into consideration all these data, we planned to test chiral half-sandwich ruthenium complexes of the general formula $[(\eta^6\text{-arene})Ru(LL^*)(H_2O)]^{2+}$ (LL* = bidentate chelate chiral ligand) as catalysts in enantioselective 1,3-dipolar cycloadditions of nitrones with methacrolein. In this paper we report the preparation of new chloride complexes of general formula $[(\eta^6\text{-arene})RuCl(LL^*)][SbF_6]$ (**1**–**4**) which are precursors of aqua solvates (**7**–**16**, Scheme 2) and the use of the latter as catalysts in the above-mentioned process. The molecular structural details of four representative complexes, determined by X-ray diffraction methods, are also included.

## Results and Discussion

### Preparation and Characterisation of the Diastereomeric Complexes 1–16

The aqua complexes **7**, **8**, **10** and **11** were prepared by treating the corresponding chloride complexes **1**–**4** with equimolar amounts of $AgSbF_6$. The latter, in turn, were prepared from the dimers[11] $[\{(\eta^6\text{-arene})RuCl\}_2(\mu\text{-}Cl)_2]$ [Equation (1)]. The previously reported chloride **5** and solvates **9**, **12** and **15** were similarly prepared.[8u,8x] The pyridylamino derivatives **6** and **16**, also prepared according to Equation (1), will be reported elsewhere.[12] The diphosphanyl complexes **13** and **14** were prepared by treatment of the dimer $[\{(\eta^6\text{-}p\text{-}MeC_6H_4iPr)RuCl\}_2(\mu\text{-}Cl)_2]$ with $AgSbF_6$, filtration of the AgCl formed and subsequent addition of the corresponding diphosphane.

$$\begin{array}{l} {}^1/_2[\{(\eta^6\text{-arene})RuCl\}_2(\mu\text{-}Cl)_2] \;+\; LL^* \\ \quad\downarrow -NaCl \;\; NaSbF_6 \\ [(\eta^6\text{-arene})RuCl(LL^*)][SbF_6] \\ \textbf{1-6} \\ \quad\downarrow -AgCl \;\; AgSbF_6 \\ [(\eta^6\text{-arene})Ru(LL^*)(H_2O)][SbF_6]_2 \\ \textbf{7-12, 15, 16} \end{array} \qquad (1)$$

The new complexes were characterised by IR and NMR spectroscopy, circular dichroism (CD), elemental analysis (see Exp. Sect.) and by the X-ray crystal structure determination of one of the epimers at the metal atom of complexes **2**, **3**, **7** and **8**.

During the formation of the chloride complexes, the ruthenium atom becomes a chiral centre and, as the chiral LL* ligand used is enantiopure, the new compounds are prepared as diastereomeric mixtures of both epimers at the metal atom. Variable degrees of diastereoselectivity are achieved, ranging from 10 to 96% *de* (see Exp. Sect.). Concerning the stereochemistry of the metal centres, it should be noted that due to the ligand priority rules,[13] different descriptors are assigned to the chlorides and to their derived aqua complexes, although both display identical spatial disposition of the ligands around the metal atom.

The absolute configurations of the new complexes were assigned through NMR spectroscopic and CD measurements. Thus, for example, irradiation of the arene protons in the $R_{Ru}$ chloride complexes (or in the $S_{Ru}$ aqua solvates) induces NOE enhancements of the $H_g$ or $H_a$ protons for

 © 2006 Wiley-VCH Verlag GmbH & Co. KGaA, Weinheim 

PN*i*Pr- or PNInd-containing complexes, respectively (see Scheme 2). Similarly, this irradiation induces, in the $S_{Ru}$ chlorides (or in the $R_{Ru}$ aqua solvates), NOE enhancements of the $H_i$ or $H_n$ protons for PN*i*Pr- or PNInd-containing complexes, respectively.

Proton shielding by aromatic ring currents can also be used to distinguish between the two epimers at the metal atom of these chiral complexes. For example, the chemical shift of the $C_6Me_6$ protons differs by 0.43 ppm for the two epimers of the PNInd-containing complex **4**. Inspection of molecular models indicates that these protons can only be efficiently shielded by the aromatic indane ring current in the $R_{Ru}$ epimers. Therefore, we assign the high-field resonance to the *R* epimer.

On the other hand, the difference in the chemical shift (ca. 1 ppm) between the signals of the two methyl protons of the PN*i*Pr ligand in complexes **1**, **2**, **7** and **8** could be explained by assuming that in these complexes the six-membered metallacycle adopts an $^1S_2$ screw boat conformation.[8v,8x,14] Such a conformation has been found in the solid state for complexes **7** and **8** (see below). In this conformation, one methyl group of the *i*Pr group lies over the *pro-R*-phenyl group of the $PPh_2$ group, becoming shielded by its aromatic ring current.

The aqua solvates **8**, **10** and **11** are fluxional. Although we have not measured the kinetic parameters for the dynamic process, the spectroscopic features encountered in the $^{31}P$ and $^1H$ NMR spectra strongly indicate that it likely consists of a flip of the phosphanyloxazoline metallacycle between the $^1S_2$ and $^2S_1$ screw boat conformations as has been previously found in the related phosphanyloxazoline aqua solvates of ruthenium, **9** and **12**.[8x]

The CD spectra of these complexes corroborate the above-assigned configurations. The main feature of the CD spectra of the $S_{Ru}$ chlorides ($R_{Ru}$ aqua complexes) is a maximum with a positive Cotton effect centred in the 360–390 nm range. The CD spectra of corresponding diastereomers with opposite configuration at the metal atom display a pseudo-enantiomorphic relationship, showing that the major contribution to the spectra corresponds to the metal atom. This transition thus gives direct insight into differences in the configurations at the metal atoms.

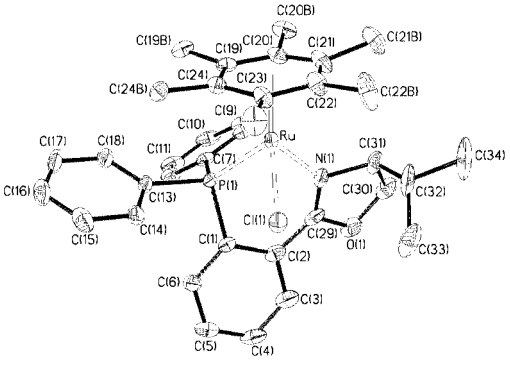


$R_{Ru}$-**2**

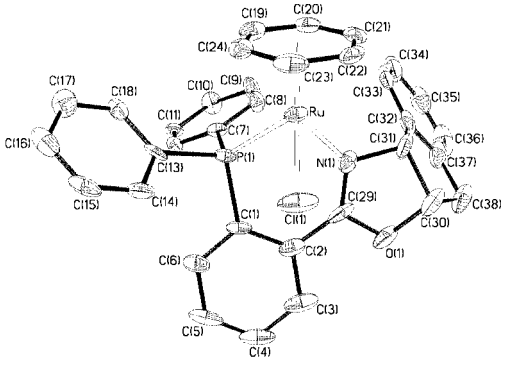


$R_{Ru}$-**3**

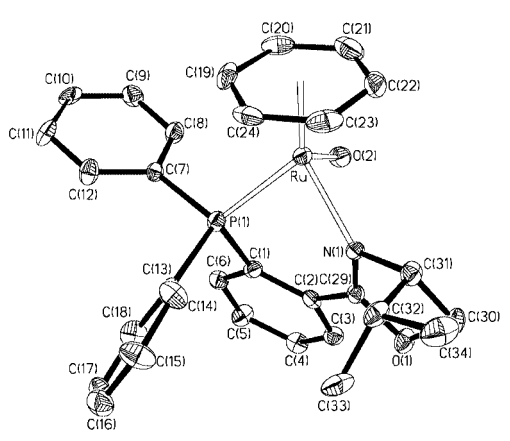


$R_{Ru}$-**7**

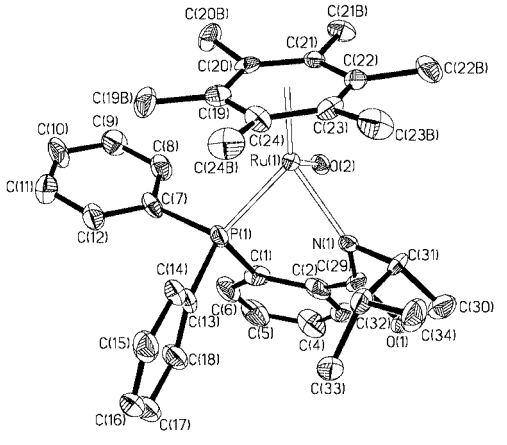


$R_{Ru}$-**8**

Figure 1. Molecular views of the cations of the complexes $R_{Ru}$-[($\eta^6$-$C_6Me_6$)RuCl(PN*i*Pr)][$SbF_6$] ($R_{Ru}$-**2**), $R_{Ru}$-[($\eta^6$-$C_6H_6$)RuCl(PNInd)][$SbF_6$] ($R_{Ru}$-**3**), $R_{Ru}$-[($\eta^6$-$C_6H_6$)Ru(PN*i*Pr)($H_2O$)][$SbF_6$]$_2$ ($R_{Ru}$-**7**) and $R_{Ru}$-[($\eta^6$-$C_6Me_6$)Ru(PN*i*Pr) ($H_2O$)][$SbF_6$]$_2$ ($R_{Ru}$-**8**).

 © 2006 Wiley-VCH Verlag GmbH & Co. KGaA, Weinheim 

Table 1. Selected bond lengths [Å] and angles [°] for $R_{Ru}$-**2**, $R_{Ru}$-**3**, $R_{Ru}$-**7** and $R_{Ru}$-**8**.

| | $R_{Ru}$-**2** | $R_{Ru}$-**3** | $R_{Ru}$-**7** | $R_{Ru}$-**8**[a] | |
|---|---|---|---|---|---|
| Ru–P(1) | 2.2920(10) | 2.3011(18) | 2.3235(15) | 2.357(2) | 2.363(2) |
| Ru–O(2)/Cl(1)[b] | 2.3973(10) | 2.3993(16) | 2.156(4) | 2.182(5) | 2.164(5) |
| Ru–N(1) | 2.133(3) | 2.125(5) | 2.095(4) | 2.115(6) | 2.138(6) |
| Ru–C(19) | 2.238(4) | 2.183(7) | 2.195(5) | 2.230(8) | 2.222(7) |
| Ru–C(20) | 2.267(4) | 2.217(6) | 2.186(6) | 2.244(7) | 2.251(8) |
| Ru–C(21) | 2.372(4) | 2.260(6) | 2.236(6) | 2.230(7) | 2.236(8) |
| Ru–C(22) | 2.338(4) | 2.269(7) | 2.271(6) | 2.288(8) | 2.278(8) |
| Ru–C(23) | 2.238(4) | 2.211(6) | 2.229(6) | 2.324(7) | 2.305(8) |
| Ru–C(24) | 2.253(4) | 2.211(6) | 2.208(6) | 2.280(8) | 2.280(8) |
| Ru-G [c] | 1.7897(17) | 1.727(3) | 1.723(2) | 1.766(3) | 1.765(3) |
| P(1)–C(1) | 1.824(4) | 1.816(6) | 1.825(6) | 1.837(8) | 1.843(8) |
| N(1)–C(29) | 1.297(6) | 1.301(8) | 1.284(7) | 1.292(10) | 1.289(10) |
| N(1)–C(31) | 1.499(5) | 1.502(9) | 1.508(7) | 1.522(11) | 1.488(9) |
| C(1)–C(2) | 1.405(5) | 1.397(10) | 1.384(7) | 1.406(12) | 1.403(11) |
| C(2)–C(29) | 1.460(6) | 1.465(10) | 1.484(8) | 1.469(12) | 1.467(11) |
| C(2)–C(3) | 1.391(6) | 1.414(9) | 1.395(8) | 1.393(11) | 1.384(10) |
| P(1)–Ru–O(2)/Cl(1)[b] | 87.00(3) | 87.06(6) | 85.43(13) | 84.50(14) | 85.79(17) |
| P(1)–Ru–N(1) | 83.73(9) | 84.12(15) | 83.03(12) | 80.47(19) | 81.17(18) |
| P(1)–Ru–G[b] | 129.21(6) | 128.69(11) | 130.68(9) | 135.27(12) | 134.54(14) |
| O(2)/Cl(1)–Ru–N(1)[b] | 84.06(8) | 83.89(16) | 80.88(16) | 81.9(2) | 80.0(2) |
| O(2)/Cl(1)–Ru–G[b,c] | 123.38(6) | 123.32(10) | 124.79(16) | 121.49(18) | 122.2(2) |
| N(1)–Ru–G[c] | 133.62(11) | 133.96(17) | 134.31(14) | 134.4(2) | 134.2(2) |
| Ru–P(1)–C(1) | 111.76(12) | 111.5(2) | 108.26(19) | 106.7(3) | 106.8(3) |
| Ru–N(1)–C(29) | 131.5(3) | 125.4(5) | 128.8(4) | 127.9(6) | 125.4(5) |
| P(1)–C(1)–C(2) | 117.8(3) | 121.1(5) | 121.0(4) | 120.1(7) | 120.1(6) |
| C(1)–C(2)–C(29) | 123.9(4) | 123.9(6) | 122.5(5) | 122.4(7) | 121.9(7) |
| N(1)–C(29)–C(2) | 129.2(4) | 130.9(7) | 130.1(5) | 127.1(7) | 131.3(7) |

[a] There were two independent molecules in the crystal. [b] Data are included for the Ru–Cl (**2** and **3**) and the Ru–O(2) (**7** and **8**) bond lengths. [c] G represents the centroid of the arene ligand C(19)–C(24).

### Molecular Structures of $R_{Ru}$-2, $R_{Ru}$-3, $R_{Ru}$-7, and $R_{Ru}$-8

Single crystals of the chlorides **2** and **3** and of the aqua complexes **7** and **8** were grown by slow diffusion of diethyl ether into dichloromethane solutions of the complexes. Their structures were determined by diffraction methods. Molecular representations of the cations of the four complexes are depicted in Figure 1 and selected structural parameters are listed in Table 1. The coordination around the ruthenium atom is pseudo-octahedral. The $\eta^6$-arene ligand ideally occupies three *fac*-coordination positions. The phosphanyloxazoline ligand, coordinated through the phosphorus and the nitrogen atoms and one chlorine atom (**2**, **3**) or one water molecule (**7**, **8**) complete the coordination sphere of the metal atom. The absolute configuration of the ruthenium centre in the four complexes is *R*, in accordance with the ligand priority sequence[13] $\eta^6$-arene > Cl > P > N (chlorides) or $\eta^6$-arene > P > O > N (aqua solvates).

The six-membered Ru–P(1)–C(1)–C(2)–C(29)–N(1) metallacycle of complexes **3**, **7** and **8** adopts a $^1S_2$ screw-boat conformation[14] with the metal and phosphorus atoms above and below the best plane, respectively. This conformation forces the *pro-R*- and *pro-S*-phenyl groups to adopt pseudo-axial and pseudo-equatorial arrays, respectively. In particular, in the solvate complexes **7** and **8**, the C(33) carbon atom of the isopropyl group lies over the *pro-R*-phenyl group of the $PPh_2$ group at 3.260(6) (**7**) and 3.405(9) Å (**8**) from the plane of the pseudo-axial phenyl group. In compound **2**, the metallacycle adopts a $^2S_1$ screw-boat conformation,[14] with the metal and phosphorus atoms below and above the best plane, respectively.

### Catalytic Reactions

Firstly, we tried the (*p*-methylisopropylbenzene)ruthenium complexes **9** and **13**–**16**, which differ in the LL* bidentate chelate chiral ligand, as catalyst precursors for the cycloaddition reaction between methacrolein and the nitrone *N*-benzylidenephenylamine *N*-oxide (nitrone **I**, Scheme 3) (Table 2). These aqua complexes efficiently catalyse the proposed cycloaddition. The catalyst precursors were treated with methacrolein in the presence of molecular sieves (4 Å) before the addition of the nitrone (see Exp. Sect.). Under these conditions, the formation of active methacrolein complexes of formula $[(\eta^6\text{-}p\text{-}MeC_6H_4iPr)\text{-}Ru(LL^*)(methacrolein)]^{2+}$ is strongly favoured at the expense of the initial aqua complexes (see below) which prevents hydrolysis of the nitrone catalysed by trace amounts of the latter.[10b] Quantitative conversions with moderate *ee* values were achieved at –25 °C after a few hours. The best results in this series were obtained when the hybrid P,N-donor phosphanyloxazoline ligand (PN*i*Pr, complex **9**) was employed as chiral source (Entry 1, Table 2). Therefore, we focused on complex **9** in subsequent catalytic experiments (Table 3). Temperature variations slightly affected both product distribution and enantioselectivity, the latter smoothly increasing as temperature decreases. The pre-

 © 2006 Wiley-VCH Verlag GmbH & Co. KGaA, Weinheim 

viously reported[8x] tetrafluoroborate and triflate complexes $[(\eta^6\text{-}p\text{-}MeC_6H_4iPr)Ru(PNiPr)(H_2O)][BF_4]_2$ (**9·BF$_4$**) and $[(\eta^6\text{-}p\text{-}MeC_6H_4iPr)Ru(PNiPr)(H_2O)][CF_3SO_3]_2$ (**9·CF$_3$SO$_3$**) were also tested as catalysts. As shown in Entries 5 and 6, the use of more coordinating anions decreased the yield, probably due to competition of the anion and the substrate for the Lewis acid site.[8o,15] The catalyst can be easily recovered and reused.

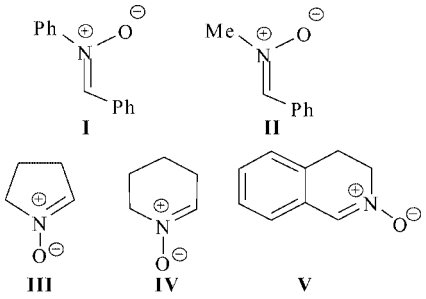


Scheme 3. Nitrones employed in the catalytic experiments.

Table 2. Enantioselective 1,3-dipolar cycloadditions of methacrolein with nitrone **I** catalysed by $[(\eta^6\text{-}p\text{-}MeC_6H_4iPr)Ru(LL^*)(H_2O)][SbF_6]_2$ complexes.[a]

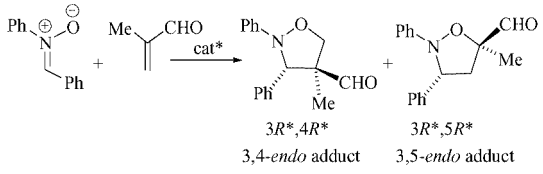


| Entry | Complex | *t* [h] | Yield [%][b,c] | 3,4-*endo*[c] | 3,5-*endo*[c] | *ee* [%][d] |
|---|---|---|---|---|---|---|
| 1 | **9** | 15 | 100 | 69 | 31 | 54:40 |
| 2 | **13** | 48 | 40 | 40 | 60 | 43/–42 |
| 3 | **14** | 15 | 90 | 32 | 68 | 6:3 |
| 4[e] | **15** | 48 | 98 | 36 | 64 | –18/–31 |
| 5[e] | **16** | 48 | 100 | 91 | 9 | –6/–4 |

[a] Reaction conditions: catalyst (0.06 mmol, 5.0 mol-%), methacrolein (1.68 mmol), molecular sieves (4 Å) (100 mg) and nitrone (1.2 mmol) in $CH_2Cl_2$ (5 mL). [b] Based on nitrone. [c] Determined by $^1$H NMR spectroscopy. [d] Determined by integration of the $^1$H NMR signals of the 3-H proton of the diastereomeric *R*-methylbenzylimine derivatives. Positive *ee* values correspond to the *endo*-3*R*,4*R* adduct. For the 3,5-*endo* adduct, positive values are arbitrarily assigned to the *ee* in the lower-field $^1$H NMR signal diastereomer. [e] Methacrolein (8.4 mmol) was used.

Consecutive runs of up to three more times were performed, producing a smooth decrease in the conversion rate. However, neither the 3,4-*endo*/3,5-*endo* ratio nor the *ee* were significantly affected (Entries 7.1–7.4).

To investigate the stereoelectronic influence of the $\eta^6$-coordinated arene ligand, we used the new benzene (**7**, **10**) and hexamethylbenzene (**8**, **11**) derivatives with PN*i*Pr or PNInd ligands as catalyst precursors for the cycloaddition of methacrolein with nitrone **I** (Table 4). Reactions carried out at –25 °C gave nearly quantitative conversions after 15 h. It seems that the PN*i*Pr ligand performs better than its PNInd congener with *ee* values of up to 74% being achieved with the former. On the other hand, no obvious trends were observed within the arene series.

Table 3. Enantioselective 1,3-dipolar cycloadditions between methacrolein and nitrone **I** catalysed by $[(\eta^6\text{-}p\text{-}MeC_6H_4iPr)Ru(PNiPr)(H_2O)]^{2+}$.[a]

| Entry | Complex | *T* [°C] | *t* [h] | Yield [%] | 3,4-*endo* | 3,5-*endo* | *ee* [%] |
|---|---|---|---|---|---|---|---|
| 1 | **9** | 0 | 15 | 100 | 57 | 43 | 40:30 |
| 2 | **9** | –10 | 24 | 100 | 62 | 38 | 46:31 |
| 3 | **9** | –25 | 15 | 100 | 69 | 31 | 54:40 |
| 4 | **9** | –45 | 48 | 93 | 74 | 26 | 56:49 |
| 5 | **9·BF$_4$** | –25 | 15 | 79 | 73 | 27 | 29:30 |
| 6 | **9·CF$_3$SO$_3$** | –25 | 15 | 5 | 72 | 28 | – |
| 7.1 | **9** | –25 | 15 | 100 | 69 | 31 | 54:40 |
| 7.2 | **9** | –25 | 15 | 92 | 70 | 30 | 56:38 |
| 7.3 | **9** | –25 | 15 | 75 | 70 | 30 | 56:39 |
| 7.4 | **9** | –25 | 15 | 62 | 68 | 32 | 56:39 |

[a] For conditions see footnote of Table 2.

Table 4. Enantioselective 1,3-dipolar cycloadditions of methacrolein with nitrone **I** catalysed by complexes **7**–**12**.[a]

| Entry | Complex | Arene | LL* | Yield [%] | 3,4-*endo* | 3,5-*endo* | *ee* [%] |
|---|---|---|---|---|---|---|---|
| 1[b] | **7** | $C_6H_6$ | PN*i*Pr | 93 | 48 | 52 | 20:52 |
| 2 | **9** | *p*-$MeC_6H_4iPr$ | | 100 | 69 | 31 | 54:40 |
| 3 | **8** | $C_6Me_6$ | | 94 | 67 | 33 | 74:45 |
| 4[b] | **10** | $C_6H_6$ | PNInd | 98 | 38 | 62 | –22/–56 |
| 5 | **12** | *p*-$MeC_6H_4iPr$ | | 98 | 62 | 38 | 25/–20 |
| 6 | **11** | $C_6Me_6$ | | 95 | 66 | 34 | –32/–34 |

[a] For conditions see footnote of Table 2. [b] Methacrolein (8.4 mmol) was used.

Finally, we examined the reaction of other acyclic as well as cyclic nitrones in the catalytic process (Scheme 3, Table 5). In general, good conversions were achieved, with

Table 5. Enantioselective 1,3-dipolar cycloadditions of methacrolein with nitrones **II**–**V**.[a]

| Entry | Complex | Nitrone | *T* [°C] | *t* [h][b] | Yield [%] | 3,5-*endo* | *ee* [%][c] |
|---|---|---|---|---|---|---|---|
| 1 | **9** | **II** | 0 | 48 | 99 | 98[d] | 27 |
| 2 | **9** | **III** | –25 | 16 | 92 | 100 | 39 |
| 3 | **9** | **IV** | –25 | 16 | 100 | 100 | 7 |
| 4 | **9** | **V** | –25 | 48 | 98 | 100 | 16 |
| 5 | **7** | **II** | 0 | 48 | 5 | 100 | 6 |
| 6 | **7** | **V** | –25 | 48 | 86 | 100 | 6 |
| 7 | **8** | **II** | 0 | 24 | 17 | 100 | –36 |
| 8 | **8** | **V** | –25 | 24 | 51 | 100 | –61 |
| 9 | **12** | **II** | 0 | 48 | 100 | 96[e] | 27 |
| 10 | **12** | **V** | –25 | 48 | 100 | 100 | 12 |

[a] Conditions were those indicated in footnote of Table 2 but using methacrolein (8.4 mmol). [b] Total reaction time; addition of nitrones was accomplished over 15 h. [c] Determined by integration of the $^1$H NMR signals of the 3-H proton of the diastereomeric *R*-methylbenzylimine (nitrone **II**) derivative, the CHO proton of the (+)-*S*-mandelic acid (nitrone **IV**) derivative or the CHO proton observed after addition of the chiral shift reagent Eu(hfc)$_3$ (nitrones **III** and **V**). Positive *ee* values correspond to the (+)-*endo*-3*R*,5*R* (nitrone **III**), (–)-*endo*-3*R*,5*R* (nitrone **IV**) and (–)-*endo*-3*S*,5*R* (nitrone **V**) adducts. For the adducts of nitrone **II**, positive values are arbitrarily assigned to the *ee* in the lower-field $^1$H NMR signal diastereomer. [d] 2% of the 3,5-*exo* isomer was also obtained. [e] 4% of the 3,4-*endo* isomer was also obtained.

 © 2006 Wiley-VCH Verlag GmbH & Co. KGaA, Weinheim 

perfect regio- and diastereoselectivity for the 3,5-*endo* isomer. In all cases, low to moderate *ee* values were achieved. The hexamethylbenzene complex $[(\eta^6\text{-}C_6Me_6)Ru(PN\text{-}i\text{Pr})(H_2O)][SbF_6]_2$ (**8**) is the least active catalyst precursor tried but the most enantioselective (61% *ee*) and the acyclic nitrone **II** generates the least active system even at higher temperature (0 °C).

### The Methacrolein Complexes $[(\eta^6\text{-arene})Ru(PN\textit{i}Pr)(methacrolein)][SbF_6]_2$ [arene = $C_6H_6$ (17), *p*-$MeC_6H_4\textit{i}Pr$ (18), $C_6Me_6$ (19)]

To obtain a deeper insight into the catalytic systems, we studied the solution behaviour of mixtures of aqua complexes $[(\eta^6\text{-arene})Ru(PN\textit{i}Pr)(H_2O)]^{2+}$ with methacrolein by NMR spectroscopy. When 4 equiv. of methacrolein were added to solutions of complexes **7**–**9** at 0 °C, the new complexes $[(\eta^6\text{-arene})Ru(PN\textit{i}Pr)(methacrolein)]^{2+}$ were formed according to $^{31}P$ NMR spectroscopic measurements. Both complexes are in equilibrium, but in the presence of molecular sieves (4 Å) the position of equilibrium is completely shifted towards the formation of the methacrolein complex. In fact, pure complexes **17**–**19** were isolated from these solutions in about 40% *de*. The new complexes were characterised by analytical and spectroscopic means. An IR band at ca. 1650 $cm^{-1}$ along with $^1H$ NMR peaks at $\delta \approx 9.50$ (CHO) and 6.60 ($=CH_2$) ppm and a $^{13}C$ NMR resonance at $\delta \approx 213$ ppm are diagnostic of coordinated methacrolein. NOE measurements allowed us to assign the absolute configuration at the metal atom in these complexes. Thus, irradiation of the arene or the CHO protons in the $S_{Ru}$ epimers produced NOE enhancement in the $H_g$ or the isopropyl methyl protons of the PN*i*Pr ligand, respectively. On the other hand, irradiation of the CHO proton in the $R_{Ru}$ epimers gave enhancement in the $H_g$ proton (Scheme 4). From these data we propose that the major epimer is the $R_{Ru}$ isomer for the benzene and hexamethylbenzene complexes **17** and **19** and the $S_{Ru}$ isomer for the *p*-$MeC_6H_4\textit{i}Pr$ complex **18**.

On the other hand, the considerable difference in the chemical shift between the two *i*Pr methyl protons of the phosphanyloxazoline ligand of the complexes ($\Delta\delta \approx 1.0$ ppm) at low temperature, could be explained by assuming that the six-membered chelate ring of the phosphanyloxazoline ligand adopts a $^1S_2$ screw-boat conformation[14] in the ground state. At higher temperature, the NMR spectroscopic data again indicate a fluxional process, most probably involving a flip of the phosphanyloxazoline metallacycle between the $^1S_2$ and $^2S_1$ screw boat conformations.

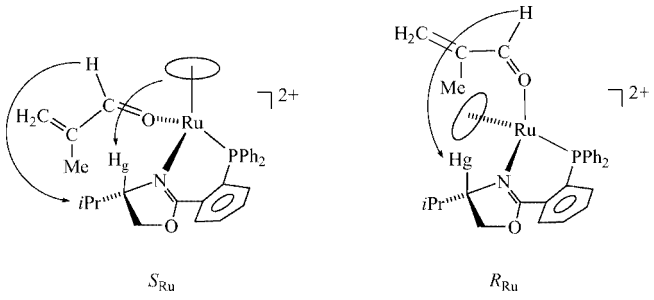


$S_{Ru}$ $R_{Ru}$

Scheme 4. NOEs observed in complexes **17**–**19**.

### Complexes $[(\eta^6\text{-}p\text{-}MeC_6H_4\textit{i}Pr)Ru(PN\textit{i}Pr)(nitrone)][SbF_6]_2$ [nitrone = I (20), II (21) and V (22)]

The reaction of the nitrone with the coordinated alkene is usually the rate- and enantio-determining step for the DCR between nitrones and enals.[7b] We therefore studied, by NMR spectroscopy, the system generated after addition of a nitrone to the methacrolein-containing complex $[(\eta^6\text{-}p\text{-}MeC_6H_4\textit{i}Pr)Ru(PN\textit{i}Pr)(methacrolein)]^{2+}$. While a partial displacement of coordinated methacrolein was observed when nitrone **I** was added to complex **18**, nitrone **II** readily substituted the coordinated enal, affording the new nitrone-containing complex $[(\eta^6\text{-}p\text{-}MeC_6H_4\textit{i}Pr)Ru(PN\textit{i}Pr)(\mathbf{II})]^{2+}$. It is important to note that in normal-electron-demand DCR, the reaction must occur by dipole attack at the coordinated dipolarophile. To circumvent this problem, we have carried out the catalysis with slow addition of nitrones **II**–**V** (see Exp. Sect.). From the solution, we have isolated and characterised the nitrone complexes **20**–**22**. One singlet in the $\delta$ = 8–8.5 ppm region of the $^1H$ NMR spectrum, along with a peak at $\delta \approx 150$ ppm in the $^{13}C$ NMR spectrum (attributed to the N=CH proton and C atom, respectively) strongly support the coordination of the nitrone ligand. Only one epimer at metal atom has been detected for these complexes from –90 °C to room temperature. NOE experiments (see Scheme 5) allow us to propose that the solely detected isomer is the $R_{Ru}$ epimer. According to the observed $\Delta\delta$ value

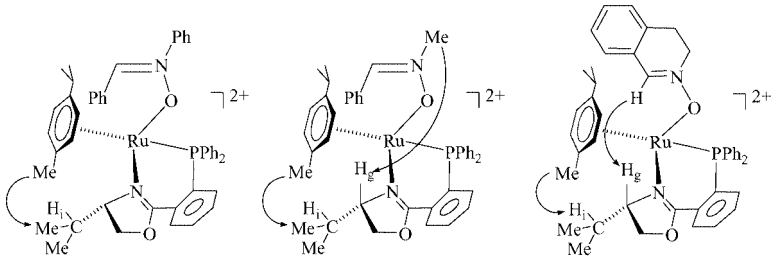


$R_{Ru}$-**20** $R_{Ru}$-**21** $R_{Ru}$-**22**

Scheme 5. NOEs observed in complexes **20**–**22**.

 © 2006 Wiley-VCH Verlag GmbH & Co. KGaA, Weinheim 

in the chemical shift of the isopropyl methyl protons of the phosphanyloxazoline ligand (see above) the metallacycle Ru–P–C–C–C–N should adopt a $^1S_2$ screw-boat conformation.[14]

## Conclusions

The half-sandwich ruthenium complexes $[(\eta^6\text{-arene})Ru(LL^*)(H_2O)]^{2+}$ are efficient catalyst precursors for the DCR of methacrolein with a series of nitrones. Typically, quantitative conversions are achieved at –25 °C in a few hours. Perfect diastereoselectivity for the *endo* adducts can be observed but only low to moderate enantioselectivity is obtained. Some structural features of the complexes involved in catalysis are illustrative. Firstly, the methacrolein complexes, presumably the active catalysts, are formed as mixtures of both epimers at the metal atom. Secondly, the metallacycle formed by coordination of the LL* ligand is conformationally labile. Thirdly, the methacrolein rotamer around the Ru–O bond is not fixed. In the related $[(\eta^5\text{-}C_5Me_5)M(R\text{-Prophos})(\text{methacrolein})]^{2+}$ (M = Rh, Ir) system, (i) only $S_M$ epimers can be detected, (ii) the metallacycle coordination only presents the $\lambda$ conformation and is not labile, (iii) O=CH···π attractive interactions set the conformation around the M–O bond in both the solid state and solution. In particular, a very strong shielding of the O=CH proton (about 2.5 ppm) indicates that this rotamer is fixed in solution. However, no significant shielding has been observed for the CHO proton of coordinated methacrolein in the ruthenium complexes reported in this work. In summary, all these structural differences could explain the distinct enantioselective behaviour encountered for these otherwise closely related half-sandwich complexes. The structural analysis carried out in this work provides a useful guide for the a priori selection of new enantioselective catalytic systems. In this context, the isolation of pure $R_{Ru}$ epimers for the nitrone complexes $[(\eta^6\text{-}p\text{-}MeC_6H_4iPr)Ru(PNiPr)(\text{nitrone})]^{2+}$ opens the door to new enantioselective processes that will be investigated in our laboratory in due course.

## Experimental Section

**General Comments:** All solvents were dried with appropriate drying agents, distilled under argon and degassed prior to use. All preparations were carried out under argon. Infrared spectra were obtained as Nujol mulls with a Perkin–Elmer 1330 spectrophotometer. Carbon, hydrogen and nitrogen analyses were performed using a Perkin–Elmer 240C microanalyser. NMR spectra were recorded with a Bruker AV-400 (400.16 MHz) or 300-ARX (300.10 MHz) instrument. Chemical shifts are expressed in ppm upfield from $SiMe_4$ or 85% $H_3PO_4$ ($^{31}P$). NOEDIFF, $^{13}C$, $^{31}P$ and $^1H$ correlation spectra were obtained using standard procedures. CD spectra were determined in acetone or dichloromethane (ca. $5\times10^{-4}$ mol L$^{-1}$ solutions) in a cell with 1 cm path length using a Jasco-710 apparatus. The nitrones were prepared according to literature procedures.[16]

**Preparation of the Complexes $[(\eta^6\text{-arene})RuCl(LL^*)][SbF_6]$ (1–4):** A mixture of the appropriate $[\{(\eta^6\text{-arene})RuCl\}_2(\mu\text{-}Cl)_2]$ (0.25 mmol), $NaSbF_6$ (129.4 mg, 0.50 mmol) and the corresponding LL* ligand (0.50 mmol) in methanol (10 mL) was stirred for 5 h. During this time, the precipitation of an orange solid was observed. The resultant suspension was vacuum-concentrated to dryness. The residue was extracted with dichloromethane (3 × 5 mL) and the solution partially concentrated under reduced pressure. Slow addition of diethyl ether gave an orange solid which was filtered off, washed with diethyl ether and air-dried. By recrystallisation from methanol/diethyl ether, pure $R_{Ru}$-**4** and mixtures of molar compositions $S_{Ru}$-**1**/$R_{Ru}$-**1** (95:5) and $S_{Ru}$-**4**/$R_{Ru}$-**4** (95:5) were obtained.

**Complex 1:** Yield 313 mg (76%), 50% *de* in $S_{Ru}$-**1**. $C_{30}H_{30}ClF_6NOPRuSb$ (823.81): calcd. C 43.74, H 3.67, N 1.70; found C 43.55, H 3.91, N 1.68. IR (Nujol): $\tilde{\nu}$ = 1603 (m, CN), 658 (s, $SbF_6$) cm$^{-1}$. CD [$Me_2CO$; $S_{Ru}$-**1**/$R_{Ru}$-**1** (95:5) mixture; maxima, minima, and nodes]: $\Theta$ ($\lambda$) = –10000 (330), 0 (340), +34000 (365), 0 (410), –4000 (430 nm). $S_{Ru}$-**1**: $^1H$ NMR ($CDCl_3$): $\delta$ = 0.12 (d, $J_{H,H}$ = 6.7 Hz, 3 H, *Me*MeCH), 1.04 (d, $J_{H,H}$ = 7.2 Hz, 3 H, Me*Me*CH), 1.90 (pseudo-sept, 1 H, MeMeC*H*), 4.53 (m, 3 H, $H_g$, $H_c$, $H_t$), 5.89 (s, 6 H, $C_6H_6$), 7.1–8.1 (m, 14 H, Ph) ppm. $^{31}P\{^1H\}$ NMR ($CDCl_3$): $\delta$ = 39.7 (s) ppm. $^{13}C$ NMR ($CDCl_3$): $\delta$ = 13.44 (*Me*MeCH), 18.76 (Me*Me*CH), 29.87 (MeMe*C*H), 68.37 ($CH_cH_t$), 80.93 ($CH_g$), 92.02 (d, $J_{P,C}$ = 3.2 Hz, $C_6H_6$), 128–134 (Ph), 167.1 (d, $J_{P,C}$ = 4.75 Hz, C=N) ppm. $R_{Ru}$-**1**: $^1H$ NMR ($CDCl_3$): $\delta$ = 0.90 (d, $J_{H,H}$ = 6.7 Hz, 3 H, *Me*MeCH), 1.19 (d, $J_{H,H}$ = 7.2 Hz, 3 H, Me*Me*CH), 2.74 (pseudo-sept, 1 H, MeMeC*H*), 4.58 (m, 2 H, $H_c$, $H_t$), 4.76 (m, 1 H, $H_g$), 5.74 (s, 6 H, $C_6H_6$), 7.1–8.1 (m, 14 H, Ph) ppm. $^{31}P\{^1H\}$ NMR ($CDCl_3$): $\delta$ = 41.1 (s) ppm. $^{13}C$ NMR ($CDCl_3$): $\delta$ = 14.74 (*Me*MeCH), 18.38 (Me*Me*CH), 29.32 (MeMe*C*H), 69.16 ($CH_cH_t$), 78.48 ($CH_g$), 91.51 (d, $J_{P,C}$ = 2.4 Hz, $C_6H_6$), 128–134 (Ph) ppm.

**Complex 2:** Yield: 427 mg (94%), 12% *de* in $R_{Ru}$-**2**. $C_{36}H_{42}ClF_6NOPRuSb$ (907.97): calcd. C 47.60, H 4.66, N 1.54; found C 47.74, H 4.30, N 1.38. IR (Nujol): $\tilde{\nu}$ = 1591 (m, CN), 657 (s, $SbF_6$) cm$^{-1}$. $S_{Ru}$-**2**: $^1H$ NMR ($CD_2Cl_2$): $\delta$ = 0.28 (d, $J_{H,H}$ = 6.8 Hz, 3 H, *Me*MeCH), 1.12 (d, $J_{H,H}$ = 7.2 Hz, 3 H, Me*Me*CH), 1.92 (s, 18 H, $C_6Me_6$), 2.01 (m, 1 H, MeMeC*H*), 4.20 (dpt, $J_{Ht,Hg}$ = 8.4 Hz, $J_{Hc,Hg} \approx J_{H,iHg}$ = 2.7 Hz, 1 H, $H_g$), 4.30 (pt, $J_{Hc,Ht}$ = 8.6 Hz, 1 H, $H_t$), 4.53 (dd, 1 H, $H_c$), 7.3–7.8 (m, 14 H, Ph) ppm. $^{31}P\{^1H\}$ NMR ($CD_2Cl_2$): $\delta$ = 42.9 (br. s) ppm. $^{13}C$ NMR ($CD_2Cl_2$) $\delta$ = 14.41 (*Me*MeCH), 15.94 ($C_6Me_6$), 18.31 (Me*Me*CH), 29.77 (MeMe*C*H), 67.57 ($CH_cH_t$), 76.30 ($CH_g$), 101.84 (d, $J_{P,C}$ = 2.8 Hz, $C_6Me_6$), 129–135 (Ph) ppm. $R_{Ru}$-**2**: $^1H$ NMR ($CD_2Cl_2$): $\delta$ = 0.67 (d, $J_{H,H}$ = 6.7 Hz, 3 H, *Me*MeCH), 1.14 (d, $J_{H,H}$ = 7.2 Hz, 3 H, Me*Me*CH), 1.87 (s, 18, $C_6Me_6$), 2.20 (m, 1 H, MeMeC*H*), 4.25 (dpt, $J_{Ht,Hg}$ = 8.4 Hz, $J_{Hc,Hg} \approx J_{Hi,Hg}$ = 2.7 Hz, 1 H, $H_g$), 4.37 (pt, $J_{Hc,Ht}$ = 8.4 Hz, 1 H, $H_t$), 4.63 (dd, 1 H, $H_c$), 7.3–7.8 (m, 14 H, Ph) ppm. $^{31}P\{^1H\}$ NMR ($CD_2Cl_2$): $\delta$= 44.5 (s) ppm. $^{13}C$ NMR ($CD_2Cl_2$): $\delta$ = 14.66 (*Me*MeCH), 16.44 ($C_6Me_6$), 18.44 (Me*Me*CH), 28.96 (MeMe*C*H), 68.56 ($CH_cH_t$), 76.02 ($CH_g$), 101,65 (d, $J_{P,C}$ = 2.8 Hz, $C_6Me_6$), 129–135 (Ph) ppm.

**Complex 3:** Yield: 370 mg (85%), 96% *de* in $R_{Ru}$-**3**. $C_{34}H_{28}ClF_6NOPRuSb$ (869.84): calcd. C 46.95, H 3.24, N 1.61; found C 46.71, H 2.94, N 1.60. IR (Nujol): $\tilde{\nu}$ = 1588 (m, CN), 659 (s, $SbF_6$) cm$^{-1}$. CD [$Me_2CO$; $S_{Ru}$-**3**/$R_{Ru}$-**3** (2:98) mixture; maxima, minima and nodes]: $\Theta$ ($\lambda$) = +16000 (330), 0 (340), –42000 (370 nm). $S_{Ru}$-**3**: $^{31}P\{^1H\}$ NMR [$(CD_3)_2CO$: $\delta$ = 39.7 (s) ppm. $^{13}C$ NMR [$(CD_3)_2CO$]: $\delta$ = 92.67 (d, $J_{P,C}$ = 2.8, $C_6H_6$) ppm. $R_{Ru}$-**3**: $^1H$ NMR [$(CD_3)_2CO$]: $\delta$ = 3.55, 3.62 (AB part of an ABX system, $J_{A,B}$ = 18.0 Hz, $J_{A,X}$ = 4.0 Hz, $J_{B,X} \approx$ 0 Hz, 2 H, $H_c$, $H_t$), 5.84 (pt, $J_{Ht,Ho} = J_{Hn,Ho}$ = 5.0 Hz, $H_o$), 6.10 (d, 1 H, $H_n$), 6.24 (s, 6 H, $C_6H_6$), 6.53 (br. d, $J_{Ha,Hb}$ = 6.2, 1 H, $H_a$), 6.83 (pt, 1 H, $H_b$), 6.9–8.1 (m, 16 H, Ph) ppm. $^{31}P\{^1H\}$ NMR [$(CD_3)_2CO$]: $\delta$ = 37.39 (br. s) ppm. $^{13}C$ NMR [$(CD_3)_2CO$]: $\delta$ = 36.54 ($CH_cH_t$), 83.03 ($CH_n$),

 © 2006 Wiley-VCH Verlag GmbH & Co. KGaA, Weinheim 

87.07 ($CH_o$); 91.90 (d, $J_{P,C}$ = 2.8, $C_6H_6$), 124–140 (Ph), 168.79 (d, $J_{P,C}$ = 4.18, C=N) ppm.

**Complex 4:** Yield: 425 mg (89%), 10% *de* in $S_{Ru}$-**4**. $C_{40}H_{40}ClF_6NOPRuSb$ (954.00): calcd. C 50.36, H 4.23, N 1.47; found C 50.42, H 4.10, N 1.38. IR (Nujol): $\tilde{\nu}$ = 1595 (m, CN), 654 (s, $SbF_6$) $cm^{-1}$. $S_{Ru}$-**4**: $^1H$ NMR [$(CD_3)_2CO$]: $\delta$ = 1.99 (s, 18 H, $C_6Me_6$), 3.52 (m, 2 H, $H_c$, $H_t$), 5.81 (d, 1 H, $J_{Hn,Ho}$ = 5.7 Hz, $H_n$), 5.85 (m, 1 H, $H_o$), 6.9–8.1 (m, Ph) ppm. $^{31}P\{^1H\}$ NMR [$(CD_3)_2$-CO]: $\delta$ = 37.4 (br. s) ppm. $^{13}C$ NMR [$(CD_3)_2CO$]: $\delta$ = 15.26 ($C_6\mathit{Me}_6$), 36.30 ($CH_cH_t$), 79.31 ($CH_n$), 89.00 ($CH_o$), 101.02 (d, $J_{P,C}$ = 3.0 Hz, $C_6Me_6$), 124–139 (Ph), 168.24 (d, $J_{P,C}$ = 7.2 Hz, C=N) ppm. $R_{Ru}$-**4**: $^1H$ NMR [$(CD_3)_2CO$]: $\delta$ = 1.56 (s, 18 H, $C_6Me_6$), 3.61 (m, 2 H, $H_c$, $H_t$), 4.55 (d, 1 H, $J_{Ho,Hn}$ = 9.0 Hz, $H_n$), 5.49 (m, $J_{Ht,Ho}$ = $J_{Hc,Ho}$ = 6.8 Hz, $H_o$), 7.1–8.5 (m, Ph) ppm. $^{31}P\{^1H\}$ NMR [$(CD_3)_2CO$]: $\delta$ = 28.66 (s) ppm. $^{13}C$ NMR [$(CD_3)_2CO$]: $\delta$ = 14.93 ($C_6\mathit{Me}_6$), 39.59 ($CH_cH_t$), 77.90 ($CH_n$), 85.61 ($CH_o$), 91.90 (d, $J_{PC}$ = 2.8 Hz), 100.79 (d, $J_{P,C}$ = 2.9 Hz, $C_6Me_6$), 125–142 (Ph), 167.54 (d, $J_{P,C}$ = 8.8 Hz, C=N) ppm.

**Preparation of the Complexes [(η⁶-arene)Ru(LL*)($H_2O$)][$SbF_6$]$_2$ (7, 8, 10, 11):** To a solution of the corresponding chloro compounds **1**–**4** (0.20 mmol) in dichloromethane (25 mL) was added $AgSbF_6$ (68.7 mg, 0.20 mmol) in acetone (2 mL). The suspension was stirred for 30 min. The AgCl formed was separated by filtration and the filtrate was partially concentrated under reduced pressure. Slow addition of hexane (20 mL) afforded an orange oil that was converted into a solid powder after vigorous stirring. The solid was filtered, washed with hexane and dried under vacuum.

**Complex 7:** Yield: 150 mg (84%), 72% *de* in $R_{Ru}$-**7**. $C_{30}H_{32}F_{12}NO_2PRuSb_2$ (1042.11): calcd. C 34.58, H 3.09, N 1.34; found C 34.71, H 3.26, N 1.30. IR (Nujol): $\tilde{\nu}$ = 3427 (m, $H_2O$), 1598 (s, CN), 658 (vs, $SbF_6$) $cm^{-1}$. CD [$Me_2CO$, $R_{Ru}$-**7**/$S_{Ru}$-**7** (90:10) mixture, maxima, minima, and nodes]: $\Theta$ ($\lambda$) = +46000 (360), 0 (400), –6000 (425 nm). $R_{Ru}$-**7**: $^1H$ NMR ($CD_2Cl_2$): $\delta$ = 0.01 (d, $J_{H,H}$ = 6.5 Hz, 3 H, *Me*MeCH), 1.03 (d, $J_{H,H}$ = 6.9 Hz, 3 H, Me*Me*CH), 1.66 (m, 1 H, MeMeC*H*), 4.64, 4.79 (m, 3 H, $H_g$, $H_c$, $H_t$), 6.13 (s, 6 H, $C_6H_6$), 7.1–8.2 (m, Ph) ppm. $^{31}P\{^1H\}$ NMR ($CD_2Cl_2$): $\delta$ = 39.05 (s) ppm. $^{13}C$ NMR [$(CD_3)_2CO$] $\delta$ = 12.79 (*Me*MeCH), 18.07 (Me*Me*CH), 29.0 (MeMe*C*H), 69.21 ($CH_cH_t$), 80.64 ($CH_g$), 90.61 (d, $J_{P,C}$ = 2.4 Hz, $C_6H_6$), 126–135 (Ph), 167.41 (d, $J_{P,C}$ = 6.7 Hz, C=N) ppm. $S_{Ru}$-**7**: $^1H$ NMR ($CD_2Cl_2$): $\delta$ = 0.86 (d, $J_{H,H}$ = 6.6 Hz, 3 H, *Me*MeCH), 1.25 (d, $J_{H,H}$ = 6.9 Hz, 3 H, Me*Me*CH), 6.00 (s, 6 H, $C_6H_6$), 7.1–8.2 (m, Ph) ppm. $^{31}P\{^1H\}$ NMR ($CD_2Cl_2$): $\delta$ = 40.2 (s) ppm. $^{13}C$ NMR [$(CD_3)_2CO$]: $\delta$ = 91.24 (d, $J_{P,C}$ = 2.4 Hz, $C_6H_6$) ppm.

**Complex 8:** Yield: 221 mg (98%), 94% *de* in $R_{Ru}$-**8**. $C_{36}H_{44}F_{12}NO_2PRuSb_2$ (1126.27): calcd. C 38.39, H 3.94, N 1.24; found C 38.27, H 3.76, N 1.13. IR (Nujol): $\tilde{\nu}$ = 3370 (w, $H_2O$), 1645 (m), 1591 (m, CN), 657 (s, $SbF_6$) $cm^{-1}$. CD [$Me_2CO$; $R_{Ru}$-**8**/$S_{Ru}$-**8** (97:3) mixture; maxima, minima and nodes]: $\Theta$ ($\lambda$) = –12000 (330), 0 (360), +18500 (390 nm). $R_{Ru}$-**8**: $^1H$ NMR ($CD_2Cl_2$): $\delta$ = 0.00 (br. d), 0.50 (br. d), 1.15 (br. d, $Me_2CH$), 1.97 (br. s), 2.12 (br. s, $C_6Me_6$), 4.55 (br. m), 4.64 (br. m, $H_c$, Ht, Hg). $^1H$ NMR [$(CD_3)_2CO$, –30 °C]: $\delta$ = –0.05 (d, $J_{H,H}$ = 6.5 Hz, 3 H, *Me*MeCH), 1.12 (d, $J_{H,H}$ = 6.8 Hz, 3 H, Me*Me*CH), 2.10 (m, 1 H, MeMeC*H*), 2.15 (s, 18 H, $C_6Me_6$), 4.66 (pt, $J_{Ht,Hc}$ = $J_{Ht,Hg}$ = 9.2 Hz, 1 H, $H_t$), 4.92 (m, 2 H, $H_c$, $H_g$), 5.20 (s, 2 H, $H_2O$), 7.4–8.2 (m, Ph) ppm. $^{31}P\{^1H\}$ NMR ($CD_2Cl_2$, –90 °C): $\delta$ = 45.0 (br. s) ppm. $^{31}P\{^1H\}$ NMR [$(CD_3)_2CO$, –30 °C]: $\delta$ = 44.73 (s) ppm. $^{13}C$ NMR [$(CD_3)_2CO$, –30 °C]: $\delta$ = 13.34 (*Me*-MeCH), 16.17 ($C_6\mathit{Me}_6$), 17.72 (Me*Me*CH), 23–30 (MeMe*C*H), 68.55 ($CH_cH_t$), 76.25 ($CH_g$), 101.35 (d, $J_{P,C}$ = 2.3 Hz, $C_6Me_6$), 125–136 (Ph), 167.91 (d, $J_{P,C}$ = 4.6 Hz, C=N). $S_{Ru}$-**8**: $^{31}P\{^1H\}$ NMR ($CD_2Cl_2$, –90 °C): $\delta$ = 42.7 (br. s) ppm.

**Complex 10:** Yield: 168 mg (77%), 86% *de* in $S_{Ru}$-**10**. $C_{34}H_{30}F_{12}NO_2PRuSb_2$ (1088.14): calcd. C 37.53, H 2.78, N 1.29; found C 37.04, H 2.80, N 1.20. IR (Nujol): $\tilde{\nu}$ = 3442 (m, $H_2O$), 1644(m), 1595 (m, CN), 660 (s, $SbF_6$) $cm^{-1}$. CD [$CH_2Cl_2$; $R_{Ru}$-**10**/$S_{Ru}$-**10** (7:93) mixture; maxima, minima and nodes]: $\Theta$ ($\lambda$) = +16000 (300), 0 (320), –62000 (360), 0 (420), +2000 (430 nm). $R_{Ru}$-**10**: $^1H$ NMR ($CD_2Cl_2$): $\delta$ = 4.56 (s, 2 H, $H_2O$), 6.13 (s, 6 H, $C_6H_6$) ppm. $^{31}P\{^1H\}$ NMR ($CD_2Cl_2$): $\delta$ = 39.4 (s) ppm. $^{13}C$ NMR ($CD_2Cl_2$): $\delta$ = 91.13 (d, $J_{P,C}$ = 2.3 Hz, $C_6H_6$) ppm. $S_{Ru}$-**10**: $^1H$ NMR ($CD_2Cl_2$): $\delta$ = 3.62 (m, 2 H, $H_c$, $H_t$), 4.90 (s, 2 H, $H_2O$), 5.94 (m, 2 H, $H_o$, $H_a$), 6.04 (d, $J_{Hn,Ho}$ = 6.04 Hz, 1 H, $H_n$), 6.24 (s, 6 H, $C_6H_6$), 6.69 (m, 1 H, $H_b$), 6.6–8.2 (m, Ph) ppm. $^{31}P\{^1H\}$ NMR ($CD_2Cl_2$): $\delta$ = 36.6 (br. s), 38.13 (s) ppm. $^{13}C$ NMR ($CD_2Cl_2$): $\delta$ = 36.53 ($CH_cH_t$), 83.51 ($CH_n$), 88.33 ($CH_o$), 90.28 (d, $J_{P,C}$ = 2.3 Hz, $C_6H_6$), 90.47 (d, $J_{P,C}$ = 3.1 Hz, $C_6H_6$), 122.65 ($CH_a$), 124–140 (Ph), 168.79 (d, $J_{P,C}$ = 4.7, C=N) ppm.

**Complex 11:** Yield: 174 mg, (73%), 40% *de* in $S_{Ru}$-**11**. $C_{40}H_{43}F_{12}NO_3PRuSb_2$ (1190.32): calcd. C 40.36, H 3.55, N 1.17; found C 39.73, H 3.75, N 1.15. IR (Nujol): $\tilde{\nu}$ = 3370 (w, $H_2O$), 1624 (s), 1596 (m, CN), 660 (m, $SbF_6$) $cm^{-1}$. CD [$Me_2CO$; $R_{Ru}$-**11**/$S_{Ru}$-**11** (30:70) mixture; maxima, minima and nodes]: $\Theta$ ($\lambda$) = +8500 (330), 0 (340), –17500 (390 nm). $R_{Ru}$-**11**: $^1H$ NMR [$(CD_3)_2$-CO]: $\delta$ = 2.27 (s, 18 H, $C_6Me_6$) ppm. $^{31}P\{^1H\}$ NMR [$(CD_3)_2CO$]: $\delta$ = 41.0 (br. s) ppm. $^{13}C$ NMR [$(CD_3)_2CO$]: $\delta$ = 17.34 ($C_6\mathit{Me}_6$), 102.32 (d, $J_{P,C}$ = 2.4 Hz, $C_6Me_6$), 171.0 (d, $J_{P,C}$ = 4.0 Hz, C=N) ppm. $S_{Ru}$-**11**: $^1H$ NMR [$(CD_3)_2CO$]: $\delta$ = 2.12 (s, 18 H, $C_6Me_6$), 3.55, 3.63 (AB part of an ABX system, $J_{A,B}$ = 18.0 Hz, $J_{A,X}$ = 4.3 Hz, $J_{B,X} \approx 0$ Hz, 2 H, $H_c$, $H_t$), 6.05 (d, 1 H, $J_{Hn,Ho}$ = 5.7 Hz, $H_n$), 6.12 (m, 1 H, $H_o$), 6.6–8.4 (m, Ph) ppm. $^{31}P\{^1H\}$ NMR [$(CD_3)_2CO$]: $\delta$ = 37.3 (br. s) ppm. $^{13}C$ NMR [$(CD_3)_2CO$]: $\delta$ = 10.61 ($C_6\mathit{Me}_6$), 37.18 ($CH_cH_t$), 80.30 ($CH_n$), 91.77 ($CH_o$), 101.77 (d, $J_{P,C}$ = 1.6 Hz, $C_6Me_6$), 126–141 (Ph), 170.73 (d, $J_{P,C}$ = 7.2 Hz, C=N) ppm.

**Preparation of the Complexes [(η⁶-*p*-$MeC_6H_4$*i*Pr)Ru(LL*)($H_2O$)][$SbF_6$]$_2$ [LL* = *R*-Prophos (13); 2,3-Bis(diphenylphosphanyl)-butane, *R*,*R*-Chiraphos (14)]:** To a suspension of [{(η⁶-*p*-$MeC_6H_4$-*i*Pr)Ru}$_2$(μ-Cl)$_2$] (102.3 mg, 0.17 mmol) in acetone (7 mL) was added $AgSbF_6$ (229.6 mg, 0.68 mmol). The resultant suspension was stirred for 30 min and the AgCl formed was filtered off. Solid LL* (0.34 mmol) was added to the filtrate and the resultant solution was stirred for 30 min. Slow addition of hexane (20 mL) afforded an orange oil which could be converted into a solid powder after vigorous stirring. The solid was filtered, washed with hexane and dried under vacuum.

**Complex 13:** Yield: 290 mg (75%), pure $S_{Ru}$-**13**. $C_{37}H_{42}F_{12}OP_2RuSb_2$ (1136.91): calcd. C 39.07, H 3.72; found C 38.94, H 3.44. IR (Nujol): $\tilde{\nu}$ = 3603 (br., $H_2O$), 1643 (m), 658 (s, $SbF_6$) $cm^{-1}$. $^1H$ NMR ($CD_2Cl_2$): $\delta$ = 0.93 (d, $J_{H,H}$ = 6.6 Hz, 3 H, *Me*MeCH), 0.95 (d, $J_{H,H}$ = 6.6 Hz, 3 H, Me*Me*CH), 1.16 (dd, $J_{P,H}$ = 12.9, $J_{H,H}$ = 6.6 Hz, 3 H, Me), 1.65 (s, 3 H, Me of *p*-$MeC_6H_4$*i*Pr), 1.95 (m, 1 H, $H_t$), 2.45 (pseudo-sept, 1 H, MeMeC*H*), 2.45(m, 1 H, $H_g$), 2.88 (br. s, 2 H, $H_2O$), 3.05 (m, 1 H, $H_c$), 5.39 (d, $J_{A,B}$ = 6.2 Hz, 1 H, $H_AH_B$), 5.97 (d, $J_{A',B'}$ = 6.6 Hz, 1 H, $H_{A'}H_{B'}$), 6.02 (d, 1 H, $H_AH_B$), 6.06 (d, 1 H, $H_{A'}H_{B'}$), 7.1–7.9 (m, Ph) ppm. $^{31}P\{^1H\}$ NMR ($CD_2Cl_2$): $\delta$ = 54.1 (d, $J_{P1,P2}$ = 42.1 Hz, $P^1$), 76.45 (d, $P^2$) ppm. $^{13}C$ NMR ($CD_2Cl_2$): $\delta$ = 15.08 (dd, $J$ = 18.3, 5.1 Hz, Me), 17.63 (Me of *p*-$MeC_6H_4$ *i*Pr), 21.55, 22.45 (*Me*MeCH), 30.46 (dd, $J_{P,C}$ = 30.7, 9.5 Hz, *C*Me), 30.96 (MeMe*C*H), 31.95 (dd, $J_{P,C}$ = 34.4, 15.4 Hz, $CH_cH_t$), 87.22, 91.95, 93.05 (d, $J_{P,C}$ = 4.4 Hz), 93.46 (C of *p*-$MeC_6H_4$*i*Pr), 109.54 (*C*Me of *p*-$MeC_6H_4$*i*Pr), 124.39 (dd, $J_{P,C}$ = 4.4, $J$ = 2.2 Hz, *C*$CMe_2$H), 121–136 (Ph) ppm.

**Complex 14:** Yield: 317 mg (81%). $C_{38}H_{34}F_{12}OP_2RuSb_2$ (1151.26): calcd. C 39.64, H 3.67; found C 40.01, H 3.39. IR (Nujol): $\tilde{\nu}$ =

 © 2006 Wiley-VCH Verlag GmbH & Co. KGaA, Weinheim 

3524 (br., $H_2O$), 1644 (s), 660 (s, $SbF_6$) $cm^{-1}$. $^1H$ NMR ($CD_2Cl_2$): $\delta$ = 0.83 (d, $J_{H,H}$ = 7.3 Hz, 3 H, *Me*MeCH), 0.88 (d, $J_{H,H}$ = 7.3 Hz, 3 H, Me*Me*CH), 0.95 (dd, $J_{P,H}$ = 13.9, $J_{H,H}$ = 6.6 Hz, 3 H, Me), 1.10 (dd, $J_{P,H}$ = 13.9, $J_{H,H}$ = 6.6 Hz, 3 H, Me), 1.62 (s, 3 H, Me of *p*-$MeC_6H_4$*i*Pr), 2.16 (pseudo-sept, 1 H, MeMeC*H*), 2.30, 2.53 (m, 2 H, C*H*Me), 5.45 (d, $J_{A,B}$ = 6.3 Hz, 1 H, $H_AH_B$), 5.58 (d, $J_{A',B'}$ = 6.3 Hz, 1 H, $H_{A'}H_{B'}$), 5.80 (d, 2 H, $H_AH_B$, $H_{A'}H_{B'}$), 7.0–7.8 (m, Ph) ppm. $^{31}P\{^1H\}$ NMR ($CD_2Cl_2$): $\delta$ = 74.9, 68.3 (d, $J_{P1,P2}$ = 48.4 Hz) ppm. $^{13}C$ NMR ($CD_2Cl_2$): $\delta$ = 13.17 (dd, $J$ = 17.6, 5.9 Hz, Me), 15.14 (dd, $J$ = 16.8, 4.4 Hz, Me), 18.13 (Me of *p*-$MeC_6H_4$*i*Pr), 21.94, 22.69 (*MeMe*CH), 30.58 (MeMe*C*H), 34.03 (dd, $J_{P,C}$ = 32.2, 11.0 Hz, *C*Me), 43.45 (dd, $J_{P,C}$ = 32.9, 15.4 Hz, *C*Me), 89.82 (d, $J_{P,C}$ = 2.2 Hz), 90.11 (d, $J_{P,C}$ = 2.9 Hz), 93.08, 93.21 (C of *p*-$MeC_6H_4$*i*Pr), 105.25 (*C*Me of *p*-$MeC_6H_4$*i*Pr), 114.23 (*C*$CMe_2H$), 121–135 (Ph) ppm.

**Catalytic Procedure:** The complexes [($\eta^6$-arene)Ru(LL*)($H_2O$)][A]$_2$ (0.06 mmol, 5 mol-%) were dissolved in $CH_2Cl_2$ (3 mL) at 0 °C. Freshly distilled methacrolein [0.14 mL (1.68 mmol) or 0.70 mL (8.40 mmol)] and activated molecular sieves (4 Å) (100.0 mg) were added and the suspension was stirred for 30 min. A solution of the corresponding nitrone (1.20 mmol) in $CH_2Cl_2$ (2 mL) was added. For nitrones **II**–**V**, the nitrone solution was added dropwise with a syringe pump over 15 h. After stirring at the appropriate temperature for the reaction time indicated in the tables, hexanes (20 mL) were added. After filtration through diatomaceous earth, the solution was concentrated to dryness. The residue was purified by chromatography ($SiO_2$) to provide a mixture of the corresponding isomers. Regioselectivity was determined on the crude mixture by $^1H$ NMR spectroscopic analysis in $C_6D_6$ (nitrones **I**, **II**, and **V**) or $CDCl_3$ (nitrones **III** and **IV**). Enantioselectivity was determined as indicated in the footnote of Tables 2 and 5.

**Preparation of the Complexes [($\eta^6$-arene)Ru(PN*i*Pr)(methacrolein)][$SbF_6$]$_2$ [arene = $C_6H_6$ (17), *p*-$MeC_6H_4$*i*Pr (18), $C_6Me_6$ (19)]:** To a solution of the corresponding aqua complex [($\eta^6$-arene)Ru(PN-*i*Pr)($H_2O$)][$SbF_6$]$_2$ (0.10 mmol) in $CH_2Cl_2$ (5 mL) at 0 °C under argon, methacrolein (33.0 μL, 0.395 mmol) and molecular sieves (4 Å) (200.0 mg) were added. The solutions were stirred for 20 min and the solvent was then vacuum-evaporated. The residues were extracted with $CH_2Cl_2$ (3 × 2 mL). Addition of dry hexane (20 mL) to the yellow filtrate afforded yellow solids which were washed with hexane and vacuum-dried.

**Complex 17:** Yield: 61 mg, (63%), 40% *de* in $R_{Ru}$-**17**. $C_{33}H_{35}F_{12}NO_2PRuSb_2$ (1093.77): calcd. C 36.23, H 3.22, N 1.28; found C 36.39, H 3.57, N 1.38. IR (Nujol): $\tilde{\nu}$ = 1687 (m, CO), 1599 (s, CN), 660 (s, $SbF_6$) $cm^{-1}$. $R_{Ru}$-**17**: $^1H$ NMR ($CD_2Cl_2$, 0 °C): $\delta$ = –0.05 (d, $J_{H,H}$ = 6.6 Hz, 3 H, *Me*MeCH), 1.01 (d, $J_{H,H}$ = 7.3 Hz, 3 H, Me*Me*CH), 1.03 [s, 3 H, CHO(C*H*$_3$)CHH], 1.63 (pseudo-sept, 1 H, MeMeC*H*), 4.63, 4.80 (m, 2 H, $H_c$, $H_t$), 4.81 (m, 1 H, $H_g$), 6.17 (s, $C_6H_6$), 6.66 [s, 2 H, CHOC(CH$_3$)C*HH*], 7.1–8.0 (m, 14 H, Ph), 9.80 (s, 1 H, COH) ppm. $^{31}P\{^1H\}$ NMR ($CD_2Cl_2$, 0 °C): $\delta$ = 39.6 (s) ppm. $^{13}C$ NMR ($CD_2Cl_2$, 0 °C): $\delta$ = 12.5 [CHOC(*C*H$_3$)CHH], 12.59 (*Me*MeCH), 18.66 (Me*Me*CH), 30.24 (MeMe*C*H), 69.51 ($CH_cH_t$), 80.29 ($CH_g$), 90.58 ($C_6H_6$), 124–135 (Ph), 145.62 [CHO*C*(CH$_3$)CHH], 149.07 [CHOC(CH$_3$)*C*HH], 166.82 (d, $J_{P,C}$ = 4.6 Hz, C=N), 214.81 (CHO) ppm. $S_{Ru}$-**17**: $^1H$ NMR ($CD_2Cl_2$, 0 °C): $\delta$ = 0.73 (d, $J_{H,H}$ = 6.6 Hz, 3 H, *Me*MeCH), 1.24 (d, $J_{H,H}$ = 6.5 Hz, 3 H, Me*Me*CH), 1.01 [s, 3 H, CHO(C*H*$_3$)CHH], 2.70 (pseudo-sept, 1 H, MeMeC*H*), 4.77 (m, 1 H, $H_g$), 6.05 (s, $C_6H_6$), 6.60, 6.63 [s, 2 H, CHOC(C*H*$_3$)C*HH*], 7.1–8.0 (m, 14 H, Ph), 9.51 (s, 1 H, CHO) ppm. $^{31}P\{^1H\}$ NMR ($CD_2Cl_2$, 0 °C): $\delta$ = 40.75 (s) ppm. $^{13}C$ NMR ($CD_2Cl_2$, 0 °C): $\delta$ = 12.75 [CHOC(*C*H$_3$)CHH], 14.23 (*Me*MeCH), 18.08 (Me*Me*CH), 29.57 (MeMe*C*H), 70.02 ($CH_cH_t$), 78.11 ($CH_g$), 91.30 ($C_6H_6$), 124–135 (Ph), 144.73 [CHO*C*(CH$_3$)CHH], 149.02 [CHOC(CH$_3$)*C*HH], 166.45 (d, $J_{P,C}$ = 9.1 Hz, C=N), 214.27 (CHO) ppm.

**Complex 18:** Yield: 102 mg (88.5%), 36% *de* in $S_{Ru}$-**18**. $C_{38}H_{44}F_{12}NO_2PRuSb_2$ (1150.30): calcd. C 39.68, H 3.85, N 1.21; found C 39.44, H 4.01, N 1.14. IR (Nujol): $\tilde{\nu}$ = 1687 (m, CO), 1598 (m, CN), 659 (s, $SbF_6$) $cm^{-1}$. $R_{Ru}$-**18**: $^1H$ NMR ($CD_2Cl_2$, –50 °C): $\delta$ = 0.14 (d, $J_{H,H}$ = 6.3 Hz, 3 H, *Me*MeCH), 1.06 (d, $J_{H,H}$ = 6.7 Hz, 3 H, Me*Me*CH), 1.11 (d, $J_{H,H}$ = 7.2 Hz, 3 H, *Me*MeCH, $MeC_6H_4$*i*Pr), 1.12 (s, 3 H, CHOC(C*H*$_3$)CHH), 1.26 (d, $J_{H,H}$ = 6.3 Hz, 3 H, Me*Me*CH, $MeC_6H_4$*i*Pr), 1.73 (pseudo-sept, 1 H, MeMeC*H*), 1.92 (s, 3 H, Me, $MeC_6H_4$*i*Pr), 2.41 (pseudo-sept, 1 H, MeMeC*H*, $MeC_6H_4$*i*Pr), 4.70–4.76 (m, 3 H, $H_g$,$H_c$,$H_t$), 5.56 (d, $J_{A,B}$ = 6.1 Hz, 1 H, $H_AH_B$), 5.82 (d, 1 H, $H_AH_B$), 6.04 (d, $J_{A',B'}$ = 6.3 Hz, 1 H, $H_{A'}H_{B'}$), 6.39 (d, 1 H, $H_{A'}H_{B'}$), 6.66 (s, 2 H, CHOC(CH$_3$)C*HH*), 7.1–8.1 (m, 14 H, Ph), 9.64 (s, 1 H, CHO) ppm. $^{31}P\{^1H\}$ NMR ($CD_2Cl_2$, –50 °C): $\delta$ = 39.0 (s) ppm. $^{13}C$ NMR ($CD_2Cl_2$, –50 °C): $\delta$ = 13.5 [CHOC(*C*H$_3$)CHH], 13.4 (Me*Me*CH), 19.0 (Me, $MeC_6H_4$*i*Pr), 18.9 (*Me*MeCH), 23.2 (*MeMe*CH, Me-$C_6H_4$*i*Pr), 30.3 (MeMe*C*H), 32.1 (MeMe*C*H, $MeC_6H_4$*i*Pr), 69.6 ($CH_cH_t$), 79.8 ($CH_g$), 86.6, 87.4, 89.7, 92.2 (C, Me*C*$_6H_4$*i*Pr), 101.7, 120.1 (d, $J_{P,C}$ = 4.3 Hz), (*C*Me and *C*$CMe_2H$, $MeC_6H_4$*i*Pr), 124–136 (Ph), 145.9 [CHO*C*(CH$_3$)CHH], 150.1 [CHOC(CH$_3$)*C*HH], 167.6 (d, $J_{P,C}$ = 5.1 Hz, C=N), 214.1 (CHO) ppm. $S_{Ru}$-**18**: $^1H$ NMR ($CD_2Cl_2$, –50 °C): $\delta$ = 0.76 (d, $J_{H,H}$ = 6.3 Hz, 3 H, *Me*-MeCH), 0.96 (d, $J_{H,H}$ = 7.2 Hz, 3 H, *Me*MeCH, $MeC_6H_4$*i*Pr), 0.98 (d, $J_{H,H}$ = 7.4 Hz, 3 H, Me*Me*CH, $MeC_6H_4$*i*Pr), 1.05 [s, 3 H, CHO(C*H*$_3$)CHH], 1.26 (d, $J_{H,H}$ = 6.3 Hz, 3 H, Me*Me*CH), 1.97 (s, 3 H, Me, $MeC_6H_4$*i*Pr), 2.49 (pseudo-sept, 1 H, MeMeC*H*, $MeC_6H_4$-*i*Pr), 2.64 (pseudo-sept, 1 H, MeMeC*H*), 4.5, 4.82 (m, 2 H, $H_c$, $H_t$) 4.63 (m, 1 H, $H_g$), 5.69 (d, $J_{A,B}$ = 6.5 Hz, 1 H, $H_AH_B$), 5.75 (d, 1 H, $H_AH_B$), 5.93 (d, $J_{A',B'}$ = 6.0 Hz, 1 H, $H_{A'}H_{B'}$), 6.24 (d, 1 H, $H_{A'}H_{B'}$), 6.69 [s, 2 H, CHOC(CH$_3$)C*HH*], 7.1–8.1 (m, 14 H, Ph), 9.56 (s, 1 H, COH) ppm. $^{31}P\{^1H\}$ NMR ($CD_2Cl_2$, –50 °C): $\delta$ = 40.4 (s) ppm. $^{13}C$ NMR ($CD_2Cl_2$, –50 °C): $\delta$ = 13.6 [CHOC(*C*H$_3$)-CHH], 14.6 (*Me*MeCH), 18.4 (Me*Me*CH), 18.5 (Me, $MeC_6H_4$*i*Pr), 21.8, 22.0 (*MeMe*CH, $MeC_6H_4$*i*Pr), 29.9 (MeMe*C*H), 32.3 (Me-Me*C*H, $MeC_6H_4$*i*Pr), 70.5 ($CH_cH_t$), 77.9 ($CH_g$), 87.9, 91.0, 91.9, 94.4 (C, Me*C*$_6H_4$*i*Pr), 99.3 (d, $J_{P,C}$ = 3.3, *C*Me, $MeC_6H_4$*i*Pr); 115.5 (d, $J_{P,C}$ = 3.3 Hz, *C*$CMe_2H$, $MeC_6H_4$*i*Pr), 124–136 (Ph), 145.3 [CHO*C*(CH$_3$)CHH], 150.0 [CHOC(CH$_3$)*C*HH], 167.4 (d, $J_{PC}$ = 8.4 Hz, C=N), 213.8 (CHO) ppm.

**Complex 19:** Yield: 111 mg, (94%), 40% *de* in $R_{Ru}$-**19**. $C_{39}H_{47}F_{12}NO_2PRuSb_2$ (1178.35): calcd. C 40.77, H 4.10, N 1.18; found C 40.44, H 4.01, N 1.12. IR (Nujol): $\tilde{\nu}$ = 1688 (m, CO), 1598 (s, CN), 660 (s, $SbF_6$) $cm^{-1}$. $R_{Ru}$-**19**: $^1H$ NMR ($CD_2Cl_2$, –30 °C): $\delta$ = 0.06 (d, $J_{H,H}$ = 6.2 Hz, 3 H, *Me*MeCH), 1.13 (m, 3 H, Me-*Me*CH), 1.20 [s, 3 H, CHO(C*H*$_3$)CHH], 1.90 (pseudo-sept, 1 H, MeMeC*H*), 1.92 ($C_6Me_6$), 4.7 (m, 3 H, $H_c$, $H_g$, $H_t$), 6.71, 6.77 [s, 2 H, CHOC(CH$_3$)C*HH*], 7.3–7.9 (m, 14 H, Ph), 9.42 (s, 1 H, COH) ppm. $^{31}P\{^1H\}$ NMR ($CD_2Cl_2$, –30 °C): $\delta$ = 43.3 (s) ppm. $^{13}C$ NMR ($CD_2Cl_2$, –30 °C): $\delta$ = 13.60 [CHOC(*C*H$_3$)CHH], 13.99 (*Me*-MeCH), 16.35 ($C_6Me_6$), 18.33 (Me*Me*CH), 30.03 (MeMe*C*H), 68.91 ($CH_cH_t$), 76.21 ($CH_g$), 101.81 (d, $J_{P,C}$ = 2.3 Hz, $C_6Me_6$), 123–135 (Ph), 145.76 [CHO*C*(CH$_3$)CHH], 149.84 [CHOC(CH$_3$)*C*HH], 167.36 (d, $J_{P,C}$ = 5.7 Hz, C=N), 212.65 (CHO) ppm. $S_{Ru}$-**19**: $^1H$ NMR ($CD_2Cl_2$, –30 °C): $\delta$ = 0.73 (d, $J_{H,H}$ = 6.7 Hz, 3 H, *Me*-MeCH), 1.29 (d, $J_{H,H}$ = 6.7 Hz, 3 H, Me*Me*CH), 1.12 [s, 3 H, CHO(C*H*$_3$)CHH], 1.89 ($C_6Me_6$), 2.10 (pseudo-sept, 1 H, Me-MeC*H*), 4.47 (m, 1 H, $H_g$), 4.62, 4.75 (m, 2 H, $H_c$, $H_t$), 6.58, 6.69 [s, 2 H, CHOC(CH$_3$)C*HH*], 7.3–7.9 (m, 14 H, Ph), 9.24 (s, 1 H, COH) ppm. $^{31}P\{^1H\}$ NMR ($CD_2Cl_2$, –30 °C): $\delta$ = 45.57 (s) ppm. $^{13}C$ NMR ($CD_2Cl_2$, –30 °C): $\delta$ = 13.42 [CHOC(*C*H$_3$)CHH], 14.97

 © 2006 Wiley-VCH Verlag GmbH & Co. KGaA, Weinheim 

(*Me*MeCH), 15.89 ($C_6Me_6$), 17.85 (Me*Me*CH), 30.22 (MeMe*C*H), 70.38 ($CH_cH_t$), 74.67 ($CH_g$), 100.90 (d, $J_{P,C}$ = 2.3 Hz, $C_6Me_6$), 123–135 (Ph), 144.77 [CHO*C*(CH$_3$)CHH], 149.58 [CHOC(CH$_3$)*C*HH], 167.83 (d, $J_{P,C}$ = 9.1, Hz, C=N), 210.68 (CHO) ppm.

**Preparation of the Complexes [(η$^6$-*p*-MeC$_6$H$_4$*i*Pr)Ru(PN*i*Pr)(nitrone)][SbF$_6$]$_2$ [nitrone = I (20), II (21), V (22)]:** A solution of [(η$^6$-*p*-MeC$_6$H$_4$*i*Pr)Ru(PN*i*Pr)(H$_2$O)][SbF$_6$]$_2$ (0.1 mmol) in $CH_2Cl_2$ (4 mL) was stirred in the presence of molecular sieves (4 Å) (200.0 mg) at 0 °C under argon for 20 min. The corresponding nitrone **I**, **II** or **V** (0.1 mmol) was then added and the suspension stirred for 20 min. Addition of hexanes (20 mL) caused the precipitation of a solid. The solvents were separated by decantation and the residue was washed with hexanes (3 × 20 mL). After washing, the residue was extracted with $CH_2Cl_2$ (5 mL). Addition of hexanes (20 mL) to the resultant solution gave an orange-red solid which was washed with hexanes and vacuum-dried.

**Complex 20:** Yield: 100 mg (78%) of pure $R_{Ru}$ epimer. $C_{47}H_{49}F_{12}N_2RuO_2PSb_2$ (1277.44): calcd. C 44.19, H 3.86, N 2.19; found C 43.93, H 3.63, N 1.98. IR (Nujol): $\tilde{\nu}$ = 1595 (s, CN), 659 (s, $SbF_6$) cm$^{-1}$. $^1$H NMR ($CD_2Cl_2$, –25 °C): $\delta$ = –0.37 (d, $J_{H,H}$ = 6.5 Hz, 3 H, *Me*MeCH), 0.83 (d, $J_{H,H}$ = 7.2 Hz, 3 H, *Me*MeCH, MeC$_6$H$_4$*i*Pr), 0.92 (d, $J_{H,H}$ = 6.8 Hz, 3 H, Me*Me*CH, MeC$_6$H$_4$*i*Pr), 0.97 (d, $J_{H,H}$ = 6.8 Hz, 3 H, Me*Me*CH), 1.37 (s, 3 H, Me, MeC$_6$H$_4$-*i*Pr), 1.72 (m, 1 H, MeMeC*H*), 1.83 (pseudo-sept, 1 H, MeMeC*H*, MeC$_6$H$_4$*i*Pr), 4.44 (m, 1 H, $H_g$), 4.62, 4.74 (m, 2 H, $H_c$, $H_t$), 5.50 (m, 1 H, $H_AH_B$), 5.57 (d, $J_{A,B}$ = 6.3 Hz, 1 H, $H_AH_B$), 5.57 (d, $J_{A',B'}$ = 6.3 Hz, 1 H, $H_{A'}H_{B'}$), 5.67 (d, 1 H, $H_{A'}H_{B'}$), 6.9–8.3 (m, Ph), 8.63 (s, 1 H, NCH) ppm. $^{31}$P{$^1$H} NMR ($CD_2Cl_2$, –25 °C): $\delta$ = 43.8 (br. s) ppm. $^{13}$C NMR ($CD_2Cl_2$, –25 °C): $\delta$ = 12.4 (*Me*MeCH), 18.8 (Me*Me*CH), 21.4 (Me, MeC$_6$H$_4$*i*Pr), 21.4, 23.3 (*MeMe*CH, MeC$_6$H$_4$*i*Pr), 30.7 (MeMe*C*H), 30.8 (MeMe*C*H, MeC$_6$H$_4$*i*Pr), 69.2 ($CH_cH_t$), 78.6 ($CH_g$), 78.8, 85.2, 85.2, 86.3 (C, Me*C*$_6$H$_4$*i*Pr), 123–137 (Ph), 155.7 (NCH), 168.2 (d, $J_{P,C}$ = 5.3 Hz, C=N) ppm.

**Complex 21:** Yield: 94 mg (77%) of pure $R_{Ru}$ epimer. $C_{42}H_{47}F_{12}N_2RuO_2PSb_2$ (1216.27): calcd. C 41.47, H 3.89, N 2.30; found C 41.19, H 4.04, N 2.21. IR (Nujol): $\tilde{\nu}$ = 1595 (s, CN), 658 (s, $SbF_6$) cm$^{-1}$. $^1$H NMR ($CD_2Cl_2$, –60 °C): $\delta$ = 0.22 (d, $J_{H,H}$ = 6.2 Hz, 3 H, *Me*MeCH), 1.01 (d, $J_{H,H}$ = 6.6 Hz, 3 H, Me*Me*CH), 1.09 (d, $J_{H,H}$ = 6.6 Hz, 3 H, *Me*MeCH, MeC$_6$H$_4$*i*Pr), 1.20 (m, 3 H, Me*Me*CH, MeC$_6$H$_4$*i*Pr), 1.50 (m, 1 H, MeMeC*H*), 1.55 (s, 3 H, Me, MeC$_6$H$_4$*i*Pr), 2.34 (pseudo-sept, 1 H, MeMeC*H*, MeC$_6$H$_4$*i*Pr), 4.15 (s, 3 H, NMe), 4.75 (m, 2 H, $H_c$, $H_t$), 4.84 (m, 1 H, $H_g$), 5.52 (m, 1 H, $H_AH_B$), 6.10 (d, $J_{A,B}$ = 5.9 Hz, 1 H, $H_AH_B$), 6.22 (d, $J_{A',B'}$ = 6.2 Hz, 1 H, $H_{A'}H_{B'}$), 6.47 (d, 1 H, $H_{A'}H_{B'}$), 7.1–8.0 (m, Ph), 8.03 (s, 1 H, NCH) ppm. $^{31}$P{$^1$H} NMR ($CD_2Cl_2$, –60 °C): $\delta$ = 37.8 (s) ppm. $^{13}$C NMR ($CD_2Cl_2$, –60 °C): $\delta$ = 13.70 (*Me*MeCH), 17.33 (Me, MeC$_6$H$_4$*i*Pr), 18.30 (Me*Me*CH), 19.76, 23.81 (*Me-Me*CH, MeC$_6$H$_4$*i*Pr); 29.65 (MeMe*C*H); 31.73 (MeMe*C*H, Me-C$_6$H$_4$*i*Pr), 51.03 (NMe), 68.67 ($CH_cH_t$), 79.67 ($CH_g$), 79.8, 88.0 (d, $J_{P,C}$ = 7.9 Hz), 88.7, 97.0 (d, $J_{P,C}$ = 3.7 Hz) (C, Me*C*$_6$H$_4$*i*Pr), 122–136 (Ph), 154.19 (NCH), 167.68 (d, $J_{PC}$ = 4.9 Hz, C=N) ppm.

**Complex 22:** Yield: 96 mg (78%) of pure $R_{Ru}$ epimer. $C_{43}H_{47}F_{12}N_2O_2PRuSb_2$ (1227.28): calcd. C 42.08, H 3.85, N 2.28; found C 42.19, H 4.01, N 2.36. IR (Nujol): $\tilde{\nu}$ = 1598 (s, CN), 659 (s, $SbF_6$) cm$^{-1}$. $^1$H NMR ($CD_2Cl_2$, –30 °C): $\delta$ = 0.18 (d, $J_{H,H}$ = 6.6 Hz, 3 H, *Me*MeCH), 1.09 (d, $J_{H,H}$ = 6.9 Hz, 3 H, Me*Me*CH), 1.11 (d, $J_{H,H}$ = 8.4 Hz, 3 H, *Me*MeCH, MeC$_6$H$_4$*i*Pr), 1.20 (d, $J_{H,H}$ = 6.6 Hz, 3 H, Me*Me*CH, MeC$_6$H$_4$*i*Pr), 1.65 (m, 1 H, MeMeC*H*), 2.01 (s, 3 H, Me, MeC$_6$H$_4$*i*Pr), 2.41 (pseudo-sept, 1 H, MeMeC*H*, MeC$_6$H$_4$*i*Pr), 2.67, 2.86, 3.10, 3.94 (m, 4 H, NCH$_2$CH$_2$), 4.40 (pt, 1 H, $J_{Hc,Ht}$ = 10.2 Hz, $J_{Hc,Hg}$ = 1.8 Hz, $H_c$), 4.68 (dd, 1 H, $H_t$), 4.96 (m, 1 H, $H_g$), 4.98 (m, 1 H, $H_AH_B$), 6.08 (m, 1 H, $H_AH_B$), 6.25 (d, $J_{A',B'}$ = 6.2 Hz, 1 H, $H_{A'}H_{B'}$), 6.77 (d, 1 H, $H_{A'}H_{B'}$), 7.2–7.9 (m, Ph), 8.11 (s, 1 H, N=CH) ppm. $^{31}$P{$^1$H} NMR ($CD_2Cl_2$, –30 °C): $\delta$ = 39.35 (s) ppm. $^{13}$C NMR ($CD_2Cl_2$, –30 °C): $\delta$ = 13.59 (*Me*MeCH), 18.19 (Me, MeC$_6$H$_4$*i*Pr), 20.43 (Me*Me*CH), 18.49, 23.11 (*MeMe*CH, MeC$_6$H$_4$*i*Pr), 27.08 (NCH$_2$*C*H$_2$), 29.83 (Me-Me*C*H), 31.73 (MeMe*C*H, MeC$_6$H$_4$*i*Pr), 56.02 (N*C*H$_2$CH$_2$), 51.03 (NMe), 69.07 ($CH_cH_t$), 79.72 ($CH_g$), 81.39, 88.36 (d, $J_{P,C}$ = 8.0 Hz), 88.94, 95.74 (d, $J_{P,C}$ = 2.3 Hz) (C, Me*C*$_6$H$_4$*i*Pr), 122–136 (Ph), 144.35 (NCH), 166.78 (d, $J_{P,C}$ = 5.7 Hz, C=N) ppm.

**Crystal Structure Determination of Complexes $R_{Ru}$-2, $R_{Ru}$-3, $R_{Ru}$-7 and $R_{Ru}$-8:** X-ray data were collected for all complexes at low temperature [100(2) K] with a Bruker SMART APEX CCD diffractometer with graphite-monochromated Mo-$K_\alpha$ radiation ($\lambda$ = 0.71073 Å). Data were corrected for absorption using a multiscan method applied with the SADABS program.[17] The structures were solved by direct methods with SHELXS-86.[18] Refinement, by full-matrix least squares on $F^2$ with SHELXL97,[18] was similar for all complexes, including isotropic and subsequently anisotropic displacement parameters for all non-hydrogen nondisordered atoms. Particular details concerning the existence of static disorder and hydrogen refinement are listed below. All the highest electronic residuals (smaller than 1.0 e Å$^{-3}$) were observed in close proximity to the metal or Sb atoms and have no chemical significance. In all structures, in addition to the internal configuration reference of the oxazoline ligand, the Flack parameter was refined as a check of the correct absolute configuration determination.[19] CCDC-297912, -297913, -297914 and -297915 contain the supplementary crystallographic data for this paper. These data can be obtained free of charge from The Cambridge Crystallographic Data Centre via http://www.ccdc.cam.ac.uk/data requested/cif.

**Crystal Data for $R_{Ru}$-2:** $C_{36}H_{42}ClF_6NOPRuSb$, $M$ = 907.95; red prism, 0.10 × 0.09 × 0.08 mm; orthorhombic, $P2_12_12_1$; $a$ = 11.7929(9), $b$ = 14.0329(10), $c$ = 21.8518(16) Å; $Z$ = 4; $V$ = 3616.2(5) Å$^3$; $D_c$ = 1.668 g cm$^{-3}$; $\mu$ = 1.334 mm$^{-1}$, min/max transmission factors 0.8762/0.9013; $2\theta_{max}$ = 57.74°; 43058 reflections collected, 8852 unique ($R_{int}$ = 0.0395); number of data/restrains/parameters = 8852/0/510; final $GoF$ = 1.103, $R_1$ = 0.0360 [8516 reflections, $I > 2\sigma(I)$], $wR_2$ = 0.0807 for all data; Flack parameter $x$ = –0.025(18); three electron residual peaks above 1 e Å$^{-3}$ were located close to the fluorine atoms (distances shorter than 1 Å) and have no chemical significance. Most of the hydrogen atoms were observed in the difference Fourier maps and included in the model as free isotropic atoms; hydrogen atoms of the terminal methyl groups were included in calculated positions and refined with positional and thermal riding parameters.

**Crystal Data for $R_{Ru}$-3:** $C_{34}H_{28}ClF_6NOPRuSb$, $M$ = 869.81; orange prism, 0.18 × 0.07 × 0.04 mm; orthorhombic, $P2_12_12_1$; $a$ = 11.1353(11), $b$ = 16.1491(16), $c$ = 17.6001(18) Å; $Z$ = 4; $V$ = 3164.9(5) Å$^3$; $D_c$ = 1.825 g cm$^{-3}$; $\mu$ = 1.531 mm$^{-1}$, min/max transmission factors 0.7669/0.9357; $2\theta_{max}$ = 57.8°; 21412 reflections collected, 7573 unique ($R_{int}$ = 0.0648); number of data/restrains/parameters = 7573/12/475; final $GoF$ = 1.059, $R_1$ = 0.0557 [6161 reflections, $I > 2\sigma(I)$], $wR_2$ = 0.0963 for all data; Flack parameter $x$ = 0.00(3); largest difference peak 1.26 e Å$^{-3}$ (close to Sb atom). Most of the hydrogen atoms were observed in the difference Fourier maps and included in the model as free isotropic atoms; the remaining hydrogen atoms were included in calculated positions and refined with positional and thermal riding parameters.

**Crystal Data for $R_{Ru}$-7:** $C_{30}H_{32}F_{12}NO_2PRuSb_2$, $M$ = 1042.11; amber irregular block, 0.15 × 0.09 × 0.06 mm; orthorhombic, $P2_12_12_1$; $a$ = 10.1400(17), $b$ = 17.020(3), $c$ = 19.899(3) Å; $Z$ = 4; $V$ = 3434.1(10) Å$^3$; $D_c$ = 2.016 g cm$^{-3}$; $\mu$ = 2.138 mm$^{-1}$, min/max trans-

 © 2006 Wiley-VCH Verlag GmbH & Co. KGaA, Weinheim 

mission factors 0.7398/0.8771; $2\theta_{max}$ = 57.96°; 23407 reflections collected, 8218 unique ($R_{int}$ = 0.0570); number of data/restrains/parameters = 8218/2/451; final *GoF* = 1.052, $R_1$ = 0.0455 [7064 reflections, $I > 2\sigma(I)$], $wR_2$ = 0.0790 for all data; Flack parameter $x$ = –0.02(2). Hydrogen atoms were included in calculated positions and refined with a positional and thermal riding model. The two hydrogen atoms of the coordinated water molecule were included from observed positions and refined as free isotropic atoms.

**Crystal Data for $R_{Ru}$-8·$C_4H_{10}O$:** $C_{80}H_{84}F_{24}N_2O_6P_2Ru_2Sb_4$, $M$ = 2376.57; red lamina, 0.23 × 0.19 × 0.01 mm; monoclinic, $P2_1$; $a$ = 11.145(5), $b$ = 17.873(5), $c$ = 23.274(5) Å; $\beta$ = 103.139(5)°; $Z$ = 2; $V$ = 4515(3) Å$^3$; $D_c$ = 1.748 g cm$^{-3}$; $\mu$ = 1.640 mm$^{-1}$, min/max transmission factors 0.7072/0.9774; $2\theta_{max}$ = 57.7°; 30335 reflections collected, 19946 unique ($R_{int}$ = 0.0297); number of data/restrains/parameters = 19946/3/1036; final *GoF* = 1.076, $R_1$ = 0.0564 [18151 reflections, $I > 2\sigma(I)$], $wR_2$ = 0.1275 for all data; Flack parameter $x$ = 0.03(2). Two independent molecules were observed in the crystal. Two of the $SbF_6^-$ anions were observed disordered and a similar model was built for both anions using two $F_6$ moieties in each case; they were refined with complementary occupancy factors. Even with this model there was some residual electronic density left in the proximity of these groups. Hydrogen atoms were included in calculated positions and refined as free isotropic atoms. At this point, several residual peaks were still present in the difference Fourier maps, clearly separated from anions and cations. They were interpreted as originated from two heavily disordered diethyl ether solvent molecules. After several attempts to include these peaks in geometrically reasonable positions without success, the highest residuals were included to take account of solvent ($C_4H_{10}O$) presence.

## Acknowledgments

This work was supported by the Dirección General de Investigación Científica y Técnica (Grants BQU 2002-1729 and BQU 2003-1096)

[1] a) *Comprehensive Asymmetric Catalysis* (Eds.: E. N. Jacobsen, A. Pfaltz, H. Yamamoto), Springer, New York, **1999**, vol. I–III, supplements 1 and 2, Springer, New York, **2004**; b) *Catalytic Asymmetric Synthesis* (Ed.: I. Ojima), VCH, Weinheim, Germany, **2000**; c) R. Noyori, *Asymmetric Catalysis in Organic Synthesis*, John Willey and Sons, New York, **1994**.

[2] *Cycloaddition Reactions in Organic Synthesis* (Eds.: S. Kobayashi, K. A. Jorgensen), Wiley-VCH, Weinheim, **2002**.

[3] a) *Synthetic Applications of 1,3-Dipolar Cycloaddition Chemistry toward Heterocycles and Natural Products* (Eds.: A. Padwa, W. H. Pearson), John Wiley & Sons, Hoboken, New Jersey, **2003**; b) K. V. Gothelf, K. A. Jorgensen, *Chem. Rev.* **1998**, *98*, 863–909.

[4] a) K. V. Gothelf, K. A. Jorgensen, *Chem. Commun.* **2000**, 1449–1458; b) J. J. Tufariello, in *1,3-Dipolar Cycloaddition Chemistry* (Ed.: A. Pawda), John Wiley & Sons, New York, **1984**, chapter 9.

[5] M. Frederickson, *Tetrahedron* **1997**, *53*, 403–425.

[6] a) F. Viton, G. Bernardinelli, E. P. Kündig, *J. Am. Chem. Soc.* **2002**, *124*, 4968–4969; b) T. Mita, N. Ohtsuki, T. Ikeno, T. Yamada, *Org. Lett.* **2002**, *4*, 2457–2460; c) N. Ohtsuki, S. Kezuka, Y. Kogami, T. Mita, T. Ashizawa, T. Ikeno, T. Yamada, *Synthesis* **2003**, 1462–1466; d) S. Kezuka, N. Ohtsuki, T. Mita, Y. Kogami, T. Ashizawa, T. Ikeno, T. Yamada, *Bull. Chem. Soc. Jpn.* **2003**, *76*, 2197–2207; e) M. Shirahase, S. Kanemasa, Y. Oderaotoshi, *Org. Lett.* **2004**, *6*, 675–678; f) M. Shirahase, S. Kanemasa, M. Hasegawa, *Tetrahedron Lett.* **2004**, *45*, 4061–4063; g) T. Kano, T. Hashimoto, K. Maruoka, *J. Am. Chem. Soc.* **2005**, *127*, 11926–11927.

[7] a) G. Consiglio, F. Morandini, *Chem. Rev.* **1987**, *87*, 761–778; b) H. Brunner, *Angew. Chem. Int. Ed.* **1999**, *38*, 1194–1208; *Angew. Chem.* **1999**, *111*, 1248–1263; c) S. G. Davies, *Pure Appl. Chem.* **1988**, *60*, 13–20; d) S. G. Davies, *Aldrichim. Acta* **1990**, *23*, 31; e) J. A. Gladysz, B. J. Boone, *Angew. Chem. Int. Ed. Engl.* **1997**, *36*, 550–583; *Angew. Chem.* **1997**, *109*, 566–602; f) J. W. Faller, Y. Ma, *Organometallics* **1992**, *11*, 2726–2729.

[8] a) J. W. Faller, J. Parr, *Organometallics* **2000**, *19*, 1829–1832; b) J. W. Faller, B. J. Grimmond, D. G. D'Alliessi, *J. Am. Chem. Soc.* **2001**, *123*, 2525–2529; c) J. W. Faller, J. Parr, *Organometallics* **2001**, *20*, 697–699; d) J. W. Faller, B. J. Grimmond, *Organometallics* **2001**, *20*, 2454–2458; e) J. W. Faller, A. Lavoie, *J. Orgonamet. Chem.* **2001**, *630*, 17–22; f) J. W. Faller, A. R. Lavoie, B. J. Grimmond, *Organometallics* **2002**, *21*, 1662–1666; g) D. L. Davies, J. Fawcett, S. A. Garratt, D. R. Russell, *Chem. Commun.* **1997**, 1351–1352; h) A. J. Davenport, D. L. Davies, J. Fawcett, S. A. Garratt, L. Lad, D. R. Russell, *Chem. Commun.* **1997**, 2347–2348; i) A. J. Davenport, D. L. Davies, J. Fawcett, S. A. Garratt, D. R. Russell, *J. Chem. Soc., Dalton Trans.* **2000**, 4432–4441; j) D. L. Davies, J. Fawcett, S. A. Garratt, D. R. Russell, *Organometallics* **2001**, *20*, 3029–3034; k) D. L. Davies, J. Fawcett, S. A. Garratt, D. R. Russell, *J. Organomet. Chem.* **2002**, *662*, 43–50; l) A. J. Davenport, D. L. Davies, J. Fawcett, D. R. Russell, *Dalton Trans.* **2004**, 1481–1492; m) E. P. Kündig, B. Bourdin, G. Bernardinelli, *Angew. Chem. Int. Ed. Engl.* **1994**, *33*, 1856–1858; *Angew. Chem.* **1994**, *106*, 1931–1934; n) M. E. Bruin, E. P. Kündig, *Chem. Commun.* **1998**, 2635–2636; o) E. P. Kündig, C. M. Saudan, G. Bernardinelli, *Angew. Chem.* **1999**, *111*, 1297–1301; *Angew. Chem. Int. Ed.* **1999**, *38*, 1219–1223; p) E. P. Kündig, C. M. Saudan, F. Viton, *Adv. Synth. Catal.* **2001**, *343*, 51–56; q) E. P. Kündig, C. M. Saudan, V. Alezra, F. Viton, G. Bernardinelli, *Angew. Chem. Int. Ed.* **2001**, *40*, 4481–4485; *Angew. Chem.* **2001**, *113*, 4613–4617; r) D. Carmona, C. Cativiela, R. García-Correas, F. J. Lahoz, M. P. Lamata, J. A. López, M. P. López-Ram de Víu, L. A. Oro, E. San José, F. Viguri, *Chem. Commun.* **1996**, 1247–1248; s) D. Carmona, C. Cativiela, S. Elipe, F. J. Lahoz, M. P. Lamata, M. P. López-Ram de Víu, L. A. Oro, C. Vega, F. Viguri, *Chem. Commun.* **1997**, 2351–2352; t) D. Carmona, F. J. Lahoz, S. Elipe, L. A. Oro, M. P. Lamata, F. Viguri, C. Mir, C. Cativiela, M. P. López-Ram de Víu, *Organometallics* **1998**, *17*, 2986–2995; u) D. Carmona, C. Vega, C. Cativiela, F. J. Lahoz, S. Elipe, L. A. Oro, M. P. Lamata, F. Viguri, R. García-Correas, C. Cativiela, M. P. López-Ram de Víu, *Organometallics* **1999**, *18*, 3364–3371; v) D. Carmona, F. J. Lahoz, S. Elipe, L. A. Oro, M. P. Lamata, F. Viguri, F. Sánchez, S. Martínez, C. Cativiela, M. P. López-Ram de Víu, *Organometallics* **2002**, *21*, 5100–5114; w) H. Brunner, F. Henning, M. Weber, D. Carmona, F. J. Lahoz, *Synthesis* **2003**, 1091–1099; x) D. Carmona, C. Vega, N. García, F. J. Lahoz, S. Elipe, L. A. Oro, M. P. Lamata, F. Viguri, R. Borao, *Organometallics* **2006**, *25*, 1592–1606.

[9] a) R. Noyori, S. Hashiguchi, *Acc. Chem. Res.* **1997**, *30*, 97–102; b) R. Noyori, M. Yamakawa, S. Hashiguchi, *J. Org. Chem.* **2001**, *66*, 7931–7944; c) D. Carmona, M. P. Lamata, L. A. Oro, *Eur. J. Inorg. Chem.* **2002**, 2239–2251; d) D. G. I. Petra, J. N. H. Reek, J.-W. Handgraaf, E. J. Meijer, P. Dierkes, P. C. J. Kamer, J. Brussee, H. S. Schoemaker, P. W. N. M. van Leeuwen, *Chem. Eur. J.* **2000**, *6*, 2818–2829; e) I. M. Pastor, P. Västilä, H. Adolfsson, *Chem. Eur. J.* **2003**, *9*, 1–15; f) P. Västilä, J. Wettergren, H. Adolfsson, *Chem. Commun.* **2005**, 4039–4041; g) M. J. Palmer, M. Wills, *Tetrahedron: Asymmetry* **1999**, *10*, 2045–2061; h) J. Hannedouche, G. J. Clarkson, M. Wills, *J. Am. Chem. Soc.* **2004**, *126*, 986–987; i) D. S. Matharu, D. J. Morris, A. M. Kawamoto, G. J. Clarkson, M. Wills, *Org. Lett.* **2005**, *7*, 5489–5491; j) A. M. Hayes, D. J. Morris, G. J. Clarkson, M. Wills, *J. Am. Chem. Soc.* **2005**, *127*, 7318–7319; For recent reviews see; k) S. E. Clapham, A. Hadzovic, R. H. Morris, *Coord. Chem. Rev.* **2004**, *248*, 2201–2237; l) S. Gladiali, E. Alberico,

 © 2006 Wiley-VCH Verlag GmbH & Co. KGaA, Weinheim 

*Chem. Soc. Rev.* **2006**, *35*, 226–236; J. S. M. Samec, J.-E. Bäckvall, P. G. Andersson, P. Brandt, *Chem. Soc. Rev.* **2006**, *35*, 237–248.
[10] a) D. Carmona, M. P. Lamata, F. Viguri, R. Rodríguez, L. A. Oro, A. I. Balana, F. J. Lahoz, T. Tejero, P. Merino, S. Franco, I. Montesa, *J. Am. Chem. Soc.* **2004**, *126*, 2716–2717; b) D. Carmona, M. P. Lamata, F. Viguri, R. Rodríguez, L. A. Oro, F. J. Lahoz, A. I. Balana, T. Tejero, P. Merino, *J. Am. Chem. Soc.* **2005**, *127*, 13386–13398.
[11] M. A. Bennett, T.-N. Huang, T. W. Matheson, A. K. Smith, *Inorg. Synth.* **1982**, *21*, 74–78.
[12] D. Carmona, M. P. Lamata, F. Viguri, unpublished work.
[13] a) R. S. Cahn, C. Ingold, V. Prelog, *Angew. Chem.* **1966**, *78*, 413; *Angew. Chem. Int. Ed. Engl.* **1966**, *5*, 385–415; b) V. Prelog, G. Helmchen, *Angew. Chem.* **1982**, *94*, 614; *Angew. Chem. Int. Ed. Engl.* **1982**, *21*, 567–583; c) C. Lecomte, Y. Dusausoy, J. Protas, J. Tirouflet, A. Dormond, *J. Organomet. Chem.* **1974**, *73*, 67–76; d) K. Stanley, M. C. Baird, *J. Am. Chem. Soc.* **1975**, *97*, 6598–6599; e) T. E. Sloan, *Top. Stereochem.* **1981**, *12*, 1.
[14] a) C. Giacovazzo, H. L. Monaco, G. Artioli, D. Viterbo, G. Ferraris, G. Gilli, G. Zanotti, M. Catti, *Fundamentals of Crystallography*, 2nd ed., Oxford University Press, Oxford, **2002**; b) D. Cremer, J. A. Pople, *J. Am. Chem. Soc.* **1975**, *97*, 1354–1358.
[15] D. A. Evans, J. A. Murry, P. von Matt, R. D. Norcross, S. J. Miller, *Angew. Chem.* **1995**, *107*, 864; *Angew. Chem. Int. Ed. Engl.* **1995**, *34*, 798–800.
[16] a) L. Tian, G.-Y. Xu, Y. Ye, L.-Z. Liu, *Synthesis* **2003**, 1329; b) S.-I. Murahashi, T. Shiota, *Tetrahedron Lett.* **1987**, *28*, 2383; c) S.-I. Murahashi, T. Shiota, Y. Imada, *Org. Synth.* **2002**, *9*, 632.
[17] a) *SAINT+, Software for CCD Diffractometers*, Bruker AXS, Madison, WI, USA, **2000**; b) G. M. Sheldrick, *SADABS, Program for Correction of Area Detector Data*, University of Göttingen, Göttingen, Germany, **1999**.
[18] a) *SHELXTL Package*, version 6.10, Bruker AXS, Madison, WI, **2000**; b) G. M. Sheldrick, *SHELXS-86 and SHELXL-97*, University of Göttingen, Göttingen, Germany, **1997**.
[19] H. D. Flack, *Acta Crystallogr. Sect. A* **1983**, *39*, 876–881.

Received: May 4, 2006
Published Online: July 19, 2006

 © 2006 Wiley-VCH Verlag GmbH & Co. KGaA, Weinheim 

DOI: 10.1002/ejic.200501062

# Transfer of Chirality in Complexes with $D_3$ Symmetry: Kinetics of the Formation Reaction of Chiral Tris[*O*,*O*′-bis(2-methylbutyl)-dithiophosphato]chromium(III) Complexes (Λ,Δ)-[Cr{(±)-Mebdtp}$_3$], Δ-(+)$_{589}$- and Λ-(–)$_{589}$-[Cr{(+)-(*S*)(*S*)-Mebdtp}$_3$]

**Paolo Biscarini,*[a] Michele Benedetti,[a][‡] Reiko Kuroda,[b] and Francesco Ferranti*[a]**

*Dedicated to Prof. Stephen F. Mason on the occasion of his 85th birthday*

**Keywords:** Chirality / Circular dichroism kinetics / UV/Vis spectroscopy / Dithiophosphate / Chromium complexes

The formation reaction of chiral racemic and diastereoisomeric title complexes, (Λ,Δ)-[Cr{(±)-Mebdtp}$_3$] and Λ-(–)$_{589}$-[Cr{(+)-(*S*)(*S*)-Mebdtp}$_3$], was monitored by absorption, UV/Vis, and circular dichroism, CD, spectroscopy, in the presence of either an excess of the racemic, (±)-Mebdtp$^-$, or the enantiopure ligand, (+)-(*S*)(*S*)-Mebdtp$^-$ = *O*,*O*′-bis[(+)-(*S*)-2-methylbutyl] dithiophosphate ion, at 25 °C in various solvents (ethanol, tetrahydrofuran, chloroform/ethanol, 9:1) and at various pH values and reactant concentrations. The kinetics of the formation reaction of the racemic complex, (Λ,Δ)-[Cr{(±)-Mebdtp}$_3$], shows three consecutive reaction steps. The relative pseudo first-order rate constants depend in different ways on the ligand and $H^+$ concentrations. Circular dichroism measurements during the formation reaction using the enantiopure ligand, as well as in the final equilibrium state, show a prevalence of the Λ-(–)$_{589}$-[Cr{(+)-(*S*)(*S*)-Mebdtp}$_3$] over the Δ-(+)$_{589}$-[Cr{(+)-(*S*)(*S*)-Mebdtp}$_3$] diastereoisomer in all solvents used. A mechanism is proposed which involves two parallel pathways each consisting of three consecutive reactions of solvent substitution by a chiral chelated ligand, interconnected by some reversible inversion reactions to obtain in solution the thermodynamic and kinetic Λ-(–)$_{589}$-[Cr{(+)-(*S*)(*S*)-Mebdtp}$_3$] as the major diastereoisomeric compound. From the equilibrated solution the more stable solid (Λ,Δ)-[Cr{(+)-(*S*)(*S*)-Mebdtp}$_3$] crystallizes as a ca. 1:1 compound of a pair of the two diastereoisomers, undergoing a crystallization-induced second-order asymmetric transformation. Δ-[Cr{(+)-(*S*)(*S*)-Mebdtp}$_3$] is the thermodynamically stable diastereoisomer in the solid state, though in solution this inverts to the more stable Λ-(–)$_{589}$-[Cr{(+)-(*S*)(*S*)-Mebdtp}$_3$].

(© Wiley-VCH Verlag GmbH & Co. KGaA, 69451 Weinheim, Germany, 2006)

## Introduction

Transfer of chirality from a chiral ligand to a coordination centre is an interesting probe to follow in the field of asymmetric catalysis, as well as in supramolecular and bioinorganic chemistry.[1] Intrinsic chirality at the metal centre can be determined by an enantiopure A[*R*] or A[*S*] ligand forming a tris-chelated octahedral OC-6 metal complex of $D_3$ symmetry, resulting as a left- or right-handed helical coordination, i.e. Λ-M(A[*R*]^A[*R*])$_3$ or Δ-M(A[*R*]^A[*R*])$_3$.[2–4] Chiral discrimination in the formation of diastereoisomeric octahedral tris-chelate complexes can be considered as the difference in the interaction of the chiral ligand molecules with the two chiral forms of intermediate complexes.

In the past, circular dichroism, CD, has been very useful to study the kinetics of the configurational inversion reaction, Λ-M(A[*R*]^A[*R*])$_3$ ⇄ Δ-M(A[*R*]^A[*R*])$_3$, of optically labile diastereoisomeric complexes, as well as to follow qualitatively the formation reaction of Λ- or Δ-M[(*R*,*R*)-bdtp]$_3$ diastereoisomers in various solvents, $M^{III}$ = Cr, Co, Rh, Ir.[3,4] Chiroptical spectroscopy is a sensitive probe for studying electronic transitions and stereochemistry of chiral transition-metal complexes. CD spectra of chiral tris-(bidentate chelate) metal complexes having octahedral coordination can show the intrinsic configurational chirality of the coordinating metal ion. Chiral octahedral complexes of $D_3$ symmetry give positive or negative differential optical density, ΔOD, during the formation reaction with enantiomeric ligands, so the kinetic of these reactions can be observed.

[a] Dipartimento di Chimica Fisica ed Inorganica, Università di Bologna,
Viale Risorgimento 4, 40136 Bologna, Italy
[b] Department of Life Sciences, Graduate School of Arts and Sciences, The University of Tokyo, JST ERATO SORST, Kuroda Chiromorphology Team
Komaba, Meguro-ku, Tokyo 153, Japan
[‡] Present address: Dipartimento di Scienze e Tecnologie Biologiche ed Ambientali, Università degli Studi di Lecce, Lecce, Italy

 © 2006 Wiley-VCH Verlag GmbH & Co. KGaA, Weinheim 

The aim of this work is to show the influence of the chiral ligand *O*,*O*′-bis[(+)-(*S*)-2-methylbutyl]dithiophosphate, (+)-(*S*)(*S*)-Mebdtp$^-$ (**1**) on the kinetics and thermodynamics of the formation reaction of diastereoisomeric coordination compounds, showing, if possible, the chirality transfer mechanisms from the ligand (**1**) to the metal centre. Our current interest is also to reveal the influence of the solvent on the formation reaction of the diastereoisomers, as well as on the configurational inversion reaction during the crystallization, to predetermine chirality on the coordination centre.

The addition of the ligand to solvated metallic ions in solution may occur in a typical three-step mechanism for octahedral tris-bidentate complexes. Two- or three-chelate ligands coordinated to a metal ion form a left-handed (Λ) or a right-handed (Δ) helix. Two-chelate ligands form a segment of helices if the two bidentate ligands do not form a common mean plane. With the title chiral ligand **1** the preferential formation of the Λ-(*S*,*S*)(*S*,*S*)(*S*,*S*) diastereoisomer in solution has been shown by CD spectroscopy.[3a]

Here we report the results of a kinetic study on the formation reaction of the title complexes, as followed by absorption (OD) and by circular dichroism (CD) to clarify the mechanism of transfer of chirality from the ligand to the metal centre and the solvent effect in this type of coordination compound.

## Results and Discussion

### Formation Reaction

The formation reaction of the chiral octahedral complex was carried out at 25 °C using either the enantiomeric dithiophosphinic acids, (+)-(*S*)(*S*)-MebdtpH or the racemic form, (±)-MebdtpH, as well as their lithium salts, as bidentate ligands, to react with $Cr^{3+}$ solvated ion in three different solvents [ethanol (EtOH), chloroform/ethanol ($CHCl_3$/EtOH, 90:10), and tetrahydrofuran (THF)] following Equation (1) and Scheme 1.

$$Cr^{3+}_{(sol)} + 3\ (\pm)\text{-Mebdtp}^-_{(sol)} \rightarrow Cr[(\pm)\text{-Mebdtp}]_{3(sol)} \quad (1)$$

This reaction was studied using an enantiopure chiral ligand by CD and UV/Vis spectroscopy to determine the influence of absolute ligand configuration and of the solvent on the kinetics and thermodynamics of diastereoselective octahedral complex formation.[3a] A faster formation of the tris{*O*,*O*′-bis[(+)-(*S*)-2-methylbutyl]dithiophosphato}chromium(III) complex, Λ-(–)$_{589}$-[Cr{(+)-(*S*)(*S*)-Mebdtp}$_3$] (**3**), than Δ-(+)$_{589}$-[Cr{(+)-(*S*)(*S*)-Mebdtp}$_3$] (**4**), was observed in solution, but in the solid phase a chiral complex (ΛΔ)-[Cr{(+)-(*S*)(*S*)-Mebdtp}$_3$] (**2**), is formed as a ca. 1:1 crystalline mixture of diastereoisomers **3** and **4** (Scheme 1).

Chiral discrimination occurs during formation of complexes in solution and also during their crystallization, as characterized by CD spectroscopy.

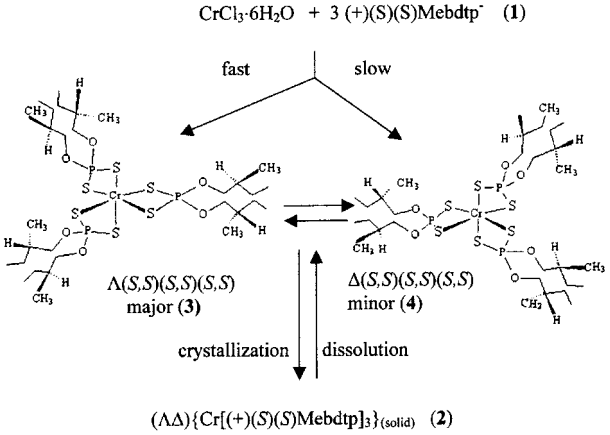


Scheme 1.

In solution the major diastereoisomer is the Λ-(–)$_{589}$-[Cr{(+)-(*S*)(*S*)-Mebdtp}$_3$] (**3**), which is in equilibrium with the minor Δ-(+)$_{589}$-[Cr{(+)-(*S*)(*S*)-Mebdtp}$_3$] (**4**).

Preferential crystallization of Δ- (**4**) together with Λ- (**3**) resulted in the formation of the hetero-chiral 1:1 complex (ΛΔ)-[Cr{(+)-(*S*)(*S*)-Mebdtp}$_3$]$_{(solid)}$ (**2**). This complex is evidently less soluble than the single diastereoisomers Λ-(**3**) or Δ- (**4**). We deduce that an inversion reaction of the major Λ-(**3**) towards the minor Δ-(**4**) complex of the equilibrium occurs during crystallization, undergoing a crystallization-induced second-order asymmetric transformation, which finally yields crystals of (ΛΔ)-[Cr{(+)-(*S*)(*S*)-Mebdtp}$_3$]$_{(solid)}$ (**2**), due to more stable hetero-chiral diastereoisomeric crystal packing as known also for some enantiomers and racemates.[2,5,6] As seen in the past, changing the stereochemical arrangement of the ligand groups and atoms causes various different dispersion forces or hydrogen bonding and different chiral discrimination forces between the molecules, in solution as well as in the solid state.[4a]

To clarify the nature of compound **2** we examined CD and absorbance spectra in solution and in the solid state (nujol, KBr pellets, thin film) or as microcrystalline powder by diffuse reflectance circular dichroism, DRCD.[7] When the solid complex **2** was dissolved in $CH_2Cl_2$, the absorption spectrum of the solution showed two bands in the range 500–700 nm. OD measures the total concentration of the complex in solution and did not change over time.[3a] In contrast, its CD spectra changed drastically: it showed a very weak almost flat spectrum at the time of dissolution, but the intensity of a positive Cotton effect at ca. 675 nm increased substantially to reach a maximum after 5–23 h (Figure 1, A). This corresponds to an equilibrium state between the major (**3**) and the minor (**4**) in $CH_2Cl_2$ solution reached through a Δ-(**4**) → Λ-(**3**) configurational inversion (Figure 1, A). This indicates the formation in the solid state of intermolecular weak interactions between hetero chiral diastereoisomers. Until now crystals suitable for X-ray structural investigation have not been obtainable, but hetero-chiral packing of a pair of octahedral enantiomeric complexes has been established in the crystalline racemic

 © 2006 Wiley-VCH Verlag GmbH & Co. KGaA, Weinheim 

compound (ΛΔ)-[Cr{ddtp}$_3$] with ddtp$^-$ = diethyl dithiophosphate ion, when the enantiomers are more soluble than the racemic compound.[2,3a,6] Hetero-chiral packing of a pair of octahedral diastereoisomeric complexes are also known.[2] The solubility of the two diastereoisomers is very high and ΛΔ-(**2**) is the less soluble complex. During crystallization the Λ-(**3**)–Δ-(**4**) packing-energy or the temperature favour the Λ → Δ configurational inversion and formation of the less soluble solid ΛΔ-(**2**).

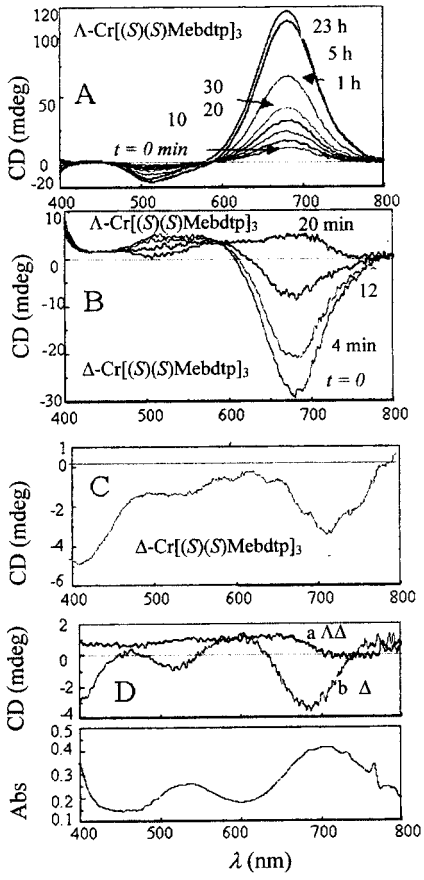


Figure 1. (A) CD spectra of ΔΛ-Cr[(*S*)(*S*)-Mebdtp]$_3$ (**2**) dissolved in $CH_2Cl_2$, positive at 678 nm at $t$ = 0 and inverted to Λ-Cr[(*S*)(*S*)-Mebdtp]$_3$ after 5–23 h. (B) CD spectra of Δ-Cr[(*S*)(*S*)-Mebdtp]$_3$ (**4**) obtained maintaining the solid ΔΛ-Cr[(*S*)(*S*)-Mebdtp]$_3$ (**2**) under vacuum at 100 °C for 3 h. The compound after dissolution in $CH_2Cl_2$ inverts from Δ to Λ showing changes at 678 nm from a negative CD at $t$ = 0, 4, 12 min to a positive CD after 20 min and over up to 5 h. (C) CD spectrum in nujol mull of solid Δ-Cr[(*S*)(*S*)-Mebdtp]$_3$ (**4**) obtained under vacuum at 100 °C for 3 h. (D) CD and UV/Vis spectra of a film over quartz: (a) ΔΛ-Cr[(*S*)(*S*)-Mebdtp]$_3$ (**2**) and (b) Δ-Cr[(*S*)(*S*)-Mebdtp]$_3$ (**4**) obtained after fast evaporation of a solution in $CH_2Cl_2$.

CD spectra of the solid **2** in nujol, KBr pellet and as a solid film (Figure 1, D, a) show a flat line in the 400–800 nm range, proving that the crystallized complex **2** is optically inactive as a ca. 1:1 solid mixture of the two diastereoisomers Λ-(**3**) and Δ-(**4**). DRCD of **2** also shows no Cotton effect in the same region as a result of the hetero-chiral equimolecular composition of the complex.

Heating of the solid **2** causes the thermodynamic Δ-(**4**) solid diastereoisomer to form. So the last complex **2**, maintained 3 h under vacuum at 100 °C, shows an inversion of configuration Λ → Δ of the inherent chiral coordination centre in the solid diastereoisomeric mixture **2**. Δ-Cr[(+)-(*S*)(*S*)-Mebdtp]$_3$ (**4**) is the major component in the new solid mixture. CD spectra of this mixture with major (**4**) and minor (**3**) diastereoisomers in nujol mull (Figure 1, C) and as a film (Figure 1, D, b) clearly show a stable negative Cotton effect in the range 680–710 nm, compared with the flat spectrum of (ΛΔ)-[Cr{(+)-(*S*)(*S*)-Mebdtp}$_3$]$_{(solid)}$ (**2**) (Figure 1, D, a).

The CD spectrum of the solution of the major (**4**) and minor (**3**) mixture shows a negative Cotton effect at 678 nm at $t$ = 0 min, immediately after dissolution in $CH_2Cl_2$; this is caused by the presence of the diastereoisomer Δ-(*S*,*S*)(*S*,*S*)(*S*,*S*) (**4**) as the major component (Figure 1, B). The CD spectrum is opposite and about enantiomeric to that of the major diastereoisomer Λ-(*S*,*S*)(*S*,*S*)(*S*,*S*) (**3**) in solution (Figure 1A). In a solution of $CH_2Cl_2$, EtOH, $CHCl_3$, or THF, the major diastereoisomer Δ- (**4**) inverts the absolute configuration of the coordination metal centre from Δ to Λ (Figure 1B) and the equilibrium between major (**3**) and minor (**4**) is once again established. In the solid state the complex Δ- (**4**) is thermodynamically more stable, but after 5 h in solution it reaches an equilibrium between the kinetic and thermodynamic major Λ- (**3**) and minor Δ- (**4**), diastereoisomeric complexes (Scheme 1, Figure 1A, B).

The less soluble complex **2** is characterized by different interconversion equilibria between the **3** and **4** diastereoisomeric species, depending on the different conditions of temperature, pressure and solvent.[3]

The preferential formation of kinetic and thermodynamic Λ-(–)$_{589}$-[Cr{(+)-(*S*)(*S*)-Mebdtp}$_3$] complex (**3**) in solution, or of thermodynamic Δ-Cr[(+)-(*S*)(*S*)-Mebdtp]$_3$ (**4**) in the solid state, can be achieved by kinetically diastereoselective steps and/or equal formation of the two Λ-(**3**), and Δ- (**4**) diastereoisomers with a parallel or consecutive Δ → Λ or Λ → Δ inversion reaction.

### Absorption and Circular Dichroism Spectra

The absorption spectra of the formation reaction solution in EtOH show two bands at ca. 675 and 530 nm, which increase with the reaction time (Figure 2). Two points in the spectra near 450 nm look somewhat like isosbestic points. However, accurate examination shows that as time increases the spectra shifts to higher wavelengths, excluding the presence of real isosbestic points and suggesting the presence of some reaction steps in the formation mechanism (see enlargement in the small window reported in Figure 2).

In the CD spectra at the beginning of the reaction a weak positive Cotton effect, growing with time, is observed, and attributed to the $^4A_{2g} \rightarrow {}^4T_{2g}$ transition corresponding to the absorbance at ca. 675 nm. Figure 3 reports the variation with time of the differential absorbance, ΔOD, in the CD spectrum in ethanol.

 © 2006 Wiley-VCH Verlag GmbH & Co. KGaA, Weinheim 

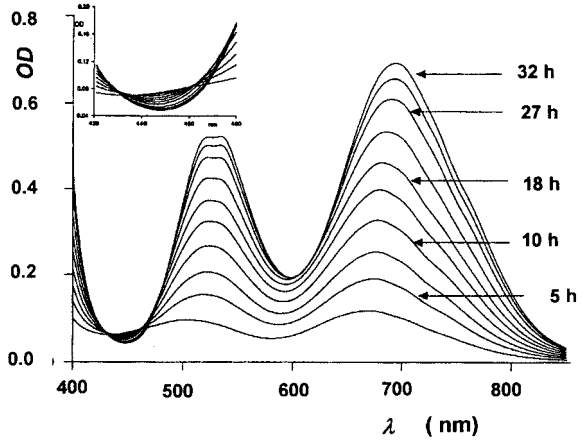


Figure 2. Variation of the OD spectra during the formation reaction of Cr[(±)-Mebdtp]$_3$. Initial concentrations: $Cr(ClO_4)_3$ 0.002 mol dm$^3$, LH 0.1 mol dm$^3$, EtOH as the solvent.

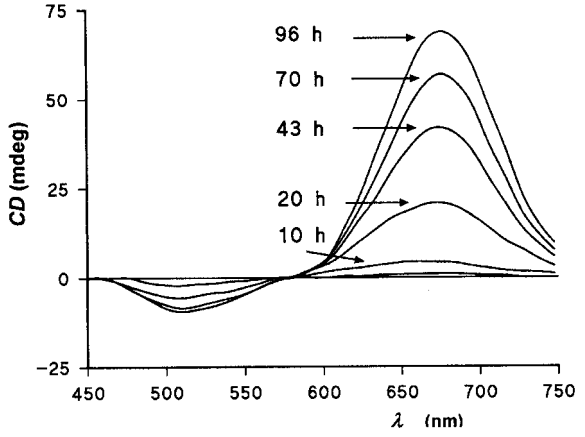


Figure 3. Variation of the CD during the formation reaction of Λ-Cr[(*S*)(*S*)-Mebdtp]$_3$ (**3**). Initial concentrations: $Cr(ClO_4)_3$ 0.002 mol dm$^3$, LH 0.1 mol dm$^3$, EtOH as the solvent.

### Kinetics by Absorption Spectra

The kinetics of the formation reaction [Equation (1) and Scheme 1] have been studied by UV/Vis and CD spectroscopy in an attempt to understand the reaction pathway of the stereoselective formation of the Λ- (**3**) diastereoisomer in solution, as well as the configuration inversion of diastereoisomeric compounds in solution and in the solid state.

Kinetic measurements of very high accuracy can offer reliable information on the formation mechanism in complex systems. OD measurements can give information on the total stoichiometric reaction. CD contributes information on the presence and reactivity of intermediate stereoisomers.

Figure 4 reports the variation in optical density with time, at 675 nm, and shows the influence on the reaction rate of three different solvents. Experimentally we measured and stored in a binary file one point OD/time every minute, so in the figure the results appear as continuous lines. OD values for the three runs at the beginning and at the end of the reactions are nearly equal, so the plot affords direct comparison of the reaction rates in the three solvents.

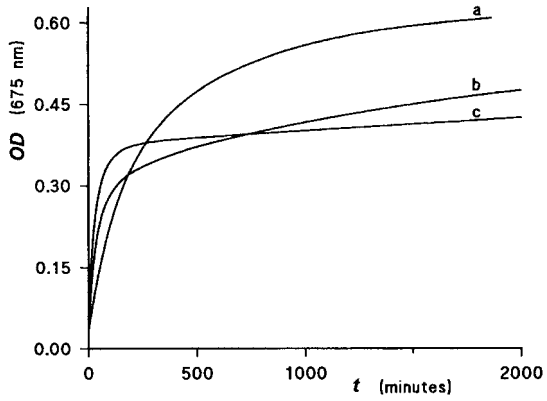


Figure 4. Increase of the optical density at 675 nm with reaction time in different solvents. (a) EtOH; (b) $CHCl_3$/EtOH, 90:10; (c) THF, initial concentrations: $Cr(ClO_4)_3$ 0.002 mol dm$^3$, LH 0.1 mol dm$^3$.

At the beginning of the reaction the OD signals in various different solvents increase with time, showing that the initial rate values differ according to the solvent in the sequence: THF > ($CHCl_3$/EtOH, 90:10) > EtOH. In the last part of the reaction the sequence is inverted, showing a lower reaction rate for THF and a higher one for EtOH.

The rate of a reaction between two ions of opposite charges, i.e. $Cr^{3+}$, $CrL^{2+}$, $CrL_2^+$ and $L^-$, should decrease with an increase in the dielectric constant of the solvent ($\varepsilon_{EtOH}$ = 25.1, $\varepsilon_{THF}$ = 7.6, $\varepsilon_{CHCl3}$ = 4.8), because the electrostatic interactions are lowered.[8] The measured rates in the solvents used do not agree well with this statement and thus, we cannot attribute the rate difference to the dielectric constants of the solvents. The more important reason for the solvent-dependent reaction rates is probably due to at least partial substitution of the water molecules in the hydration sphere of $Cr^{III}(H_2O)_6$ by solvent molecules, changing the characteristics of the activated complexes and of the reaction intermediates.

The experimental results were analyzed by applying a method of minimization of bi- or tri-exponential equations, similar to that used by N. W. Alcock et al.[9]

There are two types of mechanism, I and II, that can be hypothesized. The three rate constants, $k_a$, $k_b$, $k_c$, and the extinction coefficients, $\varepsilon_B$ and $\varepsilon_C$, of the intermediates $CrL(sol)_4^{2+}$ and $CrL_2(sol)_2^+$ were considered as adjustable parameters. The extinction coefficients $\varepsilon_A$ and $\varepsilon_D$ of the first $Cr(sol)_6^{3+}$ and the last $CrL_3$ species are accessible from the observed optical density at the beginning and at the end of the reaction.

The experimental data of the reaction in THF of Figure 4 (c) are reported in Figure 5 and Figure 6. Similar plots were obtained for reactions in other solvents.

Figure 5 shows a first-order plot, $-\log(OD_{inf} - OD)$ as a function of time. The curve only becomes linear after a rather long reaction time, while the first part of the reaction, by the nonlinearity of the curve, suggests the presence of consecutive steps.

 © 2006 Wiley-VCH Verlag GmbH & Co. KGaA, Weinheim 

$$Cr(sol)_6^{3+} + 3\,L^- \xrightarrow{k_a} CrL(sol)_4^{2+} + 2\,L^- \xrightarrow{k_b} CrL_2(sol)_2^{+} + L^- \xrightarrow{k_c} CrL_3 \quad (I)$$
$$\varepsilon_A \qquad\qquad \varepsilon_B \qquad\qquad \varepsilon_C \qquad\qquad \varepsilon_D$$

$$\text{and} \quad Cr(sol)_6^{3+} + 3\,L^- \xrightarrow{k'_a} CrL_2(sol)_2^{+} + L^- \xrightarrow{k'} CrL_3 \quad (II)$$

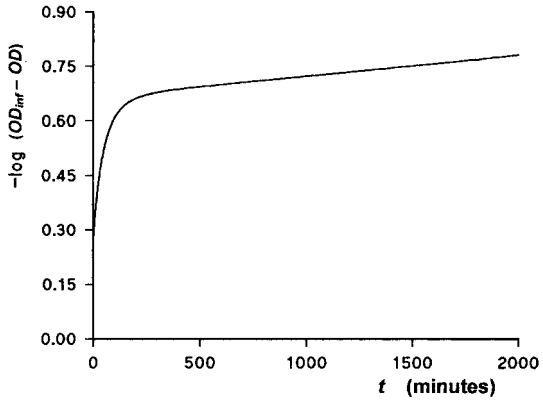


Figure 5. First-order plot of the formation reaction of Cr[(±)-Mebdtp]$_3$ in THF as the solvent. $Cr(ClO_4)_3$ 0.002 mol·dm$^{-3}$, LH 0.1 mol dm$^3$.

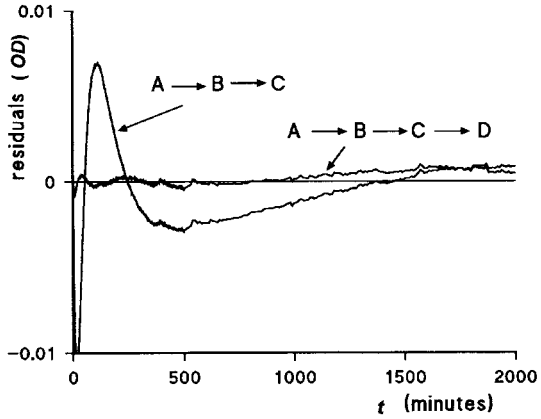


Figure 6. Differences between the observed optical density at 675 nm and that calculated according to mechanisms (I) and (II). $Cr(ClO_4)_3$ 0.002 mol dm$^3$, LH 0.1 mol dm$^3$, THF as the solvent.

Figure 6 reports the residuals (differences between the observed and calculated OD values) obtained applying the method of minimization to the three- and two-step mechanism, (I) and (II) respectively.

There is a much better agreement with mechanism (I), particularly in the first part of the reaction, the residuals being about 0.001 OD units, ca. 0.2%, of a total absorbance variation of about 0.6 OD units. The optical density varia-

Table 1. Pseudo-first-order rate constants (s$^{-1}$) for the formation reaction of Cr[(+)-(*S*)(*S*)-Mebdtp]$_3$ in different solvents and different reactant concentrations (mol dm$^3$). [$CrCl_3$·6$H_2O$] = 0.002 mol dm$^3$.

| Solvent | Reaction number | [LH][a] | [LLi][b] | [H$^+$] | $10^5\,k_a$ | $10^5\,k_b$ | $10^5\,k_c$ |
|---|---|---|---|---|---|---|---|
| | 1 | *0.050[c] | 0 | 0.20 | 5.87 | 1.93 | 1.05 |
| | 2 | *0.075 | 0 | 0.20 | 10.1 | 3.12 | 1.60 |
| | 3 | *0.10 | 0 | 0.20 | 13.9 | 4.08 | 1.85 |
| | 4 | *0.15 | 0 | 0.20 | 23.5 | 7.98 | 2.33 |
| | 5 | *0.20 | 0 | 0.20 | 46.8 | 13.3 | 2.57 |
| | 6 | *0.10 | 0 | 0.025 | 63.5 | 18.9 | 1.84 |
| | 7 | *0.10 | 0 | 0.05 | 38.6 | 12.1 | 2.35 |
| $C_2H_5OH$ | 8 | *0.10 | 0 | 0.075 | 36.2 | 9.10 | 1.96 |
| | 9 | *0.10 | 0 | 0.10 | 27.7 | 7.97 | 1.97 |
| | 10 | *0.10 | 0 | 0.15 | 20.7 | 6.15 | 1.83 |
| | 11 | *0 | 0.10 | **[c] | 1050 | 61 | 2.17 |
| | 12 | *0.05 | 0.05 | 0.05 | 39.5 | 9.7 | 2.55 |
| | 13 | 0.10 | 0 | 0.10 | 43.3 | 12.1 | 2.49 |
| | 14 | 0.05 | 0 | 0.05 | 30.2 | 9.75 | 2.0 |
| | 15 | *0 | 0.20 | ** | 3470 | 178 | 2.3 |
| | 16 | *0.20 | 0 | 0.20 | 192 | 40 | 0.55 |
| THF | 17 | 0.10 | 0 | 0.10 | 72 | 25 | 0.23 |
| | 18 | 0 | 0.050 | ** | 2200 | 38 | 2.1 |
| | 19 | 0 | 0.10 | ** | 3000 | 43 | 3.9 |
| $CHCl_3/C_2H_5OH$, | 20 | 0 | 0.05 | ** | 877 | 43 | 7.2 |
| 90:10 | 21 | 0 | 0.20 | ** | 983 | 42 | 6.3 |
| | 22 | 0.10 | 0 | 0.10 | 50 | 9.0 | 0.58 |

[a] LH = (+)-(*S*)(*S*)-MebdtpH. [b] LLi = (+)-(*S*)(*S*)-MebdtpLi. [c] * Measurement done at ionic strength $I$ = 0.212 mol dm$^{-3}$. ** Reaction solution about neutral.

 © 2006 Wiley-VCH Verlag GmbH & Co. KGaA, Weinheim 

tion as a function of time, in all runs made in THF and $CHCl_3$/EtOH (90:10), is in agreement with mechanism (I) comprehending three consecutive pseudo first-order reactions to $Cr^{III}$.

By contrast, some of the runs performed in EtOH as the solvent show a good agreement with the two-step mechanism II. Nonlinear least-square calculations, according to mechanism (I), afford poor accuracy, different results being obtained if one changes the initial set of adjustable parameters.

This discrepancy can be attributed to the too small differences between the values of the rate constants of the first and second step. To improve the reliability of the results for runs in EtOH, supposing that the reaction always occurs in three steps, the extinction coefficient, $\varepsilon_b$, of the first intermediate, $CrL^{2+}$, was measured, performing some runs with an excess of $Cr^{3+}$ over the ligand, $L^-$. The value obtained, $\varepsilon_{CrL^{2+}} = 46.7\ dm^3\,mol^{-1}\,cm^{-1}$, was then imposed as a nonadjustable parameter in mechanism I. The extinction coefficient, $\varepsilon_c$, of the second intermediate, $CrL_2^+$, was calculated as an adjustable parameter for the runs more in agreement with mechanism II. The mean value obtained, $\varepsilon_{CrL^{2+}} = 186.9 \pm 5.8\ dm^3\,mol^{-1}\,cm^{-1}$ was imposed as a nonadjustable parameter for all the runs made in EtOH following mechanism I. In every case the $k_c$ calculated values were nearly equal to the obtainable values from first-order diagrams in the last part of the reaction. We inferred that the three steps observed do correspond to the complexation of one, two and three molecules of the ligand to chromium ion, as shown in mechanism I.

In Table 1 pseudo first-order rate constants for the formation reaction of $[Cr\{(+)\text{-}(S)(S)\text{-Mebdtp}\}_3]_{(sol)}$ following the three-step mechanism I are reported. Where possible the ionic strength was maintained constant at $0.212\ mol\,dm^{-3}$, by adding tetrabutylammonium trifluoromethanesulfonate. The $H^+$ concentration was adjusted with tetrabutylammonium hydroxide or perchloric acid or using lithium salt as the ligand. The ligand LH was considered to be a strong acid, as shown by pH measurements. From the results obtained at constant ionic strength in ethanol as the solvent, it is possible to derive some information as to the reaction orders with respect to the ligand and to the $H^+$ ion.

### Reaction Order with Respect to the Ligand

The reaction order with respect to the ligand (proves 1–5 of Table 1) is bigger than one for $k_a$ and $k_b$ and smaller than one for $k_c$, in good agreement with Equations (2), (3), and (4).

$$k_a = a\,[L] + b\,[L]^2 \quad (2)$$

$$k_b = a'\,[L] + b'\,[L]^2 \quad (3)$$

$$k_c = a''\,[L]/(1 + b''\,[L]) \quad (4)$$

From the values of rate constants measured at constant $[H]^+$, $0.200\ mol\,dm^{-1}$, and a ligand concentration ranging from 0.05 and $0.2\ mol\,dm^{-1}$, values of $a = (7.49 \pm 1.70) \times 10^{-4}\ mol^{-1}\,dm^3\,s^{-1}$, $b = (7.08 \pm 1.34) \times 10^{-3}\ mol^{-2}\,dm^6\,s^{-1}$, $a' = (2.65 \pm 0.32) \times 10^{-4}\ mol^{-1}\,dm^3\,s^{-1}$, $b' = (1.88 \pm 0.25) \times 10^{-3}\ mol^{-2}\,dm^6\,s^{-1}$, $a'' = (2.7 \pm 2.9) \times 10^{-4}\ mol^{-1}\,dm^3\,s^{-1}$ and $b'' = 4.8 \pm 1.3\ mol^{-1}\,dm^3$ were calculated. A mechanism for the third reaction step in agreement with Equation (4) could involve a fast pre-equilibrium followed by a slow reaction, as in equations Equations (5) and (6).

$$CrL_2^+ + L^- \rightleftarrows CrL_2^+\cdots L^- \quad (5)$$

$$CrL_2^+\cdots L^- \rightarrow CrL_3 \quad (6)$$

In the intermediate $CrL_2^+\cdots L^-$, where we have not indicated the solvent molecules, ligand $L^-$ could be bonded to the metal by a single bond and the slow step should be a ring closure with solvent substitution. Similar mechanisms should be present in the first and second reaction steps too. The presence of a quadratic term in Equations (2) and (3) suggests parallel reaction paths of a second order with respect to the ligand. These second-order paths could be attributed to the possibility, forbidden for the third step, of forming intermediates with more than one mono-bonded ligand, followed by slow ring closure.

Alternatively these intermediates, $Cr^{3+}\cdots L^-$, $CrL^{2+}\cdots L^-$, $CrL_2^+\cdots L^-$, could be ionic pairs with the ligands and the metal somehow linked between them through the solvent molecules of the coordination sphere of the metal. In this case the rate-determining step should be substitution of a solvent molecule by the ligand, followed by a fast ring closure. The value of $b''$ seems to support the last hypothesis. In fact in the mechanism we propose, $b''$ is the formation constant of the $CrL_2^+\cdots L^-$ and corresponds, according to the Fuoss theory,[10] to a distance between the metal and the ligand in the ionic pair of 10.1 Å, a value that seems to be of the right order of magnitude.

### Reaction Order with Respect to the $H^+$ Ion

The rate constants for the first and second steps, $k_a$ and $k_b$, depend inversely on the hydrogen ion concentration in all the solvents used, taking very large values when $[H^+]$ is almost absent (proves 6–10, Table 1). Probably at the beginning of the reaction not all the water molecules in the coordination sphere of the $Cr^{3+}$ ion are substituted by the solvent and the mechanism could involve de-protonated species as shown for the first step of the reaction in Equations (7), (8) and (9).

$$Cr(OH_2)^{3+} \overset{K_a}{\rightleftarrows} Cr(OH)^{2+} + H^+ \quad (7)$$

$$k'\text{: } Cr(OH_2)^{3+} + L^- \rightarrow CrL^{2+} + H_2O \quad (8)$$

$$k''\text{: } Cr(OH)^{2+} + L^- \rightarrow CrL^{2+} + OH^- \quad (9)$$

The deprotonated species, $Cr(OH)^{2+}$ and analogously $CrL(OH)^+$ for the second step, are normally more reactive

 © 2006 Wiley-VCH Verlag GmbH & Co. KGaA, Weinheim 

than nondeprotonated species in substitution reactions.[11] The observed pseudo-first-order rate constants $k_{obs}$ should depend on the hydrogen ion concentration as in Equation (10).

$$k_{obs} = (k'\ K_a + k''\ [H^+])/([H^+] + K_a) \quad (10)$$

The experimental results of Table 1, (proves 3, 6–10, $[L^-]$ constant, 0.100 mol dm$^{-3}$, and $[H^+]$ varying from 0.025 and 0.200 mol dm$^3$) are qualitatively in agreement with Equation (10). The attempt to test Equation (10) quantitatively, however, leads to values of the acid ionization constants for $Cr(OH_2)^{3+}$, $K_a = 0.026 \pm 0.020$ mol dm$^{-3}$, and for $Cr(OH_2)$-$L^{2+}$ of the second step, $K_a = 0.018 \pm 0.008$ mol dm$^3$, that are too high compared to the value of $1.4 \cdot 10^{-4}$ mol dm$^3$ measured in aqueous solution for $Cr(OH_2)_6^{3+}$.[12] The rate constants of the third step depend very little on the hydrogen ion concentration, probably because of the low charge of the complex ion $CrL_2^+$.

### Kinetics by CD

Kinetic measurements performed by optical density cannot distinguish between Λ and Δ configuration. We then repeated the same runs as shown in Figure 4 recording the CD signal at 675 nm against time, as shown in Figure 7. The positive Cotton effect observed throughout the reaction and in all solvents used indicates a higher production in solution of the Λ-(–)$_{589}$- (**3**) than the Δ(+)$_{589}$-[Cr{(+)-(*S*)(*S*)-Mebdtp}$_3$] (**4**) complex; see Figure 1 (A), 3 and 7.

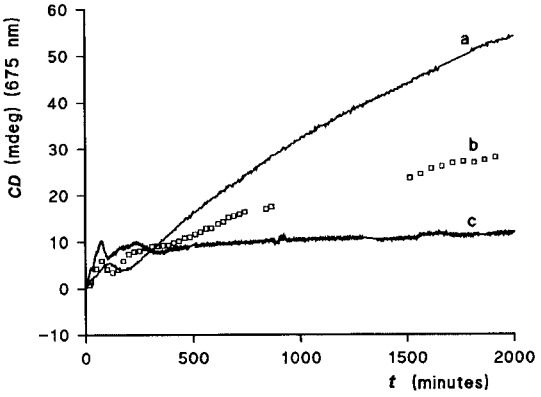


Figure 7. Variation of the CD signal at 675 nm with formation reaction time in different solvents: (a) EtOH; (b) $CHCl_3$/EtOH, (c) THF. Initial concentrations: $Cr(ClO_4)_3$ 0.002 mol dm$^3$, LH 0.1 mol dm$^3$.

The Λ-(–)$_{589}$-(**3**) is present at the final equilibrium as a major complex being stabilized by the solvent in the order: EtOH > ($CHCl_3$/EtOH, 90:10) > THF. In the first part of the reaction the positive curve is not monotonic, but shows some oscillations, with the formation of one maximum and one minimum in the case of EtOH as the solvent (Figure 7, a) and two maxima and two minima in the other two cases (Figure 7b, c). Afterwards the CD signal grows quite regularly to the end of the reaction. These oscillations can be attributed to the formation of Equilibria (11) and (12) between the Λ and Δ forms of $CrL_2^+$ (1:2) and $CrL_3$ (1:3).

$$\Lambda\text{-}CrL_2^+ \rightleftarrows \Delta\text{-}CrL_2^+ \quad (11)$$

$$\Lambda\text{-}CrL_3 \rightleftarrows \Delta\text{-}CrL_3 \quad (12)$$

Taking into account, (i) the profile of reaction (Figure 7), (ii) the three consecutive reaction steps of mechanism (I), supported by the OD measurements, and (iii) Λ and Δ, *cis* and *trans* stereoisomery of intermediates $CrL_2^+$ and final $CrL_3$ complexes, a probable mechanism of the reaction studied could be that reported in Scheme 2.

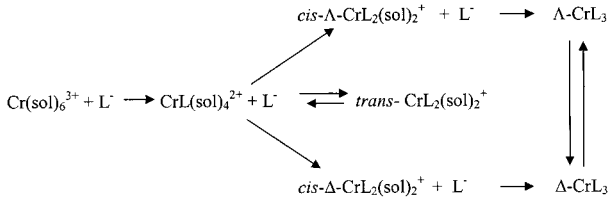


Scheme 2.

The free octahedral coordination positions, are occupied by the solvent molecules. Every reaction step, indicated by an arrow, should be of pseudo-first order with respect to $Cr^{III}$, which is very complicated because of the presence of metal complex ions that are differently solvated, protonated and forming ion pairs. The planar *trans*-intermediate $CrL_2(sol)_2^+$ in this Scheme was hypothesized as having to go back to the diastereoisomer 1:1, $CrL(sol)_4^{2+}$, to form the *cis*-Λ- or the *cis*-Δ-$CrL_2^+$, 1:2 diastereoisomer. Considering Equations (5)–(12), moreover, Scheme 2 must be considered as a simplified version of more complicated ones.

The number of parameters of Scheme 2, that influence the CD signal, e.g. rate constants and CD values, is too large for any quantitative evaluation, because of the formation of various chiral species during the reaction. Nevertheless many computer simulations have been performed to test the compatibility of the proposed reaction mechanism with the CD values oscillating in the first part of the reaction (Figure 7). We compared the experimental results of the three runs reported in Figure 7 during the first 700 min of reaction also with some other mechanisms with different numbers of intermediates and reaction steps. Every simulation used CD values of Λ-Cr[(+)-(*S*)(*S*)-Mebdtp]$_3$, (**3**) measured at the end of the reactions as a known value, and assumed approximated values for all the other parameters. The differential equations involved were resolved numerically and the theoretical values of the CD signals were compared with experimental ones. The calculation was repeated many times, alternately and by small amounts changing the values of all the parameters, until it reached the minimum possible value of the standard deviation.

Numerical values of the parameters thus obtained are not reliable because they strongly depend on the initial values used in the calculations. However, the standard deviation and the shape of the CD signal/time curve obtained with different sets of adjustable initial parameters were practically identical. One can always obtain better agreement between observed and calculated values, if more intermediate species are used, even if some levelling effect has

 © 2006 Wiley-VCH Verlag GmbH & Co. KGaA, Weinheim 

been noted. However, we think that these calculations could be useful for selecting the simplest mechanism of the hypothetical ones, which could be in sufficiently good agreement with the experimental results. Figure 8 uses continuous lines to report the calculated runs according to Scheme 2. In EtOH (Figure 8, a) the agreement is better than was the case in other solvents, though simulation cannot really reproduce the nonmonotonic behaviour of CD with time. It is interesting to note that this agreement gets worse if we try to compare the experimental results with a mechanism with only two consecutive paths instead of one with three consecutive paths. This fact supports the choice of mechanism (I) over mechanism (II) in the kinetic runs in EtOH deduced by absorbance measurements.

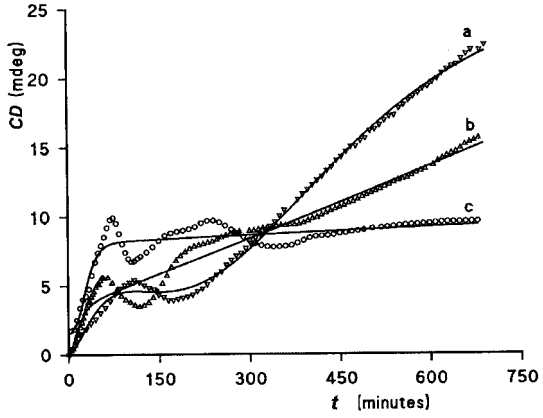


Figure 8. Simulated curves (continuous lines) CD/time, for Scheme 2 compared with experimental ones: (a) in EtOH (triangles); (b) in $CHCl_3$/EtOH, 90:10 (delta symbols); (c) in THF (circles).

The other two runs performed in the other two solvents are not in agreement with Scheme 2 and must be compared with some more complicated Schemes. Similar computer simulations were carried out for Schemes 3–5.

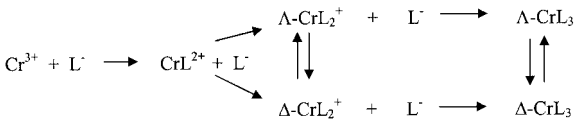


Scheme 3.

The oscillations of CD observed in THF as the solvent are more complicated and difficult to resolve but they should contain a greater amount of information about the mechanism. As the complexity of the mechanism increases, so does the agreement between the experimental points and the calculated line.

Simulated curves (see 2 in Figure 9) obtained following Scheme 2 does not agree with the experimental curve in THF (see 1 in Figure 9).

In Scheme 3 we do not consider the intermediate *trans*-$CrL_2^+$, but, instead, we suppose an interconnecting direct equilibrium between Λ- and Δ-$CrL_2(sol)_2^+$. The little improvement in respect of calculations with Scheme 2, where there is one more intermediate as *trans*-$CrL_2^+$, suggests that

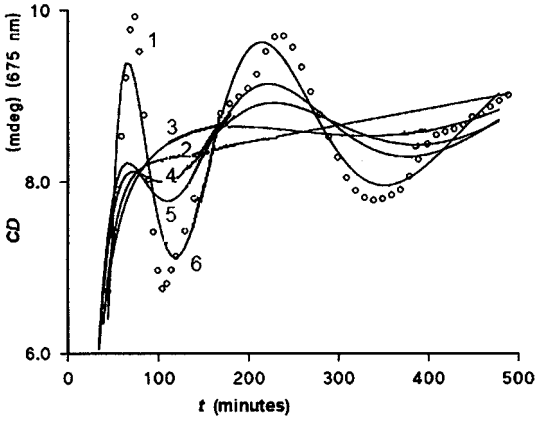


Figure 9. Experimental curve CD/time, in THF (1, line of circles), compared with simulated curves (2–6, continuous lines), obtained from various schemes of formation reaction: Scheme 2; Scheme 3, without the intermediate *trans*-$CrL^{2+}$; Scheme 4, with all intermediates and equilibria; Scheme 5, where the *cis*- and *trans*-$CrL^{2+}\cdots L^-$ intermediates were considered kinetically important; curve 6 refers to a scheme not reported here, but similar to Scheme 5, where the Λ- and Δ-$CrL^{2+}\cdots L^-$ were also considered.

the new equilibrium is an important responsible factor in the oscillations observed (see 3 in Figure 9).

In Scheme 4 it is suggested that the *trans*-$CrL_2^+$ intermediate could react further, forming equilibria with Λ- and Δ-$CrL_2(sol)_2^+$ diastereoisomers as well. The agreement grows and the two maxima and minima observed experimentally begin to appear (Figure 9 and Figure 4).

On increasing the number of direction routes (arrows) in Scheme 4, we did not obtain a much better agreement, so we have tried to increase the number of intermediates alone.

Scheme 5 supports the hypothesis, just suggested in Equations (2)–(6) of the kinetic importance of intermediates $CrL^{2+}\cdots L^-$, which should be present under two forms, one with $L^-$ mono-bonded in the *cis* position with respect to the plane of the first chelated ligand, the other linked in the *trans* position. The *cis* species should form Λ- or Δ-$CrL_2(sol)_2^+$, while the *trans* species should form Λ-$CrL_2(sol)_2^+$, Δ-$CrL_2(sol)_2^+$, or planar *trans*-$CrL_2(sol)_2^+$ (see 5 in Figure 9)

If we suppose that ion pairs of the type $CrL_2^+\cdots L^-$ are also present in the third reaction step, the agreement between calculated and experimental data increases (Figure 9, 6). However, increasing the number of intermediates we can obtain better agreement between observed and calculated values, but some levelling effect has been noted.

The experimental results point to a more complicated mechanism in THF than in EtOH. The solvent confirms its effect on the kinetic and in the thermodynamic stabilization of the various diastereoisomers formed during the reaction. All our experimental results strongly hint at the last tested mechanisms. However, Scheme 4 must be considered as a good exemplification of some more complicated mechanisms that we cannot evaluate quantitatively. For every step shown in Scheme 4 there may be a corresponding reaction path and various intermediates, as in Scheme 5 or more complicated Schemes.

 © 2006 Wiley-VCH Verlag GmbH & Co. KGaA, Weinheim 

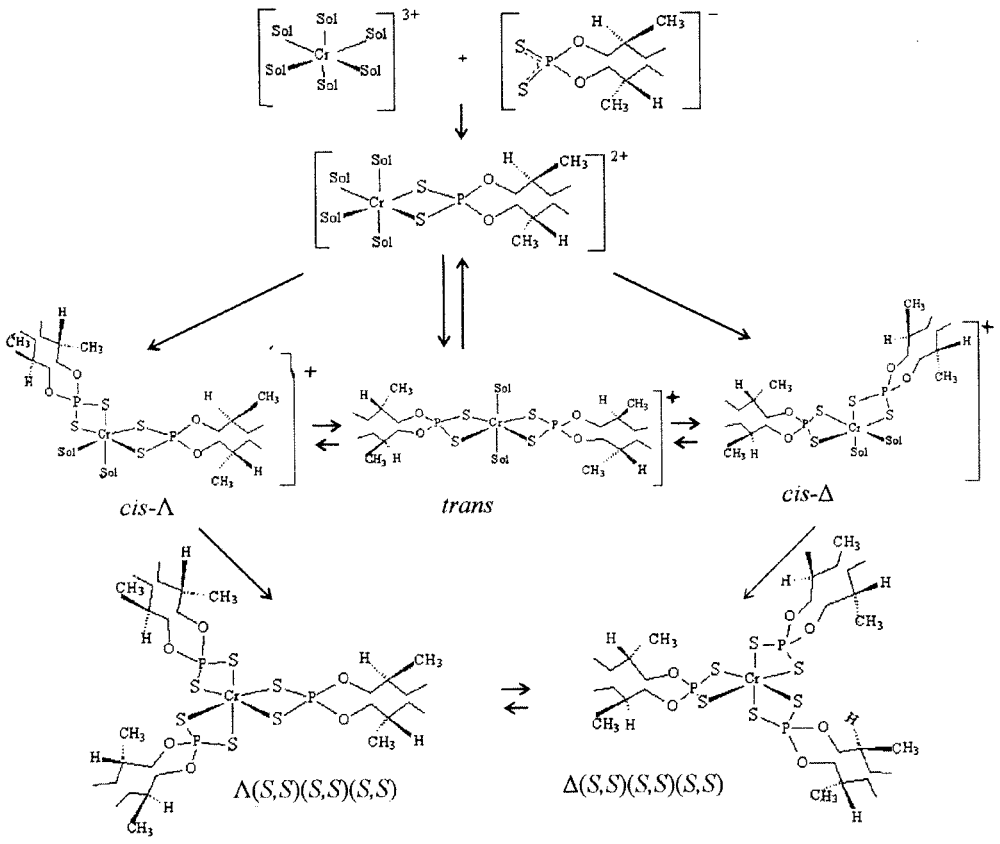


Scheme 4.

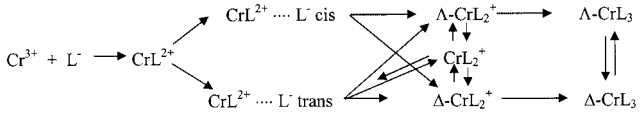


Scheme 5.

In the formation of diastereoisomeric octahedral tris-chelate complexes, chiral discrimination is active because of the difference in the interaction of the chiral chelating ligand molecules with the pro-chiral metal centre of the 1:1 ion, $CrL^{2+}$ and/or with the two chiral intermediate 1:2, *cis* bis-chelated complexed ions, Λ- or Δ-$CrL_2^+$, forming Λ- or Δ-$CrL_3$ diastereoisomeric helical complexes 1:3.

The shape and stereochemical features of the ligand molecules lead to diastereoselectivity in the formation reaction of complexes. The structure of the resulting complex and the interactions with the solvent causes thermodynamic stability of the diastereoisomers as well as chiral discrimination/recognition between molecules.

We are currently trying quantitative analysis of the configurational inversion reactions from Λ-$CrL_3$ to Δ-$CrL_3$ shown in all Schemes proposed.[13,14]

## Conclusions

This paper reports the kinetic study of the formation reaction of chiral octahedral coordination compounds by isotropic and chiroptical spectroscopy. The diastereoselective synthesis of the complex was followed kinetically by UV/Vis and CD measurements. The OD spectra suggest a three-step consecutive mechanism for tris-chelate complex formation. However, a mono-bonded ligand or ion pair could be formed before chelation and substitution of the solvent. CD spectroscopy shows new observables and adds a remarkable new contribution to the knowledge of the chirality transfer and stereoselective synthesis mechanism of chiral inorganic diastereoisomeric coordination compounds, when an enantiopure ligand is used. The CD spectra show preferential formation of Λ-(**3**) diastereoisomer in solution, and of Δ-(**4**) in the solid state. The mechanisms hypothesized on the basis of the kinetic measurements enable one to show the formation in solution of the kinetic and thermodynamic Λ-$(-)_{589}$-[Cr{(*S*)(*S*)-Mebdtp}$_3$] (**3**) complex in equilibrium with Δ-$(+)_{589}$-[Cr{(+)-(*S*)(*S*)-Mebdtp}$_3$] (**4**) through two parallel three-step consecutive pathways interconnected by some configurational inversion reactions at the metal centre.

Our experimental results show that diastereoselective synthesis of Λ-(*S*,*S*)(*S*,*S*)(*S*,*S*) or Δ-(*S*,*S*)(*S*,*S*)(*S*,*S*) can be achieved using the chiral enantiopure dithiophosphate ligand (+)-(*S*)(*S*)-Mebdtp$^-$ (**1**). The diastereoselective reaction of chiral enantiopure ligand **1** with a $Cr^{III}$ ion occurs through kinetically diastereoselective steps during the formation reaction of 1:2 metal/ligand complex, Λ-Cr[(*S*)(*S*)-Mebdtp]$_2^+$ or Δ-Cr[(*S*)(*S*)-Mebdtp]$_2^+$, and of 1:3 complex,

 © 2006 Wiley-VCH Verlag GmbH & Co. KGaA, Weinheim 

**3** or **4**. A hetero-chiral recognition occurs during crystallization, giving $(\Lambda\Delta)$-[Cr{(+)-(*S*)(*S*)-Mebdtp}$_3$]$_{(solid)}$ (**2**) which by configurational inversion gives the thermodynamic complex $\Delta$-$(+)_{589}$-[Cr{(+)-(*S*)(*S*)-Mebdtp}$_3$] (**4**) in the solid phase. Crystal packing favours a crystallization-induced second-order asymmetric transformation, shifting all equilibria towards formation of the more stable and less soluble $(\Lambda\Delta)$-[Cr{(+)-(*S*)(*S*)-Mebdtp}$_3$]$_{(solid)}$ diastereoisomer.

The transfer of chirality from the enantiomeric ligand (+)-(*S*)(*S*)-Mebdtp$^-$ to the $Cr^{III}$ centre is achieved during the formation process by stereoselecting the kinetic and thermodynamic diastereoisomer $\Lambda$-$(+)_{589}$-[Cr{(*S*)(*S*)-Mebdtp}$_3$] in all the solvents used and the thermodynamic complex $\Delta$-$(+)_{589}$-[Cr{(+)-(*S*)(*S*)-Mebdtp}$_3$] in the solid phase. The (*S*)(*S*) configuration of the chiral ligand predetermines $\Lambda$ configuration on the chromium(III) centre in solution and $\Delta$ configuration in the solid state.

## Experimental Section

### Preparation of the Compounds

Hydrated chromium(III) chloride, 2-methyl-1-butanol, and phosphorus pentasulfide (Carlo Erba and Aldrich) were used without further purification. Solvents were purified by standard methods and dehydrated to a spectroscopic degree.

Lithium *O*,*O*′-bis[(*S*)-(+)-2-methyl butyl]dithiophosphate, (+)-(*S*)(*S*)-MebdtpLi, and MebdtpLi were obtained as described, using lithium carbonate to neutralize the acid formed.[3]

$(\Lambda\Delta)$-[Cr{(+)-(*S*)(*S*)-Mebdtp}$_3$] (**2**) and the diastereoisomers $\Lambda$-$(-)_{589}$- (**3**) and $\Delta$-$(+)_{589}$-[Cr{(+)-(*S*)(*S*)-Mebdtp}$_3$] (**4**) were prepared as described.[3]

### Measurement of Formation Reaction Rates

Kinetics of the formation reaction of the complexes were analyzed by absorption, UV/Vis, and CD spectroscopy, through measurement of optical density OD and ellipticity, $\psi$, or differential absorption, $\Delta OD$, at 675 nm, with various concentrations in different solvents at 25.00 ± 0.01 °C. The ligand was always in great excess so as to maintain pseudo first-order conditions for the $Cr^{3+}$ ion.

Solutions of hydrated chromium ion, $CrCl_3 \cdot 6H_2O$ ($2 \cdot 10^{-3}$ mol dm$^3$), containing a minimum of water (ca. $10^{-2}$ mol dm$^3$), were mixed with solutions of the other reagents, in a thermostatted cell ($l$ = 1 cm), controlled by a thermocouple in contact with the same cell. In chloroform solutions it was necessary to add 10% of absolute ethanol to dissolve the chromium trichloride. Formation reactions were followed up to a state of equilibrium between the two diastereoisomers formed, and many days later a stable absorption band at 675 nm and a correspondingly stable Cotton effect were observed. The total concentration of the complexes formed, $C_{tot}$, was determined by isotropic absorbance spectra. The concentration of the major diastereoisomer formed, $C_A$, was determined by the intensity of the relative Cotton effect in CD spectra.

### Spectroscopic Measurements

The kinetics were followed at a fixed wavelength (675 nm) with a Cary/4 spectrophotometer and with a Jasco J-500 A spectropolarimeter using a 1-cm cell. UV/Vis spectra were measured with a Jasco UVIDEC 650 spectrophotometer in various solvents, between 750 and 200 nm. Circular dichroism spectra were obtained in freshly prepared solutions and in nujol mull, KBr pellets, and film between 750 and 200 nm on a Jasco J-810 spectropolarimeter.

## Acknowledgments

We thank the Italian Ministry of University and Scientific Research (MURST); the Alma Mater University of Bologna, "Finanziamento speciale alle strutture" and "Funds for Agreements with Foreign Countries".

[1] a) U. Knof, A. V. von Zelewsky, *Angew. Chem. Int. Ed.* **1999**, *38*, 302–322; b) U. Knof, A. V. von Zelewsky, *Angew. Chem.* **1999**, *111*, 312–333.
[2] S. F. Mason, *Molecular Optical Activity and the Chiral Discriminations*, Cambridge University Press, Cambridge, **1982**.
[3] a) P. Biscarini, R. Franca, R. Kuroda, *Inorg. Chem.* **1995**, *34*, 4618–4626; b) R. Kuroda, P. Biscarini, *Mol. Cryst. Liq. Cryst.* **1996**, *279*, 275–284; c) M. Benedetti, P. Biscarini, A. Brillante, *High Pressure Res.* **2000**, *18*, 285–289.
[4] a) P. Biscarini, *Inorg. Chim. Acta* **1985**, *99*, 183–188; b) P. Biscarini, R. Kuroda, *Inorg. Chim. Acta* **1988**, *154*, 209; c) P. Biscarini, *Collect. Czech. Chem. Commun.* **1991**, *56*, 3006–3011; d) R. Kuroda, P. Biscarini, *J. Chem. Soc., Dalton Trans.* **1990**, 3393–3397; e) D. Drahoňovský, U. Knof, L. Jungo, T. Belser, A. Neels, G. C. Labat, H. Stoeckli-Evans, A. von Zelewsky, *Dalton Trans.* **2006**, 1444–1454.
[5] E. L. Eliel, S. H. Wilen, L. N. Mander in *Stereochemistry of Organic Compounds*, Wiley, New York, **1994**, ch. 7, p. 316.
[6] J. Jacques, A. Collet, S. H. Wilen in *Enantiomers, Racemates and Resolutions*, Wiley, New York, **1981**, ch. 6.
[7] P. Biscarini, M. Benedetti, F. Ferranti, R. Kuroda, E. Foresti, P. Sabatino, *Chirality* **2004**, *16*, 251–262.
[8] J. W. Moore, R. G. Pearson, *Kinetics and Mechanism*, Wiley, New York, **1978**, p. 251a.
[9] N. W. Alcock, D. J. Benton, P. Moore, *Trans. Faraday Soc.* **1970**, *66*, 2210.
[10] R. M. Fuoss, *J. Am. Chem. Soc.* **1958**, *80*, 5059.
[11] R. G. Wilkins in *Kinetics and Mechanism of Reactions of Transition Metal Complexes*, 2nd ed., VCH, Weinheim, **1991**, chapter 8, p. 383.
[12] J. Burgess, *Metal Ions in Solution*, Ellis Horwood, Chichester, **1978**, p. 26.
[13] H. Ohta, M. Kita, H. Kanno, M. Kojima, *Inorg. Chim. Acta* **2000**, *311*, 75–79.
[14] a) P. Biscarini, *Inorg. Chim. Acta* **1985**, *99*, 189–194; b) P. Biscarini, F. Ferranti, paper to be published.

Received: November 28, 2005
Published Online: July 5, 2006

 © 2006 Wiley-VCH Verlag GmbH & Co. KGaA, Weinheim 

DOI: 10.1002/ejic.200501098

# Synthesis, Structure, and Magnetic Behavior of Two New 1D Polymeric Manganese Azido Complexes

**Morsy A. M. Abu-Youssef,*[a] Albert Escuer,[b] and Vratislav Langer[c]**

**Keywords:** Manganese / Coordination polymers / Azido complexes / Aqua complexes / Magnetic properties

Two new $Mn^{II}$ one-dimensional compounds with formulae $[Mn(\mu\text{-}N_3)_2(pyzamid)_2]_n$ (**1**) and $[Mn_2(3\text{-}ampy)_4(\mu\text{-}N_3)_2(N_3)_2(H_2O)_2]_n$, (**2**) (pyzamid = pyrazineamide and 3-ampy = 3-aminopyridine) were structurally and magnetically characterized. Compound **1** crystallizes in the monoclinic system, *P*2/*c* space group, and polymerizes through double end-on azido bridges giving 1D chains with the $Mn^{II}$ atoms in a $MnN_6$ environment. Compound **2** crystallizes in the triclinic system, $P\bar{1}$ space group, and consists of alternate $[Mn(3\text{-}ampy)_2(\mu\text{-}N_3)_2(N_3)_2]$ and $[Mn(3\text{-}ampy)_2(\mu\text{-}N_3)_2(H_2O)_2]$ octahedrons ($MnN_6$ – $MnN_4O_2$ environments), linked by single end-to-end azido bridges. Both chains show very uncommon topologies. Attemps to obtain manganese/azido derivatives with the qux = quinoline-4-carboxylato anion gave the recently reported compound $[Mn(\mu\text{-}qux)_2(\mu\text{-}H_2O)]_n$ (**3**), which consists of a chain with only carboxylato and aqua bridges with the $Mn^{II}$ atoms in a $MnO_6$ slightly distorted octahedron. In good agreement with the expected behavior, magnetic susceptibility measurements show weak ferromagnetic interactions for **1**, whereas compound **2** exhibits moderate antiferromagnetic coupling.

(© Wiley-VCH Verlag GmbH & Co. KGaA, 69451 Weinheim, Germany, 2006)

## Introduction

The flexidentate azide ion has been demonstrated as not only an extremely versatile ligand but also an excellent magnetic mediator, which provides complexes of great structural variety with interesting physical properties.[1–4] The versatility of this ligand is a direct consequence of its ability to link transition metal cations in $\mu\text{-}_{1,1}$ (end-on, EO), $\mu\text{-}_{1,3}$ (end-to-end, EE), $\mu\text{-}_{1,1,3}$, $\mu\text{-}_{1,1,1}$, or still other modes, easily yielding polynuclear, one-, two-, or three-dimensional species with specific topologies.[5–8] The simultaneous presence of more than one of these coordination modes in the same compound, increasing the connectivity possibilities, is not rare.[9] The interest of the magnetochemists in this ligand lies in the well-established relationship between the coordination mode and the resulting magnetic properties, which covers a wide range of ferro-, ferri-, and antiferromagnetic responses.[1] It should be pointed out that the topology of the resulting systems is far from under control because of the similar stabilities of the different coordination modes, which permit other factors such as packing forces or weak supramolecular interactions to be determinant.[10] One of the most complete series of compounds reported to date, with the general formula $[Mn(N_3)_2(R\text{-}py)_2]_n$ (R-py, substituted pyridyl ligands), is a good example of how minor differences in R can drastically change the dimensionality or the coordination mode of the azido bridges, generally because of weak effects such as hydrogen bonds, steric hindrance, or supramolecular π-π stacking interactions in the solid state. As part of our investigation on metal-azido derivatives, we have recently reported a number of transition metal coordination polymers with bidentate or tetradentate neutral organic ligands to built coordination supramolecular frameworks.[8–10]

In this paper we have studied the reaction of azido ligands with $Mn^{II}$ and several polytopic ligands such as the coligands pyzamid = pyrazineamide, 3-ampy = 3-aminopyridine, and qux = quinoline-4-carboxylato anion. These coligands, with almost one aromatic N donor, closely related with previously reported systems such as pyrimidine,[8b] nicotinate anion,[10b] 2-acetylpyridine,[10a,10e] or the same 3-aminopyridine,[10f] were chosen in order to combine the azido versatility with the possibility of a second bridging donor group such as the N pyrazinic or the amide in pyzamid, the amino function in 3-ampy or the carboxylate in qux, in a trial experiment to obtain new topologies. As a result, we present the synthesis, X-ray, and magnetic char-

[a] Chemistry Department, Faculty of Science, Alexandria University,
P. O. Box 426, Ibrahimia, 21321 Alexandria, Egypt
Fax: +2-03-3911794
E-mail: morsy5@link.net
[b] Departament de Química Inorgànica and Institut de Nanociència i Nanotecnologia de la Universitat de Barcelona (UN$^2$UB), Martí I Franqués 1–11, 08028 Barcelona, Spain
Fax: +34-934907725
E-mail: albert.escuer@qi.ub.es
[c] Environmental Inorganic Chemistry, Department of Chemical and Biological Engineering, Chalmers University of Technology,
41296 Göteborg, Sweden
Fax: +46-31-7722853
E-mail: langer@chalmers.se

 © 2006 Wiley-VCH Verlag GmbH & Co. KGaA, Weinheim 

acterization of two new polymeric manganese azido derivatives with the formula $[Mn(\mu\text{-}N_3)_2(pyzamid)_2]_n$ (**1**) and $[Mn_2(3\text{-}ampy)_4(\mu\text{-}N_3)_2(N_3)_2(H_2O)_2]_n$ (**2**). For compound **1** the pyrazineamide ligand coordinates through only one of its donor N atoms in a similar way to a classical pyridine ligand. In this case double EO azido bridges provide the second example[8a] of an EO-azido one-dimensional system. Compound **2** also has monodentate 3-aminopyridine ligands such as in $[Mn(3\text{-}ampy)_4(N_3)_2]$[10f] but the topology of the resulting system is very uncommon: alternating $[Mn(3\text{-}ampy)_2(\mu\text{-}N_3)_2\ (N_3)_2]$ and $[Mn(3\text{-}ampy)_2(\mu\text{-}N_3)_2\text{-}(H_2O)_2]$ coordination polyhedra, linked by single EE azido groups gives the 1D arrangement. The reaction with the qux ligand gave the very recently reported compound $[Mn(\mu\text{-}qux)_2(\mu\text{-}H_2O)]_n$ (**3**).[11] In this case the qux ligand only coordinates by means of the carboxylato groups while azido groups do not coordinate to the manganese atoms. The structure of **3** is closely related to the similar $[Cd(qux)_2\text{-}(H_2O)]_n$ complex.[12] The magnetic response agrees with the expected properties for the different kinds of bridges, that is to say, weak ferromagnetic interactions for the 1D EO-azido chain **1** and moderately weak antiferromagnetic coupling for the EE-azido chain **2**. Compound **3** shows weak antiferromagnetic coupling as was reported.[11]

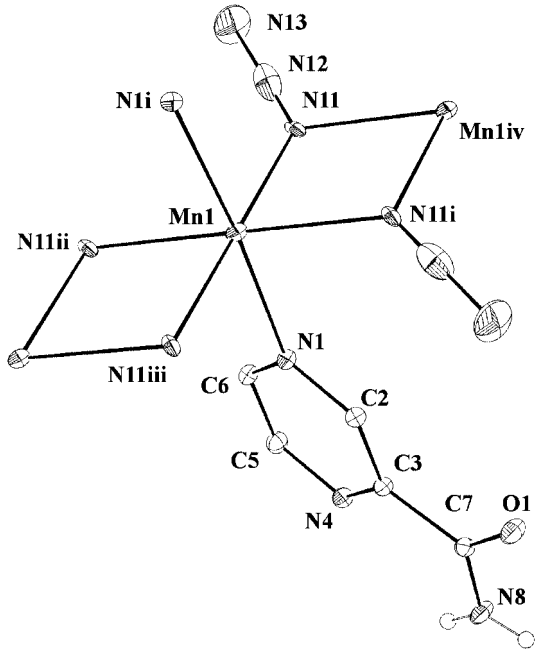


Figure 1. Numbering scheme for $[Mn(\mu\text{-}N_3)_2(pyzamid)_2]_n$ (**1**) with atomic displacement parameters shown at the 30% probability level. Symmetry codes are given in Table 1.

## Results and Discussion

### Structure of $[Mn(\mu\text{-}N_3)_2(pyzamid)_2]_n$ (1)

A labeled ORTEP plot of the structure is shown in Figure 1. Selected distances and angles are listed in Table 1.

The structure consists of neutral 1D chains of $Mn^{II}$ cations linked by double end-to-end azido bridges, along the *b* axis, see Figure 2. The manganese ions, positioned on twofold axes, are placed in a distorted octahedral geometry, $MnN_6$, linked to four bridging azides in the equatorial plane and two terminal *trans* pyzamid-groups in the apical positions. Mn–N(azido) and Mn–N(pyrazine) bond lengths are very similar lying in the range 2.328(3)–2.349(3) Å. The four-membered ring Mn1–N11–$Mn1^{iv}$–$N11^{i}$ is fully planar with Mn–N–Mn bond angles of 97.1(1)°. The Mn···Mn distance is 3.510(1) Å along the chain in the *b* direction. Aromatic rings coordinated at the *trans* sites to the manganese atoms shows a distance between the centroids of 3.510 Å, as result of the short Mn···Mn distances through the double end-on bridges, Figure 2.

The structure is stabilized in the (*a*,*c*) plane by hydrogen bonds involving the N4 atoms from the pyrazine ligands, as well as the N8 and O1 from the amide function, Table 2. The strongest interchain H bonds corresponds to N8–H···O1 [donor–acceptor distance is 2.907(4) Å with a hy-

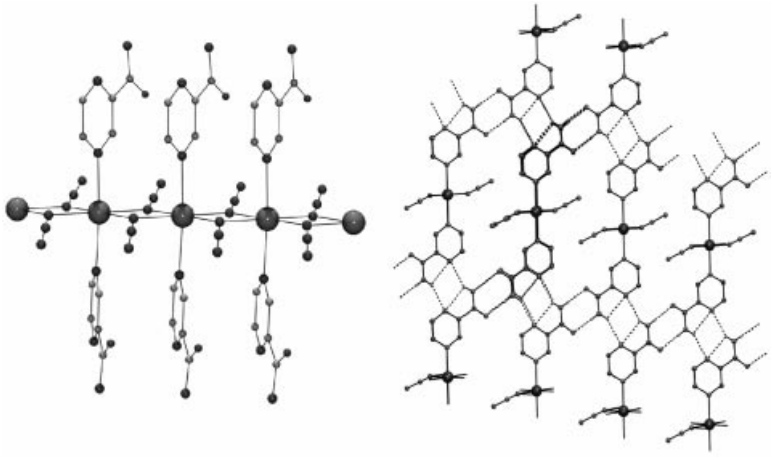

Figure 2. Left, view along the *c*-axis of the one-dimensional compound **1**, showing the double end-on azido bridges between the manganese atoms and the parallel arrangement of the pyrazine rings along the chain in the *b*-direction. Right, view of the structure of **1** projected along the *b*-direction, showing the intra and interchain H-bond network. H bonds involve the N4 atom from the pyrazine ring, O1 from the amide function, and N8 ($-NH_2$) from the same function.

 © 2006 Wiley-VCH Verlag GmbH & Co. KGaA, Weinheim 

Table 1. Selected bond lengths [Å] and bond angles [°] for complex $[Mn(\mu\text{-}N_3)_2(pyzamid)_2]_n$ (**1**).

| | | | |
|---|---|---|---|
| Mn1–N1$^{i}$ | 2.328(3) | N1–Mn1–N11 | 92.7(1) |
| Mn1–N1 | 2.328(3) | N11$^{i}$–Mn1–N11 | 83.2(2) |
| Mn1–N11$^{i}$ | 2.332(3) | N1$^{i}$–Mn1–N11$^{ii}$ | 87.3(1) |
| Mn1–N11 | 2.332(3) | N1–Mn1–N11$^{ii}$ | 89.5(1) |
| Mn1–N11$^{ii}$ | 2.349(3) | N11$^{i}$–Mn1–N11$^{ii}$ | 179.6(1) |
| Mn1–N11$^{iii}$ | 2.349(3) | N11–Mn1–N11$^{ii}$ | 97.1(1) |
| | | N1$^{i}$–Mn1–N11$^{iii}$ | 89.5(1) |
| N11–N12 | 0.960(5) | N1–Mn1–N11$^{iii}$ | 87.3(1) |
| N12–N13 | 1.236(6) | N11$^{i}$–Mn1–N11$^{iii}$ | 97.1(1) |
| | | N11–Mn1–N11$^{iii}$ | 179.6(1) |
| N1$^{i}$–Mn1–N1 | 175.8(1) | N11$^{ii}$–Mn1–N11$^{iii}$ | 82.5(2) |
| N1$^{i}$–Mn1–N11$^{i}$ | 92.7(1) | | |
| N1–Mn1–N11$^{i}$ | 90.5(1) | Mn1–N11–Mn1$^{iv}$ | 97.1(1) |
| N1$^{i}$–Mn1–N11 | 90.5(1) | N12–N11–Mn1$^{iv}$ | 121.5(3) |
| | | N11–N12–N13 | 178.9(6) |

Symmetry transformations used to generate equivalent atoms: (i): $-x+1$, $y$, $-z+1/2$; (ii): $x$, $y-1$, $z$; (iii): $-x+1$, $y-1$, $-z+1/2$; (iv): $x$, $y+1$, $z$

drogen bond angle of 180(6)°], weaker H bonds correspond to the bifurcated N8···N4 [donor–acceptor distances 2.762(4) and 3.112(4) Å, with hydrogen bond angles of 103(4)° and 146(4)°, respectively], see Figure 2, whereas weak intrachain contacts are given by the bifurcated interaction C6–H···N13. Coordination as a monodentate ligand of the pyrazine ring can be justified by two reasons: the steric hindrance of the amide group, too close to N4, and the additional stabilization of the structure provided by the H-bond network.

Table 2. H-Bond parameters for compounds **1** and **2**.

| D–H···A | *d*(D–H) [Å] | *d*(H···A) [Å] | *d*(D···A) [Å] | ∠(D–H···A) [°] |
|---|---|---|---|---|
| Compound **1** | | | | |
| N8–H8A···O1$^{v}$ | 0.77(5) | 2.14(5) | 2.907(4) | 180(6) |
| N8–H8B···N4 | 0.84(5) | 2.45(5) | 2.762(4) | 103(4) |
| N8–H8B···N4$^{vi}$ | 0.84(5) | 2.38(5) | 3.112(4) | 146(4) |
| C6–H6···N13$^{vii}$ | 0.95 | 2.44 | 3.248(6) | 143 |
| C6–H6···N13$^{viii}$ | 0.95 | 2.60 | 3.072(5) | 111 |
| Symmetry transformations used to generate equivalent atoms: (v): $-x+2$, $-y+1$, $-z+1$; (vi): $-x+2$, $y$, $-z+1/2$; (vii): $-x+1$, $-y$, $-z$; (viii): $-x+1$, $-y+1$, $-z$ | | | | |
| Compound **2** | | | | |
| O1–H1A···N23$^{iii}$ | 0.88(3) | 1.93(3) | 2.805(3) | 172(3) |
| O1–H1B···N3A$^{iv}$ | 0.82(3) | 2.04(3) | 2.856(3) | 178(3) |
| N13–H13A···N3A$^{iv}$ | 0.89(3) | 2.37(3) | 3.238(3) | 167(2) |
| N13–H13B···N3B$^{iii}$ | 0.82(3) | 2.44(3) | 3.242(3) | 163(2) |
| N23–H23A···O1$^{v}$ | 0.92(3) | 2.28(3) | 3.167(3) | 161(2) |
| N23–H23B···N13$^{ii}$ | 0.95(3) | 2.23(3) | 3.171(3) | 174(2) |
| C12–H12···N3A$^{iv}$ | 0.95 | 2.62 | 3.444(3) | 146 |
| C14–H14···N2A$^{iii}$ | 0.95 | 2.58 | 3.407(3) | 146 |
| C24–H24···N1B$^{vi}$ | 0.95 | 2.56 | 3.282(3) | 132 |
| Symmetry transformations used to generate equivalent atoms: (iii): $x-1$, $y+1$, $z$; (iv): $x-1$, $y$, $z$; (v): $-x$, $-y$, $-z$; (vi): $x$, $y-1$, $z$ | | | | |

### Structure of $[Mn_2(3\text{-ampy})_4(\mu\text{-}N_3)_2(N_3)_2(H_2O)_2]_n$ (2)

A labeled ORTEP plot of the structure is shown in Figure 3. Selected distances and angles are listed in Table 3. The structure consists of neutral 1D chains of $Mn^{II}$ along the *a* axis, in which the coordination environment around the manganese atoms shows a regular alternating chain (Figure 4).

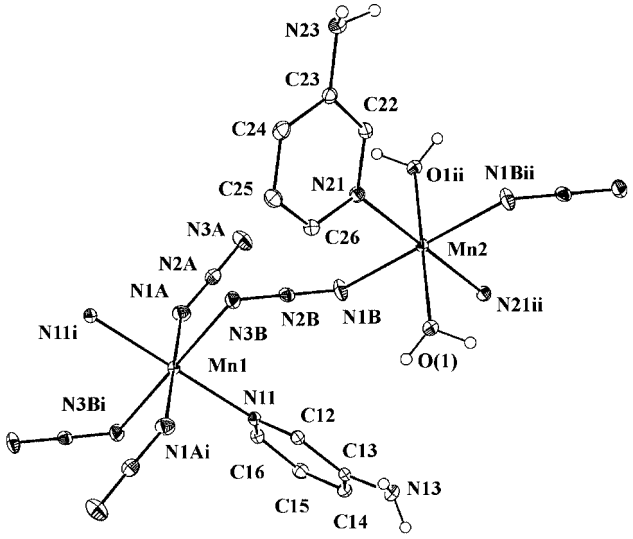


Figure 3. Numbering scheme for $[Mn_2(3\text{-ampy})_4(\mu\text{-}N_3)_2(N_3)_2(H_2O)_2]_n$ (**2**). Atomic displacement parameters are shown at the 30% probability level. Symmetry codes are given in Table 3.

Table 3. Selected bond lengths [Å] and bond angles [°] for complex $[Mn_2(3\text{-ampy})_4(\mu\text{-}N_3)_2(N_3)_2(H_2O)_2]_n$ (**2**).

| | | | |
|---|---|---|---|
| Bond lengths | | | |
| Mn1–N1A$^{i}$ | 2.216(2) | Mn2–N1B$^{ii}$ | 2.198(2) |
| Mn1–N1A | 2.216(2) | Mn2–N1B | 2.198(2) |
| Mn1–N11 | 2.251(2) | Mn2–O1$^{ii}$ | 2.229(2) |
| Mn1–N11$^{i}$ | 2.251(2) | Mn2–O1 | 2.229(2) |
| Mn1–N3B | 2.278(2) | Mn2–N21$^{ii}$ | 2.242(2) |
| Mn1–N3B$^{i}$ | 2.278(2) | Mn2–N21 | 2.242(2) |
| N1A–N2A | 1.183(3) | N1B–N2B | 1.177(3) |
| N2A–N3A | 1.176(3) | N2B–N3B | 1.180(3) |
| Bond angles | | | |
| N1A$^{i}$–Mn1–N1A | 180.0 | N1B$^{ii}$–Mn2–N1B | 180.0 |
| N1A$^{i}$–Mn1–N11 | 90.88(7) | N1B$^{ii}$–Mn2–O1$^{ii}$ | 88.81(8) |
| N1A–Mn1–N11 | 89.12(7) | N1B–Mn2–O1$^{ii}$ | 91.19(8) |
| N1A$^{i}$–Mn1–N11$^{i}$ | 89.12(7) | N1B$^{ii}$–Mn2–O1 | 91.19(8) |
| N1A–Mn1–N11$^{i}$ | 90.88(7) | N1B–Mn2–O1 | 88.81(8) |
| N11–Mn1–N11$^{i}$ | 180.0 | O1$^{ii}$–Mn2–O1 | 180.0 |
| N1A$^{i}$–Mn1–N3B | 89.59(8) | N1B$^{ii}$–Mn2–N21$^{ii}$ | 88.75(7) |
| N1A–Mn1–N3B | 90.41(8) | N1B–Mn2–N21$^{ii}$ | 91.25(7) |
| N11–Mn1–N3B | 91.20(7) | O1$^{ii}$–Mn2–N21$^{ii}$ | 89.85(7) |
| N11$^{i}$–Mn1–N3B | 88.80(7) | O1–Mn2–N21$^{ii}$ | 90.15(7) |
| N1A$^{i}$–Mn1–N3B$^{i}$ | 90.41(8) | N1B$^{ii}$–Mn2–N21 | 91.25(7) |
| N1A–Mn1–N3B$^{i}$ | 89.59(8) | N1B–Mn2–N21 | 88.75(7) |
| N11–Mn1–N3B$^{i}$ | 88.80(7) | O1$^{ii}$–Mn2–N21 | 90.15(7) |
| N11$^{i}$–Mn1–N3B$^{i}$ | 91.20(7) | O1–Mn2–N21 | 89.85(7) |
| N3B–Mn1–N3B$^{i}$ | 180.0 | N21$^{ii}$–Mn2–N21 | 180.0 |
| N2A–N1A–Mn1 | 134.7(2) | N2B–N1B–Mn2 | 143.5(2) |
| N2B–N3B–Mn1 | 129.9(2) | N1B–N2B–N3B | 179.5(2) |
| N1A–N2A–N3A | 177.8(3) | | |

Symmetry transformations used to generate equivalent atoms: (i): $-x$, $-y+1$, $-z+1$; (ii): $-x$, $-y+1$, $-z$

There are two independent manganese ions, both positioned on inversion centers giving the alternating chain. The Mn1 ion is placed in a slightly distorted octahedral geome-

 © 2006 Wiley-VCH Verlag GmbH & Co. KGaA, Weinheim 

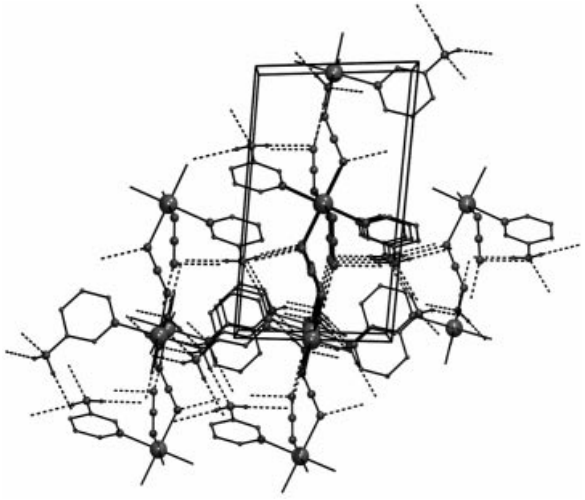

Figure 4. View of the one-dimensional compound **2** showing the interchain H bridges involving terminal azido ligands and the $-NH_2$ functions.

try, $MnN_6$. The equatorial plane is defined by two end-to-end μ-bridging azides and two terminal azides, and the axial sites are occupied by two terminal 3-ampy groups in a *trans* arrangement. The Mn1–N1A bond length (terminal azido ligand) is slightly shorter than the Mn1–N (bridging azido or 3-ampy) distances. The Mn2 ion is placed in a slightly distorted $MnN_4O_2$ octahedral environment with two end-to-end μ-bridging azides, two 3-ampy ligands in the equatorial plane, and two water molecules in the apical positions. The end-to-end azido bridge gives two slightly different bond angles with the manganese atoms, Mn1–N3B–N2B of 129.9(2)° and Mn2–N1B–N2B of 143.5(2)°, and a Mn–N–N–N–Mn dihedral angle of 165.1°.

The Mn1···Mn2 distance is 6.3507(2) Å along the chains, whereas the minimum interchain distance is equal to 7.8105(2) Å.

The structure is stabilized by a large number of strong hydrogen bonds that involve O1 from the water molecules, N13 and N23 from the amino functions, the terminal azido atoms N3A, and also one of the atoms of the bridging azido group, N3B, Table 2. One of them is an intrachain contact between the aminated groups N23–H23B···N13$^{ii}$ whereas the other contacts, involving the water molecules and the azido ligands, are all interchain contacts, Figure 4. This H-bond network gives a 3D supramolecular arrangement as occurs in compound **1**. The aromatic rings of neighbor chains interact between them by means of π-π interactions with distances between centroids of 3.394 and 3.510 Å.

### Structure of $[Mn(\mu\text{-qux})_2(\mu\text{-}H_2O)]_n$ (3)

A schematic plot of the structure of **3** is shown in Figure 5. The structure of this compound can be described as 1D chains of manganese atoms along the *c* axis, linked by two *syn-syn* carboxylates and one μ-$OH_2$ molecule. The manganese ions, positioned on inverse centers, are placed in a slightly distorted octahedral geometry, $MnO_6$, linked to four bridging quinoline-4-carboxylato ligands and two axial O atoms from bridging water molecules. The $Mn^{II}$–O(carboxylate) bond lengths lie in the range 2.103(2)–2.171(2) Å and they are shorter than the $Mn^{II}$–O(water) distances, 2.286(2) Å. The bond angle Mn–O(water)–Mn′ has a value of 114.1(2)°.

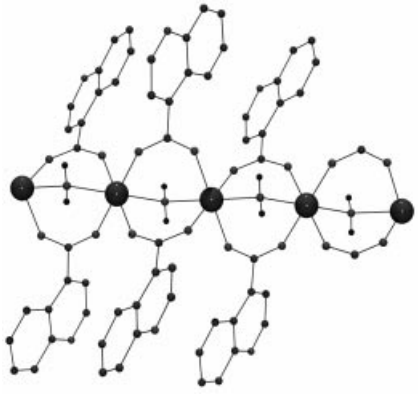

Figure 5. Schematic view of $[Mn(\mu\text{-qux})(\mu_2\text{-}H_2O)]_n$ (**3**).

The structure is stabilized in the (*a*,*b*) plane by strong interchain $O_{water}$···$N_{quinoline}$ hydrogen bonds [donor–acceptor distance is 2.742(3) Å with a hydrogen-bond angle of 179(4)°]. Each water molecule participates in two H bonds with *N*-quinoline atoms from two different chains. The aromatic rings from neighboring chains show π-π stacking with interplanar distances of 3.381(3) Å.

### Synthetic and Structural Features

Polymeric systems with exclusively end-on azido bridges, all of them characterized by $Mn^{II}$ cations, are very uncommon and only three related compounds have been reported to date. One of them is also a one-dimensional compound with the formula $[Mn(N_3)_2(2\text{-bzpy})]_n$, 2-bzpy = 2-benzoylpyridine, which stabilizes the system by means of interchain π-π stacking of the aromatic rings.[8a]

The other two are bidimensional systems in which the one-dimensional manganese-azido chains are linked between them by means of a second bridging coligand such as bis-monodentate pyrazine[5d] (pyz) or the bis-bidentate 2,2′-bipyrimidine (bpym).[13] The compound $[Mn(N_3)_2(pyz)]_n$ also shows an extensive π-π stacking of parallel pyrazine rings (distance between the rings is 3.412 Å), which contributes to stabilize the structure, Scheme 1.

Less clear are the factors that stabilize the other compound, with formula $[Mn_2(N_3)_4(bpym)]_n$, for which π-π stacking or H bonds cannot be found, but this case is not totally comparable because the coligand is bis-bidentate. In our case, compound **1** exhibits the same kind of interaction between the aromatic rings, which seems to be a quasi general factor that favors these types of compounds.

The variety of compounds that can be obtained with other pyrazines or the 3-ampy ligand are much more difficult to rationalize. As is shown in Scheme 1, nonsubstituted

 © 2006 Wiley-VCH Verlag GmbH & Co. KGaA, Weinheim

Scheme 1.

pyrazine is able to coordinate both nitrogen atoms but steric hindrance in substituted pyrazines prevents this kind of coordination and only one of the N ring atoms can act as a donor. If the function attached to the pyrazine ring contains coordinating groups, the ligand can act as bidentate, as occurs with pyrazinecarbozylate[14a] and methyl-imidopyrazinecarboxylate,[14b] which gives high-dimensional compounds in both cases. In our case, compound **1**, pyrazineamide coordinates by only one N-ring donor following the general trend for substituted pyrazines, but the poor coordinating amido functions do not act as donors and are involved in intrachain H bonds.

It should be pointed out that small differences in the synthetic procedure can produce very different compounds as occurs in the case of the ligand 3-ampy: an excess of 3-ampy (ratios of $Mn^{II}$, 3-ampy, and sodium azide 1:7:2) yield the mononuclear compound $[Mn(3\text{-ampy})_4(N_3)_2]$, which is to be expected from the large 3-ampy concentration.[10f] In contrast, similar ratios 1:2.5:2.5 or 1:2:3 give either the $[Mn_2(3\text{-ampy})_4(\mu_{1,1}\text{-}N_3)_2(\mu_{1,3}\text{-}N_3)(N_3)(H_2O)]_n$ system[15] with alternating coordination modes of the azido bridge or the above described $[Mn_2(3\text{-ampy})_4(\mu_{1,3}\text{-}N_3)_2(N_3)_2(H_2O)_2]_n$ (**2**) with alternating coordination polyhedra. This pair of compounds that differs by only one water molecule in their empirical formula, are a nice example of the similar stability of end-on and end-to-end coordinations for the azido ligand.

### Magnetic Measurements and Coupling Constant Calculations

The magnetic measurements were performed on powdered crystalline samples in the 2–300 K temperature range. The shape of the plots indicate that the overall interaction is weakly ferromagnetic for compound **1** and moderately antiferromagnetic for **2** and **3**.

Compound **1** shows a $\chi_M T$ room temperature value of 4.78 $cm^3 \cdot K \cdot mol^{-1}$, greater than the expected value of 4.375 $cm^3 \cdot K \cdot mol^{-1}$ for an isolated manganese atom. $\chi_M$ increases continuously on cooling and $\chi_M T$ also increases up to a maximum value of 8.31 $cm^3 \cdot K \cdot mol^{-1}$ at 8 K, decreasing down to 4.5 $cm^3 \cdot K \cdot mol^{-1}$ at 2 K, Figure 6. Fitting the $\chi_M T$ data as a homogeneous $S = 5/2$ chain in the 300–15 K temperature range, applying the analytical expression for a regular chain derived from the Hamiltonian $H = -JS_i \cdot S_{i+1}$ (for local $S = 5/2$),[16] gives the best fit parameters $J = +1.1(1)\ cm^{-1}$, $g = 2.045(3)$. The weak ferromagnetic response is in good agreement with the expected properties. End-on azido bridges with M–N–M bond angles around 100° gives typically ferromagnetic coupling and the $J$ value is similar to that reported for the related compound $[Mn(\mu_{1,1}\text{-}N_3)_2(2\text{-bzpy})_2]_n$ (2-bzpy = 2-benzoylpyridine), previously reported by us,[8a] and also agrees with the calculated values for the ferromagnetic interaction in $[Mn(N_3)_2(pyz)]_n$[5d] and $[Mn_2(N_3)_4(bpym)]_n$.[13] Also, the $g$ value, slightly greater than 2.00, agrees with this previously reported chain.[8a] The only difference for the $[Mn(\mu_{1,1}\text{-}N_3)_2(2\text{-bzpy})_2]_n$ compound lies in the H bonds that afford weak antiferromagnetic interchain interactions at very low temperatures; their effect can be seen in the decrease of $\chi_M T$ below 8 K. As can be expected, magnetization measurements, performed at 2 K, show a fast increase in the magnetization, reaching a value equivalent to five electrons for the manganese atom under moderate external fields, Figure 6.

In contrast, compound **2** shows a different response, with a maximum molar susceptibility at 13 K, Figure 7. On the basis of the structural data, compound **2** is an alternating one-dimensional system, which shows similar bond lengths, quite similar Mn–N–N bond angles, and identical torsion angles in the bridging region. A fit of the system was performed assuming that the two $J$ coupling constants have

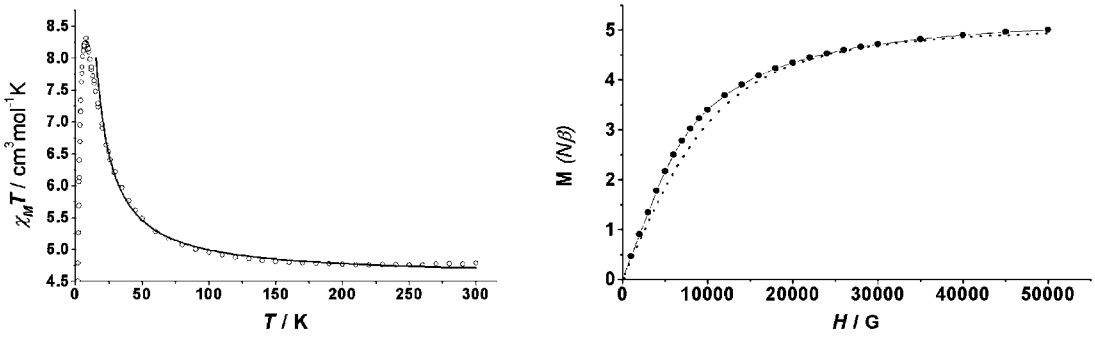


Figure 6. Plot of $\chi_M T$ for compound **1** (left plot). Solid line corresponds to the best fit (see text). Right, magnetization of compound **1**; dotted line shows the Brillouin plot for an uncoupled $S = 5/2$.

 © 2006 Wiley-VCH Verlag GmbH & Co. KGaA, Weinheim 

the same value under these conditions and by applying the analytical expression for a regular $S = 5/2$ chain; best fit parameters were $J = -3.15(2)\ cm^{-1}$ and $g = 2.000(5)$. Attempts to differentiate between the two $J$ values by means of the analytical expression for an alternating $S = 5/2$ chain[17] were unsuccessful. For the manganese–azido bridges, theoretical and experimental work on end-to-end coordination modes indicates that the coupling should be antiferromagnetic in all cases and that the large bond or torsion angles in the bridging region always give a lower interaction. Compound **2** shows one large Mn–N–N bond angle (143.5°) and a moderate dihedral angle in the Mn–N–N–N–Mn bridging region. Under these conditions a moderately low coupling can be expected, mainly derived from the large Mn–N–N bond angle.

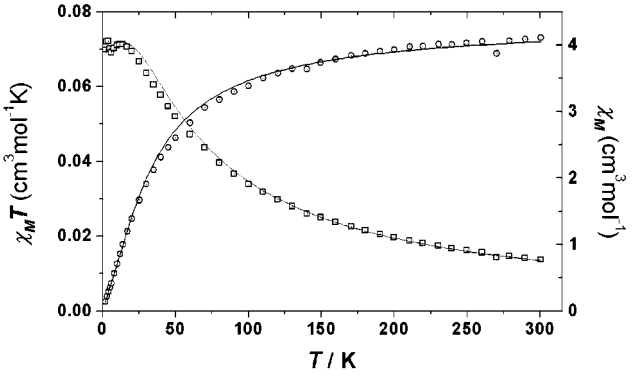


Figure 7. Plot of $\chi_M$ (open squares) and $\chi_M T$ (dot centered circles) for compound **2**. Solid line corresponds to the best fit (see text).

Remeasurement of the magnetic properties of compound **3** fully agree with the recently reported[11] data for this compound: molar susceptibility shows a maximum at 17 K, and a fit of the experimental data gives the best fit parameter $J = -2.75(2)\ cm^{-1}$. This $J$ value agrees with the values reported in the literature for simultaneous carboxylato–aqua bridges, which are always weakly antiferromagnetic.[18]

## Conclusions

Two new one-dimensional systems of $Mn^{II}$ have been obtained and characterized from structural and magnetic points of view. The effect of the coligands employed in the synthesis play a fundamental role in the topology of the final compounds: with 3-pyrazineamide (compound **1**) and 3-aminopyridine (compound **2**) the expected azido chains were obtained but weak packing interactions (π-π stacking and H-bond networks) induce either end-on or end-to-end azido derivatives. In contrast, when the coligand was quinoline-4-carboxylato (compound **3**), the azido ligand did not coordinate to the manganese atoms and one 1D system with *syn-syn* carboxylato and aqua bridges was obtained. Magnetic measurements have been performed for all of them, showing a variety of interactions closely related to the topology of the chains: ferromagnetic interactions for **1**, alternating antiferromagnetic coupling for **2**, and homogeneous antiferromagnetic interactions for **3**.

## Experimental Section

**General Remarks:** Elemental analyses (C,H,N) were carried out using a Perkin–Elmer analyzer, $Mn^{2+}$ was analyzed by a Perkin–Elmer Analyst 300, AAS atomic absorption spectrometer. Infrared spectra (4000–400 $cm^{-1}$) were recorded with a Bruker IFS-125 model FT-IR spectrophotometer using KBr pellets. Quinoline-4-carboxylic acid, pyrazineamide, and 3-aminopyridine were purchased from Aldrich and other chemicals were of analytical grade quality and used as received. Magnetic susceptibility measurements were carried out on polycrystalline samples with a Quantum Design susceptometer working in the range 20–300 K under magnetic fields of 0.3 T and under a field of 0.03 T in the range 20–2 K at the Magnetochemistry Service of the University of Barcelona. Diamagnetic corrections were estimated from Pascal Tables.

**$[Mn(\mu\text{-}N_3)_2(pyzamid)_2]_n$ (1):** A methanolic solution (10.0 mL) of manganese nitrate tetrahydrate (0.5 g, 2 mmol) was mixed with an aqueous/methanolic (1:1) solution (15 mL) of pyrazinamide (0.5 g, ca. 4 mmol). The mixture was stirred for ca. 5 min. A solution of sodium azide (0.65 g, 10 mmol) in water (10 mL) was added dropwise with vigorous stirring. The resulting clear solution was allowed to stand in a refrigerator for several weeks. Colorless needles of the ligand were formed, several days latter yellow needles suitable for X-ray measurements were collected and dried in air with a yield of ca. 45%. $C_{10}H_{10}MnN_{12}O_2$ (385.2): calcd. C 31.18, H 2.62, Mn 14.26, N 43.63; found C 31.0, H 2.5, Mn 14.4, N 43.5. IR (KBr; v: very, s: strong, m: medium, w: weak): $\tilde{\nu}$ = 3393 (s), 3294 (m), 3170 (s), 3091 (s), 2100 (vs), 1718 (vs), 1611 (s), 1590 (s), 1432 (s), 1379 (vs), 1330 (s), 1275 (m), 1187 (m), 1166 (ms), 1100 (m), 1061 (s), 1026 (s), 811 (wm), 787 (ms), 706 (w), 643 (w), 567 (s), 507 (s), 440 (s), 408 (w), 386 (w), 365 (vw), 342 (vw), 315 (vw), 292 (vw), 268 (s) $cm^{-1}$.

**$[Mn_2(3\text{-}ampy)_4(\mu\text{-}N_3)_2(N_3)_2(H_2O)_2]_n$ (2):** 3-Aminopyridine (0.19 g, ca. 2 mmol) in methanol (10.0 mL) was added to a solution (10.0 mL) of $MnCl_2{\cdot}4H_2O$ (0.20 g, ca. 1.0 mmol) in methanol. The mixture was stirred for ca. 5 min. Aqueous solutions of sodium azide (0.2 g, 3 mmol) and a few drops of saturated L-ascorbic acid, to prevent oxidation, were added successively and continuously stirred. The resulting clear solution was allowed to stand in a dark place at room temperature for several weeks. Yellowish-brown crystals suitable for X-ray measurements were collected and dried in air with a yield of ca. 65%. $C_{10}H_{14}MnN_{10}O$ (345.2): calcd. C 34.79, H 4.09, Mn 15.91, N 40.57; found C 34.7, H 3.9, Mn 15.9, N 40.5. IR (KBr; v: very, s: strong, m: medium, w: weak, br: broad): $\tilde{\nu}$ = 3343 (vs, br), 3286 (vs, br), 3062 (s), 2631 (m), 2532 (m), 2351 (w), 2310 (w), 2082 (vs), 1661 (s), 1644 (vs), 1605 (vs), 1580 (m), 1488 (vs), 1445 (vs), 1354 (m), 1313 (s), 1277 (s), 1195 (m), 1143 (m), 1096 (m), 1051 (m), 1024 (m), 989 (w), 911 (m), 858 (m), 813 (s), 797 (s), 700 (vs), 644 (s), 610 (s), 594 (s), 477 (m), 407 (m), 388 (m), 343 (w), 315 (w), 292 (w), 268 (s), 232 (s) $cm^{-1}$.

**$[Mn(\mu\text{-}qux)_2(\mu\text{-}H_2O)]_n$ (3):** Colorless crystals suitable for X-ray measurements were collected from a 2:1:4 aqueous/methanolic 1:1 solution of quinoline-4-carboxylic acid, manganese nitrate tetrahydrate, and sodium azide. From this mixture that contains a large excess of azido, the neutral chain $[Mn(\mu\text{-}qux)_2(\mu\text{-}H_2O)]_n$, containing only carboxylato bridges, was obtained instead of the expected azido derivative. $C_{20}H_{14}MnN_2O_5$ (417.3): calcd. C 57.57, H 3.38, Mn 13.17, N 6.71; found C 57.4, H 3.3, Mn 13.0, N 6.8. IR (KBr;

 © 2006 Wiley-VCH Verlag GmbH & Co. KGaA, Weinheim 

Table 4. Crystal data and structure refinement parameters for $[Mn(\mu\text{-}N_3)_2(pyzamid)_2]_n$ (**1**) and $[Mn_2(3\text{-}ampy)_4(\mu\text{-}N_3)_2(N_3)_2(H_2O)_2]_n$ (**2**).

| | $[Mn(\mu\text{-}N_3)_2(pyzamid)_2]_n$ | $[Mn_2(3\text{-}ampy)_4(\mu\text{-}N_3)_2(N_3)_2(H_2O)_2]_n$ |
|---|---|---|
| Formula | $C_{10}H_{10}MnN_{12}O_2$ | $C_{10}H_{14}MnN_{10}O$ |
| Formula mass [g·mol$^{-1}$] | 385.24 | 345.25 |
| Crystal system | monoclinic | triclinic |
| Space group | $P2/c$ | $P\bar{1}$ |
| $a$ [Å] | 14.1496(3) | 7.8105(2) |
| $b$ [Å] | 3.5097(1) | 8.3423(2) |
| $c$ [Å] | 14.6946(3) | 12.7014(3) |
| $\alpha$ [deg] | 90 | 78.663(1) |
| $\beta$ [deg] | 100.393(1) | 74.482(1) |
| $\gamma$ [deg] | 90 | 63.923(1) |
| $V$ [Å$^3$] | 717.77(3) | 713.26(3) |
| $Z$ | 2 | 2 |
| $T$ [K] | 173(2) | 173(2) |
| $\lambda$(Mo-$K_\alpha$) [Å] | 0.71073 | 0.71073 |
| $\mu$(Mo-$K_\alpha$) [mm$^{-1}$] | 0.959 | 0.946 |
| $d_{calc}$ [g·cm$^{-3}$] | 1.782 | 1.608 |
| Crystal size [mm] | 0.30 × 0.08 × 0.02 | 0.18 × 0.18 × 0.04 |
| Max./min. transmission | 0.9811/0.7618 | 0.9632/0.8482 |
| $\Theta$ min./max. [°] | 2.82/27.49 | 1.67/30.47 |
| Reflections collected | 8638 | 11546 |
| Independent reflections/$R_{int}$ | 1662/0.0396 | 4304/0.0613 |
| Data/restraints/parameters | 1662/18/122 | 4304/0/223 |
| $R$ [$I > 2\sigma I$][a] | $R_1$ = 0.0508, $wR_2$ = 0.1369 | $R_1$ = 0.0449, $wR_2$ = 0.0848 |
| $Rw$ [all][b] | $R_1$ = 0.0574, $wR_2$ = 0.1415 | $R_1$ = 0.0938, $wR_2$ = 0.1012 |

[a] $R(F_o) = \Sigma||F_o| - |F_c|| / \Sigma|F_o|$. [b] $Rw(F_o)^2 = \{\Sigma w[(F_o)^2 - (F_c)^2]^2 / [\Sigma w(F_o)^4]\}^{1/2}$.

v: very, s: strong, m: medium, w: weak, br: broad): $\tilde{\nu}$ = 3439 (m, br,) 2765 (m, br), 2353 (m), 1604 (vs), 1579 (vs), 1506 (ms), 1460 (s), 1427 (vs), 1408 (vs), 1377 (vs), 1302 (s), 1267 (m), 1206 (wm), 1153 (m), 1075 (m), 1026 (m), 995 (m), 961 (m), 874 (ms), 802 (s), 784 (s), 765 (s), 740 (ms), 652 (s), 593 (ms), 532 (wm), 510 (wm), 458 (m), 398 (s), 375 (s), 343 (m), 316 (m), 294 (m), 269 (vs) cm$^{-1}$.

**X-ray Crystallographic Study:** All diffraction data were collected using a Siemens SMART CCD diffractometer with Mo-$K_\alpha$ radiation ($\lambda$ = 0.71073 Å, graphite monochromator). The crystals were cooled to 173(2) K by a flow of nitrogen gas using the LT-2A device. A full sphere of reciprocal lattices were scanned by 0.3° steps in $\omega$ with a crystal-to-detector distance of 3.97 cm. Preliminary orientation matrices were obtained from the first frames using the SMART program.[19] The collected frames were integrated using the preliminary orientation matrices, which were updated every 100 frames. Final cell parameters were obtained by refinement on the positions of reflections with $I > 10\sigma(I)$ after integration of all the frames using the SAINT program.[19] The data were empirically corrected for absorptions and other effects using the SADABS program.[20] The structures were solved by direct methods and refined by full-matrix least-squares on all $F^2$ data using SHELXTL.[21] The non-H atoms were refined anisotropically, while hydrogen atoms were refined isotropically with the use of geometrical restraints. The crystallographic and refinement data are summarized in Table 4. Molecular graphics were prepared using the programs Diamond[22] and ORTEP3.[23] Structural determination for **3** was recently reported[11] but with a lower quality. Our refinement led to the same formula $C_{20}H_{14}MnN_2O_5$ and $C2/c$ space group with the parameters $a$ = 15.0903(7) Å, $b$ = 14.3131(7) Å, $c$ = 7.6708(4) Å, $\beta$ = 92.513(2)°, $V$ = 1655.2(1) Å$^3$, $Z$ = 4, $R_1$ = 0.0484, and $wR_2$ = 0.0772.

CCDC-291400 to -291402 contain the supplementary crystallographic data for this paper. These data can be obtained free of charge from The Cambridge Crystallographic Data Centre via www.ccdc.cam.ac.uk/data_request/cif.

## Acknowledgments

This work was supported by the SIDA (Grants 348-2002-6879 and 348-2004-5473 to M. A. and V. L.) and the CICYT (Grant PB03/0538 to A. E.).

[1] J. Ribas, A. Escuer, M. Monfort, R. Vicente, R. Cortés, L. Lezama, T. Rojo, *Coord. Chem. Rev.* **1999**, *193–195*, 1027 and references cited therein.
[2] J. M. Lehn, *Supramolecular Chemistry*, VCH, Weinheim, **1985**.
[3] R. Robin, B. F. Abrahms, R. R. Barten, R. W. Gable, B. F. Huskiness, J. Lieu, *Supramolecular Architecture*, American Chemical Society: Washington, DC, **1992**.
[4] *Molecular Magnetism, a Supramolecular Function* (Ed.: O. Kahn), Kluwer, Dordrecht, **1996**.
[5] a) E. Q. Gao, S. Q. Bai, Z. M. Wang, C. H. Yan, *J. Am. Chem. Soc.* **2003**, *125*, 4984; b) E. Q. Gao, Y. F. Yue, S. Q. Bai, Z. He, C. H. Yan, *J. Am. Chem. Soc.* **2004**, *126*, 1419; c) E. Q. Gao, S. Q. Bai, C. F. Wang, Y. F. Yue, C. H. Yan, *Inorg. Chem.* **2003**, *42*, 8456 and references cited therein; d) J. L. Manson, A. M. Arif, J. S. Miller, *Chem. Commun.* **1999**, 1479.
[6] a) A. Escuer, R. Vicente, M. A. S. Goher, F. A. Mautner, *Inorg. Chem.* **1998**, *37*, 782; b) Z. E. Serna, L. Lezama, M. K. Urtiaga, M. I. Arriortua, M. G. B. Barandika, R. Cortés, T. Rojo, *Angew. Chem. Int. Ed.* **2000**, *39*, 344; c) F. Meyer, P. Kircher, H. Pritzkow, *Chem. Commun.* **2003**, 774; d) G. C. Guo, T. C. W. Mak, *Angew. Chem. Int. Ed. Engl.* **1998**, *37*, 3286.
[7] a) M. A. S. Goher, J. Cano, Y. Journaux, M. A. M. Abu-Youssef, F. A. Mautner, A. Escuer, R. Vicente, *Chem. Eur. J.* **2000**, *6*, 778; b) G. S. Papaefstathiou, S. P. Perlepes, A. Escuer, R. Vicente, M. Font-Bardia, X. Solans, *Angew. Chem. Int. Ed.* **2001**, *40*, 884; c) A. Escuer, R. Vicente, M. A. S. Goher, F. A. Mautner, *Inorg. Chem.* **1998**, *37*, 782.
[8] a) M. A. M. Abu-Youssef, A. Escuer, D. Gatteschi, M. A. S. Goher, F. A. Mautner, R. Vicente, *Inorg. Chem.* **1999**, *38*, 5716; b) A. Escuer, R. Vicente, F. A. Mautner, M. A. S. Goher, M. A. M. Abu-Youssef, *Chem. Commun.* **2002**, 64; c) M. A. M.

 © 2006 Wiley-VCH Verlag GmbH & Co. KGaA, Weinheim 

Abu-Youssef, M. Drillon, A. Escuer, M. A. S. Goher, F. A. Mautner, R. Vicente, *Inorg. Chem.* **2000**, *39*, 5022.
[9] a) J. Cano, Y. Journaux, M. A. S. Goher, M. A. M. Abu-Youssef, F. A. Mautner, G. J. Reiß, A. Escuer, R. Vicente, *New J. Chem.* **2005**, *29*, 306; b) A. Escuer, F. A. Mautner, M. A. S. Goher, M. A. M. Abu-Youssef, R. Vicente, *Chem. Commun.* **2005**, 605; c) M. A. M. Abu-Youssef, A. Escuer, M. A. S. Goher, F. A. Mautner, G. J. Reiß, R. Vicente, *Angew. Chem. Int. Ed.* **2000**, *39*, 1624.
[10] a) M. A. M. Abu-Youssef, *J. Coord. Chem.* **2005**, *58*, 1377; b) M. A. M. Abu-Youssef, *Polyhedron* **2005**, *24*, 1829; c) F. A. Mautner, C. Gspan, K. Gatterer, M. A. S. Goher, M. A. M. Abu-Youssef, W. Sitte, E. Bucher, *Polyhedron* **2004**, *23*, 1217; d) M. A. S. Goher, A. E. H. Abdou, M. A. M. Abu-Youssef, F. A. Mautner, *Transition Met. Chem.* **2001**, *26*, 39; e) M. A. S. Goher, F. A. Mautner, M. A. M. Abu-Youssef, A. K. Hafez, A. M.-A. Badr, *J. Chem. Soc., Dalton Trans.* **2002**, 3309; f) M. A. S. Goher, A. K. Hafez, M. A. M. Abu-Youssef, A. M. A. Badr, C. Gspan, F. A. Mautner, *Polyhedron* **2004**, *23*, 2349.
[11] X. H. Bu, M. L. Tong, Y. B. Xie, J. R. Li, H. C. Chang, S. Kitagawa, J. Ribas, *Inorg. Chem.* **2005**, *44*, 9837.
[12] Z. F. Chen, P. Zhang, R. G. Xiong, D. J. Liu, X. Z. You, *Inorg. Chem. Commun.* **2002**, *5*, 35.
[13] G. De Munno, M. Julve, G. Viau, F. Lloret, J. Faus, D. Viterbo, *Angew. Chem. Int. Ed. Engl.* **1996**, *35*, 1807; R. Cortés, L. Lezama, J. L. Pizarro, M. I. Arriortua, T. Rojo, *Angew. Chem. Int. Ed. Engl.* **1996**, *35*, 1810.
[14] a) M. A. S. Goher, F. A. Mautner, A. Popitsch, *Polyhedron* **1993**, *12*, 2557; b) E. Q. Gao, Y. F. Yue, S. Q. Bai, Z. He, S. W. Zhang, C. H. Yan, *Chem. Mater.* **2004**, *16*, 1590.
[15] M. A. M. Abu Youssef, A. Escuer, M. A. S. Goher, F. A. Mautner, R. Vicente, *J. Chem. Soc., Dalton Trans.* **2000**, 413.
[16] M. E. Fisher, *Am. J. Phys.* **1964**, *32*, 343.
[17] R. Cortés, M. Drillon, X. Solans, L. Lezama, T. Rojo, *Inorg. Chem.* **1997**, *36*, 677.
[18] a) B. Ye, T. Mak, I. D. Williams, X. Li, *Chem. Commun.* **1997**, 1813; b) I. J. Kim, D. Y. Jung, *Inorg. Chem.* **2000**, *39*, 1470; c) I. J. Kim, E. W. Lee, D. Y. Jung, *Chem. Mater.* **2001**, *13*, 2684; C. Ma, C. Chen, Q. Liu, F. Chen, D. Liao, L. Li, L. Sun, *Eur. J. Inorg. Chem.* **2004**, *43*, 3316.
[19] *SMART & SAINT – Area Detector Control and Integration Software*, Siemens AXS, Madison, WI, USA, **1995**.
[20] G. M. Sheldrick, *SADABS – Program for Empirical Absorption Correction of Area Detectors* (Version 2.03), University of Göttingen, Germany, **2002**.
[21] *SHELXTL – Structure Determination Programs* (Version 6.10), Bruker AXS Inc., Madison, Wisconsin, USA, **2001**.
[22] K. Brandenburg, *Diamond – Visual Crystal Structure Information System* (Version 3.0e), Crystal Impact GbR, Bonn, Germany, **2005**.
[23] *ORTEP3* (Version 1.08): L. J. Farrugia, *J. Appl. Crystallogr.* **1997**, *30*, 565.

Received: December 7, 2005
Published Online: June 23, 2006

 © 2006 Wiley-VCH Verlag GmbH & Co. KGaA, Weinheim 

DOI: 10.1002/ejic.200600203

# Layered Double Hydroxides Containing Intercalated Zinc Sulfide Nanoparticles: Synthesis and Characterization

**Guoqing Wu,[a] Lianying Wang,[a] David G. Evans,[a] and Xue Duan*[a]**

**Keywords:** Layered compounds / Intercalations / Zinc complex / Organic–inorganic hybrid composites / ZnS nanoparticles

Nanosized ZnS has been synthesized in the interlayer galleries of Mg–Al layered double hydroxides (LDHs) by a process involving ion exchange of a $Mg_2Al$-$NO_3$ LDH precursor with a zinc–citrate complex $\{Na_2[Zn(C_6H_4O_7)]\cdot 3H_2O\}$ followed by reaction between the intercalated $[Zn(C_6H_4O_7)]^{2-}$ anions and $H_2S$. The materials have been characterized by elemental analysis, powder X-ray diffraction (XRD), transmission electron microscopy, FTIR spectroscopy, MAS $^{13}C$ NMR spectroscopy, and UV/Vis diffuse reflectance spectroscopy, and structural models have been proposed. The XRD diffraction patterns indicate that the layered structure is maintained and that the basal spacing in the intercalated materials depends on the orientation of the citrate moiety. The results confirm that cubic ZnS (sphalerite) is formed in the interlamellar domain rather than on the external surfaces and is co-intercalated with citrate dianions. The growth of ZnS particles is constrained by the layers of the LDH resulting in a large blue shift in the bandgap compared with the bulk material. The thermal decomposition process of the hybrid material has been characterized by in situ high-temperature powder XRD and thermogravimetry-differential thermal analysis (TG/DTA) coupled with mass spectrometry. The thermal stability of the zinc–citrate complex anions intercalated in LDHs is lower than that in the sodium salt. Thermal treatment below 270 °C leads to a reorientation of the citrate anions in the interlayer galleries associated with a significant interlayer contraction. No obvious changes in the XRD peaks corresponding to ZnS are apparent below 400 °C, indicating that sintering to form larger particles is successfully inhibited by the layered host; at higher temperatures the ZnS is oxidized with evolution of $SO_2$.

(© Wiley-VCH Verlag GmbH & Co. KGaA, 69451 Weinheim, Germany, 2006)

## Introduction

In recent years, semiconductor nanocrystals have attracted considerable attention because of their size- and shape-dependent optical and electronic properties as well as their potential for applications in nanodevices. ZnS is one of the most important II–VI semiconductors and has potential applications in numerous areas including optoelectronics,[1] photocatalysis,[2] and thin-film electroluminescent devices.[3] There have been many reports of attempts to control the size and morphology of ZnS including solvothermal routes,[4] thermal evaporation,[5] reverse micelle templates,[6] as well as intercalation in zeolites,[7] and mesoporous silica MCM-41.[8–10] Layered compounds have also been shown to be potential hosts: by virtue of confining the growth of nanoparticles inside the interlamellar galleries, the reaction zone is spatially constrained by the layers,[11–13] giving rise to conditions similar to those in two-dimensional nanoreactors such as Langmuir–Blodgett (LB) films and self-assembled monolayers.[14,15] One great advantage of such methods compared with lithographic fabrication is that regular nanoscale arrays of materials can be obtained with drastically reduced production costs.[16,17]

Layered double hydroxides (LDHs) are a family of lamellar solids that can be represented by the general formula $[M^{II}_{1-x}M^{III}_x(OH)_2]^{x+}A^{n-}_{x/n}\cdot mH_2O$. The structure of this class of compound, based on the stacking of positively charged layers with hydrated anions in the interlamellar domains, allows relatively high mobility of these anions.[18] It is possible to modulate their properties by changing the nature of the $M^{II}$ and $M^{III}$ cations, their molar ratio, and/or the size of the $A^{n-}$ anion.[19,20] One of the most important properties of such compounds is their high anion-exchange capacities. The lamellar structure and the anion-exchange properties of LDHs make them attractive for technological applications such as ion-exchangers, adsorbents, pharmaceutical stabilizers, and precursors of new catalytic materials.[21–23] There have been many examples of LDHs containing intercalated metal complex anions such as permanganate,[24,25] and coordination complexes.[26–30] In the case of metal oxide species, Suib et al.[24] have reported that manganese oxide species ($MnO_x$) can be prepared in LDH interlayer galleries by ion exchange followed by in situ post-treatment, whilst Lukashin et al.[31] have reported the synthesis of iron oxide nanoparticles with different morphologies and composition using an LDH as the template. However, synthesis of semiconductor nanoparticles using

[a] State Key Laboratory of Chemical Resource Engineering, Beijing University of Chemical Technology,
Box 98, 15 Beisanhuan Dong Lu, Beijing 100029, China
Fax: +86-1064425385
E-mail: duanx@mail.buct.edu.cn

 © 2006 Wiley-VCH Verlag GmbH & Co. KGaA, Weinheim 

LDHs as the host structure has not been extensively studied. Sato et al.[12,13] have reported that extremely small particles of CdS and CdS–ZnS mixtures less than 0.4 nm in thickness could be prepared by liquid–liquid reactions in the interlayers of LDH and their photocatalytic properties in respect of hydrogen evolution from $Na_2S$, $Na_2SO_3$, and/or 2-aminoethanol under irradiation by visible light have been studied. The interlayer distance of their proposed $[Cd(EDTA)]^{2-}$-intercalated LDH precursor is only 0.762 nm however, which is substantially lower than that subsequently reported for $[Ni(EDTA)]^{2-}$-intercalated LDHs.[26,32] Therefore, the $[Cd(EDTA)]^{2-}$ anions in the precursor, and hence presumably also the resulting CdS in the product, are located on the external surfaces of the LDH rather than in the interlayer galleries.

In this work, we report the synthesis of cubic ZnS (sphalerite) nanoparticles by gas–solid reaction in the confined interlayer gallery space of LDHs and the characterization of the resulting hybrid materials. An anionic zinc citrate complex $\{[Zn(Cit)]^{2-}\}$ [Cit = $C_6H_4O_7^{4-}$] is first intercalated into the LDH by ion exchange with a $Mg_2Al$-$NO_3$ LDH precursor, giving a material we denote LDH-Zn(Cit). Subsequent reaction with $H_2S$ at atmospheric pressure affords a material, denoted LDH-ZnS-$H_2$Cit, containing ZnS nanoparticles in the interlayer galleries of the LDH. Subsequent treatment of LDH-ZnS-$H_2$Cit with aqueous sodium carbonate solution gives a material, denoted LDH-$CO_3$-ZnS, containing interlayer carbonate anions and ZnS on the external surfaces of the crystallites. This method provides a simple approach for the synthesis of semiconductor particles in layered double hydroxide materials.

## Results and Discussion

The preparation of LDH-ZnS-$H_2$Cit involves four steps: preparation of $Na_2[Zn(Cit)]\cdot 3H_2O$, synthesis of an LDH-nitrate precursor, intercalation of $[Zn(Cit)]^{2-}$ by anion exchange, and, finally, reaction between $[Zn(Cit)]^{2-}$ and $H_2S$ in the interlayer galleries. The coordination chemistry of citrate is rather complex and a variety of mononuclear and polynuclear complexes have been structurally characterized.[33–37] Generally, trianionic $HCit^{3-}$ is the predominant form above pH 5.8, but it is possible to remove the proton from the hydroxy group to give a tetra-anionic $Cit^{4-}$ species at higher pH; the pH required is lowered considerably when the citrate is coordinated to a transition-metal cation. On the basis of elemental analysis (see Exp. Sect.), FTIR spectroscopy, and solid-state NMR spectroscopy (see below), it can be concluded that the tetra-anionic species was present in the zinc complex prepared under the reaction conditions employed in our work. Citrate coordination presumably involves the alkoxy group, the central carboxylate group, and one terminal carboxylate group with the octahedral coordination shell around zinc being completed by three water molecules. This is consistent with the results from both solution and structural studies of related complexes.[38,39]

### Elemental Analysis

Elemental compositions of the precursors and intercalated materials are given in the Experimental Section. The Mg/Al molar ratio in LDH-Zn(Cit) (2.00) and LDH-ZnS-$H_2$Cit (2.02) is essentially the same as that in the LDH-$NO_3$ precursor (2.03); the value is slightly lower in LDH-HCit (1.87), suggesting that part of the magnesium is leached from the layers during the synthesis of the LDH-HCit. This is commonly observed during ion-exchange reactions with LDHs.[20,21] Elemental analysis confirms that the nitrate anion in the LDH-$NO_3$ precursor is completely displaced during the exchange reactions with $[Zn(Cit)]^{2-}$ or $[HCit]^{3-}$, as no detectable amounts of nitrogen are present in either material. The data also suggest that the stoichiometry of the zinc citrate complex is unchanged after intercalation, although a small amount of carbonate anion is co-intercalated along with $[Zn(Cit)]^{2-}$. The analytical data for LDH-Zn(Cit) are consistent with the formula $[Mg_{0.69}Al_{0.33}(OH)_2][Zn(C_6H_4O_7)]_{0.16}(CO_3)_{0.01}\cdot 0.58\,H_2O$. In the case of the $[HCit]^{3-}$ intercalate, the data suggest a stoichiometry $[Mg_{0.65}Al_{0.35}(OH)_2](C_6H_5O_7)_{0.11}(CO_3)_{0.01}\cdot 0.57\,H_2O$.

When solid LDH-Zn(Cit) is reacted with gaseous $H_2S$ for 5 min, 20 min, and 1 h, the measured S/Zn molar ratio is 0.34, 0.55, and 0.70 respectively. The deviation of the S/Zn ratio from 1:1 implies that the reaction between $Zn^{2+}$ and $H_2S$ is not fully complete. However, when the reaction time was extended to 8 h, the observed S/Zn molar ratio in the resulting sample (LDH-ZnS-$H_2$Cit) was 0.96, close to the ideal value of unity. The analytical data for LDH-ZnS-$H_2$Cit are consistent with the formula $[Mg_{0.67}Al_{0.33}(OH)_2][ZnS]_{0.16}(C_6H_6O_7)_{0.16}(CO_3)_{0.01}\cdot 0.70\,H_2O$.

### X-ray Diffraction

The XRD patterns of the LDH materials are shown in Figure 1. The patterns are typical of lamellar materials, with a basal reflection and associated harmonics at low angle $2\theta$ and weaker nonbasal reflections at a higher angle. The reflections for LDHs are generally indexed in a three-layer 3R polytype with rhombohedral symmetry (space group $R\bar{3}m$), based on the structure of the mineral hydrotalcite.[40] In this case, the unit cell $c$-parameter corresponds to three times the basal spacing $d(003)$ and the value of the unit cell $a$-parameter is calculated from the position of the $d(110)$ reflection near 60° $2\theta$. The values of the cell parameters and basal spacing ($d_{obs}$) in the LDH materials are compared in Table 1. The XRD pattern of LDH-$NO_3$ shows a basal reflection at 0.867 nm, which is similar to that reported in the literature[41,42] for LDHs with Mg/Al of about 2. Intercalation of $HCit^{3-}$ leads to an increase in basal spacing to 1.15 nm, which is also comparable to the values in the literature.[43] The values of the basal spacing in LDH-Zn(Cit) and LDH-ZnS-$H_2$Cit are very similar to each other (1.21–1.22 nm) and slightly larger than that in LDH-HCit, which may indicate a different orientation of the citrate moiety within the interlayer galleries. The values of the unit cell $a$-parameter are very similar for LDH-$NO_3$,

 © 2006 Wiley-VCH Verlag GmbH & Co. KGaA, Weinheim 

LDH-Zn(Cit), LDH-ZnS-$H_2$Cit, and LDH-$CO_3$-ZnS, with a slightly smaller value being observed for LDH-HCit. The value of *a* corresponds to the average distance between metal ions in the layers and as the Shannon crystal radius of $Al^{3+}$ is smaller than that of $Mg^{2+}$, a decrease in Mg/Al ratio should lead to a lower value of *a*; the XRD data are therefore consistent with the analytical data described above.

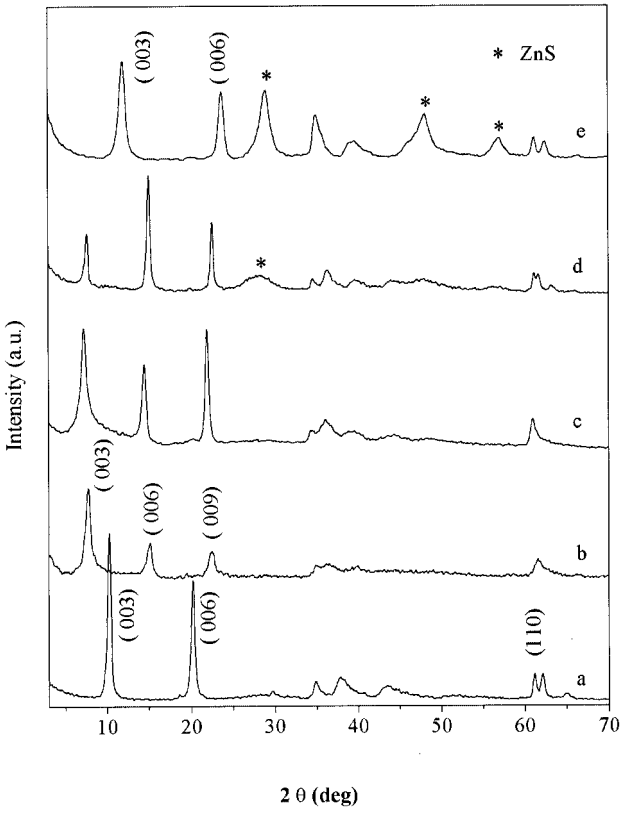


Figure 1. Powder X-ray diffraction patterns of (a) LDH-$NO_3$, (b) LDH-HCit, (c) LDH-Zn(Cit), (d) LDH-ZnS-$H_2$Cit, and (e) LDH-$CO_3$-ZnS.

Table 1. Values of unit cell parameters *a* and *c* and basal spacing *d*(003) for the LDH materials.

| Sample | *a* [nm] | *c* [nm] | *d*(003) [nm] |
|---|---|---|---|
| LDH-$NO_3$ | 0.303 | 2.601 | 0.867 |
| LDH-Zn(Cit) | 0.304 | 3.651 | 1.217 |
| LDH-ZnS-$H_2$Cit | 0.304 | 3.633 | 1.211 |
| LDH-HCit | 0.301 | 3.441 | 1.147 |
| LDH-$CO_3$-ZnS | 0.303 | 2.235 | 0.745 |

Figure 1 shows the XRD patterns of the LDH-Zn(Cit) precursor and the materials obtained after exposure to $H_2S$ for 8 hours. Although the positions of the (00*l*) (*l* = 3, 6, 9) reflections of LDH-Zn(Cit) and LDH-ZnS-$H_2$Cit are almost identical, as noted above, there is a significant variation in the relative intensities of the peaks, suggesting that structural changes have occurred within the interlayer galleries. When the interlayer anions in LDHs do not contain any atoms with large scattering power, intensities of the basal (00*l*) reflections are mainly governed by the X-ray intensity scattered by metal cations in the host layers and the intensities generally decrease as *l* increases, as is observed in Figure 1 for LDH-$NO_3$, LDH-HCit, and LDH-$CO_3$-ZnS. If the interlayer contains a transition-metal complex anion as the guest, the intensity of the (006) reflection is generally greater than that of (003), which has been attributed to an increased electron density at the midpoint of the interlayers, where the metal is presumed to be located. Reported examples include chromate or vanadate anions intercalated in [Mg–Al] LDHs,[44,45] $[MO_2]^{2-}$ (M = Co, Cu) and $[MOx_3]^{3-}$ (M = Cr, Mn, Ga) (Ox = oxalato) anions in [Zn–Al] and [Mg–Al] LDHs,[29,35] and hexachloro/hydroxoplatinum(IV) anions in [Zn–Al], [Mg–Al], and [Cu–Al] LDHs.[46] It has been reported that 1,1′-ferrocenedicarboxylate and ferrocenecarboxylate anions can be intercalated in [Zn–Al] LDHs giving materials with basal spacings of 1.55 and 2.00 nm respectively.[47] On the basis of modeling studies, these values were interpreted in terms of a monolayer and bilayer of guest species respectively. In the former case, the iron atom is located at the midpoint of the interlayer galleries and, consistent with this picture, the intensity of the (006) reflection is larger than that of (003) and (009). In the bilayer arrangement, alternate iron atoms are shifted along the *c* axis above and below the midpoint of the interlayer galleries, and in this case the intensity of the (009) reflection is larger than that of (006). In the case of LDH-Zn(Cit) (Figure 1, c), the intensity of the (009) reflection is also greater than that of (006), suggesting a similar displacement of the zinc atoms along the *c* axis. On treatment with $H_2S$, the intensity of the (006) reflection increases, with a concomitant decrease in the relative intensity of the (009) reflection. This indicates that reaction with $H_2S$ involves a change in the one-dimensional electron density distribution alone the *c* axis, which can be ascribed to the migration of the zinc atoms to the midpoint of the interlayer galleries and incorporation of sulfur.

In the case of LDH-ZnS-$H_2$Cit, a weak broad diffraction peak centered around $2\theta = 28°$ is apparent, which corresponds to the (111) lattice planes of cubic ZnS (sphalerite, JCPDS Card 5-566). The broadness of the peak is indicative of very small nanoparticles; using the Scherrer formula,[48] an average particle diameter of about $2.0 \pm 0.2$ nm in the direction perpendicular to the (111) lattice planes can be estimated.

It is well known that LDHs have a very strong affinity for carbonate anions. After treatment of LDH-ZnS-$H_2$Cit with an aqueous solution of sodium carbonate, the resulting solid has a basal spacing of 0.745 nm, which agrees with that reported in the literature for $Mg_2Al$-$CO_3$ LDH.[41,49] This indicates that the citrate ions have been displaced by carbonate from the interlayer galleries. Furthermore, the XRD pattern of the resulting material LDH-$CO_3$-ZnS (Figure 1, e) shows a series of strong and sharp diffraction peaks corresponding to cubic ZnS. This indicates the ZnS nanoparticles have also been liberated from the interlayer galleries by treatment with carbonate anions and, free of the constraint imposed by the layers, grow into larger crys-

 © 2006 Wiley-VCH Verlag GmbH & Co. KGaA, Weinheim 

tallites on the external surfaces of the LDH. An average particle diameter of about 6.0 nm can be estimated according to the Scherrer formula.[48]

### Transmission Electron Microscopy

The transmission electron microscopy (TEM) images of LDH-ZnS-$H_2$Cit and LDH-$CO_3$-ZnS are shown in Figure 2. The diameter and shape of the LDH-$CO_3$-ZnS particles are essentially identical to those of the LDH-ZnS-$H_2$Cit, which indicates that the extraction of ZnS from the interlamellar galleries does not lead to the destruction of the lamellar structure (see parts a and b in Figure 2). Even at higher magnification (Figure 2, c), there is no obvious indication of the presence of ZnS nanoparticles on the external surfaces of LDH-ZnS-$H_2$Cit. It is difficult to confirm directly the presence of ZnS in the galleries of the LDHs by the TEM method however; this is probably a result of the weak contrast between the LDH frameworks and the nanosized ZnS, as is the case for ZnS and $Fe_2O_3$ inside mesoporous hosts.[8,50] In the case of LDH-$CO_3$-ZnS however, as shown in Figure 2 (d), many ZnS crystallites of about 6.0 nm are observed on the external surfaces. The particle sizes are in agreement with those estimated from the XRD data. The above results show that the small ZnS nanoparticles can only grow in the two-dimensional gallery spaces, where they experience the confinement effect of the layers.

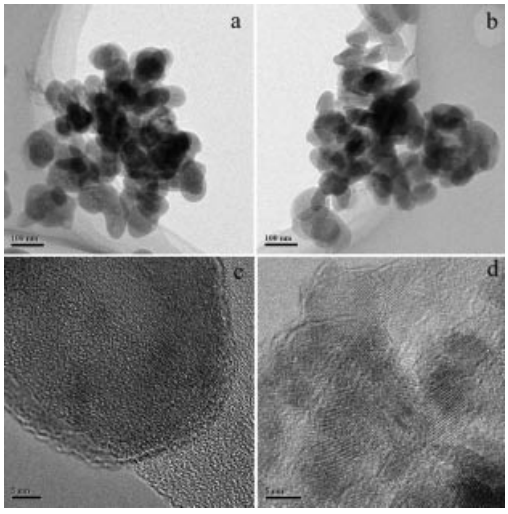


Figure 2. Transmission electron microscopy images of (a) LDH-ZnS-$H_2$Cit, (b) LDH-$CO_3$-ZnS at low magnification, (c) LDH-ZnS-$H_2$Cit, and (d) LDH-$CO_3$-ZnS at high magnification.

### FTIR Spectroscopy

FTIR spectroscopy is very helpful in the study of LDHs, especially those containing interlayer organic anions (or anions with organic moieties), as it is very sensitive to the symmetry of the organic anion and to the interactions of the anion with its environment such as hydrogen bonding and coordinate bonding.[28,39,45,51,52] The FTIR spectra of the $Na_2$[Zn(Cit)]·3$H_2O$ and $Mg_2$Al-$NO_3$ LDH precursors together with those of LDH-Zn(Cit) and LDH-ZnS-$H_2$Cit are illustrated in Figure 3. For the LDH nitrate precursor (Figure 3, a), the intense and broad absorption band centered at 3445 $cm^{-1}$ corresponds to the stretching vibrations of the hydroxy groups of both the layer hydroxide moieties and interlayer water. The broadening of this band is due to hydrogen-bond formation.[53] The band close to 1640 $cm^{-1}$ corresponds to the deformation mode ($\delta H_2O$) of water molecules. The absorption peaks at 1384 and 839 $cm^{-1}$ are usually assigned to the $v_3$ and $v_2$ vibration modes, respectively, of $NO_3^-$ with $D_{3h}$ symmetry[42,46] whilst bands around 447 and 675 $cm^{-1}$ are due to Al–O and Mg–O lattice vibrations respectively.[23] The slight broadening of the 1384 $cm^{-1}$ peak and the relatively low wavenumber for the $v_2$ mode (at 827 $cm^{-1}$) are indicative of an interaction of $NO_3^-$ anions with their surroundings,[54] namely with intercalated water, hydroxy groups, and metal cations in the brucite-type layers.

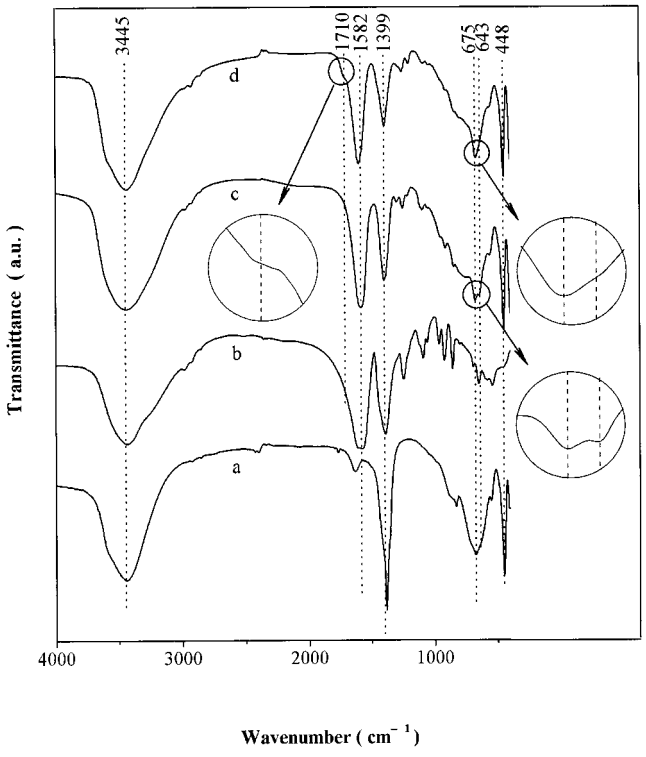


Figure 3. FTIR spectra of (a) LDH-$NO_3$, (b) $Na_2$[Zn(Cit)]·3$H_2O$, (c) LDH-Zn(Cit), and (d) LDH-ZnS-$H_2$Cit.

The FTIR spectra of the $Na_2$[Zn(Cit)]·3$H_2O$ precursor (Figure 3, b) exhibits strong characteristic absorptions of the carboxylate group of the citrate ligands in the asymmetric and symmetric vibration regions. Specifically, $v_{as}$(COO) vibrations appear at 1604 (shoulder) and 1576 $cm^{-1}$ and $v_s$(COO) vibrations are observed at 1436 (shoulder) and 1393 $cm^{-1}$. These assignments are in good agreement with those in $K_4$[$MoO_3$(Cit)]·3$H_2O$,[39] which has been structurally characterized and shown to have the same citrate coordination geometry about the metal as that proposed above for $Na_2$[Zn(Cit)]·3$H_2O$. The asymmetric $v_{as}$(COO) and

 © 2006 Wiley-VCH Verlag GmbH & Co. KGaA, Weinheim 

symmetric $\nu_s$(COO) stretching modes in the complexes are shifted to lower frequencies compared to those of free citrate, denoting the changes in the environment of the ligand upon complexation to metals. The wavenumber difference $\Delta\nu = \nu_{as} - \nu_s$ gives information about the coordination environment of the carboxylate group.[51,55] The value of $\Delta\nu$ for $Na_2[Zn(Cit)]\cdot 3H_2O$ is 183 $cm^{-1}$, indicating that the carboxylate groups are either free or coordinated to the metal in a monodentate fashion, rather than in bridging or bidentate modes. This is consistent with the structure proposed above for $Na_2[Zn(Cit)]\cdot 3H_2O$.

After exchange of $Mg_2Al\text{-}NO_3$ LDH with $Na_2[Zn(Cit)]\cdot 3H_2O$, the $\nu_3$ vibration of $NO_3^-$ disappears, and the asymmetric $\nu_{as}$(COO) and symmetric $\nu_s$(COO) stretching modes of the carboxylate groups, at 1582 and 1399 $cm^{-1}$ respectively, appear (Figure 3, c). The value of $\Delta\nu$ for LDH-Zn(Cit) (189 $cm^{-1}$) is similar to that in $Na_2[Zn(Cit)]\cdot 3H_2O$, indicating that the coordination mode of the carboxylate groups is unchanged after intercalation. The slight difference in the value of $\Delta\nu$ may be a reflection of the different intermolecular hydrogen-bonding environments experienced by the anion in the sodium salt and in the interlayer galleries of the LDH.[55–57]

After LDH-Zn(Cit) is exposed to $H_2S$, the IR spectrum of the resulting material shows a number of changes. The asymmetric $\nu_{as}$(COO) stretching mode shows a shift to 1596 $cm^{-1}$, comparable to the value for LDH-HCit (1593 $cm^{-1}$, spectrum not shown). Furthermore, the band at 643 $cm^{-1}$ (see inset of part c in Figure 3) due to the Zn–O vibration mode[23,47] is no longer detected, and an additional IR absorption band at around 1710 $cm^{-1}$, assigned to the free COOH vibration mode,[34,58,59] appears (see part d in Figure 3, inset), suggesting that (at least) one of the carboxylate groups has been protonated. In $K_4[(MoO_2)_2O(HCit)_2]\cdot 4H_2O$, where the central carboxylate group is protonated, the free COOH vibration mode is observed[39] at around 1715 $cm^{-1}$. These data all indicate that reaction of intercalated $[Zn(Cit)]^{2-}$ with $H_2S$ leads to cleavage of the Zn–O coordinate bonds in the complex, consistent with the formation of ZnS in the interlayers, according to Equations (1) and (2).

$$H_2S\ (gas) + H_2O\ (interlayer\ water) \rightarrow H_3O^+ + HS^- \quad (1)$$

$$[Zn(Cit)]^{2-} + HS^- + H_3O^+ \rightarrow ZnS + H_2Cit^{2-} + H_2O \quad (2)$$

### Solid-State NMR Spectroscopy

Figure 4 shows the solid-state MAS $^{13}C$ NMR spectra of $Na_2[Zn(C_6H_4O_7)]\cdot 3H_2O$, LDH-Zn(Cit), and LDH-ZnS-$H_2$Cit. In the spectrum of $Na_2[Zn(C_6H_4O_7)]\cdot 3H_2O$ there are resonances at $\delta$ = 184.4 and 181.4 due to the carboxyl groups, and in addition there are two signals of lower frequency at $\delta$ = 76.3 due to the alkoxy carbon and at $\delta$ = 47.9 due to the methylene carbons. The close correspondence between the MAS $^{13}C$ NMR spectra of $Na_2[Zn(C_6H_4O_7)]\cdot 3H_2O$ and LDH-Zn(Cit) indicates that the coordination mode of $[Zn(C_6H_4O_7)]^{2-}$ is preserved in LDH-Zn(Cit). In comparison with LDH-Zn(Cit), the corresponding $^{13}C$ NMR resonances for LDH-ZnS-$H_2$Cit are all shifted to high field. In particular, the α-carboxyl carbon and β-carboxyl carbon signals show large shifts of $\Delta\delta$ 7.0 and 6.7 ppm, which is a clear indication[39] of the loss of coordination of carboxyl groups to the zinc(II) cation. MAS $^{13}C$ NMR spectroscopy is unable to confirm whether the central C–O group of the citrate anion is coordinated to the zinc cation as an alcohol or alkoxide group however. Zhou et al.[39] have reported the solid-state NMR spectra of structurally characterized oxomolybdenum(VI) citrate complexes, concluding that the coordination of a deprotonated alkoxide group to molybdenum is characterized by a downfield shift in the $^{13}C$ resonance to 82–84 ppm compared with that for $KH_3Cit$ ions ($\delta$ =74 ppm). It has been reported however[60,61] that the solid-state NMR spectrum of a structurally characterized gallium citrate complex with a deprotonated alkoxide group coordinated to gallium has a peak at $\delta$ = 76 ppm. This latter value is very close to those reported for the chemical shifts (73–75 ppm) of a C–OH group in citrate coordinated to cadmium in the solid-state NMR spectra of structurally characterized $Cd^{II}$ complexes.[62] The small difference in chemical shift $\Delta\delta$ between LDH-Zn(Cit) ($\delta$ = 76.6 ppm) and LDH-ZnS-$H_2$Cit ($\delta$ = 74.6 ppm) is consistent with the presence of coordinated citrate in the former and free citrate in the latter, although whether the coordination mode in the former involves (C–O–Zn) or [C–O(H)–Zn] linkages cannot be determined. It is noteworthy that the $^{13}C$ NMR spectrum of LDH-ZnS-$H_2$Cit is similar to that of the free anion $KH_3Cit$ {$^{13}C$ NMR ($D_2O$): $\delta$ = 177.6 [$(CO_2)_\alpha$], 174.0 [$(CO_2)_\beta$], 73.6 (≡CO), 43.0 (=$CH_2$)},[39] which is consistent with the IR data.

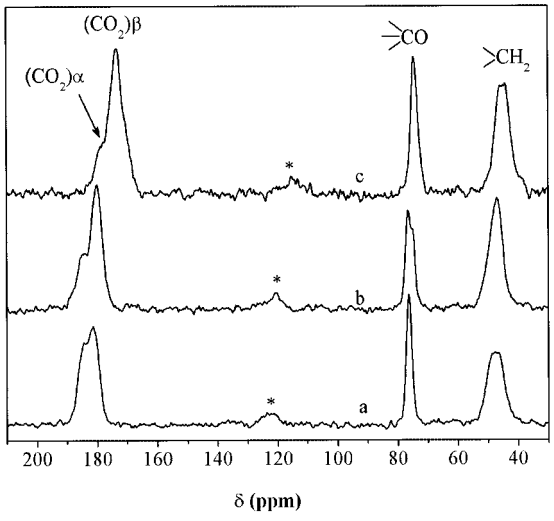


Figure 4. Solid-state $^{13}C$ MAS NMR spectra of (a) $Na_2[Zn(Cit)]\cdot 3H_2O$, (b) LDH-Zn(Cit), and (c) LDH-ZnS-$H_2$Cit; spinning sidebands are indicated with an asterisk. α, central carboxylate; β, terminal carboxylate.

 © 2006 Wiley-VCH Verlag GmbH & Co. KGaA, Weinheim 

### Optical Properties of the ZnS Nanoparticles

UV/Vis diffuse reflectance spectroscopy was used to investigate the optical properties of the ZnS nanoparticles. As shown in Figure 5, the LDH-Zn(Cit) precursor has negligible absorption above 250 nm, whereas, in contrast, both LDH-ZnS-$H_2$Cit and LDH-$CO_3$-ZnS have significant absorption in the range 250–350 nm, consistent with the presence of ZnS. In comparison with that of bulk ZnS, the absorption onset of LDH-ZnS-$H_2$Cit shows a blue shift of about 50 nm, whereas the absorption edge of LDH-$CO_3$-ZnS shows a smaller blue-shift of about 25 nm. The blue shift in UV/Vis spectra, indicating an increase in the bandgap of the material, is associated with a decrease in the particle size, characteristic of the so-called quantum size effects.[63] The smaller blue shift of LDH-$CO_3$-ZnS relative to that of LDH-ZnS-$H_2$Cit implies that the former contains larger ZnS particles,[14,64] which is consistent with the XRD data discussed above. The absorption onset for the ZnS nanoparticles is followed by a peak generally referred to as the excitonic peak. The excitonic peak position of the as-prepared ZnS particles in LDH-ZnS-$H_2$Cit is at 276 nm, corresponding to a bandgap of 4.52 eV, which is some 0.87 eV higher than that in bulk ZnS (3.65 eV).[65] The diameter of the ZnS particles in LDH-ZnS-$H_2$Cit, as calculated by the Wang equation,[4,63] is about 2.0 nm, which is comparable to the value estimated from XRD (2.0 ± 0.2 nm) as noted above.

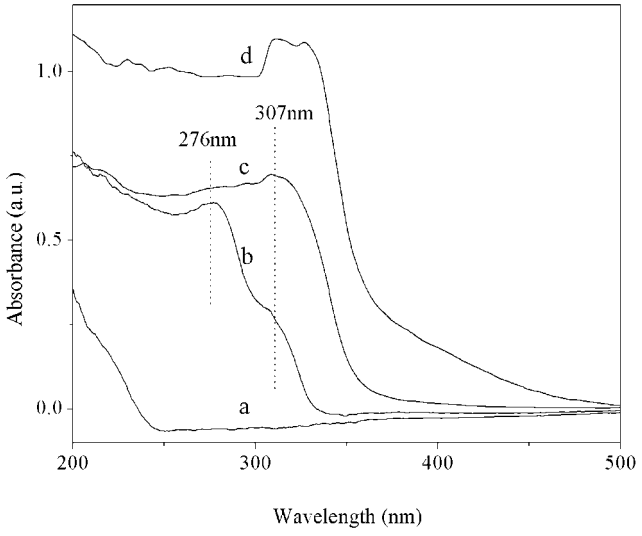


Figure 5. UV absorption spectra of (a) LDH-Zn(Cit), (b) LDH-ZnS-$H_2$Cit, (c) LDH-$CO_3$-ZnS, and (d) bulk ZnS (with particles diameter above 1 mm).

The presence of the shoulder (307 nm) on the long wavelength side of the excitonic peak in LDH-ZnS-$H_2$Cit may be an indication of an anisotropic disk or plate-like morphology of the ZnS particles induced by their confinement in the interlayer galleries. Li et al.[66] have prepared ZnS/octylamine hybrid nanosheets that show two such absorption features, and a similar phenomenon has been observed for CdS nanoparticles in LB films.[14] Alternatively, a high wavelength shoulder may be caused by a large concentration of defect sites (vacancies and interstitial anions).[67,68] Li et al.[69] reported that ZnS nanoparticles with <3 nm average diameter have two absorption features, concluding that the weak shoulder that appeared at 320 nm was caused by sulfur vacancy defects. Similar features have been observed and discussed in the literature for ZnS nanoparticles.[70,71] The spectra of our ZnS nanoparticles thus suggest that the organic component present in the sample may interact with the ZnS particles. The interface induced by the interaction between the ZnS clusters and the organic component in LDH-ZnS-$H_2$Cit may possess a large number of sulfur vacancy defects, which is consistent with the results of chemical analysis of the S/Zn ratio. Therefore, the optical properties of our ZnS nanoparticles may be similarly influenced by the presence of sulfur vacancy defects.

### Structural Model of the Intercalated Materials

All of the experimental results given above indicate that the $[Zn(Cit)]^{2-}$ anion is intercalated in the interlayer galleries and that ZnS nanoparticles are synthesized in situ by reaction with $H_2S$. If the thickness of the LDH layer ($T_{Layer}$ = 0.21 nm) and the hydrogen-bonding space between the layers and anions ($2L_H$ = 0.27 nm) are subtracted[72] from the observed basal spacing of LDH-Zn(Cit) (see Table 1), the gallery height is calculated to be 0.74 nm. As the estimated length[73] of the $[Zn(Cit)]^{2-}$ anion (with three $H_2O$ molecules) is about 0.79 nm, its long axis is probably oriented perpendicular to the layers (Figure 6, a) with the pendant carboxylate group of adjacent anions hydrogen-bonded to opposite layers. This locates the Zn atoms away from the center of the interlayer galleries, consistent with the relative intensities of the XRD reflections discussed

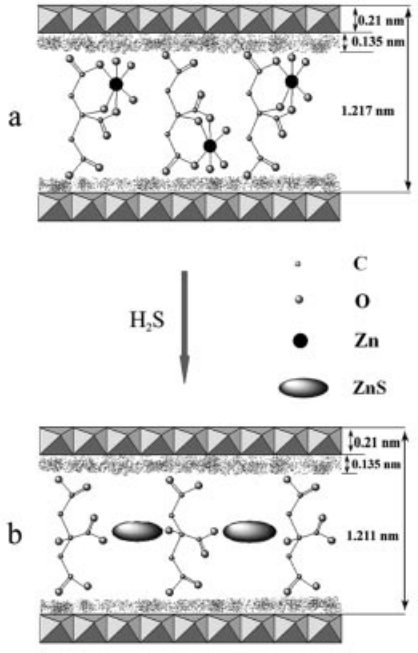


Figure 6. Schematic illustration of the structures of (a) LDH-Zn(Cit) and (b) LDH-ZnS-$H_2$Cit.

 © 2006 Wiley-VCH Verlag GmbH & Co. KGaA, Weinheim 

above [$I(009) > I(006)$]. On reaction with $H_2S$, a change in the one-dimensional electron-density distribution alone the *c* axis occurs, consistent with the formation of ZnS nanoparticles in the center of the interlayer galleries, along with co-intercalated $H_2Cit^{2-}$ anions, as shown schematically in part b of Figure 6.

As discussed above, on the basis of XRD and UV/Vis spectroscopic data, the estimated diameter of the ZnS particles is about 2.0 nm. As the gallery height in LDH-ZnS-$H_2$Cit is only 0.73 nm, this implies that the particles have a disc- or plate-like morphology. A similar observation has been reported in the literature[14,15,58,74,75] for semiconductor nanoparticles formed in the layers within LB films, where the particles adopt a disc-like morphology as result of the constraints imposed by the two-dimensional nanoreactors.

## Thermal Behavior of the Materials

### *In Situ Variable Temperature XRD Study of LDH-Zn(Cit) and LDH-Zns-$H_2$Cit*

The in situ variable temperature powder X-ray diffraction patterns of LDH-Zn(Cit) and LDH-ZnS-$H_2$Cit in the temperature range 30–900 °C are shown in Figure 7 and Figure 8 respectively. In each case, as the temperature is increased above ambient, the basal reflections move to higher angles, indicating a contraction in interlayer spacing. The magnitudes of the contraction observed on heating the two samples are very different however. The value of the basal spacing of LDH-Zn(Cit) decreases from 1.217 nm at 30 °C to 1.148 nm at 240 °C. The observed contraction of 0.069 nm can be interpreted in terms of the destruction of the hydrogen-bonding space as a result of removal of interlayer water molecules and the loss of coordinated water molecules from the complex anion (TG measurements on the $Na_2[Zn(C_6H_4O_7)]\cdot 3H_2O$ precursor show that it becomes completely dehydrated below 150 °C). It is worth mentioning that the inversion of intensity between the (006) peak and (009) peak in LDH-Zn(Cit) disappears on heating from 30 °C to 150 °C. This probably results from a disorder in the arrangement of the guests associated with the loss of water molecules from the hydrogen-bonded framework in the interlayer galleries, as water molecules play an important role in preserving interlayer order.[28,41] On further heating above 270 °C, the layer structure collapses completely, indicative of decomposition of the $[Zn(Cit)]^{2-}$ complex and dehydroxylation of the layers. At 400 °C, reflections characteristic of a cubic MgO-like phase begin to appear as a result of decomposition of the layers and at 900 °C reflections from a $MgAl_2O_4$ spinel phase and MgO are present, as is generally observed for calcined [Mg–Al] LDHs.[49,76] In addition, peaks that can be assigned to ZnO (JCPDS Card 01-1136), resulting from the decomposition of $[Zn(Cit)]^{2-}$, can be observed.

In comparison with LDH-Zn(Cit), the value of the basal spacing of LDH-ZnS-$H_2$Cit shows a much larger contraction of about 0.25 nm on heating from ambient temperature

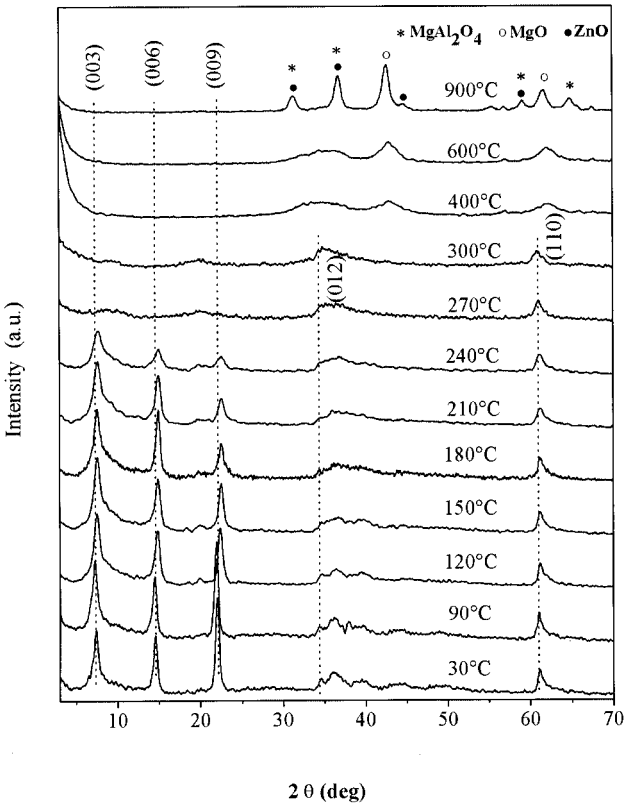


Figure 7. In situ powder X-ray diffraction patterns of LDH-Zn(Cit) in the temperature range 30–900 °C.

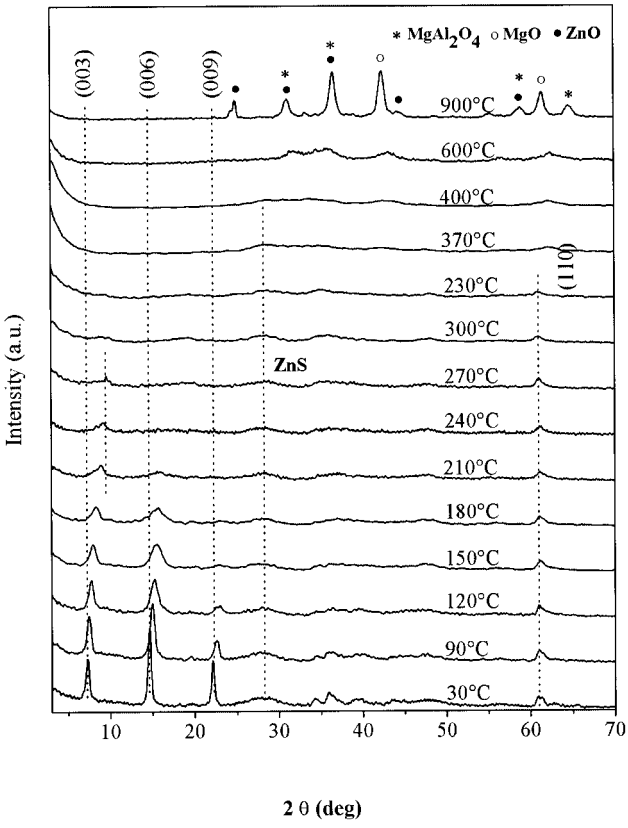


Figure 8. In situ powder X-ray diffraction patterns of LDH-ZnS-$H_2$Cit in the temperature range 30–900 °C.

 © 2006 Wiley-VCH Verlag GmbH & Co. KGaA, Weinheim 

to 240 °C, as shown in Figure 8. At 240 °C, evolution of $CO_2$ is not observed in the MS curve for LDH-ZnS-$H_2$Cit (see below), implying that decomposition of the intercalated citrate anions does not occur at this temperature. The significant decrease in basal spacing therefore probably results from a reorientation of the free citrate anions from being essentially perpendicular to the layers to being parallel to the layers; a similar phenomenon has been observed for tartrate anions intercalated in LDHs.[77] At 900 °C, peaks attributed to MgO, $MgAl_2O_4$, and ZnO appear, as for LDH-Zn(Cit).

It is noteworthy that the width of the broad diffraction peak centered around $2\theta = 28°$ corresponding to ZnS is essentially unchanged on heating from 30 to 240 °C, implying that there is no growth in particle size with increasing temperature. This provides further evidence that the ZnS nanoparticles are formed in the interlayer galleries rather on the external surfaces of the LDH, as in the latter case considerable sintering would be expected.[8] At 400 °C, the broad diffraction peak of ZnS is no longer observed, which is in agreement with the evolution of $SO_2$ observed in the MS data for LDH-ZnS-$H_2$Cit at a similar temperature (see below).

### *TG/DTA Analysis Coupled with Mass Spectrometry*

The results of the thermal analysis of the materials are presented in Figure 9, Figure 10, and Figure 11. Generally, four steps are observed in the thermal evolution of LDHs: desorption of physically adsorbed water, removal of the interlayer structural water, dehydroxylation of the brucite-like sheets, and the decomposition of the interlayer anions, although the first two steps may overlap in the temperature range 30–200 °C and the latter two steps may also overlap at higher temperatures.

For the complex $Na_2[Zn(C_6H_4O_7)]\cdot 3H_2O$ (Figure 9), the thermal decomposition clearly consists of three distinct steps. The first one (30–300 °C, 14.8% mass loss) corresponds to the removal of coordinated water. The sharp mass loss observed in the range 300–400 °C (21.1% mass loss) is due to combustion of the organic ligand, with a corresponding sharp endothermic peak ($T_m$ = 377 °C) in the DTA curve (Figure 9, a). There is a third sharp mass loss step in the range 400–600 °C (10.1% mass loss), with a corresponding strong endothermic peak ($T_m$ = 524 °C) in the DTA curve. Mass spectrometric analysis (Figure 9, b) shows that the first endothermic peak is associated with evolution of both water and carbon dioxide (*m/e* 44, $CO_2^+$), whilst the second endothermic process involves liberation of $CO_2$ alone. On this basis $Na_2[Zn(C_6H_4O_7)]\cdot 3H_2O$ decomposes on heating in air by three steps, as in Equations (3), (4), and (5).

$$Na_2[Zn(C_6H_4O_7)]\cdot 3H_2O \rightarrow Na_2Zn(C_6H_4O_7) + 3\ H_2O \quad (3)$$

$$Na_2Zn(C_6H_4O_7) + 9\ O_2 \rightarrow Na_2CO_3 + ZnCO_3 + 2\ H_2O + 4\ CO_2 \quad (4)$$

$$ZnCO_3 \rightarrow ZnO + CO_2 \quad (5)$$

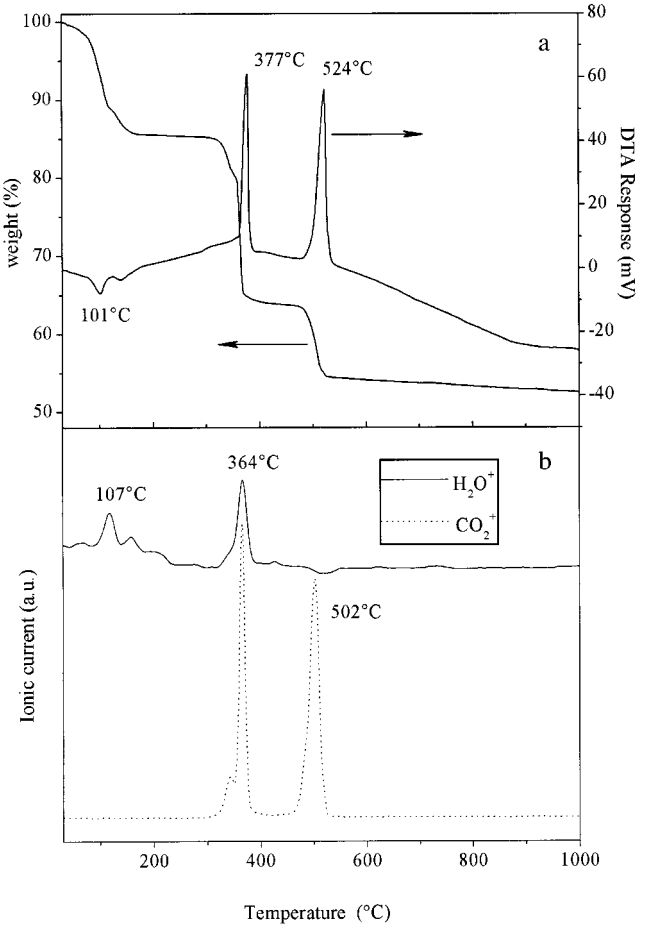


Figure 9. TG/DTA curve (a) and coupled with mass spectrometry curve (b) of $Na_2[Zn(Cit)]\cdot 3H_2O$.

The thermal decomposition of LDH-Zn(Cit) is characterized by three mass loss steps (Figure 10, a). The reduction in mass between 30 and 200 °C ($T_m$ = 120 °C, 9.9% mass loss) is due to loss of surface adsorbed and interlayer water resulting in the decrease in interlayer spacing observed in Figure 7. The latter two mass loss steps overlap to some extent (total weight loss of 37.7%) and are accompanied by exothermic peaks in the DTA at 319 and 417 °C (Figure 10, a). These two exothermic peaks occur some 58 and 107 °C below the temperatures of the corresponding DTA peaks for $Na_2[Zn(C_6H_4O_7)]\cdot 3H_2O$. Typically, the thermal stability of a complex anion intercalated in LDHs is higher than that of the precursor salt.[41] However, the opposite has been reported in the literature,[78,79] as is the case here. Although intercalation of the anion gives rise to a hydrogen-bonding interaction between the pendant terminal $COO^-$ group of the citrate ligand and the layer hydroxy groups, the strongly hydrogen-bonded network of hydrated cations and anions in the precursor salt, clearly demonstrated in the single-crystal structure of $Cu_2(C_6H_4O_7)\cdot 3H_2O$,[33] is lost on intercalation and this may be the origin of the greater thermal stability of the precursor salt. The MS trace (Figure 10, b) shows that both water and carbon dioxide are evolved simultaneously over the entire

 © 2006 Wiley-VCH Verlag GmbH & Co. KGaA, Weinheim 

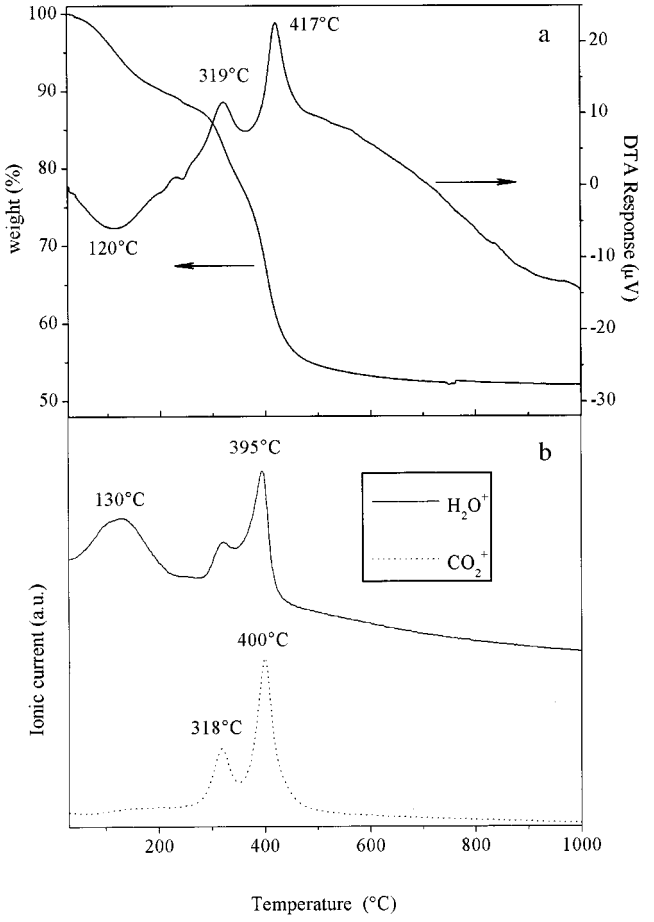


Figure 10. TG/DTA curve (a) and coupled with mass spectrometry curve (b) of LDH-Zn(Cit).

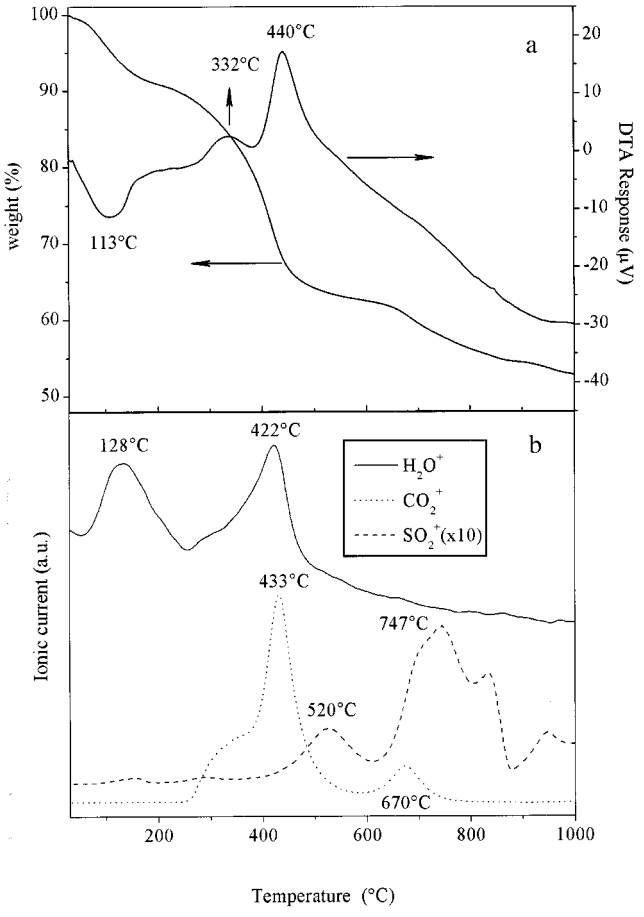


Figure 11. TG/DTA curve (a) and coupled with mass spectrometry curve (b) of LDH-ZnS-$H_2$Cit.

decomposition range, rather than in discrete steps as seen for $Na_2[Zn(C_6H_4O_7)]\cdot 3H_2O$ (Figure 9, b).

The TG trace for LDH-ZnS-$H_2$Cit (Figure 11, a) shows also three mass loss events. The first step, corresponding to the removal of surface adsorbed and interlayer water, extends from room temperature to approximately 240 °C ($T_m$ = 113 °C, 10.8% mass loss). The second step (240–540 °C, 25.9% mass loss), with two corresponding exothermic maxima at 332 and 440 °C in the DTA curve, can be assigned to partial decomposition of the citrate ligands and the dehydroxylation of the hydroxide layers. The MS trace (Figure 11, b) shows evolution of both carbon dioxide and water during this process. During the final step (540–950 °C 16.2% mass loss), a gradual weight loss is observed and the MS trace shows that both $SO_2$ (*m*/*e* 64, $SO_2^+$) and $CO_2$ are evolved. The former presumably arises from oxidation of ZnS according to Equation (5) [see Equation (6)]

$$2\ ZnS + 3\ O_2 \rightarrow 2\ ZnO + 2\ SO_2 \quad (6)$$

and is consistent with the absence of the peak assigned to ZnS from the X-ray diffraction patterns recorded above 400 °C. The $CO_2$ arises from oxidation of residual organic material and as all organic material is lost below 550 °C

Table 2. Results and interpretation of thermogravimetric measurements on precursors and products.

| Sample | Temperature range [°C] | Observed step | Experimental mass loss [%] | Calculated[a] mass loss [%] |
|---|---|---|---|---|
| $Na_2[Zn(Cit)]$ | 30–300 | dehydration | 14.8 | 15.2 |
| | 300–600 | ligand decomposition | 31.2 | 31.8 |
| LDH-Zn(Cit) | 30–200 | dehydration | 9.9 | 9.7 |
| | 200–700 | dehydroxylation + anion decomposition | 37.7 | 38.9 |
| LDH-ZnS-$H_2$Cit | 30–240 | dehydration | 10.8 | 9.2 |
| | 240–950 | dehydroxylation + anion decomposition | 42.1 | 42.9 |

[a] Mass losses are calculated based on the stoichiometries $Na_2[Zn(C_6H_4O_7)]\cdot 3H_2O$ for $Na_2[Zn(Cit)]$, $[Mg_{0.67}Al_{0.33}(OH)_2][Zn(C_6H_4O_7)]_{0.16}(CO_3)_{0.01}\cdot 0.58H_2O$ for LDH-Zn(Cit) and $[Mg_{0.67}Al_{0.33}(OH)_2][ZnS]_{0.16}(C_6H_6O_7)_{0.16}(CO_3)_{0.01}\cdot 0.70H_2O$ for LDH-ZnS-$H_2$Cit.

 © 2006 Wiley-VCH Verlag GmbH & Co. KGaA, Weinheim 

on heating LDH-Zn(Cit), this may indicate that complete combustion of intercalated citrate in LDH-ZnS-$H_2$Cit is hindered by the presence of co-intercalated ZnS.

The mass losses expected for materials with stoichiometries proposed on the basis of chemical analysis and TGA results are listed in Table 2 and correspond closely to the experimental values.

## Conclusions

Cubic sphalerite ZnS nanoparticles can be synthesized by an in situ reaction between a pre-intercalated $[Zn(Cit)]^{2-}$ anion and $H_2S$ in the interlayer galleries of an LDH. The LDH precursor is obtained by an ion-exchange reaction of $Na_2[Zn(C_6H_4O_7)]\cdot 3H_2O$ and a nitrate-containing LDH. The synthesis of the ZnS nanoparticles, involving a gas–solid reaction between the LDH and $H_2S$, provides a simple approach for the synthesis of such semiconductors in layered hosts. Structural data show that $[Zn(Cit)]^{2-}$ anions are accommodated vertically in the interlayer region as a monolayer with the zinc center in adjacent anions located alternately above and below the midpoint of the interlayer galleries. Reaction with $H_2S$ leads to the formation of co-intercalated ZnS in the interlayer galleries and citrate dianions. The ZnS nanoparticles grow only gradually in the two-dimensional gallery spaces because of the confinement effect of the layers. The material exhibits an excitonic peak at 276 nm corresponding to a bandgap of 4.52 eV, which is some 0.87 eV higher than that in the bulk. The diameter of the ZnS particles (≈ 2 nm), as estimated from XRD and UV/Vis spectroscopic data, is larger than the gallery height of the LDH (0.73 nm), demonstrating that the ZnS nanoparticles have a disc- or plate-like morphology.

## Experimental Section

**Synthesis:** In order to prevent contamination by carbonate ions arising from atmospheric $CO_2$, all procedures were carried out under constant nitrogen flow using freshly decarbonated, deionized water.

**Preparation of $Na_2[Zn(Cit)]\cdot 3H_2O$:** A mixture of ZnO (3.91 g, 0.048 mol) and citric acid monohydrate, $C_6H_8O_7\cdot H_2O$ ($H_4Cit$) (10.09 g, 0.048 mol), was stirred in water (100 mL) until the solids had completely dissolved. The reaction mixture was subsequently stirred overnight at 60 °C. Aqueous sodium hydroxide solution (1.0 M) was added until the pH reached 8.5. After concentration and slow evaporation, a white solid was obtained. The produced solid was redissolved in a water/ethanol mixture, 8:1 (v/v), under mild heating. The derived reaction mixture was allowed to slowly evaporate at room temperature. A few days later, a white crystalline material appeared at the bottom of the flask. The white crystals were isolated by filtration and dried under vacuum. $Na_2[Zn(C_6H_4O_7)]\cdot 3H_2O$ (353.43): calcd. C 20.37, H 2.83, $H_2O$ 15.28, Na 13.02, Zn 18.51; found C 20.58, H 2.56, $H_2O$ 14.87, Na 13.36, Zn 18.93 ($H_2O$ was determined by thermogravimetry as described below). $^{13}C$ MAS NMR: $\delta$ = 47.9 (=$CH_2$), 76.3 (≡CO), 181.3 [$(CO_2)_\beta$], 184.4 [$(CO_2)_\alpha$] ppm.

**LDH-Nitrate Precursor:** $Mg_2Al$-$NO_3$ LDH was prepared by a co-precipitation method at controlled pH as described in the literature.[80] The resulting white precipitate was collected by centrifugation, washed several times, and stored moist under nitrogen. $[Mg_{0.67}Al_{0.33}(OH)_2](NO_3)_{0.31}(CO_3)_{0.01}\cdot 0.47H_2O$ (87.32): calcd. C 0.15, H 3.36, Al 10.24, $H_2O$ 8.66, Mg 18.39, N 4.99; found C 0.15, H 3.25, Al 10.35, $H_2O$ 9.68, Mg 18.70, N 5.18.

**LDH-Zn(Cit):** LDH-Zn(Cit) was prepared starting from the as-synthesized LDH-nitrate without drying the solid. The wet LDH-$NO_3$ (13.75 g, about 10.0 mmol of $NO_3^-$) was suspended in a solution of $Na_2[Zn(Cit)]\cdot 3H_2O$ (14.14 g, 40.0 mmol) in water (100 mL). The mixture was stirred at room temperature for 8 h in nitrogen. The resulting product was separated by centrifugation, extensively washed, and finally air-dried at 65 °C. $[Mg_{0.67}Al_{0.33}(OH)_2]$-$[Zn(C_6H_4O_7)]_{0.16}(CO_3)_{0.01}\cdot 0.58H_2O$ (109.81): calcd. C 10.28, H 3.49, Al 8.16, $H_2O$ 9.76, Mg 14.60, Zn 9.23; found. C 10.44, H 3.47, Al 8.18, $H_2O$ 9.90, Mg 14.62, Zn 9.22. $^{13}C$ MAS NMR: $\delta$ = 47.1 (=$CH_2$), 76.6 (≡CO), 180.1 [$(CO_2)_\beta$], 184.9 [$(CO_2)_\alpha$] ppm. For comparison purposes, the $(C_6H_5O_7)^{3-}$-containing LDH (LDH-HCit) was prepared by an analogous procedure. $[Mg_{0.65}Al_{0.35}$-$(OH)_2](C_6H_5O_7)_{0.11}(CO_3)_{0.01}\cdot 0.57H_2O$ (90.62): calcd. C 8.86, H 4.07, Al 10.40, $H_2O$ 10.13, Mg 17.24; found C 8.81, H 3.94, Al 10.32, $H_2O$ 11.30, Mg 17.12.

**LDH-ZnS-$H_2$Cit:** Powdered LDH-Zn(Cit) samples were treated with gaseous $H_2S$ for 8 h. The sample is denoted LDH-ZnS-$H_2$Cit. $[Mg_{0.67}Al_{0.33}(OH)_2][ZnS]_{0.16}(C_6H_6O_7)_{0.16}(CO_3)_{0.01}\cdot 0.70H_2O$ (117.06): calcd. C 9.70, H 3.71, Al 7.63, $H_2O$ 9.65, Mg 13.70, S 4.19, Zn 8.72; found C 9.98, H 3.58, Al 7.26, $H_2O$ 10.79, Mg 13.07, S 3.97, Zn 8.39. $^{13}C$ MAS NMR: $\delta$ = 44.3 (=$CH_2$), 74.6 (≡CO), 173.4 [$(CO_2)_\beta$], 177.9 [$(CO_2)_\alpha$] ppm.

**LDH-$CO_3$-ZnS:** The reaction of LDH-ZnS-$H_2$Cit with aqueous $Na_2CO_3$ solution was carried out at 60 °C with a tenfold excess of $CO_3^{2-}/Al^{3+}$ for 2 h. The resulting product was separated by centrifugation, extensively washed, and finally air-dried at 65 °C. The sample is denoted LDH-$CO_3$-ZnS.

**Characterization:** Elemental analyses for metals and sulfur were performed by ICP emission spectroscopy using a Shimadzu ICPS-7500 instrument. Carbon, hydrogen, and nitrogen analyses were carried out using an Elementarvario elemental analysis instrument.

The in situ powder X-ray diffraction (in situ XRD) data were recorded with a Shimadzu XRD-6000 powder diffractometer in the temperature range 30–900 °C in air, using Cu-$K_\alpha$ radiation ($\lambda$ = 0.154 nm) at 40 kV and 30 mA. The samples, as unoriented powders, were step-scanned in steps of 5°/min in the $2\theta$ range from 3 to 70° using a count time of 4 s per step. The rate of temperature increase was 10 °C/min with a holding time of 5 min before each measurement.

FTIR spectra of samples in KBr matrix were recorded with a Bruker Vector 22 spectrophotometer in the range 4000–400 $cm^{-1}$. UV/Vis diffuse reflectance spectra were recorded at room temperature with a Shimadzu UV-2101PC instrument with $BaSO_4$ powder as the reference.

$^{13}C$ solid-state magic-angle spinning nuclear magnetic resonance (MAS NMR) spectra were recorded with a Bruker AV300 spectrometer operating at a frequency of 75.467 MHz for $^{13}C$ at a spinning rate of about 4500 Hz with a 5 s pulse delay.

TEM images were obtained with a JEOL 2010 FasTEM at an accelerating voltage of 200 kV. Powder samples were ultrasonically dispersed in ethanol, and the suspension was deposited on a copper grid coated with a holey carbon film.

Thermogravimetric analysis coupled to mass spectrometry was performed using a Perkin–Elmer Diamond TG apparatus linked to a

 © 2006 Wiley-VCH Verlag GmbH & Co. KGaA, Weinheim 

ThermoStar mass spectrometer by a quartz capillary transfer line heated at 190 °C. The heating rate was 10 °C/min, with an air flow rate of 200 $cm^3$/min. The TG apparatus was at atmospheric pressure, and the mass spectrometer at a working pressure of $6 \times 10^{-6}$ Torr. The mass of sample used was 10 mg in each case.

## Acknowledgments

This project was supported by the National Nature Science Foundation of China (No. 20401002), Beijing Municipal Education Commission Development Scheme (Project No. JD100100402), and National Basic Research Program (Project No. 2004CB720602).

[1] L. D. Sun, C. H. Liu, C. S. Liao, C. H. Yan, *J. Mater. Chem.* **1999**, *9*, 1655–1657.
[2] H. Fujiwara, H. Hosokawa, K. Murakoshi, Y. Wada, S. Yanagida, *Langmuir* **1998**, *14*, 5154–5159.
[3] P. Calandra, M. Goffredi, L. Turco, *Colloids Surf., A* **1999**, *160*, 9–13.
[4] Y. C. Li, X. H. Li, C. H. Yang, Y. F. Li, *J. Phys. Chem. B* **2004**, *108*, 16002–16011.
[5] Y. Jiang, X. M. Meng, Z. Y. Xie, C. S. Lee, S. T. Lee, *Adv. Mater.* **2003**, *15*, 323–327.
[6] Q. Wu, N. Zheng, Y. Ding, Y. Li, *Inorg. Chem. Commun.* **2002**, *5*, 671–673.
[7] O. Raymond, H. Villavicencio, V. Petranovskii, J. M. Siqueiros, *Mater. Sci. Eng., A* **2003**, *360*, 202–206.
[8] W. H. Zhang, J. L. Shi, H. R. Chen, Z. L. Hua, D. S. Yan, *Chem. Mater.* **2001**, *13*, 648–654.
[9] J. L. Zhang, B. X. Han, Z. S. Hou, Z. M. Liu, J. He, T. Jiang, *Langmuir* **2003**, *19*, 7616–7620.
[10] W. S. Chae, J. H. Yoon, H. N. Yu, D. J. Jang, Y. R. Kim, *J. Phys. Chem. B* **2004**, *108*, 11509–11513.
[11] O. Enea, A. J. Bard, *J. Phys. Chem.* **1986**, *90*, 301–306.
[12] T. Sato, H. Okuyama, T. Endo, M. Shimada, *React. Solids* **1990**, *8*, 63–72.
[13] T. Sato, K. Masaki, T. Yoshioka, A. Okuwaki, *J. Chem. Technol. Biotechnol.* **1993**, *58*, 315–319.
[14] S. W. Guo, L. Konopny, P. B. Ronit, H. Cohen, H. Porteanu, E. Lifshitz, M. Lahav, *J. Am. Chem. Soc.* **1999**, *121*, 9589–9598.
[15] S. W. Guo, P. B. Ronit, T. Arad, G. Hodes, L. Leiserowitz, M. Lahav, *Adv. Mater.* **1998**, *10*, 657–661.
[16] V. I. Srdanov, I. Alxneit, G. D. Stucky, C. M. Reaves, S. P. Den Baars, *J. Phys. Chem. B* **1998**, *102*, 3341–3344.
[17] J. R. Agger, M. W. Anderson, M. E. Pemble, O. Terasaki, Y. Nozue, *J. Phys. Chem. B* **1998**, *102*, 3345–3353.
[18] J. Wang, A. G. Kalinichev, J. E. Amonette, R. J. Kirkpatrick, *Am. Mineral.* **2003**, *88*, 398–409.
[19] J. H. Choy, S. Y. Kwak, Y. J. Jeong, J. S. Park, *Angew. Chem. Int. Ed.* **2000**, *39*, 4041–4045.
[20] A. I. Khan, D. O'Hare, *J. Mater. Chem.* **2002**, *12*, 3191–3198.
[21] A. Vaccari, *Catal. Today* **1998**, *41*, 53–71.
[22] B. Sels, D. De Vos, M. Buntinx, F. Pierard, K. D. Mesmaeker, P. Jacobs, *Nature* **1999**, *400*, 855–857.
[23] V. Rives, in *Layered Double Hydroxides: Present and Future* (Ed.: V. Rives), Nova Science Publishers Inc., New York, **2001**, pp. 139–192.
[24] J. C. Villegas, O. H. Giraldo, K. Laubernds, S. L. Suib, *Inorg. Chem.* **2003**, *42*, 5621–5631.
[25] M. François, J. P. Besse, *J. Solid State Chem.* **2000**, *155*, 332–341.
[26] K. A. Tarasov, D. O'Hare, *Inorg. Chem.* **2003**, *42*, 1919–1927.
[27] M. Kaneyoshi, W. Jones, *J. Mater. Chem.* **1999**, *9*, 805–811.
[28] N. H. Gutmann, L. Spiccia, T. W. Turney, *J. Mater. Chem.* **2000**, *10*, 1219–1224.
[29] P. Beaudot, M. E. De Roy, J. P. Besse, *Chem. Mater.* **2004**, *16*, 935–945.
[30] V. Rives, M. A. Ulibarri, *Coord. Chem. Rev.* **1999**, *181*, 61–120.
[31] M. P. Nikiforov, M. V. Chernysheva, A. A. Eliseev, A. V. Lukashin, Y. D. Tretyakov, Y. V. Maksimov, I. P. Suzdalev, P. Goernert, *Mater. Sci. Eng. B* **2004**, *109*, 226–231.
[32] A. I. Tsyganok, K. Suzuki, S. Hamakawa, K. Takehira, T. Hayakawa, *Chem. Lett.* **2001**, 24–25.
[33] D. Mastropaolo, D. A. Powers, J. A. Potenza, H. J. Schugar, *Inorg. Chem.* **1976**, *15*, 1444–1449.
[34] Z. H. Zhou, S. Y. Hou, H. L. Wan, *Dalton Trans.* **2004**, 1393–1399.
[35] E. R. Still, P. Wikberg, *Inorg. Chim. Acta* **1980**, *46*, 153–155.
[36] Z. H. Zhou, H. L. Wan, K. R. Tsai, S. Z. Hu, *Inorg. Chim. Acta* **1995**, *237*, 193–197.
[37] J. Strouse, S. W. Layten, C. E. Strouse, *J. Am. Chem. Soc.* **1977**, *99*, 562–572.
[38] J. P. Glusker, *Acc. Chem. Res.* **1980**, *13*, 345–352.
[39] Z. H. Zhou, H. L. Wan, K. R. Tsai, *Inorg. Chem.* **2000**, *39*, 59–64.
[40] A. S. Bookin, V. I. Cherkashin, V. Drits, *Clays Clay Miner.* **1993**, *41*, 558–564.
[41] F. Cavani, F. Trifiro, A. Vaccari, *Catal. Today* **1991**, *11*, 173–301.
[42] Z. P. Xu, H. C. Zeng, *J. Phys. Chem. B* **2001**, *105*, 1743–1749.
[43] J. Zhang, F. Zhang, L. L. Ren, D. G. Evans, X. Duan, *Mater. Chem. Phys.* **2004**, *85*, 207–214.
[44] S. Miyata, *Clays Clay Miner.* **1983**, *31*, 305–311.
[45] M. D. Arco, S. Gutiérrez, C. Martín, V. Rives, *Inorg. Chem.* **2003**, *42*, 4232–4240.
[46] P. Beaudot, M. E. De Roy, J. P. Besse, *J. Solid State Chem.* **2001**, *161*, 332–340.
[47] S. Gago, M. Pillinger, T. M. Santos, J. Rocha, I. S. Gonçalves, *Eur. J. Inorg. Chem.* **2004**, 1389–1395.
[48] Y. Wang, N. Herron, *Phys. Rev. B* **1990**, *42*, 7253–7255.
[49] E. Kanezaki, *Solid State Ionics* **1998**, *106*, 279–284.
[50] T. Abe, Y. Tachibana, T. Uematsu, M. Iwamoto, *J. Chem. Soc., Chem. Commun.* **1995**, 1617–1618.
[51] K. Nakamoto, *Infrared and Raman Spectra of Inorganic and Coordination Compounds*, 4th ed., Wiley, New York, **1986**, pp. 231–248.
[52] M. Matzapetakis, C. P. Raptopoulou, A. Tsohos, V. Papaefthymiou, N. Moon, A. Salifoglou, *J. Am. Chem. Soc.* **1998**, *120*, 13266–13267.
[53] F. M. Labajos, V. Rives, M. A. Ulibarri, *J. Mater. Sci.* **1992**, *27*, 1546–1552.
[54] Z. P. Xu, H. C. Zeng, *Chem. Mater.* **1999**, *11*, 67–74.
[55] G. B. Deacon, R. J. Phillips, *Coord. Chem. Rev.* **1980**, *33*, 227–250.
[56] Y. Tomita, K. Ueno, *Bull. Chem. Soc. Jpn.* **1963**, *36*, 1069–1073.
[57] N. Gutmann, B. Müller, H. J. Tiller, *J. Solid State Chem.* **1995**, *119*, 331–338.
[58] L. Konopny, M. Berfeld, R. Popovitz-Biro, I. Weissbuch, L. Leiserowitz, M. Lahav, *Adv. Mater.* **2001**, *13*, 580–584.
[59] X. G. Peng, S. Q. Guan, X. D. Chi, Y. S. Jiang, T. J. Li, *J. Phys. Chem.* **1992**, *96*, 3170–3174.
[60] G. E. Hawkes, P. O'Brien, H. Salacinski, M. Motevalli, I. Abrahams, *Eur. J. Inorg. Chem.* **2001**, 1005–1011.
[61] P. O'Brien, H. Salacinski, M. Motevalli, *J. Am. Chem. Soc.* **1997**, *119*, 12695–12696.
[62] E. T. Kefalas, M. Dakanali, P. Panagiotidis, C. P. Raptopoulou, A. Terzis, T. Mavromoustakos, I. Kyrikou, N. Karligiano, A. Bino, A. Salifoglou, *Inorg. Chem.* **2005**, *44*, 4818–4828.
[63] Y. Wang, A. Suna, W. Mahler, R. Kasowski, *J. Chem. Phys.* **1987**, *87*, 7315–7322.
[64] J. Nanda, S. Sapra, D. D. Sarma, *Chem. Mater.* **2000**, *12*, 1018–1024.
[65] Y. Kayanuma, *Phys. Rev. B* **1988**, *38*, 9797–9805.
[66] J. P. Li, Y. Xu, D. Wu, Y. H. Sun, *Solid State Commun.* **2004**, *130*, 619–622.

 © 2006 Wiley-VCH Verlag GmbH & Co. KGaA, Weinheim 

[67] S. Wageh, S. L. Zhao, X. R. Xu, *J. Cryst. Growth* **2003**, *255*, 332–337.
[68] J. H. Yu, J. Joo, H. M. Park, S. I. Baik, Y. W. Kim, S. C. Kim, T. Hyeon, *J. Am. Chem. Soc.* **2005**, *127*, 5662–5670.
[69] Y. D. Li, Y. Ding, Y. Zhang, Y. T. Qian, *J. Phys. Chem. Solids* **1999**, *60*, 13–15.
[70] P. Calandra, A. Longo, V. T. Liveri, *J. Phys. Chem. B* **2003**, *107*, 25–30.
[71] N. I. Kovtyukhova, E. V. Buzaneva, C. C. Waraksa, B. R. Martin, T. E. Mallouk, *Chem. Mater.* **2000**, *12*, 383–389.
[72] Q. Yuan, M. Wei, D. G. Evans, X. Duan, *J. Phys. Chem. B* **2004**, *108*, 12381–12387.
[73] E. N. Baker, H. M. Baker, B. F. Anderson, R. D. Reeves, *Inorg. Chim. Acta* **1983**, *78*, 281–285.
[74] S. Vitta, T. H. Metzger, S. S. Major, *J. Chem. Phys.* **1999**, *111*, 11088–11094.
[75] Z. Pan, J. Liu, X. Peng, T. Li, Z. Wu, M. Zhu, *Langmuir* **1996**, *12*, 851–853.
[76] B. Rebours, J.-B. d'Espinose de la Caillerie, O. Clause, *J. Am. Chem. Soc.* **1994**, *116*, 1707–1717.
[77] V. Prévot, C. Forano, J. P. Besse, *Inorg. Chem.* **1998**, *37*, 4293–4301.
[78] C. Li, G. Wang, D. G. Evans, X. Duan, *J. Solid State Chem.* **2004**, *177*, 4569–4575.
[79] V. Prévot, C. Forano, J. P. Besse, *J. Solid State Chem.* **2000**, *153*, 301–309.
[80] S. Miyata, *Clays Clay Miner.* **1975**, *23*, 369–375.

Received: March 7, 2006
Published Online: June 29, 2006

 © 2006 Wiley-VCH Verlag GmbH & Co. KGaA, Weinheim 

DOI: 10.1002/ejic.200600232

# Platinum Complexes with One Monodentate Ligand (1-Methylbenzimidazole or Antiviral Ribavirin) Flanked by Two *cis*-$NMe_2$ Groups: Informative Models for Assessing Interligand Interactions

**Leonardo Cerasino,*[a] and Giovanni Natile[a]**

**Keywords:** Platinum / Pentamethyldiethylenetriamine / 1-Methylbenzimidazole / Ribavirin / Interligand interactions

Platinum complexes with a tridentate amine ligand ($A_3$) and a nucleobase (L) represent very useful models for investigating nucleobase/*cis*-amine interactions without the complications arising from nucleobase/nucleobase interferences present in the more frequently used *cis*-$A_2PtL_2$ model systems ($A_2$ = two monodentate amines or a diamine). In this context, the $Me_3$dienPtL complexes ($Me_3$dien = *N1*,*N4*,*N7*-trimethyldiethylenetriamine), previously investigated, were particularly informative. The presence of a methyl group on each terminal nitrogen atom renders the rotation of L about the Pt–L bond slow on the NMR timescale and the two half spaces defined by the coordination plane inequivalent. Thus, guanine and deoxyguanine derivatives were found to have comparable rates of rotation by way of a H-bond interaction between the O6 atom of the rotating guanine and the NH group of the *cis*-amine. We have now extended the investigation to $Me_5$dien complexes ($Me_5$dien = *N1*,*N1′*,*N4*,*N7*,*N7′*-pentamethyldiethylenetriamine). The results indicate that the absence of a proton on the terminal nitrogen atoms not only reduces the rate of rotation of L by a factor of $10^{10}$, but also dramatically increases the difference in the rates between the L ligands mimicking guanine and deoxyguanine.
(© Wiley-VCH Verlag GmbH & Co. KGaA, 69451 Weinheim, Germany, 2006)

## Introduction

Cisplatin [*cis*-$PtCl_2(NH_3)_2$] displays exceptional anticancer activity when employed in the treatment of testicular, ovarian, cervical, head and neck, oesophageal, and non-small-cell lung cancers.[1,2] Continued research into the mechanism for the action of cisplatin[3–5] is being carried out in order to understand why it is so extraordinarily effective, especially against testicular cancer, and to allow for the rational design of new derivatives that could overcome the toxic side effects and the resistance to cisplatin of several tumors.

The major DNA adduct formed by cisplatin, the intrastrand cross-link between adjacent G groups, is mimicked by *cis*-$A_2PtG_2$ models, where $A_2$ stands for two monodentate or a bidentate amine and G is a guanine derivative. Models with bulky $A_2$ ligands, designed to reduce the rate of rotation around the Pt–G bonds, have been extensively investigated in our laboratories and have contributed to the elucidation of some relevant features of cisplatin adducts.[6–12] In some instances, in order to investigate the role of nucleotide/*cis*-amine interactions without the complications arising from interactions between *cis*-nucleotides, model compounds containing only one G group have also been constructed.

The most widely used model compound for platinum adducts with just one coordinated purine base is represented by dienPtL (dien = 1,4,7-triazaheptane = diethylenetriamine). *N4*-methyldien, *N1*,*N4*,*N7*-trimethyldien, and *N1*,*N1′*,*N4*,*N7*,*N7′*-pentamethyldien (abbreviated as Medien, $Me_3$dien, and $Me_5$dien, respectively) are systems of increasing steric bulk, which can differently affect the rate of rotation of a purine base about the Pt–N7 bond. All these ligands are nonsymmetrical with respect to the platinum coordination plane. In particular the single Me group on the N4 atom occurs only on one side of the platinum coordination plane. Therefore, coordination of a nonsymmetrical ligand L, such as a purine base, can lead to the formation of two $Me_n$dienPtL conformers differing in the orientation of the purine base with regard to the $Me_n$dien ligand (Scheme 1). The six-membered ring of the purine base and the central *N*-methyl group of $Me_n$dien can be either on the same side (*endo* rotamer) or on opposite sides (*exo* rotamer) of the platinum coordination plane.[13–17]

MedienPtL complexes[18] are very dynamic and the four hydrogen atoms on the terminal nitrogen atoms exert negligible hindrance to the *endo*/*exo* interconversion process; therefore, similar to the case of dienPtL complexes, only one set of signals, which is the coalescence of the sets of signals of the two conformers, is observed in the NMR spectra.[19]

$Me_3$dienPtL complexes represent a case in which the interconversion is sufficiently slow (already at ambient temperature) to be studied by NMR spectroscopic techniques.

[a] Università degli Studi di Bari, Dipartimento Farmaco-Chimico, via E. Orabona 4, 70125 Bari, Italy
Fax: +39-080-5442230
E-mail: cerasino@farmchim.uniba.it

 © 2006 Wiley-VCH Verlag GmbH & Co. KGaA, Weinheim 

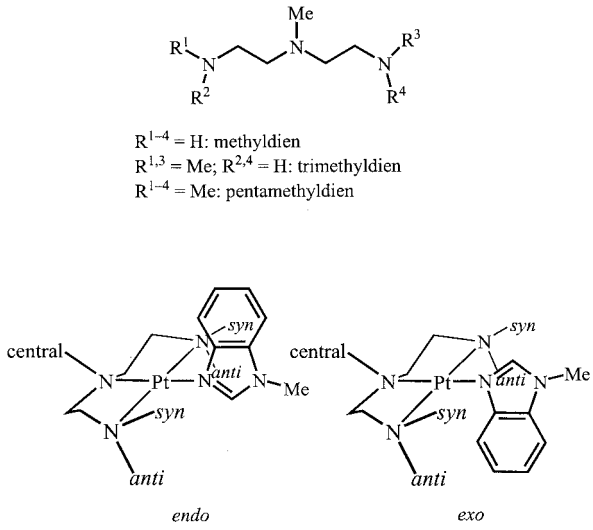


Scheme 1. Schematic view of the $Me_n$dien ligands (top) and of the two possible conformers (*endo* and *exo*) for $Me_5$dienPt(1-methylbenzimidazole) (bottom).

The rate of *endo*/*exo* interconversion has been found to depend upon the nature of the purine derivative investigated, and the factors influencing the rotation around the Pt–L bond have been elucidated.[11–14]

In particular, $Me_3$dienPtL compounds could be prepared in the form that has all three methyl groups of $Me_3$dien on the same side of the platinum coordination plane [*syn*-(*R*,*S*) isomer];[12] moreover, under acidic or neutral conditions no change in ligand configuration could be detected after several days in aqueous solution. $Me_3$dienPtL complexes were found to be the most informative for assessing steric, solvation, and electronic factors influencing stability and dynamic behavior.

A first interesting result of the investigation was the large tendency of a coordinated 5′-nucleotide to place the phosphate group on the same side of the platinum coordination plane as the NH groups of $Me_3$dien; such a conformation allows for phosphate/*cis*-amine H-bonding. Therefore, the *endo* rotamer was the exclusive form in adducts with 5′-GMP, while in adducts with 9-EtG and 3′-GMP, in which such an interaction cannot take place, the *endo* and *exo* rotamers were present in comparable amounts. The effect of the substituent at the 6-position of the purine ring on the rate of rotation about the Pt–N7 bond was also investigated. The rate of interconversion between rotamers was comparable for guanine and deoxyguanine derivatives notwithstanding the greater bulk of the C6 substituent in the guanine complex. In contrast, the rate of rotation was far slower for the adenine derivative although the bulk of the C6 substituent is comparable for adenine and guanine. Activation parameters for rotation suggest that an attractive interaction between the negatively charged O6 atom of the guanine (an H-bond acceptor) and the positively charged *N*-hydrogen atom of the *cis*-amine (an H-bond donor) could lower the rotational barrier and render the rate of rotation of guanine only one order of magnitude slower than that of deoxyguanine. Finally, in the case of adenine derivatives in which the substituent at the 6-position of the purine ring is bulky and positively charged (as positively charged as the *N*-hydrogen atoms of the triamine) the barrier to rotation could be expected to be far greater than that observed for guanine and deoxyguanine derivatives with the consequence that the interconversion between rotamers becomes very slow.

In order to prove further the correctness of the explanation given above, we extended the investigation to fully methylated dien derivatives ($Me_5$dienPtL compounds) lacking protons on the terminal aminic groups. Some $Me_5$dienPtL complexes have already been investigated (L = a guanine derivative such as 9-EtG, guanosine, 5′-dGMP, 5′-GMP,[11] and penciclovir,[10] or a deoxyguanine such as famciclovir[10]); however, in none of the cases was it possible to observe an interconversion between rotamers and the *endo*/*exo* ratio was in the range 0.6–1 in the case of the guanine derivatives and ca. 2 in the case of the deoxyguanine derivative. We therefore looked at other N-donor heterocycles that could mimic guanine and deoxyguanine derivatives but be more reactive and allow for the detection of a kinetically controlled composition, which could possibly be different from that at thermodynamic equilibrium. The search has been successful. We found two bases (Scheme 2), 1-methylbenzimidazole (bzim) and 1-D-ribose-1*H*-[1,2,4]triazole-3-carboxamide (ribavirin, riba) for which the reaction was completed in 2 d at ambient temperature. Moreover, the initially formed rotamer composition appears to be under kinetic control (*endo*/*exo* ratio of 7–8) and in one case (bzim) it has been possible to measure the rate of isomerization to the thermodynamically controlled composition and to evaluate the activation parameters.

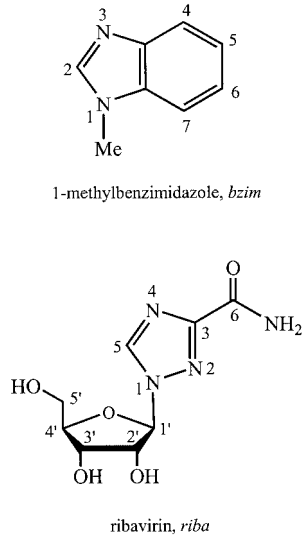


Scheme 2. Structures and numbering schemes for the two ligands L used in this work.

New insights into steric, electronic, and solvation factors influencing the dynamic behavior of these model compounds have been gained.

 © 2006 Wiley-VCH Verlag GmbH & Co. KGaA, Weinheim 

## Results

### $Me_5$dienPt(bzim)

The reaction of $[Pt(Me_5dien)(NO_3)](NO_3)$ with bzim was complete after 48 h at room temperature. In the $^1H$ NMR spectrum two sets of signals of very different intensities (ca. 8:1) were detected. For each set of signals the resonance at the lower field belongs to H2 and reveals a downfield shift with respect to the corresponding signal for the free bzim of ca. 0.8 ppm. This is a clear indication that both sets of signals belong to complex species in which bzim is *N3*-coordinated to the platinum atom. Therefore, most likely, the two sets of signals arise from the presence of two conformers, *endo* and *exo* (Table 1).

A 2D NOESY experiment showing connectivities between bzim protons and *N*-Me protons of $Me_5$dien enabled the assignment of the two sets of signals to the corresponding conformers (Figure 1). Previous investigations on strictly related compounds have demonstrated that *syn*-*N*-Me signals of $Me_5$dien are always at a higher field with respect to *anti*-*N*-Me signals and the latter are at a higher field with respect to the central *N*-Me signals.[13–17]

The major conformer exhibits intense NOE crosspeaks between bzim-H2 and *anti*-*N*-Me groups of $Me_5$dien and between bzim-H4 and *syn*-*N*-Me groups of $Me_5$dien, therefore it is identified as the *endo* rotamer (the six-membered ring of bzim is on the same side of the platinum coordination plane as the central *N*-Me group of $Me_5$dien). Consequently, the minor form is identified as the *exo* rotamer (the six-membered ring and the central *N*-Me group are on opposite sides of the platinum coordination plane). A common feature of the $Me_n$dienPtL compounds is a signal for the L proton adjacent to the coordinating nitrogen atom,

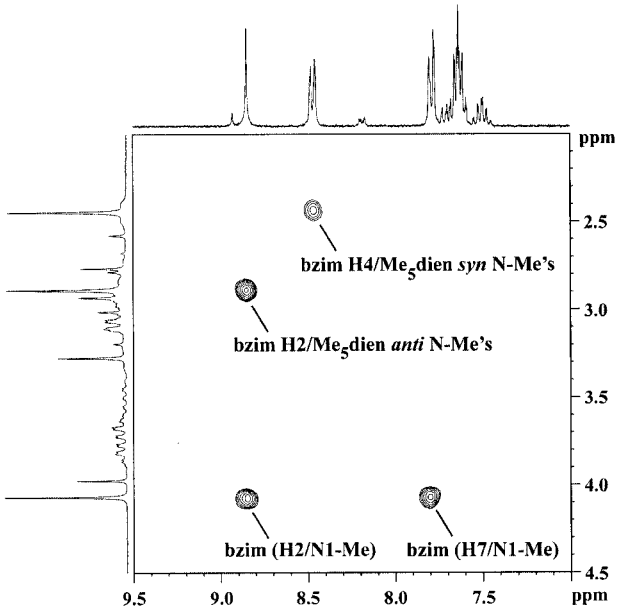


Figure 1. 2D NOESY spectrum of $Me_5$dienPt(bzim). All crosspeaks belong to the major set of signals that result from the *endo* conformer. The second set of signals has intensities that are too weak to generate observable crosspeaks, and, by exclusion, it is assigned to the *exo* rotamer.

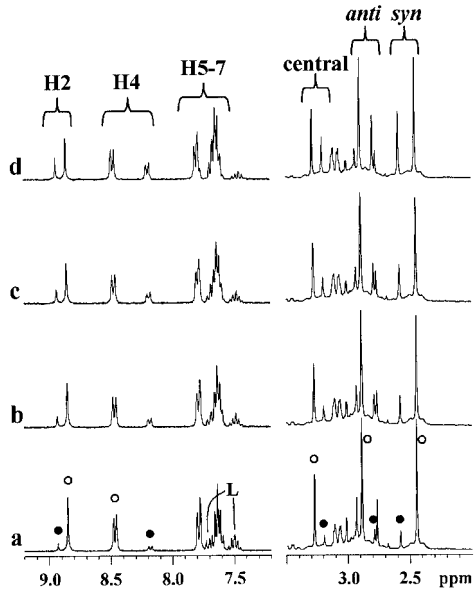


Figure 2. $^1H$ NMR spectra of $Me_5$dienPt(bzim) after standing for different times in $D_2O$ solution at 353 K (a, b, c, and d correspond to 0, 1800, 3600, and 12000 s, respectively). The signals of the bzim aromatic protons fall in the region δ = 9–7 ppm, while the $Me_5$dien protons fall in the region δ = 4–2 ppm. The intensity of the aromatic proton signals is increased by a factor of two with respect to the intensity of the aliphatic proton signals. Peaks labeled with ○ belong to the *endo* rotamer, peaks labeled with ● belong to the *exo* rotamer, and peaks labeled with L belong to unreacted bzim.

Table 1. Chemical shift values (ppm) for the $Me_5$dienPtL complexes (L = riba or bzim), and the starting $[Pt(Me_5dien)(D_2O)]^{2+}$, bzim, and riba compounds. The sugar protons of $Me_5$dienPt(riba) not listed in the table underwent rather small chemical shift changes (values for free riba are given in parenthesis): H2′ 4.75 (4.66), H3′ 4.46 (4.50), H4′ 4.30 (4.22), H5′/5′′ 3.91/3.76 (3.87/3.76).

| | | H2/H5[a] | H4 | H7 | H5 | H6 | *N1*-Me/H1′[b] | *N*-Me ($Me_5$dien) | | |
|---|---|---|---|---|---|---|---|---|---|---|
| | | | | | | | | central | *anti* | *syn* |
| $Me_5$dienPt($D_2O$) | | | | | | | | 3.04 | 2.92 | 2.75 |
| Bzim | | 8.08 | 7.72 | 7.64 | 7.51 | 7.49 | 3.86 | | | |
| $Me_5$dienPt(bzim) | *endo* | 8.85 | 8.47 | 7.79 | 7.64 | 7.62 | 4.07 | 3.27 | 2.89 | 2.44 |
| | *exo* | 8.93 | 8.18 | 7.77 | 7.63 | 7.60 | 4.08 | 3.19 | 2.79 | 2.58 |
| Riba | | 8.75 | | | | | 6.05 | | | |
| $Me_5$dienPt(riba) | *endo* | 9.81 | | | | | 6.14 | 3.21 | 2.80 | 2.47 |
| | *exo* | 9.90 | | | | | 6.15 | 3.10 | 2.71 | 2.58 |

[a] H2 for bzim and H5 for riba. [b] *N1*-Me for bzim and H1′ for riba.

 © 2006 Wiley-VCH Verlag GmbH & Co. KGaA, Weinheim 

Table 2. Experimental $C_{endo}/C_{exo}$ ratios [for $Me_5$dienPt(bzim) complex] evaluated from NMR spectroscopic data. For each temperature (first column) the $C_{endo}/C_{exo}$ value was evaluated at different time intervals (given in parenthesis) starting from the kinetically controlled composition and ending when the equilibrium composition was reached (last value on each line). The values of the equilibrium [$K = (C^{\infty}_{exo}/C^{\infty}_{endo})$] and kinetic constants ($k_{endo}$ and $k_{exo}$) are also given.

| $T$ [K] | $C_{endo}/C_{exo}$ (time [$10^3$ s]) | | | | | | | | | $K$ | $k_{endo} + k_{exo}$ ($10^{-6}$ $s^{-1}$) | $k_{endo}$ ($10^{-6}$ $s^{-1}$) | $k_{exo}$ ($10^{-6}$ $s^{-1}$) |
|---|---|---|---|---|---|---|---|---|---|---|---|---|---|
| 323 | 7.69 | 5.94 | 3.30 | 2.48 | 2.14 | 2.00 | 1.83 | 1.78 | 1.77 | 0.565 | 6.16 | 2.22 | 3.93 |
| | (0) | (18.0) | (104) | (187) | (270) | (335) | (594) | (680) | (767) | | | | |
| 333 | 6.47 | 6.00 | 4.25 | 3.83 | 2.10 | 1.83 | 1.75 | | | 0.572 | 17.1 | 6.22 | 10.9 |
| | (0) | (7.20) | (18.0) | (27.0) | (88.2) | (153) | (583) | | | | | | |
| 343 | 7.25 | 3.37 | 2.58 | 2.14 | 1.88 | 1.72 | | | | 0.583 | 146 | 53.7 | 92.1 |
| | (0) | (3.60) | (7.20) | (10.8) | (17.0) | (45.0) | | | | | | | |
| 348 | 5.51 | 4.33 | 3.61 | 2.95 | 2.40 | 2.20 | 2.06 | 1.86 | 1.71 | 0.584 | 185 | 68.1 | 117 |
| | (0) | (0.900) | (1.86) | (2.82) | (5.58) | (7.50) | (9.36) | (12.8) | (35.0) | | | | |
| 353 | 7.55 | 4.81 | 3.76 | 3.14 | 2.79 | 2.48 | 2.21 | 1.91 | 1.70 | 0.590 | 239 | 88.8 | 150 |
| | (0) | (0.900) | (1.80) | (2.70) | (3.60) | (4.50) | (6.30) | (9.90) | (12.0) | | | | |
| 363 | 6.23 | 3.09 | 2.60 | 2.13 | 1.84 | 1.78 | 1.67 | | | 0.600 | 769 | 288 | 481 |
| | (0) | (0.600) | (1.20) | (1.80) | (3.00) | (3.66) | (6.50) | | | | | | |

more shielded in the *endo* rotamer than in the *exo* rotamer.[13,14,16,17]

The 8:1 ratio between rotamers reflects a kinetic rather than a thermodynamic preference for the *endo* form. As a matter of fact, with time, the *endo*/*exo* ratio decreases until a constant value (representing the thermodynamic equilibrium) is reached (Figure 2). The rate of isomerization is very slow at room temperature, requiring weeks; however, it can be increased by increasing the temperature. In order to evaluate the activation parameters ($\Delta H^{\ddagger}$ and $\Delta S^{\ddagger}$), the rates of isomerization were measured at different temperatures in the range 323–363 K (Table 2).

The $\Delta H^{\ddagger}$ and $\Delta S^{\ddagger}$ values for the rate of isomerization of the *endo* ($k_{endo}$) and *exo* ($k_{exo}$) conformers were found to be almost identical ($\Delta H^{\ddagger} = 118 \pm 9$ and $119 \pm 9$ kJ mol$^{-1}$ for the *endo* and *exo* rotamers, respectively; and $\Delta S^{\ddagger} = 15 \pm 20$ J K$^{-1}$ mol$^{-1}$), indicating that the two rotamers have very similar ground-state enthalpy and entropy values (Table 3).

Table 3. Collection of activation enthalpies ($\Delta H^{\ddagger}$ [kJ mol$^{-1}$]) and entropies ($\Delta S^{\ddagger}$ [J K$^{-1}$ mol$^{-1}$]) for interconversion between rotamers in $Me_{3/5}$dienPtL complexes. Standard deviations are given at the 95% confidence limit.

| Compound | $\Delta H^{\ddagger}_{endo}$ | $\Delta H^{\ddagger}_{exo}$ | $\Delta S^{\ddagger}_{endo}$ | $\Delta S^{\ddagger}_{exo}$ |
|---|---|---|---|---|
| $Me_3$dienPt(penciclovir)[a] | 61 ± 2 | 54 ± 2 | –8 ± 4 | –29 ± 4 |
| $Me_3$dienPt(9-EtG)[b] | 65 ± 2 | 56 ± 2 | 2 ± 4 | –28 ± 4 |
| $Me_3$dienPt(deoxypenciclovir)[c] | 111 ± 2 | 105 ± 2 | 181 ± 4 | 159 ± 4 |
| $Me_5$dienPt(bzim) | 118 ± 9 | 119 ± 9 | 15 ± 20 | 15 ± 20 |

[a] Penciclovir = 9-[4-hydroxy-3-(hydroxymethyl)but-1-yl]guanine.[17] [b] 9-EtG = 9-ethylguanine.[16] [c] Deoxypenciclovir = 6-deoxy-9-[4-hydroxy-3-(hydroxymethyl)but-1-yl]guanine.[17]

### $Me_5$dienPt(riba)

The reaction of [Pt($Me_5$dien)($NO_3$)]($NO_3$) with riba was also complete after 48 h at room temperature. Two sets of signals (intensity ratio 7:1) were observed. For both sets of signals the chemical shift of the aromatic proton of riba (H5) is more than 1 ppm at a lower field with respect to the corresponding signal for the free ligand indicating that in both cases the riba ligand is *N4*-coordinated to the platinum atom. Therefore, the two sets of signals have to be ascribed to two conformers, most likely the *endo* and *exo* rotamers (Table 1).

As in the the case of bzim, a 2D NOESY experiment enabled the assignment of the two sets of signals to the corresponding conformers. In particular, the presence of a crosspeak between the riba H5 proton and the *anti*-*N*-Me signal of $Me_5$dien for the more intense set of signals indicates that in this case the major rotamer also has the *endo* conformation (Figure 3). No isomerization was observed for this compound, even after prolonged heating at 363 K.

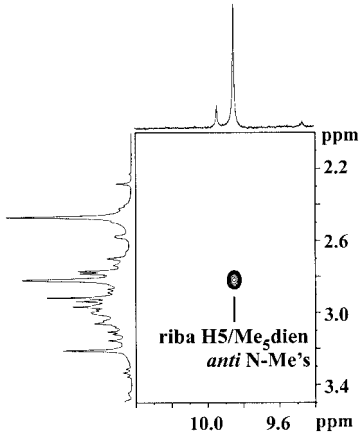


Figure 3. 2D NOESY spectrum of $Me_5$dienPt(riba). The crosspeak belongs to the major set of signals and this set is assigned to the *endo* rotamer. The second set of signals has intensities that are too weak to generate observable crosspeaks and, by exclusion, it is assigned to the *exo* rotamer.

## Discussion

In Table 3 we compare the activation parameters for rotamer interconversion in the series of $Me_{3/5}$dienPtL complexes investigated so far. In the case of $Me_3$dien complexes the most remarkable difference was between the guanine

 © 2006 Wiley-VCH Verlag GmbH & Co. KGaA, Weinheim 

and deoxyguanine derivatives. The enthalpy of activation was ca. 50 $kJ\,mol^{-1}$ higher in the case of the deoxyguanine derivative, notwithstanding the fact that deoxyguanines carry a much smaller group (H) in the 6-position of the purine ring as compared to guanines for which the substituent at the 6-position is much bulkier (O). We argued that in the transition state (in which the purine base is dragged through the platinum coordination plane) the O6 atom of the guanine ligand (negatively charged) and the *N*-hydrogen atom of the *cis*-amine (positively charged) can give rise to an attractive interaction which helps in lowering the rotational barrier. In contrast, in the case of deoxyguanine derivatives, both the purine H6 and the *cis*-amine *N*-hydrogen atom carry a partial positive charge; therefore, the electrostatic repulsion between the two positively charged moieties, when coming close to one another, would increase the rotational barrier, notwithstanding the small size of H6 as compared to O6 of guanine. In the case of deoxyguanine the greater enthalpy of activation is also accompanied by a rather large entropy of activation (average $170 \pm 4$ as compared to $-18 \pm 4\ J\,mol^{-1}\,K^{-1}$ for guanine derivatives). We suggested that, in the presence of an electrostatic repulsion between the two groups, there could be a large desolvation process (particularly of the amine groups) with the consequent release of water molecules and increase of activation entropy. The explanation given for the $Me_3$dien derivatives is fully confirmed by the behavior of the $Me_5$dien derivatives reported in this paper. The major difference between $Me_3$dien and $Me_5$dien derivatives is the absence, in the latter case, of positively charged *N*-hydrogen atoms on the *cis*-amine groups. In principle, there could also be a change in steric bulk of the terminal amines (an additional methyl group attached to each terminal nitrogen atom in the case of $Me_5$dien); however, such a change in steric bulk could be rather small. It has been widely demonstrated that the rotation of a coordinated purine base is mainly affected by substituents on the *cis*-amine, which have "quasi-equatorial" character, and $Me_3$dien and $Me_5$dien both have one "quasi-equatorial" methyl group on each terminal nitrogen atom.[14]

The $Me_5$dienPt(bzim) complex has an activation enthalpy for rotamer interconversion that is very similar to that observed for the $Me_3$dienPt(deoxyguanine) derivative. The stereochemistry of the H4 proton of bzim is coincident with that of the H6 proton of deoxyguanines; therefore, it is expected to generate a similar steric interaction with the "quasi-equatorial" *N*-Me group on the *cis*-amine, while it is dragged through the platinum coordination plane. Accordingly, the measured $\Delta H^{\ddagger}$ value for rotation is very similar for $Me_3$dienPt(deoxyguanine) and $Me_5$dienPt(bzim) complexes. In contrast, the $\Delta S^{\ddagger}$ value was much greater for $Me_3$dienPt(deoxyguanine) (average $170 \pm 4\ J\,K^{-1}\,mol^{-1}$) than for $Me_5$dienPt(bzim) (average $15 \pm 20\ J\,K^{-1}\,mol^{-1}$). The large value of $\Delta S^{\ddagger}$ for the former complex was explained by a desolvation (particularly of the amine NH group) taking place in the transition state; such a desolvation cannot occur in the $Me_5$dienPt(bzim) complex lacking amine *N*-hydrogen atoms.

The rate of interconversion was found to be extremely low for the $Me_5$dienPt(riba) complex in which the riba ligand has the O6 substituent stereochemically equivalent to the O6 atom of a guanine group. In the case of $Me_3$dienPt(guanine) derivatives the $\Delta H^{\ddagger}$ value for rotamer interconversion was found to be lowered by an electrostatic attraction between the negatively charged O6 atom and the positively charged *N*-hydrogen atom of the *cis*-amine. Such an interaction cannot take place in the $Me_5$dienPt(riba) complex lacking amine *N*-hydrogen atoms. Therefore, contrary to the case of $Me_3$dienPtL derivatives (for which the $\Delta H^{\ddagger}$ value was significantly lower for guanine as compared to deoxyguanine derivatives), $Me_5$dienPtL compounds are expected to have a much larger $\Delta H^{\ddagger}$ value for guanine-type derivatives (like the riba complex) having a bulkier substituent at the C6 position than for deoxyguanine-type derivatives (like the bzim complex) having a small proton at the C6 position. This fully explains the much slower rate of rotation observed in $Me_5$dienPt(riba) as compared to $Me_5$dienPt(bzim).

## Conclusions

This investigation has highlighted two features of $Me_5$dienPtL compounds (a kinetic preference for the *endo* rotamer and a rate of rotation depending upon the substituent at the *peri* position with respect to the coordinated L nitrogen atom) that further contribute to deepening our understanding of interactions between a rotating platinum(II)-coordinated ligand L and *cis*-amine groups. For the first time in $Me_n$dienPtL complexes, it has been shown that the kinetically preferred product has the bulkier portion of the ligand L on the sterically less hindered side of the platinum coordination plane (that is the side where the "quasi-equatorial" *N*-methyl substituents are located). In the case of $Me_3$dienPtL derivatives, the rate of rotamer interconversion was too fast to enable the observation of the kinetically controlled composition.

The investigation of rotamer interconversion in the case of $Me_5$dienPt(bzim) has fully confirmed the previous observation that an amine proton can play a key role in modulating the rate of rotation of a *cis* ligand, also in the case in which an alkyl substituent is attached to the same nitrogen atom (as in the case of $Me_3$dienPtL compounds). The presence of such a proton can increase the rate of L rotation by 10 orders of magnitude [compare the rates of rotation of L in $Me_3$dienPt(deoxyguanine)[17] and in $Me_5$dienPt(bzim)] and can greatly reduce the difference in the rate of rotation between ligands L having a bulky oxygen atom or a small proton substituent in the *peri* position with respect to the coordinated nitrogen atom. Therefore, for $Me_3$dienPtL complexes the rate of rotation is only ten times smaller in guanine than in deoxyguanine derivatives (at ambient temperature), while for $Me_5$dienPtL derivatives the rate is far smaller in the case of riba (mimicking a guanine) than in the case of bzim (mimicking a deoxyguanine).

 © 2006 Wiley-VCH Verlag GmbH & Co. KGaA, Weinheim 

Recent results from studies on oligomers led to the hypothesis that the very small size of the NH group, and not its hydrogen-bonding ability, is responsible for the good activity exhibited by antitumor Pt compounds with amine carrier ligands bearing multiple NH protons.[7,8,22] In contrast, for amines lacking NH groups, bulky substituents projecting out of the coordination plane could clash with neighboring nucleobases. Since the biological activity of cisplatin is widely considered to be associated with a definite arrangement of the nucleic bases (guanines in first place) linked by the metal center,[6–12] the lack of significant biological activity for platinum complexes bearing bulky ligands can be attributed to the conformational restrictions that the coordinated bases are subjected to in these compounds. On the other hand, it has been recently demonstrated that platinum complexes with specially designed bulky ligands can sort out other interesting effects in the case of coordination to single-strand oligonucleotides.[23] In particular, the negatively charged phosphate groups of the oligonucleotide are no longer able to wrap around the positively charged metal core with the consequence of favoring the hybridization of the oligonucleotide with the complementary strand and tightening the double-strand form. Therefore, we can envisage a possible employment of the platinum complex with $Me_5$dien in the modification of single-strand oligonucleotides to be used in antisense and antigene therapy.

## Experimental Section

**Materials:** [Pt($Me_5$dien)($NO_3$)]($NO_3$) was prepared as previously described.[20] Bzim was purchased from Sigma–Aldrich, riba was a gift from Joze Kobe of the Institute of Chemistry of Ljubljana, Slovenia.

**Preparation of the Adducts:** Solutions of the adducts were prepared by treatment of [Pt($Me_5$dien)($NO_3$)]($NO_3$) (5 mM solution in $D_2O$) with a stoichiometric amount of ligand. The reactions were monitored by $^1$H NMR spectroscopy. When the reaction was complete, the pD of the solution was found to be 7.2 in the case of both bzim and riba.

**NMR Spectroscopy:** Spectra were collected in $D_2O$ at 298 K with a Bruker DPX 300 MHz spectrometer. $^1$H NMR chemical shifts were referenced to internal TSP. For 2D NOESY experiments a standard pulse program with gradient pulses during the mixing time was used. 2048 complex points in the direct detection dimension and 256 in the indirect dimension were collected. A 3000 Hz spectral width was used in both dimensions with a 500 ms mixing time. Chemical shift values are reported in Table 1.

**Kinetic Measurements:** NMR tubes containing solutions of the bzim adduct were sealed and kept at a fixed temperature in a water bath. $^1$H NMR spectra were taken from time to time by collecting 64 scans. Selected nonexchangeable proton signals were integrated and used to determine the relative abundance of the two rotamers. Equilibrium was considered reached when the changes in signal intensities became negligible (after a time that was five-fold larger than the estimated half life at a given temperature). The kinetic constants were determined at six different temperatures covering a range of 40° (323, 333, 343, 348, 353, and 363 K). At equilibrium the *exo*/*endo* ratio ($K$) was found to be rather constant (comprised between 0.56 and 0.60). The kinetic equation for the $endo \underset{k_{exo}}{\overset{k_{endo}}{\rightleftarrows}} exo$ process has the following expression:

$$\ln \frac{KC^{t}_{endo} - C^{t}_{exo}}{KC^{0}_{endo} - C^{0}_{exo}} = -(k_{endo} + k_{exo})t$$

[in which $k_{endo}$ and $k_{exo}$ are the kinetic constants for the *endo* → *exo* and the *exo* → *endo* conversions, respectively; $K = (C^{\infty}_{exo}/C^{\infty}_{endo}) = (k_{exo}/k_{endo})$ is the equilibrium constant; $C^t$, $C^0$, and $C^\infty$ are the concentrations of a given rotamer (*endo* or *exo*) at time $t$, at time 0, and at equilibrium]. The graphical representation of the logarithmic term as a function of time (Figure 4) corresponds to a straight line whose slope gives $k_{endo} + k_{exo}$. From the values of $k_{endo}/k_{exo}$ (corresponding to the equilibrium constant $K$) and of $k_{endo} + k_{exo}$ (kinetically determined) the individual $k_{endo}$ and $k_{exo}$ constants

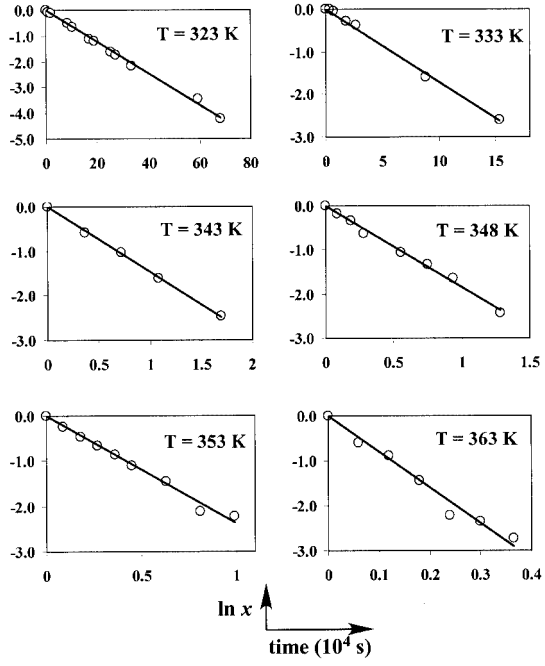


Figure 4. Plots of $\ln x$ {$x = [(KC^t_{endo} - C^t_{exo})/(KC^0_{endo} - C^0_{exo})]$} as a function of time for the isomerization of $Me_5$dienPt(bzim) at different temperatures.

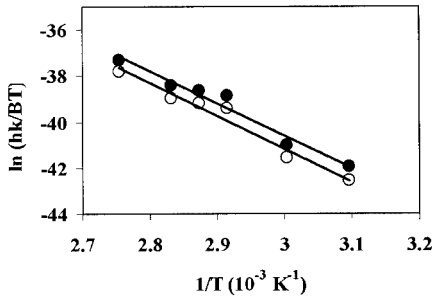


Figure 5. Plots of $\ln(h/B)\cdot(k/T)$ as a function of $1/T$ for the *endo* → *exo* (○) and *exo* → *endo* (●) interconversion of $Me_5$dienPt(bzim). According to the Eyring equation, $\Delta H^{\ddagger}$ and $\Delta S^{\ddagger}$ can be derived from the slope $[(\Delta H^{\ddagger})/R]$ and intercept $[(\Delta S^{\ddagger})/R]$ of the straight line fitting the experimental points.

 © 2006 Wiley-VCH Verlag GmbH & Co. KGaA, Weinheim 

could be determined. Enthalpies and entropies of activation ($\Delta H^{\ddagger}$ and $\Delta S^{\ddagger}$) were estimated (for direct and inverse reactions) from plots of $\ln(h/B)\cdot(k/T)$ vs. $1/T$ (Figure 5), according to the Eyring equation:

$$\ln\frac{h}{B}\frac{k}{T} = -\frac{\Delta H^{\#}}{RT} + \frac{\Delta S^{\#}}{R}$$

[$k$ = kinetic constant ($k_{endo}$ or $k_{exo}$) at temperature $T$; $h$, $B$, and $R$, are the Planck, Boltzmann, and gas constants, respectively].[21] Values of $C_{endo}/C_{exo}$ at different time intervals for a given temperature together with the estimated values of $K$, $k_{endo}$, and $k_{exo}$ are reported in Table 2. Activation parameters are reported in Table 3.

## Acknowledgments

Joze Kobe from the Institute of Chemistry of Ljubljana (Slovenia) is kindly acknowledged for providing the riba ligand. This research was supported by the University of Bari, the Italian "Ministero dell'Istruzione, Universitá e Ricerca (MIUR)" (PRIN 2004 no. 20040590-78), and the EC (COST Chemistry Projects D20/0001/2000 and D20/0003/01).

[1] B. A. Chabner, T. G. Roberts, *Nat. Rev. Cancer* **2005**, *5*, 65–72.
[2] *Cisplatin: Chemistry and Biochemistry of a Leading Anticancer Drug* (Ed.: B. Lippert), Wiley-VCH, Zurich, **1999**.
[3] J. Reedijk, *Inorg. Chim. Acta* **1992**, *198–200*, 873–881.
[4] A. Eastman, *Biochemistry* **1986**, *25*, 3912–3915.
[5] A. Gelasco, S. J. Lippard, *Biochemistry* **1998**, *37*, 9230–9239.
[6] K. M. Williams, L. Cerasino, G. Natile, L. G. Marzilli, *J. Am. Chem. Soc.* **2000**, *122*, 8021–8030.
[7] J. S. Saad, T. Scarcia, K. Shinozuka, G. Natile, L. G. Marzilli, *Inorg. Chem.* **2002**, *41*, 546–557.
[8] M. Benedetti, J. S. Saad, L. G. Marzilli, G. Natile, *Dalton Trans.* **2003**, *5*, 872–879.
[9] S. T. Sullivan, A. Ciccarese, F. P. Fanizzi, L. G. Marzilli, *Inorg. Chem.* **2000**, *39*, 836–842.
[10] L. G. Marzilli, S. O. Ano, F. P. Intini, G. Natile, *J. Am. Chem. Soc.* **1999**, *121*, 9133–9142.
[11] S. O. Ano, F. P. Intini, G. Natile, L. G. Marzilli, *J. Am. Chem. Soc.* **1997**, *119*, 8570–8571.
[12] S. O. Ano, F. P. Intini, G. Natile, L. G. Marzilli, *J. Am. Chem. Soc.* **1998**, *120*, 12017–12022.
[13] L. Cerasino, F. P. Intini, J. Kobe, E. de Clercq, G. Natile, *Inorg. Chim. Acta* **2003**, *344*, 174–182.
[14] M. Carlone, F. P. Fanizzi, F. P. Intini, N. Margiotta, L. G. Marzilli, G. Natile, *Inorg. Chem.* **2000**, *39*, 634–641.
[15] N. G. Di Masi, F. P. Intini, C. Pacifico, L. Maresca, G. Natile, *Inorg. Chim. Acta* **2000**, *310*, 27–33.
[16] M. Carlone, L. G. Marzilli, G. Natile, *Inorg. Chem.* **2004**, *43*, 584–592.
[17] M. Carlone, L. G. Marzilli, G. Natile, *Eur. J. Inorg. Chem.* **2005**, 1264–1273.
[18] F. P. Fanizzi, G. Natile, M. Lanfranchi, A. Tiripichio, R. J. H. Clark, D. J. Michael, *J. Chem. Soc., Dalton Trans.* **1989**, *1*, 1689–1696.
[19] Z. Guo, Y. Chen, E. Zang, P. J. Sadler, *J. Chem. Soc., Dalton Trans.* **1997**, 4107–4111.
[20] R. Cini, F. P. Intini, L. Maresca, C. Pacifico, G. Natile, *Eur. J. Inorg. Chem.* **1998**, 1305–1312.
[21] H. Eyring, *J. Chem. Phys.* **1935**, *3*, 107–115.
[22] L. G. Marzilli, J. S. Saad, Z. Kuklenyik, K. A. Keating, Y. Xu, *J. Am. Chem. Soc.* **2001**, *123*, 2764–2770.
[23] V. Beljanski, J. M. Villanueva, P. W. Doetsch, G. Natile, L. G. Marzilli, *J. Am. Chem. Soc.* **2005**, *127*, 15833–15842.

Received: March 14, 2006
Published Online: June 23, 2006

 © 2006 Wiley-VCH Verlag GmbH & Co. KGaA, Weinheim 

DOI: 10.1002/ejic.200600242

# Methoxyphenyl-Functionalized Diiron Azadithiolates as Models for the Active Site of Fe-Only Hydrogenases: Synthesis, Structures, and Biomimetic $H_2$ Evolution

**Li-Cheng Song,*[a] Jian-Hua Ge,[a] Xiao-Guang Zhang,[a] Yang Liu,[a] and Qing-Mei Hu[a]**

**Keywords:** Biomimetic chemistry / Diiron azadithiolate / Iron-only hydrogenases / Structural elucidation / Catalytic $H_2$ evolution

A series of methoxyphenyl-functionalized diiron azadithiolate (ADT) complexes, [{(μ-$SCH_2$)$_2$N($C_6H_4$OMe-*p*)}$Fe_2(CO)_5$L] [L = CO (**2**); $PPh_3$ (**3**); $PPh_2H$ (**4**)] and [{(μ-$SCH_2$)$_2$N-($C_6H_4$OMe-*p*)}$Fe_2(CO)_4(CN)_2$][$Et_4N$]$_2$ (**5**) as the active site models of Fe-only hydrogenases has been investigated. While model **2** was prepared in 67 % yield by a condensation reaction of *N*,*N*-bis(chloromethyl)-*p*-methoxyaniline (**1**) with [(μ-LiS)$_2Fe_2(CO)_6$], models **3**–**5** were prepared in 49–75 % yields by a CO substitution reaction of **2** with $PPh_3$, $PPh_2H$, or $Et_4NCN$, respectively. The X-ray crystal structures of **2** and **3** revealed that the methoxyphenyl substituent is attached to the N atom by an axial bond and the nitrogen lone electron pair in an equatorial position. On the basis of cyclic voltammetric studies of **2** and **4**, it was found that **2** is a catalyst for proton reduction, and an EECC mechanism is proposed for such electrocatalytic $H_2$ production catalyzed by the ADT-type models.

(© Wiley-VCH Verlag GmbH & Co. KGaA, 69451 Weinheim, Germany, 2006)

## Introduction

Hydrogen evolution and uptake in the biological energy cycle is mostly catalyzed by two types of metalloenzymes: Fe-only hydrogenases and NiFe hydrogenases.[1,2] Fe-only hydrogenases (hereafter referred to as FeHases) have recently received much more attention than NiFe hydrogenases, primarily owing to their much higher efficiency than NiFe hydrogenases in the production of hydrogen,[3] a clean and highly efficient fuel. The high-quality crystal structures of FeHases isolated from *C. pasteurianum* and *D. desulfuricans* have indicated[4] that the active site of FeHases (so-called H cluster) comprises a butterfly 2Fe2S cluster with one of the Fe atoms linked to a cuboidal 4Fe4S cluster through the S atom of a cysteinyl ligand. There are also three other ligands, namely CO, $CN^-$, and dithiolate coordinated to Fe atoms of the butterfly 2Fe2S cluster (Scheme 1). It is noteworthy that the dithiolate ligand bridged between the two iron atoms of the 2Fe2S cluster was recently suggested as an azadithiolate (ADT) $SCH_2NHCH_2S$,[5] in which the bridgehead N atom plays an important role for the heterolytic cleavage or formation of $H_2$ in the enzymatic process.[6] In spite of the biological importance of the bridgehead N atom in the H cluster, the synthetic and functional studies regarding azadithiolate (ADT) model complexes[7] have been much less investigated than diiron 1,3-propanedithiolate (PDT) model compounds.[8] So far, the PDT-type models [(μ-H)(μ-PDT)$Fe_2(CO)_4(L)_2]^+$ (L = $Me_3P$, *t*BuNC) have been reported to be catalysts for H/D exchange reactions.[9] In addition, the PDT- and ADT-type models [(μ-PDT)$Fe_2(CO)_4(CN)(Me_3P)]^-$,[10] [(μ-PDT)$Fe_2$-$(CO)_4L_2$] (L = CO, $Me_3P$),[11] and [{(μ-$SCH_2$)$_2$N(*p*-$BrC_6H_4CH_2$)}$Fe_2(CO)_6$][12] have been demonstrated to be catalysts for proton reduction to $H_2$ under electrochemical conditions. To further develop the biomimetic chemistry of FeHases, we initiated a study on the synthesis, structures and properties of a new series of diiron ADT-type model complexes, in which some substituents are attached to the N atom and Fe atoms in the diiron ADT framework [{(μ-$SCH_2$)$_2$N}$Fe_2(CO)_n$] (*n* = 4, 5). Herein we report our results obtained from this study.

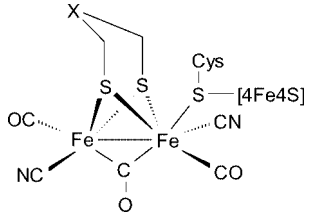


Scheme 1. Composite structure of H cluster obtained from protein crystallography (X = $CH_2$, NH, or O).

[a] Department of Chemistry, State Key Laboratory of Elemento-Organic Chemistry, Nankai University,
Tianjin 300071, China
Fax: +86-22-23504853
E-mail: lcsong@nankai.edu.cn

 © 2006 Wiley-VCH Verlag GmbH & Co. KGaA, Weinheim 

## Results and Discussion

### Synthesis and Spectroscopic Characterization of Compounds 1–5

The synthetic methods for our target compounds **2**–**5** and their precursor **1** are based on those previously reported by Rauchfuss[13] and the well-known CO substitution reactions with various 2e ligands[14] (Scheme 2). Treatment of *p*-methoxyaniline with paraformaldehyde in $CH_2Cl_2$ at room temperature followed by treatment with an excess of $SOCl_2$ gave *N*,*N*-bis(chloromethyl)-*p*-methoxyaniline (**1**) in 91% yield. Further reaction of **1** with lithium salt $[(\mu\text{-}LiS)_2Fe_2(CO)_6]$ {generated in situ from $[(\mu\text{-}S)_2Fe_2(CO)_6]$ and $Et_3BHLi$ in THF at –78 °C}[15] afforded the ADT-type model **2** in 67% yield. Models **3**–**5** could be prepared in 49–75% yields through CO substitution reactions of **2** in MeCN with $PPh_3$ in the presence of the decarbonylating agent $Me_3NO$, with $PPh_2H$ in toluene at reflux, or with $Et_4NCN$ in MeCN from 0 °C to room temperature, respectively.

Compounds **1**–**5** have been characterized by elemental analysis and IR and $^1H$ NMR spectroscopy. The $^1H$ NMR spectra of **1**–**5** each show a singlet at $\delta \approx 3.7$ ppm for their MeO groups and an AB quartet between $\delta = 6.5$ and 7.2 ppm for their *para*-disubstituted $C_6H_4$ benzene rings. While precursor **1** displays a singlet at $\delta = 5.44$ ppm for its $CH_2$ groups, **2** exhibits a singlet, **3** two doublets, **4** a multiplet, and **5** a singlet for their $CH_2$ groups at a relatively higher field. In addition, the IR spectra of **2**–**5** show three absorption bands around 2000 $cm^{-1}$ for their terminal carbonyl groups and the $\tilde{\nu}(C{\equiv}O)$ values of **3**–**5** are markedly shifted towards lower frequencies relative to those of their parent complex **2**. It follows that the $PPh_3$, $PPh_2H$, and $CN^-$ ligands in **3**–**5** are all stronger electron-donating ligands than CO.[16]

### Crystal Structures of Compounds 2 and 3

The structures of **2** and **3** have been unambiguously confirmed by X-ray crystal diffraction analysis. ORTEP diagrams of **2** and **3** are given in Figures 1 and 2, and Tables 1 and 2 list selected bond lengths and angles, respectively. Models **2** and **3**, as illustrated in Figures 1 and 2, indeed consist of a *p*-methoxyphenyl-substituted azadithiolate group that is bridged between two iron atoms to form a butterfly 2Fe2S cluster. The Fe–Fe bond of **3** [2.554(2) Å] is longer than those of **2** [2.5076(16) Å], $[\{(\mu\text{-}SCH_2)_2\text{-}NMe\}Fe_2(CO)_6]$ [2.4924(7) Å][7a] and $[(\mu\text{-}PDT)Fe_2(CO)_6]$ [2.5103(11) Å],[17] but somewhat shorter than those in the structures of enzymes *C. pasteurianum* and *D. desulfuricans* (ca. 2.6 Å).[4] The sum of the C–N–C angles around the N atom is 354.8° for **2** and 355.9° for **3**. This means that the p–π conjugation exists between the substituted benzene ring and the p-orbital of the bridgehead N atom, although it is weakened because the N atom is slightly deviated from the plane defined by the N(1), C(7), C(8), and C(9) atoms (for **2**) or by the N(1), C(24), C(25), and C(26) atoms (for **3**). Both **2** and **3** contain two fused six-membered rings: N(1)-C(7)S(1)Fe(2)S(2)C(8) and N(1)C(7)S(1)Fe(1)S(2)C(8) for **2**; N(1)C(24)S(1)Fe(1)S(2)C(25) and N(1)C(24)S(1)Fe(2)-S(2)C(25) for **3**. The former six-membered ring in **2** or **3** is in a chair conformation, while the latter ring in **2** or **3** is in a boat conformation. It should be noted that the phenyl group attached to the N(1) atom of **2** and **3** resides in an

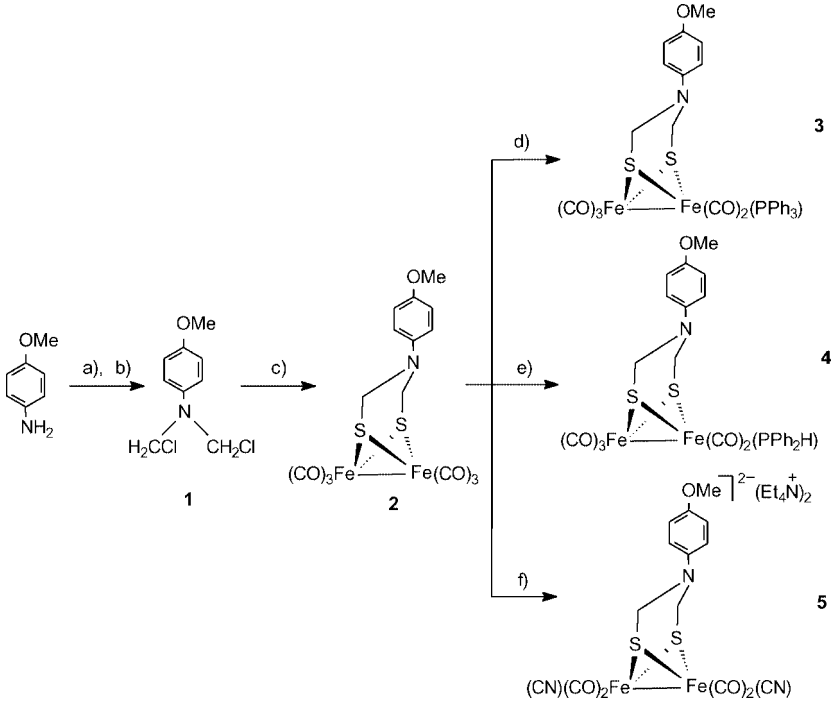


Scheme 2. (a) $(CH_2O)_n$, $CH_2Cl_2$, room temp.; (b) $SOCl_2$, room temp.; (c) $[(\mu\text{-}LiS)_2Fe_2(CO)_6]$, THF, –78 °C; (d) $PPh_3$, $Me_3NO$, MeCN, room temp.; (e) $PPh_2H$, toluene, reflux; (f) $Et_4NCN$, MeCN, 0 °C.

 © 2006 Wiley-VCH Verlag GmbH & Co. KGaA, Weinheim 

axial position and the nitrogen lone electron pair is in an equatorial position. In fact, such a conformation is also observed in other phenyl-substituted ADT-type models.[7c] Furthermore, the $PPh_3$ ligand in **3** is in an axial position of the square-pyramidal geometry of the Fe(1) atom and *trans* to the substituted benzene ring in order to reduce the steric repulsion between these two bulky structural units.

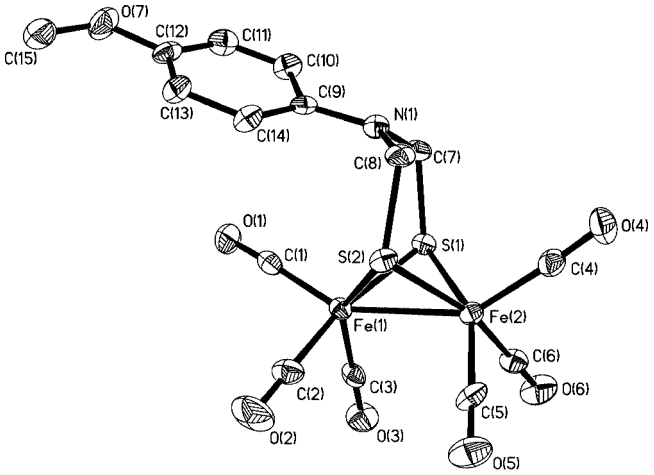


Figure 1. ORTEP view of **2** with 30% probability level ellipsoids.

Table 1. Selected bond lengths [Å] and angles [°] for **2**.

| | | | |
|---|---|---|---|
| Fe(1)–S(2) | 2.264(3) | N(1)–C(7) | 1.439(8) |
| Fe(2)–S(1) | 2.263(2) | N(1)–C(8) | 1.418(8) |
| Fe(1)–S(1) | 2.2537(19) | N(1)–C(9) | 1.419(8) |
| Fe(1)–Fe(2) | 2.5076(16) | Fe(2)–S(2) | 2.249(3) |
| S(1)–Fe(1)–S(2) | 84.42(8) | Fe(1)–S(1)–Fe(2) | 67.45(6) |
| S(1)–Fe(1)–Fe(2) | 56.45(5) | Fe(2)–S(2)–Fe(1) | 67.50(8) |
| S(2)–Fe(1)–Fe(2) | 55.97(7) | C(8)–N(1)–C(9) | 119.6(5) |
| S(2)–Fe(2)–Fe(1) | 56.54(8) | C(8)–N(1)–C(7) | 113.4(6) |
| S(1)–Fe(2)–Fe(1) | 56.10(5) | C(9)–N(1)–C(7) | 121.8(5) |

Table 2. Selected bond lengths [Å] and angles [°] for **3**.

| | | | |
|---|---|---|---|
| Fe(1)–P(1) | 2.290(2) | Fe(2)–S(1) | 2.322(2) |
| Fe(1)–S(1) | 2.314(3) | P(1)–C(6) | 1.856(7) |
| Fe(1)–S(2) | 2.320(3) | N(1)–C(24) | 1.443(8) |
| Fe(1)–Fe(2) | 2.554(2) | N(1)–C(25) | 1.452(9) |
| Fe(2)–S(2) | 2.296(3) | N(1)–C(26) | 1.438(9) |
| S(1)–Fe(1)–P(1) | 105.13(8) | S(2)–Fe(2)–S(1) | 83.44(8) |
| S(1)–Fe(1)–S(2) | 83.09(8) | S(1)–Fe(2)–Fe(1) | 56.43(7) |
| P(1)–Fe(1)–Fe(2) | 156.84(7) | Fe(1)–S(1)–Fe(2) | 66.84(8) |
| S(1)–Fe(1)–Fe(2) | 56.73(6) | C(26)–N(1)–C(24) | 118.6(6) |
| S(2)–Fe(1)–Fe(2) | 55.96(7) | C(25)–N(1)–C(24) | 114.2(6) |

### Electrochemistry of Compounds 2 and 4

The electrochemical behavior of the representative models **2** and **4** was studied in MeCN by cyclic voltammetric techniques. Table 3 lists their electrochemical data, and Figures 3 and 4 show their cyclic voltammograms, respectively.

Table 3. Electrochemical data of **2** and **4**.[a]

| Compound | $E_{pc}$ | $E_{pa}$ [V] | $E_{pa}$ | $E_{pc}$ [V] |
|---|---|---|---|---|
| **2** | –1.61 | –1.48 | +0.48 | – |
| | –2.10 | – | +0.81 | – |
| **4** | –1.78 | –1.50 | +0.26 | – |
| | –2.22 | – | +0.49 | – |

[a] All potentials in Table 3 are vs. $Fc/Fc^+$.

It has been demonstrated that **2** displays one quasi-reversible reduction, one irreversible reduction and two irreversible oxidations, whereas **4** exhibits two irreversible reductions and two irreversible oxidations. The first and second reduction peaks of **2** (–1.61 V, –2.10 V) and **4** (–1.78 V, –2.22 V) can be assigned to the one-electron reduction processes from $Fe^IFe^I$ to $Fe^IFe^0$ and $Fe^IFe^0$ to $Fe^0Fe^0$ (supported by bulk electrolysis). Similarly, the first and second oxidation peaks of **2** (+0.48 V, +0.81 V) and **4** (+0.26 V, +0.49 V) should be attributed to the one-electron oxidation processes from $Fe^IFe^I$ to $Fe^IFe^{II}$ and $Fe^IFe^{II}$ to

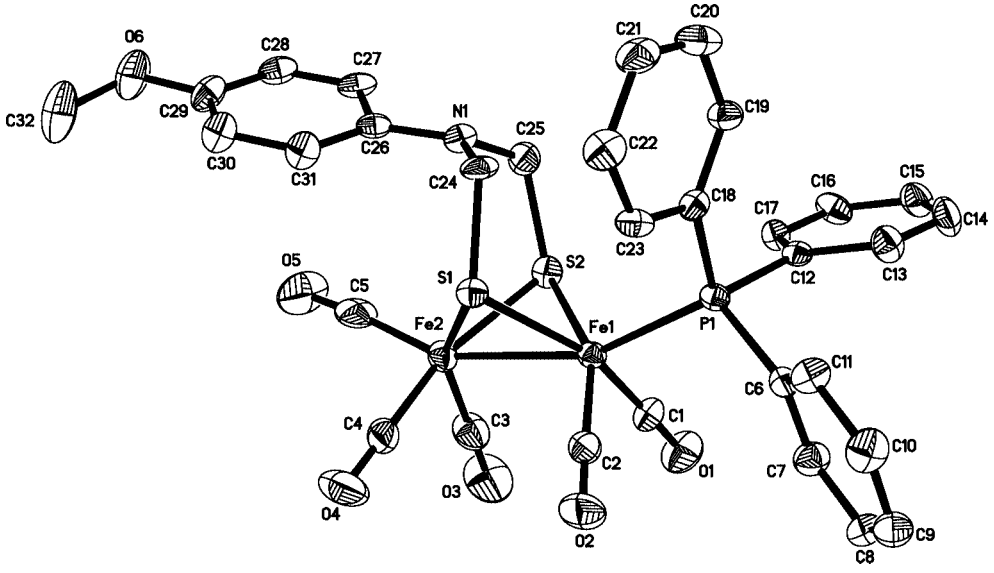


Figure 2. ORTEP view of **3** with 30% probability level ellipsoids.

 © 2006 Wiley-VCH Verlag GmbH & Co. KGaA, Weinheim 

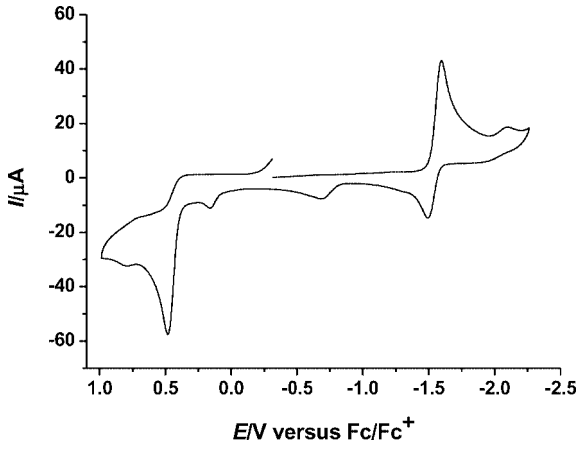


Figure 3. Cyclic voltammogram of **2** (1 mM) in 0.1 M $nBu_4NPF_6$/MeCN at a scan rate of 100 $mVs^{-1}$.

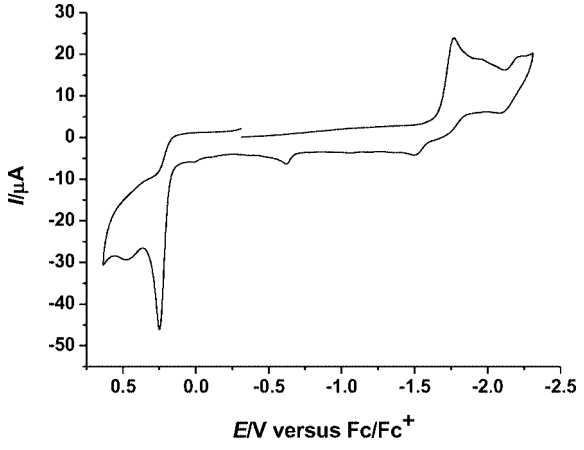


Figure 4. Cyclic voltammogram of **4** (1 mM) in 0.1 M $nBu_4NPF_6$/MeCN at a scan rate of 100 $mVs^{-1}$.

$Fe^{II}Fe^{II}$, respectively. It can be seen that the reduction and oxidation peaks of **4** (Figure 4) are apparently shifted towards more negative potentials than those corresponding to **2**. This is consistent with the substituent $PPh_2H$ being a stronger electron-donating ligand than CO. Actually, the electrochemical behavior described above resembles that displayed by those reported for ADT-, PDT-, and ODT-(oxadithiolate)-bridged analogs.[10–12,18]

We further studied the electrochemical behavior of model **2** by cyclic voltammetric techniques in the presence of HOAc (0–10 mM) in MeCN. As shown in Figure 5, the current intensity of the initial first peak at –1.61 V slightly increased when the first amount of HOAc (2 mM) was added, but it did not increase further with sequential increments of the acid concentration. However, when the first 2 mM HOAc was added, the initial second peak at –2.10 V grew considerably and increased linearly with increasing acid concentration. It is evident that such cyclic voltammetric behavior features an electrocatalytic proton reduction process.[10–12,18–21] This catalytic process was further confirmed by electrolysis of a MeCN solution of **2** (0.33 mM) with excess HOAc (6.6 mM) at –2.18 V (Figure 6). The initial rate of electrolysis is more than twice as much as it is in the absence of the catalyst. A total of 10.2 F/mol passed in 0.5 h, which corresponds to 5.1 turnovers. In such a large-scale experiment, $H_2$ evolution could clearly be seen. Gas chromatographic analysis showed that the hydrogen yield was about 90%.

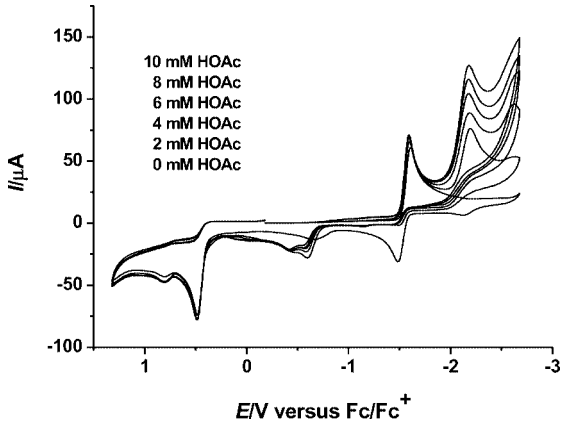


Figure 5. Cyclic voltammogram of **2** (1.0 mM) with HOAc (0–10 mM).

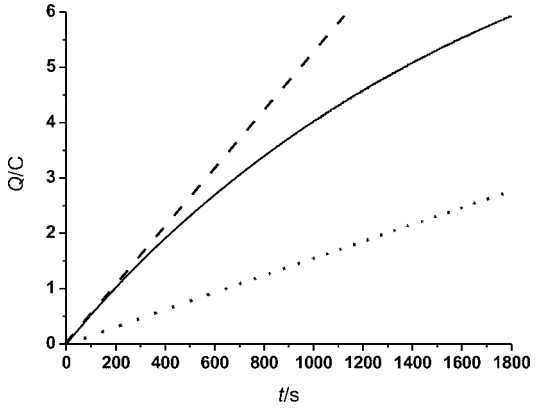


Figure 6. Bulk electrolysis of HOAc at a vitreous carbon rod electrode in the presence of **2** (——) and without **2** (·····); extrapolation of the catalytic reduction at the initial electrolysis rate (------).

On the basis of previously reported, similar cases[10–12,18–21] and the above-mentioned electrochemical observations, we can propose an EECC (E = electrochemical, C = chemical) mechanism to account for the above-described electrocatalytic $H_2$ production process. As shown in Scheme 3, model **2** can undergo a one-electron reduction at –1.61 V to give the intermediate **2a**. Further one-electron reduction of **2a** at –2.10 V affords intermediate **2b**, which is then protonated to give intermediate **2c**. Final protonation of **2c** results in $H_2$ evolution to accomplish the catalytic cycle. Apparently, this mechanism is different from the CECE mechanism for $H_2$ production from $HClO_4$ catalyzed by the benzyl-substituted model $[\{(\mu\text{-}SCH_2)_2N(p\text{-}BrC_6H_4CH_2)\}Fe_2(CO)_6]$.[12] In the CECE mechanism the bridged N atom of the benzyl-substituted model is first protonated by strong acid, $HClO_4$, whereas in our EECC mechanism the bridged N atom of model **2** is not protonated by weak acid, HOAc. In fact, the protonation of the benzyl-substituted model and the nonprotonation of **2** were

 © 2006 Wiley-VCH Verlag GmbH & Co. KGaA, Weinheim 

all confirmed by spectroscopic studies. That is, the $^1H$ NMR and IR spectroscopic data of the benzyl-substituted model determined in $HClO_4$ were obviously changed due to protonation of its bridged N atom,[12] while the corresponding data of model **2** determined by us in HOAc were almost the same as those determined in the absence of HOAc.[22] Finally, it should be noted that model **2** undergoes serious decomposition in $HClO_4$. The decomposition could be observed by its color changes from red to orange and then to light yellow. In addition, some bubbles were liberated upon addition of 5–30 equiv. of $HClO_4$ to a solution of **2** in $CD_3CN$. In fact, it is the decomposition that precluded us from further studies on its electrochemical behavior in the presence of $HClO_4$.

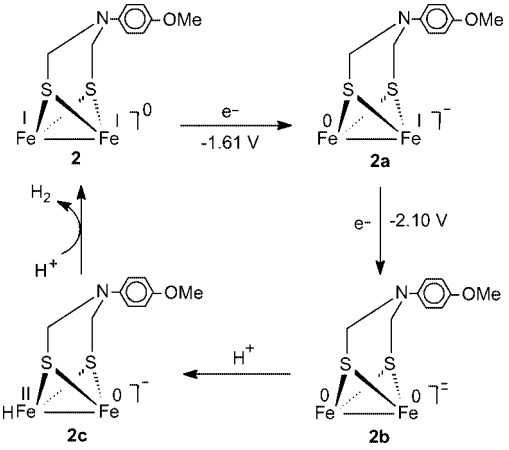


Scheme 3. Suggested EECC mechanism for $H_2$ production catalyzed by **2**. All carbonyl groups attached to Fe are omitted for clarity.

## Experimental Section

**General Comments:** All reactions were carried out under prepurified nitrogen with standard Schlenk and vacuum-line techniques. All solvents were dried and distilled prior to use. Paraformaldehyde, $SOCl_2$, $Et_3BHLi$ (1 M in THF), *p*-$MeOC_6H_4NH_2$, $Et_4NCN$, $Me_3NO{\cdot}2H_2O$, and $PPh_3$ were available commercially and used as received. $[(\mu\text{-}S)_2Fe_2(CO)_6]$[15] and $PPh_2H$[23] were prepared according to published procedures. Preparative TLC was carried out on glass plates (26 × 20 × 0.25 cm) coated with silica gel H (10–40 μm). IR spectra were recorded with a Nicolet Magna 560 FTIR or a Bruker Vector 22 infrared spectrophotometer. $^1H$ NMR spectra were recorded with a Bruker AC-P 300 NMR spectrometer. Elemental analyses was performed with an Elementar Vario EL analyzer. Melting points were determined with a Yanaco MP-500 apparatus.

**Preparation of *N*,*N*-$(ClCH_2)_2N(C_6H_4OMe\text{-}p)$ (1):** A suspension consisting of paraformaldehyde (1.50 g, 50 mmol), *p*-$MeOC_6H_4NH_2$ (2.46 g, 20 mmol), and $CH_2Cl_2$ (30 mL) was stirred at room temperature for 5 h, and then treated dropwise with $SOCl_2$ (9.52 g, 80 mmol). After the gas evolution had ceased, solvent and unreacted $SOCl_2$ were removed in vacuo. The residue was purified by extraction into $Et_2O$. Removal of $Et_2O$ afforded **1** as an orange solid (3.99 g, 91%). M.p. 38–40 °C. $^1H$ NMR (300 MHz, $CDCl_3$): $\delta$ = 7.15, 7.12, 6.84, 6.81 (AB q, 4 H, $C_6H_4$), 5.44 (s, 4 H, $2CH_2$), 3.70 (s, 3 H, $CH_3$) ppm. IR (KBr disk): $\tilde{\nu}$ = 1507 (s), 1280 (m), 1245 (s), 1183 (m), 1154 (s), 1098 (m), 1052 (m), 1023 (s), 943 (s), 820 (s) $cm^{-1}$. $C_9H_{11}Cl_2NO$ (220.10): calcd. C 49.11, H 5.04, N 6.36; found C 49.12, H 5.19, N 6.40.

**Preparation of $[\{(\mu\text{-}SCH_2)_2N(C_6H_4OMe\text{-}p)\}Fe_2(CO)_6]$ (2):** A solution of $[(\mu\text{-}S)_2Fe_2(CO)_6]$ (0.344 g, 1 mmol) in THF (20 mL) was cooled to –78 °C and treated dropwise with $Et_3BHLi$ (1 M in THF, 2 mL, 2 mmol) to give a green solution. After stirring for 15 min, **1** (0.55 g, 2.50 mmol) was added to cause an immediate color change from green to red. The mixture was warmed to room temperature and stirred for 8 h. The crude product was separated by TLC using $CH_2Cl_2$/petroleum ether (1:5) as the eluent. Compound **2** was obtained from the main band as a red solid (0.329 g, 67%). M.p. 132–135 °C. $^1H$ NMR (300 MHz, $CDCl_3$): $\delta$ = 6.90, 6.87, 6.72, 6.69 (AB q, 4 H, $C_6H_4$), 4.26 (s, 4 H, 2 $CH_2$), 3.78 (s, 3 H, $CH_3$) ppm. IR (KBr disk): $\tilde{\nu}$ = 2073 (s), 2027 (vs), 1969 (s) (C≡O) $cm^{-1}$. $C_{15}H_{11}Fe_2NO_7S_2$ (493.07): calcd. C 36.54, H 2.25, N 2.84; found C 36.42, H 2.30, N 2.86.

**Preparation of $[\{(\mu\text{-}SCH_2)_2N(C_6H_4OMe\text{-}p)\}Fe_2(CO)_5(PPh_3)]$ (3):** A mixture of **2** (0.124 g, 0.25 mmol), $PPh_3$ (0.065 g, 0.25 mmol), $Me_3NO{\cdot}2H_2O$ (0.029 g, 0.25 mmol), and MeCN (20 mL) was stirred at room temperature for 3 h. The resulting dark-brown mixture was concentrated to dryness in vacuo and the residue was separated by TLC using $CH_2Cl_2$/petroleum ether (1:2) as the eluent. Compound **3** was obtained from the main band as a red solid (0.136 g, 75%). M.p. 134 °C (dec). $^1H$ NMR (300 MHz, $CDCl_3$): $\delta$ = 7.73–7.44 (m, 15 H, $3C_6H_5$), 6.76, 6.73, 6.49, 6.46 (AB q, 4 H, $C_6H_4$), 3.82 (d, $J$ = 12.3 Hz, 2 H, 2 C*H*H), 3.73 (s, 3 H, $CH_3$), 2.90 (d, $J$ = 12.3 Hz, 2 H, 2 C*H*H) ppm. IR (KBr disk): $\tilde{\nu}$ = 2041 (vs), 1984 (vs), 1923 (s) (C≡O) $cm^{-1}$. $C_{32}H_{26}Fe_2NO_6PS_2$ (727.33): calcd. C 52.84, H 3.60, N 1.93; found C 52.80, H 3.45, N 1.87.

**Preparation of $[\{(\mu\text{-}SCH_2)_2N(C_6H_4OMe\text{-}p)\}Fe_2(CO)_5(PPh_2H)]$ (4):** A mixture of **2** (0.124 g, 0.25 mmol), $PPh_2H$ (0.047 g, 0.25 mmol), and toluene (20 mL) was stirred and refluxed for 4.5 h. The same workup used for **3** gave **4** as a red solid (0.080 g, 49%). M.p. 126–127 °C. $^1H$ NMR (300 MHz, $CDCl_3$): $\delta$ = 7.62–7.34 (m, 10 H, 2 $C_6H_5$), 6.72, 6.69, 6.51, 6.48 (AB q, 4 H, $C_6H_4$), 6.20 (d, $J$ = 349.8 Hz, 1 H, PH), 4.03–3.92 (m, 4 H, $2CH_2$), 3.68 (s, 3 H, $CH_3$) ppm. IR (KBr disk): $\tilde{\nu}$ = 2045 (vs), 1984 (vs), 1924 (s) (C≡O) $cm^{-1}$. $C_{26}H_{22}Fe_2NO_6PS_2$ (651.25): calcd. C 47.95, H 3.40, N 2.15; found C 47.92, H 3.32, N 2.19.

**Preparation of $[\{(\mu\text{-}SCH_2)_2N(C_6H_4OMe\text{-}p)\}Fe_2(CO)_4(CN)_2]\text{-}[(Et_4N)]_2$ (5):** A solution of $Et_4NCN$ (0.156 g, 1 mmol) in MeCN (5 mL) was added to a solution of **2** (0.247 g, 0.5 mmol) in MeCN (20 mL) at 0 °C, causing an immediate gas evolution. The mixture was warmed to room temperature and stirred for 4 h. The resulting brown-red solution was concentrated to dryness and the product was washed with hexane and diethyl ether, and finally dried in vacuo. Compound **5** was obtained as a red solid (0.266 g, 71%). M.p. 82–83 °C. $^1H$ NMR (300 MHz, $CD_3CN$): $\delta$ = 6.86, 6.83, 6.72, 6.68 (AB q, 4 H, $C_6H_4$), 4.16 (s, 3 H, $OCH_3$), 3.74 (s, 4 H, 2 $CH_2S$), 3.44 (q, $J$ = 6.9 Hz, 16 H, 8 C$H_2$CH$_3$), 1.14 (t, $J$ = 6.9 Hz, 24 H, 8 $CH_2CH_3$) ppm. IR (KBr disk): $\tilde{\nu}$ = 2066 (s), 2027 (s) (C≡N), 1968 (vs), 1933 (vs), 1893 (vs) (C≡O) $cm^{-1}$. $C_{31}H_{51}Fe_2N_5O_5S_2$ (749.59): C 49.67, H 6.86, N 9.34; found C 49.50, H 7.02, N 9.21.

**X-ray Structure Determination of 2 and 3:** Single crystals of **2** and **3** suitable for X-ray diffraction analyses were grown by slow concentration of their $CH_2Cl_2$/haxane solutions at about –25 °C. Each single crystal was mounted on a Bruker SMART 1000 automated diffractometer. Data were collected at room temperature, using graphite-monochromated Mo-$K_\alpha$ radiation ($\lambda$ = 0.71073 Å) in the $\omega$-2$\theta$ scanning mode. Absorption corrections were performed with the SADABS program.[24] The structures were solved by direct

 © 2006 Wiley-VCH Verlag GmbH & Co. KGaA, Weinheim 

methods using the SHELXS-97[25] program and refined by full-matrix least-squares techniques (SHELXL-97[26]) on $F^2$. Hydrogen atoms were located by using the geometric method. Details of crystal data, data collections, and structure refinements are summarized in Table 4. CCDC-293719 (**2**) and -293720 (**3**) contain the supplementary crystallographic data for this paper. These data can be obtained free of charge from The Cambridge Crystallographic Data Centre via www.ccdc.cam.ac.uk/data_request/cif.

Table 4. Crystal data and structural refinement details for **2** and **3**.

| | **2** | **3** |
|---|---|---|
| Empirical formula | $C_{15}H_{11}Fe_2NO_7S_2$ | $C_{32}H_{26}Fe_2NO_6PS_2$ |
| $M_r$ [g·mol$^{-1}$] | 493.07 | 727.33 |
| Crystal system | orthorhombic | triclinic |
| Space group | *Pca*2(1) | $P\bar{1}$ |
| *a* [Å] | 15.995(4) | 9.691(8) |
| *b* [Å] | 9.306(3) | 10.371(8) |
| *c* [Å] | 24.928(8) | 17.578(16) |
| $\alpha$ [°] | 90 | 72.857(12) |
| $\beta$ [°] | 90 | 78.003(18) |
| $\gamma$ [°] | 90 | 87.556(13) |
| *V* [Å$^3$] | 3710.7(19) | 1651(2) |
| *Z* | 8 | 2 |
| $\rho_{calcd.}$ [g·cm$^{-3}$] | 1.765 | 1.463 |
| *F*(000) | 1984 | 744 |
| $\mu$ [mm$^{-1}$] | 1.826 | 1.097 |
| $2\theta_{max}$ [°] | 52.98 | 50.02 |
| Reflections collected | 20521 | 8267 |
| Independent reflections | 6006 | 5706 |
| Index ranges | $-20 \le h \le 1\,9$ | $-11 \le h \le 9$ |
| | $-11 \le k \le 9$ | $-12 \le k \le 12$ |
| | $-22 \le l \le 31$ | $-16 \le l \le 20$ |
| *R* | 0.0463 | 0.0806 |
| *Rw* | 0.0921 | 0.1324 |
| Goodness-of-fit | 1.058 | 1.019 |
| Largest diff peak/hole [e·Å$^{-3}$] | 1.136/–0.448 | 0.731/–0.519 |

**Electrochemistry:** Acetonitrile (Fisher Chemicals, HPLC grade) was the solvent used for the electrochemistry. A solution of 0.1 M $n$Bu$_4$NPF$_6$ in MeCN was used as the electrolyte in all of the cyclic voltammetric experiments. The electrolyte solution was degassed by bubbling $N_2$ through it for 10 min before measurements were taken. Electrochemical measurements were made using a BAS Epsilon potentiostat. All voltammograms were obtained in a three-electrode cell with a 3-mm-diameter glassy carbon working electrode, a platinum counter electrode and an Ag/Ag$^+$ (0.01 M AgNO$_3$/0.1 M $n$Bu$_4$NPF$_6$ in MeCN) reference electrode under $N_2$ or CO. The working electrode was polished with 0.05 μm alumina paste and sonicated in water for 10 min. Bulk electrolysis was run on a vitreous carbon rod (ca. 3 cm$^2$) in a two-compartment, gas tight, H-type electrolysis cell containing ca. 18 mL of MeCN. All potentials are quoted against the ferrocene/ferrocenium (Fc/Fc$^+$) potential.

## Acknowledgments

We are grateful to the National Natural Science Foundation of China and the Specialized Research Fund for the Doctoral Program of Higher Education of China for financial support of this work.

[1] a) M. Y. Darensbourg, E. J. Lyon, J. J. Smee, *Coord. Chem. Rev.* **2000**, *206–207*, 533–561; b) M. Y. Darensbourg, E. J. Lyon, X. Zhao, I. P. Georgakaki, *Proc. Natl. Acad. Sci. U. S. A.* **2003**, *100*, 3683–3688; c) D. J. Evans, C. J. Pickett, *Chem. Soc. Rev.* **2003**, *32*, 268–275; d) X. Liu, S. K. Ibrahim, C. Tard, C. J. Pickett, *Coord. Chem. Rev.* **2005**, *249*, 1641–1652.

[2] a) M. Frey, *ChemBioChem* **2002**, *3*, 153–160; b) S. P. J. Albracht, *Biochem. Acta* **1994**, *1188*, 167–204; c) A. Volbeda, M. H. Charon, C. Piras, E. C. Hatchikian, M. Frey, J. C. Fontecilla-Camps, *Nature* **1995**, *373*, 580–587; d) R. Cammack, *Nature* **1999**, *397*, 214–215; e) M. W. W. Adams, E. I. Stiefel, *Science* **1998**, *282*, 1842–1843; f) J. Alper, *Science* **2003**, *299*, 1686–1687.

[3] M. W. W. Adams, *Biochim. Biophys. Acta* **1990**, *1020*, 115–145.

[4] a) J. W. Peters, W. N. Lanzilotta, B. J. Lemon, L. C. Seefeldt, *Science* **1998**, *282*, 1853–1858; b) Y. Nicolet, C. Piras, P. Legrand, C. E. Hatchikian, J. C. Fontecilla-Camps, *Struct. (London)* **1999**, *7*, 13–23.

[5] a) Y. Nicolet, B. J. Lemon, J. C. Fontecilla-Caps, J. W. Peters, *Trends Biochem. Sci.* **2000**, *25*, 138–143; b) Y. Nicolet, A. L. Lacey, X. Vernede, V. M. Fernandez, E. C. Hatchikian, J. C. Fontecilla-Camps, *J. Am. Chem. Soc.* **2001**, *123*, 1596–1601.

[6] H. Fan, M. B. Hall, *J. Am. Chem. Soc.* **2001**, *123*, 3828–3829.

[7] a) J. D. Lawrence, H. Li, T. B. Rauchfuss, M. Bénard, M.-M. Rohmer, *Angew. Chem. Int. Ed.* **2001**, *40*, 1768–1771; b) H. Li, T. B. Rauchfuss, *J. Am. Chem. Soc.* **2002**, *124*, 726–727; c) S. Ott, M. Kritikos, B. Åkermark, L. Sun, *Angew. Chem. Int. Ed.* **2003**, *42*, 3285–3288.

[8] a) X. Zhao, I. P. Georgakaki, M. L. Miller, J. C. Yarbrough, M. Y. Darensbourg, *J. Am. Chem. Soc.* **2001**, *123*, 9710–9711; b) F. Gloaguen, J. D. Lawrence, M. Schmidt, S. R. Wilson, T. B. Rauchfuss, *J. Am. Chem. Soc.* **2001**, *123*, 12518–12527; c) E. J. Lyon, I. P. Georgakaki, J. H. Reibenspies, M. Y. Darensbourg, *J. Am. Chem. Soc.* **2001**, *123*, 3268–3278; d) M. Razavet, S. C. Davies, D. L. Hughes, J. E. Barclay, D. J. Evans, S. A. Fairhurst, X. Liu, C. J. Pickett, *Dalton Trans.* **2003**, 586–595.

[9] a) X. Zhao, I. P. Georgakaki, M. L. Miller, R. Mejia-Rodriguez, C.-Y. Chiang, M. Y. Darensbourg, *Inorg. Chem.* **2002**, *41*, 3917–3928; b) J. L. Nehring, D. M. Heinekey, *Inorg. Chem.* **2003**, *42*, 4288–4292.

[10] F. Gloaguen, J. D. Lawrence, T. B. Rauchfuss, *J. Am. Chem. Soc.* **2001**, *123*, 9476–9477.

[11] D. Chong, I. P. Georgakaki, R. Mejia-Rodriguez, J. Sanabria-Chinchilla, M. P. Soriaga, M. Y. Darensbourg, *Dalton Trans.* **2003**, 4158–4163.

[12] S. Ott, M. Kritikos, B. Åkermark, L. Sun, R. Lomoth, *Angew. Chem. Int. Ed.* **2004**, *43*, 1006–1009.

[13] J. D. Lawrence, H. Li, T. B. Rauchfuss, *Chem. Commun.* **2001**, 1482–1483.

[14] L.-C. Song, *Acc. Chem. Res.* **2005**, *38*, 21–28.

[15] D. Seyferth, R. S. Henderson, L.-C. Song, *Organometallics* **1982**, *1*, 125–133.

[16] J. P. Collman, L. S. Hegedus, J. R. Norton, R. G. Finke, *Principles and Applications of Organotransition Metal Chemistry*, 2nd ed., University Science Books, Mill Valley, CA, **1987**.

[17] E. J. Lyon, I. P. Georgakaki, J. H. Reibenspies, M. Y. Darensbourg, *Angew. Chem. Int. Ed.* **1999**, *38*, 3178–3180.

[18] L.-C. Song, Z.-Y. Yang, H.-Z. Bian, Y. Liu, H.-T. Wang, X.-F. Liu, Q.-M. Hu, *Organometallics* **2005**, *24*, 6126–6135.

[19] I. Bhugun, D. Lexa, J.-M. Saveant, *J. Am. Chem. Soc.* **1996**, *118*, 3982–3983.

[20] T. Liu, M. Wang, Z. Shi, H. Cui, W. Dong, J. Chen, B. Åkermark, L. Sun, *Chem. Eur. J.* **2004**, *10*, 4474–4479.

[21] R. Mejia-Rodriguez, D. Chong, J. H. Reibenspies, M. P. Soriaga, M. Y. Darensbourg, *J. Am. Chem. Soc.* **2004**, *126*, 12004–12014.

[22] The $^1$H NMR (CD$_3$CN) data of **2** in HOAc are: $\delta$ = 7.02, 6.99, 6.91, 6.89 (AB q, 4 H, C$_6$H$_4$), 4.49 (s, 4 H, 2 CH$_2$), 3.85 (s, 3 H, CH$_3$) ppm. The IR (CH$_3$CN) data are: $\tilde{\nu}$ = 2074 (s), 2037 (vs), 1995 (vs) (C≡O) cm$^{-1}$. The $^1$H NMR (CD$_3$CN) data of **2** without HOAc are: $\delta$ = 7.02, 6.99, 6.91, 6.89 (AB q, 4 H, C$_6$H$_4$), 4.49 (s, 4 H, 2 CH$_2$), 3.85 (s, 3 H, CH$_3$) ppm. The IR

 © 2006 Wiley-VCH Verlag GmbH & Co. KGaA, Weinheim 

($CH_3CN$) data are $\tilde{\nu}$ = 2072 (s), 2037 (vs), 1995 (vs) (C≡O) $cm^{-1}$.
[23] W. Kuchen, H. Buchwald, *Chem. Ber.* **1958**, *91*, 2871–2877.
[24] G. M. Sheldrick, *SADABS, A Program for Empirical Absorption Correction of Area Detector Data*, University of Göttingen, Germany, **1996**.
[25] G. M. Sheldrick, *SHELXS97, A Program for Crystal Structure Solution*, University of Göttingen, Germany, **1997**.
[26] G. M. Sheldrick, *SHELXL97, A Program for Crystal Structure Refinement*, University of Göttingen, Germany, **1997**.
Received: March 19, 2006
Published Online: July 3, 2006

 © 2006 Wiley-VCH Verlag GmbH & Co. KGaA, Weinheim 

DOI: 10.1002/ejic.200600397

# Cationic Brønsted Acids for the Preparation of $Sn^{IV}$ Salts: Synthesis and Characterisation of $[Ph_3Sn(OEt_2)][H_2N\{B(C_6F_5)_3\}_2]$, $[Sn(NMe_2)_3(HNMe_2)_2][B(C_6F_5)_4]$ and $[Me_3Sn(HNMe_2)_2][B(C_6F_5)_4]$

**Yann Sarazin,[a] Simon J. Coles,[b] David L. Hughes,[a] Michael B. Hursthouse,[b] and Manfred Bochmann*[a]**

**Keywords:** Tin / Cations / N ligands / Anions

$Ph_3SnN(SiMe_3)_2$ (**1**) was prepared in good yields by reaction of $[\{NaN(SiMe_3)_2\}_2{\cdot}THF]$ (**2**) with $Ph_3SnF$. Treatment of **1** with $[H(OEt_2)_2][H_2N\{B(C_6F_5)_3\}_2]$ (**4**) in dichloromethane afforded the stannylium cation $[Ph_3Sn(OEt_2)][H_2N\{B(C_6F_5)_3\}_2]$ (**5**), which was characterised by $^1H$, $^{13}C\{^1H\}$, $^{11}B$, $^{19}F$ and $^{119}Sn$ NMR spectroscopy. The reaction of $Sn(NMe_2)_4$ with $[Ph_2MeNH][B(C_6F_5)_4]$ (**3**) gave the amidotin(IV) compound $[Sn(NMe_2)_3(HNMe_2)_2][B(C_6F_5)_4]$ (**6**) which proved very stable towards ligand substitution and resisted treatment with $Et_2O$, THF, TMEDA and pyrazine. Two new Brønsted acid salts $[H(NMe_2H)_2][B(C_6F_5)_4]$ (**7**) and $[(C_4H_4N_2)H{\cdot}OEt_2][H_2N\{B(C_6F_5)_3\}_2]$ (**8**) were synthesised. The reaction of **7** with $Sn(NMe_2)_4$ in $Et_2O$ allowed the preparation of **6** in a much improved yield (83 %). The treatment of **7** with $Me_3SnN(SiMe_3)_2$ in $Et_2O$ yielded $[Me_3Sn(HNMe_2)_2][B(C_6F_5)_4]$ (**9**) nearly quantitatively. Compounds **1**, **2**, **6**, **8** and **9** were characterised by single-crystal X-ray diffraction analyses; **6** is the first example of a structurally characterised amidotin(IV) cation.

(© Wiley-VCH Verlag GmbH & Co. KGaA, 69451 Weinheim, Germany, 2006)

## Introduction

Organotin(IV) compounds have long attracted interest due to their reactivity, their industrial applications and their intriguing biological activity.[1,2] In particular, organotin(IV) cations are thought to play an essential part in the cytotoxicity of organotin compounds[3] or in their catalytic activity for esterification reactions,[4] and the search for stable examples of $Sn^{IV}$ cations was initiated over half a century ago.[5–19] However, to this date only few cationic complexes of tin have been isolated. Even though in the past decade or so fundamental breakthroughs have been achieved where tin cations free of donor atoms have been characterised in the solid state,[20–25] stannylium cations stabilised by donor heteroatoms appear to be more readily accessible.[2] For instance, cationic tin species stabilised by a Y,C,Y-chelating pincer-type ligand (where Y is an heteroatom such as oxygen or nitrogen) have been prepared very successfully in the past 15 years.[26–32] The utilisation of N,C,N-coordinating ligands has even enabled the preparation of air-stable organotin cations.[33,34] Our interest in the chemistry of cationic tin species is based on our recent isolation of a thermally remarkably stable sec-alkyl carbocation that was generated by the attack of a $Me_3Sn^+$ intermediate on a suitably substituted propene (Scheme 1).[35,36]

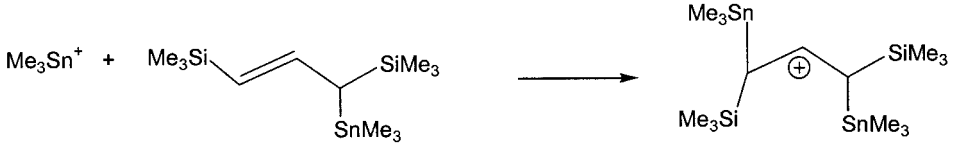


Scheme 1. Involvement of $Me_3Sn^+$ in the formation of a tin-stabilised carbocation.

This prompted us to investigate the chemistry of cationic tin species in more detail. We report here the reactions of a number of tin amides with cation-generating agents. To the best of our knowledge, simple $Sn^{IV}$-amide precursors have never been employed efficiently for this purpose.

A convenient way of generating cationic metal species is the reaction of protolysis-sensitive metal complexes with

[a] Wolfson Materials and Catalysis Centre, School of Chemical Sciences and Pharmacy, University of East Anglia, University Plain,
Norwich NR4 7TJ, UK
Fax: +44-01603-592044
E-mail: m.bochmann@uea.ac.uk
[b] School of Chemistry, University of Southampton, Highfield, Southampton SO17 1BJ, UK

 © 2006 Wiley-VCH Verlag GmbH & Co. KGaA, Weinheim 

Brønsted acidic salts of very weakly coordinating anions. For example, the oxonium ions $[H(L)_x]^+$ [L = $Et_2O$, THF, $x$ = 2; L = $(MeC{=}NC_6H_3\text{-}iPr_2\text{-}2,6)_2$, $x$ = 1] as salts of perfluorinated anions have been synthesised and used with great success in recent years;[37–43] we have shown that they can be applied as a very clean way to abstract alkyl, alkoxy and amido groups from various metals such as Mg, Zr, Zn or Cd.[43–47] For instance, the reactions of $ZnR_2$ [R = $C_6F_5$, Me, Et, $N(SiMe_3)_2$], $MgR_2$ [R = Bu, $N(SiMe_3)_2$], or $Cp_2Zr(O\text{-}iPr)_2$ with $[H(OEt_2)_2]^+[X]^-$ [X = $H_2N\{B(C_6F_5)_3\}_2$ or $B(C_6F_5)_4$] allowed the characterisation of, respectively, $[(Et_2O)_3ZnR][X]$,[44–45] $[(Et_2O)_3MgR][X]$[45] and $[Cp_2Zr(O\text{-}iPr)(HO\text{-}iPr)][X]$.[46] In addition, the anilinium salts $[PhNMe_2H][B(C_6F_5)_4]$ and $[Ph_2NMeH][B(C_6F_5)_4]$ have long been known and used as activating agents in olefin-polymerisation catalysis.[48–49]

As part of our ongoing studies on the preparation and the reactivity of main-group element cations,[43–45,47,50] we describe here the preparation and reactions of the stannylium compounds $[Ph_3Sn(OEt_2)][H_2N\{B(C_6F_5)_3\}_2]$, $[Sn(NMe_2)_3(HNMe_2)_2][B(C_6F_5)_4]$ and $[Me_3Sn(HNMe_2)_2]$-$[B(C_6F_5)_4]$. The structures of $[\{NaN(SiMe_3)_2\}_2{\cdot}THF]$, $Ph_3SnN(SiMe_3)_2$ and $[(C_4H_4N_2)H{\cdot}OEt_2][B(C_6F_5)_4]$ are also presented.

## Results and Discussion

### Synthesis and Structure of $Ph_3SnN(SiMe_3)_2$

First attempts to generate a sterically relatively unencumbered stannyl cation involved the reaction of $Ph_3SnN(SiMe_3)_2$ (**1**) with one equiv. of $[Ph_2MeNH][B(C_6F_5)_4]$ (**3**). Compound **1** is conveniently accessible from $Ph_3SnF$ and 0.5 equiv. of $[\{NaN(SiMe_3)_2\}_2{\cdot}THF]$ (**2**) in hot toluene (Scheme 2). The $^{119}Sn$ NMR spectrum of **1** exhibited a single peak at $\delta$ –106.4 ppm, i.e. there was a noticeable highfield shift of ca. 145–185 ppm when compared to other known $R_3Sn{-}NR'_2$ trialkyltin amides.[1] **1** is very soluble both in polar ($CH_2Cl_2$, $Et_2O$, THF) and non-polar (toluene, light petroleum) organic solvents.

Crystals of **1** suitable for X-ray diffraction crystallography were isolated as large colourless blocks by recrystallisation from a concentrated toluene solution stored at –26 °C. The tin atom in **1** has a tetrahedral coordination geometry, while the nitrogen atom is trigonal planar coordinated. A view of a molecule of **1** is depicted in Figure 1. Viewed down the N(4)–Sn bond, the N(4)–Si(5) bond eclipses the Sn–C(11) bond. The Si(5)–N(4)–Sn–C(11) torsion angle is 0.8(4)°. The Sn–C(11), Sn–C(21) and Sn–C(31) bond lengths in **1** of 2.149(6), 2.154(6) and 2.114(6) Å, respectively, are typical of $Sn^{IV}$–aryl bonds.[31–32,51] The Sn–N(4) bond is 2.060(5) Å, i.e. greater than the two Sn–N bond lengths reported for $(Me_2N)_2Sn(O\text{-}2,6\text{-}tBu_2\text{-}C_6H_3)_2$ [1.980(4) and 1.997(4) Å][52] and the Sn–$NMe_2$ bond length [2.013(3) Å] found in $\{(2,2,6,6\text{-}Me_4C_5H_6N){-}P{=}C(SiMe_3)\}$-$Sn\{NMe_2\}\{N(SiMe_3)_2\}_2$,[53] but comparable to the two Sn–$N(SiMe_3)_2$ bond lengths [2.070(2) and 2.080(2) Å] also identified in the latter compound. In the crystal packing, there is no stacking of parallel phenyl rings; instead, the principal packing features are those of hydrogen atoms (both of phenyl and methyl groups) pointing into the centre of phenyl rings, and of methyl–methyl interactions.

During the course of this work large crops of the crystalline sodium amide **2** were obtained fortuitously from a concentrated light petroleum solution stored at –26 °C. The molecular structure of **2** was determined and, interestingly, confirmed the presence of only 0.5 molecules of THF per sodium atom.

The molecule of **2** contains a $Na_2N_2$ ring with a $C_2$ axis passing through the two sodium atoms (Figure 2). Na(1) is bound only to the two bridging nitrogen atoms, whereas Na(2) is coordinated to the same N atoms as well as to one THF ligand. Examination of the region on the "open" side of Na(1) shows its closest neighbours to be two C(21) methyl groups of neighbouring molecules, with Na(1)···C(21′′) and Na(1)···C(21′′′) distances of 3.104(6) Å; the closest H atoms are the H(21c) atoms of these methyl groups, at 2.61 Å. The shortest distances between the methyl groups (about the twofold symmetry axis) are: C(21′′)···C(21′′′) 3.756(9), H(21b′′)···H(21b′′′) 2.62, and H(21b′′)···H(21c′′′) 2.79 Å. Because the contact distance between two hydrogen atoms is ca. 2.4 Å, there is negligible space for any other atom or group in this region; the methyl groups cover this 'open' side of Na(1). There are other short

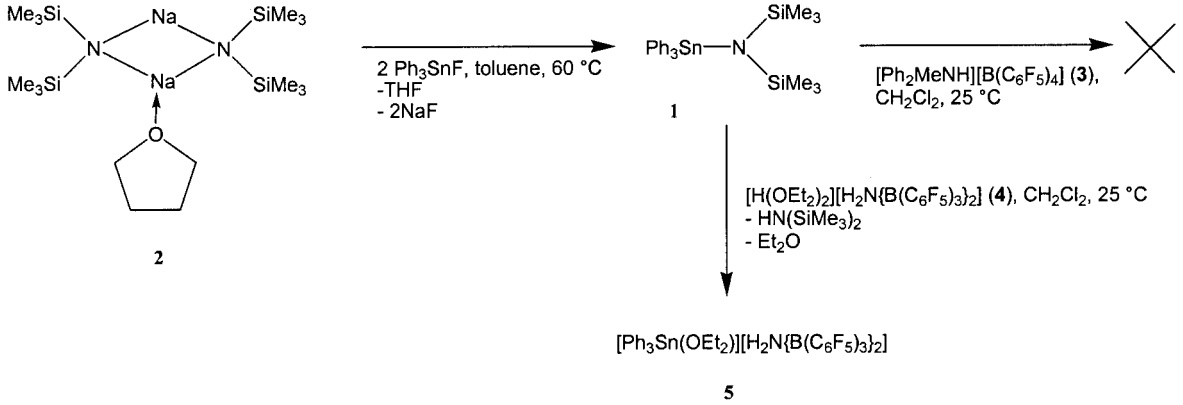


Scheme 2. Synthesis of $Ph_3SnN(SiMe_3)_2$ (**1**) and its subsequent reactions with Brønsted acids $[Ph_2MeNH][B(C_6F_5)_4]$ (**3**) and $[H(OEt_2)_2][H_2N\{B(C_6F_5)_3\}_2]$ (**4**).

 © 2006 Wiley-VCH Verlag GmbH & Co. KGaA, Weinheim 

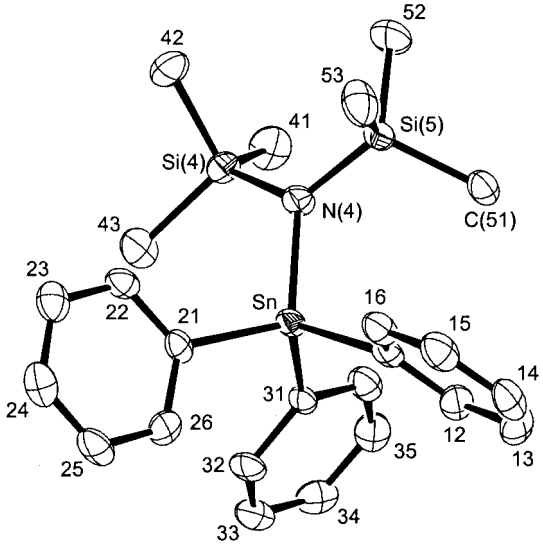


Figure 1. View of a molecule of **1**, indicating the atom numbering scheme; atoms labelled '*n*' represent the carbon atoms C(*n*). Hydrogen atoms have been omitted for clarity. Thermal ellipsoids are drawn at the 50% probability level. Selected bond lengths [Å] and angles [°]: Sn–C(11) 2.149(6), Sn–C(21) 2.154(6), Sn–C(31) 2.114(6), Sn–N(4) 2.060(5), N(4)–Si(4) 1.738(5), N(4)–Si(5) 1.743(5); C(11)–Sn–C(21) 102.5(2), C(31)–Sn–C(11) 109.5(2), C(31)–Sn–C(21) 114.0(2), N(4)–Sn–C(11) 112.9(2), N(4)–Sn–C(21) 112.8(2), N(4)–Sn–C(31) 105.3(2).

Na···H contacts of similar distance in this structure, viz. Na(1)···H(12a) 2.62, Na(1)···H(12c) 2.64 and Na(2)···H(22a) 2.66 Å. There are also Me···Me contacts between each of these C(21) groups and methyl groups of the Na(1) complex, e.g. H(12a)···H(21b′) 2.76 Å, H(21a)···H(21a′) 2.80 Å and H(11c)···H(21a′) 2.73 Å. These contacts effectively shield Na(1) from approach by any other ligand. The arrangement around Na(2) is trigonal planar, while each of the two nitrogen atoms are in a slightly distorted tetrahedral environment. The two N–Na(1)–N and N–Na(2)–N angles are almost identical [99.7(2)° and 99.0(2)°, respectively]. The presence of a THF molecule coordinated to Na(2) has very little influence on the N–Na(2) distance, because the N–Na(1) bond length of 2.388(5) Å is only marginally shorter than the 2.400(5) Å found for N–Na(2). It is remarkable that despite the presence of a unique molecule of THF in the dimeric **2**, all bond lengths and angles correspond closely to those already reported for the bis-THF adduct [{$NaN(SiMe_3)_2$}$_2$·2THF].[54] For instance, the N–Na(1), N–Na(2) and Na(2)–O(3) bond lengths of 2.388(5), 2.400(5) and 2.285(6) Å, respectively in **2** compare very well with the Na(1)–N(1) and Na(1)–O(1) lengths of 2.399 and 2.267 Å given for [{$NaN(SiMe_3)_2$}$_2$·2THF], and the N–Na(2)–N in **2** [99.0(2)°] is very close to the 101.7° found for N(1)–Na(1)–N(1) in the bis-THF adduct.

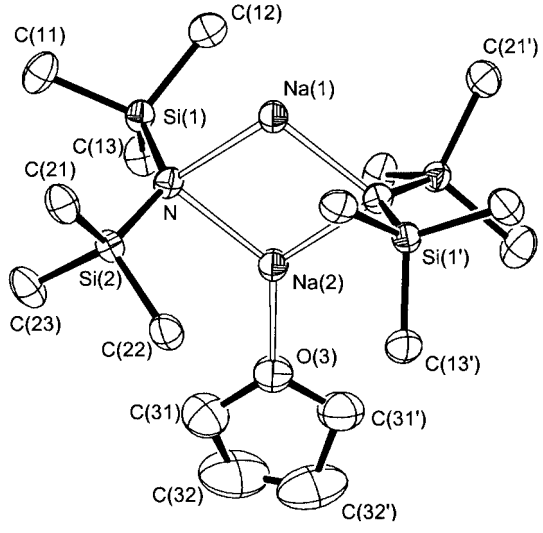


Figure 2. View of a molecule of [{$NaN(SiMe_3)_2$}$_2$·THF] (**2**), indicating the atom numbering scheme. Hydrogen atoms have been omitted for clarity. Thermal ellipsoids are drawn at the 50% probability level. Selected bond lengths [Å] and angles [°]: Na(1)–N 2.388(5), Na(2)–N 2.400(5), Na(2)–O(3) 2.285(6), N–Si(1) 1.696(5), N–Si(2) 1.688(6); N–Na(1)–N′ 99.7(2), N–Na(2)–N′ 99.0(2), N–Na(2)–O(3) 130.5(1).

### Synthesis of [$Ph_3Sn(OEt_2)$][$H_2N\{B(C_6F_5)_3\}_2$] (5)

Treatment of **1** with an equimolar amount of [$H(OEt_2)_2$]-[$H_2N\{B(C_6F_5)_3\}_2$][38] (**4**) in dichloromethane yielded a viscous oil, from which a fine white powder was obtained upon repeated washing with light petroleum. NMR spectroscopic data of this solid were consistent with the formulation [$Ph_3Sn(OEt_2)$][$H_2N\{B(C_6F_5)_3\}_2$] (**5**), and the composition was confirmed by elemental analysis. Compound **5** is very soluble in chlorinated solvents and diethyl ether, but is only sparingly soluble in toluene and insoluble in light petroleum. The $^{119}Sn$ NMR resonance for **5** was found at $\delta$ –76.0 ppm, i.e. at much higher field than reported for the free ions (mesityl)$_3Sn^+$ ($\delta$ +806 ppm)[21] and (2,4,6-triisopropylphenyl)$_3Sn^+$ ($\delta$ +714 ppm).[23] All attempts to determine the molecular structure of **5** proved unsuccessful, possibly due to its high air- and moisture-sensitivity. It was not possible to remove the coordinated $Et_2O$ molecule, even upon heating under vacuum.

Attempts to generate a stannyl cation free of coordinating ether by reacting **1** with [$Ph_2MeNH$][$B(C_6F_5)_4$] (**3**) in dichloromethane at room temperature gave dark blue mixtures from which no tractable material could be isolated.

### Synthesis, Characterisation and Reactivity of [$Sn(NMe_2)_3$-$(HNMe_2)_2$][$B(C_6F_5)_4$] (6), [$H(HNMe_2)_2$][$B(C_6F_5)_4$] (7) and [$(C_4H_4N_2)H\cdot OEt_2$][$H_2N\{B(C_6F_5)_3\}_2$] (8)

To the best of our knowledge simple amidotin(IV)–amide complexes have never been used for the preparation of organotin cations, and it prompted us to investigate the potential of these simple precursors for such purposes.

The sterically very hindered amide $MeSn[N(SiMe_3)_2]_3$ was treated with the cation-generating agents **3**, **4**, [$Ph_3C$][$H_2N\{B(C_6F_5)_3\}_2$] or $B(C_6F_5)_3$ in dichloromethane. However, none of these reactions proceeded to give the expected organotin cations, but instead the starting material $MeSn[N(SiMe_3)_2]_3$ was recovered in all cases.[55]

 © 2006 Wiley-VCH Verlag GmbH & Co. KGaA, Weinheim 

By contrast, the less encumbered $Sn(NMe_2)_4$ can be employed effectively for reactions with Brønsted acids. On addition of one equiv. of $Sn(NMe_2)_4$ to a colourless solution of **3** in dichloromethane, a pale yellow, slightly cloudy solution was obtained (Scheme 3, Method A). The crude product was isolated as a viscous yellow oil. Attempts to purify the compound adequately with light petroleum failed. Nevertheless, crystals were grown from a concentrated dichloromethane solution, and crystallographic studies carried out on these colourless plates indicated the structure $[Sn(NMe_2)_3(HNMe_2)_2][B(C_6F_5)_4]$ (**6**), with two molecules of dimethylamine coordinated to the metal centre. Elemental analysis and NMR characterisation were in agreement with the proposed structure. The $^1H$ NMR spectrum displayed a single sharp singlet for all methyl groups at $\delta$ 2.76 ppm, while the N–H protons gave rise to a broad singlet centred at $\delta$ 3.25 ppm. Whereas in the $^{119}Sn$ NMR spectrum the starting material $Sn(NMe_2)_4$ exhibited a resonance at $\delta$ –122.4 ppm, the peak for **6** was high-field shifted by about 190 ppm, to $\delta$ –311.4 ppm. The borate anion showed an $^{11}B$ NMR signal at $\delta$ –13.6 ppm, while the $^{19}F$ NMR resonances at $\delta$ –133.4, –160.6 and –166.1 ppm are typical of a noncoordinated borate. Compound **6** is highly soluble in diethyl ether, THF and dichloromethane, moderately soluble in toluene and insoluble in light petroleum. It is very air- and moisture-sensitive, but is thermally stable for periods of weeks at room temperature, and does not show any sign of deterioration upon prolonged exposure to light.

The structure of the $[Sn(NMe_2)_3(HNMe_2)_2]^+$ cation ($\mathbf{6^+}$) is shown in Figure 3. The complex is trigonal-bipyramidal, with the two dimethylamine ligands *trans* to one another [angle N(11)–Sn–N(12) 176.0(2)°; angle sum for $N_{eq}$–Sn–$N_{eq}$ 360.0°]. The Sn–N distances to the axial $HNMe_2$ ligands [Sn–N(11) 2.382(7), Sn–N(12) 2.321(7) Å] are substantially longer than those to the equatorial amido groups [Sn–N(13) 2.013(7) Å, Sn–N(14) 2.005(6) and Sn–N(15) 1.990(7) Å]. The average Sn–$N_{eq}$ length in $\mathbf{6^+}$ (2.003 Å) is somewhat shorter than the average Sn–$N_{eq}$ length of 2.038 Å found in the geometrically comparable neutral complex $Me_2NSn(MeNCH_2CH_2N)_3N$,[56] which presumably reflects the influence of the positive charge on the metal centre in $\mathbf{6^+}$. To the best of our knowledge, **6** is the first example of a structurally characterised five-coordinate amido $Sn^{IV}$-cation paired with a noncoordinating counteranion.

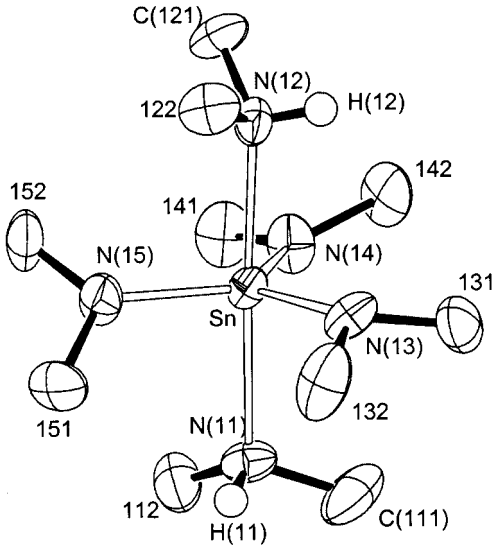


Figure 3. View of the $[Sn(NMe_2)_3(HNMe_2)_2]^+$ cation ($\mathbf{6^+}$), indicating the atom numbering scheme. Atoms labelled 'n' represent the carbon atoms C(n). Hydrogen atoms (except for the amino H atoms) have been omitted for clarity. Thermal ellipsoids are drawn at the 50% probability level. Selected bond lengths [Å] and angles [°]: Sn–N(11) 2.382(7), Sn–N(12) 2.321(7), Sn–N(13) 2.013(7), Sn–N(14) 2.005(6), Sn–N(15) 1.990(7); N(12)–Sn–N(11) 176.0(2), N(13)–Sn–N(11) 91.4(3), N(14)–Sn–N(11) 90.4(3), N(15)–Sn–N(11) 89.9(3), N(13)–Sn–N(12) 84.6(3), N(14)–Sn–N(12) 92.1(3), N(15)–Sn–N(12) 91.5(3), N(14)–Sn–N(13) 120.8(3), N(15)–Sn–N(13) 118.7(3), N(15)–Sn–N(14) 120.5(3).

The preparation described above gave **6** in low yield (24% based on Sn). Consequently, a more economical route was developed, which consisted of protonating $Sn(NMe_2)_4$ while at the same time offering a second molecule of dimethylamine (Scheme 3, Method B). For this purpose, the new Brønsted acid $[H(HNMe_2)_2][B(C_6F_5)_4]$ (**7**) was prepared. The low basicity of $NMePh_2$ compared to that of $HNMe_2$ was exploited for the nearly-quantitative synthesis of **7** (Scheme 4, top). Thus, the straightforward reaction of **3** with a large excess of $HNMe_2$ in diethyl ether at room temperature yielded a white solid after removal of the volatiles. Upon thorough washing with light petroleum, a fine white powder was obtained, and the composition of **7** was confirmed by elemental analysis and NMR spectroscopy. In the $^1H$ NMR spectrum (in $CD_2Cl_2$), all four methyl groups appear as a sharp singlet at $\delta$ 2.61 ppm, while the three N–H protons are equivalent and give rise to a sharp singlet at

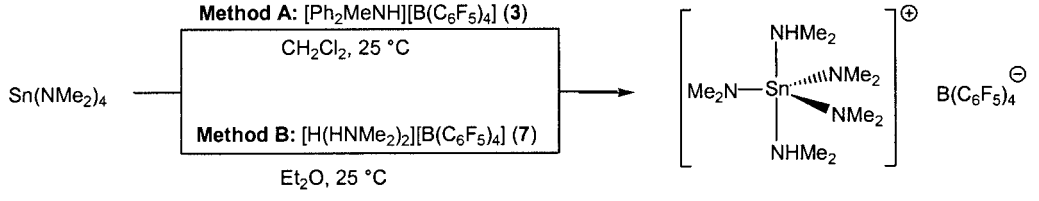


**6**

Scheme 3. Preparation of $[Sn(NMe_2)_3(HNMe_2)_2][B(C_6F_5)_4]$ (**6**).

 © 2006 Wiley-VCH Verlag GmbH & Co. KGaA, Weinheim 

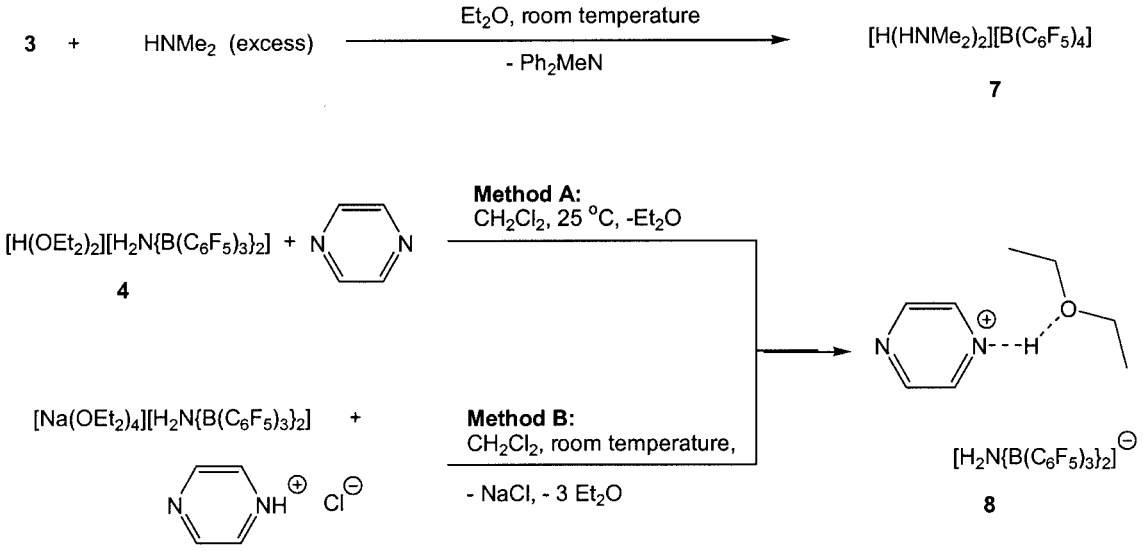


Scheme 4. Preparation of new Brønsted acids stabilised by weakly coordinating perfluorinated anions.

$\delta$ 7.04 ppm. It is worth noting that this reaction must not be conducted in dichloromethane, as in this case crystalline $Me_2NH{\cdot}HCl$ is slowly formed in quantitative yield. For this reason, highly concentrated solutions of **7** and short acquisition times were used to record its NMR spectra. Compound **7** dissolves in $Et_2O$ and THF but is hardly soluble in toluene and insoluble in light petroleum. As anticipated, the reaction of $Sn(NMe_2)_4$ with an equimolar amount of **7** in diethyl ether proceeded cleanly to yield ether-free **6** in a substantially improved yield (83%; Scheme 3, Method B).

The stability of **6** was demonstrated by its remarkable inertness towards ligand substitution. There is no reaction with diethyl ether, THF or even a chelating ligand such as tetramethylethylenediamine (TMEDA). Moreover, **6** was also isolated as the only product of the reaction between **3** and $Sn(NMe_2)_4$ carried out in $Et_2O$ or THF instead of $CH_2Cl_2$ (yield 10–20% with respect to Sn).

Because adding an excess of pyrazine to **6** proved ineffective in displacing one of the dimethylamine ligands, we envisaged adding $[(C_4H_4N_2)H{\cdot}OEt_2][H_2N\{B(C_6F_5)_3\}_2]$ (**8**) to $Sn(NMe_2)_4$, with the rationale that such reaction would lead to the formation of a $Sn^{IV}$ cation coordinated by at least one bifunctional pyrazine ligand. Thus, the new Brønsted acid **8** was conveniently prepared by addition of pyrazine to a solution of **4** in dichloromethane (Scheme 4, bottom, Method A). After removal of the volatile fraction and several washings with light petroleum, analytically pure **8** was recovered in high yield (88%). Product **8** was also readily obtained in 77% yield by reaction of solid pyrazinium chloride with $[Na(OEt_2)_4][H_2N\{B(C_6F_5)_3\}_2]$ in dichloromethane (Scheme 4, bottom, Method B). Compound **8** can easily be dissolved in $Et_2O$ and chlorinated solvents, but shows poor solubility in aromatic solvents and light petroleum. Unexpectedly, no clean product could be recovered from the reaction of $Sn(NMe_2)_4$ and **8** performed in $CH_2Cl_2$; instead a complicated mixture of products was obtained.

The anion $[H_2N\{B(C_6F_5)_3\}_2]^-$ was chosen in preference to $B(C_6F_5)_4^-$ because of its better crystallisation properties, and indeed crystals of **8** suitable for X-ray crystallography were grown as colourless shards from a concentrated

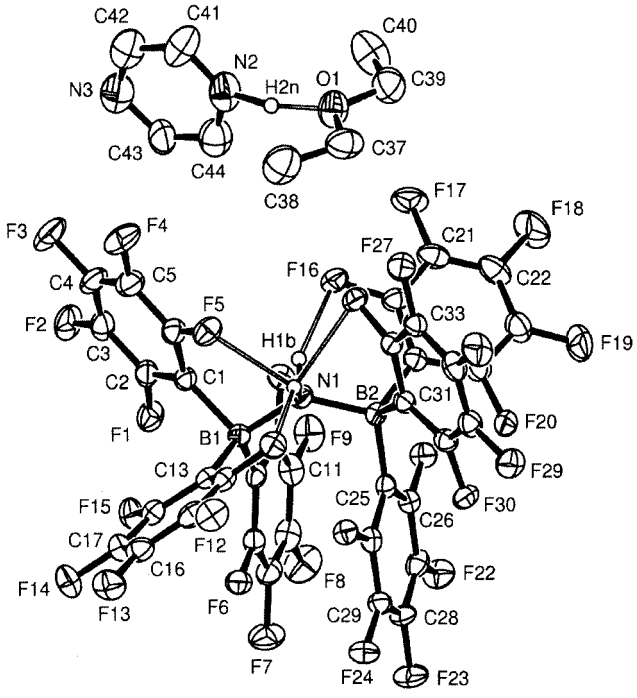


Figure 4. View of the salt $[(C_4H_4N_2)H{\cdot}OEt_2][H_2N\{B(C_6F_5)_3\}_2]$ (**8**), indicating the atom numbering scheme. Hydrogen atoms (except for the amido and acidic atoms) have been omitted for clarity. Thermal ellipsoids are drawn at the 50% probability level. Selected bond lengths [Å] and angles [°]: N(2)–H(2n) 1.27(5), O(1)–H(2n) 1.38(5), N(2)–C(41) 1.335(6), N(2)–C(44) 1.337(6), N(3)–C(42) 1.321(6), N(3)–C(43) 1.331(6), N(1)–B(1) 1.627(4), N(1)–B(2) 1.638(4), N(1)–H(1a) 0.90, N(1)–H(1b) 0.90, H(1a)–F(5) 2.24, H(1a)–F(11) 2.13, H(1a)–F(26) 2.32, H(1b)–F(16) 1.98; N(2)–H(2n)–O(1) 156(5), C(41)–N(2)–C(44) 120.6(4), C(42)–N(3)–C(43) 114.9(4), B(1)–N(1)–B(2) 133.2(2).

 © 2006 Wiley-VCH Verlag GmbH & Co. KGaA, Weinheim 

dichloromethane solution cooled to –26 °C (Figure 4). The acidic proton in the cation was refined freely. It lies between the oxygen and nitrogen atoms and is located somewhat closer to the latter [N(2)–H(2n) 1.27(5) Å, O(1)–H(2n) 1.38(5) Å]; the N(2)–H(2n)–O(1) angle is 156(5)°. The C–N bonds of the protonated nitrogen [1.335(6) and 1.337(6) Å] are marginally longer than those to the nonprotonated nitrogen atom [1.321(6) and 1.331(6) Å]. The structure of the anion resembles strongly that in $[Na(OEt_2)_2][H_2N\{B(C_6F_5)_3\}_2]$ reported previously.[38]

### Synthesis and Characterisation of $[Me_3Sn(HNMe_2)_2][B(C_6F_5)_4]$ (9)

As discussed above, no stannyl cation could be generated from $MeSn[N(SiMe_3)_2]_3$ upon treatment with various cation-generating agents. On the other hand, the sterically less hindered mono-amide $Me_3SnN(SiMe_3)_2$ reacted successfully with one equiv. of **7** in $Et_2O$ to yield $[Me_3Sn(HNMe_2)_2][B(C_6F_5)_4]$ (**9**) in a near-quantitative yield (Scheme 5). Compound **9** was fully characterised by NMR

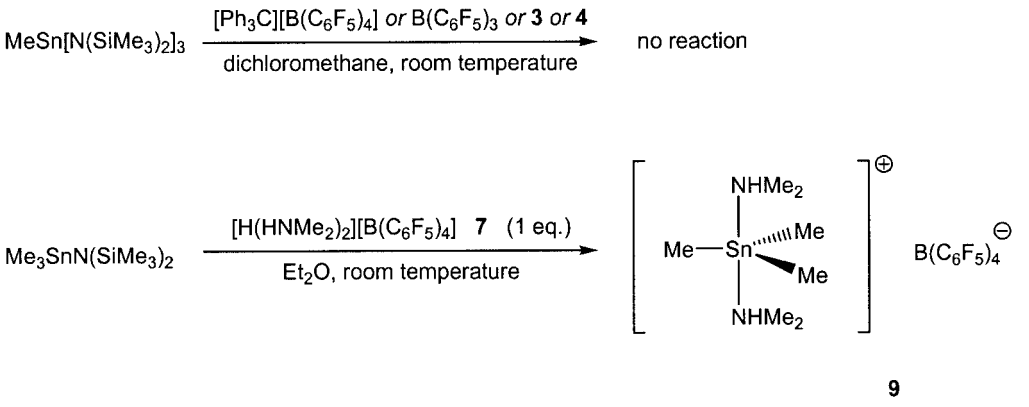


Scheme 5. Preparation of $[Me_3Sn(HNMe_2)_2][B(C_6F_5)_4]$ (**9**).

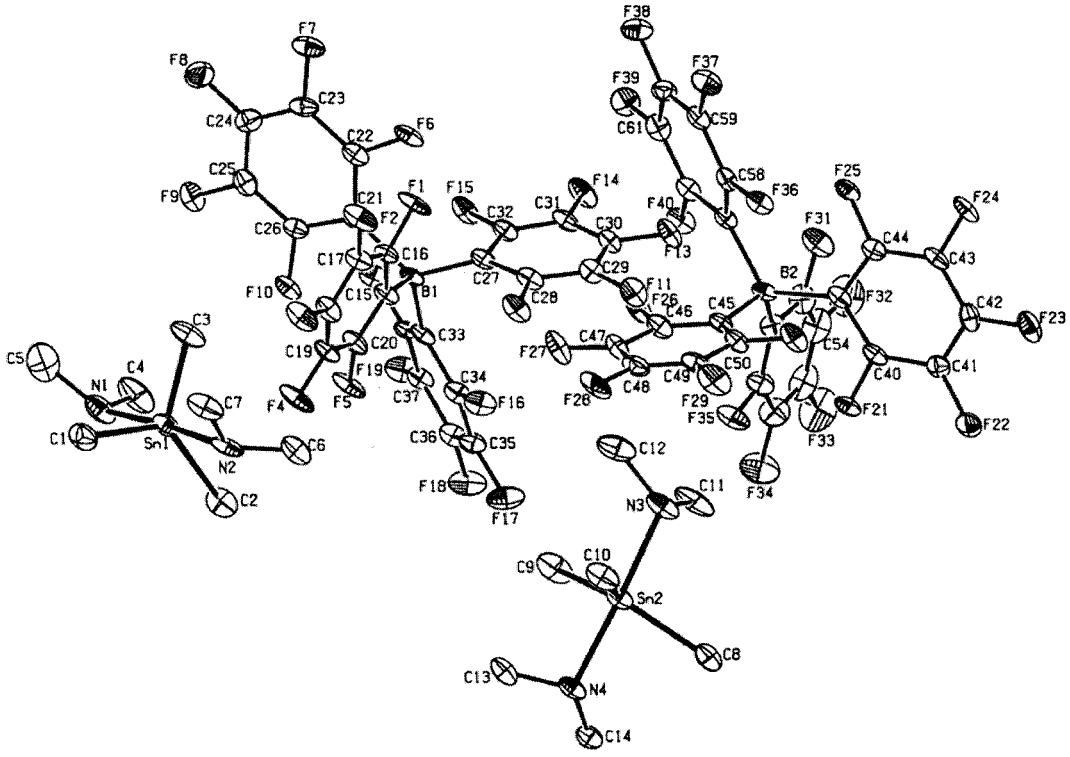

Figure 5. View of the two independent ion pairs in the salt $[Me_3Sn(HNMe_2)_2][B(C_6F_5)_4]$ (**9**), indicating the atom numbering scheme. Hydrogen atoms have been omitted for clarity. Thermal ellipsoids are drawn at the 50% probability level. Selected bond lengths [Å] and angles [°]: For the first cation, Sn(1)–N(1) 2.405(6), Sn(1)–N(2) 2.323(6), Sn(1)–C(1) 2.036(6), Sn(1)–C(2) 2.404(6), Sn(1)–C(3) 2.085(6); N(1)–Sn(1)–N(2) 176.3(2), N(1)–Sn(1)–C(1) 78.4(2), N(1)–Sn(1)–C(2) 93.0(2), N(1)–Sn(1)–C(3) 94.0(2), N(2)–Sn(1)–C(1) 100.2(2), N(2)–Sn(1)–C(2) 84.9(2), N(2)–Sn(1)–C(3) 89.7(2), C(1)–Sn(1)–C(2) 124.5(2), C(2)–Sn(1)–C(3) 127.9(2), C(1)–Sn(1)–C(3) 107.5(3). For the second cation, Sn(2)–N(3) 2.263(5), Sn(2)–N(4) 2.272(4), Sn(2)–C(8) 2.417(7), Sn(2)–C(9) 2.049(6), Sn(2)–C(10) 2.154(6); N(3)–Sn(2)–N(4) 177.0(2), N(3)–Sn(2)–C(8) 98.8(2), N(3)–Sn(2)–C(9) 80.2(2), N(3)–Sn(2)–C(10) 91.7(2), N(4)–Sn(2)–C(8) 84.0(2), N(4)–Sn(2)–C(9) 97.7(2), N(4)–Sn(2)–C(10) 87.3(2), C(8)–Sn(2)–C(9) 116.8(3), C(9)–Sn(2)–C(10) 116.1(3), C(8)–Sn(2)–C(10) 127.1(3).

 © 2006 Wiley-VCH Verlag GmbH & Co. KGaA, Weinheim 

spectroscopy in $CD_2Cl_2$, and its composition was confirmed by elemental analysis. It is readily soluble in ethers and chlorinated solvents, but only poorly soluble in aromatic hydrocarbons and totally insoluble in light petroleum. It is air- and moisture-sensitive, but is thermally stable and does not deteriorate when exposed to light.

The $^{119}Sn$ NMR spectrum of **9** consists of a single peak located at $\delta$ –25.3 ppm, i.e. it has undergone a high-field shift of about 77 ppm when compared to the starting material ($\delta$ +52.1 ppm). By contrast, the $^{119}Sn$ NMR resonance for the free $Bu_3Sn^+$ appears at the much higher frequency ($\delta$ +454 ppm).[22] In the $^1H$ NMR spectrum, the resonance for the nine Sn–$CH_3$ protons is found at $\delta$ 0.60 ppm, exhibiting a $^2J_{H,Sn}$ coupling of 30.7 Hz; the two N–H protons display a resonance at $\delta$ 2.14 ppm, and are considerably more shielded than the two analogous protons in **6** ($\delta$ 3.25 ppm). The $^{11}B$ ($\delta$ –13.6 ppm) and $^{19}F$ ($\delta$ –133.6, –164.0 and –168.0 ppm) NMR spectra are characteristic of the noncoordinating nature of the counteranion.

Single crystals of **9** were readily grown from a dichloromethane/light petroleum mixture at –28 °C as colourless slabs, suitable for X-ray diffraction. The crystal structure (Figure 5) indicates the presence of two independent ion pairs per asymmetric unit. The arrangement around the tin atoms of the two cations in **9** resembles that in **6**. Each of the cations has a distorted trigonal-bipyramidal environment, where the two dimethylamine ligands are situated in apical positions [N(1)–Sn(1)–N(2) 176.3(2)°; N(3)–Sn(2)–N(4) 177.0(2)°]. The average angle sums for $C_{eq}$–Sn(1)–$C_{eq}$ [359.9(2)°] and $C_{eq}$–Sn(2)–$C_{eq}$ [360.0(3)°] confirm the planarity of the trigonal $SnMe_3$ subunits. In both cations, one of the three equatorial Sn–C bonds is significantly longer than the other two [Sn(1)–C(2) 2.404(6) compared to Sn(1)–C(1) 2.036(6) and Sn(1)–C(3) 2.085(6) Å; Sn(2)–C(8) 2.417(7) compared to Sn(2)–C(9) 2.049(6) and Sn(2)–C(10) 2.154(6) Å], and there are considerable variations in the $C_{eq}$–Sn–$C_{eq}$ angles [$C_{eq}$–Sn(1)–$C_{eq}$ 107.5(3)–127.9(2)°; $C_{eq}$–Sn(2)–$C_{eq}$ 116.1(3)–127.1(3)°]. The axial Sn–N bond lengths in **9** differ slightly between the two independent cations [Sn(1)–N(1) 2.405(6) and Sn(1)–N(2) 2.323(6) Å; Sn(2)–N(3) 2.263(5) and Sn(2)–N(4) 2.272(4) Å], but overall compare well with those found in **6** [2.382(7) and 2.321(7) Å] and in the related ammonia complex $[Me_3Sn(NH_3)_2][N(SO_2Me)_2]$ (Sn–N 2.328 and 2.383 Å; N–Sn–N 179.2°).[57] The equatorial Sn–C bond lengths in **9** are comparable to those reported for the latter compound (Sn–C 2.117–2.124 Å).

## Conclusions

We have shown that Brønsted acids paired with weakly coordinating perfluorinated counteranions can be employed as an effective way to generate cationic tin(IV) complexes. With this aim in mind two new nitrogen-based Brønsted acids have been developed. The $Sn^{IV}$ cations formed in such fashion are highly electrophilic. In particular, $[Sn(NMe_2)_3(HNMe_2)_2]^+$ $[B(C_6F_5)_4]^-$ was synthesized as the first example of a structurally characterised cationic amidotin complex. The dimethylamine ligands exhibit a surprising resistance to substitution by other Lewis bases. Future work will involve tailor-made cationic Brønsted acids and their use in combination with other main group precursors for the development of new architectures built around cationic metal centres and weakly coordinating anions.

## Experimental Section

**General:** All manipulations were performed under argon using standard Schlenk techniques. Solvents were pre-dried, and distilled under inert atmosphere over sodium (low-sulfur toluene), sodium–benzophenone (diethyl ether, THF), sodium–potassium alloy (light petroleum, boiling point 40–60 °C) or calcium hydride (dichloromethane). NMR solvents were dried with activated 4-Å molecular sieves and degassed by several freeze–thaw cycles. NMR spectra were recorded with a Bruker Avance DPX-300 spectrometer. Chemical shifts are reported in ppm. $^1H$ NMR spectra (300.13 MHz) are referenced to the residual protons of the deuterated solvent used. $^{13}C$ NMR spectra (75.47 MHz) were referenced internally to the D-coupled $^{13}C$ resonances of the NMR solvent. $^{11}B$ (96.29 MHz), $^{19}F$ (282.38 MHz) and $^{119}Sn$ (111.91 MHz) NMR spectra were referenced externally to $BF_3{\cdot}Et_2O$, $CFCl_3$ and $SnMe_4$, respectively. $HN(SiMe_3)_2$, $NMePh_2$, $Ph_3SnF$, $SnCl_4$, $Me_3SnCl$, $MeSnCl_3$, $C_4H_4N_2$, $HNMe_2$ and *N*,*N*,*N*′,*N*′-tetramethylethylenediamine were used as purchased without further purification. $B(C_6F_5)_3$,[58–59] $[Ph_2MeNH][B(C_6F_5)_4]$ (**3**),[49] $[Na(OEt_2)_4][H_2N\{B(C_6F_5)_3\}_2]$,[38] $[H(OEt_2)_2][H_2N\{B(C_6F_5)_3\}_2]$ (**4**),[38] $[Ph_3C][H_2N\{B(C_6F_5)_3\}_2]$,[38] $MeSn[N(SiMe_3)_2]_3$,[60] $Me_3SnN(SiMe_3)_2$[61] and $Sn(NMe_2)_4$[62] were prepared according to the literature methods.

**Synthesis of $Ph_3SnN(SiMe_3)_2$ (1):** $Ph_3SnF$ (5.0 g, 13.5 mmol) was added rapidly at –78 °C to a suspension of $[\{NaN(SiMe_3)_2\}_2{\cdot}THF]$ (6.0 g, 13.5 mmol) in light petroleum (80 mL). The mixture was warmed slowly to room temperature and was stirred overnight. The volatiles were removed under vacuum, giving a white solid which was suspended in toluene (60 mL). The reaction mixture was stirred at 60 °C for 5 hours. The precipitate of NaF was then removed by filtration, and the supernatant was concentrated to 20 mL. X-ray quality crystals were obtained by recrystallisation at –26 °C. Yield: 4.8 g (70%). $^1H$ NMR ($CD_2Cl_2$, 25 °C, 300.13 MHz): $\delta$ = 7.66 (m, 6 H, Ar–*H*), 7.44 (m, 9 H, Ar–*H*), 0.10 (s, 18 H, Si*Me*$_3$) ppm. $^{13}C\{^1H\}$ NMR ($CD_2Cl_2$, 25 °C, 75.48 MHz): $\delta$ = 142.5 ($C_i$, $^1J_{C,Sn}$ = 298.9 Hz, Sn*Ph*$_3$), 137.0 ($C_o$, $^2J_{C,Sn}$ = 20.6 Hz, Sn*Ph*$_3$), 129.6 ($C_p$, $^4J_{C,Sn}$ = 6.2 Hz, Sn*Ph*$_3$), 129.1 ($C_m$, $^3J_{C,Sn}$ = 28.9 Hz, Sn*Ph*$_3$), 5.6 (Si*Me*$_3$) ppm. $^{119}Sn$ NMR ($CD_2Cl_2$, 25 °C, 111.91 MHz): $\delta$ = –106.4 ppm. $C_{24}H_{33}NSi_2Sn$ (510.4): calcd. C 56.48, H 6.52, N 2.74; found C 56.71, H 6.52, N 2.87.

**Preparation of $[\{NaN(SiMe_3)_2\}_2{\cdot}THF]$(2):** The solvent was removed from a solution of $NaN(SiMe_3)_2$ (12.0 g, 65.4 mmol) in THF (125 mL) under vacuum and the resulting solid extracted with light petroleum (2×100 mL). The filtrate was concentrated to 50 mL and stored overnight at –26 °C, affording a large crop of colourless crystals suitable for X-ray diffraction crystallography. Yield 10.0 g, 22.8 mmol, 70%. $^1H$ NMR ($CD_2Cl_2$, 25 °C, 300.13 MHz): $\delta$ = 3.41 (t, 4 H, $J$ = 6.6 Hz, $CH_2$–C*H*$_2$–O), 1.22 (m, 4 H, C*H*$_2$–$CH_2$–O), 0.26 (s, 36 H, Si*Me*$_3$) ppm. $^{13}C$ NMR ($CD_2Cl_2$, 25 °C, 75.48 MHz): $\delta$ = 68.4 ($CH_2$–*C*$H_2$–O), 25.4 (*C*$H_2$–$CH_2$–O), 7.0 (Si*Me*$_3$) ppm. $C_{16}H_{44}N_2Na_2OSi_4$ (438.9): calcd. C 43.79, H 10.11, N 6.38; found C 43.01, H 10.10, N 6.40.

 © 2006 Wiley-VCH Verlag GmbH & Co. KGaA, Weinheim 

**$[Ph_3Sn(OEt_2)][H_2N\{B(C_6F_5)_3\}_2]$ (5):** A colourless solution of **1** (0.5 g, 1.0 mmol) and **4** (1.2 g, 1.0 mmol) in $CH_2Cl_2$ (8 mL) was stirred at room temperature for 12 hours. The solvent was then removed under vacuum, leaving a sticky foam. Upon repeated washing with light petroleum a white powder was obtained which was suspended in 3 mL of light petroleum, and dichloromethane (ca. 2 mL) was added until the solid was completely dissolved. Cooling to –26 °C for several days gave a white microcrystalline solid, yield 0.5 g (30%). $^1$H NMR ($CD_2Cl_2$, 25 °C, 300.13 MHz): $\delta$ = 7.92–7.70 (m, 15 H, Ar–*H*), 5.70 (br. s, 2 H, $H_2$N), 3.61 (q, $^3J_{H,H}$ = 7.0 Hz, 4 H, $CH_3$–C$H_2$–O), 0.99 (t, $^3J_{H,H}$ = 7.0 Hz, 6 H, C$H_3$–$CH_2$–O) ppm. $^{13}$C{$^1$H} NMR ($CD_2Cl_2$, 25 °C, 75.48 MHz): $\delta$ = 149.8, 146.7, 141.2, 138.7, 137.8, 135.5 (all $ArF_5$–*C*), 136.9 ($C_i$, Sn*Ph*$_3$), 136.6 ($^2J_{C,Sn}$ = 22.8 Hz, $C_o$, Sn*Ph*$_3$), 131.1 ($C_p$, Sn*Ph*$_3$), 131.0 ($^3J_{C,Sn}$ = 33.8 Hz, $C_m$, Sn*Ph*$_3$), 67.5 ($CH_3$–*C*$H_2$–O), 13.9 (*C*$H_3$–$CH_2$–O) ppm. $^{11}$B NMR ($CD_2Cl_2$, 96.29 MHz, 25 °C): $\delta$ = –5.3 ppm. $^{19}$F NMR ($CD_2Cl_2$, 282.38 MHz, 25 °C): $\delta$ = –133.4 (d, $^3J_{F,F}$ = 19.8 Hz, 12 F, $F_o$), –160.7 (t, $^3J_{F,F}$ = 19.8 Hz, 6 F, $F_p$), –166.0 (t, $^3J_{F,F}$ = 19.8 Hz, 12 F, $F_m$) ppm. $^{119}$Sn NMR ($CD_2Cl_2$, 25 °C, 111.91 MHz): $\delta$ = –76.0 ppm. $C_{58}H_{27}B_2F_{30}NOSn$ (1464.1): calcd. C 47.58, H 1.86, N 0.96; found C 47.45, H 2.02, N 1.04.

**$[Sn(NMe_2)_3(HNMe_2)_2][B(C_6F_5)_4]$ (6). Method A:** To a colourless solution of **3** (1.3 g, 1.5 mmol) in $CH_2Cl_2$ (15 mL) was added neat $Sn(NMe_2)_4$ (0.5 g, 1.7 mmol). The solution was stirred at room temperature for 5 h, when it gradually turned pale yellow and cloudy. It was then concentrated to ca. 5 mL and crystals suitable for X-ray crystallography were obtained after several days at –26 °C. Yield 0.4 g (24% relative to Sn). $^1$H NMR ($CD_2Cl_2$, 25 °C, 300.13 MHz): $\delta$ = 3.25 (br., 2 H, N–*H*), 2.76 (s, 30 H, N–C$H_3$) ppm. $^{13}$C{$^1$H} NMR ($CD_2Cl_2$, 25 °C, 75.48 MHz): $\delta$ = 150.0, 146.8, 140.2, 138.2, 136.9, 135.0 (all $ArF_5$–*C*), 42.0 (br., N–*C*$H_3$) ppm. $^{11}$B NMR ($CD_2Cl_2$, 96.29 MHz, 25 °C): $\delta$ = –13.6 ppm. $^{19}$F NMR ($CD_2Cl_2$, 282.38 MHz, 25 °C): $\delta$ = –133.6 (d, $^3J_{F,F}$ = 19.8 Hz, 8 F, $F_o$), –164.1 (t, $^3J_{F,F}$ = 19.8 Hz, 4 F, $F_p$), –168.0 (t, $^3J_{F,F}$ = 19.8 Hz, 8 F, $F_m$) ppm. $^{119}$Sn NMR ($CD_2Cl_2$, 25 °C, 111.91 MHz): $\delta$ = –311.4 ppm. $C_{34}H_{32}BF_{20}N_5Sn$ (1020.2): calcd. C 40.03, H 3.16, N 6.87; found C 39.52, H 2.95, N 6.48.

**Method B:** Neat $Sn(NMe_2)_4$ (0.4 g, 1.4 mmol) was added to a solution of **7** (0.9 g, 1.2 mmol) in $Et_2O$ (30 mL). A white precipitate formed within 2 min. The reaction mixture was stirred overnight, and light petroleum (10 mL) was added, yielding a white precipitate. The supernatant was filtered off. The white solid residue was washed with light petroleum (4 × 30 mL) and dried in vacuo. The product proved to be identical to that prepared by Method A. Yield 1.0 g (83% relative to Sn).

**$[H(HNMe_2)_2][B(C_6F_5)_4]$ (7):** Dimethylamine (6.6 g, 14.6 mmol) was condensed into a Schlenk tube at –35 °C and transferred rapidly to a solution of **3** (1.2 g, 1.4 mmol) in $Et_2O$ (25 mL). The resulting colourless solution was stirred overnight at room temperature. The volatiles were then removed in vacuo, yielding a white solid which was washed thoroughly with light petroleum (5 × 20 mL) and dried under vacuum. Yield 0.9 g (86%). $^1$H NMR ($CD_2Cl_2$, 25 °C, 300.13 MHz): $\delta$ = 7.04 (s, 3 H, N–*H*), 2.61 (s, 12 H, N–C$H_3$) ppm. $^{13}$C{$^1$H} NMR ($CD_2Cl_2$, 25 °C, 75.48 MHz): $\delta$ = 150.0, 147.1, 140.1, 138.0, 136.7, 135.0 (all $ArF_5$–*C*), 36.7 (N–*C*$H_3$) ppm. $^{11}$B NMR ($CD_2Cl_2$, 96.29 MHz, 25 °C): $\delta$ = –11.7 ppm. $^{19}$F NMR ($CD_2Cl_2$, 282.38 MHz, 25 °C): $\delta$ = –131.8 (d, $^3J_{F,F}$ = 19.8 Hz, 8 F, $F_o$), –161.9 (t, $^3J_{F,F}$ = 19.8 Hz, 4 F, $F_p$), –165.9 (t, $^3J_{F,F}$ = 19.8 Hz, 8 F, $F_m$) ppm. $C_{28}H_{15}BF_{20}N_2$ (770.2): calcd. C 43.66, H 1.96, N 3.64; found C 43.92, H 1.82, N 3.65.

**$[(C_4H_4N_2)H{\cdot}OEt_2][H_2N\{B(C_6F_5)_3\}_2]$ (8). Method A:** Pyrazine (0.1 g, 1.2 mmol) was weighed under inert atmosphere and rapidly added to a solution of **4** (1.0 g, 0.8 mmol) in $CH_2Cl_2$ (25 mL). The colourless mixture was stirred at room temperature overnight, and the solvent was pumped off under vacuum to leave a white solid which was washed with light petroleum (3 × 25 mL) and dried in vacuo. Crystals suitable for X-ray diffraction were obtained by recrystallisation from a concentrated $CH_2Cl_2$ solution at –26 °C. Yield 0.8 g (88%). $^1$H NMR ($CD_2Cl_2$, 25 °C, 300.13 MHz): $\delta$ = 16.46 (br., 1 H, N–*H*), 10.36–8.10 (v br, 4 H, C–*H*), 5.70 (br. s, 2 H, $H_2$N), 3.86 (q, $^3J_{H,H}$ = 7.0 Hz, 4 H, $CH_3$–C$H_2$–O), 1.34 (t, $^3J_{H,H}$ = 7.0 Hz, 6 H,C$H_3$–$CH_2$–O) ppm. $^{13}$C{$^1$H} NMR ($CD_2Cl_2$, 25 °C, 75.48 MHz): $\delta$ = 148.8, 146.6, 141.1, 138.6, 137.8, 135.4 (all $ArF_5$–*C*), 142.7 ($C_4H_4N_2$), 67.7 ($CH_3$–*C*$H_2$–O), 15.0 (*C*$H_3$–$CH_2$–O) ppm. $^{11}$B NMR ($CD_2Cl_2$, 96.29 MHz, 25 °C): $\delta$ = –5.3 ppm. $^{19}$F NMR ($CD_2Cl_2$, 282.38 MHz, 25 °C): $\delta$ = –133.4 (d, $^3J_{F,F}$ = 19.8 Hz, 12 F, $F_o$), –160.6 (t, $^3J_{F,F}$ = 19.8 Hz, 6 F, $F_p$), –166.1 (t, $^3J_{F,F}$ = 19.8 Hz, 12 F, $F_m$) ppm. $C_{44}H_{17}B_2F_{30}N_3O$ (1195.2): calcd. C 44.22, H 1.43, N 3.52; found C 43.91, H 1.58, N 3.43.

**Method B:** $[Na(OEt_2)_4][H_2N\{B(C_6F_5)_3\}_2]$ (1.9 g, 1.4 mmol) was added at room temperature to a suspension of solid $C_4H_4N_2{\cdot}HCl$ (0.15 g, 1.3 mmol) in 25 mL of $CH_2Cl_2$. The pyrazinium chloride reacted immediately, and the resulting solution turned pale yellow while small amounts of NaCl precipitate persisted. The solution was filtered off after 6 h, and the volatiles were removed under vacuum. A white powder was isolated, the composition of which was essentially identical to that of the solid obtained with Method A above. Yield 1.2 g (77%).

**$[Me_3Sn(HNMe_2)_2][B(C_6F_5)_4]$ (9):** Compound **7** (0.8 g, 1.0 mmol) was rapidly added to a solution of $Me_3SnN(SiMe_3)_2$ (0.6 g, 1.8 mmol) in $Et_2O$ (30 mL). The resulting colourless solution was stirred at room temperature for 1 h. Upon removal of the volatiles in vacuo a white solid was obtained which was washed thoroughly with light petroleum (2 × 50 mL) and dried in vacuo to constant weight. Yield 0.9 g (96%). Recrystallisation from a dichloromethane/light petroleum mixture (4:1) kept at –26 °C afforded single crystals of **9** as colourless slabs. $^1$H NMR ($CD_2Cl_2$, 25 °C, 300.13 MHz): $\delta$ = 2.42 (s, 12 H, N–C$H_3$), 2.14 (br., 2 H, N–*H*), 0.60 (s, 9 H, Sn–C$H_3$) ppm. $^{13}$C{$^1$H} NMR ($CD_2Cl_2$, 25 °C, 75.48 MHz): $\delta$ = 150.1, 146.9, 140.2, 138.3, 137.0, 135.0 (all $ArF_5$–*C*), 37.8 (N–*C*$H_3$), –5.4 (Sn–*C*$H_3$) ppm. $^{11}$B NMR ($CD_2Cl_2$, 96.29 MHz, 25 °C): $\delta$ = –13.6 ppm. $^{19}$F NMR ($CD_2Cl_2$, 282.38 MHz, 25 °C): $\delta$ = –133.6 (d, $^3J_{F,F}$ = 19.8 Hz, 8 F, $F_o$), –164.0 (t, $^3J_{F,F}$ = 19.8 Hz, 4 F, $F_p$), –168.0 (t, $^3J_{F,F}$ = 19.8 Hz, 8 F, $F_m$) ppm. $^{119}$Sn NMR ($CD_2Cl_2$, 25 °C, 111.91 MHz): $\delta$ = –25.3 ppm. $C_{31}H_{23}BF_{20}N_2Sn$ (933.0): calcd. C 39.91, H 2.48, N 3.00; found C 40.07, H 2.40, N 3.06.

**X-ray Crystallography:** Crystal data and refinement results for compounds **1**, **2**, **6**, **8** and **9** are collated in Table 1. In each case, crystals were mounted on glass fibres, either in oil and fixed in the cold nitrogen stream on a Rigaku/MSC AFC7R diffractometer (samples **1**, **2** and **6**) or with epoxy resin on a Nonius KappaCCD diffractometer (samples **8** and **9**). Data were processed with the TeXsan/PROCESS[63] or DENZO program,[64] and absorption corrections applied. The structures were determined by heavy atom methods (compounds **1** and **2**) or direct methods (compounds **6**, **8** and **9**) in SHELXS.[65] Refinement was by full-matrix least-squares methods in SHELXL.[65] In all, non-hydrogen atoms were refined anisotropically; hydrogen atoms were included in idealised positions and their isotropic thermal parameters were set to ride on the $U_{eq}$ values of the parent carbon or nitrogen atoms. Scattering factors for neutral atoms were taken from ref.[66]. The relatively large difference peaks and holes were located close to the tin atoms and arise from inadequate absorption correction. No absorption correction was applied in the case of compound **1**.

 © 2006 Wiley-VCH Verlag GmbH & Co. KGaA, Weinheim 

Table 1. Crystal and structure refinement data for compounds **1**, **2**, **6**, **8** and **9**.

| Compound | **1** | **2** | **6** | **8** | **9** |
|---|---|---|---|---|---|
| Elemental formula | $C_{24}H_{33}NSi_2Sn$ | $C_{16}H_{44}N_2Na_2OSi_4$ | $C_{10}H_{32}N_5Sn$, $C_{24}BF_{20}$ | $C_8H_{15}N_2O$, $C_{36}H_2B_2F_{30}N$ | $C_{62}H_{46}B_2F_{40}N_4Sn_2$ |
| Formula weight | 510.4 | 438.9 | 1020.2 | 1195.2 | 1866.0 |
| Crystal system | triclinic | monoclinic | triclinic | orthorhombic | triclinic |
| Space group | $P\bar{1}$ (no. 2) | $C2/c$ (no. 15) | $P\bar{1}$ (no. 2) | $P2_12_12_1$ (no. 19) | $P\bar{1}$ (no. 2) |
| Unit cell dimensions [Å, °] | | | | | |
| $a$ | 11.799(14) | 11.195(13) | 12.569(10) | 13.9820(2) | 13.910(4) |
| $b$ | 12.031(12) | 21.65(2) | 14.304(12) | 17.1460(2) | 14.102(3) |
| $c$ | 9.405(11) | 11.877(13 | 10.983(8)) | 18.3470(3) | 17.786(4) |
| $\alpha$ | 95.68(9) | 90 | 91.59(7) | 90 | 88.92(2) |
| $\beta$ | 107.33(9) | 109.73(9) | 102.48(6) | 90 | 82.07(2) |
| $\gamma$ | 84.08(9) | 90 | 85.87(7) | 90 | 89.94(2) |
| Cell volume, $V$ [Å$^3$] | 1264(2) | 2710(5) | 1923(3) | 4398.43(11) | 3454.9(15) |
| No. of formula units/cell, $Z$ | 2 | 4 | 2 | 4 | 2 |
| Density (calculated) [mg/m$^3$] | 1.340 | 1.076 | 1.762 | 1.805 | 1.794 |
| $F$(000) | 524 | 960 | 1012 | 2360 | 1832 |
| Absorption coefficient [mm$^{-1}$] | 1.114 | 0.259 | 0.796 | 0.197 | 0.875 |
| Temperature [K] | 140(1) | 140(1) | 140(1) | 293(2) | 120(2) |
| Crystal colour, shape | colourless block | colourless prism | colourless plate | colourless shard | colourless slab |
| Crystal size [mm] | 0.8×0.7×0.5 | 0.5×0.25×0.2 | 0.7×0.40×0.15 | 0.27×0.02×0.02 | 0.50×0.18×0.08 |
| $\theta$ range [°] for data collection | 2.3–25.1 | 1.9–20.0 | 1.9–25.0 | 2.9–27.1 | 1.2–27.5 |
| Index ranges for $h$, $k$, $l$ | 0/14, –14/14, –11/10 | –1/10, –20/20, –11/10 | 0/13, –16/16, –12/12 | –17/16, –19/21, –23/23 | –17/17, –18/18, –22/22 |
| Absorption correction | Psi-scans | Psi-scans | Psi-scans | Semi-empirical from equivalents | Semi-empirical from equivalents |
| Max./min. transmission | 1.00/0.584 | 1.00/0.756 | 1.00/0.64 | 0.996/0.949 | 0.933/0.669 |
| Total no. of reflections measured | 4681 | 2028 | 5537 | 63610 | 70746 |
| No. of unique reflections | 4443 | 1270 | 5200 | 9638 | 14464 |
| $R_{int}$ for equivalents | 0.088 | 0.146 | 0.104 | 0.074 | 0.065 |
| No. of "observed" reflections ($I > 2\sigma_I$) | 3851 | 883 | 4053 | 7707 | 11285 |
| Refinement | | | | | |
| Data/restraints/parameters | 4443/0/254 | 1270/0/121 | 5200/0/563 | 9638/0/727 | 14464/0/1021 |
| Goodness-of-fit on $F^2$, $S$ | 1.048 | 0.999 | 0.996 | 1.065 | 1.098 |
| Final $R$ indices ("observed" data) | $R_1$ = 0.061, $wR_2$ = 0.156 | $R_1$ = 0.058, $wR_2$ = 0.114 | $R_1$ = 0.063, $wR_2$ = 0.158 | $R_1$ = 0.047, $wR_2$ = 0.104 | $R_1$ = 0.055, $wR_2$ = 0.150 |
| Final $R$ indices (all data) | $R_1$ = 0.071, $wR_2$ = 0.164 | $R_1$ = 0.094, $wR_2$ = 0.126 | $R_1$ = 0.084, $wR_2$ = 0.170 | $R_1$ = 0.068, $wR_2$ = 0.113 | $R_1$ = 0.076, $wR_2$ = 0.160 |
| Largest diff. peak and hole [e·Å$^{-3}$] | 3.23 and –1.92 | 0.22 and –0.30 | 1.52 and –2.22 | 0.60 and –0.29 | 2.07 and –1.79 |

CCDC-605857 (for **1**), -605858 (for **2**), -605859 (for **6**), -605860 (for **8**) and -605861 (for **9**) contain the supplementary crystallographic data for this paper. These data can be obtained free of charge from The Cambridge Crystallographic Data Centre via www.ccdc.cam.ac.uk/data_request/cif.

## Acknowledgments

We gratefully acknowledge support from the Engineering and Physical Sciences Research Council.

[1] A. G. Davies and P. J. Smith in: *Comprehensive Organometallic Chemistry* (Eds.: G. Wilkinson, F. G. A. Stone, E. W. Abel), Pergamon Press, **1982**, vol. 2, p. 519.
[2] A. G. Davies, *Organotin Chemistry*, 2nd ed., Wiley-VCH, **2004**.
[3] L. Pellerito, L. Nagy, *Coord. Chem. Rev.* **2002**, *224*, 111–150.
[4] S. Durand, K. Sakamoto, T. Fukuyama, A. Orita, J. Otera, A. Duthie, D. Dakternieks, M. Shulte, K. Jurkschat, *Organometallics* **2000**, *19*, 3220–3223.
[5] E. G. Rochow, D. Seyferth, *J. Am. Chem. Soc.* **1953**, *75*, 2877–2878.
[6] R. Okawara, E. G. Rochow, *J. Am. Chem. Soc.* **1960**, *82*, 3285–3287.
[7] A. B. Burg, J. R. Spielman, *J. Am. Chem. Soc.* **1961**, *83*, 2667–2668.
[8] H. C. Clark, R. J. O'Brien, *Inorg. Chem.* **1963**, *2*, 740–744.
[9] M. M. McGrady, R. S. Tobias, *Inorg. Chem.* **1964**, *3*, 1157–1163.
[10] M. Wada, R. Okawara, *J. Organomet. Chem.* **1965**, *4*, 487–488.
[11] P. M. Treichel, R. A. Goodrich, *Inorg. Chem.* **1965**, *4*, 1424–1428.
[12] W. L. Jolly, J. R. Webster, *Inorg. Chem.* **1971**, *10*, 877–879.
[13] W. J. Pietro, W. J. Hehre, *J. Am. Chem. Soc.* **1982**, *104*, 4329–4332.
[14] A. G. Davies, J. P. Goddard, M. B. Hursthouse, N. P. C. Walker, *J. Chem. Soc., Chem. Commun.* **1983**, 597–598.
[15] W. A. Nugent, R. J. McKinney, R. L. Harlow, *Organometallics* **1984**, *3*, 1315–1317.
[16] T. Birchall, V. Manivannan, *J. Chem. Soc., Dalton Trans.* **1985**, 2671–2675.
[17] J. B. Lambert, B. Kuhlmann, *J. Chem. Soc., Chem. Commun.* **1992**, 931–932.
[18] B. Wrackmeyer, G. Kehr, A. Sebald, J. Kümmerlen, *Chem. Ber.* **1992**, *125*, 1597–1603.
[19] J. B. Lambert, S. M. Ciro, C. L. Stern, *J. Organomet. Chem.* **1995**, *499*, 49–55.
[20] J. B. Lambert, Y. Zhao, *Angew. Chem. Int. Ed. Engl.* **1997**, *36*, 400–401.
[21] J. B. Lambert, Y. Zhao, H. Wu, W. C. Tse, B. Kuhlmann, *J. Am. Chem. Soc.* **1999**, *121*, 5001–5008.
[22] I. Zharov, B. T. King, Z. Havlas, A. Pardi, J. Michl, *J. Am. Chem. Soc.* **2000**, *122*, 10253–10254.
[23] J. B. Lambert, L. Lin, S. Keinan, T. Müller, *J. Am. Chem. Soc.* **2003**, *125*, 6022–6023.

 © 2006 Wiley-VCH Verlag GmbH & Co. KGaA, Weinheim 

[24] A. Sekiguchi, T. Fukawa, V. Y. Lee, M. Nakamoto, *J. Am. Chem. Soc.* **2003**, *125*, 9250–9251.
[25] I. Zharov, T.-C. Weng, A. M. Orendt, D. H. Barich, J. Penner-Hahn, D. M. Grant, Z. Havlas, J. Michl, *J. Am. Chem. Soc.* **2004**, *126*, 12033–12046.
[26] G. Van Koten, J. G. Noltes, *J. Am. Chem. Soc.* **1976**, *98*, 5393–5395.
[27] M. Mehring, C. Löw, F. Uhlig, M. Schürmann, K. Jurkschat, B. Mahieu, *Organometallics* **2000**, *19*, 4613–4623.
[28] R. Jambor, I. Císařovă, A. Růžička, J. Holeček, *Acta Crystallogr., Sect. C* **2001**, *57*, 373–375.
[29] M. Mehring, I. Vrasidas, D. Horn, M. Schürmann, K. Jurkschat, *Organometallics* **2001**, *20*, 4647–4653.
[30] R. Jambor, L. Dostál, A. Růžička, I. Císařovă, J. Brus, M. Holčapek, J. Holeček, *Organometallics* **2002**, *21*, 3996–4004.
[31] K. Peveling, M. Henn, C. Löw, M. Mehring, M. Schürmann, B. Costisella, K. Jurkschat, *Organometallics* **2004**, *23*, 1501–1508.
[32] B. Kašná, R. Jambor, L. Dostál, A. Růžička, I. Císařovă, J. Holeček, *Organometallics* **2004**, *23*, 5300–5307.
[33] J. T. B. H. Jastrzebski, P. A. Van der Schaaf, J. Boersma, G. Van Koten, M. De Wit, Y. D. Wang, Y. D. Heijdenrijk, C. H. Stam, *J. Organomet. Chem.* **1991**, *407*, 301–311.
[34] A. Růžička, L. Dostál, R. Jambor, V. Buchta, J. Brus, I. Císařovă, M. Holčapek, J. Holeček, *Appl. Organomet. Chem.* **2002**, *16*, 315–322.
[35] M. Schormann, S. Garratt, D. L. Hughes, J. C. Green, M. Bochmann, *J. Am. Chem. Soc.* **2002**, *124*, 11266–11267.
[36] M. Schormann, S. Garratt, M. Bochmann, *Organometallics* **2005**, *24*, 1718–1724.
[37] P. Jutzi, C. Müller, A. Stammler, H.-G. Stammler, *Organometallics* **2000**, *19*, 1442–1444.
[38] S. J. Lancaster, A. Rodriguez, A. Lara-Sanchez, M. D. Hannant, D. A. Walker, D. L. Hughes, M. Bochmann, *Organometallics* **2002**, *21*, 451–453.
[39] I. Krossing, A. Reisinger, *Eur. J. Inorg. Chem.* **2005**, 1979–1989.
[40] M. Finze, E. Bernhardt, M. Berkei, H. Willner, J. Hung, R. M. Waymouth, *Organometallics* **2005**, *24*, 5103–5109.
[41] D. Vagedes, G. Erker, R. Fröhlich, *J. Organomet. Chem.* **2002**, *641*, 148–155.
[42] I. Krossing, I. Raabe, *Angew. Chem. Int. Ed.* **2004**, *43*, 2066–2090.
[43] M. D. Hannant, M. Schormann, D. L. Hughes, M. Bochmann, *Inorg. Chim. Acta* **2005**, *358*, 1683–1691.
[44] D. A. Walker, T. J. Woodman, D. L. Hughes, M. Bochmann, *Organometallics* **2001**, *20*, 3772–3776.
[45] Y. Sarazin, M. Schormann, M. Bochmann, *Organometallics* **2004**, *23*, 3296–3302.
[46] E. Farrow, Y. Sarazin, D. L. Hughes, M. Bochmann, *J. Organomet. Chem.* **2004**, *689*, 4624–4629.
[47] M. D. Hannant, M. Schormann, M. Bochmann, *J. Chem. Soc., Dalton Trans.* **2002**, 4071–4073.
[48] E. Y.-X. Chen, T. J. Marks, *Chem. Rev.* **2000**, *100*, 1391–1434, and references therein.
[49] E. B. Tjaden, D. C. Swenson, R. F. Jordan, J. L. Petersen, *Organometallics* **1995**, *14*, 371–386.
[50] D. A. Walker, T. J. Woodman, M. Schormann, D. L. Hughes, M. Bochmann, *Organometallics* **2003**, *22*, 797–803.
[51] K. Claborn, B. Kahr, W. Kaminsky, *CrystEngComm* **2002**, *4*, 252–256.
[52] G. D. Smith, P. E. Fanwick, I. P. Rothwell, *Inorg. Chem.* **1990**, *29*, 3221–3226.
[53] V. D. Romanenko, A. O. Gudima, A. N. Chernega, G. Bertrand, *Inorg. Chem.* **1992**, *31*, 3493–3494.
[54] M. Karl, G. Seybert, W. Massa, K. Harms, S. Agarwal, R. Maleika, W. Stelter, A. Greiner, W. Heitz, B. Neumüller, K. Dehnicke, *Z. Anorg. Allg. Chem.* **1999**, *625*, 1301–1309.
[55] For instance, $B(C_6F_3)_3$ readily abstracts a methyl group from $MeZr[N(SiMe_3)_2]_3$ to generate highly active species for cationic polymerisation catalysis: a) A. G. Carr, D. M. Dawson, M. Bochmann, *Macromol. Rapid Commun.* **1998**, *19*, 205–207; b) J. R. Galsworthy, M. L. H. Green, N. Maxted, M. Müller, *J. Chem. Soc., Dalton Trans.* **1998**, 387–392.
[56] W. Plass, J. G. Verkade, *Inorg. Chem.* **1993**, *32*, 5153–5159.
[57] A. Blaschette, I. Hippel, J. Krahl, E. Wieland, P. G. Jones, A. Sebald, *J. Organomet. Chem.* **1992**, *437*, 279–297.
[58] A. G. Massey, A. J. Park, F. G. A. Stone, *Proc. Chem. Soc. London Proc. Chem. Soc.* **1963**, 212.
[59] J. L. W. Pohlmann, F. E. Brinckmann, *Z. Naturforsch., Teil B* **1965**, *20*, 5–11.
[60] M. Rannenberg, J. Weidlein, A. Obermeyer, *Z. Naturforsch., Teil B* **1991**, *46*, 459–467.
[61] B. Wrackmeyer, A. Pedall, J. Weidinger, *Z. Naturforsch., Teil B* **2001**, *56*, 1009–1014.
[62] K. Jones, M. F. Lappert, *Proc. Chem. Soc. London* **1962**, 358–359.
[63] TeXsan - Single Crystal Structure Analysis Software, Molecular Structure Corporation, The Woodlands, Texas, USA, **1993**.
[64] Z. Otwinowski and W, Minor, "*Processing of X-ray diffraction data collected, in: the oscillation mode*", *Methods in Enzymology*, vol. 276; Macromolecular Crystallography, part A, p. 307–326 (Eds.: C. W. Carter, R. M. Sweet Jr), Academic Press.
[65] G. M. Sheldrick, SHELX-97, Programs for crystal structure determination (SHELXS) and refinement (SHELXL), University of Göttingen, Germany, **1997**.
[66] *International Tables for X-ray Crystallography*, Kluwer Academic Publishers, Dordrecht, **1992**, vol. C, pp. 500, 219 and 193.

Received: May 1, 2006
Published Online: June 28, 2006

 © 2006 Wiley-VCH Verlag GmbH & Co. KGaA, Weinheim 

DOI: 10.1002/ejic.200600098

# Pentafluorosulfanyl ($SF_5$) Containing Energetic Salts

Haixiang Gao,[a] Chengfeng Ye,[a] Rolf W. Winter,[b] Gary L. Gard,[b] Michael E. Sitzmann,[c] and Jean'ne M. Shreeve*[a]

**Keywords:** Ionic liquids / Pentafluorosulfanylnitramide / Quaternization / Salts / Heats of formation / Energetic materials

New quaternary salts of pentafluorosulfanyl-substituted ($SF_5$) *N*-methylimidazole (**1**), 4-amino-1,2,4-triazole (**3**) or pyridine (**5**) were prepared and characterized. Most of the salts exhibit good thermal stabilities and low melting points placing them in the ionic liquid class. Their densities range between 1.4 and 1.8 g/cm$^3$. The standard enthalpies of formation for the new salts were calculated by the use of computationally feasible DFT(B3LYP) and MP2 methods in conjunction with an empirical approach based on densities of salts.
(© Wiley-VCH Verlag GmbH & Co. KGaA, 69451 Weinheim, Germany, 2006)

## Introduction

Energetic materials are vital to the improvement and advancement in our lives; essential in peace and in armed conflict. These materials are controllable energy sources which deliver power as a function of the rate at which the energy is liberated. Propellants that release energy over a period of a few milliseconds to seconds by evolving gases are useful for driving turbines or propelling rockets. However, explosives, which evolve energy at rapid rates are employed to produce intense shock waves and find great value in mining, cutting, and initiation of detonation phenomena. Nearly all of the industrially used energetics are based on ammonium nitrate, while for military purposes nitroglycerin, nitrocellulose, HMX, TNT, or RDX are most frequently used. Currently, the research in the field of energetic materials has tended to be directed towards the synthesis of simple molecules with high energy, high density, high heat resistance and low sensitivity by often focusing on the design of nitrogen-containing heterocyclic-based, energetic, low-melting salts.[1,2] Energetic materials that are salts often possess advantages over molecular analogues since they tend to exhibit lower vapor pressures and higher densities.

High on the list of important characteristics for energetic materials are density and energy released. Earlier we reported new thermally stable, pentafluorosulfanyl polyfluoroalkyl-substituted quaternary salts whose melting points were less than 0 °C and where the presence of the pentafluorosulfanyl group markedly increased the densities of these room-temperature ionic liquids vis-à-vis most of their perfluoroalkyl or alkyl analogues.[3] Based on those results and the following observations: (1) indications that the $SF_5$ group can provide energetic salts with improved properties, i.e., increased density, decreased sensitivity and good thermal stability; and (2) the larger energy release found due to formation of HF in the detonation of $SF_5$ explosives [compare the average S–F bond energy (79 kcal/mol) to that of H–F (136 kcal/mol)],[4] we examined the impact of the pentafluorosulfanyl group on the properties of energetic salts. In the present work, we report the preparation and characterization of pentafluorosulfanylalkyl-substituted imidazolium, triazolium and pyridinium salts that contain highly oxidizing anions.

## Results and Discussion

Initially, we attempted to quaternize *N*-methylimidazole (**1**), 4-amino-1,2,4-triazole (**3**) or pyridine (**5**) with $SF_5CH_2CH_2Br$ or $SF_5CH_2CH_2OTs$, but failed because major decomposition of the pentafluorosulfanyl-containing precursor occurred due to the loss of HBr or HOTs. In sharp contrast, by simply elongating the alkyl chain in the $SF_5$ electrophile from ethyl to propyl, excellent yields resulted. For example, reaction of $SF_5CH_2CH_2CH_2Br$ with *N*-methylimidazole (**1**) in a 1:1 molar ratio without solvent at 65 °C for 12 h led to the formation of the quaternary salt **2** in 90% isolated yield (Scheme 1). Analogously, reactions of $SF_5CH_2CH_2CH_2Br$ with 4-amino-1,2,4-triazole (**3**) and pyridine (**5**) gave the monoquaternary bromides **4** and **6** in >85% isolated yields. Nitrate, perchlorate, dinitramide, and pentafluorosulfanylnitramide salts were synthesized by metathesis of the monoquaternary salts with silver nitrate, silver perchlorate, ammonium dinitramide, and potassium pentafluorosulfanylnitramide,[5] respectively, in aqueous

[a] Department of Chemistry, University of Idaho, Moscow, ID 83844-2343, USA
Fax: +1-208-885-9146
E-mail: jshreeve@uidaho.edu
[b] Department of Chemistry, Portland State University, Portland, OR 97207, USA
[c] Indian Head Division, Naval Surface Warfare Center, Indian Head, MD 20640, USA

 © 2006 Wiley-VCH Verlag GmbH & Co. KGaA, Weinheim 

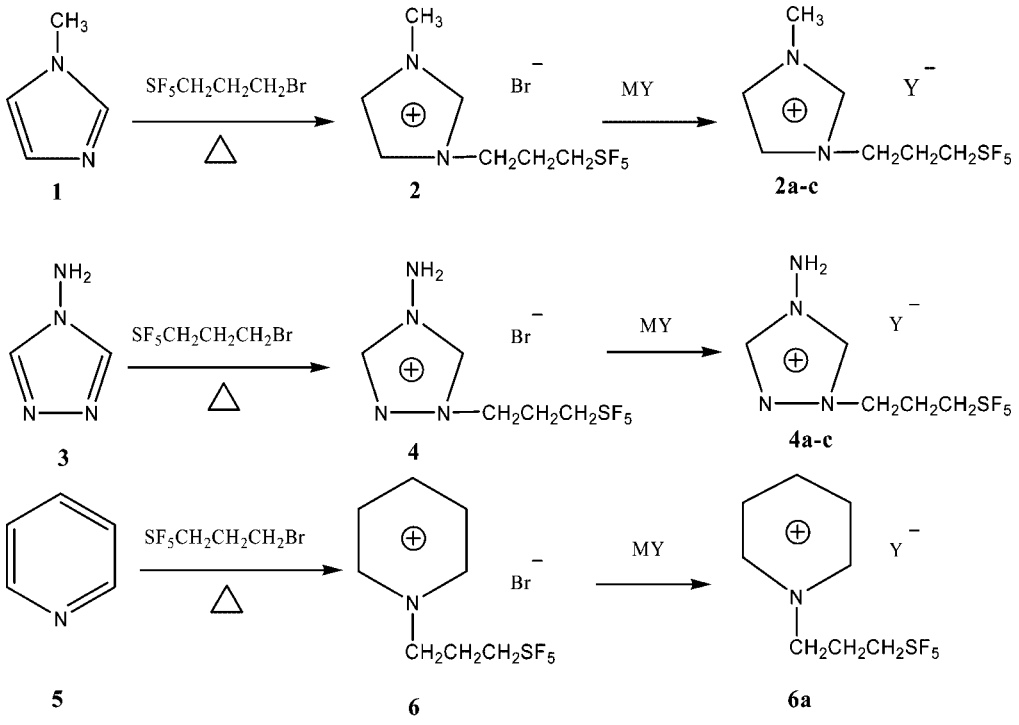


MY = $AgNO_3$, $AgClO_4$, $NH_4N(NO_2)_2$, $K(SF_5NNO_2)$

Scheme 1.

solution (Scheme 1). Because some of the nitrate salts were hygroscopic, they were dried under vacuum for 24 h and stored in a desiccator for further analysis.

Phase-transition temperatures [midpoints of melting points ($T_m$) or glass phase transition temperatures ($T_g$)] were determined by differential scanning calorimetry (DSC), and decomposition points ($T_d$) were recorded using thermogravimetric analysis (TGA) (Table 1). It is seen that the decomposition temperatures and heats of formation for the perchlorate salts are higher than those of the nitrate and dinitramide salts. The melting points of the imidazolium (**2**) and pyridinium (**6**) salts are considerably lower than that of triazolium salts (**4**).

Density is one of the important physical properties of energetic salts. Some of the experimental densities obtained by using a helium pycnometer for the new salts are also listed in Table 1. For all of the compounds, densities exceeded 1.40 g cm$^{-3}$, likely arising from the presence of the $SF_5$ moiety. This is particularly noticeable in the case of **4d**, which exhibits a density of 1.82 g/cm$^3$ due to the $SF_5$ functional groups found in both anion and cation, which markedly enhance this property.

Table 1. Structure and properties of $SF_5$-containing salts.

| Cation | Anion | No. | $T_m/T_g$ [°C] | $T_d$ [°C] | $d$ [g/cm$^3$] | $H_L$[a] | $\Delta_f H_m°$[b] (cation) | $\Delta_f H_m°$[b] (anion) | $\Delta_f H_m°$[b] (salts) | $D$[c] | $P$[d] |
|---|---|---|---|---|---|---|---|---|---|---|---|
| 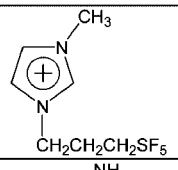 | Br | **2** | 90.5 | – | – | – | –66.3 | – | – | – | – |
| | $NO_3$ | **2a** | –33.7 | 172.3 | 1.54 | 106.5 | –66.3 | –73.6 | –246.4 | 5819 | 11.4 |
| | $ClO_4$ | **2b** | –68.0 | 247.1 | 1.46 | 102.2 | –66.3 | –66.4 | –234.8 | 5538 | 10.4 |
| | $[N(NO_2)_2]$ | **2c** | –50.7 | 201.7 | 1.52 | 102.7 | –66.3 | –26.9 | –195.9 | 6118 | 13.0 |
| 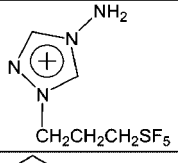 | Br | **4** | 101.3 | – | – | – | –33.3 | – | – | – | – |
| | $NO_3$ | **4a** | 58.6 | 145.8 | 1.43 | 104.4 | –33.3 | –73.6 | –211.2 | 5726 | 10.8 |
| | $ClO_4$ | **4b** | 50.7 | 242.7 | 1.41 | 101.1 | –33.3 | –66.4 | –200.8 | 5712 | 11.3 |
| | $[N(NO_2)_2]$ | **4c** | 84.8 | 160.9 | 1.44 | 101.2 | –33.3 | –26.9 | –161.4 | 6145 | 13.2 |
| | $[SF_5NNO_2]$ | **4d** | –20.6 | 188.2 | 1.82 | 102.0 | –33.3 | –284.3 | –419.5 | 6680 | 16.7 |
| 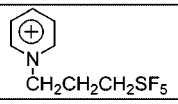 | Br | **6** | 95.4 | – | – | – | –77.9 | – | – | – | – |
| | $[N(NO_2)_2]$ | **6a** | 11.0 | 182.3 | 1.47 | 102.1 | –77.9 | –26.9 | –206.8 | 5636 | 10.7 |

[a] Lattice energy [kcal/mol]. [b] [kcal/mol]. [c] Detonation velocity [m/s]. [d] Detonation pressure [GPa].

 © 2006 Wiley-VCH Verlag GmbH & Co. KGaA, Weinheim 

### Thermochemistry

According to Born–Haber energy cycles, heats of formation of ionic salts can be simplified by the formula:

$\Delta H_f^o$ (ionic salts, 298 K) = $\Delta H_f^o$ (cation, 298 K) + $\Delta H_f^o$ (anion, 298 K) – $\Delta H_L$

where $\Delta H_L$ is the lattice energy of the ionic salts. For 1:1 salts and considering the nonlinear nature of the cation and anion we currently used, $\Delta H_L$ [kJ/mol] can be predicted by the formula suggested by Jenkins et al.[6] as:

$\Delta H_L = 1981.2 \cdot (\rho_m/M_m)^{1/3} + 108.8$

Heats of formation of the $NO_3^-$, $ClO_4^-$ and $N(NO_2)_2^-$ anions can be easily obtained by the reactions in Scheme 2.

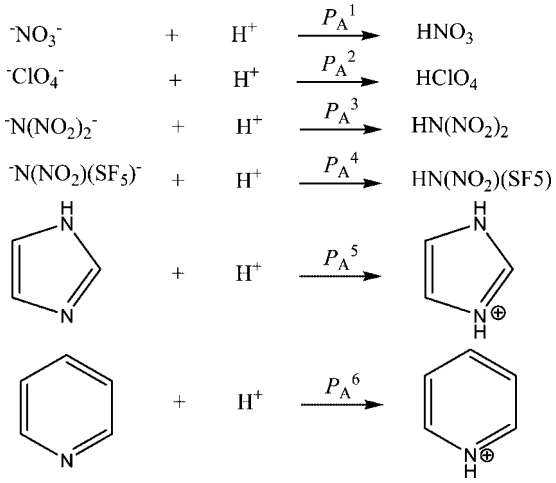


Scheme 2.

The proton affinities ($P_A$) were calculated using the G2 method or taken from the literature.[7] A value of 1528.085 kJ mol$^{-1}$ with correction of 6.197 kJ mol$^{-1}$ was adopted for $\Delta H_f^o$ ($H^+$, 298 K).[8,9] Heats of formation of $HNO_3$ and $HN(NO_2)_2$ in the gas phase are available (–32.1 and 29.9kcal/mol, respectively),[7] while the heat of formation of $HClO_4$ (g) is a little uncertain. In this work, 0.6 kcal mol$^{-1}$ was used. This was derived by computation using W1 and W2 methods.[10] This molecule exhibits particularly severe degrees of inner polarization, and as such obtaining a basis-set limit SCF component to the total atomization energy becomes a challenge. However, the G2 calculation gives 10.8 kcal/mol. Heats of formation of $NO_3^-$, $ClO_4^-$ and $N(NO_2)_2^-$ were calculated to be –73.6, –66.4, and –26.9 kcal/mol, respectively.

Then the remaining task was to determine the heats of formation of the cations, and of $N(NO_2)(SF_5)^-$, which were computed using the method of isodesmic reactions (Scheme 3). The 1,2,4-triazolium species was purposely conserved, because its heat of formation has been experimentally determined to be 835 kJ mol$^{-1}$.[8] With the experimental heat of formation of imidazole and pyridine, the imidazolium and pyridinium cations were calculated by the proton-affinity reactions shown in Scheme 2 using the G2 method. The enthalpies of reactions ($\Delta H_r^o{}_{,298}$) are obtained by combining the MP2(full)/6-311++G** energy difference for the reactions, the scaled zero-point energies, and other thermal factors. Thus, the heats of formation of the cations and of $N(NO_2)(SF_5)^-$ can be readily extracted. The results are listed in Table 1. The calculated enthalpies of formation ($\Delta_f H_m$) range from –419.5 kcal mol$^{-1}$ to –161.5 kcal mol$^{-1}$.

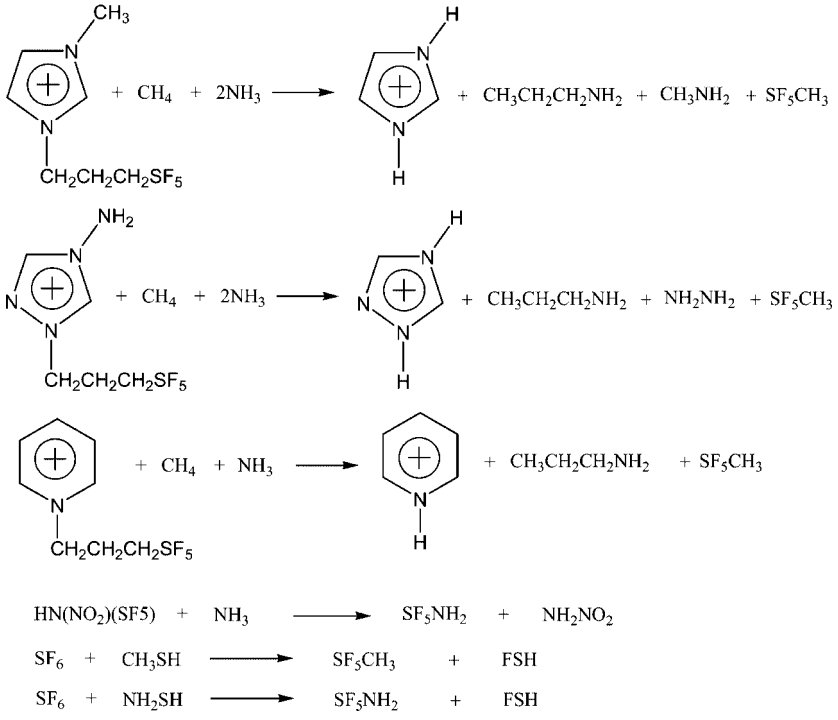


Scheme 3.

 © 2006 Wiley-VCH Verlag GmbH & Co. KGaA, Weinheim 

All of the values are negative mainly as a result of the large negative heat of formation of $SF_5$ (–216.3 kcal/mol).[11]

The expected detonation pressures ($P$) and detonation velocities ($D$) based on the traditional Chapman–Jouget thermodynamic detonation theory were calculated (Table 1).[12] For all the salts, the calculated detonation pressures lie in the range between $P$ = 10.4 GPa (**2b**) and $P$ = 16.7 GPa (**4d**). These values are similar to that of tetranitromethane (14.4 GPa).[13] Detonation velocities range between $D$ = 5538 m s$^{-1}$ and $D$ = 6630 m s$^{-1}$ (**4d**), higher than those of ammonium dinitramide ($D \geq$ 5300 m s$^{-1}$) and lead azide ($D$ = 5300 m s$^{-1}$).

Of all of the new energetic compounds, **4b** is thermally considerably more stable than **4d**, but its density is lower by 0.4 g/cm$^3$. Also, the pentafluorosulfanylnitramide derivative **4d** has a melting point which is 71 °C lower than **4b**. The densities of the new (pentafluorosulfanyl)alkyl quaternary salts are surprisingly low compared to their (pentafluorosulfanyl)polyfluoroalkyl quaternary analogs that exhibit densities around 2 g/cm$^{-3}$ making them among the most dense of any of the non-chloroaluminate salts reported to date.[14] Comparisons must be made carefully because the (pentafluorosulfanyl)polyfluoroalkyl derivatives were only studied with bis(trifluoromethanesulfonyl)amide as the anion.[3] However, it may be concluded that density may be enhanced by the presence of fluorine in fluoroalkyl and/or pentafluorosulfanyl moieties.

## Conclusions

Syntheses of $SF_5$-propyl derivatives of imidazole, 4-amino-1,2,4-triazole, and pyridine and their subsequent quaternization led to new energetic salts. Most of the new salts exhibit good physical properties, including moderately high density (>1.40 g/cm$^3$), good thermal and hydrolytic stabilities and low melting points (<100 °C). The molar enthalpies of formation were calculated by theoretical methods. Perchlorate salts have slightly higher molar enthalpies of formation than the analogous nitrates. The calculated heats of formation for dinitramide-containing salts are the highest. Utilization of pentafluorosulfanylnitramide as the anion contributes to a decrease in the melting point because of its asymmetry and of the tendency for the negative charge to be dispersed over the entire anionic structure, as is the case for dinitramide.

## Experimental Section

**Caution:** While we have experienced no difficulties with shock and friction sensitivity of these compounds with high nitrogen content and rather high heats of formation, they should be synthesized in mmol amounts and handled with extreme care.

**General Methods:** All the reagents used were analytical reagents purchased from commercial sources and used as received. $^1$H, $^{19}$F NMR and $^{13}$C NMR spectra were recorded with a 300-MHz NMR spectrometer operating at 300.13, 282 and 75.48 MHz, respectively. Chemical shifts are reported relative to $Me_4Si$ or $CCl_3F$. The solvent was $D_2O$ unless otherwise specified. The melting and decomposition points were recorded with a differential scanning calorimeter and a thermogravimetric analyzer at a scan rate of 10 °C/min, respectively. IR spectra were recorded using NaCl plates for neat liquids and KBr pellets for solids. Densities of ionic liquids were measured at room temperature using a pycnometer. Densities of solid salts were measured at room temperature using a Micromeritics Accupyc 1330 gas pycnometer. Elemental analyses were performed with an EXETER CE-440 Elemental Analyzer.

**Theoretical Study:** Computations were performed with the Gaussian03 (Revision D.01) suite of programs.[15] The geometric optimization and the frequency analyses are carried out using B3-LYP functional analyses with 6-31+G** basis set.[16] Single energy points were calculated at the $MP_2$(full)/6-311++G** level.[17,18] All of the optimized structures were characterized to be true local energy minima on the potential energy surface without imaginary frequencies.

**General Procedure:** *N*-Methylimidazole (**1**), 4-amino-1,2,4-triazole (**3**), or pyridine (**5**) (2 mmol) and $SF_5CH_2CH_2CH_2Br$ were sealed in a Pyrex glass tube in vacuo by cooling to liquid nitrogen temperature and then heated at 65 °C for 12 h. After cooling to room temperature, the tube was opened and the volatile materials were removed at reduced pressure. Washing of the crude products with an acetone/pentane mixture (1:3) gave **2**, **4**, and **6** in good yields. The nitrate, perchlorate, dinitramide and pentafluorosulfanylnitramide salts were synthesized by metathesis of the monoquaternary bromides with silver nitrate, silver perchlorate, ammonium dinitramide, and potassium pentafluorosulfanylnitramide[5] in water. Reactions of these bromides with silver salts in water in a 1:1 molar ratio were carried out at 25 °C. After 2 h, silver bromide was removed by filtration. The filtrate was concentrated and dried in vacuo to give **2a**–**b**, **3a**–**b** in high yields. Reactions of analogous substrates with ammonium dinitramide or potassium pentafluorosulfanylnitramide in water were stirred at room temperature for 2 h to give a heterogeneous mixture. The water was removed under reduced pressure at 50 °C until constant weight was reached. To the remaining suspension were added chloroform and anhydrous magnesium sulfate. After 1 h, the suspension was filtered and the volatile material was removed under reduced pressure at 30 °C for 2 h to afford the dinitramide or pentafluorosulfanylnitramide salts.

**1-Methyl-3-[3-(pentafluorosulfanyl)propyl]imidazolium Bromide (2):** Yield 90% (0.596 g). IR (KBr pellet): $\tilde{\nu}$ = 3433, 3146, 3069, 2982, 2858, 2750, 2069, 1749, 1639, 1574, 1462, 1379, 1286, 1244, 1169, 1073, 831, 624, 595, 563 cm$^{-1}$. $^1$H NMR: $\delta$ = 8.78 (s, 1 H), 7.53 (s, 1 H), 7.48 (s, 1 H), 4.34 (t, $J$ = 0.79 Hz, 2 H), 3.91 (m, 5 H), 2.58 (m, 2 H) ppm. $^{13}$C NMR: $\delta$ = 124.84, 123.05, 68.90 (m), 48.15, 36.69, 27.36 (m) ppm. $^{19}$F NMR: $\delta$ = 85.65 (m, 1 F), 64.84, (d, m, 4 F) ppm. $C_7H_{12}BrF_5N_2S$ (331.14): calcd. C 25.39, H 3.65, N 8.46; found C 25.46, H 3.59, N 8.41.

**1-Methyl-3-[3-(pentafluorosulfanyl)propyl]imidazolium Nitrate (2a):** Yield 90% (0.282 g). IR (KBr pellet): $\tilde{\nu}$ = 3433, 3149, 3092, 2395, 2289, 2067, 1631, 1571, 1377, 1169, 1082, 1037, 829, 758, 655, 627, 595, 563, 482 cm$^{-1}$. $^1$H NMR: $\delta$ = 8.80 (s, 1 H), 7.56 (s, 1 H), 7.50 (s, 1 H), 4.36 (t, $J$ = 4.82 Hz, 2 H), 3.94 (m, 5 H), 2.60 (m, 2 H) ppm. $^{13}$C NMR: $\delta$ = 137.16, 124.96, 123.14, 69.01 (m), 48.22, 36.78, 27.36 (m) ppm. $^{19}$F NMR: $\delta$ = 85.43 (m, 1 F), 64.78, (d, m, 4 F) ppm. $C_7H_{12}F_5N_3O_3S$ (313.25): calcd. C 26.84, H 3.86, N 13.41; found C 26.54, H 4.02, N 12.97.

**1-Methyl-3-[3-(pentafluorosulfanyl)propyl]imidazolium Perchlorate (2b):** Yield 89% (0.312 g). IR (KBr pellet): $\tilde{\nu}$ = 3429, 3088, 2379, 1716, 1566, 1388, 1087, 826, 754, 625, 598, 544 cm$^{-1}$. $^1$H NMR: $\delta$

 © 2006 Wiley-VCH Verlag GmbH & Co. KGaA, Weinheim 

= 9.02 (s, 1 H), 7.80 (s, 1 H), 7.71 (s, 1 H), 4.52 (t, $J$ = 4.87 Hz, 2 H), 4.06 (m, 5 H), 2.66 (m, 2 H) ppm. $^{13}$C NMR: $\delta$ = 137.11, 124.86, 123.07, 69.04 (m), 48.16, 36.67, 27.40 (m) ppm. $^{19}$F NMR: $\delta$ = 84.93 (m, 1 F), 64.34, (d, m, 4 F). $C_7H_{12}ClF_5N_2O_4S$ (350.69): calcd. C 23.97, H 3.45, N 7.99; found C 23.82, H 3.44, N 7.97 ppm.

**1-Methyl-3-[3-(pentafluorosulfanyl)propyl]imidazolium Dinitramide (2c):** Yield 84% (0.300 g). IR (KBr pellet): $\tilde{\nu}$ = 3154, 3115, 2974, 1566, 1517, 1432, 1336, 1187, 1105, 1009, 756, 624, 595, 563 cm$^{-1}$. $^1$H NMR: $\delta$ = 9.20 (s, 1 H), 7.85 (s, 1 H), 7.74 (s, 1 H), 4.56 (t, $J$ = 4.81 Hz, 2 H), 4.06 (m, 5 H), 2.67 (m, 2 H) ppm. $^{13}$C NMR: $\delta$ = $\delta$138.11, 125.02, 123.34, 69.44 (m), 48.15, 36.66, 27.85 (m) ppm. $^{19}$F NMR: $\delta$ = 84.91 (m, 1 F), 64.20, (d, m, 4 F). $C_7H_{12}F_5N_5O_4S$ (357.26): calcd. C 23.53, H 3.39, N 19.60; found C 23.68, H 3.48, N 19.32.

**4-Amino-1-[3-(pentafluorosulfanyl)propyl]triazolium Bromide (4):** Yield 84% (0.280 g). IR (KBr pellet): $\tilde{\nu}$ = 3297, 2958, 2704, 1807, 1623, 1564, 1524, 1417, 1333, 1193, 1074, 1020, 993, 914, 871, 822, 694, 615, 565, 486, 415 cm$^{-1}$. $^1$H NMR: $\delta$ = 8.87 (s, 1 H), 8.51 (s, 1 H), 4.55 (t, $J$ = 4.52 Hz), 3.98 (m, 2 H), 2.64 (m, 2 H) ppm. $^{13}$C NMR: $\delta$ = $\delta$146.45, 68.89 (m), 51.35, 26.05 (m) ppm. $^{19}$F NMR: $\delta$ = 85.75 (m, 1 F), 64.67, 2 H (d, m, 4 F). $C_5H_{10}BrF_5N_4S{\cdot}1.5\ H_2O$ (360.14): calcd. C 16.67, H 3.64, N 15.56; found C 16.58, H 3.58, N 15.43.

**4-Amino-1-[3-(pentafluorosulfanyl)propyl]triazolium Nitrate (4a):** Yield 88% (0.277 g). IR (KBr pellet): $\tilde{\nu}$ = 3451, 3305, 3196, 3121, 2395, 1762, 1627, 1525, 1385, 1194, 1073, 1012, 864, 835, 679, 618 cm$^{-1}$. $^1$H NMR: $\delta$ = 8.90 (s, 1 H), 8.79 (s, 1 H), 4.56 (t, $J$ = 4.66 Hz, 2 H), 3.99 (m, 2 H), 2.65 (m, 2 H) ppm. $^{13}$C NMR: $\delta$ = 146.46, 69.11 (m), 51.37, 26.03 (m) ppm. $^{19}$F NMR: $\delta$ = 85.32 (m, 1 F), 64.55, (d, m, 4 F) ppm. $C_5H_{10}F_5N_5O_3S$ (315.22): calcd. C 19.05, H 3.20, N 22.22; found C 19.30, H 3.25, N 22.43.

**4-Amino-1-[3-(pentafluorosulfanyl)propyl]triazolium Perchlorate (4b):** Yield 87% (0.307 g). IR (KBr pellet): $\tilde{\nu}$ = 3456, 3101, 2448, 2289, 2021, 1619, 1556, 1446, 1377, 1282, 1086, 829, 626, 561 cm$^{-1}$. $^1$H NMR ([D$_6$]acetone): $\delta$ = 9.96 (s, 1 H), 9.11 (s, 1 H), 4.74 (t, $J$ = 4.54 Hz), 4.16 (m, 2 H), 2.76 (m, 2 H) ppm. $^{13}$C NMR ([D$_6$]-acetone): $\delta$ = $\delta$142.34, 69.57 (m), 51.48, 26.24 (m) ppm. $^{19}$F NMR ([D$_6$]acetone): $\delta$ = 85.06 (m, 1 F), 64.29, 2 H (d, m, 4 F) ppm. $C_5H_{10}ClF_5N_4O_4S$ (352.67): calcd. C 17.03, H 2.86, N 15.89; found C 16.90, H 2.93, N 15.53.

**4-Amino-1-[3-(pentafluorosulfanyl)propyl]triazolium Dinitramide (4c):** Yield 78% (0.280 g). IR (KBr pellet): $\tilde{\nu}$ = 3317, 3133, 1708, 1632, 1521, 1434, 1379, 1187, 1074, 1016, 833, 759, 621, 563, 484 cm$^{-1}$. $^1$H NMR: $\delta$ = 8.88 (s,1 H), 8.69 (s,1 H), 4.55 (t, $J$ = 4.56 Hz, 2 H), 3.98 (m, 2 H), 2.64 (m, 2 H) ppm. $^{13}$C NMR: $\delta$ = 146.46, 68.91 (m), 51.35, 26.07 (m) ppm. $^{19}$F NMR: $\delta$ = 85.05 (m, 1 F), 64.25, (d, m, 4 F) ppm. $C_5H_{10}F_5N_7O_4S$ (359.23): calcd. C 16.72, H 2.81, N 27.29; found C 16.97, H 2.97, N 27.05.

**4-Amino-1-[3-(pentafluorosulfanyl)propyl]triazolium Pentafluorosulfanylnitramide (4d):** Yield 70% (0.308 g). IR (KBr pellet): $\tilde{\nu}$ = 3289, 3133, 3021, 2959, 2362, 1803, 1623, 1455, 1371, 1327, 1298, 1178, 1039, 992, 824, 736, 622, 565, 481 cm$^{-1}$. $^1$H NMR: $\delta$ = 10.71 (s,1 H), 9.1 (s,1 H), 4.83 (t, $J$ = 4.56 Hz), 4.19 (m,2 H), 2.73 (m, 2 H) ppm. $^{13}$C NMR: $\delta$ = 144.66, 69.54 (m), 50.92, 26.45 (m) ppm. $^{19}$F NMR: $\delta$ = 91.75 (m, 1 F) 84.84 (m, 1 F), 64.13 (d,, m 4 F), 64.09 (m, 4 F) ppm. $C_5H_{10}F_{10}N_6O_2S_2$ (440.29): calcd. C 13.64, H 2.29, N 19.09; found C 13.78, H 2.45, N 18.68.

**1-[3-(Pentafluorosulfanyl)propyl]pyridinium Bromide (6):** Yield 78% (0.256 g). IR (KBr pellet): $\tilde{\nu}$ = 3475, 3402, 3120, 3042, 3022, 2960, 2052, 1629, 1484, 1213, 1180, 874, 827, 785, 690,630, 557, 493, 454 cm$^{-1}$. $^1$H NMR : $\delta$ = 8.89 (d, 2 H $J$ = 3.78 Hz), 8.60 (t, $J$ = 5.25 Hz, 1 H), 8.12 (t, $J$ = 4.84 Hz, 2 H), 4.75 (t, $J$ = 5.12 Hz), 4.60 (m, 2 H), 2.72 (m, 2 H) ppm. $^{13}$C NMR: $\delta$ = $\delta$147.15, 145.34, 129.48, 68.62 (m), 60.31, 28.32 (m) ppm. $^{19}$F NMR: $\delta$ = 85.02 (m, 1 F), 64.82 (d, m, 4 F) ppm. $C_8H_{11}BrF_5NS$ (328.14): calcd. C 29.28, H 3.38, N 4.27; found C 29.43, H 3.23, N 4.10.

**1-[3-(Pentafluorosulfanyl)propyl]pyridinium Dinitramide (6a):** Yield 89% (0.315 g). IR (KBr pellet): $\tilde{\nu}$ = 3540, 3138, 3065, 2358, 2331, 1637, 1519, 1486, 1424, 1310, 1183, 1015, 814, 772, 753, 686, 626 cm$^{-1}$. $^1$H NMR: $\delta$ = 9.27 (d, $J$ = 3.62 Hz), 8.75 (t, $J$ = 5.25 Hz), 8.30 (t, $J$ = 4.79 Hz), 5.03 (t, $J$ = 5.11 Hz), 4.20 (m,2 H), 2.90 (m, 2 H) ppm. $^{13}$C NMR: $\delta$ = 147.11, 146.10,129.59, 68.18 (m), 60.27, 28.86 (m) ppm. $^{19}$F NMR: $\delta$ = 84.66 (m, 1 F), 64.35 (d, m, 4 F) ppm. $C_8H_{11}F_5N_4O_4S$ (354.25): calcd. C 27.12, H 3.13, N 15.82; found C 27.30, H 3.03, N 15.56.

## Acknowledgments

We are grateful to AFOSR (F49620-03-1-0209), NSF CHE0315275, and ONR (N00014-02-1-0600) for support of this research. The authors are particularly indebted to Drs. Jerry A. Boatz and Gregory W. Drake.

[1] a) H. Xue, R. D. Verma, J. M. Shreeve, *J. Fluorine Chem.* **2006**, *127*, *159*–176; b) R. P. Singh, R. D. Verma, D. T. Meshri, J. M. Shreeve, *Angew. Chem. Int. Ed.* **2006**, *45*, 3584–3601; and references cited therein; c) L. E. Fried, M. R. Manaa, P. F. Pagoria, R. L. Simpson, *Annu. Rev. Mater. Res.* **2001**, *31*, 291–321; d) P. F. Pagoria, G. S. Lee, A. R. Mitchell, R. D. Schmidt, *Thermochim. Acta* **2002**, *384*, 187–204; e) H. H. Krause, "New Energetic Materials", in: *Energetic Materials* (Ed.: U. Teipel), Wiley-VCH, Weinheim, **2005**, pp. 1–25; f) A. K. Sikder, N. Sikder, *J. Hazard. Mater.* **2004**, *A112*, 1–15; g) J. P. Agrawal, *Prog. Energy Combust. Sci.* **1998**, *24*, 1–30.

[2] a) K. Muralidharan, B. A. Omotowa, B. Twamley, C. Piekarski, J. M. Shreeve, *Chem. Commun.* **2005**, 5193–5195; b) D. E. Chavez, M. A. Hiskey, R. D. Gilardi, *Angew. Chem. Int. Ed.* **2000**, *39*, 1791–1793; c) D. E. Chavez, M. A. Hiskey, R. D. Gilardi, *Org. Lett.* **2004**, *6*, 2889–2891; d) K. Y. Lee, J. E. Kennedy, B. W. Asay, S. F. Son, E. S. Martin, *AIP Conference Proceedings*, Springer-Verlag, New York, **2004**, vol. 706, p. 855–858; e) J. C. Bottaro, R. J. Schmitt, M. A. Petrie, P. E. Penwell, US Patent 6255512, **2001**; f) M. S. Pevzner, *Russ. Chem. J.* **1997**, *41*, 73–83; g) M. X. Zhang, P. E. Eaton, R. D. Gilardi, *Angew. Chem. Int. Ed.* **2000**, *39*, 401–404; h) K. Karaghiosoff, T. M. Klapötke, P. Mayer, H. Piotrowski, K. Polborn, R. L. Willer, J. J. Weigand, *J. Org. Chem.* **2006**, *71*, 1295–1305.

[3] R. P. Singh, R. W. Winter, G. L. Gard, Y. Gao, J. M. Shreeve, *Inorg. Chem.* **2003**, *42*, 6142–6146.

[4] M. E. Sitzmann, W. H. Gilligan, *J. Energ. Mater.* **1990**, *8*, 352–374.

[5] M. E. Sitzmann, R. Gilardi, R. J. Butcher, W. M. Koppes, A. G. Stern, J. S. Thrasher, N. J. Trivedi, Z.-Y. Yang, *Inorg. Chem.* **2000**, *39*, 843–850.

[6] H. D. B. Jenkins, D. Tudeal, L. Glasser, *Inorg. Chem.* **2002**, *41*, 2364.

[7] J. C. Gálvez-Ruiz, G. Holl, K. Karaghiosoff, T. M. Klapötke, K. Löhnwitz, P. Mayer, H. Nöth, K. Polborn, C. J. Rohbogner, M. Suter, J. J. Weigand, *Inorg. Chem.* **2005**, *44*, 4237–4253.

[8] M. W. Gordon, M. S. Schmidt, J. A. Boatz, *J. Phys. Chem. A* **2005**, *109*, 7285–7295.

[9] M. W. Chase, C. A. Davies, J. R. Downey, D. J. Frurip, R. A. McDonald, A. N. Syverud, *J. Phys. Chem. Ref. Data* **1985**, *14*, suppl. 1.

[10] J. M. L. Martin, *J. Mol. Struct. (THEOCHEM)*, in press.

[11] M. W. Chase Jr, "NIST-JANAF Themochemical Tables", 4th ed., *J. Phys. Chem. Ref. Data*, **1998**, monograph 9, p. 1–1951.

 © 2006 Wiley-VCH Verlag GmbH & Co. KGaA, Weinheim 

[12] a) L. E. Fried, K. R. Glaesemann, W. M. Howard, P. C. Souers, *CHEETAH 4.0 User's Manual*, Lawrence Livermore National Laboratory, **2004**; b) J. P. Lu, *Evaluation of the Thermochemical Code – CHEETAH 2.0 for Modelling Explosives Performance*, DSTO-TR-1199, DSTO, Edinburgh, **2001**.
[13] R. C. Harney, *Combat Systems III: Engagement Elements*, **2005**, chapter 6, p. 405–415, http://www.nps.navy.mil/se/harney.htm.
[14] C. Ye, J. M. Shreeve, *J. Org. Chem.* **2004**, *69*, 6511–6513.
[15] M. J. Frisch, G. W. Trucks, H. B. Schlegel, G. E. Scuseria, M. A. Robb, J. R. Cheeseman, J. A. Montgomery Jr, T. Vreven, K. N. Kudin, J. C. Burant, J. M. Millam, S. S. Iyengar, J. Tomasi, V. Barone, B. Mennucci, M. Cossi, G. Scalmani, N. Rega, G. A. Petersson, H. Nakatsuji, M. Hada, M. Ehara, K. Toyota, R. Fukuda, J. Hasegawa, M. Ishida, T. Nakajima, Y. Honda, O. Kitao, H. Nakai, M. Klene, X. Li, J. E. Knox, H. P. Hratchian, J. B. Cross, V. Bakken, C. Adamo, J. Jaramillo, R. Gomperts, R. E. Stratmann, O. Yazyev, A. J. Austin, R. Cammi, C. Pomelli, J. W. Ochterski, P. Y. Ayala, K. Morokuma, G. A. Voth, P. Salvador, J. J. Dannenberg, V. G. Zakrzewski, S. Dapprich, A. D. Daniels, M. C. Strain, O. Farkas, D. K. Malick, A. D. Rabuck, K. Raghavachari, J. B. Foresman, J. V. Ortiz, Q. Cui, A. G. Baboul, S. Clifford, J. Cioslowski, B. B. Stefanov, G. Liu, A. Liashenko, P. Piskorz, I. Komaromi, R. L. Martin, D. J. Fox, T. Keith, M. A. Al-Laham, C. Y. Peng, A. Nanayakkara, M. Challacombe, P. M. W. Gill, B. Johnson, W. Chen, M. W. Wong, C. Gonzalez, J. A. Pople, *Gaussian03* (Revision D.01), Gaussian, Inc., Wallingford, CT, USA, **2004**.
[16] R. G. Parr, W. Yang, *Density Functional Theory of Atoms and Molecules*, Oxford University Press, New York, **1989**.
[17] C. M. Møller, M. S. Plesset, *Phys. Rev.* **1934**, *46*, 618.
[18] J. A. Pople, J. S. Binkely, R. Seeger, *Int. J. Quantum Chem.* **1976**, *10*, 1.

Received: February 3, 2006
Published Online: June 14, 2006

 © 2006 Wiley-VCH Verlag GmbH & Co. KGaA, Weinheim 

DOI: 10.1002/ejic.200600104

# Correlation Between Structure and Magnetic and Magnetotransport Properties of $La_{0.7}Pb_{0.3}(Mn_{1-x}Co_x)O_3$ ($0.1 \leq x \leq 0.3$) CMR Manganites

**Alazne Peña,[a] Jon Gutiérrez,*[b] Izaskun Gil de Muro,[a] Javier Campo,[c][‡] Jose Manuel Barandiarán,[b] and Teófilo Rojo[a]**

**Keywords:** Manganites / Crystal structure / Magnetic properties / Magnetoresistance / Metal–insulator transition / Perovskite phases

Structural and magnetic properties of $La_{0.7}Pb_{0.3}(Mn_{1-x}Co_x)O_3$ ($0.1 \leq x \leq 0.3$) manganites are reported. Samples were fabricated by the sol-gel low temperature method. At room temperature, the first structural characterisation of all phases gave as a result the rhombohedral space group ($R\bar{3}c$). All compositions show ferromagnetic behaviour and magnetoresistance. The measured low-temperature magnetic moment and the Curie temperature continuously decrease with respect to the undoped composition, as Mn ions are substituted progressively by Co. This is interpreted in terms of substitution of $Mn^{3+}$ by $Co^{3+}$ and the appearance of a small amount of $Co^{4+}$. The measured magnetoresistance reaches 40 % for the 10 % Co-doped one at the corresponding Curie temperature. The resistivity behaviour of all the studied compounds is determined by the intra- and intergrain conduction mechanisms, with grain sizes in the range of 10–25 nm.
(© Wiley-VCH Verlag GmbH & Co. KGaA, 69451 Weinheim, Germany, 2006)

## Introduction

Perovskite-like phases with the general formula $Ln^{3+}_{1-x}A^{2+}_xMnO_3$ ($Ln^{3+}$ = La, Pr, Nd, Sm… and $A^{2+}$ = Ca, Sr, Ba, Pb…) have attracted the attention of the scientific community because of the magnetotransport properties exhibited.[1,2] The double exchange mechanism[3] is used to explain the ferromagnetic behaviour of these phases, while the simultaneous presence of ferromagnetism and a metallic state brings about colossal magnetoresistance (CMR) when the magnetic field is changed.[4] These generic magnetic and transport properties in this type of doped manganites mainly arise from a strong on-site exchange interaction (Hund's-rule couple $J \approx 2$–$3$ eV[5]) between the localised $t_{2g}$ spins and itinerant $e_g$ electrons.[6] The rhombohedral and orthorhombic distortion of the actual crystallographic structure of the classic cubic symmetry is also an essential factor to understand the magnetic and transport properties of these samples.[7]

The substitution of the Mn ions by other transition-metal ions in perovskites of composition $Ln_{0.7}A_{0.3}Mn_{1-y}TM^{3+}_yO_3$ (TM = transition metal) gives rise to changes in the $Mn^{3+}$:$Mn^{4+}$ ratio, with important modifications in their magnetic and transport properties.[8–12] The $y = 0$ sample shows ferromagnetism and CMR. In this sense, the effect of different trivalent ions from the iron group (partially filled 3d shells) as $Fe^{3+}$ ($3d^5$), $Co^{3+}$ ($3d^6$) or $Ni^{3+}$ ($3d^7$) substitution in the Mn site is still an interesting subject.

We have shown, in previous works,[9,13] that iron enters as high-spin $t_{2g}^3\ e_g^2$ (HS, $S = 5/2$) $Fe^{3+}$ in the $La_{0.7}Pb_{0.3}Mn_{1-x}Fe_xO_3$ family of compositions because it is the most stable oxidation state for this cation, and its ionic radius is very similar to that of the $Mn^{3+}$ ion. Iron couples antiferromagnetically with Mn ions and weakens progressively the double exchange mechanism and so the ferromagnetic character (decrease of both Curie temperature and low-temperature magnetic moment value) of the compounds as the doping level increases. A 20–30% substitution of Fe leads to magnetic frustration and insulating behaviour in these compositions.[13]

The electronic and magnetic properties of the $LaCoO_3$ perovskite is still a matter of research in the scientific community. Goodenough determined that the spin state of the $Co^{3+}$ ions presents a $t_{2g}^6\ e_g^0$ diamagnetic low-spin configuration at low temperatures (LS, $S = 0$), which changes as temperature increases to a $t_{2g}^4\ e_g^2$ high-spin (HS, $S = 2$) state. The possibility of having $Co^{3+}$ in different spin states as a function of temperature arises from the close values of the intra-atomic exchange energy ($J_H$) and the crystal field splitting (10Dq) at the Co sites. The low-temperature spin state of the $Co^{III}$ ion is due to the large crystal field, which stabilises its low-spin configuration and is energetically

[a] Dpto. de Química Inorgánica, Fac. de Ciencia y Tecnología, Univ. del País Vasco/EHU, Apdo. 644, 48080 Bilbao, Spain
[b] Dpto. de Electricidad y Electrónica-Un. As. CSIC, Fac. de Ciencia y Tecnología, Univ. del País Vasco/EHU, Apdo. 644, 48080 Bilbao, Spain
Fax: +34-94-601-3071
E-mail: jon@we.lc.ehu.es
[c] Institut Laue Langevin (ILL, CRG-D1B), Rue Jules Horowitz, B. P. 156, 38042 Grenoble Cedex 9, France
[‡] New address: Instituto de Ciencia de los Materiales de Aragón, Universidad de Zaragoza, CSIC Facultad de Ciencias, 50009 Zaragoza, Spain

 © 2006 Wiley-VCH Verlag GmbH & Co. KGaA, Weinheim 

more favourable. Increasing temperature, a thermally activated spin transition from the low-temperature LS state to a paramagnetic HS state occurs; in the range 100–350 K both populations are stabilised in a dynamical equilibrium.[14,15] More recently different authors[16,17] have evidenced the existence of a transition that develops from the low-temperature $Co^{3+}$ (LS, $t_{2g}^6 e_g^0$) to an intermediate spin (occupation $t_{2g}^5 e_g^1$) state, as temperature increases, with energy differences about 10–12 meV between the ground and the first excited state. Also, in Co containing perovskite-like compounds and in particular in cobaltites, the coexistence of those ions with high-spin tetravalent $Co^{4+}$ ($t_{2g}^3 e_g^2$) has also been proposed.

In order to study such a transition and the effect of these different tri- or tetravalent Co cations, we present the results concerning the magnetic and structural properties of the $La_{0.7}Pb_{0.3}(Mn_{1-x}Co_x)O_3$ manganites when Mn is substituted progressively by Co up to 30% doping levels. Similar research work was performed in a family of manganites having Ca instead of Pb occupying the A site.[15] Briefly, it was found that even for small doping levels of Co (as low as $x = 0.05$) the ferromagnetic order of the pure manganite is severely modified. The magnetic-order temperature decreases quickly in the Mn–Co mixed compounds, with almost a constant value of 165–170 K for doping levels ranging from $x = 0.1$ to 0.3. But $Ca^{2+}$ and also $Sr^{2+}$ are cations with ionic character and when cations with a more covalent character, such as $Pb^{2+}$[13] and $Bi^{3+}$,[18] are used, the observed magnetic behaviour indicates a soft and progressive decrease of the magnetic-order temperatures in each family of compounds.

Neutron diffraction, magnetic and transport measurements have been used in order to perform this study. We have been especially careful in the analysis of the chemical and structural properties of the studied compositions, and tried to explain the observed magnetic and magnetotransport properties on the basis of those previously determined characteristics.

## Results and Discussion

The morphology of the $La_{0.7}Pb_{0.3}Mn_{0.9}Co_{0.1}O_3$ compound is shown as representative in the SEM photograph (taken with 8500 times magnification) of Figure 1. The microstructure reveals uniform and fine grain growth, less than 1 μm size, as expected from the sol-gel fabrication process used to synthesise the samples. The observed agglomeration of such fine grains is also a direct consequence of the fabrication process used.

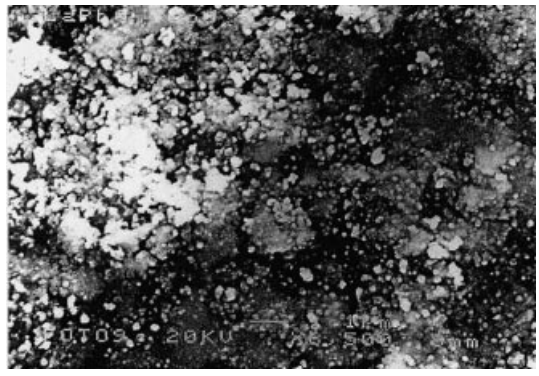

Figure 1. SEM photograph of the $La_{0.7}Pb_{0.3}Mn_{0.9}Co_{0.1}O_3$ compound.

The crystal structure of this family of compounds has been analysed in the trigonal space group ($R\bar{3}c$) (see Figure 2), hexagonal setting ($Z = 6$), using the D1B neutron powder diffraction data.

The Co cation undergoes a spin-state transition, in the range 125–230 K, that is directly correlated with the ionic radius of the cations and is reflected in the thermal evol-

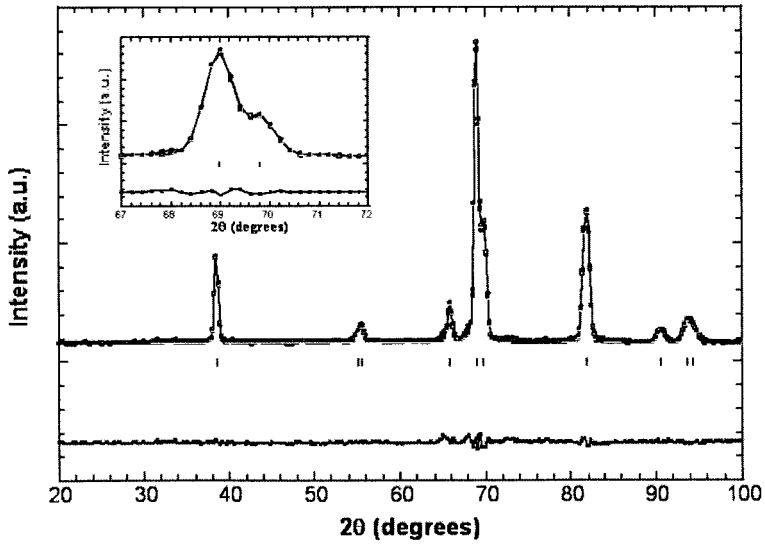


Figure 2. Rietveld fit to the neutron diffraction data (recorded at 10 K) for the $La_{0.7}Pb_{0.3}Mn_{0.7}Co_{0.3}O_3$ compound showing Bragg reflections for the $R\bar{3}c$ phase, difference curve and (inset) refinement of the main diffraction peak, around $2\theta = 69°$.

 © 2006 Wiley-VCH Verlag GmbH & Co. KGaA, Weinheim 

ution of the Mn/Co–O bond length obtained from the neutron diffraction patterns (see Figure 3). We attribute this transition to be from nonmagnetic (LS) to magnetic intermediate state (IS) of the Co cations, with the appearance of orbital ordering of occupied $e_g$ orbitals, as has been previously observed by other authors in the related compound $LaCoO_3$.[16,17] A very recent work[19] on this subject has proved that Co–O hybridisation has to be taken into account, giving rise to a "covalent" IS, $Co(t_{2g}^5\ e_g^{1.5})$–$O(2p^{5.5})$. However, in our case the Co quantity is small enough to give a precise picture of this transition.

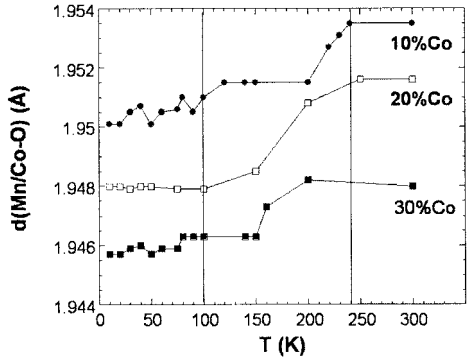


Figure 3. Thermal evolution of the bond length Mn/Co–O for these compounds.

The oxygen stoichiometry of the samples was determined by thermogravimetric analysis, the oxides being heated up to 900 °C in flowing 5% $H_2$/Ar. The samples were reduced to MnO and CoO and the observed weight losses allowed us to determine the oxygen contents of $La_{0.7}Pb_{0.3}Mn_{0.9}Co_{0.1}O_{3.10}$, $La_{0.7}Pb_{0.3}Mn_{0.8}Co_{0.2}O_{3.17}$ and $La_{0.7}Pb_{0.3}Mn_{0.7}Co_{0.3}O_{3.20}$ for the synthesised samples. The obtained excess of oxygen for all the samples is in good agreement with the quantities obtained from the redox titration, the oxygen excess being a direct consequence of the fabrication process used.

Two losses of consecutive weight based on the temperature for all the samples are observed (see Figure 4). The first loss occurs at a temperature of 437 °C. This temperature increases as the Co doping level in the sample increases, while the second loss happens at approximately the same temperature in all cases.

According to this we can affirm that first the $Mn^{4+}$ and $Co^{4+}$ ions (this one only for the 20% and 30% Co-containing compositions) are reduced to $Mn^{3+}$ and $Co^{3+}$ respectively and when all components appear in the form $Mn^{3+}$ and $Co^{3+}$ (constant amount in all the samples) the second reduction takes place, that is to say, the $Mn^{3+}$ and $Co^{3+}$ ions are reduced to $Mn^{2+}$ and $Co^{2+}$ respectively.

The obtained ZFC–FC curves, for all the compositions, are shown in Figure 5. From ZFC curves, a continuous decrease of the magnetic-order or Curie temperature from 240 K for the 10% Co-doped composition to 180 K for the 30% Co-doped one is clearly observed. This decrease in those magnetic-ordering temperatures can be directly attributed to the progressive suppression of the double exchange

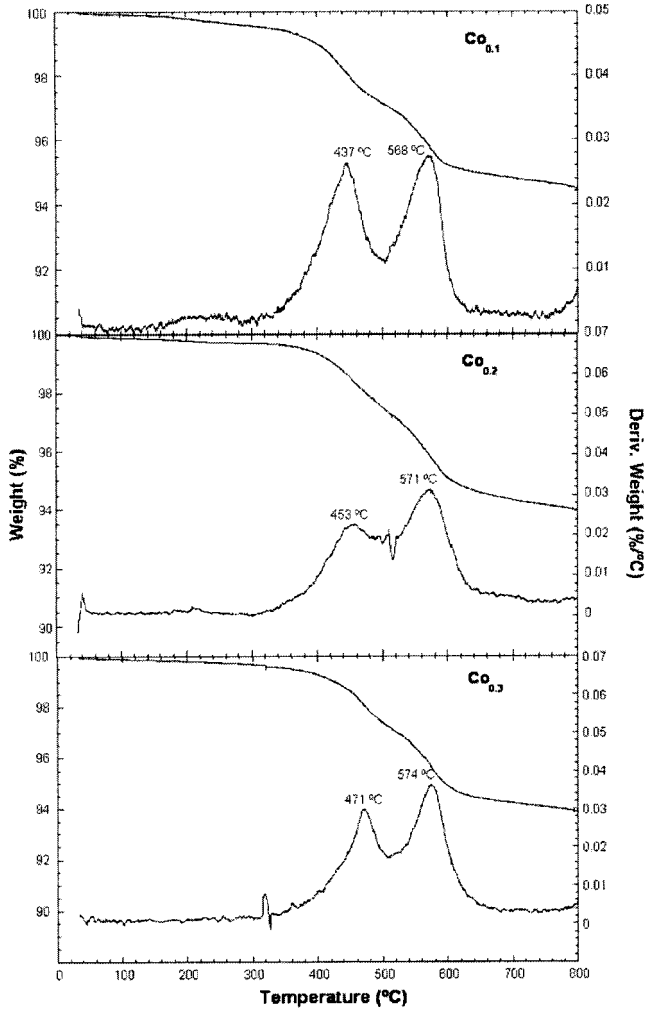


Figure 4. Thermogravimetric curves in $H_2$. It shows two steps of reduction indicating a reduction process of $TM^{4+} \rightarrow TM^{3+} \rightarrow TM^{2+}$ (TM = Mn and Co).

interaction present in the Mn host as Co content increases in the composition of the samples.

There is a remarkable similarity between this low-field magnetisation behaviour, indicating that the magnetisation process is basically the same. The degree of irreversibility of such processes is high, as indicated by the splitting between ZFC and FC curves. This bifurcation of both curves occurs at a temperature $T_b$ corresponding to the blocking temperature of the largest particles in the assembly. That is, $T_b$ defines also a temperature above which magnetisation processes are fully reversible. It is worth mentioning that the drop of the ZFC magnetisation below $T_C$ for each composition can be interpreted as a feature of cluster glass behaviour. On the other hand, a clear weakening of the ferromagnetic character of these compounds on Co substitution is observed, reflecting a decrease of the measured Curie temperature value as Co content increases in the composition of the samples.

The hysteresis loops, measured at 10 K and up to 7 T (see Figure 6), show the usual ferromagnetic behaviour, quickly reaching magnetic saturation, and the measured values of

 © 2006 Wiley-VCH Verlag GmbH & Co. KGaA, Weinheim 

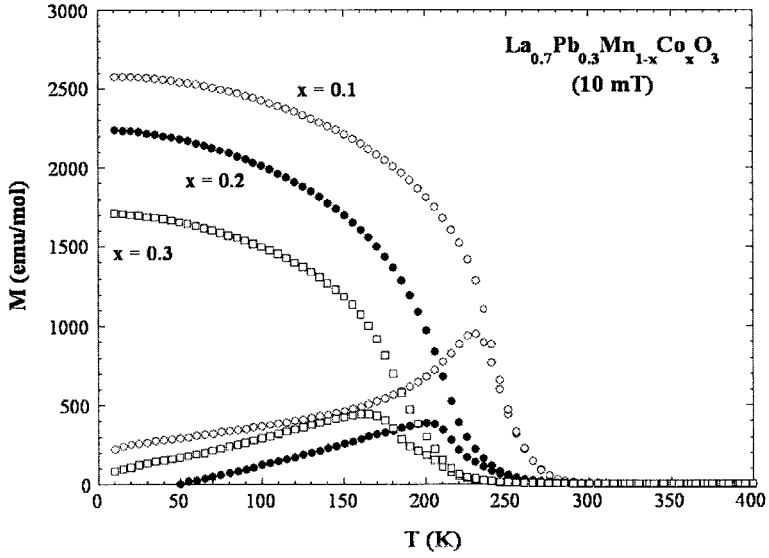


Figure 5. Zero-field cooling (ZFC) and field cooling (FC) curves measured at 10 mT.

the coercive field are 95.5, 114 and 243 kA/m for the 10, 20 and 30% Co-doped compositions, respectively. This high magnitude of the coercive field measured at low temperature can be understood as arising from the strong anisotropic nature of the Co ion.[20] The experimental value of the low-temperature magnetic moment was also determined by using Arrott plots.[21] All measured magnetic data are summarised in Table 1. Previous work from the authors[13] determined the following values for the undoped $La_{0.7}Pb_{0.3}MnO_3$ composition: low temperature $<\mu_{Mn}>_{LT}$ = 3.4 $\mu_B$, $T_C$ = 345 K, high-temperature effective moment $<\mu_{Mn}>_{HT}$ = 5.9 $\mu_B$. For the $x$ = 0.1 composition the measured low-temperature magnetic moment supports our previous supposition that Co enters in the composition only as $Co^{3+}$ (LS) (diamagnetic at low temperatures). However, this is not the case for the $x$ = 0.2 and 0.3 samples. The measured moment values do not agree with the supposition that all Co is $Co^{3+}$. To account for those measured values (and in particular for the $x$ = 0.2 composition, in which a higher degree of ferromagnetic coupling is observed) we need to assume that also $Co^{4+}$ (HS, $S$ = 5/2) is present in those compositions. In fact, a simple calculation gave us a good fit for the measured low-temperature magnetic moment values taking into account small percentages of about 9% high-spin $Co^{4+}$ for the 20% and 5% for the 30% Co-containing compositions. The existence of $Co^{4+}$ has been observed in other manganite phases.[22] Thus, the low-temperature magnetic properties of these compounds can be understood on the basis of a competition between positive $Co^{3+}$–O–$Co^{4+}$ and negative $Co^{3+}$–O–$Co^{3+}$ and $Co^{3+}$–O–$Mn^{4+}$ interactions, in which it concerns Co ions. Furthermore, a scenario in which $Co^{3+}$ ions cluster around $Co^{4+}$ ions is plausible and justifies the observed zero-field cooled magnetisation behaviour.

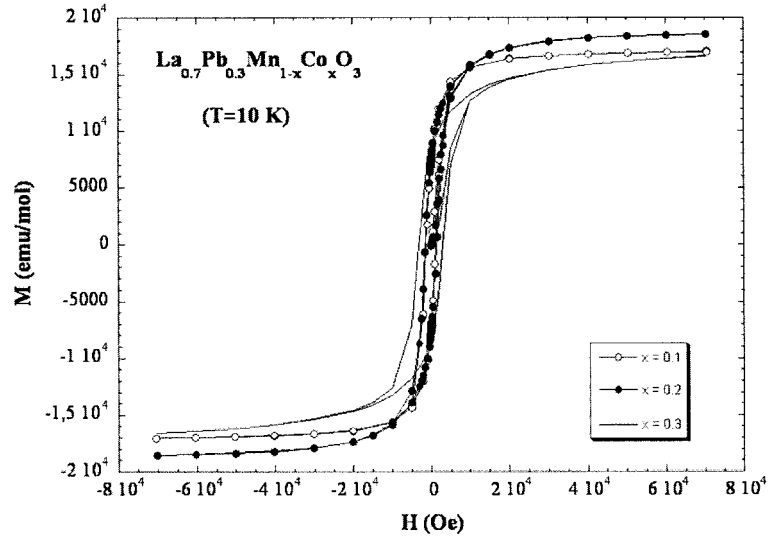


Figure 6. Hysteresis loops measured at 10 K and up to 7 T.

 © 2006 Wiley-VCH Verlag GmbH & Co. KGaA, Weinheim 

Table 1. Values of the low-temperature magnetic moment and Curie temperature for the $La_{0.7}Pb_{0.3}(Mn_{1-x}Co_x)O_3$ ($0.1 \leq x \leq 0.3$) family of compounds.

| Sample | $\mu$ [$\mu_B$][a] | $\mu$ [$\mu_B$][b] | $T_C$ [K][b] | $\mu$ [$\mu_B$][c] | $T_{order}$ [K][c] | $\mu_{eff}$ [$\mu_B$][f] | $\theta_c$ [K][f] | $\mu_t$ [$\mu_B$][g] |
|---|---|---|---|---|---|---|---|---|
| Co0.1 | 3.06 | 3.05 | 240 | 3.04[d] | 275 | 5.31 | 265 | 5.6 |
| Co0.2 | 2.72 | 3.17 | 210 | 2.72[e] | 230 | 5.27 | 244 | 5.5 |
| Co0.3 | 2.38 | 2.63 | 180 | 2.11[e] | 190 | 5.22 | 230 | 5.2 |

[a] Expected values if only $Co^{3+}$ enters in the compositions. [b] Values obtained from magnetic measurements. [c] Values obtained from neutron diffraction. [d] $T$ = 1.5 K. [e] $T$ = 10 K. [f] Values from Curie–Weiss law in the paramagnetic regime. [g] Values calculated as explained in the text.

We can check the validity of this guess by analysing the high-temperature magnetisation behaviour. In Figure 7 we show the $\chi^{-1}_{dc} = H/M_{ZFC}$ versus $T$ behaviour measured in the paramagnetic phase for the different samples. A Curie–Weiss law is clearly followed above $T_C$ and in the temperature range over which the data were taken. The effective moments $\mu_{eff}$ obtained from the Curie constants are shown in Table 1, together with the obtained paramagnetic Curie temperatures, $\theta_C$. We have also calculated the expected value $\mu_t$ of that effective moment as $\mu_t = [(1 - x)<\mu_{Mn}>^2_{HT} + x<\mu_{Co}>^2]^{1/2}$, taking into account the previous percentages of $Co^{4+}$ (HS) and that only $Co^{3+}$ (covalent IS, 2.5 $\mu_B$[19]) is present for each composition (see Table 1). As expected, all calculated values are slightly higher than the experimental ones, except for the $x$ = 0.3 compound, which shows an excellent agreement between both experimentally determined and calculated values. This sample has the lowest paramagnetic Curie temperature and as a first consequence a better accuracy in the experimental determination of $\mu_{eff}$ than the other two compounds because the temperature range used for the fitting extends to temperatures far above $T_C$.

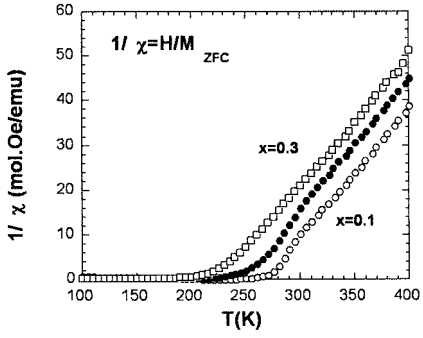


Figure 7. Curie–Weiss plot of the dc susceptibility.

The proposed magnetic behaviour for this family of Co-doped manganites is also supported by our neutron diffraction experiments. The thermal evolution of the neutron diffraction patterns for these samples was also recorded (see Figure 8). In all cases, two reflections with magnetic contribution at the same $d$ values are observed. This feature is indicative of an equivalent magnetic structure for the compounds. That is, the magnetic order does not change its structure when including 10, 20 or 30% of Co in these La-based phases. Furthermore, all magnetic reflections can be indexed with the same cell as the nuclear one, indicating an equivalent type of ferromagnetic structure with collinear magnetic moments. The magnetic contribution appears at about 275, 230 and 190 K for the 10, 20 and 30% Co-doped compositions, respectively. The best solution for the fits was obtained with a collinear magnetic structure in which the magnetic moment of the Mn ion is placed into the (101) crystallographic plane, in the hexagonal setting (parallel to the [111] direction of the perovskite cubic cell) (see Figure 9). The obtained values of the magnetic moment at the lowest temperature of the measurement (1.5 or 10 K) are 2.74, 2.72 and 2.11 $\mu_B$ for the 10, 20 and 30% Co-doped compositions, respectively. Figure 10 shows the temperature dependence of the refined magnetic moment value for the studied Co-containing compositions.

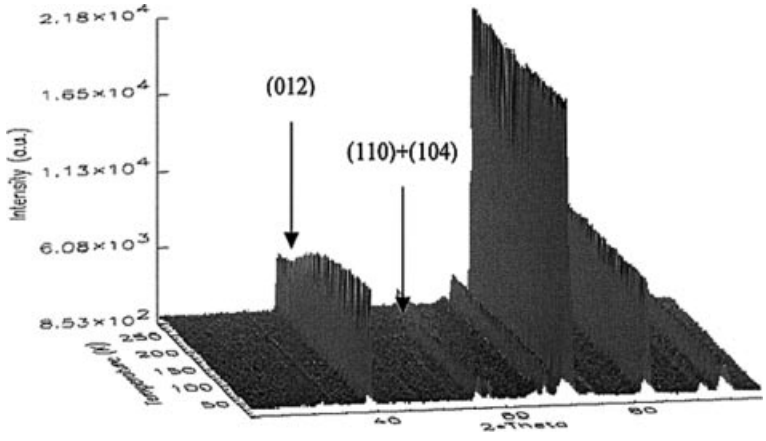


Figure 8. Thermal evolution of the neutron diffraction patterns for the $La_{0.7}Pb_{0.3}Mn_{0.8}Co_{0.2}O_3$ compound.

 © 2006 Wiley-VCH Verlag GmbH & Co. KGaA, Weinheim 

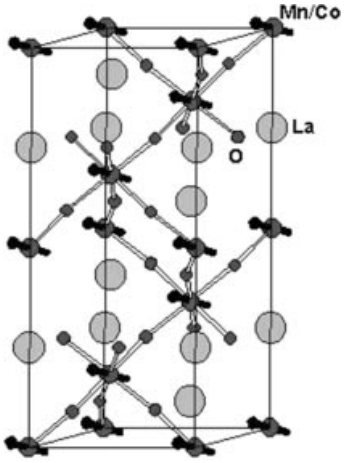


Figure 9. Magnetic structure obtained from neutron diffraction analysis for the $La_{0.7}Pb_{0.3}Mn_{0.8}Co_{0.2}O_3$ compound.

Finally, the room-temperature measured values of the resistivity are 0.098, 0.617 and 0.981 Ω·cm for the 10, 20 and 30% Co-containing samples, respectively. That is, conductivity of the samples decreases as the amount of cobalt that enters into the composition of the samples increases.

From the measured resistivity values as a function of temperature and applied magnetic field we can calculate the magnetoresistance at 6 T as MR (%) = [1 – $R$(6 T)/$R$(0 T)] × 100. The magnitude of this magnetoresistance (see Figure 11) is about 25% for the 30% Co-containing sample and reaches 40% for the 10% Co-containing one (with a local maximum arising from an intragrain magnetoresistance mechanism) at the corresponding Curie temperature of each compound. As the doping level of the cobalt increases, a progressive decrease of the MR value is observed (see Table 2).

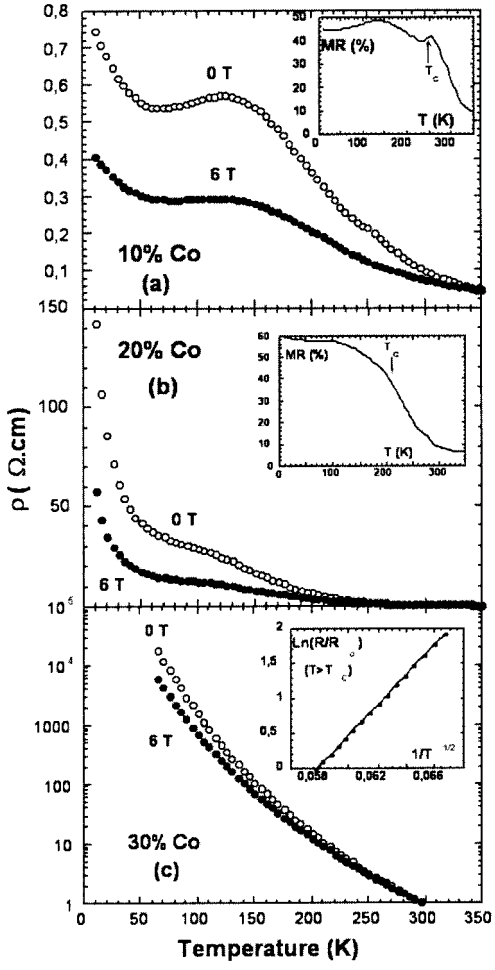


Figure 11. Temperature dependence of the electrical resistivity for all compounds, as the doping level of Co increases. The insets show: (a, b) the corresponding magnetoresistance vs. temperature behaviour and (c) the fit to the VRH mechanism for $T > T_C$.

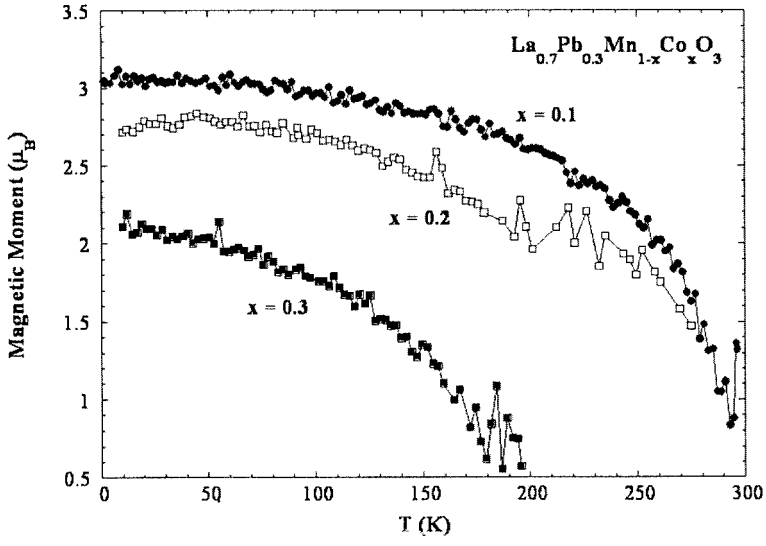


Figure 10. Temperature dependence of the magnetic moment obtained from neutron diffraction data for the Co family of compounds.

 © 2006 Wiley-VCH Verlag GmbH & Co. KGaA, Weinheim 

It is already well established that the zero-field resistivity data obtained for $T > T_C$ obey the Mott variable range hoping (VRH) mechanism[23] when the carriers are localised near the Fermi energy, as it is in the case of hole-doped manganites. Previous works[24,25] have determined also that the exponent $n = 1/2$ is the most adequate one for this law. Indeed our zero-field resistance data obey Equation (1).

$$\frac{R(T)}{R_0} \propto \exp\left(\frac{T_0}{T}\right)^{1/2} \quad (1)$$

Efros and Shklovskii[26] explained that such resistance behaviour is directly related to a form of hopping favoured by the Coulomb repulsion between carriers. Its most important consequence is the existence of an energy or Coulomb gap, which basically reflects the differences between the minimum energies of adding an electron and subtracting one from the system, without disturbing the other charges. From the obtained $T_0$ values, we have estimated values for these energy gaps ranging between 1 and 5 eV (see Table 2). In particular, the sample containing 20% of doping element exhibits a gap value higher than that obtained when $Ln_{0.7}A_{0.3}MnO_3$-type perovskites are synthesised by using the ceramic method.[27,28] Other authors have already identified such resistivity behaviour, specially at low temperatures, as arising in samples with low grain size (around 20–30 nm).[29] As previously discussed, our perovskites prepared by the sol-gel method present as one of their characteristics the fine grain obtained,[30] typically below 1 μm (see Figure 1). It is already well established that tunnelling of electric charge into small nanoparticles increases the Coulomb energy by the charging effect, strongly enhancing the tunnel resistance. The grain sizes of our compounds can be roughly estimated by using the measured values of the blocking temperature in ZFC–FC curves. This can be written as $T_b = KV/(25k_B)$, where $K$ is the anisotropy constant and $V$ is the grain volume [$V = (3\pi/4)(d/2)^3$, $d$ being the diameter of the grains, assumed to be spherical for simplicity]. From ferromagnetic resonance experiments in a similar $La_{0.67}Ba_{0.33}MnO_3$ oxide,[31] we used $K$ values in the range $2–4 \times 10^4$ J/m$^3$. Thus, from the values of $T_b = 215$ K (30% Co, the lowest one) and 255 K (10% Co, the highest one) we infer grain sizes of 10–25 nm for both compositions, in good agreement with the grain sizes obtained from our structural study. But the presence of those nanosized grains in our samples is strongly supported also by the low-temperature behaviour of the resistivity of these compounds.

Table 2. Values of the magnetoresistance at the corresponding Curie temperature and calculated energy gap for the $La_{0.7}Pb_{0.3}(Mn_{1-x}Co_x)O_3$ ($0.1 \le x \le 0.3$) family of compounds.

| Sample | $\rho_0$[a] [Ω·cm] | MR [%] | $\Delta E$ [eV][b] |
|---|---|---|---|
| Co0.1 | 0.098 | 40 | 1.9 |
| Co0.2 | 0.617 | 38 | 3.5 |
| Co0.3 | 0.981 | 25 | 4.0 |

[a] At 300 K and $H = 0$ applied field. [b] Data fitted to the variable range hopping model, $T > T_C$ range.

The resistivity of the 10% Co-doped sample shows typical features of grain boundary (intergrain) effects, that is a maximum of $\rho(T)$ at a temperature well below $T_C$ that is not shifted to higher temperatures by applying an external magnetic field (see Figure 10, a); but at low temperatures and because of the small size of the grains, it is increasingly difficult to activate this intergrain mechanism. In this situation, transport is effectively blocked, giving, as a result, a much higher upturn in the low-temperature resistivity. This is the so-called Coulomb blockade,[32] and appears much more enhanced in the 20% Co-doped composition.

Along this line of reasoning, our experimental data below 100 K fit well to the expression for granular metals [Equation (2)].[33]

$$\rho(T) \approx \exp\sqrt{(\Delta/T)} \quad (2)$$

In Equation (2) Δ is proportional to the activation or charging energy, $E_C$, of a single grain. From our fits we have obtained values of $\Delta^{1/2} = 2.4$ and 8.5 K$^{1/2}$, and gap energies of 0.5 and 6.2 meV for the Co-10% and Co-20% doped compositions, respectively, that agree with results from other authors[29,34] obtained for related compounds. We also have to mention that the fit to the $T^{-1/2}$ law is better than that to the $T^{-1}$ dependence postulated for a pure Coulomb blockade effect.

## Conclusions

In the light of our experimental work, we can conclude that Co enters in the $La_{0.7}Pb_{0.3}Mn_{1-x}Co_xO_3$ family of perovskites, giving rise to low distortion in the structure of these compounds. The measured low-temperature saturation magnetic moments are mainly due to the coexistence of $Co^{3+}$ (LS) and high spin $Co^{4+}$, as confirmed by susceptibility measurements in the paramagnetic region. The cluster glass behaviour indicated by zero-field cooled magnetisation curves is due to the fact that $Co^{3+}$ probably clusters around $Co^{4+}$ ions. A progressive increase in the doping level of Co gives rise to a subsequent decrease in the measured Curie temperature values, indicating that the long-range ferromagnetism is sensitive even to small amounts of Co.

Because of the sol-gel fabrication process used, we have obtained very homogeneous and small size of the grains (about 10–25 nm as obtained by structural methods and confirmed by magnetic measurements) for all samples. This makes the measured resistivity behaviour to be determined both by the intra- and intergrain carrier tunnelling mechanism that evolve at low temperatures to strong Coulomb blockade for the 20% Co-doped sample.

All compounds show magnetoresistance with magnitudes, at the Curie temperatures, of 40 and 25% for the 10 and 20% Co-doped samples, respectively.

## Experimental Section

Mixed oxides of nominal composition $La_{0.7}Pb_{0.3}(Mn_{1-x}Co_x)O_3$ ($0 \le x \le 0.3$) were prepared by the sol-gel method with the required

 © 2006 Wiley-VCH Verlag GmbH & Co. KGaA, Weinheim 

quantities of analytical grade of $La_2O_3$, $Pb(NO_3)_2$, $Co(NO_3)_2{\cdot}6H_2O$ and $Mn(C_2H_3O_2)_2{\cdot}4H_2O$ as the starting materials. Citric acid and ethylene glycol were used as gelling agents for the metallic ions in a nitrate solution. After drying in a sand bath for 24 h, the gel obtained was subjected to successive heat treatments at temperatures of 773, 973 and 1073 K, each of 10 h. In order to measure the electrical resistivities of the samples, the powder thus obtained was pelletised with a pressure of 7.2 MPa prior to final sintering at 1173 K for 10 h in flowing oxygen.

The $Mn^{3+}/Mn^{4+}$ content of each sample was determined by redox titration using an excess of $FeSO_4$ solution and back titration with $KMnO_4$. We have observed small deviations from the theoretical stoichiometries that could be due to an excess in the oxygen concentration, in accordance with the preparation method, or more probably to the presence of cation vacancies in the samples. We have obtained a ratio $Mn^{3+}/Mn^{4+}$ of 0.37/0.53 for the $x = 0.1$ compound that changes progressively to 0.10/0.60 for the $x = 0.3$ one. That is, as expected, the $Mn^{3+}$ content decreases as the Co doping level increases in the nominal composition of our samples.

Thermogravimetric measurements were performed in a TA instruments SDT 2960 thermobalance. Approximately 50 mg of sample was placed on an alumina crucible and heated to 900 °C at 5 °C/min in a 5% $H_2$/Ar current flow.

Scanning electron microscopic (SEM) observations were also performed to give an indication of the compound morphology and compactness using a JEOL JSM-6400 instrument.

The first crystallographic characterisation of the phases was performed by X-ray powder diffraction analysis using a Philips X-Pert diffractometer, working with Cu-$K_\alpha$1 and Cu-$K_\alpha$2 radiation, Soller slits of 0.04 rad and receiver and divergence slits of 1°. Powder diffraction patterns were Rietveld fitted using the FULLPROF program.[35]

Magnetic and resistance measurements were conducted in a Quantum Design MPMS-7 SQUID magnetometer. The zero-field cooling (ZFC) and field cooling (FC) curves were performed under an applied field of 10 mT. The order temperature, $T_C$, was determined from the ZFC curves as the temperature where the minimum of the d$M$/d$T$ derivative occurs. Hysteresis loops at 10 K and up to 7 T were also obtained. The resistance and magnetoresistance versus temperature measurements were taken by using a conventional dc four-wire system, with the magnetic field applied parallel to the current.

Neutron diffraction measurements were performed at the high-flux reactor at the Institut Laue-Langevin, Grenoble, France. In order to trace the temperature dependence of the structural and magnetic properties, measurements were carried out on D1B. We used a wavelength of 2.519 Å to study the range $2\theta$ = 20–100° at temperatures ranging from 10 to 300 K. The Rietveld analysis of the diffraction data was performed using the FULLPROF program. The line shape of the diffraction peaks was generated by a pseudo-Voigt function and the background interpolated between some fixed background points of the diagrams. In the final run the following parameters were refined: unit-cell parameters, zero-point, half-width, pseudo-Voigt and asymmetric parameters, scale factor, atomic coordinates and thermal isotropic factors. The occupancy factors were also allowed to vary in the last steps of the refinements. Because of the high correlation between the thermal and occupancy factors, in some cases the refinements did not reach the convergence. In those cases, the occupancy factors were fixed to the theoretical ones.

All structural parameters obtained from neutron diffraction experiments together with the tolerance factor ($t$) of the perovskite structure, $t = (d_{La–O})/\sqrt{2}(d_{Mn/Co–O})$ (with $d_{La–O}$ and $d_{Mn/Co–O}$ the La–O and Mn/Co–O bond lengths), are summarised in Table 3. A previous study of the related parent compound $La_{0.7}Pb_{0.3}MnO_3$ gave as the main structural parameters the following: $V$ = 353.01 Å$^3$, $t$ = 0.995, Mn–O–Mn = 166.8° and O–Mn–O = 90.71°.[13] We have observed that for our compounds the unit-cell volume decreases with increasing Co content according to the smaller size of this ion. However, this substitution produces only a minor distortion in the $MnO_6$ octahedra, the O–Mn/Co–O and Mn/Co–O–Mn/Co angles remaining rather constant. The tolerance factor does not suffer any appreciable change for the different compositions. These geometrical characteristics indicate that the distortion of the $La_{0.7}Pb_{0.3}Mn_{1-x}Co_xO_3$ perovskite structure is nearly independent of the $x$ value, in good agreement with the comparable size of $Co^{3+}$ and $Mn^{3+}$ ions. From our structural fits and using the Scherrer formula[36] we have estimated a grain size between 16 and 20 nm.

Table 3. Atomic parameters for the $La_{0.7}Pb_{0.3}(Mn_{1-x}Co_x)O_3$ ($0.1 \leq x \leq 0.3$) family of compounds after the Rietveld refinements of the D1B neutron powder diffraction data. La and Pb atoms are at 6a positions (0, 0, 1/4); Mn and Co atoms are at 6b (0, 0, 0); O atoms are at 18e ($x$, 0, 1/4). $Z$ = 6 in all cases.

| Sample | Co0.1 | Co0.2 | Co0.3 |
|---|---|---|---|
| $T$ [K] | 296 | 280 | 200 |
| Space group | $R\bar{3}c$ | $R\bar{3}c$ | $R\bar{3}c$ |
| $a$ [Å] | 5.496(2) | 5.4948(9) | 5.4859(9) |
| $c$ [Å] | 13.346(4) | 13.3374(8) | 13.2925(9) |
| $V$ [Å$^3$] | 349.1(2) | 348.7(9) | 346.4(9) |
| $t$ | 0.995 | 0.994 | 0.989 |
| La B[Å$^2$]/$F_{occ}$ | 0.247(3)/0.7 | 0.247(3)/0.7 | 0.247(3)/0.7 |
| Pb B[Å$^2$]/$F_{occ}$ | 0.247(3)/0.3 | 0.247(3)/0.3 | 0.247(3)/0.3 |
| Mn B[Å$^2$]/$F_{occ}$ | 0.247(3)/0.9 | 0.247(3)/0.8 | 0.247(3)/0.7 |
| Co B[Å$^2$]/$F_{occ}$ | 0.247(3)/0.1 | 0.247(3)/0.2 | 0.247(3)/0.3 |
| $O$ x | 0.4592(1) | 0.4565(1) | 0.4551(1) |
| O B[Å$^2$]/$F_{occ}$ | 1.4(4)/0.531 | 1.4(4)/0.531 | 1.4(4)/0.531 |
| Mn/Co–O [Å] | 1.953(3)x6 | 1.951(3)x6 | 1.948(3)x6 |
| La/Pb–O [Å] | 2.524(5)x3 | 2.508(5)x3 | 2.496(5)x3 |
| | 2.741(5)x6 | 2.741(5)x6 | 2.734(5)x6 |
| | 2.972(6)x3 | 2.986(6)x3 | 2.989(6)x3 |
| <La/Pb–O> [Å] | 2.7447 | 2.7443 | 2.7386 |
| Mn/Co–O–Mn/Co [°] | 166.81 | 165.92 | 165.48 |
| O–Mn/Co–O [°] | 90.7 | 90.77 | 90.86 |
| $R_p$ [%] | 3.41 | 4.12 | 3.64 |
| $R_{wp}$ [%] | 4.82 | 5.79 | 5.01 |
| $\chi^2$ | 2.57 | 3.59 | 3.00 |
| Bragg $R$ | 4.79 | 4.73 | 3.89 |

## Acknowledgments

We want to thank the Servicio General de Medidas Magnéticas de la UPV/EHU. We also are grateful to I. de Pedro and to Prof. J. L. Pizarro for their help in magnetic structure discussion. This work has been carried out under projects MAT2002-04178 and MAT2004-2425 of the Spanish Ministerio de Ciencia y Tecnología.

[1] S. Jin, T. H. Tiefel, M. McCormack, R. A. Fastnacht, R. Ramesh, L. H. Chen, *Science* **1994**, *264*, 413.
[2] Y. Tokura (Ed.), *Colossal Magnetoresistive Oxides*, Gordon and Breach Science Publishers, Amsterdam, The Netherlands, **2000**.
[3] C. Zener, *Phys. Rev.* **1951**, *82*, 403–405.
[4] K. Chahara, T. Ohno, M. Kasai, K. Kozono, *Appl. Phys. Lett.* **1993**, *63*, 1990–1992.

 © 2006 Wiley-VCH Verlag GmbH & Co. KGaA, Weinheim 

[5] Y. Moritomo, A. Machida, K. Matsuda, M. Ichida, A. Nakamura, *Phys. Rev. B* **1997**, *56*, 5088–5091.
[6] P. W. Anderson, H. Hasewaga, *Phys. Rev.* **1995**, *100*, 675–677.
[7] P. G. Radaelli, M. Marezio, H. Y. Hwang, S. W. Cheong, B. Batlogg, *Phys. Rev. B* **1996**, *54*, 8992–8995.
[8] L. Righi, P. Gorria, M. Insausti, J. Gutiérrez, J. M. Barandiarán, *J. Appl. Phys.* **1997**, *81*, 5767–5769.
[9] J. Gutiérrez, J. M. Barandiarán, M. Insausti, L. Lezama, A. Peña, J. J. Blanco, T. Rojo, *J. Appl. Phys.* **1998**, *83*, 7171–7173.
[10] M. Pissas, G. Kallias, E. Devlin, A. Simopoulos, D. Niarchos, *J. Appl. Phys.* **1997**, *81*, 5770–5772.
[11] K. H. Ahn, X. W. Wu, K. Liu, C. L. Chien, *Phys. Rev. B* **1996**, *54*, 15299–15302.
[12] K. Ghosh, S. B. Ogale, R. Ramesh, R. L. Greene, T. Venkatesan, K. M. Gapchup, R. Bathe, S. I. Patil, *Phys. Rev. B* **1999**, *59*, 533–537.
[13] J. Gutiérrez, A. Peña, J. M. Barandiarán, J. L. Pizarro, T. Hernández, L. Lezama, M. Insausti, T. Rojo, *Phys. Rev. B* **2000**, *61*, 9028–9035.
[14] J. B. Goodenough, *J. Phys. Chem. Solids* **1958**, *6*, 287–297.
[15] M. A. Señarís-Rodríguez, J. B. Goodenough, *J. Solid State Chem.* **1995**, *118*, 323–336.
[16] M. A. Korotin, S. Yu. Ezhov, I. V. Solovyev, V. I. Anisimov, D. I. Khomskii, G. A. Sawatzky, *Phys. Rev. B* **1996**, *54*, 5309–5316.
[17] P. Ravindran, H. Fjellvag, A. Kjekshus, P. Blaha, K. Schwarz, J. Luitz, *J. Appl. Phys.* **2002**, *91*, 291–303.
[18] L. Righi, J. Gutiérrez, J. M. Barandiarán, *J. Phys.: Condens. Matter* **1999**, *11*, 2831–2840.
[19] M. Medarde, C. Dallera, M. Grioni, J. Voigt, A. Podlesnyak, E. Pomjakushina, K. Conder, T. Neisius, O. Tjernberg, X. S. N. Barilo, *Phys. Rev. B* **2006**, *73*, 054424-1 to -10.
[20] R. L. Carlin (Ed.), *Magnetochemistry*, Springer, Berlin, Germany, **1986**.
[21] A. Arrott, *Phys. Rev.* **1957**, *108*, 1394–1396.
[22] D. Verma, A. K. Nigam, T. K. Gundu Rao, D. Bahadur, *J. Magn. Magn. Mater.* **2004**, *271*, 172–179, and references therein.
[23] N. F. Mott, *J. Non-Cryst. Solids* **1968**, *1*, 1–17.
[24] J. Gutiérrez, A. Peña, J. M. Barandiarán, J. L. Pizarro, L. Lezama, M. Insausti, T. Rojo, *J. Phys.: Condens. Matter* **2000**, *12*, 10523–10534.
[25] H. Huhtinen, R. Laiho, K. G. Lisunov, V. N. Stamov, V. S. Zakhvalinskii, *J. Magn. Magn. Mater.* **2002**, *238*, 160–167.
[26] A. L. Efros, B. I. Shklovskii, *J. Phys. C: Solid State Phys.* **1975**, *8*, L49.
[27] R. Mahendiran, R. Mahesh, A. K. Raychaudhuri, C. N. R. Rao, *Solid State Commun.* **1995**, *94*, 515–518.
[28] H. Song, W. J. Kim, S.-J. Kwon, *J. Magn. Magn. Mater.* **2000**, *213*, 126–134.
[29] L. Balcells, J. Fontcuberta, B. Martínez, X. Obradors, *Phys. Rev. B: Condens. Matter* **1998**, *58*, R14697–R14700.
[30] A. Peña, J. Gutiérrez, J. M. Barandiarán, J. P. Chapman, M. Insausti, T. Rojo, *J. Solid State Chem.* **2003**, *174*, 52–59.
[31] S. E. Lofland, S. M. Bhagat, H. L. Ju, G. C. Xiong, T. Venkatesan, R. L. Greene, *Phys. Rev. B: Condens. Matter* **1995**, *52*, 15058–15061.
[32] M. García-Hernández, F. Guinea, A. de Andrés, J. L. Martínez, C. Prieto, L. Vázquez, *Phys. Rev. B: Condens. Matter* **2000**, *61*, 9549–9552.
[33] P. Sheng, *Philos. Mag. B* **1992**, *65*, 357.
[34] J. M. D. Coey, A. E. Berkowitz, L. Balcells, F. F. Putris, A. Barry, *Phys. Rev. Lett.* **1998**, *80*, 3815–3818.
[35] J. Rodríguez-Carvajal, computer code FULLPROF, Rietveld Pattern Matching Analysis of Powder Patterns, ILL, Grenoble, **1990**.
[36] B. E. Warren (Ed.), *X-ray Diffraction: Diffraction by Imperfect Crystals*, Dover Publications, Inc., New York, USA, **1969**.

Received: February 6, 2006
Published Online: June 14, 2006

 © 2006 Wiley-VCH Verlag GmbH & Co. KGaA, Weinheim 

DOI: 10.1002/ejic.200600111

# A Ruthenium(II) Complex with a Tripodal Ligand Containing Three Imidazole Groups

**Tomoka Yamaguchi,[a] Kazutoshi Harada,[a] Yukinari Sunatsuki,[a] Masaaki Kojima,*[a] Kiyohiko Nakajima,[b] and Naohide Matsumoto[c]**

**Keywords:** Ruthenium/ Redox chemistry / Chirality / Schiff bases / N ligands / Tripodal ligands

The orange $[Ru^{II}(H_3L)](ClO_4)_2 \cdot 3H_2O$ (**1**) complex was synthesized from *cis*-$[RuCl_2(dmso)_4]$ and $H_3L$, where $H_3L$ (tris{[2-{(imidazol-4-yl)methylidene}amino]ethyl}amine) is a tripodal ligand obtained by condensation of tris(2-aminoethyl)-amine and 4-formylimidazole in a 1:3 mol ratio. The X-ray crystal structure analysis revealed that the complex has an octahedral structure coordinated by three imidazole nitrogen atoms and three Schiff base (imine) nitrogen atoms. The uncoordinated NH groups of the imidazole moieties of **1** are easily deprotonated by the action of a base. The effect of deprotonation on the $Ru^{III}/Ru^{II}$ redox potential was studied by cyclic voltammetry in methanol containing 0.1 M $LiClO_4$. Complete deprotonation shifts the $Ru^{III}/Ru^{II}$ potential to a much more negative value from –0.18 to –0.72 V vs. $Ag/Ag^+$, making it easier to oxidize. The bluish-purple $Ru^{III}$ complex, $[Ru^{III}(H_3L)]^{3+}$, was formed by controlled-potential electrolysis of **1**, and the electronic spectrum is reported.

(© Wiley-VCH Verlag GmbH & Co. KGaA, 69451 Weinheim, Germany, 2006)

## Introduction

Ruthenium complexes containing imidazole and its derivatives have attracted great attention in recent years since several of them serve as antitumor drugs.[1] For example, $(H_2im)[Ru^{III}Cl_4(Him)(dmso)]$ (Him = imidazole) and $(H_2ind)[Ru^{III}Cl_4(Hind)(dmso)]$ (Hind = indazole) are on clinical trials, the first as an antimetastatic drug and the second as an anticancer agent against primary tumors and metastases and, in particular, colon carcinomas. As a mode of antitumor action of the $Ru^{III}$ complexes, the "activation by reduction" hypothesis was proposed. The $Ru^{III}$ complexes were suggested to serve as prodrugs that are activated by reduction to $Ru^{II}$ in order to coordinate more rapidly to biomolecules.[1d] In other words, the $Ru^{III}$ complexes should possess biologically accessible reduction potentials to be active in vivo.

Recently, we reported the structures and properties of $Fe^{II}$ and $Fe^{III}$ complexes with a tripodal ligand containing three imidazole groups, $H_3L$; $H_3L$ (tris{[2-{(imidazol-4-yl)methylidene}amino]ethyl}amine) is a potentially heptadentate Schiff-base ligand derived from 1:3 condensation of tris(2-aminoethyl)amine and 4-formylimidazole (Figure 1).[2] The X-ray crystal structure analysis of $[Fe^{II}(H_3L)](BF_4)_2 \cdot 3H_2O$ revealed that the $Fe^{II}$ ion is surrounded by three Schiff base (imine) nitrogen and three imidazole nitrogen atoms in an octahedral fashion, where the tertiary amine nitrogen atom is uncoordinated. The uncoordinated imidazole NH hydrogen atoms of $[Fe^{II}(H_3L)]^{2+}$ are easily deprotonated; upon addition of up to three equiv. of NaOH, $[Fe^{II}(H_3L)]^{2+}$ in methanol under aerobic conditions shows a drastic color change from yellowish-orange, through reddish-orange and green, to deep blue.[2c] $Fe^{II}$ species are oxidized to $Fe^{III}$ by air under basic conditions, and from the final blue solution, we obtained the iron(III) complex, $[Fe^{III}(L)]$, containing the deprotonated ligand $L^{3-}$. Deprotonation of $[Fe^{II}(H_3L)]^{2+}$ induces oxidation of the metal center to generate the $[Fe^{III}(L)]^0$ species. Thus, this reaction is an example of a proton-coupled electron-transfer (PCET) reaction.[3] If we study a ruthenium complex with a ligand containing several imidazole groups such as $H_3L$, we should be able to control the redox potential by adjusting the pH of the solution because the complex will have several different $pK_a$ values. PCET is the basic mechanism of bioenergetic conversion. Small-molecule activation, redox-driven proton pumps, and hydrogen atom abstraction reactions of a wide variety of oxidases and reductases all involve the coupling of electrons to protons.[1d] Thus, $[Ru^{II}(H_3L)]^{2+}$ should be an ideal system to study the pH-dependent metal-based couples as models for PCET reactions because deprotonation should affect the stability of the oxidation state of the Ru complex.

We report here the synthesis, structure, and properties of a $Ru^{II}$ complex with a tripodal ligand containing three

[a] Department of Chemistry, Faculty of Science, Okayama University,
Tsushima-naka 3-1-1, Okayama 700-8530, Japan
Fax: +81-86-251-7842
E-mail: kojima@cc.okayama-u.ac.jp
[b] Department of Chemistry, Aichi University of Education, Kariya, Aichi 448-8542, Japan
[c] Department of Chemistry, Faculty of Science, Kumamoto University,
Kurokami 2-39-1, Kumamoto 860-8555, Japan

 © 2006 Wiley-VCH Verlag GmbH & Co. KGaA, Weinheim 

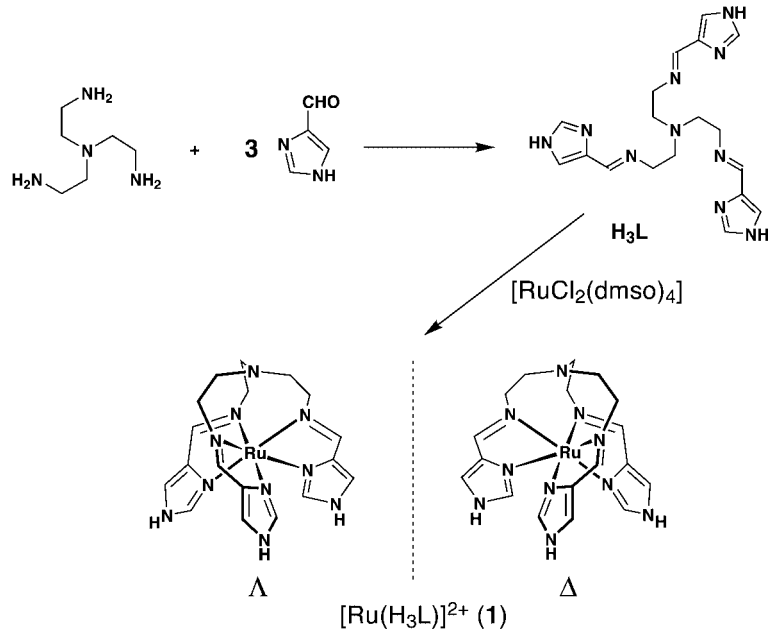


Figure 1. Synthetic procedures for the tripodal $H_3L$ ligand and $[Ru^{II}(H_3L)]^{2+}$ (**1**), and the Δ and Λ configurations of complex **1**.

imidazole groups, $[Ru(H_3L)](ClO_4)_2$ (Figure 1), with emphasis being placed on the effect of deprotonation on the cyclic voltammogram (CV) and on the electronic spectrum.

## Results and Discussion

### Synthesis and Characterization

The tripodal $H_3L$ ligand was prepared by the condensation reaction of tris(2-aminoethyl)amine and 4-formylimidazole in a 1:3 mol ratio in methanol (Figure 1). The $H_3L$ ligand was not isolated and a solution containing this ligand was used for the synthesis of $[Ru(H_3L)](ClO_4)_2\cdot 3H_2O$ (**1**). Orange $[Ru(H_3L)]^{2+}$ was prepared by mixing the ligand and *cis*-$[RuCl_2(dmso)_4]$[4] in a 10:1 mol ratio. It should be noted that the ligand/$[RuCl_2(dmso)_4]$ ratio is not 1.0, but 10. We tried to prepare the complex in different ligand/Ru ratios. A large excess of the ligand seems to be necessary to yield the desired complex. At present, we cannot explain why complex **1** does not form under the equivalent mol ratio (ligand/Ru = 1.0).

The IR spectrum of complex **1** ($4d^6$, $t_{2g}^6$) shows an intense band assignable to the Cl–O vibration of the perchlorate ion at 1088–1143 $cm^{-1}$ and an intense characteristic absorption at 1607 $cm^{-1}$ assignable to the C=N stretching vibration of the tripodal Schiff-base ligand. The position of the C=N stretching band is close to that of $[Fe^{II}(H_3L)](BF_4)_2\cdot 3H_2O$ (1610 $cm^{-1}$) in the low-spin state ($3d^6$, $t_{2g}^6$).[2f] It has been reported that the position of the C=N stretching band is sensitive to the electronic state of the complex. For example, $[Fe^{II}(H_3L)](BF_4)_2\cdot 3H_2O$ exhibits a spin crossover behavior and the high-spin species ($t_{2g}^4e_g^2$) shows the C=N stretching vibration in the Raman spectrum at a higher energy (1638 $cm^{-1}$, $T > 200$ K) than the low-spin one (1610 $cm^{-1}$, $T < 100$ K).[2f] Complex **1** in $D_2O$ shows a very simple $^1H$ NMR spectrum, and it conforms to the high symmetry ($C_3$) of the complex confirmed by X-ray crystallography.

### Crystal Structure

The crystal structure consists of a ruthenium(II) complex cation, $[Ru(H_3L)]^{2+}$, and two perchlorate ions as the counteranions. Figure 2 shows an ORTEP drawing of the cation of complex **1** with the atom numbering scheme. Selected distances and angles, with their estimated standard deviations in parentheses, are listed in Table 1. A ruthenium(II) ion with the $4d^6$, $t_{2g}^6$ electron configuration assumes an octahedral coordination environment with the $N_6$ donor set of the tripodal ligand including three imidazole and three Schiff base nitrogen atoms. The tertiary amine nitrogen atom (N1) is not coordinated, the Ru···N1 distance being 3.161(6) Å. The lengths of the six Ru–N bonds are 2.151(7)–2.232(8) Å, and are in the expected range for the given coordination number and donor atoms. The corresponding M–N bond lengths for $[Co^{III}(H_3L)](ClO_4)_3\cdot H_2O$ ($3d^6$, $t_{2g}^6$) and $[Fe^{II}(H_3L)](BF_4)_2\cdot 3H_2O$ ($3d^6$, $t_{2g}^6$) are as follows: $Co^{III}$ 1.88(1)–1.98(1) Å,[5] $Fe^{II}$ 1.981(3)–1.989(4) Å.[2f] Ionic radii (Shannon) for six-coordinate $Co^{III}$ and $Fe^{II}$ are reported to be 0.69 and 0.75 Å, respectively.[6] The ionic radius (Shannon) for $Ru^{II}$ is not available. However, on the basis of the above M–N bond lengths, we can estimate the ionic radius for $Ru^{II}$ to be ca. 0.95 Å, assuming the nature of the bonding is similar for each one of the three complexes.

The crystal consists of a dimeric unit. Two adjacent complex cations with the opposite absolute configurations (Δ and Λ) are connected in a tail-to-tail fashion by N–H···O($ClO_4^-$)···H–N hydrogen bonds through two counter-$ClO_4^-$ anions, with N(imidazole)···O($ClO_4^-$) dis-

 © 2006 Wiley-VCH Verlag GmbH & Co. KGaA, Weinheim 

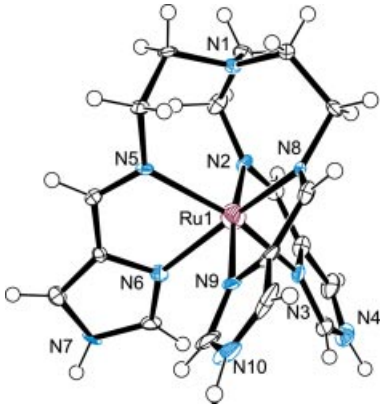


Figure 2. ORTEP drawing of the cation of $[Ru(H_3L)](ClO_4)_2$ (**1**) with atom numbering scheme showing the 50% probability ellipsoids.

tances of 3.01(1) and 2.96(1) Å and the N(imidazole)···O($ClO_4^-$)···N(imidazole) angle of 102.0(3)° (Figure 3, Table 2). Each of the other two flanking $ClO_4^-$ ions in Figure 3 (part a) are hydrogen-bonded with only one complex cation.

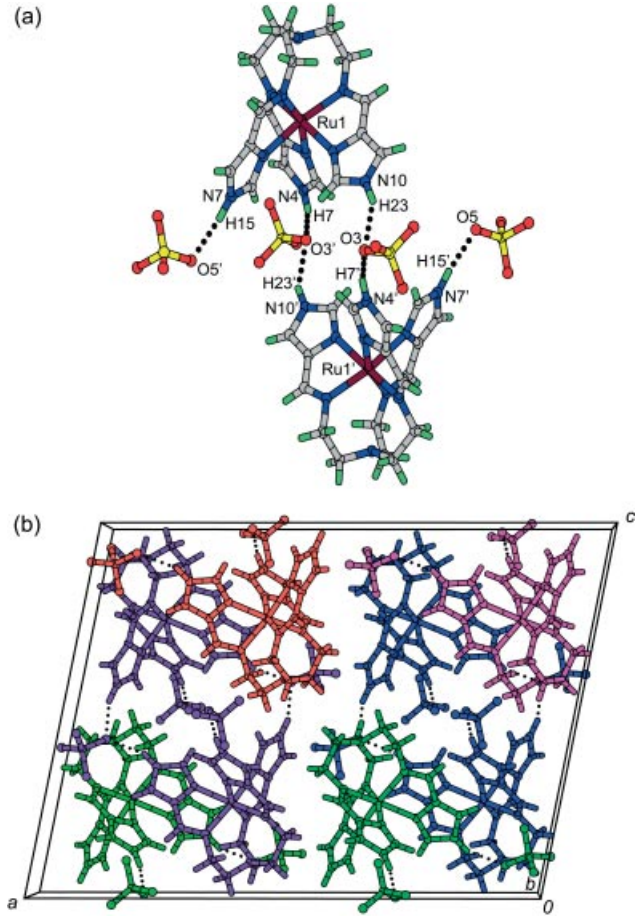


Figure 3. X-ray crystal structure of $[Ru(H_3L)](ClO_4)_2$ (**1**). (a) Two $ClO_4^-$ ions connect the two adjacent complex cations through hydrogen bonding, while the other two flanking $ClO_4^-$ ions are hydrogen bonded with only one complex cation. (b) Crystal packing showing that the two complex cations in the same color are connected by hydrogen bonding.

Table 1. Selected distances [Å] and angles [°] for $[Ru(H_3L)](ClO_4)_2$ (**1**).[a]

| | | | |
|---|---|---|---|
| Bond lengths | | | |
| Ru(1)–N(2) | 2.172(8) | Ru(1)–N(3) | 2.190(7) |
| Ru(1)–N(5) | 2.194(7) | Ru(1)–N(6) | 2.190(8) |
| Ru(1)–N(8) | 2.151(7) | Ru(1)–N(9) | 2.232(8) |
| Interatomic distances | | | |
| Ru(1)···N(1) | 3.161(6) | Ru(1)···Ru(1)$^1$ | 7.646(1) |
| Ru(1)$^1$···Ru(1)$^2$ | 7.453(1) | Ru(1)$^1$···Ru(1)$^3$ | 10.197(1) |
| Bond angles | | | |
| N(3)–Ru(1)–N(2) | 77.6(3) | N(5)–Ru(1)–N(2) | 96.7(3) |
| N(6)–Ru(1)–N(2) | 92.6(3) | N(8)–Ru(1)–N(2) | 102.6(3) |
| N(9)–Ru(1)–N(2) | 173.0(3) | N(5)–Ru(1)–N(3) | 162.5(3) |
| N(6)–Ru(1)–N(3) | 86.7(3) | N(8)–Ru(1)–N(3) | 100.5(3) |
| N(9)–Ru(1)–N(3) | 95.6(3) | N(6)–Ru(1)–N(5) | 77.0(3) |
| N(8)–Ru(1)–N(5) | 96.9(3) | N(9)–Ru(1)–N(5) | 90.3(3) |
| N(9)–Ru(1)–N(6) | 88.8(3) | N(9)–Ru(1)–N(8) | 76.6(3) |

[a] Symmetry operators: (1) $1/2-x$, $1/2+y$, $1/2-z+1$; (2) $1/2+x$, $1/2+y$, $+z$; (3) $+x$, $-y+1$, $1/2+z-1$.

Table 2. Intermolecular hydrogen bond lengths [Å] and angles [°] for $[Ru(H_3L)](ClO_4)_2$ (**1**).

| D | H | A | D···A | D–H | H···A | D–H···A |
|---|---|---|---|---|---|---|
| N(4) | H(7) | O(3′)[a] | 3.01(1) | 0.95(1) | 2.13(1) | 154(1) |
| N(10) | H(23) | O(3)[b] | 2.96(1) | 0.95(1) | 2.12(1) | 147(1) |
| N(7) | H(15) | O(5′)[c] | 3.01(1) | 0.950(9) | 2.07(1) | 167.1(8) |

[a] $1/2-x$, $1/2+y$, $3/2-z$. [b] $+x$, $-y$, $1/2+z$. [c] $+x$, $-1+y$, $z$.

## Electronic and CD Spectra

The electronic spectrum of complex **1** in methanol is shown in Figure 4. The complex is fairly stable in methanol under aerobic conditions and the spectrum stays unchanged for at least five hours. The complex shows an intense band attributable to a metal-to-ligand charge transfer (MLCT) transition in the visible region at 424 nm (13900 $M^{-1}cm^{-1}$), which obscures the weak d–d bands. The MLCT band is unsymmetrical, which may be related to the less than octahedral local symmetry ($C_3$) of the complex that leads to loss of the degeneracy of the MLCT transitions. The bands in the UV region are mainly due to intraligand transitions. The electronic spectrum of the $H_3L$ ligand in methanol is also shown in Figure 4. Comparison of the two spectra indicates that the shoulder around 330 nm of **1** is attributable to the Schiff base π–π* transition and that the intense band at 248 nm is mainly due to the imidazole moiety.

The uncoordinated NH groups of the imidazole moieties of **1** can be deprotonated by the action of a base. With the addition of $NaOCH_3$ to $[Ru(H_3L)]^{2+}$ in methanol, a slight color change from yellow to yellowish-orange was observed: aliquots of the methanolic $NaOCH_3$ solution were added up to three equiv. to $[Ru(H_3L)]^{2+}$ in methanol, and the reaction was followed spectrophotometrically (Figure 5). Although isosbestic points were observed at 375 and 440 nm, the latter is not sharp. This behavior can be ex-

 © 2006 Wiley-VCH Verlag GmbH & Co. KGaA, Weinheim 

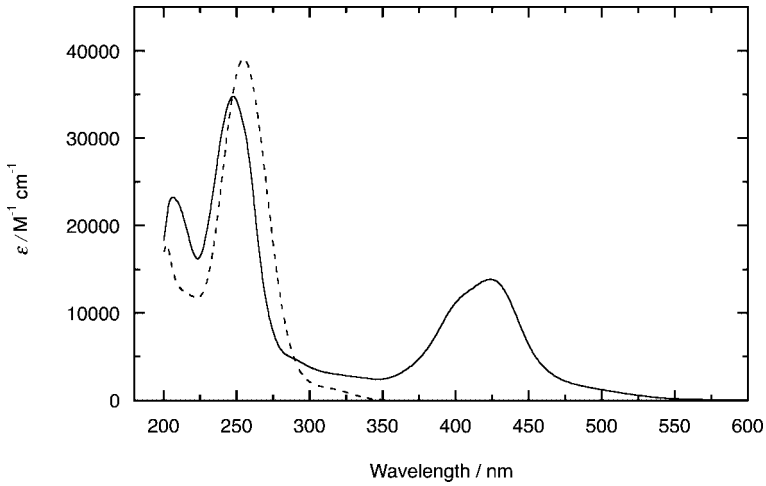


Figure 4. Electronic spectra of $[Ru(H_3L)](ClO_4)_2 \cdot 3H_2O$ (**1**, ——) and the $H_3L$ ligand (- - -) in methanol.

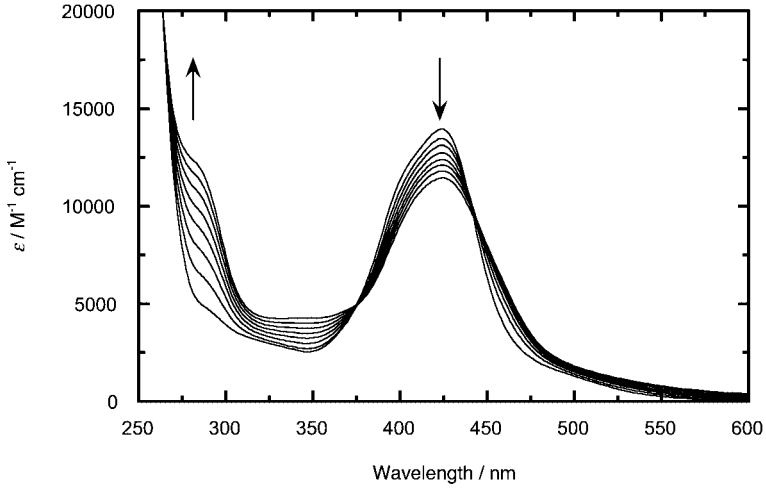


Figure 5. Electronic spectral changes of $[Ru(H_3L)](ClO_4)_2 \cdot 3H_2O$ (**1**) upon addition of $NaOCH_3$. $NaOCH_3$ in methanol was added stepwise to a methanol solution of **1** ($3.4 \times 10^{-5}$ M) up to 3.0 equiv.

plained as follows : The p$K_a$ values for $[Ru(H_3L)]^{2+}$, $[Ru(H_2L)]^{+}$, and [Ru(HL)] are similar to each other, and many species ($[Ru^{II}(H_3L)]^{2+}$, $[Ru^{II}(H_2L)]^{+}$, $[Ru^{II}(HL)]^{0}$, and $[Ru^{II}(L)]^{-}$) exist in equilibrium to obscure the isosbestic points [Equation (1)].

$$[Ru^{II}(H_3L)]^{2+} \underset{-H^+}{\overset{+H^+}{\leftrightarrows}} [Ru^{II}(H_2L)]^{+} \underset{-H^+}{\overset{+H^+}{\leftrightarrows}} [Ru^{II}(HL)] \underset{-H^+}{\overset{+H^+}{\leftrightarrows}} [Ru^{II}(L)]^{-} \quad (1)$$

In order to examine the stability of the deprotonated species under aerobic conditions, we measured the spectral change with the passage of time. After the addition of one equiv. of $NaOCH_3$, the spectrum stayed almost unchanged for at least 90 min. However, with the addition of two equiv. of $NaOCH_3$, a slight spectral change was observed after 90 min. This spectral change may be due to oxidation of $Ru^{II}$ to $Ru^{III}$. This behavior is in agreement with the cyclic voltammetry results described later. Thus, the above deprotonation reaction was carried out under an inert atmosphere. The reaction is reversible: protonation of $[Ru^{II}(L)]^{-}$ in methanol takes place upon sequential addition of $HClO_4$ in methanol, and the complex is finally converted to $[Ru^{II}(H_3L)]^{2+}$ [Equation (1)].

$[Ru(H_3L)]^{2+}$ is chiral because of a spiral coordination arrangement of the achiral $H_3L$ ligand around the $Ru^{II}$ ion. Optical resolution was carried out by column chromatography on SP-Sephadex, with 0.15 M sodium (+)-tartrate being used as the eluent.[7] The eluate was collected fractionally. The first and last fractions show CD patterns that are enantiomeric to each other, as shown in Figure 6. A strong CD band around 330 nm is attributable to the Schiff base π–π* transition. Recently, we have reported that the $Fe^{II}$ complex containing the $H_3L$ ligand, $[Fe^{II}(H_3L)](BF_4)_2 \cdot 3H_2O$, is spontaneously resolved, and X-ray crystallography revealed that the complex showing negative CD around 320 nm, attributable to the Schiff base π–π* transition, has the Δ absolute configuration.[2f] We have also resolved

 © 2006 Wiley-VCH Verlag GmbH & Co. KGaA, Weinheim 

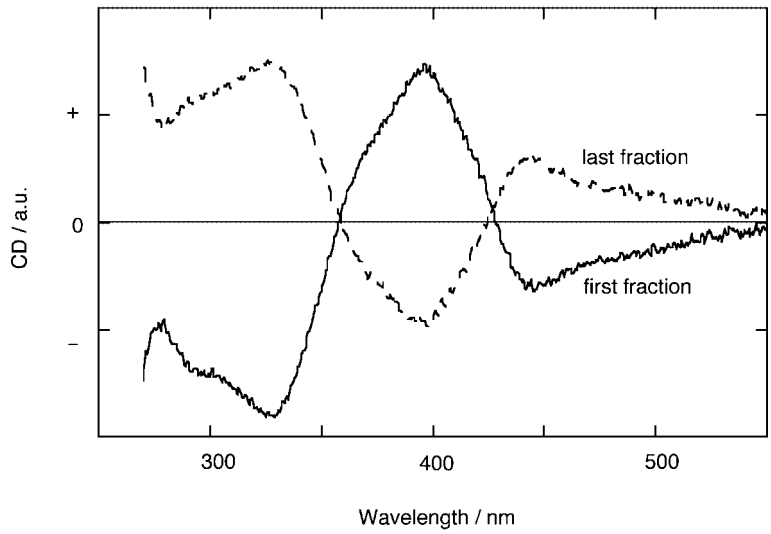


Figure 6. Circular dichroism (CD) spectra of $[Ru^{II}(H_3L)]^{2+}$ (**1**) resolved by SP-Sephadex column chromatography [eluent: 0.15 M $Na_2$(+)-tart], the first (——) and the last (- - -) fraction showing patterns that are enantiomeric to each other.

$[Co^{III}(H_2L)]^{2+}$ by fractional crystallization of the diastereomeric salt with $[Sb_2\{(+)\text{-tart}\}_2]^{2-}$ [tart = tartrate(4) ion] and have determined the absolute configuration by X-ray crystallography.[8] The less soluble diastereomeric salt, $[Co^{III}(H_2L)][Sb_2\{(+)\text{-tart}\}_2]\cdot 4H_2O$, has the Λ configuration and exhibits positive CD around 320 nm. From these results, we conclude that the faster-eluted enantiomer of $[Ru(H_3L)]^{2+}$ showing negative CD around 330 nm has the Δ absolute configuration. Exciton theory has been applied to tris(chelate)- or *cis*-bis(chelate)-type metal complexes, where chelate denotes such ligands as 2,2-bipyridine, 1,10-phenanthroline, or Schiff-base ligands, and the relationship between the CD pattern in the ligand π–π* transition region and the absolute configuration around the metal ion has been established.[9] The conclusion described above for the present complex is in agreement with the assignment based on exciton theory.

## Electrochemistry

The electrochemical properties of $[Ru^{II}(H_3L)]^{2+}$ and its deprotonated forms, $[Ru^{II}(H_2L)]^{+}$, $[Ru^{II}(HL)]^{0}$, and $[Ru^{II}(L)]^{-}$, were studied by cyclic voltammetry (CV). The measurements were performed under nitrogen using methanol solutions containing $LiClO_4$ (0.1 M) as the supporting electrolyte. The redox couple of $[Ru^{II}(H_3L)]^{2+}$ appears at –0.18 V ($E_{pc}$ = –0.21 V, $E_{pa}$ = –0.15 V) vs. $Ag/Ag^+$ irrespective of the scan rate ($10 \leq v \leq 200$ mV s$^{-1}$), the peak current ratio $i_{pa}/i_{pc}$ was found to be 1.0, ($i_{pa}$ or $i_{pc}$)/$v^{1/2}$ was independent of $v$, and the peak separation ($\Delta E_p$) was 0.060 V (Figure 7). These results are consistent with an electrochemically reversible one-electron redox process, see Equation (2).

$$[Ru^{III}(H_3L)]^{3+} + e^- \leftrightarrows [Ru^{II}(H_3L)]^{2+} \quad (2)$$

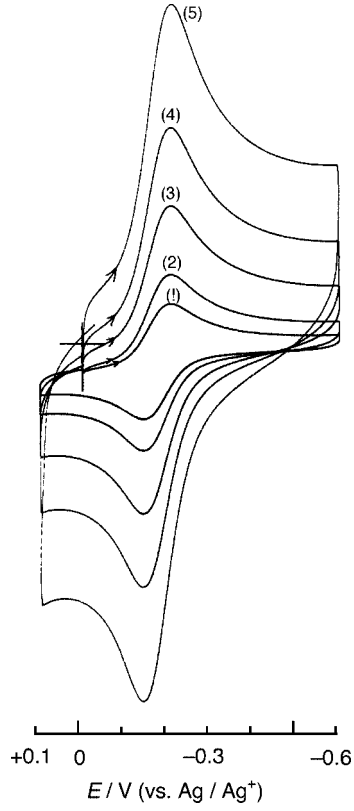


Figure 7. Cyclic voltammograms of $[Ru(H_3L)](ClO_4)_2\cdot 3H_2O$ (**1**, 0.2 mM) in methanol containing 0.1 M $LiClO_4$ at a glassy carbon electrode at sweep rates of (1) 10, (2) 20, (3) 50, (4) 100, and (5) 200 mV s$^{-1}$.

The bluish-purple $Ru^{III}$ complex, $[Ru^{III}(H_3L)]^{+}$, was formed by controlled-potential electrolysis of $[Ru^{II}(H_3L)]^{2+}$ at 0.0 V vs. $Ag/Ag^+$ in methanol containing 0.1 M ($n$-$C_4H_9)_4NBF_4$. The progress of the oxidation reaction was monitored spectrophotometrically (Figure 8). The band at

 © 2006 Wiley-VCH Verlag GmbH & Co. KGaA, Weinheim 

424 nm decreased while two bands appeared at 320 and 580 nm, and isosbestic points were observed at 370 and 480 nm. The broad moderately intense band at 580 nm can be assigned as an LMCT band.[10]

$[Ru^{II}(H_3L)]^{2+}$ in methanol undergoes reversible deprotonation and protonation upon addition of a base and an acid, respectively, as described above (deprotonation–protonation is associated with the imidazole moieties). Figure 9 shows the progress of the deprotonation reaction as monitored by cyclic voltammetry. Upon addition of one equiv. of $NaOCH_3$ to $[Ru^{II}(H_3L)]^{2+}$ in methanol (Figure 9, b), the current intensity of the initial redox couple at –0.18 V ($E_{pc}$ = –0.21 V, $E_{pa}$ = –0.15 V; Figure 9, a) diminishes and the couple shifts slightly to a more negative potential ($E_{pc}$ = –0.29 V, $E_{pa}$ = –0.18 V), and a new redox couple attributable to $[Ru^{III/II}(H_2L)]^{2+/+}$ appears at –0.67 V ($E_{pc}$ = –0.72 V, $E_{pa}$ = –0.61 V). Upon addition of one more equiv. of $NaOCH_3$ (Figure 9, c), the second redox couple shifts to a more negative potential ($E_{pc}$ = –0.75 V, $E_{pa}$ = –0.62 V) and grows at the expense of the first redox couple, and the initial redox couple shifts to a more negative potential ($E_{pc}$ = –0.35 V, $E_{pa}$ = –0.24 V). Full deprotonation at the imidazolate nitrogen moieties is achieved by adding three equiv. of base to produce $[Ru^{II}(L)]^{-}$ (see part d in Figure 9, $E^{0\prime}$ = –0.72 V, $E_{pc}$ = –0.77 V, $E_{pa}$ = –0.66 V). Complete deprotonation of the ligand shifts the $Ru^{III}/Ru^{II}$ redox potential to a more negative value from –0.18 V to –0.72 V, i.e. 180 mV per proton. Carina et al.[11] reported that deprotonation of the uncoordinated NH groups of the imidazole moieties switches the redox potential of iron by as much as 345 mV per proton. A series of reverse reactions was observed when an acid (HCl) was added to $[Ru^{II}(L)]^{-}$. These results are consistent with the acid–base equilibrium [Equation (1)]. Analysis of the CVs in Figure 9 (a–d), suggests that each $[Ru^{II}(H_{3-n}L)]^{(2-n)+}$ ($n$ = 0–3) species is characterized by a different potential of the redox couple although the redox couple for $[Ru^{III/II}(HL)]^{+/0}$ was not clearly observed; as the degree of deprotonation increases, the redox potential becomes more negative (i.e. the compound becomes easier to oxidize). These results are in accordance with the instability of the deprotonated species under aerobic conditions, as observed by electronic spectroscopy. It is worth noting that, for a metal complex with a ligand exhibiting acid–base properties in aqueous solution, the redox potential value is pH dependent; usually, however, each species (fully deprotonated, monodeprotonated, etc.) does not show an independent redox couple, but only an averaged couple is observed.[12] The $[Ru^{II}(L)]^{-}$ species exhibits another redox couple at +0.12 V (Figure 9d, $E_{pc}$ = +0.08 V,

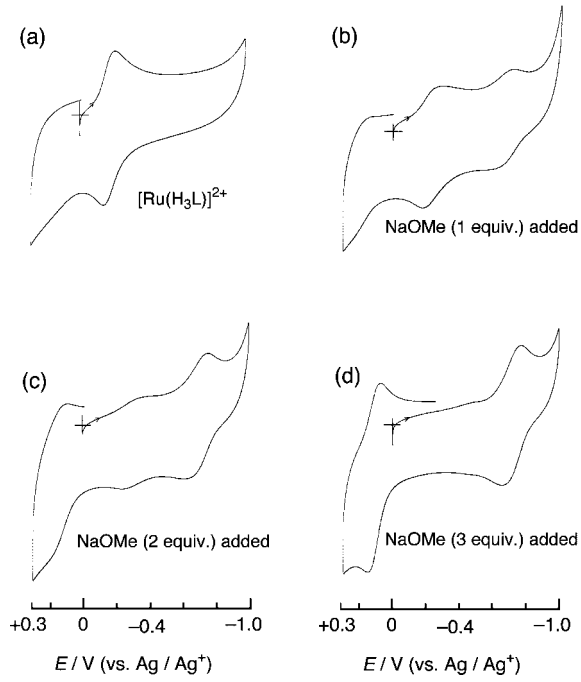


Figure 9. Progress of the deprotonation of $[Ru(H_3L)](ClO_4)_2{\cdot}3H_2O$ as monitored by cyclic voltammetry. (a)–(d): stepwise addition (0, 1, 2, and 3 equiv.) of $NaOCH_3$ in methanol to 0.2 mM $[Ru(H_3L)](ClO_4)_2{\cdot}3H_2O$ in methanol containing $LiClO_4$ (0.1 M).

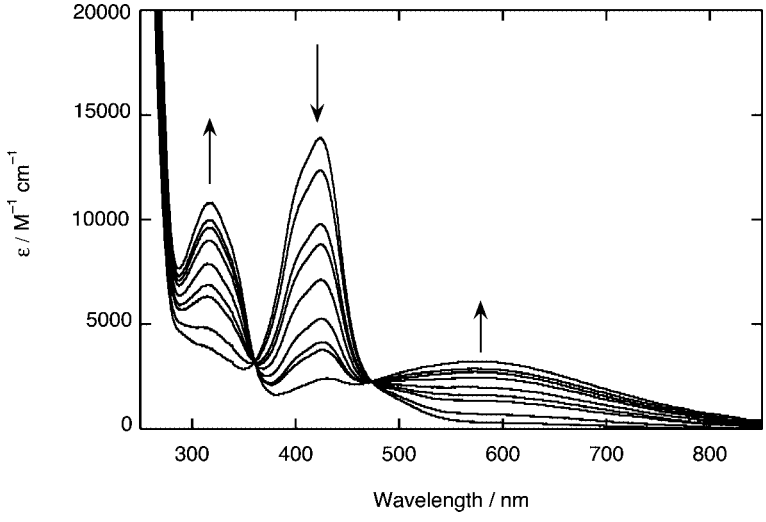


Figure 8. Electronic spectral changes accompanied by the progress of controlled-potential electrolysis (oxidation) of $[Ru(H_3L)]^{2+}$ in methanol containing 0.1 M $(n\text{-}C_4H_9)_4NBF_4$ at 0.0 V vs. $Ag/Ag^+$.

 © 2006 Wiley-VCH Verlag GmbH & Co. KGaA, Weinheim 

$E_{pa}$ = +0.16 V), and this couple may be assigned as the $Ru^{IV/III}$ process.[10]

We have demonstrated that the uncoordinated NH groups of the imidazole moieties of **1** can easily be deprotonated by the action of a base, and that deprotonation stabilizes the oxidized form, $Ru^{III}$.

## Experimental Section

**Caution!** Perchlorate salts of metal complexes are potentially explosive. Only small quantities of material should be prepared, and the samples should be handled with care.

**Materials:** All reagents and solvents in the syntheses were of reagent grade and were used without further purification. *cis*-$[RuCl_2(dmso)_4]$ was prepared according to the literature procedure.[4]

**$[Ru(H_3L)](ClO_4)_2\cdot 3H_2O$ (1):** A methanol solution (20 $cm^3$) containing tris(2-aminoethyl)amine (0.73 g, 5 mmol) and 4-formylimidazole (1.44 g, 15 mmol) was heated under reflux for 20 min to give a yellow-orange solution. This methanol solution contains the $H_3L$ ligand, and the solution was used for the preparation of the Ru complex. Nitrogen (or argon) gas was bubbled through the solution for 15 min to remove oxygen (Solution A). *cis*-$[RuCl_2(dmso)_4]$ (0.242 g, 0.5 mmol) was dissolved in oxygen-free methanol (20 $cm^3$), and the ligand solution (Solution A) was added to this solution by a syringe. The mixture was heated under reflux for 6 h. The color of the solution changed from orange to dark brown. The solution was cooled to room temperature, and a methanol solution (50 $cm^3$) of $NH_4BF_4$ (1.6 g, 15 mmol) was added to give a brown precipitate, which was collected by filtration. This product is not soluble in common organic solvents, and it is not the desired compound, but seems to be an oligomer. The filtrate was diluted with 0.01 M HCl (300 $cm^3$). The solution was passed through a column (2.7 cm I.D. × 15 cm) of SP-Sephadex C-25. The adsorbed cationic species were eluted with 0.2 M NaCl/0.01 M HCl. The eluate containing the fastest eluted orange-red band was collected, and mixed with an aqueous solution (5 $cm^3$) of $NaClO_4$ (0.2 g). The orange crystals that deposited were collected by filtration. They were recrystallized from water under nitrogen. Yield 15 mg. $C_{18}H_{30}Cl_2N_{10}O_{11}Ru_1$ = $[Ru(H_3L)](ClO_4)_2\cdot 3H_2O$: calcd. C 29.44, H 4.11, N 19.07; found C 29.34, H 3.74, N 18.88. $^1H$ NMR ($D_2O$, ref. DSS): $\delta$ = 2.8–3.5 (m, 4 H, $CH_2$), 7.25 (s, 1 H), 7.80 (s, 1 H), 8.52 (s, 1 H) ppm. IR (KBr pellet): $\tilde{\nu}$ = $\nu_{C=N}$(Schiff base), 1607 $cm^{-1}$; $\nu_{Cl-O}(ClO_4^-)$, 1088, 1115, 1143 $cm^{-1}$. UV/Vis ($CH_3OH$): $\lambda$ ($\varepsilon$) = 424 nm (13900 $M^{-1}$ $cm^{-1}$), 248 nm (34800 $M^{-1}$ $cm^{-1}$). Crystals suitable for X-ray analysis were obtained by adding a diethyl ether layer to an acetonitrile solution of the complex.

**Optical Resolution:** An aqueous solution (20 $cm^3$) of $[Ru(H_3L)](ClO_4)_2\cdot 3H_2O$ (3 mg) was adsorbed onto SP-Sephadex (1 $cm^3$) and the SP-Sephadex was placed on top of an SP-Sephadex column (1 cm ID × 30 cm). The complex was eluted with 0.15 M sodium (+)-tartrate, and the eluate was fractionally collected.[7]

**Physical Measurements:** UV/Vis absorption spectra were recorded with a JASCO Ubest-550 spectrophotometer. Infrared spectra were measured on a JASCO FT/IR-550 spectrophotometer. CD spectra were recorded with a JASCO J-720 spectropolarimeter. $^1H$ NMR spectra were recorded with a Varian Mercury 300 spectrometer ($^1H$ at 300 MHz) at ambient temperature. Cyclic voltammetry measurements were performed under nitrogen using a Fuso HECS 321B potential sweep unit with methanol solutions containing $LiClO_4$ (0.1 M) as the supporting electrolyte. The electrochemical cell was a three-electrode system consisting of a glassy-carbon working electrode, a platinum wire auxiliary electrode, and an $Ag/Ag^+$ (Ag/0.01 M $AgNO_3$) reference electrode. As an external standard, the $Fc/Fc^+$ (Fc = ferrocene) couple was observed at –0.170 V vs. $Ag/Ag^+$ under the same conditions. Controlled-potential electrolysis experiments were carried out with a platinum-gauze working electrode, with the use of a Fuso HECS 312B DC-pulse polarograph and a Model 1109 integrator. The reference electrode was the same $Ag/Ag^+$ (Ag/0.01 M $AgNO_3$) electrode used for the cyclic voltammetric experiments, and the auxiliary electrode was a platinum wire separated from the test solution by a salt bridge.

**X-ray Data Collection, Reduction, and Structure Determination:** An orange crystal of **1**, with the approximate dimensions 0.5 × 0.2 × 0.1 mm, was mounted by a loop method, and the X-ray data were collected with a Rigaku R-AXIS RAPID II imaging plate area detector using graphite-monochromated Mo-$K_\alpha$ radiation ($\lambda$ = 0.71073 Å). The crystallographic data are summarized in Table 3. The structure was solved by direct methods, and was refined using full-matrix least-squares procedures with the CrystalStructure crystallographic software package.[13] There are two possible space groups, *C*2/*c* (No.15) and *Cc* (No.9). We tried to solve the structure in both space groups. Only the space group *C*2/*c* gave rational results.

Table 3. X-ray crystallographic data for $[Ru(H_3L)](ClO_4)_2$ (**1**).

| | |
|---|---|
| Formula | $C_{18}H_{24}Cl_2N_{10}O_8Ru$ |
| Formula mass [g $mol^{-1}$] | 680.43 |
| Crystal system | monoclinic |
| Space group | *C*2/*c* (No.15) |
| *a* [Å] | 25.758(8) |
| *b* [Å] | 10.772(4) |
| *c* [Å] | 18.933(5) |
| $\alpha$ [°] | 90 |
| $\beta$ [°] | 101.57(1) |
| $\gamma$ [°] | 90 |
| *V* [$Å^3$] | 5146(2) |
| *Z* | 8 |
| $D_{calcd}$ [g $cm^{-3}$] | 1.756 |
| $\mu$ [$cm^{-1}$] | 8.82 |
| $R_1$[a] [$I > 2.0\sigma(I)$] | 0.082 |
| $wR_2$[b] [all data] | 0.243 |
| *T* [°C] | –180 |

[a] $R_1 = \Sigma||F_o| - |F_c|| / \Sigma|F_o|$. [b] $wR_2 = \{\Sigma[w(F_o^2 - F_c^2)^2]/\Sigma w(F_o^2)^2\}^{1/2}$.

CCDC-298967 contains the supplementary crystallographic data for this paper. These data can be obtained free of charge from The Cambridge Crystallographic Data Centre via www.ccdc.cam.ac.uk/data_request/cif.

## Acknowledgments

This work was supported in part by a Grant-in-Aid for Scientific Research (Nos. 17550056, 16205010, 16750050, and 17350028) from the Ministry of Education, Science, Sports, and Culture of Japan, and by the Iketani Science and Technology Foundation. T. Y. was supported by the JSPS program for Research Fellowships for Young Scientists (No. 17003601).

[1] a) E. Reisner, V. B. Arison, M. F. C. Guedes de Silva, R. Lichtenecker, A. Eichnger, B. K. Keppler, V. Yu. Kukushkin, A. J. L. Pombeiro, *Inorg. Chem.* **2004**, *43*, 7083–7093; b) A. Egger, V. B. Arison, E. Reisner, B. Cebrian-Losantos, S. Shova, G. Trettenhahm, B. K. Keppler, *Inorg. Chem.* **2005**, *44*, 122–, 132; c) E.

 © 2006 Wiley-VCH Verlag GmbH & Co. KGaA, Weinheim 

Reisner, V. B. Arison, A. Eichinger, N. Kandler, G. Giester, A. J. L. Pombeiro, B. K. Keppler, *Inorg. Chem.* **2005**, *44*, 6704–6716; d) M. J. Clarke, F. Zhu, D. R. Frasca, *Chem. Rev.* **1999**, *99*, 2511–2533; e) C. J. Chang, M. C. Y. Chang, N. H. Damrauer, D. G. Nocera, *Biochim. Biophys. Acta* **2004**, *1655*, 13–28; f) M. J. Clarke, *Coord. Chem. Rev.* **2003**, *236*, 209–233 and references cited therein.

[2] a) Y. Sunatsuki, Y. Ikuta, N. Matsumoto, H. Ohta, M. Kojima, S. Iijima, S. Hayami, Y. Maeda, S. Kaizaki, F. Dahan, J.-P. Tuchagues, *Angew. Chem. Int. Ed.* **2003**, *42*, 1614–1618; b) H. Ohta, Y. Sunatsuki, Y. Ikuta, N. Matsumoto, S. Iijima, H. Akashi, T. Kambe, M. Kojima, *Mater. Sci.* **2003**, *21*, 191–198; c) Y. Ikuta, M. Ooidemizu, Y. Yamahata, M. Yamada, S. Osa, N. Matsumoto, S. Iijima, Y. Sunatsuki, M. Kojima, F. Dahan, J.-P. Tuchagues, *Inorg. Chem.* **2003**, *42*, 7001–7017; d) M. Yamada, M. Ooidemizu, Y. Ikuta, S. Osa, N. Matsumoto, S. Iijima, M. Kojima, F. Dahan, J.-P. Tuchagues, *Inorg. Chem.* **2003**, *42*, 8406–8416; e) H. Ohta, Y. Sunatsuki, M. Kojima, S. Iijima, H. Akashi, N. Matsumoto, *Chem. Lett.* **2004**, *33*, 350–351; f) Y. Sunatsuki, H. Ohta, M. Kojima, Y. Ikuta, Y. Goto, N. Matsumoto, S. Iijima, H. Akashi, S. Kaizaki, F. Dahan, J.-P. Tuchagues, *Inorg. Chem.* **2004**, *43*, 4154–4171.

[3] S. J. Slattery, J. K. Blaho, J. Lehnes, K. A. Goldsby, *Coord. Chem. Rev.* **1998**, *174*, 391–416 and references cited therein.

[4] I. P. Evans, A. Spencer, G. Wilkinson, *J. Chem. Soc., Dalton Trans.* **1973**, 204–209.

[5] I. Katsuki, Y. Motoda, Y. Sunatsuki, N. Matsumoto, T. Nakashima, M. Kojima, *J. Am. Chem. Soc.* **2002**, *124*, 629–640.

[6] R. D. Shannon, *Acta Crystallogr., Sect. A* **1976**, *32*, 751–767.

[7] Y. Yoshikawa, K. Yamasaki, *Coord. Chem. Rev.* **1979**, *28*, 205–229.

[8] H. Nakamura, M. Fujii, T. Hamada, T. Yamaguchi, Y. Sunatsuki, N. Matsumoto, M. Kojima, to be published.

[9] a) B. Bosnich, A. T. Phillip, *J. Am. Chem. Soc.* **1968**, *90*, 6352–6359; b) J. Hidaka, B. E. Douglas, *Inorg. Chem.* **1964**, *3*, 1180–1184; c) J. W. Canary, C. S. Allen, *J. Am. Chem. Soc.* **1995**, *117*, 8484–8485; d) S. Zahn, J. W. Canary, *Angew. Chem. Int. Ed.* **1998**, *37*, 305–308; e) J. M. Castagnetto, J. W. Canary, *Chem. Commun.* **1998**, 203–204.

[10] a) S. Chakraborty, M. G. Walawalkar, G. K. Lahiri, *J. Chem. Soc., Dalton Trans.* **2000**, 2875–2883; b) S. Deoghoria, S. Sain, T. K. Karmakar, S. K. Bera, S. K. Chandra, *J. Indian Chem. Soc.* **2002**, *79*, 857–859.

[11] R. F. Carina, L. Verzegnassi, G. Bernardinelli, A. F. Williams, *Chem. Commun.* **1998**, 2681–2682.

[12] a) A. M. Bond, M. Haga, *Inorg. Chem.* **1986**, *25*, 4507–4514; b) W. Szulbinski, P. R. Warburton, D. H. Busch, N. W. Alcock, *Inorg. Chem.* **1993**, *32*, 297–302.

[13] *Crystal Structure Analysis Package*, Rigaku and MSC, **2001**.

Received: February 8, 2006
Published Online: June 28, 2006

 © 2006 Wiley-VCH Verlag GmbH & Co. KGaA, Weinheim 

DOI: 10.1002/ejic.200600169

# A Supramolecular Assembly of Organotin Complexes: Syntheses, Characterization and Crystal Structures of Organotin Complexes with *meso*-2,3-Dimercaptosuccinic Acid

**Chunlin Ma*[a,b] and Qingfu Zhang[a]**

**Keywords:** S ligands / Self-assembly / Supramolecular chemistry / Tin

A series of two types of organotin complexes, namely $[(R_3Sn)_4(dmsa)]$ (R = Ph **1**, $PhCH_2$ **2**, $CH_3$ **3**, *n*Bu **4**; $H_4$dmsa = *meso*-2,3-dimercaptosuccinic acid) and $[(R_2Sn)_2(dmsa)(Y)]\cdot L$ (R = Ph, Y = $2H_2O$, L = $H_2O$, $Et_2O$ **5**; R = $PhCH_2$ **6**; R = $CH_3$ **7**; R = *n*Bu **8**; R = *n*Bu, Y = 0.5MeOH **9**) have been synthesized. All complexes were characterized by elemental analysis and FT-IR and NMR ($^1H$, $^{13}C$ and $^{119}Sn$) spectroscopy. Among them, the strucrtures of complexes **1**, **3**, **5**, and **9** were also determined by X-ray crystallography. The structural analyses show that complexes **1** and **3** are tetranuclear triorganotin monomers, complex **5** is a dinuclear diphenyltin monomer, and complex **9** is a 3D di-*n*-butyltin coordination polymer with a metal-organic framework structure. The supramolecular structure analyses reveal that the type of organic substituent attached to the tin atoms can apparently affect the supramolecular assembly: when the substituents attached to the tin atom are aromatic groups (**1** and **5**) the supramolecular structures are dominated by intermolecular π–π (C–H···π) weak interactions, whereas when the substituents attached to the tin atom are alkyl groups (**3** and **9**) the supramolecular structures are dominated by intermolecular Sn←X (X = S, O) coordination interactions.
(© Wiley-VCH Verlag GmbH & Co. KGaA, 69451 Weinheim, Germany, 2006)

## Introduction

Recently, the design and self-assembly of metal compounds into one-, two-, or three-dimensional supramolecular architectures has been attracting considerable attention due to their potential applications and intriguing architectures.[1–9] Two main lines of study are adopted, based on the different nature and bonding energy of the interactions responsible for networking, namely (i) frameworks comprised of metal centers and di- or polydentate ligands connected through chemical (covalent or coordination) bonds, which have been widely studied in the crystal engineering of microelectronic, nonlinear optical, ferromagnetic, and catalytic materials,[2,3] (ii) networks derived by the assembly of mono- or polynuclear metal complexes through intermolecular weak interactions such as hydrogen bonds, π–π interactions, electrostatic interactions, and so on, where it has been found that these weak interactions play vital roles in highly efficient and specific biological reactions and are essential for molecular recognition and the self-organization of molecules in supramolecular chemistry.[4,5]

Both systems mentioned above have recently been widely investigated in the supramolecular chemistry of organometallic complexes[6–9] because the supramolecular structures of such complexes can be more rationally controlled by tailoring the type and number of organic substituents attached to the metal center. Among these complexes, organotin complexes are attracting more and more attention due to their wide industrial applications and antitumor activities,[10] as well as their interesting and varied supramolecular structures.[7–9] In our previous work, we have also reported several interesting supramolecular structures assembled from organotin complexes.[9] To continue our research in this area, we selected another interesting ligand − *meso*-2,3-dimercaptosuccinic acid ($H_4$dmsa). This ligand was chosen based on the following considerations: first, both the carboxy and thiol groups in this ligand can form strong covalent bonds with the organotin moiety, thus providing sufficient thermodynamic stability for them to be stable in the solid state, including toward corrosive substances such as oxygen and water; second, $H_4$dmsa is a polyfunctional chelate ligand with two carboxy and two thiol groups, so it has a rich coordination chemistry and can help to construct multidimensional coordination polymers by acting as a multidentate bridging linker; third, the conformational flexibility of this ligand will allow for the formation of various and interesting molecular and supramolecular structures; fourth, $H_4$dmsa can bond more than one organotin moiety in one discrete molecule, which will increase the opportunities for supramolecular assembly from these complexes through intermolecular weak interactions between substituents (such as π–π interactions); fifth,

[a] Department of Chemistry, Liaocheng University, Liaocheng 252059, People's Republic of China
Fax: +86-538-671-5521
E-mail: macl@lctu.edu.cn
[b] Taishan University, Taian 271021, People's Republic of China
Supporting information for this article is available on the WWW under http://www.eurjic.org or from the author.

 InterScience © 2006 Wiley-VCH Verlag GmbH & Co. KGaA, Weinheim 

$H_4$dmsa is a simple linear ligand without a complicated inner structure, which makes it easy to analyze the electronic and steric influence of the organic substituents attached to the tin atom on the supramolecular structure. In addition, although $H_4$dmsa is a mercapto-containing, water-soluble, nontoxic, orally administered metal chelator that has been used as an antidote to heavy metal (lead, mercury, arsenic, and cadmium) toxicity for more than 50 years,[11] few metal complexes with this ligand have been determined by X-ray crystallography so far.[12] Recently, we began to treat $H_4$dmsa with organotin compounds with the hope of obtaining interesting supramolecular structures by assembly of this polyfunctional ligand with different organotin compounds. Here we report the detailed syntheses of eight new organotin complexes of *meso*-2,3-dimercaptosuccinic acid of two types: $[(R_3Sn)_4(dmsa)]$ (R = Ph **1**, $PhCH_2$ **2**, $CH_3$ **3**, *n*Bu **4**) and $[(R_2Sn)_2(dmsa)(Y)]\cdot L$ (R = Ph Y = $2H_2O$ L = $H_2O$, $Et_2O$ **5**; R = $PhCH_2$ **6**; R = $CH_3$ **7**; R = *n*Bu **8**; R = *n*Bu Y = 0.5MeOH **9**). All complexes were characterized by elemental analysis and FT-IR and NMR ($^1H$, $^{13}C$, and $^{119}Sn$) spectroscopy. The structures of complexes **1**, **3**, **5**, and **9** were also determined by X-ray crystallography.

## Results and Discussion

### Syntheses

Complexes **1**–**4** were obtained by reaction of $H_4$dmsa/EtONa/$R_3SnCl$ in a 1:4:4 molar ratio in toluene/methanol (5:1) at 40 °C, while complexes **5**–**8** were obtained by reaction of $H_4$dmsa/$R_2SnO$ in a 1:2 molar ratio in toluene/methanol (5:1) at reflux. Crystals of complex **9** were obtained by solvothermal reaction of $H_4$dmsa/KOH/$R_3SnCl$ in a 1:4:4 molar ratio in methanol/water (2:1) at 150 °C. The synthetic procedures are shown in Scheme 1.

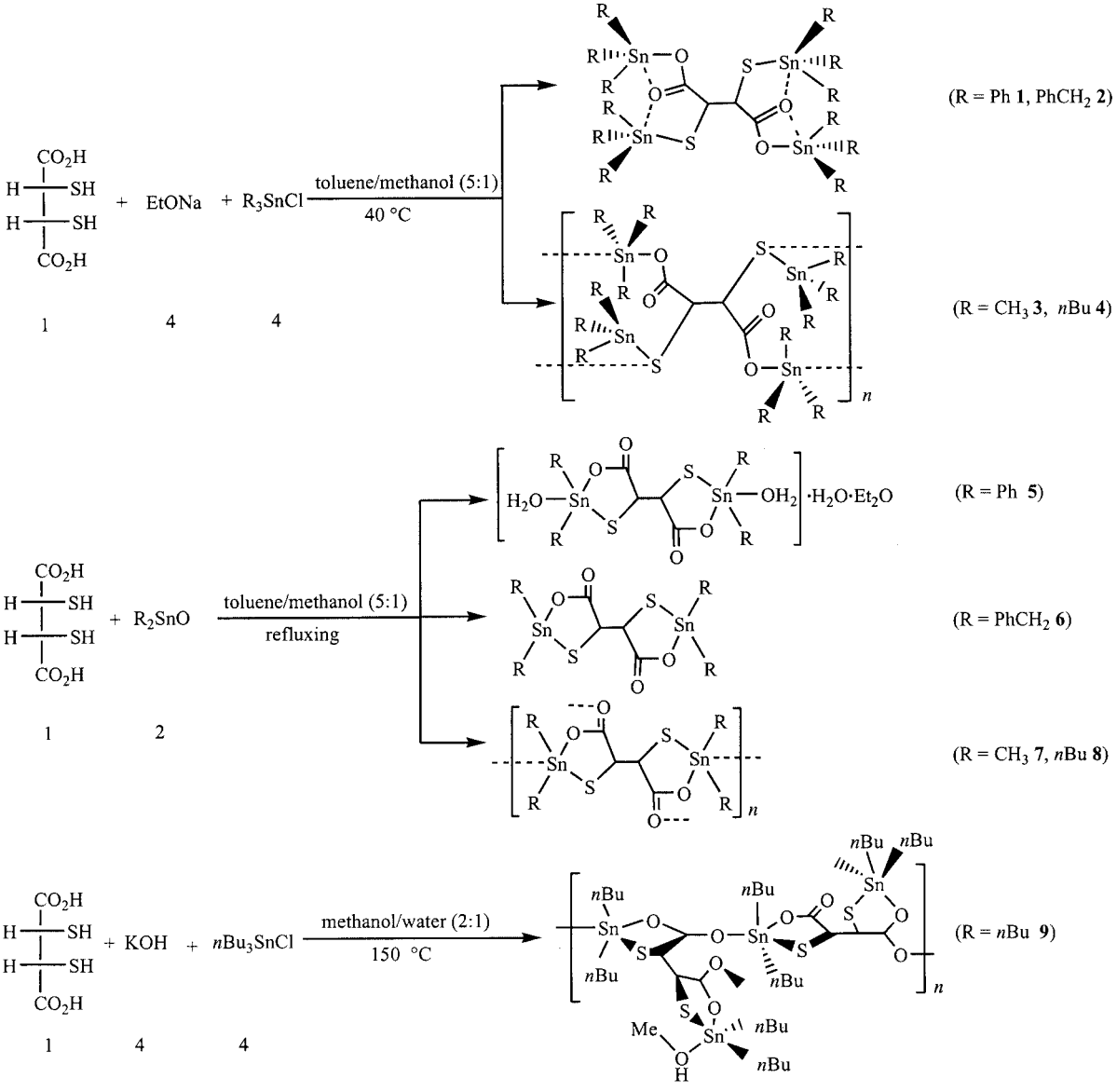


Scheme 1.

 © 2006 Wiley-VCH Verlag GmbH & Co. KGaA, Weinheim 

## Spectroscopic Studies

### *IR*

The main feature in the IR spectra of complexes **1**–**9** is the absence of bands in the region 3120–2980 and 2560–2410 $cm^{-1}$, which appear in the free ligand as $CO_2H$ and SH stretching vibrations, thus indicating metal–ligand bonding through these sites. The typical absorptions for Sn–C, Sn–O, and Sn–S vibrations in complexes **1**–**9** are all located in the normal range of similar organotin complexes.[13,14]

IR spectroscopy can provide useful information concerning the coordination of the carboxyl groups in organotin carboxylates.[15,16] When the carboxylic group coordinates the tin atom in a monodentate manner (mode **I**), the difference between the wavenumbers of the asymmetric and symmetric carboxylic stretching bonds, $\Delta\tilde{\nu}$ [$\Delta\tilde{\nu} = \tilde{\nu}(\nu_{as}CO_2^-) - \tilde{\nu}(\nu_sCO_2^-)$], is larger than that observed for ionic complexes. When the ligand chelates (mode **II**), $\Delta\tilde{\nu}$ is considerably smaller than that for ionic complexes, while in the asymmetric bidentate coordination mode the value is in the range characteristic of monodentate coordination. The characteristic wavenumber difference for mode **III** is larger than that for chelating groups and nearly the same as that observed for ionic complexes (Scheme 2).

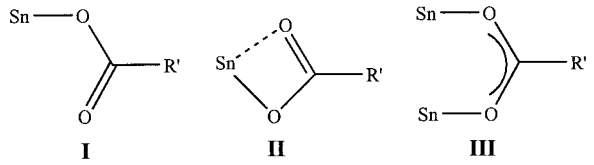


Scheme 2. Different coordination modes of the carboxylate group.

Based on the above results, it was possible to distinguish the coordination mode of the $CO_2^-$ group. The magnitude of $\Delta\tilde{\nu}$ (about 242–268 $cm^{-1}$) for **1**–**6**, compared with that for the corresponding sodium salts, reveals that the carboxylate ligands are monodentate, while the value of about 200 $cm^{-1}$ for **7**–**9** suggests a bidentate coordination mode. The conclusions drawn from the IR data are consistent with the X-ray crystallography study.

### *NMR*

The $^1H$ NMR spectra show the expected integration and peak multiplicities. In the spectra of the free ligand, the resonances observed at $\delta \approx 10.50$ and 1.65 ppm, which are absent in the spectra of the complexes, indicate removal of the $CO_2H$ and SH protons and formation of Sn–O and Sn–S bonds. This conclusion accords well with the IR data. Moreover, the $^1H$ NMR spectroscopic data show that the chemical shifts of the phenyl groups in complexes **1** and **5** ($\delta$ = 7.36–7.79 ppm), the methyl groups in complexes **3** and **7** ($\delta$ = 0.84–0.91 ppm), and the methylene groups connected directly to the tin atom in complexes **2**, **4**, **6**, **8**, and **9** ($\delta$ = 1.25–3.26 ppm) undergo an upfield shift relative to those of their precursors.

The $^{13}C$ NMR spectra of all compounds show a significant downfield shift of all carbon resonances compared with the free ligand because of an electron-density transfer from the ligand to the metal atom. Although at least two different types of carboxy groups are present, only one single resonance is observed for the $CO_2$ group in the $^{13}C$ spectra. A possible reason for this is that either accidental magnetic equivalence of the carbonyl carbon atoms occurs or the separation between the sets of resonance is too small to be resolved.

The $^{119}Sn$ NMR spectroscopic data show two signals for complexes **1**–**4** ($\delta$ = –95.1, –125.5 ppm for **1**; $\delta$ = –93.5, –118.8 ppm for **2**; $\delta$ = –96.4, –121.6 ppm for **3**; $\delta$ = –98.2, –126.1 ppm for **4**) and both of them are in the normal range for four-coordinate tin complexes,[17] thus indicating the existence of two different coordination environments around the tin atoms for complexes **1**–**4** in solution, which is similar to that found in the complexes [$(Ph_3Sn)_2$(*p*-mpspa)] and [$(Ph_3Sn)_2$(cpa)].[18] The $^{119}Sn$ NMR spectroscopic data of complexes **5**–**8** ($\delta$ = –150.2, –165.8, –175.7, and –173.8 ppm for **5**–**8**, respectively) show signals in the normal range for five-coordinate tin complexes.[17] However, complex **9** shows two signals at $\delta$ = –126.8 and –170.5 ppm, which are in the range corresponding to the coordination number 5 ($\delta$ = –90 to –190 ppm),[17] thus it can reasonably be assumed that there are also two different coordination environments around the tin atoms of complex **9** in solution.

## Crystal Structures

### *X-ray Crystallographic Study of 1 and 3*

Crystals of **1** suitable for an X-ray crystallography study were grown from dichloromethane, while crystals of **3** were grown from diethyl ether. The most relevant crystallographic data for **1** and **3** are summarized in the Experimental Section. Selected bond lengths and bond angles for **1** and **3** are given in Tables 1 and 2, respectively.

Table 1. Selected bond lengths and angles for complex **1**.

| Bond lengths [Å] | | | |
|---|---|---|---|
| Sn1–C3 | 2.122(5) | Sn1–C9 | 2.135(5) |
| Sn1–C15 | 2.114(4) | Sn1–S1 | 2.4373(13) |
| Sn1–O1 | 2.071(3) | Sn1–O2 | 2.838(3) |
| Sn2–C21 | 2.152(4) | Sn2–C27 | 2.154(5) |
| Sn2–C33 | 2.130(5) | Sn2–S1 | 2.4373(13) |
| Sn2–O2 | 2.849(3) | C1–O1 | 1.294(5) |
| C1–O2 | 1.224(5) | C2–S1 | 1.820(4) |
| **Bond angles [°]** | | | |
| C3–Sn1–C15 | 120.23(18) | C3–Sn1–O1 | 108.67(15) |
| C15–Sn1–O1 | 107.00(15) | C9–Sn1–O2 | 150.50(14) |
| C3–Sn1–C9 | 110.86(19) | C9–Sn1–C15 | 106.90(18) |
| C9–Sn1–O1 | 101.51(15) | C3–Sn1–O2 | 76.02(14) |
| C15–Sn1–O2 | 92.38(14) | O1–Sn2–O2 | 50.53(10) |
| C21–Sn2–C33 | 114.72(18) | C21–Sn2–S1 | 114.09(12) |
| C33–Sn2–S1 | 116.78(13) | C27–Sn2–O2 | 164.38(14) |
| C21–Sn2–O2 | 84.33(14) | C33–Sn2–O2 | 77.37(14) |
| S1–Sn2–O2 | 70.10(7) | C21–Sn2–C27 | 108.08(18) |
| C27–Sn2–C33 | 104.74(18) | C27–Sn2–S1 | 95.68(13) |

A perspective view of the molecular structure of complex **1** is shown in Figure 1. Complex **1** is a tetranuclear tin moi-

 © 2006 Wiley-VCH Verlag GmbH & Co. KGaA, Weinheim 

Table 2. Selected bond lengths and angles for complex **3**.

| Bond lengths [Å] | | | |
|---|---|---|---|
| Sn1–C3 | 2.100(6) | Sn1–C4 | 2.105(6) |
| Sn1–C5 | 2.114(6) | Sn1–O1 | 2.095(3) |
| Sn1–O2 | 3.092(3) | Sn2–C6 | 2.121(7) |
| Sn2–C7 | 2.130(6) | Sn2–C8 | 2.125(7) |
| Sn2–S1 | 2.4384(13) | Sn2–O2 | 3.164(4) |
| C1–O1 | 1.296(5) | C1–O2 | 1.212(5) |
| C2–S1 | 1.834(4) | | |
| **Bond angles [°]** | | | |
| C3–Sn1–C4 | 121.6(3) | C3–Sn1–C5 | 117.4(3) |
| C4–Sn1–C5 | 115.1(3) | C3–Sn1–O1 | 100.3(2) |
| C4–Sn1–O1 | 101.01(18) | C5–Sn1–O1 | 92.84(19) |
| C6–Sn2–C7 | 116.0(3) | C6–Sn2–C8 | 109.8(3) |
| C7 –Sn2–C8 | 108.4(3) | C6–Sn2–S1 | 111.5(2) |
| C7–Sn2–S1 | 111.30(19) | C8–Sn2–S1 | 98.3(2) |

ety containing two symmetrical $(Ph_3Sn)_2(SCHCO_2)$ moieties (inversion center: $-x+2$, $-y+1$, $-z$). Each tin atom in complex **1** forms four primary bonds: three from the phenyl C atoms and one from the O (for Sn1) or S (for Sn2) atom of the bridging ligand. The bond angles around the Sn1 and Sn2 atoms range from 101.51(15) to 120.23(18)° and from 95.68(13) to 116.78(13)°, respectively, suggesting apparent distortion from an ideal tetrahedron. The Sn1–O1 (2.071 Å) and Sn2–S1 [2.4373(13) Å] distances are in the normal range for Sn–O[19] and Sn–S[20] covalent bonds. There are also two weak intramolecular Sn···O interactions in complex **1** [Sn1–O2 = 2.838(3) and Sn2–O2 = 2.849(3) Å]. Although these distances are considerably longer than the normal Sn–O covalent bond, they lie in the range of Sn···O distances of 2.61–3.02 Å that have been confidently reported for intramolecular bonds.[21] As the oxygen atoms of the carboxylate groups in complex **1** are involved in weak coordination interactions with the tin atoms along one of the tetrahedral faces, the structural distortion for the tin atoms in **1** is best described as a capped tetrahedron.

Analysis of the supramolecular structure in the crystal lattice of **1** reveals that weak intermolecular C–H···π interactions play important roles in the supramolecular arrangements. The C–H···π interaction can also be viewed as an edge-to-face (as opposed to point-to-face or T-shaped) π–π interaction, and now is usually assigned to non-conventional weak hydrogen bonds.[5c,5g] Although this interaction is much weaker than covalent and coordinative interactions, and even than typical hydrogen bonds (such as O–H···O and N–H···O etc.), it clearly governs the supramolecular assembly in many compounds.[5g,22] In complex **1**, a series of parallel molecular chains connected by weak intermolecular C8–H8···Cg1 interactions (Cg1 is the centroid of the phenyl ring C9–C14) is found along the horizontal direction. Interestingly, these parallel molecular chains are further interlinked by weak intermolecular C6–H6···Cg2 interactions (Cg2 is the centroid of phenyl ring C27–C32) to form a 2D network structure in the defined plane (see Figure S1 in the Supporting Information). These C–H···π interactions in complex **1** (C8···Cg1 = 3.270, H8···Cg1 = 3.860 Å, C8–H8···Cg1 = 112.67°; C6···Cg2 = 3.752, H6···Cg2 = 2.867 Å, C6–H6···Cg2 = 159.41°) are close to those found in bis(*N*-pyridoxy-L-amino acidato)cobalt(III) complexes,[23] thereby suggesting they are strong enough to assemble these tetranuclear tin molecules into a 2D network in the solid state.

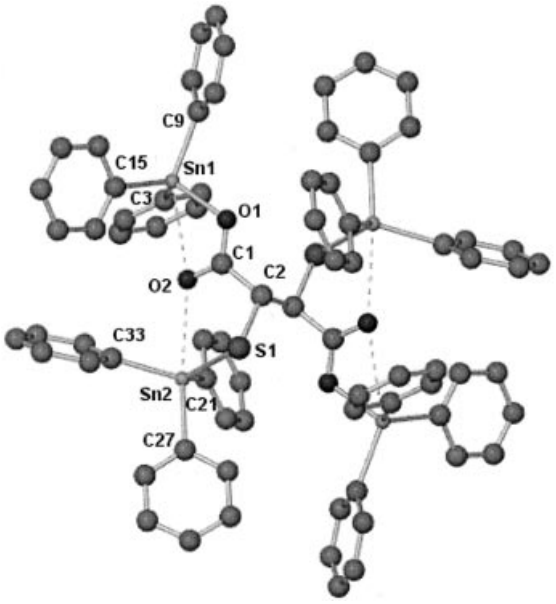


Figure 1. Molecular structure of complex **1** (all hydrogen atoms have been omitted for clarity).

A perspective view of the molecular structure of **3** is shown in Figure 2. Complex **3** is also a tetranuclear tin moiety containing two symmetrical $(Me_3Sn)_2(SCHCO_2)$ moieties (inversion center: $x$, $1-y$, $-1/2+z$). The molecular structure of **3** is similar to that of **1**, so we will not deal with many structural details here. However, a comparison of the molecular conformations and configurations of complexes **1** and **3** should be noted: first, the two intramolecular Sn···O weak interactions (Sn1···O2 = 3.092, Sn2···O2 = 3.165 Å) in complex **3** are weaker than in **1** and are out of the range of typical intramolecular Sn–O bonds (2.61–3.02 Å).[21] Therefore, these distances are almost sufficient to make this oxygen atom stereochemically inactive around the two Sn atoms; second, the Sn2 atom in complex **3** displays a distorted tetrahedral coordination sphere, with six angles ranging from 98.3(2) to 116.0(3)°. The bond angles around Sn1 (from 92.84 to 121.6°) show a larger deviation from the ideal value for a tetrahedron (109.5°), thereby indicating that there may be intermolecular contacts around Sn1 in the crystal lattice (vide infra). Finally, all the Sn–C and covalent Sn–O and Sn–S bonds around each tin atom in complex **3** are unremarkable, as expected.

To our surprise, the common intermolecular C=O→Sn interactions that can give rise to either polymeric or cyclo-oligomeric structures in trimethyltin compounds[24] are not found in complex **3**. In fact, the supramolecular structure of complex **3** is a 2D network linked by weak intermolecular Sn←S coordination interactions. As shown in Figure 3, the asymmetric unit of complex **3** is linked by weak intermolecular Sn1···S1 coordination interactions along the

 © 2006 Wiley-VCH Verlag GmbH & Co. KGaA, Weinheim 

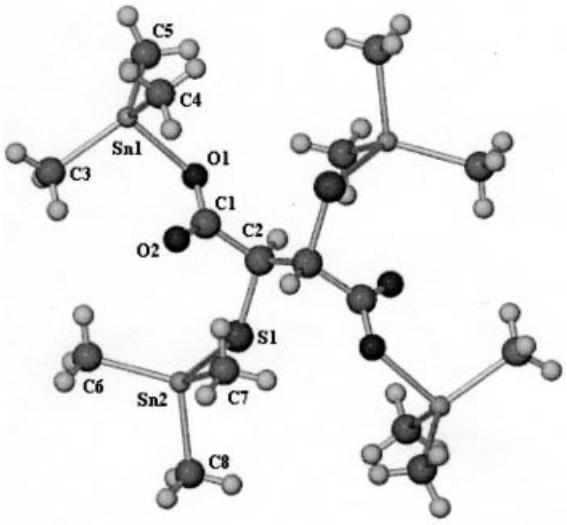


Figure 2. Molecular structure of complex **3**.

*b* and *c* axes to form a 2D layer with a 24-membered cavity in the *bc* plane. Although the loose cavities provided by these intermolecular Sn–S weak coordination interactions are large enough (7.525 × 11.265 Å) and are not completely filled by the methyl groups on the tin atoms that protrude into the interior, there are no solvent molecules in these cavities. This is not surprising in view of the fact that packing of such layers along the *a* axis produces a genuine no-cavity structure in the crystal lattice of complex **3** (see Figure S2 in the Supporting Information). Although the weak intermolecular Sn···S coordination distance in complex **3** is 3.286 Å, it still falls in the range proposed for secondary Sn···S coordination bonds (2.79–3.81 Å)[6] and is even close to the C=S···Sn distance [3.2274(8) Å] found in (5-mercapto-3-phenyl-1,3,4-thiadiazoline-2-thionato)trimethyltin.[25] If the weak Sn···S interaction is also considered, the coordination environment around the Sn1 atom in complex **3** can best be described as a distorted trigonal bipyramid.

### *X-ray Crystallographic Study of 5 and 9*

Crystals of **5** suitable for an X-ray crystallography study were grown from dichloromethane/diethyl ether, while crystals of **9** were obtained from the mother liquor of the solvothermal reaction. The most relevant crystallographic data for **5** and **9** are summarized in the Experimental Section. Selected bond lengths and bond angles for **5** and **9** are given in Tables 3 and 4, respectively.

Table 3. Selected bond lengths and angles for complex **5**.

| Bond lengths [Å] | | | |
|---|---|---|---|
| Sn1–C11 | 2.11(2) | Sn1–C5 | 2.13(2) |
| Sn1–O1 | 2.37(1) | Sn1–S1 | 2.416(4) |
| Sn1–O5 | 2.443(6) | Sn2–C23 | 2.130(9) |
| Sn2–C17 | 2.16(2) | Sn2–O3 | 2.36(1) |
| Sn2–O6 | 2.406(7) | Sn2–S2 | 2.413(4) |
| **Bond angles [°]** | | | |
| C5–Sn1–C11 | 121.7(7) | C11–Sn1–S1 | 118.4(6) |
| C5–Sn1–S1 | 116.8(5) | O1–Sn1–O5 | 167.2(3) |
| C17–Sn2–C23 | 118.7(6) | C23–Sn2–S2 | 122.2(3) |
| C17–Sn2–S2 | 116.5(6) | O3–Sn2–O6 | 167.3(3) |

A perspective view of the molecular structure of **5** is shown in Figure 4. The $[(Ph_2Sn)_2(dmsa)\cdot 2H_2O]$ asymmetric unit is a dinuclear tin moiety with two coordinated water molecules. The $[(Ph_2Sn)_2(dmsa)]$ moiety contains two five-membered SnSCCO chelate metallacycles with an envelope

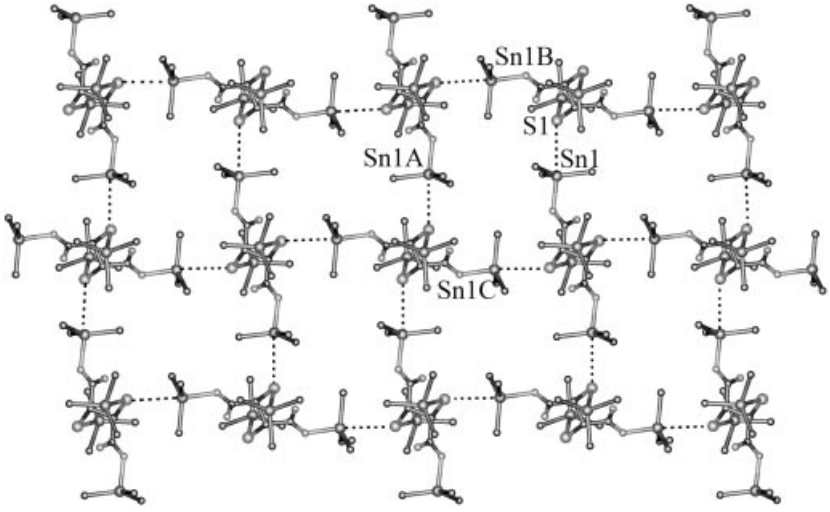


Figure 3. Supramolecular structure of complex **3** showing the 2D network linked by intermolecular Sn1···S1 coordination interactions (dotted line).

 © 2006 Wiley-VCH Verlag GmbH & Co. KGaA, Weinheim 

Table 4. Selected bond lengths and angles for complex **9**.[a]

| Bond lengths [Å] | | | |
|---|---|---|---|
| Sn1–C9 | 2.125(18) | Sn1–C13 | 2.12(2) |
| Sn1–O1 | 2.156(13) | Sn1–O9 | 2.264(15) |
| Sn1–S1 | 2.394(5) | Sn2–C17 | 2.104(182) |
| Sn2–C21 | 2.08(2) | Sn2–O3 | 2.234(10) |
| Sn2–O8B | 2.186(9) | Sn2–S2 | 2.408(4) |
| Sn3–C25 | 2.081(18) | Sn3–C29 | 2.138(19) |
| Sn3–O5 | 2.183(10) | Sn3–O4 | 2.259(9) |
| Sn3–S3 | 2.389(4) | Sn4–C33 | 2.09(2) |
| Sn4–C37 | 2.138(18) | Sn4–O2A | 2.239(11) |
| Sn4–O7 | 2.241(9) | Sn4–S4 | 2.402(4) |
| **Bond angles [°]** | | | |
| C9–Sn1–C13 | 125.0(10) | C9–Sn1–S1 | 119.5(6) |
| C13–Sn1–S1 | 115.2(8) | O1–Sn1–O9 | 167.3(5) |
| C17–Sn2–C21 | 125.4(8) | C17–Sn2–S2 | 114.5(6) |
| C21–Sn2–S2 | 119.2(5) | O3–Sn2–O8A | 164.4(4) |
| C25–Sn3–C29 | 123.5(9) | C25–Sn3–S3 | 119.3(6) |
| C29–Sn3–S3 | 117.0(7) | O4–Sn3–O5 | 162.5(4) |
| C33–Sn4–C37 | 118.1(9) | C33–Sn4–S4 | 114.4(7) |
| C37–Sn4–S4 | 127.4(6) | O7–Sn4–O2B | 163.6(4) |

[a] Symmetry codes: A: $x-1/2, -y+1/2, z-1/2$; B: $x, -y, z+1/2$.

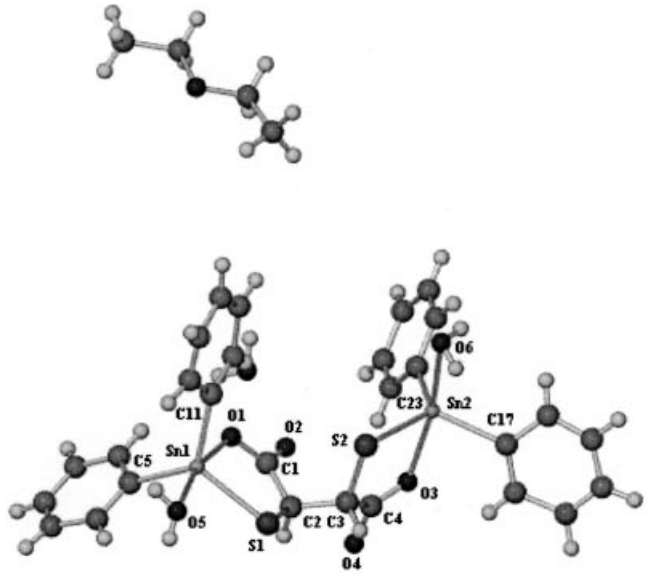


Figure 4. Molecular structure of complex **5**.

conformation, which is similar to the anion of the diorganotin carboxylate $[(n\text{Pr})_3\text{NH}][\text{Me}_2\text{Sn}(\mu^2\text{-SCH}_2\text{COO})\text{Cl}]$.[26] Each tin atom in complex **5** is a five-coordinate trigonal bipyramid, with two phenyl groups and the sulfur atom of dmsa occupying the equatorial plane and one of the carboxyl oxygen atoms (O1 or O3) and one coordinated water molecule (O5 or O6) in axial positions. Because there is a strong (O,S) chelate effect (O1–Sn1–S1 = 78.64°, O3–Sn2–S2 = 78.75°), the corresponding axial–Sn–axial angles (167.20° for Sn1 and 167.24° for Sn2) and equatorial angles (116.80°, 118.40°, 121.69° for Sn1 and 116.51°, 118.67°, 122.15° for Sn2) suggest the geometries of both tin atoms in complex **5** are distorted trigonal pyramids. The two coordinative Sn–$OH_2$ bonds (Sn1–O5 = 2.443, Sn2–O6 = 2.406 Å) are slightly longer than the corresponding covalent Sn–O bonds (Sn1–O1 = 2.367, Sn2–O2 = 2.360 Å) and are in the range of known Sn–$OH_2$ bonds [2.14(3)–2.47(2) Å].[27] Both Sn–O (Sn1–O1 = 2.367, Sn2–O2 = 2.360 Å) and Sn–S (Sn1–S1 = 2.415, Sn2–S3 = 2.413 Å) bond lengths are close to those found in diorganotin carboxylates and thiolates.[9a] In addition, there are co-crystallized water and diethyl ether molecules in complex **5**.

The supramolecular structure of complex **5** is dominated by a 1D helical molecular chain along the *c* axis linked by intermolecular C–H···π (C3–H3···Cg3, Cg3 is the centroid of phenyl C5–C10) weak hydrogen-bonding interactions (see Figure S3 in the Supporting Information); the pitch of this helix (13.337 Å) is longer than that found in $(Ph_3Sn)_2(SC_6H_4CO_2)$ (9.991 Å).[20b] The corresponding C3···Cg3, H3···Cg3, and C3–H3···Cg3 values (3.866 Å, 3.019 Å, and 145.31°) in complex **5** are close to the C–H···π values in the $CH_4/C_6H_6$ system[5g] but larger than that found in complex **1**, which is in good agreement with theoretical calculations that predict that C–H···π interactions in aliphatic/aromatic systems are weaker than in aromatic/aromatic systems.[5g]

A perspective view of the molecular structure of **9** is shown in Figure 5; for clarity, the somewhat disordered β, γ and δ carbon atoms of the butyl groups have been omitted. The structure analysis for **9** reveals that it is a 3D metal-organic framework constructed by the S-shaped building block $[(n\text{Bu}_2\text{Sn})_2(\text{dmsa})]_2\cdot\text{MeOH}$. The S-shaped asymmetric unit consists of two $[(n\text{Bu}_2\text{Sn})_2(\text{dmsa})]$ moieties and one coordinated MeOH molecule. Interestingly, every two five-membered SnSCCO chelate metallacycles in the asymmetric unit that are connected by the same dmsa ligand, such as pSn1 and pSn2, pSn3 and pSn4,[28] are not coplanar (dihedral angles between pSn1 and pSn2 and pSn3 and pSn4 are 71.51° and 60.69°, respectively), while pSn2, pSn3, and the bridging O4 atom are almost in the same plane (largest deviation: 0.071 Å; mean deviation: 0.035 Å). Each $[(n\text{Bu}_2\text{Sn})_2(\text{dmsa})]$ moiety in complex **9** also contains two five-membered SnSCCO chelate metallacycles, similar to those found in complex **5**. The coordination environment around each tin atom in complex **9** is also distorted trigonal-bipyramidal, with the equatorial positions occupied by two *n*-butyl groups and one thiol sulfur atom from the dmsa ligand and the axial positions shared by one coordinated oxygen atom from the dmsa ligand and an additional Lewis base, which may be a solvent molecule (for Sn1) or an intermolecular C=O→Sn bond (for Sn2, Sn3, and Sn4). The corresponding axial–Sn–axial skeletons are bent (ranging from 162.51° to 167.51°; av. 164.53°) due to the strong chelate effect of the O and S atoms (O–Sn–S chelate angles ranging from 80.31° to 82.68°; av. 81.36°), which is similar to that found in complex **5**. All the Sn–S and Sn–O distances lie in the range 2.389(4)–2.408(4) and 2.156(13)–2.259(9) Å, respectively, except for Sn1–O9, which is consistent with the situation reported in other organotin compounds.[9a,29] Moreover, the solvent-coordinated Sn–O bond (Sn1–O9) is only 2.264(15) Å, which is close to the

 © 2006 Wiley-VCH Verlag GmbH & Co. KGaA, Weinheim 

corresponding covalent Sn–O bond [Sn1–O1 = 2.156(13) Å] formed with carboxylate groups (the difference between these two Sn–O bonds is only 0.108 Å) and shorter than that found in [($Me_3Sn$)(TMA)]·2MeOH (2.462 and 2.586 Å),[9b] thus showing the strong coordinative interactions between guest methanol molecules and the host framework.

The supramolecular structure of complex **9** is a 3D metal-organic framework built by {[($n$Bu$_2$Sn)$_2$(dmsa)]$_2$·MeOH} units. As shown in Figure 6a, each {[($n$Bu$_2$Sn)$_2$-(dmsa)]$_2$·MeOH} unit is linked by intermolecular C=O→Sn coordination interactions along the 110 and 0$\bar{1}$1 directions, thus forming a 2D layer with 53-membered organotin rings in the defined plane. Furthermore, these layers are linked to form a 3D framework along the 010 direction to give 56-membered rhombic channels (Figure 6b). The size of the 53-membered ring channel is 26.83×11.50 Å (transannular Sn4···Sn4′ and Sn2···Sn3), while the 56-membered ring rhombic channels are only 13.551×9.658 Å in size (transannular Sn4···Sn4′′ and Sn2′···Sn3′). The solvent methanol molecules reside in the 53-membered ring channels because they are strongly coordinated to the framework Sn1 atoms. A strong H-bonding interaction is also found between the methanol molecule and the framework oxygen atom O9 (O9···O6 = 2.525 Å). These coordinating and H-bonding interactions between the methanol molecules and the framework are believed to be responsible for the formation of the framework structure. It is worth mentioning here that, although the channels in this complex are ostensibly large enough to capture the guest methanol molecules, they constitute only 4.3% of the crystal volume and are almost com-

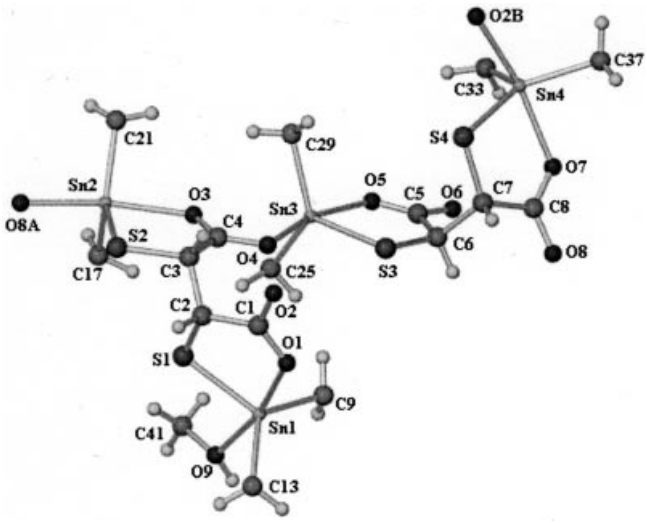


Figure 5. Molecular structure of complex **9** (the β, γ, and δ carbon atoms of the butyl groups on the tin atom have been omitted for clarity).

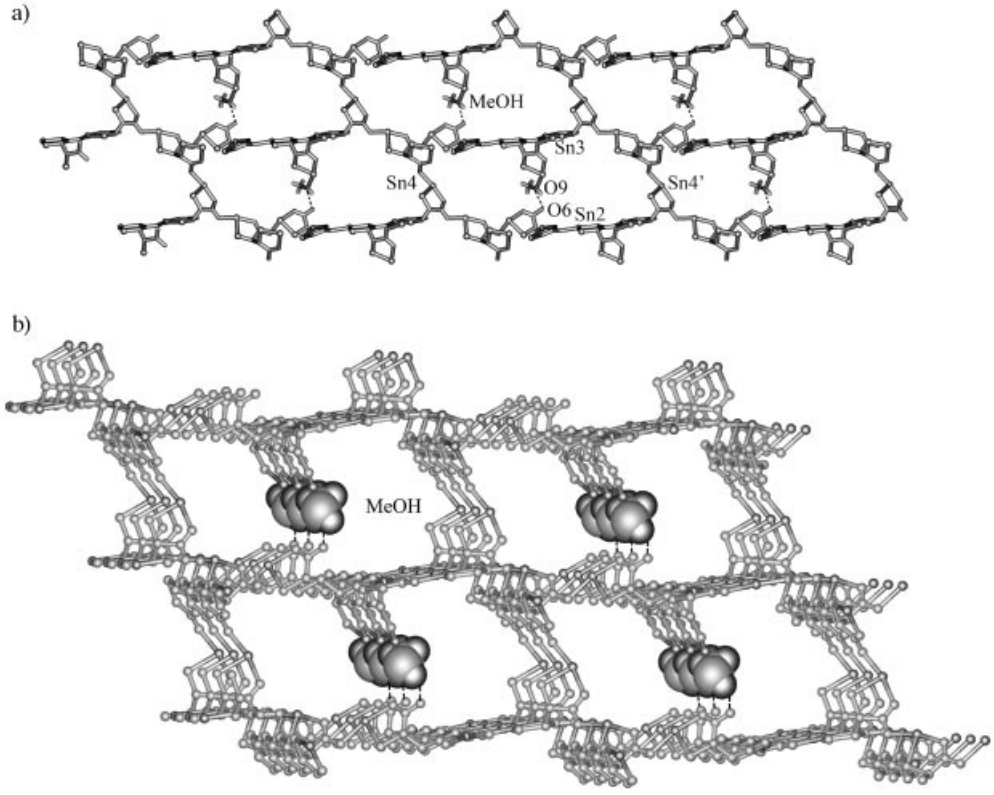


Figure 6. a) 2D "wall-like" layer and b) 3D metal-organic framework of complex **9**. The O–H···O hydrogen bonds between guest methanol molecules and the host organotin framework are shown with a broken line (the *n*-butyl groups on the tin atoms have been omitted for clarity).

 © 2006 Wiley-VCH Verlag GmbH & Co. KGaA, Weinheim 

pletely filled by the butyl groups on the tin atoms that protrude into the interior (if *n*Bu groups are omitted they constitute up to 69.7%; see Figure S4, Supporting Information).[30] This is apparently different to ionic complexes with a 3D open-framework structure, such as [{Mn(dcbp)}·$2H_2O$]$_n$ (dcbp = 4,4′-dicarboxylato-2,2′-bipyridine)[31] and [Co(bix)$_2$($H_2O$)$_2$]($SO_4$)·$7H_2O$ [bix = 1,4-bis(imidazol-1-ylmethyl)benzene],[32] which all have a large pore aperture for guest molecules (18.2% and 27%, respectively) and show reversible "desorption-adsorption" processes.

The TGA of **9** shows a continuous weight loss (found: 2.7%) from 77 to 135 °C, which is attributed to the loss of guest methanol molecules (calcd. 2.5%); the host framework is stable up to 280 °C, at which point decomposition starts. However, during thermal treatment under vacuum the crystal lattice collapses at relatively low temperatures (< 100 °C). X-ray crystallography proved that the crystalline 3D framework is transformed into an amorphous material, which is similar to that found in the organotin complex [{(*n*Bu)$_2$Sn(2,5-pdc)($H_2O$)}$_3$·$3H_2O$·*y*EtOH]$_n$.[8a] To evaluate the porosity of this material, crystals of **1** were thermally treated for a period of 1 h (100 °C at 10 Torr) and then exposed to vapors of $H_2O$, EtOH, MeOH, and $NH_3$. In all cases no solvent molecules were found by elemental analysis or integration of the $^1$H NMR spectrum in $CD_3COCD_3$, thus showing the irreversibility of the removal of the enclathrated guest molecule within the host framework. This is well in agreement with the crystal structure analysis.

## Conclusions

In summary, a series of organotin complexes based on *meso*-2,3-dimercaptosuccinic acid have been synthesized. All complexes were characterized by elemental analysis and FT-IR and NMR ($^1$H, $^{13}$C and $^{119}$Sn) spectroscopy. The structures of complexes **1**, **3**, **5**, and **9** have also been determined by X-ray diffractometry. Both the spectra and crystal structures show that when *meso*-2,3-dimercaptosuccinic acid reacts with triorganotin compounds it can form tetranuclear monomers, whereas when it reacts with diorganotin compounds it can form dinuclear monomers or 3D polymers with a metal-organic framework structure.

The supramolecular structures described in this paper demonstrate that the type of substituent attached to the tin atom has an influence on the supramolecular arrangement: when the groups attached to the tin atom are aromatic groups (**1** and **5**), the supramolecular structures are dominated by intermolecular C–H···π weak interactions, whereas when the groups attached to the tin atom are alkyl groups (**3** and **9**), the supramolecular structures are dominated by intermolecular Sn←X (X = S, O) coordination interactions. In diorganotin complexes, it also shows that the number of solvent molecules coordinated to the tin atom is crucial for the supramolecular assembly. This contribution adds several new features to the fast developing field of supramolecular chemistry and aids the fundamental understanding of molecular recognition and systematic rationalization of molecular aggregation in crystal engineering of organometallic complexes.

## Experimental Section

**Materials and Measurements:** Commercially available starting materials and solvents were used. Tribenzyltin chloride,[33] dimethyltin oxide, and dibenzyltin oxide[34] were prepared by standard methods reported in the literature. The melting points were obtained with a Kofler micro-melting point apparatus and are uncorrected. IR spectra were recorded with a Nicolet-460 spectrophotometer using KBr discs and sodium chloride optics. $^1$H, $^{13}$C, and $^{119}$Sn NMR spectra were recorded with a Varian Mercury Plus 400 spectrometer operating at 400, 100.6, and 149.2 MHz, respectively. The spectra were acquired at room temperature (298 K) unless otherwise specified; $^{13}$C NMR spectra were broadband-proton-decoupled. The chemical shifts are reported in ppm with respect to the references and are quoted relative to external tetramethylsilane (TMS) for $^1$H and $^{13}$C NMR, and to neat tetramethyltin for $^{119}$Sn NMR spectroscopy. Elemental analyses were performed with a PE-2400II apparatus.

**[($Ph_3Sn$)$_4$(dmsa)] (1):** This reaction was carried out under nitrogen. *meso*-2,3-Dimercaptosuccnic acid (0.182 g, 1 mmol) and sodium ethoxide (0.272 g, 4 mmol) were added to a mixed solution of toluene and methanol (5:1) in a Schlenk flask and stirred for 0.5 h. After the addition of triphenyltin chloride (1.542 g, 4 mmol), the mixture was stirred at 40 °C for 12 h and then filtered. The solvent was gradually removed by evaporation under vacuum until a solid product was obtained. This solid was then recrystallized from dichloromethane to give colorless crystals of **1**. Yield: 1.294 g (82%). M.p. 212–214 °C. $C_{76}H_{62}O_4S_2Sn_4$ (1578.1): calcd. C 57.84, H 3.96, S 4.06; found C 57.75, H 4.05, S 4.00. IR (KBr): $\tilde{\nu}$ = 1594 cm$^{-1}$ $\nu(COO)_{as}$, 1352 $\nu(COO)_s$, 560 $\nu$(Sn–C), 447 $\nu$(Sn–O), 320 $\nu$(Sn–S). $^1$H NMR ($CDCl_3$): $\delta$ = 4.25 (s, 2 H, CH), 7.46–7.79 (m, 60 H, $C_6H_5$) ppm. $^{13}$C NMR ($CDCl_3$): $\delta$ = 53.1, 128.1, 129.3, 136.5, 148.6, 177.4 ppm. $^{119}$Sn NMR ($CDCl_3$): $\delta$ = –95.1, –125.5 ppm.

**[{($PhCH_2$)$_3$Sn}$_4$(dmsa)] (2):** Complex **2** was prepared in the same way as compound **1**, by adding tribenzyltin chloride (1.710 g, 4 mmol) to *meso*-2,3-dimercaptosuccinic acid (0.182 g, 1 mmol) and sodium ethoxide (0.272 g, 4 mmol). The solvent was gradually removed by evaporation under vacuum until a solid product was obtained. Yield: 1.484 g (85%). M.p. 200–202 °C. $C_{88}H_{86}O_4S_2Sn_4$ (1746.6): calcd. C 60.51, H 4.96, S 3.70; found C 60.55, H 5.00, S 3.75. IR (KBr): $\tilde{\nu}$ = 1595 cm$^{-1}$ $\nu(COO)_{as}$, 1358 $\nu(COO)_s$, 575 $\nu$(Sn–C), 438 $\nu$(Sn–O), 335 $\nu$(Sn–S). $^1$H NMR ($CDCl_3$): $\delta$ = 3.24 (s, 24 H, $CH_2$), $\delta$ = 4.25 (s, 2 H, CH), 7.25–8.05 (m, 60 H, $C_6H_5$) ppm. $^{13}$C NMR ($CDCl_3$): $\delta$ = 34.8, 54.2, 126.6, 128.7, 129.7, 134.2, 135.0, 176.3 ppm. $^{119}$Sn NMR ($CDCl_3$): $\delta$ = –93.5, –118.8 ppm.

**[($Me_3Sn$)$_4$(dmsa)] (3):** Complex **3** was prepared in the same way as compound **1**, by adding trimethyltin chloride (0.800 g, 4 mmol) to *meso*-2,3-dimercaptosuccinic acid (0.182 g, 1 mmol) and sodium ethoxide (0.272 g, 4 mmol). The solvent was gradually removed by evaporation under vacuum until a solid product had formed. The solid was then recrystallized from ethanol to give colorless crystals of **3**. Yield: 0.733 g (88%). M.p. 108–110 °C. $C_{16}H_{38}O_4S_2Sn_4$ (833.34): calcd. C 23.06, H 4.60, S 7.69; found C 23.10, H 4.65, S 7.65. IR (KBr): $\tilde{\nu}$ = 1598 cm$^{-1}$ $\nu_{as}$(COO), 1360 $\nu_s$(COO), 583 $\nu$(Sn–C), 476 $\nu$(Sn–O), 357 $\nu$(Sn–S). $^1$H NMR ($CDCl_3$): $\delta$ = 0.84 (s, 36 H, $CH_3$), 4.25 (s, 2 H, CH) ppm. $^{13}$C NMR ($CDCl_3$): $\delta$ = –5.0, 2.5, 53.4, 175.5 ppm. $^{119}$Sn NMR ($CDCl_3$): $\delta$ = –96.4, –121.6 ppm.

**[($n$Bu$_3$Sn)$_4$(dmsa)] (4):** Complex **4** was prepared in the same way as compound **1**, by adding tri-*n*-butyltin chloride (1.302 g, 4 mmol)

 © 2006 Wiley-VCH Verlag GmbH & Co. KGaA, Weinheim 

to *meso*-2,3-dimercaptosuccinic acid (0.182 g, 1 mmol) and sodium ethoxide (0.272 g, 4 mmol). The solvent was gradually removed by evaporation under vacuum until a solid product was obtained. Yield: 1.137 g (85%). M.p. 152–154 °C. $C_{52}H_{110}O_4S_2Sn_4$ (1338.4): calcd. C 46.70, H 8.25, S 4.75; found C 46.66, H 8.28, S 4.79. IR (KBr): $\tilde{\nu}$ = 1590 $cm^{-1}$ $\nu_{as}$(COO), 1358 $\nu_s$(COO), 575 ν(Sn–C), 450 ν(Sn–O), 365 ν(Sn–S). $^1H$ NMR ($CDCl_3$): $\delta$ = 0.92 (t, $^3J_{H,H}$ = 7.2 Hz, 36 H, $CH_3$), 1.25–1.71 (m, 72 H, $CH_2CH_2CH_2$), 4.27 (s, 2 H) ppm. $^{13}C$ NMR ($CDCl_3$): $\delta$ = 13.4, 25.8, 26.5, 27.0, 54.0, 177.2 ppm. $^{119}Sn$ NMR ($CDCl_3$): $\delta$ = –98.2, –126.1 ppm.

**[(Ph$_2$Sn)$_2$(dmsa)(2H$_2$O)]·H$_2$O·Et$_2$O (5):** A mixture of *meso*-2,3-dimercaptosuccinic acid (0.182 g, 1 mmol) and $Ph_2SnO$ (0.580 g, 2 mmol) in toluene/methanol (5:1) was refluxed in a Dean–Stark trap for 10 h. After cooling to room temperature, the solvent was removed under vacuum to give **5** as a colorless solid. This solid was then recrystallized from diethyl ether to give colorless crystals of **5**. Yield: 0.732 g (86%). M.p. > 300°C (dec.). $C_{32}H_{38}O_8S_2Sn_2$ (852.1): calcd. C 45.10, H 4.50, S 7.55; found C 45.08, H 4.45, S 7.60. IR (KBr): $\tilde{\nu}$ = 1585 $cm^{-1}$ $\nu_{as}$(COO), 1352 $\nu_s$(COO), 558 ν(Sn–C), 460 ν(Sn–O), 375 ν(Sn–S). $^1H$ NMR ($CDCl_3$): $\delta$ = 7.68–7.36 (m, 20 H, $C_6H_5$), 4.26 (s, 2 H, CH) ppm. $^{13}C$ NMR ($CDCl_3$): $\delta$ = 51.8, 128.4, 128.8, 131.5, 150.8, 176.5 ppm. $^{119}Sn$ NMR ($CDCl_3$): $\delta$ = –150.2 ppm.

**[{(PhCH$_2$)$_2$Sn}$_2$(dmsa)] (6):** Complex **6** was prepared in the same way as complex **5**, by refluxing $(PhCH_2)_2SnO$ (0.634 g, 2 mmol) and *meso*-2,3-dimercaptosuccinic acid (0.182 g, 1 mmol). After cooling to room temperature, the solvent was removed under vacuum to give **6** as a colorless solid. Yield: 0.647 g (83%). M.p. 205–207 °C. $C_{32}H_{30}O_4S_2Sn_2$ (780.13): calcd. C 49.27, H 3.88, S 8.22; found C 49.30, H 3.85, S 8.20. IR (KBr): $\tilde{\nu}$ = 1578 $cm^{-1}$ $\nu_{as}$(COO), 1310 $\nu_s$(COO), 552 ν(Sn–C), 460 ν(Sn–O), 336 ν(Sn–S). $^1H$ NMR ($CDCl_3$): $\delta$ = 3.26 (s, 8 H, $CH_2$), 4.27 (s, 2 H, CH), 7.24–7.58 (m, 20 H, $C_6H_5$) ppm. $^{13}C$ NMR ($CDCl_3$): $\delta$ = 56.3, 125.8, 128.7, 129.3, 143.7, 177.1 ppm. $^{119}Sn$ NMR ($CDCl_3$): $\delta$ = –165.8 ppm.

**[(Me$_2$Sn)$_2$(dmsa)] (7):** Complex **7** was prepared in the same way as complex **5**, by refluxing $Me_2SnO$ (0.330 g, 2 mmol) and *meso*-2,3-dimercaptosuccinic acid (0.182 g, 1 mmol). After cooling to room temperature, the solvent was removed under vacuum to give **7** as a colorless solid. Yield: 0.418 g (88%). M.p. 221–223 °C. $C_8H_{14}O_4S_2Sn_2$ (475.74): calcd. C 20.20, H 2.97, S 13.48; found C 20.25, H 3.00 S 13.55. IR (KBr): $\tilde{\nu}$ = 1635 $cm^{-1}$ $\nu_{as}$(COO), 1326 $\nu_s$(COO), 543 ν(Sn–C), 480 ν(Sn–O), 345 ν(Sn–S). $^1H$ NMR ($CDCl_3$): $\delta$ = 0.91 (s, 12 H), 4.27 (s, CH) ppm. $^{13}C$ NMR ($CDCl_3$): $\delta$ = –0.6, 54.8, 177.5 ppm. $^{119}Sn$ NMR ($CDCl_3$): $\delta$ = –175.7 ppm.

**[(*n*Bu)$_2$Sn]$_2$(dmsa) (8):** Complex **8** was prepared in the same way as complex **5**, by refluxing $(nBu)_2SnO$ (0.498 g, 2 mmol) and *meso*-2,3-dimercaptosuccinic acid (0.182 g, 1 mmol). After cooling to room temperature, the solvent was removed under vacuum to give **8** as a colorless product. Yield: 0.515 g (80%). M.p. 310–312 °C. $C_{20}H_{38}O_4S_2Sn_2$ (644.1): calcd. C 37.30, H 5.95, S 9.96; found C 37.32, H 5.80, S 10.00. IR (KBr): $\tilde{\nu}$ = 1632 $cm^{-1}$ $\nu_{as}$(COO), 1330 $\nu_s$(COO), 558 ν(Sn–C), 464 ν(Sn–O), 328 ν(Sn–S). $^1H$ NMR ($CDCl_3$): $\delta$ = 0.80–0.93 (t, $^3J_{H,H}$ = 6.8 Hz, 12 H, $CH_3$), 1.35–1.82 (m, 24 H, $CH_2CH_2CH_2$), 4.22 (s, 2 H, CH) ppm. $^{13}C$ NMR ($CDCl_3$): $\delta$ = 13.5, 25.8, 26.3, 27.5, 52.0, 175.4 ppm. $^{119}Sn$ NMR ($CDCl_3$): $\delta$ = –173.8 ppm.

**{[(*n*Bu)$_2$Sn]$_4$(dmsa)$_2$(MeOH)}$_n$ (9):** A mixture of *meso*-2,3-dimercaptosuccinic acid (0.091 g, 0.5 mmol), KOH (0.112 g, 2 mmol), tri-*n*-butyltin chloride (0.651 g, 2 mmol), $CH_3OH$ (10 mL) and $H_2O$ (5 mL) was heated in a Teflon-lined autoclave at 150 °C for 3 d. After cooling to room temperature, colorless crystals of **9** were collected and washed with hexane. Yield: 0.280 g (85%). M.p. 298°C (dec.). $C_{41}H_{81}O_9S_4Sn_4$ (1320.5): calcd. C 37.30, H 6.11, S 9.72; found C 37.25, H 6.20, S 9.70. IR (KBr): $\tilde{\nu}$ = 3195 $cm^{-1}$ $\nu_{as}$(OH), 1625, 1555 $\nu_{as}$(COO), 1532, 1326 $\nu_s$(COO), 556 ν(Sn–C) 470 ν(Sn–O), 330 ν(Sn–S). $^1H$ NMR ($CD_3COCD_3$, $D_2O$): $\delta$ = 0.82–0.96 (t, $^3J_{H,H}$ = 7.0 Hz, 24 H, $CH_3$), 1.33–1.85 (m, 48 H, $CH_2CH_2CH_2$), 4.25 (s, 4 H, CH) ppm. $^{13}C$ NMR ($CD_3COCD_3$): $\delta$ = 13.8, 25.5, 26.2, 27.1, 52.4, 176.8 ppm. $^{119}Sn$ NMR ($CD_3COCD_3$): $\delta$ = –126.8, –170.5 ppm.

**X-ray Crystallography:** Crystals were mounted in Lindemann capillaries under nitrogen. All X-ray crystallographic data were collected with a Bruker SMART CCD 1000 diffractometer with graphite-monochromated Mo-$K_\alpha$ radiation ($\lambda$ = 0.71073 Å) at 298(2) K. A

Table 5. Crystallographic data for complexes **1**, **3**, **5**, and **9**.

| Complexes | **1** | **3** | **5** | **9** |
|---|---|---|---|---|
| Empirical formula | $C_{76}H_{62}O_4S_2Sn_4$ | $C_{16}H_{38}O_4S_2Sn_4$ | $C_{32}H_{38}O_8S_2Sn_2$ | $C_{41}H_{80}O_9S_4Sn_4$ |
| Formula mass | 1578.14 | 833.34 | 852.12 | 1320.05 |
| Crystal system | triclinic | monoclinic | triclinic | monoclinic |
| Space group | $P\bar{1}$ | *C*2/*c* | *Pna*2(1) | *Cc* |
| *a* [Å] | 11.027(2) | 18.556(3) | 9.431(2) | 23.733(9) |
| *b* [Å] | 12.329(3) | 13.3144(14) | 37.063(10) | 13.087(5) |
| *c* [Å] | 12.733(3) | 13.0162(14) | 13.337(4) | 18.598(7) |
| *a* [°] | 80.690(3) | 90 | 90 | 90 |
| *β* [°] | 86.406(3) | 105.2910(15) | 90 | 102.383(6) |
| *γ* [°] | 77.944(3) | 90 | 90 | 90 |
| Volume [Å$^3$] | 1669.7(6) | 3103.7(7) | 4662(2) | 5642(4) |
| *Z* | 1 | 4 | 4 | 4 |
| Absorption coefficient [$mm^{-1}$] | 1.590 | 3.330 | 1.196 | 1.941 |
| Crystal size [mm] | 0.42×0.35×0.19 | 0.51×0.43×0.17 | 0.31×0.27×0.12 | 0.19×0.15×0.12 |
| $D_{calcd.}$ [$g cm^{-3}$] | 1.569 | 1.809 | 1.214 | 1.554 |
| $\theta$ range for data collection [°] | 1.62–25.03 | 1.91–25.03 | 2.23–25.01 | 1.76–25.03 |
| Reflections collected | 8855 | 7895 | 23091 | 14550 |
| Unique reflections | 5842 ($R_{int}$ = 0.0196) | 2742 ($R_{int}$ = 0.0306) | 8071 ($R_{int}$ = 0.0794) | 7029 ($R_{int}$ = 0.0553) |
| Data/restraints/parameters | 5842/0/338 | 2742/0/118 | 8071/610/394 | 7029/141/516 |
| Final *R* indices [$I > 2\sigma(I)$] | $R_1$ = 0.0326, $wR_2$ = 0.0733 | $R_1$ = 0.0286, $wR_2$ = 0.0669 | $R_1$ = 0.0882, $wR_2$ = 0.2255 | $R_1$ = 0.0525, $wR_2$ = 0.1159 |
| *R* indices (all data) | $R_1$ = 0.0560, $wR_2$ = 0.0886 | $R_1$ = 0.0416, $wR_2$ = 0.0768 | $R_1$ = 0.1448, $wR_2$ = 0.2683 | $R_1$ = 0.1007, $wR_2$ = 0.1408 |

 © 2006 Wiley-VCH Verlag GmbH & Co. KGaA, Weinheim 

semiempirical absorption correction was applied to the data. The structures were solved by direct methods using SHELXS-97 and refined against $F^2$ by full-matrix least squares using SHELXL-97. Non-hydrogen atoms were refined anisotropically, while hydrogen atoms were placed in geometrically calculated positions using a riding model. Crystal data and experimental details of the structure determinations are listed in Table 5. The molecular and supramolecular structures in this paper were created with the X-Seed software package.[35] CCDC-238964 (**1**), -254168 (**3**), -254166 (**5**), and -254171 (**9**) contain the supplementary crystallographic data for this paper. These data can be obtained free of charge from The Cambridge Crystallographic Data Center via www.ccdc.cam.ac.uk/data_request/cif.

**Supporting Information** (see footnote on the first page of this article): Supromolecular structures of complexes **1**, **3**, **5**, and **9** (Figures S1–S4).

## Acknowledgments

The authors thank the National Natural Science Foundation of China (20271025) for financial support.

[1] a) J.-M. Lehn, *Science* **2002**, *295*, 2400–2403; b) J.-M. Lehn, *Supramolecular Chemistry: Concepts and Perspectives*, VCH, Weinheim, **1995**; c) J.-M. Lehn, *Angew. Chem. Int. Ed. Engl.* **1988**, *27*, 89–112; d) S. Subramanian, M. J. Zaworotko, *Coord. Chem. Rev.* **1994**, *137*, 357–401; e) C. B. Aakeroy, K. R. Seddon, *Chem. Soc. Rev.* **1993**, *22*, 397–407; f) A. D. Burrows, C.-W. Chan, M. M. Chowdhry, J. E. McGrady, D. M. P. Mingos, *Chem. Soc. Rev.* **1995**, *24*, 329–339; g) M. Munakata, L. P. Wu, T. Kuroda-Sowa, *Bull. Chem. Soc. Jpn.* **1997**, *70*, 1727–1743.

[2] a) G. J. Halder, C. J. Kepert, B. Moubaraki, K. S. Murry, J. D. Cashion, *Science* **2002**, *298*, 1762–1765; b) P. J. Hagrman, D. Hagrman, J. Zubieta, *Angew. Chem. Int. Ed.* **1999**, *38*, 2638–2684; c) A. J. Blake, N. R. Champness, P. Hubberstey, W. S. Li, M. A. Withersby, M. Schröder, *Coord. Chem. Rev.* **1999**, *183*, 117–138; d) B. Moulton, M. J. Zaworotko, *Chem. Rev.* **2001**, *101*, 1629–1658; e) O. R. Evans, W. Lin, *Acc. Chem. Res.* **2002**, *35*, 511–522; f) E. Lee, J. Heo, K. Kim, *Angew. Chem. Int. Ed.* **2000**, *39*, 2699–2701; g) A. Galet, M. C. Munoz, J. A. Real, *J. Am. Chem. Soc.* **2003**, *125*, 14224–14225; h) T. J. Prior, D. Bradshaw, S. J. Teat, M. J. Rosseinsky, *Chem. Commun.* **2003**, 500–501.

[3] a) S. Kitagawa, R. Kitaura, *Comments Inorg. Chem.* **2002**, *23*, 101–126; b) M. L. Tong, B. H. Ye, J. W. Cai, X. M. Chen, S. W. Ng, *Inorg. Chem.* **1998**, *37*, 2645–2650; c) S. S. Y. Chui, S. M. F. Lo, J. P. H. Charmant, A. G. Orpen, I. D. Williams, *Science* **1999**, *283*, 1148–1150; d) M. Eddaoudi, H. L. Li, O. M. Yaghi, *J. Am. Chem. Soc.* **2000**, *122*, 1391–1397; e) V. C. Slagt, J. N. H. Reek, P. C. J. Kamer, P. W. N. M. van Leeuwen, *Angew. Chem. Int. Ed.* **2001**, *40*, 4271–4274; f) D. de Groot, B. F. M. de Waal, J. N. H. Reek, A. P. H. J. Schenning, P. C. J. Kamer, E. W. Meijer, P. W. N. M. van Leeuwen, *J. Am. Chem. Soc.* **2001**, *123*, 8453–8458.

[4] a) G. R. Desiraju, *Acc. Chem. Res.* **2002**, *35*, 565–573; b) E. A. Meyer, R. K. Castellano, F. Diederich, *Angew. Chem. Int. Ed.* **2003**, *42*, 1210–1250; c) M. Munakata, L. P. Wu, M. Yamamoto, T. Kuroda-Sowa, M. Maekawa, *J. Am. Chem. Soc.* **1996**, *118*, 3117–3124; d) M. M. Chowdhry, D. M. P. Mingos, A. J. P. White, D. J. Williams, *Chem. Commun.* **1996**, 899–900; e) S. Kawata, S. R. Breeze, S. Wang, J. E. Greedan, N. P. Raju, *Chem. Commun.* **1997**, 717–718; f) A. Neels, B. M. Neels, H. Stoeckli-Evans, A. Clearfield, D. M. Poojary, *Inorg. Chem.* **1997**, *36*, 3402–3409.

[5] a) G. A. Jeffrey, *An Introduction to Hydrogen Bonding*, Oxford University Press, New York, **1997**; b) S. Tsuzuki, K. Honda, T. Uchimar, M. Mikami, K. Tanabe, *J. Am. Chem. Soc.* **2000**, *122*, 3746–3753; c) M. Nishio, M. Hirota, Y. Umezawa, *The CH/π Interaction: Evidence, Nature and Consequences*, Wiley, New York, **1998**; d) J. Dai, M. Yamamoto, T. Kuroda-Sowa, M. Maekawa, Y. Suenaga, M. Munakata, *Inorg. Chem.* **1997**, *36*, 2688–2690; e) M. Munakata, J. Dai, M. Maekwaw, T. Kuroda-Sowa, J. Fukui, *J. Chem. Soc., Chem. Commun.* **1994**, 2331–2332; f) T. Kuroda-Sowa, M. Munakata, H. Matsuda, S. Akiyama, M. Maekawa, *J. Chem. Soc., Dalton Trans.* **1995**, 2201–2208; g) M. Nishio, *Cryst. Eng. Commun.* **2004**, *6*, 130–158.

[6] I. Haiduc, F. T. Edelmann, *Supramolecular Organometallic Chemistry*, Wiley-VCH, Weinheim, **1999**.

[7] a) J. Lu, W. T. A. Harrison, A. J. Jacobson, *Angew. Chem. Int. Ed. Engl.* **1995**, *34*, 2557–2559; b) D. C. Apperley, N. A. Davies, R. K. Harris, A. K. Brimah, S. Eller, R. D. Fischer, *Organometallics* **1990**, *9*, 2672–2676; c) M. Hill, M. F. Mahon, J. McGinley, K. C. Molly, *J. Chem. Soc., Dalton Trans.* **1996**, 835–845; d) L. Balázs, H. J. Breunig, E. Lork, C. I. Ra, *Appl. Organomet. Chem.* **2005**, *19*, 1263–1267; e) C. Zucchi, S. Tiddia, R. Boese, C. M. Tschoerner, L. Bencze, G. Pályi, *Chirality* **2001**, *13*, 458–464; f) J. S. Casas, E. E. Castellano, J. Ellena, M. S. García-Tasende, A. Sánchez, J. Sordo, A. Touceda, *Z. Anorg. Allg. Chem.* **2005**, *631*, 2247–2252; g) Z. W. Gao, C. Y. Zhang, M. Y. Dong, L. X. Gao, G. F. Zhang, Z. T. Liu, G. F. Wang, D. H. Wu, *Appl. Organomet. Chem.* **2006**, *20*, 117–124.

[8] a) R. García-Zarracino, H. Höpfl, *Angew. Chem. Int. Ed.* **2004**, *43*, 1507–1511; b) R. García-Zarracino, H. Höpfl, *J. Am. Chem. Soc.* **2005**, *127*, 3120–3130; c) R. García-Zarracino, J. Ramos-Quiñones, H. Höpfl, *Inorg. Chem.* **2003**, *42*, 3835–3845; d) A. Goodger, M. Hill, M. F. Mahon, J. McGinley, K. C. Molly, *J. Chem. Soc., Dalton Trans.* **1996**, 847–852; e) F. Huber, B. Mundus-Glowacki, H. Preut, *J. Organomet. Chem.* **1989**, *365*, 111–121.

[9] a) C. L. Ma, Q. F. Zhang, R. F. Zhang, D. Q. Wang, *Chem. Eur. J.* **2006**, *12*, 420–428; b) C. L. Ma, Y. F. Han, R. F. Zhang, D. Q. Wang, *Eur. J. Inorg. Chem.* **2005**, 3024–3033.

[10] a) O. Lentzen, C. Moucheron, A. Kirsch-De Mesmaeker, *Metallotherapeutic Drugs and Metal-Based Diagnostic Agents*, Wiley, New York, **2005**; b) L. Pellerit, L. Nagy, *Coord. Chem. Rev.* **2002**, *224*, 111–150; c) M. Gielen, *Coord. Chem. Rev.* **1996**, *151*, 41–51; d) M. Nath, S. Pokharia, R. Yadav, *Coord. Chem. Rev.* **2001**, *215*, 99–149; e) *Tin-Based Antitumor Drugs*. NATO ASI series, vol. H37 (Ed.: M. Gielen), Springer, Berlin, **1990**; f) A. K. Saxena, F. Huber, *Coord. Chem. Rev.* **1989**, *95*, 109–123; g) M. Gielen, *Appl. Organomet. Chem.* **2002**, *16*, 481–494.

[11] a) H. V. Aposhian, *Ann. Rev. Pharmacol. Toxicol.* **1983**, *23*, 193–215; b) G. Winneke, U. Kramer, *Cent. Eur. J. Public Health* **1997**, *5*, 65–69; c) A. Jokstad, *Community Dent. Oral Epidemiol.* **1990**, *18*, 143–148; d) F. Schweinsberg, *Toxicol. Lett.* **1994**, *72*, 345–351.

[12] a) J. Singh, A. K. Powell, S. E. M. Clarke, P. J. Blower, *J. Chem. Soc., Chem. Commun.* **1991**, 1115–1117; b) G. J. Pyrka, N. Scott, Q. Fernando, *Acta Crystallogr., Sect. C* **1992**, *48*, 2007–2009.

[13] T. A. George, *J. Organomet. Chem.* **1971**, *31*, 233–238.

[14] J. R. May, W. R. McWhinnie, R. C. Poller, *Spectrochim. Acta A* **1971**, *27*, 969–974.

[15] K. Chandra, R. K. Sharma, B. S. Garg, R. P. Singh, *J. Inorg. Nucl. Chem.* **1980**, *42*, 187–193.

[16] G. Socrates, *Infrared Characteristic Group Frequencies*, Wiley-VCH, Weinheim, **1980**.

[17] a) J. Holeček, M. Nádvorník, K. Handlíř, A. Lyčka, *J. Organomet. Chem.* **1983**, *241*, 177–184.

[18] P. Álvarez-Boo, J. S. Casas, M. D. Couce, R. Farto, V. Fernández-Moreira, E. Freijanes, J. Sordo, E. Vázquez-López, *J. Organomet. Chem.* **2006**, *691*, 45–52.

[19] a) P. G. Harrison, K. Lambert, T. J. King, B. Majee, *J. Chem. Soc., Dalton Trans.* **1983**, 363–369; b) R. G. Swisher, J. F. Vollano, V. Chandrasekhar, R. O. Day, R. R. Holmes, *Inorg. Chem.* **1984**, *23*, 3147–3152.

 © 2006 Wiley-VCH Verlag GmbH & Co. KGaA, Weinheim 

[20] a) A. Kalsoom, M. Mazhar, S. Ali, M. F. Mahon, K. C. Molloy, M. I. Chaudry, *Appl. Organomet. Chem.* **1997**, *11*, 47–55; b) C. L. Ma, Q. F. Zhang, R. F. Zhang, D. Q. Wang, *J. Organomet. Chem.* **2005**, *690*, 3033–3043.
[21] a) K. C. Molloy, T. G. Purcell, K. Quill, I. W. Nowell, *J. Organomet. Chem.* **1984**, *267*, 237–247; b) A. R. Forrester, S. J. Garden, R. A. Howie, J. L. Wardell, *J. Chem. Soc., Dalton Trans.* **1992**, 2615–2621.
[22] R. Taylor, O. Kennard, *J. Am. Chem. Soc.* **1982**, *104*, 5063–5070.
[23] K. Jitsukawa, K. Iwai, H. Masuda, H. Ogoshi, H. Einaga, *J. Chem. Soc., Dalton Trans.* **1997**, 3691–3698.
[24] a) S. W. Ng, V. G. K. Das, G. Pelizzi, F. Vitali, *Heteroat. Chem.* **1990**, *1*, 433–438; b) M. Gielen, A. E. Khloufi, M. Biesemans, F. Kayser, R. Willem, *Organometallics* **1994**, *13*, 2849–2854.
[25] V. Berceanc, C. Crainic, I. Haiduc, M. F. Mahon, K. C. Molloy, M. M. Venter, P. J. Wilson, *J. Chem. Soc., Dalton Trans.* **2002**, 1036–1045.
[26] G. Y. Zhong, Q. F. Liu, X. Q. Song, G. Eng, Q. L. Xie, *J. Organomet. Chem.* **2005**, *690*, 3405–3409.
[27] a) A. M. Domingos, G. M. Sheldrick, *J. Chem. Soc., Dalton Trans.* **1974**, 477–480; b) R. E. Drew, F. W. B. Einstein, *Acta Crystallogr., Sect. B* **1972**, *28*, 345–350.
[28] For simplicity, pSn1, pSn2, pSn3, and pSn4 represent the five-membered SnSCCO chelate metallacycles that contain Sn1, Sn2, Sn3, and Sn4, respectively.
[29] a) J. F. Vollano, R. O. Day, R. R. Holmes, *Organometallics* **1984**, *3*, 750–755; b) T. P. Lockhart, *Organometallics* **1988**, *7*, 1438–1443; c) S. W. Ng, V. G. K. Das, G. Yap, A. L. Rheingold, *Acta Crystallogr., Sect. C* **1996**, *52*, 1369–1371.
[30] A. L. Spek, *PLATON – A Multipurpose Crystallographic Tool*, Utrecht University, The Netherlands, **2000**.
[31] E. Tynan, P. Jensen, P. E. Kruger, A. C. Lees, *Chem. Commun.* **2004**, 776–777.
[32] L. Carlucci, G. Ciani, D. M. Proserpio, *Chem. Commun.* **2004**, 380–381.
[33] K. Sisido, Y. Takeda, Z. Kinugawa, *J. Am. Chem. Soc.* **1961**, *83*, 538–541.
[34] M. Mehring, M. Schürmann, I. Paulus, D. Horn, K. Jurkschat, A. Orita, J. Otera, D. Dakternieks, A. Duthie, *J. Organomet. Chem.* **1999**, *574*, 176–192.
[35] a) L. J. Barbour, *J. Supramol. Chem.* **2001**, *1*, 189–191; b) J. L. Atwood, L. J. Barbour, *Cryst. Growth Des.* **2003**, *3*, 3–8.

Received: February 27, 2006
Published Online: June 21, 2006

 © 2006 Wiley-VCH Verlag GmbH & Co. KGaA, Weinheim 

DOI: 10.1002/ejic.200600223

# Metal Atom Vibrational Amplitudes in Decamethylferrocene and Related Organometallics

**Rolfe H. Herber,*[a] Israel Nowik,[a] Volker Kahlenberg,[b] Holger Kopacka,[c] and Herwig Schottenberger[c]**

**Keywords:** Sandwich complexes / Iron / Vibrational amplitudes / Mössbauer spectroscopy / Isotopic enrichment

Recent experiments have shown that root-mean-square amplitudes-of-vibration (rmsav) for iron atoms in organometallic complexes at various temperatures can be extracted from temperature-dependent $^{57}$Fe Mössbauer spectroscopic data related to the recoil-free fraction of the metal atom. The applicability of this procedure has been validated by comparison with rmsav data extracted from $U_{ij}$ values obtained from single-crystal X-ray diffraction parameters at various temperatures. This analysis has been applied in detail to a study of decamethylferrocene (DMFc), for which the agreement between the rmsav values derived from the two experimental procedures is compared in the present study. A comparison of these rmsav values for a number of related structures is also reported over a similar temperature range. An improved method for the quantitative preparation of isotopically enriched DMFc is described.
(© Wiley-VCH Verlag GmbH & Co. KGaA, 69451 Weinheim, Germany, 2006)

## Introduction

In a number of recent publications from this laboratory (HU),[1–4] it has been shown that temperature-dependent $^{57}$Fe Mössbauer effect spectroscopy (ME) can serve to elucidate the root-mean-square-amplitude-of-vibration (rmsav) of the metal atom in ferrocene-type organometallics. While such studies have led to reasonably self-consistent values for this parameter, detailed validation has only been accomplished in the case of the parent ferrocene, for which single-crystal X-ray data are available at a number of different temperatures. However, in the case of ferrocene, not only are the details of the molecular structure and arrangement complicated by the existence of a number of different crystallographic forms, but the particular crystallographic form assumed at a given temperature depends on the thermal history of the sample.[5] References to these reported X-ray data have been reported earlier.[4]

To place the inference concerning the iron atom rmsav in iron organometallics on a more reliable basis, in the present study both the X-ray structure and the detailed ME parameters of decamethylferrocene (DMFc) have been determined at a number of different temperatures, thus allowing a comparison of the values obtained by the two techniques.

[a] Racah Institute of Physics, Hebrew University of Jerusalem, 91904 Jerusalem, Israel
E-mail: Herber@vms.huji.ac.il
[b] Institut für Mineralogie/Petrographie, Universität Innsbruck, Innrain 52, 6020, Innsbruck, Austria
[c] Institut für Anorganische Chemie, Universität Innsbruck, Innrain 52a, 6020, Innsbruck, Austria

There have been a number of X-ray studies of DMFc reported in the literature, but the early work of Struchkov et al.[6] has been re-examined by Raymond et al.[7] and in neither case are the thermal parameters of the metal atom extractable from the available data. In the present study, single-crystal X-ray diffraction data for DMFc (**1**) have been acquired at 123, 173, 232, and 298 K and the rmsav data calculated from the corresponding anisotropic displacement parameters $U_{ij}$ are compared to detailed ME spectroscopic results over the range $88 < T < 385$ K. In addition, lattice dynamical parameters have been extracted from ME data for $DMFc^{+}BF_4^{-}$ (**2**), the co-crystalline solid-state adduct (intercalate) of $C_{60}$ and DMFc reported by Stanghellini et al.[8] (**3**), and the mononuclear bucky ferrocene $CpFe(CH_3)_5C_{60}$ reported by Nakamura and Matsuo et al.[9] (**4**). The details of the rmsav data for the metal atom in these structurally related complexes are described in detail in the present study.

## Results and Discussion

A representative ME spectrum of **1** at 298 K is shown in Figure 1. It consists of a single quadrupole doublet with a line width (*fwhm*) of $0.243 \pm 0.005$ mm s$^{-1}$ at room temperature. The resonance effect under these conditions is about 2.8%, and the data were treated with the "thin absorber" approximation. The hyperfine parameters [isomer shift (IS) and quadrupole splitting (QS)] for **1** have been reported earlier.[10] The area ratio of the two components of the doublet spectrum are essentially temperature independent over the range $90 < T < 370$ K, thus indicating no appreciable anisotropy in the metal atom motion parallel and perpendicu-

 © 2006 Wiley-VCH Verlag GmbH & Co. KGaA, Weinheim 

lar to the symmetry axis passing through the two five-membered rings and the Fe atom. This is in contrast to the observations made in the case of the parent ferrocene,[3,4] in which this anisotropy is significant over a similar temperature range.

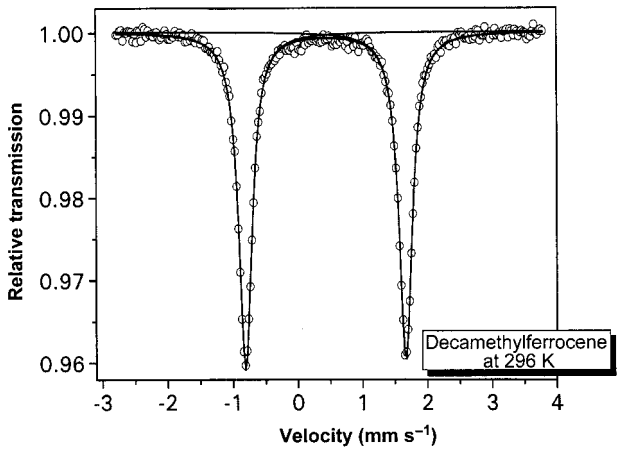


Figure 1. $^{57}$Fe Mössbauer spectrum of decamethylferrocene (**1**) at room temperature. The velocity scale is with respect to the centroid of an α-Fe absorber spectrum at room temperature.

The recoil-free fraction scales with the area ($A$) under the resonance curve in the "thin absorber" approximation; that is $\ln[A(T)/A(\mathrm{r})]$ [where $A(T)$ is the area under the resonance curve at temperature $T$, and $A(\mathrm{r})$ is a reference temperature] scales with $\ln f$. The recoil-free fraction, $f$, in turn, is given by

$$f = \exp(-k^2 \langle x_{ave}^2 \rangle)$$

where $k$ is the wave vector of the ME gamma ray (7.3039 Å$^{-1}$) and $\langle x_{ave}^2 \rangle$ is the mean square amplitude of the metal atom motion. It follows that an estimate of the msav can be extracted from the temperature-dependent spectral area values extracted from the ME data. The temperature dependence of the logarithm of the area under the resonance curve is summarized graphically in Figure 2. It is immediately obvious from these data that there is significant curvature in this dependence, especially at higher temperatures (i.e. above about 300 K), in contrast to what is usually observed in organometallic solids. Moreover, the highest temperature at which reliable ME data can be acquired is approximately 385 K, which is some 165 K below the melting point of this compound. It may be postulated that the onset of ring rotation at higher temperatures, which increases the metal–ring distances, increases the rmsav of the iron atom to the point where the ME is no longer observable. However, this assumption has been questioned on the basis of a density of states (DOS) study at 25 K, carried out at ESRF by Chumakov and van Buerck.[11] This study showed that the DOS is almost completely defined by the data within the first 9 meV and that at higher temperatures (above 100 K) all these modes are effectively populated. However, their DOS data do not directly elucidate the reason for the non-linearity referred to above except to indicate that an additional effect sets in at higher temperatures. Moreover, the X-ray data in the range $123 \leq T \leq 298$ K show that the distance from the metal atom to the centers of the five-membered rings increases by only 0.45% with increasing temperature. Extrapolation of the linear low-temperature dependence of $-\ln[A(T)]$ to 298 K shows that this extrapolation gives a value some 10% smaller than what is observed experimentally. Thus, the decrease in $f$ is not well accounted for by the onset of ring-rotation, and this dynamic may not be solely responsible for the non-linearity in the $\ln A(T)$ vs. $T$ data summarized in the figure. A "softening" of the lattice (as probed by the Fe ion) well below $T_{mp}$ must be accounted for by another mechanism. Differential scanning calorimetry data by Kobayashi et al.[12] have shown the existence of two solid phase transitions at $397 \pm 1$ and $501 \pm 2$ K involving uniaxial reorientation of the whole molecule about its $C_5$ axis. NMR spectroscopic data by Waugh et al.[13] and Pines et al.[14] have been interpreted in terms of a $2\pi/5$ jump process involving an energy barrier of about 143 and 140 meV, respectively, but these processes would not be significant in the solid in the low-temperature regime. The barrier to internal rotation for the gas-phase molecule has been reported[7b] to be 43.4 meV.

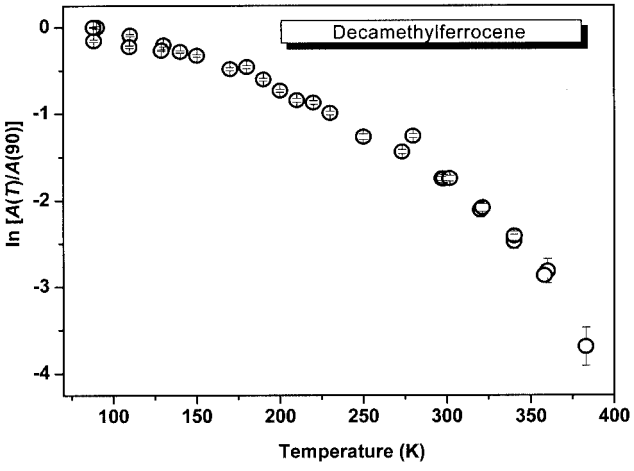


Figure 2. Temperature dependence of $\ln[A(T)/\mathrm{A}(90)]$ for **1**. The low-temperature data were obtained with a natural abundance $^{n}$Fe sample and were fitted using the optically "thin" absorber approximation. The high-temperature data were acquired using an enriched $^{57}$Fe sample as discussed in the text.

The $\ln[A(T)]$ data have been scaled so that the low-temperature regime passes through (0,0) at $T = 0$ K. The resulting curve can be well fitted by a second-order polynomial function from which $\ln A$, and hence the msav of the metal atom, can be calculated at all temperatures. These values, in turn, can be compared to those extracted from the anisotropic displacement parameters of the single-crystal X-ray diffraction experiment, and are shown in Figure 3 by the filled data points. The agreement between these two sets of values, at least up to 298 K, appears to be quite satisfactory, and validates the interpretation of the Mössbauer data in terms of $\langle x_{ave}^2 \rangle$. A similar comparison for ferrocene, based on the data of Brock and Fu,[15] has been reported earlier.[3]

 © 2006 Wiley-VCH Verlag GmbH & Co. KGaA, Weinheim 

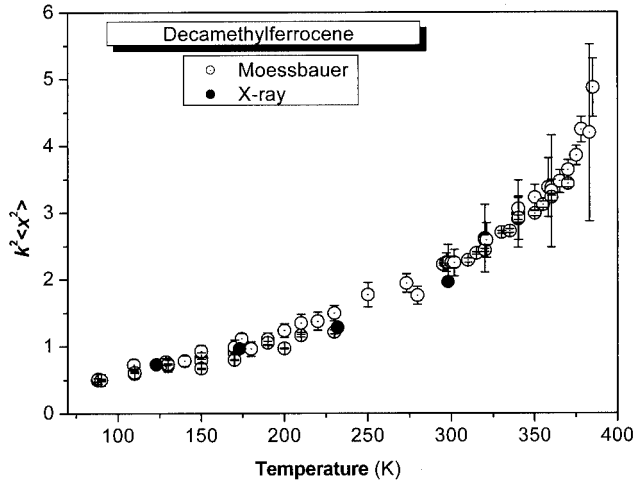


Figure 3. Temperature-dependence of the $k^2<x_{ave}^2>$ values for **1** extracted from the ME data (open circles) and from the single-crystal X-ray diffraction data (filled circles). The average errors in the X-ray values are ±0.00064, ±0.00112, ±0.0014, and ±0.00138 Å$^2$ at 298, 223, 173, and 123 K, respectively.

A summary of the rmsav of the metal atom in **1** at five different temperatures calculated from the X-ray data and the ME experiments is given in Table 1, which includes the comparable data for related systems to be discussed below. Thus, despite the uncertainty concerning the origin of the non-linearity in the ln$f$ vs. $T$ data shown in Figure 2, it is clear that the ME data can be used to estimate the rmsav of the metal atom in such organometallic solids.

Table 1. Root-mean-square amplitudes-of-vibration (rmsav; Å) of the iron atom in a number of structurally related organometallics discussed in the text.

| Ferrocene | **4** | **3** | **2** | DMFc (ME) | DMFc (X-ray) | Temp. [K] |
|---|---|---|---|---|---|---|
| 0.131 | 0.102 | 0.115 | 0.105 | 0.107 | 0.104 | 100 |
| 0.154 | 0.120 | 0.140 | 0.126 | 0.122 | 0.125 | 150 |
| 0.183 | 0.137 | 0.157 | 0.145 | 0.143 | 0.143 | 200 |
| 0.202 | 0.156 | 0.182 | 0.162 | 0.182 | 0.165 | 250 |
| 0.222 | 0.174 | 0.202 | 0.177 | 0.205 | 0.191 | 300 |

A molecular system closely related to the neutral species **1** is that obtained by one-electron oxidation of **1**, in which the cationic charge is balanced by the presence of either $BF_4^-$ or $PF_6^-$ anions. The ME spectra of the former compound, **2**, consist of a single broad resonance line which arises from spin-lattice relaxation of the paramagnetic metal site. The ME hyperfine parameters of **2** are listed in Table 2, and are similar to those of the corresponding $BF_4^-$ salt. It is, however, interesting to note that the ln[$A(T)$/$A$(90)] vs. $T$ data are well fitted by a linear regression over the temperature range 90 ≤ $T$ ≤ 360 K, in contrast to the data for **1** discussed above. The ln$A(T)$ data for **2** are shown graphically in Figure 4 (filled data points) together with those for **3** and **4** (to be discussed below). The rmsav data for **2** listed in Table 1 are very similar to those reported for **1** at a given temperature, except at 300 K, which is indicative of a similarity in the Fe–ligand interaction, especially in the lower temperature regime. Unfortunately, the relevant iron atom $U_{ij}$ data are not available in the literature, so no direct comparison with X-ray data for the cationic complex **2** can be effected at the present time.

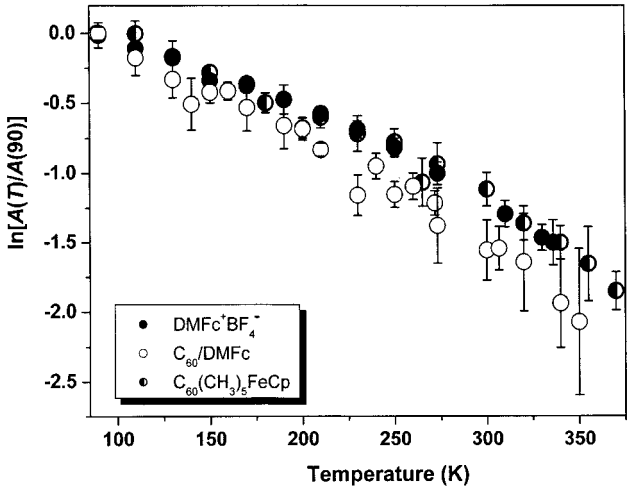


Figure 4. Temperature-dependence of the ln($A$) data (normalized to the 90 K value) for **2**, **3**, and **4**.

The data in Table 1 includes rmsav results obtained from ME experiments on the co-crystalline product $C_{60}$·DMFc (**3**) reported by Stanghellini et al.,[8] which is similar to the $C_{60}$ ferrocene intercalate reported by Crane et al.[16] for which the ME characterization has been reported from this laboratory.[17] The ME hyperfine parameters of **3** are included in Table 2. The $U_{ij}$ values for the iron atom in **3** have been determined at 150 K by Stanghellini et al.[8] and the calculated $k^2<x_{ave}^2>$ value of 1.10 is in good agreement with the ME extracted value of 1.02 at the same temperature. The remainder of the rmsav data for **3** listed in Table 1 are those derived from the ME data as described for **1** above. It is noted from these data that the rmsav of the metal atom in **3** is comparable to that in **1** at the same temperature, suggesting that this parameter reflects *intra*- rather than *inter*molecular forces. It is also worth noting

Table 2. Mössbauer effect (ME) hyperfine parameters at 90 K and related values for the compounds discussed in the text. The parenthetical number(s) are the errors associated with the last figure(s) for each entry.

| | IS(90) [mm s$^{-1}$] | QS(90) [mm s$^{-1}$] | –d(IS)/d$T$ [10$^{-4}$ mm s$^{-1}$ K$^{-1}$] | –d(ln A)/d$T$ [10$^{-3}$ K$^{-1}$] | $M_{eff}$ [Daltons] | $\Theta_M$ [K] |
|---|---|---|---|---|---|---|
| **1** | 0.492(3) | 2.473(2) | 3.17(13) | (curv.) | 131(3) | n.a. |
| **2** | 0.460(5) | 0.189(5) | 3.82(8) | 5.93(4) | 109(5) | 110(5) |
| **3** | 0.501(5) | 2.451(5) | 2.32(4) | 6.82(7) | 85(3) | 116(5) |
| **4** | 0.575(4) | 2.475(4) | 5.36(5) | 7.42(17) | 78(2) | 116(5) |

 © 2006 Wiley-VCH Verlag GmbH & Co. KGaA, Weinheim 

that the temperature dependence of the $\ln[A(T)/A(90)]$ data for **3** over the temperature range $89 \leq T \leq 350$ K are well accounted for by a linear regression (cc = 0.994 for 23 data points) so that the lattice "softening" observed in **1** is again absent in **3**. Since both the isomer shift and the recoil-free fraction data show a linear temperature-dependence over the total temperature range, it is possible to calculate[18] both an "effective vibrating mass" ($M_{eff}$) and a "Mössbauer lattice temperature" ($\Theta_M$) of 85 ± 3 D and 116 ± 5 K, respectively. Clearly, these data refer to the high-temperature limiting values, i.e. $T_{exp} > \Theta_M/2$. The difference between the calculated $M_{eff}$ (85 D) and the "bare" atom mass (57 D) reflects the covalency of the metal atom–ligand interaction, as discussed earlier.[19] The $[k^2<x^2>]^{1/2}$ values at five different temperatures, calculated from the $\ln A(T)$ data as noted above, and making the assumption that the high-temperature limiting slopes extrapolate to $f = 0$ as $T \rightarrow 0$, are summarized graphically in Figure 5.

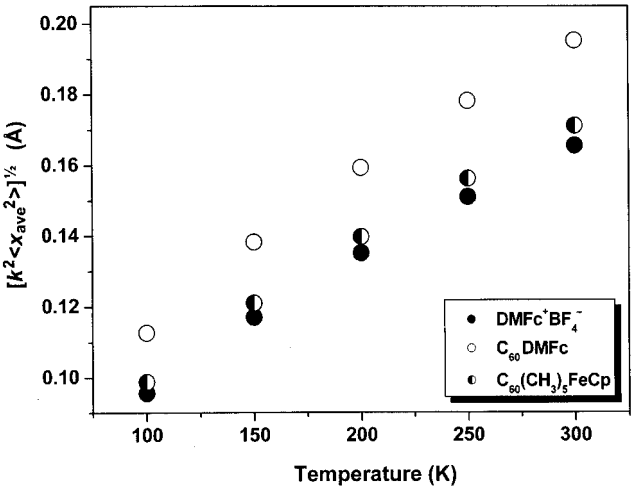


Figure 5. The $[k^2<x^2>]^{1/2}$ parameters for **2**, **3**, and **4** at five different temperatures calculated from the high temperature ($T > \Theta_M/2$) slopes of the data shown in Figure 4, as discussed in the text.

Finally, a related organometallic structure in which the iron atom is ligated to two five-membered rings and in which there are five methyl groups on the $C_{60}$ sphere, in near proximity to the metal center, is provided by the "bucky ferrocene" compound **4**, for which the details of the ME parameters have been reported earlier.[4] In this molecule the iron atom "sees" an unsubstituted Cp ring in one direction and a similar Cp ring in the opposite direction, with, however, five methyl groups attached to the next neighbor carbon atoms of the $C_{60}$ sphere. The ME hyperfine parameters and derived data are included in Table 1 and the rmsav values for the iron atom are listed in Table 2 and included in Figure 5. As in the case of **2** and **3**, the $\ln f$ vs. $T$ plot is linear over the temperature range $210 \leq T \leq 370$ K as already noted.[1] As indicated in Figure 5, the rmsav of the metal atom in **4** is very nearly identical to that in **1** and **3**. Presumably the massive fullerene moiety ligated to the Fe center plays no critical role in the magnitude of the rmsav of the metal atom in these complexes.

## Summary and Conclusions

An improved efficient synthesis of $^{57}$Fe-labeled decamethylferrocene ($^{57}$Fe DMFc) has been developed. The resulting product has been characterized by elemental and isotopic composition, single-crystal X-ray diffraction, and IR and NMR spectroscopic data. The availability of $^{57}$Fe DMFc, in turn, has made it possible to use temperature-dependent Mössbauer effect spectroscopy to elucidate the hyperfine interactions in this material at high temperatures, as well as the temperature-dependence of the recoil-free fraction of the metal atom. From these data it is possible to determine the mean-square-amplitude-of-vibration of the iron atom motion, and to compare these results with those extracted from single-crystal X-ray diffraction data. The agreement between these two data sets in the temperature range 80 to 300 K is quite satisfactory within the quoted experimental errors. The origin of the non-linearity observed in the recoil-free fraction data, as well as the vanishingly small value of this parameter at temperatures about 165 K below the melting point of DMFc is assumed to be due in part to the onset of ring rotation in the solid, but may have an additional contribution not well elucidated by the presently available data. The comparison of the Fe vibrational amplitude as a function of temperature for a number of structurally related ferrocene-type systems should lead to a clearer understanding of the relationship between the microscopic architecture and the dynamic behavior of the metal atom in these structures.

## Experimental Section

A commercial sample of **1** was recrystallized from trichloroethylene and used without further purification for the ME studies. A sample of $^{57}$Fe-enriched **1** was prepared as described below and used for acquiring data in the high-temperature regime ($T \geq 300$ K) where the recoil-free fraction values ($f$), which determine the area under the resonance curve, become so small that natural abundance samples would require inordinately long data acquisition times. Single crystal samples of **1** for the X-ray diffraction studies were grown as described below. A sample of **2** was prepared in the Innsbruck laboratory and used for Mössbauer studies as received. Complex **3** was similarly made available by Profs. Stanghellini and Viterbo and used as received. A sample of **4** was provided by Profs. Nakamura and Matsuo, and again used as received.

Temperature-dependent ME studies were carried out as described previously[1–5] and spectrometer calibration was effected using a 10.52 mg cm$^{-2}$ α-Fe foil at room temperature, which also served as the isomer-shift reference point. Temperature control was monitored using the DASWIN program of Glaberson and Brettschneider,[20] and confirmed that the indicated temperatures were constant to better than ±0.2 K over the data acquisition periods (typically 8–24 hours) at each temperature.

For the structural investigations of **1**, a rhomb-shaped crystal of good optical quality ($0.14 \times 0.14 \times 0.16$ mm$^3$ in size) was selected and mounted on a glass fiber. Data collections at four different temperatures were performed using graphite-monochromated Mo-$K_\alpha$ radiation on a Stoe IPDS-II diffractometer equipped with a 700 Series Oxford Cryostream nitrogen gas stream cooler. The mor-

 © 2006 Wiley-VCH Verlag GmbH & Co. KGaA, Weinheim 

phology of the crystals was described by external faces and an analytical absorption correction based on the indexed faces was applied. Further data reduction included Lorentz and polarization corrections. The subsequent least-squares refinements were accomplished with the program SHELX97.[21] The corresponding X-ray data for **3** have been reported in the literature.[8]

**Synthesis and Characterization of [$^{57}$Fe]Decamethylferrocene**

**Instrumentation:** Microwave reactor: Synthos 3000, Anton Paar GmbH, Austria; Kugelrohr apparatus: Buechi GKR-51, Switzerland. IR spectra were measured with a Nicolet 5700 FT-IR with an ATR diamond window, and $^{1}$H and $^{13}$C NMR spectra were recorded in $CDCl_3$ solution with a Bruker Avance DPX 300 spectrometer. All organometallic reactions were carried out under an inert atmosphere using standard Schlenk techniques. Solvents were distilled, dried, and deoxygenated prior to use. Starting compounds not specifically referred to are commercially available by several suppliers. Purchased chemicals were used without any further purification.

$^{57}$Fe-enriched iron powder (95%) was purchased from ATM, Advanced Materials Technologies. From this starting material, enriched $^{57}FeCl_2$ was prepared by oxidation with methanolic hydrogen chloride in a microwave reactor by the novel procedure described below. This synthesis is also a low-temperature preparation in solution,[22] but avoids the concomitant formation of chlorobutanol from HCl and THF, which is difficult to separate from methylated ferrocenes during workup. The $^{57}$Fe-labeled decamethylferrocene was then prepared from $^{57}FeCl_2$ by complexation with the $[CpMe_5]^-$ anion in analogy to the synthesis of [$^{57}$Fe]octamethylferrocene.[23] In contrast to octamethylferrocene, decamethylferrocene is very easily oxidized on silica and alumina-packed chromatography columns, which results in extremely reduced yields if any chromatographic purification is required. The elemental and isotopic composition of [$^{57}$Fe]decamethylferrocene was determined by means of HR mass spectrometry (Finnigan MAT 95). The exact monoisotopic molecular weight was measured using the following HR-FAB-MS conditions: Cs gun: 20 kV, 2 μA; glycerol matrix, resolution $R$ = 8000, E-scan, average over 20 scans. The determination of the $^{57}$Fe/$^{56}$Fe isotope ratio of the target compound gave a $^{57}$Fe content of >95.0%.

**Synthesis of Anhydrous $^{57}FeCl_2$:** $^{57}$Fe powder (35 mg, 0.62 mmol) was fixed on a magnetic stirring bar and placed in a Teflon-lined microwave reactor along with 6 mL of a 1.25 M solution of hydrochloric acid in methanol (6 mL required to immerse the internal temperature probe), whereupon a slight evolution of hydrogen was observable. The reaction mixture was heated to 150 °C within 1 min and held at this temperature for 50 min. Afterwards, it was cooled by the fan-device for 20 min. The liner was opened under a stream of nitrogen and the contents transferred to a Schlenk tube. The $^{57}$Fe powder was completely dissolved, although the yellowish coloration indicated the presence of iron(III) salts. Subsequently, the solvent and excess hydrogen chloride were stripped off on a vacuum line (oil pump) whilst heating to 40 °C in a water bath, and the crude iron chlorides triturated for 5 min with chlorotrimethylsilane (1 mL) in order to remove protic solvent residuals. The chlorotrimethylsilane was then pumped off whilst shaking the Schlenk tube in such a way that the crude iron chloride was deposited in a layer covering the lower part of the tube. Afterwards, the remainder was rinsed with hexamethyldisilane (1 mL) and evacuated again to yield an off-white material. Anhydrous THF (40 mL) was added to the Schlenk tube and the solution was stirred magnetically with an additional 5 mg of excess $^{57}$Fe powder adhered to the stirring bar to give a clear white solution of $FeCl_2$ within 2 min. The THF solution was cooled to –40 °C under nitrogen and used for the complexation step below.

**Synthesis of [$^{57}$Fe]Decamethylferrocene:** Anhydrous THF (60 mL) was placed in a second Schlenk tube and 1,2,3,4,5-pentamethyl-1,3-cyclopentadiene (0.95 mL, 170 mg, 1.26 mmol; Chem. Abstr. registry no. 4045-44-7) was added from a syringe. The solution was cooled to –40 °C under nitrogen and butyllithium (0.80 mL, 1.6 M in hexane) was added to give a yellowish cloudy suspension. After 30 min the external cooling bath was removed and the reaction mixture was warmed to 10 °C whilst stirring. Afterwards, the reaction mixture was again recooled to about –30 °C. The $^{57}FeCl_2$/THF solution obtained by the procedure described above was added with a cannula and the stirring bar holding the excess elemental iron powder was also transferred. The resulting reaction mixture gradually turned black. After 90 min, the cooling bath was removed and the reaction mixture was ultrasonicated for 30 min. The solvents were removed on the vacuum line and the remainder was partitioned between diethyl ether (30 mL) and water (40 mL) in a separating funnel. The aqueous layer was washed with diethyl ether (30 mL) and the combined organic phases again extracted with water (2 × 30 mL). The organic phase was dried with anhydrous sodium sulfate and filtered. Evaporation (rotary evaporator) and drying (oil pump) yielded 105 mg of crude decamethylferrocene as a yellow-orange powder (52% of theoretical yield based on $^{57}$Fe). Finally, the crude product was sublimed[24] in a Kugelrohr apparatus at 200 °C on a vacuum line. HR-MS calcd. for $C_{20}H_{30}{}^{57}Fe_1$ (DMFc): 327.1696; found 327.1705 (cation; rel. intensity 27.4); calcd. for $C_{19}{}^{13}CH_{30}{}^{57}Fe_1$ (DMFc): 328.1730; found 328.1699 (cation; rel. intensity 6.2). IR data (ATR): $\tilde{\nu}$ = 2962.5 cm$^{-1}$ s, 2943.2 m, 2891.5 s, 2851.7 m, 2712.0 w, 1473.4 m, 1448.0 m, 1424.2 m, 1371.9 s, 1353.0 w, 1259.3 m, 1068.8 s, 1024.6 vs, 867.5 w, 796.5 s, 698.7 ws, 589.4 w, 536.1 w, 507.2 w, 449.4 vs, 416.6 m. $^{1}$H NMR ($CDCl_3$): $\delta$ = 1.67 ppm (s, methyl-*H*). $^{13}$C NMR ($CDCl_3$): $\delta$ = 9.59, (methyl-*C*, $^{1}J_{C,H}$ = 125.4 Hz), 79.70 ppm (Cp-C). DMFc is only sparingly soluble in methanol; alternatively, suspending the crude material by ultrasonication then centrifuging the mixture allows removal of any organic impurities. Crystals suitable for X-ray structure determinations were grown by slow evaporation of the solvent from a solution in 2-methylbutane at ambient temperature. In order to recover any residual unreacted $^{57}$Fe material, the aqueous extracts containing precipitated iron(III) hydroxide (formed by oxidation with ambient oxygen during workup) were centrifuged. Iron(III) chloride may be reconverted to iron(II) chloride by dissolving the separated $Fe(OH)_3$ in methanolic hydrogen chloride and drying/reducing with trimethylchlorosilane/hexamethyldisilane as described above.

## Acknowledgments

The authors are indebted to Prof. H. Schottenberger both for the single crystals of **1** used in the acquisition of the X-ray data and also for providing the $^{57}$Fe-labeled samples used in the ME experiments. Similarly, we are grateful to Profs. Nakamura and Matsuo for providing a sample of **4** for study, and Profs. P. L. Stanghellini and D. Viterbo not only for providing the sample of **3** for the ME experiments but also for sharing the results of their X-ray investigation with us.

[1] R. H. Herber, I. Nowik, Y. Matsuo, M. Toganoh, Y. Kuninobu, E. Nakamura, *Inorg. Chem.* **2005**, *44*, 5629–5635.
[2] I. Nowik, M. Wagner, R. H. Herber, *J. Organomet. Chem.* **2003**, *688*, 11–14.

 © 2006 Wiley-VCH Verlag GmbH & Co. KGaA, Weinheim 

[3] R. H. Herber, I. Nowik, *Hyperfine Interact.* **2002**, *144*, 249–253.
[4] R. H. Herber, I. Nowik, *Hyperfine Interact.* **2001**, *136*, 699–703.
[5] R. H. Herber, I. Nowik, *Solid State Sci.* **2002**, *4*, 691–694 and references cited therein.
[6] Yu. T. Struchkov, V. G. Andrianov, T. N. Sal'nikova, I. R. Lyatifov, R. B. Materikove, *J. Organomet. Chem.* **1978**, *145*, 213–223.
[7] a) D. P. Freyberg, J. L. Robbins, K. N. Raymond, J. C. Smart, *J. Am. Chem. Soc.* **1979**, *101*, 892–897; b) A. Almenningen, A. Haaland, S. Samdal, J. C. Smart, *J. Organomet. Chem.* **1979**, *173*, 293–299.
[8] A. Arrais, E. Diana, R. Gobetta, M. Milanesio, D. Viterbo, P. L. Stanghellini, *Eur. J. Inorg. Chem.* **2003**, 1186–1192.
[9] M. Sawamura, Y. Kuninobu, M. Toganoh, Y. Matsuo, Y. Yamanaka, E. Nakamura, *J. Am. Chem. Soc.* **2002**, *124*, 9354–9355; Y. Matsuo, Y. Kuninobu, S. Ito, E. Nakamura, *Chem. Lett.* **2004**, 33 and references cited therein.
[10] R. H. Herber, in *Unusual Structures and Physical Properties in Organometallic Chemistry* (Eds. M. Gielen, R. Willem, B. Wrackmeyer), John Wiley & Sons, Chichester, UK, **2002**, pp. 210–211.
[11] A. Chumakov, U. van Buerke, private communication.
[12] T. Kobayashi, H. Ohki, R. Ikeda, *Mol. Cryst. Liq. Cryst. Sci. Technol., Sect. A* **1994**, *257*, 279.
[13] D. Suwelak, W. P. Rothwell, J. S. Waugh, *J. Chem. Phys.* **1980**, *73*, 2559–2569.
[14] D. E. Wemmer, D. J. Ruben, A. Pines, *J. Am. Chem. Soc.* **1981**, *103*, 28–33.
[15] C. P. Brock, Y. Fu, *Acta Crystallogr. Sect. B* **1997**, *53*, 928 (model *R*1ZH).
[16] J. D. Crane, P. B. Hitchcock, H. W. Kroto, R. Taylor, D. R. M. Walton, *J. Chem. Soc., Chem. Commun.* **1992**, 1764.
[17] P. P. R. Birkett, K. Kordatos, J. D. Crane, R. H. Herber, *J. Phys. Chem. B* **1997**, *101*, 8975–8978.
[18] R. H. Herber, in *Chemical Mossbauer Spectroscopy* (Ed.: R. H. Herber), Plenum Press, New York, **1984**, pp. 199–121.
[19] R. H. Herber, I. Nowik, D. A. Loginov, Z. A. Starikova, A. R. Kudinov, *Eur. J. Inorg. Chem.* **2004**, 3476–3483 and references cited therein.
[20] W. Glaberson, M. Brettschneider, see: www.phys.huji.ac.il/~glabersn.
[21] G. M. Sheldrick, *SHELX97 Program for Crystal Structure Analysis* (release 97-2), University of Göttingen, Germany, **1998**.
[22] M. Aresta, C. F. Nobile, D. Petruzelli, *Inorg. Chem.* **1977**, *16*, 1817.
[23] R. H. Herber, I. Nowik, H. Schottenberger, K. Wurst, N. Schuler, A. G. Mueller, *J. Organomet. Chem.* **2003**, *682*, 163; B. S. Özman, *Chem.-Ztg.* **1976**, *100*, 143.
[24] T. Kiyobayashi, M. E. Minas da Piedade, *J. Chem. Thermodyn.* **2001**, *33*, 11.

Received: March 12, 2006
Published Online: June 28, 2006

 © 2006 Wiley-VCH Verlag GmbH & Co. KGaA, Weinheim 

DOI: 10.1002/ejic.200600237

# Controlling the Size of $BaF_2$ Nanocubes from 1000 to 10 nm

Peng Gao,[a] Yi Xie,*[a] and Zhen Li[a]

**Keywords:** $BaF_2$ Nanocubes / Nanostructures / Electron diffraction / X-ray diffraction

Size control of $BaF_2$ nanocubes has been achieved by varying reaction time and pH value, thus producing nanocubes with a controllable edge length in the range 10–1000 nm. A linear relationship between cube size and reaction time has been revealed. Furthermore, a process has been developed to separate the growing $BaF_2$ nanocubes from the remaining solid products at different stages of the synthesis. On the basis of the observed crystallite morphologies, we have elucidated an "extension growing" mechanism to describe the size-controlled growth of $BaF_2$ nanocubes using this method. Photoluminescence results demonstrate that the deoxidant selenite ions prevent the incorporation of oxygen into the $BaF_2$ nanocubes effectually, which will greatly affect their performance as scintillators.
(© Wiley-VCH Verlag GmbH & Co. KGaA, 69451 Weinheim, Germany, 2006)

## Introduction

Solid inorganic fluorides have a number of uncommon properties, for example, electron-acceptor behavior, a large optical-transmission domain, high resistivity, and anionic conductivity. Inorganic nanoscale fluorides and rare-earth-doped inorganic nanoscale fluorides have attracted much interest recently because of their unique properties,[1] such as optical, electrical, and magnetic, which result from the size and shape of their particles.[2] Barium fluoride is one of the dielectric fluorides (along with $CaF_2$ and $SrF_2$) that have a wide range of potential applications in microelectronic and optoelectronic devices, such as wide-gap insulating overlayers, gate dielectrics, insulators, and buffer layers in semiconductor-on-insulator structures and more advanced 3D devices.[3] $BaF_2$ salts activated with rare-earth ions have also been reported to display unique luminescence properties and can be used as scintillators.[4] Recently, $BaF_2$ nanowires and nanocubes with arching sheet-like dendrites have been prepared in quaternary microemulsions and reverse micelles, respectively.[5] Li et al. have reported the preparation of $CaF_2$ nanocubes by a hydrothermal method in the absence of surfactants.[6] Monodispersed noble-metal and $Cu_2O$ nanocubes[7] have also been synthesized by controlled oxidation–reduction reactions. However, to the best of our knowledge, there have been no reports on large-scale preparations of $BaF_2$ nanocubes to date. Therefore, the development of simple methods for the synthesis on a large scale is a challenge. It was reported that oxygen may be incorporated into $BaF_2$ as oxygen–vacancy pairs and detrimentally affect the performance of the resulting nanocubes as scintillators,[8] thus avoiding the incorporation of oxygen into the products will be necessary in industry. We have synthesized single-crystalline $BaF_2$ nanocubes through a simple hydrothermal precipitation procedure in the presence of selenite ions, which act as deoxidants and prevent the incorporation of oxygen effectively. The morphology and size of the final products can be manipulated through controlling the synthesis parameters such as reaction time and pH value.

## Results and Discussions

### Structural and Compositional Analysis

Figure 1 shows a representative XRD pattern of samples prepared with this approach, which indicates that all the products are phase-pure crystalline $BaF_2$ [in cubic symmetry; space group (SG) *Fm*3*m*, lattice constant *a* =

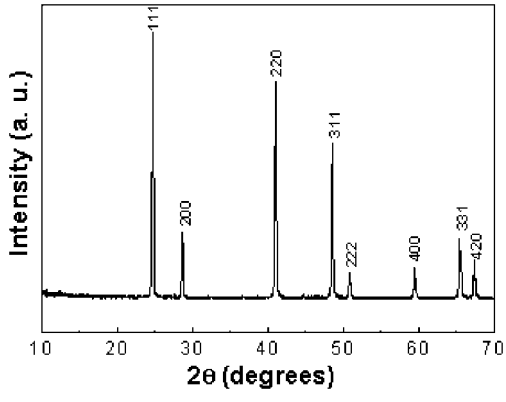


Figure 1. Powder XRD pattern of single-crystalline $BaF_2$ nanocubes with an edge length of 55 nm.

[a] Nano-materials and Nano-chemistry, Hefei National Laboratory for Physical Sciences at Microscale, University of Science & Technology of China,
Hefei, Anhui 230026, P. R. China
Fax: +86-551-3603987
E-mail: yxielab@ustc.edu.cn

 © 2006 Wiley-VCH Verlag GmbH & Co. KGaA, Weinheim 

6.19 ± 0.01 Å].[9] No other impurities have been found in the synthesized products.

Further evidence for the quality and composition of the samples was obtained by X-ray photoemission spectroscopy (XPS) of the products. An XPS measurement of the crystals shows peaks corresponding to Ba, F, O, and C (Figure 2), which agrees with results previously reported in the literature.[10] The oxygen detected in the XPS measurement may come from the atmosphere. Furthermore, low amounts of oxygen (about two percent) are frequently observed in XPS spectra. Both the results of the XRD and XPS studies leave no doubt that the product is $BaF_2$.

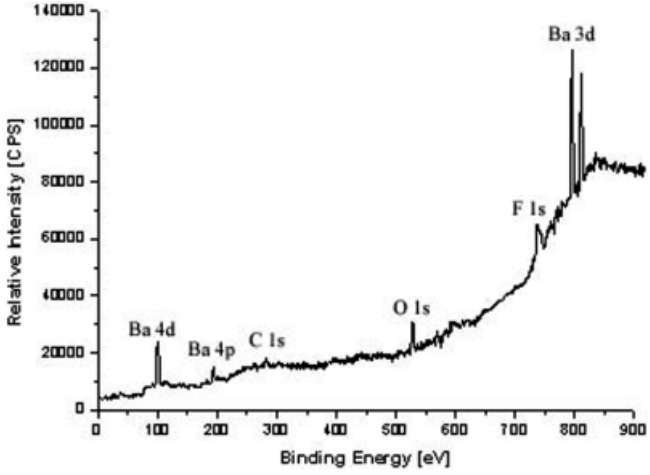


Figure 2. XPS spectrum of the $BaF_2$ nanocubes with an edge length of 55 nm.

### Morphology of the $BaF_2$ Nanocubes

As shown in Figure 3a, the $BaF_2$ products described above have perfect cubic morphology. It is also clear that more than 95% of the $BaF_2$ particles have a regular cubelike structure with a mean edge length of 55 nm. The excellent crystallinity of the $BaF_2$ nanocubes is also confirmed by an electron diffraction (ED) experiment. Figure 3c shows a spot pattern from a single-crystalline $BaF_2$ nanocube (Figure 3b). In this case, the electron beam is incident along the [001] direction, and the spot array has a fourfold axis that can be indexed with *hk*0 (i.e. [001] zone spots, in accordance with the extinction rule of electron diffraction for the space group *Fm*3*m*), which indicates cubic symmetry for the $BaF_2$ nanocubes. Figure 3d shows a typical FESEM image of the $BaF_2$ nanocubes. The inset shows a FESEM image at higher magnification that clearly displays the sharp corners and edges of these nanocubes. All these observations confirm that the particles are indeed cubelike. Moreover, the nanocubes obtained from this approach are very uniform in size.

### Size-Controlled Growths

In this work, size control of $BaF_2$ nanocubes has been achieved by varying the reaction time and adjusting the pH, and this produces $BaF_2$ nanocubes with a controllable edge length in the range 10–1000 nm.

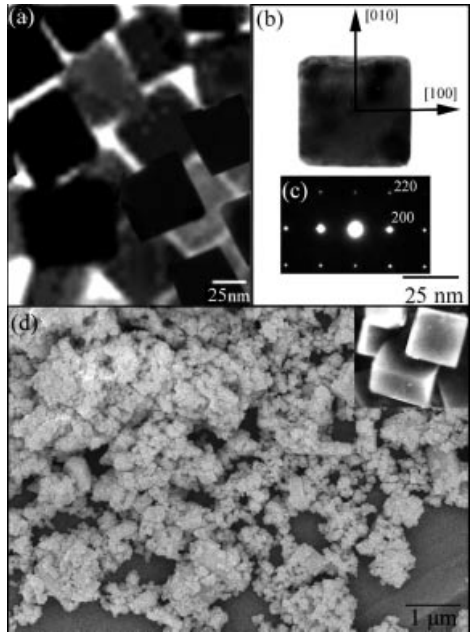


Figure 3. (a) TEM image of the $BaF_2$ nanocubes (pH = 2, 0.002 mol $SeO_2$ for 24 h). (b) TEM image of one $BaF_2$ single-crystalline nanocube. (c) Electron diffraction pattern of the nanocube in (b). (d) Typical FESEM images of the as-synthesized $BaF_2$ nanocubes. The inset shows a magnified FESEM image that illustrates the sharp corners and edges of these nanocubes.

With a simple variation in the reaction time (or ageing time), the size of these nanocubes can be controlled easily. In fact, we have obtained nanocubes as small as 10 nm (average edge length) with an ageing time of 3 h, as reported in Figure 4 and Figure 5a. After a reaction time of only 3 h, these $BaF_2$ nanoparticles started to show cubic type morphology, although they are not as well-faceted as samples obtained with longer ageing times. In principle, it is possible to capture even smaller particles by drawing samples at ageing times shorter than 3 h. However, the extremely low yield makes it impractical to do so. Nonetheless, the possibility of synthesizing even smaller (a few nanometers) and yet uniform nanocubic $BaF_2$ is positively indicated. With ageing times of 12 and 24 h (as shown in

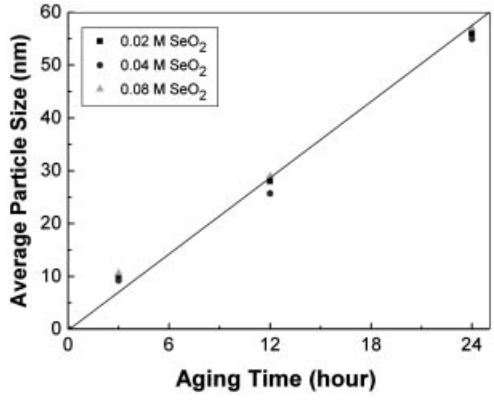


Figure 4. Average size of $BaF_2$ nanocube edges as a function of ageing time and $SeO_2$ added. The line is linearly fitted with $R^2$ = 0.98.

 © 2006 Wiley-VCH Verlag GmbH & Co. KGaA, Weinheim 

Figure 5b and Figure 3a, respectively), the particles gradually increase in size and are better faceted. As can be seen in Figure 4, the size kinetics appears to be linear with respect to time and independent of the amount of $SeO_2$ added under the synthesis conditions investigated (i.e. 0.02 M of $SeO_2$ was sufficient to generate the cubelike morphology). On the basis of the TEM image statistics, it is found that the amount of $SeO_2$ used (either 0.02 or 0.08 M) does not have a substantial influence on the sizes of the nanoparticles. Although our primary focus in this work is on $BaF_2$ nanocubes in the range 10–50 nm, this linear relationship is likely to extend further. TEM image statistics also indicate an improvement in size uniformity for the long-aged samples.

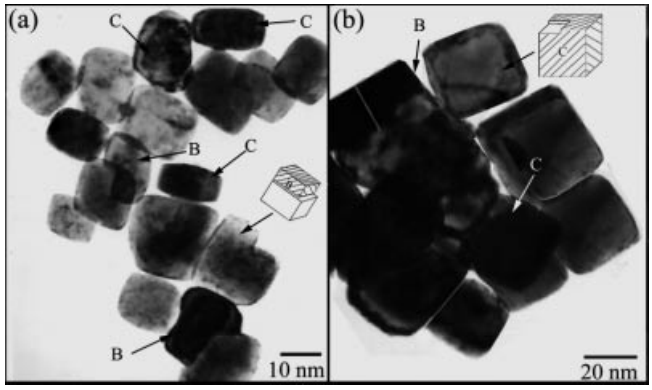


Figure 5. TEM images of $BaF_2$ nanocubes prepared (0.04 M $SeO_2$, pH = 2) with ageing times of: (a) 3 h and (b) 12 h (crystallite types B and C have been marked).

Varying the pH value of the system, while keeping other synthesis parameters unchanged, leads to a dramatic change in the size and shape of the particles. Figure 6 and Table 1 show the morphologies and sizes of the particles obtained by increasing the pH value of the system. It is found that when the pH value is small (≈2), the nanoparticles are smaller, and their shapes are cubic; When pH value ≥ 2, only larger nanocubes form; in the pH value range 2–6, a clear transition from small cubic particles is observed. Only octahedral particles with a mean edge length of 1 μm form when the pH value is raised to 7.

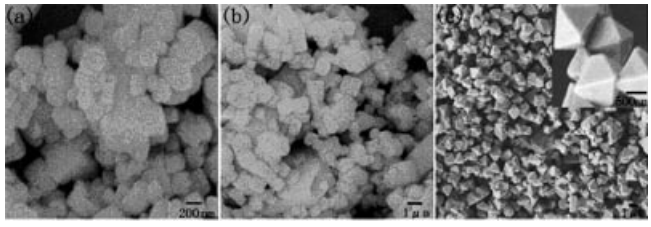


Figure 6. FESEM images of $BaF_2$ nanoparticles prepared (0.04 M $SeO_2$, ageing time 24 h) with different pH values: (a) pH = 4, (b) pH = 6 and (c) pH = 7.

Table 1. The morphologies and mean sizes of $BaF_2$ nanoparticles at different pH values.

| pH value | Morphology | Mean size [nm] |
|---|---|---|
| 2 | Cube | 55 |
| 4 | Cube | 200 |
| 6 | Cube | 1000 |
| 7 | Octahedron | 1000 |

### Growth Mechanism

In Figure 5, a considerable amount of $BaF_2$ nanoparticles (marked with arrows) show special morphologies, although the majority of the $BaF_2$ crystallites are highly symmetrical nanocubes with equal edges. Aside from the normal, perfect nanocubes (type A), there are two types of "abnormally grown" nanocubes. As illustrated further in Scheme 1, the first one, type B, indicates some sidewall extension. The second one, type C, results largely from an in-plane completing growth. All crystallites observed can be broadly classified as either type A, type B, or type C, a finding also reported for $Co_3O_4$ nanocubes.[11] As depicted in the literature, a correct sequential arrangement of these crystallite types would naturally disclose the nanocube growth mechanism, a logical repetition of the three types of nanocrystallites, i.e. $\cdots\rightarrow A_{smaller} \rightarrow B \rightarrow C \rightarrow A_{larger} \rightarrow\cdots$. Thus, the growth does not proceed in a layer-by-layer manner (atomically), but with multiple-layer growth, i.e. nucleation and growth take place simultaneously in different atomic layers.

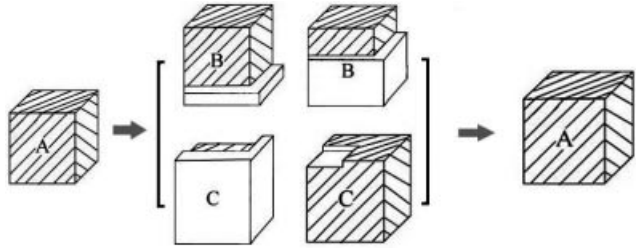


Scheme 1. Schematic illustration of the "extension growing" process based on the morphologies of intermediate crystallites (B and C) observed. The crystallite types B and Chave also been referred to in Figure 5.

In this approach, $SeO_2$ plays a critical role in the formation of the $BaF_2$ nanocubes. Firstly it acts as deoxidant, to prevent the incorporation of oxygen, which will affect the luminescence properties of $BaF_2$.[8] Photoluminescence experiments were carried out at room temperature on a Perkin–Elmer Model LS-55 fluorescence spectrometer with a Xe lamp. Photoluminescence results, as shown in Figure 7, display a weak emission peak at 453 nm (2.74 eV), which is excited at 270 nm (4.59 eV). The luminescence band at 2.74 eV results from an oxygen–vacancy complex with an oxygen on a fluorine site with a next-nearest fluorine vacancy on the surface of the nanocrystals.[12] It is believed that the deoxidant selenite ions prevent the incorporation of oxygen into $BaF_2$ effectively during the growth process, as the emission peak is so weak that it is difficult to be detected. Under the same conditions, the PL spectrum of $BaF_2$ with oxygen incorporated displays an intense peak

 © 2006 Wiley-VCH Verlag GmbH & Co. KGaA, Weinheim 

$$(SeO_2)_{bulk} + H_2O \Leftrightarrow H_2SeO_3 \Leftrightarrow 2H^+ + SeO_3^{2-} \Leftrightarrow H_2SeO_3 \Leftrightarrow (SeO_2)_{small\ crystal} + H_2O$$
$$+ \qquad +$$
$$2F^- + Ba^{2+} \Leftrightarrow BaF_2$$
$$\Updownarrow \qquad \Updownarrow$$
$$2HF \qquad BaSeO_3$$

Scheme 2.

(several hundred times that of $BaF_2$ prepared by using $SeO_2$) at the same position. The trace oxygen may come from the atmosphere when the products were examined. Secondly, it is believed that $SeO_2$ which is tetragonal in symmetry ($a$ = 8.3 Å, $c$ = 5.1 Å) acts as a seed for the growth of the $BaF_2$ nanocubes. The [001]-oriented $BaF_2$ has a fourfold-symmetric $a$ plane with $a$ = 6.2 Å, which matches well to the fourfold-symmetric $SeO_2$ (001) substrate, $4a_{BaF_2} \approx 3a_{SeO_2}$, and this results in a $c$-axis-oriented growth of $BaF_2$ on $SeO_2$ (001). A small quantity of crystalline $SeO_2$ was also found in the sample prior to washing with distilled water and anhydrous alcohol. In this solution system, $SeO_2$ undergoes a recrystallization process, which is illustrated in Scheme 2.

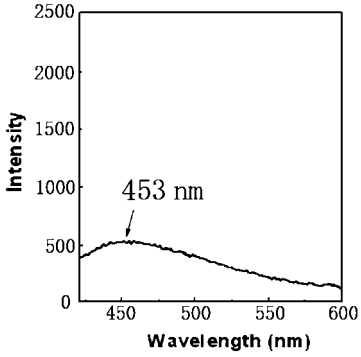


Figure 7. Photoluminescence (PL) spectra acquired from the 55-nm $BaF_2$ nanocubes excited at 270 nm.

When the pH value is lowered, more crystalline $SeO_2$ seeds form, which provides more nucleation points for the $BaF_2$ nanoparticles. This prevents the nanoparticles from aggregating and leads to the formation of smaller nanocubes, as illustrated in Table 1. When the pH value is increased to 7, only octahedral crystals are obtained. This is considered to be related to the enhanced surface energy of the $BaF_2$ nanooctahedra in the absence of $SeO_2$ seeds, which leads to more stable {111} faces being exposed. These results also indicate that the growth rate along <100> relative to that along <111> can be manipulated by adjusting the pH value, which will dictate whether nanocubes or nanooctahedra are formed. The concentration of $SeO_2$ (either 0.02 or 0.08 M) does not have a substantial influence on nanoparticle size (Figure 4) probably because at either of these concentrations, the solution is already saturated with small crystalline seeds of $SeO_2$. No $BaSeO_3$ is found in the product as a result of the acidic conditions.

## Conclusions

In summary, by controlling the reaction time and pH values, $BaF_2$ nanocubes of different sizes have been prepared in the range 10–1000 nm with high crystallite-monodispersity. The relationship between the size of the cube and reaction time is found to be linear. Furthermore, on the basis of the observed crystallite morphologies, an "extension growing" growth mechanism has been elucidated for the formation of the $BaF_2$ nanocubes. The growth of the $BaF_2$ nanocubes proceeds in a multiple-layer manner. This work may uncover new ways for preparing other nano-polyhedra.

## Experimental Section

**Preparation of $BaF_2$ Nanocubes:** In a typical growth procedure for $BaF_2$ nanocubes, $BaCl_2$ (0.002 mol), $SeO_2$ (0.002 mol), and NaF (0.004 mol) powders were combined in distilled water (30 mL) and stirred for 2 min. The solution pH was then adjusted with hydrochloric acid solution until its pH value was about 2. The sample (about 50 mL) was placed in a 60 mL autoclave with a Teflon liner, which was maintained at 140 °C for 24 h and then air cooled to room temperature. After reaction, the white precipitate was collected and washed thoroughly with distilled water and anhydrous alcohol. The product was dried in a vacuum at 50 °C for 4 h.

**Sample Characterization:** The samples were characterized by X-ray powder diffraction using a Rigaku D/max-Rapid X-ray diffractometer equipped with a copper anticathode and secondary graphite monochromator (Cu–$K_{\alpha 1,2}$, λ = 1.54178 Å). A scan rate of 0.05°/s was used to record the patterns in the 2$\theta$ range 20–70°. TEM images and ED patterns were taken on a Hitachi Model H-800 instrument with a tungsten filament, with an accelerating voltage of 200 kV. The FESEM image was obtained with a JSM-6700F field emission scanning electron microanalyser (JEOL, Japan), where the resulting powders were mounted on a copper slice. X-ray photoelectron spectroscopy (XPS) was performed with an ESCALab MKII X-ray photoelectron spectrometer, using Mg-$K_\alpha$ X-ray radiation as the excitation source. The binding energies obtained in the XPS analysis were calibrated against the C 1s peak at 284.2 eV.

## Acknowledgments

Financial support from the National Natural Science Foundation of China and the Chinese Academy of Sciences is gratefully acknowledged.

[1] a) C. M. Bender, J. M. Burlitch, D. Barber, C. Pollock, *Chem. Mater.* **2000**, *12*, 1969–1976; b) H. Lian, M. Zhang, J. Liu, Z. Ye, J. Yan, C. Shi, *Chem. Phys. Lett.* **2004**, *395*, 362–365; c)

 © 2006 Wiley-VCH Verlag GmbH & Co. KGaA, Weinheim 

R. N. Hua, C. Y. Zang, C. Sha, D. M. Xie, C. S. Shi, *Nanotechnology* **2003**, *14*, 588–591.
[2] a) J. A. Creighton, D. G. Eadon, *J. Chem. Soc., Faraday Trans.* **1991**, *87*, 3881–3891; b) Y. W. Cao, R. Jin, C. A. Mirkin, *J. Am. Chem. Soc.* **2001**, *123*, 7961–7962.
[3] R. Singh, S. Sinha, P. Chou, N. J. Hsu, F. Radpour, *J. Appl. Phys.* **1989**, *66*, 6179–6185.
[4] A. J. Wojtowicz, *Nucl. Instrum. Methods Phys. Res., Sect. A* **2002**, *486*, 201–207.
[5] a) M. H. Cao, C. W. Hu, E. B. Wang, *J. Am. Chem. Soc.* **2003**, *125*, 11196–11197; b) H. Z. Lian, Z. R. Ye, C. S. Shi, *Nanotechnology* **2004**, *15*, 1455–1458.
[6] X. M. Sun, Y. D. Li, *Chem. Commun.* **2003**, 1768–1769.
[7] a) Y. G. Sun, Y. N. Xia, *Science* **2002**, *298*, 2176–2179; b) L. F. Gou, C. J. Murphy, *Nano Lett.* **2003**, *3*, 231–234.
[8] a) J. M. Vail, E. Emberly, T. Lu, M. Gu, R. Pandey, *Phys. Rev. B* **1998**, *57*, 764–772; b) E. Radzhabov, P. Figura, *Phys. Status Solidi B* **1994**, *186*, 37–40.
[9] Joint Committee on Powder Diffraction Standards (JCPDS), file no. 4-452.
[10] L. H. Lu, H. N. Cui, W. Li, H. J. Zhang, S. Q. Xi, *Chem. Mater.* **2001**, *13*, 325–328.
[11] J. Feng, H. C. Zeng, *Chem. Mater.* **2003**, *15*, 2829–2835.
[12] U. Rogulis, S. Schweizer, J. M. Spaeth, *J. Phys.: Condens. Matter* **2002**, *14*, 6949–6956.

Received: March 16, 2006
Published Online: June 23, 2006

 © 2006 Wiley-VCH Verlag GmbH & Co. KGaA, Weinheim 

DOI: 10.1002/ejic.200600265

# Molecular Structures and NMR Studies of Lithium and Germanium(II) Complexes of a New Chelating Amido–Imino Ligand Obtained by Addition of *n*BuLi to 1,2-Bis(arylimino)acenaphthene

**Igor L. Fedushkin,*[a] Markus Hummert,[b] and Herbert Schumann[b]**

*Dedicated to Prof. Vladimir K. Cherkasov on the occasion of his 60th birthday*

**Keywords:** Lithium / N ligands / Germanium / Structure elucidation

The reaction of 1,2-bis[(2,6-diisopropylphenyl)imino]acenaphthene (dpp-bian, **1**) with 1 equiv. of *n*BuLi in diethyl ether or with 2 equiv. of *n*BuLi in hexane produces [{dpp-bian(*n*Bu)}Li($Et_2O$)] (**3**) and [{dpp-bian(*n*Bu)Li}*n*BuLi]$_2$ (**4**), respectively. Complexes **3** and **4** are formed by the transfer of an *n*Bu anion to one of the imine carbon atoms of the dpp-bian ligand. Treatment of **3** and **4** with $H_2O$ affords the *C*-alkylated *N*-protonated amino-imino compound dpp-bian(H)(*n*Bu) (**5**). The reaction of **3** with $GeCl_2$(dioxane) affords the three-coordinate germylene complex [{dpp-bian(*n*Bu)}GeCl] (**6**). The molecular structures of **3**–**6** were determined by single-crystal X-ray structure analysis. The lack of symmetry in the alkylated bian system in **3**–**6** causes the non-equivalence of all protons except those of the $CH_3$ groups of the *i*Pr substituents.

(© Wiley-VCH Verlag GmbH & Co. KGaA, 69451 Weinheim, Germany, 2006)

## Introduction

In many respects, progress in organometallic and coordination chemistry is determined by the type of organic ligands used for the preparation of these metal complexes. The use of a new ligand system usually leads to complexes with more or less novel chemical properties. During the last decade, acenaphthene-1,2-diimines (bian) have become widely used as ligands in coordination chemistry. Diimine transition metal complexes serve as catalysts in alkyne hydrogenation,[1] C–C bond formation,[2] cycloisomerization,[3] hydrosilylation,[4] polymerization of alkenes[5] and acrylic monomers,[6] as well as in the copolymerization of $CO_2$[7] and $CH_2$=$CH_2$[8] with methylenecyclopropene, of ethylene with norbornene,[9] and of CO with styrene.[10] Thus, acenaphthene-1,2-dimine late transition metal complexes, the so-called Brookhart catalysts,[11] are some of the most effective catalysts for olefin polymerization known until now. The π-acceptor capability of the acenaphthene-1,2-dimine ligand causes an electron deficiency at the respective metal center that makes these complexes highly reactive towards organic substrates.

Recently, we have demonstrated for the first time that main group metals also readily form stable bian complexes. The most widely used ligand in this field is 1,2-bis[(2,6-diisopropylphenyl)imino]acenaphthene (dpp-bian, **1**). One of the remarkable features of the dpp-bian ligand in its main group metal complexes is its ability to adopt variable oxidation states. The reduction of dpp-bian with alkali metals in diethyl ether affords the mono-, di-, tri- and tetra-anions of the ligand, i.e. [(dpp-bian)$M_n(Et_2O)_m$] (M = Li, Na; $n$ = 1–4),[12] whereas with alkaline-earth metals the reduction of dpp-bian provides only dianions, forming the complexes [(dpp-bian)M$(THF)_n$] (M = Mg, Ca; $n$ = 2–4).[13] Depending on the reaction medium, the reduction of dpp-bian with aluminum in the presence of its halides gives the complexes [(dpp-bian)$AlCl_2$], [(dpp-bian)AlI($Et_2O$)], and [(dpp-bian)AlCl($Et_2O$)].[14] Alkylaluminum complexes with dpp-bian as a radical-anionic as well as a dianionic ligand are obtained by treating (dpp-bian)Na with $R_2AlX$ (R = Me, Et, *i*Bu; X = Cl, Br).[15] Similarly, the metal-exchange reactions of (dpp-bian)$Na_2$ or (dpp-bian)Na with $GeCl_2$ give the germanium(II) derivatives [(dpp-bian)Ge][16] and [(dpp-bian)-GeCl],[17] respectively. The variability of the oxidation state of the dpp-bian ligand is impressively demonstrated by the decomposition of [(dpp-bian)Mg(*i*Pr)($Et_2O$)], which occurs with elimination of *i*Pr radicals and simultaneous reduction of the dpp-bian radical anion to the dianion.[18] The oppo-

[a] G. A. Razuvaev Institute of Organometallic Chemistry of Russian Academy of Sciences,
Tropinina 49, 603950 Nizhny Novgorod, GSP-445, Russia
Fax: +7-8312-627497
E-mail: igorfed@imoc.sinn.ru
[b] Institut für Chemie der Technischen Universität Berlin,
Straße des 17. Juni 135, 10623 Berlin, Germany
Fax: +49-30-3142-2168
E-mail: schumann@chem.tu-berlin.de

 InterScience © 2006 Wiley-VCH Verlag GmbH & Co. KGaA, Weinheim 

site process, namely oxidation of the dpp-bian dianion to the radical anion, is observed in the reactions of [(dpp-bian)-$Mg(THF)_3$] (**2**) with organic substances such as aromatic ketones.[19] The course of the reactions of **2** with ethyl halides further demonstrates the non-innocence of the dpp-bian ligand in its metal complexes. They proceed by single-electron transfer from the dianionic dpp-bian ligand to EtX to yield an ethyl radical, which, in turn, attacks the ligand, which is now a radical anion, at one of the imino carbon atoms to give [(dpp-bian)(Et)MgX$(THF)_n$].[20] Acidic substances such as aliphatic ketones, terminal alkynes, and nitriles add to complex **2** with protonation of one of the ligand nitrogen atoms to produce complexes with unsymmetrical amido–imino dpp-bian ligands.[21] The different modes of the dpp-bian ligand (**A**: neutral; **B**: radical-anion; **C**: dianion) in the reactions of **2** with organic substrates, as well as the resulting modifications of the dpp-bian ligand (**D**: amino/imine and **E**: amido/amine), are shown below.

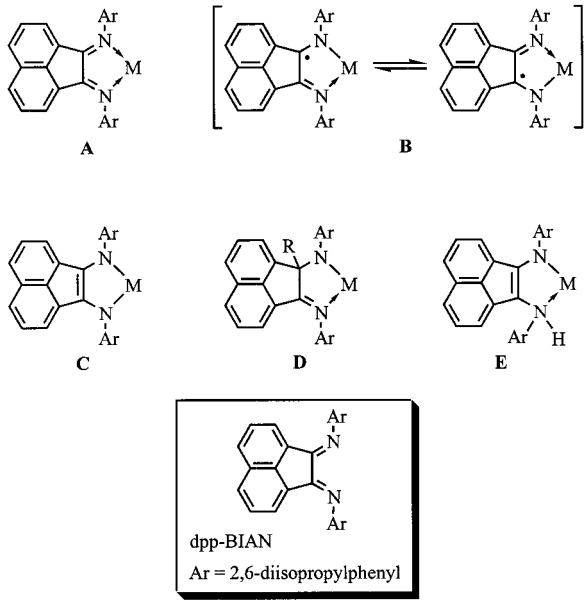


In this paper, we report on the alkylation of dpp-bian with *n*BuLi to provide the ligand system **D** and its subsequent reaction with $GeCl_2$.

## Results and Discussion

### Alkylation of dpp-bian with *n*BuLi

Addition of 1 equiv. of *n*BuLi to a suspension of dpp-bian in diethyl ether caused immediate dissolution of dpp-bian and a change in the color of the reaction mixture from yellow to blue. Crystallization of the foamy residue, remaining after removal of the solvents, from hexane afforded [dpp-bian(*n*Bu)]Li($Et_2O$) (**3**) in the form of blue, crystalline plates in 44% yield (Scheme 1).

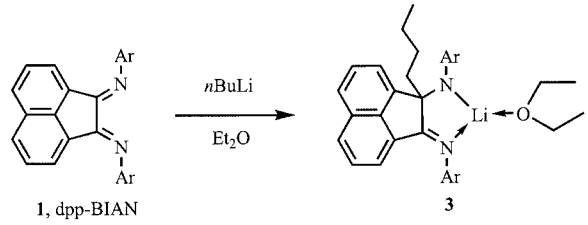


Scheme 1.

The reaction of equivalent amounts of dpp-bian and *n*BuLi also proceeded easily in hexane but produced yellow instead of blue crystals, the characterization of which by $^1H$ NMR spectroscopy in $C_6D_6$ is seriously hindered by multiple overlaps of the numerous signals. However, $[D_{10}]Et_2O$ solutions of both the blue and the yellow crystals give identical $^1H$ NMR spectra.

Addition of a twofold molar amount of *n*BuLi to a suspension of dpp-bian in hexane caused immediate precipitation of [{dpp-bian(*n*Bu)Li}*n*BuLi]$_2$ (**4**) as red crystals in 81% yield (Scheme 2).

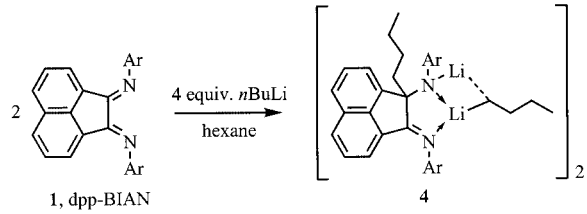


Scheme 2.

Hydrolysis of **3** and **4** resulted in the formation of the yellow, crystalline amino-imine [dpp-bian(H)(*n*Bu)] (**5**; Scheme 3).

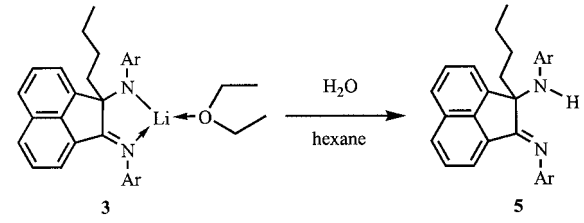


Scheme 3.

The anionic amido–imino ligand [dpp-bian(*n*Bu)]$^-$ of the lithium complex **3** can be transferred to other metal ions such as $Ge^{2+}$. Thus, the reaction of equimolar amounts of **3** and $GeCl_2$(dioxane) in $Et_2O$ afforded almost quantitative yields of red, crystalline [{dpp-bian(*n*Bu)}GeCl] (**6**), which contains three-coordinate $Ge^{II}$ (Scheme 4).

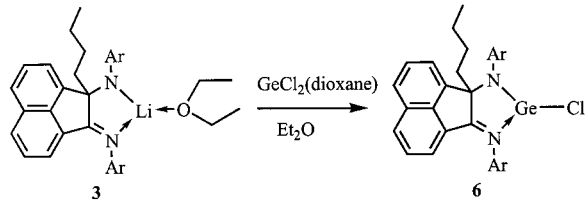


Scheme 4.

 © 2006 Wiley-VCH Verlag GmbH & Co. KGaA, Weinheim 

### Molecular Structures of Compounds 3–6

The molecular structures of **3**–**6** were determined by single-crystal X-ray analysis and are presented in the figures. Selected bond lengths and angles for **4**–**6** are presented in Tables 1 and 2, respectively. The low quality of the X-ray data obtained for **3** ($R_1$ = 0.1231) does not allow detailed information of bond lengths and angles. However, the X-ray structure of **3** (Figure 1) is good enough to indicate clearly that the reaction of *n*BuLi with dpp-bian (1:1 molar ratio) occurs with the transfer of the butyl group to the imino carbon atom C(2) of the dpp-bian ligand, thus making this carbon atom a chiral center.

Table 1. Selected bond lengths [Å] for **4**–**6**. M[a] = Li(2) for compound **4** and Ge for compound **6**.

| Compound | **4** | **5** | **6** |
|---|---|---|---|
| C(1)–N(1) | 1.285(3) | 1.274(3) | 1.286(3) |
| C(2)–N(2) | 1.485(3) | 1.497(3) | 1.468(3) |
| C(1)–C(2) | 1.561(3) | 1.542(3) | 1.533(3) |
| C(2)–C(37) | 1.561(4) | 1.535(3) | 1.558(3) |
| Li(1)–N(2) | 2.071(5) | | |
| M[a]–N(1) | 2.007(5) | | 2.1182(19) |
| M[a]–N(2) | 1.978(5) | | 1.8723(19) |
| Li(1a)–C(41) | 2.265(6) | | |
| Li(1)–C(41) | 2.321(6) | | |
| M[a]–C(41) | 2.087(6) | | |
| M[a]–Li(1) | 2.307(6) | | |
| Li(1)–Li(1a) | 2.562(10) | | |
| M[a]–Cl | | | 2.3500(7) |

Table 2. Selected bond angles [°] for **4**, **5** and **6**. M[a] = Li(2) for compound **4** and Ge for compound **6**.

| Compound | **4** | **5** | **6** |
|---|---|---|---|
| N(1)–C(1)–C(2) | 120.2(2) | 119.6(2) | 117.7(2) |
| N(2)–C(2)–C(1) | 112.5(2) | 103.41(17) | 105.22(18) |
| N(2)–C(2)–C(37) | 108.75(19) | 112.66(18) | 111.90(19) |
| C(1)–C(2)–C(37) | 106.2(2) | 112.19(18) | 110.28(18) |
| C(1)–N(1)–M[a] | 102.1(2) | | |
| C(2)–N(2)–M[a] | 101.9(2) | | |
| C(2)–N(2)–Li(1) | 130.9(2) | | |
| N(2)–Li(1)–C(41a) | 129.2(3) | | |
| N(2)–M[a]–N(1) | 93.5(2) | | 81.46(8) |
| N(2)–M[a]–C(41) | 111.2(2) | | |
| N(1)–M[a]–C(41) | 153.0(3) | | |
| N(1)–M[a]–Cl(1) | | | 93.06(5) |
| N(2)–M[a]–Cl(1) | | | 102.68(6) |

In the solid state, compound **4** (Figure 2) is the centrosymmetric dimer of the 1:1 adduct of solvent-free **3** with *n*BuLi. This dimer is formed by interaction of all four lithium atoms with the two $\mu_3$-bridging *n*Bu(Li) carbanions. Within the monomeric units, the bonding modes of the two lithium atoms relative to the [dpp-bian(*n*Bu)]$^-$ anion are different. Li(2) is connected with both N(1) and N(2) of the amido[N(2)]–imino[N(1)] ligand, while Li(1) is linked only to N(2). The amido–imino character of the alkylated dpp-bian ligand is manifested by the bond length within the N(1)–C(1)–C(2)–N(2) fragment. The length of the C(1)–N(1) bond [1.285(3) Å] is close to that of the C=N double

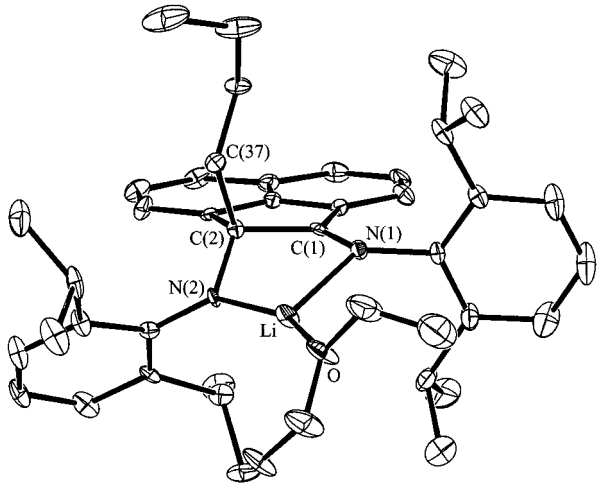


Figure 1. Molecular structure of **3**. Hydrogen atoms are omitted for clarity. Thermal ellipsoids are drawn at 30% probability.

bond in free dpp-bian [1.282(4) Å],[22] whereas the C(2)–N(2) distance [1.485(3) Å] corresponds well with the average value of carbon–nitrogen single bonds. In spite of the different functionality of the nitrogen atoms in the [dpp-bian(*n*Bu)]$^-$ anion, the N(1)–Li(2) and N(2)–Li(2) distances are very similar [2.007(5) and 1.978(5) Å, respectively]. The distance of the Li(1) atom to the amido atom N(2) is 2.071(5) Å. Both *n*-butyl carbanions act as $\mu_3$-bridges between Li(2) and the symmetry-equivalent Li(1) and Li(1a) atoms (symmetry operation: *–x*, *–y*, *–z*). The same bridging mode of *n*-butyl anions has been observed in [{(*n*BuLi)$_4$(TMEDA)}$_\infty$],[23] which exhibits a TMEDA-linked tetrameric cubane structure. The distances C(41)–Li(1) [2.321(6) Å] and C(41)–Li(1a) [2.265(6) Å], which are in the range of the Li–C distances in [{(*n*BuLi)$_4$(TMEDA)}$_\infty$], are significantly longer than the C(41)–Li(2) distance [2.087(6) Å].

The molecular structure of the metal-free amino-imine compound **5** (Figure 3) shows C–N distances that differ significantly, thus indicating an N(1)–C(1) double bond [1.274(3) Å] and an N(2)–C(2) single bond [1.497(3) Å]. The sum of the bond angles at N(2) (340°) points to a more tetrahedral (327°) than trigonal-planar (360°) arrangement.

The molecular structure of **6** (Figure 4) corresponds to a monomeric three-coordinate germylene. Because of the three different groups (chloride ion, amido- and imino-nitrogen atoms) bonded to the germanium atom and its lone electron-pair, the germanium atom is a chiral center. Taking into account that the C(2) atom in **6** is also chiral, one may expect the existence of two diastereomeric pairs of molecules, whereas in fact only one diastereomeric pair is present in the unit cell. In these two diastereomeric molecules the *n*Bu group and the chlorine atom are positioned at the same side of the plane formed by the metallacycle Ge–N(1)–C(1)–C(2)–N(2). Again, the difference between the amido and the imino functionality of the ligand is evident from the C–N distances [N(1)–C(1) = 1.286(3) and N(2)–C(2) = 1.468(3) Å]. However, in contrast to compound **4**,

 © 2006 Wiley-VCH Verlag GmbH & Co. KGaA, Weinheim 

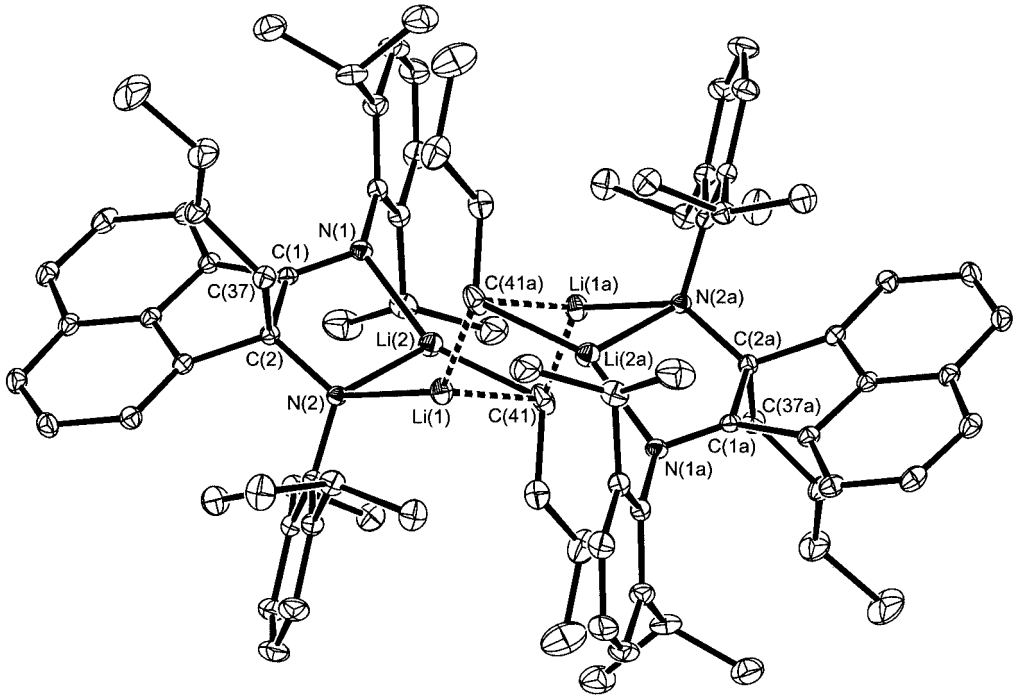


Figure 2. Molecular structure of **4**. Hydrogen atoms are omitted for clarity. Thermal ellipsoids are drawn at 30% probability.

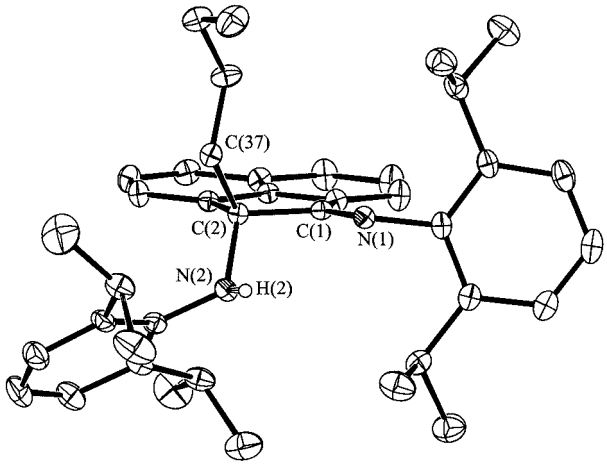


Figure 3. Molecular structure of **5**. Hydrogen atoms are omitted for clarity. Thermal ellipsoids are drawn at 30% probability.

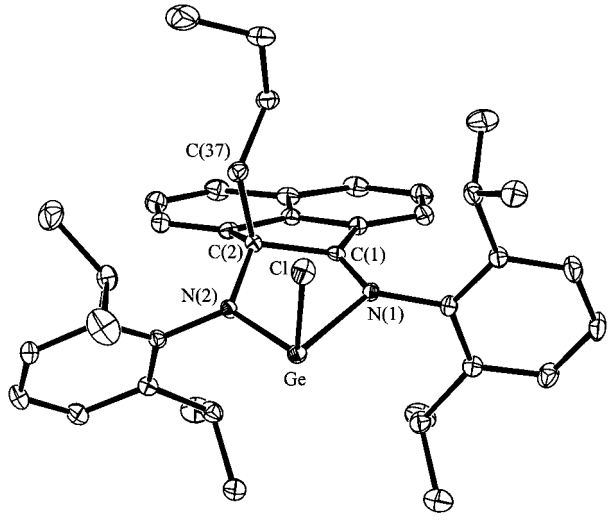


Figure 4. Molecular structure of **6**. Hydrogen atoms are omitted for clarity. Thermal ellipsoids are drawn at 30% probability.

there is also a pronounced difference in the length of the Ge–N(amido) bond [Ge–N(2) = 1.872(1) Å] and the Ge–N(imino) bond [Ge–N(1) = 2.118(1) Å]. The Ge–N(amido) distance compares well with the two Ge–N(amido) bonds in the germylene [(dpp-bian)Ge] [1.896(3) and 1.885(3) Å].[16] The Ge–Cl distance [2.3500(7) Å] is noticeably longer than the corresponding distance in the three-coordinate $Ge^{II}$ compound [(dpp-bian)GeCl] [2.2693(8) Å], which contains dpp-bian as a radical-anionic ligand.[17a] The sum of the bond angles (277.2°) at the germanium atom [81.46(8), 93.06(5), 102.68(6)°] is almost the same as in [(dpp-bian)GeCl] (276.8°).[17a]

## NMR Spectroscopy of 3–6

The addition of *n*BuLi to one of the C=N bonds of dpp-bian results in the formation of an asymmetric amido–imino structure, which, in turn, causes the inequivalence of all aromatic protons as well as of all methine protons of the isopropyl substituents (Figure 5).

The $^1$H NMR spectrum of a solution of the blue crystals of **3** in $C_6D_6$ contains twelve signals for the aromatic protons, ranging from $\delta$ = 7.48 to 6.53 ppm, and four signals for the methine protons at $\delta$ = 5.12, 3.44, 3.33, and

 © 2006 Wiley-VCH Verlag GmbH & Co. KGaA, Weinheim 

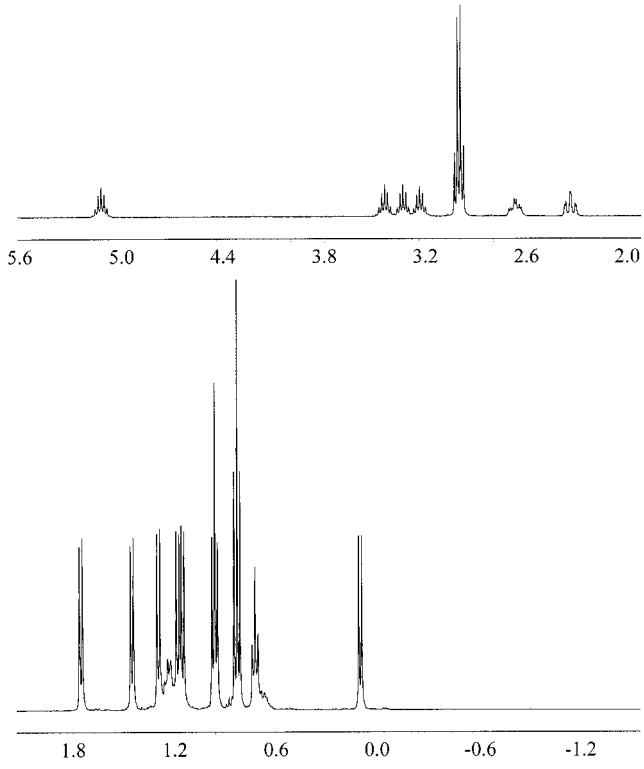


Figure 5. $^1$H NMR spectrum of **3** divided into two sections ($C_6D_6$, 400 MHz, 20 °C). The aromatic region is not shown.

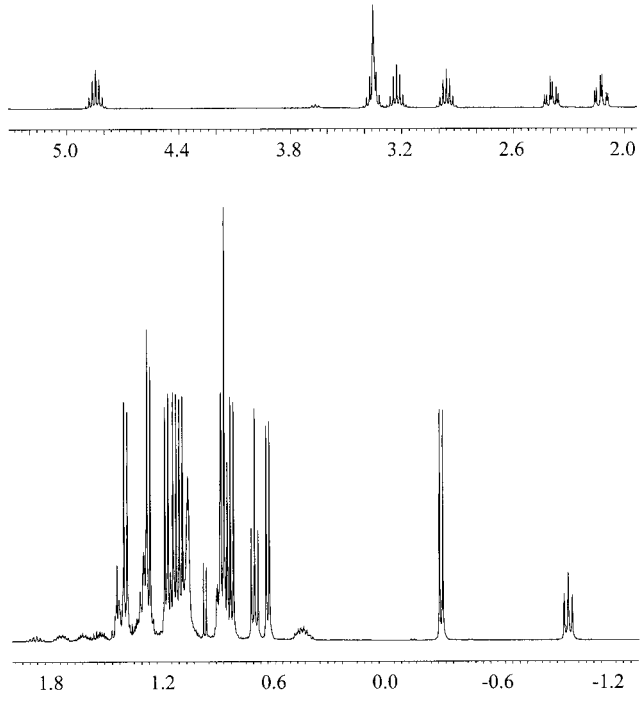


Figure 6. $^1$H NMR spectrum of **4** divided into two sections ([$D_{10}$]-$Et_2O$, 400 MHz, 20 °C). The aromatic region is not shown.

3.23 ppm (Figure 5a). Due to the restricted rotation around the N–C(*ipso*-Ph) bonds, all eight methyl groups become unequal and appear as eight doublets in the range from $\delta$ = 1.75 to 0.09 ppm (Figure 5b). The presence of the chiral carbon atom C(2) next to the methylene protons of the *n*Bu group causes the inequivalence of the α-$CH_2$(*n*Bu) protons and the appearance of two triplets of doublets at $\delta$ = 2.67 and 2.33 ppm. The $CH_3$(*n*Bu) group gives rise to a triplet at $\delta$ = 0.72 ppm, whereas the β- and γ-$CH_2$(*n*Bu) protons appear as multiplets at $\delta$ = 1.23 and 0.68 ppm. The signals of the coordinated $Et_2O$ molecule are centered at $\delta$ = 3.00 (q) and 0.83 (t) ppm. Dissolution of **3** in [$D_{10}$]$Et_2O$ does not cause significant changes in the $^1$H NMR spectrum. Thus, the four signals of the methine protons appear as septets at $\delta$ = 4.84, 3.35, 3.23 and 2.96 ppm, the nonequivalent α-$CH_2$(*n*Bu) protons give rise to two triplets of doublets at $\delta$ = 2.40 and 2.12 ppm, and the eight doublet signals for the unequal methyl groups are found between $\delta$ = 1.40 and –0.30 ppm.

The $^1$H NMR spectrum of **4** recorded in $C_6D_6$ (red solution) reveals only broadened signals, which could not be assigned. However, a simple $^1$H NMR spectrum (Figure 6) was obtained from a solution of compound **4** in [$D_{10}$]$Et_2O$ (blue solution) in which the positions of all signals of the amido–imino ligand are identical with those of the $^1$H NMR spectrum of solutions of compound **3** in [$D_{10}$]$Et_2O$.

Unexpectedly, the $^1$H NMR spectrum of compound **5** in [$D_8$]THF (Figure 7) shows signals for only eight of the twelve aromatic protons, and of the total of four methine protons belonging to the isopropyl substituents only two give distinguishable signals which are superimposed upon each other and centered at $\delta$ = 3.08 and 3.01 ppm (Figure 7). Also, only four of the eight doublet signals expected for the $CH_3$(*i*Pr) protons can be located. However, it should be noted that in the aromatic and aliphatic regions in which the missing signals would be expected, a visible raising of the baseline is observed. We attribute this to a significant broadening of those signals due to a slow (on the NMR timescale) dynamic process within the molecules of **5** in solution and suggest an umbrella-like inversion at the amino nitrogen atom N(2). Such a process affects all the protons of the 2,6-*i*$Pr_2$Ph ring bonded to N(2) and leads to a broadening of the $^1$H resonances of this substituent. In contrast, the signal of the proton connected directly to N(2)

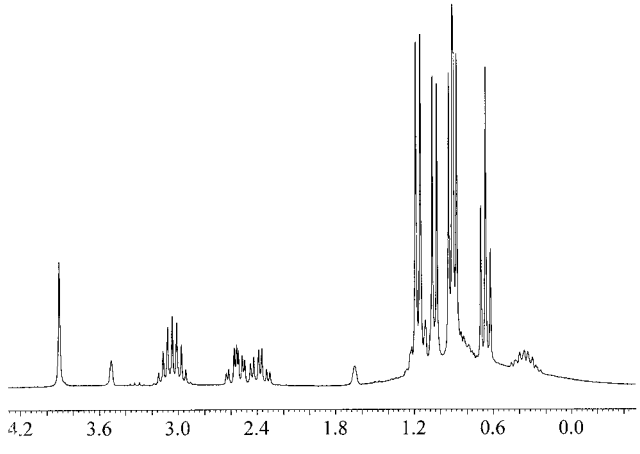


Figure 7. $^1$H NMR spectrum of **5** ([$D_8$]THF, 200 MHz, 20 °C). The aromatic region is not shown.

 © 2006 Wiley-VCH Verlag GmbH & Co. KGaA, Weinheim 

appears as a sharp singlet at $\delta$ = 3.91 ppm. The α-$CH_2$(*n*Bu) protons give rise to two triplets of doublets at $\delta$ = 2.56 and 2.38 ppm and the $CH_3$(*n*Bu) signal appears as a triplet at $\delta$ = 0.66 ppm.

The $^1$H NMR spectrum of compound **6** in [$D_8$]THF shows analogous signal sets to the $^1$H NMR spectrum of compound **3** recorded in [$D_{10}$]$Et_2O$, which differ only with respect to the chemical shifts of the signals. Nevertheless, the spectrum has one noticeable feature. In the $^1$H NMR spectrum of **6**, the α-$CH_2$(*n*Bu) protons appear at $\delta$ = 3.90 and 2.41 (2 td) ppm, thus displaying a much larger diastereotopic splitting constant (1.49 Hz) than those observed in the spectra of **3** (0.28 Hz in $Et_2O$), **4** (0.28 Hz in $Et_2O$), and **5** (0.18 Hz in THF). We believe that the high value of the splitting constant of **6** is caused by the chirality at the germanium atom.

## Conclusions

We have been able to demonstrate that the addition of *n*BuLi to one C=N bond of dpp-bian produces a new, asymmetrically chelating amido–imino ligand system which is expected to be useful for the preparation of new metal-based reagents for organic synthesis.

## Experimental Section

**General Remarks:** All manipulations were carried out under nitrogen using standard Schlenk techniques. Hexane, diethyl ether, and benzene were dried by distillation from sodium/benzophenone. *n*BuLi (2.5 M in hexane) was purchased from ACROS. The deuterated solvents [$D_8$]THF (Aldrich), $C_6D_6$ (Aldrich), and [$D_{10}$]$Et_2O$ (Euriso-top) used for NMR experiments were dried with sodium/benzophenone at ambient temperature and, just prior to use, were condensed under vacuum into the NMR tubes already containing the respective compound. Melting points were measured in sealed capillaries. IR spectra were recorded with an FTIR FSM-1201 spectrometer (Monitoring Ltd.), and $^1$H NMR spectra were obtained with Bruker DPX-200 and Bruker DRX-400 NMR spectrometers.

**[{dpp-bian(*n*Bu)}Li($Et_2O$)] (3):** Addition of 0.8 mL of *n*BuLi (2.5 M in hexane; 2.0 mmol) to a stirred suspension of dpp-bian (1.0 g, 2.0 mmol) in $Et_2O$ (20 mL) at room temperature caused immediate dissolution of dpp-bian and formation of a clear blue-green solution. The foamy residue left after evaporation of the solvent was recrystallized from hexane. The thin blue plates of compound **3** formed within 20 h were collected by decantation of the mother liquor. Yield: 0.56 g (44%); m.p. > 120 °C (dec.). $C_{44}H_{59}LiN_2O$ (638.91): calcd. C 82.72, H 9.31; found C 82.59, H 9.17. $^1$H NMR (400 MHz, $C_6D_6$, 20 °C): $\delta$ = 7.48 (dd, *J* = 7.6 and 1.7 Hz, 1 H, CH arom.), 7.42 (d, *J* = 8.0 Hz, 1 H, CH arom.), 7.29 (d, *J* = 8.0 Hz, 1 H, CH arom.), 7.26 (dd, *J* = 7.6 and 1.7 Hz, 1 H, CH arom.), 7.26 (pseudo t, *J* = 7.6 Hz, 1 H, CH arom.), 7.24 (d, *J* = 6.8 Hz, 1 H, CH arom.), 7.18 (pseudo t, *J* = 7.6 Hz, 1 H, CH arom.), 7.10 (dd, *J* = 7.6 and 1.7 Hz, 1 H, CH arom.), 7.08 (pseudo t, *J* = 7.2 Hz, 1 H, CH arom.), 6.87 (pseudo t, *J* = 7.8 Hz, 1 H, CH arom.), 6.58 (d, *J* = 7.2 Hz, 1 H, CH arom.), 6.53 (d, *J* = 6.8 Hz, 1 H, CH arom.), 5.12 [pseudo t, *J* = 6.8 Hz, 1 H, C*H*-$(CH_3)_2$], 3.44 [pseudo t, *J* = 6.8 Hz, 1 H, C*H*$(CH_3)_2$], 3.33 [pseudo t, *J* = 6.8 Hz, 1 H, C*H*$(CH_3)_2$], 3.23 [pseudo t, *J* = 6.8 Hz, 1 H, C*H*$(CH_3)_2$], 3.00 (q, *J* = 7.0 Hz, 4 H, $Et_2O$), 2.67 (td, *J* = 12.5 and 4.2 Hz, 1 H, CH*H*$(CH_2)_2CH_3$], 2.33 [td, *J* = 12.5 and 4.2 Hz, 1 H, C*H*H$(CH_2)_2CH_3$], 1.75 [d, *J* = 6.8 Hz, 3 H, CH(C*H*$_3)_2$], 1.45 [d, *J* = 6.8 Hz, 3 H, CH(C*H*$_3)_2$], 1.30 [d, *J* = 6.8 Hz, 3 H, CH(C*H*$_3)_2$], 1.18 [d, *J* = 6.8 Hz, 3 H, CH(C*H*$_3)_2$], 1.15 [d, *J* = 6.8 Hz, 3 H, CH(C*H*$_3)_2$], 0.97 [d, *J* = 6.8 Hz, 3 H, CH(C*H*$_3)_2$], 0.95 [d, *J* = 6.8 Hz, 3 H, CH(C*H*$_3)_2$], 0.83 (t, *J* = 7.0 Hz, 6 H, $Et_2O$), 0.72 [t, *J* = 7.0 Hz, 3 H, $(CH_2)_3CH_3$], 0.10 [d, *J* = 6.8 Hz, 3 H, CH(C*H*$_3)_2$] ppm.

**[{dpp-bian(*n*Bu)Li}*n*BuLi]$_2$ (4):** Addition of 1.8 mL of *n*BuLi (2.5 M in hexane; 4.4 mmol) to a stirred suspension of dpp-bian (1.0 g, 2.0 mmol) in hexane (20 mL) at room temperature caused dissolution of dpp-bian and precipitation of a red crystalline product. The product was filtered off and recrystallized from hexane (35 mL) to yield 1.08 g (81%) of compound **4** as red crystals. M.p. > 130 °C darkening, >181 °C melting (dec.). $C_{88}H_{116}Li_4N_4{\cdot}C_6H_{14}$ (1343.8): calcd. C 84.01, H, 9.75; found C 83.13, H, 9.21. $^1$H NMR (400 MHz, $Et_2O$, 20 °C): $\delta$ = 7.74 (d, *J* = 8.2 Hz, 1 H, CH arom.), 7.45 (d, *J* = 8.2 Hz, 1 H, CH arom.), 7.30 (m, 1 H, CH arom.), 7.25 (m, 2 H, CH arom.), 7.16 (pseudo t, *J* = 8.2 Hz, 1 H, CH arom.), 7.12 (pseudo t, *J* = 8.2 Hz, 1 H, CH arom.), 7.02 (dd, *J* = 7.3 and 1.9 Hz, 1 H, CH arom.), 6.68 (pseudo t, *J* = 7.3 Hz, 1 H, CH arom.), 6.61 (dd, *J* = 7.3 and 1.9 Hz, 1 H, CH arom.), 6.38 (d, *J* = 7.3 Hz, 1 H, CH arom.), 6.11 (d, *J* = 6.9 Hz, 1 H, CH arom.), 4.84 [pseudo t, *J* = 6.9 Hz, 1 H, C*H*$(CH_3)_2$], 3.35 [pseudo t, *J* = 6.9 Hz, 1 H, C*H*$(CH_3)_2$], 3.23 [pseudo t, *J* = 6.9 Hz, 1 H, C*H*-$(CH_3)_2$], 2.96 [pseudo t, *J* = 6.9 Hz, 1 H, C*H*$(CH_3)_2$], 2.40 [td, *J* = 12.7 and 4.7 Hz, 1 H, CH*H*$(CH_2)_2CH_3$], 2.12 [td, *J* = 12.7 and 3.5 Hz, 1 H, C*H*H$(CH_2)_2CH_3$], 1.40 [d, *J* = 6.9 Hz, 3 H, CH-(C*H*$_3)_2$], 1.28 [d, *J* = 6.9 Hz, 3 H, CH(C*H*$_3)_2$], 1.18 [d, *J* = 6.9 Hz, 3 H, CH(C*H*$_3)_2$], 1.14 [d, *J* = 6.9 Hz, 3 H, CH(C*H*$_3)_2$], 1.11 [d, *J* = 6.9 Hz, 3 H, CH(C*H*$_3)_2$], 0.87 [m, 8 H, $LiCH_2(CH_2)_2CH_3$], 0.83 [d, *J* = 6.9 Hz, 3 H, CH(C*H*$_3)_2$], 0.71 [t, *J* = 7.2 Hz, 3 H, $(CH_2)_3CH_3$], 0.64 [d, *J* = 6.9 Hz, 3 H, CH(C*H*$_3)_2$], –0.30 [d, *J* = 6.9 Hz, 3 H, CH(C*H*$_3)_2$], –0.98 [t, *J* = 7.0 Hz, 3 H, $LiCH_2$-$(CH_2)_2CH_3$] ppm.

**(dpp-bian)(H)(*n*Bu) (5):** Addition of $H_2O$ (0.3 mL) to a solution of **3** [prepared in situ from 1.0 g (2.0 mmol) of dpp-bian in $Et_2O$] caused an immediate yellow coloring of the reaction mixture. After evaporation of the solvent under reduced pressure, the residue was dried in vacuo for 1 h and was then recrystallized from $Et_2O$ (20 mL) to yield 0.85 g (76%) of compound **5** as yellow drusy crystals; m.p. > 179 °C. $C_{40}H_{50}N_2$ (558.82): calcd. C 85.97, H, 9.02; found C 85.88, H 8.98. IR (Nujol): $\tilde{\nu}$ = 3359 (w), 3057 (w), 1663 (vs), 1621 (w), 1598 (w), 1582 (m), 1491 (w), 1379 (s), 1363 (s), 1328 (m), 1305 (w), 1269 (w), 1252 (m), 1193 (m), 1179 (w), 1143 (w), 1113 (m), 1098 (w), 1051 (w), 1035 (m), 1019 (w), 1003 (w), 957 (w), 935 (m), 907 (w), 890 (w), 830 (s), 808 (w), 798 (s), 785 (vs), 769 (s), 755 (s), 726 (m), 708 (m), 667 (w), 649 (w), 632 (w), 606 (w), 597 (w), 559 (w), 538 (w), 522 (w), 511 (w), 469 (w), 449 (w) cm$^{-1}$. $^1$H NMR (200 MHz, [$D_8$]THF, 20 °C): $\delta$ = 7.48 (d, *J* = 8.3 Hz, 1 H, CH arom.), 6.64 (d, *J* = 8.3 Hz, 1 H, CH arom.), 7.28–7.12 (m, 4 H, CH arom.), 6.51 (d, *J* = 7.3 Hz, 1 H, CH arom.), 6.35 (d, *J* = 7.0 Hz, 1 H, CH arom.), 3.91 (s, 1 H, N–H), 3.08 [pseudo t, *J* = 6.8 Hz, 1 H, C*H*$(CH_3)_2$], 3.01 [pseudo t, *J* = 6.8 Hz, 1 H, C*H*$(CH_3)_2$], 2.56 (td, *J* = 12.2 and 3.8 Hz, 1 H, CH*H*$(CH_2)_2$-$CH_3$], 2.38 [td, *J* = 12.2 and 5.0 Hz, 1 H, C*H*H$(CH_2)_2CH_3$], 1.17 [d, *J* = 6.8 Hz, 3 H, CH(C*H*$_3)_2$], 1.05 [d, *J* = 6.8 Hz, 3 H, CH-(C*H*$_3)_2$], 0.92 [d, *J* = 6.8 Hz, 3 H, CH(C*H*$_3)_2$], 0.89 [d, *J* = 6.8 Hz, 3 H, CH(C*H*$_3)_2$], 0.66 [t, *J* = 7.3 Hz, 6 H, $(CH_2)_3CH_3$] ppm.

 © 2006 Wiley-VCH Verlag GmbH & Co. KGaA, Weinheim 

**[{dpp-bian(*n*Bu)}GeCl] (6):** Addition of a solution of **3** [prepared in situ from 1.0 g (2.0 mmol) of dpp-bian in $Et_2O$] to a stirred suspension of $GeCl_2$(dioxane) (0.46 g, 2.0 mmol) in $Et_2O$ (10 mL) caused a change of the color of the solution from blue to brown. The solution should be filtered immediately after mixing the reagents, otherwise **6** starts to crystallize from the reaction mixture on standing. Slow evaporation of the solvent from the filtrate at low pressure caused the crystallization of **6** as red crystals. Yield: 1.18 g (89%); m.p. 238 °C. $C_{40}H_{49}ClGeN_2$ (665.85): calcd. C 72.15, H 7.42; found C 72.05, H 7.30. IR (Nujol): $\tilde{\nu}$ = 1624 (s), 1589 (s), 1491 (w), 1378 (s), 1364 (w), 1315 (m), 1249 (s), 1221 (w), 1203 (m), 1187 (m), 1162 (w), 1141 (w), 1109 (m), 1099 (m), 1060 (m), 1050 (w), 1035 (m), 1005 (w), 961 (w), 933 (w), 919 (m), 884 (w), 861 (m), 833 (s), 819 (w), 800 (s), 784 (vs), 768 (w), 760 (s), 748 (m), 723 (s), 700 (w), 676 (w), 653 (w), 635 (w), 618 (m), 599 (w), 582 (w), 546 (w), 527 (w), 516 (w), 499 (w), 480 (m), 465 (w), 451 (w), 442 (w), 419 (m), 403 (m) $cm^{-1}$. $^1H$ NMR (200 MHz, [$D_8$]THF, 20 °C): $\delta$ = 8.08 (d, $J$ = 8.3 Hz, 1 H, CH arom.), 7.77 (d, $J$ = 8.3 Hz, 1 H, CH arom.), 7.54–7.31 (m, 6 H, CH arom.), 7.22 (pseudo t, $J$ = 7.3 Hz, 1 H, CH arom.), 6.97 (dd, $J$ = 7.5 and 1.7 Hz, 1 H, CH arom.), 6.55 (d, $J$ = 7.3 Hz, 1 H, CH arom.), 6.15 (d, $J$ = 7.0 Hz, 1 H, CH arom.), 4.66 [pseudo t, $J$ = 6.8 Hz, 1 H, C*H*-$(CH_3)_2$], 3.90 [td, $J$ = 13.0 and 4.0 Hz, 1 H, CH*H*$(CH_2)_2CH_3$], 3.79 [pseudo t, $J$ = 6.8 Hz, 1 H, C*H*$(CH_3)_2$], 3.01 [pseudo t, $J$ = 6.8 Hz, 1 H, C*H*$(CH_3)_2$], 2.61 [pseudo t, $J$ = 6.8 Hz, 1 H, C*H*$(CH_3)_2$], 2.41 [td, $J$ = 13.0 and 4.5 Hz, 1 H, C*H*H$(CH_2)_2CH_3$], 1.45 [d, $J$ = 6.9 Hz, 3 H, CH(C$H_3$)$_2$], 1.42 [d, $J$ = 6.9 Hz, 3 H, CH(C$H_3$)$_2$], 1.24 [d, $J$ = 6.9 Hz, 3 H, CH(C$H_3$)$_2$], 1.23 [d, $J$ = 6.9 Hz, 3 H, CH-(C$H_3$)$_2$], 1.20 [d, $J$ = 6.9 Hz, 3 H, CH(C$H_3$)$_2$], 1.13 [m, 3 H, $CH_2$(C$H_2$)$_2$C$H_3$], –0.06 [m, 1 H, $CH_2$(C$H_2$)$_2$C$H_3$], 0.90 [d, $J$ = 6.9 Hz, 3 H, CH(C$H_3$)$_2$], 0.66 [t, $J$ = 7.2 Hz, 3 H, $(CH_2)_3$C$H_3$], 0.64 [d, $J$ = 6.9 Hz, 3 H, CH(C$H_3$)$_2$], 0.05 [d, $J$ = 6.9 Hz, 3 H, CH-(C$H_3$)$_2$] ppm.

**Single-Crystal X-ray Structure Determination of 4–6:** The data were collected with a Siemens SMART CCD diffractometer (graphite-monochromated Mo-$K_\alpha$ radiation, $\omega$-scan technique, $\lambda$ = 0.71073 Å) at 173 K. **4:** $C_{88}H_{116}Li_4N_4{\cdot}C_6H_{14}$, $M$ = 1343.78, monoclinic, $a$ = 31.9219(11), $b$ = 12.7641(5), $c$ = 22.8212(8) Å, $\beta$ = 113.4070(10)°, $V$ = 8533.4(5) Å$^3$, $T$ = 173(2) K, space group $C2/c$, $Z$ = 4, $\mu$ = 0.059 $mm^{-1}$, 26677 reflections measured, 7521 unique ($R_{int}$ = 0.0895) which were used in all calculations. $R_1$ [$I > 2\sigma(I)$] = 0.0694, w$R_1$ (all data) = 0.1201. **5:** $C_{40}H_{50}N_2$, $M$ = 558.82, monoclinic, $a$ = 19.0920(8), $b$ = 9.1708(4), $c$ = 19.2750(7) Å, $\beta$ = 90.164(1)°, $V$ = 3374.8(2) Å$^3$, $T$ = 173(2) K, space group $P2_1/c$, $Z$ = 4, $\mu$ = 0.063 $mm^{-1}$, 20271 reflections measured, 5929 unique ($R_{int}$ = 0.1428) which were used in all calculations. $R_1$ [$I > 2\sigma(I)$] = 0.0593, w$R_1$ (all data) = 0.1240. **6:** $C_{40}H_{49}ClGeN_2$, $M$ = 665.85, monoclinic, $a$ = 9.7607(3), $b$ = 17.3631(6), $c$ = 21.0357(7) Å, $\beta$ = 97.9650(10)°, $V$ = 3530.7(2) Å$^3$, $T$ = 173(2) K, space group $P2_1/n$, $Z$ = 4, $\mu$ = 0.973 $mm^{-1}$, 23727 reflections measured, 6922 unique ($R_{int}$ = 0.0747) which were used in all calculations. $R_1$ [$I > 2\sigma(I)$] = 0.0409, w$R_1$ (all data) = 0.0940. The structures were solved by direct methods using SHELXS-97[24] and were refined on $F^2$ using SHELXL-97.[25] All non-hydrogen atoms were refined anisotropically and the hydrogen atoms were placed in calculated positions and assigned to an isotropic displacement parameter of 0.08 Å$^2$. SADABS[26] was used to perform area-detector scaling and absorption corrections. The geometrical aspects of the structures were analyzed with the PLATON program.[27] CCDC-605326 (**4**), -605327 (**5**), and -605328 (**6**) contain the supplementary crystallographic data for this paper. These data can be obtained free of charge from The Cambridge Crystallographic Data Centre via www.ccdc.cam.ac.uk/data_request/cif.

## Acknowledgments

This work was supported by the Russian Foundation for Basic Research (grant no. 05-03-32643), the Russian Science and Innovation Agency (grant no. 2006-RI-19.0/001/206) (I. F.) as well as the Fonds der Chemischen Industrie and the Deutsche Forschungsgemeinschaft (H. S.).

[1] a) M. W. van Laren, C. J. Elsevier, *Angew. Chem. Int. Ed.* **1999**, *38*, 3715; b) A. M. Kluwer, T. S. Koblenz, T. Jonischkeit, K. Woelk, C. J. Elsevier, *J. Am. Chem. Soc.* **2005**, *127*, 15470.
[2] a) R. van Belzen, H. Hoffmann, C. J. Elsevier, *Angew. Chem. Int. Ed. Engl.* **1997**, *36*, 1743; b) G. A. Grasa, R. Singh, E. D. Stevens, S. P. Nolan, *J. Organomet. Chem.* **2003**, *687*, 269.
[3] A. Heumann, L. Giordano, A. Tenaglia, *Tetrahedron Lett.* **2003**, *44*, 1515.
[4] J. W. Sprengers, M. de Greef, M. A. Duin, C. J. Elsevier, *Eur. J. Inorg. Chem.* **2003**, 3811.
[5] a) E. Cherian, E. B. Lobkovsky, G. W. Coates, *Chem. Commun.* **2003**, *20*, 2566; b) F. Al-Abaidi, Z. Ye, S. Zhu, *Macromol. Chem. Phys.* **2003**, *204*, 1653; c) V. Fassina, C. Ramminger, M. Seferin, R. S. Mauler, R. F. de Souza, A. L. Monteiro, *Macromol. Rapid Commun.* **2003**, *24*, 667; d) M. D. Leatherman, S. A. Svejda, L. K. Johnson, M. Brookhart, *J. Am. Chem. Soc.* **2003**, *125*, 3068; e) A. E. Cherian, J. M. Rose, E. B. Lobkovsky, G. W. Coates, *J. Am. Chem. Soc.* **2005**, *127*, 13770; f) D. H. Camacho, E. V. Salo, Z. Guan, J. W. Ziller, *Organometallics* **2005**, *24*, 4933; g) S. S. Ivanchev, V. K. Badaev, N. I. Ivancheva, E. V. Sviridova, S. Ya. Khaikin, D. G. Rogozin, A. S. Abakunchik, *Vysokomol. Soedin., Ser. A Ser. B* **2005**, *47*, 934.
[6] I. Kim, J.-M. Hwang, J. K. Lee, C. S. Ha, S. I. Woo, *Macromol. Rapid Commun.* **2003**, *24*, 508.
[7] D. Takeuchi, A. Yasuda, K. Osakada, *Dalton Trans.* **2003**, 2029.
[8] D. Takeuchi, K. Anada, K. Osakada, *Bull. Chem. Soc. Jpn.* **2005**, *78*, 1868.
[9] J. Kiesewetter, W. Kaminsky, *Chem. Eur. J.* **2003**, *9*, 1750.
[10] B. Binotti, C. Carfagna, C. Zuccaccia, A. Macchioni, *Chem. Commun.* **2005**, 92.
[11] a) B. S. Williams, M. D. Leatherman, P. S. White, M. Brookhart, *J. Am. Chem. Soc.* **2005**, *127*, 5132; b) J. Merna, J. Cihlar, M. Kucera, A. Deffieux, H. Cramail, *Eur. Polym. J.* **2005**, *41*, 303; c) W. Liu, M. Brookhart, *Organometallics* **2004**, *23*, 6099; d) D. H. Camacho, E. V. Salo, J. W. Ziller, Z. Guan, *Angew. Chem. Int. Ed.* **2004**, *43*, 1821.
[12] a) I. L. Fedushkin, A. A. Skatova, V. A. Chudakova, G. K. Fukin, *Angew. Chem. Int. Ed.* **2003**, *42*, 3294; b) I. L. Fedushkin, A. A. Skatova, V. A. Chudakova, V. K. Cherkasov, G. K. Fukin, M. A. Lopatin, *Eur. J. Inorg. Chem.* **2004**, 388.
[13] I. L. Fedushkin, A. A. Skatova, V. A. Chudakova, G. K. Fukin, S. Dechert, H. Schumann, *Eur. J. Inorg. Chem.* **2003**, 3336.
[14] A. N. Lukoyanov, I. L. Fedushkin, M. Hummert, H. Schumann, *Russ. Chem. Bull.*, in press.
[15] a) H. Schumann, M. Hummert, A. N. Lukoyanov, I. L. Fedushkin, *Organometallics* **2005**, *24*, 3891; b) A. N. Lukoyanov, I. L. Fedushkin, M. Hummert, H. Schumann, *Z. Anorg. Allg. Chem.*, in press.
[16] I. L. Fedushkin, A. A. Skatova, V. A. Chudakova, N. M. Khvoinova, A. Yu. Baurin, S. Dechert, M. Hummert, H. Schumann, *Organometallics* **2004**, *23*, 3714.
[17] a) I. L. Fedushkin, N. M. Khvoinova, A. Yu. Baurin, G. K. Fukin, V. K. Cherkasov, M. P. Bubnov, *Inorg. Chem.* **2004**, *43*, 7807; b) I. L. Fedushkin, N. M. Khvoinova, A. Yu. Baurin, V. A. Chudakova, A. A. Skatova, V. K. Cherkasov, G. K. Fukin, E. V. Baranov, *Russ. Chem. Bull.* **2006**, *55*, 74.
[18] I. L. Fedushkin, A. A. Skatova, M. Hummert, H. Schumann, *Eur. J. Inorg. Chem.* **2005**, 1601.

 © 2006 Wiley-VCH Verlag GmbH & Co. KGaA, Weinheim 

[19] I. L. Fedushkin, A. A. Skatova, V. K. Cherkasov, V. A. Chudakova, S. Dechert, M. Hummert, H. Schumann, *Chem. Eur. J.* **2003**, *9*, 5778.
[20] I. L. Fedushkin, V. M. Makarov, E. C. E. Rosenthal, G. K. Fukin, *Eur. J. Inorg. Chem.* **2006**, 827.
[21] a) I. L. Fedushkin, N. M. Khvoinova, A. A. Skatova, G. K. Fukin, *Angew. Chem. Int. Ed.* **2003**, *42*, 5223; b) I. L. Fedushkin, A. G. Morozov, O. V. Rassadin, G. K. Fukin, *Chem. Eur. J.* **2005**, *11*, 5749; c) I. L. Fedushkin, A. A. Skatova, G. K. Fukin, M. Hummert, H. Schumann, *Eur. J. Inorg. Chem.* **2005**, 2332.
[22] I. L. Fedushkin, V. A. Chudakova, G. K. Fukin, S. Dechert, M. Hummert, H. Schumann, *Russ. Chem. Bull.* **2004**, *53*, 2744.
[23] N. D. R. Barnett, R. E. Mulvey, W. Clegg, P. A. O'Neil, *J. Am. Chem. Soc.* **1993**, *115*, 1573.
[24] G. M. Sheldrick, *SHELXS-97, Program for the Solution of Crystal Structures*, University of Göttingen, **1990**.
[25] G. M. Sheldrick, *SHELXL-97, Program for the Refinement of Crystal Structures*, University of Göttingen, **1997**.
[26] G. M. Sheldrick, *SADABS, Program for Empirical Absorption Correction of Area Detector Data*, University of Göttingen, **1996**.
[27] A. L. Spek, *PLATON, A Multipurpose Crystallographic Tool*, Utrecht University, **2000**.

Received: March 27, 2006
Published Online: June 29, 2006

 © 2006 Wiley-VCH Verlag GmbH & Co. KGaA, Weinheim 

DOI: 10.1002/ejic.200600294

# A Route to Multi-Clusters Containing Half-Sandwich Rh and Ir Complexes of Chelating 1,2-Dicarba-*closo*-dodecaborane(12)-1,2-dithiolate Ligands

**Jian-Qiang Wang,[a] Chun-Xia Ren,[a] and Guo-Xin Jin*[a]**

*Dedicated to Professor Max Herberhold on the occasion of his 70th birthday*

**Keywords:** Iridium / Rhodium / Carboranes / N ligands / Cluster compounds

Reaction of the 16-electron half-sandwich rhodium and iridium complexes [Cp*M{$S_2C_2(B_{10}H_{10})$}] [M = Rh (**1a**), Ir (**1b**)] with multidentate ligands (L) such as 5,10,15,20-tetra(4-pyridyl)porphyrin) ($H_2$TPyP), 2,4,6-tri(4-pyridyl)-1,3,5-triazine (tpt), and 4,4′-azopyridine, gave the corresponding multicluster complexes [Cp*$MS_2C_2(B_{10}H_{10})]_n$(L) [M = Rh, Ir; $n$ = 4, L = $H_2$TPyP (**2**); 3, L = tpt (**3**); 2, L = 4,4′-azopyridine (**4**), *N*,*N*′-bis(4-pyridinylmethylene)biphenyl-4,4′-diamine (**5**), pyrazine, (**6**), 2,5-di(4-pyridyl)-1,3,4-oxadiazole (**7**), 1,2-di(4-pyridyl)ethylene) (**8**), diisonicotinic acid 1,4-phenylene diester (**9**), 4,4′-bipyridine (**10**)]. The X-ray structure of **2a** reveals that an $H_2$TPyP unit bridges four [Cp*$RhS_2C_2(B_{10}H_{10})$] fragments to form a tetranuclear [Cp*$RhS_2C_2(B_{10}H_{10})]_4$($H_2$TPyP) complex and the [Cp*$RhS_2C_2(B_{10}H_{10})$] units adopt a tail-to-tail contact mode, rather than a head-to-tail mode, in spite of the large steric repulsion between the two carborane ligands. In complex **3a**, three [Cp*$RhS_2C_2(B_{10}H_{10})$] units are symmetrically arranged around the periphery of one tpt core, thus forming a "bowl-shaped" structure. In **4a**, **5a**, **6a**, **8b**, and **9b**, two [Cp*$RhS_2C_2(B_{10}H_{10})$] fragments take a *trans* conformation around the linear or pseudo-linear pyridyl-based ligand core, while in **7a** they are in a *cis* conformation. All new complexes **2**–**10** were characterized by $^1$H and $^{11}$B NMR spectroscopy, and X-ray structural analyses are reported for complexes **2a**, **3a**, **4a**, **5a**, **6a**, **7a**, **8b**, and **9b**.

(© Wiley-VCH Verlag GmbH & Co. KGaA, 69451 Weinheim, Germany, 2006)

## Introduction

During the last decade, a series of mononuclear 16-electron Cp* half-sandwich complexes of Co, Rh, and Ir have been prepared that contain didentate, chelating 1,2-dicarba-*closo*-dodecaborane(12)-1,2-dichalcogenolate ligands $[(B_{10}H_{10})C_2E_2]^{2-}$ (E = S, Se).[1] These complexes exhibit a rich coordination chemistry due to both their unsaturation at the metal atom and the bridging or chelating properties of the sulfur or selenium atoms.[2] Among the types of target structures attracting attention are highly symmetrical, aesthetically appealing architectures such as star-shaped molecules.[3] The efforts to build cluster-supported molecular or supramolecular structures are expected to offer many fascinating research problems with potentially significant ramifications.[4] To the best of our knowledge, only a few examples of *ortho*-carboranyl-functionalized highly branched molecules have been reported in the search for efficient methods for assembling suitable organic or inorganic linkers into desired target metallodendrimers.[5–7] Carboranes are obvious candidates for such applications because of their synthetic versatility and well-developed derivative chemistry. Our laboratory and Herberhold et al. have already reported the synthesis of the 16-electron "pseudo-aromatic" half-sandwich complexes [Cp*M{$E_2C_2(B_{10}H_{10})$}] (M = Co, Rh, Ir; E = S, Se),[8] and a recent publication from our laboratory suggests that this species may be promising for further transformations owing to its electron deficiency at the metal center.[9] This has allowed the construction of a polycarborane molecular architecture that takes advantage of special attributes, such as an addition reaction at the metal center in a dichalcogenolato metal heterocycle.[8]

Here, we describe the assembly of soluble, air-stable supramolecular structures based on the metal-containing moieties [Cp*M{$S_2C_2(B_{10}H_{10})$}] (M = Rh **1a**; M = Ir **1b**), bridged by nitrogen-based, star-shaped organic spacers (Scheme 1).

[a] Shanghai Key Laboratory of Molecular Catalysis and Innovative Material, Department of Chemistry, Fudan University, Shanghai 200433, P. R. China
Fax: +86-21-6564-3776
E-mail: gxjin@fudan.edu.cn

 © 2006 Wiley-VCH Verlag GmbH & Co. KGaA, Weinheim 

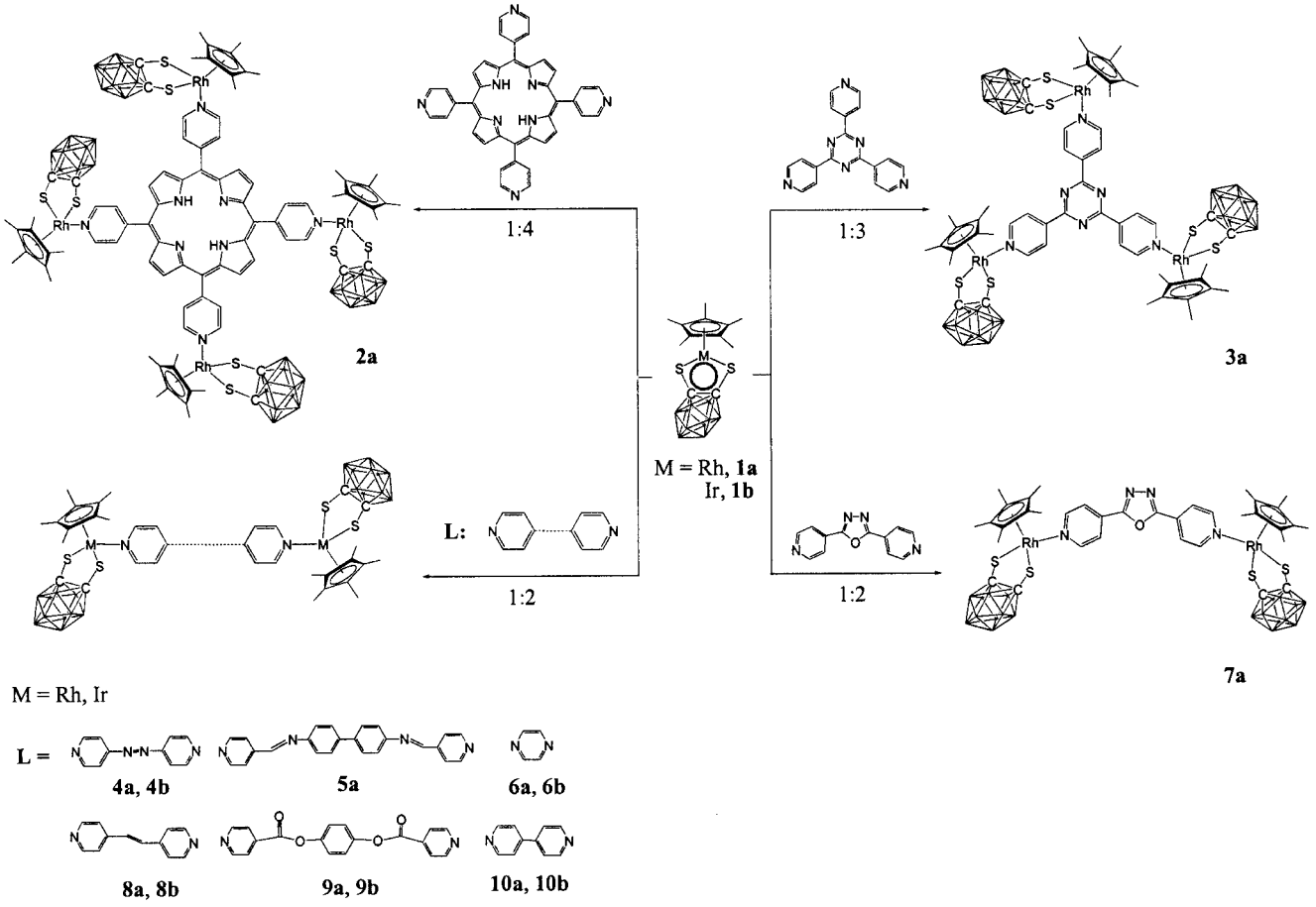


Scheme 1. Reaction of $[Cp^*MS_2C_2(B_{10}H_{10})]$ with a pyridyl-based ligand to give complexes **2**–**10**.

## Results and Discussion

### Synthesis and Characterization

We recently reported the reaction of the iridium precursor $[Cp^*IrS_2C_2(B_{10}H_{10})]$ (**1b**) with 2,4,6-tri(4-pyridyl)-1,3,5-triazine (tpt) and 4,4′-bipyridine, which leads to the formation of the multi-cluster $[Cp^*IrS_2C_2(B_{10}H_{10})]_n(L)$ [$n$ = 3, L = tpt; 2, L = 4,4′-bipyridine].[6] By using different metal complexes (**1a**, **1b**) and the linear or pseudo-linear pyridyl-based ligand that have been used as building blocks for discrete supramolecular assemblies[10] as starting materials, further neutral star-shaped molecules with $[Cp^*MS_2C_2(B_{10}H_{10})]$ (M = Rh or Ir) units can be synthesized. Scheme 1 shows the formation of star-shaped molecules **2**–**10**, which were characterized by single-crystal X-ray analysis, elemental analysis, and $^1$H NMR, $^{11}$B NMR and IR spectroscopy.

Stirring a mixture of $[Cp^*Rh\{S_2C_2(B_{10}H_{10})\}]$ (**1a**) and 5,10,15,20-tetra(4-pyridyl)porphyrin ($H_2TPyP$) in $CH_2Cl_2$ at room temperature for 24 h produced a red solution of **2a** in high yield. The IR spectrum shows a strong band at approximately 2559 cm$^{-1}$ due to the carborane group. The formation of **2a** was confirmed by the appearance of signals at $\delta$ = –2.89, 1.78, 8.20, 9.02, and 9.38 ppm in the $^1$H NMR spectrum, which are ascribed to the $H_2TPyP$ and Cp* ligands; the $^{11}$B NMR spectrum exhibits carborane (B–H) resonances at $\delta$ = –5.8, –8.2, –9.0, and –10.8 ppm.

Trinuclear complex **3a**, formulated as $[Cp^*Rh\{S_2C_2(B_{10}H_{10})\}]_3(tpt)$ from elemental analysis and $^1$H NMR spectroscopy, was formed when **1a** was treated with tpt in a 3:1 molar ratio in $CH_2Cl_2$ at room temperature (Scheme 1). The $^1$H NMR spectrum shows two kinds of resonances for each of the Cp* and tpt ligands, at $\delta$ = 1.77 ppm and $\delta$ = 8.67, 8.96 ppm respectively, suggesting the presence of configurational isomers. The signals at $\delta$ = –7.9 and –10.3 ppm in the $^{11}$B NMR spectrum suggest B–H activation.

The 16-electron "pseudo-aromatic" half-sandwich complexes **1a** and **1b** react readily with two equivalents of 4,4′-azopyridine to give dimeric complexes formulated as $[Cp^*M\{S_2C_2(B_{10}H_{10})\}]_2(C_{10}H_8N_4)$ (M = Rh **4a**, Ir **4b**). The IR spectra of **4a** and **4b** show B–H bands for the carboranes at 2568 and 2562 cm$^{-1}$, respectively. The $^1$H NMR spectrum of **4a** shows a singlet at $\delta$ = 1.77 ppm due to the methyl groups of the Cp* ligands and resonances at about $\delta$ = 7.76 and 8.85 ppm due to the 4,4′-azopyridine protons; that for **4b** has a singlet at $\delta$ = 1.87 and $\delta$ = 7.80 and 8.92 ppm. The $^{11}$B NMR spectrum exhibits a carborane (B–H) resonance at $\delta$ = –6.1, –7.5, –8.7, and –10.9 ppm for **4a** and $\delta$ = –6.2, –7.5, –8.6, and –10.5 ppm for **4b**. Detailed structures were confirmed by X-ray analysis of **4a** (see below), which re-

 © 2006 Wiley-VCH Verlag GmbH & Co. KGaA, Weinheim 

vealed that the complex is a dimer bridged by a 4,4′-azopyridine molecule.

Analogously, treatment of **1a** or **1b** with *N*,*N*′-bis(4-pyridinylmethylene)biphenyl-4,4′-diamine, pyrazine, 2,5-di(4-pyridyl)-1,3,4-oxadiazole, 1,2-di(4-pyridyl)ethylene, diisonicotinic acid 1,4-phenylene diester, or 4,4′-bipyridine also generated the dinuclear complexes $[Cp^*Rh\{S_2C_2(B_{10}H_{10})\}]_2(C_{24}H_{18}N_4)$ (**5a**), $[Cp^*M\{S_2C_2(B_{10}H_{10})\}]_2(C_4H_4N_2)$ (M = Rh **6a**, Ir **6b**), $[Cp^*Rh\{S_2C_2(B_{10}H_{10})\}]_2(C_{12}H_8N_4O)$ (**7a**), $[Cp^*M\{S_2C_2(B_{10}H_{10})\}]_2(C_{12}H_{10}N_2)$ (M = Rh **8a**, Ir **8b**), $[Cp^*Rh\{S_2C_2(B_{10}H_{10})\}]_2(C_{18}H_{12}N_2O_4)$ (M = Rh **9a**, Ir **9b**), $[Cp^*M\{S_2C_2(B_{10}H_{10})\}]_2(C_{10}H_8N_2)$ (M = Rh **10a**, Ir **10b**), respectively. All the $^1H$ NMR spectra in $CDCl_3$ show two resonances for each of the Cp* and pyridyl or pyrazine ligands and the $^{11}B$ NMR spectra in $CDCl_3$ exhibit a carborane (B–H) resonance. In the IR spectra, the B–H vibration bands of the carborane group appear at 2575–2580 $cm^{-1}$ for all of the complexes, and the C=O band appears at 1690 $cm^{-1}$ for **9a** and 1692 $cm^{-1}$ for **9b**.

### Molecular Structures

The crystal structure of **2a** consists of quadridentate units in which there are two crystallographically independent $Rh^{III}$ atoms and the $H_2TPyP$ ligand adopts a bridging mode (Figure 1, a). All of the rhodium centers adopt a three-legged piano-stool conformation with a six-coordinate geometry, assuming that the Cp* ligand functions as a three-coordinate ligand. The angles between adjacent atoms around the rhodium atoms are nearly 90°. All of the Cp* atoms fall in a fairly good plane, and the Cp* ligands are symmetrically bound to the rhodium atoms. The distances between Rh and the least-squares plane of the Cp* ring are 1.78 and 1.82 Å, which compare well with those for other rhodium complexes containing Cp*.[11,12] The dihedral angle along the S···S vector in the rhodadithiolato metallacycle ($RhS_2C_2$) is about 173° and 169°, compared to 180° in **1a**.[8b] An $H_2TPyP$ unit bridges four $[Cp^*RhS_2C_2(B_{10}H_{10})]$ fragments to form the tetranuclear $[Cp^*RhS_2C_2(B_{10}H_{10})]_4(H_2TPyP)$ complex. An interesting feature of this solid-state structure is that the $[Cp^*RhS_2C_2(B_{10}H_{10})]$ units adopt a tail-to-tail contact mode, rather than a head-to-tail mode, in spite of the large steric repulsion between the two carborane ligands, similar to that reported previously.[5] In the crystal lattice, molecules of **2a** form an extended two-dimensional layered structure. Within each layer, the molecules of **2a** interdigitate through the four legs, as depicted inpart b of Figure 1. The dihedral angle between neighboring porphyrins is 46.8°. The shortest distance between Cp* ligands in the same layer is 3.75 Å, and there is a very weak π–π interaction between the molecules. In addition, four dendrimer complexes in the same layer form a parallelogram with dimensions 15.4×18.0 $Å^2$. As illustrated in Figure 1 (b), there are channels running along the *b* axis. The overall free voids are 35.0% of the cell volume, omitting solvent molecules and hydrogen atoms.

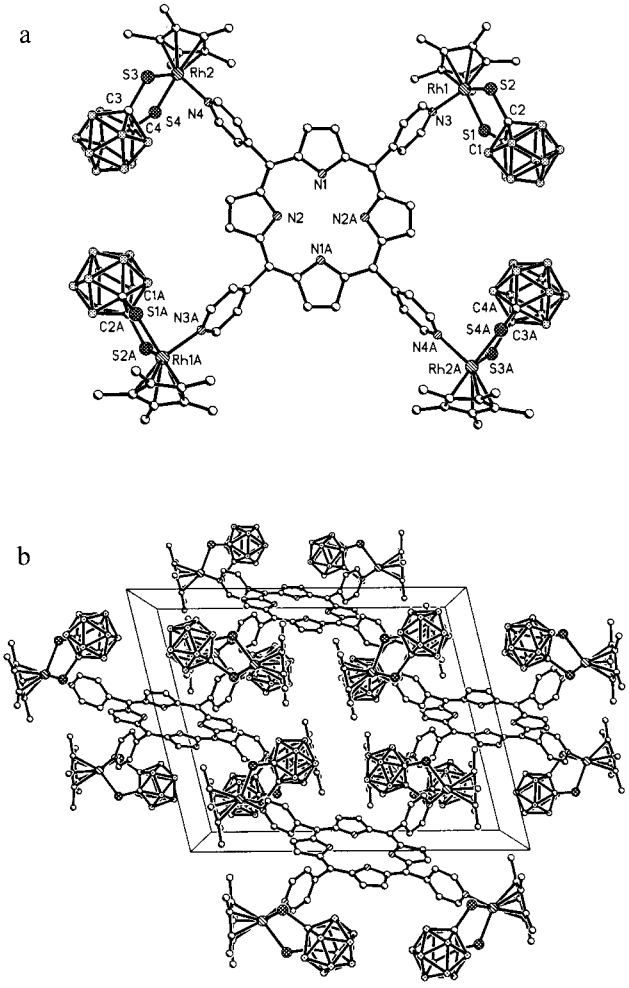


Figure 1. (a) Molecular unit of $[Cp^*RhS_2C_2(B_{10}H_{10})]_4(H_2TPyP)$ (**2a**). (b) Stacking of the molecules in crystals of **2a**, as viewed along the *b* axis. Selected distances [Å] and angles [°]: Rh(1)–N(3) 2.127(7), Rh(1)–S(1) 2.358(3), Rh(1)–S(2) 2.360(3), Rh(2)–N(4) 2.134(7), Rh(2)–S(4) 2.353(3), Rh(2)–S(3) 2.357(3), S(4)–C(4) 1.803(10), S(1)–C(1) 1.788(10), S(2)–C(2) 1.769(11), S(3)–C(3) 1.795(11), C(1)–C(2) 1.655(14), C(3)–C(4) 1.658(14); N(3)–Rh(1)–S(1) 89.3(2), N(3)–Rh(1)–S(2) 89.7(2), S(1)–Rh(1)–S(2) 90.62(10), N(4)–Rh(2)–S(4) 88.6(2), N(4)–Rh(2)–S(3) 91.9(2), S(4)–Rh(2)–S(3) 90.28(10), C(4)–S(4)–Rh(2) 106.4(3), C(1)–S(1)–Rh(1) 105.7(3), C(2)–S(2)–Rh(1) 106.0(3), C(3)–S(3)–Rh(2) 106.3(3).

Changing the ligand from $H_2TPyP$ to tpt gives **3a**, whose structure was established by X-ray structure analysis (Figure 2) and is very similar to that of $[Cp^*IrS_2C_2(B_{10}H_{10})]_3(tpt)$.[6] Three $[Cp^*RhS_2C_2(B_{10}H_{10})]$ units are symmetrically arranged around the periphery of one tpt core to form a "bowl-shaped" structure. All of the rhodium centers adopt a three-legged piano-stool conformation, which has six-coordinate geometry, assuming that the Cp* ligand functions as a three-coordinate ligand. The Rh–N bond lengths are 2.125(6)–2.144(9) Å, which are similar to those of **2a**. Each tpt ligand connects three Rh atoms related by crystallographic threefold symmetry in the tetragonal space group $P4_2/ncm$. It is interesting that the tpt ligand acts in a bifunctional tridentate fashion in **3a** through three N-donor atoms of the oligopyridyl and one triazine group. Two

 © 2006 Wiley-VCH Verlag GmbH & Co. KGaA, Weinheim 

neighboring molecules of **3a** are paired and staggered in a face-to-face fashion, with the separation between the central triazine rings being 3.46 Å, which is indicative of the presence of π–π stacking interactions. The two neighboring molecules within the stack are rotated by about 60° with respect to each other, just like two buckled bowls.

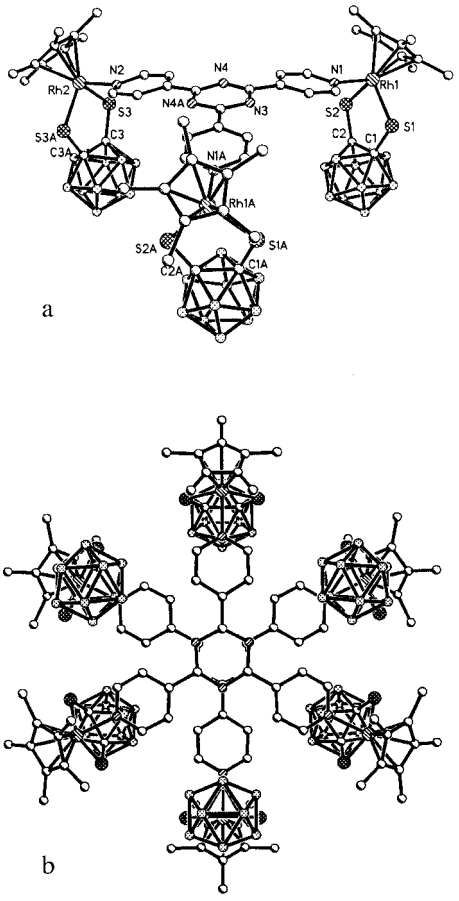


Figure 2. (a) Molecular unit of $[Cp^*RhS_2C_2(B_{10}H_{10})]_3(tpt)$ (**3a**). (b) Two units of **3a** in a staggered disposition. Selected distances [Å] and angles [°]: Rh(1)–N(1) 2.125(6), Rh(1)–S(1) 2.361(2), Rh(1)–S(2) 2.371(2), Rh(2)–N(2) 2.144(9), Rh(2)–S(3a) 2.360(3), Rh(2)–S(3) 2.360(3), S(1)–C(1) 1.765(8), S(2)–C(2) 1.776(8), S(3)–C(3) 1.760(11), C(1)–C(2) 1.690(12), C(3)–C(3a) 1.65(2); N(1)–Rh(1)–S(1) 90.72(18), N(1)–Rh(1)–S(2) 90.54(17), S(1)–Rh(1)–S(2) 91.05(8), N(2)–Rh(2)–S(3a) 90.0(2), N(2)–Rh(2)–S(3) 90.0(2), S(3a)–Rh(2)–S(3) 90.66(15), C(1)–S(1)–Rh(1) 106.0(3), C(2)–S(2)–Rh(1) 105.8(3), C(3)–S(3)–Rh(2) 105.7(4); symmetry transformation for the generation of equivalent atoms *a*: $-x+2, -y, -z+1$.

Another remarkable feature of **3a** is the packing pattern along the *c* axis. These "buckled bowls" stack along the *c* axis to form an interesting stacking structure. As shown in Figure 3, each of the eight molecules of **3a** is paired up to form two types of channels with the dimensions ranging from 3.6–4.0 Å. In other words, each molecule of **3a** is locked into position by pairing up with neighboring molecules in the crystal lattice. The packing in the crystals is such as to create infinite tunnels. It is interesting that such channels are constructed with a double-stranded helix, which consists of repeating "buckled bowl" molecules. Overall, the free voids form 40.1% of the cell volume, omitting hydrogen atoms.

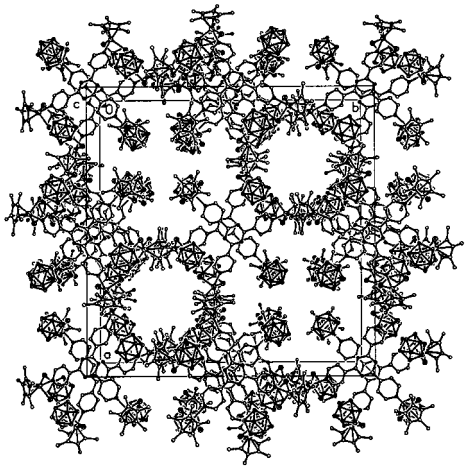


Figure 3. Crystal structure of **3a** viewed down the *c* axis. All hydrogen atoms have been omitted for clarity.

A perspective drawing of **4a** is given in Figure 4. The crystal unit has a crystallographically imposed inversion center in the middle of the Rh···Rh vector. The molecule has a dimeric structure connected by a 4,4′-azopyridine ligand. The plane of the rhodacycle has a dihedral angle of

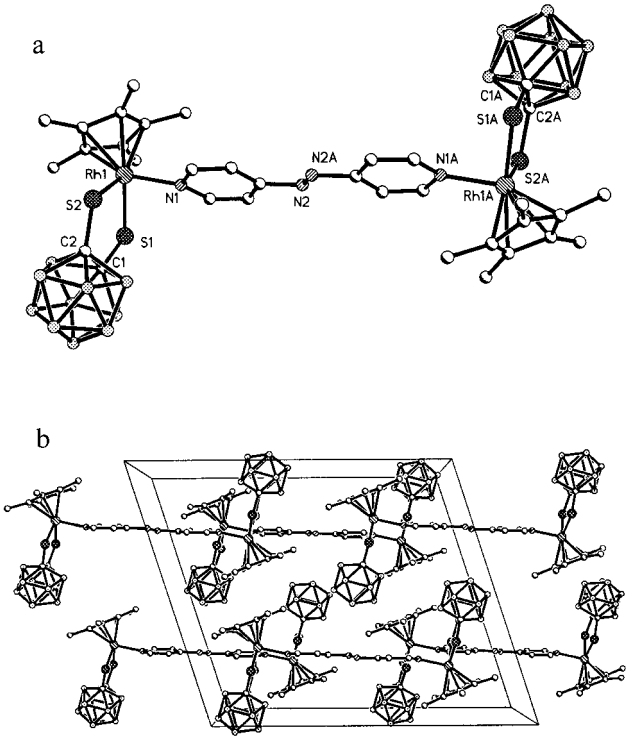


Figure 4. (a) Molecular unit of $[Cp^*Rh\{S_2C_2(B_{10}H_{10})\}]_2(C_{10}H_8N_4)$ (**4a**). (b) Crystal structure of **4a** viewed down the *b* axis. Selected distances [Å] and angles [°]: Rh(1)–N(1) 2.121(3), Rh(1)–S(2) 2.3487(11), Rh(1)–S(1) 2.3526(11), S(1)–C(1) 1.781(4), S(2)–C(2) 1.781(3), C(1)–C(2) 1.658(5); N(1)–Rh(1)–S(2) 90.23(9), N(1)–Rh(1)–S(1) 90.50(9), S(2)–Rh(1)–S(1) 91.06(4), C(1)–S(1)–Rh(1) 105.71(12), C(2)–S(2)–Rh(1) 106.30(13).

 © 2006 Wiley-VCH Verlag GmbH & Co. KGaA, Weinheim 

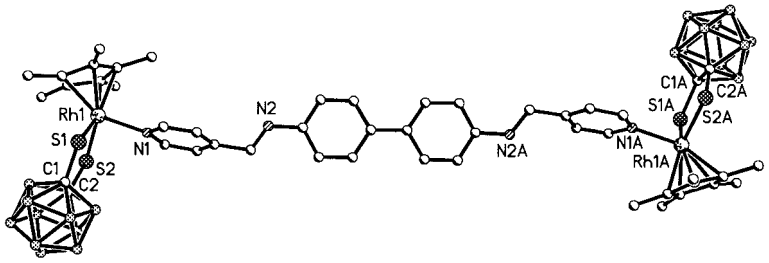


Figure 5. (a) Molecular unit of $[Cp^*Rh\{S_2C_2(B_{10}H_{10})\}]_2(C_{24}H_{18}N_4)$ $2(CHCl_3)$ (**5a**). All hydrogen atoms have been omitted for clarity. Selected distances [Å] and angles [°]: Rh(1)–N(1) 2.140(4), Rh(1)–S(2) 2.3530(17), Rh(1)–S(1) 2.3553(17), S(1)–C(1) 1.778(6), S(2)–C(2) 1.785(6), C(1)–C(2) 1.661(8); N(1)–Rh(1)–S(2) 91.32(14), N(1)–Rh(1)–S(1) 89.90(14), S(2)–Rh(1)–S(1) 91.30(6), C(1)–S(1)–Rh(1) 105.7(2), C(2)–S(2)–Rh(1) 105.7(2).

102.3° with 4,4′-azopyridine, and the Rh···Rh distance is 13.195 Å. Two neighboring molecules of **4a** are staggered in a face-to-face fashion, with the separation between the central Cp* rings being 3.64 Å, which is indicative of the presence of weak π–π stacking interactions (Figure 4, b).

The crystal structures of **5a** and **6a** are similar to that of **4a**, and also consist of $[Cp^*RhS_2C_2(B_{10}H_{10})]$ and *N*,*N*′-bis(4-pyridinylmethylene)biphenyl-4,4′-diamine or pyrazine adducts in a 2:1 molar ratio. As shown in Figures 5 and 6, each Rh is also in a three-legged piano-stool conformation. The Rh–N bond lengths are 2.129(3)–2.140(4) Å, similar to those of **2a**, **3a**, and **4a**. The crystal unit has a crystallographically imposed inversion center in the middle of the Rh···Rh vector. The molecule has a dimeric structure connected by a *N*,*N*′-bis(4-pyridinylmethylene)biphenyl-4,4′-diamine or pyrazine ligand, respectively. The plane of the rhodacycle has a dihedral angle of 100.7° with *N*,*N*′-bis(4-pyridinylmethylene)biphenyl-4,4′-diamine for **5a** and 86.7° with pyrazine for **6a**, and the Rh···Rh distance is 23.980 Å for **5** and 7.019 Å for **6a**.

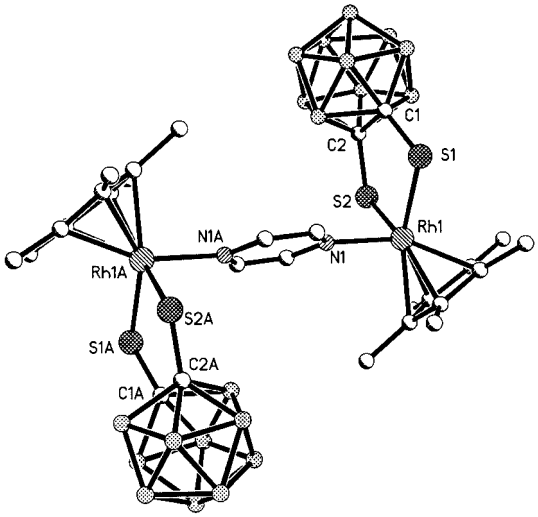


Figure 6. Molecular unit of $[Cp^*Rh\{S_2C_2(B_{10}H_{10})\}]_2(C_4H_4N_2)$ (**6a**). All hydrogen atoms have been omitted for clarity. Selected distances [Å] and angles [°]: Rh(1)–N(1) 2.129(3), Rh(1)–S(2) 2.3528(12), Rh(1)–S(1) 2.3662(12), S(1)–C(1) 1.784(4), S(2)–C(2) 1.769(4),C(1)–C(2), 1.665(5); N(1)–Rh(1)–S(2) 89.32(8), N(1)–Rh(1)–S(1) 91.26(9), S(2)–Rh(1)–S(1) 90.01(5), C(1)–S(1)–Rh(1) 105.97(14).

As shown in Figure 7, there are two crystallographically independent rhodium(III) atoms in the crystal of complex **7a**, and the stoichiometry of $[Cp^*Rh\{S_2C_2(B_{10}H_{10})\}]_2$-$(C_{12}H_8N_4O)$ is 2:1. Each $Rh^{III}$ is also located in a three-legged piano-stool conformation. The two metal atoms Rh(1) and Rh(2) are interconnected by 2,5-di(4-pyridyl)-1,3,5-oxadiazole groups to form a dimeric structure. The plane of each rhodacycle forms a dihedral angle of 88.4° and 91.6° with 2,5-di(4-pyridyl)-1,3,5-oxadiazole, respectively; the Rh(1)···Rh(2) distance is 13.820 Å. It is interesting to note that the two $[Cp^*RhS_2C_2(B_{10}H_{10})]$ fragments

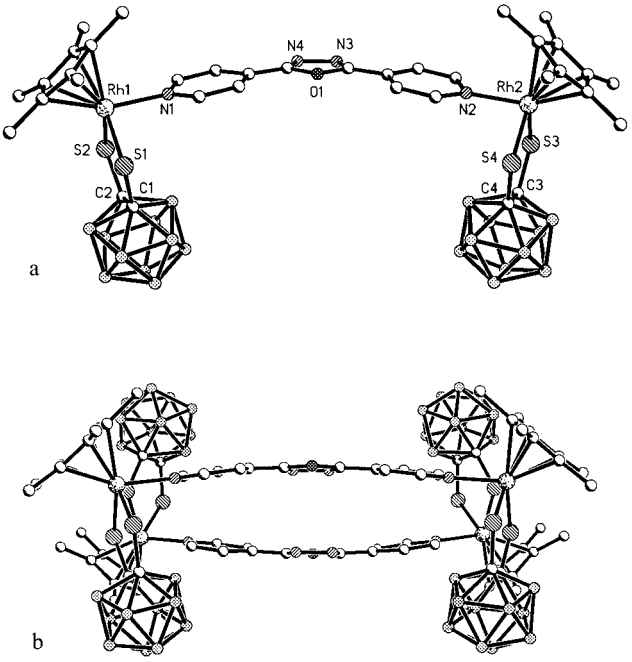


Figure 7. (a) Molecular unit of $[Cp^*Rh\{S_2C_2(B_{10}H_{10})\}]_2$-$(C_{12}H_8N_4O)\cdot(THF)$ (**7a**). (b) Two units of **7a** in a staggered disposition. All hydrogen atoms have been omitted for clarity. Selected distances [Å] and angles [°]: Rh(1)–N(1) 2.148(7), Rh(1)–S(1) 2.356(3), Rh(1)–S(2) 2.363(2), Rh(2)–N(2) 2.126(7), Rh(2)–S(4) 2.343(3), Rh(2)–S(3) 2.369(3), S(1)–C(1) 1.792(9), S(2)–C(2) 1.782(10), S(3)–C(3) 1.785(9), S(4)–C(4) 1.766(9), C(1)–C(2) 1.687(13), C(3)–C(4) 1.637(12); N(1)–Rh(1)–S(1) 91.7(2), N(1)–Rh(1)–S(2) 88.94(19), S(1)–Rh(1)–S(2) 90.38(10), N(2)–Rh(2)–S(4) 91.5(2), N(2)–Rh(2)–S(3) 88.8(2), S(4)–Rh(2)–S(3) 90.30(9), C(1)–S(1)–Rh(1) 106.7(3), C(2)–S(2)–Rh(1) 107.2(3), C(3)–S(3)–Rh(2) 105.7(3), C(4)–S(4)–Rh(2) 106.6(3).

 © 2006 Wiley-VCH Verlag GmbH & Co. KGaA, Weinheim 

are in a *cis* conformation, which is different from the *trans* conformation in **4a**, **5a**, and **6a**. It is also interesting that the 2,5-bis(4-pyridyl-1,3,5-oxadiazole) ligand is bifunctional didentate in **7a** through two N-donor atoms of the oligopyridyl and one oxadiazole group. Two neighboring molecules of **7a** are paired and staggered in a face-to-face fashion, with the separation between the central oxadiazole rings being 3.15 Å, which is indicative of the presence of strong π–π stacking interactions (Figure 7, b). The two neighboring molecules within the stack are rotated by about 180° with respect to each other, just like two buckled boxes.

The crystal structures of complexes **8b** and **9b** are quite similar to those of **4a**, **5a**, and **6a**. As shown in Figures 8 and 9, respectively, X-ray crystallographic analysis reveals that the complexes are dimers bridged by pyridyl ligands with an Ir···Ir distance of 13.461 Å for **8b** and 19.654 Å for **9b**. The plane of the iridacycle forms a dihedral angle with the pyridyl ring of 107.7° for **8b** and 97.5° for **9b**. It is interesting to note that the two [Cp*IrS$_2$C$_2$(B$_{10}$H$_{10}$)] fragments in **8b** and **9b** are in a *trans* conformation, similar to **4a**, **5a**, and **6a**.

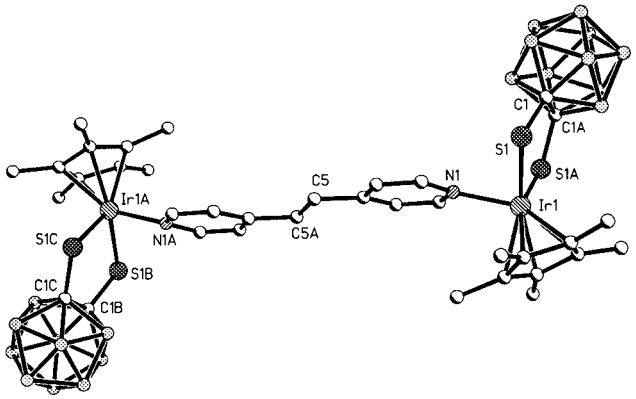


Figure 8. Molecular unit of [Cp*IrS$_2$C$_2$(B$_{10}$H$_{10}$)]$_2$(C$_{12}$H$_{10}$N$_2$) (**8b**). All hydrogen atoms have been omitted for clarity. Selected distances [Å] and angles [°]: Ir(1)–N(1) 2.115(5), Ir(1)–S(1) 2.3568(14), S(1)–C(1) 1.774(5), C(1)–C(1a) 1.662(10); N(1)–Ir(1)–S(1) 87.70(11), N(1)–Ir(1)–S(1a) 87.70(11), S(1)–Ir(1)–S(1a) 90.79(7), C(1)–S(1)–Ir(1) 105.50(17).

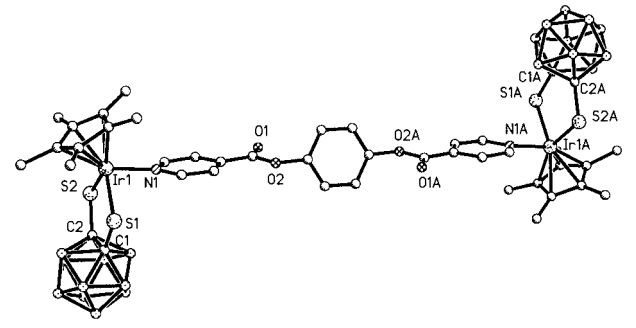


Figure 9. Molecular unit of [Cp*IrS$_2$C$_2$(B$_{10}$H$_{10}$)]$_2$(C$_{18}$H$_{12}$N$_2$O$_4$)·2(CH$_2$Cl$_2$) (**9b**). All hydrogen atoms have been omitted for clarity. Selected distances [Å] and angles [°]: Ir(1)–N(1) 2.132(8), Ir(1)–S(2) 2.3551(18), Ir(1)–S(1) 2.359(3), S(1)–C(1) 1.782(8), S(2)–C(2) 1.768(10), C(1)–C(2) 1.652(13); N(1)–Ir(1)–S(2) 90.35(17), N(1)–Ir(1)–S(1) 88.2(3), S(2)–Ir(1)–S(1) 90.71(7), C(1)–S(1)–Ir(1) 106.3(3), C(2)–S(2)–Ir(1) 105.6(3).

In summary, a new set of multi-cluster molecules has been synthesized from half-sandwich rhodium(III) and iridium(III) complexes bearing 1,2-dicarba-*closo*-dodecaborane(12)-1,2-dithiolate chelate ligands and different multidentate pyridyl ligands. This synthetic approach, which is based upon stepwise building-up of metal clusters with organic fragments, offers the potential for exquisite control over the detailed architecture of the materials, which may lead to a variety of unusual shapes.

## Experimental Section

All manipulations were performed under nitrogen using standard Schlenk techniques or in a glove box. Solvents were dried by refluxing over sodium/benzophenone ketyl (toluene, hexane, cyclohexane) and distilled just before use. [Cp*Rh{S$_2$C$_2$(B$_{10}$H$_{10}$)}] (**1a**),[12] [Cp*Ir{S$_2$C$_2$(B$_{10}$H$_{10}$)}] (**1b**),[13] 2,4,6-tri(4-pyridyl)-1,3,5-triazine,[14] 4,4′-azopyridine,[15] *N*,*N*′-bis(4-pyridinylmethylene)biphenyl-4,4′-diamine,[16] diisonicotinic acid 1,4-phenylene diester,[17] 2,5-di(4-pyridyl)-1,3,4-oxadiazole[18] were prepared by methods reported previously. IR spectra were recorded with a Nicolet AVATAR-360IR spectrometer, whereas $^1$H (500 MHz) and $^{11}$B (160 MHz) NMR spectra were obtained with a Bruker DMX-500 spectrometer in CDCl$_3$ solution. Elemental analyses were performed with an Elementar vario EI Analyzer.

**Caution!** *Perchlorate salts are explosive (especially when dry) and should be handled with care.*

**Synthesis of [Cp*Rh{S$_2$C$_2$(B$_{10}$H$_{10}$)}]$_4$(H$_2$TPyP) (2a):** A mixture of **1a** (178 mg, 0.4 mmol) and H$_2$TpyP (62 mg, 0.1 mmol) in CH$_2$Cl$_2$ (30 mL) was stirred for 24 h, whereupon the green-colored mixture gradually changed to red. The solvent was then evaporated under vacuum. The residue was washed with toluene to give a violet solid of **2a** (190 mg, 79%). C$_{88}$H$_{126}$B$_{40}$N$_8$Rh$_4$S$_8$ (2396.6): calcd. C 44.10, H 5.30, N 4.68; found C 43.85, H 5.16, N 4.57. $^1$H NMR (500 MHz, CDCl$_3$, 20 °C): $\delta$ = –2.89 (s, porphine NH, 2 H), 1.78 (s, C$_5$Me$_5$, 60 H), 8.20 (d, $^3J_{H,H}$ = 5 Hz, 3,5-pyridyl, 8 H), 9.02 (m, pyrrole, 8 H), 9.38 (d, $^3J_{H,H}$ = 5 Hz, 2,6-pyridyl, 8 H) ppm. $^{11}$B NMR (160 MHz, CDCl$_3$, 20 °C): $\delta$ = –5.8, –8.2, –9.0, –10.8 ppm. IR (KBr pellet): $\tilde{\nu}$ = 2581, 2559 ($\nu_{B-H}$), 1578, 1420, 986, 792 cm$^{-1}$.

**Synthesis of [Cp*Rh{S$_2$C$_2$(B$_{10}$H$_{10}$)}]$_3$(C$_{18}$H$_{12}$N$_6$) (3a):** A solution of **1a** (133 mg, 0.3 mmol) in CH$_2$Cl$_2$ (30 mL) was added to tpt (31 mg, 0.1 mmol) in CH$_2$Cl$_2$ (30 mL). The green-colored mixture was stirred for 24 h, whereupon it gradually changed to violet. The solvent was then evaporated under vacuum. The residue was washed with toluene to give a violet solid of **3a** (143 mg, 82%). C$_{54}$H$_{87}$B$_{30}$N$_6$Rh$_3$S$_6$ (1645.8): calcd. C 39.41, H 5.33, N 5.11; found C 39.28, H 5.27, N 5.10. $^1$H NMR (500 MHz, CDCl$_3$, 20 °C): $\delta$ = 1.77 (s, 30 H, C$_5$Me$_5$), 8.67 (br., 6 H, 3,5-pyridyl), 8.96 (br., 6 H, 2,6-pyridyl) ppm. $^{11}$B NMR (160 MHz, CDCl$_3$, 20 °C): $\delta$ = –7.9, –10.3 ppm. IR (KBr pellet): $\tilde{\nu}$ = 2573, 2559 cm$^{-1}$ ($\nu_{B-H}$).

**Synthesis of [Cp*Rh{S$_2$C$_2$(B$_{10}$H$_{10}$)}]$_2$(C$_{10}$H$_8$N$_4$) (4a):** A solution of **1a** (89 mg, 0.2 mmol) in CH$_2$Cl$_2$ (30 mL) was added to 4,4′-azopyridine (21 mg, 0.1 mmol) in CH$_2$Cl$_2$ (30 mL). The green-colored mixture was stirred for 24 h, whereupon it gradually became dark red. The solvent was then evaporated under vacuum. The residue was washed with toluene to give a red solid of **4a** (85 mg, 79%).

 © 2006 Wiley-VCH Verlag GmbH & Co. KGaA, Weinheim 

$C_{34}H_{58}B_{20}N_4Rh_2S_4$ (1073.1): calcd. C 38.05, H 5.45, N 5.22; found C 37.87, H 5.39, N 5.17. $^1$H NMR (500 MHz, $CDCl_3$, 20 °C): $\delta$ = 1.77 (s, 30 H, $C_5Me_5$), 7.76 (d, $^3J_{H,H}$ = 5 Hz, 4 H, 3,5-pyridyl), 8.85 (d, $^3J_{H,H}$ = 5 Hz, 4 H, 2,6-pyridyl) ppm. $^{11}$B NMR (160 MHz, $CDCl_3$, 20 °C): $\delta$ = –6.1, –7.5, –8.7, –10.9 ppm. IR (KBr pellet): $\tilde{\nu}$ = 2568 ($\nu_{B-H}$), 1657, 1600, 1491, 1450 cm$^{-1}$.

**Synthesis of [Cp*Ir{$S_2C_2(B_{10}H_{10})$}]$_2$($C_{10}H_8N_4$) (4b):** A solution of **1b** (106 mg, 0.2 mmol) in $CH_2Cl_2$ (30 mL) was added to 4,4′-azopyridine (21 mg, 0.1 mmol) in $CH_2Cl_2$ (30 mL). The blue-colored mixture was stirred for 24 h, whereupon it gradually became dark red. The solvent was then evaporated under vacuum. The residue was washed with toluene to give a red solid of **4b** (100 mg, 80%). $C_{34}H_{58}B_{20}Ir_2N_4S_4$ (1251.8): calcd. C 32.62, H 4.67, N 4.48; found C 32.39, H 4.61, N 4.43. $^1$H NMR (500 MHz, $CDCl_3$, 20 °C): $\delta$ = 1.87 (s, 30 H, $C_5Me_5$), 7.80 (d, $^3J_{H,H}$ = 5 Hz, 4 H, 3,5-pyridyl), 8.92 (d, $^3J_{H,H}$ = 5 Hz, 4 H, 2,6-pyridyl) ppm. $^{11}$B NMR (160 MHz, $CDCl_3$, 20 °C): $\delta$ = –6.2, –7.5, –8.6, –10.5 ppm. IR (KBr pellet): $\tilde{\nu}$ = 2562 ($\nu_{B-H}$), 1653, 1610, 1491, 1438 cm$^{-1}$.

**Synthesis of [Cp*Rh{$S_2C_2(B_{10}H_{10})$}]$_2$($C_{24}H_{18}N_4$) (5a):** A solution of **1a** (89 mg, 0.2 mmol) in $CH_2Cl_2$ (30 mL) was added to *N*,*N*′-bis(4-pyridinylmethylene)biphenyl-4,4′-diamine (36 mg, 0.1 mmol) in $CH_2Cl_2$ (30 mL). The green-colored mixture was stirred for 24 h, whereupon it gradually became dark red. The solvent was then evaporated under vacuum. The residue was washed with toluene to give a red solid of **5a** (91 mg, 73%). $C_{48}H_{68}B_{20}N_4Rh_2S_4$ (1251.4): calcd. C 46.07, H 5.48, N 4.48; found C 45.77, H 5.39, N 4.41. $^1$H NMR (500 MHz, $CDCl_3$, 20 °C): $\delta$ = 1.76 (s, 30 H, $C_5Me_5$), 7.2–7.5 (m, 8 H, biphenyl), 7.69 (s, 2 H, CH), 8.25 (br., 4 H, 3,5-pyridyl), 9.12 (br., 4 H, 2,6-pyridyl) ppm. $^{11}$B NMR (160 MHz, $CDCl_3$, 20 °C): $\delta$ = –6.1, –7.5, –8.9, –10.6, –12.2 ppm. IR (KBr pellet): $\tilde{\nu}$ = 2551, 2573 cm$^{-1}$($\nu_{B-H}$).

**Synthesis of [Cp*Rh{$S_2C_2(B_{10}H_{10})$}]$_2$($C_4H_4N_2$) (6a):** A solution of **1a** (178 mg, 0.4 mmol) in $CH_2Cl_2$ (30 mL) was added to pyrazine (17 mg, 0.2 mmol) in $CH_2Cl_2$ (30 mL). The green-colored mixture was stirred for 24 h, whereupon it gradually became dark red. The solvent was then evaporated under vacuum. The residue was washed with toluene to give a red solid of **6a** (159 mg, 82%). $C_{28}H_{54}B_{20}N_2Rh_2S_4$ (969.03): calcd. C 34.70, H 5.62, N 2.89; found C 34.59, H 5.58, N 2.83. $^1$H NMR (500 MHz, $CDCl_3$, 20 °C): $\delta$ = 1.79 (s, 30 H, $C_5Me_5$), 8.80 (s, 4 H, pyrazine) ppm. $^{11}$B NMR (160 MHz, $CDCl_3$, 20 °C): $\delta$ = –7.7, –10.2 ppm. IR (KBr pellet): $\tilde{\nu}$ = 2563 cm$^{-1}$ ($\nu_{B-H}$).

**Synthesis of [Cp*Ir{$S_2C_2(B_{10}H_{10})$}]$_2$($C_4H_4N_2$) (6b):** A solution of **1b** (213 mg, 0.4 mmol) in $CH_2Cl_2$ (30 mL) was added to pyrazine (17 mg, 0.2 mmol) in $CH_2Cl_2$ (30 mL). The green-colored mixture was stirred for 24 h, whereupon it gradually became dark red. The solvent was then evaporated under vacuum. The residue was washed with toluene to give a red solid of **6b** (197 mg, 86%). $C_{28}H_{54}B_{20}Ir_2N_2S_4$ (1147.66): calcd. C 29.30, H 4.74, N 2.44; found C 29.01, H 4.71, N 2.42. $^1$H NMR (500 MHz, $CDCl_3$, 20 °C): $\delta$ = 1.86 (s, 30 H, $C_5Me_5$), 8.81 (s, 4 H, pyrazine) ppm. $^{11}$B NMR (160 MHz, $CDCl_3$, 20 °C): $\delta$ = –7.3, –10.1 ppm. IR (KBr pellet): $\tilde{\nu}$ = 2558 cm$^{-1}$ ($\nu_{B-H}$)

**Synthesis of [Cp*Rh{$S_2C_2(B_{10}H_{10})$}]$_2$($C_{12}H_8N_4O$) (7a):** A solution of **1a** (89 mg, 0.2 mmol) in $CH_2Cl_2$ (30 mL) was added to 2,5-di(4-pyridyl)-1,3,5-oxadiazole (22 mg, 0.1 mmol) in $CH_2Cl_2$ (30 mL). The green-colored mixture was stirred for 24 h, whereupon it gradually became dark red. The solvent was then evaporated under vacuum. The residue was washed with toluene to give a red solid of **7a** (86 mg, 77%). $C_{36}H_{58}B_{20}N_4ORh_2S_4$ (1113.2): calcd. C 38.84, H 5.25, N 5.03; found C 38.49, H 5.17, N 4.98. $^1$H NMR (500 MHz, $CDCl_3$, 20 °C): $\delta$ = 1.76 (s, 30 H, $C_5Me_5$), 7.67 (d, $^3J_{H,H}$ = 5 Hz, 4 H, 3,5-pyridyl), 8.76 (d, $^3J_{H,H}$ = 5 Hz, 4 H, 2,6-pyridyl) ppm. $^{11}$B NMR (160 MHz, $CDCl_3$, 20 °C): $\delta$ = –5.7, –7.3, –8.9, –10.6 ppm. IR (KBr pellet): $\tilde{\nu}$ = 2555, 2576 cm$^{-1}$ ($\nu_{B-H}$).

**Synthesis of [Cp*Rh{$S_2C_2(B_{10}H_{10})$}]$_2$($C_{12}H_{10}N_2$) (8a):** A solution of **1a** (89 mg, 0.2 mmol) in $CH_2Cl_2$ (30 mL) was added to 1,2-di(4-pyridyl)ethylene (18 mg, 0.1 mmol) in $CH_2Cl_2$ (30 mL). The green-colored mixture was stirred for 24 h, whereupon it gradually became dark red. The solvent was then evaporated under vacuum. The residue was washed with toluene to give a red solid of **8a** (76 mg, 71%). $C_{36}H_{60}B_{20}Rh_2N_2S_4$ (1071.2): calcd. C 40.37, H 5.65, N 2.62; found C 40.19, H 5.53, N 2.55. $^1$H NMR (500 MHz, $CDCl_3$, 20 °C): $\delta$ = 1.77 (s, 30 H, $C_5Me_5$), 7.20 (m, 2 H, CH), 7.56 (br., 4 H, 3,5-pyridyl), 8.81 (m, 4 H, 2,6-pyridyl) ppm. $^{11}$B NMR (160 MHz, $CDCl_3$, 20 °C): $\delta$ = –5.8, –7.2, –8.5, –10.3 ppm. IR (KBr pellet): $\tilde{\nu}$ = 2559, 2580 cm$^{-1}$ ($\nu_{B-H}$).

**Synthesis of [Cp*Ir{$S_2C_2(B_{10}H_{10})$}]$_2$($C_{12}H_{10}N_2$) (8b):** A solution of **1b** (106 mg, 0.2 mmol) in $CH_2Cl_2$ (30 mL) was added to 1,2-di(4-pyridyl)ethylene (18 mg, 0.1 mmol) in $CH_2Cl_2$ (30 mL). The blue-colored mixture was stirred for 24 h, whereupon it gradually became dark red. The solvent was then evaporated under vacuum. The residue was washed with toluene to give a red solid of **8b** (94 mg, 75%). $C_{36}H_{60}B_{20}Ir_2N_2S_4$ (1249.8): calcd. C 34.60, H 4.84, N 2.24; found C 34.31, H 4.79, N 2.21. $^1$H NMR (500 MHz, $CDCl_3$, 20 °C): $\delta$ = 1.87 (s, $C_5Me_5$, 30 H), 7.26 (m, CH, 2 H), 7.71 (br., pyridyl, 4 H), 8.92 (br., pyridyl, 4 H) ppm. $^{11}$B NMR (160 MHz, $CDCl_3$, 20 °C): $\delta$ = –5.9, –7.1, –8.5, –10.5 ppm. IR (KBr pellet): $\tilde{\nu}$ = 2561, 2579 cm$^{-1}$ ($\nu_{B-H}$).

**Synthesis of [Cp*Rh{$S_2C_2(B_{10}H_{10})$}]$_2$($C_{18}H_{12}N_2O_4$) (9a):** A solution of **1a** (89 mg, 0.2 mmol) in $CH_2Cl_2$ (30 mL) was added to diisonicotinic acid 1,4-phenylene diester (32 mg, 0.1 mmol) in $CH_2Cl_2$ (30 mL). The green-colored mixture was stirred for 24 h, whereupon it gradually became dark red. The solvent was then evaporated under vacuum. The residue was washed with toluene to give a red solid of **9a** (98 mg, 81%). $C_{42}H_{62}B_{20}N_2O_4Rh_2S_4$ (1209.2): calcd. C 41.72, H 5.17, N 2.32; found C 41.59, H 5.08, N 2.25. $^1$H NMR (500 MHz, $CDCl_3$, 20 °C): $\delta$ = 1.78 (s, $C_5Me_5$, 20 H), 7.26 (s, phenyl, 4 H), 7.79 (d, $^3J_{H,H}$ = 5 Hz, 4 H, 3,5-pyridyl), 8.95 (s, $^3J_{H,H}$ = 5 Hz, 4 H, 2,6-pyridyl) ppm. $^{11}$B NMR (160 MHz, $CDCl_3$, 20 °C): $\delta$ = –3.2, –5.3, –7.0, –8.2, –9.7, –12.8 ppm (signal overlap). IR (KBr pellet): $\tilde{\nu}$ = 2563, 2575 cm$^{-1}$ ($\nu_{B-H}$), 1692 ($\nu_{C=O}$).

**Synthesis of [Cp*Ir{$S_2C_2(B_{10}H_{10})$}]$_2$($C_{18}H_{12}N_2O_4$) (9b):** A solution of **1b** (106 mg, 0.2 mmol) in $CH_2Cl_2$ (30 mL) was added to diisonicotinic acid 1,4-phenylene diester (32 mg, 0.1 mmol) in $CH_2Cl_2$ (30 mL). The blue-colored mixture was stirred for 24 h, whereupon it gradually became dark red. The solvent was then evaporated under vacuum. The residue was washed with toluene to give a red solid of **9b** (115 mg, 83%). $C_{42}H_{62}B_{20}Ir_2N_2O_4S_4$ (1387.9): calcd. C 36.35, H 4.50, N 2.02; found C 36.07, H 4.39, N 1.93. $^1$H NMR (500 MHz, $CDCl_3$, 20 °C): $\delta$ = 1.89 (s, $C_5Me_5$, 20 H), 7.31 (s, phenyl, 4 H), 7.89 (d, $^3J_{H,H}$ = 5 Hz, 4 H, 3,5-pyridyl), 9.01 (d, $^3J_{H,H}$ = 5 Hz, 4 H, 2,6-pyridyl) ppm. $^{11}$B NMR (160 MHz, $CDCl_3$, 20 °C): $\delta$ = –3.2, –5.3, –7.0, –8.2, –9.7, –12.8 ppm (signal overlap). IR (KBr pellet): $\tilde{\nu}$ = 2562, 2575 cm$^{-1}$ ($\nu_{B-H}$), 1690 ($\nu_{C=O}$).

**Synthesis of [Cp*Rh{$S_2C_2(B_{10}H_{10})$}]($C_{10}H_8N_2$) (10a):** A solution of **1a** (89 mg, 0.2 mmol) in $CH_2Cl_2$ (30 mL) was added to 4,4′-bipyridine (16 mg, 0.1 mmol) in $CH_2Cl_2$ (30 mL). The green-colored mixture was stirred for 24 h, whereupon it gradually became dark red. The solvent was then evaporated under vacuum. The residue was washed with toluene to give a red solid of **10a** (85 mg, 81%). $C_{34}H_{58}B_{20}N_2Rh_2S_4$ (1045.1): calcd. C 39.07, H 5.59, N 2.68; found C 38.92, H 5.46, N 2.60. $^1$H NMR (500 MHz, $CDCl_3$, 20 °C): $\delta$ = 1.78 (s, $C_5Me_5$, 30 H), 7.53 (d, $^3J_{H,H}$ = 5 Hz, 2,6-pyridyl, 4 H),

 © 2006 Wiley-VCH Verlag GmbH & Co. KGaA, Weinheim 

8.71 (d, $^3J_{H,H}$ = 5 Hz, 3,5-pyridyl, 4 H) ppm. $^{11}$B NMR (160 MHz, $CDCl_3$, 25 °C): $\delta$ = –6.5, –7.7, –8.1, –10.8 ppm. IR (KBr pellet): $\tilde{\nu}$ = 2582, 2571 cm$^{-1}$ ($\nu_{B-H}$).

**Synthesis of [Cp*Ir{$S_2C_2(B_{10}H_{10})$}]($C_{10}H_8N_2$) (10b):** A solution of **1b** (106 mg, 0.2 mmol) in $CH_2Cl_2$ (30 mL) was added to 4,4′-bipyridine (16 mg, 0.1 mmol) in $CH_2Cl_2$ (30 mL). The blue-colored mixture was stirred for 24 h, whereupon it gradually became dark red. The solvent was then evaporated under vacuum. The residue was washed with toluene to give a red solid of **10b** (106 mg, 87%). $C_{34}H_{58}B_{20}Ir_2N_2S_4$ (1223.75): calcd. C 33.37, H 4.78, N 2.29; found C 32.98, H 4.57, N 2.23. $^1$H NMR (500 MHz, $CDCl_3$, 20 °C): $\delta$ = 1.86 (s, $C_5Me_5$, 30 H), 7.57 (d, $^3J_{H,H}$ = 5 Hz, 3,5-pyridyl, 4 H), 8.77 (d, $^3J_{H,H}$ = 5 Hz, 2,6-pyridyl, 4 H) ppm. $^{11}$B NMR (160 MHz, $CDCl_3$, 25 °C): $\delta$ = –6.3, –8.1, –8.7, –10.3 ppm. IR (KBr pellet): $\tilde{\nu}$ = 2583, 2571 cm$^{-1}$ ($\nu_{B-H}$).

**X-ray Crystallographic Analysis:** Diffraction intensity data were collected with a Bruker Smart Apex CCD diffractometer. The determination of the unit cell and the collection of intensity data were performed with graphite-monochromated Mo-$K_\alpha$ radiation ($\lambda$ = 0.71073 Å). All the data were collected at room temperature using the $\omega$-scan technique. The structures were solved by direct methods using Fourier techniques, and refined on $F^2$ by a full-matrix least-squares method. SADABS[19] absorption corrections were applied to the data. All non-hydrogen atoms were refined with anisotropic

Table 1. Crystallographic data for compounds **2a**, **3a**, and **4a**.

| | **2a** | **3a** | **4a** |
|---|---|---|---|
| Empirical formula | $C_{47}H_{68}B_{20}Cl_6N_4Rh_2S_4$ | $C_{54}H_{87}B_{30}N_6Rh_3S_3$ | $C_{34}H_{58}B_{20}N_4Rh_2S_4$ |
| $M$ | 1452.01 | 1645.68 | 1073.10 |
| Crystal size [mm] | 0.20×0.18×0.15 | 0.36×0.25×0.18 | 0.15×0.12×0.10 |
| Crystal system | monoclinic | tetragonal | monoclinic |
| Space group | $P2_1/n$ | $P4_2/n$cm | $C2/c$ |
| $a$ [Å] | 17.054(5) | 35.361(8) | 18.589(6) |
| $b$ [Å] | 19.400(6) | 35.361(8) | 13.115(4) |
| $c$ [Å] | 21.333(6) | 16.106(5) | 21.696(8) |
| $\beta$ [°] | 103.470(5) | | 107.890(5) |
| $V$ [Å$^3$] | 6864(3) | 20139(9) | 5034(3) |
| $Z$ | 4 | 8 | 4 |
| $\rho_{calcd.}$ [g cm$^{-3}$] | 1.405 | 1.086 | 1.416 |
| $\mu$(Mo-$K_\alpha$) [mm$^{-1}$] | 0.872 | 0.642 | 0.854 |
| Collected reflections | 28432 | 81749 | 12471 |
| Unique | 12021 | 9069 | 5506 |
| Parameters | 748 | 464 | 304 |
| Goodness of fit | 1.040 | 1.092 | 0.779 |
| $R_1$[a] [$I > 2\sigma(I)$] | 0.0928 | 0.0835 | 0.0404 |
| $wR_2$[a] [$I > 2\sigma(I)$] | 0.2144 | 0.2436 | 0.0639 |
| Max./min. residual density [e Å$^{-3}$] | 2.006/–0.812 | 1.144/–0.502 | 0.575/–0.430 |

[a] $R_1 = \Sigma||F_o|-|F_c||$ (based on reflections with $F_o^2 > 2\sigma F^2$). $wR_2 = [\Sigma\{w(F_o^2-F_c^2)^2\}/\Sigma\{w(F_o^2)^2\}]^{1/2}$; $w = 1/[\sigma^2(F_o^2)+(0.095P)^2]$; $P = [\max(F_o^2, 0)+2F_c^2]/3$ (also with $F_o^2 > 2\sigma F^2$).

Table 2. Crystallographic data for compounds **5a**, **6a**, and **7a**.

| | **5a** | **6a** | **7a** |
|---|---|---|---|
| Empirical formula | $C_{25}H_{37}B_{10}Cl_3N_2RhS_2$ | $C_{28}H_{54}B_{20}N_2Rh_2S_4$ | $C_{40}H_{62}B_{20}N_4O_2Rh_2S_4$ |
| $M$ | 747.05 | 968.99 | 1181.20 |
| Crystal size | 0.20×0.16×0.10 | 0.20×0.15×0.10 | 0.10×0.10×0.08 |
| Crystal system | monoclinic | triclinic | monoclinic |
| Space group | $P2_1/n$ | $P\bar{1}$ | $P2_1/c$ |
| $a$ [Å] | 11.530(2) | 8.0300(16) | 12.213(4) |
| $b$ [Å] | 12.845(3) | 11.270(2) | 18.241(6) |
| $c$ [Å] | 24.066(5) | 13.560(3) | 25.984(8) |
| $\alpha$ [°] | | 95.82(3) | |
| $\beta$ [°] | 99.272(3) | 90.96(3) | 94.340(6) |
| $\gamma$ [°] | | 109.54(3) | |
| $V$ [Å$^3$] | 3517.7(12) | 1148.8(4) | 5772(3) |
| $Z$ | 4 | 1 | 4 |
| $\rho_{calcd.}$ [g cm$^{-3}$] | 1.411 | 1.401 | 1.359 |
| $\mu$(Mo-$K_\alpha$) [mm$^{-1}$] | 0.853 | 0.926 | 0.754 |
| Collected reflections | 14548 | 4868 | 24082 |
| Unique | 6213 | 4000 | 10171 |
| Parameters | 398 | 268 | 654 |
| Goodness of fit | 1.020 | 1.038 | 0.704 |
| $R_1$[a] [$I > 2\sigma(I)$] | 0.0615 | 0.0371 | 0.0520 |
| $wR_2$[a] [$I > 2\sigma(I)$] | 0.1395 | 0.0857 | 0.1141 |
| Max./min. residual density [e Å$^{-3}$] | 0.905/–0.578 | 0.338/–0.440 | 0.996/–0.472 |

[a] $R_1 = \Sigma||F_o|-|F_c||$ (based on reflections with $F_o^2 > 2\sigma F^2$). $wR_2 = [\Sigma\{w(F_o^2-F_c^2)^2\}/\Sigma\{w(F_o^2)^2\}]^{1/2}$; $w = 1/[\sigma^2(F_o^2)+(0.095P)^2]$; $P = [\max(F_o^2, 0)+2F_c^2]/3$ (also with $F_o^2 > 2\sigma F^2$).

 © 2006 Wiley-VCH Verlag GmbH & Co. KGaA, Weinheim 

Table 3. Crystallographic data for compounds **8b** and **9b**.

| | **8b** | **9b** |
|---|---|---|
| Empirical formula | $C_{19}H_{32}B_{10}Cl_2IrNS_2$ | $C_{44}H_{66}B_{20}Cl_4Ir_2N_2O_4S_4$ |
| $M$ | 709.78 | 1557.63 |
| Crystal size | 0.30×0.18×0.15 | 0.12×0.10×0.06 |
| Crystal system | orthorhombic | orthorhombic |
| Space group | *Pnnm* | *Pbca* |
| $a$ [Å] | 14.804(4) | 17.865(6) |
| $b$ [Å] | 18.493(5) | 15.210(5) |
| $c$ [Å] | 10.485(3) | 22.950(7) |
| $V$ [Å$^3$] | 2870.4(14) | 6236(3) |
| $Z$ | 4 | 4 |
| $\rho_{calcd.}$ [g cm$^{-3}$] | 1.642 | 1.659 |
| $\mu$(Mo-$K_\alpha$) [mm$^{-1}$] | 4.995 | 4.611 |
| Collected reflections | 11645 | 5575 |
| Unique | 2694 | 3395 |
| Parameters | 200 | 376 |
| Goodness of fit | 1.097 | 0.719 |
| $R_1$[a] [$I > 2\sigma(I)$] | 0.0303 | 0.0319 |
| $wR_2$[a] [$I > 2\sigma(I)$] | 0.0799 | 0.0447 |
| Max./min. residual density [e Å$^{-3}$] | 1.546/–1.030 | 0.556/–0.570 |

[a] $R_1 = \Sigma||F_o|-|F_c||$ (based on reflections with $F_o^2 > 2\sigma F^2$). $wR_2 = [\Sigma\{w(F_o^2-F_c^2)^2\}/\Sigma\{w(F_o^2)^2\}]^{1/2}$; $w = 1/[\sigma^2(F_o^2)+(0.095P)^2]$; $P = [\max(F_o^2, 0)+2F_c^2]/3$ (also with $F_o^2 > 2\sigma F^2$).

displacement coefficients, expect the solvent molecules in **2a** and **7a**. Hydrogen atoms were used in calculated positions. All the calculations were carried out using the program SHELXTL.[20] All figures were produced with the PLATON program.[21] Crystal data, data-collection parameters, and the results of the analyses of compounds **2a**, **3a**, and **4a** (Table 1), **5a**, **6a**, and **7a** (Table 2), and **8b** and **9b** (Table 3) are given below.

CCDC-298247, -298248, -298249, -298250, -298251, -298252, -298253, and -298254 contain the supplementary crystallographic data for this paper. These data can be obtained free of charge from The Cambridge Crystallographic Data Center via www.ccdc.cam.ac.uk/data_request/cif.

## Acknowledgments

Financial support by the National Nature Science Foundation of China for Distinguished Young Scholars (20531020, 20421303) and the Shanghai Science and Technology Committee (05JC14003, 05DZ22313) is gratefully acknowledged.

[1] a) G.-X. Jin, *Coord. Chem. Rev.* **2004**, *248*, 587–602; b) G.-X. Jin, in *Perspectives in Organometallic Chemistry* (Eds.: C. G. Screttas, B. R. Steele), RSC Press, Cambridge, **2003**, p. 47–63.
[2] a) D. H. Kim, J. Ko, K. Park, S. Cho, S. O. Kang, *Organometallics* **1999**, *18*, 2738–2740; b) X. Hou, X. Wang, J.-Q. Wang, G.-X. Jin, *J. Organomet. Chem.* **2004**, *689*, 2228–2235.
[3] a) J. Pang, E. J. P. Marcotte, C. Seward, R. S. Brown, S. Wang, *Angew. Chem. Int. Ed.* **2001**, *40*, 4042–4045; b) C. Seward, W.-L. Jia, R.-Y. Wang, G. D. Enright, S. Wang, *Angew. Chem. Int. Ed.* **2004**, *43*, 2933–2936; c) W.-L. Jia, R.-Y. Wang, D. Song, S. J. Ball, A. B. Mclean, S. Wang, *Chem. Eur. J.* **2005**, *11*, 832–842.
[4] a) F. A. Cotton, C. Lin, C. A. Murillo, *Acc. Chem. Res.* **2001**, *34*, 759–771; b) B. K. Roland, H. D. Selby, M. D. Carducci, Z. Zheng, *J. Am. Chem. Soc.* **2002**, *124*, 3222–3223; c) B. K. Roland, C. Carter, Z. Zheng, *J. Am. Chem. Soc.* **2002**, *124*, 6234–6235; d) H. D. Selby, B. K. Roland, Z. Zheng, *Acc. Chem. Res.* **2003**, *36*, 933–944.
[5] J.-Q. Wang, C.-X. Ren, L.-H. Weng, G.-X. Jin, *Chem. Commun.* **2006**, 162–164.
[6] J.-Q. Wang, C.-X. Ren, G.-X. Jin, *Chem. Commun.* **2005**, 4738–4740.
[7] a) D. Armspach, M. Cattalini, E. C. Constable, *Chem. Commun.* **1996**, 1823–1864; b) E. C. Constable, *Chem. Commun.* **1997**, 1073–1080.
[8] a) X.-F. Hou, X.-C. Wang, J.-Q. Wang, G.-X. Jin, *J. Organomet. Chem.* **2004**, *689*, 2228–2235; b) Q. Kong, G.-X. Jin, S. Cai, L. Weng, *Chin. Sci. Bull.* **2003**, *48*, 1733–1736.
[9] a) G.-X. Jin, J.-Q. Wang, Z. Zheng, L.-H. Weng, M. Herberhold, *Angew. Chem. Int. Ed.* **2005**, *44*, 259–262; b) J.-Q. Wang, X.-F. Hou, L.-H. Weng, G.-X. Jin, *Organometallics* **2005**, *24*, 826–830; c) J.-Q. Wang, L.-H. Weng, G.-X. Jin, *J. Organomet. Chem.* **2005**, *690*, 249–252.
[10] a) S. Leininger, B. Olenyuk, P. J. Stang, *Chem. Rev.* **2000**, *100*, 853–908; b) G. F. Swiegers, T. J. Malefetse, *Chem. Rev.* **2000**, *100*, 3483–3538; c) J. A. R. Navrro, B. Lippert, *Coord. Chem. Rev.* **2001**, *222*, 219–250.
[11] J.-Q. Wang, C.-X. Ren, G.-X. Jin, *Organometallics* **2006**, *25*, 74–81.
[12] M. Herberhold, G.-X. Jin, H. Yan, W. Milius, B. Wrackmeyer, *J. Organomet. Chem.* **1999**, *587*, 252–257.
[13] M. Herberhold, G.-X. Jin, H. Yan, W. Milius, B. Wrackmeyer, *Eur. J. Inorg. Chem.* **1999**, 873–875.
[14] H. L. Anderson, S. Anderson, J. K. M. Sanders, *J. Chem. Soc., Perkin Trans. 1* **1995**, 2231–2245.
[15] E. V. Brown, G. R. Granneman, *J. Am. Chem. Soc.* **1975**, *97*, 621–627.
[16] J. A. Nash, G. W. Gray, *Mol. Cryst. Liq. Cryst.* **1974**, *25*, 299–321.
[17] X.-B. Shao, X.-K. Jiang, X. Zhao, C.-X. Zhao, Y. Chen, Z.-T. Li, *J. Org. Chem.* **2004**, *69*, 899–907.
[18] Z.-J. Ren, E. Jiang, H.-B. Zhou, *Youji Huaxue* **1995**, *15*, 218–220.
[19] G. M. Sheldrick, *SADABS* (*2.01*), *Bruker*/*Siemens Area Detector Absorption Correction Program*, Bruker AXS, Madison, Wisconsin, USA, **1998**.
[20] G. M. Sheldrick, *SHELXL-97*; University of Gtötingen: Germany, **1997**.
[21] *PLATON*: A multi-purpose crystallographic tool, Utrecht University, The Netherlands. See: A. L. Spek, *Acta Crystallogr., Sect. A* **1990**, *46*, C34.

Received: April 3, 2006
Published Online: June 28, 2006

 © 2006 Wiley-VCH Verlag GmbH & Co. KGaA, Weinheim 

DOI: 10.1002/ejic.200600348

# Can the Clusters $Zr_6O_4(OH)_4(OOCR)_{12}$ and $[Zr_6O_4(OH)_4(OOCR)_{12}]_2$ Be Converted into Each Other?

**Michael Puchberger,[a] Franz René Kogler,[a] Myhedin Jupa,[a] Silvia Gross,[a][‡] Helmut Fric,[a] Guido Kickelbick,[a] and Ulrich Schubert*[a]**

**Keywords:** Zirconium / Zirconium oxo cluster / Hafnium oxo cluster / Metal carboxylate / Ligand exchange

Upon reaction of zirconium alkoxides, $Zr(OR)_4$, with carboxylic acids, the clusters $Zr_6O_4(OH)_4(OOCR)_{12}$ (**Zr6**) or $[Zr_6O_4(OH)_4(OOCR)_{12}]_2$ (**Zr12**) were obtained, depending on the employed carboxylic acid. The structures of **Zr12** clusters with acetate, propionate, vinyl acetate or 3,3′-dimethylacrylate ligands were determined by single-crystal X-ray diffraction, as well as that of methacrylate/acetate and methacrylate/propionate mixed-ligand clusters. The structure of the hafnium cluster $[Hf_6O_4(OH)_4(acetate)_{12}]_2$ is also reported for comparison. The **Zr12** clusters are structurally related to the **Zr6** clusters since they are composed of two **Zr6** sub-units which are bridged by four carboxylate ligands. In each compound, carboxylic acid molecules interact with the cluster by hydrogen bonding to part of the $\mu_3$-OH ligands. The clusters are highly dynamic in solution, due to site exchange of the carboxylate ligands; low-temperature NMR spectra of the clusters correspond to the solid-state structures. The **Zr6** and **Zr12** clusters can be clearly distinguished by their solution NMR spectra. Reactions between selected **Zr12** clusters and carboxylic acids led to the conclusion, that only part of the ligands is accessible for ligand exchange reactions. In contrast, all ligands were exchanged when the **Zr6** cluster $Zr_6O_4(OH)_4(methacrylate)_{12}$ was treated with an excess of propionic acid, and $Zr_6O_4(OH)_4(propionate)_{12}$ was formed. However, the **Zr12** cluster $[Zr_6O_4(OH)_4(propionate)_{12}]_2$ was obtained from the reaction of $Zr(OBu)_4$ with propionic acid. The **Zr6** and **Zr12** clusters thus do not interconvert at the given reaction conditions.
(© Wiley-VCH Verlag GmbH & Co. KGaA, 69451 Weinheim, Germany, 2006)

## Introduction

We have previously prepared a variety of carboxylate-substituted titanium and zirconium oxo clusters, mainly to use the (meth)acrylate derivatives for the preparation of cluster-crosslinked polymers.[1] During this work, we obtained several types of zirconium oxo clusters, among them $Zr_6O_4(OH)_4(OOCR)_{12}$ (**Zr6**) and the dimer $[Zr_6O_4(OH)_4(OOCR)_{12}]_2$ (**Zr12**), having the same overall stoichiometry. Previous to this work, we obtained crystalline **Zr6** clusters for RCOO = methacrylate (**1**)[2] and 5-norbornene-2-carboxylate,[3] and the **Zr12** type for RCOO = acrylate.[4] The crystal structures of both cluster types additionally contain carboxylic acid molecules interacting with the ligand shell of the clusters by hydrogen bonding (see below).

The **Zr6** clusters consist of a $Zr_6O_4(OH)_4$ cluster core in which the triangular faces of a $Zr_6$ octahedron are alternatively capped by $\mu_3$-O and $\mu_3$-OH groups. The structure of the **Zr12** cluster consists of two **Zr6** sub-units which are connected by four carboxylate bridges. This will be discussed below in more detail. In a formal manner, the **Zr12** clusters can be constructed by opening two $\mu_2$-(edge-bridging) carboxylate ligands of **Zr6** and letting two such units dimerize as shown in Figure 1.

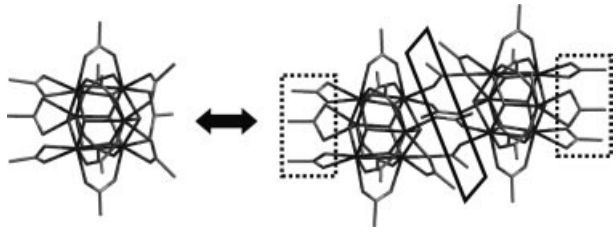

Figure 1. The schematic structures of **Zr6** $[Zr_6O_4(OH)_4(OOCR)_{12}$, left] and **Zr12** ($[Zr_6O_4(OH)_4(OOCR)_{12}]_2$, right) showing that the molecular structure of **Zr12** is derived from the **Zr6** structure. The dashed boxes mark the chelating ligands, and the box drawn with solid lines the carboxylate bridges connecting the $Zr_6$ sub-units.

The clusters were obtained when $Zr(OR')_4$ was treated with the corresponding carboxylic acid. In each case, only one cluster type was obtained, mostly in very high to quantitative yields, i.e. we never obtained mixtures of both clusters. This raises the question whether the formation of either cluster is controlled by the particular reaction conditions or by the different carboxylate ligands including the hydrogen-bonded carboxylic acid molecules. Differences in the electronic and/or steric properties could determine which cluster is formed. A related question of practical im-

[a] Institute of Materials Chemistry, Vienna University of Technology,
Getreidemarkt 9/165, 1060 Wien, Austria
[‡] Current address: Department of Chemical Sciences, University of Padova,
Via Marzolo 1, 35131 Padova, Italy

 © 2006 Wiley-VCH Verlag GmbH & Co. KGaA, Weinheim 

portance, is whether the **Zr6** and **Zr12** clusters can be converted into each other once they are formed. Since carboxylate-substituted metal alkoxides play an important role in sol-gel chemistry,[1,5] the conversion of intra-cluster bridges to inter-cluster bridges could result in the formation of oligomers or polymers made of cluster units, which could severely influence the structure of the networks formed during sol-gel processing.

We report in this article experiments proving that the two cluster types are not interconverted under the conditions employed during their synthesis. First, we will describe new **Zr12** clusters with different carboxylate ligands than previously described. Second, we will demonstrate that the **Zr6** and **Zr12** clusters can be clearly distinguished in solution by their NMR spectra. Third, we will show that each cluster type is retained when the ligands are exchanged; this renders possible the preparation of **Zr6** and **Zr12** clusters with the same ligands.

## Results and Discussion

### Preparation and Structures of New Zr12 Clusters

Cluster **1** was previously prepared by reaction of $Zr(OPr)_4$ in propanol or $Zr(OBu)_4$ in butanol with four equivalents of methacrylic acid.[2] The reported procedure is very reliable, and it is possible to prepare large quantities of this cluster per run for materials syntheses.[1] However, minor changes in the kind of employed carboxylic acid resulted in the formation of **Zr12** clusters instead. The crystalline clusters $[Zr_6O_4(OH)_4(OOCMe)_{12}]_2 \cdot 6MeCOOH \cdot 3.5CH_2Cl_2$ (**2**), $[Zr_6O_4(OH)_4(OOCCH_2Me)_{12}]_2 \cdot 6MeCH_2COOH$ (**3**), $[Zr_6O_4(OH)_4(OOCCH_2CH{=}CH_2)_{12}]_2 \cdot 6CH_2{=}CHCH_2COOH$ (**4**) and $[Zr_6O_4(OH)_4(OOCCH{=}CMe_2)_{12}]_2 \cdot 4Me_2C{=}CHCOOH$ (**5**) were formed in high yields when an 80% solution of $Zr(OBu)_4$ in *n*-butanol was treated with acetic acid (10 molar equivalents), propionic acid (2–10 molar equivalents), vinylacetic acid (7 molar equivalents) or 3,3′-dimethylacrylic acid (4 molar equivalents), respectively. Methylene chloride was used as a co-solvent in the reaction of acetic acid to obtain crystals suitable for single crystal measurements. These reactions show that the **Zr12** cluster type is obviously obtained with a much broader range of carboxylic acids than the **Zr6** cluster type.

We have previously shown that the carboxylate ligands of the **Zr6** clusters can be partially or fully exchanged, when the **Zr6** clusters are reacted with a carboxylic acid. Partial exchange resulted in mixed-ligand clusters, which can alternatively be prepared by reaction of the metal alkoxide with mixtures of two carboxylic acids.[8,6] Mixed-ligand **Zr12** clusters can also be obtained by both methods. Crystalline $[Zr_6O_4(OH)_4(OOCCH_2Me)_3\{OOC(Me){=}CH_2\}_9]_2 \cdot CH_2{=}C(Me)COOH \cdot 5MeCH_2COOH$ (**6**) was obtained by reaction of $Zr(OBu)_4$ with a 2:5 or 1:6 mixture of propionic and methacrylic acid, and $[Zr_6O_4(OH)_4(OOCMe)_8\{OOC(Me){=}CH_2\}_4]_2 \cdot 6MeCOOH$ (**7**) by reacting $Zr(OBu)_4$ with five equivalents of a 1.4:3.6 mixture of methacrylic acid and acetic acid.

The cluster $[Hf_6O_4(OH)_4(OOCMe)_{12}]_2 \cdot 6MeCOOH \cdot 6CH_2Cl_2$ (**8**) was similarly prepared by reaction of $Hf(OBu)_4$ with 10 molar equivalents of acetic acid in $CH_2Cl_2$. This **Hf12** cluster is isostructural to the zirconium cluster **2** and is therefore included in the discussion.

The solid-state structures of the **Zr12** clusters are fairly similar; differences are only observed for the carboxylic acids which are hydrogen-bonded to the cluster. We will therefore first discuss the structure of the vinyl acetate-substituted cluster **4** (Figure 2) as an example before we turn to the mixed-ligand clusters and point out differences among the different **Zr12** clusters.

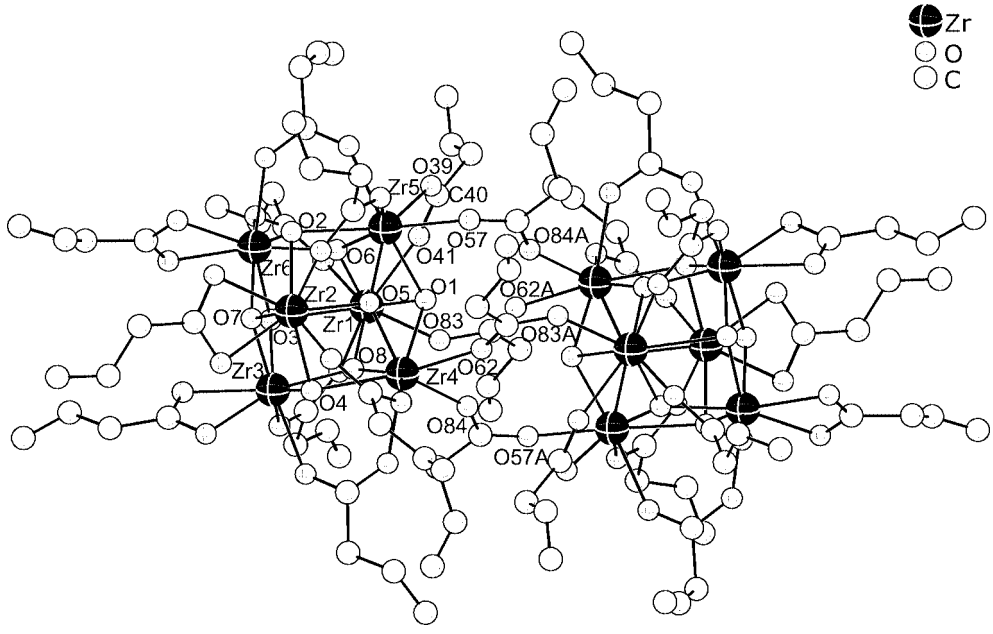


Figure 2. Structure of $[Zr_6O_4(OH)_4(OOCCH_2CH{=}CH_2)_{12}]_2$ (**4**).

 © 2006 Wiley-VCH Verlag GmbH & Co. KGaA, Weinheim 

The structure of **Zr6** (Figure 1, left) consists of a $Zr_6O_4(OH)_4$ core in which the triangular faces of a $Zr_6$ octahedron are alternatively capped by $\mu_3$-O and $\mu_3$-OH groups. The same cluster core was found in $Ce_6(OH)_4O_4$(acetylacetonate)$_{12}$.[7] Three carboxylate ligands of **Zr6** chelate the zirconium atoms at one $\mu_3$-O capped face ("chelated face"), while the other nine OOCR groups bridge all edges of the $Zr_6$ octahedron except the edges of the chelated face. Each zirconium atom is coordinated by eight oxygen atoms. The cluster core thus has a $C_{3v}$ symmetry with the $C_3$ axis passing through the center of the chelated face and the triangular face opposite to it.

The basic structural features of **Zr6** are retained in the sub-units of centrosymmetric **4** and all the other clusters of the **Zr12** type (Figure 1, right and Figure 2). The carboxylate ligands opposite the chelated face in the **Zr6** unit appear to be somewhat activated. For example, we previously obtained modifications of the **Zr6** structure, where *one* carboxylate ligand opposite the chelated face was opened to a monodendate coordination and the vacated coordination site occupied by a coordinated alcohol or a water molecule $[Zr_6O_4(OH)_4(OOCR)_{12}\cdot XOH$, X = R, H].[4,8] In **Zr12**, *two* of the bridging carboxylate ligands per $Zr_6$ unit opposite the chelated face are opened and are converted to inter-cluster bridges, i.e. the **Zr12** clusters are thus dimers of **Zr6** in which $Zr_6$ sub-units are connected by four inter-cluster carboxylate bridges. The third bridging carboxylate ligand opposite the chelated face [O(39)/C(40)/O(41)] stays bridging. This change of the coordination mode of two carboxylate units per $Zr_6$ unit from edge-bridging to inter-cluster bridging has only little effect on the geometrical parameters of the cores of the $Zr_6$ sub-units and the remaining carboxylate ligands.

The $\mu_3$-O and $\mu_3$-OH groups capping the $Zr_6$ core can be easily distinguished by their Zr–O distances. In **4**, the oxygen atoms O(5)–O(8) were $\mu_3$-O (Zr–O distances between 203.5(2) and 210.7(2) pm, where the Zr–O distances at the chelated face were slightly longer [209.0–210.7 pm]), while O(1)–O(4) were $\mu_3$-OH. While the Zr–O(1) distances (the $\mu_3$-OH group opposite the chelated face) were quite uniform [229.8(2)–233.1(2) pm], that of the other three capping OH groups showed a pattern of two short [218.3(2)–221.7(2) pm] and one long [233.1(2)–239.1(2) pm] Zr–O distance, i.e. the groups are in fact between $\mu_2$ and $\mu_3$.

The Zr–O distances of the intra-cluster bridging carboxylate ligands (218.3–223.6 pm) in **4** were in the same range as the inter-cluster bridging ligands (216.6–222.3 pm) while the distances of the chelating ligands were distinctly longer. Remarkably, each chelating carboxylate ligand had a longer [229.7(2)–230.8(2) pm] and a significantly shorter [225.3(2)–227.4(2) pm] Zr–O bond length, which is due to the hydrogen bonds described below, the *shorter* distance being the oxygen atom interacting with the hydrogen-bonded acid.

The crystal lattice of **4** contains three vinylacetic acid molecules per asymmetric unit, which interact with the cluster subunits via hydrogen bridges. The OH group of each carboxylic acid is hydrogen-bonded to an oxygen atom of a *chelating* vinyl acetate ligand [O(9)···O(87) 265.8 pm, O(15)···O(93) 262.9 pm, O(23)···O(99) 263.8 pm] and the carbonyl oxygen of each carboxylic acid is hydrogen-bonded to one of the three $\mu_3$-OH groups surrounding the chelating face [O(2)···O(85) 271.8 pm, O(3)···O(91) 275.0 pm, O(4)···O(97) 273.1 pm]. The hydrogen-bonding pattern in **4** is schematically shown in Figure 3.

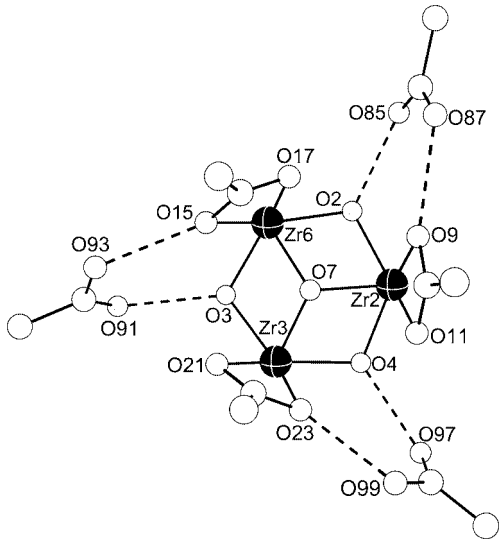


Figure 3. Hydrogen bonding patterns in **4**. The vinyl groups are omitted for clarity.

The hydrogen-bonding pattern of **4** (similar for the other **Zr12** clusters) is remarkable, as it shows that the $\mu_3$-OH groups in the clusters are efficient proton donors in hydrogen bonds and thus enable the coordination of carboxylic acid molecules at the periphery of the clusters. This may be important for carboxylate-exchange reactions as discussed below (see also ref.[8]). As we have already pointed out in a related case,[9] the simultaneous action of carboxylic acids as hydrogen donors *and* hydrogen acceptors may stabilize unusual bonding situations.

The inorganic core of the mixed-ligand clusters **6** and **7** was the same as that of the other **Zr12** clusters, but the distribution of the ligands needs to be discussed. In the following discussion we distinguish between (i) the chelating ligands, (ii) the ligands bonded to zirconium atoms at the face of the $Zr_6$ octahedron opposite the chelated face ("opposite ligands"), which are the carboxylate bridges connecting the $Zr_6$ sub-units and the remaining edge-bridging ligand at the "opposite" face, and (iii) the ligands bridging the zirconium atoms of the "chelated" face and the "opposite" face ("belt ligands", see Figure 1). Cluster **6** is again centrosymmetric and contains three propionate and nine methacrylate ligands per $Zr_6$ sub-unit. All propionate groups were "opposite" ligands (Figure 4). In the acetate/methacrylate-substituted cluster **7**, with a lower proportion of methacrylate ligands, the saturated (acetate) ligands occupied again the "opposite" ligand positions and in addition part of the "belt" positions, while the methacrylate ligands were at the chelating and part of the "belt" positions (as a matter of fact, part of the belt positions contained disordered acetate and methacrylate ligands in the

 © 2006 Wiley-VCH Verlag GmbH & Co. KGaA, Weinheim 

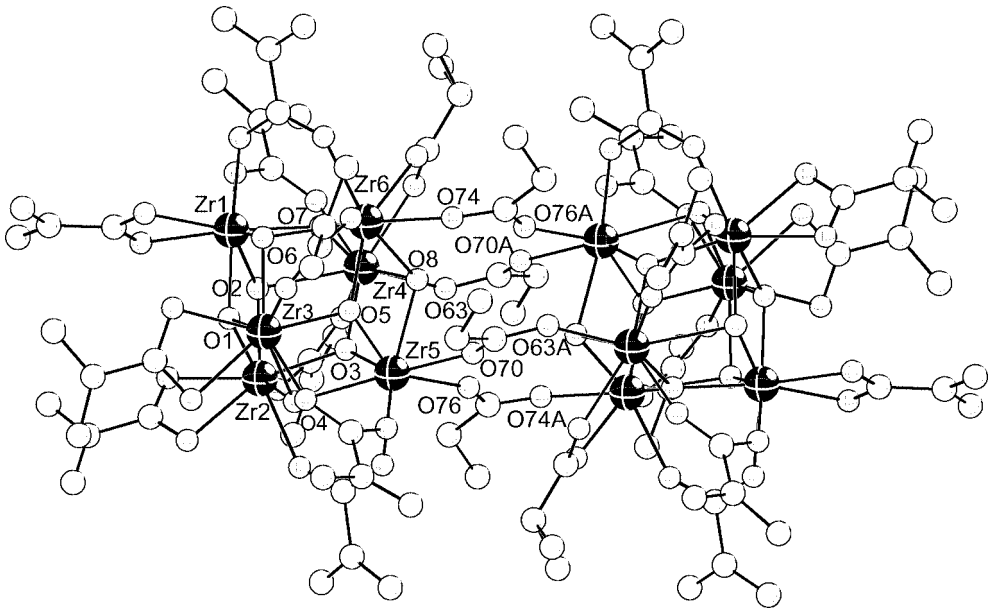


Figure 4. Structure of $[Zr_6O_4(OH)_4(OOCCH_2Me)_3\{OOCC(Me)=CH_2\}_9]_2$ (**6**).

solid-state structure). There is obviously a clear preference of the methacrylate ligands in the order chelating > belt > opposite. The reason for this preference is currently speculative. One possibility is that the $pK_a$ of methacrylic acid is slightly lower (4.66) than that of propionic acid (4.88) and acetic acid (4.76), and the site preference is thus due to the basicity of the anions. Another reason could be the slightly different steric demand of the ligands.

The molecular structures of all **Zr12/Hf12** clusters were essentially the same. However, different hydrogen-bonding patterns of the carboxylic acids were observed. In the clusters **2** and **8**, the hydrogen bonding was the same as in **4** discussed above. A second type of hydrogen bonding pattern was observed in **3**, **6** and **7**. Again, three carboxylic acid molecules are hydrogen-bonded per $Zr_6$ unit with the $\mu_3$-OH groups neighboring the chelated face as the hydrogen donors to the carbonyl oxygen atoms. However, the OH groups of the carboxylic acid molecules interact in a different manner with the chelating ligands. In **6**, two carboxylic acid molecules interact with the two oxygen atoms of *one* chelating ligand. The second chelating ligand is hydrogen-bonded as in **4**, while the third is not involved in hydrogen bonding. The structure of **3** contained two half **Zr12** molecules in the asymmetric unit. One of them had the same hydrogen-bonding pattern as in **4**, and the other as in **6**. In **7**, the OH group of one acetic acid molecule interacted with *two* chelating carboxylate ligands (with rather long O···O interactions, 286–301 pm), the second oxygen atom of which was hydrogen-bonded to the other acetic acid molecules. The dimethylacrylate derivative **5** had only four hydrogen-bonded acid molecules, probably because of their greater steric bulk. One of the dimethylacrylic acid molecules is hydrogen-bonded as described above, i.e. the carbonyl oxygen interacts with one of the $\mu_3$-OH groups [O(1)] and an oxygen of a chelating carboxylate ligand [O(30)]. The carbonyl group of the second hydrogen-bonded dimethylacrylic acid molecule interacts with the $\mu_3$-OH group O(3), but the hydrogen atom of the carboxylic OH group interacts in a bifurcated manner with one oxygen atom of both other chelating carboxylate ligands.

### NMR Spectra of Zr6 and Zr12 Clusters

For the NMR spectroscopic investigation of the clusters, the solvate molecules of the crystalline compounds were nearly completely removed by repeated dissolution/evaporation cycles, as described in the Experimental Section. We have previously reported the $^1H$ and $^{13}C$ NMR spectroscopic data of **1**,[8] where the signals in the room temperature spectra can be clearly assigned to three nonequivalent ligand positions (one chelating and two different bridging positions) according to the $C_{3v}$ symmetry of the cluster in the crystalline state. The signal ratio of the olefinic $CH_2$ protons should therefore be 2:1:1, which was approximately found by integrating the corresponding signals of the solution $^1H$ NMR spectrum; the proton signals of all methyl groups were overlapping. The three different ligands can be easily distinguished in the $^1H/^{13}C$ HMBC spectrum of **1** (Figure 5), where long-range correlations between the olefinic $CH_2$ and $CH_3$ protons to the corresponding carboxylate carbon atoms were observed. The signals at $\delta$ = 6.10/5.65 ppm ($^1H$ NMR) and 184.7 ppm ($^{13}C$ NMR) were therefore assigned to the chelating ligands, and those at 5.97/5.39 ppm ($^1H$ NMR) and 171.9 ppm ($^{13}C$ NMR) as well as those at 6.04/5.60 ppm ($^1H$ NMR) and 169.6 ppm ($^{13}C$ NMR) to the two inequivalent bridging ligands. This sequence of chemical shifts shows that $^{13}C$ NMR signals of chelating carboxylates are distinctly shifted to a lower field.

 © 2006 Wiley-VCH Verlag GmbH & Co. KGaA, Weinheim 

This is in line with previous work on zinc carboxylate clusters, where this was explained by electronic effects of the bound metal(s).[10]

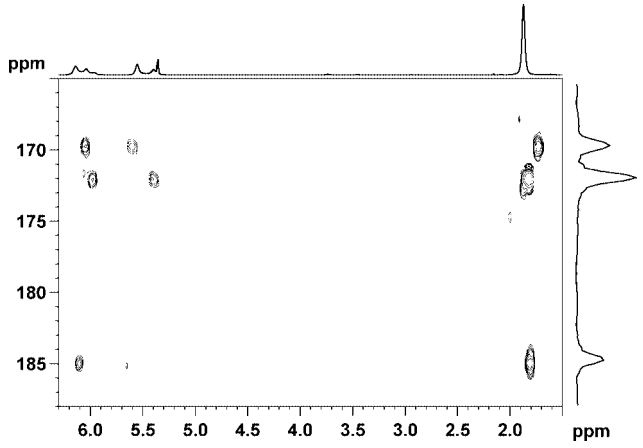


Figure 5. $^1H/^{13}C$ HMBC spectrum of **1** at room temperature in $CD_2Cl_2$.

We start the discussion of the NMR spectra of the **Zr12/Hf12** clusters with the simpler cases, i.e. the acetate-substituted clusters $[Zr_6O_4(OH)_4(OOCMe)_{12}]_2$ (**2**) and $[Hf_6O_4(OH)_4(OOCMe)_{12}]_2$ (**8**), which both show the same features in the NMR spectra. Six of the 24 acetate ligands are chelating ligands, 14 are bridging ligands within the same $Zr_6$ sub-unit and four ligands are inter-cluster bridging. The symmetry of the cluster in the crystalline state is $C_i$ with 12 inequivalent ligand positions. Neglecting a slight perturbation of the symmetry by crystal packing or slightly different conformations of the acetate ligands, the molecular symmetry is in fact $C_{2h}$ (Figure 6 (a)]. This results in seven nonequivalent ligand positions, i.e. two chelating, four bridging and one inter-cluster bridging, with a signal ratio of 1:1:2:2:2:2:2. In the case of a $C_i$ symmetry three of the 12 ligand positions are chelating, seven are bridging and two are inter-cluster bridging. Their signal intensity should be the same. A comparison of these two cases is shown in Figure 6. In passing, it should be pointed out that, in the worst case for NMR investigations, all ligands may become inequivalent due to different ligand conformations. This may lead to different isomers and an even greater number of signals or broader resonances.

Temperature-dependent $^1H$ NMR spectra of solvate-free $[Zr_6O_4(OH)_4(OOCMe)_{12}]_2$ (**2**) in $CD_2Cl_2$ are shown in Figure 7. Five separated methyl signals were observed at 20 °C. Upon cooling the solution to –40 °C two additional signals appeared; the seven nonequivalent ligand signals in an approximate ratio of 1:1:2:2:2:2:2 indicate that the cluster has indeed $C_{2h}$ symmetry in solution.

A tentative assignment of the signals was reached from a $^1H/^{13}C$ HMBC spectrum (Figure 8) and by comparison of the chemical shifts with those of compound **1**. The signal at $\delta$ = 1.75 ppm, which shows a long-range correlation to the most down-field shifted carboxylate at $\delta$ = 181.1 ppm, was assigned to a chelating acetate ligand, whereas the signal at $\delta$ = 2.05 ppm, showing a long-range correlation to

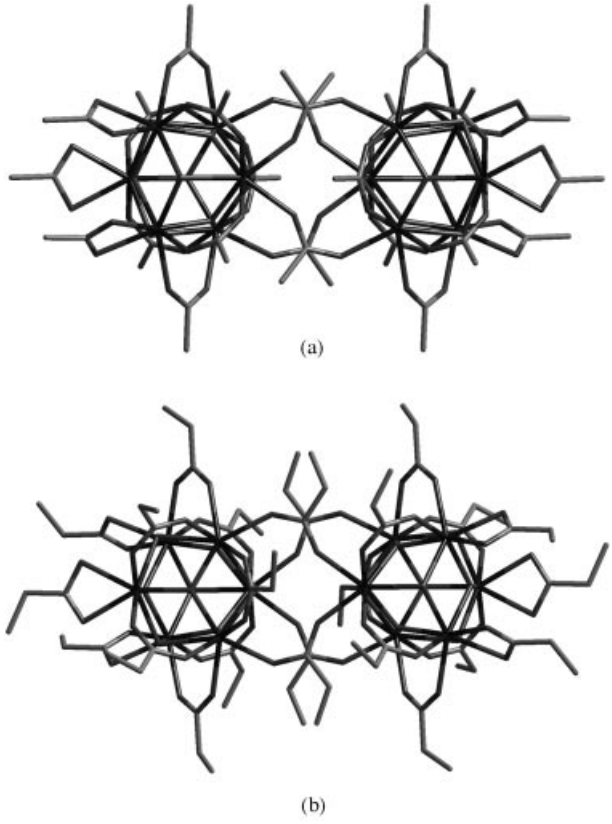


Figure 6. $[M_6O_4(OH)_4(OOCMe)_{12}]_2$ [M = Zr (**2**) or Hf (**8**); (a)] has a mirror plane whereas $[Zr_6O_4(OH)_4(OOCCH_2Me)_{12}]_2$ [**3**; (b)] only has an inversion center due to the different conformation of the ethyl groups.

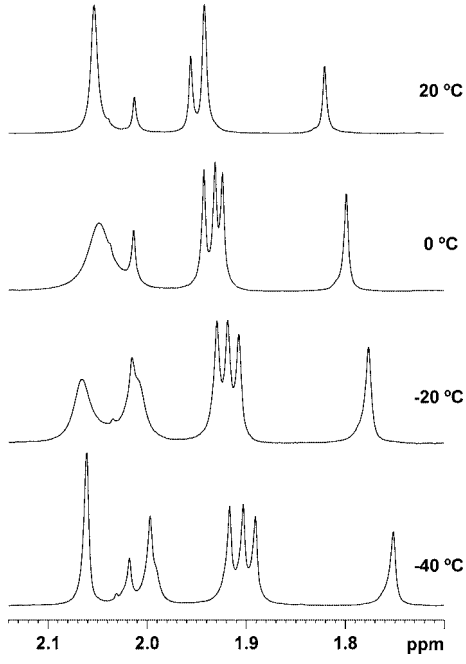


Figure 7. Temperature-dependent $^1H$ NMR spectra of $[Zr_6O_4(OH)_4(OOCMe)_{12}]_2$ (**2**) in $CD_2Cl_2$.

 © 2006 Wiley-VCH Verlag GmbH & Co. KGaA, Weinheim 

the most high-field shifted carboxylate at $\delta$ = 175.9 ppm, should correspond to a bridging ligand. The signals with long-range correlations between 2.02 ppm ($^1$H) and 176.6 ppm ($^{13}$C) as well as 2.00 ppm ($^1$H) and 176.6 ppm ($^{13}$C) appear in the $^1$H NMR spectrum only with 50% intensity and can therefore be assigned to the set of intercluster bridging ligands and to the set of chelating ligands. The remaining three signals at 1.91 ($\delta$ = 177.4 ppm), 1.90 ($\delta$ =177.3 ppm) and 1.89 ($\delta$ = 177.5 ppm) must then be signals of the other bridging acetate ligands. The carbon signals of the methyl groups are listed in the Experimental Section.

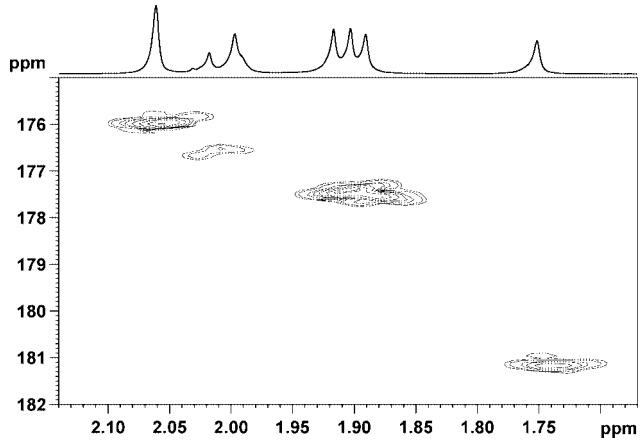


Figure 8. $^1$H/$^{13}$C HMBC spectrum of **2** at –40 °C in $CD_2Cl_2$.

A different picture was obtained for the propionate-substituted cluster $[Zr_6O_4(OH)_4(OOCCH_2Me)_{12}]_2$ (**3**) in [D$_8$]-toluene (Figure 9). The $^1$H NMR spectrum at room temperature showed sharp lines, and signals for six different ligands were observed. Five of them showed long-range correlations to carboxylate carbon atoms at 184.0, 179.9, 179.8, 179.7 and 178.4 ppm in a $^1$H/$^{13}$C HMBC spectrum, whereas no long-range correlation was observed for the broad $CH_3$ signal at $\delta$ = 1.02 ppm. This is common for fast exchanging ligands in such cluster compounds.

Cooling the sample to –40 °C changed the picture, and signals for at least ten inequivalent ligands were observed in the $^1$H NMR spectrum (not shown). This means that the symmetry of **3** is reduced to at least $C_i$ or even $C_1$ at lower temperatures. In the $^1$H/$^{13}$C HMBC spectrum at this temperature, six carboxylate signals were now resolved, and the signal, which formerly gave no long-range correlation, was shifted from 1.02 to 0.89 ppm and split into two proton signals, both of which gave a long-range correlation to the same carbon at $\delta$ = 192.0 ppm. This signal was also tentatively assigned to a chelating ligand. When the sample was further cooled to –80 °C (not shown) the lines in the spectrum became broad and unstructured. This indicated that at room temperature the symmetry is approximately $C_{2h}$ because the ligand conformations are averaged on the NMR time scale. At lower temperature, the ligand motion is restricted, and the symmetry of the cluster is thus lowered, resulting in a larger number of signals.

These examples show that the **Zr6** and **Zr12** clusters can be clearly distinguished by their molecular symmetry and therefore by their NMR spectra in solution. While the $C_{3v}$ symmetric **Zr6** cluster **1** has three sets of nonequivalent carboxylate ligands, the **Zr12** clusters have either $C_{2h}$ or $C_i$ symmetry and should therefore have either seven or 12 nonequivalent ligands. The symmetry of the cluster may even be reduced to $C_1$ and therefore the number of signals in the NMR spectra increases when the ligand motion is restricted. The NMR spectrum of **1** at room temperature had already shown signals for all three nonequivalent ligands (Figure 5). In the case of the **Zr12** clusters **2** and **3**, the room temperature NMR spectra show signals for five or six nonequivalent ligands, respectively. This indicates that site exchange of the ligands in **2** and **3** is much easier than that in the **Zr6** cluster **1**. Furthermore, it was observed that in the case of **3** the most dynamic region in this **Zr12** cluster is that of the chelating ligands.

It is worth noting at this point that the ability to distinguish clearly between a **Zr6** and a **Zr12** cluster is already a clear indication that there is no equilibrium between these two different clusters at room temperature in solution.

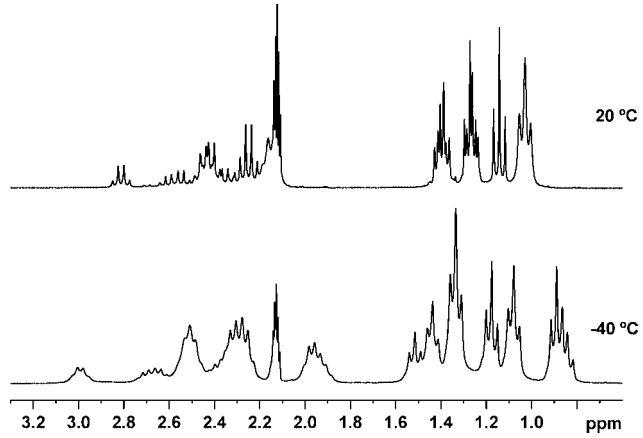


Figure 9. Temperature-dependent $^1$H NMR spectra of $[Zr_6O_4(OH)_4(OOCCH_2Me)_{12}]_2$ (**3**) in [D$_8$]toluene.

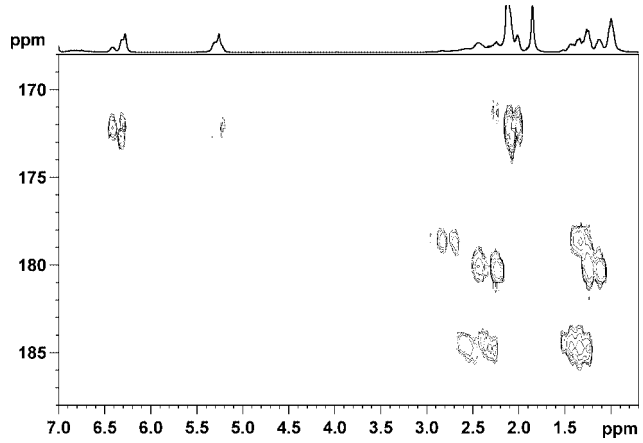


Figure 10. $^1$H/$^{13}$C HMBC spectrum of $[Zr_6O_4(OH)_4(OOCCH_2Me)_3\{OOCC(Me)=CH_2\}_9]_2$ (**6**) at room temperature in [D$_8$]toluene.

 © 2006 Wiley-VCH Verlag GmbH & Co. KGaA, Weinheim 

To explore the ability of the **Zr12** clusters to undergo ligand exchange reactions and to compare this with the already known exchange behavior of the **Zr6** clusters[8,6] we analyzed the mixed propionate-methacrylate cluster **6**. The $^1H$ NMR spectrum of **6** in [$D_8$]toluene at room temperature showed broad and unstructured lines, due to ligand exchange. The corresponding $^1H/^{13}C$ HMBC spectrum (Figure 10) of **6** showed signals for only three different methacrylate ligands and six different propionate ligands. The carboxylate carbons of the methacrylate groups appeared at 171.5, 172.0 and 172.5 ppm, and that of the propionate ligands at 178.3, 178.4, 179.7, 179.8, 184.1 and 184.2 ppm.

### Reaction of $[Zr_6O_4(OH)_4(OOCCH_2Me)_3\{OOCC(Me)=CH_2\}_9]_2$ (6) and $Zr_6O_4(OH)_4\{OOCC(Me)=CH_2\}_{12}$ (1) with Propionic Acid

Cluster **6** was treated with a large excess of propionic acid in $CH_2Cl_2$. After careful workup of the reaction product and excessive drying in vacuo, the $^1H$ NMR spectra (Figure 11) showed a complete exchange of the cluster-bonded methacrylate ligands against propionate ligands. The obtained spectrum is very similar to that of **3** directly prepared from $Zr(OBu)_4$ and propionic acid (see above). This indicated that in **Zr12** clusters at least the "outer" parts of the cluster, to which the 18 methacrylate ligands are bonded, are accessible to ligand exchange in solution.

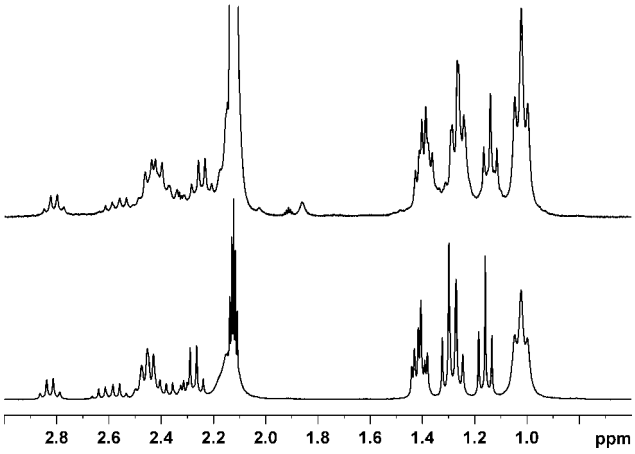


Figure 11. Top: $^1H$ NMR spectrum (in [$D_8$]toluene) of the reaction product of **6** with an excess of propionic acid in [$D_8$]toluene at room temperature. Bottom: $^1H$ NMR spectrum of solvate-free **3** for comparison.

To check whether all ligands can be exchanged, we used the propionate-substituted cluster **3**. Treatment with an excess of acetic acid should yield the acetate cluster $[Zr_6O_4(OH)_4(OOCMe)_{12}]_2$ (**2**) when all ligands are exchanged. The $^1H$ NMR spectrum of the reaction product is compared in Figure 12 (center) with the starting compound **3** (top) and **2** (bottom). It is easy to see that even after excessive treatment with acetic acids signals from propionate ligands were retained. The integration of the signals showed that the ratio of acetate to propionate was 3:1. This leads to the conclusion, that the "opposite ligands" of the **Zr12** cluster are not accessible for ligand exchange reactions in solution.

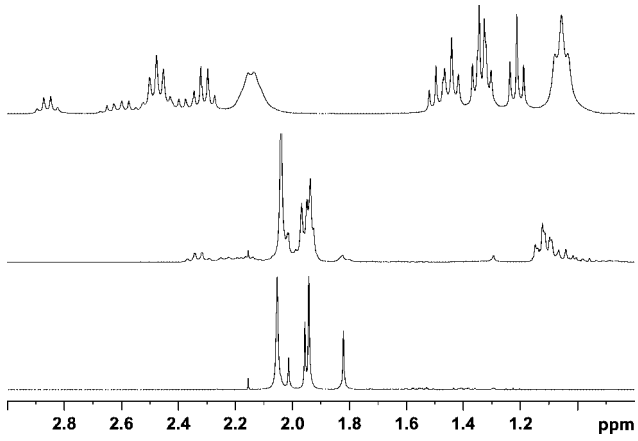


Figure 12. Top: $^1H$ NMR spectrum of $[Zr_6O_4(OH)_4(OOCCH_2Me)_{12}]_2$ (**3**). Bottom: $^1H$ NMR spectrum of $[Zr_6O_4(OH)_4(OOCMe)_{12}]_2$ (**2**), the expected reaction product. Center: Reaction product of **3** with an excess of acetic acid. All spectra were recorded at room temperature in $CD_2Cl_2$.

In contrast, when the **Zr6** cluster **1** was treated with a large excess of propionic acid, the NMR spectra clearly showed that no methacrylate ligands were left and therefore all ligands were exchanged against propionate.[8] In the $^1H/^{13}C$ HMBC spectrum of the reaction product (Figure 13), long-range correlations between the $CH_2$ and $CH_3$ protons of three different propionate groups to the corresponding carboxylate carbon atoms were observed. A comparison with the $^1H/^{13}C$ HMBC spectrum of **1** (Figure 5) showed a similar peak pattern of the signals; two of the signals appeared at a higher field (180.0 and 180.4 ppm), whereas one signal was shifted to lower field ($\delta$ = 184.0 ppm). The intensity ratio of the protons is also approximately 2:1:1 as found for **1**. This indicates strongly that the cluster core of the **Zr6** cluster was preserved during the exchange reaction, that the overall symmetry $C_{3v}$ was retained and that $Zr_6O_4(OH)_4$-(propionate)$_{12}$ was formed.

One of the key steps in the formation of zirconium oxo clusters from $Zr(OR')_4$ and carboxylic acids is the esterification reaction of the acid with the cleaved alcohol.[11] The thus-generated water is the source of the oxo and hydroxo ligands in the clusters. When mixed-ligand clusters are prepared from two different acids, the question is whether two esters were formed or just one. We therefore also monitored the formation of **6** in solution starting from $Zr(OBu)_4$ and a mixture of propionic and methacrylic acid by NMR spectroscopy, concentrating on signals from either butyl propionate or butyl methacrylate. After 6 h, the reaction was almost complete and no more ester was formed. The TOCSY spectrum (Figure 14, top) showed that the sharp triplet at $\delta$ = 3.93 ppm (marked by an arrow) can be assigned to the $CH_2O$ moiety of a butyl residue, and the $^1H/^{13}C$ HMBC spectrum (Figure 14, bottom) shows a long-range correlation from this triplet to a propionate group at $\delta$ = 173.7 ppm. The other signals in the $^1H/^{13}C$ HMBC spec-

 © 2006 Wiley-VCH Verlag GmbH & Co. KGaA, Weinheim 

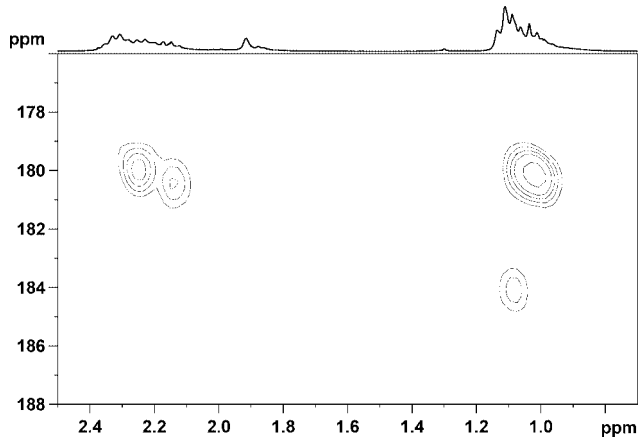


Figure 13. $^{1}H/^{13}C$ HMBC spectrum of the reaction product of **1** treated with an excess of propionic acid at room temperature in $[D_8]$toluene.

trum were due to methacrylic acid ($\delta$ = 173.0 ppm) and propionic acid ($\delta$ = 179.8 ppm). No butyl-methacrylate was formed during the reaction. This experiment shows that the formation rate of ester, and thus water, may play a key role in the formation of different cluster types.

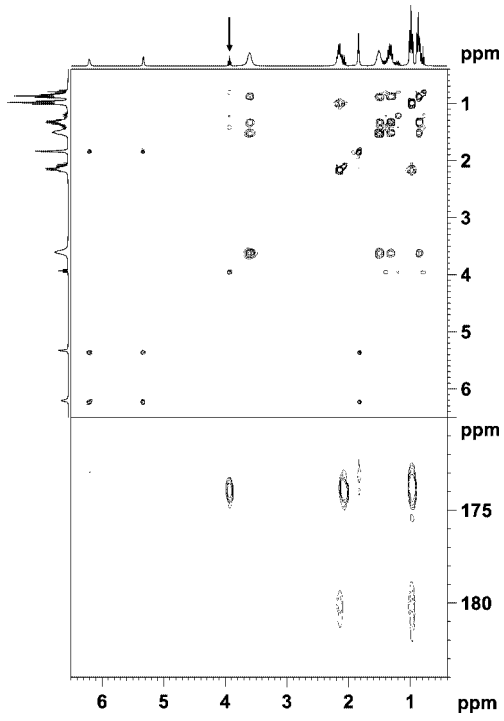


Figure 14. TOCSY spectrum (top) and $^{1}H/^{13}C$ HMBC spectrum (bottom) of the formation of $[Zr_6O_4(OH)_4(propionate)_3(methacrylate)_9]_2$ (**6**) after 6 h in $[D_8]$toluene.

## Conclusions

The most important conclusion of this work is that **Zr6** and **Zr12** clusters, despite their structural similarity, are not converted into each other in solution under the employed conditions. The first proof is that their solution NMR spectra are clearly different, especially at low temperatures. The spectra are in agreement with the molecular symmetries obtained from the solid-state structures. Second, exchange experiments showed that both $Zr_6O_4(OH)_4(propionate)_{12}$ and $[Zr_6O_4(OH)_4(propionate)_{12}]_2$ can be obtained, depending on the preparation route. The **Zr6** cluster $Zr_6O_4(OH)_4(propionate)_{12}$ was obtained by treatment of $Zr_6O_4(OH)_4(methacrylate)_{12}$ (**1**) with a large excess of propionic acid and clearly identified by NMR spectroscopy. On the other hand, the **Zr12** cluster $[Zr_6O_4(OH)_4(propionate)_{12}]_2$ was formed either when $[Zr_6O_4(OH)_4(propionate)_3(methacrylate)_9]_2$ (**6**) was treated with a large excess of propionic acid or directly from $Zr(OBu)_4$ and propionic acid. In either case, the cluster symmetry is retained upon ligand exchange.

From a structural point of view, the **Zr12** clusters are dimers of **Zr6** in which the $Zr_6$ sub-units are connected by four inter-cluster carboxylate bridges. The **Zr12** clusters could be constructed by opening two $\mu_2$- (edge-bridging) carboxylate ligands of **Zr6** and letting two such units dimerize by formation of four inter-cluster bridges. The notion that the **Zr12** clusters could be formed in this manner was imposed by the previous observation that *one* carboxylate ligand opposite the chelated face can be opened to a monodentate coordination and the vacated coordination site occupied by a coordinated alcohol or a water molecule. NMR spectra indicated that this process is reversible.[8] The process leading to the **Zr12** clusters is obviously not related to this. Why *either* **Zr6** *or* **Zr12** clusters are formed when $Zr(OR)_4$ is reacted with carboxylic acids is still an open question. The key to answering this question could be the acidity of the employed carboxylic acids. This influences both the rate of ester plus water formation and also the bond strength of the coordinated carboxylate ligands. The interplay of both probably determines how the cluster formation proceeds in the early stages of the reaction.

## Experimental Section

Acetic acid (99%, Aldrich) was dried with $CaSO_4$ and distilled before use. Methacrylic acid (99%, Aldrich) and propionic acid (99.5%, Aldrich) were distilled. $Zr(OBu)_4$ (80% in BuOH, Aldrich), $Hf(OBu)_4$ (95%, ABCR), vinylacetic acid (97%, Aldrich) and dimethylacrylic acid (97%, Aldrich) were used as received. All experiments were carried out in a moisture- and oxygen-free argon atmosphere. To remove the solvate molecules from the crystalline clusters, the compounds were dissolved in $CH_2Cl_2$ and all volatiles were removed in vacuo. This process was repeated with toluene and once more with $CH_2Cl_2$. The obtained solids were dried at room temperature and ca. $10^{-5}$ mbar.

All NMR spectra were recorded with a Bruker *Avance* 300 ($^{1}H$ at 300.13 MHz, $^{13}C$ at 75.47 MHz) equipped with a 5 mm, inverse-broadband probe head with a *z*-gradient unit. 2D experiments were measured with Bruker standard pulse sequences: COSY (Correlated Spectroscopy), TOCSY (Total Correlation Spectroscopy), HSQC (Heteronuclear Single Quantum Correlation) and HMBC (Heteronuclear Multiple Bond Correlation). Gas-tight Young tubes were used for all measurements. Solvents were either $CD_2Cl_2$ (99.8%, euriso-top) or $[D_8]$toluene (99.8%, euriso-top).

 © 2006 Wiley-VCH Verlag GmbH & Co. KGaA, Weinheim 

**Synthesis of $[Zr_6O_4(OH)_4(OOCMe)_{12}]_2$·6MeCOOH·3.5$CH_2Cl_2$ (2):** Acetic acid (2.62 g, 43.66 mmol) was added dropwise at room temperature to a solution of $Zr(OBu)_4$ (4.44 mmol, 2.13 g of a 80% solution in BuOH) in $CH_2Cl_2$ (5 mL) whilst stirring in a Schlenk tube. Within 3 h at room temperature colorless crystals were obtained. The crystals were separated and dried in vacuo. Yield: 864 mg (68%). $C_{63.5}H_{111}Cl_7O_{76}Zr_{12}$ (3433.2): calcd. C 22.22, H 3.26; found C 22.37, H 3.21. IR-ATR: $\tilde{\nu}$ = 2960 (w), 2776 (w), 2607 (w), 1757 (w), 1709 (m), 1599 (s), 1556 (s), 1449 (s), 1346 (m), 1258(m), 1046 (m), 1026 (m), 910 (w), 883 (w), 791 (w), 735 (w), 669 (m) $cm^{-1}$. $^1H$ NMR (Figure 7) ($C_7D_8$, 25 °C): $\delta$ = 1.82, 1.94, 1.96, 2.01, 2.05 (Me), 10.01 (O*H*). At –40 °C: 1.75, 1.89, 1.90, 1.92, 1.99, 2.02, 2.06 (C$H_3$), 11.51 ppm (O*H*). $^{13}C$ NMR ($C_7D_8$, 25 °C): $\delta$ = 181.0, 177.5, 176.6 (*C*O); 23.5, 23.8, 23.7, 22.9, 20.9 (Me). At –40 °C: 181.1, 177.4, 177.3, 177.5, 176.5, 175.9, 175.9 (*C*O); 23.6, 24.1, 23.9, 23.9, 22.8, 23.5, 21.0 ppm (Me).

**Synthesis of $[Zr_6O_4(OH)_4(OOCCH_2Me)_{12}]_2$·6$MeCH_2COOH$ (3):** Propionic acid (1.8 g, 24.2 mmol) was added dropwise at room temperature to a stirred mixture of $Zr(OBu)_4$ (2.37 mmol, 1.14 g of a 80% butanol solution). After 7–8 h at room temperature, colorless crystals (0.53 g) were formed. The crystals were separated and dried in vacuo. Yield 0.53 g (75%). $C_{90}H_{164}O_{76}Zr_{12}$ (3556.9): calcd. C 30.39, H 4.65; found C 29.30, H 4.30. IR-ATR: $\tilde{\nu}$ = 3402 (w), 3259 (w), 2978 (m), 2942 (w), 1717 (m, COOH), 1600 (s, sh, COO), 1533 (s, COO), 1468 (s), 1439 (s, COO), 1374 (m), 1300 (s), 1211 (m), 1078 (m), 1014 (w), 910 (w), 882 (w), 810 (m) $cm^{-1}$. $^1H$ NMR (Figure 8) ($C_7D_8$, 25 °C): $\delta$ = 1.06, 1.23, 1.35, 1.37, 1.47, 1.49 (Me); 2.20, 2.36, 2.39, 2.55, 2.69, 2.95 (C$H_2$); 11.96 ppm (O*H*). $^{13}C$ NMR ($C_7D_8$, 25 °C): $\delta$ = 180.2, 180.8, 179.9, 184.3, 178.6 (*C*O); 28.4, 30.5, 30.5, 30.6, 30.0, 30.2 (*C*$H_2$); 8.5, 9.8, 9.5, 9.5, 9.9, 10.2 ppm (Me).

**Synthesis of $[Zr_6O_4(OH)_4(OOCCH_2CH{=}CH_2)_{12}]_2$·6$CH_2$=CH-$CH_2COOH$ (4):** Vinylacetic acid (966 mg, 11.22 mmol) was added dropwise to $Zr(OBu)_4$ (1.62 mmol, 776 mg of a 80% solution in BuOH). A microcrystalline precipitate was obtained after 5 min which formed colorless crystals within 2 d at room temperature. The crystals were separated and dried in vacuo. Yield: 332 mg (63%). $C_{120}H_{164}O_{76}Zr_{12}$ (3917.2): calcd. C 36.79, H 4.22, $ZrO_2$ 37.75; found C 36.54, H 4.06, $ZrO_2$ 38.39 (TGA). IR-ATR: $\tilde{\nu}$ = 3396 (w, OH), 3080 (w, CH), 3020 (w, CH), 2982 (w, CH), 1711 (m, C=O), 1641 (w, C=C), 1603 (m, $COO_{as.}$), 1547 (sh, $COO_{as}$), 1537 (s, $COO_{as}$), 1436 (s, $COO_s$), 1417 (s, $COO_s$), 1392 (s, $COO_s$), 1314 (w), 1295 (w), 1268 (m), 1199 (m), 1121 (w), 994 (m), 914 (m, C=C), 893 (sh), 811 (m), 782 (sh), 762 (w), 724 (m, CH), 676 (sh), 627 (s, OCO) $cm^{-1}$. $^1H$ NMR ($C_7D_8$, 25 °C): $\delta$ = 6.43, 6.34, 6.32, 6.30, 5.94 (=C*H*); 5.30/5.14, 5.27/5.11, 5.26/5.17, 5.23/5.09, 5.27/5.12, 5.04/4.96 (C$H_2$=); 3.61/3.30, 3.57/3.27, 3.33/3.17, 3.29/3.14, 3.28/3.14, 3.00/2.90 (C$H_2$); 11.55, 7.36, 7.32, 6.88 ppm (O*H*). $^{13}C$ NMR ($C_7D_8$, 25 °C): $\delta$ = 182.7, 182.5, 182.3, 178.7, 176.9 (*C*O); 135.1, 133.7, 131.0 (=*C*H-); 118.5, 117.1, 115.8 (*C*$H_2$=); 42.1, 41.8, 41.6, 39.5 ppm (*C*$H_2$).

**Synthesis of $[Zr_6O_4(OH)_4(OOCCH{=}CMe_2)_{12}]_2$·4$Me_2C$=CHCOOH (5):** Dimethylacrylic acid (1.23 g, 12.3 mmol) was added to a solution of $Zr(OBu)_4$ (3.25 mmol, 1.56 g of a 80% solution in BuOH) in toluene (5 mL) whilst stirring. The mixture was allowed to stir for an additional 30 min. After 20 days at room temperature colorless crystals separated, which were dried in vacuo. Yield: 0.985 g (88%). $C_{140}H_{208}O_{72}Zr_{12}$ (4137.8): calcd. C 40.64, H 5.07, $ZrO_2$ 35.73; found C 40.58, H 4.87, $ZrO_2$ 35.29 (TGA). IR-ATR: $\tilde{\nu}$ = 3648 (w), 3355 (w, OH), 2911 (w, CH), 1696 (m, C=O), 1651 (s, C=C), 1577 (s), 1520 (br. s, $COO_{as}$), 1419 (s, $COO_s$), 1370 (m), 1314 (s), 1234 (m), 1183 (m), 1161 (m), 1077 (m), 862 (m), 819 (m), 722 (m), 638 (m) $cm^{-1}$. $^1H$ NMR ($CD_2Cl_2$, 25 °C): $\delta$ = 5.57, 5.56, 5.52, 5.57, 5.53, 5.44, 5.37 (C*H*); 2.1, 2.08, 2.07, 1.92, 1.88, 1.79, 1.47 (Me); 10.63 ppm (O*H*). $^{13}C$ NMR ($CD_2Cl_2$, 25 °C): $\delta$ = 171.5, 174.3, 171.7 (*C*O); 150.7, 152.5, 157.0 (*C*H); 118.3, 120.2, 120.5, 121.7, 121.4, 121.9, 121.1 (*C*$Me_2$), 20.0, 19.9, 20.7, 19.7, 27.0, 27.0, 27.0 ppm (Me).

**Synthesis of $[Zr_6O_4(OH)_4(OOCCH_2Me)_3\{OOCC(Me){=}CH_2\}_9]_2$·$CH_2$=C(Me)COOH·5$MeCH_2COOH$ (6):** Propionic acid (1.37 g, 18.49 mmol) and methacrylic acid (0.618 g, 7.17 mmol) were added dropwise at room temperature to a stirred mixture of $Zr(OBu)_4$ (3.72 mmol, 1.78 g of a 80% butanol solution). After 24 h at room temperature colorless crystals were formed. The crystals were separated and dried in vacuo. Yield: 995 mg (85%). $C_{109}H_{164}O_{76}Zr_{12}$ (3785.1): calcd. C 34.59, H 4.37, $ZrO_2$ 39.06; found C 33.08, H 3.87, $ZrO_2$ 39.49 (TGA). IR-ATR: $\tilde{\nu}$ = 3393 (w, OH), 2979 (m), 1718 (m, COOH), 1595 (s, sh, $COO_{as}$), 1543 (s, $COO_{as}$), 1462 (s), 1421 (s, $COO_s$), 1372 (m), 1302 (s), 1244 (m), 1203 (m), 1080 (m), 936 (m, C=$CH_2$), 826 (m), 617 (m) $cm^{-1}$. $^1H$ NMR (Figure 10) ($C_7D_8$, 25 °C): $\delta$ = 0.99, 1.11, 1.24, 1.34, 1.40 (C$H_3$ propionate); 2.11, 2.24, 2.43, 2.57, 2.71 (C$H_2$ propionate); 6.30, 5.20, 6.40, 5.29, 6.26, 5.25 (C$H_2$ methacrylate); 11.70 ppm (O*H*). $^{13}C$ NMR ($C_7D_8$, 25 °C): $\delta$ = 178.3, 179.8, 184.1 (*C*O, methacrylate); 179.8, 179.6, 178.2, 184.2, 183.7 (*C*O, propionate); 137.5, 140.1, 139.9 (*C*Me, methacrylate); 123.1; 123.2; 125.5 (*C*$H_2$, methacrylate); 27.8, 30.2, 30.3, 29.9, 30.2 (*C*$H_2$, propionate); 18.2, 18.5, 18.4 (*C*$H_3$, methacrylate); 8.3, 9.6, 9.3, 9.7, 9.8 (*C*$H_3$, propionate) ppm.

**Synthesis of $[Zr_6O_4(OH)_4(OOCMe)_8\{OOCC(Me){=}CH_2\}_4]_2$·6MeCOOH (7):** Methacrylic acid (239 mg, 2.78 mmol) and acetic acid (423 mg, 7.04 mmol) were added dropwise to $Zr(OBu)_4$ (1.97 mmol, 945 mg of a 80% solution in BuOH) whilst stirring. Colorless needles were formed after 12 h at room temperature. The crystals were washed twice with *n*-heptane (1 mL) and dried in vacuo. Yield: 540 mg (98%). IR-ATR: $\tilde{\nu}$ = 3221 (w, OH), 2980 (vw, CH), 2956 (vw, CH), 2927 (vw, CH), 2875 (vw, CH), 1711 (m, C=O), 1643 (w, C=C), 1595 (sh), 1547 (s, $COO_{as.}$), 1448 (sh), 1422 (s, $COO_s$), 1373 (m, $COO_s$), 1344 (w), 1298 (w), 1245 (s), 1207 (sh), 1179 (w), 1047 (w), 1029 (w), 1007 (w), 937 (w), 902 (w), 883 (w), 852 (w), 827 (m), 798 (m), 674 (sh), 644 (vs, OCO), 631 (sh), 612 (vs, OCO) $cm^{-1}$. $^1H$ NMR ($CD_2Cl_2$, 25 °C): $\delta$ = 6.17/5.66, 6.08/5.59, 6.06/5.59, 5.92/5.39 (C$H_2$=); 1.82, 1.77, 1.75, 1.68 (Me, methacrylate); 2.00, 1.95, 1.62, 1.47 (Me, acetate); 11.48 ppm (O*H*). $^{13}C$ NMR ($CD_2Cl_2$, 25 °C): $\delta$ = 189.5, 180.1, 176.4, 175.4, 174.1 (*C*O, acetate); 183.5, 180.1, 171.1 (*C*O, methacrylate); 138.5, 135.9, 135.7, 135.6 (-*C*-); 127.2, 127.1, 126.9, 123.8 (*C*$H_2$=); 22.9, 23.1, 20.5 (Me, acetate); 17.8, 16.6 ppm (Me, methacrylate).

**Synthesis of $[Hf_6O_4(OH)_4(OOCMe)_{12}]_2$·6MeCOOH·3$CH_2Cl_2$ (8):** Acetic acid (1.92 g, 32.0 mmol) was added dropwise at room temperature to a stirred solution of $Hf(OBu)_4$ (3.2 mmol, 1.57 g of a 95% solution in BuOH) in $CH_2Cl_2$ (3 mL). After 24 h at room temperature colorless crystals were formed. The crystals were separated and dried in vacuo. Yield: 1.15 g (98%). $C_{63}H_{110}Cl_6Hf_{12}O_{76}$ (4438.1): calcd. C 17.05, H 2.50; found C 17.00, H 2.29. IR-ATR: $\tilde{\nu}$ = 3663 (w), 3387 (w), 1710 (m), 1558 (s), 1453 (s), 1261 (m), 1029 (m), 804 (m), 652 (s), 615 (s) $cm^{-1}$. $^1H$ NMR ($CD_2Cl_2$, 25 °C): $\delta$ = 1.84, 1.94, 2.01, 2.04, 2.05 (Me), 10.32 (O*H*) ppm. $^{13}C$ NMR ($CD_2Cl_2$, 25 °C): $\delta$ = 181.9, 177.8, 176.7 (*C*O); 23.5, 23.8, 23.0, 21.8, 21.1 (Me) ppm.

**Reaction of $[Zr_6O_4(OH)_4(OOCCH_2Me)_3\{OOCC(Me){=}CH_2\}_9]_2$ (6) with Propionic Acid:** An excess (1.94 g, 26.2 mmol) of propionic acid was added to a solution of **6** (165 mg, 0.043 mmol) in benzene (5 mL). The solution was stirred for 10 min, and then all volatile

 © 2006 Wiley-VCH Verlag GmbH & Co. KGaA, Weinheim 

compounds were removed in vacuo. This process was repeated twice.

**Reaction of $Zr_6O_4(OH)_4(OMc)_{12}$ (1) with Propionic Acid:** An excess (ca. 20 mmol) of propionic acid was added to a solution of **1** (226 mg, 0.133 mmol) in toluene (15 mL). The solution was stirred for 10 min, and then all volatile compounds were removed in vacuo. This process was repeated twice.

**X-ray Structure Analyses of 2–8:** Data collection (Table 1): The crystals were mounted on a Siemens SMART diffractometer (area detector) and measured in a nitrogen stream. Mo-$K_\alpha$ radiation ($\lambda$ = 71.069 pm, graphite monochromator) was used for all measurements. The data collection covered a hemisphere of the reciprocal space, by a combination of three or four sets of exposures. Each set had a different $\varphi$ angle for the crystal, and each exposure took 15 or 20 s and covered 0.3° in $\omega$. The crystal-to-detector distance was 5 cm. The data were corrected for polarization and Lorentz effects, and an empirical absorption correction (SADABS[12]) was employed. The cell dimensions were refined with all unique reflections. The structures were solved by the direct or the Patterson method (SHELXS97[13]). Refinement was performed by the full-matrix least-squares method based on $F^2$ (SHELXL97) with aniso-

Table 1. Crystallographic and structural parameters of **2**–**8**.

| | **2** | **3** | **4** | **5** |
|---|---|---|---|---|
| Empirical formula | $C_{48}H_{80}O_{64}Zr_{12}\cdot C_{12}H_{24}O_{12}\cdot C_{3.5}H_7Cl_7$ | $C_{72}H_{128}O_{64}Zr_{12}\cdot C_{18}H_{36}O_{12}$ | $C_{96}H_{128}O_{64}Zr_{12}\cdot C_{24}H_{36}O_{12}$ | $C_{120}H_{176}O_{64}Zr_1\cdot C_{20}H_{32}O_8$ |
| Formula weight | 3425.2 | 3556.9 | 3911.2 | 4137.8 |
| Temperature [K] | 173 | 173 | 173 | 173 |
| Crystal system | monoclinic | triclinic | monoclinic | triclinic |
| Space group | $P2_1/c$ | $P\bar{1}$ | $C2/c$ | $P\bar{1}$ |
| Unit cell dimension | | | | |
| $a$ [pm] | 1253.71(6) | 1709.2(6) | 3427.6(2) | 1488.19(8) |
| $b$ [pm] | 2415.0(1) | 1935.6(6) | 2716.7(1) | 1722.83(9) |
| $c$ [pm] | 2050.9(1) | 2156.1(7) | 2075.5(1) | 1935.7(1) |
| $\alpha$ [°] | | 86.951(7) | | 90.366(1) |
| $\beta$ [°] | 104.900(1) | 88.241(8) | 125.968(1) | 93.499(1) |
| $\gamma$ [°] | | 78.973(7) | | 112.497(1) |
| Volume [pm$^3$]·10$^6$ | 6000.5(5) | 6990 (4) | 15641.3(1) | 4574.3(4) |
| $Z$ | 2 | 2 | 4 | 1 |
| Calcd. density [g/cm$^3$] | 1.896 | 1.686 | 1.660 | 1.498 |
| Absorption coeff. $\mu$ [mm$^{-1}$] | 1.255 | 0.951 | 0.859 | 0.737 |
| Crystal size [mm] | 0.34 × 0.10 × 0.09 | 0.36 × 0.28 × 0.24 | 0.37 × 0.26 × 0.25 | 0.30 × 0.30 × 0.30 |
| 2$\theta$ range [°] | 1.92–28.36 | 1.46–23.26 | 2.10–28.32 | 1.76–25.00 |
| Reflections coll./unique | 69801/14888 | 30393/19224 | 54899/19363 | 46107/16023 |
| Data/parameters | 14888/766 | 19224/1605 | 19363/940 | 16023/1009 |
| GOF on $F^2$ | 1.039 | 1.028 | 1.016 | 1.019 |
| $R$ [$I > 2\sigma(I)$] | 0.0574 | 0.070 | 0.041 | 0.041 |
| $wR_2$ | 0.1415 | 0.184 | 0.101 | 0.112 |
| Largest diff. peak/hole [e·Å$^{-3}$] | 2.293/–1.077 | 3.211/–1.466 | 1.248/–0.869 | 1.452/–1.001 |
| | **6** | **7** | **8** | |
| Empirical formula | $C_{90}H_{128}O_{64}Zr_{12}\cdot C_4H_6O_2\cdot C_{15}H_{30}O_2$ | $C_{64}H_{96}O_{64}Zr_{12}\cdot C_{12}H_{24}O_{12}$ | $C_{48}H_{80}Hf_{12}O_{64}\cdot C_{12}H_{24}O_{12}\cdot C_6H_{12}Cl_{12}$ | |
| Formula weight | 3791.1 | 3344.2 | 4678.8 | |
| Temperature [K] | 213 | 173 | 173 | |
| Crystal system | monoclinic | monoclinic | monoclinic | |
| Space group | $P2_1/n$ | $C2/m$ | $P2_1/c$ | |
| Unit cell dimensions | | | | |
| $a$ [pm] | 2274.1(2) | 3626.9(3) | 1255.93(9) | |
| $b$ [pm] | 1491.3(2) | 1574.1(2) | 2419.5(2) | |
| $c$ [pm] | 2314.5(2) | 1369.8(1) | 2049.7(2) | |
| $\alpha$ [°] | | | | |
| $\beta$ [°] | 111.519(2) | 109.385(2) | 104.993(1) | |
| $\gamma$ [°] | | | | |
| Volume [pm$^3$]·10$^6$ | 7302(1) | 7377(1) | 6016.3(8) | |
| $Z$ | 2 | 2 | 2 | |
| Calcd. density [g/cm$^3$] | 1.709 | 1.497 | 2.583 | |
| Absorption coeff. $\mu$ [mm$^{-1}$] | 0.916 | 0.896 | 10.672 | |
| Crystal size [mm] | 0.36 × 0.30 × 0.07 | 0.18 × 0.16 × 0.12 | 0.21 × 0.18 × 0.12 | |
| 2$\theta$ range [°] | 1.74–26.37 | 2.38–25.00 | 2.22–25.00 | |
| Reflections coll./unique | 43785/14908 | 20132/12844 | 38319/10582 | |
| Data/parameters | 14908/901 | 12844/772 | 10582/743 | |
| GOF on $F^2$ | 1.030 | 1.038 | 1.289 | |
| $R$ [$I > 2\sigma(I)$] | 0.037 | 0.0676 | 0.076 | |
| $wR_2$ | 0.091 | 0.1803 | 0.149 | |
| Largest diff. peak/hole [e·Å$^{-3}$] | 1.032/–0.554 | 1.259/–0.731 | 4.319/–2.227 | |

 © 2006 Wiley-VCH Verlag GmbH & Co. KGaA, Weinheim 

tropic thermal parameters for all non-hydrogen atoms. Hydrogen atoms were inserted in calculated positions and refined riding with the corresponding atom.

CCDC-604528 (**2**), -604529 (for **3**), -604530 (for **4**), -604531 (for **5**), -604532 (for **6**), -604533 (for **7**), and -604534 (for **8**) contain the supplementary crystallographic data for this paper. These data can be obtained free of charge from The Cambridge Crystallographic Data Centre via www.ccdc.cam.ac.uk/data_request/cif.

## Acknowledgments

This work was supported by the Fonds zur Förderung der wissenschaftlichen Forschung (FWF), Austria.

[1] Review articles: U. Schubert, *Chem. Mater.* **2001**, *13*, 3487; G. Kickelbick, U. Schubert, *Monatsh. Chem.* **2001**, *132*, 13.
[2] G. Kickelbick, U. Schubert, *Chem. Ber./Recueil* **1997**, *130*, 473.
[3] Y. Gao, F. R. Kogler, H. Peterlik, U. Schubert, *J. Mater. Chem.*, in press.
[4] G. Kickelbick, P. Wiede, U. Schubert, *Inorg. Chim. Acta* **1999**, *284*, 1.
[5] C. Sanchez, G. J. de Soler-Illia, F. Ribot, T. Lalot, C. R. Mayer, V. Cabuil, *Chem. Mater.* **2001**, *13*, 3061.
[6] Y. Gao, D. S. Dragan, M. Jupa, F. R. Kogler, M. Puchberger, U. Schubert, *Mat. Res. Soc. Symp. Proc.* **2005**, *847*, 539.
[7] P. Toledano, F. Ribot, C. Sanchez, *Compt. Rend. Acad. Sci. Paris, Ser. II* **1990**, *311*, 1315.
[8] F. R. Kogler, M. Jupa, M. Puchberger, U. Schubert, *J. Mater. Chem.* **2004**, *14*, 3133.
[9] M. Jupa, G. Kickelbick, U. Schubert, *Eur. J. Inorg. Chem.* **2004**, 1835.
[10] B.-H. Ye, X.-Y. Li, I. D. Williams, X.-M. Chen, *Inorg. Chem.* **2002**, *41*, 6426.
[11] G. Kickelbick, M. P. Feth, H. Bertagnolli, M. Puchberger, D. Holzinger, S. Gross, *J. Chem. Soc., Dalton Trans.* **2002**, 3892.
[12] G. M. Sheldrick, *SADABS*, University of Göttingen, **1996**.
[13] G. M. Sheldrick, *SHELXS97*, University of Göttingen, **1997**.

Received: April 19, 2006
Published Online: July 3, 2006

 © 2006 Wiley-VCH Verlag GmbH & Co. KGaA, Weinheim 

DOI: 10.1002/ejic.200600359

# Facile Synthesis of Cyclometalated Ruthenium Complexes with Substituted Phenylpyridines

**Isabelle Sasaki,*[a] Laure Vendier,[a] Alix Sournia-Saquet,[a] and Pascal G. Lacroix[a]**

**Keywords:** Metallacycles / N ligands / Ruthenium

We have developed a new strategy that uses the Kröhnke synthesis for the preparation of various substituted phenylpyridines in excellent yields (up to 88 %). Starting with the appropriate commercially available acetophenone, a variety of phenylpyridines substituted by either electron-donating (i.e. methyl, methoxy) or -withdrawing groups (i.e. bromide, nitro) on the phenyl ring are obtained in a two-step synthesis. The corresponding functionalized cyclometalated ruthenium complexes can be prepared with unusually high yields by using methanol as reaction solvent. The electrochemical data of the complexes demonstrate the strong σ-donating character of the anionic phenylpyridine ligand. X-ray analyses of four complexes show a shortening of the Ru–C bond associated with the elongation of only one of the five Ru–N bonds (*trans* effect).

(© Wiley-VCH Verlag GmbH & Co. KGaA, 69451 Weinheim, Germany, 2006)

## Introduction

(Polypyridine)ruthenium(II) complexes have attracted much interest as light absorbers, photoluminescent sensors or switches, and intermolecular energy- and electron-transfer agents.[1] Some cyclometalated counterparts of these complexes have been prepared and their physical properties reported.[2–6] In fact, cyclometalated complexes have found widespread interest as species with promising properties in various fields[7] owing to the strong σ-donor ability of the cyclometalated ligand. Typically, the coordinating ligand forms a bond to the metal center and then intramolecular C–H activation takes place to yield a five-membered chelate ring. Replacement of a nitrogen donor by a formal carbanion donor drastically increases the electron density around the metal atom[4] and the crystal-field strength.[5]

A variety of synthetic methodologies[8] for the synthesis of new pyridine derivatives have been developed. One of the most important is the transition-metal-catalyzed cross-coupling reactions of precursors developed by Negishi, Suzuki, and Stille (see refs.[9–11]). In fact, all these methods entail the preparation of functionalized intermediates.[12] In the course of our studies we have prepared a number of polypyridine ligands[13] by using the Kröhnke method.[14] By extending this procedure to aromatic ketones, we propose an easy and versatile synthesis of substituted phenylpyridines.[15] Starting from commercially available acetophenones, a variety of mono- or difunctionalized phenylpyridines substituted by electron-donating (i.e. methyl, methoxy) or -withdrawing groups (i.e. bromide, nitro) on the phenyl ring can be obtained with very good yields.

[a] Laboratoire de Chimie de Coordination, UPR 8241 du CNRS, 205 route de Narbonne, 31077 Toulouse Cedex 04, France
E-mail: sasaki@lcc-toulouse.fr

## Results and Discussion

### Synthesis

Our synthetic route starts with the preparation of the pyridinium derivative of the appropriate aromatic methyl ketone.[14] Condensation of these derivatives with methacrolein gives the corresponding phenylpyridines, as described in Scheme 1. We also checked this synthesis with tiglic aldehyde[16] to show that this methodology can be extended to other α,β-unsaturated carbonyl compounds.

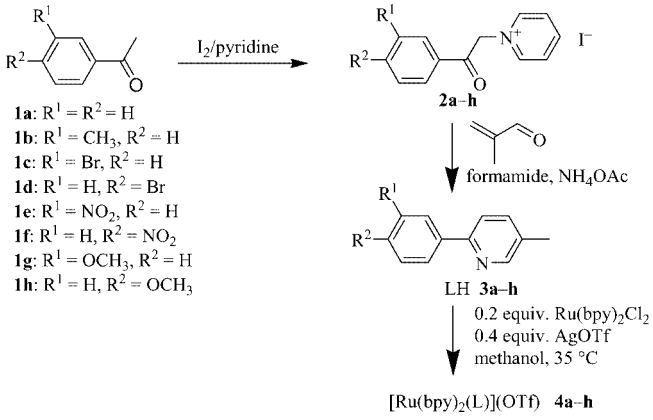


Scheme 1.

The different ligands synthesized in this work are summarized together with the few previously reported molecules in Table 1. To the best of our knowledge, no crystal structure of a phenylpyridine has been published (vide infra).

 © 2006 Wiley-VCH Verlag GmbH & Co. KGaA, Weinheim 

Table 1. List and yields of ligands LH prepared by this method.

| | | Yield [%] | Ref. |
|---|---|---|---|
| **3a**: | $R^1 = R^2 = R^3 = H$ | 88 | [15,17,18] |
| | $R^1 = R^2 = H$, $R^3 = CH_3$ | 84 | [21] |
| **3b**: | $R^1 = CH_3$, $R^2 = R^3 = H$ | 88 | [10] |
| **3c**: | $R^1 = Br$, $R^2 = R^3 = H$ | 62 | |
| **3d**: | $R^1 = R^3 = H$, $R^2 = Br$ | 82 | [20] |
| **3e**: | $R^1 = NO_2$, $R^2 = R^3 = H$ | 77 | |
| **3f**: | $R^1 = R^3 = H$, $R^2 = NO_2$ | 79 | |
| **3g**: | $R^1 = OCH_3$, $R^2 = R^3 = H$ | 81 | |
| **3h**: | $R^1 = R^3 = H$, $R^2 = OCH_3$ | 76 | [19,20] |

The different products were obtained in good yields and their characterizations were carried out by $^1H$ and $^{13}C$ NMR spectroscopy as well as by mass spectrometry (FAB or DCI) and microanalysis (see Experimental Section). These compounds offer the possibility for further reactions on both aromatic rings; for example, the Br atom on the phenyl ring can be replaced in various reactions and the $NO_2$ group can be reduced, whereas the pyridine ring can be functionalized thanks to the methyl group.[22]

The synthesis of five cyclometalated $Ru^{II}$ complexes was carried out by Constable's method[4] with a modification proposed by Coudret,[23] which uses only 5 equiv. of ligand instead of a 15-fold excess.[4] We obtained much higher yields of cyclometalated complexes (up to 90%) than according to the literature procedure by using methanol instead of dichloromethane[4] as solvent. Constable[24] has studied the effect of different solvents in the reactions of 6-phenyl-2,2′-bipyridine with ruthenium(II) and concluded that the higher the dielectric constant of the solvent the greater the proportion of the metalated product formed (as is the case with methanol compared to dichloromethane). Purification of the complexes was carried out by column chromatography, which enables recovery of the unreacted excess of ligand. This synthesis yields the corresponding functionalized ruthenium complexes directly, whereas in the literature functionalization was carried out on the ruthenium complexes. Using 3,5-dipyridylbenzene, Collin et al. converted the corresponding cyclometalated complex into the nitro derivative and subsequently into the amino derivative.[25] More recently, Coudret was able to obtain the corresponding bromo-substituted complex upon treatment of $[Ru(bpy)_2L]^+$ (L = phenpy) with NBS.[25] The synthesis of the amino derivative was also carried out.[26] The different direct functionalizations of the complex were possible only at the position *para* to the carbanion.[27] In our case, by using the appropriate starting material (acetophenone), other positions of the substituent on the ligand and therefore in the complex are accessible.

Complete assignment of the $^1H$ and $^{13}C$ NMR spectra of the complexes required 1D, 2D $^1H$-$^1H$ COSY, HMQC $^1H$-$^{13}C$ and HMBC $^1H$-$^{13}C$ experiments. The labelling of the atoms is that of the X-ray structures. For the five complexes, comparison of the $^1H$ NMR spectra shows that the peaks corresponding to the phenylpyridine ring are influenced by the electronic character of the substituents on the phenyl ring. More precisely, in the high-field region between $\delta$ = 7.3 and 5.9 ppm, the most high-field-shifted doublet is assigned to the proton of the phenyl ring (8-H) in the *ortho* position and its chemical shift varies from $\delta$ = 5.95 (methoxy derivative **4h**) to 7.3 ppm (nitro derivative **4f**). The upfield shift of the proton adjacent to the site of metalation is a common feature of compounds of this type.[4,24,28] The other shielded doublet (between $\delta$ = 6.45 and 7.05 ppm) is attributed to the proton *meta* (9-H, complex **4a**) or *para* (10-H, complexes **4b**, **4d**, and **4h**) to the metalated carbon atom. An exception is observed for **4f**, for which the proton 10-H is highly deshielded ($\delta$ = 7.69 ppm) due to the electron-withdrawing character of the nitro substituent.

## X-ray Analysis

Single crystals of ligands **3a** and **3b** were obtained after slow concentration of a mixture of pentane and ethyl acetate. The ORTEP diagrams of **3a** and **3b** are shown in Figure 1.

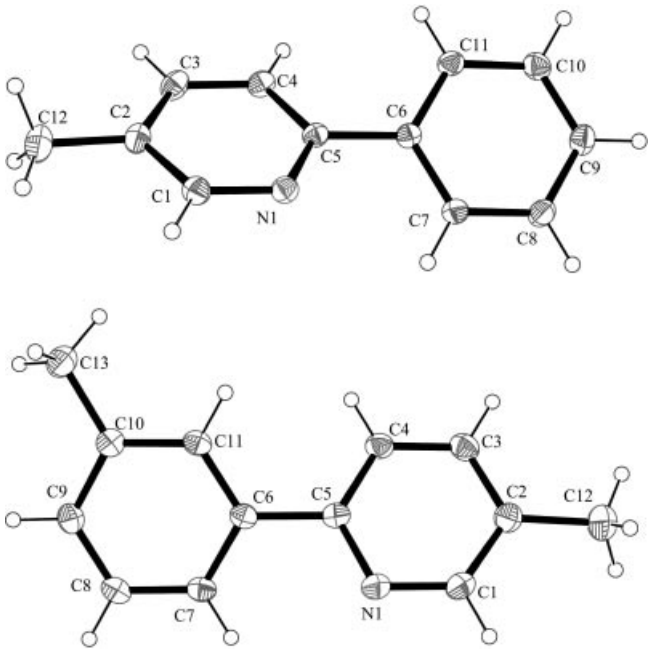


Figure 1. X-ray molecular structures of **3a** (top) and **3b** (bottom).

Ligand **3a** crystallizes in the $P2_12_12_1$ orthorhombic space group. The two aromatic rings are not planar, with an N(1)–C(5)–C(6)–C(7) torsion angle of 32.3°. Ligand **3b** crystallizes in the $P2_1/n$ monoclinic space group. The molecule is slightly more planar than **3a**, with an N(1)–C(5)–C(6)–C(7) torsion angle of 28.4°. As these compounds are not symmetrical, and as the exact position of the substituents can be unambiguously determined by NMR spectroscopy and because of the synthetic scheme, the position of the nitrogen atom is well defined. This is important for the analysis of the X-ray data of the complexes.

 © 2006 Wiley-VCH Verlag GmbH & Co. KGaA, Weinheim 

Crystals of the four complexes **4b′**, **4d**, **4f**, and **4h** were obtained for X-ray analysis (Figure 2). In one case (**4b**), good-quality crystals were available only after exchange of the trifluoromethanesulfonate counteranion by hexafluorophosphate to give complex **4b′**. Crystallization occurred upon slow diffusion of diethyl ether into acetonitrile solutions of the complexes at 5 °C.

The ruthenium complex **4b′** crystallizes in the $P2_1/n$ monoclinic space group. The asymmetric unit cell contains one ruthenium complex, one $PF_6^-$ anion, and one molecule of acetone. The phenylpyridine ligand is almost perfectly planar in the complex, with an N(1)–C(5)–C(6)–C(7) torsion angle of 0.59° against torsion angles of 2.69° and 1.73° in the bipyridine ligands with N(2)/N(3) and N(4)/N(5), respectively. The brominated complex **4d** crystallizes in the $C2/c$ monoclinic space group. The unit cell contains eight molecules of complex ($Z = 8$), and four molecules of water. The phenylpyridine ligand is roughly planar, with an N(1)–C(5)–C(6)–C(7) torsion angle of 2.95° against torsion angles of 3.00° and 0.27° in the bipyridine ligands with N(2)/N(3) and N(4)/N(5), respectively. Complex **4f** crystallizes in the $P2_1/n$ monoclinic space group, with one molecule in the asymmetric unit cell. The bipyridine ligands are nearly perfectly planar in the complex, with torsion angles of 0.30° and 0.40° for the bipyridine ligands with N(2)/N(3) and N(4)/N(5), respectively. By contrast, the torsion angle in the phenylpyridine ligand is 1.63°. Complex **4h** crystallizes in the $P\bar{1}$ triclinic space group. The asymmetric unit cell contains one ruthenium complex, one $CF_3SO_3^-$ anion, and one molecule of acetonitrile. The phenylpyridine ligand is perfectly planar (torsion angle of 0.17°), whereas the bipyridine ligands are slightly distorted, with torsion angles of 5.96° and 4.46° for the bipyridine ligands with N(2)/N(3) and N(4)/N(5), respectively.

The Cambridge Crystallographic Database contains 156 entries with a (phenylpyridine)metal unit, most of them containing platinum (55) and palladium (24). However, structures containing a $(bpy)_2$(phenpy)metal unit are far

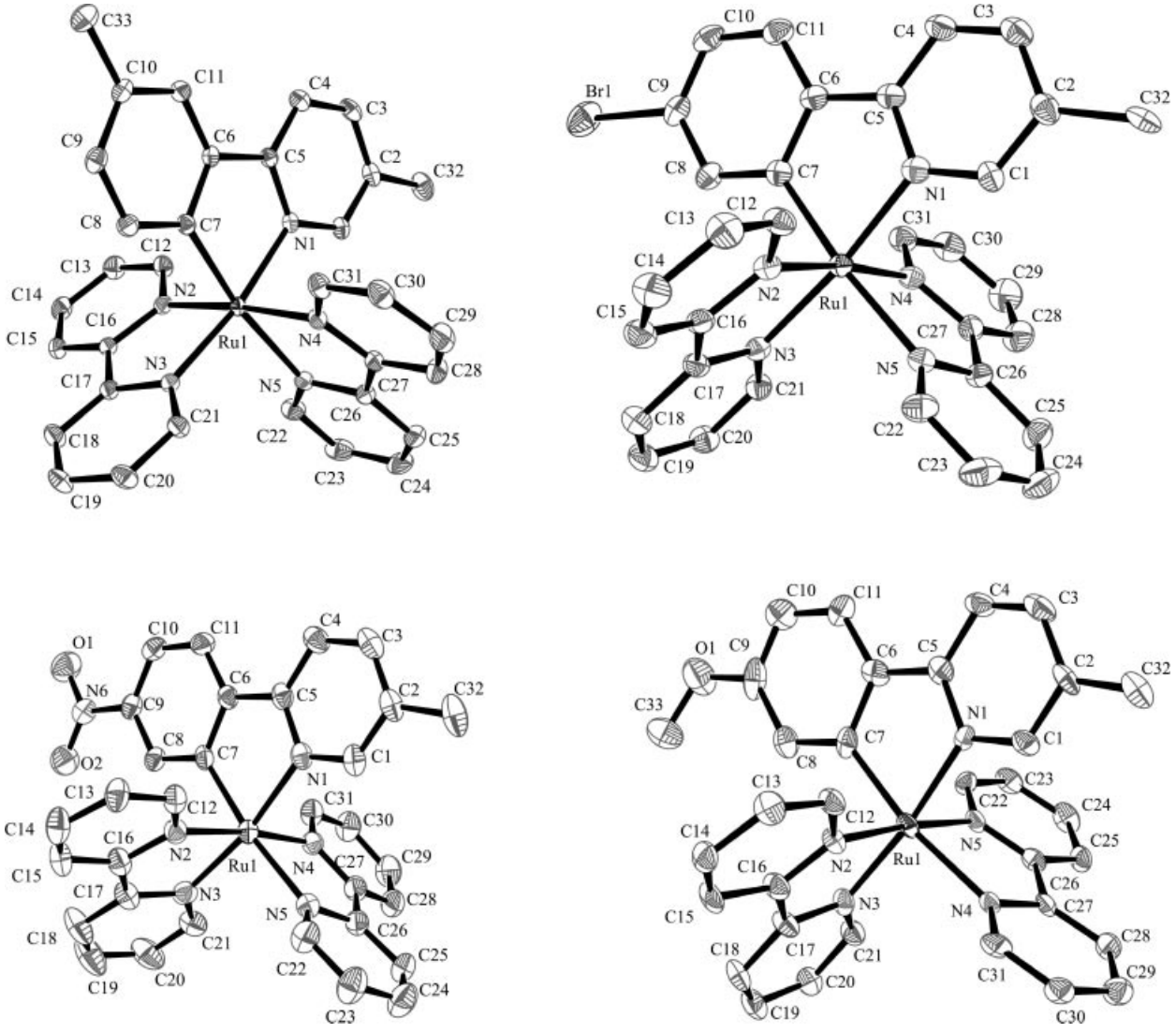


Figure 2. ORTEP representation of the X-ray structureS of **4b′** (top left), **4d** (top right), **4f** (bottom left), and **4h** (bottom right). The hydrogen atoms, solvent molecules, and counteranions are omitted for clarity.

 © 2006 Wiley-VCH Verlag GmbH & Co. KGaA, Weinheim 

Table 2. First coordination sphere (metal–ligand bond lengths [Å]) in $[Ru^{II}(bpy)_2(L)]^+$ complexes.

| Complex | Ru(1)–C(7) | Ru(1)–N(1) | Ru(1)–N(2) | Ru(1)–N(3) | Ru(1)–N(4) | Ru(1)–N(5) |
|---|---|---|---|---|---|---|
| **4b′** | 2.036(3) | 2.080(2) | 2.043(2) | 2.036(2) | 2.066(2) | 2.138(2) |
| **4d** | 2.030(5) | 2.071(4) | 2.042(4) | 2.051(4) | 2.065(4) | 2.123(4) |
| **4f** | 2.020(4) | 2.078(4) | 2.047(4) | 2.055(4) | 2.060(4) | 2.121(4) |
| **4h** | 2.031(8) | 2.067(6) | 2.047(5) | 2.042(6) | 2.066(6) | 2.121(6) |
| Av. value | 2.029(5) | 2.074(4) | 2.045(4) | 2.046(4) | 2.064(4) | 2.125(4) |
| **a**[a] | 1.997(7) | 2.075(5) | 2.040(5) | 2.056(5) | 2.086(5) | 2.140(5) |
| **b**[a] | 2.044(1) | 2.069(4) | 2.067 | 2.046 | 2.037 | 2.075 |

[a] **a**: $[Ru(bpy)_2(NPP)][BF_4]$[6] [NPP = 2-(3-nitrophenyl)pyridine]. **b**: $[Ru(bpy)_2(ppy)][PF_6]$[28] (ppy = phenylpyridine).

less common, with only four entries.[6,29–31] In two of them, namely $[Ru(bpy)_2(phenpy)][CrMn(ox)_3]$[30] and $[Rh(bpy)_2(phenpy)](PF_6)$,[31] the localization of the carbon atom was not possible. In the third complex, $[Ru(bpy)_2(phenpy)](PF_6)$,[29] the carbon atom was arbitrarily localized because its distribution was equal on the six atomic sites bonded to the Ru atom. Finally, the only crystal structure in which the carbon–metal bond was unambiguously identified is that of $[Ru^{II}(bpy)_2\{2\text{-(nitrophenyl)pyridine}\}](BF_4)$, reported by Reveco et al.[6] The description of the coordination sphere of the four new complexes **4b′**, **4d**, **4f**, and **4h** is compared to the previously reported structures in Table 2. First of all, it must be pointed out that the position of the carbon atom is unambiguous as the positions of the substituents in the unsymmetrical ligands are definite. The average metal–ligand distances for the four available structures were calculated and show the following general features: (1) whereas the Ru(1)–C(7) bond is shorter than the other metal–ligand bonds, the Ru–N bonds to both the nitrogen atom *trans* to the carbon atom [N(5)] and the one *cis* to the carbon atom [N(1)] are slightly elongated, which leads to a distorted octahedral geometry around the metal atom; (2) the Ru(1)–N(4) bond is also slightly elongated, but less than Ru(1)–N(5), probably because it belongs to the same bipyridine ligand; (3) the Ru(1)–N(2) and Ru(1)–N(3) bond lengths have similar values, thus showing that this bipyridine ligand is the least disturbed by the cyclometalating ligand. Interestingly, comparison of the Ru(1)–C(7) bond length [1.997(7) Å] in $[Ru^{II}(bpy)_2\{2\text{-(3-nitrophenyl)pyridine}\}](BF_4)$[6] and that in complex **4f** [2.020(4) Å, the smallest value in the series of complexes **4**], in which the nitro substituent is at the 4-position, demonstrates the influence of the electron-withdrawing character of the substituent. More precisely, in the *para* position, both inductive and mesomeric effects are transmitted to C(9) whereas in the *meta* position (complex **4f**) only an inductive effect is in operation.

## Electrochemistry

The ligands and ruthenium complexes were examined by cyclic voltammetry (Figure 3) and Osteryoung square-wave voltammetry (Table 3).

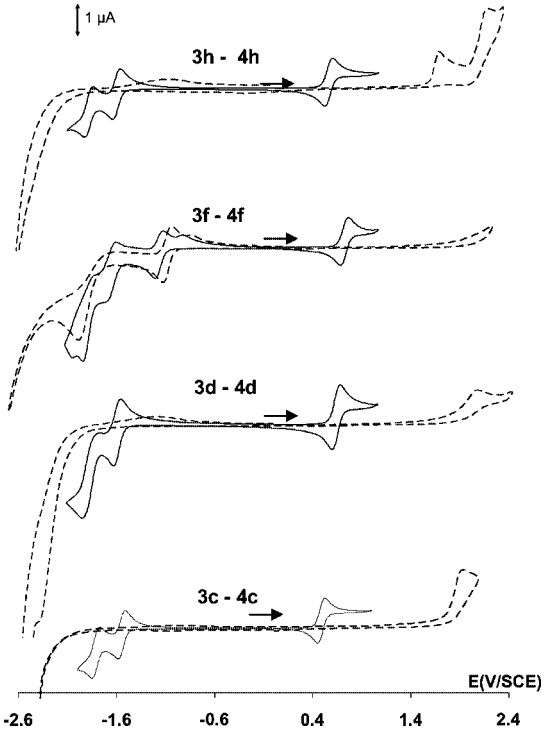


Figure 3. Cyclic voltammograms at room temperature of ruthenium complexes **4c**, **4d**, **4f**, **4h** (solid line) and ligands **3c**, **3d**, **3f**, **3h** (dashed line) in $CH_3CN$ with 0.1 M $TBABF_4$ as supporting electrolyte (Pt electrode, $v = 0.1\ V\,s^{-1}$).

Ligands **3c**, **3d**, and **3h** exhibit two processes: one in oxidation (ca. 1.9 V) and one in reduction (ca. –2.4 V). However, ligand **3h** presents another oxidation (1.55 V) due to the methoxy substituent. Ligand **3f** displays two reduction processes: a reversible redox couple at –1 V assigned to the $NO_2$ substituent and an irreversible reduction at –1.84 V (much higher than those of other ligands). This suggests that because of the electron-withdrawing properties of the $NO_2$ group, the oxidation is also dramatically shifted to higher potentials that are not measurable under the experimental conditions.

Cyclic voltammetry of the complexes exhibits three characteristic processes: one oxidation process and two reduction processes.

First, the reversible redox couple at around 0.5 V is readily assigned to the $Ru^{III}/Ru^{II}$ process.[4,32] A comparison of the potentials in Table 3 indicates that the first metal-cen-

 © 2006 Wiley-VCH Verlag GmbH & Co. KGaA, Weinheim 

Table 3. Redox potentials ([V] vs. SCE) of the ligands and ruthenium complexes in 0.1 M $TBABF_4$ in acetonitrile solutions measured at room temperature.

| | Oxidation | | | Reduction | | | |
|---|---|---|---|---|---|---|---|
| | $E_{1/2}$[a] | $E_{1/2}$[b] | $E_{1/2}$[b] | $E_{1/2}$[a] | $E_{1/2}$[a] | $E_{1/2}$[a] | $E_{1/2}$[b] |
| **3c** | | | 1.90 | | | | –2.44 |
| **3d** | | | 1.91 | | | | –2.19 |
| **3f** | | | n.d.[c] | –1.04 | | | –1.84 |
| **3h** | | 1.55 | 1.99 | | | | –2.55 |
| **4c** | 0.48 | | 1.73 | | –1.54 | –1.82 | –2.40 |
| **4d** | 0.60 | | 1.77 | | –1.51 | –1.76 | –2.24 |
| **4f** | 0.67 | | 1.99 | –1.12 | –1.57 | –1.81 | –1.94 |
| **4h** | 0.52 | 1.63 | n.d.[c] | | –1.53 | –1.79 | –2.37 |
| $Ru(bpy)_3$[33] | 1.29 | | | | –1.35 | –1.54 | –1.73 |

[a] The $E_{1/2}$ values were estimated as the average of the cathodic and anodic peak potentials in cyclic voltammetry with a scan rate of 100 mV $s^{-1}$. [b] The $E_{1/2}$ values were obtained from the square-wave voltammogram: frequency 20 Hz, step potential 5 mV, amplitude 20 mV. [c] Not observed or badly defined under the experimental conditions.

tered oxidation of the complex is shifted by about 800 mV to more cathodic potentials than that of $[Ru(bpy)_3]$.[33] This behavior demonstrates the strong σ-donating character of the phenylpyridine ligands, which stabilize $Ru^{III}$ by increasing the electron density on the metal atom.[4,7c] Moreover, the nature of the substituents affects the shift of the $Ru^{III}/Ru^{II}$ potential. The methyl and methoxy substituents with electron-donating character induce the most significant shift, whereas the electron-withdrawing groups (Br and $NO_2$), which decrease the electron density on $Ru^{III}$, lower the magnitude of the shift.

Second, the complexes exhibit two reduction processes at around –1.55 and –1.80 V (–1.35 and –1.54 V for $[Ru(bpy)_3]$). Complex **4f** displays an additional first reduction process at –1.12 V assigned to the $NO_2$ substituent. Generally, compared to $[Ru(bpy)_3]$, the bpy-centered quasi-reversible reductions are shifted to more negative potentials and are also strongly affected by the presence of the cyclometallating ligand,[7c] but the nature of the substituents does not affect significantly these processes. Moreover, the most cathodic potentials near the solvent/electrolyte limit were resolved in the square-wave experiment and were assigned to the phenylpyridine ligand.

## Conclusions

We have been able to synthesize new substituted phenylpyridines in high yields by a very simple general method from cheap, commercially available starting materials. Functionalized cyclometalated ruthenium(II) complexes were obtained in much higher yields than the few examples described in the literature. As crystals for four of them were obtained, an X-ray study highlighted specific features of the Ru–C and the *trans*-Ru–N bonds. The easiness in obtaining first the ligands and then the cyclometalated complexes is a breakthrough for the application of these complexes. By a "building block" approach, involving convergent synthesis, these compounds could lead to various polynuclear complexes[34] or to new compounds with potential NLO properties.[22]

## Experimental Section

**General:** Reagents and solvents were commercially available and were used as received. $[Ru(bpy)_2Cl_2]$ was prepared according to a literature procedure.[35] $^1H$ and $^{13}C$ NMR spectra were obtained at 298 K in $CDCl_3$, $CD_3COCD_3$, or $(CD_3)_2SO$ with a Bruker AM 250 spectrometer (250 MHz for $^1H$ NMR and 62.9 MHz for $^{13}C$) or a Bruker Avance 500 spectrometer for 2D NMR. DCI and EI mass spectra were recorded with a Thermo Finnigan TSQ 7000 and FAB mass spectra were recorded with a quadrupolar Nermag R 10-10 instrument with NBA as matrix. Elemental analyses were performed at the LCC with a Perkin–Elmer 2400 Serie II instrument. Electrochemistry data: Voltammetric measurements were carried out with a potentiostat Autolab PGSTAT 100. A home-made, airtight three-electrode cell connected to a vacuum/argon line made up of a Pt disk (0.5 mm diameter) as working electrode, a Pt gauze as auxiliary electrode, and an SCE as reference electrode. All experiments were performed at ambient temperature in $CH_3CN$ solution, with 0.1 M $nBu_4NBF_4$ as supporting electrolyte (purum electrochemical grade Fluka, purified by sublimation). The solutions used for the electrochemical studies were typically $10^{-3}$ M in ruthenium complex. Prior to measurements, the solutions were deoxygenated by bubbling with argon gas for 15 min and the working electrode was polished with a polishing machine (Presi P230); during experiments, a stream of argon was passed over the solution. All potentials are reported vs. SCE.

**X-ray Analysis:** Data collection (Table 4) was performed at low temperature (180 K) with an IPDS STOE diffractometer equipped with a graphite-monochromated Mo-$K_\alpha$ radiation source ($\lambda$ = 0.71073 Å) and an Oxford Cryosystems Cryostream Cooler Device. The final unit-cell parameters were obtained by means of a least-squares refinement performed on a set of 5000 well-measured reflections. Crystal decay was monitored during the data collection; no significant fluctuations of intensities were observed. The structures were solved by direct methods using SIR92,[36] and refined by means of least-squares procedures on $F^2$ with the aid of the program SHELXL97[37] included in the software package WinGX version 1.63.[38] Atomic scattering factors were taken from the International Tables for X-ray Crystallography.[39] All hydrogen atoms were located geometrically and refined by using a riding model. All non-hydrogen atoms were refined anisotropically, and in the last cycles of refinement a weighting scheme was used, where weights are calculated from the following formula: $w = 1/[\sigma^2(F_o^2) + (aP)^2 + bP]$ where $P = (F_o^2 + 2F_c^2)/3$. Drawings of the molecules were produced with the program ORTEP32,[40] with 30% probability displacement ellipsoids for non-hydrogen atoms. CCDC-603013 to -603018 contain the supplementary crystallographic data for this paper. These data can be obtained free of charge from The Cambridge Crystallographic Data Centre via www.ccdc.cam.ac.uk/data_request/cif.

**Typical Procedure for the Preparation of the Pyridinium Derivatives 2a–h:** A solution of sublimated iodine (5.25 g, 20.5 mmol) in 8 mL of dry pyridine was added to a solution of 20 mmol of acetophenone in 5 mL of dry pyridine. After heating at 80 °C for 6 h, then cooling, the precipitate was filtered off, rinsed once with pyridine, dried, and recrystallized from boiling ethanol. The corresponding pyridinium derivative was isolated as a beige powder.

 © 2006 Wiley-VCH Verlag GmbH & Co. KGaA, Weinheim 

Table 4. Crystal data, data collection and refinements parameters for ligands **3a** and **3b** and complexes **4b′**, **4d**, **4f**, and **4h**.

| | **3a** | **3b** | **4b′** | **4d** | **4f** | **4h** |
|---|---|---|---|---|---|---|
| Empirical formula | $C_{12}H_{11}N$ | $C_{13}H_{13}N$ | $C_{36}H_{34}F_6N_5OPRu$ | $C_{33}H_{26}BrF_3N_5O_{3.5}Ru$ | $C_{35}H_{30}F_3N_6O_{5.5}RuS$ | $C_{37}H_{31}F_3N_6O_4RuS$ |
| Formula mass | 169.22 | 183.24 | 798.72 | 818.63 | 812.78 | 801.80 |
| Crystal size [mm] | 0.5×0.3×0.07 | 0.35×0.25×0.12 | 0.375×0.11×0.05 | 0.4×0.2×0.07 | 0.45×0.1875×0.05 | 0.3×0.2×0.08 |
| Crystal system | orthorhombic | monoclinic | monoclinic | monoclinic | monoclinic | triclinic |
| Space group | $P2_12_12_1$ | $P2_1/n$ | $P2_1/n$ | $C2/c$ | $P2_1/n$ | $P\bar{1}$ |
| $a$ [Å] | 6.1173(5) | 6.338(5) | 9.0328(7) | 24.295(5) | 15.2172(16) | 9.240(5) |
| $b$ [Å] | 7.4700(5) | 7.218(5) | 13.7518(10) | 13.694(3) | 14.5676(10) | 13.611(5) |
| $c$ [Å] | 20.0874(19) | 22.561(15) | 27.824(2) | 20.137(4) | 16.8313(17) | 15.545(5) |
| $\alpha$ [°] | 90 | 90 | 90 | 90 | 90 | 66.107(5) |
| $\beta$ [°] | 90 | 96.211(5) | 87.981(10) | 105.74(3) | 112.241(11) | 83.613(5) |
| $\gamma$ [°] | 90 | 90 | 90 | 90 | 90 | 72.623(5) |
| $V$ [Å$^3$] | 917.92(13) | 1026.1(11) | 3454.1(4) | 6449(3) | 3453.5(6) | 1705.8(12) |
| $\rho_{calcd.}$ [g cm$^{-3}$] | 1.224 | 1.186 | 1.536 | 1.686 | 1.563 | 1.561 |
| $T$ [K] | 180 | 180 | 180 | 180 | 180 | 180 |
| $\mu$(Mo-$K\alpha$) [mm$^{-1}$] | 0.072 | 0.069 | 0.570 | 1.853 | 0.584 | 0.587 |
| Scan mode | $\varphi$ | $\varphi$ | $\varphi$ | $\varphi$ | $\varphi$ | $\varphi$ |
| Measured reflections | 7932 | 7840 | 32316 | 27761 | 29682 | 15476 |
| Independent reflections | 1075 | 1950 | 6770 | 5432 | 5882 | 5659 |
| Observed reflections | 1075 | 1950 | 6770 | 5432 | 5882 | 5659 |
| Criteria | $I>2\sigma(I)$ | $I>2\sigma(I)$ | $I>2\sigma(I)$ | $I>2\sigma(I)$ | $I>2\sigma(I)$ | $I>2\sigma(I)$ |
| Refinement on | $F^2$ | $F^2$ | $F^2$ | $F^2$ | $F^2$ | $F^2$ |
| No of parameters | 119 | 129 | 455 | 430 | 453 | 463 |
| H atoms | calculated | calculated | calculated | calculated | calculated | calculated |
| $R_1$ | 0.0285 | 0.0504 | 0.0319 | 0.0504 | 0.0456 | 0.0744 |
| $wR_2$ | 0.0705 | 0.1312 | 0.0706 | 0.1407 | 0.1001 | 0.1716 |
| $\Delta\rho_{max}$ [e Å$^{-3}$] | 0.125 | 0.208 | 0.551 | 1.192 | 0.558 | 1.049 |
| $\Delta\rho_{min}$ [e Å$^{-3}$] | –0.111 | –0.228 | –0.480 | –1.043 | –0.410 | –1.529 |
| GOF | 1.052 | 1.053 | 0.974 | 1.033 | 0.884 | 0.910 |

**Compound 2a:** Yield: 4.03 g (62%). $^1$H NMR ([D$_6$]DMSO): $\delta$ = 9.01 (d, $J$ = 5.5 Hz, 2 H), 8.75 (dt, $J$ = 7.9 and 1.2 Hz, 1 H), 8.29 (t, $J$ = 7.4 Hz, 2 H), 8.07 (dd, $J$ = 7 and 1.4 Hz, 2 H), 7.79 (m, 1 H), 7.67 (dt, $J$ = 7.6 and 1.7 Hz, 2 H), 6.51 (s, 2 H) ppm. $^{13}$C NMR ([D$_6$]DMSO): $\delta$ = 190.6, 146.4, 146.2, 134.7, 133.4, 129.1, 128.2, 127.8, 66.3 ppm. $C_{13}H_{12}INO$ (325.14): calcd. C 48.02, H 3.72, N 4.31; found C 47.92, H 3.38, N 4.09. FAB-MS: $m/z$ = 198 [M–I]$^+$.

**Compound 2b:** Yield: 4.27 g (63%). $^1$H NMR ([D$_6$]DMSO): $\delta$ = 8.98 (d, $J$ = 5.5 Hz, 2 H), 8.71 (t, $J$ = 7.8 Hz, 1 H), 8.24 (dd, $J$ = 7.3 and 6.6 Hz, 2 H), 7.86 (s, 1 H), 7.84 (d, $J$ = 6.3 Hz, 1 H), 7.54 (m, 2 H), 6.44 (s, 2 H), 2.44 (s, 3 H) ppm. $^{13}$C NMR ([D$_6$]DMSO): $\delta$ = 190.6, 146.3, 146.2, 138.5, 135.3, 133.5, 129.0, 128.4, 127.8, 125.5, 66.2, 20.8 ppm. $C_{14}H_{14}INO$ (339.17): calcd. C 49.58, H 4.16, N 4.13; found C 49.58, H 4.27, N 4.00. FAB-MS: $m/z$ = 212 [M–I]$^+$.

**Compound 2c:** Yield: 6.30 g (78%). $^1$H NMR ([D$_6$]DMSO): $\delta$ = 8.97 (d, $J$ = 5.5 Hz, 2 H), 8.76 (t, $J$ = 7.8 Hz, 1 H), 8.30 (dd, $J$ = 7.2 and 6.8 Hz, 2 H), 8.22 (m, 1 H), 8.1–8.0 (m, 2 H), 7.65 (t, $J$ = 7.9 Hz, 1 H), 6.48 (s, 2 H) ppm. $^{13}$C NMR ([D$_6$]DMSO): $\delta$ = 189.8, 146.5, 146.2, 137.1, 135.5, 131.4, 130.7, 127.9, 127.2, 122.3, 66.2 ppm. $C_{13}H_{11}BrINO$ (404.04): calcd. C 38.65, H 2.74, N 3.47; found C 38.71, H 2.55, N 3.33. FAB-MS: $m/z$ = 277 [M–I]$^+$.

**Compound 2d:** Yield: 6.30 g (78%). $^1$H NMR ([D$_6$]DMSO): $\delta$ = 8.97 (d, $J$ = 5.5 Hz, 2 H), 8.74 (t, $J$ = 7.8 Hz, 1 H), 8.28 (dd, $J$ = 7.1 and 7 Hz, 2 H), 8.00 (d, $J$ = 8.6 Hz, 2 H), 7.90 (d, $J$ = 8.6 Hz, 2 H), 6.45 (s, 2 H) ppm. $^{13}$C NMR ([D$_6$]DMSO): $\delta$ = 190.0, 146.4, 146.2, 132.5, 132.2, 130.1, 128.8, 127.8, 66.1 ppm. $C_{13}H_{11}BrINO$ (404.04): calcd. C 38.65, H 2.74, N 3.47; found C 38.55, H 2.50, N 3.24. FAB-MS: $m/z$ = 277 [M–I]$^+$.

**Compound 2e:** Yield: 5.55 g (75%). $^1$H NMR ([D$_6$]DMSO): $\delta$ = 8.98 (d, $J$ = 5.7 Hz, 2 H), 8.76 (m, 2 H), 8.63 (dd, $J$ = 8.2 and 2 Hz, 1 H), 8.48 (d, $J$ = 7.8 Hz, 1 H), 8.31 (dd, $J$ = 7.1 and 7 Hz, 2 H), 7.98 (t, $J$ = 8 Hz, 1 H), 6.55 (s, 2 H) ppm. $^{13}$C NMR ([D$_6$]-DMSO): $\delta$ = 189.6, 148.0, 146.6, 146.2, 134.8, 134.3, 131.0, 128.6, 127.9, 122.5, 66.3 ppm. $C_{13}H_{11}IN_2O_3$ (370.14): calcd. C 42.18, H 3.00, N 7.57; found C 42.22, H 2.92, N 7.45. FAB-MS: $m/z$ = 243 [M–I]$^+$.

**Compound 2f:** Yield: 5.33 g (72%). $^1$H NMR ([D$_6$]DMSO): $\delta$ = 8.97 (d, $J$ = 5.5 Hz, 2 H), 8.76 (t, $J$ = 7.8 Hz, 1 H), 8.48 (d, $J$ = 8.8 Hz, 2 H), 8.27–8.32 (m, 4 H), 6.51 (s, 2 H) ppm. $^{13}$C NMR ([D$_6$]-DMSO): $\delta$ = 190.0, 146.4, 146.2, 132.5, 132.2, 130.1, 128.8, 127.8, 66.1 ppm. $C_{13}H_{11}IN_2O_3$ (370.14): calcd. C 42.18, H 3.00, N 7.57; found C 42.33, H 2.95, N 7.46. FAB-MS: $m/z$ = 243 [M–I]$^+$.

**Compound 2g:** Yield: 5.82 g (82%). $^1$H NMR ([D$_6$]DMSO): $\delta$ = 8.99 (d, $J$ = 5.5 Hz, 2 H), 8.75 (t, $J$ = 7.8 Hz, 1 H), 8.29 (dd, $J$ = 7.5 and 6.6 Hz, 2 H), 7.70–7.55 (m, 2 H), 7.54 (s, 1 H), 7.39 (md, $J$ = 7.7 Hz, 1 H), 6.48 (s, 2 H), 3.87 (s, 3 H) ppm. $^{13}$C NMR ([D$_6$]-DMSO): $\delta$ = 190.4, 159.4, 146.3, 146.2, 134.7, 130.3, 127.8, 120.6, 120.4, 112.7, 66.3, 55.5 ppm. $C_{14}H_{14}INO_2$ (355.17): calcd. C 47.34, H 3.97, N 3.94; found C 47.39, H 3.97, N 4.00. FAB-MS: $m/z$ = 228 [M–I]$^+$.

**Compound 2h:** Yield: 5.11 g (72%). $^1$H NMR ([D$_6$]DMSO): $\delta$ = 9.00 (d, $J$ = 5.5 Hz, 2 H), 8.74 (t, $J$ = 7.8 Hz, 1 H), 8.27 (dd, $J$ = 7.5 and 6.7 Hz, 2 H), 8.05 (d, $J$ = 8.8 Hz, 2 H), 7.19 (d, $J$ = 8.8 Hz, 2 H), 6.45 (s, 2 H), 3.90 (s, 3 H) ppm. $^{13}$C NMR ([D$_6$]DMSO): $\delta$ = 188.8, 164.2, 146.2, 130.7, 127.7, 126.2, 114.4, 66.9, 55.8 ppm. $C_{14}H_{14}INO_2$ (355.17): calcd. C 47.34, H 3.97, N 3.94; found C 47.22, H 3.60, N 3.72. FAB-MS: $m/z$ = 228 [M–I]$^+$.

 © 2006 Wiley-VCH Verlag GmbH & Co. KGaA, Weinheim 

**Typical Procedure for the Preparation of the Phenylpyridines 3a–h:** $NH_4OAc$ (4 equiv., 8 mmol) and methacrolein (4 mmol) were added to a solution of the pyridinium derivative (2 mmol) in 5 mL of formamide. The reaction mixture was heated at 80 °C for 6 h and, after cooling, the ligand precipitated and was filtered off and rinsed with water. If the ligand did not precipitate it was extracted with $Et_2O$ (3×20 mL), the organic phase was dried with $MgSO_4$, concentrated to dryness, and purified by chromatography on silica gel with EtOAc in pentane (10:90) or methanol in dichloromethane (3:97) as eluent.

**5-Methyl-2-phenylpyridine (3a):** $^1$H NMR ($CDCl_3$): $\delta$ = 8.51 (d, $J$ = 1.2 Hz, 1 H), 7.96 (m, 2 H), 7.62 (d, $J$ = 8 Hz, 1 H), 7.54 (dd, $J$ = 8 and 2.1 Hz, 1 H), 7.49–7.35 (m, 3 H), 2.36 (s, 3 H) ppm. $^{13}$C NMR ([D$_6$]DMSO): $\delta$ = 154.7, 150.0, 139.3, 137.4, 131.6, 128.7, 128.6, 126.7, 120.0, 18.2 ppm. $C_{12}H_{11}N$(169.23): calcd. C 85.21, H 6.51, N 8.28; found C 85.29, H 6.37, N 8.21. DCI-MS: $m/z$ = 170 $[MH]^+$.

**5-Methyl-2-(3-methylphenyl)pyridine (3b):** $^1$H NMR ($CDCl_3$): $\delta$ = 8.51 (s, 1 H), 7.79 (s, 1 H), 7.71 (d, $J$ = 7.5 Hz, 1 H), 7.61 (d, $J$ = 8 Hz, 1 H), 7.53 (dd, $J$ = 8.1 and 1.9 Hz, 1 H), 7.34 (t, $J$ = 7.6 Hz, 1 H), 7.19 (d, $J$ = 7.5 Hz, 1 H), 2.42 (s, 3 H), 2.35 (s, 3 H) ppm. $^{13}$C NMR ($CDCl_3$): $\delta$ = 154.9, 150.0, 139.3, 138.3, 137.3, 131.5, 128.6, 127.4, 123.8, 120.1, 21.5, 18.1 ppm. $C_{13}H_{13}N$ (183.25): calcd. C 85.21, H 6.51, N 8.28; found C 85.29, H 6.37, N 8.21. DCI-MS: $m/z$ = 184 $[MH]^+$.

**2-(3-Bromophenyl)-5-methylpyridine (3c):** $^1$H NMR ($CDCl_3$): $\delta$ = 8.51 (s, 1 H), 7.87 (td, $J$ = 7.8 and 1.5 Hz, 1 H), 7.58 (m, 2 H), 7.50 (ddd, $J$ = 8, 1.7 and 0.8 Hz, 1 H), 7.32 (t, $J$ = 8 Hz, 1 H), 2.38 (s, 3 H) ppm. $^{13}$C NMR ($CDCl_3$): $\delta$ = 152.9, 150.1, 141.3, 137.4, 132.3, 131.4, 130.2, 129.7, 125.1, 123.0, 120.0, 18.2 ppm. $C_{12}H_{10}BrN$ (248.12): calcd. C 58.09, H 4.06, N 5.65; found C 58.15, H 3.74, N 5.52. DCI-MS: $m/z$ (%) = 248 (96), 250 (100) $[MH]^+$.

**2-(4-Bromophenyl)-5-methylpyridine (3d):** $^1$H NMR ($CDCl_3$): $\delta$ = 8.49 (d, $J$ = 0.6 Hz, 1 H), 7.83 (m, 2 H), 7.58 (m, 4 H), 2.35 (s, 3 H) ppm. $^{13}$C NMR ($CDCl_3$): $\delta$ = 153.5, 150.1, 138.2, 137.5, 132.0, 131.8, 128.2, 123.0, 119.8, 18.2 ppm. $C_{12}H_{10}BrN$ (248.12): calcd. C 58.09, H 4.06, N 5.65; found C 58.14, H 3.93, N 5.59. DCI-MS: $m/z$ (%) = 248 (100), 250 (95) $[MH]^+$.

**5-Methyl-2-(3-nitrophenyl)pyridine (3e):** $^1$H NMR ($CDCl_3$): $\delta$ = 8.81 (s, 1 H), 8.54 (s, 1 H), 8.33 (d, $J$ = 7.7 Hz, 1 H), 8.22 (dd, $J$ = 8 and 1.1 Hz, 1 H), 7.70 (d, $J$ = 8 Hz, 1 H), 7.62 (m, 2 H), 2.40 (s, 3 H) ppm. $^{13}$C NMR ($CDCl_3$): $\delta$ = 152.0, 150.4, 148.7, 141.0, 137.7, 133.1, 132.5, 129.6, 123.2, 122.5, 120.1, 18.2 ppm. $C_{12}H_{10}N_2O_2$ (214.22): calcd. C 67.28, H 4.70, N 13.08; found C 67.13, H 4.44, N 12.97. DCI-MS: $m/z$ = 215 $[MH]^+$.

**5-Methyl-2-(4-nitrophenyl)pyridine (3f):** $^1$H NMR ($CDCl_3$): $\delta$ = 8.57 (s, 1 H), 8.31 (d, $J$ = 8.9 Hz, 2 H), 8.15 (d, $J$ = 8.9 Hz, 2 H), 7.71 (d, $J$ = 8.1 Hz, 1 H), 7.62 (dd, $J$ = 8.1 and 1.8 Hz, 1 H), 2.41 (s, 3 H) ppm. $^{13}$C NMR ($CDCl_3$): $\delta$ = 152.0, 150.4, 148.7, 141.0, 137.7, 133.1, 132.5, 129.6, 123.2, 122.5, 120.1, 18.2 ppm. $C_{12}H_{10}N_2O_2$ (214.22): calcd. C 67.28, H 4.70, N 13.08; found C 67.41, H 4.34, N 12.95. DCI-MS: $m/z$ = 215 $[MH]^+$.

**2-(3-Methoxyphenyl)-5-methylpyridine (3g):** $^1$H NMR ($CDCl_3$): $\delta$ = 8.51 (d, $J$ = 1.5 Hz, 1 H), 7.60 (t, $J$ = 8 Hz, 1 H), 7.55 (m, 2 H), 7.36 (t, $J$ = 8 Hz, 1 H), 6.93 (dd, $J$ = 8.2 and 2.5 Hz, 1 H), 3.88 (s, 3 H), 2.36 (s, 3 H) ppm. $^{13}$C NMR ($CDCl_3$): $\delta$ = 160.0, 154.5, 150.0, 140.9, 137.3, 131.7, 129.6, 120.1, 119.1, 114.7, 111.7, 55.3, 18.2 ppm. $C_{13}H_{13}NO$ (199.25): calcd. C 78.39, H 6.53, N 7.03; found C 78.08, H 6.60, N 6.83. DCI-MS: $m/z$ = 200 $[MH]^+$.

**2-(4-Methoxyphenyl)-5-methylpyridine (3h):** $^1$H NMR ($CDCl_3$): $\delta$ = 8.47 (s, 1 H), 7.90 (dd, $J$ = 8.7 and 1.6 Hz, 2 H), 7.6–7.5 (m, 2 H), 6.97 (dd, $J$ = 8.8 and 1.8 Hz, 2 H), 3.86 (s, 3 H), 2.34 (s, 3 H) ppm. $^{13}$C NMR ($CDCl_3$): $\delta$ = 160.1, 154.3, 149.8, 137.2, 133.0, 130.8, 127.8, 119.2, 114.0, 55.2, 18.0 ppm. $C_{13}H_{13}NO$ (199.25): calcd. C 78.39, H 6.53, N 7.03; found C 78.30, H 6.59, N 6.96. DCI-MS: $m/z$ = 200 $[MH]^+$.

**General Procedure for the Preparation of the Complexes:** [Ru(bpy)$_2$Cl$_2$] (0.15 mmol) and AgOTf (0.30 mmol) were added to a solution of the ligand (0.75 mmol) in 5 mL of MeOH, and the mixture was refluxed in the dark for 2 h. After cooling and filtration of a brown precipitate, the filtrate was concentrated off and purification was carried out by chromatography on alumina. Elution with EtOAc/pentane (10:90) provided unreacted ligand and further elution with MeOH/$CH_2Cl_2$ (3:97) gave the pure complex.

**Complex 4a:** Yield: 98 mg (90%). $^1$H NMR ($CD_3COCD_3$): $\delta$ = 8.77 (dt, $J$ = 8.2 and 1 Hz, 1 H, H25), 8.68 (dt, $J$ = 8 and 1.1 Hz, 1 H, H28), 8.61 (dt, $J$ = 8 and 1 Hz, 1 H, H18), 8.59 (dt, $J$ = 8 and 1 Hz, 1 H, H15), 8.16 (ddd, $J$ = 5.7, 1.5 and 0.7 Hz, 1 H, H31), 8.13 (ddd, $J$ = 9.2, 5.6 and 1.5 Hz, 1 H, H24), 8.06 (d, $J$ = 8.3 Hz, 1 H, H4), 8.05 (m, 1 H, H22), 7.98–7.93 (m, 3 H, H12, H29, H19), 7.92–7.86 (m, 3 H, H11, H14, H21), 7.62 (ddd, $J$ = 8.7, 2.1 and 0.7 Hz, 1 H, H3), 7.59 (ddd, $J$ = 7.5, 5.4 and 1.2 Hz, 1 H, H23), 7.56 (m, 1 H, H1), 7.39–7.34 (m, 3 H, H20, H30, H13), 6.88 (dd, $J$ = 7.2 and 1.3 Hz, 1 H, H10), 6.81 (td, $J$ = 7.3 and 1.3 Hz, 1 H, H9), 6.18 (ddd, $J$ = 7.3, 1.3 and 0.4 Hz, 1 H, H8), 2.08 (s, 3 H, $CH_3$py) ppm. $^{13}$C NMR ($CD_3COCD_3$): $\delta$ = 191.79 (C7), 164.97 (C5), 157.88 (C27), 157.15 (C17), 156.81 (C16), 155.36 (C26), 154.15 (C31), 150.24 (C29), 149.98 (C11), 149.77 (C1), 149.10 (C22), 145.57 (C6), 136.73 (C3), 136.41 (C24), 135.18 (C8), 134.98 (C29), 133.78 (C19), 133.53 (C14), 132.07 (C2), 128.10 (C9), 127.22 (C23), 126.48 (C20), 126.29 (C30), 126.14 (C13), 123.73 (C11), 123.58 (C28), 123.34 (C25), 123.06 (C15), 123.04 (C18), 120.74 (C10), 118.39 (C4), 17.15 ($CH_3$py) ppm. FAB-MS: $m/z$ = 582 $[M–OTf]^+$.

**Complex 4b:** Yield: 98 mg (88%). Metathesis: the complex with the triflate counterion was dissolved in the minimum amount of methanol, then a saturated solution of $NH_4PF_6$ was added until no more precipitation was observed. The precipitate was filtered off, rinsed with distilled water, and dried under vacuum. $^1$H NMR ([D$_6$]-DMSO): $\delta$ = 8.76 (d, $J$ = 8.2 Hz, 1 H, H25), 8.68 (d, $J$ = 8.2 Hz, 1 H, H28), 8.61 (d, $J$ = 8.8 Hz, 1 H, H15), 8.59 (d, $J$ = 8.8 Hz, 1 H, H18), 8.09 (td, $J$ = 7.5 and 0.9 Hz, 1 H, H24), 8.04 (d, $J$ = 8.3 Hz, 1 H, H4), 7.99 (d, $J$ = 5.4 Hz, 1 H, H31), 7.91 (t, $J$ = 8.1 Hz, 1 H, H29), 7.89 (t, $J$ = 8 Hz, 1 H, H19), 7.86 (t, $J$ = 8.1 Hz, 1 H, H14), 7.81 (d, $J$ = 5.3 Hz, 1 H, H22), 7.72 (d, $J$ = 5.6 Hz, 1 H, H12), 7.68 (s, 1 H, H11), 7.62 (d, $J$ = 5.6 Hz, 1 H, H21), 7.58 (d, $J$ = 8.8 Hz, 1 H, H3), 7.56 (t, $J$ = 6.5 Hz, 1 H, H23), 7.38 (t, $J$ = 6.5 Hz, 1 H, H30), 7.36 (m, 1 H, H20), 7.35 (t, $J$ = 7 Hz, 1 H, H13), 7.28 (s, 1 H, H1), 6.61 (d, $J$ = 7.4 Hz, 1 H, H9), 6.18 (d, $J$ = 7.5 Hz, 1 H, H8), 2.22 (s, 3 H, $CH_3$phe), 2.04 (s, 3 H, $CH_3$py) ppm. $^{13}$C NMR ([D$_6$]DMSO): $\delta$ = 187.54 (C7), 164.74 (C5), 157.72 (C27), 157.0 (C16), 156.65 (C17), 155.22 (C26), 153.91 (C31), 150.03 (C21 or C12), 149.78 (C12 or C21), 149.55 (C1), 148.99 (C22), 145.55 (C10), 137.21 (C3), 136.86 (C24), 135.45 (C29), 134.94 (C8), 134.20 (C14 or C19), 133.89 (C19 or C14), 132.14 (C2), 129.78 (C9), 129.33 (C6), 127.83 (C23), 127.05 (C20 or C13), 126.87 (C13 or C20), 126.77 (C30), 124.99 (C11), 124.21 (C28), 123.94 (C25), 123.69 (C15), 123.64 (C18), 118.86 (C4), 21.27 ($CH_3$ph), 18.17 ($CH_3$py) ppm. FAB-MS: $m/z$ = 596 $[M–PF_6]^+$.

**Complex 4d:** Yield: 90 mg (74%). $^1$H NMR ($CD_3COCD_3$): $\delta$ = 8.78 (dt, $J$ = 8.2 and 1 Hz, 1 H, H25), 8.71 (dt, $J$ = 8.1 and 1 Hz, 1 H, 1 H, H28), 8.64 (dt, $J$ = 8.3 and 1 Hz, 1 H, H15), 8.62 (dt, $J$ = 8.3 and 1 Hz, 1 H, H18), 8.17 (ddd, $J$ = 5.7, 1.7 and 0.7 Hz, 1 H, H31),

 © 2006 Wiley-VCH Verlag GmbH & Co. KGaA, Weinheim 

8.14 (td, $J$ = 8.4 and 1.5 Hz, 1 H, H24), 8.09 (d, $J$ = 8.2 Hz, 1 H, H4), 8.02 (ddd, $J$ = 5.4, 1.6 and 0.8 Hz, 1 H, H22), 8.00 (ddd, $J$ = 7.6, 5 and 0.5 Hz, 1 H, H29), 7.98 (ddd, $J$ = 7.6, 5 and 0.5 Hz, 1 H, H14), 7.95 (m, 1 H, H19), 7.93 (m, 1 H, H21), 7.88 (ddd, $J$ = 5.7, 1.4 and 0.8 Hz, 1 H, H12), 7.82 (d, $J$ = 8.3 Hz, 1 H, H11), 7.64 (ddd, $J$ = 8.3, 1.1 and 0.7 Hz, 1 H, H3), 7.59 (ddd, $J$ = 7.5, 5.4 and 0.8 Hz, 1 H, H23), 7.57 (d, $J$ = 1.2 Hz, 1 H, H1), 7.44–7.37 (m, 2 H, H30, H20), 7.42 (dd, $J$ = 5.8 and 1.5 Hz, 1 H, H13), 7.04 (dd, $J$ = 8.3 and 2.1 Hz, 1 H, H10), 6.54 (d, $J$ = 2.1 Hz, 1 H, H8), 2.08 (s, 3 H, $CH_3$) ppm. $^{13}$C NMR ($CD_3COCD_3$): $\delta$ = 196.20 (C7), 163.95 (C5), 157.77 (C27), 157.07 (C16), 156.74 (C17), 155.32 (C26), 154.18 (C31), 150.39 (C21), 150.12 (C12), 149.98 (C1), 149.17 (C22), 144.86 (C6), 137.02 (C8), 136.93 (C3), 136.70 (C24), 135.38 (C29), 134.32 (C14), 134.20 (C19), 132.68 (C2), 127.27 (C23), 126.73 (C30), 126.55 (C20), 126.37 (C13), 125.32 (C11), 123.73 (C28), 123.67 (C9), 123.54 (C10), 123.45 (C25), 123.27 (C18), 123.25 (C15), 118.77 (C4), 17.19 ($CH_3$) ppm. FAB-MS: $m/z$ (%) = 662 (45), 660 (43) $[M-OTf]^+$.

**Complex 4f:** Yield: 28 mg (24%). $^1$H NMR ($CD_3COCD_3$): $\delta$ = 8.81 (d, $J$ = 8.2 Hz, 1 H, H25), 8.73 (d, $J$ = 8.1 Hz, 1 H, H28), 8.67 (d, $J$ = 8 Hz, 1 H, H15), 8.63 (d, $J$ = 8 Hz, 1 H, H18), 8.28 (d, $J$ = 8.2 Hz, 1 H, H4), 8.17 (td, $J$ = 7.9 and 1.6 Hz, 1 H, H24), 8.11 (d, $J$ = 8.6 Hz, 1 H, H11), 8.12 (m, 1 H, H31), 8.06 (ddd, $J$ = 5.3, 1.4 and 0.8 Hz, 1 H, H22), 8.03 (td, $J$ = 7.7 and 1.4 Hz, 1 H, H14), 7.98 (td, $J$ = 8 and 1.5 Hz, 1 H, H29), 7.96 (m, 1 H, H19), 7.94 (m, 1 H, H21), 7.92 (m, 1 H, H12), 7.74 (m, 1 H, H3), 7.72 (m, 1 H, H1), 7.69 (dd, $J$ = 8.5 and 2.4 Hz, 1 H, H10), 7.62 (ddd, $J$ = 7.5, 5.5 and 1.2 Hz, 1 H, H23), 7.46 (ddd, $J$ = 7.3, 5.7 and 1.3 Hz, 1 H, H13), 7.39 (ddd, $J$ = 7.3, 5.7 and 1.3 Hz, 2 H, H30, H20), 7.29 (d, $J$ = 2.4 Hz, 1 H, H8), 2.13 (s, 3 H, $CH_3$) ppm. $^{13}$C NMR ($CD_3COCD_3$): $\delta$ = 194.80 (C7), 162.76 (C5), 157.78 (C26), 157.03 (C16), 156.75 (C17), 155.30 (C26), 154.34 (C22), 152.86 (C6), 150.60 (C1), 150.47 (C21), 150.24 (C12), 149.25 (C22), 146.99 (C9), 137.12 (C3), 136.89 (C24), 135.61 (C29), 134.73 (C14), 134.57 (C19), 134.44 (C2), 128.41 (C8), 127.33 (C23), 126.93 (C13), 126.67 (C30 or C20), 126.52 (C20 or C30), 123.83 (C28), 123.65 (C11), 123.54 (C25), 123.43 (C15), 123.39 (C18), 120.39 (C4), 115.90 (C10), 17.31 ($CH_3$) ppm. FAB-MS: $m/z$ = 627 $[M-OTf]^+$.

**Complex 4h:** Yield: 95 mg (83%). $^1$H NMR ($CD_3COCD_3$): $\delta$ = 8.77 (d, $J$ = 8.2 Hz, 1 H, H25), 8.72 (d, $J$ = 8.2 Hz, 1 H, H28), 8.62 (d, $J$ = 8.1 Hz, 1 H, H18), 8.60 (d, $J$ = 8.1 Hz, 1 H, H15), 8.20 (dd, $J$ = 5.8 and 1.1 Hz, 1 H, H31), 8.12 (td, $J$ = 7.8 and 1.5 Hz, 1 H, H24), 8.05 (dd, $J$ = 5.4 and 1.3 Hz, 1 H, H22), 7.97 (m, 1 H, H29), 7.95 (m, 1 H, H12), 7.94 (m, 1 H, H21), 7.92 (d, $J$ = 8.2 Hz, 1 H, H4), 7.89 (m, 1 H, H19), 7.88 (m, 1 H, H14), 7.82 (d, $J$ = 8.5 Hz, 1 H, H11), 7.58 (ddd, $J$ = 7.5, 5.4 and 1.1 Hz, 1 H, H23), 7.55 (dd, $J$ = 8.4 and 2.1 Hz, 1 H, H3), 7.47 (m, 1 H, H1), 7.39–7.34 (m, 3 H, H13, H20, H30), 6.45 (dd, $J$ = 8.5 and 2.6 Hz, 1 H, H10), 5.95 (d, $J$ = 2.4 Hz, 1 H, H8), 3.53 (s, 3 H, $OCH_3$), 2.04 (s, 3 H, $CH_3$) ppm. $^{13}$C NMR ($CD_3COCD_3$): $\delta$ = 194.27 (C7), 164.71 (C5), 159.59 (C6), 157.84 (C27), 157.29 (C17), 156.83 (C16), 155.36 (C26), 154.06 (C31), 150.22 (C29), 150.03 (C14), 149.41 (C1), 149.11 (C22), 138.37 (C9), 136.65 (C3), 136.41 (C24), 134.99 (C12), 133.78 (C21), 133.59 (C19), 130.77 (C2), 127.19 (C23), 126.43 (C20), 126.27 (C30), 126.12 (C13), 124.99 (C11), 123.64 (C28), 123.42 (C25), 123.13 (C15), 123.07 (C18), 119.69 (C8), 117.63 (C4), 106.43 (C10), 53.73 ($OCH_3$), 17.10 ($CH_3$) ppm. FAB-MS: $m/z$ = 612 $[M-OTf]^+$.


[1] a) A. Juris, V. Balzani, F. Barigelletti, S. Campagna, P. Belser, A. Von Zelewsky, *Coord. Chem. Rev.* **1988**, *84*, 85–277; b) J. P. Sauvage, J. P. Collin, J. C. Chambron, S. Guillerez, C. Coudret, V. Balzani, F. Barigelletti, L. De Cola, L. Flamigni, *Chem. Rev.* **1994**, *94*, 993–1019.

[2] M. I. Bruce, B. L. Goodall, F. G. A. Stone, *J. Organomet. Chem.* **1973**, *60*, 343–348.

[3] K. Hiraki, Y. Obayashi, Y. Oki, *Bull. Chem. Soc. Jpn.* **1979**, *52*, 1372–1376.

[4] E. C. Constable, J. M. Holmes, *J. Organomet. Chem.* **1986**, *301*, 203–208.

[5] J. P. Collin, M. Beley, J. P. Sauvage, F. Barigeletti, *Inorg. Chim. Acta* **1991**, *186*, 91–93.

[6] P. Reveco, R. H. Schmehl, W. R. Cherry, F. R. Fronczek, J. Selbin, *Inorg. Chem.* **1985**, *24*, 4078–4082.

[7] a) A. J. Lees, *Chem. Rev.* **1987**, *87*, 711–743; b) S. Chodorowski-Kimmes, M. Beley, J. P. Collin, J. P. Sauvage, *Tetrahedron Lett.* **1996**, *37*, 2963–2966; c) F. Barigelletti, B. Ventura, J. P. Collin, R. Kayhanian, P. Gavina, J. P. Sauvage, *Eur. J. Inorg. Chem.* **2000**, 113–119.

[8] F. Mongin, G. Quéguiner, *Tetrahedron* **2001**, *57*, 4059–4090.

[9] A. Lützen, M. Hapke, *Eur. J. Org. Chem.* **2002**, 2292–2297.

[10] S. Jung, Y. Kang, H. S. Kim, Y. H. Kim, C. L. Lee, J. J. Kim, S. K. Lee, S. K. Kwon, *Eur. J. Inorg. Chem.* **2004**, 3415–3423.

[11] S. Kotha, K. Lahiri, D. Kashinath, *Tetrahedron* **2002**, *58*, 9633–9695.

[12] a) S. P. Stanforth, *Tetrahedron* **1998**, *54*, 263–304 and references cited therein; b) F. Mongin, L. Mojovic, B. Guillarnet, F. Trécourt, G. Quéguiner, *J. Org. Chem.* **2002**, *67*, 8991–8994.

[13] a) I. Sasaki, J. C. Daran, G. G. A. Balavoine, *Synthesis* **1999**, *5*, 815–820; b) M. Ziegler, V. Monney, H. Stoeckli-Evans, A. Von Zelewsky, I. Sasaki, G. Dupic, J. C. Daran, G. G. A. Balavoine, *J. Chem. Soc., Dalton Trans.* **1999**, 667–675.

[14] F. Kröhnke, *Synthesis* **1976**, 1–24.

[15] V. Bonnet, F. Mongin, F. Trécourt, G. Quéguiner, P. Knochel, *Tetrahedron* **2002**, *58*, 4429–4438.

[16] The reaction of **2a** with (*E*)-2-methyl-2-butenal (tiglic aldehyde) was carried out under the same conditions and led to 4,5-dimethyl-2-phenylpyridine in 84% yield.[21] $^1$H NMR ($CDCl_3$): $\delta$ = 8.39 (s, 1 H), 7.94 (dd, $J$ = 6.8 and 1.5 Hz, 2 H), 7.48–7.36 (m, 4 H), 2.32 (s, 3 H), 2.27 (s, 3 H) ppm. $^{13}$C NMR ($CDCl_3$): $\delta$ = 155.1, 149.9, 146.2, 139.5, 130.7, 128.7, 128.4, 126.7, 121.4, 19.4, 16.1 ppm. $C_{13}H_{13}N + 0.05\,OHCNH_2$ (185.50): calcd. C 84.50, H 7.14, N 7.93; found C 84.38, H 6.72, N 7.48. DCI-MS: $m/z$ = 183 $[M]^+$.

[17] R. F. Francis, C. D. Crews, B. S. Scott, *J. Org. Chem.* **1978**, *43*, 3227–3239.

[18] J. Mathieu, P. Gros, Y. Fort, *Tetrahedron Lett.* **2001**, *42*, 1879–1881.

[19] E. Van der Eycken, Z. Jidong, A. Kilonda, F. Compernolle, S. Toppet, G. Hoornaert, M. Van der Auweraer, C. Jackers, W. Verbouwe, F. C. De Schryver, *J. Chem. Soc., Perkin Trans. 2* **2002**, 928–937.

[20] M. S. Lowry, W. R. Hudson, R. A. Pascal Jr, S. Bernhard, *J. Am. Chem. Soc.* **2004**, *126*, 14129–14135.

[21] a) R. E. Lyle, D. L. Comins, *J. Org. Chem.* **1976**, *41*, 3250–3252; b) J. M. Bonnier, J. Court, *Bull. Soc. Chim. Fr.* **1970**, 142–146.

[22] L. Labat, J. F. Lamère, I. Sasaki, P. G. Lacroix, I. Asselberghs, J. Pérez-Monero, K. Clays, *Eur. J. Inorg. Chem.*, DOI: 10.1002/ejic.200600258.

[23] C. Coudret, private communication.

[24] E. C. Constable, M. J. Hannon, *Inorg. Chim. Acta* **1993**, *211*, 101–110.

[25] S. Chodorowski-Kimmes, M. Beley, J. P. Collin, J. P. Sauvage, *Tetrahedron Lett.* **1996**, *37*, 2963–2966.

[26] C. Coudret, S. Fraysse, J. P. Launay, *Chem. Commun.* **1998**, 663–664.

[27] C. Hortholary, F. Minc, C. Coudret, J. Bonvoisin, J. P. Launay, *Chem. Commun.* **2002**, 1932–1933.

[28] a) E. C. Constable, A. M. W. Cargill Thompson, S. Greulich, *J. Chem. Soc., Chem. Commun.* **1993**, 1444–1446; b) P. Reveco,


 © 2006 Wiley-VCH Verlag GmbH & Co. KGaA, Weinheim 

J. H. Medley, A. R. Garber, N. S. Bhacca, J. Selbin, *Inorg. Chem.* **1985**, *24*, 1096–1099.
[29] M. Brissard, M. Gruselle, B. Malézieux, R. Thouvenot, C. Guyard-Duhayon, O. Convert, *Eur. J. Inorg. Chem.* **2001**, 1745–1751.
[30] R. Andréas, M. Brissard, M. Gruselle, C. Train, J. Vaissermann, B. Malézieux, J. P. Jamet, M. Verdaguer, *Inorg. Chem.* **2001**, *40*, 4633–4640.
[31] E. C. Constable, T. A. Leese, D. A. Tocher, *Polyhedron* **1990**, *9*, 1613–1616.
[32] S. Fraysse, C. Coudret, J. P. Launay, *Eur. J. Inorg. Chem.* **2000**, 1581–1590.
[33] T. M. Pappenfus, K. R. Mann, *Inorg. Chem.* **2001**, *40*, 6301–6307.
[34] S. Fraysse, C. Coudret, J. P. Launay, *J. Am. Chem. Soc.* **2003**, *125*, 5880–5888.
[35] G. Sprintschnik, H. W. Sprintschnik, P. P. Kirsch, D. G. Whitten, *J. Am. Chem. Soc.* **1977**, *99*, 4947–4954.
[36] *SIR92 – A program for crystal structure solution*: A. Altomare, G. Cascarano, C. Giacovazzo, A. Guagliardi, *J. Appl. Crystallogr.* **1993**, *26*, 343–350.
[37] G. M. Sheldrick, *SHELX97 (includes SHELXS97, SHELXL97, CIFTAB) – Programs for Crystal Structure Analysis*, release 97-2, Institut für Anorganische Chemie der Universität, Göttingen, Germany, **1998**.
[38] *WINGX – Integrated System of Windows Programs for the Solution, Refinement and Analysis of Single Crystal X-ray Diffraction Data*, version 1.63: L. Farrugia, *J. Appl. Crystallogr.* **1999**, *32*, 837–838.
[39] D. T. Cromer, *International Tables for X-ray Crystallography*, Kynoch Press, Birmingham, UK, **1974**, vol. IV.
[40] *ORTEP3 for Windows*: L. J. Farrugia, *J. Appl. Crystallogr.* **1997**, *30*, 565.

Received: April 21, 2006
Published Online: July 5, 2006

 © 2006 Wiley-VCH Verlag GmbH & Co. KGaA, Weinheim 

EurJIC
European Journal of Inorganic Chemistry

Issue 17/2006

Pages 3305–3540

*Papers available ahead of print in Early View at www.interscience.wiley.com*

*Earliest available Table of Contents:*
*Automatically, free of charge by e-mail through*
*www.interscience.wiley.com/alerts*

## COVER PICTURE

**The cover picture shows** the supramolecular structure of an inclusion complex between the trisilanol 1,3,5-$(HOiPr_2Si)_3C_6H_3$ and *trans*-bis(4-pyridyl)ethylene (bpe). The trisilanol molecules are associated by SiO−H···O(H)Si hydrogen bonds, giving rise to the formation of 1D (horizontal) chains. The bpe molecules resemble pillars that are situated perpendicularly to the 1D chains and linked by SiO−H···N hydrogen bonds. The supramolecular motif is somewhat reminiscent of the Acropolis of Selinunte built 650 BC in Sicily, a masterpiece of classical Greek architecture. Details of synthesis and structures of supramolecular complexes between the trisilanol 1,3,5-$(HOiPr_2Si)_3C_6H_3$ and a number of 4,4′-bis(pyridine) compounds are described in the article by J. Beckmann and S. L. Jänicke on p. 3351 ff.

## MICROREVIEW

**Contents**

**3319** **P.-T. Chou,* Y. Chi***

Osmium- and Ruthenium-Based Phosphorescent Materials: Design, Photophysics, and Utilization in OLED Fabrication

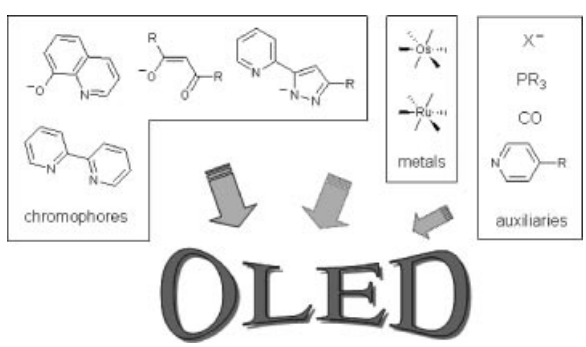


**Keywords:** Osmium / Ruthenium / N ligands / Phosphorescence / Luminescence

 © 2006 Wiley-VCH Verlag GmbH & Co. KGaA, Weinheim 

# SHORT COMMUNICATIONS


**3333** **Y. Garcia,* C. M. Grunert, S. Reiman, O. van Campenhoudt, P. Gütlich***

The Two-Step Spin Conversion in a Supramolecular Triple Helicate Dinuclear Iron(II) Complex Studied by Mössbauer Spectroscopy

**Keywords:** Spin crossover / Molecular bistability / Supramolecular chemistry / Iron(II) dinuclear compounds / Two-step conversion / Mössbauer spectroscopy


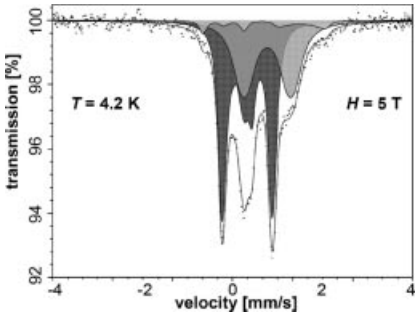



**3340** **W. J. Marshall,* G. Aullón,* S. Alvarez, K. D. Dobbs, V. V. Grushin***

"To Bend or not To Bend?" Both! The Planar and Bent Structures of $[(Ph_3P)_4Rh_2(\mu\text{-}F)_2]$

**Keywords:** Isomerism / Rhodium / Fluorine / X-ray diffraction / Theoretical calculations


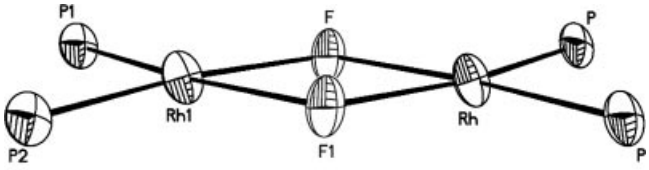


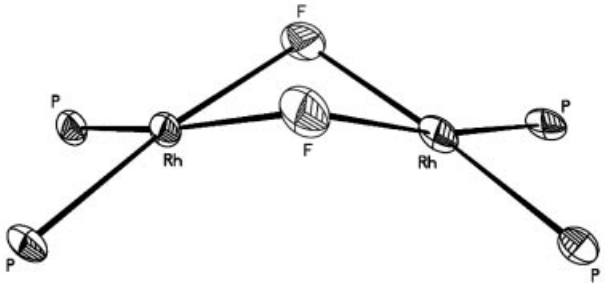



**3346** **M. Santos, J. Marçalo,* A. Pires de Matos, J. K. Gibson,* R. G. Haire**

Actinide-Transition Metal Heteronuclear Ions and Their Oxides: $\{IrUO\}^+$ as an Analogue to Uranyl

**Keywords:** Actinides / Ion−molecule reactions / Isolobal relationship / Mass spectrometry / Metal−metal interactions / Uranium


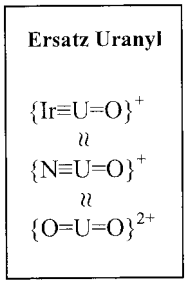


# FULL PAPERS


**3351** **J. Beckmann,* S. L. Jänicke**

Supramolecular Silanol Chemistry: Inclusion Complexes of 1,3,5-Tris(diisopropylhydroxysilyl)benzene and 4,4′-Bis(pyridines)

**Keywords:** Supramolecular chemistry / Crystal engineering / Inclusion compounds / Hydrogen bonds / Silicon


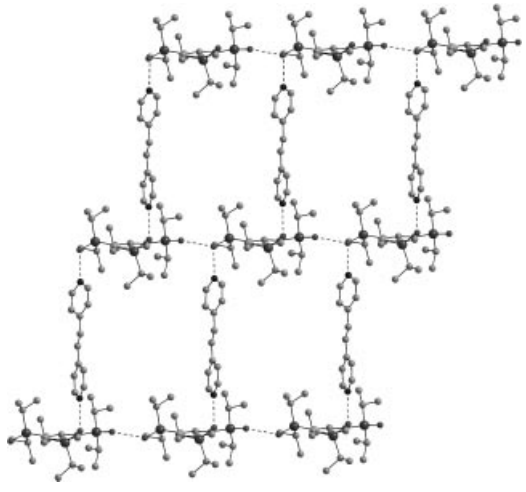

**3359** **A. Ito, Y. Nakano, M. Urabe, K. Tanaka,* M. Shiro**

Structural and Magnetic Studies of Copper(II) and Zinc(II) Coordination Complexes Containing Nitroxide Radicals as Chelating Ligands

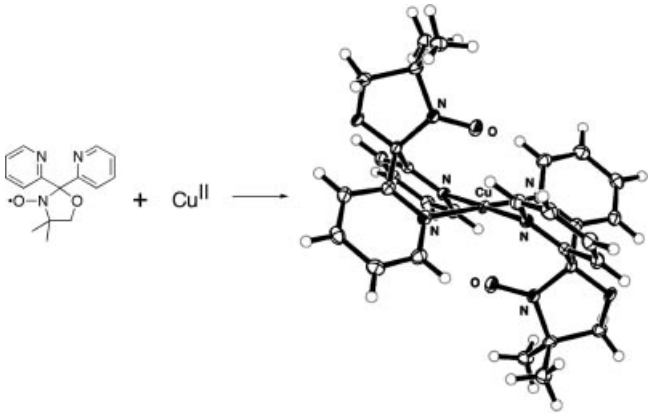

**Keywords:** Copper / Density functional calculations / Magnetic properties / Radicals / Zinc

**3369** **P. Agnihotri, E. Suresh, P. Paul,* P. K. Ghosh***

Synthesis, Crystal Structures, Cation-Binding Properties and the Influence of Intramolecular C−H···O Interactions on the Complexation Behaviour of a Family of Cone *p-tert*-Butylcalix-[4]arene-crown-5 Compounds

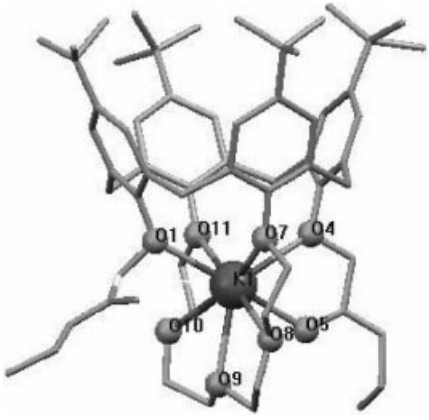

**Keywords:** Calixarenes / Crown compounds / Selectivity / Association constants

**3382** **C. E. Talbot-Eeckelaers, G. Rajaraman, J. Cano,* G. Aromí, E. Ruiz, E. K. Brechin***

Encouraging Chromium(III) Ions to Form Larger Clusters: Syntheses, Structures, Magnetic Properties and Theoretical Studies of Di- and Octametallic Cr Clusters

**Keywords:** Exchange coupling / Density functional theory / Polynuclear chromium complexes / Magnetic properties / Magneto-structural correlation

**3393** **M. Bortoluzzi,* E. De Faveri, S. Daniele, B. Pitteri**

Synthesis of a New Tetrakis(2-pyridinyl)pyrazine Complex of Gold(III) and Its Computational, Spectroscopic and Electrochemical Characterization

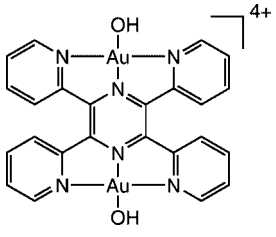

**Keywords:** Gold / N ligands / Density functional calculations / Electrochemistry

 © 2006 Wiley-VCH Verlag GmbH & Co. KGaA, Weinheim 

**3400** **A. Burkhardt, A. Buchholz, H. Görls, W. Plass***

Synthesis, Structure and Magnetic Properties of a Tetranuclear Copper(II) Complex on the Basis of a 2-Substituted Glucopyranoside Schiff Base Ligand

**Keywords:** Carbohydrates / Schiff base ligands / Copper(II) complexes / Magnetic properties

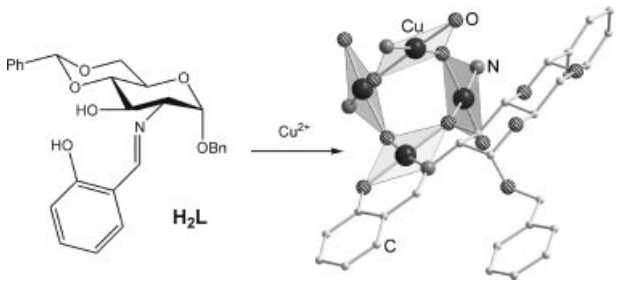


**3407** **J.-P. Zhang, Y.-Y. Lin, X.-C. Huang, X.-M. Chen***

Designed Assembly and Structures and Photoluminescence of a New Class of Discrete $Zn^{II}$ Complexes of 1*H*-1,10-Phenanthroline-2-one

**Keywords:** Zinc / Cluster compounds / Metallacycles / Photoluminescence / Solvothermal synthesis

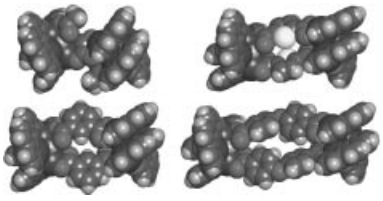

**3413** **I. M. Szilágyi,* F. Hange, J. Madarász, G. Pokol**

In situ HT-XRD Study on the Formation of Hexagonal Ammonium Tungsten Bronze by Partial Reduction of Ammonium Paratungstate Tetrahydrate

**Keywords:** Tungsten / Reduction / In situ studies / X-ray diffraction / X-ray photoelectron spectroscopy / Solid-state $^1H$ NMR spectroscopy

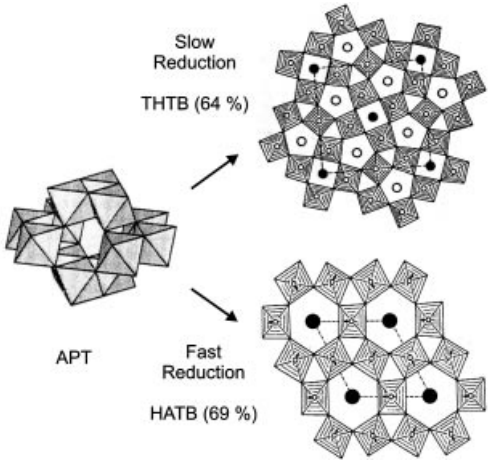


**3419** **L. Weber,* I. Domke, J. Kahlert, H.-G. Stammler**

Chemical Oxidation of 1,3,2-Diazaboroles and 1,3,2-Diazaborolidines

**Keywords:** Diazaboroles / Diazaborolidines / Diazaborolium salts / Nitrosonium hexafluorophosphate

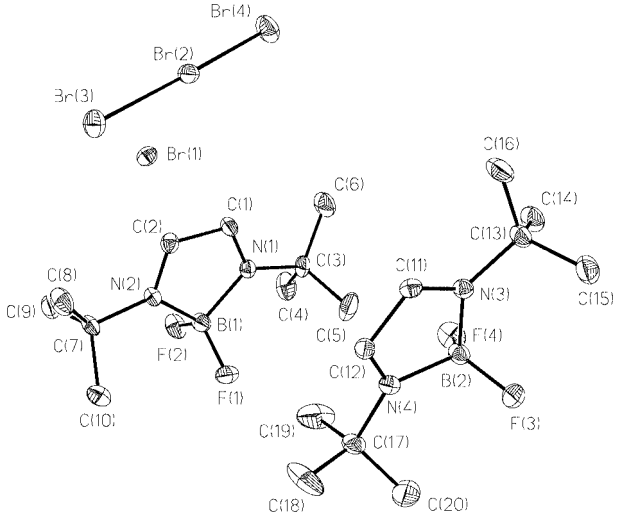


 © 2006 Wiley-VCH Verlag GmbH & Co. KGaA, Weinheim 

**3425** **J. Tedim, S. Patrício, R. Bessada, R. Morais, C. Sousa, M. B. Marques, C. Freire***

Third-Order Nonlinear Optical Properties of DA-salen-Type Nickel(II) and Copper(II) Complexes

**Keywords:** Third-order NLO properties / Z-scan technique / UV/Vis spectroscopy / Schiff bases

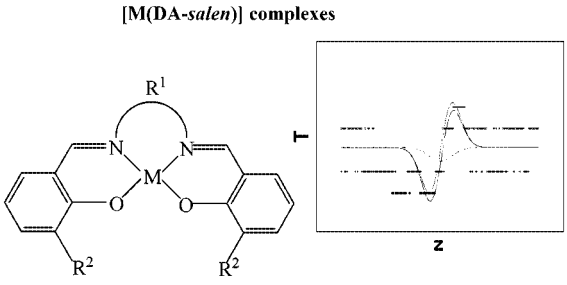


**3434** **S. Beaini, G. B. Deacon,* M. Hilder, P. C. Junk, D. R. Turner**

Organotin Compounds as Reagents for the Synthesis of Lanthanoid Complexes by Redox Transmetallation Reactions

**Keywords:** Redox transmetallation / Lanthanoid / Trimethyltin reagents / Pyrazolate / Aryl oxide / Ytterbium / Europium

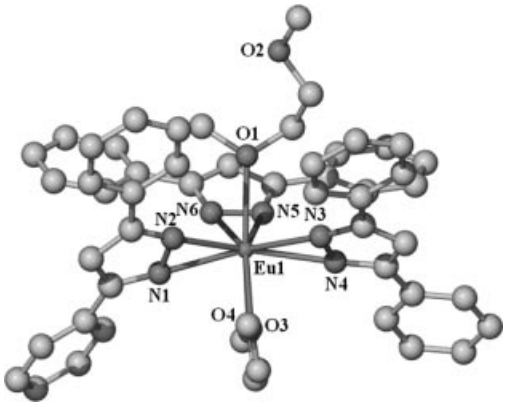


**3442** **M. Wei, X. F. Tian, J. He, M. Pu, G. Y. Rao, H. L. Yang, L. Yang, T. Liu, D. G. Evans, X. Duan***

Study of the In Situ Postintercalative Polymerization of Metanilic Anions Intercalated in NiAl-Layered Double Hydroxides under a Nitrogen Atmosphere

**Keywords:** In situ polymerization / Polyaniline / Layered double hydroxides / Nitrogen atmosphere

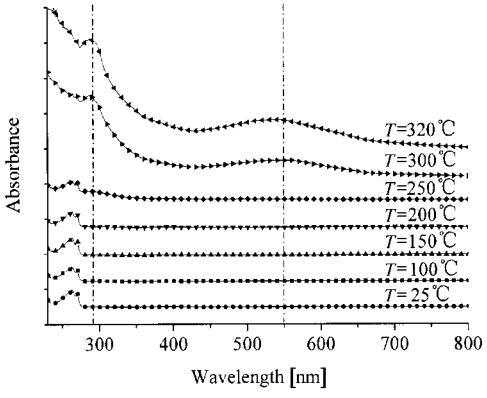


**3451** **G. Albertin,* S. Antoniutti, J. Bravo, J. Castro, S. García-Fontán, M. C. Marín, M. Noè**

Preparation of Hydroxylamine and *O*-Methylhydroxylamine Complexes of Manganese and Rhenium

**Keywords:** Hydroxylamine / *O*-Methylhydroxylamine / CO and P ligands / Manganese / Rhenium / Oxidation

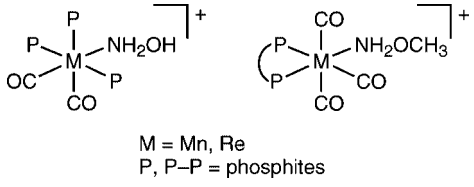


 © 2006 Wiley-VCH Verlag GmbH & Co. KGaA, Weinheim 

**3463** **P. Ramaswamy, S. Natarajan***

Amine-Intercalated Layered $Sn^{II}$ Phosphates with Open-Framework Structures

**Keywords:** Template synthesis / X-ray diffraction / Layered compounds / Hydrogen bonds / Tin / Phosphorus

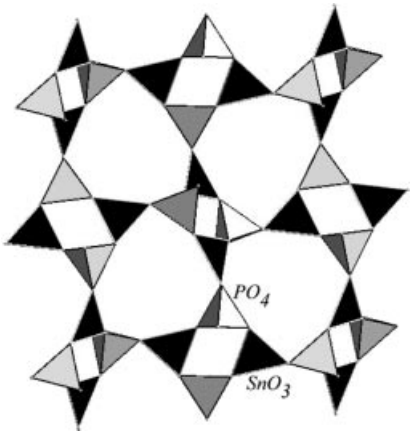


**3472** **S. El Ghachtouli, C. Cadiou, I. Déchamps-Olivier, F. Chuburu,* M. Aplincourt, T. Roisnel**

(Cyclen− and cyclam−pyridine)copper Complexes: The Role of the Pyridine Moiety in $Cu^{II}$ and $Cu^{I}$ Stabilisation

**Keywords:** Copper / Cyclen and cyclam ligands / X-ray diffraction / UV/Vis and EPR spectroscopy / Electrochemistry / Configurational isomerisation

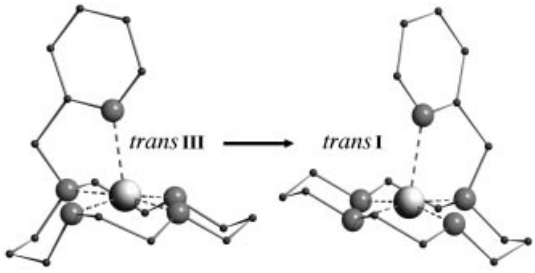


**3482** **C. Gieck, M. Schreyer, T. F. Fässler,* F. Raif, P. Claus**

Crystal Structure and Properties of $MgCo_4Ge_6$

**Keywords:** Intermetallic phases / Germanium / Heterogeneous catalysis / ELF (Electron Localization Function) / Density functional theory

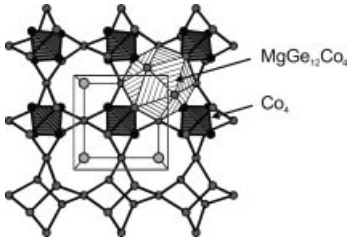


**3489** **N. Faux, F. Robin-Le Guen, P. Le Poul, B. Caro, K. Nakatani, E. Ishow, S. Golhen**

Synthesis and NLO Properties of 4-(4*H*-Chalcogenopyran-4-ylidene and 4*H*-chalcogenochromen-4-ylidene)-1-(phenylthio)but-2-enylidene Complexes − Electronic Influence of the Carbene Fragment

**Keywords:** Chalcogeno- and benzochalcogenopyran / Fischer-type thiocarbene complexes / NLO properties / X-ray structure of thiocarbene

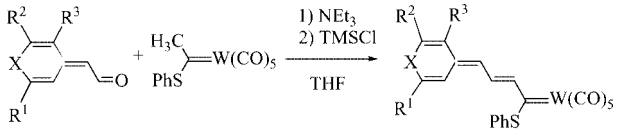


**2b** $R^1$ = Ph, $R^2$ = Ph, $R^3$ = H, X = S

$\mu\beta(CHCl_3, 1907\ nm) = 518 \cdot 10^{-48}$ esu

 © 2006 Wiley-VCH Verlag GmbH & Co. KGaA, Weinheim 

**3498** **K. Hervé, S.-X. Liu, O. Cador, S. Golhen, Y. Le Gal, A. Bousseksou, H. Stoeckli-Evans, S. Decurtins, L. Ouahab***

Synthesis of a BEDT-TTF Bipyridine Organic Donor and the First $Fe^{II}$ Coordination Complex with a Redox-Active Ligand

**Keywords:** Iron / N ligands / BEDT-TTF / Synthesis design / Redox chemistry

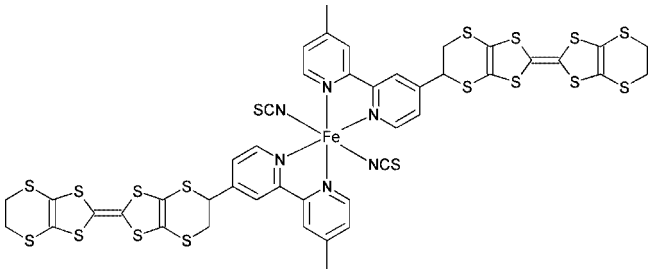


**3503** **D. John, W. Urland***

Crystal Structure and Magnetic Behaviour of the New Gadolinium Carboxylates $Gd_2(ClF_2C-COO)_6(hypy)_2$, $Gd_2(F_3CCOO)_6(hypy)_2$, $Gd_2(F_2-HCCOO)_6(hypy)_2$ and $Gd_2(Cl_2HCCOO)_6(H_2O)_2-(hypy)_2$

**Keywords:** Gadolinium / Carboxylates / O ligands / X-ray diffraction / Crystal structures / Magnetic properties

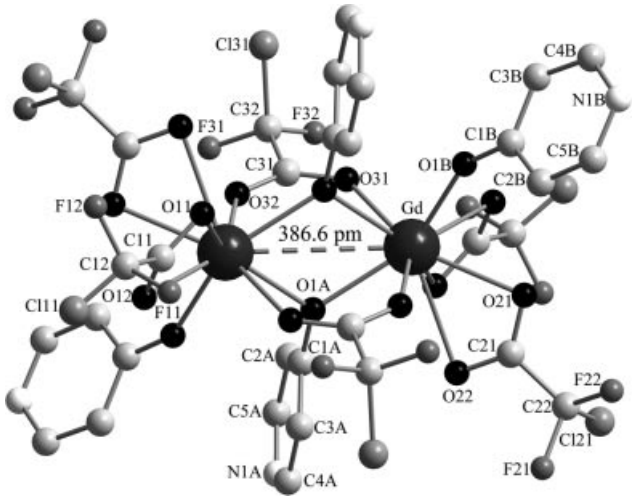


**3510** **S. Sarkar, A. Mondal, D. Chopra, J. Ribas, K. K. Rajak***

A Ferromagnetically Coupled, Bent, Trinuclear Copper(II) Complex: Synthesis, Structure, Hydrogen-Bonding Network, Magnetic Properties and DNA Interaction Study

**Keywords:** Copper / Reduced Schiff base / Magnetic properties / Hydrogen bonds / DNA recognition

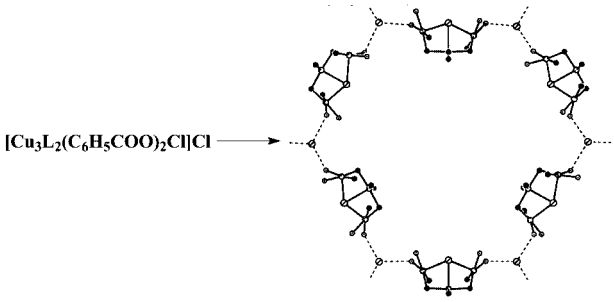


**3517** **U. Baisch, S. Pagano, M. Zeuner, W. Schnick***

Carbon Dioxide Fixation by Organolanthanides and Thermal Degradation into Amorphous and Higher Condensed Ln/O/C/N Solids

**Keywords:** Carbon dioxide fixation / Lanthanides / Organometallic precursors / IR spectroscopy

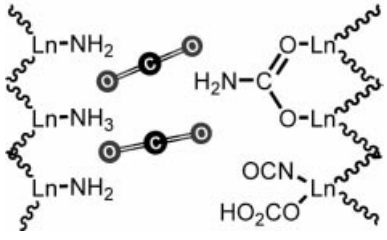


 © 2006 Wiley-VCH Verlag GmbH & Co. KGaA, Weinheim 

**3525** **S. Y. Lee, J. Seo, I. Yoon, C.-S. Kim, K. S. Choi, J. S. Kim, S. S. Lee***

A Poly(bicyclic dimer) and a Cyclic Tetramer: Ligand Isomerism of $S_2O_2$ Macrocycles During the Assembly of Supramolecular Silver(I) Complexes

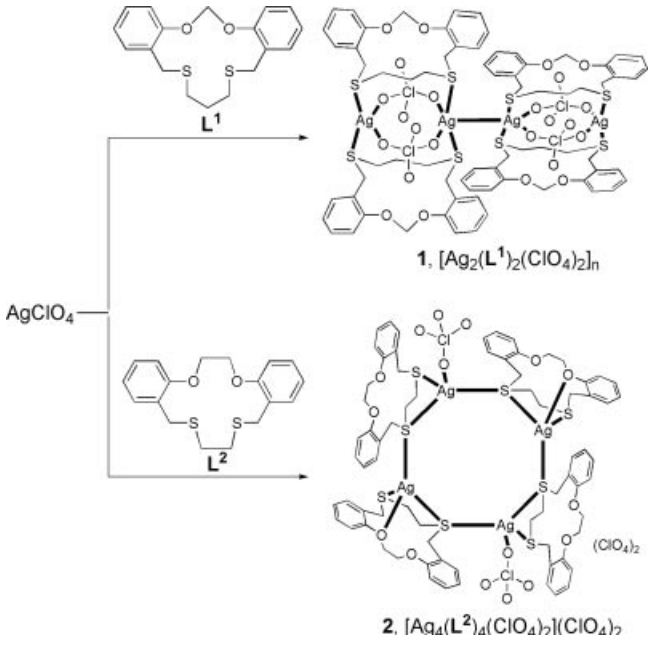


**Keywords:** Macrocycles / Silver / Self-assembly / Supramolecular chemistry / Polymers

**3532** **H.-T. Zhang,* Y.-Z. Li, T.-W. Wang, E. N. Nfor, H.-Q. Wang, X.-Z. You***

A $Zn^{II}$-Based Chiral Crystalline Nanotube

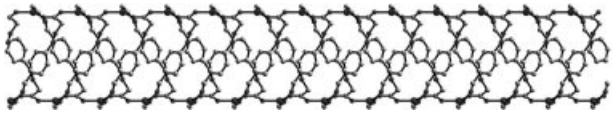

**Keywords:** Coordination polymer/ Chirality / Nanotubes / Triple helix / Nonlinear optics / Fluorescence

DOI: 10.1002/ejic.200600364

# Osmium- and Ruthenium-Based Phosphorescent Materials: Design, Photophysics, and Utilization in OLED Fabrication

**Pi-Tai Chou*[a] and Yun Chi*[b]**

**Keywords:** Osmium / Ruthenium / N ligands / Phosphorescence / Luminescence

Osmium(II) complexes possessing β-diketonate, quinolinate, diimine, and C-linked pyridyl azolate chelates reveal interesting structural and photophysical properties. Spectroscopic and dynamic measurements, in combination with theoretical analyses, have provided an important understanding of the electronically excited state properties of these complexes, such as the energy gap and nature of the lower lying states, rate for intersystem crossing, and the efficiency of corresponding radiative decay and nonradiative deactivation processes. This review also reports on the synthetic processes that lead to the neutral $Os^{II}$ and $Ru^{II}$ complexes that possess two *trans*-substituted phosphane donor ligands together with two *anti*-parallel, aligned azolate chromophores. Considerable efforts have been made to focus on utilizing these emitting materials as phosphorescent dopants for practical PLED and OLED fabrication. Consequently, the interplay between these emitting materials and device configurations is discussed.
(© Wiley-VCH Verlag GmbH & Co. KGaA, 69451 Weinheim, Germany, 2006)

## 1. Introduction

Owing to their versatility and potential in optical sensing and sensitization,[1] as well as in constructing a wide variety of photoresponsive molecular electronics,[2] research on the photophysics and photochemistry of transition-metal complexes has been revitalized and has attracted much recent attention. Particularly, a wide range of metal elements with distinctive d-shell configurations have been employed in order to study their luminescent properties. The influence of metal atoms, together with the modification of ligand architectures, continuously provides an attractive theme for further investigations. There has been an intensive investigation into the emissive $Re^{I}$ complexes, in particular those with a functionalized diimine ligand attached to the *fac*-$[Re(CO)_3]$ unit.[3] The diimine group, exhibiting diversified electronic properties, has rendered a possibility for fine-tuning the excited state properties and luminescent efficiencies. In sharp contrast, relatively less attention has been focused on the behavior of their isoelectronic and isostructural $Os^{II}$ analogues. In an attempt to explore their chemistry and corresponding photophysical properties, we have directed our research efforts specifically to the preparation and charac-

[a] Department of Chemistry, National Taiwan University, Taipei 106, Taiwan
E-mail: chop@ntu.edu.tw
[b] Department of Chemistry, National Tsing Hua University, Hsinchu 300, Taiwan
E-mail: ychi@mx.nthu.edu.tw

*Pi-Tai Chou received his Ph.D. degree from Florida State University, Tallahassee, in 1985, and is currently a Chair Professor at National Taiwan University. He was an assistant professor at University of South Carolina (1988–1994) and a professor of National Chung Cheng University, where he was the departmental chairman from 1997 to 1999. His research interests span the area of ultrafast laser spectroscopy, syntheses, and photophysics of materials suited for OLED, solar energy cell, and nanotechnology.*

*Yun Chi obtained his Ph.D. degree from UIUC, Illinois, in 1986, and was promoted to Professor of Natural Sciences at National Tsing Hua University in 2003. His past academic endeavors cover the chemistry of polymetallic carbonyl clusters, which is important for understanding the catalysts used by petroleum industries for production of new polymers and commodity organics. His current research focuses on subjects involving preparation of metal-containing thin films and nanomaterials by using chemical vapor deposition, as well as synthesis of transition-metal complexes for OLEDs and photovoltaics.*

 © 2006 Wiley-VCH Verlag GmbH & Co. KGaA, Weinheim 

terization of a great range of $Os^{II}$ complexes. With an ingenious design of ligated chromophores, we believe that the luminescent $Os^{II}$ complexes may serve as new models for probing a variety of fundamental characteristics in both ground and excited states (vide infra).

From the application point of view, organometallic complexes possessing heavy transition-metal elements are crucial for the fabrication of phosphorescent organic light-emitting diodes (OLEDs).[4] The strong spin–orbit coupling effectively promotes singlet-to-triplet intersystem crossing, as well as enhances the subsequent transition from the triplet excited state to the ground state, the results of which then facilitate strong electroluminescence by harnessing both singlet and triplet excitons. Theoretically, an internal phosphorescence quantum efficiency ($\eta_{int}$) that can be as high as 100% could be achieved,[5] such that these emitting materials would be superior to their fluorescence-only counterparts for which only singlet excitons can be utilized. This superiority leads to a continuous trend of shifting research endeavors to the heavy transition-metal-based emitters, among which intense research has been carried out on the system involving $Ir^{III}$ complexes ever since the seminal study on [Ir(ppy)$_3$] (ppy = 2-phenylpyridine).[6] In comparison, although much less explored, Os(II) complexes may gain certain advantages, such as the reduction of radiative lifetime and hence a possibility of higher luminescent efficiency, over the traditional $Ir^{III}$ and $Pt^{II}$ emitting materials in OLED applications.

On one hand, this is probably due to the fact that Os in all emissive Os complexes possesses the unique +2 oxidation state. Hence, luminescent $Os^{II}$ complexes, in general, are expected to exhibit lower electrochemical oxidation potentials in dπ orbitals relative to those of the iso-electronic $Ir^{III}$ complexes. Thus, unless $Os^{II}$ complexes are incorporated with strong π-accepting ancillary ligands such as CO, the osmium dπ orbitals will be destabilized, which results in an increase in the metal-to-ligand charge transfer (MLCT) contribution relative to typical π–π* transitions. Such a property, i.e. a short radiative decay time, may also improve the OLED device efficiencies by minimizing the unwanted triplet-triplet annihilation that occurs at a higher operating current density.[7] On the other hand, in comparison to the luminescent Pt complexes possessing a similar $Pt^{II}$ +2 oxidation state, the octahedral ligand arrangement of the $Os^{II}$ complexes would provide a prevailing environment for reducing the intermolecular interaction. This is mainly due to the fact that the planar arrangement and the $d^8$ electronic configuration of the $Pt^{II}$ complexes are subject to aggregation, which leads to a possible π–π stacking interaction in both fluid and solid solutions.[8]

Another subject of current interest is the development of luminescent, neutral $Ru^{II}$ complexes.[9] Despite the fruitful progress on the transition-metal complexes above, a practical barrier to the commercialization of phosphorescent OLED technologies may result from the prohibitive cost of noble metals. With regard to the viability of application, there is an urgent need to develop phosphorescent emitting materials from less expensive precursors, among which $Ru^{II}$ serves as an alternative. Skepticism to this approach, however, might arise as a result of the weaker ligand field strength of $Ru^{II}$ as well as its smaller heavy-atom-effect, i.e. weak spin–orbit coupling, relative to the third-row transition metals.[10] Nevertheless, recent progress has shown that $Ru^{II}$ complexes are suitable for decent OLED/PLED performance. Such success is apparently credited to the rational design of ligand structures through the standpoint of fundamental chemistry and photophysics. Accordingly, in this review, a certain focus will also be directed towards the synthesis, characterization, and utilization of the $Ru^{II}$ complexes, their excitation behavior, and the fabrication of efficient phosphorescent OLED devices.

## 2. [Os(CO)$_3$] Derivatives

### 2.1 Diketonate Complexes

Photophysical studies of lower oxidation state rhenium(I) complexes with the structural formula *fac*-[Re(CO)$_3$X(L)] (X = halides and L = bidentate heterocycles such as 2,2′-bipyridine) have received considerable attention over the past two decades.[3,11] The observed emission could originate from the ligand-centered π–π*, intra- or interligand charge transfer, or even from the metal-to-ligand charge transfer (MLCT) states, depending on the nature of heterocyclic ligands. Moreover, the central metal cation would also impose notable influence on the photophysical properties of the complexes. This gives us the motivation to initiate the heretofore unexplored osmium(II) tricarbonyl analogues.

Accordingly, a series of β-diketonate complexes with the formula [Os(CO)$_3$(tfa)(LX)] (**1**–**7**) were synthesized from the Os dimer [Os$_2$(CO)$_6$(tfa)$_2$] (tfa = trifluoroacetate) with the appropriate diketone reagent (LX)H in a Carius tube.[12]

$$[Os_2(CO)_6(tfa)_2] + (LX)H \rightarrow [Os(CO)_3(tfa)(LX)] + H_2$$

The remarkable variation in the photophysical properties of complexes **1**–**7** is summarized in Table 1. For the hexafluoroacetylacetate complex **1**, the lowest energy absorption at 336 nm, with an extinction coefficient as low as 3000 $M^{-1}cm^{-1}$, is assigned to the $^1$MLCT transition, while the corresponding emission appears at $\lambda_{max}$ = 545 nm. The phosphorescent character is ascertained by its large Stokes shift and long radiative lifetime, $\tau_r$, of ca. 7 μs, which is calculated by $\tau_r = \tau_p/\Phi$ ($\tau_p$: observed decay time, $\Phi$: emission yield). Upon replacing one $CF_3$ substituent with a *tert*-butyl or a phenyl group to form complexes **2** or **3**, respectively, the emission is still dominated by phosphorescence, as indicated by its large Stokes shifted peak wavelength and drastic $O_2$ quenching effect.

Replacement of the aromatic pendant with either α- or β-naphthalene to form **4** or **5**, respectively, also gives rise to a unique phosphorescence with a peak wavelength at 560 and 540 nm, respectively. However, in contrast to the sole phosphorescence for complexes **1**–**3** in both degassed and aerated $CH_2Cl_2$, dual emission that consists of fluorescence, i.e. 462 nm (**4**) and 455 nm (**5**), and phosphorescence was

 © 2006 Wiley-VCH Verlag GmbH & Co. KGaA, Weinheim 

Table 1. Photophysical properties of complexes **1**–**7** in $CH_2Cl_2$ at room temperature.

| | Abs. $\lambda_{max}$ [nm] ($\varepsilon \times 10^3$) | PL $\lambda_{em}$ [nm] | $\Phi$ [%][a] | $\tau_f \approx 1/k_{isc}$ [ps] | $\tau_p$ [μs] | Emitting states[b] |
|---|---|---|---|---|---|---|
| **1** | 336 (3) | 545 | 5.0 | –[c] | 0.35 | $^3$MLCT/$^3\pi\pi^*$ (11.0%) |
| **2** | 321 (7) | 507 | 4.9 | –[c] | 5.0 | $^3$MLCT/$^3\pi\pi^*$ (7.0%) |
| **3** | 347 (14.7) | 520 | 16.2 | 0.48 | 14 | $^3$MLCT/$^3\pi\pi^*$ (4.0%) |
| **4** | 375 (13.6) | 462,[d] 560 | 7.9 | 3.64 | 11 | $^3\pi\pi^*$ (1.3%) |
| **5** | 355 (17.2) | 455,[d] 540 | 13.5 | 6.71 | 19 | $^3\pi\pi^*$ (1.0%) |
| **6** | 316 (17.6), 438 (19.8) | 550, 690 | 1.2 | 120 | 14 | $^1\pi\pi^*/^3\pi\pi^*$ (≈0%) |
| **7** | 378 (20.7), 453 (11.3) | 575, 740[e] | 11.0 | 2100 | –[f] | $^1\pi\pi^*$ (≈0%) |

[a] The solution was degassed with at least three freeze-pump-thaw cycles. For **6**, the reported $\Phi$ value is the sum of florescence and phosphorescence. [b] Values in parentheses are the percentage of $^3$MLCT/$^3\pi\pi$. [c] $\tau_f$ is shorter than the system response of 150 fs. [d] The emission band was only detectable in an aerated solution. [e] The phosphorescence was acquired by laser (355 nm) excitation in a 77-K methylcyclohexane glass. [f] The phosphorescence intensity was too weak to resolve the lifetime.

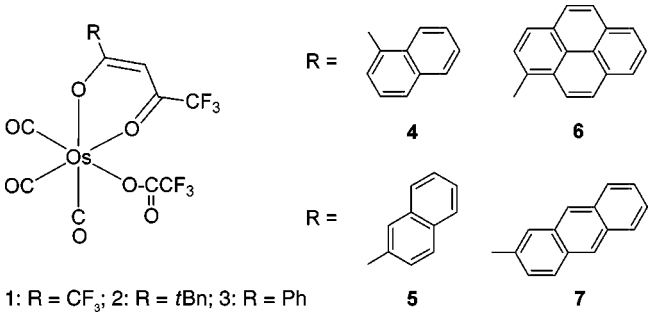


resolved for **4** and **5** under aerated conditions, which indicates their relatively slow $S_1$–$T_1$ intersystem crossing rate, $k_{isc}$. Further substitution of pyrene (**6**) reveals drastically different excitation behaviors. This is confirmed by the observation of dual fluorescence (550 nm) and phosphorescence (690 nm) with a ca. 1:1.2 intensity ratio. In contrast, complex **7** exhibits only fluorescence, regardless of whether it is in degassed or aerated $CH_2Cl_2$, as supported by the excessive short radiative lifetime of 2.1 ns. Nevertheless, weak phosphorescence with a peak wavelength at ca. 740 nm was resolved for **7** in a 77 K methylcyclohexane glass matrix.

The changes of the lowest energy excited state character can be rationalized by the π-electron conjugation introduced by the polyaromatic pendant at the diketonate chromophore, which increases (decreases) the π (π*) energy of both $S_1$ and $T_1$ states in a qualitative manner. The fast $k_{isc}$ observed in **1**–**3** can be rationalized by mixed MLCT and π–π* character in both $S_1$ and $T_1$ manifolds. If intersystem crossing takes place mainly from the $S_1 \rightarrow T_1$ pathway, the corresponding rate constant, $k_{isc}$, is proportional to $\frac{<T_1|H_{SO}|S_1>^2}{(\Delta E_{S_1-T_1})^2}$, where $H_{so}$ is the Hamiltonian for the spin–orbit coupling and $\Delta E_{S_1-T_1}$ is the energy difference between singlet ($S_1$) and triplet ($T_1$) states. The mixing of π–π* and MLCT in both $S_1$ and $T_1$ states leads to the $S_1 \rightarrow T_1$ intersystem crossing that incorporates the $<^1d_\pi\pi^*|H_{so}|^3\pi\pi^*>$ or $<^3d_\pi\pi^*|H_{so}|^1\pi\pi^*>$ term. The net result induces the change in orbital angular momentums, i.e. $d\pi \rightarrow \pi$ coupled with the flip of the electron spin, so that the transition has a significantly large first-order spin–orbit coupling term, which results in a drastic enhancement of the intersystem crossing.[13]

Accordingly, among complexes **1**–**7**, as shown in Table 1, the greatest MLCT/π–π* mixing in **1** and **2** gives rise to ultrafast, system-response–limited ($>10^{13}$ $s^{-1}$) $k_{isc}$. Because of the lack of MLCT/π–π* state mixing in **6**, $k_{isc}$ decreases drastically to $9.2 \times 10^9$ $s^{-1}$. Apparently, because of the lack of MLCT, complexes **6** and **7** mainly undergo a $^1\pi\pi^* \rightarrow {}^3\pi\pi^*$ intersystem crossing, in which the coupling between orbital and spin angular momentum, and hence the $<^1\pi\pi^*|H_{so}|^3\pi\pi^*>$ term, should be rather small owing to negligible changes in orbital angular momentum that can couple with the flip of electron spin. In other words, there is a small first-order spin–orbit coupling to enhance the intersystem crossing.

To investigate the effect of the anionic ligands X in this class of osmium(II) complexes, we prepared the dibenzoylmethanate complexes using the reaction sequence and the corresponding anion exchange protocols that is depicted.

$[Os_2(CO)_6(\mu\text{-}X)_2] + (dbm)H \rightarrow [Os(CO)_3X(dbm)]$, X = tfa (**8**) and I (**11**)

(**8**) + NaCl, NaBr or $NH_4SCN \rightarrow [Os(CO)_3X(dbm)]$, X = Cl (**9**), Br (**10**), and SCN (**12**)

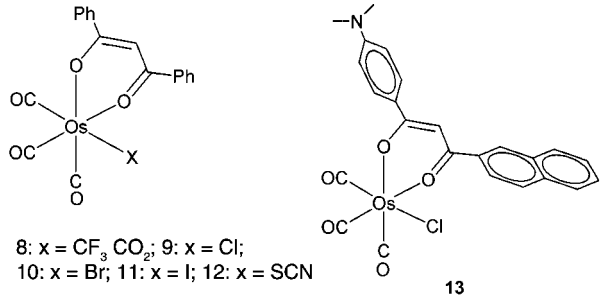


Table 2 shows their photophysical data, for which the lowest-energy absorption band in the region of ca. 367–380 nm can be assigned as an intraligand π–π* transition of the chelating dbm ligand, together with a small proportion of MLCT character.[14] The emission lifetime is unusually long (≥29 μs), giving characteristics of the long-lived phosphorescent emission and quantum yields approaching the level 0.08–0.13. The only exception is the iodide complex **11** ($\Phi$ = 0.007) − which could originate from photoinduced dissociation involving the weak Os–I bond − which exhibits a decrease in phosphorescence upon prolonged photolysis. The hypsochromic shift of the emission peak maximum follows the order tfa ≈ SCN > Cl > Br >

 © 2006 Wiley-VCH Verlag GmbH & Co. KGaA, Weinheim 

Table 2. Photophysical properties and electrochemical data of complexes **8**–**12** in $CH_2Cl_2$ at room temperature.

| | Formula | Abs. $\lambda_{max}$ [nm] ($\varepsilon \times 10^3$) | $\lambda_{em}$ [nm][a],[b] | $\tau_o$ [μs][a],[b] | $\Phi_{em}$ | $k_r$ [$10^3$ $s^{-1}$][c] |
|---|---|---|---|---|---|---|
| **8** | $[Os(CO)_3(tfa)(dbm)]$ | 280 (22), 367 (20) | 538 (541) | 64 (3.0) | 0.13 | 2.02 |
| **9** | $[Os(CO)_3Cl(dbm)]$ | 285 (19), 372 (16) | 557 (537) | 46 (9.1) | 0.13 | 2.76 |
| **10** | $[Os(CO)_3Br(dbm)]$ | 278 (19), 375 (16) | 563 (561) | 29 (4.2) | 0.08 | 2.82 |
| **11** | $[Os(CO)_3I(dbm)]$ | 278 (24), 380 (14) | 574 (602) | 0.72, 38 (2.7) | 0.007 | 0.18 |
| **12** | $[Os(CO)_3(SCN)(dbm)]$ | 277 (26), 372 (15) | 539 (545) | 53 (3.4) | 0.13 | 2.49 |

[a] Excitation wavelength: 380 nm. [b] Data in parenthesis were obtained in the thin solid films. Note that a faster decay component (<0.2 μs) was observed for **8**–**12** in the solid state possibly due to the defective sites. Its integrated intensity is <10% and is thus neglected. [c] $k_r = \Phi_{em}/\tau$.

I, which is proportional to the electron-donor strength of the anion that destabilizes the metal-centered HOMO, hence decreasing the energy gap.

We also made an attempt to probe the fundamentals of the triplet-state properties based on this inherent molecular design involving the related *fac*-$[Os(CO)_3]$ unit.[15] One intriguing topic relevant to triplet-state properties should be ascribed to the triplet-state intramolecular charge transfer (TSICT) process.[16] It has been reported that the micelle or polymer encapsulated organic chromophore, together with the external heavy atom effect, may resolve room-temperature phosphorescence.[17] However, the resulting heterogeneous and rigid environments make the investigation of the solvation-associated properties impractical. As a result, photophysical properties associated with TSICT, such as the solvation relaxation dynamics and the steady-state consequence, e.g. the phosphorescence solvatochromism, are not attainable in solvents with a low viscosity. Our strategic design, in contrast, is much more simple (c.f. complex **13**) and involves the utilization of the $[Os(CO)_3Cl]$ fragment to support an asymmetrical β-diketonate ligand, composed of an *N*,*N*-dimethylaniline and a 2-naphthylene substituent that serve as the electron donor and the acceptor, respectively.[18] As the attached heavy-metal fragment $[Os(CO)_3Cl]$ generally possesses a large energy gap for the metal dd and MLCT transitions,[19] the organic chromophore of interest, i.e. β-diketonate, is expected to lie in the lower-lying excited states.

Figure 1 shows the absorption and emission spectra of **13** in various solvents. The different relaxation dynamics of fluorescence and phosphorescence allowed us to resolve each component.[15] In aerated cyclohexane, this molecule exhibits distinct dual fluorescence at 470 nm and phosphorescence at 570 nm with a sum of near unitary quantum efficiency. As the solvent polarity increases, drastic polarity dependence in emission spectra is observed. Evidently, both the fluorescence and phosphorescence undergo notable bathochromatic shift and give rise to an exceedingly broad emission signal. Changes in dipole moment for the $S_1$ and $T_1$ states with respect to the ground state are deduced to be 18.0 and 11.9 Debye, respectively, with the Lippert–Mataga equation.[20] The appreciable difference in dipolar changes implies the intrinsic difference in the electron-density distribution between $S_1$ and $T_1$ states. Further theoretical analysis indicates that the $T_1$ state possesses a substantial contribution (≈10%) from the MLCT transition originating from the osmium dπ orbital to the π system of the 2-naphthyl moiety, whereas the $S_1$ state is dominated by a ππ* configuration. Thus, the redistribution of π electron density because of the charge transfer should be less emphasized in the $T_1$ state, rationalizing its smaller dipolar change. Such intrinsic, subtle differences in charge-transfer properties are intriguing and worthy to pursue further from a theoretical standpoint.

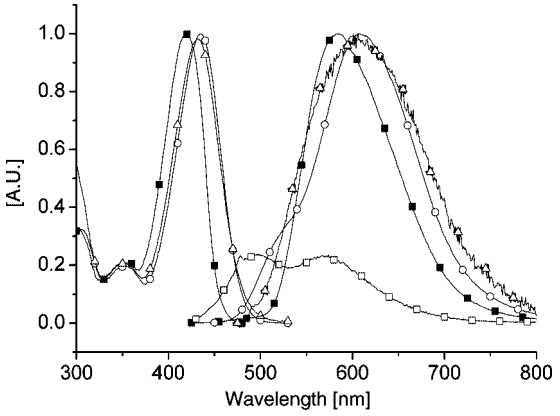


Figure 1. The absorption and steady-state emission spectra of **13** at 298 K in degassed cyclohexane (-■-), dichloromethane (-○-), and acetonitrile (-Δ-). The trace (-□-) denotes the emission spectrum of **13** in aerated cyclohexane.

### 2.2. Quinolinolate Complexes

Providing that the osmium fragment $[Os(CO)_3X]$ of β-diketonate complexes serves as a prototype to facilitate the intersystem crossing, other chelating anions such as quinolinolate have also been explored in an attempt to reveal their phosphorescent characters.[21] This issue is motivated by the consideration that aluminum quinolinolate and its homologues were extensively tested for applications as the emitting or the electron-transporting materials in OLEDs.[22]

Four osmium(II) quinolinolate complexes **14**–**17** were synthesized, which provide a good example of the structural modifications that influence the basic photophysical properties. Table 3 summarizes the peak wavelengths of the lowest-energy absorption and other important photophysical data. The room-temperature absorption and emission spectra of complexes **14**–**17** in toluene are shown in Figure 2. The lower-lying absorption peak located at near 420–450 nm is derived from a π–π* transition with a significant contribution from the intraligand charge transfer (ILCT)

 © 2006 Wiley-VCH Verlag GmbH & Co. KGaA, Weinheim 

transition.[23] This delineation is in good agreement with the ca. 20-nm bathochromic shift of a similar absorption band of **17**, for which fluorine substitution at the 5-position is expected to markedly lower the π–π energy gap of the quinolinolate fragment because of the resonance (i.e. mesomeric) effect.[24] The assignment to the MLCT band is discarded owing to the lack of electronic dependence on the metal environment in the iodide complex **15**.

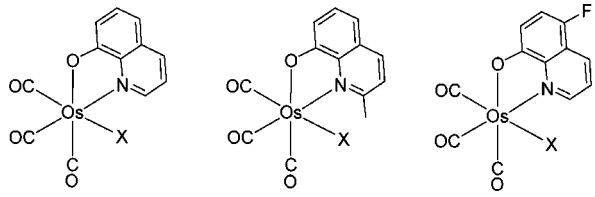


**14:** X = $CF_3CO_2$ **16:** X = $CF_3CO_2$ **17:** X = $CF_3CO_2$

**15:** X = I

As depicted in Figure 2, except for the fluorine-substituted complex **17** in which only fluorescence could be resolved, complexes **14**–**16** revealed two distinct bands, the intensity ratios of which varied according to the quinolinolate ligands and the anionic ancillary ligands. The shorter-wavelength band, showing characteristics of a short lifetime (<2 ns, see Table 3), is classified as fluorescent emission, while the longer-wavelength band can be assigned to the respective phosphorescence on the basis of its relatively much longer lifetime (>1 μm) and drastic quenching effect under oxygen. It is believed that both of these emissions are dominated by typical π–π* transition in combination with ILCT [phenolate site (π) → pyridine site (π*)] character. The latter transition, in part, incorporates the transfer of electron densities from the oxygen atom of the phenolate fragment to the π* orbitals of the fused ring system. The fluorine atom in complex **17** exhibits the mesomeric effect,[24] which results in the decrease in electronic transition energy, with a consequent bathochromic shift in both the absorption and emission bands.

The variation in the intensity of dual emissions, i.e. fluorescence vs. phosphorescence, can be correlated with the relaxation dynamics of the $S_1 \rightarrow T_1$ intersystem crossing. In comparison with complex **14**, the addition of a 2-methyl group in **16** enhances $k_{isc}$ threefold, which may be rationalized by the increase in density of the final vibronic states ($T_1$) having the same energy as the initial states ($S_1$). For complex **17**, the mesomeric effect introduced by the fluorine atom at the 5-position of the quinolinolate would result in the retardation of intersystem crossing in a qualitative manner and hence give the reduction of $k_{isc}$. However, in the case of iodide-substituted complex **15**, the phosphorescence is significantly increased, plausibly because of the additional iodide heavy-atom effect that drastically increases the rate of intersystem crossing (vide infra).[25]

Table 3. Photophysical properties of complexes **14**–**17** in degassed toluene at room temperature.

| | Abs. $\lambda_{max}$ [nm] ($\varepsilon \times 10^3$) | PL $\lambda_{max}$ [nm] | $\Phi$ [%][a] | Fluorescence [ns] | Phosphorescence [μs][b] |
|---|---|---|---|---|---|
| **14** | 424 (3.3) | 526, 635 | 1.4 | 0.55 | 33.1 |
| **15** | 430 (4.1) | 520, 650 | 2.4 | 0.15 | 3.8 |
| **16** | 421 (3.4) | 520, 650 | 0.2 | 0.21 | 21.6 |
| **17** | 443 (2.9) | 560, 689 | 1.1 | 1.10 | – |

[a] The solution was degassed with at least three freeze-pump-thaw cycles. The reported $\Phi$ value is the sum of fluorescence and phosphorescence. [b] The phosphorescence lifetime was measured by a direct laser flash experiment.

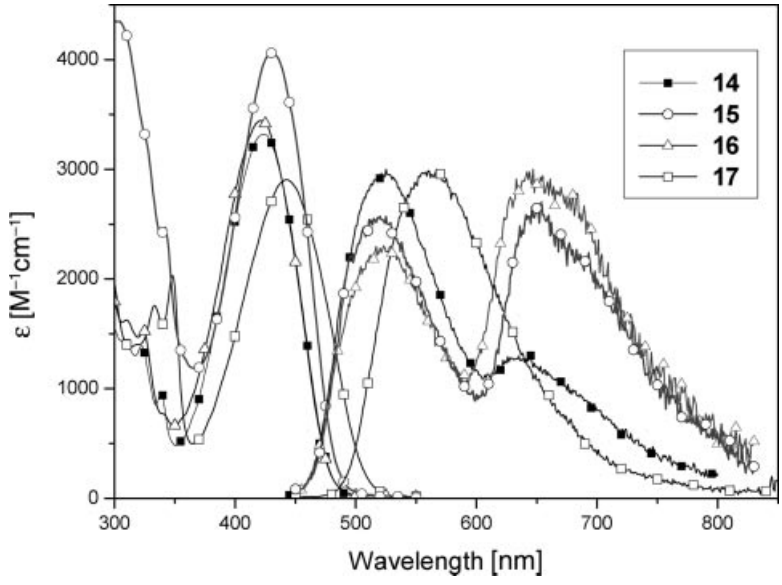


Figure 2. UV/Vis absorption and normalized emission spectra of **14** (-■-), **15** (-○-), **16** (-Δ-), and **17** (-□-) in toluene at room temperature.

 © 2006 Wiley-VCH Verlag GmbH & Co. KGaA, Weinheim 

## 3. [Os(CO)$_2$] Derivatives

### 3.1 Diimine Complexes

Dicarbonyl osmium(II) complexes of the type [Os(diimine)(CO)$_2$I$_2$] contain both π-donating iodide ligands and an accepting diimine ligand with low energy π* orbitals. These osmium(II) complexes exhibit pseudo-octahedral geometry, and the iodide and carbonyl ligands are located at the *trans* and *cis* positions, respectively.[26] The main interest in initiating this investigation was to shed light on the nature of the lowest excited state; for example, whether these complexes display the basic characteristics of the usual metal-to-ligand charge transfer excited state (MLCT) or a state with a substantial amount of the halide-to-ligand charge transfer (XLCT) character.

It is noted that these Os$^{II}$ complexes exhibit much stronger room-temperature iodide-to-ligand phosphorescence than that of their ruthenium analogues. Such a difference is attributed to an increase in the all osmium ligand bonding strength relative to that of the second row ruthenium counterparts, which affords an increase in the energy of the metal-centered dd state. Therefore, this dd state is more difficult to populate in the osmium derivatives, which shows a notable increase in luminous intensity. Conversely, if the metal-centered dd state is more easily populated, which is more likely to occur in the ruthenium complexes, the complex may relax back to the ground state through nonradiative means and exhibit a great loss in the emission efficiency.[27] DFT calculations on complex **18b** confirm that the room-temperature emission originates from mixed XLCT (≈70%) and MLCT (≈30%) as a result of the lower oxidation potential of the iodide ligand. Replacing the diimine ligand from bipyridine (or phenanthroline) with the pyridyl benzoxazole ligand leads to a significant bathochromatic shift of the emission signal. The result implies that the benzoxazole ligand of **19** possesses a lower energy π* orbital relative to that of the bipyridine (or phenanthroline) ligands, which in turn gives a reduction in the energy gap for the MLCT/XLCT excited states.

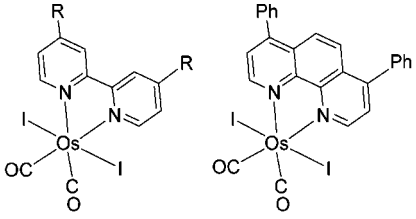

**18:** R = H; **18a:** R = *t*Bu



**18b**

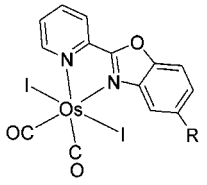

**19:** R = H; **19a:** R = *t*Bu

### 3.2 Pyridyl Azolate Complexes

The C-linked 2-pyridyl azolate belongs to a class of chelating ligands for which the large difference in the electronic properties of the pyridyl and the azolate fragment would render a larger ligand-centered π–π* energy gap. Such a property is very desirable for the generation of rarely observed blue phosphorescence. Furthermore, the disparity in electron distribution between the azolate and pyridyl fragments may provide a synergic effect such that the electron density transfers from the azolate to the cationic metal center and back to the pyridyl fragment, giving a delocalized and stabilized metal–chelate bonding interaction.

Treatment of 3-trifluoromethyl-5-(2-pyridyl)pyrazole (fppz)H and Os$_3$(CO)$_{12}$ afforded only one complex, **20**, in moderate yield.[28] For reactions with the related triazole chelate, two isomeric complexes, **21** and **22**, were observed for the direct treatment of 3-*tert*-butyl-5-(2-pyridyl)triazole (bptz)H with Os$_3$(CO)$_{12}$.[29] Separation of products was achieved by using their marked solubility differences in acetone, where the less soluble isomer **21**, which is structurally related to complex **20**, can readily be obtained as a crystalline solid, while isolation of the second complex **22** required repeated extraction and slow diffusion of hexane vapor into a saturated acetone solution at room temperature.

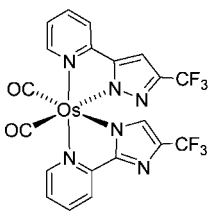

**20**

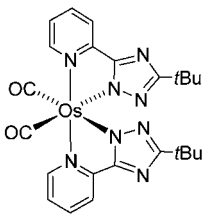

**21**

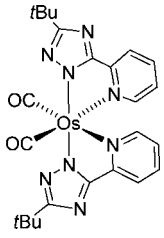

**22**

It is notable that the pyridyl fragments in complexes **20** and **21** are both located at the mutual *trans* position, while the pyridyl groups in complex **22** are located *trans* to the *cis*-oriented carbonyl ligands.

The corresponding photophysical data are summarized in Table 4. For complex **20**, the lowest-energy absorption bands at ca. 310 nm are ascribed to the ligand-centered π–π* transitions, while the corresponding MLCT transitions could be hidden under the more intense π–π* transitions. The emission spectrum exhibits a distinct vibronic feature with $\lambda_{max}$ at 430, 457, and ca. 480 nm in $CH_3CN$. The fact that the entire emission band originates from a common excited-state species is ascertained by the same fluorescence excitation spectra throughout the monitored wavelengths of 420–600 nm. This observation leads us to propose that the emissive state mainly possesses a ligand-centered $^3\pi\pi^*$ character.

Table 4. Photophysical properties of complexes **20**–**22** in degassed $CH_3CN$ at room temperature.

| | Abs. $\lambda_{max}$ [nm] | PL $\lambda_{max}$ [nm] | Q.Y. $\Phi$ | $\tau$ [μs] |
|---|---|---|---|---|
| **20** | 311 | 430, 457, 480 | 0.14 | 18.5 |
| **21** | 333 | 455, 480, 507 | 0.42 | 39.9 |
| **22** | 340 | 460, 483, 515 | 0.00046 | 0.026 |

Figure 3 shows the UV/Visible absorption and emission spectra of both **21** and **22** in acetonitrile. Similarly, a structureless band with a maximum at 310–334 nm can be assigned to a triazolate-to-pyridine intraligand π–π* transition. For their emission spectra, complex **21** exhibits strong

 © 2006 Wiley-VCH Verlag GmbH & Co. KGaA, Weinheim 

emission, with a quantum yield of 0.42, for which distinct vibronic peak maxima appear at ca. 455, 480, and 507 nm in degassed $CH_3CN$ at 298 K. Remarkable differences in emission properties were observed for **22**. Although its emission profile looks quite similar to that of **21**, this complex is nearly nonemissive with a quantum efficiency as low as $4.6\times10^{-4}$ in degassed $CH_3CN$ solution at 298 K. This weak phosphorescence also correlates well with the observed fast relaxation dynamics, in which the lifetime of phosphorescence for **22** is measured to be as short as 26 ns. It is also worth noting that a small but non-negligible fluorescence shoulder ($\lambda_{max} \approx 420$ nm, $\tau_f < 200$ ps) could be resolved in **22** (Figure 3), although the rate of intersystem crossing is very fast, as indicated by the system-response-limited rising component of the phosphorescence (<200 ps).

One possibility to account for the distinctive difference in emission behavior of **22** is that there exist certain excited states, possibly a metal-centered d–d transition (i.e. ligand field, LF, transition), which results in weakening of the metal–ligand interaction as a result of their *anti*-bonding character and may thus act as an activator for the overall radiationless transition.[30] However, this possibility was ruled out as none of the four lowest excited states, including two singlet and two triplet manifolds that were examined, possess the anticipated dd character. The inaccessibility of the dd excited state is believed to result from the strong ligand field strength of the triazolate chelates as well as of the CO ligands.

On the other hand, according to our TD–DFT calculation, a $T_1$ configuration in **22** could be reasonably attributed to a $^3\pi\pi^*$ manifold, mixed to a great extent with small amounts of the $^3$MLCT character.[31] By populating the $T_1$ excited state, a shift in the electron density from the metal center, CO ligands, and the triazolate moiety to the pyridine moiety occurs, which results in a further reduction of the already weakened Os–pyridine interactions in **22**, for which the weakened bond lengths have been confirmed by single-crystal X-ray analysis. As a result, in **22**, the potential energy surface (PES) of $T_1$ might be so shallow that, under extreme conditions, a surface crossing of PESs between $T_1$ and $S_0$ is possible. As shown in Figure 4, upon excitation, fast $S_1$–$T_n$ intersystem crossing (ISC) must take place. It is plausible that ISC proceeds from $S_1$ to $T_2$ because of their closeness in energy, followed by a fast rate for $T_2$ to $T_1$ internal conversion ($\leq 1$ ps$^{-1}$). After population equilibrium, **22** can be thermally activated to certain vibrational levels close to the section of surface crossing to execute the radiationless deactivation through facile metal–ligand bond stretching. Thus, a dominant $T_1 \rightarrow S_0$ radiationless transition caused by a "loose-bolt" effect might take place upon thermal activation.[32]

This discovery may allow a parallel comparison with the behavior of tris(cyclometalated) iridium complexes for which isolation of two geometrical isomers has been documented in the literature.[33] Structural and spectroscopic data suggest that the facial isomers have stronger and more evenly distributed metal–ligand bond interactions, and are highly emissive in both fluid and solid states at room temperature. In contrast, the meridional isomers have much greater bond length alternations caused by the differing *trans* influences of anionic phenyl and neutral nitrogen donors such as pyridine or pyrazolate, and are significantly less emissive under identical conditions at room temperature. We speculate that this greater bond strength alternation then induces a similar effect upon electronic excitation, which is more likely to be responsible for the rapid radiationless deactivation observed in this $Ir^{III}$ system.

Moreover, treatment of complex **20** with a nitrogen donor ligand led to the formation of a new series of $Os^{II}$ complexes with formula $[Os(fppz)_2(CO)(L)]$ (**23**, L = 4-dimethylaminopyridine; **24**, L = pyridine; **25**, L = 4,4′-bipyridine;

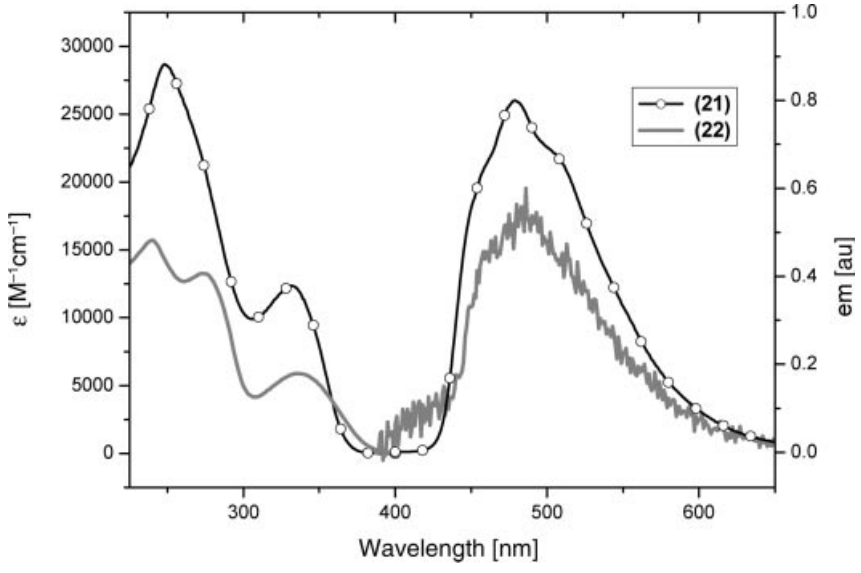


Figure 3. UV/Vis absorption and emission spectra of **21** (-o-) and **22** (—) in $CH_3CN$ solution at room temperature.

 © 2006 Wiley-VCH Verlag GmbH & Co. KGaA, Weinheim 

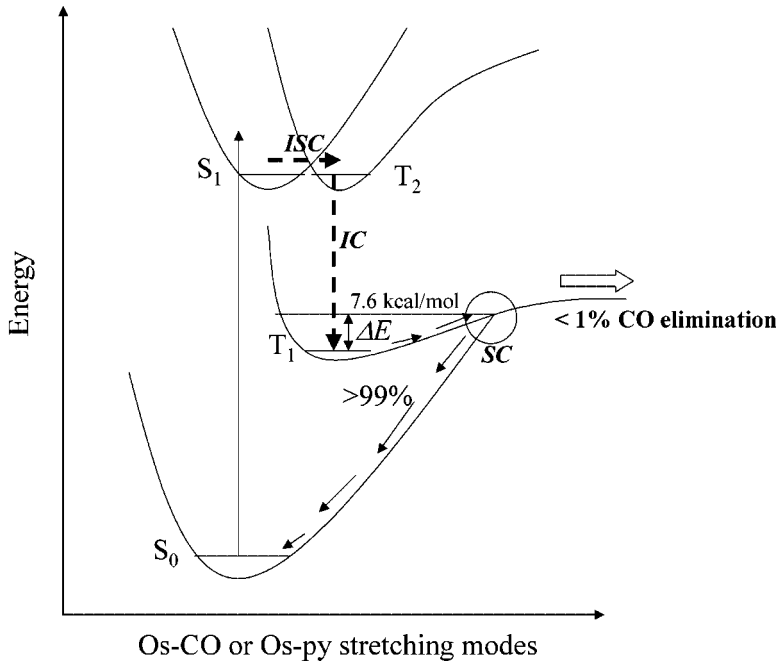


Figure 4. Energy levels of the lower-lying excited states and the proposed relaxation pathway for complex **22**. ISC: intersystem crossing, IC: internal conversion. SC: surface crossing.

**26**, L = pyridazine; **27**, L = 4-cyanopyridine); the remaining carbonyl ligands and the N-heterocyclic ligand are located at the axial positions.[34] Variation in the axial N-heterocyclic ligand leads to remarkable changes in photophysical properties such that the energy gap and the phosphorescence peak wavelength can be fine-tuned.

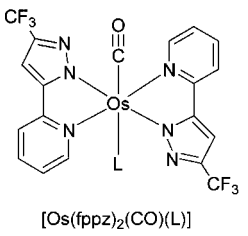


[Os(fppz)$_2$(CO)(L)]

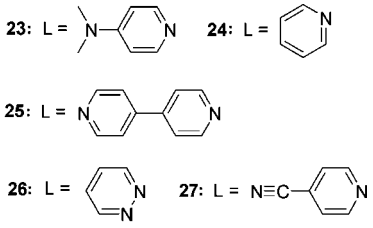


For complexes **23** and **24**, the axial nitrogen donor ligand possesses an electron-rich aromatic π system, which discourages its participation in the lowest-energy electronic transition. As a result, the phosphorescence originates from a combination of intraligand $^3\pi\pi^*$ ($^3$ILCT) and metal-to-ligand charge transfer transitions ($^3$MLCT) to the pyridyl fragments of the fppz chelates, and its peak wavelength is independent of the polarity of the solvent. This is confirmed by the observation of an only 18-nm red-shifted emission wavelength for complex **24** upon changing solvents from cyclohexane (487 nm) to acetonitrile (≈505 nm). In sharp contrast, complexes **25**–**27** exhibit mainly ligand-to-ligand charge transfer (LLCT) transitions, with a transfer of electron density from the equatorial pyrazolate fragment to the axial nitrogen donor ligand because of the excessive stabilization produced by either the extended π conjugation (4,4′-bipyridine) or the presence of an extra electronegative nitrogen atom (pyridazine and 4-cyanopyridine). The phosphorescence thus reveals strong solvent-polarity dependence, which results in a large shift in emission wavelength, e.g. from 560 (in $C_6H_{12}$) to 665 nm (in $CH_3CN$) and from 603 (in $C_6H_{12}$) to 710 nm (in $CH_3CN$) for complexes **25** and **27**, respectively. These results clearly demonstrate that a simple derivatization of the axial N-heterocyclic ligand drastically alters the excitation properties per se from intraligand charge transfer (ILCT) to the LLCT transition. The latter exhibits remarkable LLCT phosphorescence solvatochromism, so that a broad range of color tunability was achieved. Future applications to probe molecular/metal ion recognition will be of great interest and these can be achieved by applying the mechanism that incorporates solvent-polarity dependent interplay between ILCT and LLCT.[35]

## 4. Diphosphane Osmium Derivatives

An optimized synthesis was performed by the treatment of $Os_3(CO)_{12}$ with at least 6 equiv. pyridyl azole in anhydrous diethylene glycol monoethyl ether (DGME) at 180–190 °C, followed by the addition of a decarbonylation reagent, $Me_3NO$, and the phosphane ligands in sequences.[36] This one-pot synthesis strategy gives the desired $Os^{II}$ complexes **28**–**33** in good yields (>70%), and hence has a great advantage as it can be scaled up for possible industrial application.[37]

 © 2006 Wiley-VCH Verlag GmbH & Co. KGaA, Weinheim 

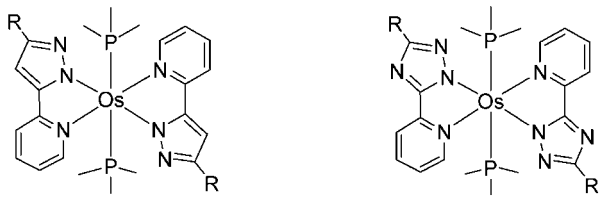

**28**: R = $CF_3$, P = $PPh_2Me$

**29**: R = $CF_3$, P = $PPhMe_2$

**30**: R = *t*Bu, P = $PPh_2Me$

**31**: R = $CF_3$, P = $PPh_2Me$

**32**: R = $C_3F_7$, P = $PPh_2Me$

**33**: R = $C_3F_7$, P = $PPhMe_2$

Figure 5 shows an ORTEP diagram of **28**, in which the metal atom is located at a crystallographic center of inversion. The two chelating pyrazolate ligands establish a nearly planar $OsN_4$ basal arrangement, together with two $PPh_2Me$ ligands located at the *trans* positions. The planar ligand arrangement is analogous to those of the porphinato ligand in metalloporphyrins such as [Os(TTP)($PPh_3$)$_2$] (TTP = *meso*-tetraphenylporphinate) and [Os(TPP)(CO)(Im)] (Im = 1-methylimidazole).[38] The measured Os–$N_{(pz)}$ distances of 2.073(2) Å in **28** are slightly shorter than the respective Os–$N_{(py)}$ bond lengths of 2.090(2) Å; both bond lengths fall in the range expected for a typical N→$Os^{II}$ dative bond. Of particular interest are the relatively weak nonbonding contacts (N3A···C1 = 3.305 Å and N3A···H1 ca. 2.50 Å) observed between the *ortho*-hydrogen atom of the pyridyl moiety and the N atom of the nearby pyrazolate fragment. It is speculated that this H-bonding, to a certain extent, is akin to that observed in the cobaloxime complexes.[39]

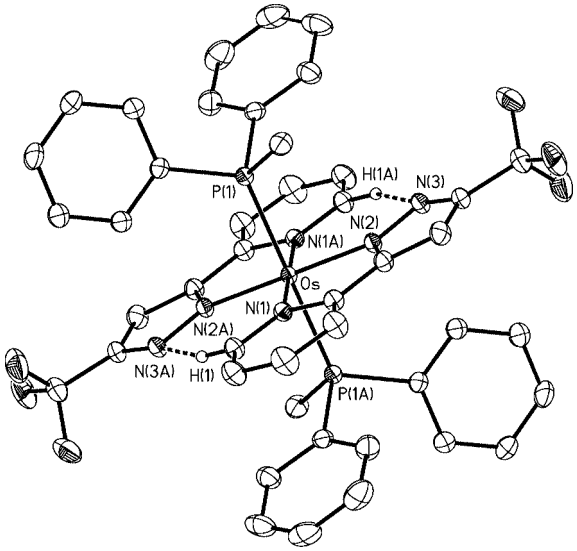


Figure 5. ORTEP diagram of **28**; selected distances: Os–P(1) = 2.3616(5), Os–N(1) = 2.090(2), Os–N(2) = 2.073(2), N(2)–N(3) = 1.349(2), N(3)···H(1A) = 2.508 Å and angles: N(1)–Os–N(2) = 76.48(7), N(1)–Os–N(2A) = 103.52(7)°.

As indicated in Table 5, the UV/Vis spectra of these osmium complexes show similar patterns, with three notable absorption maxima. The highest energy band, observed at ca. 400 nm, is naturally assigned to the spin-allowed $^1\pi\pi^*$ transition. The next lower energy absorption band, around 454–466 nm, can be ascribed to a spin-allowed metal-to-ligand charge transfer ($^1$MLCT) transition, while the third lowest energy band can be assigned to a state involving a mixture of both $^3\pi\pi^*$ and $^3$MLCT characters.

Table 5. Photophysical properties of complexes **28**–**33** in $CH_2Cl_2$ and solid state at room temperature.

| | Abs. $\lambda_{max}$ [nm] | PL $\lambda_{max}$ [nm] | Q.Y. $\Phi$[a] | $\tau$ [ns][a] |
|---|---|---|---|---|
| **28** | 405, 454, 542 | 617 (618)[a] | 0.50 (0.21) | 855 (631) |
| **29** | 411, 456, 553 | 632 (655) | 0.19 (0.29) | 725 (610) |
| **30** | 406, 466, 560 | 649 (670) | 0.25 (0.10) | 634 (440) |
| **31** | 405, 457, 543 | 617 (631) | 0.62 (0.24) | 960 (180) |
| **32** | 403, 457, 545 | 614 (618) | 0.76 (0.36) | 940 (580) |
| **33** | 410, 465, 550 | 629 (634) | 0.50 (0.21) | 810 (910) |

[a] Data in parentheses are measured in the solid state at room temperature.

For the emission spectra, in comparison with **28**, which is coordinated by two $PPh_2Me$ ligands, complex **29**, bearing the $PPhMe_2$ groups, reveals a ca. 15-nm bathochromic shift in $\lambda_{max}$ that can qualitatively be rationalized by an increase in the $Os^{II}$ d$\pi$ energy level as a result of the poor $\pi$-accepting strength of the $PPhMe_2$ ligands (see Table 5). Complexes **28** and **31**, both possessing two $PPhMe_2$ ligands, exhibit nearly identical emission in solution, $\lambda_{max}$ =617 nm. This is due to the fact that the triazolate fragment, which is more electron withdrawing relative to pyrazolate, exerts an equal amount of stabilization to both HOMO and LUMO, which are located at the $Os^{II}$ metal center and the adjacent pyridyl site, respectively. Moreover, changing the substituent on the triazolate from *tert*-butyl (**30**) to $CF_3$ (**31**) and then to $C_3F_7$ (**32**) causes a notable blue-shift as a result of the increase in the MLCT gap by lowering the metal d$\pi$ energy level.

Moreover, the observed lifetimes of ca. 0.6–0.9 μs in degassed $CH_2Cl_2$ solution are considerably shorter than those of other reported red emitting $Ir^{III}$ complexes.[40] This, in combination with decent quantum yields >0.1, implies that the OLED devices fabricated using this class of osmium complexes could exhibit reduced triplet-triplet annihilation at the higher driving voltage.[7,41]

For the preparation of light-emitting devices, we incorporated the osmium phosphor **29** into a tailor-made blue-emitting polyfluorene derivative **PF-TPA-OXD**.[42] This host polymer, which contains both hole- and electron-transporting side chains, is capable of facilitating charge injection and transport and is suitable for matching the dopant-host energy level to achieve the direct formation and confinement of an exciton at the dopant. This configuration leads to a reduction in the electrical excitation of the host polymer, which in turn decreases the degree of exciton loss arising from nonradiative decay of the host triplet. In practice, PLED devices having the configuration ITO/poly(styrenesulfonate)-doped poly(3,4-ethylenedioxythiophene) (PEDOT) (35 nm)/polymer emitting layer (50–70 nm) and dopant **29**/TPBI (30 nm)/Mg:Ag (100 nm)/Ag (100 nm) were fabricated, and the optimized dopant concentration of **29** was kept at ca. 1 mol-%. The PL profile of this device

 © 2006 Wiley-VCH Verlag GmbH & Co. KGaA, Weinheim 

contains two components, which are attributed to the polyfluorene emission of the **PF-TPA-OXD** host and the triplet emission of **29**, while the corresponding EL spectra indicate an exclusively dopant emission. The dramatic difference between the PL and EL spectra reveals that the emission would result from direct charge trapping, followed by recombination with opposite charges at the dopant sites.[43] To understand the details of the charge–transport mechanism, the HOMO and LUMO energy of **29** were estimated by using the onset potentials of the oxidations and reductions obtained with cyclic voltammetry (CV). As shown in Figure 6, holes in this device can easily be injected from PEDOT (–5.2 eV)[44] into the HOMOs (–5.3 eV) of the **PF-TPA-OXD** host upon overcoming a small energy barrier (0.1 eV). For complex **29**, the ionization potential is 0.8 eV below the HOMO of **PF-TPA-OXD**; therefore, holes can be trapped at the dopant site, followed by recombination of opposite charges (electrons) to form excitons. For comparison, this device reached a maximum external quantum efficiency of 8.37% with a peak brightness of 16720 cd m$^{-2}$. Moreover, a maximum $\eta_{ext}$ of 12.8% is reached by using a similar device configuration and by employing a tetraphenylenebiphenyldiamine (TPD) based cross-linkable hole-transport layer, as well as a layer of 1,3,5-tris(*N*-phenylbenzimidazol-2-yl)benzene (TPBI) as an electron-transport layer and complex **29** as a dopant emitter.[45]

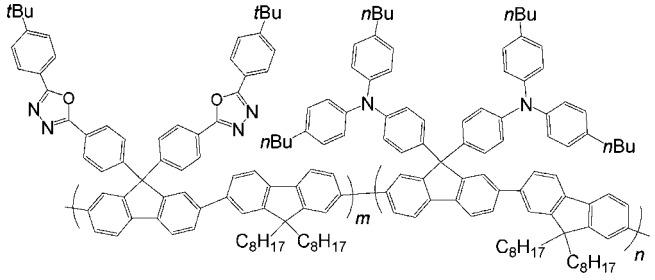


**PF-TPA-OXD**

In contrast, ionic red-emitting osmium(II) incorporating various substituted bipyridine ligands were also synthesized and tested for OLED applications.[46] The schematic drawing of two representative osmium(II) complexes, **34** and **35**, are shown.

This class of complexes features strong red MLCT phosphorescent emission ranging from 611 to 651 nm and the best quantum yields, up to 45%.[47] Electrophosphorescent

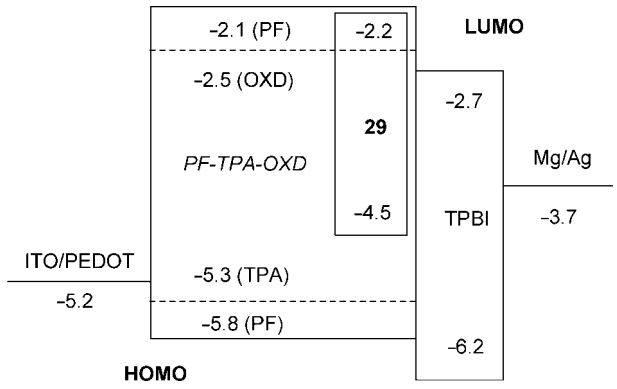


Figure 6. Proposed energy level for the devices having the configuration ITO/PEDOT/**29**: **PF-TPA-OXD**/TPBI/Mg:Ag.

devices were demonstrated by using poly(*N*-vinylcarbazole) and 2-*tert*-butylphenyl-5-biphenyl-1,3,4-oxadiazole (PVK:PBD) as the emitting layer, which give a brightness of 1400 cd m$^{-2}$. The best external quantum efficiency of 2.2%, which corresponds to a photometric efficiency of 1.9 cd A$^{-1}$, was achieved when switching the host matrix from PVK:PBD to a blend host of poly(2-vinylnaphthalene) (PVN) and PBD.[48] Moreover, it is understood that the analogous cationic osmium complexes are capable of trapping both electrons and holes, which facilitates the direct recombination of holes and electrons on the complex sites; however, the resulting devices failed to show any device data comparable to those of previously mentioned neutral osmium complexes such as **29**, even under the conditions using the copolymer **PF-TPA-OXD**, which is well known for its carefully balanced charge injection and transporting properties.[45] It is obvious that the counterions presented in this class of bipyridine complexes have seriously deteriorated the performance of the device, presumably by affecting the charge trap/transport property of the osmium complexes; hence, the use of ionic emitting materials must be avoided.

For a further comparison, we also took advantage of the high volatility of the neutral osmium(II) complexes to prepare OLEDs using direct thermal evaporation.[37] In this approach, complex **31** was selected for fabricating a series of multilayer devices with the configuration ITO/HTL(40 nm)/CBP:**31**(30 nm)/BCP(10 nm)/$Alq_3$(30 nm)/LiF(1 nm)/Al(150 nm), where CBP, BCP, and $Alq_3$ are the ab-

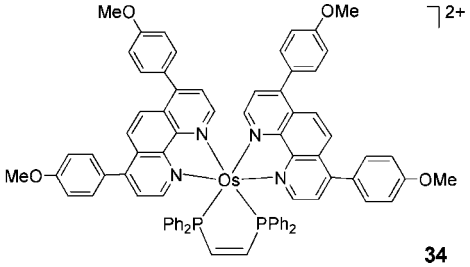


**34**

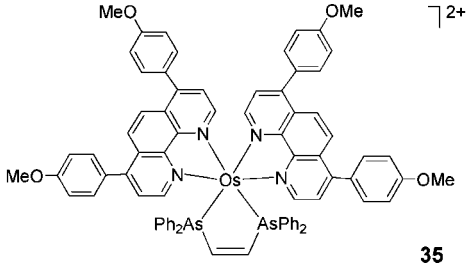


**35**

 © 2006 Wiley-VCH Verlag GmbH & Co. KGaA, Weinheim 

breviations for 4,4′-*N*,*N*′-dicarbazolyl-1,1′-biphenyl, 2,9-dimethyl-4,7-diphenyl-1,10-phenanthroline, and tris(8-hydroxyquinolinato) aluminum(III), respectively. Interestingly, upon switching the hole-transport layer (HTL) from 4,49-bis[*N*-(1-naphthyl)-*N*-phenylamino]biphenyl (NPB) and 9,9-bis{4-[bis(*p*-biphenyl)aminophenyl]}fluorene (BPAPF),[49] a very high initial external quantum efficiency of ca. 20% and luminous efficiency of 27.8 cd $A^{-1}$ are obtained at 1 mA $cm^{-2}$. These examples stand as some of the best red-emitting phosphorescent OLED devices ever fabricated.

## 5. Diphosphane Ruthenium Derivatives

It is indispensable to have neutral $Ru^{II}$ complexes that are suitable for serving as efficient phosphorescent emitters. However, the weaker ligand field strength for the second row transition elements requires the use of strong field ancillary ligands such as phosphane to increase the energy gap of the metal-centered d–d transition, such that the radiationless deactivation associated with the metal–metal and/or metal–ligand bond stretching motion can be significantly suppressed.[19,50] Moreover, the relatively high oxidation potential in $Ru^{II}$ versus that of its third-row $Os^{II}$ analogues demands the employment of extensively conjugated 1-isoquinolyl-substituted chromophores to compensate for the unfavorable metal oxidation potential for the generation of saturated red emission.

Conversely, a series of $Ru^{II}$ complexes **36**–**40** were synthesized following the synthetic scheme established for their osmium counterparts.[9] Their emission spectra are depicted in Figure 7, while photophysical data are listed in Table 6. Moderate to highly intense luminescence in the solid state is obtained for complexes **36**–**38**, with $\lambda_{max}$ at 709, 682, and 632 nm, respectively. In good agreement with the $^3$MLCT emission, the $PPh_2Me$ derivative **37** exhibits a ca. 27-nm hypsochromic shift in $\lambda_{max}$ relative to the $PPhMe_2$ anchored **36**; this result can qualitatively be rationalized in terms of a decrease in the $Ru^{II}$ dπ energy level as a result of the increase in π-accepting strength. For complex **38**, an even more notable hypsochromic shift of 50 nm is achieved. This is apparently caused by the electron-withdrawing effect of the $CF_3$ substituents on pyrazolate, which has a function of lowering the electron density at the $Ru^{II}$ metal center.

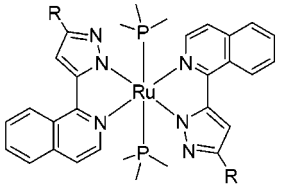

**36**: R = *t*Bu, P = $PPhMe_2$
**37**: R = *t*Bu, P = $PPh_2Me$
**38**: R = $CF_3$, P = $PPh_2Me$

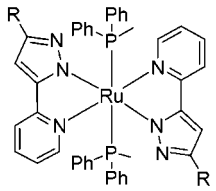

**39**: R = *t*Bu
**40**: R = $CF_3$

With the aim of reducing ligand π conjugation, replacement of the 1-isoquinolyl pyrazolate ligands with less-conjugated 2-pyridyl pyrazolate counterparts afforded the pyridyl complexes **39** and **40**.[51] Although **39** has a low chemical stability upon contact with chlorinated solvents in air, its solid sample gives a faint orange emission at $\lambda_{max}$ = 568 nm at room temperature – a result of increasing the emission gap from that of **36** ($\lambda_{max}$ = 709 nm) by reducing the π-conjugation of the LUMO orbital.

A further increase in the energy gap for **40** is expected owing to the presence of an electronegative $CF_3$ substituent on the chelating pyrazolate, which is expected to stabilize the metal dπ orbitals by lowering the electron density. This viewpoint can be firmly supported by TD–DFT calcula-

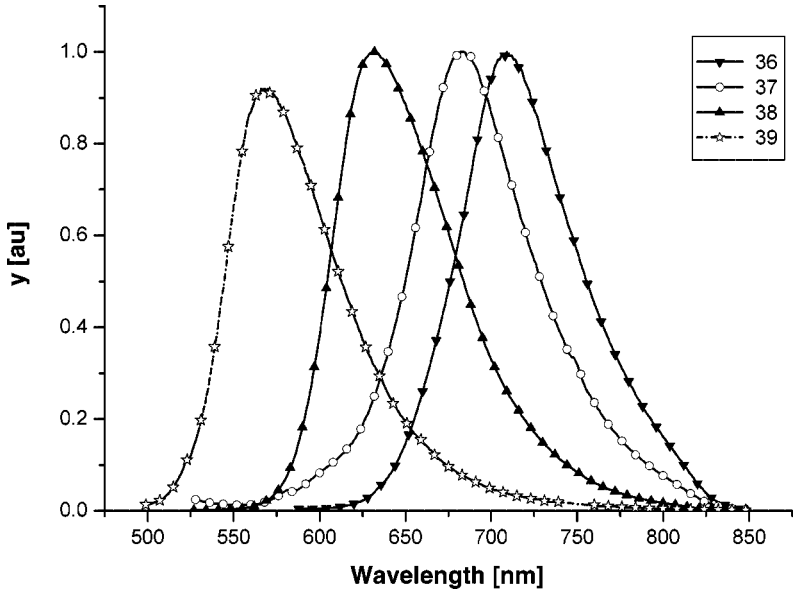


Figure 7. Photoluminescence of $Ru^{II}$ phosphors as solid film at room temperature.

 © 2006 Wiley-VCH Verlag GmbH & Co. KGaA, Weinheim 

Table 6. Photophysical properties of complexes **36**–**40** in $CH_2Cl_2$ and solid state at room temperature.

| | Abs. $\lambda_{max}$ [nm] ($\varepsilon \times 10^3$) | PL $\lambda_{max}$ [nm][a] | $\Phi$[a] | $\tau_{obs.}$ [μs][a] |
|---|---|---|---|---|
| **36** | 336 (20), 363 (14), 462 (13), ≈ 580 (0.9, br.) | 718 (709) | – (0.02) | – (1.06) |
| **37** | 332 (20), 361 (15), 455 (12), ≈ 566 (1, br.) | 700 (682) | – (0.02) | – (0.64) |
| **38** | 320 (25), 353 (13), 446 (17), ≈ 523 (1, br.) | 636 (632) | 0.01 (0.24) | 0.10 (1.82) |
| **39** | 309 (19), 395 (10), 443 (1), ≈ 493 (1, br.) | – (568) | – (0.001) | – (0.16) |
| **40** | 297 (22), 392 (12), ≈ 460 (0.7, br.) | – | – | – |

[a] Data in parentheses are measured in the solid state at room temperature.

tions. As shown by the absorption data listed in Table 6, complex **40** apparently exhibits the highest $^1$MLCT absorption (ca. 460 nm) among all other $Ru^{II}$ complexes prepared (493–580 nm). The TD–DFT results of **40** show that the lowest-energy triplet state involves metal dd character (≈64%), while the typical $^3$MLCT state increases in energy and becomes a second lowest excited state.[51]

As for the OLED applications, a multilayer device using 24 wt.-% of **38** as a dopant emitter in a CBP host and with NPB as a hole transport layer exhibits saturated red emission with an external quantum efficiency of 5.10%, luminous efficiency of 5.74 cd $A^{-1}$, and power efficiency of 2.62 lm $W^{-1}$, while incorporation of a thin layer of PEDOT/PSS between ITO and NPB gives an optimized result with external quantum efficiency of 7.03%, luminous efficiency of 8.02 cd $A^{-1}$, and power efficiency of 2.74 lm $W^{-1}$ at 20 mA $cm^{-2}$. The nonionic nature, high emission quantum efficiency, and short radiative lifetime are believed to be the key factors responsible for this unprecedented behavior. In contrast, fabrication of OLED devices using the ionic emitting materials can only produce devices with poor performances,[52] although the related $Ru^{II}$ complexes have been extensively utilized in light-emitting electrochemical cells (LECs),[53] in which the excessive mobile counterions facilitate the electrochemical redox processes required for generation of high efficiency steady-state radiance.

## 6. Concluding Remarks

With the aim of optimizing the performance of organic light-emitting diodes, research on the transition-metal complexes evidently still offers great prospects. In this review, we demonstrate the power of $Os^{II}$ and $Ru^{II}$ fragments in supporting a variety of ligands, such as those of $[Os(CO)_3]$-substituted diketonate or quinolinolate complexes, $[Os(CO)_2]$ derivatives involving diimine or pyridyl azolate complexes, diphosphane-substituted osmium and ruthenium derivatives, which result in complexes with great luminescent properties. We also show the importance of merging theoretical and experimental observations, providing timely feedback for further rational design of numerous functionalized luminescent complexes. In this regard, we formulate a fundamental issue regarding a generalized radiationless deactivation process, i.e. the first-order perturbation incorporating the spin–orbit coupling from various orbital configurations (e.g. $^3\pi\pi^*$ or $^3d_\pi\pi^*$). In this approach, mixing between $^3\pi\pi^*$ and $^3d_\pi\pi^*$ apparently gains a certain preference for facilitating the $S_1 \rightarrow T_1$ intersystem crossing rate (and likewise the $T_1 \rightarrow S_1$ process). As a result, the intersystem crossing rate can be qualitatively predicted through theoretical frontier orbital analyses in combination with, for example, X-ray structural determination. As for the case of neutral $Ru^{II}$ complexes, we trust that the design of ligands for averting the incorporation of metal dd character into the lowest triplet state plays a key role in increasing the luminescent behavior; this strategy should be equally applicable to other systems incorporating second-row transition-metal elements.

In view of OLED applications, a broad range of color tuning from red to blue has been achieved by derivatization of either pyridine or azolate segments as well as by variation in the electronic properties of the central metal atom by adjusting the ancillary ligands. Accordingly, we have reviewed a number of C-linked pyridyl azolate based $Os^{II}$ and $Ru^{II}$ complexes with regard to making OLEDs with excellent performance. It is thus possible that these pyridyl azolate based metal complexes, after full optimization, will eventually meet the expected industrial demand. Further extension of the chapter of $Os^{II}$ transition-metal complexes is also of great interest. On the basis of a similar principle, coarse as well as fine-tuning of ligands, especially the pyridyl azolate based complexes, toward the near-IR region with high luminescent efficiency is feasible, making possible their future applications in other fields such as near-IR imaging, optical communication, and photovoltaic systems, etc. We thus believe that the results as well as the perspectives presented in this review should spur continuous interest in the design and preparation of luminescence materials incorporating both $Os^{II}$ and $Ru^{II}$ elements.

[1] a) A. M. Powe, K. A. Fletcher, N. N. St. Luce, M. Lowry, S. Neal, M. E. McCarroll, P. B. Oldham, L. B. McGown, I. M. Warner, *Anal. Chem.* **2004**, *76*, 4614; b) W. R. Browne, N. M. O'Boyle, J. J. McGarvey, J. G. Vos, *Chem. Soc. Rev.* **2005**, *34*, 641; c) J. N. Demas, B. A. DeGraff, *Coord. Chem. Rev.* **2001**, *211*, 317.

[2] a) S. Leininger, B. Olenyuk, P. J. Stang, *Chem. Rev.* **2000**, *100*, 853; b) S.-S. Sun, A. J. Lees, *Coord. Chem. Rev.* **2002**, *230*, 171; c) S. M. Woessner, J. B. Helms, J. F. Houlis, B. P. Sullivan, *Inorg. Chem.* **1999**, *38*, 4380; d) V. W.-W. Yam, *Chem. Commun.* **2001**, 789.

[3] a) F. Li, M. Zhang, J. Feng, G. Cheng, Z. Wu, Y. Ma, S. Liu, J. Sheng, S. T. Lee, *Appl. Phys. Lett.* **2003**, *83*, 365; b) D. Xu, K. T. Khin, W. E. Van der Veer, J. W. Ziller, B. Hong, *Chem.*

 © 2006 Wiley-VCH Verlag GmbH & Co. KGaA, Weinheim 

*Eur. J.* **2001**, *7*, 2425; c) P. Spellane, R. J. Watts, A. Vogler, *Inorg. Chem.* **1993**, *32*, 5633.
[4] a) M. A. Baldo, D. F. O'Brien, Y. You, A. Shoustikov, S. Sibley, M. E. Thompson, S. R. Forrest, *Nature* **1998**, *395*, 151; b) E. Holder, B. M. W. Langeveld, U. S. Schubert, *Adv. Mater.* **2005**, *17*, 1109; c) X. Gong, J. C. Ostrowski, G. C. Bazan, D. Moses, A. J. Heeger, *Appl. Phys. Lett.* **2002**, *81*, 3711.
[5] a) Y. Kawamura, K. Goushi, J. Brooks, J. J. Brown, H. Sasabe, C. Adachi, *Appl. Phys. Lett.* **2005**, *86*, 071104; b) C. Adachi, M. A. Baldo, M. E. Thompson, S. R. Forrest, *J. Appl. Phys.* **2001**, *90*, 5048.
[6] a) M. A. Baldo, M. E. Thompson, S. R. Forrest, *Pure Appl. Chem.* **1999**, *71*, 2095; b) C. Adachi, M. A. Baldo, S. R. Forrest, M. E. Thompson, *Appl. Phys. Lett.* **2000**, *77*, 904.
[7] a) H. Zhen, C. Jiang, W. Yang, J. Jiang, F. Huang, Y. Cao, *Chem. Eur. J.* **2005**, *11*, 5007; b) J. Kalinowski, J. Mezyk, F. Meinardi, R. Tubino, M. Cocchi, D. Virgili, *Appl. Phys. Lett.* **2005**, *98*, 063532; c) M. A. Baldo, C. Adachi, S. R. Forrest, *Phys. Rev. B* **2000**, *62*, 10967.
[8] a) S.-W. Lai, C.-M. Che, *Top. Curr. Chem.* **2004**, *241*, 27; b) B. Ma, P. I. Djurovich, M. E. Thompson, *Coord. Chem. Rev.* **2005**, *249*, 1501; c) J. Kavitha, S.-Y. Chang, Y. Chi, J.-K. Yu, Y.-H. Hu, P.-T. Chou, S.-M. Peng, G.-H. Lee, Y.-T. Tao, C.-H. Chien, A. J. Carty, *Adv. Funct. Mater.* **2005**, *15*, 223.
[9] Y.-L. Tung, S.-W. Lee, Y. Chi, L.-S. Chen, C.-F. Shu, F.-I. Wu, A. J. Carty, P.-T. Chou, S.-M. Peng, G.-H. Lee, *Adv. Mater.* **2005**, *17*, 1059.
[10] E. A. Medlycott, G. S. Hanan, *Chem. Soc. Rev.* **2005**, *34*, 133.
[11] a) V. W.-W. Yam, V. C.-Y. Lau, L.-X. Wu, *J. Chem. Soc. Dalton Trans.* **1998**, 1461; b) A. Vogler, H. Kunkely, *Coord. Chem. Rev.* **2000**, *200–202*, 991; c) D. R. Striplin, G. A. Crosby, *Coord. Chem. Rev.* **2001**, *211*, 163.
[12] Y.-L. Chen, S.-W. Li, Y. Chi, Y.-M. Cheng, S.-C. Pu, Y.-S. Yeh, P.-T. Chou, *ChemPhysChem* **2005**, *6*, 2012.
[13] J. Li, P. I. Djurovich, B. D. Alleyne, M. Yousufuddin, N. N. Ho, J. C. Thomas, J. C. Peters, R. Bau, M. E. Thompson, *Inorg. Chem.* **2005**, *44*, 1713.
[14] Y.-L. Chen, C. Sinha, I.-C. Chen, K.-L. Liu, Y. Chi, J.-K. Yu, P.-T. Chou, T.-H. Lu, *Chem. Commun.* **2003**, 3046.
[15] J.-K. Yu, Y.-M. Cheng, Y.-H. Hu, P.-T. Chou, Y.-L. Chen, S.-W. Lee, Y. Chi, *J. Phys. Chem. B* **2004**, *108*, 19908.
[16] a) D. S. Tyson, C. R. Luman, X. Zhou, F. N. Castellano, *Inorg. Chem.* **2001**, *40*, 4063; b) L.-Q. Song, J. Feng, X.-S. Wang, J.-H. Yu, Y.-J. Hou, P.-H. Xie, B.-W. Zhang, J.-F. Xiang, X.-C. Ai, J.-P. Zhang, *Inorg. Chem.* **2003**, *42*, 3393; c) W. Goodall, J. A. G. Williams, *Chem. Commun.* **2001**, 2514; d) A. Del Guerzo, S. Leroy, F. Fages, R. H. Schmehl, *Inorg. Chem.* **2002**, *41*, 359.
[17] a) S. Shtykov, G. Melnikov, I. Goryacheva, *J. Mol. Struct.* **1999**, *482–483*, 699; b) J. A. Murillo Pulgarin, A. A. Molina, M. T. Alanon Pardo, *Anal. Chim. Acta* **2000**, *423*, 85; c) T. Perez-Ruiz, C. Martinez-Lozano, V. Tomas, J. Martin, *J. Pharm. Biomed. Anal.* **2003**, *32*, 225.
[18] Y. Sato, M. Morimoto, H. Segawa, T. Shimidzu, *J. Phys. Chem.* **1995**, *99*, 35.
[19] S. Zalis, I. R. Farrell, A. Vlcek, *J. Am. Chem. Soc.* **2003**, *125*, 4580.
[20] J. R. Lakowicz, *Principles of Fluorescence Spectroscopy*, Kluwer Academic/Plenum Publishers, New York, **1999**, ch. 6.
[21] Y.-M. Cheng, Y.-S. Yeh, M.-L. Ho, P.-T. Chou, P.-S. Chen, Y. Chi, *Inorg. Chem.* **2005**, *44*, 4594.
[22] a) M. Muccini, M. A. Loi, K. Kenevey, R. Zamboni, N. Masciocchi, A. Sironi, *Adv. Mater.* **2004**, *16*, 861; b) V. A. Montes, G. Li, R. Pohl, J. Shinar, P. Anzenbacher Jr, *Adv. Mater.* **2004**, *16*, 2001; c) M. Colle, J. Gmeiner, W. Milius, H. Hillebrecht, W. Brutting, *Adv. Funct. Mater.* **2003**, *13*, 108.
[23] R. Ballardini, G. Varani, M. T. Indelli, F. Scandola, *Inorg. Chem.* **1986**, *25*, 3858.
[24] M. Klessinger, M J. Michl, *Excited States and Photochemistry of Organic Molecules*, VCH, New York, **1995**, ch. 2.
[25] H. Kunkely, A. Vogler, *Chem. Phys. Lett.* **2003**, *376*, 226.
[26] Y.-L. Chen, S.-W. Lee, Y. Chi, K.-C. Hwang, S. B. Kumar, Y.-H. Hu, Y.-M. Cheng, P.-T. Chou, S.-M. Peng, G.-H. Lee, S.-J. Yeh, C.-T. Chen, *Inorg. Chem.* **2005**, *44*, 4287.
[27] a) P. A. Anderson, F. R. Keene, T. J. Meyer, J. A. Moss, G. F. Strouse, J. A. Treadway, *J. Chem. Soc. Dalton Trans.* **2002**, 3820; b) G. H. Allen, R. P. White, D. P. Rillema, T. J. Meyer, *J. Am. Chem. Soc.* **1984**, *106*, 2613.
[28] P.-C. Wu, J.-K. Yu, Y.-H. Song, Y. Chi, P.-T. Chou, S.-M. Peng, G.-H. Lee, *Organometallics* **2003**, *22*, 4938.
[29] J.-K. Yu, Y.-H. Hu, Y.-M. Cheng, P.-T. Chou, S.-M. Peng, G.-H. Lee, A. J. Carty, Y.-L. Tung, S.-W. Lee, Y. Chi, C.-S. Liu, *Chem. Eur. J.* **2004**, *10*, 6255.
[30] a) A. Vogler, H. Kunkely, *Top. Curr. Chem.* **2001**, *213*, 143; b) M. M. Glezen, A. J. Lees, *J. Am. Chem. Soc.* **1988**, *110*, 3892.
[31] P. J. Hay, *J. Phys. Chem. A* **2002**, *106*, 1634.
[32] N. J. Turro, *Modern Molecular Photochemistry*, University Science Books, Mill Valley, California, **1991**, ch. 6, p. 170.
[33] a) A. B. Tamayo, B. D. Alleyne, P. I. Djurovich, S. Lamansky, I. Tsyba, N. N. Ho, R. Bau, M. E. Thompson, *J. Am. Chem. Soc.* **2003**, *125*, 7377; b) T. Karatsu, T. Nakamura, S. Yagai, A. Kitamura, K. Yamaguchi, Y. Matsushima, T. Iwata, Y. Hori, T. Hagiwara, *Chem. Lett.* **2003**, *32*, 886.
[34] S.-W. Li, Y.-M. Cheng, Y.-S. Yeh, C.-C. Hsu, P.-T. Chou, S.-M. Peng, G.-H. Lee, Y.-L. Tung, P.-C. Wu, Y. Chi, F.-I. Wu, C.-F. Shu, *Chem. Eur. J.* **2005**, *11*, 6347.
[35] M.-L. Ho, F.-M. Hwang, P.-N. Chen, Y.-H. Hu, Y.-M. Cheng, K.-S. Chen, G.-H. Lee, Y. Chi, P.-T. Chou, *Org. Biomol. Chem.* **2006**, *4*, 98.
[36] Y.-L. Tung, P.-C. Wu, C.-S. Liu, Y. Chi, J.-K. Yu, Y.-H. Hu, P.-T. Chou, S.-M. Peng, G.-H. Lee, Y. Tao, A. J. Carty, C.-F. Shu, F.-I. Wu, *Organometallics* **2004**, *23*, 3745.
[37] Y.-L. Tung, S.-W. Lee, Y. Chi, Y.-T. Tao, C.-H. Chien, Y.-M. Cheng, P.-T. Chou, S.-M. Peng, C.-S. Liu, *J. Mater. Chem.* **2005**, *15*, 460.
[38] C. M. Che, T. F. Lai, W. C. Chung, W. P. Schaefer, H. B. Gray, *Inorg. Chem.* **1987**, *26*, 3907.
[39] B. D. Gupta, V. Singh, R. Yamuna, T. Barclay, W. Cordes, *Organometallics* **2003**, *22*, 2670.
[40] a) A. Tsuboyama, H. Iwawaki, M. Furugori, T. Mukaide, J. Kamatani, S. Igawa, T. Moriyama, S. Miura, T. Takiguchi, S. Okada, M. Hoshino, K. Ueno, *J. Am. Chem. Soc.* **2003**, *125*, 12971; b) F.-M. Hwang, H.-Y. Chen, P.-S. Chen, C.-S. Liu, Y. Chi, C.-F. Shu, F.-I. Wu, P.-T. Chou, S.-M. Peng, G.-H. Lee, *Inorg. Chem.* **2005**, *44*, 1344.
[41] F.-I. Wu, P.-I. Shih, C.-F. Shu, Y.-L. Tung, Y. Chi, *Macromolecules* **2005**, *38*, 9028.
[42] F.-I. Wu, P.-I. Shih, Y.-H. Tseng, G.-Y. Chen, C.-H. Chien, C.-F. Shu, Y.-L. Tung, Y. Chi, A. K.-Y. Jen, *J. Phys. Chem. B* **2005**, *109*, 14000.
[43] a) Y.-Y. Noh, C.-L. Lee, J.-J. Kim, K. Yase, *J. Chem. Phys.* **2003**, *118*, 2853; b) M. Uchida, C. Adachi, T. Koyama, Y. Taniguchi, *J. Appl. Phys.* **1999**, *86*, 1680; c) F.-C. Chen, S. C. Chang, G. He, S. Pyo, Y. Yang, M. Kurotaki, J. Kido, *J. Polym. Sci., Part B: Polym. Phys.* **2003**, *41*, 2681.
[44] T. M. Brown, J. S. Kim, R. H. Friend, F. Cacialli, R. Daik, W. J. Feast, *Appl. Phys. Lett.* **1999**, *75*, 1679.
[45] Y.-H. Niu, Y.-L. Tung, Y. Chi, C.-F. Shu, J. H. Kim, B. Chen, J. Luo, A. J. Carty, A. K.-Y. Jen, *Chem. Mater.* **2005**, *17*, 3532.
[46] a) B. Carlson, G. D. Phelan, W. Kaminsky, L. Dalton, X. Jiang, S. Liu, A. K.-Y. Jen, *J. Am. Chem. Soc.* **2002**, *124*, 14162; b) X. Jiang, A. K.-Y. Jen, B. Carlson, L. R. Dalton, *Appl. Phys. Lett.* **2002**, *80*, 713.
[47] X. Jiang, A. K. Y. Jen, B. Carlson, L. R. Dalton, *Appl. Phys. Lett.* **2002**, *81*, 3125.
[48] J. H. Kim, M. S. Liu, A. K.-Y. Jen, B. Carlson, L. R. Dalton, C.-F. Shu, R. Dodda, *Appl. Phys. Lett.* **2003**, *83*, 776.
[49] C.-W. Ko, Y.-T. Tao, *Synth. Met.* **2002**, *126*, 37.
[50] M. K. Nazeeruddin, R. Humphry-Baker, D. Berner, S. Rivier, L. Zuppiroli, M. Graetzel, *J. Am. Chem. Soc.* **2003**, *125*, 8790.

 © 2006 Wiley-VCH Verlag GmbH & Co. KGaA, Weinheim 

[51] Y.-L. Tung, L.-S. Chen, Y. Chi, S.-W. Lee, P.-T. Chou, Y.-M. Cheng, E. Y. Li, G.-H. Lee, C.-F. Shu, F.-I. Wu, A. J. Carty, C.-S. Liu, *Adv. Funct. Mater.* **2006**, *16*, 1615–1626.
[52] a) H. Xia, C. Zhang, X. Liu, S. Qiu, P. Lu, F. Shen, J. Zhang, Y. Ma, *J. Phys. Chem. B* **2004**, *108*, 3185; b) J. Yang, K. C. Gordon, *Chem. Phys. Lett.* **2003**, *372*, 577.
[53] a) G. Kalyuzhny, M. Buda, J. McNeill, P. Barbara, A. J. Bard, *J. Am. Chem. Soc.* **2003**, *125*, 6272; b) H. Rudmann, S. Shimada, M. F. Rubner, *J. Appl. Phys.* **2003**, *94*, 115; c) J. D. Slinker, A. A. Gorodetsky, M. S. Lowry, J. Wang, S. Parker, R. Rohl, S. Bernhard, G. G. Malliaras, *J. Am. Chem. Soc.* **2004**, *126*, 2763.

Received: April 24, 2006
Published Online: July 13, 2006

 © 2006 Wiley-VCH Verlag GmbH & Co. KGaA, Weinheim 

DOI: 10.1002/ejic.200600365

# The Two-Step Spin Conversion in a Supramolecular Triple Helicate Dinuclear Iron(II) Complex Studied by Mössbauer Spectroscopy

**Yann Garcia,*[a] C. Matthias Grunert,[b] Sergey Reiman,[b] Olivier van Campenhoudt,[a] and Philipp Gütlich*[b]**

*Dedicated to Professor Hans-Georg von Schnering on the occasion of his 75th birthday*

**Keywords:** Spin crossover / Molecular bistability / Supramolecular chemistry / Iron(II) dinuclear compounds / Two-step conversion / Mössbauer spectroscopy

The triple helicate dinuclear iron(II) complex, $[Fe_2(L)_3](ClO_4)_4 \cdot 2H_2O$ (**1**), previously reported by Tuna et al. (*Chem. Eur. J.* **2004**, *10*, 5737), was prepared and characterised by detailed SQUID and $^{57}Fe$ Mössbauer measurements. Compound **1** exhibits a thermochromic two-step spin conversion at $T_{SC}^{(1)}$ ca. 240 K and $T_{SC}^{(2)}$ ca. 120 K, but does not switch its spin state further below 20 K as proven by Mössbauer spectroscopy. The sharp variation of the susceptibility below 20 K is due to zero-field splitting of the remaining iron(II) high-spin species. Applied field $^{57}Fe$ Mössbauer spectroscopy experiments at 4.2 K indicate that the gradual thermal spin conversion from [HS–HS] pairs to [LS–LS] pairs is complete for one half of the $Fe^{II}$ active sites. The presence of a step tracked in the spin-conversion curve and through the variation of the Mössbauer parameters of an uncoupled iron(II) site call for the occurrence of an [LS–HS] intermediate spin state in the plateau region.

(© Wiley-VCH Verlag GmbH & Co. KGaA, 69451 Weinheim, Germany, 2006)

## Introduction

The spin crossover (SCO) phenomenon presumably belongs to one of the most exciting and active field of research in molecular and coordination chemistry[1] as probed by the constantly increasing amount of papers.[2] This phenomenon has been observed for coordination compounds of 3d transition metals such as $d^4$ ($Cr^{II}$, $Mn^{III}$), $d^5$ ($Fe^{III}$, $Mn^{II}$), $d^6$ ($Fe^{II}$, $Co^{III}$) and $d^7$ ($Co^{II}$) ions.[3] Yet, most of the synthetic efforts and physical investigations have been carried out for $Fe^{II}$ mononuclear complexes displaying a wide range of SCO behaviours.[1,2] Recently, synthetic approaches combining the tools of supramolecular and coordination chemistry have been developed because it was realised that bridging active sites through noncovalent and/or covalent bonds could enhance cooperative effects associated to the spin-state change of individual molecules.[4] Such strategy is appealing because it can lead to the observation of a bistability domain that is of great importance for potential applications.[5] It should, however, be used with caution as strong cooperative interactions between spin-changing molecules in the crystal lattice can disfavour, in some cases, the occurrence of spin-state crossover itself.[6,7] The understanding of complex magnetic behaviour as developed in SCO coordination polymers[8] requires a full understanding of the SCO occurring in much simpler compounds such as monomers and oligomers.[9–10] As such, dinuclear $Fe^{II}$ complexes exhibiting a SCO between the high-spin (HS, $^5T_{2g}$) state and the low-spin (LS, $^1A_{1g}$) state in the liquid and solid state have been the subject of intensive preparation and investigations during the last three years.[11–19] The quest for new complexes is motivated by the understanding of the nature and the determination of the proportion of the existing spin pairs for these materials exhibiting gradual, abrupt or stepwise spin conversions. Another motivation stems from the possibility to combine both magnetic exchange and SCO phenomena in the same dinuclear unit[20] leading to multifunctional materials.[21]

Several modules have been used to link the active SCO sites in these binuclear systems: one bridging ligand such as μ-bpym (bpym = 2,2′-bipyrimidine)[11,12,17b] or μ-dicyanamide,[15] two ligands constituting a μ-pyrazolato[16,17] or μ-triazolato bridge,[18] or three benzimidazole bridging ligands leading to an helicate structure presenting a spin con-

[a] Unité de Chimie des Matériaux Inorganiques et Organiques, Département de Chimie, Faculté des Sciences, Université Catholique de Louvain,
Place Louis Pasteur 1, 1348 Louvain-la-Neuve, Belgium
Fax: +32-1047-2330
E-mail: garcia@chim.ucl.ac.be
[b] Institut für Anorganische Chemie und Analytische Chemie, Johannes Gutenberg Universität Mainz,
Staudingerweg 9, 55099 Mainz, Germany
Fax: +49-6131-3922990
E-mail: guetlich@uni-mainz.de

Supporting information for this article is available on the WWW under http://www.eurjic.org or from the author.

 © 2006 Wiley-VCH Verlag GmbH & Co. KGaA, Weinheim 

version in solution.[19] A new series of triple helicate dinuclear $Fe^{II}$ complexes of the type $[Fe_2(L)_3]A_4 \cdot n$Solvent with A = $PF_6^-$, $BF_4^-$ and $ClO_4^-$ was also recently communicated.[22] L is a Schiff base resulting from the condensation of 3*H*-imidazole-4-carbaldehyde with 4,4′-methylenedianiline in methanol. Their crystal structure reveals that the $Fe^{II}$ centres are in a six-coordinate pseudo-octahedral coordination environment bound to three imidazolimine units originating from three different ligand strands. Each ligand strand binds to two metals, and the three ligands wrap around the metal–metal axis leading to a triple helical dinuclear structure (Figure 1). CH···π interactions are noted in the centre of the helix, the Fe···Fe distance being of 11.584(3) Å.[22] These compounds, that were investigated by SQUID measurements over the temperature range 1.8–340 K, where shown to display a thermally induced spin-state conversion. The perchlorate complex of formula $[Fe_2(L)_3](ClO_4)_4 \cdot 2H_2O$ (**1**) attracted our special interest, because it was reported to exhibit a two-step spin conversion with one gradual step at $T_{sco} \approx 180$ K and another very abrupt spin conversion was proposed to take place below ca. 20 K. On this basis, the authors concluded on the existence of a "tristability" phenomenon[22] although no hysteresis effect was observed. Our attention has been drawn to this compound for two main reasons:

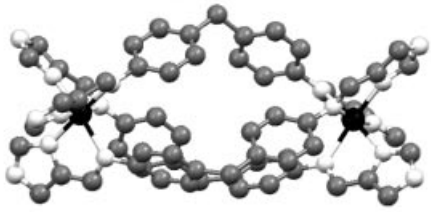

Figure 1. View of the triple-helicate cation in complex **1** adapted from ref.[22]. Hydrogen atoms and perchlorate anions are omitted for clarity. White and grey small spheres correspond to nitrogen and carbon atoms, respectively. The larger black spheres correspond to $Fe^{II}$ ions.

(i) To our experience it is very unlikely, for kinetic reasons, that thermal spin conversion occurs at such low temperatures as below 20 K. The sharp decrease of the $\chi_M T$ values below 20 K may be rather due to zero-field splitting (ZFS) of the approximately 50% of the $Fe^{II}$ ions in the HS state still present in the plateau around 50 K.

(ii) The spin conversion observed between 260 and 50 K gives rise to the question whether it takes place simultaneously in the $Fe^{II}$ dinuclear units, viz. via [HS–HS] ↔ [LS–LS] pairs, or via the intermediate [HS–LS] pairs in the sequence [HS–HS] ↔ [HS–LS] ↔ [LS–LS], as demonstrated to occur in other dinuclear $Fe^{II}$ complexes.[11a,12,14]

We thus re-synthesised and characterised compound **1** in order to clarify its thermally induced spin conversion by a set of precise SQUID and $^{57}$Fe Mössbauer measurements over the temperature range 1.8–300 K. The full differentiation of the existing spin pairs is not a routine exercise, and can only be solved using applied field Mössbauer spectroscopy,[23] which has also been carried out at 4.2 K.

## Results

### Synthesis and Characterisation

Complex **1** was prepared according to the described procedure.[22] The ligand L was first obtained as shown by $^1$H NMR and IR spectroscopy. The complex was also successfully obtained, as an orange powder, as shown by electrospray ionisation mass spectrometry (ESI), C,H,N analysis, IR and UV/Vis spectroscopy. No thermogravimetric measurement was carried out due to the presence of perchlorate anions in this complex. The use of $^{57}$Fe Mössbauer spectroscopy (vide infra), confirmed the nonoxidation of this material since no ferric species were observed for this $Fe^{II}$ compound. Interestingly, this material reveals a distinct colour change on cooling from orange (293 K) to wine brown (77 K). This reversible thermochromic phenomenon was not previously reported.[22]

### Magnetic Susceptibility Measurements

The magnetic data were collected every K over the temperature range 300–1.8 K on cooling and warming modes with an applied field of 10 kOe. The temperature dependence of the molar magnetic susceptibility is displayed in Figure 2 in the form of a $\chi_M T$ vs. $T$ plot, $\chi_M$ being the molar magnetic susceptibility corrected for diamagnetic contributions and $T$ the temperature. At room temperature, $\chi_M T$ is equal to 7.23 $cm^3 mol^{-1} K$, which indicates $Fe^{II}$ ions in the HS state with a $g$ value of 2.197. As $T$ is lowered, $\chi_M T$ initially remains constant down to ca. 280 K and then smoothly decreases in two steps as a result of a HS to LS conversion, reaching a plateau value of 3.43 $cm^3 mol^{-1} K$ at 66 K. The conversion is thus incomplete, ca. 50% of molecules remaining in the HS state. Between 65 and 30 K, the $\chi_M T$ product decreases very slightly, a behaviour that might be attributed to weak antiferromagnetic interactions between paramagnetic spin carriers, as confirmed by applied field $^{57}$Fe Mössbauer spectroscopy. Below 20 K, $\chi_M T$ decreases sharply and falls to 0.96 $cm^3 mol^{-1} K$ at 1.8 K. This behaviour can be attributed to the presence of ZFS splitting due to spin-orbit coupling of the HS $Fe^{II}$ ions, and the preferred Boltzmann population of the lowest levels with decreasing temperatures. The absence of any spin-state crossover at this temperature is unambiguously demonstrated by zero-field $^{57}$Fe Mössbauer spectroscopy (see next section). The spin conversion occurs in two steps with transition temperatures near 240 K and 120 K, respectively. It is of interest to note that the mean transition temperature around 180 K roughly corresponds to the transition temperature deduced from the gradual spin conversion of the first step presented in.[22] As $T$ is increased, the same magnetic behaviour was observed indicating no hysteresis effect in none of the spin conversion branches. This measurement thus confirms the absence of a bistability domain for **1** and does not support the tristability behaviour interpreted in ref.[22]. The calculated $\chi_M T$ values for the nonsolvated dinuclear complex in ref.[22] of 7.70 $cm^3 K mol^{-1}$ and

 © 2006 Wiley-VCH Verlag GmbH & Co. KGaA, Weinheim 

3.81 $cm^3 K mol^{-1}$ at room temperature and 66 K, respectively, are noticeably higher than in Figure 2 of the present study. These magnetic data were not calculated for the non-solvated complex as indicated in the caption to Figure 1 in ref.[22] because considering the molecular mass (1718.93 $g mol^{-1}$) and diamagnetic correction (–220.68·$10^{-6}$ $cm^3 mol^{-1}$) for the crystals of $[Fe_2(L)_3](ClO_4)_4 \cdot 4MeOH \cdot H_2O$, we could fully recover the magnetic data presented in ref.[22]. The calculations in ref.[22] are thus not correct because these SQUID measurements were performed on powders of $[Fe_2(L)_3](ClO_4)_4 \cdot 2H_2O$ as done in our study.

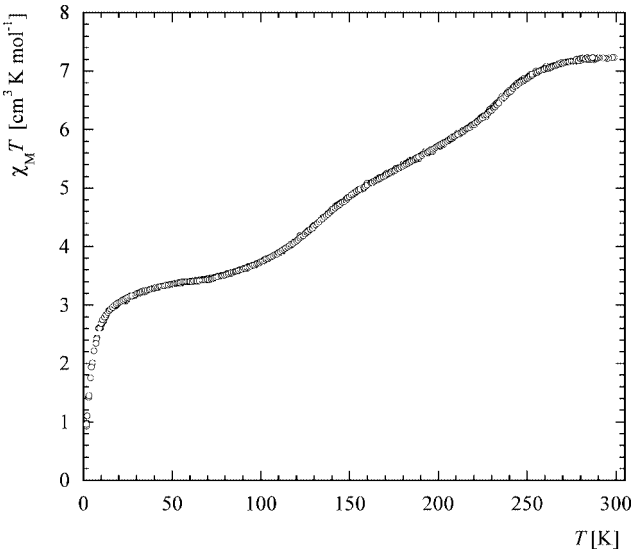


Figure 2. $\chi_M T$ vs. $T$ plot for **1** over the 300–1.8 K range.

### Zero-Field $^{57}Fe$ Mössbauer Spectroscopy

$^{57}Fe$ Mössbauer spectra were recorded for **1** at variable temperatures between 300 K and 4.2 K. Selected spectra are displayed in Figure 3, and detailed values of the Mössbauer parameters at 19 temperatures deduced from least-squares fitting procedures are listed in Table S1 (supp. inf.; for supporting information see also the footnote on the first page of this article). The spectrum at 300 K could be fitted best with two quadrupole doublets. The isomer shift, $\delta$, is 0.98 mm/s for both doublets, the quadrupole splitting, $\Delta$, is 1.20 mm/s and 0.79 mm/s, respectively. Both signals refer to $Fe^{II}$ in the HS state, one denoted as HS(A) with area fraction of ca. 10% and the other as HS(B) with area fraction of ca. 90%. This result is consistent with the magnetic measurements recorded at 300 K that also indicated 100% of HS $Fe^{II}$ ions. On decreasing the temperature the quadrupole splitting of these two $Fe^{II}$ HS species increases (see Figure 4); this is typical for $Fe^{II}$ HS species, where the electric field gradient is dominated by the temperature-dependent valence-electron contribution. The difference between the quadrupole-splitting values of HS(A) and HS(B) is caused by different lattice contributions of opposite sign to that of the valence-electron contributions. The HS(B) signal loses intensity on lowering the temperature at the favour of

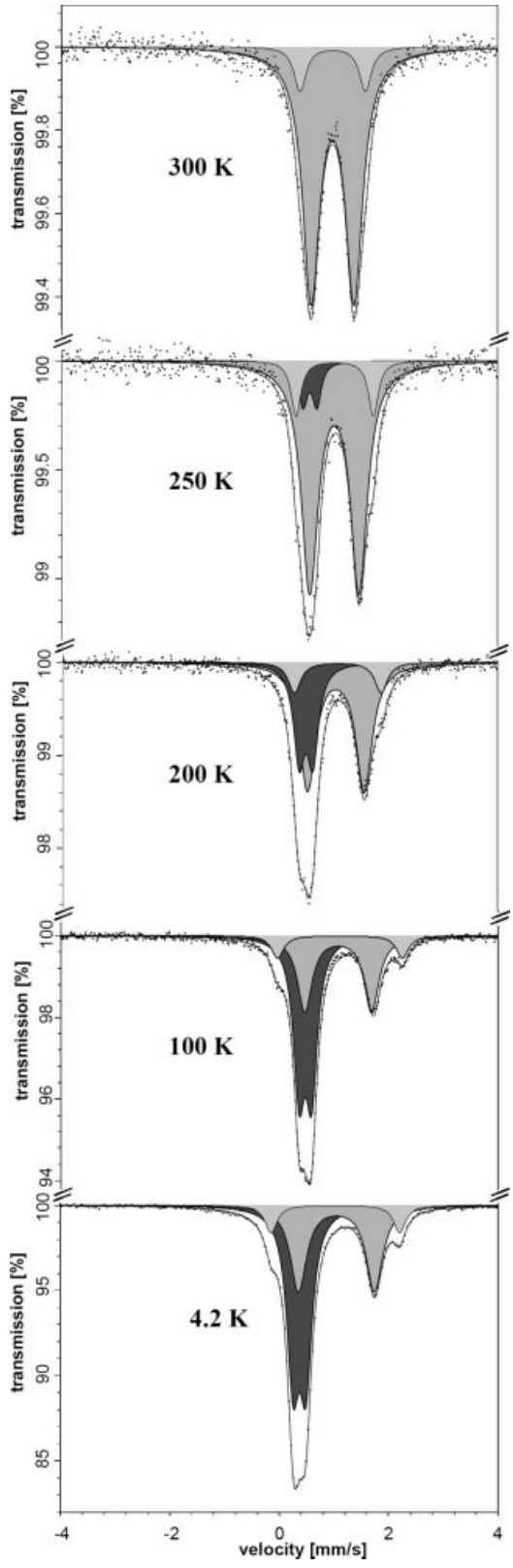


Figure 3. Selected $^{57}Fe$ Mössbauer spectra for **1** over the temperature range 300–4.2 K. The integrals of HS species (A and B) are filled in light grey and grey, respectively, and the LS species (B) in black.

 © 2006 Wiley-VCH Verlag GmbH & Co. KGaA, Weinheim 

a new signal, a poorly resolved quadrupole doublet with parameter values $\delta$ = 0.57 mm/s and $\Delta$ = 0.25 mm/s typical of iron(II) in the LS state, LS(B) that is seen from 270 K downwards. Thus HS(B) undergoes partial thermal spin conversion to reach a plateau, that is also seen in the $\chi_M T$ curve, corresponding to ca. 40% HS(B) and ca. 50% LS(B) at 4.2 K, while the ca. 10% of HS(A) remains essentially constant over the whole temperature range (Figure 5). The partial spin conversion is completed at about 80 K as noted in the $\chi_M T$ curve. The spectrum obtained at 4.2 K shows, in comparison to the spectrum at 61 K, that the strong decrease of the $\chi_M T$ values to very low temperatures, seen in Figure 2, is not caused by a further decrease of the HS molar fraction and, therefore, not caused by a spin transition. The ZFS with increasing Boltzmann population of the lowest electronic levels on lowering the temperature is responsible for the abrupt decrease below 20 K.

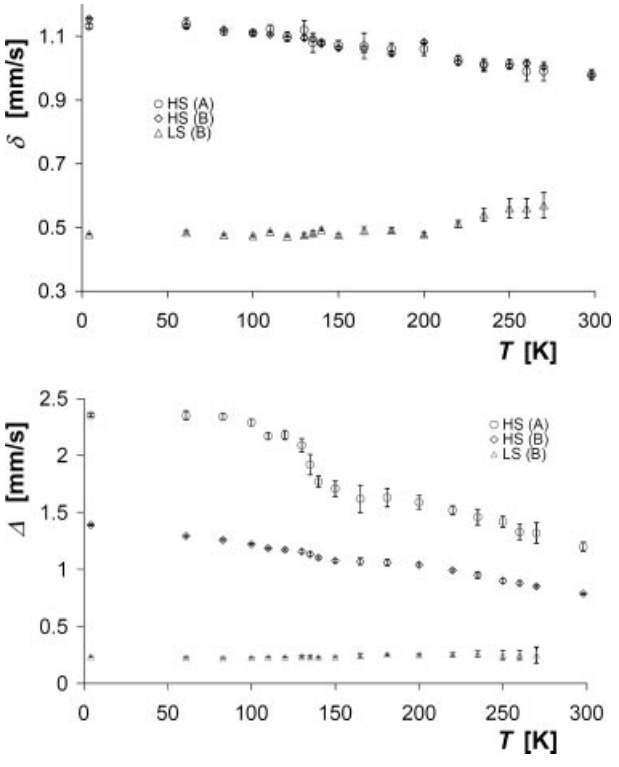


Figure 4. Temperature dependence of isomer shift ($\delta$) and quadrupole splitting values $\Delta$ for site A: ○ (HS) and site B: ◊ (HS), Δ (LS) in **1** over the temperature range 300–4.2 K.

The SCO dinuclear units are thus represented by the HS(B) site. But the nature of the HS(A) site should be discussed. The HS(A) site does not refer to an impurity as a result of oxidation because no ferric species were detected (the isomer shift corresponds to $Fe^{II}$ ions[24] and signal A is present over the whole temperature range of investigation – see Figure 5). It cannot be attributed to the iron starting material, too, for two reasons: (i) The isomer shift of HS(A) is exactly the same as the one of the dinuclear units HS(B) (see Figure 4) (ii) We did not observed a gradual replacement of the lines for this site between ca. 200 K and 250 K, as reported for $[Fe(H_2O)_6](ClO_4)_2$.[25] Therefore,

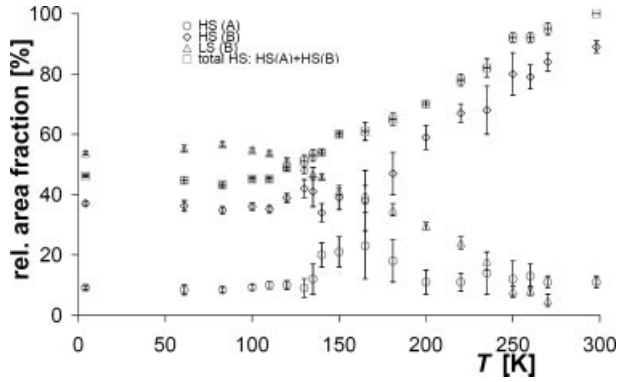


Figure 5. Temperature dependence of the relative area fraction for site A: ○ (HS) and site B: ◊ (HS), Δ (LS) in **1** over the temperature range 300–4.2 K. The HS molar fraction (□) is also given.

HS(A) should correspond to nonswitched complexes that could be either $[Fe_2L_3]^{4+}$ dinuclear units or dinuclear units with one vacant metal centre. Applied field Mössbauer experiments (see next section) have revealed that these species are uncoupled at 4.2 K. We thus favour the hypothesis of the presence of mononuclear species, that is interestingly supported by the detection of mononuclear species in the ESI analysis of **1**.

### Applied Field $^{57}$Fe Mössbauer Spectroscopy

To answer the second question of this study, whether the spin conversion occurs via intermediates of [HS–LS] pair formation or directly from [HS–HS] to [LS–LS] pairs, we have performed a $^{57}$Fe Mössbauer experiment in applied parallel magnetic field (50 kOe) at 4.2 K (Figure 6), as the zero-field Mössbauer spectrum gives only access to the fraction of HS and LS components, irrespective of the nature of the spin pairs involved. The effective hyperfine magnetic field $H_{eff}$ at the iron nuclei of a paramagnetic nonconducting sample in an external field $H_{ext}$ may be estimated as $H_{eff} \approx H_{ext} - [220 - 600(g-2)]\langle S \rangle$, where $\langle S \rangle$ is the atomic spin moment and $g$ the Landé splitting factor.[26,27] The difference between the expectation values of $S$ for $Fe^{II}$ in the LS and in the HS states in [LS–LS], [HS–LS] and [HS–HS] pairs enables one to distinguish unambiguously between the dinuclear units consisting of two possible spin states in an external magnetic field.[11a] To do so, the strength of the external magnetic field should be sufficiently high, and the temperature sufficiently low, in order to avoid magnetic relaxation taking place within the characteristic time window of a Mössbauer experiment ($\approx 10^{-7}$ s). The black spectrum with area fraction of 57% refers to $Fe^{II}$–LS split by a local effective field of 49.4 kOe, which corresponds to the applied magnetic field of 50 kOe, as expected for $\langle S \rangle = 0$ of the LS centres in the [LS–LS]. The grey doublet with area fraction of 37% shows considerable line broadening arising from the interaction with the external field. The value of the effective field calculated from this spectrum is 13 kOe. The two iron HS centres of the [HS–HS] pairs are antiferromagnetically coupled and the resulting spin ladder is thermally popu-

 © 2006 Wiley-VCH Verlag GmbH & Co. KGaA, Weinheim 

lated leading to the expectation value <S> of ca. 0.4, derived from the formula above. This value results from a weak antiferromagnetic coupling between the two HS $Fe^{II}$ centres of the dinuclear species. The light-grey magnetically split spectrum with area fraction of ca. 6% is typical for uncoupled $Fe^{II}$–HS centres with S = 2 each. This fraction corresponds to the HS(A) site. The calculated effective field is 56 kOe. Thus, no [HS–LS] pairs were detected at 4.2 K.

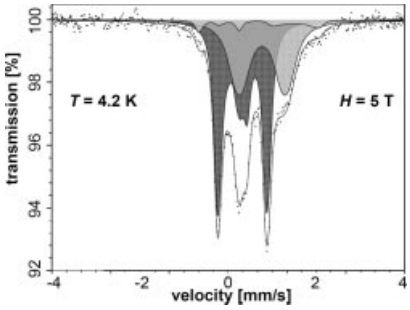


Figure 6. $^{57}$Fe Mössbauer spectrum of **1** recorded at 4.2 K in an external magnetic field of 50 kOe. The signals in black, grey, and light grey refer to LS ions in [LS–LS] pairs, HS ions in [HS–HS] pairs and to uncoupled HS ions, respectively.

## Discussion

The field experiments at 4.2 K may call for the occurrence of thermal spin conversion in the present triple helicate dinuclear system directly from [HS–HS] to [LS–LS] species, contrary to what was observed for the series {[Fe(L)(NCX)$_2$]$_2$(μ-bpym)} (L = bpym, X = S or Se) and (L = bt = 2,2′-bithiazoline and X = S)[23] and for {[Fe(phdia)(NCS)$_2$]$_2$(phdia)} (phdia = 4,7-phenanthroline-5,6-diamine)[14] using the same physical method. According to Real, the predominant factor that determines the existence of [HS–LS] pairs is the strength of intermolecular interactions in these compounds.[28] Indeed, weak intermolecular interactions were taken responsible for the direct [HS–HS] to [LS–LS] transformation observed by applied field Mössbauer spectroscopy in {[Fe(dpa)(NCS)$_2$]$_2$-(bpym)} (dpa = 2,2′-dipyridylamine),[13] but such interactions can be hardly evaluated because this material was not structurally characterised. This is in line with a density functional theory (DFT) study recently reported by Zein and Borshch.[29] These authors have studied the energetics of five binuclear SCO complexes exhibiting different ligand-field strength and different structural arrangements of the bridging ligands. It could be shown that spin transition via the intermediate [HS–LS] pairs occurs only in those cases, where the energy of the [HS–LS] pairs lies below the halfway point between the energies of [LS–LS] and [HS–HS] states. Favourable for this to occur seems to be a planar bridging structure. On the contrary, a strong distortion of the bridging ligand breaks the electronic communication between the metal centres and destabilises the [HS–LS] spin-state shifting it above the halfway point. In such systems, a direct spin transition from [HS–HS] to [LS–LS] is expected and has indeed been observed on the basis of X-ray measurements, for two other binuclear complexes: [(pypzH)(NCSe)Fe(μ-pypz)$_2$Fe(NCSe)(pypzH)]·2H$_2$O displaying an abrupt spin transition[17a] and [{Fe(NCBH$_3$)(4-phpy)}$_2$(μ-bpypz)$_2$] (4phpy = 4-phenylpyridine) presenting a stepwise transition.[16a] This also appears to be the case in the triple helicate system under study that displays a gradual spin conversion despite the fact that all noncoordinated species (perchlorate anions, water and methanol solvent molecules) are involved in hydrogen bonding with the triple-helicate cation in the crystal structure of [Fe$_2$(L)$_3$](ClO$_4$)$_4$·4MeOH·H$_2$O.[22] The use of the very flexible L thus does not propagate efficiently cooperative effects associated with the spin-state change within the dinuclear unit as earlier observed for some Fe coordination polymers exhibiting a gradual SCO behaviour.[30] Interestingly, according to the above mentioned DFT calculations,[29] the step in the spin conversion curve around 180 K (see Figure 2) calls for the presence of an intermediate spin state involving [LS–HS] pairs. This situation is supported by the Zero-field Mössbauer study looking at the evolution of the HS(A) fraction as well as its Mössbauer parameters. On cooling, in the region slightly below the step, the quadrupole splitting increases rather abruptly and follows from then on the usual increase of the quadrupole splitting with decreasing temperature (Figure 4). The jump in quadrupole splitting falls together with the formation of the [LS–LS] pairs. If we consider that the transition would directly occur from [HS–HS] to [LS–LS], we would then rather expect a continuous increase in quadrupole splitting as is commonly observed for iron(II) HS compounds. The ca. 50% gradual spin conversion of **1** thus occurs via [LS–HS] pairs formation and is complete for the involved fraction since these pairs are not present at 4.2 K. A quantitative evaluation of the population of these mixed species could not be obtained by applied field Mössbauer spectroscopy due to the high temperature range of the plateau (≈ 180 K) that would have prevented the trapping of the sample to 4.2 K by rapid cooling. During the pronounced change of the quadrupole splitting of HS(A) the area fraction of this site increases and decreases again (see Figure 5). This indicates transient stiffening of the nearby lattice which shows that these HS sites, although presumably not directly linked to the dinuclear complexes, may take part in the cooperative elastic interactions accompanying the spin conversion process.

## Conclusions

The spin-state-crossover phenomenon in [Fe$_2$(L)$_3$](ClO$_4$)$_4$·2H$_2$O (**1**) investigated by precise SQUID magnetic measurements performed over the temperature range (300–1.8 K) occurs in two steps at ca. 240 K and ca. 120 K. $^{57}$Fe Mössbauer data recorded at 4.2 K have demonstrated that half of the $Fe^{II}$ ions remains in the HS state, and that the second drop of $\chi_M T$ observed below ca. 20 K cannot be attributed to a spin-state conversion. The absence of any hysteresis effect also disapproves the "multistability" char-

 © 2006 Wiley-VCH Verlag GmbH & Co. KGaA, Weinheim 

acter reported for **1**,[22] and confirms the noncooperative character of the spin conversion. Applied field Mössbauer measurements demonstrate the occurrence of a complete thermal spin conversion for half of the iron(II) ions from [HS–HS] to [LS–LS] species because no [LS–HS] species were identified at 4.2 K. The mechanism of this spin-state conversion should, however, involve [LS–HS] species that should be responsible of the presence of the plateau around 180 K in the magnetic measurements (Figure 2) and which are sensed in the Mössbauer parameters of an uncoupled iron(II) site. Further experiments are planned to confirm the presence of these mixed species in this novel system.

## Experimental Section

**General:** All reagents and solvents were used as received from commercial sources. $^1$H NMR spectra were recorded with a Gemini 200–92, 200 MHz spectrometer. The solvent residual peak has been set as a reference. CHN analyses have been performed by the Zentrale Analytik of the Institute für Organische Chemie (Mainz). IR spectra were collected with a BioRad FTS-135 spectrometer using KBr pellets. UV spectra in solution were recorded with a Cary 50 spectrometer and diffuse reflectance spectra on solids were recorded with a CARY 5E spectrophotometer using polytetrafluoroethylene as a reference. Mass spectra were recorded with a Thermo Finnigan LCQ Ion Trap spectrometer using ESI mode and detecting positive ions. Magnetic susceptibilities were measured over the temperature range 1.8–300 K with a cooling and heating rate of 2 K/min with a Quantum Design MPMS*XL* SQUID magnetometer equipped with a 50-kOe magnet operating at 10 kOe. Magnetic data were corrected for diamagnetic contributions, which were estimated from Pascal's constants. $^{57}$Fe Mössbauer spectra were recorded in transmission geometry with a conventional constant-acceleration spectrometer with a room temperature $^{57}$Co(Rh) source over the temperature range (300–83 K). The samples were sealed in a Plexiglas sample holder. For the 4.2 K experiment, the samples were mounted in a helium-bath cryostat with a $^{57}$Co(Rh) source that was kept at 4.2 K. A superconducting magnet was applied to create a magnetic field directed parallel to the wave vector of the $\gamma$-quanta. The spectra were fitted to Lorentzians using Recoil 1.05 Mössbauer Analysis Software[31] assuming equal Debye–Waller factors of the HS and LS states of the $Fe^{II}$ ions. All isomer shifts refer to natural Fe at room temperature.

**Synthesis of L:** The L ligand has been prepared as a white solid by a condensation reaction of 4,4′-methylenedianiline and 3*H*-imidazole-4-carboxaldehyde in methanol according to ref.[22]. $^1$H NMR (200 MHz, DMSO, 25 °C): $\delta$ = 8.43 (s, 1 H, $H^{im}$), 7.82 (s, 1 H, $H^{2/4}$); 7.64 (s, 1 H, $H^{2/4}$), 7.24 (d, $J$ = 7.6 Hz, 2 H, $H^{Ph}$), 7.15 (d, $J$ = 7.6 Hz, 2 H, $H^{Ph}$), 3.96 ppm (s, 1 H, $CH_2$) ppm. IR (KBr): $\tilde{\nu}$ = 3021 (w), 2907 (w), 2827 (*w*), 1629 (vs), 1600 (s), 1541 (vw), 1501 (s), 1437 (m), 1414 (*w*), 1351 (w), 1330 (*w*), 1299 (w), 1222 (*m*), 1201 (*w*), 1170 (w), 1148 (sh), 1109 (w), 1093 (m), 1014 (w), 990 (m), 977 (sh), 918 (w), 873 (m), 844 (m), 808 (w), 787 (w), 753 (w), 709 (w), 622 (s), 601 (w), 539 (m) cm$^{-1}$.

**Synthesis of 1:** The complex $[Fe_2L_3](ClO_4)_4{\cdot}2H_2O$ was prepared as an orange powder according to a procedure slightly adapted from that in ref.[22] substituting the addition of $LiClO_4$ by $Fe(ClO_4)_2{\cdot}6H_2O$ to avoid the presence of unwanted cationic species and a few mg of ascorbic acid to prevent oxidation of $Fe^{II}$ ions. Yield: 0.097 g (67%). $C_{63}H_{58}Cl_4Fe_2N_{18}O_{18}$ (1608.77): calcd. C 47.04, H 3.63, N 15.67; found C 47.10, H 3.67, N 15.58. IR (KBr): $\tilde{\nu}$ = 3131 (br), 2932 (w), 2853 (w), 1620 (vs), 1599 (s), 1558 (w), 1540 (w), 1506 (s), 1501 (sh), 1437 (m), 1294 (m), 1232 (w), 1207 (w), 1090 (vs), 1009 (m), 935 (vw), 892 (m), 861 (w), 814 (m), 756 (w), 708 (w), 625 (s), 544 (w) cm$^{-1}$. UV/Vis (PTFE): $\lambda_{max}$ = 470 nm (MLCT), 880 nm ($^5E \leftarrow {}^5T_2$). UV/Vis (MeCN): $\lambda_{max}$ = 282 ($\pi$–$\pi^*$), 306 ($\pi$–$\pi^*$), 460 (MLCT), 825 ($^5E \leftarrow {}^5T_2$). ESI-MS (MeCN): *m*/*z* = 1473 $[Fe_2(L)_3(ClO_4)_3]^+$, 1118 $[Fe_2(L)_2(ClO_4)_3]^+$, 817 $[Fe_2(L\text{-}H)(L\text{-}2H)]^+$, 686 $[Fe_2(L)_3(ClO_4)_2]^{2+}$, 636 $[Fe_2(L)_2(L\text{-}H)(ClO_4)]^{2+}$, 586 $[Fe_2(L)(L\text{-}H)_2]^{2+}$, 459 $[Fe_2(L)(L\text{-}H)(ClO_4)]^{2+}$, 409 $[Fe(L\text{-}H)]^+$, 355 $[HL]^+$. The synthesis carried out with the same reagents as in ref.[22] led to the same analytical results.

***CAUTION!*** No problems were encountered during the preparation of the perchlorate complex described in this work. However, suitable care must be taken when handling such potentially explosive materials.

**Supporting Information** (see footnote on the first page of this article): Overview of the $^{57}$Fe-Mössbauer parameters for **1**.

## Acknowledgments

This work was partly funded by the Deutsche Forschungsgemeinschaft (Priority Programme No.1137, Molecular Magnetism, and the CNRS-DFG project Gu 95/59), the Fonds der Chemischen Industrie, the Materialwissenschaftliches Forschungszentrum der Universität Mainz and the Fonds Special de Recherche de l'Université Catholique de Louvain.

[1] a) P. Gütlich, A. Hauser, H. Spiering, *Angew. Chem.* **1994**, *106*, 2109; *Angew. Chem. Int. Ed. Engl.* **1994**, *33*, 2024; b) P. Gütlich, Y. Garcia, H. A. Goodwin, *Chem. Soc. Rev.* **2000**, *29*, 419; c) P. Gütlich, Y. Garcia, H. Spiering, "From Molecules to Materials, IV", Wiley-VCH, **2003**, *8*, 271.

[2] P. Gütlich, H. A. Goodwin (Eds.), "Spin Crossover in Transition Metal Compounds", *Top. Curr. Chem.* **2004**, *233–235*, Springer, Berlin, Heidelberg.

[3] Y. Garcia, P. Gütlich, in: "Spin Crossover in Transition Metal Compounds, II", (Eds.: P. Gütlich, H. A. Goodwin), *Top. Curr. Chem.* **2004**, *234*, 49.

[4] a) O. Kahn, E.Codjovi, Y. Garcia, P. J. van Koningsbruggen, R. Lapouyade, L. Sommier, in: Molecule-Based Magnetic Materials (Eds: M. M. Turnbull, T. Sugimoto, L. K. Thompson), *ACS Symposium Series*, American Chemical Society: Washington, **1996**, *644*, p. 298; b) O. Kahn, Y. Garcia, J.-F. Létard, C. Mathonière, in *Supramolecular Engineering of Synthetic Metallic Materials. Conductors and Magnets* (Eds.: J. Veciana, C. Rovira, D. B. Amabilino), *NATO ASI Series C*, **1999**, vol. 518, Kluwer Academic Publishers: Dordrecht, p. 127.

[5] a) O. Kahn, J. Kröber, C. Jay, *Adv. Mater.* **1992**, *4*, 718; b) O. Kahn, C. Jay-Martinez, *Science* **1998**, *279*, 44.

[6] D. L. Reger, J. R. Gardinier, M. D. Smith, A. M. Shahin, G. J. Long, L. Rebbouh, F. Grandjean, *Inorg. Chem.* **2005**, *44*, 1582.

[7] Y. Garcia, G. Bravic, C. Gieck, D. Chasseau, W. Tremel, P. Gütlich, *Inorg. Chem.* **2005**, *44*, 9723.

[8] Y. Garcia, V. Niel, M. C. Muñoz, J. A. Real, *Top. Curr. Chem.* **2004**, *233*, 229.

[9] a) Y. Garcia, P. Guionneau, G. Bravic, D. Chasseau, J. A. K. Howard, O. Kahn, V. Ksenofontov, S. Reiman, P. Gütlich, *Eur. J. Inorg. Chem.* **2000**, 1531; b) G. Psomas, N. Bréfuel, F. Dahan, J.-P. Tuchagues, *Inorg. Chem.* **2004**, *43*, 4590.

[10] a) E. Breuning, M. Ruben, J.-M. Lehn, F. Renz, Y. Garcia, V. Ksenofontov, P. Gütlich, E. K. Wegelius, K. Rissanen, *Angew. Chem.* **2000**, *112*, 2563; *Angew. Chem. Int. Ed.* **2000**, *39*, 2504; b) M. Ruben, E. Breuning, J.-M. Lehn, V. Ksenofontov, F. Renz, P. Gütlich, G. B. M. Vaughan, *Chem. Eur. J.* **2003**, *9*, 4422; c) M. Nihei, M. Ui, M. Yokota, L. Han, A. Maeda, H.

 © 2006 Wiley-VCH Verlag GmbH & Co. KGaA, Weinheim 

Kishida, H. Okamoto, H. Oshio, *Angew. Chem.* **2005**, *117*, 6642; *Angew. Chem. Int. Ed.* **2005**, *44*, 6484.
[11] a) J. A. Real, A. B. Gaspar, M. C. Muñoz, P. Gütlich, V. Ksenofontov, H. Spiering, *Top. Curr. Chem.* **2004**, *233*, 167; b) K. S. Murray, C. J. Kepert, *Top. Curr. Chem.* **2004**, *233*, 195.
[12] a) J. A. Real, H. Bolvin, A. Bousseksou, A. Dworkin, O. Kahn, F. Varret, J. Zarembowitch, *J. Am. Chem. Soc.* **1992**, *114*, 4650; b) N. Moussa, G. Molnar, S. Bonhommeau, A. Zwick, S. Mouri, K. Tanaka, J. A. Real, A. Bousseksou, *Phys. Rev. Lett.* **2005**, *94*, 107205/1.
[13] A. B. Gaspar, V. Ksenofontov, J. A. Real, P. Gütlich, *Chem. Phys. Lett.* **2003**, *373*, 385.
[14] V. Ksenofontov, A. B. Gaspar, S. Reiman, V. Niel, J. A. Real, P. Gütlich, *Chem. Eur. J.* **2004**, *10*, 1291.
[15] N. Ortega-Villar, A. L. Thompson, M. C. Muñoz, V. M. Ugalde-Saldivar, A. E. Goeta, R. Moreno-Esparza, J. A. Real, *Chem. Eur. J.* **2005**, *11*, 5721.
[16] a) K. Nakano, N. Suemura, S. Kawata, A. Fuyuhiro, T. Yagi, S. Nasu, S. Morimoto, S. Kaizaki, *Dalton Trans.* **2004**, 982; b) K. Nakano, N. Suemura, K. Yoneda, S. Kawata, S. Kaizaki, *Dalton Trans.* **2005**, *4*, 740; c) K. Nakano, S. Kawata, K. Yoneda, A. Fuyuhiro, T. Yagi, S. Nasu, S. Morimoto, S. Kaizaki, *Chem. Commun.* **2004**, *24*, 2892.
[17] a) B. A. Leita, B. Moubaraki, K. S. Murray, J. P. Smith, J. D. Cashion, *Chem. Commun.* **2004**, 156; b) S. R. Batten, J. Bjernemose, P. Jensen, B. A. Leita, K. S. Murray, B. Moubaraki, J. P. Smith, H. Toftlund, *Dalton Trans.* **2004**, 3370.
[18] M. H. Klingele, B. Moubaraki, J. D. Cashion, K. S. Murray, S. Brooker, *Chem. Commun.* **2005**, *8*, 987.
[19] a) L. J. Charbonière, A. F. Williams, C. Piguet, G. Bernarinelli, E. Rivara-Minten, *Chem. Eur. J.* **1998**, *4*, 485; b) S. G. Telfer, B. Bocquet, A. F. Williams, *Inorg. Chem.* **2001**, *40*, 4818.
[20] S. Brooker, P. G. Plieger, B. Moubaraki, K. S. Murray, *Angew. Chem.* **1999**, *111*, 424; *Angew. Chem. Int. Ed.* **1999**, *38*, 408.
[21] A. B. Gaspar, V. Ksenofontov, M. Seredyuk, P. Gütlich, *Coord. Chem. Rev.* **2005**, *249*, 2661.
[22] F. Tuna, M. R. Lees, G. J. Clarkson, M. J. Hannon, *Chem. Eur. J.* **2004**, *10*, 5737.
[23] a) V. Ksenofontov, H. Spiering, S. Reiman, Y. Garcia, A. B. Gaspar, N. Moliner, J. A. Real, P. Gütlich, *Chem. Phys. Lett.* **2001**, *348*, 381; b) V. Ksenofontov, H. Spiering, S. Reiman, Y. Garcia, A. B. Gaspar, J. A. Real, P. Gütlich, *Hyperfine Interact.* **2002**, *141/142*, 47.
[24] N. N. Greenwood, T. C. Gibb, Mössbauer spectroscopy, Chapman and Hall Ltd, London, **1971**.
[25] I. Deszi, L. Keszthelyi, *Solid State Commun.* **1966**, *4*, 511.
[26] R. Zimmermann, G. Ritter, H. Spiering, *Chem. Phys.* **1974**, *4*, 133.
[27] R. Zimmermann, G. Ritter, H. Spiering, D. L. Nagy, *J. Phys.* **1974**, *35*, C6.
[28] J. A. Real, A. B. Gaspar, M. Carmen Muñoz, *Dalton Trans.* **2005**, 2062.
[29] S. Zein, S. A. Borshch, *J. Am. Chem. Soc.* **2005**, *127*, 16197.
[30] a) P. J. van Koningsbruggen, Y. Garcia, O. Kahn, H. Kooijman, A. L. Spek, J. G. Haasnoot, J. Moscovici, K. Provost, A. Michalowicz, L. Fournès, F. Renz, P. Gütlich, *Inorg. Chem.* **2000**, *39*, 1891; b) G. S. Matouzenko, G. Molnar, N. Bréfuel, M. Perrin, A. Bousseksou, S. A. Borshch, *Chem. Mater.* **2003**, *15*, 550; c) S. Imatomi, R. Kitashima, T. Hamamatsu, M. Okeda, Y. Ogawa, N. Matsumoto, *Chem. Lett.* **2006**, *35*, 502.
[31] K. Lagarec, D. G. Rancourt, *Nucl. Instrum. Methods Phys. Res. B* **1997**, *129*, 266.

Received: April 24, 2006
Published Online: July 24, 2006

 © 2006 Wiley-VCH Verlag GmbH & Co. KGaA, Weinheim 

DOI: 10.1002/ejic.200600523

# "To Bend or not To Bend?" Both! The Planar and Bent Structures of $[(Ph_3P)_4Rh_2(\mu\text{-}F)_2]$

**William J. Marshall,*[a] Gabriel Aullón,*[b] Santiago Alvarez,[b] Kerwin D. Dobbs,[a] and Vladimir V. Grushin*[a]**

**Keywords:** Isomerism / Rhodium / Fluorine / X-ray diffraction / Theoretical calculations

The first experimental evidence is presented for planar–bent isomerism of complexes of the type $[L_4M_2(\mu\text{-}X)_2]$. Both the planar and bent forms have been detected for *the same composition*, $[(Ph_3P)_4Rh_2(\mu\text{-}F)_2]$, with full exclusion of any variation in such factors as the nature of the metal, ligand, counterion, and solvent of co-crystallization. Computational studies point to weak C–H···F intramolecular bonding as an additional factor affecting the choice between the planar and bent geometries.

(© Wiley-VCH Verlag GmbH & Co. KGaA, 69451 Weinheim, Germany, 2006)

In 1998, two of us published a paper entitled "To Bend or Not To Bend: Dilemma of the Edge-Sharing Binuclear Square Planar Complexes of $d^8$ Transition Metal Ions".[1] This publication provided a structural and theoretical analysis of complexes of the type $[L_4M_2(\mu\text{-}X)_2]$ which are ubiquitous in the chemistry of catalytically important metals such as Ni, Pd, Pt, Rh, and Ir.[1–3] A remarkable feature of such dinuclear complexes is their ability to exist in either planar or bent forms, with the bending angle $\theta$ (Scheme 1) showing a bimodal distribution with maxima at 130 and 180°. Analysis of well over 100 X-ray structures of $[L_4M_2(\mu\text{-}X)_2]$ (X = halogen or chalcogen) indicated that for M = Rh, Pd, and Pt, both bent and planar geometries are commonly observed.[1] The energy cost of bending for such complexes is normally low, often only a few kcal mol$^{-1}$,[1,4] suggesting that both forms could be found experimentally for a single species. Both almost planar and more bent molecules have been found in the crystal structure of *non-square-planar* $[Co_2(\mu\text{-}PPh_2)_2(CO)_6]$.[5] The $Pt_2(\mu\text{-}S)_2$ moiety in complexes of the type $[L_4Pt_2(\mu\text{-}S)_2]$ is commonly bent,[1] though for L = 2-(diphenylphosphanyl)pyridine, a planar structure was reported.[6] Depending on the nature of the counterion X in $[Pt_2(NH_3)_4(\mu\text{-}OH)_2]X_2$, both the planar (X = $NO_3$[7] or 1/2$CO_3$, dihydrate[8]) and bent (X = $ClO_4$[9]) forms of the cation can exist in the crystalline state. The angle $\theta$ for these structures is apparently governed by H-bonding interactions involving the anion, as well as by different packing requirements for different X. There have been no literature reports describing a compound of the type $[L_4M_2(\mu\text{-}X)_2]$, for which *both* planar and bent forms have been detected for *the same composition*, with full exclusion of any variation in the ligand, counterion, solvent of crystallization, and so forth. In this communication, we report the first example of such a complex, $[(Ph_3P)_4Rh_2(\mu\text{-}F)_2]$.

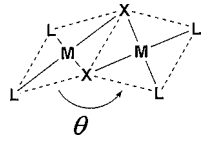


Scheme 1.

Some of us recently reported[10,11] that the fluoro congener of Wilkinson's catalyst, $[(Ph_3P)_3RhF]$, exhibits intriguing reactivity patterns. For instance, heating of $[(Ph_3P)_3RhF]$ in benzene (at 80 °C for 2.5 h) leads to F transfer to one of the P atoms, as shown in Equation (1).[10]

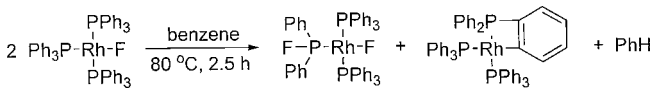


(1)

The reaction occurs by reversible Ph/F exchange as the first key step.[11] In order to determine if the resulting fluoride complex, *trans*-$[(Ph_3P)_2(Ph_2PF)RhF]$, was also capable of undergoing such Ph/F exchange, the thermolysis was conducted for longer periods of time. After 5–6 h at 80 °C, complex reaction mixtures were produced, as judged by $^{19}F$

[a] Central Research and Development, E. I. DuPont de Nemours & Co., Inc., Experimental Station, Wilmington, Delaware 19880-0328, USA
Fax: +1-302-695-8281
E-mail: will.j.marshall@usa.dupont.com
vlad.grushin-1@usa.dupont.com
[b] Departament de Química Inorgànica, Universitat de Barcelona, Diagonal 647, 08028 Barcelona, Spain
Fax: +34-93-490-7725
E-mail: gabriel.aullon@qi.ub.es

Supporting information for this article is available on the WWW under http://www.eurjic.org or from the author.

 © 2006 Wiley-VCH Verlag GmbH & Co. KGaA, Weinheim 

and $^{31}P$ NMR analysis. Because the NMR spectroscopic data did not allow for unambiguous characterization of new compounds, a series of attempts were made to isolate some of the products by fractional crystallization. After the reaction solutions were concentrated and treated with ether and/or hexane, single crystals were obtained. X-ray analysis of one of the gold-yellow square plates revealed the structure of ideally planar ($\theta$ = 180°) $[(Ph_3P)_4Rh_2(\mu\text{-}F)_2]$ (**1**).[12] Poor quality, disordered structures of $\mathbf{1}\cdot 2C_6H_6$ and $\mathbf{1}\cdot 2C_6H_5CH_3$ have been mentioned before.[10] The formation of $[(PPh_3)_4Rh_2(\mu\text{-}F)_2]$ is easily accounted for by dissociation and decomposition of the (in its free form[13,14]) unstable $Ph_2PF$ from $[(Ph_3P)_2(Ph_2PF)RhF]$ to give "$[(PPh_3)_2RhF]$" which would undergo dimerization to **1**.

In another experiment under similar reaction and crystallization conditions, growth of very thin, "two-dimensional" looking yellow plates was noticed. Although the bulkiest crystal in the batch appeared to be only ca. 0.005 mm thick, its X-ray analysis was achieved with a Bruker Smart Apex-II CCD instrument. To our surprise, the crystal was comprised of the same dimer $[(Ph_3P)_4Rh_2(\mu\text{-}F)_2]$ but in a *bent* form ($\theta$ = 133.7°). The planar (**1-p**) and bent (**1-b**) structures are shown in Figures 1 and 2, respectively.[12] The quality of the structure of **1-b** was limited by the crystal size/shape, and structure subtleties such as bond lengths and angles should be looked at with care. Most importantly, the bent geometry was established beyond any doubt.

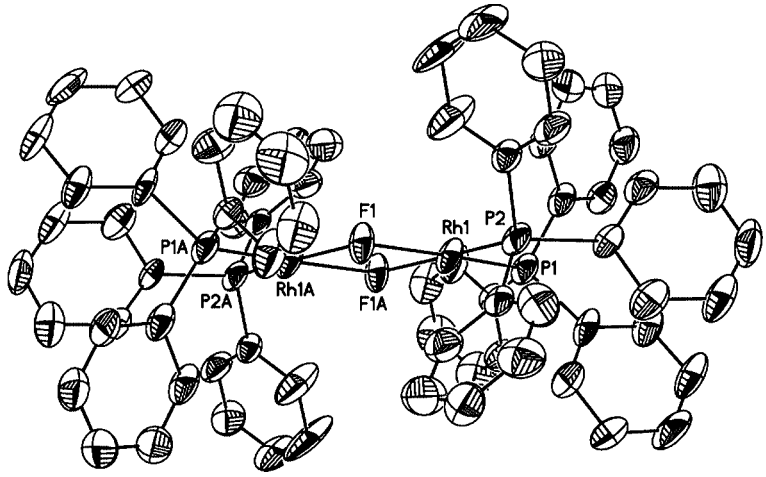


Figure 1. ORTEP view of the planar form of **1** (**1-p**) with thermal ellipsoids drawn to the 50% probability level. Selected bond lengths [Å] and angles [°]: Rh(1)–F(1) 2.131(5), Rh(1)–F(1A) 2.141(5), Rh(1)–P(1) 2.161(3), Rh(1)–P(2) 2.185(3); F(1)–Rh(1)–F(1A) 77.3(2), F(1)–Rh(1)–P(1) 171.4(2), F(1A)–Rh(1)–P(1) 94.2(1), F(1)–Rh(1)–P(2) 93.2(2), F(1A)–Rh(1)–P(2) 170.1(1), P(1)–Rh(1)–P(2) 95.4(1).

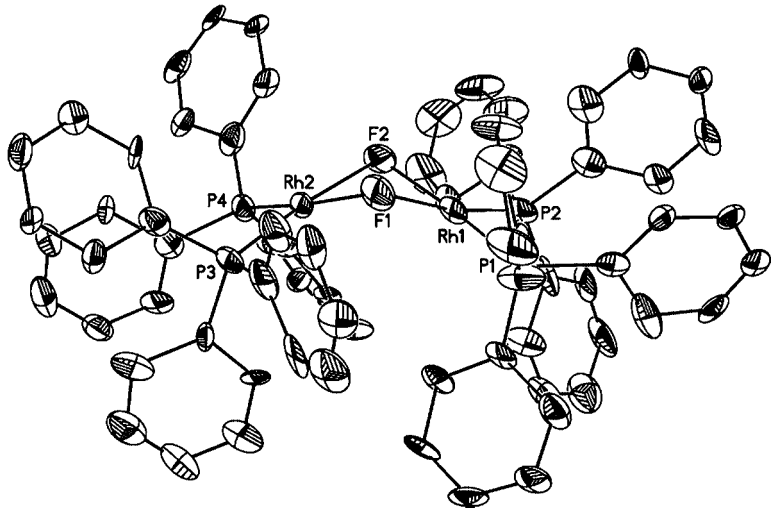


Figure 2. ORTEP view of the bent form of **1** (**1-b**) with thermal ellipsoids drawn to the 50% probability level. Selected bond lengths [Å] and angles [°]: Rh(1)–F(1) 2.02(1), Rh(1)–F(2) 2.07(1), Rh(1)–P(2) 2.116(6), Rh(1)–P(1) 2.146(7), Rh(1)–Rh(2) 2.972(6), Rh(2)–F(1) 2.04(1), Rh(2)–F(2) 2.08(1), Rh(2)–P(4) 2.109(6), Rh(2)–P(3) 2.115(6); F(1)–Rh(1)–F(2) 76.1(5), F(1)–Rh(1)–P(2) 169.8(4), F(2)–Rh(1)–P(2) 95.7(3), F(1)–Rh(1)–P(1) 93.9(4), F(2)–Rh(1)–P(1), 170.0(3), P(2)–Rh(1)–P(1) 94.3(2), F(1)–Rh(1)–Rh(2) 43.1(4), F(2)–Rh(1)–Rh(2) 44.5(3), P(2)–Rh(1)–Rh(2) 133.0(2), P(1)–Rh(1)–Rh(2) 126.82(14), F(1)–Rh(2)–F(2) 75.6(5), F(1)–Rh(2)–P(4) 167.7(3), F(2)–Rh(2)–P(4) 92.1(4), F(1)–Rh(2)–P(3) 95.6(4), F(2)–Rh(2)–P(3) 170.6(4), P(4)–Rh(2)–P(3) 96.6(2), F(1)–Rh(2)–Rh(1) 42.8(3), F(2)–Rh(2)–Rh(1) 44.3(4), P(4)–Rh(2)–Rh(1) 126.6(2), P(3)–Rh(2)–Rh(1) 126.6(2).

 © 2006 Wiley-VCH Verlag GmbH & Co. KGaA, Weinheim 

The structures of **1-p** and **1-b** were carefully examined to see if the Rh centers could be bridged by OH, rather than F. There was no evidence from the X-ray data that either structure contained OH based upon occupancy refinement or the location of hydrogen atoms from difference maps. However, the X-ray data from structures of this quality cannot rule out completely the presence of OH either partially or fully occupied in the bridging position. While direct X-ray evidence cannot be obtained for the lack of OH in the crystals, a number of experimental facts support the formulation $[(Ph_3P)_4Rh_2(\mu\text{-}F)_2]$. Complex **1** has been found[15a] uncommonly stable toward hydrolysis. Rigorously anhydrous conditions[11] were used all through the experiments, from the thermolysis to the fractional crystallization steps. The starting material, $[(Ph_3P)_3RhF]$, was free of $[(Ph_3P)_4Rh_2(\mu\text{-}OH)_2]$ (NMR), the "would-be" product of its hydrolysis. Because there is no fast exchange between $[(Ph_3P)_3RhF]$ and $[(Ph_3P)_4Rh_2(\mu\text{-}OH)_2]$,[15a] the presence of the latter would have been easily detected. The reaction mixtures were studied by $^{19}F$ and $^{31}P$ NMR prior to fractional crystallization in a dry-box. The NMR spectra indicated the presence of **1**[10] and no detectable amounts of $[(Ph_3P)_4Rh_2(\mu\text{-}OH)_2]$ with the characteristic chemical shift and $J$(Rh–P) coupling constant.[15b] It is also noteworthy that unlike **1**, $[(Ph_3P)_4Rh_2(\mu\text{-}OH)_2]$ crystallizes with 2 molecules of benzene under similar conditions.[15c] Measuring NMR spectra of the crystals in bulk supported the formulation $[(Ph_3P)_4Rh_2(\mu\text{-}F)_2]$.[10] The ultimate solution to the problem, however (as also suggested by a referee), would be obtaining NMR spectroscopic data for the very crystals used in the X-ray determination. This, however, is not experimentally feasible. The masses of the crystals of **1-p** ($0.420 \times 0.420 \times 0.030$ mm; $d = 1.454$ g cm$^{-3}$) and **1-b** ($0.320 \times 0.300 \times$ ca. 0.005 mm; $d = 1.618$ g cm$^{-3}$) were ca. 0.0077 mg and 0.00078 mg, respectively. Such quantities are not amenable to a solution NMR study.

The difference in energy between the planar and bent forms ($\Delta E$) of **1** is expected to be small. For instance, the $\Delta E$ value from the ab initio (MP2) study of the planar ($\theta = 180°$) and bent ($\theta = 139.1°$) forms of $[(PH_3)_4Rh_2(\mu\text{-}F)_2]$ has been computed at about 3 kJ mol$^{-1}$,[1] the smallest difference among the series of analogous halide-bridged rhodium complexes. This small value suggests that the observed deviation from the planar geometry of **1** may be easily forced by weak ligand–ligand interactions or different crystal-packing requirements, e.g., due to co-crystallization with different solvents. Remarkably, however, both X-ray-analyzed crystals contained only molecules of **1** and no other co-crystallized species. Examination of the X-ray structures of **1-p** and **1-b** did not reveal any conclusive evidence that the crystal packing might influence the bending along the F···F hinge.

Both structures exhibit intramolecular CH···F close contacts, as defined by being shorter than the sum of the van der Waals radii (2.67 Å). Such CH···F interactions are common for late transition metal fluoride complexes.[16] In the planar form (**1-p**) each F atom interacts with *two ortho*-hydrogen atoms of two different phenyl groups of the same phosphane ligand with the H···F distances of 2.45 and 2.49 Å and corresponding C···F distances of 3.11 and 3.21 Å. In contrast, each fluorine atom of the bent form (**1-b**) exhibits only *one* short CH···F contact. Within the bent molecule, the two non-symmetry related H···F distances are observed at 2.26 and 2.64 Å with C···F distances of 3.02 and 2.92 Å, respectively. At difference with the planar form, the bent form (**1-b**, Figure 2) presents three intermolecular contacts shorter than 3.0 Å to the bridging fluorine atoms. It should be emphasized that because of the limited quality of the structures the presented H···F distances should be interpreted with care.

The unusual existence of both the planar and the bent forms of $[(Ph_3P)_4Rh_2(\mu\text{-}F)_2]$ prompted us to perform exploratory electronic structure calculations in search for an explanation, using DFT at the B3LYP level.[17] First, we verified that the DFT calculations do reproduce the qualitative expectations of the higher level MP2 calculations, using the simplified model complexes $[(R_3P)_4Rh_2(\mu\text{-}F)_2]$ (R = H, Me) in which the phenyl rings in the phosphane ligands were substituted by the computationally affordable H atoms or Me groups. Energy optimization of their bent and planar forms tells us that the two geometries correspond to two nearly isoenergetic minima (characterized through a vibrational analysis; geometries provided in the Supporting Information). We note also that B3LYP calculations have been shown to provide excellent results for the analysis of bending of dinuclear complexes similar to the ones studied here.[18]

These results, combined with the structural information of the short contacts between the bridging fluoride ions and the phenyl groups of the phosphanes, suggest that the F···Ph interactions may govern the choice between the planar and bent forms. Therefore, we studied the interaction between $[(H_3P)_4Rh_2(\mu\text{-}F)_2]$ and an independent benzene molecule. Two energy minima were found for the $[(H_3P)_4Rh_2(\mu\text{-}F)_2]\cdots C_6H_6$ adduct. In one of them, one C–H···F contact is formed while the $Rh_2F_2$ core remains practically planar ($\theta = 165°$). The slight degree of bending is most likely an artefact of the choice of only one benzene ring to study this interaction, because in the experimental planar structure each fluorine atom interacts with one phenyl proton at each side of the molecular plane. In the other minimum found for the adduct, two C–H···F contacts appear between two *ortho*-hydrogen atoms of the *exo*-phenyl group and the two bridging fluorine atoms, quite similar to the intermolecular interaction found in the experimental bent structure **1b**. Moreover, the optimized adduct presents a minimum only at a bent geometry ($\theta = 148°$), thus giving support to the idea that the intermolecular C–H···F contacts favor the bent structure.[19] Further support to the effect of the weak hydrogen bonds governing the molecular geometry comes from calculations on $[(H_2PhP)_4Rh_2(\mu\text{-}F)_2]$, in which the phenyl substituents pointing to the central part of the molecule have been retained. This complex has only one energy minimum with a planar geometry and two short intramolecular F···H contacts (2.14 Å) per fluorine atom.

 © 2006 Wiley-VCH Verlag GmbH & Co. KGaA, Weinheim 

Let us concisely review the factors influencing the bending in $[L_4M_2(\mu\text{-}X)_2]$,[1] as applied to **1**.

**The Nature of the Metal.** Of the metals that may present both planar and bent structures (Rh, Ir, Pd, and Pt), rhodium is the one that favors the most diverse distribution. For the other metals, planar structures prevail for palladium and platinum, while only bent structures are found for iridium.

**The Nature of the Bridging Atom.** Of all the halogens, fluorine is apparently the one, for which the smallest $\Delta E$ value is expected. The ab initio (MP2) calculated values for $\Delta E$ in $[(PH_3)_4Rh_2(\mu\text{-}X)_2]$ are 3, 17, 26, and 31 kJ mol$^{-1}$, for X = F, Cl, Br, and I, respectively.[1]

**The Nature of the Terminal Ligand.** It has been concluded[1] that bent structures for $[L_4M_2(\mu\text{-}X)_2]$ are favored by monodentate ligands L that are good σ-donors/π-acceptors. Strongly σ-donating organic tertiary phosphanes $R_3P$ are also recognized[20] as π-acids, the combination of electronic properties that might be important for stabilization of the M–F bond in late transition metal fluorides.[15a] With regards to steric properties, the bending in **1** is surprising due to the presence of four bulky $PPh_3$ ligands which normally favor only planar structures.[1]

**The Substituents of the Phosphane Ligand.** Given the small energy difference between the planar and bent forms to be expected for the $[(PR_3)_4Rh_2(\mu\text{-}F)_2]$ compounds, the ability of the R groups to form weak hydrogen bonds with the bridging fluorine atoms, combined with the different orientation of the $PR_3$ groups in the planar and bent forms, may stabilize the form with the larger number of short H···F contacts for R = Ph, but not for R = Me.[19]

Very poor solubility of **1** precludes its low-temperature NMR studies in solution. More easily soluble Werner's Rh–F dimer $[(i\text{Pr}_3P)_4Rh_2(\mu\text{-}F)_2]$[21] has been found[11,15a] planar in the solid state. A detailed solution NMR study[21] did not reveal the presence of two or more isomers of $[(i\text{Pr}_3P)_4Rh_2(\mu\text{-}F)_2]$ at room temperature. Because the $^{19}F$ and $^{31}P$ spectral parameters of **1** are similar,[10] the barrier to planar–bent isomerization of both $[(i\text{Pr}_3P)_4Rh_2(\mu\text{-}F)_2]$ and **1** may be low enough to regard **1-p** and **1-b** as conformational isomers.

It is worth mentioning in this communication one more unexpected result obtained during our studies of decomposition of $[(Ph_3P)_3RhF]$ at prolonged heating. After a benzene solution of $[(Ph_3P)_3RhF]$ in glass had been kept at 80 °C for 48 h, the formation of well-shaped yellow crystals was noticed. Although the amount of these crystals was insufficient for full characterization in bulk, single-crystal X-ray analysis was carried out to reveal the astounding structure of a cationic $Rh^I$ complex $[(dppbz)_2Rh]^+X^-$ (**2**)[12] where dppbz = 1,2-bis(diphenylphosphanyl)benzene [Equation (2); Figure 3].[22] The nature of the counterion $X^-$ could not be established unambiguously. In the X-ray analysis, the anion refined well as tetrahedral $[F_3SiO]^-$. Indeed, when the experiment was repeated in a teflon reactor, no precipitation was observed, indicating that the bis(chelate) was not produced. Although the formation of $[(dppbz)_2Rh]^+$ from $[(Ph_3P)_3RhF]$ in glass is certainly remarkable, we did not carry out a detailed study of this reaction [Equation (2)], as it was beyond the scope of this project. It is noteworthy, however, that monitoring the long-term decomposition of $[(Ph_3P)_3RhF]$ by $^{31}P$ and $^{19}F$ NMR spectroscopy indicated intermediate formation of several Rh species bearing $PhPF_2$ as a ligand, i.e. triplets of multiplets with large triplet coupling constants of ca. 900–1100 Hz in the $^{31}P$ NMR spectra. Hence, the originally formed $Ph_2PF$ ligand [Equation (1)] is apparently capable of undergoing further Ph/F exchange with fluoride on Rh, albeit at considerably slower rates.

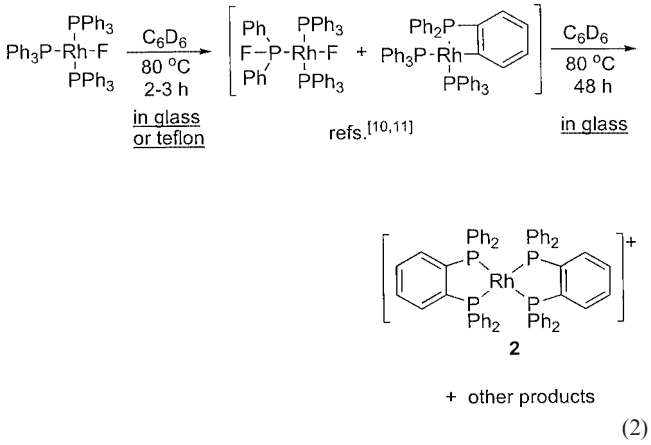


(2)

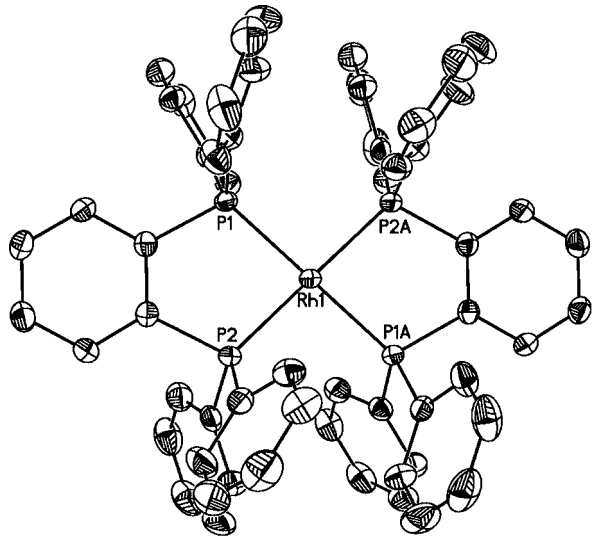


Figure 3. ORTEP view of the cation of **2** with thermal ellipsoids drawn to the 50% probability level. Selected bond lengths [Å] and angles [°]: Rh(1)–P(2A) 2.2807(7), Rh(1)–P(2) 2.2807(7), Rh(1)–P(1) 2.2975(7), Rh(1)–P(1A) 2.2976(7); P(2A)–Rh(1)–P(2) 174.93(3), P(2A)–Rh(1)–P(1) 95.03(2), P(2)–Rh(1)–P(1) 85.00(2), P(2A)–Rh(1)–P(1A) 85.00(2), P(2)–Rh(1)–P(1A) 95.03(2), P(1)–Rh(1)–P(1A) 179.29(3).

In conclusion, we have obtained the first experimental evidence for the existence of a single compound of the type $[L_4M_2(\mu\text{-}X)_2]$ in *both* planar and bent forms. Most importantly, the two forms have been detected for *the same composition*, $[(Ph_3P)_4Rh_2(\mu\text{-}F)_2]$, with full exclusion of any varia-

 © 2006 Wiley-VCH Verlag GmbH & Co. KGaA, Weinheim 

tion in such factors as the nature of the metal, ligand, counterion, and solvent of co-crystallization. For the first time, experimental support has been provided to the previous theoretical results predicting a very small difference in energy between the planar and bent forms for dimers of the type $[L_4M_2(\mu\text{-}X)_2]$. The preliminary DFT study suggests that the hydrogen bonding pattern will govern whether the planar or bent form is isolated.

**Supporting Information** (see footnote on the first page of this article): Tables containing atomic coordinates of the B3LYP optimized geometries of $[(H_3P)_4Rh_2(\mu\text{-}F)_2]$ and $[(Me_3P)_4Rh_2(\mu\text{-}F)_2]$ in their planar and bent conformations, of the adducts formed by benzene and $[(H_3P)_4Rh_2(\mu\text{-}F)_2]$ in the *exo* and *endo* orientations, and of $[(H_2PhP)_4Rh_2(\mu\text{-}F)_2]$. Figures showing the energy of interaction between a benzene molecule and $[Rh_2(\mu\text{-}F)_2(PH_3)_4]$ as a function of the intermolecular F···H distance, calculated at the B3LYP and MP2 levels, and the relative B3LYP energy of $[(Me_3P)_4Rh_2(\mu\text{-}F)_2]$ as a function of the bending angle $\theta$.

## Acknowledgments

This is DuPont CRD Contribution No. 8618. We thank Professor Agustí Lledós for fruitful discussions. Support from Dirección General de Investigación (MEC, project CTQ2005-08123-C02-01/BQU) to G. A. and S. A. is thankfully acknowledged.

[1] G. Aullón, G. Ujaque, A. Lledós, S. Alvarez, P. Alemany, *Inorg. Chem.* **1998**, *37*, 804.
[2] G. Aullón, G. Ujaque, A. Lledós, S. Alvarez, *Chem. Eur. J.* **1999**, *5*, 1391.
[3] G. Aullón, A. Lledós, S. Alvarez, *Inorg. Chem.* **2000**, *39*, 906.
[4] P. Seuret, J. Weber, T. A. Wesolowski, *Mol. Phys.* **2003**, *101*, 2537.
[5] A. D. Harley, R. R. Whittle, G. L. Geoffroy, *Organometallics* **1983**, *2*, 383.
[6] V. W.-W. Yam, P. K.-Y. Yeung, K.-K. Cheung, *J. Chem. Soc., Chem. Commun.* **1995**, 267.
[7] R. Faggiani, B. Lippert, C. J. L. Lock, B. Rosenberg, *J. Am. Chem. Soc.* **1977**, *99*, 777.
[8] B. Lippert, C. J. L. Lock, B. Rosenberg, M. Zvagulis, *Inorg. Chem.* **1978**, *17*, 2971.
[9] K. Sakai, Y. Konno, N. Takayama, S. Takahashi, *Acta Crystallogr., Sect. B* **2004**, *60*, 255.
[10] V. V. Grushin, W. J. Marshall, *J. Am. Chem. Soc.* **2004**, *126*, 3068.
[11] S. A. Macgregor, D. C. Roe, W. J. Marshall, K. M. Bloch, V. I. Bakhmutov, V. V. Grushin, *J. Am. Chem. Soc.* **2005**, *127*, 15304.
[12] Data for all structures were collected at –100 °C using a Bruker APEX-II CCD system equipped with Mo-$K_\alpha$ radiation. Indexing and integration were performed using the Bruker APEX-II software suite and the structures were solved and refined on $|F^2|$ using the SHELXTL software suite. All of the hydrogen atoms were idealized using a riding model. Extra redundant reflections were collected and a SADABS correction was applied to help minimize absorption effects. Specific parameters are as follows. **1-p:** Square plate, $0.42\times0.42\times0.03$ mm, triclinic, $P\bar{1}$, $a$ = 9.130(7), $b$ = 13.311(10), $c$ = 14.106(11) Å, $\alpha$ = 67.872(14), $\beta$ = 71.577(16), $\gamma$ = 72.832(18)°, $V$ = 1476(2) Å$^3$, $\rho_{calcd.}$ = 1.454 g/cm$^3$, $\mu$(Mo) = 0.72 mm$^{-1}$, total data = 18279, unique data = 5507, $2\theta$ range = 3.20–51.40°, parameters = 362, $R$ indices [$I>4\sigma(I)$]: $R_1$ = 0.089, $wR_2$ = 0.203, $R$ indices (all data): $R_1$ = 0.166, $wR_2$ = 0.223, max. difference peak/hole = 2.55/–2.11 e/Å$^3$. **1-b:** Thin plate, $0.320\times0.300\times$ca. 0.005 mm, monoclinic, $P21/c$, $a$ = 13.32(3), $b$ = 34.39(8), $c$ = 13.04(3) Å, $\beta$ = 117.31(4)°, $V$ = 5307(21) Å$^3$, $\rho_{calcd.}$ = 1.618 g/cm$^3$, $\mu$(Mo) = 0.80 mm$^{-1}$, total data = 32033, unique data = 10735, $2\theta$ range = 3.64–52.74°, parameters = 716, restraints = 1365, $R$ indices [$I>4\sigma(I)$]: $R_1$ = 0.168, $wR_2$ = 0.347, $R$ indices (all data): $R_1$ = 0.274, $wR_2$ = 0.381, max. difference peak/hole = 2.97/–2.62 e/Å$^3$. The overall quality of this structure was poor due to the small crystal size. A number of restraints were used to help stabilize the refinement including SAME, FLAT, SIMU and ISOR commands. **2:** Irregular block, $0.17\times0.17\times0.12$ mm, monoclinic, $C2/c$, $a$ = 16.062(3), $b$ = 15.054(3), $c$ = 23.422(4) Å, $\beta$ = 104.797(3)°, $V$ = 5475.6(18) Å$^3$, $\rho_{calcd.}$ = 1.425 g/cm$^3$, $\mu$(Mo) = 0.50 mm$^{-1}$, total data = 21929, unique data = 6807, $2\theta$ range = 3.60–56.66°, parameters = 383, restraints = 13, $R$ indices [$I>4\sigma(I)$]: $R_1$ = 0.039, $wR_2$ = 0.094, $R$ indices (all data): $R_1$ = 0.064, $wR_2$ = 0.101, max difference peak/hole = 0.62/–0.60 e/Å$^3$. CCDC-295809 (**1-p**), -295810 (**1-b**), and -295811 (**2**) contain the supplementary crystallographic data for this paper. These data can be obtained free of charge from The Cambridge Crystallographic Data Centre via www.ccdc.cam.ac.uk/data_request/cif.
[13] C. Brown, M. Murray, R. Schmutzler, *J. Chem. Soc. C* **1970**, 878.
[14] L. Riesel, J. Haenel, G. Ohms, *J. Fluorine Chem.* **1988**, *38*, 335.
[15] a) W. J. Marshall, V. V. Grushin, *Organometallics* **2004**, *23*, 3343; b) V. V. Grushin, V. F. Kuznetsov, C. Bensimon, H. Alper, *Organometallics* **1995**, *14*, 3927; c) H. A. Brune, R. Hemmer, J. Unsin, K. Holl, U. Thewalt, *Z. Naturforsch., Teil B* **1988**, *43*, 487.
[16] For a review, see: L. Brammer, E. A. Bruton, P. Sherwood, *Cryst. Growth Des.* **2001**, *1*, 277.
[17] DFT calculations at the B3LYP level were performed using the LANL2DZ valence double-ζ basis set with pseudopotentials for the innermost core orbitals of the Rh atom, and a similar description for the phosphorus orbitals, supplemented with a d polarization function, while the 6-31g* basis set was used for C, H and F atoms. Interaction energies were corrected for the basis set superposition error by means of the counterpoise method. All calculations were performed with the Gaussian package: M. J. Frisch, G. W. Trucks, H. B. Schlegel, G. E. Scuseria, M. A. Robb, J. R. Cheeseman, V. G. Zakrzewski, J. A. Montgomery, Jr., R. E. Stratmann, J. C. Burant, S. Dapprich, J. M. Millam, A. D. Daniels, K. N. Kudin, M. C. Strain, O. Farkas, J. Tomasi, V. Barone, M. Cossi, R. Cammi, B. Mennucci, C. Pomelli, C. Adamo, S. Clifford, J. Ochterski, G. A. Petersson, P. Y. Ayala, Q. Cui, K. Morokuma, P. Salvador, J. J. Dannenberg, D. K. Malick, A. D. Rabuck, K. Raghavachari, J. B. Foresman, J. Cioslowski, J. V. Ortiz, A. G. Baboul, B. B. Stefanov, G. Liu, A. Liashenko, P. Piskorz, I. Komaromi, R. Gomperts, R. L. Martin, D. J. Fox, T. Keith, M. A. Al-Laham, C. Y. Peng, A. Nanayakkara, M. Challacombe, P. M. W. Gill, B. Johnson, W. Chen, M. W. Wong, J. L. Andres, C. Gonzalez, M. Head-Gordon, E. S. Replogle, J. A. Pople, *Gaussian 98* (Revision A.11), Gaussian, Inc., Pittsburgh, PA, **2001**.
[18] R. Mas-Ballesté, G. Aullón, P. A. Champkin, W. Clegg, C. Mégret, P. González-Duarte, A. Lledós, *Chem. Eur. J.* **2003**, *9*, 5023.
[19] Calculations on the corresponding methane adduct $[(H_3P)_4Rh_2(\mu\text{-}F)_2]\cdots CH_4$ at the B3LYP level gives an interaction energy of less than 1 kJ mol$^{-1}$, pointing to an almost negligible effect of the C–H···F contact. This is in contrast with the non-negligible effect (4 kJ mol$^{-1}$ at the same level of theory) for the benzene adduct $[(H_3P)_4Rh_2(\mu\text{-}F)_2]\cdots C_6H_6$. The attractive nature of the weak hydrogen bonds in the $[(H_3P)_4Rh_2(\mu\text{-}F)_2]\cdots C_6H_6$ adduct has been verified by re-calculating the interaction energy curve at the MP2 level (with correction for the basis set superposition error), that indicates a bonding interaction of some 13 kJ mol$^{-1}$ at an optimum distance of 2.5 Å, and

 © 2006 Wiley-VCH Verlag GmbH & Co. KGaA, Weinheim 

still significant interaction (11 kJ mol$^{-1}$) at 3.0 Å (see Supporting Information, Figure S1).
[20] P. B. Dias, M. E. Minas de Piedade, J. A. Martinho Simões, *Coord. Chem. Rev.* **1994**, *135/136*, 737.
[21] J. Gil-Rubio, B. Weberndorfer, H. Werner, *J. Chem. Soc., Dalton Trans.* **1999**, 1437.
[22] The cation $[(dppbz)_2Rh]^+$ has been reported before, although without structural characterization, see: W. A. Fordyce, G. A. Crosby, *Inorg. Chem.* **1982**, *21*, 1455; C. A. Helms, T. A. Reynolds, G. A. Crosby, *Chem. Phys. Lett.* **1987**, *142*, 99.

Received: June 1, 2006
Published Online: July 21, 2006

 © 2006 Wiley-VCH Verlag GmbH & Co. KGaA, Weinheim 

DOI: 10.1002/ejic.200600562

# Actinide-Transition Metal Heteronuclear Ions and Their Oxides: $\{IrUO\}^+$ as an Analogue to Uranyl

**Marta Santos,[a] Joaquim Marçalo,*[a] António Pires de Matos,[a] John K. Gibson,*[b] and Richard G. Haire[b]**

**Keywords:** Actinides / Ion–molecule reactions / Isolobal relationship / Mass spectrometry / Metal–metal interactions / Uranium

Recent theoretical calculations have shown that Ir should behave as a chemical analogue to N, with the result that $IrUO^+$, like known $NUO^+$, is predicted to be a stable species isoelectronic with $UO_2^{2+}$, the uranyl dication. The target heterometallic analogue to uranyl has now been prepared by direct laser desorption/ionization of a U/Ir alloy, and by oxidation of $UIr^+$ with $N_2O$ and $C_2H_4O$. Properties of $UIr^+$, $UPt^+$, and $UAu^+$ bimetallic ions have been studied. They demonstrate direct actinide–transition metal bonding, and support the concept of "autogenic isolobality".
(© Wiley-VCH Verlag GmbH & Co. KGaA, 69451 Weinheim, Germany, 2006)

## Introduction

Despite that actinide–transition metal (An–$M_{nd}$) bonding has been an important goal in molecular actinide chemistry, remarkably few complexes have been characterized in which an An–$M_{nd}$ bond has been clearly identified (An = Th, U).[1,2] In these complexes, the An–$M_{nd}$ bonding is either mediated by phosphido bridges,[1] or is between the An and a $M_{nd}$-containing fragment, $M_{nd}Cp(CO)_2$ (Cp = *cyclo*-$C_5H_5$),[2] which can be considered an "organometallic pseudohalogen".[3] Accordingly, there to date seem to be no well-established molecular complexes with a direct, unsupported covalent An–$M_{nd}$ bond.

Gaseous $AnM_{nd}$ bimetallics are elementary molecular species incorporating distinct An–$M_{nd}$ bonding. The ThRu, ThRh, ThIr, ThPt, and URh molecules, synthesized in high-temperature vapors, have bond energies of 500 to 600 kJ mol$^{-1}$.[4] Direct An–$M_{5d}$ bonding was also demonstrated with the preparation of the $ThFe^+$ and $UFe^+$ ions by collision-induced dissociation (CID) of $AnFe(CO)_x^+$ ($x$ = 2, 3).[5] In a recent theoretical study, Gagliardi and Pyykkö[6] predicted several stable triatomic species which would incorporate covalent bonds between uranium and 5d transition metals ($M_{5d}$), including $IrUO^+$. According to the concept of "autogenic isolobality",[6,7] Au can behave as a pseudohalogen, Pt as a pseudochalcogen, and Ir as a pseudopnictogen. Thus, $IrUO^+$ can be formally represented as $\{Ir{\equiv}U{=}O\}^+$, which is nominally isoelectronic with $\{N{\equiv}U{=}O\}^+$ and $\{O{=}U{=}O\}^{2+}$ (the uranyl dication);[6] both of the latter have been prepared in the gas phase.[8,9]

In view of recent theoretical predictions of strong U–$M_{5d}$ covalent bonds and stable triatomic species incorporating such bonds, we employed laser desorption/ionization (LDI) of binary An/$M_{5d}$ alloys to synthesize gaseous $AnM_{5d}^+$ bimetallic ions. The synthesis of these ions, and their reactions with nitrous oxide, ethylene oxide, and ethane, are interpreted in the context of "autogenic isolobality",[6,7] and the nature of An–$M_{5d}$ bonds.[6]

## Results and Discussion

In the initial experiments that employed dilute (≈ 2–5 wt.-%) An/Pt alloys (An = Th, Pa, U, Np, Pu, Am, Cm),[10] several diatomic and triatomic ions were produced. These included the bimetallics, $ThPt^+$, $PaPt^+$, $UPt^+$, $NpPt^+$, $PuPt^+$, $AmPt^+$ and $CmPt^+$, the trimetallics $ThPt_2^+$ and $UPt_2^+$, and the bimetallic oxides $OThPt^+$, $OPaPt^+$, $OUPt^+$ and $ONpPt^+$. The appearance of the $OAnPt^+$ (from O contamination in the alloys) only for Th through Np reflects the particularly strong O–$An^+$ bonds there;[10] the suggested atomic connectivities of the oxides are consistent with this strong bonding.

Generation of the $AnPt^+$ ions motivated a LDI study of U/$M_{5d}$ alloys ($M_{5d}$ = Os, Ir, Pt, Au; ≈ 20 wt.-% U). The following three bimetallics were produced in the indicated order of relative yields: $UAu^+ > UPt^+ > UIr^+$; $UOs^+$ was not observed. Illustrative LDI spectra are shown in Figure 1. For each U/$M_{5d}$ ($M_{5d}$ = Au, Pt, Ir) alloy, $U^+$ and $M_{5d}^+$ were produced by LDI, both in an abundance very roughly an order of magnitude greater than that of $UM_{5d}^+$.

[a] Departamento de Química, Instituto Tecnológico e Nuclear, 2686-953 Sacavém, Portugal
Fax: +351-21-994-6185
E-mail: jmarcalo@itn.pt
[b] Chemical Sciences Division, Oak Ridge National Laboratory, Oak Ridge, TN 37831-6375, USA
Fax: +1-865-574-4987
E-mail: gibsonjk@ornl.gov

 © 2006 Wiley-VCH Verlag GmbH & Co. KGaA, Weinheim 

In analogy with high-temperature synthesis of $AnM_{nd}$,[4] the $UM_{5d}^+$ (and other $AnM_{5d}^+$) are presumably formed by coalescence of a neutral atom and monopositive ion in the laser-desorption plume. As the four IE[$M_{5d}$] are in the range of 8.7 eV (Os) to 9.2 eV (Au) and IE[U] = 6.2 eV,[11] electron transfer from U to $M_{5d}^+$ is exothermic by ≥ 2.5 eV and should predominate over U/$M_{5d}^+$ coalescence. A probable mechanism for generation of the $UM_{5d}^+$ is instead association of $U^+$ with $M_{5d}$. It is not possible to be conclusive regarding the bimetallic formation mechanism(s) or the relative yields. However, several atomic properties that might account for the relative $UM_{5d}^+$ yields vary monotonically between Os and Au; for example, the electron affinities {EA/eV}[11] are: Os {1.1} < Ir {1.6} < Pt {2.1} < Au {2.3}. Another factor that likely affects the propensity for coalescence during alloy LDI is the relative volatilities of the transition-metal constituents, as indicated by their vapor pressures at 2500 K{P/Torr}:[12] Os {3·10$^{-6}$} < Ir {6·10$^{-4}$} < Pt {0.04} < Au {17}. In a general sense, the relative yields can be considered to be related to the different electronic structures of the $M_{5d}$. LDI also resulted in the formation of the trimetallics $UAu_2^+$ and (minor) $UPt_2^+$, but not $UIr_2^+$ or $UOs_2^+$. Bimetallic monoxides were also produced by LDI, with the following average relative abundances: $OUAu^+ > OUPt^+ > OUIr^+$ ($OUOs^+$ was not observed). The $OUIr^+$ ion has been predicted as a species comprising a strong formally triple U≡Ir bond, which renders it isoelectronic with dipositive uranyl, $O{=}U{=}O^{2+}$,[6] and $N{\equiv}U{=}O^+$.[8]

Some bimetallic ions were subjected to collision-induced dissociation (CID). Whereas $UAu^+$ fragmented into $U^+$ and Au, there was no evidence for dissociation of $UPt^+$ or $UIr^+$. Although these results suggest a relatively weak $U^+$–Au bond, consistent with single- rather than multiple-bond character, such CID studies are only qualitative. Electronic structure calculations should be performed to assess the validity of these somewhat speculative interpretations of the CID results regarding the relative bond energies. The CID of $OUAu^+$ and $OUPt^+$ resulted exclusively in fragmentation to $OU^+$ and Au or Pt, suggesting that the U–$M_{5d}$ bonds are weaker than the U–O bonds (there was insufficient $OUIr^+$ for a CID study). These latter CID results support the proposed O–U–$M_{5d}$ connectivity – for both the U–$M_{5d}$–O and U–O–$M_{5d}$ connectivities, some $M_{5d}O$ loss would be expected.

To further probe the nature of these $UM_{5d}^+$, they and the constituent atomic metal ions were treated with $N_2O$, $C_2H_4O$ (ethylene oxide) and $C_2H_6$. The results of the primary ion–molecule reactions are summarized in Table 1. In some cases, secondary and higher order reactions were observed, but these are not discussed here.

For a reaction of thermalized ions to occur, the overall process must be exothermic regardless of kinetic considerations. If a reaction does not proceed it may be due to a kinetic barrier rather than endothermicity. Here we only consider thermodynamic limits based on the requirement for exothermicity; no assumptions are made regarding kinetics. In accord with previous results, both $Ir^+$[13a] and $Pt^+$[13] were oxidized to the monoxides by $N_2O$, consistent with the requirement that $D[Ir^+–O]$ ca. 250 kJ mol$^{-1}$[14] and $D[Pt^+–O]$ ca. 322 kJ mol$^{-1}$[15] exceed $D[N_2–O]$ = 167 kJ mol$^{-1}$.[14] That $Au^+$ is unreactive with $N_2O$[13a] may reflect a kinetic or thermodynamic barrier. As reported previously,[8,10a] $U^+$ reacts with $N_2O$ to give $UO^+$ and $UN^+$. The three $UM_{5d}^+$ ions react with $N_2O$ to give $OUAu^+$, $OUPt^+$ and $OUIr^+$, along with $UO^+$ (and $AuN_2$, $PtN_2$ and $IrN_2$ as presumed neutral products). Given the inert charac-

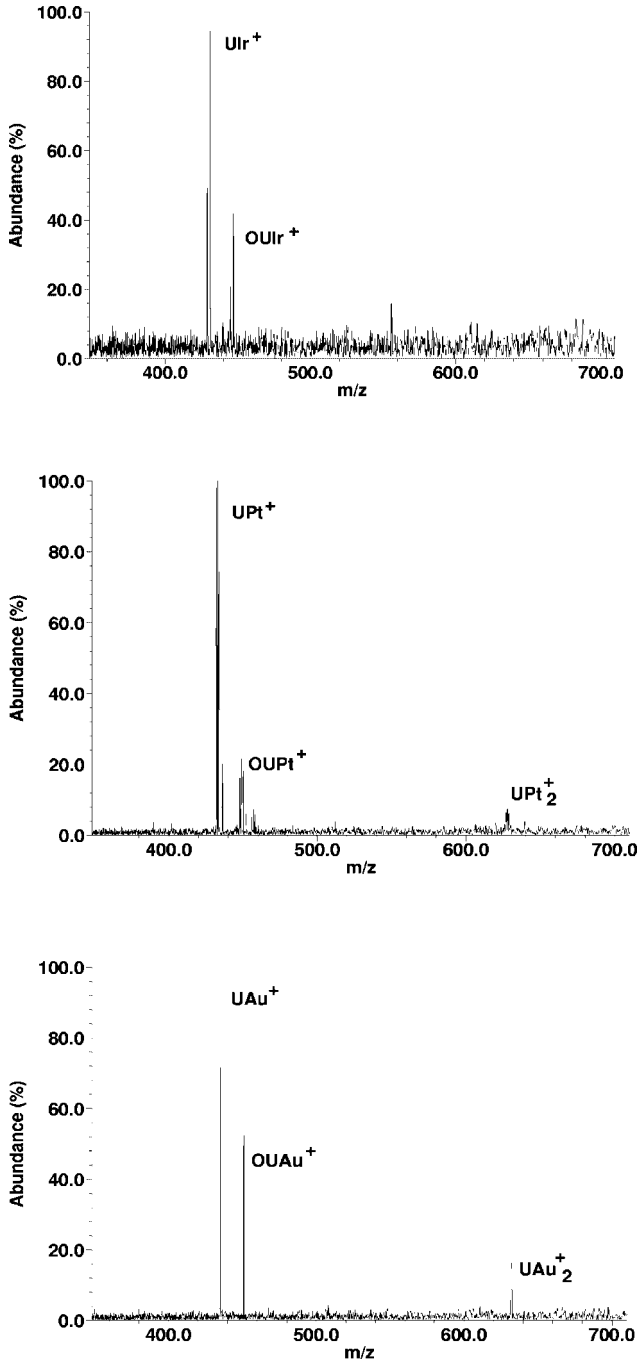


Figure 1. Direct LDI mass spectra for U/Ir (top), U/Pt (middle), and U/Au (bottom) alloys. The two isotopes of Ir and several isotopes of Pt are evident. The minor peaks in the middle spectrum at $m/z$ = 456–460 correspond to the composition $UPtC_2^+$.

 © 2006 Wiley-VCH Verlag GmbH & Co. KGaA, Weinheim 

Table 1. Products, rate constants, and efficiencies for primary reactions of atomic and bimetallic ions.[a]

| Reactant Ion | $N_2O$ Product(s) | $k$ | $k/k_{COL}$ | $C_2H_4O$ Product(s) | $k$ | $k/k_{COL}$ | $C_2H_6$ Product(s) | $k$ | $k/k_{COL}$ |
|---|---|---|---|---|---|---|---|---|---|
| $U^{+}$[b] | $UO^{+}$(60) $UN^{+}$(40) | 3.26 | 0.47 | $UO^{+}$ | 5.89 | 0.34 | – | <0.01 | <0.001 |
| $Ir^{+}$ | $IrO^{+}$ | 1.38 | 0.19 | $IrCH_2^{+}$ | 3.59 | 0.21 | $IrC_2H_4^{+}$(50) $IrC_2H_2^{+}$(50) | 2.21 | 0.23 |
| $Pt^{+}$ | $PtO^{+}$ | 0.17 | 0.024 | $PtCH_2^{+}$ | 2.82 | 0.16 | $PtC_2H_4^{+}$(60) $PtC_2H_2^{+}$(40) | 2.29 | 0.24 |
| $Au^{+}$ | – | <0.01 | <0.001 | $AuCH_2^{+}$ | 1.98 | 0.11 | $AuC_2H_4^{+}$ | 1.86 | 0.19 |
| $UIr^{+}$ | $OUIr^{+}$(70) $UO^{+}$(30) | 0.65 | 0.098 | $OUIr^{+}$ | 4.01 | 0.24 | – | <0.01 | <0.001 |
| $UPt^{+}$ | $OUPt^{+}$(80) $UO^{+}$(20) | 0.64 | 0.095 | $OUPt^{+}$ | 3.50 | 0.21 | – | <0.01 | <0.001 |
| $UAu^{+}$ | $OUAu^{+}$(40) $UO^{+}$(40) $UN^{+}$(20) | 1.93 | 0.29 | $OUAu^{+}$(60) $UO^{+}$(40) | 4.60 | 0.28 | – | <0.01 | <0.001 |

[a] Where more than one product was formed, the relative abundances (%) are indicated in parentheses. Rate constants ($k$) are in units of $10^{-10}$ $cm^3 molecule^{-1} s^{-1}$; $k/k_{COL}$ are the reaction efficiencies.[10c] Absolute rate constants are uncertain by ±50%; relative uncertainties are ±20%. [b] Results for the $U^{+}/N_2O$ and $U^{+}/C_2H_4O$ reactions are from ref.[10a].

ter of bare $Au^{+}$ toward $N_2O$, the formation of $OUAu^{+}$ supports the proposed atomic connectivity. The $OUIr^{+}$ connectivity had been predicted from theory.[6] The $UAu^{+}/N_2O$ reaction produced $NUAu^{+}$, for which the thermodynamic requirement is $D$[N–$UAu^{+}$] ≥ {$D$[N–NO] = 482 kJ mol$^{-1}$}.[14] That both $UO^{+}$[8,10a] and $UPt^{+}$ are oxidized by $N_2O$ is in agreement with the isolobal analogy between $UPt^{+}$ and $UO^{+}$.[6,7] The observation that $UN^{+}$ is unreactive with $N_2O$, while formally isoelectronic $UIr^{+}$ is oxidized to $OUIr^{+}$ by $N_2O$, illustrates that the "autogenic isolobality" concept does not imply absolute correspondence, but rather chemical analogy.[6,7]

Whereas $U^{+}$ is oxidized to $UO^{+}$ by $C_2H_4O$,[10a] the three $M_{5d}^{+}$ react to give carbenes, $M_{5d}CH_2^{+}$ (Table 1). Thus, if the neutral product of the $M_{5d}^{+}/C_2H_4O$ reactions is formaldehyde ($CH_2O$), the thermodynamic requirement is $D$[$M_{5d}^{+}$–$CH_2$] ≥ 334 kJ mol$^{-1}$; if instead the neutral products are CO + $H_2$, the thermodynamic requirement is $D$[$M_{5d}^{+}$–$CH_2$] ≥ 332 kJ mol$^{-1}$.[14] Previous experimental studies have established $D$[$Ir^{+}$–$CH_2$] = 474 ± 3 kJ mol$^{-1}$,[16] $D$[$Pt^{+}$–$CH_2$] ≥ 464 kJ mol$^{-1}$,[17] and $D$[$Au^{+}$–$CH_2$] ≥ 397 kJ mol$^{-1}$.[18] The formation of the triatomic oxides, rather than carbenes, from the $UM_{5d}^{+}/C_2H_4O$ reactions is reminiscent of the $U^{+}/C_2H_4O$ reaction. This suggests that the reactivities of the $UM_{5d}^{+}$ are dominated by the oxophilicity of the uranium metal center, and that the product oxides can be represented as $OUM_{5d}^{+}$. In analogy with the ethane results discussed below, the $U^{+}$-like, rather than $M_{5d}^{+}$-like, reactivity of the $UM_{5d}^{+}$ with $C_2H_4O$ suggests that the transition-metal center has been rendered inert. The thermodynamic requirement for the $C_2H_4O$ oxidation reactions is $D$[O–$UM_{5d}^{+}$] ≥ 354 kJ mol$^{-1}$[14] ($M_{5d}$ = Ir, Pt, Au). The oxidation of the three $UM_{5d}^{+}$ in a similar manner to bare $U^{+}$ provides a further indication of the O–U–$M_{5d}$ connectivities proposed above. Additional calculations are required to establish the energy differences between the different isomers, as well as whether the species are linear (like $UO_2^{2+}$) or bent (like $ThO_2$). The calculations by Gagliardi and Pyykkö[6] indicate that some triatomic uranium-transition metal species adopt a linear structure but the bond angle for $OUIr^{+}$ (or other $OUM_{5d}^{+}$) was not reported.[6]

The appearance of $UO^{+}$ (+ $AuC_2H_4$) from the $UAu^{+}/C_2H_4O$ reaction is consistent with a weaker $U^{+}$-Au bond as compared with the $U^{+}$–Ir and $U^{+}$–Pt bonds. Neither the $UIr^{+}/C_2H_4O$ nor $UPt^{+}/C_2H_4O$ reactions result in $UO^{+}$ (+ $M_{5d}C_2H_4$). This distinctive behavior of $UAu^{+}$ supports the interpretation of the CID results discussed above in terms of the relative U–$M_{5d}$ bond strengths.

The results in Table 1 for reactions with ethane are in agreement with earlier reports for $U^{+}/C_2H_6$,[19] $Ir^{+}/C_2H_6$,[17] and $Au^{+}/C_2H_6$;[18] in an ion beam study of the $Pt^{+}/C_2H_6$ reaction,[20] only $PtC_2H_4^{+}$ (+ $H_2$) was reported, not $PtC_2H_2^{+}$ (+ $2H_2$). In contrast to the bare $M_{5d}^{+}$, but like bare $U^{+}$, the three $UM_{5d}^{+}$ were unreactive towards $C_2H_6$: the reactivity of the transition metal center is evidently "shut off" in the $UM_{5d}^{+}$, in distinct contrast to $Pt_2^{+}$, which is as effective at dehydrogenating $C_2H_6$ as is atomic $Pt^{+}$.[20] The reduced reactivity of $UM_{5d}^{+}$ also contrasts with ions such as $PtCu^{+}$, $PtAg^{+}$ and $PtAu^{+}$, which dehydrogenate methane with an efficiency comparable to that of $Pt_2^{+}$.[21] According to the concept of "autogenic isolobality",[6,7] it can be considered that there are no non-bonding valence electrons at the transition metal centers in Au–$U^{+}$, Pt =$U^{+}$ and Ir≡$U^{+}$. With the lack of available valence electrons at the $M_{5d}$ center, reactivity would disappear, as is observed.

In conclusion, we have synthesized several new $AnPt^{+}$ (An = Th through Cm), and examined the chemistries of $UIr^{+}$, $UPt^{+}$, and $UAu^{+}$ in the general context of "autogenic isolobality", and the prediction of strong actinide–transition metal bonds.[6,7] Our experimental results are consistent with the predicted bonding for these species – specifically, the reactivities of the transition-metal centers are apparently "shut off" in the $UM_{5d}^{+}$ bimetallics. With each of the three reagents, $N_2O$, $C_2H_4O$ and $C_2H_6$, the reactivities of the $UM_{5d}^{+}$ ions were evidently dominated by the U metal center, in agreement with the concept of "autogenic isolobality".[6] To further probe Ir as a pseudopnictogen, Pt as a pseudochalcogen, and Au as a pseudohalogen or pseudohydrogen,[22,23] our future efforts will compare directly reactivities of the $UM_{5d}^{+}$ ($M_{5d}$ = Ir, Pt, Au) and isoelectronic $UX^{+}$, where X is a pnictogen, chalcogen, or halogen (or H). One noteworthy result of the present work was the synthesis

 © 2006 Wiley-VCH Verlag GmbH & Co. KGaA, Weinheim 

of $IrUO^+$, which was predicted to exist as a stable species isoelectronic with uranyl, $OUO^{2+}$.[6]

## Experimental Section

The experimental procedures, described in detail elsewhere,[5,9,10] are briefly summarized here. The atomic and bimetallic ions were produced by direct LDI of arc-melted actinide–transition metal alloys,[10] An/Pt (An = natural Th-232, Pa-231, depleted U, Np-237, Pu-242, Am-243, Cm-248) and $U/M_{5d}$ ($M_{5d}$ = Os, Ir, Pt, Au). The LDI ions directly entered the source cell of a dual cell Finnigan FT/MS 2001-DT FTICR mass spectrometer equipped with a 3-T magnet and controlled by an Odyssey data system; all experiments were performed in the source cell. The $N_2O$ and $C_2H_6$ were commercial gases (>99%); the $C_2H_4O$ was a commercial liquid (>99%) degassed prior to use. The reagents were introduced into the spectrometer through a leak valve to pressures of $3{\cdot}10^{-8}$ to $2{\cdot}10^{-7}$ Torr. Isolation of ions was achieved using single-frequency, frequency-sweep, or SWIFT excitation. The reactant ions were thermalized by collisions with argon, introduced through a leak valve to a constant pressure in the range of $(1–5)\times10^{-6}$ Torr, concurrent with the reagent gas. Thermalization of the reactant ions was confirmed by standard procedures.[5,9,10] The CID experiments were carried out by ion excitation and collision with argon.[5] The pseudo-first-order rate constants, $k$, were determined from the reactant ion decay as a function of time; the collisional rate constants, $k_{COL}$, were calculated as described previously.[10c]

## Acknowledgments

This work was supported by Fundação para a Ciência e a Tecnologia (FCT) and POCI 2010 (co-financed by FEDER), under contract POCI/QUI/58222/2004; and by the Office of Basic Energy Sciences, U.S. Department of Energy under contract DE-AC05-00OR22725 with Oak Ridge National Laboratory. M. Santos is grateful to FCT for a Ph.D. grant.

[1] a) J. M. Ritchey, A. J. Zozulin, D. A. Wrobleski, R. R. Ryan, H. J. Wasserman, D. C. Moody, R. T. Paine, *J. Am. Chem. Soc.* **1985**, *107*, 501–503; b) P. J. Hay, R. R. Ryan, K. V. Salazar, D. A. Wrobleski, A. P. Sattelberger, *J. Am. Chem. Soc.* **1986**, *108*, 313–315.
[2] a) R. S. Sternal, C. P. Brock, T. J. Marks, *J. Am. Chem. Soc.* **1985**, *107*, 8270–8272; b) R. S. Sternal, T. J. Marks, *Organometallics* **1987**, *6*, 2621–2623.
[3] B. E. Bursten, K. J. Novo-Gradac, *J. Am. Chem. Soc.* **1987**, *109*, 904–905.
[4] a) K. A. Gingerich, *Chem. Phys. Lett.* **1973**, *23*, 270–274; b) K. A. Gingerich, *Chem. Phys. Lett.* **1974**, *25*, 523–526; c) K. A. Gingerich, S. K. Gupta, *J. Chem. Phys.* **1978**, *69*, 505–511.
[5] M. C. Vieira, J. Marçalo, A. Pires de Matos, *J. Organomet. Chem.* **2001**, *632*, 126–132.
[6] L. Gagliardi, P. Pyykkö, *Angew. Chem. Int. Ed.* **2004**, *43*, 1573–1576.
[7] P. Pyykkö, M. Patzschke, J. Suurpere, *Chem. Phys. Lett.* **2003**, *381*, 45–52.
[8] C. Heinemann, H. Schwarz, *Chem. Eur. J.* **1995**, *1*, 7–11.
[9] a) H. H. Cornehl, C. Heinemann, J. Marçalo, A. Pires de Matos, H. Schwarz, *Angew. Chem. Int. Ed. Engl.* **1996**, *35*, 891–894; b) J. K. Gibson, R. G. Haire, M. Santos, J. Marçalo, A. Pires de Matos, *J. Phys. Chem. A* **2005**, *109*, 2768–2781.
[10] a) M. Santos, J. Marçalo, A. Pires de Matos, J. K. Gibson, R. G. Haire, *J. Phys. Chem. A* **2002**, *106*, 7190–7194; b) M. Santos, J. Marçalo, J. P. Leal, A. Pires de Matos, J. K. Gibson, R. G. Haire, *Int. J. Mass Spectrom.* **2003**, *228*, 457–465; c) M. Santos, A. Pires de Matos, J. Marçalo, J. K. Gibson, R. G. Haire, R. Tyagi, R. M. Pitzer, *J. Phys. Chem. A* **2006**, *110*, 5751–5759.
[11] NIST Chemistry WebBook – NIST Standard Reference Database Number 69, June **2005** release (http://webbook.nist.gov/chemistry).
[12] O. Kubaschewski, C. B. Alcock, *Metallurgical Thermochemistry*, 5th ed., Pergamon, Oxford, **1979**, pp. 358–377.
[13] a) V. V. Lavrov, V. Blogojevic, G. K. Koyanagi, G. Orlova, D. K. Bohme, *J. Phys. Chem. A* **2004**, *108*, 5610–5624; b) M. Brönstrup, D. Schröder, I. Kretzschmar, H. Schwarz, J. N. Harvey, *J. Am. Chem. Soc.* **2001**, *123*, 142–147; c) X.-G. Zhang, P. B. Armentrout, *Eur. J. Mass Spectrom.* **2004**, *10*, 963–975.
[14] S. G. Lias, J. E. Bartmess, J. F. Liebman, J. L. Holmes, R. D. Levin, W. G. Mallard, *J. Phys. Chem. Ref. Data* **1988**, *17 (Suppl. 1)*.
[15] M. Pavlov, M. R. A. Blomberg, P. E. M. Siegbahn, R. Wesendrup, C. Heinemann, H. Schwarz, *J. Phys. Chem. A* **1997**, *101*, 1567–1579.
[16] F.-X. Li, X.-G. Zhang, P. B. Armentrout, *Int. J. Mass Spectrom.* (published online on March 29, **2006**).
[17] K. K. Irikura, J. L. Beauchamp, *J. Phys. Chem.* **1991**, *95*, 8344–8351.
[18] A. K. Chowdhury, C. L. Wilkins, *J. Am. Chem. Soc.* **1987**, *109*, 5336–5343.
[19] C. Heinemann, H. H. Cornehl, H. Schwarz, *J. Organomet. Chem.* **1995**, *501*, 201–209.
[20] T. Hanmura, M. Ichihashi, T. Kondow, *J. Phys. Chem. A* **2002**, *106*, 11465–11469.
[21] K. Koszinowski, D. Schröder, H. Schwarz, *Angew. Chem. Int. Ed.* **2004**, *43*, 121–124, and references therein.
[22] P. Pyykkö, *Angew. Chem. Int. Ed.* **2004**, *43*, 4412–4456.
[23] L. Gagliardi, *J. Am. Chem. Soc.* **2003**, *125*, 7504–7505.

Received: June 16, 2006
Published Online: July 24, 2006

 © 2006 Wiley-VCH Verlag GmbH & Co. KGaA, Weinheim 

DOI: 10.1002/ejic.200600383

# Supramolecular Silanol Chemistry: Inclusion Complexes of 1,3,5-Tris(diisopropylhydroxysilyl)benzene and 4,4′-Bis(pyridines)

**Jens Beckmann*[a] and Sanna L. Jänicke[a]**

**Keywords:** Supramolecular chemistry / Crystal engineering / Inclusion compounds / Hydrogen bonds / Silicon

The trisilanol 1,3,5-(HO*i*Pr$_2$Si)$_3$C$_6$H$_3$ (**5**), a novel building block for applications in supramolecular chemistry, has been prepared via the intermediates 1,3,5-(H*i*Pr$_2$Si)$_3$C$_6$H$_3$ (**6**) and (Cl*i*Pr$_2$Si)$_3$C$_6$H$_3$ (**7**). The inclusion complexes **5**·0.5H$_2$O, **5**·bpy·0.5H$_2$O, **5**·bpe, **5**·azpy and **5**·bpa have been investigated by X-ray crystallography [bpy = 4,4′-bipyridine, bpe = (*E*)-bis(4-pyridyl)ethylene, azpy = 4,4′-azopyridine, bpa = bis(4-pyridyl)aceylene]. The ratio between donor and acceptor molecules is always 1:1 and the crude supramolecular motifs are very similar for **5**·bpy·0.5H$_2$O, **5**·bpe, **5**·azpy and **5**·bpa. The trisilanol molecules form 1D chains, which are connected by nearly perpendicular 4,4′-bis(pyridine) molecules to give rise to formation of 2D grid networks featuring O–H···O(H)Si and O–H···N hydrogen bonds. Differences are observed in the shape and size of the voids defined by the 2D grids. The smaller voids are blocked by trisilanol molecules of adjacent 2D networks in case of **5**·bpy·0.5H$_2$O and **5**·bpe. In case of **5**·azpy, the larger voids are filled by interpenetration of the same 2D networks.

(© Wiley-VCH Verlag GmbH & Co. KGaA, 69451 Weinheim, Germany, 2006)

## Introduction

Organosilanols are well known for their extensive self-organisation in the solid state, which has led to the observation of a great variety of different hydrogen-bond patterns.[1] In most cases organosilanols form hydrogen bonds with themselves, but occasionally co-crystals with alcohols,[2] ethers[3] and amines[4] have been observed. Whilst the majority of these complexes has been formed inadvertently with solvent and reagent molecules, recently a small number of inclusion complexes has been prepared deliberately by co-crystallisation studies.[5] However, the vast potential of organosilanols in molecular recognition has not yet been exploited for applications in supramolecular chemistry and crystal engineering. The organosilanols used in previous studies lack topological pre-organisation of the silanol sites on a molecular level, a prerequisite for genuine control of supramolecular structures.

Gaining control over solid-state structures requires the judicious choice of molecular building blocks ("synthons") possessing adhesive functional groups ("tectons") with prefixed directionality.[6] 1,3,5-Trimesic acid, 1,3,5-(HOOC)$_3$C$_6$H$_3$ (**1**), the prime building block for organic supramolecular chemistry fulfils this criterion and gives rise to formation of honeycomb ("chicken-wire") networks containing nano-dimensional cavities in the solid state, which may be useful for applications in host–guest chemistry (Scheme 1).[7] Organometallic chemistry can extend the range of useful building blocks for supramolecular chemistry by a wealth of adhesive functional groups.[8] For instance, 1,3,5-benzenetriphosphonic acid, 1,3,5-(H$_2$O$_3$P)$_3$C$_6$H$_3$ (**2**), has been used for co-crystallisation studies with

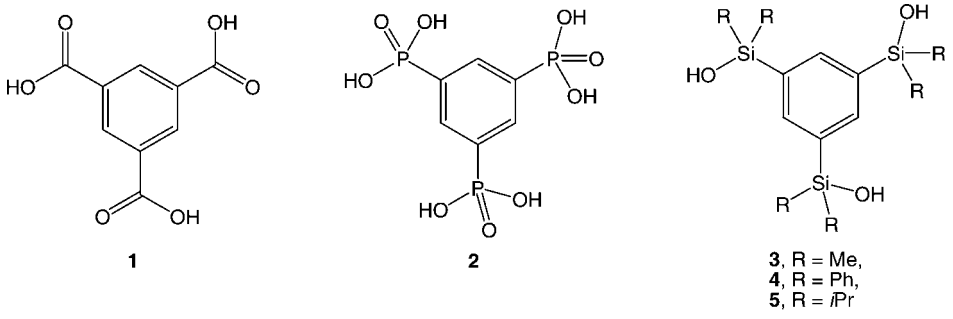


Scheme 1.

[a] Institut für Chemie und Biochemie, Freie Universität Berlin, Fabeckstr. 34–36, 14195 Berlin, Germany

 © 2006 Wiley-VCH Verlag GmbH & Co. KGaA, Weinheim 

a number of amines, which has given rise to formation of inclusion complexes revealing N–H···OP hydrogen-bond contacts (Scheme 1).[9]

Recently, we have prepared 1,3,5-(hydroxydiorganosilyl)-benzenes, 1,3,5-$(HOR_2Si)_3C_6H_3$ (**3**, R = Me; **4**, R = Ph) and investigated their supramolecular structures (Scheme 1).[10] Unfortunately, all attempts to prepare inclusions complexes of 1,3,5-(hydroxydiorganosilyl)benzenes and amines have not yet been successful. In case of **3**, the amines have base-catalysed the condensation and formation of siloxanes, whereas in case of **4**, C–H···π stacking is presumably the predominant crystal-packing force, precluding the formation of inclusion complexes with amines.[11] We have now prepared a novel 1,3,5-(hydroxydiorganosilyl)benzene, 1,3,5-$(HO{i}Pr_2Si)_3C_6H_3$ (**5**) possessing bulky and aliphatic isopropyl groups, which are able to circumvent the difficulties encountered with **3** and **4** in co-crystallisation studies with amines. Herein, we describe co-crystals of **5** with 4,4′-bipyridine (bpy), (*E*)-bis(4-pyridyl)ethylene (bpe), 4,4′-azopyridine (azpy) and bis(4-pyridyl)aceylene (bpa) that exhibit similar supramolecular motifs featuring 2D grid networks of O–H···O(H)Si and O–H···N hydrogen bonds.

## Results and Discussion

The synthesis of the trisilanol 1,3,5-$(HO{i}Pr_2Si)_3C_6H_3$ (**5**) has been achieved in three steps starting from commercially available 1,3,5-tribromobenzene (Scheme 2). The diisopropylsilyl groups have been introduced by the in situ Grignard reaction of 1,3,5-$Br_3C_6H_3$ with $i$Pr$_2$SiHCl/Mg affording 1,3,5-$(H{i}Pr_2)_3C_6H_3$ (**6**) as a distillable oil. Chlorination of **6** using $SO_2Cl_2$ has provided the corresponding chlorosilane 1,3,5-$(Cl{i}Pr_2)_3C_6H_3$ (**7**) as distillable oil that solidifies upon standing at room temperature. The base hydrolysis of **7** provides the trisilanol 1,3,5-$(HO{i}Pr_2Si)_3C_6H_3$ (**5**) as a low-melting crystalline solid.

### Solid-State Structure of 5

After recrystallisation from $CH_2Cl_2$/hexane, the trisilanol 1,3,5-$(HO{i}Pr_2Si)_3C_6H_3$ (**5**) has been obtained free of crystal water. The IR spectrum (KBr pellet) of this material exhibits two absorptions at 3694 cm$^{-1}$ (sharp, intense) and 3345 cm$^{-1}$ (broad, very intense), which were assigned to stretching vibrations of hydroxy groups that are free and involved in hydrogen bonding, respectively.[12] This assignment is supported by a preliminary X-ray structure analysis,[13] which reveals that only one silanol group is engaged in hydrogen bonding, whereas the other two are free. Unfortunately, severe disorder or twining has precluded the satisfying refinement of the X-ray data. When slowly crystallised from toluene the trisilanol was isolated as a hemihydrate, **5**·0.5$H_2O$, which has been investigated by X-ray diffraction. A perspective view of the supramolecular structure of **5**·0.5$H_2O$ is shown in Figure 1. Crystal and refinement data are collected in Table 6. The asymmetric unit contains three crystallographically independent molecules of **5** (denoted A, B and C) and water. Twelve O···O distances between 2.684(3) and 2.871(3) Å are indicative for weak to medium-strength hydrogen bonding and are listed in Table 1. The exact donor–acceptor relationship could not be established from the erratic refinement of the hydrogen positions. However, from the close proximity of the water molecules (O11–O12) to four oxygen atoms of the silanol groups it can be deduced that each water molecule serves twice as donor and acceptor for a total of four hydrogen bonds. The supramolecular motif around the water molecules can be described best as a spirocyclic arrangement of two eight-membered rings each consisting of four oxygen

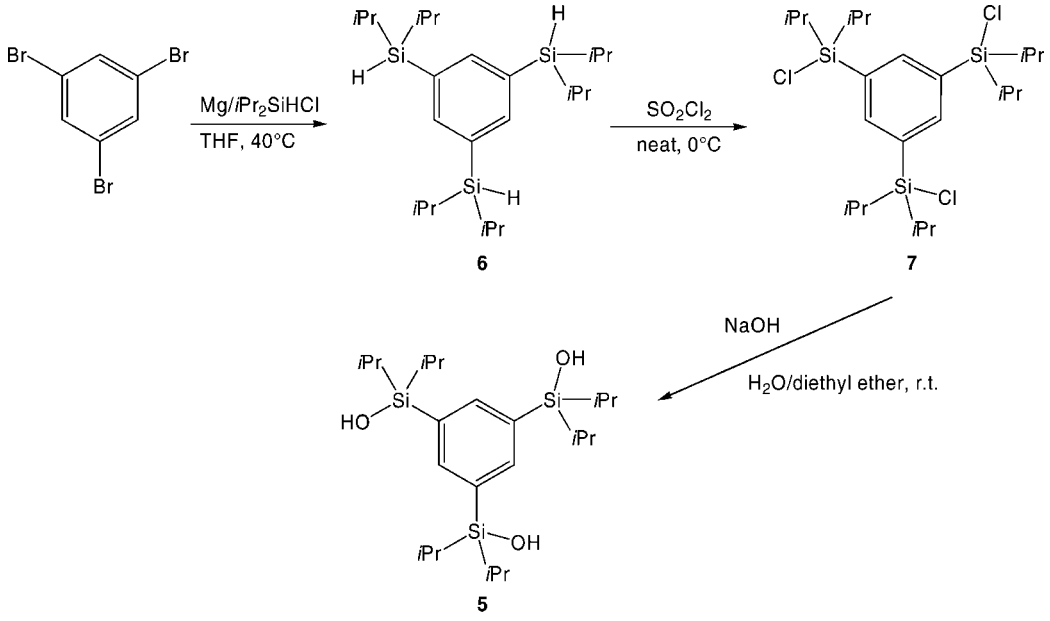


Scheme 2.

 © 2006 Wiley-VCH Verlag GmbH & Co. KGaA, Weinheim 

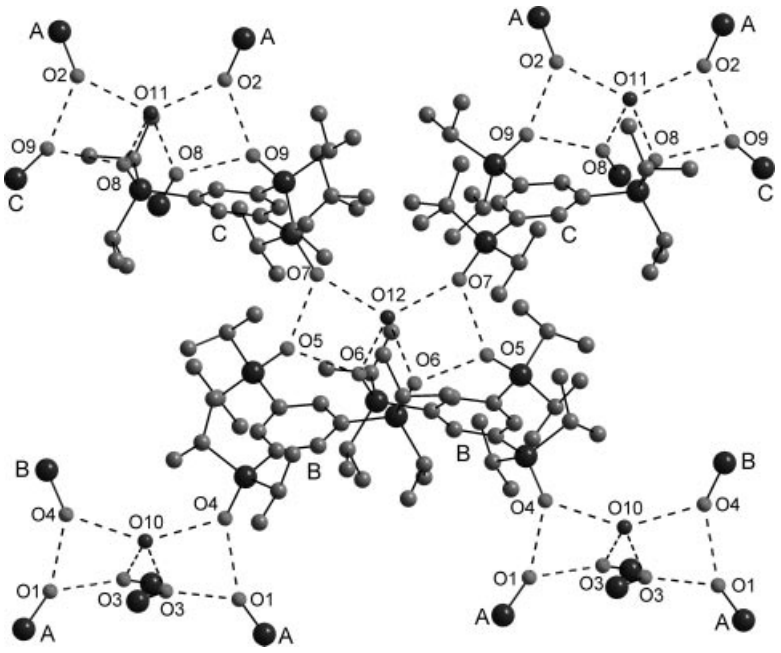


Figure 1. Perspective view of the inclusion complex **5**·0.5$H_2O$ (only SiO groups of the outer trisilanol molecules are shown for clarity).

and four hydrogen atoms. The eight-membered rings feature one water molecule and three silanol groups and therefore somewhat resemble the hydrogen-bond motif observed for the hydrate of **4**.[10] The participation of all silanol groups in hydrogen bonding is confirmed by an IR spectrum (KBr) of **5**·0.5$H_2O$, which shows one absorption at 3357 $cm^{-1}$ (broad, very intense).

Table 1. Donor acceptor distances [Å] of the hydrogen bonds of **5**·0.5$H_2O$.

| O–H···O(H)Si | | O–H···$OH_2$ | |
|---|---|---|---|
| O1···O3 | 2.719(2) | O2···O11 | 2.757(5) |
| O1···O4 | 2.778(2) | O3···O10 | 2.761(3) |
| O2···O9 | 2.700(3) | O4···O10 | 2.791(5) |
| O5···O6 | 2.739(3) | O6···O12 | 2.861(3) |
| O5···O7 | 2.675(3) | O7···O12 | 2.809(5) |
| O8···O9 | 2.771(3) | O8···O11 | 2.783(3) |

### Inclusion Complexes of 5 with 4,4′-Bis(pyridines)

Co-crystals of **5** with 4,4′-bipyrdine (bpy), (*E*)-bis(4-pyridyl)ethylene (bpe), 4,4′-azopyridine (azpy) and bis(4-pyridyl)acetylene (bpa) have been obtained and investigated by X-ray crystallography. Crystal and refinement data are collected in Table 6. To account for the fact that the trisilanol **5** and the 4,4′-bis(pyridines) contain three potential H-donors sites and two potential H-acceptor sites, respectively, the ratio of the reactants was originally intended to be 2:3. However, all isolated co-crystals consist of equimolar amounts of the trisilanol **5** and the acceptor molecule, which has been confirmed by microanalyses and $^1H$ NMR spectroscopy. The same co-crystals are also formed when an excess of the trisilanol **5** is used.

A perspective view of the inclusion complex **5**·bpy·0.5$H_2O$ is shown in Figure 2. Hydrogen-bond parameters are collected in Table 2. The asymmetric unit contains two crystallographically independent molecules of **5** (denoted as A and B) and bpy as well as one water molecule, which are associated through hydrogen bonding. The donor–acceptor relationship has been unambiguously established by complete refinement of all relevant hydrogen atoms. The trisilanol molecules are linked by hydrogen bonds (O3–H3···O4/O6–H6···O1) into 1D chains, in which the benzene rings are nearly coplanar. These 1D chains are connected by two bpy pillars and one water molecule giving rise to the formation of a 2D grid structure. The connection between the 1D chains and the bpy pillars is realised by two hydrogen-bond junctions (O1–H1···N1/O7–H7A···N2/O2–H···O7 and O4–H4···N3/O5–H5···N4) running approximately in parallel. This 2D grid network is linked to adjacent networks by an additional hydrogen bond (O7–H7B···O5) being associated with the water molecule. Adjacent network layers are aligned parallel without penetration and are shifted with respect to each other by half length of the supramolecular repeating unit, so that the 1D chains are situated in close proximity to the bpy pillars of the adjacent layers. This crystal packing avoids larger cavities in the lattice.

A perspective view of the inclusion complex **5**·bpe is shown in Figure 3. Hydrogen-bond parameters are collected in Table 3. The asymmetric unit contains only one molecule of **5** and one bpe molecule, which are linked by hydrogen bonding. The position of all relevant hydrogen atoms has been located during the X-ray data refinement. The supramolecular motif can be described best as 2D brick-wall structure. Therein, the trisilanol **5** forms 1D chains, in which the individual molecules are linked by hy-

 © 2006 Wiley-VCH Verlag GmbH & Co. KGaA, Weinheim 

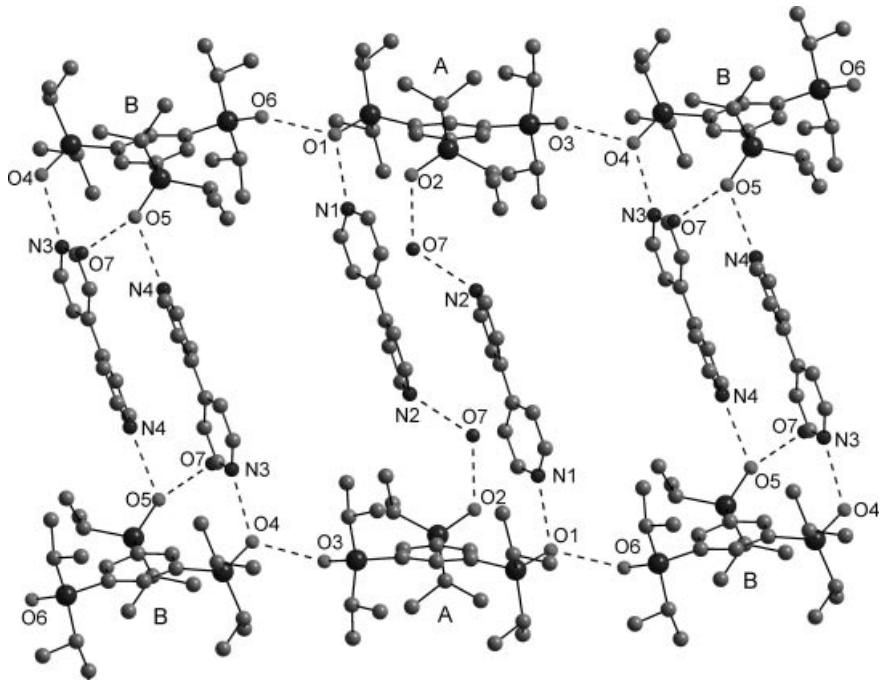


Figure 2. Perspective view of the inclusion complex **5**·bpy·0.5$H_2O$.

Table 2. Hydrogen-bond parameters [Å, °] of **5**·bpy·0.5$H_2O$.

| O–H···A | O–H | H···A | O···A | O–H···A |
|---|---|---|---|---|
| O1–H1···N1 | 0.75(3) | 2.02(3) | 2.761(8) | 176(3) |
| O2–H2···O7 | 0.80(4) | 2.01(4) | 2.779(7) | 164(3) |
| O3–H3···O4 | 0.72(5) | 2.05(5) | 2.764(4) | 172(5) |
| O4–H4···N3 | 0.82(4) | 1.95(4) | 2.767(8) | 177(3) |
| O5–H5···N4 | 0.77(5) | 2.09(5) | 2.859(8) | 171(5) |
| O6–H6···O1 | 0.69(3) | 2.16(3) | 2.842(4) | 173(4) |
| O7–H7A···N2 | 0.96(7) | 1.87(7) | 2.796(8) | 162(6) |
| O7–H7B···O5 | 0.79(4) | 2.13(4) | 2.91(1) | 168(3) |

drogen bridges (O2–H2···O1) and the phenyl rings are coplanar. The bpe molecules are situated approximately perpendicular to the 1D chains to which they are associated

Table 3. Hydrogen-bond parameters [Å, °] of **5**·bpe.

| O–H···A | O–H | H···A | O···A | O–H···A |
|---|---|---|---|---|
| O1–H1···N2 | 0.82(3) | 1.90(3) | 2.716(5) | 176(3) |
| O2–H2···O3 | 0.73(4) | 2.03(4) | 2.752(4) | 171(4) |
| O3–H3···N1 | 0.76(5) | 2.00(4) | 2.755(5) | 175(5) |

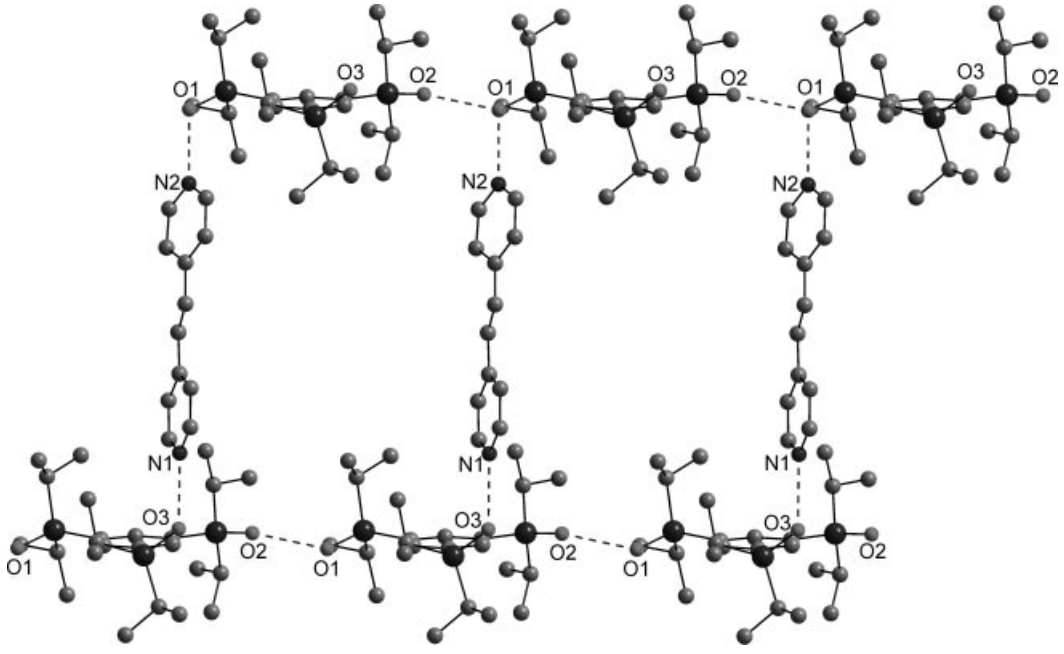


Figure 3. Perspective view of the inclusion complex **5**·bpe (only half of the outer bpe molecules are shown for clarity).

 © 2006 Wiley-VCH Verlag GmbH & Co. KGaA, Weinheim 

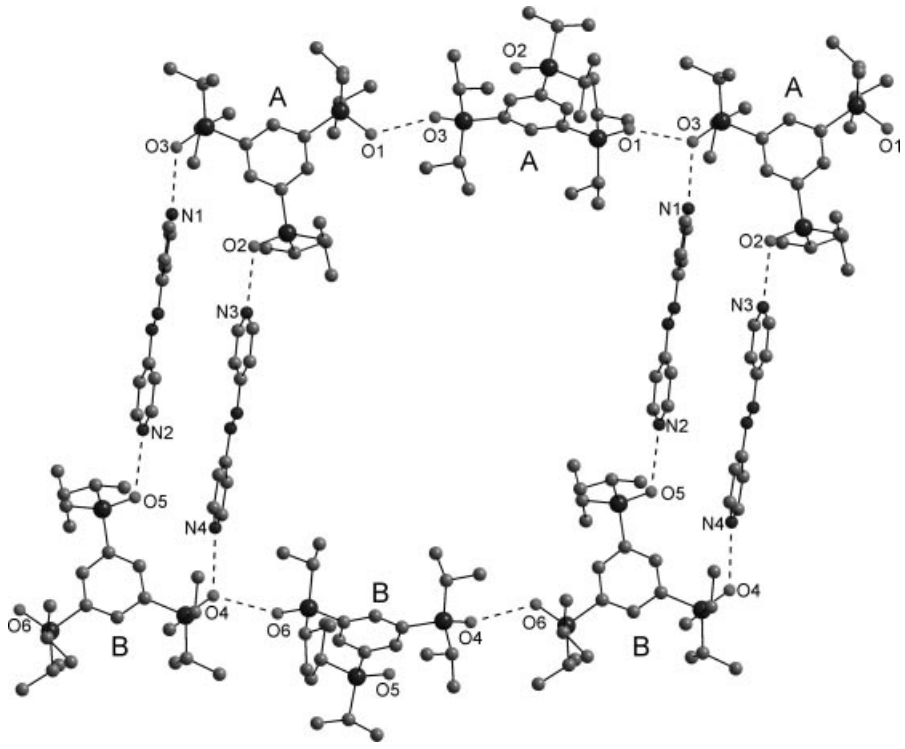


Figure 4. Perspective view of the inclusion complex **5**·azpy.

Table 4. Hydrogen-bond parameters [Å, °] of **5**·azpy.

| O–H···A | O–H | H···A | O···A | O–H···A |
|---|---|---|---|---|
| O1–H1···O3 | 0.87(4) | 1.91(4) | 2.765(9) | 165(4) |
| O2–H2···N3 | 0.84(4) | 1.96(5) | 2.783(4) | 167(4) |
| O3–H3···N1 | 0.67(5) | 2.15(5) | 2.817(5) | 176(6) |
| O4–H4···N4 | 0.71(5) | 2.16(5) | 2.866(4) | 175(5) |
| O5–H5···N2 | 0.61(4) | 2.24(4) | 2.832(4) | 169(4) |
| O6–H6···O4 | 0.64(4) | 2.19(4) | 2.81(1) | 164(5) |

through hydrogen bonding (O1–H1···N2/O3–H3···N1). The almost square-like voids defined by this 2D brick-wall net-

Table 5. Hydrogen-bond parameters [Å, °] of **5**·bpa.

| O–H···A | O–H | H···A | O···A | O–H···A |
|---|---|---|---|---|
| O1–H1···N1 | 0.67(5) | 2.20(5) | 2.871(7) | 171(5) |
| O2–H2···N2 | 0.78(5) | 2.07(5) | 2.828(6) | 166(5) |
| O3–H3···O2 | 0.85(5) | 1.95(5) | 2.782(7) | 165(4) |

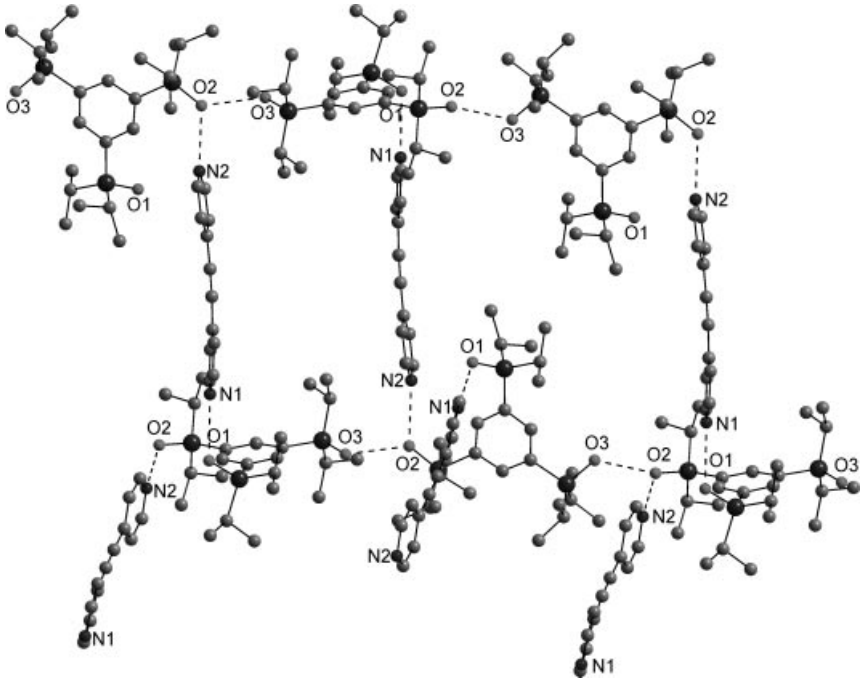


Figure 5. Perspective view of the inclusion complex **5**·bpa.

 © 2006 Wiley-VCH Verlag GmbH & Co. KGaA, Weinheim 

work are approximately 10 × 10 Å and blocked mostly by trisilanol molecules of adjacent layers running parallel.

A perspective view of the inclusion complex **5**·azpy is shown in Figure 4. Hydrogen-bond parameters are collected in Table 4. The asymmetric unit contains two crystallographically independent molecules of **5** (denoted as A and B) and azpy. All hydrogen atoms related to hydrogen bonds have been located during the X-ray data refinement. Similar as observed for the two previous structures, the trisilanol molecules are associated through hydrogen bonds (O1–H1···O3/O6–H6···O4) and give rise to the formation of 1D chains. However, unlike the two previous structures, the phenyl rings are not coplanar. The overall supramolecular motif may be also described as 2D brick-wall structure. The azpy pillars occur pair-wise and are situated approximately perpendicular to the 1D chains to which they are associated through hydrogen bonds (O2–H2···N3/O3–H3···N1/O4–H4···N4/O5–H5···N2). The almost square-like voids defined by the supramolecular arrangement are approximately 16 × 16 Å and filled by the same interpenetrating 2D brick-wall network. To the best of our knowledge interpenetrating networks[14] have not yet been observed for silanol structures.[1]

A perspective view of the inclusion complex **5**·bpa is shown in Figure 5. Hydrogen-bond parameters are collected in Table 5. The asymmetric unit contains one molecule of **5** and bpa. All hydrogen atoms associated with hydrogen bonding have been located during the refinement. As observed in the structures before, the trisilanol molecules are associated through hydrogen bonds (O3–H3···O2) giving rise to the formation of 1D chains, in which the phenyl groups are not coplanar. The bpa pillars are situated approximately perpendicular to the 1D chains to which they are associated through hydrogen bonding (O1–H1···N1/O2–H2···N2). The almost square-like voids defined by the supramolecular pattern are approximately 8 × 8 Å.

The close examination of hydrogen-bond parameters (Tables 1–5) reveals no significant difference between O–H···O(H)Si and O–H···N hydrogen bonds. The donor–acceptor distances of the hydrogen bridges of all four structures range from 2.684(3) to 2.91(1) Å with an average of 2.78(1) Å and compare well with previously reported experimental values[1–5] as well as parameters established computationally in the gas phase for $H_3SiOH\cdots O(H)SiH_3$ (2.863 Å) and $H_3SiOH\cdots$pyridine (2.815 Å) at the B3LYP/6-311+(2d,p) level of theory.[15]

Applications in supramolecular chemistry and crystal engineering require that the molecular building blocks are rigid and that the functional groups possess a pre-fixed directionality.[7] In an effort to qualitatively examine the conformational flexibility of the silanols groups, the O–Si–C–C torsion angles have been assessed and compared for all structures. The absolute torsion angles can vary between 2.5(2) and 70.3(2)°; however, most values are close to the average of 25.5(2)° for all structures. The average of these values for each individual trisilanol molecule varies only between 20.6(2) and 31.4(2)°, which apparently suggests that the silanol groups cannot adopt conformations that are entirely independent from the influence of the other two silanol groups attached to the same phenyl ring.

## Conclusions

Regardless of the stoichiometric ratio of the reactants applied, the inclusion complexes between **5** and 4,4′-bis(pyridines), namely **5**·bpy·0.5$H_2O$, **5**·bpe and **5**·azpy, contain the same number of donor and acceptor molecules, which are associated by hydrogen bonding. The thermodynamic driving force of the co-crystallisation is the energy gain associated with the formation of O–H···N hydrogen bonds. This energy gain needs to be higher than that of the competitive O–H···O(H)Si hydrogen bonds. We have recently shown that the BSSE-corrected hydrogen-bond energies of the model compounds $H_3SiOH\cdots O(H)SiH_3$ and $H_3SiOH\cdots$pyridine are –3.47 and –6.47 kcal mol$^{-1}$, respectively, at the B3LYP/6-311+(2d,p) level of theory.[15] These values suggest that the highest energy gain should be observed when the ratio between trisilanol and 4,4′-bis(pyridine) is 2:3, allowing a maximum of three O–H···N hydrogen bridges. However, the loss of symmetry in a 2:3 complex and the associated increase of entropy, apparently, cannot be compensated entirely by the O–H···N hydrogen-bond energy. The formation of 1:1 complexes might be a compromise between the gain of hydrogen-bond energy and the loss of symmetry.

One of the more ambitious goals in supramolecular chemistry is the prediction of solid-state architectures.[6] Interestingly, the crude supramolecular motifs are very similar for **5**·bpy·0.5$H_2O$, **5**·bpe and **5**·azpy. In all three structures, the trisilanol molecules form 1D chains, which are interconnected by nearly perpendicular 4,4′-bis(pyridine) pillars to give rise to formation of 2D grid networks. However, the inevitable voids between the 2D grids differ substantially in size and shape for all four structures. The small voids of **5**·bpa (8 × 8 Å) are unfilled, the medium-sized voids of **5**·bpy·0.5$H_2O$ (10 × 12 Å) and **5**·bpe (10 × 10 Å) are blocked by trisilanol molecules of adjacent 2D networks, whereas the larger voids of **5**·azpy (16 × 16 Å) are filled by interpenetration. It might be interesting to see if these voids can be also filled with guest molecules that may possibly interact with the C–C and N–N double bonds of the bpe and azpy pillars.

## Experimental Section

**General:** 1,3,5-Tribromobenzene, chlorodiisopropylsilane, 4,4′-bipyridine (bpy) and (*E*)-bis(4-pyridyl)ethylene (bpe) are commercially available, whereas 4,4′-azopyridine (azpy) and bis(4-pyridyl)-acetylene (bpa) have been prepared according to known routes.[16] NMR spectra were collected using a Jeol JNM-LA 400 FT spectrometer and are referenced against $Me_4Si$. IR spectra were recorded with a 5 SXC Nicolet DTGS FT-IR spectrometer. Microanalyses were obtained with a Vario EL elemental analyser.

**1,3,5-Tris(diisopropylsilyl)benzene (6):** A 250-mL three-neck flask equipped with a septum, dropping funnel and reflux condenser was

 © 2006 Wiley-VCH Verlag GmbH & Co. KGaA, Weinheim 

charged with Mg turnings (4.75 g, 195 mmol), *i*$Pr_2$SiHCl (24.0 g, 159 mmol) and THF (100 mL). The Mg was activated by addition of 1,2-dibromoethane (250 μL) through a syringe. 1,3,5-Tribromobenzene (15.3 g, 49.0 mmol) dissolved in THF (100 mL) was slowly added. The temperature was maintained at 40 °C for 12 h, before the mixture was hydrolysed by the addition of $H_2O$ (50 mL). The organic layer was washed with water (3 × 20 mL) and dried with $Na_2SO_4$. Removal of the solvent and fractional distillation of the crude product in vacuo afforded **6** as an almost colourless viscous oil [11.5 g, 27.3 mmol (56%); b.p. 200–220 °C/7.5 $10^{-3}$ Torr]. $^1$H NMR ($CDCl_3$, 399.65 MHz): $\delta$ = 7.56 (s, 3 H, Ph), 3.86 [s, $^1J(^1H-^{29}Si)$ = 182 Hz, 3 H, Si*H*], 1.16 (m, 6 H, C*H*Me$_2$), 0.98, 0.90 (d, 36 H, CH*Me$_2$*) ppm. $^{13}C\{^1H\}$ NMR ($CDCl_3$, 100.40 MHz): $\delta$ = 143.4, 131.8 (Ph), 18.7, 18.4 (*C*HMe$_2$), 10.8 (CH*Me$_2$*) ppm. $^{29}Si\{^1H\}$ NMR ($CDCl_3$, 79.30 MHz): $\delta$ = 5.3 [s, $^1J(^{29}Si-^1H)$ = 184 Hz] ppm. IR (KBr plates): $\tilde{\nu}$ = 2101 (SiH) $cm^{-1}$. $C_{24}H_{48}Si_3$ (420.52): calcd. C 68.55, H 11.41; found C 68.53, H 11.45.

**1,3,5-Tris(chlorodiisopropylsilyl)benzene (7):** A 50-mL Schlenk flask with gas outlet was charged with **6** (10.5 g, 25 mmol) and sealed with a septum. An excess of $SO_2Cl_2$ (7 mL, 93 mmol) was slowly added through a syringe. After a short induction delay, a strongly exothermic reaction occurred and $SO_2$ gas vigorously evolved. During the reaction, the mixture was cooled with an ice bath. After the addition was complete, the mixture was stirred at room temperature for 24 h and at 40 °C for 1 h. Unreacted $SO_2Cl_2$ was removed in vacuo and the remaining crude product was purified by kugelrohr distillation to give **7** as a colourless low-melting solid [9.37 g, 17.9 mmol (72%); b.p. 220–240 °C/7.5 $10^{-3}$ Torr]. $^1$H NMR ($CDCl_3$, 399.65 MHz): $\delta$ = 7.89 (s, 3 H, Ph), 1.45 (m, 6 H, C*H*Me$_2$), 1.09, 1.01 (d, 36 H, CH*Me$_2$*) ppm. $^{13}C\{^1H\}$ NMR ($CDCl_3$, 100.40 MHz): $\delta$ = 141.6, 130.7 (Ph), 16.9, 16.7 (*C*HMe$_2$), 13.7 (CH*Me$_2$*) ppm. $^{29}Si\{^1H\}$ NMR ($CDCl_3$, 79.30 MHz): $\delta$ = 26.4 (s) ppm. $C_{24}H_{45}Cl_3Si_3$ (523.87): calcd. C 54.99, H 8.65; found C 54.90, H 9.03.

**1,3,5-Tris(hydroxydiisopropylsilyl)benzene (5):** Compound **7** (8.23 g, 16 mmol) dissolved in diethyl ether (40 mL) was treated with an aqueous solution (40 mL) of NaOH (5.28 g, 132 mmol). The mixture was stirred at room temperature for 3 h before the layers were separated. The organic layer was washed with $H_2O$ (3 × 40 mL) and dried with $Na_2SO_4$. The removal of the solvent in vacuo produced a colourless solid that was recrystallised from $CH_2Cl_2$/hexane to furnish **5** as colourless crystals [3.2 g, 6.8 mmol (43%); m.p. 90–91 °C]. $^1$H NMR ($CDCl_3$, 399.65 MHz): $\delta$ = 7.74 (s, 3 H, Ph), 2.39 (s, OH), 1.20 (m, 6 H, C*H*Me$_2$), 1.00, 0.92 (d, 36 H, CH*Me$_2$*) ppm. $^{13}C\{^1H\}$ NMR ($CDCl_3$, 100.40 MHz): $\delta$ = 140.7, 132.7 (Ph), 17.1, 16.9 (*C*HMe$_2$), 12.4 (CH*Me$_2$*) ppm. $^{29}Si\{^1H\}$ NMR ($CDCl_3$, 79.30 MHz): $\delta$ = 7.0 (s) ppm. IR (KBr pellet): $\tilde{\nu}$ = = 3694, 3345 (OH) $cm^{-1}$. $C_{24}H_{48}O_3Si_3$ (468.89): calcd. C 61.48, H 10.32; found C 61.53, H 10.62. Slow recrystallisation from toluene afforded **5**·0.5$H_2O$. $C_{48}H_{98}Si_6O_7$ (955.80): calcd. C 61.32, H 10.33; found C 60.13, H 10.50.

**Synthesis of the Inclusion Complexes of 5 with 4,4′-Bis(pyridines):** Compound **5** (50 mg, 0.107 mmol) and the appropriate amount of the 4,4′-bis(pyridines) (byp: 10.7 mg, bpe: 13.0 mg, azpy: 13.7 mg, 0.070 mmol) were dissolved in $CH_2Cl_2$/hexane (3:2). Slow concentration of the solution furnished colourless or orange crystals. The yields were not optimised. **5·byp·0.5$H_2O$:** Yield 20 mg (30%). $C_{68}H_{113}N_4O_7Si_6$ (1267.19): calcd. C 64.40, H 9.06, N 4.42; found

Table 6. Crystal data and structure refinement of **5**·0.5$H_2O$, **5**·bpy·0.5$H_2O$, **5**·bpe, **5**·azpy and **5**·bpa.

| | **5**·0.5$H_2O$ | **5**·bpy·0.5$H_2O$ | **5**·bpe | **5**·azpy | **5**·bpa |
|---|---|---|---|---|---|
| Empirical formula | $C_{48}H_{90}O_7Si_6$ | $C_{68}H_{113}N_4O_7Si_6$ | $C_{36}H_{58}N_2O_3Si_3$ | $C_{34}H_{56}N_4O_3Si_3$ | $C_{36}H_{56}N_2O_3Si_3$ |
| Formula mass [g mol$^{-1}$] | 947.75 | 1267.18 | 651.11 | 653.10 | 649.10 |
| Crystal system | monoclinic | triclinic | monoclinic | monoclinic | monoclinic |
| Crystal size [mm] | 0.60 × 0.63 × 0.83 | 0.11 × 0.22 × 0.42 | 0.01 × 0.15 × 0.05 | 0.02 × 0.14 × 0.50 | 0.05 × 0.07 × 0.37 |
| Space group | *C*2/c | *P*$\bar{1}$ | $P2_1$/c | *P*n | *C*2/c |
| *a* [Å] | 17.910(2) | 11.068(3) | 10.763(2) | 17.054(4) | 34.326(9) |
| *b* [Å] | 43.010(6) | 16.077(4) | 23.687(5) | 11.947(3) | 11.798(3) |
| *c* [Å] | 23.406(3) | 22.753(5) | 16.169(4) | 20.495(5) | 21.652(5) |
| *α* [°] | 90 | 103.633(6) | 90 | 90 | 90 |
| *β* [°] | 94.643(4) | 98.387(5) | 108.016(5) | 110.609(5) | 117.209(7) |
| *γ* [°] | 90 | 101.752(5) | 90 | 90 | 90 |
| *V* [Å$^3$] | 17970(4) | 3771.2(15) | 3920.1(15) | 3908.5(15) | 7798(3) |
| *Z* | 12 | 2 | 4 | 4 | 8 |
| $\rho_{calcd.}$ [Mg·m$^{-3}$] | 1.051 | 1.116 | 1.103 | 1.110 | 1.106 |
| *T* [K] | 143 | 133 | 173 | 173 | 173 |
| $\mu$(Mo-$K_\alpha$) [mm$^{-1}$] | 0.180 | 0.160 | 0.155 | 0.157 | 0.155 |
| *F*(000) | 6216 | 1378 | 1416 | 1416 | 2816 |
| $\theta$ range [°] | 0.95 to 25.00 | 0.94 to 25.00 | 1.58 to 25.00 | 1.34 to 25.00 | 0.98 to 25.00 |
| Index ranges | $-16 \le h \le 21$<br>$-51 \le k \le 51$<br>$-27 \le l \le 15$ | $-13 \le h \le 13$<br>$-17 \le k \le 19$<br>$-22 \le l \le 27$ | $-12 \le h \le 11$<br>$-28 \le k \le 28$<br>$-19 \le l \le 19$ | $-12 \le h \le 11$<br>$-28 \le k \le 28$<br>$-19 \le l \le 19$ | $-17 \le h \le 40$<br>$-14 \le k \le 13$<br>$-24 \le l \le 25$ |
| No. of reflections collected | 44816 | 25707 | 31128 | 23848 | 16008 |
| Completeness to $\theta_{max}$ | 99.3% | 97.6% | 99.9% | 99.6% | 98.0% |
| No. independent reflections | 15720 | 12955 | 6905 | 10302 | 6736 |
| No. obsd. reflns. with $[I > 2\sigma(I)]$ | 11896 | 9210 | 4799 | 9097 | 2649 |
| No. refined parameters | 835 | 798 | 409 | 817 | 409 |
| GooF($F^2$) | 1.010 | 1.035 | 1.069 | 1.103 | 0.876 |
| $R_1(F)$ $[I > 2\sigma(I)]$ | 0.048 | 0.050 | 0.0519 | 0.0366 | 0.0660 |
| $wR_2(F^2)$ (all data) | 0.151 | 0.140 | 0.1561 | 0.1042 | 0.1980 |
| $(\Delta/\sigma)_{max}$ | 0.002 | 0.002 | 0.001 | 0.002 | 0.001 |
| Largest diff peak/hole [e·Å$^{-3}$] | 2.498/–0.391 | 0.768/–0.253 | 0.546/–0.363 | 0.376/–0.217 | 0.374/–0.380 |

 © 2006 Wiley-VCH Verlag GmbH & Co. KGaA, Weinheim 

C 63.78, H 9.40, N 4.06. **5·bpe:** Yield 30 mg (43%). $C_{36}H_{58}N_2O_3Si_3$ (651.13): calcd. C 66.41, H 8.98, N 4.30; found C 66.35, H 9.19, N 4.27. **5·azpy:** Yield 40 mg (57%). $C_{34}H_{56}N_4O_3Si_3$ (653.09): calcd. C 62.53, H 8.64, N 8.58; found C 62.31, H 8.58, N 8.44. **5·bpa:** Yield 40 mg (57%). $C_{36}H_{56}Si_3N_2O_3$ (648.10): calcd. C 66.61, H 8.70, N 4.32; found C 66.12, H 8.71, N 4.19.

**X-ray Crystallography:** Intensity data were collected with a Bruker SMART 1000 CCD diffractometer with graphite-monochromated Mo-$K_\alpha$ (0.7107 Å) radiation. Data were reduced using the program SAINT.[17] The structures were solved by direct methods and difference Fourier synthesis using SHELXS-97 implemented in the program WinGX 2002.[18] Full-matrix least-squares refinements on $F^2$, using all data, were carried out with anisotropic displacement parameters applied to all non-hydrogen atoms. Disorder of an isopropyl group in **5**·0.5$H_2O$ was resolved with split occupancies of 0.6 and 0.4 for C81 and C81′. The large residual electron density (2.498 e·Å$^{-3}$) might be indicative for disorder (of O12) or an unaccounted solvent molecule; however, all attempts of modelling failed. Hydrogen atoms attached to carbon atoms were included in geometrically calculated positions using a riding model and were refined isotropically. Hydrogen atoms attached to oxygen atoms were located from the electron-density maps of **5**·bpy·0.5$H_2O$, **5**·bpe, **5**·azpy and **5**·bpa and refined isotropically without restraints. The absolute configuration of **5**·azpy has been determined by the refinement of the Flack parameter [0.00(8)]. Figures were created using DIAMOND.[19] Further details are listed in Table 6. CCDC-605353 (**5**·0.5$H_2O$), -605354 (**5**·bpy·0.5$H_2O$), -605355 (**5**·bpe), -605356 (**5**·azpy) and -605357 (**5**·bpa) contain the supplementary crystallographic data for this paper. These data can be obtained free of charge from The Cambridge Crystallographic Data Centre via www.ccdc.cam.ac.uk/data_request/cif.

## Acknowledgments

Mrs. Irene Brüdgam (Freie Universität Berlin) is gratefully acknowledged for the X-ray data collection.

[1] a) P. D. Lickiss, *Adv. Inorg. Chem.* **1995**, *42*, 147–262; b) V. Chandrasekhar, R. Boomishankar, S. Nagendran, *Chem. Rev.* **2004**, *104*, 5847–5910.
[2] a) S. A. Bourne, L. R. Nassimbeni, K. Skobridis, E. Weber, *J. Chem. Soc., Chem. Commun.* **1991**, 282–283; b) M. Schneider, B. Neumann, H. G. Stammler, P. Jutzi, *Monatsh. Chem.* **1999**, *130*, 33–44.
[3] a) E. A. Babaian, M. Huff, F. A. Tibbals, D. C. Hrncir, *J. Chem. Soc., Chem. Commun.* **1990**, 306–307; b) S. A. Bourne, L. Johnson, C. Marais, L. R. Nassimbeni, E. Weber, K. Skobridis, F. Toda, *J. Chem. Soc. Perkin Trans. 2* **1991**, 1707–1713; c) K. F. Bowes, C. Glidewell, J. N. Low, *Acta Crystallogr., Sect. C* **2002**, *58*, o409–o415.
[4] a) K. A. Ruud, J. S. Sepeda, F. A. Tibbals, D. C. Hrncir, *J. Chem. Soc., Chem. Commun.* **1991**, 629–630.
[5] a) I. Baxter, L. D. Cother, C. Dupuy, P. D. Lickiss, A. J. P White, D. J. Williams, published electronically in **1997** at http://www.ch.ic.ac.uk/ectoc/ectoc-3/pub/010/index.html, accessed on 12.04.**2002**; b) B. O'Leary, T. R. Spalding, G. Ferguson, C. Glidewell, *Acta Crystallogr. Sect. B* **2000**, *56*, 273–286; c) A. E. Goeta, S. E. Lawrence, M. M. Meehan, A. O'Dowd, T. R. Spalding, *Polyhedron* **2002**, *21*, 1689–1694; d) U. Klingebiel, P. Neugebauer, I. Müller, M. Noltemeyer, I. Usón, *Eur. J. Inorg. Chem.* **2002**, 717–722; e) K. F. Bowes, G. Ferguson, A. J. Lough, C. Glidewell, *Acta Crystallogr. Sect. B* **2003**, *59*, 277–286; f) D. E. Turkington, A. J. Lough, G. Ferguson, C. Glidewell, *Acta Crystallogr. Sect. B* **2004**, *60*, 238–248; g) G. Prabusankar, R. Murugavel, R. J. Butcher, *Organometallics* **2004**, *23*, 2305–2314.
[6] a) G. R. Desiraju, *Crystal engineering – The design of organic solids*, Elsevier, Amsterdam, The Netherlands, **1989**; b) M. C. Etter, *Acc. Chem. Res.* **1990**, *23*, 120–126; c) G. R. Desiraju, *Angew. Chem. Int. Ed. Engl.* **1995**, *34*, 2311–2327; d) G. R. Desiraju, *Chem. Commun.* **1997**, 1475–1482.
[7] a) S. V. Kolotuchin, E. E. Fenlon, S. R. Wilson, C. J. Loweth, S. C. Zimmerman, *Angew. Chem. Int. Ed. Engl.* **1996**, *34*, 2654–2657; b) K. Biradha, D. Dennis, V. A. MacKinnon, C. V. K. Sharma, M. J. Zaworotko, *J. Am. Chem. Soc.* **1998**, *120*, 11894–11903; c) A. S. Abd-El-Aziz, C. R. de Denus, M. J. Zaworotko, C. V. K. Sharma, *Chem. Commun.* **1998**, 265–266; d) S. V. Kolotuchin, P. A. Thiessen, E. E. Fenlon, S. R. Wilson, C. J. Loweth, S. C. Zimmerman, *Chem. Eur. J.* **1999**, *5*, 2537–2547; e) S. Chatterjee, V. R. Pedireddi, A. Ranganathan, C. N. R. Rao, *J. Mol. Struct.* **2000**, *520*, 107–115; f) R. Liu, K. F. Mok, S. Valiyaveettil, *New J. Chem.* **2001**, *25*, 890–892.
[8] I. Haiduc, F. T. Edelmann, *Supramolecular Organometallic Chemistry*, Wiley-VCH, Weinheim, Germany, **1999**.
[9] a) M. Mehring, *Eur. J. Inorg. Chem.* **2004**, 3240–3246; b) D. Kong, A. Clearfield, J. Zoń, *Cryst. Growth Des.* **2005**, *5*, 1767–1773.
[10] J. Beckmann, A. Duthie, G. Reeske, M. Schürmann, *Organometallics* **2004**, *23*, 4630–4635.
[11] J. Beckmann, G. Reeske, unpublished results, **2003**.
[12] R. West, R. H. Baney, *J. Am. Chem. Soc.* **1959**, *81*, 6145–6148.
[13] Crystal system: tetragonal, space group: $P\bar{4}$, cell dimensions: $a$ = 11.3732(10), $c$ = 11.1566(21) Å.
[14] S. R. Batten, R. Robson, *Angew. Chem. Int. Ed.* **1998**, *37*, 1460–1494.
[15] J. Beckmann, S. Grabowsky, manuscript in preparation.
[16] a) E. V. Brown, G. R. Granneman, *J. Am. Chem. Soc.* **1975**, *97*, 621–627; b) B. J. Coe, J. L. Harries, J. A. Harris, B. S. Brunschwig, S. J. Coles, M. E. Light, M. B. Hursthouse, *Dalton Trans.* **2004**, *18*, 2935–2942.
[17] *SMART*, *SAINT*, *SADABS*, Siemens Analytical X-ray Instruments Inc., Madison, Wisconsin, USA, **1999**.
[18] L. J. Farrugia, *J. Appl. Crystallogr.* **1999**, *32*, 837–838.
[19] *DIAMOND*, V2.1d, Crystal Impact, K. Brandenburg & M. Berndt GbR, **2002**.

Received: April 27, 2006
Published Online: July 25, 2006

 © 2006 Wiley-VCH Verlag GmbH & Co. KGaA, Weinheim 

DOI: 10.1002/ejic.200600085

# Structural and Magnetic Studies of Copper(II) and Zinc(II) Coordination Complexes Containing Nitroxide Radicals as Chelating Ligands

**Akihiro Ito,[a] Yoshiaki Nakano,[a] Masashi Urabe,[a] Kazuyoshi Tanaka,*[a,b] and Motoo Shiro[c]**

**Keywords:** Copper / Density functional calculations / Magnetic properties / Radicals / Zinc

The mononuclear transition metal complexes $[Cu(CF_3SO_3)_2\mathbf{1}_2]$ (**1a**), $[Zn(CF_3SO_3)_2\mathbf{1}_2]$ (**1b**), $[Cu(CF_3SO_3)_2\mathbf{2}_2]\cdot 2CH_3CN$ (**2a**), and $[Zn(CF_3SO_3)_2\mathbf{2}_2]\cdot 2CH_3CN$ (**2b**) have been prepared from the newly synthesized doxyl nitroxide ligands 4,4-dimethyl-2,2-di(2-pyridyl)oxazolidine-*N*-oxyl (**1**) and 4,4-dimethyl-2,2-bis[2-(3-methylpyridyl)]oxazolidine-*N*-oxyl (**2**) and $M(CF_3SO_3)_2$ (M = $Cu^{II}$ or $Zn^{II}$). These metal–nitroxide complexes have been structurally and magnetically characterized. In all complexes, the four pyridyl groups coordinate in equatorial coordination sites and the two nitroxide groups in axial coordination sites, which means that the central metal ion acquires a distorted $N_4O_2$ octahedral configuration. The variable-temperature magnetic susceptibility data show that complexes **1b** and **2b** exhibit paramagnetic behavior, and hence a very weak intraligand magnetic interaction could be estimated [$J_{NO-NO}$ = –0.64 (**1b**) and 0.14 $cm^{-1}$ (**2b**)]. The $\chi_m T$ values of **1a** and **2a** decrease continuously with decreasing temperature until they reach a nearly constant value at around 50 K, thereby indicating an intramolecular antiferromagnetic interaction between the $Cu^{II}$ ion and the nitroxide ligands for both **1a** and **2a** [$J_{Cu-NO}$ = –81.6 (**1a**) and –78.1 $cm^{-1}$ (**2b**)]. These magnetic behaviors are supported by density functional theory calculations and are discussed in connection with the specific structural features.
(© Wiley-VCH Verlag GmbH & Co. KGaA, 69451 Weinheim, Germany, 2006)

## Introduction

Studies in multi-spin systems consisting of paramagnetic metal ions and organic radicals are drawing much attention in the field of molecular magnetism.[1] The advantage of using metal–radical compounds resides not only in the fact that both building blocks afford spin centers but also that a higher dimensional molecular architecture can be constructed by versatile coordination patterns of paramagnetic metal ions. Moreover, the radical ligands have the possibility of mediating a stronger magnetic interaction between the adjacent paramagnetic metal ion centers even though the metal–metal distance is large. Therefore, the metal–radical approach has become one of the most promising strategies for large hetero-spin assemblies of exchange-coupled species.

On the other hand, as is the case with metal–radical complexes in which the radical centers are directly bound to the paramagnetic metal ions, intramolecular magnetic interactions are governed by direct overlap between their magnetic orbitals.[2,3] Hence, the nature of the magnetic interaction depends strongly on the coordination geometry around the paramagnetic metal ion. For example, the magnetic interactions in copper(II)–radical complexes range from strong antiferromagnetic interactions to weak ferromagnetic ones.[2] Therefore, the development of organic radical ligands is important to control the magnetic interaction. Several kinds of organic radical ligands have been studied in this context.[4–7] In particular, nitroxide radicals have often been used as paramagnetic ligand molecules because of their stability and ease of chemical modification.[3] However, nitroxides are generally considered as weak Lewis bases and hence they cannot coordinate to metal ions unless the Lewis acidity of the metal center is enhanced by using electron-withdrawing co-ligands such as hexafluoroacetylacetonato (hfac). Consequently, their weak ligating ability to metal ions prevents the formation of metal–nitroxide complexes with high-dimensional structures.[3] Actually, the dimensionality is restricted due to the prior occupation of coordination sites by the electron-withdrawing co-ligands.[8,9] Two strategies have been developed to overcome this difficulty. One approach is to use a high-spin poly(nitroxide radical) as a polydentate bridging ligand to connect the paramagnetic metal ions.[10,11] The other approach is to incorporate nitroxide groups into normal organic ligands with powerful ligating ability such as pyridine,[12] 2,2′-bipyridine,[13] triazole,[14] imidazole,[15] and piperazine,[16]

[a] Department of Molecular Engineering, Graduate School of Engineering, Kyoto University,
Sakyo-ku, Kyoto 606-8501, Japan
E-mail: a51053@sakura.kudpc.kyoto-u.ac.jp
[b] CREST, Japan Science and Technology Agency (JST), Japan
[c] Rigaku Corporation, X-ray Research Laboratory, Matsubaracho 3-9-12, Akishima, Tokyo 196-8666, Japan

 © 2006 Wiley-VCH Verlag GmbH & Co. KGaA, Weinheim 

which allows a facile coordination to metal ions through the chelate effect.

In the present work, two new organic radical ligands bearing pyridyl groups, namely 4,4-dimethyl-2,2-di(2-pyridyl)oxazolidine-*N*-oxyl (**1**) and 4,4-dimethyl-2,2-bis[2-(3-methylpyridyl)]oxazolidine-*N*-oxyl (**2**), were synthesized to have a suitable ligating ability to metal ions. The selection of copper(II) and zinc(II) as the metal ion centers stems from two reasons: (i) $Cu^{II}$ has a $d^9$ configuration with spin-1/2, which simplifies the magnetic interaction between the metal ion and the organic radical ligand,[3] and (ii) $Zn^{II}$ has a closed-shell $d^{10}$ configuration with no unpaired electrons, and hence we can extract the direct magnetic interaction between the paramagnetic ligand molecules. More conveniently, the ionic radius for $Cu^{II}$ (0.87 Å) is almost the same as that for $Zn^{II}$ (0.88 Å).[17] Structural characterization by X-ray crystallographic studies and measurement of the magnetic properties with a SQUID magnetometer for the newly prepared metal–radical complexes were performed. For the $Cu^{II}$ and $Zn^{II}$ complexes with **1**, a theoretical analysis was also carried out on the basis of density functional calculations.

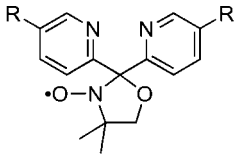

**1**: R = H
**2**: R = $CH_3$

## Results and Discussion

### Synthesis

The novel radical ligands **1** and **2** were synthesized as illustrated in Scheme 1.

Coupling of the dipyridyl ketone **3** (or **4**), with 2-amino-2-methylpropan-1-ol in toluene gives the oxazolidine **5** (or **6**), in high yield. A long reaction time (several days) and continuous water removal by means of a Dean–Stark trap were needed for successful preparation of **5** and **6**. Dipyridyl ketone **4** was prepared by reaction of ethyl chloroformate with lithiated 2-bromo-5-methylpyridine, whereas **3** is commercially available. Oxidation of **5** and **6** with MCPBA in $Et_2O$ finally gave **1** and **2** in relatively high yield. The four complexes **1a**, **1b**, **2a**, and **2b** were obtained by treatment of an acetonitrile solution of $M(CF_3SO_3)_2$ (M = $Cu^{II}$ and $Zn^{II}$) with the corresponding radical ligand, **1** and **2**; vapor diffusion of $Et_2O$ into the reaction mixtures afforded single crystals of these complexes. Elemental analyses of complexes **1a** and **1b** confirmed that the two radical ligands coordinate to a single metal ion. On the other hand, efflorescence was observed with complexes **2a** and **2b**, which suggests that some solvent molecules are included in the crystals. Consequently, we could not determine the chemical formulae of **2a** and **2b** from the elemental analyses; they were finally determined by the X-ray structure analyses, as discussed below.

### Crystal Structures

The structures of complexes **1a**, **1b**, **2a**, and **2b** were determined by X-ray crystallography at 103 or 123 K. All the

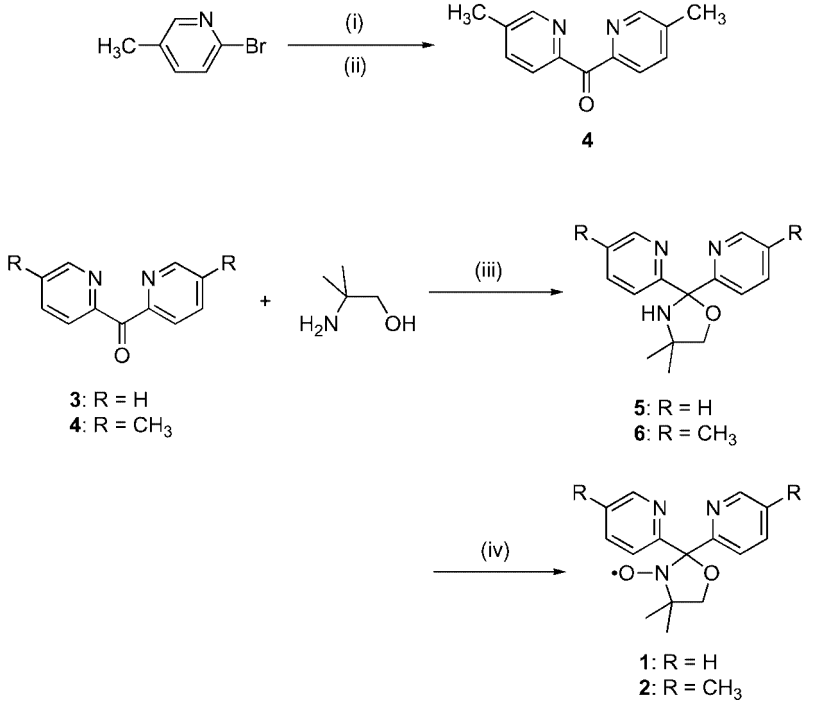

Scheme 1. Synthesis of **1** and **2**: (i) *n*BuLi, THF, –80 °C; (ii) $ClCO_2Et$, THF, –80 °C; (iii) toluene, $H_2SO_4$, reflux (–$H_2O$); (iv) MCPBA, $Et_2O$, 0 °C.

 © 2006 Wiley-VCH Verlag GmbH & Co. KGaA, Weinheim 

Table 1. Selected bond lengths [Å], bond angles [°], and dihedral angles [°] for **1a**, **1b**, **2a**, and **2b**.

| | **1a** | **1b** | **2a** | | **2b** | |
|---|---|---|---|---|---|---|
| M–N2 | 2.001(1) | 2.101(1) | 2.014(2) | 2.025(2) | 2.101(2) | 2.096(2) |
| M–N3 | 2.033(1) | 2.144(1) | 2.028(2) | 2.001(2) | 2.134(2) | 2.119(2) |
| M–O1 | 2.333(1) | 2.163(1) | 2.333(2) | 2.309(2) | 2.165(1) | 2.155(2) |
| N2–M–N3 | 86.52(6) | 85.24(5) | 86.53(8) | 87.66(8) | 85.03(7) | 86.46(6) |
| M–O1–N1 | 110.3 | 114.2 | 110.9 | 109.7 | 114.7 | 113.3 |
| $\varphi$[a] | 90.5 | 91.4 | 94.8 | 83.8 | 85.5 | 96.4 |
| $\theta$[b] | 6.0 | 5.6 | 5.9 | 4.7 | 5.8 | 5.1 |

[a] Dihedral angle between the equatorial plane and the nitroxide plane (see text). [b] Tilt angle of the $Cu^{II}$–$O_{NO}$ coordination bond from the line perpendicular to the equatorial plane of the $Cu^{II}$ ion (see text).

complexes crystallize in the triclinic system with space group $P\bar{1}$; they are isostructural. The nitroxide ligand molecule **1** or **2** in these complexes behaves as a tridentate ligand through two pyridyl N-atoms ($N_{pyridyl}$) and one nitroxide O-atom ($O_{NO}$). All the equatorial coordination sites around the central metal ion are occupied by the $N_{pyridyl}$ atoms, with the remaining axial coordination sites occupied by $O_{NO}$ atoms. As a result, the central metal ion has a distorted $N_4O_2$ octahedral configuration. The triflate anions are not coordinated. Selected bond lengths, bond angles, and dihedral angles are given in Table 1, where the dihedral angle, $\varphi$, is defined as that between the equatorial plane (defined by the central metal ion and the four $N_{pyridyl}$ atoms) and the nitroxide plane (defined by the nitroxide N- and O-atoms and two carbon atoms adjacent to the nitroxide N-atom). The tilt angle, $\theta$, is defined as the difference between the line along the $Cu^{II}$–$O_{NO}$ coordination bond and the line perpendicular to the equatorial plane of the $Cu^{II}$ ion.

### *[Cu(CF$_3$SO$_3$)$_2$1$_2$] (1a) and [Zn(CF$_3$SO$_3$)$_2$1$_2$] (1b)*

The molecular structures of **1a** and **1b** are shown in Figure 1. The central $Cu^{II}$ and $Zn^{II}$ ions reside at the inversion center of a distorted octahedron. In the equatorial plane, a considerable deviation from the ideal square geometry is seen in **1a**: the two kinds of $Cu^{II}$–$N_{pyridyl}$ bond lengths are Cu–N2 = 2.001(1) and Cu–N3 = 2.033(1) Å, and the N2–Cu–N3 angle is 86.52(6)°. The axially coordinated $Cu^{II}$–$O_{NO}$ bond [Cu–O1 = 2.333(1) Å] is longer than the equatorially coordinated $Cu^{II}$–$N_{pyridyl}$ bonds. As is well-known for a $d^9$ electron configuration like the $Cu^{II}$ ion, the octahedral geometry does not remain perfect at equilibrium and is inevitably distorted along one axis (the Jahn–Teller effect).[18]

A similar deviation from the ideal square geometry is also observed in **1b** [Zn–N2 = 2.101(1), Zn–N3 = 2.144(1) Å; N2–Zn–N3 = 85.24(5)°]. The elongation along the axial axis is not conspicuous due to the $d^{10}$ electron configuration of the $Zn^{II}$ ion [Zn–O1 = 2.163(1) Å]. The dihedral ($\varphi$) and tilt ($\theta$) angles in **1a** (and **1b**) are 90.5° (91.4°) and 6.0° (5.6°), respectively. As the elongation axis is through O1–Cu1–O1*, the magnetic orbital of $Cu^{II}$ is considered to be $d_{x^2-y^2}$, which is directed toward the nitrogen atoms of the pyridyl groups. As shown in part a of Figure 2, neighboring complex molecules in **1a** (and also **1b**) are well separated in the crystal [the shortest distances between the adjacent metal ions for **1a** and **1b** are 7.5928(5) and 7.6792(4) Å, respectively]. The shortest $O_{NO}$–$O_{NO}$ distances between intermolecular nitroxide groups for **1a** and **1b** are 5.680(2) and 5.953(2) Å, respectively. There is a short C–C contact [3.337(3) Å for **1a** and 3.323(3) Å for **1b**] that is less than the sum of the van der Waals radii (3.40 Å)[19] between the adjacent complex molecules along the *a*-axis.

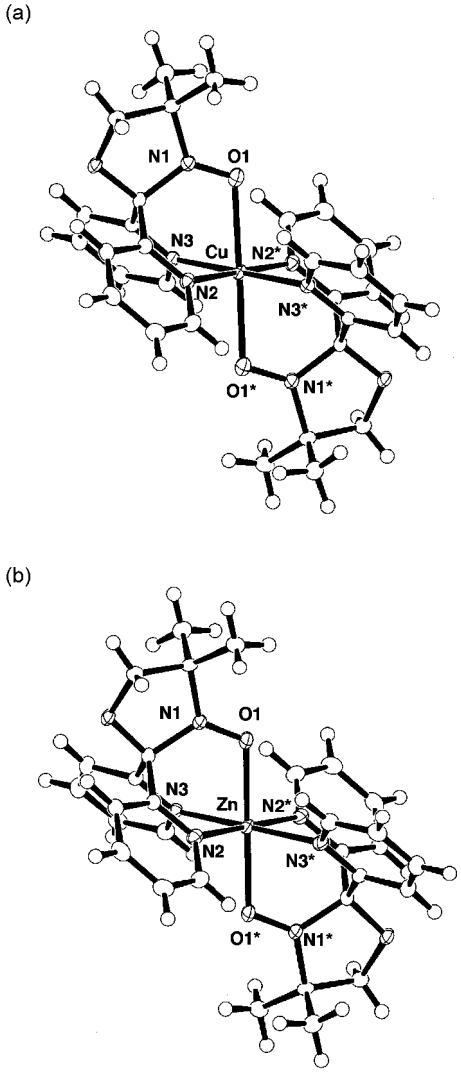


Figure 1. ORTEP view (50% probability ellipsoids) and atom labeling scheme of a) [Cu(CF$_3$SO$_3$)$_2$**1**$_2$] (**1a**) and b) [Zn(CF$_3$SO$_3$)$_2$**1**$_2$] (**1b**). The non-coordinated triflate anions have been omitted for clarity. The atom labeling for compounds **2a** and **2b** is identical.

 © 2006 Wiley-VCH Verlag GmbH & Co. KGaA, Weinheim 

As described later, however, the spin density on the C atoms with the short contact is so small that a strong magnetic interaction via this molecular contact cannot be expected. Consequently, the magnetic systems of **1a** and **1b** can be considered to be an assemblage of well-isolated three- and two-spin systems, respectively. Moreover, **1a** and **1b** have similar molecular and crystal structures, and therefore we can compare the magnetic interactions in the three-spin systems with those in the two-spin system without the central spin-1/2 moiety within the same geometrical configuration.

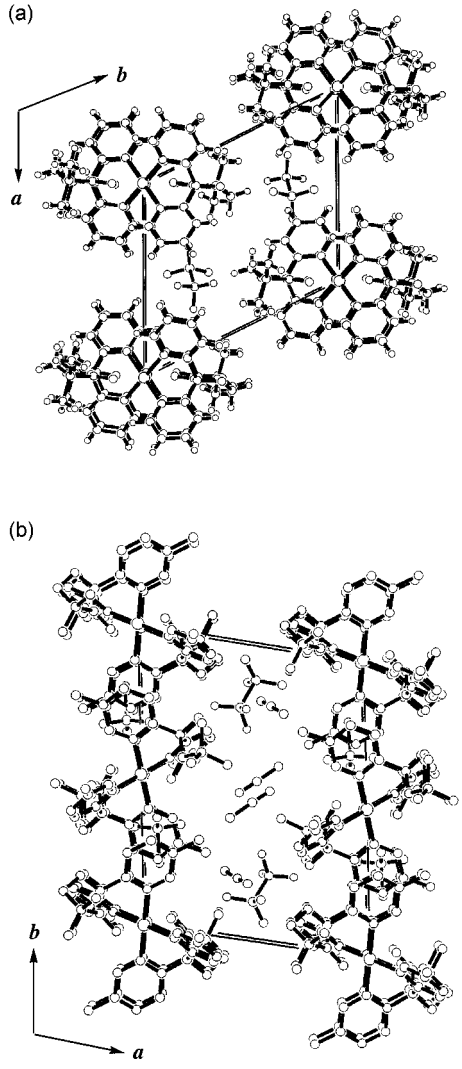


Figure 2. Views of the crystal packing for **1a** (a) and **2a** (b).

### *[Cu(CF$_3$SO$_3$)$_2$2$_2$]·2CH$_3$CN (2a) and [Zn(CF$_3$SO$_3$)$_2$2$_2$]·2CH$_3$CN (2b)*

The crystal structure of **2a** is shown in Figure 2 (b). The crystal of **2a** (and also **2b**) contains two acetonitrile molecules per molecular unit and is different from **1a** (and **1b**) as there are two crystallographically independent molecules in which the central metal ion resides on the inversion center. The molecular structures of **2a** and **2b** are similar to those of **1a** and **1b**. The characteristic geometrical parameters of **2a** are as follows: Cu–O1 = 2.333(2) [2.309(2)], Cu–N2 = 2.014(2) [2.025(2)], Cu–N3 = 2.028(2) Å [2.001(2) Å]; the N2–Cu–N3 angle is 86.53(8)° [87.66(8)°]. The corresponding parameters in **2b** are also similar to those of **1b**: Zn–O1 = 2.165(1) [2.155(2)], Zn–N2 = 2.101(2) [2.096(2)], Zn–N3 = 2.134(2) Å [2.119(2) Å], N2–Zn–N3 = 85.03(7)° [86.46(6)°]. Moreover, the dihedral ($\varphi$) and tilt ($\theta$) angles in **2a** (and **2b**) are 94.8° [83.8°] (85.5° [96.4°]) and 5.9° [4.7°] (5.8° [5.1°]), respectively. The deviation of the dihedral angle between the equatorial plane and the nitroxide plane from 90° in **2a** and **2b** is larger than that in **1a** and **1b**. The intermolecular distances in **2a** and **2b** are larger than those in **1a** and **1b** due to the steric hindrance of the crystallized acetonitrile molecules and the methyl group of ligand **2** (the shortest distances between the adjacent metal ions for **2a** and **2b** are 7.97 and 8.16 Å, respectively). The shortest $O_{NO}$–$O_{NO}$ distances between intermolecular nitroxide groups for **2a** and **2b** are 7.477(3) and 7.465(3) Å, respectively. In addition, there is no intermolecular contact less than the sum of the van der Waals radii (3.40 Å for C–C; 3.22 Å for C–O)[19] between the adjacent complex molecules. Therefore, the intermolecular magnetic interactions in **2a** and **2b** are expected to be weaker than those in **1a** and **1b**.

### Magnetic Properties

The temperature-dependent magnetic susceptibility of complexes **1a**, **1b**, **2a**, and **2b** was measured in the temperature range 2–300 K; $\chi_m T$ values are plotted as a function of

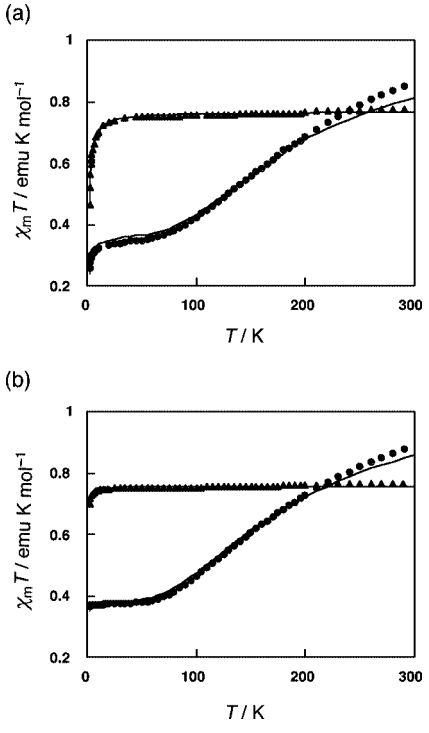


Figure 3. Temperature-dependence of the magnetic susceptibilities of a) **1a** (solid circle) and **1b** (solid triangle) and b) **2a** (solid circle) and **2b** (solid triangle). The solid curves represent the best theoretical fit to the data (see text).

 © 2006 Wiley-VCH Verlag GmbH & Co. KGaA, Weinheim 

the temperature in Figure 3, where $\chi_m$ is the molar magnetic susceptibility per molecular unit.

### *[Cu(CF$_3$SO$_3$)$_2$I$_2$] (1a) and [Zn(CF$_3$SO$_3$)$_2$I$_2$] (1b)*

As shown in Figure 3 (a), the $\chi_m T$ value for **1b** is nearly constant at around 0.75 emu K mol$^{-1}$, which corresponds to two magnetically uncoupled spins-1/2 per molecular unit. This result is reasonable for the complex of a diamagnetic $Zn^{II}$ ion with two spin-1/2 radical ligands. Moreover, the crystal structural analysis shows that the shortest $O_{NO}$–$O_{NO}$ distance between intermolecular nitroxide groups (5.95 Å) is longer than that between intramolecular nitroxide groups (4.33 Å). This indicates that the spin system in **1b** can be regarded as an assemblage of approximately isolated two-spin clusters. Taking these results into account, the magnetic data for **1b** were analyzed by using the Bleaney–Bowers equation[20] for a two-spin cluster composed of a pair of nitroxide radical ligands ($H = -2J_{NO-NO}\boldsymbol{S}_{NO}\cdot\boldsymbol{S}_{NO}$, where $\boldsymbol{S}_{NO}$ is the spin-1/2 operator for the nitroxide radical ligand and $J_{NO-NO}$ is the exchange coupling constant between two intramolecular nitroxide spins). Furthermore, the Curie–Weiss law can be used to describe inter-cluster magnetic interactions [Equation (1)], where $f$ is the purity factor of the sample, $N_A$ the Avogadro number, $g$ the isotropic $g$-factor (assuming $g = 2$), $\theta$ the Weiss temperature, $k_B$ the Boltzmann constant, and $\mu_B$ the Bohr magneton.

$$\chi_m T = f\frac{2N_A g^2 \mu_B^2 T}{k_B(T-\theta)}\frac{1}{3+exp\left(-\frac{2J_{NO-NO}}{k_B T}\right)} \quad (1)$$

The best fit parameters were found to be $f = 1.02$, $J_{NO-NO} = -0.64$ cm$^{-1}$, and $\theta = -0.4$ K ($-0.26$ cm$^{-1}$). The small values of $J_{NO-NO}$ and $\theta$ indicate that the intra- and intermolecular magnetic interaction between the nitroxide radical spins in **1b** can be ignored as compared to the magnetic interaction between the d$^9$ $Cu^{II}$ spin and the nitroxide radical spin in the complex molecule of **1a**, as discussed below.

In contrast, the $\chi_m T$ value for **1a** at room temperature is smaller than the theoretical value ($\chi_m T$ = 1.125 emu K mol$^{-1}$) for three spins-1/2 per molecular unit. Furthermore, on lowering the temperature, the $\chi_m T$ value decreases gradually and reaches a nearly constant value close to a theoretical value for a single spin-1/2 per molecular unit ($\chi_m T$ = 0.375 emu K mol$^{-1}$) at around 50 K. These results indicate that a relatively strong antiferromagnetic interaction is present in the crystal of **1a**. As indicated by the crystal structure analysis of **1a**, the shortest intra- and intermolecular $O_{NO}$–$O_{NO}$ distances between the nitroxide radical ligands (4.67 and 5.68 Å, respectively) and the shortest intermolecular $Cu^{II}$–$Cu^{II}$ distance (7.59 Å) are longer than the $Cu^{II}$–$O_{NO}$ distance (2.333 Å). This indicates that the spin system in **1a** can be regarded as an assemblage of approximately isolated three-spin clusters consisting of a $Cu^{II}$ ion and two nitroxide radical ligands. Moreover, the direct intramolecular magnetic interaction between the nitroxide ligand molecules in **1a** can be neglected due to the magnetic behavior of **1b**. Therefore, the arrangement of the three-spin clusters in complex **1a** can be regarded as a linear three-spin model [$\boldsymbol{S}_{NO(1)}$–$\boldsymbol{S}_{Cu}$–$\boldsymbol{S}_{NO(2)}$]. The spin Hamiltonian can be written as shown in Equation (2) using an exchange coupling constant, $J_{Cu-NO}$, between the $Cu^{II}$ spin and the nitroxide radical spin.

$$H = -2J_{Cu-NO}[\boldsymbol{S}_{NO(1)}\cdot\boldsymbol{S}_{Cu} + \boldsymbol{S}_{Cu}\cdot\boldsymbol{S}_{NO(2)}] \quad (2)$$

for which the eigenvalues are

$$E_1(S = 1/2) = 2\,J_{Cu-NO}$$

$$E_2(S = 1/2) = 0$$

$$E_3(S = 3/2) = -\,J_{Cu-NO}$$

Hence, the temperature dependence of $\chi_m T$ is given by Equation (3).

$$\chi_m T = f\frac{N_A g^2 \mu_B^2 T}{4k_B(T-\theta)}\frac{1+exp\left(-\frac{2J_{Cu-NO}}{k_B T}\right)+10exp\left(\frac{J_{Cu-NO}}{k_B T}\right)}{1+exp\left(-\frac{2J_{Cu-NO}}{k_B T}\right)+2exp\left(\frac{J_{Cu-NO}}{k_B T}\right)} \quad (3)$$

The parameters in this equation are the same as in Equation (1). This equation was fitted well to the experimental data, and the best-fit parameters were $f = 0.99$, $J_{Cu-NO} = -81.6$ cm$^{-1}$, and $\theta = -1.1$ K ($-0.77$ cm$^{-1}$). The sign of $J_{Cu-NO}$ is opposite to that found for $Cu^{II}$–nitroxide complexes where the $O_{NO}$ atoms occupy the axial positions (+10 to +70 cm$^{-1}$).[2,21] However, the magnitude of $J_{Cu-NO}$ is smaller than that observed for $Cu^{II}$–nitroxide complexes where the $O_{NO}$ atoms occupy the equatorial positions (ca. $-600$ cm$^{-1}$).[2,21] This discrepancy in the sign of $J_{Cu-NO}$ suggests that the overlap mode between the π* orbital of the nitroxide group and the magnetic orbital ($d_{x^2-y^2}$) of the $Cu^{II}$ ion differs between the present complex and the previously reported axially coordinated $Cu^{II}$–nitroxide complexes.[22] The relatively small $J_{Cu-NO}$ value arises from the fact that the Cu–$O_{NO}$ distance is fairly long (ca. 2.3 Å) owing to the Jahn–Teller distortion as compared to that for the equatorially coordinated $Cu^{II}$–nitroxide complexes (ca. 2.0 Å).[21,23,24]

### *[Cu(CF$_3$SO$_3$)$_2$2$_2$]·2CH$_3$CN (2a) and [Zn(CF$_3$SO$_3$)$_2$2$_2$]·2CH$_3$CN (2b)*

The $\chi_m T$ vs. $T$ plots for **2a** and **2b** are shown in Figure 3 (b). The temperature dependence of the $\chi_m T$ value for **2a** and **2b** is similar to those for **1a** and **1b**, respectively. The X-ray structural analysis shows that the intermolecular distance and shortest contacts in **2a** and **2b** are larger than those in **1a** and **1b**. However, the temperature dependence of their magnetic properties remains unchanged. This means that the main magnetic interaction observed in the crystals of **1a** and **2a** can be ascribed to the intramolecular antiferromagnetic interaction between the $Cu^{II}$ spin and the nitroxide radical spin. Hence, the magnetic data were again fitted to Equations (1) and (3). The best fit, shown in Figure 3 (b) as a solid line, afforded the following parameters:

 © 2006 Wiley-VCH Verlag GmbH & Co. KGaA, Weinheim 

$f$ = 1.03, $J_{Cu-NO}$ = –78.1 cm$^{-1}$, and $\theta$ = –0.2 K (–0.15 cm$^{-1}$) for **2a** and $f$ = 1.01, $J_{NO-NO}$ = 0.14 cm$^{-1}$, and $\theta$ = –0.3 K (–0.19 cm$^{-1}$) for **2b**. The value of $J_{Cu-NO}$ is similar to that for **1a**, which supports the assumption that the spin alignment in **1a** and **2a** is governed by an intramolecular antiferromagnetic interaction between the Cu$^{II}$ ion and the nitroxide ligands.

### Theoretical Considerations

On the basis of the obtained X-ray structures of **1a** and **1b** we performed quantum chemical calculations in order to examine the electronic structures of the present metal–radical complexes. First of all, we investigated the spin-density distribution of complexes **1a** and **1b**. As density functional theory (DFT) calculations often give good results for both signs and magnitudes of spin densities of open-shell molecules, we carried out calculations using the hybrid HF/DF method (B3LYP/LANL2DZ).[25] The partially occupied spin-free natural orbitals from the B3LYP/LANL2DZ calculations for the $^4A_u$ state of **1a** and the selected spin densities of the low- and high-spin states of **1a** and **1b** are shown in Figures 4 and 5, respectively. In both of the doublet and quadruplet states of **1a**, the spin densities are mainly localized on the Cu$^{II}$ ion and the nitroxide groups. In **1b**, the spin densities for the singlet and triplet states are localized only on the nitroxide groups of the two ligands. On the other hand, the spin densities over the peripheral pyridyl groups of **1a** and **1b** are quite small. These results are consistent with the experimental result that the intermolecular magnetic interactions in all four complexes are very weak.

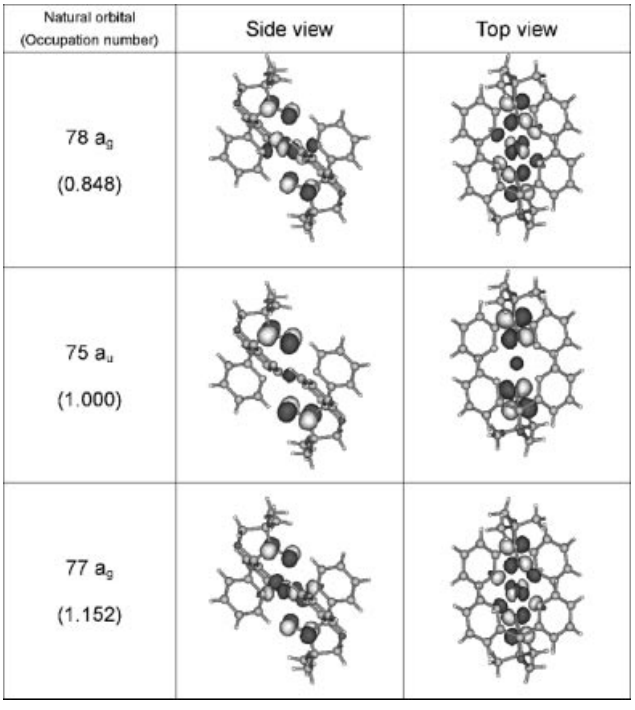


Figure 4. Three partially occupied natural orbitals for the $^2A_u$ state of **1a** at the UB3LYP/LANL2DZ level of theory.

Moreover, the sign of the spin density on the Cu$^{II}$ ion in the doublet state of **1a** is opposite to that in the quadruplet state, while the magnitudes of the spin densities on the Cu$^{II}$ and nitroxyl groups remain unchanged. This indicates that an antiferromagnetic spin alignment occurs in the doublet state of **1a**, while a ferromagnetic spin alignment occurs in the quadruplet state of **1a**. In addition, the natural orbital occupation number indicates that the $^2A_u$ state of **1a** has a doublet triradical character.

Energetically, the doublet state ($^2A_u$) in **1a** was estimated to be more stable than the quadruplet state ($^4A_u$) by 223 cm$^{-1}$. In addition, the exchange coupling constant, $J$, can be estimated to be 110 cm$^{-1}$ by using the approximate spin projection method[26–29] given by Equation (4),

$$J = \frac{E(^2A_u) - E(^4A_u)}{\langle S^2\rangle(^4A_u) - \langle S^2\rangle(^2A_u)} \quad (4)$$

where $E(^2A_u)$ and $E(^4A_u)$ are the total energies for the $^2A_u$ and $^4A_u$ states and $<S^2>(^2A_u)$ and $<S^2>(^4A_u)$ the expectation values for the total spin angular momentums of $^2A_u$ and $^4A_u$ states. The estimated $J$ value gives a good agreement with the $J_{Cu-NO}$ value determined from the magnetic

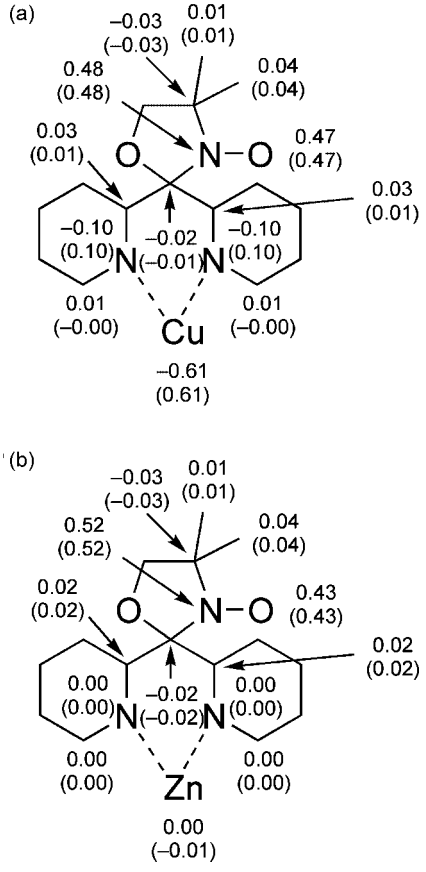


Figure 5. Mulliken spin density for a) the doublet and quadruplet states (in parentheses) of **1a** and b) the singlet and triplet states (in parentheses) of **1b** at the UB3LYP/LANL2DZ level of theory. The centrosymmetric atoms have the same spin density (having the opposite sign only for the singlet state of **1b**), hence one of the two ligands has been omitted for clarity.

 © 2006 Wiley-VCH Verlag GmbH & Co. KGaA, Weinheim 

measurements. On the other hand, the singlet ($^1A_u$) and triplet ($^3A_u$) states of **1b** were found to be virtually degenerate. This indicates that effective magnetic interactions between the two nitroxide ligands via the diamagnetic $Zn^{II}$ ion do not occur.

The present axially coordinated $Cu^{II}$–nitroxide complexes **1a** and **2a** show antiferromagnetic coupling between the metal center and the nitroxide ligand molecule, although the $Cu^{II}$–nitroxide magnetic interaction in the axially coordinated $Cu^{II}$–nitroxide complexes is usually ferromagnetic.[3,22] Schweizer and co-workers have clearly shown the spin-density distribution of an axially coordinated $Cu^{II}$–nitroxide complex on the basis of a neutron diffraction analysis; their results strongly suggest that the ferromagnetic interaction between the $Cu^{II}$ ion and the nitroxide ligand is derived from orthogonality between the corresponding magnetic orbitals (the $3d_{x^2-y^2}$ atomic orbital for $Cu^{II}$ and the π* orbital for the nitroxide).[30] In general, the exchange parameter is approximately expressed as Equation (5),

$$J_{dir} \approx \rho_{x^2-y^2} J(3d_{x^2-y^2}, \pi^*) \quad (5)$$

$$J(3d_{x^2-y^2}, \pi^*) \sim < 3d_{x^2-y^2}\,\pi^* \mid \pi^*\,3d_{x^2-y^2} > + 2S < \pi^* \mid h \mid 3d_{x^2-y^2} > - S^2 [\, \varepsilon_{xy} + \varepsilon_{\pi^*} + < 3d_{x^2-y^2}\,3d_{x^2-y^2} \mid \pi^*\,\pi^* > ]$$

where $\rho_{x^2-y^2}$ is the density of the unpaired electron on the $3d_{x^2-y^2}$ atomic orbital, $S = <3d_{x^2-y^2}|\pi^*>$ is the overlap integral between the magnetic orbitals, $\varepsilon_{xy}$ and $\varepsilon_{\pi^*}$ are the orbital energies, $<3d_{x^2-y^2}\pi^*|\pi^*\,3d_{x^2-y^2}>$ and $<3d_{x^2-y^2}\,3d_{x^2-y^2}|\pi^*\,\pi^*>$ are the two-electron integrals of the exchange and Coulomb types, respectively, and $h$ is the one-electron Hamiltonian. According to Musin and co-workers,[31] the strong antiferromagnetic coupling ($J \approx -500\ cm^{-1}$)[3] in equatorially coordinated $Cu^{II}$–nitroxide complexes can be explained by the above-mentioned direct exchange interaction $J_{dir}$. The third term of $J(3d_{x^2-y^2}, \pi^*)$ in Equation (5) becomes dominant due to the large overlap integral $S \approx 10^{-1}$ ($J_{dir} \approx -500\ cm^{-1}$).

On the other hand, in axially coordinated $Cu^{II}$–nitroxide complexes, slight delocalization of the unpaired electron from the π* orbital of the nitroxide group to the $3d_{z^2}$ atomic orbital of the $Cu^{II}$ ion takes place. Hence, the delocalized π* orbital is approximately expressed as $\pi^* + c_{z^2}3d_{z^2}$. As a result, the exchange parameter contains two main contributions, $J \approx J_{dir} + J_{del}$. The exchange parameter due to the delocalization mechanism $J_{del}$ takes the form shown in Equation (6),

$$J_{dir} \approx \rho_{x^2-y^2}\rho_{z^2} <3d_{x^2-y^2}\,3d_{z^2}|3d_{z^2}\,3d_{x^2-y^2}> \quad (6)$$

where $\rho_{z^2} = c_{z^2}$, the spin density due to delocalization from the nitroxide group to $Cu^{II}$. In the axially coordinated $Cu^{II}$–nitroxide complexes, the values of $S$ are estimated to be very small because of orthogonality between the $3d_{x^2-y^2}$ atomic orbital for the $Cu^{II}$ ion and the π* orbital of nitroxide group. Hence, the direct exchange term $J_{dir}$ only gives a very small positive value. On the other hand, in spite of the smallness of the delocalization $\rho_{z^2}$, the large intra-atomic exchange integral [Equation (6)] leads to a major contribution from the delocalized exchange term $J_{del}$ (ca. 10–65 $cm^{-1}$).[31]

In the present complexes **1a** and **1b** the nitroxide groups are axially coordinated to the $Cu^{II}$ ion. However, the determined exchange parameter is antiferromagnetic ($J_{exp} \approx 80\ cm^{-1}$), which is contrary to the expected ferromagnetic interaction in axially coordinated $Cu^{II}$–nitroxide complexes. This can be explained by the difference of overlap mode between the magnetic orbitals of the $Cu^{II}$ ion and the nitroxide groups. As shown in Figure 6 (a), when the symmetry plane containing the π* orbital of the nitroxide group is orthogonal to the equatorial plane of the $Cu^{II}$ ion, the tilting of the $Cu^{II}$–$O_{NO}$ coordination bond from the line

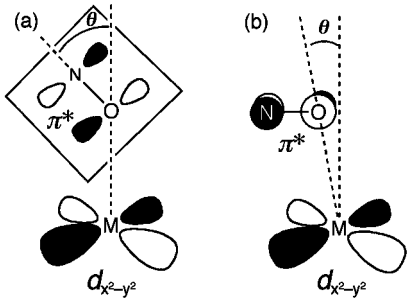


Figure 6. Schematic views of possible orbital interactions between the magnetic orbitals ($3d_{x^2-y^2}$) of the $Cu^{II}$ ion ($3d_{x^2-y^2}$) and the nitroxide radical (π*). $\theta$ is the tilt angle of the $Cu^{II}$–$O_{NO}$ coordination bond from the line perpendicular to the equatorial plane of the $Cu^{II}$ ion.

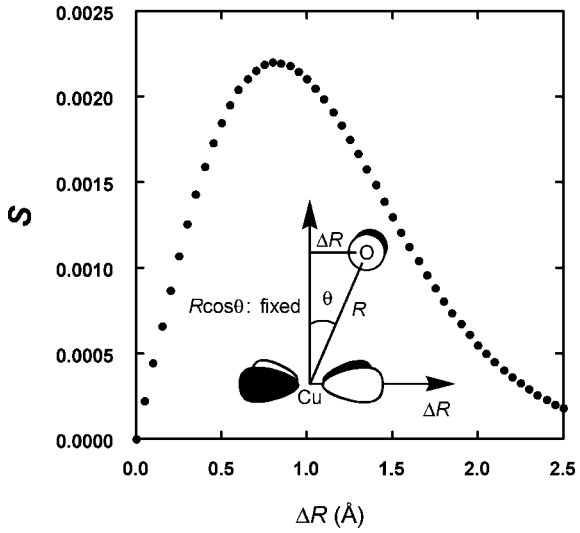


Figure 7. Dependence of the overlap integral between the Slater 2p atomic orbital of the oxygen atom and the Slater $3d_{x^2-y^2}$ atomic orbital of the Cu atom on the distance $\Delta R$ (in Å) defined in the inset ($R\cos\theta$ was fixed to 2.3202 Å, which corresponds to complex **1a**). $\Delta R$ can be related to the tilt angle $\theta$ in Table 1 and Figure 6 by the formula $\sin\theta = \Delta R/R$. We adopted 2.275 and 2.95 for the values of $\zeta$ of the oxygen 2p orbital and the copper 3d orbital, respectively [see: J. A. Pople, D. L. Beveridge, *Approximate Molecular Orbital Theory*, McGraw-Hill, New York, **1970**.]. In the case of complex **1a**, the corresponding overlap integral was estimated to be 0.001 [$\Delta R = 0.2438$].

 © 2006 Wiley-VCH Verlag GmbH & Co. KGaA, Weinheim 

perpendicular to the equatorial plane causes an effective overlap between the π* orbital of the nitroxide group and the $3d_{z^2}$ atomic orbital of the $Cu^{II}$ ion. Therefore, the delocalization mechanism [Equation (6)] leads to a relatively large ferromagnetic interaction. On the other hand, as shown in Figure 6 (b), in the present $Cu^{II}$–nitroxide complexes the symmetry plane containing the π* orbital of the nitroxide group is nearly parallel to the equatorial plane of the $Cu^{II}$ ion. Hence, the overlap integral between the π* orbital of the nitroxide group and the $3d_{z^2}$ atomic orbital of the $Cu^{II}$ ion is virtually negligible. Thus, we can ignore the above-mentioned delocalization mechanism in complexes **1a** and **1b**. More importantly, the $Cu^{II}$–$O_{NO}$ coordination bond tilts from the line perpendicular to the equatorial plane ($\theta \approx 5°$) in the present coordination mode [Figure 6 (b)]. Therefore, the finite overlap integral between the π* orbital of the nitroxide group and $3d_{x^2-y^2}$ atomic orbital of the $Cu^{II}$ ion is expected. However, the overlap integral is expected to be small compared to the equatorially coordinated $Cu^{II}$–nitroxide complexes, as shown in Figure 7 ($S \approx 0.001$). Such a specific overlap mode leads to a relatively weak antiferromagnetic interaction ($J \approx 80\ cm^{-1}$) in complexes **1a** and **1b** due to the direct exchange mechanism.

## Concluding Remarks

The synthesis, magnetic properties, and theoretical analysis of $Cu^{II}$ complexes **1a** and **2a** and $Zn^{II}$ complexes **1b** and **2b** containing radical ligands **1** and **2** have been described. It has been shown that the combination of the metal ion and these radical ligands results in formation of isostructural mononuclear complexes. The magnetic properties of the $Zn^{II}$ complex indicate that there is a weak intramolecular magnetic interaction between two nitroxide ligands. On the other hand, the exchange coupling constant $J_{Cu–NO}$ between the $Cu^{II}$ and the nitroxide ligands for **1a** and **2a** was determined to be –81.6 and –78.1 $cm^{-1}$, respectively, thereby indicating an antiferromagnetic interaction. The DFT calculations show that the ground $^2A_u$ state of **1a** has a doublet triradical character and give a reasonable exchange coupling constant $J_{Cu–NO}$ (–110 $cm^{-1}$). Although the present axially coordinated $Cu^{II}$–nitroxide complexes show an antiferromagnetic interaction, this interaction can be attributed to the specific structural features of the coordination pattern of the nitroxide ligand molecules. Unfortunately, the present nitroxide ligand molecules **1** and **2** are contained in mononuclear transition metal complexes. However, it may be possible to build highly dimensional magnetic materials by using radical ligands containing 3- or 4-pyridyl groups to avoid coordination of all the pyridyl groups to a single metal ion.

## Experimental Section

**General Procedures and Materials:** $^1H$ and $^{13}C$ NMR spectra were recorded with a JEOL AL-300 spectrometer, and chemical shifts are given in ppm relative to internal tetramethylsilane (TMS; $\delta$ = 0.0 ppm) for $^1H$ and to $CDCl_3$ for $^{13}C$ NMR spectroscopy. Elemental analyses were performed by the Center for Organic Elemental Microanalysis of Kyoto University. Toluene was distilled from over calcium hydride. 2-Amino-2-methylpropan-1-ol was distilled from over calcium hydride under reduced pressure. THF was distilled from over potassium/benzophenone under argon. *m*-Chloroperbenzoic acid (MCPBA) was obtained commercially (70–75% purity) and used without further purification. All the other purchased reagents and solvents were used without further purification.

**4,4-Dimethyl-2,2-di(2-pyridyl)oxazolidine (5):** This compound was prepared by a modified literature procedure.[32,33] A mixture of bis(2-pyridyl) ketone (9.71 g, 51.7 mmol), freshly distilled 2-amino-2-methylpropan-1-ol (110 mL, 1130 mmol), and concentrated $H_2SO_4$ (25 drops) in toluene (200 mL) was refluxed for 4 d. The water generated was removed by means of a Dean–Stark trap containing 4-Å molecular sieves. The reaction mixture was then cooled to room temperature and concentrated under reduced pressure. Water (200 mL) and $Et_2O$ (100 mL) were added to the resulting residue and then the organic layer was separated. The aqueous layer was extracted with $CH_2Cl_2$ (2 × 100 mL). The combined organic layers were dried with $MgSO_4$ and the solvents evaporated in vacuo. The residue was recrystallized from cyclohexane to afford **5** (4.39 g, 33%) as a white solid. The mother liquor was evaporated and chromatographed on aluminum oxide (ethyl acetate/*n*-hexane = 1:1 as eluent) to afford additional **5** (8.54 g, 65%). The total yield was 98%. $^1H$ NMR (300 MHz, $CDCl_3$): $\delta$ = 8.55 (d, $J$ = 4.0 Hz, 2 H), 7.75 (d, $J$ = 7.9 Hz, 2 H), 7.63 (td, $J$ = 7.7, 1.6 Hz, 2 H), 7.11–7.16 (m, 2 H), 4.26 (br., 1 H), 3.68 (s, 2 H), 1.21 (s, 6 H) ppm. $^{13}C$ NMR (75.5 MHz, $CDCl_3$): $\delta$ = 162.3, 148.5, 136.3, 122.3, 121.2, 98.9, 77.9, 59.6, 26.6 ppm. $C_{15}H_{17}N_3O$: calcd. C 70.56, H 6.71, N 16.46, O 6.27; found C70.28, H 6.71, N 16.55, O 6.30.

**4,4-Dimethyl-2,2-di(2-pyridyl)oxazolidine-*N*-oxyl (1):** This compound was also prepared by a modified literature procedure.[32] Thus, a solution of MCPBA (4.34 g, ca. 17.6 mmol) in $Et_2O$ (40 mL) was added dropwise to an ice-cooled solution of **5** (3.01 g, 11.8 mmol) in $Et_2O$ (40 mL). The resulting solution was allowed to stand for 4 h. Cold 5% $Na_2CO_3$ aqueous solution (40 mL) was then added to the reaction mixture and the aqueous layer was separated. The organic layer was extracted with cold 5% $Na_2CO_3$ aqueous solution (4 × 40 mL) and the aqueous phases were combined. The aqueous phase was extracted with $CH_2Cl_2$ (5 × 40 mL). The combined organic phase was washed with cold 5% $Na_2CO_3$ solution (2 × 40 mL), dried with $MgSO_4$, and the solvents evaporated in vacuo. The resulting orange solid was chromatographed on silica gel (acetone as eluent). A fraction ($R_f$ = 0.61) afforded **1** as an orange solid (1.99 g, 62%). ESR (X-band, toluene): $g$ = 2.0094 and $a_N$ = 13.7 G. $C_{15}H_{16}N_3O_2$: calcd. C 66.65, H 5.97, N 15.55, O 11.84; found C66.74, H 5.92, N 15.48, O 11.84.

**Bis[2-(3-methylpyridyl)] Ketone (4):** Compound **4** was prepared by a modified literature procedure.[34] *n*BuLi (10.5 mmol, 1.5 M in hexane) was added dropwise to a solution of 2-bromo-5-methylpyridine (1.93 g, 11.0 mmol) in THF (15 mL) at –90 °C (petroleum ether/liquid nitrogen) under argon. The resulting solution was stirred at –90 °C for 1 h, and then a solution of ethyl chloroformate (0.58 g, 5.18 mmol) in THF (2 mL) was added rapidly. After stirring overnight, the reaction mixture was concentrated and $CH_2Cl_2$ (100 mL) and water (100 mL) were added. The organic layer was separated and the aqueous layer was extracted with $CH_2Cl_2$ (4 × 50 mL). The combined organic layer was washed with 10% aqueous $NaHCO_3$, dried with $MgSO_4$, and the solvents evaporated in vacuo. The crude product was chromatographed on silica gel (ethyl acetate as eluent). A fraction ($R_f$ = 0.38) afforded **4** as a pale-

 © 2006 Wiley-VCH Verlag GmbH & Co. KGaA, Weinheim 

yellow solid (yield 0.40 g, 36%). $^1$H NMR (300 MHz, $CDCl_3$): $\delta$ = 8.57 (dd, $J$ = 1.5, 0.7 Hz, 2 H), 8.01 (d, $J$ = 7.9 Hz, 2 H), 7.67 (ddd, $J$ = 7.9, 2.2, 0.7 Hz, 2 H), 2.43 (s, 6 H) ppm. $^{13}$C NMR (75.5 MHz, CDCl3): $\delta$ = 192.8, 152.1, 149.7, 137.0, 136.7, 125.0, 18.7 ppm. $C_{13}H_{12}N_2O$: calcd. C 73.56, H 5.70, N 13.20, O 7.54; found C73.28, H 5.85, N 13.06, O 7.48.

**4,4-Dimethyl-2,2-bis[2-(3-methylpyridyl)]oxazolidine (6):** Compound **6** was obtained from **4** by the same procedure as **5**. The reaction mixture was chromatographed on aluminum oxide (ethyl acetate as eluent) to afford **6** as a pale-yellow solid ($R_f$ = 0.83, yield 97%). $^1$H NMR (300 MHz, $CDCl_3$): $\delta$ = 8.37 (s, 2 H), 7.60 (d, $J$ = 7.9 Hz, 2 H), 7.43 (d, $J$ = 8.1 Hz, 2 H), 4.21 (br., 1 H), 3.67 (s, 2 H), 2.27 (s, 6 H), 1.20 (s, 6 H) ppm. $^{13}$C NMR (75.5 MHz, $CDCl_3$): $\delta$ = 159.7, 148.9, 136.9, 131.6, 120.7, 98.9, 77.9, 59.7, 26.7, 18.0 ppm. $C_{17}H_{21}N_3O$: calcd. C 72.06, H 7.47, N 14.83, O 5.65; found C 72.15, H 7.68, N 14.58, O 5.52.

**4,4-Dimethyl-2,2-bis[2-(3-methylpyridyl)]oxazolidine-*N*-oxyl (2):** Compound **2** was obtained from **6** by the same procedure as **1**. The reaction mixture was chromatographed on a silica gel column (acetone as eluent) to afford **2** as an orange solid ($R_f$ = 0.72, yield 73%). $C_{17}H_{20}N_3O_2$: calcd. C 68.43, H 6.76, N 14.08, O 10.72; found C 68.25, H 6.84, N 13.91, O 10.54.

**General Procedure for the Synthesis of Complexes 1a, 1b, 2a, and 2b:** A solution of the radical ligand (2.0 mmol) in acetonitrile (10 mL) was added to a solution of the appropriate triflate salt (1.0 mmol) in acetonitrile (15 mL). The color of the solution changed to dark green (for the $Cu^{II}$ complexes) or pale yellow (for the $Zn^{II}$ complexes). The resulting solution was filtered and $Et_2O$ vapor was slowly diffused into the solution. The single crystals obtained were suitable for X-ray studies.

**[Cu(CF$_3$SO$_3$)$_2$2$_2$] (1a):** Dark green blocks. $C_{32}H_{32}CuF_6N_6O_{10}S_2$: calcd. C 42.60, H 3.57, N 9.31; found C 42.68, H 3.57, N 9.34.

**[Cu(CF$_3$SO$_3$)$_2$2$_2$]·2CH$_3$CN (2a):** Efflorescent dark-green needles. $C_{40}H_{46}CuF_6N_8O_{10}S_2$: calcd. C 46.17, H 4.46, N 10.77; found C 44.19, H 4.31, N 8.39.

**[Zn(CF$_3$SO$_3$)$_2$1$_2$] (1b):** Yellow blocks. $C_{32}H_{32}F_6N_6O_{10}S_2Zn$: calcd. C 42.51, H 3.57, N 9.30; found C 42.57, H 3.59, N 9.19.

**[Zn(CF$_3$SO$_3$)$_2$2$_2$]·2CH$_3$CN (2b):** Efflorescent yellow needles. $C_{40}H_{46}F_6N_8O_{10}S_2Zn$: calcd. C 46.09, H 4.45, N 10.75; found C 44.55, H 4.26, N 9.15.

**X-ray Crystallographic Studies:** The measurements were performed on a Rigaku/MSC Mercury CCD diffractometer (for **1a**) or a Rigaku RAXIS imaging plate area detector (for **1b**, **2a**, and **2b**) with graphite-monochromated Mo-$K_\alpha$ radiation. The data were collected at a temperature of 103 K (for **1a**) or 123 K (for **1b**, **2a**, and **2b**) to a maximum $2\theta$ value of 54.9° (for **1a** and **2a**) or 60.1° (for **1b** and **2b**). After correction of the raw data for Lorentz and polarization effects, the structure was solved by direct methods (SIR97[35]). The non-hydrogen atoms were refined anisotropically. Hydrogen atoms were included but not refined. For **2a**, hydrogen atoms were refined isotropically. However, for **1a**, **1b**, and **2b** hydrogen atoms were included but not refined. Crystallographic data for these complexes are listed in Table 2.

CCDC-267140 (for **1a**), -267141 (for **2a**), -267142 (for **1b**), and -267143 (for **2b**) contain the supplementary crystallographic data for this paper. These data can be obtained free of charge from The Cambridge Crystallographic Data Center via www.ccdc.cam.ac.uk/data_request/cif.

**Magnetic Susceptibility Measurements:** The magnetic susceptibility was measured on polycrystalline samples of **1a** and **1b** or powder samples of **2a** and **2b** in the 2–300 K temperature range under a field of 500 G with a SQUID magnetometer (Quantum Design MPMS-5S). The data were corrected for magnetization of the sample holder and the magnetic susceptibility was corrected for diamagnetism of the constituent atoms using the Pacault method.[36]

**Calculational Methods:** Density functional theory (DFT) calculations were carried out by using a hybrid method (B3LYP) that combines Becke's three-parameter non-local exchange functional[21] with the non-local correlation functional of Parr and co-workers.[37] All of the computations were performed with the Gaussian 98 package[38] using the LANL2DZ basis set where the pseudopotential proposed by Hay and Wadt[39] is applied to the Cu atom, and the Dunning/Huzinaga valence double-ζ basis set[40] to the H, C, O, and N atoms. We employed the geometrical parameters of the isolated complex molecules of **1a** and **1b** determined by the X-ray crystallography as the geometry for the quantum chemical calculations, without geometry optimizations. DFT doublet, triplet, and quadruplet energies were calculated in straightforward unrestricted fashion (UB3LYP). The open-shell singlet energy for **1b** was estimated by the sum method.[41] Generally speaking, the UB3LYP calculations for the open-shell singlet state give the so-called

Table 2. Crystallographic data for **1a**, **1b**, **2a**, and **2b**.

| | **1a** | **1b** | **2a** | **2b** |
|---|---|---|---|---|
| Empirical formula | $C_{32}H_{32}CuF_6N_6O_{10}S_2$ | $C_{32}H_{32}F_6N_6O_{10}S_2Zn$ | $C_{40}H_{46}CuF_6N_8O_{10}S_2$ | $C_{40}H_{46}F_6N_8O_{10}S_2Zn$ |
| Formula mass | 902.30 | 904.13 | 1040.51 | 1042.34 |
| Crystal system | triclinic | triclinic | triclinic | triclinic |
| Space group | $P\bar{1}$ | $P\bar{1}$ | $P\bar{1}$ | $P\bar{1}$ |
| $a$ [Å] | 7.5928(5) | 7.6792(4) | 13.1699(8) | 12.2718(9) |
| $b$ [Å] | 11.050(1) | 11.1243(9) | 15.9376(8) | 12.9988(2) |
| $c$ [Å] | 12.656(2) | 12.3578(6) | 12.3034(6) | 16.309(1) |
| $\alpha$ [°] | 62.580(2) | 114.878(1) | 97.677(3) | 95.983(6) |
| $\beta$ [°] | 79.239(1) | 99.148(2) | 115.045(1) | 98.322(4) |
| $\gamma$ [°] | 86.508(1) | 93.366(3) | 95.896(1) | 114.940(4) |
| $V$ [Å$^3$] | 925.6(2) | 936.2(1) | 2281.9(2) | 2294.2(2) |
| $Z$ | 1 | 1 | 2 | 2 |
| $T$ [K] | 103 | 123 | 123 | 123 |
| $D_{calcd.}$ [g cm$^{-3}$] | 1.619 | 1.604 | 1.514 | 1.509 |
| Goodness of fit | 1.21 | 1.04 | 0.19 | 1.09 |
| $R$ | 0.051 | 0.047 | 0.038 | 0.074 |
| $R_W$ | 0.075 | 0.104 | 0.042 | 0.096 |

 © 2006 Wiley-VCH Verlag GmbH & Co. KGaA, Weinheim 

broken-symmetry state.[42] In the weak bonding regime, the following relationship is deduced between the energies of the broken-symmetry state ($E_{BS}$) and those of the pure (open-shell) singlet ($E_S$) and triplet states ($E_T$) from which we can estimate the pure singlet energy for complex **1b** [see Equation (7)].

$$E_{BS} = (E_S + E_T)/2 \quad (7)$$

## Acknowledgments

This work was supported by CREST (Core Research for Evolutional Science and Technology) of the Japan Science and Technology Agency (JST) and by a Grant-in-Aid for Scientific Research from the Japan Society for Promotion of Science (JSPS). Calculations were partly carried out at the Supercomputer Laboratory of the Institute for Chemical Research of Kyoto University.

[1] O. Kahn, *Molecular Magnetism*, Wiley-VCH, Weinheim, **1993**.
[2] A. Caneschi, D. Gatteschi, R. Sessoli, *Acc. Chem. Res.* **1989**, *22*, 392.
[3] A. Caneschi, D. Gatteschi, P. Rey, *Prog. Inorg. Chem.* **1991**, *39*, 331.
[4] C. G. Pierpont, C. G. Lange, *Prog. Inorg. Chem.* **1994**, *41*, 331.
[5] D. J. R. Brook, V. Lynch, B. Conklin, M. A. Fox, *J. Am. Chem. Soc.* **1997**, *119*, 5155.
[6] B. D. Koivisto, R. G. Hicks, *Coord. Chem. Rev.* **2005**, *249*, 2612.
[7] M. Jenings, K. E. Preuss, J. Wu, *Chem. Commun.* **2006**, 341.
[8] A. Caneschi, D. Gatteschi, P. Rey, R. Sessoli, *J. Am. Chem. Soc.* **1987**, *109*, 2191.
[9] D. Luneau, P. Rey, J. Laugier, P. Fries, A. Caneschi, D. Gatteschi, R. Sessoli, *J. Am. Chem. Soc.* **1991**, *113*, 1245.
[10] K. Inoue, H. Iwamura, *J. Am. Chem. Soc.* **1994**, *116*, 3173.
[11] K. Inoue, T. Hayamizu, H. Iwamura, D. Hashizume, Y. Ohashi, *J. Am. Chem. Soc.* **1996**, *118*, 1803.
[12] G. Francese, F. M. Romero, A. Neels, H. Stoeckli-Evans, S. Decurtins, *Inorg. Chem.* **2000**, *39*, 2087.
[13] D. Luneau, F. M. Romero, R. Ziessel, *Inorg. Chem.* **1998**, *37*, 5078.
[14] Y. Pei, A. Lang, P. Bergerat, O. Kahn, M. Fettouhi, L. Ouahab, *Inorg. Chem.* **1996**, *35*, 193.
[15] K. Fegy, D. Luneau, T. Ohm, C. Paulsen, P. Rey, *Angew. Chem. Int. Ed.* **1998**, *37*, 1270.
[16] K. E. Vostrikova, E. Belorizky, J. Pécaut, P. Rey, *Eur. J. Inorg. Chem.* **1999**, 1181.
[17] R. D. Shannon, *Acta Crystallogr., Sect. A* **1976**, *32*, 751.
[18] F. A. Cotton, G. Wilkinson, *Advanced Inorganic Chemistry*, Wiley, New York, **1980**.
[19] A. Bondi, *J. Phys. Chem.* **1964**, *68*, 441.
[20] B. Bleaney, K. Bowers, *Proc. R. Soc. London*, *Ser. A* **1952**, *214*, 451.
[21] S. Fokin, V. Ovcharenko, G. Romanenko, V. Ikorskii, *Inorg. Chem.* **2004**, *43*, 969.
[22] A. Caneschi, D. Gatteschi, A. Grand, J. Laugier, L. Pardi, P. Rey, *Inorg. Chem.* **1988**, *27*, 1031, and references cited therein.
[23] Y. Y. Lin, R. S. Drago, *Inorg. Chem.* **1972**, *11*, 1334.
[24] L. C. Porter, R. J. Doedens, *Inorg. Chem.* **1985**, *24*, 1006.
[25] K. Ragavachari, *Theor. Chem. Acc.* **2000**, *103*, 361 and references cited therein.
[26] L. Noodleman, *J. Chem. Phys.* **1981**, *74*, 5737.
[27] M. Nishino, S. Yamanaka, Y. Yoshioka, K. Yamaguchi, *J. Phys. Chem. A* **1997**, *101*, 705.
[28] E. Ruiz, J. Cano, S. Alvarez, P. Alemany, *J. Comput. Chem.* **1999**, *20*, 1391.
[29] T. Onishi, D. Yamaki, K. Yamaguchi, Y. Takano, *J. Chem. Phys.* **2003**, *118*, 9747.
[30] E. Ressouche, J.-X. Boucherle, B. Gillon, P. Rey, J. Schweizer, *J. Am. Chem. Soc.* **1993**, *115*, 3610.
[31] R. N. Musin, P. V. Schastnev, S. A. Malinovskaya, *Inorg. Chem.* **1992**, *31*, 4118.
[32] J. F. W. Keana, S. B. Keana, D. Beetham, *J. Am. Chem. Soc.* **1967**, *89*, 3055.
[33] G. R. Newkome, H. C. R. Taylor, F. R. Fronczek, T. J. Delord, *J. Org. Chem.* **1984**, *49*, 2961.
[34] G. R. Newkome, G. E. Kiefer, Y. A. Frere, M. Onishi, V. K. Gupta, F. R. Fronczek, *Organometallics* **1986**, *5*, 348.
[35] A. Altomare, M. C. Burla, M. Camalli, G. L. Cascarano, C. Giacovazzo, A. Guagliardi, A. G. G. Moliterni, G. Polidori, R. Spagna, *J. Appl. Crystallogr.* **1999**, *32*, 115.
[36] R. R. Gupta, *Landolt-Börnstein, New Series II* (Eds.: K.-H. Hellwege, A. M. Hellwege), Springer Verlag, Berlin, **1986**, vol. 16 (Diamagnetic Susceptibility).
[37] C. Lee, W. Yang, R. G. Parr, *Phys. Rev. B* **1998**, *37*, 785.
[38] M. J. Frisch, G. W. Trucks, H. B. Schlegel, G. E. Scuseria M. A. Robb, J. R. Cheeseman, V. G. Zakrzewski, J. A. Montgomery Jr, R. E. Stratmann, C. J. Burant, S. Dapprich, J. M. Millam, A. M. Daniels, K. N. Kudin, M. C. Strain, O. Farkas, J. Tomasi, V. Barone, M. Cossi, R. Cammi, B. Mennuchi, C. Pomelli, C. Adamo, S. Clifford, J. Ochterski, A. G. Petersson, Y. P. Ayala, Q. Cui, K. Morokuma, K. D. Malick, D. A. Rabuck, K. Raghavachari, B. J. Foresman, J. Cioslowski, J. V. Ortiz, B. B. Stefanov, G. Liu, A. Liashenko, P. Piskorz, I. Komaromi, R. Gomperts, R. L. Martin, D. J. Fox, T. Keith, M. A. Al-Laham, C. Y. Peng, A. Nanayakkara, V. G. Zakrzewski, M. Challacombe, P. Y. Ayala, W. Chen, M. W. Wong, J. L. Andres, C. Gonzalez, M. Head-Gordon, E. S. Replogle, J. A. Pople, *Gaussian 98*, *Revision A.9*, Gaussian Inc., Pittsburgh, PA, **1998**.
[39] P. J. Hay, W. R. Wadt, *J. Chem. Phys.* **1985**, *82*, 299.
[40] T. H. Dunning Jr, P. J. Hay, *Modern Theoretical Chemistry* (Ed.: H. F. Schafer, III), Plenum, New York, **1976**, vol. 3, pp. 1–28.
[41] C. J. Cramer, B. A. Smith, *J. Phys. Chem.* **1996**, *100*, 9664.
[42] J. Cano, P. Alemany, S. Alvarez, M. Verdaguer, E. Ruiz, *Chem. Eur. J.* **1998**, *4*, 476.

Received: January 27, 2006
Published Online: July 24, 2006

 © 2006 Wiley-VCH Verlag GmbH & Co. KGaA, Weinheim 

DOI: 10.1002/ejic.200600354

# Synthesis, Crystal Structures, Cation-Binding Properties and the Influence of Intramolecular C–H···O Interactions on the Complexation Behaviour of a Family of Cone *p-tert*-Butylcalix[4]arene-crown-5 Compounds

**Pragati Agnihotri,[a] Eringathodi Suresh,[a] Parimal Paul,*[a] and Pushpito K. Ghosh*[a]**

**Keywords:** Calixarenes / Crown compounds / Selectivity / Association constants

A family of cone *p-tert*-butylcalix[4]arene-crown-5 compounds with various substituents (H, $COCH_3$, $CH_2CO_2C_2H_5$ and $CH_2CO_2H$) appended at the opposite phenolic oxygen atoms have been synthesised to evaluate their efficiency and selectivity towards different alkali and alkaline-earth metal ions, and also to ascertain the role of the appended side-arms in the complexation process. The selectivity of these ionophores towards $Na^+$, $K^+$, $Mg^{2+}$, and $Ca^{2+}$ has been evaluated with an aqueous solution containing an equimolar mixture of these ions. The concentration of metal ion in the extract (organic phase) has been estimated by ion chromatographic assay. Among these ions, $K^+$ shows the highest selectivity in all cases except one, where the two phenolic oxygen atoms contain $COCH_3$ substituents. All the ionophores show poor selectivity towards $Mg^{2+}$ and $Ca^{2+}$. Association constants ($K_a$) for the binding of $Na^+$ and $K^+$ to these ionophores have been determined spectrophotometrically. $K_a$ ($7.2\times10^7$) is highest for the binding of $K^+$ to the ionophore with $CH_2CO_2C_2H_5$ substituents. The molecular structures of four of the ionophores and four of the metal complexes have been established by single-crystal X-ray crystallography. Analysis of the structures revealed that in case of the ionophore with two $COCH_3$ substituents, the C–H···O interactions form an eight-membered zigzag ring almost perpendicular to the crown ring, which prevents entry of the metal ions into the calix-crown cavity. The ionophore with $CH_2CO_2C_2H_5$ substituents, where no such interaction is observed, forms metal complexes easily and exhibits the highest association constant. $^1H$ and $^{13}C$ NMR studies have also been carried out to investigate the conformational behaviour of these ionophores and their metal complexes in solution.

(© Wiley-VCH Verlag GmbH & Co. KGaA, 69451 Weinheim, Germany, 2006)

## Introduction

Calixarenes, which are macrocyclic oligomers made up of phenol units linked by a methylene bridge, are receiving increasing attention because of their ability to bind guest molecules or ions.[1] In the calixarene family, calix[4]arenes are most popular because of their rigid structures, which make them ideal candidates for the complexation of neutral molecules or ions.[1,2] This chemistry has become even more versatile because of the ease with which calix[4]arenes can be modified with functional groups at either the lower or upper rims, or both, depending on the requirements. These modified calixarenes provide a highly pre-organized architecture for the assembly of converging binding sites.[3] Among these calixarene derivatives, calix[4]arene-crown ethers have attracted intense interest as selective alkali metal extractants.[4] The ion selectivity of this class of compounds is controlled mainly by the conformation of the calixarene platform, the size of the crown ether ring, the substituents at the upper rim of the calixarene and the appended functional groups at the two sides of the crown ring. Among various conformations of the calixarene, 1,3-alternate conformers have been studied more extensively as complexing agent for alkali metal ions.[4b,4c,4f,5] Other conformers have also been prepared but metal ion complexation studies are rare.[4a,4d] Among various crown ether rings, crown-5- and crown-6-containing calixarene derivatives have been found to be more suitable for complexation with alkali metal ions.[4] A number of calix[4]-bis(crown ethers) and their complexation behaviour, mainly with cations of large size, have also been reported.[6]

It has been observed that the substituents at the lower rim determine the conformations of the calixarenes. Calix[4]arene-crown ether derivatives in 1,3-alternate conformation have been studied most since they are more efficient and selective in the complexation of potassium ions.[5] The ionophores *p-tert*-butylcalix[4]arene-crown derivatives, which have not been studied extensively, exist in cone, partial cone and 1,3-alternate conformations.[4a,4g,7] In the latter case, the desired conformation can be obtained by manipulating the experimental conditions and reagents.[4g,8] It should be noted that the selectivity and efficiency of extraction of alkali and alkaline-earth metal ions is maximal with

[a] Analytical Science Division, Central Salt and Marine Chemicals Research Institute,
Bhavnagar 364002, India
E-mail: ppaul@csmcri.org
pkghosh@csmcri.org

Supporting information for this article is available on the WWW under http://www.eurjic.org or from the author.

 © 2006 Wiley-VCH Verlag GmbH & Co. KGaA, Weinheim 

the cone conformation of *p-tert*-butylcalix[4]arene-crown derivatives, except for one report in which a partial cone conformation was reported to exhibit high $K^+/Na^+$ selectivity.[4a]

As part of our effort to identify suitable options for selective extraction of $K^+$ from natural sources such as brine and bittern, which mainly contain $Na^+$, $K^+$, $Ca^{2+}$ and $Mg^{2+}$,[9] we here report our studies on competitive binding of these ions with *p-tert*-butylcalix[4]arene-crown-5 derivatives in the cone conformation (Figure 1). The effect of appended substituents on complexation and the structural features of the ionophores before and after complexation in solution and the solid state, as probed by NMR spectroscopic and single-crystal X-ray studies, are reported. These studies have enabled us to unravel structural features of the ionophores and their complexes; in particular, the influence of intramolecular hydrogen bonding on complexation.

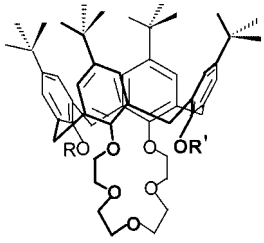


Figure 1. Structures of the ionophores (**1**–**5**) used in this study.

## Results and Discussion

### Synthesis of Ligands 1–5

The compound *p-tert*-butylcalix[4]arene-crown-5 (**1**) was synthesised by the reaction of *p-tert*-butylcalix[4]arene, tetraethylene glycol ditosylate and *t*BuOK (Scheme 1) according to a modified literature procedure.[4a] The conformation of the calix-crown products depends on the reaction conditions and reagents used; the cone conformation needed for the complexation study could be obtained in good yield. For the synthesis of acetyl derivatives of **1**, we attempted the reaction at room temperature with acetyl chloride and acetyl bromide, using NaH as base and diethyl ether as solvent. However, a mixture of mono- and diacetyl derivatives was obtained, with the former as the major product even after extended (3 d) stirring. We optimised the reaction conditions in diethyl ether to maximize the yield of the monoacetyl derivative, and compound **2** was obtained in cone conformation after purification by column chromatography. By switching the solvent from diethyl ether to THF and conducting the synthesis under reflux conditions, we were successful in obtaining the diacetyl derivative **3** in good yield. Compound **4** was obtained in cone conformation by the reaction of **1** with ethyl bromoacetate in the presence of $K_2CO_3$ under reflux in acetonitrile. Hydrolysis of **4** yielded the corresponding acid **5** in good yield. During preparation of this manuscript, a paper has appeared on the synthesis of **4** and **5** and use of the latter as a proton di-ionisable extractant for $Mg^{2+}$, $Ca^{2+}$, $Sr^{2+}$ and $Ba^{2+}$; however, this study is quite different from that reported here.[10]

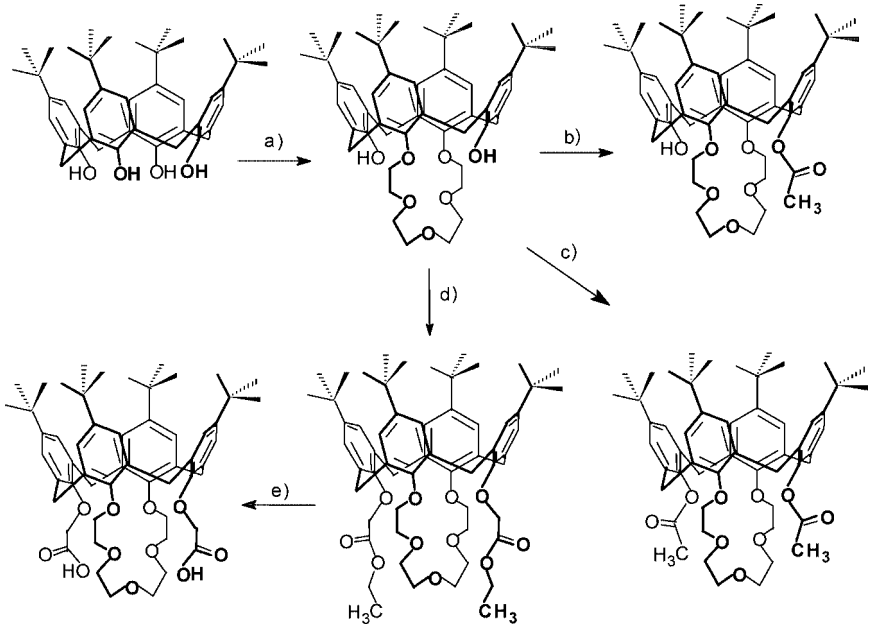


Scheme 1. Synthesis of *p-tert*-butylcalix[4]arene-crown-5 compounds; a) $OTsCH_2(CH_2OCH_2)_2CH_2OTs$, *t*BuOK, benzene; b) $CH_3COBr$, NaH, diethyl ether; c) $CH_3COBr$, NaH, THF; d) $BrCH_2CO_2C_2H_5$, $K_2CO_3$, $CH_3CN$; e) NaOH, ethanol.

 © 2006 Wiley-VCH Verlag GmbH & Co. KGaA, Weinheim 

### Synthesis of $Na^+$ and $K^+$ Complexes of 1–5

Reaction of the ligands with a ten-fold excess of metal picrate in chloroform resulted in the formation of 1:1 metal complexes. In the case of **3**, however, the $Na^+$ complex (**3**·$Na^+Pic^-$, Pic = picrate) was only obtained in poor yield, and virtually no complex formation took place with $K^+$, as evident from the $^1H$ NMR spectrum. Hence, the $K^+$ complex of **3** is not discussed further.

All of these ligands and metal complexes gave satisfactory C, H, and N analyses. The mass spectra of all these ligands and metal complexes were recorded and the observed *m*/*z* values show excellent agreement with the calculated values. It may be noted that the *m*/*z* values (100%) of all ligands correspond to the $Na^+$ adduct [ligand + Na]$^+$, which is a well-known phenomenon in LC mass spectrometry. The potassium and sodium complexes of the ligands (complex formation was confirmed by NMR studies and X-ray structure determination; vide infra) exhibit molecular ion peaks corresponding to [ligand + K]$^+$ and [ligand + Na]$^+$, respectively.

### NMR Study

The $^1H$ and $^{13}C$ NMR spectra of all compounds were recorded in $CDCl_3$ and the data are presented in the Experimental Section. The NMR spectroscopic data established the conformation of the ligands and complexes in solution. The $^1H$ NMR spectra of these compounds exhibit two signals for the aromatic protons, two doublets for the bridging methylene groups of the calixarene unit and two singlets for the *tert*-butyl groups. In the case of **2** and its complexes, however, the spectra are more complex because of asymmetric substituents at the *p*-hydroxy positions of the opposite benzene rings (OH and $COCH_3$). In all of these ionophores and complexes, a typical AB pattern was observed for the methylene bridge (Ar$CH_2$Ar) protons, that is, two widely separated doublets at $\delta$ = 3.90–4.65 and 3.12–3.36 ppm ($J$ = 12–13.8 Hz), which suggests that these ionophores exist in a cone conformation in solution.[4a,11] The low-field doublet is due to the axial H atom and the high-field doublet is due to the equatorial H atom of the methylene bridge. The chemical shift difference ($\Delta\delta$) between $H_{axial}$ and $H_{equatorial}$ serves as a measure of the "flattening" of each phenyl unit.[1a,12] In general, $\Delta\delta$ = 0.9 ppm for a system in the regular cone conformation, and for a more "flattened" conformation the value of $\Delta\delta$ decreases. For compounds **1**–**5**, the $\Delta\delta$ values are 0.78, 0.89 (1.31 for another ring), 0.78, 1.48 and 1.10 ppm, respectively. These data indicate that the "flattening" of the phenyl rings is greater in **1** and **3** and lesser in **4** and **5** than that of the regular cone conformation.[4a] The reduced "flattening" in **4** and **5** is because of steric crowding caused by bulky substituents at the narrow lower rim of the calix[4]arene-crown moiety. The $\Delta\delta$ values for the metal complexes of **1**–**3** could not be calculated because of the overlapping of signals from the high-field doublet and crown moiety. However, for the complexes of **4** and **5** these values are in the range 1.07–1.12 ppm, thus indicating that the structures of the metal complexes in solution are close to a regular cone conformation. The difference between the two signals due to phenyl groups and also due to *tert*-butyl groups observed for the free ligand are significantly reduced ($\leq$0.1) in the complexed state. This is presumably because insertion of a metal ion into the crown cavity provides a similar geometrical shape of the complexed molecule. It should be noted that the two appended $CH_2CO_2C_2H_5$ groups of **4**·$Na^+Pic^-$ and **4**·$K^+Pic^-$ exhibit one set of signals [$\delta$ = 4.77 (s), 4.32 (q) and 1.33 (t) ppm for **4**·$Na^+Pic^-$ and $\delta$ = 4.57 (s), 4.32 (q) and 1.33 (t) ppm for 4·$K^+Pic^-$ (Figure 2)] thus indicating that both groups in each compound are chemically equivalent in solution. A similar observation was also noted for the complexes of **3** and **5**, in which two appended $COCH_3$ and $CH_2CO_2H$ groups are present, respectively. Interestingly, the crystal structures of **4**·$Na^+Pic^-$, **4**·$K^+Pic^-$ and **5**·$K^+Pic^-$ (see below) show that only one of the two appended groups in each complex is connected to a metal ion through its oxygen atom. Therefore, two sets of signals for two non-equivalent appended groups in each complex are expected. The appearance of only one set of signals suggests exchange of coordination between the appended groups and the metal ion in solution. This exchange process is fast enough on the NMR timescale to make them indistinguishable. Another unprecedented observation is noted for the signals for the phenyl and *tert*-butyl protons of the complexes of **1**. Ligand **1** shows two signals for the phenyl protons and two signals for the *tert*-butyl protons. However, in the complexes one of the signals (high-field) of the phenyl protons is found to split to produce two signals at $\delta$ = 6.73 (1 H) and 6.63 (3 H) ppm for **1**·$Na^+Pic^-$ and $\delta$ = 6.74 (1 H) and 6.61 (3 H) ppm for **1**·$K^+Pic^-$. The high-field signal for *tert*-butyl is also seen to split to produce signals at $\delta$ = 1.20 (3 H), 0.92 (3 H) and 0.83 (12 H) ppm for **1**·$Na^+Pic^-$ and $\delta$ = 1.20 (3 H), 0.93 (3 H) and 0.81 (12 H) ppm for **1**·$K^+Pic^-$. The possibility of the formation of other conformations can be ruled out on the basis of full NMR spectroscopic data. The crystal structure of **1**·$K^+Pic^-$ shows that the picrate anion is coordinated to the metal ion in a bidentate fashion through the oxygen atoms of the deprotonated phenolic group and one of the nitro groups. Beer et al. have noted similar observations in the lanthanide picrate complexes of their *tert*-butylcalix[4]arene diamide ligand.[13]

Analysis of the crystal structure of **1**·$K^+Pic^-$ shows that the benzene ring of the picrate anion is in proximity, and almost parallel to, one of the benzene rings of the calixarene ($C_g$–$C_g$ distance is 3.76 Å and the dihedral angle between the planes of the rings is 13.72°). The structural analysis shows that one of the phenyl protons and a few of the *tert*-butyl protons of one of the benzene rings of the calixarene are pointed towards the deshielding zone of the benzene ring of the picrate anion, which results in a splitting of the signals for the phenyl and *tert*-butyl protons.[14] Because of this deshielding effect, the signals of one of the phenyl protons and two methyl groups of the *tert*-butyl moiety are shifted downfield; the shift of one of the methyl groups is quite pronounced.

 © 2006 Wiley-VCH Verlag GmbH & Co. KGaA, Weinheim 

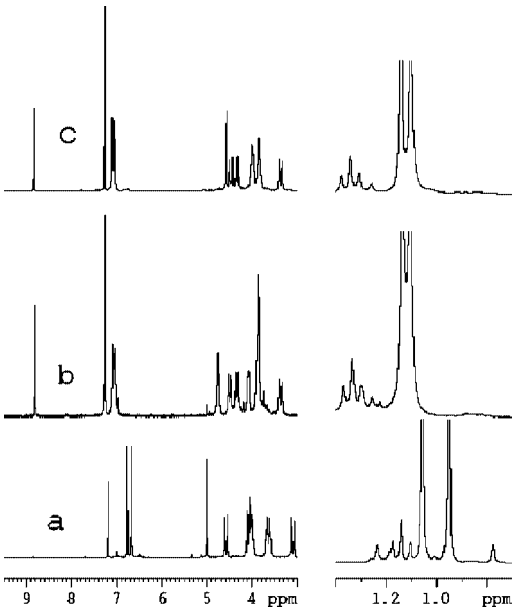


Figure 2. $^1$H NMR spectra of ionophore **4** (a), its $Na^+$ (**4**·$Na^+Pic^-$) (b) and $K^+$ complexes (**4**·$K^+Pic^-$) (c), recorded in $CDCl_3$ at room temperature.

In the $^{13}$C NMR spectra, the signals of the carbon atoms of the four methylene bridges (Ar$CH_2$Ar) appear at the same position (one peak), with a chemical shift of $\delta \approx$ 31 ppm, which is typical for the cone conformation of *tert*-butylcalix[4]arene derivatives.[4g,15] The other observation is that the C-1 and C-4 carbon atoms (see Figure 3 for the numbering scheme) show two signals each, which could be due to different substituents attached to the carbon atoms at the lower rim of the calixarene. In the metal complexes, the $^{13}$C NMR signals are consistent with the cone conformation of the calixarene moiety albeit with some changes in chemical shift for the carbon atoms of the crown moiety, due to complex formation, compared to the free ligand.

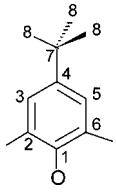


Figure 3. Numbering scheme for carbon atoms of the *p-tert*-butylcalix[4]arene used in the NMR discussion.

## Crystal Structures

X-ray crystal structures of four ionophores and four complexes have been determined; ORTEP views of the ionophores are displayed in Figure 4. The structures of the ionophores clearly show the flattened cone conformation, as suggested by the NMR spectroscopic data. However, the extent of flattening differs from ligand to ligand. The interplanar angles between the two opposite rings are 71.89° and 41.10° (82.67° and 35.60° for the other molecule in the unit cell) for **1**, 87.00° and 7.40° for **2**, 60.66° and 39.82° for **3** and 78.10° and 29.18° for **4**. The opposite benzene rings, which are connected to the crown moiety, are less flattened, as evident from their low inter-planar angles. The wide variations in flattening of the rings are due to steric overcrowding of the bulky substituents at the lower rim of the rings and also due to intramolecular C–H···O interactions. It should be noted that the oxygen atoms of the CO groups of the $COCH_3$ substituent in **2** and **3** and the $CH_2COOC_2H_5$ substituent of **4** are directed away from the polyether rings, which could be due to minimisation of the electrostatic repulsion between the lone pairs of the oxygen atoms of the CO and polyether rings. Most of the appended groups show hydrogen-bonding interactions with the oxygen atoms of the polyether rings. There are many examples of hydrogen-bonding interactions involving OH groups at the lower rim of the calixarene,[16] although hydrogen-bonding interactions involving other groups are not common. In case of **1**, the hydrogen atoms of the OH groups (O6–H6 and O7–H7) make strong O–H···O interactions with O5 and O1, which act as donors; O7, on the other hand, acts as an acceptor, making C–H···O interactions with H48A and H50B of the methylene groups of the polyether ring. The interesting feature of the packing is the dimeric association of the two ligands A and B present in the asymmetric unit. This occurs by an intermolecular C–H···O interaction involving H10K attached to C101 and the phenolic oxygen atom O6. Two such hydrogen-bonded dimers are further associated by a C–H···π interaction to form a tetrameric unit (Figure 5). Details of C–H···O, C–H···N, and C–H···π interactions of **1**–**3** and **4** are given in Table S1 in the Supporting Information. In the case of **2**, the hydrogen atom (H1) of the phenolic oxygen atom O1 is involved in a strong intramolecular O–H···O interaction with O4. Two of the methyl hydrogen atoms of the acetyl moiety (H46B and H46C) make intramolecular C–H···O interactions with O4 and O8 of the crown moiety. A packing diagram of **2** showing the one-dimensional array formed by intermolecular hydrogen-bonding interactions between adjacent molecules is depicted in Figure S1 (Supporting Information).

The intramolecular hydrogen-bonding pattern of **3** is interesting and provides important information regarding its robustness towards complexation with $K^+$. In this compound, it has been observed that the two H atoms of each methyl group of the two appended $COCH_3$ groups (H46B, H48C and H46C, H48B) are close to the oxygen atoms of the polyether ring and are held strongly by C–H···O interactions with O6 and O8 of the crown moiety (Table 1) In fact, this hydrogen bonding forms an eight-membered puckered ring, which is nearly perpendicular to the crown ring (79.33°) and crosses it through the middle (Figure 6). We believe this interaction also exists in solution and, therefore, metal ions such as $K^+$ cannot enter into the cavity to form metal complexes. The packing diagram of **3**, which shows a dimeric association of the molecule through intermolecular interactions involving surrounding lattice solvent molecules, is shown in Figure S2 (Supporting Information).

 © 2006 Wiley-VCH Verlag GmbH & Co. KGaA, Weinheim 

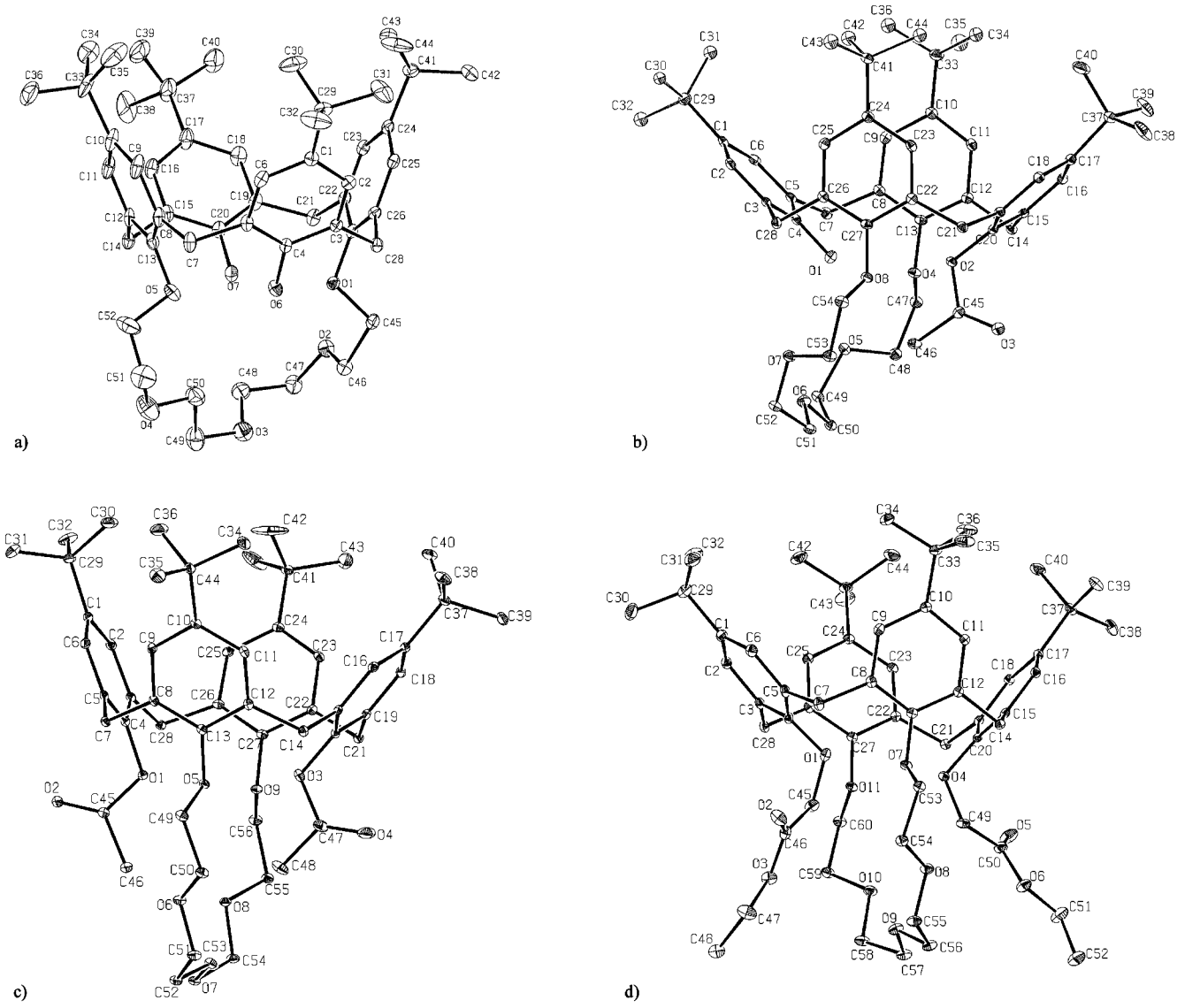


Figure 4. ORTEP views of compounds **1** (a), **2** (b), **3** (c) and **4** (d).

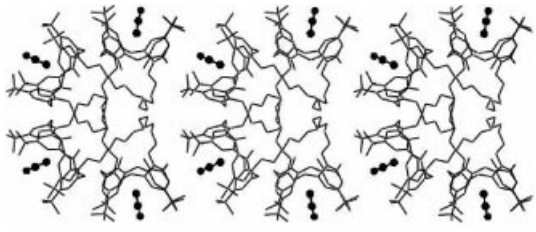

Figure 5. Packing diagram of **1** viewed along the *a*-axis showing the tetrameric association of the compound with acetonitrile (ball-and-stick model) in the cavity of the calix cone.

Table 1. Intramolecular C–H···O interactions involving methyl hydrogen atoms of $COCH_3$ and oxygen atoms of the crown ring for **3**.

| D–H···A | H···A [Å] | D···A [Å] | <(D–H···A) [°] |
|---|---|---|---|
| C46–H46B···O6 | 2.30 | 3.240(3) | 167 |
| C46–H46C···O8 | 2.32 | 3.269(3) | 168 |
| C48–H48B···O8 | 2.44 | 3.315(4) | 151 |
| C48–H48C···O6 | 2.40 | 3.255(4) | 149 |

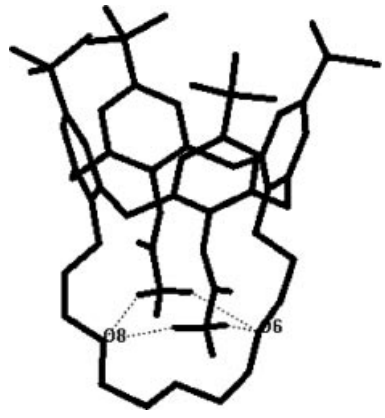


Figure 6. Capped stick model of compound **3**, showing C–H···O interactions (dotted line) involving methyl hydrogen atoms of $COCH_3$ groups and oxygen atoms (O6 and O8) of the crown moiety.

 © 2006 Wiley-VCH Verlag GmbH & Co. KGaA, Weinheim 

In the case of **4** the C–H···O interactions involving the crown ring are not significant. The only interaction observed is that between the hydrogen atoms (H49A) of the $CH_2COOC_2H_5$ moiety and O9 of the crown ring. However, the oxygen atoms of the CO groups of both $CH_2COOC_2H_5$ moieties form C–H···O interactions with the hydrogen atoms of the bridging methylene group. The packing diagram of **4** is also available as Supporting Information (Figure S3).

All of the above ligands contain lattice solvent molecule(s) and these appear to play a role in crystal formation. One of the acetonitrile molecules present in the crystal occupies the cone cavity of the calixarene unit in all cases. This acetonitrile molecule is held in the cavity and forms C–H···N interactions with the hydrogen atom of one of the bridging ethylene groups and C–H···π interactions with the benzene rings of the calixarene moiety.

The crystal structures of the metal complexes reveal that the $K^+$ ion is coordinated to eight oxygen atoms in all complexes whereas the $Na^+$ ion in **4**·$Na^+Pic^-$ is coordinated to six oxygen atoms (Figure 7). In **1**·$K^+Pic^-$, where eight coordination sites with oxygen atoms as donor are not available,

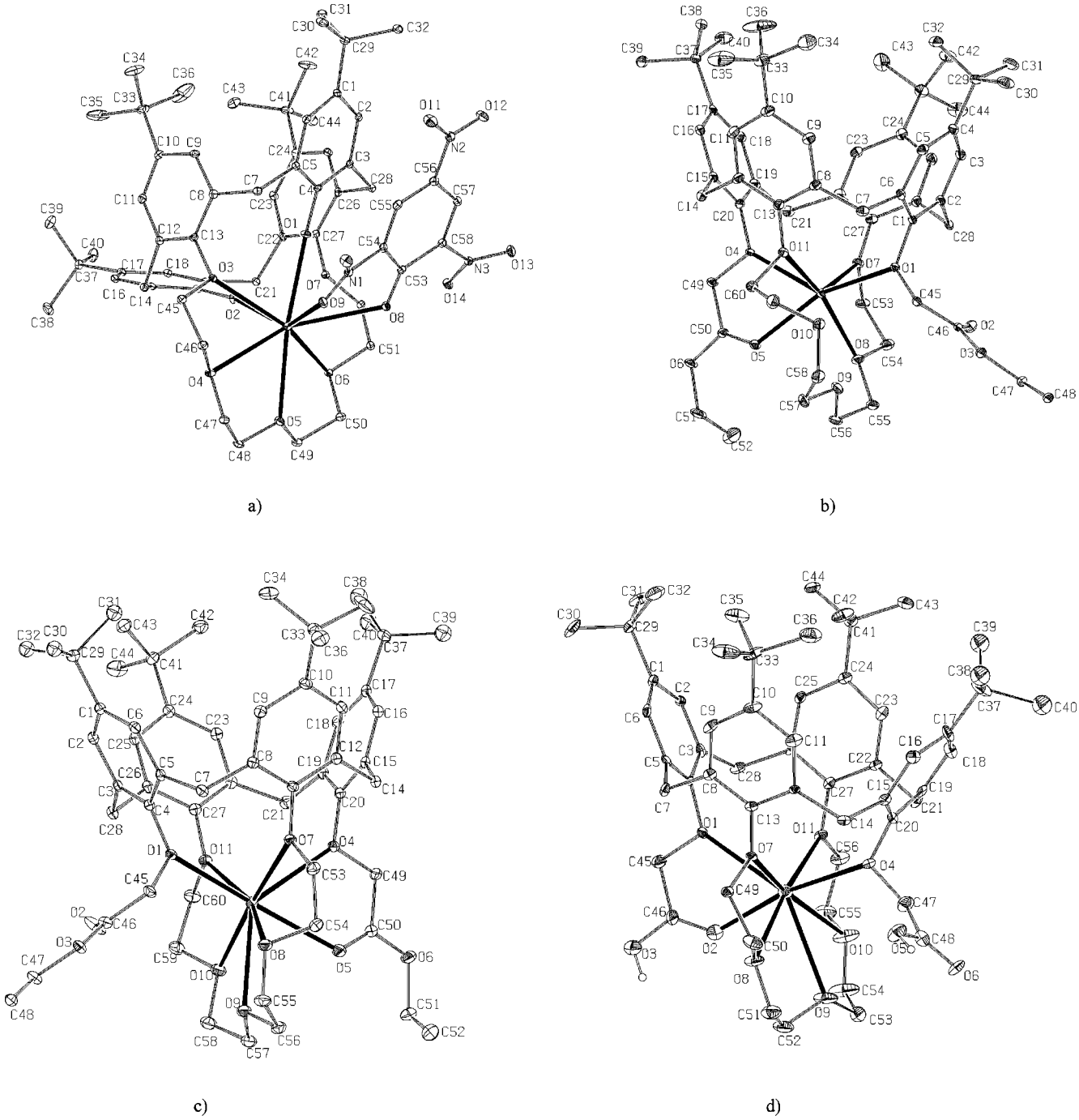


Figure 7. ORTEP views of complexes **1**·$K^+Pic^-$ (a), **4**·$Na^+Pic^-$ (b), **4**·$K^+Pic^-$ (c), and **5**·$K^+Pic^-$ (d).

 © 2006 Wiley-VCH Verlag GmbH & Co. KGaA, Weinheim 

the picrate anion acts as a bidentate ligand to make $K^+$ octacoordinate. For complexes **4**·$Na^+Pic^-$, **4**·$K^+Pic^-$ and **5**·$K^+Pic^-$, out of two $CH_2CO_2C_2H_5$ and $CH_2CO_2H$ appended arms, the oxygen atom of the CO group of one arm is coordinated to $K^+$. In the case of **4**·$Na^+Pic^-$, however, two oxygen atoms (O9 and O10) of the crown moiety are not coordinated to $Na^+$. The M–O distances of all complexes are given in Table 2. In the metal complexes, the cone conformations of the calixarene moieties are more symmetric than those of the corresponding free ligands. For example, all the four phenyl rings of **4**·$K^+Pic^-$ make similar angles of intersection with the plane of the four rim methylene groups (64.50–69.92°) and the inter-planar angles between the two opposite rings are 45.63° and 54.25°, which suggests an almost symmetric cone conformation of the calixarene unit.

Table 2. Metal–oxygen bond lengths [Å] for complexes **1**·$K^+Pic^-$, **4**·$Na^+Pic^-$, **4**·$K^+Pic^-$, and **5**·$K^+Pic^-$.

| | | | |
|---|---|---|---|
| **1**·$K^+Pic^-$ | | | |
| K1–O9 | 2.700(2) | K1–O2 | 2.824(2) |
| K1–O5 | 2.703(2) | K1–O4 | 2.845(2) |
| K1–O1 | 2.711(2) | K1–O8 | 2.890(2) |
| K1–O3 | 2.726(2) | K1–O6 | 3.013(2) |
| **4**·$Na^+Pic^-$ | | | |
| Na1–O5 | 2.367(3) | Na1–O7 | 2.405(3) |
| Na1–O11 | 2.375(3) | Na1–O8 | 2.420(3) |
| Na1–O1 | 2.394(3) | Na1–O4 | 2.543(3) |
| **4**·$K^+Pic^-$ | | | |
| K1–O1 | 2.657(2) | K1–O7 | 2.801(2) |
| K1–O5 | 2.659(3) | K1–O4 | 2.803(2) |
| K1–O11 | 2.712(2) | K1–O9 | 2.836(3) |
| K1–O10 | 2.758(3) | K1–O8 | 2.931(3) |
| **5**·$K^+Pic^-$ | | | |
| K1–O1 | 2.742(6) | K1–O8 | 2.760(6) |
| K1–O2 | 2.561(8) | K1–O9 | 2.971(8) |
| K1–O4 | 2.566(5) | K1–O10 | 2.926(6) |
| K1–O7 | 2.703(4) | K1–O11 | 2.704(4) |

Analysis of the crystal structures revealed that each of these structures make a number of intra- and intermolecular C–H···O interactions, leading to layered or zigzag chain network of packing. Packing diagrams (Figures S4–S7) and a table of hydrogen-bonding interactions (Table S2) for all these complexes are available as Supporting Information. Some of the solvent molecules and picrate anions are highly disordered, as discussed in the Experimental Section.

## Selectivity

The selectivities of these ionophores toward metal ions such as $Na^+$, $K^+$, $Mg^{2+}$ and $Ca^{2+}$ were determined by a two-phase extraction method followed by ion chromatographic assay of the metal ions in the extract.[9] The experiments were carried out with an aqueous solution containing equimolar amounts of $Na^+$, $K^+$, $Mg^{2+}$ and $Ca^{2+}$ as their picrate salts, as described in the Experimental Section. Chromatograms of the original solution and that of the extract obtained using **4** are given in Figure 8. The distributions of metal ions in the organic extracts, together with values of the observed selectivity ratios, are given in Table 3. As can be seen from the data, all ionophores except **3** show high selectivity towards $K^+$, this selectivity being highest for **4** (82.1%). From the crystal structures it appears that the calix-crown cavity fits well with $K^+$, allowing it to coordinate to all the oxygen donors of the cavity. $Na^+$ also coordinates, but it does not fit well in the cavity and leaves two oxygen atoms of the crown ring uncoordinated. $Mg^{2+}$ and $Ca^{2+}$ show poor selectivity.

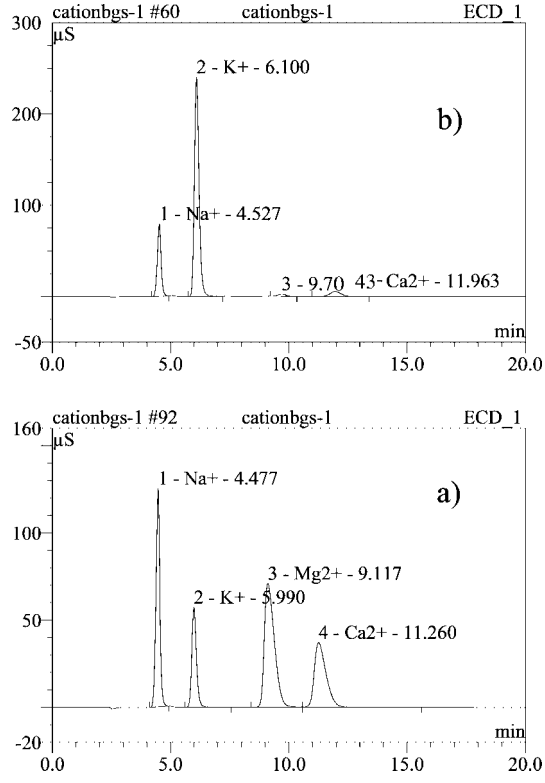


Figure 8. Ion chromatograms of a) a solution containing an equimolar mixture of $Na^+$, $K^+$, $Mg^{2+}$, and $Ca^{2+}$ and b) the extract obtained from the equimolar mixture by two-phase extraction using ionophore **4**.

Apart from cavity size, the C–H···O interactions involving oxygen atoms of the crown ring observed in some of these compounds play an important role in complex formation. In the ionophores **2**–**5**, the main coordination core (calix-crown moiety) for all of them is the same, with one of the appended arms taking part in coordination. However, the selectivity for a particular metal ion (e.g. $K^+$) differs significantly. The crystal structures show that in the case of **2**, one side of the crown ring is blocked by strong C–H···O interactions between two of the methyl protons of $COCH_3$ and the oxygen atoms of the crown rings. For **3**, both the sides are blocked (Figure 6), and in this case the effect is so severe that $K^+$ cannot enter into the cavity for complex formation. For **4**, however, the C–H···O interaction involving oxygen atoms of the crown ring is not significant and the metal ion can interact easily with the calix-

 © 2006 Wiley-VCH Verlag GmbH & Co. KGaA, Weinheim 

Table 3. Concentration of metal ions in the extract and selectivity ratio with respect to potassium ion.

| Compound | Concentration [%] of metal ion in extract[a] | | | | Selectivity ratio[b] | | |
|---|---|---|---|---|---|---|---|
| | $Na^+$ | $K^+$ | $Mg^{2+}$ | $Ca^{2+}$ | $K^+/Na^+$ | $K^+/Mg^{2+}$ | $K^+/Ca^{2+}$ |
| **1** | 22.0 | 63.8 | 3.2 | 10.9 | 1.7 | 12.2 | 6.0 |
| **2** | 28.3 | 57.5 | 2.15 | 12.0 | 1.2 | 16.5 | 4.9 |
| **3** | 56.5 | 25.3 | –[c] | 18.1 | 0.3 | – | 1.4 |
| **4** | 17.9 | 82.1 | –[c] | –[c] | 2.7 | – | – |
| **5** | 26.6 | 69.4 | 0.7 | 4.2 | 1.5 | 60.9 | 16.9 |

[a] Concentration [%] of metal ion in the original solution (before extract): $Na^+$ = 18.2, $K^+$ = 30.9, $Mg^{2+}$ = 19.9, $Ca^{2+}$ = 31.7. [b] Ratio calculated by [% of $K^+$ in the extract][% of $M^{n+}$ in the original solution]/[% of $M^{n+}$ in the extract][% of $K^+$ in the original solution]. [c] Trace amount.

crown moiety. This is consistent with the selectivity data and the association constants determined. It should be noted that apart from the appended arms, the remainder of all five ionophores is identical, therefore the observed variation in complex formation/selectivity is obviously due to the effect of the appended arms. Steric crowding is not a significant factor in this case as the ionophore with the most bulky appended arms (**4**) shows the highest selectivity. This suggests that the intramolecular hydrogen-bonding interactions involving the lower rim of the ionophore play an important role in complex formation with metal ions. The appended functional groups, which are expected to act cooperatively as an axial ligand to stabilise the complex, may not always work in this manner and could even inhibit complex formation.

### Association Constants

The association constants ($K_a$) of the ionophores **1**–**5** with $Na^+$ and $K^+$ picrates were determined spectrophotometrically, as described in the Experimental Section. Metal picrates in aqueous solution were extracted with chloroform both in the presence and absence of host. The amount of picrate ion in the chloroform layer was determined from its extinction coefficient at 380 nm after appropriate dilution in $CH_3CN$. The association constants were determined using Equation (1), where $K_a$ is the association constant, $K_d$ the distribution constant, $R$ the molar ratio of picrate to host in the organic layer, $[G_i]_{H_2O}$ the initial concentration of the guest (metal ion/picrate), $[H_i]_{CHCl_3}$ the initial concentration of the host (ionophore) in chloroform, $V_{CHCl_3}$ the volume of the organic layer (chloroform) and $V_{H_2O}$ the volume of the aqueous layer.[17]

$$K_a = \frac{R}{(1-R)K_d\{[G_i]_{H_2O} - [H_i]_{CHCl_3}(V_{CHCl_3}/V_{H_2O})\}^2} \quad (1)$$

The molar ratios of picrate to host ($R$) were determined from Equation (2), where $A$ is the observed absorbance in the aqueous phase, $D$ the dilution factor, $\varepsilon$ the extinction coefficient of the picrate salt at 380 nm in $CH_3CN$ ($\varepsilon$ = 16900), $[G_i^+]$ the initial concentration of guest in the aqueous phase, $V_{aq}$ the volume of the aqueous phase, $V_{org}$ the volume of the organic phase, and $[H_i^*]$ the initial concentration of the host in the $CHCl_3$ phase.[18]

$$R_{CHCl_3} = \frac{\{[G_i^+] - A(D/\varepsilon)\}(V_{aq}/V_{org})}{[H_i^*]} \quad (2)$$

The distribution constants were determined using Equation (3).[17]

$$K_d = \frac{[G^+X^-]_{CHCl_3}}{[G^+]_{H_2O}[X^-]_{H_2O}} \quad (3)$$

The values of association constants ($K_a$) and $R$ for all ionophores are given in Table 4. The data show that the values of $K_a$ for $K^+$ with various ionophores decrease in the order **4** > **5** > **1** > **2** >> **3**, which is consistent with the selectivity data and the C–H···O interactions observed in the crystal structures. For $Na^+$, the values of $K_a$ are approximately 10–100 times lower than those for $K^+$, in line with the selectivity data.

Table 4. Molar ratio of picrate/host in the organic layer ($R$) and association constants ($K_a$) with $Na^+$ and $K^+$.

| Ionophore | $R$ | | $K_a$ | |
|---|---|---|---|---|
| | $Na^+$ | $K^+$ | $Na^+$ | $K^+$ |
| **1** | 0.02 | 0.24 | $1.06\times10^4$ | $1.82\times10^6$ |
| **2** | 0.02 | 0.08 | $8.70\times10^4$ | $3.25\times10^5$ |
| **3** | 0.01 | – | $5.17\times10^4$ | – |
| **4** | 0.26 | 0.68 | $3.12\times10^6$ | $7.20\times10^7$ |
| **5** | 0.34 | 0.66 | $5.96\times10^6$ | $5.80\times10^7$ |

## Conclusions

A series of *p*-*tert*-butylcalix[4]arene-crown ethers with various substituents attached to the opposite phenolic oxygen atoms have been synthesised in the cone conformation to evaluate their performance as ionophores towards $Na^+$, $K^+$, $Mg^{2+}$ and $Ca^{2+}$. NMR and crystal structure studies suggest that these ionophores exist in a "flattened" cone conformation both in solution and the solid state. $Na^+$ and $K^+$ complexes of these ionophores have been synthesised and the crystal structures show that, in all cases, one of the two appended substituents coordinates to the metal ion and the size of the calix-crown cavity is most suited to $K^+$ among the ions studied. The $^1H$ NMR study also revealed that there is fast exchange of coordination between the two appended groups and the metal ion in solution. The selectivity study with a mixture of cations showed the highest

 © 2006 Wiley-VCH Verlag GmbH & Co. KGaA, Weinheim 

selectivity towards $K^+$; the association constants also follow the same order. The one exception is compound **3**, where access to the metal ion is blocked as a result of strong C–H···O interactions between the pendant $COCH_3$ substituents and the crown moiety. Such deleterious interactions are apparently nonexistent in the case of the $CH_2CO_2C_2H_5$ substituents as the ligand interacts strongly with the metal ions. Evidently, although appended functional groups (like "lariat" crown ethers) are known to act as a stabilizing axial ligand, these may, in fact, act in the opposite way if strong intramolecular hydrogen bond involving the crown ring is operational. The X-ray structure determination of the ionophores therefore provides an insight into the effect of intramolecular interactions on the structure–selectivity correlation.

## Experimental Section

**Reagents and Methods:** The ligand *p-tert*-butylcalix[4]arene was synthesised according to a literature procedure.[19] Metal picrate salts were prepared by the reaction of picric acid and the metal hydroxide in aqueous media. All the reagents used in this study were purchased from Aldrich and S. D. Fine Chemicals. All solvents were of analytical grade and purified by standard procedures before use.[20] Milli-Q (Millipore Corporation) water was used for extraction and ion chromatographic study. Elemental analyses (C and H) were performed with a model 2400 Perkin–Elmer elemental analyzer. NMR spectra were recorded with a model DPX 200 Bruker FT-NMR instrument. Infrared spectra were recorded with a Perkin–Elmer Spectrum GX FT-IR system. Mass spectra were recorded with a Q-TOF Micro™ LC-MS instrument. The UV/Vis spectra were recorded with a model 8452A Hewlett–Packard diode array spectrophotometer. Cation concentration was measured with a Dionex 500 ion chromatograph. Single crystal structures were determined using a Bruker SMART 1000 (CCD) diffractometer.

**Synthesis of 1:** A mixture of *p-tert*-butylcalix[4]arene (1.46 g, 2.25 mmol) and *t*BuOK (0.23 g, 2 mmol) in 150 mL of dry benzene was refluxed under an inert gas with stirring for 1.5 h, then tetraethylene glycol ditosylate (1.06 g, 2 mmol) was added. After refluxing for 24 h, a second portion of *t*BuOK (0.23 g, 2 mmol) was added, and the reaction mixture was refluxed for an additional 24 h. It was then cooled to room temperature, treated with 1 N HCl (125 mL), and extracted five or six times with 30 mL of diethyl ether each time. The combined organic layers were finally washed three times with water (100 mL each time) and the solvent was removed by rotary evaporation. The crude product was purified by column chromatography using silica gel as packing material and dichloromethane/ethyl acetate (4:1) as eluent. Yield: 0.75 g (43%). $^1$H and $^{13}$C NMR spectroscopic data are similar to those reported earlier.[4a,10] LC-MS: *m*/*z* = 829.51 (calcd. for [**1** + $Na^+$] 829.50). $C_{52}H_{71}O_{7.5}$ (**1**·0.5$H_2O$, 815.50): calcd. C 76.59, H 8.78; found C 76.48, H, 8.69.

**Synthesis of 2:** Compound **1** (0.27 g, 0.3 mmol), NaH (0.04 g, 1.75 mmol), and acetyl bromide (0.4 mL, 5.4 mmol) were dissolved in 70 mL of diethyl ether and the mixture was stirred at room temperature under an inert gas for 3 d. After removing the solvent with a rotary evaporator, the solid mass was treated with 10% HCl (50 mL) and extracted with dichloromethane (50 mL). The organic layer was washed twice with water (50 mL each time) and the solvent was removed by rotary evaporation. The product was purified by column chromatography using silica gel as packing material and ethyl acetate/hexane (1:5) as eluent. Initially, some starting materials were separated and then the desired product was eluted. The solvent was removed from the desired fraction and the solid compound was dried in vacuo. Yield: 0.11 g (39%). $^1$H NMR (200 MHz, [$D_3$]chloroform): $\delta$ = 7.20 (s, 2 H, ArH), 7.08 (s, 2 H, ArH), 6.79 (s, 1 H, OH), 6.64 (d, *J* = 2.4 Hz, 2 H, ArH), 6.59 (d, *J* = 2.4 Hz, 2 H, ArH), 4.55 (d, *J* = 13.0 Hz, 2 H, Ar*CH*$_2$Ar), 4.13 (d, *J* = 12.8 Hz, 2 H, Ar*CH*$_2$Ar), 4.07–3.46 (m, 16 H, crown-*CH*$_2$), 3.24 (dd, $J_1$ = 13.1, $J_2$ = 3.6 Hz, 4 H, Ar*CH*$_2$Ar), 2.90 (s, 3 H, O*CH*$_3$), 1.35 (s, 9 H, *t*Bu), 1.34 (s, 9 H, *t*Bu), 0.83 (s, 18 H, *t*Bu) ppm. $^{13}$C NMR: $\delta$ = 171.18 (*CO*$CH_3$), 151.45, 151.25, 150.44 (C-1), 147.43, 146.24 (C-4), 135.71, 135.44, 133.11, 132.01, 131.96 (C-2, C-6), 128.47, 126.05, 125.58, 125.36, 125.33, (C-3, C-5), 74.98, 72.39, 71.69, 71.52, 70.99, 70.38, (O*CH*$_2$*CH*$_2$O*CH*$_2$*CH*$_2$O), 32.49, 32.29, (C-7), 32.40, 31.62 (C-8), 31.97 (Ar*CH*$_2$Ar), 22.10 (CO*CH*$_3$) ppm. LC-MS: *m*/*z* = 871.7 (calcd. for [**2** + $Na^+$]: 871.53). $C_{54}H_{73}O_{8.5}$ (**2**·0.5$H_2O$, 857.53): calcd. C 75.63, H 8.58; found C 75.64, H 8.55.

**Synthesis of 3:** NaH (0.02 g, 0.8 mmol) was added to a solution of **1** (0.20 g, 0.25 mmol) in THF (70 mL) and the reaction mixture was refluxed. After 30 min of reflux, a solution (10 mL) of acetyl bromide (0.5 mL, 7.0 mmol) in THF was added dropwise to the reaction mixture and refluxing was continued. After 6 h, the solution was cooled to room temperature, filtered and the solvent of the filtrate was removed by rotary evaporation. The residue was treated with 2 N HCl (50 mL), the mixture filtered and the solid mass washed twice with water (25 mL each time). The product thus obtained was recrystallised from dichloromethane/acetonitrile. Yield: 0.16 g (81%). $^1$H NMR (200 MHz, [$D_3$]chloroform): $\delta$ = 7.06 (s, 4 H, ArH), 6.48 (s, 4 H, ArH), 4.28–4.06 (m, 8 H, crown-*CH*$_2$), 3.90 (d, *J* = 12.8 Hz, 4 H, Ar*CH*$_2$Ar), 3.77–3.61 (m, 8 H, crown-*CH*$_2$), 3.12 (d, *J* = 12.8 Hz, 4 H, Ar*CH*$_2$Ar), 2.56 (s, 6 H, O*CH*$_3$), 1.25 (s, 18 H, *t*Bu), 0.78 (s, 18 H, *t*Bu) ppm. $^{13}$C NMR: $\delta$ = 171.39 (*CO*$CH_3$), 154.95, 152.44 (C-1), 146.66, 145.43 (C-4), 135.53 (C-2), 132.16 (C-6), 126.68, 125.51 (C-3, C-5), 74.02, 73.62, 71.89, 71.57 (O*CH*$_2$*CH*$_2$O*CH*$_2$*CH*$_2$O), 32.42, 31.82, 31.74 (C-7, C-8), 32.04 (Ar*CH*$_2$Ar), 22.25 (CO*CH*$_3$) ppm. LC-MS: *m*/*z* = 913.53 (calcd. for [**3** + $Na^+$]: 913.52). $C_{56}H_{76}O_{10}$ (**3**·$H_2O$, 908.52): calcd. C 74.03, H 8.43; found C 74.12, H, 8.07.

**Synthesis of 4:** A mixture of **1** (0.20 g, 0.25 mmol) and $K_2CO_3$ (0.08 g, 0.53 mmol) in 70 mL of acetonitrile was refluxed with stirring for 3 h, then ethyl bromoacetate (0.09 g, 0.53 mmol) was added dropwise and refluxing was continued for 24 h. The reaction mixture was then cooled to room temperature, treated with 5% HCl (50 mL) and extracted with 50 mL of dichloromethane. The organic layer thus obtained was washed twice with water (50 mL in each time) and the solvent was removed by rotary evaporation. The crude product was recrystallised from dichloromethane/acetonitrile. Yield: 0.18 g (71%). $^1$H NMR (200 MHz, [$D_3$]chloroform): $\delta$ = 6.84 (s, 4 H, ArH), 6.74 (s, 4 H, ArH), 5.07 (s, 4 H, O*CH*$_2$CO), 4.65 (d, *J* = 12.6 Hz; 4 H, Ar*CH*$_2$Ar), 4.20–4.05 (m, 8 H, crown-*CH*$_2$), 3.76–3.66 (m, 8 H, crown-*CH*$_2$), 3.17 (d, *J* = 12.6 Hz, 4 H, Ar*CH*$_2$Ar), 1.21 (t, *J* = 6.8 Hz, 6 H, $CH_3$), 1.13 (s, 18 H, *t*Bu), 1.01 (s, 18 H, *t*Bu) ppm. $^{13}$C NMR: $\delta$ = 171.53 (OCH$_2$*CO*OCH$_2$CH$_3$) 153.98, 152.79 (C-1), 145.28, 145.13 (C-4), 134.67 (C-2), 134.09 (C-6), 125.46 (C-3, C-5), 73.40, 71.81, 71.49, 71.18, (O*CH*$_2$*CH*$_2$O*CH*$_2$-*CH*$_2$O), 70.98 (O*CH*$_2$COOCH$_2$CH$_3$), 60.69 (OCH$_2$COO*CH*$_2$CH$_3$), 34.37, 34.25 (C-7), 32.68 (Ar*CH*$_2$Ar), 32.18, 31.83 (C-8), 14.82 (OCH$_2$COOCH$_2$*CH*$_3$) ppm. LC-MS: *m*/*z* = 1001.58 (calcd. for [**4** + $Na^+$]: 1001.57). $C_{60}H_{86}O_{13}$ (**4**·2$H_2O$, 1014.6): calcd. C 71.03, H 8.54; found C 71.01, H, 8.46.

 © 2006 Wiley-VCH Verlag GmbH & Co. KGaA, Weinheim 

**Synthesis of 5:** An aqueous solution (0.25 mL) of NaOH (15%) was added to an ethanolic solution (70 mL) of **4** (0.10 g, 0.1 mmol) and the reaction mixture was heated under reflux. After 24 h, it was cooled to room temperature and the solvent was removed by rotary evaporation. Then, 50 mL of cold water was added to the solid mass and 30% HCl was added dropwise with vigorous stirring until the pH of the solution reached 1. The solid product thus produced was isolated by filtration. The crude product was then dissolved in chloroform (50 mL) and washed with HCl (30%) followed by concentrated brine. The organic layer was separated, the solvent removed, and the product dried in vacuo. Yield: 0.065 g (70%). $^1$H NMR (200 MHz, [D$_3$]chloroform): $\delta$ = 7.12 (s, 4 H, ArH), 6.60 (s, 4 H, ArH), 5.29 (s, 4 H, O*CH$_2$*CO), 4.37 (d, *J* = 12.0 Hz, 4 H, Ar*CH$_2$*Ar), 4.08–3.85 (m, 16 H, crown-CH$_2$), 3.27 (d, *J* = 12.0 Hz, 4 H, Ar*CH$_2$*Ar), 1.33 (s, 18 H, *t*Bu), 0.83 (s, 18 H, *t*Bu) ppm. $^{13}$C NMR: $\delta$ = 172.99 (OCH$_2$*CO*OH), 153.69, 152.18 (C-1), 146.69, 146.19 (C-4), 135.49 (C-2), 132.89 (C-6), 126.39, 126.19 (C-3, C-5), 74.09, 71.13, 71.07, 70.99 (O*CH$_2$CH$_2$*O*CH$_2$CH$_2$*O), 70.44 (O*CH$_2$*-COOH), 34.89, 34.39 (C-7), 32.89 (Ar*CH$_2$*Ar), 32.39, 31.99 (C-8) ppm. LC-MS: *m*/*z* = 945.52 (calcd. for [**5** + Na$^+$]: 945.51). $C_{56}H_{80}O_{14}$ (**5**·3H$_2$O, 976.51): calcd. C 68.87, H 8.26; found C 69.14, H, 8.32.

**General Procedure for the Synthesis of Na$^+$ and K$^+$ Complexes of 1–5:** A mixture of 0.05 mmol of the required ionophore (**1**–**5**) and Na$^+$/K$^+$ picrate (0.5 mmol, ten-fold excess) was stirred in chloroform at room temperature for 24 h. The reaction mixture was then filtered to remove unreacted picrate salt and the complex was obtained by removing the solvent from the filtrate by rotary evaporation. The yellow complex thus obtained was dissolved in a minimum amount (ca. 3 mL) of dichloromethane (in which Na$^+$/K$^+$ picrate is almost insoluble) and filtered to remove trace quantities of unreacted Na$^+$/K$^+$ picrate. The solvent was then removed from the filtrate and the yellow product was dried in vacuo. The $^1$H NMR spectra of the product did not show any signal corresponding to free ligand or excess picrate anion. Yield: 90–95%.

**Sodium Complex of 1 (1·Na$^+$Pic$^-$):** $^1$H NMR (200 MHz, [D$_3$]chloroform): $\delta$ = 8.69 (s, 2 H, picrate), 7.03 (s, 2 H, OH), 7.03 (s, 4 H, ArH), 6.73 (s, 1 H, ArH), 6.63 (s, 3 H, ArH), 4.22–4.16 (m, 12 H, Ar*CH$_2$*Ar and crown-*CH$_2$* overlapped), 3.98–3.80 (m, 8 H, crown-*CH$_2$*), 3.30 (d, *J* = 13.6 Hz, 4 H, Ar*CH$_2$*Ar), 1.29 (s, 18 H, *t*Bu), 1.20 (s, 3 H, *t*Bu), 0.92, 0.83 (s, 15 H, *t*Bu) ppm. $^{13}$C NMR: $\delta$ = 150.15, 148.15 (C-1), 143.27, 142.18 (C-4), 132.61 (C-2), 128.62 (C-6), 127.50 (C-3), 126.35 (C-5), 125.99 (picrate), 75.84, 71.27, 70.24 (O*CH$_2$CH$_2$*O*CH$_2$CH$_2$*O), 34.59 (C-7), 32.40, 32.24, 31.60 (C-8), 31.93 (Ar*CH$_2$*Ar) ppm. LC-MS: *m*/*z* = 829.10 (calcd. for [**1** + Na$^+$]: 829.50). $C_{58}H_{72}N_3NaO_{14}$ (1057.51): calcd. C 65.84, H 6.85, N 3.96; found C 65.46, H, 6.49, N 3.68.

**Potassium Complex of 1 (1·K$^+$Pic$^-$):** $^1$H NMR (200 MHz, [D$_3$]chloroform): $\delta$ = 8.70 (s, 2 H, picrate), 7.05 (s, 2 H, OH), 7.05 (s, 4 H, ArH), 6.74, (s, 1 H, ArH), 6.61 (s, 3 H, ArH), 4.37–4.18 (m, 12 H, Ar*CH$_2$*Ar and crown-*CH$_2$*), 3.90–3.73 (m, 8 H, crown-*CH$_2$*), 3.30 (d, *J* = 13.8 Hz, 4 H, Ar*CH$_2$*Ar), 1.30 (s, 18 H, *t*Bu), 1.20 (s, 3 H, *t*Bu), 0.93 (s, 3 H, *t*Bu), 0.81 (s, 12 H, *t*Bu) ppm. $^{13}$C NMR: $\delta$ = 50.35, 148.17 (C-1), 143.74, 142.15 (C-4), 132.65 (C-2), 129.03 (C-6), 127.74 (C-3), 126.55 (C-5), 125.89 (picrate), 75.75, 71.56, 71.35, 70.14 (O*CH$_2$CH$_2$*O*CH$_2$CH$_2$*O), 34.69, 34.59 (C-7), 32.43, 32.26, 31.62 (C-8), 31.85 (Ar*CH$_2$*Ar) ppm. LC-MS: *m*/*z* = 845.41 (calcd. for [**1** + K$^+$]: 845.50). $C_{58}H_{72}KN_3O_{14}$ (1073.5): calcd. C 64.89, H 6.76, N 3.91; found C 65.15, H 6.54, N 3.67.

**Sodium Complex of 2 (2·Na$^+$Pic$^-$):** $^1$H NMR (200 MHz, [D$_3$]chloroform): $\delta$ = 8.78 (s, 2 H, picrate), 7.05 (s, 2 H, ArH), 6.98 (s, 2 H, ArH), 6.66 (br., 2 H, ArH), 6.63 (br., 2 H, ArH), 4.30–3.62 (m, 20 H, ArCH$_2$, crown-CH$_2$), 3.30 (d, *J* = 12.8 Hz, 4 H, ArCH$_2$), 2.27 (s, 3 H, OCH$_3$), 1.35 (s, 9 H, *t*Bu), 1.30 (s, 9 H, *t*Bu), 0.82 (s, 18 H, *t*Bu) ppm. $^{13}$C NMR: $\delta$ = 171.36 (*CO*CH$_3$), 150.34, 150.06, (C-1), 148.59, 148.00 (C-4), 132.55 (C-2), 128.51 (C-6), 127.22, 126.44 (C-3, C-5), 125.85 (picrate), 75.88, 71.93, 71.21, 70.22 (O*CH$_2$CH$_2$*-O*CH$_2$CH$_2$*O), 34.57, 32.20 (C-7), 32.30, 31.51 (C-8), 31.83 (Ar-*CH$_2$*Ar), 21.74 (CO*CH$_3$*) ppm. LC-MS: *m*/*z* = 871.9 (calcd. for [**2** + Na$^+$]: 871.53). $C_{60}H_{76}N_3NaO_{16}$ (with H$_2$O, 1117.5): calcd. C 64.49, H 6.86, N 3.76; found C 64.23, H 6.88, N 3.57.

**Potassium Complex of 2 (2·K$^+$Pic$^-$):** $^1$H NMR (200 MHz, [D$_3$]chloroform): $\delta$ = 8.72 (s, 2 H, picrate), 7.20 (s, 1 H, ArH), 7.08 (s, 1 H, ArH), 7.06 (s, 2 H, ArH), 6.79 (s, 1 H, OH), 6.64–6.56 (m, 4 H, ArH), 4.16–3.46 (m, 20 H, ArCH$_2$, crown-CH$_2$), 3.33–3.19 (m, 4 H, ArCH$_2$), 2.90 (s, 3 H, OCH$_3$), 1.34 (s, 9 H, *t*Bu), 1.30 (s, 9 H, *t*Bu), 0.83 (s, 18 H, *t*Bu) ppm. $^{13}$C NMR: $\delta$ = 174.56 (*CO*CH$_3$),150.56, 150.33 (C-1), 147.88, 146.28 (C-4), 132.80 (C-2), 128.75 (C-6), 127.49, 126.31 (C-3, C-5), 125.73 (picrate), 75.01, 72.39, 71.44, 70.43 (O*CH$_2$CH$_2$*O*CH$_2$CH$_2$*O), 34.46, 32.48 (C-7), 32.28, 31.56 (C-8), 31.85 (Ar*CH$_2$*Ar), 21.82 (CO*CH$_3$*) ppm. LC-MS: *m*/*z* = 887.57 (calcd. for [**2** + K$^+$]: 887.53). $C_{60}H_{74}KN_3O_{15}$ (1115.5): calcd. C 64.60, H 6.69, N 3.76; found C 65.13, H 6.37, N 3.85.

**Sodium Complex of 3 (3·Na$^+$Pic$^-$):** $^1$H NMR (200 MHz, [D$_3$]chloroform): $\delta$ = 8.82 (s, 2 H, picrate), 7.16 (s, 4 H, ArH), 6.53 (s, 4 H, ArH), 4.28–3.72 (m, 20 H, ArCH$_2$, crown-CH$_2$), 3.35 (d, *J* = 13.0 Hz, 4 H, ArCH$_2$), 2.61 (s, 6 H, OCH$_3$), 1.26 (s, 18 H, *t*Bu), 0.75 (s, 18 H, *t*Bu) ppm. $^{13}$C NMR: $\delta$ = 171.58 (*CO*CH$_3$), 151.77, 151.51 (C-1), 146.64, 144.50 (C-4), 135.67 (C-2), 132.38 (C-6), 127.20 (picrate), 126.71, 125.88 (C-3, C-5), 75.23, 71.98, 71.17, 70.53 (O*CH$_2$CH$_2$*O*CH$_2$CH$_2$*O), 34.70, 32.32, 32.20, 31.93 (C-7, C-8), 31.49 (Ar*CH$_2$*Ar), 21.34 (CO*CH$_3$*) ppm. LC-MS: *m*/*z* = 914.0 (calcd. for [**3** + Na$^+$]: 913.52). $C_{62}H_{77}N_3NaO_{16.5}$ (with 0.5H$_2$O, 1150.5): calcd. C 64.73, H 6.75, N 3.65; found C 64.75, H, 6.92, N 3.32.

**Sodium Complex of 4 (4·Na$^+$Pic$^-$):** $^1$H NMR (200 MHz, [D$_3$]chloroform): $\delta$ = 8.80 (s, 2 H, picrate), 7.10 (s, 4 H, ArH), 7.04 (s, 4 H, ArH), 4.77 (s, 4 H, O*CH$_2$*CO), 4.48 (d, *J* = 12.4 Hz, 4 H, Ar-*CH$_2$*Ar), 4.32 (q, *J* = 7.4 Hz, 4 H, O*CH$_2$*CH$_3$), 4.09 (m, 4 H, crown-*CH$_2$*), 3.86 (br., 12 H, crown-*CH$_2$*), 3.36 (d, *J* = 12.2 Hz, 4 H,Ar), 1.33 (t, *J* = 7.0 Hz, 6 H, OCH$_2$*CH$_3$*), 1.13 (s, 18 H, *t*Bu), 1.10 (s, 18 H, *t*Bu) ppm. $^{13}$C NMR: $\delta$ = 171.44 (OCH$_2$*CO*OCH$_2$CH$_3$) 151.85, 150.53 (C-1), 148.78, 148.23 (C-4), 134.73 (C-2, C-6), 127.16 (picrate), 126.60 (C-3, C-5), 77.04, 73.93, 71.27, 70.33, (O*CH$_2$CH$_2$*-O*CH$_2$CH$_2$*O), 70.57 (O*CH$_2$*COOCH$_2$CH$_3$), 62.60 (OCH$_2$-COO*CH$_2$*CH$_3$), 34.83, 34.80 (C-7), 31.95 (C-8), 31.10 (Ar*CH$_2$*Ar), 14.84 (OCH$_2$COOCH$_2$*CH$_3$*) ppm. LC-MS: *m*/*z* = 1001.57 (calcd. for [**4** + Na$^+$]: 1001.57). $C_{66}H_{84}N_3NaO_{18}$ (1229.6): calcd. C 64.47, H 6.89, N 3.42; found C 64.77, H 6.88, N 3.66.

**Potassium Complex of 4 (4·K$^+$Pic$^-$):** $^1$H NMR (200 MHz, [D$_3$]chloroform): $\delta$ = 8.82 (s, 2 H, picrate), 7.10 (s, 4 H, ArH), 7.06 (s, 4 H, ArH), 4.57 (s, 4 H, O*CH$_2$*CO), 4.46 (d, *J* = 12.2 Hz, 4 H, Ar-*CH$_2$*Ar), 4.32 (q, *J* = 7.4 Hz, 4 H, O*CH$_2$*CH$_3$), 4.40–3.84 (m, 16 H, crown-*CH$_2$*), 3.36 (d, *J* = 12.6 Hz, 4 H, Ar*CH$_2$*Ar), 1.33 (t, *J* = 6.8 Hz, 6 H, CH$_3$), 1.13 (s, 18 H, *t*Bu), 1.10 (s, 18 H, *t*Bu) ppm. $^{13}$C NMR: $\delta$ = 170.76 (OCH$_2$*CO*OCH$_2$CH$_3$) 151.76, 151.12 (C-1), 148.31, 147.74 (C-4), 134.47, 134.37 (C-2, C-6), 127.17 (picrate), 126.68 (C-3, C-5), 77.13, 73.87, 71.50, 70.64, (O*CH$_2$CH$_2$*O*CH$_2$-*CH$_2$*O), 70.57 (O*CH$_2$*COOCH$_2$CH$_3$), 62.63 (OCH$_2$COO*CH$_2$*CH$_3$), 34.79 (C-7), 31.97 (C-8), 30.16 (Ar*CH$_2$*Ar), 14.86 (OCH$_2$-COOCH$_2$*CH$_3$*) ppm. LC-MS: *m*/*z* = 1017.1 (calcd. for [**4** + K$^+$]: 1017.6). $C_{66}H_{84}KN_3O_{18}$ (1245.6): calcd. C 63.66, H 6.79, N 3.37; found C 64.15, H, 6.94, N 3.40.

 © 2006 Wiley-VCH Verlag GmbH & Co. KGaA, Weinheim 

**Sodium Complex of 5 (5·$Na^+Pic^-$):** $^1$H NMR (200 MHz, [$D_3$]chloroform): $\delta$ = 8.85 (s, 2 H, picrate) 7.06 (s, 4 H, ArH), 7.10 (s, 4 H, ArH), 4.65 (s, 4 H, $OCH_2CO$), 4.43 (d, $J$ = 12.0 Hz, 4 H, $ArCH_2$), 4.08–3.86 (m, 16 H, crown-$CH_2$), 3.36 (d, $J$ = 12.0 Hz, 4 H, $ArCH_2$), 1.14 (s, 18 H, *t*Bu), 1.11 (s, 18 H, *t*Bu) ppm. $^{13}$C NMR: $\delta$ = 172.23 ($OCH_2$*CO*OH), 151.61, 150.18 (C-1), 148.77, 148.24 (C-4), 134.75 (C-2, C-6), 126.69 (picrate), 126.60, 126.49 (C-3, C-5), 74.03, 71.45, 70.68, 69.96 (O*CH*$_2$*CH*$_2$O*CH*$_2$*CH*$_2$O), 68.25 (O*CH*$_2$-COOH), 34.81, 34.74 (C-7), 31.93, 31.89 (C-8) 30.37 (Ar*CH*$_2$Ar) ppm. LC-MS: $m/z$ = 945.0 (calcd. for [**5** + $Na^+$]: 945.51). $C_{62}H_{78}N_3NaO_{19}$ (with $H_2O$, 1191.5): calcd. C 62.50, H 6.60, N 3.52; found C 62.67, H, 6.75, N 3.64.

**Potassium Complex of 5 (5·$K^+Pic^-$):** $^1$H NMR (200 MHz, [$D_3$]chloroform): $\delta$ = 8.87 (s, 2 H, picrate), 7.12 (s, 4 H, ArH), 7.04 (s, 4 H, ArH), 4.65 (s, 4 H, $OCH_2CO$), 4.47 (d, $J$ = 12.0 Hz, 4 H, $ArCH_2$), 4.07–3.82 (m, 16 H, crown-$CH_2$), 3.36 (d, $J$ = 12.2 Hz, 4 H, $ArCH_2$), 1.17 (s, 18 H, *t*Bu), 1.07 (s, 18 H, *t*Bu) ppm. $^{13}$C NMR: $\delta$ = 171.50 ($OCH_2$*CO*OH), 153.81, 152.13 (C-1), 148.43 (C-4), 134.56, 134.38 (C-2, C-6), 126.83, 126.63 (picrate, C-3, C-5), 74.05, 71.62, 70.69, 70.32 (O*CH*$_2$*CH*$_2$O*CH*$_2$*CH*$_2$O), 68.72, (O*CH*$_2$-COOH), 34.77 (C-7), 32.01, 31.90 (C-8) 30.37 (Ar*CH*$_2$Ar) ppm. LC-MS: $m/z$ = 961.57 (calcd. for [**5** + $K^+$]: 961.51). $C_{62}H_{78}KN_3O_{19}$ (with $H_2O$, 1207.5): calcd. C 61.67, H 6.51, N 3.48; found C 61.16, H, 6.80, N 3.24.

**Determination of Selectivity of the Ionophores:** The selectivity of the ionophores towards $Na^+$, $K^+$, $Mg^{2+}$, and $Ca^{2+}$ was determined using an equimolar mixture of the picrate salts of these ions according to a procedure described in the literature.[9] In a typical procedure, equal volumes (15 mL) of an aqueous solution of an equimolar mixture of picrate salts ($Na^+$, $K^+$, $Mg^{2+}$, $Ca^{2+}$; 0.005 M each) and a $CH_2Cl_2$ solution (15 mL) of the required ionophore (0.005 M) were mixed and vigorously shaken in a vortex mixer for 15 min. The solution was then transferred to a separating funnel and allowed to stand for 4–5 h. The dichloromethane layer was then separated and transferred to a crucible, stripped of solvent by gentle heating in a water bath, and then heated in a furnace at 550 °C for 4–5 h. The residue was dissolved in deionized water (ca. 5 mL) and filtered through 0.2-μm filter paper. The relative concentrations of the cations in the filtrate were determined by ion chromatography on an Ion Pac CS12 (2 mm) analytical column and 20 mM methylsulfonic acid as eluent with a flow rate of 0.25 mL min$^{-1}$. Quantification was made using a standard solution containing a mixture of NaCl, KCl, $MgCl_2$, and $CaCl_2$ (15 ppm each). A blank experiment, without added ionophore, was carried out under similar experimental conditions; no detectable amount of picrate was observed in the dichloromethane layer.

**Determination of Association Constants ($K_a$) with $Na^+$ and $K^+$ Picrate:** Association constants of the ionophores **1**–**5** with $Na^+$ and $K^+$ were determined according to a published procedure using picrate as anion.[17,18] This involves two-phase (water/chloroform) extraction of the metal complex followed by determination of the ratios of picrate to host ($R$) in the organic phase and determination of the distribution constants ($K_d$) of the picrate salts between water and chloroform [Equations (1)–(3)].

**Determination of Molar Ratio of Picrate/Host in the Organic Layer ($R$):** Aqueous solutions were prepared that were 0.01 M in the picrate of $Na^+$ and $K^+$. Into each of two 10-mL centrifuge tubes was transferred 1 mL of the appropriate picrate solution with a syringe; 1-mL aliquots of a previously prepared chloroform solution that was 0.01 M in host were then added with a syringe to each tube. The tube was covered immediately with a rubber septum to prevent evaporation and the two layers in each tube were mixed thoroughly with a Vortex Genie mixer for 5 min. The tubes were then placed in a centrifuge for 15 min. Aliquots of 0.5 mL of the organic phase were carefully removed from each phase with a syringe and transferred to a 10-mL volumetric flask, which was brought to the mark with acetonitrile. The absorbance of each sample was then determined ($\lambda$ = 380 nm) after appropriate dilution (to make absorbance within measuring limit). The molar ratio of picrate/host ($R$) was then calculated from Equation (2).

**Determination of Distribution Constants ($K_d$) of Picrate Anion:** A 0.02 M metal picrate solution in 100 mL of water was added to 100 mL of chloroform and the mixture was shaken in a separating funnel for 5–6 h. The layers of the mixture were then allowed to separate overnight (ca. 12 h). The lower layer (chloroform) was then carefully transferred into a round-bottomed flask and the solvent evaporated with a rotary evaporator. The residue was quantitatively transferred with acetonitrile to a 10-mL volumetric flask and diluted with acetonitrile up to the mark. The absorbance of the organic layer was measured spectrophotometrically and the value of $K_d$ was determined from Equation (3).

**X-ray Crystallography for 1–4, 1·$K^+Pic^-$, 4·$Na^+Pic^-$, 4·$K^+Pic^-$ and 5·$K^+Pic^-$:** Crystal data collection and refinement parameters for all eight compounds are given in Table 5. A suitable crystal of each compound was selected, coated with Paratone oil and mounted with epoxy cement on the tip of a fine glass fibre. Data sets were obtained with a Bruker Smart APEX diffractometer with a CCD area detector using graphite-monochromated Mo-$K_\alpha$ radiation ($\lambda$ = 0.71073 Å) at liquid nitrogen temperature (100 K). Data frames were processed using the Bruker SAINT program.[21] Intensities were corrected for Lorentz, polarisation, decay effects and an absorption correction was applied using SADABS.[22] The structure was solved by direct methods using SHELXS-97[23] and refined on $F^2$ using SHELXL-97.[24] The non-hydrogen atoms were located directly by successive Fourier calculations and were refined anisotropically in all the solvated ligand structures except for **2**. In **2**, three of the *tert*-butyl groups attached to the phenyl rings were found to be disordered over two positions (with occupancy factor 0.50) and these disordered *tert*-butyl groups were refined only isotropically. In the case of **1**·$K^+Pic^-$, the lattice THF molecule is disordered extensively, and in the case of **4**·$K^+Pic^-$ two of the *tert*-butyl groups, the lattice solvent molecules (benzene and THF) and the nitrate groups of the picrate anions showed dynamic disorder; all these disordered atoms were refined isotropically. Since it was very difficult to determine the dynamic disorder present in both the *tert*-butyl groups and lattice solvent molecules, these disorders were taken care of by assigning a tentative occupancy factor for the reasonably good peaks appearing in the difference Fourier map depending upon their peak heights. Anisotropic full-matrix refinement of all atoms, except the disordered atoms, was carried out using SHELXL-97 until convergence was reached (no significant peaks in the difference Fourier map). The inclusion of all the disordered atoms with the occupancy factor tentatively assigned, depending upon the peak height, significantly reduced the refinement parameters, thus implying the correct treatment of the disorder; a constrained or rigid model refinement was not possible in this case. In the case of **4**·$Na^+Pic^-$, it was not possible to locate the picrate anions and severely disordered solvents (THF and toluene from which crystals for X-ray study were grown) present in the lattice from the difference Fourier map. A suitable disorder model was not obtained and the picrate anion and solvent contribution was subtracted from the reflection data using the program SQUEEZE.[25] A combination of SQUEEZE and PLATON was applied to resolve severely disordered molecules of solvents (THF and toluene) within the asymmetric unit, which also contains one

 © 2006 Wiley-VCH Verlag GmbH & Co. KGaA, Weinheim 

Table 5. Experimental data for the X-ray diffraction studies on single crystals of **1**–**4**, **1**·$K^+Pic^-$, **4**·$Na^+Pic^-$, **4**·$K^+Pic^-$, and **5**·$K^+Pic^-$.

| Compound | **1** | **2** | **3** | **4** | **1**·$K^+Pic^-$ | **4**·$Na^+Pic^-$ | **4**·$K^+Pic^-$ | **5**·$K^+Pic^-$ |
|---|---|---|---|---|---|---|---|---|
| Empirical formula | $C_{108}H_{142}N_2O_{14}$ | $C_{58}H_{51}N_2O_8$ | $C_{76}H_{84}N_3O_9$ | $C_{64}H_{88}N_2O_{11}$ | $C_{62}H_{72}KN_3O_{15}$ | $C_{60}H_{82}NaNO_{12}$ | $C_{82}H_{70}KN_3O_{19}$ | $C_{62}H_{58}N_3KO_{19}$ |
| Formula mass | 1692.24 | 904.01 | 1133.68 | 1061.36 | 1138.33 | 1002.25 | 1440.51 | 1188.21 |
| *a* [Å] | 12.2085(12) | 20.9878(13) | 14.3741(9) | 12.9539(9) | 12.4879(11) | 13.570(3) | 15.4140(12) | 19.1372(13) |
| *b* [Å] | 35.618(4) | 12.7867(8) | 14.7658(9) | 13.7659(9) | 15.1378(13) | 32.711(8) | 20.1863(16) | 16.0996(12) |
| *c* [Å] | 46.261(5) | 21.2898(13) | 17.2358(11) | 16.9973(11) | 16.1659(14) | 19.403(5) | 24.673(2) | 20.0525(14) |
| *α* [°] | 90 | 90 | 66.2500(10) | 82.6790(10) | 92.793(2) | 90 | 90 | 90 |
| *β* [°] | 90 | 111.2090(10) | 78.6250(10) | 88.1120(10) | 94.146(2) | 105.859(5) | 97.7120(10) | 97.772(2) |
| *γ* [°] | 90 | 90 | 67.2500(10) | 80.4720(10) | 100.515(2) | 90 | 90 | 90 |
| *Z* | 8 | 4 | 2 | 2 | 2 | 4 | 4 | 4 |
| *V* [Å$^3$] | 20116(4) | 5326.4(6) | 3084.2(3) | 2964.6(3) | 2990.8(4) | 8285(3) | 7607.6(10) | 6121.5(8) |
| Crystal system | orthorhombic | monoclinic | triclinic | triclinic | triclinic | monoclinic | monoclinic | monoclinic |
| Space group | *Pbca* | $P2_1/c$ | $P\bar{1}$ | $P\bar{1}$ | $P\bar{1}$ | *P*21/*n* | *P*21/*n* | *P*21/*c* |
| *λ* [Å] | 0.71073 | 0.71073 | 0.71073 | 0.71073 | 0.71073 | 0.71073 | 0.71073 | 0.71073 |
| $\rho_{calcd.}$ [g cm$^{-3}$] | 1.118 | 1.127 | 1.221 | 1.189 | 1.264 | 0.804 | 1.258 | 1.289 |
| *μ* [mm$^{-1}$] | 0.073 | 0.075 | 0.205 | 0.080 | 0.157 | 0.059 | 0.143 | 0.162 |
| *F*(000) | 7328 | 1908 | 1212 | 1148 | 1208 | 2164 | 3032 | 2488 |
| Temp. [K] | 100 | 100 | 100 | 100 | 100 | 100 | 100 | 100 |
| Rflns collected/unique | 60303/13142 | 20483/6939 | 18195/13407 | 25645/13342 | 18244/13194 | 39935/14475 | 44443/17616 | 24283/7976 |
| *R*(int) | 0.1332 | 0.0247 | 0.0172 | 0.0160 | 0.0247 | 0.0981 | 0.0367 | 0.084 |
| GOF on $F^2$ | 1.065 | 1.195 | 1.013 | 1.038 | 1.009 | 0.856 | 1.044 | 1.073 |
| $R_1/wR_2$ ($[I>2\sigma(I)]$ | 0.1203/ 0.2972 | 0.0764/ 0.2149 | 0.0651/ 0.1669 | 0.0518/ 0.1427 | 0.0665/ 0.1633 | 0.0910/ 0.2134 | 0.0945/ 0.2720 | 0.1180/ 0.3039 |
| $R_1/wR_2$ (all data) | 0.1867/ 0.3498 | 0.0816/ 0.2184 | 0.0809/ 0.1801 | 0.0592/ 0.1492 | 0.0908/ 0.1778 | 0.1527/ 0.2404 | 0.1360/ 0.3056 | 0.1631/ 0.3356 |

crystallographically independent picrate anion. Within the 3460 Å$^3$ void space occupied by solvent molecules and the unresolved anion, a total of 810 electrons were calculated per unit cell. After correction for the one unresolved counteranion per asymmetric unit, corresponding to 115 electrons, the rest of the electron density per asymmetric unit (87.6) can be equated for by the presence of approximately one molecule of THF and one molecule of toluene in the asymmetric unit. A refinement using reflections modified by the SQUEEZE procedure behaved well, and the geometry of **4**·$Na^+Pic^-$ and, of course, the *R* factors and GOF values were significantly improved. H atoms (except for the H atoms attached to the disordered non-hydrogen atoms and some of the lattice solvent hydrogen atoms) were calculated on the basis of geometric criteria and were treated with a riding model in subsequent refinements using the SHELXL default parameters. The molecular graphics of the crystal structures were generated using ORTEP, PLATON and Mercury.[26–28] CCDC-297554 to -297561 (for complexes **1**–**4**, **1**·$K^+Pic^-$, **4**·$Na^+Pic^-$, **4**·$K^+Pic^-$, and **5**·$K^+Pic^-$, respectively) contain the supplementary crystallographic data for this paper. These data can be obtained free of charge from The Cambridge Crystallographic Data Centre via www.ccdc.cam.ac.uk/data_request/cif.

**Supporting Information Available** (see footnote on the first page of this article): Tables S1 and S2 contain hydrogen-bonding parameters of the ionophores and metal complexes, respectively. Figures S1–S7 show packing diagrams of **2**–**4**, **1**·$K^+Pic^-$, **4**·$Na^+Pic^-$, **4**·$K^+Pic^-$, and **5**·$K^+Pic^-$, respectively.

## Acknowledgments

We are grateful to the Department of Science and Technology (DST), Government of India, for financial support. We also thank CSIR, New Delhi for generous support towards infrastructure and core competency. P. A. gratefully acknowledges CSIR for awarding a Senior Research Fellowship (SRF).

[1] a) C. D. Gutsche, *Calixarenes*, The Royal Society of Chemistry, Cambridge, UK, **1989**; b) *Calixarenes*, *A Versatile Class of Macrocyclic Compounds* (Eds.: J. Vicens, V. Bohmer), Kluwer, Dordrecht, Netherlands, **1991**; c) V. Boehmer, *Angew. Chem.* **1995**, *107*, 785; *Angew. Chem. Int. Ed. Engl.* **1995**, *34*, 713; d) A. Ikeda, S. Shinkai, *Chem. Rev.* **1997**, *97*, 1713; e) C. D. Gutsche, *Calixarenes Revisited*, The Royal Society of Chemistry, Cambridge, UK, **1998**; f) *Calixarenes in Action* (Eds.: L. Mandolini, R. Ungaro), Imperial College Press, London, **2000**; g) F. Arnaud-Neu, M. A. McKervey, M. J. Schwing-Weill, *Calixarenes 2001* (Eds.: Z. Asfari, V. Bohmer, J. Harrowfield, J. Vicens), Kluwer Academic Publishers, Dordrecht, The Netherlands, **2001**; h) A. Casnati, F. Sansone, R. Ungaro, *Adv. Supramol. Chem.* **2003**, *9*, 165–218.

[2] a) F. Arnaud-Neu, E. M. Collins, M. Deasy, G. Ferguson, S. J. Harris, B. Kaitner, A. J. Lough, M. A. McKervey, E. Marques, B. L. Ruhl, M. J. Schwing-Weill, E. M. Seward, *J. Am. Chem. Soc.* **1989**, *111*, 8681; b) A. Ikeda, S. Shinkai, *J. Am. Chem. Soc.* **1994**, *116*, 3102; c) S. Leon, D. A. Leigh, F. Zerbetto, *Chem. Eur. J.* **2002**, *8*, 4854; d) G. Guillemot, E. Solari, C. Rizzoli, C. Floriani, *Chem. Eur. J.* **2002**, *8*, 2072; e) A. Shivanyuk, M. Saadioui, F. Broda, I. Thondorf, M. O. Vysotsky, K. Rissanen, E. Kolehmainen, V. Boehmer, *Chem. Eur. J.* **2004**, *10*, 2138.

[3] a) P. L. H. M. Cobben, R. J. M. Egberink, J. G. Bomer, P. Bergveld, W. Verboom, D. N. Reinhoudt, *J. Am. Chem. Soc.* **1992**, *114*, 10573; b) M. H. B. G. Gansey, W. Verboom, F. C. J. M. van Veggel, V. Vetrogon, F. Arnaud-Neu, M.-J. Schwing-Weill, D. N. Reinhoudt, *J. Chem. Soc., Perkin Trans. 2* **1998**, 2351; c) J. Rebek Jr, *Chem. Commun.* **2000**, 637; d) D. Diamond, K. Nolan, *Anal. Chem.* **2001**, *73*, 22A (invited A-Section article); e) A. F. D. de Namor, D. Kowalska, E. E. Castellano, O. E. Piro, F. J. S. Velarde, J. V. Salas, *Phys. Chem. Chem. Phys.* **2001**, *3*, 4010; f) S. E. Matthews, P. Schmitt, V. Felix, M. G. B. Drew, P. D. Beer, *J. Am. Chem. Soc.* **2002**, *124*, 1341; g) P. R. A. Webber, A. Cowley, M. G. B. Drew, P. D. Beer, *Chem. Eur. J.* **2003**, *9*, 2439.

 © 2006 Wiley-VCH Verlag GmbH & Co. KGaA, Weinheim 

[4] a) E. Ghidini, F. Ugozzoli, R. Ungaro, S. Harkema, A. A. El-Fadl, D. N. Reinhoudt, *J. Am. Chem. Soc.* **1990**, *112*, 6979; b) A. Casnati, A. Pochini, R. Ungaro, F. Ugozzoli, F. Arnaud, S. Fanni, M.-J. Schwing, R. J. M. Egberink, F. de Jong, D. N. Reinhoudt, *J. Am. Chem. Soc.* **1995**, *117*, 2767; c) A. Ikeda, T. Tsudera, S. Shinkai, *J. Org. Chem.* **1997**, *62*, 3568; d) J. Guillon, J.-M. Leger, P. Sonnet, C. Jarry, M. Robba, *J. Org. Chem.* **2000**, *65*, 8283; e) K. Takahashi, A. Gunji, D. Guillaumont, F. Pichierri, S. Nakamura, *Angew. Chem. Int. Ed.* **2000**, *39*, 2925; f) J. S. Kim, O. J. Shon, J. W. Ko, M. H. Cho, I. Y. Yu, J. Vicens, *J. Org. Chem.* **2000**, *65*, 2386; g) H. Zhou, K. Surowiec, D. W. Purkiss, R. A. Bartsch, *Org. Biomol. Chem.* **2005**, *3*, 1676; h) J. Luo, Q.-Y. Zheng, C.-F. Chen, Z.-T. Huang, *Chem. Eur. J.* **2005**, *11*, 5917; i) I. Oueslati, R. Abidi, P. Thuery, M. Nierlich, Z. Asfari, J. Harrowfield, J. Vicens, *Tetrahedron Lett.* **2000**, *41*, 8263; j) L. Prodi, F. Bolletta, M. Montalti, N. Zaccheroni, A. Casnati, F. Sansone, R. Ungaro, *New J. Chem.* **2000**, *24*, 155; k) A. Casnati, N. Della Ca, F. Sansone, F. Ugozzoli, R. Ungaro, *Tetrahedron* **2004**, *60*, 7869.

[5] a) R. Ungaro, A. Casnati, F. Ugozzoli, A. Pochini, J.-F. Dozoli, C. Hill, H. Rouquette, *Angew. Chem. Int. Ed. Engl.* **1994**, *33*, 1506; b) V. Lamare, J.-F. Dozol, F. Ugozzoli, A. Casnati, R. Ungaro, *Eur. J. Org. Chem.* **1998**, 1559; c) J. S. Kim, J. H. Pang, I. Y. Yu, W. K. Lee, I. H. Suh, J. K. Kim, M. H. Cho, E. T. Kim, D. Y. Ra, *J. Chem. Soc., Perkin Trans. 2* **1999**, *2*, 837; d) A. Casnati, A. Pochini, R. Ungaro, C. Bocchi, F. Ugozzoli, R. J. M. Egberink, H. Struijk, R. Lugtenberg, F. D. Jong, D. N. Reinhoudt, *Chem. Eur. J.* **1996**, *2*, 436.

[6] a) J. S. Kim, I. H. Suh, J. K. Kim, M. H. Cho, *J. Chem. Soc., Perkin Trans. 1* **1998**, 2307; b) J. S. Kim, W. K. Lee, I. H. Suh, J.-G. Kim, J. Yoon, J. H. Lee, *J. Org. Chem.* **2000**, *65*, 7215; c) I. Leray, Z. Asfari, J. Vicens, B. Valeur, *J. Chem. Soc., Perkin Trans. 2* **2002**, 1429; d) J. S. Kim, O. J. Shon, S. H. Yang, J. Y. Kim, M. J. Kim, *J. Org. Chem.* **2002**, *67*, 6514; e) S. H. Lee, J. Y. Kim, J. Ko, J. Y. Lee, J. S. Kim, *Org. Chem.* **2004**, *69*, 2902; f) Z. Asfari, C. Bressot, J. Vicens, C. Hill, J.-F. Dozol, H. Rouquette, S. Eymard, V. Lamare, B. Tournois, *Anal. Chem.* **1995**, *67*, 3133; g) F. Arnaud-Neu, Z. Asfari, B. Souley, J. Vicens, *New J. Chem.* **1996**, *20*, 453.

[7] Z. Brzozka, B. Lammerink, D. N. Reinhoudt, *J. Chem. Soc., Perkin Trans. 2* **1993**, 1037.

[8] H. Tsue, T. Takimoto, R. Tamura, C. Kikuchi, S. Tanaka, *Lett. Org. Chem.* **2004**, *1*, 276.

[9] a) E. Suresh, P. Agnihotri, B. Ganguly, P. Bhatt, P. S. Subramanian, P. Paul, P. K. Ghosh, *Eur. J. Inorg. Chem.* **2005**, 2198; b) P. Agnihotri, E. Suresh, B. Ganguly, P. Paul, P. K. Ghosh, *Polyhedron* **2005**, *24*, 1023.

[10] H. Zhou, K. Surowiec, D. W. Purkiss, R. A. Bartsch, *Org. Biomol. Chem.* **2006**, Advance Article in Web.

[11] a) D. N. Reinhoudt, P. J. Dijkstra, P. J. A. in't Veld, K. E. Bugge, S. Harkema, R. Ungaro, E. Ghidini, *J. Am. Chem. Soc.* **1987**, *109*, 4761; b) P. J. Dijkstra, J. A. J. Bbrunink, K. E. Bugge, D. N. Reinhoudt, S. Harkema, R. Ungaro, F. Ugozzoli, E. Ghidini, *J. Am. Chem. Soc.* **1989**, *111*, 7567.

[12] a) C. D. Gutsche, M. Iqbal, K. Nam, I. Alam, *Pure Appl. Chem.* **1988**, *60*, 483; b) K. Iwamoto, S. Shinkai, *J. Org. Chem.* **1992**, *57*, 7066.

[13] P. D. Beer, M. G. B. Drew, A. Grieve, M. I. Ogden, *J. Chem. Soc., Dalton Trans.* **1995**, 3455.

[14] a) R. P. Thummel, Y. Jahng, *Inorg. Chem.* **1986**, *25*, 2527; b) R. P. Thummel, F. Lefoulon, J. D. Korp, *Inorg. Chem.* **1987**, *26*, 2370; c) P. Paul, B. Tyagi, A. K. Bilakhiya, M. M. Bhadbhade, E. Suresh, G. Ramachandraiah, *Inorg. Chem.* **1998**, *37*, 5733.

[15] C. Jaime, J. de Mendoza, P. Prados, P. M. Nieto, C. Sanchez, *J. Org. Chem.* **1991**, *56*, 3372.

[16] a) I. Oueslati, R. Abidi, P. Thuery, M. Nierlich, Z. Asfari, J. Harrowfield, J. Vicens, *Tetrahedron Lett.* **2000**, *41*, 8263; b) I. Oueslati, R. Abidi, P. Thuery, J. Vicens, *J. Inclusion Phenom.* **2003**, *47*, 173; c) S. Banthia, A. Samanta, *Org. Biomol. Chem.* **2005**, *3*, 1428; d) A. Dubes, K. A. Udachin, P. Shahgaldian, A. N. Lazar, A. W. Coleman, J. A. Ripmeester, *New J. Chem.* **2005**, *29*, 1141.

[17] S. S. Moore, T. L. Tarnowski, M. Newcomb, D. J. Cram, *J. Am. Chem. Soc.* **1977**, *99*, 6398.

[18] a) K. E. Koeing, G. M. Lein, P. Stuckler, T. Kaneda, D. J. Cram, *J. Am. Chem. Soc.* **1979**, *101*, 3553; b) D. J. Cram, G. M. Lein, *J. Am. Chem. Soc.* **1985**, *107*, 3657.

[19] C. D. Gutsche, M. Iqwal, *Org. Synth.* **1989**, *68*, 234.

[20] D. D. Perrin, W. L. F. Armarego, D. R. Perrin, *Purification of Laboratory Chemicals*, 2nd ed., Pergamon Press, Oxford, U. K., **1980**.

[21] Bruker Analytical X-ray Instruments, Inc., Madison, WI.

[22] G. M. Sheldrick, University of Göttingen, Göttingen, Germany, **1996**.

[23] G. M. Sheldrick, *SHELXS97*, *a program for crystal structure solution*, University of Göttingen, Germany, **1997**.

[24] G. M. Sheldrick, *SHELXL97*, *a program for crystal structure refinement*, University of Göttingen, Germany, **1997**.

[25] A. L. Spek, *SQUEEZE*, University of Utrecht, The Netherlands, **1992**.

[26] C. K. Johnson, *ORTEP II*, Report ORNL-5138, Oak Ridge National Laboratory, Oak Ridge, TN, **1976**.

[27] A. L. Spek, *PLATON-97*, University of Utrecht, The Netherlands, **1997**.

[28] *Mercury 1.3*, supplied with Cambridge Structural Database CCDC, Cambridge, UK, **2003–2004**.

Received: April 20, 2006
Published Online: July 25, 2006

 © 2006 Wiley-VCH Verlag GmbH & Co. KGaA, Weinheim 

DOI: 10.1002/ejic.200600377

# Encouraging Chromium(III) Ions to Form Larger Clusters: Syntheses, Structures, Magnetic Properties and Theoretical Studies of Di- and Octametallic Cr Clusters

**Caytie E. Talbot-Eeckelaers,[a] Gopalan Rajaraman,[a] Joan Cano,*[b,c,d] Guillem Aromí,[b] Eliseo Ruiz,[b,c] and Euan K. Brechin*[a,e]**

**Keywords:** Exchange coupling / Density functional theory / Polynuclear chromium complexes / Magnetic properties / Magneto-structural correlation

Reaction of anhydrous $CrCl_2$ with the tripodal ligands 1,1,1-tris(hydroxymethyl)ethane ($H_3$thme), 1,1,1-tris(hydroxymethyl)propane ($H_3$tmp) and pentaerythritol ($H_4$peol) produces three new $Cr^{III}$ clusters that have been structurally and magnetically characterised. The dimeric complex $[Cr_2(H_2tmp)_2Cl_4]\cdot 2MeOH$ (**1**·2MeOH) is generated under reflux. An analogous reaction, but under solvothermal conditions produces the octametallic species $[Cr_8O_2(thme)_2(Hthme)_4Cl_6]\cdot 2MeOH$ (**2**·2MeOH) and $[Cr_8O_2(Hpeol)_2(H_2peol)_4Cl_6]\cdot 3MeOH$ (**3**·3MeOH). Complex **1** is a simple dimeric species whereas the structures of **2** and **3** are based on the decametallate $\{M_{10}O_{28}\}^{26-}$ ion. Variable-temperature direct-current (dc) magnetic susceptibility data were collected for complexes **1** and **2** in the 1.8–300 K temperature range in fields up to 5.0 T. Complex **1** has a ground state of S = 0 with the best-fit parameters $J = -12.30 \pm 0.04$ cm$^{-1}$ and $g = 1.990 \pm 0.003$. Electronic structure calculations based on density functional theory (DFT) on **1** and **2** have been carried out and good agreement with the experimental data was found for **1**. For **2**, the theoretical results have been used as starting point to fit the $J$ values to the experimental data, revealing the presence of competing antiferromagnetic ($J_{4,7} = -39.0$ cm$^{-1}$; $J_{3,7} = J_{4,6} = +1.1$ cm$^{-1}$, $J_{4,5} = J_{3,4} = -20.0$ cm$^{-1}$, $J_{3,6} = -16.0$ cm$^{-1}$ and $J_{1,3} = J_{1,6} = J_{1,4} = J_{1,7} = -4.8$ cm$^{-1}$) exchange interactions between the $Cr^{III}$ centres that suggests a singlet ground state with very close S = 1, 2, 3 and 4 excited states. Magneto-structural correlations developed on a model complex based on **1** show a strong dependence of $J$ with Cr–O–Cr angle. A similar magneto-structural correlation is found for the $J$ values obtained by theoretical calculations on **2**.
(© Wiley-VCH Verlag GmbH & Co. KGaA, 69451 Weinheim, Germany, 2006)

## Introduction

Polymetallic clusters of chromium remain relatively rare, and in terms of nuclearity, relatively small. Whereas clusters of Mn, Fe, Ni, Co and Cu have, in some cases, contained more than eighty metal centres, the largest known $Cr^{III}$ clusters contain only twelve metal ions.[1–20] The kinetically inert nature of the $Cr^{III}$ ion usually requires reactions to be carried out at high temperatures, and the most successful synthetic routes have involved either the direct heating of the basic Cr carboxylates $[Cr_3O(O_2CR)_6(H_2O)_3]^+$ or the heating of the $Cr^{III}$ salt in the presence of a carboxylic acid. For example, the use of a combination of $CrF_3$ and pivalic acid leads to a family of clusters based on wheels,[1] as does the solvothermal heating of $[Cr_3O(O_2CR)_6(H_2O)_3]^+$ in alcohol.[2] An interesting aspect of this chemistry is that homometallic Cr clusters all contain bridging carboxylates, the majority have topologies that are based on either cubes or wheels, and most are characterised by S = 0 spin ground states. The exceptions to this are a $Cr_{12}$ centred-pentacapped trigonal prism with S = 6,[3] a ferromagnetic $Cr_{10}$ wheel,[2] and a tetrametallic cluster with S = 6.[4]

Theoretical calculations based on density functional theory of magnetic exchange coupling constants ($J$) in binuclear and polynuclear transition-metal complexes have gained much attention recently because these methods have proven to give good numerical estimates of $J$ values as well as providing insight into the electronic structure of the molecule of interest.[11,21–40] For polynuclear transition-metal complexes, the best way to experimentally obtain a good set of $J$ values (or other spin Hamiltonian parameters such as zero-field splitting) is Inelastic Neutron Scattering (INS) or Frequency Domain Magnetic Resonance Spec-

[a] Department of Chemistry, The University of Manchester, Oxford Road, Manchester, M13 9PL, UK
[b] Departament de Química Inorgànica, Facultat de Química, Universitat de Barcelona, Diagonal 647, 08028 Barcelona, Spain
Fax: +34-93-4907725
E-mail: joan.cano@qi.ub.es
[c] Centre de Recerca en Química Teòrica, Universitat de Barcelona, 08028 Barcelona, Spain
[d] Institució Catalana de Recerca i Estudis Avançats (ICREA), Spain
[e] School of Chemistry, The University of Edinburgh, West Mains Road, Edinburgh, EH9 3JJ, UK
E-mail: ebrechin@staffmail.ed.ac.uk
Supporting information for this article is available on the WWW under http://www.eurjic.org or from the author.

 © 2006 Wiley-VCH Verlag GmbH & Co. KGaA, Weinheim 

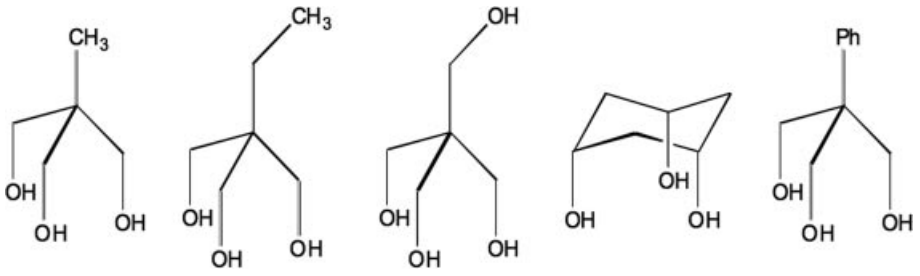


Scheme 1.

troscopy (FDMRS).[5–7] INS allows the direct spectroscopic determination (in zero-applied field) of such parameters, but unfortunately these measurements are somewhat uncommon because of restrictive sample requirements.[5] These constants can also be evaluated from magnetic susceptibility (fitting of $\chi_M$ or $\chi_M T$ vs. $T$ curves), heat capacity or EPR measurements, but the obtained values are only correct if certain requirements are fulfilled, namely: (i) as well as in the INS experiments, the choice of an accurate spin Hamiltonian that properly describes the magnetic properties of the system; (ii) the presence of critical points in the experimental curves that allow for a better assessment of the variable parameters in the fitting; and (iii) avoidance of over-parameterisation, i.e. using too many parameters ($J$ constants) in the spin Hamiltonian. In this latter case, obtaining a set of $J$ values from theoretical calculations as a starting point for the fitting procedure is a very useful alternative.

We have been using the tripodal ligand 1,1,1-tris(hydroxymethyl)ethane ($H_3$thme, Scheme 1) and its analogues in the synthesis of Mn, Fe, Ni and Co clusters[8] and herein report our first attempts to make polymetallic $Cr^{III}$ clusters including a novel dinuclear cluster and a related octametallic $Cr^{III}$ cluster whose structure is based on the decametallate $\{M_{10}O_{28}\}^{26-}$ ion. Both complexes are formed from similar reaction schemes, but the dimeric cluster is isolated under reflux and the octametallic species isolated under solvothermal conditions. In order to elucidate the magnetic properties of these compounds, we have also studied their electronic structure. The relevant exchange coupling constants have been calculated and several magneto-structural correlations have been found and interpreted according to the Cr–O–Cr angle for different families displaying several bridging ligands (oxo, alkoxo).

## Results and Discussion

### Synthesis

When $CrCl_2$, $H_3$tmp and NaOMe are stirred in MeOH at room temperature no isolable products are obtained, even if the solvent is evaporated and the resultant solid extracted into a variety of solvents. When the reaction is repeated, but under reflux, the dimeric species **1** is obtained when the original MeOH solution is stripped off and the resultant solid redissolved in MeCN. No isolable product is obtained from the initial MeOH solution or from any other solvents, or when the reaction is repeated with the tripodal ligands $H_3$thme or $H_4$peol. Superheating a methanolic solution containing equivalent amounts of $CrCl_2$, $H_3$thme or $H_4$peol and NaOMe in a sealed high-pressure vessel at 100 °C for 12 h followed by slow cooling to room temperature generates crystals of compounds **2** and **3**, respectively, directly from the reaction mixture in high yield. It is likely that the $Cr^{II}$ ions are oxidised almost immediately upon dissolution, but the analogous reactions – under both refluxing and solvothermal conditions – using $Cr^{III}$ halides failed to yield any isolable products.

### Structure Description

Complex **1** (Figure 1) crystallises in the monoclinic space group $P2_1/c$. Selected bond lengths and angles are given in Table 1. The structure consists of two $Cr^{III}$ ions related by an inversion centre, bridged by two singly deprotonated $H_2tmp^-$ ligands. The deprotonated arms (O1 and O1A) act as μ-bridges with the protonated arms (O2, O3A and symmetry equivalents), each bonding in a terminal fashion. These are H-bonded to the MeOH solvent molecules [e.g. O4···O2, 2.552(3) Å] and their bonds to Cr are slightly longer [1.983(2)–2.017(2) Å] than the bridging Cr–O distances [1.954(2)–1.964(2) Å]. Two terminal chloride ions (Cl1, Cl2 and symmetry equivalents) complete the coordination spheres of the $Cr^{III}$ ions, and these H-bond to the

Figure 1. Perspective view of the dinuclear complex $[Cr_2(H_2tmp)_2Cl_4]$ (**1**).

 © 2006 Wiley-VCH Verlag GmbH & Co. KGaA, Weinheim 

Table 1. Selected bond lengths, intermetal distances and angles for **1**.

| | | | |
|---|---|---|---|
| Cr1–O1 | 1.954(2) | Cr1–Cl1 | 2.338(2) |
| Cr1–O1A | 1.964(2) | Cr1–Cl2 | 2.309(2) |
| Cr1–O2 | 1.983(2) | Cr1···Cr1A | 3.022(2) |
| Cr1–O1–Cr1A | 100.9(2) | O1A–Cr1–Cl1 | 173.1(1) |
| O1–Cr1–O1A | 79.1(2) | O2–Cr1–Cl1 | 90.0(2) |
| O1–Cr1–O2 | 90.6(2) | O3–Cr1–Cl1 | 91.4(2) |
| O1A–Cr1–O2 | 87.8(2) | O1–Cr1–Cl2 | 171.8(2) |
| O1–Cr1–O3 | 86.9(2) | O1A–Cr1–Cl2 | 93.5(2) |
| O1A–Cr1–O3 | 90.5(2) | O2–Cr1–Cl2 | 92.6(2) |
| O2–Cr1–O3 | 177.3(2) | O3–Cr1–Cl2 | 89.7(2) |
| O1–Cr1–Cl1 | 94.4(2) | Cl1–Cr1–Cl2 | 93.2(1) |

oxygen arms of the tripodal ligands on neighbouring molecules (Cl···O, 3.06–3.18 Å). The $Cr^{III}$ ions are in distorted octahedral geometries with *cis* angles in the range 79.1(1)–94.43(7)° and *trans* angles of 171.77(7)–177.25(9)°. In the crystal the $Cr_2$ units pack in 2D sheets as mediated by the Cl···O and O(tripod)···O(MeOH) H-bonds, with these "metallic" sheets separated from each other by the organic tails of the tripodal ligands and the chloride ions. Here, the closest intermolecular interactions are of the order 3.5–4.0 Å. Complex **1** is structurally related to the vanadium dimers of general formula $[V_2O_2(H_2tripod)_2Cl_2]$, in which one of the chloride ions on each metal has been replaced by an oxygen.[9]

Complex **2**, $[Cr_8O_2(thme)_2(Hthme)_4Cl_6]$ crystallises in the triclinic space group $P\bar{1}$, whereas complex **3**, $[Cr_8O_2(Hpeol)_2(H_2peol)_4Cl_6]$ crystallises in the monoclinic space group $C2/c$. Both structures are essentially the same, and thus we will confine our discussion to complex **2** (Table 2 and Table 3). Differences in the packing arrangements between **2** and **3** are discussed afterwards (Figure S1). The core of **2** (Figure 2) consists of two $[Cr_5O]^{13+}$ square-based pyramids, related by an inversion centre, which share one edge forming a central $[Cr_8O_2]^{20+}$ unit. The core can be regarded as part of the decametallate $\{M_{10}O_{28}\}^{26-}$ ion of two edge-sharing octahedra, but with two of the apical metal centres missing and with the bridging and terminal oxo groups replaced by a combination of oxygen atoms from tripodal ligands and chloride ions. The tripodal ligands are of two types: the two fully deprotonated $thme^{3-}$ ligands, each bound to the open triangular face of the square-based pyramid with each oxygen (O5, O6, O10A) arm bridging in a $\mu_2$-fashion between either the apical $Cr^{III}$ ion (e.g. Cr3A) and basal ion (e.g. Cr2) or between two basal $Cr^{III}$ ions (e.g. Cr4A, Cr2). The remaining four tripodal ligands are doubly deprotonated, $Hthme^{2-}$, and occupy four of the "faces" surrounding the vacant apical Cr sites: one deprotonated arm bonds in a $\mu_2$-fashion between apical and basal $Cr^{III}$ ions (e.g. O9) – thus linking the two square-based pyramids together; the second deprotonated arm bridges between two basal sites (e.g. O8), with the third protonated arm (e.g. O7) binding in a terminal fashion to a basal $Cr^{III}$ site. There are six chloride ions in the structure which each bond terminally to $Cr^{III}$ ions on the open triangular faces of the square-based pyramids. The two $O^{2-}$ ions are five-coordinate and square-based pyramidal, each bound to four basal and one apical $Cr^{III}$ ion, with *cis* angles in the range 89.2–95.3° and *trans* angles 170.8–172.0° (Table 2). The result is an $\{M_8L_{26}\}$ unit, equivalent to the $\{M_{10}O_{28}\}^{26-}$ decametallate ion minus the two {ML} apices. The terminal Cr–O bonds of the $Hthme^{2-}$ ligand are significantly longer (2.020–2.064 Å) than the μ-bridging oxygen

Table 2. Selected bond lengths and angles for **2**.

| | | | | | |
|---|---|---|---|---|---|
| Cr1–O1 | 2.084(2) | Cr2–O5 | 1.963(3) | Cr3–O9 | 1.979(3) |
| Cr1–O1A | 2.087(2) | Cr2–O6 | 1.962(3) | Cr3–O10 | 1.971(3) |
| Cr1–O2 | 1.958(3) | Cr2–O7 | 2.064(3) | Cr4–O1 | 2.108(2) |
| Cr1–O3 | 1.928(3) | Cr2–O8 | 1.978(3) | Cr4–O3 | 1.961(3) |
| Cr1–O8 | 1.933(3) | Cr3–O1 | 2.060(3) | Cr4–O4 | 2.020(3) |
| Cr1–O9 | 1.977(3) | Cr3–O2 | 1.978(3) | Cr4–O6 | 1.950(3) |
| Cr2–O1 | 2.083(2) | Cr3–O5 | 1.984(3) | Cr4–O10 | 1.954(3) |
| Cr2–Cl1 | 2.273(1) | Cr3–Cl2 | 2.292(1) | Cr4–Cl3 | 2.282(1) |
| Cr1–O1–Cr1A | 89.3(1) | Cr1–O1–Cr2 | 170.9(1) | Cr1–O1–Cr3 | 95.2 (1) |
| Cr1–O1–Cr4 | 89.1(1) | Cr2–O1–Cr3 | 93.9 (1) | Cr2–O1–Cr4 | 90.4(1) |
| Cr3–O1–Cr4 | 93.6(1) | Cr1–O1A–Cr2 | 89.9(1) | Cr1–O1A–Cr3 | 94.3(1) |
| Cr1–O1A–Cr4 | 172.1(1) | Cr3–O1A–Cr4 | 101.5(1) | Cr1–O2–Cr3 | 101.1(1) |
| Cr2–O5–Cr3 | 100.2(1) | Cr2–O6–Cr4 | 99.0(1) | Cr1–O8–Cr2 | 97.7(1) |
| Cr1–O9–Cr3 | 101.36(1) | O1–Cr1–O8 | 172.7(1) | O1A–Cr1–O3 | 173.5(1) |
| O2–Cr1–O9 | 172.9(1) | O1–Cr1–O3 | 87.0 (1) | O1A–Cr1–O8 | 86.7(1) |
| O1A–Cr1–O9 | 93.2(1) | O3–Cr1–O8 | 96.3(1) | O3–Cr1–O9 | 92.54(1) |
| O5–Cr2–O7 | 170.8(1) | O6–Cr2–O8 | 170.4 (1) | O1A–Cr2–Cl1 | 179.22(1) |
| O1A–Cr2–O6 | 85.4(1) | O1A–Cr2–O8 | 85.6(1) | O5–Cr2–O8 | 92.1(1) |
| O6–Cr2–O7 | 89.7(1) | O6–Cr2–Cl1 | 93.9(1) | O7–Cr2–Cl1 | 92.2(2) |
| O2A–Cr3–O10 | 165.1(1) | O5A–Cr3–O9 | 165.0(1) | O1–Cr3–Cl2 | 179.5(1) |
| O1–Cr3–O2A | 82.4(1) | O2A–Cr3–O9 | 85.5(1) | O5A–Cr3–O10 | 88.9(1) |
| O9–Cr3–O10 | 90.0(1) | O9–Cr3–Cl2 | 98.3(1) | O10–Cr3–Cl2 | 96.8(1) |
| O3–Cr4–O6A | 169.3(1) | O4–Cr4–O10 | 172.7(1) | O1–Cr4–Cl3 | 177.1(1) |
| O1–Cr4–O3 | 85.5(1) | O1–Cr4–O6A | 85.0(1) | O1–Cr4–O10 | 82.0(1) |
| O3–Cr4–O10 | 93.2(1) | O6A–Cr4–Cl3 | 95.6(1) | O10–Cr4–Cl3 | 95.1(1) |

 © 2006 Wiley-VCH Verlag GmbH & Co. KGaA, Weinheim 

Table 3. Selected bond lengths, intermetal distances and angles for **3**.

| | | | | | |
|---|---|---|---|---|---|
| Cr1–O1 | 2.088(2) | Cr2–O2 | 1.988(2) | Cr3–O8A | 1.955 (2) |
| Cr1–O1A | 2.086(2) | Cr2–O4 | 2.039(2) | Cr3–O10 | 1.964(2) |
| Cr1–O2 | 1.937(2) | Cr2–O8 | 1.951(2) | Cr4–O1A | 2.040(2) |
| Cr1–O3 | 1.968(2) | Cr2–O9 | 1.960(2) | Cr4–O3 | 1.978(2) |
| Cr1–O5 | 1.924(2) | Cr3–O1A | 2.116(2) | Cr4–O6A | 1.978 (2) |
| Cr1–O6 | 1.959(2) | Cr3–O5 | 1.972(2) | Cr4–O9A | 1.983(2) |
| Cr2–O1 | 2.080(2) | Cr3–O7 | 2.008(2) | Cr4–O10 | 1.971(2) |
| Cr2–Cl1 | 2.286(1) | Cr3–Cl2 | 2.268(1) | Cr4–Cl3 | 2.297(1) |
| Cr1···Cr1A | 2.931(1) | Cr1···Cr2 | 2.937(1) | Cr1···Cr3 | 2.949(1) |
| Cr1···Cr4 | 3.033(1) | Cr1···Cr4A | 3.037(1) | Cr2···Cr3A | 2.988(1) |
| Cr2···Cr4 | 3.026(1) | Cr3···Cr4 | 3.025(1) | O11···O13 | 2.656(1) |
| Cr1–O1–Cr1A | 89.2(1) | Cr3A–O1–Cr4A | 93.4(1) | Cr1A–O1–Cr2 | 170.9(1) |
| Cr1–O1–Cr2 | 89.6(1) | Cr1–O2–Cr2 | 96.9 (1) | Cr1–O1–Cr3A | 171.9(1) |
| Cr1A–O1–Cr3A | 89.1(1) | Cr2–O1–Cr3A | 90.8 (1) | Cr1–O1–Cr4 | 94.7(1) |
| Cr2–O1–Cr4A | 94.6(1) | Cr1A–O1–Cr4A | 94.6(1) | Cr1–O3–Cr4 | 100.4(1) |
| Cr1–O5–Cr3 | 98.4(1) | Cr1–O6–Cr4A | 100.9(1) | Cr2–O8–Cr3A | 99.8(1) |
| Cr2–O9–Cr4A | 100.24(1) | O1–Cr1–O5 | 173.7(1) | O1A–Cr1–O2 | 173.2(1) |
| O3–Cr1–O6 | 173.4(1) | O1–Cr1–O1A | 90.8(1) | O1–Cr1–O2 | 87.2(1) |
| O1–Cr1–O3 | 93.3(1) | O1A–Cr1–O3 | 82.0(1) | O1A–Cr1–O5 | 87.2(1) |
| O1A–Cr1–O6 | 93.5(1) | O2–Cr1–O5 | 95.4(1) | O3–Cr1–O6 | 92. 4(1) |
| O2–Cr2–O8 | 170.9(1) | O4–Cr2–O9 | 171.9(1) | O3–Cr2–Cl1 | 178.9(1) |
| O1–Cr2–O2 | 86.1(1) | O1–Cr2–O4 | 89.5(1) | O1–Cr2–O8 | 85.2(1) |
| O2–Cr2–O9 | 91.6(1) | O4–Cr2–Cl1 | 90.9(1) | O3–Cr2–Cl1 | 93.8(1) |
| O5–Cr3–O8A | 168.4(1) | O7–Cr3–O10 | 171.2(1) | O1A–Cr3–Cl2 | 178.2(1) |
| O1A–Cr3–O5 | 85.2(1) | O1A–Cr3–O8A | 84.1(1) | O5–Cr3–O7 | 87.8(1) |
| O5–Cr3–O10 | 92.9(1) | O7–Cr3–Cl2 | 92.6(10) | O8A–Cr3–Cl2 | 96.6(1) |
| O3–Cr4–O9A | 165.7(1) | O6A–Cr4–O10 | 166.5(1) | O1A–Cr4–Cl3 | 178.3(1) |
| O1A–Cr4–O6A | 82.6(1) | O3–Cr4–O6A | 86.2(1) | O3–Cr4–O10 | 91.0(1) |
| O9A–Cr4–O10 | 96.7(1) | O3–Cr4–Cl3 | 95.5(1) | O9A–Cr4–Cl3 | 98.7(1) |

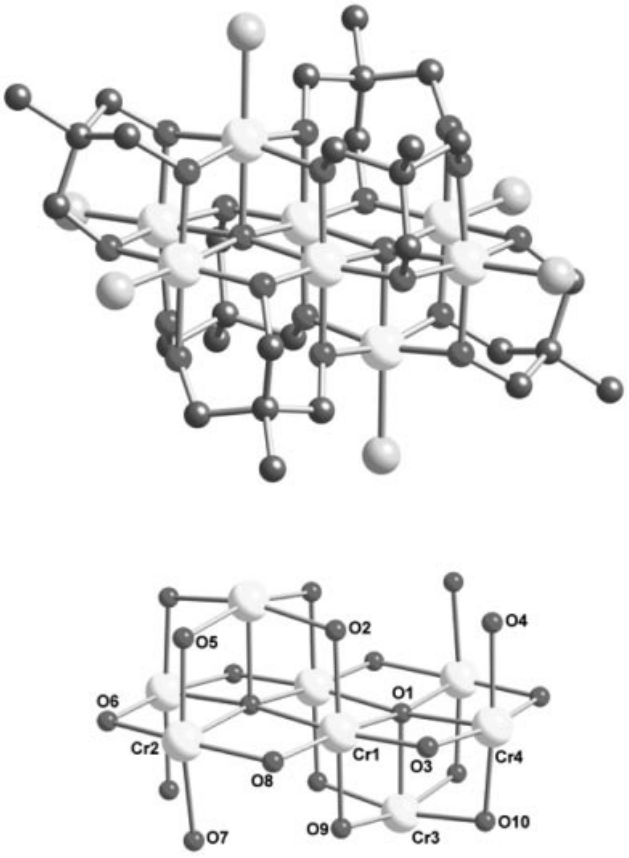


Figure 2. Perspective view of the octanuclear complex $[Cr_8O_2(thme)_2(Hthme)_4Cl_6]$ (**2**) (top) and its metal–oxygen core (bottom).

bond lengths (1.949–1.984 Å), with O4 and O7A hydrogen bonded both to each other and a MeOH solvate molecule (e.g. O4···O7A, 2.737 Å; O4···O11, 2.662 Å) (Table 2). All the $Cr^{III}$ ions are in distorted octahedral geometries with their oxidation states confirmed by a combination of BVS calculations, bond lengths and overall charge balance considerations.

In the crystal the molecules pack in columns with one $Cr_8$ unit sitting directly above and below its nearest neighbours. Here, the closest intermolecular interactions are between the terminal chloride ions and the tripodal ligands (≈ 3.5–3.7 Å). Intermolecular interactions between the columns are mediated through a combination of Cl···C (tripod) H-bonds (in the region of ≈ 3.5–3.7 Å), and the Cl···O (MeOH) H-bonds. For complex **3**, the pendant alcohol group of the pentaerythritol ligand is found to greatly influence the packing within the crystal lattice. These additional OH groups form hydrogen bonds to molecules in adjacent planes (e.g. O11···O13, O11A···O13A) at a distance of ca. 2.65 Å and result in these planes packing in a perpendicular fashion. The terminal chloride ions are also involved in two intermolecular H-bonding interactions; one OH···Cl interaction with an uncoordinated $H_2peol^-$ ligand arm (e.g. O12···Cl3, 3.25 Å), and the other with a MeOH solvent molecule (O17···Cl2, 3.21 Å).

The edge-sharing $[M_8(\mu_5\text{-}O_2)]^{n+}$ core adopted by **2** and **3** is somewhat unusual. Other examples of this octanuclear fragment are restricted to the Ba clusters $[Ba_8O_2]^{12+}$, $[Sr_6Ba_2O_2]^{12+}$ and $[Ba_8Eu_2O_2]^{12+}$ where the principal bridging ligand is also an alkoxo group.[10,11] Similar cores can, however, be found in the decanuclear transition-metal

 © 2006 Wiley-VCH Verlag GmbH & Co. KGaA, Weinheim 

clusters $[Fe_{10}O_2Cl_8(tmp)_6]$, $[(VO)_2Fe_8O_2Cl_6(tmp)_6]$ and $(NEt_4)_2[Mn_{10}O_2Cl_8(thme)_6]$.[9,12,13]

### Magnetic Measurements

Solid-state dc magnetisation measurements were performed on **1** and **2** in the temperature range 1.8–300 K in a field of 5.0 kG and the Irreducible Tensor Operator (ITO) formalism was employed to fit the experimental data by means of the programme VPMAG.[14] For complex **1**, the room temperature $\chi_M T$ value of approximately 3.75 $cm^3 \cdot K \cdot mol^{-1}$ is that expected for two non-interacting $Cr^{III}$ centres (Figure 3). As the temperature is lowered, the value of $\chi_M T$ drops very gradually until approximately 100 K where it begins to fall more dramatically, reaching a value close to 0 $cm^3 \cdot K \cdot mol^{-1}$ at 1.8 K. At 27 K a maximum in $\chi_M$ is reached ($\chi_M$ = 0.0512 $cm^3 \cdot K \cdot mol^{-1}$). This behaviour is indicative of relatively weak antiferromagnetic exchange coupling between the $Cr^{III}$ ions with an $S = 0$ spin ground state. Using the spin Hamiltonian $\hat{H} = -J\hat{S}_1 \cdot \hat{S}_2$, the best fit (Figure 3 solid line) was obtained for the following parameters: $J = -12.30 \pm 0.04$ $cm^{-1}$ and $g = 1.990 \pm 0.003$, resulting in an S = 0 spin ground state. The agreement factor of the fit, defined as

$F = \{\Sigma[\chi_i^{exp.} - \chi_i^{calcd.}]^2\}/\{\Sigma[\chi_i^{calcd.}]^2\}$, is good ($F = 1.1 \cdot 10^{-5}$).

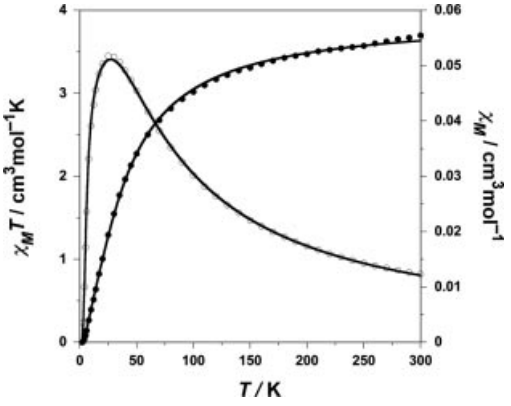


Figure 3. Plot of $\chi_M$ and $\chi_M T$ vs. $T$ for complex **1**. The solid lines are fits to the experimental data. See text for details.

For complex **2**, the $\chi_M T$ value of approximately 10.8 $cm^3 \cdot K \cdot mol^{-1}$ at 300 K is smaller than that expected for eight noninteracting $S = 3/2$ metal centres (15 $cm^3 \cdot K \cdot mol^{-1}$, with $g = 2.0$). Below 300 K, the value of $\chi_M T$ drops gradually with temperature reaching a pseudo-plateau with a value of approximately 3.2 $cm^3 \cdot K \cdot mol^{-1}$ at 10 K (Figure 4). This behaviour is indicative of dominant antiferromagnetic exchange between the $Cr^{III}$ ions, resulting in a relatively small spin ground state ($S = 2$). Below 10 K the $\chi_M T$ value falls again to approximately 2 $cm^3 \cdot K \cdot mol^{-1}$ at 1.8 K. The decrease of $\chi_M T$ in this last region is probably due to intermolecular interactions, the magnetic anisotropy of the ground spin state, or (less probably) the presence of more stable states displaying lower spin angular momenta.

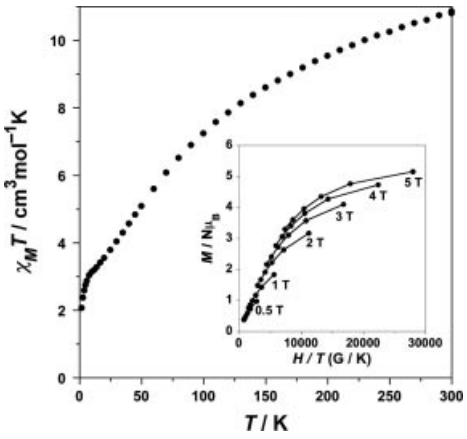


Figure 4. Plot of $\chi_M T$ vs. $T$ for complex **2** and (inset) magnetisation ($M$) vs. field ($H$) data taken in the ranges 1.8–6.2 K and 0.5–5.0 T.

Magnetisation measurements in the 1.8–6.2 K temperature range were performed under constant magnetic fields of 0.5–5.0 T (Figure 4, inset). The isofield lines are not superimposable and the values of reduced magnetisation ($M/N\mu_B$) become higher than expected for the postulated spin ground state ($M/N\mu_B \approx 4$ for $S = 2$). This is probably caused by population of low-lying excited states with higher spin numbers which become more stable with increasing fields. For this reason a fit of the magnetisation data to a Brillouin equation was not attempted, because a well-isolated spin ground state is required for such a model to apply. The possibility of slow relaxation of the magnetisation was investigated by collection of ac susceptibility data taken in a range of frequencies. However, no out-of-phase ($\chi_M''$) signal was observed over the whole temperature range (1.8–6.2 K) indicating that **2** is not a single-molecule magnet.

Unfortunately, there are few examples of $Cr^{III}$ compounds in the literature that actually possess similar bridging ligands to the ones found in **2** and **3**, and even these contain other bridging co-ligands (e.g. carboxylates etc.).[15–23] Moreover, there exists little magnetic characterisation of these species and/or their magnetic properties have not been quantitatively analysed because the complexity of the system.[24–30] Thus, it is very difficult to compare and contrast any results with other $Cr^{III}$ complexes. In addition, in such complicated multiple $J$ systems it is usually possible to find several sets of $J$ values that can reproduce the experimental magnetic behaviour equally well. We therefore decided to carry out calculations based on DFT in order to either have good estimated $J$ values to use them as a starting point in a fit.

### Theoretical Study of the Magnetic Exchange Coupling

#### *Complex 1*

An exchange coupling constant, $J = -7.5$ $cm^{-1}$, has been obtained from DF calculations on complex **1** using the broken symmetry approach. Although the theoretical study correctly reproduces the nature of the magnetic interaction, the magnitude of the $J$ constant is slightly lower than the

 © 2006 Wiley-VCH Verlag GmbH & Co. KGaA, Weinheim 

experimental value (–12.3 $cm^{-1}$). Despite the fact that only a few compounds display the $[Cr_2(OX)_2]^{4+}$ core (X = H, Me or Et), there does exist a magneto-structural correlation for this unit based on experimental structural parameters which relates the magnetic exchange constant to the Cr–O–Cr angle ($\alpha$), the Cr–O distance ($d_{CrO}$), and the dihedral angle formed between the OR group and $Cr_2O_2$ plane ($\theta$).[31] Here, we have revisited this correlation bringing up to date the experimental data (Table 4), as well as performing a theoretical analysis by electronic structure calculations. The Cr–O distance remains essentially unchanged along the series of compounds, so we have focused our efforts in the study of the influence of the $\alpha$ and $\theta$ angles. We have used the model complex $[Cr_2(OMe)_2(H_2O)_4Cl_4]$ (**1A**) built from the experimental structural parameters of **1** (Figure S2). In this magneto-structural correlation only the $\alpha$ angles have been modified with the remaining parameters constant. It is important to stress that the molecular geometry of the most stable compound corresponds to an $\alpha$ angle equal to 100.85° – similar to that experimentally found (100.93°, Figure 5). This $\alpha$ value is the same in the singlet (ground state) and triplet state. The thermal energy at room temperature allows the $\alpha$ angle to achieve any value between 98.8 and 102.8° and so, in agreement with the experimental data (Table 4), we can conclude that the experimental $\alpha$ angles in the $[Cr_2(OR)_2]^{4+}$ complexes will take similar values.

At $\alpha$ = 101.3° ($\alpha_{min}$), near the more stable molecular geometry, the antiferromagnetic exchange coupling reaches a minimum value ($J$ = –5.2 $cm^{-1}$). At lower $\alpha$ angles the exchange coupling becomes strongly antiferromagnetic because the inter-metal distance is short enough to allow direct interaction between the paramagnetic centres ($\alpha < 95°$). However, as has been observed in bis-alkoxo dinuclear copper(II) complexes,[32,33] there is an experimental and theoretical correlation between the $\alpha$ and $\theta$ (dihedral) angles (Figure S3). However, no qualitative changes occur in the magneto-structural correlation between the $J$ constant and the $\alpha$ angle (Figure 5). Most complexes display an $\alpha$ value of around 100–101°, but in some cases where bulky alkoxo bridging ligands are used, the $\alpha$ angle can take larger values.

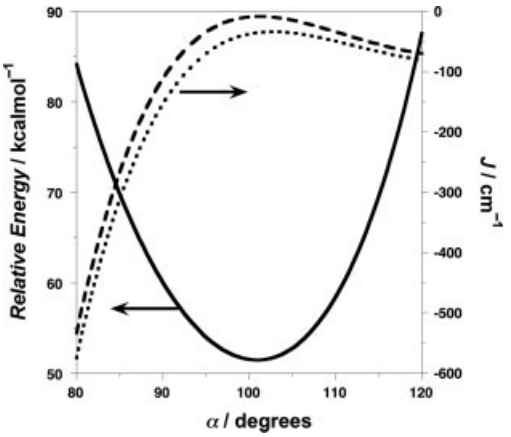


Figure 5. Relative energy (in kcal/mol, solid line) of the singlet ground state and magnetic exchange coupling as a function of the bridging angle Cr–O–Cr ($\alpha$) angle. The dotted and dashed lines correspond to the $J$ values obtained on model **1A** when the $\theta$ angle is or is not optimised, respectively.

In these cases the alkoxo group is almost coplanar with the $[Cr_2(OR)_2]^{4+}$ unit and the antiferromagnetic coupling becomes stronger (Table 4), as predicted by theoretical calculations.[22,34–41] We have analysed this magneto-structural correlation in order to find the electronic factors that govern it (Figure S4). In agreement with previous work, we have concluded that the contribution from the $d_{xy}$ magnetic orbitals is responsible for the correlation between the $J$ constant and the $\alpha$ angle.[31] A more detailed analysis can be found in the Supporting Information.

The thme ligand provides two possible exchange pathways to mediate the magnetic exchange coupling between the $Cr^{III}$ centres: (a) by one alkoxo oxygen only; and (b) by the more extended O–C–C–C–O network (see Figure 1). In previous work, we demonstrated that the more extended pathway is an inefficient route for magnetic communication between $Fe^{III}$ ions where $t_{2g}$ and $e_g$ magnetic orbitals are present.[42] In this case, calculations on the full experimental molecule and on the simpler model lead to the same conclusion. The calculations on the model, where only the shortest pathway is present, give a theoretical $J$ value (–5.2 $cm^{-1}$)

Table 4. Experimental structural data and exchange coupling constants[a] for $[Cr_2(OR)_2]^{4+}$ compounds.

| Compound | $d_{CrO}$ | $\alpha$ | $\theta$ | $J$[b] | Refcode[c] | Ref. |
|---|---|---|---|---|---|---|
| $[Cr(L_1)(Cl)]_2(ClO4)_2$·DMF | 1.963 | 99.27 | 149.77 | – | FEBXIT | [36] |
| $[Cr(L_2)(OMe)(H_2O)]_2(ClO4)_2$ | 1.958 | 100.79 | 154.07 | – | DESRIC | [37] |
| $[Cr(H_2tmp)Cl_2]_2$·2MeOH | 1.959 | 100.93 | 142.93 | –12.3 (–7.5) | – | this work |
| $[Cr(acac)_2(OMe)]_2$ | 1.962 | 101.03 | 150.19 | –9.8 | BIKVAS | [22] |
| $[Cr(3\text{-}Cl\text{-}acac)_2(OMe)]_2$ | 1.959 | 101.09 | 155.58 | –9.8 | MXCACR10 | [34] |
| $[Cr(3\text{-}Br\text{-}acac)_2(OMe)]_2$ | 1.956 | 101.44 | 154.48 | –8.5 | MXBACR10 | [34] |
| $[Cr(tmjd)_2Cr(OMe)]_2$ | 1.954 | 101.74 | 148.77 | –8.9 | CUVVAQ | [38] |
| $[Cr(3\text{-}Br\text{-}acac)_2(OEt)]_2$ | 1.958 | 101.75 | 161.58 | –17.9 | EXBACR10 | [34] |
| $[Cr(DpyF)(OMe)(Cl)]_2$ | 1.977 | 101.88 | 159.69 | –12.5 | WOXFIY | [39] |
| $[Cr(L^S)(OMe)(MeOH)]_2$·MeOH | 1.981 | 103.10 | 175.41 | –16.6 | VACROH | [40] |
| $[Cr(L^{Se})(OMe)(MeOH)]_2$ | 1.968 | 103.58 | 177.32 | –18.0 | VACREX | [40] |
| $[Cr(L_3)(MeOH)]_2$·MeOH | 1.984 | 104.17 | 167.07 | – | QOZRIG | [41] |

[a] All angles in °; distance in Å and constants in $cm^{-1}$. [b] Because various magnetic models have been used in the literature, $J$ refers to the energy of the triplet states as calculated from the observed susceptibility data. Theoretical value obtained from electronic structure calculations is in parentheses. [c] Codes for locating structural data in the Cambridge Structural Database.[58]

 © 2006 Wiley-VCH Verlag GmbH & Co. KGaA, Weinheim 

similar to that obtained for the full molecule (–7.5 $cm^{-1}$). Moreover, the experimental $J$ value of **1** (–12.3 $cm^{-1}$) agrees well with those observed in previous complexes presenting similar $\alpha$ angles via the shortest M–O–M pathway only (–9.8 $cm^{-1}$). Therefore, the longest M–O–C–C–C–O–M pathway should not be relevant in these complexes as it leads to weak contributions. The contribution of $e_g$ magnetic orbitals – not present in the $Cr^{III}$ ion – are mainly responsible for the magnetic exchange coupling in $Fe^{III}$ complexes and it is strongly weakened when the exchange pathway is lengthened.

### *Complex 2*

As was shown in the structural section, the metal ions in complexes **2** and **3** are connected in three different ways: (a) by two $\mu_5$-oxo bridging ligands ($J_1$); (b) by one $\mu_5$-oxo ion ($J_2$); and (c) by one $\mu_5$-oxo ion and one μ-alkoxo ($J_3$). However, this simple model infers a higher molecular symmetry than that experimentally found (Figure 6). The lower molecular symmetry is related to the different Cr–O bond lengths and Cr–O–Cr angles, and in reality we can take into account ten possible exchange coupling constants and, thus, the spin Hamiltonian (Equation (1):

$$\hat{H} = -J_{4,7}\hat{S}_4 \cdot \hat{S}_7 - J_{3,7}(\hat{S}_3 \cdot \hat{S}_7 + \hat{S}_4 \cdot \hat{S}_8) - J_{4,6}(\hat{S}_4 \cdot \hat{S}_6 + \hat{S}_5 \cdot \hat{S}_7) - J_{4,5}(\hat{S}_4 \cdot \hat{S}_5 + \hat{S}_6 \cdot \hat{S}_7) - J_{3,4}(\hat{S}_3 \cdot \hat{S}_4 + \hat{S}_7 \cdot \hat{S}_8) - J_{3,6}(\hat{S}_3 \cdot \hat{S}_6 + \hat{S}_5 \cdot \hat{S}_8) - J_{1,3}(\hat{S}_1 \cdot \hat{S}_3 + \hat{S}_2 \cdot \hat{S}_8) - J_{1,6}(\hat{S}_1 \cdot \hat{S}_6 + \hat{S}_2 \cdot \hat{S}_5) - J_{1,4}(\hat{S}_1 \cdot \hat{S}_4 + \hat{S}_2 \cdot \hat{S}_7) - J_{1,7}(\hat{S}_1 \cdot \hat{S}_7 + \hat{S}_2 \cdot \hat{S}_4) \quad (1)$$

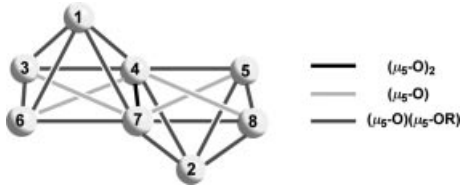


Figure 6. Scheme of the interactions employed in the study of the magnetic properties of **2** and **3**.

where the subindex in the $J$ constants refers to the paramagnetic centres involved in the exchange coupling. We have performed a least-squares fitting to the fourteen-equation system obtained from the differences in the energy between the fifteen spin distributions ($SD_i$) shown in Table S1. The results are shown in the Table 5. In Figure 7 is displayed a spin density map of the most stable configuration, $SD_3$. A more detailed description of this study is able in the Supporting Information.

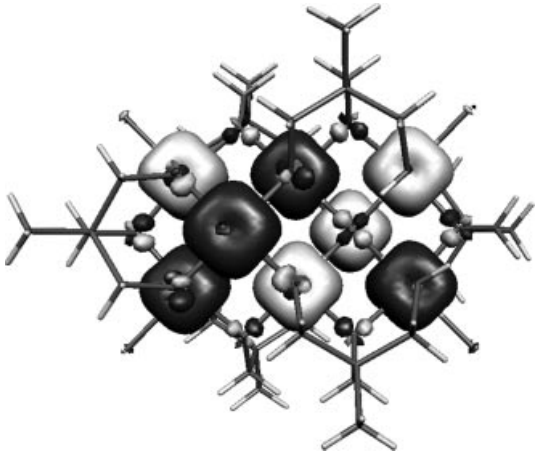

Figure 7. Spin density map calculated at the B3LYP level for the spin ground state of **2** (light and dark contours indicate positive and negative spin populations, respectively). The isodensity surface corresponds to a value of 0.005 $e^-/bohr^3$.

Although the $[Cr_2O_2]$ unit has a relatively low symmetry, a good magneto-structural correlation is found between the exchange coupling constants and the Cr–O–Cr angle in the cases where one oxo and one alkoxo groups act as bridges between metal ions (interaction 4–5, 3–4, 3–6, 1–3. 1–6, 1–4, 1–7; see Table 5). A change of the nature of the magnetic interaction is observed at $\alpha$ ca. 98°, where the ferro- and antiferromagnetic contributions are counter-balanced and a zero value for the $J$ constant is expected (Figure 8). This correlation is also found with the metal–metal distance because the Cr–O distances are almost constant within this small family. Only one system is not in accord with this correlation, displaying a weaker antiferromagnetic interaction than that expected, probably due to the longer Cr–O bond length (2.026 Å, Table 5) weakening the metal–ligand overlap and thus the magnetic exchange.

Table 5. Description of the bridging ligands, average Cr···Cr distances, Cr–O bond lengths, Cr–O–Cr bond angles and calculated exchange coupling constants $J_{i,j}$ (in $cm^{-1}$).

| $i,j$ | Bridging ligands | $d$(Cr···Cr)[a] | $d$(Cr–O)[a] | Cr–O–Cr ($\alpha$)[a] | $J_{i,j}$ |
|---|---|---|---|---|---|
| 4,7 | $(\mu_5\text{-}O^{2-})_2$ | 2.930 (2.930) | 2.085 (2.087) | 89.3 (89.2) | –52.7 |
| 3,7 | $(\mu_5\text{-}O^{2-})$ | 4.154 (4.152) | 2.084 (2.083) | 170.9 (170.9) | –3.8 |
| 4,6 | $(\mu_5\text{-}O^{2-})$ | 4.165 (4.194) | 2.097 (2.102) | 172.1 (171.9) | –2.8 |
| 4,5 | $(\mu_5\text{-}O^{2-})(\mu\text{-OR})$ | 2.942 (2.949) | 2.021 (2.025) | 93.7 (93.8) | –26.2 |
| 3,4 | $(\mu_5\text{-}O^{2-})(\mu\text{-OR})$ | 2.946 (2.937) | 2.020 (2.023) | 93.8 (93.3) | –25.7 |
| 3,6 | $(\mu_5\text{-}O^{2-})(\mu\text{-OR})$ | 2.974 (2.987) | 2.026 (2.026) | 94.7 (95.3) | –10.6 |
| 1,3 | $(\mu_5\text{-}O^{2-})(\mu\text{-OR})$ | 3.029 (3.026) | 2.023 (2.020) | 97.1 (97.4) | –4.8 |
| 1,6 | $(\mu_5\text{-}O^{2-})(\mu\text{-OR})$ | 3.039 (3.025) | 2.023 (2.023) | 97.6 (96.9) | –3.9 |
| 1,4 | $(\mu_5\text{-}O^{2-})(\mu\text{-OR})$ | 3.039 (3.033) | 2.021 (2.017) | 97.7 (97.8) | –1.4 |
| 1,7 | $(\mu_5\text{-}O^{2-})(\mu\text{-OR})$ | 3.061 (3–037) | 2.023 (2.018) | 98.3 (97.5) | +0.8 |

[a] The values corresponding to **3** are displayed in parentheses. Angles and distances are given in ° and Å.

 © 2006 Wiley-VCH Verlag GmbH & Co. KGaA, Weinheim 

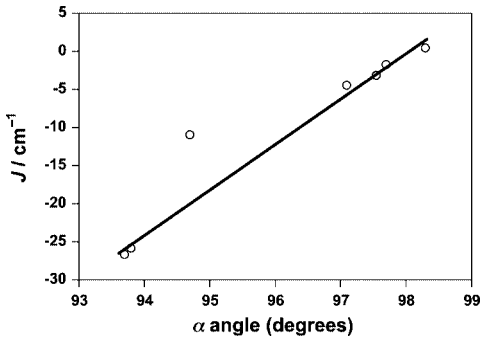


Figure 8. Dependence of the calculated exchange coupling constant ($J$) in **2** for the $[Cr_2O_2]^{2+}$ core with the Cr–O–Cr($\alpha$) angle.

There are two exchange interactions that mediate only through one $\mu_5$-oxo bridge (interaction 3–7, 4–6; see Table 5) where the $J$ constants are found to be –3.8 $cm^{-1}$ and –2.8 $cm^{-1}$. These values are very similar because both $[Cr_2O_2]$ units have similar $\alpha$ values (170.9° and 172.1°). The magnetic coupling in this case is expected to be governed by the Cr–O distance, so the stronger of the two $J$ constants is the one with the shortest Cr–O bond length. The stronger magnetic interactions found in **2** where two $\mu_5$-oxo bridges are present (interaction 4–7) should thus be due to the extremely small $\alpha$ values (Table 5).

Unfortunately, it is difficult to find similar compounds in the literature that have been structurally and magnetically characterised. In fact, only two such dinuclear complexes and one dodecanuclear $Cr^{III}$ complex exist.[17,29,30] For the dinuclear complexes there are no reported magnetic measurements and for the $Cr_{12}$ cluster the measurements have not been analysed due to the complexity of the system. The crystal structures of two $Cr^{III}$ dimers displaying a linear or quasi-linear $[Cr_2O]^{4+}$ core are known,[24,25] but, as is often the case, there are no studies of the magnetic properties, meaning we have no way to check the validity of our theoretical results.

The magnetic behaviour of **2** can be simulated by exact diagonalisation of the energy matrix built using the irreductible tensors operator approach. We have obtained the $\chi_M T$ vs. $T$ curve for **2** from the calculated $J$ values and find that they are in qualitatively acceptable agreement with the experimental curve (Figure 9). We have also carried out a fit using these $J$ values as starting point and to avoid overparameterisation, we have reduced the number of variables in the way shown in Table 6. The best fit was obtained for the following parametes: $J_{4,7}$ = –39.0 $cm^{-1}$; $J_{3,7}$ = $J_{4,6}$ = +1.1 $cm^{-1}$, $J_{4,5}$ = $J_{3,4}$ = –20.0 $cm^{-1}$, $J_{3,6}$ = –16.0 $cm^{-1}$, $J_{1,3}$ = $J_{1,6}$ = $J_{1,4}$ = $J_{1,7}$ = –4.8 $cm^{-1}$ and $g$ = 1.919. The $J$ values are in good agreement with the calculated ones. However, the $g$ factor is slightly smaller than that expected for a chromium(III) ion (1.98–1.99). This fact can be explained by a partial hydration of the sample observed when it is exposed to the environment modifying the formula mass. According to the magneto-structural correlation observed in **2** (Figure 8), when one oxo and one alkoxo group act as bridges, a strong antiferromagnetic coupling is expected for small angles (89.3°) such as it occurs for $J_{4,7}$. Probably, for this $\alpha$ value a short metal–metal distance is found favouring the direct interaction between two metal ions, as proposed in the previous theoretical study on dinuclear models (compound **1**). It is also possible to find a set of $J$ parameters with a $g$ factor near to 1.98–2.00; however, this set is discarded because the obtained $J_{4,7}$ value is too large (–122.9 $cm^{-1}$). In fact, the $J_{4,7}$ value expected from the magneto-structural correlation shown in Figure 8 (–53.3 $cm^{-1}$) is lower and closer to that obtained from DF calculations. In the curves obtained with the calculated and fitted $J$ values, as the temperature decreases the value of $\chi_M T$ is close to reaching a plateau ($\chi_M T \approx 3.2$ $cm^3 \cdot K \cdot mol^{-1}$) in agreement with the experimental curve. At lower temperatures the value of $\chi_M T$ falls to reach a value equal to zero corresponding to a singlet ground state. Thus, we can reject possible intermolecular interactions or magnetic anisotropy as a cause of the magnetic behaviour at lower temperature. Regardless, the chosen set of $J$ values must explain the be-

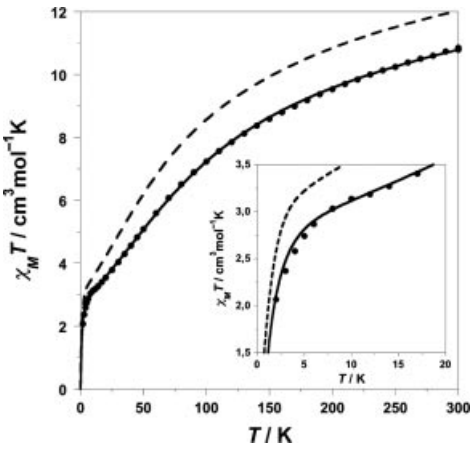


Figure 9. Magnetic susceptibility curves for **2** obtained from the calculated $J$ values (dashed line) and fitted $J$ values (solid line) that are shown in Table 6. The experimental data is displayed as black circles.

Table 6. Exchange coupling constants ($J_{i,j}$, $cm^{-1}$) obtained for **2** from theoretical calculations (A) and fitted values (B) in the temperature range 300–20 K. We also indicate the $g$ factor, agreement factor ($F$), the spin ground state (GS) and the relative energy of first excited state ($E_1$, in $cm^{-1}$).

| $J_{i,j}$ | A | B |
|---|---|---|
| $J_{4,7}$ | –52.7 | –39.0 |
| $J_{3,7}$ | –3.8 | +1.1 |
| $J_{4,6}$ | –2.8 | +1.1 |
| $J_{4,5}$ | –26.2 | –20.0 |
| $J_{3,4}$ | –25.7 | –20.0 |
| $J_{3,6}$ | –10.6 | –16.0 |
| $J_{1,3}$ | –4.8 | –4.8 |
| $J_{1,6}$ | –3.9 | –4.8 |
| $J_{1,4}$ | –1.4 | –4.8 |
| $J_{1,7}$ | +0.8 | –4.8 |
| $g$ factor | – | 1.919 |
| $F$ | – | $5.1 \cdot 10^{-5}$ |
| GS | 0 | 0 |
| $E_1$[a] | 0.23 (1) | 0.18 (1) |

[a] $S$ value of the first excited state in parentheses.

 © 2006 Wiley-VCH Verlag GmbH & Co. KGaA, Weinheim 

haviour observed for the dependence of the magnetisation with magnetic field at several temperatures. From an energy-level diagram obtained from calculated $J$ values (Figure S5), we observe that some singlet, triplet, quintet and septet states are very close to the ground spin state. At slightly higher energy we can also find the first nonet state. Thus, when the applied magnetic field is increased some *ms* eigenfunctions of low-lying excited states with higher multiplicity will be populated reaching a non-zero-saturation value. In this situation the shape of the magnetisation curve and the saturation value are dependent on the temperature, because low-lying excited states will be populated at higher temperature. A similar behaviour is observed with the parameters obtained in the fit.

## Conclusions

In conclusion, the reactions between $CrCl_2$ and the tripodal ligands $H_3$thme, $H_3$tmp, and $H_4$peol have produced new di- and octanuclear $Cr^{III}$ clusters. Complex **1** can only be made under reflux and complexes **2** and **3** only under solvothermal conditions. Complexes **2** and **3** represent rare examples of "large" Cr clusters containing no bridging carboxylates with structures derived from the decametallate core commonly seen in polyoxometallate chemistry. As such, **1**–**3** may represent the first examples in a large family of Cr clusters and variations of the above reaction schemes may lead to the isolation of diverse metal polyhedra exhibiting novel magnetic properties. Magneto-structural correlations for $[Cr_2(OR)_2]^{4+}$ and $[Cr_2O_2]^{2+}$ complexes have been found, which we hope will help the analysis of the magnetic properties in new polynuclear $Cr^{III}$ clusters. Electronic-structure calculations based on density functional theory have allowed us to understand the electronic factors that govern these correlations. Electronic structure calculations have been performed on **1** and **2** and good estimates of the $J$ values have been obtained. Different sets of $J$ values have been found to reproduce the magnetic behaviour of **2**. An analysis of the theoretical results and those obtained in the fitting procedure by diagonalisation of the Hamiltonian matrix allowed us to select one among the fitted $J$ value sets.

## Experimental Section

**$[Cr_2(H_2tmp)_2Cl_4]\cdot 2MeOH$ (1·2MeOH):** Anhydrous $CrCl_2$ (0.5 g, 4.0 mmol), $H_3$tmp (0.545 g, 4.0 mmol) and NaOMe (0.110 g, 2.0 mmol) were heated at reflux in MeOH (30 mL) for 3 h. The reaction mixture was filtered and the resulting dark green solution cooled. The solvent was then removed under reduced pressure and the resulting dark green solid recrystallised from MeCN (20 mL). Green crystals of **1** appeared upon $Et_2O$ diffusion over 2 weeks. Yield based on $Cr^{III}$: 0.230 g (20%). $C_{14}H_{32}Cl_4Cr_2O_8$ (574.22): calcd. C 29.18, H 5.95; found C 28.99, H 5.85. IR (KBr pellet): $\tilde{\nu}$ = 3424 (s), 3170 (s), 2978 (s), 2604 (m), 1630 (w), 1453 (m), 1384 (m), 1299 (m), 1265 (w), 1189 (w), 1100 (s), 1040 (s), 940 (s), 773 (w), 592 (m), 560 (s), 509 (m), 443 (w) $cm^{-1}$. $[Cr_2(H_2tmp)_2Cl_4]\cdot$ 2MeOH (576.22): calcd. C 29.18, H 5.95; found: C 28.99, H 5.85.

**$[Cr_8O_2(thme)_2(Hthme)_4Cl_6]\cdot 2MeOH$ (2·2MeOH):** This complex was synthesised by heating $CrCl_2$ (0.3 g, 2.4 mmol), $H_3$thme (0.29 g, 2.4 mmol) and NaOMe (0.13 g, 2.4 mmol) in MeOH (9 mL) in a teflon-lined autoclave at 100 °C for 12 h. Slow cooling to room temperature yielded dark green crystals of **2**. Yield based on $Cr^{III}$: 0.130 g (30%). $C_{32}H_{62}Cl_6Cr_8O_{29}$ (1427.28): calcd. C 26.85, H 4.65; found C 26.28, H 4.67. IR (KBr pellet): 3420 (s), 2930 (s), 2361 (m), 1636 (w), 1464 (w), 1385 (w), 1124 (m), 1044 (s), 630 (m), 580 (s), 536 (m), 468 (w) $cm^{-1}$.

**$[Cr_8O_2(Hpeol)_2(H_2peol)_4Cl_6]\cdot 3MeOH$ (3·3MeOH):** The complex was synthesised as **2**, replacing $H_3$thme with $H_4$peol. $C_{33}H_{60}Cl_6Cr_8O_{22}$ (1549.27): calcd. C 25.31, H 4.89; found C 25.63, H 4.97. IR (KBr pellet): $\tilde{\nu}$ = 3450 (s), 2931 (m), 2874 (m), 1636 (w), 1472 (w), 1388 (w), 1224 (w), 1115 (s), 1060 (s), 653 (m), 593 (s), 537 (m), 506 $cm^{-1}$ (w).

Table 7. Crystallographic data for complexes **1**–**3**.

| | **1** [$Cr_2$] | **2** [$Cr_8$thme] | **3** [$Cr_8$peol] |
|---|---|---|---|
| Formula | $C_{14}H_{34}Cl_4Cr_2O_8$ | $C_{32}H_{66}Cl_6Cr_8O_{22}$ | $C_{33}H_{70}Cl_6Cr_8O_{27}$ |
| $M$ [g·mol$^{-1}$] | 576.12 | 1427.52 | 1565.62 |
| Crystal system | monoclinic | triclinic | monoclinic |
| Space group | $P2_1/c$ | $P\bar{1}$ | $C2/c$ |
| $a$ [Å] | 9.3936(32) | 10.0553(19) | 13.1762(6) |
| $b$, Å | 10.0550(34), | 10.968(2) | 17.5288(8) |
| $c$ [Å] | 12.4914(42) | 12.671(2) | 22.9112(11) |
| $\alpha$ [°] | 90 | 79.722(15) | 90 |
| $\beta$ [°] | 99.812(6) | 67.844(18) | 99.468(4) |
| $\gamma$ [°] | 90 | 89.221(15) | 90 |
| $V$ [Å$^3$] | 1162.6(7) | 1271.3(4) | 5219.6(4) |
| $T$ [K] | 100(2) | 100(2) | 100(2) |
| $Z$ | 2 | 2 | 4 |
| $\rho_{calcd.}$ [g cm$^{-3}$] | 1.646 | 1.870 | 1.985 |
| Crystal shape and colour | green block | green block | green block |
| Crystal size [mm] | 0.08 × 0.04 × 0.01 | 0.37× 0.20× 0.08 | 0.35× 0.24 × 0.13 |
| $\mu$ [mm$^{-1}$] | 1.430 | 2.032 | 1.998 |
| Unique data | 1676 | 7850 | 8477 |
| Unique data, [$I > 2\,\theta\,(F)$] | 1430 | 6443 | 6309 |
| $R_1$, $wR_2$ | 0.0290, 0.0705 | 0.0572, 0.1572 | 0.0572, 0.1469 |
| Goodness of fit | 1.060 | 1.090 | 1.022 |

 © 2006 Wiley-VCH Verlag GmbH & Co. KGaA, Weinheim 

**X-ray Crystallography:** Data were collected with either Bruker SMART APEX CCD (1) or Oxford Diffraction Crysalis CCD diffractometers (**2**, **3**) at 100(2) K using Mo-$K_\alpha$ radiation ($\lambda$ = 0.71073 Å). Both structures were solved by direct methods and refined (on $F^2$ for all reflections) using SHELXTL.[43,44] Absorption corrections were applied using SADABS (**1**) and software built into the Crysalis CCD program (**2**, **3**). All non-hydrogen atoms were refined anisotropically. Excessive thermal motion of the chlorine atoms in **1** required thermal and angular restraints to be applied. Neither refinement nor absorption corrections reduced the residual electron density in the core of **2**. The hydrogen atoms in **2** could not be found so were added in calculated positions. Relevant crystallographic information for the compounds is summarised in Table 7. CCDC-285702–285704 contain the supplementary crystallographic data for this paper. These data can be obtained free of charge from The Cambridge Crystallographic Data Centre via www.ccdc.cam.ac.uk/data_request/cif.

**Magnetic Measurements:** Variable-temperature, solid-state direct current (dc) magnetic susceptibility data down to 1.80 K were collected with a Quantum Design MPMS-XL SQUID magnetometer equipped with a 5.5-T dc magnet at the University of Barcelona. Diamagnetic corrections were applied to the observed paramagnetic susceptibilities using Pascal's constants.

**Computational Details:** All theoretical calculations were carried out with the hybrid B3LYP method,[45–47] as is implemented in the Gaussian03 program.[48] Double-ζ (SV) and triple-ζ (TZV) quality basis sets proposed by Ahlrichs and co-workers have been used for all atoms.[49,50] For the chromium ions, two extra p functions have been added. The electronic configurations used as starting points have been created using Jaguar 6.0 software. The broken-symmetry approach has been employed to describe the unrestricted solutions of the antiferromagnetic spin states.[51–53] No molecular modelling has been done, with the full experimental geometry of **2** used for the calculations. A quadratic convergence method was employed to determine the more stable wave functions in the SCF process.[54] The atomic spin densities were obtained from Natural Bond Orbital (NBO) analysis.[55–57]

**Other Measurements:** Elemental analyses were performed by the University of Manchester Microanalysis Service. IR spectra were recorded as KBr pellets on a Nicolet model 510P spectrophotometer.

## Acknowledgments

This work was supported by the Lloyds of London Tercentenary Foundation (UK), EPSRC (UK), The Leverhulme Trust (UK), Dirección General de Enseñanza Superior (DGES) and Comissió Interdepartamental de Ciència i Tecnologia (CIRIT) through the grants CTQ2005-08123-C02-02/BQU and 2005SGR-00036, respectively. The computing resources were generously made available in the Centre de Computació de Catalunya (CESCA) with a grant provided by Fundació Catalana per a la Recerca (FCR) and the Universitat de Barcelona.

[1] E. J. L. McInnes, S. Piligkos, G. A. Timco, R. E. P. Winpenny, *Coord. Chem. Rev.* **2005**, *249*, 2577.
[2] R. H. Laye, E. J. L. McInnes, *Eur. J. Inorg. Chem.* **2004**, 2811.
[3] D. Collison, M. Murrie, V. S. Oganesyan, S. Piligkos, N. R. J. Poolton, G. Rajaraman, G. M. Smith, A. J. Thomson, G. A. Timko, W. Wernsdorfer, R. E. P. Winpenny, E. J. L. McInnes, *Inorg. Chem.* **2003**, *42*, 5293.
[4] A. Bino, D. C. Johnston, D. P. Goshorn, T. R. Halbert, E. I. Stiefel, *Science* **1988**, *241*, 1479.
[5] R. Basler, C. Boskovic, G. Chaboussant, H. U. Güdel, M. Murrie, S. T. Ochsenbein, A. Sieber, *ChemPhysChem* **2003**, *4*, 910.
[6] J. Telser, J. van Slageren, S. Vongtragool, M. Dressel, W. M. Reiff, S. A. Zvyagin, A. Ozarowski, J. Krzystek, *Magn. Reson. Chem.* **2005**, *43*, S130.
[7] S. Piligkos, G. Rajaraman, M. Soler, N. Kirchner, J. van Slageren, R. Bircher, S. Parsons, H. U. Güdel, J. Kortus, W. Wernsdorfer, G. Christou, E. K. Brechin, *J. Am. Chem. Soc.* **2005**, *127*, 5572.
[8] E. K. Brechin, *Chem. Commun.* **2005**, 5141.
[9] M. I. Khan, J. Zubieta, *Prog. Inorg. Chem.* **1995**, *43*, 1.
[10] K. G. Caulton, M. H. Chisholm, S. R. Drake, K. Folting, J. C. Huffman, *Inorg. Chem.* **1993**, *32*, 816.
[11] W. J. Evans, D. G. Giarikos, M. A. Greci, J. W. Ziller, *Eur. J. Inorg. Chem.* **2002**, 453.
[12] R. C. Finn, J. Zubieta, *J. Cluster Sci.* **2000**, *11*, 461.
[13] M. Cavaluzzo, Q. Chen, J. Zubieta, *J. Chem. Soc., Chem. Commun.* **1993**, 131.
[14] J. Cano, in *VPMAG, Revision C01*, Universitat de València, Valencia, **2004**.
[15] I. M. Atkinson, C. Benelli, M. Murrie, S. Parsons, R. E. P. Winpenny, *Chem. Commun.* **1999**, 285.
[16] F. E. Mabbs, E. J. L. McInnes, M. Murrie, S. Parsons, G. M. Smith, C. C. Wilson, R. E. P. Winpenny, *Chem. Commun.* **1999**, 643.
[17] S. Parsons, A. A. Smith, R. E. P. Winpenny, *Chem. Commun.* **2000**, 579.
[18] B. G. Gafford, R. E. Marsh, W. P. Schaefer, J. H. Zhang, C. J. Oconnor, R. A. Holwerda, *Inorg. Chem.* **1990**, *29*, 4652.
[19] B. G. Gafford, R. A. Holwerda, *Inorg. Chem.* **1990**, *29*, 4353.
[20] N. K. Dalley, X. L. Kou, C. J. O'Connor, R. A. Holwerda, *Inorg. Chem.* **1996**, *35*, 2196.
[21] M. Eshel, A. Bino, *Inorg. Chim. Acta* **2002**, *329*, 45.
[22] H. R. Fischer, J. Glerup, D. J. Hodgson, E. Pedersen, *Inorg. Chem.* **1982**, *21*, 3063.
[23] J. J. H. Edema, S. Gambarotta, W. J. J. Smeets, A. L. Spek, *Inorg. Chem.* **1991**, *30*, 1380.
[24] M. Divaira, F. Mani, *Inorg. Chem.* **1984**, *23*, 409.
[25] B. G. Gafford, R. A. Holwerda, H. J. Schugar, J. A. Potenza, *Inorg. Chem.* **1988**, *27*, 1126.
[26] F. Bottomley, D. E. Paez, L. Sutin, P. S. White, F. H. Kohler, R. C. Thompson, N. P. C. Westwood, *Organometallics* **1990**, *9*, 2443.
[27] F. Bottomley, D. E. Paez, P. S. White, *J. Am. Chem. Soc.* **1981**, *103*, 5581.
[28] F. Bottomley, D. E. Paez, P. S. White, *J. Am. Chem. Soc.* **1982**, *104*, 5651.
[29] N. J. Robertson, M. J. Carney, J. A. Halfen, *Inorg. Chem.* **2003**, *42*, 6876.
[30] K. B. P. Ruppa, K. Feghali, I. Kovacs, K. Aparna, S. Gambarotta, G. P. A. Yap, C. Bensimon, *J. Chem. Soc., Dalton Trans.* **1998**, 1595.
[31] D. J. Hodgson, in: *Magneto-Structural Correlations in Exchange Coupled Systems, Vol. 140* (Eds.: R. D. Willet, D. Gatteschi, O. Kahn), NATO ASI Series C, Dordrecht, **1985**, p. 497.
[32] E. Ruiz, P. Alemany, S. Alvarez, J. Cano, *Inorg. Chem.* **1997**, *36*, 3683.
[33] E. Ruiz, P. Alemany, S. Alvarez, J. Cano, *J. Am. Chem. Soc.* **1997**, *119*, 1297.
[34] E. D. Estes, R. P. Scaringe, W. E. Hatfield, D. J. Hodgson, *Inorg. Chem.* **1976**, *15*, 1179.
[35] E. D. Estes, R. P. Scaringe, W. E. Hatfield, D. J. Hodgson, *Inorg. Chem.* **1977**, *16*, 1605.
[36] D. A. House, V. McKee, P. J. Steel, *Inorg. Chem.* **1986**, *25*, 4884.
[37] W. Clegg, *Acta Crystallogr., Sect. C* **1985**, *41*, 1830.
[38] H. R. Fischer, D. J. Hodgson, E. Pedersen, *Inorg. Chem.* **1984**, *23*, 4755.

 © 2006 Wiley-VCH Verlag GmbH & Co. KGaA, Weinheim 

[39] R. Clerac, F. A. Cotton, C. A. Murillo, X. P. Wang, *Chem. Commun.* **2001**, 205.
[40] T. K. Paine, T. Weyhermuller, K. Wieghardt, P. Chaudhuri, *Inorg. Chem.* **2002**, *41*, 6538.
[41] M. V. Barybin, P. L. Diaconescu, C. C. Cummins, *Inorg. Chem.* **2001**, *40*, 2892.
[42] R. Carrasco, J. Cano, T. Mallah, L. F. Jones, D. Collison, E. K. Brechin, *Inorg. Chem.* **2004**, *43*, 5410.
[43] G. M. Sheldrick, in *SHELXL-97*, University of Gottingen, Germany, **1997**.
[44] P. T. Beurskens, G. Beurskens, W. P. Bosman, R. de Gelder, S. Garcia-Granada, R. O. Gould, R. Israel, J. M. M. Smits, in *DIRDIF96 Program System*, Technical Report of the Crystallography Laboratory, University of Nijmegen, The Netherlands, **1996**.
[45] A. D. Becke, *Phys. Rev. A* **1988**, *38*, 3098.
[46] C. T. Lee, W. T. Yang, R. G. Parr, *Phys. Rev. B* **1988**, *37*, 785.
[47] A. D. Becke, *J. Chem. Phys.* **1993**, *98*, 5648.
[48] M. J. Frisch, G. W. Trucks, H. B. Schlegel, G. E. Scuseria, M. A. Robb, J. R. Cheeseman, J. Montgomery, J. A., T. Vreven, K. N. Kudin, J. C. Burant, J. M. Millam, S. S. Iyengar, J. Tomasi, V. Barone, B. Mennucci, M. Cossi, G. Scalmani, N. Rega, G. A. Petersson, H. Nakatsuji, M. Hada, M. Ehara, K. Toyota, R. Fukuda, J. Hasegawa, M. Ishida, T. Nakajima, Y. Honda, O. Kitao, H. Nakai, M. Klene, X. Li, J. E. Knox, H. P. Hratchian, J. B. Cross, V. Bakken, C. Adamo, J. Jaramillo, R. Gomperts, R. E. Stratmann, O. Yazyev, A. J. Austin, R. Cammi, C. Pomelli, J. W. Ochterski, P. Y. Ayala, K. Morokuma, G. A. Voth, P. Salvador, J. J. Dannenberg, V. G. Zakrzewski, S. Dapprich, A. D. Daniels, M. C. Strain, O. Farkas, D. K. Malick, A. D. Rabuck, K. Raghavachari, J. B. Foresman, J. V. Ortiz, Q. Cui, A. G. Baboul, S. Clifford, J. Cioslowski, B. B. Stefanov, G. Liu, A. Liashenko, P. Piskorz, I. Komaromi, R. L. Martin, D. J. Fox, T. Keith, M. A. Al-Laham, C. Y. Peng, A. Nanayakkara, M. Challacombe, P. M. W. Gill, B. Johnson, W. Chen, M. W. Wong, C. Gonzalez, J. A. Pople, in *Gaussian 03, Revision C.02*, Gaussian 03, Revision C.02 ed., Gaussian, Inc. Wallingford CT, **2004**.
[49] A. Schäfer, H. Horn, R. Ahlrichs, *J. Chem. Phys.* **1992**, *97*, 2571.
[50] A. Schäfer, C. Huber, R. Ahlrichs, *J. Chem. Phys.* **1994**, *100*, 5829.
[51] E. Ruiz, J. Cano, S. Alvarez, P. Alemany, *J. Comput. Chem.* **1999**, *20*, 1391.
[52] E. Ruiz, S. Alvarez, A. Rodríguez-Fortea, P. Alemany, Y. Puoillon, C. Massobrio, in: *Magnetism: Molecules to Materials, Vol. II* (Eds.: J. S. Miller, M. Drillon), Wiley-VCH, Weinheim, **2001**, pp. 5572.
[53] E. Ruiz, A. Rodriguez-Fortea, J. Cano, S. Alvarez, P. Alemany, *J. Comput. Chem.* **2003**, *24*, 982.
[54] G. B. Bacskay, *Chem. Phys.* **1981**, *61*, 385.
[55] J. E. Carpenter, F. Weinhold, *J. Mol. Struct. (Theochem)* **1988**, *169*, 41.
[56] A. E. Reed, L. A. Curtiss, F. Weinhold, *Chem. Rev.* **1988**, *88*, 899.
[57] F. Weinhold, J. E. Carpenter, *The Structure of Small Molecules and Ions*, Plenum, **1988**.
[58] F. H. Allen, O. Kennard, *Chem. Des. Autom. News* **1993**, *8*, 31.
Received: May 24, 2006
Published Online: July 11, 2006

 © 2006 Wiley-VCH Verlag GmbH & Co. KGaA, Weinheim 

DOI: 10.1002/ejic.200600380

# Synthesis of a New Tetrakis(2-pyridinyl)pyrazine Complex of Gold(III) and Its Computational, Spectroscopic and Electrochemical Characterization

**Marco Bortoluzzi,*[a] Eddy De Faveri,[b] Salvatore Daniele,[b] and Bruno Pitteri[a]**

**Keywords:** Gold / N ligands / Density functional calculations / Electrochemistry

The cationic dinuclear (hydroxo)$Au^{III}$ complex $[Au_2(OH)_2(tppz)]Cl_4$ [tppz = 2,3,5,6-tetrakis(2-pyridinyl)pyrazine] was prepared by allowing the ligand tppz to react with $K[AuCl_4]\cdot 2H_2O$ in refluxing methanol. Its NMR and IR spectra support the formation of a symmetric hydroxo derivative instead of the expected chloro complex. DFT B3PW91 calculations were performed with various basis sets to give better insights into the properties of the prepared complex and to compare it with the known derivative $[Au(OH)(terpy)]^{2+}$ (terpy = 2,2′:6′,2′′-terpyridine). The electrochemical behaviour of $[Au_2(OH)_2(tppz)]Cl_4$ was investigated by cyclic voltammetry and it was found that two main irreversible reduction processes occurred. In particular, a four-electron process, leading to the formation of gold(I) complex species in solution, and a two-electron process affording metallic gold were observed. The electronicity involved in the two processes was verified by macroelectrolysis at controlled potential.
(© Wiley-VCH Verlag GmbH & Co. KGaA, 69451 Weinheim, Germany, 2006)

## Introduction

Pyridine-derived polydentate ligands play a fundamental role in inorganic chemistry and one of the most interesting molecules of this kind is the terdentate ligand 2,2′:6′,2′′-terpyridine (terpy; Scheme 1), whose coordination chemistry with $Au^{III}$ has been studied in the past few years. In particular, chloro- and hydroxogold(III)–terpy complexes of the type $[AuL(terpy)]^{2+}$ (L = Cl, OH) are known that have been structurally characterized.[1,2] In the field of gold complexes with pyridine-based polydentate ligands, much less attention has been devoted to the ligand 2,3,5,6-tetrakis(2-pyridinyl)pyrazine (tppz; Scheme 1), even though it can be approximately considered as a "double terpyridine" and, therefore, is suited to coordinate two metal fragments to form complexes having a strong electronic delocalization.

A number of tppz complexes of transition metals such as ruthenium and osmium,[3] iron,[4] rhodium,[5] iridium,[6] nickel,[7] palladium,[8] copper[7,9,10] and zinc[10] have been prepared, whereas, to the best of our knowledge, no example of a gold derivative of 2,3,5,6-tetrakis(2-pyridinyl)pyrazine has been published in the literature. The previous works regarding tetrakis(2-pyridinyl)pyrazine coordination chemistry demonstrated that both mono- and dinuclear tppz complexes can be synthesized and that it is also possible to obtain mixed-metal tppz derivatives. Many of these tetrakis(2-pyridinyl)pyrazine complexes have shown intriguing spectroelectrochemical and electrochemical properties due to the characteristics of the tppz ligand.

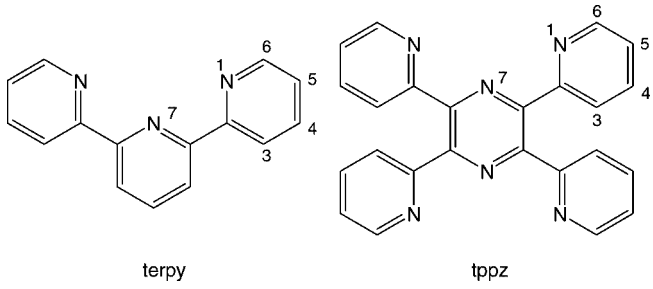


Scheme 1. 2,2′:6′,2′′-Terpyridine (terpy) and 2,3,5,6-tetrakis(2-pyridinyl)pyrazine (tppz) and the numbering of their hydrogen and nitrogen atoms.

In this paper the synthesis of a tetrakis(2-pyridinyl)pyrazine derivative of gold, the dinuclear hydroxo complex $[Au_2(OH)_2(tppz)]Cl_4$, is reported for the first time. DFT B3PW91 calculations are also performed to give better insights into the electronic and steric properties of the prepared compound and to compare it with the known $[Au(OH)(terpy)]^{2+}$ cation. Cyclic voltammetric experiments and macroelectrolysis at controlled potential are performed to understand the redox properties of $[Au_2(OH)_2(tppz)]Cl_4$ and to ascertain an eventual formation of stable tetrakis(2-pyridinyl)pyrazine derivatives of gold(I) in solution.

## Results and Discussion

### Preparation and Characterization of the Complex

The hydroxo complex $[Au_2(OH)_2(tppz)]Cl_4$ was prepared by treating the ligand 2,3,5,6-tetrakis(2-pyridinyl)pyrazine

[a] Dipartimento di Chimica, Università Ca' Foscari di Venezia, Dorsoduro 2137, 30123 Venezia, Italy
E-mail: markos@unive.it
[b] Dipartimento di Chimica Fisica, Università Ca' Foscari di Venezia, Dorsoduro 2137, 30123 Venezia, Italy

 © 2006 Wiley-VCH Verlag GmbH & Co. KGaA, Weinheim 

(tppz) with potassium tetrachloroaurate dihydrate $K[AuCl_4]\cdot 2H_2O$ in refluxing methanol (see Scheme 2). On the basis of previous works with the terpy ligand,[1,2] the formation of the chloro complex $[Au_2Cl_2(tppz)]^{2+}$ was expected. However, both the IR and the $^1H$ NMR spectra of the reaction product support the presence of a coordinated hydroxo ligand. Thus, an O–H stretching is observable in the IR spectrum (3412 $cm^{-1}$) and the hydrogen atoms of the OH ligands give a broad signal in the $^1H$ NMR spectrum. The chemical shift of this signal is, as expected, quite dependent upon the temperature. The formation of a hydroxo ligand is probably due to the presence of water in the reaction mixture coming from the starting precursor $K[AuCl_4]\cdot 2H_2O$. All the pyridine rings are magnetically equivalent, and only four signals attributable to coordinated tppz can be observed in the $^1H$ NMR spectrum. Also, the $^{13}C\{^1H\}$ NMR spectrum shows signals of only four primary carbon atoms and two quaternary carbon atoms. This means that the prepared compound is dinuclear and that both the gold atoms have the same coordination environment. Finally, the elemental analyses (C, H, Cl, N) are also in agreement with the proposed formulation, the deviations between found and calculated values being less than 0.4%.

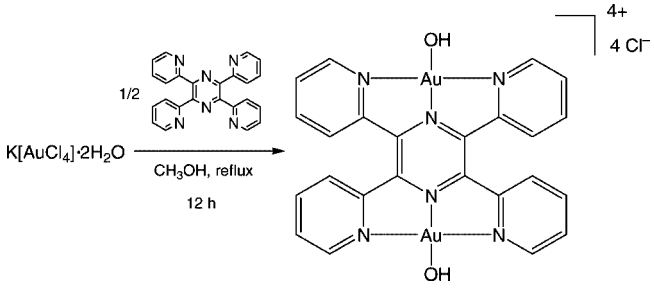


Scheme 2. Synthesis of $[Au_2(OH)_2(tppz)]Cl_4$.

## DFT Studies

To better understand the electronic and steric properties of the prepared compound, computational geometry optimisations of the cations $[Au(OH)(terpy)]^{2+}$ and $[Au_2(OH)_2(tppz)]^{4+}$ were performed using the DFT B3PW91 method. Table 1 shows the $r_{Au-O}$, $r_{Au-N7}$ and the average $r_{Au-N1}$ bond lengths of $[Au(OH)(terpy)]^{2+}$ and $[Au_2(OH)_2(tppz)]^{4+}$. The average C6–N1–Au–O dihedral angle and the Mulliken charge of the coordinated [AuOH] fragments are also included. The differences between the DFT-calculated bond lengths and the bond lengths found in the X-ray structure analysis of $[Au(terpy)(OH)](ClO_4)_2$[2] are always less than 2.2%; the greatest deviation between calculated and experimental $r_{Au-O}$ bond lengths is less than 1.2%.

The average $r_{Au-N1}$ and $r_{Au-O}$ bond lengths for both optimised cations are almost identical to within three significant figures, whereas the Au–N7 bond in the $[Au_2(OH)_2(tppz)]^{4+}$ complex is about 0.03 Å longer than that in the monomer. The coordination of two gold fragments strongly twists the molecule from planarity because of the steric hindrance between the H3 atoms of the pyridine rings. The degree of twisting can be quantified by comparing the C6–N1–Au–O dihedral angles of $[Au(OH)(terpy)]^{2+}$ and $[Au_2(OH)_2(tppz)]^{4+}$: the terpy derivative is approximately planar, with an average C6–N1–Au–O dihedral angle of less than 1°, while the dinuclear [tetrakis(2-pyridinyl)pyrazine]gold derivative has an average C6–N1–Au–O dihedral angle of between 9.0° and 9.8°, depending upon the basis set. A similar deviation of the tetrakis(2-pyridinyl)pyrazine ligand from planarity has already been observed in the X-ray structures of dinuclear tppz derivatives of various transition metals.[3,5–10]

From the calculated geometries, a $C_{2h}$ symmetry can be ascribed to the $[Au_2(OH)_2(tppz)]^{4+}$ cation, which is in agreement with the corresponding $^1H$ NMR and $^{13}C\{^1H\}$ NMR spectra. The DFT B3LYP/BS3 optimised geometry of $[Au_2(OH)_2(tppz)]^{4+}$ is shown in Figure 1.

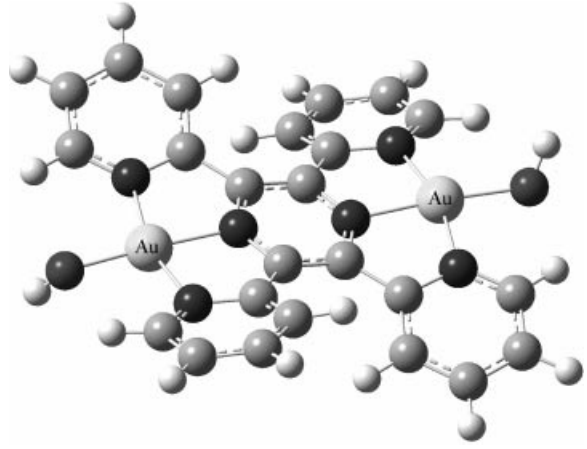


Figure 1. DFT B3LYP/BS3 optimised geometry of the $[Au_2(OH)_2(tppz)]^{4+}$ cation.

Table 1. Selected bond lengths and angles for the cations $[Au(OH)(terpy)]^{2+}$ and $[Au_2(OH)_2(tppz)]^{4+}$ and the Mulliken charge of the coordinated [AuOH] fragment. **BS1**: CEP-121G, CEP-31G on Au; **BS2**: D95V, SDD on Au; **BS3**: D95, LANL2DZ on Au.

| Complex | $r_{Au-N1}$ [Å] | $r_{Au-N7}$ [Å] | $r_{Au-O}$ [Å] | C6–N1–Au–O [°] | [AuOH] charge |
|---|---|---|---|---|---|
| **BS1** | | | | | |
| $[Au(OH)(terpy)]^{2+}$ | 2.0484 | 1.9916 | 1.9796 | 0.4 | 0.786 |
| $[Au_2(OH)_2(tppz)]^{4+}$ | 2.0421 | 2.0224 | 1.9646 | 9.4 | 0.891 |
| **BS2** | | | | | |
| $[Au(OH)(terpy)]^{2+}$ | 2.0370 | 1.9871 | 1.9897 | 0.6 | 0.886 |
| $[Au_2(OH)_2(tppz)]^{4+}$ | 2.0312 | 2.0194 | 1.9764 | 9.0 | 0.953 |
| **BS3** | | | | | |
| $[Au(OH)(terpy)]^{2+}$ | 2.0423 | 1.9855 | 1.9763 | 0.9 | 0.831 |
| $[Au_2(OH)_2(tppz)]^{4+}$ | 2.0377 | 2.0151 | 1.9597 | 9.8 | 0.915 |

 © 2006 Wiley-VCH Verlag GmbH & Co. KGaA, Weinheim 

The Mulliken charge of the [AuOH] fragments in the $[Au_2(OH)_2(tppz)]^{4+}$ cation is always higher than that calculated for the $[Au(OH)(terpy)]^{2+}$ complex (see Table 1). This means that the tetrakis(2-pyridinyl)pyrazine derivative has less basic hydroxo ligands and more electrophilic gold centres and this fact can be ascribed to the lower ability of the tppz ligand, if compared with two terpy molecules, to delocalize the positive charge on its aromatic rings. The mechanism of formation of the mononuclear $[Au(OH)(terpy)]^{2+}$ cation from the chloro complex $[AuCl(terpy)]^{2+}$ and the equilibrium between this hydroxo derivative and the corresponding aqua complex $[Au(OH_2)(terpy)]^{3+}$ has been studied in a previous paper.[2] It was found that the water molecule coordinated to the $[Au(terpy)]^{3+}$ fragment behaves as a strong acid ($K_a \geq 0.8$ M). It therefore seems reasonable to hypothesise that the mechanism leading to the $[Au_2(OH)_2(tppz)]Cl_4$ complex could be similar to that of the analogous terpy derivative. Thus, the reaction between tppz and $AuCl_4^-$ probably leads to the initial formation of an intermediate chloro species. This may react with water present in the reaction medium to give a very acidic aqua species which, on the basis of the DFT calculations, would be even more acidic than the corresponding $[Au(OH_2)(terpy)]^{3+}$ complex and, consequently, would deprotonate to provide the final $[Au_2(OH)_2(tppz)]Cl_4$ hydroxo species. It must be considered that, although the formation of (aqua)-$Au^{III}$–tppz derivatives is disfavoured by the experimental conditions, the driving force of the whole reaction is the immediate deprotonation of the coordinated water molecules. The $[Au_2(OH)_2(tppz)]Cl_4$ product should be very stable as the square-planar hydroxo species is known to be inert towards nucleophilic substitution.[11] Besides, the very similar values of the calculated $r_{Au-O}$ bond lengths in $[Au_2(OH)_2(tppz)]^{4+}$ and $[Au(OH)(terpy)]^{2+}$ (see Table 1) and the fact that the terpy derivative is rather stable allowed us to conclude that the same lack of reactivity occurs for the dinuclear $Au^{III}$ complex prepared in this work.

On the other hand, because the formation of a 6+ diaquo intermediate of the type $[Au_2(OH_2)_2(tppz)]^{6+}$ in solution is rather improbable as its acidity should be even higher than that of a 5+ aquo species like $[Au_2Cl(OH_2)(tppz)]^{5+}$ or $[Au_2(OH)(OH_2)(tppz)]^{5+}$, a possible reaction pathway leading to the hydroxo derivative from the intermediate chloro species is that summarized in Scheme 3.

## Electrochemical Characterisation

The redox properties of $[Au_2(OH)_2(tppz)]Cl_4$ were investigated by cyclic voltammetry (CV) with both conventional and microelectrodes.[13,14] Figure 2 shows a typical cyclic voltammogram recorded for $[Au_2(OH)_2(tppz)]Cl_4$ at 50 mV s$^{-1}$ with a 3 mm glassy carbon electrode, displaying a rather complex pattern. In particular, in the forward scan, two main irreversible cathodic processes occurring at –0.030 and –0.70 V (**A** and **B**, respectively, in Figure 2), and a series of smaller processes, which occur over the potential region from –1.5 to –2.2 V, are observed. In the reverse scan, apart from the small peaks associated with the latter processes, two major peaks, occurring at 0.56 and 1.16 V (**C** and **D**, respectively, in Figure 2), are observed. Direct anodic scans, starting from 0.3 V, also displayed peak **D**, which is characterised by its much smaller height (see Figure 2 dashed line). This finding suggests that a bulk solution species is responsible for the latter electrode process. Voltammetric measurements performed in DMF solutions containing the supporting electrolyte and increasing amounts of $[BzEt_3N]Cl$ allowed us to assign peak **D** as being due to the oxidation of free $Cl^-$ ions. Similarly, the series of small cathodic and anodic patterns over the potential region from –1.5 to –2.2 V were assigned to an electrode process involving free tppz ligand, as checked in solutions of pure sample. Peaks **A** and **B** probably involve the metal centres and our attention was therefore mainly devoted to these processes. It should be noted that peak **B** is rather broad, and a closer examination of its shape suggests that at least two overlapping peaks are present in it.

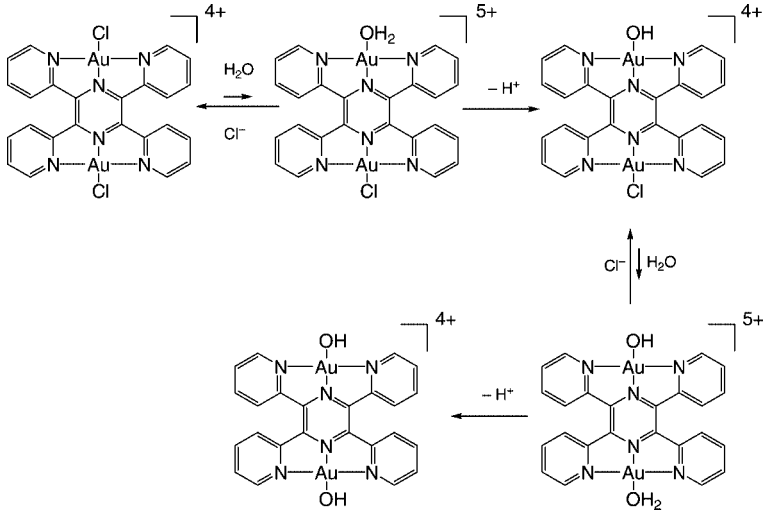


Scheme 3. Mechanism of formation of the $[Au_2(OH)_2(tppz)]Cl_4$ complex.

 © 2006 Wiley-VCH Verlag GmbH & Co. KGaA, Weinheim 

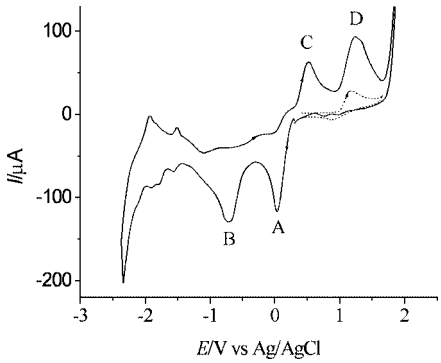


Figure 2. Cyclic voltammograms of 2 mM $[Au(OH)_2(tppz)]Cl_4$ in DMF + 0.1 M TBAP; (—) direct cathodic scan, (- - -) direct anodic scan. Glassy carbon electrode (3 mm diameter); scan rate: 50 mV s$^{-1}$.

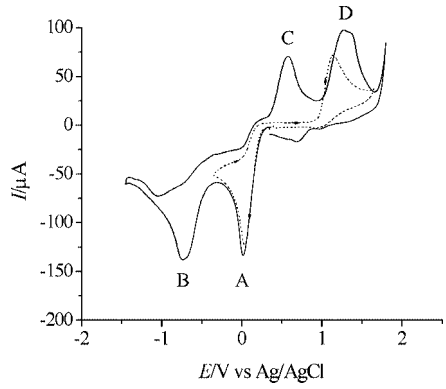


Figure 3. Cyclic voltammograms of 2 mM $[Au(OH)_2(tppz)]Cl_4$ in DMF + 0.1 M TBAP; (—) reversal of the scan direction after peak **B**, (- - -) reversal of the scan direction after peak **A**. Glassy carbon electrode (3 mm diameter); scan rate: 50 mV s$^{-1}$.

Figure 3 shows the cyclic voltammograms obtained for the $[Au_2(OH)_2(tppz)]Cl_4$ solution on reversal of the scan direction soon after either peak **A** or **B** were traversed. It is evident that peak **C** originates from the second cathodic process, while peak **D** increases strongly in current height after peak **A** has been traversed. This current increase indicates that a larger amount of $Cl^-$ ions is formed at the electrode surface following the first reduction process. This circumstance, along with the conductivity value found for a $10^{-3}$ M $[Au_2(OH)_2(tppz)]Cl_4$ solution in DMF at 25 °C ($\Lambda_M$ = 159 $\Omega^{-1}$ mol$^{-1}$ cm$^2$), which is lower than that expected for a 4:1 electrolyte (i.e. in the range 250–300 $\Omega^{-1}$ mol$^{-1}$ cm$^2$[12]), suggests that the $[Au_2(OH)_2(tppz)]^{4+}$ cation forms relatively stable ionic couples with chloride ions in DMF. Evidence for association of cationic gold(III) complexes of the type $[AuCl_2(N–N)]^+$ (N–N = sp$^2$-nitrogen-donating chelate ligands like 2,2′-bipyridine and 1,10-phenanthroline) with chloride in solution is known in the literature;[17] therefore, both the low conductivity value and the growth of peak **D** after the first reduction process were not unexpected. The above scenario did not change when performing cyclic voltammetric measurements at different scan rates over the range 0.01–0.5 V s$^{-1}$. The analysis of peak current ($I_p$) as a function of the square root of scan rate ($v^{1/2}$) was linear for both peaks **A** and **B**, thus indicating that they are diffusion-controlled processes.[13] An analysis of the peak potential ($E_p$) and the half-peak potential ($E_p - E_{p/2}$) ($E_{p/2}$ is the potential at $I_p/2$) as a function of scan rate over the above range was also performed. However, because of the complex nature of peak **B**, only the characteristics of peak **A** were examined from a quantitative point of view. It was found that $E_{p(A)}$ shifts by about 90 mV towards more negative potentials with a tenfold change of scan rate, although ($E_{p(A)} - E_{p/2}$) is equal to 106(±7) mV regardless of the scan rate. These findings are consisent with the occurrence of an irreversible electrode process.[13] The irreversible character of process **A** was further confirmed by CV measurements performed at higher scan rates with a platinum microdisk electrode. In fact, no oxidation process was directly associated to peak **A**, even when performing CV measurements at scan rates up to 500 V s$^{-1}$.[13]

Cyclic voltammetric measurements with the microelectrodes were also performed at low scan rates, and Figure 4 shows a typical CV obtained at 20 mV s$^{-1}$. Under these conditions sigmoidal waves, which are typical for microelectrodes working under steady-state conditions, were obtained.[14] The number of both cathodic and anodic processes observed, and their positions, are identical to those obtained with the conventional electrode. The shape of the voltammogram either confirmed or gave additional information with respect to that obtained with the conventional electrode. In particular, the analysis of wave **A** in terms of the Tomes difference ($E_{1/4} - E_{3/4}$)[15] (i.e. the difference between the potentials recorded at 1/4 and 3/4 of the steady-state limiting current of the forward waves) gave a value of 81(±2) mV, which is considerably higher than the value of 56.5/$n$ mV ($n$ is the number of electrons) expected theoretically for a reversible process at 24 °C.[13] This confirms the irreversible character of process **A**. The CV pattern on reversal of the scan direction from the second cathodic wave displays a current cross-over to which wave **C** is associated (see Figure 4). This behaviour is typical for metal deposition and growth on the electrode surface.[16] Therefore, the formation of metallic gold is conceivably occurring over the reduction process of the second wave. Consequently, wave **C** could be assigned to the stripping of metallic gold from the electrode surface.

The involvement of metallic gold in the correspondence of peak **C** was verified by performing a series of measurements with a conventional gold electrode in DMF solutions containing TBAP and, in consecutive steps, $[BzEt_3N]Cl$ and the tppz ligand. It was observed that the anodization of the gold electrode in the presence of $[BzEt_3N]Cl$ provided the peak at 0.56 V (peak **C**), probably due to the formation of gold chloride species.

The number of electrons involved in the two cathodic processes **A** and **B** was evaluated by preparative macroelectrolysis at controlled potential.[13] Exhaustive reduction performed at –0.4 V (where only **A** is reduced) yielded a charge consumption corresponding to a total of four electrons per mol of $[Au_2(OH)_2(tppz)]Cl_4$, i.e. an overall two-electron

 © 2006 Wiley-VCH Verlag GmbH & Co. KGaA, Weinheim 

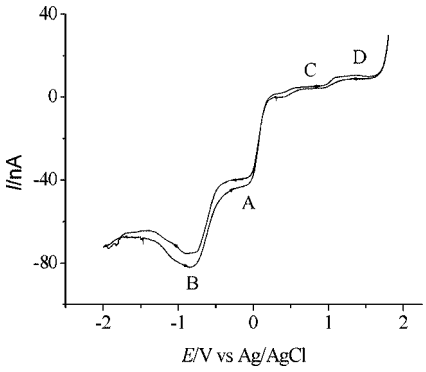


Figure 4. Cyclic voltammogram of 2 mM $[Au_2(OH)_2(tppz)]Cl_4$ in DMF + 0.1 M TBAP at a 12.5-μm Pt disk; scan rate: 20 mV s$^{-1}$.

process for each Au centre. During this experiment the solution turned from bright yellow to colourless. Cyclic voltammetric analysis of the electrolysed solution performed with a glassy carbon electrode displayed peak **B** in the cathodic scan and peaks **C** and **D** upon reversal of the scan direction. Only peak **D** was present in the direct anodic scan. It is also interesting to note that the voltammetric analysis performed on an electrolysed solution after a charge consumption corresponding to a an overall two electrons per mol of $[Au_2(OH)_2(tppz)]Cl_4$ still displays peak **A** with a height equal to half of its initial value, while peak **B** maintains almost the same height as in Figure 2. This suggests that the reduction of $[Au_2(OH)_2(tppz)]Cl_4$ provides only the species responsible for peak **B**, and that the electrons consumed are shared between the two $Au^{III}$ centres, conceivably providing $Au^{I}$ species.

Macroelectrolysis performed at –1.5 V (i.e. at peak **B**) required an overall two electrons per mol of the $[Au_2(OH)_2(tppz)]Cl_4$ complex, thus indicating a one-electron reduction process for each central atom. This reduction process affords metallic gold, as indicated by the fact that during electrolysis the platinum gauze becomes covered by a yellow film, conceivably due to a thick deposit of metallic gold,

Peak **A**

$$[Au^{III}_2(OH)_2(tppz)]Cl_4 \rightleftharpoons [Au_2(OH)_2(tppz)]Cl_{(4-i)}^{i+} + i\,Cl^-$$

$$[Au_2(OH)_2(tppz)]Cl_{(4-i)}^{i+} \xrightarrow{4\,e^-} Au_2(OH)_2(tppz) + (4-i)\,Cl^-$$

$$Au_2(OH)_2(tppz) \xrightarrow[fast]{} [Au_2(tppz)]^{2+} + 2\,OH^-$$

$i$ = number of free $Cl^-$

Peak **B**

$$[Au_2(tppz)]^{2+} \xrightarrow{e^-} [Au_2(tppz)]^{+}$$

$$[Au_2(tppz)]^{+} \xrightarrow[fast]{} [Au(tppz)]^{+} + Au$$

$$[Au(tppz)]^{+} \xrightarrow{e^-} Au(tppz)$$

$$Au(tppz) \xrightarrow[fast]{} tppz + Au$$

Scheme 4. Reduction pathway at peaks **A** and **B**.

and at the same time the colour of the solution turned from almost colourless to yellow-orange. Voltammetric analysis of the electrolysed solution displayed only a series of peaks from –1.5 to –2.5 V in the cathodic region, and peak **D** during the anodic scan. The latter peak was also observed by direct scan in the anodic potential window. Consequently, the final reduction products are metallic gold, free tppz ligand and $Cl^-$ ions.

On the basis of the voltammetric and macroelectrolysis experiments, the possible reduction pathways for processes **A** and **B** can be described as shown in Scheme 4.

## Concluding Remarks

The first gold complex of 2,3,5,6-tetrakis(2-pyridinyl)-pyrazine has been synthesized and spectroscopically characterised. DFT B3PW91 calculations have allowed us to understand some steric and electronic properties of the prepared compound, while electrochemical measurements have allowed us to determine the tetraelectronic nature of the reduction process, which leads to the formation of a stable gold(I)–tppz derivative in solution. Further studies will be carried out in order to obtain new complexes having a gold ion linked by the bridging ligand tppz to another transition metal ion, which could be really interesting from an electrochemical point of view.[3]

## Experimental Section

**Materials:** The salt $K[AuCl_4]\cdot 2H_2O$ was prepared according to a standard procedure starting from metallic Au (99.99%). The ligand 2,3,5,6-tetrakis(2-pyridinyl)pyrazine, the supporting electrolyte tetrabutylammonium perchlorate (TBAP) and benzyltriethylammonium chloride $[BzEt_3N]Cl$ were purchased from Aldrich. Solvents were dried using standard techniques.

**Preparation of $[Au_2(OH)_2(tppz)]Cl_4$:** This complex was prepared by adding solid 2,3,5,6-tetrakis(2-pyridinyl)pyrazine (0.194 g, 0.5 mmol) to a solution of $K[AuCl_4]\cdot 2H_2O$ (0.414 g, 1.0 mmol) in methanol (25 mL). The reaction mixture was heated to reflux for 12 h. During this time the white, insoluble ligand slowly changed to a bright yellow precipitate, which was filtered after cooling the reaction mixture to room temperature and dried in vacuo. The product was purified by dissolving the solid in the minimum volume of DMF (ca. 6 mL) and filtering the resulting solution. Dropwise addition of diethyl ether (ca. 20 mL) caused the product to precipitate, and this solid was filtered, washed with diethyl ether and dried in vacuo. The complex was obtained in nearly quantitative yield. $C_{24}H_{18}Au_2Cl_4N_6O_2$ (958.18): calcd. C 30.08, H 1.89, Cl 14.80, N 8.77; found C 30.20, H 1.90, Cl 14.85, N 8.80. $^1$H NMR [$(CD_3)_2SO$, 298 K]: $\delta$ = 8.53 (dd, $^3J_{H,H}$ = 5.1, $^4J_{H,H}$ = 1.2 Hz, 4 H, 6-H), 8.26 (dd, $^3J_{H,H}$ = 7.2, $^4J_{H,H}$ = 1.5 Hz, 4 H, 3-H), 8.21 (ddd, $^3J_{H,H}$ = 7.2, $^3J_{H,H}$ = 6.9, $^4J_{H,H}$ = 1.2 Hz, 4 H, 4-H), 7.66 (ddd, $^3J_{H,H}$ = 5.1, $^3J_{H,H}$ = 6.9, $^4J_{H,H}$ = 1.5 Hz, 4 H, 5-H), 6.01 (br. s, 2 H, OH) ppm. $^{13}C\{^1H\}$ NMR [$(CD_3)_2SO$, 298 K]: $\delta$ = 153.5, 147.6 (tppz quaternary C atoms), 147.1, 140.2, 125.7, 125.5 ppm (tppz primary C atoms). IR (nujol): $\tilde{\nu}$ = 3412 [$\nu$(O–H)] cm$^{-1}$. $\Lambda_M$ (DMF, 298 K) = 159 $\Omega^{-1}$ mol$^{-1}$ cm$^2$.

**Physical Measurements:** Infrared spectra (4000–400 cm$^{-1}$, nujol mulls) were recorded with a Perkin–Elmer Spectrum One spectro-

 © 2006 Wiley-VCH Verlag GmbH & Co. KGaA, Weinheim 

photometer. $^1$H NMR, $^1$H COSY and $^{13}$C{$^1$H} NMR spectra were obtained with an Avance 300 Bruker spectrometer in $(CD_3)_2SO$ at temperatures between 298 and 338 K. $^1$H and $^{13}$C{$^1$H} NMR spectra are referenced to internal tetramethylsilane. The SwaN-MR and MestRe-C software packages were used to treat the NMR spectroscopic data.[18] Elemental analyses (C, H, Cl, N) were performed by the microanalytical laboratory at the Department of Pharmaceutical Sciences, University of Padua. The conductivity of $10^{-3}$ M solutions of the complexes in DMF at 25 °C was measured with a Radiometer CDM 83 instrument.

**Computational Details:** Computational geometry optimisation of the cations $[Au(OH)(terpy)]^{2+}$ and $[Au_2(OH)_2(tppz)]^{4+}$ was performed in vacuo using the restricted DFT B3PW91 method[19,20] without symmetry constraints. The basis sets used were CEP-121G (CEP-31G on the Au atom) (**BS1**),[21] D95V (SDD on the Au atom) (**BS2**) and D95 (LANL2DZ on the Au atom) (**BS3**).[22] Geometry convergence was accelerated using the GDIIS algorithm. All of the resultant stationary points were characterized as true minima (i.e., no imaginary frequencies). Atomic charges were derived from a Mulliken population analysis. All calculations were carried out with computers equipped with Intel Pentium 4 660 processors (Prescott 2M) operating at 3.6 GHz. The software used was Gaussian 98.[23]

**Electrochemical Apparatus and Procedure:** Voltammetric experiments were performed in an air-tight, three-electrode cell, which was located in a Faraday cage to avoid external noise. Working electrodes of both conventional and micrometric dimensions were employed. The working electrodes of conventional size were either a glassy carbon or a platinum disk of about 3 mm diameter. Preliminary voltammetric tests showed that similar results were obtained whether conventional glassy carbon or platinum disk electrodes were employed as working electrodes, therefore the general voltammetric behaviour of the investigated complex at the conventional glassy carbon electrode is discussed in the text. The microelectrode was a Pt microdisk (25 μm diameter), which was prepared by sealing a 25-μm-diameter wire directly in glass, as reported elsewhere.[16] A platinum spiral was used as counter electrode, and aqueous Ag/AgCl saturated with KCl was used as reference electrode. It was separated from the cell by a salt bridge containing the same solvent and supporting electrolyte solution as used in the cell. All working electrodes were polished mechanically with graded alumina powder (1, 0.3 down to 0.05 μm) on a polishing microcloth. Cyclic voltammetric experiments were performed with a potentiostat/galvanostat PAR 283 A (EG&G) controlled by 270 PAR (EG&G) software using a PC. For experiments with conventional electrodes, positive feedback corrections of the uncompensated resistance (i.r. drop) were performed. Steady-state voltammograms with the microelectrode were recorded at 20 mV s$^{-1}$. Macroelectrolyses were carried out in an H-shaped cell with the cathodic and anodic compartments separated by a sintered glass disk. As the compound examined displayed comparable voltammetric behaviours on glassy carbon and platinum electrodes, the working electrode used in macroelectrolysis was a large-area platinum gauze, while a platinum spiral served as counter electrode. In controlled-potential electrolyses, an Amel model 552 potentiostat coupled to an Amel model 731 integrator was employed. Unless otherwise stated, voltammetric and coulometric measurements were performed at room temperature using 2 mM $[Au_2(OH)_2(tppz)]Cl_4$ and 0.1 M supporting electrolyte (TBAP) DMF solutions. The cells were degassed with pure nitrogen (99.99%), which was first passed through sulfuric acid solution to remove traces of water and then equilibrated to the vapour pressure of DMF, prior to the measurements.

## Acknowledgments

We thank the Ca' Foscari University of Venice for financial support (Ateneo fund 2004).

[1] L. S. Hollis, S. J. Lippard, *J. Am. Chem. Soc.* **1983**, *105*, 4293.
[2] B. Pitteri, G. Marangoni, F. Visentin, T. Bobbo, V. Bertolasi, P. Gilli, *J. Chem. Soc., Dalton Trans.* **1999**, 677.
[3] a) N. Chanda, R. Laye, S. Chakraborty, R. L. Paul, J. C. Jeffery, M. D. Ward, G. K. Lahiri, *J. Chem. Soc., Dalton Trans.* **2002**, 3496; b) N. Chanda, B. Sarkar, J. Fiedler, W. Kaim, G. K. Lahiri, *Dalton Trans.* **2003**, 3550; c) C. M. Hartshorn, N. Daire, V. Tondreau, B. Loeb, T. J. Meyer, P. S. White, *Inorg. Chem.* **1999**, *38*, 3200; d) C. R. Arana, H. D. Abruña, *Inorg. Chem.* **1993**, *32*, 194; e) R. G. Brewer, G. E. Jensen, K. J. Brewer, *Inorg. Chem.* **1994**, *33*, 124; f) L. M. Vogler, K. J. Brewer, *Inorg. Chem.* **1996**, *35*, 818; g) N. Chanda, B. Sarkar, S. Kar, J. Fiedler, W. Kaim, G. K. Lahiri, *Inorg. Chem.* **2004**, *43*, 5128; h) L. M. Vogler, S. W. Jones, G. E. Jensen, R. G. Brewer, K. J. Brewer, *Inorg. Chim. Acta* **1996**, *250*, 155; i) S. W. Jones, L. M. Vrana, K. J. Brewer, *J. Organomet. Chem.* **1998**, *554*, 29; j) R. R. Ruminski, J. L. Kiplinger, *Inorg. Chem.* **1990**, *29*, 4581; k) D. M. Dattelbaum, C. M. Hartshorn, T. J. Meyer, *J. Am. Chem. Soc.* **2002**, *124*, 4938; l) S. Fantacci, F. De Angelis, J. Wang, S. Bernhard, A. Selloni, *J. Am. Chem. Soc.* **2004**, *126*, 9715.
[4] R. Ruminski, J. Kiplinger, T. Cockroft, C. Chase, *Inorg. Chem.* **1989**, *28*, 370.
[5] a) J. Bera, C. S. Campos-Fernández, C. Rodolphe, K. Dunbar, *Chem. Commun.* **2002**, 2536; b) R. R. Ruminski, C. Letner, *Inorg. Chim. Acta* **1989**, *162*, 175; c) J. Lee, L. M. Vrana, E. R. Bullock, K. J. Brewer, *Inorg. Chem.* **1998**, *37*, 3575.
[6] L. M. Vogler, B. Scott, K. J. Brewer, *Inorg. Chem.* **1993**, *32*, 898.
[7] M. Graf, H. Stoeckli-Evans, A. Escuer, R. Vicente, *Inorg. Chim. Acta* **1997**, *257*, 89.
[8] Y. Yamada, Y. Miyashita, K. Fujisawa, K. Okamoto, *Bull. Chem. Soc. Jpn.* **2000**, *73*, 1843.
[9] J. Carranza, C. Brennan, J. Sletten, J. M. Clemente-Juan, F. Lloret, M. Julve, *Inorg. Chem.* **2003**, *42*, 8716.
[10] M. Graf, B. Greaves, H. Stoeckli-Evans, *Inorg. Chim. Acta* **1993**, *204*, 239.
[11] F. Basolo, R. G. Pearson, *Mechanism of Inorganic Reactions*, 2nd ed., Wiley, New York, **1967**.
[12] W. Geary, *Coord. Chem. Rev.* **1971**, *7*, 81.
[13] A. J. Bard, L. R. Faulkner, *Electrochemical Methods*, Wiley, New York, **2001**.
[14] M. I. Montenegro, M. A. Queiros, J. L. Daschbach, *Microelectrodes: Theory and Applications*, NATO ASI Series, **1991**, vol. E197.
[15] J. Tomes, *Collect. Czech. Chem. Commun.* **1937**, *9*, 150.
[16] S. Daniele, M. A. Baldo, M. Corbetta, G. A. Mazzocchin, *J. Electroanal. Chem.* **1994**, *379*, 261.
[17] R. J. Puddephatt, *Comprehensive Coordination Chemistry*, vol. 5 (Ed.: G. Wilkinson), Pergamon, Oxford, **1987**, p. 896 and references cited therein.
[18] a) G. Balacco, *J. Chem. Inf. Comput. Sci.* **1994**, *34*, 1235; b) J. C. Cobas Gómez, F. J. Sardina López, *MestRe-C*, Universidad de Santiago de Compostela, Spain.
[19] R. G. Parr, W. Yang, *Density-Functional Theory of Atoms and Molecules*, Oxford University Press, Oxford, **1989**.
[20] a) A. D. Becke, *J. Chem. Phys.* **1993**, *98*, 5648; b) K. Burke, J. P. Perdew, Y. Wang, in *Electronic Density Functional Theory: Recent Progress and New Directions* (Eds.: J. F. Dobson, G. Vignale, M. P. Das), Plenum, New York, **1998**.
[21] T. R. Cundari, W. J. Stevens, *J. Chem. Phys.* **1993**, *98*, 5555.
[22] T. H. Dunning Jr., P. J. Hay, *Modern Theoretical Chemistry*, vol. 3 (Ed.: H. F. Schafter), Plenum, New York, **1976**.
[23] a) M. J. Frisch, G. W. Trucks, H. B. Schlegel, G. E. Scuseria, M. A. Robb, J. R. Cheeseman, V. G. Zakrzewski, J. A. Montgomery Jr, R. E. Stratmann, J. C. Burant, S. Dapprich, J. M.

 © 2006 Wiley-VCH Verlag GmbH & Co. KGaA, Weinheim 

Millam, A. D. Daniels, K. N. Kudin, M. C. Strain, O. Farkas, J. Tomasi, V. Barone, M. Cossi, R. Cammi, B. Mennucci, C. Pomelli, C. Adamo, S. Clifford, J. Ochterski, G. A. Petersson, P. Y. Ayala, Q. Cui, K. Morokuma, D. K. Malick, A. D. Rabuck, K. Raghavachari, J. B. Foresman, J. Cioslowski, J. V. Ortiz, A. G. Baboul, B. B. Stefanov, G. Liu, A. Liashenko, P. Piskorz, I. Komaromi, R. Gomperts, R. L. Martin, D. J. Fox, T. Keith, M. A. Al-Laham, C. Y. Peng, A. Nanayakkara, M. Challacombe, P. M. W. Gill, B. Johnson, W. Chen, M. W. Wong, J. L. Andres, C. Gonzalez, M. Head-Gordon, E. S. Replogle, J. A. Pople, *Gaussian 98*, Gaussian, Inc., Pittsburgh PA, **1998**. We thank Dr. A. Zambon for the use of his software package.

Received: April 26, 2006
Published Online: July 21, 2006

 © 2006 Wiley-VCH Verlag GmbH & Co. KGaA, Weinheim 

DOI: 10.1002/ejic.200600404

# Synthesis, Structure and Magnetic Properties of a Tetranuclear Copper(II) Complex on the Basis of a 2-Substituted Glucopyranoside Schiff Base Ligand

**Anja Burkhardt,[a] Axel Buchholz,[a] Helmar Görls,[a] and Winfried Plass*[a]**

*Dedicated to Professor Ernst-Gottfried Jäger on the occasion of his 70th birthday*

**Keywords:** Carbohydrates / Schiff base ligands / Copper(II) complexes / Magnetic properties

Condensation of a derivatized 2-aminoglucose fragment with salicylaldehyde affords the new sugar-based Schiff base ligand benzyl 4,6-*O*-benzylidene-2-deoxy-2-salicylideneamino-α-D-glucopyranoside ($H_2L$). The reaction of the dibasic ligand $H_2L$ with $[Cu(CH_3COO)_2]\cdot H_2O$ leads to the formation of the tetranuclear copper(II) complex $[\{Cu(L)\}_4]$ (**3**) by a self-assembly process. The X-ray structural analysis of complex **3** which crystallizes together with two molecules of chloroform and one molecule of ethanol in the space group $P2_12_12_1$ revealed for all copper atoms a $NO_3$ coordination environment with a square-planar geometry. The tetranuclear molecule **3** consists of four chiral building blocks {Cu(L)} with the rare 2,3-coordination of the *trans*-configured donor atoms of the sugar backbone. The observed coordination mode of the building blocks exemplifies how chitosan-derived polysaccharide ligands can act as a chiral support for transition-metal complexes. The C-3 alcoholate oxygen atoms of the carbohydrate unit is bridging adjacent {Cu(L)} moieties resulting in an eight-membered $Cu_4O_4$ ring with a boat-like conformation. Temperature-dependent magnetic measurements of **3** indicate moderate antiferromagnetic interactions between the four copper(II) ions with a coupling constant of $J = -130\ cm^{-1}$.

(© Wiley-VCH Verlag GmbH & Co. KGaA, 69451 Weinheim, Germany, 2006)

## Introduction

Carbohydrates are the most abundant biogenic class of compounds involved in a wide range of functions in living organisms. In case of cellulose, sugars act as scaffolding material in plants. Monosaccharide fragments are participating in glycolipids and glycoproteins and play an important role in various biological processes e.g. as building blocks for nucleotides and of the ADP/ATP energy-storage system.[1] Many sugar-metabolizing enzymes have been revealed to function with alkaline earth and transition metal ions in the active sites.[2–10]

Although the importance of sugar–metal interaction is known for many years, the field of sugar–metal complexes is still largely unexplored. Only for the past two decades, sugars received a growing interest as ligand components in bioorganic chemistry due to their enantiomerically pure natural abundance and their polyfunctionality. The vicinal functional groups feature many donor atoms forming stable chelate complexes.[11–15] Furthermore, carbohydrates combine interesting properties like stable chiral scaffold and supramolecular arrangement. Well-known modification strategies for introducing additional donor groups into the sugar backbone are *N*-glycosylation with polyamines[16–22] and nucleophilic substitution of bromoethyl-*O*-glycosides.[23–28] A further method is the condensation of amino saccharides and carbonyl components resulting in tridentate Schiff base ligands.[29–31]

The corresponding transition-metal complexes show a large tendency for coordinative saturation via coligation or self-assembly to polynuclear compounds by oxo-bridging. Many naturally available copper-containing enzymes like catechol oxidase[32] or ascorbate oxidase[33] exhibit a polynuclear active site. Thus, polynuclear sugar-modified copper(II) complexes are interesting concerning their biorelevance as structural and/or functional models for various metalloenzymes. However, the rare examples described in literature are linear trinuclear and cyclic di- or tetranuclear copper(II) complexes which are based on either C-1 or C-6 amino functionalized carbohydrate fragments.[34–38]

Amino precursors have to be synthesized by *N*-glycosylation or a laborious six-step synthesis with participation of various protecting groups. 2-Aminoglucose is the monomer unit of chitosan which could be obtained from acidic deacetylation of chitin (see Scheme 1). The β-(1-4)-linked polysaccharide is the structural element in the exoskeleton of crustaceans. The vision of creating polymeric catalysts provoked us to more detailed studies of the coordination

[a] Institut für Anorganische und Analytische Chemie, Friedrich-Schiller-Universität Jena,
Carl-Zeiss-Promenade 10, 07745 Jena, Germany
Fax: +49-3641-948132
E-mail: Sekr.Plass@uni-jena.de

 © 2006 Wiley-VCH Verlag GmbH & Co. KGaA, Weinheim 

chemistry of Schiff base ligands derived from the monomeric chitosan fragment 2-aminoglucose.

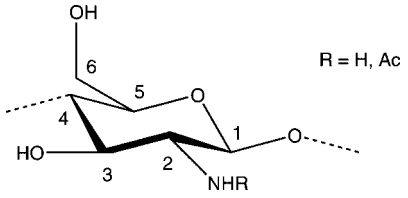


Scheme 1. 2-Aminoglucose backbone as found in chitosan.

## Results and Discussion

### Synthesis and Characterization

Starting from benzyl 2-amino-4,6-*O*-benzylidene-2-deoxy-α-D-glucopyranoside (**1**)[39,40] the Schiff base ligand $H_2L$ (**2**) was prepared by condensation with salicylaldehyde in methanol as depicted in Scheme 2. The synthesized Schiff base ligand **2** was characterized by IR, NMR and ESI-MS studies as well as elemental analysis. The IR band at 1637 $cm^{-1}$ is attributed to the valence vibration of the imino group. In the NMR spectra the corresponding resonances of the imino group are present at $\delta$ = 167.8 ppm ($^{13}C$ NMR) and at $\delta$ = 9.91 ppm ($^{1}H$ NMR). The proton on C-1 of the D-glucose moiety leads to a doublet in the $^{1}H$ NMR spectrum with $^{3}J_{12}$ = 3.7 Hz indicative for the exclusive presence of the α-anomer of the saccharide unit associated with the *cis* position of the protons attached to C-1 and C-2. Due to its hydrophobic phenyl groups the sugar ligand **2** is soluble in less polar solvents.

For complexation an aqueous solution of $[Cu(CH_3COO)_2]\cdot H_2O$ was added to a chloroform solution of **2** in a 1:1 molar ratio at room temperature. Ethanol was added under vigorous stirring for homogenization of the generated two-phase system. Slow evaporation of the dark green solution affords crystals of $[\{Cu(L)\}_4]\cdot 2CHCl_3\cdot EtOH$ (**3**·$2CHCl_3$·EtOH) as green prisms after 4 d. Due to its volatility, chloroform is removed first from the reaction mixture leading to an increasing polarity of the remaining solution. Owing to the poor solubility of **3** in polar solvents the formed copper(II) complex can be isolated in very high yields.

In accordance with the molecular ion peaks at 2092 ($[\{Cu(L)\}_4+H]^+$) and 2113 ($[\{Cu(L)\}_4+Na]^+$) obtained from ESI-MS measurements, complex **3** also appears to exist as undissociated tetranuclear species in solution. UV/Vis studies of the green copper(II) complex **3** performed in chloroform solution exhibit two charge–transfer bands at 277 and 370 nm and a third band at 628 nm attributed to a d–d transition. No weight loss can be found up to the decomposition temperature by TGA measurement indicating that all solvent molecules are removed during the air-drying process consistent with the formula $[\{Cu(L)\}_4]$ for complex **3**. This is further corroborated by the results obtained from elemental analysis.

To the best of our knowledge complex **3** is the first tetranuclear transition-metal complex derived from the monomeric chitosan unit 2-aminoglucose. Copper(II) structures on the basis of C-1-salicylidene-functionalized Schiff base ligands of 1-amino-D-sorbitol[35] and 1-amino-4,6-*O*-ethylidene-β-D-glucopyranose[38] have recently been reported. Furthermore, **3** is the first transition-metal complex characterized by X-ray crystallography featuring a *trans*-configured coordination of donor atoms at C-2 and C-3 of the sugar moiety. From literature 2-aminoglucose-derived *cis*-dioxomolybdenum(VI) complexes are known with the metal center coordinated by the imino nitrogen atom and the alcoholate oxygen atom at the anomeric carbon atom C-1.[41]

### Structure Description

Figure 1 shows the molecular structure of the complex $[\{Cu(L)\}_4]$ (**3**) which was found in crystals of **3**·$2CHCl_3$·EtOH. The observed space group $P2_12_12_1$ is consistent with the appearance of only one diastereomer formed by self-assembly of the four neutral mononuclear chiral building blocks {Cu(L)}. Selected distances and angles are given in Table 1. Each copper(II) center is coordinated in a square-planar environment by a phenolate oxygen atom of the salicylidene residue, a nitrogen atom of the C-2 imino group and a C-3 alcoholate oxygen atom of the sugar backbone. The fourth position is occupied by an additional C-3 alcoholate group from an adjacent sugar unit.

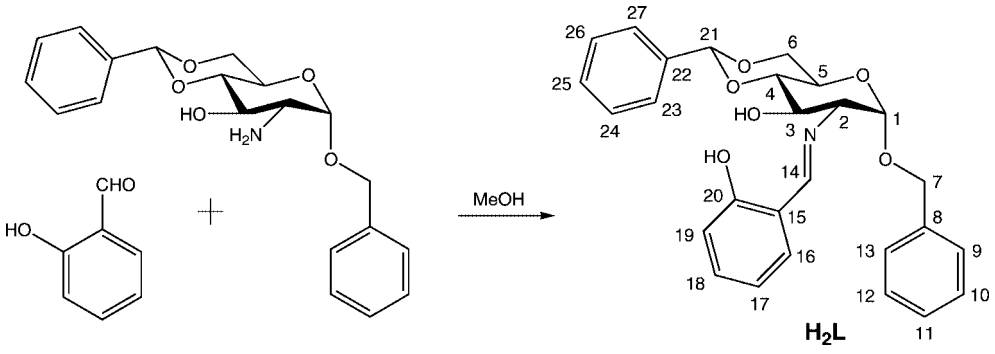


Scheme 2. Reaction scheme for the synthesis of ligand $H_2L$ (**2**).

 © 2006 Wiley-VCH Verlag GmbH & Co. KGaA, Weinheim 

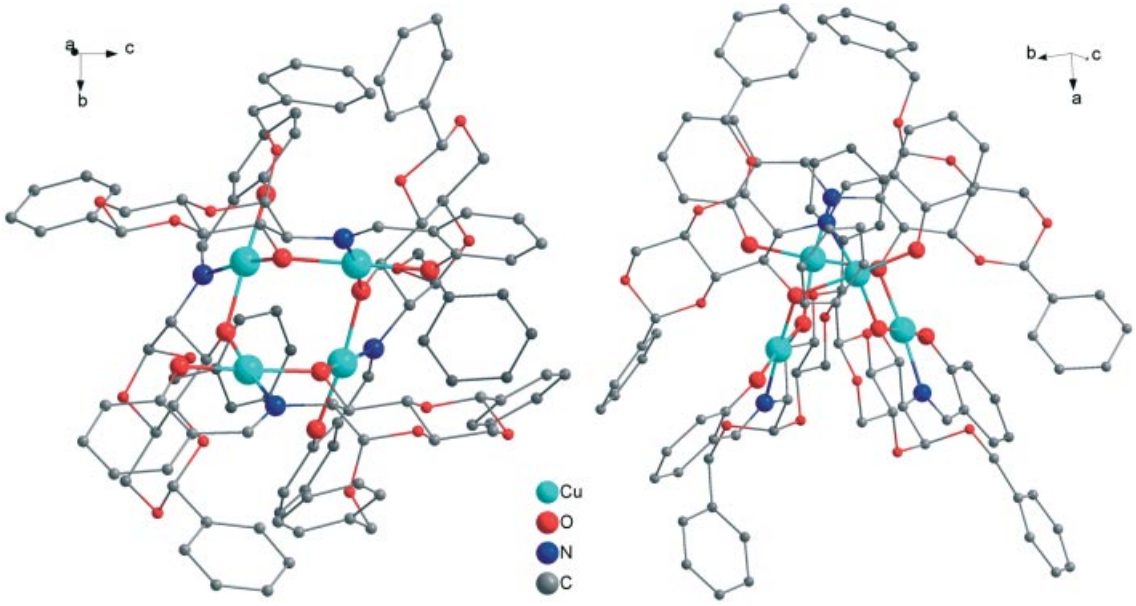


Figure 1. Molecular structure of [{Cu(L)}$_4$] (**3**) in crystals of **3**·2CHCl$_3$·EtOH. Solvent molecules and hydrogen atoms are omitted for clarity. (left) View approximately along the pseudo $S_4$ axis of the central Cu$_4$ tetrahedron. (right) Side view, indicating the boat-like conformation of the Cu$_4$O$_4$ metallocycle.

All 2-aminoglucose moieties adopt the more stable $^4C_1$ chair conformation. The copper(II) centers are included well in each NO$_3$ coordination plane with deviations less than 0.05 Å from the corresponding mean planes. The N–Cu–O and O–Cu–O angles are varying from 83.9 to 94.5° and from 170.5 to 177.1°, which is consistent with a slightly distorted square-planar geometry at the copper atoms.

The tetranuclear complex **3** is formed by a self-assembly process of four chiral building blocks {Cu(L)}, with the C-3 alcoholate oxygen atoms being the bridging links between adjacent {Cu(L)} moieties. The resulting eight-membered Cu$_4$O$_4$ ring depicted in Figure 2 is folded in a boat-like conformation. The metal centers occupy the vertices of a distorted tetrahedron which is bisected by the distorted tetragonal plane [torsion angle $\tau$(O13–O23–O33–O43) = 51.8°] composed of the linker alcoholate oxygen atoms O*i*3 (*i* is the running number assigned to the {Cu(L)} moieties) with its normal vector almost collinear to the pseudo $C_2$ axis of the [{Cu(L)}$_4$] molecule. This results in a non-coplanar orientation of the coordination planes of the four {Cu(L)} moieties given by Cu*i*, N*i*, O*i*3, O*i*6 and O*j*3 (*i* and *j* are the running numbers of the {Cu(L)} moieties). The angles between adjacent planes are ranging from 68.4 to 88.9°, whereas the angles between opposite planes are 43.0 (Cu1 and Cu3) and 45.7° (Cu2 and Cu4).

In accordance with the Cu*i*–O*i*3 distances ranging from 1.917 to 1.957 Å the C-3 alcoholate groups are deprotonated affording a dianionic ligand unit and finally complex **3** as a neutral species. All bond lengths and angles of complex **3** are in the expected range (see Table 1). Unlike the square-planar coordination found for the metal centers in **3**, the only two other sugar-based tetranuclear copper(II) complexes described in literature[35,38] exhibit a square-pyramidal coordination environment at the copper(II) ions. In the latter cases, the apical position is occupied by an additional alcoholate group from the sugar backbone. The absence of an auxiliary accessible donor function in H$_2$L (**2**) may be the reason for the observed coordination number four in complex **3**. Unsaturated copper(II) centers are interesting with respect to catalysis due to a possible substrate binding at the unoccupied fifth position.

Table 1. Selected distances [Å] and angles [°] for [{Cu(L)}$_4$] (**3**) in crystals of **3**·2CHCl$_3$·EtOH.

| | | | |
|---|---|---|---|
| Distances | | | |
| Cu1–N1 | 1.926(3) | Cu2–N2 | 1.982(3) |
| Cu1–O13 | 1.957(3) | Cu2–O23 | 1.917(3) |
| Cu1–O16 | 1.900(3) | Cu2–O26 | 1.908(3) |
| Cu1–O43 | 1.938(3) | Cu2–O13 | 1.939(3) |
| Cu3–N3 | 1.953(3) | Cu4–N4 | 1.956(3) |
| Cu3–O23 | 1.933(3) | Cu4–O33 | 1.928(3) |
| Cu3–O33 | 1.925(3) | Cu4–O43 | 1.947(3) |
| Cu3–O36 | 1.890(3) | Cu4–O46 | 1.917(3) |
| Cu1···Cu2 | 3.395(4) | Cu2···Cu3 | 3.407(6) |
| Cu1···Cu3 | 3.610(5) | Cu2···Cu4 | 3.881(5) |
| Cu1···Cu4 | 3.435(5) | Cu3···Cu4 | 3.454(5) |
| Angles | | | |
| N1–Cu1–O13 | 84.56(12) | N2–Cu2–O23 | 83.91(12) |
| N1–Cu1–O16 | 93.49(12) | N2–Cu2–O26 | 92.05(13) |
| N1–Cu1–O43 | 170.50(13) | N2–Cu2–O13 | 173.43(13) |
| O13–Cu1–O16 | 171.96(13) | O23–Cu2–O26 | 175.53(12) |
| O13–Cu1–O43 | 88.49(11) | O23–Cu2–O13 | 89.92(11) |
| O16–Cu1–O43 | 94.26(12) | O26–Cu2–O13 | 94.05(12) |
| N3–Cu3–O33 | 85.32(12) | N4–Cu4–O43 | 84.11(13) |
| N3–Cu3–O36 | 93.68(13) | N4–Cu4–O46 | 91.61(13) |
| N3–Cu3–O23 | 171.75(13) | N4–Cu4–O33 | 176.11(13) |
| O33–Cu3–O36 | 177.16(13) | O43–Cu4–O46 | 174.41(11) |
| O33–Cu3–O23 | 86.59(12) | O43–Cu4–O33 | 92.49(12) |
| O36–Cu3–O23 | 94.48(12) | O46–Cu4–O33 | 91.65(12) |
| Cu1–O13–Cu2 | 121.21(13) | Cu2–O23–Cu3 | 124.47(13) |
| Cu1–O43–Cu4 | 124.30(14) | Cu3–O33–Cu4 | 127.34(14) |

 © 2006 Wiley-VCH Verlag GmbH & Co. KGaA, Weinheim 

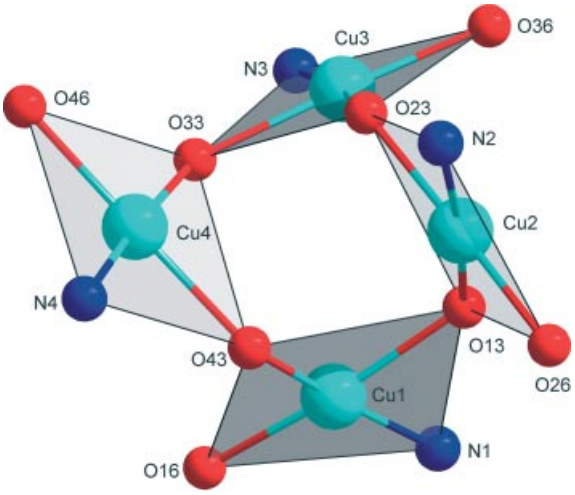


Figure 2. Representation of the central $Cu_4O_4$ core of complex **3**.

## Magnetic Properties

Magnetic susceptibility measurements of powder samples of **3** were carried out in the temperature range of 2–300 K at an applied magnetic field of 500 Oe. The magnetic data are represented as $\chi_M$ vs. $T$ and $\chi_M T$ vs. $T$ plots in Figure 3. The molar paramagnetic susceptibility $\chi_M$ is corrected for the diamagnetic contributions using Pascal's constants. $\chi_M$ goes through a maximum at about 150 K and is increasing again below 25 K due to the presence of paramagnetic impurities. The observed low-temperature value of $\chi_M T$ is in accordance with an $S = 0$ ground state of **3**. The high-temperature value of 1.41 $cm^3 K mol^{-1}$ at 300 K is slightly below the expected spin-only value for four independent copper(II) ions. The temperature dependence of $\chi_M T$ clearly indicates antiferromagnetic exchange interactions within the tetranuclear core of complex **3**.

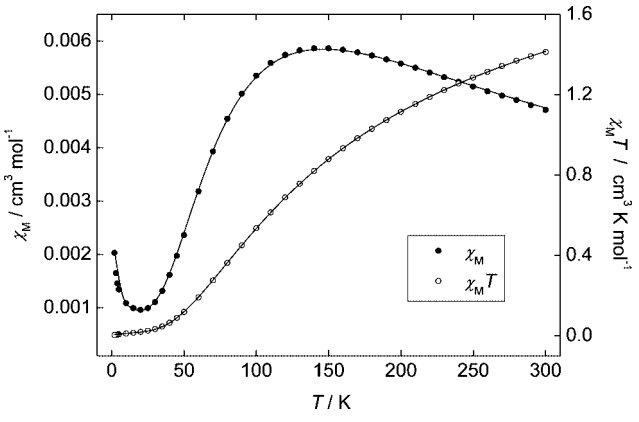


Figure 3. Plots of $\chi_M$ vs. $T$ (●), $\chi_M T$ vs. $T$ (○) for **3**. The solid lines represent the best fit to the experimental data (see text).

On the basis of the Cu···Cu distances ranging from 3.39 to 3.88 Å and the unfavorable relative orientations of the copper coordination planes, direct interactions between the metal centers are not very likely. Therefore, the prominent interaction is most likely superexchange through the alcoholate bridges. In the majority of cases the central $Cu_4O_4$ unit of tetranuclear copper(II) complexes exhibits a cubane-like structure treated as a dimer of $Cu_2O_2$ fragments. In complex **3** the $Cu_4O_4$ metallocyclic core unit adopts the unusual boat-like conformation found for only two other magnetically studied examples.[35,42]

Because of the similarity of the Cu*i*–O*i*3 distances ranging from 1.917 to 1.957 Å and the Cu*i*–O*i*3–Cu*j* bridging angles ranging from 121.2 to 127.3°, only one coupling constant $J$ is employed. This assumption is confirmed by the obtained quality of the best fit (solid lines in Figure 3) on the basis of the Heisenberg spin Hamiltonian given in Equation (1)[43] to the experimental data, which results in a coefficient of determination of $r^2 = 0.99999$. The fit parameters $g = 2.15$, $J = -130\ cm^{-1}$, $\rho = 0.0024$ and $\chi_{TIP} = 6.9 \cdot 10^{-4}\ cm^3 mol^{-1}$ were obtained by least-square methods utilizing Equation (2) ($\chi_{TIP}$ = temperature-independent paramagnetism). To account for small amounts of paramagnetic impurity in the sample indicated by the $\chi_M$ vs. $T$ plot, the additional constant $\rho$ (fraction of paramagnetic impurity) was included in Equation (2). The contributions of $\rho$ become significant at temperatures below 20 K.

$$H = -J\,(S_1 S_2 + S_2 S_3 + S_3 S_4 + S_1 S_4) \tag{1}$$

$$\chi_M \cdot T = \frac{2Ng^2\beta^2}{k}\left[(1-\rho)\left(\frac{e^{\frac{J}{kT}} + 2e^{\frac{2J}{kT}} + 5e^{\frac{3J}{kT}}}{1 + 3e^{\frac{J}{kT}} + 7e^{\frac{2J}{kT}} + 5e^{\frac{3J}{kT}}}\right) + \frac{\rho}{2}\right] + \chi_{TIP} \cdot T \tag{2}$$

For dinuclear copper complexes with a planar $Cu_2O_2$ core magneto-structural correlations between the Cu–O(R)–Cu bridging angle ($\alpha$) and the singlet-triplet splitting ($J$) have been reported depending on the nature of the bridging unit (R = H, alkyl, aryl).[44] On the basis of the Cu*i*–O*i*3–Cu*j* bridging angles observed for complex **3**, ranging from 121 to 127°, the relationship found for alcoholate-bridged copper(II) complexes ($J = 82.1\alpha - 7857$) would estimate a very strong antiferromagnetic interaction of about 2000 $cm^{-1}$, which is a rather poor prediction. Although this difference may be related to the variation of the number of bridges, this cannot account for the overall effect. More important is the fact that for planar $Cu_2O_2$ arrangements the bridging angle is a sufficient parameter to describe the interaction of the magnetic orbitals based on their given coplanar orientation, whereas this is not the case for complexes with single alcoholate bridges. Therefore, additional parameters are essential in order to describe the relative orientation of the magnetic orbitals for systems with single alcoholate bridges, as found in the case of complex **3**. An important structural feature in this context is the torsion angle between adjacent copper coordination planes.[45] For complex **3** the relevant torsion angles range from 68 to 89°. This missing coplanarity of the adjacent Cu coordination planes is associated with poor overlap of the magnetic orbitals.[46] Hence, this can explain the comparatively low value of $J$ observed for complex **3**.

 © 2006 Wiley-VCH Verlag GmbH & Co. KGaA, Weinheim 

## Conclusions

The reaction of the sugar-derived Schiff base ligand $H_2L$ (**2**), obtained from the condensation of benzyl 2-amino-4,6-*O*-benzylidene-2-deoxy-α-D-glucopyranoside (**1**) and salicylaldehyde, with $[Cu(CH_3COO)_2]\cdot H_2O$ affords the tetranuclear complex $[\{Cu(L)\}_4]$ (**3**) by a self-assembly process of the chiral building blocks {Cu(L)}. The structure determination by X-ray crystallography revealed the exclusive presence of square-planar coordination environments for the copper(II) ions, which to the best of our knowledge is as yet unprecedented in literature for oligonuclear complexes with sugar-derived Schiff base ligands. The square-planar coordination of the copper centers is given by a phenolate oxygen atom of the salicylidene residue, a nitrogen atom of the C-2 imino group and a C-3 alcoholate oxygen atom of the sugar backbone as well as the bridging C-3 alcoholate oxygen atom of the adjacent {Cu(L)} building block. The four adjacent {Cu(L)} moieties are linked by the C-3 alcoholate oxygen atoms resulting in an eight-membered $Cu_4O_4$ metallocycle adopting a boat-like conformation. This is uncommon for such a tetranuclear oxygen atom bridged core unit, for which usually a cubane-like structure is observed. Magnetic studies of complex **3** show moderate antiferromagnetic interactions between the copper(II) centers with a coupling constant of $J = -130\ cm^{-1}$. Regarding to the obtuse Cu*i*–O*i*3–Cu*j* bridging angles of more than 120° much larger exchange interactions would be predicted on the basis of magneto-structural correlations derived from binuclear complexes. This is mainly because of the missing coplanarity of the adjacent Cu coordination planes and hence the magnetic orbitals. As first example for 2-amino sugar-derived transition-metal complexes exhibiting a 2,3-coordination of the *trans*-configured donor atoms of the sugar backbone, **3** provides useful insight to the opportunity of constructing polysaccharide-based coordination compounds, in particular chitosan-derived polymer complexes.

## Experimental Section

**Material:** The precursor ligand benzyl 2-amino-4,6-*O*-benzylidene-2-deoxy-α-D-glucopyranoside (**1**) was obtained by a three-step synthesis starting from *N*-acetyl-α-D-glucopyranosamine following reported procedures.[39,40] All other chemicals were purchased from commercial suppliers and used without further purification.

**Physical Measurements:** Melting points are given uncorrected and were determined with a VEB Analytik Dresden HMK 72/41555. Thermogravimetric analysis (TGA) for powdered samples was performed with a Netzsch STA409PC Luxx apparatus under constant flow of nitrogen ranging from room temperature up to 1000 °C with a heating rate of 1 °C/min. Infrared and Raman spectra were recorded with a Bruker IFS55/EQUINOX spectrometer. $^1H$ and $^{13}C$ NMR experiments were carried out with a Bruker AVANCE DRX 400 spectrometer. The exact interpretation was accomplished by additional two-dimensional experiments. For the labeling scheme see Scheme 2. UV/Vis spectra were recorded with a Varian CARY 5000 UV/Vis-NIR spectrometer. Mass spectra were measured with a Bruker MAT SSQ 710 spectrometer. Elemental analyses were determined with a Leco CHNS/932 elemental analyzer and a VARIO EL III. Magnetic susceptibilities were obtained from powdered samples using a Quantum-Design MPMSR-5S SQUID magnetometer equipped with a 5-Tesla magnet in the range from 300 to 2 K. The diamagnetic correction of the sample was estimated from Pascal's constants.

**Crystallographic Study:** Crystallization of complex **3** from a mixture of chloroform, ethanol and water afforded green prismatic crystals of $[\{Cu(L)\}_4]\cdot 2CHCl_3\cdot EtOH$ (**3**·$2CHCl_3$·EtOH) suitable for X-ray measurements. Single crystals were selected while still covered with mother liquor under a polarizing microscope and fixed on fine glass fibers. X-ray measurements were carried out with a Nonius Kappa CCD diffractometer using graphite-monochromated Mo-$K_\alpha$ radiation ($\lambda = 0.71073$ Å). The crystallographic data is summarized in Table 2. The structure was solved by direct methods with SHELXS-97[47] and was full-matrix least-squares refined against $F^2$ using SHELXL-97.[47] The refinement afforded a Flack parameter of 0.004(8). Anisotropic thermal parameters were used for all non-hydrogen atoms except the ethanol solvent molecules. Hydrogen atoms were calculated and treated as riding atoms with fixed thermal parameters. CCDC-602321 contains the supplementary crystallographic data for this paper. These data can be obtained free of charge from The Cambridge Crystallographic Centre via www.ccdc.cam.ac.uk/data-request/cif.

Table 2. Crystallographic data and structure refinement parameters for **3**·$2CHCl_3$·EtOH.

| | |
|---|---|
| Empirical formula | $C_{112}H_{108}Cl_6Cu_4N_4O_{25}$ |
| Formula mass [g/mol] | 2376.88 |
| Crystal size [mm] | 0.5 × 0.5 × 0.5 |
| Crystal system | orthorhombic |
| Space group | $P2_12_12_1$ |
| $a$ [Å] | 15.137(3) |
| $b$ [Å] | 26.021(5) |
| $c$ [Å] | 26.987(5) |
| $V$ [Å$^3$] | 10629(4) |
| $T$ [K] | 183(2) |
| $Z$ | 4 |
| $\rho_{calcd.}$ [g/cm$^{-1}$] | 1.485 |
| $\mu$ [mm$^{-1}$] | 1.017 |
| $\theta$ range [°] | 1.09–27.48 |
| Unique data | 24107 |
| Observed data [$I > 2\sigma(I)$] | 17801 |
| Parameters | 1362 |
| Goodness-of-fit on $F^2$ | 1.077 |
| $R_1$ for observed data | 0.0464 |
| $wR_2$ for all data | 0.1270 |

**Synthesis of Benzyl 4,6-*O*-Benzylidene-2-deoxy-2-salicylideneamino-α-D-glucopyranoside ($H_2L$) (2):** Salicylaldehyde (0.65 mL; 6.10 mmol) was added to a suspension of **1** (2.00 g, 4.33 mmol) in 60 mL methanol at room temperature. A clear yellow solution was obtained within 2 min. After stirring additional 10 min a yellow solid precipitated. The mixture was subsequently stirred for another 20 min before the precipitate was collected by filtration. The product was washed with a small amount of methanol and then dried in air. Yield: 2.40 g (93%). $C_{27}H_{27}NO_6$ (461.52): calcd. C 70.27, H 5.90, N 3.04; found C 69.12, H 6.00, N 2.70. M.p. 94–96 °C. IR (KBr): $\tilde{\nu}$ = 3447 (ν O–H), 3064, 3032 (ν C–H arom.), 2909 ($\nu_{as}$ $CH_2$), 2870 ($\nu_s$ $CH_2$), 1637 (ν CH=N), 1580, 1498 (ν C=C), 1454 (δ $CH_2$), 1374, 1351, 1316, 1282, 1211, 1151 (ν C–O), 1050 (ν C–O), 1024 (ν C–O), 984, 754, 733, 697 cm$^{-1}$. $^1H$ NMR (400 MHz, $CDCl_3$, 25 °C): $\delta$ = 3.45 (dd, $^3J_{2,1}$ = 3.7, $^3J_{2,3}$ = 9.5 Hz,

 © 2006 Wiley-VCH Verlag GmbH & Co. KGaA, Weinheim 

1 H, 2-H), 3.63 (dd, $^3J_{4,3} = {}^3J_{4,5} = 9.5$ Hz, 1 H, 4-H), 3.81 (dd, $^2J_{6a,6e} = {}^3J_{6a,5} = 10.4$ Hz, 1 H, 6a-H), 4.09 (ddd, $^3J_{5,6a} = 9.9$, $^3J_{5,6e} = 4.9$ Hz, 1 H, 5-H), 4.29–4.36 (m, 2 H, 3-H and 6e-H), 4.61 and 4.81 (2d, $^2J_{7a,7b} = 12.2$ Hz, each 1 H, 7a-H and 7b-H), 4.92 (d, $^3J_{1,2} = 3.7$ Hz, 1 H, 1-H), 5.59 (s, 1 H, 21-H), 6.89 (dt, $J_d = 1.1$, $J_t = 7.5$ Hz, 1 H, Ph), 7.01 (d, $J_d = 8.2$ Hz, 1 H, Ph), 7.26–7.41 (m, 10 H, Ph), 7.50–7.53 (m, 2 H, Ph), 9.91 (s, 1 H, 14-H), 13.50 (s, 1 H, 20-OH) ppm. $^{13}C$ NMR (100 MHz, $CDCl_3$, 25 °C): $\delta$ = 62.9 (C5), 69.0 (C3, C6), 69.8 (C7), 72.6 (C2), 81.9 (C4), 98.5 (C1), 102.2 (C21), 117.3, 118.5, 118.6, 126.36, 127.9, 128.0, 128.4, 128.5, 129.3, 131.8, 132.8, 136.9, 137.1 (all Ph), 161.6 (C20), 167.8 (C14) ppm. ESI-MS: *m/z* (%) = 484 $[(H_2L) + Na]^+$ (100).

**Synthesis of [{Cu(L)}$_4$] (3):** A solution of $[Cu(CH_3COO)_2]\cdot H_2O$ (174 mg, 0.87 mmol) in 5 mL water was added dropwise to a solution of **2** (400 mg, 0.87 mmol) in 15 mL chloroform at room temperature. Subsequently 30 mL ethanol were added under vigorous stirring. Complex **3** was obtained in form of green crystals of $[\{Cu(L)\}_4]\cdot 2CHCl_3\cdot EtOH$ suitable for X-ray measurements after 4 d. The crystals have been isolated, washed with a small amount of ethanol and dried in air affording a solvent-free material. Yield: 417 mg (92%). $C_{108}H_{100}Cu_4N_4O_{24}$ (2092.23): calcd. C 62.00, H 4.82, N 2.69; found C 61.95, H 4.79, N 2.57. Decomposition interval: 284–307 °C. IR (KBr): $\tilde{\nu}$ = 3447 (ν O–H), 3063, 3030 (ν C–H arom.), 2929 and 2910 ($\nu_{as}$ $CH_2$), 2884 and 2860 ($\nu_s$ $CH_2$), 1636 (ν CH=N), 1603 and 1533 (ν C=C), 1452 (δ $CH_2$), 1387, 1349, 1332, 1192, 1148 (ν C–O), 1119 (ν C–O), 1097 (ν C–O), 1065 (ν C–O), 1024 (ν C–O), 913, 756, 737, 699, 653 $cm^{-1}$. Raman (solid): $\tilde{\nu}$ = 3052 (ν C–H arom.), 2962, 2937 ($\nu_{as}$ $CH_2$), 2889, 2870, 2860 ($\nu_s$ $CH_2$), 1637 (ν C=N), 1603, 1535 (ν C=C), 1457, 1451 (δ $CH_2$), 1359, 1350, 1249, 1209, 1027 and 1003 (ν C–O), 808 $cm^{-1}$. UV/Vis ($CHCl_3$): $\lambda_{max}$ ($\varepsilon$) = 277 ($4.21\cdot10^4$), 370 ($2.17\cdot10^4$), 632 nm ($4.97\cdot10^2$ l $mol^{-1}$ $cm^{-1}$). ESI-MS: *m/z* (%) = 2092 $[\{Cu(L)\}_4 + H]^+$ (11); 2113 $[\{Cu(L)\}_4 + Na]^+$ (100).

## Acknowledgments

We are grateful to the Deutsche Forschungsgemeinschaft for financial support.

[1] J. F. Kennedy, C. A. White, *Bioactive Carbohydrates in Chemistry, Biochemistry and Biology*, John Wiley & Sons, New York, **1983**.
[2] R. W. Gracy, E. A. Noltmann, *J. Biol. Chem.* **1968**, *243*, 4109–4116.
[3] K. D. Hardman, R. C. Agarwal, M. J. Freiser, *J. Mol. Biol.* **1982**, *157*, 69–86.
[4] R. L. Root, J. R. Durrwachter, C.-H. Wong, *J. Am. Chem. Soc.* **1985**, *107*, 2997–2999.
[5] G. K. Farber, A. Glasfeld, G. Tiraby, D. Ringe, G. A. Petsko, *Biochemistry* **1989**, *28*, 7289–7297.
[6] J. Jenkins, J. Janin, F. Rey, M. Chiadmi, H. Van Tilbeurgh, I. Lasters, M. D. Maeyer, D. V. Belle, S. J. Wodak, M. Lauwereys, P. Stanssens, N. T. Mrabet, J. Snauwaert, G. Matthyssens, A.-M. Lambeir, *Biochemistry* **1992**, *31*, 5449–5458.
[7] Y. Zhang, J.-Y. Liang, S. Huang, H. Ke, W. N. Lipscomb, *Biochemistry* **1993**, *32*, 1844–1857.
[8] A. Lavie, K. N. Allen, G. A. Petsko, D. Ringe, *Biochemistry* **1994**, *33*, 5469–5480.
[9] K. K.-S. Ng, W. I. Weis, *Biochemistry* **1997**, *36*, 979–988.
[10] K. K.-S. Ng, S. Park-Snyder, W. I. Weis, *Biochemistry* **1998**, *37*, 17965–17976.
[11] N. Habermann, G. Jung, M. Klaassen, P. Klüfers, *Chem. Ber.* **1992**, *125*, 809–814.
[12] J. Burger, C. Gack, P. Klüfers, *Angew. Chem.* **1995**, *107*, 2950–2951; *Angew. Chem. Int. Ed. Engl.* **1995**, *34*, 2647–2649.
[13] P. Klüfers, T. Kunte, *Angew. Chem.* **2001**, *113*, 4356–4358; *Angew. Chem. Int. Ed.* **2001**, *40*, 4210–4212.
[14] P. Klüfers, T. Kunte, *Eur. J. Inorg. Chem.* **2002**, 1285–1289.
[15] P. Klüfers, O. Krotz, M. Oßberger, *Eur. J. Inorg. Chem.* **2002**, 1919–1923.
[16] S. Yano, *Coord. Chem. Rev.* **1988**, *92*, 113–156.
[17] T. Tanase, M. Nakagoshi, A. Teratani, M. Kate, Y. Yamamoto, S. Yano, *Inorg. Chem.* **1994**, *33*, 5–6.
[18] T. Tanase, T. Onaka, M. Nakagoshi, I. Kinoshita, K. Shibata, M. Doe, J. Fujii, S. Yano, *Chem. Commun.* **1997**, 2115–2116.
[19] T. Tanase, Y. Yasuda, T. Onaka, S. Yano, *J. Chem. Soc. Dalton Trans.* **1998**, 345–351.
[20] T. Tanase, T. Onaka, M. Nakagoshi, I. Kinoshita, K. Shibata, M. Doe, J. Fujii, S. Yano, *Inorg. Chem.* **1999**, *38*, 3150–3159.
[21] T. Tanase, S. Tamakoshi, M. Doi, M. Mikuriya, H. Sakurai, S. Yano, *Inorg. Chem.* **2000**, *39*, 692–704.
[22] T. Tanase, H. Inukai, T. Onaka, M. Kato, S. Yano, S. J. Lippard, *Inorg. Chem.* **2001**, *40*, 3943–3953.
[23] Y. Mikata, Y. Shinohara, K. Yoneda, Y. Nakamura, K. Esaki, M. Tanahashi, I. Brudziñska, S. Hirohara, M. Yokoyama, K. Mogami, T. Tanase, T. Kitayama, K. Takashiba, K. Nabeshima, R. Takagi, M. Takatani, T. Okamoto, I. Kinoshita, M. Doe, A. Hamazawa, M. Morita, F. Nishida, T. Sakakibara, C. Orvig, S. Yano, *J. Org. Chem.* **2001**, *66*, 3783–3789.
[24] S. Yano, Y. Mikita, *Bull. Chem. Soc. Jpn.* **2002**, *75*, 2097–2113.
[25] Y. Mikata, Y. Sugai, S. Yano, *Inorg. Chem.* **2004**, *43*, 4778–4780.
[26] T. Storr, Y. Sugai, C. A. Barta, Y. Mikata, M. J. Adam, S. Yano, C. Orvig, *Inorg. Chem.* **2005**, *44*, 2698–2705.
[27] T. Storr, M. Obata, C. L. Fisher, S. R. Bayly, D. E. Green, I. Brudziñska, Y. Mikata, B. O. Patrick, M. J. Adam, S. Yano, C. Orvig, *Chem. Eur. J.* **2005**, *11*, 195–203.
[28] Y. Mikata, Y. Sugai, M. Obata, M. Harada, S. Yano, *Inorg. Chem.* **2006**, *45*, 1543–1551.
[29] J. C. Irvine, J. C. Earl, *J. Chem. Soc.* **1922**, *121*, 2376–2381.
[30] A. K. Sah, C. P. Rao, P. K. Saarenketo, E. K. Wegelius, E. Kolehmainen, K. Rissanen, *Eur. J. Inorg. Chem.* **2001**, *11*, 2773–2781.
[31] M. E. Cucciolito, R. D. Litto, G. Roviello, F. Ruffo, *J. Mol. Catal. A* **2005**, *236*, 176–181.
[32] T. Klabunde, C. Eicken, J. C. Sacchettini, B. Krebs, *Nat. Struct. Biol.* **1998**, *5*, 1084–1090.
[33] A. Messerschmidt, A. Rossi, R. Ladenstein, R. Huber, M. Bolognesi, G. Gatti, A. Marchesini, R. Petruzzelli, A. Finazzi-Agró, *J. Mol. Biol.* **1989**, *206*, 513–529.
[34] R. Wegner, M. Gottschaldt, H. Görls, E.-G. Jäger, D. Klemm, *Angew. Chem.* **2000**, *112*, 608–612; *Angew. Chem. Int. Ed.* **2000**, *39*, 595–599.
[35] A. Fragoso, M. L. Kahn, A. Castineiras, J.-P. Sutter, O. Kahn, R. Cao, *Chem. Commun.* **2000**, 1547–1548.
[36] A. K. Sah, C. P. Rao, P. K. Saarenketo, K. Rissanen, G. A. Van Albada, J. Reedijk, *Chem. Lett.* **2002**, 348–349.
[37] A. K. Sah, M. Kato, T. Tanase, *Chem. Commun.* **2005**, 675–677.
[38] A. K. Sah, T. Tanase, M. Mikuriya, *Inorg. Chem.* **2006**, *45*, 2083–2092.
[39] P. H. Gross, R. W. Jeanloz, *J. Org. Chem.* **1967**, *32*, 2759–2763.
[40] Z. Györgydeák, *Liebigs Ann. Chem.* **1991**, 1291–1300.
[41] J. Zhao, X. Zhou, A. M. Santos, E. Herdtweck, C. C. Romão, F. E. Kühn, *Dalton Trans.* **2003**, 3736–3742.
[42] C. J. Matthews, K. Avery, Z. Xu, L. K. Thompson, L. Zhao, D. O. Miller, K. Biradha, K. Poirier, M. J. Zaworotko, C. Wilson, A. E. Goeta, J. A. K. Howard, *Inorg. Chem.* **1999**, *38*, 5266–5276.
[43] O. Kahn, in: *Molecular Magnetism*, VCH, Weinheim, **1993**.
[44] F. Tuna, L. Patron, Y. Journaux, M. Andruh, W. Plass, J.-C. Trombe, *J. Chem. Soc. Dalton Trans.* **1999**, 539–545.

 © 2006 Wiley-VCH Verlag GmbH & Co. KGaA, Weinheim 

[45] L. Merz, W. Haase, *J. Chem. Soc. Dalton Trans.* **1978**, 1594–1598.
[46] E. Ruiz, C. De Graaf, P. Alemany, S. Alvarez, *J. Phys. Chem. A* **2002**, *106*, 4938–4941.
[47] G. Sheldrick, *SHELXS* and *SHELXL*, University of Göttingen, **1997**.

Received: May 3, 2006
Published Online: July 27, 2006

 © 2006 Wiley-VCH Verlag GmbH & Co. KGaA, Weinheim 

DOI: 10.1002/ejic.200600417

# Designed Assembly and Structures and Photoluminescence of a New Class of Discrete $Zn^{II}$ Complexes of 1*H*-1,10-Phenanthroline-2-one

**Jie-Peng Zhang,[a] Yan-Yong Lin,[a] Xiao-Chun Huang,[a] and Xiao-Ming Chen*[a]**

**Keywords:** Zinc / Cluster compounds / Metallacycles / Photoluminescence / Solvothermal synthesis

The hydrothermal reaction of 1*H*-1,10-phenanthroline-2-one (Hophen), zinc acetate, benzoic acid (Hba), and triethylamine (3.0 mL) yields the tetranuclear complex $[Zn_4(\mu_3\text{-}OH)_2(ophen)_4(ba)_2]$ (**2**), which features a chair-like $Zn_4(\mu_3\text{-}OH)_2$ cluster with two ba ligands centrosymmetrically oriented. $[(OAc)\{Zn_3(\mu_3\text{-}OH)(ophen)_3\}(ox)\{Zn_3(\mu_3\text{-}OH)(ophen)_3\}(OAc)]$ (**3**; ox = oxalate) was isolated when less triethylamine (1.0 mL) was used. Two $Zn_3(\mu_3\text{-}OH)(ophen)_3$ clusters in **3** are linked together by an oxalate to form a dumbbell-like structure in which the acetate and oxalate ligands point outward from the $Zn_3(\mu_3\text{-}OH)(ophen)_3$ cluster with an acute bending angle. A geometric analysis reveals that $Zn_3(\mu_3\text{-}OH)(ophen)_3$ and dicarboxylate with an obtuse bending angle cannot form an infinite zigzag chain, whereas the ring isomer can. With isophthalate (ipa), thiophene-2,5-dicarboxylate (tda), and 4,4′-oxybis(benzoate) (oba) instead of the acetate of **3** three new complexes, namely $[\{Zn_3(\mu_3\text{-}OH)(ophen)_3\}(ipa)_2\{Zn_3(\mu_3\text{-}OH)(ophen)_3\}]\cdot 0.5H_2O$ (**4**), $[\{Zn_3(\mu_3\text{-}OH)(ophen)_3\}(tda)_2\{Zn_3(\mu_3\text{-}OH)(ophen)_3\}]$ (**5**), and $[\{Zn_3(\mu_3\text{-}OH)(ophen)_3\}(oba)_2\{Zn_3(\mu_3\text{-}OH)(ophen)_3\}]$ (**6**), were obtained in which two $Zn_3(\mu_3\text{-}OH)(ophen)_3$ clusters are linked by a pair of ipa, tda, or oba ligands to form isostructural, cluster-based 2:2 metallomacrocycles. Photoluminescence studies of **2**–**6** revealed that their luminescent properties are derived from ophen-based $\pi\text{-}\pi^*$ excited states.

(© Wiley-VCH Verlag GmbH & Co. KGaA, 69451 Weinheim, Germany, 2006)

## Introduction

The rational design of supramolecular metal–organic compounds has received considerable attention. Due to the lack of control over the self-assembly of individual metal ions or ligands, chemists have introduced metal clusters as molecular building blocks as they offer greater structural rigidity and predictable coordination geometries.[1] This strategy has been successfully combined with net-based or reticular approaches to assemble many pre-designed cluster-based coordination polymers,[2] and has recently been extended to discrete metal–organic polyhedra.[3] Discrete metal–organic polygons and polyhedra have been widely studied[4] and continue to be one of the most interesting research topics.[3,5–9] Generally, the vertices or the edges of these polygons and polyhedra are occupied by single metal ions such as *cis*-protected $Pt^{II}$ and $Pd^{II}$,[4–7] while reported cluster-based polygons or polyhedra are rare.[3,8,9] Systematic studies of cluster-based polygons have mainly been concerned with *cis*-protected $Mo_2^{4+}$ and $Rh_2^{4+}$ dimetal units.[8] It should be noted that common metal clusters can possess more than two leaving groups, for example there are six substitutable acetates in $[Zn_4O(OAc)_6]$, whereas a polygon requires uniquely two-connected building blocks. Therefore, known cluster-based metal–organic polygons are extremely rare, especially for trinuclear or larger metal clusters. In this context, the key strategy for the rational construction of cluster-based polygons is to select metal clusters with only two substitutable monotopic ligands.

Another problem in the controlled assembly of metal–organic polygons comes from the phenomenon of supramolecular isomerism. Both polygons and infinite zigzag chains as possible extended superstructures can be obtained for a given set of two-connected angular and/or linear molecular building blocks.[10] The kinetically favored infinite framework structures are usually the dominant species for highly insoluble metal–organic systems, especially those neutral ones such as metal polyazolates/polycarboxylates. Therefore, the reaction conditions should also be controlled to avoid the formation of infinite chain isomers.

Recently, we discovered a novel chelating/bridging ligand, namely 1*H*-1,10-phenanthroline-2-one (Hophen), which tends to form polynuclear metal clusters such as $[Cu_2(ophen)_2]$,[11] $[Cd_3(ophen)_5Cl]$, and $[Zn_4(\mu_4\text{-}O)(ophen)_4(OAc)_2]$ (**1**).[12] Obviously, the two acetate ligands located on two opposite sides of the centrosymmetric cluster of **1** might be substituted by angular dicarboxylates to form infinite chains or finite rings. Unfortunately, our preliminary trials of substituting the acetates in **1** by dicarbox-

[a] MOE Laboratory of Bioinorganic and Synthetic Chemistry/State Key Laboratory of Photoelectronic Materials and Technologies, School of Chemistry and Chemical Engineering, Sun Yat-Sen University,
Guangzhou 510275, China
Fax: +86-20-8411-2245
E-mail: cxm@mail.sysu.edu.cn

Supporting information for this article is available on the WWW under http://www.eurjic.org or from the author.

 © 2006 Wiley-VCH Verlag GmbH & Co. KGaA, Weinheim 

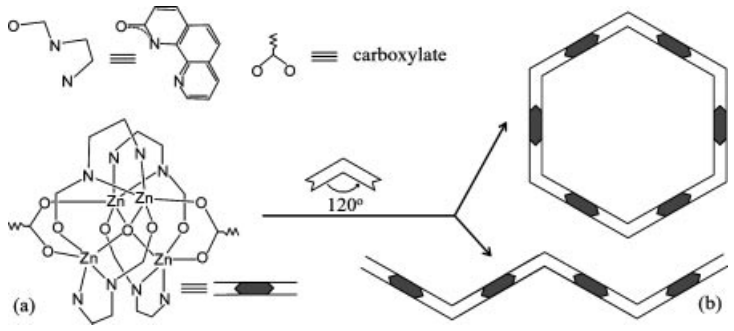


Scheme 1. Simplification of **1** as a linear two-connected building block (a) and two typical supramolecular isomers formed by using a bent dicarboxylate to substitute the two acetates of **1** (b).

ylates failed. From a geometrical point of view, centrosymmetric $Zn_4(\mu_4\text{-}O)(ophen)_4$ is a linear two-connector since the two acetates are located on two opposite sides of the $Zn_4(\mu_4\text{-}O)$ core. When a common rigid angular dicarboxylate such as isophthalate is used, the hypothetical cluster-based hexagonal ring of $Zn_4(\mu_4\text{-}O)(ophen)_4$ should be expected. Similar to the approaches for copper(I) imidazolate rings,[6a] the inner cavity of this hexagon is too large for common templates. Although we can use dicarboxylates with smaller bending angles (much smaller than 120°) to reduce the difficulty, such rigid angular dicarboxylates are not readily available. Alternatively, we can also shift our attention to reducing the bending angle by modifying the $Zn^{II}$ cluster.

Since acidity can play an important role in controlling the degree of aggregation and the structure of oxo/hydroxo-bridged $Zn^{II}$ clusters, we anticipated being able to synthesize new $Zn^{II}$ clusters by varying the reaction conditions, especially the pH. Simple carboxylates like acetate and benzoate were used as the potential leaving groups. Herein, we report our step-by-step approach toward the rational design and synthesis of a new series of cluster-based metallacycles (Scheme 1).

## Results and Discussion

### Synthesis and Structure

We first obtained the discrete, tetranuclear cluster $[Zn_4(\mu_3\text{-}OH)_2(ophen)_4(ba)_2]$ (**2**; ba = benzoate) using triethylamine (3.0 mL) as base, while the oxo-bridged **1** was synthesized by using the very strong base $NaOCH_3$. The four $Zn^{II}$ ions of **2** are bridged by two $\mu_3$-$OH^-$ groups [Zn–O1 1.932(2)–2.018(2) Å] to form a centrosymmetric, chair-like $Zn_4(\mu_3\text{-}OH)_2$ core. The $Zn^{II}$ ions are also chelated by the bipyridyl fragments of ophen ligands [Zn–N 2.028(2)–2.127(2) Å] (Figure 1). The ketone oxygen atoms of the ophen ligands further bridge the $Zn_4(\mu_3\text{-}OH)_2$ core either by coordinating to $Zn^{II}$ ions [Zn1–O3 2.018(2) Å] or by hydrogen bonding to the hydroxo groups (O1···O2 2.562(2) Å, O1–H···O2 166(3)°]. The outer $Zn^{II}$ ions are further coordinated by ba ligands in a chelating mode [Zn2–O4 2.247(2), Zn2–O5 2.088(2) Å]. According to the above discussion, **2** is not a good candidate for the construction of cluster-based metallacycles as the ba ligands are oriented centrosymmetrically, as in **1**.

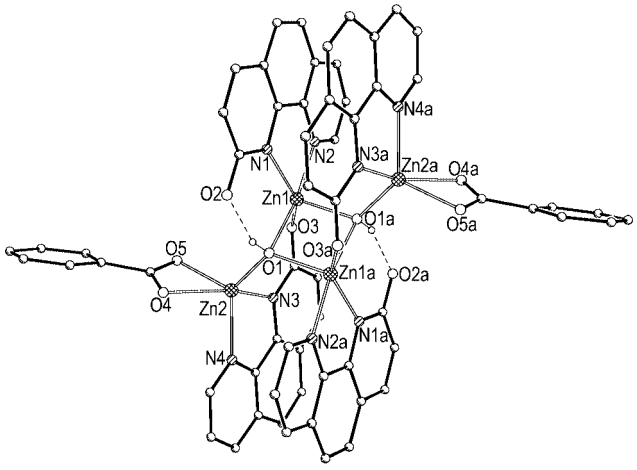


Figure 1. Perspective view of the molecular structure of **2** (a: $-x$, $1-y$, $-z$).

The chair-like $Zn_4(\mu_3\text{-}OH)_2$ cluster is composed of two edge-sharing triangular $Zn_3(\mu_3\text{-}OH)$ clusters. One may expect that changing the pH value would either prevent or promote the expansion of the $Zn_3(\mu_3\text{-}OH)$ cluster, and consequently modify the size and symmetry of the $Zn^{II}$ cluster. For example, $Zn_4(\mu_4\text{-}O)$ or $Zn_5(\mu_3\text{-}OH)_2$ might be generated at higher pH, while $Zn_3(\mu_3\text{-}OH)$ might be generated at lower pH. When the experiments were carried out using less triethylamine (1.0 mL), we managed to isolate several new complexes with the expected $Zn_3(\mu_3\text{-}OH)(ophen)_3$ clusters. A discrete, hexanuclear complex $[(OAc)\{Zn_3(\mu_3\text{-}OH)(ophen)_3\}(ox)\{Zn_3(\mu_3\text{-}OH)(ophen)_3\}(OAc)]$ (**3**; ox = oxalate) was isolated in 20% yield by the solvothermal reaction of $Zn(OAc)_2$, Hophen, triethylamine, and benzoic acid in water. We subsequently found that **3** could also be synthesized in a higher yield (40%) in the absence of benzoic acid. The $Zn_3(\mu_3\text{-}OH)$ cluster in **3** [Zn–O1 1.983(2)–2.037(2) Å] replicates part of the $Zn_4(\mu_3\text{-}OH)_2$ core in **2**. Each of the three $Zn^{II}$ ions is also chelated by a corresponding ophen ligand through its bipyridyl fragment [Zn–N 2.062(2)–2.193(2) Å]. Each ketone oxygen atom of the ophen ligands further ligates another $Zn^{II}$ ion [Zn–O 1.962(2)–2.125(2) Å]. An acetate ligand coordinates to the outer sphere of $Zn_3(\mu_3\text{-}OH)(ophen)_3$ by ligation to the $Zn^{II}$

 © 2006 Wiley-VCH Verlag GmbH & Co. KGaA, Weinheim 

ion [Zn–O 2.053(2) Å] and hydrogen bonding to the hydroxy ion (O1···O8 2.594(3) Å, O1–H···O8 170(3)°]. Finally, two $\{Zn_3(\mu_3\text{-OH})(phen)_3\}(OAc)$ moieties are linked by a bis-chelating, *exo*-tetradentate oxalate ligand [Zn–O 2.011(2)–2.169(2) Å]. This unexpected oxalate ligand must be derived from an acetate since no oxalic acid or oxalate was added. An oxalate ligand can be generated by oxidation of ethanol or oxidative coupling of methanol under solvothermal conditions using nitrate as the oxidant.[13] It has also been reported that oxalate can be generated by the decarboxylative coupling of isonicotinates under solvothermal conditions.[14] Since no obvious oxidant was added in our experiment, we believe that the oxalate in **3** might be derived from the decarboxylative coupling of an acetate (Figure 2).

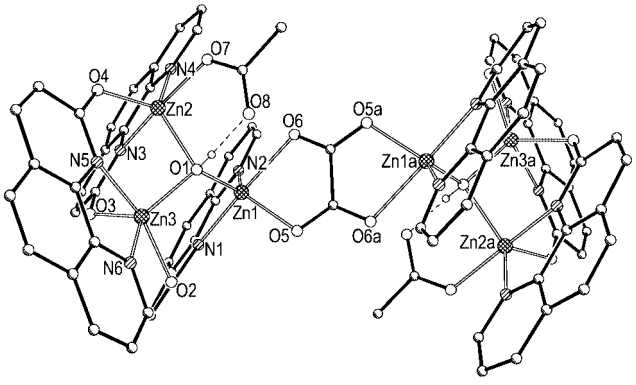


Figure 2. Perspective view of the molecular structure of **3** (a: $-x$, $-y$, $1 - z$).

Two carboxylate vectors ($OAc^-$ and $ox^{2-}$) in **3** point outward from $Zn_3(\mu_3\text{-OH})(phen)_3$ with a bending angle of around 30° (or turning angle of around 150°). Therefore, we can construct a 2:2 cluster-based metallacycle by substituting the carboxylates by dicarboxylates with a bending angle of about 150° (or turning angle of about 30°). Interestingly, these two types of two-connected molecular building blocks, which individually contain an acute or an obtuse bending angle, cannot be self-assembled into an infinite zigzag chain, as illustrated in Scheme 1. Geometrically, this phenomenon can be explained by considering the geometric criteria for these isomers. For the ring isomers, the overall turning angle is equal to $360° = n(x + y)$ ($x \geq 0$, $y \geq 0$, $x \neq y$, $n \geq 2$), whereas for the zigzag chain isomers the overall turning angle is equal to $0° \neq n(x - y)$ ($x \geq 0$, $y \geq 0$, $x \neq y$, $n \geq 2$), where $x$ and $y$ are the turning angles of the molecular building blocks and $n$ is the number of repeat units. In other words, a finite ring-like structure would be much more easily obtained in such a self-assembly system because it does not contain infinite zigzag chain isomers (Scheme 2).

We therefore used isophthalate (ipa), thiophene-2,5-dicarboxylate (tda), and 4,4′-oxybis(benzoate) (oba) as the obtuse dicarboxylates to replace the acetate and oxalate. Three new, isostructural, centrosymmetric, cluster-based metallacycles, namely $[\{Zn_3(\mu_3\text{-OH})(phen)_3\}(ipa)_2\{Zn_3(\mu_3\text{-OH})(phen)_3\}]\cdot 0.5H_2O$ (**4**), $[\{Zn_3(\mu_3\text{-OH})(phen)_3\}(tda)_2\{Zn_3(\mu_3\text{-OH})(phen)_3\}]$ (**5**), and $[\{Zn_3(\mu_3\text{-OH})(phen)_3\}(oba)_2\{Zn_3(\mu_3\text{-OH})(phen)_3\}]$ (**6**), were obtained in high yields under solvothermal conditions similar to that of **3**. It should be noted that no zigzag chain isomer or other crystalline product was isolated in these experiments (Figure 3).

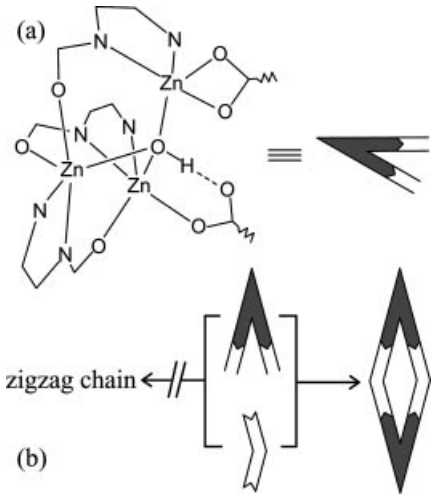


Scheme 2. Simplification of the $Zn_3(\mu_3\text{-OH})(phen)_3$ cluster as an angular building block (a) and possible extended structures for combining two different types of angular building blocks (b).

The $Zn_3(\mu_3\text{-OH})(phen)_3$ clusters in **4**–**6** are isostructural to that of **3** with similar structural parameters [Zn–OH 1.950(1)–2.059(1), Zn–N 2.022(2)–2.177(2), $Zn–O_{ophen}$ 1.968(2)–2.196(2) Å], while the acetate and oxalate ligands in **3** are now replaced by dicarboxylate ligands. The coordination/hydrogen-bonding mode of the carboxylate group of the acetate in **3** is retained in **4**–**6** [Zn2–O7a 2.042(2)–2.056(2), O1···O8a 2.613(2)–2.668(3) Å; O1–H···O8a 160(3)–168(3)°]. The stable five-membered chelating mode of the oxalate in **3** is not available for ipa, tda, or oba, and is replaced by four-membered chelating carboxylate groups in **4**–**6**. Two Zn–O bond lengths of the chelating carboxylate groups in **4**–**6** show remarkable structure-related differences. Two carboxylate groups in an ipa moiety are oriented with a bending angle of about 120°, which is significantly smaller than the required angle of 150°. This structural deviation is compensated for by distorting the very energetically stable, ideal chelating carboxylate to a quasi-monodentate one [Zn1–O5 1.946(2), Zn1–O6 2.560(2) Å]. On the other hand, two carboxylate groups in tda are oriented with a bending angle of about 140°, and the difference in the Zn–O bond lengths in **5** [Zn1–O5 2.039(2), Zn1–O6 2.283(2) Å] is much smaller than that in **4**. A short intramolecular S···S contact [3.461(2) Å] is also found in **5**. Furthermore, the bending angle of oba (ca. 130°) and the difference in Zn–O bond lengths in **6** [Zn1–O5 2.002(2), Zn1–O6 2.366(2) Å] lies between those of ipa and tba.

Two $Zn_3(\mu_3\text{-OH})(phen)_3$ clusters are linked by different dicarboxylates to give nanosized supermolecules. According to the lengths of the dicarboxylates, the sizes of **3**–**6** vary from 1.76 to 2.15, 2.20, and 2.72 nm, respectively. Similar to **1**, intermolecular, head-to-tail π-π stacking interactions are the major supramolecular interactions between the dis-

 © 2006 Wiley-VCH Verlag GmbH & Co. KGaA, Weinheim 

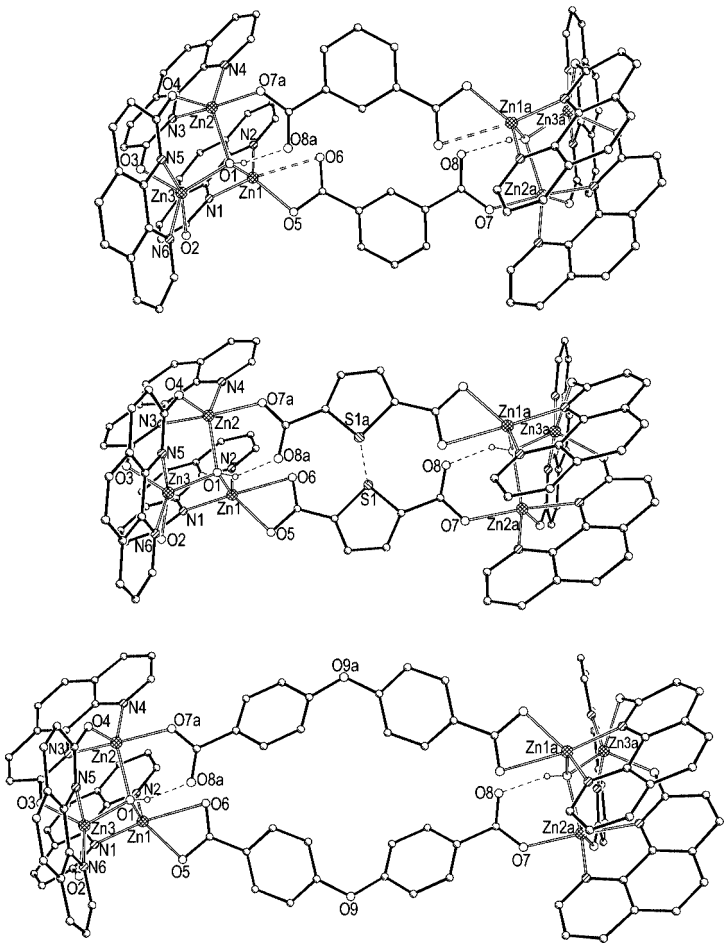


Figure 3. Perspective view of the molecular structures of **4** (a: $-x$, $-y$, $1-z$), **5** (a: $1-x$, $-y$, $1-z$), and **6** (a: $-x$, $-y$, $-z$).

crete molecules in **2**–**6**. Significant intramolecular, head-to-head π-π stacking interactions are also found in **1**–**6**. Although **2**–**6** are discrete, neutral molecules, they are barely soluble in common solvents. This interesting phenomenon has also been observed in other solvothermally synthesized discrete complexes and may be partially ascribed to the significant three-dimensional packing of the molecules (see Supporting Information).

## Photoluminescence

Compounds **2**–**6** display bright blue to green photoluminescence upon UV irradiation. The photoluminescence parameters of **2**–**6** are summarized in Table 1 and the emission and excitation spectra of **2**–**6** are shown in Figure 4. The solid-state photoluminescent properties of **2**–**6** are very similar to those of **1**,[12] thus implying that the carboxylate ligands may not influence the nature or energy of the luminescence-related electronic ground state or excited state. The carboxylate ligands in **1**–**6** have much smaller π-conju-

Table 1. Photoluminescence properties of **2**–**6**.

| | Excitation [nm] | Emission [nm] | Lifetime [ns] |
|---|---|---|---|
| **2** | 383 sh, 402 sh, 418 | 487 | 3.43(5) |
| **3** | 375, 404 sh | 464 | 3.58(4) |
| **4** | 383, 402 sh, 409 sh | 468 | 6.97(1) |
| **5** | 383, 401 sh, 413 | 469 | 7.70(2) |
| **6** | 376, 393 sh, 406 | 477 | 7.57(4) |

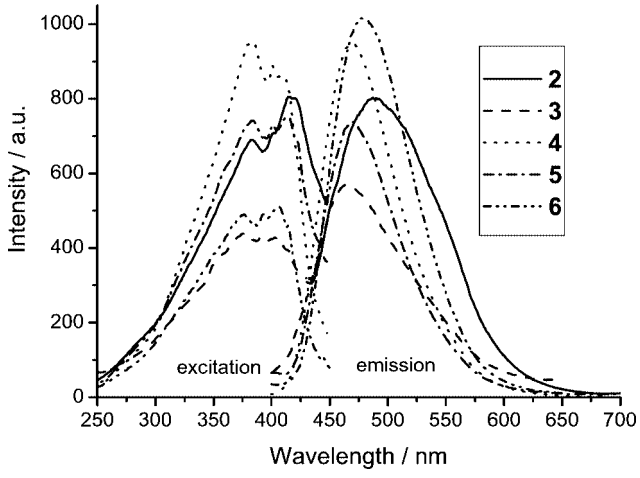


Figure 4. Photoluminescence spectra of **2**–**6**.

 © 2006 Wiley-VCH Verlag GmbH & Co. KGaA, Weinheim 

gated systems than that of the ophen ligand, therefore the lowest lying HOMO–LUMOs should be mainly localized on the ophen ligand, which results in an ophen-based π-π* excitation mechanism. Compared with that of oxo-bridged **1** (15 ns), the shorter luminescence lifetime of **2**–**6** (3.4–7.7 ns) may be attributed to the quenching effect of the OH stretch.

## Conclusions

Based on geometrical considerations and a strategy of controlling the reaction condition, we have successfully synthesized a new series of cluster-based metallacycles. Our results demonstrate that the degree of aggregation of the hydroxy- or oxo-bridged Zn–ophen cluster can be simply controlled by varying the reaction conditions, generating $[Zn_4(\mu_4\text{-}O)(ophen)_4]^{2+}$, $[Zn_4(\mu_3\text{-}OH)_2(ophen)_4]^{2+}$, or $[Zn_3(\mu_3\text{-}OH)(ophen)_3]^{2+}$ from very high (NaOMe) to relatively low basicity (triethylamine). Although the above Zn clusters are potential candidates for the construction of cluster-based metallacycles, we have demonstrated that $[Zn_3(\mu_3\text{-}OH)(ophen)_3]^{2+}$, which binds two carboxylate groups in an acute angle, can easily form 2:2 metallacycles with different dicarboxylate ligands with obtuse bending angles. The self-assembly principle has been rationalized in the context of supramolecular isomerism, in which the infinite zigzag chain isomer is excluded by the geometrical requirements of the molecular building blocks. Owing to its tendency to form metal clusters, ophen may be an excellent ligand for paramagnetic transition metal ions to form metal clusters of significance in molecular magnetism.

## Experimental Section

**General Remarks:** Commercially available reagents were used as received without further purification. Hophen was prepared by our previously reported method.[12] IR spectra were obtained from KBr pellets on a Bruker EQUINOX 55 FT IR spectrometer in the 400–4000 $cm^{-1}$ region. Elemental analyses (C, H, N) were performed with a Perkin–Elmer 240 elemental analyzer. The steady-state fluorescent and fluorescence lifetimes were determined with an Edinburgh Instrument FLS920 fluorescence spectrophotometer. Single-crystal samples were used in photoluminescence analyses.

**Synthesis of $[Zn_4(\mu_3\text{-}OH)_2(ophen)_4(ba)_2]$ (2):** Reaction of a mixture of $Zn(OAc)_2{\cdot}2H_2O$ (0.220 g, 1.0 mmol), Hophen (0.196 g, 1.0 mmol), benzoic acid (0.060 g, 0.5 mmol), triethylamine (3.0 mL), and water (10.0 mL) in a 23-mL Teflon-lined bomb at 160 °C for 80 h afforded yellow, block-like crystals (yield: 0.20 g, 60%). $C_{62}H_{40}N_8O_{10}Zn_4$ (1318.6): calcd. C 56.47, H 3.06, N 8.50; found C 56.34, H 3.09, N 8.39. IR: $\tilde{\nu}$ = 3059 $cm^{-1}$ w, 1624 s, 1593 s, 1560 s, 1534 s, 1483 s, 1391 s, 1313 w, 1136 m, 845 s, 723 m, 657 m, 473 w.

**Synthesis of $[(OAc)\{Zn_3(\mu_3\text{-}OH)(ophen)_3\}(ox)\{Zn_3(\mu_3\text{-}OH)(ophen)_3\}(OAc)]$ (3):** Reaction of a mixture of $Zn(OAc)_2{\cdot}2H_2O$ (0.220 g, 1.0 mmol), Hophen (0.196 g, 1.0 mmol), triethylamine (1.0 mL), and water (10.0 mL) in a 23-mL Teflon-lined bomb at 160 °C for 80 h afforded yellow, block-like crystals (yield: 0.12 g, 40%). $C_{76}H_{44}N_{12}O_{16}Zn_6$ (1773.6): calcd. C 51.47, H 2.50, N 9.48; found C 51.36, H 2.54, N 9.40. IR: $\tilde{\nu}$ = 3409 $cm^{-1}$ w, 3057 w, 2921 w, 1652 s, 1624 s, 1560 s, 1526 s, 1481 s, 1389 s, 1309 m, 1138 m, 943 w, 846 s, 734 m, 659 m, 496 m.

**Synthesis of $[\{Zn_3(\mu_3\text{-}OH)(ophen)_3\}(ipa)_2\{Zn_3(\mu_3\text{-}OH)(ophen)_3\}]{\cdot}0.5H_2O$ (4):** Reaction of a mixture of $Zn(OAc)_2{\cdot}2H_2O$ (0.220 g, 1.0 mmol), Hophen (0.196 g, 1.0 mmol), isophthalic acid (0.041 g, 0.25 mmol), triethylamine (1.0 mL), and water (10.0 mL) in a 23-mL Teflon-lined bomb at 160 °C for 80 h afforded yellow, block-like crystals (yield: 0.19 g, 80%). $C_{88}H_{53}N_{12}O_{16.5}Zn_6$ (1934.8): calcd. C 54.63, H 2.76, N 8.69; found C 54.67, H 2.68, N 8.72. IR: $\tilde{\nu}$ = 3411 $cm^{-1}$ w, 3057 w, 1624 s, 1561 s, 1528 s, 11484 s, 1388 s, 1307 w, 1140 w, 944 w, 846 s, 737 m, 657 m, 496 w.

**Synthesis of $[\{Zn_3(\mu_3\text{-}OH)(ophen)_3\}(tda)_2\{Zn_3(\mu_3\text{-}OH)(ophen)_3\}]$ (5):** Reaction of a mixture of $Zn(OAc)_2{\cdot}2H_2O$ (0.220 g, 1.0 mmol), Hophen (0.196 g, 1.0 mmol), thiophene-2,5-dicarboxylic acid (0.043 g, 0.25 mmol), triethylamine (1.0 mL), and water (10.0 mL) in a 23-mL Teflon-lined bomb at 160 °C for 80 h afforded yellow, block-like crystals (yield: 0.16 g, 65%). $C_{84}H_{48}N_{12}O_{16}S_2Zn_6$ (1937.8): calcd. C 52.06, H 2.50, N 8.67, S 3.31; found C 52.17, H 2.51, N 8.59; S 3.18. IR: $\tilde{\nu}$ = 3421 $cm^{-1}$ w, 3059 w, 1624 s, 1563 s, 1526 s, 1482 s, 1391 s, 1141 w, 943 w, 846 s, 735 m, 656 w, 498 w.

**Synthesis of $[\{Zn_3(\mu_3\text{-}OH)(ophen)_3\}(oba)_2\{Zn_3(\mu_3\text{-}OH)(ophen)_3\}]$ (6):** Reaction of a mixture of $Zn(OAc)_2{\cdot}2H_2O$ (0.220 g, 1.0 mmol),

Table 2. Crystallographic data and structure refinement for **2**–**6**.

| Compound | **2** | **3** | **4** | **5** | **6** |
|---|---|---|---|---|---|
| Formula | $C_{62}H_{40}N_8O_{10}Zn_4$ | $C_{76}H_{44}N_{12}O_{16}Zn_6$ | $C_{88}H_{53}N_{12}O_{16.5}Zn_6$ | $C_{84}H_{48}N_{12}O_{16}S_2Zn_6$ | $C_{100}H_{60}N_{12}O_{18}Zn_6$ |
| Formula weight | 1318.50 | 1803.52 | 1934.64 | 1937.68 | 2109.82 |
| Space group | $P2_1/c$ (no. 14) | $P\bar{1}$ (no. 2) | $P\bar{1}$ (no. 2) | $P\bar{1}$ (no. 2) | $P\bar{1}$ (no. 2) |
| $a$ [Å] | 10.3041(6) | 10.5382(6) | 10.4276(5) | 10.4076(5) | 11.1842(5) |
| $b$ [Å] | 13.5436(8) | 10.8562(6) | 10.8019(6) | 10.6861(5) | 14.1429(6) |
| $c$ [Å] | 18.8727(11) | 17.2856(10) | 20.1650(10) | 18.5376(9) | 15.7344(8) |
| $\alpha$ [°] | 90 | 81.156(1) | 91.529(1) | 98.675(1) | 64.734(2) |
| $\beta$ [°] | 104.884(1) | 76.051(1) | 104.170(1) | 96.148(1) | 87.895(2) |
| $\gamma$ [°] | 90 | 61.021(1) | 118.809(1) | 116.608(1) | 73.613(2) |
| $V$ [Å$^3$] | 2545.4(3) | 1677.35(16) | 1901.49(17) | 1786.32(15) | 2149.23(17) |
| $Z$ | 2 | 1 | 1 | 1 | 1 |
| $D_c$ [g cm$^{-3}$] | 1.720 | 1.785 | 1.689 | 1.801 | 1.630 |
| $\mu$ [mm$^{-1}$] | 1.938 | 2.197 | 1.945 | 2.126 | 1.729 |
| Final $R$ indices[a] | $R_1$ = 0.0492 | $R_1$ = 0.0499 | $R_1$ = 0.0346 | $R_1$ = 0.0450 | $R_1$ = 0.0395 |
| All data[a] | $wR_2$ = 0.0917 | $wR_2$ = 0.0938 | $wR_2$ = 0.0795 | $wR_2$ = 0.0955 | $wR_2$ = 0.0938 |
| GooF | 1.039 | 1.002 | 1.046 | 1.033 | 1.028 |

[a] $R_1 = \Sigma||F_o| - |F_c||/\Sigma|F_o|$; $wR_2 = [\Sigma w(F_o^2 - F_c^2)^2/\Sigma w(F_o^2)^2]^{1/2}$.

 © 2006 Wiley-VCH Verlag GmbH & Co. KGaA, Weinheim 

Hophen (0.196 g, 1.0 mmol), 4,4′-oxybis(benzoic acid) (0.060 g, 0.25 mmol), triethylamine (1.0 mL), and water (10.0 mL) in a 23-mL Teflon-lined bomb at 160 °C for 80 h afforded yellow, block-like crystals (yield 0.18 g, 70%). $C_{100}H_{60}N_{12}O_{18}Zn_6$ (2110.0): calcd. C 56.92, H 2.87, N 7.97; found C 56.87, H 2.95, N 7.83. IR: $\tilde{\nu}$ = 3418 $cm^{-1}$ w, 3051 w, 1625 s, 1595 s, 1559 s, 1534 s, 1484 s, 1390 s, 1243 s, 1161 m, 849 s, 781 m, 734 m, 704 m, 661 m, 496 w.

**X-ray Crystallographic Study:** Diffraction intensities were collected at 293(2) K on a Bruker Smart APEX CCD area-detector diffractometer (Mo-$K_\alpha$, $\lambda$ = 0.71073 Å). Absorption corrections were applied by using the multi-scan program SADABS.[15] The structures were solved by direct methods and refined with a full-matrix least-squares technique with the SHELXTL program package.[16] Anisotropic thermal parameters were applied to all non-hydrogen atoms. The organic hydrogen atoms were generated geometrically (C–H: 0.96 Å); hydroxy hydrogen atoms were located from difference maps and refined with isotropic temperature factors. Crystal data as well as details of data collection and refinements for the complexes are summarized in Table 2.

CCDC-291301 to -291305 (for **2**–**6**) contain the supplementary crystallographic data for this paper. These data can be obtained free of charge from The Cambridge Crystallographic Data Centre via www.ccdc.cam.ac.uk/data_request/cif.

## Acknowledgments

This work was supported by the Guangdong Provincial Science and Technology Bureau and the National Natural Science Foundation of China (grant no. 20131020).

[1] M. Eddaoudi, D. B. Moler, H.-L. Li, B.-L. Chen, T. M. Reineke, M. O'Keeffe, O. M. Yaghi, *Acc. Chem. Res.* **2001**, *34*, 319–330.

[2] a) R. Robson, *J. Chem. Soc., Dalton Trans.* **2000**, 3735–3744; b) O. M. Yaghi, M. O'Keeffe, N. W. Ockwig, H. K. Chae, M. Eddaoudi, J. Kim, *Nature* **2003**, *423*, 705–714.

[3] a) M. Eddaoudi, J. Kim, J. B. Wachter, H. K. Chae, M. O'Keeffe, O. M. Yaghi, *J. Am. Chem. Soc.* **2001**, *123*, 4368–4369; b) J.-P. Lang, Q.-F. Xu, Z.-N. Chen, B. F. Abrahams, *J. Am. Chem. Soc.* **2003**, *125*, 12682–12683; c) A. C. Sudik, A. R. Millward, N. W. Ockwig, A. P. Côté, J. Kim, O. M. Yaghi, *J. Am. Chem. Soc.* **2005**, *127*, 7110–7118; d) Z. Ni, A. Yassar, T. Antoun, O. M. Yaghi, *J. Am. Chem. Soc.* **2005**, *127*, 12752–12753.

[4] a) M. Fujita, *Chem. Soc. Rev.* **1998**, *27*, 417–425; b) S. Leininger, B. Olenyuk, P. J. Stang, *Chem. Rev.* **2000**, *100*, 853–908.

[5] a) H. Abourahma, B. Moulton, V. Kravtsov, M. J. Zaworotko, *J. Am. Chem. Soc.* **2002**, *124*, 9990–9991; b) G.-F. Liu, B.-H. Ye, Y.-H. Ling, X.-M. Chen, *Chem. Commun.* **2002**, 1442–1443.

[6] a) X.-C. Huang, J.-P. Zhang, X.-M. Chen, *J. Am. Chem. Soc.* **2004**, *126*, 13218–13219; b) J.-P. Zhang, Y.-Y. Lin, X.-C. Huang, X.-M. Chen, *Chem. Commun.* **2005**, 1258–1260; c) X.-C. Huang, J.-P. Zhang, Y.-Y. Lin, X.-M. Chen, *Chem. Commun.* **2005**, 2232–2233.

[7] a) M.-C. Hong, Y.-J. Zhao, W.-P. Su, R. Cao, M. Fujita, Z.-Y. Zhou, A. S.-C. Chan, *J. Am. Chem. Soc.* **2000**, *122*, 4819–4920; b) M. Tominaga, K. Suzuki, M. Kawano, T. Kusukawa, T. Ozeki, S. Sakamoto, K. Yamaguchi, M. Fujita, *Angew. Chem. Int. Ed.* **2004**, *43*, 5621–5625; c) K.-W. Chi, C. Addicott, A. M. Arif, P. J. Stang, *J. Am. Chem. Soc.* **2004**, *126*, 16569–16574.

[8] F. A. Cotton, C. Lin, C. A. Murillo, *Acc. Chem. Res.* **2001**, *34*, 759–771.

[9] a) Y. Li, Z.-Y. Lin, W.-T. Wong, *Eur. J. Inorg. Chem.* **2001**, 3163–3173; b) R.-H. Wang, M.-C. Hong, J.-H. Luo, R. Cao, J.-B. Weng, *Eur. J. Inorg. Chem.* **2002**, 3097–3100.

[10] B. Moulton, M. J. Zaworotko, *Chem. Rev.* **2001**, *101*, 1629–1659.

[11] X.-M. Zhang, M.-L. Tong, M.-L. Gong, H.-K. Lee, L. Luo, K.-F. Li, Y.-X. Tong, X.-M. Chen, *Chem. Eur. J.* **2002**, *8*, 3187–3194.

[12] S.-L. Zheng, J.-P. Zhang, X.-M. Chen, Z.-L. Huang, Z.-Y. Lin, W.-T. Wong, *Chem. Eur. J.* **2003**, *9*, 3888–3896.

[13] O. R. Evans, W.-B. Lin, *Cryst. Growth Des.* **2001**, *1*, 9–11.

[14] J. Y. Lu, J. Macias, J.-G. Lu, J. E. Cmaidalka, *Cryst. Growth Des.* **2002**, *2*, 485–487.

[15] G. M. Sheldrick, *SADABS 2.05*, University of Göttingen.

[16] G. M. Sheldrick, *SHELXTL*, Version 6.10, Siemens Industrial Automation Inc., Madison, Wisconsin, USA, **2000**.

Received: May 7, 2006
Published Online: July 25, 2006

 © 2006 Wiley-VCH Verlag GmbH & Co. KGaA, Weinheim 

DOI: 10.1002/ejic.200500875

# In situ HT-XRD Study on the Formation of Hexagonal Ammonium Tungsten Bronze by Partial Reduction of Ammonium Paratungstate Tetrahydrate

**Imre Miklós Szilágyi,*[a] Ferenc Hange,[b] János Madarász,[a] and György Pokol[a]**

**Keywords:** Tungsten / Reduction / In situ studies / X-ray diffraction / X-ray photoelectron spectroscopy / Solid-state $^1$H NMR spectroscopy

Hexagonal ammonium tungsten bronze, $(NH_4)_{0.33-x}WO_{3-y}$, is a possible constituent of the intermediate "tungsten blue oxide" in non-sag (NS) tungsten production and a material of chromogenic and sensor interest. Its formation has been studied by in situ high-temperature powder X-ray diffraction (HT-XRD) accompanied by semiquantitative phase analysis through the partial thermal reduction of ammonium paratungstate tetrahydrate, $(NH_4)_{10}[H_2W_{12}O_{42}]\cdot 4H_2O$, in flowing 10 % $H_2$/He. The effect of the heating program on the formation of the title compound has been discussed. Highly crystalline, monophasic hexagonal ammonium tungsten bronze prepared by partial reduction of ammonium paratungstate tetrahydrate has been characterised by high-precision powder XRD, X-ray photoelectron spectroscopy (XPS), chemical analysis and solid-state $^1$H NMR spectroscopy ($^1$H-MAS-NMR).
(© Wiley-VCH Verlag GmbH & Co. KGaA, 69451 Weinheim, Germany, 2006)

## Introduction

Hexagonal ammonium tungsten bronze (HATB), $(NH_4)_{0.33-x}WO_{3-y}$, is one of the compounds that may be intermediates in the powder metallurgical production of tungsten lamp filaments. Partial reduction of the starting material, ammonium paratungstate tetrahydrate (APT), $(NH_4)_{10}[H_2W_{12}O_{42}]\cdot 4H_2O$, between 400 and 600 °C produces an intermediate product (called "tungsten blue oxide"), which is a possible mixture of different phases. It is doped with K, Al and Si that ensure, after complete reduction in hydrogen, an overlapping crystallite structure of tungsten powder, which finally provides appropriate mechanical stability (a so-called "non-sag" feature) to tungsten filaments even at high operating temperatures in lamps.[1–3] Among the possible constituents of "tungsten blue oxide" (an X-ray amorphous phase, $WO_3$, $WO_{2.9}$, $WO_{2.72}$, $WO_2$ and tungsten bronzes[1,2,4–7]), hexagonal ammonium tungsten bronze may have an important role in the doping process because of its ion-exchange property.[4,5,8,9]

Furthermore, for applications in electrochromic devices,[1,10–14] humidity[15,16] and gas sensors[17–21] as well as secondary batteries,[22] metastable tungsten oxides and oxide bronzes have attracted much attention in the past decades due to their open-tunnel structures.[1,2,23,24] Hexagonal ammonium tungsten bronze is an interesting member of these compounds because of its mixed proton and electron conductivity[25] and, in addition, hexagonal $WO_3$ can be produced by its oxidation,[26] the latter being one of the most studied tungsten oxides.[22,27–29] Besides hydrothermal[25,30] and solvothermal[31,32] synthetic methods, the partial reduction of APT is also a viable way of preparing the hexagonal ammonium tungsten bronze for these fields of interest.

For further studies on the various aforementioned reactions and applications of the title compound, it is advisable to obtain a deeper insight into its formation through the partial reduction of APT. In previous studies, when heating APT at a rate of 5–10 °C min$^{-1}$, hexagonal ammonium tungsten bronze readily appeared between 350 and 600 °C but was accompanied by some other phases (monoclinic, orthorhombic or hexagonal $WO_3$ in air,[1,2,33–37] tetragonal hydrogen tungsten bronze, $WO_{2.9}$, $WO_{2.72}$ and $WO_2$ in reducing gases[1,2,7,37–40] and X-ray amorphous phase in all cases). On the other hand, a monophasic, crystalline and/or partly amorphous hexagonal ammonium tungsten bronze could be produced when APT was decomposed in a furnace between 300 and 500 °C in reducing[41–45] or inert gases.[46]

In an attempt to explain the effect of the heating conditions on the partial reduction of APT, we report here our results obtained by in situ high-temperature powder X-ray diffraction (HT-XRD) in flowing 10 % $H_2$/He on the formation and thermal stability of hexagonal ammonium tungsten bronze. Supported by the results of our HT-XRD measurements and also by earlier studies,[1,2,7,37–46] we have proposed a model for the formation of the title compound through the partial reduction of APT. In harmony with this model, HATB has been prepared in a monophasic, highly

[a] Institute of General and Analytical Chemistry, Budapest University of Technology and Economics,
Szt. Gellért tér 4, 1111 Budapest, Hungary
Fax: +36-1-463-3408
E-mail: imre.szilagyi@mail.bme.hu
[b] GE Hungary ZRt., GE Consumer & Industrial Lighting,
Váci út 77, 1340 Budapest, Hungary

 © 2006 Wiley-VCH Verlag GmbH & Co. KGaA, Weinheim 

crystalline form and its composition and structure have been studied by high-precision powder XRD, X-ray photoelectron spectroscopy (XPS), chemical analysis and solid-state $^1$H NMR spectroscopy ($^1$H-MAS-NMR).

## Results and Discussion

### Formation and Thermal Stability of Hexagonal Ammonium Tungsten Bronze

On the basis of earlier studies,[43–45] an annealing temperature of 400 °C seemed to be the most suitable for the formation of the monophasic title compound when heating APT in a furnace in a reducing gas. This process (fast heating of APT followed by an isothermal period) has been modelled by in situ HT-XRD measurements in flowing 10% $H_2$/He.

Straight after (1 min) rapid heating (100 °C min$^{-1}$) of APT to 400 °C, hexagonal ammonium tungsten bronze, HATB (ICDD 42-0452), tetragonal hydrogen tungsten bronze, THTB, $H_xWO_{3-y}$ (ICDD 23-1448), and an X-ray amorphous phase were identified in the XRD pattern (Figure 1). The $2\theta$ = 23.702° reflection of HATB ($I/I_0$ = 65%) and the $2\theta$ = 22.980° reflection of THTB ($I/I_0$ = 50%) were used for semiquantitative phase analysis. The amounts of crystalline hexagonal bronze and tetragonal bronze were 69% and 31%, respectively (Figure 2). This is much higher than in the case of heating APT slowly (5 °C min$^{-1}$) to 450 °C, whereby the proportion of HATB was 34%.[47]

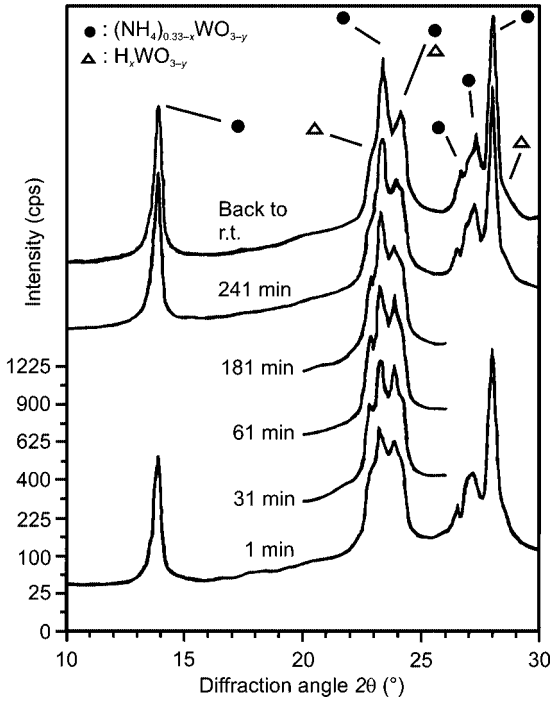


Figure 1. In situ HT-XRD patterns at 400 °C after rapid heating (100 °C min$^{-1}$) of APT in 10% $H_2$/He.

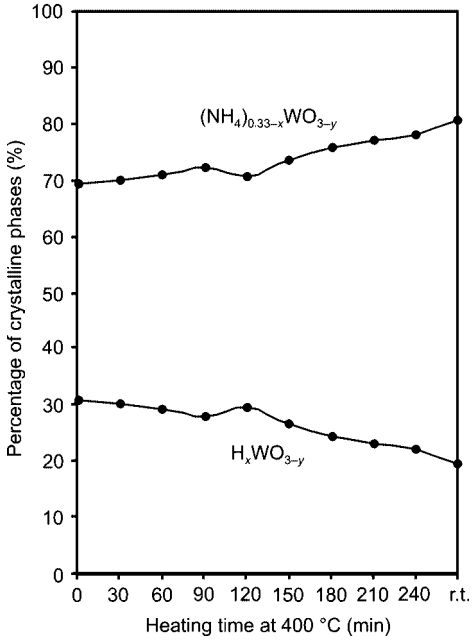


Figure 2. Amount of the formed crystalline tungsten bronzes from APT at 400 °C after rapid heating (100 °C min$^{-1}$) in 10% $H_2$/He.

During consecutive heating at 400 °C, the sample became more crystalline. This is indicated by the growth in intensity of reflections from both the hexagonal and tetragonal bronzes (Figure 1). On the other hand, the ratio of the hexagonal phase increased steadily (Figure 2). A further increase in the crystallinity of the sample and the amount of the hexagonal bronze (80%) accompanied cooling of the sample to room temperature (r.t.), which followed the 4 h isothermal heating period.

Our present study, as well as a comparison of earlier results,[1,2,7,37–46] shows that the heating conditions of APT in a reducing gas influence the formation of the bronzes, i.e. formation of the hexagonal bronze is favoured when APT is heated rapidly whereas for the formation of the tetragonal bronze, slow heating is favourable. We propose an explanation in terms of structure for this phenomenon.

The structure of APT is basically determined by the paratungstate ion, $[H_2W_{12}O_{42}]^{10-}$, which is built up from twelve $WO_6$ octahedra. These large ions are bound together by water molecules and ammonium ions.[48] When annealing APT at 250–300 °C (in fact this is the third main decomposition step of APT[1,2,37]), ammonia and water are released, structural collapse and rearrangement take place, i.e. some $WO_6$ octahedra from separate paratungstate ions become linked together and an amorphous phase is formed.[49] In this structure, a certain number of water molecules, ammonium ions as well as ammonia molecules are trapped and therefore cannot be released in this temperature region. From the amorphous phase, tungsten bronzes and then tungsten oxides form on further heating at 300–600 °C.

We suppose that the heating rate of APT determines the process of $WO_6$ octahedra linking and the amount of trapped molecules and ions. This then also determines the possibility of the formation of hexagonal and tetragonal

 © 2006 Wiley-VCH Verlag GmbH & Co. KGaA, Weinheim 

bronzes. Ammonia molecules and ammonium ions fit in the hexagonal channels of HATB the best. Therefore, the faster APT is heated, the more ammonia molecules and ammonium ions (as well as water molecules) are trapped in the cages between the $WO_6$ octahedra. This results in a higher proportion of hexagonal bronze.

The growth in the amount of HATB during the isothermal period must also be explained. One solution might be that the tetragonal bronze becomes transformed into the hexagonal material.[39] The other possibility is that right after (1 min; Figure 2) the rapid heating of APT, only a part of the sample crystallised. Since under such circumstances the formation of the hexagonal phase seems to be favoured, during the isothermal period, when the other part of the sample also crystallised, HATB was formed to a greater extent than THTB resulting in a growth in the percentage of the hexagonal bronze.

It should be mentioned that we observed only a phase mixture at all stages of the reaction and that the hexagonal bronze was accompanied by small amounts of the tetragonal bronze even after 4 h of annealing. We assume that the difference of the decomposition conditions for APT in a furnace and in a high-temperature camera may be the reason why a monophasic HATB finally did not form in our experiments.

However, we clearly detected that during fast heating and then during isothermal heating of APT, much more hexagonal bronze than tetragonal bronze formed. We also observed that during the isothermal stage the sample became more crystalline. Our results and assumptions together with earlier studies[41–46] thus show that when HATB is required in a highly crystalline, monophasic form, APT has to be heated rapidly, preferably at 400 °C in a reducing gas, and kept under these conditions for several hours, which in practice corresponds to heating APT in a furnace.

It is very interesting that in air formation of the tetragonal hydrogen tungsten bronze was not observed as described earlier and that hexagonal ammonium tungsten bronze was accompanied by an X-ray amorphous phase and/or by crystalline monoclinic, orthorhombic or hexagonal $WO_3$.[1,2,33–37] In this case, oxidation might also have an effect on the linking process of paratungstate ions, which should be responsible for the absence of the tetragonal bronze during the decomposition sequence of APT in air.

## Characterisation of Hexagonal Ammonium Tungsten Bronze

In order to check our model of how highly crystalline, monophasic hexagonal ammonium tungsten bronze is formed through the partial reduction of APT, ammonium paratungstate tetrahydrate was annealed at 400 °C for 6 h in $H_2$. The structure and composition of the resultant HATB sample were determined by high-precision powder XRD, XPS, chemical analysis and $^1$H-MAS-NMR spectroscopy.

### *Characterisation of Hexagonal Ammonium Tungsten Bronze by High-Precision XRD*

XRD analysis showed that the HATB sample contained only the hexagonal ammonium tungsten bronze phase, which was identified by the ICDD 42-0452 card in space group $P6_3/mcm$, no. 193.[46] The sample was highly crystalline [the signal/background ratio for the (2,0,0) reflection was 6050 cps/60 cps] and an X-ray amorphous phase was not detected. Thus, a monophasic, highly crystalline hexagonal ammonium tungsten bronze could be successfully produced by partial thermal reduction of APT, in agreement with our model.

To check the cell parameter refining program, we recalculated the cell parameters of the title compound on the basis of the measured reflections of HATB found in the literature[8,44,46] and this showed the reliability of our program (Table 1). The slight difference in literature cell parameters[8,44,46] might have been caused mostly by the differences in the compositions of hexagonal ammonium tungsten bronze samples.[5]

In order to obtain precise XRD data, we used all the simulated reflections of the $P6_3/mcm$, no. 193 space group for finding and indexing the reflections in the measured XRD pattern of the HATB sample. The simulated reflections were calculated with PulverX using cell parameters of HATB reported by Dickens et al.[44] Deconvolution of peaks, base line correction, splitting of peaks from Cu-$K_{\alpha1}$ and -$K_{\alpha2}$ radiation, profile fitting and, finally, correction of reflections on the basis of an Si internal standard were then performed. The obtained reflections of HATB are listed in Table 2.

The following cell parameters of the HATB sample were obtained: $a = 0.7381 \pm 0.0001$ nm, $c = 0.7540 \pm 0.0002$ nm.

While we could detect all the measurable 77 reflections of HATB, Kiss et al.[8] observed 49 reflections, Dickens et al.[44] listed 20 and Volkov[46] detected 25 of them. Interestingly, Kiss et al.[8] reported indices (3,0,1) and (5,0,3), which are in contrast to the extinction rule of the space group $P6_3/mcm$, no. 193.

### *Characterisation of Hexagonal Ammonium Tungsten Bronze by XPS*

In tungsten bronzes, the tungsten atoms may appear in different oxidation states.[1,2] To check this for our HATB

Table 1. Recalculation of cell parameters of HATB samples for which *d* values have been previously published.[8,44,46]

| Source | Compound | $a$ [nm] | $\sigma_a$ [nm] | $c$ [nm] | $\sigma_c$ [nm] |
|---|---|---|---|---|---|
| Ref.[46] ICDD 42-0452 | $(NH_4)_{0.33}WO_3$ | 0.7392 | 0.0002 | 0.7512 | 0.0003 |
| Recalculated ref.[46] | | 0.7391 | 0.0001 | 0.7512 | 0.0002 |
| Ref.[44] | $(NH_4)_{0.25}WO_3$ | 0.7388 | 0.0003 | 0.7551 | 0.0006 |
| Recalculated ref.[44] | | 0.7388 | 0.0003 | 0.7550 | 0.0006 |
| Ref.[8] | $(NH_4)_{0.1135}WO_{2.9832}\cdot(H_2O)_{0.14}$ | 0.7389 | not given | 0.7514 | not given |
| Recalculated ref.[8] | | 0.7379 | 0.0005 | 0.7508 | 0.0009 |

 © 2006 Wiley-VCH Verlag GmbH & Co. KGaA, Weinheim 

Table 2. Powder XRD data of HATB.

| *d* [nm] | $I/I_0$ [%] | *hkl* | *d* [nm] | $I/I_0$ [%] | *hkl* |
|---|---|---|---|---|---|
| 0.6407 | 41.4 | 100 | 0.1277 | 0.3 | 500 |
| 0.3771 | 66.7 | 002 | 0.1267 | 0.4 | 323 |
| 0.3696 | 17.9 | 110 | 0.1257 | 0.8 | 006 |
| 0.3308 | 7.5 | 111 | 0.1233 | 0.9 | 106 |
| 0.3246 | 18.8 | 102 | 0.1226 | 0.9 | 330 |
| 0.3197 | 100.0 | 200 | 0.1220 | 3.0 | 413 |
| 0.2638 | 9.7 | 112 | 0.1219 | 3.0 | 404 |
| 0.2439 | 55.9 | 202 | 0.1216 | 1.5 | 331 |
| 0.2413 | 2.5 | 210 | 0.1210 | 2.1 | 502 |
| 0.2303 | 4.4 | 211 | 0.1209 | 1.7 | 420 |
| 0.2132 | 2.8 | 300 | 0.1188 | 0.5 | 116 |
| 0.2076 | 1.5 | 113 | 0.1170 | 1.8 | 206 |
| 0.2035 | 2.6 | 212 | 0.1168 | 1.5 | 332 |
| 0.1885 | 8.7 | 004 | 0.1158 | 0.9 | 324 |
| 0.1857 | 2.9 | 302 | 0.1152 | 2.8 | 422 |
| 0.1846 | 17.0 | 220 | 0.1149 | 2.0 | 315 |
| 0.1808 | 2.9 | 104 | 0.1148 | 1.5 | 510 |
| 0.1774 | 4.6 | 310 | 0.1136 | 2.2 | 511 |
| 0.1741 | 2.0 | 213 | 0.1121 | 0.6 | 414 |
| 0.1726 | 6.3 | 311 | 0.1114 | 0.2 | 216 |
| 0.1678 | 2.8 | 114 | 0.1105 | 1.1 | 333 |
| 0.1657 | 15.6 | 222 | 0.1098 | 0.9 | 512 |
| 0.1624 | 18.1 | 204 | 0.1082 | 0.2 | 306 |
| 0.1603 | 6.5 | 312 | 0.1066 | 0.6 | 600 |
| 0.1599 | 5.1 | 400 | 0.1052 | 0.3 | 325 |
| 0.1484 | 1.7 | 214 | 0.1050 | 0.2 | 430 |
| 0.1473 | 6.9 | 402 | 0.1045 | 2.0 | 513 |
| 0.1470 | 3.1 | 320 | 0.1040 | 0.9 | 431 |
| 0.1450 | 3.3 | 313 | 0.1038 | 1.5 | 226 |
| 0.1441 | 0.6 | 321 | 0.1035 | 0.5 | 117 |
| 0.1413 | 0.9 | 304 | 0.1030 | 0.6 | 334 |
| 0.1400 | 0.7 | 115 | 0.1026 | 0.6 | 316 |
| 0.1395 | 0.8 | 410 | 0.1025 | 1.0 | 602 |
| 0.1374 | 2.5 | 411 | 0.1024 | 0.4 | 415 |
| 0.1367 | 0.6 | 322 | 0.1023 | 0.4 | 520 |
| 0.1320 | 7.2 | 224 | 0.1018 | 2.7 | 424 |
| 0.1310 | 1.1 | 412 | 0.1015 | 0.7 | 521 |
| 0.1292 | 1.8 | 314 | 0.1011 | 0.1 | 432 |
| 0.1280 | 0.1 | 215 | | | |

sample, the $WO_3$ reference sample was investigated first. Besides O atoms (O1s = 530.7 eV) only $W^{VI}$ atoms were detected (Figure 3a), the W4f values of which ($W4f_{7/2}$ = 36.9 eV and $W4f_{5/2}$ = 34.8 eV) were in agreement with earlier results.[27,50,51]

After refining the XPS spectrum belonging to the HATB sample (Figure 3b), $W^{IV}$ atoms ($W4f_{7/2}$ = 35.2 eV and $W4f_{5/2}$ = 33.2 eV) and $W^{V}$ atoms ($W4f_{7/2}$ = 35.9 eV and $W4f_{5/2}$ = 33.5 eV) were also observed besides $W^{VI}$ atoms.[52–54] Zhan et al.[32] also investigated a hexagonal ammonium tungsten bronze sample by XPS but they did not report the presence of $W^{IV}$ and $W^{V}$ atoms.

Furthermore, in our HATB sample, $NH_3$ molecules (N1s = 399.7 eV) were also detected in addition to $NH_4^+$ ions (N1s = 401.9 eV).[50,51] Up to this time ammonia molecules were only detected in HATB by $^1$H-MAS-NMR spectroscopy[4,5] whereas they were not detected by XPS.[32]

Depth profiling by $Ar^+$ ion sputtering was not informative because sputtering distorted the structure so much that, due to oxygen loss, even $W^0$ species ($W4f_{7/2}$ = 32.5 eV and $W4f_{5/2}$ = 30.5 eV) appeared.[54–56]

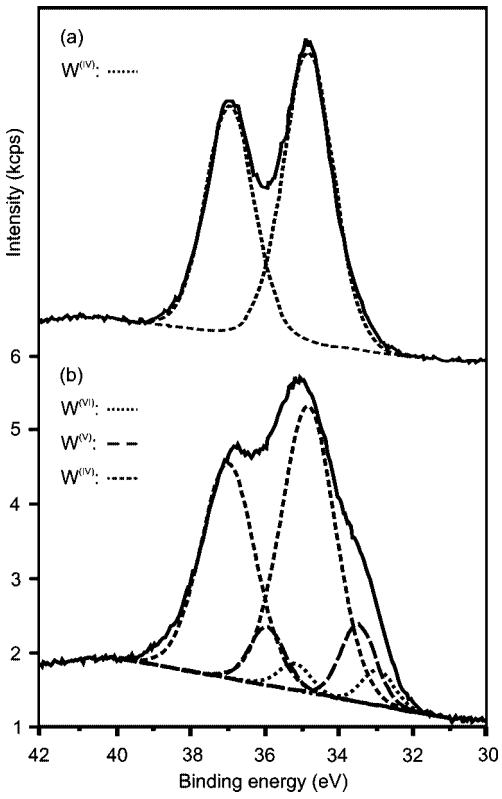


Figure 3. XPS spectra of (a) $WO_3$ and (b) HATB.

### *Chemical Analysis of Hexagonal Ammonium Tungsten Bronze*

In order to determine the composition of the HATB sample, it was first heated at 800 °C in argon in a Setaram TG-DTA 92 thermobalance to form $WO_{3-x}$ and was then heated at 800 °C in air to form $WO_3$. From the corresponding weight changes, the W and O contents of the sample were calculated. The N content was determined by titration of the ammonia released when the HATB sample was heated in nitrogen. The ratio of $NH_4^+$ ions to $NH_3$ molecules was measured by XPS. The total amount of $H_2O$ present in the sample was calculated by complementing to 100% (m/m). The weight loss of the sample up to 100 °C, i.e. corresponding to adsorbed water was not taken into account when calculating the stoichiometry. Thus, the formula of the HATB sample was determined as $(NH_4)_{0.07}(NH_3)_{0.04}(H_2O)_{0.09}WO_{2.95}$. XPS analysis showed no impurities in the sample.

In the case of HATB samples, for which cell parameters and *d* values were published previously[8,44,46] (Table 1), the chemical analysis of samples was not detailed enough. The presence of $NH_3$ molecules was not checked in any of the reports corresponding to refs.[8,44,46] and the rate of reduction, i.e. the oxygen index, was not taken into account in refs.[44,46].

### *Characterisation of Hexagonal Ammonium Tungsten Bronze by $^1$H-MAS-NMR Spectroscopy*

Because of the possible presence of some proton-containing species ($NH_3$, $NH_4^+$, $H_2O$ and OH group) in hexagonal

 © 2006 Wiley-VCH Verlag GmbH & Co. KGaA, Weinheim 

ammonium tungsten bronze, the HATB sample was also characterised by solid-state $^1$H NMR spectroscopy.

In the $^1$H-MAS-NMR spectrum of the $WO_3$ reference sample, only a small peak was observed at $\delta$ = 0.8 ppm, which was also noticeable in the $^1$H-MAS-NMR spectrum of HATB (Figure 4). Since this peak was also present in the $^1$H-MAS-NMR spectrum of the sample holder, we could not check the presence of OH groups on the surface of $WO_3$ and HATB particles.[4,5,57]

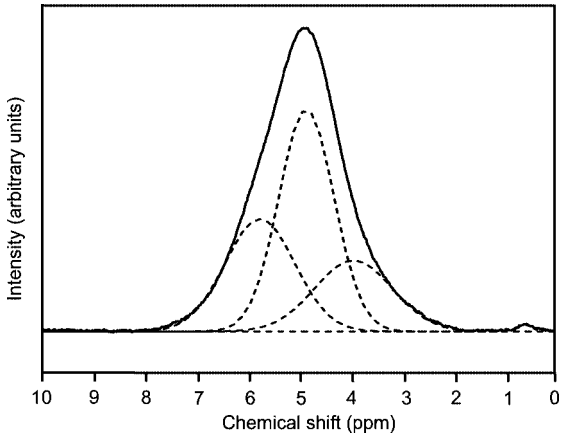


Figure 4. $^1$H-MAS-NMR spectrum of HATB.

In the$^1$H-MAS-NMR spectrum of HATB, the large peak at $\delta \approx 5$ ppm seemed to be asymmetric and we could not fit it properly with one or two but only with three peaks. The peak at $\delta$ = 4.9 ppm was assigned to the ammonium ions situated in the hexagonal channels, in accordance with ref.[5] We suppose that the peak at $\delta$ = 5.8 ppm is due to ammonia molecules in the hexagonal channels, an idea which is also supported by our XPS measurements and also by earlier results.[5] The peak at $\delta$ = 4.0 ppm may come from water molecules bound to the surface of or inside the bronze particles.

## Conclusions

On the basis of in situ HT-XRD measurements and earlier results,[1,2,7,37–45] we propose that the heating program of APT influences the process of linking of $WO_6$ octahedra of paratungstate ions. This probably determines the likelihood, as a result of structural factors, of the formation of hexagonal ammonium tungsten bronze. Formation of monophasic hexagonal bronze is favoured the most when APT is heated rapidly at 400 °C in a reducing gas. On the basis of this model, the preparation of a highly crystalline, monophasic HATB sample was successful.

Chemical analysis of the resultant hexagonal ammonium tungsten bronze sample showed a composition of $(NH_4)_{0.07}(NH_3)_{0.04}(H_2O)_{0.09}WO_{2.95}$. The presence of $W^{IV}$, $W^{V}$ and $W^{VI}$ species detected by XPS supports the electron-conducting properties while the presence of $NH_3$ molecules and $NH_4^+$ ions detected by XPS and $^1$H-MAS-NMR spectroscopy supports the proton-conducting properties of the title compound. With powder XRD analysis more reflections of hexagonal ammonium tungsten bronze were detected than previously observed.

## Experimental Section

**Ammonium Paratungstate Tetrahydrate:** Ammonium paratungstate tetrahydrate (H. C. Starck GmbH), $(NH_4)_{10}[H_2W_{12}O_{42}]\cdot 4H_2O$ (ICDD 40-1470) was used as purchased (analysis: measured $WO_3$ 89.6%, $NH_3$ 5.1%; calculated $WO_3$ 88.8%, $NH_3$ 5.4%). XRD measurements did not show any impurities in the APT sample.

**Hexagonal Ammonium Tungsten Bronze:** Hexagonal ammonium tungsten bronze was produced by annealing APT at 400 °C for 6 h in $H_2$ since, on the basis of earlier results[43–45] and our HT-XRD measurements, these conditions seemed to be the best for the formation of highly crystalline, monophasic HATB.

**Tungsten Trioxide:** Monoclinic tungsten trioxide, $WO_3$ (ICDD 83-0951), was produced as a reference sample for XPS and $^1$H-MAS-NMR spectroscopic analysis by heating APT at 600 °C for 2 h in air. XRD, XPS and $^1$H-MAS-NMR spectroscopic measurements did not show any impurities in the $WO_3$ sample.

**In situ High-Temperature Powder X-ray Diffraction (HT-XRD):** HT-XRD patterns were recorded with a device consisting of a Müller Mikro 111 generator, a Philips PW 1710 diffractometer control unit and a Philips PW 1050 goniometer between $2\theta$ = 10–30° and 20–26° at (0.02° per 0.5 s) with Cu-$K_{\alpha 1,2}$ radiation. Heating of samples was performed in an Anton Paar HTK 16 high-temperature camera in flowing 10% $H_2$/He. Deconvolution of peaks, base-line correction, splitting of peaks from Cu-$K_{\alpha 1}$ and -$K_{\alpha 2}$ radiation as well as profile fitting were carried out using Profit for Windows 1.0. The relative ratio of the crystalline phases was calculated by semiquantitative phase analysis.

**Powder X-ray Diffraction (XRD):** X-ray diffraction pattern of the title compound was recorded with a Philips MPD 1880 X-ray diffractometer using Si (ICDD 27-1402) as an internal standard between $2\theta$ = 5 and 100° at (0.01° per 3 s) with Cu-$K_{\alpha 1,2}$ radiation. The same program and method were used to obtain the Cu-$K_{\alpha 1}$ reflections as in the case of in situ HT-XRD experiments. Measured reflections were indexed on the basis of simulated reflections of the $P6_3/mcm$, no. 193 space group, which were calculated by PulverX using cell parameters of HATB reported by Dickens et al.[44] A linear interpolation was made between the deviations of measured and standard $d$ values at each Cu-$K_{\alpha 1}$ reflection belonging to the Si internal standard and, using the function obtained this way, the $d$ values of HATB sample were corrected. The cell parameters of hexagonal ammonium tungsten bronze were refined using a gwbasic language program, which used non-linear fitting (least square of $1/d^2$, Gauss–Newton–Marquardt method) without weighting.[58]

**X-ray Photoelectron Spectroscopy (XPS):** XPS data were collected with a VG Microtech instrument consisting of an XR3E2 X-ray source, a twin anode (Mg-$K_\alpha$ and Al-$K_\alpha$) and a CLAM 2 hemispherical analyser using Mg-$K_\alpha$ radiation. Survey scans were obtained in the 0–1100 eV range with a 20 eV pass energy at 0.4 eV per 0.1 s. Detailed scans were recorded with a 50 eV pass energy at 0.05 eV per 1.5 s. The spectrometer was calibrated by using the binding energy of the C 1s line (284.5 eV).

**Solid-State $^1$H NMR Spectroscopy ($^1$H-MAS-NMR):** $^1$H-MAS-NMR spectra were recorded with a Varian Unity 300 spectrometer supplied with a Doty XC5 solid-phase $^1$H head at a rotor spinning frequency of 4000 Hz in an XC5 insert (special sample holder), which was set inside an $Si_3N_4$ rotor.

 © 2006 Wiley-VCH Verlag GmbH & Co. KGaA, Weinheim 

## Acknowledgments

G. Szalontai (NMR Laboratory, Pannon University, Veszprém, Hungary) as well as V. K. Josepovits and H. Lovas (Department of Atomic Physics, Budapest University of Technology and Economics, Hungary) are greatly acknowledged for their help in performing $^1$H-MAS-NMR and XPS measurements, respectively. One of the authors (I. M. S.) is grateful for an Aschner scholarship of GE Hungary ZRt, GE Consumer & Industrial Lighting.

[1] E. Lassner, W.-D. Schubert, *Tungsten. Properties, Chemistry, Technology of the Element, Alloys, and Chemical Compounds*, Kluwer Academic/Plenum Publishers, New York, **1999**.
[2] "Special Issue on the Chemistry of Non-Sag Tungsten" (Eds.: L. Bartha, E. Lassner, W.-D. Schubert, B. Lux), *Int. J. Refract. Met. Hard Mater.* **1995**, *13*, 1–164.
[3] E. Pink, L. Bartha, *The Metallurgy of Doped/Non-Sag Tungsten*, Elsevier, London, **1989**.
[4] H.-J. Lunk, B. Ziemer, M. Salmen, D. Heidemann, *Int. J. Refract. Met. Hard Mater.* **1993–1994**, *12*, 17–26.
[5] H.-J. Lunk, M. Salmen, D. Heidemann, *Int. J. Refract. Met. Hard Mater.* **1998**, *16*, 23–30.
[6] A. Lackner, T. Molinari, P. Paschen, *Scand. J. Metall.* **1996**, *25*, 115–121.
[7] J. W. van Put, T. W. Zegers, *Int. J. Refract. Met. Hard Mater.* **1991**, *10*, 115–122.
[8] B. A. Kiss, G. Rom Berendné, G. Gyarmathy, Z. Kutasi Feketéné, *Magy. Kem. Foly* **1987**, *93*, 97–106.
[9] L. Bartha, G. Gyarmati, B. A. Kiss, T. Németh, A. Salamon, T. Szalay, *Acta Chim. Acad. Sci. Hung.* **1979**, *101*, 127–138.
[10] C. G. Grandqvist, *Handbook of Inorganic Electrochromic Materials*, Elsevier, Amsterdam, **1995**.
[11] C. G. Granqvist, *J. Eur. Ceram. Soc.* **2005**, *25*, 2907–2912.
[12] A. Azens, E. Avendano, J. Backholm, L. Berggren, G. Gustavsson, R. Karmhag, G. A. Niklasson, A. Roos, C. G. Granqvist, *Mater. Sci. Eng., B* **2005**, *119*, 214–223.
[13] A. A. Argun, P. H. Aubert, B. C. Thompson, I. Schwedeman, C. L. Gaupp, J. Hwang, N. J. Pinto, D. B. Tanner, A. G. MacDiarmid, J. R. Reynolds, *Chem. Mater.* **2004**, *16*, 4401–4412.
[14] C. G. Granqvist, A. Avendano, A. Azens, *Thin Solid Films* **2003**, *442*, 201–211.
[15] G. V. Kunte, U. Ail, S. A. Shivashankar, A. M. Umarji, *Bull. Mater. Sci.* **2005**, *28*, 243–248.
[16] I. Tsuyomoto, T. Kudo, *Sens. Actuators, B* **1996**, *30*, 95–99.
[17] G. Shaw, I. P. Parkin, K. F. E. Pratt, D. E. Williams, *J. Mater. Chem.* **2005**, *15*, 149–154.
[18] C. J. Jin, T. Yamazaki, Y. Shirai, T. Yoshiwaza, T. Kikuta, N. Nakatani, H. Takeda, *Thin Solid Films* **2005**, *474*, 255–260.
[19] R. Ionescu, A. Hoel, C. G. Granqvist, E. Llobet, P. Heszler, *Sens. Actuators, B* **2005**, *104*, 124–131.
[20] X. L. Li, T. J. Lou, X. M. Sun, Y. D. Li, *Inorg. Chem.* **2004**, *43*, 5442–5449.
[21] L. Zhuang, X. Xu, H. Shen, *Surf. Coat. Technol.* **2003**, *167*, 217–220.
[22] W. Han, M. Hibino, T. Kudo, *Solid State Ionics* **2000**, *128*, 25–32.
[23] M. S. Wittingham, *Solid State Ionics* **2004**, *168*, 255–263.
[24] B. Gérand, L. Seguin, *Solid State Ionics* **1996**, *84*, 199–204.
[25] L. Huao, H. Zhao, F. Mauvy, S. Fourcade, C. Labrugere, M. Pouchard, J.-C. Grenier, *Solid State Sci.* **2004**, *6*, 679–688.
[26] B. Schlasche, R. Schollhorn, *Rev. Chim. Miner.* **1982**, *19*, 534–544.
[27] O. Y. Khyzhun, Y. M. Solonin, V. F. Dobrovolsky, *J. Alloys Compd.* **2001**, *320*, 1–6.
[28] J. Pfeifer, C. Balázsi, B. A. Kiss, B. Pécz, A. L. Tóth, *J. Mater. Sci. Lett.* **1999**, *18*, 1103–1105.
[29] W. Han, M. Hibino, T. Kudo, *Bull. Chem. Soc. Jpn.* **1998**, *71*, 933–937.
[30] T. E. Gier, D. C. Pease, A. W. Sleight, T. A. Bither, *Inorg. Chem.* **1968**, *7*, 1646–1647.
[31] A. Michailovski, F. Krumeich, G. R. Patzke, *Chem. Mater.* **2004**, *16*, 1433–1440.
[32] J. H. Zhan, X. G. Yang, Y. Xie, B. F. Li, Y. T. Qain, Y. B. Jia, *Solid State Ionics* **1999**, *126*, 373–377.
[33] J. Madarász, I. M. Szilágyi, F. Hange, G. Pokol, *J. Anal. Appl. Pyrolysis* **2004**, *72*, 197–201.
[34] N. E. Fouad, A. K. H. Nohman, M. A. Mohamed, M. I. Zaki, *J. Anal. Appl. Pyrolysis* **2000**, *56*, 23–31.
[35] Z. Zhang, M. Muhammed, *Thermochim. Acta* **2003**, *400*, 235–245.
[36] A. B. Kiss, L. Chudik-Major, *Acta Chim. Acad. Sci. Hung.* **1973**, *78*, 237–251.
[37] O. Kirilenko, F. Girgsdies, R. E. Jentoft, T. Ressler, *Eur. J. Inorg. Chem.* **2005**, *11*, 2124–2133.
[38] I. M. Szilágyi, J. Madarász, F. Hange, G. Pokol, *Solid State Ionics* **2004**, *172*, 583–586.
[39] M. Mészáros, J. Neugebauer, F. Hange, *High Temp. Mater. Processes* **1996**, *15*, 111–115.
[40] N. E. Fouad, A. K. H. Nohman, M. I. Zaki, *Thermochim. Acta* **2000**, *343*, 139–143.
[41] R. C. T. Slade, P. G. Dickens, D. A. Claridge, D. J. Murphy, T. K. Halstead, *Solid State Ionics* **1990**, *38*, 201–206.
[42] L. D. Clark, M. S. Wittingham, R. A. Huggins, *J. Solid State Chem.* **1972**, *5*, 487–493.
[43] J. Bludská, J. Vondrák, I. Jakubec, *Electrochim. Acta* **1994**, *39*, 2045–2048.
[44] P. G. Dickens, A. C. Halliwell, D. J. Murphy, M. S. Wittingham, *Trans. Faraday Soc.* **1971**, *67*, 794–800.
[45] Y. Yamamoto, S. Yamada, S. Honkawa, N. Shigaki, *Funtai oyobi Funmatsu Yakin* **1993**, *40*, 1126–1130.
[46] a) V. L. Volkov, *Izv. Akad. Nauk SSSR. Neorg. Mater. (Russ.)* **1990**, *26*, 125–129; b) V. L. Volkov, *Inorg. Mater. (Engl. Transl.)* **1990**, *26*, 101; c) $(NH_4)_{0.33}WO_3$, International Centre for Diffraction Data (ICDD), file no. 42-0452.
[47] I. M. Szilágyi, J. Madarász, F. Hange, G. Pokol, to be published.
[48] H. D'Amour, R. Allman, *Z. Kristallogr.* **1972**, *136*, 23–47.
[49] M. A. Mohamed, S. A. A. Mansour, M. I. Zaki, *Thermochim. Acta* **1989**, *138*, 309–317.
[50] *Handbook of X-ray Photoelectron Spectroscopy* (Eds.: C. D. Wagner, W. M. Riggs, L. E. Davis, J. F. Moulder, G. E. Muilenberg), Perkin–Elmer Corporation, Division of Electronics Division, Minessota, **1979**.
[51] B. V. Crist, *Handbook of Monochromatic XPS Spectra*, vol. 1 ("The Elements and Nature Oxides"), XPS International, California, **1999**.
[52] A. Henningson, H. Rensmo, A. Sandell, S. Södergen, H. Siegbahn, *Thin Solid Films* **2004**, *461*, 237–242.
[53] D. Gogova, K. Gesheva, A. Kakanakova-Georgieva, M. Surtchev, *Eur. Phys. J. Appl. Phys.* **2000**, *11*, 167–174.
[54] H. Y. Wong, C. W. Ong, R. W. M. Kwok, K. W. Wong, S. P. Wong, W. Y. Cheung, *Thin Solid Films* **2000**, *376*, 131–139.
[55] W. B. Cross, I. P. Parkin, S. A. O'Neil, P. A. Williams, M. F. Mahon, K. C. Molloy, *Chem. Mater.* **2003**, *15*, 2786–2796.
[56] S. Santucci, C. Cantalini, M. Crivellari, L. Lozzi, L. Ottaviano, M. Passacantando, *J. Vac. Sci. Technol. A* **2000**, *18*, 1077–1082.
[57] J. Z. Hu, J. H. Kwak, J. E. Herrera, Y. Wang, C. H. F. Peden, *Solid State Nucl. Magn. Reson.* **2005**, *27*, 200–205.
[58] P. Valkó, S. Vajda, *Advanced Scientific Computing in BASIC with Applications in Chemistry, Biology and Pharmacology*, Elsevier Science Publishers, New York, **1989**.

Received: September 29, 2005
Published Online: July 24, 2006

 © 2006 Wiley-VCH Verlag GmbH & Co. KGaA, Weinheim 

DOI: 10.1002/ejic.200600006

# Chemical Oxidation of 1,3,2-Diazaboroles and 1,3,2-Diazaborolidines

**Lothar Weber,*[a] Imme Domke,[a] Jan Kahlert,[a] and Hans-Georg Stammler[a]**

**Keywords:** Diazaboroles / Diazaborolidines / Diazaborolium salts / Nitrosonium hexafluorophosphate

Oxidation of the 1,3,2-diazaborole *t*BuN$^a$CH=CHN$^b$(*t*Bu)-BBr(*N$^a$*–*B*) (**1h**) with $NO^+PF_6^-$ afforded the diazaborolium salts [*t*BuN$^a$=CH–CH=N$^b$(*t*Bu)$BF_2$(*N$^a$*–*B*)]$^+X^-$ (X = $Br^-$, $Br_3^-$, $PF_6^-$) (**3h**) as the result of different oxidation processes. The same product was obtained when the 1,3,2-diazaborolidine *t*BuN$^a$$CH_2CH_2$N$^b$(*t*Bu)BBr(*N$^a$*–*B*) (**2h**) was subjected to reaction with $NO^+PF_6^-$. In contrast to this, oxidation of **1h** and **2h** with $NO^+BF_4^-$ cleanly furnished [*t*BuN$^a$CH–CH=N$^b$(*t*Bu)-BFBr(*N$^a$*–*B*)]$^+BF_4^-$ (**6h**). Treatment of the 1,3,2-diazaboroles *t*BuN$^a$CH=CHN$^b$(*t*Bu)BR(*N$^a$*–*B*) [R = H (**1e**), CN (**1i**), C≡CH (**1j**)] with $NO^+PF_6^-$ under comparable conditions led to the borolium salts [*t*BuN$^a$=CH–CH=N$^b$(*t*Bu)BRF(*N$^a$*–*B*)]$^+PF_6^-$ [R = H (**3e**), CN (**3i**), C≡CH (**3j**)]. All the borolium salts investigated in this study were reversibly reduced by cyclic voltammetry. The novel products were characterized by elemental analyses and NMR spectra ($^1$H, $^{11}$B, $^{13}$C, $^{19}$F, $^{31}$P). The X-ray structure analysis of **3h** reveals two independent planar cations in the asymmetric unit, accompanied by one bromide and one tribromide ion.

(© Wiley-VCH Verlag GmbH & Co. KGaA, 69451 Weinheim, Germany, 2006)

## Introduction

The reactivity of the 1,3,2-diazaboroles **I** towards a broad range of nucleophiles has been investigated intensively and described in detail in the literature some years ago.[1] More recently, the redox chemistry of these compounds and of their saturated analogs, the 1,3,2-diazaborolidines **II** (Scheme 1), has been studied by cyclic voltammetry and He(I)-UV-photoelectron spectroscopy.[2]

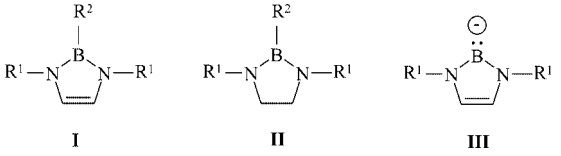

Scheme 1. Diazaborole **I**, diazaborolidine **II** and boranide ion **III**.

The electrochemical reduction of diazaboroles to afford the boranide ion **III**, however, has never been observed. This is consistent with the results of their chemical reduction with sodium/potassium alloy, which also did not lead to anions of the type **III**. The latter would be analogous to Denk's silylene[3] or to the related germylene.[4] The alkali metal reduction of **IV**[5] and **VI**[6] afforded the diboranes(4) **V** and **VII**. Treatment of diazaborole **1h**, however, did not furnish the corresponding diborane(4) (Scheme 2).

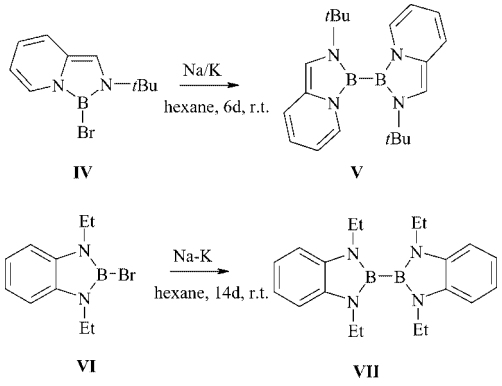

Scheme 2. Chemical reduction of 1,3,2-diazaboroles **IV** and **VI**.

The electrochemical oxidation of *N*,*N*-di-*tert*-butyldiazaboroles **1a**–**i** by cyclic voltammetry displayed clean, but irreversible waves, whereby the oxidation potentials $E_{ox,1/2}$ vary strongly in dependence of the substitution pattern at the boron center (Table 1). Thus, the amino-substituted borole **1a** as well as the methoxy-substituted heterocycle **1c** were oxidized much easier than the cyano- or bromodiazaboroles, **1h** or **1i**, which was rationalized by the donor and acceptor abilities of the functional groups at the boron atom. The corresponding saturated 1,3,2-diazaborolidines with identical ligands at the boron atom exhibited the same trend, but in general they were less easy oxidized. This trend was confirmed by photoelectron spectroscopy of the heterocycles in the gas phase.[2]

[a] Fakultät für Chemie der Universität Bielefeld,
Universitätsstrasse 25, 33615 Bielefeld, Germany
Fax: +49-521-106-6146
E-mail: lothar.weber@uni-bielefeld.de

 © 2006 Wiley-VCH Verlag GmbH & Co. KGaA, Weinheim 

Table 1. Oxidation potentials of **1a**–**i** in $CH_2Cl_2$ vs. Fc/Fc$^+$.

| 1 | a | b | c | d | e | f | g | h | i |
|---|---|---|---|---|---|---|---|---|---|
| R | $NH_2$ | OMe | Me | $NMe_2$ | H | SMe | $SnMe_3$ | Br | CN |
| $E_{ox}$ [mV] | –288 | –58 | 124 | 158 | 310 | 354 | 396 | 576 | 752 |

## Results and Discussion

With respect to the irreversible electrochemical oxidation of diazaboroles, we were interested in the nature of the oxidation products and thus decided to oxidize these heterocycles chemically. The reaction of 1 equiv. of bromoborole **1h** with 2 equiv. of $NO^+PF_6^-$ in $CH_2Cl_2$/hexane led to the quantitative formation of the difluoroborolium salt **3h** as yellow crystals (Scheme 3). The counterion in the product, however, was not uniform. Obviously, the bromo ligand of **1h** was displaced by fluoride, which was released from a $PF_6^-$ ion before, and serves now as a counterion in the salt in addition to the $PF_6^-$ ion and the tribromide ion. The presence of a $Br_3^-$ anion indicates that additional redox processes have taken place. It could be formed from $Br^-$ by the oxidation with excessive $NO^+PF_6^-$. In contrast to other 1,3,2-diazaborolium salts with bromo or chloro substituents, **3h** was excellently soluble in dichloromethane and moderately soluble in toluene.

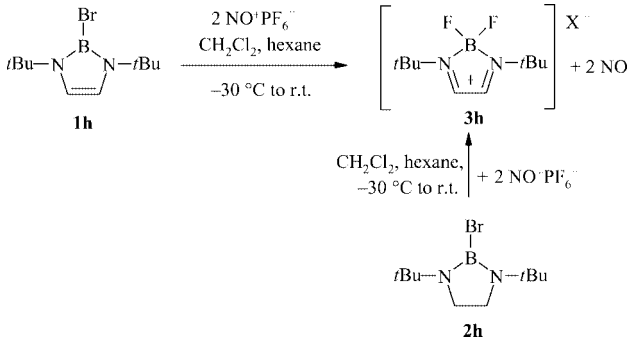


Scheme 3. Oxidation of the bromoborole **1h** and bromoborolidine **2h** with $NO^+PF_6^-$ (X = Br, $Br_3$, $PF_6$).

The reaction of the 1,3,2-diazaborolidine **2h** with $NO^+PF_6^-$ under the same conditions also led to the formation of product **3h** (Scheme 3). The employment of 4 equiv. of $NO^+PF_6^-$ did not lead to an improved yield. Instead 2 equiv. of the nitrosonium salt were recovered unaffected after the reaction.

Another situation was encountered when the 1,3,2-diazaborole was substituted by poor leaving groups, like the hydrido, ethynyl or cyano units. Here, only one fluoride atom was added to the boron center and borolium ions with two different ligands were formed. Thus, the reaction of the hydroborole **1e**, the cyanoborole **1i** or the ethynylborole **1j** with 2 equiv. of $NO^+PF_6^-$ afforded the intensely yellow (**3e**) or red borolium salts (**3i** and **3j**) in moderate to high yields (Scheme 4).

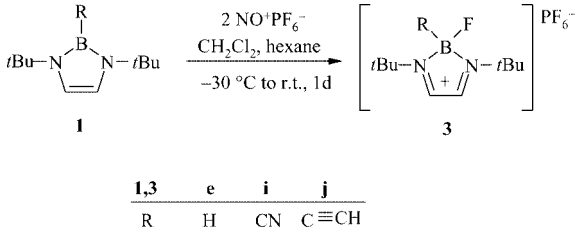


Scheme 4. Oxidation of diazaborole **1e**, **i**, **j** with $NO^+PF_6^-$.

Here, the hexafluorophosphate was observed as the sole counterion. The formation of the different diazaborolium salts studied here requires a twofold electron transfer. Principally, this could lead to the liberation of 2 equiv. of NO. At the top of the reaction vessel, where the released gases came into contact with air, an acidic reaction at a moist indicator paper was observed ($HNO_3$). The oxidation of the diazaborolidine **2h** to **3h**, however, required the removal of four electrons. According to experimental evidence this is accomplished by only 2 equiv. of the nitrosonium salt. Obvioulsy, here $NO^+$ is reduced to a nitrogen species with an oxidation number smaller than +II ($N_2$?). The treatment of diazaboroles containing electron-donating substituents on the boron atom, like dimethylamino- or methoxy-functionalized derivatives **1d** and **1b** with $NO^+PF_6^-$, did not lead to the borolium salts. Here, a ring opening took place with the formation of *N*,*N*′-di-*tert*-butyldiazabutadiene (**4**), $[Me_2NBF_2]_2$ (**5d**) or $[MeOBF_2]_n$ (**5b**), which were identified by comparison of their $^1H$ and $^{11}B$ NMR spectra with those of authentic samples (Scheme 5).

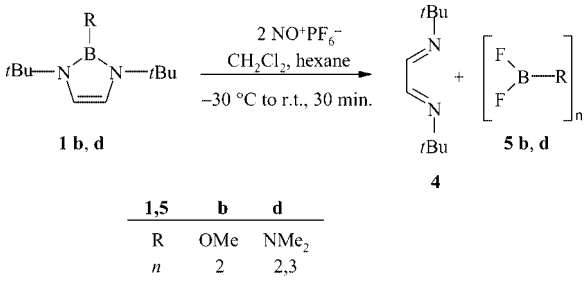


Scheme 5. Oxidation of diazaboroles **1b**, **d** with $NO^+PF_6^-$.

The 1,3,2-diazaboroles **1c**, **1k** (R = Ph) with methyl or phenyl substituents at the boron center were reluctant towards oxidation with $NO^+PF_6^-$ despite the fact that the methyl-substituted diazaborole **1c** and its saturated analog were easily oxidized electrochemically. Even an excess of the oxidant and stirring in boiling toluene for hours did not lead to the oxidation of the heterocycle.

Some of these experiments were repeated with $NO^+BF_4^-$ and $AgPF_6$ With the hexafluorophosphate, the results of the reaction with $NO^+PF_6^-$ were reproduced. In contrast to this, the reaction of **1h** and **2h** with $NO^+BF_4^-$ led to the mixed borolium salt **6h** (Scheme 6). In addition to elemental analysis, the identity of **6h** was evidenced by ESI mass spectroscopy. The signal of the cation of **6h** (*m*/*z* = 356 [M$^+$]) was observed with the correct isotopic distribution.

 © 2006 Wiley-VCH Verlag GmbH & Co. KGaA, Weinheim 

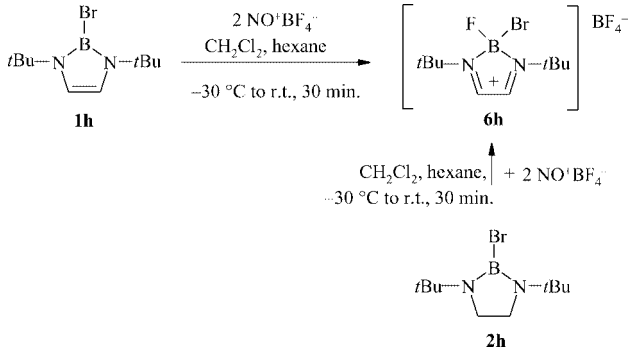


Scheme 6. Reaction of **1**, **2h** with $NO^+BF_4^-$.

With $AgPF_6$ as an oxidation agent, side reactions were observed depending on the stoichiometry of both reactants. Equimolar amounts of bromoborole **1h** and $AgPF_6$ led to the formation of equal portions of *t*BuN$^a$CH=CHN$^b$(*t*Bu)-BF($N^a$–*B*) (**1l**) and salt **3h**. The formation of the fluoroborole **1l** was avoided by the use of 2 equiv. of $AgPF_6$, and borolium salt **3h** was then isolated as the only product.

## Spectra and Structural Data

The $^{11}B\{^1H\}$ NMR spectrum of **3h** displays several signals in the typical area for tetracoordinate boron ($\delta \approx$ 6 ppm), due to the various borolium salts present.[7] In the $^1H$ NMR spectrum the ring protons absorb as broad singlets at $\delta$ = 8.87 ppm. The NMR spectroscopic data of the other borolium salts **3e**,**i**,**j** and **6h** are similar. ESI mass spectra of all the different borolium salts were obtained, whereby the cations represent the base peak. The products of the reaction of 1,3,2-diazaboroles with electron-donating groups (**1b**,**d**) were identified by comparison of the $^1H$ and $^{11}B\{^1H\}$ NMR spectroscopic data with authentic samples. In both cases, the $^1H$ NMR spectrum displays two characteristic singlets at $\delta$ = 1.10 and 8.09 ppm for the free *N*,*N*′-di-*tert*-butyldiazabutadiene. In addition to that, in the $^1H$ NMR spectrum of the reaction of **1b** with $NO^+PF_6^-$, another singlet at $\delta$ = 1.24 ppm is present, which belongs to the boron-bound methoxy group of the difluoro(methoxy)-borane **5b**. The product of the reaction of **1d** with $NO^+PF_6^-$, the difluoro(dimethylamino)borane **5d**, shows in the $^1H$ NMR spectrum a singlet at $\delta$ = 1.36 ppm. In the $^{11}B\{^1H\}$ NMR spectrum, the signals for $[F_2BOMe]_n$ ($n$ = 2,3) are observed at $\delta$ = 0.66 ppm and for $[F_2BNMe_2]_2$ at $\delta$ = 1.08 ppm, in agreement with the data of authentic samples.

## X-ray Structural Analysis of 3h

Yellow single crystals of **3h** suitable for an X-ray diffraction study (Table 2) were grown from a dichloromethane/hexane (1:1) mixture. Two independent diazaborolium cations are in the asymmetric unit in addition to one bromide and one tribromide anion. There are no bonding contacts between the cations and anions. The tribromide ion is slightly bent [Br(3)–Br(2)–Br(4) 175.65(1)°] with bond lengths Br(2)–Br(3) of 2.5811(4) Å and Br(2)–Br(4) of 2.5325(4) Å. In the symmetric anion of $(Me_3NH)Br_3$ the Br–Br bond length amounts to 2.54 Å (Br–Br–Br 171°), whereas in the nonsymmetric anion of $(PBr_4)Br_3$ (Br–Br–Br 177.3°) the Br–Br bond lengths are 2.39(1) and 2.91(1) Å.[8]

As the bonding parameters of both cations do not differ significantly, only the ring constructed of the atoms B(1), N(1), N(2), C(1) and C(2) is discussed in detail (Figure 1). The structure features a planar five-membered heterocycle (sum of bond angles 539.9°) with a tetracoordinate boron atom. The bond lengths B(1)–F(1) [1.366(3) Å] and B(1)–F(2) [1.369(3) Å] are slightly shorter than the B–F contacts in the $BF_4^-$ ion of $[\{Mes^*P{=}C(NMe_2)\}_2Cu]BF_4$, which range from 1.379(2) to 1.403(2) Å.[9] The boron–nitrogen bonds [B(1)–N(1) 1.607(3) Å, B(1)–N(2) 1.611(3) Å] are significantly longer than the average B–N single-bond of 1.59 Å found in amine–boranes.[10] Consistently, in compound **VIII** the B–N distance amounts to 1.588(3) Å.[11] An extremely long B–N bond was found in the Dewar borazine **IX** [1.752 Å].[12]

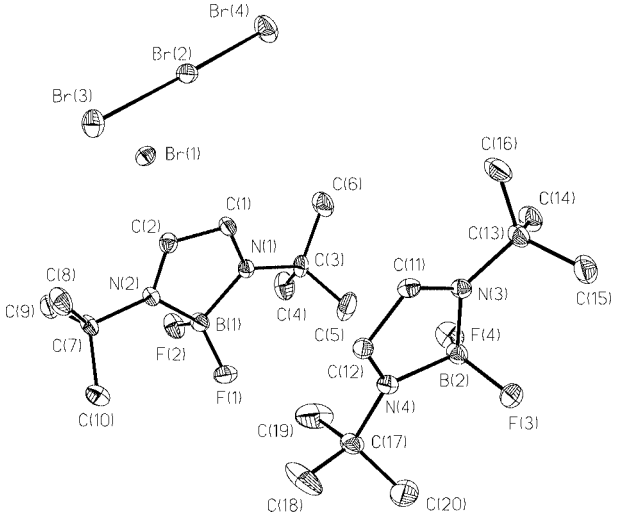


Figure 1. Crystal structure of **3h**; H atoms have been omitted for clarity. Selected bond lengths [Å] and angles [°]: B(1)–N(1) 1.607(3), B(1)–N(2) 1.611(3), B(1)–F(1) 1.366(3), B(1)–F(2) 1.369(3), N(1)–C(1) 1.282(3), N(2)–C(2) 1.290(3), N(1)–C(3) 1.513(3), N(2)–C(7) 1.511, C(1)–C(2) 1.491(3); N(1)–B(1)–N(2) 97.2(2), B(1)–N(1)–C(1) 110.4(2), B(1)–N(2)–C(2) 109.8(2), N(1)–C(1)–C(2) 111.0(2), N(2)–C(2)–C(1) 111.2(2), N(1)–B(1)–F(1) 110.9(2), N(1)–B(1)–F(2) 112.1(2), N(2)–B(1)–F(1) 112.4(2), N(2)–B(1)–F(2) 109.7(2), F(1)–B(1)–F(2) 113.3(2), B(1)–N(1)–C(3) 124.9(2), B(1)–N(2)–C(7) 125.2(2), C(1)–N(1)–C(3) 124.7(2), C(2)–N(2)–C(7) 124.4(2).

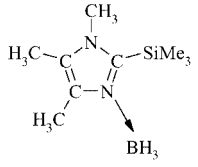


**VIII**

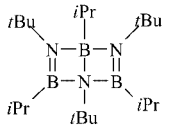


**IX**

In the precursor molecules, the 1,3,2-diazaborole B–N bond lengths range from 1.40–1.45 Å [e.g., (trimethylstannyl)diazaborole **1g**: B–N 1.439(7) and 1.450(7) Å].[1b] The

 © 2006 Wiley-VCH Verlag GmbH & Co. KGaA, Weinheim 

endocyclic C–N bond lengths [C(1)–N(1) 1.282(3) Å; C(2)–N(2) 1.290(3) Å] are characteristic for double bonds which are well comparable with those in the cyclic ketiminoborane **X** [1.273(3)–1.277(2) Å].[13]

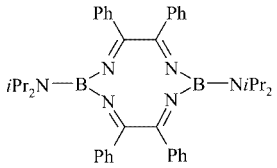


**X**

The carbon–carbon bond length in the cation [1.491(3) Å] indicates a bond order of unity, whereas in the precursor diazaboroles double bonds [e.g., 1.344(8) Å in **1g**] are typical. In the course of the oxidation process the angle at the boron atom N(1)–B(1)–N(2) (in diazaboroles ca. 105°) was compressed to 97.42(16)° in **3h**, whereas the endocyclic angles B(1)–N(1)–C(1) [110.41(17)°], B(1)–N(2)–C(2) [109.8(2)°], N(1)–C(1)–C(2) [111.0(2)°] and N(2)–C(2)–C(1) [111.2(2)°] are similar to those in **1g** [107.1(4)–110.2(5)°].

### Electrochemical Data

The established protocol for the synthesis of 2-halo-1,3,2-diazaboroles involves the reduction of the corresponding diazaborolium salts with a strong reducing agent, e.g. sodium amalgam.[1d] This preparative result is supported by reductive cyclovoltammetric experiments. All borolium salts **3e**,**h**,**i**,**j** and **6h** show a clean, reversible curve in the range of 0 to –2 V, performed in dichloromethane or acetonitrile as a solvent. The reductive cyclovoltammogram of **3j** is shown as a representative in Figure 2 with scan rates from 10 to 100 mV/s.

The distance between the two extrema (120 mV) exceeds the theroretical value of 58 mV and could be an indicator for quasireversibility.

The reductive potentials $E_{1/2}$ of the various borolium salts, taken from square-wave voltammetry, vary from –731 mV (**3e**) to –742 mV (**3j**), vs. the ferrocene/ferrocinium standard. As expected, no electrochemical oxidation was observed in the range of 0–3.2 V.

## Conclusions

A number of 1,3,2-diazaboroles with different substituents at the boron atom can be irreversibly oxidized using cyclic voltammetry; the potentials $E^o$, taken from square-wave voltammetry, vary strongly, subject to the functional group at the boron atom. We were interested in the nature of the oxidation products and decided to study the chemical oxidation of a series of 1,3,2-diazaboroles **1b**–**e** and **1h**,**i**,**j**. The products were either borolium salts with two fluoride ligands at the boron atom as given with **3h**, or borolium salts with one fluoride substituent in addition to the functional group at the boron center. The latter situation was observed with diazaboroles containing poor leaving groups as given in **1e**,**i**,**j**. With electron-donating groups at the boron atom (**1b**,**d**) oligomers of difluoroboranes were detected as products. Interestingly, the alkyl- or aryl-substituted diazaboroles can not be oxidized chemically, although the oxidative cyclovoltammogram of the methyl-substituted borole **1c** shows a clean, irreversible signal. The chemical oxidation of the 2-bromodiazaborolidine **2h** suprisingly led to the same product **3h** as in the case of the unsaturated analog.

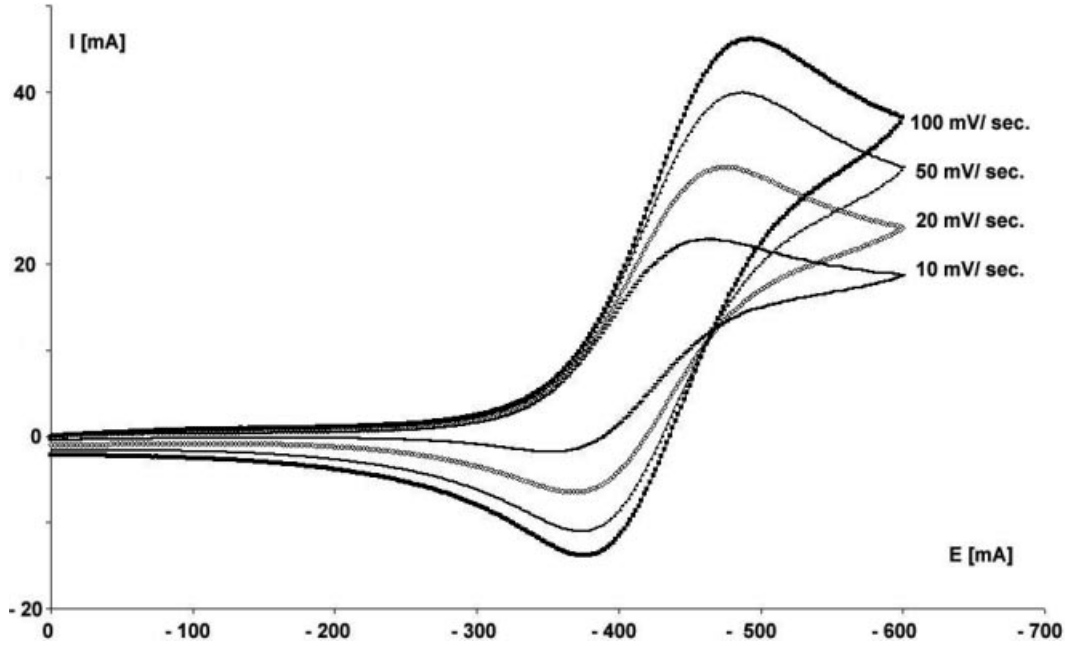


Figure 2. Reductive multiscan cyclovoltammogram of the borolium salt **3j**, 0 to –700 mV, $CH_2Cl_2$ with TBAPF at scan rates 10, 20, 50 and 100 mV/s.

 © 2006 Wiley-VCH Verlag GmbH & Co. KGaA, Weinheim 

The borolium salts **3e**,**h**,**i**,**j** and **6h** are deeply colored, air-stable compounds and prone for reduction by cyclic voltammetry. Hereby, the values of $E_{1/2}$ [ca. –735 mV] do not vary significantly.

## Experimental Section

**General:** All manipulations were performed under dry nitrogen. Solvents were rigorously dried with appropriate drying agents and distilled before use. The boron-containing heterocycles were prepared as described in the literature: *t*BuN$^a$=CH–CH=N$^b$(*t*Bu)-BR(*N*$^a$–*B*) (**1b**–**e**,**h**,**i**,**j**; R = OMe,[5] Me,[14] NMe$_2$,[1a] H,[1b] Br,[1d] CN,[1a] C$_2$H[1a]) and *t*BuN$^a$CH$_2$CH$_2$N$^b$(*t*Bu)BBr(*N*$^a$–*B*) (**2h**).[2] NMR spectra were recorded in $CD_2Cl_2$ with a Bruker AM Avance DRX 500 spectrometer ($^1$H, $^{11}$B, $^{13}$C, $^{19}$F) using $SiMe_4$, $BF_3{\cdot}OEt_2$ and $CFCl_3$ as external standards, mass spectra with a VG Autospec sector-field mass spectrometer (Micromass). The electrochemical experiments were performed with a PAR Model 270A instrument and the relevant software (Model 270). A system of microelectrodes with a three-electrode array was used. As working electrode a platinum wire was used (1.5 cm length, 0.5 mm diameter), which was formed to a helix around the counter electrode. A silver wire (1.5 cm length, 1 mm diameter) served as pseudo-reference electrode. All experiments were conducted in a glass device, which was flame dried prior to use and filled with dry dinitrogen. The determinations were performed in a 0.1 M solution of tetrabutylammonium hexafluorophosphate (TBAPF) in $CH_2Cl_2$ and MeCN with concentrations of the analyte of ca. $1{\cdot}10^{-4}$ mol L$^{-1}$ in the range of 0–3 V. The cyclovoltammograms were recorded with scan rates of 5–700 mV s$^{-1}$, whereby the results presented here were obtained with scan rates of 10, 20, 50 and 100 mV s$^{-1}$. All published potentials were confirmed by square-wave voltammetry (frequency: 5 Hz). The oxidation potentials were referenced vs. the ferrocene/ferrocinium couple ($E_{ox}$ = 0 eV) as a standard.

**[(*t*BuN$^a$=CH–CH=N$^b$*t*Bu)BF$_2$(*N*$^a$–*B*)]X (X = Br$^-$, Br$_3^-$, PF$_6^-$) (3h). Path a:** Compound **1h** (1.00 g, 3.86 mmol) was dissolved in a mixture of 20 mL of $CH_2Cl_2$ and 20 mL of hexane and cooled to –30 °C. Then solid $NOPF_6$ (1.36 g, 7.72 mmol) was added. The color of the solution turned pale yellow and after 2 h at 20 °C to orange. After 2 d at 4 °C, the product **3h** crystallized with different counterions (1.61 g). **Path b:** Analogous protocol with **2h** instead of **1h**. **Path c:** Analogous protocol with $AgPF_6$ instead of $NOPF_6$. $^1$H NMR: $\delta$ = 1.54 (s, 18 H, *t*Bu), 8.87 (s, 2 H, NCH) ppm. $^{13}$C NMR ($CD_2Cl_2$): $\delta$ = 27.7 [s, C(*C*H$_3$)$_3$], 60.8 [s, *C*(CH$_3$)$_3$], 151.2 (s, NCH) ppm. $^{11}$B{$^1$H} NMR: $\delta$ = 6.1 ppm. $^{19}$F{$^1$H} NMR: $\delta$ = –69.7 (d, $^2J$ = 710.0 Hz, PF$_6^-$), –148.8 (s, BF) ppm. $^{31}$P{$^1$H} NMR: $\delta$ = –144 (sept, $^2J$ = 710.0 Hz, PF$_6$) ppm. Due to different counterions the elemental analysis was meaningless. ESI MS: *m*/*z* = 217 [*t*BuN$^a$=CH–CHN$^b$(*t*Bu)BF$_2$(*N*$^a$–*B*)]$^+$.

**[(*t*BuN$^a$=CH–CH=N*t*Bu)BBrF(*N*$^a$–*B*)]BF$_4$ (6a):** To a chilled solution (–30 °C) of **1h** (1.00 g, 3.86 mmol) in a mixture of $CH_2Cl_2$ (20 mL) and hexane (20 mL), solid $NOBF_4$ (0.90 g, 7.72 mmol) was added. The color of the solution turned pale yellow and after 2 h at room temp. it changed to orange. After 3 d at 4 °C, pure **6a** (1.24 g, 88%) was collected as yellow crystals. $^1$H NMR: $\delta$ = 1.44 (s, 18 H, *t*Bu), 8.80 (s, 2 H, NCH) ppm. $^{13}$C NMR: $\delta$ = 27.9 [s, C(*C*H$_3$)$_3$], 61.2 [s, *C*(CH$_3$)$_3$], 151.7 (s, NCH) ppm. $^{11}$B{$^1$H} NMR: $\delta$ = 5.2 ppm. $^{19}$F{$^1$H} NMR: $\delta$ = –69.7 (d, $^2J$ = 710.0 Hz, PF$_6^-$), –148.5 (s, BFBr) ppm. $C_{10}H_{20}B_2BrF_5N_2$ (364.80): calcd. C 32.92, H 5.53, N 7.68; found C 33.44, H 6.13, N 7.99. ESI MS: *m*/*z* = 278 [*t*BuN$^a$=CH–CHN$^b$(*t*Bu)BBrF(*N*$^a$–*B*)]$^+$.

**[(*t*BuN$^a$=CH–CH=N$^b$*t*Bu)BHF(*N*$^a$–*B*)]PF$_6$ (3e):** Solid $NOPF_6$ (1.94 g, 11.10 mmol) was added to a solution (–30 °C) of **1e** (1.00 g, 5.55 mmol) in $CH_2Cl_2$ (20 mL) and hexane (20 mL). Again, the color of the solution changed during the reaction from colorless to orange. After 2 d of stirring at room temp., the solution was stored at –4 °C for 4 d, and 1.28 g (67%) was obtained as yellow crystals. $^1$H NMR: $\delta$ = 1.41 (s, 18 H, *t*Bu), 3.75 (br. s, BH), 8.53 (s, 2 H, NCH) ppm. $^{13}$C NMR: $\delta$ = 27.3 [s, C(*C*H$_3$)$_3$], 60.8 [s, *C*(CH$_3$)$_3$], 158.3 (s, NCH) ppm. $^{11}$B{$^1$H} NMR: $\delta$ = 5.2 ppm. $^{19}$F{$^1$H} NMR: $\delta$ = –69.7 (d, $^1J$ = 710.0 Hz, PF$_6^-$), –147.7 (s, BFBr) ppm. $^{31}$P{$^1$H} NMR: $\delta$ = –144 (sept, $^1J$ = 710.0 Hz, PF$_6^-$) ppm. No reliable analysis was obtained. ESI MS: *m*/*z* = 199 [*t*BuN$^a$=CH CHN$^b$(*t*Bu)-HBF(*N*$^a$–*B*)]$^+$.

**[(*t*BuN$^a$=CH–CH=N$^b$*t*Bu)B(CN)F(*N*$^a$–*B*)]PF$_6$ (3i):** A solution of **3i** (1.00 g, 4.88 mmol) and $NOPF_6$ (1.70 g, 9.76 mmol) was stirred in a mixture of $CH_2Cl_2$/hexane (1:1) for 3 d, whereby the color changed from yellow to red. The solution was stored at 4 °C for at least 5 d; then 1.39 g of the product (77%) was obtained as a red solid. $^1$H NMR: $\delta$ = 1.45 (s, 18 H, *t*Bu), 7.81 (s, 2 H, NCH) ppm. $^{13}$C{$^1$H} NMR: $\delta$ = 28.9 [s, C(*C*H$_3$)$_3$], 59.6 [s, *C*(CH$_3$)$_3$], 155.1 (s, NCH) ppm. $^{11}$B{$^1$H} NMR: $\delta$ = 5.1 ppm. $^{19}$F{$^1$H} NMR: $\delta$ = –69.7 (d, $^1J$ = 710.0 Hz, PF$_6^-$), –148.5 (s, BFCN) ppm. $^{31}$P{$^1$H} NMR: $\delta$ = –144 (sept, $^1J$ = 710.0 Hz, PF$_6$) ppm. $C_{11}H_{20}BF_7N_3P$ (369.11): calcd. C 35.79, H 5.46, N 11.38; found C 35.38, H 6.11, N 11.99. ESI MS: *m*/*z* = 224 [*t*BuN$^a$=CH CHN$^b$(*t*Bu)B(CN)F(*N*$^a$–*B*)]$^+$.

**[(*t*BuN$^a$=CH–CH=N$^b$*t*Bu)B(C$_2$H)F(*N*$^a$–*B*)]PF$_6$ (3j):** Neat $NOPF_6$ (1.72 g, 9.80 mmol) and **3j** (1.00 g, 4.90 mmol) were stirred in a mixture of $CH_2Cl_2$/hexane (1:1) for 1 d, whereby the solution turned from colorless to cherry-red. After 4 d at 4 °C, 1.25 g of the product was collected as a red solid (69%). $^1$H NMR: $\delta$ = 1.69 (s, 18 H, *t*Bu), 2.51 (s, C$_2$CH), 8.77 (s, 2 H, NCH) ppm. $^{13}$C NMR: $\delta$ = 29.0 [s, C(*C*H$_3$)$_3$], 66.0 [s, *C*(CH$_3$)$_3$], 89.8 (s, C$_2$H), 161.3 (s, NCH) ppm. $^{11}$B{$^1$H} NMR: $\delta$ = 5.1 ppm. $^{19}$F{$^1$H} NMR: $\delta$ = –69.7 (d, $^1J$ = 710.0 Hz, PF$_6^-$), –148.5 (s, BFC$_2$H) ppm. $^{31}$P{$^1$H} NMR: $\delta$

Table 2. Crystal data and collection parameters.

| | **3h** |
|---|---|
| Empirical formula | $C_{10}H_{20}BBr_3F_2N_2$ |
| $M_r$ [mg mol$^{-1}$] | 1.621 |
| Crystal dimensions [mm] | 0.30 × 0.21 × 0.15 |
| Crystal system | triclinic |
| Space group | $P\bar{1}$ |
| *a* [Å] | 10.1840(12) |
| *b* [Å] | 11.5580(11) |
| *c* [Å] | 14.1300(10) |
| *α* [°] | 84.033(7) |
| *β* [°] | 69.445(7) |
| *γ* [°] | 83.944(8) |
| *V* [Å$^3$] | 1544.6(3) |
| *Z* | 2 |
| $\rho_{calcd.}$ [Mg·m$^{-3}$] | 1.621 |
| $\mu$ [mm$^{-1}$] | 5.251 |
| *F*(000) | 748 |
| *Θ* [°] | 2.14–30.00 |
| No. refl. collected | 61803 |
| No. refl. unique | 8984 |
| *R*(int) | 0.0523 |
| No. refl. [$I > 2\sigma(I)$] | 6835 |
| Refined parameters | 468 |
| GOF | 1.048 |
| $R_F$ [$I > 2\sigma(I)$] | 0.0308 |
| $wR_{F2}$ [$I > 2\sigma(I)$] | 0.0517 |
| $\Delta\rho_{max/min}$ [e·Å$^{-3}$] | 0.770/–0.705 |

 © 2006 Wiley-VCH Verlag GmbH & Co. KGaA, Weinheim 

= –144 (sept, $^1J$ = 710.0 Hz, $PF_6$) ppm. $C_{12}H_{21}BF_7N_2P$ (368.12): calcd. C 39.15, H 6.15, N 7.61; found C 39.33, H 6.12, N 7.78. ESI MS: *m*/*z* = 223 [*t*BuN$^a$=CH CHN$^b$(*t*Bu)B($C_2$H)F($N^a$–*B*)]$^+$.

**Reaction of 1b with $NOPF_6$:** Compound **1b** (1.00 g, 4.48 mmol) and neat $NOPF_6$ (1.72 g, 9.80 mmol) were stirred in a mixture of hexane/$CH_2Cl_2$ (1:1) for 7 d. The solvent was removed in vacuo and 0.18 g (50%) of $[F_2BOMe]_n$ (*n* = 2, 3) was collected as a yellow oil. $^1$H NMR: $\delta$ = 1.24 (s, 3 H, OMe) ppm. $^{11}$B{$^1$H} NMR: $\delta$ = 0.66 ppm. $^{19}$F{$^1$H} NMR: $\delta$ = –152.6 ppm.

**Reaction of 1d with $NOPF_6$:** Compound **1d** (1.00 g, 4.75 mmol) and neat $NOPF_6$ (1.67 g, 9.5 mmol) were stirred in a mixture of hexane/$CH_2Cl_2$ (1:1) for 9 d. The solution turned red after minutes (a borolium salt is formed, but not stable). After removal of the solvent, 0.40 g (98%) of **5d** was collected as a colorless solid. $^1$H NMR: $\delta$ = 1.36 (s, 6 H, $NMe_2$) ppm. $^{11}$B{$^1$H} NMR: $\delta$ = 1.09 ppm. $^{19}$F{$^1$H} NMR: $\delta$ = –162.6 ppm.

**X-ray Structural Analysis:** Details are listed in Table 2. CCDC-292358 contains the supplementary crystallographic data for this paper. These data can be obtained free of charge from The Cambridge Crystallographic Data Centre via www.ccdc.cam.ac.uk/data_request/cif.


[1] a) L. Weber, E. Dobbert, A. Rausch, H.-G. Stammler, B. Neumann, *Z. Naturforsch., Teil B* **1999**, *54*, 363; b) L. Weber, E. Dobbert, A. Rausch, H.-G. Stammler, R. Boese, *Eur. J. Inorg. Chem.* **1999**, 491; c) L. Weber, E. Dobbert, R. Boese, M. T. Kirchner, D. Bläser, *Eur. J. Inorg. Chem.* **1998**, 1145; d) L. Weber, E. Dobbert, H.-G. Stammler, B. Neumann, R. Boese, D. Bläser, *Chem. Ber./Recueil* **1997**, *130*, 705.

[2] L. Weber, I. Domke, W. Greschner, A. Chrostowska, K. Miquieu, P. Baliére, *Organometallics* **2005**, *24*, 5455.

[3] a) M. Denk, R. Lennon, R. Hayashi, R. West, A. V. Belyakov, H. P. Verbe, A. Haaland, M. Wagner, N. Metzler, *J. Am. Chem. Soc.* **1984**, *116*, 2691; b) B. Gehrhus, M. F. Lappert, *J. Organomet. Chem.* **2001**, *617–618*, 209; c) M. Haaf, A. Schmiedl, T. A. Schmedake, D. R. Powell, A. J. Millevolte, M. Denk, R. West, *J. Am. Chem. Soc.* **1998**, *120*, 12714.

[4] W. A. Herrmann, M. Denk, J. Behm, W. Scherer, F.-R. Klingan, H. Bock, B. Solouki, M. Wagner, *Angew. Chem.* **1992**, *104*, 1489; *Angew. Chem. Int. Ed. Engl.* **1992**, *31*, 1485.

[5] L. Weber, M. Schnieder, P. Lönnecke, *J. Chem. Soc., Dalton Trans.* **2001**, 3459.

[6] L. Weber, H.-B. Wartig, H.-G. Stammler, B. Neumann, *Z. Anorg. Allg. Chem.* **2001**, *627*, 2663.

[7] S. C. Piers, W. E. Bourke, K. D. Conroy, *Angew. Chem.* **2005**, *117*, 5142; *Angew. Chem. Int. Ed.* **2005**, *44*, 5016.

[8] N. N. Greenwood, A. Earnshaw, *Chemie der Elemente*, VCH, Weinheim, **1988**, 1083.

[9] L. Weber, J. Krümberg, H.-G. Stammler, B. Neumann, *Z. Anorg. Allg. Chem.* **2006**, *632*, 879.

[10] P. Paetzold, *Adv. Inorg. Chem.* **1987**, *31*, 123.

[11] A. Wacker, H. Pritzkow, W. Siebert, *Eur. J. Inorg. Chem.* **1999**, 789.

[12] P. Paetzold, C. von Plotho, G. Schmid, R. Boese, *Z. Naturforsch., Teil B* **1984**, *39*, 1069.

[13] N. Weis, H. Pritzkow, W. Siebert, *Eur. J. Inorg. Chem.* **1999**, 7.

[14] G. Schmid, J. Schulze, *Chem. Ber.* **1977**, *110*, 2744.


Received: January 4, 2006
Published Online: July 11, 2006

 © 2006 Wiley-VCH Verlag GmbH & Co. KGaA, Weinheim 

DOI: 10.1002/ejic.200600017

# Third-Order Nonlinear Optical Properties of DA-salen-Type Nickel(II) and Copper(II) Complexes

João Tedim,[a][‡] Sónia Patrício,[a] Rosa Bessada,[a] Rui Morais,[b,c] Carla Sousa,[a][‡‡] Manuel B. Marques,[b,c] and Cristina Freire*[a]

**Keywords:** Third-order NLO properties / Z-scan technique / UV/Vis spectroscopy / Schiff bases

Third-order nonlinear and linear optical properties of nickel(II) and copper(II) complexes with salen ligands, functionalised with electron donor/acceptor groups (DA-salen), have been investigated in solution by the Z-scan technique using an Nd:YAG laser ($\lambda_{inc}$ = 1064 nm) and UV/Vis spectroscopy. The [M(DA-*salen*)] complexes exhibit positive nonresonant nonlinear refractive indexes ($n_2^I$) in the range 27.0–8.50·$10^{-21}$ $m^2 W^{-1}$ and nonlinear absorption coefficients ($\alpha_2^I$) within the range 1.80–26.0·$10^{-17}$ $m W^{-1}$. The latter values correspond to less than 10 % of the overall magnitude of the third-order susceptibility, $|\chi_3|$, which is the result of the absence of electronic transitions near $\lambda_{inc}$ = 1064 nm. For the group of $Ni^{II}$ complexes, the highest $n_2^I$ values are exhibited by the complexes with aromatic diimine bridges and large π-electron delocalisation, which leads to intense electronic charge-transfer bands ($\varepsilon > 16000$ $mol^{-1} dm^3 cm^{-1}$) in the region $\lambda$ = 275–500 nm. The complexes that exhibit charge-transfer bands near $\lambda_{inc}/2$ = 532 nm, also show the highest $\alpha_2^I$ values, a consequence of multiphoton absorption processes. For the group of $Cu^{II}$ complexes, the highest $n_2^I$ value is also observed by the complex that exhibits the most intense charge-transfer bands in the region $\lambda$ = 275–475 nm. Between $Ni^{II}$ and $Cu^{II}$ complexes with the same DA-salen ligands, those of copper show always higher $n_2^I$ values, indicating that NLO responses can also be fine-tuned by the metal centre.
(© Wiley-VCH Verlag GmbH & Co. KGaA, 69451 Weinheim, Germany, 2006)

## Introduction

During the last decade there has been a continuous demand for new materials capable of faster responses in optical information processing.[1] More specifically, the search has been focused on materials possessing high nonresonant nonlinear optical (NLO) responses. This implies that the materials must have not only high nonlinear refractive indexes, but also small linear and nonlinear absorptions; otherwise the slow photothermal effects arising from absorptive processes dominate the desirable fast photorefractive effects.[2]

Molecules with high NLO responses must possess small differences between the ground and low excited states; the corresponding electronic transitions should also correspond to strong absorptions and there must be a large difference between the dipole moments of the ground and excited states.[3] These properties can be accomplished by compounds with a D-π-A structure, where an electron donor (D) group and an electron acceptor (A) group are placed away from each other in the molecule through a π-conjugated system, therefore creating a high asymmetry in the electronic density.

Organic compounds with extensive π-delocalisation have emerged as promising NLO materials instead of inorganic solids, due to their ultrafast NLO responses, good processability as thin-film devices and enhanced nonresonant NLO responses.[4] More recently, transition metal complexes have appeared as an important alternative for the design of NLO materials, since the metal centre can impart important structural and electronic properties to the organic ligands, and consequently to the NLO responses.[5] Among transition-metal complexes, those with porphyrins and their derivatives exhibit great potential application due to their two-dimensional structures and unique electronic properties.[6] The $N_2O_2$ Schiff-base ligands derived from salicyladehyde and diamines (generically named as salen ligands) can be used as alternative building blocks for the design/preparation of NLO compounds owing to their synthetic versatility relative to the introduction of electron donor/acceptor functionalities and creation of extensive π-delocalisation to in-

[a] REQUIMTE/Departamento de Química, Faculdade de Ciências, Universidade do Porto,
Rua do Campo Alegre, 4169-007 Porto, Portugal
Fax: +351-22-6082959
E-mail: acfreire@fc.up.pt
[b] Departamento de Física, Faculdade de Ciências, Universidade do Porto,
4169-007 Porto, Portugal
[c] .INESC/Porto, Departamento de Física, Faculdade de Ciências, Universidade do Porto,
4169-007 Porto, Portugal
[‡] Current address: Department of Chemistry, University of Leicester, Leicester LE1 7RH, UK
[‡‡] Current address: Faculdade de Ciências da Saúde, Universidade Fernando Pessoa, Rua Carlos da Maia no. 296, 4200-150 Porto, Portugal

 © 2006 Wiley-VCH Verlag GmbH & Co. KGaA, Weinheim 

duce large electron asymmetry.[7] Furthermore, they can also coordinate several transition metal cations, in different oxidation states, which can additionally fine-tune the NLO responses.

The second-order NLO properties of metal complexes with salen-type ligands functionalised with electron donor and acceptor groups with a D-π-A structure have been extensively studied by Di Bella and Lacroix[8–14] and some important conclusions have been presented on the relationship between complex molecular structure and second-order NLO properties. It has been shown that second-order NLO responses of salen-type complexes were related to the presence of intense low-energy metal-to-ligand, ligand-to-metal charge transfer and intraligand transitions. The importance of the metal centre in these complexes was shown in the surveys carried out by the same authors and others.[11,14,15] Inclusion of metal centres in Schiff-base ligands was always accompanied by an enhancement of second-order NLO responses, compared to that of the free ligands and the role of the metal centre could be twofold, as it could act as both the donor of the D-π-A structure and/or as part of the π-bridging moiety.

With the work presented here we endeavour to extend the previous study on NLO properties of salen complexes to third-order and exploit the potential application of these compounds as building blocks for the preparation of materials with NLO properties suitable for ultrafast switching technologies. Several nickel(II) and copper(II) complexes with salen-type ligands functionalised with electron donor/acceptor groups – denoted here by [M(DA-salen)] complexes (Scheme 1) – were investigated by the Z-scan technique and their nonlinear refractive index and nonlinear absorption determined and the relationship between molecular NLO properties and complex molecular structure exploited. To the best of our knowledge, this is the first study on third-order NLO properties of (salen)nickel(II) and -copper(II) complexes in solution, although recently, the third-order NLO properties of some related bis(salicylaldiminato)$Ni^{II}$ and -$Cu^{II}$ complexes were measured by a coupling Z-scan technique and degenerate four-wave mixing.[16] The study presented here can also be the starting point for a survey of the NLO properties of electroactive films based on the same [M(DA-salen)] complexes, as previous works have shown that (salen)nickel(II) and -copper(II) complexes can be electropolymerized as electroactive films that exhibit interesting electrochromic properties.[17]

The potential application of these compounds/films in ultrafast switching technologies has determined the choice of the wavelength to study the third-order NLO responses, $\lambda_{inc}$ = 1064 nm, as the operating wavelength in ultrafast switching technologies is generally in the near infrared region ($\lambda$ = 1000–1500 nm).[18] It must be mentioned that very few of the organic materials reported so far are suitable for implementation in devices working in the near infrared.[4] In fact, the absolute magnitude of the nonlinear refractive index can be enhanced by one- or two-photon resonant transitions when the compound has strong absorptions close to $\lambda_{in}$ (1064 nm) and $\lambda_{in}/2$ (532 nm), and for the organic compounds with the largest nonlinear refractive index, strong electronic transitions are usually observed at $\lambda$ = 500–600 nm, leading to strong absorption losses.[19] In this context, the attempt to produce new molecular compounds with the referred and desired properties still remains an actual area of research. The divalent transition-metal complexes with salen ligands have square-planar geometries leading to strong electronic transitions (CT and intraligand) in the UV/Vis region and medium-intense d–d bands in the far visible region;[20] these electronic characteristics make them potential candidates for the preparation of materials with third-order nonlinear optical properties to be used in ultrafast optical communications.

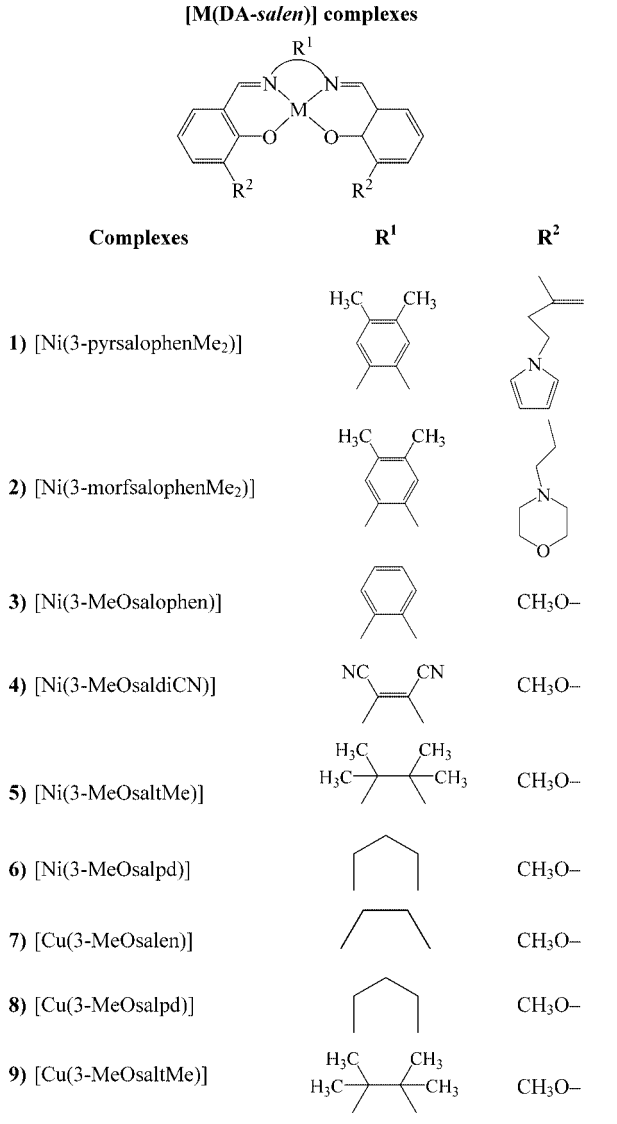


Scheme 1. Structures of [M(DA-salen)] complexes, M = Ni and Cu.

## Results and Discussion

The linear and nonlinear optical properties of the $Ni^{II}$ and $Cu^{II}$ complexes with DA-salen ligands summarised in

 © 2006 Wiley-VCH Verlag GmbH & Co. KGaA, Weinheim 

Scheme 1 have been investigated as a function of the different combinations of the electron donor/acceptor groups introduced in the ligand in the 3-position of the aldehyde fragment (methoxy group, pyrrol or morpholine derivatives) and in the diimine bridge (several aromatic and aliphatic diimine bridges). These $N_2O_2$ tetradentate ligands with delocalised π-systems impart strong ligand fields leading to almost square-planar geometries and low-spin ground states for the metal complexes (for those that have more than one spin ground state), inducing high degrees of covalence/delocalisation within the metal–ligand bonds. The presence of these electronic properties, which are important in the design of molecules with high nonlinear optical properties, can be firstly surveyed from the study of the linear optical properties of the metal complexes.

## UV/Vis Spectra

The UV/Vis spectra of $Ni^{II}$ and $Cu^{II}$ complexes with DA-salen ligands are very similar and present typically high intense bands ($\varepsilon$ higher than 1000 $mol^{-1}\,dm^3\,cm^{-1}$) occurring at $\lambda < 400$ nm, due to metal-to-ligand and ligand-to-metal charge transfer and intra-ligand transitions and one broad band in the visible region at $\lambda$ = 500–650 nm with $\varepsilon$ values ranging from 70 to 400 $mol^{-1}\,dm^3\,cm^{-1}$, corresponding to the nonresolved d-d transitions from the four low-lying d orbitals ($d_{xz}$, $d_{yz}$, $d_{z^2}$, $d_{x^2-y^2}$) to the empty (in the case of Ni) or half filled (in the case of Cu) $d_{xy}$ orbital.[20] This latter broad electronic band is not observed in the nickel complexes that have an extended π-system including the aldehyde moiety and the diimine bridge, as the more intense CT bands are shifted to higher wavelengths, therefore preventing its observation. This is a general trend that is observed for nickel and copper complexes with salen ligands that have an extended π-system and is a consequence of the high degree of π-delocalisation between the metal centre and the ligand, which in turn induces an increase in $\varepsilon$ values. The $\lambda_{max}$ bands for all the complexes and the corresponding $\varepsilon$ values are summarised in Table 1. The electronic spectra of nickel and copper complexes with salen complexes functionalised with methoxy groups are shown in Figures 1 and 2 as examples.

The energy of the broad band assigned to d-d transitions can provide a rough estimate of the equatorial ligand-field strength, since one of the electronic transitions comprised in the band envelope is $d_{xy} \leftarrow d_{x^2-y^2}$ and the energy associated with this transition is $10Dq$-$C$.[7,20] No comparison is possible between energies for d-d transitions for the Ni complexes with aliphatic imine bridges (complexes **5** and **6**) to those with aromatic imine bridges (complexes **1** to **4**), as they are not observed in the latter complexes. However, for those with aliphatic bridges (Ni and Cu complexes) it can be inferred that an increase in the number of bridging carbon atoms is associated with a small decrease in ligand field, as can be gathered from the lower energies of d-d

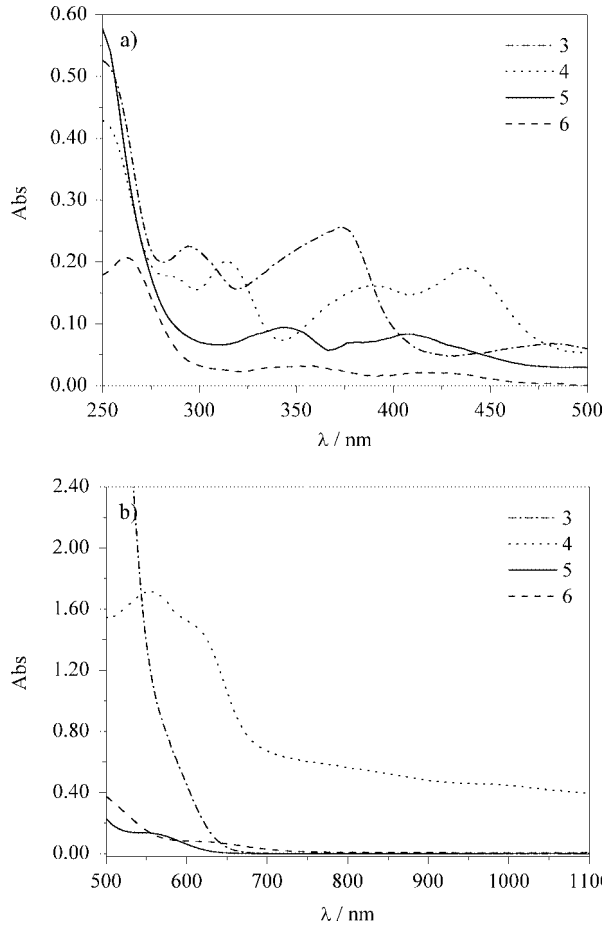


Figure 1. UV/Vis spectra of [Ni(3-MeOsalen)]-based complexes in solution recorded in the range: (a) $\lambda$ = 250–500 nm (complex concentration $1{\cdot}10^{-5}$ mol $dm^{-3}$) and (b) $\lambda$ = 500–1100 nm (complex concentration $1{\cdot}10^{-3}$ mol $dm^{-3}$).

Table 1. Electronic bands ($\lambda_{max}$) and respective absorption coefficients ($\varepsilon$) for the [M(DA-salen)] complexes.

| Complex | $\lambda_{max}$ [nm] ($\varepsilon$ [$mol^{-1}\,dm^3\,cm^{-1}$]) |
|---|---|
| **1** | 254 (42800), 294 (16400), 312 (18800), 376 (22700), 447 (14300)[a], 471(9000) |
| **2** | 258 (34400), 294 (16100)[a], 374 (18800), 478 (6000), 666 (100) |
| **3** | 294 (22600), 396 (19900)[a], 356 (23100)[a], 372 (25600), 482 (6800), 560 (1000)[a] |
| **4** | 254 (42100)[a], 286 (17800), 314 (20300), 388 (16200), 438 (19100), 510 (1400)[a], 556 (1600), 612 (1400)[a] |
| **5** | 330 (8400)[a], 344 (9400), 376 (6900)[a], 408 (8300), 554 (100)[a] |
| **6** | 262 (20700), 346 (3100), 358 (3300), 416 (2100), 630 (100)* |
| **7** | 278 (34200), 360 (9600)[a], 372 (10400), 378 (10000)[a], 574 (400) |
| **8** | 280 (28800), 366 (7700)[a], 372 (7900), 378 (7700)[a], 610 (300) |
| **9** | 280 (25900), 360 (7700)[a], 366 (8100), 378 (7700), 566 (400) |

[a] Inflections.

 © 2006 Wiley-VCH Verlag GmbH & Co. KGaA, Weinheim 

transitions for the complexes with the 1,3-propanediamine bridge; this decrease must be due to an increase in the size of the ligand cavity. On the other hand, for Cu complexes the introduction of methyl groups in the ethylene bridge leads to a slight increase in ligand field strength due to the donor capacity of these groups. No trend in the values of $\lambda_{max}$ of the d-d band was detected when comparison is made between the nickel and the copper complexes with the same ligands.

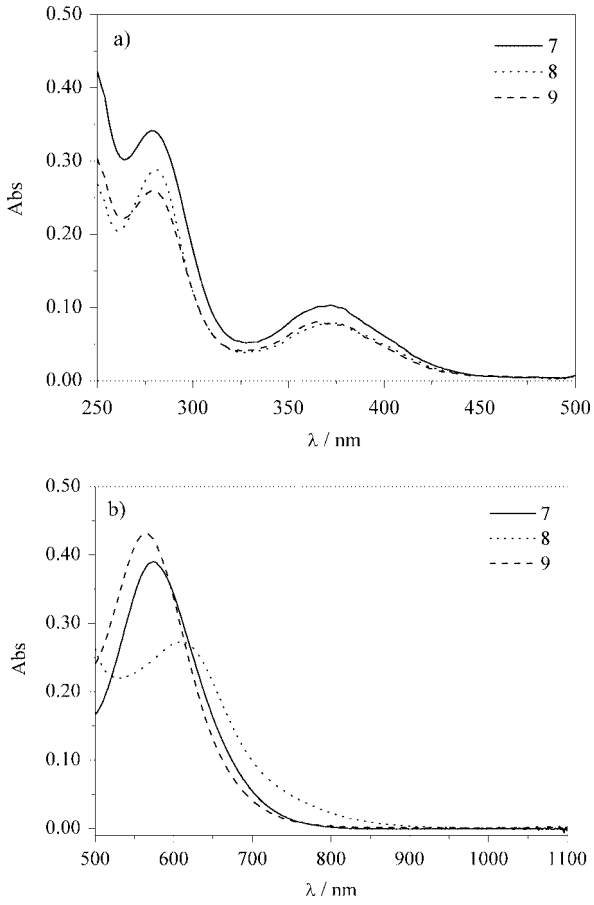


Figure 2. UV/Vis spectra of [Cu(3-MeOsalen)]-based complexes in solution recorded in the range: (a) $\lambda$ = 250–500 nm (complex concentration $1 \cdot 10^{-5}$ mol dm$^{-3}$) and (b) $\lambda$ = 500–1100 nm (complex concentration $1 \cdot 10^{-3}$ mol dm$^{-3}$).

Another key aspect to analyse in terms of the linear optical properties is the values of $\varepsilon$, for both types of electronic bands: d-d and charge-transfer bands. In this context it must be mentioned that the $\varepsilon$ values (d-d and CT bands) for the Cu complexes are always higher than those of the Ni homologues, and complexes with aromatic diimine bridges show higher values than those with aliphatic diimine bridges, with the complex **1** showing the most intense bands of the group of DA-salen studied in this work. These can be related to the degree of covalence in the M–L bonds, and thus copper complexes will have a high degree of covalence when compared with the homologous nickel complexes.

## Z-Scan Measurements

The Z-scan technique used to evaluate the NLO properties was developed by Sheik-Bahae et al.[21,22] and is based on the transformation of phase distortion during beam propagation. By using a single Gaussian laser beam, the transmittance of a nonlinear medium is measured as a function of the sample position (Z), measured with respect to the focal plane; further details on the Z-scan technique can be gathered from the literature.[21,22] This technique requires relatively simple experimental apparatus, when compared with other common techniques, such as nonlinear interferometry, degenerate four-wave mixing (DFWM) and third harmonic generation (THG) and provides the direct measurement of both nonlinear refractive index and absorption coefficient, along with their sign,[23] which allows the estimation of the third-order susceptibility coefficient $|\chi_3|$ in its real and imaginary components, respectively. Moreover, the measurement of third-order optical properties is not limited by restrictions in the system symmetry, which is an important advantage when compared with second-order techniques, which can only be used on noncentrosymmetric systems.

The experimental setup of the Z-scan technique was validated using carbon disulfide, which has been extensively studied in the literature.[2,21,22] Figure 3a shows the $CS_2$ Z-scan results and respective fitting curve obtained by the least-squares method: it shows the expected peak-valley curve with a pre-focal minimum followed by a post-focal maximum, which demonstrates a nonlinear refraction index with a positive sign. When compared with published works[21,22] the curve shape allows us to ignore nonlinear effects arising from nonelectronic processes, mostly thermal effects, since the refractive processes depend on the temperature and the use of high-energetic lasers could be a contribution to the rise in the local temperature of the sample region where the laser is focused. Under these conditions, if the complexes present nonlinear refractive indexes, they will be only due to electronic processes. The nonlinear refractive index of $CS_2$ was measured and is $1.09 \cdot 10^{-18}$ m$^2$ W$^{-2}$, which is very close to the reported value.[2]

All the complexes show a peak-valley curve with a pre-focal minimum followed by a post-focal maximum, which demonstrates a nonlinear refraction index with a positive sign. The almost symmetrical shape of the Z-scan plots of the complexes shows that nonlinear refraction effects dominate any nonlinear absorption. In Figure 3b a typical closed Z-scan result and the corresponding fitting curve are depicted for complex **3**.

The nonlinear refractive indexes of the complexes, $n_2^I$, were calculated using the $CS_2$ nonlinear refractive index by applying Equations (1) and (2), deduced from the theory inherent to the Z-scan technique[21] and considering the experimental conditions unchanged during all the measurements performed. The nonlinear absorption coefficients, $\alpha_2^I$, were calculated using Equation (3), based on the Beer–Lambert law, in which $\Delta T_{p,v}$ is the difference of normalized transmittance peak-valley due to nonlinear refraction,

 © 2006 Wiley-VCH Verlag GmbH & Co. KGaA, Weinheim 

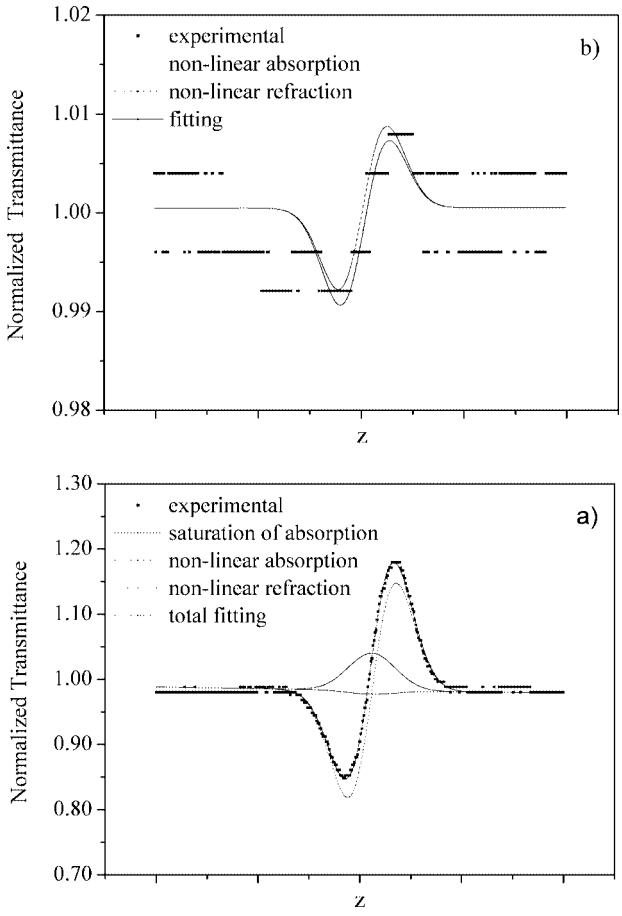


Figure 3. Closed Z-scan measurement at $\lambda_{inc}$ = 1064 nm; normalised transmission plotted as a function of sample position $z$ of: (a) $CS_2$ and (b) a solution of complex **3** in $CH_3CN$.

$\Delta T_{v(absorption)}$ is the difference of normalized transmittance occurring in the valley due to nonlinear absorption. Both $\Delta T$ values were obtained using the least-squares method, $L$ is the sample length and $a$ is the linear absorption coefficient.

$$n_2^I(sample) = \left(\frac{L_{eff\,(reference)}}{L_{eff\,(sample)}}\right) \times \left(\frac{\Delta T_{p,v(sample)}}{\Delta T_{p,v(reference)}}\right) \times n_2^I(reference) \quad (1)$$

$$L_{eff} = \left(\frac{1 - e^{-\alpha L}}{\alpha}\right) \quad (2)$$

$$\alpha_2^I = \left(\frac{\ln(1 - \Delta T_{v(absorption)} \cdot e^{\alpha L}}{I_0}\right) \quad (3)$$

The nonlinear refractive index and nonlinear absorption coefficients allow the estimation of the third-order susceptibility coefficient, $|\chi_3|$, in its real and imaginary components, respectively using Equations (4) and (5);[2] $n_0$ is the linear refractive index, $n_2^I$ is the nonlinear refractive index, $a_2^I$ is the nonlinear absorption coefficient, $c$ is the light velocity and $k$ the magnitude of the wave vector, $k = 2\pi/\lambda$, where $\lambda$ is the wavelength.

$$\chi_3^{(real)} = 2n_2^I \cdot {n_0}^2 \cdot {\varepsilon_0}^2 \cdot c \quad (4)$$

$$\chi_3^{(imaginary)} = \left(\frac{10^8 \cdot {n_0}^2 \cdot \alpha_2^I \cdot \varepsilon_0}{(2\pi \cdot k \cdot c)}\right) \quad (5)$$

In Table 2 are summarised the normalized values for nonlinear refractive indexes ($n_2^I$), nonlinear absorption coefficients ($a_2^I$) and the third-order susceptibility coefficient ($|\chi_3|$) and its real and imaginary components; data is normalised for a complex concentration of 1 mmol dm$^{-3}$.

The complexes show nonlinear refractive indexes ($n_2^I$) at $\lambda$ = 1064 nm in the range of 27.0–8.50·10$^{-21}$ m$^2$ W$^{-1}$and nonlinear absorption coefficients ($a_2^I$) within the range of 1.80–26.0·10$^{-17}$ m W$^{-1}$. The contribution of nonlinear refractive indexes and the nonlinear absorption coefficients to the overall magnitude of the third-order susceptibility

Table 2. Values of nonlinear refractive indexes ($n_2^I$), nonlinear absorption coefficients ($a_2^I$) and third-order susceptibility coefficients ($|\chi_3|$), real and imaginary components, for the [M(DA-salen)] complexes.[a]

| Complex | Solvent | $n_2^I \cdot 10^{21}$ [m$^2$ W$^{-1}$] | $a_2^I \cdot 10^{17}$ [m W$^{-1}$] | $\lvert\chi_3\rvert^{(real)} \cdot 10^{34}$ [m$^2$ V$^{-2}$] | $\lvert\chi_3\rvert^{(imag)} \cdot 10^{35}$ [m$^2$ V$^{-2}$] | $\lvert\chi_3\rvert \cdot 10^{34}$ [m$^2$ V$^{-2}$] |
|---|---|---|---|---|---|---|
| **7** | $CH_3CN$ | 26.7 | 1.85 | 25.4 | 2.65 | 25.4 |
| **1** | $CH_2Cl_2$ | 20.5 | 16.8 | 19.5 | 24.1 | 19.6 |
| **9** | $CH_3CN$ | 17.1 | 8.18 | 16.3 | 11.8 | 16.4 |
| **4** | $CH_3CN$ | 12.6 | 25.4 | 12.1 | 36.5 | 12.6 |
| **3** | $CH_3CN$ | 12.6 | 4.63 | 12.0 | 6.66 | 12.0 |
| **8** | $CH_3CN$ | 11.3 | 10.6 | 10.8 | 15.2 | 10.9 |
| **6** | $CH_2Cl_2$ | 11.1 | 11.6 | 10.6 | 16.7 | 10.7 |
| **2** | $CH_3CN$ | 9.53 | 4.07 | 9.09 | 5.85 | 9.11 |
| **5** | $CH_3CN$ | 8.52 | 3.90 | 8.13 | 5.61 | 8.14 |

[a] The complexes are displayed by decreasing values of $n_2^I$. All values are normalised for complex concentration of 1 mmol dm$^{-3}$. The values of $|\chi_3|$ have been calculated with the following expression: $|\chi_3| = \sqrt{\left|\chi_3^{real}\right|^2 + \left|\chi_3^{imaginary}\right|^2}$.

 © 2006 Wiley-VCH Verlag GmbH & Co. KGaA, Weinheim 

coefficient is presented in Figure 4. Analysis of the plot indicates that in general, the imaginary part of $|\chi_3|$, associated with $a_2{}^I$, contributes less than 10% to the overall $|\chi_3|$. Therefore, we can conclude that the NLO responses of [M(DA-salen)] complexes investigated in this work are mainly controlled by nonlinear refractive processes and this is an important result for our main objective of designing molecules with potential application for optical communications.

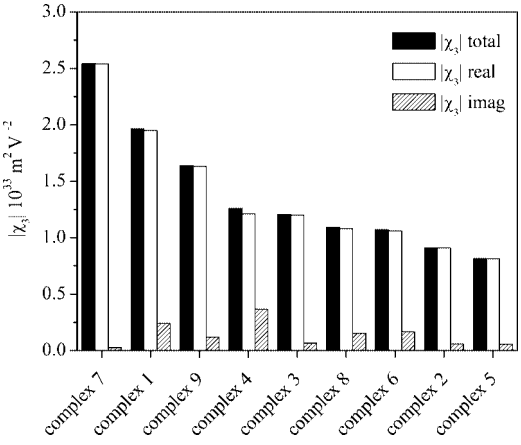


Figure 4. Different contributions for $|\chi_3|$ in [M(DA-salen)] complexes, M = Ni and Cu.

As mentioned previously, low values of $a_2{}^I$ are compatible with the absence of electronic transitions near $\lambda_{inc}$ and $\lambda_{inc}/2$. In fact, none of the complexes showed electronic transitions at $\lambda_{inc}$ = 1064 nm (see UV/Vis spectra). Nevertheless, complexes **1** and **4** show two intense electronic transitions in the vicinity of $\lambda_{inc}/2$ = 532 nm, the wavelength at which the double-photonic transitions occur, and thus are responsible for their highest nonlinear absorption coefficients.

The bis(salicylaldiminato)Ni$^{II}$ and -Cu$^{II}$ analogues[16] of the complexes described in this work show a similar trend for their third-order NLO properties measured at $\lambda$ = 532 nm: values of $n_2{}^I$ around $10^{-19}$ m$^2$ W$^{-1}$ and a small contribution of the nonlinear absorption to the overall $|\chi_3|$. This similarity can be attributed to the same geometry, ligand coordinating atoms and electronic structure of the metal centres in both types of complexes.

### Effect of the Substituents on the NLO Responses

For the group of Ni$^{II}$ complexes functionalised with methoxy groups in 3-position of the aldehyde moiety, complexes **3** to **6**, the highest NLO responses are shown by complexes with aromatic diimine bridges with electron acceptor properties, [Ni(3-MeOsaldiCN)] (**4**) and [Ni(3-MeOsalophen)] (**3**). The highest NLO response of these complexes is the result of the presence of intense low-energy charge-transfer bands that are associated with a high variation of the transition dipolar moment vector. These are induced by the high degree of aromaticity, and the proper combination between the π-donor properties of the methoxy group in the aldehyde moiety and the π-acceptor properties of the imine bridges; on the contrary the σ-donor groups ($CH_3$ and $CH_2$) in the aliphatic imine bridges of complexes **6** and **5** decrease the charge asymmetry and thus the NLO responses. Comparison between Ni$^{II}$ complexes with the same diimine bridge derived from 4,5-Me$_2$-1,2-phenylenediimine and different substituents in the aldehyde, complexes **1** and **2**, show that the former complex, which exhibits the largest number and most intense electronic bands is the one that presents the highest NLO response; in this case the proper combination between substituents to enhance the NLO response is the $CH_3$ σ-donor groups within the aromatic imine bridge and the pyrrol derivative in the 3-position of the aldehyde, that have electron-acceptor properties.

Within the Cu complexes, that are also functionalised with methoxy groups in the 3-position of the aldehyde, but have aliphatic imine bridges, the nonlinear refractive index of [Cu(3-MeOsalen)] (**7**) is considerably higher than those of [Cu(3-MeOsalpd)] (**8**) and [Cu(3-MeOsaltMe)] (**9**), following the same trend of the $\varepsilon$ values associated with the CT transitions. In this case, the NLO responses decrease with the increase in the number of $CH_3$ or $CH_2$ electron-donor groups in the aliphatic bridge, suggesting, as referred for Ni complexes, that methoxy groups still act as π-donor groups.

Between Ni$^{II}$ and Cu$^{II}$ complexes with the same DA-salen ligands, those of copper show higher $n_2{}^I$ values, indicating that, besides the presence of DA electron groups within the salen ligand, NLO responses can also be fine-tuned by the metal centre. The increase in the NLO responses on going from (DA-salen)Ni$^{II}$ to -Cu$^{II}$ complexes have also been observed in the studies performed by Di Bella and Lacroix on the second-order NLO properties of similar complexes[11,12] and in the study of the third-order NLO properties (at $\lambda$ = 532 nm) of the bis(salicylaldiminato)Ni$^{II}$ and -Cu$^{II}$ complexes.[16] Some insights into a possible explanation can be gathered from their UV/Vis spectra, although the number of complexes to be compared is small.

The UV/Vis spectra of homologous Ni$^{II}$ and Cu$^{II}$ complexes, **5**, **6**, **8** and **9**, in the range of $\lambda$ = 250–500 nm (Figure 5a) show no significant differences in the $\varepsilon$ values of the CT bands, suggesting that the differences within the NLO responses may depend on other factors. Nevertheless, analysis of the spectra in the range $\lambda$ = 500–1100 nm, Figure 5b, where d-d bands appear, show some interesting features: the d-d bands of the Cu$^{II}$ complexes are more intense than those of the Ni$^{II}$ analogues, and the intensity differences are higher for the complexes with the tetramethylethylene bridge; the NLO response follows exactly the same trend. The differences in third-order nonlinear responses for these complexes with salen ligands with aliphatic bridges suggests that the metal centre displays an important role in the variation of the molecular transition dipole moment and thus in the NLO response.

 © 2006 Wiley-VCH Verlag GmbH & Co. KGaA, Weinheim 

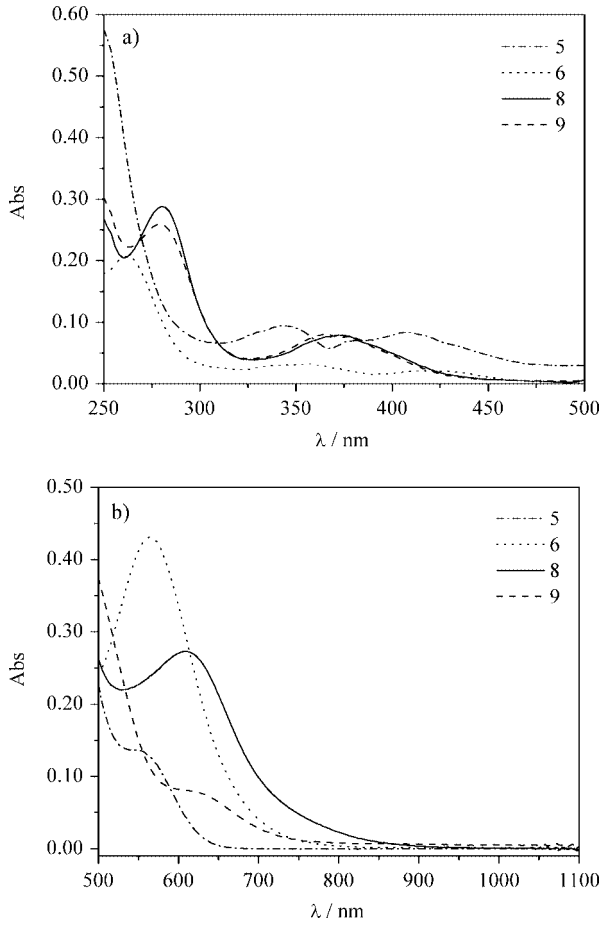


Figure 5. Comparison between UV/Vis spectra of $Ni^{II}$ and $Cu^{II}$ with the same DA-salen ligands in the range: (a) $\lambda$ = 250–500 nm (complex concentration $1 \cdot 10^{-5}$ mol dm$^{-3}$) and (b) $\lambda$ = 500–1100 nm (complex concentration $1 \cdot 10^{-3}$ mol dm$^{-3}$).

It is worthwhile to mention that [Cu(3-MeOsalen)] (**7**) is the complex with the highest $n_2^I$ of the compounds studied in this work, beyond those of nickel with high extensive π-delocalisation and efficient DA groups to create charge asymmetry. As the number of copper complexes used in this work is limited, no further conclusions can be made on the role of this cation in the NLO responses of Schiff-base ligands. Several Cu complexes with DA-salen ligands are now being prepared and their third-order NLO properties evaluated.

## Conclusions

The linear and third-order NLO properties of some nickel(II) and copper(II) complexes with salen ligands functionalised with donor/acceptor groups, [M(DA-salen)], were investigated by combining electronic spectroscopy and the Z-scan technique.

The [M(DA-salen)] complexes exhibit positive nonresonant nonlinear refractive indexes ($n_2^I$) in the range of 27.0–$8.50 \cdot 10^{-21}$ m$^2$ W$^{-1}$ and nonlinear absorption coefficients ($a_2^I$) within the range of 1.80–$26.0 \cdot 10^{-17}$ m$^2$ W$^{-1}$. The nonlinear absorption contribution is less than 10% of the overall magnitude of the third-order susceptibility, $|\chi_3|$, which is the result of the absence of electronic transitions near $\lambda_{inc}$ = 1064 nm or strong absorption near $\lambda_{in}/2$ = 532 nm, a consequence of the square-planar geometry of all the complexes coupled with a strong in-plane ligand field imposed by the DA-salen ligands.

The NLO responses follow the same trends observed for the number and ε values of the metal complexes electronic bands in the UV/Vis region, and therefore UV/Vis spectroscopy has been shown to be an important tool to complement the study of NLO properties for [M(DA-salen)] complexes.

The combination of electron-donor/acceptor groups in [M(DA-salen)] complexes strongly affects the nature and value of NLO response; nevertheless, more important than the strength of individual donor and/or acceptor groups is the combination of both D/A groups to achieve a high nonlinear response.

The results presented in this work also show that replacement of $Ni^{II}$ for $Cu^{II}$ in DA-salen with aliphatic bridges leads to a significant improvement in the NLO response; however, no further explanations could be anticipated, because of the low number of complexes that have been studied. In future, we intend to prepare more $Cu^{II}$ complexes with DA-salen and other metal complexes in order to better understand the role of the metal centre within the third-order NLO responses.

## Experimental Section

**Materials:** All the solvents were obtained from Merck; nickel(II) acetate 4-hydrate and copper(II) acetate 1-hydrate were obtained from Riedel–de Haën, and diaminomaleonitrile from Fluka. The reagents 2-hydroxy-3-methoxybenzaldehyd, 4,5-dichloro-1,2-phenylenediamine, 4,5-dimethyl-1,2-phenylenediamine, 1,2-phenylenediamine, 1,3-diamino-2-propanol, ethylenediamine, 1,3-diaminopropane and 2,3-dimethyl-2,3-dinitrobutane were obtained from Aldrich; all the chemicals were used as received. The compound 2,3-diamino-2,3-dimethylbutane was prepared by the method of Sayre,[24] and 4-(ethoxymethyl)morpholine was prepared as described elsewhere.[25] The DA-salen ligands were prepared by the standard method of refluxing an ethanolic solution containing stoichiometric amounts of the aldehyde and the diamines:[26] typically 10 mmol of the aldehyde was treated with 5 mmol of the diamines, leading to yields in the range of 70–90%. An exception was the preparation of the ligand 1,2-(4,5-dimethyl)phenylenbis(3-oxyethylpyrrole)salicylideneimine that was synthesised as described in the literature.[27] Similarly, the respective complexes were prepared by the usual method of refluxing an ethanolic solution of the DA-salen ligand and the metallic acetate in stoichiometric quantities[10,26] (typically 5 mmol of each reagent), leading to yields in the range of 50–80%. An exception was the complex [Ni(3-MeOsaldiCN)] (**4**), which was prepared by a procedure described in the literature.[12]

**[Ni(3-pyrsalophen$Me_2$)] (1):** $^1$H NMR (300 MHz, $CDCl_3$): $\delta$ = 7.78 (s, 2 H, C*H*N), 7.56 (s, 2 H, $H_{arom}$), 6.85–6.71 (m, 8 H, $H_{arom}$), 6.33–6.20 (t, 6 H, $H_{arom}$), 4.31–4.23 (t, 4 H, $CH_2$), 2.99–2.96 (t, 4 H, $CH_2$), 1.90 (s, 6 H, $CH_2$) ppm. $C_{36}H_{32}N_4NiO_6$ (675.4): calcd. C 64.0, H 4.8, N 8.3; found C 64.0, H 4.8, N 8.2.

 © 2006 Wiley-VCH Verlag GmbH & Co. KGaA, Weinheim 

**[Ni(3-morphsalophenMe$_2$)] (2):** $^1$H NMR (300 MHz, DMSO): $\delta$ = 8.78 (s, 2 H, C*H*N), 7.95 (s, 2 H, H$_{arom}$), 6.75–7.49 (m, 6 H, H$_{arom}$), 3.52–3.60 (m, 12 H, C$H_2$O, C$H_2$N), 2.37–2.46 (m, 8 H, C$H_2$), 2.30 (s, 6 H, C$H_3$) ppm. $C_{32}H_{36}N_4NiO_4$ (599.4): calcd. C 64.1, H 6.1, N 9.4; found C 63.1, H 6.1, N 9.4.

**[Ni(3-MeOsalophen)]·H$_2$O (3):** $^1$H NMR (300 MHz, $CDCl_3$): $\delta$ = 8.22 (s, 2 H, C*H*N), 7.71–6.30 (m, 10 H, H$_{arom}$), 3.84 (s, 6 H, OC$H_3$) ppm. $C_{22}H_{18}N_2NiO_4·H_2O$ (451.1): calcd. C 58.6, H 4.5, N 6.2; found C 58.6, H 4.6, N 6.3.

**[Ni(3-MeOsaldiCN)]·H$_2$O (4):** $^1$H NMR (300 MHz, $CDCl_3$): $\delta$ = 8.08 (s, 2 H, C*H*N), 7.01–6.74 (m, 6 H, H$_{arom}$), 3.07 (s, 6 H, OC$H_3$) ppm. $C_{20}H_{14}N_4NiO_4·H_2O$ (451.1): calcd. C 53.3, H 3.6, N 12.4; found C 53.7, H 3.1, N 12.3.

**[Ni(3-MeOsaltMe)] (5):** $^1$H NMR (300 MHz, $CDCl_3$): $\delta$ = 7.50 (s, 2 H, C*H*N), 6.70–6.50 (m, 6 H, H$_{arom}$), 3.80 (s, 6 H, OC$H_3$), 1.40 (s, 12 H, C$H_3$) ppm. $C_{22}H_{26}N_2NiO_4$ (441.2): calcd. C 59.9, H 5.9, N 6.3; found C 59.9, H 6.0, N 6.3.

**[Ni(3-MeOsalpd)]·2H$_2$O (6):** $^1$H NMR (300 MHz, $CDCl_3$): $\delta$ = 7.90 (s, 2 H, C*H*N), 6.96–6.74 (m, 6 H, H$_{arom}$), 3.91 (s, 6 H, OC$H_3$), 3.77–3.71 (m, 4 H, C$H_2$), 2.17–2.00 (m, 2 H, C$H_2$) ppm. $C_{19}H_{20}N_2NiO_4·2H_2O$ (435.1): calcd. C 52.4, H 5.6, N 6.4; found C 52.0, H 5.6, N 6.3.

**[Cu(3-MeOsalen)]·H$_2$O (7):** $C_{18}H_{18}CuN_2O_4·H_2O$ (407.9): calcd. C 53.0, H 4.9, N 6.9; found C 53.5, H 5.3, N 6.9.

**[Cu(3-MeOsalpd)] (8):** $C_{19}H_{20}CuN_2O_4$ (403.9): calcd. C 56.5, H 5.0, N 6.9; found C 56.6, H 4.9, N 6.9.

**[Cu(3-MeOsaltMe)]·1.5H$_2$O (9):** $C_{22}H_{26}CuN_2O_4·1.5H_2O$ (473.0): calcd. C 55.9, H 6.2, N 5.9; found C 55.5, H 6.1, N 5.8.

**Physical Measurements:** The solution UV/Vis spectra of the complexes were recorded with a Unicam UV-2 spectrometer in the ranges of $\lambda$ = 250–500 nm (complex concentration $1·10^{-5}$ mol dm$^{-3}$) and $\lambda$ = 500–1100 nm (complex concentration $1·10^{-3}$ mol dm$^{-3}$), using quartz cells with a 1-cm optical path. The Z-scan technique measurements were carried out using a 6-ns pulse Nd:YAG laser ($\lambda$ = 1064 nm) with a repetition rate of 10 Hz. The focal distance $f$ was 20 cm, the energy per pulse $E$ in the focus was 0.2 mJ, the beam radius at half-maximum in the focus $r_{1/2}$ was 1.5 mm and the aperture diameter $D$ was 2.2 mm (oscilloscope and photodiode). The spatial pulses were considered to be in the Gaussian transverse mode (TEM$_{00}$) and the sample is regarded as optically thin, because its length is small enough such that changes in the beam diameter within the sample due to either diffraction or nonlinear refraction can be neglected. The solutions were placed in a 1-cm quartz cuvette which was fixed in a controlled translation stage moving along the $z$-direction. All the Z-scan measurements were performed with the finite aperture placed in front of the photodiode: *closed* Z-scan mode. The possibility of analysing the contribution of different NLO processes to the overall NLO response (nonlinear absorption and nonlinear refraction) by using only the *closed* Z-scan mode, is described elsewhere.[22] This can be achieved because each process affects the transmittance through the aperture in a distinctive way: nonlinear absorption processes cause a symmetrical decrease of the transmittance with a minimum located in the focal point, linear processes are detected by a symmetrical rise in the transmittance around the focal point and nonlinear refractive processes are detected by the presence of a peak-valley profile, where the height and shape of the peaks are equal to the valley homologues, with an inflexion point placed at the focus. The fitting of experimental data was performed using a mathematical function composed of three different components that account for each phenomenon present within the sample: (i) a negative Gaussian associated with the nonlinear absorption coefficient, (ii) its first derivative which evaluates the nonlinear refractive index,[22] and (iii) a Gaussian component with positive sign to evaluate linear processes. The experimental data fitting was obtained using least-squares methods. None of the solvents used in the preparation of the complex solution showed nonlinear optical behaviour; the complex concentrations used were within the range of 4.5–6.0 mmol dm$^{-3}$.

## Acknowledgments

This work was partially funded by Reitoria da Universidade do Porto and Fundação Ilídio Pinho, Porto Portugal through Projecto de Investigação Científica na Pré-Graduação – 2004. We acknowledge the CLOQ Laboratory for the laser facilities. R. B. and C. S. thank Fundação para a Ciência e a Tecnologia (Portugal) for fellowships.

[1] M. Bass, J. M. Enoch, E. W. V. Stryland, W. L. Wolfe (Eds.), *Handbook of Optics IV, Fiber Optics & Nonlinear Optics*, 2nd ed., McGraw-Hill, New York, **2001**.
[2] J. G. Breitzer, D. D. Dlott, L. K. Iwaki, S. M. Kirkpatrick, T. B. Rauchfuss, *J. Phys. Chem. A* **1999**, *103*, 6930–6937.
[3] a) L. T. Cheng, W. Tam, S. H. Stevenson, G. R. Meredith, G. Rikken, S. R. Marder, *J. Phys. Chem.* **1991**, *95*, 10631–10643; b) L. T. Cheng, W. Tam, S. R. Marder, A. E. Stirgman, G. Rikken, C. W. Sprangler, *J. Phys. Chem.* **1991**, *95*, 10643–10652.
[4] H. S. Nalwa, S. Miyata (Eds.), *Nonlinear Optics of Organic Molecules and Polymers*, CRC Press, Boca Raton, **1997**.
[5] B. J. Coe in *Comprehensive Coordination Chemistry II* (Eds.: J. A. McCleverty, T. J. Meyer), Elsevier Pergamon, Oxford, U. K., **2004**, vol. 9, p. 621–628.
[6] a) H. L. Anderson, S. J. Martin, D. D. C. Bradley, *Angew. Chem. Int. Ed. Engl.* **1994**, *33*, 655–657; b) H. S. Nalwa, A. KaKuta, A. Mukoh, *Chem. Phys. Lett.* **1993**, *203*, 109–113; c) H. S. Nalwa, A. Kakuta, A. Mukoh, *J. Phys. Chem.* **1993**, *97*, 10515–10517.
[7] a) C. Freire, B. de Castro, *J. Chem. Soc., Dalton Trans.* **1998**, 1491–1497; b) C. Freire, B. de Castro, *Polyhedron* **1998**, *17*, 4227–4235.
[8] S. Di Bella, I. Fragalà, I. Ledoux, T. J. Marks, *J. Am. Chem. Soc.* **1995**, *117*, 9481–9485.
[9] S. Di Bella, I. Fragalà, T. J. Marks, M. A. Ratner, *J. Am. Chem. Soc.* **1996**, *118*, 12747–12751.
[10] S. Di Bella, I. Fragalà, I. Ledoux, M. A. Diaz-Garcia, T. J. Marks, *J. Am. Chem. Soc.* **1997**, *119*, 9550–9557.
[11] P. G. Lacroix, *Eur. J. Inorg. Chem.* **2001**, 339–348.
[12] P. G. Lacroix, S. Di Bella, I. Ledoux, *Chem. Mater.* **1996**, *8*, 541–545.
[13] S. Di Bella, I. Fragalà, *Synth. Met.* **2000**, *115*, 191–196.
[14] S. Di Bella, *Chem. Soc. Rev.* **2001**, *30*, 355–366.
[15] J.-B. Gaudry, L. Capes, P. Langot, S. Marcén, M. Kollmannsberger, O. Lavastre, E. Freysz, J.-F. Létard, O. Kahn, *Chem. Phys. Lett.* **2000**, *324*, 321–329.
[16] J. M. Floyd, G. M. Gray, A. G. V. Spivey, C. M. Lawson, T. M. Prichett, M. J. Ferry, R. C. Hoffman, A. G. Mott, *Inorg. Chim. Acta* **2005**, *358*, 3773–3785.
[17] a) M. Vilas-Boas, C. Freire, B. De Castro, A. R. Hillman, P. A. Christensen, *Inorg. Chem.* **1997**, *36*, 4919–4929; b) M. Vilas-Boas, C. Freire, B. De Castro, A. R. Hillman, *J. Phys. Chem. B* **1998**, *102*, 8533–8540; c) M. Vilas-Boas, C. Freire, B. De Castro, P. A. Christensen, A. R. Hillman, *Chem. Eur. J.* **2001**, *7*, 139–150.
[18] B. J. Coe, *Chem. Eur. J.* **1999**, *5*, 2464–2471.
[19] F. Chérioux, A.-J. Attias, H. Maillote, *Adv. Funct. Mater.* **2002**, *12*, 203–208.

 © 2006 Wiley-VCH Verlag GmbH & Co. KGaA, Weinheim 

[20] A. B. P. Lever, *Inorganic Electronic Spectroscopy*, 2nd ed., Elsevier, New York, **1984**.
[21] M. Sheik-Bahae, A. A. Said, E. W. Van Stryland, *Opt. Lett.* **1989**, *14*, 955–957.
[22] M. Sheik-Bahae, A. A. Said, T. Wei, D. A. Hagan, E. W. Van Stryland, *IEEE J. Quantum Electron.* **1990**, *26*, 760–769.
[23] S. L. Gómez, F. L. S. Cuppo, A. M. Figueiredo Neto, *Braz. J. Phys.* **2003**, *33*, 813–820.
[24] R. Sayre, *J. Am. Chem. Soc.* **1955**, *77*, 6689–6690.
[25] H. Adams, N. A. Bailey, D. E. Fenton, G. Papageorgiu, *J. Chem. Soc., Dalton Trans.* **1995**, 1883–1886.
[26] R. H. Holm, G. W. Everett, A. Chakravorty, *Prog. Inorg. Chem.* **1966**, *7*, 183–214.
[27] M. Andrade, C. Sousa, J. E. Borges, C. Freire, *J. Phys. Org. Chem.* **2005**, *18*, 935–940.

Received: January 10, 2006
Published Online: July 13, 2006

 © 2006 Wiley-VCH Verlag GmbH & Co. KGaA, Weinheim 

DOI: 10.1002/ejic.200600045

# Organotin Compounds as Reagents for the Synthesis of Lanthanoid Complexes by Redox Transmetallation Reactions

Samar Beaini,[a] Glen B. Deacon,*[a] Matthias Hilder,[a] Peter C. Junk,[a] and David R. Turner[a]

**Keywords:** Redox transmetallation / Lanthanoid / Trimethyltin reagents / Pyrazolate / Aryl oxide / Ytterbium / Europium

Redox transmetallation reactions between trimethyltin compounds, $SnMe_3L$ [L = 3,5-diphenylpyrazolate ($Ph_2pz$), 2,6-di-*tert*-butyl-4-methylphenolate (OAr), or $C_6F_5$] and lanthanoid metals have yielded $[Ln(Ph_2pz)_2(DME)_2]$ (Ln = Eu, Yb), $[Ln(Ph_2pz)_3(DME)_2]$ (Ln = Y, La, Nd, Eu), $[Ln(Ph_2pz)_3(THF)_3]$ (Ln = Nd, Sm), $[Ln(Ph_2pz)_3(THF)_2]$ (Ln = Y, Yb), $[Sm(OAr)_3(THF)]$, $[Yb(OAr)_2(THF)_3]$, and $[Yb(C_6F_5)_2(THF)_4]$ complexes in yields generally competitive with those from other methods, and hexamethylditin. The crystal structures of $[Nd(Ph_2pz)_3(DME)_2]\cdot DME$, $[Eu(Ph_2pz)_3(DME)_2]\cdot 2DME$, and $[Sm(Ph_2pz)_3(THF)_3]\cdot 3THF$ were determined. All have nine-coordination of the lanthanoid atom and three $\eta^2$-$Ph_2pz$ ligands, the first two also having an $\eta^1$- and an $\eta^2$-DME ligand and the last having three THF ligands.
(© Wiley-VCH Verlag GmbH & Co. KGaA, 69451 Weinheim, Germany, 2006)

## Introduction

Redox transmetallation reactions between lanthanoid metals and mercury or thallium compounds [Equations (1) and (2); $n$ = 2, 3] have become an important route to rare earth organometallic compounds, organoamides, aryl oxides,[1] and thiolates.[2]

$$Ln + n/2\ HgL_2 \rightarrow Ln(L)_n + n/2\ Hg \quad (1)$$

$$Ln + n\ TlL \rightarrow Ln(L)_n + n\ Tl \quad (2)$$

On the other hand, there has been only one example of redox transmetallation between a tin reagent and a lanthanoid metal; viz formation of an ytterbium(II) organoamide from an $Sn^{II}$ precursor,[3] despite the widespread use of tin reagents in *non-redox* transmetallations.[4] Trialkyltin compounds can be envisaged as potential redox transmetallation reagents for the preparation of lanthanoid complexes [Equation (3)].

$$Ln + n\ SnR_3L \rightarrow Ln(L)_n + n/2\ Sn_2R_6 \quad (3)$$

Encouragement that such syntheses may be possible comes from the oxidation of bis(*tert*-butylcyclopentadienyl)-samarium(II) by trimethyltin fluoride to give the corresponding organosamarium(III) fluoride [Equation (4)].[5]

$$6\ [Sm(\eta^5\text{-}C_5H_4tBu)_2(THF)_2] + 6\ SnMe_3F \rightarrow 2\ [Sm(\eta^5\text{-}C_5H_4tBu)_2F]_3 + 3\ Sn_2Me_6 \quad (4)$$

However, the reduction of hexaphenylditin and triphenyltin halide by ytterbium giving $[Yb(SnPh_3)_2]$[6] sends a note of warning especially if excess Ln metal is used, despite the high $E_0$ value (–2.9 V) for reduction of $Ph_3SnSnPh_3$.[7]

Lead(II) compounds have also been used as oxidants,[8] and an attempted use in redox transmetallation unexpectedly gave a Pb/La dimetallic compound.[9] We now report proof of concept of reaction according to Equation (3) by syntheses of a range of lanthanoid pyrazolates and aryl oxides generally in good yield from appropriate trimethyltin reagents. In addition, in situ formation of $Yb(C_6F_5)_2$ from $SnMe_3(C_6F_5)$ has been demonstrated.

## Results and Discussion

The outcomes of the reactions of trimethyltin 3,5-diphenylpyrazolate [$SnMe_3(Ph_2pz)$],[10] trimethyltin 2,6-di-*tert*-butyl-4-methylphenolate [$SnMe_3(OAr)$] and trimethyl(pentafluorophenyl)tin with lanthanoid metals in 1,2-dimethoxyethane and tetrahydrofuran are summarised in Scheme 1. Reactions with $SnMe_3(Ph_2pz)$ gave both trivalent $[Ln(Ph_2pz)_3(DME)_2]$ (Ln = Y, La, Nd, Eu), $[Ln(Ph_2pz)_3(THF)_3]$ (Ln = Nd, Sm), $[Ln(Ph_2pz)_3(THF)_2]$ (Ln = Y, Yb) and divalent $[Ln(Ph_2pz)_2(DME)_2]$ (Ln = Eu, Yb) pyrazolate complexes [Equations (5) and (6); L = $Ph_2pz$; S = DME or THF].

[a] School of Chemistry, Monash University,
P. O. Box 23, Clayton, Victoria 3800, Australia
Fax: +61-3-9905-4597
E-mail: glen.deacon@sci.monash.edu.au

 © 2006 Wiley-VCH Verlag GmbH & Co. KGaA, Weinheim 

$$2\ Ln + 6\ SnMe_3L \xrightarrow{S} 2\ [LnL_3(S)_n] + 3\ Sn_2Me_6 \quad (5)$$

$$Ln + 2\ SnMe_3L \xrightarrow{S} [LnL_2(S)_n] + Sn_2Me_6 \quad (6)$$

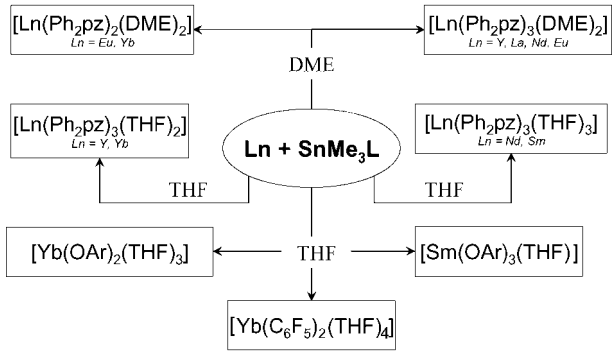


Scheme 1. Redox transmetallation reactions between $SnMe_3L$ and Ln metals.

Similarly, $[Sm(OAr)_3(THF)]$ and $[Yb(OAr)_2(THF)_3]$ were obtained from analogous reactions of lanthanoid metals with $SnMe_3(OAr)$ in tetrahydrofuran [reactions according to Equations (5) and (6); Ln = Sm, Yb; L = OAr; S = THF]. Formation of hexamethylditin in all reactions was established by $^1H$ NMR spectroscopy[11] and in one case also by $^{119}Sn$ NMR spectroscopy.[12] Thus, the $^{119}Sn$ NMR spectrum of the filtrate after isolation of $[Yb(OAr)_2(THF)_3]\cdot THF$ showed the presence of a resonance attributable to $Sn_2Me_6$.[12] There was no resonance near $\delta$ = –95 ppm where the signal of the Yb–Sn-bonded species $[Yb\{Sn(CH_2tBu)_3\}_2(THF)_2]$ is observed,[13] suggesting significant amounts of $Yb(SnMe_3)_2$ are not formed despite the use of a large excess of Yb metal. Reactions were carried out with activation of the lanthanoid metal by Hg metal. Without activation, reactions occurred, but were slower. Initiation of reactions was faster in DME than in THF. Variation of the excess of europium metal in the reactions of $SnMe_3(Ph_2pz)$ in DME enabled either the $Eu^{II}$ or $Eu^{III}$ product to be obtained (Scheme 1) in good yield. On the other hand, the corresponding reaction of Yb metal has a solvent-dependent outcome, yielding a $Yb^{II}$ complex in DME but a $Yb^{III}$ complex in THF (Scheme 1), even though a greater excess of Yb metal was utilised for the latter. In THF, a deep orange-red colour suggestive of some $Yb^{II}$ was observed after sonication, but the solution turned yellow after removal from the excess of Yb due to oxidation by $SnMe_3(Ph_2pz)$ [Equation (7)].

$$2\ Yb(Ph_2pz)_2 + 2\ SnMe_3(Ph_2pz) \rightarrow 2\ Yb(Ph_2pz)_3 + Sn_2Me_6 \quad (7)$$

Reactions according to Equations (5) and (6) generally give yields comparable with those of alternative routes (Table 1). However, $[Nd(Ph_2pz)_3(DME)_2]$, $[Nd(Ph_2pz)_3(THF)_3]$, and $[Sm(Ph_2pz)_3(THF)_3]$ are obtained in higher yield by the present method, but $[Ln(Ph_2pz)_3(THF)_2]$ (Ln = Y, Yb) in lower yield. In addition, $[Ln(Ph_2pz)_3(DME)_2]$ (Ln = Y, Eu), and $[Sm(Ph_2pz)_3(THF)_3]$ are new complexes, while $[Nd(Ph_2pz)_3(DME)_2]\cdot DME$ is a new solvate. The last complex has previously been isolated as an unsolvated powder[14] and as a $C_6D_6$ solvate.[15] Of special interest is the formation of $[Yb(Ph_2pz)_3(THF)_2]$ by reaction according to Equation (5), as attempts to prepare this complex from Yb metal, $Hg(C_6F_5)_2$ and $Ph_2pzH$ led to gross decomposition,[16a] and the corresponding reaction using $HgPh_2$, and redox transmetallation between Yb metal and $Tl(Ph_2pz)$ both yielded $Yb^{II}$ complexes.[16b] Thus, previous access to $[Yb(Ph_2pz)_3(THF)_2]$ required a two-step synthesis[17] (Table 1). Attempted reaction of Yb metal with $SnMe_3(C_6F_5)$ in tetrahydrofuran at room temperature for 2 d failed, but, after 1 d of ultrasonication, incomplete formation of $Yb(C_6F_5)_2$ [Equation (6); Ln = Yb; L = $C_6F_5$] was detected. By contrast, redox transmetallation between Yb and $Hg(C_6F_5)_2$ in tetrahydrofuran requires only a few minutes induction and is complete in 4 h.[1c]

Table 1. Comparison of yields of $Ln(L)_n$ complexes of the current study with literature methods.

| $Ln(Ph_2pz)_n(S)_m$ | Ln + $SnMe_3L$ | Reported | Method |
|---|---|---|---|
| $[Y(Ph_2pz)_3(DME)_2]\cdot DME$ | 80 | – | – |
| $[La(Ph_2pz)_3(DME)_2]$ | 82 | 77[a] | La/$Ph_2pzH$/$Hg(C_6F_5)_2$[a] |
| $[Nd(Ph_2pz)_3(DME)_2]\cdot DME$ | 79 | 17[a] | Nd/$Ph_2pzH$/$Hg(C_6F_5)_2$[a] |
| $[Eu(Ph_2pz)_2(DME)_2]$ | 88 | 90[b] | Eu/$Tl(Ph_2pz)$[b] |
| $[Eu(Ph_2pz)_3(DME)_2]\cdot 2DME$ | 70 | – | – |
| $[Yb(Ph_2pz)_2(DME)_2]$ | 80 | 66[c] | several[c] |
| $[Y(Ph_2pz)_3(THF)_2]$ | 54 | 76[d] | Y/$Ph_2pzH$/$Hg(C_6F_5)_2$[d] |
| $[Nd(Ph_2pz)_3(THF)_3]\cdot THF$ | 97 | 69[e] | Nd/$Ph_2pzH$/$Hg(C_6F_5)_2$[e] |
| $[Sm(Ph_2pz)_3(THF)_3]\cdot 3THF$ | 96 | 72[f] | Sm/$Ph_2pzH$/$Hg(C_6F_5)_2$[f] |
| $[Yb(Ph_2pz)_3(THF)_2]$ | 51 | 64[g] | Yb/$Tl(Ph_2pz)$ + oxid. with $Tl(Ph_2pz)$[g] |
| $[Sm(OAr)_3(THF)]\cdot THF$ | 45 | 49[h] | metathesis[h] |
| $[Yb(OAr)_2(THF)_3]\cdot THF$ | 87 | 76[i] | several[i] |

[a] Ref.[14] [b] Ref.[16a] [c] Ref.[16b] [d] Ref.[18] [e] Ref.[19] [f] This work. [g] Ref.[17] [h] Ref.[20] [i] Ref.[21]

Known complexes (Table 1) were characterised by lanthanoid metal analyses, IR spectroscopy and $^1H$ NMR spectroscopy, which confirmed the DME or THF/$Ph_2pz$ or OAr ratio. However, 4-H(pz) and *o*-H(Ph) resonances of $[Nd(Ph_2pz)_3(THF)_3]\cdot THF$ were too broad for satisfactory integrations. Furthermore, single crystals of $[Nd(Ph_2pz)_3(THF)_3]\cdot THF$, $[Yb(Ph_2pz)_2(DME)_2]$ and $[Yb(OAr)_2(THF)_3]\cdot THF$ were grown, and their unit cells are in agreement with the reported data.[16,19,20] In the case of the known[16a] $[Eu(Ph_2pz)_2(DME)_2]$, fifteen of sixteen single crystals examined had unit cell data corresponding to that reported for *trans*-$[Eu(Ph_2pz)_2(DME)_2]$,[16a] the product of redox transmetallation between Eu metal and $Tl(Ph_2pz)$.[16a] However, the values for one crystal were close to those for *cis*-$[Yb(Ph_2pz)_2(DME)_2]$,[16b] and can be attributed to *cis*-$[Eu(Ph_2pz)_2(DME)_2]$. It previously seemed surprising that $[Eu(Ph_2pz)_2(DME)_2]$ crystallised with the $Ph_2pz$ ligands mutually *transoid* when the complex of the

 © 2006 Wiley-VCH Verlag GmbH & Co. KGaA, Weinheim 

adjacent Sm was isolated *cisoid*[16a] as was *cis*-[Yb($Ph_2pz$)$_2$($DME$)$_2$].[16b] Although only one crystal of *cis*-[Eu($Ph_2pz$)$_2$($DME$)$_2$] was identified from the reaction according to Equation (6), its existence is established.

The composition of the new complex Y($Ph_2pz$)$_3$($DME$)$_3$ was established by microanalysis, metal analysis, and the DME/$Ph_2pz$ ratio by $^1$H NMR spectroscopy. Single crystals could not be obtained, but as $Y^{3+}$ has a similar size to $Er^{3+}$, which gives a nine-coordinate [Er($Ph_2pz$)$_3$($\eta^2$-DME)($\eta^1$-DME)][14] complex, it is likely the yttrium complex is a nine-coordinate mono-DME solvate [Y($Ph_2pz$)$_3$($DME$)$_2$]·DME. Besides characterisation by IR and NMR spectroscopy, and lanthanoid metal analyses, the new complexes [Eu($Ph_2pz$)$_3$($DME$)$_2$]·2DME, [Sm($Ph_2pz$)$_3$($THF$)$_3$]·3THF and the new solvate [Nd($Ph_2pz$)$_3$($DME$)$_2$]·DME were characterised by single-crystal X-ray structure determinations (below). For the Nd complex, both 4-H(pz) and *o*-H(Ph) resonances were severely broadened. The DME of solvation was readily lost from crystals of the Eu complex and the %Eu value for the dried complex corresponded to the composition [Eu($Ph_2pz$)$_3$($DME$)$_2$], whilst the $^1$H NMR spectra from two separate preparations showed a DME/$Ph_2pz$ ratio of 4:3, as in single crystals, and 3:3. Similarly, the dried product from one preparation of the samarium complex showed a THF/$Ph_2pz$ ratio of 6:3 as in the single crystals, and the product from another a THF/$Ph_2pz$ ratio of 5:3. No other products showed a similar loss of lattice solvent of crystallisation.

The structures of [Eu($Ph_2pz$)$_3$($DME$)$_2$]·2DME (Figure 1) and the new solvate [Nd($Ph_2pz$)$_3$($DME$)$_2$]·DME have nine-coordinate lanthanoid atoms with three $\eta^2$-$Ph_2pz$ ligands, one chelating DME and one (less usual[22]) unidentate DME. Selected bond lengths and angles are given in Table 2. The complexes have similar connectivity to unsolvated [Er($Ph_2pz$)$_3$($DME$)$_2$][14] and [Nd($Ph_2pz$)$_3$($DME$)$_2$]·2$C_6D_6$,[15] but there are differences in the structural details. Notably, the uncoordinated end of the unidentate DME points away from the metal atom in the present complexes [Eu···O(2)$_{nonbonding}$ 5.47 Å, Nd···O(2)$_{nonbonding}$ 5.41 Å; Eu–O(1)···O(2) 162°, Nd–O(1)···O(2) 153°] more markedly than in the erbium complex (4.62 Å/122°) and the neodymium $C_6D_6$ solvate (4.92 Å/129°). Plausibly, packing effects associated with differing solvation in the crystals [2 DME (Eu), 1 DME (Nd) (this study); 0 DME (Er);[14] 2 $C_6D_6$ (Nd)[15]] affect the arrangements of the $\eta^1$-DME ligand. All $Ph_2pz$ and $\eta^2$-DME ligands are nearly symmetrically chelating with only a small divergence in Ln–N (0.01–0.05 Å) and Ln–O ($\eta^2$-DME) (0.01–0.03 Å) bond lengths (Table 2). Nevertheless, the differences between Nd–N bond lengths of each chelating pair in the DME solvate (0.018, 0.054, 0.012 Å) (Table 2) are slightly larger than in the $C_6D_6$ solvate (0.008, 0.026, 0.005 Å).[15] For [Eu($Ph_2pz$)$_3$($DME$)$_2$]·2DME (Table 2) and [Nd($Ph_2pz$)$_3$($DME$)$_2$]·2$C_6D_6$,[15] the Ln–O ($\eta^1$-DME) distance lies between the values for Ln–O ($\eta^2$-DME), whereas for [Nd($Ph_2pz$)$_3$($DME$)$_2$]·DME (Table 2) and the Er complex[14] Ln–O ($\eta^1$-DME) is the shortest Ln–O distance. Moreover, the pairings here do not conform to the $\eta^1$-DME conformational pairings. Whilst the <Ln–N(O)> distances decline in the sequence Nd, Eu, Er as expected from the lanthanoid contraction, <Eu-N>

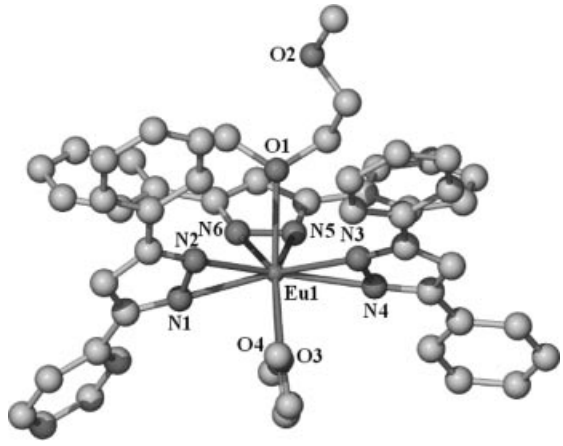


Figure 1. Molecular structure of [Eu($Ph_2pz$)$_3$($DME$)$_2$]·2DME. Selected bond lengths [Å] and angles [°] for this structure and the near isostructural Nd complex are given in Table 2. Only one disordered position of $\eta^2$-DME shown for clarity.

Table 2. Selected bond lengths [Å] and angles [°] for the new Ln($Ph_2pz$)$_n$ complexes.

| | [Nd($Ph_2pz$)$_3$($DME$)$_2$]·DME | [Eu($Ph_2pz$)$_3$($DME$)$_2$]·2DME | [Sm($Ph_2pz$)$_3$($THF$)$_3$]·3THF | | | |
|---|---|---|---|---|---|---|
| Bond lengths | | | Molecule 1 | | Molecule 2 | |
| Ln(1)–N(1) | 2.452(3) | 2.411(3) | Sm(1)–N(1) | 2.428(4) | Sm(2)–N(7) | 2.439(4) |
| Ln(1)–N(2) | 2.470(3) | 2.424(3) | Sm(1)–N(2) | 2.463(4) | Sm(2)–N(8) | 2.423(4) |
| Ln(1)–N(3) | 2.485(3) | 2.454(3) | Sm(1)–N(3) | 2.435(4) | Sm(2)–N(9) | 2.450(4) |
| Ln(1)–N(4) | 2.430(3) | 2.418(3) | Sm(1)–N(4) | 2.418(4) | Sm(2)–N(10) | 2.425(4) |
| Ln(1)–N(5) | 2.451(2) | 2.436(3) | Sm(1)–N(5) | 2.415(4) | Sm(2)–N(11) | 2.467(4) |
| Ln(1)–N(6) | 2.462(2) | 2.423(3) | Sm(1)–N(6) | 2.460(4) | Sm(2)–N(12) | 2.428(4) |
| Ln(1)–O(1) | 2.526(2) | 2.505(2) | Sm(1)–O(1) | 2.507(3) | Sm(2)–O(4) | 2.627(3) |
| Ln(1)–O(3) | 2.558(2) | 2.532(3) | Sm(1)–O(2) | 2.588(3) | Sm(2)–O(5) | 2.520(3) |
| Ln(1)–O(4) | 2.576(2) | 2.504(2) | Sm(1)–O(3) | 2.517(3) | Sm(2)–O(6) | 2.498(3) |
| Bond angles | | | | | | |
| O(1)–Ln(1)–O(3) | 140.87(7) | 134.91(8) | O(1)–Sm(1)–O(2) | 76.25(11) | O(4)–Sm(2)–O(5) | 74.47(11) |
| O(1)–Ln(1)–O(4) | 156.04(7) | 160.42(8) | O(1)- Sm(1)–O(3) | 159.00(12) | O(4)–Sm(2)–O(6) | 131.23(11) |
| O(3)–Ln(1)–O(4) | 63.05(7) | 64.14(8) | O(2)–Sm(1)–O(3) | 124.48(11) | O(5)–Sm(2)–O(6) | 153.80(11) |

 © 2006 Wiley-VCH Verlag GmbH & Co. KGaA, Weinheim 

exceeds <Er-N> by more (0.09 Å) than than expected (0.06 Å) from ionic radii,[23] whereas the corresponding <Ln–O> difference is less (0.03 Å) than expected.

$[Sm(Ph_2pz)_3(THF)_3]\cdot 3THF$ has nine-coordination for samarium with three $\eta^2$-$Ph_2pz$ and three THF ligands (Figure 2). It is isostructural with $[Nd(Ph_2pz)_3(THF)_3]\cdot THF$, which was isolated as a mono-THF solvate,[19] whereas the present complex has two closely related independent molecules and six THF solvent molecules in the asymmetric unit. The Sm–O bond lengths are very similar to the Nd–O bond lengths,[23] despite the expectation of a 0.03 Å difference based on ionic radii.[23] Molecule 2 has almost identical O–Ln–O angles to those of the Nd complex, but molecule 1 shows some deviation. More symmetrical $\eta^2$-$Ph_2pz$ bonding is observed in the present complex, and <Sm–N> is 0.02 Å shorter than <Nd–N>, near ionic radius expectations.[23]

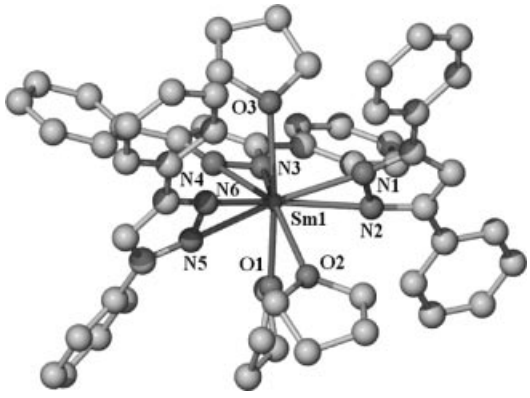


Figure 2. Molecular structure of $[Sm(Ph_2pz)_3(THF)_3]\cdot 3THF$. One of the two independent but closely related molecules is displayed.

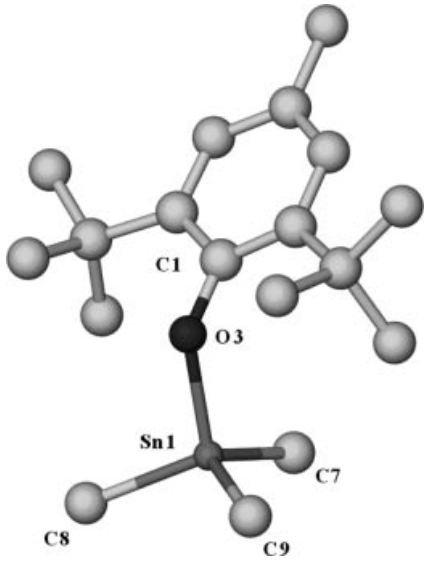


Figure 3. Molecular structure of $[SnMe_3(OAr)]$. Selected bond lengths [Å] and angles [°]: Sn(1)–O(3) 2.0082(15), O(3)–C(1) 1.363(3), Sn(1)–C(7) 2.127(2), Sn(1)–C(8) 2.139(3), Sn(1)–C(9) 2.127(3); C(1)–O(3)–Sn(1) 133.77(14), O(3)–Sn(1)–C(7) 105.56(9), O(3)–Sn(1)–C(8) 104.31(9), O(3)–Sn(1)–C(9) 106.44(9), C(7)–Sn(1)–C(8) 113.92(11), C(7)–Sn(1)–C(9) 117.10(11), C(8)–Sn(1)–C(9) 108.42(11).

An X-ray crystal structure was also obtained for the $[SnMe_3(OAr)]$ reagent (Figure 3). The compound is essentially isostructural with the known $[SiMe_3(OAr)]$.[24] The coordination environment around the tin atom is distorted tetrahedral. However, the C–O–Sn angle is significantly smaller than the C–O–Si angle within the silicon analogue,[24] presumably owing to reduced steric crowding by the *tert*-butyl groups due to the increased ionic radius of tin.

## Conclusions

This study shows that organotin(IV) compounds can be used in redox transmetallation reactions with lanthanoid elements to provide metal–organic lanthanoid complexes [Equations (5) and (6)]. Although their initial reactivity is somewhat lower than that of the analogous $Tl^I$ reagents or redox transmetallation with $HgR_2$ and LH, comparable or in some cases better yields have been obtained with the tin reagents (Table 1). Moreover, the different reactivity has enabled both $Eu^{II}$ and $Eu^{III}$ complexes to be isolated and a different Yb oxidation state outcome than with previous redox transmetallation methods. Besides variation of the alkyl groups, there is opportunity for considerable modulation of the tin reagents, e.g. (i) use of $SnMe_3Ar$ reagents with lanthanoid metals and protic reagents such as pyrazoles, phenols, and amines in redox transmetallation/ligand exchange, and (ii) exploration of $Sn^{VI} \rightarrow Sn^{II}$ reduction with the potentially more transfer efficient $SnMe_2L_2$ reagents. Evidence that Yb metal reacts with $SnMe_3(C_6F_5)$ to give $Yb(C_6F_5)_2$ in solution provides encouragement for the use of this compound in redox transmetallation/ligand exchange.

## Experimental Section

**General Remarks:** All reactions were carried out under dry nitrogen using standard Schlenk and dry-box equipment. THF was freshly distilled from sodium/benzophenone, while DME was distilled from sodium. Infrared spectra (4000–650 $cm^{-1}$) were recorded as Nujol mulls with a Perkin–Elmer 1600 FTIR spectrophotometer. $^1H$ NMR spectra were recorded with a Bruker DPX 300 MHz spectrometer using dry degassed deuteriobenzene or deuteriotetrahydrofuran solvents at 25 °C; resonances were referenced to residual hydrogen from the solvent. $^{119}Sn$ NMR spectra were obtained with a Bruker DRX 400 spectrometer and were referenced to tetramethyltin. $^{19}F$ NMR spectra were recorded with a Bruker DPX 300 spectrometer and were referenced to external $CFCl_3$. $^1H$ NMR spectra of all solutions following reactions of lanthanoid metals with $SnMe_3L$ reagents showed the presence of $Sn_2Me_6$ ($\delta$ = 0.20 ppm; $J_{^{117}Sn-CH_3}$ = 46.4 Hz, $J_{^{119}Sn-CH_3}$ = 48.4 Hz).[11] Metal analyses of the lanthanoid complexes were performed by EDTA titration with xylenol orange indicator following digestion in concentrated nitric and sulfuric acids and buffering with hexamine.[16a] Microanalysis samples were sealed in glass ampoules under purified $N_2$ and were determined by the Campbell Microanalytical service, University of Otago, New Zealand. 3,5-Diphenylpyrazole and

 © 2006 Wiley-VCH Verlag GmbH & Co. KGaA, Weinheim 

$SnMe_3(Ph_2pz)$ were prepared as reported.[25,10] A modification ($LiC_6F_5$ instead of $MgC_6F_5Br$) of the reported method[26] was used to obtain $SnMe_3(C_6F_5)$, which was distilled under reduced pressure and had IR and $^{19}F$ NMR spectra as reported.[26] Bis(pentafluorophenyl)mercury $Hg(C_6F_5)_2$ was prepared by a literature method.[27]

**(2,6-Di-*tert*-butyl-4-methylphenolato)trimethyltin(IV). Method (a):** *n*-Butyllithium (11.2 mL, 1.6 M in hexanes, 18.0 mmol) was added dropwise to pre-dried 2,6-di-*tert*-butyl-4-methylphenol (3.30 g, 15.0 mmol) in $Et_2O$ (50 mL), and the mixture was stirred for 1 h. Trimethyltin chloride (14.97 mL, 1.0 M in hexanes, 14.97 mmol) was then added dropwise. After stirring the reaction mixture overnight, the diethyl ether solution was filtered and the filtrate concentrated to crystallisation. Data of the crude product, which contained traces of lithium phenolate (NMR identification): IR: $\tilde{\nu}$ = 2726 w, 1603 w, 1418 vs, 1346 s, 1263 s, 1233 s, 1216 m, 1194 m, 1118 w, 1023 w, 918 w, 886 s, 861 m, 822 m, 772 m, 722 m $cm^{-1}$. $^1H$ NMR ($C_6D_6$): $\delta$ = 0.34 (s, $^2J_{H,^{117}Sn}$ = 53 Hz, $^2J_{H,^{119}Sn}$ = 57 Hz, 9 H, $Me_3Sn$), 1.51 (s, 18 H, *t*Bu), 2.32 (s, 3 H, Me), 7.20 (s, 2 H, 3,5-H) ppm. Extraction with hexane and concentration of the solvent yielded pure $SnMe_3OAr$ as colourless crystals (1.99 g, 35%), identified by X-ray crystallography (below). $^{119}Sn\{^1H\}$ NMR (149 MHz, $C_6D_6$, 25 °C): $\delta$ = 131.5 ppm. **Method (b):** Excess of $SnMe_3Cl$ (1.80 g; 9.05 mmol) was added to a solution of lithium 2,6-di-*tert*-butyl-4-methylphenolate (LiOAr) (1.33 g; 5.90 mmol) in $Et_2O$ (50 mL), and the resulting solution was stirred at room temperature overnight. After filtration through a filter cannula, the $Et_2O$ was removed under vacuum yielding a very fine crystalline material, which was washed with 3×10 mL of hexane to remove $SnMe_3Cl$. M.p. 138–140 °C;1.35 g, 55%. The $^1H$ NMR spectrum ($C_6D_6$) as above, was void of LiOAr resonances. $C_{18}H_{32}OSn$ (383.16): calcd. C 56.42, H 8.41; found C 56.56, H 8.22.

**Redox Transmetallation Reactions**

**Preparation of Bis(3,5-diphenylpyrazolato)lanthanoid(II) and Tris(3,5-diphenylpyrazolato)lanthanoid(III) Complexes:** DME or THF (50 mL) was added to excess lanthanoid metal (powder or filings), $SnMe_3(Ph_2pz)$ and 1–2 drops of mercury. The resulting mixture was stirred or sonicated at room temperature usually for 5 d. A colour change was observed for most reactions within 4 h (Yb: 1 h). The filtrate was collected by a filter cannula, and the solvent volume reduced to 15 mL. Crystalline or powdered $Ln(Ph_2pz)_n$ ($n$ = 2,3) compounds were obtained by cooling of the concentrated solutions to –20 °C. In all cases, the $^1H$ NMR spectrum of the crude product was obtained to verify $Sn_2Me_6$ formation.[11] The product was then washed with hexane to remove $Sn_2Me_6$, and dried briefly under vacuum.

**$[Y(Ph_2pz)_3(DME)_2]\cdot DME$:** Y metal powder (0.59 g; 6.62 mmol) and $SnMe_3(Ph_2pz)$ (0.50 g; 1.32 mmol) in DME, stirred for 5 d, gave colourless crystals;0.36 g, 80%. IR: $\tilde{\nu}$ = 1603 m, 1512 w, 1420 w, 1260 m, 1225 w, 1192 w, 1154 w, 1130 w, 1107 m, 1072 m, 1057 s, 1026 m, 1000 w, 972 vs, 912 m, 872 s, 804 m, 794 m, 758 vs, 704 s, 696 vs, 688 s $cm^{-1}$. $^1H$ NMR ($C_6D_6$): $\delta$ = 2.98 (br. s, 18 H, $CH_3$-*DME*), 3.10 (br. s, 12 H, $CH_2$-*DME*), 7.04–7.07 (br. t, 6 H, *p*-H), 7.08 (s, 3 H, 4-H), 7.14 (br. s, 12 H, *m*-H), 7.90–7.93 (br. d, 12 H, *o*-H) ppm. $C_{57}H_{63}N_6O_6Y$ (1017.05): calcd. C 67.31, H 6.24, N 8.26, Y 8.74; found C 66.73, H 6.60, N 8.22, Y 8.91.

**$[La(Ph_2pz)_3(DME)_2]$:** La powder (1.03 g; 7.44 mmol) and $SnMe_3(Ph_2pz)$ (0.50 g; 1.31 mmol) in DME, stirred for 5 d, gave a white powder; 0.35 g, 82%. The IR spectrum is similar to that reported.[14] $^1H$ NMR ($C_6D_6$): $\delta$ = 3.02 (br. s, 12 H, $CH_3$-*DME*), 3.17 (br. s, 8 H, $CH_2$-*DME*), 7.01–7.12 (m, 21 H, *m*-H, *p*-H, 4-H), 7.86 (br. s, 12 H, *o*-H) ppm. $C_{53}H_{53}LaN_6O_4$ (976.93): calcd. La 14.22; found La 14.51.

**$[Nd(Ph_2pz)_3(DME)_2]\cdot DME$:** Nd metal powder (0.94 g; 6.55 mmol) and $SnMe_3(Ph_2pz)$ (0.52 g; 1.36 mmol) in DME, stirred for 5 d, gave lavender-blue crystals; 0.38 g, 79%. The IR spectrum is in agreement with that of $[Nd(Ph_2pz)_3(DME)_2]$.[15] $^1H$ NMR ($C_6D_6$): $\delta$ = –3.41 (br. s, 12 H, $CH_2$-*DME*), 0.29 (s, 18 H, $CH_3$-*DME*), 8.08-8.22 (m, 18 H, *m*-H, *p*-H), 12.4 (v. br. s, *o*-H), 17.8 (v. br. s, 4-H) ppm. $C_{57}H_{63}N_6NdO_6$ (1072.39): calcd. Nd 13.45; found Nd 13.71. X-ray crystallography established the composition $[Nd(Ph_2pz)_3(DME)_2]\cdot DME$.

**$[Eu(Ph_2pz)_2(DME)_2]$:** Eu metal filings (2.52 g, 16.6 mmol) and $SnMe_3(Ph_2pz)$ (0.60 g, 1.57 mmol) in DME, sonicated for 5 d, gave deep yellow crystals; 1.06 g, 88%. The IR spectrum is identical with that reported.[16a] $^1H$ NMR ($C_6D_6$): $\delta$ = 0.43 (br. s, 8 H, $CH_2$-*DME*), 0.92 (br. s, 12 H, $CH_3$-*DME*), 1.32–2.09 (br. m, 22 H, 4-H, *p*-, *m*-, *o*-H) ppm. $C_{38}H_{42}EuN_4O_4$ (770.73): calcd. Eu 19.73; found Eu 19.26. X-ray crystallographic examination of the yellow crystals gave *one* crystal: monoclinic, space group $P2_1/a$, $a$ = 7.8740, $b$ = 18.8715, $c$ = 23.9260 Å; $\beta$ = 91.042°, $V$ = 3554.67 $Å^3$; isomorphous with *cis*-$[Yb(Ph_2pz)_2(DME)_2]$[16b] [monoclinic, space group $P2_1/a$, $a$ = 7.882(4), $b$ = 18.959(3), $c$ = 24.080(14) Å; $\beta$ = 91.03(2)°, $V$ = 3598(3) $Å^3$] and *fifteen* crystals of *trans*-$[Eu(Ph_2pz)_2(DME)_2]$, monoclinic, space group $P2/c$, $a$ = 14.9771, $b$ = 12.5269, $c$ = 19.6728 Å; $\beta$ = 109.398°, $V$ = 3481.40 $Å^3$, in agreement with reported data[16a] [monoclinic, space group $P2/c$, $a$ = 19.746(3), $b$ = 12.635(2), $c$ = 15.396(2) Å; $\beta$ = 110.12(1)°, $V$ = 3607 $Å^3$].

**$[Eu(Ph_2pz)_3(DME)_2]\cdot 2DME$:** Eu metal chunks (0.73 g, 4.80 mmol) and $SnMe_3(Ph_2pz)$ (0.53 g, 1.38 mmol) in DME, stirred for 3 d, gave golden yellow crystals; 0.38 g, 70%. IR: $\tilde{\nu}$ = 1604 m, 1246 w, 1192 m, 1124 m, 1107 m, 1057 s, 1026 m, 971 s, 916 w, 865 m, 800 w, 758 vs, 724 w, 696 s, 684 s, 666 w $cm^{-1}$. $^1H$ NMR ($C_6D_6$): $\delta$ = 0.23 (s, 3 H, 4-H), 2.09-3.68 (br. s, 40 H, $CH_3$ and $CH_2$-DME), 7.01-8.56 (m, 30 H, *o*-, *m*-, *p*-H) ppm. Metal analysis on dried crystals for $C_{53}H_{53}EuN_6O_4$ (loss of DME of solvation) (989.99): calcd. Eu 15.35; found Eu 15.36. Single crystals were obtained from another preparation that involved sonication of the DME mixture of Eu metal chunks and $SnMe_3(Ph_2pz)$ for 3 d (yield <5%). X-ray crystallographic examination revealed the composition $[Eu(Ph_2pz)_3(DME)_2]\cdot 2DME$. The $^1H$ NMR spectrum in $[D_8]THF$ showed loss of 1DME of solvation ($C_4D_8O$): $\delta$ = 3.47–3.59 (m, 30 H, $CH_3$-, $CH_2$-*DME*), 5.16 (s, 3 H, 4-H), 7.35 (br. t, 18 H, *m*- and *p*-H), 7.84 (d, 12 H, *o*-H) ppm.

**$[Yb(Ph_2pz)_2(DME)_2]$:** Yb metal filings (1.20 g, 6.96 mmol) and $SnMe_3(Ph_2pz)$ (0.66 g, 1.72 mmol) in DME, sonicated for 5 d, gave deep red crystals; 0.54 g, 80%. The IR spectrum is in agreement with that reported.[16b] $^1H$ NMR ($C_6D_6$): $\delta$ = 3.12 (br. s, 20 H, $CH_3$, $CH_2$-*DME*), 7.22 (br. s, 6 H, *p*-H, 4-H), 7.33 (br. s, 8 H, *m*-H), 8.10 (br. s, 8 H, *o*-H) ppm (reasonable agreement with data for a solution in $C_4D_8O$).[16b] $C_{38}H_{42}N_4O_4Yb$ (791.80): calcd. Yb 21.85; found Yb 20.32. A unit cell, monoclinic, space group $P2_1/a$, $a$ = 7.7214, $b$ = 18.7327, $c$ = 23.8207 Å; $\beta$ = 91.03°, $V$ = 3445.20 $Å^3$ is in agreement with that of *cis*-$[Yb(Ph_2pz)_2(DME)_2]$[16b] [monoclinic, space group $P2_1/a$, $a$ = 7.882(4), $b$ = 18.959(3), $c$ = 24.080(14) Å; $\beta$ = 91.03(2)°, $V$ = 3598(3) $Å^3$].

**$[Y(Ph_2pz)_3(THF)_2]$:** Y metal powder (1.01 g; 11.36 mmol) and $SnMe_3(Ph_2pz)$ (0.61 g; 1.60 mmol) in DME, sonicated for 5 d, gave a white powder; 0.26 g, 54%. The IR spectrum is identical with that reported.[18] $^1H$ NMR ($C_6D_6$): $\delta$ = 1.36 (s, 8 H, $CH_2$-*THF*), 3.43 (br. s, 8 H, $CH_2$-*THF*), 6.91 (br. s, 6 H, *p*-H), 7.02 (br. t, 12 H, *m*-H), 7.17 (br. s, 3 H, 4-H), 7.71 (br. s, 12 H, *o*-H) ppm. $C_{53}H_{49}N_6O_2Y$ (890.90): calcd. Y 9.98; found Y 9.28.

**$[Nd(Ph_2pz)_3(THF)_3]\cdot THF$:** Nd metal powder (0.95 g; 6.57 mmol) and $SnMe_3(Ph_2pz)$ (0.57 g; 1.49 mmol) in THF, stirred for 5 d, gave

 © 2006 Wiley-VCH Verlag GmbH & Co. KGaA, Weinheim 

lavender-blue crystals; 0.51 g, 97%. The IR spectrum is identical with that reported.[19] $^1$H NMR ($C_6D_6$): $\delta$ = –5.59 (br. s, 16 H, $CH_2$-*THF*), –2.78 (br. s, 16 H, $CH_2$-*THF*), 7.90–8.01 (br. s, 18 H, *m*-H, *p*-H), 12.37–12.62 (v. br. s, *o*-H), 17.95–17.98 (v. br. s, 4-H) ppm. $C_{61}H_{65}N_6NdO_4$ (1090.45): calcd. Nd 13.22; found Nd 13.58. A unit cell on the lavender blue crystals, orthorhombic, space group $P2_12_12_1$, $a$ = 14.18(2), $b$ = 16.26(1), $c$ = 22.78(2) Å; $V$ = 5254(8) Å$^3$ is identical with that of $[Nd(Ph_2pz)_3(THF)_3]\cdot THF$[19] [orthorhombic, space group $P2_12_12_1$, $a$ = 14.009(9), $b$ = 16.280(8), $c$ = 22.640(16) Å; $V$ = 5163(5) Å$^3$].

**$[Sm(Ph_2pz)_3(THF)_3]\cdot 3THF$. Method (a). $SnMe_3(Ph_2pz)$ with Sm Metal in THF:** Sm metal powder (1.59 g; 10.6 mmol) and $SnMe_3(Ph_2pz)$ (0.52 g; 1.36 mmol) in THF, stirred for 5 d, then sonicated for 1 d, gave a brownish/yellow precipitate; 0.54 g, 96%. IR $\tilde{\nu}$ = 1602 m, 1562 w, 1424 w, 1298 w, 1225 w, 1154 w, 1071 m, 1050 (sh), 1026 m, 970 s, 915 m, 869 m, 803 w, 757 s, 697 m, 669 w cm$^{-1}$. $^1$H NMR ($C_6D_6$): $\delta$ = 0.91 (m, 24 H, $CH_2$-*THF*), 2.66 (m, 24 H, $CH_2$-*THF*), 7.29 (t, 6 H, *p*-H), 7.60 (t, 12 H, *m*-H), 7.83 (s, 3 H, 4-H), 9.48 (d, 12 H, *o*-H) ppm. $C_{69}H_{81}N_6O_6Sm$ (1240.78): calcd. Sm 12.12; found Sm 11.98. In a similar reaction, sonicating the same amounts of Sm and $SnMe_3(Ph_2pz)$ for 6 d, the filtrate, after isolation of the bulk product as a powder, was allowed to stand for a few months and deposited single crystals of $[Sm(Ph_2pz)_3(THF)_3]\cdot 3THF$ (0.16 g, 30%). The IR spectrum and $^1$H NMR chemical shifts agree with those of the above preparation, but the solid had lost 1THF of solvation. An X-ray structure determination of the colourless crystals found two $[Sm(Ph_2pz)_3(THF)_3]\cdot 3THF$ molecules in the unit cell (see below). **Method (b):** Sm powder (0.22 g; 1.50 mmol), bis(pentafluorophenyl)mercury (0.80 g; 1.50 mmol) and 3,5-diphenylpyrazole (0.66 g; 3.00 mmol) were stirred in THF (30 mL) at room temperature for 5 d. After filtration through a diatomaceous earth pad, the pale yellow filtrate was concentrated to 2 mL. Petroleum spirit (20 mL) was added causing formation of a white precipitate, which was dried under vacuum for 3.5 h; 0.89 g, 0.72 mmol, 72%. The IR spectrum is as above. $C_{69}H_{81}N_6O_6Sm$ (1240.78): calcd. Sm 12.12; found Sm 12.30.

**$[Yb(Ph_2pz)_3(THF)_2]$:** Yb metal filings (1.36 g; 7.89 mmol) and $SnMe_3(Ph_2pz)$ (0.55 g; 1.44 mmol) in THF were sonicated for 5 d. The initial deep orange-red solution lightened to a yellow colour after filtration and concentration. A white powder was obtained after evaporation of THF; 0.24 g, 51%. The IR spectrum is similar to that reported.[17] $C_{53}H_{49}N_6O_2Yb$ (975.03): calcd. Yb 17.75; found Yb 18.34.

### Preparation of (2,6-Di-*tert*-butyl-4-methylphenolato)lanthanoid(II) and 2,6-Di-*tert*-butyl-4-(methylphenolato)lanthanoid(III) Complexes

**$[Sm(OAr)_3(THF)]\cdot THF$:** THF (50 mL) was added to a mixture of Sm metal powder (1.52 g; 10.1 mmol), $SnMe_3(OAr)$ (0.89 g; 2.33 mmol) and 2 drops of Hg metal, and the resulting solution was sonicated for 5 d. The deep-coloured solution was filtered through a filter cannula, and THF was removed under vacuum. The precipitate was washed with hexane to remove $Sn_2Me_6$, giving a yellow powder; 0.33 g, 45%. IR $\tilde{\nu}$ = 1602 w, 1550 w, 1420 m, 1272 s, 1217 w, 1196 w, 1040 s, 918 m, 888 m, 862 m, 818 s, 802 s. 789 s, 722 w, 668 w cm$^{-1}$. $^1$H NMR ($C_6D_6$): $\delta$ = 1.24 (br. s, 8 H, $CH_2$-*THF*), 1.71 (s, 54 H, *t*Bu), 2.43 (s, 9 H, Me), 3.19 (br. s, 8 H, $CH_2$-*THF*), 7.42 (s, 6 H, 3,5-H) ppm. $C_{53}H_{85}O_5Sm$ (952.60): calcd. Sm 15.78; found Sm 16.08.

**$[Yb(OAr)_2(THF)_3]\cdot THF$:** THF (50 mL) was added to a mixture of $SnMe_3(OAr)$ (1.10 g, 2.87 mmol), Yb metal filings (1.70 g, 9.82 mmol) and 2 drops of Hg metal, and the resulting mixture was ultrasonicated for 5 d. After allowing the suspension to settle, the deep orange supernatant solution was filtered and concentrated to 25 mL, resulting in golden-yellow crystalline $[Yb(OAr)_2(THF)_3]\cdot THF$; 1.12 g, 87%. The IR spectrum corresponds to that reported.[21b] $C_{46}H_{78}O_6Yb$ (900.15): calcd. Yb 19.22; found Yb 19.92. The unit cell, monoclinic, space group $P2_1$, $a$ = 9.7489, $b$ = 15.2423, $c$ = 15.3858 Å; $\beta$ = 95.62°, $V$ = 2277.68 Å$^3$, is in agreement with that reported[21a] [monoclinic, space group $P2_1$, $a$ = 15.393(4), $b$ = 15.619(5), $c$ = 9.859(2) Å; $\beta$ = 95.62(2)°, $V$ = 2359 Å$^3$]. A $^{119}$Sn{$^1$H} NMR (149 MHz, $C_6D_6$, 25 °C) spectrum of the filtrate shows the presence of $Sn_2Me_6$: $\delta$ = –109.0 ppm (reported: $\delta$ = –108.7 ppm)[12] but no $SnMe_3(OAr)$ signal. The $^1$H NMR spectrum ($C_6D_6$) of the concentrated solution shows phenolate resonances: $\delta$ = 2.18 (s, 6 H, Me), 7.42 (s, 4 H, 3,5-H) ppm (*t*Bu methyl resonances hidden by the residual THF solvent resonances).

**$SnMe_3(C_6F_5)$ with Yb Metal in THF:** $SnMe_3(C_6F_5)$ (1 mL, 8.03 mmol) was added under $N_2$ to a stirred mixture of Yb filings (1.14 g, 6.60 mmol) and 2 drops of Hg metal in THF (50 mL). After 2 d, no colour change was observed. The reaction mixture was ultrasonicated for 1 d resulting in a deep-coloured solution. A $^{19}$F NMR spectrum (282 MHz, 25 °C) of the solution showed $[Yb(C_6F_5)_2(THF)_4]$[28] and $SnMe_3(C_6F_5)$[26] in a 2:1 ratio: $\delta$ = –108.3 (br. m, 8 F, *o*-F, $[Yb(C_6F_5)_2(THF)_4]$), –121.5 [m, 2 F, *o*-F, $SnMe_3(C_6F_5)$], –154.0 [m, 1 F, *p*-F, $SnMe_3(C_6F_5)$], –161.5 (m, 14 F, *m*-F, $SnMe_3(C_6F_5)$ and *m*-, *p*-F, $[Yb(C_6F_5)_2(THF)_4]$) ppm (in agreement with the respective reported data {$[Yb(C_6F_5)_2(THF)_4]$:[28] $\delta$ = –108.3 (*o*-F) and –161.4 (*m*-, *p*-F) ppm; $SnMe_3C_6F_5$:[26] $\delta$ = –122.2 (*o*-F), –153.9 (*p*-F), –161.4 (*m*-F) ppm}.

**X-ray Crystallography:** Crystalline samples of $SnMe_3(OAr)$, $[Nd(Ph_2pz)_3(DME)_2]\cdot DME$, $[Nd(Ph_2pz)_3(THF)_3]\cdot THF$, $[Eu(Ph_2pz)_2(DME)_2]$, $[Eu(Ph_2pz)_3(DME)_2]\cdot 2DME$, $[Yb(Ph_2pz)_2(DME)_2]$, $[Sm(Ph_2pz)_3(THF)_3]\cdot 3THF$, and $[Yb(OAr)_2(THF)_3]\cdot THF$ were mounted on glass fibres in viscous hydrocarbon oil. Crystal data were collected using an Enraf–Nonius Kappa CCD instrument (Sn, Sm, Eu, Yb) or Bruker ApexII diffractometer (Nd) both equipped with monochromated Mo-$K_\alpha$ radiation, $\lambda$ = 0.71073 Å. All data were collected at 123 K, maintained using an open flow of nitrogen from an Oxford Cryostreams cryostat. X-ray data were processed using the DENZO program (Nonius)[29] or SAINT package (Bruker).[30] Structural solution and refinement was carried out using SHELXL-97[31] and SHELXS-97[32] utilising the graphical interface X-Seed.[33] For $[Eu(Ph_2pz)_3(DME)_2]\cdot 2DME$ there was one disordered DME molecule in the lattice which was modelled over two sites. The $\eta^2$-DME contains two disordered positions of the $C_2$ backbone, also successfully modelled. For $[Sm(Ph_2pz)_3(THF)_3]\cdot 3THF$ there were three THF molecules in the lattice with varying degrees of disorder. These were refined isotropically and no hydrogen atoms were attached. For $[Nd(Ph_2pz)_3(DME)_2]\cdot DME$, one $Ph_2pz$ phenyl group was successfully modelled as being disordered over two positions. The corresponding phenyl group of the same $Ph_2pz$ ligand also showed signs of disorder but this could not be satisfactorily modelled. The $\mu_2$-DME showed signs of being disordered in an analogous manner to that in the Eu complex but could not be modelled adequately. Crystal data and refinement parameters for all complexes are compiled below. CCDC-288000 to -288002 and -607830 contain the supplementary crystallographic data for this paper. These data can be obtained free of charge from The Cambridge Crystallographic Data Centre via www.ccdc.cam.ac.uk/data_request/cif.

**Crystal Data for $SnMe_3(OAr)$:** $C_{18}H_{32}OSn$, $M$ = 383.16, 0.5 × 0.5 × 0.375 mm, monoclinic, space group $P2_1/c$ (No. 14), $a$ = 13.421(3), $b$ = 15.265(3), $c$ = 9.0962(18) Å, $\beta$ = 93.34(3)°, $V$ = 1860.5(6) Å$^3$, $Z$ = 4, $D_c$ = 1.368 g/cm$^3$, $F(000)$ = 792, $2\theta_{max}$ = 55.8°, 19949 reflections collected, 4416 unique ($R_{int}$ = 0.0434). Final *GooF*

 © 2006 Wiley-VCH Verlag GmbH & Co. KGaA, Weinheim 

= 1.103, $R_1$ = 0.0316, $wR_2$ = 0.0851, $R$ indices based on 3616 reflections with $I > 2\sigma(I)$ (refinement on $F^2$), 182 parameters, 0 restraints. Lp and absorption corrections applied, $\mu$ = 1.369 mm$^{-1}$. The complex is isostructural with $SiMe_3(OAr)$.[24]

**Crystal Data for [Nd(Ph$_2$pz)$_3$(DME)$_2$]·DME:** $C_{57}H_{63}N_6NdO_6$, $M$ = 1072.39, blue block, 0.24×0.18×0.10 mm, monoclinic, space group $P2_1/c$ (No. 14), $a$ = 12.3824(2), $b$ = 16.0973(4), $c$ = 26.7915(7) Å, $\beta$ = 97.5260(10)°, $V$ = 5294.2(2) Å$^3$, $Z$ = 4, $D_c$ = 1.345 g/cm$^3$, $F(000)$ = 2220, $2\theta_{max}$ = 55.0°, 42938 reflections collected, 12144 unique ($R_{int}$ = 0.0263). Final *GooF* = 1.076, $R_1$ = 0.0413, $wR_2$ = 0.0963, $R$ indices based on 10980 reflections with $I > 2\sigma(I)$ (refinement on $F^2$), 674 parameters, 9 restraints. Lp and absorption corrections applied, $\mu$ = 1.036 mm$^{-1}$.

**Crystal Data for [Eu(Ph$_2$pz)$_3$(DME)$_2$]·2DME:** $C_{61}H_{73}EuN_6O_8$, $M$ = 1170.21, yellow block, 0.35×0.30×0.20 mm, monoclinic, space group $P2_1/n$ (No. 14), $a$ = 11.785(2), $b$ = 25.600(5), $c$ = 20.106(4) Å, $\beta$ = 106.03(3)°, $V$ = 5830(2) Å$^3$, $Z$ = 4, $D_c$ = 1.333 g/cm$^3$, $F(000)$ = 2432, $2\theta_{max}$ = 55.0°, 23569 reflections collected, 13230 unique ($R_{int}$ = 0.0657). Final *GooF* = 0.951, $R_1$ = 0.0442, $wR_2$ = 0.0748, $R$ indices based on 8144 reflections with $I > 2\sigma(I)$ (refinement on $F^2$), 711 parameters, 0 restraints. Lp and absorption corrections applied, $\mu$ = 1.134 mm$^{-1}$.

**Crystal Data for [Sm(Ph$_2$pz)$_3$(THF)$_3$]·3THF:** $C_{69}H_{81}N_6O_6Sm$, $M$ = 1240.75, colourless block, 0.20×0.10×0.10 mm, triclinic, space group $P\bar{1}$ (No. 2), $a$ = 13.343(3), $b$ = 18.579(4), $c$ = 25.270(5) Å, $\alpha$ = 76.58(3), $\beta$ = 85.19(3), $\gamma$ = 87.35(3)°, $V$ = 6070(2) Å$^3$, $Z$ = 4, $D_c$ = 1.358 g/cm$^3$, $F(000)$ = 2588, $2\theta_{max}$ = 55.0°, 51382 reflections collected, 27663 unique ($R_{int}$ = 0.0737). Final *GooF* = 1.018, $R_1$ = 0.0598, $wR_2$ = 0.1171, $R$ indices based on 17199 reflections with $I > 2\sigma(I)$ (refinement on $F^2$), 1471 parameters, 280 restraints. Lp and absorption corrections applied, $\mu$ = 1.025 mm$^{-1}$.

## Acknowledgments

The authors gratefully acknowledge the continued financial support of the Australian Research Council, and Dr. Joanna Cosgriff for the parallel synthesis of the samarium complex.

[1] a) D. C. Bradley, R. C. Mehrotra, I. P. Rothwell, A. Singh, *Alkoxo and Aryloxo Derivatives of Metals*, Academic Press, London, **2001**; b) M. N. Bochkarev, L. N. Zakharov, G. S. Kalinina, *Organoderivatives of the Rare Earth Elements*, Kluwer, Dordrecht, **1995**; c) *Synthetic Methods of Organometallic and Inorganic Chemistry* (Herrmann/Brauer) (Ed.: W. A. Herrmann), Thieme, New York, **1997**, vol. 6 (vol. Ed.: F. T. Edelmann); d) G. B. Deacon, C. M. Forsyth, S. Nickel, *J. Organomet. Chem.* **2002**, *647*, 50–60; e) G. B. Deacon, C. M. Forsyth, in: *Inorganic Chemistry Highlights* (Eds.: G. Meyer, D. Naumann, L. Wesemann), Wiley-VCH, Germany, Weinheim, **2002**, chapter 7, p. 139.

[2] J. H. Melman, T. M. Emge, J. G. Brennan, *Inorg. Chem.* **2001**, *40*, 1078–1081; J. H. Melman, C. Rhode, T. J. Emge, J. G. Brennan, *Inorg. Chem.* **2002**, *41*, 28–33.

[3] B. Cetinkaya, P. B. Hitchcock, M. F. Lappert, R. G. Smith, *J. Chem. Soc., Chem. Commun.* **1992**, 932–934.

[4] A. G. Davies, "Tin" (vol. 2, chapter 6), T. Sato, "Tin" (vol. 11, chapter 8), in: *Comprehensive Organometallic Chemistry II* (Eds.: E. W. Abel, F. G. A. Stone, G. Wilkinson), Pergamon, Oxford, **1995**; A. G. Davies, P. W. Smith, "Tin" (vol. 2, chapter 11), in: *Comprehensive Organometallic Chemistry I* (Eds.: G. Wilkinson, F. G. A. Stone, E. W. Abel), Pergamon, Oxford, **1982**; P. Oulie, N. Brefuel, L. Vendier, C. Duhayon, M. Etienne, *Organometallics* **2005**, *24*, 4306–4314.

[5] H. Schumann, M. R. Keitsch, J. Winterfeld, J. Demtschuk, *J. Organomet. Chem.* **1996**, *525*, 279–281.

[6] L. N. Bochkarev, O. V. Grachev, S. F. Ziltsov, L. N. Zakharov, Y. T. Struchkov, *J. Organomet. Chem.* **1992**, *436*, 299–311.

[7] R. E. Dessy, W. Kitching, T. Chivers, *J. Am. Chem. Soc.* **1966**, *88*, 453–459.

[8] a) W. J. Evans, C. A. Seibel, J. W. Ziller, *J. Am. Chem. Soc.* **1998**, *120*, 6745–6752; b) W. J. Evans, K. J. Forrestal, J. T. Leman, J. W. Ziller, *Organometallics* **1996**, *15*, 527–531; see also the related W. J. Evans, G. W. Nyce, M. A. Johnston, J. W. Ziller, *J. Am. Chem. Soc.* **2000**, *122*, 12019–12020.

[9] P. B. Hitchcock, M. F. Lappert, A. V. Protchenko, *Main Group Metal Chemistry*, RSC, Dalton Division Meeting, UCL, 9/8/**2005**.

[10] G. B. Deacon, E. E. Delbridge, C. M. Forsyth, P. C. Junk, B. W. Skelton, A. H. White, *Aust. J. Chem.* **1999**, *52*, 733–739.

[11] T. L. Brown, G. L. Morgan, *Inorg. Chem.* **1963**, *2*, 736–740.

[12] T. N. Mitchell, G. Walter, *J. Chem. Soc., Perkin Trans. 2* **1977**, 1842–1847. .

[13] F. G. N. Cloke, C. I. Dalby, P. B. Hitchcock, H. Karamallakis, G. A. Lawless, *J. Chem. Soc., Chem. Commun.* **1991**, *11*, 779–781.

[14] J. E. Cosgriff, G. B. Deacon, G. D. Fallon, B. M. Gatehouse, H. Schumann, R. Weimann, *Chem. Ber.* **1996**, *129*, 953–958.

[15] G. B. Deacon, E. E. Delbridge, G. D. Fallon, C. Jones, D. E. Hibbs, M. B. Hursthouse, B. W. Skelton, A. H. White, *Organometallics* **2000**, *19*, 1713–1721.

[16] a) G. B. Deacon, E. E. Delbridge, B. W. Skelton, A. H. White, *Eur. J. Inorg. Chem.* **1999**, 751–761; b) G. B. Deacon, E. E. Delbridge, B. W. Skelton, A. H. White, *Eur. J. Inorg. Chem.* **1998**, 543–545.

[17] G. B. Deacon, C. M. Forsyth, A. Gitlits, B. W. Skelton, A. H. White, *Dalton Trans.* **2004**, 1239–1247.

[18] J. E. Cosgriff, G. B. Deacon, B. M. Gatehouse, P. R. Lee, H. Schumann, *Z. Anorg. Allg. Chem.* **1996**, *622*, 1399–1403.

[19] J. E. Cosgriff, G. B. Deacon, B. M. Gatehouse, *Aust. J. Chem.* **1993**, *46*, 1881–1896.

[20] G. Qi, Y. Lin, J. Hu, Q. Shen, *Polyhedron* **1995**, *14*, 413–415.

[21] a) G. B. Deacon, P. B. Hitchcock, S. A. Holmes, M. F. Lappert, P. MacKinnon, R. H. Newnham, *J. Chem. Soc., Chem. Commun.* **1989**, 935–937; b) G. B. Deacon, T. Feng, P. MacKinnon, R. H. Newnham, S. Nickel, B. W. Skelton, A. H. White, *Aust. J. Chem.* **1993**, *46*, 387–399; c) J. R. van den Hende, P. B. Hitchcock, S. A. Holmes, M. F. Lappert, *J. Chem. Soc., Dalton Trans.* **1995**, 1435–1440; d) T. D. Tilley, PhD Thesis, University of California, **1982**.

[22] a) M. J. McGeary, P. S. Coan, K. Folting, W. E. Streib, K. G. Caulton, *Inorg. Chem.* **1991**, *30*, 1723–1735; b) P. S. Coan, W. E. Streib, K. G. Caulton, *Inorg. Chem.* **1991**, *30*, 5019–5023; c) M. J. McGeary, R. H. Cayton, K. Folting, J. C. Huffman, K. G. Caulton, *Polyhedron* **1992**, *11*, 1369–1382; d) F. E. Hahn, M. Keck, K. N. Raymond, *Inorg. Chem.* **1995**, *34*, 1402–1407; e) M. N. Bochkarev, I. L. Fedushkin, A. A. Fagin, T. V. Petrovskaya, J. W. Ziller, R. N. R. Broomhall-Dillard, W. J. Evans, *Angew. Chem. Int. Ed. Engl.* **1997**, *36*, 133–135.

[23] R. D. Shannon, *Acta Crystallogr., Sect. A* **1976**, *32*, 751–767.

[24] M. D. Healy, A. R. Barron, *J. Organomet. Chem.* **1990**, *381*, 165–172.

[25] R. V. Rothenburg, *Ber. Dtsch. Chem. Ges.* **1894**, *27*, 1097.

[26] R. D. Chambers, T. Chivers, *J. Chem. Soc.* **1964**, 4782–4790.

[27] G. B. Deacon, R. N. M. Smith, *Russ. J. Org. Chem.* **1982**, *18*, 1584.

[28] G. B. Deacon, W. D. Raverty, D. G. Vince, *J. Organomet. Chem.* **1977**, *135*, 103–114.

[29] Z. Otwinowski, W. Minor, in: *Macromolecular Crystallography*, Part A ("Methods in Enzymology") (Eds.: C. W. Carter Jr, R. M. Sweet), Academic Press, New York, **1997**, vol. 276, p. 307.

[30] SAINT is part of the ApexII software package, Bruker AXS, Madison, WI.

 © 2006 Wiley-VCH Verlag GmbH & Co. KGaA, Weinheim 

[31] G. M. Sheldrick, *SHELXL-97*, University of Göttingen, Germany, **1997**.
[32] G. M. Sheldrick, *SHELXS-97*, University of Göttingen, Germany, **1997**.
[33] L. J. Barbour, *J. Supramol. Chem.* **2001**, *1*, 189–191.
Received: January 16, 2006
Published Online: July 11, 2006

 © 2006 Wiley-VCH Verlag GmbH & Co. KGaA, Weinheim 

DOI: 10.1002/ejic.200600215

# Study of the In Situ Postintercalative Polymerization of Metanilic Anions Intercalated in NiAl-Layered Double Hydroxides under a Nitrogen Atmosphere

Min Wei,[a] Xiaofei Tian,[a] Jing He,[a] Min Pu,[a] Guoying Rao,[a] Heli Yang,[a] Lan Yang,[a] Tao Liu,[b] David G. Evans,[a] and Xue Duan*[a]

**Keywords:** In situ polymerization / Polyaniline / Layered double hydroxides / Nitrogen atmosphere

A new route has been developed for preparing polyaniline (PANI) layered double hydroxide (LDH) nanocomposites through in situ chemical oxidative polymerization of metanilic anions ($m$-$NH_2C_6H_4SO_3^-$) intercalated in NiAl LDHs under a nitrogen atmosphere by using pre-intercalated nitrate as an oxidizing agent. The interlayer space of NiAl LDHs has been used as an original nanoreactor for the in situ polymerization of the intercalated monomer. The whole process involves the synthesis of the precursor LDH [$Ni_2Al(OH)_6(NO_3)\cdot nH_2O$], the intercalation of the monomer metanilic anions into the LDH and its in situ polymerization between the layers by thermal treatment under a nitrogen atmosphere. The interlayer polymerization reaction was monitored by thermogravimetric analysis (TG), differential thermal analysis (DTA), mass spectrometry (MS), UV/Vis absorption spectroscopy, in situ X-ray absorption near edge structure (XANES) spectroscopy, in situ high-temperature X-ray diffraction (HT-XRD) and in situ Fourier transform infrared (FTIR) spectroscopy. The UV/Vis spectra provide evidence for the polymerization of the intercalated metanilic anions, and an increase in the interlayer distance from 16.0 to 17.2 Å is observed by HT-XRD. It has been found by the in situ techniques that the pre-intercalated nitrate anions act as the oxidizing agent that induces the polymerization of the interlayer monomer under a nitrogen atmosphere upon heating at 300 °C. The orientation of the interlayer polymerization product has also been proposed.

(© Wiley-VCH Verlag GmbH & Co. KGaA, 69451 Weinheim, Germany, 2006)

## Introduction

In recent years, considerable interest has been devoted to nanocomposites prepared from the assembly of an organic polymer and an inorganic layered material. Polymer intercalation nanocomposites prepared by using layered materials are expected to consist of a high degree of polymeric ordering and to exhibit advanced physicochemical properties compared with the individual parts.[1–5]

Among the organic polymers, polyaniline (PANI) has been and continues to be extensively studied as an organic component in such systems. Polyaniline is a promising conjugated polymer because of its simple synthesis, high conductivity, and excellent environmental stability, although it is associated with rather poor properties with respect to processing. Consequently, there are many reports focusing on the preparation of novel nanocomposites consisting of PANI with various layered materials such as $V_2O_5$ xerogel,[6] $MoO_3$ bronze,[7] graphitic oxide,[8] α-$RuCl_3$,[9] montmorillonite,[10] and layered metal phosphates.[11]

As for the layered materials, LDHs have received considerable attention because of their special intercalation properties. LDHs, which are widely known as a class of anionic clays, can be represented by the general formula $[M_{1-x}^{II}M_x^{III}(OH)_2]^{x+}(A^{n-})_{x/n}\cdot mH_2O$, where $M^{II}$ and $M^{III}$ are divalent and trivalent metal cations, respectively. $A^{n-}$ is an exchangeable inorganic or organic anion and the $x$ value, i.e. the charge density, is equal to the molar ratio $M^{III}/(M^{III} + M^{II})$. LDHs have positively charged layers, and a wide variety of charge-balancing anionic species have been intercalated into the gallery region.[12] As a result, LDHs are now well established as excellent anion-exchange materials and their extensive intercalation chemistry has widespread applications in the area of organic/inorganic nanocomposites.[13]

PANI/LDH nanocomposites were first reported by Challier and Slade.[14] Prior to the incorporation, the LDH host structure was exchanged with terephthalate or hexacyanoferrate anions in order to expand the basal spacing. The pre-swollen LDH materials were then heated at reflux with pure aniline. Analysis of the XRD patterns of the products confirmed the presence of multiple phases. More recently, interlayer polymerization methods have concentrated on heat treatment after polymeric monomer intercalation into the LDH. This process is the so called "soft thermal treatment", which is a two-step soft chemistry route that in-

[a] State Key Laboratory of Chemical Resource Engineering, Beijing University of Chemical Technology, Beijing 100029, P. R. China
[b] Institute of High Energy Physics, Chinese Academy of Science, Beijing 100039, P. R. China
E-mail: duanx@mail.buct.edu.cn

 © 2006 Wiley-VCH Verlag GmbH & Co. KGaA, Weinheim 

cludes the intercalation of aniline sulfonic acid between the sheets of the LDHs and its subsequent in situ polymerization at a temperature below 200 °C in air. This approach can avoid the ion-exchange reaction competing with the interlayer polymerization as well as the destruction of the layered structure by external oxidizing agents. As in the case of other lamellar nanocomposites, atmospheric oxygen was found to play a major role in the polymerization process.[15–17]

In the present study, we report a new route for preparing PANI/LDH nanocomposites by using pre-intercalated nitrates as the oxidizing agent. In situ chemical oxidative polymerization of metanilic anions ($m$-$NH_2C_6H_4SO_3^-$) intercalated in NiAl LDHs under a nitrogen atmosphere has been performed for the first time. The whole process involves the synthesis of the precursor LDH [$Ni_2Al(OH)_6(NO_3)\cdot nH_2O$], the intercalation of the monomer metanilic anions into the LDH and its in situ polymerization between the layers by thermal treatment under nitrogen. Advantages of this method are: (1) the restricted interlayer region of the LDH makes it easier to obtain nanosized oligomers with uniform size; (2) the pre-intercalated $NO_3^-$ acting as an oxidizing agent can prevent the influence of mass transfer and diffusion on the polymerization reaction of the interlayer monomer. A combination of techniques, including TG–DTA–MS, UV/Vis, in situ XANES, in situ HT-XRD, and in situ FTIR spectroscopy, was used for the characterization of intercalated metanilic anions and their in situ interlayer polymerization. UV/Vis spectroscopy provides evidence for the polymerization of the intercalated monomer, and an increase in the interlayer distance from 16.0 to 17.3 Å is observed by HT-XRD. It has been found by the in situ techniques that the pre-intercalated nitrate anions act as the oxidizing agent, which induces the polymerization of the interlayer monomer upon heating at 300 °C under nitrogen. The orientation of the interlayer polymerization product has also been proposed.

## Results and Discussion

### Structure of NiAl-Metanilic LDHs

The X-ray diffraction patterns of the precursor NiAl-$NO_3$ LDH and the metanilic anion intercalated LDH are shown in Figure 1. In each case, the reflections can be indexed to a hexagonal lattice with $R$-3$m$ rhombohedral symmetry, commonly used for the description of the LDH structures.[19] The main diffraction peaks for NiAl-$NO_3$ LDH appear at 9.9° (003), 19.9° (006), 29.5° (009), and 62.1° (110) (Figure 1a), while the corresponding peaks for NiAl-metanilic LDH are observed at 5.4°, 11.1°, 16.8°, and 61.7° (Figure 1b), respectively. Apparently, the XRD pattern for NiAl-metanilic LDH exhibits the characteristic reflections of LDH materials with a series of (00$l$) peaks, which are evidence for the layered character. The interlayer distance for the NiAl-$NO_3$ LDH is 8.9 Å which is larger than that reported by Prinetto et al. (8.3 Å, for the existence of a large amount of $CO_3^{2-}$).[20] After the intercalation of metanilic acid, the value of the interlayer distance increased to 16.3 Å, which is 7.4 Å larger than that of NiAl-$NO_3$ LDH. The expansion of the basal spacing was due to the intercalation of metanilic anions into the LDH lamellar. Thus, the interaction of NiAl-$NO_3$ LDH with an aqueous solution of metanilic acid at pH 7.0 led to the anion exchange of $NO_3^-$ for the metanilic anions with conservation of the layered structure. As for the (110) reflection, no obvious shift was observed after intercalation, indicating that no significant change occurred in the LDH layer.

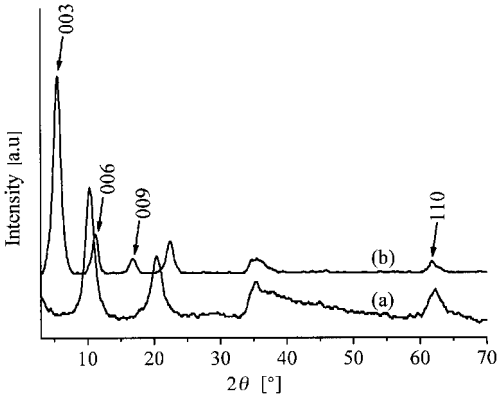


Figure 1. XRD patterns for (a) NiAl-$NO_3$ LDH and (b) NiAl-metanilic LDH.

The size of the gallery height of 11.5 Å, obtained by subtracting the thickness of the aluminium hydroxide layer (4.8 Å) from the interlayer distance (16.3 Å),[21] was much longer than a single perpendicular anion height (6.4 Å, calculated with Chemwin 6.0) but shorter than its double value. This may indicate that the guest anions are accommodated with an interpenetrating arrangement, leaving interstitial gaps between the monomers and the hydroxide sheets. Water molecules and nitrate anions occupy these interstitial spaces.

Compared with the NiAl-$NO_3$ LDH precursor (Figure 2a), three strong bands at 1599, 1484, and 1454 $cm^{-1}$ and two weak bands at 1257 and 1315 $cm^{-1}$ are observed in the FTIR spectrum of NiAl-metanilic LDH (Figure 2b), which can be attributed to the characteristic absorptions of metanilic anions.[22] The remarkable absorption band at 1384 $cm^{-1}$ resulting from the stretching vibration of $NO_3^-$ is also observed. It can be seen that not all of the $NO_3^-$ anions have been exchanged by metanilic anions, and similar results have also been reported by other researchers in studies of the intercalation of large anions into $NO_3$-LDH precursors.[23,24] Furthermore, elemental analysis data show that the chemical composition of the NiAl-metanilic LDH is $Ni_{0.66}Al_{0.34}(OH)_2(C_6H_4NH_2SO_3)_{0.23}(NO_3)_{0.11}\cdot 0.78H_2O$, which is consistent with the results of XRD and IR spectroscopy.

The structure of an LDH is based on brucite-like layers in which octahedrally coordinated metal ions share edges to form infinite sheets.[25] The area of each $[Ni_{1-x}Al_x(OH)_2]^{x+}$ octahedral unit is related to the unit cell parameter $a$ by the formula: $S = \sqrt{3}(a^2/2)$.[26] The value of $a$ can be

 © 2006 Wiley-VCH Verlag GmbH & Co. KGaA, Weinheim 

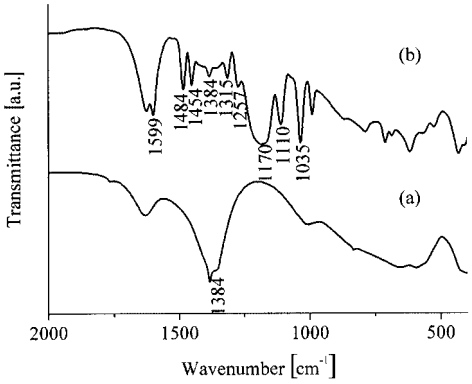


Figure 2. FT IR spectra for (a) NiAl-$NO_3$ LDH and (b) NiAl-metanilic LDH.

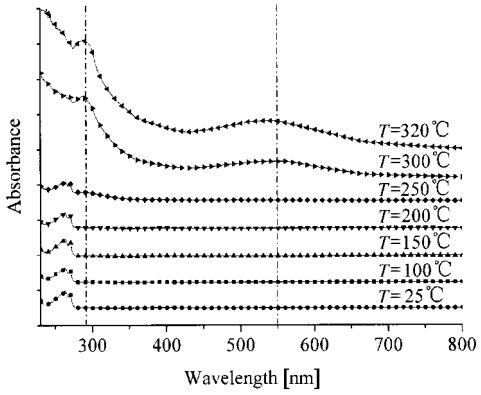


Figure 4. UV/Vis spectra of NiAl-metanilic LDH after heat treatment at different temperatures under nitrogen.

calculated from the XRD pattern in Figure 1b ($a = 2d_{110}$ = 2.99 Å). The area of each octahedral unit is therefore 7.74 Å$^2$, giving one positive charge per 23 Å$^2$ in the case of $x = 0.34$ (based on the chemical composition of NiAl-metanilic LDH given above). The maximum dimensions of the anion are calculated as 6–7 Å (calculated with Chemwin 6.0), and the corresponding cross-sectional area of the complex anions can thus be estimated to be in the range of 28–38 Å$^2$. Consequently, it is impossible for metanilic anions alone to balance the positive charge of the host layer, thereby accounting for the co-intercalation of $NO_3^-$.

On the basis of the discussion above, the structure of NiAl-metanilic LDHs can be represented as alternating NiAl-OH hydroxide layers and layers containing metanilic anions, $NO_3^-$, and water molecules. The schematic model of NiAl-metanilic LDHs is proposed in Figure 3.

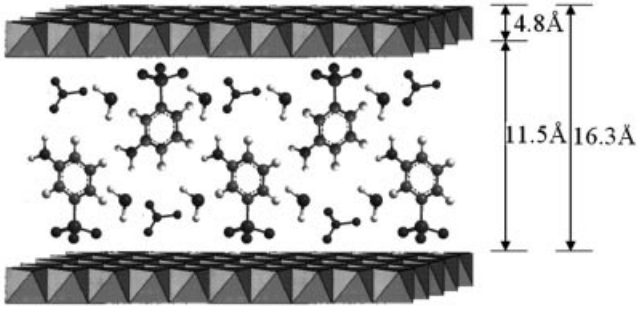


Figure 3. A schematic representation of the possible arrangement for NiAl-metanilic LDHs.

## UV/Vis Spectroscopy

Results obtained by UV/Vis spectroscopy give evidence for the polymerization of metanilic anions intercalated in NiAl LDHs by heat treatment under nitrogen. Figure 4 shows the optical absorption spectra, in the wavelength range 230–800 nm, of the synthesized NiAl-metanilic LDH and the resultant products after heat treatment at different temperatures.

It can be seen from Figure 4 that two absorption bands at 262 and 269 nm at room temperature are observed, which are associated with the phenyl group of the metanilic monomer. Along with the heat treatment, a strong absorption band (centered at 296 nm) corresponding to the $\pi_B$–$\pi_B$* transition appears when the temperature reaches 300 °C,[27] indicating that the polymerization of the intercalated monomer occurrs and the polymeric product possesses alternative benzenoid units (see structure A). The absorption band centered at 550 nm, attributable to charge transfer from the benzoid to the quinoid segments ($\pi_B$–$\pi_Q$*), becomes more obvious when the temperature increases to 320 °C (see structures B and C).[28] The $\pi_B$–$\pi_Q$* transition provides direct evidence that quinoid units are produced and the interlayer polyaniline sulfonic (PANIS) is present in its highly oxidized form. This result is consistent with reports on the study, by optical absorption spectroscopy, of the interconversion of polyaniline oxidation states.[27,29,30]

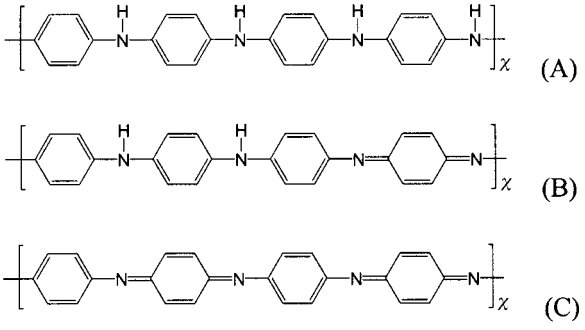


## In Situ XANES

Previous studies on PANI/CuCr LDH nanocomposites show that oxidative $Cu^{2+}$ has been used to induce the reaction of the oxidative polymerization of aniline in the interlayer galleries of pillared hosts.[14] In order to study whether $Ni^{2+}$ in the host layer participates in the interlayer polymerization in this system, in situ X-ray absorption near edge structure (XANES) measurements were carried out at the Ni *K*-edge. The features in the absorption edge are sensitive

 © 2006 Wiley-VCH Verlag GmbH & Co. KGaA, Weinheim 

to the immediate Ni environment and local geometry. For the *K* edge, the existence of a pre-edge and its intensity are closely related to the degree of d–p orbital mixing, and loss of centrosymmetry can cause a large intensity of this peak. The dominant jump at the edge arises from the dipolar-allowed transition related to final electronic 4p states. Therefore, it is sensitive to the variation of the oxidation state of Ni.[31]

Figure 5 shows the normalized XANES spectra at the Ni *K*-edge of NiAl-metanilic LDH heated under nitrogen. The pre-edge peak (A) can be observed and this arises from the quadrupolar 1s→3d transition, which is directly related to the occupation of the 3d orbital and to the local symmetry. Peak C reflects the long-range ordering of the Ni–O or Ni–Ni shell.[32] During the heat treatment, a broadening of both peaks B and C was observed as a result of the thermal disorder. However, no significant shifts in the three peaks could be observed, implying that no dramatic redox process involving Ni occurred during the heat treatment. The results therefore demonstrate that $Ni^{2+}$ in the host layer does not serve as the oxidant for the interlayer oxidative polymerization and thus maintains the same valence in the temperature range 25–320 °C.

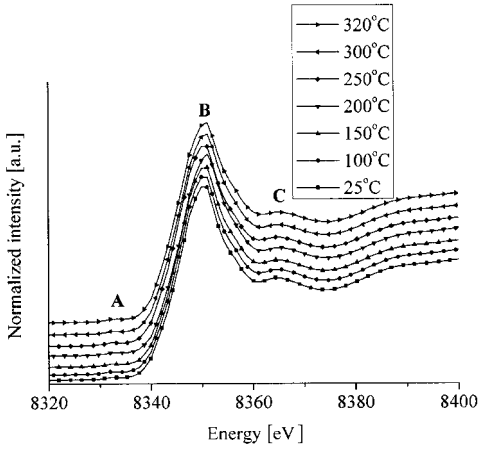


Figure 5. In situ XANES spectra at the Ni *K*-edge of NiAl-metanilic LDH heated from 25 to 320 °C under nitrogen.

## TG–DTA–MS Analyses

Simultaneous thermogravimetric (TG) and–differential thermal analyses (DTA) combined with analysis by mass spectrometry was found to be useful for following the in situ thermal behavior of the organic/inorganic nanocomposites over a wide temperature range.[33]

The TG, DTG, and DTA profiles for the pristine metanilic acid are shown in Figure 6. It can be seen that metanilic acid exhibits rather high thermal stability from room temperature to 400 °C under nitrogen. Two consecutive weight losses occur between 400 and 500 °C, with two corresponding strong endothermic peaks in the DTA curve attributable to the decomposition of metanilic anions.

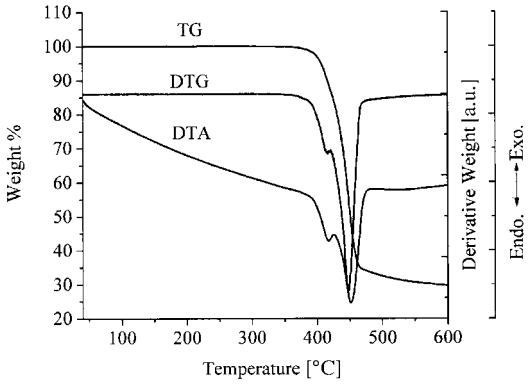


Figure 6. TG–DTA profiles of the pristine metanilic acid heated under nitrogen.

In the case of NiAl-metanilic LDH (Figure 7), the TG–DTA–MS determination shows that the thermal behavior under nitrogen can basically be described in four steps: the first step is observed between ambient temperature to about 100 °C. The TG curve displays a small weight loss with an endothermic peak in the DTA curve, and the corresponding MS determination (Figure 8 and Table 1) reveals one $H_2O^+$ ($m/z$ = 18) peak at ca. 100 °C. This process is associated with the volatilization of the adsorbed water in the composite.

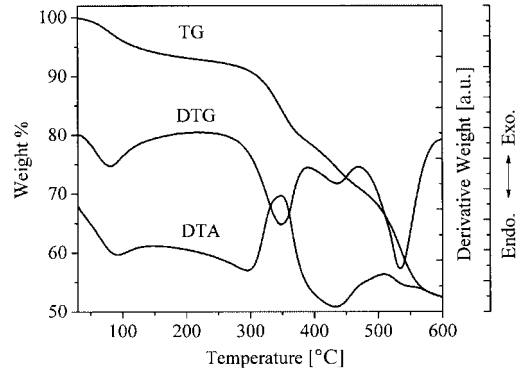


Figure 7. TG–DTA profiles of NiAl-metanilic LDH heated under nitrogen.

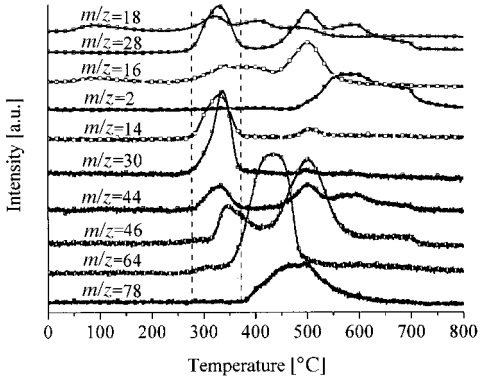


Figure 8. Mass analyses of NiAl-metanilic LDH heated under helium.

 © 2006 Wiley-VCH Verlag GmbH & Co. KGaA, Weinheim 

Table 1. Results for MS analyses of NiAl-metanilic LDH.

| Proposed positive ion | $H_2^+$ | $N^+$ | $O^+$ | $H_2O^+$ | $N_2^+$ | $NO^+$ | $N_2O^+$ | $NO_2^+$ | $SO_2^+$ | $C_6H_4^+$ |
|---|---|---|---|---|---|---|---|---|---|---|
| *m*/*z* | 2 | 14 | 16 | 18 | 28 | 30 | 44 | 46 | 64 | 76 |
| Intensity [A] | $10^{-11}$ | $10^{-11}$ | $10^{-11}$ | $10^{-10}$ | $10^{-10}$ | $10^{-11}$ | $10^{-11}$ | $10^{-12}$ | $10^{-12}$ | $10^{-13}$ |

The second step takes place in the temperature range 300–350 °C. The TG curve shows a big weight loss accompanied by a strong exothermic peak in the DTA curve. Several fragments assigned to $N_2^+$ (*m*/*z* = 28), $NO^+$ (*m*/*z* = 30), $N_2O^+$ (*m*/*z* = 44), $H_2O^+$ (*m*/*z* = 18), and $NO_2^+$ (*m*/*z* = 46) appear in the corresponding MS curves. For the nitrate-containing LDHs, the release of $NO_2$ and NO was generally attributable to the pyrolysis of nitrates, whereas the interlayer nitrate would be evolved as NO and $N_2O$ only during the TPR experiment under hydrogen.[34] In this work, the release of $N_2$, NO, and $N_2O$ at the same time provides evidence that the co-intercalated nitrate anions are involved in an interlayer redox reaction. The $NO_2^+$ peak lags behind the $N_2^+$, $NO^+$, $N_2O^+$, and $H_2O^+$ peaks, indicating that pyrolysis of the pre-intercalated nitrates occurs after reduction. The DTA curve in this step displays a strong exothermic peak at about 320 °C, which was not found in the DTA curve of the pristine metanilic acid. Roland-Swanson et al. have reported DTA traces with such an exothermic peak assigned to the polymerization of the 3-sulfopropyl methacrylate potassium salt (SPMA) intercalated in ZnAl LDHs by thermal treatment.[35] Because the reaction was complete without the use of any external chemical agent, the polymerization process was interpreted as an oxidative reaction induced by atmospheric oxygen. In the present study, this strong exothermic peak and the reduction of the co-intercalated nitrates correspond to the emergence of the new absorption bands attributable to the $\pi_B$–$\pi_B$* and $\pi_B$–$\pi_Q$* transitions in UV/Vis spectra, which demonstrates the polymerization of metanilic anions intercalated NiAl LDHs in the same temperature range. On the basis of the discussion above and of the comparison with other studies on the thermal behavior of the polymeric monomer/LDH nanocomposites, the strong exothermic process under an inert atmosphere in this work can be assigned to the chemical oxidative polymerization of the interlayer monomer with the co-intercalated nitrates acting as the oxidizing agent. This will be further discussed in the next sections.

The third weight loss (350–450 °C) is due to the pyrolysis of the hydroxide layers and the interlayer organic materials, which results in an enhanced signal of $H_2O^+$ (*m*/*z* = 18) and $SO_2^+$ (*m*/*z* = 64). The corresponding endothermic peak is observed at ca. 430 °C. The complete thermal decomposition of the nanocomposite occurs in the fourth step (450–600 °C).

### In Situ FTIR

Figure 9 shows the in situ FTIR spectra for NiAl-metanilic LDH heated to different scheduled temperatures under nitrogen. Table 2 summarizes the assignments of the IR absorption bands for metanilic-intercalated LDH and its thermal products.[36,37]

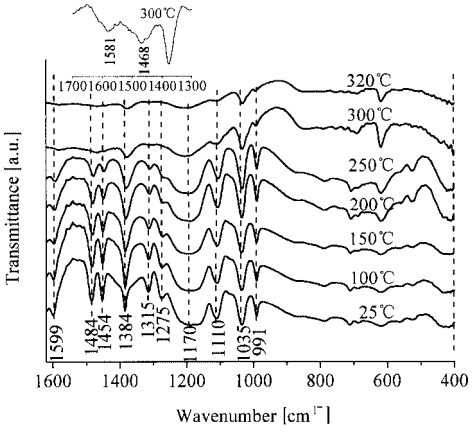


Figure 9. In situ FTIR spectra for the thermal polymerization of NiAl-metanilic LDH.

Table 2. Assignments for IR absorption bands for metanilic-intercalated LDH and its thermal products.[a]

| Frequency [$cm^{-1}$] | Assignment |
|---|---|
| 1599 | disorder-induced C–C ring stretching |
| 1581 | stretching of N=Q=N |
| 1484 | ring stretching of C=C |
| 1468 | stretching of N=B=N |
| 1453 | stretching of benzene ring |
| 1315 | N–H in or out of plane bending |
| 1275 | C–H bending or C–N stretching |
| 1170 | C–H bending in plane |
| 1110 | C–S bending in plane |
| 1035 | S=O bending |
| 991 | C–H bending out of plane |

[a] Abbreviations: B, benzenoid unit; Q, quinonoid unit.

It can be seen that very little change is observed for the three strong bands at 1599, 1484, and 1454 $cm^{-1}$ and the weak band at 1315 $cm^{-1}$, which are characteristic absorptions of metanilic anions from room temperature to 250 °C. When the temperature increases to 300 °C, the former four characteristic bands weaken remarkably because of the increase in the conjugated degree of the polymerization products upon thermal treatment. Moreover, the emergence of the bands at 1581 and 1468 $cm^{-1}$ in the spectrum of NiAl-metanilic LDH at 300 °C indicates that the polymerization product is in a high oxidation state.[38] The comparison of the IR spectrum of the original metanilic-intercalated LDH and those of its oxidation products after treatment at 300 °C reveals a sharp decrease in the intensity of the bands at 1170 ($\upsilon_{C-H}$ in plane), 1275, and 1315 $cm^{-1}$, which points to a substantial decrease in the number of amino groups ($-NH_2$). This further confirms the formation of an interlayer polyconjugated system. Moreover, the intensity of the band at 1384 $cm^{-1}$ attributable to cointercalated $NO_3^-$ decreases sharply as the temperature reaches 300 °C, thereby giving evidence that $NO_3^-$ is engaged in the interlayer redox reaction. This is in agreement with the results of UV/Vis spectroscopy and TG–MS.

 © 2006 Wiley-VCH Verlag GmbH & Co. KGaA, Weinheim 

### In Situ HT-XRD

In order to get further insight into the thermal polymerization process of the monomer intercalated NiAl LDH, in situ X-ray measurements were carried out. The temperatures at which the X-ray data were collected were defined on the basis of TG–DTA analysis. The in situ HT-XRD patterns of the intercalation product NiAl-metanilic LDH in the temperature range 25–320 °C under nitrogen are shown in Figure 10. The variation in the $d_{003}$ basal spacing of NiAl-metanilic LDH with temperature is displayed in Figure 11.

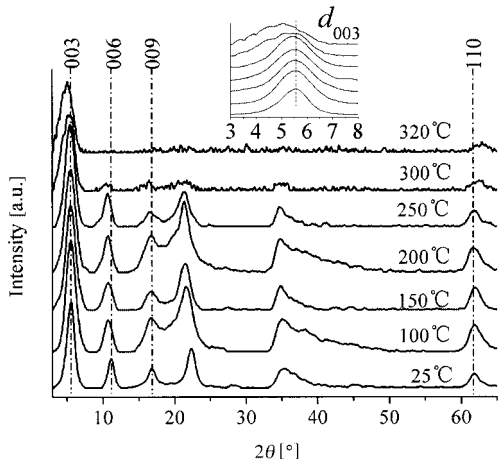


Figure 10. In situ HT-XRD patterns of NiAl-metanilic LDH in the temperature range 25–320 °C.

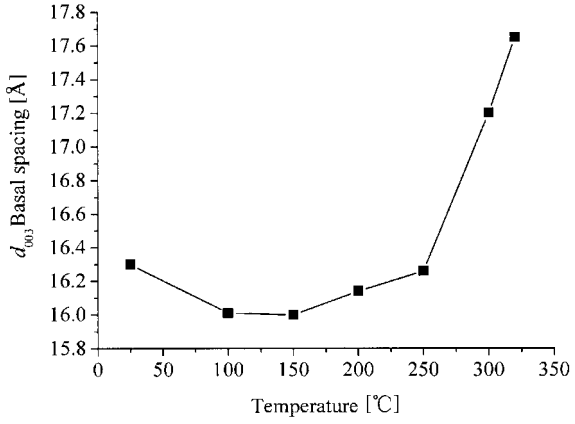


Figure 11. The relationship between the $d_{003}$ basal spacing and temperature.

Upon increasing the temperature, the (003), (006), and (009) reflections of NiAl-metanilic LDH move to a slightly higher $2\theta$ angle (as shown in Figure 10), and the (003) basal spacing decreases from 16.3 to 16.0 Å (Figure 11) when the material was heated from 25 °C to 150 °C. This contraction may result from the loss of absorbed water and parts of gallery water.[39] However, the value of $d_{003}$ slowly increases from 16.0 Å at 150 °C to 16.2 Å at 250 °C. This might be due to the reorientation of the interlayer monomer accompanied by the loss of the gallery water.

When the temperature reaches 300 °C, the (003) reflection of the nanocomposite becomes broader and moves to a remarkably lower $2\theta$ angle. The interlayer distance increases drastically from 16.2 Å at 250 °C to 17.2 Å at 300 °C, indicating that interlayer polymerization of the interlamellar species occurs. This phenomenon was also observed in the case of post-intercalative polymerization of aniline and its derivatives in layered metal phosphates after thermal treatment at 130 °C in air.[11] In addition, the color of the nanocomposite turns from bright green to dark brown after the heat treatment. The broadening of the (003) reflection and the decrease in intensity of other diffraction peaks of the nanocomposite at 300 °C indicate the decrease in ordered stacking sequences and in crystallinity during the polymerization process. Nevertheless, the diffraction maximum between the $2\theta$ values of 62 and 63° (the spectrum at 300 °C in Figure 10) can still be observed, indicating the conservation of the lamellar structure with no substantial structural collapse during the interlayer polymerization reaction.

The coupling between the monomers and the arrangement of their subsequent dimerization or polymerization have been discussed in term of the gap sizes, which can be calculated by using the peak fit program of XRD-6000 Version 4.1.[17] The geometry and atomic charges of the possible dimers have been optimized by using the MOPAC semi-empirical method, employing the PM3 Hamiltonian.[40]

Figure 12 shows the peak fit results of $d_{003}$ at 300 °C, at which the interlayer polymerization occurs. Three different $d_{003}$ values, i.e. 15.77, 17.48, and 20.07 Å were obtained in this case, and the corresponding gallery heights were calculated to be 10.97, 12.68, and 15.27 Å, respectively, by subtracting the inorganic layer thickness of 4.8 Å. The polymerization between monomers located on different layers (opposite inner side) may proceed iso- or syndiotactically, and the coupling between monomers may occur by a linkage (α,β), (β,β), or (N,N). The calculated lengths of the three possible dimers are 10.43, 11.63, and 12.42 Å (as shown in Scheme 1), respectively. It can be concluded that the coupling between monomers most likely occurs by the linkages (α,β) and (N,N) since the calculated lengths of the two possible dimers (10.43 and 12.42 Å) correspond well with the two gallery heights of 10.97 and 12.68 Å. As a result, the coupling between monomers on different layers hereinbefore should give rise to the quasi-monolayer arrangement by the linkage (α,β) (Figure 13a), whereas the gallery height of 15.27 Å may result from the bilayer arrangement when polymerization occurs between the two monomers on the same layer (Figure 13b).[17] The linkage of N and N charac-

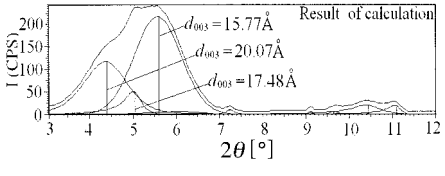


Figure 12. The peak fit results of $d_{003}$ of NiAl-metanilic LDH at 300 °C.

 © 2006 Wiley-VCH Verlag GmbH & Co. KGaA, Weinheim 

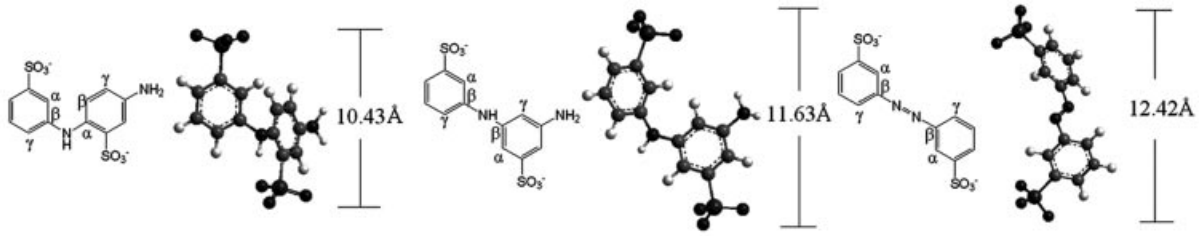


Scheme 1. The structure for the three possible dimers of metanilic anions formed by different linkages: (a) (α,β), (b) (β,β), and (c) (N,N).

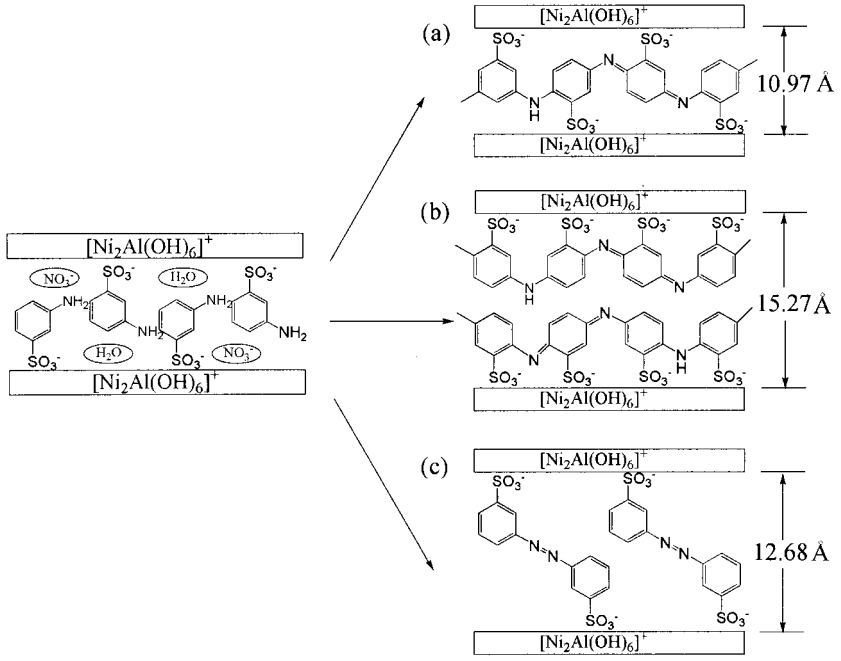


Figure 13. Schematic representations of the interlayer polymerization products.

teristics, which results from the "head-to-head" coupling (Figure 13c), was observed only in the spectra of products prepared under neutral or basic conditions. For instance, the formation of azobenzene derivatives in basic or in an acetonitrile/pyridine medium has also been reported by Wawzonek and MacIntyre.[41] On the basis of the discussion above, it can be concluded that the coupling between monomers most likely occurs by the (α,β) and (N,N) linkages, and the main coupling likely occurs by an (α,β) linkage. This is in agreement with the much earlier work of Mohilner et al., in which aniline oxidation products obtained in neutral or weakly acidic media have a predominantly "head-to-tail" arrangement.[42]

## TEM

The TEM micrographs of the prepared materials are illustrated in Figure 14. It can be seen that NiAl-metanilic LDH exhibits the characteristic LDH platelet, an ill-defined shape with a uniform size from 200 to 300 Å (Figure 14a). This morphological result is consistent with that from HT-XRD analysis. The polymerization product PANIS shows a similar platelike morphology (Figure 14b) with average particle size of 50–100 Å. Such a small size is possibly due to the restriction on the chain growth of PANIS afforded by the layers of LDH.

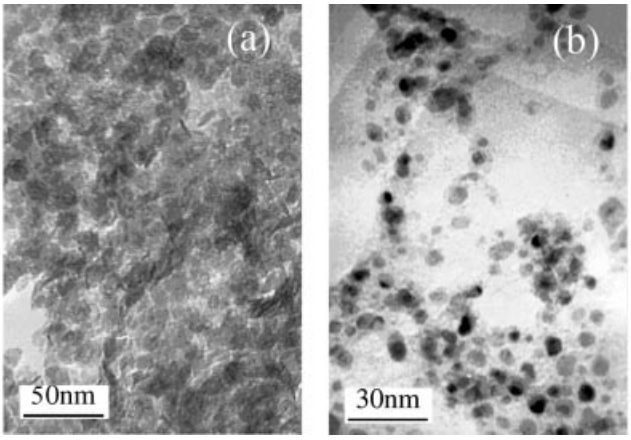


Figure 14. TEM images of (a) NiAl-metanilic LDH and (b) the polymerization product (PANIS).

 © 2006 Wiley-VCH Verlag GmbH & Co. KGaA, Weinheim 

## Conclusions

The in situ chemical oxidative polymerization of metanilic anions ($m$-$NH_2C_6H_4SO_3^-$) intercalated in NiAl LDH has been performed for the first time by the use of pre-intercalated nitrate as the oxidizing agent. From the characterization by XRD, IR spectroscopy, elemental analysis, and geometrical considerations, the schematic model of NiAl-metanilic LDH has been proposed in which the structure can be represented as alternating NiAl-OH hydroxide layers and layers containing metanilic anions, $NO_3^-$ ions, and water molecules.

Results obtained by UV/Vis spectroscopy give evidence for the polymerization of the metanilic anions intercalated NiAl LDH when the temperature reaches 300 °C. The particle sizes of 50–100 Å of the interlayer polymerization product determined by TEM microscopy indicates the low conjugation extent of the interlayer PANIS.

In situ XANES demonstrates that $Ni^{2+}$ in the host layer does not serve as the oxidant for interlayer oxidative polymerization. According to the results of TG–DTA–MS for the pristine metanilic acid and the NiAl-metanilic LDH under nitrogen, we propose that the pre-intercalated nitrate anions act as the oxidant, which induces the polymerization of the interlayer monomer under nitrogen upon heating at 300 °C.

In situ FTIR and in situ HT-XRD provide further insight into the thermal polymerization process. The basal spacing increases from 16.0 to 17.2 Å, and the characteristic vibrational absorptions of polyaniline emerge at 300 °C under nitrogen. It can be concluded, on the basis of the peak fit program and the MOPAC semi-empirical method, that the coupling between monomers most likely occurs by the (α,β) and (N,N) linkages. The possible schematic arrangement for the interlayer products has also been proposed.

## Experimental Section

**Reagents:** All chemicals used in this synthesis including $Ni(NO_3)_2{\cdot}6H_2O$, $Al(NO_3)_3{\cdot}9H_2O$, NaOH, and metanilic acid ($m$-$NH_2C_6H_4SO_3^-$) were of analytical grade and were purchased from Aldrich and used without any further purification. High purity nitrogen gas ($O_2 < 1$ ppm) and high purity helium gas ($O_2 < 1$ ppm) were purchased from the Beijing Chemical Plant Limited. All solutions were prepared with distilled and decarbonated water.

**Synthesis:** The precursor LDH $[Ni_2Al(OH)_6(NO_3)]{\cdot}nH_2O$ was prepared following a standard aqueous coprecipitation and thermal crystallization method.[18] A solution of NaOH (8.0 g, 0.20 mol) in water (100 mL) was added dropwise over 2 h to a solution (100 mL) containing $Ni(NO_3)_2{\cdot}6H_2O$ (19.4 g, 0.066 mol) and $Al(NO_3)_3{\cdot}9H_2O$ (12.5 g, 0.033 mol), with vigorous stirring under nitrogen. The pH value of the solution at the end of addition was 7.0. The resultant gelatinous precipitate was maintained at 100 °C for 72 h, centrifuged, and washed thoroughly with water before drying at 70 °C for 24 h under vacuum.

The metanilic intercalated NiAl-LDH was prepared following the ion-exchange method. A solution (100 mL) of metanilic acid (10.4 g, 6.0 mmol) with a pH value adjusted to 7.0 using NaOH (2.0 M) was added to a suspension of NiAl-$NO_3$ LDH (5.0 g, *ca.* 1.5 mmol) in water (100 mL). The mixture was held at 30 °C under nitrogen for 72 h. The product was washed extensively with water, centrifuged, and dried under vacuum for 24 h.

For the thermal treatment, the hybrid phase was placed in a tube furnace heated at 25, 100, 150, 200, 250, 300, or 320 °C for 0.5 h under nitrogen.

**Characterization Techniques:** Powder X-ray diffraction (XRD) measurements were performed on a Rigaku XRD-6000 diffractometer, using Cu-$K_\alpha$ radiation ($\lambda$ = 1.5418 Å) at 40 kV and 30 mA. Data were collected over the angular range of $2\theta$ from 3° to 70° at a scanning rate of 0.02° per second at room temperature. The UV/Vis spectra were collected in reflectance mode using a Shimadzu UV-2401 spectrophotometer in the 230–800 nm region (the samples were dissolved in 0.1 M hydrochloric acid). Fourier transform infrared (FTIR) spectra were recorded using a Vector 22 (Bruker) spectrophotometer in the range 4000 to 400 $cm^{-1}$ with 2 $cm^{-1}$ resolution. The standard KBr disk (1 mg of sample in 100 mg of KBr) was used. In situ XANES spectra were collected at the XAFS station (beam line 4W1B) of the Beijing Synchrotron Radiation Facility. The storage ring energy was 2.2 GeV and the current was 50–60 mA. The X-rays were monochromated by using a Si (111) single crystal. Samples were shaped into ingots with a thickness of about 1 mm. X-ray absorption spectra of the Ni $K$-edge were collected at ambient temperature up to 320 °C with a heating rate of 5 °C $min^{-1}$ under nitrogen in the transmission mode. The incident and transmission X-ray intensities were detected using ion chambers which were installed in front of and behind the sample, respectively. In situ HT-XRD measurements were performed on a Rigaku D/max 2500VB2+/PC diffractometer in the temperature range 25–320 °C under nitrogen by using Cu-$K_\alpha$ radiation ($\lambda$ = 1.5418 Å) at 40 kV and 30 mA. The samples as disoriented powders were scanned in steps of 0.02° in the $2\theta$ range 3°–70° by using a count time of 4 s per step. An α-$Al_2O_3$ substrate was used. In situ FTIR spectra were recorded with a Nicolet 60sxb spectrometer in the range 4000 to 400 $cm^{-1}$ with 2 $cm^{-1}$ resolution. The spectra were obtained every 10° with a heating rate of 5 °C $min^{-1}$ under nitrogen. The standard KBr disk method (1 mg of sample in 100 mg of KBr) was used. TG–DTA analyses were carried out under nitrogen (flux of 100 mL $min^{-1}$) with a Seiko 6300 simultaneous DTA–TGA apparatus from Seiko Instruments, at a heating rate of 5 °C $min^{-1}$, with $Al_2O_3$ as a reference. Simultaneous TG–MS analyses were performed with a Pyris Diamond TG–DTA instrument coupled to a ThermoStar™ QM220 mass spectrometer by a quartz capillary transfer line at 180 °C. The heating rate was 5 °C $min^{-1}$, with a helium flow of 100 mL $min^{-1}$. The scanning speed of mass was 1 a.m.u $s^{-1}$, with a filtering time 0.03 s. The TGA apparatus operated at atmospheric pressure, and the mass spectrometer at a working pressure of $3 \times 10^{-6}$ mPa and an electron energy of 70 eV. The proposed mass number, the ion current intensity, and the amplifying rate are listed in Table 1. Elemental analyses were performed with a Shimadzu ICPS-7500 instrument. C, H, and N content were determined by using an Elementarvario elemental analysis instrument. TEM images were obtained by using a JEOL JEM-1200 instrument operating at an acceleration voltage of 80 kV. The TEM samples were ultrasonically dispersed in water, and then a suspension was deposited onto a holey carbon film deposited on a Cu grid.

## Acknowledgments

This project was supported by the National Natural Science Foundation Key Project of China (Project No.: 20531010), the National

 © 2006 Wiley-VCH Verlag GmbH & Co. KGaA, Weinheim 

Natural Science Foundation Major International Joint Research Program (Project No.: 20620130108), the Beijing Nova Program (No.: 2004A13), and the Program for Changjiang Scholars and the Innovative Research Team at the University (PCSIRT). We also acknowledge the Beijing Synchrotron Radiation Facility (BSRF) for provision of synchrotron radiation facilities and thank Dr. Tao Liu and Yaning Xie for assistance in using beamline 4W1B.

[1] A. I. Khan, D. O'Hare, *J. Mater. Chem.* **2002**, *12*, 3191–3198.
[2] F. Leroux, J. P. Besse, *Chem. Mater.* **2001**, *13*, 3507–3515.
[3] R. Schollhorn, *Chem. Mater.* **1996**, *8*, 1747–1757.
[4] L. Vieille, E. M. Moujahid, C. Taviot-Guého, J. Cellier, J. P. Besse, F. Leroux, *J. Phys. Chem. Solids* **2004**, *65*, 385–393.
[5] E. M. Moujahid, F. Leroux, M. Dubois, J. P. Besse, *C. R. Chim.* **2003**, *6*, 259–264.
[6] M. G. Kanatzidis, C. G. Wu, H. O. Marcy, C. R. Kannewurf, *J. Am. Chem. Soc.* **1989**, *111*, 4139–4141.
[7] T. A. Kerr, H. Wu, L. F. Nazar, *Chem. Mater.* **1996**, *8*, 2005–2015.
[8] P. Liu, K. Gong, *Carbon* **1999**, *37*, 706–707.
[9] L. Wang, P. Brazis, M. Rocci, C. R. Kannewurf, M. G. Kanatzidis, *Chem. Mater.* **1998**, *10*, 3298–3300.
[10] H. Inoue, H. J. Yoneyama, *J. Electroanal. Chem.* **1987**, *233*, 291–294.
[11] Y. J. Liu, M. G. Kanatzidis, *Chem. Mater.* **1995**, *7*, 1525–1533.
[12] C. B. Koch, *Hyperfine Interact.* **1998**, *117*, 131–157.
[13] F. Cavani, F. Trifiro, A. Vaccari, *Catal. Today* **1991**, *11*, 173–301.
[14] T. Challier, R. C. T. Slade, *J. Mater. Chem.* **1994**, *4*, 367–371.
[15] E. M. Moujahid, M. Dubois, J. P. Besse, F. Leroux, *Chem. Mater.* **2002**, *14*, 3799–3807.
[16] V. P. Isupov, L. E. Chupakhina, M. A. Ozerova, V. G. Kostrovsky, V. A. Poluboyarov, *Solid State Ionics* **2001**, *141–142*, 231–236.
[17] E. M. Moujahid, M. Dubois, J. P. Besse, F. Leroux, *Chem. Mater.* **2005**, *17*, 373–382.
[18] J. Wilson, T. Olorunyolemi, A. Jaworski, L. Borum, D. Young, A. Siriwat, E. Dickens, *Appl. Clay Sci.* **1999**, *15*, 265–279.
[19] N. T. Whilton, P. J. Vickers, S. Mann, *J. Mater. Chem.* **1997**, *7*, 1623–1629.
[20] F. Prinetto, D. Tichit, R. Teissier, B. Coq, *Catal. Today* **2000**, *55*, 103–116.
[21] J. Zhang, F. Z. Zhang, L. L. Ren, D. G. Evans, X. Duan, *Mater. Chem. Phys.* **2004**, *85*, 207–214.
[22] T. A. Huber, *A Literature Survey of Polyaniline*, Defence R&D Canada – Atlantic, **2003**, p. 014.
[23] N. T. Whilton, P. J. Vickers, S. Mann, *J. Mater. Chem.* **1997**, *7*, 1623–1629.
[24] A. Fudala, I. Palinko, I. Kiricsi, *Inorg. Chem.* **1999**, *38*, 4653–4658.
[25] G. W. Brindley, S. Kikkawa, *Am. Mineral.* **1979**, *64*, 836–843.
[26] S. K. Yun, T. J. Pinnavaia, *Chem. Mater.* **1995**, *7*, 348–354.
[27] J. E. de Albuquerque, L. H. C. Mattoso, M. Faria, J. G. Masters, A. G. MacDiarmid, *Synth. Met.* **2004**, *146*, 1–10.
[28] B. A. Deore, I. Yu, M. S. Freund, *J. Am. Chem. Soc.* **2004**, *126*, 52–53.
[29] V. Luca, S. Thomson, *J. Mater. Chem.* **2000**, *10*, 2121–2126.
[30] L. W. Shacklette, J. F. Wolf, S. Gould, R. H. Baughman, *J. Chem. Phys.* **1988**, *88*, 3955–3961.
[31] F. Leroux, P. J. Dewar, M. Intissar, G. Ouvrard, L. F. Nazar, *J. Mater. Chem.* **2002**, *12*, 3245–3253.
[32] M. Jiménez-Ruiz, C. Prieto, J. L. Martínez, J. M. Alonso, *J. Solid State Chem.* **1998**, *140*, 278–284.
[33] C. W. Lu, Z. He, T. G. Xi, Y. X. Chen, L. Luo, *Thermochim. Acta* **1999**, *334*, 149–155.
[34] D. Tichit, F. Medina, B. Coq, R. Dutartre, *Appl. Catal. A* **1997**, *159*, 241–258.
[35] C. Roland-Swanson, J. P. Besse, F. Leroux, *Chem. Mater.* **2004**, *16*, 5512–5517.
[36] M. C. Miras, C. Barbero, O. Haas, *Synth. Met.* **1991**, *43*, 3081–3084.
[37] Y. Furukawa, F. Ueda, Y. Hyodo, I. Harada, T. Nakajima, T. Kawagoe, *Macromolecules* **1988**, *21*, 1297–1305.
[38] E. T. Kang, K. G. Neoh, K. L. Tan, *Prog. Polym. Sci.* **1998**, *23*, 277–324.
[39] M. Wei, J. Wang, J. He, D. G. Evans, X. Duan, *Microporous Mesoporous Mater.* **2005**, *78*, 53–61.
[40] A. M. Aicken, I. S. Bell, P. V. Coveney, W. Jones, *Adv. Mater.* **1997**, *9*, 496–500.
[41] S. Wawzonek, T. W. MacIntyre, *J. Electrochem. Soc.* **1972**, *119*, 1350–1357.
[42] D. M. Mohilner, R. N. Adams, W. J. Argersinger, *J. Am. Chem. Soc.* **1962**, *84*, 3618–3622.

Received: March 9, 2006
Published Online: July 11, 2006

 © 2006 Wiley-VCH Verlag GmbH & Co. KGaA, Weinheim 

DOI: 10.1002/ejic.200600251

# Preparation of Hydroxylamine and *O*-Methylhydroxylamine Complexes of Manganese and Rhenium

**Gabriele Albertin,*[a] Stefano Antoniutti,[a] Jorge Bravo,[b] Jesús Castro,[b] Soledad García-Fontán,[b] Mª Carmen Marín,[b] and Marco Noè[a]**

**Keywords:** Hydroxylamine / *O*-Methylhydroxylamine / CO and P ligands / Manganese / Rhenium / Oxidation

Hydroxylamine and *O*-methylhydroxylamine complexes $[M(NH_2OH)(CO)_nP_{5-n}]BPh_4$ and $[M(NH_2OCH_3)(CO)_nP_{5-n}]BPh_4$ [M = Mn, Re; $n$ = 1, 2, 3; P = $P(OEt)_3$, $PPh(OEt)_2$, $PPh_2OEt$] were prepared by allowing hydrides $MH(CO)_nP_{5-n}$ to react first with triflic acid and then with an excess of hydroxylamine. Bidentate phosphane and phosphite can also be used to prepare both $NH_2OH$ and $NH_2OCH_3$ complexes of manganese and rhenium of the $[M(NH_2OR)(CO)_2(P–P)\{P(OEt)_3\}]BPh_4$ and $[M(NH_2OR)(CO)_3(P–P)]BPh_4$ [R = H, $CH_3$; P–P = $Ph_2POCH_2CH_2OPPh_2$, $Ph_2PO(CH_2)_3OPPh_2$, $Ph_2PN(CH_3)CH_2CH_2N(CH_3)PPh_2$] types with the use of $MH(CO)_2(P–P)\{P(OEt)_3\}$ and $MH(CO)_3(P–P)$ as precursors. The complexes were characterized spectroscopically and by the X-ray crystal-structure determination of $[Re(NH_2OCH_3)(CO)_2\{PPh(OEt)_2\}_3]BPh_4$ and $[Re(NH_2OCH_3)(CO)_3\{Ph_2PO(CH_2)_3OPPh_2\}]BPh_4$. Oxidation of the hydroxylamine complexes with $Pb(OAc)_4$ was studied at –40 °C and led to an unstable compound tentatively characterized as a nitroxyl [M]–N(H)=O derivative.

(© Wiley-VCH Verlag GmbH & Co. KGaA, 69451 Weinheim, Germany, 2006)

## Introduction

Despite the very large number of transition-metal complexes that contain monodentate nitrogenous ligands[1] such as ammonia, amines, imine, nitrile, nitrogen monoxide, hydrazine, etc., the coordination chemistry of hydroxylamine, $NH_2OH$, may be considered somewhat unexplored. A glance through the literature, in fact, shows that hydroxylamine complexes are very scarce,[2] and only recently have some examples of complexes of the $[MX(NH_2OH)(CO)_2(PPh_3)_2]CF_3SO_3$ (M = Ru, Os; X = Cl, Br) and $[Re(NH_2OH)(CO)_3(PPh_3)_2]CF_3SO_3$ types been reported.[3]

This feature is rather surprising in view of the fact that the hydrazine molecule, $NH_2NH_2$, which is isoelectronic to and somewhat similar to $NH_2OH$ forms a number of stable and isolable transition-metal complexes.[4,5] A reason for the scarce number of hydroxylamine derivatives may be a result of the presence of the OH group that is bonded to $NH_2$, which makes the $NH_2OH$ a poor ligand either as an *N*-bonded, or as an *O*-bonded group. However, the instability of the $NH_2OH$ molecule in the free state may also contribute to the fact that the synthesis of hydroxylamine derivatives is somewhat difficult.

We have interest in the chemistry of transition metal complexes with nitrogen-containing ligands and have reported the synthesis and the reactivity of hydrazine complexes of Mn, Re, Fe, Ru, and Os stabilized by phosphite ligands.[6] Recently, we have focused our attention on the $NH_2OH$ molecule and reported the preparation of both mono- and bis(hydroxylamine) complexes of ruthenium and osmium of the $[MH(NH_2OH)P_4]^+$ and $[M(NH_2OH)_2P_4]^{2+}$ types (M = Ru, Os; P = phosphites).[7]

These studies have now been extended to manganese and rhenium as a central metal to determine whether the synthesis of hydroxylamine complexes can be achieved for these metals and, if possible, to compare these complexes with related hydrazine derivatives.[6a,6g] The results of these studies, which allow the synthesis of the first hydroxylamine and methylhydroxylamine complexes of manganese and of new examples for rhenium, are reported here.

## Results and Discussion

The synthesis of hydroxylamine complexes of manganese(I) and rhenium(I) was achieved by the reaction of the $MH(CO)_nP_{5-n}$ hydride[6a,8] first with an equimolar amount of triflic acid (HOTf) and then with an excess of hydroxylamine, as shown in Scheme 1 and Scheme 2.

Protonation of the $MH(CO)_nP_{5-n}$ hydride with HOTf leads to the evolution of $H_2$ and the formation of the triflate complexes $M(\kappa^1\text{-OTf})(CO)_nP_{5-n}$.[6a,8] Substitution of the labile $\kappa^1$-OTf ligand with $NH_2OH$ afforded the final hydroxylamine complexes, which were isolated in good yields and characterized. Crucial for the success of the synthesis is to carry out the reaction at 0 °C for 5–8 hours and to use a large excess of free $NH_2OH$. Otherwise, either intractable

[a] Dipartimento di Chimica, Università Ca′ Foscari di Venezia, Dorsoduro 2137, 30123 Venezia, Italy
[b] Departamento de Química Inorgánica, Universidade de Vigo, Facultade de Química, Edificio de Ciencias Experimentais, 36310 Vigo, Galicia, Spain

 © 2006 Wiley-VCH Verlag GmbH & Co. KGaA, Weinheim 

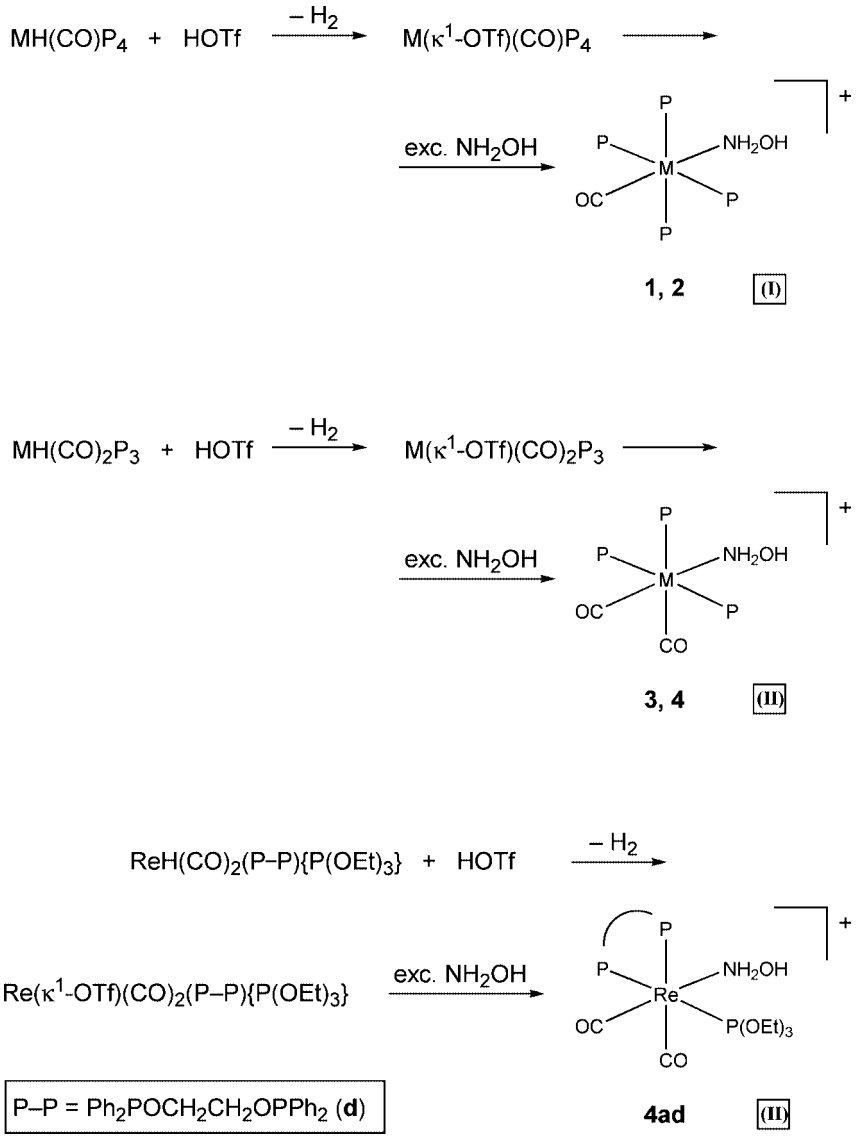


Scheme 1. M = Mn (**1**, **3**), Re (**2**, **4**); P = $P(OEt)_3$ (**a**), $PPh(OEt)_2$ (**b**); OTf = $CF_3SO_3$.

mixtures of products, or very low yields in the complexes are obtained. It should also be noted that only the mono- $[M(CO)P_4]$ and the dicarbonyl $[M(CO)_2P_3]$ fragments with $P(OEt)_3$ and $PPh(OEt)_2$ ligands allow the synthesis of hydroxylamine complexes. With tricarbonyl complexes $[M(CO)_3P_2]$, a different phosphane such as $PPh_2OEt$ or $Ph_2PN(Me)CH_2CH_2N(Me)PPh_2$ (P–P) must be used to yield hydroxylamine complexes $[Mn(NH_2OH)(CO)_3(PPh_2OEt)_2]BPh_4$ (**5c**) and $[Re(NH_2OH)(CO)_3(P–P)]BPh_4$ (**6e**) [Scheme 2].

It seems, therefore, that the electronic properties of the $[M(CO)_nP_{5-n}]$ (M = Mn, Re) fragment are important in determining the synthesis and the stabilization of the $NH_2OH$ complexes. In particular, it seems that an electron-poor metal center is not able to stabilize the coordination of $NH_2OH$. With good π-acceptor[9] phosphanes such as $P(OEt)_3$ and $PPh(OEt)_2$ only mono- and dicarbonyl compounds $[M(NH_2OH)(CO)P_4]^+$ and $[M(NH_2OH)(CO)_2P_3]^+$ were obtained, while stable tricarbonyl cations $[M(NH_2OH)(CO)_3P_2]^+$could only be prepared through the use of phosphanes that are less π-acidic than $PPh(OEt)_2$, such as $PPh_2OEt$ and P–P, which were used in complexes **5c** and **6e**. The presence of four strong π-acceptor carbonyl ligands in the $[M(CO)_4P]$ fragment makes the metal center so electron-poor that it does not allow for the preparation of hydroxylamine complexes with any phosphane used.

A comparison between the behavior of $NH_2OH$ and the somewhat related $NH_2NH_2$ ligands toward the $[M(CO)_nP_{5-n}]$ fragment reveals that when hydrazine was used the synthesis of mixed-ligand complexes of manganese and rhenium with carbonyl and phosphite compounds was easily achieved with every $[M(CO)_nP_{5-n}]$ fragment,[6a,6g] and stable complexes were even obtained with the tetracarbonyl $[M(NH_2NH_2)(CO)_4P]^+$ cation, but hydroxylamine was found to be a more problematic ligand. Only appropriate fragments, in fact, allow for the synthesis of the corresponding hydroxylamine derivatives, which highlights the fact that $NH_2OH$ is a molecule that is hard to coordinate.

 © 2006 Wiley-VCH Verlag GmbH & Co. KGaA, Weinheim 

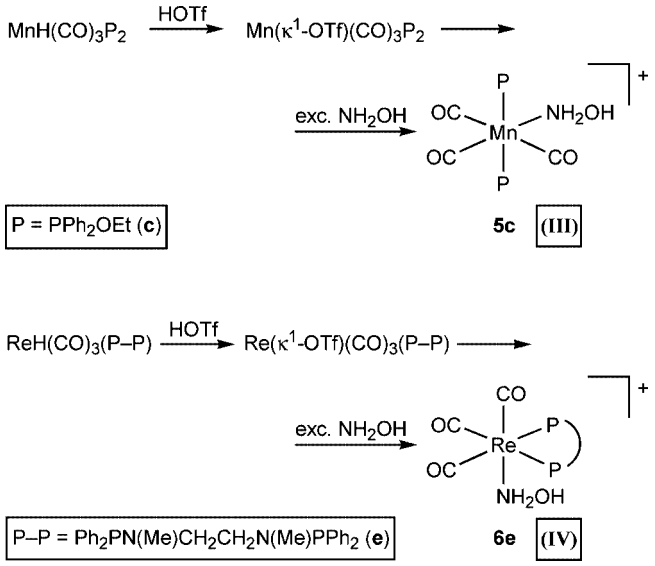


Scheme 2.

However, the use of the triflate complex $M(\kappa^1\text{-OTf})(CO)_nP_{5-n}$ ($n$ = 1, 2, 3) as a precursor allows for the synthesis of the first hydroxylamine complexes of manganese, in addition to new examples of rhenium derivatives. Only one example, in fact, of $NH_2OH$ complexes of rhenium[3b] is reported in the literature, while only quantum chemical calculations[10] are reported for hydroxylamine complexes of manganese.

The results obtained with hydroxylamine prompted us to extend our study to the use of both *N*- and *O*-substituted $NH_2OH$ as a ligand. We began to investigate the behavior of the *N*-methyl, $NH(CH_3)OH$, and hydroxylamine towards the triflate complex $M(\kappa^1\text{-OTf})(CO)_nP_{5-n}$, but in no case was an *N*-methylhydroxylamine complex obtained. The steric hindrance of the methyl group probably prevents the *N*-coordination of the $NH(CH_3)OH$ molecule.

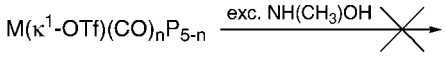


The *O*-methylhydroxylamine, on the other hand, quickly reacts with the triflate complexes $M(\kappa^1\text{-OTf})(CO)_nP_{5-n}$ containing monodentate phosphite ligands (P) to give the $NH_2OCH_3$ derivatives **7**–**11** which were isolated in good yield and characterized (Scheme 3).

The reaction also proceeds with triflate precursors $Re(\kappa^1\text{-OTf})(CO)_2(P–P)\{P(OEt)_3\}$ and $Re(\kappa^1\text{-OTf})(CO)_3(P–P)$, containing bidentate phosphane ligands, to yield the related $NH_2OCH_3$ complexes **9**–**11**, as shown in Scheme 4.

The syntheses of the $NH_2OCH_3$ complexes **7**–**11** can be carried out at room temperature and do not need particular attention to give the final complexes in good yields. Furthermore, in contrast to $NH_2OH$, the tricarbonyl fragment $M(CO)_3P_2$ afforded stable *O*-methylhydroxylamine complexes with all the phosphites used. These results may be attributed to the presence of the methoxy group in $NH_2OCH_3$, which makes *O*-methylhydroxylamine a better σ-donor than $NH_2OH$. As a result, more thermally stable

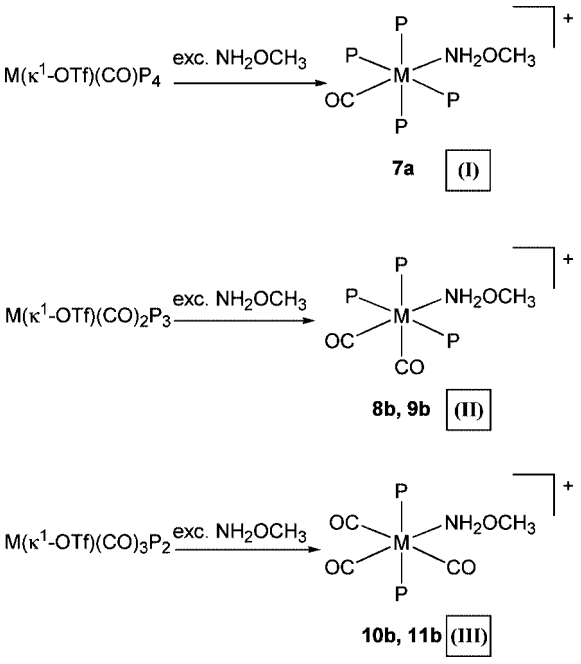


Scheme 3. M = Re (**7**, **9**, **11**), Mn (**8**, **10**); P = $P(OEt)_3$ (**a**), $PPh(OEt)_2$ (**b**).

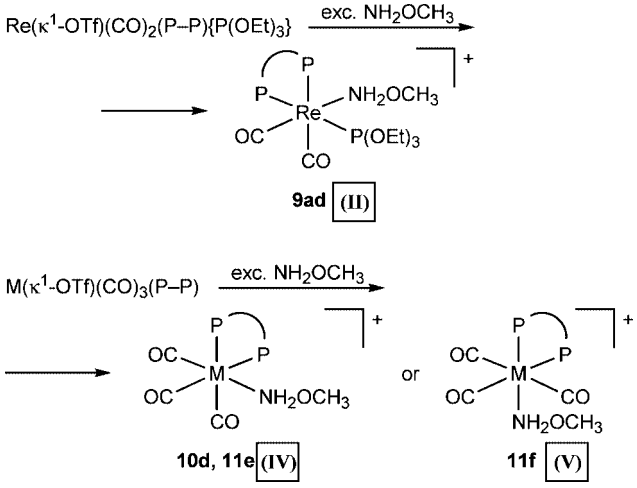


Scheme 4. M = Mn (**10**), Re (**11**); P–P = $Ph_2POCH_2CH_2OPPh_2$ (**d**), $Ph_2PN(CH_3)CH_2CH_2N(CH_3)PPh_2$ (**e**), $Ph_2PO(CH_2)_3OPPh_2$ (**f**).

complexes were obtained with the $NH_2OCH_3$ ligand, and suitable crystals for X-ray crystal-structure determination were also obtained with the *O*-methylhydroxylamine complexes **9b** and **11f**.

Once crystallized, both the hydroxylamine complexes **1**–**6** and the *O*-methylhydroxylamine complexes **7**–**11** are stable as solids and in a solution of polar organic solvents, in which they behave like 1:1 electrolytes.[11] The complexes were characterized spectroscopically (Table 1 and Table 2) and by the X-ray crystal-structure determination of $[Re(NH_2OCH_3)(CO)_2\{PPh(OEt)_2\}_3]BPh_4$ (**9b**) and $[Re(NH_2OCH_3)(CO)_3\{Ph_2PO(CH_2)_3OPPh_2\}]BPh_4$ (**11f**), whose ORTEP drawings are shown in Figure 1 and Figure 2.

 © 2006 Wiley-VCH Verlag GmbH & Co. KGaA, Weinheim 

Table 1. Selected IR and 300 MHz NMR spectroscopic data for manganese and rhenium complexes.

| | Compound | IR[a] $\tilde{\nu}$ [cm$^{-1}$] | Assign-ment | $^1$H NMR[b,c] $\delta$ [ppm] $J$ [Hz] | Assign-ment | Spin system | $^{31}$P{$^1$H}NMR[b,d] $\delta$ [ppm] $J$ [Hz] |
|---|---|---|---|---|---|---|---|
| **1b** | $[Mn(NH_2OH)(CO)\{PPh(OEt)_2\}_4]BPh_4$ | 3415 m, br | $\nu_{OH}$ | 6.11 br[e] | OH | $A_4$[e] | 196.4 s |
| | | 3303 m | $\nu_{NH}$ | 5.30 br | $NH_2$ | | |
| | | 3222 m | | 3.48 m, br | $CH_2$ | | |
| | | 1884 s | $\nu_{CO}$ | 3.19 m, br | | | |
| | | | | 1.11 t | $CH_3$ | | |
| **2a** | $[Re(NH_2OH)(CO)\{P(OEt)_3\}_4]BPh_4$ | 3434 m, br | $\nu_{OH}$ | 6.39 t[e] | OH | $A_4$[e] | 118.0 s |
| | | 3316 w | $\nu_{NH}$ | $J_{H,H}$ = 2.3 | | | |
| | | 3230 m | | 6.17 m, br | $NH_2$ | | |
| | | 1888 s | $\nu_{CO}$ | $J_{P,H}$ = 3.0 | | | |
| | | | | 4.01 q | $CH_2$ | | |
| | | | | 1.27 t | $CH_3$ | | |
| **3b** | $[Mn(NH_2OH)(CO)_2\{PPh(OEt)_2\}_3]BPh_4$ | 3414 m | $\nu_{OH}$ | 6.16 br[f] | OH | $A_2B$[f] | $P_A$: 189.6 |
| | | 3289 m | $\nu_{NH}$ | 5.68 t, br | $NH_2$ | | $P_B$: 182.0 |
| | | 3217 m | | 3.78 m | $CH_2$ | | $J_{A,B}$ = 84.0 |
| | | 2000 s | $\nu_{CO}$ | 1.25 m | $CH_3$ | | |
| | | 1909 s | | | | | |
| **4a** | $[Re(NH_2OH)(CO)_2\{P(OEt)_3\}_3]BPh_4$ | 3390 m | $\nu_{OH}$ | 5.50 t, br[e] | OH | $AB_2$[e] | $P_A$: 142.0 |
| | | 3277 m | $\nu_{NH}$ | 5.05 m, br | $NH_2$ | | $P_B$: 135.1 |
| | | 3221 m | | 4.10–3.30 m | $CH_2$ | | $J_{A,B}$ = 36.7 |
| | | 1986 s | $\nu_{CO}$ | 1.31 m | $CH_3$ | | |
| | | 1902 s | | 1.14 t | | | |
| **4b** | $[Re(NH_2OH)(CO)_2\{PPh(OEt)_2\}_3]BPh_4$ | 3417 m | $\nu_{OH}$ | 5.79 t, br | OH | $AB_2$ | $P_A$: 139.3 |
| | | 3287 m | $\nu_{NH}$ | 5.60 m, br | $NH_2$ | | $P_B$: 137.4 |
| | | 3218 m | | 3.94 m | $CH_2$ | | $J_{A,B}$ = 36.1 |
| | | 1998 s | $\nu_{CO}$ | 3.84 m | | | |
| | | 1915 s | | 1.37 m | $CH_3$ | | |
| | | | | 1.35 t | | | |
| **4ad** | $[Re(NH_2OH)(CO)_2(Ph_2POCH_2CH_2OPPh_2)\{P(OEt)_3\}]BPh_4$ | 3383 m, br | $\nu_{OH}$ | 4.95 m, br | $NH_2$ | ABC | $P_A$: 124.0 |
| | | 3348 m | $\nu_{NH}$ | 4.59 m, br | OH | | $P_B$: 121.3 |
| | | 3215 m | | 4.50–3.88 m | $CH_2$ | | $P_C$: 112.6 |
| | | 1988 s | $\nu_{CO}$ | 4.10 m | | | $J_{A,B}$ = 34.0 |
| | | 1889 s | | 1.16 t | $CH_3$ | | $J_{A,C}$ = 248.1 |
| | | | | | | | $J_{B,C}$ = 27.2 |
| **5c** | $[Mn(NH_2OH)(CO)_3(PPh_2OEt)_2]BPh_4$ | 3395 m | $\nu_{OH}$ | 4.65 m, br[g] | $NH_2$ | $A_2$[f] | 158.1 |
| | | 3269 m | $\nu_{NH}$ | 4.41 br | OH | | |
| | | 3223 m | | 3.56 m | $CH_2$ | | |
| | | 2065 m | $\nu_{CO}$ | 1.15 t, br | $CH_3$ | | |
| | | 1973 s | | | | | |
| | | 1940 s | | | | | |
| **6e** | $[Re(NH_2OH)(CO)_3\{Ph_2PN(CH_3)CH_2CH_2N(CH_3)PPh_2\}]BPh_4$ | 3381 m, br | $\nu_{OH}$ | 4.87 t, br | OH | $A_2$ | 66.1 s |
| | | 3243 m | $\nu_{NH}$ | 3.54 m, br | $NH_2$ | | |
| | | 3212 m | | 3.80 m | $CH_2$ | | |
| | | 2047 s | $\nu_{CO}$ | 3.28 m | | | |
| | | 1979 s | | 2.50 s | $NCH_3$ | | |
| | | 1913 s | | | | | |
| **7a** | $[Re(NH_2OCH_3)(CO)\{P(OEt)_3\}_4]BPh_4$ | 3263 w | $\nu_{NH}$ | 6.19 qnt[g] | $NH_2$ | $A_4$[g] | 119.0 s |
| | | 3230 m | | 4.00 m | $CH_2$ | | |
| | | 1881 s | $\nu_{CO}$ | 3.49 s | $OCH_3$ | | |
| | | | | 1.26 t | $CH_3$ phos | | |
| **8b** | $[Mn(NH_2OCH_3)(CO)_2\{PPh(OEt)_2\}_3]BPh_4$ | 3269 m | $\nu_{NH}$ | 4.88 t[g] | $NH_2$ | $A_2B$ [f] | $P_A$: 194.1 |
| | | 3223 m | | $J_{P,H}$ = 6 | | | $P_B$: 187.9 |
| | | 1993 s | $\nu_{CO}$ | 3.95 m | $CH_2$ | | $J_{A,B}$ = 93.0 |
| | | 1907 s | | 2.88 s | $OCH_3$ | | |
| | | | | 1.36 m | $CH_3$ phos | | |
| | | | | 1.34 t | | | |
| | | | | 1.30 t | | | |
| **9b** | $[Re(NH_2OCH_3)(CO)_2\{PPh(OEt)_2\}_3]BPh_4$ | 3238 m | $\nu_{NH}$ | 4.75 t[g] | $NH_2$ | $AB_2$[g] | $P_A$: 139.1 |
| | | 2025 s | $\nu_{CO}$ | $J_{P,H}$ = 6 | | | $P_B$: 138.4 |
| | | 1909 s | | 4.09–3.80 m | $CH_2$ | | $J_{A,B}$ = 34.9 |
| | | | | 2.70 s | $OCH_3$ | | |
| | | | | 1.37 m | $CH_3$ phos | | |
| | | | | 1.32 t | | | |

 © 2006 Wiley-VCH Verlag GmbH & Co. KGaA, Weinheim 

Table 1. *Continued*

| | Compound | IR[a] $\tilde{\nu}$ [$cm^{-1}$] | Assignment | $^1H$ NMR[b,c] $\delta$ [ppm] $J$ [Hz] | Assignment | Spin system | $^{31}P\{^1H\}$NMR[b,d] $\delta$ [ppm] $J$ [Hz] |
|---|---|---|---|---|---|---|---|
| **9ad** | $[Re(NH_2OCH_3)(CO)_2(Ph_2POCH_2CH_2OPPh_2)\{P(OEt)_3\}]BPh_4$ | 3245 m | $\nu_{NH}$ | 4.32 m, br | $NH_2$ | ABC | $P_A$: 131.0 |
| | | 3215 m | | 4.08 m | $CH_2$ | | $P_B$: 113.1 |
| | | 1995 s | $\nu_{CO}$ | 4.55–4.27 m | | | $P_C$: 109.4 |
| | | 1891 s | | 2.64 s | $OCH_3$ | | $J_{A,B}$ = 33.2 |
| | | | | 1.14 t | $CH_3$ phos | | $J_{A,C}$ = 245.2 |
| | | | | | | | $J_{B,C}$ = 30.2 |
| **10b** | $[Mn(NH_2OCH_3)(CO)_3\{PPh(OEt)_2\}_2]BPh_4$ | 3261 m | | 4.83 t[e] | $NH_2$ | $A_2$[e] | 188.7 s, br |
| | | 3228 m | | $J_{P,H}$ = 6 | | | |
| | | 2056 m | | 4.05 m | $CH_2$ | | |
| | | 1975 s | | 2.90 s | $OCH_3$ | | |
| | | 1943 s | | 1.38 t | $CH_3$ phos | | |
| **10d** | $[Mn(NH_2OCH_3)(CO)_3(Ph_2POCH_2CH_2OPPh_2)]BPh_4$ | 3257 m | $\nu_{NH}$ | 4.58 m, br | $NH_2$ | $A_2$ | 165.8 s |
| | | 3225 m | | 4.35–4.00 m | $CH_2$ | | |
| | | 2042 s | $\nu_{CO}$ | 3.23 s | $OCH_3$ | | |
| | | 1977 s | | | | | |
| | | 1945 s | | | | | |
| **11b** | $[Re(NH_2OCH_3)(CO)_3\{PPh(OEt)_2\}_2]BPh_4$ | 3259 m | $\nu_{NH}$ | 5.48 t | $NH_2$ | $A_2$ | 135.2 s |
| | | 3215 m | | $J_{P,H}$ = 4.5 | | | |
| | | 2072 w | $\nu_{CO}$ | 4.08 m | $CH_2$ | | |
| | | 1981 s | | 2.99 s | $OCH_3$ | | |
| | | 1949 s | | 1.44 s | $CH_3$ phos | | |
| **11e** | $[Re(NH_2OCH_3)(CO)_3\{Ph_2PN(CH_3)CH_2CH_2N(CH_3)PPh_2\}]BPh_4$ | 3271 w | $\nu_{NH}$ | 4.32 m | $NH_2$ | $A_2$ | 66.1 s |
| | | 3235 w | | 3.81 m | $CH_2$ | | |
| | | 2044 s | $\nu_{CO}$ | 3.26 m | | | |
| | | 1971 s | | 2.54 s, br | $OCH_3$ + | | |
| | | 1925 s | | | $NCH_3$ | | |
| **11f** | $[Re(NH_2OCH_3)(CO)_3(Ph_2POCH_2CH_2CH_2OPPh_2\}]BPh_4$ | 3246 m | $\nu_{NH}$ | 4.76 s, br | $NH_2$ | AB | $P_A$: 110.0 |
| | | 3217 m | | 3.72 m | $OCH_2$ | | $P_B$: 115.0 |
| | | 2066 m | $\nu_{CO}$ | 3.50 m | | | $J_{A,B}$ = 32.5 |
| | | 1971 s | | 2.39 s | $OCH_3$ | | |
| | | 1950 s | | 1.95 m | $CH_2$ | | |

[a] In KBr pellets. [b] In $CD_2Cl_2$ at 20 °C, unless otherwise noted. [c] Phenyl proton resonances omitted. [d] Positive shift downfield from 85% $H_3PO_4$. [e] At –30 °C. [f] At –70 °C. [g] At 0 °C.

Compound **9b** does not show any interaction between the complex cation and the $BPh_4^-$ anion, but in the case of **11f** an interionic interaction, with parameters: distance H···Ct1 = 2.66(3) Å, distance N···Ct1 = 3.530(3) Å and angle NHCt1 = 167(3)° (where Ct1 is the centroid of one of the phenyl rings of the anion) indicates an NH-π hydrogen bond between the nitrogen of the *O*-methylhydroxylamine and a phenyl ring of the $BPh_4^-$ anion. Compound **11f** crystallized with a molecule of $CH_2Cl_2$ solvent to give a supramolecular arrangement of the crystal through a hydrogen-bonded network involving the cation [parameters, H···Ct2 = 2.98 Å, C···Ct2 = 3.805(4) Å, angle CHCt2 = 141.2°; H···O4′ = 2.74 Å, C···O4′ = 3.649(5) Å, angle CHO4′ = 152.4°. Symmetry operation 2–*x*, 2–*y*, 2–*z*; Ct2 stands for the centroid of the phenyl ring labeled as C31 to C36.]

In both cationic complexes the rhenium atom is coordinated in a slightly distorted octahedral fashion. In **9b** there are three meridional phosphonite ligands $PPh(OEt)_2$, two *cis* carbonyl ligands and an *N*-coordinated *O*-methylhydroxylamine. In **11f** there are three *mer* carbonyl ligands, two phosphorus atoms of the bidentated phosphinite ligand $PPh_2\{O(CH_2)_3O\}PPh_2$, and an *N*-coordinated *O*-methylhydroxylamine. The coordination polyhedra in **11f** is more irregular; the *cis* angles range from 86.26(9) to 95.47(3)°, and 95.47(3) is the largest value that corresponds to the chelate angle of the bidentate ligand. This fact was already observed in other compounds that bear this ligand[8d] and it is probably due to the steric requirement of the ligand.

For **11f**, the eight-membered ring adopts the disposition of a chair, in such a way that the phosphorus and the oxygen atoms are in a planar situation (rms deviation of 0.0229) with the rhenium atom slightly below the plane [0.463(2) Å], and the three carbon atoms form another almost parallel plane, [dihedral angle of 4.5(4)°] at 1.21(1) Å (average for the two nearest carbon atoms). This conformation was previously found for complexes with this ligand.[8d]

The Re–P bond lengths are in the range observed for complexes with phosphonite or phosphinite ligands.[8d,12] For **9b**, the Re–P distances for the mutually *trans* phosphonite ligands [2.381(3) Å (average)] are shorter than that of the phosphonite *trans* to a carbonyl ligand [2.413(3) Å] because of the stronger π-acceptor character of the CO group. The same behavior is observed in compound **11f** in which the Re–P1 distance is shorter [2.3647(8) Å] than Re–P2 [2.4608(8) Å].

The Re–C bond lengths in **9b** also show the different *trans* influence of the ligand: Re–C2 (*trans* to a P atom) is 0.063 Å longer than Re–C3 (*trans* to an N atom) because

 © 2006 Wiley-VCH Verlag GmbH & Co. KGaA, Weinheim 

Table 2. 300 MHz $^{13}C\{^1H\}$ NMR spectroscopic data for selected manganese and rhenium complexes.

| | Compound | $^{13}C\{^1H\}$NMR[a] $\delta$ [ppm], $J$ [Hz] | Assignment |
|---|---|---|---|
| **3b** | $[Mn(NH_2OH)(CO)_2\{PPh(OEt)_2\}_3]BPh_4$[b] | 221.1 m | CO |
| | | 216.5 m | |
| | | 65.7 d | $CH_2$ |
| | | 64.8 d | |
| | | 16.3 s | $CH_3$ |
| | | 16.1 s | |
| **4b** | $[Re(NH_2OH)(CO)_2\{PPh(OEt)_2\}_3]BPh_4$[b] | 198.3 m | CO |
| | | 195.5 m | |
| | | 63.5 m | $CH_2$ |
| | | 16.3 m | $CH_3$ |
| **4ad** | $[Re(NH_2OH)(CO)_2(Ph_2POCH_2CH_2OPPh_2)\{P(OEt)_3\}]BPh_4$[c] | 196.9 m | CO |
| | | 193.2 m | |
| | | 65.2 s, br | $CH_2$ bident. |
| | | 64.8 s, br | |
| | | 63.0 d, $J_{C,P}$ = 8 | $CH_2$ |
| | | 15.7 d, $J_{C,P}$ = 6 | $CH_3$ |
| **7a** | $[Re(NH_2OCH_3)(CO)\{P(OEt)_3\}_4]BPh_4$[b] | 196.3 qnt | CO |
| | | 66.8 s | $OCH_3$ |
| | | 61.7 t | $CH_2$ |
| | | 16.3 s | $CH_3$ |
| **8b** | $[Mn(NH_2OCH_3)(CO)_2\{PPh(OEt)_2\}_3]BPh_4$[b] | 221.8 m | CO |
| | | 217.9 m | |
| | | 67.1 s | $OCH_3$ |
| | | 65.2 d | $CH_2$ |
| | | 64.1 d | |
| | | 16.5 s | $CH_3$ |
| | | 16.2 s | |
| **9ad** | $[Re(NH_2OCH_3)(CO)_2(Ph_2POCH_2CH_2OPPh_2)\{P(OEt)_3\}]BPh_4$[c] | 197.3 m | CO |
| | | 193.4 m | |
| | | 66.7 s | $OCH_3$ |
| | | 65.3 s, br | $CH_2$ bident. |
| | | 64.1 s, br | |
| | | 62.9 d, $J_{C,P}$ = 8 | $CH_2$ |
| | | 15.8 d, $J_{C,P}$ = 7 | $CH_3$ |
| **11b** | $[Re(NH_2OCH_3)(CO)_3\{PPh(OEt)_2\}_2]BPh_4$[b] | 190.1 t, $J_{C,P}$ = 8 | CO |
| | | 189.8 t, $J_{C,P}$ = 10 | |
| | | 67.9 s | $OCH_3$ |
| | | 64.7 m | $CH_2$ |
| | | 16.3 m | $CH_3$ |
| **11e** | $[Re(NH_2OCH_3)(CO)_3\{Ph_2PN(CH_3)CH_2CH_2N(CH_3)PPh_2\}]BPh_4$[c] | 194.2 m | CO |
| | | 188.3 m | |
| | | 66.2 s | $OCH_3$ |
| | | 52.1 t, $J_{C,P}$ = 7 | $CH_2$ |
| | | 39.5 t, $J_{C,P}$ = 3 | $NCH_3$ |
| **11f** | $[Re(NH_2OCH_3)(CO)_3(Ph_2POCH_2CH_2CH_2OPPh_2\}]BPh_4$[c] | 191.0 m | CO |
| | | 189.1 m | |
| | | 65.4 s | $OCH_3$ |
| | | 64.7 s, br | $OCH_2$ |
| | | 63.4 s, br | |
| | | 29.6 s, br | $-CH_2-$ |

[a] Phenyl resonances omitted. [b] In $CD_2Cl_2$ at 20 °C. [c] In $CDCl_3$ at 20 °C.

of the stronger π-acceptor character of the phosphonite ligand.

In both cases, the geometrical parameters of the *O*-methylhydroxylamine ligand are in accordance with an $sp^3$ character for both the oxygen and the nitrogen atom,[13] and the conformation of the ligand is such that all the atoms belong to the same plane (Re–N1–O1–C1) (rms deviation of 0.0173 and 0.0405, respectively). The Re–N bonds are similar to those found in previously reported[3b] hydroxylaminerhenium(I) complexes.

The presence of the $NH_2OH$ or $NH_2OCH_3$ ligand in the complexes can be determined by IR and NMR spectroscopy (Table 1). The IR spectra of the hydroxylamine derivatives show one medium-intensity band at $\tilde{\nu}$ = 3381–3434 $cm^{-1}$ for the $\nu$OH stretch, and two bands at $\tilde{\nu}$ = 3212–3348 $cm^{-1}$ attributed to the $\nu$NH stretch of the $NH_2OH$ ligand. In the spectra of the related $NH_2OCH_3$ complexes only two medium-intensity bands at $\tilde{\nu}$ = 3215–3271 $cm^{-1}$ for the $\nu$NH stretch were observed.

 © 2006 Wiley-VCH Verlag GmbH & Co. KGaA, Weinheim 

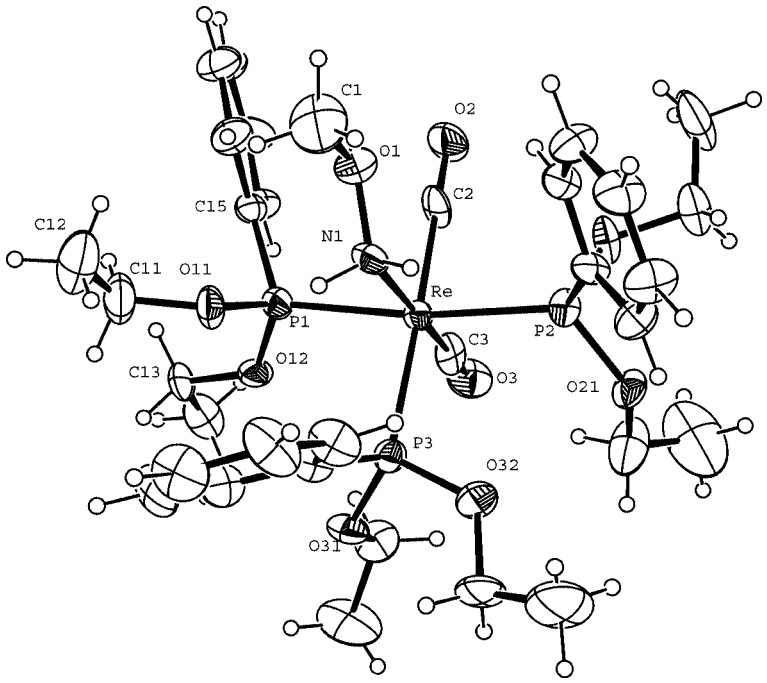


Figure 1. The cation of $[Re(NH_2OCH_3)(CO)_2\{PPh(OEt)_2\}_3]BPh_4$ (**9b**) drawn at 30% probability level.

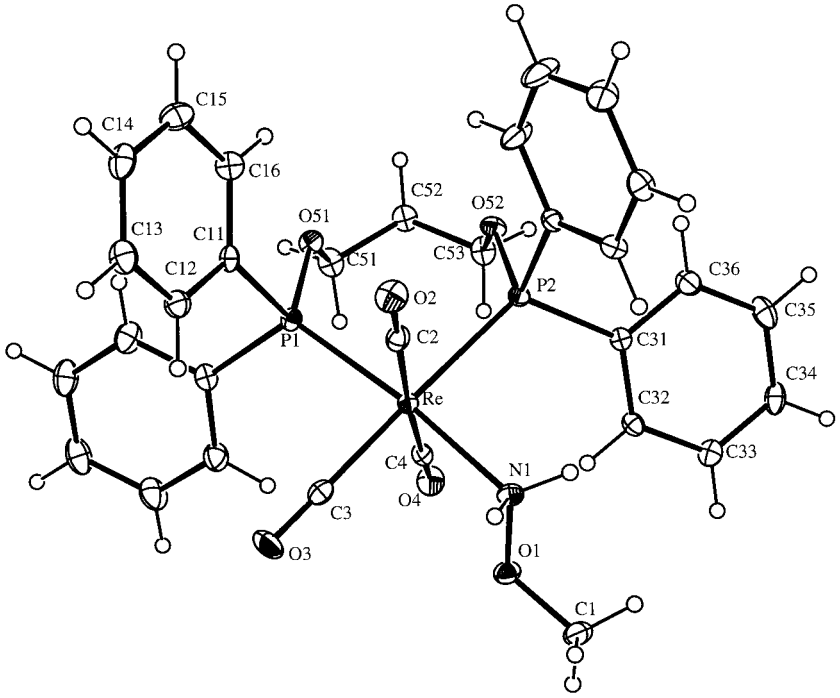


Figure 2. The cation of $[Re(NH_2OCH_3)(CO)_3\{Ph_2PO(CH_2)_3OPPh_2\}]BPh_4$ (**11f**) drawn at 30% probability level.

The NMR spectra of the $NH_2OH$ complexes **1**–**5**, which contain monodentate phosphite ligands, indicate that they are fluxional. The slightly broad signal that appears at room temperature in the proton spectra, in fact, resolves into two signals for the ligands at 243 K. At this temperature the spectra show, besides the signals for the phosphite and the $BPh_4$ anion, a triplet at $\delta$ = 4.41–6.39 ppm ($J_{H,H}$ = 2.3 Hz) attributed to the OH protons of the $NH_2OH$ ligand and one slightly broad multiplet at $\delta$ = 3.54–6.17 ppm for the $NH_2$ protons of $NH_2OH$ group. Decoupling experiments and COSY spectra were used to confirm these assignments and to determine the value of $J_{H,P}$ for the $NH_2$ protons. Values between $J_{H,P}$ = 2 and 3 Hz were determined for the $NH_2OH$ complexes **1**–**5**, which strongly supports the presence of an *N*-bonded $NH_2OH$ ligand.

 © 2006 Wiley-VCH Verlag GmbH & Co. KGaA, Weinheim 

The proton spectra of complexes **4ad** and **6e**, which contain the bidentate phosphane ligand show, apart from no fluxionality, the characteristic signals for the $NH_2$ and the OH protons , in agreement, also in this case, with the presence of the hydroxylamine ligand.

The $^1H$ NMR spectra of the $NH_2OCH_3$ derivatives show a singlet at $\delta$ = 2.39–3.49 ppm attributed to the methoxy group, $OCH_3$, and a multiplet at $\delta$ = 4.32–6.19 ppm for the $NH_2$ protons of the *O*-methylhydroxylamine ligand. Decoupling experiments indicate that the multiplet for the $NH_2$ protons is a result of the coupling of the phosphorus nuclei of the phosphane to the $NH_2OCH_3$ ligand with $J_{H,P}$ = 4–6 Hz, which is in agreement with the *N*-bonded coordination of the $NH_2OCH_3$ ligand.

The $^{31}P\{^1H\}$ NMR spectra of the monocarbonyl complexes $[M(NH_2OH)(CO)P_4]^+$ and $[M(NH_2OCH_3)(CO)P_4]^+$ (**1**, **2**, **7**) appear as a slightly broad signal at room temperature, which resolves into a sharp singlet at 243 K, in agreement with the magnetic equivalence of the four phosphite ligands. On the basis of these data, a geometry of type **I** (Scheme 1 and Scheme 3), with the carbonyl and the hydroxylamine ligands in a mutually *trans* position, can reasonably be proposed.

The IR spectra of the dicarbonyl complexes $[M(NH_2OR)(CO)_2P_3]^+$ (**3**, **4**, **8**, **9**) (R = H, $CH_3$) show two strong *v*CO bands which indicate a mutually *cis* position of the two carbonyl ligands. These two CO groups, however, are not magnetically equivalent, because they show two well-separated multiplets at 221.8 and 193.2 ppm in the $^{13}C$ NMR spectra (Table 2). At room temperature, the $^{31}P\{^1H\}$ NMR spectra of the dicarbonyl complexes that contain the monodentate phosphite ligands (**3b**, **4a**, **4b**, **8b**, **9b**) show a rather broad multiplet which resolves into an $AB_2$ pattern at temperatures between 0 and –70 °C. This indicates that there are two phosphites that are magnetically equivalent but different from the third phosphite. On the basis of these data, a *mer-cis* geometry of type **II** (Scheme 1 and Scheme 3) similar to that observed in the solid state for **9b** can reasonably be proposed for these dicarbonyl-hydroxylamine derivatives.

In the temperature range between +20 and –80 °C, the $^{31}P\{^1H\}$ NMR spectra of the dicarbonyl complexes **4ad** and **9ad** appear as an ABC multiplet, which can be easily simulated with the parameters reported in Table 1. These parameters indicate that, while two of the $J_{P,P}$ values are comparable($J_{P,P}$ = 27–34 Hz) the third is considerably higher than the others ($J_{P,P}$ = 245–248 Hz), which suggests that two of the three phosphanes are in a mutually *trans* position. Taking into account that the IR spectra suggest the presence of two CO groups in a mutually *cis* position, we can then reasonably propose a *mer-cis* geometry of type **II** (Scheme 1 and Scheme 4) for the complexes containing a bidentate phosphane ligand.

At room temperature, the $^{31}P$ NMR spectra of the tricarbonyl cations $[M(NH_2OH)(CO)_3P_2]^+$ (**5c**) and $[M(NH_2OCH_3)(CO)_3P_2]^+$ (**10b**, **11b**) appear as a rather broad signal which resolves into a sharp singlet as the temperature is lowered, which indicates the magnetic equivalence of the two phosphane ligands. The IR spectra show, in the *v*CO region, three bands; one band of medium intensity and two strong bands, which suggests a *mer* arrangement of the three carbonyl ligands. On the basis of these data, a *mer-trans* geometry **III** may be proposed for the tricarbonyl complexes **5c**, **10b**, **11b**.

The IR spectra of the tricarbonyl complexes **6e**, **10d** and **11e**, containing bidentate phosphane ligands, show three strong absorptions in the *v*CO region, which indicates a *fac* arrangement of the three carbonyl ligands. In the temperature range between +20 and –80 °C the $^{31}P\{^1H\}$ NMR spectra appear as a sharp singlet, in agreement with the magnetic equivalence of the two phosphite ligands. On the basis of these data, a *fac* geometry (**IV**) can reasonably be proposed for these hydroxylamine complexes. Finally, a *mer-cis* geometry of type **V** (Scheme 4), like that found in the solid state, can be proposed for the tricarbonyl complex $[Re(NH_2OCH_3)(CO)_3\{Ph_2PO(CH_2)_3OPPh_2\}]BPh_4$ (**11f**), whose IR spectrum shows one medium-intensity band and two strong bands in the *v*CO region. The $^{31}P$ NMR spectrum has an AB multiplet.

The *mer-cis* geometry observed for compound **11f** is unusual as compared with those of related complexes **10d**, **11e** that contain bidentate phosphane ligands and may be attributed to the steric requirement of the $Ph_2PO(CH_2)_3OPPh_2$ ligand, because the π-acceptor properties of the P–P phosphites are very similar in complexes **10d** and **11f**.

The fluxional behavior observed in some of our hydroxylamine complexes may be due to an intermolecular process that involves dissociation of $NH_2OR$ or phosphite ligands. NMR experiments in the presence of free phosphite or hydroxylamine, however, seem to exclude such a process. Therefore, it is plausible to assume that the fluxional process simply results in the inter-exchange of the position of both the P- and the $NH_2OR$ ligands at room temperature, and the progressive decrease of this change as the temperature is lowered leads to a static $A_2B$ or ABC system at –70 °C.

Reactivity studies of the hydroxylamine complexes were undertaken, and the preliminary results indicate that they are relatively robust complexes. Substitution of the $NH_2OH$ or $NH_2OCH_3$ ligand by carbonyl or phosphane is very slow at room temperature, while reflux conditions cause the decomposition of the complexes.

Oxidation reactions with $Pb(OAc)_4$ were also tested, and the results show (Scheme 5) that, while the *O*-methylhydroxylamine complexes **7**–**11** do not react with $Pb(OAc)_4$ under any conditions, hydroxylamines **1**–**6** quickly react with $Pb(OAc)_4$ at –40 °C to give a pale-yellow solution. Unfortunately, the solid separated from this solution is not a pure species, but its $^1H$ NMR spectrum shows, in the case of the oxidation of complex $[Re(NH_2OH)(CO)_2\{PPh(OEt)_2\}_3]BPh_4$ (**4b**), a slightly broad signal at $\delta$ = 19.7 ppm. This resonance may be attributed[2b,3b] to the NH proton of the N(H)=O group of the $[Re\{N(H)=O\}(CO)_2\{PPh(OEt)_2\}_3]^+$ cation, formed by selective oxidation of the $NH_2OH$ ligand, as shown in Scheme 5.

 © 2006 Wiley-VCH Verlag GmbH & Co. KGaA, Weinheim 

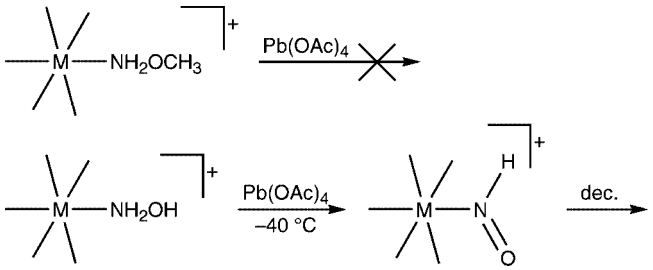


Scheme 5. M = Mn, Re.

Unfortunately, the nitroxyl $[Re\{N(H)=O\}(CO)_2P_3]^+$ derivatives are unstable even at –40 °C and were separated only as traces. The IR spectrum of the separated solid did not show a signal for the nitrosyl [Re]–NO complex, which would result from the deprotonation of [Re]-N(H)=O . This observation suggests that the deprotonation does not take place. Our results, therefore, prove that the $M(CO)_nP_{5-n}$ fragment is able to stabilize the coordination of the hydroxylamine group, but not that of the nitroxyl ligand.

## Conclusions

In this report we have highlighted that the synthesis of the unprecedented hydroxylamine and the *O*-methylhydroxylamine complexes of manganese can be achieved through the use of mixed-ligand $Mn(OTf)(CO)_nP_{5-n}$ complexes with mono- or bidentate phosphites and carbonyls as precursors. New $NH_2OH$ and $NH_2OCH_3$ derivatives of rhenium were also prepared which allowed for the first structural parameters of an *O*-methylhydroxylamine complex to be obtained. Oxidation of the hydroxylamine complexes with $Pb(OAc)_4$ at –40 °C was also studied and led to the unstable [M]–N(H)O nitroxyl derivative.

## Experimental Section

**General:** All synthetic work was carried out under an inert atmosphere by using standard Schlenk techniques or a ffacuum Atmosphere dry-box. Once isolated, the complexes were found to be relatively stable in air, but were stored under an inert atmosphere at –25 °C. All solvents were dried with appropriate drying agents, degassed on a vacuum line and distilled into vacuum-tight storage flasks. The phosphite $P(OEt)_3$ (Aldrich) was purified by distillation under nitrogen, while $PPh(OEt)_2$ and $PPh_2OEt$ were prepared by the method of Rabinowitz and Pellon.[14] The bidentate phosphanes $Ph_2PO(CH_2)_nOPPh_2$ ($n$ = 2, 3) and $Ph_2PN(CH_3)CH_2CH_2N(CH_3)PPh_2$ were prepared by the reported methods.[8c,8d,15] $Re_2(CO)_{10}$ was purchased from Pressure Chemical Co. (U.S.A.) while $Mn_2(CO)_{10}$ was purchased from Aldrich, and both compounds were used as received. Hydroxylamine ($NH_2OH$), *N*-methylhydroxylamine [$NH(CH_3)OH$], and *O*-methylhydroxylamine ($NH_2OCH_3$) were prepared by a slight modification of a reported method,[16] which involved the treatment of hydroxylamine hydrochloride with sodium ethylate in ethanol. The free $NH_2OH$ was isolated as a white solid, while $NH(CH_3)OH$ and $NH_2OCH_3$ were prepared in solution just prior to use. Other reagents were purchased from commercial sources in the highest available purity and used as received. Infrared spectra were recorded with a Nicolet Magna 750 FT-IR or Perkin–Elmer Spectrum One spectrophotometer. NMR spectra ($^1H$, $^{13}C$, $^{31}P$) were obtained with Bruker AC200, AVANCE 300, and ARX 400 spectrometers at temperatures varying between –90 and +30 °C, unless otherwise noted. $^1H$- and $^{13}C$ spectra are referred to internal tetramethylsilane, while $^{31}P\{^1H\}$ chemical shifts are reported with respect to 85% $H_3PO_4$, with downfield shifts considered positive. The COSY, HMQC, and HMBC NMR experiments were performed with their standard programs. The SwaN-MR and g-NMR software packages[17] were used to treat the NMR spectroscopic data and for the simulation. The conductivity of $10^{-3}$ mol·dm$^{-3}$ solutions of the complexes in $CH_3NO_2$ at 25 °C was measured with a Radiometer CDM 83 instrument.

**Preparation of the Complexes:** The hydride complexes $MH(CO)_nP_{5-n}$ [M = Mn, Re; P = $P(OEt)_3$, $PPh(OEt)_2$, $PPh_2OEt$; $n$ = 1, 2, 3, 4] were prepared by following the previously reported method.[6e,8a,8b] The related complexes $MH(CO)_2(P–P)\{P(OEt)_3\}$ and $MH(CO)_3(P–P)$ [P–P = $Ph_2POCH_2CH_2OPPh_2$, $Ph_2PO(CH_2)_3OPPh_2$, $Ph_2PN(CH_3)CH_2CH_2N(CH_3)PPh_2$] were also obtained by a known method.[8c,8d]

**$[Mn(NH_2OH)(CO)_nP_{5-n}]BPh_4$ (1b, 3b, 5c) [P = $PPh(OEt)_2$ (b), $PPh_2OEt$ (c); $n$ = 1 (1); $n$ = 2 (3); $n$ = 3 (5)]:** An equimolar amount of $CF_3SO_3H$ (0.2 mmol, 18 μL) was added to a solution of the appropriate hydride $MnH(CO)_nP_{5-n}$ (0.2 mmol) in $CH_2Cl_2$ (10 mL) cooled to –196 °C. The reaction mixture was brought to room temperature, stirred for 1 h, and then cooled again to –196 °C. An excess of hydroxylamine (1 mmol, 0.91 mL of a 1.1 M solution in ethanol) was added, and the resulting solution was brought to 0 °C and stirred for 8 h. The solvent was removed under reduced pressure. The oil that was obtained was treated with ethanol (1.5 mL) containing an excess amount of $NaBPh_4$ (0.4 mmol, 137 mg). A yellow solid slowly separated out from the resulting solution, which was allowed to stand at –25 °C overnight to complete the precipitation. The solid was filtered and crystallized at 0 °C from $CH_2Cl_2$ and ethanol. Yield: 115 mg for **1b** (47%), 131 mg for **3b** (62%), and 103 mg for **5c** (54%).

**1b:** $C_{65}H_{83}BMnNO_{10}P_4$ (1228.01): calcd. C 63.58, H 6.81, N 1.14; found C 63.82, H 6.95, N 1.10. $\Lambda_M$ = 55.5 $\Omega^{-1}$ mol$^{-1}$ cm$^2$.

**3b:** $C_{56}H_{68}BMnNO_9P_3$ (1057.82): calcd. C 63.58, H 6.48, N 1.32; found C 63.45, H 6.57, N 1.27. $\Lambda_M$ = 56.0 $\Omega^{-1}$ mol$^{-1}$ cm$^2$.

**5c:** $C_{55}H_{53}BMnNO_6P_2$ (951.72): calcd. C 69.41, H 5.61, N 1.47; found C 69.35, H 5.75, N 1.44. $\Lambda_M$ = 51.9 $\Omega^{-1}$ mol$^{-1}$ cm$^2$.

**$[Re(NH_2OH)(CO)_nP_{5-n}]BPh_4$ (2a, 4a, 4b) [P = $P(OEt)_3$ (a), $PPh(OEt)_3$ (b); $n$ = 1 (2); $n$ = 2 (4)]:** These complexes were prepared as per the related manganese complexes **1**, **3**, **5** with the use of hydride $ReH(CO)_nP_{5-n}$ as a precursor. The reaction mixture was stirred for 4 h at room temperature. Yield: 175 mg for **2a** (71%), 142 mg for **4a** (65%), and 147 mg for **4b** (62%).

**2a:** $C_{49}H_{83}BNO_{14}P_4Re$ (1231.10): calcd. C 47.81, H 6.80, N 1.14; found C 48.02, H 6.90, N 1.06. $\Lambda_M$ = 53.8 $\Omega^{-1}$ mol$^{-1}$ cm$^2$.

**4a:** $C_{44}H_{68}BNO_{12}P_3Re$ (1092.95): calcd. C 48.35, H 6.27, N 1.28; found C 48.44, H 6.25, N 1.19. $\Lambda_M$ = 54.3 $\Omega^{-1}$ mol$^{-1}$ cm$^2$.

**4b:** $C_{56}H_{68}BNO_9P_3Re$ (1189.09): calcd. C 56.57, H 5.76, N 1.18; found C 56.66, H 5.90, N 1.12. $\Lambda_M$ = 54.7 $\Omega^{-1}$ mol$^{-1}$ cm$^2$.

**$[Re(NH_2OH)(CO)_2(Ph_2POCH_2CH_2OPPh_2)\{P(OEt)_3\}]BPh_4$ (4ad):** This complex was prepared as per the related rhenium complexes **2** and **4** with the use of $ReH(CO)_2(Ph_2POCH_2CH_2OPPh_2)\{P(OEt)_3\}$ as a precursor. The reaction mixture was stirred at room temperature for 6 h. Yield: 131 mg (55%). $C_{58}H_{62}BNO_8P_3Re$

 © 2006 Wiley-VCH Verlag GmbH & Co. KGaA, Weinheim 

(1191.06): calcd. C 58.49, H 5.25, N 1.18; found C 58.62, H 5.29, N 1.15. $\Lambda_M$ = 50.0 $\Omega^{-1}$ mol$^{-1}$ cm$^2$.

**[Re(NH$_2$OH)(CO)$_3${Ph$_2$PN(Me)CH$_2$CH$_2$N(Me)PPh$_2$}]BPh$_4$ (6e):** This complex was prepared as per the related rhenium complexes with the use of hydride ReH(CO)$_3$(Ph$_2$PN(CH$_3$)CH$_2$CH$_2$N(CH$_3$)PPh$_2$). The reaction was stirred for 7 h at 0 °C; yield 175 mg (81%). $C_{55}H_{53}BN_3O_4P_2Re$ (1079.00): calcd. C 61.22, H 4.95, N 3.89; found C 61.05, H 4.88, N 3.68. $\Lambda_M$ = 52.6 $\Omega^{-1}$ mol$^{-1}$ cm$^2$.

**[Re(NH$_2$OMe)(CO)$_n$P$_{5-n}$]BPh$_4$ (7a, 9b, 11b) and [Mn(NH$_2$OMe)(CO)$_n$P$_{5-n}$]BPh$_4$ (8b, 10b) [P = P(OEt)$_3$ (a), PPh(OEt)$_2$ (b); *n* = 1 (7); *n* = 2 (8, 9); *n* = 3 (10, 11)]:** An equimolar amount of $CF_3SO_3H$ (0.2 mmol, 18 μL) was added to a solution of the appropriate hydride MH(CO)$_n$P$_{5-n}$ (0.2 mmol) in $CH_2Cl_2$ (5 mL) cooled to –196 °C. The reaction mixture was brought to room temperature, stirred for 1 h, and then cooled again to –196 °C. An excess of $NH_2OCH_3$ (2 mmol, 1.54 mL of a 1.3 M solution in ethanol) was added, and the resulting solution was brought to room temperature and stirred for about 5 h. The solvent was removed under reduced pressure. The oil that was obtained was treated with ethanol (1.5 mL) containing an excess of $NaBPh_4$ (0.4 mmol, 137 mg). A white or pale-yellow solid slowly separated out from the resulting solution, which was allowed to stand at –25 °C overnight to complete the precipitation. The solid was filtered and crystallized from $CH_2Cl_2$ and ethanol. Yield: 167 mg for **7a** (67%), 133 mg for **8b** (62%), 176 mg for **9b** (73%), 123 mg for **10b** (68%), and 155 mg for **11b** (75%).

**7a:** $C_{50}H_{85}BNO_{14}P_4Re$ (1245.12): calcd. C 48.23, H 6.88, N 1.12; found C 48.45, H 6.94, N 1.08. $\Lambda_M$ = 56.9 $\Omega^{-1}$ mol$^{-1}$ cm$^2$.

**8b:** $C_{57}H_{70}BMnNO_9P_3$ (1071.85): calcd. C 63.87, H 6.58, N 1.31; found C 63.80, H 6.67, N 1.27. $\Lambda_M$ = 55.9 $\Omega^{-1}$ mol$^{-1}$ cm$^2$.

**9b:** $C_{57}H_{70}BNO_9P_3Re$ (1203.11): calcd. C 56.90, H 5.86, N 1.16; found C 57.04, H 5.95, N 1.11. $\Lambda_M$ = 53.5 $\Omega^{-1}$ mol$^{-1}$ cm$^2$.

**10b:** $C_{48}H_{55}BMnNO_8P_2$ (901.66): calcd. C 63.94, H 6.15, N 1.55; found C 64.10, H 6.41, N 1.49. $\Lambda_M$ = 52.1 $\Omega^{-1}$ mol$^{-1}$ cm$^2$.

**11b:** $C_{48}H_{55}BNO_8P_2Re$ (1032.92): calcd. C 55.82, H 5.37, N 1.36; found C 55.60, H 5.35, N 1.25. $\Lambda_M$ = 55.0 $\Omega^{-1}$ mol$^{-1}$ cm$^2$.

**[Re(NH$_2$OMe)(CO)$_2$(Ph$_2$POCH$_2$CH$_2$OPPh$_2$){P(OEt)$_3$}]BPh$_4$ (9ad):** This compound was prepared as per the related rhenium complexes **7**, **9**, **11** with the use of hydride ReH(CO)$_2$(Ph$_2$POCH$_2$CH$_2$OPPh$_2$){P(OEt)$_3$}. Yield: 137 mg (57%). $C_{59}H_{64}BNO_8P_3Re$ (1205.09): calcd. C 58.80, H 5.35, N 1.16; found C 59.04, H 5.49, N 1.18. $\Lambda_M$ = 49.6 $\Omega^{-1}$ mol$^{-1}$ cm$^2$.

**[Mn(NH$_2$OMe)(CO)$_3$(Ph$_2$POCH$_2$CH$_2$OPPh$_2$)]BPh$_4$ (10d) and [Re(NH$_2$OMe)(CO)$_3$(P–P)]BPh$_4$ (11e, 11f) [P–P = Ph$_2$PN(Me)CH$_2$CH$_2$N(Me)PPh$_2$ (e), Ph$_2$PO(CH$_2$)$_3$OPPh$_2$ (f)]:** These complexes were prepared as per the related complexes **7**–**11** with the use of hydride MH(CO)$_3$(P–P). The reaction was stirred for 5 h. Yield: 108 mg for **10d** (58%), 168 mg for **11e** (77%), and 162 mg for **11f** (75%).

**10d:** $C_{54}H_{49}BMnNO_6P_2$ (935.25): calcd. C 69.32, H 5.28, N 1.50; found C 69.25, H 5.43, N 1.47. $\Lambda_M$ = 55.6 $\Omega^{-1}$ mol$^{-1}$ cm$^2$.

**11e:** $C_{56}H_{55}BN_3O_4P_2Re$ (1093.03): calcd. C 61.54, H 5.07, N 3.84; found C 61.49, H 5.13, N 3.80. $\Lambda_M$ = 52.3 $\Omega^{-1}$ mol$^{-1}$ cm$^2$.

**11f:** $C_{55}H_{51}BNO_6P_2Re$ (1080.97): calcd. C 61.11, H 4.76, N 1.30; found C 61.25, H 4.87, N 1.24. $\Lambda_M$ = 50.7 $\Omega^{-1}$ mol$^{-1}$ cm$^2$.

**Oxidation Reaction:** The oxidation of the hydroxylamine and *O*-methylhydroxylamine complexes was carried out at low temperature (–40 °C) by using Pb(OAc)$_4$ as a reagent. In a typical experi-

Table 3. Crystal data and structure refinement for [Re(NH$_2$OCH$_3$)(CO)$_2${PPh(OEt)$_2$}$_3$]BPh$_4$ (**9b**) and [Re(NH$_2$OCH$_3$)(CO)$_3${Ph$_2$PO(CH$_2$)$_3$OPPh$_2$}]BPh$_4$ (**11f**).

| Identification code | **9b** | **11f** |
|---|---|---|
| Empirical formula | $C_{57}H_{70}BNO_9P_3Re$ | $C_{56}H_{53}BCl_2NO_6P_2Re$ |
| Formula weight | 1203.06 | 1165.84 |
| Temperature | 293(2) K | 173(2) K |
| Wavelength | 0.71073 Å | 0.71073 Å |
| Crystal system | monoclinic | triclinic |
| Space group | $P2_1/c$ | $P\bar{1}$ |
| Unit cell dimensions | $a$ = 12.707(2) Å | $a$ = 10.0187(7) Å |
| | $b$ = 27.279(5) Å | $b$ = 15.7038(11) Å |
| | $c$ = 17.486(3) Å | $c$ = 17.9835(13) Å |
| | $\alpha$ = 90° | $\alpha$ = 94.267(1)° |
| | $\beta$ = 106.130(5)° | $\beta$ = 104.823(1)° |
| | $\gamma$ = 90° | $\gamma$ = 105.249(1)° |
| Volume | 5822.9(18) Å$^3$ | 2608.3(3) Å$^3$ |
| $Z$ | 4 | 2 |
| Density (calculated) | 1.372 Mg/m$^3$ | 1.484 Mg/m$^3$ |
| Absorption coefficient | 2.222 mm$^{-1}$ | 2.544 mm$^{-1}$ |
| $F$(000) | 2464 | 1176 |
| Crystal size | 0.14 × 0.11 × 0.07 mm | 0.36 × 0.23 × 0.22 mm |
| Theta range for data collection | 1.42 to 28.08° | 1.36 to 28.01° |
| Index ranges | $-15 \le h \le 16$; $-35 \le k \le 27$; $-20 \le l \le 22$ | $-12 \le h \le 13$; $-20 \le k \le 18$; $-23 \le l \le 18$ |
| Reflections collected | 30713 | 17230 |
| Independent reflections | 12872 [$R$(int) = 0.1441] | 11960 [$R$(int) = 0.0424] |
| Reflections observed (>2σ) | 3713 | 10213 |
| Data completeness | 0.908 | 0.949 |
| Max. and min. transmission | 1.000 and 0.753 | 1.000 and 0.739 |
| Data/restraints/parameters | 12872/0/656 | 11960/0/632 |
| Goodness-of-fit on $F^2$ | 0.637 | 0.953 |
| Final $R$ indices [$I$>2σ($I$)] | $R_1$ = 0.0555 $wR_2$ = 0.0631 | $R_1$ = 0.0301 $wR_2$ = 0.0608 |
| $R$ indices (all data) | $R_1$ = 0.2593 $wR_2$ = 0.1031 | $R_1$ = 0.0400 $wR_2$ = 0.0629 |
| Largest diff. peak and hole | 0.837 and –0.600 e·Å$^{-3}$ | 0.989 and –0.890 e·Å$^{-3}$ |

 © 2006 Wiley-VCH Verlag GmbH & Co. KGaA, Weinheim 

ment, a sample of the appropriate complex, $[M(NH_2OH)(CO)_nP_{5-n}]BPh_4$ or $[M(NH_2OCH_3)(CO)_nP_{5-n}]BPh_4$ (0.10 mmol), was placed in a three-necked, 25-mL, round-bottomed flask fitted with a solid-addition sidearm containing an equimolar amount of $Pb(OAc)_4$ (44 mg, 0.10 mmol). The system was evacuated, $CH_2Cl_2$ (10 mL) was added, the solution cooled to –40 °C, and the $Pb(OAc)_4$ was added portionwise over 10–20 min to the cold solution with stirring. The reaction mixture was then warmed to 0 °C, stirred for 10 min, and the solvent was removed under reduced pressure. The oil obtained was treated at 0 °C with ethanol (2 mL) containing $NaBPh_4$ (42 mg, 0.12 mmol), but no solid compound was separated from the resulting solution.

**X-ray Crystal-Structure Determination of $[Re(NH_2OCH_3)(CO)_2\{PPh(OEt)_2\}_3]BPh_4$ (9b) and $[Re(NH_2OCH_3)(CO)_3\{Ph_2PO(CH_2)_3OPPh_2\}]BPh_4$ (11f):** Suitable crystals for X-ray analysis were obtained by slow cooling of a saturated solution of the complexes in ethanol and $CH_2Cl_2$. The data was collected with a SIEMENS Smart CCD area-detector diffractometer with graphite-monochromated Mo-$K_\alpha$ radiation, at room temperature in the case of **9b** and at –100 °C in the case of **11f**. Absorption corrections were carried out with SADABS with the use of semi-empirical methods from equivalents.[18] The structures were solved by direct methods in the case of **9b** and by Patterson methods in the case of **11f**. Both were refined by a full-matrix least-squares analysis based on $F^2$.[19] Non-hydrogen atoms were refined with anisotropic displacement parameters. Hydrogen atoms were included in idealized positions and refined with isotropic displacement parameters, except those bonded to the nitrogen atom in **11f**, which were located on the density map and refined isotropically. Atomic scattering factors and anomalous dispersion corrections for all atoms were taken from the International Tables for X-ray Crystallography (Tables 3, 4 and 5).[20]

Table 4. Selected bond lengths [Å] and angles [°] for $[Re(NH_2OCH_3)(CO)_2\{PPh(OEt)_2\}_3]BPh_4$ (**9b**).

| | | | |
|---|---|---|---|
| Re–C3 | 1.838(12) | Re–C2 | 1.901(10) |
| Re–N1 | 2.223(8) | Re–P1 | 2.378(3) |
| Re–P2 | 2.385(3) | Re–P(3) | 2.413(3) |
| O1–C1 | 1.426(11) | O1–N1 | 1.432(8) |
| C3–Re–C2 | 86.1(5) | C3–Re–N1 | 176.3(4) |
| C2–Re–N1 | 91.3(4) | C3–Re–P1 | 91.5(3) |
| C2–Re–P1 | 87.6(3) | N1–Re–P1 | 85.6(2) |
| C3–Re–P2 | 91.0(3) | C2–Re–P2 | 85.4(3) |
| N1–Re–P2 | 91.5(2) | P1–Re–P2 | 172.41(10) |
| C3–Re–P3 | 96.2(3) | C2–Re–P3 | 177.6(3) |
| N1–Re–P3 | 86.33(19) | P1–Re–P3 | 91.53(9) |
| P2–Re–P3 | 95.31(9) | C1–O1–N1 | 111.2(8) |
| O1–N1–Re | 110.5(5) | | |

Table 5. Selected bond lengths [Å] and angles [°] for $[Re(NH_2OCH_3)(CO)_3\{Ph_2PO(CH_2)_3OPPh_2\}]BPh_4$ (**11f**).

| | | | |
|---|---|---|---|
| Re–C3 | 1.962(4) | Re–C4 | 1.977(3) |
| Re–C2 | 1.998(3) | Re–N1 | 2.232(3) |
| Re–P1 | 2.3647(8) | Re–P2 | 2.4608(8) |
| N1–O1 | 1.440(3) | O1–C1 | 1.436(3) |
| C3–Re–C4 | 92.80(13) | C3–Re–C2 | 91.70(13) |
| C4–Re–C2 | 175.41(13) | C3–Re–N1 | 86.45(12) |
| C4–Re–N1 | 90.57(11) | C2–Re–N1 | 90.62(11) |
| C3–Re–P1 | 86.98(9) | C4–Re–P1 | 91.47(9) |
| C2–Re–P1 | 87.85(9) | N1–Re–P1 | 173.21(9) |
| C3–Re–P2 | 176.74(9) | C4–Re–P2 | 89.29(9) |
| C2–Re–P2 | 86.26(9) | N1–Re–P2 | 91.03(8) |
| P1–Re–P2 | 95.47(3) | O1–N1–Re | 107.26(16) |
| C1–O1–N1 | 111.3(2) | | |

Details of crystal data and structural refinement are given in Table 3; selected bond lengths and angles are listed in Table 4 and Table 5. CCDC-297494 and -297495 contain the supplementary crystallographic data for this paper. These data can be obtained free of charge from The Cambridge Crystallographic Data Centre via www.ccdc.cam.ac.uk/data_request/cif.

## Acknowledgments

The financial support from MIUR (Rome, Italy) - PRIN 2004, the Xunta de Galicia (Project PGIDT04PXIC31401PN), and the Spanish Ministry of Education (Project BQU2003–06783) is gratefully acknowledged. We thank the University of Vigo, CACTI services, for collecting X-ray data and recording NMR spectra. We also thank Daniela Baldan, University of Venice, for technical assistance.

[1] a) B. L. Haymore, J. R. Dilworth in *Comprehensive Coordination Chemistry* (Eds.: G. Wilkinson, R. D. Gillard, J. A. McCleverty), Pergamon Press, Oxford, UK, **1987**; b) A. B. P. Lever in *Comprehensive Coordination Chemistry II* (Eds.: J. A. McCleverty, T. J. Meyer), Elsevier Pergamon, Oxford, UK, **2003**, vol. 1 and 2.

[2] a) K. R. Grundy, C. A. Reed, W. R. Roper, *J. Chem. Soc., D* **1970**, 1501; b) R. Melenkivitz, G. Hillhouse, *Chem. Commun.* **2002**, 660–661; c) D.-W. Feng, M. D. Ryan, *Inorg. Chem.* **1987**, *26*, 2480–2483.

[3] a) T.-Y. Cheng, A. Ponce, A. L. Rheingold, G. L. Hillhouse, *Angew. Chem. Int. Ed. Engl.* **1994**, *33*, 657–659; b) J. S. Southern, G. L. Hillhouse, A. L. Rheingold, *J. Am. Chem. Soc.* **1997**, *119*, 12406–12407.

[4] a) D. Sutton, *Chem. Rev.* **1993**, *93*, 995–1022; b) H. Kisch, P. Holzmeier, *Adv. Organomet. Chem.* **1992**, *34*, 67–109; c) H. Zollinger, *Diazo Chemistry II*, VCH, Weinheim, Germany, **1995**; d) R. A. Henderson, G. J. Leigh, C. J. Pickett, *Adv. Inorg. Chem. Radiochem.* **1983**, *25*, 197–292; e) F. Bottomley, *Q. Rev. Chem. Soc.* **1970**, *24*, 617.

[5] a) K. D. Demadis, S. M. Malinak, D. Coucouvanis, *Inorg. Chem.* **1996**, *35*, 4038–4046; b) C. J. Davies, I. M. Dodd, M. M. Harding, B. T. Heaton, C. Jacob, J. Ratnam, *J. Chem. Soc., Dalton Trans.* **1994**, 787–792; c) D. Sellmann, K. Engl, F. W. Heinemann, *Eur. J. Inorg. Chem.* **2000**, 423–429; d) T. E. Glassman, M. G. Vale, R. R. Schrock, *J. Am. Chem. Soc.* **1992**, *114*, 8098–8109; e) M. Kawano, C. Hoshino, K. Matsumoto, *Inorg. Chem.* **1992**, *31*, 5158–5159.

[6] a) G. Albertin, S. Antoniutti, A. Bacchi, E. Bordignon, F. Busatto, G. Pelizzi, *Inorg. Chem.* **1997**, *36*, 1296–1305; b) G. Albertin, S. Antoniutti, A. Bacchi, E. Bordignon, P. M. Dolcetti, G. Pelizzi, *J. Chem. Soc., Dalton Trans.* **1997**, 4435–4444; c) G. Albertin, S. Antoniutti, A. Bacchi, M. Bergamo, E. Bordignon, G. Pelizzi, *Inorg. Chem.* **1998**, *37*, 479–489; d) G. Albertin, S. Antoniutti, E. Bordignon, F. Menegazzo, *J. Chem. Soc., Dalton Trans.* **2000**, 1181–1189; e) G. Albertin, S. Antoniutti, A. Bacchi, E. Bordignon, G. Perinello, *J. Organomet. Chem.* **2001**, *625*, 217–230; f) G. Albertin, S. Antoniutti, E. Bordignon, F. Chimisso, *Inorg. Chem. Commun.* **2001**, *4*, 402–404; g) G. Albertin, S. Antoniutti, M. T. Giorgi, *Eur. J. Inorg. Chem.* **2003**, 2855–2866; h) G. Albertin, S. Antoniutti, A. Bacchi, B. Fregolent, G. Pelizzi, *Eur. J. Inorg. Chem.* **2004**, 1922–1938; i) G. Albertin, S. Antoniutti, M. Bortoluzzi, J. Castro-Fojo, S. García-Fontán, *Inorg. Chem.* **2004**, *43*, 4511–4522.

[7] G. Albertin, S. Antoniutti, S. Beraldo, F. Chimisso, *Eur. J. Inorg. Chem.* **2003**, 2845–2854.

[8] a) G. Albertin, S. Antoniutti, M. Bettiol, E. Bordignon, F. Busatto, *Organometallics* **1997**, *16*, 4959–4969; b) G. Albertin, S. Antoniutti, S. García-Fontán, R. Carballo, F. Padoan, *J. Chem. Soc., Dalton Trans.* **1998**, 2071–2081; c) S. Bolaño, J. Bravo, R. Carballo, S. García-Fontán, U. Abram, E. M.

 © 2006 Wiley-VCH Verlag GmbH & Co. KGaA, Weinheim 

Vázquez-López, *Polyhedron* **1999**, *18*, 1431–1436; d) S. Bolaño, J. Bravo, J. Castro, S. García-Fontán, M. C. Marín, P. Rodríguez-Seoane, *J. Organomet. Chem.* **2005**, *690*, 4945–4958; e) S. Bolaño, J. Bravo, J. Castro, F. Fernández-García, S. García-Fontán, E. Lamas, M. C. Marín, P. Rodríguez-Seoane, manuscript in preparation.
[9] a) C. A. Tolman, *Chem. Rev.* **1977**, *77*, 313–348; b) M. M. Rahaman, H. Y. Liu, K. Eriks, A. Prock, W. P. Giering, *Organometallics* **1989**, *8*, 1–7.
[10] M. M. Raikhshtat, V. V. Zhogina, *Russ. J. Coord. Chemm.* **1994**, *20*, 915–917.
[11] W. J. Geary, *Coord. Chem. Rev.* **1971**, *7*, 81–122.
[12] F. Fernández-García, S. Bolaño, R. Carballo, S. García-Fontán, J. Bravo, *Polyhedron* **2001**, *20*, 2675–2681.
[13] Y. Li, W. T. Wong, *Dalton Trans.* **2003**, 398–405.
[14] R. Rabinowitz, J. Pellon, *J. Org. Chem.* **1961**, *26*, 4623–4626.
[15] M. S. Balakrishna, M. G. Walawalker, *J. Organomet. Chem.* **2001**, *628*, 76–80.
[16] C. D. Hurd, *Inorg. Synth.* **1939**, *1*, 87–89.
[17] a) G. Balacco, *J. Chem. Inf. Comput. Sci.* **1994**, *34*, 1235–1241; b) P. H. M. Budzelaar, *gNMR, Version 4.1*, Cherwell Scientific Limited, Oxford, UK, **1999**.
[18] G. M. Sheldrick, *SADABS. An Empirical Absorption Correction Program for Area Detector Data*, University of Göttingen, Germany, **1996**.
[19] G. M. Sheldrick, *SHELX-97. Program for the Solution and Refinement of Crystal Structures*, University of Göttingen, Germany, **1997**.
[20] *International Tables for X-ray Crystallography*, *Vol. C*, Ed. Kluwer, Dordrecht, The Netherlands, **1992**.

Received: March 21, 2006
Published Online: July 24, 2006

 © 2006 Wiley-VCH Verlag GmbH & Co. KGaA, Weinheim 

DOI: 10.1002/ejic.200600273

# Amine-Intercalated Layered $Sn^{II}$ Phosphates with Open-Framework Structures

**Padmini Ramaswamy[a] and Srinivasan Natarajan*[a]**

**Keywords:** Template synthesis / X-ray diffraction / Layered compounds / Hydrogen bonds / Tin / Phosphorus

Three new $Sn^{II}$ phosphate materials, $[NH_3(CH_2)_3NH_2(CH_2)_2NH_2(CH_2)_3NH_3]\cdot 2[Sn_2P_2O_8]$ (**I**), $[(N_2C_5H_{14})_2][Sn_4P_4O_{16}]\cdot 3H_2O$ (**II**) and $[(N_2C_5H_{14})][Sn_2P_2O_8]\cdot H_2O$ (**III**), have been synthesised by means of hydrothermal methods using *N*,*N*′-bis(3-aminopropyl)ethylenediamine (BAPEN; for **I**) and homopiperazine (H-PIP; for **II** and **III**), respectively, as the structure-directing organic amines. The solids **I**–**III** have layered architectures. The structures of all three compounds consist of strictly alternating vertex-sharing trigonal-pyramidal $SnO_3$ and tetrahedral $PO_4$ moieties forming infinite layers possessing apertures bound by 4- and 8-T atoms (T = Sn, P). The distorted 4- and 8-membered apertures within the layers suggest the subtle influence of the lone-pair of electrons of $Sn^{II}$ on the structure. The interlamellar space is occupied by the protonated organic amine molecules which interact with the framework through N–H···O hydrogen bonding. The compounds **I**–**III** bear some structural relationship to the layered zinc phosphite phases.
(© Wiley-VCH Verlag GmbH & Co. KGaA, 69451 Weinheim, Germany, 2006)

## Introduction

The wide structural diversity along with the potential applications in the areas of catalysis, sorption and separation processes are the reasons for the continued interest in the area of open-framework materials.[1] The continuing research has clearly established that new materials with novel structures can be made in the presence of structure-directing organic amines.[2] It is now firmly established that tin(II) phosphates exhibiting open-framework structures can be prepared employing hydrothermal methods.[3–13] The chemistry of divalent tin and its related compounds, especially the phosphates[3–13] and the phosphonates,[14–16] continues to yield unexpected results with the lone-pair associated with $Sn^{II}$ playing a significant role. In the family of tin phosphates, the isolation of solids having zero-,[3] one-,[4,5] two-[6–8] and three-dimensionally[9–13] extended networks clearly indicates that the system is versatile like the other family of open-framework phosphates. It is noteworthy that one of the basic structural building blocks, present in most of the phosphate based open-framework solids, is a four-membered ring made of $[M_2P_2O_4]$ units. The analogue with M = Sn has also been isolated and characterised.[3] The main structural features present in all the tin phosphate and phosphonate materials are the presence of either three- and/or four-coordinated $Sn^{II}$ atoms that are vertex-linked to $PO_4$ tetrahedra forming channels and cavities. In general, it is observed that the Sn/P ratio in many of the tin phosphates is >1. In this paper, we report the hydrothermal synthesis and structures of three simple open-framework tin(II) phosphates, $[NH_3(CH_2)_3NH_2(CH_2)_2NH_2(CH_2)_3NH_3]\cdot 2[Sn_2P_2O_8]$ (**I**), $[(N_2C_5H_{14})_2][Sn_4P_4O_{16}]\cdot 3H_2O$ (**II**) and $[(N_2C_5H_{14})][Sn_2P_2O_8]\cdot H_2O$ (**III**), having an Sn/P ratio of 1.0. The compounds were prepared in the presence of *N*,*N*′-bis(3-aminopropyl)ethylenediamine (BAPEN; for **I**) and homopiperazine (H-PIP; for **II** and **III** ), respectively, as the structure-directing agent.

## Results and Discussion

Three new $Sn^{II}$ phosphates, $[\{NH_3(CH_2)_3NH_2(CH_2)_2NH_2(CH_2)_3NH_3\}_2]\cdot 2[Sn_2P_2O_8]$ (**I**), $[(N_2C_5H_{14})_2][Sn_4P_4O_{16}]\cdot 3H_2O$ (**II**) and $[(N_2C_5H_{14})][Sn_2P_2O_8]\cdot H_2O$ (**III**), were synthesised using hydrothermal methods. As a result of the synthesis being kinetically controlled solvent-mediated reactions, there is no relationship between the starting synthesis mixture composition and the stoichiometry of the final solid product. The compounds **I**–**III** have similar structures consisting of layers that are intercalated by the structure-directing organic amine molecules. The structures are based on a network of strictly alternating $SnO_3$ and $PO_4$ units. These units form infinite layers with the incorporation of the organic amine in the fully protonated form.

The asymmetric unit of **I** contains 18 independent non-hydrogen atoms, of which two Sn and P atoms are crystallographically independent. The structure of **I** is constructed from a network of $SnO_3$ and $PO_4$ units forming infinite layers which are anionic. The connectivity between these moieties creates 4- and 8-membered rings along the *b*-axis. The polyhedral connectivity between the $SnO_3$ and $PO_4$ units forming the two-dimensional layer is shown in Fig-

[a] Framework Solids Laboratory, Solid State and Structural Chemistry Unit, Indian Institute of Science
Bangalore 560012, India
E-Mail: snatarajan@sscu.iisc.ernet.in
Supporting information for this article is available on the WWW under http://www.eurjic.org or from the author.

 © 2006 Wiley-VCH Verlag GmbH & Co. KGaA, Weinheim 

ure 1. As can be noted, each four-membered ring within the layer is connected to four eight-membered rings and each eight-membered ring is attached to four four-membered rings. The organic amine molecules (BAPEN) balance the charges of the anionic layers and are located in the spaces between the layers. The individual layers are held together by the fully protonated BAPEN molecules through hydrogen bonding interactions (Figures 2a and b).

The asymmetric unit of **II** contains 42 independent non-hydrogen atoms, of which 24 atoms belong to the framework and the remaining atoms to the lattice water and amine guest molecules. There are four Sn and P atoms that

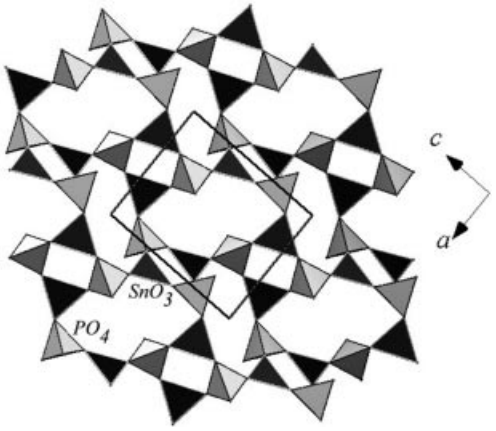


Figure 1. Polyhedral view of a single layer in $[NH_3(CH_2)_3NH_2(CH_2)_2NH_2(CH_2)_3NH_3]\cdot 2[Sn_2P_2O_8]$ (**I**) in the *ac* plane.

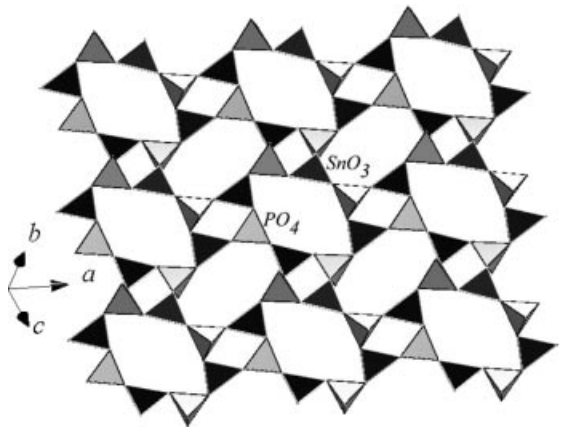


Figure 3. Polyhedral view of a single layer in $[(N_2C_5H_{14})_2][Sn_4P_4O_{16}]\cdot 3H_2O$ (**II**).

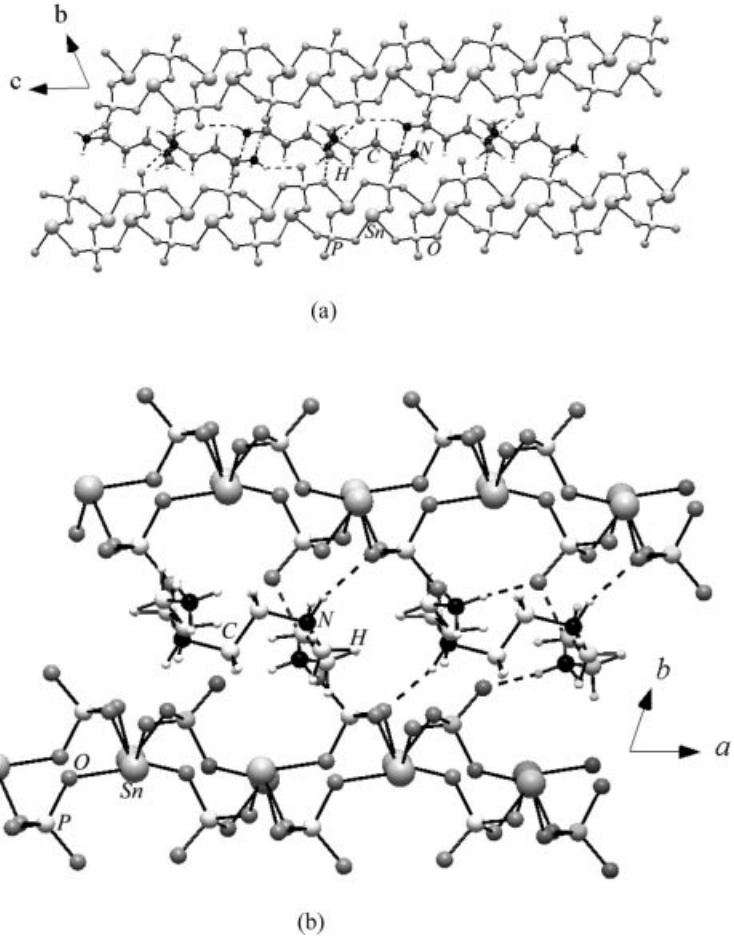


Figure 2. (a) Arrangement of the layers in **I** in the *bc* plane. (b) Arrangement of the layers in **I** in the *ab* plane. The dotted lines in both the cases represent possible hydrogen-bonding interactions.

 © 2006 Wiley-VCH Verlag GmbH & Co. KGaA, Weinheim 

are crystallographically independent. Similar to **I**, the structure of **II** is constructed by a network of $SnO_3$ and $PO_4$ units forming infinite layers that are anionic. The connectivity between these moieties creates 4- and 8-membered rings in the *ab* plane (Figure 3). In **II**, there appear to be two types of 4- and 8-membered apertures, the arrangement of which gives a three-dimensional character to the layers. The differences in the sizes and shapes of the apertures may be attributed to the relative positioning of the lone-pair of electrons on $Sn^{II}$. The charge-compensating protonated organic amine cations (H-PIP) are located in the inter-lamellar regions and are involved in hydrogen bonding through N–H···O, C–H···O and O–H···O interactions (Figure 4).

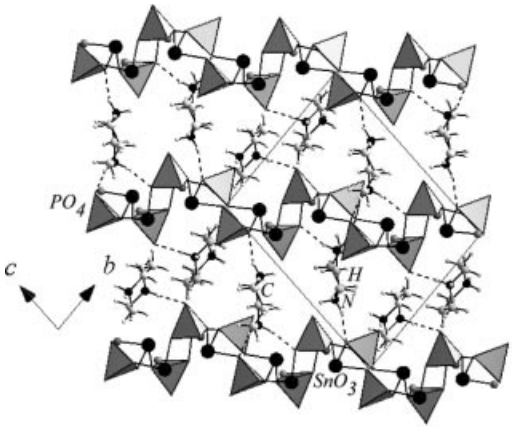


Figure 4. Arrangement of the layers in **II** in the *bc* plane. Dotted lines represent possible hydrogen-bonding interactions. The lattice water molecules are not shown.

The asymmetric unit of **III** contains 20 independent non-hydrogen atoms, of which two Sn and P atoms are crystallographically independent. The connectivity between the $SnO_3$ and $PO_4$ units creates 4- and 8-membered rings within the layer in the *bc* plane. The polyhedral connectivity of a single layer is shown in Figure 5. As can be noted, each 4-membered ring within the layer is connected to four 8-membered rings and each 8-membered ring is attached to four 4-membered rings. The 8-membered rings are considerably more distorted compared with those in the structures of **I** and **II**. The organic amine molecules (H-PIP) balance the charges of the anionic layers and are located in the spaces between the layers. The individual layers are held together by the protonated H-PIP molecules through hydrogen-bonding interactions (Figure 6).

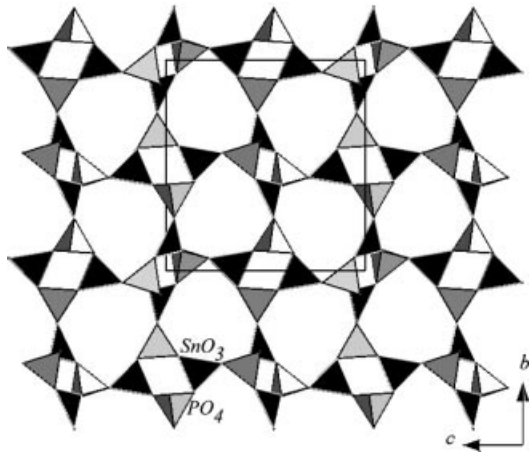


Figure 5. Polyhedral view of a single layer in $[(N_2C_5H_{14})][Sn_2P_2O_8]\cdot H_2O$ (**III**) in the *bc* plane.

Compounds **I**–**III** therefore represent examples of open-framework solids possessing alternating anionic and cationic layers. It may be noted that one of the basic building units present in many of the tin phosphates and other related materials, namely $M_2P_2O_4$ units (M = Sn in the present case),[3] can be observed in all the structures.

The Sn–O bond lengths are in the range from 2.0635(18) to 2.1234(17) Å and the O–Sn–O bond angles are between 82.76(6) and 93.42(14)° which is typical of three-coordinate $Sn^{II}$ centres[3–13] (Tables 1, 2 and 3). The Sn atoms are linked to P by means of the oxygen links. The P atoms are

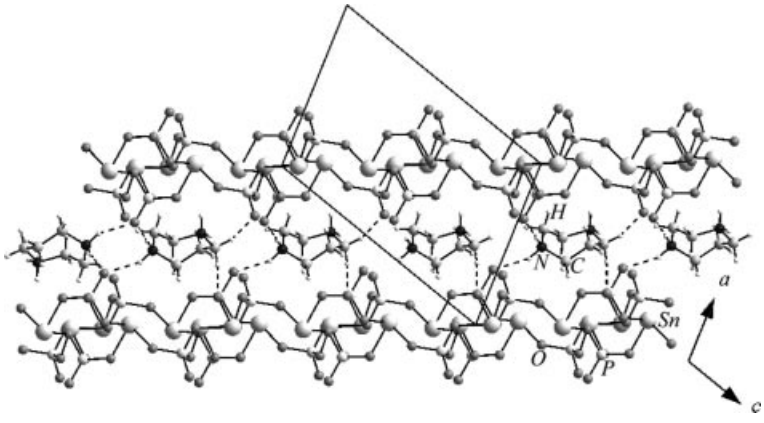


Figure 6. Arrangement of layers in **III** in the *ac* plane. Dotted lines represent possible hydrogen-bonding interactions. The lattice water molecules are not shown.

 © 2006 Wiley-VCH Verlag GmbH & Co. KGaA, Weinheim 

Table 1. Selected bond lengths [Å] and bond angles [°] for $[NH_3(CH_2)_3NH_2(CH_2)_2NH_2(CH_2)_3NH_3]\cdot 2[Sn_2P_2O_8]$ (**I**).

| | | | |
|---|---|---|---|
| Sn(1)–O(1) | 2.0911(17) | P(1)–O(5)[a] | 1.5412(17) |
| Sn(1)–O(2) | 2.0899(18) | P(1)–O(6)[b] | 1.5475(17) |
| Sn(1)–O(3) | 2.1035(16) | P(1)–O(3) | 1.5510(16) |
| Sn(2)–O(4) | 2.0635(18) | P(2)–O(8) | 1.4928(18) |
| Sn(2)–O(5) | 2.0957(18) | P(2)–O(4) | 1.5268(17) |
| Sn(2)–O(6) | 2.1234(17) | P(2)–O(1) | 1.5442(18) |
| P(1)–O(7) | 1.5022(18) | P(2)–O(2)[c] | 1.5448(19) |
| O(2)–Sn(1)–O(1) | 89.12(8) | O(8)–P(2)–O(4) | 111.89(12) |
| O(2)–Sn(1)–O(3) | 86.52(7) | O(8)–P(2)–O(1) | 109.78(11) |
| O(1)–Sn(1)–O(3) | 82.76(6) | O(4)–P(2)–O(1) | 107.85(11) |
| O(4)–Sn(2)–O(5) | 84.62(7) | O(8)–P(2)–O(2)[c] | 112.26(13) |
| O(4)–Sn(2)–O(6) | 88.67(7) | O(4)–P(2)–O(2)[c] | 107.20(11) |
| O(5)–Sn(2)–O(6) | 88.13(7) | O(1)–P(2)–O(2)[c] | 107.65(11) |
| O(7)–P(1)–O(5)[a] | 108.40(11) | P(2)–O(1)–Sn(1) | 119.79(10) |
| O(7)–P(1)–O(6)[b] | 112.81(11) | P(2)[c]–O(2)–Sn(1) | 122.75(11) |
| O(5)[a]–P(1)–O(6)[b] | 108.79(10) | P(1)–O(3)–Sn(1) | 122.80(9) |
| O(7)–P(1)–O(3) | 110.93(10) | P(2)–O(4)–Sn(2) | 130.82(11) |
| O(5)[a]–P(1)–O(3) | 109.29(10) | P(1)[d]–O(5)–Sn(2) | 126.37(11) |
| O(6)[b]–P(1)–O(3) | 106.55(9) | P(1)[b]–O(6)–Sn(2) | 120.31(10) |

Symmetry transformations used to generate equivalent atoms: [a] $x, y, z + 1$. [b] $-x, -y, -z$. [c] $-x + 1, -y, -z$. [d] $x, y, z - 1$.

Table 2. Selected bond lengths [Å] and bond angles [°] for $[(N_2C_5H_{14})_2][Sn_4P_4O_{16}]\cdot 3H_2O$ (**II**).

| | | | |
|---|---|---|---|
| Sn(1)–O(1) | 2.082(4) | P(1)–O(4) | 1.545(4) |
| Sn(1)–O(2) | 2.092(4) | P(1)–O(6) | 1.558(4) |
| Sn(1)–O(3) | 2.124(4) | P(2)–O(14) | 1.510(4) |
| Sn(2)–O(4)[a] | 2.079(4) | P(2)–O(5) | 1.535(4) |
| Sn(2)–O(5)[b] | 2.101(4) | P(2)–O(11) | 1.546(4) |
| Sn(2)–O(6) | 2.112(4) | P(2)–O(2) | 1.547(4) |
| Sn(3)–O(7) | 2.095(4) | P(3)–O(15) | 1.517(4) |
| Sn(3)–O(8) | 2.107(4) | P(3)–O(10)[c] | 1.532(4) |
| Sn(3)–O(9) | 2.115(3) | P(3)–O(7) | 1.540(4) |
| Sn(4)–O(10) | 2.082(4) | P(3)–O(9)[d] | 1.551(4) |
| Sn(4)–O(11) | 2.099(4) | P(4)–O(16) | 1.500(4) |
| Sn(4)–O(12) | 2.115(4) | P(4)–O(8) | 1.533(4) |
| P(1)–O(13) | 1.499(4) | P(4)–O(3) | 1.554(4) |
| P(1)–O(1) | 1.535(4) | P(4)–O(12) | 1.557(4) |
| O(1)–Sn(1)–O(2) | 85.96(15) | O(15)–P(3)–O(10)[c] | 109.4(2) |
| O(1)–Sn(1)–O(3) | 90.65(15) | O(15)–P(3)–O(7) | 110.6(2) |
| O(2)–Sn(1)–O(3) | 92.12(15) | O(10)[c]–P(3)–O(7) | 108.2(2) |
| O(4)[a]–Sn(2)–O(5)[b] | 89.10(15) | O(15)–P(3)–O(9)[d] | 110.6(2) |
| O(4)[a]–Sn(2)–O(6) | 88.93(15) | O(10)[c]–P(3)–O(9)[d] | 109.3(2) |
| O(5)[b]–Sn(2)–O(6) | 85.25(14) | O(7)–P(3)–O(9)[d] | 108.6(2) |
| O(7)–Sn(3)–O(8) | 89.12(15) | O(16)–P(4)–O(8) | 110.8(2) |
| O(7)–Sn(3)–O(9) | 88.60(14) | O(16)–P(4)–O(3) | 110.2(2) |
| O(8)–Sn(3)–O(9) | 87.21(14) | O(8)–P(4)–O(3) | 109.5(2) |
| O(10)–Sn(4)–O(11) | 85.27(14) | O(16)–P(4)–O(12) | 111.7(2) |
| O(10)–Sn(4)–O(12) | 86.81(14) | O(8)–P(4)–O(12) | 108.4(2) |
| O(11)–Sn(4)–O(12) | 93.42(14) | O(3)–P(4)–O(12) | 106.1(2) |
| O(13)–P(1)–O(1) | 111.9(2) | P(1)–O(1)–Sn(1) | 129.0(2) |
| O(13)–P(1)–O(4) | 112.3(2) | P(2)–O(2)–Sn(1) | 123.0(2) |
| O(1)–P(1)–O(4) | 107.7(2) | P(4)–O(3)–Sn(1) | 119.1(2) |
| O(13)–P(1)–O(6) | 109.4(2) | P(1)–O(4)–Sn(2)[a] | 127.4(2) |
| O(1)–P(1)–O(6) | 106.6(2) | P(2)–O(5)–Sn(2)[b] | 126.5(2) |
| O(4)–P(1)–O(6) | 108.7(2) | P(1)–O(6)–Sn(2) | 121.2(2) |
| O(14)–P(2)–O(5) | 111.4(2) | P(3)–O(7)–Sn(3) | 122.2(2) |
| O(14)–P(2)–O(11) | 109.5(2) | P(4)–O(8)–Sn(3) | 131.4(2) |
| O(5)–P(2)–O(11) | 109.3(2) | P(3)[d]–O(9)–Sn(3) | 123.2(2) |
| O(14)–P(2)–O(2) | 110.9(2) | P(3)[c]–O(10)–Sn(4) | 129.3(2) |
| O(5)–P(2)–O(2) | 107.8(2) | P(2)–O(11)–Sn(4) | 123.8(2) |
| O(11)–P(2)–O(2) | 107.9(2) | P(4)–O(12)–Sn(4) | 121.6(2) |

Symmetry transformations used to generate equivalent atoms: [a] $-x + 1, -y + 1, -z + 1$. [b] $-x, -y + 1, -z + 1$. [c] $-x, -y, -z + 2$. [d] $-x + 1, -y, -z + 2$.

tetrahedrally linked to oxygen atoms with P–O distances in the range of 1.493(2) to 1.558(4) Å and O–P–O bond angles in the range of 106.1(2) to 112.8(2)°. The P(1)–O(7) and P(2)–O(8) bonds with distances of 1.5022(18) and 1.4928(18) Å for **I**, P(1)–O(13), P(2)–O(14), P(3)–O(15) and P(4)–O(16) bonds with distances of 1.499(4), 1.510(4), 1.517(4) and 1.500(4) Å for **II** and P(1)–O(7) and P(2)–O(8) bonds with distances of 1.506(3) and 1.510(3) Å for **III** are all formally P=O double bonds. Terminal P=O groups in, for example $H_3PO_4\cdot 0.5H_2O$, are 1.485 and 1.495 Å in length.[17] The various bond lengths and angles observed in compounds **I**–**III** are in good agreement with other tin phosphate open-framework structures.[3–13] Selected bond lengths and angles are listed in Tables 1, 2 and 3 for **I**, **II** and **III**, respectively.

Table 3. Selected bond lengths [Å] and bond angles [°] for $[N_2C_5H_{14}][Sn_2P_2O_8]\cdot H_2O$ (**III**).

| | | | |
|---|---|---|---|
| Sn(1)–O(1) | 2.075(3) | P(1)–O(4)[a] | 1.546(3) |
| Sn(1)–O(2) | 2.086(3) | P(1)–O(6)[b] | 1.547(3) |
| Sn(1)–O(3) | 2.100(3) | P(1)–O(1) | 1.548(3) |
| Sn(2)–O(4) | 2.081(3) | P(2)–O(8) | 1.510(3) |
| Sn(2)–O(5) | 2.114(3) | P(2)–O(5) | 1.546(3) |
| Sn(2)–O(6) | 2.114(3) | P(2)–O(2)[c] | 1.546(3) |
| P(1)–O(7) | 1.506(3) | P(2)–O(3) | 1.550(3) |
| O(1)–Sn(1)–O(2) | 87.32(11) | O(8)–P(2)–O(5) | 111.61(16) |
| O(1)–Sn(1)–O(3) | 85.90(11) | O(8)–P(2)–O(2)[c] | 109.41(16) |
| O(2)–Sn(1)–O(3) | 90.42(11) | O(5)–P(2)–O(2)[c] | 108.12(16) |
| O(4)–Sn(2)–O(5) | 84.35(11) | O(8)–P(2)–O(3) | 112.58(16) |
| O(4)–Sn(2)–O(6) | 88.91(12) | O(5)–P(2)–O(3) | 106.81(15) |
| O(5)–Sn(2)–O(6) | 86.08(11) | O(2)[c]–P(2)–O(3) | 108.15(16) |
| O(7)–P(1)–O(4)[a] | 110.40(16) | P(1)–O(1)–Sn(1) | 129.44(17) |
| O(7)–P(1)–O(6)[b] | 112.59(16) | P(2)[c]–O(2)–Sn(1) | 124.39(16) |
| O(4)[a]–P(1)–O(6)[b] | 108.16(16) | P(2)–O(3)–Sn(1) | 123.33(15) |
| O(7)–P(1)–O(1) | 110.33(16) | P(1)[d]–O(4)–Sn(2) | 125.01(17) |
| O(4)[a]–P(1)–O(1) | 108.82(17) | P(2)–O(5)–Sn(2) | 123.74(15) |
| O(6)[b]–P(1)–O(1) | 106.39(16) | P(1)[e]–O(6)–Sn(2) | 123.96(16) |

Symmetry transformations used to generate equivalent atoms: [a] $-x + ½, y + ½, -z + ½$. [b] $x + ½, -y + ½, z + ½$. [c] $-x, -y + 1, -z$. [d] $-x + ½, y - ½, -z + ½$. [e] $x - ½, -y + ½, z - ½$.

The proton-decoupled $^{31}P$ pulsed MAS NMR spectra of **I** and **III**, shown in Figures 7a and b, clearly indicate the presence of two phosphorus sites with chemical shifts of $\delta_{iso}$ = 2.58 and 0.116 ppm for **I** and $\delta_{iso}$ = –3.475 and –4.507 ppm for **III**. The differences in the chemical shifts may be attributed to the involvement of the phosphate tetrahedra in hydrogen-bonding interactions. The observation of two distinct chemical shift peaks in the MAS NMR spectra indicates the presence of two crystallographically independent P sites which is in agreement with the single-crystal X-ray crystallographic data. Similar chemical shift values have been observed in other phosphate compounds.[18]

The lone pair of electrons on $Sn^{II}$ appears to play an important role in the present structures. The stereoactive lone-pair of electrons manifests itself in the lattice by creating open spaces between the two layers in the tin phosphates. It is likely that the differences in the arrangement of the 4- and 8-membered apertures within the layers, observed in the present compounds, are also subtly influenced by the presence of the lone-pair electrons. The lone-pair of

 © 2006 Wiley-VCH Verlag GmbH & Co. KGaA, Weinheim 

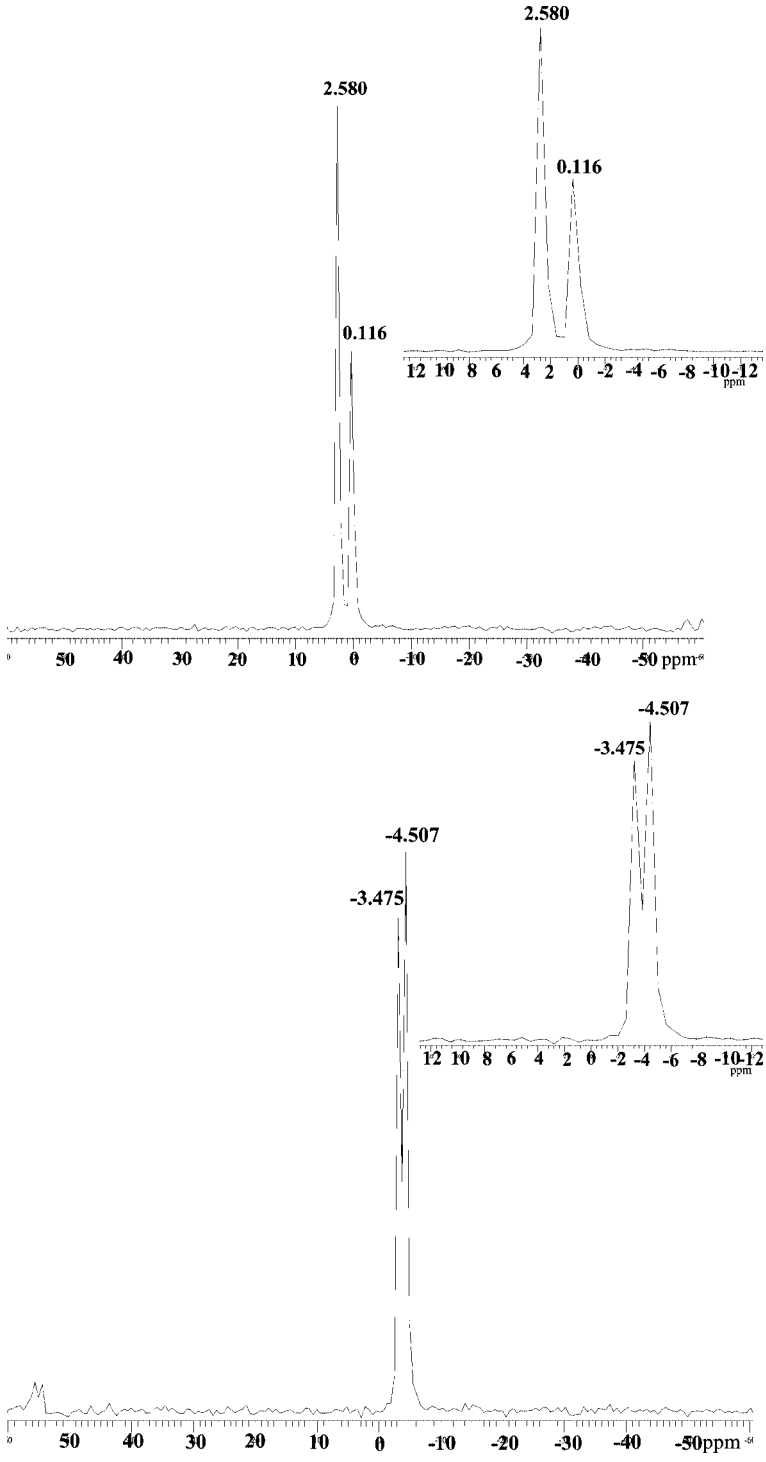


Figure 7. $^{31}$P-CPMAS NMR spectra for (a) $[NH_3(CH_2)_3NH_2(CH_2)_2NH_2(CH_2)_3NH_3]\cdot 2[Sn_2P_2O_8]$ (**I**) and (b) $[(N_2C_5H_{14})][Sn_2P_2O_8]\cdot H_2O$ (**III**).

electrons on $Sn^{II}$ generally points in a direction perpendicular to the plane of the layers. This is also expected since the amine molecules are cationic and located between the layers which would facilitate favourable interactions with the lone-pair of electrons. Similar lone-pair electron positions have been observed in many other layered $Sn^{II}$ phosphate materials.[6–8]

Multipoint hydrogen-bonding interactions help maintain structural stability and possibly help in the formation of many of the open-framework materials that have low-dimensional character.[3–8,19–24] In the present structures **I**–**III**, the hydrogen atoms of the amine molecule interact strongly with the framework oxygen atoms, especially with the double-bonded ones. Thus, a large number of N–H···O

 © 2006 Wiley-VCH Verlag GmbH & Co. KGaA, Weinheim 

and C–H···O hydrogen-bonding interactions has been observed in **I**–**III**. In addition, the lattice water molecules also participate in hydrogen-bonding O–H···O interactions. Selected hydrogen-bonding interactions, observed in **I**–**III**, are listed in Table 4. The present compounds **I**–**III** thus provide good examples of multipoint hydrogen bonding and illustrate the importance of them in the structural stability of two-dimensional solids.

Table 4. Selected hydrogen-bonding interactions in $[NH_3(CH_2)_3NH_2(CH_2)_2NH_2(CH_2)_3NH_3]\cdot 2[Sn_2P_2O_8]$ (**I**), $[(N_2C_5H_{14})_2][Sn_4P_4O_{16}]\cdot 3H_2O$ (**II**) and $[(N_2C_5H_{14})][Sn_2P_2O_8]\cdot H_2O$ (**III**).

| Moiety | D–H | A–H | D–A | D–H···A |
|---|---|---|---|---|
| **I** | | | | |
| N(1)–H(1)···O(5)[a] | 0.89 | 2.40 | 3.215(3) | 152 |
| N(1)–H(2)···O(8)[a] | 0.89 | 1.90 | 2.765(3) | 162 |
| N(1)–H(3)···O(8)[b] | 0.89 | 1.87 | 2.717(3) | 158 |
| N(2)–H(10)···O(7)[c] | 0.90 | 1.78 | 2.665(3) | 166 |
| N(2)–H(11)···O(3)[d] | 0.90 | 1.95 | 2.828(3) | 163 |
| **II** | | | | |
| N(1)–H(1)···O(100) | 0.90 | 1.83 | 2.664(8) | 154 |
| N(1)–H(2)···O(14)[d] | 0.90 | 1.99 | 2.774(7) | 175 |
| N(2)–H(9)···O(200) | 0.90 | 1.79 | 2.687(8) | 175 |
| N(2)–H(10)···O(15)[d] | 0.90 | 1.78 | 2.672(7) | 170 |
| N(3)–H(15)···O(300)[b] | 0.90 | 1.85 | 2.728(8) | 165 |
| N(3)–H(16)···O(9)[b] | 0.90 | 2.05 | 2.891(7) | 155 |
| N(4)–H(23)···O(3) | 0.90 | 1.95 | 2.828(7) | 166 |
| N(4)–H(24)···O(6) | 0.90 | 1.94 | 2.789(7) | 158 |
| O(100)–H(101)···O(14)[b] | 0.86 | 1.91 | 2.668(7) | 148 |
| O(100)–H(102)···O(15)[e] | 0.86 | 1.81 | 2.634(7) | 161 |
| O(200)–H(201)···O(13)[a] | 0.86 | 1.80 | 2.630(7) | 165 |
| O(200)–H(202)···O(16)[b] | 0.85 | 1.96 | 2.760(9) | 157 |
| C(5)–H(13)···O(7) | 0.97 | 2.39 | 3.198(8) | 141 |
| C(7)–H(20)···O(13)[b] | 0.97 | 2.52 | 3.442(9) | 159 |
| C(8)–H(22)···O(2)[b] | 0.97 | 2.53 | 3.446(8) | 158 |
| C(10)–H(27)···O(100) | 0.97 | 2.58 | 3.424(15) | 145 |
| C(10)–H(28)···O(16) | 0.97 | 2.47 | 3.438(16) | 174 |
| **III** | | | | |
| N(1)–H(1)···O(8)[a] | 0.90 | 1.94 | 2.773(5) | 153 |
| N(1)–H(2)···O(8)[c] | 0.90 | 1.85 | 2.744(5) | 175 |
| C(2)–H(5)···O(2)[c] | 0.97 | 2.45 | 3.364(5) | 157 |
| C(2)–H(6)···O(7)[b] | 0.97 | 2.39 | 3.348(5) | 172 |
| C(3)–H(4)···O(5) | 0.97 | 1.98 | 2.918(4) | 161 |
| C(3)–H(8)···O(7)[c] | 0.97 | 1.73 | 2.664(5) | 160 |

Symmetry transformations used to generate equivalent atoms: **I**: [a] $-x, 1-y, 1-z$. [b] $1-x, 1-y, -z$. [c] $x, y, 1+z$. [d] $-x, 1-y, -z$. **II**: [a] $1-x, 1-y, 1-z$. [b] $-x, 1-y, 1-z$. [c] $1-x, -y, 1-z$. [d] $1+x, y, -1+z$. [e] $x, y, -1+z$. **III**: [a] $½+x, ½-y, -½+z$. [b] $½+x, ½-y, ½+z$. [c] $-x, ½+y, ½-z$.

Structurally, the present compounds possess many features that are similar to other previously known open-framework solids, especially in $Sn^{II}$ phosphates with two-dimensional structures.[6–8] The layered arrangements in **II** and **III**, however, appear to be unique. Additionally, the $Sn^{II}$ phosphates can be compared with the structures of the recently discovered layered zinc phosphite networks.[23,24] While the $Sn^{II}$ phosphate structures are built up from $SnO_3$ trigonal pyramids and $PO_4$ tetrahedra, the $ZnO_4$ tetrahedra and $PO_3$ pseudo-tetrahedral units are vertex-linked in the zinc phosphite structures. Thus, the net available vertices for bonding in both the cases are similar. In the zinc phosphites, the fourth vertex of the pseudo-tetrahedra is occupied by a P–H bond and in the $Sn^{II}$ phosphates the fourth vertex is occupied by the lone-pair of electrons of the $Sn^{II}$ ions. Illustrative examples of some of the previously reported zinc phosphite structures in which the layers have 4- and 8-membered apertures along with the layer arrangement of **I** and **II** are shown in Figure 8. In the zinc phosphites, $[C_2N_2H_{10}][Zn_2(HPO_3)_3]$[23] and $[(C_4N_2H_{12})(C_5NH_4)]_4[Zn_6(HPO_3)_8]$,[24] (Figures 8a and b), the 8-membered rings are connected edge-wise and are separated by edge-sharing 4-membered rings. In the zinc phosphite $[C_3NH_{10}]_2[Zn_3(HPO_3)_4]$,[24] the connectivity within the layers is identical to that found in **I** (Figures 8c and d) which clearly establishes the net available vertices for bonding in both the structures. The structural features observed in the structures of **II** and **III** (Figures 8e and f) appear to be unique and, to the best of our knowledge, there are no corresponding zinc phosphite structures known in the literature. It may be noted that the 8-membered rings in **III** are distorted compared with those in **I** and **II**, indicating the subtle control exhibited, on the structure of **III**, by the lone-pair of electrons on $Sn^{II}$. In general, the layered phosphate/phosphite structures are held together by strong hydrogen-bonding interactions involving the P=O groups and the organic amine template molecules. The presence of trigonal-pyramidal $SnO_3$ and tetrahedral $PO_4$ units linking to form the layers and the interactions with the organic amine molecule renders the unique architectures seen in these materials.

## Conclusions

The synthesis of three new layered tin(ii) phosphate materials, $[NH_3(CH_2)_3NH_2(CH_2)_2NH_2(CH_2)_3NH_3]\cdot 2[Sn_2P_2O_8]$ (**I**), $[(N_2C_5H_{14})_2][Sn_4P_4O_{16}]\cdot 3H_2O$ (**II**) and $[(N_2C_5H_{14})][Sn_2P_2O_8]\cdot H_2O$ (**III**), consisting of alternating inorganic and organic layers has been accomplished. These materials, together with the previously reported $Sn^{II}$ phosphate and phosphonate solids, illustrate the profound structural influences of relatively minor modifications in the reaction conditions and/or changes in the starting source of tin. The present solids represent another example illustrating the importance of multipoint hydrogen bonding in the synthesis and stability of lower dimensional open-framework materials. The structures appear to a have close similarity to the phosphite-based ones. The stereoactive lone-pair of electrons on $Sn^{II}$ appears to subtly control the formation of the structure by manifesting itself in the open spaces. Our continuing research on the $Sn^{II}$ phosphates indicates that other related structures are formed under hydrothermal conditions in the presence of other structure-directing agents. While the isolation of a two-dimensional solid with strictly alternating $SnO_3$ and $PO_4$ moieties provides information about the stereochemical consequences of the $Sn^{II}$ lone-pair of electrons, further evaluation is required to exploit the structure-directing influences of this unit in the presence of other organic amines in the synthesis of open-framework materials.

 © 2006 Wiley-VCH Verlag GmbH & Co. KGaA, Weinheim 

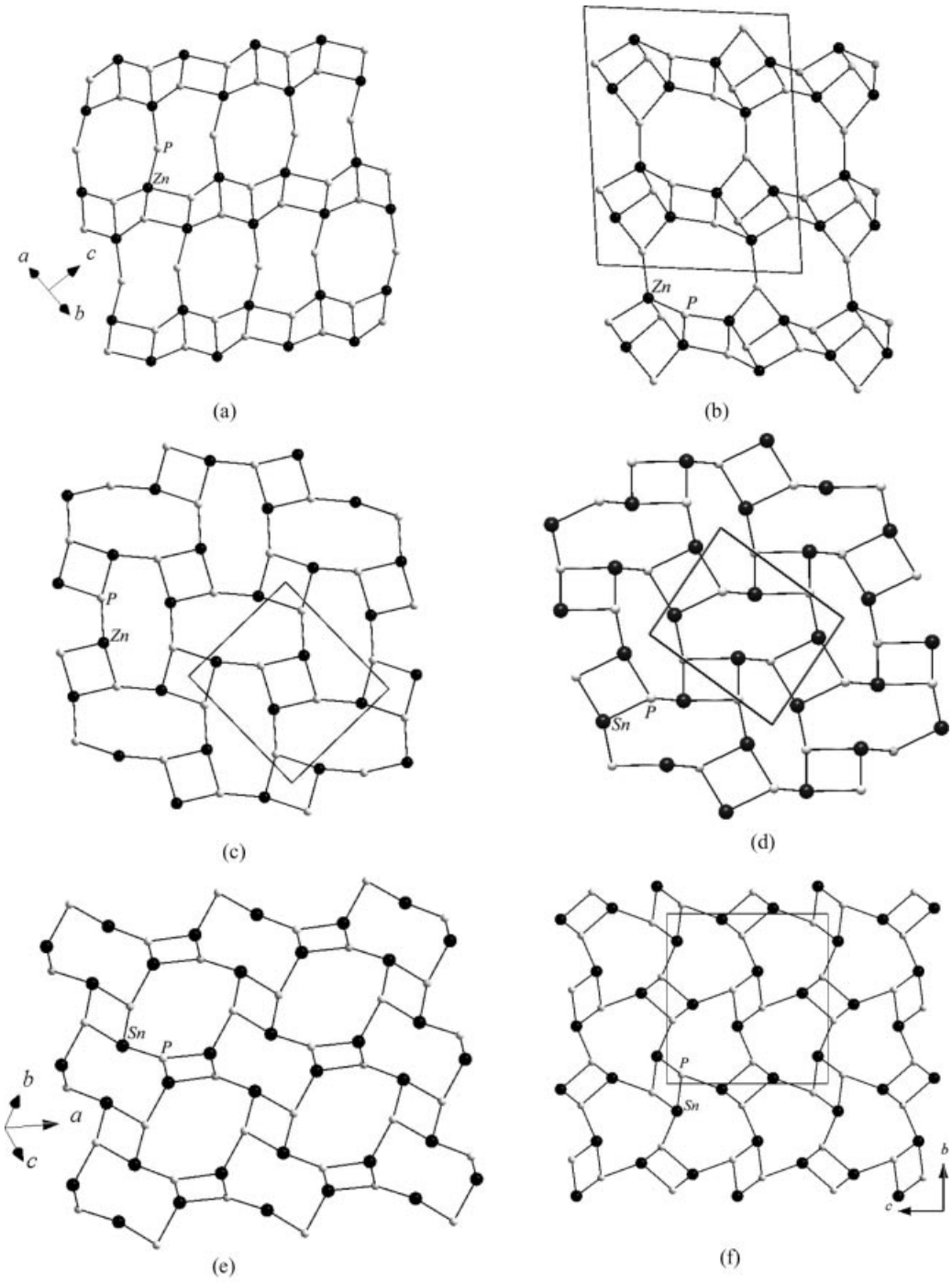


Figure 8. (a) View of the T-atom (T = Zn, P) connectivity within the layer in the zinc phosphite $[C_2N_2H_{10}][Zn_2(HPO_3)_3]$.[23] (b) View of the T-atom (T = Zn, P) connectivity within the layer in the zinc phosphite $[(C_4N_2H_{12})(C_5NH_4)]_4[Zn_6(HPO_3)_8]$.[24] (c) View of the T-atom (T = Zn, P) connectivity within the layer in the zinc phosphite $[C_3NH_{10}]_2[Zn_3(HPO_3)_4]$.[24] (d) T- atom (T = Sn, P) connectivity in **I** within the layer. Note the close similarity with the zinc phosphite structure (c). (e) T-atom (T = Sn, P) connectivity in **II** within the layer. (f) T-atom (T = Sn, P) connectivity in **III** within the layer.

## Experimental Section

**NMR Spectroscopy:** Solid-state NMR experiments were carried out with a Bruker DSX 300 spectrometer operating at 7 T with a resonance frequency of 121 MHz for $^{31}P$. A Bruker 5 mm double resonance probe was used for the experiments. The $^{31}P$ MAS spectra were recorded using standard cross-polarisation (CP) procedures and high proton decoupling employing a magic angle spinning (MAS) frequency of 7 kHz. In a typical experiment, radio-frequency fields of 120 kHz were used. The chemical shifts are reported relative to 85% $H_3PO_4$ as an external standard.

 © 2006 Wiley-VCH Verlag GmbH & Co. KGaA, Weinheim 

**Synthesis:** Compounds **I**–**III** were synthesised by hydrothermal methods starting from a tin phosphate gel and employing *N*,*N*′-bis(3-aminopropyl)ethylenediamine (BAPEN; for **I**) and homopiperazine (H-PIP; for **II** and **III**) as the structure-directing agents, respectively. For the synthesis of compound **I**, $Sn^{II}$ oxalate was used as the source of tin, whereas $SnCl_2{\cdot}2H_2O$ was employed for **II** and **III**. In a typical synthesis for **I**, tin(II) oxalate (0.211 g) was dispersed in distilled water (1 mL). To this were added 85% aq. $H_3PO_4$ (0.07 mL) and BAPEN (0.19 mL) and the mixture was stirred at room temperature until homogeneous (ca. 30 min.). The final reaction mixture with the composition $1.0SnC_2O_4/1.0H_3PO_4/1.0BAPEN/55H_2O$ was heated in a 23 mL PTFE-lined stainless steel autoclave at 180 °C for 72 h. The initial pH of the mixture was 9.0 and there was no appreciable change in pH after the reaction. The resultant product contained large quantities of block-shaped colourless crystals along with a small quantity of white powder. The yield of the product was ca. 70% based on the metal source. For **II**, a reaction mixture with the composition $1.0SnCl_2{\cdot}2H_2O/1.0H_3PO_4/3.0(H\text{-}PIP)/55H_2O$ was heated in a 23 mL PTFE-lined stainless steel autoclave at 150 °C for 48 h. The initial pH of the mixture was 7.0 and there was no change in pH during the reaction. The product contained predominantly unidentified powder with a few isolated plate-like single crystals. The white powder product was found to be poorly crystalline and did not correspond to the structure of **II**. In spite of our repeated attempts, we were not able to prepare **II** in pure form and hence other than the single-crystal structure, we have not been able to characterise the compound completely. For **III**, a reaction mixture with the composition $1.0SnCl_2{\cdot}2H_2O/1.0H_3PO_4/3.0(H\text{-}PIP)/110H_2O$ was heated at 150 °C for 24 h resulting in large quantities of block-like single crystals (yield 60%). In all the preparations, the products were washed with deionised water and dried under ambient conditions.

**Single-Crystal Structure Determinations:** A suitable colourless single crystal of each compound was carefully selected under a polarising microscope and glued to a thin glass fibre. The single-crystal diffraction data were collected with a Bruker AXS Smart Apex CCD diffractometer at room temperature (293 K). The X-ray generator was operated at 50 kV and 35 mA using Mo-$K_\alpha$ ($\lambda$ = 0.71073 Å) radiation. Data were collected with $\omega$-scans of width 0.3°. A total of 606 frames were collected in three different settings of $\varphi$ (0, 90 and 180°), keeping the sample-to-detector distance fixed at 6 cm and the detector position fixed at –25°. Pertinent experimental details of the structure determinations are listed in Table 5. The data were reduced using SAINTPLUS[25] and an empirical absorption correction was applied using the SADABS program.[26] The crystal structures were solved and refined by direct methods using SHELXL-97 present in the WinGX suite of programs.[27] The hydrogen atoms were placed in geometrically idealised positions and refined using the riding model. The last cycles in the refinements included all the atomic positions, anisotropic thermal parameters for all the non-hydrogen atoms and isotropic thermal parameters for all the hydrogen atoms. Full-matrix least-squares structure refinement against $|F|^2$ was carried out using the WinGX suite of programs.[27] CCDC-299664, -299665 and -602825 contain the supplementary crystallographic data for this paper. These data can be obtained free of charge from The Cambridge Crystallographic Data Centre via www.ccdc.cam.ac.uk/data_request/cif.

**Initial Characterisations:** The initial characterisations of **I** and **III** were carried out using elemental analysis, powder X-ray diffraction (XRD), thermogravimetric analysis (TGA) and infrared spectroscopy (IR). Elemental analyses of the crystals were carried out using atomic absorption spectroscopy (ThermoFinnigan FLASH EA 1112 CHNS analyser). TGA measurements were performed in an atmosphere of flowing oxygen (flow rate 50 mL min$^{-1}$) in the temperature range 30–800 °C (heating rate 5 °C min$^{-1}$). Infrared spectra were recorded in the range 400–4000 cm$^{-1}$ using KBr pellets (Perkin-Elmer SPECTRUM 1000 instrument). The powder X-ray diffraction patterns were recorded on crushed single crystals in the $2\theta$ range 5–50° using Cu-$K_\alpha$ radiation (Philips X'pert Pro). The C,

Table 5. Crystal data and structure refinement parameters for $[NH_3(CH_2)_3NH_2(CH_2)_2NH_2(CH_2)_3NH_3]{\cdot}2[Sn_2P_2O_8]$ (**I**), $[(N_2C_5H_{14})_2][Sn_4P_4O_{16}]{\cdot}3H_2O$ (**II**) and $[(N_2C_5H_{14})][Sn_2P_2O_8]{\cdot}H_2O$ (**III**).

| | **I** | **II** | **III** |
|---|---|---|---|
| Empirical formula | $C_8H_{26}N_4O_{16}P_4Sn_4$ | $C_{10}H_{32}N_4O_{19}P_4Sn_4$ | $C_5H_{14}N_2O_9P_2Sn_2$ |
| Formula mass | 1033.04 | 1111.04 | 545.50 |
| Crystal system | triclinic | triclinic | monoclinic |
| Space group | $P\bar{1}$ (no.2) | $P\bar{1}$ (no. 2) | $P2_1/n$ (no. 14) |
| $a$ [Å] | 8.010(1) | 10.065(3) | 8.956(2) |
| $b$ [Å] | 9.449(1) | 11.677(3) | 12.997(2) |
| $c$ [Å] | 9.742(1) | 14.404(4) | 12.911(2) |
| $\alpha$ [°] | 68.54(1) | 76.438(4) | 90 |
| $\beta$ [°] | 85.65(1) | 73.189(4) | 107.187(3) |
| $\gamma$ [°] | 71.88(1) | 71.766(4) | 90 |
| Volume [Å$^3$] | 651.51(2) | 1519.7(7) | 1435.8(4) |
| $Z$ | 2 | 2 | 4 |
| $\rho_{calcd.}$ [g cm$^{-3}$] | 2.633 | 2.428 | 2.524 |
| $\lambda$ (Mo-$K_\alpha$) [Å] | 0.71073 | 0.71073 | 0.71073 |
| $\mu$ [mm$^{-1}$] | 4.111 | 3.542 | 3.744 |
| $\theta$ range [°] | 2.25–28.00 | 1.50–24.71 | 2.28–28.03 |
| Total data collected | 7527 | 13678 | 12260 |
| Unique data | 3021 | 5116 | 3362 |
| Observed data [$I > 2\sigma(I)$] | 2889 | 3985 | 3046 |
| Refinement method | full-matrix least squares on $\|F\|^2$ | full-matrix least squares on $\|F\|^2$ | full-matrix least squares on $\|F\|^2$ |
| $R$ indices [$I > 2\sigma(I)$] | $R_1$ = 0.0177,[a] $wR_2$ = 0.0456[b] | $R_1$ = 0.0352,[a] $wR_2$ = 0.0916[b] | $R_1$ = 0.0278,[a] $wR_2$ = 0.0618[b] |
| $R$ indices (all data) | $R_1$ = 0.0177,[a] $wR_2$ = 0.0456[b] | $R_1$ = 0.0491,[a] $wR_2$ = 0.0990[b] | $R_1$ = 0.0324,[a] $wR_2$ = 0.0639[b] |
| Largest difference peak/hole [e Å$^{-3}$] | 0.508/–0.706 | 1.191/–1.217 | 0.928/–0.749 |

[a] $R_1 = \Sigma||F_o| - |F_c||/\Sigma|F_o|$. [b] $wR_2 = \{\Sigma[w(F_o^2 - F_c^2)^2]/\Sigma[w(F_o^2)^2]\}^{1/2}$. $w = 1/[\sigma^2(F_o)^2 + (aP)^2 + bP]$, $P = [\max.(F_o^2,0) + 2(F_c)^2]/3$, where $a$ = 0.0225 and $b$ = 0.2629 for **I**; $a$ = 0.0517 and $b$ = 2.3068 for **II** and $a$ = 0.0181 and $b$ = 3.1629 for **III**.

 © 2006 Wiley-VCH Verlag GmbH & Co. KGaA, Weinheim 

H and N analyses of **I** and **III** are as follows: **I**: calcd. C 9.29, H 2.52, N 5.42; found C 9.92, H 2.64, N 5.49; **III**: calcd. C 10.97, H 2.92, N 5.12; found C 11.36, H 3.14, N 5.18. The powder X-ray diffraction patterns (XRD) for **I** and **III** indicated that the patterns were new and being entirely consistent with those simulated from the single-crystal structures.[28] The XRD pattern of the powder sample, obtained along with **I**, also indicated that it belongs to the structure of **I**. The IR spectra of **I** and **III** show similar features and the following bands were observed: **I**: $\tilde{\nu}$ = 3000 [$\nu_s$(N–H)], 2824 [$\nu_s$(C–H)], 1602 [δ(N–H)], 1465 [δ(C–H)], 1406 [$\nu_s$(C–N)], 1334 [$\nu_s$(C–C)], 1153 [$\nu_{as}(PO_4)$], 755 [$\nu_s(PO_4)$], 625 [δas($PO_4$)], 583 [δs($PO_4$)] $cm^{-1}$; **III**: $\tilde{\nu}$ = 3554 [$\nu_s$(O–H)], 3099 [$\nu_s$(N–H)], 2804 [$\nu_s$(C–H)], 1619 [δ(O–H)], 1505 [δ(N–H)], 1431 [δ(C–H)], 1377 [$\nu_s$(C–N)], 1238 [$\nu_s$(C–C)], 1109 [$\nu_{as}(PO_4)$], 843 [$\nu_s(PO_4)$], 638 [δas($PO_4$)], 587 [δs($PO_4$)] $cm^{-1}$. The TGA studies on **I** were carried out in flowing air (50 mL $min^{-1}$) in the temperature range 25–800 °C (heating rate 10 °C $min^{-1}$). The results indicate one sharp weight loss in the at around 325 °C with a tail up to 475 °C followed by a small increase in the weight. The observed weight loss of ca. 15% in the range 325–500 °C corresponds to the loss of the amine molecule (calcd. 17.2%). The weight gain of 3% after 500 °C is probably the result of the oxidation of $Sn^{II}$ to $Sn^{IV}$ in the oxygen atmosphere (calcd. 3.74%). The TGA studies of **III** showed an initial weight loss followed by a prominent one. The initial continuous weight loss of 4.14% in the temperature range 30–200 °C corresponds to the loss of the lattice water and some adsorbed water (calcd. 3.30%). The second and more prominent weight loss of 15.5% in the range 300–700 °C corresponds to the loss of the amine molecule (calcd. 18.6%). Similar to **I**, beyond 700 °C there was a small weight gain of 2.75% which may be due to the oxidation of $Sn^{II}$ to $Sn^{IV}$ in the oxygen atmosphere. In both cases, the powder X-ray diffraction pattern of the decomposed samples indicated a poorly crystalline $Sn^{IV}P_2O_7$ phase (JCPDS: 29-1352). It seems likely that an amorphous phase with a ratio Sn/P > 1:1 is also present.

**Supporting Information** (for details see the footnote on the first page of this article): Asymmetric units for all the compounds (**I**–**III**), experimental and simulated powder XRD patterns, IR spectra and TGA curves for compounds **I** and **III**.

## Acknowledgments

S. N. thanks the Department of Science and Technology (DST), Government of India for the award of a research grant. The authors also thank DST-IRPHA for the BRUKER-CCD facility.

[1] A. K. Cheetham, T. Loiseau, G. Ferey, *Angew. Chem. Int. Ed.* **1999**, *38*, 3268–3292.
[2] C. N. R. Rao, S. Natarajan, A. Choudhury, S. Neeraj, A. A. Ayi, *Acc. Chem. Res.* **2001**, *34*, 80–87.
[3] S. Ayyappan, A. K. Cheetham, S. Natarajan, C. N. R. Rao, *J. Solid State Chem.* **1998**, *139*, 207–210.
[4] S. Natarajan, *J. Mater. Chem.* **1998**, *8*, 2757–2760.
[5] S. Ayyappan, X. Bu, A. K. Cheetham, S. Natarajan, C. N. R. Rao, *Chem. Commun.* **1998**, 2181–2182.
[6] S. Natarajan, A. K. Cheetham, *J. Solid State Chem.* **1998**, *140*, 435–439.
[7] R. Vaidhyanathan, S. Natarajan, *J. Mater. Chem.* **1999**, *9*, 1807–1811.
[8] Y.-L. Liu, G.-S. Zhu, J.-S. Chen, L.-Y. Na, J. Hua, W.-Q. Pang, R.-R. Xu, *Inorg. Chem.* **2000**, *39*, 1820–1822.
[9] S. Natarajan, M. P. Attfield, A. K. Cheetham, *Angew. Chem. Int. Ed. Engl.* **1997**, *36*, 978–980.
[10] S. Natarajan, A. K. Cheetham, *Chem. Commun.* **1997**, 1089–1090.
[11] S. Natarajan, S. Ayyappan, A. K. Cheetham, C. N. R. Rao, *Chem. Mater.* **1998**, *10*, 1627–1631.
[12] S. Natarajan, M. Eswaramoorthy, A. K. Cheetham, C. N. R. Rao, *Chem. Commun.* **1998**, 1561–1562.
[13] S. Natarajan, *J. Solid State Chem.* **1999**, *148*, 50–55.
[14] G. H. Bonavia, R. C. Haushalter, S. Lu, C. J. O'Conner, J. Zubieta, *J. Solid State Chem.* **1997**, *132*, 144–150.
[15] P. J. Zapf, D. J. Rose, R. C. Haushalter, J. Zubieta, *J. Solid State Chem.* **1996**, *125*, 182; P. J. Zapf, D. J. Rose, R. C. Haushalter, J. Zubieta, *J. Solid State Chem.* **1997**, *132*, 438–442.
[16] B. Adair, S. Natarajan, A. K. Cheetham, *J. Mater. Chem.* **1998**, *8*, 1477–1479.
[17] B. Dickens, E. Prince, L. W. Schroeder, T. H. Jordan, *Acta Crystallogr. Acta Crystallogr. Sect. B* **1974**, *30*, 1470–1473.
[18] S. Natarajan, L. van Wullen, W. Klein, M. Jansen, *Inorg. Chem.* **2003**, *42*, 6265–6273.
[19] W. T. A. Harrison, Z. Bircsak, L. Hanooman, Z. Zhang, *J. Solid State Chem.* **1998**, *136*, 93–102.
[20] A. M. Chippindale, C. Turner, *J. Solid State Chem.* **1997**, *128*, 318–322.
[21] S. Natarajan, *J. Mater. Chem.* **1998**, *8*, 2757–2760.
[22] R. H. Jones, A. M. Chippindale, S. Natarajan, J. M. Thomas, *J. Chem. Soc., Chem. Commun.* **1994**, 565–566.
[23] Z. E. Lin, J. Zhang, S. T. Zheng, G. Y. Yang, *Solid State Sci.* **2004**, *6*, 371–376.
[24] S. Mandal, S. Natarajan, *Solid State Sci.* **2006**, *8*, 388–396.
[25] SMART (v. 5.628), SAINT (v. 6.45a), XPREP and SADABS, Bruker AXS Inc. Madison, Wisconsin, USA, **2004**.
[26] G. M. Sheldrick, *SADABS, Siemens Area Detector Absorption Correction Program*, University of Göttingen, Göttingen, Germany, **1994**.
[27] WinGX (v. 1.64.05), Crystallograhic Program for Windows, **2003**.
[28] W. Krauss, G. Notze, *Powder Cell for Windows*, v. 2.4, Federal Institute for Materials Research and Testing, Berlin, Germany, **2000**.

Received: March 28, 2006
Published Online: July 11, 2006

 © 2006 Wiley-VCH Verlag GmbH & Co. KGaA, Weinheim 

DOI: 10.1002/ejic.200600297

# (Cyclen– and cyclam–pyridine)copper Complexes: The Role of the Pyridine Moiety in $Cu^{II}$ and $Cu^{I}$ Stabilisation

Sanae El Ghachtouli,[a] Cyril Cadiou,[a] Isabelle Déchamps-Olivier,[a] Françoise Chuburu,*[a] Michel Aplincourt,[a] and Thierry Roisnel[b]

**Keywords:** Copper / Cyclen and cyclam ligands / X-ray diffraction / UV/Vis and EPR spectroscopy / Electrochemistry / Configurational isomerisation

The protonation constants of cyclen– and cyclam–pyridine [1-(pyridin-2-ylmethyl)-1,4,7,10-tetraazacyclododecane ($\mathbf{L^1}$) and 1-(pyridin-2-ylmethyl)-1,4,8,11-tetraazacyclotetradecane ($\mathbf{L^2}$), respectively] and the stability constants ($\log\beta_{110}$) of the corresponding copper complexes ($[Cu\mathbf{L^1}]^{2+}$ and $[Cu\mathbf{L^2}]^{2+}$) were determined by potentiometric titrations. The complexes were subsequently isolated and characterised by X-ray diffraction, UV/Vis spectroscopy and electrochemical studies. The $[Cu\mathbf{L^2}]^{2+}$ complex adopts two distinct and stable geometries (*trans* I and III), which mainly differ by the macrocycle configuration. The *trans* III configurational isomer can be converted into the *trans* I one by electron transfer.
(© Wiley-VCH Verlag GmbH & Co. KGaA, 69451 Weinheim, Germany, 2006)

## Introduction

The coordination chemistry of tetraazamacrocyclic receptors like cyclen and cyclam is always of interest, as new fields like diagnostic imaging or therapeutic agent development have recourse to such ligands. Gadolinium complexes of polyamino carboxylate ligands are frequently used as contrast agents for magnetic resonance imaging (MRI) to improve the images.[1] Therapeutic metalloradiopharmaceuticals designed to localise tumour sites and deliver a cytotoxic radiation dose have become widespread.[2] These molecules are made up of a bifunctional chelator, which coordinates the metal ion and is covalently attached to a targeting molecule. The design of the chelator depends on the metal ion and, for instance, the complexation of copper radionucleides is provided by *N*-functionalised cyclams.[3] High thermodynamic and kinetic complex stabilities constitute crucial parameters for their in vivo applications. For this purpose, tetraazamacrocyclic receptors are very well suited, as the donor atoms, the ligand denticity and, above all, the ligand preorganisation ensure such stabilities. Finally, stereochemistry is often important when targeting complexes to specific receptors and, as far as tetraazamacrocyclic ligands are concerned, the orientation of the N–H bonds is important for receptor recognition.[4] It was recently shown that modifications of the macrocyclic substitution pattern can act directly on the stereochemistry and the properties of the metal complexes.[5–7] In particular, in metal complexes of *N*,*N*′,*N*′′,*N*′′′-tetrasubstituted tetraazamacrocycles, topological reorganisations can be induced by electron transfer. For these reasons, the preparation and characterisation of coordination compounds with tetraazamacrocyclic ligands bearing pendant substituents are still of interest. *N*-functionalisation may enhance the metal complexation and the coordination ability of the pendant arms may affect the stereochemistry of the metal complexes.

In this study, we focused on the copper coordination of cyclen– and cyclam–pyridine ($\mathbf{L^1}$ and $\mathbf{L^2}$, respectively; Scheme 1) in aqueous solution. The stability constants of the 1:1 copper complexes were determined. The complexes' stereochemistry was studied in solution (UV/Vis and EPR measurements) and supported by X-ray data. Finally, electrochemical experiments were carried out to give an insight into the behaviour of the copper complexes in solution.

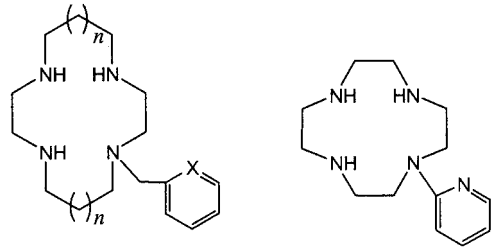


X = N: $n = 0$ $\mathbf{L^1}$; $n = 1$ $\mathbf{L^2}$

X = C: $n = 0$ $\mathbf{L^4}$; $n = 1$ $\mathbf{L^5}$

$\mathbf{L^3}$

Scheme 1.

[a] GRECI, Université de Reims Champagne-Ardenne, B. P. 1039, 51687 Reims Cedex 2, France
[b] UMR CNRS 6511, Institut de Chimie de Rennes, CS 74205, 35042 Rennes Cedex, France
E-mail: francoise.chuburu@univ-reims.fr
Supporting information for this article is available on the WWW under http://www.eurjic.org or from the author.

 © 2006 Wiley-VCH Verlag GmbH & Co. KGaA, Weinheim 

## Results and Discussion

The ligands **L¹** and **L²** were prepared according to the bis(aminal) methodology.[8] The protonation constants of the ligands and the overall formation constants of the copper complexes (see Experimental Section) were determined by means of potentiometric titrations at 20 °C in a 1 mol·L$^{-1}$ $KNO_3$ medium.

### Acid/Base Behaviour of L¹ and L²

The titration of the **L¹** and **L²** solutions gave rise to neutralisation curves with a single inflexion point at pH ≈ 7 for both ligands. A nonlinear least-squares refinement of six independent data sets with PROTAF software[9] allowed the determination of the $\log K_{01h}$ values, which are summarised in Table 1 with those of cyclen, cyclam and a monopyridyl relevant derivative, **L³** (Scheme 1), for comparison. For both ligands, one should expect five protonation constants, four for the nitrogen atoms of the macrocycle and one for the pyridinic nitrogen atom ($N_{pyr}$).

For **L¹**, the first two constants, $\log K_{011}$ (10.6) and $\log K_{012}$ (9.77), are close to those determined for the parent cyclen.[10] It means that the beginning of the protonation pattern of **L¹** is similar to the cyclen one and that the first two added protons are bound inside the macrocyclic cavity. The same proposal can be formulated for the cyclam analogue **L²**, as the first two protonation constants ($\log K_{011}$ = 11.31 and $\log K_{012}$ = 10.47) are similar to the ones determined for the parent cyclam.[11]

For **L¹**, only the third protonation constant ($\log K_{013}$ = 3.42) can be reached, while the last two are too weak to be determined with sufficient accuracy, unlike **L²**, for which three additional protonation constants ($\log K_{013}$ = 2.88, $\log K_{014}$ = 2.32 and $\log K_{015}$ = 1.73) are calculated. For each ligand, the purpose is to identify as much as possible when the $N_{pyr}$-protonation occurs. In fact, for the ligands incorporating a pyridine moiety, the $N_{pyr}$-protonation occurs in a wide pH range: for example the $N_{pyr}$ protonation constant is $\log K_{012}$ = 2.46[12a] for the 2-pyridinylmethanamine, and $\log K_{013}$ = 3.91 for the relevant ligand cyclen–pyridine **L³** (Table 1[12b]). Consequently, for the studied ligands, the identification of the third (**L¹**) or third and fourth (**L²**) protonation sites remains ambiguous, as these protonation steps occur at pH < 3.5, and in this pH range at least two sites are in competition, the first one being the $N_{pyr}$ atom, the second one being a nitrogen atom from the macrocyclic cavity. This is particularly true for the cyclam ligand **L²**. In order to gain an insight into the protonation pattern of **L¹** and **L²**, UV absorption and $^1$H NMR evolutions taking place upon protonation were investigated. For **L¹** and **L²**, the acidification of the medium induces in the UV absorption spectra (Figure 1) the characteristic hyperchromic shift of the pyridine chromophore,[13] which begins to appear at pH = 3.7 for **L¹**, at pH = 2.9 for **L²** and increases with decreasing pH to a maximum for **L¹** at pH = 1.5 and for **L²** at pH = 1.6. The protonation patterns of **L¹** and **L²** ligands were then examined by recording $^1$H NMR spectra at different pH values. The proton assignment was firstly elucidated with the help of two-dimensional $^1$H-$^1$H COSY, $^1$H-$^{13}$C HMQC and $^1$H-$^{13}$C HMBC correlation charts. For **L¹** (Figure 2, see also SI-1 in the Supporting Information), the chemical shifts of the aromatic protons ($H_{ar}$) are sensitive reporters of the protonation state of the ligand amino

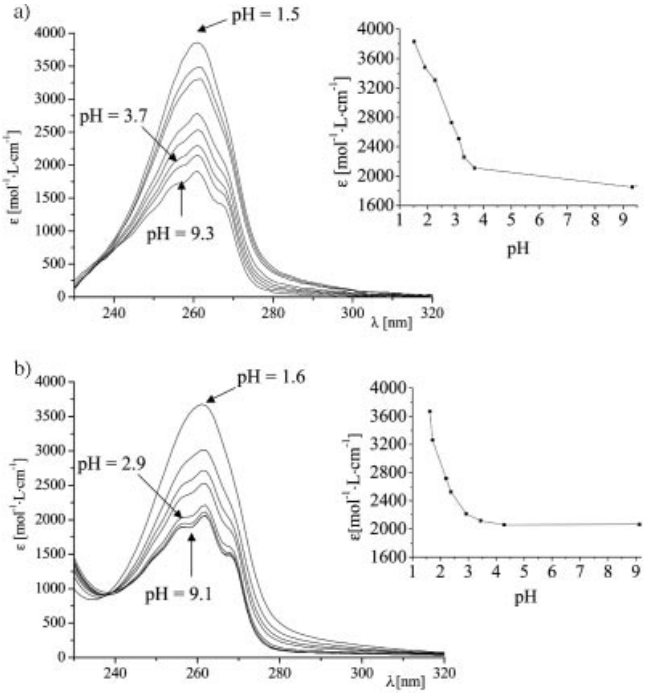


Figure 1. Spectrophotometric titrations of **L¹** and **L²** by KOH (0.1 mol·L$^{-1}$): (a) [**L¹**] = 3.9 × 10$^{-4}$ mol·L$^{-1}$ in HCl (1 mol·L$^{-1}$), pH ∈ [1.5; 9.3]. (b) [**L²**] = 2.34 × 10$^{-4}$ mol·L$^{-1}$ in HCl (1 mol·L$^{-1}$), pH ∈ [1.6; 9.1]. $T$ = 20 °C; $l$ = 1 cm [inset: $\varepsilon$ (mol$^{-1}$·L·cm$^{-1}$) = $f$(pH)].

Table 1. Ligand protonation constants $\log K_{01h}$ and overall formation constants $\beta_{110}$ of the 1:1 copper complexes. Values in parentheses represent 2σ standard deviation.

| | L¹[a] | L²[a] | L³[b] | L⁴[a] | L⁵[a] | Cyclen[c] | Cyclam[c,d] |
|---|---|---|---|---|---|---|---|
| $L + H^+ \rightleftharpoons LH^+$ | 10.6(1) | 11.31(1) | 10.99(5) | 10.80(6) | 11.5(1) | 10.97 | 11.58 |
| $LH^+ + H^+ \rightleftharpoons LH_2^{2+}$ | 9.77(8) | 10.47(6) | 7.16(5) | 9.23(3) | 9.31(3) | 9.87 | 10.62 |
| $LH_2^{2+} + H^+ \rightleftharpoons LH_3^{3+}$ | 3.42(5) | 2.88(8) | 3.91(5) | <2 | 2.46(4) | <2 | 1.61 |
| $LH_3^{3+} + H^+ \rightleftharpoons LH_4^{4+}$ | <2 | 2.32(1) | <3 | <2 | 2.29(7) | <2 | 2.42 |
| $LH_4^{4+} + H^+ \rightleftharpoons LH_5^{5+}$ | <2 | 1.73(5) | | | | | |
| $Cu^{2+} + L \rightleftharpoons CuL^{2+}$ | 21.0(2) | 23.0(2) | | 20.4(3) | 22.0(2) | 23.3 | 26.5 |

[a] Potentiometric titrations experimented at 20.0(1) °C, $I$ = 1 mol·L$^{-1}$ ($KNO_3$) (this work). [b] Ref.[12b] at 25 °C, $I$ = 0.1 mol·L$^{-1}$ ($NaClO_4$). [c] Ref.[10] at 25 °C, $I$ = 1 mol·L$^{-1}$ ($KNO_3$). [d] Ref.[11]

 © 2006 Wiley-VCH Verlag GmbH & Co. KGaA, Weinheim 

functions. In the pH range 4–12, no significant evolution of the $^1H_{ar}$ chemical shifts is observed (see also molecular modelling of **L¹**), which means that the first two protons bind the macrocycle (**L¹**H⁺ and **L¹**$H_2^{2+}$ species). In the pH range 2–4, a marked downfield shift is observed for the signals of the aromatic protons. This observation, in agreement with the UV data, strongly suggests that the third protonation step in **L¹** occurs on the $N_{pyr}$ atom.[14] For **L²** (Figure 3, see also SI-2,3 in the Supporting Information), the best reporters of the protonation steps are the $H_{ar}$ and the protons in the β-position with respect to the macrocyclic nitrogen atoms. In the pH range 9–12, a downfield shift is observed for the signals of the aliphatic protons, confirming that the first two protons added (species **L²**H⁺ and **L²**$H_2^{2+}$) bind to the macrocyclic cavity. In the pH range 1.5–3, a concomitant downfield shift of the signals of $H_{ar}$ and β-H is observed. In this region, the distribution diagram of the protonated **L²** species indicates that the existence domains of **L²**$H_3^{3+}$, **L²**$H_4^{4+}$ and **L²**$H_5^{5+}$overlap. It is worth noting that the coexistence of these three species induces a deep modification of the β-H signals with the coalescence of the β-H signals at pH ≈ 2 (see SI-3 of the Supporting Information). All these arguments mean that, for **L²**, the third and fourth protonation steps cannot be unambiguously attributed to the $N_{pyr}$ atom and to a macrocyclic nitrogen atom, respectively.

It is worth noting too that, for **L¹**, the difference between $\log K_{012}$ and $\log K_{013}$ is important. The third protonation constant attributed to the $N_{pyr}$ atom in **L¹** ($\log K_{013}$ = 3.42) is about two orders of magnitude smaller than that for the $N_{pyr}$-protonation in pyridine ($pK_a$ = 5.25[15]). This difference reflects the free-energy cost of protonating the third amino group in **L¹**, that is, the protonation of the $N_{pyr}$ atom is more difficult when the pyridine group is appended in proximity to the macrocyclic ring. At least two reasons can be invoked to explain this behaviour.[16] The first one takes into account the stabilisation of the diprotonated structure by intramolecular hydrogen bonding with the pyridine nitrogen atom (the protonation of this atom then induces hydrogen bond break-up). The second one corresponds to a conformational reorganisation upon protonation. To check these assumptions, molecular modelling of **L¹** and its protonated forms was undertaken.

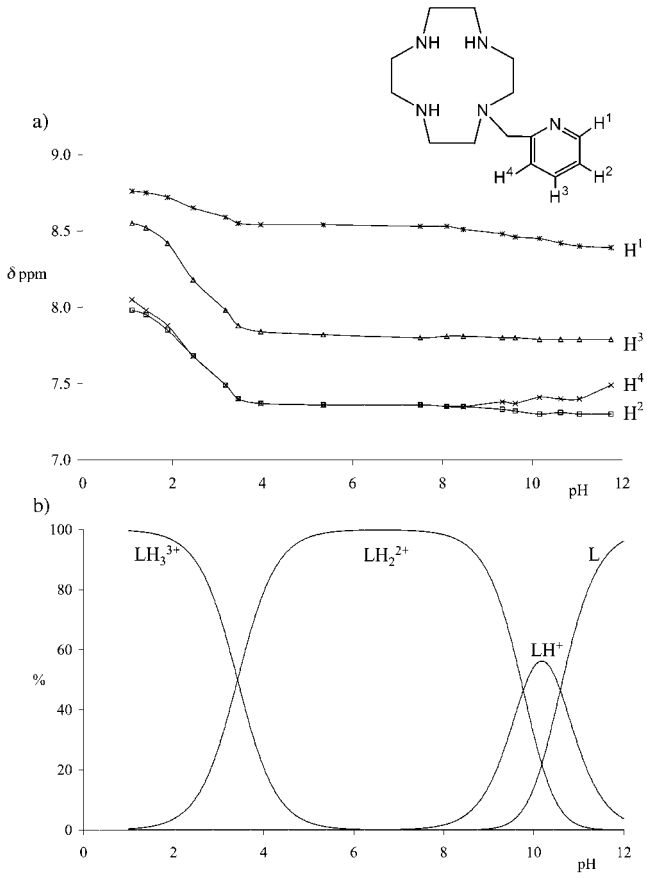


Figure 2. (a) pH dependence of the $^1H$ aromatic NMR signals of **L¹**. (b) Distribution diagram of the **L¹** protonated forms ([**L¹**] = $1.5\times10^{-3}$ mol·L$^{-1}$, $I$ = 1 mol·L$^{-1}$).

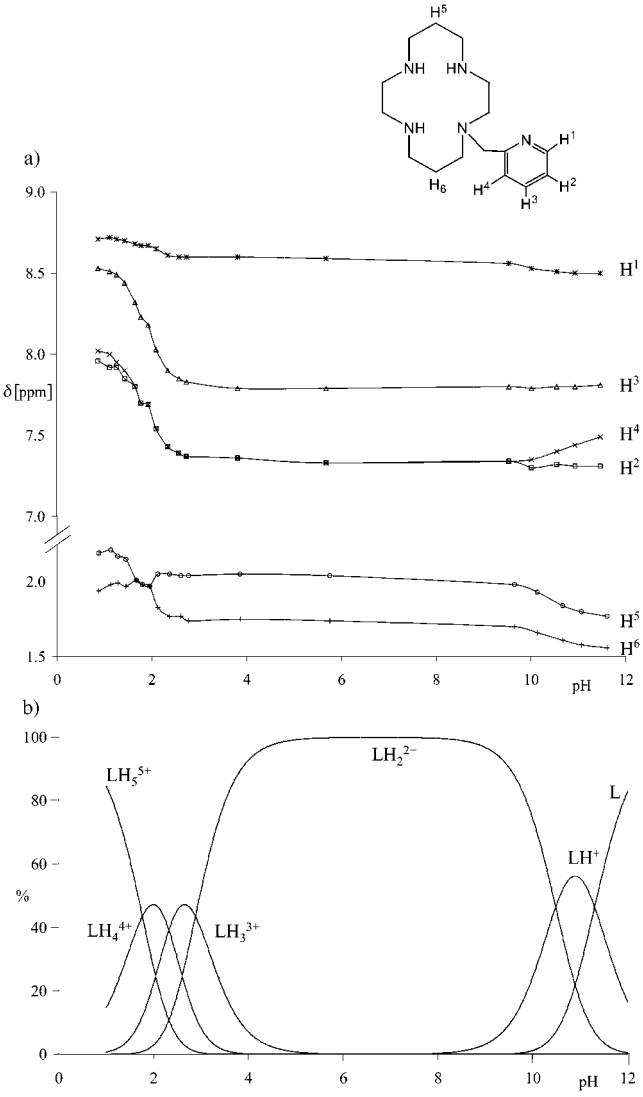


Figure 3. (a) pH dependence of the $^1H$ aromatic and β-H NMR signals of **L²**. (b) Distribution diagram of the **L²** protonated forms ([**L²**] = $1.5\times10^{-3}$ mol·L$^{-1}$, $I$ = 1 mol·L$^{-1}$).

 © 2006 Wiley-VCH Verlag GmbH & Co. KGaA, Weinheim 

### Molecular Modelling of $L^1$ and Its Protonated Forms

Low-energy conformers generated by a conformational search performed at the semiempirical level (AM1 calculations) were optimised using the Gaussian package[17a] under DFT/B3LYP/6-31G* formalism. The results concerning the **L¹** ligand are gathered in Table 2.

Table 2. DFT-optimised molecular structures of **L¹**, $[\mathbf{L^1}H]^{1+}$, $[\mathbf{L^1}H_2]^{2+}$and $[\mathbf{L^1}H_3]^{3+}$. For the sake of clarity, only the pertinent hydrogen atoms are represented. The dashed lines correspond to hydrogen bonds.

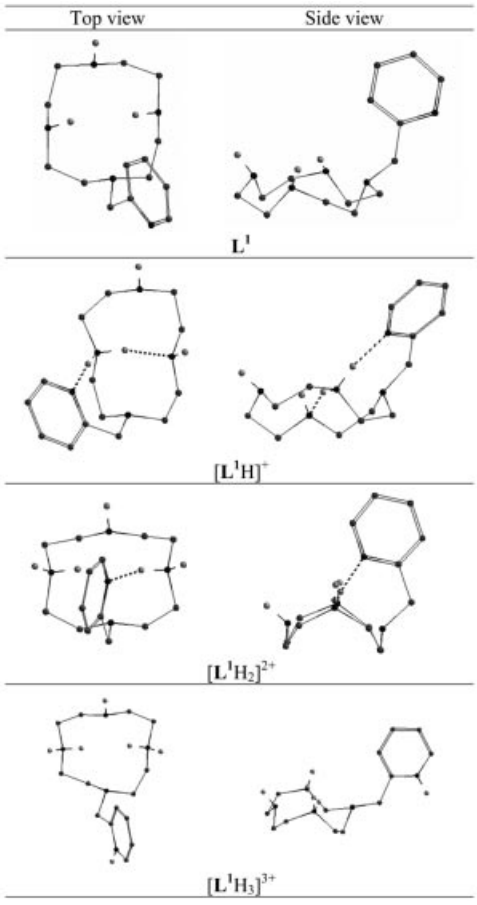


The lowest-energy structure computed for the neutral ligand **L¹** shows an outward orientation of the pyridine moiety relative to the macrocyclic cavity. The macrocycle has two of the three hydrogen atoms of the secondary amine functions directed towards the centre of the cavity. For the stepwise addition of protons, all the protonation sites were considered and the most stable situations are reported in Table 2. As the first proton is added, the pyridine moiety moves towards the inside of the macrocyclic cavity. The optimised geometry shows that the added proton is stabilised by a hydrogen bond with the $N_{pyr}$ atom, the overall structure being stabilised by two intramolecular hydrogen bonds. These characteristics are reinforced when the addition of the second proton is considered. The diprotonated structure is symmetrical, the symmetry plane including the pyridine ring. The pyridine moiety is then in an apical position towards the macrocyclic cavity, the $N_{pyr}$ atom stabilising the added proton by hydrogen bonds. Finally, the addition of the third proton occurs on the $N_{pyr}$ atom and the pyridine moiety is moved outward the macrocyclic cavity. The $N_{pyr}$ atom can no longer stabilise the first two added protons, as the hydrogen bonds are broken up. Moreover, the comparison of the calculated macrocyclic shapes for the **L¹** ligand and its protonated forms shows conformational modifications. The reorganisation of the macrocyclic cavity as a function of an increased number of protons is a way to accommodate positive charges in proximity. The modification is particularly important between $[\mathbf{L^1}H_2]^{2+}$ and $[\mathbf{L^1}H_3]^{3+}$ structures, as it corresponds to the shift of the pyridine ring away from the cyclen cavity. All these considerations indicate that the protonation of the $[\mathbf{L^1}H_2]^{2+}$ species is difficult, which is in good agreement with the small $\log K_{013}$ value determined for **L¹**.

### Copper Complexation of $L^1$ and $L^2$

#### *Thermodynamic Stability of the Complexes $[CuL^1]^{2+}$ and $[CuL^2]^{2+}$*

The pH titration of the ligands **L¹** and **L²** in the presence of 1 equiv. of copper(II) showed the formation of $[Cu\mathbf{L^1}]^{2+}$ and $[Cu\mathbf{L^2}]^{2+}$ complexes. From the analysis of the titration data, the complexation constants $\log\beta_{110}$ of $[Cu\mathbf{L^1}]^{2+}$ (21.0 ± 0.2) and $[Cu\mathbf{L^2}]^{2+}$ (23.0 ± 0.2) were determined (Table 1). The comparison of these values with those determined for (cyclen)- and (cyclam)copper complexes shows that the *N*-functionalisation of the cavity provokes a decrease of the complexes' stability (Table 1). This decrease is, however, less pronounced than for the benzyl complexes $[Cu\mathbf{L^4}]^{2+}$ and $[Cu\mathbf{L^5}]^{2+}$ (Table 1). This suggests that in solution the pyridine moiety is weakly involved in copper coordination.

#### *Molecular Structures of the Complexes*

To provide a proof of the stoichiometry and the structure of the complexes, a crystallographic study of the copper(II) complexes of **L¹** and **L²** was carried out.

For the $[Cu\mathbf{L^1}]^{2+}$ complex, X-ray quality blue single crystals were grown from diffusion of diethyl ether into an acetonitrile solution of the complex. Selected geometrical parameters are given in Table 3. The X-ray structure of $[Cu\mathbf{L^1}]^{2+}$ showed that the metal ion is pentacoordinate (Figure 4), the coordination sphere of the copper centre consisting of the four macrocyclic nitrogen atoms and the pyridinic $N_{pyr}$ atom. The Cu–N(secondary) bond lengths [2.013(4)–2.022(4) Å] are in the range expected for a copper ion coordinated in a cyclen cavity;[18] the Cu–N(tertiary) bond length of 2.058(3) Å, longer than the average of the Cu–N(secondary) ones (2.018 Å), is a consequence of the macrocyclic *N*-alkylation.[19] The $N_{pyr}$ atom is coordinated to the copper ion and the Cu–$N_{pyr}$ bond length is rather short [2.164(4) Å] by comparison with the same situation in the corresponding bis(macrocyclic) compound (2.266 Å).[18] This leads, in the solid state, to an efficient five-membered

 © 2006 Wiley-VCH Verlag GmbH & Co. KGaA, Weinheim 

chelate ring, as the $N_{pyr}$–Cu–N4 angle of 80.65(14)°, where the N4 atom bears the pyridine arm, is noticeably smaller than the other three $N_{pyr}$–Cu–N angles [99.00(17)–126.74(16)°].

Table 3. Selected bond lengths [Å] and angles [°] in $[CuL^1]^{2+}$.

| | | | |
|---|---|---|---|
| Cu–N1 | 2.013(4) | N1–Cu–N2 | 86.31(16) |
| Cu–N2 | 2.020(4) | N1–Cu–N3 | 146.94(18) |
| Cu–N3 | 2.022(4) | N1–Cu–N4 | 85.44(14) |
| Cu–N4 | 2.058(3) | N1–Cu–N5 | 111.24(16) |
| Cu–N5 | 2.164(4) | N2–Cu–N3 | 86.10(16) |
| | | N2–Cu–N4 | 152.46(17) |
| | | N2–Cu–N5 | 126.74(16) |
| | | N3–Cu–N4 | 86.62(15) |
| | | N3–Cu–N5 | 99.00(17) |
| | | N4–Cu–N5 | 80.65(14) |

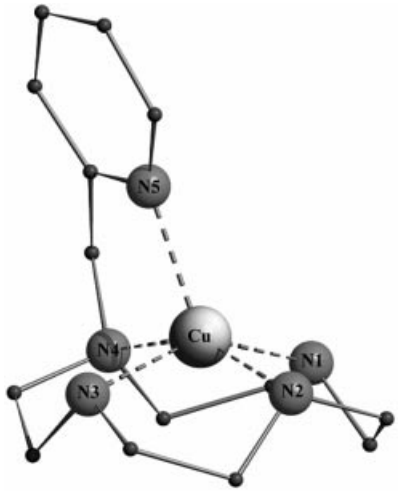


Figure 4. SCHAKAL diagram of $[CuL^1]^{2+}$.

For the $[CuL^2]^{2+}$ complex, as far as metal cation coordination by a cyclam derivative is concerned, one may expect the formation of stereoisomers for the complexes, according to the relative orientation of the NH group towards the macrocyclic cavity. The most frequently encountered configurational isomers are *trans* I (*R*,*S*,*R*,*S*) (++++) and *trans* III (*R*,*R*,*S*,*S*) (+–+–), where + indicates that the NH group is above the plane of the macrocycle and – indicates that it is below the plane.[20] Recently, it was demonstrated that, according to the redox state of the copper centre, different coordination modes around the metal ion are reached and can be responsible for the formation of the *trans* I and the *trans* III isomers.[6] Thus, depending on the experimental conditions, *trans* I and *trans* III isomers of $[CuL^2]^{2+}$ were isolated and characterised in the solid state. A $[CuL^2]^{2+}$ complex was easily obtained as a blue solid when the synthesis was performed with copper perchlorate in $CH_3OH$. The X-ray structure of the corresponding complex (Figure 5, Table 4a) showed that it adopts the *trans* I arrangement. The copper ion is pentacoordinate in a distorted square-pyramidal environment. The $N_{pyr}$ atom is therefore coordinated to the metal centre [2.220(2) Å]. The bond angles around the copper ion are different from those expected in an ideal square-pyramidal structure [e.g. N1CuN2, N4CuN1, N2CuN4, N3CuN1 of 86.20(5), 95.83(5), 170.96(5), 164.19(5)°, respectively]. The four macrocyclic nitrogen atoms define a plane and the copper ion is out of this plane by 0.218 Å.

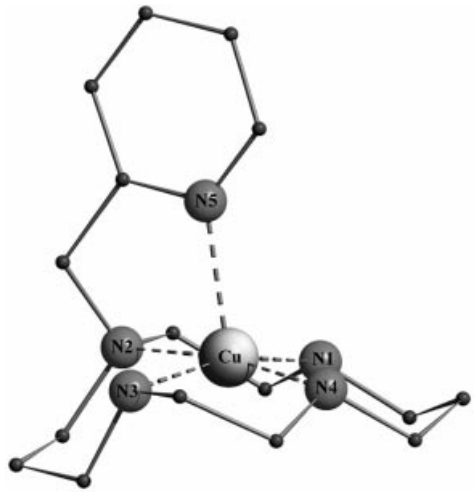


Figure 5. SCHAKAL diagram of $[CuL^2]^{2+}$ *trans* I.

Table 4. Selected bond lengths [Å] and angles [°] of $[CuL^2]^{2+}$ *trans* I (a) and $[CuL^2]^{2+}$ *trans* III (b).

| | | | |
|---|---|---|---|
| a | | | |
| Cu–N1 | 2.010(2) | N1–Cu–N2 | 86.20(5) |
| Cu–N2 | 2.080(2) | N1–Cu–N3 | 164.19(5) |
| Cu–N3 | 2.024(2) | N1–Cu–N4 | 95.83(5) |
| Cu–N4 | 2.037(2) | N1–Cu–N5 | 95.39(5) |
| Cu–N5 | 2.220(2) | N2–Cu–N5 | 78.66(5) |
| | | N3–Cu–N2 | 90.33(5) |
| | | N3–Cu–N4 | 85.34(5) |
| | | N3–Cu–N5 | 99.05(5) |
| | | N4–Cu–N2 | 170.96(5) |
| | | N4–Cu–N5 | 109.84(5) |
| b | | | |
| Cu–N1 | 2.038(2) | N1–Cu–N3 | 169.05(8) |
| Cu–N2 | 2.025(2) | N1–Cu–N5 | 109.70(8) |
| Cu–N3 | 2.092(2) | N2–Cu–N1 | 90.92(9) |
| Cu–N4 | 2.024(2) | N2–Cu–N3 | 85.64(9) |
| Cu–N5 | 2.250(2) | N2–Cu–N5 | 95.11(8) |
| | | N3–Cu–N5 | 80.99(8) |
| | | N4–Cu–N1 | 84.71(9) |
| | | N4–Cu–N2 | 165.38(9) |
| | | N4–Cu–N3 | 96.05(9) |
| | | N4–Cu–N5 | 99.50(8) |

When the complexation was performed with $L^2$ and $Cu(CH_3CN)_4PF_6$ as $Cu^I$ salt in $CH_3OH$ under aerobic conditions,[6] a violet solid resulting from the oxidation of $Cu^I$ by dioxygen was formed. The X-ray structure of the complex (Figure 6, Table 4b) highlighted the fact that it adopts a *trans* III configuration. The copper environment is still pentacoordinate, the $N_{pyr}$–Cu bond being a little longer [2.250(2) Å] than the corresponding one in the *trans* I complex. The main geometrical parameters are more or less the same as those observed for the *trans* I isomer, the copper ion being out of the macrocyclic plane by 0.224 Å.

 © 2006 Wiley-VCH Verlag GmbH & Co. KGaA, Weinheim 

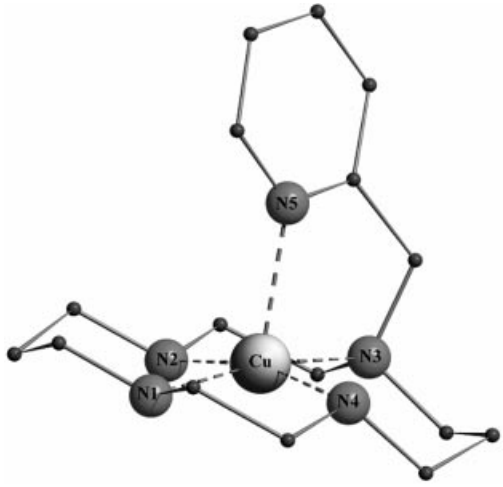


Figure 6. SCHAKAL diagram of $[CuL^2]^{2+}$ *trans* III.

### UV/Vis Spectral Properties and EPR Studies of the $[CuL^{1,2}]^{2+}$ Complexes

The UV/Vis absorption maxima of the complexes $[CuL^{1,2}]^{2+}$ in water and in acetonitrile together with the corresponding solid-reflectance spectra are listed in Table 5.

Table 5. UV/Vis data $\{\lambda$ [nm] $(\varepsilon$ [mol$^{-1}$·L·cm$^{-1}$])$\}$ of $[CuL^{1,2}]^{2+}$ complexes in $H_2O$, $CH_3CN$ solutions and in the solid state.

| | $H_2O$ | $CH_3CN$ | Solid state |
|---|---|---|---|
| $[CuL^1]^{2+}$ | 595 (218) | 601 (247) | 600 |
| $[CuL^2]^{2+}$ *trans* I | 602 (129) | 588 (144) | 580 |
| $[CuL^2]^{2+}$ *trans* III | 541 (228) | 550 (125) | 551 |

In the $[CuL^2]^{2+}$ *trans* I/III complexes, with regard to the copper band, the spectrum of the *trans* I complex exhibits a $\lambda_{max}$ = 602 nm in $H_2O$ (588 nm in $CH_3CN$) and a $\lambda_{max}$ = 580 nm in the solid state. The concordance of solid-state and solution UV/Vis spectra means that on going from the solid state to solution, the copper environment is maintained. The $\lambda_{max}$ values are consistent with a pentacoordinate copper centre,[19b,21] where the pyridyl group coordination has to be considered, according to the X-ray data for the $[CuL^2]^{2+}$ *trans* I complex ($CuN_5$ chromophore). For the *trans* III complex, a $\lambda_{max}$ = 541 nm in $H_2O$ (550 nm in $CH_3CN$) and a $\lambda_{max}$ = 551 nm in the solid state were determined. The $\lambda_{max}$ values suggest then that the pyridyl group in the *trans* III complex is still coordinated to the metal centre ($CuN_5$ chromophore). When a 5 M perchloric acid solution was added to aqueous solutions of $[CuL^2]^{2+}$ *trans* I/III complexes, a blue shift was observed for the absorption maxima (from 602 to 531 nm for $[CuL^2]^{2+}$ *trans* I and from 541 to 511 nm for $[CuL^2]^{2+}$ *trans* III). The positions of the resulting bands (531 and 511 nm) are typical of a $CuN_4$ chromophore where the metal ion is held in an *N*-monofunctionalised cyclam cavity.[22] Then the acid addition triggered the pyridine decoordination.

In the $[CuL^1]^{2+}$ complex, the spectrum exhibits a broad band at $\lambda_{max}$ = 595 nm in $H_2O$ (601 nm in $CH_3CN$) and at $\lambda_{max}$ = 600 nm in the solid state. The positions of these bands are typical of a square-pyramidal complex[18] where the copper centre is pentacoordinate. The concordance of solid-state and solution UV/Vis spectra seems to indicate that the copper coordination is again the same in the solid state and in solution. On the basis of the X-ray structure, it means that the pyridine moiety participates in the metal coordination ($CuN_5$ chromophore). To test this proposal, a 5 M perchloric acid solution was added to an aqueous solution of the $[CuL^1]^{2+}$ complex. Under these conditions, no blue shift of the absorption maximum was observed. In fact, this is not surprising if we consider that under acidic conditions the pyridine moiety can be decoordinated and replaced by a water molecule, as it is well known that in the cyclen cavity the copper ion is always pentacoordinate.[18] The acidification of the $[CuL^1]^{2+}$ solution can lead to chromophore modification from $CuN_5$ to $CuN_4O$.

Electron paramagnetic resonance corroborates the coordination geometry proposed for the copper ion in $CuL^1]^{2+}$ and $[CuL^2]^{2+}$ *trans* I/III complexes. The EPR spectra of the three complexes were recorded in a DMF solution at 150 K to ensure good glasses, and the corresponding simulated anisotropic parameters are listed in Table 6. The X-band EPR spectra of $[CuL^1]^{2+}$ and $[CuL^2]^{2+}$ *trans* I/III frozen solutions exhibit a strong absorption at about 3200 G, imputable to the allowed transitions $\Delta M_S = 1$. The shapes of the spectra consisted of four equidistant absorptions in the parallel region as expected for the coupling of the unpaired copper electron to the copper nucleus ($I$ = 3/2) (SI-4 in the Supporting Information). These spectra with $g_\parallel > g_\perp$ and $G > 4$ are typical of axially symmetric $d^9$ copper(II) complexes in a ground-state doublet with the unpaired electron in the $d_{x^2-y^2}$ orbital.[21] Moreover, for $[CuL^2]^{2+}$ complexes, the $g_\parallel$ values are slightly larger than that for [Cu(cyclam)]$^{2+}$ (2.186),[23] which is again consistent with the *N*-alkylation of the macrocyclic cavity.[22] The hyperfine coupling constant $A_\parallel$ is also a good indicator of distortion from square-planar to square-pyramidal coordination in copper(II) complexes, with smaller values implying distortion.

Table 6. EPR parameters of $[CuL^{1,2}]^{2+}$ complexes in frozen solution (DMF) at 150 K.

| | $g_\parallel$ | $g_\perp$ | [a] | $A_\parallel$ [$10^{-4}$ cm$^{-1}$] | $A_\perp$ [$10^{-4}$ cm$^{-1}$] |
|---|---|---|---|---|---|
| $[CuL^1]^{2+}$ | 2.192 | 2.045 | 4.26 | 175.0 | 15.6 |
| $[CuL^2]^{2+}$ *trans* I | 2.190 | 2.045 | 4.22 | 177.5 | 25.5 |
| $[CuL^2]^{2+}$ *trans* III | 2.197 | 2.045 | 4.37 | 188.7 | 22.5 |
| [Cu(cyclen)]$^{2+}$[b] | 2.198 | 2.057 | | 184 | |
| [Cu(cyclam)]$^{2+}$[b] | 2.186 | 2.049 | | 205 | |

[a] $G = (g_\parallel - 2)/(g_\perp - 2)$. [b] Ref.[23]

 © 2006 Wiley-VCH Verlag GmbH & Co. KGaA, Weinheim 

The $A_{\parallel}$ values for $[Cu\mathbf{L^1}]^{2+}$and $[Cu\mathbf{L^2}]^{2+}$ *trans* I/III are smaller than the corresponding $A_{\parallel}$ values for $[Cu(cyclen)]^{2+}$ and $[Cu(cyclam)]^{2+}$ (Table 6), which is consistent with $[Cu\mathbf{L^1}]^{2+}$and $[Cu\mathbf{L^2}]^{2+}$ *trans* I/III X-ray structures and pentacoordinate copper centres.

### Redox Properties of the $[CuL^{1,2}]^{2+}$ Complex

The electrochemical behaviour of $[Cu\mathbf{L^1}]^{2+}$ in acetonitrile was determined. The reduction was quasireversible and occurred at $E_{1/2}^{red}$ = –0.89 V versus $Fc^+$/Fc ($\Delta E_p$ = 80 mV); the oxidation was irreversible with a peak potential at $E_p^{ox}$ = 1.55 V versus $Fc^+$/Fc. No change in the CV waves was observed when full scans were performed except a drop in the current intensities when the system was investigated at high potentials, because of the irreversible oxidation.

Electrochemical studies of acetonitrile solutions of $[Cu\mathbf{L^2}]^{2+}$ *trans* I/III were only performed on the $Cu^{II}/Cu^{I}$ reduction system as oxidation to $Cu^{III}$ is irreversible and produces highly oxidative species giving very high anodic currents.[24] For the *trans* I complex, a single quasireversible reduction system was observed at $E_{1/2}^{red}$ = –1.145 V versus $Fc^+$/Fc ($\Delta E_p$ = 130 mV) and the voltammogram was fully reproducible from the first scan to several scans in reduction. This means that the electrogenerated $[Cu\mathbf{L^2}]^{+}$ *trans* I complex is stable, as it does not evolve within the voltammetry timescale.[7] For the *trans* III complex, the reduction yielded the short-lived $[Cu\mathbf{L^2}]^{+}$ *trans* III complex, for which an irreversible wave was located at $E_p^{red}$ = –1.05 V versus $Fc^+$/Fc. The comparison of the reduction potential of $[Cu\mathbf{L^2}]^{2+}$ *trans* I and $[Cu\mathbf{L^2}]^{2+}$ *trans* III shows that the *trans* I complex is more difficult to reduce than the *trans* III one. This has to be correlated with the Cu–$N_{pyr}$ distances obtained from crystallographic measurements. For the *trans* I complex, the Cu–$N_{pyr}$ distance is 2.220 Å, while for the *trans* III one this distance is 2.250 Å; for the *trans* I isomer, the ligand field is therefore stronger. Consequently, the *trans* I isomer's antibonding $e_g$* orbitals are destabilised compared to the *trans* III ones, making, for the *trans* I isomer, the removal of an electron easier and its withdrawal more difficult.[22]

The electrogenerated $[Cu\mathbf{L^2}]^{+}$ *trans* III complex is a transient species. Effectively, it readily isomerises as the reversible *trans* I system at $E_{1/2}^{red}$ = –1.15 V versus $Fc^+$/Fc ($\Delta E_p$ = 140 mV) is immediately observed after the irreversible *trans* III one. On cycling, the consecutive voltammograms exhibit only the *trans* I system. This behaviour has been observed until now only on tetrasubstituted (cyclam)copper complexes,[6,7] and indicates that the topological rearrangement process of the electrogenerated $[Cu\mathbf{L^2}]^{+}$ *trans* III complex to a $[Cu\mathbf{L^2}]^{+}$ *trans* I complex is rapid. One can also conclude that the pyridine moiety greatly enhances the $[Cu\mathbf{L^2}]^{+}$ stabilities, particularly for the *trans* I complex, as it does not evolve towards other species within the voltammetry timescale.[7] Finally, as the *trans* III → *trans* I conversion has not been observed by other techniques, electrochemical experiments illustrate the relevance of electron transfer in mediating topological reorganisation of the functionalised cyclam cavity.

## Conclusion

In cyclen– and cyclam–pyridine ligands and their copper complexes, the pyridine moiety behaves as a "non-innocent" fragment and its influence can be felt at several levels.

In the ligands, it participates through intramolecular hydrogen bonds in the stabilisation of two added protons in the macrocyclic cavity. In the copper complexes, the pyridine nitrogen atom participates as a fifth coordination site for the metal ion, both in the solid state and in solution. Regarding the complexes' structures, the pyridine moiety does not significantly affect the flexibility of the macrocyclic shape, as two configurational (cyclam–pyridine)copper complexes (*trans* I and *trans* III) can be synthesised. Finally, the pyridine moiety facilitates the stabilisation of copper(I) complexes and, as a result, helps the mediated electron transfer topological reorganisation of the *trans* III complex into the *trans* I one.

## Experimental Section

**Syntheses:** The metal salts were purchased from Aldrich. All the other reagents were of the highest grade commercially available and used without further purification.

**Ligand Synthesis:** The ligands $\mathbf{L^1}$ and $\mathbf{L^2}$ were synthesised according to a published procedure.[8]

#### Preparation of the Copper Complexes

**$[Cu\mathbf{L^1}](ClO_4)_2$:** Copper perchlorate hexahydrate (130 mg, 0.35 mmol) in methanol (5 mL) was added dropwise to a solution of $\mathbf{L^1}$ (100 mg, 0.32 mmol) in methanol (15 mL). The blue solution was refluxed for 2 h and then concentrated by solvent evaporation. The blue solid complex was precipitated upon addition of diethyl ether, and collected by filtration under vacuum. This solid was further dissolved in acetonitrile and the diffusion of a diethyl ether solution produced blue monocrystals of $[Cu\mathbf{L^1}](ClO_4)_2$, suitable for X-ray analysis. $C_{14}H_{25}Cl_2CuN_5O_8{\cdot}H_2O$ (543.84): calcd. C 30.92, H 5.00, N 12.88; found C 31.06, H 4.72, N 12.70. ESI-MS; *m*/*z* (%): calcd. for $[Cu\mathbf{L^1}(ClO_4)]^+$ 425, found 425 (100); calcd. for $[Cu\mathbf{L^1}H_{-1}]^+$ 325, found 325 (75).

**$[Cu\mathbf{L^2}](ClO_4)_2$ *trans* I:** A similar procedure to that described for $[Cu\mathbf{L^1}](ClO_4)_2$ was used. Blue single crystals suitable for X-ray diffraction analysis were obtained by diffusion of diethyl ether in the acetonitrile solution of $[Cu\mathbf{L^2}](ClO_4)_2$. $C_{16}H_{29}Cl_2CuN_5O_8$ (553.88): calcd. C 34.70, H 5.28, N 12.64; found C 34.65, H 5.01, N 12.48. ESI-MS; *m*/*z* (%): calcd. for $[Cu\mathbf{L^2}(ClO_4)]^+$ 453, found 453 (100); calcd. for $[Cu\mathbf{L^2}H_{-1}]^+$ 353, found 353 (60).

***CAUTION:*** Perchlorate-containing complexes are potentially explosive and appropriate precautions should be in place for their preparation, handling and storage.

**$[Cu\mathbf{L^2}](PF_6)_2$ *trans* III:** $Cu(CH_3CN)_4PF_6$ (62 mg, 0.17 mmol, white powder) in methanol (5 mL) was added dropwise to $\mathbf{L^2}$ (50 mg, 0.17 mmol) in methanol (10 mL). The solution, which immediately turned blue, was stirred at room temperature in aerobic conditions for 1 d and then concentrated by solvent evaporation. The violet solid complex was precipitated upon addition of diethyl ether, and

 © 2006 Wiley-VCH Verlag GmbH & Co. KGaA, Weinheim 

collected by filtration. This solid was further dissolved in methanol and the diffusion of a diethyl ether solution produced violet single crystals of $[Cu\mathbf{L^2}](PF_6)_2$, suitable for an X-ray analysis. $C_{16}H_{29}CuF_{12}N_5P_2{\cdot}CH_3OH$ (676.95): calcd. C 30.16, H 4.91, N 10.35; found C 30.29, H 4.73, N 10.45. ESI-MS; *m*/*z* (%): calcd. for $[Cu\mathbf{L^2}(PF_6)]^+$ 499, found 499 (70); calcd. for $[Cu\mathbf{L^2}H_{-1}]^+$ 353, found 353 (100).

**Potentiometric Measurements:** Potentiometric titrations were carried out with an automatic titrator composed of a microprocessor burette Metrohm Dosimat 665 and a Metrohm pH-Meter 713 connected to a computer. The titration procedure was fully automated.[25] All measurements were performed within a thermoregulated cell at 20.0 ± 0.1 °C under an argon stream to avoid the dissolution of carbon dioxide. The ionic strength was adjusted to 1 with potassium nitrate. The combined "U"-type Metrohm glass electrode used had a very low alkaline error. Solutions of ligand ($1\times10^{-3}$ to $2\times10^{-3}$ mol·L$^{-1}$) and ligand/copper nitrate mixture (ligand/metal ratio in the range 1.2–2) were titrated with a 0.1 mol·L$^{-1}$ KOH solution. For the complex titrations, an equilibration period of 1 month at 40 °C at acidic pH was observed until pH stabilisation. The potentiometric data were processed by using the PROTAF program[9] to obtain the best-fit chemical model and refined overall constants $\beta_{mlh}$.

$$m\,M + l\,L + h\,H^+ \rightleftharpoons M_mL_lH_h \qquad \beta_{mlh} = \frac{[M_mL_lH_h]}{[M]^m[L]^l[H^+]^h}$$

The stepwise protonation constants ($K_{0lh}$) related to the equilibrium of Equation (1) are defined by Equation (2) and were deduced from the refined ($\beta_{0lh}$) values by Equation (3).

$$LH_{h-1}^{(h-1)+} + H^+ \overset{K_{0lh}}{\rightleftharpoons} LH_h^{h+} \quad (1)$$

$$K_{0lh} = \frac{[LH_h^{h+}]}{[LH_{h-1}^{(h-1)+}][H^+]} \quad (2)$$

$$\beta_{0lh} = \prod_{i=1}^{h} K_{0li} \quad (3)$$

**Spectroscopic Measurements:** $^1$H and $^{13}$C NMR spectra were recorded with a Bruker DRX 500 spectrometer. $^1$H-$^1$H and $^1$H-$^{13}$C 2D correlation experiments were performed to assign the signals. In $^1$H NMR titrations, the pD was adjusted by additions of small amounts of a 4% diluted NaOD solution or a 3.5% diluted DCl solution to $D_2O$ solutions containing ligand $\mathbf{L^1}$ or $\mathbf{L^2}$ ($1.5\times10^{-3}$ mol·L$^{-1}$). The pH was calculated from the measured pD values using Equation (4).[26]

$$pH = pD - 0.40 \quad (4)$$

For both ligands, NMR measurements were performed after an equilibration time of 1 d. Mass spectra in acetonitrile were recorded with a Micromass Q-TOF instrument by electrospray positive ionisation. Electronic spectra in aqueous or acetonitrile solutions were all measured in the 200–900 nm range with a Perkin–Elmer Lambda 6 spectrophotometer. Solid-state spectra were obtained by depositing the complexes on a "Schleicher and Schüll" paper. EPR spectra were recorded with a Bruker ESP 300e spectrometer equipped with a Bruker E035M gaussmeter and an HP 5350B microwave frequency counter. Samples were prepared at a concentration of 5 mmol·L$^{-1}$ in DMF frozen solutions (150 K, Bruker ER4111VT variable-temperature unit). The simulation of the high-field EPR spectra was performed using XSophe software version

Table 7. Crystal data and details of the structure determination for $[Cu\mathbf{L^{1,2}}]^{2+}$complexes.

| | $[Cu\mathbf{L^1}](ClO_4)_2$, $CH_3CN$ | $[Cu\mathbf{L^2}]$ *trans* I $(ClO_4)_2$ | $[Cu\mathbf{L^2}]$ *trans* III $(PF_6)_2$ |
|---|---|---|---|
| Empirical formula | $C_{16}H_{28}Cl_2CuN_6O_8$ | $C_{16}H_{29}Cl_2CuN_5O_8$ | $C_{16}H_{29}CuF_{12}N_5P_2$ |
| Formula mass | 566.88 | 553.88 | 644.92 |
| Temperature [K] | 120 | 120 | 120 |
| Crystal system | monoclinic | monoclinic | monoclinic |
| Space group | *P*21/*n* | *P*21/*c* | *P*21/*n* |
| Colour | blue | blue | violet |
| *a* [Å] | 11.911(5) | 9.978(5) | 9.2090(2) |
| *b* [Å] | 13.695(5) | 14.867(5) | 17.0482(3) |
| *c* [Å] | 14.837(5) | 15.254(5) | 15.5835(3) |
| *α* [°] | 90 | 90 | 90 |
| *β* [°] | 98.444 | 97.635(5) | 100.95(10) |
| *γ* [°] | 90 | 90 | 90 |
| Volume [Å$^3$] | 2394(16) | 2242(15) | 2402.01(8) |
| *Z* | 4 | 4 | 4 |
| $D_{calcd.}$ [g·cm$^{-3}$] | 1.573 | 1.640 | 1.783 |
| Absorption coefficient [mm$^{-1}$] | 1.189 | 1.266 | 1.152 |
| *F*(000) | 1172 | 1148 | 1308 |
| $\lambda$(Mo-$K_\alpha$) [Å] | 0.71069 | 0.71069 | 0.71073 |
| Largest diff. peak/hole [e·Å$^{-3}$] | 1.719/–1.065 | 0.566/–0.544 | 0.952/–0.705 |
| No. independent reflections | 5427 | 7794 | 5490 |
| No. reflections [$I > 2.0\sigma(I)$] | 3924 | 6564 | 4527 |
| $R_1$ | 0.0641 | 0.0338 | 0.0424 |
| $wR_2$ | 0.1719 | 0.0822 | 0.1078 |
| Goodness-of-fit on $F^2$ | 1.006 | 1.053 | 1.043 |

 © 2006 Wiley-VCH Verlag GmbH & Co. KGaA, Weinheim 

1.1.4 for Mandriva 2006 x86-64 developed by the centre for Magnetic Resonance and the Department of Mathematics of the University of Queensland, Brisbane, Australia, for Bruker Biospin GmbH.[27] The software uses an angular dependence of *g* linewidth model and a Hooke and Jeeves optimisation method with the copper element in a natural abundance (for $[Cu\mathbf{L^1}]^{2+}$: linewidth in the parallel region $23.7\times10^{-4}$ cm$^{-1}$, in the perpendicular region $19.8\times10^{-4}$ cm$^{-1}$; for $[Cu\mathbf{L^2}]^{2+}$ *trans* I: linewidth in the parallel region $35.0\times10^{-4}$ cm$^{-1}$, in the perpendicular region $27.0\times10^{-4}$ cm$^{-1}$; for $[Cu\mathbf{L^2}]^{2+}$ *trans* III: linewidth in the parallel region $32.5\times10^{-4}$ cm$^{-1}$, in the perpendicular region $17.5\times10^{-4}$ cm$^{-1}$).

**Electrochemical Measurements:** Voltammetric data were recorded with an "Autolab with PGSTAT12" potentiostat (ECO Chemie) associated to a conventional three-electrode electrochemical cell, the working electrode being a glassy carbon disk. A platinum plate was used as a counter electrode and a silver electrode separated from the complex solution was used as a pseudoreference. In acetonitrile, the potential of the pseudoreference was measured versus the ferricinium/ferrocene couple. Complex concentrations were always close to $10^{-3}$ mol·L$^{-1}$ and tetrabutylammonium hexafluorophosphate $10^{-1}$ mol·L$^{-1}$ was used as the supporting electrolyte.

**Computational Details:** The input geometries were obtained by a conformational search performed on each structure, $\mathbf{L^1}$, $[\mathbf{L^1}H^+]$, $[\mathbf{L^1}H^{2+}]$, $[\mathbf{L^1}H^{3+}]$, at the semiempirical level (AM1 calculations, Spartan software[17b]) to determine the lowest conformer for each. The low-energy conformers generated were then minimised using the Gaussian 98 program package.[17a] Both geometry and energy calculations were performed at the DFT/B3LYP/6-31G* level. Each molecular structure was fully optimised and characterised as a minimum by frequency calculations.

**Crystal Structure Determination:** The crystal diffraction data were collected with a Kappa CCD diffractometer (Centre de Diffractométrie X, Univ. Rennes, France) using monochromated Mo-$K_\alpha$ radiation ($\lambda$ = 0.71073 Å) at 120 K. Data collection was performed with the COLLECT program.[28] Frames integration and data reduction procedures were realised using the DENZO and SCALEPACK program of the KappaCCD software package, respectively,[29] for the $Cu\mathbf{L^1}$ and $Cu\mathbf{L^2}$ *trans* I/III compounds and with EVAL[30] and SADABS[31] programs. The structures were solved using the direct-methods program SIR97,[32] which revealed all non-hydrogen atoms. SHELXL97[33] was used to refine the structure. Finally, hydrogen atoms were placed geometrically and held in riding mode in the least-squares refinement procedure. Final difference maps revealed no significant maxima. Further details are given in Table 7. CCDC-602318 ($[Cu\mathbf{L^1}]^{2+}$), -602319 ($[Cu\mathbf{L^2}]^{2+}$ *trans* I) and -602320 ($[Cu\mathbf{L^2}]^{2+}$ *trans* III) contain the supplementary crystallographic data for this paper. These data can be obtained free of charge from The Cambridge Crystallographic Data Centre via www.ccdc.cam.ac.uk/data_request/cif.

**Supporting Information** (see footnote on the first page of this article): Stack plots of $^1$H NMR spectra (aromatic region), EPR spectra, and Z-matrix of DFT-minimised (B3LYP/6-31G*) lowest-energy conformers.

## Acknowledgments

We thank Dr. J. M. Nuzillard and H. Ballia (Université de Reims Champagne Ardenne, France) for their help in the 2D NMR measurements. D. Harakat is thanked for ESI-MS measurements. Prof. G. R. Hanson (University of Queensland, Australia) is gratefully acknowledged for his valuable assistance during the implementation of XSophe.

[1] P. Caravan, J. J. Ellison, T. J. McMurry, R. B. Lauffer, *Chem. Rev.* **1999**, *99*, 2293–2352.
[2] S. Liu, D. S. Edwards, *Bioconjugate Chem.* **2001**, *12*, 7–34.
[3] C. J. Anderson, M. J. Welch, *Chem. Rev.* **1999**, *99*, 2219–2234.
[4] S. J. Paisey, P. J. Sadler, *Chem. Commun.* **2004**, 306–307.
[5] L. Siegfried, T. A. Kaden, *Dalton Trans.* **2005**, 3079–3082.
[6] C. Bucher, J. C. Moutet, J. Pécaut, G. Royal, E. Saint-Aman, F. Thomas, S. Torelli, M. Ungureanu, *Inorg. Chem.* **2003**, *42*, 2242–2252.
[7] C. Amatore, J. M. Barbe, C. Bucher, E. Duval, R. Guilard, J. N. Verpeaux, *Inorg. Chim. Acta* **2003**, *356*, 267–278.
[8] M. Le Baccon, F. Chuburu, L. Toupet, H. Handel, M. Soibinet, I. Déchamps-Olivier, J. P. Barbier, M. Aplincourt, *New J. Chem.* **2001**, *25*, 1168–1174.
[9] a) R. Fournaise, C. Petitfaux, *Talanta* **1987**, *34*, 385–395; b) R. Fournaise, C. Petitfaux, *Analusis* **1990**, *18*, 242–249.
[10] A. Bianchi, M. Micheloni, P. Paoletti, *Coord. Chem. Rev.* **1991**, *110*, 17–113.
[11] R. D. Hancock, R. J. Motekaitis, J. Mashishi, I. Cukrowski, J. H. Reibenspies, A. E. Martell, *J. Chem. Soc., Perkin Trans. 2* **1996**, 1925–1929.
[12] a) Y. Couturier, C. Petitfaux, *Bull. Soc. Chim. Fr.* **1974**, 855–862; b) S. Aoki, D. Kagata, M. Shiro, K. Takeda, E. Kimura, *J. Am. Chem. Soc.* **2004**, *126*, 13377–13390.
[13] G. J. Bridger, R. T. Skerlj, S. Padmanabhan, S. A. Martellucci, G. W. Henson, M. J. Abramo, H. C. Joao, M. Witvrouw, K. De Vreese, R. Pauwells, E. De Clercq, *J. Med. Chem.* **1996**, *39*, 109–119.
[14] C. Bazzicalupi, A. Bencini, E. Berni, A. Bianchi, L. Borsari, C. Giorgi, B. Valtancoli, C. Lodeiro, J. C. Lima, A. J. Parola, F. Pina, *Dalton Trans.* **2004**, 591–597.
[15] K. J. Powell, Academic software Mini SCDatabase, version 5.3, **1999**.
[16] a) L. Frémond, E. Espinosa, M. Meyer, F. Denat, R. Guilard, V. Huch, M. Veith, *New J. Chem.* **2000**, *24*, 959–966; b) M. Meyer, L. Frémond, A. Tabard, E. Espinosa, G. Y. Vollmer, R. Guilard, Y. Dory, *New J. Chem.* **2005**, *29*, 99–108.
[17] a) M. J. Frisch, G. W. Trucks, H. B. Schlegel, G. E. Scuseria, M. A. Robb, J. R. Cheesemen, V. G. Zakrzewski, J. A. Montgomery, R. E. Stratmann, J. C. Burant, S. Dapprich, J. M. Millam, A. D. Daniels, K. N. Kudin, M. C. Strain, O. Farkas, J. Tomasi, V. Barone, M. Cossi, R. Cammi, M. Mennucci, C. Pomelli, C. Adamo, S. Clifford, J. Ochterski, G. A. Petersson, P. Y. Ayala, Q. Cui, K. Morokuma, D. K. Malik, A. D. Rabuk, K. Raghavachari, J. B. Foresman, J. Cioslowski, J. V. Ortiz, B. B. Stefanov, G. Liu, A. Liashenko, P. Piskorz, I. Komaromi, R. Gomperts, R. L. Martin, D. J. Fox, T. Keith, M. A. Al-Laham, C. Y. Peng, A. Nanayakkara, G. Gonzalez, M. Challacombe, P. M. W. Gill, B. G. Johnson, W. Chen, M. W. Wong, J. L. Andres, M. Head-Gordon, E. S. Replogle, J. A. Pople, *Gaussian 98* (Revision A.1), Gaussian Inc., Pittsburgh, PA, **1998**; b) *Spartan04*, Wavefunction, Inc., Irvine, CA.
[18] S. El Ghachtouli, C. Cadiou, I. Déchamps-Olivier, F. Chuburu, M. Aplincourt, V. Turcry, M. Le Baccon, H. Handel, *Eur. J. Inorg. Chem.* **2005**, 2658–2668.
[19] a) A. E. Goeta, J. A. K. Howard, D. Maffeo, H. Puschmann, J. A. Gareth Williams, D. S. Yufit, *J. Chem. Soc., Dalton Trans.* **2000**, 1873–1880; b) V. J. Thorn, C. C. Fox, J. C. A. Boeynes, R. D. Hancock, *J. Am. Chem. Soc.* **1984**, *106*, 3198–3207.
[20] B. Bonisch, C. K. Poon, M. L. Tobe, *Inorg. Chem.* **1965**, *4*, 1102–1108.
[21] B. J. Hathaway, A. A. G. Tomlinson, *Coord. Chem. Rev.* **1970**, *5*, 1–43.
[22] Y. Dong, G. A. Lawrence, L. F. Lindoy, P. Turner, *Dalton Trans.* **2003**, 1567–1576.
[23] K. Miyoshi, H. Tanaka, E. Kimura, S. Tsuboyama, S. Murata, H. Shimizu, K. Ishizu, *Inorg. Chim. Acta* **1983**, *78*, 23–30.
[24] a) C. Bisi Castellani, M. Licchelli, A. Perotti, A. Poggi, *J. Chem. Soc., Chem. Commun.* **1984**, 806–808.

 © 2006 Wiley-VCH Verlag GmbH & Co. KGaA, Weinheim 

[25] M. Soibinet, I. Déchamps-Olivier, E. Guillon, J. P. Barbier, M. Aplincourt, F. Chuburu, M. Le Baccon, H. Handel, *Eur. J. Inorg. Chem.* **2003**, 1984–1994.
[26] A. K. Covington, M. Paabo, R. A. Robinson, R. G. Bates, *Anal. Chem.* **1968**, *40*, 700–706.
[27] M. Griffin, A. Muys, C. Noble, D. Wang, C. Eldershaw, K. E. Gates, K. Burrage, G. R. Hanson, *Mol. Phys. Rep.* **1999**, *26*, 60–84.
[28] *COLLECT*, KappaCCD software, Nonius BV, Delft, The Netherlands.
[29] Z. Otwinowski, W. Minor in *Methods in Enzymology* (Ed.: C. W. Carter Jr, R. M. Sweet), Academic Press, New York, **1997**, vol. 276, p. 307.
[30] A. Altomare, M. C. Burla, M. Camalli, G. Cascarano, C. Giacovazzo, A. Guagliardi, A. G. G. Moliterni, G. Polidori, R. Spagna, *J. Appl. Crystallogr.* **1999**, *32*, 115–119.
[31] G. M. Sheldrick, *SHELX97*, Program for the Refinement of Crystal Structures, University of Göttingen, Germany, **1997**.
[32] A. J. M. Duisenberg, *Reflections on Area detectors*, Thesis, Utrecht, **1998**.
[33] G. M. Sheldrick, *SADABS*, version 2.03, Bruker AXS Inc., Madison, WI, USA, **2002**.

Received: April 4, 2006
Published Online: July 21, 2006

 © 2006 Wiley-VCH Verlag GmbH & Co. KGaA, Weinheim 

DOI: 10.1002/ejic.200600298

# Crystal Structure and Properties of $MgCo_4Ge_6$

**Christine Gieck,[a] Martin Schreyer,[a] Thomas F. Fässler,*[a] Fabian Raif,[b] and Peter Claus[b]**

**Keywords:** Intermetallic phases / Germanium / Heterogeneous catalysis / ELF (Electron Localization Function) / Density functional theory

$MgCo_4Ge_6$ is a novel compound in the ternary system Mg-Co-Ge. Single crystals for a structure analysis were obtained from mixtures of the elements at high temperatures in sealed tantalum ampoules. The tetragonal structure [$I\bar{4}_2m$; $a$ = 6.1725(9) and $c$ = 8.660(2) Å; $YRu_4Sn_6$ structure type] was determined by X-ray single crystal analysis and refined to $R_1$ = 0.027 for all data. The electronic structure is discussed by means of density of states and band-structure analyses on the basis of density functional theory. Chemical bond analysis is performed using the electron localization function (ELF). The catalytic properties of the polar intermetallic alloy with respect to the selective hydrogenation of α,β-unsaturated aldehydes are discussed and compared with those of the recently investigated $MgCo_6Ge_6$.
(© Wiley-VCH Verlag GmbH & Co. KGaA, 69451 Weinheim, Germany, 2006)

## Introduction

The synthesis of polar intermetallic alloys with a well-defined stoichiometry is attempted in order to obtain substitutes for the expensive platinum group metal catalysts currently used for the selective hydrogenation of α,β-unsaturated aldehydes. While both the electronic and structural properties of intermetallic compounds, as well as the catalytic properties of some alloys on ceramic supports, have been studied extensively, no systematic investigations on the catalytic properties of well-defined alloys have been reported yet. A comparison of the ternary tetrelides of cobalt and ruthenium shows that isotypic compounds are obtained in many cases.[1–4] Besides this isotypic relationship, which can be taken as evidence for the similarity of the chemical properties of the two metals involved, we have also found that specific element combinations in alloys lead to an unexpected catalytic activity. In this context, we have recently reported the catalytic properties of $Mg_2Sn$[5] and $MgCo_6Ge_6$,[6] both of which show a remarkable activity and a high selectivity for the hydrogenation of *cis*/*trans* citral to geraniol and nerol. Since alloys of such compositions have not yet been considered as catalytically active materials, we extended our systematic study to other compounds in the ternary phase diagram Mg-Co-Ge and report here on the novel representative $MgCo_4Ge_6$.

[a] Department Chemie, Technische Universität München, Lichtenbergstr. 4, 85747 Garching, Germany
Fax: +49-89-289-13186
E-mail: thomas.faessler@lrz.tum.de
[b] Ernst-Berl-Institute/Chemical Technology II, Department of Chemistry, Technical University Darmstadt, Petersenstr. 20, 64287 Darmstadt, Germany

## Results and Discussion

### Crystal Structure

$MgCo_4Ge_6$ crystallizes in the $YRu_4Sn_6$ structure type and can be derived from the $Au_3Cu$ structure.[7,8] The relationship between the structure of $MgCo_4Ge_6$ and that of $Au_3Cu$ is emphasized in Figure 1. The $Au_3Cu$ structure derives from a cubic close packing of Au atoms by replacing every fourth Au by a Cu atom in each close packed layer, whilst maintaining the Au triangles. The cubic packing of those trigonal layers labeled as A, B, and C is shown in Figure 1 (a). Replacement of every second Mg atom in the hypothetical, corresponding $MgGe_3$ structure by a $C_{2v}$ distorted tetrahedral $Co_4$ unit in an ordered manner (Figure 1, b) leads to the title compound ($Mg_2Ge_6$ → $MgCo_4Ge_6$). In the $Au_3Cu$ structure, Cu is cube-octahedrally coordinated by 12 Au atoms, and in $MgCo_4Ge_6$ Mg is similarly coordinated by 12 Ge atoms, although in a strongly distorted cube-octahedral manner. Two opposite squares of the six present in a cube-octahedron are rhomboidally distorted, with the orientation of the two short diagonals perpendicular to each other. The lengths of the short diagonals are in the range of the other Ge–Ge contacts within the cube-octahedron. The rhomboidal distorted squares of the $Ge_{12}$ cube-octahedra are strongly bent, thereby retaining the convex nature of the polyhedron. The remaining four squares of the cube-octahedron are capped by Co atoms. The resulting 16-vertex polyhedron $Mg@Ge_{12}Co_4$ is shown in Figure 2 (a). These polyhedra form a tetragonal body-centered packing and are interconnected by common vertices and external Co–Co bonds (Figure 2, b).

 © 2006 Wiley-VCH Verlag GmbH & Co. KGaA, Weinheim 

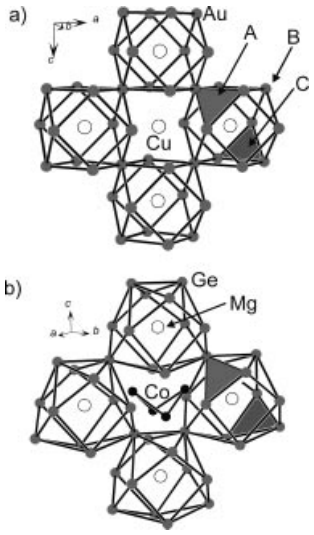


Figure 1. The relation between the $MgCo_4Ge_6$ and the $Au_3Cu$ structure. a) The $Au_3Cu$ structure; labels indicate atoms and the cubic stacking sequence of the layers A, B, and C; the $Au_3$ triangles of each layer are highlighted in grey. b) Related packing of $MgGe_{12}$ polyhedra in $MgCo_4Ge_6$, with inserted $Co_4$ units in black.

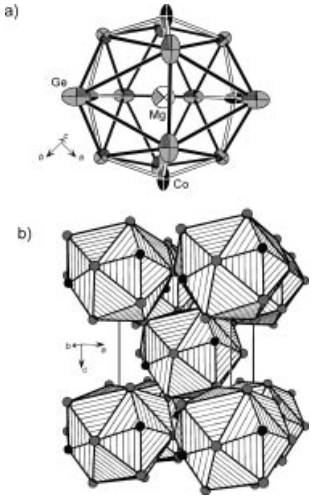


Figure 2. a) The $Ge_{12}Co_4$ coordination polyhedron around the Mg atom. All thermal ellipsoids are shown at 90% probability. b) Tetragonal body-centered packing of $Ge_{12}Co_4$ polyhedra (Co in black, Ge in grey).

An alternative description arises from the Ge sub-lattice, where the connection of the Ge atoms leads to layers of vertex-sharing $Ge_8$ units in the *ab* plane, with a close analogy between these units and the arrangement in the molecular compound $P_4S_4$ (Figure 3, a). The Ge substructure forms two-dimensional slabs in the *ab* plane that are stacked in the *c* direction, with each subsequent layer shifted by (1/2, 1/2, 1/2) to form the body-centered packing (Figure 3, b). The $P_4S_4$-like $Ge_8$ cages are "filled" with distorted tetrahedral $Co_4$ units (Figures 3, a and c), and the cavities formed by four vertex-sharing Ge atoms and four bridging Ge atoms host the Mg atoms. The coordination sphere of the Mg atoms is completed by two Ge–Ge contacts of − with respect to the Ge sub-lattice − three-connected Ge atoms of the previous and next Ge layers along the *c* direction (Figure 3, c). The Ge–Ge distances [2.906(1) and 2.987(1) Å] of the Ge sub-structure are longer than in typical covalently connected Ge atoms in Zintl phases, which are about 2.6 Å. Another interesting feature is the $Co_4$ unit that is present in the $P_4S_4$-type $Ge_8$ cages. These show two longer and four shorter Co–Co distances of 3.102(1) and 2.581(2) Å, respectively. The shorter distances

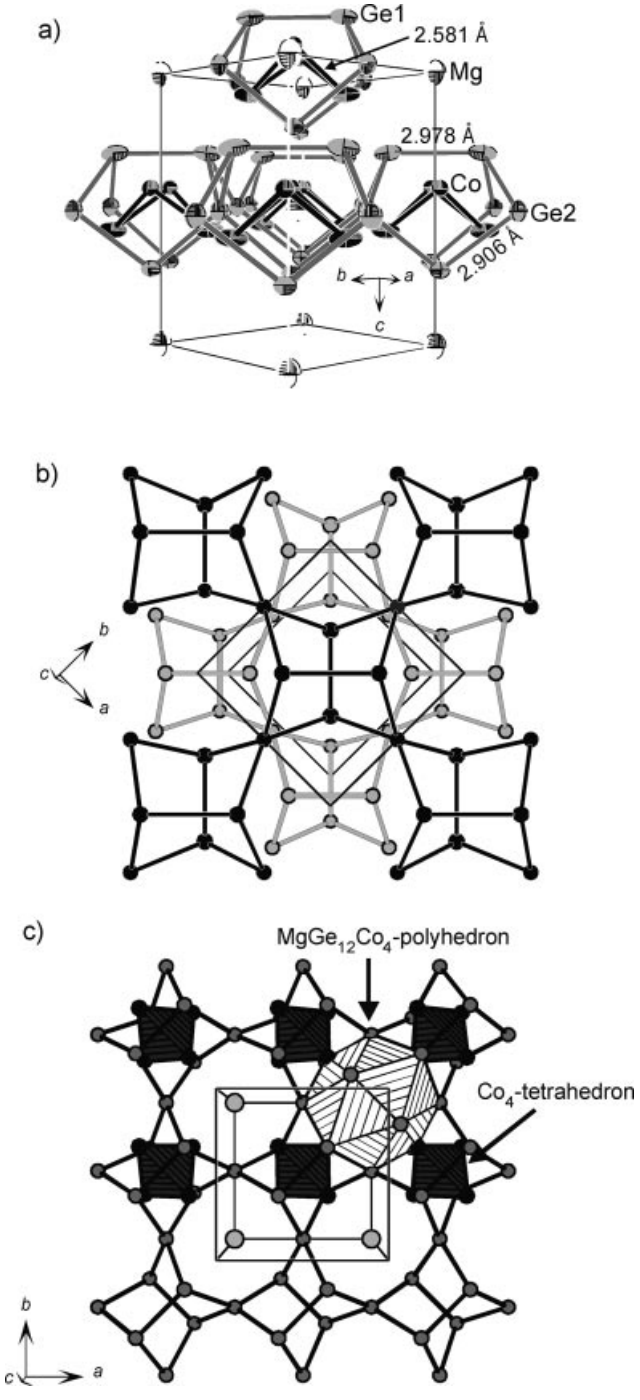


Figure 3. a) Crystal structure of $MgCo_4Ge_6$ as a combination of the Ge substructure centered by $Co_4$ units. All thermal ellipsoids are shown at 90% probability. b) [001] stacking of the germanium layers. c) Combination of the two views of a) and b).

 © 2006 Wiley-VCH Verlag GmbH & Co. KGaA, Weinheim 

are close to that observed in α-Co (2.506 Å).[9] Some binary cobalt germanides have even shorter Co–Co contacts, with the shortest being 2.377 Å in $Co_5Ge_7$.[10] Figure 3 (c) shows the combined picture of the packed polyhedra and the homoatomic Ge substructure: four 16-vertex polyhedra are interconnected in the *ab* plane by four fourfold-connected atoms of one $P_4S_4$-type $Ge_8$ entity. Further external interconnections between the polyhedra occur via the shorter Co–Co contacts of the $C_{2v}$ distorted $Co_4$ tetrahedra.

### Catalytic Properties

GC analysis revealed that citral undergoes no conversion in hydrogenation experiments under the reaction conditions described in the Experimental Section (reaction time: 150 min). Therefore, the experiments were repeated with a larger amount of $MgCo_4Ge_6$ (up to 500 mg) under $H_2$ pressure (7.5 MPa) for a longer reaction time (360 min) in a batch reactor (300 mL, Parr), but again, no conversion was observed. The absence of any catalytic activity is in contrast to the behavior of the intermetallic compound $MgCo_6Ge_6$, for which a citral conversion of 17% was observed at 453 K.[6]

### Quantum Chemical Calculations

The TB-LMTO band-structure calculations (Figure 4, a) reveal individual bands with a large dispersion crossing the Fermi level. The Fermi level is located at a local minimum of the density of states (DOS). Thus, $MgCo_4Ge_6$ is clearly a metal with delocalized states at the Fermi level. An analysis of the partial contributions to the DOS shows that the states at the Fermi level have predominantly Co orbital character (Figure 4, b). Ge orbital contributions are located well below the Fermi level, whereas there are virtually no Mg orbital contributions at all. This is consistent with the fact that Mg is the most electropositive element in the compound. The COHP curve in Figure 4 (c) indicates that bonding Ge–Co interactions are optimized up to $E_F$. Antibonding interactions occur only above $E_F$. The corresponding COHP curves of Ge–Ge contacts show that these interactions are much weaker. There is a noticeable flat COHP

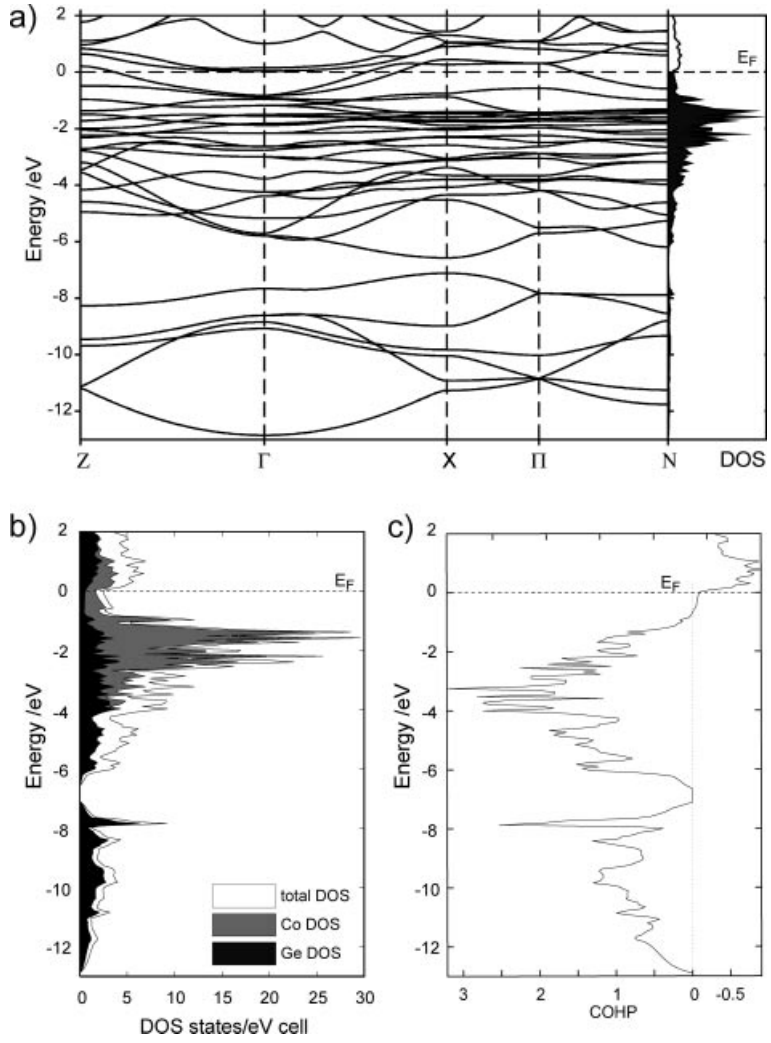


Figure 4. a) Band structure and DOS of $MgCo_4Ge_6$. b) Partial contributions of Co and Ge to the density of states.

 © 2006 Wiley-VCH Verlag GmbH & Co. KGaA, Weinheim 

region in Figure 4 (c) as well as in the Ge–Ge COHP diagram (not shown) right below $E_F$. Since there are considerable Ge and Co contributions in the DOS plot of Figure 4 (b) those states must belong to nonbonding states. In order to detect nonbonding domains, chemical bonding was further analyzed by means of the electron localization function (ELF).

Figure 5 shows several two-dimensional cross-sections of the function parallel to the *ab* plane. The color of each pixel corresponds to a certain value of ELF, as illustrated by the color bar at the bottom of Figure 5 (d). Contour lines illustrate ELF isobars and are superimposed onto the pictures. The left-hand column of Figure 5 represents the ELF calcu-

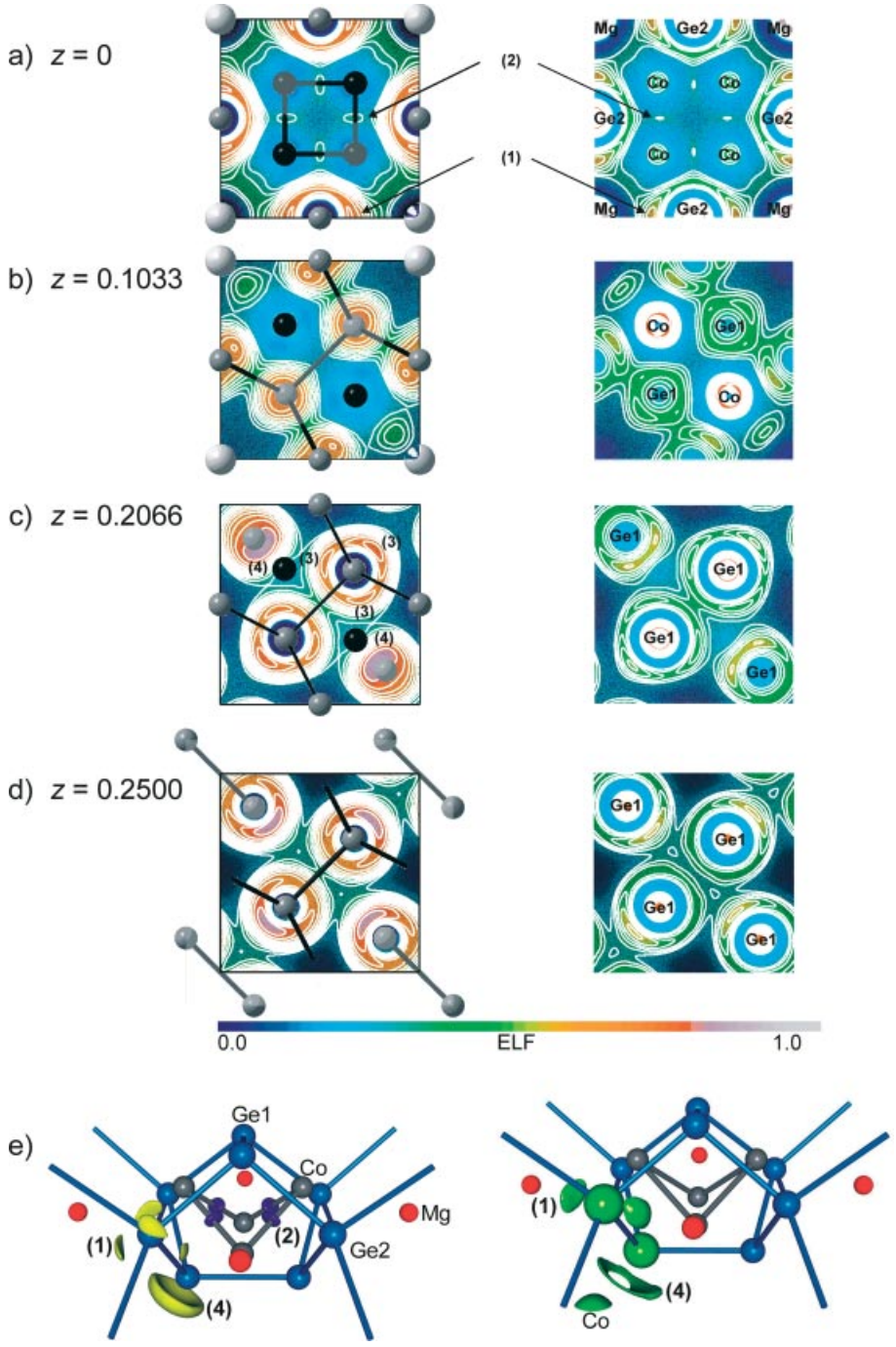


Figure 5. Two-dimensional cross-sections of the ELF in the *ab* plane at different values along the *c* direction. Isobars for $0.3 \leq \text{ELF} \leq 0.8$, with a step width of 0.05, are superimposed on the colored maps. Valence ELF is presented to the left, with all-electron ELF to the right. Structural motifs are superimposed on the valence ELF pictures. e) Left-hand side: 3D Isosurfaces of the ELF around selected atoms. Yellow: valence ELF (ELF = 0.759) at the two germanium sites. Violet: valence ELF (ELF = 0.3) between the cobalt atoms; right-hand side: as in Figure 5 (e), but all-electron ELF (ELF = 0.545 in green) around the germanium sites.

 © 2006 Wiley-VCH Verlag GmbH & Co. KGaA, Weinheim 

lated from a valence-electron treatment, while the right-hand column illustrates the ELF calculated from the electron density of all electrons, including core electrons. The atoms in the plane and their next neighbors are overlaid. At $z = 0$ the *ab* plane cuts though the Mg and Ge2 atoms and the four centers of the shorter Co–Co bonds of the $C_{2v}$ distorted tetrahedron (Figure 5, a). In both valence and all-electron ELF, maximum values of ELF are observed close to the Ge2 atoms pointing towards the neighboring Mg atoms. The regions (1) can be interpreted as lone-pair-type localization domains since the Ge2 and Mg atoms are ultimately separated by minimum values of ELF. Another small maximum (2) of the function with ELF = 0.3 is observed at the center of the Co–Co bonds, thus indicating a certain degree of covalency for these bonds. The second slice at $z = 0.1033$ (Figure 5, b) cuts through the center of the bonds between the three-connected Ge1 and four-connected Ge2 atoms. No maximum is observed here, and these contacts do not show any covalent contribution. The third cut (Figure 5, c), at $z = 0.2066$, cuts through the Ge1 positions. Three maxima are observed in a staggered position around each Ge1 atom with respect to the three Ge1–Ge2 contacts. Additionally, ELF maxima (4) that can be attributed to the Ge1 atoms of the adjacent layer become visible. In the valence-ELF picture these maxima point directly towards the Co atoms of adjacent layers, while, due to the repulsion between the core and the valence electrons, they appear to be separated into two smaller maxima in the case of the all-electron ELF. Finally, the cut at $z = 0.25$ (Figure 5, d) is located in the middle between two $P_4S_4$-type layers of $Ge_8$ cages, where no Ge–Ge bonds can be detected.

The situation in the vicinity of the $Ge_8$ cages is also outlined in Figure 5 (e), which shows the 3D isosurfaces of the valence ELF to the left and the all-electron ELF to the right. The yellow isosurfaces correspond to an ELF value of 0.76 of the valence ELF. There are five basins and these which must be interpreted as being of a lone-pair type since their ELF maxima are not located on an atom–atom connection vector. The larger one (4) is attached to the Ge1 atom and points away from the three Ge1–Ge2 contacts. Consistent with the 2D images (Figure 5, c) it points towards a Co atom of the adjacent Ge–Co layer. The four smaller, bean-shaped maxima are found around the four-bonded Ge2 atom; the positions of the four local maxima are due to the tetrahedrally oriented Ge2–Ge1 contacts. The valence-ELF isosurface with ELF = 0.3 is superimposed in violet color. The maxima are located at the centers of the shorter Co–Co contacts and confirm a certain degree of covalency, as already deduced from the 2D plots. The right-hand side of Figure 5 (e) shows the all-electron ELF isosurfaces of ELF = 0.545 around the two different germanium sites. The picture differs from that of the valence-ELF: the lone-pair attached to the Ge1 site is significantly flattened as compared to the one in the valence-ELF, and is turned into a crest due to the repulsion of the adjacent cobalt atom by the core electrons. The bean-shaped basins around the Ge2 atoms are contracted to two basins, which are oriented directly towards the adjacent Mg sites.

## Conclusions

Our search for other catalytically active alloys in the ternary phase system Mg–Co–Ge has led to the discovery of the novel compound $MgCo_4Ge_6$, which crystallizes in the $YRu_4Sn_6$ structure type first described by Venturini et al. The structure can be regarded as a coloring of the cubic-close packing observed in the $Au_3Cu$ structure. A closer investigation of the interatomic distances reveals peculiar and unprecedented homoatomic substructures for each of the Ge and Co atoms (Table 1). With respect to the dimensionality of the Ge sub-lattice, the structure is similar to $MgCo_6Ge_6$, which contains a graphite-type Ge sub-lattice with Ge–Ge contacts of about 2.9 Å. Quantum chemical investigations on the DFT level as well as the ELF interpretation of both compounds show that the Ge–Ge contacts of the Ge sub-lattices do not indicate any covalent bond contributions. However, in $MgCo_6Ge_6$ additional $Ge_2$ dimers with considerably localized bond character in the range of a Ge–Ge single bond were observed. In $MgCo_4Ge_6$ a combination of chemical bond types is found, with the main bonding contributions originating from Co–Ge interactions. ELF analysis reveals lone-pairs at the three-connected Ge atoms of the Ge subnet. These lone-pairs are oriented toward the Co atoms and thus a dative bonding between Ge and Co atoms can be formulated. Further small covalent contributions are found between the transition metal atoms.

Table 1. Interatomic distances [Å] for $MgCo_4Ge_6$.

| | | | |
|---|---|---|---|
| Ge(1)–Ge(2) | 2.906(1) (2×) | Mg(1)–Co(1) | 2.894(2) (4×) |
| Ge(1)–Ge(1) | 2.978(1) | Co(1)–Ge(1) | 2.285(2) |
| Co(1)–Co(1) | 2.581(2) (2×) | Co(1)–Ge(2) | 2.371(1) (2×) |
| Co(1)–Co(1) | 3.102(1) | Co(1)–Ge(1) | 2.419(2) (2×) |
| Mg(1)–Ge(1) | 2.945(1) (4×) | Co(1)–Ge(1) | 2.469(2) |
| Mg(1)–Ge(2) | 3.086(1) (4×) | | |

Despite some similarities with respect to chemical bonding properties, such as two-dimensional Ge networks and composition, all attempts to catalyze citral hydrogenation with $MgCo_4Ge_6$ failed, which is in contrast to the catalytic behavior of the intermetallic compound $MgCo_6Ge_6$.[6] This difference indicates that catalytic properties might also depend on the structure type and thus on the electronic properties and not only on the nature of the metals involved.

## Experimental Section

**Synthesis:** $MgCo_4Ge_6$ was synthesized by heating a stoichiometric mixture of the elements in a tantalum crucible to 750 °C for two days, followed by slow cooling of the reaction product to room temperature. The product consisted of xenomorphous crystals with a metallic luster, which were embedded in a microcrystalline silver-metallic matrix. The purity of the sample was established crystallographically, using a STOE STADI P powder diffractometer with a Cu-$K_\alpha$ source. The powder diffractogram, which could be indexed[11] with the help of the theoretical powder pattern calculated for $MgCo_4Ge_6$, showed only slight impurities of elementary Ge.

 © 2006 Wiley-VCH Verlag GmbH & Co. KGaA, Weinheim 

**Crystal Structure Determination:** The crystal structure was determined from single-crystal X-ray diffraction data. A single crystal was selected from the reaction mixture and placed into an oil-filled glass capillary. The measurement was performed on a Nonius DIP 2020 diffractometer equipped with a monochromatic Mo-$K_\alpha$ source ($\lambda$ = 0.71073 Å). Data were collected by a scan of 2° in $\varphi$ in 180 frames. The exposure time was 300 seconds per frame. The collection of the intensity data was carried out with the HKL2000 program.[12] Cell parameters were initially calculated from reflections taken from five frames of reflections. The final lattice parameters were calculated from all reflections observed in the actual data collection. The data from the data collection were processed with the Scalepack[12] program and corrected for absorption using the PLATON[13] program suite. A summary of the experimental and crystallographic data is given in Table 2.

Table 2. Crystallographic data for $MgCo_4Ge_6$.

| | |
|---|---|
| Empirical formula | $MgCo_4Ge_6$ |
| Formula weight | 695.57 |
| Temperature | 293(2) K |
| Wavelength | 0.71073 Å |
| Crystal system | tetragonal |
| Space group | $I\bar{4}_2m$ |
| Unit cell dimensions | $a$ = 6.1725(9) Å |
| | $c$ = 8.660(2) Å |
| Volume | 329.94(9) Å$^3$ |
| $Z$ | 2 |
| Density (calculated) | 7.001 g cm$^{-3}$ |
| Absorption coefficient | 36.664 mm$^{-1}$ |
| $F_{000}$ | 624 |
| Crystal size | 0.1 × 0.1 × 0.15 mm |
| Theta range for data collection | 4.05 to 27.54° |
| Index ranges | $-5 \le h \le 5$, $0 \le k \le 8$, $0 \le l \le 11$ |
| Reflections collected | 2645 |
| Independent reflections | 212 |
| Completeness to $\theta$ = 27.54° | 100.0% |
| Absorption correction | PLATON[13] |
| Refinement method | full-matrix least-squares on $F^2$ |
| Data/restraints/parameters | 212/0/19 |
| Goodness-of-fit on $F^2$ | 1.367 |
| Final $R$ indices [$I > 2\sigma(I)$] | $R_1$ = 0.027, $wR_2$ = 0.077 |
| $R$ indices (all data) | $R_1$ = 0.027, $wR_2$ = 0.077 |
| Largest diff. peak and hole | 1.530 and –0.977 e Å$^{-3}$ |

The structure was solved by direct methods, which revealed the atomic positions and was refined with the SHELXL-97 program.[14] The final coordinates and equivalent isotropic temperature factors of all atoms are given in Table 3.

Table 3. Atomic coordinates (×10$^4$) and equivalent isotropic displacement parameters [Å$^2$ × 10$^3$] for $MgCo_4Ge_6$. $U_{(eq)}$ is defined as one third of the trace of the orthogonalized $U_{ij}$ tensor.

| Atom | Wyck. | $x$ | $y$ | $z$ | $U_{(eq)}$ |
|---|---|---|---|---|---|
| Mg | 2a | 0 | 0 | 0 | 20(1) |
| Co | 8i | 8223(2) | 8223(2) | 4215(2) | 17(1) |
| Ge1 | 8i | 8294(1) | 8294(1) | 7066(1) | 18(1) |
| Ge2 | 4c | 0 | 5000 | 0 | 13(1) |

Further details of the crystal structure investigation may be obtained from the Fachinformationzentrum Karlsruhe, 76344 Eggenstein-Leopoldshafen, Germany (Fax: +49-7247-808-666; E-mail: crysdata@fiz-karlsruhe.de) on quoting the depository number CSD-416401.

**Hydrogenation Reaction:** The hydrogenation of citral (3,7-dimethyl-2,6-octadienal), which has three unsaturated bonds including conjugated C=C and C=O groups as well as an isolated C=C bond, was chosen as a test reaction. Hydrogenation was carried out in a high-pressure batch reactor system described earlier.[15] The reactor was filled with a solution of 1 mL of citral in 9 mL of hexane. After the addition of 100 mg of $MgCo_4Ge_6$ (particle size < 63 mm), the reaction mixture was stirred at 850 rpm, the reactor was flushed four times with argon (2 MPa), and heated up to 453 K within 45 min (0.8 MPa argon pressure was left in the reactor). The reaction was started by setting the hydrogen pressure to 7 or 9 MPa, respectively. Analysis of the reaction mixture by GC (HP 5890, flame ionization detector, DB-WAX capillary column) showed no conversion products.

**Quantum Chemical Calculations:** The electronic structure was investigated by means of the ab initio full-potential linear muffin-tin orbital (LMTO) method in the atomic sphere approximation (ASA), using the tight-binding (TB) program (TB-LMTO-ASA).[16] The calculations were based on the local-density approximation (LDA), and the Hedin–Lundquist parameterization was employed for exchange and correlation potentials.[17] The radii of the muffin-tin spheres and empty spheres were determined according to Jepsen and Andersen.[18] For the calculations, s, p, and "down-folded" d-partial waves for Ge, s, p, and "down-folded" d-partial waves for Mg, and s, p, and d-partial waves for Co were used. COHP (crystal orbital Hamilton populations) plots[24] show DOS curves, which were weighted by the contributions of each crystal orbital to some measure of the strength of a given bond. The contribution of the covalent part of a particular interaction to the total bonding energy of the crystal can be obtained from COHP analyses. All COHP curves presented here are in the following format: positive and negative values are bonding and antibonding, respectively.

For further insight into the chemical bonding in intermetallic compounds a topographical analysis of the electron density distribution using the Electron Localization Function (ELF), which was originally introduced for the deduction of the shell structure of atoms from the electron density, was performed.[19] ELF values were scaled between 0 and 1, with high ELF values and local ELF maxima corresponding to areas and centers of localized electrons, and low ELF values defining the spatial area around these maxima. The resulting partition of space into areas of high electron localization can be interpreted in terms of bonding and nonbonding electron pairs and reveals their three-dimensional shape. Thus, spatial domains of localized electrons become visible.[20–23] These calculations were carried out both with valence electrons only and with all electrons.

## Acknowledgments

This work was supported by the Deutsche Forschungsgemeinschaft (project number FA 198/4-1 and CL 168/3-1: "Polare Legierungen als Mehrkomponenten-Katalysatoren"). The authors would like to thank Dr. Annette Schier for her help with the correction of the manuscript.

[1] $Tb_2CoGe_2$: O. I. Bodak, V. K. Pecharskii, P. K. Starodub, P. S. Salamakha, O. Ya. Mruz, V. A. Bruskov, *Izv. Akad. Nauk SSSR, Met.* **1986**, *4*, 214–216.
[2] $Tb_2RuGe_2$: P. Boulet, F. Weitzer, K. Hiebl, H. Noel, *Physik* **2000**, *292*, 302–319.
[3] $Sc_3Co_2Si_3$: E. I. Gladyshevskii, B. Ya. Kotur, *Kristallografiya* **1978**, *23*, 946–950.

 © 2006 Wiley-VCH Verlag GmbH & Co. KGaA, Weinheim 

[4] $Ho_3Ru_2Ge_3$: O. L. Sologub, Yu. M. Prots, P. S. Salamakha, O. I. Bodak, *J. Alloys Compd.* **1994**, *209*, 107–109.
[5] P. Claus, F. Raif, S. Cavet, S. Cemirel-Gülen, M. Schreyer, T. F. Fässler, *Catal. Commun.* **2006**, *7*, 618.
[6] C. Gieck, M. Schreyer, T. F. Fässler, S. Cavet, P. Claus, *Chem. Eur. J.* **2006**, *12*, 1924–1930.
[7] R. Pöttgen, R.-D. Hoffmann, E. V. Sampathkumaran, I. Das, B. D. Mosel, R. Müllmann, *J. Solid State Chem.* **1997**, *134*, 326–331.
[8] G. Venturini, B. Chafik El Idrissi, J. F. Marêché, B. Malaman, *Mater. Res. Bull.* **1999**, *25*, 1541.
[9] A. Taylor, R. W. Floyd, *Acta Crystallogr.* **1950**, *3*, 285–289.
[10] E. Stolz, K. Schubert, *Chem. Erde* **1962**, *22*, 709–711.
[11] W. Kraus, G. Nolze, *J. Appl. Crystallogr.* **1996**, *29*, 301–303.
[12] Z. Otwinowski, W. Minor, "Processing of X-ray Diffraction Data Collected, in Oscillation Mode", *Methods in Enzymology*, vol. 276: Macromolecular Crystallography, part A (Eds.: C. W. Carter Jr., R. M. Sweet), Academic Press, New York, p. 307–326, **1997**.
[13] A. L. Spek, *J. Appl. Crystallogr.* **2003**, *36*, 7–13.
[14] G. Sheldrick, SHELXS-97, *Program for the Solution of Crystal Structures*, University of Göttingen, **1997**; G. M. Sheldrick, SHELXL-97, *Program for the Refinement of Crystal Structures*, University of Göttingen, **1997**.
[15] M. Lucas, P. Claus, *Chem. Ing. Tech.* **2001**, *73*, 252–257.
[16] M. van Schilfgarde, T. A. Paxton, O. Jepsen, O. K. Andersen, G. Krier, *Programm TB-LMTO*, Max-Planck-Institut für Festkörperforschung, Stuttgart, **1994**.
[17] U. Barth, L. Hedin, *J. Phys. Chem.* **1972**, *5*, 1629–1972.
[18] O. Jepsen, O. K. Andersen, *Z. Phys. B* **1995**, *97*, 35–37.
[19] A. D. Becke, E. J. Edgecombe, *Chem. Phys.* **1990**, *92*, 5397–5403.
[20] A. Savin, A. D. Becke, J. Flad, R. Nesper, H. G. von Schnering, *Angew. Chem.* **1991**, *103*, 421–424; *Angew. Chem. Int. Ed. Engl.* **1991**, *30*, 409–412.
[21] B. Silvi, A. Savin, *Nature* **1994**, *371*, 683–686.
[22] A. Savin, R. Nesper, S. Wengert, T. F. Fässler, *Angew. Chem.* **1997**, *109*, 1892–1915; *Angew. Chem. Int. Ed. Engl.* **1997**, *36*, 1809–1832.
[23] R. F. W. Bader, *Coord. Chem. Rev.* **2000**, *197*, 71–94.
[24] R. Dronskowski, P. E. Blöchl, *J. Phys. Chem.* **1993**, *97*, 8617.

Received: April 4, 2006
Published Online: July 27, 2006

 © 2006 Wiley-VCH Verlag GmbH & Co. KGaA, Weinheim 

DOI: 10.1002/ejic.200600300

# Synthesis and NLO Properties of 4-(4*H*-Chalcogenopyran-4-ylidene and 4*H*-chalcogenochromen-4-ylidene)-1-(phenylthio)but-2-enylidene Complexes – Electronic Influence of the Carbene Fragment

**Nadège Faux,[a] Françoise Robin-Le Guen,[b] Pascal Le Poul,[b] Bertrand Caro,*[b] Keitaro Nakatani,[c] Eléna Ishow,[c] and Stéphane Golhen[d]**

**Keywords:** Chalcogeno- and benzochalcogenopyran / Fischer-type thiocarbene complexes / NLO properties / X-ray structure of thiocarbene

The synthesis of 4-(4*H*-chalcogenopyran-4-ylidene and 4*H*-chalcogenochromen-4-ylidene)-1-(phenylthio)but-2-enylidene complexes is described and their non-linear optical (NLO) properties have been investigated (as $\mu\beta$ by EFISH). NMR studies and X-ray crystallographic analyses show that the (phenylthio)carbene fragment has a better electron-withdrawing capability than the methoxy analogues and, likewise, the corresponding thiocarbenes have a more significant pyrylium character. The $\mu\beta$ values of these complexes were obtained from EFISH experiments. The microscopic NLO response is sensitive to the nature of the intracyclic chalcogen atom, the nature of the metal centre and the benzo-annulation of the heterocycle.

(© Wiley-VCH Verlag GmbH & Co. KGaA, 69451 Weinheim, Germany, 2006)

## Introduction

Due to the strong electron-withdrawing effect of the (carbene)pentacarbonylmetal fragment, alkenyl Fischer carbene complexes have been exploited extensively for synthetic purposes. The utility of these unsaturated organometallic reagents in the Dötz reaction[1] in 1,2-, 1,4- and 1,6-addition reactions[2] or in the synthesis of heterocyclic compounds by means of various cycloaddition processes[3] is well documented. In the field of organometallic complex utilisation for NLO applications,[4] this electronic ability has made the pentacarbonyl(methoxy- or aminocarbene)metal fragments attractive candidates as acceptors in push-pull structures.[5] Association by means of a π-spacer to classic organic or organometallic donors such as *para*-(dimethylamino)benzyl[6] or ferrocenyl[7] groups has proved the efficiency of this method. High values of the first molecular hyperpolarisability $\beta$ have been determined by Hyper Raleigh Scattering (HRS). The influences of the metal (W or Cr),[5] the unsaturated chain length[6,7] and the solvent[7] on the $\beta$ values have been investigated. The results have been analysed in the context of the two-level model developed by Oudar and Chemla[8] which is based on the predominance of a single electronic transition despite the presence of more than one electronic transition in the visible region.[7]

In fact, the role of the organometallic carbene fragment is not well understood. For aminocarbene complexes, polarisation of the π-cloud by the electronic inductive effect of the $M(CO)_5$ moiety is responsible for the important NLO response.[6] The influence of an MLCT transition is minimised due to the lack of conjugation between the unsaturated chain and the carbene fragment.[9] On the other hand, noticeable $\beta$ values were also obtained for highly π-conjugated unsaturated methoxycarbene complexes.[5] It is worth noting that despite significant electronic differences between these two classes of carbenes, a systematic comparison between them has never been carried out. In addition, surprisingly, there are no reports on the NLO properties of unsaturated (alkylthio)- or (phenylthio)carbene complexes.

In fact, unlike their alkoxy or amino counterparts, (alkenyl)(thio)carbene complexes are rare compounds.[10] Their properties and reactivity require further elucidation.[11] Only some unsaturated (alkylthio)- and (phenylthio)carbenes have been reported by Aumann et al. using a condensation reaction between non-enolizable aldehydes (benzaldehyde, cinnamaldehyde) and the carbanion of $CH_3(SR)$-

[a] Laboratoire de Chimie Bio-Organique, UMR CNRS 7015 – Université de Haute Alsace, Ecole Nationale Supérieure de Chimie de Mulhouse,
3 rue Alfred Werner, 68093 Mulhouse cedex, France
[b] U.M.R. 6226 Sciences Chimiques de Rennes, CNRS – I.U.T. Lannion,
Rue E. Branly, 22300 Lannion, France
Fax: +33-2-96485797
E-mail: bertrand.caro@univ-rennes1.fr
[c] Laboratoire de Photophysique et de Photochimie Supramoléculaires et Macromoléculaires, UMR CNRS 8531, Ecole Normale Supérieure de Cachan,
61 avenue du président Wilson, 94235 Cachan Cedex, France
[d] Laboratoire de Chimie du Solide et Inorganique Moléculaire, UMR 6226,
Campus de Beaulieu, 35042 Rennes Cedex, France

Supporting information for this article is available on the WWW under http://www.eurjic.org or from the author.

 © 2006 Wiley-VCH Verlag GmbH & Co. KGaA, Weinheim 

C=M(CO)$_5$ (M = Cr, W).[10] The low p$K_a$ values which characterise these complexes[12] [p$K_a$ = 8.37 for $CH_3$-($SCH_3$)C=W(CO)$_5$ compared with 12.36 for $CH_3$($OCH_3$)-C =W(CO)$_5$] enabled deprotonation by $NEt_3$. On the other hand, we have previously shown that 4*H*-pyran-4-ylidene fragments act as efficient electron-donors in push-pull methoxy Fischer-type carbene complexes.

The pyrylium character of these molecules was evaluated by using NMR spectroscopy, X-ray crystallographic measurements, DFT calculations and from their reactivity towards nucleophilic reagents.[2b,13] More recently, we have reported the NLO properties (as $\mu\beta$ by EFISH) of (4*H*-chalcogenopyran-4-ylidene and 4*H*-chalcogenochromen-4-ylidene)-1-methoxyalkenylidene complexes.[14] The $\mu\beta$ product is sensitive to the length of the unsaturated spacer, the nature of the chalcogen atom and to benzo-annulation of the heterocycle. Herein, we wish to report the formation and, for the first time, the first hyperpolarisability measurements of (phenylthio)carbene complexes. In addition, from NMR spectroscopic studies and X-ray structure analyses, we have shown that the carbonyl[(phenylthio)carbene]metal fragment acts as a powerful electron-withdrawing group. Comparison with analogous methoxycarbenes has been carried out.

## Results and Discussion

### Synthesis

To obtain the expected donor-acceptor structures, we first chose to repeat Aumann's procedure[10] using the appropriate heterocyclic aldehydes **1a**–**1e**[15] and the carbanion produced from $CH_3$(PhS)C=W(CO)$_5$ by treatment with $NEt_3$, but this was unsuccessful. Addition of chlorotrimethylsilane (TMSCl) to the reaction mixture induced an instant colour change from red-orange to blue. After hydrolysis and purification by silica-gel chromatography, the intense dark blue condensation products **2a**–**2e** could be isolated. The moderate to low yields reported (Scheme 1) are the consequence of a decomplexation reaction which arises during the workup leading to the corresponding thioester.[16] The lack of reactivity without the assistance of TMSCl could be due to the high zwitterionic character of the heterocyclic aldehydes which prevents the carbanion addition on the carbon atom of the carbonyl function (Scheme 1).

We suggest that addition of the chlorosilane reagent produces alkenylpyrylium salts and favours the conjugated addition of the carbanion as the first step in this reaction. Such a zwitterionic form is insignificant in benzaldehyde and cinnamaldehyde and the condensation reaction does not require the use of TMSCl.[10,17]

The new heterocyclic carbene complexes **2a**–**2e** were characterised by $^1$H and $^{13}$C NMR spectroscopy, UV/Vis spectroscopy, FTIR spectroscopy, elemental analysis and high resolution mass spectrometry (for **2a**). All the data are consistent with the proposed structures. In particular, the $^3J_{H,H}$ coupling constant values (ca. 13 Hz) are in agreement with an (*E*) configuration for the C2–C3 double bond of the unsaturated chain (Scheme 1).

### NMR Studies – Evaluation of the Pyrylium Character of the Heterocyclic Complexes 2 in Solution

To obtain information about the pyrylium character of complexes **2** in solution, three NMR spectroscopic criteria were taken into account: (i) the chemical shift values of the 2-H and 3-H signals, (ii) the differences in $^3J_{H,H}$ values ($\Delta J$) across adjacent C=C and C–C bonds of the unsaturated chain and (iii) the $^{13}$C NMR chemical shift of the carbene carbon signal. First, with regards to the $^1$H NMR spectra of all compounds **2**, the chemical shift values of 2-H and 3-H display an oscillatory behaviour [$\delta$(3-H) > $\delta$(2-H) > $\delta$(4-H)] (Scheme 1). In particular the respective 3-H, 2-H signal position, which leads to positive $\Delta$ values [$\delta$(3-H) – $\delta$(2-H)]

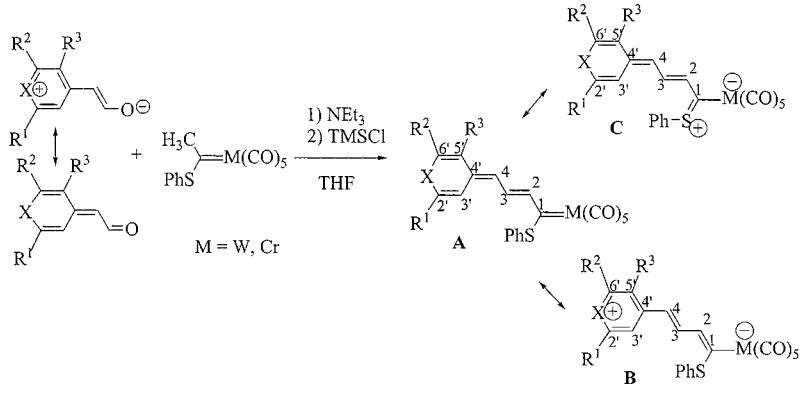


**1a** $R^1$ = Ph, $R^2$ = Ph, $R^3$ = H, X = O
**1b** $R^1$ = Ph, $R^2$ = Ph, $R^3$ = H, X = S
**1c** $R^1$ = Ph, $R^2$ = $R^3$ = –CH=CH–CH=CH–, X = O
**1d** $R^1$ = *t*Bu, $R^2$ = $R^3$ = –CH=CH–CH=CH–, X = O
**1e** $R^1$ = Ph, $R^2$ = $R^3$ = –CH=CH–CH=CH–, X = S

**2a** (40%) $R^1$ = Ph, $R^2$ = Ph, $R^3$ = H, X = O, M = W
**2b** (60%) $R^1$ = Ph, $R^2$ = Ph, $R^3$ = H, X = S, M = W
**2c** (17%) $R^1$ = Ph, $R^2$ = $R^3$ = –CH=CH–CH=CH–, X = O, M = W
**2'c** (20%) $R^1$ = Ph, $R^2$ = $R^3$ = –CH=CH–CH=CH–, X = O, M = Cr
**2d** (37%) $R^1$ = *t*Bu, $R^2$ = $R^3$ = –CH=CH–CH=CH–, X = O, M = W
**2e** (34%) $R^1$ = Ph, $R^2$ = $R^3$ = –CH=CH–CH=CH–, X = S, M = W

Scheme 1. Preparation of push-pull (phenylthio)carbene complexes **2**.

 © 2006 Wiley-VCH Verlag GmbH & Co. KGaA, Weinheim 

Table 1. NMR spectroscopic data for complexes **2**–**3**.[a]

| | **2a**[b] | **2b**[b] | **2c**[b] | **2d**[b] | **2e**[b] | **2′c**[b][14] | **3a**[c][14] | **3b**[c][14] | **3c**[c]14] | **3d**[c][15c] | **3e**[c][14] |
|---|---|---|---|---|---|---|---|---|---|---|---|
| $\Delta$ [$\delta$(3-H) – $\delta$(2-H)] [ppm] | 1.44 | 1.44 | 1.33 | 1.29 | 1.28 | 1.12 | 0.94 | 0.79 | 0.59 | 0.79 | 0.45 |
| $\Delta J$[d] [Hz] | –0.6 | –0.6 | 0.2 | 0.1 | 0.2 | 0.6 | 0.4 | 0.7 | 1.8 | 1.5 | 0.6 |
| $\delta^{13}$C [ppm] | 261.6 | 263.5 | 273.1 | 272.1 | 274.3 | 301.7 | 289.0 | 292.9 | 296.5 | 295.8 | 297.9 |

[a] NMR spectra were recorded in [$D_8$]THF solution. [b] Scheme 1. [c] Figure 1. [d] $\Delta J$ values: difference in $^3J_{H,H}$ values across adjacent C(2)=C(3) and C(3)–C(4) bonds for compounds **2**–**3**.

(Table 1), suggests a highly conjugated push-pull structure for which the zwitterionic resonance form **B** is of importance in the valence bond description of the heterocyclic molecules (Scheme 1). As shown in Table 1, a similar trend has been observed for the methoxycarbene **3**,[14,18] analogously to **2** (Figure 1).

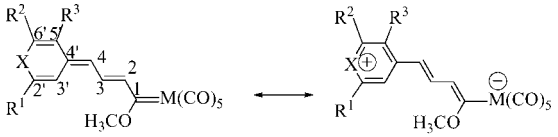


**3a** $R^1$ = Ph, $R^2$ = Ph, $R^3$ = H, X = O, M = W
**3b** $R^1$ = Ph, $R^2$ = Ph, $R^3$ = H, X = S, M = W
**3c** $R^1$ = Ph, $R^2$ = $R^3$= –CH=CH–CH=CH–, X = O, M = W
**3d** $R^1$ = *t*Bu, $R^2$ = $R^3$= –CH=CH–CH=CH–, X = O, M = Cr
**3e** $R^1$ = Ph, $R^2$ = $R^3$= –CH=CH–CH=CH–, X = S, M = W

Figure 1. Molecular structure of methoxycarbene complexes **3**.

As noted previously,[13a] this result differs from that found for other push-pull methoxy- and aminocarbene containing ferrocenyl,[7] *para*-(dimethylamino)phenyl[19] or 3,4-(methylenedioxy)phenyl groups[6] for which 2-H is more deshielded than 3-H (Table 2, Figure 2). For aminocarbenes, the predominance in solution of a conformation in which the (carbene)carbonylmetal fragment is perpendicular to the unsaturated part of the molecule would be responsible for this feature.[6,9] Owing to the low π-overlap, the inductive effect of the (carbene)carbonylmetal fragment controls the $^1$H NMR chemical shift values of the unsaturated chain and $\delta$(2-H) > $\delta$(3-H).

Table 2. $^1$H NMR spectroscopic data for push-pull alkenylidene complexes (Figure 2).

| R | Y | M | $\Delta$ [$\delta$(3-H) – $\delta$(2-H)] [ppm] | $\Delta J_{av.}$ [Hz][a] | Solvent |
|---|---|---|---|---|---|
| Fc[7] | OMe | W | –0.22[b] | 3.8[b] | $CDCl_3$ |
| *p*-$N(CH_3)_2C_6H_4$[19] | OMe | W | –0.11[b] | 3.9[b] | $CD_2Cl_2$ |
| 3,4-$CH_2O_2C_6H_4$[6] | $N(CH_2)_4$ | Cr | –0.10[b] | – | $CDCl_3$ |

[a] $\Delta J_{av.}$ values: average difference in $^3J_{H,H}$ values across adjacent C=C and C–C bonds. [b] Evaluated from NMR values found in refs.[6,7,19]

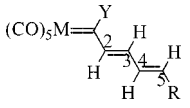


Figure 2. Structure of alkenyl Fischer-type carbene complexes.

It can be noted that the $\Delta$ values [$\delta$(3-H) – $\delta$(2-H)] of the (phenylthio)carbenes **2** are larger than those of methoxycarbenes **3**, indicating that the contribution of the pyrylium resonance structure in **3** is of lesser importance than in **2**. However, the $^1$H NMR chemical shift differences should reflect other factors such as the anisotropic effect of the phenyl group linked to the sulfur atom. Therefore, a comparison between the electronic influence of the methoxy- and the (phenylthio)carbene group requires other criteria.

Previously, it has been emphasised that the variation of $^3J_{H,H}$ values along a conjugated polyene chain provides a good estimate of the C–C bond lengths (or bond orders).[20] In push-pull molecules containing a similar donor (acceptor), the so-called bond length alternation (BLA) depends on the strength of the acceptor (donor). As a consequence, the difference $\Delta J$ between the coupling constant $^3J_{H,H}$ of concomitant C–C bonds ranges from 6.5 Hz for unconjugated molecules to 0 Hz for molecules in which all the C–C bond lengths are equal (cyanine limit). As shown in Table 1, calculated $\Delta J$ values for carbenes **2** and **3** are slightly negative or positive, in accordance with a reduced bond length alternation and, therefore, indicating a large degree of intramolecular charge transfer. Two features are noteworthy:

(1) The phenylthio complexes display lower $\Delta J$ values than those of their methoxy counterparts, in agreement with the better electron-withdrawing ability of the thiocarbene group as found above from the $\Delta$ [$\delta$(3-H) – $\delta$(2-H)] criterion. The negative values found for **2a** and **2b** strongly suggest that these molecules approach or even surpass the cyanine limit (predominance of resonance structure **B**) (Scheme 1). As proposed by Ali and Bernasconi from p$K_a$ values and kinetic constant determinations for both classes of complexes, the electronic difference can be mainly attributed to the smaller π-donor effect of the SR group compared with that of the methoxy group.[12] As a consequence, in complexes of type **2**, the conjugation between the ends of the molecule through the unsaturated chain is increased. However, concerning the π-effect strength of the SR group in Fischer-type carbene complexes, it should be noted that opposite conclusions were drawn from X-ray crystallographic data[21] and dynamic NMR studies (Figure 3).[22] In this context, the $^{13}$C NMR chemical shift values of the carbene carbon atom are of interest. In Fischer-type carbenes, the large upfield shift of the carbene carbon signal, when the heteroatom substituent is changed from an alkoxy to an amino group, has been attributed to the greater ability of the nitrogen atom to participate in dative π-bonding with the carbene carbon atom.[23] As shown in Table 3, such a

 © 2006 Wiley-VCH Verlag GmbH & Co. KGaA, Weinheim 

difference exists in (4*H*-pyran-4-ylidene)alkenylidene complexes (comparison between the carbene carbon chemical shifts of complexes **4** and **3a**). Accordingly, the intramolecular charge transfer in donor-acceptor unsaturated amino complexes[13] is limited due to the predominance of a resonance form involving the lone pair of the nitrogen atom of the amino group and the p-orbital of the carbene carbon atom. The chemical shift difference $\Delta$ [$\delta$(3-H) – $\delta$(2-H)] and the $\Delta J$ value found for the unsaturated aminocarbene complex **4** also support this electronic description. Since the PhS group in complex **2** seems to possess a lesser π-electron-donating capability compared with that of a methoxy group, the upfield shift observed for the carbene carbon signal of **2a** (Table 3) seems, at first glance, to be surprising. This finding, which is in sharp contrast to the usually observed chemical shift [$\delta(C_{carb,thio}) > \delta(C_{carb,methoxy})$],[24] should again reflect the donor-acceptor intramolecular charge transfer enhancement for the thiocarbene complexes. It is actually well established that along a series, the $^{13}C$ NMR carbene carbon chemical shift is sensitive to the electronic influence of the ligand.[13b]

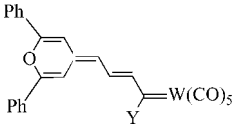


Figure 3. Structure of (4*H*-pyran-4-ylidene)alkenylidene complexes.

Table 3. NMR spectroscopic data for selected push-pull (4*H*-pyran-4-ylidene)alkenylidene complexes (Figure 3).

| | Y | $\Delta$ [$\delta$(3-H) – $\delta$(2-H)] [ppm] | $\Delta J$ [Hz] | $^{\delta 13}C$ [ppm] |
|---|---|---|---|---|
| **3a** | OMe | 0.94 | 0.4 | 289 |
| **4**[13a] | $N(CH_2)_4$ | –0.03 | 3.8 | 244 |
| **2a** | SPh | 1.44 | –0.6 | 261 |

(2) For the same organometallic phenylthio or methoxy fragment, $\Delta J$ values appear to increase from the pyran to the benzopyran series (methoxy and thiocarbene) (Table 1). This trend, which does, however, have an exception (see NMR values of **3e**), suggests a decrease in the electron-donor strength upon benzo-annulation (Table 1). Accordingly, the pyrylium characters of molecules **2a**, **2b**, **3a** and **3b** are greater than those of **2c**, **2d**, **3c** and **3d**, respectively. This view is corroborated by the low-field chemical shift values of the carbene carbon signals observed (even for **3e**) for the fused ring compounds. It should be noted that the chemical shift difference $\delta(C_{carb,benzopyran}) - \delta(C_{carb,pyran})$ is more pronounced for the (phenylthio)carbene indicating the great sensitivity of these complexes to π-electronic effects.

Very recently, effects of successive benzo-fusions for pyridinium acceptors in push-pull zwitterionic chromophores have been reported.[25] In such cases, and in agreement with the present results, it has been found that the annulation favours the neutral form thanks to the aromatic character of the fused benzene ring.

Finally, it is worth noting that the $\Delta J$ values reported here and those found for analogous derivatives of **3** increasing length[14,15] are much smaller than those calculated from previous studies for unsaturated methoxy complexes containing ferrocenyl[7] or *para*-(dimethylamino)phenyl donor groups[19] ($\Delta J_{av.} > 3.5$ Hz) (Table 2, Figure 2). This once again confirms the great electron-donor capability of the proaromatic pyran and benzopyran heterocycles and the powerful electron-withdrawing ability of the carbonyl-[(phenylthio)carbene]metal group.

## X-ray Analysis of 2a

Blue single crystals of **2a** suitable for the X-ray analysis were obtained by slow concentration of a diethyl ether/petroleum ether solution. The molecular view with the atom labelling is shown in Figure 4. As indicated by the ORTEP drawing, the determination of the (*E*) stereochemistry based on the *J* coupling constant values is correct. The molecule exhibits a nearly planar conformation. However, the phenyl ring linked to the sulfur atom is in a *syn* conformation and is twisted by 88.8(5)° with respect to the plane of the conjugated chain. In addition, C(3) and C(4) lie slightly away from the ideal plane. The –CH=CH–C(SPh)=W(CO)$_5$ fragment is in an *syn* conformation.

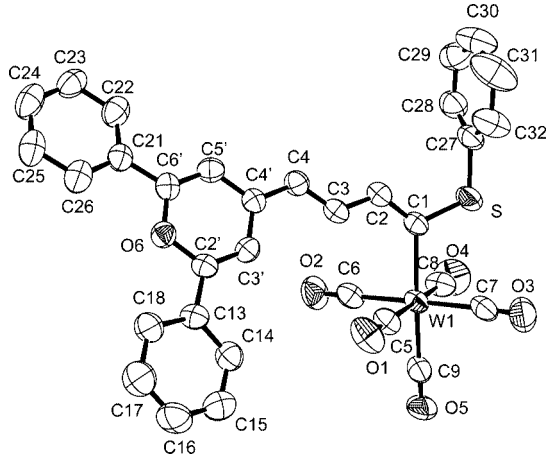


Figure 4. ORTEP drawing of **2a** showing the atom numbering. Hydrogen atoms are omitted for clarity. Thermal ellipsoids are drawn at the 50% probability level. Selected bond lengths [Å]: W(1)–C(1) 2.251(7), S–C(1) 1.719(7), C(1)–C(2) 1.398(10), C(2)–C(3) 1.377(9), C(3)–C(4) 1.373(9), C(4)–C(4′) 1.389(9), O(6)–C(6′) 1.359(8), O(6)–C(2′) 1.370(8), C(2′)–C(3′) 1.336(10), C(3′)–C(4′) 1.429(10), C(6′)–C(5′) 1.350(10), C(5′)–C(4′) 1.435(9).

Assuming that the solid-state molecular structure reflects the conformation of **2a** in solution, this situation should have an influence on the NLO properties (see below). In accordance with the NMR investigations, the nearly equal C(2)–C(3), C(3)–C(4) bond lengths together with the large C(1)–W bond length [2.251(7) Å] are indicative of significant delocalisation between the heterocyclic oxygen atom and the metal centre through the unsaturated backbone (large pyrylium character). On the pyran side, the intracyclic C–C and C–O bond length values appear to be close to those found for other (4*H*-pyran-4-ylidene)alkenylidene complexes for which DFT calculations and X-ray analyses

 © 2006 Wiley-VCH Verlag GmbH & Co. KGaA, Weinheim 

have indicated a pyrylium character.[13] It is noticeable that the 2,6-diphenylpyrylium salts bearing a 4-(dimethylamino)benzyl group donor display similar intraheterocyclic C–O and C–C bond lengths due to pronounced 4*H*-pyran-4-ylidene character.[26] Again, in accordance with the significant contribution from the pyrylium form, the exocyclic C=C bond length (1.389 Å) has single-bond character. This value is greater than that determined for lesser conjugated bis(4*H*-pyrans) (1.375 Å)[27] and is close to those reported by us for other methoxy(4*H*-pyran-4-ylidene)alkenylidene complexes.[2b,13b] Moreover, it is worth remarking that in chromenylideneacetaldehyde hydrazone containing $[(\eta^6\text{-arene})CpFe]^+$ as an electron-accepting group, the exocyclic C=C bond is 1.354 Å long indicating a weak benzopyrylium form.[28] Finally, the C–SPh distance (1.719 Å), which lies within the normal range (C–S, C=S),[20] provides evidence for back-bonding donation from the heteroatom lone pair and the carbene carbon atom (resonance structure **C**) (Scheme 1). It is noticeable that a lower value was reported from the pentacarbonyl[methyl(phenylthio)carbene]chromium complex X-ray analysis.[20b]

### Linear and Non-Linear Optical Properties

The UV/Vis electronic spectra of molecules **2** were recorded in four solvents of varying polarity (Table 4). For **2a**, **2b**, **2c** and **2′c**, a rapid decomplexation reaction occurs in DMSO ($\varepsilon_{25\,°C}$ = 48.9) leading to the corresponding thioester.[10] In such cases $CH_3CN$ ($\varepsilon_{25\,°C}$ = 37.5) was used. The UV/Vis spectra of the (phenylthio)carbenes **2** consist of two intense absorption bands in the visible region (Table 4). By comparison with the spectra of analogous methoxycarbene complexes, for which DFT computations have been performed,[13b] the lower and the higher energy bands can be assigned to the metal-to-ligand charge transfer transition (MLCT), corresponding to the HOMO–LUMO transition, and the intraligand charge transfer transition (ILCT or $\pi\rightarrow\pi^*$), respectively. In these complexes, the HOMO and the LUMO electronic density is mainly located on the metal centre and on the ligand, respectively.[13] However, despite the great similarity of the spectra, it can be noted that compared with their methoxy counterparts **3**, the corresponding electronic transitions of **2** are red-shifted, possibly as a consequence of a lowering of the π*-level (LUMO). On the other hand, under the intracyclic O→S atom substitution, a bathochromic shift can be observed for the two bands. Such a trend, also found for the methoxycarbenes,[14] should be a consequence of a decrease in the HOMO–LUMO and π→LUMO gaps. MNDO calculations have shown that such HOMO–LUMO gap lowering upon O→S substitution exists in push-pull chalcogenopyrylium salts.[29] Substitution of the Cr atom for W (**2c**, **2′c** comparison) leads to a clear bathochromic shift.

As expected, the MLCT band appears to be more sensitive to the metal change. The presence of a *t*Bu electron-donating group in **2d** (which, unlike a phenyl substituent, is not capable of conjugative interaction with the chalcogenobenzopyran ring) increases the energy of both transitions. Finally, influence of the benzo-annulation on the maximum absorptions seems more complex and depends on the nature of the chalcogen atom (Table 4) and on the solvent polarity. Thus, for **2a** and **2b**, the two characteristic CT bands exhibit a hypsochromic shift when the solvent polarity is increased, as expected from the zwitterionic character of the ground state (see above). It is worth remarking that for the less zwitterionic methoxy complexes **3a** and **3b** (Figure 1), analogous to **2a** and **2b**, a bathochromic shift occurs for the MLCT transition.[14] For the chalcogenobenzopyran complexes **2c**, **2d** and **2e**, a weak solvent influence can be observed for both electronic transitions, and an inversion of the solvatochromism cannot be totally excluded. The behaviour of the carbenechromium complex **2′c** differs from that of **2c** since the solvent change has a small influence on the $\pi\rightarrow\pi^*$ transition and the MLCT transition is only sensitive to the less polar solvents utilised ($CCl_4$, $CH_2Cl_2$ and $CH_3COCH_3$) (observation of a hypsochromic shift). In conclusion, the presence of two intense electronic transitions in the visible region should make the interpretation of the NLO results more difficult and precludes relevant analysis based on the two-level model.[8]

Second-order nonlinear properties were studied in $CHCl_3$ solution ($\varepsilon_{25\,°C}$ = 4.7) at 1907 nm by the electric-field-induced second-harmonic generation technique (EFISH) which provides information about the scalar product $\mu\beta$ ($2\omega$) of the vector component of the first hyperpolarisability tensor $\beta$ and the dipole moment vector. This product

Table 4. UV/Vis absorption properties of compounds **2** in various solvents.

| | Solvent | $\lambda_{max}$ [nm] ($\varepsilon\times10^{-4}$) | | | | | |
|---|---|---|---|---|---|---|---|
| | | **2a** | **2b** | **2c** | **2d** | **2e** | **2′c** |
| $\lambda_1$ ($\varepsilon$) | $CCl_4$ | 538 (4.8) | 565 (3.2) | 541 (2.9) | 526 (3.7) | 563 (3.3) | 549 (3.5) |
| $\lambda_1$ ($\varepsilon$) | $CH_2Cl_2$ | 532 (4.1) | 561 (3.2) | 540 (3.4) | 524 (3.4) | 567 (2.3) | 549 (3.7) |
| $\lambda_1$ ($\varepsilon$) | $(CH_3)_2CO$ | 521 (4.2) | 551 (2.5) | 536 (1.1) | 519 (3.0) | 562 (2.3) | 544 (3.8) |
| $\lambda_1$ ($\varepsilon$) | $CH_3CN$ | 518 (3.1) | 547 (2.0) | 534 (2.2) | 518 (2.5) | 561 (1.4) | 544 (3.0) |
| $\lambda_1$ ($\varepsilon$) | DMSO | [a] | [a] | 538 (1.9) | 522 (2.5) | [a] | [a] |
| $\lambda_2$ ($\varepsilon$) | $CCl_4$ | 673 (3.4) | 695 (2.5) | 663 (1.7) | 649 (2.0) | 679 (2.2) | 690 (1.3) |
| $\lambda_2$ ($\varepsilon$) | $CH_2Cl_2$ | 658 (5.4) | 693 (4.3) | 657 (3.0) | 638 (3.1) | 682 (2.3) | 670 (1.8) |
| $\lambda_2$ ($\varepsilon$) | $(CH_3)_2CO$ | 652 (8.1) | 689 (5.0) | 652 (1.3) | 631 (3.5) | 681 (2.9) | 662 (2.3) |
| $\lambda_2$ ($\varepsilon$) | $CH_3CN$ | 648 (6.4) | 687 (4.4) | 654 (2.6) | 630 (3.2) | 682 (1.9) | 663 (1.9) |
| $\lambda_2$ ($\varepsilon$) | DMSO | [a] | [a] | 663 (3.1) | 636 (4.0) | [a] | [a] |

[a] In DMSO, decomplexation reactions occur.

 © 2006 Wiley-VCH Verlag GmbH & Co. KGaA, Weinheim 

Table 5. $\mu\beta$ values for **2**–**3**.

| | **2a** | **2b** | **2c** | **2d** | **2e** | **2′c** | **3a**[14] | **3b**[14] | **3c**[14] | **3d**[15c] | **3e**[14] |
|---|---|---|---|---|---|---|---|---|---|---|---|
| $\mu\beta$ [$10^{-48}$ esu][a] | 173 | 518 | 420 | 374 | 421 | 140 | 505 | 665 | 219 | 310 | 402 |

[a] $\mu\beta(2\omega)$ at 1907 nm in $CHCl_3$. Molecular concentrations used for the measurements were in the range $10^{-3}$ to $10^{-2}$ M; 3-methyl-4-nitroaniline (MNA) for which $\mu\beta(CHCl_3) = 71.06 \times 10^{-48}$ esu was used as an external reference. $\mu\beta \pm 20\%$.

is derived according to Equation (1) and, considering $\gamma_0(-2\omega,\omega,\omega,0)$, the third-order term is negligible for the push-pull compounds under study. This approximation is usually used for push-pull organic and organometallic molecules.

$$\gamma_{EFISH} = \mu\beta/5kT + \gamma_0(-2\omega,\omega,\omega,0) \quad (1)$$

All complexes were thus tested away from resonance. It should be noted that the sign and values of $\mu\beta$ depend on the "direction" of the transition implied in the NLO phenomena and on the direction of the ground-state dipole moment. When $\beta$ and $\mu$ are parallel (antiparallel), positive (negative) maxima $\mu\beta$ values are reached.

DFT calculations performed on analogous methoxycarbenes have shown that the ground-state dipole moment is governed by the pyrylium character of these molecules (Figure 5).[13b] However, a slight variation in the dipole moment orientation can occur according to the degree of *syn* or *anti* conformation of the complexes (see X-ray analysis of **2a**).[30]

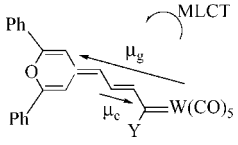


Figure 5. Orientations of the ground-state and excited-state (MLCT) dipole moment vectors.

As for the methoxycarbenes[14] **3**, all the $\mu\beta$ values of complexes **2** (Table 5) are large and positive, indicative of the implied transition(s) of the first excited states which are more polarized than the ground states and a vectorial $\beta$ with almost the same direction as the ground-state dipole moment. This is not in accordance with the negative solvatochromism or the low solvent polarity influence observed for the MLCT and π-π* transitions in **2a**–**2e** and **2′c**. Moreover, the MLCT charge transfer direction implies an excited dipole moment vector $\mu_e$ opposite to the ground-state dipole moment $\mu_g$ vector.[8] Therefore, this transition may only play a minor role in the first hyperpolarisability, since positive $\mu\beta$ values are found. On the other hand, the π→π* charge transfer implies a corresponding $\mu_e$ almost parallel to $\mu_g$. A positive or a negative $\mu\beta$ value could be expected with respect to the contribution of the two limit forms **A** and **B** (Scheme 1). Despite the complexity of this situation, important information can be deduced from the $\mu\beta$ values shown in Table 5.

First, substitution of W by Cr (**2c**, **2′c** comparison) lowers the first hyperpolarisability response. This shift, as previously[5] proposed, should be the consequence of a more polarisable metal electron shell for the W atom. However, a part of the $\mu\beta$ decrease should reflect the variation of the dipole moment (see NMR: $\Delta J$ values). From a comparison of **2a** and **2b** it seems once again (see **3a**, **3b**, **3c** and **3e** $\mu\beta$ values, Table 5)[14] that the presence of an intracyclic pyran sulfur atom favours the hyperpolarisability response. This effect could be relevant to the greater polarisability of the electrons of the sulfur compared with the electrons of the oxygen. However, it can be noted that this heteroatomic influence is not operative in the chalcogenobenzopyran structure, since similar responses are found for **2c** and **2e**. It seems that the presence of a fused benzene ring produces subtle electronic differences which make the analysis more difficult. On the other hand, annulation produces an increase in $\mu\beta$ for O-heterocycles and a decrease for S-heterocycles. This last result is in line with the behaviour of analogous methoxycarbenes (see **3a**, **3c** and **3b**, **3e** $\mu\beta$ values, Table 5).[14] It should be the consequence of the lower π-electron mobility in **2e** owing to the aromatic character of the appending benzene ring. The low $\mu\beta$ value observed for the pyran complex **2a**, which is responsible for the inverse $\mu\beta$ evolution for the two series, merits comments. As stated from NMR spectroscopic data, the pyrylium character of **2a** is important and is close to the thiopyrylium character of **2b** (see $\Delta J$ value, Table 1). Consequently, the greater aromaticity of the pyran ring in **2a**[29,31] should in part explain the lower NLO response. Finally, for the (phenylthio)carbenes, substitution of a phenyl group by a tertiary butyl group slightly reduced the $\mu\beta$ value (**2c**, **2d** comparison). The opposite trend (slight increase) may be observed for the methoxycarbenes (**3c**, **3d** comparison). In conclusion, from $\mu\beta$ and $\Delta J$ value comparison, it seems that the BLA factor has a minor influence on the NLO behaviour of these complexes.

## Conclusion

In the 4-(4*H*-chalcogenopyran-4-ylidene and 4*H*-chalcogenochromen-4-ylidene)-1-(phenylthio)but-2-enylidene complexes **2**, the carbonyl[(phenylthio)carbene]metal fragment acts as an exceptional electron-accepting group. Consequently, the pyrylium character is important and some of the complexes under investigation surpass the cyanine limit in [$D_8$]THF. From comparisons of NMR spectroscopic data, it seems that the carbonyl[(phenylthio)carbene]metal group in complexes **2** is a better electron-withdrawing group than a carbonyl(methoxycarbene)metal group. A single-crystal X-ray diffraction analysis of compound **2a** has shown an electronic structure which enables conjugation between the intracyclic oxygen atom and the metal centre which is in accordance with the pronounced pyrylium character of the heterocycle. The first hyperpolarisability of the

 © 2006 Wiley-VCH Verlag GmbH & Co. KGaA, Weinheim 

thiocarbenes have been measured by the EFISH technique. The $\mu\beta$ values are close to those found for methoxycarbenes of similar lengths[14] and are sensitive to the intracyclic heteroatom, the benzo-annulation and the metal. However, the presence of two absorption bands in the visible region precludes analysis based only on a simple model. Theoretical calculations should be necessary to obtain more information on the electronic transitions and excited states implied by the NLO properties.

## Experimental Section

**General Remarks:** All preparations involving organometallic (4*H*-pyran-4-ylidene)alkenylidene compounds were carried out under dry nitrogen. Solvents were dried and distilled before use according to standard procedures.[32] $^1$H and $^{13}$C NMR spectra were recorded in [D$_8$]THF using a Bruker 500 MHz spectrometer. Infrared spectra were recorded with a Perkin–Elmer FTIR-1000 spectrometer using KBr plates. Microanalyses were performed using a Microanalyseur Flash EA 1112 instrument and mass spectra were obtained using a high-resolution MS/MS Zab spec Tof micromass system at the Centre Régional de Mesures Physiques de l'Ouest Université de Rennes 1. Optical absorption spectra were measured with a Perkin–Elmer Lambda 25 spectrophotometer.

**X-ray Structure Determination:** Blue single crystals of **2a** suitable for X-ray analysis were obtained by slow concentration of a diethyl ether/petroleum ether solution and were mounted on a Nonius four-circle diffractometer equipped with a CCD camera and a graphite-monochromated Mo-$K_\alpha$ radiation source ($\lambda$ = 0.71073 Å) at the Centre de Diffractométrie (CDFIX), Université de Rennes 1, France. Data collection was performed at 293(2) K. $C_{32}H_{20}O_6SW$, $M$ = 716.39, monoclinic, $P2_1/c$, $a$ = 9.0690(2), $b$ = 14.7950(2), $c$ = 21.4990(5) Å, $\beta$ = 100.432(1)°, $V$ = 2836.9(1) Å$^3$, $Z$ = 4, $\rho_{calcd.}$ = 1.677 g cm$^{-3}$. 12109 structure factors were collected before merging to yield 6506 unique intensities ($R_{int}$ = 0.0482). The structure was solved with SHELXS-97.[33] The refinement of 361 parameters against $F^2$ of 6506 unique intensities [4246 observed intensities $I > 2\sigma(I)$] was performed with SHELXL-97[34] with anisotropic thermal parameters for all non-hydrogen atoms. Hydrogen atoms were added to the structure model in calculated positions. Final residuals: $R$ = 0.0548, $wR$ = 0.1247. CCDC-297214 contains the supplementary crystallographic data for this paper. These data can be obtained free of charge from The Cambridge Crystallographic Data Centre via www.ccdc.cam.ac.uk/data_request/cif.

**Synthetic Methodology: General Procedure for the Synthesis of Complexes 2a–2e:** A solution of the aldehydes[15] **1a**–**1e** ($1.1\times10^{-3}$ mol) with 1 equiv. of $CH_3(SPh)C{=}W(CO)_5$[10,35] ($1.1\times10^{-3}$mol), 3 equiv. of $(CH_3)_3SiCl$ (TMSCl) and 3 equiv. of $(C_2H_5)_3N$ in THF (20 mL) was stirred at room temperature. The reaction, monitored by TLC, showed that the starting carbene complex quickly disappeared. Degassed water was poured onto the blue reaction mixture and the product was extracted with diethyl ether. The extract was dried with magnesium sulfate and the solvent was removed under reduced pressure. The residue was purified by chromatography on silica gel plates (elution with petroleum ether/dichloromethane, 70:30). The condensation products **2a**–**2e** were isolated after evaporation of the solvent and recrystallised from diethyl ether/petroleum ether solutions.

**Synthesis of Analogous Complex 2′c:** The above procedure was applied, but using the (phenylthio)carbene complex $CH_3(SPh)C{=}Cr(CO)_5$.

**Complex 2a:** Decomposition > 250 °C. MS (FAB): calcd. for $C_{29}H_{20}O_3SW$ [M – 3 CO]$^{+\cdot}$ 632.0643, found 632.0660. IR (KBr pellet): $\tilde{\nu}$ = 2049, 1928, 1893, 1641, 1519, 1502, 1482, 1342, 1245, 1156, 963, 934, 882, 792, 767, 680, 591 cm$^{-1}$. $^1$H NMR ([D$_8$]THF): $\delta$ = 8.39 (t, $^3J$ = 12.9 Hz, 1 H, 3-H), 7.99 (m, 4 H, Ph), 7.59 (m, 3 H, Ph), 7.58 (s, 1 H, 3-H), 7.54 (m,3 H, Ph), 7.48 (m, 5 H, Ph), 7.24 (d, $^4J$ = 1.5 Hz, 1 H, 5-H), 6.95 (d, $^3J$ = 12.6 Hz, 1 H, 2-H), 6.04 (d, $^3J$ = 13.2 Hz, 1 H, 4-H) ppm. $^{13}$C NMR ([D$_8$]THF): $\delta$ = 261.6 (C-1), 205.8 (C, CO), 200.8 (C, CO), 160.4 (C-2′), 160.2 (C-6′), 157.3 (C-3), 152.3 (C-4′), 138.95 (C-2), 134.2 (C, Ph), 132.6 (C, Ph), 132.4 (C, Ph), 132.2 (C, Ph), 130.4 (C, Ph), 130.3 (C, Ph), 130.2 (C, Ph), 130.1 (C, Ph), 126.8 (C, Ph), 126.7 (C, Ph), 118.0 (C-4), 111.9 (C-5′), 105.1 (C-3′) ppm.

**Complex 2b:** M.p. 162 °C. IR (KBr pellet): $\tilde{\nu}$ = 2051, 1902, 1878, 1529, 1472, 1276, 1168, 805, 747 cm$^{-1}$. $C_{30}H_{20}S_2W$ (628): calcd. C 52.47, H 2.75, S 8.75; found C 52.78, H 3.05, S 8.66. $^1$H NMR ([D$_8$]THF): $\delta$ = 8.40 (t, $^3J$ = 12.9 Hz, 1 H, 3-H), 7.93 (s, 1 H, 3′-H), 7.74 (m, 4 H, Ph), 7.56 (m, 3 H, Ph), 7.52 (m, 3 H, Ph), 7.50 (s, 1 H, 5′-H), 7.47 (m, 5 H, Ph), 6.97 (d, $^3J$ = 12.6 Hz, 1 H, 2-H), 6.24 (d, $^3J$ = 12.6 Hz, 1 H, 4-H) ppm. $^{13}$C NMR ([D$_8$]THF ): $\delta$ = 263.5 (C-1), 206.0 (C, CO), 200.6 (C, CO), 155.8 (C-3), 152.1 (C-4′), 150.1 (C-2′), 149.2 (C-6′), 139.8 (C-2), 138.8 (C, Ph), 137.4 (C, Ph), 137.1 (C, Ph), 134.2 (C, Ph), 132.0 (C, Ph), 130.6 (C, Ph), 130.5 (C, Ph), 130.4 (C, Ph), 128.5 (C-5′), 127.5 (C, Ph), 127.3 (C, Ph), 121.0 (C-3′) ppm.

**Complex 2c:** Decomposition > 250 °C. IR (KBr pellet): $\tilde{\nu}$ = 2052, 1906, 1615, 1529, 1505, 1487, 1350, 1272, 1170, 1123, 1011, 907, 795, 764, 682 cm$^{-1}$. $C_{30}H_{18}O_6SW$ (690): calcd.C 52.19, H 2.63, S 4.64; found C 52.56, H 2.89, S 4.78. $^1$H NMR ([D$_8$]THF ): $\delta$ = 8.55 (t, $^3J$ = 12.8 Hz, 1 H, 3-H), 8.11 (d, $^3J$ = 8.2 Hz, 1 H, benzo), 8.01 (2 H, m, Ph-H), 7.67 (ddd, $^3J$ = 8.4 Hz, $^3J$ = 7.1 Hz, 1 H, benzo), 7.60 (1 H, s, 3′-H), 7.56 (m, 4 H, benzo, Ph), 7.52 (m, 3 H, Ph), 7.50 (2 H, m, Ph), 7.36 (ddd, $^3J$ = 8.2 Hz, $^3J$ = 7.1 Hz, 1 H, benzo), 7.22 (d, $^3J$ = 12.9 Hz, 1 H, 2-H), 6.80 (d, $^3J$ = 12.7 Hz, 1 H, 4-H) ppm. $^{13}$C NMR ([D$_8$]THF): $\delta$ = 273.1 (C-1), 206.0 (C, CO), 200.4 (C, CO), 157.6 (C-2′), 156.9 (C-3), 154.0 (C-6′), 147.0 (C-4′), 141.2 (C-2), 139.0 (C, Ph), 134.0 (C, benzo), 133.8 (C, Ph), 132.8 (C, Ph), 132.3 (C, Ph), 130.8 (C, Ph), 130.6 (C, Ph), 130.1 (C, Ph), 126.9 (C, benzo), 126.8 (C, Ph), 125.3 (C-5′), 119.3 (C, benzo), 115.3 (C-4), 102.7 (C-3′) ppm.

**Complex 2d:** M.p. 170 °C. IR (KBr pellet): $\tilde{\nu}$ = 2052, 1914, 1622, 1563, 1534, 1508, 1477, 1462, 1349, 1309, 1267, 1232, 1183, 1164, 1135, 1104, 1024, 960, 936, 882, 862, 836, 808, 761, 751 cm$^{-1}$. $C_{28}H_{22}O_6SW$ (670): calcd. C 50.17, H 3.31, S 4.78; found C 50.30, H 3.41, S 4.56. $^1$H NMR ([D$_8$]THF): $\delta$ = 8.56 (t, $^3J$ = 12.8 Hz, 1 H, 3-H), 8.07 (dd, $^3J$ = 8.3 Hz, $^4J$ = 1.3 Hz, 1 H, benzo), 7.63 (ddd, $^3J$ = 8.4 Hz, $^3J$ = 7.2 Hz, $^4J$ = 1.3 Hz, 1 H, benzo), 7.52 (m, 3 H, Ph), 7.48 (m, 2 H, Ph), 7.43 (dd, $^3J$ = 8.4 Hz, $^4J$ = 1.0 Hz, 1 H, benzo), 7.33 (ddd, $^3J$ = 8.3 Hz, $^3J$ = 7.2 Hz, $^4J$ = 1.0 Hz, 1 H, 6′-H), 7.17 (d, $^3J$ = 12.9 Hz, 1 H, 2-H), 7.01 (s, 1 H, 3′-H), 6.72 (d, $^3J$ = 12.8 Hz, 1 H, 4-H), 1.40 (s, 9 H, $CH_3$) ppm. $^{13}$C NMR ([D$_8$]-THF): $\delta$ = 272.1 (C-1), 205.7 (C, CO), 200.3 (C, CO), 170.4 (C-2′), 157.9 (C-3), 154.4 (C-6′), 148.1 (C-4′), 140.5 (C-2), 139.0 (C, Ph), 133.9 (C, benzo), 133.9 (C, Ph), 130.8 (C, Ph), 130.6 (C, Ph), 126.6 (C, benzo), 125.3 (C, benzo), 122.1 (C-5′), 119.1 (C, benzo), 114.1 (C-4), 110.9 (C-3′), 37.2 [C, $C(CH_3)_3$], 28.2 (C, $CH_3$) ppm.

**Complex 2e:** Decomposition > 250°. IR (KBr pellet): $\tilde{\nu}$ = 2050, 1902, 1526, 1500, 1485, 1258, 1163, 1085, 962, 823, 750, 689 cm$^{-1}$. $C_{30}H_{18}O_5S_2W$ (706): calcd. C 51.01, H 2.57, S 9.08; found C 51.64, H 2.67, S 9.87. $^1$H NMR ([D$_8$]THF): $\delta$ = 8.54 (t, $^3J$ = 12.7 Hz, 1 H, 3-H), 8.28 (d, $^3J$ = 8.4 Hz, 1 H, benzo), 8.03 (s, 1 H, 3-H), 7.78 (dd, $^3J$ = 5.5 Hz, $^4J$ = 2.8 Hz, 2 H, Ph), 7.71 (d, $^3J$ = 8.0 Hz, 1 H,

 © 2006 Wiley-VCH Verlag GmbH & Co. KGaA, Weinheim 

benzo), 7.58 (m, 1 H, benzo), 7.55 (m, 6 H, Ph), 7.51 (m, 2 H, Ph), 7.49 (m, 1 H, benzo), 7.26 (d, $^3J$ = 12.9 Hz, 1 H, 2-H), 7.07 (d, $^3J$ = 12.7 Hz, 1 H, 4-H). $^{13}$C NMR ([D$_8$]THF): $\delta$ = 274.3 (C-1), 206.1 (C, CO), 200.1 (C, CO), 156.2 (C-3), 148.2 (C-4′), 146.1 (C-2′), 142.1 (C-2), 138.9 (C, Ph), 138.0 (C, Ph), 131.0 (C, Ph), 130.7 (C, Ph), 130.4 (C, Ph), 129.8 (C-5′), 129.6 (C, benzo), 128.4 (C, benzo), 127.5 (C, Ph), 121.1 (C-4), 119.3 (C-3′) ppm.

**Complex 2′c:** Decomposition > 250°. IR (KBr pellet): $\tilde{\nu}$ = 2041, 1907, 1625, 1512, 1488, 1463, 1350, 1322, 1273, 1154, 1123, 1112, 964, 909, 884, 814, 763, 688, 654 cm$^{-1}$. $C_{30}H_{18}O_6SCr$ (558): calcd. C 64.51, H 3.25, S 5.74, found C 64.47, H 3.52, S 6.14. $^1$H NMR ([D$_8$]THF): $\delta$ = 8.55 (t, $^3J$ = 12.8 Hz, 1 H, 3-H), 8.07 (dd, $^3J$ = 8.2 Hz, $^4J$ = 1.3 Hz, 1 H, 5-H), 7.59 (s, 1 H, 3-H), 7.56 (m, 3 H, Ph), 7.42 (m, 4 H, 8-H, Ph), 7.45 (m, 2 H, Ph), 7.42 (d, $^3J$ = 13.1 Hz, 1 H, 2-H), 7.35 (ddd, $^3J$ = 8.2 Hz, $^3J$ = 7.2 Hz, $^4J$ = 1.0 Hz, 1 H, 6-H), 6.76 (d, $^3J$ = 12.6 Hz, 1 H, 4-H) ppm. $^{13}$C NMR ([D$_8$]THF): $\delta$ = 301.7 (C-1′), 227.6 (C, CO), 219.7 (C, CO), 157.2 (C-2), 153.9 (C-9), 153.2 (C-3′), 146.2 (C-4), 140.2 (C-2′), 133.8 (C, Ph), 132.9 (C, Ph), 132.2 (C, Ph), 130.8 (C, Ph), 130.5 (C, Ph), 130.1 (C, Ph), 126.7 (C-6 + C, Ph), 125.3 (C-5), 122.1 (C-10), 119.2 (C-8), 115.3 (C-4′), 102.3 (C-3) ppm.

**NLO Measurements:** NLO measurements were carried out using the Electric Field Induced Second Harmonic (EFISH) technique.[36] The data were recorded using a nanosecond Nd:YAG pulsed (10 Hz) laser operating at 1064 nm, equipped with a hydrogen cell (1 m long, 40 bar) for Raman shifting. The 1907 nm beam was selected and used as the fundamental for EFISH. The compounds were dissolved in chloroform at various concentrations (typically in the range of $1 \times 10^{-3}$ to $9 \times 10^{-3}$ mol L$^{-1}$) and a specific cell mounted on a translation stage was used. The centrosymmetry of the solution was broken by dipolar orientation of the chromophores with a high voltage pulse (5 kV) synchronized with the laser pulse. The SHG signal was selected through a suitable interference filter, detected by a photomultiplier, and recorded by an oscilloscope. Translation of the cell allowed us to obtain the typical Maker fringes. The NLO response was analysed according to an already published procedure. 2-Methyl-4-nitroaniline was used as a reference ($\mu\beta = 71 \times 10^{-48}$ esu at 1907 nm) to determine the $\mu\beta$ value of our compounds.

**Supporting Information** (see footnote on the first page of this article): Table S1 lists the UV/Vis absorption properties of complexes **3** in various solvents.

## Acknowledgments

CNRS, le Conseil Général des Côtes d'Armor, la Communauté des Communes du Trégor and le Ministère de l'Education Nationale de la Recherche et de la Technologie (MENRT; grant to N. F.) are gratefully acknowledged for their financial support.

[1] a) H. Wang, W. D. Wulff, *J. Am. Chem. Soc.* **1998**, *120*, 10573–10574; b) M. L. Waters, T. A. Brandvold, L. Isaacs, W. D. Wulff, A. L. Rheingold, *Organometallics* **1998**, *17*, 4298–4308; c) M. Torrent, M. Duran, M. Sola, *J. Am. Chem. Soc.* **1999**, *121*, 1309–1316; d) J. Barluenga, F. Aznar, I. Gutierrez, A. Martin, S. Garcia-Granda, M. A. Llorca-Baragano, *J. Am. Chem. Soc.* **2000**, *122*, 1314–1324; e) J. Barluenga, L. A. Lopez, S. Martinez, M. Tomas, *Tetrahedron* **2000**, *56*, 4967–4975.

[2] a) J. Barluenga, J. Florez, F. Fatanas, *J. Organomet. Chem.* **2001**, *624*, 5–17; b) B. Caro, P. Le Poul, F. Robin-Le Guen, M.-C. Sénéchal-Tocquer, J.-Y. Saillard, S. Kahlal, L. Ouahab, S. Gohlen, *Eur. J. Org. Chem.* **2000**, 577–581.

[3] for reviews see: a) H. Rudler, A. Parlier, S. Bezennine-Lafollée, J. Vaissermann, *Eur. J. Org. Chem.* **1999**, 2825–2833; b) R. Aumann, *Eur. J. Org. Chem.* **2000**, 17–31; c) J. W. Herndon, *Tetrahedron* **2000**, *56*, 1257–1280; d) J. Barluenga, J. Santamaria, M. Tomas, *Chem. Rev.* **2004**, *104*, 2259–2284.

[4] a) N. J. Long, *Angew. Chem. Int. Engl.* **1995**, *34*, 21–38; b) D. R. Kanis, M. A. Ratner, T. J. Marks, *J. Am. Chem. Soc.* **1992**, *114*, 10338–10357; c) D. R. Kanis, M. A. Ratner, T. J. Marks, *Chem. Rev.* **1994**, *94*, 195–242; d) D. R. Kanis, P. G. Lacroix, M. A. Ratner, T. J. Marks, *J. Am. Chem. Soc.* **1994**, *116*, 10089–10102; e) S. H. Lecours, H. W. Guan, S. G. DiMagno, C. H. Wang, M. J. Therien, *J. Am. Chem. Soc.* **1996**, *118*, 1497–1503; f) E. Hendrickx, A. Persoons, S. Samson, G. R. Stephenson, *J. Organomet. Chem.* **1997**, *542*, 295–297; g) G. Roth, H. Fischer, T. Meyer-Friedrichsen, J. Heck, S. Houbrechts, A. Persoons, *Organometallics* **1998**, *17*, 1511–1516; h) M. P. Cifuentes, J. Driver, M. G. Humphrey, I. Asselberghs, A. Persoons, M. Samoc, B. Luther-Davies, *J. Organomet. Chem.* **2000**, *607*, 72–77; i) H. Wong, T. Meyer-Friedrichsen, T. Farrell, C. Mecker, J. Heck, *Eur. J. Inorg. Chem.* **2000**, 631–646; j) H. Le Bozec, T. Renouard, *Eur. J. Inorg. Chem.* **2000**, 229–239; k) S. Barlow, S. R. Marder, *Chem. Commun.* **2000**, 1555–1562; l) J. A. Mata, E. Falomir, R. Llusar, E. Peris, *J. Organomet. Chem.* **2000**, *616*, 80–88; m) D. Roberto, R. Ugo, S. Bruni, E. Cariati, F. Cariati, P. C. Fantucci, I. Invernizzi, S. Quici, I. Ledoux, J. Zyss, *Organometallics* **2000**, *19*, 1775–1788; n) R. D. A. Hudson, A. R. Manning, J. F. Gallagher, M. H. Garcia, N. Lopes, I. Asselberghs, R. Van Boxel, A. Persoons, A. J. Lough, *J. Organomet. Chem.* **2002**, *655*, 70–88; o) M. Pizzotti, R. Ugo, D. Roberto, S. Bruni, P. Fantucci, C. Rovizzi, *Organometallics* **2002**, *21*, 5830–5840; p) A. Hameed, A. Rybarczyk-Pirek, J. Zakrzewski, *J. Organomet. Chem.* **2002**, *656*, 102–107; q) I. Janowska, J. Zakrzewski, K. Nakatani, J. A. Delaire, M. Palusiak, M. Walak, H. Scholl, *J. Organomet. Chem.* **2003**, *675*, 35–41; r) F. Cariati, U. Caruso, R. Centore, A. De Maria, M. Fusco, B. Panunzi, A. Roviello, A. Tuzi, *Inorg. Chim. Acta* **2004**, *357*, 548–555; s) G. Martin, M. V. Martinez-Diaz, G. de la Torre, I. Ledoux, J. Zyss, F. Agullo-Lopez, T. Torres, *Synth. Met.* **2003**, *139*, 95–98; t) E. Peris, *Coord. Chem. Rev.* **2004**, *248*, 279–297; u) F. Cariati, U. Caruso, R. Centore, A. De Maria, M. Fusco, B. Panunzi, A. Roviello, A. Tuzi, *Optical Materials* **2004**, *27*, 91–97; v) P. G. Lacroix, F. Averseng, I. Malfant, K. Nakatani, *Inorg. Chim. Acta* **2004**, *357*, 3825–3835; w) P. M. Cifuentes, M. G. Humphrey, *J. Organomet. Chem.* **2004**, *689*, 3968–3981; x) C. E. Powell, M. G. Humphrey, *Coord. Chem. Rev.* **2004**, *248*, 725–756.

[5] S. Maiorana, A. Papagni, E. Licandro, A. Persoons, K. Clays, S. Houbrechts, W. Porzio, *Gazz. Chim. Ital.* **1995**, *125*, 377–379.

[6] E. Licandro, S. Maiorana, A. Papagni, P. Hellier, L. Capella, A. Persoons, S. Houbrechts, *J. Organomet. Chem.* **1999**, *583*, 111–119.

[7] K. N. Jayaprakash, P. C. Ray, I. Matsuoka, M. M. Bhadbhade, V. G. Puranik, P. K. Das, H. Nishihara, A. Sarkar, *Organometallics* **1999**, *18*, 3851–3858.

[8] a) J. L. Oudar, D. S. Chemla, *J. Chem. Phys.* **1977**, *66*, 2664–2668. In this simplified model $\beta \propto \Delta\mu \cdot f_{ge}/E^3$ where $\Delta\mu = \mu_e - \mu_g$ ($\mu_g$ is the ground-state dipole moment value and $\mu_e$ is the dipole moment value of the excited state), $f_{ge}$ and $E$ are the oscillator strength and the energy of the electronic transition, respectively. b) B. F. Levine, C. G. Betha, *J. Chem. Phys.* **1976**, *65*, 1989–1993.

[9] B. A. Anderson, W. D. Wulff, T. S. Powers, S. Tribbitt, A. Rheingold, *J. Am. Chem. Soc.* **1992**, *114*, 10784–10798. In this case, a conformation in which the carbon–carbon double bond is perpendicular to the carbene fragment is preferred.

[10] R. Aumann, J. Schröder, *Chem. Ber.* **1990**, *123*, 2053–2058.

[11] For example, a recent theoretical study (DFT calculation) related to electronic properties of $(CO)_5Cr{=}C(X)R$ does not take into account the (alkylthio)- or (phenylthio)carbene (X = SR;

 © 2006 Wiley-VCH Verlag GmbH & Co. KGaA, Weinheim 

R = alkyl, $C_6H_5$). M. Cases, G. Frenking, M. Duran, M. Sola, *Organometallics* **2002**, *21*, 4182–4191.
[12] C. F. Bernasconi, M. Ali, *J. Am. Chem. Soc.* **1999**, *121*, 3039–3045.
[13] a) F. Robin-Le Guen, P. Le Poul, B. Caro, R. Pichon, N. Kervarec, *J. Organomet. Chem.* **2001**, *626*, 37–42; b) B. Caro, P. Le Poul, F. Robin-Le Guen, J.-Y. Saillard, S. Kahlal, C. Moinet, N. Le Poul, J. Vaissermann, *Tetrahedron* **2002**, *58*, 7519–7530.
[14] N. Faux, B. Caro, F. Robin-Le Guen, P. Le Poul, K. Nakatani, E. Ishow, *J. Organomet. Chem.* **2005**, *690*, 4982–4988.
[15] a) Aldehyde **1a** was obtained from the action of DMF on the corresponding 4-methylpyrylium salts followed by hydrolysis of the iminium salts by a 2% NaOH solution. G. A. Reynolds, J. A. van Allan, *J. Org. Chem.* **1969**, *34*, 2736–2741; b) Aldehydes **1b**–**1e** are formed by treatment of 4-unsubstituted chalcogenopyrylium salts with $NEt_3/I_2$ followed by $K_2CO_3$ salt action.D. H. Wadsworth, M. R. Detty, B. J. Murray, C. H. Weidner, N. F. Haley, *J. Org. Chem.* **1984**, *49*, 2676–2681; c) N. Faux, Thesis dissertation, Université de Rennes 1, **2004**.
[16] Hydrolysis performed with cold water decreases the thioester formation.
[17] Addition of chlorosilane reagents to heterocyclic aldehydes in $CH_2Cl_2$ solution gives a yellow precipitate of pyrylium salts: B. Caro, unpublished results. Another mechanism proposed by one referee is that the alkenylylidene complexes are produced in a two-step reaction. The first step is the reversible addition of a carbanion to the carbonyl group. This reaction occurs in any case (for benzaldehyde and heterocyclic aldehyde) but in the absence of TMSCl does not undergo the elimination to complexes **2a**–**2e** due to the electron-donating effect of the 4*H*-pyran-4-ylidene group.
[18] Carbene complex **3d** (Figure 1) is obtained from aldehyde **1d** (Scheme 1) and $CH_3(OCH_3)C{=}W(CO)_5$ by treatment with $NEt_3$ in the presence of TMSCl; see ref.[15c]
[19] C. Cosset, I. Del Rio, H. Le Bozec, *Organometallics* **1995**, *14*, 1938–1944.
[20] a) G. Scheibe, W. Seiffert, G. Hohlneicher, C. Jutz, H. J. Springer, *Tetrahedron Lett.* **1966**, *7*, 5053–5059; b) R. Radeglia, S. Dähne, *J. Mol. Struct.* **1970**, *5*, 399–411; c) M. Blanchard-Desce, V. Alain, P. V. Bedworth, S. R. Marder, A. Fort, C. Runser, M. Barzoukas, S. Lebus, R. Wortmann, *Chem. Eur. J.* **1997**, *3*, 1091–1104.
[21] R. J. Hoare, O. S. Mills, *J. Chem. Soc., Dalton Trans.* **1972**, 653–656.
[22] O. E. Fischer, M. Leupold, C. G. Kreiter, J. Müller, *Chem. Ber.* **1972**, *105*, 599–608.
[23] C. V. Senoff, J. E. H. Ward, *Inorg. Chem.* **1975**, *14*, 278–282.
[24] P. D. Woodgate, H. S. Sutherland, C. E. F. Rickard, *J. Organomet. Chem.* **2001**, *629*, 114–130.
[25] a) A. Abbotto, L. Beverina, S. Bradamante, A. Facchetti, C. Klein, G. A. Pagani, M. Redi-Abshiro, R. Wortmann, *Chem. Eur. J.* **2003**, *9*, 1991–2007; b) Z. Sainudeen, P. C. Ray, *J. Phys. Chem. A* **2005**, *109*, 9095–9103. It can be noted that the electronic structures of the zwitterionic merocyanines studied are sensitive to changes in the solvent.
[26] I. Turowska-Tyrk, T. M. Krygowski, P. Millart, *J. Mol. Struct.* **1991**, *263*, 235–245.
[27] J. J. Doney, C. H. Chen, H. R. Luss, *Tetrahedron Lett.* **1982**, *23*, 1747–1750.
[28] L. Millán, M. Fuentealba, C. Manzur, D. Carrillo, N. Faux, B. Caro, F. Robin-Le Guen, S. Sinbandhit, I. Ledoux-Rak, J. R. Hamon, *Eur. J. Inorg. Chem.* **2006**, 1131–1138.
[29] a) M. R. Detty, J. M. McKelvey, H. R. Luss, *Organometallics* **1988**, *7*, 1131–1147.
[30] R. Aumann, J. Schröder, *Chem. Ber.* **1990**, *123*, 2053–2058.
[31] For a recent review, see: A. T. Balaban, D. C. Onicia, A. R. Katrizky, *Chem. Rev.* **2004**, *104*, 2777–2812.
[32] D. D. Perrin, W. L. F. Armarego, D. R. Perrin, *Purification of Laboratory Chemicals*, Pergamon Press, New York, **1980**.
[33] G. M. Sheldrick, *SHELXS-97, Program for Crystal Structure Solution*, Göttingen, **1997**.
[34] G. M. Sheldrick, *SHELXL-97, Program for Crystal Structure Refinement*, Göttingen, **1997**.
[35] C. H. Lam, C. V. Senoff, J. E. H. Ward, *J. Organomet. Chem.* **1974**, *70*, 273–281.
[36] a) I. Maltey, J. A. Delaire, K. Nakatani, P. Wang, X. Shi, S. Wu, *Adv. Mater. Opt. Electron.* **1996**, *6*, 233–238; b) C. Bosshard, G. Knöpfle, P. Prêtre, P. Günter, *J. Appl. Phys.* **1992**, *71*, 1594–1605.

Received: April 4, 2006
Published Online: July 11, 2006

 © 2006 Wiley-VCH Verlag GmbH & Co. KGaA, Weinheim 

DOI: 10.1002/ejic.200600351

# Synthesis of a BEDT-TTF Bipyridine Organic Donor and the First $Fe^{II}$ Coordination Complex with a Redox-Active Ligand

**Katel Hervé,[a] Shi-Xia Liu,[b] Olivier Cador,[a] Stéphane Golhen,[a] Yann Le Gal,[a] Azzedine Bousseksou,[c] Helen Stoeckli-Evans,[d] Silvio Decurtins,[b] and Lahcène Ouahab*[a]**

**Keywords:** Iron / N ligands / BEDT-TTF / Synthesis design / Redox chemistry

The synthesis of the new ligand, BEDT-TTF-bipy [4,5-ethylenedithio-4′,5′-(4′-methyl-2,2′-dipyrid-4-ylethylenedithio)-tetrathiafulvalene] is reported. The first $Fe^{II}$ coordination complex, namely $[Fe(NCS)_2(BEDT\text{-}TTF\text{-}bipy)_2]\cdot CHCl_3$, with this redox-active ligand is obtained. Magnetic measurements and Mössbauer spectroscopy revealed the coexistence of high-spin and low-spin $Fe^{II}$ species with a ratio of 40:60 in this compound.
(© Wiley-VCH Verlag GmbH & Co. KGaA, 69451 Weinheim, Germany, 2006)

## Introduction

Charge transfer (CT) complexes based on organic donors such as TTF (tetrathiafulvalene) and its derivatives have been intensively studied.[1] Considerable efforts are currently devoted to the synthesis and investigations of new molecule-based materials involving interplay and synergy between multiple physical properties, such as electrical conductivity or superconductivity and magnetic effects, optical and magnetic properties or spin crossover.[2] Construction of such materials appears to be a challenging target for synthetic chemists who are faced with the difficult control of the self-assembly of molecular building blocks. This is indeed a crucial step to obtain a supramolecular compound that has the desired structure, stability and physical properties. Some significant achievements have been obtained in different directions: (i) light-induced magnetization[3] observed in a Prussian blue derivative, namely $K_{0.2}Co_{1.4}[Fe(CN)_6]\cdot 6.9H_2O$,[3c,3d] which exhibits a reversible photo-induced magnetization as a result of oxidation state changes for the metal ions from [$Co^{III}$, $S = 0$ and $Fe^{II}$, $S = 0$] to [$Co^{II}$, $S = 3/2$ and $Fe^{III}$, $S = 1/2$]; (ii) synergy between spin-crossover and magnetic interactions:[4] $[Fe(mnt)_2(rad)]$ [mnt = maleonitriledithiolate; rad = 2-(*para*-*N*-methylpyridinio)-4,4,5,5-tetramethylimidazolin-1-oxyl] exhibits a spin crossover between $S_{Fe} = 5/2$ at high temperature and $S_{Fe} = 1/2$ at low temperature and also an antiferromagnetic (AF) interaction at low temperature between the radical unit and $Fe^{III}$; (iii) electrical conductivity and magnetic interactions:[5–7] conducting materials incorporating localized spins are currently a subject of intense investigations and many compounds of this kind were obtained and characterized, such as $(BEDT\text{-}TTF)_3[MnCr(C_2O_4)_3]$ [BEDT-TTF = bis(ethylenedithio)tetrathiafulvalene (or ET)],[6a] $(BETS)_2FeCl_4$ [BETS = bis(ethylenedithio)tetraselenafulvalene],[6b] $(C1\text{-}TET\text{-}TTF)_2FeX_4$ [X = Cl, Br; C1-TET-TTF = 4,5-bis-(methylthio)-4′,5′-ethylenedithiotetrathiafulvalene].[2a]

Only two examples of hybrids with a combination of a spin cross-over property and electrical conductivity have been reported so far, namely $Fe(abpt)_2(TCNQ)_2$[8] and $[Fe(sal_2\text{-}trien)][Ni(dmit)_2]$.[9] However, in both cases no conductivity was observed. In order to enhance interactions between the two subsystems, a strategy consisting of the covalent linkage of paramagnetic transition-metal ions to redox-active ligands has been addressed.[7] However, to the best of our knowledge, there is no example of such a system with TTF derivatives as ligands. As a first attempt in this direction, we report here a detailed study on the synthesis and characterizations of the new ligand BEDT-TTF-bipy as well as its $Fe^{II}$ complex, namely $[Fe(NCS)_2(BEDT\text{-}TTF\text{-}bipy)_2]\cdot CHCl_3$.

## Results and Discussion

### Synthesis

The synthesis of ligand **6** was performed as shown in Scheme 1 by a phosphate-mediated cross-coupling method between chalcogenones **4** and **5**. The former was prepared by transchalcogenation of the corresponding thione **3**, the synthesis of which was based on the thermal depolymerization of oligomer **1** on heating, followed by Diels–Alder re-

[a] Equipe Organométalliques et Matériaux Moléculaires, UMR CNRS 6226 Sciences Chimiques de Rennes,
Campus de Beaulieu, 35042 Rennes Cedex, France
E-mail: lahcene.ouahab@univ-rennes1.fr
[b] Departement für Chemie und Biochemie, Universität Bern, Freiestrasse 3, 3012 Bern, Switzerland
[c] Laboratoire de Chimie de Coordination du CNRS, UPR 8241, 205 route de Narbonne, 31077 Toulouse Cedex, France
[d] Institut de Chimie, Université de Neuchâtel, Avenue de Bellevaux 51, 2007 Neuchâtel, Switzerland

 © 2006 Wiley-VCH Verlag GmbH & Co. KGaA, Weinheim 

action with 4-methyl-4′-vinyl-2,2′-bipyridine (**2**). All compounds were easily purified by chromatographic separation or precipitation and have been fully characterized. Compound **7** (Scheme 2) was obtained by allowing $Fe(NCS)_2$ to react with **6** in chloroform.

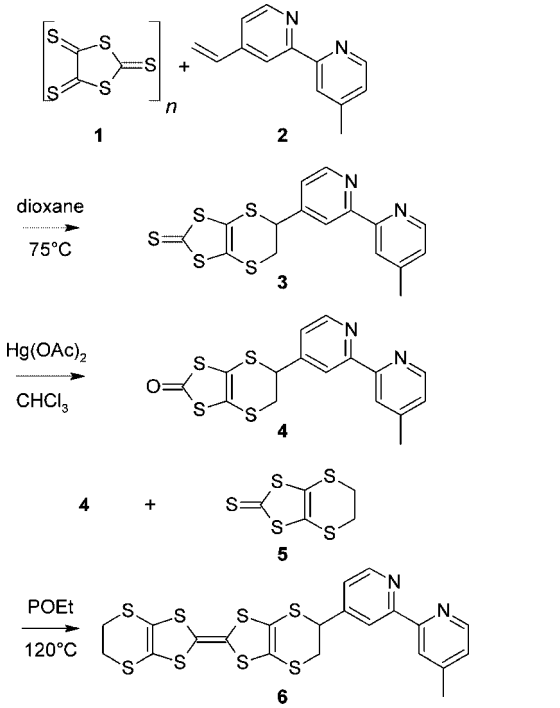


Scheme 1. Synthesis of BEDT-TTF-bipy (**6**).

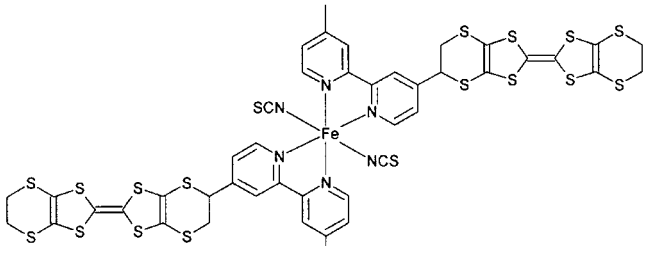


Scheme 2. One of the possible isomers of the $Fe^{II}$ complex **7**.

## Single-Crystal Structure of Compound 4

An ORTEP plot of molecule **4** with the atomic numbering scheme is shown in Figure 1.

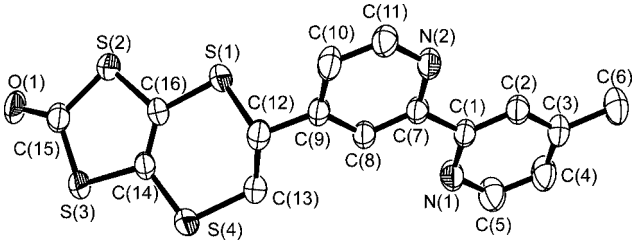


Figure 1. ORTEP (50% probability ellipsoids) structure of compound **4**. Hydrogen atoms are omitted for clarity. Selected bond lengths [Å]: S1–C16 1.754(2), S2–C16 1.745(2), S2–C15 1.765(3), S3–C14 1.748(2), S3–C15 1.765(3), S4–C14 1.747(3), S1–C12 1.839(3), S4–C13 1.808(3), O1–C15 1.207(3).

Molecule **4** contains an essentially planar moiety, comprising atoms C(14), C(15), C(16), O(1) and all four sulfur atoms; this plane forms an angle of 126.5° with the mean plane calculated from the C(7)–C(8)–C(9)–C(10)–C(11)–N(2) atoms belonging to the pyridyl ring. All atoms of the bipyridyl moiety lie almost perfectly within one plane with atoms N1 and N2 situated in *anti* orientation. As expected, S(1)–C(12) and S(4)–C(13) are typical single bonds, while the other C–S bonds are considerably shorter than that of a single C–S bond, indicating some delocalized π-bonding through the interaction of the sulfur d-orbitals with the C=C and C=O π-bonds. These C–S bond-length differences have been found in other analogous compounds.[10]

## Single Crystal Structure of Compound 6

Although the quality of the crystal of compound **6** was poor, it was possible to determine its crystal structure. An ORTEP plot of the molecule with the atomic numbering scheme is shown in Figure 2. Compared to compound **4**, the nitrogen atoms of the bipyridyl moiety also lie in an *anti* position, but an angle of 11.8(11)° is observed between the two pyridyl rings. The mean plane calculated from the pyridyl ring [C(11)–C(12)–C(13)–C(14)–C(15)–N(1)] directly bonded to the BEDT-TTF moiety, forms an angle of 75.2(5)° (see Figure 3) with the almost planar TTF skeleton [S(3)–S(4)–C(5)–C(6)–S(5)–S(6)]. As usual, a boat conformation is observed for the ET molecule. One can notice that the S(7)–C(9) and S(8)–C(10) bonds are significantly shorter than the corresponding ones [S(1)–C(12) and S(4)–C(13)] observed in compound **4** (see Figures 1 and 2).

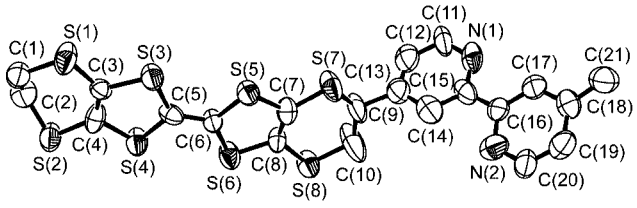


Figure 2. ORTEP structure of **6** with 50% probability ellipsoids. Hydrogen atoms are omitted for clarity. Selected bond lengths [Å]: S6–C8 1.723(16), S6–C6 1.734(15), S3–C5 1.720(17), S3–C3 1.787(16), S8–C8 1.731(17), S8–C10 1.78(2), S4–C5 1.753(16), S4–C4 1.76(2), S5–C6 1.731(16), S5–C7 1.762(19), C5–C6 1.42(2), C8–C7 1.38(3), C4–C3 1.32(3), S7–C9 1.72(3), S7–C7 1.729(18).

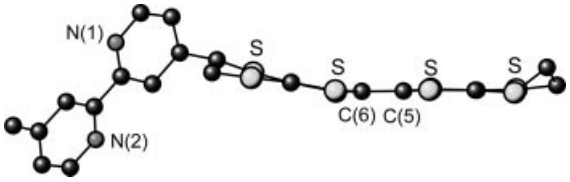


Figure 3. View of compound **6** showing the angle of 75.2(5)° between the TTF skeleton and the $N(1)C_5$ pyridyl ring.

## TGA of Compound 7

The detection of the temperature dependence of weight loss of $[Fe(NCS)_2(BEDT\text{-}TTF\text{-}bipy)_2]\cdot CHCl_3$ was carried

 © 2006 Wiley-VCH Verlag GmbH & Co. KGaA, Weinheim 

out on a powdered sample between 25 and 150 °C, where the compound starts to decompose. In total, a weight loss of 8.1% is observed within the range 25–65 °C. The gas analysis by means of mass spectrometry coupled to TGA revealed the presence of chloroform only. The calculated weight loss for one molecule of $CHCl_3$ is equal to 8.5%.

### Electrochemical Measurements of Compound 7

The solution redox properties of the new donor ligand **6** and of the target compound **7** were investigated by cyclic voltammetry (CV), in dichloromethane. Table 1 gives these results and those obtained for BEDT-TTF (ET) under the same conditions. In each case, two typical reversible single-electron redox couples are observed, corresponding to respective formations of the monocation followed by the dication. No difference is observed between ET and donor **6** redox potentials, showing that the methylbipyridyl group has no effect on the redox potentials. The first potential of compound **7** remains unaffected while the second potential decreases.

Table 1. Cyclic voltammetric data[a].

| Compound | $E_1^{1/2}$ [V] | $E_2^{1/2}$ [V] | $E(Fe^{2+}/Fe^{3+})$ [mV] | $\Delta E = E_2^{1/2} - E_1^{1/2}$ [mV] |
|---|---|---|---|---|
| ET | 0.52 | 0.94 | | 420 |
| **6** | 0.55 | 0.95 | | 400 |
| **7** | 0.55 | 0.86 | 1100 | 310 |

[a] All oxidation potentials were determined under $N_2$ in $CH_2Cl_2$ vs. ESC at room temperature. Measurements have been performed at a scan rate of 100 mV·s$^{-1}$ using 0.1 M $(Bu_4N)PF_6$ as the electrolyte and Pt as the working electrode.

### UV/Vis Spectra of Compound 7

The room-temperature UV/Vis absorption spectra of BEDT-TTF-bipy and $[Fe(NCS)_2(BEDT\text{-}TTF\text{-}bipy)_2]$ in DMF solution are shown in Figure 4. The spectra mainly reveal that upon complexation, an intense broad band appears at around 19000 cm$^{-1}$. This band is characteristic of the Fe–bipyridine metal-to-ligand charge transfer (MLCT).[11,12] The presence of this MLCT band reflects the formation of the complex $[Fe(NCS)_2(BEDT\text{-}TTF\text{-}bipy)_2]$. The intense absorption band observed at energies > 25000 cm$^{-1}$ corresponds to the tail of the intra-ligand charge transfer π-π*.[13,14]

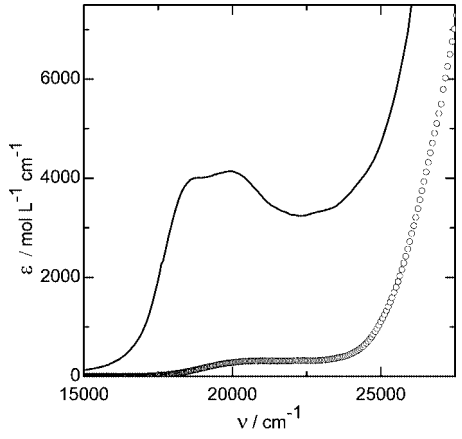


Figure 4. Absorption spectra of **6** (circles) and $[Fe(NCS)_2(BEDT\text{-}TTF\text{-}bipy)_2]$ (—) in dimethylformamide solution.

### Magnetic Susceptibility of Compound 7

The thermal dependence of the $\chi_M T$ product of $[Fe(NCS)_2(BEDT\text{-}TTF\text{-}bipy)_2]\cdot CHCl_3$ is represented in Figure 5. At room temperature, $\chi_M T$ is equal to 1.65 cm$^3$·K·mol$^{-1}$ and the value remains almost constant down to 60 K where it starts to decrease. The room-temperature value is, on the one hand, much lower than the expected value for a high-spin (HS) $Fe^{II}$ species ($\chi_M T \approx$ 3.7 cm$^3$·K·mol$^{-1}$)[15] and, on the other hand, much higher than the expected value for a purely low-spin (LS) $Fe^{II}$ species ($\chi_M T \approx$ 0.1 cm$^3$·K·mol$^{-1}$).[16] We may therefore conclude that both HS and LS $Fe^{II}$ species are mixed together, the ratio being close to 40:60. It may also be the result of the presence of *cis*/*trans* configurations in the complex, but this could not be answered conclusively. The lowering of $\chi_M T$ at low temperatures can be due to the zero-field splitting of $Fe^{II}$[17] and intermolecular antiferromagnetic interactions between the metal centres.

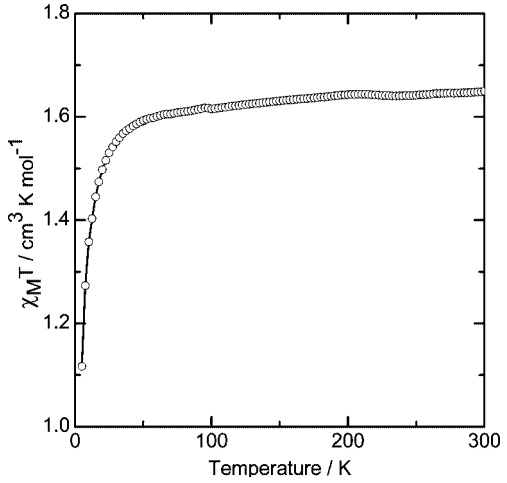


Figure 5. Thermal variation of $\chi_M T$ for a powdered sample of $[Fe(NCS)_2(BEDT\text{-}TTF\text{-}bipy)_2]\cdot CHCl_3$.

### Mössbauer Spectroscopy of Compound 7

The Mössbauer spectrum of $[Fe(NCS)_2(BEDT\text{-}TTF\text{-}bipy)_2]\cdot CHCl_3$ at 80 K is shown in Figure 6. The spectrum shows unambiguously the presence of two spin states for $Fe^{II}$: a high-spin state, characterized by a doublet with quadrupole splitting $\Delta E_Q$ = 2.70(1) and an isomer shift $IS$ = 1.000(6) mm·s$^{-1}$ and a low-spin state, characterized by a second quadrupolar doublet with quadrupole splitting $\Delta E_Q$ = 0.369(2) and an isomer shift $IS$ = 0.367(1) mm·s$^{-1}$. These Mössbauer parameters are in good agreement with those

 © 2006 Wiley-VCH Verlag GmbH & Co. KGaA, Weinheim 

observed in the literature for high-spin and low-spin $Fe^{II}$ compounds.[18] On the basis of equal Debye–Waller factors ($f$) for HS and LS $Fe^{II}$, the ratios $A_{HS}/A_{TOT}$ and $A_{LS}/A_{TOT}$ result in 0.25(1) and 0.75(1), respectively. However, this parameter for the resonating nuclei can differ distinctly for HS and LS $Fe^{II}$,[19] whereby the determined LS area ($A_{LS}$) overestimates the LS molar fraction if $f_{HS} = f_{LS}$ is assumed. Consequently, an HS $Fe^{II}$ fraction in the order of 0.3–0.4 can be estimated in fairly good agreement between the magnetic and the Mössbauer measurements.

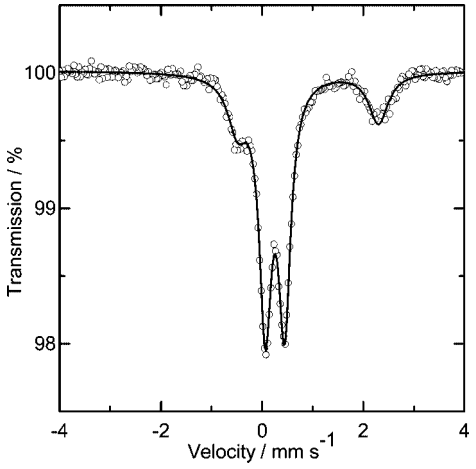


Figure 6. Mössbauer spectrum of $[Fe(NCS)_2(BEDT\text{-}TTF\text{-}bipy)_2]\cdot CHCl_3$ at 80 K. The spectrum is characterized by two quadruple doublet characteristics of high-spin and low-spin states of $Fe^{II}$, respectively.

## Conclusions

We reported in this contribution a detailed synthesis and structure of a new ligand, namely BEDT-TTF-bipy as well as the first $Fe^{II}$ coordination complex, namely $[Fe(NCS)_2(BEDT\text{-}TTF\text{-}bipy)_2]\cdot CHCl_3$ with this redox-active ligand. Although it was not possible to obtain single crystals of this complex, the use of different techniques (TGA, elemental analysis, cyclic voltammetry, magnetic measurements, UV and Mössbauer spectroscopy) allowed us to fully characterize this material. Magnetic measurements and Mössbauer spectroscopy showed a mixture of high-spin and low-spin $Fe^{II}$ species with a ratio of 40:60 in this complex. Moreover, one of the reasons for the lack of crystallization might be the existence of several possible isomers for this compound. In order to limit the number of isomers, work is underway to prepare the corresponding ligand with a terminal C=C double bond [C(9)–C(10) in Figure 2].

## Experimental Section

**General:** X-ray data for compound **4** were collected at 253 K with a Stoe Image Plate Diffraction System,[20] while for compound **6** data were collected at room temperature with an Enraf–Nonius four-circle diffractometer equipped with a CCD camera (CDFIX centre of Université de Rennes 1). Both sets of data were collected using an Mo-$K_\alpha$ graphite-monochromated radiation source ($\lambda$ = 0.71073 Å). The room-temperature UV/Vis absorption spectra were obtained with a BIO-TEK Instruments UVIKON-XL spectrophotometer. The magnetic susceptibility $\chi_M$ was recorded with a Quantum Design MPMS SQUID magnetometer operating in the 2–300 K temperature range at a field of 1 T. The experimental data have been corrected from the diamagnetism of the sample holder and the intrinsic diamagnetism of the materials evaluated with Pascal's tables. Mössbauer measurements were obtained on a constant-acceleration spectrometer with a 50 mCi source of $^{57}Co$ (Rh matrix). The isomer shift values (*IS*) are given with respect to metallic iron at room temperature. The absorber was a sample of microcrystalline powder enclosed in a 2 cm diameter cylindrical plastic sample holder, the size of which was determined to optimize the absorption. The 80 K spectrum was obtained by using an MD306 Oxford cryostat, the thermal scanning being monitored by an Oxford ITC4 servocontrol device (±0.1 K). Fitting parameters for all spectra were obtained by using a least-squares computer program. The standard deviations of statistical origin of the Mössbauer parameters are given in parentheses. Cyclic voltammetry measurements were conducted with an EDAC EA161 Potentiostat. Thermogravimetric analysis was performed with a SETARAM LABSYS DTA-TG/DSC apparatus coupled to a Pfeiffer Omnistar mass spectrometer.

**Synthesis:** All reagents were of analytical grade and used as received. All reactions were carried out under argon, using freshly distilled and degassed solvents. The $[C_3S_5]_x$ oligomer **1**[21] and 4-methyl-4′-vinyl-2,2′-bipyridine (**2**)[22] were prepared according to literature procedures.

**4,5-[(4′-Methyl-2,2′-dipyrid-4-yl)ethylenedithio]-1,3-dithiole-2-thione (3):** A mixture of oligomer **1** (1 g) and compound **2** (1 g, 5.1 mmol) in dioxane (20 mL) was heated to 75 °C and stirred for 1.5 h. The resulting mixture was filtered hot and the precipitate was further washed with dichloromethane (3 × 25 mL) to completely extract the product. The filtrate and combined washings were treated with activated charcoal. After filtration, the solvent was evaporated under vacuum to give a yellow oil that was purified by chromatography on silica gel with dichloromethane/ethyl acetate (1:1) to afford a yellow powder (1.44 g, 72%). $C_{16}H_{12}N_2S_5\cdot 0.3C_4H_8O_2$ (419.05): calcd. C 49.30, H 3.46, N 6.69; found C 49.50, H 3.16, N 6.64.

**4,5-(4′-Methyl-2,2′-dipyrid-4-ylethylenedithio)-1,3-dithiol-2-one (4):** To a solution of **3** (0.4 g, 1 mmol) in chloroform (55 mL) and acetic acid (7 mL), was added $Hg(OAc)_2$ (0.935 g, 2.9 mmol). The mixture was stirred at room temperature for 45 min. During this period, the suspension changed colour from yellow to white. The resulting white precipitate was filtered off using Celite and washed thoroughly with $CHCl_3$. The filtrate and combined washings were neutralized with a saturated $Na_2CO_3$ aqueous solution and then extracted with water (3 × 40 mL). After drying with $Na_2SO_4$, the combined organic phases were concentrated under vacuum. The resulting oily product was solidified upon the addition of diethyl ether to give **4** as a pale yellow powder (0.28 g, 73%). $C_{16}H_{12}N_2OS_4\cdot 0.2C_4H_{10}O$ (391.36): calcd. C 51.56, H 3.60, N 7.16; found C 50.70, H 3.57, N 6.90.

**4,5-Ethylenedithio-4′,5′-(4′-methyl-2,2′-dipyrid-4-ylethylenedithio)-tetrathiafulvalene (6):** A suspension of 4,5-ethylenedithio-1,3-dithiole-2-thione (**5**)[23] (0.26 g, 1.16 mmol) and compound **4** (0.3 g, 0.54 mmol) in triethyl phosphite (5 mL) under nitrogen was heated to 120 °C and stirred for 2 h. After cooling to room temperature, a red precipitate had formed, which was filtered off and washed with diethyl ether to afford analytically pure **6** as a red powder

 © 2006 Wiley-VCH Verlag GmbH & Co. KGaA, Weinheim 

(0.19 g, 44%). $C_{21}H_{16}N_2S_8{\cdot}0.5H_2O$ (561.89): calcd. C 44.89, H 2.85, N 4.99; found C 44.88, H 2.90, N 4.57.

**$[Fe(NCS)_2(BEDT\text{-}TTF\text{-}bipy)_2]{\cdot}CHCl_3$ (7):** A mixture of $FeSO_4{\cdot}7H_2O$ (25.2 mg, 0.09 mmol), KNCS (17.6 mg, 0.18 mmol) and a pinch of ascorbic acid in 3 mL of freshly distilled methanol was stirred at room temperature for 30 min. After filtration, the resulting colourless solution of $Fe(NCS)_2$ was added dropwise to a solution of compound **6** (100 mg, 0.18 mmol) in distilled chloroform (22 mL). A red-brown precipitate formed immediately, which was filtered off and washed with MeOH and $CHCl_3$ to give the desired $Fe^{II}$ complex as a dark-purple powder (87 mg, 75%). $C_{44}H_{32}FeN_6S_{18}{\cdot}CHCl_3$ (1397.17): calcd. C 38.68, H 2.38; N 6.01, S 41.31; Fe 4.00; found C 38.97, H 2.45, N 6.46, S 39.95, Fe 4.42.

**X-ray Crystallography. 4:** A pale-yellow, rod-like crystal of compound **4** ($0.42\times0.15\times0.11$ mm) was obtained by slow concentration of a solution of compound **4** in a mixture of $CH_2Cl_2$ and ethyl acetate. The intensity data were collected at 253 K. This compound crystallized in the $P\bar{1}$ triclinic space group with the following parameters: $a$ = 5.6428(7) Å, $b$ = 10.1851(13) Å, $c$ = 15.158(2) Å, $\alpha$ = 105.847(15)°, $\beta$ = 94.448(16)°, $\gamma$ = 103.526(15)°, $V$ = 805.5(2) Å$^3$, $Z$ = 2, $\mu$ = 0.594 mm$^{-1}$, 2911 unique for 5724 collected reflections, $R_1$ = 0.0392, $wR_2$ = 0.1039. **6:** Compound **6** was dissolved in a mixture of $CH_2Cl_2$ and ethyl acetate and heated in an ultrasonic bath. The resulting solution was filtered and a few drops of methanol were added to the solution. After slow concentration, a few crystals of **6** of very low quality were obtained. The intensity data were collected at room temperature. This compound crystallized in the monoclinic space group $P2_1/c$ with the following parameters: $a$ = 6.8420(4) Å, $b$ = 17.6760(11) Å, $c$ = 19.2560(14) Å, $\beta$ = 96.146(2)°, $V$ = 2315.4(3) Å$^3$, $Z$ = 4, $\mu$ = 0.785 mm$^{-1}$, 4026 unique for 13627 collected reflections, $R_1$ = 0.1949, $wR_2$ = 0.4551. All structures were solved by direct methods using the program SHELXS-97.[24] The refinement and all further calculations were carried out using SHELXL-97.[25] H-atom positions were calculated as a riding model. Non-H atoms were refined anisotropically, using weighted full-matrix least squares on $F^2$. CCDC-287337 and -600718 contain the supplementary crystallographic data for this paper. These data can be obtained free of charge from The Cambridge Crystallographic Data Centre via www.ccdc.cam.ac.uk/data_request/cif.

## Acknowledgments

This work was supported by the CNRS, the EU through MAGMANet, the Germaine de Staël exchange program no. 05410TD and La Région Bretagne with projects SIE no. 05012917 and PRIR no. 05013053.

[1] a) T. Ishiguro, K. Yamaji, G. Saito, *Organic Superconductors*, 2nd ed., Springer, Heidelberg, Germany, **1998**; b) J. M. Williams, J. R. Ferraro, R. J. Thorn, K. D. Carlson, U. Geiser, H. H. Wang, A. M. Kini, M. H. Whangbo, *Organic Superconductors. Synthesis Structure, Properties and Theory*, Prentice Hall, Englewood Cliffs, New Jersey, **1992**; c) J. L. Segura, N. Martín, *Angew. Chem. Int. Ed.* **2001**, *40*, 1372 and references cited therein.

[2] a) A. Miyazaki, T. Enoki, *Chem. Rev.* **2004**, *104*, 5449; b) E. Coronado, P. Day, *Chem. Rev.* **2004**, *104*, 5419; c) L. Ouahab, T. Enoki, *Eur. J. Inorg. Chem.* **2004**, *5*, 933; d) L. Ouahab, *Chem. Mater.* **1997**, *9*, 1909.

[3] a) O. Sato, T. Iyoda, A. Fujishima, K. Hashimoto, *Science* **1996**, *272*, 704; b) S. Ohkoshi, A. Fujishima, K. Hashimoto, *J. Am. Chem. Soc.* **1998**, *120*, 5349; c) O. Kahn, O. Cador, J. Larionova, C. Mathonière, J.-P. Sutter, L. Ouahab, *Mol. Cryst., Liq. Cryst.* **1997**, *305*, 1; d) S. Turner, C. Michaut, O. Kahn, L. Ouahab, A. Lecas, E. Amouyal, *New J. Chem.* **1995**, *19*, 773.

[4] J.-P. Sutter, M. Fettouhi, C. Michaut, L. Li, L. Ouahab, O. Kahn, *Angew. Chem. Int. Ed. Engl.* **1996**, *35*, 2113.

[5] a) S. S. Turner, C. Michaut, S. Durot, P. Day, T. Gelbrich, M. B. Hursthouse, *J. Chem. Soc., Dalton Trans.* **2000**, 905; b) F. Setifi, S. Golhen, L. Ouahab, A. Miyazaki, K. Okabe, T. Enoki, T. Toita, J. Yamada, *Inorg. Chem.* **2002**, *41*, 3786.

[6] a) E. Coronado, J. R. Galan-Mascaros, C. J. Gomez-García, V. N. Laukhin, *Nature* **2000**, *408*, 447; b) H. Fujiwara, E. Fujiwara, Y. Nakazawa, B. Z. Narymbetov, K. Kato, H. Kobayashi, A. Kobayashi, M. Tokumoto, P. Cassoux, *J. Am. Chem. Soc.* **2001**, *123*, 306.

[7] a) F. Setifi, L. Ouahab, S. Golhen, Y. Yoshida, G. Saito, *Inorg. Chem.* **2003**, *42*, 1791; b) F. Iwahori, S. Golhen, L. Ouahab, R. Carlier, J.-P. Sutter, *Inorg. Chem.* **2001**, *40*, 6541; c) S.-X. Liu, S. Dolder, P. Franz, A. Neels, H. Stoeckli-Evans, S. Decurtins, *Inorg. Chem.* **2003**, *42*, 4801; d) N. Arvarvari, M. Fourmigué, *Chem. Commun.* **2004**, 1300; e) T. Sugawara, *Mol. Cryst. Liq. Cryst.* **1999**, *334*, 257.

[8] P. J. Kunkeler, P. J. van Koningsbruggen, J. P. Cornelissen, A. N. van der Horst, A. M. van der Kraan, A. L. Spek, J. G. Haasnoot, J. Reedijk, *J. Am. Chem. Soc.* **1996**, *118*, 2190.

[9] S. Dorbes, L. Valade, J. A. Real, C. Faulmann, *Chem. Commun.* **2005**, 69.

[10] G.-Q. Liu, W.-T. Yu, G. Xue, Z. Liu, Q. Fang, *Acta Crystallogr. Sect. E* **2002**, *58*, o514.

[11] S. Schenker, P. C. Stein, J. A. Wolny, C. Brady, J. J. McGarvey, H. Toftlund, A. Hauser, *Inorg. Chem.* **2001**, *40*, 134.

[12] G. Chastanet, C. Carbonera, C. Mingotaud, J.-F. Létard, *J. Mater. Chem.* **2004**, *14*, 3516.

[13] E. König, K. Madeja, *Inorg. Chem.* **1967**, *6*, 1.

[14] E. König, K. Madeja, K. J. Watson, *J. Am. Chem. Soc.* **1968**, *90*, 1146.

[15] J.-F. Létard, G. Chastanet, O. Nguyen, S. Marcén, M. Marchivie, P. Guionneau, D. Chasseau, P. Gütlich, *Monatsh. Chem.* **2003**, *134*, 165.

[16] S. Decurtins, P. Gütlich, K. M. Hasselbach, A. Hauser, H. Spiering, *Inorg. Chem.* **1985**, *24*, 2174.

[17] A. Bousseksou, M. Verelst, H. Constant-Machado, G. Lemercier, J.-P. Tuchagues, F. Varret, *Inorg. Chem.* **1996**, *35*, 110.

[18] S. Decurtins, P. Gütlich, C. P. Köhler, H. Spiering, *J. Chem. Soc., Chem. Commun.* **1985**, 430.

[19] P. Poganiuch, S. Decurtins, P. Gütlich, *J. Am. Chem. Soc.* **1990**, *112*, 3270.

[20] Stoe & Cie, *IPDS Software*, Stoe & Cie GmbH, Darmstadt, Germany, **2000**.

[21] N. Svenstrup, J. Becher, *Synthesis* **1995**, 215.

[22] H. D. Abruna, A. I. Breikss, D. B. Collum, *Inorg. Chem.* **1985**, *24*, 987.

[23] K. S. Varma, A. Bury, N. J. Harris, A. E. Underhill, *Synthesis* **1987**, 837.

[24] SHELXS-97, Program for Crystal Structure Determination: G. M. Sheldrick, *Acta Crystallogr. Sect. A* **1990**, *46*, 467.

[25] G. M. Sheldrick, *SHELXL-97*, University of Göttingen, Göttingen, Germany, **1999**.

Received: April 20, 2006
Published Online: July 21, 2006

 © 2006 Wiley-VCH Verlag GmbH & Co. KGaA, Weinheim 

DOI: 10.1002/ejic.200600353

# Crystal Structure and Magnetic Behaviour of the New Gadolinium Carboxylates $Gd_2(ClF_2CCOO)_6(hypy)_2$, $Gd_2(F_3CCOO)_6(hypy)_2$, $Gd_2(F_2HCCOO)_6(hypy)_2$ and $Gd_2(Cl_2HCCOO)_6(H_2O)_2(hypy)_2$

**Daniela John[a] and Werner Urland*[a]**

**Keywords:** Gadolinium / Carboxylates / O ligands / X-ray diffraction / Crystal structures / Magnetic properties

Four complexes with the formulae $Gd_2(ClF_2CCOO)_6(hypy)_2$ (**1**), $Gd_2(F_3CCOO)_6(hypy)_2$ (**2**), $Gd_2(F_2HCCOO)_6(hypy)_2$ (**3**) and $Gd_2(Cl_2HCCOO)_6(H_2O)_2(hypy)_2$ (**4**) have been synthesised and characterised by single-crystal X-ray diffraction methods at room temperature. The title compounds have been obtained by reaction of the corresponding gadolinium carboxylates with 4-hydroxypyridine in a solution of ethanol and water. They crystallise in the triclinic space group $P\bar{1}$ ($Z$ = 2) [**1**: $a$ = 999.8(4) pm, $b$ = 1061.8(5) pm, $c$ = 1283.6(6) pm, $\alpha$ = 91.23(5)°, $\beta$ = 111.29(5)° and $\gamma$ = 105.27(5)°; **2**: $a$ = 972.4(4) pm, $b$ = 1053.5(5) pm, $c$ = 1252.4(6) pm, $\alpha$ = 94.23(5)°, $\beta$ = 110.21(5)° and $\gamma$ = 104.84(5)°; **3**: $a$ = 883.3(4) pm, $b$ = 1051.3(4) pm, $c$ = 1284.9(6) pm, $\alpha$ = 100.46(5)°, $\beta$ = 109.87(5)° and $\gamma$ = 97.43(5)°; **4**: $a$ = 913.7(4) pm, $b$ = 1079.0(5) pm, $c$ = 1137.5(5) pm, $\alpha$ = 93.41(5)°, $\beta$ = 109.36(5)° and $\gamma$ = 99.53(5)°]. The crystal structures consist of dinuclear $Gd^{3+}$–$Gd^{3+}$ units. The corresponding residuals (all data) for the refined structures are 4.82 % (**1**), 5.93 % (**2**), 5.68 % (**3**) and 4.04 % (**4**). The magnetic behaviour of the compounds was investigated over the temperature range 1.76–300 K. The magnetic data were interpreted by considering exchange interactions within the dimeric units [$J_{ex}$ = –0.019 $cm^{-1}$ (**1**), $J_{ex}$ = –0.034 $cm^{-1}$ (**2**), $J_{ex}$ = –0.064 $cm^{-1}$ (**3**), $J_{ex}$ = –0.011 $cm^{-1}$ (**4**)].

(© Wiley-VCH Verlag GmbH & Co. KGaA, 69451 Weinheim, Germany, 2006)

## Introduction

In connection with the investigations of the structural chemistry of polynuclear complexes of lanthanides that are of importance for the study of magnetic interactions,[1–16] we paid attention to the carboxylates $Gd_2(X_kH_mCCOO)_6(H_2O)_n(hypy)_2$ [X = Cl, F; $k$ = 2, 3; $m$ = 0, 1; $n$ = 0, 2; hypy: tautomerised 4-hydroxypyridine = 4-(1*H*)-pyridone]. There are no simple rules to predict the occurrence of ferro- or antiferromagnetic coupling, unlike those of Goodenough and Kanamori for compounds of d elements.[17] In order to eliminate this nescience we determined the magnetic behaviour of the title compounds. The magnetic data were interpreted by considering magnetic exchange coupling in the dinuclear $Gd^{3+}$–$Gd^{3+}$ units.[17,18]

## Results and Discussion

### Crystal Structures

The crystal data and details of the refinements for **1**, **2**, **3** and **4** are summarised in Table 1, selected bond lengths can be found in Table 2.

[a] Institut für Anorganische Chemie der Universität Hannover, Callinstrasse 9, 30167 Hannover, Germany
Fax: +49-511-762-19032
E-Mail: urland@acc.uni-hannover.de

The title compounds crystallise in the triclinic space group $P\bar{1}$ (Z = 2) with **1**: $a$ = 999.8(4) pm, $b$ = 1061.8(5) pm, $c$ = 1283.6(6) pm, $\alpha$ = 91.23(5)°, $\beta$ = 111.29(5)° and $\gamma$ = 105.27(5)°; **2**: $a$ = 972.4(4) pm, $b$ = 1053.5(5) pm, $c$ = 1252.4(6) pm, $\alpha$ = 94.23(5)°, $\beta$ = 110.21(5)° and $\gamma$ = 104.84(5)°; **3**: $a$ = 883.3(4) pm, $b$ = 1051.3(4) pm, $c$ = 1284.9(6) pm, $\alpha$ = 100.46(5)°, $\beta$ = 109.87(5)° and $\gamma$ = 97.43(5)°; **4**: $a$ = 913.7(4) pm, $b$ = 1079.0(5) pm, $c$ = 1137.5(5) pm, $\alpha$ = 93.41(5)°, $\beta$ = 109.36(5)° and $\gamma$ = 99.53(5)°.

#### *$Gd_2(ClF_2CCOO)_6(hypy)_2$ (1)*

The crystal structure is shown in Figure 1. The $Gd^{3+}$ ions are connected ($Gd^{3+}$–$Gd^{3+}$ distance is 386.6 pm) through two carboxylate groups ($\mu_2$-carboxylato-$\kappa^1O$:$\kappa^1O'$) and two 4-(1*H*)-pyridone molecules ($\mu_2$-pyridone-1:2$\kappa^2O$) to form dimers (Figure 2). In addition each $Gd^{3+}$ ion is chelated by two chlorodifluoroacetate ions and one pyridone molecule (Figure 2). The central ion is ninefold coordinated by oxygen atoms originating from the carboxylate groups ($Gd^{3+}$–O distances are 240.2–268.3 pm) and three pyridone molecules ($Gd^{3+}$–O distances are 226.4–246.6 pm).

The 4-(1*H*)-pyridone molecules form the extended structure through π–π stacking interactions (Figure 3).[19,20] The shortest orthogonal distance between two aromatic fragments is 325.4 pm.

 © 2006 Wiley-VCH Verlag GmbH & Co. KGaA, Weinheim 

Table 1. Crystallographic data for $Gd_2(ClF_2CCOO)_6(hypy)_2$ (**1**), $Gd_2(F_3CCOO)_6(hypy)_2$ (**2**), $Gd_2(F_2HCCOO)_6(hypy)_2$ (**3**) and $Gd_2(Cl_2HCCOO)_6(H_2O)_2(hypy)_2$ (**4**).

| Compound | **1** | **2** | **3** | **4** |
|---|---|---|---|---|
| Crystal system | triclinic | triclinic | triclinic | triclinic |
| Space group | $P\bar{1}$ | $P\bar{1}$ | $P\bar{1}$ | $P\bar{1}$ |
| Lattice constants [pm,°] | $a$ = 999.8(4) | $a$ = 972.4(4) | $a$ = 883.3(4) | $a$ = 913.7(4) |
| | $b$ = 1061.8(5) | $b$ = 1053.5(5) | $b$ = 1051.3(4) | $b$ = 1079.0(5) |
| | $c$ = 1283.6(6) | $c$ = 1252.4(6) | $c$ = 1284.9(6) | $c$ = 1137.5(5) |
| | $\alpha$ = 91.23(5) | $\alpha$ = 94.23(5) | $\alpha$ = 100.46(5) | $\alpha$ = 93.41(5) |
| | $\beta$ = 111.29(5) | $\beta$ = 110.21(5) | $\beta$ = 109.87(5) | $\beta$ = 109.36(5) |
| | $\gamma$ = 105.27(5) | $\gamma$ = 104.84(5) | $\gamma$ = 97.43(5) | $\gamma$ = 99.53(5) |
| $V$ [pm$^3$] | $1214.4(9)\times10^6$ | $1145.1(9)\times10^6$ | $1079.7(8)\times10^6$ | $1035.4(8)\times10^6$ |
| $Z$ | 2 | 2 | 2 | 2 |
| $\rho$ (X-ray) [g·cm$^3$] | 2.012 | 1.991 | 1.946 | 2.098 |
| Absorption coefficient $\mu$ [mm$^{-1}$] | 3.151 | 3.013 | 3.168 | 4.014 |
| $F$(000) | 706 | 658 | 610 | 626 |
| Crystal dimensions [mm] | $0.333\times0.222\times0.222$ | $0.407\times0.333\times0.2405$ | $0.222\times0.992\times0.407$ | $0.481\times0.666\times0.148$ |
| Temperature [K] | 293(2) | | | |
| Wavelength | Mo-$K_\alpha$ ($\lambda$ = 71.073 pm) | | | |
| $\theta$ range [°] | $2.29 \le 2\theta \le 26.25$ | $2.34 \le 2\theta \le 26.23$ | $2.32 \le 2\theta \le 26.24$ | $2.41 \le 2\theta \le 26.20$ |
| Index range ($h$, $k$, $l$) | $-12 \le h \le 12$ | $-11 \le h \le 11$ | $-10 \le h \le 10$ | $-11 \le h \le 11$ |
| | $-13 \le k \le 13$ | $-13 \le k \le 13$ | $-12 \le k \le 12$ | $-13 \le k \le 13$ |
| | $-15 \le l \le 15$ | $-15 \le l \le 15$ | $-15 \le l \le 15$ | $-14 \le l \le 14$ |
| No. of collected reflections | 17685 | 16568 | 15712 | 15064 |
| No. of independent reflections | 4519 | 4243 | 4007 | 3849 |
| Observed reflections with $F > 2\sigma$ | 4139 | 3876 | 3527 | 3647 |
| $R_{int}$ | 0.0697 | 0.0912 | 0.0858 | 0.0705 |
| Structure refinement | Full-matrix, least-squares | | | |
| No. of refined parameters | 325 | 327 | 298 | 252 |
| Goodness-of-fit[a] | 1.095 | 1.122 | 1.078 | 1.094 |
| Residuals [$I > 2\sigma(I)$][a] | $R_1$ = 0.0446 | $R_1$ = 0.0559 | $R_1$ = 0.0506 | $R_1$ = 0.0386 |
| | $wR_2$ = 0.1187 | $wR_2$ = 0.1445 | $wR_2$ = 0.1329 | $wR_2$ = 0.1013 |
| Residuals (all data)[a] | $R_1$ = 0.0482 | $R_1$ = 0.0593 | $R_1$ = 0.0568 | $R_1$ = 0.0404 |
| | $wR_2$ = 0.1241 | $wR_2$ = 0.1545 | $wR_2$ = 0.1384 | $wR_2$ = 0.1045 |
| Largest differential hole and peak [e pm$^{-3}$] | $-1.758\times10^{-6}$/ $1.431\times10^{-6}$ | $-0.551\times10^{-6}$/ $0.622\times10^{-6}$ | $-2.691\times10^{-6}$/ $1.319\times10^{-6}$ | $-2.012\times10^{-6}$/ $1.684\times10^{-6}$ |
| CCDC deposition number[27] | 604198 | 604200 | 604199 | 604197 |

[a] Definition given in the literature.[25]

Table 2. Selected interatomic distances [pm] for $Gd_2(ClF_2CCOO)_6(hypy)_2$ (**1**), $Gd_2(F_3CCOO)_6(hypy)_2$ (**2**), $Gd_2(F_2HCCOO)_6(hypy)_2$ (**3**) and $Gd_2(Cl_2HCCOO)_6(H_2O)_2(hypy)_2$ (**4**).

| **1** | | **2** | | **3** | | **4** | |
|---|---|---|---|---|---|---|---|
| Gd–Gd[a] | 386.6(3) | Gd–Gd[a] | 387.7(3) | Gd–Gd[a] | 388.0(3) | Gd–Gd[b] | 405.1(2) |
| Gd–O(1B) | 226.4(4) | Gd–O(1A) | 224.8(6) | Gd–O(1A) | 228.1(5) | Gd–O(1A) | 224.6(4) |
| Gd–O(1A) | 235.7(4) | Gd–O(1B) | 234.6(5) | Gd–O(1B) | 233.7(5) | Gd–O11 | 230.4(4) |
| Gd–O32 | 240.2(5) | Gd–O31 | 240.3(5) | Gd–O31 | 241.1(6) | Gd–O31 | 237.8(3) |
| Gd–O31 | 241.7(5) | Gd–O32 | 240.8(6) | Gd–O32 | 242.8(6) | Gd–O22 | 239.0(4) |
| Gd–O(1A)[a] | 246.6(4) | Gd–O(1B)[a] | 247.3(5) | Gd–O22 | 247.1(7) | Gd–O(1W) | 239.3(4) |
| Gd–O21 | 248.6(5) | Gd–O22 | 250.4(6) | Gd–O(1B)[a] | 249.6(6) | Gd–O21 | 239.8(4) |
| Gd–O12 | 253.2(6) | Gd–O12 | 253.4(6) | Gd–O11 | 257.8(7) | Gd–O32 | 250.3(4) |
| Gd–O11 | 267.4(6) | Gd–O21 | 266.3(7) | Gd–O12 | 259.2(8) | Gd–O31[b] | 263.8(4) |
| Gd–O22 | 268.3(6) | Gd–O11 | 267.2(7) | Gd–O21 | 268.0(7) | | |

Symmetry transformations used to generate atoms: [a] $-x+1,-y+1,-z+1$; [b] $-x+1,-y+1,-z+2$.

### *$Gd_2(F_3CCOO)_6(hypy)_2$ (2) and $Gd_2(F_2HCCOO)_6(hypy)_2$ (3)*

The crystal structures of **2** (Figure 4) and **3** (Figure 5) comprise dimers [shown in Figure 6 (**2**) and Figure 7 (**3**); $Gd^{3+}$–$Gd^{3+}$ distance is 387.7 pm for **2** and 388.0 pm for **3**]. The structural characteristics are as described for **1**. The $Gd^{3+}$–carboxylate O distances for **2** are 240.3–267.2 pm and 241.1–268.0 pm for **3**. The $Gd^{3+}$–pyridone O distances for **2** are 224.8–247.3 pm and 228.1–249.6 pm for **3**.

The extended structures are also formed by the 4-(1*H*)-pyridone molecules through π–π stacking interactions as in **1**.[19,20] The shortest orthogonal distances between the two aromatic fragments are 331.1 (**2**) and 325.6 pm (**3**).

 © 2006 Wiley-VCH Verlag GmbH & Co. KGaA, Weinheim 

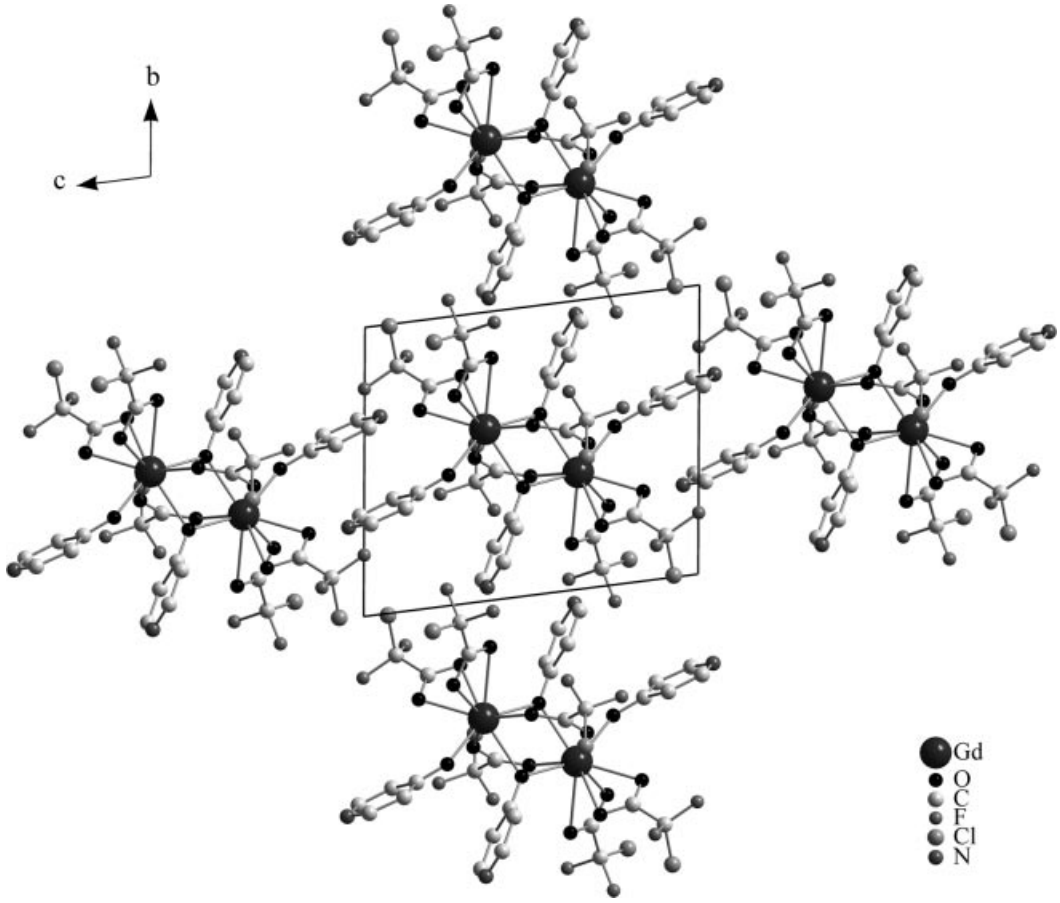


Figure 1. Crystal structure of $Gd_2(ClF_2CCOO)_6(hypy)_2$ (**1**). The triclinic unit cell is given; H atoms are not displayed.

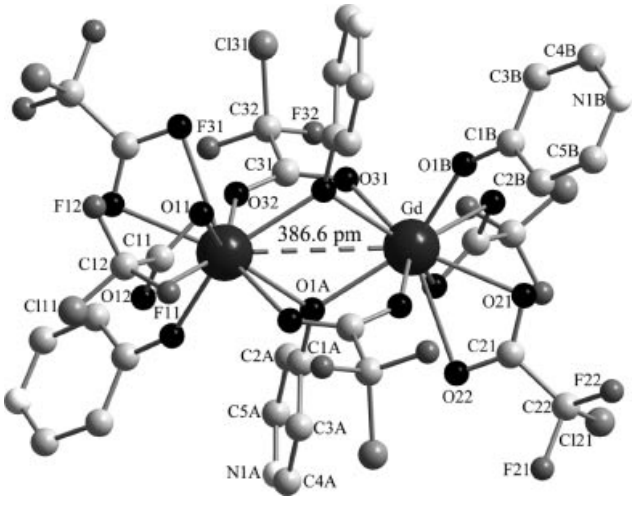


Figure 2. Dimeric unit in $Gd_2(ClF_2CCOO)_6(hypy)_2$ (**1**). The dashed line shows the $Gd^{3+}$–$Gd^{3+}$ distance; H atoms are not displayed.

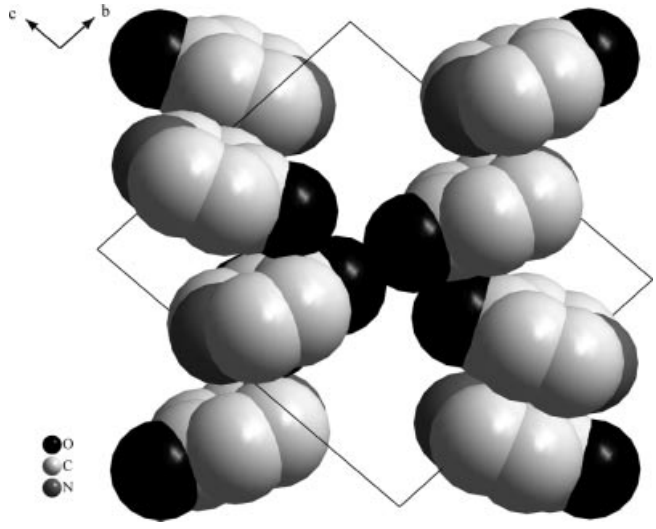


Figure 3. π–π stacking of the 4-(1*H*)-pyridone molecules in $Gd_2(ClF_2CCOO)_6(hypy)_2$ (**1**). The unit cell is given; H atoms are not displayed.

### *$Gd_2(Cl_2HCCOO)_6(H_2O)_2(hypy)_2$ (4)*

The crystal structure of **4** is shown in Figure 8. The structure comprises discrete dimers ($Gd^{3+}$–$Gd^{3+}$ distance is 405.1 pm) with two kinds of bridging carboxylate groups ($\mu_2$-carboxylato-$\kappa^1O$:$\kappa^1O'$ and $\mu_2$-$O'$;$\kappa^2O,O'$) along with a chelating dichloroacetate ion, a water and a 4-(1*H*)-pyridone molecule (Figure 9). The $Gd^{3+}$ ion is eightfold coordinated by oxygen atoms originating from five carboxylate

 © 2006 Wiley-VCH Verlag GmbH & Co. KGaA, Weinheim 

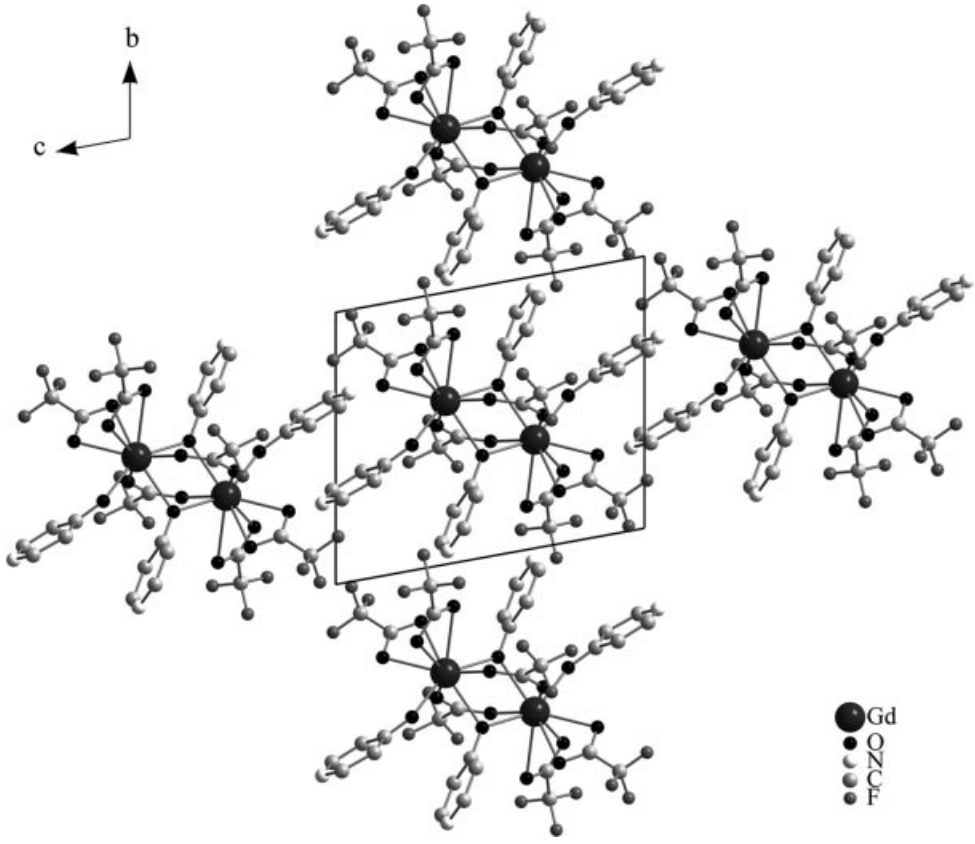


Figure 4. Crystal structure of $Gd_2(F_3CCOO)_6(hypy)_2$ (**2**). The triclinic unit cell is given; H atoms are not displayed.

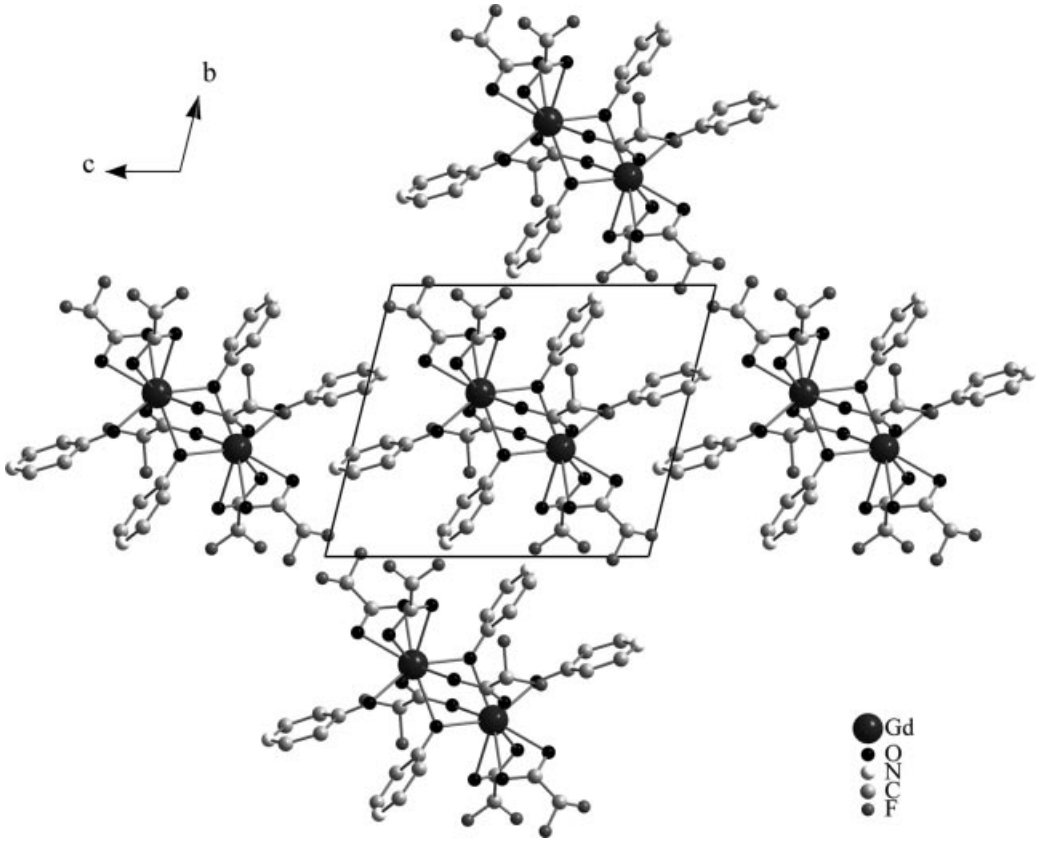


Figure 5. Crystal structure of $Gd_2(F_2HCCOO)_6(hypy)_2$ (**3**). The triclinic unit cell is given; H atoms are not displayed.

 © 2006 Wiley-VCH Verlag GmbH & Co. KGaA, Weinheim 

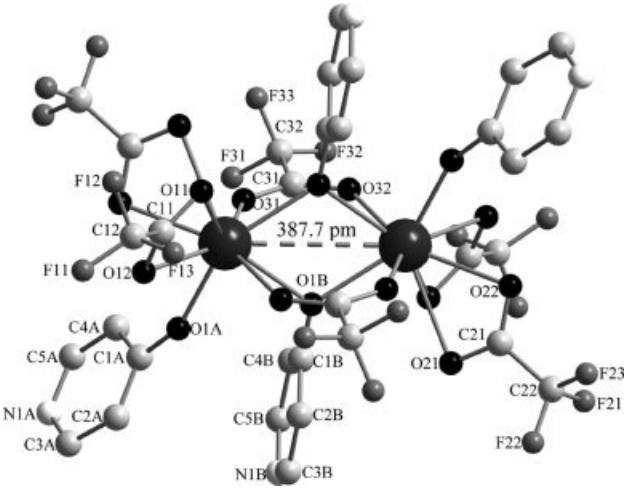


Figure 6. Dimeric unit in $Gd_2(F_3CCOO)_6(hypy)_2$ (**2**). The dashed line shows the $Gd^{3+}$–$Gd^{3+}$ distance; H atoms are not displayed.

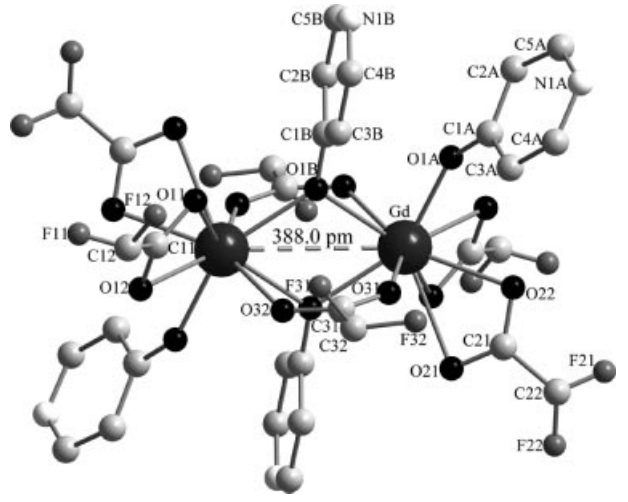


Figure 7. Dimeric unit in $Gd_2(F_2HCCOO)_6(hypy)_2$ (**3**). The dashed line shows the $Gd^{3+}$–$Gd^{3+}$ distance; H atoms are not displayed.

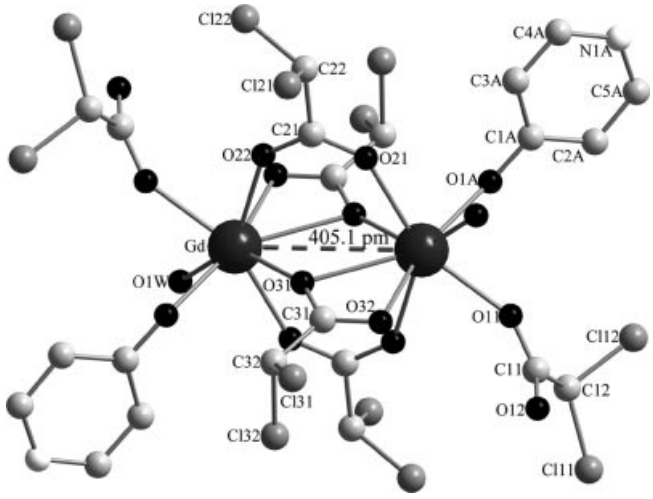


Figure 9. Dimeric unit in $Gd_2(Cl_2HCCOO)_6(H_2O)_2(hypy)_2$ (**4**). The dashed line shows the $Gd^{3+}$–$Gd^{3+}$ distance; H atoms are not displayed.

groups, one water and one pyridone molecule ($Gd^{3+}$–O distances are 224.6–263.8 pm).

Former results have shown that the $\mu_2$-*O*′;$\kappa^2$*O*,*O*′ mode is responsible for a ferromagnetic interaction, whereas the $\mu_2$-carboxylato-$\kappa^1$*O*:$\kappa^1$*O*′ bridging mode leads to an antiferromagnetic interaction.[21,10–16] The obtained crystal structures of the compounds **1-3** are of interest for magnetic investigations in order to study the influence of the bridging pyridone oxygen atom and of the $\mu_2$-carboxylato-$\kappa^1$*O*:$\kappa^1$*O*′ bridging mode of the carboxylate group. Compound **4** is interesting for magnetic investigations in order to study the influence of the coexistence of the $\mu_2$-*O*′;$\kappa^2$*O*,*O*′- and the $\mu_2$-carboxylato-$\kappa^1$*O*:$\kappa^1$*O*′ bridging modes.

### Magnetic Behaviour

The presentation of the magnetic data follows the recommendation of Hatscher et al.[22] Figures 10, 11, 12 and 13

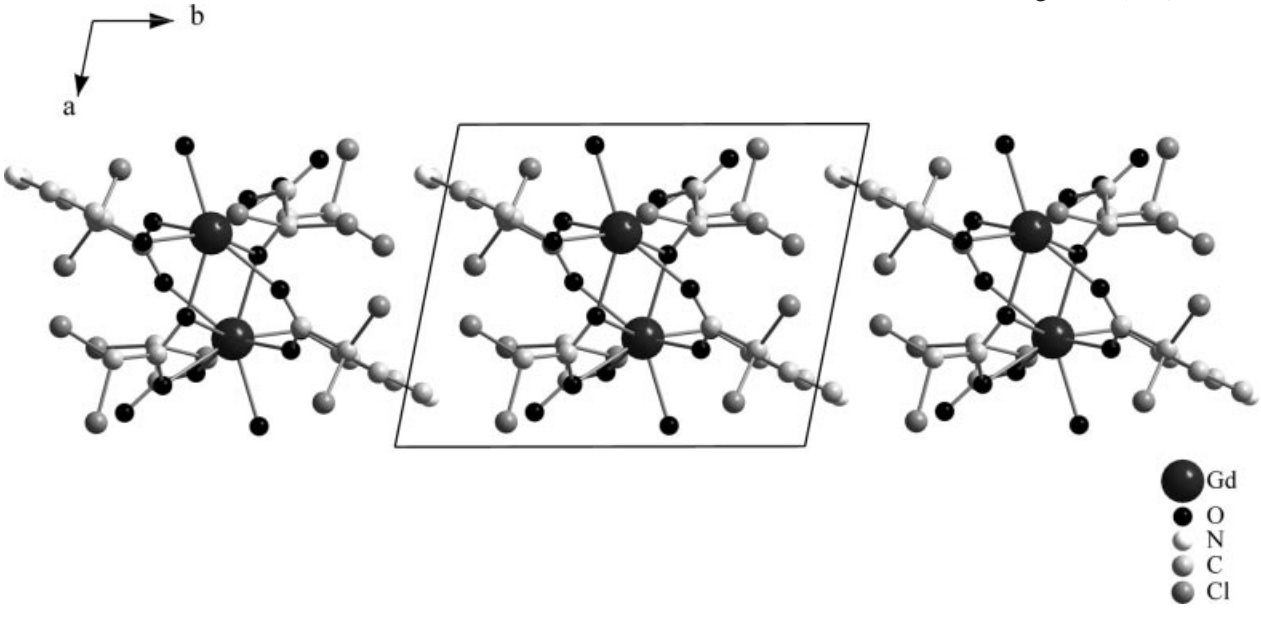


Figure 8. Crystal structure of $Gd_2(Cl_2HCCOO)_6(H_2O)_2(hypy)_2$ (**4**). The triclinic unit cell is given; H atoms are not displayed.

 © 2006 Wiley-VCH Verlag GmbH & Co. KGaA, Weinheim 

display the measured effective Bohr magneton numbers ($\mu_{eff}$) of **1**–**4** in the temperature range 1.76–300 K ($H^{(ir)}$ = 500 and 1000 Oe). The curve progression shows antiferromagnetic behaviour in each case. The measured magnetic susceptibility ($\chi_m^{(ir)}$) is interpreted by Equation (1) given below, where the intramolecular interaction within the dimeric unit is described by the Heisenberg model with a spin Hamiltonian $\hat{H}_{ex} = -2J_{ex}\hat{\boldsymbol{S}}_{Gd1}\cdot\hat{\boldsymbol{S}}_{Gd2}$ ($S_{Gd1} = S_{Gd2} = 7/2$):[18]

$$\chi_m^{(ir)} = \frac{N_A\mu_B^2 g^2}{k_B T}\cdot\frac{e^{2x}+5e^{6x}+14e^{12x}+30e^{20x}+55e^{30x}+91e^{42x}+140e^{56x}}{1+3e^{2x}+5e^{6x}+7e^{12x}+9e^{20x}+11e^{30x}+13e^{42x}+15e^{56x}}$$

$$\text{with} \quad x = J_{ex}/k_B T \tag{1}$$

where $N_A$ is the Avogadro constant, $\mu_B$ the Bohr magneton, $g$ the Landé factor, $k_B$ the Boltzmann constant, $T$ the absolute temperature and $J_{ex}$ the magnetic excoohange parameter.

The fitting procedure leads to $J_{ex}$ = –0.019 cm$^{-1}$ (**1**), $J_{ex}$ = –0.034 cm$^{-1}$ (**2**), $J_{ex}$ = –0.064 cm$^{-1}$ (**3**) and $J_{ex}$ = –0.011 cm$^{-1}$ (**4**), with $g$ = 2.00. The agreement between the measured and calculated $\mu_{eff}$ values [$\mu_{eff} = 2.8279\text{-}(T\chi_m^{(ir)})^{1/2}$] are shown in Figures 10–13.

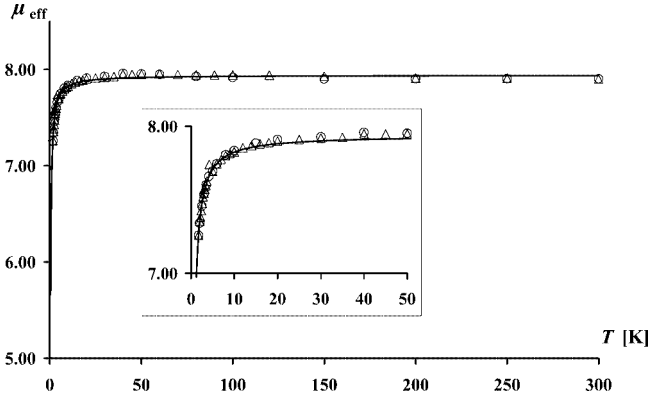


Figure 10. Comparison of measured (Δ, $H^{(ir)}$ = 0.5 kOe; ○, $H^{(ir)}$ = 1.0 kOe) and calculated (−) effective Bohr magneton numbers for $Gd_2(ClF_2CCOO)_6(hypy)_2$ (**1**).

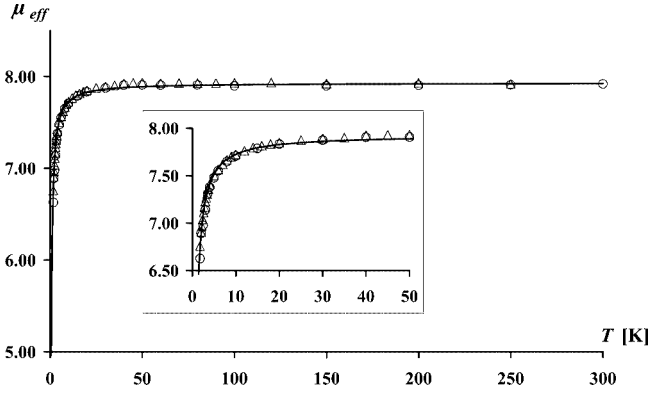


Figure 11. Comparison of measured (Δ, $H^{(ir)}$ = 0.5 kOe; ○, $H^{(ir)}$ = 1.0 kOe) and calculated (−) effective Bohr magneton numbers for $Gd_2(F_3CCOO)_6(hypy)_2$ (**2**).

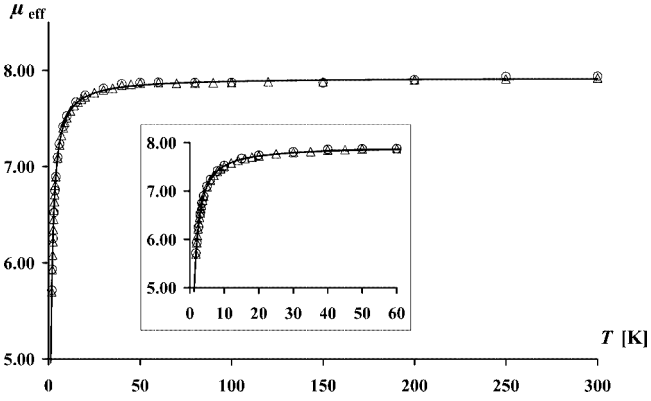


Figure 12. Comparison of measured (Δ, $H^{(ir)}$ = 0.5 kOe; ○, $H^{(ir)}$ = 1.0 kOe) and calculated (−) effective Bohr magneton numbers for $Gd_2(F_2HCCOO)_6(hypy)_2$ (**3**).

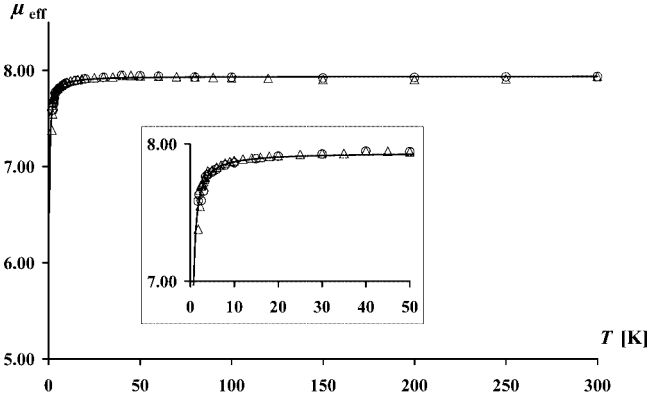


Figure 13. Comparison of measured (Δ, $H^{(ir)}$ = 0.5 kOe; ○, $H^{(ir)}$ = 1.0 kOe) and calculated (−) effective Bohr magneton numbers for $Gd_2(Cl_2HCCOO)_6(H_2O)_2(hypy)_2$ (**4**).

The values of $J_{ex}$ for the title compounds are comparable with those of other carboxylates containing $Gd^{3+}$. The coexistence of the $\mu_2$-pyridone-1:2$\kappa^2O$- or $\mu_2$-$O'$;$\kappa^2O,O'$ bridging mode and the $\mu_2$-carboxylato-$\kappa^1O$:$\kappa^1O'$ bridging mode in **1**–**4** leads to a negative exchange parameter (Table 3). Thus, only in the case where the carboxylate group exclusively bridges the $Gd^{3+}$ ions in a $\mu_2$-$O'$;$\kappa^2O,O'$ bridging mode is a ferromagnetic interaction observed.

## Experimental Section

Transparent, colourless, air stable single crystals of **1**–**4** have been obtained by reaction of the corresponding gadolinium carboxylate with 4-hydroxypyridine (Fluka, ≥95.0%) [molar ratio 2:1 for **1**, **2** and **4**; 1:2 for **3**] in a solution of ethanol (Sigma–Aldrich, 99.8%) and water (1:1). The starting compounds $Gd(ClF_2CCOO)_3(H_2O)_3$, $Gd(CF_3COO)_3(H_2O)_3$, $Gd(HF_2CCOO)_3(H_2O)_2{\cdot}H_2O$ and $Gd_3(H_2ClCCOO)_9(H_2O)_5$ were prepared as given in the literature.[11,16,21,23]

Well-grown single crystals were mounted on a STOE imaging plate diffractometer. The data collection was carried out at room temperature. The structures were solved by Patterson methods and

 © 2006 Wiley-VCH Verlag GmbH & Co. KGaA, Weinheim 

Table 3. Comparison of $J_{ex}$ [$cm^{-1}$], bridging mode and $Gd^{3+}$–$Gd^{3+}$ distance [pm] for $Gd_2(ClF_2CCOO)_6(hypy)_2$ (**1**), $Gd_2(F_3CCOO)_6(hypy)_2$ (**2**), $Gd_2(F_2HCCOO)_6(hypy)_2$ (**3**), $Gd_2(Cl_2HCCOO)_6(H_2O)_2(hypy)_2$ (**4**), $Gd_2(ClH_2CCOO)_6(bipy)_2$ (**A**), $Gd(CF_2HCOO)_3(phen)$ (**B**), $Gd(F_2HCCOO)_3(H_2O)_2{\cdot}H_2O$ (**C**), $[NH_3CH_3][Gd(Cl_2HCCOO)_4]$ (**D**), $[NH_3C_2H_5][Gd(Cl_2HCCOO)_4]$ (**E**) and $Gd(H_3CCOO)_3(H_2O)_2{\cdot}2H_2O$ (**F**).

| Compound | $J_{ex}$ | Bridging mode | $Gd^{3+}$–$Gd^{3+}$ Distance | Reference |
|---|---|---|---|---|
| **3** | –0.064 | $\mu_2$-pyridone-1:2$\kappa^2O$ and $\mu_2$-carboxylato-$\kappa^1O$:$\kappa^1O'$ | 388.0 | this work |
| **2** | –0.034 | $\mu_2$-pyridone-1:2$\kappa^2O$ and $\mu_2$-carboxylato-$\kappa^1O$:$\kappa^1O'$ | 387.7 | this work |
| **A** | –0.020 | $\mu_2$-$O'$;$\kappa^2O,O'$ and $\mu_2$-carboxylato-$\kappa^1O$:$\kappa^1O'$ | 399.0 | [15] |
| **1** | –0.019 | $\mu_2$-pyridone-1:2$\kappa^2O$ and $\mu_2$-carboxylato-$\kappa^1O$:$\kappa^1O'$ | 386.6 | this work |
| **B** | –0.016 | $\mu_2$-$O'$;$\kappa^2O,O'$ and $\mu_2$-carboxylato-$\kappa^1O$:$\kappa^1O'$ | 403.4 | [14] |
| **4** | –0.011 | $\mu_2$-$O'$;$\kappa^2O,O'$ and $\mu_2$-carboxylato-$\kappa^1O$:$\kappa^1O'$ | 405.1 | this work |
| **C** | –0.012 | $\mu_2$-carboxylato-$\kappa^1O$:$\kappa^1O'$ | 445.6 | [21] |
| **D** | –0.007 | $\mu_2$-carboxylato-$\kappa^1O$:$\kappa^1O'$ | 451.6 | [12] |
| **E** | 0.029 | $\mu_2$-$O'$;$\kappa^2O,O'$ | 418.1 | [13] |
| **F** | 0.025 | $\mu_2$-$O'$;$\kappa^2O,O'$ | 420.6 | [10] |
| **D** | 0.023 | $\mu_2$-$O'$;$\kappa^2O,O'$ | 418.4 | [12] |

were refined with anisotropic displacement parameters based on $F^2$ by using the SHELXS-97[24] and SHELXL-97[25] programs. Each data analysis indicated the $P\bar{1}$ space group. The final refinement yielded $R_1$ (all data) = 4.82% (**1**), $R_1$ (all data) = 5.93% (**2**), $R_1$ (all data) = 5.68% (**3**) and $R_1$ (all data) = 4.04% (**4**). Hydrogen atoms were always included by using a riding model. The crystal data and details of the refinements are summarised in Table 1. Selected bond lengths can be found in Table 2.

Elemental analysis (Vario EL, Elementar Analysesysteme GmbH, Hanau, Germany) for **1** $C_{16}H_{10}Cl_3F_6GdN_2O_8$ (735.86): calcd. C 26.12, H 1.37, N 3.81; found C 26.03, H 1.41, N 3.78. For **2** $C_{16}H_{10}F_9GdN_2O_8$ (686.50): calcd. C 27.99, H 1.47, N 4.08; found C 28.01, H 1.49, N 4.00. For **3** $C_{16}H_{13}F_6GdN_2O_8$ (632.53): calcd. C 30.38, H 2.07, N 4.43; found C 30.36, H 2.10, N 4.41. For **4** $C_{11}H_{10}Cl_6GdNO_8$ (654.17): calcd. C 20.20, H 1.54, N 2.14; found C 20.26, H 1.59, N 2.14.

Pulverised single crystals of the title compounds were measured with a SQUID magnetometer (MPMS5, Quantum Design) over the temperature range 1.76–300 K at magnetic fields ($H^{(ir)}$) of 500 and 1000 Oe. No field dependence of the magnetic data was observed. The sample was weighed into the lid of a gelatine capsule. To avoid orientation effects during the measurement, another gelatine capsule was pressed on the sample to fix it. Subsequently, the container was sewn in a plastic straw. The raw magnetic data were corrected for diamagnetism of the sample carrier and the sample by using the increments of Haberditzl.[26]


[1] G. Oczko, J. Legendziewicz, J. Mrozinski, G. Meyer, *J. Alloys Compd.* **1998**, *275–277*, 219–224.
[2] T. Kido, Y. Ikuta, Y. Sunatsuki, Y. Ogawa, N. Matsumoto, *Inorg. Chem.* **2003**, *42*, 398–408.
[3] C. Benelli, D. Gatteschi, *Chem. Rev.* **2002**, *102*, 2369–2388, and references cited therein.
[4] A. Figuerola, C. Diaz, J. Ribas, V. Tangoulis, J. Granell, F. Lloret, J. Mahia, M. Maestro, *Inorg. Chem.* **2003**, *42*, 641–649.
[5] J.-P. Costes, F. Dahan, A. Dupuis, J.-P. Laurent, *Chem. Eur. J.* **1998**, *4*, 1616–1620.
[6] J.-P. Costes, F. Nicodeme, *Chem. Eur. J.* **2002**, *8*, 3442–3447.
[7] J. Legendziewicz, M. Borzechowska, G. Oczko, G. Meyer, *New J. Chem.* **2000**, *24*, 53–59.
[8] J. Legendziewicz, M. Borzechowska, G. Oczko, J. Mronzinski, *Spectrochim. Acta* **1998**, *A54*, 2197–2205.
[9] G. Oczko, J. Legendziewicz, M. Wickleder, G. Meyer, *J. Alloys Compd.* **2002**, *341*, 255–262.
[10] S. T. Hatscher, W. Urland, *Angew. Chem.* **2003**, *115*, 2969–2971; *Angew. Chem. Int. Ed.* **2003**, *42*, 2862–2864.
[11] A. Rohde, W. Urland, *Z. Anorg. Allg. Chem.* **2004**, *630*, 2434–2437.
[12] A. Rohde, W. Urland, *Z. Anorg. Allg. Chem.* **2005**, *631*, 417–420.
[13] A. Rohde, W. Urland, *J. Alloys Compd.* **2005**, *408–412*, 618–621.
[14] D. John, W. Urland, *Z. Anorg. Allg. Chem.* **2005**, *631*, 2635–2637.
[15] D. John, W. Urland, *Eur. J. Inorg. Chem.* **2005**, 4486–4489.
[16] D. John, A. Rohde, W. Urland, *Z. Naturforsch., B: Chem. Sci.* **2006**, *61*, 699–707.
[17] O. Kahn, *Molecular Magnetism*, 1st ed., VCH, Weinheim, **1993**.
[18] H. Lueken, *Magnetochemie*, 1st ed., Teubner, Stuttgart, **1999**.
[19] C. Janiak, *J. Chem. Soc., Dalton Trans.* **2000**, 3885–3896.
[20] M. D. Curtis, J. Cao, J. W. Kampf, *J. Am. Chem. Soc.* **2004**, *126*, 4318–4328.
[21] A. Rohde, S. T. Hatscher, W. Urland, *J. Alloys Compd.* **2004**, *374*, 137–141.
[22] S. Hatscher, H. Schilder, H. Lueken, W. Urland, *Pure Appl. Chem.* **2005**, *77*, 497–511.
[23] A. Rohde, W. Urland, *Z. Anorg. Allg. Chem.* **2003**, *629*, 2069–2071.
[24] G. M. Sheldrick, *SHELXS-97, Program for crystal structure solution*, University of Göttingen, Göttingen, Germany, **1997**.
[25] G. M. Sheldrick, *SHELXL-97, Program for the refinement of crystal structures from diffraction data*, University of Göttingen, Göttingen, Germany, **1997**.
[26] W. Haberditzl, *Angew. Chem.* **1966**, *78*, 277–288; *Angew. Chem. Int. Ed. Engl.* **1966**, *5*, 288–298.
[27] CCDC 604198 (**1**), -604200 (**2**), -604199 (**3**) and -604197 (**4**) contain the supplementary crystallographic data for this paper. These data can be obtained free of charge from The Cambridge Crystallographic Data Centre via www.ccdc.cam.ac.uk/data_request/cif.


Received: April 20, 2006
Published Online: July 19, 2006

 © 2006 Wiley-VCH Verlag GmbH & Co. KGaA, Weinheim 

DOI: 10.1002/ejic.200600378

# A Ferromagnetically Coupled, Bent, Trinuclear Copper(II) Complex: Synthesis, Structure, Hydrogen-Bonding Network, Magnetic Properties and DNA Interaction Study

**Sumana Sarkar,[a] Amrita Mondal,[a] Deepak Chopra,[b] Joan Ribas,[c] and Kajal Krishna Rajak*[a]**

**Keywords:** Copper / Reduced Schiff base / Magnetic properties / Hydrogen bonds / DNA recognition

A bent trinuclear copper(II) complex (**1**) incorporating μ-phenoxo, μ-*syn*-*syn* carboxylato, and $\mu_3$-chloro bridges and an *O*,*N*,*N*-coordinated reduced Schiff-base ligand is reported. The complex shows an intramolecular ferromagnetic interaction in the solid state. The EPR spectra also support the magnetic behaviour of the complex. In the compound, each copper centre has a square-pyramidal geometry. The separation between the adjacent copper ions is about 3.05 Å and that between the terminal copper ions is about 5.0 Å. The complex forms a supramolecular architecture through N–H···Cl hydrogen bonding between the amine group of the reduced Schiff-base ligand and the counter chloride anions. Absorption and fluorescence spectral studies and viscosity measurements have been performed to determine the type of interaction with calf-thymus DNA. The nuclease activity of the complex with plasmid DNA is also studied.
(© Wiley-VCH Verlag GmbH & Co. KGaA, 69451 Weinheim, Germany, 2006)

## Introduction

The chemistry of multinuclear copper complexes has aroused considerable interest in recent years as copper has been found in the active sites of a large number of metalloproteins[1,2] as well as because of their interesting magnetic properties.[3] Among the multicentred copper proteins, the active sites of particulate methane monooxygenase (pMMO),[4] laccase[5] and ascorbate oxidase[6] contain trinuclear copper(II) sub-units. It has been documented that trinuclear copper(II) centres exhibit the $S = 3/2$ ground state in the fully oxidised form of pMMO.[7] It is also reported that the oxidised form of the active site of ascorbate oxidase consists of an angled trinuclear copper(II) moiety with a Cu···Cu separation in the range 3.66–3.90 Å, with appropriate $C_2$ symmetry.[6] Although a few ferromagnetically coupled trinuclear copper(II) complexes have been reported,[8,9] to the best of our knowledge studies on mixed-bridged bent trinuclear copper(II) complexes are rare.[10] Thus, there is an increasing demand for mixed-bridged angular trinuclear copper(II) systems in order to better understand the underlying chemistry as well as the magnetic properties of biomolecules. Furthermore, the studies of such systems may be helpful in order to develop the fundamental knowledge about the exchange interactions between the paramagnetic centres of such systems and in the design of molecular-based ferromagnetic materials. These considerations have generated a lot of interest in the synthesis and characterisation of ferromagnetically coupled mixed-bridge bent trinuclear copper(II) complexes using conformationally labile reduced Schiff-base ligands.

The study of the interaction of polynuclear copper(II) complexes with DNA and their nuclease activity is also of abiding interest in the field of bioinorganic chemistry of copper.[11] This is because such polynuclear complexes might interact with DNA by different pathways and exhibit DNA cleavage activity.[8a,12] Thus, developments in the field of DNA interaction and cleavage studies with small molecules have prompted us to explore the binding of trinuclear copper(II) complexes with DNA and their nuclease activity.

Besides the importance of understanding the chemistry, magnetic properties and DNA interaction studies with biologically related polynuclear copper(II) complexes, the design of polynuclear coordination clusters by self-assembly of small building blocks has also received a great deal of attention in the context of crystal engineering, molecular recognition and supramolecular chemistry.[13–15] One particularly interesting method in the construction of self-assembled clusters involves using a ligand that can be involved in coordination and hydrogen-bonding interactions simultaneously, such that the transition metal cationic centres are linked through anions by hydrogen bonding to form a self-assembled cluster. Reduced Schiff-base ligands

[a] Inorganic Chemistry Section, Department of Chemistry, Jadavpur University,
Kolkata 700032, India
E-mail: kajalrajak@hotmail.com
[b] Solid State and Structural Chemistry Unit, Indian Institute of Science,
Bangalore 560012, India
[c] Department de Química Inorgánica, Universitat de Barcelona, Diagonal 6487, 08028 Barcelona, Spain

 © 2006 Wiley-VCH Verlag GmbH & Co. KGaA, Weinheim 

have great potential in the organisation of the primary molecule in the solid state by intermolecular hydrogen bonding.[16] This has also motivated us to undertake the task of designing a supramolecular cluster in the solid state by self-assembly with bifunctional reduced Schiff-base ligands.

Here we describe the synthesis of a mixed-bridge (μ-phenoxo, μ-carboxylato, and $\mu_3$-chloro) trinuclear copper(II) complex incorporating an *O*,*N*,*N*-coordinated reduced Schiff-base ligand. The X-ray structure of the complex has been determined, which allows the secondary interactions in the solid state to be investigated thoroughly. Variable temperature magnetic susceptibility measurements confirm the ferromagnetic behaviour, and the EPR spectra also support the magnetic behaviour. The solution properties are studied, and the interaction with DNA and nuclease activity of the complex is scrutinized.

## Results and Discussion

The reduced Schiff base ligand (**HL**) used in this work was prepared by $NaBH_4$ reduction of the corresponding Schiff base in methanol.[17]

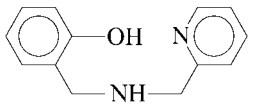


**HL**

The stoichiometric reaction of copper(II) chloride dihydrate with **HL** and benzoic acid in the presence of piperazine in methanol afforded a dark coloured complex of formula $[Cu_3L_2(C_6H_5COO)_2Cl]Cl$ in good yield. This complex displays carboxylate stretches near 1560 and 1420 $cm^{-1}$, respectively. The splitting between the two peaks is 140 $cm^{-1}$, which indicates that the carboxylate group bridges the two copper ions in a *syn-syn* fashion.[18] The band at around 1200 $cm^{-1}$ is assigned to the $\nu(C–O_{phenolate})$ vibration. The hydrogen-bonded NH vibration occurs as a broad band near 3400 $cm^{-1}$.

The electronic spectra were recorded in Tris-HCl/NaCl buffer solution; the data are summarised in the Exp. Sect. The complex exhibits a single d-d absorption band near 650 nm which is characteristic of square-pyramidal copper(II) complexes.[19] The allowed intense band observed near 420 nm is believed to be due to an LMCT transition between bridging phenoxide and copper(II) ions.[19]

### Molecular Structure

The crystal structure of $[Cu_3L_2(C_6H_5COO)_2Cl]Cl$ (**1**) was determined. The asymmetric unit consists of one half of a centrosymmetric molecule; Figure 1 shows the cationic part of the molecular structure and the bond parameters are listed in Table 1.

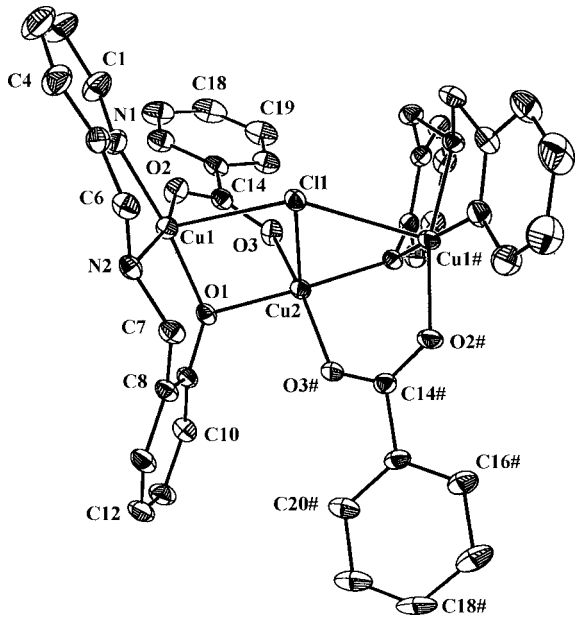


Figure 1. Perspective view and atom-labelling scheme for the cationic part of $[Cu_3L_2(C_6H_5COO)_2Cl]Cl$ (**1**). All non-hydrogen atoms are represented by 30% thermal probability ellipsoids.

Table 1. Selected bond lengths [Å] and angles [°] for $[Cu_3L_2(C_6H_5COO)_2Cl]Cl$.

| | |
|---|---|
| Cu(1)–N(2) | 1.981(4) |
| Cu(1)–O(1)# | 1.947(3) |
| Cu(1)–O(2) | 1.929(3) |
| Cu(1)–Cl(1) | 2.732(2) |
| Cu(2)–O(1) | 1.973(3) |
| Cu(2)–O(3) | 1.926(4) |
| Cu(2)–Cl(1) | 2.654(2) |
| Cu(1)···Cu(2) | 3.055(8) |
| Cu(1)···Cu(1)# | 5.104(8) |
| N(1)–Cu(1)–N(2) | 82.00(19) |
| N(1)–Cu(1)–O(1)# | 173.79(16) |
| N(1)–Cu(1)–O(2) | 91.40(18) |
| N(1)–Cu(1)–Cl(1) | 98.74(15) |
| N(2)–Cu(1)–O(1)# | 94.14(16) |
| N(2)–Cu(1)–O(2) | 165.73(18) |
| N(2)–Cu(1)–Cl(1) | 91.22(14) |
| O(1)#–Cu(1)–O(2) | 91.28(15) |
| O(1)#–Cu(1)–Cl(1) | 86.16(10) |
| O(2)–Cu(1)–Cl(1) | 102.32(12) |
| O(1)–Cu(2)–O(1)# | 175.67(19) |
| O(1)–Cu(2)–O(3) | 90.10(14) |
| O(1)–Cu(2)–O(3)# | 90.70(14) |
| O(1)–Cu(2)–Cl(1) | 87.83(10) |
| O(3)–Cu(2)–O(3)# | 159.0(3) |
| O(3)–Cu(2)–Cl(1) | 100.50(13) |
| Cu(1)#–O(1)–Cu(2) | 102.40(14) |
| Cu(1)–Cl(1)–Cu(2) | 69.10(3) |
| Cu(1)–Cl(1)–Cu(1)# | 138.20(7) |
| Cu(1)–Cu(2)–Cu(1)# | 113.31(3) |

Symmetry operation for Cu(1)#, O(1)# and O(3)#: 2/3 + *x*, –2/3 + *y*, 1/6 – *z*.

The compound possesses a twofold axis through the central copper atom. In the cationic part, the adjacent copper atoms are bridged by the phenoxy oxygen atom of the deprotonated ligand L and two oxygen atoms of a didentate

 © 2006 Wiley-VCH Verlag GmbH & Co. KGaA, Weinheim 

*syn-syn* benzoato group to give a bent trinuclear entity. The three copper atoms in the trinuclear moiety form an isosceles triangle with an adjacent Cu···Cu distance of 3.055(8) Å and a terminal Cu···Cu distance of 5.104(8) Å. The Cu(1)–Cu(2)–Cu(1)# and Cu–$O_{phenoxo}$–Cu angles are 113.31(3)° and 102.40(14)°, respectively. The geometry of each copper ion is distorted square-pyramidal in which the basal plane of the terminal copper atoms consists of two nitrogen (pyridine and amine) and two oxygen (phenoxo and benzoato) atoms while that of the central copper atom contains four oxygen atoms. The equatorial planes are essentially planar (mean deviation = 0.0649 and 0.2128 Å) and the dihedral angle between the terminal and central basal planes is 65.7°. The apical site of each copper ion is occupied by the $\mu_3$-chloro group. The Cu–($\mu_3$-Cl) bond lengths span the range 2.654(2) to 2.732(2) Å and are significantly larger than the terminal Cu–Cl bond. Cu(1) is displaced by 0.1550 Å whereas Cu(2) is shifted by 0.1381 Å towards the apical chloride group. The Cu–N and Cu–O bond lengths are normal.

## Hydrogen Bonding

The primary structure of the compound is remarkably different from its solid-state structure due to the involvement of secondary interactions in the lattice. In the extended solid-state structure a self-assembled cluster compound is formed by simultaneous coordinative and hydrogen-bonding interactions. The amine hydrogen atom of both the reduced Schiff-base ligands in the trinuclear entity engage in hydrogen bonding. The chloride ion is symmetrically hydrogen bonded with the amine hydrogen atom [Cl···N = 3.163(6) Å] of one of the reduced Schiff-base ligands of three different molecules. The basic unit of the cluster is shown in Figure 2. The remaining three amine hydrogen atoms of the three different molecules of the small building blocks are anchored within an extended hydrogen-bonding network. This interaction leads to the formation of macrocyclic cavities with six molecules of average diameter 25.0 Å; the hydrogen-bonded macrocyclic cavity is shown in Figure 3. The hexameric synthons are again assembled in the crystal lattice through similar types of intermolecular contacts to form a honeycomb-like supramolecular array. This honeycomb network is shown in Figure 4.

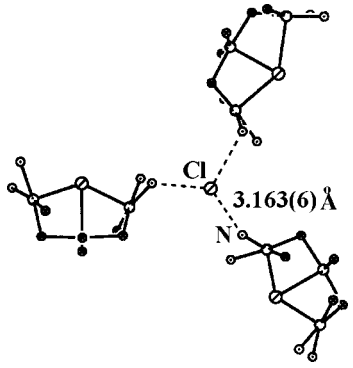


Figure 2. Basic unit of secondary interactions of $[Cu_3L_2(C_6H_5COO)_2Cl]Cl$ (**1**); carbon and hydrogen atoms have been excluded for clarity.

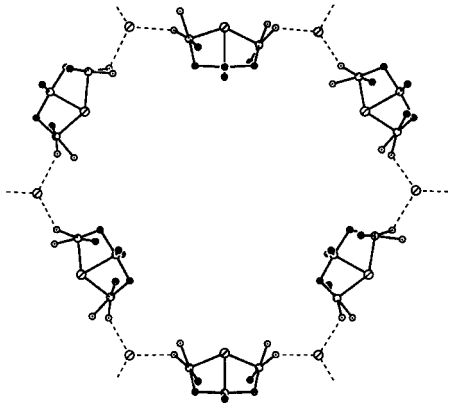

Figure 3. Hexameric macrocycle of **1**; carbon and hydrogen atoms have been excluded for clarity.

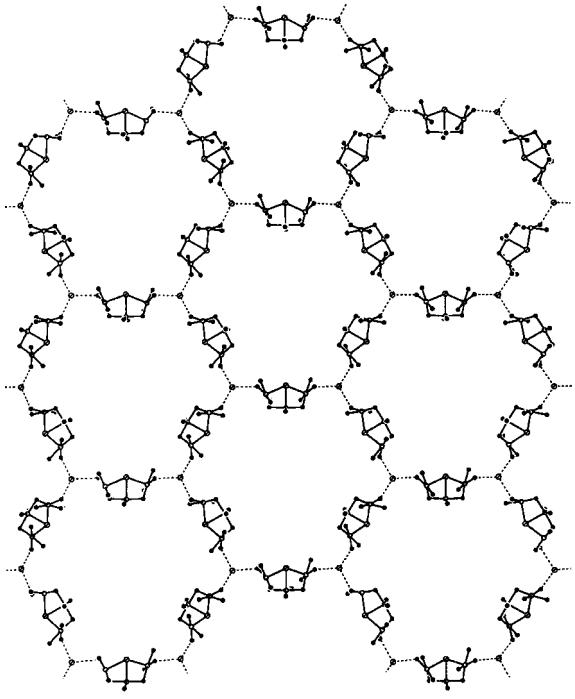

Figure 4. Supramolecular network in the lattice of **1**; carbon and hydrogen atoms have been excluded for clarity.

## Magnetic Studies

The variable-temperature magnetic susceptibility, $\chi_M$, per trinuclear copper(II) unit was measured in the temperature range 2–300 K. A $\chi_M T$ value of 1.32 $cm^3 mol^{-1} K$ is observed for **1** at 300 K, which is as expected for three magnetically quasi-isolated spin doublets ($g > 2.00$). Upon decreasing the temperature the $\chi_M T$ value increased to 1.87 $cm^3 mol^{-1} K$ at 7 K. Such magnetic behaviour is characteristic of a predominant ferromagnetic exchange coupling in a trinuclear copper(II) system. The plot of $\chi_M T$ vs.

 © 2006 Wiley-VCH Verlag GmbH & Co. KGaA, Weinheim 

$T$ is given in Figure 5. After passing through the maximum, the $\chi_M T$ value decreases quickly to 1.60 $cm^3 mol^{-1} K$ at 2 K. The magnetic orbitals of the terminal copper ions in **1** have predominantly $d_{x^2-y^2}$ character. A significant exchange interaction between two terminal copper atoms through the bridging chloride ligand may be excluded in the isolated trinuclear moiety because the delocalisation of an unpaired electron towards the apical chloride ion is likely to be less effective due to the large Cu–($\mu_3$-Cl) bond length.[20] The decrease of $\chi_M T$ at low temperature is probably either due to a zero-field splitting effect ($D$ parameter) for the $S = 3/2$ ground state or inter-cluster antiferromagnetic interactions ($J'$). Both $D$ and $J'$ exhibit the same behaviour in the low-temperature regime. However, in the case of copper(II), the possible $D$ parameters of the $S = 3/2$ ground state must be very small due only to the dipolar interactions. Therefore, for simplification, the $D$ parameter was not taken into consideration when fitting the experimental data. The fit of the susceptibility data was carried out using the molecular field approximation, with the $J'$ parameter, according to the method given by Kahn,[3] with the Hamiltonian

$$H = -J(S_1S_2 + S_2S_3) + g\beta H\mathbf{S}_z - zJ'\langle\mathbf{S}_z\rangle\mathbf{S}_z$$

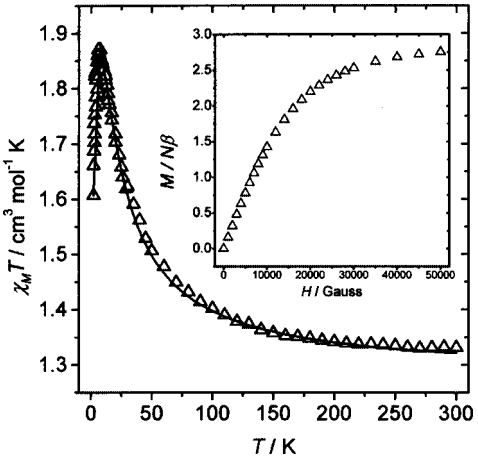


Figure 5. Plot of $\chi_M T$ vs. $T$ for $[Cu_3L_2(C_6H_5COO)_2Cl]Cl$ (**1**) (open points are the experimental data and the solid line represents the best fit obtained). Plot of the reduced magnetisation, $M/N\beta$, vs. $H$ for **1** at 2 K (see inset).

With this molecular field approach (neglecting $D$ parameter), the best-fit parameters for complex **1** are: $J = 20.8 \pm 0.2$ $cm^{-1}$, $J' = -0.4 \pm 0.2$ $cm^{-1}$, $g = 2.13 \pm 0.01$ and $R = 1.2 \times 10^{-4}$ [$R = \Sigma(\chi_M^{calc} - \chi_M^{obs})^2/\Sigma(\chi_M^{obs})^2$].

The nature of the reduced molar magnetisation is shown in the inset of Figure 5. The $M/N\beta$ value at 5 T is close to $3N\beta$ and this value indicates the tendency to have three unpaired electrons ($S = 3/2$) at 2 K.

The ferromagnetic interaction in the present complex can be explained by considering the dihedral angle between the equatorial planes of the terminal and central copper(II) centres.[21] It is known that spin coupling between the paramagnetic centres becomes ferromagnetic when the dihedral angle decreases from 180°. In complex **1** the dihedral angle of 65.7° deviates significantly from the value of 180°. These results also support the ferromagnetic interactions.

## EPR Spectra

Variable-temperature EPR spectra of the complex were recorded to find out more about the behaviour of the unpaired electron within the trinuclear cluster in the solid state. The X-band EPR spectra of polycrystalline powdered complex at different temperatures are shown in Figure 6.

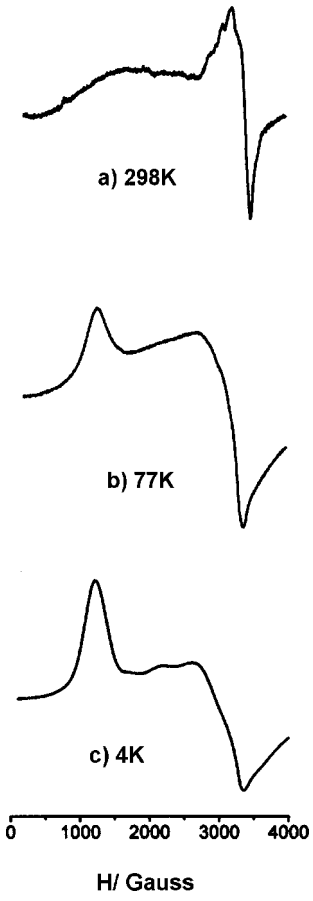


Figure 6. Solid powder X-band EPR spectra of $[Cu_3L_2(C_6H_5COO)_2Cl]Cl$ (**1**).

The EPR spectrum at 4 K is dominated by a transition at 1215 G (Figure 6, c), which unambiguously identifies the $S = 3/2$ ground spin-state. At this temperature the signals within the ±1/2 and ±3/2 Kramer's doublets are observed. It is clear from the variable-temperature studies (Figure 6) that the intensity of the $M_S = \pm 1/2$ EPR spectra increases with decreasing temperature. At 4 K the effective $g_\perp$ value is found at 5.2; this value may arise due to the transition within $M_S = \pm 1/2$ of the Kramer doublet of quadruplets state ($S = 3/2$). The corresponding $g_\parallel$ value is observed at 2.15. It is interesting to note that the strong signal at low field gradually broadens and almost disappears with increasing temperature (Figure 6). However, the signal corresponding to $g \approx 2.0$ remains almost unchanged. These

 © 2006 Wiley-VCH Verlag GmbH & Co. KGaA, Weinheim 

spectral features have been attributed to the increasing population of the two $S = 1/2$ excited states with a rise in temperature. As a consequence, there is compensation of the $S = 3/2$ ground state and the room-temperature spectrum is more reminiscent of the $S = 1/2$ term. All the spectral observations are in good agreement with the magnetic moment of the complex.

### Interaction Between DNA and the Complex

Electronic absorption spectroscopic techniques are often employed to investigate the binding of DNA with complexes. To achieve this, the absorption spectra of the complex in the absence and presence of calf-thymus DNA at different concentrations were measured. The UV/Vis spectral change with increasing DNA concentration for **1** is shown in Figure 7. A considerable hypochromicity without appreciable change in wavelength of the d-d and charge-transfer transitions can be attributed to an interaction[22] between the surface of the DNA molecule and the trinuclear complex. The binding constant between DNA and the complex was determined from the UV/Vis spectroscopic data using the following equation[23]

$$[DNA]/(\varepsilon_a - \varepsilon_f) = [DNA]/(\varepsilon_b - \varepsilon_f) + 1/K_b(\varepsilon_a - \varepsilon_f)$$

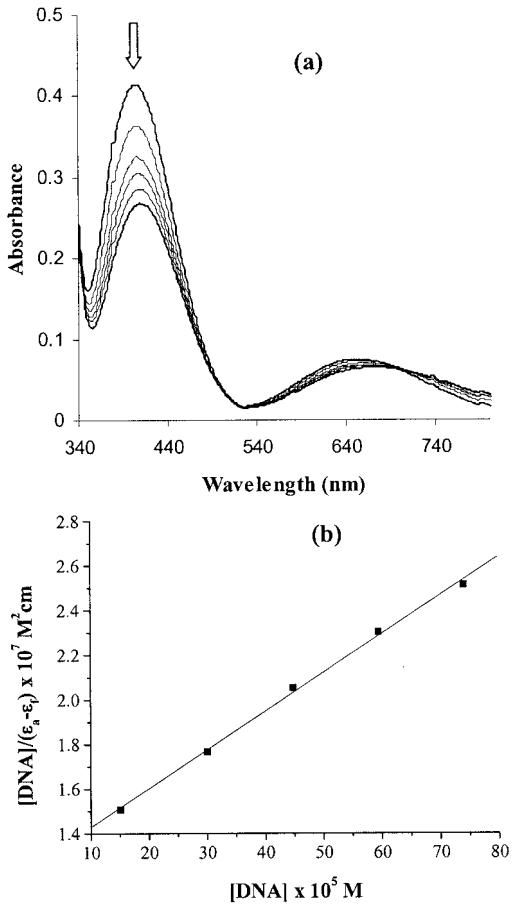


Figure 7. (a) Absorption spectra of $[Cu_3L_2(C_6H_5COO)_2Cl]Cl$ (**1**) in 50 mM Tris-HCl and 18 mM NaCl buffer (pH 7.2) in the presence of increasing amounts of DNA ([DNA] = 0–75 μM). (b) Plot of $[DNA]/(\varepsilon_a - \varepsilon_f)$ vs.[DNA].

where $\varepsilon_a$, $\varepsilon_f$ and $\varepsilon_b$ correspond to $A_{obs.}/[Cu]$, the extinction coefficient of the free copper complex and the extinction coefficient of the copper complex in the fully bound form, respectively. The binding constant obtained is $1.38 \times 10^5$ M$^{-1}$.

Fluorescence spectra of the ethidium bromide–DNA intercalative adduct were recorded in the presence of the complex. No considerable quenching of fluorescence intensity was observed in the presence of **1**, which suggests that there is no significant intercalation between DNA and the metal complex.

Viscosity measurement is an important tool to ascertain the interaction mode[24] of DNA with complexes. It has been established that a significant enhancement in viscosity of a DNA solution is observed in the case of classical intercalative binding of complexes.[25] However, groove-face, electrostatic or surface binding of the compounds results in less or no change of viscosity of the DNA solution.[26] The $\eta/\eta_0$ values are given in Table 2. The results show that there is a slight decrease in relative viscosity of calf-thymus DNA solution in the presence of this trinuclear complex and this is probably due to interaction of the complex with the DNA surface.

Table 2. Data for DNA viscosity in the presence of complex **1**.

| [complex]/[DNA][a] | $\eta/\eta_0$ |
|---|---|
| 0.0 | 1.00 |
| 0.13 | 0.992 |
| 0.17 | 1.002 |
| 0.22 | 0.990 |
| 0.26 | 0.971 |
| 0.31 | 0.952 |
| 0.35 | 0.950 |

[a] [DNA] = 200 μM.

In summary, the UV/Vis spectral, fluorescence and viscosity measurements reveal that the trinuclear complex interacts with the DNA surface and is inhibited from intercalation with the DNA molecule. This interaction mode is different from that of previously reported trinuclear copper species.[8a]

### Cleavage of pUC18 DNA by $[Cu_3L_2(C_6H_5COO)_2Cl]Cl$ (1)

The cleavage of supercoiled pUC18 DNA by the complex was studied by gel electrophoresis in Tris-HCl/NaCl buffer. Figure 8 shows the gel electrophoresis separation of plasmid DNA induced by our mixed-bridge, bent, trinuclear copper(II) complex. From this figure it can be seen (lane 5) that the complex itself converts plasmid supercoiled pUC18 DNA into a mixture of supercoiled (Form I) and nicked (Form II). The activity increases remarkably in the presence of $H_2O_2$ (lane 6). However, there is no significant increase (lane 7) in the conversion on addition of 2-mercaptoethanol to the complex and $H_2O_2$. Incubation with $H_2O_2$, 2-mercaptoethanol or both $H_2O_2$ and 2-mercaptoethanol without the complex does not cause strand scission of supercoiled DNA. These experimental results demonstrate that complex **1** exhibits DNA cleavage activity that is enhanced by the addition of hydrogen peroxide. We assume that there is a

 © 2006 Wiley-VCH Verlag GmbH & Co. KGaA, Weinheim 

possibility of formation of copper-oxo species during the DNA cleavage reaction in the absence or presence of $H_2O_2$.[27] This copper species is probably responsible for the cleavage of DNA by the trinuclear complex alone (lane 5). Besides the copper-oxygen species, the generation of hydroxy radicals in the presence of $H_2O_2$ enhances the DNA cleavage activity (lane 6).[27]

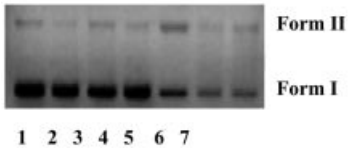


Figure 8. Electrophoretic separation of pUC18 DNA by $[Cu_3L_2(C_6H_5COO)_2Cl]Cl$ (**1**). DNA alone (lane 1), DNA + 2-mercaptoethanol (lane 2), DNA + $H_2O_2$ (lane 3), DNA + $H_2O_2$ + 2-mercaptoethanol (lane 4), DNA + **1** (lane 5), DNA + **1** + 100 μM $H_2O_2$ (lane 6), DNA + **1** + $H_2O_2$ + 2-mercaptoethanol (lane 7).

## Conclusions

A conformationally labile reduced Schiff-base ligand having coordinating and hydrogen-bonding sites has been successfully utilized to synthesise a phenoxo, carboxylato, chloro-bridged bent trinuclear copper(II) complex in good yields. The separations between the copper ions in the complex fall in the range 3.05–5.10 Å, which is in agreement with the trinuclear active sites of the oxidized form of ascorbate oxidase.[6] The ferromagnetic behaviour of the complex also resembles the oxidized form of particulate methane monooxygenase.[7] The variable-temperature EPR spectral measurements support the magnetic behaviour. Spectral and viscosity measurements reveal the surface binding of **1** to calf thymus DNA. Cleavage of pUC18 by **1** indicates that the complex exhibits nuclease activity. Interesting supramolecular structures are obtained in the solid state through the combination of hydrogen bonding between the chloride ion and the NH group of the reduced Schiff-base ligand. The results presented herein may be helpful in understanding the chemistry and magnetic properties of biomolecules containing trinuclear sub-units in their active sites. In addition, the studies also provide valuable insights into the synthesis of supramolecules by self-assembly of reduced Schiff-base ligands. Further research aimed at the synthesis of polynuclear mixed-bridged copper complexes containing different reduced Schiff-base ligands, investigation of their DNA interaction and clarification of the cleavage mechanism, along with their solid- and solution-state behaviour is currently in progress.

## Experimental Section

**Materials:** All the starting chemicals were analytically pure and were used without further purification. The ligand was prepared by reduction of the corresponding Schiff base derived from salicylaldehyde and 2-(aminomethyl)pyridine with $NaBH_4$.[17] Calf thymus (CT) DNA and supercoiled pUC18 DNA were obtained from Sigma. The concentration of calf thymus DNA (200 μM) was estimated spectrophotometrically from the extinction coefficient of DNA (6600 $M^{-1}cm^{-1}$) at 260 nm.[28] Agarose (molecular biology grade), 2-mercaptoethanol, and ethidium bromide were purchased from Sigma.

**Physical Measurements:** UV/Vis spectra were recorded with a Perkin–Elmer LAMBDA25 spectrophotometer and IR spectra were measured with a Perkin–Elmer L-0100 spectrometer. Electrochemical measurements were performed (acetonitrile solution) with a CH620A electrochemical analyzer using a platinum electrode. Tetraethylammonium perchlorate (TEAP)[29] was used as supporting electrolyte and the potentials are referenced to the standard calomel electrode (SCE) without junction correction. EPR spectra were recorded with a Bruker 300E automatic spectrometer, varying the temperature between 4–300 K. Magnetic measurements were carried out on polycrystalline samples with a Quantum Design MPMS XL SQUID susceptometer operating at a magnetic field of 0.1 T between 2 and 300 K. The diamagnetic corrections were evaluated from Pascal's constants. Elemental analyses (C, H, N) were performed with a Perkin–Elmer 2400 Series II elemental analyzer.
Viscosity measurements were performed with an Ubbelohde viscometer at 27 ± 0.1 °C. The concentration of DNA was 200 μM. The flow times were determined with a digital stop clock and each measured point is the average of four readings. Viscosity values are presented as $\eta/\eta_0$ vs. [complex]/[DNA], where $\eta$ is the viscosity of DNA in the presence of complex and $\eta_0$ is the viscosity of DNA solution alone.
The gel electrophoresis experiments were performed by incubation at 37 °C for 1 h as follows: pUC18 DNA (200 ng), complex (40 μM), $H_2O_2$ (100 μM), and 2-mercaptoethanol (100 μM) in 50 mM Tris-HCl/18 mM NaCl buffer (pH 7.2). The sample was electrophoresed for 2 h at 40 V on 1% agarose gel using Tris-boric acid-EDTA buffer (pH 8.3). After electrophoresis, the gel was stained using 1 μg mL ethidium bromide and photographed under UV light.

**$[Cu_3L_2(C_6H_5COO)_2Cl]Cl$ (1):** A methanolic solution (5 mL) of benzoic acid (70 mg, 0.6 mmol) containing piperazine (45 mg) was added to a solution of $CuCl_2{\cdot}2H_2O$ (90 mg, 0.6 mmol) in methanol (15 mL). A methanolic solution of **HL** (107 mg, 0.5 mmol) was added to the resulting solution. Slow evaporation of the dark-green solution yielded a dark-green crystalline product. Yield: 70% (340 mg). $C_{40}H_{34}Cl_2Cu_3N_4O_6$ (927.5): calcd. C 51.75, H 3.67, N 6.04; found C 51.4, H 3.4, N 5.9 ppm. IR (KBr): ν(C–$O_{phenolate}$) 1240; ν($COO^-$) 1420, 1560; ν(NH) 3400 $cm^{-1}$. UV/Vis [Tris-HCl/NaCl buffer]: $\lambda_{max}$ (ε) = 650 nm (1480 $M^{-1}cm^{-1}$), 420 (8260). $E_{pa}$ ($Cu_3^{II}/Cu_2^{II}Cu^{III}$ couple): 1.1 V (irr); $E_{pc}$ ($Cu_3^{II}/Cu_2^{II}Cu^{I}$ couple): –0.5 V (irr).

**Crystallographic Studies:** Suitable crystals of complex **1** were grown by slow evaporation of a methanolic solution. The X-ray intensity data were measured at 293 K with a Bruker AXS SMART APEX CCD diffractometer (Mo-$K_\alpha$, $\lambda$ = 0.71073 Å). The detector was placed at a distance of 6.03 cm from the crystal. A total of 606 frames were collected with a scan width of 0.3° in different settings of $\varphi$. The data were reduced with SAINTPLUS[30] and an empirical absorption correction was applied using the SADABS package.[30] Metal atoms were located by direct methods and the rest of the non-hydrogen atoms emerged from successive Fourier synthesis. The structure was refined by full-matrix least-square procedures on $F^2$. All non-hydrogen atoms were refined anisotropically. The amine hydrogen atoms were located directly in the difference Fourier maps and the remaining hydrogen atoms were included in calculated positions. Calculations were performed with the SHELXTL V5.03[31] program package. Relevant crystal data are given in Table 3.

 © 2006 Wiley-VCH Verlag GmbH & Co. KGaA, Weinheim 

Table 3. Crystallographic data for **1**.

| | |
|---|---|
| Formula | $C_{40}H_{34}Cl_2Cu_3N_4O_6$ |
| $M_w$ | 927.5 |
| Space group | *R*-3*c* |
| *a* [Å] | 21.773(3) |
| *b* [Å] | 21.773(3) |
| *c* [Å] | 51.579(8) |
| *α* [°] | 90 |
| *β* [°] | 90 |
| *γ* [°] | 120 |
| *V* [Å$^3$] | 21176.0(5) |
| *Z* | 21 |
| *T* [K] | 293(2) |
| $\rho_{calcd.}$ [mg m$^{-3}$] | 1.311 |
| $\mu$ (Mo-$K_\alpha$) [mm$^{-1}$] | 1.483 |
| *R*1,[a] *wR*2[b] [$I > 2\sigma(I)$] | 0.0654, 0.1909 |

[a] $R1 = \Sigma||F_o| - |F_c||/\Sigma|F_o|$. [b] $wR2 = [\Sigma w(F_o^2 - F_c^2)^2/\Sigma w(F_o^2)^2]^{1/2}$.

CCDC-275218 contains the supplementary crystallographic data for this paper. These data can be obtained free of charge from The Cambridge Crystallographic Data Centre via www.ccdc.cam.ac.uk/data_request/cif.

## Acknowledgments

Financial support from the Department of Science and Technology, New Delhi, India, and from the Council of Scientific and Industrial Research, New Delhi, India, is gratefully acknowledged. We are thankful to the DST for the data collection on the CCD facility setup (Indian Institute of Science, Bangalore, India) under the IRHPA-DST program. We are also thankful to Mr. Arnab China of IISc, Bangalore, and Dr. Parimal Karmakar of Jadavpur University for valuable discussions on DNA cleavage and the interaction study. Joan Ribas acknowledges financial support from the Spanish Government (grant BQU2003/00539).

[1] a) *Handbook of Metalloproteins* (Eds.: A. Messerschmidt, R. Huber, T. Poulos, K. Wieghardt), J. Wiley & Sons, Chichester, New York, Weinheim, Brisbane, Singapore, Toronto, **2001**; b) K. D. Karlin, Z. Tyeklar, *Bioinorganic Chemistry of Copper*, Chapman & Hall, New York, **1993**.
[2] E. I. Solomon, U. M. Sundaram, T. E. Machonkin, *Chem. Rev.* **1996**, *96*, 2563.
[3] O. Kahn, *Molecular Magnetism*; VCH Publishers, New York, **1993**.
[4] H.-H. T. Nguyen, A. K. Shiemke, S. J. Jacobs, B. J. Hales, M. E. Linstrom, S. I. Chan, *J. Biol. Chem.* **1994**, *269*, 14995.
[5] a) R. Huber, *Angew. Chem.* **1989**, *101*, 849; *Angew. Chem. Int. Ed. Engl.* **1989**, *28*, 848; b) S.-K. Lee, S. DeBeer George, W. E. Antholine, B. Hedman, K. O. Hodgson, E. I. Solomon, *J. Am. Chem. Soc.* **2002**, *124*, 6180.
[6] a) A. Messerschmidt, A. Rossi, R. Ladenstein, R. Huber, M. Bolognesi, G. Gatti, A. Marchesini, T. Petruzzelli, A. Finazzi-Agro, *J. Mol. Biol.* **1989**, *206*, 513; b) A. Messerschmidt, H. Leucke, R. Huber, *J. Mol. Biol.* **1993**, *230*, 997.
[7] a) H.-H. T. Nguyen, K. H. Nakagawa, B. Hedman, S. J. Elliott, M. E. Lidstrom, K. O. Hodgson, S. I. Chan, *J. Am. Chem. Soc.* **1996**, *118*, 12766; b) S. S. Lumos, H. Yuan, M. L. Perille Collins, W. E. Antholine, *Curr. Top. Biophys.* **2002**, *26*, 43.
[8] a) M. González-Alvarez, G. Alzuet, J. Borrás, B. Macías, A. Castiñeiras, *Inorg. Chem.* **2003**, *42*, 2992; b) R. Boča, L. Dlháň, G. Mezei, T. Ortiz-Pérez, R. G. Raptis, J. Telser, *Inorg. Chem.* **2003**, *42*, 5801; c) S.-L. Ma, W.-X. Zhu, S. Gao, Q.-L. Guo, M.-Q. Xu, *Eur. J. Inorg. Chem.* **2004**, 1311.
[9] a) S. Gehring, H. Astheimer, W. Haase, *J. Chem. Soc., Faraday Trans. 2* **1987**, *83*, 347; b) M. P. Suh, M. Y. Han, J. H. Lee, K. S. Min, C. Hyeon, *J. Am. Chem. Soc.* **1998**, *120*, 3819; c) L. Gutierrez, G. Alzuet, J. A. Real, J. Cano, J. Borrás, A. Castiñeiras, *Inorg. Chem.* **2000**, *39*, 3608; d) L. Gutierrez, G. Alzuet, J. A. Real, J. Cano, J. Borrás, A. Castiñeiras, *Eur. J. Inorg. Chem.* **2002**, 2094.
[10] a) S. Gehring, P. Fleischauer, H. Paulus, W. Haase, *Inorg. Chem.* **1993**, *32*, 54; b) S. Meenakumari, S. K. Tiwary, A. R. Chakravarty, *Inorg. Chem.* **1994**, *33*, 2085.
[11] a) J. Liu, T.-B. Lu, H. Li, Q.-L. Zhang, L.-N. Ji, *Transition Met. Chem.* **2002**, *27*, 686; b) S. Dhar, M. Nethaji, A. R. Chakravarty, *Dalton Trans.* **2004**, 4180.
[12] a) W. K. Pogozelski, T. D. Tullius, *Chem. Rev.* **1998**, *98*, 1089; b) K. J. Humphreys, K. D. Karlin, S. E. Rokita, *J. Am. Chem. Soc.* **2001**, *123*, 5588; c) K. J. Humphreys, K. D. Karlin, S. E. Rokita, *J. Am. Chem. Soc.* **2002**, *124*, 8055; d) C. Tu, Y. Shao, N. Gan, Q. Xu, Z. Guo, *Inorg. Chem.* **2004**, *43*, 4761.
[13] a) G. Seeber, P. Kögeler, B. M. Kariuki, L. Cronin, *Chem. Commun.* **2004**, 1580; b) U. Suksangpanyu, A. J. Blake, E. M. Cade, P. Hubberstey, D. J. Parker, C. Wilson, *CrystEngComm* **2004**, *6*, 159.
[14] a) M. T. Allen, A. D. Burrows, M. F. Mahon, *J. Chem. Soc., Dalton Trans.* **1999**, 215; b) Z. Qin, M. C. Jennings, R. J. Puddephatt, *Inorg. Chem.* **2002**, *41*, 5174; c) D. Vujovic, H. G. Raubenheimer, L. R. Nassimbeni, *Dalton Trans.* **2003**, 631.
[15] a) J. M. Lehn, *Supramolecular Chemistry*, VCH, Weinheim, **1995**; b) G. R. Desiraju, *Angew. Chem. Int. Ed. Engl.* **1995**, *34*, 2311; c) D. Braga, F. Frepioni, G. R. Desiraju, *Chem. Rev.* **1998**, *98*, 1375.
[16] C.-T. Yang, M. Vetrichelvan, X. Yang, B. Moubaraki, K. S. Murray, J. J. Vittal, *Dalton Trans.* **2004**, 113.
[17] S. Larsen, K. Michelsen, E. Pedersen, *Acta Chem. Scand. Sect. A* **1986**, *40*, 63.
[18] G. B. Deacon, R. J. Phillips, *Coord. Chem. Rev.* **1980**, *33*, 227.
[19] S. Torelli, C. Belle, I. Gautier-Luneau, J. L. Pierre, E. Saint-Aman, J. M. Latour, L. LePape, D. Luneau, *Inorg. Chem.* **2000**, *39*, 3526.
[20] G. V. R. Chandramouli, T. K. Kundu, P. T. Manoharan, *Aust. J. Chem.* **2003**, *56*, 1239.
[21] a) T. Tokii, N. Hamamura, M. Nakashima, Y. Muto, *Bull. Chem. Soc. Jpn.* **1992**, *65*, 1214; b) W. B. Tolman, R. L. Rardin, S. J. Lippard, *J. Am. Chem. Soc.* **1989**, *111*, 4532.
[22] M. Asadi, E. Safari, B. Ranjbar, L. Hasani, *New J. Chem.* **2004**, *28*, 1227.
[23] A. Wolfe, G. H. Shimer, T. Meehan, *Biochemistry* **1987**, *26*, 6392.
[24] S. Satyanarayana, J. C. Daborusak, J. B. Chaires, *Biochemistry* **1992**, *31*, 9319.
[25] a) J. A. Pachter, C.-H. Huang, V. H. Duvernay, A. W. Prestayko, *Biochemistry* **1982**, *21*, 1541; b) D. H. Tjahjono, S. Mima, T. Akutsu, N. Yoshioka, H. Inoue, *J. Inorg. Biochem.* **2001**, *85*, 219.
[26] a) T. M. Kelly, A. B. Tossi, D. J. McConnell, T. C. Strekas, *Nucleic Acids Res.* **1985**, *13*, 6017; b) J. Liu, T. Zhang, L. Qu, H. Zhou, Q. Zhang, J. Liangnian, *J. Inorg. Biochem.* **2002**, *91*, 269.
[27] a) S. Borah, M. S. Melvin, N. Lindquist, R. A. Manderville, *J. Am. Chem. Soc.* **1998**, *120*, 4557; b) D. S. Sigman, *Acc. Chem. Res.* **1986**, *19*, 180.
[28] M. E. Reichmann, S. A. Rice, C. A. Thomas, P. Doty, *J. Am. Chem. Soc.* **1954**, *76*, 3047.
[29] G. K. Lahiri, S. Bhattacharya, B. K. Ghosh, A. Chakravorty, *Inorg. Chem.* **1987**, *26*, 4324.
[30] *SMART*, *SAINT*, *SADABS*, *XPREP*, *SHELXTL*; Bruker AXS Inc., Madison, WI, **1998**.
[31] G. M. Sheldrick, *SHELXTL*, version 5.03; Siemens Analytical Instruments, Inc., Madison, WI, **1994**.

Received: April 26, 2006
Published Online: July 27, 2006

 © 2006 Wiley-VCH Verlag GmbH & Co. KGaA, Weinheim 

DOI: 10.1002/ejic.200600406

# Carbon Dioxide Fixation by Organolanthanides and Thermal Degradation into Amorphous and Higher Condensed Ln/O/C/N Solids

**Ulrich Baisch,[a] Sandro Pagano,[a] Martin Zeuner,[a] and Wolfgang Schnick*[a]**

**Keywords:** Carbon dioxide fixation / Lanthanides / Organometallic precursors / IR spectroscopy

Ammine[tris(cyclopentadienyl)]-, amido[bis(cyclopentadienyl)]lanthanides, and tris[bis(trimethylsilylamido)]cerium have been studied with respect to $CO_2$ absorption under various reaction conditions. Subsequent thermal treatment of these complexes under gaseous and supercritical $CO_2$ yielded new higher condensed lanthanide Ln/O/C/N solids. IR spectroscopic studies of the $CO_2$-activated species reveal the formation of various oxonitridocarbonates, in particular carbamates ($O_2CNH_2^-$), imidocarbonates ($O_2CNH^{2-}$), isocyanates ($OCN^-$), and carbonates ($CO_3^{2-}$), which function as multidentate linkers between the lanthanide ions. Thereby, inorganic polymers are formed, which represent single-source precursors for application in various deposition methods and can therefore be utilized as pre-organized reagents in solid-state chemistry. In this context, we report on the structural characterization of one of the molecular precursors [$Cp_3YbNH_3$] [reticular pseudomerohedral twin, $P2_1/c$, $a$ = 826.8(2), $b$ = 1103.8(2), $c$ = 1482.0(3) pm, $\beta$ = 101.60(3)°, $Z$ = 4, $V$ = 1309.0(5)·$10^6$ pm$^3$]. Crystals of [$Cp_3YbNH_3$] appear red, orange, yellow, and dark green depending on the orientation under plane-polarized light (pleochroism).

(© Wiley-VCH Verlag GmbH & Co. KGaA, 69451 Weinheim, Germany, 2006)

## Introduction

Carbon dioxide ($CO_2$) is an interesting reagent for various synthetic approaches in the chemistry of catalysis and represents a reagent of growing interest in other fields of chemistry.[1–6] Novel methods to sufficiently activate $CO_2$ for an application in organic and inorganic solvent reactions have been reported emphasizing the potential of this compound in various processes.[7–12] We have discovered a novel approach for this "green" reagent as a pre-organized C/O donor in solid-state reactions for the synthesis of novel mixed N-containing lanthanide derivatives of carbonato compounds, which can be described as oxonitridocarbonates (i.e. $O_2CNH_2^-$, $O_2CNH^{2-}$, $O_3C_3N_3H^{2-}$, $OCN^-$). These groups can be envisaged to function as bidentate or multidentate linkers between the Ln ions (Ln = lanthanide = La–Lu) resulting in crosslinked inorganic polymers.

The present study revealed that several kinds of oxonitridocarbonates were formed by the reaction of $CO_2$ with N-containing inorganic complexes and it was therefore intended to investigate these $CO_2$ absorbants for the use as single-source precursors and potential Ln/O/C/N-dopants for applications in solid-state reactions. (Nitrido)lanthanide materials are of particular interest in materials chemistry of optically active or semiconducting compounds. Research previously carried out in our laboratory revealed that the introduction of oxygen into Ln nitridosilicates results in interesting luminescent properties.[13–17] The $CO_2$ reactivity studies of these precursor compounds reported herein enlarge the potential of amorphous O/C/N-containing solids as future reagents for materials science.

In this context we have focused on the study of the solid-state reactivity of activated ammine- and amidolanthanide compounds towards carbon dioxide under various reaction conditions. In particular we report the use of tris[bis(trimethylsilyl)amido]cerium (Ce-BTMSA) as well as ammine-[tris(cyclopentadienyl)]lanthanides (Ln-$NH_3$, cyclopentadienyl = Cp) and amido[bis(cyclopentadienyl)]lanthanides (Ln-$NH_2$) as reactive complexes for the absorption and insertion of $CO_2$ in the solid state.

[Ce{N(SiMe$_3$)$_2$}$_3$] (Ce-BTMSA) has been used as a dopant in materials chemistry yielding SrS:Ce.[18] Because of the sterically demanding nature of the BTMSA moiety, the central atom exhibits free coordination sites above and below the cerium atom, and – caused by the electron deficiency at the Ce center – these complexes can be considered to be highly reactive with respect to a variety of O-containing reagents and in particular against $CO_2$.

Lanthanide metallocenes have been shown to be interesting molecular reagents in materials chemistry.[19] Recently, the synthesis of aggregated nanocrystalline lanthanide nitride materials was reported to be successful using [$Cp_3LnNH_3$] and [{$Cp_2LnNH_2$}$_2$] as precursors.[20] These amido- and ammine(cyclopentadienyl)lanthanide com-

[a] Department Chemie und Biochemie, Lehrstuhl für Anorganische Festkörperchemie, Ludwig-Maximilians-Universität München,
Butenandtstraße 5–13 (D), 81377 München, Germany
E-mail: wolfgang.schnick@uni-muenchen.de

Supporting information for this article is available on the WWW under http://www.eurjic.org or from the author.

 © 2006 Wiley-VCH Verlag GmbH & Co. KGaA, Weinheim 

plexes are volatile under vacuum ($10^{-3}$ mbar) and at temperatures as low as 150–250 °C, which makes them potentially relevant for chemical vapor deposition (CVD) processes.[21,22]

These complexes have been described in the literature;[23–27] however, neither further applications nor crystal structure determinations have been reported for $[Cp_3YbNH_3]$. In the course of our work the crystal structure of $[Cp_3YbNH_3]$ (Yb-$NH_3$) has been determined successfully. Pleochroic behavior was observed viewing the crystals under plane-polarized light. Yb-$NH_3$ can therefore be considered as an interesting material for optical applications.

For further degradation processes, the Cp rings can be removed easily by thermal treatment or using inorganic bases like $LiNH_2$ or $CaH_2$.[20] The mild-temperature conditions, under which supercritical carbon dioxide is used, are of special interest for these precursor compounds.[2,5,10] In this manner, Yb-$NH_3$ can be carboxylated before thermal degradation of the Cp ligands occurs. Thus, this $CO_2$-activated compound represents a molecular single-source precursor.

The absorption of $CO_2$ and the resulting amorphous products have been studied by IR spectroscopy, elemental analysis, and temperature-dependent in-situ mass spectrometry (MS) studies. The higher condensed O/C/N materials obtained are rather difficult to characterize. Solid-state NMR studies can be considered to be rather inappropriate, because of the anisotropic environment around the metal ions resulting in very large quadrupole moments. Furthermore, most $Ln^{III}$ complexes exhibit unpaired electrons (paramagnetism).

As an important reference substance for IR spectroscopy, ammonium carbamate was used and re-characterized[28] more accurately by IR spectroscopy and X-ray structure analysis. This compound was synthesized by the reaction of liquid ammonia with gaseous $CO_2$. Whereas the reaction of these gases under normal conditions (pressure, temperature) always yields ammonium carbamate, amido and ammine metal complexes react with carbon dioxide in a different way.[7,29–35] Scheme 1 shows possible species formed by the nonstoichiometric reaction of $CO_2$ with $NH_3$. Apparently, some of these products are not stable in the protonated form, but are known as anionic ligands in inorganic chemistry.

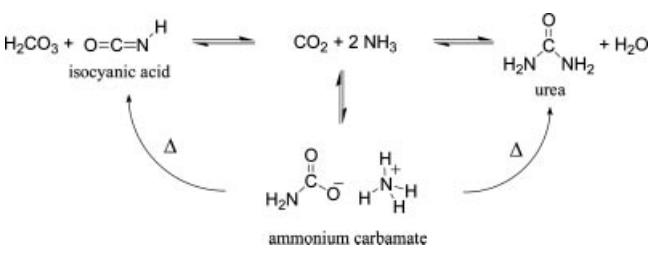


Scheme 1. Protonated species formed by the reaction of $CO_2$ and $NH_3$.

## Results and Discussion

### Characterization and Reactivity of $[Cp_3YbNH_3]$ and $[\{Cp_2YbNH_2\}_2]$

The molecular structure of $[Cp_3YbNH_3]$ (Yb-$NH_3$) has been determined by X-ray diffraction analysis and is illustrated in Figure 1. The $Yb^{III}$ ion shows a coordination number CN = 10 taking into account only the binding electron pairs of the Cp and $NH_3$ ligands. The centroids (Ctr) of the Cp rings and the coordinated $NH_3$ ligand form a distorted tetrahedral environment around the Yb center. Selected bond lengths and angles are given in Table 1.

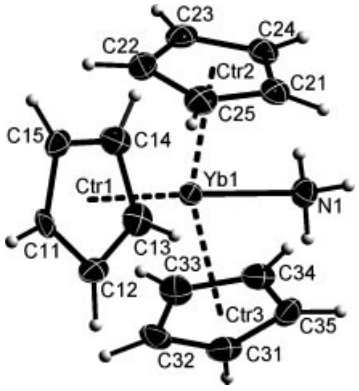


Figure 1. Molecular structure of $[Cp_3YbNH_3]$ at 130 K (50% probability ellipsoids). The hydrogen atoms were calculated and refined using a riding model with fixed isotropic thermal parameters.

Table 1. Selected bond lengths [pm] and angles [°] for $[Cp_3YbNH_3]$.

| $[Cp_3YbNH_3]$ | |
|---|---|
| Yb–N | 242.0(4) |
| Yb–Ctr(1) | 241.1(3) |
| Yb–Ctr(2) | 242.2(3) |
| Yb–Ctr(3) | 240.0(3) |
| N–Yb–Ctr(1) | 97.23(2) |
| N–Yb–Ctr(2) | 98.65(2) |
| N–Yb–Ctr(3) | 98.55(2) |
| Ctr(1)–Yb–Ctr(2) | 117.98(2) |
| Ctr(1)–Yb–Ctr(3) | 118.04(2) |
| Ctr(2)–Yb–Ctr(3) | 118.06(2) |

The three Cp ligands are $\eta^5$-coordinated to the central ion and the Yb–Ctr bond lengths lay within the expected ranges from 240.0(3) to 242.2(3) pm. The Yb–N bond is only slightly shorter [242.0(4) pm] compared with other reported structures of $[Cp_3LnNH_3]$ (Ln = Gd, Dy, Ho, Er).[20] Additional intermolecular interaction was observed for one Cp ring (Ctr1) to a neighboring ammonia ligand of another complex molecule. Intermolecular distances Yb–Ctr1 of 319.6(4) and 263.5(4) pm for C(15)–H(1N) were observed. The formation of a weak N–H–C interaction is probable as one proton of the coordinated ammonia is slightly acidic (Figure 2).

 © 2006 Wiley-VCH Verlag GmbH & Co. KGaA, Weinheim 

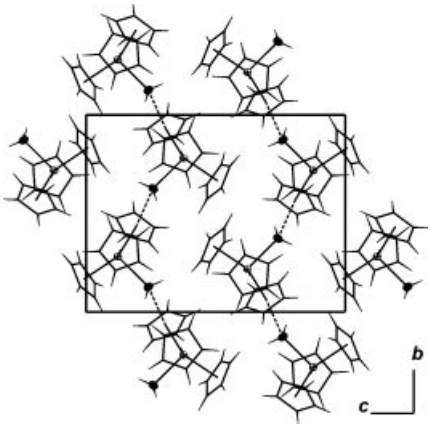


Figure 2. Projection of the unit cell of [$Cp_3YbNH_3$], view along axis *a*. Intermolecular interactions are depicted with dotted lines.

Crystals of Yb–$NH_3$ appear in different colors depending on the orientation of plane-polarized light under which they are viewed (pleochroism). In the literature, Cp-containing ytterbium complexes have been discussed controversially towards their colors. Often, explanations for this discrepancy were given taking into account also the presence of $Yb^{II}$. In the case of Yb-$NH_3$ all colors given elsewhere have been described correctly.[24,26,27] Along the crystal faces the crystallites appear red, orange, yellow, and dark green. Figure 3 displays two crystals at different orientations towards the light source. The emerald green powder of Yb-$NH_3$ sealed in an ampule is shown as well.

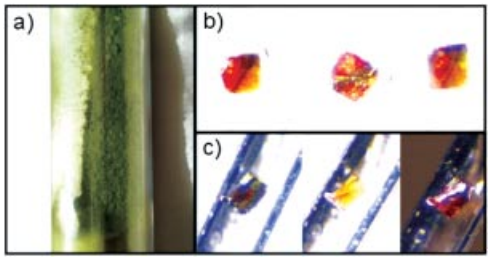


Figure 3. a) Yb–$NH_3$ sealed in an ampule under argon. b, c) Two crystals of Yb-$NH_3$ viewed under plane-polarized light and in three different orientations towards the light source.

Thermal treatment of Yb-$NH_3$ under argon (250 °C) causes deprotonation of the coordinated $NH_3$ ligand and abstraction of one cyclopentadiene molecule ($C_5H_6$) forming the more stable and sublimable dinuclear complex [{$Cp_2YbNH_2$}$_2$] (Yb-$NH_2$). The crystal structure of this complex has been determined recently.[20] The Yb–Ctr and Yb–N distances of 234.3(6)–234.6(7) pm and 229(1) and 233(1) pm, respectively, were observed to be significantly shorter than in the ammonia-coordinated derivative.

Yb-$NH_3$ has been characterized by IR spectroscopy (Figure 4). The coordinated ammonia can be identified by the strong N–H stretching vibrations at 3365, 3330, and 3250 $cm^{-1}$ and by the intense asymmetric and symmetrical N–H deformation and reticular vibrations at 1600, 1225, and 500 $cm^{-1}$. The vibrations differ only slightly within a range of ±7 $cm^{-1}$ from the corresponding ammine complexes of Sm, Gd, Dy, Ho, and Er.[20] The seven typical stretching [2 $\nu_{(CH)}$, 2 $\nu_{(CC)}$] and deformation vibrations [1 $\delta_{(CH)}$ parallel, 2 $\delta_{(CH)}$ perpendicular] of the cyclopentadienyl rings at 3090, 3070, 1440, 1360, 1010, 790, and 775 $cm^{-1}$ were also observed.[36]

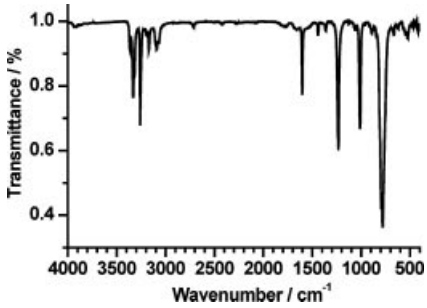


Figure 4. IR spectrum of Yb-$NH_3$.

In contrast to Ln-$NH_3$, the amido complexes (Ln-$NH_2$) are stable up to 360 °C until melting and decomposition to LnN occurs. Thus, the ammonia complex can be considered as a reactive reagent for low-temperature carboxylation reactions whereas the Ln-$NH_2$ compounds are interesting for solid-state reactions up to 350 °C under normal pressure. Both species (Ln = Ho, Yb) were used for decomposition reactions utilizing gaseous and supercritical carbon dioxide.

### Characterization of Ammonium Carbamate $[NH_4]^+[O_2CNH_2]^-$

The solid-state structure of thin colorless plate-like crystals was re-determined by X-ray diffraction analysis. The crystal parameters reported in older literature data were confirmed and the bond lengths and angles of the ammonium ion and the amido moiety were determined more accurately.[28] Ammonium carbamate crystallizes in the orthorhombic space group *Pbca*, with $a$ = 653.5(2), $b$ = 675.4(2), $c$ = 1711.9(4) pm, $V$ = 755.73(3)·$10^6$ $pm^3$.

The compound is stable in closed vessels or under $CO_2$. The IR spectrum was used as an important reference for further investigations, as it shows vibrations of an oxonitridocarbonate without any metal interaction (Figure 5).

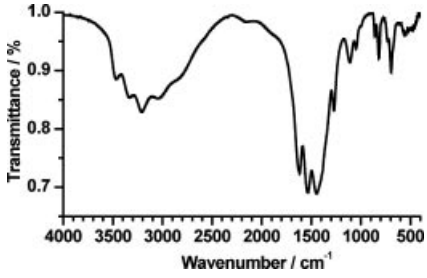


Figure 5. IR spectrum of ammonium carbamate.

Broad N–H and O–H stretching vibrations between 3500 and 2500 $cm^{-1}$ indicate the presence of N···H···O-bridging ligands of the carbonyl and the ammonium moiety. Three intense signals are attributed to the O=C and N=C valences of the carbamate ligand at 1615, 1535, and 1445 $cm^{-1}$.[29,32]

 © 2006 Wiley-VCH Verlag GmbH & Co. KGaA, Weinheim 

Additionally, the deformation vibrations of N–H and O–C–N can be located at 1272, 1112, 859, and 695 $cm^{-1}$.[29,32]

### Heterogeneous Solid-Gas Reactivity of $[Ce\{N(SiMe_3)_2\}_3]$ Towards $CO_2$

The structure of Ce-BTMSA has been determined elsewhere[18] and revealed a mononuclear species with the $Ce^{III}$ ion in the center of the three BTMSA ligands (CN = 3). It has been shown that the central atom displays a disorder in the *z* direction, occupying two sites positioned above and below the plane formed by the ligand nitrogen atoms. The compound has been described to be isostructural with other Ln derivatives.

Crystalline Ce-BTMSA was heated under argon to 150 °C and then brought into reaction with a slow stream of pure gaseous $CO_2$. The beige solid (Ce-1a) was analyzed by IR spectroscopy and showed 40.3% loss of weight. Subsequent thermal treatment of the reaction product under $NH_3$ to 650 °C resulted in the formation of a brown amorphous solid (Ce-1b). Further loss of weight was observed and IR spectroscopic measurements and elemental analysis were carried out. The product showed a composition of Ce/O/C/N = 4:14:7:4. Figure 6 represents the vibrational spectra of the reagent Ce-BTMSA and also includes the carboxylation product after thermal treatment at 150 °C and 650 °C.

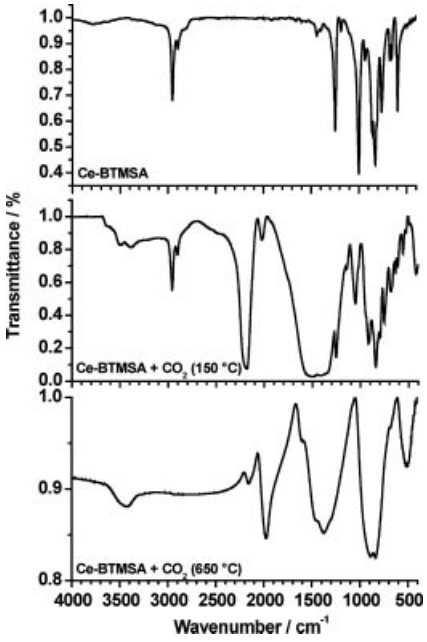


Figure 6. IR spectra of Ce-BTMSA (top) and the carboxylation products after annealing at 150 °C under $CO_2$ (center) and 650 °C (bottom).

Ce-1a heated to 150 °C still shows sharp signals at 2960, 1250, 1055, and 840 $cm^{-1}$, indicating the presence of stretching and deformation vibrations of Si–C and Si–N moieties.[37] A broad and intense absorption between 1700 and 1300 $cm^{-1}$ is characteristic of both carbonate and carbamate groups.[29,38] Additionally, an intensive large and a weak vibration are located between 2150 and 2250 and at 2015 $cm^{-1}$. They can be assigned to several kinds of molecular fragments: Strong absorptions can be observed in the region 2250–1950 $cm^{-1}$ if isocyanates are present.[38,39] Signals of weak and strong intensities have been reported upon occurrence of agostic Si–H or $CO_2$ adducts.[37,40] The formation of OCN groups can be regarded as improbable due to the low reaction temperature and the specific energy necessary for the conversion of a carbamic ligand into carbonate and isocyanate moieties according to Scheme 1.

The ammonolysis reaction of Ce-1a at 650 °C yielded a product (Ce-1b) with a largely different IR spectrum (Figure 6). Less-resolved vibrations typical of amorphous, more condensed solid-state compounds are present, thus proving further decomposition into an O/C/N-containing material. Considering the thermal conditions and peak profiles, this spectrum closely corresponds to typical isocyanato vibrations reported in the literature.[39] N–C–O stretching and deformation modes can be attributed to the signals at 2160 and 1975 as well as 887 and 837 $cm^{-1}$, respectively. Absorptions at 1595, 1455, and 1375 are situated in the characteristic region for both carbamato and carbonato ligands.[29,38]

A formula for the amorphous compound (Ce-1b) with composition $Ce_4O_{14}C_7N_4$ (according to elemental analysis) can be formulated as $[Ce_4(OCN)_3(O_3C)(O_2CN)]$. Further decomposition of the compounds at higher temperatures resulted in the formation of $Ce_2O_3$. The overall thermal treatment of Ce-BTMSA under $CO_2$ can by summarized as Equations (1) and (2).

$$4\ Ce\{N(SiMe_3)_2\}_3 + 7\ CO_2 \xrightarrow{150\ °C} "Ce_4\{N(SiMe_3)_2\}_{12}(CO_2)_7" + 4\ NH_3 \quad (1)$$

$$"Ce_4\{N(SiMe_3)_2\}_{12}(CO_2)_7" \xrightarrow{650\ °C} Ce_4O_{14}C_7N_4 + 12\ HN(SiMe_3)_2 \quad (2)$$

### Heterogeneous Solid-Gas Reactivity of $[\{Cp_2HoNH_2\}_2]$ Towards $CO_2$

Crystalline Ho-$NH_2$ was heated under purified gaseous $CO_2$, $H_2$, and $N_2$ ($CO_2/H_2/N_2$ = 1:1:1). The pink crystallites of Ho-$NH_2$ did not show reaction with the gases below a temperature of 200 °C. During the reaction, the compound decolorized forming a beige solid (Ho-1a). Subsequent heating to a temperature of 350 °C was carried out to achieve a complete thermal degradation of the Cp ligands. A brownish reaction product (Ho-1b) was isolated and analyzed by X-ray diffraction, elemental analysis, and IR spectroscopy. The solid was observed to be amorphous and showed a composition of Ho/O/C/N/H = 2:8:12:1:11. The vibrational spectra of the starting material Ho-$NH_2$ and the carboxylation product after thermal treatment at 200 °C and 350 °C are depicted in Figure 7.

Compared with Ho-$NH_2$ the N–H valence vibrations at 3504 $cm^{-1}$ are broadened in the spectrum of Ho-1a. Similar signals were observed in the IR spectrum of ammonium carbamate (vide supra) and indicate the formation of

 © 2006 Wiley-VCH Verlag GmbH & Co. KGaA, Weinheim 

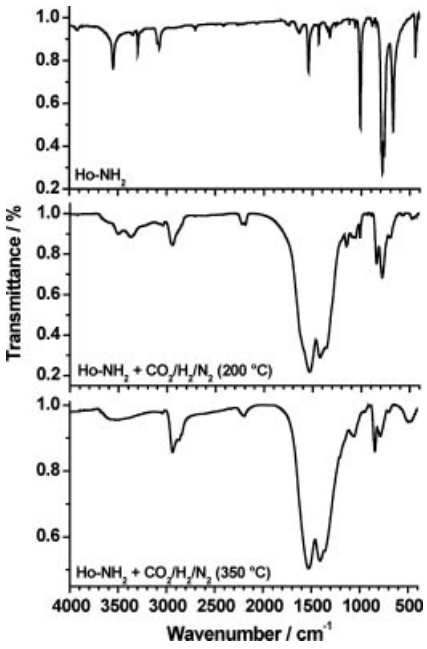


Figure 7. IR spectra of Ho-$NH_2$ (top) and the carboxylation products after annealing under $CO_2/H_2/N_2$ at 200 °C (center) and 350 °C (bottom).

N···H···N-bridged molecular units in the solid. Absorptions around 2950 and 2850 $cm^{-1}$ indicate the occurrence of $C_5H_6$ formed by degradation of the Cp ligands under $H_2$.[26]

Intense broad vibrations at 1620, 1598, and 1530 $cm^{-1}$ are characteristic of CO and CN moieties in carbamato derivatives.[38] Together with additional strong signals between 1480 and 1290 $cm^{-1}$ these absorptions confirm the formation of carbamates or carbonates.[29,32,38] Especially the shoulders at 1620, 1598, and 1290 $cm^{-1}$ are in accordance with vibrations observed for other lanthanide carbamates and ammonium carbamate. The C–O deformations can be attributed to the 950–750 $cm^{-1}$ region.

Only weak intensities were observed between 2250 and 2100 $cm^{-1}$. The presence of isocyanato moieties can therefore be excluded, but signals of similar shape and intensity in this region were described for several adduct complexes of $CO_2$ and $H_2$. The temperature conditions (200 °C) could still justify the occurrence of these species. As a matter of fact, the spectrum of Ho-1b clearly shows that the stretching vibrations for the $CO_2$ and $NCO_2$ fragments in the region 2250–1550 $cm^{-1}$ are diminished and thus a further thermal degradation apparently occurred.

For Ho-1a a possible formula can be formulated as $[Ho_2(CO_3)_2(O_2CNH)]_n$. A further thermal treatment of this compound at higher temperatures resulted in the formation of holmium carbonate, confirmed by X-ray powder diffraction. Therefore, the thermal treatment of Ho-$NH_2$ with $CO_2/H_2/N_2$ at temperatures between 200 and 350 °C can be written as Equation (3).

$$(Cp_2HoNH_2)_2 + 4\ CO_2 + 2\ H_2 \xrightarrow{200\ °C} Ho_2(CO_3)_2(O_2CNH) + 4\ C_5H_6 + NH_3 \quad (3)$$

In order to detect volatile species being potentially evolved during the degradation process of Ho-1a, mass spectra were acquired while heating an evacuated sample in a furnace up to 300 °C. Until 160 °C, a peak of relatively low intensity with $m/z$ = 18 dominates the spectra, which can be attributed to water adsorbed on the sample and adhering to the inside wall of the spectrometer and glass tube. A peak at $m/z$ = 44 shows increasing intensity between 80 and 180 °C; at 200 °C it dominates the spectra. Ammonia ($m/z$ = 17) simultaneously appears in the diagram between 140 and 260 °C, the associated intensity, however, being orders of magnitude smaller as compared to that of $CO_2$. The degradation of cyclopentadiene ($C_5H_6$, $m/z$ = 66) was detected beyond 200 °C. At temperatures above 220 °C the relative intensity of $CO_2$ ($m/z$ = 44) decreases, while the $m/z$ = 66 peak was observed to be the dominating species in the defragmentation pattern until the final temperature of 300 °C was reached. The MS measurement of Ho-1a proved the insertion of $CO_2$ into the N–H bond and showed that $C_5H_6$ was built during the degradation process. N–H moieties must have been present in the carboxylation product, otherwise a formation of $NH_3$ would not be observable.

### Heterogeneous Solid-Gas Reaction of $[Cp_3YbNH_3]$ in Supercritical $CO_2$

Yb-$NH_3$ shows high reactivity against supercritical $CO_2$ at 40–50 °C and at a pressure of 250–280 bar. The emerald green amido complex adsorbed $CO_2$ forming an orange-yellow solid (Yb-1). During the carboxylation process, Yb-$NH_3$ was transformed into Yb-$NH_2$. Under normal pressure conditions this reaction was observed to require temperatures between 200 and 290 °C. Yb-$NH_2$ formed in the first reaction stage as well as the reaction product Yb-1 and both were analyzed by IR spectroscopy. The spectra are depicted in Figure 8.

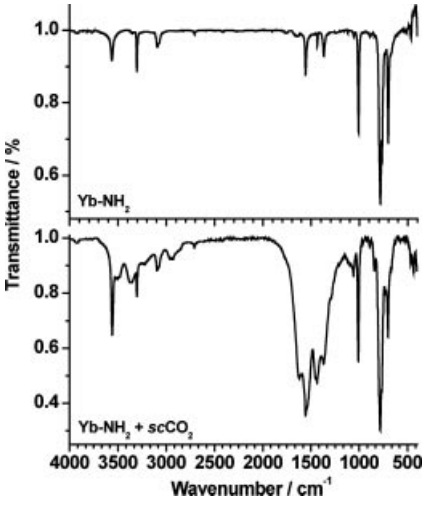


Figure 8. IR spectra of Yb-$NH_2$ (top) and the carboxylation product (bottom) after the reaction in supercritical $CO_2$ ($T$ = 50 °C, $p$ = 250–280 bar).

The $\mu_2$-bridged amido ligands of the dinuclear complex Yb-$NH_2$ can be identified by the intense N–H stretching

 © 2006 Wiley-VCH Verlag GmbH & Co. KGaA, Weinheim 

vibrations around 3350 and 3290 $cm^{-1}$, and the asymmetric and symmetric N–H deformation modes around 1540, 670, and 440 $cm^{-1}$.[20] An intense vibration mode at 3500 $cm^{-1}$, probably due to a combination of two lower signals, is typical of these amido compounds.[20]

The characteristic stretching and deformation vibrations of Yb-$NH_2$ are observed in both spectra. Therefore, a degradation of the Cp ring did not occur, probably due to the mild thermal conditions under which the experiment was carried out. Additionally, broad N–H stretching vibrations can be identified in the 3500–3000 $cm^{-1}$ region and can be interpreted as N–H-bridging moieties (vide infra). Signals at 2950 $cm^{-1}$ indicate the occurrence of $C_5H_6$ formed by the decomposition process of Yb-$NH_3$ to Yb-$NH_2$. The most characteristic vibrations in the spectra of Yb-1 are the intense absorptions at 1640, 1540, 1450, and 1379 $cm^{-1}$. They fit well in the expected ranges of CO and CN stretching vibrations of carbamato complexes.[29] The deformation modes for these kinds of carbamato ligands can be observed at 841 and 670 $cm^{-1}$. Therefore, the formation of an isolated or higher condensed carbamato complex with the formula [{CpYb}$_2$O$_2$CNH] is very probable.

The synthesized oxonitridocarbonates were observed to be amorphous and not soluble in any common polar and nonpolar solvent. Attempts to crystallize these products by thermal treatment resulted in the decomposition of these precursors to the corresponding oxides or oxide cyanamides.

## Conclusions

Ce-BTMSA, Ln-$NH_3$, and Ln-$NH_2$ have been shown to be considerable molecular precursor compounds for thermal degradation reactions resulting in novel highly condensed lanthanide O/C/N materials. The carbonato, imidocarbonato, and carbamato species were synthesized using different kinds of heterogeneous solid-gas reactions.

The Ce-BTMSA precursor absorbs $CO_2$, leading to the formation of a mixed carbamato(carbonato)isocyanato compound. The IR spectra of the products differ significantly from the results reported for carboxylation reactions in solution or in sealed ampules.[35,41] The cerium precursor Ce-BTMSA is activated with $CO_2$ in the first step. According to the results of the elemental analysis two molecules of $CO_2$ are absorbed by one molecule of Ce-BTMSA. Subsequently, the $CO_2$ inserts into the Ce–N bond yielding a carbamato species. According to Scheme 1 further ammonolysis of the compound at higher temperatures results in the formation of an carbonato(isocyanato)cerium compound. The flowing gas stream provides for a better degradation of the $Me_3Si$ groups.

Lanthanide metallocenes were observed to be quite stable against thermal treatment under an inert gas, but they represent a highly reactive molecular precursor species under $CO_2$ at temperatures above 200 °C. The use of both a reducing ($H_2$) and oxidizing agent ($CO_2$) with $N_2$ as the carrier gas gave satisfying results forming a polymeric (imidocarbonato)holmium complex. The Cp ligands can be split off easily by the presence of $H_2$ with $CO_2$ occupying the free coordination sites of the lanthanide ion. The activation or doping of the surface of various materials with lanthanide carbonates or carbamates could therefore be achieved in this way.

The carboxylation reaction of Yb-$NH_3$ in supercritical carbon dioxide showed, that the temperature necessary for the $CO_2$ insertion into the Yb–N bond can be lowered significantly. The complex molecule reacted with $CO_2$ without simultaneous degradation of the Cp ligands. Thus, a molecular single-source precursor with the tentative formula [{CpYb}$_2$O$_2$CNH] has been synthesized. It represents an adequate compound for the deposition of predefined Ln/O/C/N material on various surfaces in materials chemistry.[19]

Furthermore, the observed pleochroism of [$Cp_3YbNH_3$] is a promising optical property for further applications of this compound as a future dopant in solid-state sciences. Thus, small amounts of this compound introduced during the synthesis of materials could change significantly the optical properties of the final products. The high volatility of [$Cp_3YbNH_3$] facilitates significantly the doping process using CVD techniques at very convenient conditions (180 °C, $10^{-3}$ mbar).

## Experimental Section

**General Procedures:** All manipulations described below were performed with rigorous exclusion of oxygen and moisture in flame-dried Schlenk-type glassware or tubes of silica glass, interfaced to a vacuum ($10^{-3}$ mbar) line. Argon was purified by passage through columns of silica gel, molecular sieve, KOH, $P_4O_{10}$, titanium sponge (650 °C), hydrogen and nitrogen by passage through columns of silica gel, molecular sieve, KOH, $P_4O_{10}$, BTS,[42] and $Cr^{II}$ oxide catalyst.[43] Carbon dioxide was purified by passage through columns of $P_4O_{10}$ and BTS catalyst.[42] Anhydrous lanthanide(III) chlorides were purchased from Alfa Aesar (99.99%, ultra dry) and were used without any further purification. The complexes [$Cp_3YbNH_3$] (Ln-$NH_3$) and [{$Cp_2LnNH_2$}$_2$] (Ln-$NH_2$, with Ln = Ho, Yb) as well as [Ce{N(SiMe$_3$)$_2$}$_3$] were prepared according to known procedures[20,25,44] and sublimed twice before use ($10^{-3}$ mbar, 120–250 °C). For thermal degradation experiments a Reetz collapsible tube furnace (LK-1100-45-250) handled by an Omron (RE.LB.1.P16) temperature controller was used. For $CO_2$ experiments under supercritical conditions a Parr high-pressure vessel (Type 4740) with a Parr gage block (Type 4316) was used. FT-IR spectra were recorded with a Bruker IFS 66v/S spectrometer with DTGS detector. The samples were thoroughly mixed with dried KBr and the preparation procedures were performed in a glovebox under dried argon. The spectra were collected in a range from 400 to 4000 $cm^{-1}$ with a resolution of 2 $cm^{-1}$. During the measurement, the sample chamber was evacuated. Elemental analysis was performed by Mikroanalytisches Labor Pascher, Remagen, Germany. Each element of the sample was analyzed twice. Temperature-dependent mass spectra were recorded using DEI+ (70 eV) with the sample contained in an evacuated ($10^{-4}$ mbar) Schlenk tube (length 330 mm, diameter 10 mm) connected with the gas inlet system of the spectrometer by glass tubes of about 200 mm total length, thus providing dynamic vacuum conditions. The Schlenk tube was placed horizontally in a Carbolite furnace

 © 2006 Wiley-VCH Verlag GmbH & Co. KGaA, Weinheim 

equipped with a Eurotherm temperature controller (Type 2132). The sample was heated up to 573 K in steps of 5 K min$^{-1}$ and mass spectra of the volatile decomposition products were acquired successively at intervals of 20 K.

**X-ray Crystallography:** Reflection data were collected with a STOE IPDS diffractometer. The Stoe IPDS software package was used for the determination of the unit-cell parameters, the data collection, and to transform the raw data into the reflection data file. Subsequent calculations after the determination of the unit-cell parameters and data reduction to the *hkl* format were carried out using the SHELXS[45] and SHELXL[46] program. The analytical scattering factors for neutral atoms were used throughout the analysis. Hydrogen atoms were either treated isotropically, if found in the Fourier maps, or were otherwise included manually using a riding model. Absorption correction was carried out using the Stoe IPDS program package. All non-hydrogen atoms were refined anisotropically. X-ray diffraction experiments on powder samples at room temperature were conducted with a STOE Stadi P diffractometer with Ge(111)-monochromated Cu-$K_{\alpha1}$ radiation ($\lambda$ = 154.06 pm). **[$Cp_3YbNH_3$]:** The structure of Yb-$NH_3$ was solved by direct methods and refined on $F^2$ by full-matrix least-squares techniques. Intrinsic reticular pseudo-merohedral twinning was observed for each of the isolated crystals.[47] The compound crystallizes as emerald-green or ruby (depending on the viewing direction and lighting) brick-shaped crystals. An appropriate extracted crystal was used and two data sets for each twin domain were extracted from the diffraction data. Yb-$NH_3$ showed pseudo-orthorhombic symmetry, but X-ray powder diffraction experiments (XRD) confirmed a monoclinic cell setting. The diffraction symmetry was 2/*m* and the systematic absences were consistent with the centrosymmetric monoclinic space group $P2_1/c$. The reflections were isolated unifying all of the overlapping reflections of the two domains to one reflection set of the most appropriate individual. Subsequent determination of the twin law and refinement of the data resulted in a satisfying crystal structure refinement, taking into account the problems encountered during the isolation and weighting of the overlapping reflections in the reciprocal space. Tables 1 and 2 show the crystallographic data as well as bond lengths and angles, and Figure 1 the molecular structure of Yb–$NH_3$. CCDC-603950 (for [$Cp_3YbNH_3$]) and -603951 (for $[NH_4]^+$-$[O_2CNH_2]^-$) contain the supplementary crystallographic data for this paper. These data can be obtained free of charge from The Cambridge Crystallographic Data Centre via www.ccdc.cam.ac.uk/data_request/cif.

Table 2. Summary of crystallographic data for [$Cp_3YbNH_3$].

| | [$Cp_3YbNH_3$] |
|---|---|
| Empirical formula | $C_{15}H_{15}NYb$ |
| Formula mass [g mol$^{-1}$] | 385.34 |
| Crystal system | Monoclinic |
| Space group | $P2_1/c$ (no. 14); reticular pseudo-merohedral twinning |
| Diffractometer device | Stoe IPDS |
| Crystal size [mm] | 0.20 × 0.14 × 0.06 |
| Wavelength $\lambda$ [pm] | 71.073 (Mo-$K_\alpha$) |
| Temperature $T$ [K] | 120 |
| Twin law | $\begin{pmatrix} -0.12 & 0 & -0.565 \\ 0 & -1 & 0 \\ -1.745 & 0 & 0.12 \end{pmatrix}$ |
| Twin ratio | 0.027(2) |
| Lattice constants [pm, °] | $a$ = 826.8(2)<br>$b$ = 1103.8(2)<br>$c$ = 1482.0(3)<br>$\beta$ = 101.60(3) |
| Cell volume [10$^6$ pm$^3$] | 1309.0(5) |
| Formula units/cell | 4 |
| $\rho_{calcd.}$ [g cm$^{-3}$] | 1.955 |
| $\mu$ [mm$^{-1}$] | 7.12 |
| $F$(000) | 740 |
| 2$\theta$ range [°] | 2.53–30.61 |
| Measured refl. | 15421 |
| Independent refl. | 3952 |
| Refl. with $F_o^2 = 2\sigma(F_o^2)$ | 12103 |
| No. of refined parameters | 155 |
| Max. peak/min. hole [e·Å$^{-3}$] | 1.684/–1.485 |
| $R_{int}/R_\sigma$ | 0.0459/0.0342 |
| $R_1$ [$I > 2\sigma(I)$] | 0.0457 |
| $wR_2$ | 0.1224 |
| GooF | 1.152 |

**Synthesis. Ce-1:** Ce-BTMSA was ground in a mortar, placed in an alumina boat and transferred into a silica tube situated in a tube furnace. First, the solid was heated under flowing argon to 150 °C and than predried $CO_2$ was added to the gas stream. Melting of the yellow Ce-BTMSA was observed immediately after the first contact with $CO_2$ and the yellow fluid solidified within 30 min yielding a beige product (Ce-1a). The solid was cooled slowly to room temperature and a small part of the solid was used for IR spectroscopic analysis. The residue was re-introduced into the silica tube and heated to 650 °C under flowing predried ammonia. Ammonia was dried by passage over KOH pellets, $Cr^{II}$ catalyst and condensed over Na and K before use. A dark-brown solid (Ce-1b) was isolated after the sample was cooled to room temperature (4 h) and analyzed by elemental analysis, IR spectroscopy, and X-ray powder diffraction. Ce-1b (0.0615 g) was isolated after the reaction process using an argon-filled glovebox. **Ho-1:** Ho-$NH_2$ was ground in a mortar, placed in an alumina boat and transferred into a silica tube situated in a tube furnace. The solid was heated under a flowing gas stream of a mixture of $CO_2/H_2/N_2$ = 1:1:1 and heated slowly to 200 °C. The temperature was maintained for 4 h. Cooling of the sample to room temperature yielded a beige solid (Ho-1a). A small part of the solid was used for IR spectroscopic analysis and the residue was re-introduced into the silica tube and heated to 350 °C (4 h) under the same conditions as described above. A dark-brown solid (Ho-1b) was isolated after the sample was cooled to room temperature (2 h) and analyzed by elemental analysis, IR spectroscopy, and X-ray powder diffraction. **Yb-1:** Yb-$NH_3$ was introduced into a high-pressure vessel and connected with a gas vacuum line. Purified carbon dioxide was desublimated by cooling the vessel to –80 °C until sufficient solid $CO_2$ was present. The reaction vessel was closed and warmed slowly to 50 °C. A pressure of 250–280 bar was observed during the reaction. After 1 d, the pressure was reduced carefully by opening the valve of the unit and the vessel was opened in an argon-filled glovebox. A yellow-orange powder (Yb-1) was isolated and analyzed by X-ray diffraction methods, IR spectroscopy, and elemental analysis.

**Supporting Information** (see footnote on the first page of this article): Tables of crystal data, structure solution and refinement, bond lengths and angles for $[NH_4]^+[O_2CNH_2]^-$ as well as figures of the crystal structure.

## Acknowledgments

The authors are indebted to Dr. Oliver Oeckler for conducting single-crystal X-ray diffractometry measurements [Department Chemie und Biochemie, Universität München (LMU)]. Financial

 © 2006 Wiley-VCH Verlag GmbH & Co. KGaA, Weinheim 

support by the Deutsche Forschungsgemeinschaft (DFG) (Schwerpunktprogramm SPP 1166, Lanthanoidspezifische Funktionalitäten in Molekül und Material, project SCHN377/10) and the Fonds der Chemischen Industrie is gratefully acknowledged.

[1] J. Alauzun, A. Mehdi, C. Reyé, J. P. Corriu, *J. Am. Chem. Soc.* **2005**, *127*, 11204–11205.
[2] J. A. Behles, J. M. DeSimone, *Pure Appl. Chem.* **2001**, *73*, 1281–1285.
[3] V. Iota, J. H. Park, C. S. Yoo, *Phys. Rev. B: Condens. Matter* **2004**, *69*, 064106.
[4] J. H. Park, C. S. Yoo, V. Iota, H. Cynn, M. F. Nicol, T. Le Bihan, *Phys. Rev. B: Condens. Matter* **2003**, *68*, 014107.
[5] P. Raveendran, Y. Ikushima, S. L. Wallen, *Acc. Chem. Res.* **2005**, *38*, 478–485.
[6] Y. Zou, A. E. Rodrigues, *Adsorpt. Sci. Technol.* **2001**, *19*, 255–266.
[7] D. Belli Dell'Amico, F. Calderazzo, L. Labella, F. Marchetti, G. Pampaloni, *Chem. Rev.* **2003**, *103*, 3857–3898.
[8] P. G. Jessop, T. Ikariya, R. Noyori, *Science (Washington, DC)* **1995**, *269*, 1065.
[9] A. M. Scurto, S. N. V. K. Aki, J. F. Brennecke, *J. Am. Chem. Soc.* **2002**, *124*, 10276–10277.
[10] M. Solinas, J. Jiang, O. Stelzer, W. Leitner, *Angew. Chem. Int. Ed.* **2005**, *44*, 2291–2295; *Angew. Chem.* **2005**, *117*, 2331–2335.
[11] K. Wittmann, W. Wisniewski, R. Mynott, W. Leitner, C. L. Kranemann, T. Rische, P. Eilbracht, S. Kluwer, J. M. Ernsting, C. J. Elesevier, *Chem. Eur. J.* **2001**, *7*, 4584–4589.
[12] D. Belli Dell'Amico, F. Calderazzo, L. Labella, F. Marchetti, G. Pampaloni, *Inorg. Chem. Commun.* **2002**, *5*, 733–745.
[13] W. Schnick, R. Bettenhausen, B. Götze, H. A. Höppe, H. Huppertz, E. Irran, K. Köllisch, R. Lauterbach, M. Orth, S. Rannabauer, T. Schlieper, B. Schwarze, F. Wester, *Z. Anorg. Allg. Chem.* **2003**, *629*, 902–912.
[14] T. Juestel, P. Schmidt, H. Höppe, W. Schnick, W. Mayr (Philips Intellectual Property & Standards GmbH, Germany; Koninklijke Philips Electronics N.V.; Lumileds Lighting U. S. LLC), WO 2004055910, A1, 24 pp., *PCT Int. Appl.* **2004** [*Chem. Abstr.* **2004**, *141*, 96377].
[15] T. Juestel, P. Schmidt, W. Schnick, F. M. Stadler (Philips Intellectual Property & Standards G.m.b.H., Germany; Koninklijke Philips Electronics N.V.; Lumileds Lighting Us, LLC), WO 2006006099, A1, 31 pp., *PCT Int. Appl.* **2006** ; [*Chem. Abstr.* **2006**, *144*, 138595].
[16] P. Schmidt, T. Juestel, H. Höppe, W. Schnick, W. Mayr (Philips Intellectual Property & Standards GmbH, Germany; Koninklijke Philips Electronics N.V.; Lumileds Lighting, US LLC), WO 2005116163, A1, 35 pp., *PCT Int. Appl.* **2005**; [*Chem. Abstr.* **2004**, *144*, 29519].
[17] R. Mueller-Mach, G. Mueller, M. R. Krames, H. A. Höppe, F. Stadler, W. Schnick, T. Juestel, P. Schmidt, *Phys. Status Solidi A* **2005**, *202*, 1727–1732.
[18] W. S. Rees, O. Just, D. S. Van Derveer, *J. Mater. Chem.* **1999**, *9*, 249–252.
[19] Y. K. Gun'ko, F. T. Edelmann, *Comments Inorg. Chem.* **1997**, *19*, 153–184.
[20] U. Baisch, S. Pagano, M. Zeuner, N. Barros, L. Maron, W. Schnick, *Chem. Eur. J.* **2006**, *12*, 4785–4798.
[21] S. Mathur, M. Veith, T. Rügamer, E. Hemmer, H. Shen, *Chem. Mater.* **2004**, *16*, 1304–1312.
[22] S. Mathur, M. Veith, H. Shen, S. Huefner, M. H. Jilavi, *Chem. Mater.* **2002**, *14*, 568–582.
[23] J. M. Birmingham, G. Wilkinson, *J. Am. Chem. Soc.* **1956**, *78*, 42–44.
[24] F. Calderazzo, R. Pappalardo, S. Losi, *J. Inorg. Nucl. Chem.* **1965**, *28*, 987–999.
[25] E. O. Fischer, H. Fischer, *J. Organomet. Chem.* **1966**, *6*, 141–148.
[26] H. Fischer, PhD Thesis, Technische Hochschule München, **1965**.
[27] R. G. Hayes, J. L. Thomas, *Inorg. Chem.* **1969**, *8*, 2521–2522.
[28] J. M. Adams, R. W. H. Small, *Acta Crystallogr., Sect. B* **1973**, *29*, 2317–2319.
[29] U. Baisch, D. Belli Dell'Amico, F. Calderazzo, L. Labella, F. Marchetti, A. Merigo, *Eur. J. Inorg. Chem.* **2004**, 1219–1224.
[30] K. Bouzouita, J. Desmaison, *J. Alloys Compd.* **2002**, *336*, 270–279.
[31] F. Calderazzo, G. Dell′Amico, R. Netti, M. Pasquali, *Inorg. Chem.* **1978**, *17*, 471–473.
[32] M. H. Chisholm, M. W. Extine, *J. Am. Chem. Soc.* **1977**, *99*, 792–802.
[33] C. Jegat, M. Fouassier, J. Mascetti, *Inorg. Chem.* **1991**, *30*, 1521–1529.
[34] C. Jegat, M. Fouassier, M. Tranquille, J. Mascetti, *Inorg. Chem.* **1991**, *30*, 1529–1536.
[35] Y. F. Rad′kov, E. A. Fedorova, S. Y. Khorshev, G. S. Kalinina, M. N. Bochkarev, *Zh. Obshch. Khim.* **1986**, *56*, 386–389; *Russ. J. Gen. Chem.* **1986**, *56*, 336–339.
[36] H. P. Fritz, *Adv. Organomet. Chem.* **1964**, *1*, 239–316.
[37] R. Anwander, O. Runte, J. Eppinger, G. Gerstberger, E. Herdtweck, M. Spiegler, *J. Chem. Soc., Dalton Trans.* **1998**, 847–858.
[38] K. Nakamoto, *Infrared Spectra of Inorganic and Coordination Compounds*, 2nd ed., Wiley, New York, London, Sydney, Toronto, **1970**.
[39] J. L. Burmeister, S. D. Patterson, E. A. Deardorff, *Inorg. Chim. Acta* **1969**, *3*, 105–109.
[40] J. C. Dobrowolski, M. H. Jamroz, *J. Mol. Struct.* **1992**, *275*, 211–219.
[41] M. N. Bochkarev, E. A. Fedorova, Y. F. Rad'kov, S. Y. Khorshev, G. A. Razuvaev, *J. Organomet. Chem.* **1983**, *258*, C29–C30.
[42] G. Brauer, *Handbuch der Präparativen Anorganischen Chemie*, 3rd ed., Ferdinand Enke, Stuttgart, **1975**, vol. 1.
[43] H. L. Krauss, H. Stach, *Z. Anorg. Allg. Chem.* **1969**, *366*, 34–42.
[44] F. T. Edelmann, *Synthetic Methods of Organometallic and Inorganic Chemistry* (Eds.: W. A. Herrmann, G. Brauer), 1st ed., Georg Thieme, Stuttgart, New York, **1997**, vol. 6, pp. 88–90.
[45] G. M. Sheldrick, *SHELXS-97*, University of Göttingen, Göttingen, Germany, **1997**.
[46] G. M. Sheldrick, *SHELXL-97*, University of Göttingen, Göttingen, Germany, **1997**.
[47] R. Herbst-Irmer, G. M. Sheldrick, *Acta Crystallogr., Sect. B: Struct. Sci.* **1998**, *54*, 443–449.

Received: May 3, 2006
Published Online: July 13, 2006

 © 2006 Wiley-VCH Verlag GmbH & Co. KGaA, Weinheim 

DOI: 10.1002/ejic.200600290

# A Poly(bicyclic dimer) and a Cyclic Tetramer: Ligand Isomerism of $S_2O_2$ Macrocycles During the Assembly of Supramolecular Silver(I) Complexes

So Young Lee,[a] Joobeom Seo,[a] Il Yoon,[a] Chung-Sik Kim,[b] Kyu Seong Choi,[b] Jae Sang Kim,[a] and Shim Sung Lee*[a]

**Keywords:** Macrocycles / Silver / Self-assembly / Supramolecular chemistry / Polymers

Two isomeric $S_2O_2$ macrocycles ($\mathbf{L^1}$ and $\mathbf{L^2}$) with a 14-membered cavity have been synthesised as a model system with different binding modes. Self-assembly reactions of $\mathbf{L^1}$ and $\mathbf{L^2}$ with silver perchlorate afford the respective ligand-directed cyclic oligomer complexes with different shapes: a poly(bicyclic dimer) (**1**) and a discrete cyclic tetramer (**2**). The formation of these supramolecular complexes is discussed in terms of conformational discrimination of two isomeric macrocycles due to ring rigidity and interdonor distances.

(© Wiley-VCH Verlag GmbH & Co. KGaA, 69451 Weinheim, Germany, 2006)

## Introduction

The programmed self-assembly of discrete supramolecular complexes and coordination networks has attracted intense interest not only for their potential applications as new functional materials but also their fascinating structural topologies.[1] A cyclic oligomer complex, which is one of the entities in the former category, has been reported to be capable of selective recognition and separation of guest species, including small molecules and anions.[2] As a methodology of emerging significance in supramolecular chemistry, there is an interest in understanding the factors that influence the way in which metal complexes self-assemble into cyclic oligomers. Rigid rod-like didentate ligands such as 4,4′-bipyridyl derivatives, together with corner-piece complexes based on late transition metal ions, are known to form a range of metallacycles.[3]

Besides its formation of numerous cyclic oligomer complexes with multidentate N-donor ligands, the soft silver(I) ion has a high affinity for sulfur ligands, such as linear thioethers, and such compounds can be used as building blocks to construct discrete metallomacrocyclic frameworks as well as network species. For their supramolecular assembly, the choice of length of the spacer unit in the ligand, anions and solvent are crucial to the structure of the final product.

Recently, we proposed the *exo* coordination properties of S/O or S/O/N donor macrocycles, which afford diverse types of supramolecular complexes, including cyclic oligomer silver(I) complexes, upon varying donor atoms, counteranions and solvents.[4] This approach is attractive because the *exo* coordination of sulfur donors[5] to the metal ion offers the possibility of linking the ligand building blocks in diverse modes. We are interested in extending this to a ligand-directed approach, such as ligand isomerism,[6] in order to construct new supramolecular structures, including cyclic oligomer complexes based on dithiaoxa macrocycles. By using two positional isomers with different interdonor distances ($\mathbf{L^1}$ and $\mathbf{L^2}$), we succeeded in generating two different cyclic oligomer complexes (**1** and **2**).

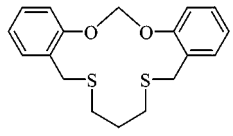

$\mathbf{L^1}$

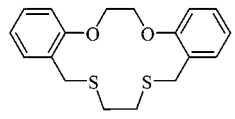

$\mathbf{L^2}$

## Results and Discussion

### Synthesis and Characterisation of Ligands

Synthesis of the ligands began with salicylaldehyde (Scheme 1). Dichlorides ($m$ = 0 and 1) were prepared using a known procedure,[7] and $\mathbf{L^1}$ and $\mathbf{L^2}$ were obtained by macrocyclisation coupling reactions between these dichlorides and dithiols in the presence of $Cs_2CO_3$ under high-dilution condition in reasonable yield (28 and 41%, respectively). The $^1H$ and $^{13}C$ NMR spectra together with elemental analyses and mass spectra are clearly in agreement with the proposed structures.

[a] Department of Chemistry and Research Institute of Natural Sciences, Gyeongsang National University, Chinju 660-701, Korea
Fax: +82-55-753-7614
E-mail: sslee@gsnu.ac.kr
[b] Department of Chemistry, Kyungnam University, Masan 630-701, Korea

 © 2006 Wiley-VCH Verlag GmbH & Co. KGaA, Weinheim 

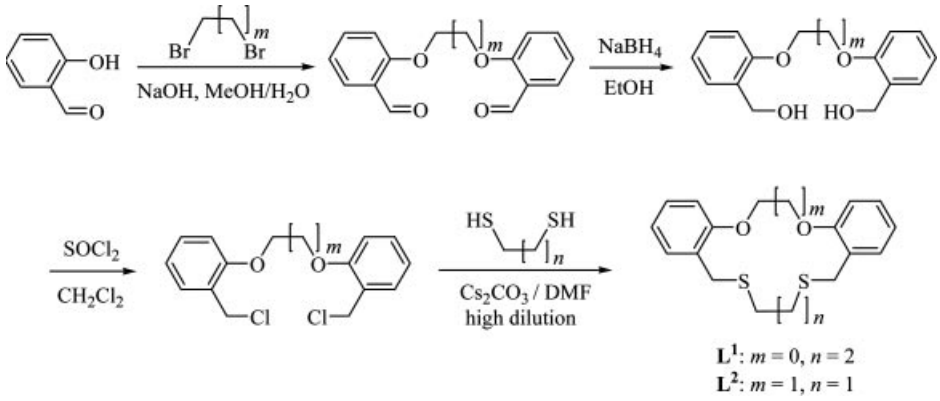


Scheme 1. Synthesis of ligands.

The structures of these macrocycles were also characterised in the solid state by single-crystal X-ray crystallography. Colourless crystals of **L¹** and **L²** suitable for X-ray analysis were obtained by slow concentration of their respective solutions in methanol (**L¹**) or dichloromethane (**L²**). Crystals of **L¹** and **L²** (Figure 1) have the acentric space groups *Pc* and $P2_12_12_1$, respectively. The conformations of the ring cavities in the two molecules differ only in their inter-donor distances. In both cases, the macrocyclic rings are relatively flattened and the two oxygen atoms are oriented endodentate, whilst the two sulfur atoms are arranged exodentate with respect to the ring cavity.[5] As expected, the observed S···S distance in **L¹** (5.627 Å) is significantly longer than that of **L²** (4.387 Å).

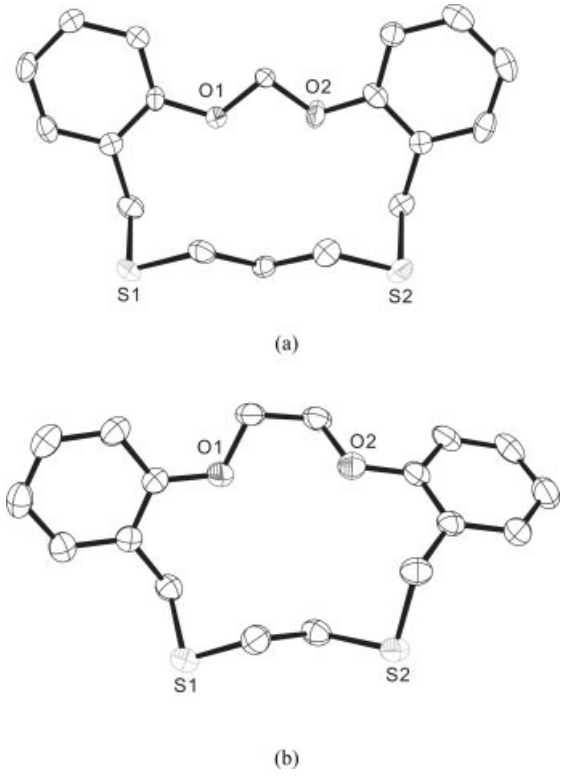


Figure 1. Molecular structures of **L¹** (a) and **L²** (b). Thermal ellipsoids are drawn at the 30% probability level. Selected interatomic distances [Å]: **L¹**: S1···S2 5.627(2); **L²**: S1···S2 4.387(1).

## Complex Syntheses and Structural Description

Two crystalline supramolecular complexes were obtained from the assembly reactions of the ligands with silver perchlorate. A colourless precipitate was obtained from **L¹** and $AgClO_4$ in methanol/water, and colourless single crystals of **1** suitable for X-ray analysis were obtained by vapour diffusion of diethyl ether into a nitromethane solution of this complex. Similarly, a colourless precipitate was obtained from **L²** and $AgClO_4$ in dichloromethane/methanol, and colourless single crystals of **2** suitable for X-ray analysis were obtained by vapour diffusion of diethyl ether into its DMF solution (Scheme 2).

The X-ray analysis revealed that **1** is a poly(bicyclic dimer) $[\{Ag_2(\mathbf{L^1})_2(ClO_4)_2\}CH_3NO_2]_n$ (Figure 2a). The bicyclic dimer unit of **1** contains two bridging Ag atoms, two macrocycles, two perchlorate ions and one noncoordinating nitromethane molecule (not shown). Each five-coordinate Ag atom[8] that lies outside the cavity bridges two S donors from two different macrocycles in a bent fashion [S1–Ag1–S1C 161.95(6)°] such that the two metal centres point towards each other. However, the separation of the two Ag atoms [Ag1···Ag1A 4.8611(12) Å] is far from the range of an argentophilic interaction.[9] Interestingly, two diagonally opposite $ClO_4^-$ anions weakly bridge two Ag atoms in a bidentate manner to form a three-dimensional bicycle. It is known that in most reported $AgClO_4$ complexes with dithioether ligands, the $ClO_4^-$ anions usually take the role of a monodentate ligand or intercalating anion. However, the $ClO_4^-$ anions in **1** coordinate to two Ag atoms in the rare $\eta^2$-double-bridge mode through two O atoms to form an eight-membered ring.[8] Several cases of bicyclic dimeric $AgClO_4$ complexes with acyclic dithioethers[8] were ex-

 © 2006 Wiley-VCH Verlag GmbH & Co. KGaA, Weinheim 

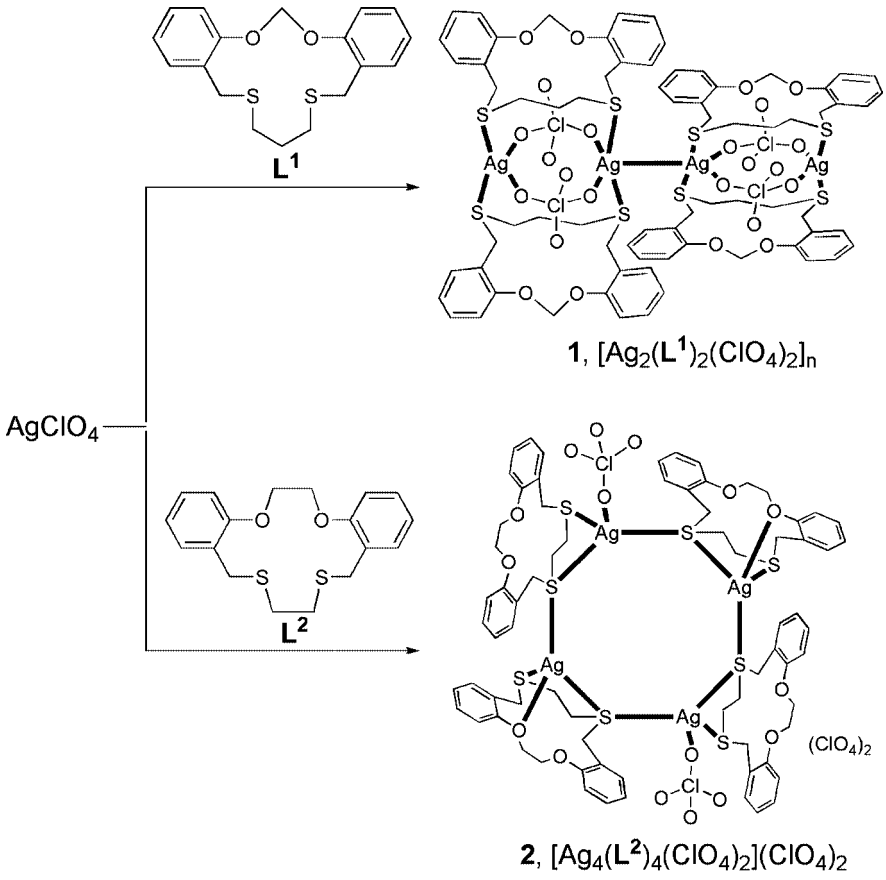


Scheme 2. Complexes prepared.

tracted from the Cambridge Crystallographic Database (CCDC).[10] As we understand, however, this is the first example of a bicyclic dimeric $AgClO_4$ complex based on a cyclic analogue. The bicyclic dimer unit is further held together by Ag–Ag contacts[9] [3.129(1) Å] to form a polymeric chain of the bicyclic dimer unit. Some $d^{10}$ metal ions show a tendency to form metal–metal bonds, and Ag–Ag contacts in the range 2.80–3.30 Å have been reviewed.[9] The two repeating adjacent bicyclic dimer units of **1** are perpendicular to each other and show a propeller-like side view (Figure 2b). In this case, no significant change of the S···S distance (5.622 Å for **1**) is observed compared with that for $\mathbf{L^1}$ (5.627 Å).

In the packing structure (Figure 2c), each 1D network is arranged side by side with an adjacent one such that they form an offset face-to-face-type π-π stacking interaction[11] through the aromatic rings. The dihedral angle between the two aromatic rings is 13.0(3)°, thereby indicating a slightly tilted orientation. The intercentroid distance between two aromatic rings is 4.153 Å, which falls at the mean of the literature range (3.7–4.6 Å) for such an interaction.[11]

The reaction of $\mathbf{L^2}$ with $AgClO_4$ in dichloromethane/methanol afforded a colourless precipitate. Vapour diffusion of diethyl ether into a DMF solution of this precipitate gave a crystalline product **2**. An X-ray analysis revealed that **2** is a cyclic tetramer $[Ag_4(\mathbf{L^2})_4(ClO_4)_2](ClO_4)_2{\cdot}2MeOH$ with inversion symmetry (Figure 3a). Tetranuclear $Ag^I$ complexes $[Ag_4\mathbf{L}_4]^{4+}$ of trithiamacrocycles (**L**) with similar cyclic tetrameric structure have been reported by Loeb et al.[12] Ag1, which lies outside the cavity, is bonded to one O and two S atoms of one macrocycle as well as to one S atom of the adjacent macrocycle to form a distorted tetragonal environment, whereas tetrahedrally coordinated Ag2 is surrounded by two S atoms of one macrocycle and one S atom of an adjacent macrocycle. The fourth site is occupied by an O atom of $ClO_4^-$ in a monodentate manner. Consequently, the repeating Ag1–S–Ag2–S bonding leads to an octagonal scaffold with an $Ag_4S_4$ core. The two coordinating $ClO_4^-$ ions are attached to the exterior and two other $ClO_4^-$ ions are included in the octagonal cavity. The resulting 3D structure of **2** is "doughnut"-like and has a diameter of approximately 13.8 Å and a thickness of 7.4 Å. The S···S distances in **2** (3.432 and 3.635 Å) are shorter than that in $\mathbf{L^2}$ (4.387 Å) due to conversion of the torsion angle between the two S atoms from *anti* to *gauche* upon complexation.

The FAB mass spectra of **1** and **2** contain peaks at *m*/*z* = 439 and 979, which correspond to $[Ag_2(\mathbf{L^1})_2]^{2+}$ and $[Ag_4(\mathbf{L^2})_4(ClO_4)_2]^{2+}$, respectively, according to their isotope patterns (Figure 4).

 © 2006 Wiley-VCH Verlag GmbH & Co. KGaA, Weinheim 

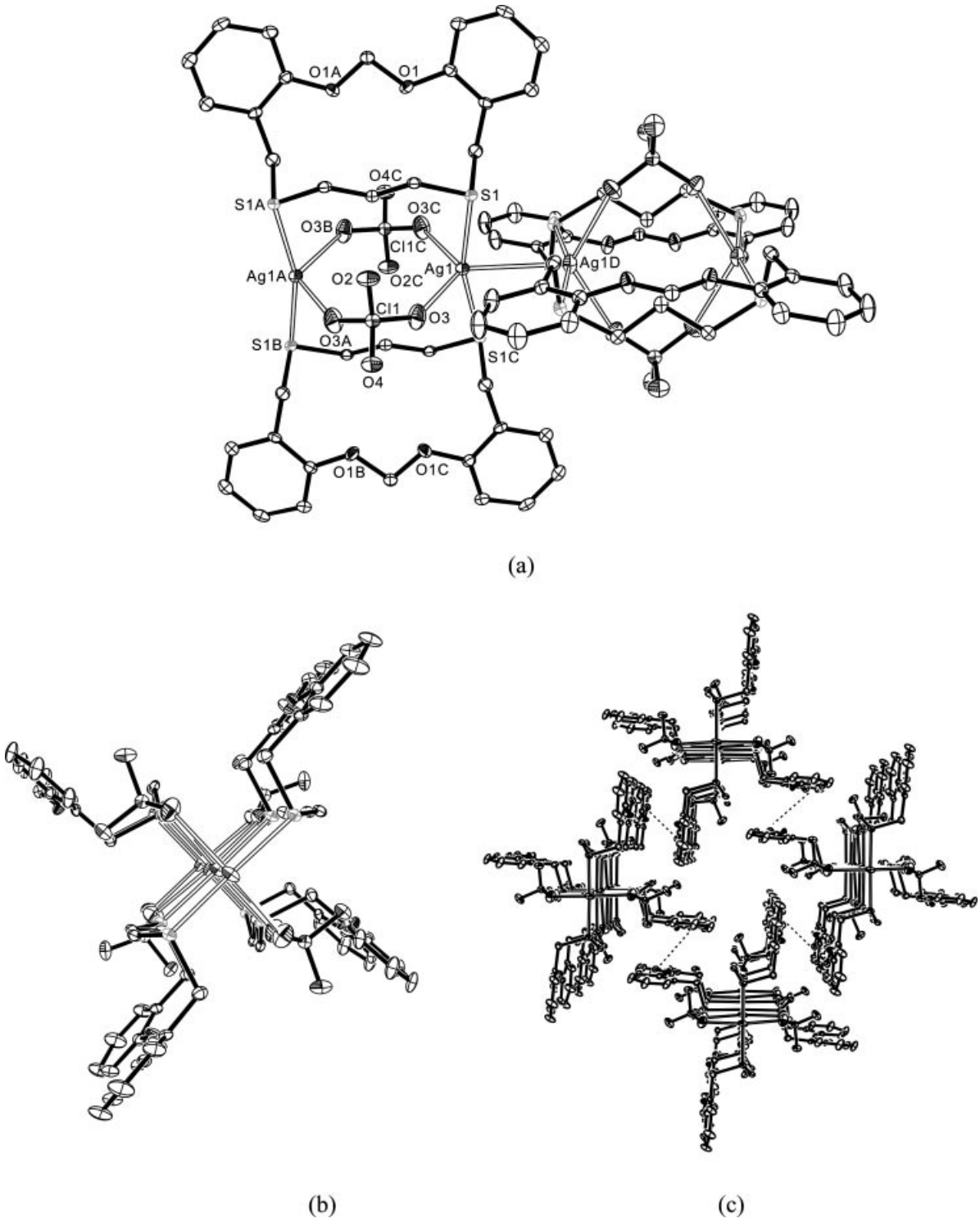


Figure 2. Poly(bicyclic dimer) structure of **1**: (a) general view, (b) side view and (c) packing arrangement showing π-π stacking (dashed line). Hydrogen atoms and non-coordinating nitromethane molecules have been omitted for clarity. Thermal ellipsoids are drawn at the 30% probability level. Selected bond lengths [Å] and angles [°]: Ag1–S1 2.4243(14), Ag1–S1C 2.4243(13), Ag1–Ag1D 3.1285(11), Ag1···Ag1A 4.8611(12), S1···S1A 5.6217(24); S1–Ag1–S1C 161.95(6), S1C–Ag1–Ag1D 80.98(3), S1–Ag1–Ag1D 80.98(3). Symmetry operations: A: *x*, *y*, *–z* + 1; B: 2 – *x*, *–y*, 1 – *z*; C: *–x* + 2, *–y*, *z*; D: *y* + 1, *–x* + 1, *–z* + 3/2.

## Conclusion

The preparation and structural characterisation of two types of cyclic oligomer silver(I) complexes derived from isomeric $S_2O_2$ macrocycles have been presented. The tendency to adopt these respective arrangements shows the possibility that the metal coordination mode can be controlled by tuning the inter-donor distances in the backbone of each bound ligand.

 © 2006 Wiley-VCH Verlag GmbH & Co. KGaA, Weinheim 

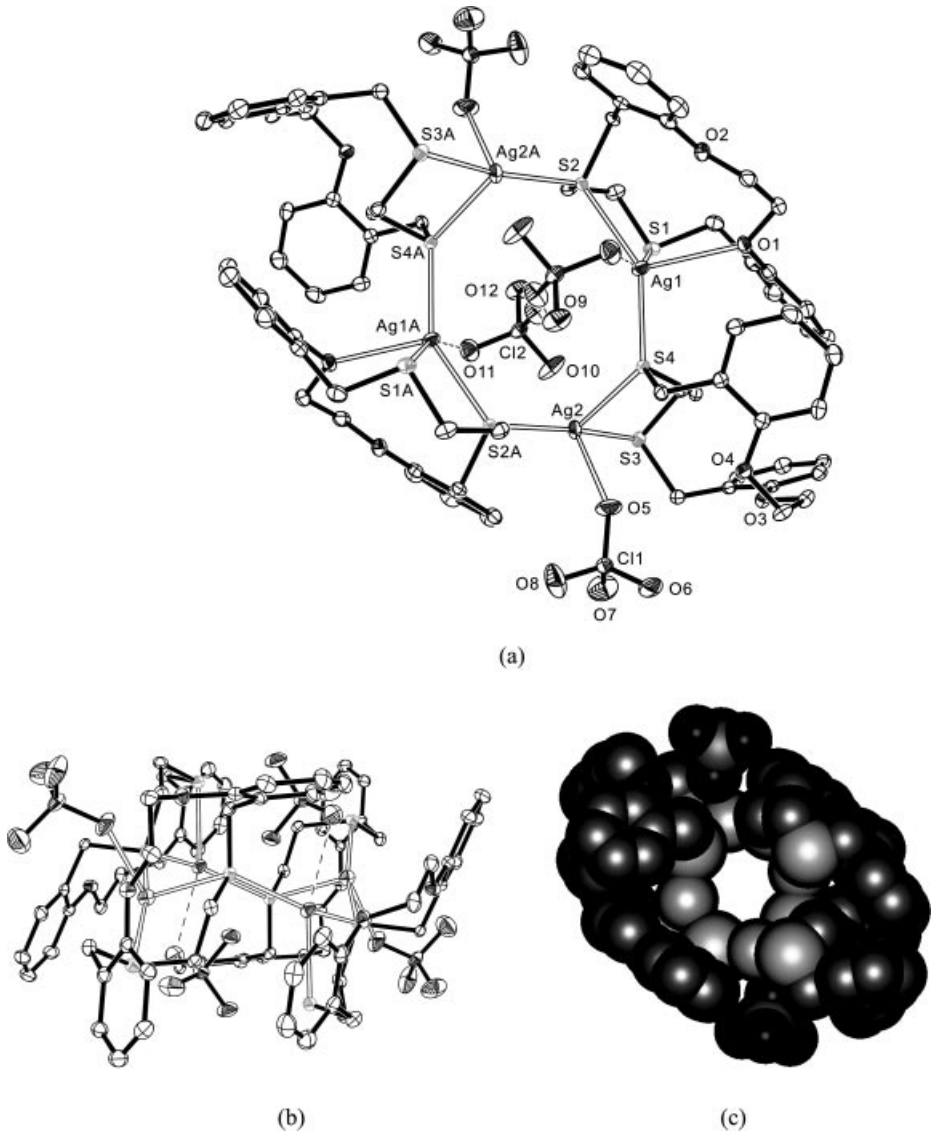


Figure 3. Cyclic tetramer structure of **2**: (a) top view, (b) side view and (c) space-filling view (noncoordinating anions are omitted). Hydrogen atoms and noncoordinating methanol molecules have been omitted for clarity. Thermal ellipsoids are drawn at the 30% probability level. Selected bond lengths [Å] and angles [°]: Ag1–S1 2.6102(14), Ag1–S2 2.6322(14), Ag1–S4 2.5245(12), Ag2–S3 2.4855(13), Ag2–S4 2.6990(13); S1–Ag1–S2 81.79(4), S4–Ag1–S2 145.60(4), S4–Ag1–S1 113.43(4), S3–Ag2–S4 88.92(4), Ag1–S4–Ag2 120.60(5); S1···S2 3.4320(18), S3···S4 3.6346(17), Ag1···Ag2 4.5381(7), Ag1···Ag1A 5.6148(9). Symmetry operation: A: $-x + 1, -y + 1, -z + 1$.

## Experimental Section

**General Remarks:** Chemical reagents and solvents were purchased commercially and used as received without further purification. Infrared spectra were measured with a Mattson Genesis Series FTIR spectrophotometer, and the NMR spectra were recorded with a Bruker 300 MHz spectrometer. Mass spectra were obtained with a JEOL JMS-700 spectrometer at the Central Laboratory of Gyeongsang National University.

**Synthesis and Characterisation of $L^1$:** Cesium carbonate (11.22 g, 34.46 mmol) was dissolved in DMF (1000 mL) in a 3-L, round-bottomed flask. 1,3-Propanedithiol (2.12 g, 22.5 mmol) and the dichloride (6.7 g, 22.5 mmol) were dissolved in DMF (30 mL) and this solution was taken up in a 50-mL glass syringe. Under nitrogen, the contents of the syringe were added dropwise (0.6 mL $h^{-1}$) to the DMF solution of $Cs_2CO_3$ at 45–50 °C over 50 h. The reaction mixture was rapidly stirred for a further 10 h, cooled to room temperature and filtered. The filtrate was concentrated and the residue was partitioned between water and dichloromethane. The aqueous phase was separated and extracted with two further portions of dichloromethane. The combined organic phases were dried with anhydrous sodium sulfate and then concentrated to dryness. Flash column chromatography on silica gel with 20% ethyl acetate/*n*-hexane as the eluent led to the isolation of $\mathbf{L^1}$ as a colourless crystalline product in 28% yield. M.p. 78–80 °C. $C_{18}H_{20}O_2S_2$ (332.48): calcd. C 65.02, H 6.06; found C 64.79, H 6.12. IR (KBr): $\tilde{\nu}$ = 2924, 2290, 1590, 1491, 1415 $cm^{-1}$. $^1H$ NMR (300 MHz, $CDCl_3$): $\delta$ = 7.60–7.04 (m, 8 H, Ar), 5.83 (s, 2 H, $OCH_2$), 3.69 (s, 4 H, $ArCH_2$), 2.34 (t, $J$ = 7.57 Hz, 4 H, $SCH_2CH_2$), 1.63 (t, $J$ = 2.24 Hz, 2 H, $SCH_2CH_2$) ppm. $^{13}C$ NMR (125 MHz, $CDCl_3$): $\delta$ =

 © 2006 Wiley-VCH Verlag GmbH & Co. KGaA, Weinheim 

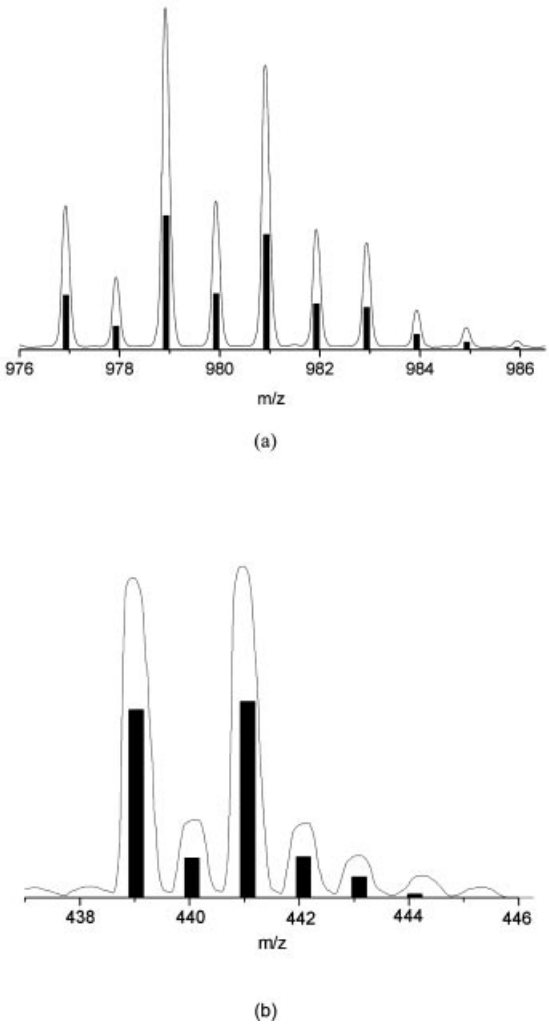


Figure 4. Observed isotopic distribution for $\mathbf{1}^{2+}$ (a) and $\mathbf{2}^{2+}$ (b) in the FAB mass spectra of **1** and **2**. The bars represent the predicted mass spectral distribution for this ion.

154.73, 130.95, 128.21, 123.09, 114.58, 92.19, 31.10, 29.82, 28.81 ppm. FAB-MS: $m/z$ = 332 [$M^+$].

**Synthesis and Characterisation of $L^2$:** The synthetic procedure was almost the same as for $\mathbf{L^1}$ except for the use of a different dichloride ($m$ = 1) and 1,2-ethanedithiol as the thiol (Scheme 2). Flash column chromatography ($SiO_2$; *n*-hexane/ethyl acetate, 1:1) afforded the product as a white solid in 41% yield. M.p. 128–130 °C. $C_{18}H_{20}O_2S_2$ (332.48): calcd. C 65.02, H 6.06, S 19.29; found C 64.88, H 6.25, S 19.47. IR (KBr): $\tilde{\nu}$ = 2921, 2358, 1592, 1490, 1452, 1288 $cm^{-1}$. $^1H$ NMR (500 MHz, $CDCl_3$): $\delta$ = 6.87–7.38 (m, 8 H, Ar), 4.34 (s, 4 H, $OCH_2$), 3.78 (s, 4 H, $ArCH_2$), 2.73 (s, 4 H, $SCH_2CH_2S$) ppm. $^{13}C$ NMR (125 MHz, $CDCl_3$): $\delta$ = 155.95, 131.02, 128.59, 128.06, 121.52, 111.07, 66.65, 31.61, 28.17 ppm. FAB-MS: $m/z$ = 332 [$M^+$].

**$[Ag_2(L^1)_2(ClO_4)_2]\cdot 2H_2O$ (1):** A colourless precipitate was obtained by mixing of equimolar amounts of $\mathbf{L^1}$ and $AgClO_4$ in methanol/water. The product was filtered off and washed with methanol and dried under vacuum. Yield: 78%. M.p. 180–181 °C. $C_{36}H_{44}Ag_2Cl_2O_{14}S_4$ (1115.63): calcd. C 38.76, H 3.98, S 11.50; found C 38.75, H 3.96, S 11.49. IR (KBr): $\tilde{\nu}$ = 2928, 1595, 1492, 1454, 1418, 1294, 1226, 1097 ($ClO_4^-$), 1001, 756, 621 $cm^{-1}$. FAB-MS: $m/z$ = 439 $[Ag_2(\mathbf{L^1})_2]^{2+}$.

**$[Ag_4(L^2)_4(ClO_4)_2](ClO_4)_2\cdot 1.5MeOH$ (2):** Reaction of $\mathbf{L^2}$ with $AgClO_4$ in dichloromethane/methanol afforded a colourless precipitate. Vapour diffusion of diethyl ether into a DMF solution gave rise to a crystalline product. The product for microanalysis was dried under vacuum. Yield: 90%. M.p. 159–160 °C. $C_{73.5}H_{86}Ag_4Cl_4O_{25.5}S_8$ (2207.26): calcd. C 40.44, H 4.28; found C 40.00, H 3.93. IR (KBr): $\tilde{\nu}$ = 2932, 1593, 1493, 1452, 1246, 1097 ($ClO_4^-$), 930, 758, 621 $cm^{-1}$. FAB-MS: $m/z$ = 979 $[Ag_4(\mathbf{L^2})_4]^{2+}$.

***CAUTION!*** *Perchlorate salts of metal complexes are potentially explosive and should be handled with great care.*

**X-ray Crystallography:** All data were collected with a Bruker Smart diffractometer equipped with a graphite-monochromated Mo-$K_\alpha$ ($\lambda$ = 0.71073 Å) radiation source and a CCD detector; 45 frames of two-dimensional diffraction images were collected and processed to obtain the cell parameters and orientation matrix. The first 50 frames were retaken after complete data collection. The crystal showed no significant decay. The frame data were processed with

Table 1. Crystal and experimental data.

| | $\mathbf{L^1}$ | $\mathbf{L^2}$ | **1** | **2** |
|---|---|---|---|---|
| Empirical formula | $C_{18}H_{20}O_2S_2$ | $C_{18}H_{20}O_2S_2$ | $C_{37}H_{43}Ag_2Cl_2NO_{14}S_4$ | $C_{74}H_{88}Ag_4Cl_4O_{26}S_8$ |
| Formula mass | 332.46 | 332.46 | 1140.60 | 2223.20 |
| Temperature [K] | 173(2) | 298(2) | 173(2) | 173(2) |
| Crystal system | monoclinic | orthorhombic | tetragonal | monoclinic |
| Space group | *Pc* | $P2_12_12_1$ | $P4_2/m$ | $P2_1/c$ |
| *Z* | 2 | 4 | 2 | 2 |
| *a* [Å] | 4.6632(4) | 8.7160(8) | 11.7322(8) | 16.8393(9) |
| *b* [Å] | 11.9310(11) | 11.6729(11) | 11.7322(8) | 13.5962(7) |
| *c* [Å] | 14.8994(13) | 16.7701(15) | 15.979(2) | 20.7473(11) |
| $\beta$ [°] | 97.685(2) | 90 | 90 | 110.8510(10) |
| *V* [Å$^3$] | 821.51(13) | 1706.2(3) | 2199.5(3) | 4439.0(4) |
| $D_X$ [g cm$^{-3}$] | 1.344 | 1.294 | 1.722 | 1.663 |
| $2\theta_{max}$ [°] | 56.56 | 56.52 | 52.7 | 56.6 |
| *R* | 0.0645 | 0.0476 | 0.0455 | 0.0511 |
| *wR* | 0.1247 | 0.0994 | 0.0856 | 0.1442 |
| No. of reflection used [$I > 2\sigma(I)$] | 3271 ($R_{int}$ = 0.0532) | 4096 ($R_{int}$ = 0.0658) | 2342 ($R_{int}$ = 0.1156) | 10421 ($R_{int}$ = 0.0311) |

 © 2006 Wiley-VCH Verlag GmbH & Co. KGaA, Weinheim 

SAINT to give the structure factors.[13] The structure was solved by direct methods and refined by full-matrix least-squares methods on $F^2$ for all data with SHELXTL.[14] The non-hydrogen atoms were refined anisotropically. In **2**, the ten peaks which were found to have an electron density of more than 1 e Å$^{-3}$ in the final difference Fourier map are the ghosts of methanol. Relevant crystal data collection and refinement data for the crystal structures of **L$^1$**, **L$^2$**, **1** and **2** are summarised in Table 1. CCDC-292047 (**L$^1$**), -292048 (**L$^2$**), -292049 (**1**) and -292050 (**2**) contain the supplementary crystallographic data for this paper. These data can be obtained free of charge from The Cambridge Crystallographic Data Centre via www.ccdc.ac.uk/data_request/cif.

## Acknowledgments

This work was supported by KOSEF (R01-2004-000-10321-0).

[1] a) *Comprehensive Supramolecular Chemistry* (Eds.: J. L. Atwood, J. E. D. Davies, D. D. MacNicol, F. Vögtle), Pergamon, Oxford, **1996**, vol. 9; b) *Crystal Engineering* (Eds.: C. B. Aakeröy, A. S. Borovik), *Coordination Chemistry Reviews*, Elsevier, Amsterdam, **1999**, vol. 183; c) *Design of Organic Solids* (Ed.: E. Weber), *Topics in Current Chemistry*, Springer, Berlin, **1998**, vol. 198; d) *Crystal Engineering: The Design of Organic Solids* (Ed.: G. R. Desiraju), Elsevier, Amsterdam, **1989**.

[2] a) K. A. Hirsch, S. R. Wilson, J. S. Moore, *J. Am. Chem. Soc.* **1997**, *119*, 10401–10412; b) J. Liu, H.-K. Liu, X.-L. Feng, H.-X. Zhang, Z.-Y. Zhou, A. S. C. Chan, B.-S. Kang, *Inorg. Chem. Commun.* **2001**, *4*, 674–677; c) S. P. Crabtree, A. S. Batsanov, J. A. K. Howard, M. Kilner, *Polyhedron* **1998**, *17*, 367–372; d) J. Seo, S.-T. Moon, J. Kim, S. S. Lee, K.-M. Park, *Bull. Korean Chem. Soc.* **2003**, *24*, 1393–1395.

[3] a) S. Leininger, B. Olenyuk, P. J. Stang, *Chem. Rev.* **2000**, *100*, 853–908; b) P. J. Stang, D. H. Cao, K. Chen, G. M. Gray, D. C. Muddiman, R. D. Smith, *J. Am. Chem. Soc.* **1997**, *119*, 5163–5168; c) M. Fujita, J. Yazaki, K. Ogura, *J. Am. Chem. Soc.* **1990**, *112*, 5645–5647; d) P. Teo, L. L. Koh, T. S. A. Hor, *Inorg. Chem.* **2003**, *42*, 7290–7296; e) H. Chun, D. Kim, D. N. Dybtsev, K. Kim, *Angew. Chem. Int. Ed.* **2004**, *43*, 971–974; f) L. Tei, A. J. Blake, P. A. Cooke, C. Caltagirone, F. Demartin, V. Lippolis, F. Morale, C. Wilson, M. Schröder, *J. Chem. Soc., Dalton Trans.* **2002**, 1662–1670.

[4] a) Y. Jin, I. Yoon, J. Seo, J.-E. Lee, S.-T. Moon, J. Kim, S. W. Han, K.-M. Park, L. F. Lindoy, S. S. Lee, *Dalton Trans.* **2005**, 788–796; b) I. Yoon, J. Seo, J.-E. Lee, M. R. Song, S. Y. Lee, K. S. Choi, O.-S. Jung, K.-M. Park, S. S. Lee, *Dalton Trans.* **2005**, 2352–2354; c) K.-M. Park, I. Yoon, J. Seo, J.-E. Lee, J. Kim, K. S. Choi, O.-K. Jung, S. S. Lee, *Cryst. Growth Des.* **2005**, *5*, 1707–1709; d) J. Seo, I. Yoon, J.-E. Lee, M. R. Song, S. Y. Lee, S. H. Park, T. H. Kim, K.-M. Park, B. G. Kim, S. S. Lee, *Inorg. Chem. Commun.* **2005**, *8*, 916–919; e) K.-M. Park, Y. H. Lee, Y. Jin, J. Seo, I. Yoon, S. C. Lee, S. B. Park, M.-S. Gong, M. L. Seo, S. S. Lee, *Supramol. Chem.* **2004**, *16*, 51–58.

[5] a) S. Wolfe, *Acc. Chem. Res.* **1972**, *5*, 102–111; b) R. E. Wolf Jr, J. R. Hartman, J. M. E. Storey, B. M. Foxman, S. R. Cooper, *J. Am. Chem. Soc.* **1987**, *109*, 4328–4335.

[6] J. Seo, M. R. Song, J.-E. Lee, S. Y. Lee, I. Yoon, K.-M. Park, J. Kim, J. H. Jung, S. B. Park, S. S. Lee, *Inorg. Chem.* **2006**, *45*, 952–954.

[7] a) I. M. Atkinson, L. F. Lindoy, O. A. Matthews, G. V. Meehan, A. N. Sobolev, A. H. White, *Aust. J. Chem.* **1994**, *47*, 1155–1162; b) I. Yoon, J. Seo, J.-E. Lee, K.-M. Park, J. S. Kim, M. S. Lah, S. S. Lee, *Inorg. Chem.*, in press.

[8] a) R.-Q. Zou, J.-R. Li, Y.-B. Xie, R.-H. Zhang, X.-H. Bu, *Cryst. Growth Des.* **2004**, *4*, 79–84; b) L. R. Falvello, J. Forniés, A. Martín, R. Navarro, V. Sicilia, P. Villarroya, *Chem. Commun.* **1998**, 2429–2430; c) W. Chen, M. Du, X.-H. Bu, R.-H. Zhang, T. C. M. Mak, *CrystEngComm* **2003**, *5*, 96–100; d) S. Kitagawa, M. Kondo, S. Kawata, S. Wada, M. Maekawa, M. Munakata, *Inorg. Chem.* **1995**, *34*, 1455–1465; e) P. L. Caradoc-Davies, L. R. Hanton, *Dalton Trans.* **2003**, 1754–1758.

[9] M. Jansen, *Angew. Chem. Int. Ed. Engl.* **1987**, *26*, 1098–1110.

[10] Cambridge Crystallographic Data Centre, Cambridge Structure Database System Software ConQuest 1.8, Cambridge, **2006**.

[11] I. Dance, M. Scudder, *Chem. Eur. J.* **1998**, *2*, 481–486.

[12] H. A. Jenkins, S. J. Loeb, A. M. I. Riera, *Inorg. Chim. Acta* **1996**, *246*, 207–215.

[13] Bruker, *SMART and SAINT, Area Detector Control and Integration Software*, Ver. 6.22, Bruker Analytical X-ray Instruments, Madison, Wisconsin, **2001**.

[14] Bruker, *SHELXTL, Structure Determination Programs*, Ver. 6.10, Bruker Analytical X-ray Instruments, Madison, Wisconsin, **2000**.

Received: April 1, 2006
Published Online: July 24, 2006

 © 2006 Wiley-VCH Verlag GmbH & Co. KGaA, Weinheim 

DOI: 10.1002/ejic.200600302

# A $Zn^{II}$-Based Chiral Crystalline Nanotube

Hong-Tao Zhang,*[a] Yi-Zhi Li,[a] Tian-Wei Wang,[a] Emmanuel N. Nfor,[a] Hua-Qin Wang,[b] and Xiao-Zeng You*[a]

**Keywords:** Coordination polymer/ Chirality / Nanotubes / Triple helix / Nonlinear optics / Fluorescence

A novel metal-organic chiral nanotube, $\{[Zn(C_{14}H_{10}N_2O_4)\cdot(H_2O)_4]_2\cdot H_2O\}_n$ (**1**), with the walls consisting of homochiral triple-stranded right-handed (*P*) helices has been constructed by the reaction of acyclic ligands and zinc ions. All guest water molecules are arranged in a helical fashion inside the hydrophilic channel of the nanotube. This coordination polymer shows blue-emitting fluorescence and displays a second harmonic generation (SHG) response in the solid state.

(© Wiley-VCH Verlag GmbH & Co. KGaA, 69451 Weinheim, Germany, 2006)

## Introduction

Nanotubular supramolecular architectures are currently of intense interest in chemistry, biology, and materials science, owing to their potential applications in mimicking ion channels, water channels, and as small molecule transport systems.[1,2] The construction of synthetic nanotubes is achieved through the self-assembly of suitable cyclic building blocks such as cyclic peptides[3] and cyclic oligoureas.[4] Another motif in the formation of nanotubes is achieved by the self-assembly of acyclic oligopeptides which, like cyclic peptides, are building blocks that can also result in chiral tubular structures.[5] However, most of the previously reported nanotubes are made up of synthetic organic molecules and to date, the construction of metal-containing nanotubular structures has received scant attention.[6] In forming channel structures, the coordination polymer approach has the advantage of preparative convenience, functionalization, and thermal stability.[7] The metal-organic nanotubes could be generated through the self-assembly of metal ions with organic ligands and such metal-organic nanotubes might display opto-electronic or magnetic properties induced by the coordination moiety. Furthermore, the employment of chiral organic molecules can induce a noncentrosymmetric structure in the resulting nanotubes which may be useful in the field of nonlinear optics (NLO) applications.[8] In view of the above, we present herein the construction of a novel metal-organic chiral nanotube, ZnL (**1**) [L = (2*S*,2′*S*)-2,2′-(benzene-1,4-dicarboxamido)dipropionate], with the walls consisting of homochiral triple-stranded right-handed (*P*) helices and its optical properties.

[a] Coordination Chemistry Institute, The State Key Laboratory of Coordination Chemistry, Nanjing University, Nanjing 210093, P. R. China
E-mail: hongtaozhang2000@yahoo.com
xyz@netra.nju.edu.cn
[b] Center of Materials Analysis, Nanjing University, Nanjing 210093, P. R. China.

## Results and Discussion

### Crystal Structure

Compound **1** was obtained by the reaction of zinc acetate with the chiral ligand $H_2L$. The crystal structure of **1** reveals that, there is one zinc ion, one ligand dianion, and two coordination water molecules as well as half of one guest water molecule in the asymmetric unit. Crystallographic data of **1** is summarized in Table 1. As shown in Figure 1, the coordination motif of the zinc ion has a trigonal-bipyramidal geometry. Two coordinated water O atoms (O1 and O2) occupy an axial position of the Zn trigonal

Table 1. Crystallographic data for complex **1**.

| | **1** |
|---|---|
| Empirical formula | $C_{28}H_{38}N_4O_{17}Zn_2$ |
| Formula mass | 833.36 |
| Crystal system | monoclinic |
| Space group | P $2_1$ |
| Temperature [K] | 298(2) |
| $a$ [Å] | 11.755(2) |
| $b$ [Å] | 4.9670(10) |
| $c$ [Å] | 14.654(3) |
| $\beta$ [°] | 92.27(3) |
| $V$ [Å$^3$] | 854.9(3) |
| Z | 1 |
| $D_{calcd.}$ [mg m$^{-3}$] | 1.619 |
| $\mu$ [mm$^{-1}$] | 1.485 |
| $R_{int}$ | 0.0208 |
| Reflections collected | 3396 |
| Unique reflections | 2959 |
| $N$(parameters/restraints)$_{refined}$ | 237/1 |
| Goodness-of-fit on $F^2$ | 1.047 |
| $R_1$ [$I > 2\sigma(I)$][a] | 0.0544 |
| $wR_2$ [$I > 2\sigma(I)$][b] | 0.1145 |
| $R_1$ (all data)[a] | 0.0633 |
| $wR_2$ (all data)[b] | 0.1166 |

[a] $R_1 = \Sigma||F_o| - |F_c||/\Sigma|F_o|$. [b] $wR_2 = [\Sigma w(|F_o^2| - |F_c^2|)^2/\Sigma w(|F_o^2|)^2]^{1/2}$.


© 2006 Wiley-VCH Verlag GmbH & Co. KGaA, Weinheim

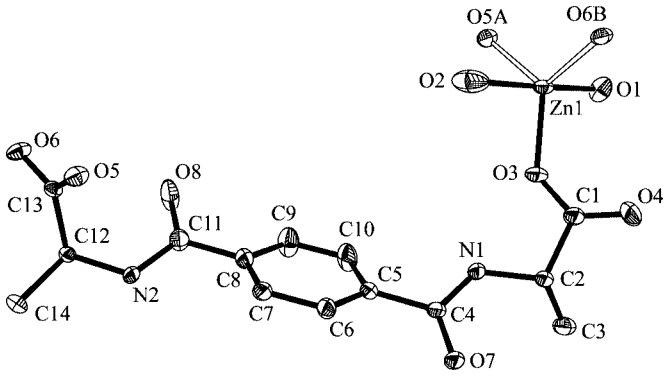


Figure 1. ORTEP view of compound **1** showing 30% probability displacement ellipsoids. All H atoms and the guest water molecule are omitted for clarity. Symmetric codes: A: $-x$, $y - 1/2$, $-z + 1$; B: $-x$, $y - 3/2$, $-z + 1$.

Table 2. Selected bond lengths [Å], angles [°], and torsion angles [°] for **1**.

| | | | |
|---|---|---|---|
| Zn(1)–O(3) | 1.952(4) | Zn(1)–O(6)[a] | 1.976(5) |
| Zn(1)–O(5)[b] | 1.982(4) | Zn(1)–O(1) | 2.071(4) |
| Zn(1)–O(2) | 2.252(4) | O(3)–Zn(1)–O(6)[a] | 119.07(17) |
| O(3)–Zn(1)–O(5)[b] | 125.79(18) | O(6)[a]–Zn(1)–O(5)[b] | 113.21(18) |
| O(3)–Zn(1)–O(1) | 97.38(18) | O(6)[a]–Zn(1)–O(1) | 94.22(19) |
| O(5)[b]–Zn(1)–O(1) | 92.03(17) | O(3)–Zn(1)–O(2) | 83.90(17) |
| O(6)[a]–Zn(1)–O(2) | 87.6(2) | O(5)[b]–Zn(1)–O(2) | 84.95(19) |
| O(1)–Zn(1)–O(2) | 176.9(2) | C(4)–N(1)–C(2)–C(3) | 81.1(7) |
| C(4)–N(1)–C(2)–C(1) | –155.8(6) | C(11)–N(2)–C(12)–C(14) | 176.8(6) |
| C(11)–N(2)–C(12)–C(13) | –62.2(7) | N(1)–C(2)–C(1)–O(3) | –6.2(8) |
| N(2)–C(12)–C(13)–O(5) | –34.3(7) | N(2)–C(12)–C(13)–O(6) | 145.5(4) |

[a] Symmetry transformations used to generate equivalent atoms: $-x$, $y - 3/2$, $-z + 1$. [b] Symmetry transformations used to generate equivalent atoms: $-x$, $y - 1/2$, $-z + 1$.

bipyramid, while three carboxylato O atoms (O3, O5A, and O6B) bond to the equatorial positions. At one end of the ligand, the side methyl group C14 is almost coplanar with the amide group O8/C11/N2 with a torsion angle of 176.8(6)° for C11–N2–C12–C14, while the carboxyl group O5/C13/O6 is almost perpendicular to the amide plane. At the other end of the ligand, the methyl group C3 is vertical on the amide plane O7/C4/N1 with a torsion angle of 81.1(7)° for C4–N1–C2–C3. The carboxyl group O4/C1/O3 lies slightly out of the plane of the amide group O7/C4/N1 with a torsion angle of –6.2(8)° for N1–C2–C1–O3 (selected bond lengths, angles, and torsion angles are listed in Table 2). Thus, the two sides of the phenyl ring are not equivalent with each other, owing to the different coordination modes of the two carboxylate groups (O3/C1/O4 as a monodentate ligand and O5/C13/O6 as a carboxyl bridge) and their conformations. Consequently, two ligands connect a pair of zinc ions in a head-to-tail fashion through the O3 and O6 atoms, thus forming a right-handed twofold single-

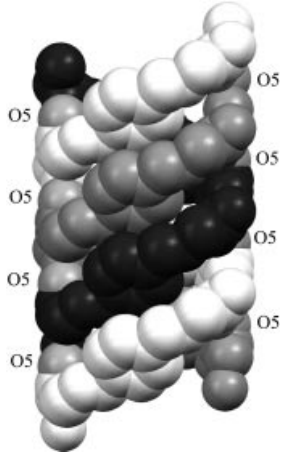


Figure 2. Triple-stranded right-handed helix. All water molecules, amide O atoms, H atoms, and the side α-methyl groups are omitted for clarity.

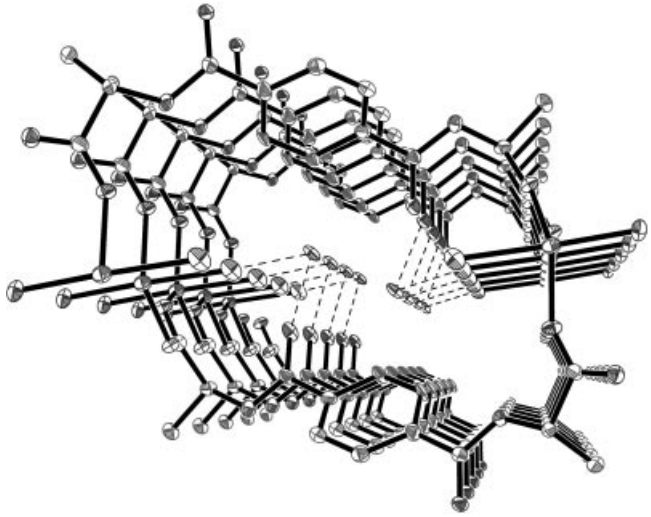

Figure 3. 1D tube-like coordination polymer with hydrophilic channel including water molecules.

 © 2006 Wiley-VCH Verlag GmbH & Co. KGaA, Weinheim 

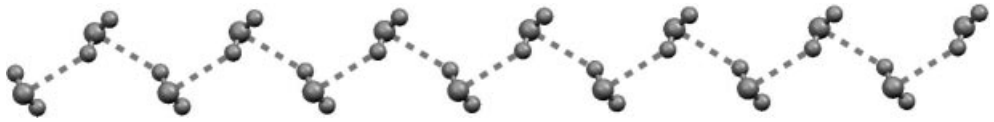

Figure 4. Guest water molecules are arranged in a helical fashion inside the polymeric structure.

Table 3. Hydrogen bonds for **1**.

| D–H···A | *d*(D–H) [Å] | *d*(H···A) [Å] | *d*(D···A) [Å] | <(D–H···A) [°] |
|---|---|---|---|---|
| N(2)–H(6)···O(7)[c] | 0.86 | 2.19 | 3.004(7) | 158.8 |
| O(1)–H(1B)···O(4)[d] | 0.96 | 1.92 | 2.620(6) | 127.4 |
| O(1)–H(1A)···O(1)[d] | 0.96 | 1.99 | 2.943(4) | 170.8 |
| O(2)–H(2B)···O(1W)[e] | 0.96 | 1.82 | 2.500(10) | 125.3 |
| O(1W)–H(1WC)···O(8)[e] | 0.85 | 2.39 | 3.094(9) | 141.1 |
| O(2)–H(2B)···O(8)[b] | 0.96 | 2.49 | 3.430(7) | 167.6 |
| O(2)–H(2C)···O(8)[a] | 0.96 | 1.82 | 2.776(6) | 171.0 |

[a] Symmetry transformations used to generate equivalent atoms: $-x$, $y - 3/2$, $-z + 1$. [b] Symmetry transformations used to generate equivalent atoms: $-x$, $y - 1/2$, $-z + 1$. [c] Symmetry transformations used to generate equivalent atoms: $-x + 1$, $y + 1/2$, $-z + 1$. [d] Symmetry transformations used to generate equivalent atoms: $-x$, $y + 1/2$, $-z + 2$. [e] Symmetry transformations used to generate equivalent atoms: $-x + 1$, $y - 1/2$, $-z + 1$.

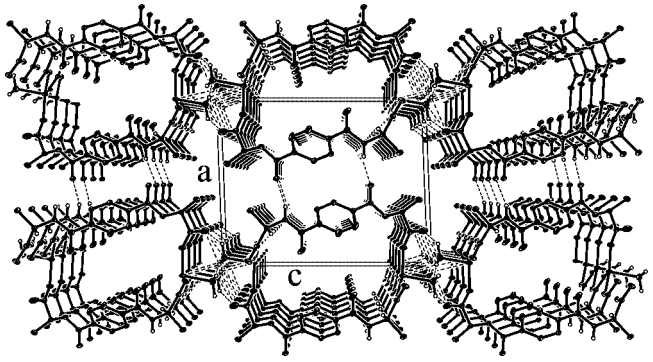


Figure 5. The nanotube arrays in complex **1**. The guest water molecules and H atoms except for the amide H atoms are omitted for clarity.

stranded helix propagating along the *b*-axis. The O5 atoms at "the head" and at "the tail" link two zinc ions from different single-stranded helices, respectively, thus constructing a homochiral triple-stranded (*P*) helix as depicted in Figure 2. In the previously reported triple helical coordination polymers, the interwoven helices just form rod-like structures owing to the small screw diameter.[9] However, in complex **1**, the triple-stranded helix around the screw axis generates an open-ended tube with an average internal diameter of 5 Å including the van der Waals contact (approximately 3 Å excluding the van der Waals contact), which is attributed to the expansion of the screw diameter by the phenyl ring. The interior of the channel is hydrophilic owing to the presence of the guest water molecules as shown in Figure 3. All guest water molecules are arranged in a helical fashion inside the polymeric structure (Figure 4). In the lattice, as depicted in Figure 5, all nanotubes are packed together to produce three-dimensional arrays by means of the inter-tubular hydrogen-bonding interactions between amide groups, coordination water molecules and guest water molecules as well as carboxylate groups (for details see Table 3).

## Thermal and Optical Properties

The TGA performed under flowing $N_2$ shows a gradual weight loss of 1.95% in the temperature range of 30–64 °C corresponding to the guest water molecule's liberation from the channels (calcd. 2.16%). The weight loss of 8.29% in the range 64–135 °C is attributed to the removal of coordination water molecules (calcd. 8.64%) and the decomposition of compound **1** starts at 386 °C. A crystal of compound **1** was stable at room temperature; however, it cracked when it had been left to stand at 45 °C for 14 d in order to release guest water molecules. Compound **1** is insoluble in water and common organic solvents such as methanol, ethanol, acetone, acetonitrile, DMF, and DMSO.

As shown in Figure 6, compound **1** exhibits a blue-fluorescent emission around 439 nm upon excitation at 338 nm in the solid state at room temperature. This has a blue shift and an enhancement of intensity in comparison with the emission of the ligand (a very weak emission is observed for the free ligand around 450 nm upon excitation at 348 nm in the solid state). This indicates that the emission is neither MLCT (metal-to-ligand charge transfer) nor LMCT (ligand-to-metal charge transfer) in nature and can thus be tentatively assigned to intraligand fluorescent emission.[10] The significant enhancement of fluorescent intensity is probably ascribed to the coordination of ligand to the Zn ion, increasing the ligand conformational rigidity, thereby reducing the nonradiative decay of the intraligand $^1(\pi\text{-}\pi^*)$ excited state.[11]

Given that **1** crystallizes in a noncentrosymmetric space group, its powder second harmonic generation (SHG) measurement was performed according to the method previously reported by Kurtz.[12] When a beam at $\lambda = 1064$ nm fundamental wavelength from a Q-switched Nd:YAG laser falls onto compound **1**, a green light can be seen with the naked eye. The preliminary experimental result shows that the powder SHG intensity of **1** is about 0.6 times that of urea. This intensity is comparable to the previously reported helical coordination polymers.[13]

 © 2006 Wiley-VCH Verlag GmbH & Co. KGaA, Weinheim 

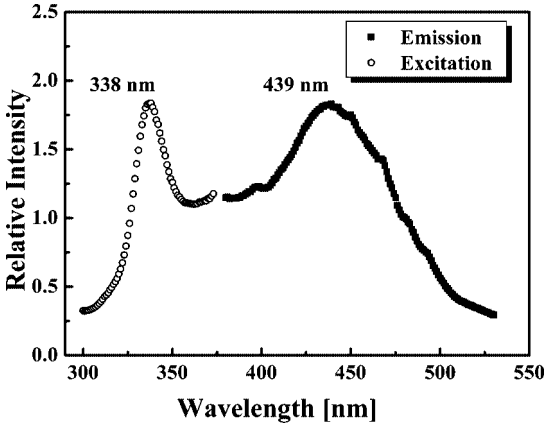


Figure 6. Fluorescent spectra of **1** in the solid state at room temperature.

## Conclusions

In conclusion, the reported nanotubular coordination polymer **1** has hydrophilic channels surrounded by homochiral triple helices, emits an enhanced blue fluorescence, and exhibits a second harmonic generation response. The transparency of the complex and its insolubility in common solvents, such as water, methanol, and ethanol among others, makes it an attractive candidate for blue-emitting fluorescent materials and in nonlinear optics (NLO) applications. Therefore, it can be developed towards a new motif in the formation of chiral nanotubes with opto-electronic properties.

## Experimental Section

**General:** Elemental analyses were carried out with a Perkin–Elmer 240C elemental analyzer. IR spectra were recorded with a Bruker VECTOR22 FT-IR spectrometer using the KBr pellet technique. Thermogravimetric analyses (TGA) were performed with a TA-SDT 2960 thermal analyzer at a heating rate of 10 °C min$^{-1}$ from room temperature to 600 °C under flowing nitrogen. The solid-state excitation-emission spectrum was acquired with an AMINCO Bowman Series AB2 Luminescence Spectrometer at room temperature. Approximate estimations of second-order NLO intensity were obtained by a comparison of the results from a powdered sample, in the form of a pellet (Kurtz powder test),[12] with those obtained for urea. A pulsed Q-switched Nd:YAG laser at a wavelength of 1064 nm was used to generate an SHG signal from samples. The backward-scattered SHG light was collected using a spherical concave mirror and passed through a filter that transmits only 532 nm radiation.

**$\{[Zn(C_{14}H_{10}N_2O_4)\cdot(H_2O)_4]_2\cdot H_2O\}_n$ (1):** The diacid, (2*S*,2′*S*)-2,2′-(benzene-1,4-dicarboxamido)dipropionic acid ($H_2L$), was synthesized by treating 1,4-benzenedicarbonyl dichloride with L-alanine ethyl ester according to a published procedure.[14] The ligand $H_2L$ (31.0 mg, 0.1 mmol) and zinc acetate dihydrate (22.0 mg, 0.1 mmol) were dissolved in water (10 mL). The resulting solution was left to stand for several weeks at room temperature. Colorless block crystals that formed were collected by filtration (16.0 mg, yield 40%). $C_{28}H_{38}N_4O_{17}Zn_2$ (833.36): calcd. C 40.35, H 4.60, N 6.72; found C 40.30, H 4.68, N 6.69. IR (KBr): $\tilde{\nu}$ = 3392 (m), 3268 (m), 2994 (w), 1654 (s), 1619 (s), 1578 (s), 1550 (s), 1490 (s), 1396 (m), 1320 (m), 1176 (w), 1055 (w), 870 (w), 746 (w), 594 (w) cm$^{-1}$.

**Crystallography:** A single crystal with dimensions 0.6 × 0.4 × 0.3 mm was used for structural determination with an Enraf–Nonius CAD-4 diffractometer with graphite-monochromatized Mo-$K_\alpha$ radiation ($\lambda$ = 0.71073 Å) using a $\omega$-2$\theta$ scan mode at 298 K. Intensity data were collected in the $\theta$ range of 1.39–25.97°, data reduction was made with the MolEN package.[15] Absorption corrections from $\psi$ scans were applied. The structure was solved by direct methods using SHELXS-97[16] and refined by least-squares treatment on $F^2$ by full-matrix least squares using SHELXL-97 with anisotropic displacement parameters for all non-hydrogen atoms.[17] The guest water molecule O1W was refined as occupancy disorder. CCDC-279580 contains the supplementary crystallographic data for this paper. These data can be obtained free of charge from The Cambridge Crystallographic Data Centre via www.ccdc.cam.ac.uk/data_request/cif.

## Acknowledgments

We are grateful to The National Natural Science Foundation of China (G200077500), the Natrual Science Foundation of Jiangsu Province (No. BK2004414) and The Postdoctoral Research Foundation of Nanjing University (No. 2003022) for the financial supports. E. N. N. gratefully acknowledges The Third World Academy of Science (TWAS) for Postdoctoral Fellowship.

[1] a) D. T. Bong, T. D. Clark, J. R. Granja, M. R. Ghadiri, *Angew. Chem. Int. Ed.* **2001**, *40*, 989–1011; b) J. G. Moralez, J. Raez, T. Yamazaki, R. K. Motkuri, A. Kovalenko, H. Fenniri, *J. Am. Chem. Soc.* **2005**, *127*, 8307–8309.

[2] a) J. Sánchez-Quesada, H. S. Kim, M. R. Ghadiri, *Angew. Chem. Int. Ed.* **2001**, *40*, 2503–2506; b) M. Engels, D. Bashford, M. R. Ghadiri, *J. Am. Chem. Soc.* **1995**, *117*, 9151–9158.

[3] a) K. Rosenthal-Aizman, G. Svensson, A. Unden, *J. Am. Chem. Soc.* **2004**, *126*, 3372–3373; b) S. Leclair, P. Baillargeon, R. Skouta, D. Gauthier, Y. Zhao, Y. L. Dory, *Angew. Chem. Int. Ed.* **2004**, *43*, 349–353.

[4] a) L. S. Shimizu, A. D. Hughes, M. D. Smith, M. J. Davis, B. P. Zhang, H.-C. zur Loye, K. D. Shimizu, *J. Am. Chem. Soc.* **2003**, *125*, 14972–14973; b) V. Semetey, C. Didierjean, J. P. Briand, A. Aubry, G. Guichard, *Angew. Chem. Int. Ed.* **2002**, *41*, 1895–1898.

[5] a) S. Ray, D. Haldar, M. G. B. Drew, A. Banerjee, *Org. Lett.* **2004**, *6*, 4463–4465; b) C. H. Görbitz, *Chem. Eur. J.* **2001**, *7*, 5153–5159.

[6] a) Z. Fei, D. Zhao, T. J. Geldbach, R. Scopelliti, P. J. Dyson, S. Antonijevic, G. Bodenhausen, *Angew. Chem. Int. Ed.* **2005**, *44*, 5720–5725; b) T. Yamaguchi, S. Tashiro, M. Tominaga, M. Kawano, T. Ozeki, M. Fujita, *J. Am. Chem. Soc.* **2004**, *126*, 10818–10819; c) F. Chang, Z.-M. Wang, H.-L. Sun, S. Gao, G.-H. Wen, X.-X. Zhang, *Dalton Trans.* **2005**, 2976–2978.

[7] a) M. Eddaoudi, D. B. Moler, H. Li, B. Chen, T. M. Reineke, M. O'Keeffe, O. M. Yaghi, *Acc. Chem. Res.* **2001**, *34*, 319–330; b) B. F. Abrahams, M. Moylan, S. D. Orchard, R. Robson, *Angew. Chem. Int. Ed.* **2003**, *42*, 1848–1851; c) S. Kitagawa, R. Kitaura, S.-I. Noro, *Angew. Chem. Int. Ed.* **2004**, *43*, 2334–2375.

[8] a) O. R. Evans, W. Lin, *Acc. Chem. Res.* **2002**, *35*, 511–522; b) P. A. Maggard, C. L. Stern, K. R. Poeppelmeier, *J. Am. Chem. Soc.* **2001**, *123*, 7742–7743.

[9] a) M. Elhabiri, J. Hamacek, J. C. G. Bünzli, A. M. Albrecht-Gary, *Eur. J. Inorg. Chem.* **2004**, 51–62; b) D. M. Ciurtin, N. G. Pschirer, M. D. Smith, U. H. F. Bunz, H.-C. zur Loye, *Chem. Mater.* **2001**, *13*, 2743–2745; c) M. Cantuel, G. Bernardinelli, G. Muller, J. P. Riehl, C. Piguet, *Inorg. Chem.* **2004**, *43*, 1840–

 © 2006 Wiley-VCH Verlag GmbH & Co. KGaA, Weinheim 

1849; d) B. Venkataramanan, Z. Ning, J. J. Vittal, S. Valiyaveettil, *CrystEngComm* **2005**, *7*, 108–112.
[10] a) For a recent review on luminescent $Zn^{II}$ coordination complexes see: S.-L. Zheng, X.-M. Chen, *Aust. J. Chem.* **2004**, *57*, 703–712; b) R. Bertoncello, M. Bettinelli, M. Casarin, A. Gulino, E. Tondello, A. Vittadini, *Inorg. Chem.* **1992**, *31*, 1558–1565; c) W. Yang, H. Schmider, Q. Wu, Y.-S. Zhang, S. Wang, *Inorg. Chem.* **2000**, *39*, 2397–2404; d) Y.-P. Tong, S.-L. Zheng, X.-M. Chen, *Eur. J. Inorg. Chem.* **2005**, 3734–3741; e) C. Jiang, Z. Yu, C. Jiao, S. Wang, J. Li, Z. Wang, Y. Cui, *Eur. J. Inorg. Chem.* **2004**, 4669–4674; f) J. Pang, E. J.-P. Marcotte, C. Seward, R. S. Brown, S. Wang, *Angew. Chem., Int. Ed.* **2001**, *40*, 4042–4045; g) X.-L. Wang, C. Qin, E.-B. Wang, Z.-M. Su, *Chem. Eur. J.* **2006**, *12*, 2680–2691.
[11] C. Seward, J. Pang, S. Wang, *Eur. J. Inorg. Chem.* **2002**, 1390–1399.
[12] S. K. Kurtz, T. T. Perry, *J. Appl. Phys.* **1986**, *39*, 3798–3813.
[13] a) B. Yan, M. D. Capracotta, P. A. Maggard, *Inorg. Chem.* **2005**, *44*, 6509–6511; b) R. Fu, H. Zhang, L. Wang, S. Hu, Y. Li, X. Huang, X. Wu, *Eur. J. Inorg. Chem.* **2005**, 3211–3213.
[14] B. Gong, C. Zheng, Y. Yan, *J. Chem. Crystallogr.* **1999**, *29*, 649–652.
[15] C. K. Fair, *MolEN, Structure Solution Procedures*, Enraf–Nonius, Delft, Holland, **1990**.
[16] G. M. Sheldrick, *SHELXS-97, Program for Crystal Structure Solution*, University of Göttingen, Göttingen, Germany, **1990**.
[17] G. M. Sheldrick, *SHELXS-97, Program for the Refinement of Crystal Structure from Diffraction Data*, University of Göttingen, Göttingen, Germany, **1997**.

Received: April 5, 2006
Published Online: July 24, 2006

 © 2006 Wiley-VCH Verlag GmbH & Co. KGaA, Weinheim 

# METALLOENZYMES AND CHEMICAL BIOMIMETICS

**Luigi Casella[a]**

Bioinorganic enzymology, the chemistry of metalloenzymes and closely related areas dealing with metalloprotein functions, is a broad interdisciplinary research field, representing an intellectually attractive and experimentally demanding frontier in modern chemical and biological sciences. Inorganic chemists should play a major role in this area because metal ions and their properties/reactivity are a primary feature characterizing these biological systems. Metalloproteins are basically highly elaborated metal complexes where the ligand is a structured polypeptide chain. They contain one or more metal ions in the active site and are optimally designed to accomplish evolutionary directed functions. The ultimate goal of biological inorganic chemistry research is to gain an understanding of these functions in terms of structure and reactivity. Inorganic chemists, in particular, recognize that the structural and electronic properties of biological metal centres are often modulated from those of small molecules containing the same metal ion. Understanding these differences is essential for understanding function, and for this reason the contribution of synthetic and biomimetic chemistry is extremely important for the progress of this field.

**Major role for Inorganic Chemisty**

The significance of the metal-centred chemistry performed by metalloenzymes is not limited to the biological environment. It has a strong impact on the medical sciences (e.g. generation of oxygen radicals, production and reactions of nitric oxide), pharmacological sciences (e.g. enzyme inhibition, protein receptors, metal toxicity), and environmental sciences (e.g. nitrogen and sulphur cycles, soil and water detoxification). But the capacity of metalloenzymes to carry out energetically difficult processes efficiently under mild conditions should also be attractive to chemical industry, with the aim of developing environmentally friendly processes.

As with other interdisciplinary research fields, it is clear that bringing together scientists with different expertise is essential for the progress in the area. The key importance of metallobiochemistry has been recognized at the European level with the launch of several COST Actions, and ultimately D21 (2000−2006) had the objective of coordinating the research efforts by a large number of European groups on topics of timely and relevant interest, and promoting more intensive exchange between individual groups. More than 100 laboratories were involved in this programme, which developed along the following priority areas: (a) structural, mechanistic and spectroscopic studies of metalloenzymes; (b) synthetic studies of mononuclear and polynuclear metal complexes with biomimetic ligands as active site models and biomimetic catalysts; (c) structural and spectro-

**Interdisciplinary exchange promoted**

[a] Professor Luigi Casella
Chairperson, European COST Chemistry Action D21 Metalloenzymes and chemical biomimetics
Dipartimento di Chimica Generale
University of Pavia, Italy
E-mail: bioinorg@unipv.it

 © 2006 Wiley-VCH Verlag GmbH & Co. KGaA, Weinheim 

scopic studies on electron transfer proteins; (d) characterisation and biological role of metal-protein interactions; (e) small molecules activation at biological and biomimetic metal centres. A large body of high quality scientific progress has been made during the years through this COST Action. Much of this would have probably been made also in the absence of this programme, but it is true that facilitating the collaborations increased the scientific impact that would have been obtained if individual groups carried out their research independently. Given the dimension of COST D21, a huge number of papers have been published in the literature within this programme. A "flavour" of the broad scope of D21 "Metalloenzymes and chemical biomimetics" is given by the fully peer-reviewed microreviews and research papers appearing in the present and following issues of the European Journal of Inorganic Chemistry. These papers span several research topics which characterized D21, and in particular focus on insulin mimetic vanadium complexes (Gätjens et al., Kiss et al.), DNA cleavage by artificial nucleases (Borras et al.), metal-protein interactions (Kiss et al.), enzyme inactivation by radical species (Golding et al.), protein-protein interactions (Moura et al.), enzymatic production of toxic small inorganic molecules (Obinger et al.), inhibition of zinc enzymes (Santos et al.), distribution of vanadate in human blood (Gorzsas et al.), biomimetic chemistry of dinuclear zinc complexes (Meyer et al.), vanadium complexes (Pessoa et al., Geraldes et al.) and manganese clusters (McKenzie et al.), and engineering of electron transfer proteins (Canters et al.). We hope that this collection will stimulate more inorganic chemists to be involved into the field of metallobiochemistry, perhaps initiating interdisciplinary collaborations.

**Collaboration raised scientific impact**

 © 2006 Wiley-VCH Verlag GmbH & Co. KGaA, Weinheim 

EurJIC
European Journal of Inorganic Chemistry

Issue 18/2006

Pages 3541–3776

*Papers available ahead of print in Early View at www.interscience.wiley.com*

*Earliest available Table of Contents:*
*Automatically, free of charge by e-mail through*
*www.interscience.wiley.com/alerts*

## COVER PICTURE

**The cover picture shows** a symbolic representation of the fate of vanadate in human blood. Since the transition metal vanadium is named after Vanadis, the Nordic goddess of beauty, she is represented by the famous Venus de Milo sculpted in metal. Her cloth is decorated with the functional groups of the ligands that can form a complex ("dress") with the metal while travelling in the blood vessels, the latter being symbolised by the caverns in the background. The water in the caves represents the aqueous solutions in which speciation studies have been carried out in the group of Professor Lage Pettersson. Further references to these studies are found as cave paintings on the walls: a distribution diagram and a set of $^{51}V$ NMR spectra. The studies have been carried out in the framework of the COST D21/009 working group. The geographical locations of the research groups within this working group are shown by illuminated dots on the map of Europe in the background. The goal of the studies was to better understand the ability of vanadium to lower blood glucose levels (represented by the sugar cubes washed ashore on the left) and thus its potential as an orally applicable drug against diabetes. A Microreview, covering the results of the above mentioned speciation studies dealing with the fate of vanadate in human blood, is represented by A. Gorzsás, I. Andersson, and L. Pettersson on p. 3559ff. The digital artwork for this cover was created by András Gorzsás.

## MICROREVIEW

**Contents**

**3559** **A. Gorzsás,* I. Andersson, L. Pettersson**

On the Fate of Vanadate in Human Blood

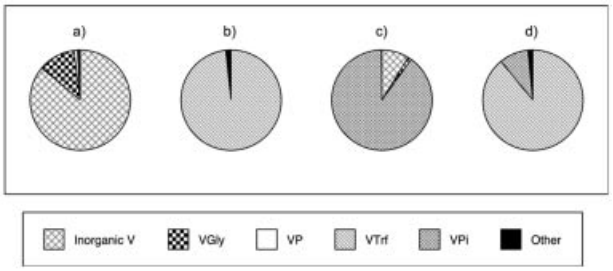


**Keywords:** Vanadium / Bioinorganic chemistry / Equilibria in aqueous solution / Diabetes

 © 2006 Wiley-VCH Verlag GmbH & Co. KGaA, Weinheim 

# SHORT COMMUNICATIONS


**3567** **A. Kobayashi, A. Tokunaga, R. Ikeda, H. Sagayama, Y. Wakabayashi, H. Sawa, M. Hedo, Y. Uwatoko, H. Kitagawa***

Pressure-Induced Metal−Semiconductor−Metal Transitions in an MMX-Chain Complex, $Pt_2(C_2H_5CS_2)_4I$

**Keywords:** Mixed-valent compounds / Conducting materials / MMX chain / Metal−insulator transition / High pressure


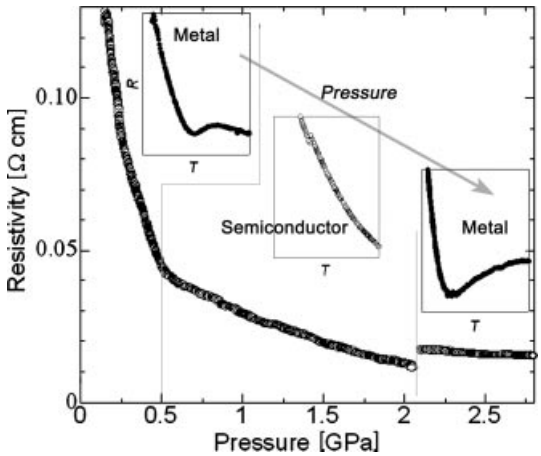



**3571** **A. Galet, A. B. Gaspar, G. Agusti, M. C. Muñoz, G. Levchenko, J. A. Real***

Pressure Effect Investigations on the Spin Crossover Systems $\{Fe[H_2B(pz)_2]_2(bipy)\}$ and $\{Fe[H_2B(pz)_2]_2(phen)\}$

**Keywords:** Spin transition / Bistability / Cooperative effects / Pressure / Phase Transitions


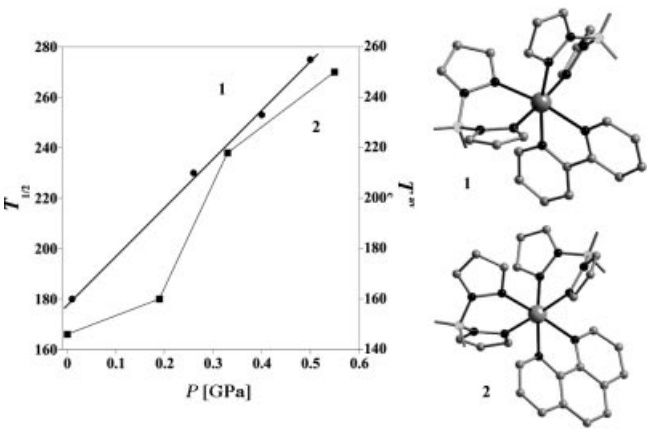


# FULL PAPERS


**3575** **J. Gätjens,* B. Meier, Yu. Adachi, H. Sakurai, D. Rehder**

Characterization and Insulin-Mimetic Potential of Oxidovanadium(IV) Complexes Derived from Monoesters and -carboxylates of 2,5-Dipicolinic Acid

**Keywords:** Vanadium / N,O Ligands / Picolinates / Insulin mimesis


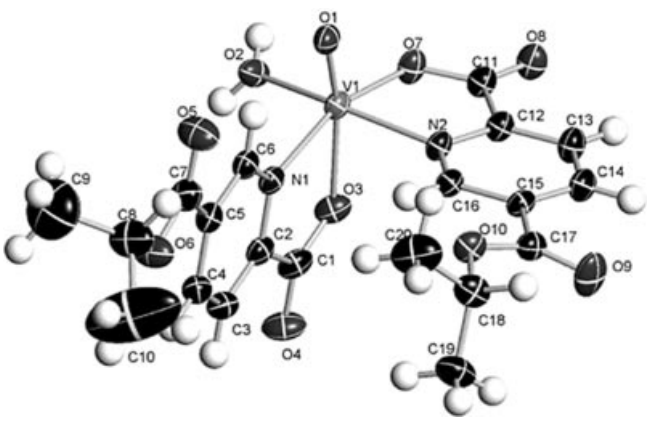

**3586** **F. Avecilla,* C. F. G. C. Geraldes, A. L. Macedo, M. M. C. A. Castro***

Crystal Structure of the $V^V$ Dimer $[V_2O_2(\mu\text{-}O)(dmpp)_2(OCH_3)_2]$ and Its Equilibrium with the $V^V$ Trimer $[V_3O_3(\mu\text{-}O)_3(dmpp)_3(H_2O)](H_2O)_2$ in Methanol/Water Solutions

**Keywords:** Vanadium / Pyridinone complexes / NMR spectroscopy / X-ray crystallography

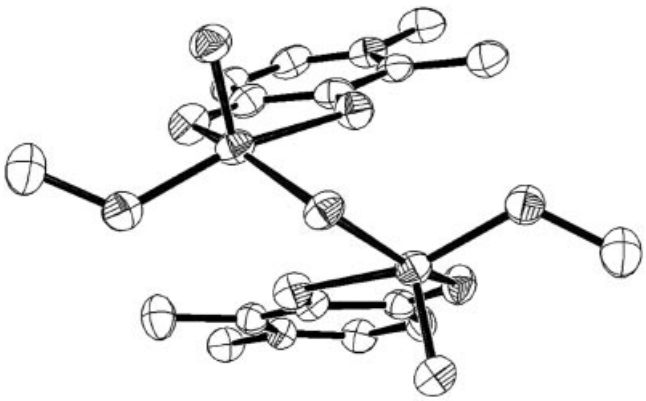

**3595** **J. Costa Pessoa,* S. Marcão, I. Correia, G. Gonçalves, A. Dörnyei, T. Kiss,* T. Jakusch, I. Tomaz, M. M. C. A. Castro, C. F. G. C. Geraldes, F. Avecilla**

Vanadium (IV and V) Complexes of Reduced Schiff Bases Derived from the Reaction of Aromatic *o*-Hydroxyaldehydes and Diamines Containing Carboxyl Groups

**Keywords:** Salen-like ligands / N,O ligands / Vanadium / Coordination modes / Equilibrium and structural studies

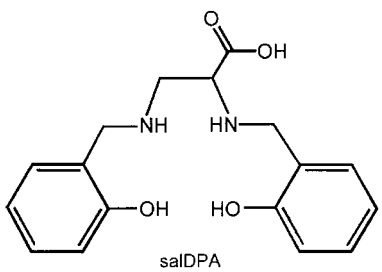


**3607** **T. Kiss,* T. Jakusch, S. Bouhsina, H. Sakurai, É. A. Enyedy**

Binding Constant of $V^{IV}O$ to Transferrin

**Keywords:** $V^{IV}O$–Transferrin complexes / EPR spectroscopy / UV spectroscopy / Stability constants

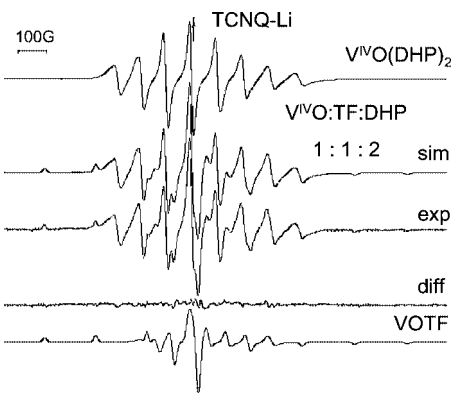


**3614** **Á. Dörnyei, S. Marcão, J. Costa Pessoa,* T. Jakusch, T. Kiss***

Interactions of Insulin-Mimetic Vanadium Complexes with the Cell Constituents ATP and Glutathione

**Keywords:** Insulin mimetics / Vanadium oxido complexes / Coordination modes

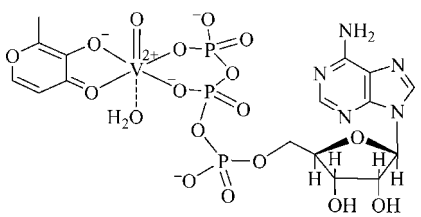


 © 2006 Wiley-VCH Verlag GmbH & Co. KGaA, Weinheim 

**3622** **W. Buckel,* A. J. Pierik, S. Plett, A. Alhapel, D. Suarez, S. Tu, B. T. Golding***

Mechanism-Based Inactivation of Coenzyme $B_{12}$-Dependent 2-Methyleneglutarate Mutase by (*Z*)-Glutaconate and Buta-1,3-diene-2,3-dicarboxylate

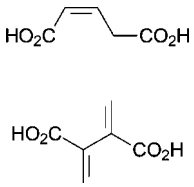


**Keywords:** 2-Methyleneglutarate / Mutase / Coenzyme $B_{12}$ / Inhibition / Buta-1,3-diene-2,3-dicarboxylic acid / Glutaconic acid

**3627** **G. Pilet,* J. Grins, M. Edén, S. Esmaeilzadeh**

$La_{17}Si_9Al_4N_{32-x}O_x$ ($x \leq 1$): A Nitridoaluminosilicate with Isolated Si/Al-N/O Clusters

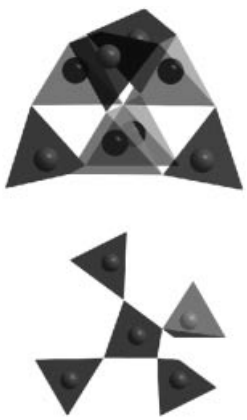

**Keywords:** Aluminosilicates / Anions / Lanthanides

**3634** **J.-P. Guo, W.-K. Wong,* W.-Y. Wong**

The Template Effect of Palladium(II): Synthesis, Characterization, and Crystal Structures of 2,4-Substituted 1,3,5-Triazapentadienatopalladium-(II) Complexes

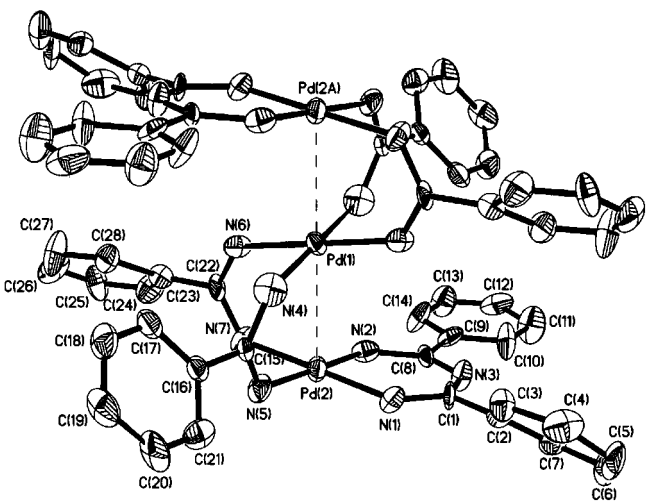


**Keywords:** Amidinate ligands / Hydrogen bonds / Palladium / N ligands

**3641** **X. Cai, G. Zhu,* W. Zhang, H. Zhao, C. Wang,* S. Qiu, Y. Wei***

Diatom-Templated Synthesis of Ordered Meso/Macroporous Hierarchical Materials

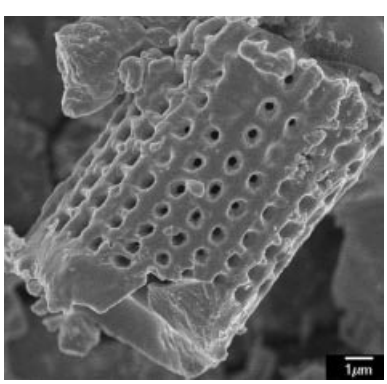


**Keywords:** Hierarchical materials / Nanomaterials / Porosity / So−gel processes / Template synthesis

 © 2006 Wiley-VCH Verlag GmbH & Co. KGaA, Weinheim 

**3646** **P. Thuéry***

Solvothermal Synthesis and Crystal Structure of Uranyl Complexes with 1,1-Cyclobutanedicarboxylic and (1*R*,3*S*)-(+)-Camphoric Acids − Novel Chiral Uranyl-Organic Frameworks

**Keywords:** Uranium / Carboxylate ligands / Metal-organic frameworks / Solvothermal synthesis / Structure elucidation

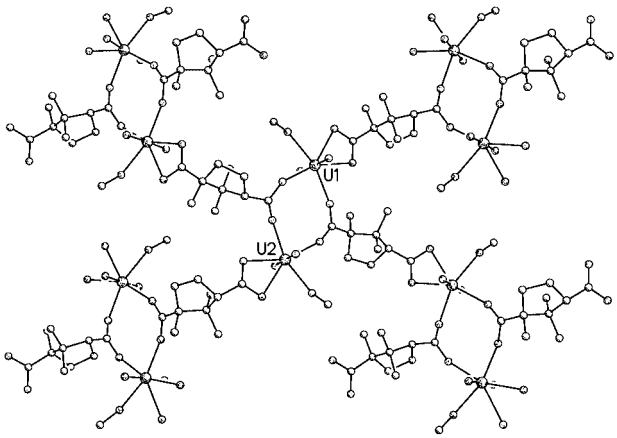


**3652** **A. Alaaeddine, A. Amgoune, C. M. Thomas, S. Dagorne, S. Bellemin-Laponnaz, J.-F. Carpentier***

Bis[bis(oxazolinato)] Complexes of Yttrium and Lanthanum: Molecular Structure and Use in Polymerization of DL-Lactide and DL-β-Butyrolactone

**Keywords:** Homogeneous catalysis / Lanthanides / N ligands / Polymerization

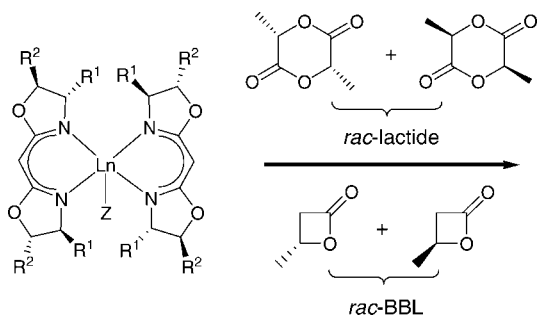


**3659** **X.-L. Hong, J. Bai,* Y. Song, Y.-Z. Li, Y. Pan***

Luminescent Open-Framework Antiferromagnet − Hydrothermal Syntheses, Structures, and Luminescent and Magnetic Properties of Two Novel Coordination Polymers: $[Zn(pdoa)(bipy)]_n$ and $\{[Mn(pdoa)(bipy)](bipy)\}_n$ [pdoa = 2,2′-(1,3-phenylenedioxy)bis(acetate); bipy = 4,4′-bipyridine]

**Keywords:** Functional coordination polymers / Polycarboxylate ligands / 4,4′-Bipyridine / Luminescence

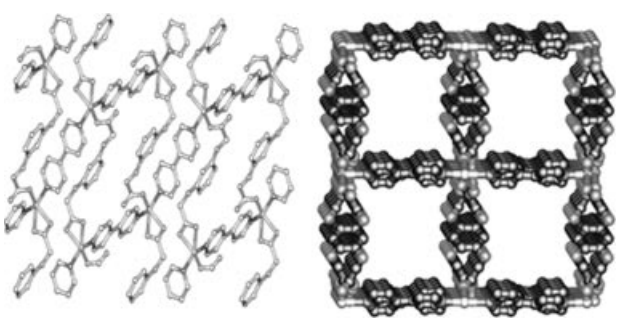

**3667** **C. Lin, H. Wang, D. Kong, M. Yu, X. Liu, Z. Wang, J. Lin***

Silica Supported Submicron $SiO_2@Y_2SiO_5:Eu^{3+}$ and $SiO_2@Y_2SiO_5:Ce^{3+}/Tb^{3+}$ Spherical Particles with a Core−Shell Structure: Sol−Gel Synthesis and Characterization

**Keywords:** Sol−gel processes / Luminescence / Core−shell structures / Silicates / Materials science

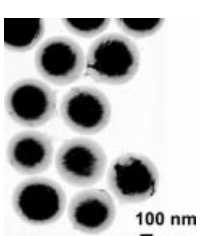


 © 2006 Wiley-VCH Verlag GmbH & Co. KGaA, Weinheim 

**3676** **K. Ono,* M. Joho, K. Saito, M. Tomura, Y. Matsushita, S. Naka, H. Okada, H. Onnagawa**

Synthesis and Electroluminescence Properties of *fac*-Tris(2-phenylpyridine)iridium Derivatives Containing Hole-Trapping Moieties

**Keywords:** Amines / Charge-carrier injection / Doping / Iridium / Luminescence

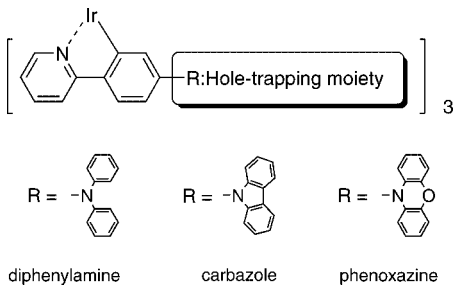


**3684** **F. Michel, F. Thomas,* S. Hamman, C. Philouze, E. Saint-Aman, J.-L. Pierre**

Galactose Oxidase Models: Creation and Modification of Proton Transfer Coupled to Copper(II) Coordination Processes in Pro-Phenoxyl Ligands

**Keywords:** Copper / Phenoxyl / Tripodal ligands / Proton transfer / Radicals

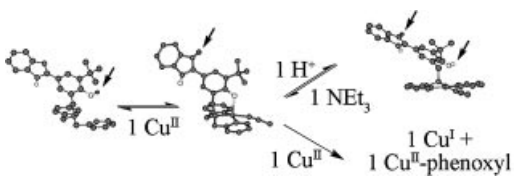


**3697** **B. Gadenne, P. Hesemann, V. Polshettiwar, J. J. E. Moreau***

Highly Ordered Functional Organosilicas by Template-Directed Hydrolysis-Polycondensation of Chiral Camphorsulfonamide Precursors

**Keywords:** Mesoporous materials / Organic-inorganic hybrid composites / Sol−gel processes / Supported catalysts / Template synthesis

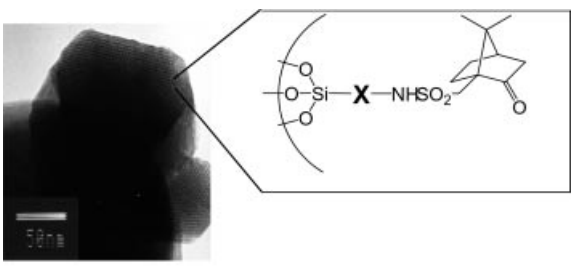


**3703** **G. Lu, M. Bai, R. Li, X. Zhang, C. Ma, P.-C. Lo, D. K. P. Ng, J. Jiang***

Lanthanide(III) Double-Decker Complexes with Octaphenoxy- or Octathiophenoxyphthalocyaninato Ligands − Revealing the Electron-Withdrawing Nature of the Phenoxy and Thiophenoxy Groups in the Double-Decker Complexes

**Keywords:** Phthalocyanine / Rare earth / Double-decker / Phenoxy group / Thiophenoxy group

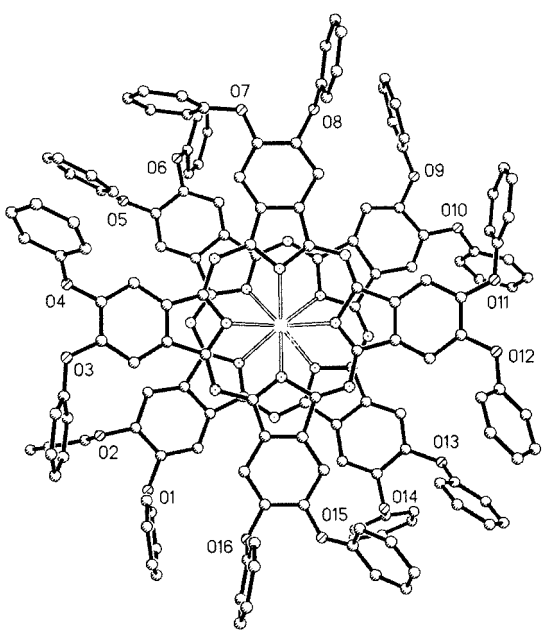


 © 2006 Wiley-VCH Verlag GmbH & Co. KGaA, Weinheim 

**3710** **V. Psycharis,* C. P. Raptopoulou, A. K. Boudalis, Y. Sanakis, M. Fardis, G. Diamantopoulos, G. Papavassiliou**

Syntheses, Structural, and Physical Studies of Basic $Cr^{III}$ and $Fe^{III}$ Benzilates and Benzoates: Evidence of Antisymmetric Exchange and Distributions of Isotropic and Antisymmetric Exchange Parameters

**Keywords:** Trinuclear oxo-centered chromium(III) and iron(III) complexes / Magnetic properties / Crystal structures / EPR spectroscopy / Mössbauer spectroscopy

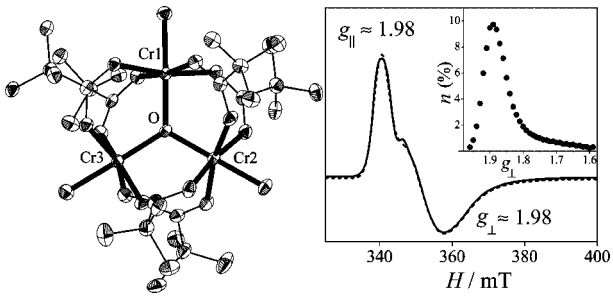


**3724** **L. Ray, V. Katiyar, M. J. Raihan, H. Nanavati, M. M. Shaikh, P. Ghosh***

First Example of a Gold(I) *N*-Heterocyclic-Carbene-Based Initiator for the Bulk Ring-Opening Polymerization of L-Lactide

**Keywords:** Carbenes / Functionalized NHC / Ring-opening polymerization (ROP) / Organometallic catalysis / Silver−NHC complex / Gold−NHC complex

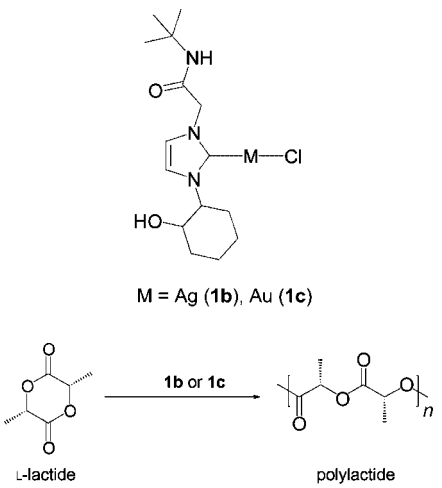


**3731** **L.-H. Gao, M. Guan, K.-Z. Wang,* L.-P. Jin, C.-H. Huang**

A Comparative Study of the Optical and Electroluminescent Properties of $Eu^{III}$ Complexes with TTA and 2-(2′-Pyridyl)azoles: The Crystal Structure of $[Eu(TTA)_3(PBO)]$

**Keywords:** X-ray diffraction / Luminescence / Chelates / N,O ligands / Lanthanides

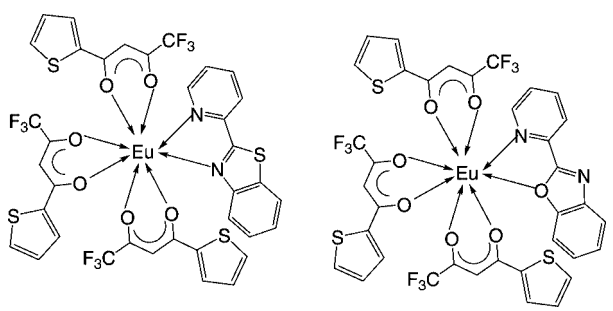


**3738** **S. Del Piero, P. Di Bernardo, R. Fedele, A. Melchior,* P. Polese, M. Tolazzi***

Affinity of Polypyridines Towards $Cd^{II}$ and $Co^{II}$ Ions: a Thermodynamic and DFT Study

**Keywords:** Cadmium(II) / Cobalt(II) / Pyridine complexes / Thermodynamics / Density functional calculations

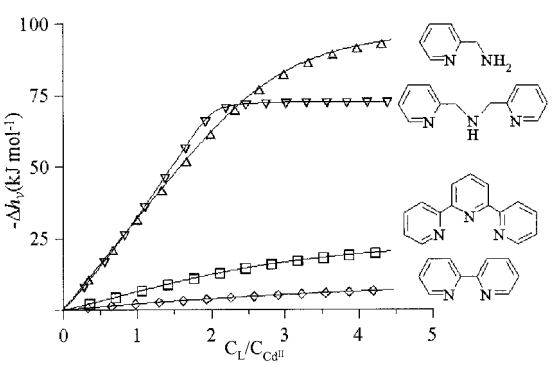


 © 2006 Wiley-VCH Verlag GmbH & Co. KGaA, Weinheim 

**3746** **C. Rothenburger, M. Galanski,* V. B. Arion, H. Görls, W. Weigand,* B. K. Keppler***

Synthesis and Characterization of [(1*R*,2*R*)-*trans*-Diaminocyclohexane]platinum(II) Coordinated to Sulfur and Selenium Amino Acids

**Keywords:** Bioinorganic chemistry / Platinum / Amino acids / Sulfur / Selenium

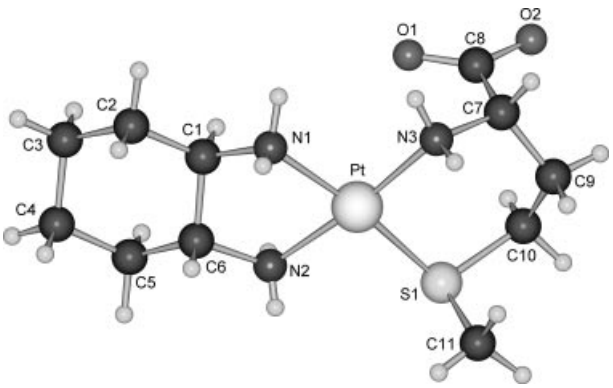


**3753** **T. Yano, H. Arii, S. Yamaguchi, Y. Funahashi, K. Jitsukawa, T. Ozawa,* H. Masuda***

$Co^{III}$ Complexes with Square-Planar $N_2S_2$- and $N_2(SO_2)_2$-Type Ligands as An Active Site Structural Model for Nitrile Hydratase − Biological Implications of an Amidate Coordination

**Keywords:** Nitrile hydratase / Cobalt / Amidate ligand / Electrophilic interactions / Lewis acids

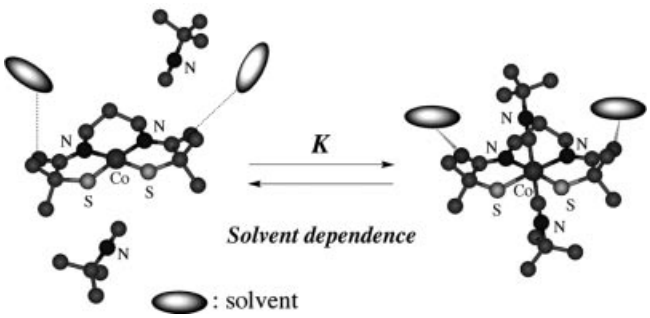


**3762** **S. González-Montiel, N. Andrade-López, J. G. Alvarado-Rodríguez***

Synthesis, Characterisation and Properties of *As*-Monohalogenated Dibenzoarsocines $S(C_6H_4S)_2AsHal$ (Hal = Cl, Br, I) − A Study of the Transannular Interaction S→As

**Keywords:** Arsenic complexes / Main group elements / Hypervalent compounds / Structure elucidation

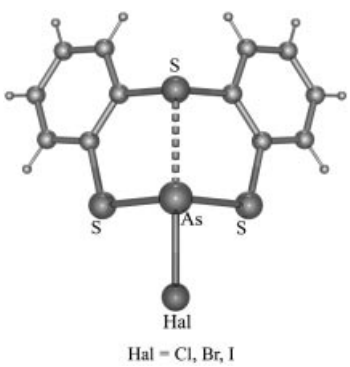


**3769** **E. Ortega, N. Kleigrewe, G. Kehr, G. Erker,* R. Fröhlich**

Product Diversity in the Reaction of [(norbornadiene){CpP(*i*Pr)$_2$}Rh] with Alkyl Iodides

**Keywords:** Rhodium / Phosphonium salts / Dimetallic complexes / Cyclopentadienyl ligands / Phosphorus ylides

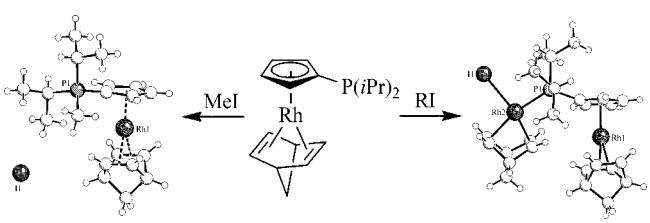



 © 2006 Wiley-VCH Verlag GmbH & Co. KGaA, Weinheim 

DOI: 10.1002/ejic.200600360

# On the Fate of Vanadate in Human Blood

**András Gorzsás,*[a][‡] Ingegärd Andersson,[a] and Lage Pettersson[a]**

**Keywords:** Vanadium / Bioinorganic chemistry / Equilibria in aqueous solution / Diabetes

As a summary of recent activities at our research group, a model describing the distribution of pentavalent vanadium (referred to as vanadate throughout the present work) in human blood has been constructed based on our speciation studies performed in the physiological medium of 0.150 M Na(Cl) with various blood constituents. In addition, other data (most notably with the high mass serum constituents albumin and transferrin) have also been used to give as broad a view as possible. Two antidiabetic drug candidate ligands, picolinate and maltol, have also been included in order to investigate the stability of their vanadium complexes in the presence of blood constituents, i.e. to account for ligand-exchange possibilities. The model predicts transferrin to be the major carrier of vanadium in the bloodstream. It is capable of almost completely replacing the vanadium-bound picolinate even if the latter is in large excess. Maltol, on the other hand, can retain most of the vanadium when it is supplied in about a 5 mM concentration. The model still has certain limitations but it serves as a useful base for investigating structure, stability, relationship effects and provides insight into the fate of vanadate in human blood.

(© Wiley-VCH Verlag GmbH & Co. KGaA, 69451 Weinheim, Germany, 2006)

## Introduction

Arguably the biggest contribution to the renewed interest in the bioinorganic chemistry of vanadium originates from the discovery of the insulin-enhancing properties of this transition metal and its compounds. *Diabetes mellitus*, with its explosively increasing incidence worldwide[1] and many global and societal implications,[2] is one of the most threatening and costly "epidemics" of our times. Currently insulin is used as the core treatment in both type I and type II diabetes. Although it is extremely important, there is need for substitutes, especially when dealing with type II diabetes. In addition, being destroyed in the stomach, insulin cannot be administered orally in mammals and the constant use of subcutaneous injections is inconvenient. Thus, the ideal substitute would be orally applicable and effective, particularly in the case of type II diabetes. It also should meet other criteria regarding its absorption, stability in body fluids, a desired high specificity and low toxicity.[3]

[a] Department of Chemistry, Inorganic Chemistry, Umeå University,
90187 Umeå, Sweden
Fax: +46-90-786-9195
E-mail: Andras.Gorzsas@genfys.slu.se
[‡] Present address: Department of Forest Genetics and Plant Physiology, Umeå Plant Science Centre,
90183 Umeå, Sweden

Vanadium compounds have long been shown to exert insulin-like effects both in vitro,[4–8] and in vivo,[3,9,10,11–20] the first example being documented as early as 1899.[21] In all these tests, vanadium has been demonstrated to perform insulin-like actions in virtually all respects.[9,22,23] The amount of vanadium needed to induce the required metabolic effects has been found to be in the range of micromolar to millimolar concentrations,[4,6,7,8,24] depending not only on the nature of the compound but also on the time course of the management (generally lower doses are needed when long-term treatment is applied). It is worth noting that usually a longer time has been required during in vivo experiments to observe the desired insulin-like effects as compared to in vitro tests. On the other hand, the effects have mostly been long lasting, even after stopping the administration of the compounds. These indicate a possible accumulation of the active component(s) in the body,[9] as has been shown in the case of bones.[25,19,20] It is also important to point out that plasma insulin levels have not been increased during the treatments. Thus, the glucose-lowering effects are not due to a vanadium-induced increase in insulin secretion,[14,26] but rather they are realised by mechanisms that are (at least partly) different from that of insulin.[3,27] However, these mechanisms are not yet completely elucidated. In addition, different vanadium compounds operate along (partially) different pathways, further complicating the picture.[9,28,29]

**MICROREVIEWS:** This feature introduces the readers to the authors' research through a concise overview of the selected topic. Reference to important work from others in the field is included.

 © 2006 Wiley-VCH Verlag GmbH & Co. KGaA, Weinheim 

Unfortunately, mostly owing to the low adsorption and specificity of vanadium, problems with toxicity and side effects arise. On the other hand, these problems can in theory be overcome by applying the proper ligands. In fact a great advantage of vanadium compounds is that virtually all of their important features, such as stability, oral availability, as well as absorption, toxicity, etc. can be fine-tuned by means of different ligands. While investigating the effects of different vanadium complexes, it has also been suggested that it is always the uncomplexed vanadium that is the active component, irrespective of the introduced species.[30] In other words, the only role of the ligand could be to deliver vanadium as efficiently as possible, including translocation across the cell membrane. In opposition to this hypothesis, different mechanisms of action have been suggested for different vanadium complexes, depending on the nature of the compound.[9,28] Whatever the case may be, ligands may still play an important role in facilitating the uptake and/or transport of vanadium, thereby reducing toxicity and side effects and possibly increasing effectiveness.

It should also be noted that the incidence of diabetes is increasing among pets, for similar reasons as in the case of humans, namely sedentary lifestyle and obesity.[31] Food supplies often contain nutrients in much higher amounts than the natural diet of the animal would do or require. For instance, there is a large amount of carbohydrates in certain commercial cat foods, despite the well-known fact that cats are strict carnivores, and hence their diet naturally is based mostly on protein and fat with very little carbohydrates.[32] This causes serious malnutrition as the high carbohydrate diet leads to decreased insulin sensitivity in cats.[33] However, applying regular injections in animal treatment is even more troublesome than in the case of humans. Thus, oral medication is also desired in veterinary practices, and vanadium compounds may represent one type of solution.

Finally, it has to be pointed out that, although research in this field involves vanadium in its +4 and +5 oxidation states (as well as +3, to a much lesser extent), in the present article we focus solely on the +5 oxidation state. Thus, from here on, vanadium in the text refers to vanadium(V), unless otherwise specified.

## Speciation Studies and Modelling

Numerous drugs are known to be bound to plasma proteins when entering the bloodstream. The extent and nature of this interaction has a profound effect on the distribution of the drug into other compartments and on its therapeutic as well as toxic effects.[34–36]

Complete speciation studies are of great value in the fundamental research of this field. By the pH-independent formation constants obtained from such studies modelling of physiological conditions can be done, which is of fundamental interest in revealing vanadium interactions in humans as well as in drug design and production. Once vanadium speciation is established with all the major components in blood, including mixed ligand species, modelling can be used to determine the fate of any particular vanadium complex under physiological conditions, provided that

*András Gorzsás was born in Hajdúböszörmény, Hungary. He graduated in chemistry and English special translator majors at Lajos Kossuth University (now Debrecen University), Debrecen, Hungary, in 1999. He received his PhD in inorganic chemistry from Umeå University in 2005. He is currently a postdoctoral fellow at Umeå Plant Science Centre, working on the chemical analysis of wood cell walls by FT-IR microspectroscopy.*

*Ingegärd Andersson was born in Röbäck, close to Umeå, Sweden. She became an engineer in chemistry in 1965 in Skellefteå, Sweden. She has been working at the Department of Chemistry, Inorganic Chemistry, Umeå University since then.*

*Lage Pettersson was born in Holmsund, close to Umeå, Sweden. He received his MSc degree at the University of Uppsala (Sweden) in 1965. He joined Umeå University in 1966 and received his PhD in chemistry there in 1974. He became professor in inorganic chemistry at Umeå University in 1995. His group has specialised in equilibrium and structure studies of vanadium bioinorganic systems and polyoxometallate systems with molybdenum and vanadium.*

 © 2006 Wiley-VCH Verlag GmbH & Co. KGaA, Weinheim 

the speciation with the given ligand in the complex is also known. This paper represents such an attempt. Although some of the constituents of human blood had to be excluded (see below), our ongoing series of investigations,[37–39] have provided us with enough data to form a base for model calculations that are of interest to researchers in this field.

Albumin is found in approximately 630 μM concentration (Table 1) in human blood, and it (together with $\alpha_1$-acid glycoprotein) is one of the most common nonspecific binding proteins. Transferrin is another binding protein that is important in the case of metal transportation[40,41] (especially with iron, hence the name). It is present in human blood in about a 37 μM concentration (Table 1), and has two binding sites per protein to accommodate metal ions.[42] In normal serum, only about 30% of the total binding sites are occupied by iron.[43] This means that there are still sites available for other metal ions, without needing to replace the tightly bound iron. It has to be noted that there is a bidentate carbonate in the active site, usually referred to as the synergistic anion,[44,45] without which practically no iron–transferrin binding occurs.

Since both albumin and transferrin play important roles in the distribution and transportation of different compounds, they cannot be ignored when evaluating the interactions of any introduced vanadium-containing drugs in human blood. Indeed, it has been demonstrated that vanadium binds to both of these proteins,[46–54] although the binding is approximately 1000-times stronger to transferrin than to albumin.[55] Interestingly, vanadium has been found to be bound to transferrin even in the absence of $HCO_3^-$.[56]

Beside these two proteins, other constituents should also be included in a model that attempts to elucidate the fate of vanadium in human blood. Table 1 lists five additional low mass bioligands: glycine, lactate, phosphate, citrate and histidine, with their respective concentrations in human blood. Some constituents, such as carbonate, sulfate, cysteine, etc. have been excluded owing to the lack of (reliable) formation constants for their vanadate complexes. Of these excluded ligands, only hydrogen carbonate should be of considerable importance, because of its high concentration in blood (almost 25 mM).

In addition to the physiological concentrations of the selected blood constituents, Table 1 also lists the complexes they form with vanadate. These species have been included in the model calculation. Unfortunately, some of the formation constants given in Table 1 have not been determined in the physiological medium, which introduces an error in the model calculations. Moreover, in the case of transferrin, another simplification has been made. As explained earlier, transferrin is capable of binding two metals per protein, which could lead to the formation of a $V_2$Trf-type complex with vanadium. On the other hand, iron is present and competes with vanadium for the binding sites under physiological conditions. What is more, the binding of iron is favoured over other metal ions by transferrin. Since no iron is included in the model calculation, this kind of competitive binding has to be included in another way. It has been achieved by performing the calculation with VTrf-type complexes only. The other binding site can then be occupied by iron, as is most probably the case. Thus, the complex VTrf can in fact be considered as FeVTrf. Although this is a rather arbitrary simplification, it should give satisfactorily accurate results, since the amount of vacant binding sites of transferrin is estimated to be around 40 μM in human serum in the presence of iron.[42]

Table 1. Vanadate complexes with selected constituents in human blood. The concentrations of the ligands in healthy human subjects are given according to ref.[57] Maltol and picolinate are included to represent drug candidate ligands. The simplified notations for the complexes represent only their nuclearities and charges. Whenever charge is not indicated, it has not been determined in the study. Asterisks denote complexes with the same composition but different structures. The higher number of asterisks, the less dominating the species is. Formation constants for the complexes are shown at 25 °C, and the ionic media in which they have been determined are also noted.

| Ligand (Abbreviation) | Concentration in human blood | Complex notation | log$\beta$ | Medium |
|---|---|---|---|---|
| Glycine (Gly) | 2.3 mM | VGly | 1.8[a,i] | 1.0 M KCl, HEPES buffer |
| Lactate ($Lac^-$) | 1.51 mM | $VLac^{2-}$ | 0.88[b] | 0.15 M Na(Cl) |
| | | $VLac^-$ | 6.92[b] | |
| Phosphate ($P^-$) | 1.1 mM | $VP^{3-}$ | –5.68[c] | 0.15 M Na(Cl) |
| | | $VP^{2-}$ | 1.51[c] | |
| | | $VP_2^{4-}$ | –3.94[c] | |
| | | $VP_2^{3-}$ | 2.36[c] | |
| Citrate ($Cit^{3-}$) | 99 μM | $VCit^{2-}$ | 14.19[d] | 0.15 M Na(Cl) |
| Histidine (His) | 77 μM | VHis | 0.2[e,i] | 0.15 M NaCl |
| | | *VHis | –0.2[e,i] | |
| Albumin (Alb) | 630 μM | VAlb | 3.0[a,i] | 1.0 M KCl, HEPES buffer |
| Transferrin (Trf) | 37 μM | VTrf | 6.5[f,i] | 0.1 M HEPES buffer |
| Picolinate ($Pi^-$) | – | $VPi_2^-$ | 18.92[g] | 0.15 M Na(Cl) |
| | | *$VPi_2^-$ | 18.77[g] | |
| | | **$VPi_2^-$ | 18.24[g] | |
| | | $VPi^-$ | 9.31[g] | |
| | | *$VPi^-$ | 8.70[g] | |
| Maltol (Ma) | – | $VMa^-$ | 2.66[h] | 0.15 M Na(Cl) |
| | | $VMa^{2-}$ | –7.37[h] | |
| | | $VMa_2^-$ | 7.02[h] | |

[a] Ref.[51] [b] Ref.[37] [c] Ref.[38] [d] Ref.[39] [e] Ref.[58] [f] Ref.[48] [g] Ref.[59] [h] Ref.[60] [i] Constants are log $K$ values, not log $\beta$.

 © 2006 Wiley-VCH Verlag GmbH & Co. KGaA, Weinheim 

In all cases, only those mononuclear complexes that may be relevant at the pH of human blood have been listed. Higher nuclearity species have been omitted completely, as they are extremely unlikely to be present at very low total concentrations of vanadium. For the present modelling $[V]_{tot}$ = 1 μM has been chosen, since vanadate species have shown insulin-like effects at this concentration, but no toxicity.[8] For a more complete list of vanadate species formed with a given ligand at various pH values and total concentrations, consult the references.

In order to represent an introduced vanadium-containing drug, either vanadate–picolinate or vanadate–maltol complexes (Table 1) have also been included in the model. This has been done to investigate whether the carrier ligand gets replaced by any of the blood constituents. Picolinate and maltol have been chosen since they form very stable mononuclear complexes with vanadium.[59,60] Extensive clinical research and in vitro tests have been carried out on complexes of vanadium and either of these ligands (or derivatives).[15,61,62,63–66] In addition, both ligands bind to vanadium over a wide pH range, covering conditions from acidic (stomach) to nearly neutral and slightly alkaline (blood, small intestines). This is of importance when taking a designed drug orally.

The calculations presented here have been performed using WINSGW,[67] a programme package based on the SOLGASWATER algorithm.[68] For the species formed in the $H^+$–$H_2VO_4^-$ binary system, formation constants have been taken from ref.[69] In cases of the different ternary $H^+$–$H_2VO_4^-$ ligand systems, only the complexes listed in Table 1 have been taken into consideration with the formation constants given there. For the model, $[V]_{tot}$ = 1 μM and pH = 7.4 have been used, with $[Ligand]_{tot}$ set to values given in Table 1 for each of the ligands. Thus, the matrix consisted of inorganic vanadates together with all the vanadate–ligand complexes given in Table 1.

Figure 1 shows the results of one of the model calculations. As can be seen, when there is no carrier ligand introduced with vanadium and the high mass serum constituents (HMS), albumin and transferrin, are excluded from the model, most of the metal is present as inorganic monovanadate, $H_2VO_4^-$ and $HVO_4^{2-}$ (Figure 1, a). Approximately 12% of vanadium is bound to glycine, and about 1–2% to other constituents (mostly phosphate). When the proteins are also included, however, more than 98% of the total vanadium is bound to transferrin (Figure 1, b). To illustrate the strength of picolinate itself as a carrier ligand in the absence of HMS, the distribution is also shown for that case (Figure 1, c). The diagram shows that a substantial fraction of vanadium (about 90%) is bound to picolinate when neither of the proteins is present. However, when HMS are included the transferrin binds almost all of the vanadium (approximately 90%), despite the high concentration of picolinate (20 mM, Figure 1, d). This is in accordance with the results obtained with canine blood,[47] where it has been shown that almost 80% of vanadium is bound to transferrin, regardless of what kind of inorganic vanadium species has been injected originally. It is also in accordance with the fact that introduced vanadium seems to be targeted towards iron-rich cells,[70] i.e. the transport route of vanadium follows that of iron.

Interesting results are found when doing the same kind of modelling with maltol, instead of picolinate (Figure 2). Using the same concentration for maltol as for picolinate in the previous calculation (20 mM), it is obvious how much stronger this ligand binds to vanadate at physiological pH (Figure 2, a). Even in the presence of HMS, almost 97% of the total vanadium is bound as $VMa_2^-$ (Figure 2, b). When lowering the total concentration of maltol to 5 mM, more vanadium is bound to transferrin, but still not more than approximately 34% (Figure 2, c). This means that although transferrin binds vanadium very strongly, a considerable fraction of the metal can still be bound to its original carrier if an appropriate ligand is applied. Certainly the ligand needs to be in excess, but it does not have to be at extreme concentrations to be able to effectively compete with the HMS. In contrast, recent findings with vanadium(IV)–bismaltolato complexes suggest that transferrin is capable of

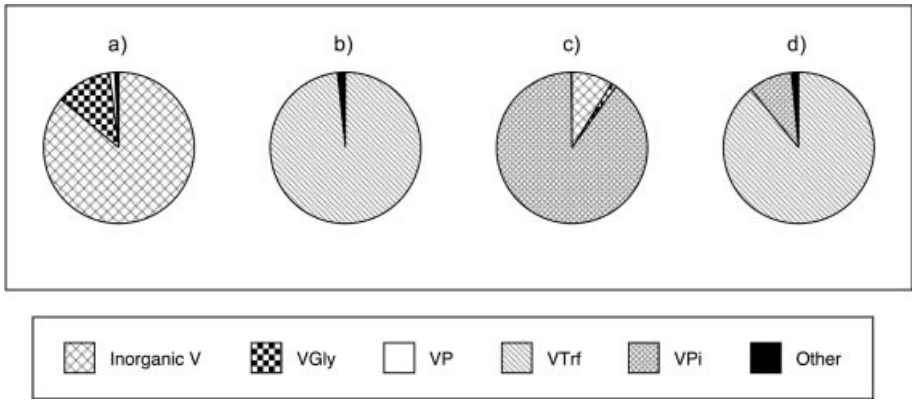


Figure 1. Distribution of vanadate in the presence of different blood constituents at pH = 7.4. $[V]_{tot}$ = 1 μM in all cases, concentrations of the constituents are according to Table 1. HMS is short for the high mass serum constituents, albumin and transferrin. Gly stands for glycine, P for phosphate, Trf for transferrin and Pi for picolinate in the legend. From left to right: (a) No HMS, no Pi (b) No Pi, HMS included (c) No HMS, $[Pi]_{tot}$ = 20 mM (d) $[Pi]_{tot}$ = 20 mM, HMS included.

 © 2006 Wiley-VCH Verlag GmbH & Co. KGaA, Weinheim 

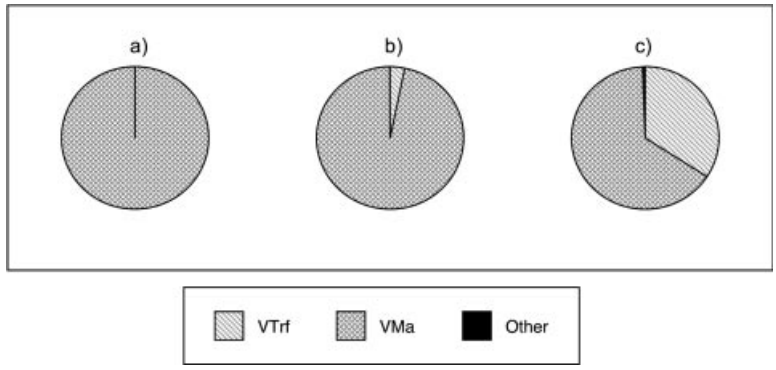


Figure 2. Distribution of vanadate in the presence of blood constituents at pH = 7.4. $[V]_{tot}$ = 1 μM in all cases, concentrations of blood constituents are according to Table 1. HMS is short for high mass serum constituents (albumin and transferrin). Trf stands for transferrin and Ma for maltol in the legend. From left to right: (a) No HMS, $[Ma]_{tot}$ = 20 mM (b) HMS included, $[Ma]_{tot}$ = 20 mM (c) HMS included, $[Ma]_{tot}$ = 5 mM.

replacing the maltol ligand(s) of the introduced complex at certain concentration ratios.[71] However, it is worth noting that vanadium(IV) has a higher affinity to transferrin than does vanadium(V).[56] In other words, vanadium(V) complexes generally have a better chance to avoid ligand replacement by transferrin than the corresponding ones with vanadium(IV). This is especially interesting when comparing the vanadium–bismaltolato complexes in each oxidation state. Vanadium(IV)–maltol (or derivative) complexes have been extensively studied,[61–65] and have shown promising insulin-enhancing properties. However, the corresponding vanadium(V) species seems to be considerably less active in this regard.[72] Why that is so is hard to explain by our speciation model alone, especially when taking into account the ease by which vanadium(V) and (IV) could interconvert under physiological conditions. Our model indicates that vanadium(V) forms very strong complexes with maltol (Figure 2), but says nothing about the kinetic lability of the formed species. A too inert species may effectively remove vanadium from the system by binding it too tightly and thereby prohibiting its interactions with other compounds. Additionally, it could be a charge effect. The bismaltolato complex of vanadium(IV) is neutral, whereas the corresponding vanadium(V) species is –1 charged. This certainly affects the way the complex can enter the cells and might be at least one of the reasons why they show different insulin-enhancing activities.

It has to be mentioned that limitations do apply to the models presented above. First of all, the formation constants used are from different media and a considerable simplification has been made when considering only VTrf but not $V_2$Trf in the model. In addition, mixed ligand vanadate complexes so far have only been determined with lactate and citrate[39] out of all the bioligands shown in Table 1. Although these are extremely weak complexes, others (with phosphate, for instance) might not necessarily be. In addition, recent data on the interactions of the vanadium(IV)–bismaltolato complex with HMS indicated that albumin may take part in the formation of such mixed-ligand complexes (in that case a vanadium(IV)–maltol–albumin species).[71] While no such species have yet been reported with vanadium(V) complexes, their existence cannot be ruled out. Nevertheless, these are not likely to cause major changes in the overall picture, and the model should be valid for all the major features and trends.

## Concluding Remarks

Speciation studies are very useful for the bioinorganic and medicinal chemistry of vanadium compounds in many respects. First of all, they provide insight to the complex formation patterns and preferences of vanadate in the presence of various biologically important or potential drug candidate ligands. This is extremely valuable, since it helps in tailoring the properties of the complex and also casts light on the fate of vanadium in the presence of e.g. blood constituents. In addition, by means of the formation constants obtained from such studies, parameters can be optimised for crystallisation studies or in general to obtain a maximum yield in the synthesis of a given complex. Moreover, physiological conditions can also be modelled (with certain restrictions) to predict what happens to any introduced vanadium compound when it enters e.g. the stomach, bloodstream, etc. Naturally, care must be taken to use the proper ionic medium for the studies (e.g. 0.150 M Na(Cl), to represent the ionic strength of human blood). A series of speciation studies with pentavalent vanadium has been carried out with different blood constituents in this context.[37–39] As incomplete as this series is, it forms a solid base for model calculations aiming to elucidate the fate of vanadate (compounds) in human blood. Although certain limitations apply to the model presented in this paper, the major features should be valid nonetheless, providing a useful overview and practical guidelines.

## Acknowledgments

This work has been supported by the Swedish Research Council and the European Union (COST project D21/009-01). The authors would like to thank the members of the various working groups within the COST framework, especially Prof. Dieter Rehder.

 © 2006 Wiley-VCH Verlag GmbH & Co. KGaA, Weinheim 

[1] H. King, R. Aubert, W. Herman, *Diabetes Care* **1998**, *21*, 1414–1431.
[2] P. Zimmet, K. G. M. M. Alberti, J. Shaw, *Nature* **2001**, *414*, 782–787.
[3] Y. Shechter, I. Goldwaser, M. Mironchik, M. Fridkin, D. Gefel, *Coord. Chem. Rev.* **2003**, *237*, 3–11.
[4] Y. Shechter, S. J. Karlish, *Nature* **1980**, *284*, 556–558.
[5] D. M. Barnes, D. B. Sykes, Y. Shechter, D. S. Miller, *J. Cell. Physiol.* **1995**, *162*, 154–161.
[6] E. L. Tolman, E. Barris, M. Burns, A. Pansini, R. Partridge, *Life Sci.* **1979**, *25*, 1159–1164.
[7] L. Agius, W. J. Vaartjes, *Biochem. J.* **1982**, *202*, 791–794.
[8] D. Rehder, J. Costa Pessoa, C. F. G. C. Geraldes, M. M. C. A. Castro, T. Kabanos, T. Kiss, B. Meier, G. Micera, L. Pettersson, M. Rangel, A. Salifoglou, I. Turel, D. Wang, *J. Biol. Inorg. Chem.* **2002**, *7*, 384–396.
[9] I. Goldwaser, D. Gefel, E. Gershonov, M. Fridkin, *J. Inorg. Biochem.* **2000**, *80*, 21–25.
[10] C. E. Heyliger, A. G. Tahiliani, J. H. McNeill, *Science* **1985**, *227*, 1474–1477.
[11] S. M. Brichard, J. C. Henquin, *Trends Pharmacol. Sci.* **1995**, *16*, 265–270.
[12] J. L. Domingo, M. Gomez, D. J. Sanchez, J. M. Llobet, C. L. Keen, *Diabetes* **1994**, *43*, 1267–1267.
[13] R. A. Pederson, S. Ramanadham, A. M. Buchan, J. H. McNeill, *Diabetes* **1989**, *38*, 1390–1395.
[14] M. Bendayan, D. Gingras, *Diabetologia* **1989**, *32*, 561–567.
[15] K. H. Thompson, J. H. McNeill, C. Orvig, *The 4th International Symposium on Chemistry and Biological Chemistry of Vanadium*, Szeged, Hungary, September 3–5, **2004**, poster session.
[16] M. Halberstam, N. Cohen, P. Shlimovich, L. Rossetti, H. Shamoon, *Diabetes* **1996**, *45*, 659–666.
[17] N. Cohen, M. Halberstam, P. Shlimovich, C. J. Chang, H. Shamoon, L. Rossetti, *J. Clin. Invest.* **1995**, *95*, 2501–2509.
[18] A. B. Goldfine, D. C. Simonson, F. Folli, M. E. Patti, C. R. Kahn, *J. Clin. Endocrinol. Metab.* **1995**, *80*, 3311–3320.
[19] D. M. Facchini, V. G. Yuen, M. L. Battell, J. H. McNeill, M. D. Grynpas, *Bone* **2006**, *38*, 368–377.
[20] A. L. Edel, M. Kopilas, T. A. Clark, F. Aguilar, P. K. Ganguly, C. E. Heyliger, G. N. Pierce, *Metab. Clin. Exp.* **2006**, *55*, 263–270.
[21] B. M. Lyonett, E. Martin, *La Press Medicale* **1899**, *1*, 191.
[22] N. Sekar, J. Li, Y. Shechter, *Crit. Rev. Biochem. Mol. Biol.* **1996**, *31*, 339–359.
[23] Y. Shechter, *Diabetes* **1990**, *39*, 1–5.
[24] I. G. Fantus, F. Ahmad, G. Deragon, *Endocrinology* **1990**, *127*, 2716–2725.
[25] S. A. Dikanov, B. D. Liboiron, C. Orvig, *J. Am. Chem. Soc.* **2002**, *124*, 2969–2978.
[26] S. M. Brichard, J. C. Henquin, *Trends Pharmacol. Sci.* **1995**, *16*, 265–270.
[27] Z.-W. Yu, *Insulin-like actions of vanadium compounds in fat cells*, PhD Thesis, Dept. of Medicine, University of Umeå, Inst. of Internal Medicine, University of Göteborg, **1998**, Umeå, Sweden.
[28] A. Shisheva, Y. Shechter, *Endocrinology* **1993**, *133*, 1562–1568.
[29] M. Z. Mehdi, A. K. Srivastava, *Arch. Biochem. Biophys.* **2005**, *440*, 158–164.
[30] K. G. Peters, M. G. Davis, B. W. Howard, M. Pokross, V. Rastogi, C. Diven, K. D. Greis, E. Eby-Wilkens, M. Maier, A. Evdokimov, S. Soper, F. Genbauffe, *J. Inorg. Biochem.* **2003**, *96*, 321–330.
[31] M. Hoenig, *Mol. Cell. Endocrinol.* **2002**, *197*, 221–229.
[32] J. W. S. Bradshaw, D. Goodwin, V. Legrad-Defretin, H. M. R. Nott, *Comput. Biochem. Physiol.* **1996**, *114*, 205–209.
[33] M. Hoenig, C. Reusch, M. E. Peterson, *Vet. Immunol. Immunopathol.* **2000**, *77*, 93–102.
[34] B. Fichtl, A. von Nieciecki, K. Walter, *Adv. Drug. Res.* **1991**, *30*, 117–166.
[35] P. du Spuich, J. Verges, S. Erill, *Clin. Pharmacokinet.* **1993**, *24*, 435–440.
[36] J. D. Wright, F. D. Boudinot, M. R. Ujhelyi, *Clin. Pharmacokinet.* **1996**, *30*, 445–462.
[37] A. Gorzsás, I. Andersson, L. Pettersson, *Dalton Trans.* **2003**, 2503–2511.
[38] I. Andersson, A. Gorzsás, C. Kerezsi, I. Tóth, L. Pettersson, *Dalton Trans.* **2005**, 3658–3666.
[39] A. Gorzsás, K. Getty, I. Andersson, L. Pettersson, *Dalton Trans.* **2004**, 2873–2882.
[40] W. R. Harris, *Struct. Bonding (Berlin)* **1998**, *92*, 122–162.
[41] H. Sun, H. Li, P. J. Sadler, *Chem. Rev.* **1999**, *99*, 2817–2842.
[42] W. R. Harris, L. Messori, *Coord. Chem. Rev.* **2002**, *228*, 237–262.
[43] N. D. Chasteen, *Coord. Chem. Rev.* **1977**, *22*, 1–36.
[44] S. Bailey, R. W. Evans, R. C. Garratt, B. Gorinsky, S. Hasnain, C. Horsburgh, H. Jhoti, P. F. Lindley, A. Mydin, R. Sarra, J. L. Watson, *Biochemistry* **1988**, *27*, 5804–5812.
[45] R. T. A. MacGillivray, S. A. Moore, J. Chen, B. F. Anderson, H. Baker, Y. Luo, M. Bewley, C. A. Smith, M. E. P. Murphy, Y. Wang, A. B. Mason, R. C. Woodworth, G. D. Brayer, E. N. Baker, *Biochemistry* **1998**, *37*, 7919–7928.
[46] N. D. Chasteen, J. K. Grady, C. E. Holloway, *Inorg. Chem.* **1986**, *25*, 2754–2760.
[47] W. R. Harris, S. B. Friedman, D. Silberman, *J. Inorg. Biochem.* **1984**, *20*, 157–169.
[48] W. R. Harris, C. J. Carrano, *J. Inorg. Biochem.* **1984**, *22*, 201–218.
[49] A. Butler, M. J. Danzitz, *J. Am. Chem. Soc.* **1987**, *109*, 1864–1865.
[50] A. Butler, H. Eckert, *J. Am. Chem. Soc.* **1989**, *111*, 2802–2809.
[51] D. C. Crans, R. L. Bunch, L. A. Theisen, *J. Am. Chem. Soc.* **1989**, *111*, 7597–7607.
[52] M. W. Makinen, M. J. Brady, *J. Biol. Chem.* **2002**, *277*, 12215–12220.
[53] D. Rehder, M. Časný, R. Große, *Magn. Reson. Chem.* **2004**, *42*, 745–749.
[54] D. C. Crans, J. J. Smee, E. Gaidamauskas, L. Yang, *Chem. Rev.* **2004**, *104*, 849–902.
[55] G. Heinemann, B. Fichtl, M. Mentler, W. Vogt, *J. Inorg. Biochem.* **2002**, *90*, 38–42.
[56] M. H. Nagaoka, T. Yamazaki, T. Maitani, *Biochem. Biophys. Res. Commun.* **2002**, *296*, 1207–1214.
[57] W. R. Harris, *Clin. Chem.* **1992**, *38*, 1809–1818.
[58] M. Fritzsche, V. Vergopoulos, D. Rehder, *Inorg. Chim. Acta* **1993**, *211*, 11–16.
[59] I. Andersson, A. Gorzsás, L. Pettersson, *Dalton Trans.* **2004**, 421–428.
[60] K. Elvingson, A. González Baró, L. Pettersson, *Inorg. Chem.* **1996**, *35*, 3388–3393.
[61] K. H. Thompson, V. G. Yuen, J. H. McNeill, C. Orvig, in: *Vanadium Compounds: Chemistry, Biochemistry and Therapeutic Applications* (Eds.: A. S. Tracey, D. C. Crans), ACS Symposium Series 711, ACS Publications, Washington DC, **1998**, chapter 26.
[62] J. H. McNeill, V. G. Yuen, H. R. Hoveyda, C. Orvig, *J. Med. Chem.* **1992**, *35*, 1489–1491.
[63] H. Sakurai, K. Fujii, H. Watanabe, H. Tamura, *Biochem. Biophys. Res. Commun.* **1995**, *214*, 1095–1101.
[64] K. Fukui, Y. Fujisawa, H. Ohya-Nishiguchi, H. Kamada, H. Sakurai, *J. Inorg. Biochem.* **1999**, *77*, 215–224.
[65] K. H. Thompson, J. H. McNeill, C. Orvig, *Chem. Rev.* **1999**, *99*, 2561–2572.
[66] J. Gätjens, B. Meier, T. Kiss, E. M. Nagy, P. Buglyó, H. Sakurai, K. Kawabe, D. Rehder, *Chem. Eur. J.* **2003**, *9*, 2924–2935.
[67] For more information and availability, please visit the website www.chem.umu.se/dep/inorgchem/samarbeta/WinSGW_eng.stm.
[68] G. Eriksson, *Anal. Chim. Acta* **1979**, *112*, 375–383.


 © 2006 Wiley-VCH Verlag GmbH & Co. KGaA, Weinheim 

[69] H. Schmidt, I. Andersson, D. Rehder, L. Pettersson, *Chem. Eur. J.* **2001**, *7*, 251–257.
[70] N. D. Chasteen, E. M. Lord, H. J. Thompson, J. K. Grady, *Biochim. Biophys. Acta* **1986**, *884*, 84–92.
[71] B. D. Liboiron, K. H. Thompson, G. R. Hanson, E. Lam, N. Aebischer, C. Orvig, *J. Am. Chem. Soc.* **2005**, *127*, 5104–5115.
[72] V. G. Yuen, P. Caravan, L. Gelmini, N. Glover, J. H. McNeill, I. A. Setyawati, Y. Zhou, C. Orvig, *J. Inorg. Biochem.* **1997**, *68*, 109–116.

Received: April 21, 2006
Published Online: July 24, 2006

 © 2006 Wiley-VCH Verlag GmbH & Co. KGaA, Weinheim 

DOI: 10.1002/ejic.200600506

# Pressure-Induced Metal–Semiconductor–Metal Transitions in an MMX-Chain Complex, $Pt_2(C_2H_5CS_2)_4I$

**Atsushi Kobayashi,[a] Aya Tokunaga,[b] Ryuichi Ikeda,[b] Hajime Sagayama,[c] Yusuke Wakabayashi,[c] Hiroshi Sawa,[c] Masato Hedo,[d] Yoshiya Uwatoko,[d] and Hiroshi Kitagawa*[a]**

**Keywords:** Mixed-valent compounds / Conducting materials / MMX chain / Metal–insulator transition / High pressure

The electrical conductivity and X-ray diffraction measurements were performed for a highlyconductive halogen-bridged binuclear-metal mixed-valence complex (the so-called MMX chain), $Pt_2(C_2H_5CS_2)_4I$, under high pressure up to 2.5 GPa. The complex exhibited pressure-induced metal–semiconductor–metal transitions at 0.5 and 2.1 GPa. The X-ray diffuse scatterings were observed at $k = n+0.5$ ($n$: integer) under ambient pressure, which are derived from the charge-density wave (CDW: ···$Pt^{2+}$–$Pt^{2+}$···I–$Pt^{3+}$–$Pt^{3+}$–I···) fluctuation in the MMX chain. Above 0.5 GPa, where the pressure-induced metal–semiconductor transition occurred, these scatterings disappeared. The electronic phases under high pressure ($P$) were found to be attributable to the metallic averaged-valence state (AV: –$Pt^{2.5+}$–$Pt^{2.5+}$–I–$Pt^{2.5+}$–$Pt^{2.5+}$–I–) with CDW fluctuation of $P < 0.5$ GPa, semiconducting charge-polarization state (CP: ···$Pt^{2+}$–$Pt^{3+}$–I···$Pt^{2+}$–$Pt^{3+}$–I···) of $0.5 < P < 2.1$ GPa, and metallic AV state of $P > 2.1$ GPa. The electronic state of $Pt_2(C_2H_5CS_2)_4I$ is very sensitive to pressure, which implies that the phase competition among the CP, CDW, and AV phases is present in the MMX chain.
(© Wiley-VCH Verlag GmbH & Co. KGaA, 69451 Weinheim, Germany, 2006)

## Introduction

One-dimensional (1D) halogen-bridged mixed-valence binuclear-metal complexes (MMX chain) have drawn much attention because of their various electronic structures that originate from the internal degree of freedom of charge distribution in metal-dimer units as follows:[1–2]

(1) Averaged-valence (AV) phase
–$M^{2.5+}$–$M^{2.5+}$–X–$M^{2.5+}$–$M^{2.5+}$–X–

(2) Charge-polarization (CP) phase
···$M^{2+}$–$M^{3+}$–X···$M^{2+}$–$M^{3+}$–X···

(3) Charge-density wave (CDW) phase
···$M^{2+}$–$M^{2+}$···X–$M^{3+}$–$M^{3+}$–X···

(4) Alternate-charge-polarization (ACP) phase
···$M^{2+}$–$M^{3+}$–X–$M^{3+}$–$M^{2+}$···X···

$Pt_2(C_2H_5CS_2)_4I$, which is an MMX chain complex as shown in Figure 1, exhibits a high electrical conduction and a metal–insulator (M–I) transition at 205 K.[3] This M–I transition temperature ($T_{MI}$) is relatively lower than typical 1D $d$-electron conductors in comparison with transition-metal complexes such as $K_2Pt(CN)_4Br_{0.3}\cdot nH_2O$ (commonly called KCP(Br); $T_{MI}$ = 250 K at 0 GPa).[4] It was revealed that the electronic state changes variously with decreasing temperature; the AV phase occurs with CDW fluctuation

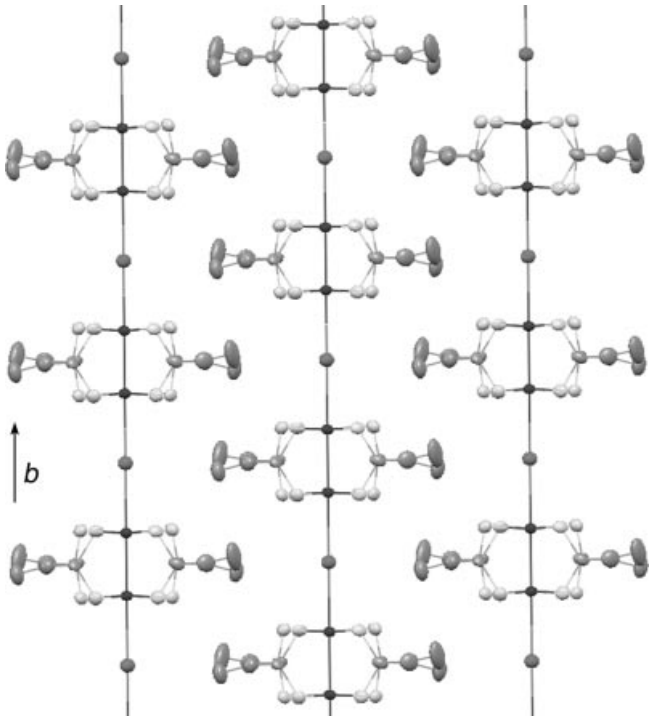


Figure 1. Chain structure of $Pt_2(C_2H_5CS_2)_4I$.

[a] Department of Chemistry, Faculty of Science, Kyushu University,
Hakozaki 6-10-1, Higashi-ku, Fukuoka 812-8581, Japan
[b] Department of Chemistry, University of Tsukuba,
Tennodai 1-1-1, Tsukuba, Ibaraki 305-8571, Japan
[c] Photon Factory, Institute of Materials Structure Science, High Energy Accelerator Research Organization,
Oho 1-1, Tsukuba, Ibaraki 305-0801, Japan
[d] Institute for Solid State Physics, The University of Tokyo,
Kashiwanoha 5-1-5, Kashiwa, Chiba 277-8581, Japan

 © 2006 Wiley-VCH Verlag GmbH & Co. KGaA, Weinheim 

above 205 K, the CP phase between 160–205 K, and the ACP phase below 160 K.[3,5] This phase competition is derived from the fact that the several interactions, such as the electron transfer integral ($t$), electron correlation (on-site ($U$) and inter-site ($V$) Coulombic repulsive energies), and electron-lattice interaction ($S$) are antagonistic to each other in this complex.[1d,1e,6]

The application of a high pressure to low-dimensional complexes gives rise to a drastic change in their physical properties because of an increase in the electron transfer integral $t$ and a suppression of electron-lattice interaction $S$.[7] For example, $(CH_3)_4N[Ni(dmit)_2]_2$ shows a pressure-induced transition at 0.32 GPa from the normal metallic state to the superconducting state below 3 K.[8] Since the title complex exhibits various electronic states, the application of pressure may create a novel electronic phase. Therefore, we have investigated the electronic state of the MMX-chain complex under high pressure by electrical resistivity and X-ray diffuse scattering measurements.

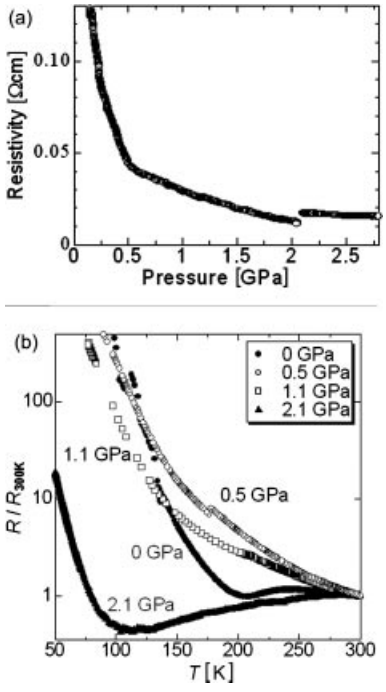


Figure 2. (a) Pressure dependence of the electrical resistivity at 298 K up to 2.5 GPa. (b) Temperature dependence of the electrical resistivity under several pressures (0, 0.5, 1.1 and 2.1 GPa).

## Results and Discussion

Figure 2(a) shows the pressure dependence of the electrical resistivity along the $b$-axis (parallel to the 1D chain) at 298 K. As the pressure is increased, the resistivity decreases rapidly up to 0.5 GPa and gradually between 0.5 and 2.1 GPa. The pressure coefficients of the resistivity below and above 0.5 GPa are –1.8 and –0.16 $GPa^{-1}$, respectively. Above 2.1 GPa, the resistivity is almost constant. The change in the pressure coefficients at 0.5 and 2.1 GPa implies that some phase transitions occur at these pressure points. A small resistance jump observed at 2.1 GPa is due to the resistance hysteresis derived from a cycle of cooling and heating processes in the electrical conductivity measurements.

The temperature dependences of the electrical resistivity at 0, 0.5, 1.1, and 2.1 GPa along the $b$-axis are shown in Figure 2(b). The resistivity is normalized at 300 K. At ambient pressure, $Pt_2(C_2H_5CS_2)_4I$ exhibited metallic conduction ($\approx$ 5 $Scm^{-1}$ at 300 K) and underwent a metal–insulator transition at 205 K, which is consistent with our previous work.[3] As a little pressure was applied, a pressure-induced metal–semiconductor transition occurred at 0.5 GPa; the metallic conduction disappeared and a behavior consistent with a semiconductor was observed in the whole temperature range. This pressure-induced metal–semiconductor transition is in agreement with the discontinuity of the pressure coefficient observed at 0.5 GPa [Figure 2(a)]. The activation energy decreased with applied pressures from 72 meV at 0.5 GPa to 54 meV at 1.1 GPa, which is considered to be due to an increase in the bandwidth $W$ ($\approx 4t$ for 1D electronic system). At 2.1 GPa, metallic behavior was again observed, and an M–I transition occurred at 114 K. This pressure-induced semiconductor–metal transition is also in agreement with the discontinuity of the pressure coefficient observed at 2.1 GPa. Compared with the $T_{MI}$ = 210 K of KCP(Br) under 3.2 GPa,[4d] the transition temperature 114 K is a significantly lower value, which means that the metallic state of $Pt_2(C_2H_5CS_2)_4I$ is very stable as a 1D electronic system.

To clarify the electronic state under high pressure, an X-ray diffraction measurement was performed on a single-crystal with a diamond-anvil cell at room temperature.[8] Figure 3(a) shows the X-ray diffraction photograph taken at 0.1 GPa. Diffuse scatterings were clearly observed at $k = n + 0.5$ ($n$: integer), which corresponds to the CDW fluctuation that exists at ambient pressure as mentioned above. The intensities of the pixels located on the solid-line arrow from A to B in Figure 3(a) are shown in Figure 3(b). These scatterings observed at $k = n + 0.5$ disappeared gradually with increasing pressure, and were hardly observed above 0.5 GPa. The disappearance of these diffuse scatterings indicates that the CDW fluctuation is lost above 0.5 GPa where the pressure coefficient changed, as shown in Figure 2. Since no remarkable change in X-ray diffraction photographs was observed in the pressure region between 0.5 and 2.5 GPa, the superstructures with twofold periodic ordering such as CDW or ACP are absent in the high-pressure range.

In general, the application of high pressure to the complex suppresses the electron-lattice interaction $S$ and increases the electron transfer integral $t$ because of the increase in the elastic energy and the decrease in the interatomic distance. This in turn results in an increase in the conductivity, and the behavior of the complex tends to change from an insulator to a semiconductor or a metallic species.[7] Actually, with pressure the conductivity of

 © 2006 Wiley-VCH Verlag GmbH & Co. KGaA, Weinheim 

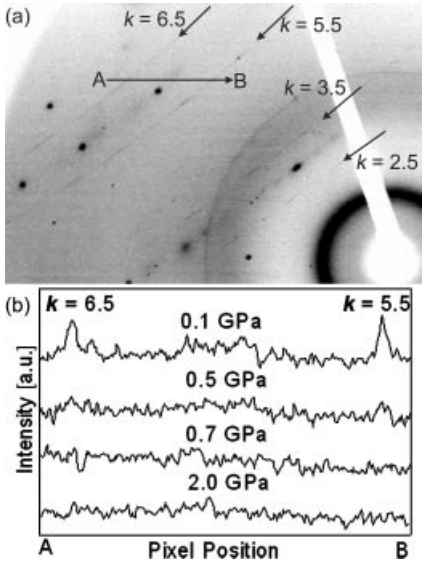


Figure 3. (a) X-ray diffraction photograph under 0.1 GPa at room temperature. (b) Intensity on the solid-line arrow from A to B in Figure 3(a) under several pressures (0.1, 0.5, 0.7 and 2.0 GPa).

$Pt_2(C_2H_5CS_2)_4I$ increased drastically and the CDW fluctuation of ···$Pt^{2+}$–$Pt^{2+}$···I–$Pt^{3+}$–$Pt^{3+}$–I··· was suppressed, which would disturb the itinerancy of the conduction of the electrons. The pressure-induced metal–semiconductor transition was nevertheless observed at 0.5 GPa. Recent theoretical calculations performed by Yamamoto et al. pointed out that the inter-site Coulombic repulsive energy $V$ increases as the interatomic distance is decreased with pressure, and in the case of $V > t$, the CP phase of ···$Pt^{2+}$–$Pt^{3+}$–I···$Pt^{2+}$–$Pt^{3+}$–I··· could be stabilized.[6a,6b] The CP phase can be regarded as a charge-ordered (or charge-localized) state, that is, a Mott insulating state.[9] With the consideration of the absence of any twofold structures, the semiconducting state of the complex in the region of 0.5–2.1 GPa is attributable to the CP phase. Above 2.1 GPa, the metallic phase appeared again in the temperature range of 114–300 K, which would be derived from the AV state of –$Pt^{2.5+}$–$Pt^{2.5+}$–I–$Pt^{2.5+}$–$Pt^{2.5+}$–I– under the delicate competitive condition of $t > V$. No twofold structures were observed, which is not in conflict with the AV state.

In summary, the electrical conductivity and X-ray diffraction measurements under high pressure have been performed for a highly conductive MMX-chain complex, $Pt_2(C_2H_5CS_2)_4I$. Pressure-induced metal–semiconductor–metal transitions were observed at 0.5 and 2.1 GPa, which is considered to be derived from the phase transitions of the metallic AV state with CDW fluctuation to the semiconducting CP state, and from the CP state to the metallic AV state, respectively. The electronic state of $Pt_2(C_2H_5CS_2)_4I$ is very sensitive to pressure, which implies that the phase competition among the CP, CDW, and AV phases is present in the MMX chain. To determine the origin of these metal–semiconductor–metal transitions, theoretical calculations, Raman and IR spectroscopic studies under high pressure, are in progress.

## Experimental Section

**Synthesis:** Single-crystals of $Pt_2(C_2H_5CS_2)_4I$ were prepared according to the literature (see ref.[3a]).

**Electrical Conductivity:** The dc electrical resistivity of $Pt_2(C_2H_5CS_2)_4I$ along the *b*-axis (parallel to the 1D chain) was measured for several single-crystals with the four-probe-method with the use of a clump-cell and a cubic-anvil press system at the ISSP, the University of Tokyo.

**X-ray Diffraction:** X-ray diffraction measurements under high pressure were performed with a diamond-anvil cell at the BL-1B beamline in KEK-PF ($\lambda$ = 0.688 Å). Pressure was calibrated by the ruby luminescence technique.

## Acknowledgments

This work was partly supported by a Grant-in-Aid for Scientific Research on Priority Areas (Chemistry of Coordination Space, No. 16074212) and the Joint Project for Chemical Synthesis Core Research Institutions, from the Ministry of Education, Culture, Sports, Science and Technology, Japan, a Grant-in-Aid for Scientific Researches (B) Nos. 14340215, 16350033, and 18350031 from the Japan Society for the Promotion of Science and the Kurata Memorial Hitachi Science and Technology Foundation.

[1] a) C. Bellitto, A. Flamini, L. Gastaldi, L. Scaramuzza, *Inorg. Chem.* **1983**, *22*, 444–449; b) C. Bellitto, G. Dessy, V. Fares, *Inorg. Chem.* **1985**, *24*, 2815–2820; c) H. Kitagawa, N. Onodera, J.-S. Ahn, T. Mitani, *Synth. Met.* **1997**, *86*, 1931–1932; d) H. Kitagawa, T. Mitani, *Coord. Chem. Rev.* **1999**, *190–192*, 1169–1184; e) H. Kitagawa, N. Onodera, T. Sonoyama, M. Yamamoto, T. Fukawa, T. Mitani, M. Seto, Y. Maeda, *J. Am. Chem. Soc.* **1999**, *121*, 10068–10080; f) H. Kitagawa, T. Sonoyama, T. Mitani, *Synth. Met.* **1999**, *103*, 2159–2160; g) Y. Miyazaki, Q. Wang, A. Sato, K. Saito, M. Yamamoto, H. Kitagawa, T. Mitani, M. Sorai, *J. Phys. Chem. B* **2002**, *106*, 197–202.

[2] a) C.-M. Che, H. F. Herbstein, P. W. Schaefer, E. R. Marsh, H. B. Gray, *J. Am. Chem. Soc.* **1983**, *105*, 4604–4607; b) L. G. Butler, M. H. Zietlow, C.-M. Che, W. P. Schaefer, S. Sridhar, P. J. Grunthaner, B. I. Swanson, R. J. Clark, H. B. Gray, *J. Am. Chem. Soc.* **1988**, *110*, 1155–1162; c) H. Matsuzaki, T. Matsuoka, H. Kishida, K. Takizawa, H. Miyasaka, K. Sugiura, M. Yamashita, *Phys. Rev. Lett.* **2003**, *90*, 046401; d) H. Matsuzaki, H. Kishida, H. Okamoto, K. Takizawa, S. Matsunaga, S. Takaishi, H. Miyasaka, K. Sugiura, M. Yamashita, *Angew. Chem. Int. Ed.* **2005**, *44*, 3240–3243.

[3] a) M. Mitsumi, T. Murase, H. Kishida, T. Yoshinari, Y. Ozawa, K. Toriumi, T. Sonoyama, H. Kitagawa, T. Mitani, *J. Am. Chem. Soc.* **2001**, *123*, 11179–11192; b) M. Mitsumi, K. Kitamura, A. Morinaga, Y. Ozawa, M. Kobayashi, K. Toriumi, Y. Iso, H. Kitagawa, T. Mitani, *Angew. Chem. Int. Ed.* **2002**, *41*, 2767–2771; c) A. Kobayashi, H. Kitagawa, R. Ikeda, S. Kitao, M. Seto, M. Mitsumi, K. Toriumi, *Synth. Met.* **2003**, *135–136*, 405–406; d) A. Kobayashi, T. Kojima, R. Ikeda, H. Kitagawa, *Inorg. Chem.* **2006**, *45*, 322–327.

[4] a) K. Krogmann, *Angew. Chem. Int. Ed. Engl.* **1969**, *8*, 35; b) D. Kuze, H. R. Zeller, *Phys. Rev. Lett.* **1971**, *27*, 1060–1063; c) H. R. Zeller, A. Beck, *J. Phys. Chem. Solids* **1974**, *35*, 77–80; d) M. Thielemans, R. Deltour, D. Jerome, J. R. Cooper, *Solid State Commun.* **1976**, *19*, 21–27.

[5] Y. Wakabayashi, A. Kobayashi, H. Sawa, H. Ohsumi, N. Ikeda, H. Kitagawa, *J. Am. Chem. Soc.* **2006**, *128*, 6676–6682.

[6] a) S. Yamamoto, *J. Phys. Chem. Solids* **2002**, *63*, 1489–1493; b) S. Yamamoto, *J. Phys. Soc. Jpn.* **2001**, *70*, 1198–1201; c) M. Kuwabara, K. Yonemitsu, *J. Mater. Chem.* **2001**, *11*, 2163–2175.

 © 2006 Wiley-VCH Verlag GmbH & Co. KGaA, Weinheim 

[7] a) E. Conwell, *Semiconductors and Semimetals*, Academic Press, London, **1988**, vol. 27, ch. 3, pp. 166–170; b) J. S. Miller (Ed.), *Extended Linear Chain Compounds*, Plenum, New York, 1982, vol. 1, ch. 9, p. 435; c) L. V. Interrante, K. W. Browall, F. P. Bundy, *Inorg. Chem.* **1974**, *13*, 1162–1166.
[8] a) A. Kobayashi, H. Kim, Y. Sasaki, R. Kato, H. Kobayashi, S. Moriyama, Y. Nishino, K. Kajita, W. Sasaki, *Chem. Lett.* **1987**, 1819–1822; b) K. Kajita, Y. Nishino, S. Moriyama, R. Kato, H. Kobayashi, W. Sasaki, A. Kobayashi, H. Kim, Y. Sasaki, *Solid State Commun.* **1988**, *65*, 361–363; c) H. Kim, A. Kobayashi, Y. Sasaki, R. Kato, H. Kobayashi, *Chem. Lett.* **1987**, 1799–1802.
[9] a) N. F. Mott, *Metal–Insulator Transitions*, Taylor and Francis, London, **1974**; b) I. G. Austin, N. F. Mott, *Science* **1970**, *168*, 71–77; c) A. Zylbersztejn, N. F. Mott, *Phys. Rev. B* **1975**, *11*, 4383–4395.

Received: May 31, 2006
Published Online: August 10, 2006

 © 2006 Wiley-VCH Verlag GmbH & Co. KGaA, Weinheim 

DOI: 10.1002/ejic.200600517

# Pressure Effect Investigations on the Spin Crossover Systems {Fe[$H_2B(pz)_2]_2$(bipy)} and {Fe[$H_2B(pz)_2]_2$(phen)}

**Ana Galet,[b] Ana Belén Gaspar,[a] Gloria Agusti,[a] M. Carmen Muñoz,[b] Georgii Levchenko,[c] and José Antonio Real*[a]**

**Keywords:** Spin transition / Bistability / Cooperative effects / Pressure / Phase Transitions

Pressure effect studies on the spin crossover behaviour of the mononuclear compounds {Fe[$H_2B(pz)_2]_2$(bipy)}(**1**) and {Fe[$H_2B(pz)_2]_2$(phen)}(**2**) have been performed in the range of $10^5$ Pa–1.02 GPa at variable temperatures (100–310 K). Continuous spin transitions and displacement of its characteristic temperature has been observed for **1** with increasing pressure. Meanwhile the response of **2** under applied pressures is quite unexpected, and can only be understood in terms of a crystallographic phase transition or change in the bulk modulus of the compound.
(© Wiley-VCH Verlag GmbH & Co. KGaA, 69451 Weinheim, Germany, 2006)

## Introduction

The ability of spin crossover (SCO) materials to change their magnetic, structural, dielectric and optical properties, induced by a variation of temperature and/or pressure or light, has led to an increase in the interest of their potential use in technological applications. Because of their switching properties, SCO materials are potentially useful for rewritable optical, thermal or pressure memories at a nanometric scale.[1–6]

While thermally induced spin crossover behaviour in $Fe^{II}$ complexes is increasingly common, pressure induce high and low spin (HS and LS) $Fe^{II}$ complexes are scarcely reported in the literature. Systematic and detailed studies related to the concerted action of both temperature and pressure variation on SCO compounds have only recently become possible with the development of special hydrostatic pressure cells in connection with magnetic susceptibility, optical and Mössbauer measurements, EXAFS and vibrational spectroscopy.[7–8] Here we present pressure effect investigations on the magnetic behaviour of {Fe[$H_2B(pz)_2]_2$(bipy)}(**1**) and {Fe[$H_2B(pz)_2]_2$(phen)} (**2**) complexes carried out in the range of $10^5$ Pa–1.2 GPa.

Both **1** and **2** undergo thermal- and light-induced SCO.[9] The thermal spin transition of **2** is more cooperative than that of **1**, as shown by the more abrupt spin transition that takes place with hysteresis (with characteristic temperatures of $T_c\downarrow$ = 165 K and $T_c\uparrow$ = 169 K). Structural data has been previously reported for both the HS and LS states.[10] As illustrated in Figure 1, the structures of **1** and **2** are composed of mononuclear neutral species where the positive charge of the iron(II) ion is neutralized by the coordination of two bidentate dihydrobis(pyrazolyl)borate $[H_2B(pz)_2]^-$ anions; bipy or phen neutral ligands are then used to fill the iron(II) coordination sphere. The molecular structures for both compounds are very similar with Fe–N bond lengths in the 2.212–2.158 Å and 2.007–1.996 Å range for the HS and LS states, respectively. Contrary to **1**, the spin transition of **2** is accompanied by a crystallographic phase transition [*C*2/*c* (HS) and $P\bar{1}$(LS)].[10]

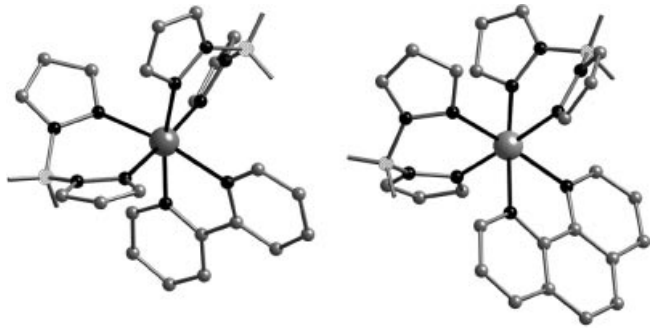

Figure 1. Molecular structure of **1** (left) and **2** (right).

## Results and Discussion

Figure 2 gathers a collection of $\chi_M T$ versus $T$ curves ($\chi_M$ is the molar magnetic susceptibility, and $T$ the temperature) at different hydrostatic pressures for complex **1**. The measurements have been performed at the rate of 1 K·min$^{-1}$ on single-microcrystals. At 300 K and $10^5$ Pa, a $\chi_M T$ value of 3.52 cm$^3$·K·mol$^{-1}$ indicates a S = 2 spin state configuration

[a] Institut de Ciència Molecular/Departament de Química Inorgànica, Universitat de València, Edifici de Instituts de Paterna, Apartat de Correus 22085, 46071 València, Spain
[b] Departament de Física Aplicada, Universitat Politécnica de València, Camí de Vera s/n, 46022, València, Spain
[c] Donetsk Physico-Thechnical Institute, NAS of Ukraine, R. Luxemburg 72, 83114 Donetsk, Ukraine

 © 2006 Wiley-VCH Verlag GmbH & Co. KGaA, Weinheim 

for the iron(II) ions. $\chi_M T$ remains constant down to 220 K, where it progressively diminishes as a consequence of the spin transition to the S = 0 spin state and attains a value of 0.06 $cm^3 \cdot K \cdot mol^{-1}$ at 100 K. The transition is complete and relatively abrupt. The temperature at which the number of molecules in the HS and LS states is equal, $T_{1/2}$, is 160 K. Application of pressures as high as 0.26 GPa have a strong effect on the $T_{1/2}$ value and shifts it upwards to 210 K. At this pressure, the $\chi_M T$ value at 300 K is slightly lower than that observed at atmospheric pressure which indicates that a small amount of molecules are in the LS state (300 K: 3.42 $cm^3 \cdot K \cdot mol^{-1}$, 97% HS molecules). An increase in the pressure up to 0.4 and 0.5 Gpa results in a displacement of $T_{1/2}$ to 233 K and 255 K, respectively. At room temperature, the $\chi_M T$ value at these two last pressures also decreases to 3.23 $cm^3 \cdot K \cdot mol^{-1}$ and 3.12 $cm^3 \cdot K \cdot mol^{-1}$, respectively.

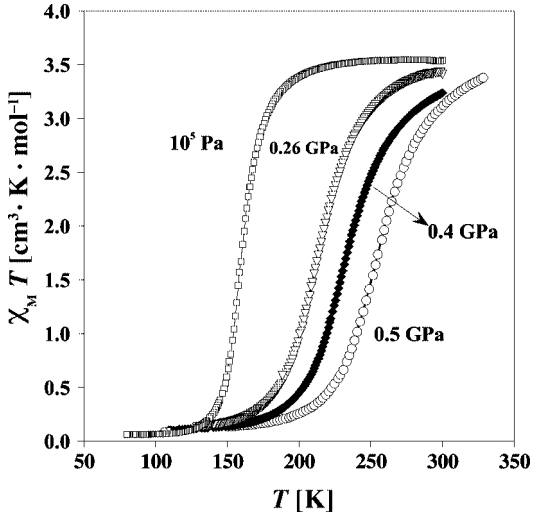


Figure 2. Thermal dependence of $\chi_M T$ at different pressures for **1**.

It is worth mentioning the remarkable continuous character of the spin transition as pressure is increased. The spin crossover takes place in temperature intervals of 150 K, whereas at $10^5$ Pa the spin crossover occurs within 70 K. Also, the linear pressure dependence of $T_{1/2}$ for **1** should be noted. The slope of the line in the $T_{1/2}$ versus $P$ plot, $dT_{1/2}/dP$ = 187.5 $K \cdot GPa^{-1}$ (Figure 4), is in the range of values observed for several mononuclear compounds such as $[Fe(abpt)_2(NCS)_2]$ polymorph B,[11] $[Fe(phen)_2(NCS)_2]$ polymorph II,[12] $[Fe(dpa)_2(NCS)_2]$[13] and $[Fe(pic)_3]Cl_2 \cdot EtOH$[14] (Table 1).

Table 1. $dT_{1/2}/dP$ in $K \cdot GPa^{-1}$.

| | |
|---|---|
| $[Fe(abpt)_2(NCS)_2]$ | 176 |
| $[Fe(phen)_2(NCS)_2]$ polymorph II | 220 |
| $[Fe(dpa)_2(NCS)_2]$ | 187.5 |
| $[Fe(pic)_3]Cl_2 \cdot EtOH$ | 150 |

Figure 3 shows the thermal dependence of **2** for $\chi_M T$ at different pressures. As for **1**, the measurements have been performed on single-microcrystals in the cooling and warming modes at a rate of 1 $K \cdot min^{-1}$. At 300 K and atmospheric pressure, the $\chi_M T$ value is 3.60 $cm^3 \cdot K \cdot mol^{-1}$, which indicates a HS configuration of the iron(II) ions. This value remains virtually constant up to the point of the spin transition, which takes place abruptly at $T_c\downarrow$ = 165 K and $T_c\uparrow$ = 169 K. The application of a hydrostatic pressure of 0.19 GPa dramatically influences the spin crossover behaviour of **2** particularly in the width of the hysteresis loop. Indeed, $\Delta T_c$ is equal to 20 K. Meanwhile, at atmospheric pressure $\Delta T_c$ is only 4 K. At 0.19 GPa, the critical temperature for the cooling mode is $T_c\downarrow$ = 169 K and for the warming mode it is $T_c\uparrow$ = 189 K. Another remarkable fact is the decrease in the abruptness of the spin transition in the cooling mode. This is in contrast to the transition in the warming mode, which remains steep. A further increase in the pressure up to 0.33 GPa results in a considerable shift of the spin transition to higher temperatures, $T_c\downarrow$ = 238 K and $T_c\uparrow$ = 240 K, with the hysteresis width being very narrow. A complete transformation to a second order phase transition occurs at 0.55 GPa, where $T_{1/2}$ is approximately 270 K. At 1.02 GPa, almost all of the molecules are in the LS state at room temperature. Reversibility of these measurements was checked after a complete relaxation of the pressure because the magnetic behaviour of **2** at $10^5$ Pa was perfectly reproducible. Moreover, the magnetic behaviour of **2** in the range of $10^5$ Pa–1.02 GPa was investigated in two independent experiments, and the exact same results were obtained.

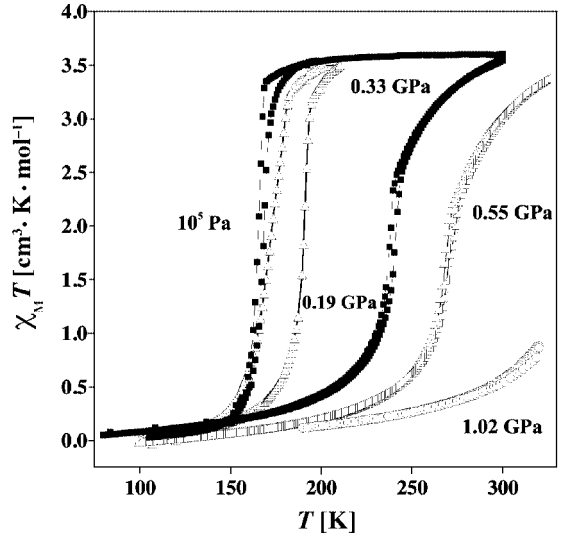


Figure 3. Thermal dependence of $\chi_M T$ at different pressures for **2**.

Figure 4 displays the pressure dependence of the average $T_c^{av}$ values calculated as $T_c^{av} = (T_c^{down} + T_c^{up})/2$ for **2**. As it can be seen, there is a strong nonlinearity in the case of compound **2** that contrasts the almost linear dependence observed for **1**. This is an unexpected result in view of the fact that the mean field theory of phase transitions in SCO compounds predicts a decrease in the hysteresis width and in the slope of the transition curve with an increase in the pressure. The hysteresis vanishes at a critical pressure, and at even higher pressures the transition transforms into a second order continuous phase transition.[7,8,15] However, there are several SCO systems in which the effect of pres-

 © 2006 Wiley-VCH Verlag GmbH & Co. KGaA, Weinheim 

sure on the SCO behaviour cannot be adequately described by this theory. Occurrence of structural phase transitions and/or a change in the bulk modulus of the materials under the applied pressure has been proposed for the observed anomalous behaviour (e.g. increase in the hysteresis width, nonlinear behaviour of $T_c(P)$ versus $P$).[5,7,8,16]

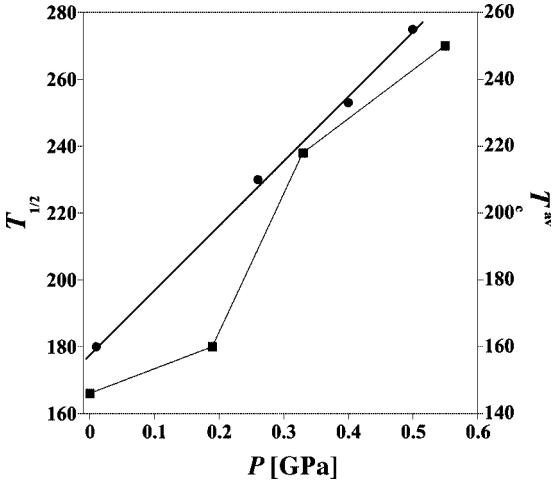


Figure 4. $T_{1/2}$ versus $P$ plots for **1** (filled circles) and $T_{av}$ versus $P$ plot for **2** (filled squares). The straight line corresponds to the linear fit for **1**.

As mentioned above, the crystallographic phase transition that involves the space group change $C2/c$ (HS) ↔ $P\bar{1}$(LS) takes place concomitantly with the thermally induced HS ↔ LS spin transition in **2**. The response of **2** under the applied pressures increases the hysteresis width at 0.19 GPa, and the nonlinear behaviour of $T_{1/2}$ versus $P$ could be due to the occurrence of a crystallographic phase transition under these applied pressures. The unexpected pressure effects will be understood from the crystal structure determination under applied pressure and, of course, at variable temperature.

## Experimental Section

**Synthesis of 1 and 2:** Single-crystals of both compounds were obtained as discussed previously in the literature.[9]

**Magnetic Susceptibility Measurements Under Hydrostatic Pressure:** The variable-temperature magnetic susceptibility measurements were performed on small single-crystals with a Quantum Design MPMS2 SQUID susceptometer equipped with a 5.5 T magnet and operated at 1 T and 1.8–375 K. The hydrostatic pressure cell was made of hardened beryllium bronze with silicon oil as the pressure-transmitting medium, and was operated in the pressures range $10^5$ Pa–1.2 GPa (accuracy $\approx \pm 0.025$ GPa). Cylindrically shaped powder sample holders with dimensions of 1 mm in diameter and 5–7 mm in length were used. The pressure dependence of the superconducting transition temperature of the built-in pressure sensor, which is made of high purity tin, was used to measure the pressure.[17] Experimental data were corrected for diamagnetism with Pascal's constants.

## Acknowledgments

Financial support is acknowledged from the Spanish Ministerio de Educacion y Ciencia (MEC) (CTQ 2004-03456/BQU) and Generalitat Valenciana (ACOMP06/048). A. G. thanks the Universitat Politécnica de València for a predoctoral fellowship. A. B. G. thanks the Spanish MEC for a research contract (Programa Ramón y Cajal).

[1] P. Gütlich, H. A. Goodwin (Eds.), *Topics in Current Chemistry Vols. 233–235: Spin Crossover in Transition Metal Compounds*, Springer, Berlin, **2004**.
[2] a) J. A. Real, A. B. Gaspar, M. C. Muñoz, *Dalton Trans.* **2005**, 2062; b) A. B. Gaspar, V. Ksenofontov, M. Seredyuk, P. Gütlich, *Coord. Chem. Rev.* **2005**, *249*, 2661.
[3] J. A. Real, A. B. Gaspar, V. Niel, M. C. Muñoz, *Coord. Chem. Rev.* **2003**, *236*, 121.
[4] P. Gütlich, A. Hauser, H. Spiering, *Angew. Chem. Int. Ed. Engl.* **1994**, *33*, 2024.
[5] A. Galet, A. B. Gaspar, M. C. Muñoz, G. V. Bukin, G. Levchenko, J. A. Real, *Adv. Mater.* **2005**, *17*, 2949.
[6] a) O. Kahn, C. J. Martinez, *Science* **1998**, *279*, 44; b) O. Kahn, J. Kröber, C. Jay, *Adv. Mater.* **1992**, *4*, 718.
[7] P. Gütlich, V. Ksenofontov, A. B. Gaspar, *Coord. Chem. Rev.* **2005**, *249*, 1811.
[8] V. Ksenofontov, A. B. Gaspar, P. Gütlich, *Top. Curr. Chem.* **2004**, *235*, 23.
[9] a) J. A. Real, M. C. Muñoz, J. Faus, X. Solans, *Inorg. Chem.* **1997**, *36*, 3008; b) N. Moliner, L. Salmon, L. Capes, M. C. Muñoz, J. F. Lètard, A. Bouseksou, J. P. Tuchages, J. J. McGarvey, A. C. Dennis, M. Castro, R. Burriel, J. A. Real, *J. Phys. Chem. B* **2002**, *106*, 4276.
[10] A. L. Thompson, A. E. Goeta, J. A. Real, A. Galet, M. C. Muñoz, *Chem. Commun.* **2004**, 1390.
[11] A. B. Gaspar, M. C. Muñoz, N. Moliner, V. Ksenofontov, G. Levchenko, P. Gütlich, J. A. Real, *Monatsh. Chem.* **2003**, *134*, 285.
[12] V. Ksenofontov, A. B. Gaspar, G. Levchenko, B. Fitzsimmons, P. Gütlich, *J. Phys. Chem. B* **2004**, *108*, 7723.
[13] A. B. Gaspar, G. Agustí, V. Martínez, M. C. Muñoz, G. Levchenko, J. A. Real, *Inorg. Chim. Acta* **2005**, *358*, 4089.
[14] C. P. Köhler, R. Jakobi, E. Meissner, H. Wiehl, H. Spiering, P. Gütlich, *J. Phys. Chem. Solids* **1990**, *51*, 239.
[15] C. P. Slichter, H. G. Drickamer, *J. Chem. Phys.* **1972**, *56*, 2142.
[16] V. Ksenofontov, H. Spiering, A. Schreiner, G. Levchenko, H. A. Goodwin, P. Gütlich, *J. Phys. Chem. Solids* **1999**, *60*, 393.
[17] M. Baran, V. P. Dyakonov, L. Gladczuk, G. G. Levchenko, S. Piechota, G. Szymczak, *Physica C* **1995**, *241*, 383.

Received: June 2, 2006
Published Online: August 7, 2006

 © 2006 Wiley-VCH Verlag GmbH & Co. KGaA, Weinheim 

DOI: 10.1002/ejic.200600130

# Characterization and Insulin-Mimetic Potential of Oxidovanadium(IV) Complexes Derived from Monoesters and -carboxylates of 2,5-Dipicolinic Acid

**Jessica Gätjens,*[a][‡] Beate Meier[b] Yusuke Adachi,[c] Hiromu Sakurai,[c] and Dieter Rehder[a]**

**Keywords:** Vanadium / N,O Ligands / Picolinates / Insulin mimesis

The monomethyl ester 2MeOdipicH (**1**) of 2,5-dipicolinic acid, characterized as its magnesium salt $[Mg(H_2O)_6](2MeOdipic)_2$, was converted, via the diesters 2MeO-5ROdipic and the copper complexes $[Cu(5ROdipic)_2]$, to the ligands 5ROdipicH (R = *i*Pr **2a**, (*S*)-2-Bu **2b**). The proligands 2MeO-5ROdipic (with R = diisopropyl-D-galactose **2c**, *myo*-inositol-orthoformate **2d**) and 2MeO-5R′NHdipic (where R′ represents the ethyl-protected L-amino acid residues Gly **3a**, Ala **3b**, Val **3c** and Phe **3d**) were obtained from 2-MeO-5Cldipic and the amino acid ethyl esters. Reaction of **2** and **3** with $VOSO_4$ afforded the complexes $[VO(H_2O)(5ROdipic)_2]$ (**4a–d**) and $[VO(H_2O)(5R'NHdipic)_2]$, **5a–d**, respectively. $[Mg(H_2O)_6](2MeOdipic)_2{\cdot}4H_2O$, **2b**, **3a** and **4a**$\cdot 0.5H_2O$ were characterized by single-crystal X-ray diffraction analysis. Selected type **4** and **5** complexes were submitted to in vitro tests (fibroblasts, SV 3T3 mice fibroblasts) for their uptake kinetics and insulin-mimetic behavior. The compounds were comparable to insulin in their ability to stimulate cellular glucose uptake and metabolism. In vitro tests with rat adipocytes showed that the complexes also mimic the ability of insulin to inhibit lipolysis.

(© Wiley-VCH Verlag GmbH & Co. KGaA, 69451 Weinheim, Germany, 2006)

## Introduction

During the last two decades, in vitro and in vivo studies have demonstrated the potential of many vanadium compounds as insulin-mimetic (or insulin-enhancing) agents.[1–3] Among those which have been shown to be effective are bis(maltolato)oxidovanadium complexes,[4a] which successfully passed clinical tests phase I,[4b] $[VO(pic)_2]$ which normalizes serum glucose and fatty acid levels in rats with streptozotozin-induced diabetes type 1,[5] and $[VO_2(H_2O)(2,6\text{-dipic})]^-$, which had beneficial effects in cats suffering from diabetes type 2.[6] Picolinato complexes of vanadium appear to be generally effective,[7] the extent, however, to which they actually mimic the involvement of insulin in the glucose and lipid metabolisms is subject to variations in the coordination periphery. We have recently shown that the methyl ester derivative $[VO(H_2O)(5MeOdipic)_2]$, where 5MeOdipic is the monomethyl ester of 2,5-dipicolinate, is clearly more effective than the corresponding ethyl ester both in the ability to trigger cellular glucose uptake (and metabolism) and to inhibit lipolysis.[8] These differences in impact correlate with the net amount of vanadium taken up by the cells, possibly indicative for a balanced hydro/lipophilicity being a key factor in efficacy.

An apparent advantage of vanadium complexes in the treatment of *diabetes mellitus* type 1 (lacking insulin production) and type 2 (tolerance/resistance against insulin) is their application per os, and the possibility to design the compounds so as to provide minimal toxicity and optimal efficiency along with stability against redox- and hydrolytic break-down. The compound has to survive the acidic conditions pertinent to the stomach (pH typically around 2), as well as the slightly alkaline conditions in the small intestines (pH 7–8) and the blood stream (pH 7.35). It has to resist to a certain extent competing ligands such as the plasma constituents citrate, phosphate and transferrin in order to preserve the information implanted by the specific properties of the ligands used in the synthesis of the potential drug. The complex should be easily absorbed in the gastrointestinal tract, transported by the blood stream at least partly intact, and traffic across the cell membrane. Oxidovanadium complexes carrying monoesters of 2,5-dipicolinic acid as ligands have been shown to fulfil several of these conditions.[8] Picolinates are natural metabolites; toxicity by degradation of the complexes thus will be minimized. In order to improve the trans-membrane transport, a fine-tuning of the hydro/lipophilicity by choosing the "correct" sub-

[a] Institute of Inorganic and Applied Chemistry, University of Hamburg,
Martin-Luther-King-Platz 6, 20146 Hamburg, Germany
E-Mail: jgaetjens@yahoo.de
dieter.rehder@chemie.uni-hamburg.de
[b] bcm-research,
Entrischenbrunn 12, 85307 Entrischenbrunn, Germany
[c] Department of Analytical and Bioinorganic Chemistry, Kyoto Pharmaceutical University,
Kyoto, 607-8414, Japan
[‡] Present address: Department of Chemistry, University of Michigan,
930 N. University Ave., Ann Arbor, MI 48109, USA,
Fax: +1-734-936-7628

 © 2006 Wiley-VCH Verlag GmbH & Co. KGaA, Weinheim 

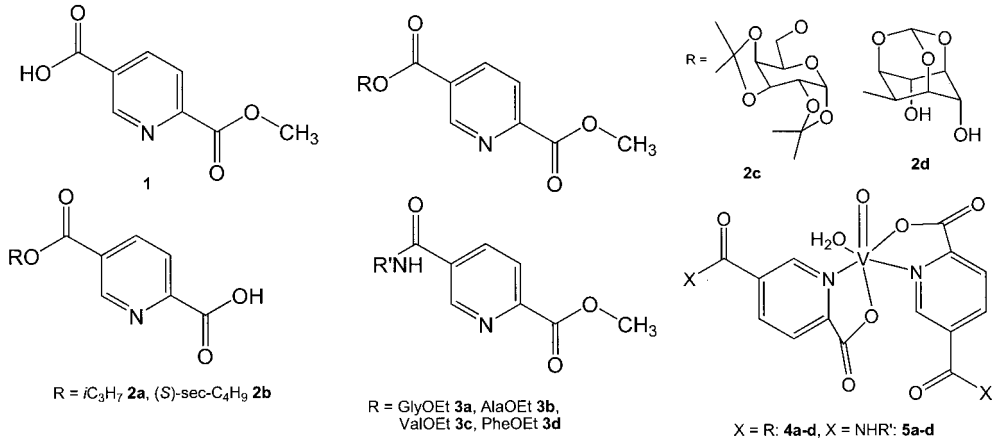


Scheme 1.

stituents in the ligand periphery is one option. A second option is to attach groups to the periphery for which membrane receptors exist and which can thus be recognized by the cell. Following these concepts, we have extended earlier investigations on picolinates to galactose and inositol derivatives on the one hand, and carboxamides derived from amino acids on the other hand. Scheme 1 gives an overview of the types of compounds discussed in the present work. Along with the vanadium complexes and their in vitro insulin-mimetic properties, structural features of ligands and ligand precursors will be described.

## Results and Discussion

### Synthesis, Characterization and Structure Determination

The syntheses of the ligands **2a**–**b** followed the route depicted in Scheme 2. 6-(Methoxycarbonyl)pyridine-3-carboxylic acid (**1**) was converted into the corresponding acyl chloride by reaction with thionyl chloride. Addition of a solution of the acid chloride in toluene to a solution of the alcohol ROH (R = *i*Pr, (*S*)-*s*Bu, in 1.4 fold excess) in pyridine yielded the mixed diesters 2MeO-5ROdipic, which were converted via the copper complexes [Cu(5ROdipic)$_2$] into the acids 5ROdipicH, **2a**–**b**. For the structure of the anion of **1**, **1**H$_{-1}$, see below.

Single crystals of **2b** were grown from aqueous acetone solution. **2b** crystallizes in the monoclinic space group $P2_1$. Bond lengths and angles are in the expected range (Table 1). The molecular structure and a picture showing the hydrogen-bonding network are displayed in Figure 1. The molecules are linked through OH···N hydrogen bonds, comparable to the features exhibited by other members of this family of dipicolinic acid derivatives.[8]

The proligands **2c**–**d** were synthesized in analogy to the ligands **2a**–**b**, with the modification that equimolar amounts of acyl chloride and alcohol were reacted. The deprotection step via the copper complexes was omitted. The cleavage of the methyl ester group occurred in situ under the conditions chosen for the synthesis of the vanadium complexes and concomitantly with the coordination of the carboxylate function to vanadium.

For the syntheses of the amino acid derivatives **3a**–**d**, cf. Scheme 2, a solution of the acyl chloride in dichloromethane was treated with a solution containing the amino acid ethyl ester hydrochloride and triethylamine in $CH_2Cl_2$,

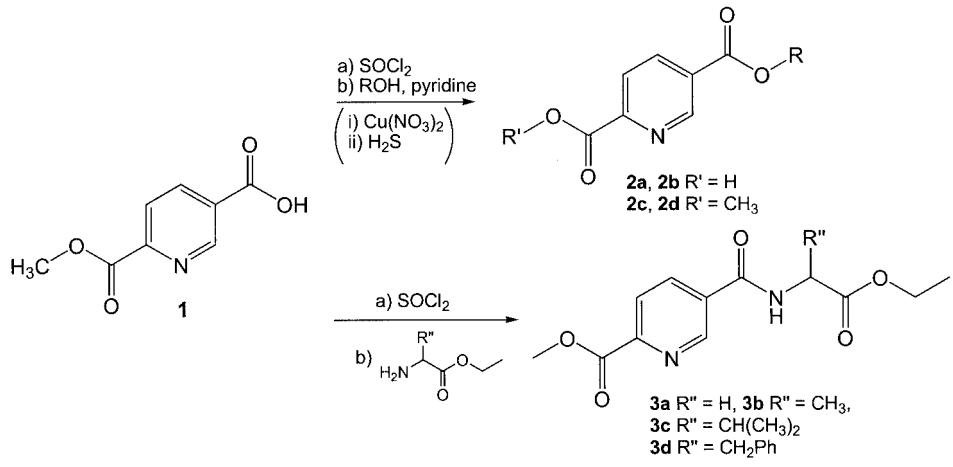


Scheme 2.

 © 2006 Wiley-VCH Verlag GmbH & Co. KGaA, Weinheim 

Table 1. Selected bond lengths [Å] and angles [°] for $[Mg(H_2O)_6](\mathbf{1}H_{-1})_2 \cdot 4H_2O$, **2b** and **3a**.

| $[Mg(H_2O)_6](\mathbf{1}H_{-1})_2 \cdot 4H_2O$ | | **2b** | | **3a** | |
|---|---|---|---|---|---|
| C1–O1 | 1.4516(13) | C1–C2 | 1.499(4) | C1–O1 | 1.458(2) |
| C2–O1 | 1.3251(14) | C1–O1 | 1.323(4) | C2–O1 | 1.328(2) |
| C2–O2 | 1.2080(13) | C1–O2 | 1.197(4) | C2–C3 | 1.504(3) |
| C2–C3 | 1.4960(14) | C5–C7 | 1.492(4) | C6–C8 | 1.503(2) |
| C6–C8 | 1.5083(13) | C7–O3 | 1.198(4) | C8–N2 | 1.337(2) |
| C8–O3 | 1.2716(13) | C7–O4 | 1.340(4) | C8–O3 | 1.227(2) |
| C8–O4 | 1.2390(13) | C8–O4 | 1.479(4) | C9–N2 | 1.442(2) |
| C1–O1–C2 | 116.05(9) | O1–C1–O2 | 125.5(3) | O1–C2–O2 | 124.31(18) |
| O1–C2–O2 | 124.91(10) | O3–C7–O4 | 124.91(10) | O3–C8–N2 | 122.13(17) |
| O3–C8–O4 | 125.91(10) | | | | |

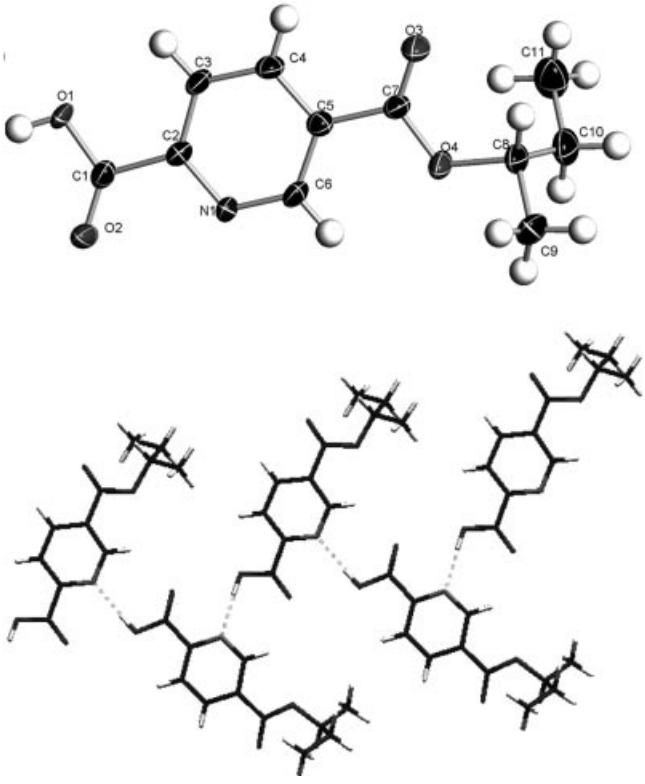


Figure 1. Top: XSHELL plot of **2b** (50% probability level). Bottom: Hydrogen bonding network for **2b** (Mercury, vers. 1.1).

which led to the formation of the desired products in good yields. The compounds were characterized by the standard spectroscopic and spectrometric methods. In the case of the glycine ethyl ester derivative **3a**, colorless single crystals were grown from dichloromethane/hexane at room temperature. **3a** crystallizes in the monoclinic space group $P2_1/c$. The molecular structure is shown in Figure 2. Bond lengths and angles are in the expected range (Table 1).

The magnesium salt of **1**, $[Mg(H_2O)_6](\mathbf{1}H_{-1})_2 \cdot 4H_2O$, was isolated in low yields as a by-product of the synthesis of the amino acid derivatives and characterized by IR and $^1H$ NMR spectroscopy. The magnesium apparently stemmed from $MgSO_4$ employed as a drying agent for the solvents. Single crystals grew from a methanolic solution by slow evaporation of the solvent. The compound crystallizes in the monoclinic space group $P2_1/c$ with two independent molecules in the asymmetric unit. The magnesium cation is octahedrally coordinated by six water ligands. The molecular structure is depicted in Figure 3, bonding parameters are contained in Table 2. There are hydrogen bonds between the waters of crystallization O8 and O9 (2.74 Å), O8 and the pyridine-N (2.83 Å), and O9 and water coordinated to $Mg^{2+}$ (2.79 Å).

Following a procedure described previously,[8] the vanadium(IV) complexes **4a**–**b** were isolated from the reaction of vanadyl sulfate and the acids **2a**–**b** as green microcrystalline powders. Green single crystals of compound $\mathbf{4a} \cdot 0.5H_2O$ were obtained from a hot aqueous solution on slow cooling.

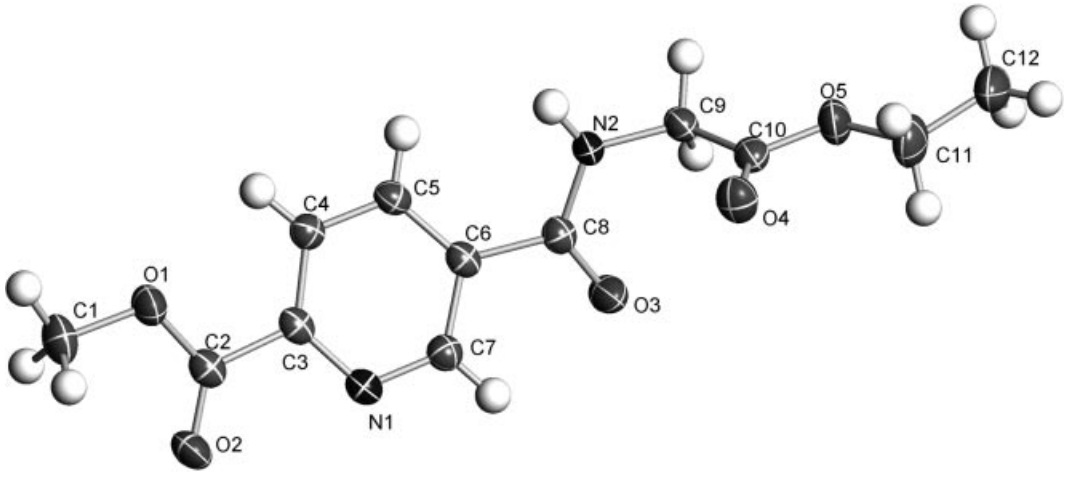


Figure 2. XSHELL plot of **3a** (50% probability level).

 © 2006 Wiley-VCH Verlag GmbH & Co. KGaA, Weinheim 

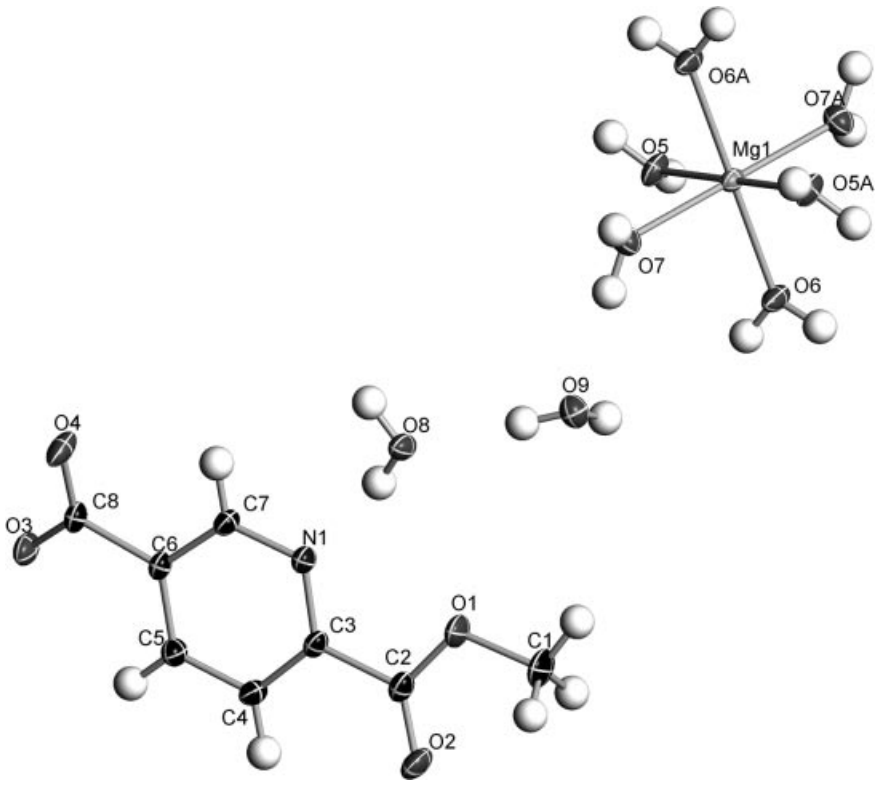


Figure 3. XSHELL plot of $[Mg(H_2O)_6](\mathbf{1}H_{-1})_2 \cdot 4H_2O$ (50% probability level). Only one of the anions $\mathbf{1}H_{-1}$ and two of the waters of crystallization are shown.

Table 2. Crystal data and structure refinement for $(\mathbf{1}H_{-1})_2$, **2b**, **3a**, **4a**.

| | $[Mg(H_2O)_6](2\text{-MeOdipic})_2$ | **2b** | **3a** | **4a**·0.5$H_2O$ |
|---|---|---|---|---|
| Emperical formula | $C_{16}H_{32}MgN_2O_{18}$ | $C_{11}H_{13}NO_4$ | $C_{12}H_{14}N_2O_5$ | $C_{20}H_{23}N_2O_{10.5}V$ |
| $M$ [g mol$^{-1}$] | 564.75 | 223.23 | 266.25 | 510.35 |
| Crystal system | monoclinic | monoclinic | monoclinic | triclinic |
| Space group | $P2(1)/c$ | $P2(1)$ | $P2(1)/c$ | $P\bar{1}$ |
| Cell dimensions | | | | |
| $a$ [Å] | 13.7795(7) | 4.4079(15) | 13.0421(17) | 10.9185(5) |
| $b$ [Å] | 7.5126(4) | 9.434(3) | 6.8948(9) | 13.4119(5) |
| $c$ [Å] | 13.8657(8) | 13.354(4) | 15.465(2) | 17.6792(8) |
| $\alpha$ [°] | 90 | 90 | 90 | 69.6350(10) |
| $\beta$ [°] | 117.2500(10) | 91.478(6) | 112.338(2) | 78.2570(10) |
| $\gamma$ [°] | 90 | 90 | 90 | 77.8200(10) |
| $V$ [Å$^3$]/$Z$ | 1276.07(12)/2 | 555.1(3)/2 | 1286.3(3)/4 | 2348.42(17)/4 |
| $\rho$(calcd.) [g cm$^{-3}$] | 1.470 | 1.335 | 1.375 | 1.440 |
| $\mu$ [mm$^{-1}$] | 0.156 | 0.102 | 0.108 | 0.481 |
| $F$(000) | 596 | 236 | 560 | 996 |
| Crystal size [mm] | 0.41×0.34×0.10 | 0.55×0.26×0.07 | 0.65×0.10×0.07 | 0.50×0.250×0.10 |
| $\theta$ range [°] | 2.94–32.50 | 2.64–27.49 | 1.69–27.49 | 2.14–29.00 |
| Index ranges | –20<$h$<20, –11<$k$<11, –20<$l$<20 | –5<$h$<5, –12<$k$<12, –16<$l$<16 | –16<$h$<16, –8<$k$<8, –19<$l$<19 | –14<$h$<14, –18<$k$<18, –24<$l$<24 |
| Reflections collected | 33675 | 6338 | 14783 | 57316 |
| Independent reflections ($R_{int}$) | 4587 (0.0457) | 1328 (0.0746) | 2916 (0.0460) | 12361 (0.0478) |
| Restraints/parameters | 15/200 | 1/148 | 0/175 | 13/661 |
| GooF on $F^2$ | 1.004 | 0.928 | 1.055 | 0.969 |
| Final $R$ ($I > 2\sigma I_0$), $R_1/wR_2$ | 0.0414/0.0985 | 0.0473/0.0871 | 0.0464/0.0942 | 0.0470/0.1208 |
| $R$ indices (all data), $R_1/wR_2$ | 0.0582/0.1050 | 0.0694/0.0932 | 0.0765/0.1200 | 0.0748/0.1348 |
| Largest diff. peak and hole [e·Å$^{-3}$] | 0.555/–0.259 | 0.225/–0.184 | 0.518/–0.430 | 1.099/–0.521 |

The compound crystallizes in the monoclinic space group $P\bar{1}$ with two independent molecules and one water of

 © 2006 Wiley-VCH Verlag GmbH & Co. KGaA, Weinheim 

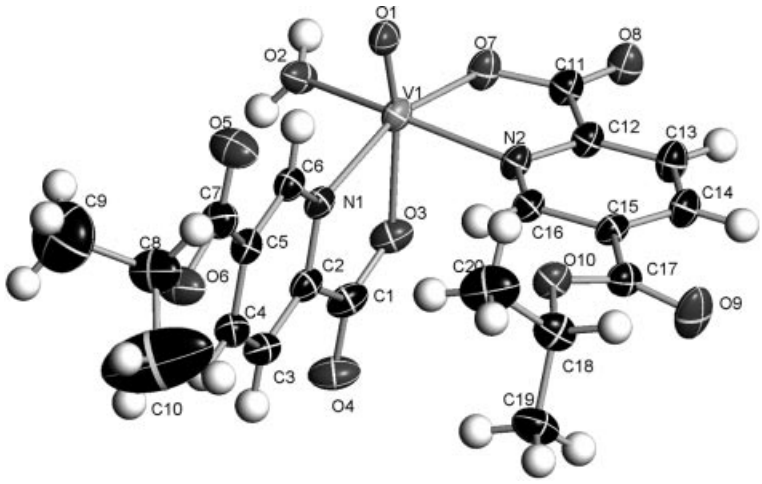


Figure 4. XSHELL plot of **4a** (50% probability level). Only one of the two independent molecules, containing one of the *i*Pr substituents in a disordered state, is shown. Water of crystallization omitted. Selected bonding parameters: V1–O1 1.5989(14), V1–O2 2.0175(14), V1–O3 1.1290(15), V1–O7 1.9890(15), V1–N1 2.1503(17), V1–N2 2.1072(16) Å; O1–V1–O3 164.55(7), O2–V1–N2 164.62(7), O7–V1–N1 161.62(6)°.

crystallization, disordered over two positions, in the asymmetric unit. Two ligands coordinate in the expected bidentate manner to form, together with an aqua ligand (O2) in the equatorial plane and an oxo ligand (O1) in the apical position, a distorted octahedron, Figure 4. The oxygen O3 of one of the carboxylato groups occupies the axial position *trans* to the oxo ligand, leading to the rather long V1–O3 distance 2.1290(15) Å due to the *trans* influence of the doubly bonded oxygen. The isopropyl group of one of the ligands is disordered over two positions (1:1) in one of the two independent molecules. The bonding parameters for the coordinated ligand anion are the same within the error limits as in the free ligand **2a** (Table 1). The water of crystallization is in hydrogen-bonding contact with the carboxylate oxygens O4 (2.79 Å) and O3 (2.83 Å).

For the synthesis of the vanadium(IV) complexes **4c**–**d** and **5a**–**d**, an aqueous solution of vanadylsulfate was mixed with a solution of the proligand and sodium acetate in THF/water and heated to reflux for 6 h. Under these conditions, the deprotection of the 2-position of the ligand precursor and the subsequent formation of the desired vanadium complex took place. The resulting dark green solution was evaporated to dryness. Recrystallization from THF yielded complexes **4c**–**d** and **5a**–**d** as green solids. All analyses confirmed the coordination of two ligand molecules to the metal center plus a solvent molecule, commonly water; cf. Scheme 1 and **4a** in Figure 4.

### Insulin-Mimetic Tests

The biological tests with regard to glucose uptake and metabolism were carried out with a modified (see below) MTT reduction assay using Simian virus transformed mice fibroblasts as described earlier.[16] In this assay, yellow soluble MTT is reduced to insoluble formazan blue by reduction equivalents generated by the metabolism of glucose by the mitochondrial respiratory chain. The amount of formazan blue is determined photometrically and correlates with the ability of either insulin or the vanadium compound to stimulate cellular glucose uptake and metabolism by the cells. The cells were grown to sub-confluency, and incubated in insulin-free medium for 24 h in order to minimize effects other than those imparted by the vanadium compound. This procedure was followed by 3 h incubation with the medium supplemented with the vanadium compound. This modified MTT test has previously been verified using D-[C6–$^3$H]glucose.[16] In order to determine the time dependent effect, a sample was taken every 15–30 minutes. Compounds included in this study are **4c**, **5a**, **5c**, **5d**, $VOSO_4$, and [VO(5MeOdipic)$_2$], the insulin-mimetic activity of which has been established earlier, and which proved most effective among the alkyl derivatives [VO(5ROdipic)$_2$].[8] The amino acid derivative with alanine, **5b**, displayed a behavior similar to the glycine derivative **5a**.

Figure 5 shows the absorbance for different concentrations of the vanadium compounds relative to a control group (without vanadium or insulin), and cells incubated with insulin instead of the vanadium compound. The data after 60 minutes incubation time are shown. During this time, about 90% of the overall effect is observed (see below). Except for the glycine derivative **5a**, all compounds exhibit insulin-mimetic properties in the concentration range (1 μM $\leq c \leq$ 200 μM) tested. The most promising results are those for the phenylalanine derivative **5d**, showing comparable stimulation of glucose uptake and metabolism as insulin. Particularly noteworthy is the fact that even at rather low concentrations ($c <$ 10 μM) the vanadium complexes are still active (Figure 5).

The time-dependent effect of compounds **4c** and **5a**, [VO(5MeOdipic)$_2$] and [VO(pic)$_2$] is shown in Figure 6. At an intermediate vanadium concentration of $c$ = 40 μM the maximum level of activity is reached after an incubation time of approximately 90 minutes. Similar results have been found for other concentrations and other complexes. The

 © 2006 Wiley-VCH Verlag GmbH & Co. KGaA, Weinheim 

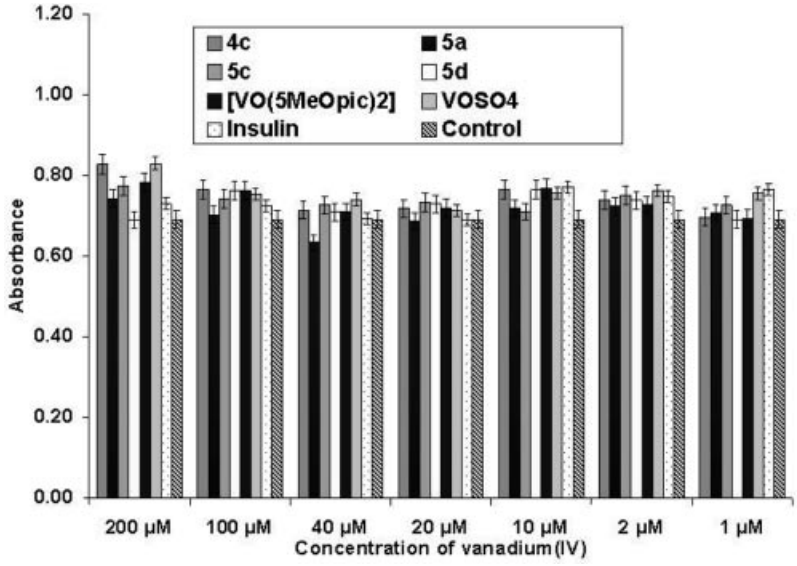


Figure 5. Glucose uptake stimulated by the vanadium picolinates **4c**, **5a**, **5c** and **5d** after 60 min. The absorbance, shown relative to a control group, reflects the efficacy of the compounds. The diagram also shows the data for $[VO(5MeOdipic)_2]$, $VOSO_4$, and a group of cells where insulin was added instead of vanadium.

time dependence in activity for the compounds apparently is not as significant as one might expect when considering the differences in the ligand spheres. Further, Figure 6 clearly shows that the galactose derivative **4c** exhibits, at this specific concentration, an insulin-mimetic activity comparable to the well established efficiency of $[VO(pic)_2]$[5] and $[VO(5MeOdipic)_2]$.[8] The time dependent insulin-mimetic effect of **4c** at different concentrations reveals that the maximum level of activity at high concentrations ($c$ = 400 µM and 200 µM) is already reached after an incubation time of approx. 45 minutes, cf. Figure 7. In this respect, **4c** is unique, since all of the other compounds considered in this study displayed the highest activity after 60 to 90 minutes, even at high concentrations (not shown). Furthermore, the effect promoted by **4c** at $c$ = 400 µM and 200 µM is significantly higher than the activity of insulin itself.

Testing of compounds **4c** and **5a**–**c** with respect to their ability to inhibit lipolysis in rat adipocytes required the presence of 1 mM ascorbic acid as a reducing agent. In the absence of ascorbic acid, aerial oxidation ($^{51}V$ NMR evidence) in the Krebs–Ringer buffer to species of low activity occurred. Figure 8 shows the effects on the release of free fatty acids (FFA) by $[V^{IV}O(pic)_2]$, the four vanadium(IV) complexes **4c** and **5a**–**c**, and the two dioxidovanadium(V) complexes $K[VO_2(pic)_2]$ and $K[VO_2(2,5dipic)_2]$. All of the compounds show an inhibitory effect with respect to the control C (epinephrine [= adrenalin], which works as an effective antagonist to insulin), an effect which increases as concentration is increased from 0.1 to 1 mM. The results obtained with insulin (B in Figure 8) are not quite reached. There is no sizeable difference in efficiency between the neutral oxidovanadium(IV) and the anionic dioxidovanadi-

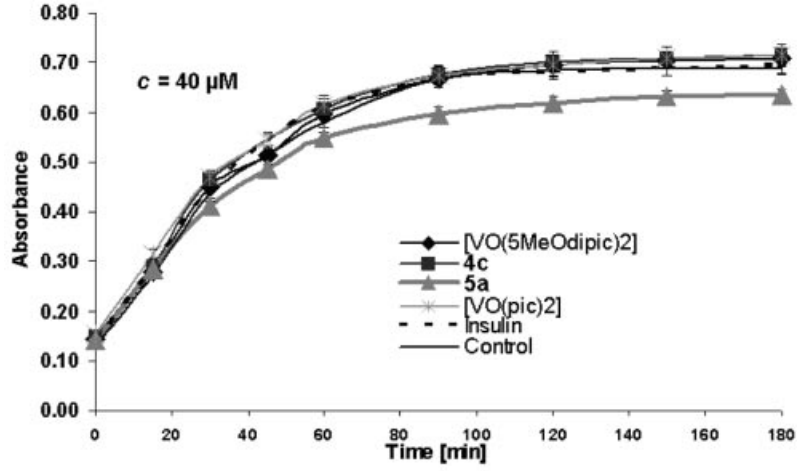


Figure 6. Glucose uptake stimulated by **4c** and **5a** ($c$ = 40 µM) presented as a function of time. This diagram also includes the results for $[VO(pic)_2]$, $[VO(5MeOdipic)_2]$ and insulin. Data are not corrected for background.

 © 2006 Wiley-VCH Verlag GmbH & Co. KGaA, Weinheim 

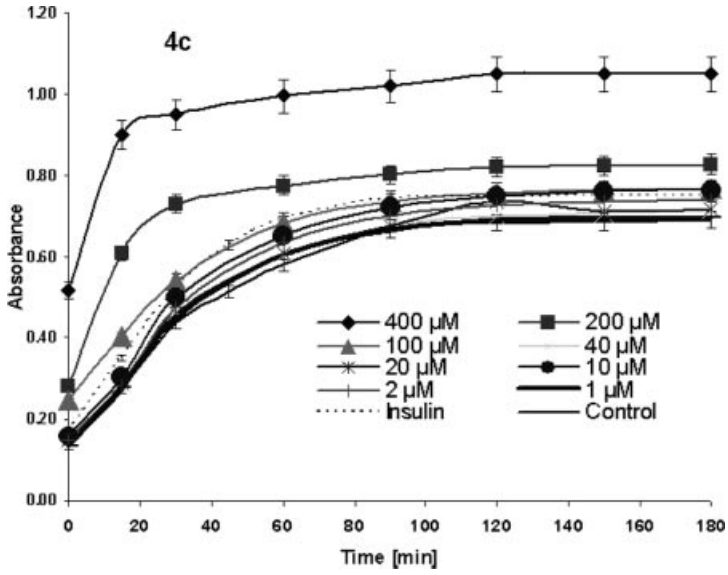


Figure 7. Glucose uptake stimulated by the galactosyl derivative **4c** as a function of time over a wide concentration range. Data are not corrected for background.

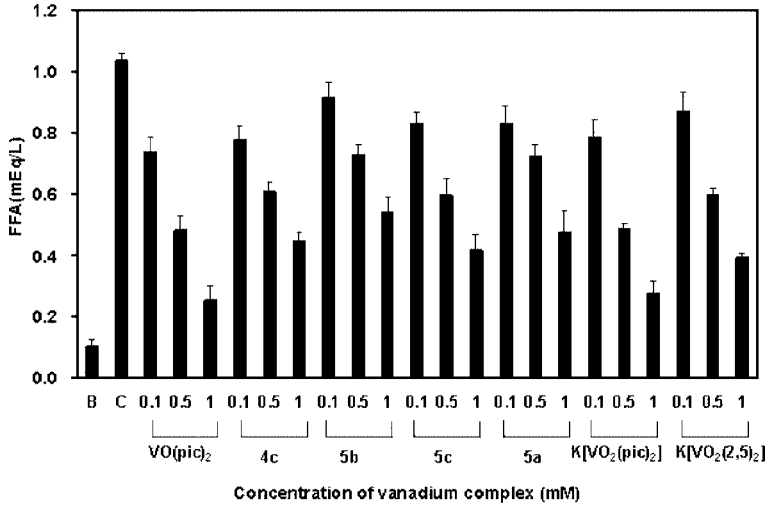


Figure 8. Inhibitory effects of vanadium complexes on FFA-release from rat adipocytes treated with epinephrine. Data are expressed as the means ± SDs for three experiments. B: adipocytes treated with insulin. C: adipocytes pre-incubated with saline for 30 min before treatment with 10 µM epinephrine for 3 h.

um(V) compounds, nor between the different picolinate derivatives. The ligands themselves did not show any appreciable activity (data not shown).

## Conclusions

In extension of earlier work,[8] we have introduced here a new concept for the design of potentially insulin-mimetic vanadium(IV) compounds. The framework represented by pyridine-2,5-dicarboxylic acid was extended by introducing, into the 5-position, organic molecules into the ligand sphere for which membrane receptors exist and/or which modify the hydro/lipophilicity of the dipicolinatovanadium complexes. Here, we have employed amino acids, galactose and inositol residues, along with alkyl derivatives for comparison. Selected compounds were subjected to in vitro studies of their ability to stimulate glucose uptake and oxidative degradation by modified fibroblasts on the one hand, and to inhibit lipolysis by adipocytes on the other hand. Except for the glycine and L-alanine derivatives, all compounds were effective insulin-mimetics in the glucose uptake experiments in the concentration range 200 to 1 µM. The galactose containing complex initiated an earlier saturation of glucose uptake in the time-dependent studies than other compounds, which can be interpreted in terms of a faster uptake of the galactosyl complex by the cells. All of the complexes also showed insulin-mimetic activity in the inhibition of li-

 © 2006 Wiley-VCH Verlag GmbH & Co. KGaA, Weinheim 

polysis, in particular at relatively high concentrations of 1 mM.

## Experimental Section

**General and Chemicals:** All preparations of vanadium complexes in the oxidation state +IV were carried out under nitrogen atmosphere, using Schlenk techniques. For further handling of the complexes, Schlenk techniques were dispensable. Chemicals were obtained from Merck, Aldrich and Fluka and used without further purification unless stated otherwise. Solvents were dried and purified by standard procedures. Tetrahydrofuran (THF) was dried and deoxygenated by refluxing for at least three hours over $LiAlH_4$ and distilled in an $N_2$ stream. Triethylamine was distilled (88–90 °C) and stored over molecular sieves (4 Å). Dichloromethane was refluxed for 24 h over calcium hydride. Toluene was refluxed for 24 h over sodium and then distilled in an $N_2$ stream. Pyridine ($H_2O \leq 0.005\%$) was stored over molecular sieve. Deionized water was degassed before use. Products were dried at room temperature under vacuum and stored under $N_2$. The following compounds were prepared according to published procedures: 6-(methoxycarbonyl)-pyridine-3-carboxylic acid (**1**),[9] methyl 5-(chlorocarbonyl)pyridine-2-carboxylate,[10] *myo*-inositol-orthoformate,[11,12] 1,2:3,4-di-*O*-isopropylidene-*α*-D-galactose,[13] [VO(pic)$_2$],[14]K[$VO_2$(pic)$_2$],[14] K[$VO_2$(2,5dipic)].[15]

**Analyses and Methods:** Elemental analyses were carried out in the Analytical Laboratory of the Chemistry Department, University of Hamburg. Infrared spectra were recorded as KBr pellets on a Perkin–Elmer 1720 FT–IR spectrometer. NMR spectra were obtained either on a Varian Gemini 200 BB or a Bruker Avance 400 spectrometer at room temperature in 5 mm tubes. Chemical shifts $\delta$ are reported in ppm (parts per million) relative to TMS for $^1H$ and $^{13}C$ NMR spectra. Coupling constants ($J$) are quoted in Hertz. Mass spectrometry was carried out at the Institute of Organic Chemistry, University of Hamburg, with the usual spectrometer settings on a Varian MAT 311A (70 eV, EI) or a VG Analytical 70–250 S (FAB). EPR spectra of **4a**–**d** and **5a**–**d** were scanned at ca. 9.6 GHz (X-band) on a Bruker ESP-300 E spectrometer at room temperature and 100 K. Parameter adaptations by simulation were achieved by using the Bruker software SimFonia. X-ray structure analyses were carried out at 153(2) K using Mo-$K_\alpha$ irradiation ($\lambda$ = 0.71073 Å, graphite monochromator) on a Smart Apex CCD diffractometer. Hydrogen atoms were usually found, and otherwise calculated into idealized positions and included in the last cycles of refinement. Absorption corrections were carried out by SADABS. Structure solution and refinement were carried out using the SHELXTL-Plus software package (G. M. Sheldrick, Version 5.1, Bruker AXS, 1998). For crystal data and structure refinement see Table 2.

CCDC-22102, -285853, -225187, and -257605 contain the supplementary crystallographic data for this paper. These data can be obtained free of charge from The Cambridge Crystallographic Data Centre via www.ccdc.cam.ac.uk/data_request/cif.

**Insulin-Mimetic Tests:** Tests for the glucose uptake activity were based on the MTT (MTT = 3-(4,5-dimethylthiazol-2-yl)-2,5-diphenyl-2*H*-tetrazolium bromide) reduction assay.[16] The cells were cultured in glucose-rich DMEM medium (Dulbecco's modification of Eagle's medium) supplemented with 10% fetal calf serum at 37 °C/5% $CO_2$ to subconfluency. Afterwards, the cells were passed to an insulin-free, DMEM high glucose medium for 24 h. For the MTT tests, DMEM (without phenol red) supplemented with MTT (Sigma; 0.5 g/L) and solutions of the vanadium complexes in different concentrations were added to the cells and incubated for up to 3 h at 37 °C in a 5% $CO_2$ atmosphere. The cells were separated from the medium and the reaction was stopped by addition of 0.1 M HCl in 2-propanol. The insoluble dye was extracted by HCl/2-propanol, and the amount of formazan blue formed by reduction of MTT was measured at 570 nm in a multi-well reader (SLT 340 ATC). All measurements were carried out in triplicate; standard deviations for the absorbances typically amount to 4 ± 2%.

Tests for the inhibition of free fatty acid (FFA) release were performed on epidymal fat pads, excised from male Wistar rats (7 weeks) anesthetized with diethyl ether. The pads were cut into appropriately sized pieces and were incubated with collagenase in KRB buffer (Krebs–Ringer hydrogen carbonate buffer; 120 mM NaCl, 1.27 mM $CaCl_2$, 1.2 mM $MgSO_4$, 4.75 mM KCl, 1.2 mM $KH_2PO_4$, and 24 mM $NaHCO_3$; pH 7.4) containing 2% BSA at 37 °C with gentle shaking at 100 cycle/min for 1 h. At the end of the incubation period, the prepared cells were filtered through sterilized cotton gauze and washed three times with the KRB buffer. The cells were incubated at 37 °C for 30 min with the vanadium complexes, dissolved in DMSO, at various concentrations (0.1–1.0 mM), including 1 mM ascorbic acid to prevent their oxidations in KRB buffer containing 2% DMSO. A 10 μM solution of epinephrine was then added to the reaction mixtures, and the resulting solutions were incubated at 37 °C for 3 h. The mixtures were centrifuged at 3000 rpm for 10 min at 4 °C. On the outer solution of the cells, the FFA level was determined with a FFA kit (NEFA C test; Wako, Osaka, Japan).

All animal experiments in the present study were approved by the Experimental Animal Research Committee of Kyoto Pharmaceutical University (KPU), and were performed according to the Guideline for Animal Experimentation of the KPU.

**Synthesis and Characterization**

For the NMR assignments, the numbering of the ring-H and -C atoms follows the usual one. C1 and C7 refer to the carboxylic carbons in the ring positions 2 and 5, respectively.

**[$Mg(H_2O)_6$](1H$_{-1}$)$_2$:** This compound was obtained in low yields as a by-product during the syntheses of the amino acid derivatives **3a**–**d** (see below). Single crystals were grown by slow evaporation of a methanolic solution. IR (KBr) $\tilde{\nu}$ = 3114, 3075 (ar. C–H); 2955, 2924, 2851 (C–H); 1730 (sh), 1708 (C=O); 1636, 1605, 1561 (C=C), (C=N); 1479, 1439, 1391, 1324 (C–H); 1287, 1258 (C=C), (C=N); 1158, 1122, 1072, 1030, 1005 (C–O–C); 818 (ar. C–H), ν(C–$CO_2$); 746 (ar. C–H) cm$^{-1}$. $^1H$ NMR (400 MHz, $CD_3OD$/TMS): $\delta$ = 9.19 (m, 1 H, H-2), 8.47–8.45 (m, 1 H, H-4), 8.18–8.16 (m, 1 H, H-5), 3.98 (s, 3 H, H-1) ppm.

**General Procedure for the Syntheses of the Ligands 2a–b:** To a solution of methyl 5-(chlorocarbonyl)pyridine-2-carboxylate (1.5 g, 7.56 mmol) in toluene (5 mL) was added dropwise and with cooling a 1.4 fold excess of the alcohol in pyridine (15 mL). After the addition of a catalytic amount of 4-(dimethylamino)pyridine, the resulting dark solution was stirred overnight at room temperature. The solvent was evaporated and the residue dissolved in water. The aqueous solution was extracted with dichloromethane (5 × 30 mL). The organic layer was dried with $Na_2SO_4$ and the solvent evaporated. Purification was carried out using column chromatography on silica gel, elutant ethyl acetate/*n*-hexane, 1:1, to give a light yellow solid (yield 59–65%) which was treated with an equimolar amount of $Cu(NO_3)_2 \cdot 3H_2O$, followed by treatment with hydrogen sulfide as has been described earlier[8] to produce the ligands as white solids in yields of 50–85%.

**5-(Isopropyloxycarbonyl)-2-pyridinecarboxylic Acid (2a):** Yield 44% (0.69 g). $C_{10}H_{11}NO_4$ (209.20): calcd. C 57.41, H 5.30, N 6.70; found

 © 2006 Wiley-VCH Verlag GmbH & Co. KGaA, Weinheim 

C 57.34, H 5.31, N 6.67. IR (KBr) $\tilde{\nu}$ = 3053 (ar. C–H); 2980, 2875, 2767 (C–H); 1718 (C=O); 1600, 1583, 1498 (C=C), (C=N); 1471, 1459, 1377 (C–H), (O–H); 1301, 1269 (C=C), (C=N); 1108, 1036 (C–O–C); 750 (ar. C–H) $cm^{-1}$. $^1H$ NMR (200 MHz, [D$_6$]DMSO): $\delta$ = 9.12 (dd, $^4J_{6,4}$ = 2.17 Hz, $^5J_{6,3}$ = 0.82 Hz, 1 H, H-6), 8.40 (dd, $^4J_{4,6}$ = 2.17 Hz, $^3J_{4,3}$ = 8.10 Hz, 1 H, H-4), 8.13 (dd, $^5J_{3,6}$ = 0.82 Hz, $^3J_{3,4}$ = 8.10 Hz, 1 H, H-3), 5.16 (h, $^3J$ = 6.23 Hz, 1 H, C*H*(CH$_3$)$_2$), 1.32 (d, $^3J$ = 6.23 Hz, 6 H, CH(C*H*$_3$)$_2$) ppm. $^{13}C$ NMR (50 MHz, [D$_6$]DMSO): $\delta$ = 166.17 (C-1), 164.21 (C-7), 152.32 (C-2), 150.39 (C-6), 138.82 (C-4), 128.98 (C-5), 125.24 (C-3), 69.95 (*C*H(CH$_3$)$_2$), 22.21 (CH(*C*H$_3$)$_2$) ppm. MS (70 eV, EI): *m*/*z* (%): 209 (5) ($M^{+\cdot}$), 168 (42) (M – $C_3H_5$), 165 (34) (M – $CO_2$), 150 (100) (M – $C_3H_7O$), 123 (41) (M – $C_4H_6O_2$), 43 (21) ($C_2H_4N^+$).

**5-[(*S*)-*sec*-Butyloxycarbonyl]-2-pyridinecarboxylic Acid (2b):** Yield 50% (0.84 g). $C_{10}H_{11}NO_4$ (223.23): calcd. C 59.19, H 5.87, N 6.27; found C 58.88, H 5.91, N 6.31. IR (KBr) $\tilde{\nu}$ = 3047 (ar. C–H); 2976, 2935, 2878, 2768 (C–H); 1715 (C=O); 1599, 1581 (C=C), (C=N); 1457, 1419, 1372 (C–H), (O–H); 1297, 1267 (C=C), (C=N); 1119, 1109, 1035 (C–O–C); 749 (ar. C–H) $cm^{-1}$. $^1H$ NMR (200 MHz, [D$_6$]DMSO): $\delta$ = 9.17 (br. m, 1 H, H-6), 8.46 (m, 1 H, H-4), 8.19 (br. m, 1 H, H-3), 5.06 (tq, $^3J$ = 6.2 Hz, 1 H, C*H*(CH$_3$)CH$_2$CH$_3$), 1.78–1.64 (m, 2 H, CH(CH$_3$)C*H*$_2$CH$_3$), 1.33 (d, $^3J$ = 6.23 Hz, 3 H, CH(C*H*$_3$)CH$_2$CH$_3$), 0.94 (t, $^3J$ = 7.4 Hz, 3 H, CH(CH$_3$)-CH$_2$C*H*$_3$) ppm. $^{13}C$ NMR (50 MHz, [D$_6$]DMSO): $\delta$ = 165.87 (C-1), 163.84 (C-7), 151.9 (C-2), 148.88 (C-6), 138.24 (C-4), 128.26 (C-5), 124.75 (C-3), 73.63 (*C*H(CH$_3$)CH$_2$CH$_3$), 28.26 (CH(CH$_3$)-*C*H$_2$CH$_3$), 19.21 (CH(*C*H$_3$)CH$_2$CH$_3$), 9.53 (CH(CH$_3$)-CH$_2$*C*H$_3$) ppm. MS (70 eV, EI): *m*/*z* (%): 223 (1) ($M^{+\cdot}$), 168 (60) (M – $C_4H_7$), 150 (100) (M – $C_4H_9O$), 122 (25) (M – $C_5H_9O_2$).

**Preparation of the Galactose/Inositol Derivatives 2c, 2d:** To a solution of methyl 5-(chlorocarbonyl)pyridine-2-carboxylate (600 mg, 3.0 mmol) in toluene (10 mL) in an ice bath was added a solution of the corresponding alcohol (3.0 mmol) in pyridine (15 mL). After addition of a catalytic amount of 4-(dimethylamino)pyridine, the resulting solution was stirred for 12 h at room temperature. The solvent was evaporated and the residue extracted with toluene (10 mL), followed by dichloromethane (10 mL). The galactose derivative was dissolved in 1-butanol and the organic phase washed with water and a diluted solution of $Na_2CO_3$. The organic layer was dried with $MgSO_4$ and the solvent was evaporated to yield a yellow oil. The inositol derivative was dissolved in water and the aqueous phase was extracted with ethyl acetate. The organic layer was dried with $MgSO_4$ and the solvent was evaporated to yield a light yellow solid.

**2MeO-5GalOdipic (2c):** Yield 89% (0.98 g). $C_{20}H_{25}NO_9{\cdot}2H_2O{\cdot}0.5(C_4H_{10}O)$ (496.51): calcd. C 53.22, H 6.90, N 2.82; found C 53.56, H 6.52, N 2.66. IR (KBr) $\tilde{\nu}$ = 3112, 2989 (ar. C–H); 2933, 2851 (C–H); 1728, 1716 (sh) (C=O); 1627, 1597, 1580, 1479 (C=C), (C=N); 1439, 1384 (C–H); 1311, 1275, 1255, 1213, 1168, 1139, 1071, 1003 (C–O), (C–N), (C–O–C); 748 (ar. C–H) $cm^{-1}$. $^1H$ NMR (400 MHz, CD$_3$OD/TMS): $\delta$ = 9.22–9.15 (m, 1 H, H-7), 8.56–8.53 (m, 1 H, H-5), 8.27–8.22 (m, 1 H, H-4), 5.52–5.50 (m, 1 H, H-1′), 4.64–4.61 (m, 1 H, H-5′), 4.36–4.28 (m, 2 H, H-2′, H-3′), 4.02 (s, 3 H, H-1), 3.89–3.85 (m, 1 H, H-4′), 3.69–3.66 (m, 2 H, H-6′), 1.53, 1.41, 1.34, 1.33 (s, 12 H, H-9′, H-10′, H-11′, H-12′) ppm. $^{13}C$ NMR (100 MHz, CD$_3$OD/TMS): $\delta$ = 165.9, 165.4 (C-8, C-2), 151.8 (C-3), 151.3 (C-7), 140.0 (C-5), 130.3 (C-6), 126.1 (C-4), 110.8, 109.7 (C-7′, C-8′), 97.7 (C-1′), 72.4 (C-2′), 72.2 (C-3′), 71.9 (C-4′), 67.5 (C-5′), 66.0 (C-6′), 53.5 (C-1), 26.3, 26.2, 25.1, 24.6 (C-9′, C-10′, C-11′, C-12′) ppm. MS (70 eV, EI): *m*/*z* (%): 408 (100) (M – $CH_3$), 183 (27) ($C_8H_9NO_4^+$), 164 (50) ($C_8H_6NO_3^+$), 115 (26) ($C_6H_{11}O_2^+$), 100 (45) ($C_5H_8O_2^+$), 85 (24) ($C_5H_9O^+$), 81 (57) ($C_5H_5O^+$), 59 (29) ($C_2H_3O_2^+$), 43 (53) ($C_3H_7^+$).

**2MeO-5-Inodipic (2d):** Yield 69% (0.73 g). $C_{15}H_{15}N_{1.3}O_9$ (357.48): calcd. C 50.39, H 4.23, N 5.09; found C 51.90, H 4.35, N 5.18. IR (KBr) $\tilde{\nu}$ = 3399, 3326 (O–H), 3013 (ar. C–H); 2952, 2924, 2852 (C–H); 1729, 1717 (C=O); 1627, 1597, 1580, 1478 (C=C), (C=N); 1440, 1385 (C–H); 1275, 1162, 1139, 1060, 1007, 993, 960 (C–O), (C–N), (C–O–C); 748 (ar. C–H) $cm^{-1}$. $^1H$ NMR (200 MHz, CD$_3$OD/TMS): $\delta$ = 9.21–9.20 (m, 1 H, H-7), 8.28–8.22 (m, 1 H, H-5), 7.98–7.88 (m, 1 H, H-4), 5.41 (d, $^4J$ = 1.28 Hz, 1 H, H-7′), 4.44–4.40 (m, 2 H, H-1′, H-4′), 4.18–4.06 (m, 4 H, H-2′, H-3′, H-5′, H-6′), 4.01 (s, 3 H, H-1) ppm. $^{13}C$ NMR (100 MHz, CD$_3$OD/TMS): $\delta$ = 166.9, 165.9 (C-8, C-2), 151.5 (C-7), 147.9 (C-3), 140.3 (C-5), 131.3 (C-6), 126.1 (C-4), 103.9 (C-7′), 76.0 (C-2′, C-6′), 70.6 (C-4′), 69.1 (C-3′, C-5′), 61.1 (C-1′), 53.5 (C-1) ppm. MS (70 eV, EI): *m*/*z* (%): 352 (3) ($M^{+\cdot}$-H), 236 (10) (M – $C_7H_3NO$), 182 (44) ($C_8H_8NO_4^+$) 164 (100) ($C_8H_6NO_3^+$), 137 (26) ($C_7H_7NO_2^+$), 106 (20) ($C_6H_4NO^+$), 73 (41) ($C_3H_5O_2^+$), 44 (41) ($CO_2^+$).

**General Procedure for Compounds (2MeO-5R′NHdipic) 3a–d:** To a solution of the L-amino acid ethyl ester hydrochloride (5.0 mmol) in dichloromethane (10 mL) was added triethylamine (1.52 mL, 1.11 g, 11.0 mmol). The resulting mixture was stirred for 5 minutes (sometimes formation of a white precipitate was observed). Then a solution of methyl 5-(chlorocarbonyl)pyridine-2-carboxylate (1.0 g, 5.0 mmol) in dichloromethane (10 mL) was added drop wise with cooling (5–10 °C). The resulting yellow solution was stirred for 12 h at room temperature. The solvent was removed by evaporation and the residue was dissolved in ethylacetate. The solution was filtered, and the precipitate washed with a small amount of ethylacetate. The filtrate was concentrated. Purification was carried out using column chromatography on silica gel; elutant ethyl acetate/*n*-hexane, 1:1. The products were isolated as slightly yellow oils, which solidified upon cooling. Yields were 36 to 66%. Single crystals of compound **3a** were obtained by slow diffusion of *n*-hexane into a saturated solution of the compound in dichloromethane.

**2MeO-5GlyNHdipic (3a):** Yield 36% (0.50 g). $C_{12}H_{14}N_2O_5$ (266.25): calcd. C 54.13, H 5.30, N 10.52; found C 54.15, H 5.57, N 9.71. IR (KBr): $\tilde{\nu}$ = 3355 (N–H); 3063 (ar. C–H); 2977, 2961 (C–H); 1753, 1727, 1664 (C=O); 1595, 1531, 1480 (C=C), (C=N), (N–H); 1440, 1383 (C–H); 1311, 1253, 1200, 1169, 1128, 1024 (C–O), (C–N), (C–O–C); 753 (ar. C–H) $cm^{-1}$. $^1H$ NMR (400 MHz, CDCl$_3$/TMS): $\delta$ = 9.14–9.13 (m, 1 H, H-7), 8.33–8.30 (m, 1 H, H-5), 8.21–8.19 (m, 1 H, H-4), 7.36 (br. t, 1 H, N*H*), 4.28–4.23 (m, 4 H, H-9, H-11), 4.03 (s, 3 H, H-1), 1.31 (t, $^3J_{12,11}$ = 7.1 Hz, 3 H, H-12) ppm. $^{13}C$ NMR (100 MHz, CDCl$_3$/TMS): $\delta$ = 169.74 (C-8), 164.96 (C-2), 164.90 (C-10), 149.81 (C-3), 148.36 (C-7), 136.63 (C-5), 132.22 (C-6), 124.77 (C-4), 61.78 (C-11), 53.18 (C-1), 41.90 (C-9), 14.13 (C-12) ppm. MS (70 eV, EI): *m*/*z* (%): 266 (6) ($M^{+\cdot}$), 208 (33) (M – $C_3H_6O$), 193 (13) (M – $C_3H_5O_2$), 164 (100) (M – $C_5H_{10}O_2$), 40 (16) ($C_3H_4^+$).

**2MeO-5AlaNHdipic (3b):** Yield 66% (0.92 g). $C_{13}H_{16}N_2O_5$ (280.28): calcd. C 55.71, H 5.75, N 9.99; found C 55.74, H 5.52, N 9.74. IR (KBr) $\tilde{\nu}$ = 3296 (N–H); 3067 (ar. C–H); 2985, 2951, 2854 (C–H); 1744, 1718, 1645 (C=O); 1595, 1540 (C=C), (C=N), (N–H); 1455, 1442, 1381 (C–H); 1311, 1291, 1246, 1214, 1177, 1136, 1020 (C–O), (C–N), (C–O–C); 744 (ar. C–H) $cm^{-1}$. $^1H$ NMR (400 MHz, CDCl$_3$/TMS): $\delta$ = 9.13–9.12 (m, 1 H, H-7), 8.28–8.21 (m, 2 H, H-4, H-5), 6.94 (br. d, 1 H, N*H*), 4.82–4.75 (dq, $^3J_{9,NH}$ = 7.1 Hz, $^3J_{9,10}$ = 7.14 Hz, 1 H, H-9), 4.27 (q, $^3J_{12,13}$ = 7.14 Hz, 2 H, H-12), 4.04 (s, 3 H, H-1), 1.56 (d, $^3J_{10,9}$ = 7.14 Hz, 3 H, H-10), 1.33 (t, $^3J_{13,12}$ = 7.14 Hz, 3 H, H-13) ppm. $^{13}C$ NMR (50 MHz, CDCl$_3$/TMS): $\delta$ = 172.90 (C-8), 164.86 (C-2), 164.25 (C-11), 149.74 (C-3), 148.41 (C-7), 136.43 (C-5), 132.27 (C-6), 124.81 (C-4), 61.82 (C-12), 53.16 (C-1), 48.83 (C-9), 18.09 (C-10), 14.12 (C-13) ppm.

 © 2006 Wiley-VCH Verlag GmbH & Co. KGaA, Weinheim 

MS (70 eV, EI): *m/z* (%): 280 (33) ($M^{+\cdot}$), 235 (13) (M – $C_2H_5O$), 208 (34) (M – $C_3H_4O_2$), 207 (100) (M – $C_3H_5O_2$), 165 (33) (M – $C_6H_{11}O_2$), 164 (76) (M – $C_6H_{12}O_2$), 136 (21) (M – $C_6H_{10}NO_3$), 106 (20) (M – $C_7H_{12}NO_4$), 78 (25) ($C_5H_4N^+$).

**2MeO-5ValNHdipic (3c):** Yield 66% (1.01 g). $C_{15}H_{20}N_2O_5$ (308.33): calcd. C 58.43, H 6.54, N 9.09; found C 58.43, H 6.25, N 8.94. IR (KBr) $\tilde{\nu}$ = 3307 (N–H); 3103 (ar. C–H); 2971, 2932, 2872 (C–H); 1746, 1713, 1645 (C=O); 1597, 1569, 1523 (C=C), (C=N), (N–H); 1472, 1437, 1393, 1373 (C–H); 1313, 1301, 1248, 1190, 1160, 1139, 1021 (C–O), (C–N), (C–O–C); 698 (ar. C–H) $cm^{-1}$. $^1H$ NMR (400 MHz, $CDCl_3$/TMS): $\delta$ = 9.14–9.13 (m, 1 H, H-7), 8.29–8.19 (m, 2 H, H-4, H-5), 6.74 (br. d, 1 H, N*H*), 4.81–4.78 (dd, $^3J_{9,NH}$ = 8.44 Hz, $^3J_{9,10}$ = 4.70 Hz, 1 H, H-9), 4.38–4.14 (m, 2 H, H-13), 4.04 (s, 3 H, H-1), 2.32 (dq, $^3J_{10,9}$ = 4.70 Hz, $^3J_{10,11/11'}$ = 6.91 Hz, 1 H, H-10), 1.33 (t, $^3J_{14,13}$ = 7.14 Hz, 3 H, H-14), 1.03, 1.01 (d, d, $^3J_{11/11',10}$ = 6.91 Hz, 6 H, H-11, H-11′) ppm. $^{13}C$ NMR (100 MHz, $CDCl_3$/TMS): $\delta$ = 175.56 (C-8), 164.92 (C-2), 164.64 (C-12), 149.99 (C-3), 148.41 (C-7), 136.20 (C-5), 132.53 (C-6), 124.87 (C-4), 61.69 (C-9), 57.74 (C-13), 53.20 (C-1), 31.38 (C-10), 19.01, 18.00 (C-11, C-11′), 14.30 (C-14) ppm. MS (70 eV, EI): *m/z* (%): 308 (5) ($M^{+\cdot}$), 235 (85) (M – $C_3H_5O_2$), 181 (32) (M – $C_7H_{11}O_2$), 164 (100) (M – $C_6H_{10}NO_3$), 78 (12) ($C_5H_4N^+$).

**2MeO-5PheNHdipic (3d):** Yield 54% (0.96 g). $C_{19}H_{20}N_2O_5$ (356.37): calcd. C 64.04, H 5.66, N 7.86; found C 63.88, H 5.66, N 7.74. IR (KBr) $\tilde{\nu}$ = 3321 (N–H); 3137, 3068, 3029 (ar. C–H); 2980, 2946, 2870 (C–H); 1734, 1647 (C=O); 1595, 1568, 1526, 1498 (C=C), (C=N), (N–H); 1455, 1439, 1375 (C–H); 1309, 1285, 1194, 1161, 1117, 1099, 1022 (C–O), (C–N), (C–O–C); 748, 700 (ar. C–H) $cm^{-1}$. $^1H$ NMR (400 MHz, $CDCl_3$/TMS): $\delta$ = 9.00–8.99 (m, 1 H, H-7), 8.21–8.16 (m, 2 H, H-4, H-5), 7.32–7.24 (m, 3 H, H-13, H-14, H-15), 7.15–7.12 (m, 2 H, H-12, H-16), 6.67 (br. d, 1 H, N*H*), 5.09–5.04 (dt, $^3J_{9,NH}$ = 7.49 Hz, $^3J_{9,10}$ = 5.93 Hz, 1 H, H-9), 4.25 (q, $^3J_{18,19}$ = 7.16 Hz, 2 H, H-18), 4.03 (s, 3 H, H-1), 3.34–3.23 (m, 2 H, H-10), 1.31 (t, $^3J_{19,18}$ = 7.16 Hz, 3 H, H-19) ppm. $^{13}C$ NMR (100 MHz, $CDCl_3$/TMS): $\delta$ = 171.27 (C-8), 164.87 (C-2), 164.15 (C-17), 150.01 (C-3), 148.14 (C-7), 136.26 (C-5), 135.49 (C-11), 132.34 (C-6), 129.28 (C-12, C-16), 128.74 (C-13, C-15), 127.40 (C-14), 124.91 (C-4), 61.96 (C-18), 53.66 (C-9), 53.21 (C-1), 37.70 (C-10), 14.15 (C-19) ppm. MS (70 eV, EI): *m/z* (%): 356 (6) ($M^{+\cdot}$), 283 (14) (M – $C_3H_5O_2$), 176 (97) (M – $C_{11}H_{16}O_2$), 164 (100) (M – $C_{11}H_{14}NO_2$), 148 (11) (M – $C_{12}H_{16}O_3$), 131 (18) (M – $C_{12}H_{19}NO_3$), 91 (19) ($C_7H_7^+$), 78 (12) ($C_5H_4N^+$).

**Preparation of the Vanadium(IV) Compounds 4a–d and 5a–d. 4a–b:** A solution of the ligand (1.0 mmol) and sodium acetate·$3H_2O$ (136 mg, 1.0 mmol) in water (10 mL) and THF (1 mL) was mixed with a solution of $VOSO_4$·$5H_2O$ (127 mg, 0.5 mmol) in water (2 mL) at 50 °C to yield light green solids. **4c–d**, **5a–d:** To a solution of the proligand (1.0 mmol) and sodium acetate·$3H_2O$ (136 mg, 1.0 mmol) in water (3 mL) and THF (6 mL) was added a solution of vanadyl sulfate·$5H_2O$ (127 mg, 0.5 mmol) in water (3 mL). The resulting green slurry was kept at reflux for ca. 6 h to yield a clear green solution. The solvent was evaporated, the residue was dissolved in THF and filtered. Evaporation to dryness yielded green solids.

**[VO(5-*i*PrOdipic)$_2$] (4a):** Yield 74% (185 mg). $C_{20}H_{20}N_2O_9V$·$H_2O$ (501.34): calcd. C 47.91, H 4.42, N 5.59; found C 47.56, H 4.45, N 5.08. IR (KBr) $\tilde{\nu}$ = 3114, 3058 (ar C–H); 2983, 2873 (C–H); 1730 (C=O); 1687, 1652 $\nu_{as}(CO_2^-)$; 1609 (C=C), (C=N); 1484, 1397, 1353 (C–H), $\nu_s(CO_2^-)$; 1289 (C=C), (C=N); 1108, 1051 (C–O–C); 967 (V=O); 848 (ar. C–H), (C–$CO_2$); 750 (ar. C–H) $cm^{-1}$. MS (FAB): *m/z* = 484 (M – $H_2O$]. EPR (293 K, ethanol): $g_0$ = 1.975, $A_0$ = 93·$10^{-4}$ $cm^{-1}$; (100 K, ethanol): $g_\perp$ = 1.985, $A_\perp$ = 60·$10^{-4}$ $cm^{-1}$, $g_{II}$ = 1.945, $A_{II}$ = 167·$10^{-4}$ $cm^{-1}$.

**[VO(5-*s*BuOdipic)$_2$] (4b):** Yield 65% (190 mg). $C_{22}H_{24}N_2O_9V$·THF (583.49): calcd. C 53.52, H 5.53, N 4.80; found C 52.70, H 5.47, N 4.98. IR (KBr) $\tilde{\nu}$ = 3116, 3080 (ar C–H); 2974, 2931, 2880, 2854 (C–H); 1727 (C=O); 1687 $\nu_{as}(CO_2^-)$; 1643, 1627, 1606, 1578 (C=C), (C=N); 1485, 1457, 1419, 1357 (C–H), $\nu_s(CO_2^-)$; 1283 (C=C), (C=N); 1130, 1108, 1046 (C–O–C); 977 (V=O); 851 (ar. C–H), (C–$CO_2$); 748 (ar. C–H) $cm^{-1}$. MS (FAB): *m/z* = 512 (M – THF]. EPR (100 K, ethanol): $g_\perp$ = 1.983, $A_\perp$ = 60·$10^{-4}$ $cm^{-1}$, $g_{II}$ = 1.945, $A_{II}$ = 165·$10^{-4}$ $cm^{-1}$.

**[VO(5-GalOdipic)$_2$] (4c):** Yield 84% (530 mg). $C_{38}H_{44}N_2O_{19}V$·4THF·0.75$Na_2SO_4$ (1260.64): calcd. C 51.45, H 6.08, N 2.22; found C 51.01, H 5.93, N 2.13. IR (KBr) $\tilde{\nu}$ = 3114, 3081 (ar C–H); 2988, 2936 (C–H); 1731 (C=O); 1681 $\nu_{as}(CO_2^-)$; 1642, 1608, 1578 (C=C), (C=N); 1457, 1437, 1415, 1383 (C–H), $\nu_s(CO_2^-)$; 1282, 1256, 1283, 1212 (C=C), (C=N); 1168, 1113, 1070, 1002 (O–CH); 973 (V=O); 898, 863 (ar. C–H), (C–$CO_2$); 747 (ar. C–H) $cm^{-1}$. MS (FAB): *m/z* = 884 (M + 1). EPR (293 K, THF): $g_0$ = 1.975, $A_0$ = 95·$10^{-4}$ $cm^{-1}$; (100 K, ethanol): $g_\perp$ = 1.983, $A_\perp$ = 60·$10^{-4}$ $cm^{-1}$, $g_{II}$ = 1.945, $A_{II}$ = 165·$10^{-4}$ $cm^{-1}$.

**[VO(5-InoOdipic)$_2$] (4d):** Yield 85% (331 mg). $C_{28}H_{24}N_2O_{19}V$·$2H_2O$ (779.47): calcd. C 43.15, H 3.62, N 3.59; found C 43.06, H 4.17, N 3.65. IR (KBr) $\tilde{\nu}$ = 3075 (ar C–H); 2929, 2851 (C–H); 1724 (C=O); 1664 (sh) $\nu_{as}(CO_2^-)$; 1635, 1577 (C=C), (C=N); 1488, 1397, 1348 (C–H), $\nu_s(CO_2^-)$; 1287 (C=C), (C=N); 1162, 1124, 1090, 1048, 1006 (O–CH); 985 (V=O); 752 (ar. C–H) $cm^{-1}$. MS (FAB): *m/z* = 778 (M – 1]. EPR (293 K, THF): $g_0$ = 1.97, $A_0$ = 100·$10^{-4}$ $cm^{-1}$; (100 K, water): $g_\perp$ = 1.983, $A_\perp$ = 60·$10^{-4}$ $cm^{-1}$, $g_{II}$ = 1.945, $A_{II}$ = 165·$10^{-4}$ $cm^{-1}$.

**[VO(5-GlyOEtdipic)$_2$] (5a):** Yield 73% (241 mg). $C_{22}H_{22}N_4O_{11}V$·THF·$H_2O$ (659.50): calcd. C 47.35, H 4.89, N 8.50; found C 47.30, H 4.59, N 9.11. IR (KBr) $\tilde{\nu}$ = 3067 (ar C–H); 2981, 2953, 2873 (C–H); 1745 (C=O); 1670 $\nu_{as}(CO^{2-})$; 1597, 1542 (C=C), (C=N); 1437, 1417, 1377, 1353 (C–H), $\nu_s(CO_2^-)$; 1311, 1248, 1207 (C=C), (C=N); 1119, 1029 (O–CH); 975 (V=O); 873, 829 (ar. C–H), (C–$CO_2$); 749 (ar. C–H) $cm^{-1}$. MS (FAB): *m/z* = 570 (M), 592 [M + Na]. EPR (100 K, ethanol): $g_\perp$ = 1.99, $A_\perp$ = 60·$10^{-4}$ $cm^{-1}$, $g_{II}$ = 1.95, $A_{II}$ = 170·$10^{-4}$ $cm^{-1}$.

**[VO(5-AlaOEtdipic)$_2$] (5b):** Yield 65% (235 mg). $C_{24}H_{26}N_4O_{11}V$·THF·$H_2O$·0.25$Na_2SO_4$ (723.06): calcd. C 46.51, H 5.02, N 7.75; found C 46.15, H 4.45, N 7.99. IR (KBr) $\tilde{\nu}$ = 3070 (ar C–H); 2986, 2936, 2854 (C–H); 1738 (C=O); 1665 $\nu_{as}(CO_2^-)$; 1605, 1575, 1541 (C=C), (C=N); 1484, 1452, 1418, 1370, 1343 (C–H), $\nu_s(CO_2^-)$; 1284, 1212, 1179 (C=C), (C=N); 1123, 1047 (O–CH); 977 (V=O); 851 (ar. C–H), (C–$CO_2$); 749 (ar. C–H) $cm^{-1}$. MS (FAB): *m/z* = 598 (M), 620 [M + Na]. EPR (100 K, ethanol): $g_\perp$ = 1.985, $A_\perp$ = 60·$10^{-4}$ $cm^{-1}$, $g_{II}$ = 1.950, $A_{II}$ = 163·$10^{-4}$ $cm^{-1}$.

**[VO(5-ValOEtdipic)$_2$] (5c):** Yield 69% (228 mg). $C_{22}H_{22}N_4O_{11}V$·THF·$H_2O$ (659.50): calcd. C 47.35, H 4.89, N 8.50; found C 47.30, H 4.59, N 9.11. IR (KBr) $\tilde{\nu}$ = 3065 (ar C–H); 2967, 2937, 2876 (C–H); 1739 (C=O); 1651 $\nu_{as}(CO_2^-)$; 1570, 1538 (C=C), (C=N); 1438, 1419, 1393, 1373 (C–H), $\nu_s(CO_2^-)$; 1312, 1249, 1197 (C=C), (C=N); 1157, 1021 (O–CH); 975 (V=O); 862, 823 (ar. C–H), (C–$CO_2$); 744, 697 (ar. C–H) $cm^{-1}$. MS (FAB): *m/z* = 654 (M + 1], 676 [M + Na]. EPR (100 K, ethanol): $g_\perp$ = 1.981, $A_\perp$ = 60·$10^{-4}$ $cm^{-1}$, $g_{II}$ = 1.945, $A_{II}$ = 166·$10^{-4}$ $cm^{-1}$.

**[VO(5-PheOEtdipic)$_2$] (5d):** Yield 50% (203 mg). $C_{36}H_{34}N_4O_{11}V$·0.5THF·$1.5H_2O$ (812.71): calcd. C 56.16, H 5.08, N 6.89; found C 56.35, H 5.19, N 6.78. IR (KBr) $\tilde{\nu}$ = 3061, 3030 (ar C–H); 2980, 2952, 2929, 2868 (CH); 1739 (C=O); 1665

 © 2006 Wiley-VCH Verlag GmbH & Co. KGaA, Weinheim 

$\nu_{as}(CO_2^-)$; 1602, 1536, 1497 (C=C), (C=N); 1455, 1438, 1374 (C–H), $\nu_s(CO_2^-)$; 1309, 1247, 1197, 1157 (C=C), (C=N); 1122, 1025 (O–CH); 966 (V=O); 855 (ar. C–H), (C–$CO_2$); 745, 700 (ar. C–H) $cm^{-1}$. MS (FAB): $m/z$ = 750 (M + 1]. EPR (100 K, ethanol): $g_\perp$ = 1.983, $A_\perp = 60 \cdot 10^{-4}$ $cm^{-1}$, $g_{II}$ = 1.945, $A_{II} = 165 \cdot 10^{-4}$ $cm^{-1}$.

## Acknowledgments

This work was supported by the Hanseatic City of Hamburg, the Deutsche Forschungsgemeinschaft (grants RE 431/13-1 and /18-1) and the European Union (COST D21 0009/01).

[1] T. Kiss, T. Jakusch, *Metallotherapeutic Drugs and Metal-Based Diagnostic Agents: The Use of Metals in Medicine* (Eds.: M. Gielen, E. Tiekink), Wiley-VCH, Weinheim, **2005**, chapter 8.
[2] K. H. Thompson, C. Orvig, *J. Chem. Soc., Dalton Trans* **2000**, 2885–2892.
[3] a) K. H. Thompson, J. H. McNeill, C. Orvig, *Chem. Rev.* **1999**, *99*, 2561–2571; b) C. Orvig, K. H. Thompson, personal communication.
[4] S. Semiz, C. Orvig, J. H. McNeill, *Molec. Cell Biochem.* **2002**, *231*, 23–35.
[5] H. Sakurai, K. Fujii, H. Watanabe, H. Tamura, *Biochem. Biophys. Res. Commun.* **1995**, *214*, 1095–1101.
[6] D. C. Crans, L. Yang, T. Jakusch, T. Kiss, *Inorg. Chem.* **2000**, *39*, 4409–4416.
[7] H. Sakurai, Y. Kojima, Y. Yoshikawa, K. Kawabe, H. Yasui, *Coord. Chem. Rev.* **2002**, *226*, 187–198.
[8] J. Gätjens, B. Meier, T. Kiss, E. M. Nagy, P. Buglyó, H. Sakurai, K. Kawabe, D. Rehder, *Chem. Eur. J.* **2003**, *9*, 4924–4935.
[9] K. Isagawa, M. Kawai, Y. Fushizaki, *Nippon Kaguku Zasshi* **1967**, *88*, 553.
[10] K. Ohta, E. Kawachi, N. Inoue, H. Fukasawa, Y. Hashimoto, A. Itai, H. Kagechika, *Chem. Pharm. Bull.* **2000**, *48*, 1504–1513.
[11] H. W. Lee, Y. Kishi, *J. Org. Chem.* **1985**, *50*, 4402–4404.
[12] S. Ozaki, Y. Koga, L. Ling, Y. Watanabe, Y. Kimura, M. Hirata, *Bull. Chem. Soc. Jpn.* **1994**, *67*, 1058–1063.
[13] S. R. Tipson, *Methods Carbohydr. Chem.* **1963**, *2*, 246–250.
[14] M. Melchior, K. H. Thompson, J. M. Jong, S. J. Rettig, E. Shuter, V. G. Yuen, Y. Zhou, J. H. McNeill, C. Orvig, *Inorg. Chem.* **1999**, *38*, 2288–2293.
[15] K. Wieghardt, *Inorg. Chem.* **1978**, *17*, 57–64.
[16] D. Rehder, J. Costa Pessoa, C. F. G. C. Geraldes, M. M. C. A. Castro, T. Kabanos, T. Kiss, B. Meier, G. Micera, L. Pettersson, M. Rangel, A. Salifoglou, I. Turel, D. Wang, *J. Biol. Inorg. Chem.* **2002**, *7*, 384–396.

Received: February 15, 2006
Published Online: May 30, 2006

 © 2006 Wiley-VCH Verlag GmbH & Co. KGaA, Weinheim 

DOI: 10.1002/ejic.200600301

# Crystal Structure of the $V^V$ Dimer $[V_2O_2(\mu\text{-}O)(dmpp)_2(OCH_3)_2]$ and Its Equilibrium with the $V^V$ Trimer $[V_3O_3(\mu\text{-}O)_3(dmpp)_3(H_2O)](H_2O)_2$ in Methanol/Water Solutions

**Fernando Avecilla,*[a] Carlos F. G. C. Geraldes,[b] Anjos L. Macedo,[c] and M. Margarida C. A. Castro*[b]**

**Keywords:** Vanadium / Pyridinone complexes / NMR spectroscopy / X-ray crystallography

The behaviour of the cyclic trimeric $V^V$ complex $[V_3O_3(\mu\text{-}O)_3(dmpp)_3(H_2O)](H_2O)_2$, $V_3L_3$, (L = Hdmpp = 3-hydroxy-1,2-dimethyl-4-pyridinone) was studied in methanol and methanol/water solutions by using $^{51}V$ and 1D- and 2D $^1H$ NMR spectroscopy. Red crystals, isolated from a highly concentrated methanol solution of the trimeric complex, were analysed by X-ray crystallography. The solid-state structure of the compound showed the presence of a new dinuclear $V^V$ cluster and allowed for its formulation as a $[V_2O_2(\mu\text{-}O)(dmpp)_2(OCH_3)_2]$ complex, $V_2Y_2L_2$ (Y = $OCH_3$). This complex crystallises in the monoclinic system: $P2_1/c$, $a$ = 8.4573(11) Å, $b$ = 15.034(2) Å and $c$ = 15.849(2) Å, $\beta$ = 105.300(2)°, $V$ = 1943,7(4) Å$^3$, $Z$ = 2, and $R_1(wR_2)$ = 0.0492(0.1706). The trimer $V_3L_3$ complex dissolved in a dry methanol solution fully decomposes, as shown by the $^{51}V$ NMR signals at –388, –450 and –551 ppm, which are assigned to a monomer complex $[VO(OMe)(dmpp)_2]$ ($VYL_2$), the dimer $V_2Y_2L_2$ and the monomethyl ester of monovanadate, $V_1Y$ ($V_1$ = monovanadate; Y = $OCH_3$), respectively. In methanol/water solutions, a new $^{51}V$ NMR signal appears at $\delta$ = –492 ppm, which is assigned to the $[VO_2(dmpp)(H_2O)_2]$ (VL) complex. When the percentage of water in the mixture increases, the relative intensities of the $V_2Y_2L_2$ and $V_1Y$ signals decrease sharply, and a broad signal at –488 ppm appears, corresponding to the original $V^V$ trimer complex, which is the only species present in 94 % water. A temperature-dependent $^1H$ NMR study of a $CD_3OD$ solution of $V_3L_3$ confirmed the presence, at room temperature, of the dinuclear $V_2L_2$ complex and the $VL_2$ species. At temperatures below 0 °C down to –50 °C, the appearance of new signals reflects the presence of isomers for the $V_2Y_2L_2$ and $VYL_2$ species with different stabilities and symmetries. 2D $^1H$ homonuclear NMR exchange experiments (EXSY) allowed us to establish the isomeric equilibria that take place in solution, and indicates intramolecular exchange between the two ligands of the major isomer of $VYL_2$ and intermolecular exchange between the major and minor isomers of species of different nuclearity, $V_2Y_2L_2$ and $VYL_2$. However, no evidence was found for intermolecular exchange between the major isomers and between the minor isomers of species of different nuclearity or between isomers of species of the same nuclearity.

(© Wiley-VCH Verlag GmbH & Co. KGaA, 69451 Weinheim, Germany, 2006)

## Introduction

Vanadium is an essential biological trace element of the utmost importance.[1,2] It is present in some biological systems in high concentrations, where it seems to have a relevant role, such as in the *Amanita muscaria* mushroom as the amavadin complex[3] and in some ascideas in the form of tunichromes.[4] Vanadium is the cofactor of some enzymes, like the vanadium-dependent haloperoxidases in algae and lichens[5] and the vanadium-nitrogenases in some bacteria.[6] It also interferes with the activity of certain enzymes, in particular those involved in phosphorylations,[7] where it acts as a phosphate analogue, and it is responsible for many physiological and metabolic effects observed in different organisms, where it is essential at low concentrations although toxic at concentrations higher than 1 mM.[8] Vanadium in biological systems mainly occurs as the anionic vanadate ($V^V$), which is isostructural to phosphate, or the cationic vanadyl ($V^{IV}$), depending on the redox properties of the medium.[8] The insulin-mimetic properties of inorganic vanadate and vanadyl,[9] as well as of some $V^{IV}$ and $V^V$ complexes,[10] have stimulated the search for a vanadium complex that can be used as an effective oral substitute for insulin. The well-recognised biological importance of vanadium has attracted much interest for its coordination and redox chemistry both in the $V^{IV}$ and $V^V$ oxidation states and both in the solid state and in solution. The interest extends to the modeling of the interaction of vanadium

[a] Departamento de Química Fundamental, Universidade da Coruña,
Campus de A Zapateira s/n, 15071, A Coruña, Spain
E-mail: avecil@udc.es
[b] Departamento de Bioquímica, Centro de Espectroscopia RMN e Centro de Neurociências e Biologia Celular, Faculdade de Ciências e Tecnologia, Universidade de Coimbra,
Apartado 3126, 3001-401 Coimbra, Portugal
E-mail: gcastro@ci.uc.pt
[c] REQUIMTE, C.Q.F.B., Departamento de Química, Faculdade de Ciências e Tecnologia, Universidade Nova de Lisboa,
2829-516 Caparica, Portugal

 © 2006 Wiley-VCH Verlag GmbH & Co. KGaA, Weinheim 

with living systems, with particular focus on the structural and functional biological activity of this element.

The aqueous chemistry of vanadium(V) is very complex. Hydrolysis, redox and oligomerization reactions can occur in solution, resulting in different species, depending on the pH, ionic strength and total vanadium concentration in the medium,[11] which together determine the coordination properties of vanadium(V). The structure and reactivity of vanadate in other solvents, in particular alcohols, have been largely studied.[12] Vanadium complexes with different geometries and coordination modes containing O and/or N and/or S as donor atoms in their structures[6b,11,13] have been useful model compounds to understand the coordination chemistry of vanadium in living systems. In particular, the solid-state structures of $V^{IV}$ and $V^V$ compounds with ligands from the class of pyrones and pyridinones (with one ketonic and one enolic group as donor atoms) have been determined by X-ray crystallography[14a,15] and EXAFS.[16] The speciation of these vanadium compounds in solution has been extensively studied by using potentiometry, UV/Vis, $^{51}V$ and $^1H$ NMR and EPR spectroscopy.[14a,16–18] Compound bis(maltolato)oxidovanadium(IV) [BMOV, $VO(ma)_2$, ma = maltolate] was the first example to be used as an insulin-mimetic complex,[14,19] and phase 1 clinical trials in humans have been completed on bis(ethylmaltolato)oxidovanadium(IV) (BEOV).[20] Several other oxovanadium(IV) complexes have also been reported to exhibit insulin-mimetic properties in vivo.[21] The compound bis(3-hydroxy-1,2-dimethyl-4-pyridinone)oxidovanadium(IV), $VO(dmpp)_2$ (see Scheme 1 for the structure of the ligand Hdmpp), as well as the ternary systems formed with low molecular mass components of blood serum have also been studied in aqueous solution under anaerobic and aerobic conditions.[17,18] At physiological pH, $VO(dmpp)_2$ showed low toxicity in erythrocyte suspensions[22] and promising in vitro insulin-like properties in fibroblast cell lines[23a] and in rat adipocytes.[23b]

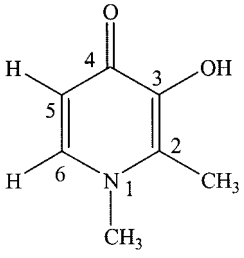


Scheme 1.

The interaction of vanadate with the ligand Hdmpp in aqueous solution has been extensively studied by us.[18] A new trinuclear oxovanadium(V) complex was isolated from aqueous solution at a pH of 4–5 and was characterised in the solid state by X-ray crystallography as $[V_3O_3(\mu\text{-}O)_3(dmpp)_3(H_2O)](H_2O)_2$ that contains a cyclic $V^V$ cluster and in aqueous solution by mass spectrometry and $^{51}V$ and $^1H$ NMR spectroscopy.[24] In this work, we report on the behaviour of this trinuclear $V^V$ compound in methanol and methanol/water solutions investigated by $^{51}V$ NMR spectroscopy and 1D and 2D $^1H$ NMR spectroscopy. The red crystals that formed from a highly concentrated $CD_3OD$ solution of the $V^V$ trimer were structurally analysed, and the X-ray crystallographic data obtained indicated the formation of a new dinuclear $V^V$ compound $[V_2O_2(\mu\text{-}O)(dmpp)_2(OCH_3)_2]$.

## Results and Discussion

### X-ray Structure

The X-ray structure obtained for the crystalline $[V_2O_2(\mu\text{-}O)(dmpp)_2(OCH_3)_2]$ complex ($V_2Y_2L_2$) is shown in Figure 1 with the atomic numbering scheme, and the corresponding bond lengths and angles are listed in Table 1. It consists of a dinuclear oxovanadium(V) complex with two anionic dmpp ligands, one oxygen atom bridge and two methoxy groups, each coordinated to one vanadium atom. The oxygen atom bridge links the two vanadium atoms, each one of which is also coordinated to one oxo group. Both V1 and V2 atoms adopt a distorted six-coordinate octahedral geometry (Figure 2). The V1 coordination sphere is composed of an enolate oxygen atom [V1–O6 = 2.040(3) Å], a ketonic oxygen atom [V1–O7 = 1.989(3) Å], a deprotonated alkoxide oxygen atom of a methoxy group [V1–O1M = 1.787(4) Å], a terminal oxo atom [V1–O1 = 1.594(3) Å] and a second oxo atom [V1–O4 = 1.824(3) Å] that forms a strong bridge to V2 [V2–O4 = 1.804(3) Å]. The remainder of the V2 coordination sphere is completed by an enolate oxygen [V2–O3 = 2.060(3) Å], a ketonic oxygen atom [V2–O5 = 1.972(3) Å], an alkoxide oxygen atom of the other methoxy ligand [V2–O2M = 1.783(3) Å] and a terminal oxo atom [V2–O2 = 1.594(3) Å]. A second, weaker

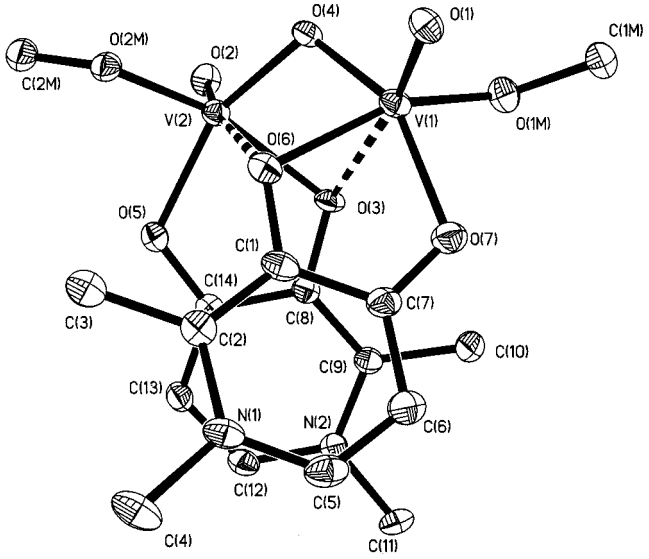


Figure 1. X-ray crystal structure of the complex $[V_2O_2(\mu\text{-}O)(dmpp)_2(OCH_3)_2]$ showing the atomic numbering scheme. Hydrogen atoms have been omitted for simplicity. The ORTEP plot is at the 30% probability level.

 © 2006 Wiley-VCH Verlag GmbH & Co. KGaA, Weinheim 

bridge between V1 and V2 is formed by an enolate oxygen (O3) of the ligand coordinated to V2 (see Table 1) and an enolate oxygen (O6) of the ligand coordinated to V1. The V2–O3 and V1–O6 distances are 2.060(3) Å and 2.040(3) Å, respectively, as compared with the V1–O3 and V2–O6 bond lengths of 2.464(3) Å and 2.589(3) Å, respectively. The vanadium atom V1 is located at 0.33697 Å from the axial plane defined by O4, O6, O7 and O1M, and the vanadium atom V2 is 0.4010 Å from the basal plane defined by O3, O4, O5 and O2M (Figure 2). Both vanadium atoms have a strong V=O bond, as the values of the V1–O1 and V2–O2 distances are compatible with those found in other similar structures.[25] All bond lengths are in the range of the values reported in the literature for other known polynuclear vanadium(V) complexes.[14a,15,26]

Table 1. Selected bond lengths [Å] and angles [°] for $[V_2O_2(\mu\text{-}O)(dmpp)_2(OCH_3)_2]$ with estimated standard deviations in parentheses. M indicates the methoxy oxygen atoms.

| Bond lengths | | | |
|---|---|---|---|
| V(1)–O(1) | 1.594(3) | V(2)–O(2) | 1.594(3) |
| V(1)–O(1M) | 1.787(4) | V(2)–O(2M) | 1.783(3) |
| V(1)–O(3) | 2.464(3) | V(2)–O(3) | 2.060(3) |
| V(1)–O(4) | 1.824(3) | V(2)–O(4) | 1.804(3) |
| V(1)–O(6) | 2.040(3) | V(2)–O(5) | 1.972(3) |
| V(1)–O(7) | 1.989(3) | V(2)–O(6) | 2.589(3) |
| **Bond angles** | | | |
| O(1)–V(1)–O(1M) | 99.94(17) | O(2)–V(2)–O(2M) | 101.51(17) |
| O(1)–V(1)–O(4) | 104.13(17) | O(2)–V(2)–O(4) | 104.61(17) |
| O(1M)–V(1)–O(4) | 103.30(16) | O(2M)–V(2)–O(4) | 102.85(15) |
| O(1)–V(1)–O(7) | 101.56(17) | O(2)–V(2)–O(5) | 100.86(17) |
| O(1M)–V(1)–O(7) | 86.57(16) | O(2M)–V(2)–O(5) | 87.46(15) |
| O(4)–V(1)–O(7) | 150.29(15) | O(4)–V(2)–O(5) | 149.83(15) |
| O(1)–V(1)–O(6) | 99.11(16) | O(2)–V(2)–O(3) | 101.90(16) |
| O(1M)–V(1)–O(6) | 158.03(16) | O(2M)–V(2)–O(3) | 154.64(15) |
| O(4)–V(1)–O(6) | 82.46(14) | O(4)–V(2)–O(3) | 80.46(14) |
| O(7)–V(1)–O(6) | 78.95(14) | O(5)–V(2)–O(3) | 78.69(13) |
| O(1)–V(1)–O(3) | 171.68(16) | O(2)–V(2)–O(6) | 171.03(15) |
| O(1M)–V(1)–O(3) | 87.04(14) | O(2M)–V(2)–O(6) | 85.82(14) |
| O(4)–V(1)–O(3) | 69.59(12) | O(4)–V(2)–O(6) | 68.37(12) |
| O(7)–V(1)–O(3) | 83.25(13) | O(5)–V(2)–O(6) | 84.49(13) |
| O(6)–V(1)–O(3) | 74.99(12) | O(3)–V(2)–O(6) | 71.85(12) |
| | | V(2)–O(3)–V(1) | 81.85(11) |
| | | V(2)–O(4)–V(1) | 110.33(16) |
| | | V(1)–O(6)–V(2) | 79.12(11) |

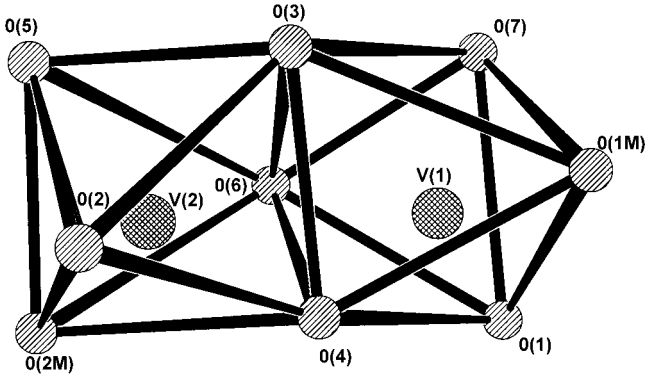


Figure 2. Coordination polyhedra in the crystal structure of the vanadium cluster in the dimeric species $[V_2O_2(\mu\text{-}O)(dmpp)_2(OCH_3)_2]$.

The oxido and methoxido ligands of the $V_2Y_2L_2$ dimer, which exert a strong *trans* influence, are *cis* to one another. The preference of these ligands for a *cis* configuration in such complexes has been demonstrated in VO(OMe)(L) compounds {where L represents the tetradentate Schiff bases *N*,*N*′-2,2-dimethyltrimethylenebis[salicylidenaminato(2–)] (salnptn) and *N*,*N*′-ethylenebis[salicylideneaminato(2–)] (salen)}.[27] In these complexes, a *cis*-VO(OMe) arrangement was allowed by forcing the normally planar tetradentate Schiff base ligands into three equatorial and one axial coordination positions. The oxido and methoxido ligands are also *cis* to one another in the *cis*-VO(OMe)-$(ma)_2$ complex, which results from aerobic oxidation of the bis(maltolato)oxidovanadium(IV) complex $[VO(ma)_2$, BOMV] in methanol.[14a,15a]

The $V_2Y_2L_2$ dimer complex has an enolic dmpp oxygen atom (O3 in V1) that is *trans* and four dmpp oxygen atoms (enolic O6 and ketonic O7 in V1, and enolic O3 and ketonic O5 in V2) that are *cis* relative to the strong V=O bond in each vanadium atom.[14a,15a] The dmpp oxygen atoms belonging to the enolic groups are deprotonated (O3 and O6). The *trans* position is destabilised with respect to the other positions, as shown by the length of the V1–O3 and V2–O6 bonds in the $V_2Y_2L_2$ species, in a manner similar to that in other dimeric and monomeric compounds.[28] The dmpp ligand has a strong preference for meridional coordination, except when a methoxy group or a water molecule competes with it for the *cis* position relative to the oxo group.

The dinuclear complex contains the $V_2O_3$ framework,[15b] which exhibits one bridging oxygen atom (O4) and the formal enolic oxygen atoms (O3 and O6) of the two dmpp groups. From the X-ray results one could not unambiguously distinguish between a keto-O5 and an enolate-O3 structure for this bifunctional binding group, as the C–O bond lengths to the formal keto and enolate oxygen atoms in the C–O–V–O–C chain are almost the same {e.g. C8–O3 [1.338(5) Å], C14–O5 [1.317(6) Å] for the V2 cycle}. It is possible that the π electron cloud is delocalised over all the atoms that form each C–O–V–O–C cycle, giving an intermediate character to all the formal ketonic and enolic oxygen atoms of each dmpp molecule.[24] As expected, the doubly bridging (O3 and O6) dmpp atoms have V–O bond [2.464(3) and 2.060(3) Å for (O3), 2.040(3) Å and 2.589(3) Å for (O6)] that are longer than the V–O bond for the bridging oxygen atom (O4) [1.824(3) and 1.804(3) Å]. The V2–O6 distance [2.589(3) Å] is even longer than the V1–O3 distance. The average value of the V–O–V bond lengths is 1.81(2), which is similar to that obtained for other polynuclear vanadium compounds.[29] In the $V_2O_3$ framework, the bond angle V1–O4–V2 [110.35(16)°] is very different from the bond angles V1–O3–V2 [81.81(11)°] and V1–O6–V2 [79.12(11)°]. This is in agreement with the results published for the trimeric species $[V_3O_3(\mu\text{-}O)_3(dmpp)_3(H_2O)](H_2O)_2$.[24]

Figure 3 shows an upper view of the complex along the pseudo-$C_2$ axis, which passes along the oxygen atom O4.

 © 2006 Wiley-VCH Verlag GmbH & Co. KGaA, Weinheim 

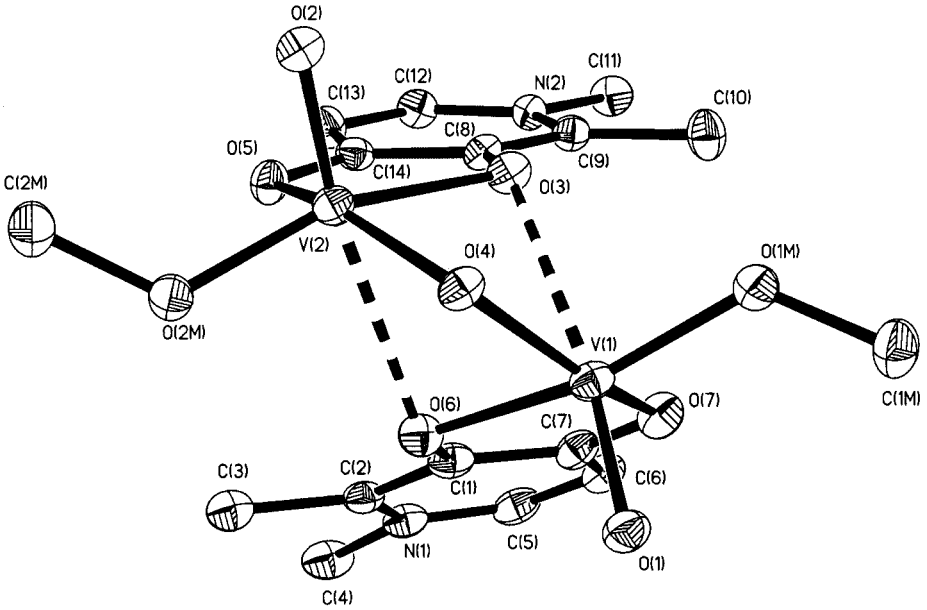


Figure 3. Upper view of the complex $[V_2O_2(\mu\text{-}O)(dmpp)_2(OCH_3)_2]$. Hydrogen atoms have been omitted for simplicity. The ORTEP plot is at the 30% probability level.

This view clearly illustrates the pseudo-$C_2$ symmetry of the complex. Each of the two methoxy groups is coordinated to each of the two vanadium atoms. The angle between the planes of the two dmpp ligands is 34.6°. In this view, it is easy to foresee that a dynamic equilibrium between different isomers can occur in solution.

## Solution Studies

### *$^{51}V$ NMR Spectroscopic Studies*

The behaviour of the cyclic $V^V$ trimer compound $[V_3O_3(\mu\text{-}O)_3(dmpp)_3(H_2O)](H_2O)_2$, $(V_3L_3)$[24] was studied as a function of solvent composition by $^{51}V$ NMR spectroscopy. Dissolution of black crystals of $V_3L_3$ in dry methanol gives a $^{51}V$ NMR spectrum that shows four signals with different intensities at –386 (shoulder), –388, –450 and –551 ppm (Figure 4A), which indicates the presence of four different vanadium(V) species in solution. The signal at –551 ppm corresponds to the monomethyl ester of vanadate $V_1Y$ ($V_1$ = monovanadate; Y = $OCH_3$),[12c] which was previously detected as one of the products resulting from the aerobic oxidation in methanol solution of $VO(ma)_2$ to $[VO(OCH_3)(ma)_2]$ and was described as $[VO(OCH_3)]^{2+}$.[15a] The signal at –450 ppm, with the highest intensity, was assigned to the dimer $V^V$ complex $V_2Y_2L_2$. This assignment is corroborated by the observation of $^{51}V$ high frequency shifts of the signals for the dimer with respect to those of the monomer in other systems, such as the oxovanadium alkoxides $VO(OR)_3$ or vanadate complexes of hydroxy acids such as glycerate or lactate.[30]

In a highly concentrated methanol solution, this compound precipitates as red crystals, which were analysed by X-ray crystallography. The crystal structure is presented in this work. The signal at –388 ppm was assigned to *cis*-$[VO(OCH_3)(dmpp)_2]$ ($VYL_2$) containing one methoxy

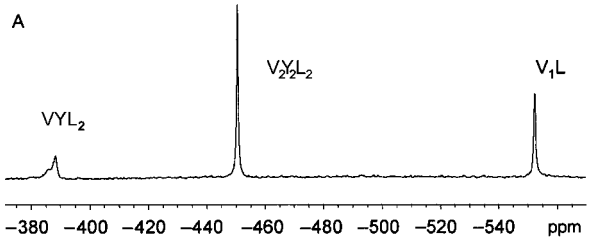


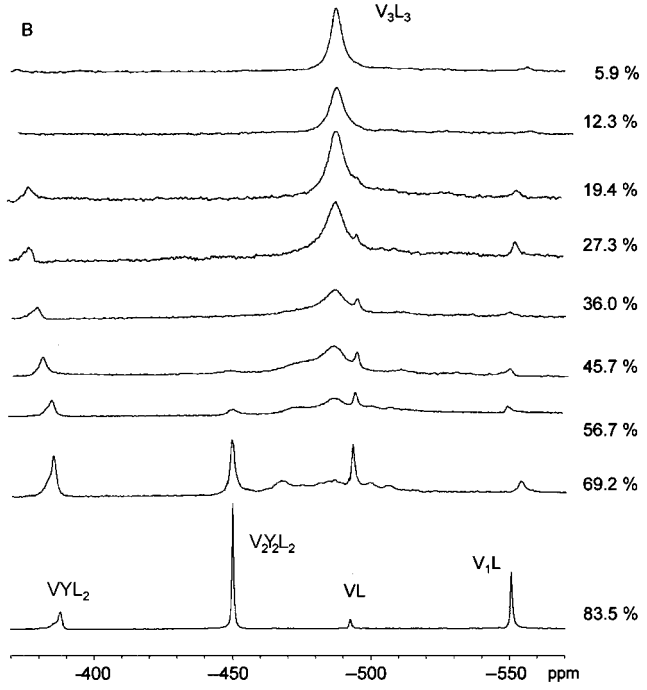


Figure 4. $^{51}V$ NMR spectra of solutions of the crystalline $V^V$ compound $[V_3O_6(dmpp)_3(H_2O)]\cdot(H_2O)_2$ obtained at 131.404 MHz and at 22.0 ± 0.5 °C in (A) dry $CH_3OH$; (B) $CH_3OH/H_2O$ mixtures, at pH ≈ 4 and different $CH_3OH/H_2O$ mol ratios. The $CH_3OH$ mol% is shown in the figure.

 © 2006 Wiley-VCH Verlag GmbH & Co. KGaA, Weinheim 

group, analogous to the bis(maltolato) complex $[VO(OCH_3)(ma)_2]$,[14a,15a] and its shoulder at –386 ppm to the corresponding *trans* isomer.

The $^{51}V$ NMR spectra of the trimer $V_3L_3$ dissolved in methanol/water solutions with different percentages of the two solvents dramatically change with the solvent composition, as shown in Figure 4B. In a solution where the mol fraction of $CH_3OH$ is 83.5%, a new signal appears at $\delta$ = –492 ppm, in addition to those already present. This signal, which is absent in pure methanol and only appears when water is present in solution, was assigned to the $[VO_2(dmpp)(H_2O)_2]$ (VL) complex with no methoxy group in its structure, which, at pH ≈ 4 appears at –492 ppm, as previously reported.[18] The relative intensities of the $V_2Y_2L_2$ and $V_1Y$ signals decrease sharply when the percentage of water in the solution increases. The first signal completely disappears at 36.0% $CH_3OH$ and the second one at 12.3% $CH_3OH$. The signals for the VL and $VYL_2$ species disappear at 12.3% $CH_3OH$. Furthermore, the $VYL_2$ signals gradually shift with increasing water content, up to a value of –376 ppm, reflecting the formation of the $[VO(OH)(dmpp)_2]$ complex, which dominates in water solution at pH ≈ 4.[18] In addition, at 69.2% $CH_3OH$, a broad signal appears at –488 ppm. Its intensity increases with the percentage of water, and when water is present at 94.1%, it is the only signal observed in the $^{51}V$ NMR spectrum (Figure 4B). This signal corresponds to the original $V^V$ trimer complex $V_3L_3$, whose $^{51}V$ NMR signal in aqueous solution at pH ≈ 4 has already been reported.[24] This was confirmed by slowly evaporating the methanol from a water/methanol solution of the $V^V$ trimer at room temperature, which leads to an aqueous solution that gives a $^{51}V$ NMR spectrum consisting of the same single, broad signal at –488 ppm. After some time, black crystals were isolated from the solution, and characterisation of their structure by X-ray crystallography confirmed that these are indeed crystals of the $V^V$ trimer $V_3L_3$ compound, whose structure had been previously reported.[24]

### *$^1$H NMR Spectroscopic Studies*

$^1$H NMR spectra of solutions of the $V^V$ trimer, $[V_3O_3(\mu\text{-}O)_3(dmpp)_3(H_2O)](H_2O)_2$, in dry [D$_4$]MeOH ($CD_3OD$, no water present) were obtained at different temperatures. Figure 5A shows the signals for the $H^5$ and $H^6$ aromatic dmpp protons (6.0–8.0 ppm) from 25 °C down to –40 °C, while Figure 5B shows the signals corresponding to the $H^5$ (6.0–7.0 ppm) and C(2)–$CH_3$ (1.5–3.0 ppm) dmpp protons at –50 °C.[14,19] At 25 °C (Figure 5A) two doublets are observed at $\delta$ = 7.69 ppm and 7.55 ppm, corresponding to the $H^6$ protons of the $V_2Y_2L_2$ and $VYL_2$ species, respectively, and a doublet at $\delta$ = 6.55 ppm and a broad signal at $\delta$ = 6.28 ppm, assigned to the $H^5$ protons of the $V_2Y_2L_2$ and $VYL_2$ species, respectively. These assignments were made taking into account the $^{51}V$ NMR spectra previously discussed, which show the absence of the VYL and VL species when no water is present.

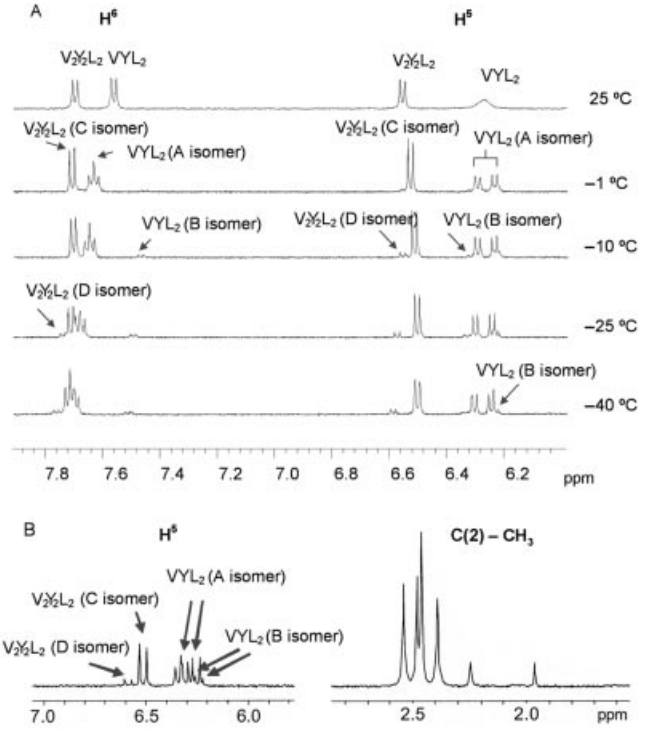


Figure 5. (**A**) 400 MHz $^1$H NMR spectra of solutions of the crystalline $V^V$ compound $[V_3O_6(dmpp)_3(H_2O)]\cdot(H_2O)_2$ in $CD_3OD$, at different temperatures, showing only the signals corresponding to the $H^5$ and $H^6$ protons of the ligand dmpp; (**B**) 200 MHz $^1$H NMR spectrum of a solution of the crystalline $V^V$ compound $[V_3O_6(dmpp)_3(H_2O)]\cdot(H_2O)_2$ in $CD_3OD$, at –50 °C, showing only the signals corresponding to the $H^5$ (6–7 ppm) and C(2)–$CH_3$ (1.5–3 ppm) protons of the ligand dmpp. The assignments in the spectra of Figure 5A are made according to the structures of the isomers presented in Figure 6.

The $^1$H NMR spectra at lower temperatures become more complex, revealing the presence of isomers of these complexes in solution. At –1 °C, the 6.28 ppm (25 °C) broad signal splits into two doublets at $\delta$ = 6.32 ppm and 6.25 ppm, while the 7.55 ppm (25 °C) signal originates from the triplet centred at $\delta$ = 7.63 ppm formed by two partially overlapping doublets (Figure 5A, b), which correspond to the nonequivalent $H^5$ and $H^6$ protons of the two ligands of the $VYL_2$ compound.[14a,14c,19] These features reflect the slowing down of the intramolecular dynamic processes, which, at higher temperature, average the two different environments of the $H^5$ and $H^6$ protons of the two ligands in the dominant *cis* isomer of $VYL_2$ compound (isomer A, Figure 6A), making them nonequivalent. At –10 °C, the new low-intensity doublets appearing at $\delta$ = 6.32 ppm and $\delta$ = 7.45 ppm (Figure 5A) are indicative of the presence of isomeric forms, and correspond to the $H^5$ and $H^6$ protons of the less stable *trans* isomer of the $VYL_2$ species (isomer B, Figure 6B), respectively. The doublet at $\delta$ = 6.56 ppm with a weak intensity corresponds to the $H^5$ proton of an isomer of the $V_2Y_2L_2$ dimer with the methoxy groups in a *cis* position (Figure 6D); this isomer is less stable than the major isomer with *trans* methoxy groups (Figure 6C), which is similar to the structure obtained in the crystal form. This

 © 2006 Wiley-VCH Verlag GmbH & Co. KGaA, Weinheim 

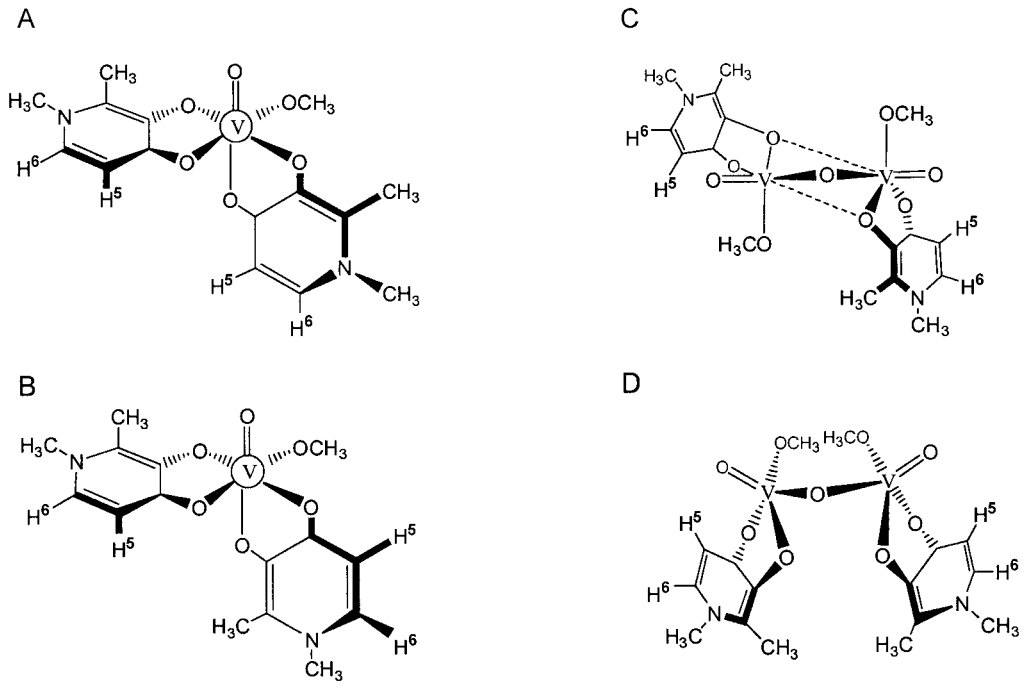


Figure 6. Schematic representation of the chemical structures of the possible isomers of: (A) the more stable and (B) the less stable isomers of the $VYL_2$ species [$VO(dmpp)_2(OMe)$]; and (C) the more stable and (D) the less stable isomers of the $V_2Y_2L_2$ species [$V_2O_2(\mu\text{-}O)(dmpp)_2(OCH_3)_2$], in methanol solution.

doublet is shifted to 6.57 ppm at –25 °C and to 6.58 ppm at –40 °C (Figure 5A). At –10 °C the $H^6$ signal of this isomer is not observed, as it overlaps with the large $H^6$ signal of the major $V_2Y_2L$ isomer. However, at –25 °C it can be seen at $\delta$ = 7.75 ppm and it shifts to 7.76 ppm at –40 °C. At lower temperatures the signals of the $H^6$ proton of the two isomers of $VYL_2$ are shifted to higher frequencies– the signal of the major isomer (isomer A) becomes superimposed with the $H^6$ proton signals of the $V_2Y_2L_2$ compound.

A schematic representation of the proposed chemical structures of the two isomers for each of these two species, which is in agreement with the NMR spectroscopic data, is presented in Figure 6. From the $^1H$ NMR spectroscopic data, it is expected that the two $H^6$ protons of the dmpp ligands in the $V_2Y_2L_2$ compound are equivalent in each isomer; the same can be said for the two $H^5$ protons (Figure 6C and D). These protons in the $VYL_2$ species are nonequivalent in both isomers (Figure 6A and B), although they are indistinguishable at 25 °C (Figure 5A) because of the presence of intramolecular averaging processes that are fast on the NMR time-scale. The structures A and C of Figure 6 are assumed to represent the more stable isomers of $VYL_2$ and $V_2Y_2L_2$, respectively. This assumption is based on the present X-ray crystal structure data for $V_2L_2$ and on the literature data for $VYL_2$ (L = ma).[14,15] However, a more precise knowledge of the relative stability of the structures in solution would require a study involving theoretical energy calculations.

Figure 5B presents an $^1H$ NMR spectrum obtained at –50 °C that shows the spectral regions 5.8–7.0 ppm, corresponding to the $H^5$ protons, and 1.5–3.0 ppm, corresponding to the protons of the $CH_3$ group attached to the C(2) atom of the dmpp molecule. The different doublets corresponding to the $H^5$ protons in the different species in solution are better resolved and corroborate the presence of two isomers for the $V_2Y_2L_2$ complex (one doublet at $\delta$ = 6.51 ppm for the more stable isomer C and one doublet at $\delta$ = 6.59 ppm for the less stable isomer D) and two isomers of the $VYL_2$ compound (two doublets at $\delta$ = 6.24 ppm and 6.35 ppm for the less stable isomer B and two doublets at $\delta$ = 6.25 ppm and 6.31 ppm for the more stable isomer A). With respect to the protons of the C(2)–$CH_3$ group, six singlets are observed: two signals are assigned to the $CH_3$ protons of the two isomers of the $V_2Y_2L_2$ complex, each one corresponding to the six protons of the two equivalent $CH_3$ groups of each isomer, and the other four signals correspond to the four $CH_3$ groups (two nonequivalent $CH_3$ groups in each isomer of the $VYL_2$ complex).

### *2D NMR Spectroscopic Experiments*

Two-dimensional (2D) $^1H$ NMR experiments, COSY (*J* correlated spectroscopy) and EXSY [exchange correlated spectroscopy, obtained using a phase-sensitive nuclear Overhauser spectroscopy (NOESY) pulse sequence], were carried out to further investigate the existence of different isomeric forms in solution, complementing the data obtained through one-dimensional (1D) $^1H$ NMR spectra at low temperature (–1 °C to –50 °C).

Figure 7 shows the low field region (6.0–8.0 ppm) of the 2D-COSY (Figure 7A) and 2D-EXSY (Figure 7B) spectra at –10 °C. This temperature value and the region in which the $H^5$ and $H^6$ signals of the dmpp ligand appear proved to

 © 2006 Wiley-VCH Verlag GmbH & Co. KGaA, Weinheim 

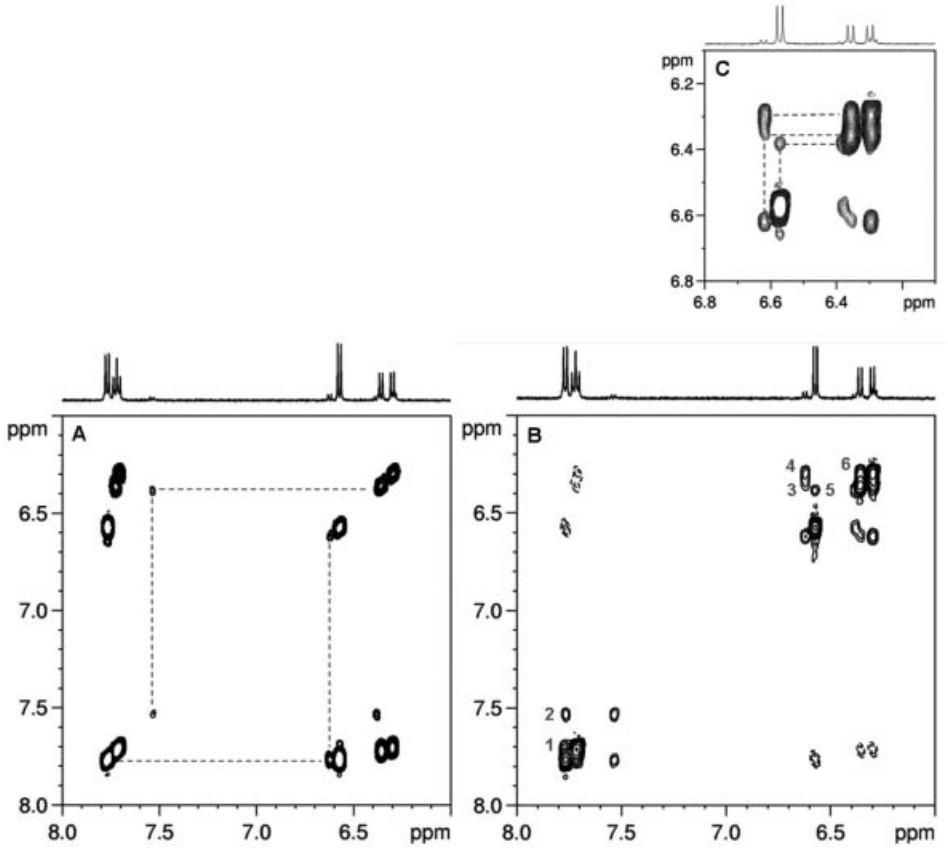


Figure 7. 400 MHz 2D $^1$H homonuclear NMR spectra (spectral region 6–8 ppm) of solutions containing the $V^V$ compound $[V_3O_6(dmpp)_3(H_2O)]\cdot(H_2O)_2$, in $CD_3OD$, at –10 °C: (A) COSY spectrum; and (B) EXSY spectrum (mixing time 800 ms) with (C) an expansion of the $H^5$ proton region. The contours of positive and negative peaks are defined by continuous and dashed lines, respectively.

give the most relevant information. In the COSY spectrum, cross-peaks correlating the protons $H^5$ and $H^6$ of each species in solution are expected. One cross-peak for each of the isomers C and D of $V_2Y_2L_2$, two cross-peaks for the two ligands of the major isomer of $VYL_2$ (isomer A) and only one of the two expected for its minor isomer (isomer B) can be observed. These observations confirm the assignments described above for the 1D $^1$H NMR spectra.

The phase sensitive 2D-EXSY spectrum in the pure double absorption mode contains two types of cross-peaks. For small molecules, like those studied here, the cross-peaks resulting from nuclear Overhauser effects (nOes) that are based on the intramolecular dipolar interactions of protons $H^5$ and $H^6$ of the same ligand, which are close in space, have negative intensities and appear at the same positions as the COSY cross-peaks. Only three nOe cross-peaks are observed, two for the major isomer (A) of $VL_2$ and one for the major isomer (C) of $V_2Y_2L_2$, as those for the minor isomers could not be detected. The diagonal peaks and the exchange cross-peaks resulting from the exchange processes that occur between different species and/or between the isomeric forms of a given species have positive intensities. The exchange cross-peaks observed for mixing times $\tau_m > 1/R$, where $R = k_{ex}/\Delta\upsilon_o$ is the ratio of the exchange rate constant and the chemical shift difference between the exchanging peaks of the same proton in the two species, give useful information about the dynamic equilibria in solution.[31] Their intensities are related to the corresponding exchange rate constants of the exchange equilibrium. A qualitative analysis of the exchange patterns of Figure 7B shows six cross-peaks, two in the $H^5$ region and four in the $H^6$ region. In the $H^5$ region, there are two stronger correlations – one between the two ligands of the major isomer of $VYL_2$ (A) and one between the minor isomer of $V_2Y_2L_2$ (D) and one of the two $H^5$ protons of the major isomer of $VYL_2$ (A). Two weaker correlations in the $H^5$ region are observed between the minor isomer of $V_2Y_2L_2$ (D) and the other $H^5$ protons of the major isomer of $VL_2$ (A), and between the major isomer of $V_2Y_2L_2$ (C) and the minor isomer of $VYL_2$ (B). In the $H^6$ region, two weak cross-peaks are observed – one involving correlation of the major or minor isomers of $V_2Y_2L_2$ (C or D) with the major isomer of $VYL_2$ (A) and the other with its minor isomer (B). This uncertainty results from the overlap of the $H^6$ resonances of isomers C and D of $V_2Y_2L_2$. However, taking into account the exchange pattern observed for the $H^5$ protons, the A↔D and B↔C correlations between the $H^6$ protons are more plausible. There is no evidence of cross-peaks correlating the $H^5$ or $H^6$ protons of the two isomers of the same species.

In conclusion, the $^{51}$V NMR spectroscopic data show that two different oligomeric species containing $V^V$ and dmpp can be isolated in water and methanol. Their X-ray

 © 2006 Wiley-VCH Verlag GmbH & Co. KGaA, Weinheim 

crystal structures show that the water species is a cyclic $V_3L_3$ trimer, $[V_3O_3(\mu\text{-}O)_3(dmpp)_3(H_2O)](H_2O)_2$, while the methanol species is a $V_2Y_2L_2$ dimer, $[V_2O_2(\mu\text{-}O)(dmpp)_2(OCH_3)_2]$. Dissolution of black crystals of the $V_3L_3$ trimer in methanol leads to its complete dissociation into a $V_2Y_2L_2$ dimer, a $VYL_2$ monomer and monovanadate, each of which has one methoxy group coordinated to the $V^V$ atoms. Red crystals of the dimer were isolated from the methanol solution. Increasing the amount of water in mixtures with methanol leads successively to the appearance of VL, the disappearance of $V_2Y_2L_2$ and the monomer species, while the trimer dominates at high water content.

On the basis of the results from the 2D-EXSY NMR experiments, the following intermolecular exchange equilibria between the different species were detected in a $CD_3OD$ solution of the trimer $V^V$ complex:

$V_2Y_2L_2$ (C isomer) ⇆ $VYL_2$ (B isomer)

$V_2Y_2L_2$ (D isomer) ⇆ $VYL_2$ (A isomer)

These equilibria involve exchange between the major isomer and the minor isomer of species of different nuclearity. Intramolecular exchange was also detected between the two ligands of $VYL_2$ (isomer A), but no evidence was found for intermolecular exchange between the major and minor isomers of species of different nuclearity or between isomers of species of the same nuclearity.

## Experimental Section

**Reagents:** Sodium metavanadate, $NaVO_3$, and methanol were purchased from Sigma, and the ligand 1,2-dimethyl-3-hydroxy-4-pyridinone (Hdmpp) from ACROS Organics and used without further purification. KOH, HCl and $CH_3OH$ were obtained from Merck, while KOD, DCl, $D_2O$ (99.9 atom% D) and $CD_3OD$ (99.9 atom% D) from Cambridge Isotope Laboratories. All the experiments were carried out under aerobic conditions.

**Synthesis:** The synthesis of the trimer $[V_3O_3(\mu\text{-}O)_3(dmpp)_3(H_2O)](H_2O)_2$ was carried out following the procedure described in the literature.[24] Red crystals of $[V_2O_2(\mu\text{-}O)(dmpp)_2(OCH_3)_2]$ were isolated from methanolic solution of the trimer; however, under atmospheric conditions these crystals turn black after replacement of methanol by water.

**Solutions:** Solutions of the trimer $[V_3O_3(\mu\text{-}O)_3(dmpp)_3(H_2O)](H_2O)_2$ used for the $^{51}V$ NMR spectroscopic experiments contained $CH_3OH$ or $CH_3OH/H_2O$ mixtures, and were prepared by dissolving the appropriate amount of the solid compound in the solvent (or solvents) in order to have the desired concentrations. The $CH_3OH/H_2O$ mol ratios were checked by integration of the $^1H$ NMR signals of the solvents. 1D $^1H$ NMR spectra as well as 2D $^1H$ COSY and EXSY NMR spectra were acquired in $CD_3OD$ solutions. pH values were measured by using a Crison MicropH 2002 pH meter with an Ingold 405-M5 combined electrode.

### Methods

**NMR Spectroscopy:** $^{51}V$ NMR spectra at 22.0 ± 0.5 °C were recorded with a Varian Unity-500 Spectrometer operating at 131.404 MHz, using a 5 mm broad band probe. $^{51}V$ NMR chemical shifts were externally referenced to a $VOCl_3$ solution at 0 ppm. The $^{51}V$ NMR acquisition parameters were: 33 kHz spectral width, 25 μs pulse width, 0.5 s acquisition time and 10 Hz line broadening. $^1H$ NMR spectra were obtained by using a pre-saturation pulse sequence to eliminate the residual water signal. The low-temperature 1D and the 2D $^1H$ NMR spectra were obtained with a Bruker ARX400 NMR Spectrometer operating at 400.13 MHz, using a 5 mm inverse probe and a controlled-temperature unit. Magnitude COSY and phase sensitive NOESY (800 ms mixing time) were acquired with a spectral width of 4000 Hz in both F1 and F2, with 1024×256 data points. Spectra were processed with unshifted sine bell (COSY) and sine$^2$ (NOESY) functions. The $^1H$ NMR spectrum at –50 °C was obtained with a Bruker AC 200 F Spectrometer operating at 200.13 MHz, using a 5-mm probe and a controlled-temperature unit.

**ES Mass Spectrum:** Electron spray (ES) mass spectra were recorded with an MSD spectrometer with a fragmentation of 50 V in a mixture of 98% methanol/2% formic acid: $m/z$ = 457 $[V_2O_3(C_7H_8O_2N)_2(OCH_3)]^+$, 343 $[VO(C_7H_8O_2N)_2]^+$, 236 $[VO(C_7H_8O_2N)(OCH_3)]^+$.

**X-ray Crystallography:** The crystalline trimer $[V_3O_3(\mu\text{-}O)_3(dmpp)_3(H_2O)](H_2O)_2$ was dissolved in methanol until saturation was reached. After a few hours, slow evaporation of this solution gave dark red crystals of X-ray quality. A suitable crystal of $[V_2O_2(\mu\text{-}O)(dmpp)_2(OCH_3)_2]$ was coated with Fomblin oil, placed at the end of a silica fibre and mounted on a goniometer head of a Bruker SMART CCD diffractometer in a stream of cold nitrogen gas. These crystals are unstable and turn black when left in contact with atmospheric conditions.

Selected crystallographic data are shown in Table 2. Three-dimensional X-ray data were collected at low temperature (173 K) in the range $1.90 < 2\theta < 28.32°$ with a Siemens SMART 1000 CCD diffractometer by the $\Omega$-scan method. Complex scattering factors were taken from the programme package SHELXTL.[32] The structure was solved by direct methods and refined by using full-matrix least-squares methods on $F^2$. The data were processed and corrected for Lorentz and polarisation effects and for absorption (semi-empirical method). The non-hydrogen atoms were refined with anisotropic thermal parameters in all cases. The hydrogen atoms were refined to carbon, which were placed in idealised positions and refined by using a riding mode. A final difference Fourier map showed no residual density outside –1.064 to +0.845 e Å$^{-3}$. Selected bond lengths and bond angles appear in Table 1.

Table 2. Crystallographic data for the complex $[V_2O_2(\mu\text{-}O)(dmpp)_2(OCH_3)_2]$.

| | |
|---|---|
| Empirical formula | $C_{16}H_{22}N_2O_9V_2$ |
| Formula mass [g mol$^{-1}$] | 488.24 |
| Crystal system | monoclinic |
| Space group | $P2_1/c$ |
| $a$ [Å] | 8.4573(11) |
| $b$ [Å] | 15.034(2) |
| $c$ [Å] | 15.849(2) |
| $\beta$ [°] | 105.300(2) |
| $V$ [Å$^3$] | 1943.7(4) |
| Z | 2 |
| $T$ [K] | 173(2) |
| $\lambda$ [Å] | 0.71073 |
| $D_{calcd.}$ [g·cm$^{-3}$] | 1.668 |
| $F$ (000) | 1000 |
| No. of reflections collected | 10939 |
| No. of observed reflections | 3038 |
| $R_1$[a] | 0.0492 |
| $wR_2$ (all data) | 0.1706 |
| Largest diff peak and hole [e Å$^{-3}$] | 0.845/–1.064 |

[a] $R_1 = \Sigma||F_o| - |F_c|| / \Sigma|F_o|$, $wR_2 = \{\Sigma[w(|F_o|^2 - |F_c|^2)^2] / \Sigma[w(F_o^4)]\}^{1/2}$.

 © 2006 Wiley-VCH Verlag GmbH & Co. KGaA, Weinheim 

CCDC-602237 contains the supplementary crystallographic data for this paper. These data can be obtained free of charge from The Cambridge Crystallographic Data Centre via www.ccdc.cam.ac.uk/data_request/cif.

## Acknowledgments

We are grateful for the financial support from Fundação para a Ciência e Tecnologia, Portugal (FCT Project POCTI/QUI//56949/2004) and FEDER. F. A. thanks Xunta de Galicia and the University of A Coruña for the grants to visit the University of Coimbra and the Spanish-Portuguese Bilateral Programme (Accion Integrada HP2004-0074). This work was carried out within the working group "Vanadium Compounds as Insulin-Mimetic Agents" of the COST D21 Action of the E. U.

[1] N. D. Chasteen (Ed.), *Vanadium in Biological Systems*, Kluwer, Dordrecht, The Netherlands, **1990**.
[2] H. Sigel, A. Sigel (Eds.), *Metal Ions in Biological Systems*, Marcel Dekker, Inc., New York, **1995**, vol. 31.
[3] E. M. Armstrong, R. L. Beddoes, L. J. Calviou, J. M. Charnock, D. Collison, N. Ertok, J. H. Naismith, C. D. Garner, *J. Am. Chem. Soc.* **1993**, *115*, 807–808.
[4] a) M. J. Smith, *Experiencia* **1989**, *45*, 452; b) S. W. Taylor, B. Kammerer, E. Bayer, *Chem. Rev.* **1997**, *97*, 333–346.
[5] H. Vilter, *Phytochemistry* **1984**, *23*, 1387–1390.
[6] a) R. L. Robson, R. R. Eady, T. H. Richardson, R. W. Miller, M. Hawkins, J. R. Postgate, *Nature (London)* **1986**, *322*, 388–390; b) D. Rehder, *Coord. Chem. Rev.* **1999**, *182*, 297–322; c) R. R. Eady, *Coord. Chem. Rev.* **2003**, *237*, 23–30.
[7] a) P. J. Stankiewicz, A. S. Tracey and D. C. Crans, "Vanadium and its Role in Life" in *Metal Ions in Biological Systems* (Eds.: H. Sigel, A. Sigel), Marcel Dekker, New York, **1995**, vol. 31, ch. 9; b) A. B. Goldfine, G. Willksy, C. R. Kahn in *Vanadium Compounds: Biochemistry Chemistry, and Therapeutic Applications* (Eds.: A. S. Tracey, D. C. Crans), American Chemical Society, Washington, DC, **1998**.
[8] N. D. Chasteen, "The Biochemistry of Vanadium" in *Structure and Bonding* **1983**, *53*, 105–138.
[9] a) Y. Shechter, S. J. D. Karlish, *Nature* **1980**, *284*, 556–558; b) H. Sakurai, K. Tsuchiya, M. Nukatsuka, M. Sofue, J. Kawada, *J. Endocrinol.* **1990**, *126*, 451–459; c) K. Kawabe, M. Tadokoro, Y. Kojima, Y. Fujisawa, H. Sakurai, *Chem. Lett.* **1998**, 9–10.
[10] a) D. C. Crans, L. Yang, J. A. Alfano, L.-H. Chi, W. Jin, M. Mahroof-Tahir, K. Robbins, M. M. Toloue, L. K. Chan, A. J. Plante, R. Z. Grayson, G. R. Willsky, *Coord. Chem. Rev.* **2003**, *237*, 13–22; b) H. Sakurai, H. Yasui, Y Adachi, *Expert Opin. Invest. Drugs* **2003**, *12*, 1189–1203.
[11] D. Rehder, *Angew. Chem. Int. Ed. Engl.* **1991**, *30*, 148–167.
[12] a) M. J. Gresser, A. S. Tracey, *J. Am. Chem. Soc.* **1986**, *108*, 1935–1939; b) A. S. Tracey, M. J. Gresser, *Can. J. Chem.* **1988**, *66*, 2570–2574; c) A. S. Tracey, M. J. Gresser, B. Galeffi, *Inorg. Chem.* **1988**, *27*, 157–161.
[13] D. C. Crans, J. J. Smee, E. Gaidamauskas, L. Yang, *Chem. Rev.* **2004**, *104*, 849–902.
[14] a) P. Caravan, L. Gelmini, N. Glover, F. G. Herring, H. Li, J. H. McNeill, S. J. Rettig, I. A. Setyawati, E. Shuter, Y. Sun, A. S. Tracey, V. G. Yuen, C. Orvig, *J. Am. Chem. Soc.* **1995**, *117*, 12759–12770; b) J. H. McNeil, V. G. Yuen, H. R. Hoveyda, C. Orvig, *J. Med. Chem.* **1992**, *35*, 1489–1491; c) G. R. Hanson, Y. Sun, C. Orvig, *Inorg. Chem.* **1996**, *35*, 6507–6512.
[15] a) Y. Sun, B. R. James, S. J. Rettig, C. Orvig, *Inorg. Chem.* **1996**, *35*, 1667–1673; b) Y. Sun, M. Melchior, D. A. Summers, R. C. Thompson, S. J. Rettig, C. Orvig, *Inorg. Chem.* **1998**, *37*, 3119–3121.
[16] J. Burgess, B. de Castro, C. Oliveira, M. Rangel, W. Schlindwein, *Polyhedron* **1997**, *16*, 789–794.
[17] a) M. M. C. A. Castro, C. F. G. C. Geraldes, P. Gameiro, E. Pereira, B. Castro, M. Rangel, *J. Inorg. Biochem.* **2000**, *80*, 177–179; b) M. Rangel, *Transition Met. Chem.* **2001**, *26*, 219–223.
[18] a) M. M. C. A. Castro, F. Avecilla, C. F. G. C. Geraldes, B. de Castro, M. Rangel, *Inorg. Chim. Acta* **2003**, *356*, 142–154; b) P. Buglyo, T. Kiss, E. Kiss, D. Sanna, E. Garriba, G. Micera, *J. Chem. Soc., Dalton Trans.* **2002**, 2275–2282.
[19] A. Katoh, K. Kazutoshi, R. Saito, Y. Fujisawa, T. Takino, H. Sakurai, *Heterocycles* **2003**, *60*, 1147–1159.
[20] K. H. Thompson, B. D. Liboiron, Y. Sun, K. D. D. Bellman, I. A. Setyawati, B. O. Patrick, V. Karunaratne, G. Rawji, J. Wheeler, K. Sutton, S. Bhanot, C. Cassidy, J. H. McNeill, V. G. Yuen, C. Orvig, *J. Biol. Inorg. Chem.* **2003**, *8*, 66–74.
[21] a) P. Poucheret, R. Gross, A. Cadene, M. Manteguetti, J. Serrano, G. Ribes, G. Cross, *Mol. Cell. Biochem.* **1995**, *153*, 197–204; b) H. Sakurai, K. Fujii, H. Watanabe, H. Tamura, *Biochem. Biophys. Res. Commun.* **1995**, *214*, 1095–1101; c) H. Sakurai, K. Tsuchiya, M. Nukatsuka, J. Kawada, S. Ischikawa, H. Yoshida, M. Komatsu, *J. Clin. Biochem. Nutr.* **1990**, *8*, 193–200; d) H. Watanabe, M. Nakai, K. Komazawa, H. Sakurai, *J. Med. Chem.* **1994**, *37*, 876–877; e) J. H. McNeill, V. G. Yuen, S. Dai, C. Orvig, *Mol. Cell. Biochem.* **1995**, *153*, 175–180; f) H. Sakurai, K. Fujii, S. Fujimoto, Y. Fujisawa, K. Takechi and H. Yasui in *ACS Symposium Series 711* (Ed.: A. S. Tracey and D. C. Crans), American Chemical Society, Washington D.C., **1998**, p. 344; g) H. Sakurai, Y. Fujisawa, S. Fujimoto, H. Yasui, T. Takino, *J. Trace Elem. Exp. Med.* **1999**, *12*, 393–401.
[22] T. C. Delgado, A. I. Tomaz, I. Correia, J. C. Pessoa, J. G. Jones, C. F. G. C. Geraldes, M. M. C. A. Castro, *J. Inorg. Biochem.* **2005**, *99*, 2328–2339.
[23] a) D. Rehder, J. C. Pessoa, C. F. G. C. Geraldes, M. M. C. A. Castro, T. Kabanos, T. Kiss, B. Maier, G. Micera, L. Petterson, M. Rangel, A. Salifoglou, I. Turel, D. Wang, *J. Biol. Inorg. Chem.* **2002**, *7*, 384–396; b) M. Rangel, A. Tamura, C. Fukushima, H. Sakurai, *J. Biol. Inorg. Chem.* **2001**, *6*, 128–132.
[24] F. Avecilla, C. F. G. C. Geraldes, M. M. C. A. Castro, *Eur. J. Inorg. Chem.* **2001**, 3135–3142.
[25] F. Jiang, P. A. Oren, S. M. Miller, J. Chen, M. Mahroof-Tahir, D. C. Crans, *Inorg. Chem.* **1998**, *37*, 5439–5451.
[26] a) K. Isobe, S. I. Ooi, Y. Nakamura, S. Kawaguchi, H. Kuroya, *Chem. Lett.* **1975**, 35–38; b) C. R. Cornman, J. Kampf, M. S. Lah, V. L. Pecoraro, *Inorg. Chem.* **1992**, *31*, 2035–2043; c) X. Li, M. S. Lah, V. L. Pecoraro, *Inorg. Chem.* **1988**, *27*, 4657–4664.
[27] S. A. Fairhust, D. L. Hughes, U. Kleinkes, J. G. Leigh, J. R. Sanders, J. Weisner, *J. Chem. Soc., Dalton Trans.* **1995**, 321–326.
[28] C. J. Carrano, C. M. Nunn, R. Quan, J. A. Bonadies, V. L. Pecoraro, *Inorg. Chem.* **1990**, *29*, 944–951.
[29] a) I. Cavaco, J. Costa-Pessoa, M. T. Duarte, P. M. Matias, R. T. Henriques, *Polyhedron* **1993**, *12*, 1231–1237; b) W. Priebsch, D. Rehder, M. von Oeynhausen, *Chem. Ber.* **1991**, *124*, 761–764; c) H. Rieskamp, P. Gietz, R. Mattes, *Chem. Ber.* **1976**, *109*, 2090–2096.
[30] a) D. Paulsen, D. Rehder, D. Thoennes, *Z. Naturforsch., Teil A* **1978**, *33*, 834–839; b) D. Rehder, *Bull. Magn. Reson.* **1982**, *4*, 33–83; c) A. S. Tracey, M. Gresser, K. M. Parkinson, *Inorg. Chem.* **1987**, *26*, 629–638.
[31] a) G. Otting, E. Liepinsh, K. Wüthrich, *J. Am. Chem. Soc.* **1990**,*113*, 4363–4364; b) D. Neuhaus, M. Williamson (Eds.), "The Nuclear Overhauser Effect" in *Structural and Conformational Analysis*, 2nd ed., Wiley-VCH Inc., Chichester, United Kingdom, **2000**.
[32] G. M. Sheldrick, *SHELXTL Bruker Analytical X-ray System*, ver. 5.01, Madison, WI, **1997**.

Received: April 4, 2006
Published Online: July 24, 2006

 © 2006 Wiley-VCH Verlag GmbH & Co. KGaA, Weinheim 

DOI: 10.1002/ejic.200600309

# Vanadium (IV and V) Complexes of Reduced Schiff Bases Derived from the Reaction of Aromatic *o*-Hydroxyaldehydes and Diamines Containing Carboxyl Groups

**João Costa Pessoa,*[a] Susana Marcão,[a] Isabel Correia,[a] Gisela Gonçalves,[a] Agnes Dörnyei,[b] Tamás Kiss,*[b] Tamás Jakusch,[b,c] Isabel Tomaz,[a,d] M. Margarida C. A. Castro,[d] Carlos F. G. C. Geraldes,[d] and Fernando Avecilla[e]**

**Keywords:** Salen-like ligands / N,O ligands / Vanadium / Coordination modes / Equilibrium and structural studies

The reduced Schiff bases of salicylaldehyde [and *o*-vanillin (*o*-van)] with D,L- and L-diaminopropionic acid (DPA), designated by salDPA, and L-2,4-diaminopentanoic acid [ornithine (Orn)], designated by salOrn, as well as the $V^{IV}O^{2+}$ and $V^{V}O_2^{+}$ complexes of salDPA were prepared. The compounds were characterised in the solid state and in solution. The structure of $H_4$salDPA$^+$Cl$^-$ was determined by X-ray diffraction. Complexation of $V^{IV}O^{2+}$ and $V^{V}O_2^{+}$ with salDPA and salOrn (only the $V^{IV}O$ system) in aqueous solution was studied by potentiometry, UV/Visible spectroscopy and circular dichroism, as well as by EPR spectroscopy for the $V^{IV}O$–salDPA system and by $^1$H- and $^{51}$V NMR spectroscopy for the $V^{V}O_2$–salDPA system. Stoichiometries and complex formation constants were determined by potentiometry at 25 °C and $I$ = 0.2 M KCl. Practically only 1:1 complexes were formed in both systems with composition (VO)$LH_2$ and (VO)L in the $V^{IV}O$–salDPA system, and with composition ($VO_2$)LH and ($VO_2$)L in the $V^{V}O_2$–salDPA system. Spectroscopic data provided information about the most probable binding modes of each stoichiometry.
(© Wiley-VCH Verlag GmbH & Co. KGaA, 69451 Weinheim, Germany, 2006)

## Introduction

The presence of vanadium in biological systems, its insulin-enhancing action[1–4] and anticancer activity[5–7] has driven a considerable amount of research. Particular interest has been given to the study of the potential benefits of vanadium compounds as oral insulin substitutes for the treatment of diabetes.[8–12] Coordinated ligands should be able to improve the absorption and possibly the transport of vanadium to the cells, reducing the dose necessary for producing an equivalent effect. Several vanadium complexes of the dianionic tetradentate Schiff base salen (*N*,*N*′-disalicylideneethylenediamine)-type ligands have been proposed for use as insulin-enhancing agents, and for treatment of obesity and hypertension.[13–15] Durai and Saminathan[13] reported the ability of $V^{IV}O$(salen) to reverse the hyperglycemic condition of alloxan-induced diabetic rats to near normal, thereby exerting insulin-like action. However, rats tended to become hypoglycemic, and withdrawal of treatment brought about an immediate return of the hyperglycemia. Oxidovanadium(IV) complexes of hydroxysalen derivatives have also been reported to possess nuclease activity in the presence of an activating agent (mercaptopropionic acid or Oxone).[16]

Salen-type ligands present versatile steric, electronic and lipophilic properties. They may be easily prepared by the condensation of two compounds: (i) an aromatic *o*-hydroxyaldehyde and (ii) a diamine, the hydrophilic–lipophilic balance being easily fine-tuned by choosing the appropriate amine precursors and ring substituents of the aldehyde. However, Schiff base (SB) ligands have the disadvantage that they hydrolyse in solution. This instability can be overcome by the reduction of the SB to give an amine, i.e. ligands often designated as salan compounds. This presents interesting possibilities, as the reduced SB will be more flexible and not restrained to remain planar when coordinated to a metal centre. Moreover, some of the $V^{IV}O^{2+}$ and $V^{V}O_2^{+}$ complexes with salan ligands have been shown to be several orders of magnitude more stable than the corresponding salen compounds.[15,17]

[a] Centro Química Estrutural, Instituto Superior Técnico, Av. Rovisco Pais, 1049–001 Lisboa, Portugal
[b] Department of Inorganic and Analytical Chemistry University of Szeged, PO Box 440, 6701 Szeged, Hungary
[c] Bioinorganic Chemistry Research Group of the Hungarian Academy of Sciences, Department of Inorganic and Analytical Chemistry, University of Szeged, PO Box 440, 6701 Szeged, Hungary
[d] Departamento de Bioquímica, Centro de RMN e Centro de Neurociênciase Biologia Celular, Universidade de Coimbra, 3000 Coimbra, Portugal
[e] Departamento de Química Fundamental, Universidaded de Coruña, Campus de A Zapateira s/n, 15071, A Coruña, Spain
Supporting information for this article is available on the WWW under http://www.eurjic.org or from the author.

 © 2006 Wiley-VCH Verlag GmbH & Co. KGaA, Weinheim 

We report the preparation of salan compounds derived from the condensation of salicylaldehyde [in one case also of *o*-vanillin (*o*-van)] with D,L- and L-diaminopropionic acid (DPA), L-2,4-diaminopentanoic acid (L-ornithine) and L-2,5-diamino-hexanoic acid (L-lysine), which are designated by salDPA (**1**), salOrn (**2**) and salLys (**3**), respectively, and the preparation of $V^{IV}O$– and $V^{V}O_2$–salDPA complexes. The compounds were characterised in the solid state and in solution. The molecular formulas of two of the salan compounds prepared (salDPA and salOrn) are depicted in Scheme 1.

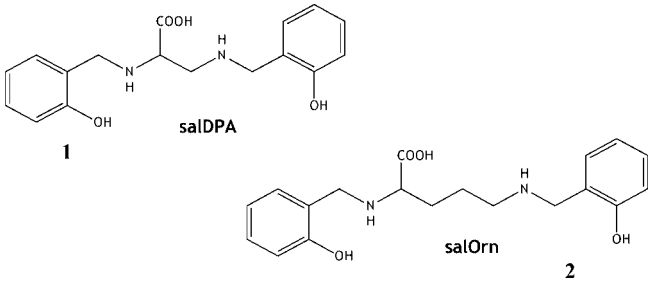


Scheme 1. Molecular formulae of two of the ligands prepared. Those of salLys (**3**) and vanDPA (**4**) are represented in the Supporting Information. The totally protonated compound **1** corresponds to $H_5salDPA^{2+}$. We obtained two different solid compounds: $H_3salDPA$ (**1**) and $H_4salDPA^+Cl^-$ (**1A**). When designating these and the other salan compounds obtained in this work without specific attention to their protonation state, we will omit the protonation state, e.g. we will normally designate **1** as salDPA.

Most of the biologically important reactions of vanadium occur in water-based environments such as blood plasma or other biological fluids and intracellular media. Therefore, the knowledge of the distribution and chemical speciation of the vanadium compounds in aqueous solution is of utmost importance. Most of the salen-type ligands and their vanadium complexes prepared so far are not water-soluble. The vanadium compounds prepared using salDPA are moderately soluble in water; therefore, they may be useful for therapeutic use. The salOrn ligand (**2**) was obtained in a low yield and only a few studies were made using this compound. However, as salLys (**3**) is not soluble in water or in ethanol/water at least up to 10% ethanol, this compound was characterised in the solid state but was not further studied.

Studies of moderately water-soluble Schiff bases and their hydrolytically more stable salan derivatives were previously reported,[15,17] namely several $V^{IV}O$– and $V^{V}O_2$–pyran complexes [pyran = *N*,*N*′-ethylenebis(piridoxylaminato)] were prepared and their properties studied. The ligands were found to form basically similar complexes coordinating through the O and N atoms ($2\times O_{phenolate}$, $2\times N_{amine/imine}$). EPR spectroscopic ($V^{IV}O$–pyran system) and $^1H$- and $^{51}V$ NMR spectroscopic ($V^{V}O_2$–pyran system) studies indicated the presence of various isomeric species in solution. The additional carboxylate group of salDPA may alter the structure and stability of the complexes. In fact salDPA forms very stable complexes with $Cu^{II}$ and $Fe^{III}$,[18] and in this work we also find that it is an effective ligand for $V^{IV}O^{2+}$ and $V^{V}O_2^+$. Moreover, the pendant carboxylate group may help with the coupling of the salan moiety to other molecules that may target the compound to specific biological sites, thereby anticipating the possibility of minimising its toxicity and increasing its efficacy.

## Results and Discussion

### Synthesis and Characterisation

The reduced SBs **1**–**2** depicted in Scheme 1 were prepared by the condensation of two equivalents of the appropriate aldehyde derivative with one equivalent of the diamine derivative. Treatment of these condensation products with sodium borohydride resulted in the reduction of the two imine bonds, yielding the reduced SBs (salan compounds) depicted in Scheme 1. The compounds gave good elemental analysis and were characterised by $^1H$ NMR spectroscopy. A reduced SB derived from the reaction of *o*-vanillin and DPA [vanDPA (**4**)] was also obtained and characterised in the solid state.

Crystals of $H_4salDPA^+Cl^-$ (**1A**) suitable for X-ray diffraction studies were obtained and more details are given in the Supporting Information. The amine nitrogen atoms are both protonated and the carboxylate group is not protonated. An ORTEP diagram with the molecular structure is depicted in Figure 1.

The bond lengths found for **1A** are within the expected range, and are similar to those of two related Schiff base compounds,[19] except for the C=N distance. In these com-

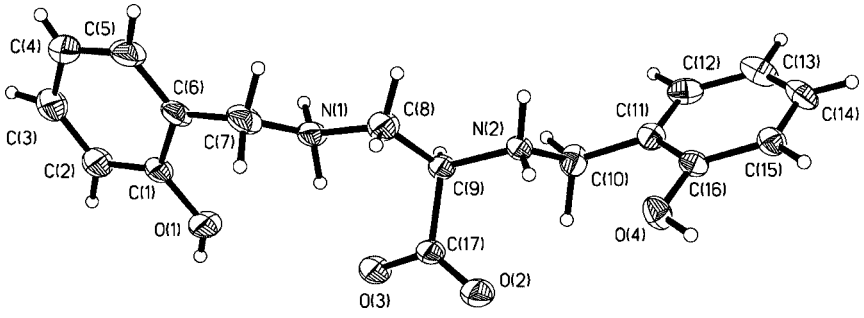


Figure 1. ORTEP diagram of $H_4salDPA^+\cdot Cl^-$ (**1A**) with the thermal ellipsoids of the non-hydrogen atoms drawn at the 30% probability level.

 © 2006 Wiley-VCH Verlag GmbH & Co. KGaA, Weinheim 

pounds this distance is 1.248(6) and 1.277(4) Å, and in **1A** it corresponds to two single C–N bonds [1.491(7) and 1.524(6) Å, for N(1)–C(7) and N(2)–C(10), respectively].

Some selected IR data for the ligands and vanadium complexes are shown in the Supporting Information (Table S1)[20–23]. The $\nu_{as}$(COO) bands appear at 1620–1650 $cm^{-1}$, while the $\nu_s$(COO) bands are assigned to the bands observed at 1415–1480 $cm^{-1}$. The characteristic $\nu$(V=O) band appears as a strong band at 960 $cm^{-1}$ in the IR spectrum of $V^{IV}O$(salDPA). For Na[$V^{V}O_2$(salDPA)] the strong $\nu$(V=O) bands appear at 880 and 906 $cm^{-1}$.

## Solution Studies

### *salDPA and salOrn*

The totally protonated form of compound **1** (Scheme 1) corresponds to $H_5$salDPA$^{2+}$. The protonation constants and respective p$K_a$ values derived from the potentiometric titrations are listed in Table 1. These values agree well with those obtained by Jancsó et al.,[18] for a different medium. The p$K_a$ of the carboxyl group is too low to be determined by potentiometric measurements, this is because of the strong electron-withdrawing effect of the neighbouring amino groups and/or H-bond formation involving these groups. In the Supporting Information (Section 2), we include Figure S1 where the $^1$H NMR chemical shifts of salDPA are represented as a function of pD. The chemical shift of the proton attached to C(9) (proton b) shows important changes at pD < 2, but the protons attached to C(8) (protons c) also show some much less important changes in this pH range. The $H_4L^+$ form is dominant in the pH range 2–5 and its deprotonation (p$K_{a2}$ = 5.91) is well separated from the following consecutive deprotonation steps. Since practically no change in the UV spectra occurs during this step, this can be assigned to the deprotonation of an amino group.[18] In Figure S1 it is clear that only the chemical shifts of the protons attached to C atoms close to the $N_{amine}$ atoms show significant changes at pD ≈ 6, in particular the proton attached to C(9) shows important changes. This indicates that p$K_{a2}$ is mainly associated with the deprotonation of atom N(2). Further deprotonation processes are followed by a continuous increase of the absorption bands at 238 and 292 nm, attributed to intramolecular transitions of the phenolate rings. In Figure S1, for pD > 8 there is a progressive change in the chemical shifts of all protons (except for proton b) as pD is increased. Therefore, the three consecutive deprotonations of $H_3$salDPA involve overlapping deprotonation processes related to the second amino group and the two phenol OH groups. However, the behaviour of the chemical shifts of the H atoms of C(7) (proton d) and C(8) (proton c) suggests that the second –$NH_2^+$– group is slightly more acidic than the two phenol protons whose deprotonation occurs at higher pD values, as shown particularly by the changes in the chemical shifts of the aromatic H atoms of C(4) and C(13) (protons $f_1$) and of C(2) and C(15) (protons $f_2$) (see Figure S1).

The protonation constants and p$K_a$ values of salOrn, determined by potentiometry, are also included in Table 2. The p$K_a$ values of salOrn (**2**) are higher than those of salDPA by a factor of 0.3–1.8 units. Since one of the amino groups is two carbon atoms further from the carboxyl group, when compared with salDPA, the p$K_a$(COOH) is higher for salOrn and could be determined by potentiometric measurements. The difference |p$K_{a2}^{salOrn}$ – p$K_{a2}^{salDPA}$| (equal to 1.8) suggests that the –$NH_2^+$– group associated with this deprotonation is the one that is closer to the $COO^-$ group.

Table 1. Formation constants (log$\beta_{pqr}$ for species $M_pL_qH_r$)[a] for the proton, $V^{IV}O^{2+}$ and $V^{V}O_2^+$ complexes of salDPA and salOrn,[b] and some derived data ($I$ = 0.2 M KCl and 25 °C).

| *pqr*/$H_mL^x$/p$K_{an}$ | salDPA | salDPA | salOrn |
|---|---|---|---|
| 015/$H_5L^{2+}$/p$K_{a1}$ | –/<1.6 | | 40.31(9)/1.70 |
| 014/$H_4L^+$/p$K_{a2}$ | 35.54(6)/5.91 | | 38.61(8)/7.71 |
| 013/$H_3L$/p$K_{a3}$ | 29.60(6)/8.45 | | 30.90(6)/8.84 |
| 012/$H_2L^-$/p$K_{a4}$ | 21.15(6)/10.07 | | 22.06(6)/10.45 |
| 011/$HL^{2-}$/p$K_{a5}$ | 11.09(9)/11.09 | | 11.61(9)/11.61 |
| 010/$L^{3-}$/– | | | |
| *pqr*/$M_pL_qH_r^x$[c] | log$\beta$ ($V^{IV}O^{2+}$)[d] | log$\beta$ ($V^{V}O_2^+$)/p$K_a$ | log$\beta$ ($V^{IV}O^{2+}$)/p$K_a$ |
| 112/(VO)$LH_2$ | 31.28(3) | | 33.23(3)/6.33 |
| 111/(VO)$LH^-$ | – | | 26.9(1)/5.9 |
| 110/(VO)$L^{2-}$ | 23.39(3) | | 20.99(6) |
| 210/$(VO)_2L$ | 25.7(3) | | – |
| 112/{$(VO_2)LH_2$}[d] | | {48.1(2)}[e]/5.08 | |
| 111/$(VO_2)LH^-$ | | 43.02(9)/8.62 | |
| 110/$(VO_2)L^{2-}$ | | 34.40(9) | |

[a] Three times the standard deviation is reported in parentheses. [b] A figure with a species distribution diagram for the complexes formed in the $V^{IV}O$–salOrn system is included in Section 4 of the Supporting Information. [c] M = (VO) for $V^{IV}O$ complexes and M = ($VO_2$) for $V^{V}O_2$ complexes. [d] One of the "good" equilibrium models obtained with PSEQUAD from the potentiometric data included stoichiometry (VO)$LH_{-1}$ with log$\beta$ = 12.92 (other constants have similar log$\beta$ values). However, for this different model, (VO)$LH_{-1}$ starts forming at pH = 9 and this is not compatible with the Vis spectroscopy and CD results. [e] A $V^{V}$–salDPA complex forms at pH < ca. 5.5, but precipitation of a grey solid and the possible occurrence of redox reactions precluded the reliable determination of its stoichiometry and log$\beta$.

 © 2006 Wiley-VCH Verlag GmbH & Co. KGaA, Weinheim 

Table 2. Spin Hamiltonian parameters for the $V^{IV}O$–salDPA complexes, obtained by computer simulation of the experimental spectra, and $A_z^{est}$ values estimated for particular binding modes.

| | $g_z$[a]<br>$g_{x,y}$[a] | $A_z$ ($\times 10^4$ cm$^{-1}$)[a]<br>$A_{x,y}$ ($\times 10^4$ cm$^{-1}$)[a] | Possible binding modes | $A_z^{est}$<br>($\times 10^4$ cm$^{-1}$) |
|---|---|---|---|---|
| $VOLH_2$ (**II**) | 1.948 | 171.1 | $(COO^-, N_{amine}, 2\times H_2O)_{eq}$ | 173.3 |
| | 1.963 | 50.9 | $(O^-_{Phen}, N_{amine}, 2\times H_2O)_{eq}(COO^-)_{ax}$ | 170.2 |
| VOL (**IIIA**) | 1.944 | 167.9 | $(COO^-, 2\times O^-_{Phen}, H_2O)_{eq}(N_{amine})_{ax}$ | 165.5 |
| | 1.978 | 58.0 | | |
| VOL (**IIIB**) | 1.954 | 161.4 | $(2\times O^-_{Phen}, COO^-, N_{amine})_{eq}(N_{amine})_{ax}$ | 160.0 |
| | 1.978 | 57.2 | $(2\times N_{amine}, COO^-, O^-_{Phen})_{eq}(O^-_{Phen})_{ax}$ | 161.2 |

[a] Spin Hamiltonian parameters obtained by the simulation of the experimental spectra by using the computer programme of Rockenbauer and Korecz.[30]

### *$V^{IV}O$ Complexes*

The complex formation constants calculated from the potentiometric titrations carried out at different vanadium/salDPA ratios are also included in Table 1.[24] Slow equilibration of the solutions only occurred at pH > 10.5 (some potentiometric measurements) or at pH > 11 (some spectroscopic measurements). With $V^{IV}O^{2+}$ the concentration distribution diagram (Figure 2) includes the stoichiometries (oxidation state and charges omitted): VO, $(VO)LH_2$, $(VO)_2L$ (minor species) and (VO)L. For pH > ca. 12 the CD spectra recorded indicate the formation of a distinct $V^{IV}O$–salDPA complex [stoichiometry probably $(VO)LH_{-1}$]; however, a reliable log$\beta$ for this species could not be obtained (see below).

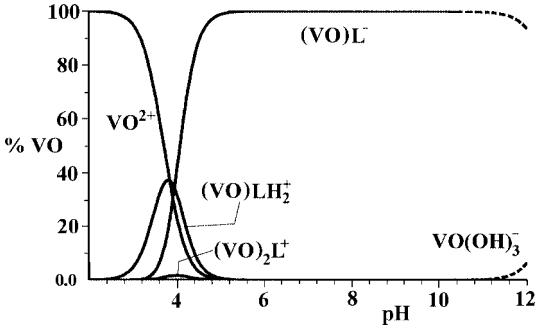


Figure 2. Species distribution diagram for the complexes formed in the $V^{IV}O$–salDPA system for solutions for which $C_{VO}$ = 1.0 mM and L/M = 1 (25 °C and $I$ = 0.2 M KCl).

It is clear from the speciation diagram that the salDPA ligand forms very stable complexes with $V^{IV}O^{2+}$, its hydrolysis products are not formed in measurable concentration at least in the pH range 2–11 and $(VO)L^-$ corresponds to ca. 100% of total V in the pH range 5–11 (at the experimental conditions specified). In $(VO)LH_2^+$ the tridentate coordination of the ligand seems to be the most probable, then by the cooperative deprotonation of the other half of the molecule a significant rearrangement of the coordinating donors occurs, which results in the formation of a joint chelate-ring system (for the possible binding modes see later).

Potentiometric pH measurements were also carried out to determine the equilibrium model and formation constants for the $V^{IV}O$–salOrn system. The best model includes the stoichiometries $(VO)LH_2$, (VO)LH and (VO)L; the corresponding log$\beta$ values are included in Table 2, and a calculated species distribution diagram is shown in the Supporting Information (Section 3, Figure S2). Compound salOrn also forms stable complexes with $V^{IV}O^{2+}$, but the hydrolysis products of oxidovanadium(IV), namely $[(VO)_2(OH)_5^-]_n$ and $VO(OH)_3^-$,[25] have a much higher relative importance in the pH range for the formation of species VOL in the $V^{IV}O$–salOrn system than for the $V^{IV}O$–salDPA system. This results from the lower stability of this VOL species, as one ring of the joint chelate system formed with salOrn is larger than that formed with salDPA (the carbon chain between the two NH groups is two carbon atoms longer in Orn than in DPA).

Figure 3 includes some of the CD spectra recorded in solutions containing $V^{IV}O^{2+}$ and sal-L-DPA. Globally the CD spectra agree well with the speciation diagram included in Figure 2. Up to pH 2.60, as the only V-containing species present in solution is $VO(H_2O)_5^{2+}$, the CD signal in the wavelength range 400–1000 nm (where vanadium-related bands are expected to show up) is almost zero. As $(VO)LH_2^+$ forms, spectra with the band pattern (–,+,–) are recorded up to pH ca. 3.4 with $\lambda_{max} < 400$ nm ($\Delta\varepsilon_m < 0$), ca. 565 nm ($\Delta\varepsilon_m > 0$) and ca. 790 nm ($\Delta\varepsilon_m < 0$). For pH > 3.5 and up to 5.0, the band pattern gradually changes (see Figure 3), but in the pH range 5–10.5 the CD spectra remain the same, with two main bands at 585 nm ($\Delta\varepsilon_m$ = –0.23 mol$^{-1}$ dm$^3$ cm$^{-1}$) and 945 nm ($\Delta\varepsilon_m$ = +1.46 mol$^{-1}$ dm$^3$ cm$^{-1}$), and only show small changes in the pH range 10.5–11.5.

The PSEQUAD computer programme[24] and the CD spectra obtained at different pH values were used to calculate the log$\beta$ and/or the spectrum of each individual species formed in the $V^{IV}O$–salDPA system. The calculated log$\beta$ values agree reasonably well with those obtained from the potentiometry (within ±0.1 log unit), and reasonable CD spectra could be calculated for $VOLH_2$ and VOL (see Figure 3d). This confirms that the speciation model proposed and the stability constants calculated from the potentiometric measurements are correct and reliable.

Figure 4 includes some of the visible absorption (Vis) spectra recorded with solutions containing $V^{IV}O^{2+}$ and salDPA. Globally the Vis spectra also agree well with the speciation diagram included in Figure 2. At pH < 2.60 the Vis spectra are quite similar to the spectrum of $VO(H_2O)_5^{2+}$ (see Figure 4a). For pH > 2.6 bands II ($d_{xy} \rightarrow$

 © 2006 Wiley-VCH Verlag GmbH & Co. KGaA, Weinheim 

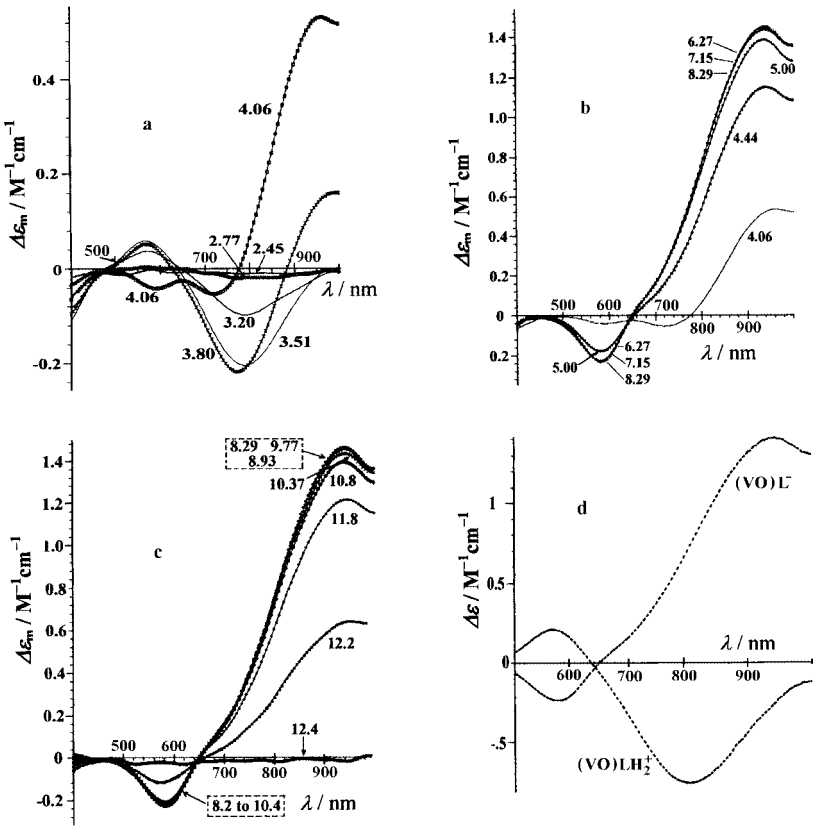


Figure 3. In a, b and c some CD spectra recorded for the $V^{IV}O$–salDPA system at a 1:1 metal ion/ligand ratio at several pH values (indicated) and $C_{VO}$ = 1 mM are represented. The $\Delta\varepsilon_m$ values recorded at pH = 1.96, 2.18, 2.45, 12.4 are close to zero. Spectra in d are the individual CD spectra calculated for stoichiometries $(VO)LH_2$ and (VO)L by the PSEQUAD programme[24] from the experimental CD spectra and the equilibrium constants included in Table 2.

$d_{x^2-y^2}$) and I ($d_{xy} \rightarrow d_{xz}$, $d_{yz}$) separate gradually, indicating an increase in the field strength. In the pH range 5.5–11.0 the Vis spectra do not change much (Figure 4b) showing two bands at ca. 575 nm ($\varepsilon_m \approx 65$ $mol^{-1}\,dm^{-3}\,cm^{-1}$) and ca. 910 nm ($\varepsilon_m \approx 43$ $mol^{-1}\,dm^{-3}\,cm^{-1}$), which indicate the presence of a single predominating species, VOL.

There is an important increase in the absorbance at ca. 400 nm between pH ca. 2.6 and 3.0, a less important one between 3.0 and 4.0, and then not much change up to pH 12 (Supporting Information, Section 5, Figure S3). This means that the equatorial coordination of the $O^-_{Phen}$ donors is already important at relatively low pH, and its contribution to the $\varepsilon_m$ values at 380–400 nm does not increase at pH > 4.0. At pH > 5 the absorbance at ca. 400 nm is sensitive to small percentages of hydrolysis or oxidation of the metal ion, but for this system the $\varepsilon_m$ values do not change much in this pH range.

EPR spectra were measured in "frozen" solutions (77 K) to check the speciation model and to elucidate the binding modes of the species. Some of the EPR spectra obtained for the $V^{IV}O$–salDPA system, in the region corresponding to $M_I$ = 5/2 and 7/2, are depicted in Figure 5. Table 2 shows the spin Hamiltonian parameters obtained by simulation of the experimental spectra. For the $V^{IV}O$–systems Chasteen[26] developed an additivity rule to estimate the hyperfine coupling constant $A_z^{est}$ [Equation (1)], on the basis of the contributions $A_{z,i}$ of each of the four equatorial donor groups. The estimated accuracy of $A_z^{est}$ is $\pm 3 \times 10^{-4}$ $cm^{-1}$.

$$A_z^{cst} = \sum_{i=1}^{4} A_{z,i} \quad (1)$$

Most of the $A_{z,i}$ relevant for this work were presented by Chasteen.[26] The contribution of the carboxylate ($COO^-$) donor in Equation (1) was estimated by Chasteen as $42.7 \times 10^{-4}$ $cm^{-1}$, on the basis of the $A_z$ of the VO-(oxalato)$_2^{2-}$ complex, assuming that the four $COO^-$ groups coordinate equatorially. However, the solution structure presumably involves the set $(3 \times COO^-, H_2O)_{eq}$,[27] so this contribution should be $42.1 \times 10^{-4}$ $cm^{-1}$, the value used in the present work. This data can be used to establish the most probable binding mode of the complexes formed, but care must be taken as the contributions of the donor groups to the hyperfine coupling may depend e.g. on their orientation,[28] or the charge of the ligand.[29] The influence of the axial donor groups (if any) is not taken into account.

Table 2[30] summarises the EPR parameters obtained, mostly from the simulation of the spectra by using the computer programme of Rockenbauer and Korecz.[30] Globally the EPR spectra (Figure 5) agree well with the speciation diagram depicted in Figure 2. Namely, for pH < 3 the only species detected is the aqua complex $[VO(H_2O)_5^{2+} \equiv VO \equiv$

 © 2006 Wiley-VCH Verlag GmbH & Co. KGaA, Weinheim 

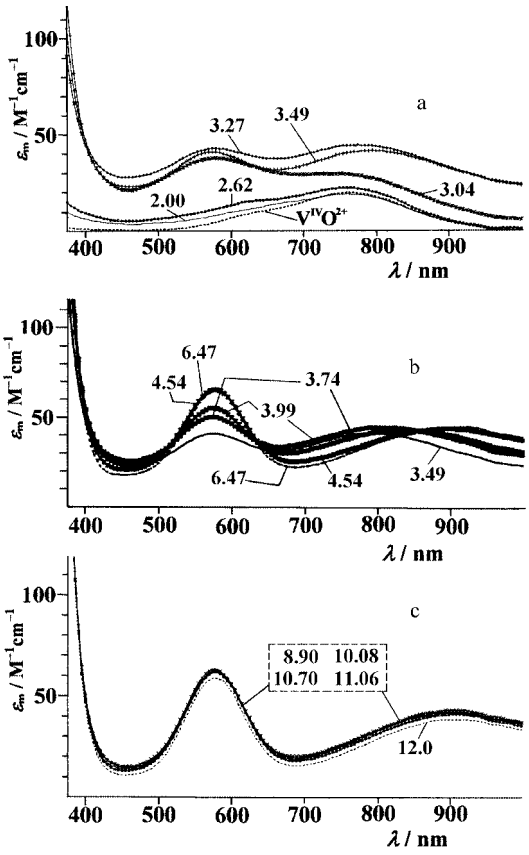


Figure 4. Some of the Vis absorption spectra recorded with aqueous solutions containing $V^{IV}O^{2+}$ and salDPA at a 1:1 metal ion/ligand ratio at several pH values (indicated) and $C_{VO}$ ca. 3 mM.

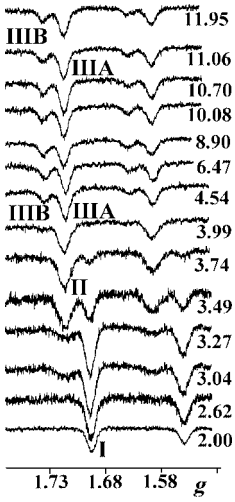


Figure 5. High field region of the EPR spectra (77 K) of frozen solutions containing $V^{IV}O^{2+}$ and salDPA at several pH values, with L/M = 1 and $C_{VO}$ ca. 3 mM. Four main components are detected: **I**-$[VO(H_2O)_5]^{2+}$, **II**-$(VO)LH_2^+$, **IIIA**-$(VO)L^-$ and **IIIB**-$(VO)L^-$.

**I**]. At pH = 3.04, besides a signal for VO, a signal corresponding to $(VO)LH_2^+$ (**II**) can already be detected. At pH 3.49 the signals corresponding to VO and $(VO)LH_2^+$ show similar intensities, but it should be noted that one of the signals corresponding to $(VO)L^-$ (**IIIA**) also starts appearing in this field range. In the pH range ca. 4.5–12 only two EPR components, designated by **IIIA** and **IIIB** and corresponding to $A_z$ values of 167.9 and $161.4\times10^{-4}$ cm$^{-1}$, respectively, are detected. Their relative intensity is always the same so they must correspond to isomeric structures of the same stoichiometry, $(VO)L^-$. Up to pH 12 apparently no other species forms, and this is consistent with the Vis and CD spectra obtained. If any small amount of $VO(OH)_3^-$ is present at high pH, as its $A_z$ is ca. $162\times10^{-4}$ cm$^{-1}$, it would not be distinguished from the lines of $(VO)L^-$ (**IIIB**).

It has been previously emphasised[25] that, as the V atom in most oxidovanadium(IV) complexes is a stereogenic centre, most complexes in solution correspond to two enantiomers. If the ligand contains stereogenic centres and/or if one of the coordinating atoms becomes a stereogenic centre, several isomers corresponding to the same binding mode necessarily form. This is the case of the $V^{IV}O$–salDPA system where C(9) is a stereogenic centre. Moreover, for the same stoichiometry more than one type of binding mode may form. Some may yield distinct EPR signals, others not.

Species $(VO)LH_2^+$ may correspond to binding modes [($COO^-$, $N_{amine}$, $2\times H_2O)_{eq}$($N_{amine}$ or $O_{Phen}$)$_{ax}$] **BMa**, [($O_{Phen}$, $N_{amine}$, $2\times H_2O)_{eq}$($H_2O$ or $COO^-$)$_{ax}$] **BMb**, or [($O_{Phen}$, $COO^-$, $2\times H_2O)_{eq}$ ($N_{amine}$)$_{ax}$] **BMc** (see Scheme 2). These binding modes correspond to $A_z^{est}$ values of 173.5, 170.2 or $172.3\times10^{-4}$ cm$^{-1}$, respectively. The Vis spectra (Figure 4) indicate a significant equatorial coordination of $O_{Phen}$ starting at pH < 3; this rules out **BMa1** and **BMa2**. As the calculated CD spectrum for $VOLH_2$ is quite strong (Figure 3d), this suggests that the $COO^-$ group is coordinated equatorially, since this group should induce a strong CD effect and is near the stereogenic centre. Therefore, the predominant binding mode is probably **BMc**, where a set of (5+6)-membered chelate rings forms, the part of the salDPA molecule involved in the coordination being the one closer to the stereogenic centre.

Species $(VO)L^-$ involves at least two types of isomers, corresponding to species **IIIA** ($A_z = 167.9\times10^{-4}$ cm$^{-1}$) and **IIIB** ($A_z = 161.4\times10^{-4}$ cm$^{-1}$) detected in the EPR spectra (e.g. Figure 5). Species with binding mode [($2\times O_{Phen}$, $2\times N_{amine})_{eq}$($H_2O$ or $COO^-$)$_{ax}$] correspond to $A_z^{est}$ = $157.9\times10^{-4}$ cm$^{-1}$, quite different from the experimental $A_z$; therefore, this binding mode does not form significantly. Species **IIIB** may correspond to binding modes such as [($O_{Phen}$, $COO^-$, $2\times N_{amine})_{eq}$($O_{Phen}$)$_{ax}$] (**BMe**) corresponding to $A_z^{est}$ = $161.2\times10^{-4}$ cm$^{-1}$, or [($2\times O_{Phen}$, $COO^-$, $N_{amine})_{eq}$($N_{amine}$)$_{ax}$] (**BMf**) corresponding to $A_z^{est}$ = $160.0\times10^{-4}$ cm$^{-1}$ (see Scheme 2). On the other hand, given the donor groups available, species **IIIA** corresponds to quite a high $A_z$ value. The highest reasonable $A_z^{est}$ is obtained for the binding mode [($2\times O_{Phen}$, $COO^-$, $H_2O)_{eq}$-($N_{amine}$)$_{ax}$] (**BMd**), which corresponds to $A_z^{est}$ = $165.5\times10^{-4}$ cm$^{-1}$, compatible with the experimental value ($167.9\times10^{-4}$ cm$^{-1}$). However, this binding mode assumes that the amino group N(2)H is deprotonated and noncoordinated, which is hardly probable, even if, not considering the carboxylate, this group has a lower macroscopic p$K_a$

 © 2006 Wiley-VCH Verlag GmbH & Co. KGaA, Weinheim 

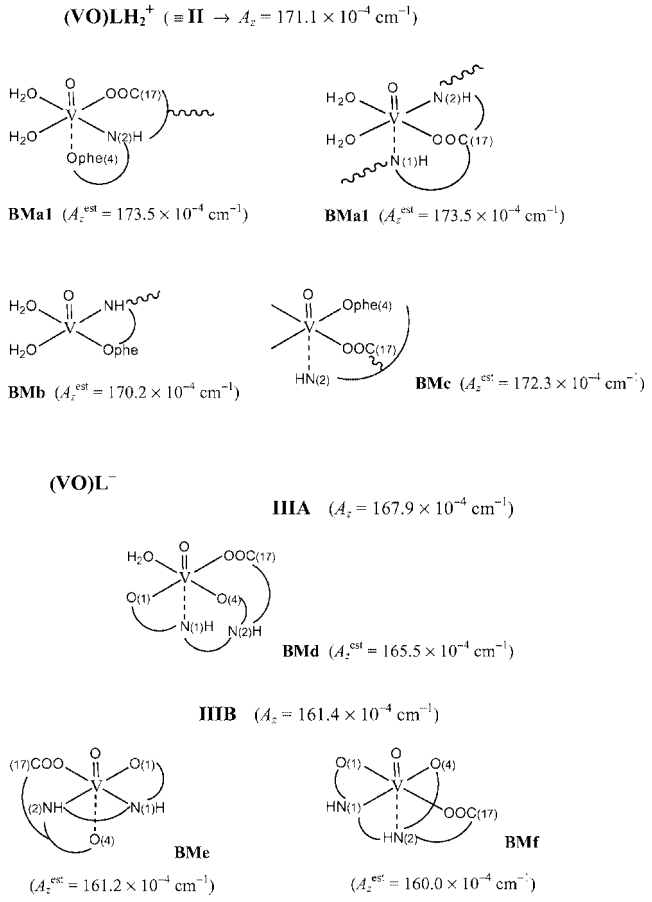


Scheme 2. Schematic representation of the plausible structures for the main stoichiometries that form in the $V^{IV}O$–salDPA system; the corresponding $A_z^{est}$ values are also included. In some of these representations the numbering of atoms of salDPA used in Figure 1 is also included to specify more clearly to which atoms they correspond. For the EPR component **IIIA**, other plausible binding modes cannot be ruled out (see text).

($pK_{a2}$ = 5.91) value. Possible binding modes that involve coordination of all groups with high $pK_a$ values are: e.g. [($O_{Phen}$, $H_2O$, $2\times N_{amine})_{eq}(O_{Phen})_{ax}$] ($A_z^{est}$ = $164.6\times10^{-4}$ cm$^{-1}$) and [($2\times O_{Phen}$, $H_2O$, $N_{amine})_{eq}(N_{amine})_{ax}$] ($A_z^{est}$ = $163.8\times10^{-4}$ cm$^{-1}$), these also correspond to relatively high $A_z$ values and cannot be completely ruled out. Scheme 2 summarises the set of the most plausible binding modes for $VOLH_2$ and VOL.

The CD spectrum of the isolated Na[$V^{IV}O$(sal-L-DPA)] complex (see Figure S4) resembles the CD spectrum corresponding to $(VO)L^-$ (Figure 3d). The spectrum in Figure 3d is the calculated spectrum for stoichiometry $(VO)L^-$; therefore, it is a weighted average of the CD spectra of all isomeric complexes present, i.e. all complex species corresponding to the EPR components **IIIA** and **IIIB**.

### *$V^VO_2$ Complexes*

The complex formation constants derived from the potentiometric titrations carried out at different salDPA/vanadium(V) ratios are also included in Table 2. For the $V^V$–salDPA system, the distribution diagram (Figure 6) includes the stoichiometries (oxidation state and charges omitted) M, $MLH_2$, MLH and ML ($M=V^VO_2$). Hereafter, $MLH_2$, MLH and ML will be designated by $(VO_2)LH_2$, $(VO_2)LH^-$ and $(VO_2)L^{2-}$, respectively. The system was also studied by $^{51}$V- and $^1$H NMR and CD spectroscopy. Some of the $^{51}$V NMR spectra recorded are included in Figure 7 and the CD spectra are included in Figure 8. Under the experimental conditions used to obtain these spectra, as the pH was decreased the colour changed from yellow to yellow-grey and then to grey (pH ≈ 4). For pH < 5 the pH was not stable and a solid precipitated. At pH ≈ 4 there was no important concentration of $V^V$ in solution as was indicated by the low intensity of the $^{51}$V NMR spectra. In the potentiometric titrations similar observations were made but in the experiments at lower vanadium concentrations (0.5–1 mM) no precipitation of any solid compound was detected upon decreasing the pH. However, as the pH readings were not stable, only titration points for pH > 5

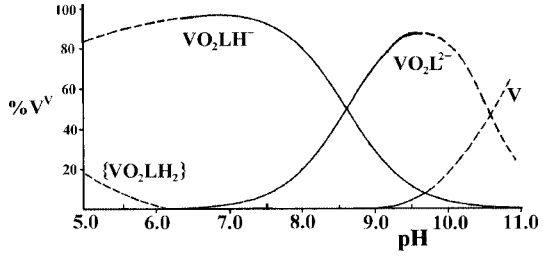


Figure 6. Approximate species distribution diagram for the complexes formed in the $V^V$–salDPA system for solutions for which $C_V$ ca. 3.0 mM and L/M = 1 (t = 25 °C, $I$ = 0.2 M KCl). The potentiometric data suggest that the $V^V$–salDPA species that forms for pH < 6 corresponds to a $(VO_2)LH_2$ stoichiometry. The full lines were calculated from the log$\beta$ values included in Table 1. The dashed lines are an estimate of the relative importance of the $V^V$–species present in solution, partly on the basis of the relative areas of the $^{51}$V NMR peaks.

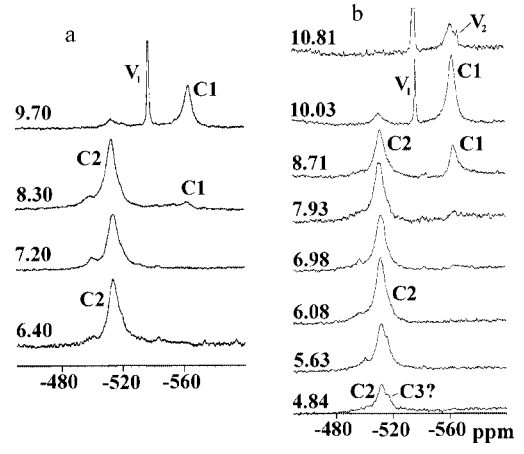


Figure 7. $^{51}$V NMR spectra, obtained at 131.404 MHz and at 25.0 ± 0.5 °C, of solutions containing sodium vanadate and salDPA. Spectra corresponding to two different sets of experiments are shown, (a) $C_V$ ca. 3.0 mM and L/M = 1.27 ($D_2O$ solution), the pD values are indicated in each spectrum; (b) $C_V$ ca. 4.0 mM and L/M = 1.2 ($H_2O$ solution), the pH values are indicated in each spectrum.

 © 2006 Wiley-VCH Verlag GmbH & Co. KGaA, Weinheim 

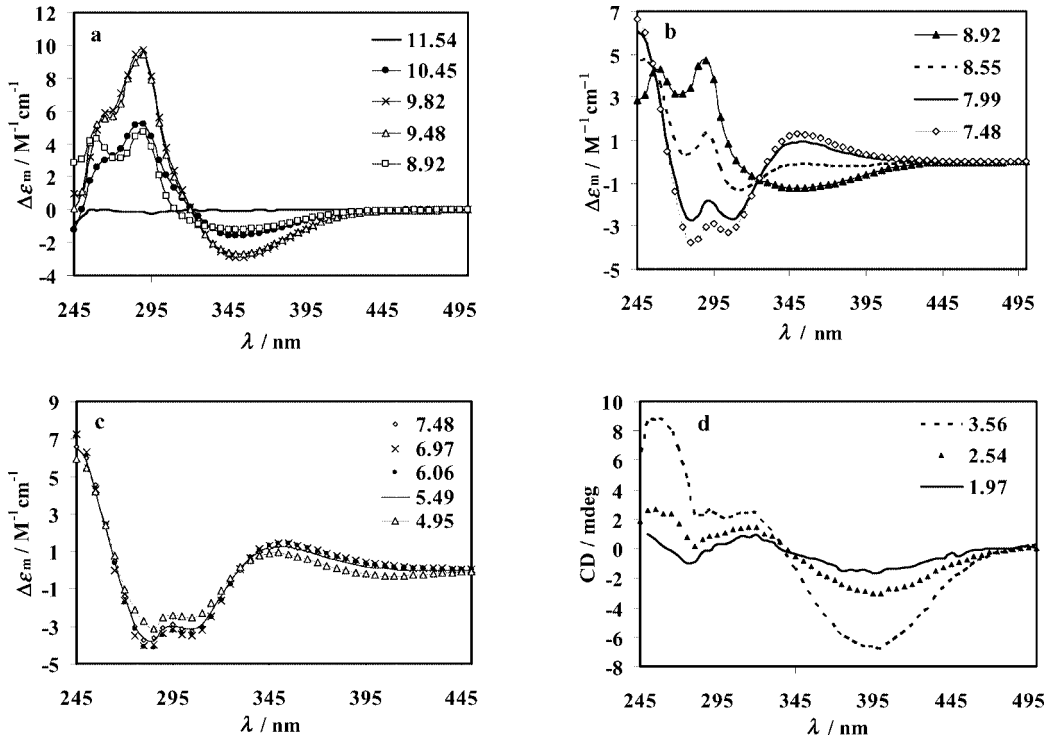


Figure 8. Some CD spectra recorded for the $V^{V}O_2$–salDPA system at a 1.2:1 ligand/metal ion ratio at several pH values (indicated) and $C_V$ = ca. 3 mM. The measurements started at pH ca. 11.5 and were made by making successive additions of an HCl solution. For pH < 5 a grey precipitate started to form, and the amount of this precipitate increased for pH < 4. The CD spectra for pH < 4 were recorded from clear samples after filtration of the mixture. The CD spectra of species $(VO_2)LH^-$ and $(VO_2)LH^{2-}$ calculated with the PSEQUAD programme[24] by using the log$\beta$ values included in Table 1 are shown in Section 8 of the Supporting Information.

were used in the calculations with the PSEQUAD programme.

In Figure 7 the $^{51}V$ NMR peak at –563 ppm (**C1**), detected between ca. pH 11 and 7.6, corresponds to the $(VO_2)L^{2-}$ species. In this complex the ligand is probably tetradentate and is coordinated by the two phenolate and two amine donors (see **BMg** in Scheme 3), as was observed in the $V^V$–pyran system where $^{51}V$ NMR peaks also appeared at ca. –565 ppm.[15] However, as this complex corresponds to a relatively intense CD signal (see below), structures involving the coordination of the $COO^-$ group instead of one $O_{phen}$ or one $NH_{amine}$ cannot be ruled out.

The broad peak around –512 ppm (**C2**), has a peak/shoulder at –500 ± 2 ppm, and shoulder(s) may also be seen at ≈–516 ± 2 ppm. Apparently, the relative intensity of the peaks at ca. –512 and ca. –500 ppm does not change with pH, so they correspond to isomeric forms of the same stoichiometry, $(VO_2)LH^-$. Scheme 3 includes several plausible structures for these species.

As mentioned above, for pH < 5 a precipitate forms, most of the $V^V$ is removed from the solution, and the $^{51}V$ NMR signals are very weak. Upon addition of an HCl solution, this grey precipitate dissolves, forming a blue solution; therefore, the solid contains a $V^{IV}$ species. However, as neither the grey solid nor its mother solution show an EPR signal, most of it is probably vanadyl hydroxide (see also Section 6 in the Supporting Information).

In solutions initially containing 3 mM $V^V$ and salDPA, a weak signal at ca. –515 ppm (**C3**) could be detected between ca. pH 5.6 and 4.0 (together with the peak **C2** and at least four other peaks which presumably correspond to oligomeric vanadates, not shown in Figure 7). The dashed line in the pH range 5–6 in Figure 6 was estimated on the basis of these observations. It is reasonable to assume that this $^{51}V$ NMR peak corresponds to complex $(VO_2)LH_2$, as suggested by the potentiometric calculations.

CD spectra were recorded for aqueous solutions containing sal-L-DPA at several pH values, but the $\Delta\varepsilon_m$ values were approximately zero in the range 240–700 nm. Several CD spectra recorded for the $V^V$–salDPA system are included in Figure 8. The sal-L-DPA ligand itself has no significant CD spectrum for $\lambda$ > 240 nm and no absorption for $\lambda$ > 320 nm; therefore, the CD bands observed must mainly be metal-related induced CD signals. We expect that the efficiency of the sal-L-DPA donor groups in inducing dissymmetry in the metal-related bands follows the order $COO^-$ > N(2) > N(1) >> $O_{Phen}$,[31] i.e. strong CD signals are expected only when N(2) and particularly $COO^-$ are coordinated to the metal centre.

At pH ca. 11.5 the $\Delta\varepsilon_m$ values are approximately zero, so there are no $V^V$–sal-L-DPA complexes in solution. At pH 10.5 the pattern of the CD spectrum is the same as that observed at pH 9.8 or 9.5, but $|\Delta\varepsilon_m|^{pH10.4} \approx 1/2|\Delta\varepsilon_m|^{pH9.8\text{ or }9.4}$ (see Figure 8a). These CD spectra correspond to the species $(VO_2)L^{2-}$. Between pH 11.4 and 9.5, all CD spectra cross at ca. 325 nm, $\Delta\varepsilon_m$ = 0, indicating the presence of only one optically active species in equilibrium with the $V^V$ hydrolysis products. For pH < 9.4 the pattern

 © 2006 Wiley-VCH Verlag GmbH & Co. KGaA, Weinheim 

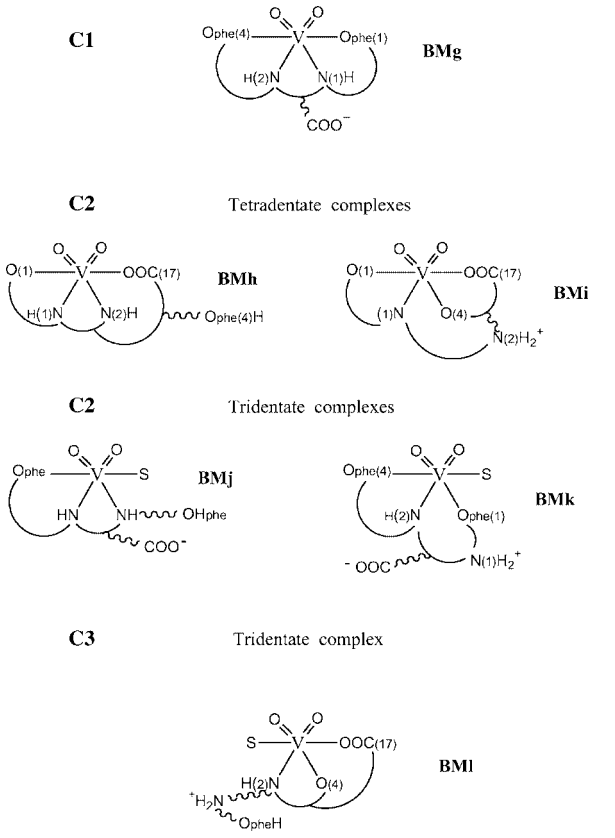


Scheme 3. Schematic representation of the plausible structures for the main stoichiometries that form in the $V^{V}O_2$–salDPA system. In some of these representations the numbering of atoms of salDPA used in Figure 1 is also included to specify more clearly to which atoms they correspond. Note that, for each of the schematic binding modes represented, (i) more than one isomer may form, (ii) other plausible binding modes can be envisaged.

of the CD spectra gradually change, and between pH 8.9 and 7.0 they show an isodichroic point, indicating the presence of two types of optically active species, $VO_2L^{2-}$ and $VO_2LH^{-}$ (Figure 8b). Between pH 7.5 and 5.0, the spectra remain approximately the same and correspond to $(VO_2)LH^{-}$ (Figure 8c).

For lower pH values, precipitation of a dark-grey solid occurs. CD spectra could be obtained after filtering the mixture. Figure 8d includes some of the spectra recorded, but $\Delta\varepsilon_m$ values could not be obtained as the $V^{V}$ concentration in these solutions is not known. The pattern of these CD spectra differs from that corresponding to $(VO_2)LH^{-}$ (Figure 8c), so this optically active complex corresponds to a distinct stoichiometry, $(VO_2)LH_2$, as suggested by the potentiometric data.

Species **C3**, detected by $^{51}V$ NMR and CD spectroscopy, probably corresponds to the binding mode **BMl** indicated in Scheme 3. This is the only reasonable way to obtain an optically active $V^{V}$–salDPA complex with a $(VO_2)LH_2$ stoichiometry, i.e. the (5+6)-chelate rings containing atoms O(2 or 3)–C(17)–C(9)–N(2)–C(10)–C(11)–C(16)–O(4) (see Figure 1), which are involved in the chelate rings.

Species **C2** corresponds to the CD spectra shown in Figure 8c (and in Figure S6) and to more than one isomer, as indicated by the $^{51}V$ NMR spectrum, where at least two distinct broad peaks are detected: an intense one at $-512 \pm 2$ ppm and a weaker one at $-500 \pm 2$ ppm; the difference in chemical shift between **C1** and **C2** indicates quite different binding modes. The broadness of the peaks may suggest a nonsymmetrical binding mode, **BMh** and **Bmi**, corresponding to a plausible hypothesis. For the tridentate structures such as **BMk** and particularly **BMj**, we would expect a weak CD signal (see above), but this is not the case here. However, tridentate structures cannot be ruled out, as this appears to be the most reasonable explanation for the large difference in chemical shift between **C1** and **C2**.

## Conclusions

The reduced Schiff bases of salicylaldehyde with diaminopropionic acid (salDPA) and ornithine (salOrn), as well as the $V^{IV}O^{2+}$ and $V^{V}O_2^{+}$ complexes of salDPA were prepared and characterised in the solid state and in solution. The structure of one of the protonated forms of salDPA, $H_4$salDPA$^{+}Cl^{-}$, was determined by X-ray diffraction. Complexation of $V^{IV}O^{2+}$ and $V^{V}O_2^{+}$ with salDPA in aqueous solution was studied by potentiometry, UV/Visible spectroscopy and circular dichroism, as well as by EPR spectroscopy for the $V^{IV}O$–salDPA system and by $^{1}H$- and $^{51}V$ NMR spectroscopy for the $V^{V}O_2$–salDPA system. The $V^{IV}O$–salOrn system was studied by potentiometry.

These reduced Schiff base ligands are less susceptible to hydrolysis than their corresponding Schiff base compounds, which we did not isolate in pure form. They also form much more stable complexes than the corresponding Schiff bases. As expected for a salen-type ligand derived from an ethylenediamine rather than a butylenediamine moiety, the $V^{IV}O$ complexes formed with salDPA are much more stable than those formed with salOrn. In fact, in aqueous solutions containing 1:1 ligand/metal stoichiometry, no $V^{IV}O$ hydrolytic products were detected in the pH range 4 to 11 in the salDPA system, while for the salOrn system significant concentrations of $[(VO)_2(OH)_5^{-}]_n$[25] formed in the pH ranges 5–7.5 and 10.5–12.

Practically only 1:1 complexes are formed. The main species formed have the composition $(VO)LH_2^{+}$ and $(VO)L^{-}$ in the $V^{IV}O$–salDPA system, $(VO)LH_2^{+}$, (VO)LH and $(VO)L^{-}$ in the $V^{IV}O$–salOrn system and $(VO_2)LH^{-}$ and $(VO_2)L^{2-}$ in the $V^{V}O_2$–salDPA system. Spectroscopic data provided information about the most probable binding mode of each stoichiometry of the vanadium–salDPA systems. In most cases, the $COO^{-}$ groups are involved in the coordination to $V^{IV}O^{2+}$ or $V^{V}O_2^{+}$, so the binding modes of the ligand may differ from those typically found in vanadium–salen systems.

Globally salDPA is a very effective ligand for $V^{IV}O^{2+}$ and $V^{V}O_2^{+}$, namely in the pH range 6–9. The pendant carboxylate group may help the coupling of the salan moiety to other molecules that may target the compound to specific

 © 2006 Wiley-VCH Verlag GmbH & Co. KGaA, Weinheim 

biological sites. Therefore, we anticipate the possibility of using salDPA systems as carriers of vanadium or other metal ions for this purpose.

## Experimental Section

### Synthesis of Solid Compounds

**salDPA (1):** Triethylamine (3 g, 29.8 mmol) was added to a suspension of L- or D,L-2,3-diaminopropionic acid (DPA) (2 g, 14.2 mmol) in methanol (50 mL) in order to neutralise the mixture. Small portions of a solution of salicylaldehyde in MeOH (3.6 g, 29.1 mmol) were slowly added to this mixture. The mixture became yellow, and this colour became stronger and stronger until the dissolution of DPA was completed. The solution was cooled in ice, and sodium borohydride (2.4 g, 63.9 mmol) was slowly added. A white solid soon precipitated; it was filtered and suspended in MeOH for 3 h. The solid was then filtered, washed with water and MeOH and dried under vacuum. Yield 62%. The number of molecules of water of crystallization found in the several syntheses performed varied from 0 to 1 and the values reported are only examples of some of those found. Yield: 2.8 g, 60%. For $H_3$sal-D,L-DPA, $C_{17}H_{20.6}N_2O_{4.3}$ [$C_{17}H_{20}N_2O_4{\cdot}0.3H_2O$] (321.7): calcd. C 63.46, H 6.45, N 8.71; found C 63.6, H 6.7, N 8.6. $^1$H NMR (300 MHz, $D_2O$, ≈25 °C): 4.30 (s, 5 H, Ar–CH2–N and –CH–*N*–), 3.55 (d, 2 H, NH–$CH_2$), 6.92 (s, 4 H, $CH_{aromatic}$), 7.28 (d, 4 H, $CH_{aromatic}$) ppm. A second method was also used; in the final stage the white solid was suspended in MeOH, and the pH was lowered with a methanol solution of HCl (pH < 1.5). The solid dissolved, and ca. 30 min later another white solid precipitated. This was filtered and washed with water and MeOH. (Yield: 37%). From the mother solution, kept at room temperature for one week, white crystals (small needles) suitable for single-crystal X-ray diffraction were obtained. Yield: 0.132 g, 37%. For $H_4$sal-D,L-DPA·Cl (**1A**), $C_{17}H_{21}N_2O_4Cl$ (358.2): calcd. C 57.87, H 6.00, N 7.94; found C 58.0, H 6.3, N 7.9. For $H_4$sal-L-DPA·Cl, $C_{17}H_{21.6}N_2O_{4.3}Cl$ [$C_{17}H_{21}N_2O_4Cl{\cdot}0.3H_2O$] (358.2): calcd. C 56.99, H 6.08, N 7.82; found C 57.1, H 6.3, N 7.7.

**sal-L-Orn (2):** An ethanol solution (5 mL) of salicylaldehyde (0.230 mL; 2.2 mmol) was added to an aqueous solution (20 mL) of L-ornithine (0.169 g, 1 mmol). The yellow solution was stirred for ca. 1 h and then cooled to ca. 0 °C. As a solution of sodium borohydride (0.095 g, 2.5 mmol) in ethanol (2 mL) containing a few drops of a NaOH (4 M) solution was slowly added, the yellow colour gradually disappeared. After ca. 2 h, the pH was set to ca. 5.2 with HCl (3 M). The solution was kept in a refrigerator at ca. 4 °C for one week. A small amount of a white precipitate formed, which was filtered, washed with cold water, ethanol and ether and dried in vacuo. Yield: 0.051 g, 13%. For $H_3$sal-L-Orn, $C_{19}H_{28.4}N_2O_{6.7}$ [$C_{19}H_{24}N_2O_4{\cdot}2.7H_2O$] (393.0): calcd. C 58.06, H 7.54, N 7.13; found C 58.0, H 7.5, N 7.1.

**sal-L-Lys (3):** The procedure was identical to the one used for sal-L-Orn, but the white solid sal-L-Lys precipitated overnight. Yield: 28%. The number of molecules of water of crystallization found in the several solids obtained varied from 2 to 3, and the value included here corresponds to one of the batches. Yield: 0.114 g, 28%. For $H_3$sal-L-Lys, $C_{20}H_{31.4}N_2O_{6.7}$ [$C_{20}H_{26}N_2O_4{\cdot}2.7H_2O$] (407.0): calcd. C 59.01, H 7.77, N 6.88; found C 59.0, H 7.8, N 6.8. The compound is not soluble in water or in ethanol/water (at least up to 10% ethanol).

**van-D,L-DPA (4):** A methanol solution (5 mL) of *o*-vanillin (0.339 g, 2.2 mmol) was added to a suspension of D,L-2,3-diaminopropionic acid (DPA) (0.142 g, 1 mmol) in methanol (10 mL). Triethylamine was added in order to obtain a pH value of ca. 7.0. The yellow solution was stirred for 3 h at room temperature and then cooled to ca. 0 °C. Sodium borohydride was then slowly added (0.113 g, 3.0 mM), and the solution became colourless. A small amount of a white solid precipitated, which was washed with cooled water (ca. 4 °C), methanol and ether and then dried in vacuo. Yield: 0.092 g, ca. 22%. For $H_3$van-D,L-DPA, $C_{19}H_{28.8}N_2O_{8.4}$ [$C_{19}H_{24}N_2O_6{\cdot}2.4H_2O$] (419.6): calcd. C 54.38, H 6.92, N 6.65; found C 54.4, H 6.4, N 6.6.

**Na[$V^{IV}O$(salDPA)]:** salDPA was (0.322 g, 1 mmol) dissolved in 20 mL of ethanol/water (1:3), and a few drops of NaOH (4 M) were added to promote total dissolution. An aqueous solution (2 mL) of sodium acetate (0.675 g, 5 mmol) was then added, followed by the addition of an aqueous solution (2 mL) of $VOSO_4{\cdot}5H_2O$ (0.26 g, 1 mmol). The solution became pink, and a pink solid precipitated, which was filtered, washed with cold water (≈4 °C), ethanol and ether, and dried under vacuum. Yield: 0.0987 g, 23%. For Na[$V^{IV}O$(sal-D,L-DPA)], $C_{17}H_{16}N_2NaO_5V$ [$C_{17}H_{16}N_2O_5VNa{\cdot}1.5H_2O$] (429.2): calcd. C 47.57, H 4.46, N 6.53, Na 5.36; found C 47.8, H 4.7, N 6.5, Na 6.3. All procedures were performed under $N_2$ and both Na[$V^{IV}O$(sal-D,L-DPA)] and Na[$V^{IV}O$(sal-L-DPA)] were prepared.

**Na[$V^{V}O_2$(salDPA)]:** sal-D,L-DPA (0.322 g, 1 mmol) was dissolved in 25 mL of water, and a few drops of NaOH (4 M) were added to promote total dissolution. An aqueous solution (5 mL) of ammonium vanadate was prepared, also containing a few drops of NaOH (4 M). Under vigorous stirring, the vanadate solution was slowly added to the salDPA solution. A solution of HCl (3 M) was then slowly added until pH ca. 8 was obtained. While adding the acid, a dark solid first appeared, but it disappeared upon stirring. The initial yellow colour became greenish. After 2 h of stirring, a greyish solid formed, it was filtered, and the filtrate was kept. After ca. 20 h a lemon-green solid was formed, which was filtered and washed with cold water (≈4 °C), ethanol and ether, and dried under vacuum. Yield: 0.188 g, 40%. For Na[$VO_2$(sal-D,L-DPA)], $C_{17}H_{20}N_2NaO_7V$ [$C_{17}H_{16}N_2O_5VNa{\cdot}2H_2O$] (470.2): calcd. C 44.95, H 4.44, N 6.17, Na 5.05; found C 44.9, H 4.4, N 6.0, Na 4.6.

### Potentiometric Measurements

All measurements were made in aqueous solution. The purity of the ligands was checked potentiometrically and the exact concentration of solutions was determined by the Gran method.[32] The stock solution of $V^{IV}O$ was prepared and standardised as reported earlier.[33,34] The $H_3O^+$ concentration in the stock solutions were determined by potentiometry. The $V^V$ stock solution was prepared by dissolving $KVO_3$ (Sigma–Aldrich) in an accurately measured volume of a KOH solution of known molarity (0.1977 M), and its $OH^-$ concentration was calculated by taking into account the total volume of the $V^V$ stock solution prepared.

All solutions were manipulated in an inert atmosphere (high purity $N_2$ or purified argon). The ionic strength was adjusted to 0.20 M KCl and the temperature was 25.0 ± 0.1 °C. The pH was measured with an Orion 710A precision digital pH meter equipped with an Orion Ross 8103BN type combined glass electrode, calibrated for hydrogen ion concentration as described earlier.[33] The ionic product of water was $pK_w$ = 13.76.

The protonation constants of salDPA were determined from five titration curves of 4- to 8-mL samples with initial concentrations in the range 0.002 to 0.01 M. Those of sal-L-Orn were determined from five titration curves of 2- to 4-mL samples with a similar concentration range.

Stability constants of the $V^{IV}O$–salDPA system were determined by potentiometric titrations of six 10.0-mL samples. The metal con-

 © 2006 Wiley-VCH Verlag GmbH & Co. KGaA, Weinheim 

centrations were in the range 0.0005–0.003 M, and the L/M ratio was from 0.7 to 4. Titrations were normally performed from pH 2.0 up to 11, unless very extensive hydrolysis, precipitation (only for L/M = 0.7, at pH = 4.0) or very slow equilibration was detected, with KOH solution of known concentration (ca. 0.2 M) under a purified argon atmosphere. For the $V^{IV}O$–sal-L-Orn system, the metal concentrations were in the range 0.001–0.004 M, and the L/M ratios varied from 1 to 4. Titrations were normally performed from pH 2.0 up to 11 in a 5-mL thermostatted cell, by using the same criteria as for the $V^{IV}O$–salDPA system.

The stability constants of the $V^{V}O_2$–salDPA system were also determined by potentiometric titrations of six 10.0 mL samples from pH 12 to ca. 4 (or down to pH ca. 5 for the more concentrated samples, as some precipitation was detected at pH < 5) with an HCl solution of known concentration (ca. 0.2 M). The reversibility of the $V^{V}$ complexation was checked for three L/M ratios by titrating samples starting from pH ca. 5. The reproducibility of titration points included in the evaluation was within 0.005 pH units in the pH range 5–11.

The concentration stability constants $\beta_{pqr} = [M_pL_qH_r]/[M]^p[L]^q[H]^r$ were calculated by using the PSEQUAD computer programme.[24] The formation of the following $V^{IV}O$ hydroxido complexes was taken into account: $[V^{IV}O(OH)]^+$, $[(V^{IV}O)_2(OH)_2]^{2+}$, $[(V^{IV}O)_2(OH)_5]^-$ and $[V^{IV}O(OH)_3]^-$.[25,35,36] As is discussed in ref.[25], the $\log\beta$ of $[(V^{IV}O)_2(OH)_5]^-$ and $[V^{IV}O(OH)_3]^-$ are not known accurately. Therefore, the calculations for pH > 4 may not be entirely reliable, particularly for systems and experimental conditions where these $V^{IV}O$-hydroxido complexes have significant concentrations. For the $V^{IV}O$–salDPA this is not the case, but for the salOrn system some inaccuracies may result from this. For the $V^{V}$ systems, the stability constants were similarly defined, where M refers to $VO_2^+$. The speciation of vanadate into monomeric, dimeric, tetrameric, pentameric and decameric species[37] was taken into account.

### Spectroscopic Measurements

**General:** IR spectra were recorded either with a BioRad FTS 3000 MX FTIR or with a Jasco FTIR 430 spectrometer. Visible spectra were recorded either with a Hitachi U-2000 or a Perkin–Elmer Lambda 9 UV/Vis/NIR spectrophotometer. The CD spectra were recorded with a JASCO 720 spectropolarimeter, either with a red-sensitive photomultiplier (EXEL-308) suitable for the 400–1000 nm range or with the photomultiplier suitable for the 200–700 nm range. The EPR spectra were recorded at 77 K (with glass made by freezing solutions in liquid nitrogen) with a Bruker ESP 300E X-band spectrometer. The $^1$H- and $^{51}$V NMR spectra were obtained with a Varian Unity-500 NMR spectrometer operating at 499.824 and 131.404 MHz, respectively, by using a 5-mm-broadband probe and a controlled-temperature unit set at 25 ± 1 °C. Most of the $^1$H NMR spectra were obtained with a Varian Unity 300 spectrometer also at ca. 25 °C.

**UV/Vis and CD Spectroscopy:** All measurements were made in water. The temperature was kept at 25.0 ± 0.3 °C with circulating water. Unless otherwise stated, by visible (Vis) or circular dichroism (CD) spectra we mean a representation of $\varepsilon_m$ or $\Delta\varepsilon_m$ values vs. $\lambda$ [$\varepsilon_m$: absorption/($bC_M$) and $\Delta\varepsilon_m$: differential absorption/($bC_M$), where $b$: optical path and $C_M$: total $V^{IV}$ or $V^{V}$ concentration]. The spectral range covered was normally 350–900 (Vis) and either 240–600 or 400–1000 nm (CD). All measurements and operations of the spectropolarimeter were computer-controlled. Normally the spectra were recorded by changing the pH with approximately fixed total vanadium and ligand concentrations. The CD spectra of polycrystalline samples were obtained as described in ref.[38]

**EPR Spectroscopy:** In the absence of ethylene glycol, a relatively broad background was present in most of the frozen solution EPR spectra; therefore, most spectra were run with aqueous solutions containing 5% of ethylene glycol. The $V^{IV}O$ EPR spectra were simulated by using a programme by Rockenbauer and Korecz.[30] The EPR spectra help to elucidate which groups coordinate in solution.[26] For the $V^{IV}O$ systems, we used the additivity rule to estimate the hyperfine coupling constant $A_z^{est}$ (see above).

**$^1$H- and $^{51}$V NMR Spectroscopy:** All samples were prepared at room temperature immediately before the acquisition of the NMR spectra. Ligand solutions for the $^1$H NMR pH titrations were prepared in $D_2O$ (99.995%D) by weighing the appropriate amount of the ligand in order to have the desired concentration. The pD values of these solutions were adjusted with DCl and $CO_2$-free NaOD solutions, and measured by using either a Crison MicropH 2002 pH-meter with an Ingold 405-M5 combined electrode, or a Thermo Orion 420A+ pH meter with a Mettler Toledo U402-M3-S7/200 combined microelectrode (all calibrated at 20 ± 1 °C with standard aqueous buffers at pH 4.0 and 7.0). The final values of pD were determined from pD = pH* + 0.40, where pH* corresponds to the reading of the pH meter.[39] To obtain $^{51}$V NMR spectra, the solutions containing the $V^{V}$–salDPA complexes were normally prepared by adding the appropriate amounts of the ligand salDPA to aqueous sodium vanadate solutions of known concentrations and at pH ca. 11–12 in order to have the desired L/M ratios (L/M = 1–1.2). The initial $V^{V}$ concentration in the samples was 3 to 5 mM. The measurements normally started at pH ca. 12 and were continued down to pH 4 (in one set of experiments down to pD 1.8) by addition of an HCl solution. In these experiments, a dark grey precipitate formed at pH < 4–5 (depending on the concentrations), but as the solid settled at the bottom of the NMR tubes, NMR spectra could be obtained from the clear solution. For the acquisition of $^1$H NMR spectra from which data shown in Figure S1 was obtained, a ca. 5-mM solution of salDPA was prepared at pD ca. 13 in $D_2O$, by addition of $CO_2$-free NaOD. The measurements were performed down to pH 1 by addition of DCl (or NaOD, whenever necessary). For pH < 5 the salDPA started to precipitate, but as it agglomerated at the bottom of the NMR tubes, the spectra could be obtained from the clear solution in the upper part. The $^1$H- and $^{51}$V NMR chemical shifts were referenced to DSS (sodium [2,2,3,3-$D_4$]-3-trimethylsilylpropionate) at 0 ppm and to a $VOCl_3$ external solution at 0 ppm, respectively. $^{51}$V NMR acquisition parameters were: 33 kHz spectral width, 30 μs pulse width, 1 s acquisition time and 10 Hz line broadening. The signal intensities of the NMR resonances were obtained by using the line-fitting routine supplied with the NUTS™ PC-based NMR spectral analysis programme.[40]

**X-ray Crystal Structure Determination of 1:** Three-dimensional room temperature X-ray data were collected with a Bruker Smart 1000 CCD instrument by the $\varphi$-$\omega$ scan method. Reflections were measured from a hemisphere of data collected from frames each covering 0.3° in $\omega$. Of the 10878 reflections measured, all were corrected for Lorentz and polarization effects and for absorption by multiscan methods based on symmetry-equivalent and repeated reflections, and 1765 independent reflections exceeded the significance level ($|F|/\sigma|F|$) > 4.0. Complex scattering factors were taken from the programme package SHELXTL,[41] implemented on a Pentium computer. The structures were solved by direct methods and refined by full-matrix least-squares on $F^2$. Hydrogen atoms were left to refine freely with isotropic thermal parameters, except for hydrogen atoms of N(1), O(4), C(8) and C(9), which were localised in the Fourier map and then fixed to the corresponding atoms. Refinement was performed with the allowance for thermal anisot-

 © 2006 Wiley-VCH Verlag GmbH & Co. KGaA, Weinheim 

ropy of all non-hydrogen atoms. Complex scattering factors were taken from the programme package SHELXTL. Further details of the crystal structure determination and X-ray data are given in the Supporting Information (Section 10). CCDC 602814 (for **1A**) contains the supplementary crystallographic data for the structure reported in this paper. These data can be obtained free of charge from the Cambridge Crystallographic Data Centre via www.ccdc.cam.ac.uk/data_request/cif.

**Supporting Information** (see footnote on the first page of this article):

1. Infrared spectra of the compounds.

2. $^{1}H$ NMR chemical shifts of salDPA as a function of pD.

3. Speciation in the $V^{IV}O$–salOrn system.

4. CD spectra of $V^{IV}O$–salDPA solutions at pH > 11.

5. Representation of $\varepsilon_m$ values vs. pH for $V^{IV}O$–salDPA solutions.

6. Circular dichroism spectra of solid polycrystalline samples.

7. Structures of ligands synthesized in this work for which complex formation in solution was not studied.

8. Circular dichroism spectra of $(VO_2)LH^-$ and $(VO_2)L^{2-}$.

9. Comparison of the $V^V$–salDPA species concentration estimated from the $^{51}V$ NMR spectra and the distribution diagram.

10. Crystal and structural data for $H_4salDPA^+ \cdot Cl^-$ (**1A**).

## Acknowledgments

This work was carried out in the frame of a COST D21 project. The authors are grateful to the National Research Fund (OTKA NI61786 and OTKA T49417), to the Hungarian Academy of Sciences, the Fundo Europeu para o Desenvolvimento Regional, Fundação para a Ciência e Tecnologia, the POCI Programme (project POCI/56949/QUI/2004 and POCI/55985/QUI/2004), the Hungarian-Portuguese Intergovernmental S & T Cooperation Programme for 2004–2005, University of A Coruña and the Spanish-Portuguese Bilateral Programme (Acção Integrada E-56/05). We also thank Tamás Gajda for supplying some of the sal-D,L-DPA ligand used in the preliminary experiments.

[1] K. H. Thompson, J. H. McNeill, C. Orvig, *Chem. Rev.* **1999**, *99*, 2561–2571.
[2] K. H. Thompson, C. Orvig, *J. Chem. Soc., Dalton Trans.* **2000**, 2885–2892.
[3] C. Orvig, K. H. Thompson, *Coord. Chem. Rev.* **2001**, *219–221*, 1033–1053.
[4] H. Sakurai, Y. Kojima, Y. Yoshikawa, K. Kawabe, H. Yasui, *Coord. Chem. Rev.* **2002**, *226*, 187–198.
[5] A. E. Evangelou, *Crit. Rev. Oncol./Hematol.* **2002**, *42*, 249–265.
[6] P. Kopf-Maier, H. Kopf, *Z. Naturforsch., Teil B* **1979**, *84*, 805.
[7] C. Djorgevitz in *Metal Ions in Biological Systems* (Eds.: H. Sigel, A. Sigel), Marcel Dekker, New York, **1995**, vol. 31, p. 596.
[8] S. J. D. Karlish, Y. Shechter, *Nature* **1980**, *284*, 556.
[9] G. R. Dubyak, A. Kleinzeller, *J. Biol. Chem.* **1980**, *255*, 5306.
[10] C. E. Heyliger, A. G. Tahiliani, J. H. McNeill, *Science* **1985**, *227*, 1474.
[11] J. Meyerovitch, Z. Farfel, J. Sack, Y. Schechter, *J. Biol. Chem.* **1987**, *262*, 609.
[12] A. S. Tracey, M. J. Gresser, *Proc. Natl. Acad. Sci. USA* **1986**, *83*, 609.
[13] N. Durai, G. Saminathan, *J. Clin. Biochem. Nutr.* **1997**, *22*, 31–39.
[14] J. M. Lacoste, J. Duhault, D. Ravel, EUR Pat. Appl. EP 521,787, **1993**.
[15] I. Correia, J. Costa Pessoa, M. T. Duarte, R. T. Henriques, M. F. Minas da Piedade, L. Veiros, T. Jakusch, A. Dornyei, T. Kiss, M. M. C. A. Castro, C. F. G. C. Geraldes, F. Avecilla, *Chem. Eur. J.* **2004**, *10*, 2301–2317.
[16] G. Verquin, G. Fontaine, M. Bria, E. Zhilinskaya, E. Abi-Aad, A. Aboukais, B. Baldeyrou, C. Bailly, J. L. Bernier, *J. Biol. Inorg. Chem.* **2004**, *9*, 345–353.
[17] I. Correia, J. Costa Pessoa, M. T. Duarte, M. F. Minas da Piedade, T. Jackush, T. Kiss, M. M. C. A. Castro, C. F. G. C. Geraldes, F. Avecilla, *Eur. J. Inorg. Chem.* **2005**, 732–744.
[18] A. Jancsó, Z. Paksi, S. Mikkola, A. Rockenbauer, T. Gajda, *J. Inorg. Biochem.* **2005**, *99*, 1480–1489.
[19] P. O'Brien, S. Mahmood, M. A. Malik, M. Motevalli, P. B. Nunn, *Tetrahedron* **1998**, *54*, 5721–5730.
[20] D. H. Williams, I. Fleming in *Spectroscopic Methods in Organic Chemistry*, 5th ed., McGraw-Hill, London, **1995**, pp. 42–49.
[21] G. Socrates, *Infrared and Raman Characteristic Group Frequencies. Tables and Charts*, 3rd ed., John Wiley & Sons, Chichester, **2001**, pp. 108–113.
[22] R. M. Silverstein, G. C. Bassler, T. C. Morril, "IR Spectroscopy" in *Spectrometric Identification of Organic Compounds*, 5th ed., John Wiley & Sons, New York, **1991**, pp. 122–125.
[23] R. L. Shriner, C. K. F. Hermann, T. C. Morrill, D. Y. Curtin, R. C. Fuson, *The Systematic Identification of Organic Compounds*, 8th ed., John Wiley & Sons, **2004**, p. 194–227.
[24] L. Zekany, I. Nagypal in *Computational Methods for the Determination of Stability Constants* (Ed.: D. Leggett), Plenum, New York, **1985**, pp. 291–353.
[25] L. F. Vilas Boas, J. Costa Pessoa, "Vanadium" in *Comprehensive Coordination Chemistry* (Eds.: G. Wilkinson, R. D. Gillard, J. A. McCleverty), Pergamon, Oxford, **1987**, vol. 3, ch. 33, pp. 453–583.
[26] N. D. Chasteen in *Biological Magnetic Resonance* (Eds.: J. Lawrence, L. J. Berliner, J. Reuben), Plenum, New York, **1981**; vol. 3, ch. 2, pp. 53–119.
[27] T. Jakusch, P. Buglyó, I. Tomaz, J. Costa Pessoa, T. Kiss, *Inorg. Chim. Acta* **2002**, *339*, 119–128.
[28] T. S. Smith, C. A. Root, J. W. Kampf, P. G. Rasmussen, V. L. Pecoraro, *J. Am. Chem. Soc.* **2000**, *122*, 767–775.
[29] A. J. Tasiopoulos, A. N. Troganis, A. E. Evangelou, C. P. Raptopoulou, A. Terzis, Y. Deligiannakis, T. A. Kabanos, *Eur. J. Chem.* **1999**, *5*, 910–921.
[30] A. Rockenbauer, L. Korecz, *Appl. Magn. Reson.* **1996**, *10*, 29–43.
[31] H. Sigel, R. B. Martin, *Chem. Rev.* **1982**, *82*, 385–426.
[32] G. Gran, *Acta Chem. Scand.* **1950**, *4*, 559–575.
[33] J. Costa Pessoa, T. Gajda, R. D. Gillard, T. Kiss, S. M. Luz, J. J. G. Moura, I. Tomaz, J. P. Telo, I. Torok, *J. Chem. Soc., Dalton Trans.* **1998**, 3587–3600.
[34] I. Nagypál, I. Fábián, *Inorg. Chim. Acta* **1982**, *61*, 109–113.
[35] A. Komura, M. Hayashi, H. Imanaga, *Bull. Chem. Soc. Jpn.* **1977**, *50*, 2927–2931.
[36] R. P. Henry, P. C. H. Mitchell, J. E. Prue, *J. Chem. Soc., Dalton Trans.* **1973**, 1156–1159.
[37] L. Pettersson, B. Hedman, I. Andersson, N. Ingri, *Chem. Scr.* **1983**, *22*, 254–264.
[38] J. Costa Pessoa, M. J. Calhorda, I. Cavaco, P. J. Costa, I. Correia, D. Costa, L. Vilas-Boas, V. Felix, R. D. Gillard, R. T. Henriques, R. Wiggins, *Dalton Trans.* **2004**, 2855–2866.
[39] P. K. Glasoe, F. A. Long, *J. Phys. Chem.* **1960**, *64*, 188–190.
[40] NUTS-NMR, *Spectroscopic Data Processing Software*, Acorn NMR, Fremont, CA, USA, **1999**.
[41] G. M.Sheldrick, *SHELXTL Bruker Analytical X-ray System*, Madison, WI, **1997**.

Received: April 5, 2006
Published Online: August 24, 2006

 © 2006 Wiley-VCH Verlag GmbH & Co. KGaA, Weinheim 

DOI: 10.1002/ejic.200600314

# Binding Constant of $V^{IV}O$ to Transferrin

**Tamás Kiss,*[a,b] Tamás Jakusch,[b] Saâd Bouhsina,[c] Hiromu Sakurai,[d] and Éva Anna Enyedy[a]**

**Keywords:** $V^{IV}O$–Transferrin complexes / EPR spectroscopy / UV spectroscopy / Stability constants

The interactions of bis-$V^{IV}O$-1,2-dimethyl-3-hydroxy-4(1*H*)-pyridinone (DHP) with apotransferrin (apoTF) were followed by means of electron paramagnetic resonance spectroscopy (EPR) at room temperature and at liquid nitrogen temperature. Partial ligand displacement between DHP and apoTF was observed, and the reaction was used to determine the binding constant of $V^{IV}O$ to apoTF. A value of $\log K = 14.3 \pm 0.6$ was obtained for the binding of the first $V^{IV}O$ to apoTF. In order to confirm the validity of the binding constant, UV spectroscopy was used to monitor the displacement reaction between $V^{IV}O$–apoTF and nitrilotriacetic acid (NTA). The difference between the binding constants obtained by the two different methods (ca. one log unit) was explained in terms of the possible ternary complex formation between $V^{IV}O$–apoTF and the displacing ligand. The binding constants obtained exhibit a reasonably good agreement with the linear free energy relationship (LFER) estimation.

(© Wiley-VCH Verlag GmbH & Co. KGaA, 69451 Weinheim, Germany, 2006)

## Introduction

There is considerable interest in the binding strength of metal ions to human serum transferrin (TF) because of its natural, therapeutic, diagnostic and toxicological importance.[1] The serum transport protein TF has two very similar metal binding sites (C-lobe and N-lobe), and their affinities for metal ions differ only slightly. Each lobe contains a distorted octahedral site consisting of two Tyr-$O^-$ anions, one His-N group, one Asp-$COO^-$ anion and one usually bidentate hydrogen carbonate anion (the synergistic anion).[2,3] Normally, the two stepwise binding constants ($\log K$ values) differ by approximately one unit, which is beyond the purely statistical factor of four (0.6 log unit), because of a slight difference in the intrinsic binding affinities of the two lobes. The mode of binding of metal ions at the two sites depends upon the nature of the metal ion, the synergistic anion and the pH, but binding is generally a little more preferred at the C-terminal site than at the N-terminal site.[2]

[a] Department of Inorganic and Analytical Chemistry, University of Szeged,
P. O. Box 440, 6701 Szeged, Hungary
Fax: +36-62-420505
E-mail: tkiss@chem.u-szeged.hu
[b] Biocoordination Chemistry Research Group of the Hungarian Academy of Sciences,
P. O. Box 440, 6701 Szeged, Hungary
[c] Laboratoire Interdisciplinaire en Sciences de l'Environment, Université du Littoral Côte d'Opale, ELICO ESA 8013,
32 Avenue Foch, 62930 Wimereux, France
[d] Department of Analytical and Bioinorganic Chemistry, Kyoto Pharmaceutical University,
5 Nakauchi-cho, Misasagi, Yamashina-ku, Kyoto 607-8414, Japan

A number of experimental techniques have been used to determine the stability constants of metal–TF complexes. Difference UV spectroscopy, based on the production of new absorption bands at ca. 240 nm and ca. 295 nm[2] on the complexation of metal ions to the phenolic groups of the Tyr residues, has been applied most frequently.[4–9] Other methods include equilibrium dialysis, EPR[5] and multinuclear NMR spectroscopy,[10] the latter two also being used to distinguish the modes of metal ion binding between the two sites.[11–14]

Interest in the biochemistry of vanadium has increased enormously in the past twenty years partly because of its insulin-mimetic or more precisely insulin-enhancing properties.[15] It has been proposed that the transport of vanadium in higher organisms is mediated by TF,[16] and it was recently proved that most of the vanadium in the serum is bound to TF.[17,18] The complexation of vanadium to TF in oxidation states of +3,[19–22] +4[13,14,20–27] or +5[21–24,28–30] has been extensively studied by various research groups. The results uniformly indicate that two vanadium ions are bound to the metal-ion-free apoTF, at the usual specific $Fe^{III}$ binding sites. Using X-band and Q-band EPR spectroscopic methods, Chasteen et al.[13,14] distinguished three $V^{IV}O$ binding environments at a physiological pH (ca. 7.4), all having similar O-donor-rich environments, but with slightly different conformations. One possibly has the normally preferred square-pyramidal or square-bipyramidal $V^{IV}O$ geometry, in which the $V^{IV}O$ oxygen atom occupies an apical position (A environment), while for the other two ($B_1$ and $B_2$) [although in-plane anisotropy (rhombic spectra) is not observed] the noncoincidence of the magnetic axes suggests significant distortion around the $V^{IV}O$ ar-

 © 2006 Wiley-VCH Verlag GmbH & Co. KGaA, Weinheim InterScience 

rangement. The relative intensities of the A and B resonances are strongly pH dependent. The two interconvertible A and B conformational states are believed to belong to the C-terminal and N-terminal binding sites of the protein, respectively.[31]

The binding of $V^{IV}O$ to TF is strong, and thus only stoichiometric formation of the complexes can be observed.[13,14,21] We are not aware of any attempt to characterise the complexation of $V^{IV}O$ with TF in a quantitative way; only the competition between $V^{IV}O$ and $Fe^{II}$ binding to ferritin[26] and the equilibrium distribution of $V^{IV}O$ between albumin and TF have been studied.[24] Sun et al.[2] suggested that the LFER between the binding constants ($\log K_1$) of metal ions to the first lobe of TF and the stability constants, $\log K_{OH^-}$ for the binding of hydroxide, can be used for the prediction of unknown stability constants of metal-ion–TF complexes. Other possible correlations between the metal ion binding to TF and small N,O-donor ligands such as nitrilotriacetic acid (NTA), oxalate, acetate, glycine, malonate and lactate were also examined but none of them were as good as that with $OH^-$. This suggests that the two Tyr moieties at the metal-binding site of TF play predominant roles in determining the strength of the metal binding.[2] We used the above approach in our previous work in order to describe the speciation of various insulin-mimetic $V^{IV}O$ complexes in blood serum,[32] and obtained a value of $\log K_1(TF) = 13.2 \pm 1.6$ for $V^{IV}O$ binding to TF. During the study EPR spectroscopy revealed a partial displacement of apoTF by one of the low-molecular-mass carrier ligands, 1,2-dimethyl-3-hydroxy-4(1*H*)-pyridinone (DHP). It was decided to make use of this reaction to assess the binding of $V^{IV}O$ to apoTF.

Accordingly, in this paper we report, to the best of our knowledge, the first binding constants of $V^{IV}O$ to human serum TF obtained by means of EPR and UV spectral monitoring of the ligand displacement reactions between the $V^{IV}O$ complexes formed with apoTF and DHP or NTA.

## Results and Discussion

The EPR spectra of the $V^{IV}O$–apoTF system at a metal-ion-to-ligand ratio of 1:1 at pH 7.5 at room temperature and at 77 K (LNT: liquid nitrogen temperature) are depicted in Figure 1. In agreement with the earlier result,[33] the room temperature spectrum of [$V^{IV}O$(apoTF)] (Figure 1, II) is axial because of the slow tumbling motion of the protein. However, on the parallel part only two types of vanadium species are clearly observable (A and B), while the not completely perfect simulation of the spectrum might indicate the presence of a third species ($B_2$). The measured ratio of environments A and B is almost identical, but the difference between the two –7/2 peaks is only 1.5 mT (instead of 2.5 mT as reported earlier in ref.[33]).

The –3/2 peak of the perpendicular part of the LNT X-band spectra clearly shows three species in contrast with Chasteen's earlier findings, where only the Q-band spectra could differentiate between the $B_1$ and $B_2$ environments. In

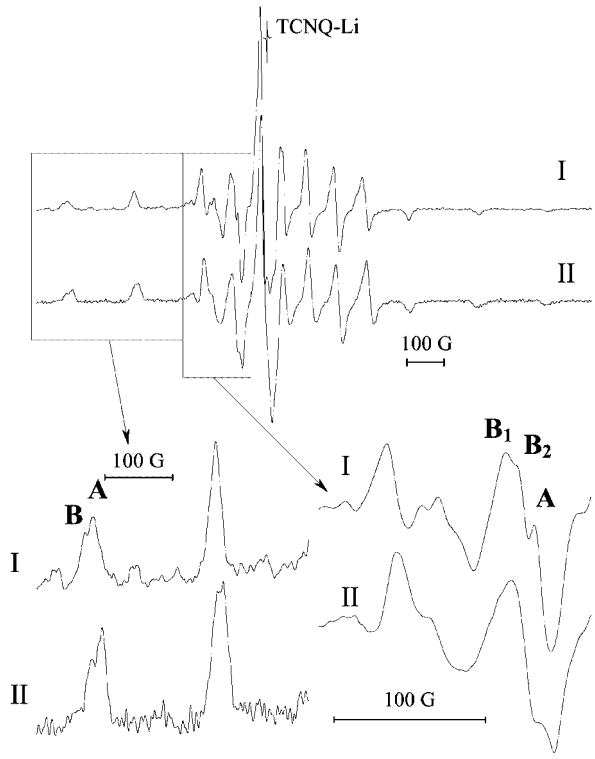


Figure 1. EPR spectra of $V^{IV}O$–apoTF, 1:1 at pH 7.5 (I) at liquid nitrogen temperature and (II) at room temperature.

the parallel part of the spectra, the peaks strongly overlap and accordingly $g_{\|}$ and $A_{\|}$ parameters were not determined.

The mechanism of the insulin-enhancing effect of $V^{IV}O$ compounds is still unknown, and the speciation of the $V^{IV}O$ insulin-mimetic compounds in the blood is therefore interesting.[34–37] The estimated [$V^{IV}O$(apoTF)] stability constants obtained from the LFER prediction clearly demonstrated that in most cases of the insulin-mimetic $V^{IV}O$ complexes (with maltol, picolinic acid, 6-Me-picolinic acid, 2-OH-pyridine *N*-oxide and 2-SH-pyridine *N*-oxide)[32,36] apoTF completely displaces the carrier ligands in equimolar concentration. Orvig et al. recently reached a similar conclusion with regard to the interactions of [$V^{IV}O(maltol)_2$] with the serum proteins albumin and apoTF:[38] TF is capable of binding two equivalents of the complex to produce a [$(V^{IV}O)_2$(TF)] species in which the metal ions occupy both $Fe^{III}$ binding sites with the concomitant release of the free maltol. The bis complex of DHP seems to be an exception – only partial displacement of the DHP occurred because it forms exceptionally stable complexes with $V^{IV}O$.[37] Although [$V^{IV}O(DHP)_2$] is present exclusively at pH 7.5 (see speciation in Figure 2), the EPR spectrum obtained at this pH (Figure 3a: LNT, 3b: room temperature) indicates the presence of two isomers. The formation of *cis* and *trans* isomers (see Scheme 1) among the bis-$V^{IV}O$ complexes of chelating O-donor ligands is well documented in the literature.[34–37] There is no general rule regarding the preferential formation of one or other of the isomers, but it has been found, for instance, that the charge of the coordinating ligands and the size of the chelate ring can affect this.[39] The

 © 2006 Wiley-VCH Verlag GmbH & Co. KGaA, Weinheim 

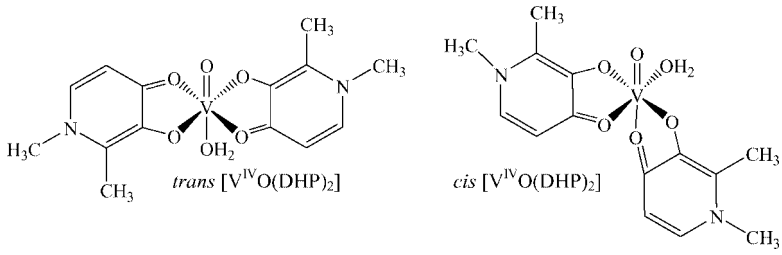


Scheme 1. Binding modes of the *cis* and *trans* isomers of $[V^{IV}O(DHP)_2]$.

EPR parameters of the bis complexes of $V^{IV}O$ and DHP, together with the ratios of the two isomers, are given in Table 1. The data reveal that *trans* isomer formation is favoured with DHP, when a water molecule is *trans* to the oxo group of $V^{IV}O$.

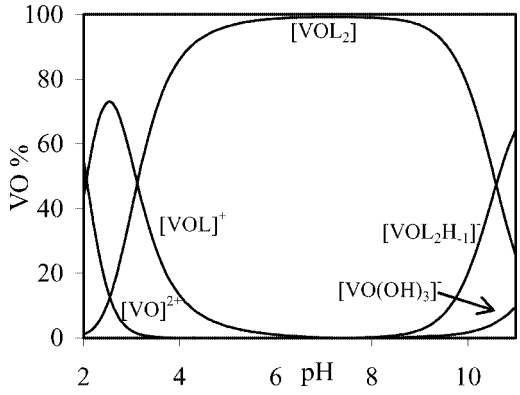


Figure 2. Speciation curves for complexes formed in the $V^{IV}O$–DHP system at a 1:2 metal-ion-to-ligand ratio, $[V^{IV}O]$ = 0.001 M. Calculated with stability constants, $\log\beta(HL)$ = 9.76, $\log\beta(H_2L)$ = 13.46, $\log\beta([V^{IV}OL]^+)$ = 12.18, $\log\beta([V^{IV}OL_2])$ = 22.83, $\log\beta([V^{IV}OL_2H_{-1}]^-)$ = 12.24, $\log\beta([V^{IV}OL_3H_2]^+)$ = 38.5, $\log\beta([V^{IV}O_2L_2H_{-2}]^{2-})$ = 16.43, taken from ref.[40]

After the detailed equilibrium and EPR spectral description of the binary systems, measurements were made on the ternary system $V^{IV}O$–apoTF–DHP at different metal-ion-to-ligand ratios at both room temperature and 77 K. For easier comparison, the room temperature spectra of the $V^{IV}O$–apoTF (1:1), $V^{IV}O$–DHP (1:2) and $V^{IV}O$–apoTF–DHP (1:1:2) systems are depicted together in Figure 4. It is clearly seen that the ternary spectrum is a composite of the isotropic spectrum of the $[V^{IV}O(DHP)_2]$ and the axial one of the $[(V^{IV}O)(apoTF)]$. This observation indicates partial displacement of the carrier ligand by apoTF or vice versa, i.e. $[V^{IV}O(DHP)_2]$ + apoTF ⇌ $[(V^{IV}O)(apoTF)]$ + 2 DHP. (As a first approximation, ternary complex formation with the protein and the carrier ligand was neglected in order to make further calculations possible.) The +7/2 and +5/2 parts of the LNT spectra of these three systems are depicted together in Figure 5.

As a first step in the quantitative evaluation of the spectral changes, the extent of ligand displacement was determined by calculating the ratio of the concentrations of $V^{IV}O$ bound to the two ligands through double integration

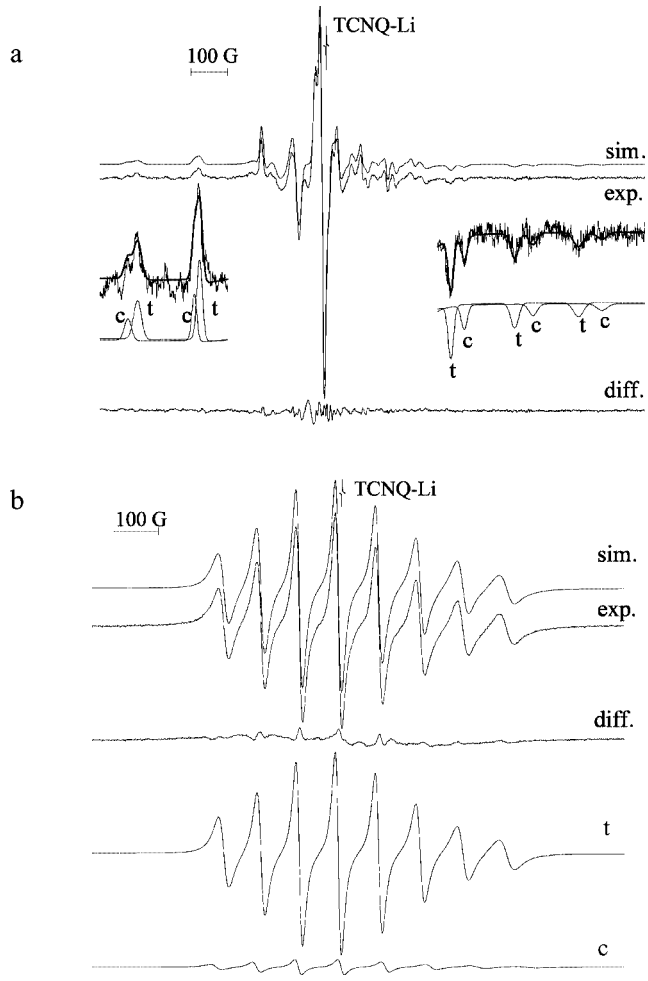


Figure 3. EPR spectra (sim. = simulated, exp. = experimental) of $V^{IV}O$–DHP, 1:2 at pH 7.5 (a) at liquid nitrogen temperature and (b) at room temperature, *t* = *trans* isomer, *c* = *cis* isomer.

of the enlarged sections of the simulated EPR spectra shown in Figure 5. From these data, the concentrations ($[V^{IV}O(apoTF)]$, [DHP], $[V^{IV}O(DHP)_2]$ and [apoTF]) and the displacement constant $K = [[V^{IV}O(apoTF)]]\cdot[[DHP]]^2/[[V^{IV}O(DHP)_2]]\cdot[[apoTF]]$ can be calculated. We used this displacement constant ($\log K = -3.6 \pm 0.3$) to obtain the binding constant for the $V^{IV}O$–apoTF interaction. The conditional stability constant for the competitive complex $[V^{IV}O(DHP)_2]$ at pH 7.5 was first calculated by taking into account the protonation equilibria of the ligand DHP, Equation (1):

 © 2006 Wiley-VCH Verlag GmbH & Co. KGaA, Weinheim 

Table 1. EPR parameters[a] for the $V^{IV}O$–apoTF, $V^{IV}O$–DHP and $V^{IV}O$–apoTF–DHP systems obtained by computer simulation[44] of the experimental spectra, together with some earlier literature results.

| | $g_x$, $g_y$ | $g_z$ | $A_x$, $A_y$ | $A_z$ | Ratio | pH | Ref. |
|---|---|---|---|---|---|---|---|
| **$V^{IV}O$–apoTF** | | | | | | | |
| *RT* | | | | | | | |
| A | 1.974(1) | 1.940(2) | 60.1(5) | 166.8(9) | | 7.5 | [b] |
| B | 1.969(1) | 1.934(3) | 56(1) | 170(3) | | 7.5 | [b] |
| *LN* | | | | | | | |
| A | 1.973(1) | 1.939–1.944[d] | 55.6(8) | 166–171[d] | | 7.5 | [b] |
| $B_1$ | 1.972(1) | 1.939–1.944[d] | 57.4(4) | 166–171[d] | | 7.5 | [b] |
| $B_2$ | 1.976(1) | 1.939–1.944[d] | 59.7(7) | 166–171[d] | | 7.5 | [b] |
| A | 1.973 | 1.938 | 56.6 | 168.0 | 50 | 7.6 | [14] |
| $B_1$ | 1.979 | 1.941 | 57.7 | 170.3 | 25 | 7.6 | [14] |
| $B_2$ | 1.977 | 1.937 | 60.9 | 172.4 | 25 | 7.6 | [14] |
| A | 1.973 | 1.938 | 57.5 | 168.0 | | 8.0 | [27] |
| B | 1.978 | 1.9375 | 54.0 | 170.0 | | 8.0 | [27] |
| Rat TF | 1.968 | 1.937 | 57.9 | 167.7 | | 8.3 | [33] |
| **$V^{IV}O$–DPH** | | | | | | | |
| *RT* | | | | | | | |
| $V^{IV}O(L)_2$ *trans*[c] | 1.973(1) | | 84.2(2) | | 88(5) | | [b] |
| $V^{IV}O(L)_2$ *cis*[c] | 1.967(2) | | 92(2) | | 12(5) | | [b] |
| *LN* | | | | | | | |
| $V^{IV}O(L)_2$ *trans* | 1.987(1), 1.981(1) | 1.954(1) | 43.2(3), 54.4(1) | 158.1(2) | 64(4) | | [b] |
| $V^{IV}O(L)_2$ *cis* | 1.978(1) | 1.943(1) | 58.1(4) | 168.3(2) | 36(4) | | [b] |
| **$V^{IV}O$–apoTF–DHP** | | | | | | | |
| *RT* | | | | | | | |
| $V^{IV}O$(apoTF) A (?) | 1.972(1) | 1.940(1) | 57.5(1) | 164.9(2) | | 7.5 | [b] |
| $V^{IV}O(L)_2$ *trans*[c] | 1.973(1) | | 84.2(4) | | | 7.5 | [b] |
| $V^{IV}O(L)_2$ *cis*[c] | 1.967(2) | | 92(1) | | | 7.5 | [b] |

[a] In the case of the axial geometry: $g_x = g_y = g_\perp$; $A_x = A_y = A_\perp$; $g_z = g_\parallel$ and $A_z = A_\parallel$. A is given in $10^4$ $cm^{-1}$. [b] This work. [c] Isotropic spectra $g_x = g_y = g_z = g_0$ and $A_x = A_y = A_z = A_0$. [d] The parameters are not resolved.

$$\log \beta^c([V^{IV}O(DHP)_2]) = \log \{\beta([V^{IV}O(DHP)_2])/(1 + \beta_1^{II}(DHP)\ 10^{-pH} + \beta_2^{II}(DHP)\ 10^{-2pH})^2\} \quad (1)$$
$$= \log (10^{22.83}/(1 + 10^{9.76}10^{-7.5} + 10^{13.46}10^{-15.0})^2 = 18.31$$

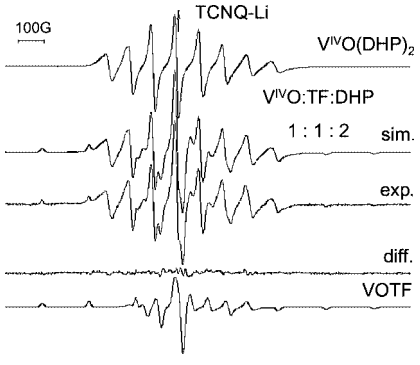


Figure 4. Room-temperature EPR spectra of (a) the binary $V^{IV}O$–DHP 1:2 (simulation), (b) the ternary $V^{IV}O$–apoTF–DHP 1:1:2 and (c) the $V^{IV}O$–apoTF 1:1 systems (simulation) at pH 7.5. Simulations were performed with EPR parameters given in Table 1.

A value of $\log\beta^c([V^{IV}O(DHP)_2]) = 18.31 \pm 0.06$ was obtained. (Stability constants for the formation of the proton and $V^{IV}O$ complexes were taken from ref.[40]) The conditional binding constant could now be calculated as $\log K_1^c([V^{IV}O(apoTF)]) = \log\beta^c([V^{IV}O(DHP)_2]) + \log K_{displacement} = 18.31 - 3.6 = 14.7$. The ratios ($[V^{IV}O(apoTF)]/[V^{IV}O(DHP)_2]$) and the $\log K_1^c([V^{IV}O(apoTF)])$ values determined for all spectra are listed in Table 2. From EPR spectroscopic studies, where formation of both the ternary complex and $[(V^{IV}O)_2(apoTF)]$ was neglected, $K_1^c([V^{IV}O(apoTF)]) = 14.7 \pm 0.3$ was determined. The binding constant $\log K_2^c$, characteristic of the binding of the second $V^{IV}O$ to apoTF, can be estimated by using the observed difference between the stepwise binding constants for transition metal ions (ca. one log unit),[2] as $\log K_2^c([V^{IV}O(apoTF)]) = 13.7 \pm 0.5$.

 © 2006 Wiley-VCH Verlag GmbH & Co. KGaA, Weinheim 

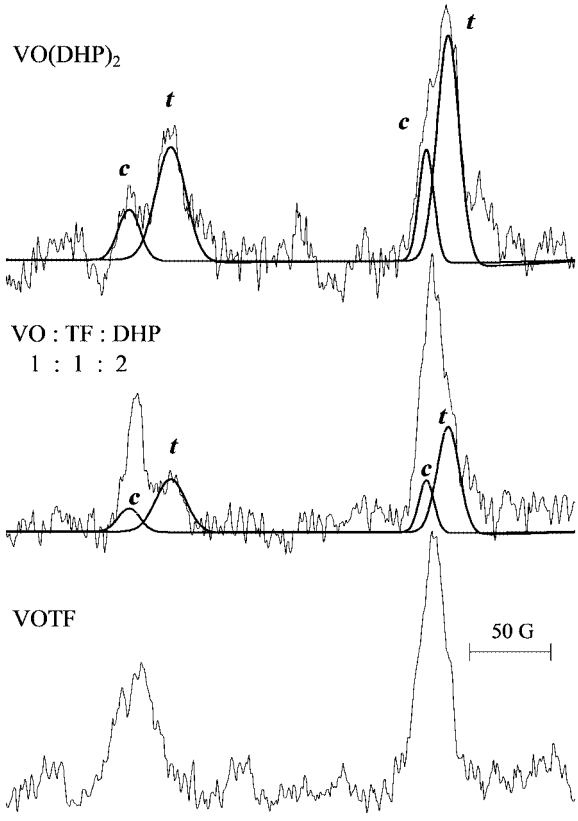


Figure 5. Lowfield region (parallel +7/2, +5/2 peaks) LNT EPR spectra of (a) the binary $V^{IV}O$–DHP 1:2, (b) the ternary $V^{IV}O$–apoTF–DHP 1:1:2 and (c) the $V^{IV}O$–apoTF 1:1 systems at pH 7.5.

In order to confirm the conditional [$V^{IV}O$(apoTF)] binding constants obtained, UV spectrophotometry was also used in the hope that this would furnish more accurate binding constants. In this case, we had to apply a rather low apoTF concentration (8 μM) so as to be able to measure the UV absorbance, and we used a different second ligand, NTA, to displace apoTF from the vanadium coordination sphere. The shape and the intensity of the individual difference spectra (see Figure 6) are in good agreement with that reported by Bertini et al. earlier.[20]

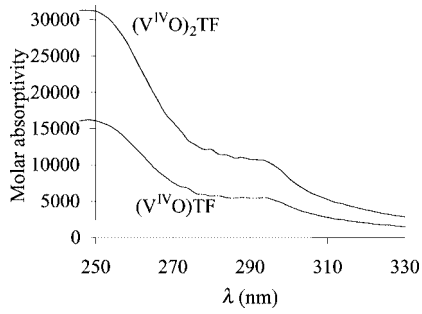


Figure 6. Individual difference spectra of [$V^{IV}O$(apoTF)] and [$(V^{IV}O)_2$(apoTF)] calculated from UV spectroscopic measurements.

The determined $\log K_1^c$ and $\log K_2^c$ values are listed in Table 2. Unfortunately, there is a 0.7 unit difference in the $\log K_1^c$ values determined with DHP and NTA, and both are outside the uncertainty range of the same constants determined by EPR spectroscopy.

Table 2. Stepwise stability constants {$V^{IV}O^{2+}$ + apoTF ⇌ [$V^{IV}O$(apoTF)] ($\log K_1^c$) and $VO^{2+}$ + [$V^{IV}O$(apoTF)] ⇌ [$(V^{IV}O)_2$(apoTF)]} ($\log K_2^c$) determined by different methods {pH 7.5, [$HCO_3^-$] = 0.025 M, $T$ = 25 °C}.

| Method | System | [$V^{IV}O$(apoTF)]: [$V^{IV}O(DHP)_2$] | $\log K_1^c$ | | $\log K_2^c$ | | Numb. of spectra | Fitting[a] |
|---|---|---|---|---|---|---|---|---|
| **LNT EPR** | $V^{IV}O$–apoTF–DHP (mM) | | | | | | | |
| | 0.5 : 0.5: 1.0 | 40 : 60 | 15.0 | ±0.3 | | | 1 | |
| | 0.5 : 0.75 : 1.5 | 25 : 75 | 14.6 | ±0.3 | | | 1 | |
| **RT EPR** | $V^{IV}O$–apoTF–DHP (mM) | | | | 13.7[b] | ±0.5 | | |
| | 1 : 1 : 2 | 37 : 63 | 14.9 | ±0.1 | | | 1 | |
| | 1 : 0.5 : 1 | 47 : 53 | 14.6 | ±0.1 | | | 1 | |
| | 1 : 1 : 1 | 59 : 41 | 14.3 | ±0.2 | | | 1 | |
| **UV–VIS** | | | | | | | | |
| | $V^{IV}O$–apoTF–DHP | | 14.0 | ±0.2 | 11.5 | ±0.6 | 70 | $5.9\times10^{-3}$ |
| | $V^{IV}O$–apoTF–NTA | | 13.4 | ±0.2 | 11.9 | ±0.5 | 85 | $3.9\times10^{-3}$ |
| | $V^{IV}O$–apoTF–DHP–NTA | | 13.7 | ±0.2 | 11.8 | ±0.5 | 129 | $5.7\times10^{-3}$ |
| **Average** | | | **14.3** | **±0.6** | **11.7** | **±0.6** | | |

[a] Square root of the average of the square difference between the measured and simulated absorbance; sqrt{$\Sigma[(A_{exp} - A_{fitt})^2]/n$}, $n$ is the number of degrees of freedom. [b] Estimated value from ref.[2] (see text).

 © 2006 Wiley-VCH Verlag GmbH & Co. KGaA, Weinheim 

The difference between the binding constants determined from the EPR and UV spectra may be explained in part by the slightly different experimental conditions: different total concentrations of apoTF, ca. 1 mM for EPR and ca. 0.01 mM for UV spectroscopic measurements; different solvents, 10% (v/v) DMSO for the LNT EPR spectroscopy and water for the other measurements; and different temperatures, ca. –5 °C for the LNT measurements and 25 °C for the others.

The rather low value obtained for $\log K_2^c$ by UV spectroscopy is more worrying. However, this value is probably very uncertain because of the very low concentration of the ligand used in the UV spectroscopic measurements, and thus the rather high error from any disturbing circumstances affecting the concentration of the interacting species, or from the light absorption of the sample, such as slight oxidation of the metal ion. Accordingly, $\log K_2^c$ determined by means of UV spectroscopic measurements can be considered only a tentative value. The constants $K_1^c$ and $K_2^c$ are conditional constants for pH 7.5 and 25 mM hydrogen carbonate concentration.

The differences between the binding constants $\log K_1^c$ obtained by the three experimental methods (room-temperature EPR spectroscopy, LNT EPR and UV spectroscopy) are about 0.5–1.5 orders of magnitude higher than that obtained from the LFER prediction ($13.2 \pm 1.6$) (see Figure 6 in ref.[32]), although they are within the uncertainty range of the latter.

As mentioned above, the absence of ternary complex formation between [$V^{IV}O$(apoTF)] and the competitor ligand had to be assumed as a precondition for the calculation of the binding constant. This has not been proven,[38] and NMRD measurements[41] have suggested that displaced DHP ligand(s) do not move far away from the metal ions, which to some extent continues to feel their presence. More detailed studies are currently being carried out in our laboratories in order to explore the possibility of ternary complex formation between $V^{IV}O$–apoTF and low molecular mass carrier ligands. This process may be the reason for the differing LFER estimated value.

Although the measurements reported here were carried out with metal-ion-free apoTF, the binding constants determined can be applied with a good approximation to the interaction of $V^{IV}O$ with TF, as only ca. 30% of the metal-binding sites of the protein are saturated with $Fe^{III}$ under normal conditions, and thus there are enough free sites to bind other, mostly hard metal ions (e.g. $Al^{III}$ or $V^{IV}O$) and to transport them in the blood stream.

## Materials and Methods

### Chemicals

DHP, NTA and human apotransferrin (apoTF) were obtained from Sigma Co. The purities of the small organic ligands were checked, and the exact concentrations of their solutions were determined by the Gran method.[42] The concentrations of protein solutions were estimated from their UV absorption ($\varepsilon_{280}$(TF) = 92.300 $m^{-1} cm^{-1}$[24]). The $V^{IV}O$ stock solution was prepared as described in ref.[43] and standardised for metal ion concentration by a permanganate titration.

### EPR Spectroscopic Measurements

As a consequence of the ready oxidation of $V^{IV}O$ to $V^{V}$ under neutral or basic conditions, extreme care was taken to exclude oxygen during the preparation of the samples and during the measurements. It has been reported that $V^{IV}O$ ions bound to human serum TF are very unstable towards aerobic oxidation,[24] and the half-life for the oxidation is estimated to be between 5 and 13 min. Aqueous solutions (0.5 mL) of samples containing DHP and apoTF in ratios of 0.001 M:0.0005 M, 0.0015 M:0.0005 M and 0.001 M:0.0008 M were prepared in 0.1 M HEPES buffer and 0.025 M sodium hydrogen carbonate adjusted to pH 7.5. The solutions were carefully purged with argon and then sealed under an argon atmosphere. A $V^{IV}O$ stock solution (5 μL) was then added to each sample through a rubber septum with a Hamilton syringe. Samples for the EPR spectroscopic measurements were taken out by syringe and were immediately transferred into the EPR tube (LNT) or into the capillary (room temperature). X-band EPR spectra (9.59 or 9.40 GHz) were recorded in aqueous solution at LNT (77 K) and at room temperature with a Bruker EMX or JEOL JES-RE-1X spectrometer. The samples for low-temperature measurements contained 10% (v/v) of DMSO to ensure good glass formation (dilution of the samples was taken into account). The EPR spectra were evaluated and simulated with the EPR computer programme of Rockenbauer and Korecz.[44]

### UV Spectroscopic Measurements

At physiological pH, vanadium(IV) undergoes extensive hydrolysis. Hence, the stability constants of apoTF were determined by a displacement reaction with NTA and with DHP. Both ligands form appropriately stable complexes with $V^{IV}O$, and the stability constants are available at 25 °C and $I$ = 0.2 M (KCl).[40,45] However, while NTA does not exhibit significant UV absorption at pH 7.5, which simplifies the determination, at pH 7.5 the complex $[V^{IV}OL]^-$ of NTA is partly hydrolysed and a ternary complex, $[V^{IV}OL(OH)]^{2-}$, is formed, which makes the system somewhat more complicated. On the other hand, DHP forms a single $[V^{IV}OL_2]$ complex at pH 7.5, but both the complex and the ligand exhibit significant UV absorption, which imposes a limit to the use of a high excess of the ligand.

In contrast with the difference UV spectroscopic method (frequently applied by Harris and coworkers to determine the stability constants of TF complexes with different metal ions[4–9]), we simply measured the absorbance and fitted the data (wavelength range 250–330 nm) and individual spectra by using the computer programme PSEQUAD.[46]

The apoTF concentration was 8 μM, the molar ratio between apoTF and NTA was 1:0, 0:1, 1:1, 1:5, 1:25 or 1:120 and that between apoTF and DHP was 0:1, 1:1, 1:2.5 or 1:5 at 25 °C in 0.025 M $HCO_3^-$, and $I$ = 0.2 M (KCl) in 0.1 M HEPES buffer adjusted to pH 7.5. The starting volume was 2.0 mL and at each titration point 25 μL of 0.16 mM $V^{IV}OCl_2$ was added until an apoTF to $V^{IV}O$ ratio of 1:4 was reached. (When the calculation suggested hydrolysis of $V^{IV}O$ at a titration point, the data of the spectrum were omitted from the calculation.) An HP 8452 diode array spectrophotometer was used with a silica cell with a pathlength of 1.00 cm. During measurements, the cell was closed, and during the addition of $V^{IV}O$, argon was bubbled through the sample to exclude air.

 © 2006 Wiley-VCH Verlag GmbH & Co. KGaA, Weinheim 

## Acknowledgments

This work was performed in the frame of a COST D21 collaboration and supported by the Hungarian Research Fund (OTKA grants NI61786 and T049417). The authors thank Dr E. A. Aad (Universite du Littoral) for his help with the EPR spectroscopic measurements.

[1] G. Berthon (Ed.), *Handbook of Metal-Ligand Interactions in Biological Fluids: Bioinorganic Medicine*, Dekker, New York, **1995**, vol. 1, part I.
[2] H. Sun, M. C. Cox, H. Li, P. J. Sadler, *Struct. Bond.* **1997**, *88*, 71–102.
[3] W. R. Harris, L. Messori, *Coord. Chem. Rev.* **2002**, *228*, 237–262.
[4] W. R. Harris, B. Yang, S. Abdollahi, Y. Hamada, *J. Inorg. Biochem.* **1999**, *76*, 231–242.
[5] W. R. Harris, Y. Chen, *J. Inorg. Biochem.* **1994**, *54*, 1–19.
[6] W. R. Harris, Y. Chen, *Inorg. Chem.* **1992**, *31*, 5001–5006.
[7] W. R. Harris, *J. Inorg. Biochem.* **1986**, *27*, 41–49.
[8] W. R. Harris, J. *Sheldo*, *Inorg. Chem.* **1990**, *29*, 119–124.
[9] W. R. Harris, Y. Chen, K. Wein, *Inorg. Chem.* **1994**, *33*, 4991–4998.
[10] D. C. Harris, P.Aisen in *Iron Carriers and Iron Proteins* (Ed.: T. M. Loehr), VCH, Weinheim, Germany, **1989**, pp. 239–299.
[11] G. Kubal, A. B. Mason, S. U. Patel, P. J. Sadler, A. Tucker, R. C. Woodworth, *Biochemistry* **1993**, *32*, 3387–3393.
[12] G. Kubal, A. B. Mason, P. J. Sadler, A. Tucker, R. C. Woodworth, *J. Biochem.* **1995**, *285*, 711–718.
[13] J. Cannon, N. D. Chasteen, *Biochemistry* **1975**, *14*, 4573–4577.
[14] L. K. White, N. D. Chasteen, *J. Phys. Chem.* **1979**, *83*, 279–284.
[15] K. H. Thompson, J. H. McNeill, C. Orvig, *Chem. Rev.* **1999**, *99*, 2561–2571.
[16] L. C. Cantley, M. Resh, G. Guidotti, *Nature* **1978**, *272*, 552.
[17] K. De Cremer, M. Van Hulle, C. Chery, R. Cornelis, K. Strijckmans, R. Dams, N. Lameire, R. Vanholder, *J. Biol. Inorg. Chem.* **2002**, *7*, 884–890.
[18] C. C. Chery, K. De Cremer, E. Dumont, R. Cornelis, L. Moens, *Electrophoresis* **2002**, *23*, 3284–3288.
[19] I. Bertini, G. Canti, C. Luchinat, *Inorg. Chim. Acta* **1982**, *67*, 21–22.
[20] I. Bertini, C. Luchinat, I. Messori, *J. Inorg. Biochem.* **1985**, *25*, 57–60.
[21] C. A. Smith, E. W. Ainscough, A. M. Brodie, *J. Chem. Soc., Dalton Trans.* **1995**, 1121–1126.
[22] M. H. Nagaoka, T. Yamazaki, T. Maitani, *Biochem. Bioph. Res. Commun.* **2002**, *296*, 1207–1214.
[23] W. R. Harris, C. J. Carrano, *J. Inorg. Biochem.* **1984**, *22*, 201–218.
[24] N. D. Chasteen, J. K. Grady, C. E. Holloway, *Inorg. Chem.* **1986**, *25*, 2754–2760.
[25] S. S. Eaton, J. Dubach, K. M. More, G. R. Eaton, G. Thurman, D. R. Ambruso, *J. Biol. Chem.* **1989**, *264*, 4776–4781.
[26] P. M. Hanna, N. D. Chasteen, A. Rottman, A. Aisen, *Biochemistry* **1991**, *30*, 9210–9216.
[27] D. Mustafi, E. V. Galtseva, J. Krzystek, L. C. Brunuel, M. W. Makinen, *J. Phys. Chem. A* **1999**, *103*, 11279–11286.
[28] A. Butler, M. J. Danzitz, H. Eckert, *J. Am. Chem. Soc.* **1987**, *109*, 1864–1871.
[29] A. Butler, H. Eckert, *J. Am. Chem. Soc.* **1989**, *111*, 2802–2809.
[30] J. A. Saponja, H. J. Vogel, *J. Inorg. Biochem.* **1996**, *62*, 253–270.
[31] N. D. Chasteen in *Biological Magnetic Resonance* (Eds.: J. Lawrence, L. J. Berliner, J. Reuben), Plenum, New York, **1981**, vol 3, pp. 53–119.
[32] T. Kiss, E. Kiss, E. Garribba, H. Sakurai, *J. Inorg. Biochem.* **2000**, *80*, 65–73.
[33] N. D. Chasteen, E. M. Lord, H. J. Thompson, J. K. Grady, *Biochim. Biophys. Acta* **1986**, *884*, 84–92.
[34] P. Caravan, L. Gelmini, N. Glover, F. G. Herring, H. Li, J. H. McNeill, S. J. Rettig, I. A. Setyawati, E. Shuter, Y. Sun, A. S. Tracey, V. G. Yuen, C. Orvig, *J. Am. Chem. Soc.* **1995**, *117*, 12759–12766.
[35] G. R. Hanson, Y. Sun, C. Orvig, *Inorg. Chem.* **1996**, *35*, 6507–6512.
[36] E. Kiss, E. Garribba, G. Micera, T. Kiss, H. Sakurai, *J. Inorg. Biochem.* **2000**, *78*, 97–108.
[37] S. S. Amin, K. Cryer, B. Y. Zhang, S. K. Dutta, S. S. Eaton, O. P. Anderson, S. M. Miller, B. A. Reul, S. M. Brichard, D. C. Crans, *Inorg. Chem.* **2000**, *39*, 406–416.
[38] B. D. Liboiron, K. H. Thompson, G. R. Hanson, E. Lam, N. Aebischer, C. Orvig, *J. Am. Chem. Soc.* **2005**, *127*, 5104–5114.
[39] P. Buglyó, E. Kiss, I. Fábián, T. Kiss, D. Sanna, E. Garribba, G. Micera, *Inorg. Chim. Acta* **2000**, *306*, 174–183.
[40] P. Buglyó, T. Kiss, E. Kiss, D. Sanna, E. Garribba, G. Micera, *J. Chem. Soc., Dalton Trans.* **2002**, 2275–2282.
[41] D. Hollender, K. Nerinovski C. Luchinat, T. Kiss, I. Bertini, unpublished results.
[42] G. Gran, *Acta Chem. Scand.* **1950**, *4*, 559–573.
[43] I. Nagypál, I. Fábián, *Inorg. Chim. Acta* **1982**, *61*, 109–116.
[44] A. Rockenbauer, L. Korecz, *Appl. Magn. Reson.* **1996**, *10*, 29–43.
[45] D. Sanna, I. Bódi, S. Bouhsina, G. Micera, T. Kiss, *J. Chem. Soc., Dalton Trans.* **1999**, 3275–3282.
[46] L. Zékány, I. Nagypál in *Computational Methods for the Determination of Stability Constants* (Ed.: D. Leggett), Plenum, New York, **1985**, pp. 291–353.

Received: April 6, 2006
Published Online: August 15, 2006

 © 2006 Wiley-VCH Verlag GmbH & Co. KGaA, Weinheim 

DOI: 10.1002/ejic.200600385

# Interactions of Insulin-Mimetic Vanadium Complexes with the Cell Constituents ATP and Glutathione

Ágnes Dörnyei,[a] Susana Marcão,[b] João Costa Pessoa,*[b] Tamás Jakusch,[c] and Tamás Kiss*[a,c]

**Keywords:** Insulin mimetics / Vanadium oxido complexes / Coordination modes

In order to assess the molecular form of vanadium insulin-mimetic complexes in cells, the interactions of $V^{IV}O$–maltolate and $V^{IV}O$–dipicolinate systems with adenosine 5′-triphosphate (ATP) and glutathione (GSH) in aqueous solution were studied by employing pH potentiometry, and EPR, CD and UV/Vis spectroscopy. The stoichiometries and stability constants of the complexes formed were determined at 25 °C with an ionic strength of $I = 0.2\ mol\,dm^{-3}$ (KCl). The most probable binding mode of the complexes formed in solution was determined by means of various spectral methods. The results suggest that from among the important cell constituents, GSH mostly takes part in the reduction of $V^{V}$ to $V^{IV}$ and helps keep $V^{IV}$ in this oxidation state. ATP, which is a strong $V^{IV}O$ binder, chelates the metal ion, forming binary and/or ternary complexes. The results of this work strongly suggest that ATP binds relevant $V^{IV}O$ species under cellular conditions and thus might somehow be involved in the insulin-mimetic action of $V^{IV}O$ compounds.
(© Wiley-VCH Verlag GmbH & Co. KGaA, 69451 Weinheim, Germany, 2006)

## Introduction

Since the insulin-mimetic effects of vanadium compounds were first reported, a large number of vanadium complexes in the oxidation states III to V and as peroxo complexes have been prepared, tested biologically and found to be efficient,[1–3] but only one of them, bis(maltolato)oxidovanadium(IV) ($VO(malt)_2$), has participated in clinical studies; it passed the phase I test in Canada.[2,4] In vitro, vanadium compounds may enter cells by several pathways, including passive diffusion, whereas when given orally vanadium(III,IV,V) complexes undergo parallel ligand exchange and redox reactions with the endogenous or exogenous bioligands of the human body;[1,5,6] this is mostly independent of the original form, and depends primarily on the nature of the interacting bioligand.

For this reason, the interactions of various insulin-mimetic $V^{IV}O$ compounds have been studied with the high molecular mass (h.m.m.) serum components, albumin and transferrin, and also with some of the low molecular mass (l.m.m.) components, such as lactate, oxalate, phosphate and citrate, which may be potential transporters of $V^{IV}O$ in the blood.[7–13] Detailed speciation studies led to the suggestions concerning the actual chemical forms of the vanadium compounds formed from the original carrier complex during their transport in the blood. We found that little of the vanadium remains bound to the original carrier: l.m.m. serum components (citrate) and h.m.m serum components (transferrin) displace most of the carrier molecules.[6,11–13] Accordingly, vanadium can enter cells in the oxidation state IV through the iron path, and in part in the oxidation state V through the phosphate path.

In the intracellular medium, reducing agents can interact in a redox manner with vanadium(V,IV) complexes. The most frequently discussed candidate for reduction is glutathione (GSH).[14,15] The extent to which vanadium is reduced in the redox equilibrium largely depends on the stabilisation of vanadium(IV,V) by complexation. A high intracellular excess of GSH (the usual concentration level is millimolar), i.e. about three orders of magnitude more than the biologically relevant concentration of vanadium (the usual concentration level is micromolar) increases the possibility of vanadium being present in lower oxidation states. Excess GSH and also GSSG (oxidized glutathione) readily coordinate to $V^{IV}O$.[16,17] The vanadium complexes thus formed may undergo ligand exchange with a variety of l.m.m. and h.m.m. biogenic ligands available in cells. Among the l.m.m. binders, adenosine 5′-triphosphate (ATP) may be of importance[18] as it efficiently binds $V^{IV}O$ and is present in millimolar concentrations in cells.

Sakurai and Tsuji considered the most relevant oxidation state of vanadium in the cell to be IV because of the reducing agents present in the cell (e.g. GSH or cysteine).[19] We

[a] Department of Inorganic and Analytical Chemistry, University of Szeged,
P. O. Box 440, 6701 Szeged, Hungary
[b] Centro Química Estrutural, Instituto Superior Técnico,
Av. Rovisco Pais, 1049-001 Lisboa, Portugal
[c] Bioinorganic Chemistry Research Group of the Hungarian Academy of Sciences, Department of Inorganic and Analytical Chemistry, University of Szeged,
P. O. Box 440, 6701 Szeged, Hungary
Supporting information for this article is available on the WWW under http://www.eurjic.org or from the author.

 © 2006 Wiley-VCH Verlag GmbH & Co. KGaA, Weinheim 

accepted this and studied vanadium only in the $V^{IV}O$ form, even though reoxidation of $V^{IV}O$ to $V^{V}$ is an obvious assumption, which can have different importance at different compartments of the cell. Accordingly, the aim of the present work was to attain a better understanding of the behaviour of $V^{IV}O$ insulin-mimetic complexes as they enter cells and interact with l.m.m. cell constituents. Of the $V^{IV}O$ complexes, we chose the $V^{IV}O$–dipicolinate and $V^{IV}O$–maltolate systems, and as cell constituents we selected GSH and ATP (see Scheme 1). The equilibria in the systems were studied by a combination of pH potentiometry and spectroscopic methods [electron paramagnetic resonance (EPR), electronic absorption (UV/Vis) and circular dichroism (CD)].

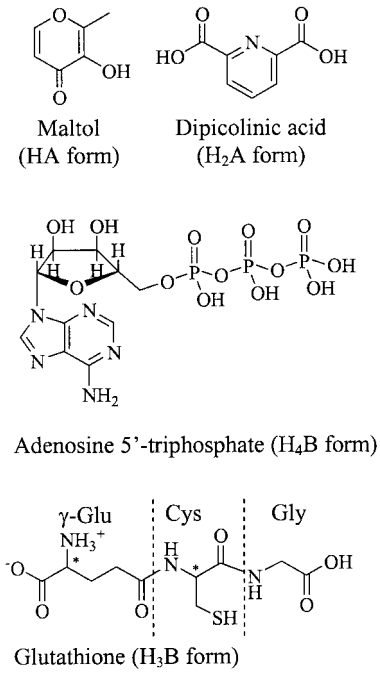


Scheme 1.

The complex-forming properties of $V^{IV}O$ with dipicolinate (dipic),[12] maltolate (malt),[7,8,20] ATP[18] and GSH[17] have been studied, and stability constants measured under similar experimental conditions have been reported previously.

Maltolate forms mono and bis complexes with the $V^{IV}O$ ion by the formation of five-membered ($O^-$, = O) chelates. The neutral bis complex $[VO(malt)_2(H_2O)]$ is the predominant species in the pH range 5–7. It occurs in two geometrical isomeric forms depending on the position of the solvent molecule; the water molecule can be either *cis* or *trans* to the oxido group of $V^{IV}O$. In aqueous solution at room temperature and neutral pH, the EPR spectra clearly indicate that the *cis* form predominates.[7,8,20] In a recent paper based on detailed EPR and ENDOR spectroscopic studies, Mustafi and Makinen concluded that in aqueous solution at room temperature maltolate coordinates to $V^{IV}O$ only in the *cis* form.[21]

Dipicolinate forms mono and bis complexes with the $V^{IV}O$ ion.[12] In the neutral mono complex, $[VO(dipic)(H_2O)_2]$, the ligand coordinates in a tridentate manner; the coordinating donor groups are two carboxylates, besides the two water molecules, and the pyridyl-N atom is in an axial position (*trans* to the oxido group). Bis complex formation in the $V^{IV}O$–dipic system is not as favoured as it is with maltolate. In $[VO(dipic)_2]^{2-}$, the first ligand coordinates in a tridentate manner, and the second ligand in a bidentate manner, having an uncoordinated carboxylate group. At the biologically relevant neutral pH values, dipicolinate is not a very efficient $V^{IV}O$ binder; mixed hydroxo and oligonuclear binary hydroxo species of $V^{IV}O$ are present in the solution, besides the neutral mono complex and the double negatively charged bis complex.[12]

## Results and Discussion

### $V^{IV}O$ Ternary Systems with ATP

ATP was found to coordinate to $V^{IV}O$ through the terminal phosphate donor(s) in the weakly acidic and neutral pH range to yield $[VOBH_x]^{x-2}$ ($x$ = 2, 1, 0) and $[VOB_2]^{6-}$.[18] In the basic pH range, at low excess, ATP is not a very efficient $V^{IV}O$ binder because oligonuclear hydroxo species $\{[(VO)_2(OH)_5]^-\}_n$ are present in the solution besides the $V^{IV}O$–ATP complexes. At pH 7–8 the pH readings drift and pH equilibrium is reached within 10 min; in the pH range 8.8–10.4, pH stabilization was not reached within this time even at a 10-fold excess of ATP. Thus, the formation constants of the species formed in this pH region are only estimates. In contrast with our earlier report,[18] the formation of dinuclear species had to be assumed either to fit the pH-metric data or to explain the slight decrease in intensity of the EPR spectra. In the earlier work, formation of the binary hydroxo-bridged hydrolysed $V^{IV}O$ species $[(VO)_2(OH)_5]^-$ was not considered, though it is undoubtedly formed[22,23] and may be responsible for the decrease in the intensity of the signal rather than the dihydroxo-bridged $V^{IV}O$–ATP species: $[(VO)_2B_2H_x]^{x-4}$ ($x$ = –2, –3, –4).

In the cells, ATP is present in high excess relative to $V^{IV}O$ and also relative to the carrier ligands. As the proton competition for the alcoholate donors decreases the ribose moiety becomes a more efficient binding site. In the slightly basic pH range, the complex $[VOB_2H_{-2}]^{8-}$ forms involving a mixed binding mode with one ATP coordinating through the phosphate chain and the other through the ribose moiety. In the species $[VOB_2H_{-4}]^{10-}$, both ATP molecules coordinate to the $V^{IV}O$ species through the ribose residue.[18] The CD spectra furnish information on the species in which the ribose moiety is coordinated to the $V^{IV}O$; these species are mostly formed above the physiological pH. In the highly basic pH range an extra deprotonation is detected by pH potentiometry and also by CD spectroscopy (see ESI-1), corresponding to the formation of $[VOB_2H_{-5}]^{11-}$. In this species the extra proton is probably lost from a coordinated water molecule.

### $V^{IV}O$–dipic–ATP System

Our speciation calculations indicated that, in the ternary system with dipicolinic acid, ATP, as a stronger $V^{IV}O$

 © 2006 Wiley-VCH Verlag GmbH & Co. KGaA, Weinheim 

binder, will displace one of the dipicolinates from the coordination sphere of $V^{IV}O$. As a result, ternary complexes will exist, besides the binary ATP complexes, at physiological pH. The potentiometric data could be fitted by assuming the formation of the species $[VOAB]^{4-}$, $[VOABH_{-1}]^{5-}$ and $[VOABH_{-2}]^{6-}$ (see Table 1). The distribution diagram for the $V^{IV}O$–dipic–ATP system (Figure 1) reveals that the formation of the ternary complex $[VOAB]^{4-}$ is favoured in the weakly acidic pH range. Besides the carboxylate groups of dipic, the phosphate groups of ATP are expected to be coordinated in this complex while in $[VOABH_{-2}]^{6-}$, formed in the neutral pH range, the deprotonated ribose alcoholate groups are in equatorial positions.

Table 1. Stability constants of mixed ligand $V^{IV}O$ complexes of dipicolinate and maltolate (ligands A) with ATP (ligand B).

| Ligand A | VOAB | $VOABH_{-1}$ | $VOABH_{-2}$ |
|---|---|---|---|
| Dipicolinate | 11.0(1) | 4.3(2) | –2.5(1) |
| Maltolate | 13.5(2) | – | –2.8(9) |

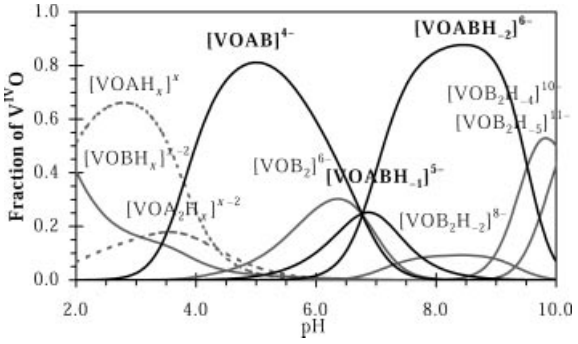


Figure 1. Concentration distribution diagram of the $V^{IV}O$–dipic(A)–ATP(B) system at 1:2:10 metal ion-to-ligand ratio, $C_{VO} \approx 0.004$ mol dm$^{-3}$.

The X-band EPR spectra of frozen solutions of the $V^{IV}O$–dipic binary system and the ternary system with ATP at pH < 8 could be simulated as axial spectra. At pH > 8, the species with the $(O^-,O^-)(O^-,O^-)$ donor set has a rhombic EPR spectrum. The high-field region corresponding to $A_\parallel$ or $A_z$ and $M_I$ = 5/2 and 7/2 yields more information on the type and number of species formed. As may be seen in Figure 2, the EPR spectra for the $V^{IV}O$–dipic–ATP system resemble those recorded for the $V^{IV}O$–ATP system; no new signals could be detected. Ternary complex formation is accompanied only by phosphate/carboxylate substitution in the equatorial plane, and does not result in any significant change in the EPR parameters. The EPR parameters of the binary complexes VOA of dipic and $[VOB_2]^{6-}$ of ATP with carboxylate or phosphate groups in the equatorial plane of $V^{IV}O$ are also expected to be the same within the uncertainties of the parameters (see Table 2). However, as dipic retards the hydrolysis of the $V^{IV}O$ complexes present in the basic pH range, an improved signal-to-noise ratio may be observed in the ternary system as compared with the binary $V^{IV}O$–ATP system; dipic helps to keep $V^{IV}O$ in solution. A similar observation may be made concerning the CD spectra; they are more intense for the ternary system.

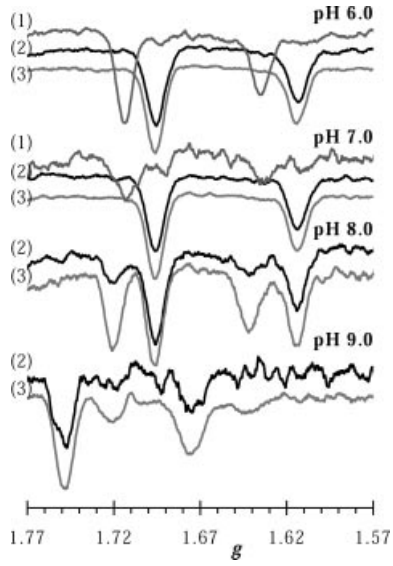


Figure 2. High field range of the first-derivative EPR spectra at 77 K of frozen solutions containing: (1) $V^{IV}O$ – dipic 1:2, (2) $2V^{IV}O$ – ATP 1:10, (3) $V^{IV}O$ – dipic – ATP 1:2:10 metal ion-to-ligand ratio, $C_{VO} \approx 0.004$ mol dm$^{-3}$. The pH values are indicated.

Table 2. EPR parameters ($g_\parallel$, $A_\parallel$)[a] for the binary and ternary complexes of $V^{IV}O$ formed with dipicolinate, maltolate and ATP.

| Species | $g_\parallel$ | $A_\parallel$ ($\times 10^4$ cm$^{-1}$) | Chelating set |
|---|---|---|---|
| $[VO(H_2O)_5]^{2+}$ | 1.933 | 182.6 | $4\times H_2O$ |
| Dipicolinate | | | |
| VOA | 1.931 | 178.4 | $(COO^-,COO^-)\ 2\times H_2O$ |
| $[VOA_2]^{2-}$ | 1.939 | 167.8 | $(COO^-,COO^-)(COO^-,$pyridyl–N$)$ |
| Maltolate | | | |
| $[VOA]^+$ | 1.937 | 175.1 | $(O^-,=O)\ 2\times H_2O$ |
| $VOA_2$ | 1.938 | 171.4 | $(O^-,=O)\ (O^-,=O_{ax})\ H_2O$ |
| $[VOA_2H_{-1}]^-$ | 1.942 | 166.8 | $(O^-,=O)\ (O^-,=O_{ax})\ OH^-$ |
| ATP | | | |
| $[VOBH_x]^{x-2}$ | 1.930 | 181.8 | $(PO_3^{2-}–O–PO_2^-–O–PO_2^-–)\ 2\times H_2O$ |
| $[VOB_2]^{6-}$ | 1.933 | 178.4 | $2\times(PO_3^{2-}–O–PO_2^-–O–PO_2^-–)$ |
| $[VOB_2H_{-2}]^{8-}$ | 1.946 | 166.8 | $(PO_3^{2-}–O–PO_2^-–O–PO_2^-–)\ (O^-,O^-)$ |
| $[VOB_2H_{-4}]^{10-}$ | 1.958 | 151.8 | $(O^-,O^-)\ (O^-,O^-)$ |
| Dipicolinate + ATP | | | |
| $[VOAB]^{4-}$ | 1.933 | 178.1 | $(COO^-,COO^-)\ (PO_3^{2-}–O–PO_2^-–O–PO_2^-–)$ |
| $[VOABH_{-1}]^{5-}$ | – | – | [b] |
| $[VOABH_{-2}]^{6-}$ | 1.946 | 167.0 | $(COO^-,COO^-)\ (O^-,O^-)$ |
| Maltolate + ATP | | | |
| $[VOAB]^{3-}$ | 1.941 | 169.1 ? | $(O^-,=O)\ (PO_3^{2-}–O–PO_2^-–O–PO_2^-–)$ |
| $[VOABH_{-2}]^{5-}$ | 1.943 | 166.4 ? | $(O^-,=O)\ (O^-,O^-)$ |

[a] The relative uncertainty in the calculation of the parameters is estimated to be ca. 0.005 for $g_\parallel$ and ca. 1.0 for $A_\parallel$. In the case of rhombic distortion $g_\parallel$ and $A_\parallel$ are in fact $g_z$ and $A_z$, respectively. [b] A log$\beta$ value for this stoichiometry was obtained from the pH-potentiometric data and calculations. However, its EPR signals are possibly under the complex pattern of other signals recorded and we did not find a distinct signal for this complex. Therefore we do not propose any binding mode.

In accordance with the pH-potentiometric speciation results, electronic absorption spectroscopy unambiguously revealed a new species ($[VOAB]^{4-}$) in the pH range 2.5–5.5,

 © 2006 Wiley-VCH Verlag GmbH & Co. KGaA, Weinheim 

with an extra band in the CT region, caused by the coordination of dipic (not shown). The difference between the CD spectra of the $V^{IV}O$–ATP and $V^{IV}O$–dipic–ATP systems (ESI-2) indicates the formation of a new type of ternary complex above the physiological pH range, where the ribose moiety becomes a more efficient binding site ($[VOABH_{-2}]^{6-}$).

### $V^{IV}O$–Maltolate–ATP System

Under physiological conditions (pH ≈ 7), maltolate is a stronger $V^{IV}O$ binder than dipic. For this reason, participation of maltolate in in vivo binding (even in binary complexes) can be expected to be more significant than was found in the case of dipic. The potentiometric data were fitted with a speciation model[24] with the assumption of two mixed-ligand complexes, $[VOAB]^{3-}$ and $[VOABH_{-2}]^{5-}$ (see Table 1). The concentration distribution diagram for $V^{IV}O$–maltolate–ATP depicted in Figure 3 displays the species formed under the conditions of the spectroscopic measurements. The pH-metric measurements demonstrate that ternary complex formation is not as dominant as with dipic, where binary bis complexes of maltolate are present in significant amounts.

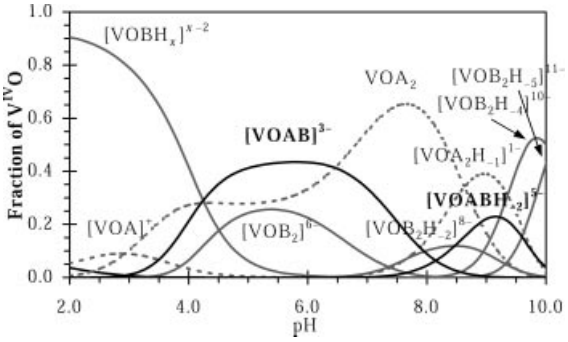


Figure 3. Concentration distribution diagram of the $V^{IV}O$ – maltol(A) – ATP(B) system at 1:2:10 metal ion-to-ligand ratio, $C_{VO} \approx 0.004$ mol dm$^{-3}$.

The EPR spectra of the systems $V^{IV}O$–maltolate, $V^{IV}O$–ATP and $V^{IV}O$–maltolate–ATP are presented in Figure 4, and the EPR parameters of the mixed-ligand species are listed in Table 2. Because of the difference in the type of donor groups involved in the coordination ternary complex formation is clearly indicated. Below pH 7, water and a carbonyl group are substituted by one or two phosphates, resulting in a detectable change ($A_{\parallel}$ from $171.4 \times 10^{-4}$ cm$^{-1}$ for $VOA_2$ to $169.1 \times 10^{-4}$ cm$^{-1}$ for $[VOAB]^{3-}$) in the EPR parameters.

A new signal from the formation of the complex $[VOABH_{-2}]^{5-}$ with a sugar-like binding mode of the ATP is not clearly seen as it is formed only from ca. 20% of the total V according to the speciation calculations. This species could be characterised by pH potentiometry only with a large uncertainty since the species distribution for the $V^{IV}O$–ATP (see above) and $V^{IV}O$–maltolate binary systems at pH > 9 is also uncertain as a result of the slight aerobic

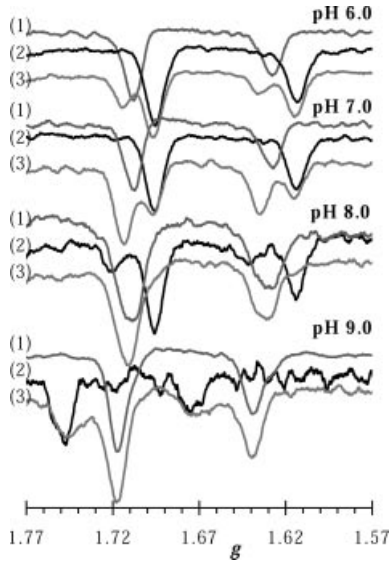


Figure 4. High field range of the first-derivative EPR spectra at 77 K of frozen solutions containing: (1) $V^{IV}O$–maltol 1:2, (2) $V^{IV}O$–ATP 1:10, (3) $V^{IV}O$–maltol–ATP 1:2:10 metal ion-to-ligand ratios; $C_{VO} \approx 0.004$ mol dm$^{-3}$. The pH values are indicated.

redox reaction of $V^{IV}O$–maltolate that may take place,[20] and/or the slow hydroxo complex formation processes.[13] However, in the CD spectra (ESI-3), a new type of signal can be observed at pH 8–9, unambiguously indicating coordination of the ribose residue corresponding to the formation of $[VOABH_{-2}]^{5-}$. At pH ≥ 9, the CD spectra for the binary and ternary systems become very similar, in agreement with the speciation results: both carrier molecules are displaced by the ribose-coordinated nucleotide ligands, resulting in the formation of the binary ATP complex $[VOB_2H_{-4(-5)}]^{7-(8-)}$.

### $V^{IV}O$ Ternary Systems with GSH

GSH is a cysteine-containing tripeptide (γ-Glu-Cys-Gly) with eight potential donor atoms. As mentioned above, it is possible that GSH plays an important role in relation to the biochemistry of vanadium. It is present in high excess in cells, but GSH is a much weaker $V^{IV}O$ binder than ATP. For $V^{IV}O$ concentrations above ca. 1 mM and more than a 10-fold excess of the ligand, the bis amino acid type binding mode ($[VOB_2H_2]^{2-}$) with the donor set $2\times(COO^-, NH_2)_{eq}$ is relevant in the pH range 5.0–6.5.[15,17,25,26] Participation of the thiolate donor may occur above pH ca. 7, forming the complex $[VOBH_{-1}]^{2-}$. This $[VOBH_{-1}]^{2-}$ stoichiometry corresponds to two different EPR components, and coordination of the deprotonated $N_{amide}$ group can be assumed in the minor isomer.[17] At a 10-fold excess of GSH, ternary complex formation could be detected only with rather high uncertainty in the pH-potentiometric titrations (see Table 3), and this excess of GSH was not enough to prevent the hydrolysis of the metal ion at pH > 6.5 for the dipic system and at pH > 8.0 for the maltolate system. Higher GSH concentrations could not be used in the pH potent-

 © 2006 Wiley-VCH Verlag GmbH & Co. KGaA, Weinheim 

iometry because of the high buffer capacity of the ligand, and thus there was even higher uncertainty in the pH-potentiometric calculations. Most of the measured pH effect resulted from deprotonation of the excess ligand, and only a very small amount of it related to the metal-induced proton displacement reaction. Hence, complex formation between $V^{IV}O$ and GSH could be monitored by pH potentiometry only with great uncertainty. Accordingly, mostly spectroscopic measurements (EPR, UV/Vis and CD) were used to detect the formation of ternary complexes.

Table 3. Stability constants of mixed ligand $V^{IV}O$ complexes of dipicolinate and maltolate (ligands A) with GSH (ligand B).

| Ligand A | $VOABH_2$ | $VOA_2BH_2$ | $VOA_2BH$ |
|---|---|---|---|
| Dipicolinate | 25.9(8) | – | – |
| Maltolate | 28.6(3) | 35.5(8) | 27.7(5) |

### $V^{IV}O$–dipic–GSH System

A concentration distribution diagram for the $V^{IV}O$–dipic–GSH system with the metal ion-to-ligand ratio and $V^{IV}O$ concentration used in the spectroscopic measurements is depicted in Figure 5 (the formation constants of the binary complexes used in the speciation calculation were taken from ref.[12] and ref.[17]).

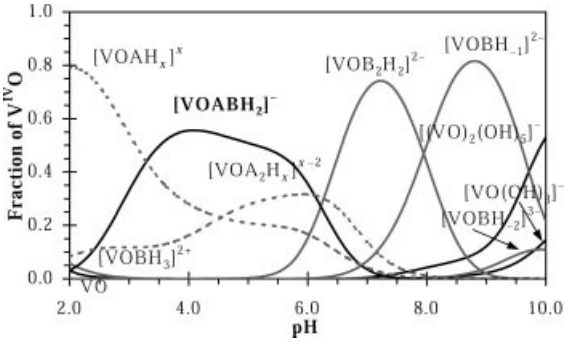


Figure 5. Concentration distribution diagram of the $V^{IV}O$–dipic(A)–GSH(B) system at a 1:2:50 metal ion-to-ligand ratio, $C_{VO} \approx 0.004$ mol dm$^{-3}$.

The speciation calculations suggested that $V^{IV}O$ starts to coordinate to dipic at pH < 2. At a 10-fold or higher excess of GSH, besides the binary species, a ternary complex $[VOABH_2]^-$ could be detected in which GSH most probably coordinates in a monodentate way through the C-terminal $COO^-$ or with the possibility of chelation together with the peptide carbonyl-O. Neither CD nor EPR spectroscopy can distinguish between these two different binding modes. This complex can be determined potentiometrically only with high uncertainty because the coordinating carboxylate donor is in the deprotonated form over most of the pH range of formation (p$K$(COOH) ca. 3.5),[17] and thus its coordination does not result in a direct pH change. At pH > 6, binary complexes of GSH are formed. Subsequently, because of the significantly weaker $V^{IV}O$-binding ability of GSH, even a 10-fold excess of GSH was not sufficient to prevent hydrolysis of the metal ion and formation of the oligonuclear hydroxo species $\{[(VO)_2(OH)_5]^-\}_n$.

By EPR spectroscopy (Figure 6, Table 4) a new species could be detected in the pH range 3–6; this is probably the ternary species $[VOABH_2]^-$. However, at pH ca. 7, the EPR spectrum of the $V^{IV}O$–dipic–GSH system coincides fully with that of $V^{IV}O$–GSH, indicating that GSH completely displaces the carrier ligands from the coordination sphere of the metal ion. Although GSH is a weaker vanadium binder than dipic, it is present at a 50–100-fold excess relative to dipic.

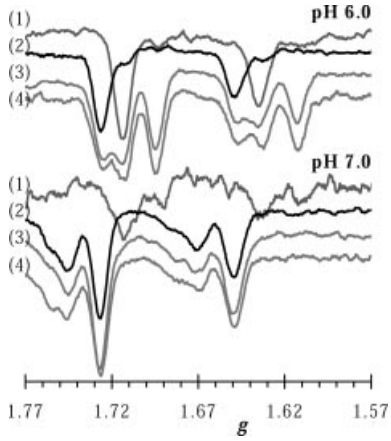


Figure 6. High-field range of the first-derivative EPR spectra at 77 K of frozen solutions containing: (1) $V^{IV}O$–dipic 1:2, (2) $V^{IV}O$–GSH 1:50, (3) $V^{IV}O$–dipic–GSH 1:2:50 and (4) 1:2:100 metal ion-to-ligand ratios, $C_{VO} \approx 0.004$ mol dm$^{-3}$. The pH values are indicated.

Table 4. EPR parameters ($g_\parallel$, $A_\parallel$)[a] for the binary and ternary complexes of $V^{IV}O$ formed with dipicolinate, maltolate and GSH.

| Species | $g_\parallel$ | $A_\parallel$ ($\times 10^4$ cm$^{-1}$) | Chelating set |
|---|---|---|---|
| GSH | | | |
| $[VOBH_2]^+$ | 1.937 | 174.2 | |
| VOBH | 1.941 | 170.0 | |
| $[VOB_2H_2]^{2-}$ | 1.948 | 163.8 | 2×($COO^-$, $NH_2$) |
| $[VOBH_{-1}]^{2-}$ (I) | 1.956 | 154.5 | ($COO^-$/amide-O, $NH_2$, $S^-$) $OH^-$ |
| $[VOBH_{-1}]^{2-}$ (II) | 1.959 | 147.0 | |
| Dipicolinate + GSH | | | |
| $[VOABH_2]^-$ | 1.930 | 177.2 | ($COO^-$,$COO^-$) ($COO^-$, amide-O/$H_2O$) |
| Maltolate + GSH | | | |
| $VOABH_2$ | 1.936 | 174.2 | ($O^-$, =O) ($COO^-$, amide-O/$H_2O$) |
| $[VOA_2BH_2]^-$ | 1.941 | 169.0 | ($O^-$, =O) ($O^-$, $=O_{ax}$) $COO^-$ |
| $[VOA_2BH]^{2-}$ | 1.949 | 159.1 | ($O^-$, =O) ($O^-$, $=O_{ax}$) $S^-$ |

[a] The relative uncertainty in the calculation of the parameters is estimated to be ca. 0.005 for $g_\parallel$ and ca. 1.0 for $A_\parallel$. In the case of rhombic distortion $g_\parallel$ and $A_\parallel$ are in fact $g_z$ and $A_z$, respectively.

### $V^{IV}O$–Maltolate–GSH System

A concentration distribution diagram of the $V^{IV}O$–maltolate–GSH system under the experimental conditions of the spectral measurements is depicted in Figure 7. In accord-

 © 2006 Wiley-VCH Verlag GmbH & Co. KGaA, Weinheim 

ance with the species distribution, new EPR signals could be detected that can be assigned to the ternary species (see Table 4).

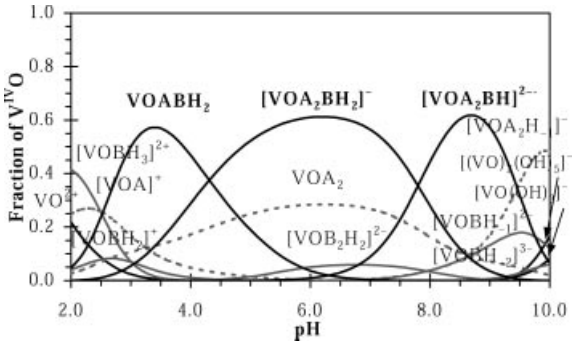


Figure 7. Concentration distribution diagram of the $V^{IV}O$–maltolate(A)–GSH(B) system at a 1:2:50 metal ion-to-ligand ratio, $C_{VO} \approx 0.004$ mol dm$^{-3}$.

In the pH range 2.5–4.0, besides the signals from the species $[VOBH_x]^{x-1}$ ($x$ = 2, 3), a new complex ($g_{\|}$ = 1.941 and $A_{\|} = 169.5 \times 10^{-4}$ cm$^{-1}$) was detected that was not seen in the EPR spectra of the binary systems. In the pH range 6–7, this signal was slightly shifted ($g_{\|}$ = 1.941 and $A_{\|} = 168.6 \times 10^{-4}$ cm$^{-1}$), but remained in the uncertainty range of the EPR parameters. Above pH 7, another new signal appeared at $g_{\|}$ = 1.949 and $A_{\|} = 159.1 \times 10^{-4}$ cm$^{-1}$. Some of the EPR spectra recorded by varying the B ligand concentration at pH 7.0 are shown in Figure 8.

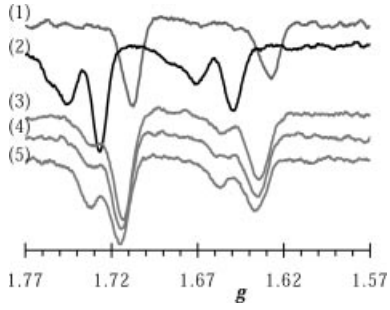


Figure 8. High field range of the first-derivative EPR spectra at 77 K of frozen solutions containing: (1) $V^{IV}O$–maltolate 1:2, (2) $V^{IV}O$–GSH 1:50, (3) $V^{IV}O$–maltolate–GSH 1:2:25,(4) 1:2:50 and (5) 1:2:100 metal ion-to-ligand ratios, $C_{VO} \approx 0.004$ mol dm$^{-3}$ at pH 7.0.

The EPR spectra clearly indicate ternary complex formation in the $V^{IV}O$–maltolate–GSH system at a 25-fold excess of GSH. Considering the EPR parameters (Table 4) and the low CD signals recorded (not shown), we conclude that GSH most probably coordinates at the Gly end through ($COO^-$, O-amide/$H_2O$) donors, while participation of the thiolate donor occurs only at pH > 7. The most likely binding modes of the complexes formed in the $V^{IV}O$–maltolate–GSH system are shown in Table 4. In the complex $VOABH_2$ formed in the slightly acidic pH range, GSH coordinates bidentately or monodentately in the equatorial plane, while in $[VOA_2BH_2]^-$ formed in the neutral pH range, GSH coordinates in a monodentate manner through the C-terminal $COO^-$ function to the fourth equatorial position of $V^{IV}O$. In the case of $VOA_2$, the *cis* complex, with one empty equatorial coordination site, is the predominant or the exclusive isomeric form. In the species $[VOA_2BH]^{2-}$, when Equation (1) is applied to the equatorial donor set, (2 × ($O^-$, =O), $S^-$) may be assumed. The estimated value $A_{\|}^{est}$ = $157.6 \times 10^{-4}$ cm$^{-1}$ agrees fairly well with the experimental value $A_{\|} = 159.1 \times 10^{-4}$ cm$^{-1}$. This suggests equatorial thiolate coordination.

### $V^{IV}O$–Carrier Ligand–ATP–GSH Systems

When ATP and GSH are simultaneously considered as potential $V^{IV}O$ binders, GSH is not expected to be able to compete with ATP for binding to $V^{IV}O$ since ATP is a much stronger ligand. The competition reaction was studied by EPR spectroscopy (see Figure 9) in the absence and in the presence of the insulin-mimetic complexes. In the case of dipic, no spectral changes could be detected between the spectra measured in the presence or absence of GSH, in agreement with what was found in the $V^{IV}O$–dipic–ATP system. Therefore, EPR spectroscopy does not give any information on the changes that might have occurred in the coordination sphere because of the high similarity of the partial contributions of the coordinating donors to the $A_{\|}$ value (see above).

For the $V^{IV}O$–ATP–GSH ternary system, when ATP was in a 10-fold excess relative to $V^{IV}O$, only the EPR signals of the $V^{IV}O$–ATP complexes were detected. New signals appeared only at a 2.5-fold excess (EPR parameters: $A_{\|}$ = $172.1 \times 10^{-4}$ cm$^{-1}$ and $165.7 \times 10^{-4}$ cm$^{-1}$). Comparison of the EPR spectra of solutions containing $V^{IV}O$, maltolate, ATP and GSH at pH ca. 7 (see Figure 9) revealed significant changes only when ATP was not present in at least a 10-

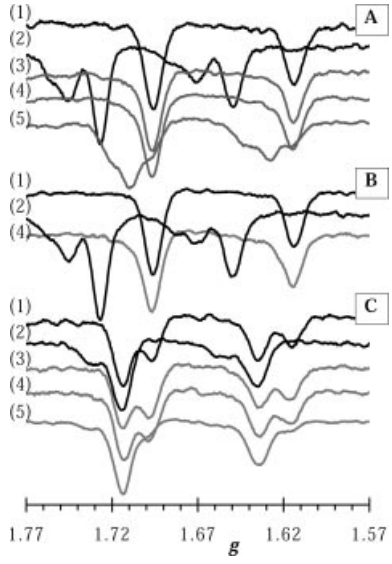


Figure 9. High field range of the first-derivative EPR spectra at 77 K of frozen solutions: (A) without carrier ligand, (B) with 8 mM dipicolinate, (C) with 8 mM maltolate, (1) $V^{IV}O$–ATP 1:10, (2) $V^{IV}O$–GSH 1:50, (3) $V^{IV}O$–ATP–GSH 1:10:25,(4) 1:10:50 and (5) 1:2.5:50 metal ion-to-ligand ratios; $C_{VO} \approx 0.004$ mol dm$^{-3}$ at pH 7.0.

 © 2006 Wiley-VCH Verlag GmbH & Co. KGaA, Weinheim 

fold excess (see above). Below such an excess of ATP, the changes in the ratio of the predominating signals seem to indicate the participation of GSH in complex formation.

## Conclusions

With respect to the two important cell constituents GSH and ATP, our results indicate that if the carrier ligands can somehow find a way to enter the cell strong $V^{IV}O$-binder cell constituents will partly displace the carrier ligands and ternary complexes with relevant biomolecules of the cell will be formed. Some of the ternary species are highly anionic, which are partly neutralised and probably undergo ion paring with cations, $K^+$ and $Mg^{2+}$, of the cell.

From among the important cell constituents, GSH will possibly take part in the reduction of $V^V$ to $V^{IV}$ and will help keep $V^{IV}$ in this oxidation state. As a strong $V^{IV}O$ binder, ATP will chelate the metal ion, forming binary and/or ternary complexes. The results of this work strongly suggest that ATP binds relevant $V^{IV}O$ species under cell conditions, and thus might somehow be involved in the insulin-mimetic action of $V^{IV}O$ compounds. However, the time courses of these parallel redox and complexation reactions require further investigations.

## Experimental Section

**Materials:** The ligands investigated were Sigma products of the highest analytical purity. They were used without further purification, but their purities were checked and the exact concentrations of their solutions was determined by the Gran method.[27] The $V^{IV}O$ stock solution, prepared as described earlier,[28] was standardized for metal ion concentration by permanganate titration and for hydrogen ion concentration by potentiometry, using the appropriate Gran function. The ionic strength was adjusted to 0.20 mol dm$^{-3}$ KCl. The temperature was 25.0 ± 0.1 °C for potentiometric measurements, and 25.0 ± 0.3 °C for CD and Vis spectra.

**Potentiometric Measurements:** For potentiometric titrations, an automatic titration set, including a Dosimat 665 autoburette, an Orion 710A precision digital pH meter and an IBM-compatible personal computer was used. A Metrohm 6.0234.100 semimicro combined glass electrode was calibrated for hydrogen ion concentration according to the method of Irving et al.[29] The ionic product of water was taken as $pK_w = 13.76 \pm 0.01$.

When we refer to the stoichiometries of complexes present in solution, the notation $M_pA_qB_rH_s$ is used, where M = $V^{IV}O^{2+}$, $H_2A$ or HA refers to the fully protonated form of dipicolinate acid or maltolate, respectively, and $H_5B^+$ denotes totally protonated ATP. However two of the four protons of the triphosphate chain dissociate in very acidic media (pH < 1). $H_4B^+$ refers to totally protonated GSH. The concentration stability constants, $\beta_{pqrs} = [M_pA_qB_rH_s]/([M]^p[A]^q[B]^r[H]^s)$, were calculated by using the computer programme PSEQUAD.[30] The equilibria corresponding to the formation of hydroxo complexes of $V^{IV}O$ were taken into account in the calculation of the stability constants of the complexes. The following stability constants ($\log\beta$) were assumed for these complexes: $[VO(OH)]^+$ ($\log\beta_{100-1} = -5.94$); $[(VO)_2(OH)_2]^{2+}$ ($\log\beta_{200-2} = -6.95$), calculated from the data published by Henry et al.,[31] using the Davies equation to take into account the different ionic strengths; $[VO(OH)_3]^-$ ($\log\beta_{100-3} = -18.00$);[22] and $[(VO)_2(OH)_5]^-$ ($\log\beta_{200-5} = -22.50$),[22,23] were taken from the literature.

**Spectroscopic Measurements:** The CD spectra were recorded with a JASCO 720 spectropolarimeter with a red-sensitive photomultiplier (EXWL-308). Visible spectra were recorded with a Perkin–Elmer Lambda 9 spectrophotometer. The spectral range covered was normally 400–900 nm (Vis) and 400–1000 nm (CD). By Vis and CD spectra, we mean representations of $\varepsilon_m$ or $\Delta\varepsilon_m$ values vs. $\lambda$ [$\varepsilon_m$ = absorption/($bC_{VO}$) and $\Delta\varepsilon_m$ = differential absorption/($bC_{VO}$), where $b$ = optical path and $C_{VO}$ = total $V^{IV}O$ concentration].

The EPR spectra were recorded at 77 K with a Bruker ESR-ER 200D X-band spectrometer. The spin-Hamiltonian parameters were obtained by simulation of the spectra with the aid of the modified computer programme of Rockenbauer and Korecz.[32] The EPR spectra of the $V^{IV}O$ systems help to elucidate the binding mode of the complexes formed in solution; Chasteen developed an additivity rule to estimate the hyperfine coupling constant $A_z^{est}$ [Equation (1)], based on the contributions $A_{z,i}$ of each of the four equatorial donor groups.[33] The estimated accuracy of $A_z^{est}$ is ca. $3 \times 10^{-4}$ cm$^{-1}$.

$$A_z^{est} = \sum_{i=1}^{4} A_{z,i} \quad (1)$$

Most of the $A_{z,i}$ data relevant for this work were presented by Chasteen.[33] For the carboxylate ($COO^-$) donor, Chasteen estimated its contribution in Equation (1) to be $42.7 \times 10^{-4}$ cm$^{-1}$, based on the $A_z$ of the VO(oxalato)$_2^{2-}$ complex, assuming that the four $COO^-$ groups coordinate equatorially. However, the solution structure presumably involves the set ($3 \times COO^-$, $H_2O)_{eq}$,[34] so this contribution should be $42.1 \times 10^{-4}$ cm$^{-1}$, the value used in the present work. The contribution of each O donor of maltolate in Equation (1) was taken to be $41–42 \times 10^{-4}$ cm$^{-1}$. This value was calculated from the $A_z$ parameters of *cis* and *trans* complexes of VO(malt)$_2$, determined by assuming the [($O^-$, =O)($O^-$, $=O_{ax}$) $H_2O$] and [($O^-$, =O)($O^-$, =O)] sets, respectively.[8] These data can be used to establish the most probable binding mode of the complexes formed, but care must be taken as the contributions of the donor groups to the hyperfine coupling may depend, for instance on their orientation,[35] or the charge of the ligand.[36] The influence of the axial donor groups (if any) is not taken into account. In the absence of ethylene glycol, a relatively broad background was present in most of the frozen solution EPR spectra, and therefore most spectra were obtained from aqueous solutions containing 5% of ethylene glycol.

## Acknowledgments

This work was carried out in the frame of the COST D21/009/01 project (Insulin-Mimetic Vanadium Compounds). The authors are grateful to the National Research Fund (OTKA NI61786 and OTKA T49417), the Hungarian Academy of Sciences, the Fundo Europeu para o Desenvolvimento Regional, Fundação para a Ciência e Tecnologia, the POCI Programme (project POCI/56949/QUI/2000), and the Hungarian-Portuguese Intergovernmental S & T Co-operation Programme for 2004–2005.

[1] D. Rehder, J. Costa Pessoa, C. F. G. C. Geraldes, M. M. C. A. Castro, T. Kabanos, T. Kiss, B. Meier, G. Micera, L. Pettersson, M. Rangel, A. Salifoglou, I. Turel, D. Wang, *J. Biol. Inorg. Chem.* **2002**, *7*, 384–396.

[2] K. H. Thompson, J. H. McNeill, J. H. Orvig, *Chem. Rev.* **1999**, *99*, 2561–2571.

 © 2006 Wiley-VCH Verlag GmbH & Co. KGaA, Weinheim 

[3] K. H. Thompson, C. Orvig, *J. Chem. Soc., Dalton Trans.* **2000**, *17*, 2885–2892.
[4] K. H. Thompson, C. Orvig, *Dalton Trans.* **2006**, *6*, 761–764.
[5] D. Rehder, *Inorg. Chem. Commun.* **2003**, *6*, 604–617.
[6] T. Kiss, T. Jakusch, in: *Metallotherapeutic Drugs and Metal-based Diagnostic Agents* (Eds.: M. Gielen, E. R. T. Tiekink), Wiley, Chichester, **2005**, pp. 143–158.
[7] T. Kiss, E. Kiss, G. Micera, D. Sanna, *Inorg. Chim. Acta* **1998**, *283*, 202–210.
[8] P. Buglyó, E. Kiss, I. Fábián, T. Kiss, D. Sanna, E. Garribba, G. Micera, *Inorg. Chim. Acta* **2000**, *306*, 174–183.
[9] E. Kiss, E. Garribba, G. Micera, T. Kiss, H. Sakurai, *J. Inorg. Biochem.* **2000**, *78*, 97–108.
[10] E. Kiss, K. Petrohán, D. Sanna, E. Garribba, G. Micera, T. Kiss, *Polyhedron* **2000**, *19*, 55–61.
[11] T. Kiss, E. Kiss, E. Garribba, H. Sakurai, *J. Inorg. Biochem.* **2000**, *80*, 65–73.
[12] T. Jakusch, W. Jin, L. Yang, T. Kiss, D. C. Crans, *J. Inorg. Biochem.* **2003**, *95*, 1–13.
[13] P. Buglyó, T. Kiss, E. Kiss, D. Sanna, E. Garribba, G. Micera, *J. Chem. Soc., Dalton Trans.* **2002**, *11*, 2275–2282.
[14] H. Degani, M. Gochin, S. J. D. Karlish, Y. Shechter, *Biochemistry* **1981**, *20*, 5795–5799.
[15] T. Goda, H. Sakurai, T. Yashimura, *Nippon Kagaku Kaishi* **1988**, 654–661.
[16] J. Costa Pessoa, I. Tomaz, T. Kiss, P. Buglyó, *J. Inorg. Biochem.* **2001**, *84*, 259–270.
[17] J. Costa Pessoa, I. Tomaz, T. Kiss, E. Kiss, P. Buglyó, *J. Biol. Inorg. Chem.* **2002**, *7*, 225–240.
[18] E. Alberico, D. Dewaele, T. Kiss, G. Micera, *J. Chem. Soc., Dalton Trans.* **1995**, *3*, 425–430.
[19] H. Sakurai, A. Tsuji, in: *Vanadium in the Environment*, Part 2, *Health Effects* (Ed.: J. O. Nrigau), Wiley, New York, **1998**, p. 301.
[20] a) P. Caravan, L. Gelmini, N. Glover, F. G. Herring, H. Li, J. H. McNeill, S. J. Rettig, I. A. Seyawati, E. Shuter, Y. Sun, A. S. Tracey, V. G. Yuen, C. Orvig, *J. Am. Chem. Soc.* **1995**, *117*, 12759–12770; b) Y. Sun, B. R. James, S. J. Rettig, C. Orvig, *Inorg. Chem.* **1996**, *35*, 1667–1673; c) G. R. Hanson, Y. Sun, C. Orvig, *Inorg. Chem.* **1996**, *35*, 6507–6512.
[21] D. Mustafi, M. W. Makinen, *Inorg. Chem.* **2005**, *44*, 5580–5590.
[22] L. F. Vilas Boas, J. Costa Pessoa, in: *Comprehensive Coordination Chemistry*, (Eds.: G. Wilkinson, R. D. Gillard, J. A. McCleverty), Pergamon Press, Oxford, **1987**, vol. 3, pp. 453–583.
[23] A. Komura, M. Hayashi, H. Imanaga, *Bull. Chem. Soc. Jpn.* **1977**, *50*, 2927–2931.
[24] T. Kiss, E. Kiss, G. Micera, D. Sanna, *Inorg. Chim. Acta* **1998**, *283*, 202–210.
[25] A. Dessi, G. Micera, D. Sanna, *J. Inorg. Biochem.* **1993**, *52*, 275–286.
[26] A. J. Tasiopoulos, A. N. Troganis, A. Evangelou, C. P. Raptopoulou, A. Terzis, Y. G. Deligiannakis, T. A. Kabanos, *Chem. Eur. J.* **1999**, *5*, 910–921.
[27] G. Gran, *Acta Chem. Scand.* **1950**, *4*, 559–577.
[28] I. Nagypál, I. Fábián, *Inorg. Chim. Acta* **1982**, *61*, 109–113.
[29] H. M. Irving, M. G. Miles, L. D. Pettit, *Anal. Chim. Acta* **1967**, *38*, 475–488.
[30] L. Zékány, I. Nagypál, in: *Computational Methods for the Determination of Stability Constants* (Ed.: D. Leggett), Plenum, New York, **1985**, p. 291.
[31] R. P. Henry, P. C. H. Mitchell, J. E. Prue, *J. Chem. Soc., Dalton Trans.* **1973**, *11*, 1156–1159.
[32] A. Rockenbauer, L. Korecz, *Appl. Magn. Reson.* **1996**, *10*, 29–43.
[33] N. D. Chasteen, Vanadyl(IV) EPR Spin Probes. Inorganic and Biochemical Aspects, vol. 3, in: *Biological Magnetic Resonance* (Eds.: J. Lawrence, L. J. Berliner, J. Reuben), Plenum: New York, **1981**; chapter 2, pp. 53–119.
[34] T. Jakusch, P. Buglyó, A. I. Tomaz, J. Costa Pessoa, T. Kiss, *Inorg. Chim. Acta* **2002**, *339*, 119–128.
[35] T. S. Smith, C. A. Root, J. W. Kampf, P. G. Rasmussen, V. L. Pecoraro, *J. Am. Chem. Soc.* **2000**, *122*, 767–775.
[36] A. J. Tasiopoulos, A. N. Troganis, A. E. Evangelou, C. P. Raptopoulou, A. Terzis, Y. Deligiannakis, T. A. Kabanos, *Chem. Eur. J.* **1999**, *5*, 910–921.

Received: April 27, 2006
Published Online: August 7, 2006

 © 2006 Wiley-VCH Verlag GmbH & Co. KGaA, Weinheim 

DOI: 10.1002/ejic.200600405

# Mechanism-Based Inactivation of Coenzyme $B_{12}$-Dependent 2-Methyleneglutarate Mutase by (*Z*)-Glutaconate and Buta-1,3-diene-2,3-dicarboxylate

**Wolfgang Buckel,*[a] Antonio J. Pierik,[a] Sandra Plett,[a] Ashraf Alhapel,[a] Diana Suarez,[b] Shang-min Tu,[b] and Bernard T. Golding*[b]**

**Keywords:** 2-Methyleneglutarate / Mutase / Coenzyme $B_{12}$ / Inhibition / Buta-1,3-diene-2,3-dicarboxylic acid / Glutaconic acid

In the presence of *holo* 2-methyleneglutarate mutase, buta-1,3-diene-2,3-dicarboxylate and (*Z*)-glutaconate [(*Z*)-pent-2-ene-1,5-dicarboxylate], but not (*E*)-glutaconate, each induced homolysis of the Co–C bond of coenzyme $B_{12}$ to afford cob(II)alamin and the 5′-deoxyadenosyl radical. The latter probably added to the double bond in (*Z*)-glutaconate and one of the double bonds in buta-1,3-diene-2,3-dicarboxylate to afford a corresponding "radical adduct". The formation of new radicals and cob(II)alamin was diagnosed by UV/Visible and EPR spectroscopy. (*Z*)-Glutaconate rapidly inactivated the mutase with formation of aquocobalamin, which was possibly derived by electron transfer from cob(II)alamin to the radical adduct. In contrast, buta-1,3-diene-2,3-dicarboxylate was a much slower inactivator. In this case, the spectroscopic data revealed a relatively stable complex of the radical adduct with cob(II)alamin in the active site of the enzyme.
(© Wiley-VCH Verlag GmbH & Co. KGaA, 69451 Weinheim, Germany, 2006)

## Introduction

Coenzyme $B_{12}$-dependent enzymes comprise eliminases and mutases, both of which catalyse molecular rearrangements, whereby a functional group undergoes a 1,2-shift enabling conversion of substrate to product. In the eliminases, the migrating group is amino or hydroxy, whereas in the mutases it is either amino or a carbon-based group. The mechanisms of these reactions have been extensively discussed and reviewed.[1–3] For the mutases, experimental and theoretical data have recently led to the proposal that in the mutases cob(II)alamin assists the group migration by stabilising intermediate methylene radicals.[3]

2-Methyleneglutarate mutase from the strict anaerobic bacterium *Eubacterium barkeri*, formerly called *Clostridium barkeri*, catalyses the reversible carbon-skeleton rearrangement of 2-methyleneglutarate (**1a**) to (*R*)-3-methylitaconate (**2a**, 2-methylene-3-methylsuccinate) in the pathway of nicotinate fermentation.[4] Binding of the substrate **1a** to the enzyme induces homolytic cleavage of the Co–C σ bond in the prosthetic group coenzyme $B_{12}$ to afford cob(II)alamin and the 5′-deoxyadenosyl radical. This highly reactive methylene radical abstracts the 4-*Re*-hydrogen atom from 2-methyleneglutarate to yield the substrate-derived 2-methylene-4-ylglutarate radical (**1b**) and 5′-deoxyadenosine. Cob(II)alamin coupled to an organic radical, possibly 2-methylene-4-ylglutarate (**1b**), can be observed by EPR spectroscopy.[5] It has been proposed that the substrate radical either fragments into acrylate and the 2-acrylate radical ($CH_2{=}C^{\cdot}HCO_2^-$), which recombine to the product-related (*R*)-3-methylene-itaconate radical (**2b**), or the latter radical is derived via an intermediate 1,2-dicarboxycyclopropylmethyl radical (**3**) (see Scheme 1).[5] Recently, Newcomb and Miranda have proposed a variant ("polar/heterolytic") of fragmentation–recombination in which the intermediates are the 2-carbanion of acrylate ($CH_2{=}C^-CO_2^-$) and the carboxyl radical of acrylate ($CH_2{=}CHCO_2^{\cdot}$).[6] The reaction cycle is completed by a H-atom transfer from 5′-deoxyadenosine to the 3-methylene-itaconate radical (**2b**) yielding the product **2a**. Finally, the coenzyme is regenerated by combining cob(II)alamin and the 5′-deoxyadenosyl radical, thereby reforming the Co–C σ-bond. In this paper we report the use of stable analogues of the proposed intermediate radicals with π bonds at those carbon atoms that during catalysis are converted into the $sp^2$ centres of radicals. In principle, these compounds could either competitively inhibit the enzyme or the 5′-deoxyadenosyl radical might add at a double bond to form an adduct radical and cob(II)alamin, thus leading to inactive enzyme. We synthesised (*Z*)-glutaconic acid [**4a**, (*Z*)-pent-2-ene-1,5-dicarboxylic acid] as a potential analogue of the 2-methylene-4-ylglutar-

[a] Laboratorium für Mikrobiologie, Fachbereich Biologie, Philipps-Universität,
35032 Marburg, Germany
E-mail: buckel@staff.uni-marburg.de
[b] School of Natural Sciences – Chemistry, Bedson Building, Newcastle University,
Newcastle upon Tyne, NE1 7RU, UK
E-mail: b.t.golding@ncl.ac.uk

 © 2006 Wiley-VCH Verlag GmbH & Co. KGaA, Weinheim 

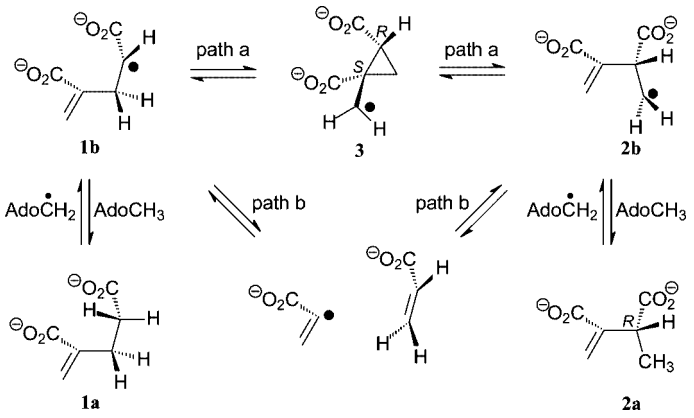


Scheme 1. Proposed reaction pathways for 2-methyleneglutarate mutase. (Path a) Addition-elimination mechanism with the participation of an intermediate 1-methylene-1,2-cyclopropanedicarboxylate radical **3**, for which the (1*S*,2*R*)-isomer is shown {$AdoCH_2$ = 5′-deoxyadenosyl; $AdoCH_3$ = 5′-deoxyadenosine}. (Path b) Fragmentation–recombination mechanism for 2-methyleneglutarate mutase involving an acrylate molecule and a 2-acrylate radical.

ate radical (**1b**), as well as buta-1,3-diene-2,3-dicarboxylic acid (**5**) as an analogue of the (*R*)-3-methyleneitaconate radical (**2b**). The commercially available (*E*)-glutaconic acid (**4b**) was also studied. Interestingly, compounds **4a** and **5** were inactivators of 2-methyleneglutarate mutase, whereas **4b** had no effect on the enzyme.

## Synthesis of Inhibitors

The synthesis of (*Z*)-glutaconic acid (**4a**, Scheme 2) was based on the procedure described in ref.[7] (Scheme 2). Thus, laevulinic acid (**6**) was cleanly dibrominated to 3,5-dibromolaevulinic acid (**7**), which underwent a Favorski rearrangement on treatment with potassium hydrogen carbonate to give exclusively (*Z*)-glutaconic acid with no trace of the (*E*)-isomer **4b** according to $^1$H NMR analysis.

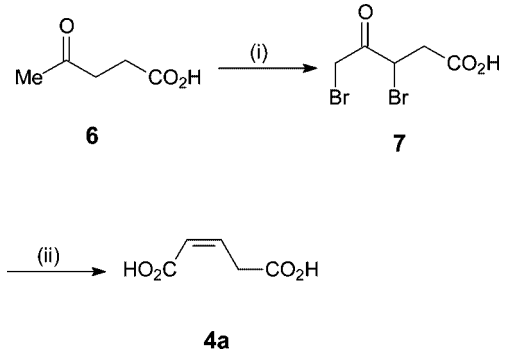


Scheme 2. Synthesis of (*Z*)-glutaconic acid (**4a**) [reagents: (i) $Br_2$, aq. 48% HBr; (ii) aq. $KHCO_3$].

The synthesis of buta-1,3-diene-2,3-dicarboxylic acid (**5**, Scheme 3) was performed via the corresponding di-*tert*-butyl ester, the preparation of which was closely modelled on that of dimethyl buta-1,3-diene-2,3-dicarboxylate.[8] Thus, *tert*-butyl acrylate (**8**) was treated with bromine to give *tert*-butyl 2,3-dibromopropionate (**9**), which was dehydrobrominated to *tert*-butyl 2-bromoacrylate (**10**) using triethylamine as base. The *tert*-butyl 2-bromoacrylate was subjected to nickel(0)-induced coupling to afford di-*tert*-butyl buta-1,3-diene-2,3-dicarboxylate (**11**), which was deprotected with trifluoroacetic acid to give buta-1,3-diene-2,3-dicarboxylic acid (**5**).

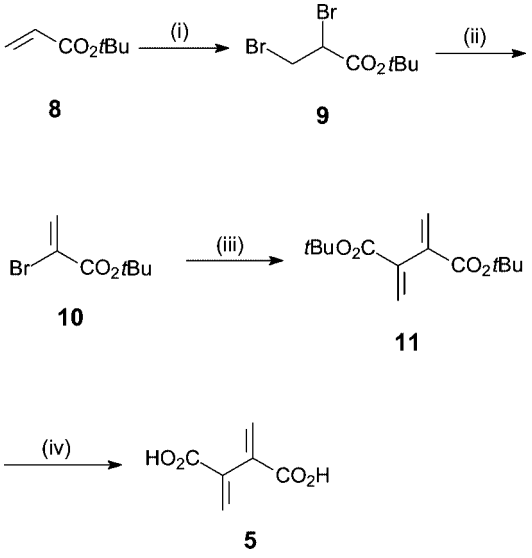


Scheme 3. Synthesis of buta-1,3-diene-2,3-dicarboxylic acid (**5**) [reagents and conditions: (i) $Br_2$, DCM, <10 °C; (ii) $Et_3N$, diethyl ether, 0 °C to room temperature; (iii) $(cycloocta\text{-}1,5\text{-}diene)_2Ni$, $Ph_3P$, diethyl ether, 25 °C, 4.5 h; (iv) TFA, room temperature].

## Enzyme Inhibition Studies

The activity of 2-methyleneglutarate mutase was determined in a coupled assay using 3-methylitaconate Δ-isomerase as an auxiliary enzyme.[5] The formation of 2,3-dimethylmaleate was followed spectrophotometrically at $\lambda$ = 256 nm. At first all three compounds were checked for their ability to inhibit or inactivate the isomerase. Whereas the glutaconates (**4a**, **4b**) did not affect the enzyme at all, 1 mM buta-1,3-diene-2,3-dicarboxylate (**5**) caused complete inactivation within 3 min under the conditions of the assay. Possibly a cysteine residue at the active site of the isomerase

 © 2006 Wiley-VCH Verlag GmbH & Co. KGaA, Weinheim 

added to one of the conjugated double bonds of this substrate analogue. This interesting result was not pursued further for the time being.

Because both glutaconates did not inhibit the isomerase, their action on the mutase could be studied directly in the coupled assay. It was found that 0.2 mM (*Z*)-glutaconate (**4a**) already inactivated the mutase by 60% within 1 min; after 5 min the inactivation was complete. Furthermore, whereas 1 mM (*Z*) isomer **4a** completely inactivated the mutase within 1 min, 1 mM (*E*) isomer **4b** exhibited no effect during this time. Only with 4 mM **4b** was there a slight deviation from the control observed after the first minute. $^1$H NMR spectroscopy revealed that the commercial **4b** used in this study contained ca. 2% **4a**. This was deduced from the integrated signal at $\delta$ = 6.55 ppm (β-H of **4a**) as compared to 7.03 ppm (**4b**). Hence the observed inactivation is completely specific for the (*Z*) isomer **4a**. In order to show that inactivation of 2-methyleneglutarate mutase only occurred with the *holo*-enzyme, coenzyme $B_{12}$-free *apo*-2-methyleneglutarate mutase was incubated for 10 min with **4a**, which was then removed by gel filtration through Sephadex G25. Following the addition of coenzyme $B_{12}$ to the recovered *apo*-enzyme, the reconstituted *holo*-enzyme was found to be fully active towards 2-methyleneglutarate.

The effect of **5** on the enzyme was assessed with 15 μM *apo*-2-methyleneglutarate mutase (subunit $m$ = 67 kDa), 100 μM coenzyme $B_{12}$, 2 mM dithiothreitol and 1 mM **5** in 100 mM potassium phosphate (pH 7.4) which were incubated for 30 min at 25 °C. Afterwards, the inhibitor was removed by gel filtration and the activity of the recovered enzyme was measured in the coupled assay. The results showed that incubation of the *holo*-enzyme with **5** decreased the activity of the enzyme by 45 ± 2% as compared to that of a control without **5**. We also studied the mutase under steady-state conditions and found that in the presence of excess of coenzyme $B_{12}$ and 10 mM 2-methyleneglutarate the *apo*-mutase lost 80% of its activity after 20 min (50% after 10 min) or about 6 million turnovers; within the next 20 min the decrease was much slower, leading to 15% residual activity. In the absence of either coenzyme $B_{12}$ or substrate the enzyme remained stable during this time.

UV/Visible spectroscopy of the reconstituted (*holo*) 2-methyleneglutarate mutase, from which the excess of coenzyme $B_{12}$ had been removed by gel filtration, exhibited a broad peak at 535 nm and a shoulder at around 570 nm (Figure 1). Upon addition of 25 mM 2-methyleneglutarate the absorbance of both features decreased, and the peak shifted by about 5 nm to 530 nm. A new peak arose at 470 nm indicating the formation of cob(II)alamin. These spectral changes were already observed after 1 min; incubation for a further 5 min revealed only a slight increase in the intensities of the new peaks. Addition of 10 mM **5** to *holo*-mutase resulted in the same changes but with a twofold increase in intensity. An almost identical spectrum was obtained after 30 min incubation of the apoenzyme with 1 mM **5** and an excess of coenzyme $B_{12}$, followed by removal of the unbound small molecules through gel filtration. Different spectral changes were observed by addition of 10 mM **4a** to the *holo*-enzyme. The peak at 535 nm shifted to 521 nm and a new peak arose at 495 nm. The same concentration of the (*E*) isomer **4b** modified the spectrum in a similar manner but to a lesser extent, and is ascribed to 2% **4a** as an impurity. The new peaks revealed the formation of aquocobalamin, the oxidation product of cob(II)alamin.

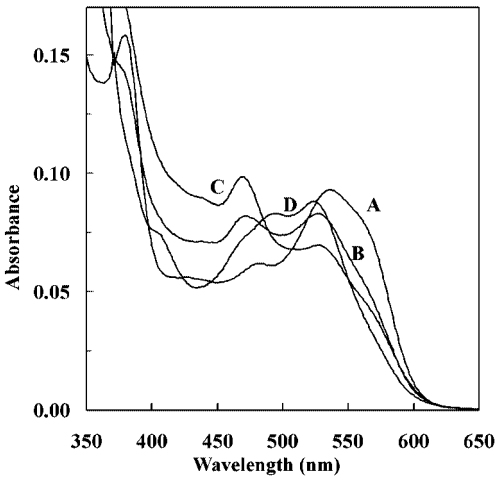


Figure 1. Visible spectra of 20 μM reconstituted *holo*-2-methyleneglutarate mutase (A) in the presence of 25 mM 2-methyleneglutarate (B) or 10 mM buta-1,3-diene-2,3-dicarboxylate (**5**, C) or 10 mM (*Z*)-glutaconate (**4a**, D). The addition of the dicarboxylate caused 10% dilution. The spectra were run 6 min after the additions.

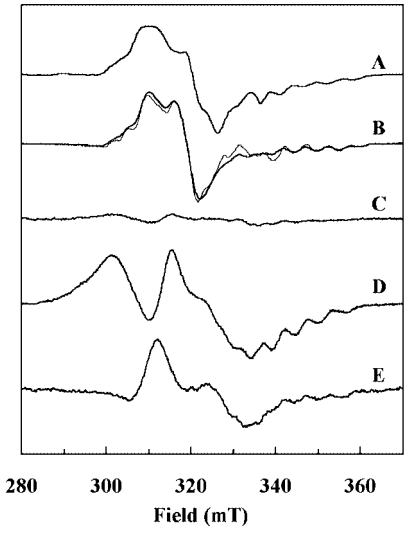


Figure 2. EPR spectra of 270 μM 2-methyleneglutarate mutase incubated in the presence of 1.6 mM coenzyme $B_{12}$ and 40 mM of 2-methyleneglutarate (A) or acrylate (B) or [2,3,3-$^2H_3$]acrylate (B, sharper trace) or (*E*)-glutaconate (**4b**, C) or (*Z*)-glutaconate (**4a**, D) or buta-1,3-diene-2,3-dicarboxylate (**5**, E). EPR conditions: temperature, 40 K for A, 77 K for B–E; microwave power 2 mW (A), 1.3 mW (B), 10 mW for C–E; microwave frequency 9463 ± 1 MHz (A) or 9435 ± 2 MHz (B–E); modulation amplitude 0.5 mT (A), 1.25 mT (B–E). Spectra were normalised to identical amplitudes, except for (*E*)-glutaconate. Thus, the spectra of the glutaconates can be directly compared.

 © 2006 Wiley-VCH Verlag GmbH & Co. KGaA, Weinheim 

EPR spectra were obtained by mixing 270 μM *apo*-methyleneglutarate mutase (final concentration; 18 mg protein $mL^{-1}$) in 50 mM Tris/HCl (pH 7.5) and 75 mM NaCl with 1.6 mM coenzyme $B_{12}$, and 40 mM substrate or inactivator, followed by freezing in liquid pentane/$N_2$ within 30 s. The results are shown in Figure 2. The spectra revealed that 2-methyleneglutarate, as well as the inactivators **4a** and **5**, led to the formation of stable enzyme-bound organic radicals, which interact with cob(II)alamin.[5] In the case of **4a** the concentration dependence of the EPR signal was studied. Saturation was observed with an apparent $K_i$ of $0.9 \pm 0.1$ mM. The determination of the nature of the radicals (see below) has to await the syntheses of $^2H$- and $^{13}C$-labelled inactivators. Interestingly, acrylate also induced the formation of radicals even though it was recently shown not to act as an inhibitor.[5] This result was confirmed with perdeuterated acrylate, which sharpened the signal.

## Discussion

In this paper we describe two mechanism-based inactivators of 2-methyleneglutarate mutase. Buta-1,3-diene-2,3-dicarboxylate (**5**) can be regarded as a close analogue of the product (*R*)-3-methylitaconate (**2a**): just the methyl group is converted to a second methylene group. Unfortunately we were not able to perform steady-state kinetics with **5**, because it reacted rapidly and irreversibly with the auxiliary enzyme, the isomerase. However, incubation of **5** with the mutase resulted in partial inactivation, formation of oxygen-insensitive cob(II)alamin and induction of an organic radical interacting with cob(II)alamin. Interestingly the same features were observed with the substrate 2-methyleneglutarate (**1a**) itself; only the EPR spectrum was somewhat different. Hence **5** behaved superficially like 2-methyleneglutarate. However, whereas the 5′-deoxyadenosyl radical abstracts a hydrogen atom from C-4 of 2-methyleneglutarate, with **5** the 5′-deoxyadenosyl radical most likely added at one of its methylene groups leading to an allyl radical **12**. A similar proposal has been made for the inactivation of glutamate mutase induced by 2-methyleneglutarate.[9] The partial inactivation of 2-methyleneglutarate mutase by **5** suggests that the proposed radical addition may be reversible. The substrate analogue **5** may fit sufficiently well into the enzyme active site that the adduct produced by the interaction of **5** with the 5′-deoxyadenosyl radical protects cob(II)alamin from interaction with oxygen.

The inactivator **4a** is not so closely related to the substrate 2-methyleneglutarate because it lacks the *exo*-methylene group. However, it apparently fits well into the active site, possibly because the distance between the two carboxylates is similar to that in the enzyme-bound conformation of (*R*)-3-methylitaconate. This could be the explanation for the inability of the (*E*) isomer **4b** to inactivate the enzyme. The (*Z*) isomer reacts rapidly with the mutase as shown by activity measurements and EPR spectroscopy. Already 60 s after mixing under anoxic conditions an organic radical interacting with cob(II)alamin was detected. In the visible spectra, however, which were taken after 1 and 6 min (Figure 1), only aquocob(III)alamin rather than cob(II)alamin could be seen. This could be due to an electron transfer from cob(II)alamin to the initially derived adduct radical from **4a** and the 5′-deoxyadenosyl radical.

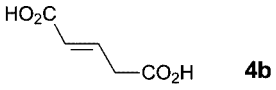


**4b**

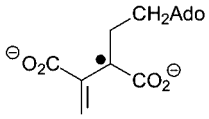


**12**

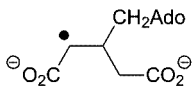


**13**

(AdoCH$_2$ = 5'-deoxyadenosyl)

The adduct radical is possibly **13**, arising from addition of the 5′-deoxyadenosyl radical to C-3 of **4a**. Similar electron transfers have been observed from cob(II)alamin to substrate-derived radicals in β-lysine 5,6-aminomutase[10] and in variants of methylmalonyl-CoA mutase.[11]

## Experimental Section

**Enzymology:** The preparation and assay of 2-methyleneglutarate mutase and 3-methylitaconate Δ-isomerase, as well as the method of recording the EPR spectra, have been described previously.[5] In the standard assay, 2-methyleneglutarate mutase activity (0.05–0.1 unit) was measured with 10 mM 2-methyleneglutarate as substrate in 100 mM potassium phosphate (pH 7.4, 25 °C) using 3-methylitaconate isomerase (10–30 units/mL) as auxiliary enzyme. The 2,3-dimethylmaleate formed was measured by its UV absorbance ($\varepsilon_{256}$ = 0.66 $mM^{-1} cm^{-1}$). For the inactivation studies (*E*)- and (*Z*)-glutaconate and buta-1,3-diene-2,3-dicarboxylate were dissolved in aqueous KOH to give 0.1 M solutions (pH ca. 7). In order to remove small molecules from the enzymes, PD-10-desalting columns containing Sephadex® G-25 Medium from GE Healthcare (Amersham Biosciences) were used. Concentrations (mM or μM) given in this paper are the final concentration for a particular component in the reaction mixture.

**3,5-Dibromolaevulinic Acid (7):** Bromine (13.7 g, 86 mmol) was added dropwise to a mixture of laevulinic acid (5.0 g, 43 mmol) and 48% aqueous HBr (4.3 mL, 38 mmol) at 0 °C over 30 min. The mixture was stirred at 0 °C for 4 h. The excess of bromine was removed using a nitrogen flow. The resulting solution was stirred overnight at 0 °C to give a solid, which was taken up in ethyl acetate (40 mL) and washed with saturated aqueous sodium metabisulfite (3 × 25 mL). After drying ($MgSO_4$), the solvent was removed to afford crude product as a pale yellow solid. Recrystallisation from ethyl acetate/petroleum ether afforded the title compound as a white solid (7.83 g, 66% yield). M.p. 110–112 °C (lit.[7] m.p. 111–113). $^1H$ NMR (300 MHz, $CDCl_3$): $\delta$ = 2.97 (dd, $J$ = 5.6 and 17.6 Hz, 1 H, C*H*$HCO_2H$), 3.29 (dd, $J$ = 8.1 and 17.4 Hz, 1 H, CH*H*$CO_2H$), 4.07 (d, $J$ = 13.2 Hz, 1 H, C*H*HBr), 4.28 (d, $J$ = 12.9 Hz, 1 H, CH*H*Br), 4.94 (br. t, $J$ = 6.0 Hz, 1 H, CHBr) ppm. $^{13}C$ NMR (75 MHz, $CDCl_3$): $\delta$ = 30.9 (C-2), 38.4 (C-5), 41.1 (C-3), 174.5 (C-1), 194.4 (C-4) ppm. $C_5H_6O_3Br_2$: calcd. C 21.93, H 2.21, found C 22.02, H 2.27. IR (KBr disc): $\tilde{\nu}$ = 3000 (m), 1724 (s), 1700 (s), 611 (m) $cm^{-1}$.

 © 2006 Wiley-VCH Verlag GmbH & Co. KGaA, Weinheim 

**(*Z*)-Glutaconic Acid (4a):** $KHCO_3$ (17.0 g, 169 mmol) in water (210 mL) was added to 3,5-dibromolaevulinic acid (5.5 g, 21 mmol). The mixture was vigorously stirred for 19 h. When constant titration values against methyl orange were obtained, the reaction was quenched by acidification (aq. HCl) and extracted with diethyl ether (10 × 30 mL). After drying the combined organic extracts ($Na_2SO_4$) the solvent was removed. The resulting yellow solid was recrystallised from acetonitrile (decolourisation by charcoal) to give the title compound as a white solid (0.21 g, 8% yield). M.p. 130–132 °C (lit.[7] m.p. 136–136.5, lit.[12] 136–136.5). $^1$H NMR (300 MHz, $CD_3OD$): $\delta$ = 3.71 (dd, $J$ = 3.0 and 7.0 Hz, 2 H, $CH_2CO_2H$), 5.93 (dt, $J$ = 2.0 and 11.5 Hz, 1 H, CH), 6.52 (dt, $J$ = 7.0 and 11.6 Hz, 1 H, CH) ppm. $^{13}$C NMR [$\delta_C$ (75 MHz, $CD_3OD$)]: $\delta$ = 35.2 (C-4), 123.5 (C-3), 142.2 (C-2), 169.5 (C-1), 174.7 (C-5) ppm. $C_5H_6O_4$: calcd. C 46.16, H 4.65; found C 45.99, H 4.62. IR (KBr disc): $\tilde{\nu}$ = 3066 (m), 1686 (s), 1649 (s) cm$^{-1}$.

***tert*-Butyl 2,3-Dibromopropionate (9):** Bromine (2.9 ᴍ ) in DCM (10 mL) was added dropwise to *tert*-butyl acrylate (2.0 g, 15.6 mmol) in DCM (20 mL), cooled below 10 °C over 20 min. The mixture was stirred at ca. 5 °C for 2 h at which stage an orange colour persisted. The solvent was removed to afford the title compound as a colourless oil (4.41 g, 90% yield). $^1$H NMR (300 MHz, $CDCl_3$): $\delta$ = 1.43 [s, 9 H, $C(CH_3)_3$], 3.57 (dd, $J$ = 4.4 and 9.8 Hz 1 H, CH*H*Br), 3.81 (dd, $J$ = 9.8 and 11.3 Hz, 1 H, C*H*HBr), 4.27 (dd, $J$ = 4.4 and 11.3 Hz, 1 H, $CHBr_2$) ppm. $^{13}$C NMR (75 MHz, $CDCl_3$): $\delta$ = 28.1 [$C(CH_3)_3$], 41.0 (C-3), 43.3 (C-2), 83.9 [$C(CH_3)_3$], 166.8 (C-1) ppm.

***tert*-Butyl 2-Bromoacrylate (10):** Triethylamine (0.77 g, 0.80 mL, 7.7 mmol) in diethyl ether (5 mL) was added dropwise to *tert*-butyl 2,3-dibromopropionate (3.0 g, 7.0 mmol) in dry diethyl ether (15 mL), cooled to 0 °C . The mixture was stirred overnight at room temperature and then filtered. The filtrate was washed with water (3 × 10 mL), dried ($Na_2SO_4$) and the solvent was removed. The title compound was obtained as a pale yellow oil for which no further purification was needed (1.72 g, 80% yield). $^1$H NMR (300 MHz, $CDCl_3$): $\delta$ = 1.45 [s, 9 H, $C(CH_3)_3$], 6.13 (d, $J$ = 1.5 Hz, 1 H, CH*H*), 6.77 (d, $J$ = 1.5 Hz, 1 H, C*H*H) ppm. $^{13}$C NMR (75 MHz, $CDCl_3$): $\delta$ = 28.3 [$C(CH_3)_3$], 83.4 [$C(CH_3)_3$], 123.8 (C-3), 129.2 (C-2), 161.1 (C-1) ppm.

**Di-*tert*-butyl Buta-1,3-diene-2,3-dicarboxylate (11):** Bis(1,5-cyclooctadiene)nickel(0) (1.5 g, 5.3 mmol) and triphenylphosphane (2.8 g, 10.6 mmol) were suspended in dry diethyl ether (20 mL) at 25 °C under nitrogen in a flame-dried Schlenk tube. Neat *tert*-butyl 2-bromoacrylate (1.87 g, 8.9 mmol) was added rapidly via syringe and the reaction mixture was stirred at 25 °C for 4.5 h. The mixture was diluted with diethyl ether (20 mL), washed with water (2 × 25 mL), dried ($MgSO_4$) and the solvent was removed. The crude product was purified by medium pressure chromatography (silica, elution with 5% ethyl acetate in petrol). The product containing fractions ($R_f$ = 0.36 on silica, same solvent system) were collected and the solvent was removed to afford the title compound as a colourless oil (0.48 g, 47% yield). $^1$H NMR (300 MHz, $CDCl_3$): $\delta$ = 1.42 [s, 18 H, $C(CH_3)_3$], 5.60 (d, $J$ = 1.7 Hz, 2 H, CH*H*), 6.06 (d, $J$ = 1.7 Hz, 2 H, C*H*H) ppm. $^{13}$C NMR (75 MHz, $CDCl_3$): $\delta$ = 28.4 [$C(CH_3)_3$], 81.3 [$C(CH_3)_3$], 116.6 ($CH_2$), 126.0 (C-2, C-3), 165.3 (C-1) ppm.

**Buta-1,3-diene-2,3-dicarboxylic Acid (5):** Trifluoroacetic acid (TFA) (1.0 mL) was added to di-*tert*-butyl buta-1,3-diene-2,3-dicarboxylate (0.16 g, 0.63 mmol) in DCM (2 mL). The resulting solution was stirred at room temperature for 20 min. The solvent was removed and the title compound was obtained as a white solid (0.08 g, 90% yield). Recrystallisation from acetonitrile gave an analytically pure sample. M.p. 184–186 °C (lit.[13] m.p. 186–188, lit.[8] 192–192.5). $^1$H NMR (300 MHz, $CD_3OD$): $\delta$ = 5.85 (d, $J$ = 1.5 Hz, 2 H, C*H*H), 6.22 (d, $J$ = 1.5 Hz, 2 H, CH*H*) ppm. $^{13}$C NMR (75 MHz, $CD_3OD$): $\delta$ = 128.1 ($CH_2$), 140.1 (C-2, C-3), 167.1 (C-1) ppm. IR (KBr disc): $\tilde{\nu}$ = 3066 (m), 1675 (s), 1614 (s) cm$^{-1}$.

## Acknowledgments

We are grateful to the European Commission, Deutsche Forschungsgemeinschaft, and Fonds der Chemischen Industrie for funding this work.

[1] R. Banerjee, *Chemistry and Biochemistry of $B_{12}$*, John Wiley & Sons Inc., New York, **1999**.
[2] K. L. Brown, *Chem. Rev.* **2005**, *105*, 2075–2149.
[3] W. Buckel, C. Kratky, B. T. Golding, *Chem. Eur. J.* **2006**, *12*, 352–362.
[4] W. Buckel, G. Bröker, H. Bothe, A. J. Pierik, B. T. Golding, in *Chemistry and Biochemistry of $B_{12}$*, John Wiley & Sons, Inc., New York, **1999**, p. 757.
[5] A. J. Pierik, D. Ciceri, R. F. Lopez, F. Kroll, G. Bröker, B. Beatrix, W. Buckel, B. T. Golding, *Biochemistry* **2005**, *44*, 10541–10551.
[6] M. Newcomb, N. Miranda, *J. Am. Chem. Soc.* **2003**, *125*, 4080–4086.
[7] C. Rappe, R. Adeström, *Acta Chem. Scand.* **1965**, *19*, 383–389.
[8] M. F. Semmelhack, P. Helquist, L. D. Jones, L. Keller, L. Mendelson, L. S. Ryono, J. G. Smith, R. D. Stauffer, *J. Am. Chem. Soc.* **1981**, *103*, 6460–6471.
[9] M. S. Huhta, D. Ciceri, B. T. Golding, E. N. G. Marsh, *Biochemistry* **2002**, *41*, 3200–3206.
[10] K. H. Tang, C. H. Chang, P. A. Frey, *Biochemistry* **2001**, *40*, 5190–5199.
[11] M. D. Vlasie, R. Banerjee, *Biochemistry* **2004**, *43*, 8410–8417.
[12] R. Malachowski, *Ber. Dtsch. Chem. Ges.* **1929**, *62*, 1323–1326.
[13] S. G. Deshpande, N. P. Argade, *Synthesis* **1999**, *8*, 1306–1308.

Received: May 3, 2006
Published Online: August 2, 2006

 © 2006 Wiley-VCH Verlag GmbH & Co. KGaA, Weinheim 

DOI: 10.1002/ejic.200600270

# $La_{17}Si_9Al_4N_{32-x}O_x$ ($x \leq 1$): A Nitridoaluminosilicate with Isolated Si/Al-N/O Clusters

**Guillaume Pilet,*[a,b] Jekabs Grins,[a] Mattias Edén,[c] and Saeid Esmaeilzadeh[a]**

**Keywords:** Aluminosilicates / Anions / Lanthanides

A nitrogen-rich aluminosilicate with nominal composition $La_{17}Si_9Al_4N_{33}$ has been synthesised at 1500–1650 °C under a $N_2$ atmosphere by reaction of La metal, AlN and $Si_3N_4$. Its crystal structure was solved and refined in space group $F\bar{4}3m$, with $a$ = 15.4279(6) Å and $Z$ = 4, to $R_f$ = 1.9 %. The structure contains two novel types of discrete tetrahedral aluminosilicate clusters, with respective nominal compositions $Al_4Si_4N_{17}$ and $Si_5N_{16}$, with La atoms in between. Bulk samples were also investigated by powder X-ray and electron diffraction. The $^{29}Si$ and $^{27}Al$ solid-state NMR results indicate that the phase contains minor amounts of oxygen and has a narrow compositional range with probable end limits $La_{17}Si_9Al_4N_{33}$ and $La_{16.67}Si_9Al_4N_{32}O$.

(© Wiley-VCH Verlag GmbH & Co. KGaA, 69451 Weinheim, Germany, 2006)

## Introduction

Nitridosilicates and sialons are well known to exhibit useful physical properties, such as high strength, good wear resistance, high decomposition temperature, good oxidation resistance, excellent thermal-shock properties and resistance to corrosive environments. They have traditionally been investigated with an aim towards applications such as cutting tools, burners, welding nozzles, heat exchangers and engine applications. Phase-formation conditions and phase-compatibility relationships have therefore been systematically studied in many M-Si-Al-O-N sialon systems [e.g. M = Ca, Y and rare-earth (RE) elements].[1] During the last decades, however, more efforts have also been directed towards the synthesis of novel compounds with more complex crystal structures.[2] In particular, the use of electropositive metals as starting materials has proven to be a successful synthesis route.[3] The new compounds found have crystal structures that exhibit features that are distinctly different from those found for oxosilicates.[4–6] For example, whereas the O atoms in oxosilicates are connected to either one or two Si atoms,[7] the N atoms in nitridosilicates and sialons may also be shared by three, and even four, Si tetrahedra.[8,9] The network connectivity for nitridosilicates is therefore, as a rule, higher than for oxosilicates.

We report here on the structure determination and bulk synthesis of a new nitridoaluminosilicate with nominal composition $La_{17}Si_9Al_4N_{33}$. Two features make it noteworthy. First, its crystal structure does not contain any continuous linkage of tetrahedra, but instead two types of isolated Si-(Al)-N/(O) clusters. The same type of clusters is found in the similar structure of $Pr_{63}Si_{40}Al_{12}O_{20}N_{115}$,[10] the first known example of a nitridosilicate structure with all Al and Si atoms in isolated clusters. However, $Pr_{63}Si_{40}Al_{12}O_{20}N_{115}$ crystallises with a cubic *primitive* unit cell, in space group $P\bar{4}3m$ with $Z$ = 1 and $a$ = 15.185(2) Å, and the clusters are different with respect to their composition and connectivity, as described further below. Counterparts to the cluster types are also found in oxosilicate structures, although obviously they contain O instead of N atoms. Secondly, $La_{17}Si_9Al_4N_{33}$ is, according to its formal composition, a rare example of a pure nitridoaluminosilicate. The few other members include the wurtzite-type phases $MAlSiN_3$ (M = Be, Mg, Mn, Ca),[11,12] filled α-$Si_3N_4$-type compounds,[13] $Ca_5Si_2Al_2N_8$[12] and $Ca_4SiAl_3N_7$.[12]

However, although it is clear that the phase is very rich in nitrogen, it cannot be ruled out that it may contain minor amounts of oxygen, considering, for example, that the starting materials were not free of oxygen. In order to obtain local structural insight, $^{27}Al$ and $^{29}Si$ NMR spectra were therefore recorded. The NMR results indicate that there is a minor substitution of N by O and that the phase is likely a solid solution with end limits $La_{17}Si_9Al_4N_{33}$ and $La_{16.67}Si_9Al_4N_{32}O$. In what follows, the nominal composition will first be assumed, the NMR results presented, and conclusions about compositional variations then addressed in the Discussion.

[a] Arrhenius Laboratory, Division of Inorganic Chemistry, Stockholm University,
10691 Stockholm, Sweden
[b] Laboratoire des Multimatériaux et Interfaces, Groupe de Cristallographie et Ingénierie Moléculaire, Université Claude Bernard Lyon 1,
Bâtiment Jules Raulin, Campus de la Doua, 69622 Villeurbanne Cedex, France
E-mail: guillaume.pilet@univ-lyon1.fr
[c] Arrhenius Laboratory, Division of Physical Chemistry, Stockholm University,
106 91 Stockholm, Sweden

 © 2006 Wiley-VCH Verlag GmbH & Co. KGaA, Weinheim 

## Results

### Crystal Structure Determination and Refinement

The single-crystal data for $La_{17}Si_9Al_4N_{33}$ could be indexed with a cubic F-centred unit cell with $a$ = 15.410(1) Å. The F-centring, and the absence of further reflection conditions, was confirmed by electron diffraction (ED). The [011] zone axis pattern in Figure 1a shows the absence of 00l reflections with $l \neq 2n$ and $hk0$ reflections with $h + k \neq 2n$. Tilting of the sample (see Figure 1b) showed that an equivalent set of reflections appear in the first-order Laue zone (FOLZ), thus implying the extinction symbol F---.[14] The structure was solved in the space group $F23$ by direct methods, using the SIR97 program[15] in combination with Fourier difference syntheses. It was refined against $F$ using the CRYSTALS program[16] and reflections with $I/\sigma(I) > 3$. An inspection of refined atomic positions showed that the space group symmetry could be increased to $F\bar{4}3m$ (no. 216), and the final refinements made using this space group yielded a weighted $R_f$ value of 1.9% for 294 unique reflections. Thermal displacement parameters were refined anisotropically for Si and La atoms, and isotropically for N atoms. Refinement data are given in the Experimental Section, with structural parameters in Table 1 and selected bond lengths in Table 2.

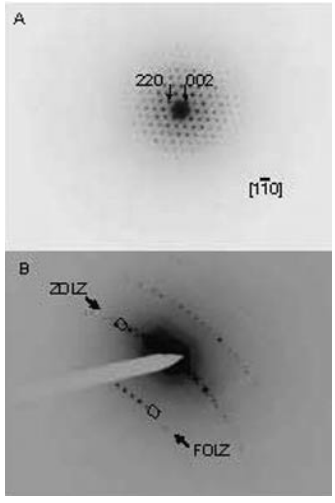


Figure 1.(a) [011] zone axis ED pattern of $La_{17}Si_9Al_4N_{33}$, showing the absence of 00$l$ reflections with $l \neq 2n$ and $hk0$ reflections with $h + k \neq 2n$. (b) A corresponding tilted ED pattern, showing an equivalent set of reflections in the first-order Laue zone (FOLZ).

Table 1. Atomic parameters for $La_{17}Si_9Al_4N_{33}$; cubic, $a$ = 15.4279(6) Å, $V$ = 3672.13 Å$^3$, $F\bar{4}3m$, $Z$ = 4.

| Atom | Site | $x$ | $y$ | $z$ | $U_{eq}$ [Å$^2$] |
|---|---|---|---|---|---|
| La1 | 24$f$ | 1/2 | 0.29365(6) | 0 | 0.0098 |
| La2 | 24$g$ | 3/4 | 1/4 | 0.01012(8) | 0.0141 |
| La3 | 16$e$ | 0.40995(6) | 0.09005(6) | –0.09005(6) | 0.0230 |
| La4 | 4$d$ | 3/4 | 1/4 | 1/4 | 0.0176 |
| Si1 | 4$a$ | 1/2 | 1/2 | 0 | 0.0064 |
| Si2 | 16$e$ | 0.6354(3) | 0.1354(3) | –0.1354(3) | 0.0107 |
| Si3 | 16$e$ | 0.6338(3) | 0.3662(3) | 0.1338(3) | 0.0070 |
| Al1 | 16$e$ | 0.8199(3) | 0.1801(3) | –0.1801(3) | 0.0116 |
| N1 | 48$h$ | 0.6134(5) | 0.2577(7) | 0.1134(5) | 0.013(3) |
| N2 | 48$h$ | 0.3854(6) | 0.2476(8) | 0.1146(6) | 0.029(3) |
| N3 | 16$e$ | 0.5665(8) | 0.4335(8) | 0.0665(8) | 0.013(4) |
| N4 | 16$e$ | 0.575(1) | 0.075(1) | –0.075(1) | 0.054(8) |
| N5 | 4$c$ | 3/4 | 1/4 | –1/4 | 0.02(1) |

Table 2. Atomic distances [Å] in $La_{17}Si_9Al_4N_{33}$.

| Si–N | | | | Average | |
|---|---|---|---|---|---|
| Si1–N3 | 1.77(2) 4× | | | 1.77 | |
| Si2–N2 | 1.79(1) 3× | Si2–N4 | 1.63(3) | 1.75 | |
| Si3–N1 | 1.73(1) 3× | Si3–N3 | 1.80(2) | 1.75 | |
| Al–N | | | | | |
| Al1–N2 | 1.81(1) 3× | Al1–N5 | 1.866(7) | 1.82 | |
| La–N | | | | | |
| La1–N1 | 2.53(1) 2× | La1–N2 | 2.60(1) 2× | La1–N3 | 2.5971(9) 2× |
| La2–N1 | 2.642(2) 4× | La2–N2 | 2.837(1) 4× | | |
| La3–N4 | 2.56(2) 3× | La3–N1 | 2.63(1) 3× | | |
| La4–N1 | 2.98(1) 12× | | | | |

### Structure Description

The unit cell contains four nominal formula units of $La_{17}Si_9Al_4N_{33}$. Possible deviations from this formula are addressed in the Discussion. There are four tetrahedral T (T = Si/Al) sites in the structure. One site has a considerably larger average T–N distance than the other ones and is concluded to be occupied by Al atoms. The other three T sites are accordingly occupied by only Si atoms. The structure contains two types of isolated tetrahedral clusters. One type has a composition of $Al_4Si_4N_{17}^{-23}$ and is illustrated in Figure 2 (a). In each $Al_4Si_4N_{17}$ unit, a central N atom, on the

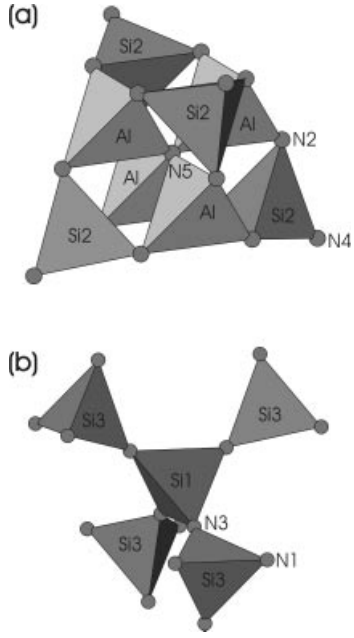


Figure 2. The two types of tetrahedral clusters found in the structure of $La_{17}Si_9Al_4N_{33}$. (a) The $Al_4Si_4N_{17}$ cluster centred at the 4$c$ site at (1/4,1/4,1/4). (b) The $Si_5N_{16}$ cluster centred at the 4$a$ site at (0,0,0).

 © 2006 Wiley-VCH Verlag GmbH & Co. KGaA, Weinheim 

4*c* site at (1/4,1/4,1/4), is common to four $AlN_4$ tetrahedra. Each of four $SiN_4$ tetrahedra then shares three of its N corner atoms with separate $AlN_4$ tetrahedra, and has one free apex N atom pointing outwards from the unit. A crystal-chemical formula[17] for the crystal is $[Al_4^{1;6}Si(2)_4^{1;3}N(4)^{[1]}N(2)_{12}^{[2]}N(5)^{[4]}]^{23-}$. A similar cluster is found in the structure of $Pr_{63}Si_{40}Al_{12}O_{20}N_{115}$.[10] This has the composition $Al_4Si_4N_{13}O_4^{-19}$ and differs by having O atoms on the Si tetrahedra apex atom sites. An identical atomic arrangement is also found for the $Be_4Si_4O_{17}$ cluster in the structure of $Na_{10}Be_4Si_4O_{17}$.[18]

The other type of cluster, illustrated in Figure 2 (b), has a composition of $Si_5N_{16}^{-28}$ and a crystal-chemical formula of $[Si(1)^{[1;4]}Si(3)_3^{[1;1]}N(1)_{12}^{[1]}N(3)^{[2]}]^{28-}$. It has at its centre, on the 4*a* site at (0,0,0), a $SiN_4$ tetrahedron that is connected by corner-sharing to four surrounding $SiN_4$ tetrahedra. Similar clusters, with composition $Si_5O_{16}$, are found in the structure of zunyite $[Al_{13}Si_5O_{20}(OH)_{18}Cl]$.[19] The structure of $Pr_{63}Si_{40}Al_{12}O_{20}N_{115}$ also contains $Si_5N_{16}$ zunyite-type clusters, but four such clusters are further interlinked by four additional $SiON_3$ tetrahedra to form a much larger cluster with composition $Si_{24}N_{64}O_4^{-104}$. The arrangement of two types of clusters in the unit cell of $La_{17}Si_9Al_4N_{33}$ is illustrated in Figure 3. There are four different La atom positions in the structure; the coordination of N atoms around them is illustrated in Figure 4. La1 is coordinated by six N atoms at 2.53–2.60 Å that form a distorted square bipyramid, La2 by a distorted cube of eight N atoms at 2.64–2.84 Å, La3 by a distorted octahedron of six N atoms at 2.56–2.63 Å, and La4 by 12 N atoms that form a cube-octahedron.

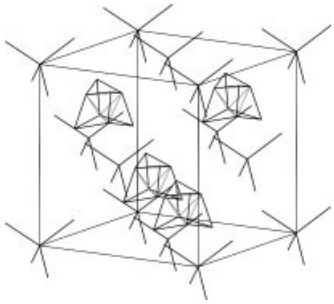

Figure 3. An illustration of the arrangement of the two types of clusters in the unit cell of $La_{17}Si_9Al_4N_{33}$. The drawn lines connect tetrahedral atom positions.

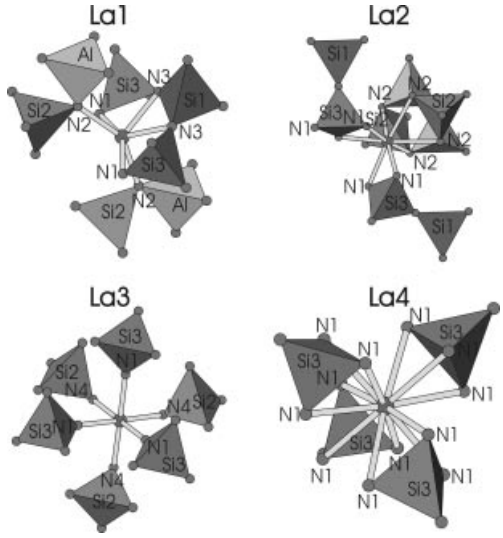


Figure 4. The coordination of N atoms around the four crystallographically different La atoms in the structure of $La_{17}Si_9Al_4N_{33}$.

## Bulk Synthesis

Initial syntheses showed that the $La_{17}Si_9Al_4N_{33}$ phase could be obtained together with LaN in the presence of a large excess (double amount) of La metal. The crystallinity was good, but the sample decomposed over a period of about one week, simultaneously with hydrolysis of the LaN, when left in contact with air. When stoichiometric amounts of the starting materials were used, and also when adding a smaller excess (10%) of La, yellow to yellow-green coloured samples were obtained after applying two consecutive heat treatments at 1500 and 1600 °C. These samples contained two minority phases in addition to $La_{17}Si_9Al_4N_{33}$. The reflections of one could be indexed using a small monoclinic unit cell with $a$ = 5.2582(9), $b$ = 5.5717(9), $c$ = 3.9909(6) Å, and $\beta$ = 92.35(1)°, thus indicating that its structure may be perovskite related. The reflections of the second could be indexed with an *I*-centred tetragonal unit cell with $a$ = 6.821(2) and $c$ = 11.133(6) Å. The cell strongly suggests that the phase is related to $La_3AlO_3N_2$, which crystallises in *I*4/*mcm* with $a$ = 6.855(2) and $c$ = 11.199(5) Å.[20] A third heat treatment did not decrease the amounts of these secondary phases. However, their amounts could be drastically reduced by mixing the obtained samples with 3 wt.-% fine-grained carbon and then further heat-treating them at 1500 °C, i.e. by a carbothermal reduction and nitridation of the secondary phases. The powder pattern of the stoichiometric, yellow sample then only contained two weak reflections, with relative intensities below 1.5%, for the impurity phases. A good agreement was found between the observed reflection intensities and the intensities calculated from the single crystal data. The obtained unit-cell parameter was $a$ = 15.4279(6) Å and the indexed powder pattern is given in Table 3. Unfortunately, we were not able to obtain samples with this level of purity in larger amounts, for example to perform neutron powder diffraction or physical property measurements.

To find an alternative synthetic route, a 4-g stoichiometric mixture of LaN, $Si_3N_4$ and AlN was hot-pressed at 1600 °C and 50 MPa for 4 h. The powder pattern of the prepared sample contained, however, only broad reflections from unreacted starting materials, cuspidine-type $La_4Si_2O_7N_2$ and unidentified phases. In order to investigate whether Al and O can be simultaneously incorporated into $La_{17}Si_9Al_4N_{33}$ according to the common sialon substitution mechanism ($Si^{4+} + N^{3-} \leftrightarrow Al^{3+} + O^2$) three 1.5-g samples of $La_{17}Si_{9-x}Al_{4+x}N_{33-x}O_x$, with $x$ = 2, 4, and 6, were prepared with $SiO_2$ as oxygen source. The powder patterns of

 © 2006 Wiley-VCH Verlag GmbH & Co. KGaA, Weinheim 

Table 3. Observed and calculated $2\theta$ values for the Guinier–Hägg diffraction pattern of $La_{17}Si_9Al_4N_{33}$ up to the 20th observed line. $a$ = 15.4279(6) Å, $\Delta 2\theta = 2\theta_{obs.} - 2\theta_{calcd.}$, $\lambda$ = 1.5406 Å. Cell figure-of-merit: $M_{20}$ = 131, $F_{20}$ = 152 (0.0055, 24).

| *hkl* | $2\theta_{obs.}$ [°] | $\Delta 2\theta$ | $d_{obs}$ [Å] | $I/I_0$ |
|---|---|---|---|---|
| 111 | 9.930 | 0.007 | 8.90 | 12 |
| 220 | 16.233 | –0.004 | 5.45 | 1 |
| 400 | 23.046 | 0.005 | 3.856 | 36 |
| 331 | 25.139 | –0.001 | 3.540 | 20 |
| 420 | 25.813 | 0.008 | 3.449 | 6 |
| 422 | 28.320 | 0.003 | 3.149 | 28 |
| 511 | 30.067 | –0.007 | 2.970 | 83 |
| 440 | 32.805 | –0.007 | 2.728 | 100 |
| 600 | 34.871 | 0.007 | 2.571 | 13 |
| 620 | 36.814 | –0.002 | 2.440 | 1 |
| 533 | 38.218 | –0.005 | 2.353 | 3 |
| 622 | 38.697 | 0.015 | 2.325 | 5 |
| 444 | 40.473 | –0.002 | 2.227 | 21 |
| 711 | 41.774 | –0.005 | 2.161 | 5 |
| 640 | 42.199 | –0.007 | 2.140 | 2 |
| 642 | 43.879 | –0.001 | 2.062 | 5 |
| 731 | 45.100 | –0.003 | 2.009 | 12 |
| 800 | 47.081 | –0.005 | 1.929 | 10 |
| 733 | 48.242 | –0.003 | 1.885 | 10 |
| 820 | 48.640 | 0.013 | 1.870 | 7 |

the samples with $x$ = 2 and 4 showed no change in the unit-cell parameter for $La_{17}Si_9Al_4N_{33}$ and the presence of several additional phases, among them AlN and the two secondary phases described above. The sample with $x$ = 6 contained no $La_{17}Si_9Al_4N_{33}$ at all. These results show that the $La_{17}Si_9Al_4N_{33}$ phase does not accept any significant simultaneous incorporation of Al and O. A comparison of the obtained unit-cell parameters for all preparations of $La_{17}Si_9Al_4N_{33}$ showed, however, very small but significant variations. The largest unit-cell parameter was observed for the sample prepared with a large excess of La [$a$ = 15.4402(9) Å], and the smallest one for the stoichiometric sample that was further heat-treated with added carbon at 1500 °C [$a$ = 15.4279(6) Å]. The difference is very small [0.012(1) Å], but indicates nevertheless that $La_{17}Si_9Al_4N_{33}$ shows smaller compositional variations. It may be noted that the two samples have nominally the same Al/Si ratio. Finally, attempts were made to prepare isostructural phases with the rare-earths Pr, Sm, Gd and Y at 1500–1650 °C. These were not successful, but in the case of Y yielded a very distinct powder pattern from YN and a hexagonal phase with $a$ = 9.8027(4) and $c$ = 10.6235(6) Å. The unit-cell parameters indicate that the phase is isostructural with $Y_{6+x/3}Si_{11}N_{20+x}O_{1-x}$,[21] a structure type that can also incorporate Al according to the more general formula $RE_{6+x/3}Si_{11-y}Al_yN_{20+x+y}O_{1-x+y}$, e.g. $Nd_7Si_8Al_3N_{20}$.[22]

## Solid-State NMR Spectroscopy

### *$^{27}$Al NMR*

Figure 5 shows $^{27}$Al MAS and 3QMAS[24] NMR spectra recorded for a freshly prepared sample of $La_{17}Si_9Al_4N_{33}$. The MAS spectrum displays two signals at around $\delta$ = 112 and 90 ppm, which were assigned to $AlN_4$ and $AlN_3O$ tetrahedra, respectively, on the basis of typical chemical shifts for such units.[25,26]

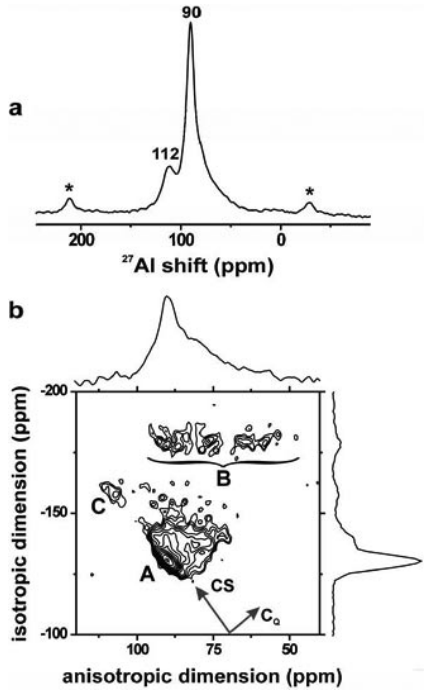


Figure 5. (a) Zoom around the centre-band region of an $^{27}$Al MAS spectrum recorded for $La_{17}Si_9Al_4N_{33}$ at a MAS frequency of 12.5 kHz. It results from the summation of 192 signal transients, each obtained using a relaxation delay of 200 s and short excitation pulse of flip angle ca. 12°. The nutation frequency was 94 kHz, measured relative to $Al^{3+}$(aq). 200 Hz full width at half maximum height (FWHM) Lorentzian broadening was applied prior to Fourier transformation. Chemical shift values are displayed on the top of the peak maxima and asterisks indicate spinning sidebands. (b) 3QMAS spectrum recorded by the shifted-echo technique[23] at 13.3 kHz MAS, using 96 transients per $t_1$-value and relaxation delays of 30.5 s. Arrows indicate the direction of peak displacement due to changes in isotropic chemical shifts and quadrupolar coupling constants.

However, the higher spectral resolution in the 3QMAS spectrum reveals a significantly more complex signal pattern than hinted from the 1D MAS spectrum. The signal region labelled A corresponds to the peak at $\delta$ = 90 ppm in the MAS spectrum. From the 3QMAS data, we estimated the isotropic chemical shift as $\delta_{iso}$ = 92 ppm. As the asymmetry parameter of the electric-field tensor could not be determined for any of the sites discussed below, we have henceforth assumed that $\eta$ = 0, for site A, which results in a corresponding quadrupolar coupling constant $C_Q = e^2qQ/h$ = 1.7 MHz. The same chemical shift value was obtained by using the frequency positions of central and satellite transition peaks, as described previously.[26] Signal A extends along both spectral dimensions due to spreads in isotropic chemical shifts as well as quadrupolar coupling constants. In the MAS spectrum in part a of Figure 5, these dispersions are manifested as the signal "tail" extending towards lower shifts (ppm values). However, the broad peak labelled B (Figure 5, b) also contributes to this spectral re-

 © 2006 Wiley-VCH Verlag GmbH & Co. KGaA, Weinheim 

gion. Signal B is associated with an aluminium site experiencing a significant quadrupolar coupling constant (estimated as $CQ$ = 7.4 MHz), but unlike the other sites, it is not associated with dispersions in quadrupolar couplings or chemical shifts. Based on its isotropic chemical shift ($\delta_{iso}$ = 108 ppm), this peak is assigned to an $AlN_4$ environment.[25,26]

The 3QMAS spectral intensities are not quantitative[24] due to the widely differing quadrupolar coupling constant of site B compared to A and C. This is evident, for example, from the fact that the anisotropic MAS projection of Figure 5 (b) differs from the 1D MAS spectrum in Figure 5 (a), as is the incomplete excitation of the peak around $\delta$ = 112 ppm (corresponding to signal C in Figure 5, b).

The MAS spectrum was deconvoluted into three components (not shown), from which the relative integrated intensities for A–C were estimated. This (highly uncertain) calculation showed that 55, 34 and 11% of the total signal portion derives from A, B and C, respectively. It now remains to reconcile the information from the $^{27}$Al NMR spectrum, which shows signals from (at least) three distinct Al environments (for the proposed structure of $La_{17}Si_9Al_4N_{33}$ only a *single* tetrahedral $AlN_4$ site is expected). Several scenarios of O↔N and Si↔Al substitution were considered. It turned out to be most plausible that (i) the weak signal C derives from a minor impurity phase that is not detected by XRD (incidentally, its NMR parameters are almost identical to those of AlN) and (ii) the remaining two sites may be accounted for by noting that if oxygen substitutes for nitrogen at the 4*c* position, four $AlN_4$ units are converted into four $AlN_3O$ units for every N→O replacement. After renormalising the integrals of A and B, this implies that the structure contains 62% $AlN_3O$ and 38% $AlN_4$ units, which translates roughly into 62% oxygen substitution at the 4*c* positions and the net formula $La_{17}Si_9Al_4N_{32.4}O_{0.6}$.

### *$^{29}$Si NMR*

The corresponding $^{29}$Si MAS spectrum is shown in Figure 6. It has a poor signal-to-noise ratio due to the very slow $^{29}$Si T1 relaxation coupled to relatively broad NMR signals, and displays two main groups of peaks, one extending between $\delta$ = –51 and –56 ppm and another centred at $\delta$ = –70 ppm. Both signals are attributed to $SiN_4$ tetrahedra. However, whereas the chemical shift of the former peak is representative for such units, a shift of around $\delta$ = –70 ppm is more typical of $SiN_2O_2$ groups.[27–29] Therefore, $^{29}$Si NMR spectroscopy alone cannot exclude additional oxygen substitution leading to "mixed" $SiN_nO_{4-n}$ environments. Nevertheless, we note that a relatively broad span of $^{29}$Si NMR chemical shifts has already been found from a still fairly small collection of nitridosilicates, ranging from $\delta$ = –36 ppm in $Y_3Si_6N_{11}$ to $\delta$ = –65 ppm in $LaSi_3N_5$.[27–29] Thus the very strong shielding of the $^{29}$Si nuclei of the $SiN_4$ tetrahedra may originate from a unique combination of structural factors (bond lengths and angles) in the present compound. From the single-crystal XRD analysis, we expect three distinct $^{29}$Si signals with relative intensities 1:4:4. It is possible to reconcile the spectrum of Figure 6 with the proposed structure of $La_{17}Si_9Al_4N_{33}$ by noting that if the $^{29}$Si signals from the two Si 16*e* sites overlap, a spectrum with two peaks of relative intensity 1:8 would result. This is not unlikely when considering that overlap between signals from *distinct* $SiN_nO_{4-n}$ environments has previously been reported in the $^{29}$Si NMR spectra of oxynitridosilicates.[27,28,30] In fact, the width (FWHM ≈ 10 ppm) of the peak centred at $\delta$ = 70 ppm (Figure 6) is exceptional for a crystalline nitridosilicate. As neither of the two peaks from $La_{17}Si_9Al_4N_{33}$ fitted well to a single Lorentzian, Gaussian or mixed lineshape, this indeed suggests that they either arise from several partially overlapping signals or that the peaks are broadened by residual MAS non-averaged dipolar couplings between $^{29}$Si and the quadrupolar spins in its surroundings ($^{14}$N, $^{27}$Al and $^{139}$La).[27,31] The ratio between the integrated peaks in Figure 6 was estimated to be 1:(8.5 ± 2). The deviation from the ratio 1:8 may be due to different degrees of saturation of the three $^{29}$Si sites caused by differing $T_1$ relaxation times or possibly from interfering signals of minor impurity phases.

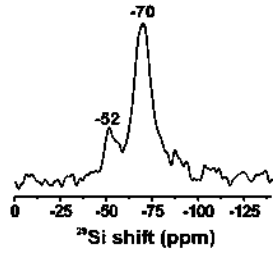


Figure 6. $^{29}$Si MAS spectrum recorded at 9.4 T employing MAS at 6.5 kHz. It is the result of 68 co-added signal transients using 30° excitation pulses and 50 min relaxation delays. 150 Hz FWHM Lorentzian broadening was applied in the data processing.

## Discussion

EDS microanalysis was performed on both the obtained crystals and the powder bulk samples and yielded 57(2)% La, 30(1)% Si, 13.3(9)% Al and 56(3)% La, 30(2)% Si, 13(1)% Al, which correspond to the formulae $La_{17.0(6)}Si_{9.0(4)}Al_{4.0(3)}$ and $La_{16.8(7)}Si_{9.1(5)}Al_{3.9(3)}$, respectively. The analytical results are thus in very good agreement with the structural cation composition $La_{17}Si_9Al_4$, obtained by placing Al atoms on the 16*e* sites with $x$ = 0.1800(3) and Si atoms on the remaining tetrahedral sites. Therefore, if all cation and anion positions are fully occupied, one can conclude by charge balancing that all anions are $N^{3-}$ and that the compound formula is $La_{17}Si_9Al_4N_{33}$.

Considering the diffraction data alone, it cannot be ruled out, however, that the phase contains smaller amounts of oxygen. First, the starting materials $Si_3N_4$ and AlN contain some oxygen, corresponding to an estimated O/N ratio in the final, fully nitrided mixture of about 0.5:33, which may partly explain why pure bulk samples were not obtained using stoichiometric metal compositions. Secondly, oxygen might also have been taken up by the sample during the

 © 2006 Wiley-VCH Verlag GmbH & Co. KGaA, Weinheim 

heat treatment, as we have observed for other syntheses, even though it was performed in a graphite furnace under a $N_2$ gas flow. Furthermore, as described above, the amounts of the formed secondary phases could be significantly reduced by further carbothermal reduction and nitridation of the samples.

$^{27}$Al NMR spectroscopy has provided direct evidence of O substitution at the N5 4*c* position by showing the presence of both $AlN_3O$ and $AlN_4$ tetrahedral units, whereas the $^{29}$Si NMR spectroscopic data could not rule out additional oxygen substitution. The smaller total anion charge resulting from O substitution is probably compensated by vacancies on some of the La sites, leading to a formula $La_{17-x/3}Si_9Al_4N_{33-x}O_x$ ($x \leq 1$). However, no reliable conclusions concerning La vacancies could be drawn from structure refinements. We see no way of incorporating more substantial amounts of oxygen without larger changes in the cation composition, which would contradict the results of the EDS analysis, the single crystal diffraction data, and the observed near constancy of the unit-cell parameter for bulk samples. We therefore conclude that the compound has a formula very close to $La_{17}Si_9Al_4N_{33}$ but that it contains variable minor amounts of oxygen, with probable end-limit compositions being $La_{17}Si_9Al_4N_{33}$ and $La_{16.67}Si_9Al_4N_{32}O$.

The unit-cell parameters and atomic coordinates of $La_{17}Si_9Al_4N_{33}$ suggest that its structure could be a $4\times4\times4$ superstructure of the perovskite type, similar to $Ce_{16}Si_{15}O_6N_{32}$ for example,[6,9] which is notable as its structure contains silicon octahedrally coordinated by nitrogen. Following Liebau,[6] the latter formula may accordingly be rewritten as $Ce_{16}(Si^{[6]}Si_{14}^{[4]}\square)(O_6N_{32}\square_{10})$. The relationship to the cubic perovskite $ABX_3$ structure rests on the fact that the atoms corresponding to A and B do not deviate significantly from the highly symmetrical positions in the ideal perovskite structure, even when the coordination number for B atoms is reduced from six to four. The anion X positions may, however, deviate extensively from their ideal positions and are expected to contain vacancies due to the decreased coordination number of the B atoms.

For $La_{17}Si_9Al_4N_{33}$ the relationship with perovskite is not so close. While many of the La atoms are found in positions corresponding to perovskite A atoms, this set of positions is in addition occupied by Si1 atoms (at the centres of the $Si_5N_{16}$ zunyite-type clusters), N1 atoms (at the centres of the $Al_4Si_4N_{17}$ clusters), and also contains vacancies [at the 4b sites (1/2,1/2,1/2)]. Further, the Al atom positions are significantly displaced from the positions corresponding to perovskite B atoms and the $Al_4Si_4N_{17}$ clusters cannot readily be described as part of a perovskite structure. It should also be noted that the $Al_4Si_4N_{17}$ clusters cannot be described as being a part of an anion close packing.

According to the formula $La_{17}Si_9Al_4N_{33}$, the compound is one of the rare examples of a pure nitridoaluminosilicate. More noteworthy, however, is that $La_{17}Si_9Al_4N_{33}$ is a nitrido(alumino)silicate with a structure where all the tetrahedral atoms are part of isolated complex anions or clusters that contain only, or predominantly, N atoms. Nitridosilicate crystal chemistry differs from that of oxosilicates mainly due to the common occurrence of $N^{(3)}$, and to a much less extent of $N^{(4)}$, atoms.[9] For oxonitridosilicates and sialons, the crystal chemistry is more similar to that of oxosilicates, especially for low N/O ratios. As the T/X ratio increases [T = (Si/Al) and X = (N/O)] the structures exhibit a condensation of the tetrahedra in the sequence of isolated $TX_4$ tetrahedra → isolated $T_2X_7$ groups → rings or chains of tetrahedra → layers of tetrahedra → frameworks of tetrahedra.[11] Structures containing more complex isolated clusters built up from $TX_4$ tetrahedra are virtually non-existent for all of these types of silicates. The compound $La_{17}Si_9Al_4N_{33}$ has a T/X ratio of 1:2.54, from which one might anticipate a structure containing rings, chains or sheets of tetrahedra. Instead, the structure contains isolated tetrahedral clusters and 48.5% $N^{(1)}$, 48.5% $N^{(2)}$ and 3.0% $N^{(4)}$ atoms. Despite its high nitrogen and silicon content, there are no $N^{(3)}$ atoms, which are the common structural characteristic for nitridosilicates.

## Experimental Section

Powder samples of $La_{17}Si_9Al_4N_{33}$ were prepared at 1500–1650 °C in a graphite furnace under nitrogen, from La metal (Chempure, 99.9%), $Si_3N_4$ (UBE, SN-E10) and AlN (H. C. Starck, Berlin, grade A) as starting materials. During the synthesis the La metal reacts with $N_2$ to form reactive LaNd. The powders were mixed, in amounts of ca. 1 g, and ground in a dry-box under argon to prevent oxidation of the La metal, and then placed in Nb tubes that were sealed with parafilm during the transfer to the furnace. In a typical run, the sample was heated to the synthesis temperature over 2 h, kept there for 12 h, then cooled to 1200 °C over 4 h, whereupon the furnace was switched off. Yellow to orange single crystals were found in preparations at 1650 °C.

The heat-treated powder samples were characterised by their X-ray powder patterns, which were recorded with a Guinier–Hägg camera, using Cu-$K_{\alpha1}$ radiation and Si as internal standard. The data were evaluated using a film scanner system[32] and, for the majority of patterns, the Rietveld program FullProf.[33] Energy-dispersive X-ray (EDX) microanalyses of the metal composition were made using a JEOL 820 scanning electron microscope equipped with a LINK AN10000 EDX system. Electron diffraction (ED) studies were carried out with a JEOL 200FX transmission electron microscope (TEM), operating at 200 kV, in order to confirm the crystal system and space group. Single-crystal X-ray diffraction (XRD) data for $La_{17}Si_9Al_4N_{33}$ were collected with a STOE image-plate detector system (IPDS), using a Siemens rotating anode and Mo-$K_\alpha$ radiation, up to $2\theta = 52°$ and *d*-values ≥ 0.81 Å (Table 4). The STOE IPDS software package[34] was used for indexing and integration.

Further details of the crystal-structure investigations may be obtained from the Fachinformationzentrum, 76344 Eggenstein-Leopoldshafen, Germany, on quoting the depository number CSD-416358.

Magic-angle spinning (MAS) NMR experiments were carried out on a finely ground powder of $La_{17}Si_9Al_4N_{33}$ using a Varian/Chemagnetics Infinity-400 spectrometer at a magnetic field of 9.4 T, with the Larmor frequencies 79.50 and –104.28 MHz for $^{29}$Si and $^{27}$Al, respectively. 6-mm and 4-mm probeheads were employed for $^{29}$Si and $^{27}$Al acquisitions, respectively. Chemical shifts are reported in

 © 2006 Wiley-VCH Verlag GmbH & Co. KGaA, Weinheim 

Table 4. Refinement data for $La_{17}Si_9Al_4N_{33}$.

| | |
|---|---|
| Crystal form | cube |
| Crystal size [mm] | 0.02 × 0.02 × 0.02 |
| Radiation [Å] | Mo-$K_\alpha$ (0.71073 Å) |
| $\mu$ ($mm^{-1}$) | 19.80 |
| Absorption correction | numerical from shape |
| Range of $h$, $k$, $l$ | $-10 \rightarrow h \rightarrow 10$<br>$0 \rightarrow k \rightarrow 13$<br>$1 \rightarrow l \rightarrow 18$ |
| No. of measured reflections | 6463 |
| No. of independent reflections | 410 |
| No. of observed reflections | 294 |
| Criterion for observed reflections | $I > 3\sigma(I)$ |
| $R_{int}$ | 0.063 |
| $2\theta$ max. [°] | 52.0 |
| Refinement on | $F$ |
| No. of reflections used in the refinement | 294 |
| No. of parameters used | 34 |
| $R$ [$I > 3\sigma(I)$] | 0.019 |
| $wR$ [$I > 3\sigma(I)$] | 0.019 |
| $R$ (all) | 0.031 |
| $wR$ (all) | 0.023 |
| $S$ | 1.15 |
| $\Delta\rho_{max}$, $\Delta\rho_{min}$ ($e^- Å^{-3}$) | +1.5, –1.0 |

deshielding ($\delta$) units of ppm, referenced with respect to TMS ($^{29}Si$) and $Al^{3+}$(aq) ($^{27}Al$). Additional experimental parameters are given in the figure captions.

## Acknowledgments

We thank Z. Weng for instrumental NMR support, A. Sohier and L. Del Villano for their help during the syntheses and NMR characterisations, respectively, Dr. J. Garcia-Garcia for the EDS analyses, and Prof. W. Schnick for valuable discussions. S.E. holds a research fellowship from the Royal Academy of Sciences financed by the Knut and Alice Wallenberg Foundation. This work was supported by the Swedish Research Council (VR) and by the Carl Tryggers Foundation.

[1] T. Ekström, M. Nygren, *J. Am. Ceram. Soc.* **1992**, *75*, 259.
[2] W. Schnick, H. Huppertz, *Chem. Eur. J.* **1997**, *3*, 679.
[3] W. Schnick, H. Huppertz, R. Lauterbach, *J. Mater. Chem.* **1999**, *9*, 289.
[4] H. Huppertz, W. Schnick, *Chem. Eur. J.* **1997**, *3*, 249.
[5] H. Yamane, F. J. DiSalvo, *J. Alloys Compd.* **1996**, *240*, 33.
[6] K. Köllisch, W. Schnick, *Angew. Chem. Int. Ed.* **1999**, *38*, 357.
[7] F. Liebau, *Structural Chemistry of Silicates*, Springer-Verlag, Berlin, **1985**.
[8] H. Huppertz, W. Schnick, *Angew. Chem. Int. Ed.* **1996**, *35*, 1983.
[9] F. Liebau, *Angew. Chem. Int. Ed.* **1999**, *38*, 1733.
[10] K. Köllisch, PhD Thesis, University of Bayreuth, Germany, **2001**.
[11] D. P. Thompson, *Mater. Sci. Forum* **1989**, *47*, 21.
[12] F. Ottinger, PhD Thesis, Eidgenössische Techische Hochschule, Zürich, Diss. ETH Nr. 15624, **2004**.
[13] J. Grins, S. Esmaeilzadeh, Z. Shen, *J. Am. Ceram. Soc.* **2003**, *86*, 727.
[14] J. P. Morniroli, J. W. Steeds, *Ultramicroscopy* **1992**, *45*, 219.
[15] A. Altomare, M. C. Burla, M. Camalli, G. L. Cascarano, C. Giacovazzo, A. Guagliardi, A. G. G. Moliterni, G. Polidori, R. Spagna, *J. Appl. Crystallogr.* **1999**, *32*, 115.
[16] D. J. Watkin, C. K. Prout, J. R. Carruthers, P. W. Betteridge, *CRYSTALS Issue 11*, Chemical Crystallography Laboratory, Oxford, UK, **1999**.
[17] J. Lima-De-Faria, E. Hellner, F. Liebau, E. Makovicky, E. Parthé, *Acta Crystallogr. Sect. A* **1990**, *46*, 1.
[18] W. B. Kamb, *Acta Crystallogr.* **1960**, *13*, 15.
[19] J. Fernández-Urban, S. Esmaeilzadeh, manuscript to be published.
[20] M. Woike, W. Jeitschko, *J. Solid State Chem.* **1997**, *129*, 312.
[21] K. Köllisch, H. A. Höppe, H. Huppertz, M. Orth, W. Schnick, *Z. Anorg. Allg. Chem.* **2001**, *627*, 1371.
[22] A. Medek, J. S. Harwood, L. Frydman, *J. Am. Chem. Soc.* **1995**, *117*, 1279.
[23] D. Massiot, B. Touzo, D. Trumeau, J. P. Coutures, J. Virlet, P. Florian, P. J. Grandinetti, *Solid State NMR* **1996**, *6*, 73.
[24] M. E. Smith, *J. Phys. Chem.* **1992**, *96*, 1444.
[25] R. Dupree, M. H. Lewis, M. E. Smith, *J. Appl. Crystallogr.* **1988**, *21*, 109.
[26] E. Lippmaa, A. Samoson, M. Mägi, *J. Am. Chem. Soc.* **1986**, *108*, 1730.
[27] R. Dupree, M. H. Lewis, M. E. Smith, *J. Am. Chem. Soc.* **1989**, *111*, 5125.
[28] R. K. Harris, M. J. Leach, D. P. Thompson, *Chem. Mater.* **1989**, *1*, 336.
[29] T. C. Ekström, K. J. D. MacKenzie, M. J. Ryan, I. W. M. Brown, G. V. White, *J. Mater. Chem.* **1997**, *7*, 505.
[30] A. Koroglu, D. P. Thompson, D. C. Apperley, R. K. Harris, *J. Solid State Chem.* **2004**, *177*, 2530.
[31] R. K. Harris, A. A. Olivieri, *Prog. Nucl. Magn. Reson. Spectrosc.* **1992**, *24*, 435.
[32] K. E. Johansso, T. Palm, P.-E. Werner, *J. Phys. E* **1980**, *13*, 1289.
[33] J. Rodriguez-Carjaval, *FullProf98* and *WinPLOTR*: New Windows 95/NT Applications for Diffraction Commission for Powder Diffraction, International Union for Crystallography, Newsletter no. 20 (May–August), summer **1998**.
[34] *STOE IPDS software manual*, version 2.87, December **1997**.

Received: March 28, 2006
Published Online: August 3, 2006

 © 2006 Wiley-VCH Verlag GmbH & Co. KGaA, Weinheim 

DOI: 10.1002/ejic.200600275

# The Template Effect of Palladium(II): Synthesis, Characterization, and Crystal Structures of 2,4-Substituted 1,3,5-Triazapentadienatopalladium(II) Complexes

Jian-Ping Guo,[a] Wai-Kwok Wong,*[a] and Wai-Yeung Wong[a]

**Keywords:** Amidinate ligands / Hydrogen bonds / Palladium / N ligands

The reaction of $LiN(SiMe_3)_2$ with two equivalents of 2-, 3-, or 4-cyanopyridine followed by the addition of half an equivalent of $[PdCl_2(PhCN)_2]$ gives neutral 1,3,5-triazapentadienato complexes of the general formula $[Pd\{HNC(Py)NC(Py)NH\}_2]$ (Py = 2-pyridyl **1**, 3-pyridyl **2**, 4-pyridyl **3**). When the above reaction was carried out with benzonitrile and then 3- or 4-cyanopyridine was added followed by half an equivalent of $[PdCl_2(PhCN)_2]$ neutral unsymmetrical 1,3,5-triazapentadienato complexes of the general formula $[Pd\{HNC(Ph)NC(Py)NH\}_2]$ (Py = 3-pyridyl **4**, 4-pyridyl **5**) were obtained. When $LiN(SiMe_3)_2$ was treated with one equivalent of benzonitrile in THF, followed by the addition of a quarter of an equivalent of anhydrous palladium chloride and workup in air, the trinuclear complex tetrakis(benzamidinato)bis(2,4-diphenyl-1,3,5-triazapentadienato)tripalladium(II) (**6**) was obtained as yellow crystals in 19% yield. All complexes were fully characterized by elemental analysis, $^1H$ NMR spectroscopy, and mass spectrometry. The solid-state structures of compounds **2**, **3**, and **6** were determined by X-ray crystallography. Structural analyses revealed that the 2,4-bis(pyridyl)-1,3,5-triazapentadienyl ligands in **2** and **3** behave as didentate ligands to form six-membered rings with the metal ion. For **6**, the 2,4-diphenyl-1,3,5-triazapentadienyl ligands also behave as didentate ligands to form six-membered rings with the metal ion, whereas the amidinato ligands behave as bridging didentate ligands.
(© Wiley-VCH Verlag GmbH & Co. KGaA, 69451 Weinheim, Germany, 2006)

## Introduction

Didentate, monoanionic, nitrogen-based L–X$^-$ ligands and their complexes are one of the subjects of intense study in the field of amidinates.[1] Among this class of compounds, the coordination chemistry and potential application in catalysis of β-diketiminato ligands and their metal complexes have received significantly increasing attention recently. A series of β-diketiminate complexes have been synthesized by the nucleophilic addition reaction of α-hydrogen-free nitriles to substituted methyllithiums, and the catalytic properties of some of these complexes have been investigated.[2,3] Similar diimine ligands, namely *N*-phosphanyl-β-diimine ligands,[4] sterically demanding aromatic diimine ligands,[5] and their complexes have also been developed. Many metal β-diiminate complexes, such as magnesium,[6] aluminum,[7] nickel and palladium,[8] zirconium,[9] rhodium,[10] gallium,[11] and scandium[12] etc. have been reported. Moreover, these diimine and similar complexes have been found to be effective catalysts for the polymerization of ethylene.[8,13]

However, there are very few reports on the isoelectronic 1,3,5-triazapentadienato ligands and their complexes. Transition metal complexes with chelating 1,3,5-triazapentadienato ligands have been isolated by (i) evaporating a methanol solution of nickel chloride hexahydrate and acetamidine,[14] (ii) treating lithium benzamidinate with $[PtCl_2(PhCN)_2]$,[15] (iii) treating acetonitrile with the dinuclear nickel complex $[Ni_2(\mu\text{-}OH)_2(tpa)_2](ClO_4)_2$ [tpa = tris(2-pyridylmethyl)-amine],[16] (iv) treating triazine with copper acetate,[17] and (v) a coupling reaction between amidine and ligated nitriles.[18] Bis(perfluoroalkyl)triazapentadiene and its transition metal complexes have also been synthesized.[19,20]

We have synthesized the complex bis[2,4-bis(*n*-pyridyl)-1,3,5-triazapentadienato]nickel(II) (*n* = 3 or 4) in about 30% yield by the reaction of anhydrous nickel(II) chloride with the addition product of cyanopyridine with $LiN(SiMe_3)_2$.[21] We have since extended our study to $[PdCl_2(PhCN)_2]$ and the results are described here. Depending on the nature of the aryl group, $[PdCl_2(PhCN)_2]$ reacts with the addition product of lithium *N*,*N*′-bis(trimethylsilyl)arylamidinate, $[(Me_3Si)N(Li)C(Ar)N(SiMe_3)]$ (Ar = phenyl, 2-pyridyl, 3-pyridyl, 4-pyridyl) and an aryl nitrile to give the neutral mononuclear triazapentadienyl complexes bis(2-Ar-4-Ar′-1,3,5-triazapentadienato)palladium(II) (Ar = Ar′ = 2-pyridyl **1**; Ar = Ar′ = 3-pyridyl **2**; Ar = Ar′ = 4-pyridyl **3**; Ar = Ph, Ar′ = 3-pyridyl **4**; Ar = Ph, Ar′ = 4-pyridyl **5**) and trinuclear triazapentadienyl complex tetrakis(benzamidinato)bis(2,4-diphenyl-1,3,5-triazapentadienato)tripalladium(II) (**6**; Scheme 1). This is in contrast to the reaction of $[MCl_2(PhCN)_2]$ (M = Pd or Pt) with lithium *N*,*N*′-diphenylbenzamidinate [PhN(Li)C(Ph)NPh],

[a] Department of Chemistry, Hong Kong Baptist University, Waterloo Road, Kowloon Tong, Hong Kong, P. R. China
Fax: +852-3411-5862
E-mail: wkwong@hkbu.edu.hk

 © 2006 Wiley-VCH Verlag GmbH & Co. KGaA, Weinheim 

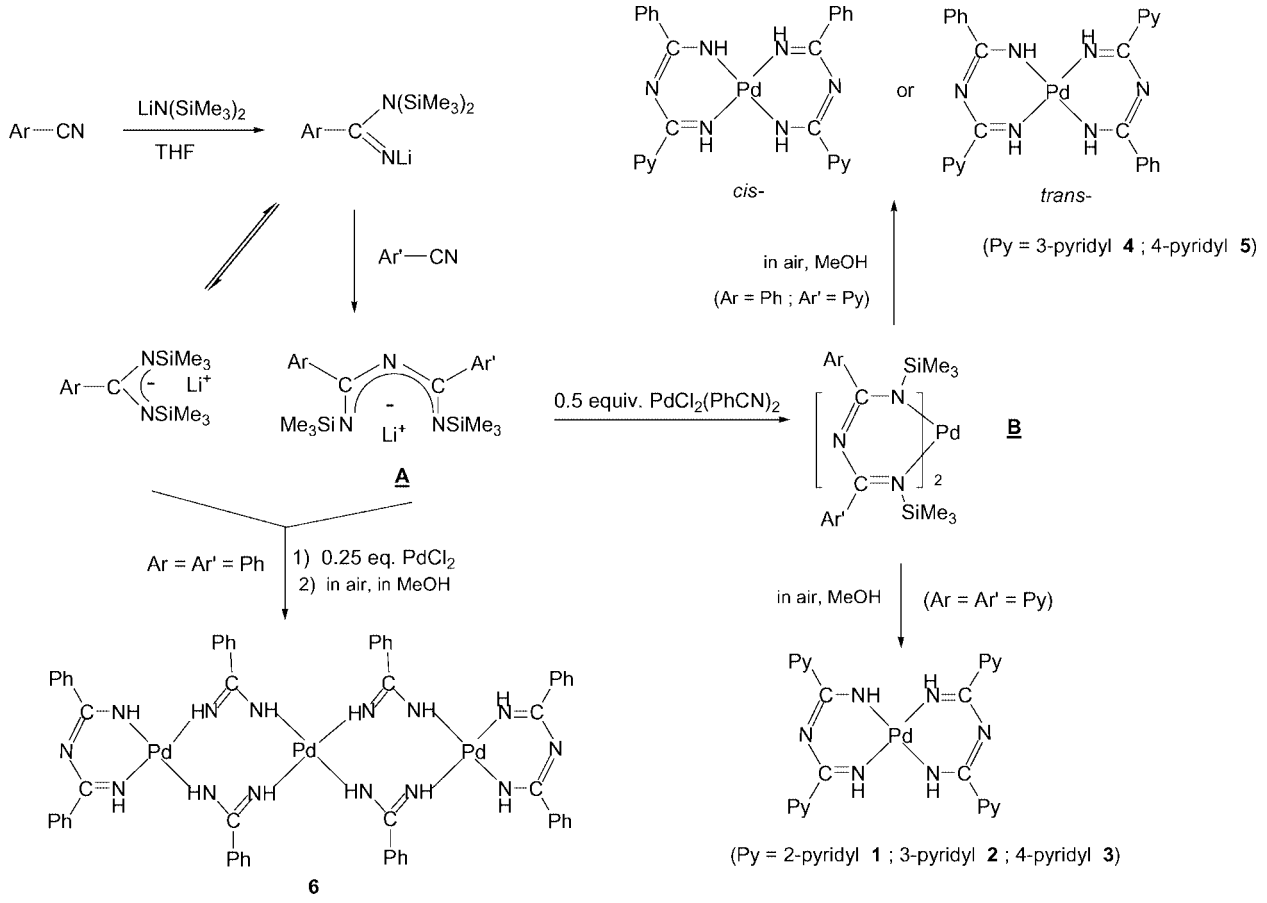


Scheme 1.

which gives the bis(amidinato) complexes [M{PhNC(Ph)NPh}$_2$].[22] The fact that the palladium complexes are isolated with higher yields than the related nickel complexes and the formation of compound **6** suggest that palladium plays a more evident template role in the synthesis of 1,3,5-triazapentadienato metal complexes. In other words, palladium may be specially suited to stabilizing the six-membered ring formed by palladium and the 1,3,5-triazapentadienato ligand.

## Result and Discussion

### Synthesis and Structural Characterization

Yellow crystals of the neutral, symmetrical 2,4-disubstituted 1,3,5-triazapentadienato complexes [Pd{HNC(Py)NC(Py)NH}$_2$] (Py = 2-pyridyl **1**; 3-pyridyl **2**; 4-pyridyl **3**), were obtained in good yields (71, 70, and 71%, respectively) when LiN(SiMe$_3$)$_2$ was treated with two equivalents of 2-, 3-, or 4-cyanopyridine in THF, followed by the addition of half an equivalent of [PdCl$_2$(PhCN)$_2$] and workup in air. Elemental analyses and electrospray ionization high resolution mass spectroscopic (ESI-HRMS) data confirmed the formulation of the compounds. The ESI mass spectra (positive mode) of **1**–**3** exhibit the $[M+1]^+$ peak at *m*/*z* 555.0947, 555.0944, and 555.1032, respectively, which deviate less than 10 ppm from the theoretical value of 555.0985 for the elemental composition $C_{24}H_{21}N_{10}Pd$. The observed isotopic distribution patterns of these peaks also match the expected theoretical signals.

Compounds **1**–**3** should have a similar structure. The solid-state structures of **2** and **3** were ascertained by X-ray crystallography. Perspective drawings of **2** and **3** are shown in Figures 1 and 2, respectively; selected bond lengths and angles are given in Table 1.

The structural analyses of **2** and **3** revealed that their structures are similar to the corresponding nickel(II) complexes [Ni{HNC(Py)NC(Py)NH}$_2$][21] and the analogous Pt complex [Pt{HNC(Ph)NC(Ph)NH}$_2$].[15] Both **2** and **3** are centrosymmetric with the palladium(II) ion adopting a square-planar geometry. The palladium(II) ion in **2** is located at the center of the plane defined by the four nitrogen atoms of the two didentate 1,3,5-triazapentadieno ligands [HNC(3-Py)NC(3-Py)NH]$^-$, with Pd–N distances of 1.980(3) [Pd(1)–N(1)] and 1.974(3) Å [Pd(1)–N(2)], and an N(1)–Pd(1)–N(2) angle of 87.12(12)°. Each didentate 1,3,5-triazapentadienato ligand forms a six-membered metallacycle with the metal ion. This six-membered ring is nearly planar with a mean deviation of 0.0278 Å from the plane. Within the 1,3,5-triazapentadieno ligand, the N(1)–C(1) [1.299(5) Å], C(1)–N(3) [1.353(5) Å], N(3)–C(7) [1.344(4) Å], and C(7)–N(2) [1.307(4) Å] distances are very

 © 2006 Wiley-VCH Verlag GmbH & Co. KGaA, Weinheim 

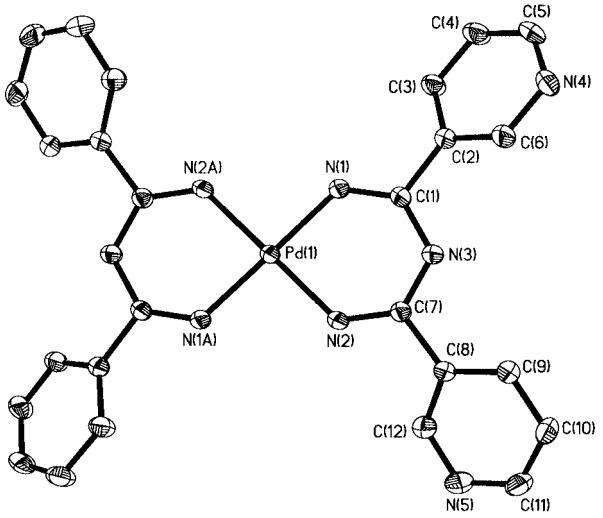


Figure 1. ORTEP drawing (30% probability level) of the molecular structure of **2**. Hydrogen atoms have been omitted for clarity.

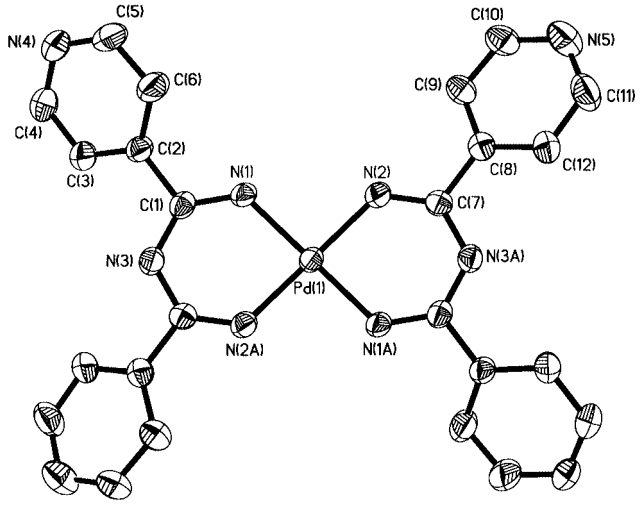


Figure 2. ORTEP drawing (30% probability level) of the molecular structure of **3**. Hydrogen atoms have been omitted for clarity.

similar, thereby indicating complete delocalization within the N–C–N–C–N framework. The plane of the six-membered ring forms dihedral angles of 37.8° and 30.7° with the N(4)- and N(5)-pyridyl planes, respectively, thus indicating that the N(4)-pyridyl and N(5)-pyridyl rings are not coplanar with the metal-containing six-membered ring.

Figure 2 shows the palladium(II) ion of **3** positioned at the center of the N(1)N(2)N(1A)N(2A) plane, with Pd–N distances of 1.980(4) [Pd(1)–N(1)] and 1.971(4) Å [Pd(1)–N(2)], and an N(1)–Pd(1)–N(2) angle of 92.38(16)°. Each didentate 1,3,5-triazapentadienato ligand forms a six-membered metallacycle with the metal ion. This six-membered ring is almost planar, with a mean deviation of 0.0086 Å from the plane. Within the 1,3,5-triazapentadienato ligand, the similarity between the N(1)–C(1) [1.316(6) Å], C(1)–N(3) [1.339(6) Å], N(3)–C(7A) [1.339(6) Å], and C(7A)–N(2A) [1.304(3) Å] distances shows complete delocalization within the N–C–N–C–N framework. The planes of the N(4)-pyridyl and N(5A)-pyridyl rings are not coplanar with the metal six-membered ring; they form a dihedral angle of 27.1° and 26.8° with the plane of the six-membered metallacycle, respectively.

When $LiN(SiMe_3)_2$ was treated with one equivalent of benzonitrile, then one equivalent of 3- or 4-cyanopyridine in THF, followed by the addition of half an equivalent of $[PdCl_2(PhCN)_2]$ and workup in air, the unsymmetrical complexes $[Pd\{HNC(Ph)NC(Py)NH\}_2]$ (Py = 3-pyridyl **4**; 4-pyridyl **5**) were obtained as yellow crystals in 31 and 27% yields, respectively. The formulation of the compounds was confirmed by elemental analyses and ESI-HRMS data. The ESI mass spectra (positive mode) of both compounds in methanol exhibit the corresponding $[M+1]^+$ peak at *m*/*z* 553.1106 for **4** and 553.1049 for **5**, both of which deviate by less than 10 ppm from the theoretical value of 553.1080 for the elemental composition $C_{26}H_{23}N_8Pd$. The observed isotopic distribution patterns of the $[M+1]^+$ peak also match the expected theoretical signals. It is clear that the lithium benzamidinate undergoes a nucleophilic addition reaction with 3-cyanopyridine or 4-cyanopyridine

Table 1. Selected bond lengths [Å] and bond angles [°] for compounds **2**, **3**, and **6**.

| **2** | | **3** | | **6** | | | |
|---|---|---|---|---|---|---|---|
| Pd(1)–N(1) | 1.980(3) | Pd(1)–N(1) | 1.980(4) | Pd(1)–N(4) | 1.986(10) | N(4)–Pd(1)–N(6) | 88.5(4) |
| Pd(1)–N(2) | 1.974(3) | Pd(1)–N(2) | 1.971(4) | Pd(1)–N(6) | 2.067(9) | N(1)–Pd(2)–N(2) | 88.3(4) |
| N(1)–C(1) | 1.299(5) | N(1)–C(1) | 1.316(6) | Pd(2)–N(1) | 1.998(9) | N(5)–Pd(2)–N(7) | 86.8(4) |
| C(1)–N(3) | 1.353(5) | C(1)–N(3) | 1.339(6) | Pd(2)–N(2) | 1.931(8) | Pd(1)–N(4)–C(15) | 131.9(9) |
| N(3)–C(7) | 1.344(4) | N(3)–C(7A) | 1.339(6) | Pd(2)–N(5) | 2.022(9) | N(4)–C(15)–N(5) | 120.0(12) |
| C(7)–N(2) | 1.307(4) | C(7)–N(2) | 1.304(6) | Pd(2)–N(7) | 2.044(8) | C(15)–N(5)–Pd(2) | 125.9(9) |
| C(1)–C(2) | 1.497(5) | C(1)–C(2) | 1.487(6) | N(1)–C(1) | 1.360(13) | Pd(1)–N(6)–C(22) | 130.2(9) |
| C(7)–C(8) | 1.498(5) | C(7)–C(8) | 1.489(6) | C(1)–N(3) | 1.238(15) | N(6)–C(22)–N(7) | 125.9(11) |
| N(1)–Pd(1)–N(2) | 87.12(12) | N(1)–Pd(1)–N(2) | 92.38(16) | N(3)–C(8) | 1.306(15) | C(22)–N(7)–Pd(2) | 121.2(9) |
| Pd(1)–N(1)–C(1) | 127.9(3) | Pd(1)–N(1)–C(1) | 126.7(3) | C(8)–N(2) | 1.391(12) | Pd(2)–N(1)–C(1) | 124.4(9) |
| Pd(1)–N(2)–C(7) | 128.3(3) | Pd(1)–N(2)–C(7) | 128.4(4) | C(1)–C(2) | 1.445(17) | N(1)–C(1)–N(3) | 128.0(12) |
| N(1)–C(1)–N(3) | 127.4(3) | N(1)–C(1)–N(3) | 128.2(4) | C(8)–C(9) | 1.500(17) | C(1)–N(3)–C(8) | 127.9(11) |
| C(1)–N(3)–C(7) | 121.7(3) | C(1)–N(3)–C(7A) | 122.0(4) | N(4)–C(15) | 1.332(15) | N(3)–C(8)–N(2) | 122.9(12) |
| N(3)–C(7)–N(2) | 127.0(3) | N(3A)–C(7)–N(2) | 127.0(5) | C(15)–N(5) | 1.305(15) | C(8)–N(2)–Pd(2) | 128.2(9) |
| N(1)–C(1)–C(2) | 119.8(3) | N(1)–C(1)–C(2) | 117.8(4) | N(6)–C(22) | 1.239(14) | | |
| N(2)–C(7)–C(8) | 118.8(3) | N(2)–C(7)–C(8) | 119.6(4) | C(22)–N(7) | 1.336(15) | | |
| | | | | C(15)–C(16) | 1.504(15) | | |
| | | | | C(22)–C(23) | 1.448(14) | | |

 © 2006 Wiley-VCH Verlag GmbH & Co. KGaA, Weinheim 

and $[PdCl_2(PhCN)_2]$ to form the respective palladium(II) complex. Attempts to grow crystals of **4** and **5** suitable for an X-ray diffraction study were unsuccessful. However, the structures of **4** and **5** are expected to be similar to those of **2** and **3**. Compounds **4** and **5** could adopt either a *cis* or a *trans* configuration (Scheme 1). Unfortunately, the existing spectroscopic data cannot distinguish between these two configurations.

When $LiN(SiMe_3)_2$ was treated with an excess amount of benzonitrile followed by addition of a quarter of an equivalent of $PdCl_2$, the neutral trinuclear palladium complex $[Pd_3\{[HNC(Ph)NC(Ph)NH]_2[\mu_2\text{-}HNC(Ph)NH]_4\}]$ (**6**) was isolated in low yield (19%). This contrasts with the reaction with anhydrous $NiCl_2$, which gave the ionic salt $[Ni\{H_2NC(Ph)NH\}_4]Cl_2$.[21] The solid-state structure of **6** was ascertained by X-ray crystallography; a perspective drawing is shown in Figure 3. Selected bond lengths and angles are also given in Table 1. This structural analysis revealed that **6** is centrosymmetric, with Pd(1) at the inversion center. There are two kinds of coordinated anions − benzamidinato and 2,4-diphenyl-1,3,5-triazapentadienato − and three palladium atoms in the molecule of **6**. All three palladium(II) ions adopt a square-planar geometry. The distance between two neighboring palladium atoms is 2.933 Å, which is too long for any significant interaction between the two metal centers. The N(2)–Pd(2)–N(1) and N(5)–Pd(2)–N(7) angles are 88.3(4)° and 86.8(4)°, respectively, and the N(4)–Pd(1)–N(6) angle is 88.5(4)°. The lengths of the bonds between palladium and the coordinated nitrogen atoms of the 2,4-bis(phenyl)-1,3,5-triazapentadienato ligand are 1.998(9) [Pd(2)–N(1)] and 1.931(8) Å [Pd(2)–N(2)], respectively. The Pd–N bond lengths between the palladium atoms and the coordinated nitrogen atoms of benzamidinato are 2.022(9) [Pd(2)–N(5)], 2.044(8) [Pd(2)–N(7)], 1.986(10) [Pd(1)–N(4)], and 2.067(9) Å [Pd(1)–N(6)], which are similar to the Pd–N distance [2.038(3) Å] in $[Pd\{PhNC(Ph)NPh\}_2]$.[22] The didentate 1,3,5-triazapentadienato ligand forms a six-membered metallacycle with the metal ion. This six-membered ring is nearly planar, with a mean deviation of 0.0224 Å from the plane. Within the 1,3,5-triazapentadieno ligand, the N(1)–C(1) [1.360(13)], C(1)–N(3) [1.238(15)], N(3)–C(8) [1.306(15)], and C(8)–N(2) [1.391(12) Å] distances are similar, thus indicating delocalization within the N–C–N–C–N framework. The plane of the six-membered ring forms dihedral angles of 35.1° and 2.5° with the C(2)–C(7) and C(9)–C(14) phenyl planes, respectively, presumably due to solid-state packing effects. This indicates that the C(9)–C(14) phenyl plane is coplanar with the metal six-membered ring.

There are two benzamidinato anions in half a molecule of **6**. Each of them forms a five-membered ring with two palladium ions. The five-membered rings Pd(1)N(4)C(15)N(5)Pd(2) and Pd(1)N(6)C(22)N(7)Pd(2) are nearly planar with a mean deviation of 0.0615 and 0.0399 Å from the plane, respectively. The N(4)–C(15) [1.332(15) Å] and C(15)–N(5) [1.305(15) Å] bond lengths are indicative of delocalization within the N–C–N framework, which is also the case for the N(6)–C(22) [1.239(14) Å] and C(22)–N(7) [1.336(15) Å] bonds. The Pd(1)N(4)C(15)N(5)Pd(2) and Pd(1)N(6)C(22)N(7)Pd(2) planes form a dihedral angle of 36.3° and 53.0° with the C(16)–C(21) and C(23)–C(28) phenyl planes, respectively. The dihedral angle between the two five-membered planes is 87.9°.

### Template Effect of Palladium(II) for the Formation of 1,3,5-Triazapentadienato Complexes

The above discussion can be summarized as follows:
(1) Under the same reaction conditions, the yields of compounds **2** (70%) and **3** (71%) are much higher than those

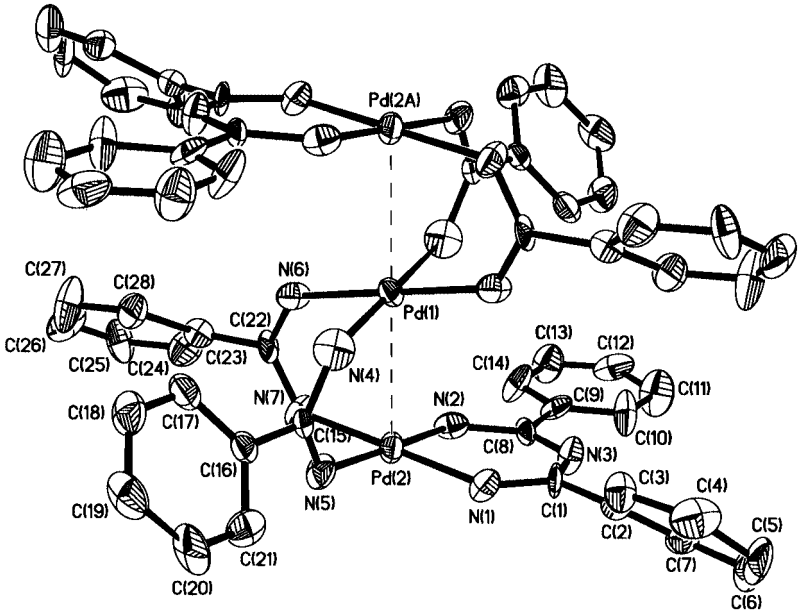


Figure 3. ORTEP drawing (30% probability level) of the molecular structure of **6**. Hydrogen atoms have been omitted for clarity.

 © 2006 Wiley-VCH Verlag GmbH & Co. KGaA, Weinheim 

for the corresponding nickel complexes (28 and 30%, respectively).[21]

(2) If $[PdCl_2(PhCN)_2]$ is replaced by $ZnCl_2$, under the same reaction conditions as for the preparation of compound **3**, the product is 4-pyridylamidinatozinc chloride instead of bis[2,4-bis(pyridyl)-1,3,5-triazapentadienato]zinc.[23]

(3) The ligand 2,4-bis(pyridyl)-1,3,5-triazapentadiene $[HN=C(4\text{-}Py)N=C(4\text{-}Py)\text{-}NH_2]$ is not stable in air as it could not be isolated from the hydrolysis products obtained from the hydrolysis of the intermediate derived from reaction of lithium 4-pyridylamidinate with 4-cyanopyridine. If the hydrolysis product was analyzed very quickly after the hydrolysis, the $[M+1]^+$ peak (226.1198) could be found in the ESI spectra. Moreover, MS-MS analysis of the $[M+1]^+$ peak showed that $[HN=C(4\text{-}Py)N=C(4\text{-}Py)NH_2]$ is cleaved into 4-cyanopyridine and 4-pyridylamidine.

(4) Rapid mass spectral analysis of the hydrolysis products derived from reaction of lithium benzamidinate with benzonitrile did not locate the $[M+1]^+$ peak of the ligand 2,4-diphenyl-1,3,5-triazapentadiene $[HN=C(Ph)\text{–}N=C(Ph)\text{-}NH_2]$. This indicates that the ligand cannot exist in air.

(5) Under the same reaction conditions as for compound **6**, but with nickel chloride instead of palladium chloride, the product was tetrakis(benzamidine)nickel chloride rather than the analogous nickel complex.[21]

From the observations mentioned above it is clear that the nickel or palladium center plays a key role in the formation of 1,3,5-triazapentadienato complexes. The lithium arylamidinate attacks another aryl nitrile followed by a 1,3-silyl shift to produce the 1,3,5-triazapentadienatolithium intermediate **A** (see Scheme 1). When palladium chloride is added to the reaction system, the 1,3,5-triazapentadienato metal intermediate complexes **B** are produced, and these are hydrolyzed during work up in air to give the stable bis(2,4-aryl-1,3,5-triazapentadienato)-coordinated metal complexes. It is clear that the square-planar geometry of nickel and palladium ions leads to a template effect in the synthesis. Moreover, the high yield of palladium complexes and the formation of compound **6** indicate that palladium is a very effective template for the formation of bis(2,4-aryl-1,3,5-triazapentadienato)palladium complexes.

## Conclusions

We have developed a simple and effective method for the synthesis of symmetric and unsymmetrical 1,3,5-triazapentadienyl-based transition metal complexes. The 1,3,5-triazapentadienyl ligands, which are generated in situ by the interaction of amidinate with aryl nitrile, react with palladium and nickel ions to form a six-membered planar metallacycle. Structural analyses have revealed that the N–C–N–C–N framework within the 1,3,5-triazapentadienyl ligand is completely delocalized.

## Experimental Section

**General Procedures:** All reactions were carried out under nitrogen in flame-dried Schlenk-type glassware on a dual manifold Schlenk line unless otherwise stated. Solvents were pre-dried prior to use. All chemicals used were of reagent grade and obtained from Aldrich or Fisher Scientific Chemical Company. NMR spectra were measured in $[D_6]$DMSO either on a Varian INOVA 400 MHz FT-NMR or a Bruker DRX-300 spectrometer. Fast atom bombardment (FAB) mass spectra were recorded with a Finnigan MAT SSQ710 mass spectrometer, and electrospray ionization high resolution mass spectra (ESI-HRMS) with a quadrupole time-of-flight (Q-TOF) mass spectrometer equipped with a turbo ionspray source (PE SCIEX API QSTAR Pulsar i, Applied Biosystem). IR spectra (KBr pellets) were recorded with a Perkin–Elmer Paragon 1000PC or Nicolet Nagan-IR 550 Series II FTIR spectrometer. Elemental analyses were performed with a Vario EL-III instrument.

**Preparation of Bis[2,4-bis(2-pyridyl)-1,3,5-triazapentadienato]palladium(II) (1):** 2-Cyanopyridine (0.416 g, 4.0 mmol) and $LiN(SiMe_3)_2$ (0.334 g, 2.0 mmol) were placed in THF (20 mL) at 0 °C. The resultant red solution was warmed to room temperature and stirred for an additional 2 h before cooling down to –78 °C. Anhydrous $[PdCl_2(PhCN)_2]$ (0.383 g, 1.0 mmol) was then added to the reaction mixture which was stirred at –78 °C for an hour before warming up to room temperature and allowed to react overnight. Solvent was then removed in vacuo. The reaction system was exposed to air, methanol (20 mL) was added to the residue and the solution was filtered. Slow evaporation of the methanol solution gave yellow crystals of **1**. Yield: 0.392 g (0.708 mmol, 71%); m.p. > 300 °C. MS (FAB, +ve): *m/z* 554.4 $[M]^+$. ESI-HRMS (in methanol, +ve) calcd. for $C_{24}H_{21}N_{10}Pd$: 555.0985; found 555.0947 $[M+H]^+$. $^1$H NMR ($[D_6]$DMSO): NH protons: $\delta$ = 9.31 (s, 4 H); 2-pyridyl protons: $\delta$ = 8.79 (dd, $J$ = 5.6 and 1.6 Hz, 4 H), 8.65 (d, $J$ = 7.6 Hz, 4 H), 8.04 (td, $J$ = 7.6 and 1.6 Hz, 4 H), 7.62 ppm (ddd, $J$ = 7.6, 5.6 and 1.6 Hz, 4 H). IR (KBr): $\tilde{\nu}$ = 3448 m, 3286 s, 3057 w, 1576 s, 1550 vs, 1483 m, 1431 vs, 1265 w, 1241 w, 1057 m, 1997 m, 813 mm, 751 s, 708 s cm$^{-1}$. See also Table 2. $C_{24}H_{20}N_{10}Pd\cdot 2H_2O$ (590.94): calcd. C 48.78, H 4.09, N 23.70; found C 48.65, H 4.14, N 23.50.

Table 2. Characteristic $^1$H NMR and IR data for compounds **1**–**6**.

| | $^1$H NMR NH protons [ppm] | IR [cm$^{-1}$] $\nu_{N-H}$ | $\nu$[24] for the 1,3,5-triazapentadienyl skeleton |
|---|---|---|---|
| **1** | 9.31 (s, 4×1 H) | 3448, 3286 | 1483, 1431 and 1265 |
| **2** | 8.81 (s, 4×1 H) | 3406, 3299 | 1462, 1411 and 1302 |
| **3** | 9.01 (s, 4×1 H) | 3327, 3283 | 1464, 1410 and 1301 |
| **4** | 9.26 (d, 2×1 H)<br>8.76 (s, 2×1 H) | 3299 | 1472, 1421 and 1285 |
| **5** | 8.85 (s, 2×1 H)<br>8.79 (s, 2×1 H) | 3430, 3317, 3231 | 1452, 1402 and 1295 |
| **6** | 8.22 (s, 2×1 H)<br>8.03 (m, 2×2 H)<br>7.75 (m, 2×2 H)<br>6.83 (s, 2×1 H) | 3404, 3375, 3357 | 1472, 1445 and 1273 |

**Preparation of Bis[2,4-bis(3-pyridyl)-1,3,5-triazapentadienato]palladium(II) (2):** Compound **2** was prepared under the same reaction conditions as **1** from 3-cyanopyridine (0.416 g, 4 mmol), $LiN(SiMe_3)_2$ (0.334 g, 2.0 mmol), and anhydrous $[PdCl_2(PhCN)_2]$ (0.383 g, 1 mmol). Yellow crystals of **2** were obtained. Yield: 0.389 g (0.702 mmol, 70%); m.p. > 300 °C. MS (FAB, +ve): *m/z*: 554 $[M]^+$. ESI-HRMS (in methanol, +ve) calcd. for $C_{24}H_{21}N_{10}Pd$: 555.0985; found 555.0944 $[M+H]^+$. $^1$H NMR ($[D_6]$DMSO): NH protons: $\delta$ = 8.82 (s, 4 H); 3-pyridyl protons: $\delta$ = 9.23 (s), 8.67 (d, $J$ = 6.0 Hz, 4 H), 8.42 (d, $J$ = 9.0 Hz, 4 H), 7.51 ppm (dd, $J$ = 9.0 and 6.0 Hz, 4 H). IR (KBr): $\tilde{\nu}$ = 3576 w, 3406 w, 3299 s, 3061 m, 1589 s, 1548 s, 1462 s, 1411 s, 1302 s, 1196 w, 1028 m, 827 m, 732 s,

 © 2006 Wiley-VCH Verlag GmbH & Co. KGaA, Weinheim 

697 s $cm^{-1}$. See also Table 2. $C_{24}H_{20}N_{10}Pd{\cdot}2H_2O$ (590.94): calcd. C 48.78, H 4.09, N 23.70; found C 48.93, H 3.93, N 23.39.

**Preparation of Bis[2,4-bis(4-pyridyl)-1,3,5-triazapentadienato]palladium(II) (3):** Compound **3** was prepared under the same reaction conditions as **1** from 4-cyanopyridine (0.416 g, 4 mmol), $LiN(SiMe_3)_2$ (0.334 g, 2.0 mmol), and anhydrous $[PdCl_2(PhCN)_2]$ (0.383 g, 1 mmol). Yellow crystals of **3** were obtained. Yield: 0.392 g (0.708 mmol, 71%); m.p. > 300 °C. MS (FAB, +ve): *m*/*z* 554.4 $[M]^+$. ESI-HRMS (in methanol, +ve) calcd. for $C_{24}H_{21}N_{10}Pd$: 555.0985; found 555.1032 $[M+H]^+$. $^1H$ NMR ([D$_6$]-DMSO): NH protons: $\delta$ = 9.02 (s, 4×1 H); 4-pyridyl protons: $\delta$ = 8.76 (d, $J$ = 4.8 Hz, 8 H) and 8.02 (d, $J$ = 4.8 Hz, 8 H). IR (KBr): $\tilde{\nu}$ = 3327 s, 3283 s, 3037 m, 1605 s, 1581 s, 1540 s, 1464 s, 1410 s, 1301 s, 1062 w, 1043 w, 1004 m, 841 m, 749 m, 704 s $cm^{-1}$. See also Table 2. $C_{24}H_{20}N_{10}Pd{\cdot}2H_2O{\cdot}0.5CH_3OH$ (606.96): calcd. C 48.48, H 4.32, N 23.08; found C 48.48, H 4.28, N 22.31.

**Preparation of Bis[2-phenyl-4-(3-pyridyl)-1,3,5-triazapentadienato]-palladium(II) (4):** Compound **4** was prepared under similar reaction conditions to **1**. Benzonitrile (0.26 mL, 2.5 mmol) and $LiN(SiMe_3)_2$ (0.418 g, 2.5 mmol) were placed in THF (20 mL) at 0 °C. The resultant yellow solution was warmed to room temperature and stirred for an additional 2 h. 3-Cyanopyridine (0.26 g, 2.5 mmol) was then added at room temperature and allowed to react overnight. Anhydrous $[PdCl_2(PhCN)_2]$ (0.479 g, 1.25 mmol) was then added to the reaction mixture at –78 °C which was stirred at this temperature for an hour before warming up to room temperature and allowed to react overnight. Solvent was then removed under vacuum. The reaction mixture was exposed to air, saturated with methanol (20 mL), and filtered. Slow evaporation of the methanol filtrate gave yellow crystals of **4**. Yield: 0.189 g (0.34 mmol, 27%); m.p. > 300 °C. ESI-HRMS (in methanol, +ve) calcd. for $C_{26}H_{23}N_8Pd$: 553.1080; found 553.1106 $[M+H]^+$. $^1H$ NMR ([D$_6$]-DMSO): $\delta$ = 9.26 (d, $J$ = 2.4 Hz, 2×1 H, NH) 8.76 (s, 2×1 H, NH), 8.69 (m, 2×2 H), 8.43 (m, 2×1 H), 8.08 (m, 2×2 H), 7.52 (m, 2×4 H). IR (KBr): $\tilde{\nu}$ = 3299 bm, 3062 w, 1593 m, 1544 vs, 1473 s, 1421 s, 1285 s, 1029 m, 822 w, 720 s $cm^{-1}$. See also Table 2. $C_{26}H_{22}N_8Pd{\cdot}0.5H_2O$ (561.94): calcd. C 55.58, H 4.13, N 19.93; found C 55.53, H 4.11, N 19.51.

**Preparation of Bis[2-phenyl-4-(4-pyridyl)-1,3,5-triazapentadienato]-palladium(II) (5):** Compound **5** was prepared under the same reaction conditions as compound **4** from benzonitrile (0.41 mL, 4.0 mmol), $LiN(SiMe_3)_2$ (0.67 g, 4.0 mmol), 4-cyanopyridine (0.41 g, 4.0 mmol), and anhydrous $[PdCl_2(PhCN)_2]$ (0.77 g, 2.0 mmol). Slow evaporation of the methanol filtrate gave yellow crystals of **5**. Yield: 0.34 g (0.62 mmol, 31%); m.p. > 300 °C. ESI-HRMS (in methanol, +ve) calcd. for $C_{26}H_{23}N_8Pd$: 553.1080; found 553.1049 $[M+H]^+$. $^1H$ NMR ([D$_6$]DMSO): NH protons: $\delta$ = 8.85 (s, 2×1 H), 8.79 (s, 2×1 H, NH); 4-pyridyl protons: $\delta$ = 8.74 (m, 2×2 H), 8.08 (m, 2×2 H), 8.01 (m, 2×2 H), 7.52 (m, 2×3 H) ppm. $^{13}C$ NMR ([D$_6$]DMSO): $\delta$ = 121.7, 127.6, 128.3, 130.2, 138.4, 145.7, 150.1, 158.5, 160.7 ppm. IR (KBr): $\tilde{\nu}$ = 3430 bw, 3317 bm, 3231 bm, 3042 bw, 1602 w, 1585 m, 1565 m, 1535 vs, 1453 s, 1403 vs, 1295 s, 1064 m, 844 w, 825 w, 712 s, 530 w $cm^{-1}$. See also Table 2. $C_{26}H_{22}N_8Pd{\cdot}H_2O$ (570.95): calcd. C 54.70, H 4.24, N 19.62; found C 54.69, H 4.04, N 19.08.

**Preparation of Tetrakis(benzamidinato)bis(2,4-diphenyl-1,3,5-triazapentadienato)tripalladium(II) (6):** Benzonitrile (0.412 mL, 4 mmol) and $LiN(SiMe_3)_2$ (0.67 g, 4 mmol) were placed in THF (20 mL) at 0 °C. The resultant red solution was warmed to room temperature and stirred for an additional 2 h before cooling down to –78 °C. Anhydrous $PdCl_2$ (0.177 g, 1 mmol) was then added to the reaction mixture, which was stirred at –78 °C for an hour before warming up to room temperature and allowed to react overnight. Solvent was then removed under vacuum. The mixture was exposed to air, dichloromethane (20 mL) was added to the residue, and the solution was filtered. The solvent of the filtrate was removed in vacuo to give a dark-red oily product. The product was dissolved in THF (10 mL) and the solvent was allowed to evaporate slowly in air to afford yellow crystals of **6**. Yield: 0.12 g (0.097 mmol, 19%), m.p > 300 °C. $^1H$ NMR ([D$_6$]DMSO): NH protons, $\delta$ = 8.22 (s, 2×1 H), 8.03 (m, 2×2 H), 7.75 (m, 2×2 H), 6.83 (s, 2×1 H); phenyl protons: 7.66–7.45 ppm (m, 2×20 H). IR (KBr): $\tilde{\nu}$ = 3404 m, 3375 s, 3357 m, 3057 w, 3021 w, 1648 w, 1559 vs, 1540 vs, 1472 s, 1445 s, 1273 m, 1218 w, 1028 w, 783 w, 697 vs, 651 m $cm^{-1}$. See also Table 2. $C_{56}H_{52}N_{14}Pd_3{\cdot}0.5H_2O$ (1247.2): calcd. C 53.88, H 4.28, N 15.72; found C 53.85, H 4.14, N 15.33.

**X-ray Crystallography:** Crystals of **2**·2$CH_3OH$, **3**·2$CH_3OH$, and **6** suitable for X-ray diffraction were grown by slow evaporation of the respective methanol solution of these compounds in air. The intensity data were collected with a Bruker AXS SMART 1000 CCD area-detector diffractometer with graphite-monochromated Mo-$K_\alpha$ radiation ($\lambda$ = 0.71073 Å) at 293 K. The collected frames were processed with the proprietary software SAINT[25] and an absorption correction was applied (SADABS[26]) to the collected reflections. The structures of these molecules were solved by direct methods and expanded by standard difference Fourier syntheses using the software SHELXTL.[27] Structure refinements were made on $F^2$ using the full-matrix least-squares technique. All non-hydrogen atoms were refined with anisotropic displacement parameters. Hydrogen atoms were placed in their idealized positions and allowed to ride on the respective carbon atoms. Pertinent crystallographic data and other experimental details are summarized in Table 3.

Table 3. Crystal data and refinement for compounds **2**, **3** and **6**.

| | **2**·2$CH_3OH$ | **3**·2$CH_3OH$ | **6** |
|---|---|---|---|
| Empirical formula | $C_{26}H_{28}N_{10}O_2Pd$ | $C_{26}H_{28}N_{10}O_2Pd$ | $C_{56}H_{52}N_{14}Pd_3$ |
| Molecular mass | 618.98 | 618.98 | 1240.32 |
| Crystal system | triclinic | monoclinic | triclinic |
| Space group | $P\bar{1}$ (no. 2) | $P2_1/c$ (no. 14) | $P\bar{1}$ (no. 2) |
| $a$ [Å] | 7.518(2) | 5.5416(9) | 9.6938(8) |
| $b$ [Å] | 7.865(3) | 18.296(3) | 10.5983(8) |
| $c$ [Å] | 12.645(4) | 13.962(2) | 25.0385(19) |
| $\alpha$ [°] | 86.156(6) | 90 | 95.411(2) |
| $\beta$ [°] | 78.994(5) | 97.950(3) | 96.251(2) |
| $\gamma$ [°] | 63.959(5) | 90 | 96.4450(10) |
| $V$ [Å$^3$] | 659.4(4) | 1401.9(4) | 2526.1(3) |
| $Z$ | 1 | 2 | 2 |
| $F$(000) | 316 | 632 | 1248 |
| $D_{calcd.}$ [g $cm^{-3}$] | 1.559 | 1.466 | 1.631 |
| $\mu$(Mo-$K_\alpha$) [$mm^{-1}$] | 0.749 | 0.704 | 1.111 |
| Rflns. collected | 3249 | 8182 | 12876 |
| Unique rflns. | 2629 | 3159 | 8860 |
| Obsd. rflns. | 2294 | 1790 | 3374 |
| GOF on $F^2$ | 1.002 | 0.917 | 0.999 |
| $R_1$, $wR_2$ [$I > 2\sigma(I)$] | 0.0448, 0.1050 | 0.0526, 0.1309 | 0.0434, 0.1043 |
| $R_1$, $wR_2$ (all data) | 0.0523, 0.1087 | 0.0973, 0.1497 | 0.1345, 0.1362 |

CCDC-602853 (for **2**), -602854 (for **3**) and -602855 (for **6**) contain the supplementary crystallographic data for this paper. These data can be obtained free of charge from The Cambridge Crystallographic Data Centre via www.ccdc.cam.ac.uk/data_request/cif.

 © 2006 Wiley-VCH Verlag GmbH & Co. KGaA, Weinheim 

## Acknowledgments

We thank the Hong Kong Baptist University and the Hong Kong Research Grants Council (HKBU 2021/99P) for financial support.

[1] L. Bourget-Merie, M. F. Lappert, J. R. Severn, *Chem. Rev.* **2002**, *102*, 3031–3066 and references cited therein.
[2] a) P. B. Hitchcock, M. F. Lappert, D.-S. Liu, *J. Chem. Soc., Chem. Commun.* **1994**, 1699–1700; b) P. B. Hitchcock, M. F. Lappert, M. Layh, D.-S. Liu, R. Sablong, T. Shun, *J. Chem. Soc., Dalton Trans.* **2000**, 2301–2312; c) P. B. Hitchcock, M. F. Lappert, M. Layh, *J. Chem. Soc., Dalton Trans.* **2001**, 2409–2416.
[3] B.-J. Deelman, M. F. Lappert, H.-K. Lee, T. C. W. Mak, W.-P. Leung, P.-R. Wei, *Organometallics* **1997**, *16*, 1247–1252.
[4] A. Maraval, D. Arquier, A. Igau, Y. Coppel, B. Donnadieu, J.-P. Majoral, *Organometallics* **2001**, *20*, 1716–1718.
[5] S. Nückel, P. Burger, *Organometallics* **2000**, *19*, 3305–3311.
[6] V. C. Gibson, J. A. Segal, A. J. P. White, D. J. Williams, *J. Am. Chem. Soc.* **2000**, *122*, 7120–7121.
[7] a) C. E. Radzewich, I. A. Guzei, R. F. Jordan, *J. Am. Chem. Soc.* **1999**, *121*, 8673–8674; b) C. Cui, H. W. Roesky, H. Hao, H.-G. Schmidt, M. Noltemeyer, *Angew. Chem.* **2000**, *112*, 1885–1887; *Angew. Chem. Int. Ed.* **2000**, *39*, 1815–1817.
[8] J. Feldman, S. J. McLain, A. Parthasarathy, W. J. Marshall, J. C. Calabrese, S. D. Arthur, *Organometallics* **1997**, *16*, 1514–1516.
[9] B. Qian, W. J. Scanlon, M. R. Smith, D. H. Motry, *Organometallics* **1999**, *18*, 1693–1698.
[10] P. H. M. Budzelaar, R. Gelder, A. W. Gal, *Organometallics* **1998**, *17*, 4121–4123.
[11] N. J. Hardman, B. E. Eichler, P. P. Power, *Chem. Commun.* **2000**, 1991–1992.
[12] L. W. M. Lee, W. E. Piers, M. R. J. Elsegood, W. Clegg, M. Parvez, *Organometallics* **1999**, *18*, 2947–2949.
[13] a) L. K. Johnson, S. Mecking, M. Brookhart, *J. Am. Chem. Soc.* **1996**, *118*, 267–268; b) B. L. Small, M. Brookhart, A. M. A. Bennett, *J. Am. Chem. Soc.* **1998**, *120*, 4049–4050; c) G. J. P. Britovsek, V. C. Gibson, B. S. Kimberley, P. J. Maddox, S. J. McTavish, G. A. Solan, A. J. P. White, D. J. Williams, *Chem. Commun.* **1998**, 849–850.
[14] R. Norrestam, *Acta Crystallogr., Sect. C* **1984**, *40*, 955–957.
[15] J. Barker, M. Kilner, M. M. Mahmoud, S. C. Wallwork, *J. Chem. Soc., Dalton Trans.* **1989**, 837–841.
[16] S. V. Kryatov, M. B. Smith, E. V. Rybak-Akimova, A. Y. Nazarenko, *Chem. Commun.* **2001**, 1174–1175.
[17] T. Kajiwara, A. Kamiyama, T. Ito, *Chem. Commun.* **2002**, 1256–1257.
[18] a) M. N. Kopylovich, A. J. L. Pombeiro, A. Fischer, L. Kloo, V. Yu. Kukushkin, *Inorg. Chem.* **2003**, *42*, 7239–7248; b) N. A. Bokach, T. V. Kuznetsova, S. A. Simanova, M. Haukka, A. J. L. Pombeiro, V. Yu. Kukushkin, *Inorg. Chem.* **2005**, *44*, 5152–5160.
[19] a) A. R. Siedle, R. J. Webb, F. E. Behr, R. A. Newmark, D. A. Weil, K. Erickson, R. Naujok, M. Brostrom, M. Mueller, S.-H. Chou, V. G. Young Jr, *Inorg. Chem.* **2003**, *42*, 932–934; b) A. R. Siedle, R. J. Webb, M. Brostrom, R. A. Newmark, F. E. Behr, V. G. Young Jr, *Organometallics* **2004**, *23*, 2281–2286.
[20] H. V. R. Dias, S. Singh, *Inorg. Chem.* **2004**, *43*, 5786–5788.
[21] J. Guo, W.-K. Wong, W.-Y. Wong, *Eur. J. Inorg. Chem.* **2004**, 267–275.
[22] a) J. Barker, M. Kilner, R. O. Gould, *J. Chem. Soc., Dalton Trans.* **1987**, 2687–2693; b) J. Barker, N. Cameron, M. Kilner, M. M. Mahoud, S. C. Wallwork, *J. Chem. Soc., Dalton Trans.* **1986**, 1359–1365.
[23] J. Guo, W.-K. Wong, unpublished work.
[24] D. Lin-Vien, N. B. Colthup, W. G. Fateley, J. G. Grasselli, *The Handbook of Infrared and Raman Characteristic Frequencies of Organic Molecules*, Academic Press, Inc., **1991**.
[25] *SAINT*, *Reference manual*, Siemens Energy and Automation, Madison, WI, **1994–1996**.
[26] G. M. Sheldrick, *SADABS*, *Empirical Absorption Correction Program*, University of Göttingen, Germany, **1997**.
[27] G. M. Sheldrick, *SHELXTL*™, *Reference manual*, version 5.1, Siemens, Madison, WI, **1997**.

Received: March 29, 2006
Published Online: July 28, 2006

 © 2006 Wiley-VCH Verlag GmbH & Co. KGaA, Weinheim 

DOI: 10.1002/ejic.200600339

# Diatom-Templated Synthesis of Ordered Meso/Macroporous Hierarchical Materials

Xiaohui Cai,[a,b] Guangshan Zhu,*[b] Weiwei Zhang,[b] Huanyu Zhao,[b] Ce Wang,*[a] Shilun Qiu,[b] and Yen Wei*[c]

**Keywords:** Hierarchical materials / Nanomaterials / Porosity / Sol–gel processes / Template synthesis

Ordered meso/macroporous hierarchical silica materials have been prepared using block copolymer P123 ($EO_{20}$-$PO_{70}EO_{20}$) and an inverse carbon replica of diatom as templates. The silica wall of the diatom was replaced by ordered mesoporous silica, while the micron-sized diatom architecture was replicated by using an inverse carbon replication technique. The mesoporous silica was found to have macroporous structures of both columnar and discoid diatom templates. The presence of hierarchical meso/macroporous systems was confirmed by the results from scanning and transmission electron microscopy, powder X-ray diffraction, and nitrogen adsorption–desorption studies. The materials with columnar and discoid morphologies have BET surface areas of about 400 $m^2 g^{-1}$.
(© Wiley-VCH Verlag GmbH & Co. KGaA, 69451 Weinheim, Germany, 2006)

## Introduction

In recent years hierarchical porous materials with two or more levels of porosities have attracted much attention owing to their potential applications in catalysis, separation, and ion-exchange.[1–7] Such materials improve the diffusion of the guest molecules through the inorganic network of pores and channels, because larger pores allow for better molecular accessibility while the smaller pores provide high surface areas and large pore volumes.[8] Zhao et al. reported that sponge-like silica membranes with 3D mesoporous/macroporous structures were obtained by a multiphase process of acid-catalyzed silica sol–gel chemistry.[9] Wood cells were used to prepare micro/macroporous materials by a zeolite-seeded growth method.[10] Many nonsiliceous hierarchical porous materials, for example carbon or metal oxide monoliths, were replicated from porous silica monoliths by Smått et al.[11] During the preparation of hierarchical porous materials, the simplicity of the synthesis and abundance of raw materials are important considerations. For example, a micro/macroporous composite material was prepared readily with the use of abundant diatomaceous earth.[12]

[a] Alan G. MacDiarmid Institute, Jilin University, Changchun 130012, China
Fax: +86-431-5168292
E-mail: cwang@jlu.edu.cn
[b] State Key Laboratory of Inorganic Synthesis and Preparative Chemistry, Jilin University, Changchun 130012, China
Fax: +86-431-5168331
E-mail: zhugs@mail.jlu.edu.cn
[c] Department of Chemistry, Drexel University, Philadelphia, PA 19104, USA
E-mail: weiyen@drexel.edu

Diatoms are microscopic aquatic, single-celled algae.[13] Diatomaceous earth, the residue of decayed diatoms, largely consists of amorphous silica with a macroporous architecture.[14] Diatomaceous earth is extremely abundant and available at low cost.[15] It is commonly used in sound and heat insulation, abrasives, filters, absorbents, and explosives.[16] The introduction of mesoporosity or microporosity to macroporous diatom architecture may extend or improve their use in many applications. Diatom zeolitization is a method of obtaining micro/macroporous hierarchical materials.[12,17] A meso/macroporous material with a BET surface area of 284 $m^2 g^{-1}$ has been prepared using hexadecyltrimethylammonium bromide (CTAB) ($C_{16}$TMABr) as the template in a previous investigation.[8] The technique of introducing ordered mesoporosity into the macrostructure of diatoms is based on "pseudomorphic synthesis", which has been utilized by Di Renzo and co-workers to prepare discrete micrometer-sized spherical particles of MCM-48, MCM-41, and large-pore micelle-templated silica (MTS).[18–20] However, when it was used to rearrange the silica wall of diatoms, both ordered and disordered mesostructures co-existed.[8]

Carbon is often used as the hard template to prepare zeolite or mesoporous materials because of its easy removal. Zeolite hollow fibers have been prepared by employing carbon fibers as the hard template.[21–23] Carbon nanofibers and carbon black aggregates were also capable of acting as a template for preparing mesoporous materials.[24,25] ZSM-5 zeolite/porous carbon composite has been prepared from carbonized rice husk.[26] Carbon aerogel was employed as the template to produce zeolite of mesoporous channels.[27,28] Zeolite single crystals of mesoporous channels were synthesized by using carbon particles as the tem-

 © 2006 Wiley-VCH Verlag GmbH & Co. KGaA, Weinheim InterScience 

plate.[29] Activated carbon is another template for making nanoporous silica.[30]

Since ordered mesoporous carbons were prepared by Ryoo et al.,[31] many ordered mesoporous silica materials and zeolites have been prepared using mesoporous carbon as the hard template.[32–36] However, to the best of our knowledge, there has been no report in the literature on the use of carbon replicas of biomaterials as templates. Here, we present the first synthesis of ordered meso/macroporous hierarchical materials using carbon replicas of biomaterials as hard templates for macroporosity and a block copolymer as the templating surfactant for mesoporosity. The nonionic block copolymer and the inverse carbon replica of diatom are used as direct templates under acidic conditions. Although the diatom is an indirect template, it is vital for keeping the microscopic morphology of the hierarchical materials. In this process the silica wall of the diatom is replaced by ordered mesoporous silica completely and the near perfect macroporous diatom architecture is well replicated.

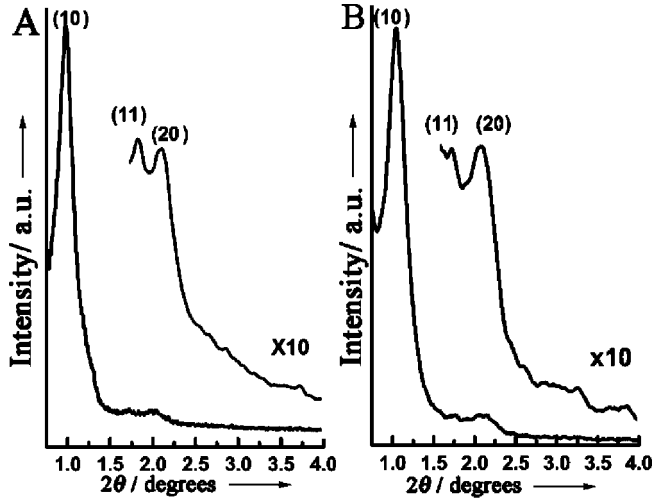


Figure 1. Powder XRD patterns of hierarchical porous materials templated by the diatoms with (A) columnar and (B) discoid morphologies.

## Results and Discussion

The preparation of ordered meso/macroporous hierarchical materials with carbon replicas of diatoms as templates is achieved as follows: sucrose was first introduced in the macropores of the diatom; after carbonizing the sucrose and etching the diatom, the carbon replica of the diatom was prepared; using the carbon replica of the diatom as the hard template, a solid product with both carbon and silica was obtained through the solvent evaporation technique.[39] After removing the carbon replica and the organic template, the ordered meso/macroporous hierarchical materials were finally prepared.

Figure 1 shows small-angle X-ray diffraction (XRD) patterns for the hierarchical porous materials that were prepared using columnar and discoid diatoms as templates. Three resolved peaks appearing at low angles in Figure 1 A and Figure 1 B can be indexed as 10, 11, and 20 reflections associated with two-dimensional hexagonal pore ordering in the *p6mm* space group.[37] The morphologies of the initial diatoms were revealed by scanning electron microscopy (SEM). Figure 2 shows the diatoms with columnar and discoid morphologies. The columnar diatoms have a diameter of about 7 μm and a length of about 15 μm (Figure 2 A). A high-magnification image (Figure 2 B) shows that the diameter of subpores is about 0.6 μm. The top of the hollow columnar diatom presents a hole with a diameter of about 5 μm, as shown in Figure 2 C. Low-magnification images display the discoid diatoms with a diameter of about 30 μm (Figure 2 D). From high-magnification observations of the surface, the subpore sizes range from approximately 350 to 550 nm (Figure 2 E). The thickness of the discoid diatom is about 5 μm, as identifiable from the side view in Figure 2 F. There is a cavum in each type of diatom. Part of the diatom wall is represented in Scheme 1 a.

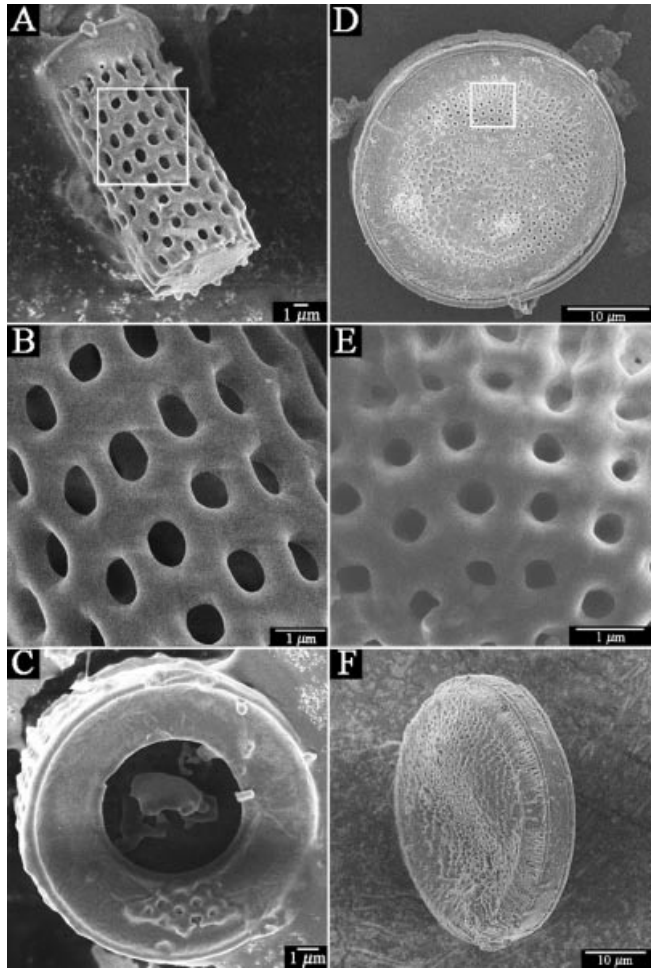


Figure 2. SEM images of initial diatoms with (A, B, C) columnar and (D, E, F) discoid morphologies.

The extent of carbonization depends on the amount of sucrose adsorbed on the inner surface of the diatom. After the diatom was dissolved in HF solution, a carbon frame-

 © 2006 Wiley-VCH Verlag GmbH & Co. KGaA, Weinheim 

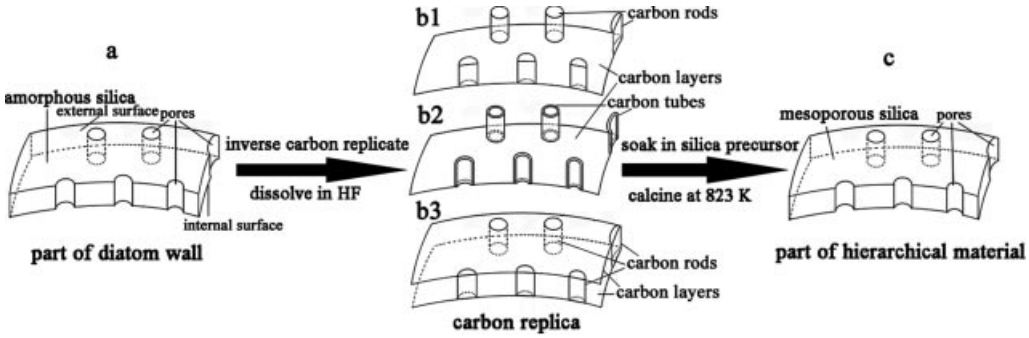


Scheme 1. Schematic illustration of the preparation of the meso/macroporous hierarchical porous materials.

work as an inverse replica of the diatom was obtained, as shown in Figure 3. Figure 3 A–C show the inverse carbon replicas of columnar diatoms, while Figure 3 D shows the carbon replica of the discoid diatom. At a high weight ratio of sucrose/diatom, it is a carbon rod that inversely replicates the subpores of diatoms (Figure 3 A–C), which is illustrated in Scheme 1 b1. When the sucrose is in large excess, the carbon layers are formed not only on the internal surface but also on the external surface of the diatoms (Figure 3 C), which is represented in Scheme 1 b3. When the weight ratio of sucrose/diatom is low, insufficient sucrose is absorbed on the surface of the subpores, which is transformed not to carbon rods but carbon tubes (Figure 3D), as illustrated in Scheme 1 b2.

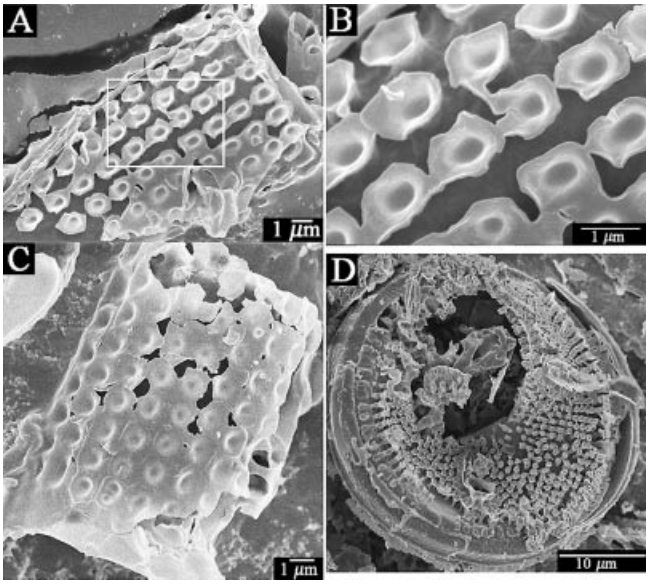


Figure 3. SEM images of inverse carbon replicas of diatoms with (A, B, C) columnar and (D) discoid morphologies.

After the inverse carbon replicas were immersed in the silica reaction mixture, they were coated with mesoporous silica upon evaporation of ethanol. When the carbon and the surfactant were removed by calcination, the diatom-replicated silica framework possessing an ordered mesostructure was obtained as depicted in Scheme 1 c and evidenced by SEM images (Figure 4) for the resultant mesoporous silicas with columnar (Figure 4 A and B) and discoid (Figure 4 C and D) morphologies. It is apparent that both the macroporous structure and the morphology of the initial diatom can be replicated by this method. As observed from the TEM images in Figure 5, the wall of the above final

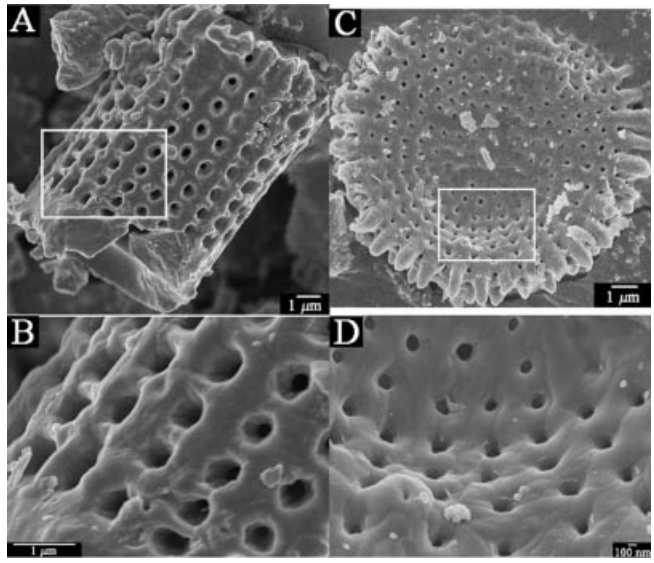


Figure 4. SEM images of hierarchical porous materials templated by diatoms with (A, B) columnar and (C, D) discoid morphologies.

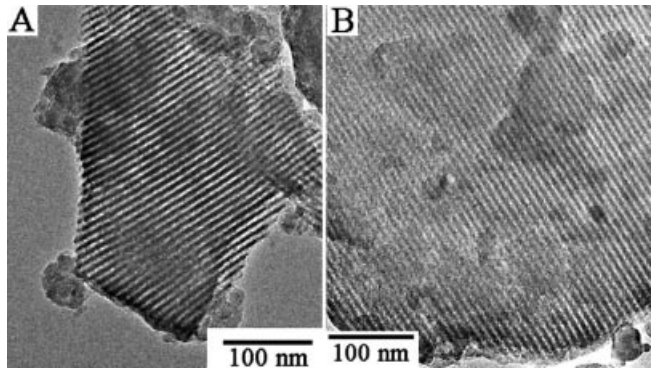


Figure 5. TEM images of hierarchical porous materials templated by diatoms with (A) columnar and (B) discoid morphologies.

 © 2006 Wiley-VCH Verlag GmbH & Co. KGaA, Weinheim 

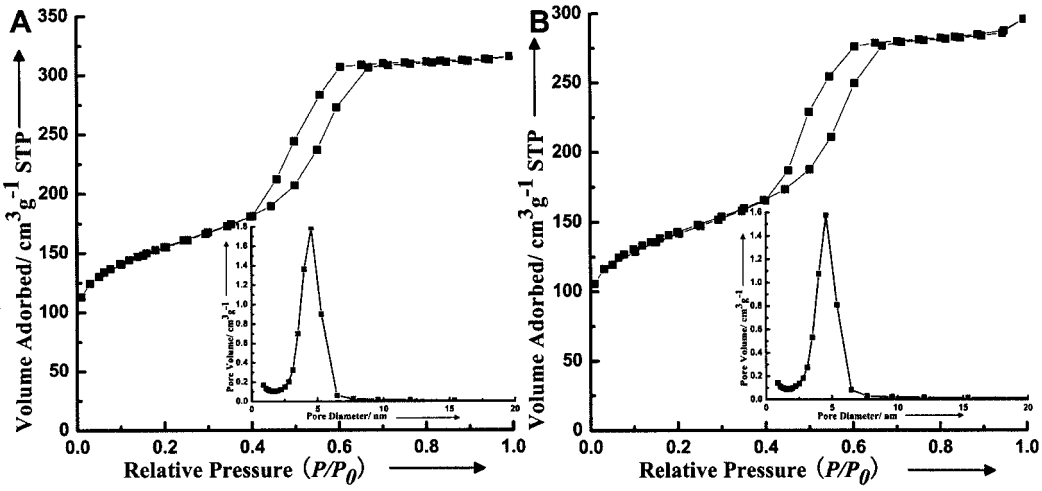


Figure 6. $N_2$ adsorption–desorption isotherms and pore-size distribution (inset) of hierarchical porous materials templated by diatoms with (A) columnar and (B) discoid morphologies.

hierarchical porous silica possesses ordered mesopores, which is in agreement with results of powder X-ray diffraction (Figure 1).

Nitrogen adsorption–desorption isotherm measurements were performed on both columnar (Figure 6 A) and discoid (Figure 6 B) hierarchical porous silica materials. In both cases, type IV isotherms with large hystereses were obtained, which are characteristic of mesoporous materials. The BET surface areas of the columnar and discoid hierarchical porous materials are 405 and 381 $cm^2 g^{-1}$ and the pore volumes are 0.41 and 0.37 $cm^3 g^{-1}$, respectively. It is noted that the BET surface area of about 400 $m^2 g^{-1}$ as obtained here because of the presence of mesoporosity is much higher than that of previously reported materials templated by diatoms.[8] The average pore diameter of both hierarchical materials is about 4.5 nm, as calculated from the BJH method of mesopore size analysis on the adsorption branch of the $N_2$ isotherms.

## Conclusions

We have demonstrated the synthesis of ordered hierarchical porous silica using block copolymer P123 and a carbon replica of a diatom as dual templates. The P123 functions as a soft template for the formation of mesoporosity and the inverse carbon replica as a direct hard template for macroporous structures. The macrostructure of the diatom is inversely replicated by the carbon replica. The weight ratio of sucrose/diatom was found to be important for the preparation of carbon replicas. High sucrose/diatom ratios lead to the formation of carbon layers on both internal and external surfaces of diatoms and of carbon rods in the subpores of diatoms; while low ratios resulted in the formation of a carbon layers only on the internal surface and of carbon tubes in pores. SEM results show that hierarchical materials with macropores 350–550 nm in diameter exhibit columnar and discoid morphologies. Nitrogen sorption studies indicate that the materials have high BET surface areas of about 400 $m^2 g^{-1}$. Powder XRD and TEM results indicate that the mesopore in the hierarchical structure has a two-dimensional hexagonal pore ordering. These ordered hierarchical porous materials have the advantages of both mesoporosity and macroporosity, which may find a broad range of potential applications in catalysis, adsorption, and separation.

## Experimental Section

Two types of diatomaceous earth (consisting of columnar and discoid diatoms) were purchased from Aldrich (Celatom FW80) and Tianjin Chemical Graduate School, respectively, and were purified further by sedimentation and ultrasonication. A sedimentary method in deionized water was used to remove the mixed scrappy mineral and ultrasonication in ethanol solution was performed to separate the clay from the diatom. The inverse carbon replication technique that was used in this work was adopted from the literature.[38] Thus, the purified diatom was impregnated with an aqueous solution of sucrose in the presence of sulfuric acid, and then the resulting mixture was dried and carbonized at 373 K and subsequently at 433 K. Diatom silica was removed by HF. The detailed procedure is as follows: purified diatom (1 g) was added to a solution obtained by dissolving sucrose (0.6 g) and $H_2SO_4$ (0.14 g) in $H_2O$ (5 g). The mixture was placed in a drying oven at 373 K for 6 h, and subsequently the oven temperature was increased to 433 K for another 6 h. After dissolving the diatom in an aqueous solution of HF for 12 h, the inverse carbon replica was obtained. A silica reaction mixture was prepared as follows:[39] P123 (0.3 g) was dissolved in ethanol (4.5 g), followed by addition of an aqueous HCl solution (0.03 g, 2 M), deionized water (0.24 g), and tetraethyl orthosilicate (TEOS) (0.7 g), whilst stirring. The mixture was stirred at room temperature for 2 h. Inverse carbon replica (0.23 g) was added to the above reaction mixture under agitation and the whole mixture was transferred to an uncovered vessel until the air bubbles in the solution disappeared. The volatiles were evaporated under a flow of air after almost 12 h. The black solid was isolated after the weight of the mixture had lost about 60% by evaporation of ethanol and was dried at 373 K; it was then calcined at 823 K for 5 h to remove the inverse carbon replica and surfactant. The final product was a white powder. We also employed other silica sources,

 © 2006 Wiley-VCH Verlag GmbH & Co. KGaA, Weinheim 

including water glass, silica sol, and fumed silica, and so forth, but so far no good results have been obtained under the same experimental conditions. When triblock copolymer F127 ($EO_{106}$-$PO_{70}EO_{106}$) was used instead of P123, meso/macroporous hierarchical materials could also be prepared and the mesoporous structure had a cubic *Im*3*m* space-group symmetry with a pore size of 5–6 nm. X-ray diffraction (XRD) measurements were conducted with a Siemens D5005 diffractometer using Cu-$K_\alpha$ radiation ($\lambda$ = 1.54 Å). Transmission electron micrograph was obtained with a JEM-3010 using a copper grid-type sample holder. Scanning electron microscopy was performed with a JSM-6700F. Nitrogen adsorption–desorption isotherms were measured at the temperature of liquid nitrogen using a Micromeritics ASAP 2010 system. The samples were degassed at 573 K for 10 h before the measurements.

## Acknowledgments

This work was supported in part by the State Basic Research Project (G2000077507), the National Natural Science Foundation of China (Grant nos. 29873017 and 20101004), National 973 Project (no. 2001CB610500), NSFC (nos. 50173009 and 20320120169), and NIH (Grant no. DE09848).

[1] B. T. Holland, L. Abrams, A. Stein, *J. Am. Chem. Soc.* **1999**, *121*, 4308–4309.
[2] G. Zhu, S. Qiu, F. Gao, D. Li, Y. Li, R. Wang, B. Gao, B. Li, Y. Guo, R. Xu, Z. Liu, O. Terasaki, *J. Mater. Chem.* **2001**, *11*, 1687–1693.
[3] K. H. Sandhage, M. B. Dickerson, P. M. Huseman, M. A. Caranna, J. D. Clifton, T. A. Bull, T. J. Heibel, W. R. Overton, M. E. A. Schoenwaelder, *Adv. Mater.* **2002**, *14*, 429–433.
[4] A. Dong, Y. Wang, Y. Tang, Y. Zhang, N. Ren, Z. Gao, *Adv. Mater.* **2002**, *14*, 1506–1510.
[5] T. Sen, G. J. T. Tiddy, J. L. Casci, M. W. Anderson, *Angew. Chem. Int. Ed.* **2003**, *42*, 4649–4653.
[6] D. Brandhuber, V. Torma, C. Raab, H. Peterlik, A. Kulak, N. Hüsing, *Chem. Mater.* **2005**, *17*, 4262–4271.
[7] D. Kuang, T. Brezesinski, B. Smarsly, *J. Am. Chem. Soc.* **2004**, *126*, 10534–10535.
[8] C. E. Fowler, Y. Hoog, L. Vidal, B. Lebeau, *Chem. Phys. Lett.* **2004**, *398*, 414–417.
[9] D. Zhao, P. Yang, B. F. Schmelka, G. D. Stucky, *Chem. Mater.* **1999**, *11*, 1174–1178.
[10] A. Dong, Y. Wang, Y. Tang, N. Ren, Y. Zhang, Y. Yue, Z. Gao, *Adv. Mater.* **2002**, *14*, 926–929.
[11] a) A. H. Lu, J. H. Smått, M. Lindén, *Adv. Funct. Mater.* **2005**, *15*, 865–871; b) J. H. Smått, B. Spliethoff, J. B. Rosenholm, M. Lindén, *Chem. Commun.* **2004**, 2188–2189; c) J. H. Smått, C. Weidenthaler, J. B. Rosenholm, M. Lindén, *Chem. Mater.* **2006**, *18*, 1443–1450.
[12] M. W. Anderson, S. M. Holmes, N. Hanif, C. S. Cundy, *Angew. Chem. Int. Ed.* **2000**, *39*, 2707–2710.
[13] E. G. Vrieling, T. P. M. Beelen, R. A. van Santen, W. W. C. Gieskes, *J. Biotechnol.* **1999**, *70*, 39–51.
[14] S. Mann, G. A. Ozin, *Nature* **1996**, *382*, 313–318.
[15] D. Werner, *The Biology of Diatoms*, University of California Press, Berkeley, CA, **1977**.
[16] Y. Wang, Y. Tang, A. Dong, X. Wang, N. Ren, Z. Gao, *J. Mater. Chem.* **2002**, *12*, 1812–1818.
[17] S. M. Holmes, C. Markert, R. J. Plaisted, J. O. Forrest, J. R. Agger, M. W. Anderson, C. S. Cundy, J. Dwyer, *Chem. Mater.* **1999**, *11*, 3329–3332.
[18] T. Martin, A. Galarneau, F. Di Renzo, F. Fajula, D. Plee, *Angew. Chem. Int. Ed.* **2002**, *41*, 2590–2592.
[19] B. Lefèvre, A. Galarnear, J. Iapichella, C. Petitto, F. Di Renzo, F. Fajula, Z. Bayram-Hahn, R. Skudas, K. Unger, *Chem. Mater.* **2005**, *17*, 601–607.
[20] C. Petitto, A. Galarneau, M. F. Driole, B. Chiche, B. Alonso, F. Di Renzo, F. Fajula, *Chem. Mater.* **2005**, *17*, 2120–2130.
[21] V. Valtchev, B. J. Schoeman, J. Hedlund, S. Mintova, J. Sterte, *Zeolites* **1996**, *17*, 408–415.
[22] Y. J. Wang, Y. Tang, X. D. Wang, W. L. Yang, Z. Gao, *Chem. Lett.* **2000**, 1344–1345.
[23] C. Ke, W. L. Yang, Z. Ni, Y. J. Wang, Y. Tang, Y. Gua, Z. Gao, *Chem. Commun.* **2001**, 783–784.
[24] M. A. Ermakova, D. Y. Ermakov, G. G. Kuvshinov, *Kinet. Catal.* **2002**, *43*, 427–432.
[25] A. H. Janssen, I. Schmidt, C. J. H. Jacobsen, A. J. Koster, K. P. de Jong, *Microporous Mesoporous Mater.* **2003**, *65*, 59–75.
[26] H. Katsuki, S. Furuta, T. Watari, S. Komarneni, *Microporous Mesoporous Mater.* **2005**, *86*, 145–151.
[27] Y. Tao, Y. Hattori, A. Matumoto, H. Kanoh, K. Kaneko, *J. Phys. Chem. B* **2005**, *109*, 194–199.
[28] Y. S. Tao, H. Kanoh, K. Kaneko, *J. Phys. Chem. B* **2003**, *107*, 10974–10976.
[29] M. Y. Kustova, P. Hasselriis, C. H. Christensen, *Catal. Lett.* **2004**, *96*, 205–211.
[30] a) Q. Xu, K. L. Ding, L. M. He, J. B. Li, Y. Q. Guo, H. J. Fan, *Mater. Sci. Eng., B* **2005**, *121*, 266–271; b) H. Wakayama, Y. Fukushima, *Chem. Mater.* **2000**, *12*, 756–761.
[31] R. Ryoo, S. H. Joo, S. Jun, *J. Phys. Chem. B* **1999**, *103*, 7743–7746.
[32] A. H. Lu, W. Schmidt, B. Spliethoff, F. Schuth, *Chem. Eur. J.* **2004**, *10*, 6085–6092.
[33] J. Y. Kim, S. B. Yoon, J. S. Yu, *Chem. Mater.* **2003**, *15*, 1932–1934.
[34] Z. X. Yang, Y. D. Xia, R. Mokaya, *Adv. Mater.* **2004**, *16*, 727–732.
[35] L. F. Wang, K. F. Lin, Y. Di, D. L. Zhang, C. J. Li, Q. Yang, C. Y. Yin, Z. H. Sun, D. Z. Jiang, F. S. Xiao, *Microporous Mesoporous Mater.* **2005**, *86*, 81–88.
[36] S. Jun, S. H. Joo, R. Ryoo, M. Kruk, M. Jaroniec, Z. Liu, T. Ohsuna, O. Terasaki, *J. Am. Chem. Soc.* **2000**, *122*, 10712–10713.
[37] D. Zhao, J. Feng, Q. Huo, B. F. Chmelka, G. D. Stucky, *Science* **1998**, *279*, 548–552.
[38] M. Kruk, M. Jaroniec, S. H. Joo, R. Ryoo, *J. Phys. Chem. B* **2003**, *107*, 2205–2213.
[39] L. Huang, H. Wang, C. Y. Hayashi, B. Tian, D. Zhao, Y. Yan, *J. Mater. Chem.* **2003**, *13*, 666–668.

Received: April 18, 2006
Published Online: August 1, 2006

 © 2006 Wiley-VCH Verlag GmbH & Co. KGaA, Weinheim 

DOI: 10.1002/ejic.200600358

# Solvothermal Synthesis and Crystal Structure of Uranyl Complexes with 1,1-Cyclobutanedicarboxylic and (1*R*,3*S*)-(+)-Camphoric Acids – Novel Chiral Uranyl-Organic Frameworks

**Pierre Thuéry*[a]**

**Keywords:** Uranium / Carboxylate ligands / Metal-organic frameworks / Solvothermal synthesis / Structure elucidation

Reaction of the 1,1-cyclobutanedicarboxylic ($H_2L^1$) or (1*R*,3*S*)-(+)-camphoric ($H_2L^2$) acids with uranyl nitrate under solvothermal conditions gives novel uranyl-organic assemblages. The complex $[Hpy]_2[UO_2L^1(NO_3)]_2$ (**1**), obtained in pyridine, is a dimeric, dinuclear species in which the closeness of the two carboxylate groups prevents the formation of a more extended architecture. The chiral complexes $[UO_2L^2(py)_2]\cdot py$ (**2**) and $[UO_2L^2MeOH]\cdot MeOH$ (**3**), obtained with the enantiopure, divergent camphorate ligand in either pyridine (**2**) or methanol/water (**3**), are comprised of zigzag chains defining channels and a microporous assemblage or of undulated sheets based on tessellated 8- and 32-membered rings, respectively. Apart from a zinc(II) complex previously described, compounds **2** and **3** are the only examples of metal complexes with camphoric acid crystallographically characterized.
(© Wiley-VCH Verlag GmbH & Co. KGaA, 69451 Weinheim, Germany, 2006)

## Introduction

Several research groups have recently illustrated the potential of hydrothermal methods for the synthesis of uranyl-organic polymers, with a particular emphasis on obtaining microporous or luminescent materials.[1] Most of the compounds thus investigated include organic polycarboxylic acids as ligands and exploit the huge variety of this class of molecules. Even polyacid complexes recalcitrant to other crystallization procedures can be obtained in this way, as evidenced lately by the cases of uranyl citrate and tricarballylate.[2] Among organic polyacids, particularly interesting are those which, through a proper choice of geometry and rigidity, can assemble uranyl ions to form metallacycles, as is the case for tetrahydrofuran-2*r*,3*t*,4*t*,5*c*-tetracarboxylic acid.[3] The latter reacts with uranyl ions in organic solvents at room temperature to give tri- or tetranuclear cyclic species. Other candidates that seemed promising in this context are 1,1-cyclobutanedicarboxylic ($H_2L^1$) and (1*R*,3*S*)-(+)-camphoric ($H_2L^2$) acids, but these two ligands, when treated with uranyl nitrate in the presence of bases such as triethylamine or alkali metal hydroxides, did not give crystals, neither in organic solvents at room temperature nor under hydrothermal conditions. Suitable crystals could only be obtained, albeit in very low yields, under solvothermal conditions, using pyridine or methanol/water as the solvent and the crystal structures of the three species thus characterized are reported herein. A search of the Cambridge Structural Database (CSD, Version 5.27)[4] indicates that, apart from a polymeric terbium(III) complex,[5] all the metal complexes of 1,1-cyclobutanedicarboxylic acid which have been crystallographically characterized include 3d ions [platinum(II) and palladium(II) in particular]. In the case of (1*R*,3*S*)-(+)-camphoric acid, only one zinc(II) complex has been reported.[6] The present complexes are thus the first with an actinide ion for both ligands and with an f element for the second. Much work has recently been devoted to the synthesis of chiral nanoporous materials, with potential applications in enantioselective separation or heterogeneous asymmetric catalysis.[7] A particularly simple way to obtain such assemblages is the use of enantiopure chiral ligands, such as L- or D-tartaric acid,[7e,7g,7h] as metal bridges. The present results show that (1*R*,3*S*)-(+)-camphoric acid deserves to be considered as a useful building block in this context.

## Results and Discussion

In the presence of pyridine, the diacid $H_2L^1$ gives the centrosymmetric, dinuclear complex $[Hpy]_2[UO_2L^1(NO_3)]_2$ (**1**), represented in Figure 1. The $L^1$ dianions chelate each of the metal ions, one of them through one oxygen atom of each acid group (O3, O5) and the other by a single acid group (O5, O6). The oxygen atoms O5 and O5′ are thus bridging the two metal centres in a $\mu_2$ fashion. The four U–$O_{carboxy}$ bond lengths are quite different (Table 1), likely as a result of the constraints arising from the rigid geometry of the ligand, the shortest being U–O3 and the longest U–O6′; the average U–(O5,O5′) bond [2.45(3) Å] is longer

[a] CEA/Saclay, DSM/DRECAM/SCM (CNRS URA 331), Bât. 125,
91191 Gif-sur-Yvette, France
E-mail: pierre.thuery@cea.fr

 © 2006 Wiley-VCH Verlag GmbH & Co. KGaA, Weinheim 

than U–O3 due to the bridging nature of these oxygen atoms. All these values are in the range of U–$O_{carboxy}$ distances for uranyl complexes reported in the CSD, 2.24–2.64 Å [mean value 2.42(7)]. The coordination sphere of the metal atom is completed by a bidentate nitrate ion, with an average U–O bond length of 2.509(3) Å, close to the mean value for bidentate nitrate ions in the CSD, 2.52(3) Å. The uranium atom is thus in a hexagonal-bipyramidal environment, quite usual when small-bite bidentate ligands are used, and is located at 0.0820(8) Å from the mean plane defined by the six equatorial donor atoms (r.m.s. deviation 0.039 Å). The coordination polyhedra of the two metal atoms share a common edge (O5–O5′), with a U···U′ distance of 4.2896(3) Å. A similar coordination mode is observed with other diacids, such as adipic acid, in which case the uranyl dimers are further linked in a three-dimensional network.[1c] The double negative charge of the complex is balanced by the positive charges of two pyridinium ions, which are involved in hydrogen bonds with the uncoordinated carboxylic oxygen atoms O4 and O4′ [N2···O4 2.677(4) Å, N2–H2···O4 170°]. It appears that, in contrast with tetrahydrofuran-2*r*,3*t*,4*t*,5*c*-tetracarboxylic acid, in which the acid groups are in the β- or γ-position relative to one another, their α-position in $L^1$ and the ensuing easy chelation of the metal ion through one oxygen atom from each result in these acid groups being nearly coplanar [dihedral angle between the two COO planes 34.3(4)°]. This ligand thus appears badly adapted to the synthesis of cyclic uranyl complexes.

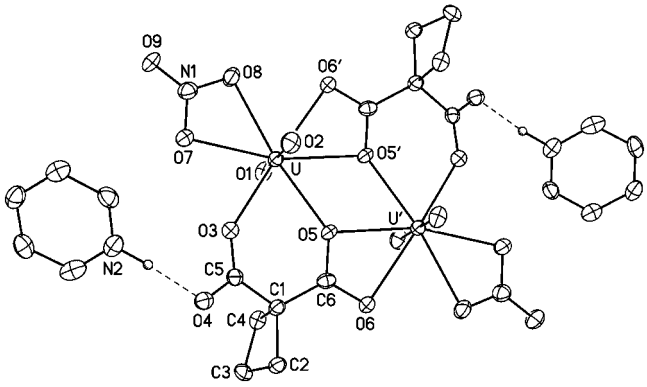


Figure 1. View of the complex $[Hpy]_2[UO_2L^1(NO_3)]_2$ (**1**). Hydrogen atoms not involved in hydrogen bonds have been omitted for clarity. Hydrogen bonds are shown as dashed lines. Displacement ellipsoids are drawn at the 50% probability level. Symmetry code: ′: 1 – *x*, 1 – *y*, 2 – *z*.

When treated with uranyl nitrate under conditions similar to those leading to complex **1**, $H_2L^2$ gives the complex $[UO_2L^2(py)_2]\cdot py$ (**2**). The two acid groups being in γ-positions with respect to one another and separated by the bulky methyl substituents, metal ion chelation through one atom from each group is no longer possible. Each acid group chelates a metal ion instead, giving rise to a one-dimensional polymer in which the motifs are related to one another by a binary screw axis (Figure 2a). The uranium atom is in a hexagonal-bipyramidal environment, being

Table 1. Environment of the uranium atoms: selected bond lengths [Å] and angles [°].

| | | | | |
|---|---|---|---|---|
| **1**[a] | U–O1 | 1.766(3) | O1–U–O2 | 177.47(13) |
| | U–O2 | 1.758(3) | O3–U–O5 | 68.09(10) |
| | U–O3 | 2.327(4) | O5–U–O5′ | 58.01(14) |
| | U–O5 | 2.424(2) | O5′–U–O6′ | 51.36(9) |
| | U–O5′ | 2.481(3) | O6′–U–O8 | 63.40(10) |
| | U–O6′ | 2.544(3) | O8–U–O7 | 51.03(11) |
| | U–O7 | 2.512(3) | O7–U–O3 | 68.02(9) |
| | U–O8 | 2.506(3) | | |
| **2**[b] | U–O1 | 1.759(6) | O1–U–O2 | 178.6(3) |
| | U–O2 | 1.772(7) | O3–U–O4 | 52.3(2) |
| | U–O3 | 2.420(6) | O4–U–N1 | 63.7(2) |
| | U–O4 | 2.471(6) | N1–U–O5′ | 65.4(2) |
| | U–O5′ | 2.464(6) | O5′–U–O6′ | 52.6(2) |
| | U–O6′ | 2.441(6) | O6′–U–N2 | 63.6(2) |
| | U–N1 | 2.552(6) | N2–U–O3 | 63.0(2) |
| | U–N2 | 2.569(7) | | |
| **3**[c] | U1–O1 | 1.766(9) | O1–U1–O2 | 177.4(4) |
| | U1–O2 | 1.753(8) | O5–U1–O9 | 85.5(3) |
| | U1–O5 | 2.312(9) | O9–U1–O13 | 76.9(3) |
| | U1–O9 | 2.354(8) | O13–U1–O11′ | 71.1(2) |
| | U1–O11′ | 2.519(7) | O11′–U1–O12′ | 52.8(2) |
| | U1–O12′ | 2.414(7) | O12′–U1–O5 | 74.1(3) |
| | U1–O13 | 2.393(8) | | |
| | U2–O3 | 1.741(8) | O3–U2–O4 | 178.1(4) |
| | U2–O4 | 1.755(8) | O6–U2–O10 | 79.4(3) |
| | U2–O6 | 2.330(8) | O10–U2–O7" | 77.3(3) |
| | U2–O10 | 2.294(7) | O7"–U2–O8" | 52.6(3) |
| | U2–O7" | 2.412(8) | O8"–U2–O14 | 72.8(3) |
| | U2–O8" | 2.497(7) | O14–U2–O6 | 78.1(3) |
| | U2–O14 | 2.365(8) | | |

[a] Symmetry code: ′: 1 – *x*, 1 – *y*, 2 – *z*. [b] Symmetry code: ′: 1.5 – *x*, –*y*, 0.5 + *z*. [c] Symmetry codes: ′: 1 – *x*, 0.5 + *y*, 1 – *z*; ″: –*x*, *y* – 0.5, –*z*.

bound, in addition to the two oxo atoms, to four carboxylic oxygen atoms [mean U–$O_{carboxy}$ bond length 2.45(2) Å] and two pyridine molecules in *trans* positions [mean U–N bond length 2.561(8) Å]. The metal atom is located at 0.010(3) Å from the mean equatorial plane (r.m.s. deviation 0.083 Å) and the dihedral angle between the equatorial planes of two successive metal atoms along the chain is 72.80(11)°. The geometry of the rigid ligand is not modified by metal ion coordination since the dihedral angle between the two COO planes is 63.2(8)° in **2**, whereas values in the range 61.9–63.4° are observed in the uncomplexed camphoric acid.[8,9] Such a value of the angle between uranyl equatorial planes and the overall coordination geometry could in principle lead to a cyclic species, but five units would be necessary for ring closure, giving a large complex probably less stable than the chiral, undulated chain which is formed instead. The packing of these chains gives rise to chiral channels directed along the *a*-axis in the crystal structure, in which the solvent pyridine molecules are located (Figure 2b) and which could in principle be interesting for the recognition of chiral guests. The absence of any significant π-stacking or CH···π interactions between host and guest suggests that the included pyridine molecules, held primarily by van der Waals interactions, have at most little contribution in the framework formation. This assemblage presents some similitude with several hydrogen-bonded organic-organic polymers including $H_2L^2$ and polyamines recently re-

 © 2006 Wiley-VCH Verlag GmbH & Co. KGaA, Weinheim 

ported.[9] With polyamines such as 1,2-bis(4-pyridyl)ethane or DABCO (1,4-diazabicyclo[2.2.2]octane), zigzag chains with curved parts defined by camphoric acid are observed, whereas 4,4′-bipyridine gives a spiral arrangement and other polyamines give more intricate sheets or frameworks. The coordination bonds with uranyl ions being much more directional than hydrogen bonds, the chains in **2** appear more regular (the polyamine complexes are highly disordered) and the separation between camphoric acid units is reduced. Moreover, no channels are formed in the case of the organic-organic chains analogous to those in complex **2**. This analogy between linear spacers such as 4,4′-bipyridine, which is much used, in association with 3d transition metal ions, to generate squares, boxes or cubes,[10] and the stereochemically constrained uranyl ion has been pointed out previously and several examples have been given of the use of uranyl ions as edge- or face-defining units.[3,11]

The presence of coordinated pyridine in complex **2** can be thought of as preventing the formation of a more extended assemblage. For this reason, the reaction between camphoric acid and uranyl nitrate under solvothermal conditions was repeated in a methanol/water solution and in the presence of NaOH as a base. The chiral complex thus obtained, $[UO_2L^2MeOH]\cdot MeOH$ (**3**), differs markedly from **2**. Each camphorate dianion bridges three uranium atoms, two of them in a monodentate ($\mu_2$-carboxylato-*O*,*O*′) and the other in a bidentate, chelating fashion (Figure 3a). Each metal atom is bound in its turn to three $L^2$ molecules [average $U–O_{carboxy}$ bond length 2.32(2) Å for the $\mu_2$-carboxylato-*O*,*O*′ groups and 2.46(5) Å for the chelating groups] and its environment is completed by a methanol molecule [average U–O bond length 2.379(14) Å, in agreement with the mean value from the CSD, 2.39(11) Å]. The metal atom environment is thus pentagonal-bipyramidal, as

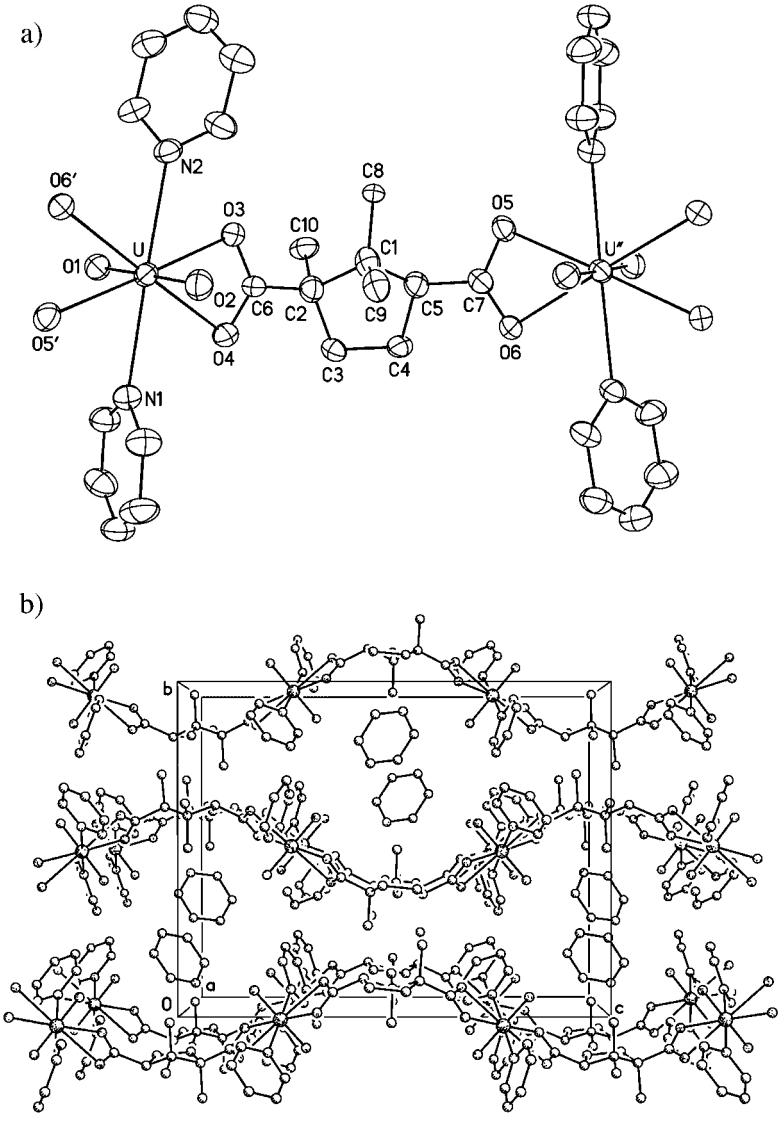


Figure 2. (a) View of the complex $[UO_2L^2(py)_2]\cdot py$ (**2**). Hydrogen atoms and solvent molecules have been omitted for clarity. Displacement ellipsoids are drawn at the 30% probability level. Symmetry codes: ′: 1.5 – *x*, –*y*, 0.5 + *z*; ″: 1.5 – *x*, –*y*, *z* – 0.5. (b) View of the packing along the *a*-axis. A single chain is shown at the top.

 © 2006 Wiley-VCH Verlag GmbH & Co. KGaA, Weinheim 

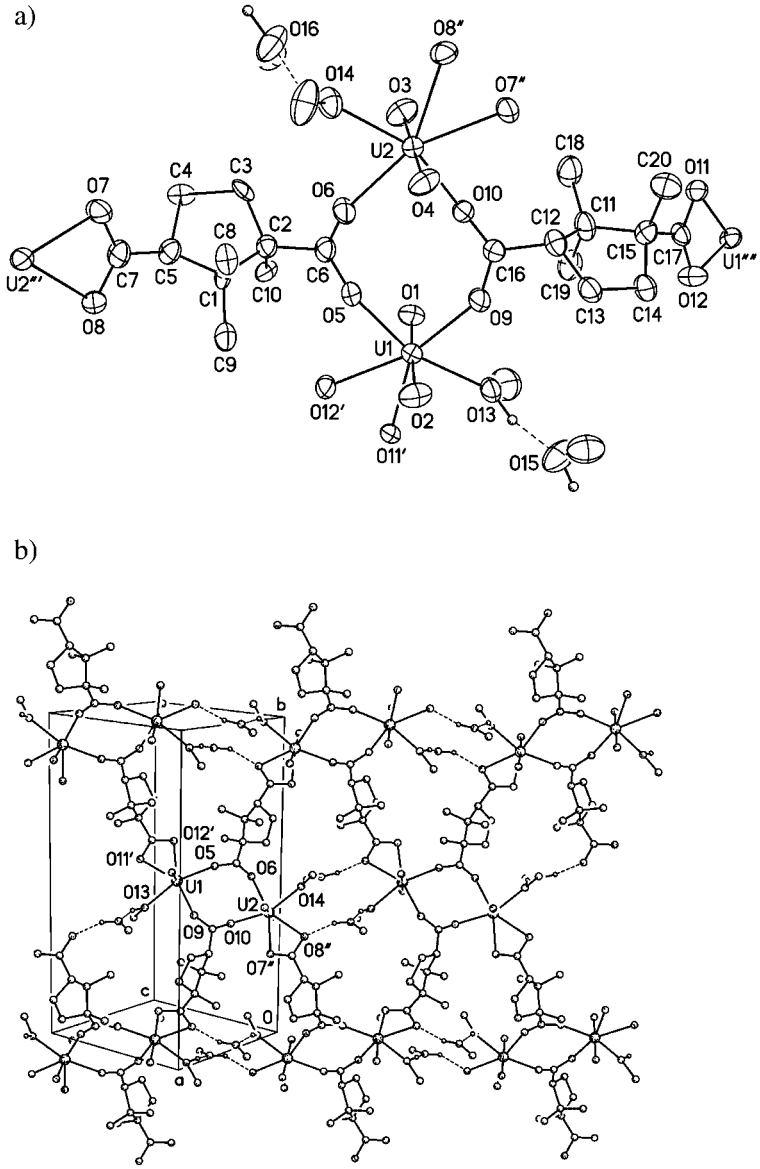


Figure 3. (a) View of the complex $[UO_2L^2MeOH]\cdot MeOH$ (**3**). Hydrogen atoms not involved in hydrogen bonds have been omitted for clarity. Hydrogen bonds are shown as dashed lines. Displacement ellipsoids are drawn at the 50% probability level. Symmetry codes: ′: 1 – *x*, 0.5 + *y*, 1 – *z*; ″: –*x*, *y* – 0.5, –*z*; ‴: –*x*, 0.5 + *y*, –*z*; ⁗: 1 – *x*, *y* – 0.5, 1 – *z*. (b) View of the two-dimensional assemblage in **3**.

expected since only one ligand is chelating. The metal centres are displaced by 0.004(4) and 0.003(4) Å from the associated equatorial mean planes (r.m.s. deviations 0.09 and 0.04 Å). The two uranium atoms linked by the $\mu_2$-carboxylato-*O*,*O*′ groups are separated by 5.5737(5) Å and they are part of a nearly planar eight-membered ring subunit [the dihedral angle between the two average uranyl equatorial planes is 7.2(4)°]. The four $L^2$ molecules which diverge from each subunit further assemble these subunits to form undulated sheets in which the curved parts correspond to the $L^2$ linkers [dihedral angle between the two COO planes: 66.2(12) and 63.3(10)° in the two independent molecules]. Larger, 32-membered elongated rings are formed in the process, which unite four $L^2$ ligands and four uranyl ions and are doubly bridged in their centre by the hydrogen-bonded and coordinated methanol molecules (Figure 3b). However, no channel is formed through the packing of these sheets, which does not involve inter-sheet hydrogen bonding. By contrast with the case of compound **2** in which it behaves as a simple spacer, $L^2$ appears in **3** to be able to act as a ring assembler, although not as a molecular metallacycle linker.

## Conclusions

The two acids investigated in this work present some characteristics, such as multiple coordination sites and rigidity, which make them attractive ligands for the synthesis of uranyl complexes, in the wake of the results previously obtained with other polyacids. However, the proximity of the two carboxylic groups in the α-diacid $H_2L^1$ favours ura-

 © 2006 Wiley-VCH Verlag GmbH & Co. KGaA, Weinheim 

nyl chelation through one oxygen atom from each group, leading, with further chelation of a second metal atom by one of the carboxylate groups, to the formation of a dimeric, dinuclear species. Conversely, the separation of the two carboxylic acid functions in the γ-diacid $H_2L^2$ prevents similar chelation, but, due to the insufficient curvature of the ligand, either chiral zigzag chains or undulated sheets are formed instead of a molecular metallacycle, which should likely be pentanuclear. Camphoric acid appears nevertheless to be a versatile ligand for metal complexation, leading to very different, one- or two-dimensional assemblages upon varying reaction conditions, and it should therefore benefit from a reappraisal in metal coordination chemistry, particularly for its potential in the synthesis of built-in chiral frameworks. The present results also illustrate the potential of solvothermal synthesis, which can permit the obtention of species unattainable through the more widely used hydrothermal method and also the synthesis of different species from the same building blocks with different organic solvents.

## Experimental Section

**Starting Materials:** 1,1-Cyclobutanedicarboxylic acid and (1*R*,3*S*)-(+)-camphoric acid were purchased from Aldrich and used without further purification.

**$[Hpy]_2[UO_2L^1(NO_3)]_2$ (1):** 1,1-Cyclobutanedicarboxylic acid (57 mg, 0.40 mmol), $UO_2(NO_3)_2{\cdot}6H_2O$ (100 mg, 0.20 mmol) and pyridine (3 mL) were placed in a 15-mL tightly closed vessel and heated at 145 °C under autogenous pressure. A few light-yellow single crystals of complex **1** were obtained in about two weeks.

**$[UO_2L^2(py)_2]{\cdot}py$ (2):** (1*R*,3*S*)-(+)-Camphoric acid (61 mg, 0.30 mmol), $UO_2(NO_3)_2{\cdot}6H_2O$ (151 mg, 0.30 mmol) and pyridine (4 mL) were placed in a 20-mL tightly closed vessel and heated at 125 °C under autogenous pressure. Light-yellow single crystals of complex **2** were obtained within 2 d.

**$[UO_2L^2MeOH]{\cdot}MeOH$ (3):** (1*R*,3*S*)-(+)-Camphoric acid (61 mg, 0.30 mmol), $UO_2(NO_3)_2{\cdot}6H_2O$ (151 mg, 0.30 mmol), NaOH (12 mg, 0.30 mmol), demineralized water (1.5 mL) and methanol (3 mL) were placed in a 20-mL tightly closed vessel and heated at 140 °C under autogenous pressure. Light-yellow single crystals of complex **3** were obtained within 3 d.

**X-ray Crystallography:** The data were collected at 100(2) K with a Nonius Kappa-CCD area detector diffractometer[12] using graphite-monochromated Mo-$K_\alpha$ radiation ($\lambda$ = 0.71073 Å). The crystals were introduced in glass capillaries with a protecting "Paratone-N" oil (Hampton Research) coating. The unit-cell parameters were determined from ten frames, then refined on all data. The data ($\varphi$- and $\omega$-scans) were processed with HKL2000.[13] The structures were solved by Patterson map interpretation (**1** and **2**) or by direct methods (**3**) with SHELXS-97 and subsequent Fourier difference synthesis and refined by full-matrix least squares on $F^2$ with SHELXL-97.[14] Absorption effects were corrected empirically with SCALEPACK.[13] All non-hydrogen atoms were refined with anisotropic displacement parameters. The solvent pyridine molecule in **2** was refined as an idealized hexagon with restraints on displacement parameters. The hydrogen atoms bound to the nitrogen atom of the pyridinium ion in compound **1** and to the oxygen atoms of the methanol molecules in **3** were found on Fourier difference maps and all the others were introduced at calculated positions; all were treated as riding atoms with an isotropic displacement parameter equal to 1.2 (OH, NH, CH, $CH_2$) or 1.5 ($CH_3$) times that of the parent atom. The absolute configuration in compounds **2** and **3** indicated by the value of the Flack parameter[15] is in agreement with that of the uncomplexed ligand $H_2L^2$. Crystal data and struc-

Table 2. Crystal data and structure refinement details.

| | **1** | **2** | **3** |
|---|---|---|---|
| Empirical formula | $C_{22}H_{24}N_4O_{18}U_2$ | $C_{25}H_{29}N_3O_6U$ | $C_{12}H_{22}O_8U$ |
| Formula mass | 1108.51 | 705.54 | 532.33 |
| Crystal system | triclinic | orthorhombic | monoclinic |
| Space group | $P\bar{1}$ | $P2_12_12_1$ | $P2_1$ |
| $a$ [Å] | 8.5930(4) | 9.6288(4) | 8.9042(4) |
| $b$ [Å] | 8.8937(5) | 14.7667(8) | 18.4850(11) |
| $c$ [Å] | 11.4899(7) | 19.1379(11) | 9.8137(5) |
| $\alpha$ [°] | 96.053(3) | 90 | 90 |
| $\beta$ [°] | 107.979(3) | 90 | 91.599(4) |
| $\gamma$ [°] | 113.464(3) | 90 | 90 |
| $V$ [Å$^3$] | 739.45(8) | 2721.1(2) | 1614.65(15) |
| $Z$ | 1 | 4 | 4 |
| $D_{calcd.}$ [Mg·m$^{-3}$] | 2.489 | 1.722 | 2.190 |
| $\mu$ (Mo-$K_\alpha$) [mm$^{-1}$] | 11.026 | 6.006 | 10.086 |
| $F$(000) | 512 | 1360 | 1000 |
| Reflections collected | 31496 | 56216 | 71395 |
| Independent reflections | 2797 | 5139 | 6083 |
| Observed reflections [$I > 2\sigma(I)$] | 2684 | 4761 | 5880 |
| $R_{int}$ | 0.071 | 0.067 | 0.033 |
| Parameters | 208 | 307 | 390 |
| $R_1$ | 0.023 | 0.039 | 0.036 |
| $wR_2$ (all data) | 0.049 | 0.106 | 0.104 |
| $S$ | 1.031 | 1.064 | 1.045 |
| Flack parameter | – | 0.006(14) | 0.003(13) |
| $\Delta\rho_{min.}$ [e·Å$^{-3}$] | –1.91 | –1.09 | –0.84 |
| $\Delta\rho_{max.}$ [e·Å$^{-3}$] | 1.37 | 1.20 | 1.36 |

 © 2006 Wiley-VCH Verlag GmbH & Co. KGaA, Weinheim 

ture refinement details are given in Table 2. The molecular plots were drawn with SHELXTL.[16] CCDC-604884 to -604886 contain the supplementary crystallographic data for this paper. These data can be obtained free of charge from The Cambridge Crystallographic Data Centre via www.ccdc.cam.ac.uk/data_request/cif.


[1] a) J. Y. Kim, A. J. Norquist, D. O'Hare, *Chem. Mater.* **2003**, *15*, 1970–1975; b) J. Y. Kim, A. J. Norquist, D. O'Hare, *Dalton Trans.* **2003**, 2813–2814; c) L. A. Borkowski, C. L. Cahill, *Inorg. Chem.* **2003**, *42*, 7041–7045; d) W. Chen, H. M. Yuan, J. Y. Wang, Z. Y. Liu, J. J. Xu, M. Yang, J. S. Chen, *J. Am. Chem. Soc.* **2003**, *125*, 9266–9267; e) Z. T. Yu, Z. L. Liao, Y. S. Jiang, G. H. Li, G. D. Li, J. S. Chen, *Chem. Commun.* **2004**, 1814–1815; f) M. Frisch, C. L. Cahill, *Dalton Trans.* **2005**, 1518–1523; g) Y. Z. Zheng, M. L. Tong, X. M. Chen, *Eur. J. Inorg. Chem.* **2005**, 4109–4117; h) W. Zhang, J. Zhao, *Inorg. Chem. Commun.* **2006**, *9*, 397–399; i) Y. S. Jiang, Z. T. Yu, Z. L. Liao, G. H. Li, J. S. Chen, *Polyhedron* **2006**, *25*, 1359–1366.

[2] P. Thuéry, *Chem. Commun.* **2006**, 853–855.

[3] P. Thuéry, C. Villiers, J. Jaud, M. Ephritikhine, B. Masci, *J. Am. Chem. Soc.* **2004**, *126*, 6838–6839.

[4] F. H. Allen, *Acta Crystallogr., Sect. B: Struct. Sci.* **2002**, *58*, 380–388.

[5] Z. Rzaczynska, A. Bartyzel, T. Głowiak, *J. Coord. Chem.* **2003**, *56*, 1525–1530.

[6] A. D. Burrows, R. W. Harrington, M. F. Mahon, S. J. Teat, *Eur. J. Inorg. Chem.* **2003**, 766–776.

[7] a) J. S. Seo, D. Whang, H. Lee, S. I. Jun, J. Oh, Y. J. Jeon, K. Kim, *Nature* **2000**, *404*, 982–986; b) Y. Cui, H. L. Ngo, P. S. White, W. Lin, *Chem. Commun.* **2002**, 1666–1667; c) T. Moriuchi, K. Yoshida, T. Hirao, *J. Organomet. Chem.* **2003**, *668*, 31–34; d) Z. L. Lü, W. Chen, J. Q. Xu, L. J. Zhang, C. L. Pan, T. G. Wang, *Inorg. Chem. Commun.* **2003**, *6*, 244–248; e) C. D. Wu, C. Z. Lu, S. F. Lu, H. H. Zhuang, J. S. Huang, *Dalton Trans.* **2003**, 3192–3198; f) D. Bradshaw, J. B. Claridge, E. J. Cussen, T. J. Prior, M. J. Rosseinsky, *Acc. Chem. Res.* **2005**, *38*, 273–282; g) S. Thushari, J. A. K. Cha, H. H. Y. Sung, S. S. Y. Chui, A. L. F. Leung, Y. F. Yen, I. D. Williams, *Chem. Commun.* **2005**, 5515–5517; h) A. S. F. Au-Yeung, H. H. Y. Sung, J. A. K. Cha, A. W. H. Siu, S. S. Y. Chui, I. D. Williams, *Inorg. Chem. Commun.* **2006**, *9*, 507–511.

[8] J. C. Barnes, J. D. Paton, C. S. Blyth, R. A. Howie, *Acta Crystallogr., Sect. C: Cryst. Struct. Commun.* **1991**, *47*, 1888–1892.

[9] C. M. Zakaria, G. Ferguson, A. J. Lough, C. Glidewell, *Acta Crystallogr., Sect. B: Struct. Sci.* **2003**, *59*, 118–131.

[10] J. W. Steed, J. L. Atwood, *Supramolecular Chemistry*, 1st ed., John Wiley & Sons, Chichester, UK, **2000**, pp. 478–497.

[11] P. Thuéry, B. Masci, *Supramol. Chem.* **2003**, *15*, 95–99.

[12] *COLLECT Software*, Nonius BV, Delft, The Netherlands, **1998**.

[13] Z. Otwinowski, W. Minor, *Methods Enzymol.* **1997**, *276*, 307–326.

[14] G. M. Sheldrick, *SHELXS-97* and *SHELXL-97*, University of Göttingen, Germany, **1997**.

[15] H. D. Flack, *Acta Crystallogr., Sect. A: Found. Crystallogr.* **1983**, *39*, 876–881.

[16] G. M. Sheldrick, *SHELXTL*, version 5.1, Bruker AXS Inc., Madison, WI, USA, **1999**.


Received: April 20, 2006
Published Online: July 28, 2006

 © 2006 Wiley-VCH Verlag GmbH & Co. KGaA, Weinheim 

DOI: 10.1002/ejic.200600437

# Bis[bis(oxazolinato)] Complexes of Yttrium and Lanthanum: Molecular Structure and Use in Polymerization of DL-Lactide and DL-β-Butyrolactone

**Ali Alaaeddine,[a] Abderramane Amgoune,[a] Christophe M. Thomas,[a] Samuel Dagorne,[b] Stéphane Bellemin-Laponnaz,[b] and Jean-François Carpentier*[a]**

**Keywords:** Homogeneous catalysis / Lanthanides / N ligands / Polymerization

Bis[bis(oxazolinato)]lanthanide complexes of general type $[Box]_2Ln[N(SiHMe_2)_2]$ (Ln = Y, La; Box = deprotonated chiral and nonchiral 2,2′-methylene[bis(oxazoline)] ligands) have been prepared by amine elimination protocols. The complexes have been characterized by $^1H$ and $^{13}C$ NMR spectroscopy and elemental analysis. The solid-state structure of the first bis[bis(oxazolinato)]-lanthanide complex, i.e. $\{2,2'$-(α-methylmethylene)bis(4,4-dimethyl-2-oxazolinato)$\}_2$-$Y[N(SiHMe_2)_2]$ (**1**), is reported. Complex **1** features a five-coordinate yttrium center in a distorted trigonal bipyramidal geometry, where the Box ligands adopts a conformation to minimize nonbonded interactions. The prepared complexes are among the most active initiators known in the ring-opening polymerization of DL-lactide and DL-β-butyrolactone, with TOF up to 31200 $h^{-1}$ at room temperature, and are highly productive (TON up to 2400). The produced poly(lactide)s and poly(hydroxybutyrate)s have narrow polydispersities ($M_w/M_n$ = 1.08–1.44) and controlled number-average molecular masses ($M_n$ up to 182000 g $mol^{-1}$). However, whether chiral or nonchiral Box ligands are used, the polymers show an atactic microstructure.

(© Wiley-VCH Verlag GmbH & Co. KGaA, 69451 Weinheim, Germany, 2006)

## Introduction

Ring-opening polymerization (ROP) of lactides (LA) and related lactone monomers has become a quite topical research field in recent years.[1] A reason for this interest is that the resulting biodegradable/biocompatible polymers, in addition to their high-tech applications,[1a,1b] could replace conventional polyolefinic materials.[2] An interesting challenge in this chemistry is to control the stereoselective ROP of *racemic* monomers, to produce in turn either syndiotactic, heterotactic, or isotactic stereoblock polymers, which each have their own peculiar physico-chemical properties.[1] Group 3 metal complexes are among the best catalysts/initiators for such ROP reactions.[1b,1c] For instance, we have recently reported that discrete group 3 complexes having a tetradentate [amino-ether-bis(phenolate)] ligand are highly active single-site initiators in the synthesis of heterotactic and syndiotactic poly(lactide) (PLA) from *rac*-lactide and *meso*-lactide, respectively.[3] The same complexes are also very active and stereoselective initiators for the controlled polymerization of *rac*-β-butyrolactone (BBL), generating highly syndiotactic poly(3-hydroxybutyrate) (PHB).[4]

Bis(oxazoline) (Box) are some of the most effective transition-metal ligands for a variety of asymmetric catalytic transformations.[5] Although the synthesis of mono- and bis[bis(oxazolinato)] organogroup 3 metal complexes has been known since 1999,[6] their use in catalysis has been so far limited to asymmetric hydroamination.[7] In this study we synthesized chiral and nonchiral bis[bis(oxazolinato)]-lanthanide complexes for the ROP of *rac*-lactide and *rac*-BBL. Their activity and degree of control have been investigated. The first X-ray-characterized bis[bis(oxazolinato)]-lanthanide catalyst precursor is also presented.

[a] Catalyse et Organométalliques, UMR 6226 CNRS-Université de Rennes 1,
35042 Rennes Cedex, France
Fax: +33-223-236-939
E-mail: jean-francois.carpentier@univ-rennes1.fr
[b] Laboratoire DECOMET, UMR 7177-LC3, Institut Le Bel, 4, rue Blaise Pascal, 67070 Strasbourg Cedex, France

## Results and Discussion

### Synthesis of Complexes

Bis[bis(oxazolinato)]-lanthanide complexes **1**–**6** of the type $[Box]_2Ln[N(SiHMe_2)_2]$ (Ln = Y, La; Box = deprotonated ligand) were prepared following the general σ-bond metathesis procedure reported by Anwander et al.[6,7] The reaction between 2 equiv. of a neutral Box ligand and a homoleptic precursor $Ln[N(SiHMe_2)_2]_3(THF)_2$ in benzene or toluene resulted in the protonolysis of two of the bulky (dimethylsilyl)amido ligands by the relatively acidic methine (**1**–**3**) or methylene (**4**–**6**) protons (Scheme 1). Yttrium and lanthanum were chosen for this study because they are representative of small and large lanthanides, respectively, and allow straightforward NMR studies thanks to their diamagnetism. The reaction is readily monitored by $^1H$ NMR spectroscopy. For all the ligand/metal systems investigated, the resulting reaction mixture remains a clear, homogeneous

 © 2006 Wiley-VCH Verlag GmbH & Co. KGaA, Weinheim 

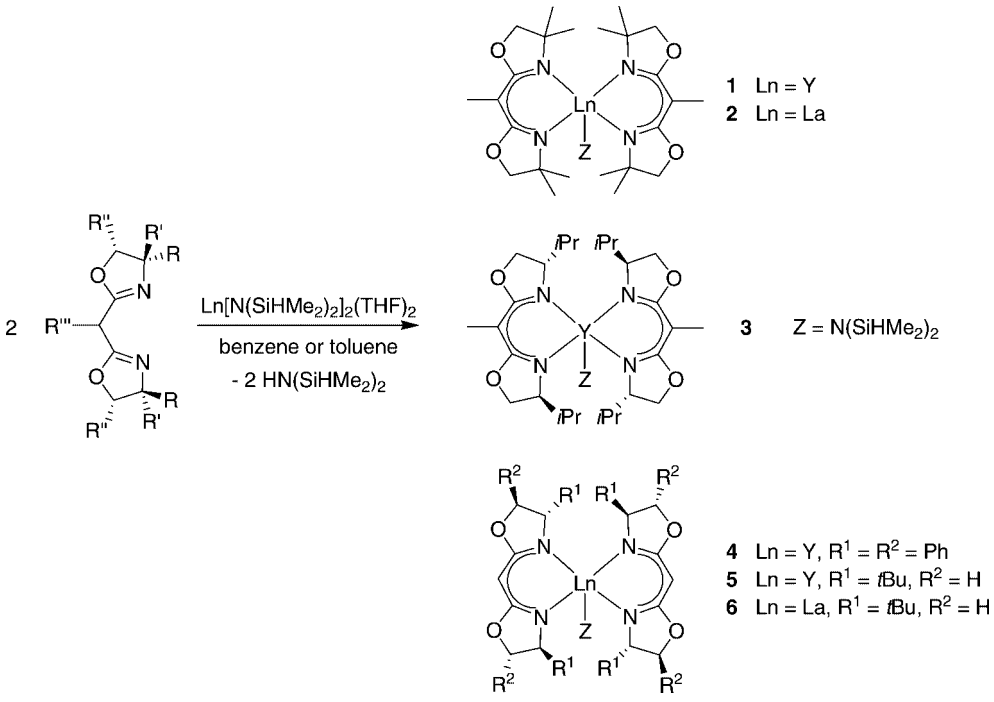


Scheme 1.

solution, and complete conversion of reagents is observed within 2 h at 20 °C. The resulting crude NMR shows clean release of 2 equiv. of $HN(SiHMe_2)_2$, with resonances for one major or exclusive (>95–99%) product $[Box]_2$-$Ln[N(SiHMe_2)_2]$. This good reactivity and selectivity allowed us to generate effectively in situ some of the complexes, and thus investigate the performances of a broad range of polymerization precursors (only a few of these are described in this report).

In addition to previously reported compounds **5** and **6**,[6] the identity of new complexes **1**–**4** was fully established by means of 1D and 2D $^1H/^{13}C$ NMR experiments and elemental analyses. Key NMR spectroscopic data include a single set of $^1H$ and $^{13}C$ resonances for two Box ligands equivalent on the NMR timescale at 20 °C. Also, two distinct $^{13}C$ resonances for inequivalent $SiH\mathit{Me}_2$ groups are observed in **1** ($\delta$ = 3.58, 3.29), **3** ($\delta$ = 3.71, 3.57) and **4** ($\delta$ = 3.51, 2.84); this is further confirmed by $^1H$ NMR spectroscopy in **3** ($\delta$ = 0.35, 0.32) and **4** ($\delta$ = 0.35, 0.18), but does not appear in the lower field $^1H$ NMR spectra (200–300 MHz) of **1**. The 300 MHz $^1H$ and 125 MHz $^{13}C$ NMR spectra of **2** show a single resonance for the $SiH\mathit{Me}_2$ groups, though incidental overlapping cannot be discarded.[6] Comparable to the case of **5** and **6**,[6] coordination of the chiral ligands in **3** and **4** renders the $SiHMe_2$ groups diastereotopic and inequivalent; however, this explanation cannot stand for the achiral complex **1**. On the other hand, the chemical shifts of the SiH protons (**1**, $\delta$ = 5.26; **2**, $\delta$ = 5.34; **3**, $\delta$ = 5.01; **4**, $\delta$ = 4.82 ppm) argue against any significant Si–H–Y β-agostic interaction.[8]

### Molecular Structure of {1,1-Bis[4,4-dimethyl-1,3-oxazolin-2-yl]}$_2$Y[N(SiHMe$_2$)$_2$] (1)

To gain a better insight into the above-mentioned structural features, an X-ray diffraction study was conducted on **1**. This is the first molecular structure reported for a bis-[bis(oxazolinato)]-lanthanide compound[9] and it can be compared to the only two examples of mono[bis(oxazolinato)]-lanthanide complexes that have been characterized so far in the solid state.[6,7] Suitable crystals of **1** were grown at room temperature from a saturated benzene solution. The unit cell contains two independent molecules (**A** and **B**), which feature overall the same structural arrangement and coordination geometry, but noticeable differences in bond lengths and angles; nonetheless, structural trends remain comparable within both molecules and mostly data of molecule **A** will be discussed below. An ORTEP view of molecule **A** is presented in Figure 1 and a partial list of bond lengths and angles for both molecules **A** and **B** is given in Table 1; complete details of the crystallographic analysis are given in Table 3.

Compound **1** is monomeric in the solid state, with a five-coordinate yttrium center ligated by the four nitrogen atoms of the two Box ligands, and one $N(SiHMe_2)_2$ group. The geometry at the yttrium center is distorted trigonal bipyramidal, with the apical sites being occupied by two Box nitrogen atoms [N(101) and N(121) in molecule **A**]. An approximate [noncrystallographic] $C_2$ symmetry axis exists through the $Y^{3+}$ and $N(SiHMe_2)_2$ centers. The Box ligands are oriented away from the $N(SiHMe_2)_2$ group in a horse

 © 2006 Wiley-VCH Verlag GmbH & Co. KGaA, Weinheim 

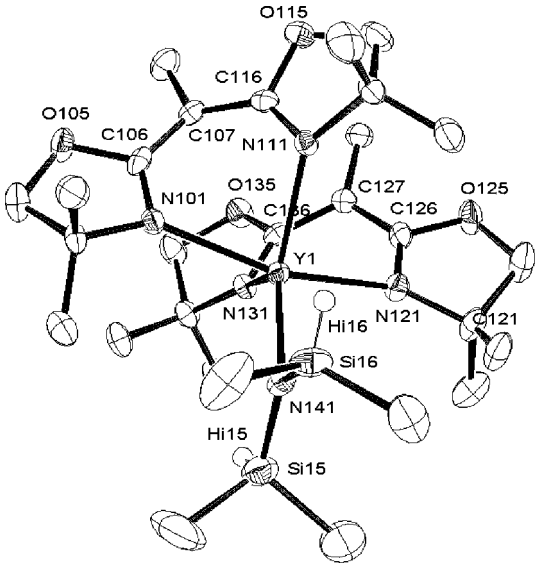


Figure 1. Molecular structure of $[Me_2Box]_2Y[N(SiHMe_2)_2]$ (**1**) (only molecule **A** is displayed). All hydrogen atoms, except those on Si atoms (Hi15 and Hi16), are omitted for reasons of clarity. Ellipsoids are drawn at the 50% probability level.

saddle fashion, thus minimizing steric hindrance. Comparable to that found in mono(Box)-lanthanide,[6,7] -copper,[10a] -rhodium,[10b] -aluminum,[11a] and -gallium[11b] complexes, significant delocalization of the ligand negative charge is suggested by the elongated N(101)–C(106) and N(111)–C(116) distances [1.321(3) and 1.322(3) Å, respectively] and the shortened C(106)–C(107) and C(116)–C(107) distances [1.401(4) and 1.406(4) Å, respectively]. The bis(oxazolinato) ligands in molecule **A** are somewhat dissymmetrically coordinated as apparent from the ca. 0.05–0.06 Å difference between the Y(1)–N(101)/Y(1)–N(111), and Y(1)–N(131)/Y(1)–N(131) distances, but the dissymmetry is less pronounced in molecule **B** (0.01–0.03 Å). Those Y–N(Box) distances in **1** [2.325(2)–2.389(2) Å] are longer than those in the four-coordinate mono[bis(oxazolinato)]-yttrium complex $[t\text{BuBox}]Y[N(SiHMe_2)_2]_2$ reported by Anwander et al. [2.288(5) Å],[6] reflecting the hindrance induced by the second Box ligand. Steric crowding in **1** is also reflected by the twisting angle between the two oxazoline ring planes relative to one another [mean plane N(101)/mean plane N(111), 32.7°; N(121)/N(131), 31.9°; N(201)/N(211), 32.4°; N(221)/N(231), 32.7°], values which are sig-

Table 1. Selected bond lengths [Å] and angles [°] for $[Me_2Box]_2Y[N(SiHMe_2)_2]$ (**1**).

| Molecule A | | Molecule B | |
|---|---|---|---|
| Bond lengths | | | |
| Y(1)–N(141) | 2.253(2) | Y(2)–N(241) | 2.241(2) |
| Y(1)–N(131) | 2.325(2) | Y(2)–N(231) | 2.355(2) |
| Y(1)–N(121) | 2.389(2) | Y(2)–N(221) | 2.366(2) |
| Y(1)–N(111) | 2.336(2) | Y(2)–N(211) | 2.365(2) |
| Y(1)–N(101) | 2.388(2) | Y(2)–N(201) | 2.332(2) |
| Y(1)–C(136) | 3.008(3) | Y(2)–C(236) | 3.041(3) |
| Y(1)–C(126) | 3.077(3) | Y(2)–C(226) | 3.088(3) |
| Y(1)–C(116) | 3.023(3) | Y(2)–C(216) | 3.087(3) |
| Y(1)–C(106) | 3.099(3) | Y(2)–C(206) | 3.039(3) |
| N(101)–C(106) | 1.321(3) | N(201)–C(206) | 1.326(3) |
| C(106)–C(107) | 1.401(4) | C(206)–C(207) | 1.408(3) |
| C(107)–C(116) | 1.406(3) | C(207)–C(216) | 1.407(3) |
| N(111)–C(116) | 1.322(3) | N(211)–C(216) | 1.317(3) |
| Si(15)–C(152) | 1.839(4) | Si(26)–C(262) | 1.864(3) |
| Si(15)–C(151) | 1.854(4) | Si(26)–C(261) | 1.872(3) |
| Si(16)–C(161) | 1.859(3) | Si(27)–C(271) | 1.856(3) |
| Si(16)–C(162) | 1.869(3) | Si(27)–C(272) | 1.868(3) |
| Bond angles | | | |
| N(141)–Y(1)–N(131) | 119.32(8) | N(241)–Y(2)–N(201) | 123.28(8) |
| N(141)–Y(1)–N(111) | 128.74(7) | N(241)–Y(2)–N(231) | 128.36(8) |
| N(131)–Y(1)–N(111) | 111.94(7) | N(201)–Y(2)–N(231) | 108.36(8) |
| N(141)–Y(1)–N(101) | 99.83(7) | N(241)–Y(2)–N(221) | 97.57(7) |
| N(131)–Y(1)–N(101) | 92.57(7) | N(201)–Y(2)–N(221) | 93.59(7) |
| N(111)–Y(1)–N(101) | 77.01(7) | N(201)–Y(2)–N(211) | 77.42(7) |
| N(141)–Y(1)–N(121) | 99.35(7) | N(241)–Y(2)–N(211) | 99.33(7) |
| N(131)–Y(1)–N(121) | 77.62(7) | N(231)–Y(2)–N(221) | 77.62(7) |
| N(111)–Y(1)–N(121) | 91.26(7) | N(231)–Y(2)–N(211) | 91.52(7) |
| N(101)–Y(1)–N(121) | 160.81(7) | N(211)–Y(2)–N(221) | 163.10(7) |
| C(106)–N(101)–Y(1) | 109.98(16) | C(206)–N(201)–Y(2) | 109.22(16) |
| N(101)–C(106)–C(107) | 129.3(2) | N(201)–C(206)–C(207) | 130.3(2) |
| C(106)–C(107)–C(116) | 119.3(2) | C(206)–C(207)–C(216) | 119.4(2) |
| N(111)–C(116)–C(107) | 130.4(2) | N(211)–C(216)–C(207) | 129.1(2) |
| C(116)–N(111)–Y(1) | 108.25(15) | C(216)–N(211)–Y(2) | 110.70(15) |
| Si(15)–N(141)–Y(1) | 119.96(11) | Si(26)–N(241)–Y(2) | 116.15(11) |
| Si(16)–N(141)–Y(1) | 111.66(11) | Si(27)–N(241)–Y(2) | 122.48(12) |
| Si(15)–N(141)–Si(16) | 128.35(13) | Si(25)–N(241)–Si(26) | 121.05(13) |

 © 2006 Wiley-VCH Verlag GmbH & Co. KGaA, Weinheim 

nificantly larger than those observed in mono[bis(oxazolinato)]-lanthanide complexes [12.4°, 15.7°].[6,7] On the other hand, the Y(1)–N(141) [2.253(2) Å] and Y(2)–N(241) [2.241(2) Å] silylamide bonds compare well to those in the four-coordinate [*t*BuBox]Y[N(SiHMe$_2$)$_2$]$_2$ [2.222(6) Å] and in the five-coordinate precursor amide complex [2.229(4)–2.276(4) Å].[12] The normal angles at the silylamide nitrogen atom and the long Y···H contact distances (>3.03 Å) argue against any significant β(Si–H)-Y agostic interaction, which is consistent with the NMR spectroscopic data (vide supra).

### Ring-Opening Polymerization of *rac*-Lactide and *rac*-β-Butyrolactone

The prepared bis[bis(oxazolinato)]-lanthanide complexes are very active in the ROP of *rac*-lactide and *rac*-β-butyrolactone under mild conditions (Scheme 2, Table 2); polymerization experiments conducted with mono[bis(oxazolinato)]-yttrium complexes, e.g. [*t*BuBox]Y[N(SiHMe$_2$)$_2$]$_2$, gave poorly reproducible results. Complexes **1**–**4** allow complete conversion of 100 equiv. of lactide within 5–10 min at room temperature in either toluene or THF solutions at [*rac*-LA] = 0.5–1.0 mol/L. The yttrium complex **5** that bears bulky *tert*-butyl-substituted BOX ligands is inactive in toluene (entry 4), which possibly reflects the large steric crowding at the metal center. However, this complex shows good activity in THF (entry 5), stressing the crucial importance of solvent in these ROPs.[3,4,13] Disappointingly, the use of chiral Box ligands in the initiators does not lead to stereocontrol of the polymerization: all PLA and PHB polymers, including also those produced with the achiral initiators **1** and **2**, show atactic (or slightly isotactic-enriched) microstructures, as determined by NMR analysis.[4,14] Contrary to our previous observations with [amino-ether-bis-

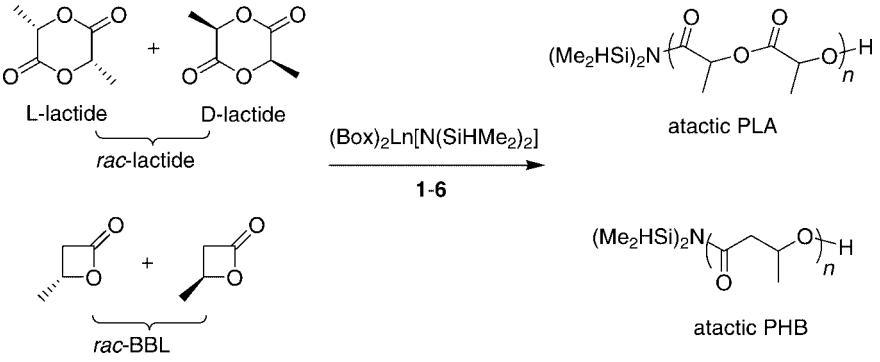


Scheme 2.

Table 2. Polymerization of *rac*-lactide and *rac*-β-butyrolactone with bis[bis(oxazolinato)]-lanthanide complexes.[a]

| Entry | M | [M]/[Ln] | Complex | Solvent | Time[b] | Conv.[c] | $M_{n,th}$[d] | $M_{n,exp}$[e] | $M_w/M_n$[e] |
|---|---|---|---|---|---|---|---|---|---|
| | | | | | [min] | [mol-%] | [g mol$^{-1}$] | [g mol$^{-1}$] | |
| 1 | *rac*-LA | 100 | **3** | toluene | 5 | >98 | 14400 | 18300 | 1.32 |
| 2 | *rac*-LA | 100 | **3** | THF | 5 | >98 | 14400 | 36400 | 1.34 |
| 3 | *rac*-LA | 100 | **4** | toluene | 10 | >98 | 14400 | 22400 | 1.29 |
| 4 | *rac*-LA | 100 | **5** | toluene | 20 | 0 | 14400 | – | – |
| 5 | *rac*-LA | 100 | **5** | THF | 20 | >98 | 14400 | 37000 | 1.36 |
| 6 | *rac*-LA | 100 | **6** | THF | 10 | 95 | 13700 | 18000 | 1.18 |
| 7 | *rac*-LA | 500 | **6** | THF | 1 | 95 | 68400 | 63000 | 1.29 |
| 8 | *rac*-LA | 100 | **1** | toluene | 5 | >98 | 14400 | 27600 | 1.25 |
| 9 | *rac*-LA | 100 | **1** | THF | 10 | >98 | 14400 | 33000 | 1.27 |
| 10 | *rac*-LA | 100 | **2** | THF | 10 | >98 | 14400 | 19000 | 1.22 |
| 11 | (*S*)-LA | 500 | **1** | THF | 5 | >98 | 72000 | 89000 | 1.44 |
| 12 | *rac*-LA | 500 | **1** | THF | 5 | 95 | 68400 | 68300 | 1.14 |
| 13[f] | *rac*-LA | 500 | **1** | THF | 10 | >98 | 14400 | 6000 | 1.07 |
| 14 | *rac*-LA | 1000 | **1** | THF | 120 | >98 | 144000 | 138000 | 1.24 |
| 15[g] | *rac*-LA | 1000 | **1** | THF | 20 | 95 | 45600 | 33000 | 1.08 |
| 16 | *rac*-LA | 2000 | **1** | THF | 5 | 95 | 273600 | 182000 | 1.37 |
| 17 | *rac*-LA | 4000 | **1** | THF | 5 | 65 | 374400 | ns[h] | ns[h] |
| 8 | *rac*-BBL | 200 | **1** | THF | 2 | 60 | 9900 | 8000 | 1.21 |
| 19 | *rac*-BBL | 200 | **5** | THF | 2 | >98 | 16800 | 17000 | 1.19 |
| 20 | *rac*-BBL | 200 | **5** | toluene | 2 | >98 | 16800 | 19000 | 1.14 |

[a] General conditions: [M] = 0.5–1.0 mol L$^{-1}$, $T$ = 20 °C. [b] Reaction time was not necessarily optimized. [c] Conversion of monomer M as determined by $^1$H NMR spectroscopy. [d] $M_n$ Value calculated from the relation: Molecular weight of M × conv. × [M]/[Ln]. [e] Experimental (uncorrected) $M_n$ and $M_w/M_n$ values determined by GPC in THF vs. polystyrene standards. [f] Reaction run in the presence of 5 equiv. (vs. Ln) of *i*PrOH. [g] Reaction run in the presence of 3 equiv. (vs. Ln) of *i*PrOH. [h] Polymer insoluble in hot THF.

 © 2006 Wiley-VCH Verlag GmbH & Co. KGaA, Weinheim 

(phenolate)]-lanthanide systems,[3,4] decreasing the temperature down to –20 °C and changing the solvent (toluene, THF) resulted in no enhancement in stereoselectivity. Polymerization of L-lactide by **1** (entry 11) or **3** resulted in pure isotactic PLA; the decoupled $^1$H NMR spectrum of the polymer showed one sharp resonance for the methine region. This observation supports the lack of base-promoted epimerization of L-lactide or PLA and argues against an anionic polymerization mechanism being operative.[15]

Because of the absence of stereocontrol with [Box]$_2$-Ln[N(SiHMe$_2$)$_2$] catalysts, further experiments aimed at investigating the degree of control of polymerization were carried out with the nonchiral systems **1** and **2** (entries 8–18). All the PLAs and PHBs obtained with amido complexes showed monomodal GPC traces with relatively narrow polydispersity values ($M_w/M_n$ = 1.14–1.44). In most cases, the experimental (uncorrected) number-average molecular mass ($M_n$) values are close to the theoretical ones (calculated on the assumption that each silylamide group initiates the polymerization). As shown by the monotonous relationship between the monomer-to-metal ratio and $M_n$ values (Figure 2), which is linear at least up to LA-to-Y = 1000, a good control of *rac*-LA polymerization is achieved with **1**. Even a catalyst loading of 0.05% yielded almost quantitatively PLA with $M_n$ as high as 182000 g mol$^{-1}$ (entry 16). The productivity of this system is remarkable, enabling high conversion for an unprecedented high *rac*-LA-to-Y ratio of 4000 within 5 min (TOF = 31200 h$^{-1}$) (entry 17). Very narrow polydispersities of 1.07–1.08 were obtained by pre-reacting the amido complex **1** with 2-propanol, to generate in situ the corresponding isopropoxide bis[bis(oxazolinato)] species (entries 13, 15). It is well known that isopropoxide is usually a better initiating group than amido [-N(SiMe$_3$)$_2$, -N(SiHMe$_2$)$_2$] for the ROP of *rac*-lactide at room temperature.[3b,16]

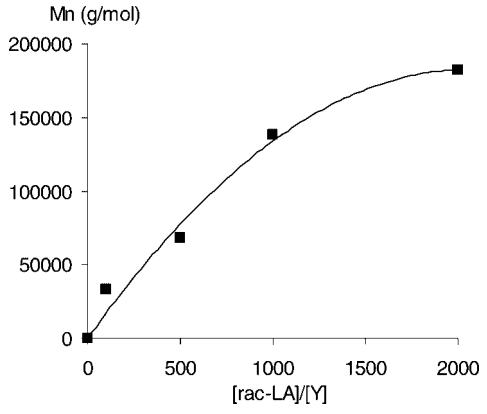


Figure 2. Variation of number-average molecular masses ($M_n$) with monomer-to-yttrium ratio in the polymerization of *rac*-lactide with complex **1** (see Table 2 for conditions).

The ROP of 200 equiv. of *rac*-BBL proceeded also in a controlled manner (entries 18–20). Surprisingly, the apparent rate is faster with **5** (TOF > 6000 h$^{-1}$) than **1** (TOF = 3600 h$^{-1}$). Even when the polymerization is conducted in toluene, **5** enables fast conversion of *rac*-BBL, i.e. the opposite trend to that observed for *rac*-lactide polymerization (entry 4). Reasons for this contradictory trend remain unclear to date, but concur with the peculiar behaviors of LA and BBL monomers in ROPs.

## Conclusions

Amido-bis[bis(oxazolinato)] complexes of yttrium and lanthanum, readily prepared from a tris(amido) lanthanide precursor and a Box ligand, are very active single-site initiators for the ROP polymerization of *rac*-lactide and *rac*-β-butyrolactone. Their performances in terms of kinetics and productivity compare favorably with the best systems so far disclosed. The polymerizations proceed in a controlled fashion, leading to PLAs and PHBs with relatively narrow polydispersities and number-average molecular masses in good agreement with calculated values. However, such complexes based on well-known chiral Box ligands appear unable to control the microstructure of the polymer: only atactic PLAs and PHBs are produced, which can be achieved as well with a cheaper nonchiral bis[bis(oxazolinato)]-lanthanide complex.

## Experimental Section

**General Considerations:** Synthesis of lanthanide complexes and polymerization experiments were carried out under purified argon using standard Schlenk techniques or in a high-performance (<1 ppm $O_2$, <2 ppm $H_2O$) glove box. Solvents (toluene, THF) and deuterated solvents ([D$_6$]benzene, [D$_8$]toluene, [D$_8$]THF/99.5% D, Eurisotop) were freshly distilled from Na/K alloy under nitrogen and degassed thoroughly by freeze-thaw-vacuum cycles prior to use. Bis(oxazoline) ligands were prepared following reported procedures[11a] or purchased from Aldrich and used as received. Lanthanide precursors Y[N(SiHMe$_2$)$_2$]$_3$(THF)$_2$ and La[N(SiHMe$_2$)$_2$]$_3$-(THF)$_2$,[17] and complexes **5** and **6**,[6] were prepared following literature procedures. Racemic lactide and *S*-lactide (Aldrich) were recrystallized twice from dry toluene and then sublimed under vacuum at 50 °C. Racemic β-butyrolactone (Aldrich) was freshly distilled from $CaH_2$ alloy under nitrogen and degassed thoroughly by freeze-thaw-vacuum cycles prior to use.

**Instruments and Measurements:** NMR spectra were recorded with Bruker AC-200, AC-300, and AC-500 spectrometers in Teflon valve NMR tubes. $^1$H and $^{13}$C chemical shifts are reported in ppm vs. SiMe$_4$ and were determined by reference to the residual solvent peaks. Assignment of signals was made from multinuclear 1D [$^1$H, $^{13}$C{$^1$H}] and 2D (COSY, HMQC, HMBC) NMR experiments. Coupling constants are given in Hertz. Size exclusion chromatography (SEC) of PLAs and PHBs was performed in THF at 20 °C using a Waters SIS HPLC pump, a Waters 410 refractometer, a DAD-UV detector, and Waters styragel columns (HR2, HR3, HR4, HR5E) or PL-GEL Mixte B and 100A columns. The number average molecular masses ($M_n$) and polydispersity index ($M_w/M_n$) of the resultant polymers were calculated with reference to a polystyrene calibration. The microstructure of PLAs was measured by homodecoupling $^1$H NMR spectroscopy at 20 °C in $CDCl_3$ with a Bruker AC-500 spectrometer. The microstructure of PHBs was measured by analyzing the carbonyl region of $^{13}$C{$^1$H} NMR spectra at 40 °C in $CDCl_3$ with a Bruker AC-500 spectrometer operating at 125 MHz.

 © 2006 Wiley-VCH Verlag GmbH & Co. KGaA, Weinheim 

**{2,2′-(α-Methylmethylene)bis(4,4-dimethyl-2-oxazolinato)}$_2$Y[N(SiHMe$_2$)$_2$] (1):** A solution of 2,2′-(α-methylmethylene)bis[4,4-dimethyl-2-oxazoline] (100 mg, 0.446 mmol) in toluene (5 mL) was added slowly under an inert atmosphere to a solution of Y[N(SiHMe$_2$)$_2$]$_3$(THF)$_2$ (140 mg, 0.223 mmol) in toluene (5 mL) at room temperature. The mixture was warmed at 70 °C and then stirred for 12 h. Volatiles were removed in vacuo and the resulting white solid was washed with cold hexane (1.0 mL), and dried under vacuum to give **1** (95 mg, 62%). $^1$H NMR (200 MHz, $C_6D_6$): $\delta$ = 5.26 (m, 2 H, Si*H*Me$_2$), 3.58 (d, $J$ = 7.7, 4 H, C*H*$_2$O), 3.45 (d, $J$ = 7.7, 4 H, C*H*$_2$O), 2.23 (s, 6 H, C*H*$_3$CCN), 1.43 (s, 12 H, C*H*$_3$), 1.04 (s, 12 H, C*H*$_3$), 0.45 (d, $J$ = 2.8 Hz, 12 H, Si*H*Me$_2$) ppm. $^{13}$C{$^1$H} NMR (75 MHz, $C_6D_6$): $\delta$ = 171.40 (N*C*O), 77.28 (*C*H$_2$O), 67.94 (Me*C*CN), 66.20 (*C*Me$_2$), 28.20 (C*Me*$_2$), 26.31 (C*Me*$_2$), 11.23 (*Me*CCN), 3.58 (SiH*Me*Me), 3.29 (SiHMe*Me*) ppm. $C_{28}H_{52}N_5O_4Si_2Y$ (667.82): calcd. C 50.36, H 7.85, N 10.49; found C 49.86, H 7.98, N 10.25.

**{2,2′-(α-Methylmethylene)bis(4,4-dimethyl-2-oxazolinato)}$_2$La[N(SiHMe$_2$)$_2$] (2):** Using the same procedure as used for synthesizing **1** (vide supra), compound **2** was obtained from La[N(SiHMe$_2$)$_2$]$_3$(THF)$_2$ (26.0 mg, 0.038 mmol) as a white solid (15 mg, 54%). $^1$H NMR (300 MHz, $C_6D_6$): $\delta$ = 5.34 [m, 2 H, Si*H*(CH$_3$)$_2$], 3.64 (m, 8 H, C*H*$_2$O), 2.35 (s, 6 H, C*H*$_3$CCN), 1.46 (s, 12 H, C*H*$_3$), 1.33 (s, 12 H, C*H*$_3$), 0.56 (d, $J$ = 2.8, 12 H, Si*H*Me$_2$) ppm. $^{13}$C{$^1$H} NMR (75 MHz, $C_6D_6$): $\delta$ = 169.90 (N*C*O), 77.39 (*C*H$_2$O), 64.57 (Me*C*CN), 62.21 (*C*Me$_2$), 29.99 (C*Me*Me), 27.62 (CMe*Me*), 11.62 (*Me*CCN), 2.81 (SiH*Me*$_2$) ppm. $C_{28}H_{52}LaN_5O_4Si_2$ (717.82): calcd. C 46.85, H 7.30, N 9.76; found C 46.12, H 7.68, N 9.65.

**{2,2′-(α-Methylmethylene)bis[(4*S*)-4-isopropyl-2-oxazolinato]}$_2$Y[N(SiHMe$_2$)$_2$] (3):** Using the same procedure as used for synthesizing **1** (vide supra), compound **3** was obtained from 2,2′-(α-methylmethylene)bis[(4*S*)-4-isopropyl-2-oxazoline] (100 mg, 0.400 mmol) and Y[N(SiHMe$_2$)$_2$]$_3$(THF)$_2$ (165 mg, 0.200 mmol) in benzene (10 mL) at 20 °C, and recovered as a white solid (73 mg, 66%). $^1$H NMR (500 MHz, $C_6D_6$): $\delta$ = 5.01 (m, 2 H, Si*H*Me$_2$), 3.92 (d, $J$ = 10.2, 4 H, C*H*$_2$O), 3.86 (d, $J$ = 10.2, 4 H, C*H*$_2$O), 3.65 (m, 2 H, NC*H*), 2.27 (s, 6 H, C*H*$_3$CCN + sept, 4 H, C*H*i Pr), 0.81 (d, $J$ = 6.7, 12 H, C*H*$_3$ *i*Pr), 0.72 (d, $J$ = 7.0, 12 H, C*H*$_3$ *i*Pr), 0.36 (d, $J$ = 1.9, 6 H, SiH*Me*$_2$), 0.32 (d, $J$ = 1.9, 6 H, SiH*Me*$_2$) ppm. $^{13}$C{$^1$H} NMR (125 MHz, $C_6D_6$): $\delta$ = 173.25 (N*C*O), 68.77 (*C*HN), 66.16 (*C*H$_2$O), 64.90 (Me*C*CN), 32.80 (*C*H *i*Pr), 19.80 (*C*H$_3$ *i*Pr), 15.06 (*C*H$_3$ *i*Pr), 12.26 (*Me*CCN), 3.71 (SiH*Me*Me), 3.57 (SiHMe*Me*) ppm. $C_{20}H_{32}N_5O_4Si_2Y$ (551.58): calcd. C 43.55, H 5.85, N 12.70; found C 43.26, H 5.93, N 12.67.

**NMR Scale Generation of {2,2′-Methylenebis[(4*S*,5*S*)-4,5-diphenyl-2-oxazolinato]}$_2$-Y[N(SiHMe$_2$)$_2$] (4):** Using the same procedure as used for synthesizing **3** (vide supra), compound **4** was generated at the NMR scale from Y[N(SiHMe$_2$)$_2$]$_3$(THF)$_2$ (14.0 mg, 0.022 mmol) and 2 equiv. of 2,2′-methylenebis[(4*S*,5*S*)-4,5-diphenyl-2-oxazoline] (20.0 mg, 0.044 mmol). NMR spectroscopy revealed complete conversion of the reagents to **4** with release of 2 equiv. of HN(SiHMe$_2$)$_2$ ($^1$H NMR: $\delta$ = 4.71, 0.11 ppm. $^{13}$C NMR: $\delta$ = 0.23 ppm). $^1$H NMR (200 MHz, $C_6D_6$): $\delta$ = 6.89 (m, 40 H, *Ph*), 5.94 [d, $J$ = 7.7, 4 H, C*H*Ph(O)], 5.56 [d, $J$ = 7.6, 4 H, C*H*PhN], 5.32 (s, 2 H, C*H*CCN), 5.06 (m, 2 H, Si*H*Me$_2$), 0.35 (d, $J$ = 2.8, 6 H, SiH*Me*$_2$), 0.18 (d, $J$ = 1.9, 6 H, SiH*Me*$_2$) ppm. $^{13}$C{$^1$H} NMR (75 MHz, $C_6D_6$): $\delta$ = 174.47 (N*C*O), 139.37 ($C_q$ Ph), 135.83 ($C_q$ Ph), 127.89 (*Ph*), 127.36 (*Ph*), 126.65 (*Ph*), 85.48 (*C*HPh), 71.77 (*C*HPh), 58.56 (*C*HCN), 3.51 (SiH*Me*Me), 2.84 (SiHMe*Me*) ppm.

**Crystal Structure Determination of 1:** A suitable single crystal of **1** was mounted onto a glass fiber using the "oil-drop" method. Diffraction data were collected at 100 K with an APEX 2 AXS-Bruker diffractometer with graphite monochromatized Mo-$K_\alpha$ radiation. The crystal structure was solved by means of direct methods, the remaining atoms were located from difference Fourier synthesis, followed by full-matrix least-squares refinement based on $F^2$ (program SIR-97).[18] Many hydrogen atoms could be found from the Fourier difference. Carbon-bound hydrogen atoms were placed at calculated positions and forced to ride on the attached carbon atom. The hydrogen atom contributions were calculated but not refined. All non-hydrogen atoms were refined with anisotropic displacement parameters. The unit cell of **1** was found to contain two independent molecules. The main crystallographic data are summarized in Table 3.

Table 3. Crystal data and structure refinement for **1**.

| | |
|---|---|
| Empirical formula | $C_{28}H_{52}N_5O_4Si_2Y$ |
| Formula weight | 667.83 |
| Temperature | 100(2) K |
| Wavelength | 0.71073 Å |
| Crystal system | monoclinic |
| Space group | $P2_1/c$ (no. 14) |
| Unit cell dimensions | $a$ = 11.762(3) Å |
| | $b$ = 34.259(9) Å |
| | $c$ = 17.378(5) Å |
| | $\beta$ = 91.914(13)° |
| Volume | 6999(3) Å$^3$ |
| $Z$ | 8 |
| Density (calculated) | 1.268 Mg m$^{-3}$ |
| Absorption coefficient | 1.771 mm$^{-1}$ |
| $F$(000) | 2832 |
| Crystal size | 0.30 × 0.25 × 0.20 mm |
| Theta range for data collection | 1.31 to 27.54° |
| Index ranges | $-12 \le h \le 15$, $-35 \le k \le 44$, |
| | $-22 \le l \le 22$ |
| Reflections collected | 73433 |
| Independent reflections | 15947 |
| Max. and min. transmission | –0.465 and 0.632 |
| Refinement method | Full-matrix least-squares on $F^2$ |
| Data/restraints/parameters | 15947/0/721 |
| Goodness-of-fit on $F^2$ | 1.037 |
| Final $R$ indices [$I > 2\sigma(I)$] | $R_1$ = 0.0423, $wR_2$ = 0.0845 |

CCDC-603139 contains the supplementary crystallographic data for this paper. These data can be obtained free of charge from The Cambridge Crystallographic Data Centre via www.ccdc.cam.ac.uk/data_request/cif.

**General Procedure for Lactide Polymerization:** In the glovebox, a Schlenk flask was charged with a solution of the initiator (typically 0.019 mmol, ca. 10 mg) in toluene (0.2 mL) or THF (0.2 mL). To this solution was added rapidly a solution of the monomer (*rac*-LA, S-LA, BBL) in the appropriate ratio in toluene or THF (3.0 mL). The mixture was immediately stirred with a magnetic stir bar at room temperature. Aliquots were periodically removed with a pipette for monitoring by $^1$H NMR spectroscopy. After the desired time, the reaction was quenched with acidic methanol (0.5 mL of a 1.2 M HCl solution), and the polymer was precipitated with excess methanol (100 mL). The polymer was then dried under vacuum to constant weight.

**General Procedure for *rac*-β-Butyrolactone Polymerization:** In the glovebox, a Schlenk flask was charged with a solution of the initiator (typically 0.014 mmol, ca. 10 mg) in toluene (1.0 mL) or THF (1.0 mL). *rac*-β-Butyrolactone (typically 2.64 mmol, 216 μL) was then syringed in dropwise under vigorous stirring at room temperature. After a small sample of the crude material was removed with a pipette for characterization by $^1$H NMR, the reaction was

 © 2006 Wiley-VCH Verlag GmbH & Co. KGaA, Weinheim 

quenched with acidic methanol (0.5 mL of a 1.2-M HCl solution in MeOH), and the polymer was precipitated with excess methanol (ca. 100 mL). The polymer was then dried under vacuum to constant weight.

## Acknowledgments

This research was in part supported by the Region Bretagne (COPOBIO program to AA) and the CNRS (ATIPE program to JFC). We gratefully thank Dr. Thierry Roisnel (X-ray diffraction center, University of Rennes 1) for the determination of the molecular structure of **1**.

[1] a) M. Okada, *Prog. Polym. Sci.* **2002**, *27*, 87–133; b) O. Dechy-Cabaret, B. Martin-Vaca, D. Bourissou, *Chem. Rev.* **2004**, *104*, 6147–6176; c) J. Wu, T.-L. Yu, C.-T. Chen, C.-C. Lin, *Coord. Chem. Rev.* **2006**, *250*, 602–626.

[2] R. E. Drumright, P. R. Gruber, D. E. Henton, *Adv. Mater.* **2000**, *12*, 1841–1846.

[3] a) C.-X. Cai, A. Amgoune, C. W. Lehmann, J.-F. Carpentier, *Chem. Commun.* **2004**, 330–331; b) A. Amgoune, C. M. Thomas, T. Roisnel, J.-F. Carpentier, *Chem. Eur. J.* **2006**, *12*, 169–179.

[4] A. Amgoune, C. M. Thomas, S. Ilinca, T. Roisnel, J.-F. Carpentier, *Angew. Chem. Int. Ed.* **2006**, *45*, 2782–2785.

[5] a) A. K. Ghosh, G. Bilcer, S. Fidanze in *The Chemistry of Heterocyclic Compounds* (Ed.: D. C. Palmer), Wiley, Hoboken, NJ, **2004**, *60*, pp. 529–594; b) D. Rechavi, M. Lemaire, *Chem. Rev.* **2002**, *102*, 3467–3493; c) J. S. Johnson, D. A. Evans, *Acc. Chem. Res.* **2000**, *33*, 325–335; d) A. K. Ghosh, P. Mathivanan, J. Cappiello, *Tetrahedron: Asymmetry* **1998**, *9*, 1–45.

[6] H. W. Gorlitzer, M. Spiegler, R. Anwander, *J. Chem. Soc., Dalton Trans.* **1999**, 4287–4288.

[7] S. Hong, S. Tian, M. V. Metz, T. J. Marks, *J. Am. Chem. Soc.* **2003**, *125*, 14768–14783.

[8] J. Eppinger, M. Spiegler, W. Hieringer, W. A. Herrmann, R. Anwander, *J. Am. Chem. Soc.* **2000**, *122*, 3080–3096 and references cited therein.

[9] For the crystal structure of a bis[bis(oxazoline)] complex, i.e. {[2,2′-(α,α-dimethylmethylene)bis{(4*R*,*S*)-4-phenyl-2-oxazoline}]$_2$Zn}[$ClO_4$]$_2$, see: S. Crosignani, G. Desimoni, G. Faita, S. Filippone, A. Mortoni, P. P. Righetti, M. Zema, *Tetrahedron Lett.* **1999**, *40*, 7007–7010.

[10] a) J. Hall, J.-M. Lehn, A. DeCian, J. Fischer, *Helv. Chim. Acta* **1991**, *74*, 1–6; b) J. M. Brown, P. J. Guiry, D. W. Price, M. B. Hursthouse, S. Karalulov, *Tetrahedron: Asymmetry* **1994**, *5*, 561–564.

[11] a) S. Dagorne, S. Bellemin-Laponnaz, R. Welter, *Organometallics* **2004**, *23*, 3053–3061; b) S. Dagorne, S. Bellemin-Laponnaz, A. Maisse-François, M.-N. Rager, L. Jugé, R. Welter, *Eur. J. Inorg. Chem.* **2005**, 4206–4214.

[12] W. A. Herrmann, F. C. Munck, G. R. J. Artus, O. Runte, R. Anwander, *Organometallics* **1994**, *16*, 682–688.

[13] E. L. Marshall, V. C. Gibson, H. S. Rzepa, *J. Am. Chem. Soc.* **2005**, *127*, 6048–6051.

[14] a) K. A. M. Thakur, R. T. Kean, E. S. Hall, J. J. Kolstad, T. A. Lindgren, M. A. Doscotch, J. I. Siepmann, E. J. Munson, *Macromolecules* **1994**, *30*, 2422–2428; b) J. E. Kasperczyk, *Macromolecules* **1995**, *28*, 3937–3939.

[15] a) B. M. Chamberlain, Y. Sun, J. R. Hagadorn, E. W. Hemmesch, V. G. Young Jr, M. Pink, M. A. Hillmyer, W. B. Tolman, *Macromolecules* **1999**, *32*, 2400–2402; b) M. H. Chisholm, N. W. Eilerts, *Chem. Commun.* **1996**, 853–854.

[16] a) M. Cheng, A. B. Attygalle, E. B. Lobkovsky, G. W. Coates, *J. Am. Chem. Soc.* **1999**, *121*, 11583–11584; b) H. Ma, J. Okuda, *Macromolecules* **2005**, *38*, 2665–2673.

[17] a) K. C. Hultzsch, P. Voth, K. Beckerle, T. P. Spaniol, J. Okuda, *Organometallics* **2000**, *19*, 228–243; b) R. Anwander, O. Runte, J. Eppinger, G. Gerstberger, E. Herdtweck, M. Spiegler, *J. Chem. Soc., Dalton Trans.* **1998**, 847–858.

[18] a) A. Altomare, M. C. Burla, M. Camalli, G. Cascarano, C. Giacovazzo, A. Guagliardi, A. G. G. Moliterni, G. Polidori, R. Spagna, *J. Appl. Crystallogr.* **1999**, *32*, 115–119; b) G. M. Sheldrick, *SHELXL-97*, University of Göttingen, Göttingen, Germany, **1999**.

Received: May 10, 2006
Published Online: July 27, 2006

 © 2006 Wiley-VCH Verlag GmbH & Co. KGaA, Weinheim 

DOI: 10.1002/ejic.200600198

# Luminescent Open-Framework Antiferromagnet – Hydrothermal Syntheses, Structures, and Luminescent and Magnetic Properties of Two Novel Coordination Polymers: $[Zn(pdoa)(bipy)]_n$ and $\{[Mn(pdoa)(bipy)](bipy)\}_n$ [pdoa = 2,2′-(1,3-phenylenedioxy)bis(acetate); bipy = 4,4′-bipyridine]

**Xian-Lan Hong,[a,b] Junfeng Bai,*[a] You Song,[a] Yi-Zhi Li,[a] and Yi Pan*[a]**

**Keywords:** Functional coordination polymers / Polycarboxylate ligands / 4,4′-Bipyridine / Luminescence

Two coordination polymers of mixed ligands, 2,2′-(1,3-phenylenedioxy)bis(acetate) (pdoa) and 4,4′-bipyridine (bipy), namely $[Zn(pdoa)(bipy)]_n$ (**1**) and $\{[Mn(pdoa)(bipy)](bipy)\}_n$ (**2**), have been hydrothermally synthesized and characterized by single-crystal X-ray diffraction and IR spectra. Complex **1** crystallizes in the triclinic space group $P\bar{1}$ with $a$ = 6.8826(18) Å, $b$ = 11.202(3) Å, $c$ = 12.295(3) Å, $\alpha$ = 86.854(4)°, $\beta$ = 85.759(5)°, $\gamma$ = 72.629(4)° and is a novel folded-paper-shaped coordination compound with polymeric sheets formed by the five-coordinate $Zn^{II}$ centers and bridging pdoa and bipy. Complex **2** crystallizes in the monoclinic space group $P2_1/c$ with $a$ = 11.507(2) Å, $b$ = 23.254(5) Å, $c$ = 9.8710(19) Å, $\beta$ = 96.418(4)° and exhibits a robust three-dimensional framework with nanosized rectangular channels (11.627 × 11.507 Å). They both display blue fluorescent emission and could be considered as new luminescent materials. In addition, the magnetic properties of complex **2** were investigated and the magnetic susceptibility data were rationally fitted with $g$ = 2.072(5), $J$ = –1.11(4) $cm^{-1}$, and $zJ'$ = –0.161(7) $cm^{-1}$, showing it is an unprecedented luminescent open-framework antiferromagnet.

(© Wiley-VCH Verlag GmbH & Co. KGaA, 69451 Weinheim, Germany, 2006)

## Introduction

In recent years, metal-organic coordination polymers based on multicarboxylate ligands have been of great interest because of their fascinating molecular topologies and crystal-packing motifs along with their outstanding properties in spectroscopy, magnetism, and catalysis, and potential applications as functional materials.[1] Much work has been focused on rigid ligands and flexible ligands such as benzenedicarboxylates[2] and aliphatic carboxylates,[3] respectively. However, there are few examples of ligands containing both aromatic and aliphatic features.[4] Moreover, the combination of both dicarboxylate and 4,4′-bipyridine ligands helps to assemble higher-dimensional supramolecular networks.[5] Meanwhile, chemists have been pursuing multifunctional materials for molecule devices. But, to the best of our knowledge, porous coordination networks usually exhibit a single functionality, such as luminescence or magnetic ordering.[6–9]

[a] State Key Laboratory of Coordination Chemistry & School of Chemistry and Chemical Engineering, Nanjing University, Nanjing 210093, P. R. China
E-mail: bjunfeng@nju.edu.cn
yipan@nju.edu.cn
[b] School of Public Health and Tropical Medicine, Southern Medical University,
Guangzhou 510515, P. R. China
E-mail: hongxianlan@yahoo.com.cn

We are interested in the utilization of polycarboxylate ligands with characteristics of both flexibility and rigidity, such as 2,2′-(1,4-phenylenedioxy)bis(acetate) and 2,2′-(1,3-phenylenedioxy)bis(acetate), which were initially investigated as herbicides and remained almost unexplored in the field of crystal engineering and supramolecular chemistry to construct coordination polymers.[10] The $–OCH_2–$ group makes these ligands more flexible in comparison with the corresponding benzenedicarboxylate, whilst the existence of the benzene ring provides a rigid element. Herein, we report hydrothermal syntheses, crystal structures, and solid-state photoluminescent and magnetic properties of two novel coordination polymers with mixed ligands, 2,2′-(1,3-phenylenedioxy)bis(acetate) (pdoa) and 4,4′-bipyridine (bipy), $[Zn(pdoa)(bipy)]_n$ (**1**) and $\{[Mn(pdoa)(bipy)](bipy)\}_n$ (**2**), in which complex **1** is an interesting 2D folded-paper-shaped structure, whereas complex **2** is an intriguing 3D framework structure with rectangular nanosized channels. Both, **1** and **2** display blue fluorescent emission, and complex **2** exhibits the characteristics of a weak antiferromagnetic coupling between metal ions in the system mediated by both types of the bridging ligands. Interestingly, to the best of our knowledge, complex **2** is the first example of an open-framework coordination polymer with conjugation of blue fluorescent emission and antiferromagnetic long-range ordering.

 © 2006 Wiley-VCH Verlag GmbH & Co. KGaA, Weinheim 

## Results and Discussion

### Description of the Crystal Structures

The asymmetric unit of compound **1** contains one $Zn^{2+}$ ion, one 2,2′-(1,3-phenylenedioxy)bis(acetate) ligand, and two half bipy molecules (Figure 1a). The zinc ion is five-coordinate in a distorted square-pyramidal environment of asymmetry with three oxygen atoms of two different carboxylate groups, one bipy nitrogen atom in the basal plane (O1, O2, O5, N2), and one nitrogen atom of another bipy ligand at the apex position (N1). Two carboxylate groups in the same pdoa molecule have different coordination modes, in which one acts as a chelating bidentate and the other serves as a monodentate ligand. The unequal coordination of two oxygen atoms (O1 and O5) from the chelating bidentate carboxylate moiety of pdoa results from the asymmetrical five-coordination environment. From the crystallographic data and selected bond lengths and angles for the title complexes (Tables 1 and 2), the lengths of Zn1–O1 [2.244(2) Å] and Zn1–O5 [2.131(2) Å] are similar to those, relative to the chelating bidentate carboxylate ligand, found in $[Zn_3(Hcit)_2(H_2O)_2]_n$ [2.318(2)–2.071(2) Å][11a] and $[Zn_4(OH)_2(fa)_3(bipy)_2]$ [2.367(4)–2.089(4) Å][11b] (Hcit and fa denote citric acid anion and fumarate, respectively). However, the separation of Zn1 from O2 of the monodentate $COO^-$ group [Zn1–O2 1.9369(18) Å] is significantly shorter than those relative to the chelating bidentate carboxylate ligand, but consistent with those referring to the monodentate carboxylate ligand in $[Zn_3(\mu_3\text{-}OH)(\mu_2\text{-}OH)(bipy)_{0.5}(oba)_2]\cdot 0.5H_2O$ [1.939(4) Å, oda = 4,4′-oxybis-(benzoate)][11c] and $[Zn_3(Hcit)_2(H_2O)_2]_n$ [2.028(2) Å],[11a] implying the existence of a certain tension in the four-membered ring formed between the chelating bidentate $COO^-$ group and the zinc ion. The Zn–N distances [Zn1–N1 2.048(2) Å and Zn1–N2 2.090(2) Å] are slightly shorter than those in structurally related polymers $[Zn(tp)(4,4'\text{-bipy})]_n$ [2.154(2) and 2.186 Å] (tp denotes terephthalate).[12] The $Zn^{2+}$ ions are linked by pdoa ligands forming infinite straight-linear chains along the *b*-axis. Furthermore, such linear chains are bridged at the point of $Zn^{2+}$ ions by bipy ligands to form two-dimensional sheets (Figure 2a), which have an interesting folded-paper-like topology as illustrated in Figure 2b. The two pyridine rings of the bipy molecule are almost coplanar (dihedral angle about 0.93°) and there is an inversion center at the midpoint of the C1–C1′ bond of each bipy ligand. The adjacent Zn···Zn distance due to the pdoa ligand in the same chain is 11.202(3) Å and the Zn···Zn distance between adjacent chains due to bipy is 11.170 (2) Å. Furthermore, the resulting 2D wave-like sheets superpose on each other with crest to crest, forming a 3D supramolecular lattice of noninterpenetration by weak C–H···O H bonds [C17#1–H17#1···O20 or C17–H17···O20#1, with a C···O distance of 3.468 Å and a C–H···O angle of 148.86°; symmetry code: #1: $1 - x$, $1 - y$, $1 - z$] and the offset face-to-face π–π stacking interactions between the pyridine ring of bipy and the phenyl ring of pdoa (represented as *α* and *β* in Figure 3, respectively, with a separation of 3.397 Å from *α* to *β*, and with an angle of 164.1° between them). These weak H bonds and π–π interactions are important in the construction of supramolecules, as is well documented in the literature.[13] Another interesting feature of the structure is that the pdoa ligands jut out and stand on the crests of folded-paper-like sheets, filling the voids among the layers (Figure 3).

As shown in Figure 1b, the asymmetric unit of complex **2** contains one $Mn^{2+}$ ion, one pdoa ligand, one coordinated, and one free bipy molecule. The Mn atom is in an octahedral environment with two bipy nitrogen donors (N1, N2#3) occupying the axial positions and four oxygen atoms (O2, O3#2, O5#4, O6#1) from four different pdoa ligands in the equatorial plane (symmetry codes: #1: $-1 + x$, $y$, $-1 + z$; #2: $x$, $1.5 - y$, $-0.5 + z$; #3: $1 - x$, $0.5 + y$, $0.5 - z$; #4: $-1 + x$, $1.5 - y$, $-0.5 + z$). The two pyridine rings of each coordinated or guest bipy molecule are not coplanar, and twisted around each other with dihedral angles 6.63(2)° and 6.75(2)° for coordinated and guest bipy, respectively, in contrast to those in complex **1** in which they are virtually coplanar. The axial Mn–N distances [Mn–N1 2.386(3);

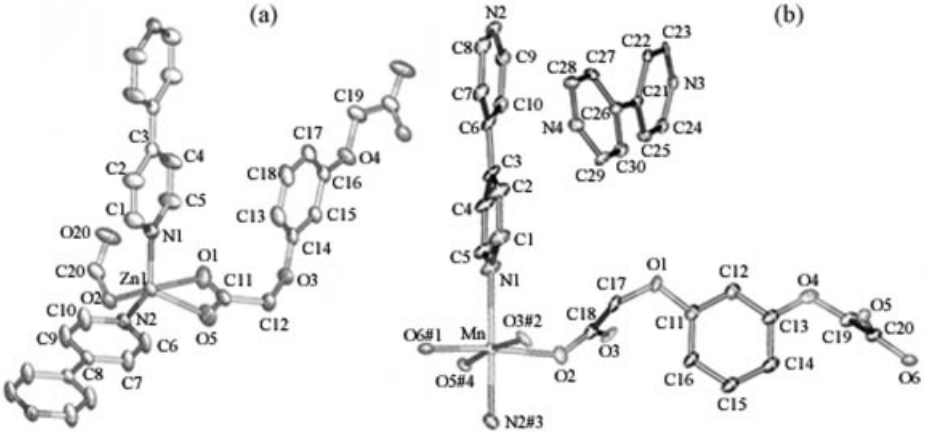


Figure 1. Structural plots showing the asymmetric unit and the metal ion's coordination environment for complexes **1** (a) and **2** (b); thermal ellipsoids are drawn at 30% probability and all the H atoms are omitted for clarity (symmetry codes: #1: $-1 + x$, $y$, $-1 + z$; #2: $x$, $1.5 - y$, $-0.5 + z$; #3: $1 - x$, $0.5 + y$, $0.5 - z$; #4: $-1 + x$, $1.5 - y$, $-0.5 + z$).

 © 2006 Wiley-VCH Verlag GmbH & Co. KGaA, Weinheim 

Table 1. Crystal data and details of the structure determination for complexes **1** and **2**.

| | **1** | **2** |
|---|---|---|
| Empirical formula | $C_{20}H_{16}N_2O_6Zn$ | $C_{30}H_{24}MnN_4O_6$ |
| Formula mass | 445.74 | 591.47 |
| Crystal system | triclinic | monoclinic |
| Space group | $P\bar{1}$ | $P2_1/c$ |
| $b$ [Å] | 11.202(2) | 23.254(5) |
| $c$ [Å] | 12.295(3) | 9.8710(19) |
| $\alpha$ [°] | 86.854(4) | 90 |
| $\beta$ [°] | 85.759(5) | 96.418(4) |
| $Z$ | 2 | 4 |
| $V$ [Å$^3$] | 901.7(4) | 2624.7(9) |
| $d_{calcd.}$ [g cm$^{-3}$] | 1.642 | 1.497 |
| $\mu$ [mm$^{-1}$] | 1.405 | 0.557 |
| $F$ (000) | 456 | 1220 |
| Crystal size [mm] | 0.30×0.30×0.20 | 0.32×0.22×0.18 |
| $\theta$ range [°] | 2.49–28.02 | 1.75–26.00 |
| Reflections collected | 5344 | 14053 |
| Unique reflections | 3954 [$R$(int) = 0.0730] | 5149 [$R$(int) = 0.0258] |
| $R$ indices [$I > 2\sigma(I)$] | $R_1$ = 0.0442, $wR_2$ = 0.1158 | $R_1$ = 0.0489, $wR_2$ = 0.1079 |
| $R$ indices (all data) | $R_1$ = 0.0485, $wR_2$ = 0.1182 | $R_1$ = 0.0742, $wR_2$ = 0.1151 |

Table 2. Selected bond lengths [Å] and angles [°] for complexes **1** and **2**.[a]

| | | | |
|---|---|---|---|
| **1** | | | |
| Zn1–O1 | 2.244(2) | Zn1–O2 | 1.9369(18) |
| Zn1–O5 | 2.131(2) | Zn1–N1 | 2.048(2) |
| Zn1–N2 | 2.090(2) | | |
| O1–Zn1–O2 | 100.70(8) | O1–Zn1–O5 | 59.11(8) |
| O1–Zn1–N2 | 149.44(9) | O2–Zn1–O5 | 133.92(10) |
| O2–Zn1–N1 | 116.57(8) | O2–Zn1–N2 | 97.15(8) |
| O5–Zn1–N1 | 106.05(10) | O5–Zn1–N2 | 90.75(8) |
| O1–Zn1–N1 | 92.71(9) | N1–Zn1–N2 | 101.23(8) |
| **2** | | | |
| Mn–O(6)#1 | 2.108(2) | Mn–O(3)#2 | 2.1422(17) |
| Mn–N(2)#3 | 2.164(2) | Mn–O(2) | 2.2044(19) |
| Mn–O(5)#4 | 2.2379(18) | Mn–N(1) | 2.386(3) |
| O(6)#1-Mn–O(3)#2 | 92.63(7) | O(6)#1-Mn–N(2)#3 | 85.42(8) |
| O(3)#2-Mn–N(2)#3 | 88.25(8) | O(6)#1-Mn–O(2) | 174.60(7) |
| O(3)#2-Mn–O(2) | 86.24(7) | N(2)#3-Mn–O(2) | 89.27(8) |
| O(6)#1-Mn–O(5)#4 | 93.08(7) | O(3)#2-Mn–O(5)#4 | 172.66(7) |
| N(2)#3-Mn–O(5)#4 | 87.62(7) | O(2)–Mn–O(5)#4 | 87.65(7) |
| O(6)#1-Mn–N(1) | 92.55(8) | O(3)#2-Mn–N(1) | 88.62(8) |
| N(2)#3-Mn–N(1) | 176.19(8) | O(2)–Mn–N(1) | 92.70(8) |
| O(5)#4-Mn–N(1) | 95.73(7) | | |

[a] Symmetry codes: #1: –1 + $x$, $y$, –1 + $z$; #2: $x$, 1.5 – $y$, –0.5 + $z$; #3: 1 – $x$, 0.5 + $y$, 0.5 – $z$; #4: –1 + $x$, 1.5 – $y$, –0.5 + $z$.

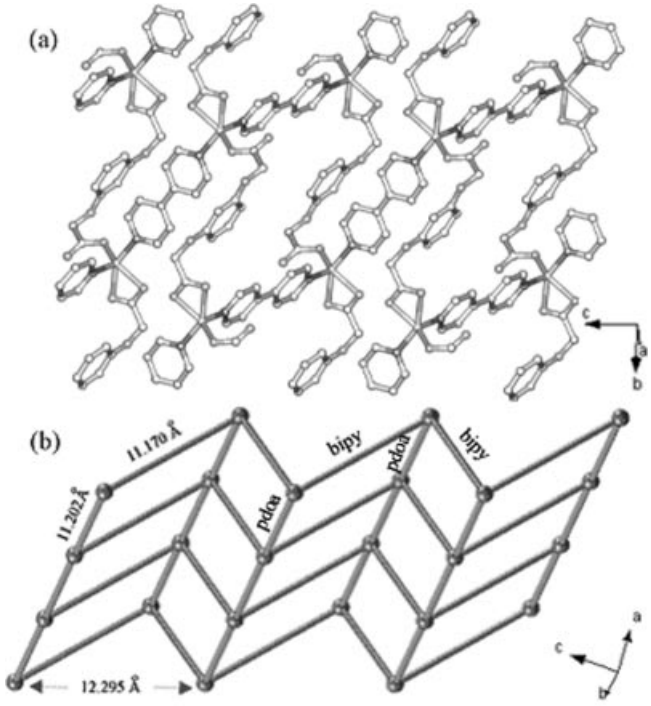


Figure 2. (a) Schematic illustration of the 2D network with all the H atoms omitted for clarity; (b) folded-paper-like topologic diagram of $[Zn(pdoa)(bipy)]_n$ (gray spheres denote zinc atoms).

Mn–N2#3 2.164(2)] and the Mn–O distances [Mn–O2 2.2044(19) Å; Mn–O3#2 2.1422(17) Å; Mn–O5#4 2.2379(18) Å; Mn–O6#1 2.108(2) Å] are comparable to those of analogous complexes,[14] indicating the manganese asymmetric coordination environment in terms of diversities of bond strength. All the carboxylate groups act as bis(unidentate) ligands and each pdoa ligand links four different manganese ions to form an equatorial $[Mn(pdoa)]_n$ sheet (Figure 4a), in which all the phenyl rings are parallel to each other and vertical to the crystallographic *ac* plane. The Mn···Mn separation due to pdoa is 11.507(3) Å, significantly larger than that of $[Mn(5\text{-methylpyrazole})_2(tp)]_n$ (9.655–9.659 Å) based on a tp ligand.[14b] It can be easily seen, from the view of the $[Mn(pdoa)]_n$ layer along the *c*-axis (Figure 4b), that all the manganese ions are not in one plane, instead alternatively situated above and below the plane between them. Interestingly, as shown in Figure 4a, this sheet contains distinctive duplex helixes of –Mn–O–C–O–Mn– with $Mn(O–C–O–)_2Mn$ eight-membered rings; the Mn···Mn distance relative to the bridging carboxylate group is 4.999(2) Å, similar to that of $[Mn(5\text{-methylpyrazole})_2(tp)]_n$ (4.917 Å),[14b] and shorter than that of $[Mn(bipy)(H_2O)(C_4H_4O_4)]\cdot 0.5bipy$ [5.264(1) Å, $C_4H_4O_4$ = succinate dianion].[14c] The analogous duplex helix was found in $Tb(bdc)NO_3\cdot 2DMF$ (bdc = 1,4-benzenedicarboxylate).[15]

 © 2006 Wiley-VCH Verlag GmbH & Co. KGaA, Weinheim 

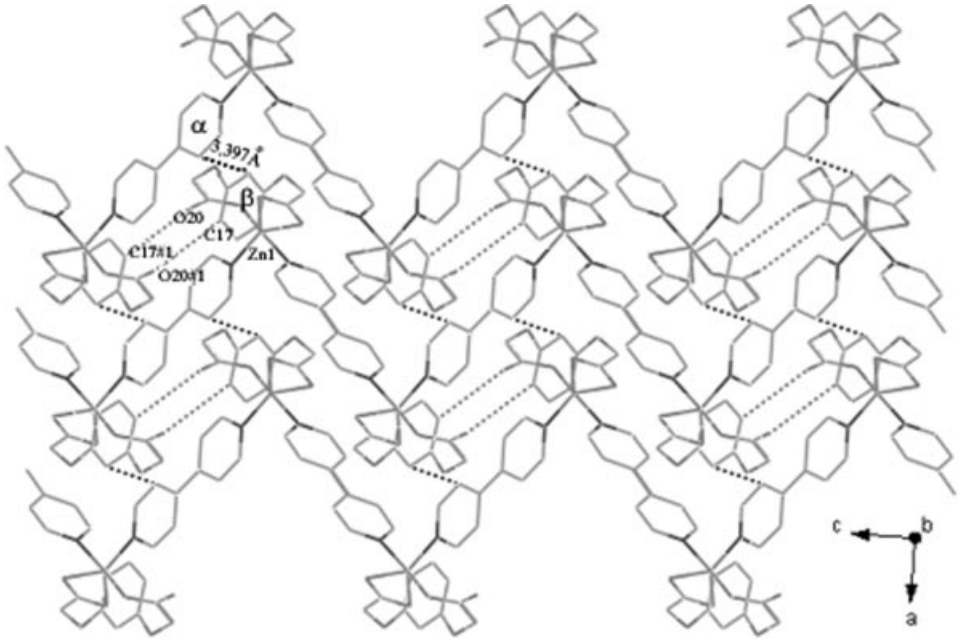


Figure 3. Perspective view along the *b*-axis of complex **1** showing the weak C–H···O H bonds (gray dotted lines) and the offset face-to-face π–π stacking interactions (dark gray dotted lines) between the puckered layers. All the H atoms have been omitted for clarity (symmetry code: #1: 1 – *x*, 1 – *y*, 1 – *z*).

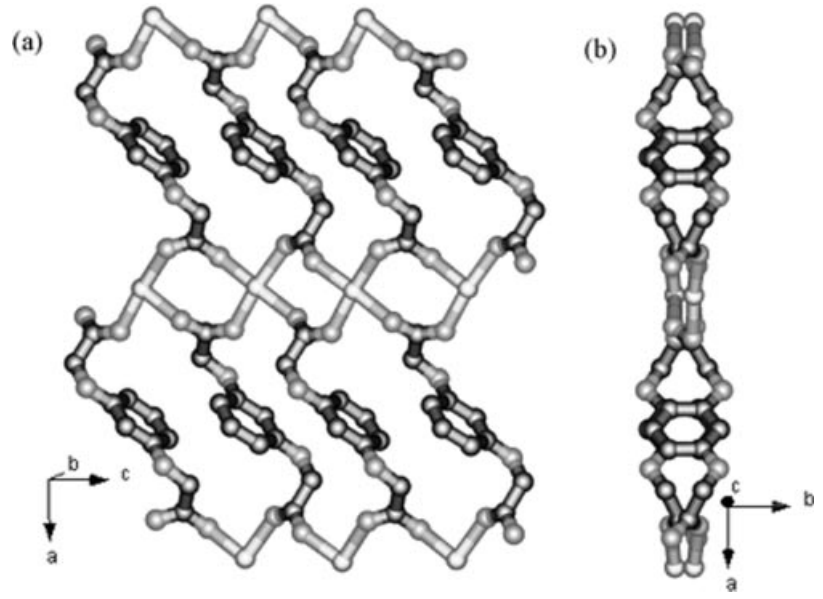


Figure 4. (a) Representation of the $[Mn(pdoa)]_n$ plane in complex **2**. (b) View of the $[Mn(pdoa)]_n$ plane in complex **2** along the *c*-axis. All hydrogen atoms have been omitted for clarity.

It is noteworthy that such a uniform $Mn^{II}$ carboxylate 2D sheet with only one coordination mode of the carboxylate moiety acting as bis(unidentate) bridging ligand to connect four metal ions in complex **2** is unprecedented.

Furthermore, the $[Mn(pdoa)]_n$ sheets are pillared by the rigid μ-4,4′-bipyridine ligands to form a 3D open framework exhibiting one-dimensional rectangular tunnels along the *c*-axis with dimensions of 11.627 × 11.507 Å (Figure 5a), which is considerably larger than that of reported manganese analogues.[14a,14c] To the best of our knowledge, this manganese inorganic-organic hybrid polymer with a noninterpenetration three-dimensional framework exhibits the largest channel among similar $Mn^{II}$ pillar-layered structures documented to date.[14]

The free bipy ligands as guest molecules and templates, like the examples,[16] reside at the 1D channel (Figure 5b). Unfortunately, removing the guest bipy molecules will give rise to collapse of the framework and decomposition of the whole complex, which was confirmed by thermal gravimetric analyses. Moreover, there exist weak H bonds between the guest and coordinated bipy molecules, as represented in Figure 5b, C4#5–H4#5···N3 and C4#7–H4#7···N3#6

 © 2006 Wiley-VCH Verlag GmbH & Co. KGaA, Weinheim 

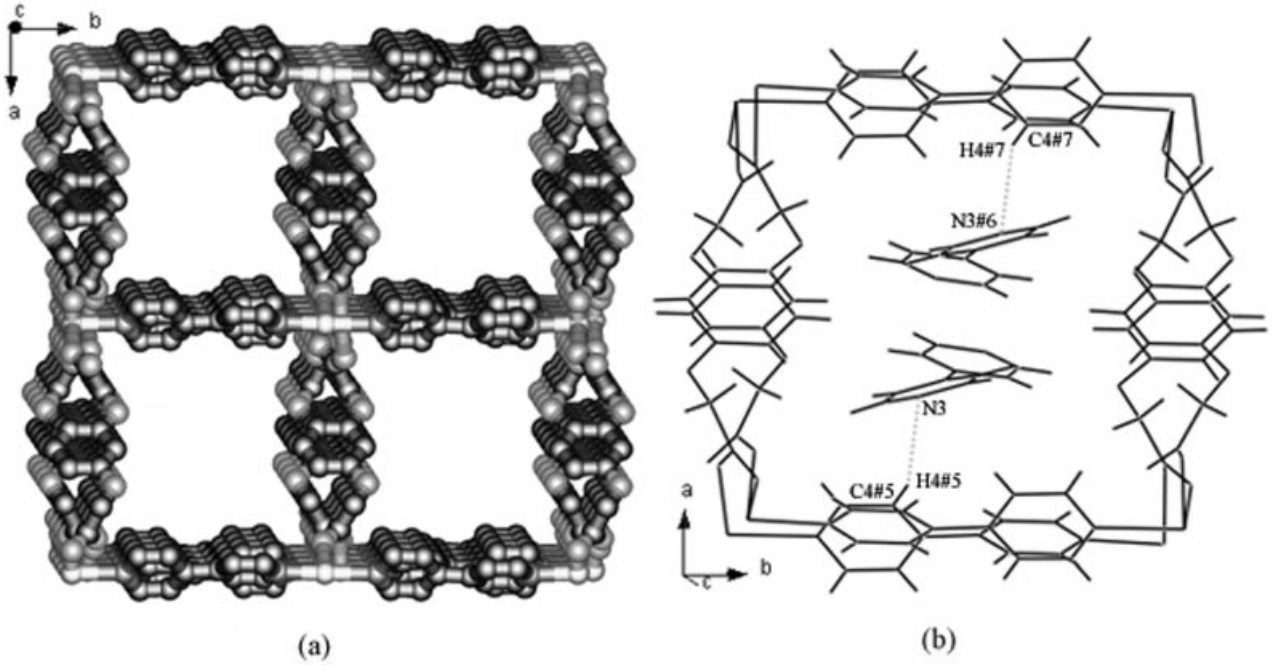


Figure 5. (a) Projection of the 3D network showing the rectangular channels along the *c*-axis in complex **2**. All hydrogen atoms and guest 4,4′-bipyridine molecules have been omitted for clarity. (b) A part of the side view of the 3D structure of **2** showing the guest 4,4′-bipyridine molecules residing at the 1D channel and the weak H bonds (C–H···N, shown as gray dotted lines) between the coordinated and guest 4,4′-bipyridine molecules (symmetry codes: #5: 1 – *x*, 1 – *y*, 1 – *z*; #6: 2 – *x*, 1 – *y*, 1 – *z*; #7: 1 + *x*, *y*, *z*).

(symmetry codes: #5: 1 – *x*, 1 – *y*, 1 – *z*; #6: 2 – *x*, 1 – *y*, 1 – *z*; #7: 1 + *x*, *y*, *z*); the C···N distance and the angle of C–H···N are 3.30 Å and 146.05°, respectively.

### IR Spectrum

As well documented in the literature,[17] IR spectra are very helpful in diagnosing characteristic coordination modes of carboxylate groups and determining the whole structure of previously unknown carboxylate complexes. The crystal structures provide us with an opportunity to investigate the IR spectral characters of pdoa complexes with three coordination modes [unidentate, chelating bidentate, and bridging bis(monodentate)]; representative data of IR spectra for pdoa, **1**, and **2** are tabulated in Table 3. Although the IR spectra of both complexes are complicated because of the overlap of the absorption of pdoa and bipy, several strong bands can be assigned in comparison with those of pdoa, bipy and other related complexes. The absence of the $\nu$(COOH) band at 1762 $cm^{-1}$ and the $\nu$(C–OH) band at 1267 $cm^{-1}$ of $H_2$pdoa in **1** and **2** suggests that all the carboxylate groups are completely deprotonated. The bands at 3086 and 3048 $cm^{-1}$ for **1** and **2** can be assigned to the C–H stretching vibration of the pdoa ligand in contrast to that of $H_2$pdoa (3083 $cm^{-1}$).[18] For complex **1**, the values of $\nu_{asym}$(OCO) and $\nu_{sym}$(OCO) corresponding to the unidentate mode are 1622 $cm^{-1}$ and 1380 $cm^{-1}$ respectively, which are similar to those of some carboxylate complexes with only unidentate coordination of the carboxylate group, such as [Zn(Pht)(py)$_2$] ($\nu_{asym}$: 1618 $cm^{-1}$; $\nu_{sym}$: 1390 $cm^{-1}$), [Zn(Pht)(mepy)$_2$] ($\nu_{asym}$: 1622 $cm^{-1}$; $\nu_{sym}$: 1372 $cm^{-1}$; here Pht, py, and mepy denote *o*-phthalic dianion, pyridine, and 3-methylpyridine, respectively),[19a] $ZnCl_2$(Hpipe-2)$_2$ ($\nu_{asym}$: 1635 $cm^{-1}$; $\nu_{sym}$: 1397 $cm^{-1}$), $ZnCl_2$(Hpipe-3)$_2$·3$H_2O$ ($\nu_{asym}$: 1626 $cm^{-1}$, $\nu_{sym}$ = 1387 $cm^{-1}$; Hpipe-2 = DL-piperidine-2-carboxylic acid, Hpipe-3 = DL-piperidine-3-carboxylic acid).[19b] However, the values of $\nu_{asym}$(OCO) and $\nu_{sym}$(OCO) relative to those of the chelating bidentate carboxylate group are 1608 $cm^{-1}$ and 1537 $cm^{-1}$, respectively, similar to those of [Zn(ip)(bipy)$_2$][Zn(ip)(bipy)]·0.25$H_2O$ ($\nu_{asym}$: 1615 $cm^{-1}$; $\nu_{sym}$: 1555 $cm^{-1}$; ip = iosphthalate).[19c] Because the $COO^-$ group has only one coordination mode in complex **2**, the very strong absorptions at 1596 and 1407 $cm^{-1}$ are assigned to $\nu_{asym}$(OCO) and $\nu_{sym}$(OCO), which are both highly blue-shifted in comparison with an analogous compound, [Mn(5-methylpyrazole)$_2$(tp)]$_n$ ($\nu_{asym}$: 1558 $cm^{-1}$; $\nu_{sym}$: 1374 $cm^{-1}$).[14b] Conclusively, the order of the separation between the asymmetric and symmetric stretching vibrations resulting from complexes **1** and **2** is Δ(unidentate, 242 $cm^{-1}$) > Δ(bridging bidentate, 189 $cm^{-1}$) > Δ(chelating bidentate, 71 $cm^{-1}$), supposing that the effects of variation of metal ions are relatively little to the value of Δ($\nu_{asym}$ – $\nu_{sym}$), which are well in accordance with the documented results of Deacon and Phillips.[17] In addition, the IR characteristics of bipy in complexes **1** and **2** are different. For complex **1**, the two pyridyl rings of bipy acting as a bidentate ligand are almost coplanar. Meanwhile, the bipy molecule has a center of symmetry, as indicated in the X-ray structure, and the in-plane C–H bending vibration (about 1215 $cm^{-1}$) loses its IR activity. However, for **2**, the two pyridyl rings of each free and coordinated bipy molecule are not coplanar; the IR properties of bipy in **2** are thus similar

 © 2006 Wiley-VCH Verlag GmbH & Co. KGaA, Weinheim 

Table 3. The data of IR spectra for $H_2$pdoa and complexes **1** and **2**.

| | |
|---|---|
| $H_2$pdoa | 3083 (w), 1762 (vs), 1710 (vs), 1596 (vs), 1494 (vs), 1433 (vs), 1340 (m), 1267 (s), 1248 (s), 1192 (vs), 1156 (s), 1087 (vs), 960 (m), 847 (s), 769 (s) |
| **1** | 3086 (w), 1638 (vs), 1608 (vs), 1537 (s), 1418 (s), 1380 (s), 1292 (s), 1220 (m), 1157 (vs), 1068 (s), 848 (m), 810 (vs), 764 (s), 725 (s), 638 (s) |
| **2** | 3048 (w), 1596 (vs), 1486 (w), 1407 (vs), 1322 (w), 1283 (s), 1181 (s), 1156 (vs), 1067 (s), 832 (m), 807 (vs), 717 (s), 626 (s), 605 (m) |

to those of pyridine. The strong absorption band at 1181 $cm^{-1}$ can be rationally attributed to the in-plane C–H bending vibration of bipy according to the literature.[20]

### Luminescent Properties

The excitation and emission spectra for $H_2$pdoa, $[Zn(pdoa)(bipy)]_n$, and $\{[Mn(pdoa)(bipy)](bipy)\}_n$ are shown in Figure 6. The excitation bands at 350 nm for $H_2$pdoa could be assigned to π→π* transitions of the O–$C_6H_4$–O group. Accordingly, the emissions spectra ($\lambda_{ex}$ = 350 nm) centered approximately at 394 nm can be assigned to the transition emission from the $T_1\pi,\pi^*$ and $T_1n,\pi^*$ to the ground state of the –$OC_6H_4O$– group.[21] For complex **1**, the band at 358 nm in the excitation spectra, similar to that of $H_2$pdoa, is associated with the π→π* transition of the O–$C_6H_4$–O unit. The band at 473 nm with a shoulder band at 530 nm in the emission spectrum is obviously different to that of $H_2$pdoa, and accordingly may be assigned to ligand-to-metal charge transfer (LMCT).[11b,11c,22] The excitation and emission spectra of **2** are very similar to those of **1** both in shape and position and are not characteristic of $Mn^{2+}$, with $3d^5$ electron configuration and octahedral coordination sphere according to the literature,[23] thus the excitation band at 356 nm can be assigned to the π→π* transition of the O–$C_6H_4$–O group, and the emission at 472 nm with the shoulder band at 535 nm to LMCT. Conclusively, both **1** and **2** may be used as blue-light-emitting functional materials. Complex **2**, with a combination of luminescent and magnetic properties (see below), may especially be a promising candidate for luminescent molecular magnetic materials.

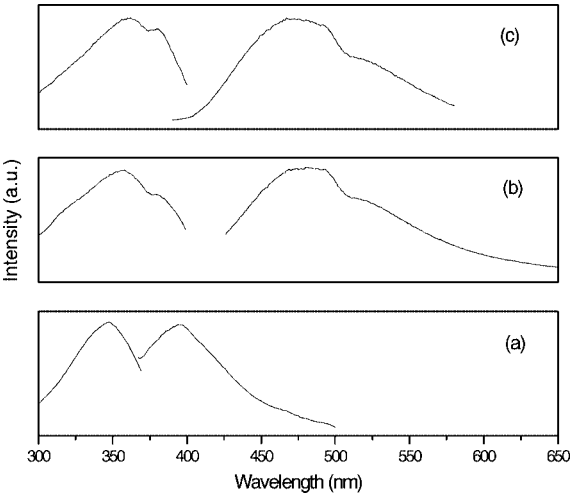


Figure 6. Solid-state excitation-emission spectra of $H_2$pdoa (a), complex **1** (b), and complex **2** at room temperature (c).

### Magnetic Properties

The temperature dependence of the magnetic susceptibility of complex **2** is depicted in Figure 7 in the form of the product $\chi_M T$ versus $T$ in the range of 300–1.8 K. The magnetic susceptibility is corrected for diamagnetism by using Pascal's constants. At room temperature, the product is 4.41 emu K $mol^{-1}$, which is the same as the spin-only value for $Mn^{2+}$ ($s$ = 5/2 and $g$ = 2.008 determined by EPR). As the temperature is lowered, the product $\chi_M T$ decreases steadily in the whole temperature range to 0.4 emu K $mol^{-1}$ at 1.8 K, indicating the antiferromagnetic interaction between $Mn^{II}$ ions through both bridging ligands bipy and carboxylate. Equally, a maximum was observed in the plot of $\chi_M$ versus $T$ (Figure 7), which is the nature of antiferromagnetic coupling between $Mn^{II}$ ions. The magnetic susceptibility data were fitted assuming that the carboxylate bridges between $Mn^{II}$ ions form a uniform chain with exchange constant $J$ and then bipy and pdoa connect the chains to form the 3D structure of this complex with an exchange constant $zJ'$. Thus, the expression in the literature can be written as Equations (1) and (2) for the magnetic fittings,[24] where $u = \coth[JS(S+1)/kT] - kT/JS(S+1)$.

$$\chi_{chain} = \frac{Ng^2\beta^2}{3kT}\frac{1+u}{1-u}S(S+1) \quad (1)$$

$$\chi_M = \frac{\chi_{chain}}{1-\chi_{chain}(2zJ'/Ng^2\beta^2)} \quad (2)$$

The best parameters obtained by a standard least-squares fitting were $g$ = 2.072(5), $J$ = –1.11(4) $cm^{-1}$, and $zJ'$ = –0.161(7) $cm^{-1}$ with $R = 4.3\times10^{-6}$ [$R = \sum|(\chi_M)_{exp} - (\chi_M)_{calc}|^2/\sum(\chi_M)^2_{exp}$]. Thus, the bipy and pdoa ligands mediate the very weak antiferromagnetic interaction between the $Mn^{II}$ ions in this system.

For a 3D antiferromagnetic complex, an observed maximum in the plot of $\chi_M$ versus $T$ implies the presence of a possible long-range anriferromagnetic ordering. It is confirmed by the specific heat ($C_p$) determination with a physical property measurement system (PPMS) at $10^{-4}$ Torr and zero field. The total specific heat ($C_p$) of complex **2** at low temperatures in the range of 1.8–8.5 K was determined ex-

 © 2006 Wiley-VCH Verlag GmbH & Co. KGaA, Weinheim 

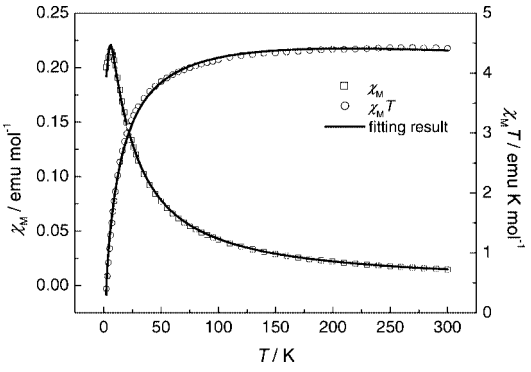


Figure 7. Temperature dependence of magnetic properties of complex **2** in the form of $\chi_M T$ (○) vs. $T$ and $\chi_M$ (□) vs. $T$; the solid line is the fitting of experimental data.

perimentally and the result is shown in Figure 8. It is accepted that the lattice-specific heats generally vary smoothly with the temperature and are not influenced greatly by the details of the structure. Therefore, we can gain insight into the magnetic properties from the variance of the total specific heat with the change of temperature. As seen in Figure 8, a peak is observed at 1.9 K and the lambda shape is similar to those of some one-dimensional antiferromagnetic compounds, such as $CsMnCl_3 \cdot 2H_2O$, $MnF_2$, and $(CH_3)_4NMnCl_3$.[25] The plot of $C_p$ versus $T$ further confirms the antiferromagnetic interaction between the $Mn^{II}$ ions in complex **2**; there is long-range ordering below 1.9 K (Neel temperature). Similar behavior was found in $[Mn_2(pm)]$, where pm represents 1,2,4,5-benzenetetracarboxylate.[26] To the best of our knowledge, complex **2** represents the first example of an open-framework coordination polymer with conjugation of blue fluorescent emission and antiferromagnetic long-range ordering, a promising candidate for multifunctional materials, such as luminescent molecular magnetic materials.

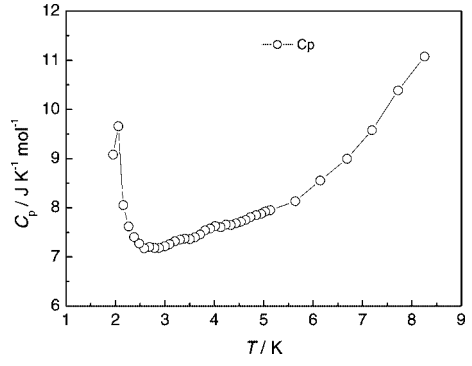


Figure 8. Total specific heat, $C_p$, plotted against temperature, $T$, for complex **2** between 1.8 and 8.5 K.

## Conclusions

Two coordination polymers containing 2,2′-(1,3-phenylenedioxy)bis(acetate) (pdoa) and 4,4′-bipyridine (bipy) with formulae $[Zn(pdoa)(bipy)]_n$ (**1**) and $\{[Mn(pdoa)(bipy)](bipy)\}_n$ (**2**) have been synthesized and characterized by single-crystal X-ray diffraction analyses and IR spectra and their luminescent properties and the magnetic behaviors have been investigated. The reactions of $ZnCl_2$ and $Mn(OOCCH_3)_2$ with pdoa and bipy under the same conditions result in strikingly different structures. Complex **1** has an interesting 3D noninterpenetration supramolecular structure, whereas complex **2** forms under the same reaction conditions an intriguing 3D open-framework structure with rectangular nanosized channels. The order of the separation between the asymmetric and symmetric stretching vibration is Δ(unidentate) > Δ(bridging bidentate) > Δ(chelating bidentate) according to the IR data. Both **1** and **2** display blue fluorescent emission, indicating that they are potentially luminescent materials. The magnetic studies in the range 300–1.8 K indicate that complex **2** displays the characteristics of a weak antiferromagnetic coupling between metal ions in the system mediated by both types of bridging ligands between the $Mn^{II}$ ions. Complex **2** is the first example of an open-framework coordination polymer with conjugation of blue fluorescent emission and antiferromagnetic long-range ordering, a promising candidate for multifunctional materials, such as luminescent molecular magnetic materials.

## Experimental Section

**Materials and Methods:** 2,2′-(1,3-Phenylenedioxy)bis(acetatic acid) was prepared according to a literature method;[10c] other reagents were commercially available and used without further purification.

**Synthesis of $[Zn(pdoa)(bipy)]_n$ (1):** A mixture of $ZnCl_2$ (0.07 g, 0.5 mmol), 4,4′-bipyridine (0.078 g, 0.5 mmol), 2,2′-(1,3-phenylenedioxy)bis(acetic acid) (0.113 g, 0.5 mmol), methanol (10 mL), and $H_2O$ (10 mL) was placed in a 25-mL Teflon-lined autoclave and heated to 120 °C for 72 h. Then the solution was cooled to room temperature and prismatic yellow crystals were obtained, which were filtered and washed with water and air-dried. Yield (based on $ZnCl_2$): 0.0141 g (20.1%). $C_{20}H_{16}N_2O_6Zn$ (445.74): C 53.89, H 3.62, N 6.28; found C 53.71, H 3.34, N 6.08.

**Synthesis of $\{[Mn(pdoa)(bipy)](bipy)\}_n$ (2):** Synthesized as brown block-shaped crystals in an identical manner to that of **1** with manganese(II) acetate tetrahydrate (0.122 g, 0.5 mmol) in place of $ZnCl_2$. Yield [based on $Mn(CH_3COO)_2 \cdot 4H_2O$]: 0.020 g (16.4%). $C_{30}H_{24}MnN_4O_6$ (591.47): C 60.92, H 4.09, N 9.47; found C 60.71, H 3.82, N 9.23.

**Physical Measurements:** Elemental analyses were carried out with a PE-2400CHN analyzer. The IR spectra were recorded with a Bruker VECTOR22 FTIR spectrometer in KBr pellets. Fluorescence measurements were performed with an AMINCO-Bowman Series $AB_2$ Luminescence Spectrometer. EPR spectra were measured with a Bruker EMX 10/12 EPR spectrometer. Magnetic susceptibility data on a crushed polycrystalline sample of **2** were collected over a temperature range of 300–1.8 K using a Quantum Design MPMS-XL superconducting quantum interference device (SQUID) magnetometer and diamagnetic corrections were made using Pascal's constants. The specific heat measurements were performed using a Quantum Design PPMS Heat Capacity System in the temperature range 300–1.8 K.

**X-ray Data Collection and Structure Determination:** Suitable single crystals of complexes **1** and **2** were mounted on a Pyrex fiber with

 © 2006 Wiley-VCH Verlag GmbH & Co. KGaA, Weinheim 

epoxy and affixed to a brass pin for the X-ray experiment. The intensity data were collected at room temperature with a Bruker Smart Apex CCD diffractometer with graphite-monochromated Mo-$K_\alpha$ radiation ($\lambda$ = 0.71073 Å). The data were collected over a hemisphere of the reciprocal space by a combination of three sets of exposures; each set had a different $\varphi$ angle (0°, 88°, and 180°) for the crystal and each exposure of 30 s covered 0.3° in $\omega$. The crystal–detector distance was 4 cm and the detector swing angle was –35°. Coverage of the unique set was over 99% complete. The 30 initial frames were recollected at the end of data collection to monitor crystal decay by analyzing the duplicate reflections, but no significant decays were observed. The raw data collected were reduced and corrected for Lorentz and polarization effects using the SAINT program and for absorption using the SADABS program.[27] The structures were solved by direct methods using SHELXS 97[28a] and all the non-hydrogen atoms were refined anisotropically by full-matrix least squares based on $F^2$ values.[28b] The largest residual density peak was close to the metal atom. Hydrogen atoms were added geometrically and were not refined. CCDC-294484 (for **1**) and -294485 (for **2**) contain the supplementary crystallographic data for this paper. These data can be obtained free of charge from The Cambridge Crystallographic Data Center via www.ccdc.cam.ac.uk/data_request/cif.

## Acknowledgments

We thank Prof. Manfred Scheer for his helpful suggestions and acknowledge support for this work from Jiangsu Planned Projects for Postdoctoral Research Funds, the Talent Development Foundation of Nanjing University, the Twenty-First Century Talent Foundation of the Ministry of Education, the Foundation for the Returnee of the Ministry of Education, and the Measurement Foundation of Nanjing University and the National Natural Science Foundation of China (No. 20301010).

[1] a) S. Kitagawa, R. Kitaura, S. Noro, *Angew. Chem. Int. Ed.* **2004**, *43*, 2334–2375; b) O. M. Yaghi, M. O'Keeffe, N. W. Ockwig, H. K. Chae, M. Eddaoudi, J. Kim, *Nature* **2003**, *423*, 705–714; c) C. N. R. Rao, S. Natarajan, R. Vaidhyanathan, *Angew. Chem. Int. Ed.* **2004**, *43*, 1466–1496.

[2] a) M. Eddaoudi, J. Kim, N. Rosi, D. Vodak, J. Wachter, M. O'Keeffe, O. M. Yaghi, *Science* **2002**, *295*, 469–472; b) B. Moulton, M. J. Zaworotko, *Chem. Rev.* **2001**, *101*, 1629–1658.

[3] G. Férey, *Chem. Mater.* **2001**, *13*, 3084–3098.

[4] L. Pan, K. M. Adams, H. E. Hernandez, X. Wang, C. Zheng, Y. Hattori, K. Kaneko, *J. Am. Chem. Soc.* **2003**, *125*, 3062–3067.

[5] a) J. Li, H. Zeng, J. Chen, Q. Wang, X. Wu, *Chem. Commun.* **1997**, 1213–1214; b) C. Seward, W.-L. Jia, R.-Y. Wang, G. D. Enright, S. Wang, *Angew. Chem. Int. Ed.* **2004**, *43*, 2933–2939 and references cited therein.

[6] a) L. G. Beauvais, J. R. Long, *J. Am. Chem. Soc.* **2002**, *124*, 12096–12097; b) Z. Wang, B. Zhang, H. Fujiwara, H. Kobayashi, M. Kurmoo, *Chem. Commun.* **2004**, 416–417.

[7] a) J. Bai, A. V. Virovets, M. Scheer, *Angew. Chem. Int. Ed.* **2002**, *41*, 1737–1740; b) J. Bai, J. Zuo, W. Ji, W. Tan, Z. Shen, X. You, H. K. Fun, K. Chinmakaly, I. A. Razak, *J. Mater. Chem.* **1999**, *9*, 2419–2423; c) Y. Yang, Y. Li, J. Wei, X. You, T. Wang, J. Bai, *Chin. J. Inorg. Chem.* **2004**, *20*, 683–687.

[8] Y. Q. Zheng, J. L. Lin, Z. P. Kang, *Inorg. Chem.* **2004**, *43*, 2590–2596.

[9] D.-S. Li, Y.-Y. Wang, X.-J. Luan, P. Liu, C.-H. Zhou, H.-R. Ma, Q.-H. Shi, *Eur. J. Inorg. Chem.* **2005**, 2678–2684.

[10] a) JP 04173764[92,173,764]; b) J. W. Liu, L. H. Huo, S. Gao, H. Zhao, Z. B. Zhu, J. G. Zhao, *Chin. J. Inorg. Chem.* **2004**, *20*, 707–710; c) J.-F. Zhang, Y.-H. Hu, D.-Z. Wang, *J. Cent. South Univ. Technol. (Engl. Ed.)* **2001**, *32*, 146–149.

[11] a) G. Zhang, G. Yang, J. S. Ma, *Cryst. Growth Des.* **2006**, *6*, 375–381; b) J. Tao, M.-L. Tong, J.-X. Shi, X.-M. Chen, S. W. Ng, *Chem. Commun.* **2000**, 2043–2044; c) J. Tao, J.-X. Shi, M.-L. Tong, X.-X. Zhang, X.-M. Chen, *Inorg. Chem.* **2001**, *40*, 6328–6330.

[12] J. Tao, M.-L. Tong, X.-M. Chen, *J. Chem. Soc., Dalton Trans.* **2000**, 3669–3674.

[13] a) G. R. Desiraju, *Acc. Chem. Res.* **1996**, *29*, 441–449; b) J. W. Steed, J. L. Atwood, *Supramolecular Chemistry*, John Wiley & Sons, Chichester, **2000**, p. 26.

[14] a) T. K. Maji, S. Sain, G. Mostafa, T.-H. Lu, J. Ribas, M. Monfort, N. R. Chaudhuri, *Inorg. Chem.* **2003**, *42*, 709–716; b) C. S. Hong, Y. Do, *Inorg. Chem.* **1997**, *36*, 5684–5685; c) Y.-Q. Zheng, J.-L. Lin, Z.-P. Kang, *Inorg. Chem.* **2004**, *43*, 2590–2596.

[15] T. M. Reineke, M. Eddaudi, M. O'Keeffe, O. M. Yaghi, *Angew. Chem. Int. Ed.* **1999**, *38*, 2590–2594.

[16] a) E. Y. Choi, Y.-U. Kwon, *Inorg. Chem.* **2005**, *44*, 538–545; b) X.-Z. Sun, Y.-F. Sun, B.-H. Ye, X.-M. Chen, *Inorg. Chem. Commun.* **2003**, *6*, 1412–1412.

[17] G. B. Deacon, R. J. Phillips, *Coord. Chem. Rev.* **1980**, *33*, 227–250.

[18] K. Nakamoto, *Infrared Spectra of Inorganic and Coordination Compounds*, 4th ed., John Wiley & Sons, New York, **1986**.

[19] a) S. G. Baca, Y. A. Simonov, N. V. Gerbeleu, M. Gdaniec, P. N. Bourosh, G. A. Timco, *Polyhedron* **2001**, *20*, 831–837; b) Y. Inomata, K. Sasaki, H. Umehara, F. S. Howell, *Inorg. Chim. Acta* **2001**, *313*, 95–99; c) Y.-M. Dai, E. Ma, E. Tang, J. Zhang, Z.-J. Li, X.-D. Huang, Y.-G. Yao, *Cryst. Growth Des.* **2005**, *5*, 1313–1315.

[20] J. Metz, O. Schneider, M. Hanack, *Spectrochim. Acta, Part A* **1982**, *38*, 1265–1273.

[21] J. Sun, W. Xie, L. Yuan, K. Zhang, Q. Wang, *Mater. Sci. Eng., B* **1999**, *64*, 157–160.

[22] a) C. Kutal, *Coord. Chem. Rev.* **1990**, *99*, 213–252; b) J.-H. Yang, W. Li, S.-L. Zheng, X.-M. Chen, *Aust. J. Chem.* **2003**, *56*, 1175–1178; c) R. Bertoncello, M. Bettinelli, M. Cassrin, A. Gulino, E. Tondello, A. Vittadini, *Inorg. Chem.* **1992**, *31*, 1558–1565; d) W. Chen, J.-Y. C. Chen, Q. Yue, H.-M. Yuan, J.-S. Chen, S.-N. Wang, *Inorg. Chem.* **2003**, *42*, 944–946.

[23] a) L. E. Orgel, *J. Chem. Phys.* **1955**, *23*, 1004–1014; b) S. Fernandez, J. L. Mesa, J. L. Pizarro, L. Lezama, M. I. Arriortua, R. Olazcuaga, T. Rojo, *Chem. Mater.* **2000**, *12*, 2092–2098.

[24] R. Cortés, M. Drillon, X. Solans, L. Lezama, T. Rojo, *Inorg. Chem.* **1997**, *36*, 677–683.

[25] a) K. Kopinga, T. de Neef, W. J. M. de Jonge, *Phys. Rev. B* **1975**, *11*, 2364–2369; b) J. W. Stout, E. Catalano, *J. Chem. Phys.* **1955**, *23*, 2013–2022; c) W. O. J. Boo, J. W. Stout, *J. Chem. Phys.* **1976**, *65*, 3929–3934; d) W. J. M. de Jonge, C. H. W. Swuste, K. Kopinga, K. Takeda, *Phys. Rev. B* **1975**, *12*, 5858–5863.

[26] H. Kumagai, K. W. Chapman, C. J. Kepert, M. Kurmoo, *Polyhedron* **2003**, *22*, 1921–1927.

[27] *SMART* (Version 5.0), *SAINT-plus* (Version 6), *SHELXTL* (Version 6.1) and *SADABS* (Version 2.03), Bruker AXS Inc., Madison, WI, USA, **2000**.

[28] a) G. M. Sheldrick, *SHELXS-97, Program for X-ray Crystal Structure Solution*, University of Göttingen, Göttingen, Germany, **1997**; b) G. M. Sheldrick, *SHELXL-97, Program for X-ray Crystal Structure Refinement*, University of Göttingen, Göttingen, Germany, **1997**.

Received: March 3, 2006
Published Online: July 31, 2006

 © 2006 Wiley-VCH Verlag GmbH & Co. KGaA, Weinheim 

DOI: 10.1002/ejic.200600256

# Silica Supported Submicron $SiO_2@Y_2SiO_5:Eu^{3+}$ and $SiO_2@Y_2SiO_5:Ce^{3+}/Tb^{3+}$ Spherical Particles with a Core–Shell Structure: Sol–Gel Synthesis and Characterization

**Cuikun Lin,[a] Huan Wang,[b] Deyan Kong,[a] Min Yu,[b] Xiaoming Liu,[a] Zhenling Wang,[a] and Jun Lin*[a]**

**Keywords:** Sol–gel processes / Luminescence / Core–shell structures / Silicates / Materials science

$X_1$-$Y_2SiO_5:Eu^{3+}$ and $X_1$-$Y_2SiO_5:Ce^{3+}$ and/or $Tb^{3+}$ phosphor layers have been coated on nonaggregated, monodisperse, submicron spherical $SiO_2$ particles by a sol–gel process, followed by surface reaction at high temperature (1000 °C), to give core/shell structured $SiO_2@Y_2SiO_5:Eu^{3+}$ and $SiO_2@Y_2SiO_5:Ce^{3+}/Tb^{3+}$ particles. X-ray diffraction (XRD), field emission scanning electron microscopy (FESEM), TEM, photoluminescence (PL), low voltage cathodoluminescence (CL), and time-resolved PL spectra and lifetimes are used to characterize these materials. The XRD results indicate that $X_1$-$Y_2SiO_5$ layers have been successfully coated on the surface of $SiO_2$ particles, as further verified by the FESEM and TEM images. The PL and CL studies suggest that $SiO_2@Y_2SiO_5:Eu^{3+}$, $SiO_2@Y_2SiO_5:Tb^{3+}$ (or $Ce^{3+}/Tb^{3+}$), and $SiO_2@Y_2SiO_5:Ce^{3+}$ core/shell particles exhibit red ($Eu^{3+}$, 613 nm: $^5D_0$–$^7F_2$), green ($Tb^{3+}$, 542 nm: $^5D_4$–$^7F_5$), or blue ($Ce^{3+}$, 450 nm: 5d-4f) luminescence, respectively. PL excitation, emission, and time-resolved spectra demonstrate that there is an energy transfer from $Ce^{3+}$ to $Tb^{3+}$ in the $SiO_2@Y_2SiO_5:Ce^{3+},Tb^{3+}$ core/shell particles.
(© Wiley-VCH Verlag GmbH & Co. KGaA, 69451 Weinheim, Germany, 2006)

## Introduction

The synthesis of nanostructured inorganic materials with hierarchical morphologies has attracted considerable attention in the fields of catalysis, separation technology, microelectronic devices, and biomaterials engineering.[1] In particular, the term core/shell nowadays comprises a huge area of particles that are in the broadest sense defined by a core of matter that is surrounded by a shell of different matter.[2] Core/shell materials can be used to protect drugs or other materials from dissolving or hydrolysis and to strength polymeric materials,[3] and a gold core has been found to act as an antenna that absorbs light that is then transferred to a bound rare-earth oxide shell, thereby enhancing the oxide luminescence.[4] There are numerous methods for preparing core/shell structured materials, including vapor deposition, plasma-assisted techniques, chemical reduction, self-assembly, and co-precipitation.[5] In most cases, however, the degree of surface coverage is low and the coating is not uniform.[6] The sol–gel process is an effective method for preparing such materials since the reactants can be homogeneously mixed at molecular level in solution.

The current demand for high-resolution, high brightness, and high efficiency in phosphors for cathode-ray tubes, field-emissive displays, and plasma display panels has promoted the development of new phosphors, particularly those with a nonagglomerated, monodisperse, spherical (<2 μm) morphology as they offer higher packing density, lower scattering of light, brighter luminescent performance, higher definition, and more improved screen packing.[7] Nowadays, many synthetic routes have been developed to control the size, morphology, and distribution of phosphor particles, such as spray pyrolysis[8] and flux precipitation,[9] but it is still difficult to obtain highly monodisperse and spherical phosphor particles by these methods.

It is well known that monodisperse and spherical silica particles in the nano- to submicron range can be prepared by the hydrolysis and condensation of tetraethoxysilane (TEOS) catalyzed by ammonia.[10] If the silica spheres are coated with phosphors layers, a kind of core/shell phosphor material with spherical morphology will be obtained and the size of the phosphor particles can be controlled by the silica cores. Furthermore, because silica is cheaper than most of the phosphor materials, which often employ expensive rare-earth elements as activators and/or host components, core/shell phosphor materials should be cheaper than the pure phosphor materials. $Y_2SiO_5$ is an important material that shows many interesting properties, and rare-earth (RE) oxyorthosilicates [$(RE)_2SiO_5$] doped with $Eu^{3+}$,

[a] Key laboratory of Rare Earth Chemistry and Physics, Changchun Institute of Applied Chemistry, Chinese Academy of Sciences, Changchun 130022; and Graduate School of the Chinese Academy of Sciences,
Beijing 100049, P. R. China
Fax: +86-431-569-8041
E-mail: jlin@ns.ciac.jl.cn
[b] Department of Chemistry, Northeast Normal University, Changchun 130024, P. R. China
Supporting information for this article is available on the WWW under http://www.eurjic.org or from the author.

 © 2006 Wiley-VCH Verlag GmbH & Co. KGaA, Weinheim 

$Ce^{3+}$, and $Tb^{3+}$ are well-known luminescent materials.[11–13] It is well known that $Y_2SiO_5$ is a good laser host[14] and $Y_2SiO_5$:Tb is one of the best green-emitting cathodoluminescent phosphors.[15] $Y_2SiO_5$:Eu has also been found to be a promising candidate for coherent time-domain optical memory (CTDOM) applications.[16] Therefore, rare-earth-doped yttrium orthosilicates have been attracting the attention of many research groups.

In this paper, we employ monodisperse $SiO_2$ spheres as supporting cores to prepare $SiO_2@Y_2SiO_5:Eu^{3+}$ and $SiO_2@Y_2SiO_5:Ce^{3+}/Tb^{3+}$ core/shell-structured phosphor particles by a sol–gel process, and thoroughly characterize the structure, morphology, and luminescent properties of these samples.

## Results and Discussion

The procedures for preparation of monodisperse core/shell-structured $SiO_2@Y_2SiO_5:Eu^{3+}$ and $SiO_2@Y_2SiO_5:Ce^{3+}/Tb^{3+}$ submicron spherical particles together with their luminescence photos are given in Figure S1 (see Supporting Information). The synthesis of the monodisperse $SiO_2$ core particles was carried out by the well-known Stöber method, i.e., hydrolysis of TEOS in an ethanol solution containing water and ammonia.[10] This process yielded a colloidal solution of silica particles with a narrow size distribution in the submicron range, with the particle size of silica dependent on the relative concentration of the reactants. A sol–gel technique was used for the deposition of the $Y_2SiO_5:Eu^{3+}$ and $Y_2SiO_5:Ce^{3+}/Tb^{3+}$ shells on the $SiO_2$ cores to produce core/shell-structured $SiO_2@Y_2SiO_5:Eu^{3+}$ and $SiO_2@Y_2SiO_5:Ce^{3+}/Tb^{3+}$ particles.

### Formation and Morphology of Core–Shell Particles

The formation and morphology of the core/shell particles were performed representatively for $SiO_2@Y_{1.9}Tb_{0.1}SiO_5$ by X-ray diffraction (XRD), field emission scanning electron microscopy (FESEM), and TEM. The results for the other compounds were similar to those of $SiO_2@Y_{1.9}Tb_{0.1}SiO_5$ and will not be discussed further.

The oxyorthosilicates $(RE)_2SiO_5$ of the larger rare-earth ions (RE = La–Tb) possess a monoclinic $X_1$-type structure with the space group $P2_1/C$ (no. 14),[17] whereas the smaller ones (RE = Dy–Lu, Sc) have an $X_2$-type structure with the space group $B2/b$ (no. 15).[18] $Y_2SiO_5$ crystallizes in the $X_1$ structure when annealed at a temperature below 1190 °C and in the $X_2$ structure above this temperature.[19] Figure S2 (Supporting Information) shows the structure of $X_1$-$Y_2SiO_5$. This structure contains isolated $SiO_4$ tetrahedra and nonsilicon-bonded oxygen. There are two types of Y positions. Y1 is coordinated by nine oxygen atoms, eight of which are bonded to silicon, and Y2 is coordinated by seven atoms, four of which are bonded to silicon.[20]

Figure 1 shows the XRD profiles for the pure $Y_{1.9}Tb_{0.1}SiO_5$ powder (a) and $SiO_2@Y_{1.9}Tb_{0.1}SiO_5$ (b), both annealed at 1000 °C, as well as the JCPDS 21-1456 card for $X_1$-$Y_2SiO_5$ (c) as the reference. For the $SiO_2@Y_{1.9}Tb_{0.1}SiO_5$ sample (Figure 1, b), besides the broad band at $2\theta = 22°$ due to amorphous $SiO_2$,[7] all the diffraction peaks can be indexed according to the standard data of $X_1$-$Y_2SiO_5$ (JCPDS 21-1456). This agrees well with the pure $Y_{1.9}Tb_{0.1}SiO_5$ powder sample annealed at 1000 °C, which also crystallizes with the $X_1$-$Y_2SiO_5$ phase structure. No second phase was detected. In general, the nanocrystallite size can be estimated from the Scherrer formula: $D_{hkl} = K\lambda/(\beta\cos\theta)$, where $\lambda$ is the X-ray wavelength (0.15405 nm), $\beta$ is the full-width at half-maximum, $\theta$ is the diffraction angle, $K$ is a constant (0.89), and $D_{hkl}$ is the size along the ($hkl$) direction.[21] Here, we use diffraction data at 29.60°, 31.02°, 32.58°, and 33.64° to calculate the crystallite size, which give an estimated average crystallite size of 22 nm for $Y_{1.9}Tb_{0.1}SiO_5$ on the $SiO_2$ sphere and 29 nm for pure $Y_{1.9}Tb_{0.1}SiO_5$. The unit cell parameters and crystallite size of $Y_2SiO_5$ powder and $SiO_2@Y_{1.9}Tb_{0.1}SiO_5$ core/shell particles, as well as the internuclear distances and angles of the $SiO_2@Y_{1.9}Tb_{0.1}SiO_5$ core/shell particles, were calculated using Jade 5.0 and CASTEP,[22] respectively. The results are listed in Table 1 and Table S1, respectively.

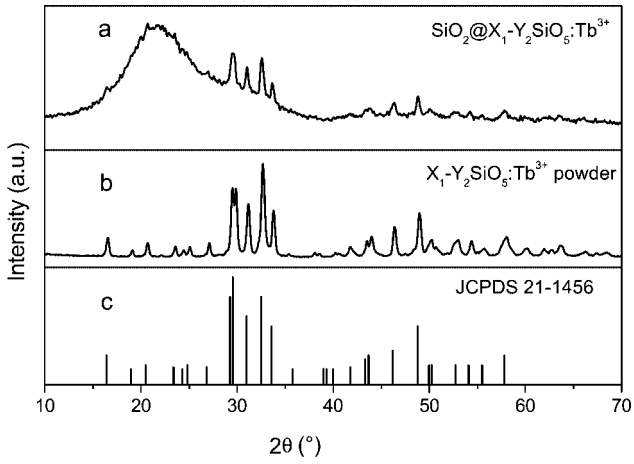


Figure 1. XRD patterns of $SiO_2@Y_{1.9}Tb_{0.1}SiO_5$ (a) and $SiO_2@Y_{1.9}Tb_{0.1}SiO_5$ (b) particles annealed at 1000 °C as well as the standard data for JCPDS No. 21-1456 (c) as a reference.

Table 1. Calculated unit-cell parameters and crystalline size of $Y_2SiO_5$ powder and $SiO_2@Y_2SiO_5$:Tb core/shell particles.

| Sample | *a* [nm] | *b* [nm] | *c* [nm] | *β* [°] | Crystal size [nm] |
|---|---|---|---|---|---|
| $Y_2SiO_5$ powder | 0.905 | 0.690 | 0.664 | 106.41 | 29 |
| $SiO_2@Y_2SiO_5$:Tb core/shell particles | 0.899 | 0.694 | 0.662 | 106.48 | 22 |

Figure 2 shows the SEM micrographs of the as-formed $SiO_2$ particles (a) and $SiO_2@Y_{1.9}Tb_{0.1}SiO_5$ (coated four times) core/shell particles (b). From the SEM micrograph in Figure 2 (see part a), we can see that the as-formed $SiO_2$ sample consists of spherical particles with an average size of 385 nm and that these particles are nonaggregated and have a narrow size distribution. After functionalizing the silica particles by coating four times with $Y_{1.9}Tb_{0.1}SiO_5$, the

 © 2006 Wiley-VCH Verlag GmbH & Co. KGaA, Weinheim 

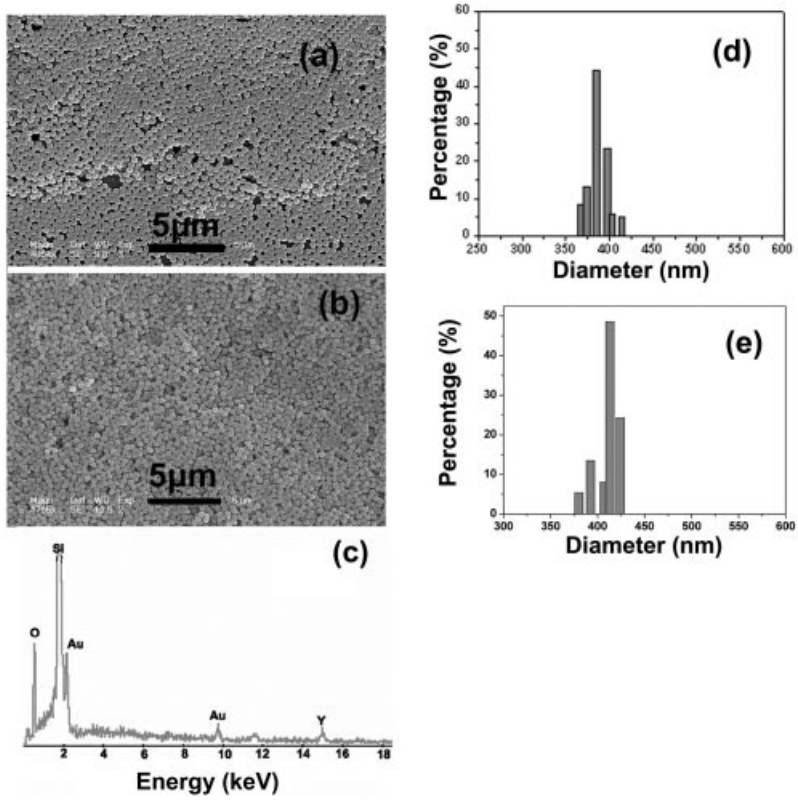


Figure 2. FESEM micrographs of amorphous $SiO_2$ (a) and core/shell-structured $SiO_2@Y_{1.9}Tb_{0.1}SiO_5$ particles (b) as well as the histograms for their size distribution (d for a, e for b) and EDX analysis of the core/shell-structured $SiO_2@Y_{1.9}Tb_{0.1}SiO_5$ particles (c).

resultant $SiO_2@Y_{1.9}Tb_{0.1}SiO_5$ particles are still spherical and uniform and keep the morphological properties of the silica particles, as shown in Figure 2 (b). The mean size of these particles is about 413 nm, which is a little larger than pure silica. The core/shell spheres were examined by energy-dispersive X-ray (EDX) analysis, which confirmed the presence of Y, Si, and O on the surface (Figure 2, c). Tb was not detected due to its low concentration, although it can be detected in the luminescence spectra (see below).

In order to investigate the inner structure of $SiO_2@Y_{1.9}Tb_{0.1}SiO_5$, TEM was performed. Figure 3 shows the $SiO_2$ particles coated by four layers of $Y_{1.9}Tb_{0.1}SiO_5$ shells; the core/shell structure of the sample can be seen clearly due to the different electron penetrability of the core and shell. The core can be seen as a black sphere with an average size of 350 nm and the shells have a gray color and an average thickness of 50 nm. Electron diffraction measurements were performed at the interface region of the core and shell of a particle, as shown in the inset of Figure 3 (b). The electron-diffraction rings demonstrate the existence of a crystalline phase at the surface of the core/shell particles.

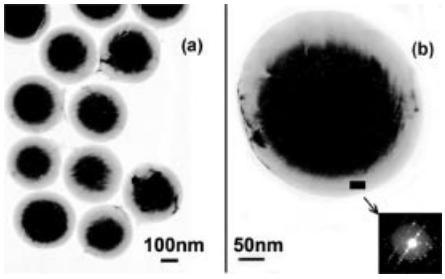


Figure 3. TEM micrographs of $SiO_2@$ $Y_{1.9}Tb_{0.1}SiO_5$ (a, b). The inset in (b) is the electron-diffraction pattern of the selected region.

## Photoluminescence Properties

The as-prepared core/shell particles of $SiO_2@Y_2SiO_5:Eu^{3+}$, $SiO_2@Y_2SiO_5:Tb^{3+}$ (or $Ce^{3+}/Tb^{3+}$), and $SiO_2@Y_2SiO_5:Ce^{3+}$ can be dispersed in solvents such as ethanol and water to form a relatively stable colloidal solution. Under UV excitation, these colloidal solutions show bright red ($SiO_2@Y_2SiO_5:Eu^{3+}$), blue ($SiO_2@Y_2SiO_5:Ce^{3+}$), and green ($SiO_2@Y_2SiO_5:Tb^{3+}$ and $SiO_2@Y_2SiO_5:Ce^{3+},Tb^{3+}$) luminescence, as shown in Figure S1.

### *$SiO_2@Y_2SiO_5:Eu^{3+}$*

$SiO_2@Y_2SiO_5:Eu^{3+}$ core/shell particles exhibit a strong red emission under UV irradiation. Figure 4 (a) shows the excitation and emission spectra of $SiO_2@Y_{1.8}Eu_{0.2}SiO_5$ core/shell particles. The excitation spectrum (Figure 4, part a, left) consists of a broad, intense band, with a maximum at 253 nm, and some weak lines. The former is due to the charge-transfer band (CTB) of $Eu^{3+}$–$O^{2-}$, and the latter are

 © 2006 Wiley-VCH Verlag GmbH & Co. KGaA, Weinheim 

due to f-f transitions within the $Eu^{3+}$ $4f^6$ electron configuration (320: $^7F_0 \rightarrow {}^5H_6$; 364: $^7F_0 \rightarrow {}^5D_4$; 384: $^7F_0 \rightarrow {}^5G_2$; 397: $^7F_0 \rightarrow {}^5L_6$, 468: $^7F_0 \rightarrow {}^5D_2$).[23] Upon excitation into the CTB at 253 nm, the emission spectrum was found to be composed of $^5D_0 \rightarrow {}^7F_J$ ($J$ = 0, 1, 2, 3, 4) emission lines of $Eu^{3+}$, with the hypersensitive red emission $^5D_0 \rightarrow {}^7F_2$ (612 nm) transition being the most prominent group (Figure 6, part a, right). When the $Eu^{3+}$ is located at a low-symmetry local site (without an inversion center), the hypersensitive $^5D_0 \rightarrow {}^7F_2$ transition is often dominant in its emission spectrum.[24] This is actually the case for $X_1$-$Y_2SiO_5$, which adopts a monoclinic structure with a space group of $P2_1/c$ where the two $Y^{3+}$ sites have a $C_1$ point symmetry (without an inversion center).[12,24] The doped $Eu^{3+}$ ions occupy the $Y^{3+}$ sites in the $SiO_2@X_1$-$Y_2SiO_5$ core/shell particles, which results in the hypersensitive red emission $^5D_0 \rightarrow {}^7F_2$ transition of $Eu^{3+}$ being the most prominent group in its emission spectrum.

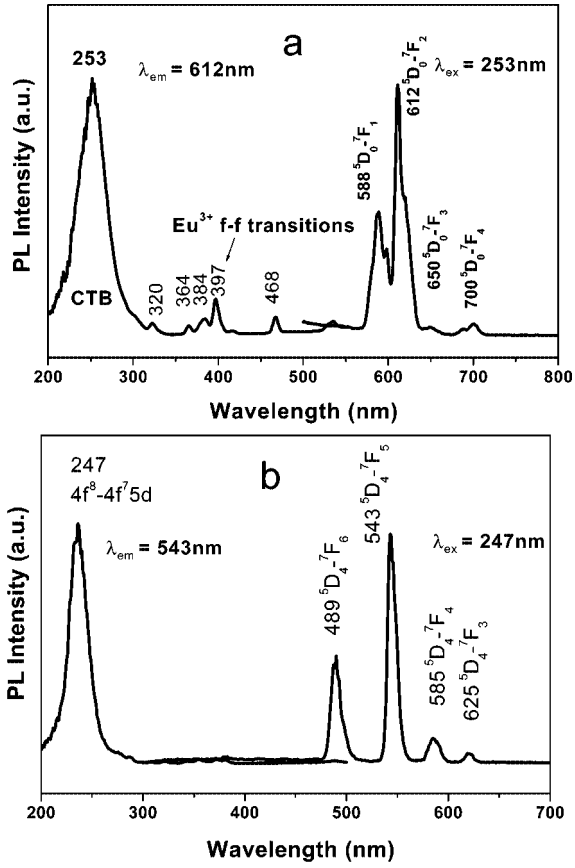


Figure 4. Excitation (left) and emission (right) spectra for $SiO_2@Y_{1.8}Eu_{0.2}SiO_5$ core/shell particles (a) and excitation (left) and emission (right) spectra for $SiO_2@Y_{1.9}Tb_{0.1}SiO_5$ core/shell particles (b).

The decay curve for the $^5D_0 \rightarrow {}^7F_2$ transition of $Eu^{3+}$ in $SiO_2@Y_{1.8}Eu_{0.2}SiO_5$ core/shell particles is shown in Figure S3; it can be well fitted to a single-exponential function as $I = A\exp(-\tau/\tau_0)$[25] (the fitting parameters are shown in the figure). A lifetime, $\tau$, of 2.31 ms is obtained for the $^5D_0 \rightarrow {}^7F_2$ emission of $Eu^{3+}$.

Because of the invariability of the $Eu^{3+}$ $^5D_0 \rightarrow {}^7F_1$ transition intensity, it can be taken as a reference for the calculation of luminescent quantum yield.[26,27] On obtaining the intensity parameters of the $Eu^{3+}$ emission spectra, the total radiative rate of $^5D_0$ can be expressed by Equation (1),[27,28]

$$k_r = k_{r(0-1)} \frac{\sum_{J=0}^{4} S_{(0-J)}}{S_{(0-1)}} \quad (1)$$

where $S_{(0\rightarrow J)}$ and $S_{(0\rightarrow 1)}$ are the integral intensities of the $^5D_0 \rightarrow {}^7F_J$ and $^5D_0 \rightarrow {}^7F_1$ transitions, respectively, and $k_{r(0\rightarrow 1)}$ is the radiative rate of the $^5D_0 \rightarrow {}^7F_1$ transition. Since $[k_{r(0\rightarrow 1)}]_{vac}$ is 14.65 $s^{-1}$,[29] when an average index of refraction, $n$, equal to 1.506 is considered, the value of $k_{0-1}$ is equal to $n^3[k_{r(0\rightarrow 1)}]_{vac}$, about 50 $s^{-1}$.[26,29–32]

The total radiative rate of $^5D_0$ was determined to be 0.137 $ms^{-1}$ from Equation (1). All the $^5D_0$ decay curves determined for the samples could be fitted well to a single-exponential function, which reflects the existence of the $Eu^{3+}$ local site symmetry.[33,34] The fitted lifetime is 2.31 ms. From these data, the total decay rate of $^5D_0$ ($K_{tot}$), which can be given as Equation (2), is 0.433 $ms^{-1}$. Finally, the absolute emission quantum yield ($\eta$) determined from Equation (3) is around 32%. This quantum value seems rather low considering that the materials have been annealed at 1000 °C, which generally leads to high quantum yields for this rare-earth ion. This may be due to the concentration quenching effect. It should be noted that Equation (3) describes the quantum efficiency of the $Eu^{3+}$ $^5D_0$ level and not the absolute emission quantum yield of the $SiO_2@Y_2SiO_5$:$Eu^{3+}$ core/shell particles, and that the absolute emission quantum yield is a more general quantity that involves the ratio between light absorption and light emission. Therefore, the absolute emission quantum yield and the quantum efficiency of the $^5D_0$ level are equal if all the energy absorbed is transferred to the $^5D_0$ level.

$$k_{tot} = \frac{1}{\tau} = k_r + k_{nr} \quad (2)$$

$$\eta = \frac{k_r}{k_r + k_{nr}} \quad (3)$$

### *$SiO_2@Y_2SiO_5$:$Tb^{3+}$*

$SiO_2@Y_2SiO_5$:$Tb^{3+}$ core/shell particles exhibit a strong green emission under UV irradiation. Figure 4 (b) shows the excitation and emission spectra of $SiO_2@Y_{1.9}Tb_{0.1}SiO_5$ core/shell particles. The excitation spectrum (Figure 4, part b, left) contains an intense, broad band with a maximum at 247 nm due to the spin-allowed $4f^8 \rightarrow 4f^75d$ transition ($\Delta S$ = 0) of $Tb^{3+}$.[34] The excitation lines in the longer wavelength regions within the $Tb^{3+}$ $4f^8$ electron configuration cannot be seen at this magnification due to their weak intensity.

 © 2006 Wiley-VCH Verlag GmbH & Co. KGaA, Weinheim 

Excitation into the spin-allowed $4f^8 \rightarrow 4f^7 5d$ band at 247 nm yields the characteristic emission lines of $Tb^{3+}$ $^5D_4 \rightarrow {}^7F_J$ ($J$ = 3, 4, 5, 6) transitions, with the $^5D_4 \rightarrow {}^7F_5$ (543 nm) green emission as the most prominent group (Figure 4, part b, right).

The decay curve for $^5D_4 \rightarrow {}^7F_5$ of $Tb^{3+}$ in $SiO_2@Y_{1.9}Tb_{0.1}SiO_5$ core/shell particles is shown in Figure S4, which can also be well fitted to a single-exponential function like the situation for $Eu^{3+}$ in $SiO_2@Y_{1.8}Eu_{0.2}SiO_5$; the fitting parameters are shown in the figure. A lifetime value of 3.29 ms is obtained for the $^5D_4 \rightarrow {}^7F_5$ emission of $Tb^{3+}$.

The PL intensity of $SiO_2@Y_{1.9}Tb_{0.1}SiO_5$ core/shell particles can be tuned by the number of coatings. Figure 5 shows the PL intensity of the sample as a function of the coating number. Obviously, the PL intensity increases with an increase of coating number, which can be attributed to an increase of the thickness of the $Y_{1.9}Tb_{0.1}SiO_5$ shells on the $SiO_2$ spheres. The PL intensity of the four-layer $SiO_2@Y_{1.9}Tb_{0.1}SiO_5$ core/shell particles reaches about 62% of that of the pure $Y_{1.9}Tb_{0.1}SiO_5$ sample, as indicated in Figure 5.

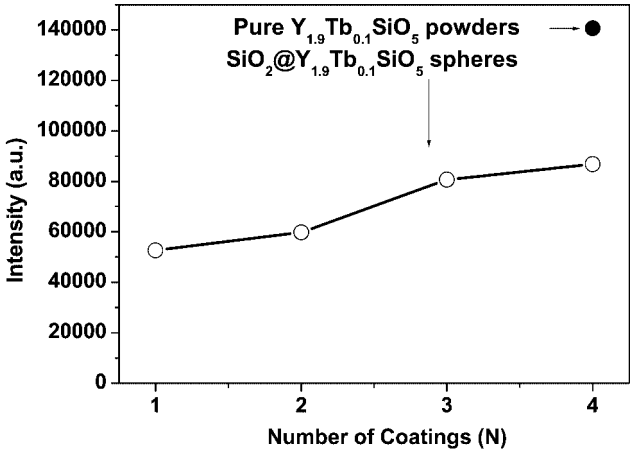


Figure 5. The photoluminescence intensity of $Tb^{3+}$ as a function of the number of coatings (N) of $SiO_2@Y_{1.9}Tb_{0.1}SiO_5$ core/shell particles. The photoluminescence intensity of pure $Y_{1.9}Tb_{0.1}SiO_5$ is also given for comparison.

### *$SiO_2@Y_2SiO_5:Ce^{3+}$ and $SiO_2@Y_2SiO_5:Ce^{3+},Tb^{3+}$*

The $SiO_2@Y_2SiO_5:Ce^{3+}$ core/shell particles show a blue emission under longer wavelength UV excitation. The excitation (a) and emission (b) spectra of $SiO_2@Y_{1.94}Ce_{0.06}SiO_5$ core/shell particles are shown in Figure 6. The excitation spectrum mainly consists of a strong band with a maximum at 370 nm and a weak band at 282 nm, corresponding to the transitions from the ground state $^2F_{5/2}$ to the excited 5d states of $Ce^{3+}$. The emission of $Ce^{3+}$ includes a broad band with a maximum at 443 nm, which is assigned to the parity-allowed transitions of the lowest component of the 5d state to the ground state of $Ce^{3+}$.[35]

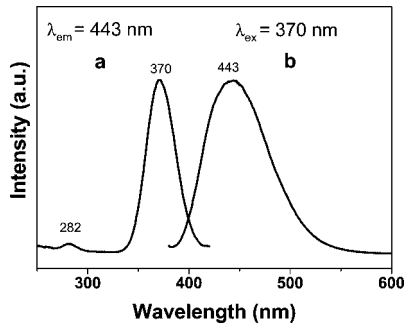


Figure 6. Excitation (a) and emission (b) spectra for $SiO_2$ @ $Y_{1.94}Ce_{0.06}SiO_5$ core/shell particles.

$SiO_2@Y_{1.84}Ce_{0.06}Tb_{0.1}SiO_5$ core/shell particles show a blue-green emission under UV excitation. The excitation spectrum monitored with the 543 nm emission ($^5D_4 \rightarrow {}^7F_5$) of $Tb^{3+}$ contains an intense band at 247 nm, a weak band at 282 nm, and a strong band with a maximum at 370 nm. By comparison with the excitation spectra for $SiO_2@Y_{1.9}Tb_{0.1}SiO_5$ (Figure 4, b) and $SiO_2@Y_{1.94}Ce_{0.06}SiO_5$ (Figure 5), we can easily ascribe the former band at 247 nm to the $4f^8 \rightarrow 4f^7 5d$ transitions of $Tb^{3+}$, and the latter bands at 282 and 370 nm to 4f–5d transitions of $Ce^{3+}$ in Figure 7 (a). The presence of the excitation bands of $Ce^{3+}$ in the excitation spectrum monitored with $Tb^{3+}$ emission indicates that an energy transfer has occurred from $Ce^{3+}$ to $Tb^{3+}$ in the $SiO_2@Y_{1.84}Ce_{0.06}Tb_{0.1}SiO_5$ sample. Excitation into the $Ce^{3+}$ excitation band at 370 nm yields both the emission of $Ce^{3+}$ (380–470 nm, which is identical to the emission spectrum of $SiO_2@Y_{1.94}Ce_{0.06}SiO_5$ core/shell particles, dotted line) and that of $Tb^{3+}$ ($^5D_4 \rightarrow {}^7F_J$ at 488, 543, 586, 625 nm), as shown in Figure 7 (b), and is further indicative of the energy transfer from $Ce^{3+}$ to $Tb^{3+}$ in $SiO_2@Y_{1.84}Ce_{0.06}Tb_{0.1}SiO_5$.

The kinetic decay curves for the emission of $Ce^{3+}$ in $SiO_2@Y_{1.94}Ce_{0.06}SiO_5$ and in $SiO_2@Y_{1.84}Ce_{0.06}Tb_{0.1}SiO_5$ were also measured (see Supporting Information, Figure S4, parts a and b, respectively). Both of the decay curves for $Ce^{3+}$ can be well-fitted to a single-exponential function, and the lifetimes ($\tau$) for $Ce^{3+}$ were determined to be 39.8 ns in the former and 20.1 ns in the latter. The shortening of the lifetime in $SiO_2@Y_{1.94}Ce_{0.06}SiO_5$ with respect to $SiO_2@Y_{1.84}Ce_{0.06}Tb_{0.1}SiO_5$ is due to the occurrence of the energy transfer from $Ce^{3+}$ to $Tb^{3+}$ in the latter sample. The $Ce^{3+} \rightarrow Tb^{3+}$ energy transfer is not complete due to the presence of the strong $Ce^{3+}$ emission. The energy-transfer efficiency from a donor ($Ce^{3+}$) to an acceptor ($Tb^{3+}$) can be calculated according to the formula $\eta_{ET} = 1 - I_d/I_{d0}$ (= $1 - \tau/\tau_0$), where $I_d$ ($\tau$) and $I_{d0}$ ($\tau_0$) are the corresponding luminescence intensities (lifetimes) of the donor ($Ce^{3+}$) in the presence and absence of the acceptor ($Tb^{3+}$) for the same donor concentration, respectively.[36] The energy-transfer efficiency from $Ce^{3+}$ to $Tb^{3+}$ is 48%, as calculated from the lifetimes of $Ce^{3+}$.

In order to study the energy-transfer process from $Ce^{3+}$ to $Tb^{3+}$ in $SiO_2@Y_{1.84}Ce_{0.06}Tb_{0.1}SiO_5$ in more detail, the time-resolved emission spectra were measured by excitation

 © 2006 Wiley-VCH Verlag GmbH & Co. KGaA, Weinheim 

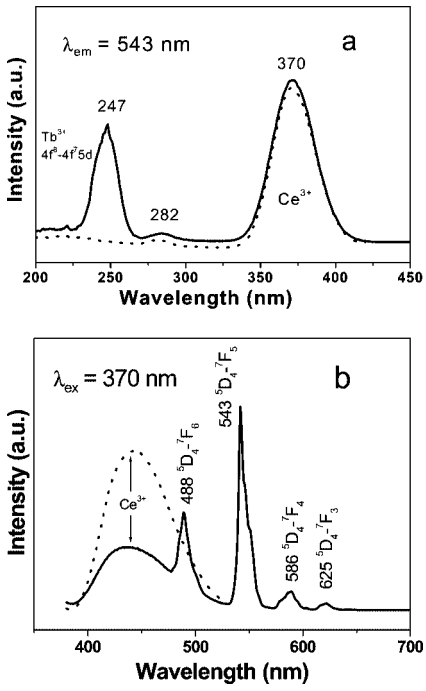


Figure 7. Excitation (a) and emission (b) spectra for $SiO_2@Y_{1.84}Ce_{0.06}Tb_{0.1}SiO_5$ core/shell particles.

into the $Ce^{3+}$ band with a 370-nm laser. The emission spectra collected at different delay times $t$ are shown in Figure 8. When $t$ = 0.25 μs, only the broad emission of $Ce^{3+}$ is observed; no $Tb^{3+}$ emission is present because the excitation energy of $Ce^{3+}$ has not been transferred to $Tb^{3+}$ within this short time. When $t$ = 1.25 μs, the emission of $Ce^{3+}$ starts to decreases and is accompanied by a $Tb^{3+}$ emission due to the energy transfer from $Ce^{3+}$. The emission of $Ce^{3+}$ decreases gradually with further increase of the delay time, while that of $Tb^{3+}$ begins to increase (a large part of the $Tb^{3+}$ emission is from the $^5D_3$ level) due to transfer of more excitation energy from $Ce^{3+}$ to $Tb^{3+}$. When $t$ = 7.75 μs, the emission of $Ce^{3+}$ disappears, and the emission spectrum contains exclusively that of $Tb^{3+}$. The emission from the $^5D_3$ level of $Tb^{3+}$ then begins to decrease until it is quenched completely at $t$ = 100 μs. This quenching of the $^5D_3$ emission of $Tb^{3+}$ is due to cross-relaxation between two adjacent $Tb^{3+}$ ions, i.e. $Tb^{3+}$ ($^5D_3$) + $Tb^{3+}$ ($^7F_6$) → $Tb^{3+}$ ($^5D_4$) + $Tb^{3+}$ ($^7F_0$), which occurs at a longer delay time.[36]

The mechanism of nonradiative energy transfer from $Ce^{3+}$ (5d-level) to $Tb^{3+}$ (mainly the $^5D_3$ level) is an inductive resonant process. Since the concentration of $Ce^{3+}$ ions is not great, a dipole–dipole interaction between $Ce^{3+}$ and $Tb^{3+}$ in the excited state is the most likely one.[37,38] The absolute constant of the energy-transfer rate can be defined by the formula $K_t = 1/\tau - 1/\tau_0$, where $\tau$ and $\tau_0$ are the decay times of luminescence for the donor ions with and without the acceptor, respectively.[38,39] So, for $SiO_2@Y_{1.84}Ce_{0.06}Tb_{0.1}SiO_5$, the energy-transfer rate from $Ce^{3+}$ to $Tb^{3+}$ is 25 $\mu s^{-1}$ (at room temperature). This is much faster than the radiative rate of $Tb^{3+}$.[40] As a result, the excited state of $Tb^{3+}$ ($^5D_4$) can be populated many times by energy transfer from $Ce^{3+}$ before the depopulation occurs, which result in the increase of emission intensity during this period. Thus, the emission characteristics of $Ce^{3+}$ and $Tb^{3+}$ in Figure 8 can be understood.

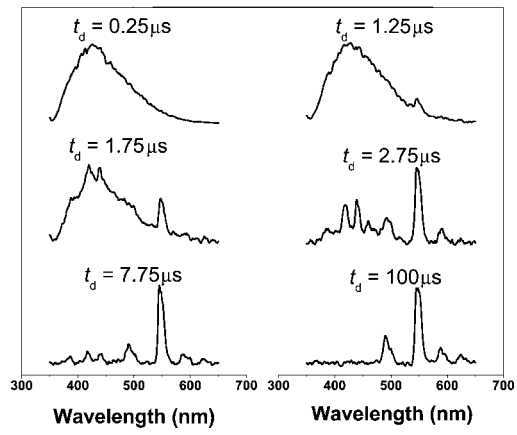


Figure 8. Time-resolved PL spectra of $SiO_2@Y_{1.84}Ce_{0.06}Tb_{0.1}SiO_5$ core/shell particles ($\lambda_{ex}$ = 370 nm).

A summary of the emission and energy-transfer processes in $SiO_2@Y_{1.84}Ce_{0.06}Tb_{0.1}SiO_5$ is shown schematically in Figure 9.[41] An electron on $Ce^{3+}$ ion is excited from the ground state (4f) to the excited state (5d) by UV light. In the excited state, this electron either relaxes to the lowest 5d crystal-field-splitting state then returns to the ground state to produce the blue emission, or transfers its excitation energy to the higher excited energy levels of $Tb^{3+}$ ($4f^8$), which relax to the $^5D_4$ level, where the green emission ($^5D_4 \rightarrow {}^7F_J$) takes place.[41] Competition between the above two processes results in the occurrence of emission from $Ce^{3+}$ and $Tb^{3+}$ simultaneously in $SiO_2@Y_{1.84}Ce_{0.06}Tb_{0.1}SiO_5$ (Figure 9, b)

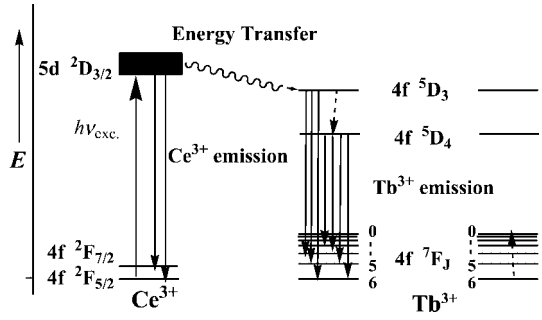


Figure 9. Scheme of energy transfer from $Ce^{3+}$ to $Tb^{3+}$.

## Cathodoluminescence Properties

Similar to the emission under UV excitation, the $SiO_2@Y_{1.9}Tb_{0.1}SiO_5$, $SiO_2@Y_{1.94}Ce_{0.06}SiO_5$, and $SiO_2@Y_{1.84}Ce_{0.06}Tb_{0.1}SiO_5$ core/shell particles also exhibit strong red-green, blue, and blue-green luminescence, respectively, upon excitation with an electron beam (3 kv). Typical

 © 2006 Wiley-VCH Verlag GmbH & Co. KGaA, Weinheim 

emission spectra are shown in Figure 10 (a–c), respectively. These emission spectra basically agree with the corresponding PL emission spectra (Figure 4 and Figure 7). The CL emission for $SiO_2$ particles coated with four layers of $Y_{1.94}Ce_{0.06}SiO_5$, $Y_{1.9}Tb_{0.1}SiO_5$, $Y_{1.84}Ce_{0.06}Tb_{0.1}SiO_5$ were investigated as a function of accelerating voltage, as shown in Figure S6 (a–c, respectively). When the filament is fixed at 14 mA, the CL intensities of $SiO_2@Y_{1.94}Ce_{0.06}SiO_5$, $SiO_2@Y_{1.9}Tb_{0.1}SiO_5$, and $SiO_2@Y_{1.84}Ce_{0.06}Tb_{0.1}SiO_5$ core/shell particles increase upon raising the acceleration voltage from 1 to 5 kV. For cathodoluminescence, the $Ce^{3+}$ and $Tb^{3+}$ ions are excited by the plasmons produced by the incident electrons. The electron penetration depth can be estimated by Equation (4)[42,43]

$$L\,[\text{Å}] = 250\left(\frac{A}{\rho}\right)\left(\frac{E}{Z^{\frac{1}{2}}}\right)^{n} \quad (4)$$

where $n = 1.2/(1 - 0.29\cdot\log_{10} Z)$, and A is the atomic weight, $\rho$ is the density, $Z$ is the atomic number, and $E$ is the accelerating voltage (V).[44] For $SiO_2@X_1$-$Y_2SiO_5:Tb^{3+}$ and $SiO_2@X_1$-$Y_2SiO_5:Ce^{3+}$, the electron penetration depth at 5 kV is 16.5 nm. This value is within the $X_1$-$Y_2SiO_5:Tb^{3+}$, $X_1$-$Y_2SiO_5:Ce^{3+}$, and $SiO_2@Y_{1.84}Ce_{0.06}Tb_{0.1}SiO_5$ shell for the $SiO_2@X_1$-$Y_2SiO_5:Tb^{3+}$, $SiO_2@X_1$-$Y_2SiO_5:Ce^{3+}$, and $SiO_2@Y_{1.84}Ce_{0.06}Tb_{0.1}SiO_5$ core/shell particles, respectively. With the increase of accelerating voltage, more plasmons will be produced by the incident electrons, which results in more $Ce^{3+}$ and $Tb^{3+}$ions being excited and thus a higher CL intensity. The increase in electron energy is attributed to deeper penetration of the electron into the shell, which is governed by Equation (4).

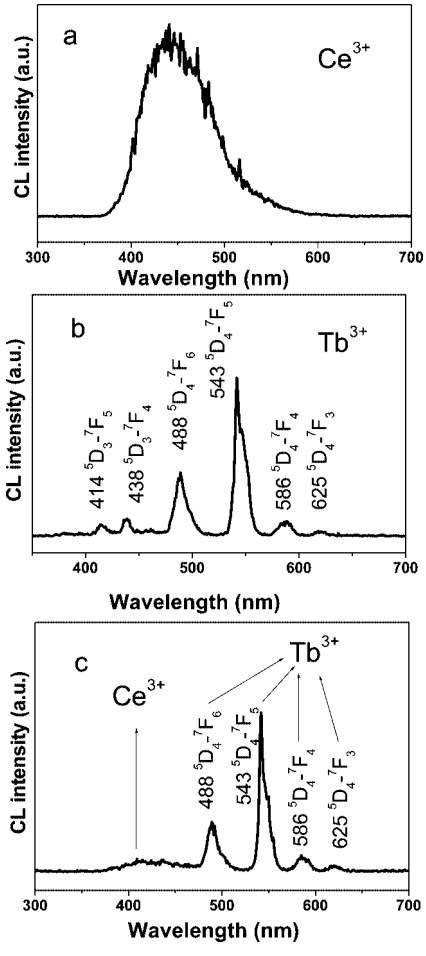


Figure 10. CL spectra of $SiO_2@Y_{1.94}Ce_{0.06}SiO_5$ (a), $SiO_2@Y_{1.9}Tb_{0.10}SiO_5$ (b), and $SiO_2@Y_{1.84}Ce_{0.06}Tb_{0.10}SiO_5$ (c) core/shell particles (voltage: 3 kV).

The deeper penetration of electrons into the shell results in an increase in the electron–solid interaction volume in which excitation of $Ce^{3+}$ and $Tb^{3+}$ions, which is responsible for light emission, takes place. Therefore, an increase in interaction volume, which effectively determines the generation of light inside the shell, with an increase in electron energy brings about an increase in the CL brightness of $SiO_2@Y_2SiO_5:Tb^{3+}$ and $SiO_2@Y_2SiO_5:Ce^{3+}$ core/shell particles.[45]

## Conclusions

A simple and effective sol–gel process has been developed to coat $X_1$-$Y_2SiO_5$: $RE^{3+}$ (RE = $Eu^{3+}$, $Ce^{3+}$, and/or $Tb^{3+}$) phosphor layers on monodisperse spherical $SiO_2$ particles. The obtained $SiO_2@Y_2SiO_5:Eu^{3+}$, $SiO_2@Y_2SiO_5:Tb^{3+}$, $SiO_2@$-$Y_2SiO_5:Ce^{3+}$, and $SiO_2@Y_2SiO_5:Ce^{3+},Tb^{3+}$ core/shell-structured phosphors maintain the spherical morphology, submicrometer size, and narrow size-distribution of the originals. Under the excitation of UV light and electron beams, these core/shell phosphors show red, green, blue, and green luminescence, respectively. An energy transfer from $Ce^{3+}$ to $Tb^{3+}$ exists in $SiO_2@Y_2SiO_5:Ce^{3+},Tb^{3+}$ core/shell phosphors, and this has been studied by time-resolved spectroscopic methods. This process can be extended to prepare other phosphor materials with a homogeneous spherical morphology.

## Experimental Section

The core/shell samples with general compositions $SiO_2@Y_{1.8}Eu_{0.2}$-$SiO_5$, $SiO_2@Y_{1.9}Tb_{0.1}SiO_5$, $SiO_2@Y_{1.94}Ce_{0.06}SiO_5$, and $SiO_2@Y_{1.84}Ce_{0.06}Tb_{0.1}SiO_5$ were prepared by a sol–gel process. The main starting materials were $Y_2O_3$ (99.99%), $Eu_2O_3$ (99.99%), $Ce_2(CO_3)_3$ (99.99%), and $Tb_4O_7$ (99.99%), all of which were purchased from Shanghai Yuelong Nonferrous Metals Limited, tetraethyl orthosilicate $Si(OC_2H_5)_4$ (TEOS, 99 wt.-%, analytical reagent, Beijing Beihua Chemicals Co., Ltd.), polyethylene glycol (PEG, molecular weight 10000, analytical reagent), and ammonium hydroxide (25 wt.-%, analytical reagent, Beijing Beihua Chemicals Co., Ltd.).

First, monodisperse silica spheres were prepared by the well-known Stöber method.[10] In a typical experiment, 7.8 mL of TEOS, 18 mL of deionized $H_2O$, and 98 mL of $NH_4OH$ were added to 75 mL of absolute ethanol and stirred at room temperature for 3 h to give a white silica colloidal suspension. The silica particles were centrifugally separated from the suspension and washed with ethanol three times. Then, coating of the $SiO_2$ particles with $Y_2SiO_5$-based phos-

 © 2006 Wiley-VCH Verlag GmbH & Co. KGaA, Weinheim 

phor layers was performed by a sol–gel process. According to the compositions in the above formulae, stoichiometric amounts of $Y_2O_3$, $Eu_2O_3$, $Tb_4O_7$, and $Ce_2(CO_3)_3$ were dissolved in dilute $HNO_3$ with vigorous stirring. Then, a certain amount of TEOS and water/ethanol (v/v = 1:7) was added to the solution and PEG was added with a concentration of 0.1 g/mL. The solution was stirred for 3 h to form a sol, and then silica particles were added with stirring. After stirring for 3 h, the silica particles were separated by centrifugation. The samples were immediately dried at 100 °C for 1 h. The dried samples were annealed to 1000 °C at a heating rate of 2 °C $min^{-1}$ and held there for 2 h in air (for samples containing Eu) or in a reducing atmosphere (CO for samples containing Ce and/or Tb). The above process was repeated several times to increase the thickness of the phosphor shells. For comparison, the coating sol was evaporated in a similar way to produce the pure $Y_2SiO_5$-based powder phosphors. The whole process is shown schematically in Figure 1.

X-ray diffraction (XRD) studies of the powder samples were performed with a Rigaku-Dmax-IIB spectrometer with using Cu-$K_\alpha$ radiation ($\lambda$ = 0.15405 nm). The morphology of the samples was inspected with a field emission scanning electron microscope (FE-SEM, XL30, Philips) and a transmission electron microscope (JEOL-2010, 200 kV). The excitation and emission spectra were recorded with a Hitachi F-4500 spectrofluorimeter equipped with a 150-W xenon lamp and 1–6-kv electron gun (self-made) as the excitation source. Luminescence decay curves were obtained with a Lecroy Wave Runner 6100 Digital Oscilloscope (1 GHz) using a 250-nm laser (pulse width: 4 ns, gate: 50 ns) as the excitation source (Continuum Sunlite OPO). All the measurements were performed at room temperature.

**Supporting Information** (see also the footnote on the first page of this article): Figure S1. Formation process of $SiO_2@Y_2SiO_5:Eu^{3+}$, $SiO_2@Y_2SiO_5:Ce^{3+}$, $SiO_2@Y_2SiO_5:Tb^{3+}$, and $SiO_2@Y_2SiO_5:Ce^{3+},Tb^{3+}$ core/shell particles with the corresponding luminescent photos under UV irradiation. Figure S2. The crystal structure of $X_1$-$Y_2SiO_5$. Figure S3. Decay curves for the luminescence of $Eu^{3+}$ in $SiO_2@Y_{1.8}Eu_{0.2}SiO_5$ core/shell particles. Figure S4. Decay curve for the luminescence of $Tb^{3+}$ in $SiO_2@Y_{1.9}Tb_{0.1}SiO_5$ core/shell particles. Figure S5. Decay curves for the luminescence of $Ce^{3+}$ in $SiO_2@Y_{1.94}Ce_{0.06}SiO_5$ (a) and in $SiO_2@Y_{1.84}Ce_{0.06}Tb_{0.1}SiO_5$ (b) core/shell particles. Figure S6. CL emission intensity of $SiO_2@Y_{1.94}Ce_{0.06}SiO_5$ (a) $SiO_2@Y_{1.9}Tb_{0.10}SiO_5$ (b), and $SiO_2@Y_{1.84}Ce_{0.06}$ $Tb_{0.10}SiO_5$ (c) core/shell particles as a function of accelerating voltage. Table S1. Calculated internuclear distances and angles of $SiO_2@Y_2SiO_5$:Tb core/shell particles.

## Acknowledgments

This project was financially supported by the "Bairen Jihua" foundation of the Chinese Academy of Sciences, the National Natural Science Foundation of China (50225205, 50572103, and 20431030) and the MOST of China (no. 2003CB314707). Dr M. Yu is grateful for a special starting research fund for awardees of the President Prize of the Chinese Academy of Sciences (2005–2007).

[1] I. L. Radtchenko, G. B. Sukhorukov, N. Gaponik, A. Kornowski, A. L. Rogach, H. Mohwald, *Adv. Mater.* **2001**, *13*, 1684–1687; C. T. Kresge, M. E. Leonowicz, W. J. Roth, J. C. Vartuli, J. S. Beck, *Nature* **1992**, *359*, 710–712; H. Yang, N. Coombs, G. A. Ozin, *Nature* **1997**, *386*, 692–695; D. Zhao, J. Feng, Q. Huo, N. Melosh, G. H. Fredrickson, B. F. Chmelka, G. D. Stucky, *Science* **1998**, *279*, 548–552; P. V. Braun, P. Osenar, S. I. Stupp, *Nature* **1996**, *380*, 325–328; J. Liu, Y. Shin, Z. Nie, J. H. Chang, L. Q. Wang, G. E. Fryxell, W. D. Samuels, G. J. Exarhos, *J. Phys. Chem. A* **2000**, *104*, 8328–8339; C. W. Guo, Y. Cao, S. H. Xie, W. L. Dai, K. N. Fan, *Chem. Commun.* **2003**, 700–701.

[2] J. J. Schneider, *Adv. Mater.* **2001**, *13*, 529–533; C. J. Zhong, M. M. Maye, *Adv. Mater.* **2001**, *13*, 1507–1511; M. S. Fleming, T. K. Mandal, D. R. Walt, *Chem. Mater.* **2001**, *13*, 2210; M. Yu, J. Lin, J. Fang, *Chem. Mater.* **2005**, *17*, 1783–1791.

[3] J. H. Lee, T. G. Park, H. K. Choi, *J. Microencapsulation* **1999**, *16*, 715–729; R. Schirrer, R. Lenke, J. Boudouaz, *Polym. Eng. Sci.* **1997**, *37*, 1748–1760.

[4] C. Louis, S. Roux, G. Ledoux, L. Lemelle, P. Gillet, O. Tillement, P. Perriat, *Adv. Mater.* **2004**, *16*, 2163–2166.

[5] Z. J. Jiang, C. Y. Liu, *J. Phys. Chem. B* **2003**, *107*, 12411; H. Giesche, E. Matijevic, *J. Mater. Res.* **1994**, *9*, 436–450.

[6] R. A. Caruso, M. I. Antoniett, *Chem. Mater.* **2001**, *13*, 3272–3282.

[7] X. Jing, T. G. Ireland, C. Gibbons, D. J. Barber, J. Silver, A. Vecht, G. Fern, P. Trogwa, D. Morton, *J. Electrochem. Soc.* **1999**, *146*, 4654–4658; A. Vecht, C. Gibbons, D. Davies, X. Jing, P. Marsh, T. G. Ireland, J. Silver, A. Newport, *J. Vac. Sci. Technol. B* **1999**, *17*, 750–757; Y. D. Jiang, Z. L. Wang, F. Zhang, H. G. Paris, C. J. Summers, *J. Mater. Res.* **1998**, *13*, 2950–2955.

[8] Y. H. Zhou, J. Lin, X. M. Han, S. B. Wang, H. J. Zhang, *Mater. Res. Bull.* **2003**, *38*, 1289–1299; S. H. Cho, J. S. Yoo, J. D. Lee, *J. Electrochem. Soc.* **1998**, *145*, 1017–1019.

[9] A. Celikkaya, M. Akinc, *J. Am. Ceram. Soc.* **1990**, *73*, 2360–2365.

[10] W. Stöber, A. Fink, *J. Colloid Interf. Sci.* **1968**, *26*, 62–69; G. H. Bogush, M. A. Tracy, C. F. Zukoskiiv, *J. Non-Cryst. Solids* **1988**, *104*, 95–106.

[11] J. Lin, Q. Su, S. B. Wang, H. J. Zhang, *J. Mater. Chem.* **1996**, *6*, 265–269; Q. Y. Zhang, K. Pita, W. Ye, W. X. Que, C. H. Kam, *Chem. Phys. Lett.* **2002**, *356*, 161–167; Y. Liu, C. N. Xu, H. Matsui, T. Imamura, T. Watanabe, *J. Lumin.* **2000**, *87*, 1297–1299; S. H. Shin, D. Y. Jeon, K. S. Suh, *Jpn. J. Appl. Phys.* **2001**, *40*, 4715–4719; M. Yin, W. Zhang, L. Lou, S. Xia, J.-C. Krupa, *Physica B* **1998**, *254*, 141–147.

[12] C. Cannas, M. Mainas, A. Musinu, G. Piccaluga, A. Speghini, M. Bettinelli, *Opt. Mater.* **2005**, *27*, 1506–1510.

[13] A. Sennaroglu, *Prog. Quantum Electron.* **2002**, *26*, 287–352; M. Yin, C. K. Duan, W. P. Zhang, S. D. Xia, J. C. Krupa, *J. Appl. Phys.* **1999**, *86*, 3751–3757; W. P. Zhang, P. B. Xie, C. K. Duan, K. Yan, M. Yin, L. R. Lou, S. D. Xia, J. C. Krupa, *Chem. Phys. Lett.* **1998**, *292*, 133–136; M. Yin, W. P. Zhang, L. R. Lou, S. D. Xia, J. C. Krupa, *Spectrosc. Lett.* **1998**, *31*, 767–778; M. Yin, W. P. Zhang, S. D. Xia, J. C. Krupa, *J. Lumin.* **1996**, *68*, 335–339.

[14] T. Aitasalo, J. Holsa, M. Lastusaari, J. Niittykoski, F. Pelle, *Opt. Mater.* **2005**, *27*, 1511–1515; C. Li, C. Wyon, R. Moncorge, *IEEE J. Quantum Electron.* **1992**, *28*, 1209–1221.

[15] T. E. Peters, *J. Electrochem. Soc.* **1969**, *116*, 985–989; H. S. Kang, Y. C. Kang, H. D. Park, Y. G. Shul, *Appl. Phys. A* **2005**, *80*, 347–351.

[16] M. Mitsunaga, R. Yano, N. Uesugi, *Opt. Lett.* **1991**, *16*, 1890–1892; R. Yano, M. Mitsunaga, N. Uesugi, *J. Opt. Soc. Am. B – Opt. Phys.* **1992**, *9*, 992–997.

[17] N. F. M. Henry, K. Lonsdale, *International Tables for X-ray Crystallography*, vol. 1, Kynoch Press, Birmingham UK, **1952**.

[18] J. Felsche, *Struct. Bond.* **1973**, *13*, 99; J. Ito, H. Johnson, *Am. Miner.* **1968**, *53*, 1940–1946.

[19] T. Aitasalo, J. Holsa, M. Lastusaari, J. Niittykoski, F. Pelle, *Opt. Mater.*, in press.

[20] J. G. Wang, S. J. Tian, G. B. Li, F. H. Liao, X. P. Jing, *Mater. Res. Bull.* **2001**, *36*, 1855–1861.

[21] L. S. Birks, H. Friedman, *J. Appl. Phys.* **1946**, *17*, 687–692.

 © 2006 Wiley-VCH Verlag GmbH & Co. KGaA, Weinheim 

[22] M. D. Segall, P. L. D. Lindan, M. J. Probert, C. J. Pickard, P. J. Hasnip, S. J. Clark, M. C. Payne, *J. Phys.: Condens. Matter* **2002**, *14*, 2717–2744.
[23] C. Louis, K. Lebbou, M. A. Flores-Gonzalez, R. Bazzi, B. Hautefeuille, B. Mercier, S. Roux, P. Perriat, C. Olagnon, O. Tillement, *J. Crystal Growth* **2004**, *265*, 459–465; C. Louis, R. Bazzi, M. A. Flores-Gonzalez, W. Zheng, K. Lebbou, O. Tillement, B. Mercier, C. Dujardin, P. Perriat, *J. Solid State Chem.* **2003**, *173*, 335–341; G. Ledoux, B. Mercier, C. Louis, C. Dujardin, O. Tillement, P. Perriat, *Radiation Measurements* **2004**, *38*, 763–766.
[24] C. Duan, M. Yin, K. Yan, M. F. Reid, *J. Alloy Comput.* **2000**, *303–305*, 371–375; C. Duan, S. Xia, W. Zhang, M. Yin, J.-C. Krupa, *J. Alloy Comput.* **1998**, *275–277*, 450–454.
[25] M. Yu, J. Lin, J. Fu, H. J. Zhang, Y. C. Han, *J. Mater. Chem.* **2003**, *13*, 1413–1419.
[26] R. C. G. Naber, P. W. M. Blom, G. H. Gelinck, A. W. Marsman, D. M. de Leeuw, *Adv. Mater.* **2005**, *17*, 2692–2695.
[27] C. Peng, H. Zhang, J. Yu, Q. Meng, L. Fu, H. Li, L. Sun, X. Guo, *J. Phys. Chem. B* **2005**, *109*, 15278–15287.
[28] T. Yamase, T. Kobayashi, M. Sugeta, H. Naruke, *J. Phys. Chem. A* **1997**, *101*, 5046–5053.
[29] M. H. V. Werts, R. T. F. Jukes, J. W. Verhoeven, *Phys. Chem. Chem. Phys.* **2002**, *4*, 1542–1548.
[30] M. Sugeta, T. Yamase, *Bull. Chem. Soc. Jpn.* **1993**, *66*, 444–449.
[31] L. D. Carlos, Y. Messadeq, H. F. Brito, R. A. Sa-Ferreira, V. de Zea Bermudz, S. J. L. Ribeiro, *Adv. Mater.* **2000**, *12*, 594–598.
[32] M. F. Hazenkamp, G. Blasse, *Chem. Mater.* **1990**, *2*, 105–110.
[33] S. J. L. Ribeiro, K. Dahmouche, C. A. Ribeiro, C. V. Santilli, S. H. J. Pulcinelli, *J. Sol-Gel Sci. Technol.* **1998**, *13*, 427–432.
[34] T. R. Zhang, C. Spitz, M. Antonietti, C. F. J. Faul, *Chem. Eur. J.* **2005**, *11*, 1001–1009.
[35] See ref. 19.
[36] M. Yu, J. Lin, J. Fu, Y. C. Han, *Chem. Phys. Lett.* **2003**, *371*, 178–183.
[37] G. Blasse, A. Bril, *J. Chem. Phys.* **1967**, *47*, 1920–1926.
[38] V. A. Pustovarov, B. V. Shulgin, S. A. Smirnov, E. I. Zinin, *Nucl. Instrum. Methods Phys. Res., Sect. A* **1998**, *405*, 396–399.
[39] I. M. Batayev, S. U. Morev, *Opt. Spectrosk.* **1966**, *80*, 85–89.
[40] W. van Schaik, S. H. M. Poort, J. J. H. Schlotter, E. Dorrestijn, G. Blasse, *J. Electrochem. Soc.* **1994**, *141*, 2201–2207.
[41] M. T. Jose, A. R. Lakshmanan, *Opt. Mater.* **2004**, *24*, 651–659; J.-C. Bourcet, F. K. Fong, *J. Chem. Phys.* **1974**, *60*, 34–39; Z. L. Wang, Z. W. Quan, J. Lin, J. Fang, *J. Nanosci. Nanotech.* **2005**, *5*, 1532–1536.
[42] H. A. Bette, *Ann. Phys. (Leipzig)* **1930**, *5*, 325.
[43] H. Wang, C. K. Lin, X. M. Liu, J. Lin, M. Yu, *Appl. Phys. Lett.* **2005**, *87*, 181907.
[44] C. Feldman, *Phys. Rev.* **1960**, *117*, 455–459.
[45] D. Kumar, K. G. Cho, Z. Chen, V. Craciun, P. H. Holloway, R. K. Singh, *Phys. Rev. B* **1999**, *60*, 13331–13334.

Received: March 24, 2006
Published Online: August 2, 2006

 © 2006 Wiley-VCH Verlag GmbH & Co. KGaA, Weinheim 

DOI: 10.1002/ejic.200600285

# Synthesis and Electroluminescence Properties of *fac*-Tris(2-phenylpyridine)-iridium Derivatives Containing Hole-Trapping Moieties

**Katsuhiko Ono,*[a] Michitoshi Joho,[a] Katsuhiro Saito,[a] Masaaki Tomura,[b] Yosuke Matsushita,[c] Shigeki Naka,[c] Hiroyuki Okada,[c] and Hiroyoshi Onnagawa[c]**

**Keywords:** Amines / Charge-carrier injection / Doping / Iridium / Luminescence

In order to investigate an effective method for carrier injection into the phosphor of organic electroluminescent (EL) devices, we synthesized *fac*-tris(2-phenylpyridine)iridium [Ir(ppy)$_3$] derivatives containing hole-trapping moieties, such as diphenylamine, carbazole, and phenoxazine. Their photoluminescent maxima were observed around the maximum of Ir(ppy)$_3$. These values were slightly shifted depending on the hole-trapping moieties: redshifted due to diphenylamine and blueshifted due to carbazole and phenoxazine. Further, these moieties affected the oxidation potentials of Ir complexes in cyclic voltammetry. EL devices using an Ir complex with diphenylamine exhibited high EL performance because 1,1-bis[4-(di-*p*-tolylamino)phenyl]cyclohexane (TAPC) was employed as a hole-transporting layer. The maximum external quantum efficiency ($\eta_{ext}$) was recorded as 12.2 %. This value is comparable to that observed in a device using Ir(ppy)$_3$. These results indicate that the diphenylamino substituent is favorable to serve as a hole-trapping moiety of Ir(ppy)$_3$.
(© Wiley-VCH Verlag GmbH & Co. KGaA, 69451 Weinheim, Germany, 2006)

## Introduction

Currently, organic electroluminescent (EL) devices are an active area of research because of their potential applications in flat-panel displays.[1] The research to synthesize phosphorescent materials with heavy metals such as platinum and iridium has attracted considerable attention[2,3] because an internal quantum efficiency of 100% can be achieved by the energy transfer from both the singlet and triplet states to the phosphor triplet state at the emitting layer.[4,5] *fac*-Tris(2-phenylpyridine)iridium [Ir(ppy)$_3$] is a well-known green emitter.[3,6] A phosphorescent EL device using Ir(ppy)$_3$ demonstrated a high performance with a maximum external quantum efficiency of 19.2%.[3e] This value was comparable to the theoretical limit of around 20% obtained from simple classical optics.[7] However, further investigation of phosphorescent materials is still required for the research and development of phosphorescent EL devices. Also, synthetic studies on various materials such as Ir,[8,9] Pt,[10] and other metal[11] complexes have been conducted. These substances are used as dopants at the emitting layer. For example, the addition of an amount of ca. 6 wt.-% of Ir(ppy)$_3$ to the host material afforded the highest external quantum efficiency.[3a,3b] Therefore, the combination of phosphorescent and host materials is crucial for effective injection of holes and electrons into the

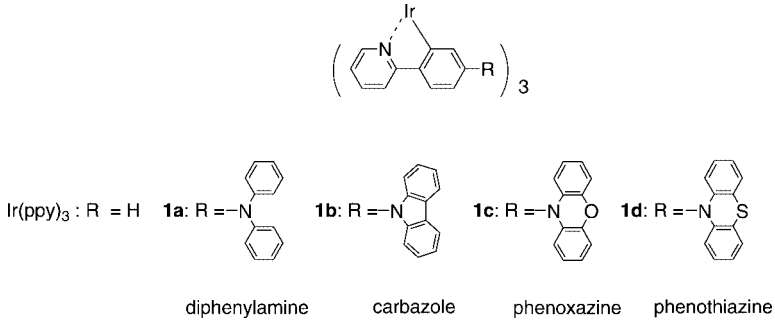


Scheme 1. Structures of Ir complexes **1**.

[a] Department of Materials Science and Engineering, Nagoya Institute of Technology, Gokiso,
Showa-ku, Nagoya 466-8555, Japan
Fax: +81-52-735-5407
E-mail: ono.katsuhiko@nitech.ac.jp
[b] Institute for Molecular Science,
Myodaiji, Okazaki 444-8585, Japan
[c] Department of Electric and Electronic Engineering, Faculty of Engineering, University of Toyama,
Gofuku, Toyama 930-8555, Japan

 © 2006 Wiley-VCH Verlag GmbH & Co. KGaA, Weinheim 

phosphor. 4,4′-Bis(carbazol-9-yl)-1,1′-biphenyl (CBP), which is an aromatic amine, is generally employed as the host material.[2b] Thus, we synthesized $Ir(ppy)_3$ derivatives as new types of phosphorescent materials, which are composed of aromatic amines such as diphenylamine, carbazole, phenoxazine, and phenothiazine[12] (see Scheme 1); these amine units act as effective hole-trapping moieties.[13] As a compound related to **1a**, its acetylacetonate (acac) complex $[Ir(ppy\text{-}NPh_2)_2(acac)]$ has been recently synthesized.[14] It was reported that the phosphorescent EL performance of this complex was better than that of $Ir(ppy)_2(acac)$. In this paper, we report the synthesis and properties of Ir complexes **1** and their applications in the study of phosphorescent EL devices.

## Results and Discussion

### Preparation and Properties of Ir Complexes Containing Hole-Trapping Moieties

The synthesis of the Ir complexes **1** is illustrated in Scheme 2. 2-(4-Bromophenyl)pyridine (**3**) was synthesized with a yield of 43% by the reaction of 2-fluoropyridine (**2**) with 4-bromophenyllithium;[15] this was utilized as the key compound in the following amination reaction. The ligands **4a**–**d** were prepared with yields of 82–91% by the Pd-catalyzed cross-coupling reaction of **3** with aromatic amines such as diphenylamine, carbazole, phenoxazine, and phenothiazine.[16] This reaction required a selective use of an additive base. Sodium *tert*-butoxide was selected for the reaction of diphenylamine, and potassium carbonate was employed for those of rigid amines, namely, carbazole, phenoxazine, and phenothiazine. The ligands **4a**–**c** produced the cyclometalated $Ir^{III}$ μ-chloro-bridged dimers **5a**–**c** with yields of 80–88% by treatment with $IrCl_3{\cdot}nH_2O$ in 2-ethoxyethanol and water at 120 °C.[6a] However, the Ir dimer **5d** was not obtained. The Ir complexes **1a**–**c** were prepared with yields of 48–78% by stirring **4** and **5** in glycerol with $K_2CO_3$ at 240 °C.[17] These Ir complexes were obtained in the form of orange solids for **1a** and yellow solids for **1b** and **1c**. Their melting points were above 300 °C. Structural determination was performed by using $^1H$ NMR, MALDI-TOF mass spectrometry, and elemental analysis. The stereochemistry of these complexes was determined to be that of facial isomers because the NMR chemical shifts observed in the three ligands were equivalent. In order to investigate the molecular structures of the Ir complexes, an X-ray crystallographic analysis of **1a** was performed. Two crystallographically independent molecules existed in this crystal. The structure of one of these molecules is shown in Figure 1. Three sets of linear C–Ir–N bonds are observed, indi-

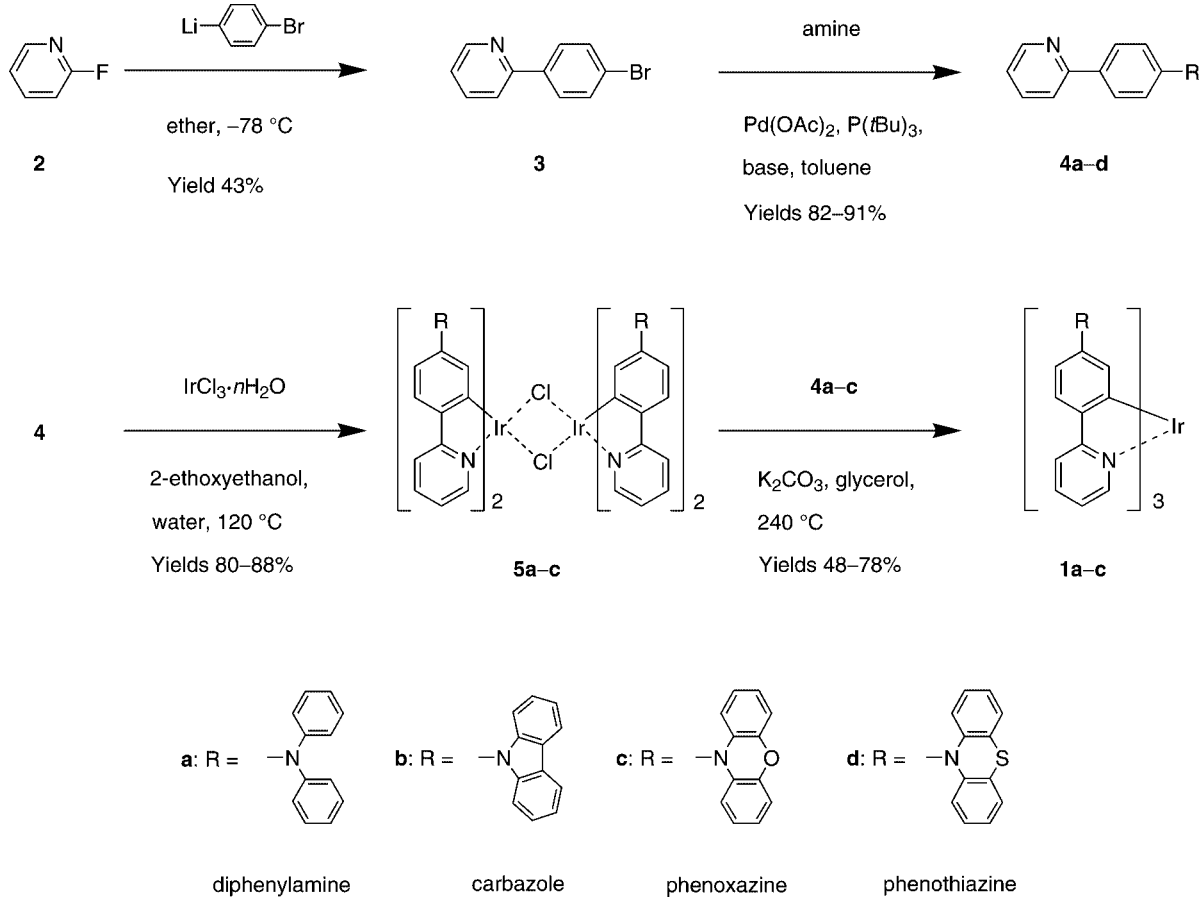


Scheme 2. Synthesis of ligands **4** and Ir complexes **1**.

 © 2006 Wiley-VCH Verlag GmbH & Co. KGaA, Weinheim 

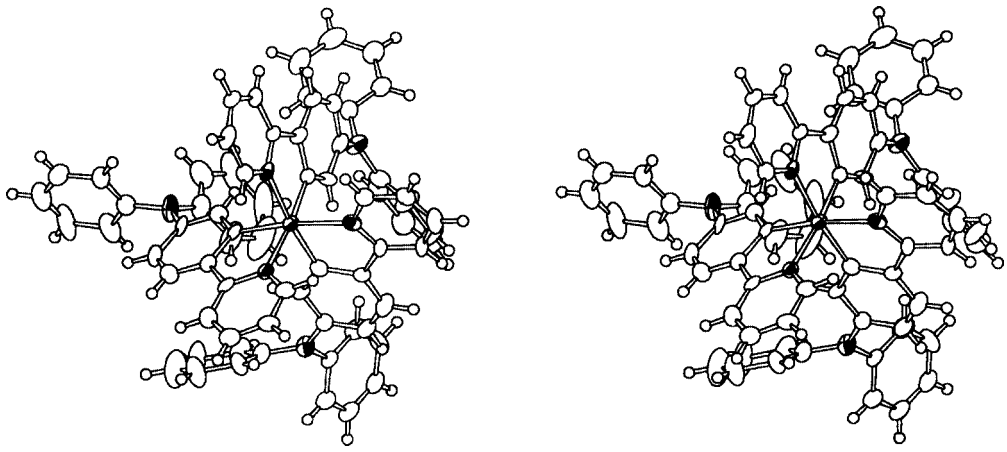

Figure 1. Molecular structure of Ir complex **1a** (stereo view). Ir and N atoms are depicted as shaded octants.

cating that complex **1a** is a facial isomer. Three diphenylamine moieties, resembling antennas, exist on the side of the $Ir(ppy)_3$ core.

The ligands **4** exhibited photoluminescence (PL) maxima between 400 and 540 nm in dichloromethane. The emission and absorption maxima are listed in Table 1. The Stokes shifts (Δ) for **4c**–**d** are greater than those for **4a**–**b**, indicating that the insertion of chalcogens such as O and S atoms into the carbazole moieties results in large Stokes shifts. The PL spectra of Ir complexes **1** are shown in Figure 2, and their emission and absorption maxima are listed in Table 2. The absorption maxima of the Ir complexes are redshifted as compared to those of the ligands. These maxima can be attributed to the metal–ligand charge-transfer (MLCT) excitation. The PL maxima of **1** are almost similar to that of $Ir(ppy)_3$, indicating the $Ir(ppy)_3$ cores as the source of the emission. The emission maxima marginally shifted depending on the molecular structure of the hole-trapping moiety. The maximum of **1a**, possessing a flexible amine, is redshifted from that of $Ir(ppy)_3$, and the maxima of **1b** and **1c**, possessing rigid amines, are blueshifted. The redshift is attributed to the resonance effect of the diphenylamino substituent, which reduced the energy gap between HOMO and LUMO. On the other hand, the π-conjugation on the rigid frameworks of carbazole and phenoxazine prevents the electron donation to the phenylpyridine (ppy) chelates. Furthermore, the emission maxima of the Ir complexes **1a** and **1b** are redshifted by ca. 100 nm from those of the ligands **4a** and **4b**, and the maximum of **1c** is similar to that of **4c** because of the large Stokes shift in the ligand. In addition, the emission maximum of **1a** is comparable to that of $Ir(ppy\text{-}NPh_2)_2(acac)$ ($\lambda_{em}$ = 530 nm).[14] The PL quantum yields of **1a**–**c** were measured in dichloromethane using $Ir(ppy)_3$ as the standard ($\Phi_{PL}$ = 0.40),[6b] and these values are listed in Table 2. The quantum yield of **1b** is greater than those of **1a** and **1c**.

In order to investigate the redox properties of the Ir complexes **1**, cyclic voltammetry (CV) was performed in dimethylformamide (DMF) with 0.1 M $nBu_4NClO_4$ as the supporting electrolyte. The voltammograms of **1** indicated reversible redox waves. The half-wave oxidation potentials of **1a**–**c** were recorded as +0.19, +0.48, and +0.23 V vs. $Fc/Fc^+$, respectively.[18] The values of **1a** and **1c** were lower than that of $Ir(ppy)_3$ (+0.32 V), indicating higher electron-donating abilities of **1a** and **1c**. On the other hand, the electron-donating ability of **1b** was lower than that of $Ir(ppy)_3$ owing to the introduction of a carbazole moiety. These results were attributed to the redox behavior of the ligands **4a**–**c**. The half-wave oxidation potentials of **4a** and **4c** (quasi-reversible and reversible waves) were measured to be +0.54 and

Table 1. PL and absorption maxima of ligands **4**.[a]

| Ligand | $\lambda_{em}$ [nm] | $\lambda_{abs}$ [nm] | Δ [nm] |
|---|---|---|---|
| **4a** | 435 | 346 | 89 |
| **4b** | 406 | 318 | 88 |
| **4c** | 520 | 326 | 194 |
| **4d** | 535 | 320 | 215 |

[a] In $CH_2Cl_2$.

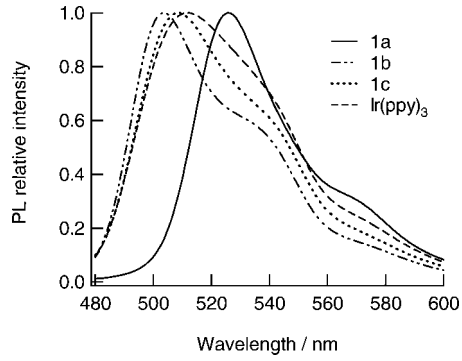


Figure 2. PL spectra of Ir complexes **1** in dichloromethane.

Table 2. PL and absorption maxima and quantum yields of Ir complexes **1**.[a]

| Complex | $\lambda_{em}$ [nm] | $\lambda_{abs}$ [nm] | $\Phi_{PL}$[b] |
|---|---|---|---|
| **1a** | 526 | 398 | 0.14 |
| **1b** | 504 | 378 sh | 0.38 |
| **1c** | 509 | 375 sh | 0.17 |
| $Ir(ppy)_3$ | 512 | 377 | 0.40 |

[a] In $CH_2Cl_2$. [b] Measured relative to $Ir(ppy)_3$, $\lambda_{ex}$ = 380 nm.

 © 2006 Wiley-VCH Verlag GmbH & Co. KGaA, Weinheim 

+0.30 V, respectively. The peak oxidation potential of **4b** (irreversible wave) was observed as +0.91 V. In addition, the half-wave reduction potentials of ligands **4a**–**c** were observed as –2.78, –2.69, and –2.64 V, respectively. Thus, the hole-trapping moieties affected the oxidation states of Ir complexes **1**.

### EL Properties of Ir Complex 1a Compared to Those of Ir(ppy)$_3$

An organic EL device using Ir complex **1a** as the emitter was fabricated, and its performance was investigated. The structure of ITO/TPD (50 nm)/Ir complex/CBP (20 nm)/BCP (30 nm)/LiF (1 nm)/Al (70 nm) was examined. *N*,*N*′-Diphenyl-*N*,*N*′-bis(3-methylphenyl)-1,1′-biphenyl-4,4′-diamine (TPD), Ir complex (5 wt.-%), and CBP were employed as the hole-transporting layer, emitter, and carrier combination host, respectively. 2,9-Dimethyl-4,7-diphenyl-1,10-phenanthroline (BCP) was used as an electron-transporting and hole-blocking layer. Figure 3(a) demonstrates the luminance/current density (*L*/*J*) characteristics of the EL devices using **1a** and Ir(ppy)$_3$ as the emitters. The EL from **1a** was over 40000 cd m$^{-2}$ at 14.4 V, although the emission from **1a** was weak as compared to that from Ir(ppy)$_3$ at the same current density. This result indicated that Ir complex **1a** as well as Ir(ppy)$_3$ were good emitters. The turn-on voltage was 4.8 V; this value was greater than that observed in the device with Ir(ppy)$_3$ (3.0 V). The external quantum efficiency ($\eta_{ext}$) of the device with **1a** also was lower than that of the device with Ir(ppy)$_3$ [Figure 3(b)]. Figure 3(c) shows the EL spectra. The spectrum from **1a** is similar to its PL spectrum shown in Figure 2. The EL maximum from **1a** was observed at 528 nm, which was slightly redshifted as compared to that from Ir(ppy)$_3$ (514 nm). In addition, a weak EL emission from TPD was observed in the wavelength region between 390 and 470 nm. This result indicated that an energy transfer occurred from the MLCT singlet state of **1a** to the singlet state of TPD by the Förster mechanism.

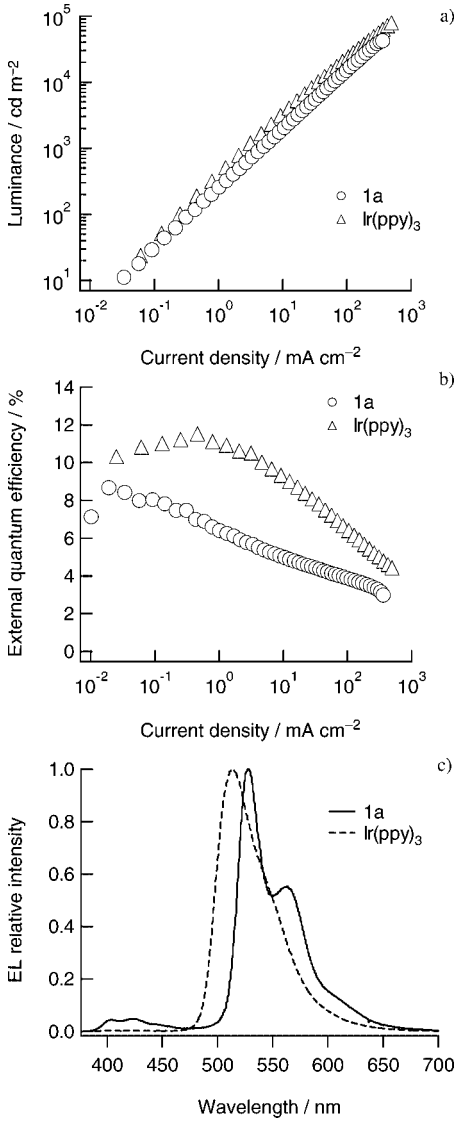


Figure 3. EL characteristics of ITO/TPD (50 nm)/Ir complex (5 wt.-%)/CBP (20 nm)/BCP (30 nm)/LiF (1 nm)/Al (70 nm). Ir complex = **1a** (circles), Ir(ppy)$_3$ (triangles). (a) Luminance (*L*)/current density (*J*) plots. (b) External quantum efficiency ($\eta_{ext}$)/current density (*J*) plots. (c) EL spectra.

### Scope and Limitations of Ir Complexes Containing Hole-Trapping Moieties

Because the EL emission from TPD was observed in the device with **1a**, 1,1-bis[4-(di-*p*-tolylamino)phenyl]cyclohexane (TAPC) was employed as a hole-transporting layer. The EL structure of ITO/TAPC (50 nm)/Ir complex/CBP (20 nm)/BCP (30 nm)/LiF (1 nm)/Al (70 nm) was examined. As an emitter, 5 wt.-% of **1a** was employed. Figure 4(a) shows the plots of the variation of the external quantum efficiency ($\eta_{ext}$) vs. the current density (*J*), indicating that the efficiency increased by replacing TPD (circles) with TAPC (triangles) as the hole-transporting layer (HTL). Thus, a maximum external quantum efficiency of 9.6% was observed at 7.4 V. The EL from **1a** was over 26000 cd m$^{-2}$ at 14.4 V. According to the EL spectrum shown in Figure 4(b), emission from the hole-transporting layer (TAPC) was not observed. This result implied that the energy transfer from **1a** to the hole-transporting layer was suppressed because the HOMO–LUMO energy gap of TAPC is larger than that of TPD (TAPC: 3.4 eV; TPD: 3.1 eV). Further, the phosphor triplet excitons were effectively confined by the TAPC layer, thereby leading to the high EL efficiency.[19]

An optimized amount of the Ir complex dopant was used at the emitting layer. The highest EL efficiency was observed when an amount of approximately 10 wt.-% of **1a** was doped. The molar ratio of the optimized amount was slightly higher as compared to that used for Ir(ppy)$_3$. The luminance (*L*) of **1a** was observed as 51900 cd m$^{-2}$ at 13.0 V. This resulted in the maximum external quantum efficiency ($\eta_{ext}$) of 12.2% [Figure 4(a)]. This value is comparable to those observed in devices using Ir(ppy)$_3$ [$\eta_{ext}$ = 11.5%, Figure 3(b)] and Ir(ppy-NPh$_2$)$_2$(acac) ($\eta_{ext}$ = 11.8%).[14] Table 3

 © 2006 Wiley-VCH Verlag GmbH & Co. KGaA, Weinheim 

Table 3. EL properties of devices using Ir complexes **1**.[a]

| Complex | wt.-% [%] | Turn-on voltage [V] | $\eta_{ext}$ [%,V] | $L$ [cd·m$^{-2}$, V] | $\eta_p$ [lm·W$^{-1}$, V] | $\lambda_{max}$ [nm] | CIE ($x$, $y$) |
|---|---|---|---|---|---|---|---|
| **1a** | 10 | 4.0 | 12.2, 6.6 | 51900, 13.0 | 24.8, 6.0 | 528 | 0.33, 0.64 |
| **1b** | 12 | 3.6 | 9.1, 4.8 | 14600, 13.6 | 22.5, 4.4 | 506 | 0.24, 0.64 |
| **1c** | 11 | 3.8 | 8.7, 6.4 | 31000, 13.0 | 15.2, 6.4 | 513 | 0.26, 0.64 |

[a] Device structure: ITO/TAPC (50 nm)/Ir complex/CBP (20 nm)/BCP (30 nm)/LiF (1 nm)/Al (70 nm).

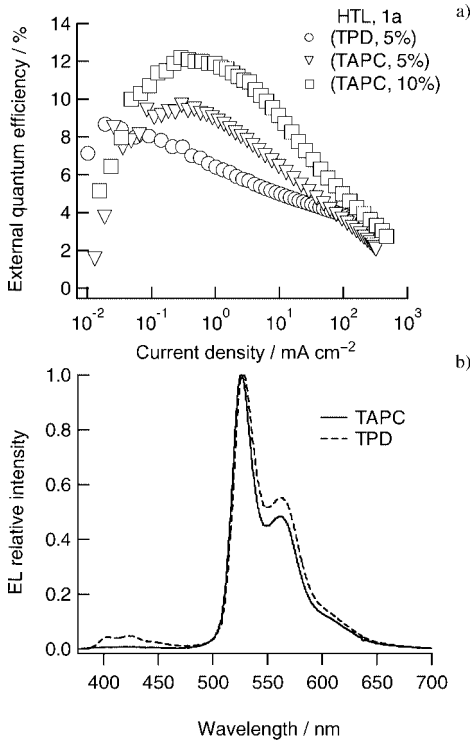


Figure 4. EL characteristics of ITO/HTL (50 nm)/**1a**/CBP (20 nm)/BCP (30 nm)/LiF (1 nm)/Al (70 nm). (a) External quantum efficiency ($\eta_{ext}$)/current density ($J$) plots. HTL/**1a** with TPD (5 wt.-%, circles), TAPC (5 wt.-%, triangles), TAPC (10 wt.-%, squares). (b) EL spectra.

summarizes the EL performances of devices with Ir complexes **1a**–**c**. The luminance increased in the following order: **1b**, **1c**, and **1a**. This may be attributed to their redox behavior as explained in the CV study. The EL efficiency of **1a** is higher than those of **1b** and **1c**. These results indicate that the diphenylamine moiety with a branched structure is acceptable as the hole-trapping moiety of Ir(ppy)$_3$.

## Conclusions

We prepared *fac*-tris(2-phenylpyridine)iridium [Ir(ppy)$_3$] derivatives containing hole-trapping moieties such as diphenylamine (**1a**), carbazole (**1b**), and phenoxazine (**1c**). Their PL maxima were observed around the maximum of Ir(ppy)$_3$. These values were marginally shifted depending on the hole-trapping moieties: redshifted for **1a** and blueshifted for **1b** and **1c**. The electron-donating ability of Ir(ppy)$_3$ was increased due to the diphenylamine and phenoxazine moieties, and the oxidation state became more unstable due to the carbazole unit. Organic EL devices using Ir complex **1a** as the emitter exhibited stronger luminance than devices that used **1b** and **1c**. Particularly, high EL efficiency was observed when TAPC was used as the hole-transporting layer. The maximum external quantum efficiency from the device was comparable to that observed in a device that used Ir(ppy)$_3$. Therefore, the introduction of a branched aromatic amine into phosphor is effective for the research and development of new phosphorescent materials.

## Experimental Section

**General:** Iridium trichloride *n*-hydrate ($IrCl_3 \cdot nH_2O$) was purchased from Soekawa Chemicals. Melting points were measured with a Yanaco micro melting point apparatus and are uncorrected. IR, UV/Vis, and PL spectra were obtained with JASCO FT/IR-5300, V-550, and FP-6300 spectrometers, respectively. Mass spectra were determined with a Hitachi M-2000S mass spectrometer (EI) operating at 70 eV by a direct inlet system and a Voyager-DE STR mass spectrometer (MALDI-TOF) using dithranol as a matrix. Elemental analyses were performed with a Perkin–Elmer 2400II analyzer. $^1$H and $^{13}$C NMR spectra were recorded with Varian GEMINI spectrometers (300 and 50 MHz) and a Bruker AVANCE 600 spectrometer (600 and 150 MHz) with tetramethylsilane as an internal standard.

**Preparation of 2-(4-Bromophenyl)pyridine (3):** *n*BuLi in hexane (1.60 M, 16.0 mL, 25.6 mmol) was added dropwise to a suspension of 1,4-dibromobenzene (5.90 g, 25.0 mmol) in dry diethyl ether (40 mL) at –78 °C under nitrogen. 2-Fluoropyridine (**2**) (1.72 mL, 20.0 mmol) was added after stirring for 30 min. The mixture was stirred at –78 °C for 1 h and at room temperature for 1 h. The reaction mixture was poured into water (50 mL), and diethyl ether (50 mL) was added. The organic layer was separated and the aqueous layer was extracted with diethyl ether (50 mL × 2). The combined organic solutions were extracted with a 5% HCl solution (200 mL × 3), and the aqueous layer was adjusted to an alkaline pH with KOH (63 g). The aqueous layer was extracted with diethyl ether (200 mL × 3). The organic solution was dried with $MgSO_4$ and concentrated. The residue was sublimed at 65–70 °C under $10^{-2}$ Torr to afford compound **3** (2.02 g, 43%) as colorless needles. M.p. 60–62 °C. IR (KBr): $\tilde{\nu}$ = 3052, 3007, 1586, 1462, 1433, 1391, 1154, 1100, 1071, 1005, 841, 774 cm$^{-1}$. $^1$H NMR ($CDCl_3$, 300 MHz): $\delta$ = 7.23–7.28 (m, 1 H), 7.60 (dt, $J$ = 8.8, 2.2 Hz, 2 H), 7.68–7.79 (m, 2 H), 7.88 (dt, $J$ = 8.8, 2.2 Hz, 2 H), 8.69 (ddd, $J$ = 4.8, 1.8, 1.1 Hz, 1 H) ppm. $^{13}$C NMR ($CDCl_3$, 50 MHz): $\delta$ = 120.3, 122.4, 123.4, 128.4, 131.8, 136.9, 138.2, 149.7, 156.2 ppm. MS (EI): $m/z$ (%) = 235 (100) [M$^+$], 233 (99) [M$^+$], 154 (84). $C_{11}H_8BrN$ (234.09): calcd. C 56.44, H 3.44, N 5.98; found C 56.47, H 3.55, N 5.89.

**Preparation of Ligands 4a–d:** A solution of $Pd(OAc)_2$ (28 mg, 0.12 mmol) and $t$Bu$_3$P (90 mg, 0.44 mmol) in toluene (4 mL) was

 © 2006 Wiley-VCH Verlag GmbH & Co. KGaA, Weinheim 

added to a suspension of compound **3** (0.94 g, 4.0 mmol), diphenylamine (0.68 g, 4.0 mmol), and *t*BuONa (0.47 g, 4.9 mmol) in toluene (4 mL) under nitrogen. The mixture was refluxed for 3 h. After cooling, the reaction mixture was poured into water (10 mL), and ethyl acetate (10 mL) was added. The organic layer was separated and the aqueous layer was extracted with ethyl acetate (10 mL × 2). The combined organic solutions were dried with $Na_2SO_4$ and concentrated. The residue was chromatographed on alumina gel (hexane/$CH_2Cl_2$, 2:1) to give ligand **4a** (1.17 g, 91%) as pale yellow needles. M.p. 177–177.5 °C (from ethanol). IR (KBr): $\tilde{\nu}$ = 3057, 1586, 1491, 1466, 1433, 1325, 1279, 787, 756, 698, 515 $cm^{-1}$. $^1H$ NMR ($CDCl_3$, 300 MHz): $\delta$ = 7.05 (tt, $J$ = 7.3, 1.4 Hz, 2 H), 7.12–7.20 (m, 7 H), 7.24–7.31 (m, 4 H), 7.65–7.74 (m, 2 H), 7.87 (dt, $J$ = 8.8, 2.4 Hz, 2 H), 8.65 (ddd, $J$ = 4.9, 1.7, 1.0 Hz, 1 H) ppm. $^{13}C$ NMR ($CDCl_3$, 50 MHz): $\delta$ = 117.8, 119.8, 121.4, 123.2, 124.7, 127.7, 129.3, 133.1, 136.6, 147.5, 148.7, 149.6, 157.1 ppm. MS (EI): $m/z$ (%) = 322 (100) [$M^+$]. UV/Vis ($CH_2Cl_2$): $\lambda_{max}$ (log$\varepsilon$) = 346 (4.42), 308 (4.23) nm. $C_{23}H_{18}N_2$ (322.40): calcd. C 85.68, H 5.63, N 8.69; found C 85.63, H 5.80, N 8.56. Similar reaction conditions were applied to the synthesis of ligands **4b**–**d**. These were carried out using $K_2CO_3$ (3 equiv.) as a base instead of *t*BuONa. The reaction mixtures were refluxed for 24 h. **4b:** Yield 87% (0.56 g). Pale yellow crystals (from ethanol). M.p. 179–180.5 °C. IR (KBr): $\tilde{\nu}$ = 1603, 1516, 1453, 1366, 1335, 1318, 1235, 779, 750, 725 $cm^{-1}$. $^1H$ NMR ($CDCl_3$, 300 MHz): $\delta$ = 7.27–7.33 (m, 3 H), 7.40–7.51 (m, 4 H), 7.69 (dt, $J$ = 8.8, 2.2 Hz, 2 H), 7.81–7.83 (m, 2 H), 8.16 (d, $J$ = 7.8 Hz, 2 H), 8.23 (dt, $J$ = 8.8, 2.2 Hz, 2 H), 8.76 (dt, $J$ = 4.9, 1.1 Hz, 1 H) ppm. $^{13}C$ NMR ($CDCl_3$, 50 MHz): $\delta$ = 109.8, 120.1, 120.3, 120.5, 122.4, 123.5, 126.0, 127.2, 128.4, 136.9, 138.3, 138.4, 140.7, 149.8, 156.5 ppm. MS (EI): $m/z$ (%) = 320 (100) [$M^+$]. UV/Vis ($CH_2Cl_2$): $\lambda_{max}$ (log$\varepsilon$) = 318 (4.25), 292 (4.30), 240 (4.68) nm. $C_{23}H_{16}N_2$ (320.39): calcd. C 86.22, H 5.03, N 8.74; found C 86.01, H 5.19, N 8.62. **4c:** Yield 84% (0.86 g). Pale yellow crystals (from methanol). M.p. 173–174.5 °C. IR (KBr): $\tilde{\nu}$ = 1589, 1491, 1341, 1273, 743, 729 $cm^{-1}$. $^1H$ NMR ($CDCl_3$, 300 MHz): $\delta$ = 6.01 (dd, $J$ = 7.8, 1.5 Hz, 2 H), 6.57–6.72 (m, 6 H), 7.27–7.31 (m, 1 H), 7.45 (d, $J$ = 8.7 Hz, 2 H), 7.80 (m, 2 H), 8.21 (d, $J$ = 8.7 Hz, 2 H), 8.74 (d, $J$ = 4.7 Hz, 1 H) ppm. $^{13}C$ NMR ($CDCl_3$, 50 MHz): $\delta$ = 113.3, 115.4, 120.7, 121.4, 122.5, 123.2, 129.6, 131.1, 134.2, 137.1, 139.4, 139.6, 143.9, 149.7, 156.4 ppm. MS (EI): $m/z$ (%) = 336 (100) [$M^+$], 182 (69). UV/Vis ($CH_2Cl_2$): $\lambda_{max}$ (log$\varepsilon$) = 326 (3.95), 276 (4.21), 240 (4.75) nm. $C_{23}H_{16}N_2O$ (336.39): calcd. C 82.12, H 4.79, N 8.33; found C 82.28, H 4.82, N 8.32. **4d:** Yield 82% (0.42 g). Pale yellow crystals (from ethanol). M.p. 174–175.5 °C. IR (KBr): $\tilde{\nu}$ = 1589, 1464, 1437, 1310, 1260, 1244, 1046, 920, 783, 743 $cm^{-1}$. $^1H$ NMR ($CDCl_3$, 300 MHz): $\delta$ = 6.34 (dd, $J$ = 7.7, 1.9 Hz, 2 H), 6.80–6.90 (m, 4 H), 7.05 (dd, $J$ = 6.9, 2.1 Hz, 2 H), 7.25–7.30 (m, 1 H), 7.49 (dt, $J$ = 8.7, 2.2 Hz, 2 H), 7.77–7.81 (m, 2 H), 8.20 (dt, $J$ = 8.7, 2.2 Hz, 2 H), 8.74 (dt, $J$ = 4.7, 1.4 Hz, 1 H) ppm. $^{13}C$ NMR ($CDCl_3$, 50 MHz): $\delta$ = 116.6, 120.6, 120.9, 122.4, 122.7, 126.8, 126.9, 129.2, 130.5, 136.9, 139.0, 141.9, 144.0, 149.8, 156.5 ppm. MS (EI): $m/z$ (%) = 352 (100) [$M^+$]. UV/Vis ($CH_2Cl_2$): $\lambda_{max}$ (log$\varepsilon$) = 320 (3.87), 257 (4.74) nm. $C_{23}H_{16}N_2S$ (352.45): calcd. C 78.38, H 4.58, N 7.95; found C 78.32, H 4.53, N 7.89.

**Preparation of Ir Dimers 5a–c:** A mixture of ligand **4a** (0.65 g, 2.0 mmol) and $IrCl_3{\cdot}nH_2O$ (0.36 g, 1.0 mmol) in a solution of 2-ethoxyethanol (12 mL) and water (4 mL) was stirred under nitrogen at 120 °C for 24 h. After cooling, the precipitate was filtered and washed with methanol, diethyl ether, and hexane to afford Ir dimer **5a** (0.69 g, 80%) as yellow solid. M.p. > 300 °C. $^1H$ NMR ($CDCl_3$, 300 MHz): $\delta$ = 5.48 (d, $J$ = 2.2 Hz, 4 H), 6.21 (t, $J$ = 6.5 Hz, 4 H), 6.45 (dd, $J$ = 8.5, 2.2 Hz, 4 H), 6.85–6.94 (m, 24 H), 7.09 (t, $J$ = 7.8 Hz, 16 H), 7.22–7.28 (m, 8 H), 7.43 (d, $J$ = 7.7 Hz, 4 H), 8.89 (d, $J$ = 6.5 Hz, 4 H) ppm. $^{13}C$ NMR ($CDCl_3$, 50 MHz): $\delta$ = 114.3, 117.3, 120.4, 122.7, 122.9, 123.8, 125.4, 128.8, 135.4, 137.2, 146.1, 147.3, 147.7, 151.0, 167.4 ppm. MALDI-TOF MS: $m/z$ = 1741.40 [$M^+$ + 1], 1705.41 [$M^+$ – Cl], 870.19 [$M^+$/2], 835.22 [$M^+$/2 – Cl]. $C_{92}H_{68}Cl_2Ir_2N_8$ (1740.9): calcd. C 63.47, H 3.94, N 6.44; found C 63.41, H 3.83, N 6.36. Similar reaction conditions were applied to the synthesis of Ir dimers **5b** and **5c**. **5b:** Yield 85% (0.36 g). Yellow solid. M.p. > 300 °C. MALDI-TOF MS: $m/z$ = 1733.37 [$M^+$ + 1], 1697.40 [$M^+$ – Cl], 866.22 [$M^+$/2], 831.25 [$M^+$/2 – Cl]. $C_{92}H_{60}Cl_2Ir_2N_8$ (1732.9): calcd. C 63.77, H 3.49, N 6.47; found C 63.15, H 3.43, N 6.32. **5c:** Yield 88% (0.43 g). Yellow solid. M.p. > 300 °C. MALDI-TOF MS: $m/z$ = 1761.33 [$M^+$ – Cl], 898.23 [$M^+$/2], 863.26 [$M^+$/2 – Cl]. $C_{92}H_{60}Cl_2Ir_2N_8O_4$ (1796.9): calcd. C 61.50, H 3.37, N 6.24; found C 60.57, H 3.25, N 6.01.

**Preparation of *fac*-Ir Complexes 1a–c:** A mixture of Ir dimer **5a** (130 mg, 0.075 mmol), ligand **4a** (49 mg, 0.15 mmol) and $K_2CO_3$ (106 mg, 0.77 mmol) in glycerol (5 mL) was stirred under nitrogen at 240 °C for 11 h. After cooling, water (5 mL) and dichloromethane (10 mL) were added. The organic layer was separated and the aqueous layer was extracted with dichloromethane (10 mL × 2). The combined organic solutions were dried with $Na_2SO_4$ and concentrated. The residue was chromatographed on silica gel ($CH_2Cl_2$) to afford *fac*-Ir complex **1a** (82 mg, 48%) as orange solid. M.p. > 300 °C (from $CH_2Cl_2$). $^1H$ NMR ($CDCl_3$, 600 MHz): $\delta$ = 6.24 (dd, $J$ = 8.4, 2.1 Hz, 3 H), 6.58 (d, $J$ = 2.1 Hz, 3 H), 6.78 (t, $J$ = 6.4 Hz, 3 H), 6.83 (d, $J$ = 7.7 Hz, 12 H), 6.87 (t, $J$ = 7.7 Hz, 6 H), 7.09 (t, $J$ = 7.7 Hz, 12 H), 7.27 (d, $J$ = 8.4 Hz, 3 H), 7.52–7.55 (m, 6 H), 7.68 (d, $J$ = 8.0 Hz, 3 H) ppm. $^{13}C$ NMR ($CDCl_3$, 150 MHz): $\delta$ = 114.6, 117.7, 120.5, 122.2, 124.5, 124.8, 128.6, 130.2, 135.4, 137.6, 147.2, 147.6, 148.2, 161.9, 166.2 ppm. MALDI-TOF MS: $m/z$ = 1156.42 [$M^+$]. UV/Vis ($CH_2Cl_2$): $\lambda_{max}$ (log$\varepsilon$) = 398 (4.68), 367 (4.70), 320 (4.67), 261 (4.69), 227 (4.80) nm. $C_{69}H_{51}IrN_6$ (1156.4): calcd. C 71.67, H 4.45, N 7.27; found C 71.65, H 4.32, N 7.33. Similar reaction conditions, stirring at 240 °C for 48 h and 24 h, were applied to the synthesis of *fac*-Ir complexes **1b** and **1c**, respectively. **1b:** Yield 78% (0.27 g). Yellow solid. M.p. > 300 °C. $^1H$ NMR ($CDCl_3$, 300 MHz): $\delta$ = 6.87 (br. m, 6 H), 6.96–7.03 (m, 18 H), 7.20 (d, $J$ = 2.2 Hz, 3 H), 7.71 (td, $J$ = 8.0, 1.5 Hz, 3 H), 7.76 (d, $J$ = 4.7 Hz, 3 H), 7.81 (d, $J$ = 8.2 Hz, 3 H), 7.94 (d, $J$ = 7.1 Hz, 6 H), 7.99 (d, $J$ = 8.0 Hz, 3 H) ppm. MALDI-TOF MS: $m/z$ = 1150.35 [$M^+$]. UV/Vis ($CH_2Cl_2$): $\lambda_{max}$ (log$\varepsilon$) = 378 sh (4.40), 346 (4.70), 238 (5.18) nm. $C_{69}H_{45}IrN_6$ (1150.4): calcd. C 72.04, H 3.94, N 7.31; found C 72.20, H 4.03, N 7.26. **1c:** Yield 54% (0.20 g). Yellow solid. M.p. > 300 °C. $^1H$ NMR ($CDCl_3$, 300 MHz): $\delta$ = 5.69 (dd, $J$ = 7.8, 1.4 Hz, 6 H), 6.01 (td, $J$ = 7.8, 1.4 Hz, 6 H), 6.39 (td, $J$ = 7.8, 1.4 Hz, 6 H), 6.52 (dd, $J$ = 7.8, 1.4 Hz, 6 H), 6.72 (d, $J$ = 2.0 Hz, 3 H), 6.76 (dd, $J$ = 8.1, 2.0 Hz, 3 H), 7.02 (t, $J$ = 5.9 Hz, 3 H), 7.69–7.73 (m, 6 H), 7.81 (d, $J$ = 8.1 Hz, 3 H), 7.92 (d, $J$ = 7.7 Hz, 3 H) ppm. MALDI-TOF MS: $m/z$ = 1198.34 [$M^+$]. UV/Vis ($CH_2Cl_2$): $\lambda_{max}$ (log$\varepsilon$) = 375 sh (4.23), 330 (4.52), 283 (4.85), 241 (5.20) nm. $C_{69}H_{45}IrN_6O_3$ (1198.4): calcd. C 69.16, H 3.78, N 7.01; found C 69.14, H 3.90, N 6.89.

**X-ray Crystallographic Analysis for *fac*-Ir Complex 1a:** A single crystal was obtained as a greenish brown platelet by recrystallization of **1a** from a mixture of dichloromethane and ethyl acetate. Crystal data for **1a**: 0.15 × 0.13 × 0.03 mm, $C_{69}H_{51}IrN_6$, $M$ = 1156.42, monoclinic, space group $P2_1/n$, $a$ = 13.9742(9), $b$ = 17.1467(9), $c$ = 44.590(3) Å, $\beta$ = 98.158(3)°, $V$ = 10576(1) $Å^3$, $Z$ = 8, $D_c$ = 1.452 $g\,cm^{-3}$, $\mu$ = 25.82 $cm^{-1}$, $F(000)$ = 4672. A total of 21884 unique reflections for $2\theta_{max}$ = 55° was collected [$I > 2\sigma(I)$] with a Rigaku MSC MercuryCCD diffractometer (Mo-$K_\alpha$ radiation, $\lambda$ = 0.71070 Å, graphite monochromator) at 173 K. A numerical absorption correction was applied. The structure was solved

 © 2006 Wiley-VCH Verlag GmbH & Co. KGaA, Weinheim 

using the direct method (SHELXS-97)[20] and refined by the full-matrix least-squares analysis (SHELXL-97)[21] giving values of $R_1$ = 0.088, $R_w$ = 0.165, $S$ = 1.26, $\rho_{max}/\rho_{min}$ = 3.44/–2.31 e·Å$^{-3}$. All calculations were performed using the teXsan programs.[22] CCDC-294487 contains the supplementary crystallographic data for this paper. The data can be obtained free of charge from the Cambridge Crystallographic Data Centre via www.ccdc.cam.ac.uk/data_request/cif.

**Electrochemical Measurements:** CV was performed with a Toho Technical Research polarization unit PS-07 potentiostat/galvanostat. The CV studies of compounds **1** and **4** were carried out in DMF with 0.1 M $n$Bu$_4$NClO$_4$ using Pt and SCE electrodes. The values are expressed in potentials vs. Fc/Fc$^+$.

**Electroluminescence Measurements:** An ITO-coated glass substrate was patterned and cleaned by scrubbing, ultrasonication, and irradiation in a UV/ozone chamber. Organic layers were deposited on the ITO at an evaporating rate of 1 nm/s. The cathode of a LiF/Al bilayer was formed by sequential deposition. The rate and thickness of the films were monitored with a quartz oscillator. The sample area was 2×2 mm. Current and luminance on applied voltage were measured with an HP 4145A semiconductor parameter analyzer, which was connected with a Topcon BM-3 luminance meter. The electroluminescence spectra were measured with an Ocean Optics S2000 spectrometer. The external quantum efficiency ($\eta_{ext}$) was calculated from the luminance, the current density, and the emission spectrum of each device assuming that the observed emission was the Lambertian one.

## Acknowledgments

This work was supported by a Grant-in-Aid (nos. 17750037, 17550033) from the Ministry of Education, Culture, Sports, Science and Technology, Japan and a grant from Innovation Plaza Tokai ("Investigation of organic device integration using self-alignment technology"). K. O. wishes to thank the Yazaki Memorial Foundation for Science and Technology and Research Foundation for the Electrotechnology of Chubu for financial support. We would like to thank the Research Center for Molecular-Scale Nanoscience, Institute for Molecular Science, for the crystal analysis.

[1] a) C. W. Tang, S. A. VanSlyke, *Appl. Phys. Lett.* **1987**, *51*, 913–915; b) C. Adachi, S. Tokito, T. Tsutsui, S. Saito, *Jpn. J. Appl. Phys.* **1988**, *27*, L713–L715.

[2] a) M. A. Baldo, D. F. O'Brien, Y. You, A. Shoustikov, S. Sibley, M. E. Thompson, S. R. Forrest, *Nature* **1998**, *395*, 151–154; b) D. F. O'Brien, M. A. Baldo, M. E. Thompson, S. R. Forrest, *Appl. Phys. Lett.* **1999**, *74*, 442–444.

[3] a) M. A. Baldo, S. Lamansky, P. E. Burrows, M. E. Thompson, S. R. Forrest, *Appl. Phys. Lett.* **1999**, *75*, 4–6; b) T. Tsutsui, M.-J. Yang, M. Yahiro, K. Nakamura, T. Watanabe, T. Tsuji, Y. Fukuda, T. Wakimoto, S. Miyaguchi, *Jpn. J. Appl. Phys.* **1999**, *38*, L1502–L1504; c) M. A. Baldo, M. E. Thompson, S. R. Forrest, *Nature* **2000**, *403*, 750–753; d) C. Adachi, M. A. Baldo, S. R. Forrest, M. E. Thompson, *Appl. Phys. Lett.* **2000**, *77*, 904–906; e) M. Ikai, S. Tokito, Y. Sakamoto, T. Suzuki, Y. Taga, *Appl. Phys. Lett.* **2001**, *79*, 156–158.

[4] a) C. Adachi, M. A. Baldo, M. E. Thompson, S. R. Forrest, *J. Appl. Phys.* **2001**, *90*, 5048–5051; b) B. W. D'Andrade, M. A. Baldo, C. Adachi, J. Brooks, M. E. Thompson, S. R. Forrest, *Appl. Phys. Lett.* **2001**, *79*, 1045–1047.

[5] H. Yersin, *Top. Curr. Chem.* **2004**, *241*, 1–26.

[6] a) S. Lamansky, P. Djurovich, D. Murphy, F. Abdel-Razzaq, R. Kwong, I. Tsyba, M. Bortz, B. Mui, R. Bau, M. E. Thompson, *Inorg. Chem.* **2001**, *40*, 1704–1711; b) K. A. King, P. J. Spellane, R. J. Watts, *J. Am. Chem. Soc.* **1985**, *107*, 1431–1432.

[7] G. Gu, D. Z. Garbuzov, P. E. Burrows, S. Venkatesh, S. R. Forrest, M. E. Thompson, *Opt. Lett.* **1997**, *22*, 396–398.

[8] a) X. Gong, M. R. Robinson, J. C. Ostrowski, D. Moses, G. C. Bazan, A. J. Heeger, *Adv. Mater.* **2002**, *14*, 581–585; b) A. Tsuboyama, H. Iwawaki, M. Furugori, T. Mukaide, J. Kamatani, S. Igawa, T. Moriyama, S. Miura, T. Takiguchi, S. Okada, M. Hoshino, K. Ueno, *J. Am. Chem. Soc.* **2003**, *125*, 12971–12979; c) S.-C. Lo, N. A. H. Male, J. P. J. Markham, S. W. Magennis, P. L. Burn, O. V. Salata, I. D. W. Samuel, *Adv. Mater.* **2002**, *14*, 975–979; d) H. Z. Xie, M. W. Liu, O. Y. Wang, X. H. Zhang, C. S. Lee, L. S. Hung, S. T. Lee, P. F. Teng, H. L. Kwong, H. Zheng, C. M. Che, *Adv. Mater.* **2001**, *13*, 1245–1248; e) V. V. Grushin, N. Herron, D. D. LeCloux, W. J. Marshall, V. A. Petrov, Y. Wang, *Chem. Commun.* **2001**, 1494–1495; f) E. J. Nam, J. H. Kim, B.-O. Kim, S. M. Kim, N. G. Park, Y. S. Kim, Y. K. Kim, Y. Ha, *Bull. Chem. Soc. Jpn.* **2004**, *77*, 751–755.

[9] a) B. M. J. S. Paulose, D. K. Rayabarapu, J.-P. Duan, C.-H. Cheng, *Adv. Mater.* **2004**, *16*, 2003–2007; b) J.-P. Duan, P.-P. Sun, C.-H. Cheng, *Adv. Mater.* **2003**, *15*, 224–228; c) T. Tsuzuki, N. Shirasawa, T. Suzuki, S. Tokito, *Adv. Mater.* **2003**, *15*, 1455–1458; d) Y.-J. Su, H.-L. Huang, C.-L. Li, C.-H. Chien, Y.-T. Tao, P.-T. Chou, S. Datta, R.-S. Liu, *Adv. Mater.* **2003**, *15*, 884–888; e) B. W. D'Andrade, M. E. Thompson, S. R. Forrest, *Adv. Mater.* **2002**, *14*, 147–151; f) C. Adachi, R. C. Kwong, P. Djurovich, V. Adamovich, M. A. Baldo, M. E. Thompson, S. R. Forrest, *Appl. Phys. Lett.* **2001**, *79*, 2082–2084; g) S. Lamansky, P. Djurovich, D. Murphy, F. Abdel-Razzaq, H.-E. Lee, C. Adachi, P. E. Burrows, S. R. Forrest, M. E. Thompson, *J. Am. Chem. Soc.* **2001**, *123*, 4304–4312; h) R. Zhu, J. Lin, G.-A. Wen, S.-J. Liu, J.-H. Wan, J.-C. Feng, Q.-L. Fan, G.-Y. Zhong, W. Wei, W. Huang, *Chem. Lett.* **2005**, *34*, 1668–1669.

[10] a) C. Adachi, M. A. Baldo, S. R. Forrest, S. Lamansky, M. E. Thompson, R. C. Kwong, *Appl. Phys. Lett.* **2001**, *78*, 1622–1624; b) J. Kavitha, S.-Y. Chang, Y. Chi, J.-K. Yu, Y.-H. Hu, P.-T. Chou, S.-M. Peng, G.-H. Lee, Y.-T. Tao, C.-H. Chien, A. J. Carty, *Adv. Funct. Mater.* **2005**, *15*, 223–229; c) S.-Y. Chang, J. Kavitha, S.-W. Li, C.-S. Hsu, Y. Chi, Y.-S. Yeh, P.-T. Chou, G.-H. Lee, A. J. Carty, Y.-T. Tao, C.-H. Chien, *Inorg. Chem.* **2006**, *45*, 137–146; d) W. Lu, B.-X. Mi, M. C. W. Chan, Z. Hui, N. Zhu, S.-T. Lee, C.-M. Che, *Chem. Commun.* **2002**, 206–207; e) J. Nishida, A. Maruyama, T. Iwata, Y. Yamashita, *Chem. Lett.* **2005**, *34*, 592–593; f) R. C. Kwong, S. Sibley, T. Dubovoy, M. Baldo, S. R. Forrest, M. E. Thompson, *Chem. Mater.* **1999**, *11*, 3709–3713.

[11] a) J. Kido, H. Hayase, K. Hongawa, K. Nagai, K. Okuyama, *Appl. Phys. Lett.* **1994**, *65*, 2124–2126; b) M. D. McGehee, T. Bergstedt, C. Zhang, A. P. Saab, M. B. O'Regan, G. C. Bazan, V. I. Srdanov, A. J. Heeger, *Adv. Mater.* **1999**, *11*, 1349–1354; c) Y.-H. Niu, Y.-L. Tung, Y. Chi, C.-F. Shu, J. H. Kim, B. Chen, J. Luo, A. J. Carty, A. K.-Y. Jen, *Chem. Mater.* **2005**, *17*, 3532–3536; d) Y.-L. Tung, S.-W. Lee, Y. Chi, L.-S. Chen, C.-F. Shu, F.-I. Wu, A. J. Carty, P.-T. Chou, S.-M. Peng, G.-H. Lee, *Adv. Mater.* **2005**, *17*, 1059–1064; e) A. R. Hosseini, C. Y. Koh, J. D. Slinker, S. Flores-Torres, H. D. Abruña, G. G. Malliaras, *Chem. Mater.* **2005**, *17*, 6114–6116.

[12] Complex **1d** has not been obtained yet. Further investigations are underway.

[13] W.-Y. Wong, G.-J. Zhou, X.-M. Yu, H.-S. Kwok, B.-Z. Tang, *Adv. Funct. Mater.* **2006**, *16*, 838–846.

[14] J. Nishida, H. Echizen, T. Iwata, Y. Yamashita, *Chem. Lett.* **2005**, *34*, 1378–1379.

[15] M. T. DuPriest, C. L. Schmidt, D. Kuzmich, S. B. Williams, *J. Org. Chem.* **1986**, *51*, 2021–2023.

[16] a) T. Yamamoto, M. Nishiyama, Y. Koie, *Tetrahedron Lett.* **1998**, *39*, 2367–2370; b) M. Watanabe, M. Nishiyama, T. Yamamoto, Y. Koie, *Tetrahedron Lett.* **2000**, *41*, 481–483.

[17] A. B. Tamayo, B. D. Alleyne, P. I. Djurovich, S. Lamansky, I. Tsyba, N. N. Ho, R. Bau, M. E. Thompson, *J. Am. Chem. Soc.* **2003**, *125*, 7377–7387.

 © 2006 Wiley-VCH Verlag GmbH & Co. KGaA, Weinheim 

[18] Complex **1a** showed three oxidation waves with the half-wave potential of +0.19 V and the peak potentials of +0.39 V and +0.48 V.
[19] K. Goushi, R. Kwong, J. J. Brown, H. Sasabe, C. Adachi, *J. Appl. Phys.* **2004**, *95*, 7798–7802.
[20] G. M. Sheldrick, *SHELXS-97, Program for the Solution of Crystal Structures*, University of Göttingen, Göttingen, Germany, **1997**.
[21] G. M. Sheldrick, *SHELXL-97, Program for the Refinement of Crystal Structures*, University of Göttingen, Göttingen, Germany, **1997**.
[22] *teXsan, Crystal Structure Analysis Package*, Molecular Structure Corporation, **1985**, **1999**.

Received: March 31, 2006
Published Online: August 3, 2006

 © 2006 Wiley-VCH Verlag GmbH & Co. KGaA, Weinheim 

DOI: 10.1002/ejic.200600286

# Galactose Oxidase Models: Creation and Modification of Proton Transfer Coupled to Copper(II) Coordination Processes in Pro-Phenoxyl Ligands

**Fabien Michel,[a] Fabrice Thomas,*[a] Sylvain Hamman,[a] Christian Philouze,[a] Eric Saint-Aman,[b] and Jean-Louis Pierre[a]**

**Keywords:** Copper / Phenoxyl / Tripodal ligands / Proton transfer / Radicals

Two tripodal ligands containing two pyridyl and one 4-(benzimidazol-2-yl)-2-*tert*-butylphenol ($HL^H$) and one 2-*tert*-butyl-4-(*N*-methylbenzimidazol-2-yl)phenol ($HL^{Me}$) unit have been synthesized. They possess a $N_3O$ donor set that is known to stabilize phenoxyl radicals more efficiently than the corresponding $N_2O_2$ donor unit. Reaction of one molar equiv. of $Cu(ClO_4)_2{\cdot}6H_2O$ with $HL^H$ or $HL^{Me}$ affords the zwitterionic benzimidazolium phenolate complexes $[Cu^{II}(HL^H)]^{2+}$ and $[Cu^{II}(HL^{Me})]^{2+}$ via a proton transfer reaction coupled to copper(II) coordination. Addition of $HClO_4$ to $[Cu^{II}(HL^H)]^{2+}$ and $[Cu^{II}(HL^{Me})]^{2+}$ results in the formation of the benzimidazolium phenol complexes $[Cu^{II}(H_2L^H)]^{3+}$ and $[Cu^{II}(H_2L^{Me})]^{2+}$, while addition of $NEt_3$ affords the benzimidazol-phenolate complexes $[Cu^{II}(L^H)]^{2+}$ and $[Cu^{II}(L^{Me})]^{2+}$, respectively. The phenol's $pK_a$ is remarkably low due to the strong withdrawing effect of the benzimidazolium substituent. X-ray crystallographic analysis of the copper(II) complexes shows that deprotonation of the axial phenol forces the metal to move out of the square plane towards the oxygen atom, and one (or two) $Cu–N_{pyridine}$ equatorial bond length increases. The copper(II) phenoxyl species $[Cu^{II}(HL^H)]^{\cdot 3+}$ and $[Cu^{II}(HL^{Me})]^{\cdot 3+}$ were prepared electrochemically, or by addition of two molar equiv. of copper(II) to $HL^H$ or $HL^{Me}$. Under these conditions, radical formation has never been observed for tripodal ligands containing two pyridyl and one 2,4-di-*tert*-butylphenol group. This difference is explained in terms of the proton transfer mechanism and redox potentials.

(© Wiley-VCH Verlag GmbH & Co. KGaA, 69451 Weinheim, Germany, 2006)

## Introduction

Galactose Oxidase (GO) is a copper(II) enzyme that catalyses the oxidation of primary alcohols to the corresponding aldehydes, with concomitant reduction of dioxygen to hydrogen peroxide.[1–11] This two electron chemistry is promoted by a single copper atom, working in synergy with a tyrosyl radical from the protein. Galactose Oxidase possesses a $N_2O_2$ donor set: One oxygen atom, from the $Tyr_{272}^{\cdot}$ radical residue, is the organic redox center, while the other (from $Tyr_{495}$) controls the proton transfer process. The mechanism by which the radical is generated is of major interest. It has been shown recently that mixing apo-GO with copper (I or II) in the presence of $O_2$ affords the $Cu^{II}$ radical enzyme.[12–15] During the last few years, several model compounds for the GO active site have been developed.[16–48] Tripodal ligands have been widely used, and it has been shown that they are good structural models, which reproduce quite well the spectroscopic signatures of GO, and sometimes are able to model GO's reactivity towards alcohol oxidation.[17,25,27,28,35,38,41,45] It has also been shown that tripodal ligands possessing a $N_3O$ donor set stabilize more efficiently copper(II) coordinated phenoxyl radicals than the corresponding $N_2O_2$ set.

We have recently developed a biomimetic approach to radical cofactor formation. In this context, we have studied the solution chemistry of several tripodal ligands,[49] involving one pro-phenoxyl group (mimicking the amino acids of the GO active site), under various copper(II), base, and dioxygen reagent conditions.[50] We have shown that $Cu^{II}$ phenoxyl radical species could be obtained by adding two equiv. of copper(II) to ligands possessing a $N_3O$ coordination moiety, such as $HLt^{Bu}$ (Scheme 1), in the presence of one equiv. of triethylamine ($O_2$ is not involved in the reaction). In the absence of base, only a small amount of radical species is formed. In order to bypass this base requirement for radical formation, and thus to obtain more biologically relevant systems, we have synthesized the ligands $HL^H$ and $HL^{Me}$ (Scheme 1). Their structures are also tripodal, with two pyridyl and one phenol moiety joined together by a pivotal amino nitrogen atom. The 2-*tert*-butylphenol unit is substituted at its 4-position (with respect to the coordinating oxygen atom) by a benzimidazole ($HL^H$) or *N*-methylbenzimidazole ($HL^{Me}$) group in order to control the proton transfer processes, as do some non-coordinating histidine

[a] Laboratoire de Chimie Biomimétique, LEDSS, UMR CNRS 5616, ICMG FR CNRS 2607, Université J. Fourier, B. P. 53, 38041 Grenoble cedex 9, France
Fax: +33-4-7651-4836
E-mail: Fabrice.Thomas@ujf-grenoble.fr
[b] Pr. E. Saint-Aman, LEOPR, UMR CNRS 5630, ICMG FR CNRS 2607, Université J. Fourier, B. P. 53, 38041 Grenoble Cedex 9, France

 © 2006 Wiley-VCH Verlag GmbH & Co. KGaA, Weinheim 

residues in enzymes. This substituent is also known to stabilize phenoxyl radicals.[51–52] Another aspect highlighting the originality of $HL^H$ and $HL^{Me}$ is their ability to manage the two proton/two electron shuttle process (like GO), unlike other copper(II) complexes containing $N_3O$ ligands. The phenoxyl oxygen atom and the copper(II) ion may control the two electron transfer, while the benzimidazolium/benzimidazole and phenol/phenoxyl acidobasic couples may be involved in the transfer of two protons. Their chemistry is therefore close to that of copper complexes of ligands possessing a $N_2O_2$ donor set, while their $N_3O$ donor set is expected to enhance the stability of the phenoxyl radicals.

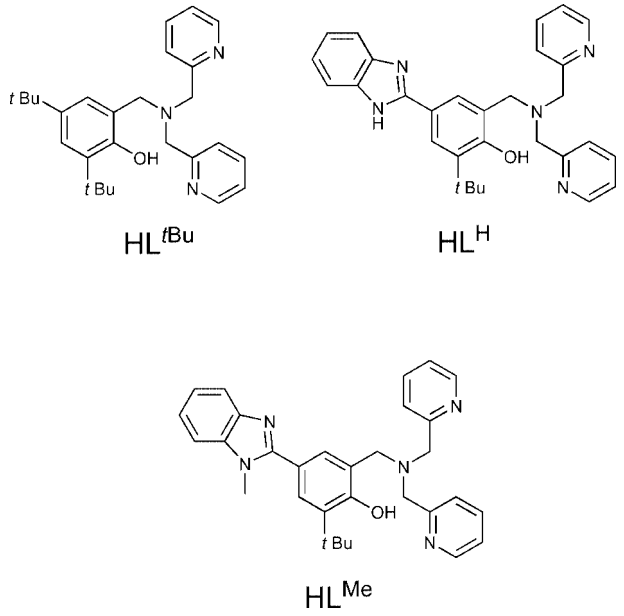


Scheme 1. Formulae for the ligands.

The coordination and solution chemistry of the copper(II) complexes of $HL^H$ and $HL^{Me}$ are described in this paper, and compared to that of an already published system based on the ligand $HLt^{Bu}$ (Scheme 1).[50]

## Results and Discussion

### Synthesis of the Ligands

The ligands $HL^H$ and $HL^{Me}$ were obtained by using a Mannich reaction: In a one-pot synthesis, $HL^H$ is obtained by mixing bis(2-pyridylmethyl)amine and 4-(1*H*-benzoimidazol-2-yl)-2-*tert*-butylphenol in the presence of one equiv. of formaldehyde. Ligand $HL^{Me}$ is obtained by mixing bis(2-pyridylmethyl)amine and 2-*tert*-butyl-4-(1-methyl-1*H*-benzoimidazol-2-yl)phenol in the presence of one equiv. of formaldehyde.

The phenol benzimidazole (and not phenolate benzimidazolium) protonation state was confirmed by $^1H$ NMR ([$D_6$]DMSO) due to the hydroxy proton resonance ($\delta$ = 11.73 ppm and 11.76 ppm for $HL^H$ and $HL^{Me}$ respectively). Its structural attributes were confirmed by GHMBC and QHMQC sequences, showing $^3J$ correlations between the C2 carbon atom ($\delta$ = 136.9 ppm and 136.8 ppm for $HL^H$ and $HL^{Me}$ respectively), the *tert*-butyl protons ($\delta$ = 1.50 ppm and 1.49 ppm for $HL^H$ and $HL^{Me}$ respectively) and the hydroxy proton (see ESI).

### Structures of the Copper(II) Complexes

The copper(II) phenolate complexes $[Cu^{II}(HL^H)]^{2+}$ and $[Cu^{II}(HL^{Me})]^{2+}$ were obtained by mixing stoichiometric amounts of the ligands and $Cu(ClO_4)_2{\cdot}6H_2O$ in acetonitrile. Dark blue single crystals were obtained on slow diffusion of di-*iso*-propyl ether into acetonitrile solutions of the complexes (Table 1). The ORTEP views of the phenolate complexes $[Cu^{II}(HL^H)]^{2+}$ and $[Cu^{II}(HL^{Me})]^{2+}$ are depicted in

Table 1. Crystallographic data for $[Cu^{II}(H_2LH)]^{3+}$, $[Cu^{II}(HLH)]^{2+}$, $[Cu^{II}(H_2LMe)]^{3+}$ and $[Cu^{II}(HLMe)]^{2+}$.

| | $[Cu^{II}(H_2LH)]^{3+}$ | $[Cu^{II}(HLH)]^{2+}$ | $[Cu^{II}(H_2LMe)]^{3+}$ | $[Cu^{II}(HLMe)]^{2+}$ |
|---|---|---|---|---|
| Formula | $C_{34}H_{38}Cl_3CuN_7O_{13}$ | $C_{36}H_{40}Cl_2CuN_8O_9$ | $C_{37}H_{43}Cl_3CuN_8O_{15.33}$ | $C_{35}H_{39}Cl_2CuN_7O_{9.66}$ |
| $M$ | 922.62 | 863.21 | 1015.03 | 846.80 |
| Crystal system | monoclinic | triclinic | triclinic | monoclinic |
| Space group | *C*2/*c* | *P*-1 | *P*-1 | *P*21/*n* |
| $a$ [Å] | 32.92(4) | 8.142(2) | 8.487(2) | 8.460(3) |
| $b$ [Å] | 15.38(2) | 11.656(2) | 15.076(2) | 22.356(4) |
| $c$ [Å] | 19.91(2) | 21.504(4) | 19.185(3) | 20.324(7) |
| $\alpha$ [°] | 90 | 96.99(2) | 94.57(1) | 90 |
| $\beta$ [°] | 121.13(1) | 95.82(2) | 101.33(1) | 101.5(3) |
| $\gamma$ [°] | 90 | 105.53(2) | 100.05(1) | 90 |
| $V$ [Å$^3$] | 8630(16) | 1932.4(8) | 2353.3(8) | 3766(1) |
| $Z$ | 8 | 2 | 2 | 4 |
| $T$ [K] | 150 | 150 | 150 | 150 |
| $D_c$ [g cm$^{-3}$] | 1.420 | 1.483 | 1.432 | 1.493 |
| $\mu$ [cm$^{-1}$] | 0.758 | 0.768 | 0.707 | 0.787 |
| Monochromator | graphite | graphite | graphite | graphite |
| Wavelength | Mo-$K_\alpha$ (0.71073 Å) | Mo-$K_\alpha$ (0.71073 Å) | Mo-$K_\alpha$ (0.71073 Å) | Mo-$K_\alpha$ (0.71073 Å) |
| Reflections collected | 47630 | 48235 | 40692 | 27910 |
| Independent reflections ($R_{int}$) | 11386 (0.10131) | 11277 (0.08692) | 7530 (0.11620) | 6410 (0.09244) |
| Observed reflections | 11386 [$I > 2\sigma(I)$] | 7923 [$I > 2\sigma(I)$] | 4975 [$I > 2\sigma(I)$] | 4624 [$I > 2\sigma(I)$] |
| $R$ | 0.0922 | 0.0403 | 0.0931 | 0.0887 |
| $R_w$ | 0.1366 | 0.0530 | 0.1264 | 0.1310 |

 © 2006 Wiley-VCH Verlag GmbH & Co. KGaA, Weinheim 

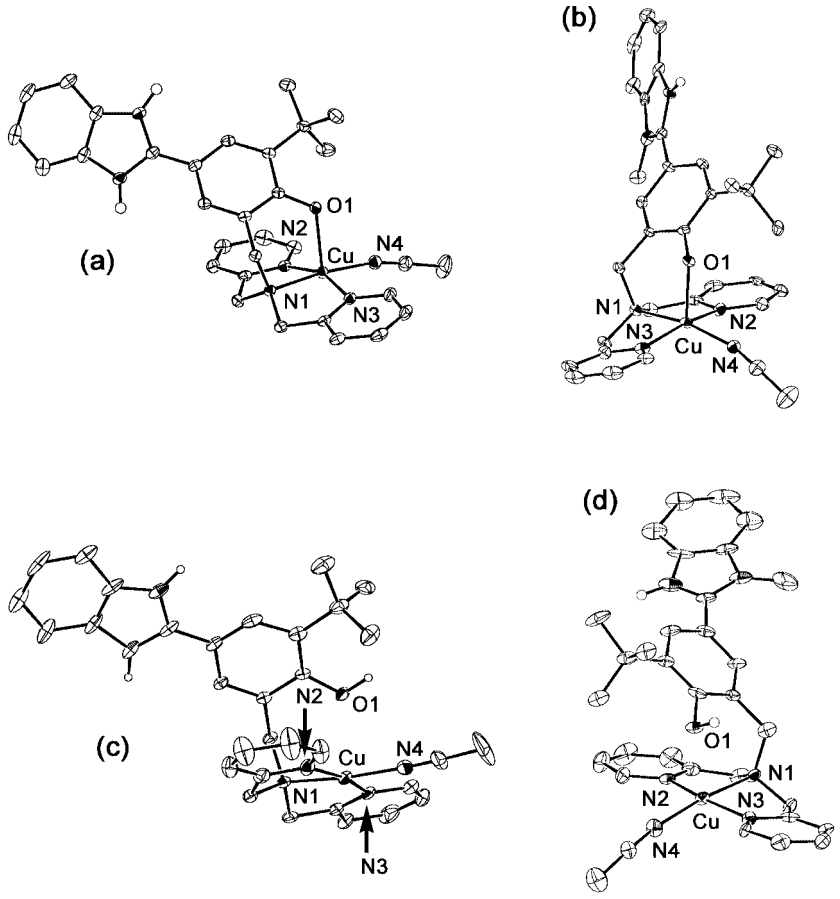


Figure 1. ORTEP view showing 35% displacement ellipsoids, and partial atomic labelling for (a) $[Cu^{II}(HL^{H})]^{2+}$, (b) $[Cu^{II}(HL^{Me})]^{3+}$, (c) $[Cu^{II}(H_2L^{H})]^{2+}$ and (d) $[Cu^{II}(H_2L^{Me})]^{3+}$. Hydrogen atoms, except the phenolic proton as well as the iminium protons, have been omitted for clarity. Weakly coordinating perchlorates are not shown (see text). Selected distances and angles are reported in Table 2.

Figure 1 (see parts a and b, respectively), and selected bond lengths and angles listed in Table 2. The geometry around the metal center is octahedral, with the copper(II) ion coordinated in a square plane by one tertiary nitrogen atom, N1, two pyridine nitrogen atoms, N2 and N3, and one acetonitrile nitrogen atom, N4. The phenolate oxygen atom, O1, occupies one axial position, and one perchlorate oxygen atom, O8, is very weakly coordinated at the opposite axial position.

In $[Cu^{II}(HL^{H})]^{2+}$ (Figure 1, a), the bond lengths are 2.021(1) Å (Cu–N1), 1.982(2) Å (Cu–N2), 1.978(1) Å (Cu–N3), 1.973(2) Å (Cu–N4), 2.156(1) Å (Cu–O1) and 2.813(2) Å (Cu–O8), while the angles N1–Cu–N2, N1–Cu–N3, N2–Cu–N4 and N3–Cu–N4 differ only slightly from 90° [83.8(1)°, 82.9(1)°, 96.2(1)° and 95.1(1)° respectively]. The mean deviation from the least square plane defined by atoms N1, N2, N3, N4, and Cu is 0.0801 Å, and the copper atom is displaced 0.205(2) Å above the basal plane towards the axial O1 oxygen atom.

In $[Cu^{II}(HL^{Me})]^{2+}$ (Figure 1, b), the Cu–N1, Cu–N2, Cu–N3, and Cu–N4 bond lengths are 2.039(5), 1.995(5), 1.999(5) and 1.981(3) Å respectively. The mean deviation from the least square plane defined by atoms N1, N2, N3, N4, and Cu is 0.036 Å. The copper atom is displaced 0.245(6) Å above the basal plane towards the axial oxygen atom, with a Cu–O1 bond length of 2.133(4) Å [the Cu–O8 distance is 2.875(5) Å].

In both $[Cu^{II}(HL^{H})]^{2+}$ and $[Cu^{II}(HL^{Me})]^{2+}$, the benzimidazolium (or *N*-methylbenzimidazolium) rings of two separate molecules, of the same complex, are π-stacked head-to-tail, with distances between the phenyl and imidazolium centroids of 3.45 and 3.53 Å for $[Cu^{II}(HL^{H})]^{2+}$ and $[Cu^{II}(HL^{Me})]^{2+}$ respectively. In both $[Cu^{II}(HL^{H})]^{2+}$ and $[Cu^{II}(HL^{Me})]^{2+}$ the iminium hydrogen atom, H1, is hydrogen bonded to the O9 oxygen atom of a perchlorate molecule.

Adding one equiv. of $HClO_4$ to acetonitrile solutions of $[Cu^{II}(HL^{H})]^{2+}$ and $[Cu^{II}(HL^{Me})]^{2+}$ affords the copper(II) phenol complexes $[Cu^{II}(H_2L^{H})]^{3+}$ and $[Cu^{II}(H_2L^{Me})]^{3+}$ that were recrystallized by diffusion of diisopropyl ether into the solution (Table 1). In $[Cu^{II}(H_2L^{H})]^{3+}$ and $[Cu^{II}(H_2L^{Me})]^{3+}$ (Figure 1, c and d, respectively) the copper(II) atoms have similar octahedral geometry. The square plane is defined by one tertiary nitrogen atom, N1, two pyridine nitrogen atoms, N2 and N3, and one acetonitrile nitrogen atom, N4. The phenolic oxygen atom, O1, and one perchlorate oxygen atom (O7 for $[Cu^{II}(H_2L^{Me})]^{3+}$ and O20 for $[Cu^{II}(H_2L^{H})]^{3+}$) occupy the apical positions.

The Cu–N1, Cu–N2 and Cu–N4 bond lengths in $[Cu^{II}(H_2L^{H})]^{3+}$ (phenol copper) are similar to those ob-

 © 2006 Wiley-VCH Verlag GmbH & Co. KGaA, Weinheim 

Table 2. Selected bond lengths [Å] and angles [°] for $[Cu^{II}(HL^{H})]^{2+}$, $[Cu^{II}(H_2L^{H})]^{3+}$, $[Cu^{II}(HL^{Me})]^{2+}$, $[Cu^{II}(H_2L^{Me})]^{3+}$ and $[Cu^{II}(HL^{tBu})]^{2+}$.

| | | | | | |
|---|---|---|---|---|---|
| $[Cu^{II}(HL^{H})]^{2+}$ | | | | | |
| Cu–N1 | 2.021(1) | Cu–N2 | 1.982(2) | Cu–N3 | 1.978(1) |
| Cu–N4 | 1.973(2) | Cu–O1 | 2.156(1) | Cu–O8 | 2.813(2) |
| N1–Cu–N2 | 83.77(6) | N1–Cu–N3 | 82.90(6) | N1–Cu–N4 | 172.84(6) |
| N2–Cu–N3 | 159.37(6) | N2–Cu–N4 | 96.18(6) | N3–Cu–N4 | 95.10(6) |
| O1–Cu–N1 | 93.50(5) | O1–Cu–N2 | 92.86(5) | O1–Cu–N3 | 103.60(5) |
| O1–Cu–N4 | 93.65(6) | | | | |
| $[Cu^{II}(H_2L^{H})]^{3+}$ | | | | | |
| Cu–N1 | 2.021(5) | Cu–N2 | 1.980(6) | Cu–N3 | 1.964(5) |
| Cu–N4 | 1.972(6) | Cu–O1 | 2.509(5) | Cu–O20 | 2.432(6) |
| N1–Cu–N2 | 83.4(2) | N1–Cu–N3 | 82.8(2) | N1–Cu–N4 | 174.9(2) |
| N2–Cu–N3 | 165.7(2) | N2–Cu–N4 | 96.6(2) | N3–Cu–N4 | 97.5(3) |
| $[Cu^{II}(HL^{Me})]^{2+}$ | | | | | |
| Cu–N1 | 2.039(5) | Cu–N2 | 1.995(5) | Cu–N3 | 1.999(5) |
| Cu–N4 | 1.981(6) | Cu–O1 | 2.133(4) | Cu–O8 | 2.875(5) |
| N1–Cu–N2 | 84.6(2) | Cu–N3 | 82.5(2) | N1–Cu–N4 | 167.9(2) |
| N2–Cu–N3 | 160.2(2) | N2–Cu–N4 | 95.9(2) | N3–Cu–N4 | 93.7(2) |
| O1–Cu–N1 | 94.2(2) | O1–Cu–N2 | 96.1(2) | O1–Cu–N3 | 99.7(2) |
| O1–Cu–N4 | 97.8(2) | | | | |
| $[Cu^{II}(H_2L^{Me})]^{3+}$ | | | | | |
| Cu–N1 | 2.031(5) | Cu–N2 | 1.967(6) | Cu–N3 | 1.972(6) |
| Cu–N4 | 1.984(5) | Cu–O1 | 2.401(5) | Cu–O7 | 2.714(7) |
| N1–Cu–N2 | 83.6(2) | N1–Cu–N3 | 83.2(2) | N1–Cu–N4 | 172.3(2) |
| N2–Cu–N3 | 165.6(2) | N2–Cu–N4 | 97.6(2) | N3–Cu–N4 | 94.8(2) |
| $[Cu^{II}(HL^{tBu})]^{2+}$ | | | | | |
| Cu–N1 | 2.037(4) | Cu–N2 | 1.987(4) | Cu–N3 | 1.977(4) |
| Cu–N4 | 1.974(6) | Cu–O1 | 2.456(3) | | |
| N1–Cu–N2 | 83.4(2) | N1–Cu–N3 | 83.6(2) | N1–Cu–N4 | 178.5(2) |
| N2–Cu–N3 | 164.4(2) | N2–Cu–N4 | 95.4(2) | N3–Cu–N4 | 97.4(2) |

served for $[Cu^{II}(HL^{H})]^{2+}$ (phenolate copper). This is not the case for the Cu–N3 bond length that is 1.964(5) Å for $[Cu^{II}(H_2L^{H})]^{3+}$, which is 0.015 Å shorter than in $[Cu^{II}(HL^{H})]^{2+}$ [1.978(1) Å]. One can also notice that the Cu–O1 bond length in $[Cu^{II}(H_2L^{H})]^{3+}$ is much longer than in $[Cu^{II}(HL^{H})]^{2+}$, it is 2.509(5) Å in $[Cu^{II}(H_2L^{H})]^{3+}$ but only 2.156(1) Å in $[Cu^{II}(HL^{H})]^{2+}$. The $Cu–O_{perchlorate}$ distance in $[Cu^{II}(H_2L^{H})]^{3+}$ [Cu–O20, 2.432(6) Å] is shorter than observed in $[Cu^{II}(HL^{Me})]^{2+}$ [Cu–O8, 2.813(2) Å].

Even more marked geometric variations, were observed for $[Cu^{II}(H_2L^{Me})]^{3+}$. The Cu–N1 and Cu–N4 bond lengths in $[Cu^{II}(H_2L^{Me})]^{3+}$ are similar to those observed in $[Cu^{II}(HL^{Me})]^{2+}$, while both the Cu–N2 and Cu–N3 bond lengths are 0.02 Å shorter (1.967(6) and 1.972(6) Å, respectively for $[Cu^{II}(H_2L^{Me})]^{3+}$, 1.995(5) and 1.999(5) Å, respectively for $[Cu^{II}(HL^{Me})]^{2+}$). The Cu–O1 bond length in $[Cu^{II}(H_2L^{Me})]^{3+}$ is significantly longer than in $[Cu^{II}(HL^{Me})]^{2+}$ (2.401(5) Å in $[Cu^{II}(H_2L^{Me})]^{3+}$, 2.133(4) Å in $[Cu^{II}(HL^{Me})]^{2+}$). The copper(II) atom is less displaced above the mean basal plane towards the axial oxygen atom in $[Cu^{II}(H_2L^{Me})]^{3+}$ [0.121(7) Å] than in $[Cu^{II}(HL^{Me})]^{2+}$ [0.245(6) Å]. The Cu–O7 distance in $[Cu^{II}(H_2L^{Me})]^{3+}$ [2.714(7) Å] is shorter than observed in $[Cu^{II}(HL^{Me})]^{2+}$. A weak π-stacking interaction (rings are slightly eclipsed) exists between the phenol unit and the imidazole ring of $[Cu^{II}(H_2L^{H})]^{3+}$, and between the *N*-methylbenzimidazolium rings of two $[Cu^{II}(H_2L^{Me})]^{3+}$ complexes, the rings are stacked head-to-tail, as in $[Cu^{II}(HL^{Me})]^{2+}$. Hydrogen bonds are present between the two iminium hydrogen atoms, H2 and H3, of $[Cu^{II}(H_2L^{H})]^{3+}$ and the perchlorate oxygen atoms, O4 and O14. One hydrogen bond is present between the iminium hydrogen atom, H2, of $[Cu^{II}(H_2L^{Me})]^{3+}$ and the perchlorate oxygen atom, O15, while another is present between the phenolic proton, H1, and the oxygen atom, O2, of one perchlorate molecule.

In these structures, another important point of note is the torsion angle between the phenol(ate) and the *para* substituent of the ring. It is significantly higher for the *N*-methylbenzimidazole (40° and 35° for $[Cu^{II}(H_2L^{Me})]^{3+}$ and $[Cu^{II}(HL^{Me})]^{2+}$, respectively) than for the benzimidazole (4° and 27° for $[Cu^{II}(H_2L^{H})]^{3+}$ and $[Cu^{II}(HL^{H})]^{2+}$, respectively), this may be explained, at least partially, by consideration of the steric hindrance of the methyl group. The consequence of this difference will be weaker electronic communication between the groups in the former case.

Complexes $[Cu^{II}(HL^{H})]^{2+}$ and $[Cu^{II}(HL^{Me})]^{2+}$ belong to the small class of structurally characterized mononuclear copper(II) complexes of tripodal ligands, in which the phenolate group occupies the unusual axial position. The complexes that belong to this class usually involve only one coordinating phenolate, and exhibit a relatively long Cu–O bond (higher than 2.17 Å).[24] In $[Cu^{II}(HL^{H})]^{2+}$, and espe-

 © 2006 Wiley-VCH Verlag GmbH & Co. KGaA, Weinheim 

cially in $[Cu^{II}(HL^{Me})]^{2+}$, the Cu–O1 distances are shorter [2.156(1) and 2.133(4) Å, respectively], making them the shortest bonds reported for axially coordinated phenolates.

We have previously reported the X-ray crystal structures of both the copper(II) phenol and the copper(II) phenolate complexes of $HL^{NO2}$, the structures of which are related to $HL^{H}$ (they bear a nitro instead of a benzimidazole substituent).[49] Unfortunately, the exogenous ligand was different in these structures, an acetonitrile molecule in the phenol form, and a chloride ion in the phenolate form. Thus, the influence of the protonation of the axial phenolate on the equatorial bonds could not be visualized. Here, we report X-ray structures in which the phenolate and phenol forms have been crystallized with the same exogenous ligand (acetonitrile molecule) coordinated to the metal center. To the best of our knowledge, this is the first example in which changes in the copper(II) ion geometry, induced by deprotonation of the axial phenol, could be visualized so clearly: the metal moves out of the basal plane towards the oxygen atom as a consequence of a stronger axial bond, and one (or both) Cu–$N_{pyridine}$ bond length(s) increase, reflecting the weakening of the equatorial bonds (Figure 2).

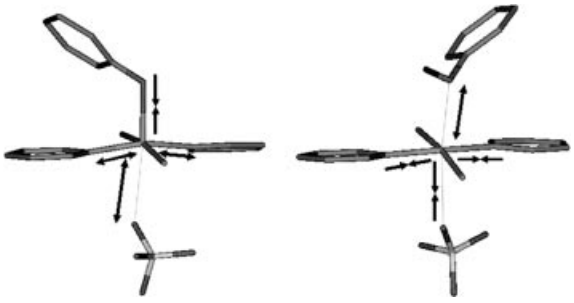

Figure 2. Influence of the phenol protonation state on the Cu–O and Cu–N bond lengths in $[Cu^{II}(HL^{Me})]^{2+}$ (left) and $[Cu^{II}(H_2L^{Me})]^{3+}$ (right).

## Spectroscopic Properties of the Copper(II) Complexes

The electronic spectra of acetonitrile solutions of $[Cu^{II}(H_2L^{H})]^{3+}$ and $[Cu^{II}(H_2L^{Me})]^{3+}$ show d-d transitions at around 600 nm (Table 3, Figure 3). This suggests that the phenol subunit remains protonated in solution, and that the copper(II) atom resides within an octahedral (with a very weakly coordinated perchlorate) or square pyramidal coordination sphere (without the perchlorate). The EPR spectra of frozen $CH_3CN$ solutions of $[Cu^{II}(H_2L^{H})]^{3+}$ and $[Cu^{II}(H_2L^{Me})]^{3+}$ are typical of axial mononuclear copper(II) complexes, and similar to that of $[Cu^{II}(HL^{tBu})]^{2+}$ (Table 4).[49] In all three complexes, the copper(II) atoms have roughly similar geometry, in agreement with the X-ray diffraction analysis. The influence of the phenol *para* substituent cannot be visualized in the EPR spectra, as a consequence of the very weak phenolic oxygen–copper(II) bond (see above). Complexes $[Cu^{II}(HL^{H})]^{2+}$ and $[Cu^{II}(HL^{Me})]^{2+}$ exhibit, in their electronic spectra, the phenolate-to-copper(II) CT transition centered at 524 and 508 nm, respectively (Figure 3, Table 3). The low energy tail in the 700–900 nm region originates from d-d transitions. On addition of one equiv. of $NEt_3$ to $CH_3CN$ solutions of

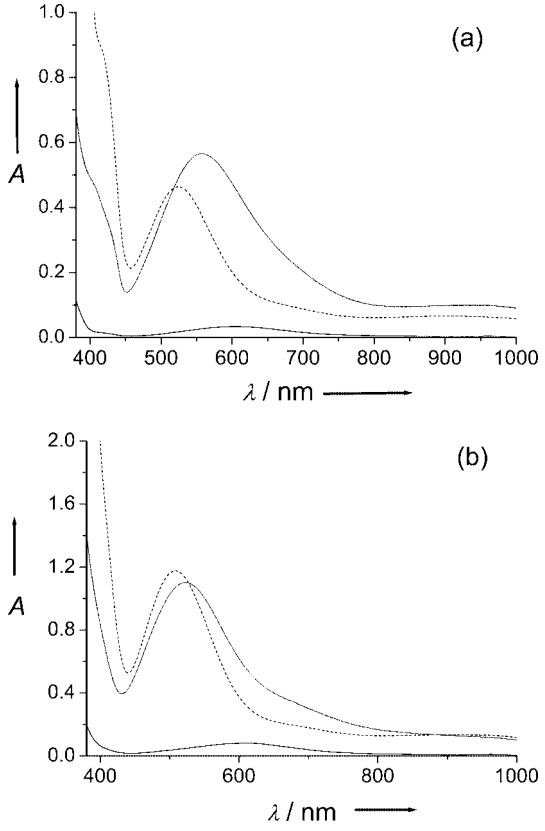


Figure 3. 298 K electronic spectra of $CH_3CN$ solutions of: (a) 0.1 mM $[Cu^{II}(H_2L^{H})]^{3+}$ (solid line), $[Cu^{II}(HL^{H})]^{2+}$ (dashed line) and $[Cu^{II}(L^{H})]^{+}$ (dotted line); (b) 0.2 mM $[Cu^{II}(H_2L^{Me})]^{3+}$ (solid line), $[Cu^{II}(HL^{Me})]^{2+}$ (dashed line) and $[Cu^{II}(L^{Me})]^{+}$ (dotted line).

Table 3. Electronic and electrochemical properties of the copper(II) complexes in $CH_3CN$ solutions.[a]

| Complex | $\lambda_{max}$ (nm) [$\varepsilon$ ($M^{-1}cm^{-1}$)] | $E_{1/2}$[a] |
|---|---|---|
| $[Cu^{II}(H_2L^{H})]^{3+}$ | 601 br [85] | 1.01[b] |
| $[Cu^{II}(HL^{H})]^{2+}$ | 415 sh [2240], 524 [1160], 700 sh [220], 900 br [165] | 0.50[c] |
| $[Cu^{II}(L^{H})]^{+}$ | 405 sh [1180], 556 [1415], 700 sh [510], 900 br [245] | 0.23 |
| $[Cu^{II}(H_2L^{Me})]^{3+}$ | 615 br [85] | 0.95[b] |
| $[Cu^{II}(HL^{Me})]^{2+}$ | 508 [1180], 664 sh [210], 900 br [135] | 0.60 |
| $[Cu^{II}(L^{Me})]^{+}$ | 521 [1100], 682 sh [340], 900 br [135] | 0.31 |
| $[Cu^{II}(HL^{tBu})]^{2+}$ | 600 [180] | >0.8[b,d] |
| $[Cu^{II}(L^{tBu})]^{+}$ | 553 [935], 950 br [180] | 0.15 |

[a] V vs. $Fc/Fc^{+}$. [b] Irreversible, the value given is $E_p^a$. [c] Shoulder. [d] Taken from ref.[49].

 © 2006 Wiley-VCH Verlag GmbH & Co. KGaA, Weinheim 

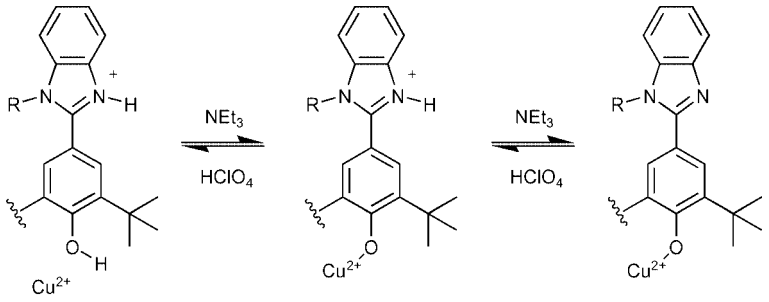


| | | | |
|---|---|---|---|
| R = Me | $[Cu^{II}(H_2L^{Me})]^{3+}$ | $[Cu^{II}(HL^{Me})]^{2+}$ | $[Cu^{II}(L^{Me})]^{+}$ |
| R = H | $[Cu^{II}(H_2L^{H})]^{3+}$ | $[Cu^{II}(HL^{H})]^{2+}$ | $[Cu^{II}(L^{H})]^{+}$ |

Scheme 2. Protonation equilibria for $[Cu^{II}(HL^{Me})]^{2+}$ and $[Cu^{II}(HL^{H})]^{2+}$.

$[Cu^{II}(HL^{H})]^{2+}$ and $[Cu^{II}(HL^{Me})]^{2+}$ the phenolate-to-copper(II) CT transition is displaced towards lower energy regions (556 nm and 521 nm, respectively). Such a shift can be explained by the increased donor ability of the *p*-phenolate substituent, and the subsequent deprotonation of the *N*-methylbenzimidazolium and benzimidazolium groups by $NEt_3$, affording the phenolate benzimidazole complexes $[Cu^{II}(L^{H})]^{+}$ and $[Cu^{II}(L^{Me})]^{+}$. Both the phenolate benzimidazolium and phenolate benzimidazole forms exhibit, in their EPR spectra, a signal typical of mononuclear copper(II) complexes (Table 4). The phenolate oxygen atom does not bridge two copper atoms (as observed when the phenolate *ortho* substituent is not sufficiently sterically hindered). The protonation equilibria involving $[Cu^{II}(HL^{H})]^{2+}$ and $[Cu^{II}(HL^{Me})]^{2+}$ are summarized in Scheme 2.

Table 4. EPR parameters of the copper(II) complexes of $HL^{Me}$ and $HL^{H}$ in $CH_3CN$ at 100 K.

| | $g_{xx} = g_{yy}$ | $g_{zz}$ | $A_{xx}$[a] | $A_{yy}$[a] | $A_{zz}$[a] |
|---|---|---|---|---|---|
| $[Cu^{II}(L^{Me})]^{+}$ | 2.083 | 2.248 | 0.5 | 0.5 | 17.2 |
| $[Cu^{II}(HL^{Me})]^{2+}$ | 2.067 | 2.240 | 0.5 | 0.5 | 17.2 |
| $[Cu^{II}(H_2L^{Me})]^{3+}$ | 2.060 | 2.229 | 1 | 1 | 18.4 |
| $[Cu^{II}(L^{H})]^{+}$ | broad | | | | |
| $[Cu^{II}(HL^{H})]^{2+}$ | 2.056 | 2.235 | 1/1.5 | 1.5 | 18.0 |
| $[Cu^{II}(H_2L^{H})]^{3+}$ | 2.060 | 2.233 | 1/1.5 | 1.5 | 18.0 |

[a] Values in mT.

### Protonation Constants of the Complexes

The protonation constants were determined from pH-metric titrations that were monitored by UV/Vis spectroscopy (Figure 4). After dissolution of single crystals of $[Cu^{II}(H_2L^{H})]^{3+}$ and $[Cu^{II}(H_2L^{Me})]^{3+}$ into a $CH_3CN/H_2O$ (1:1) mixture (the complexes are poorly soluble in pure $H_2O$), the $^{s}_{w}$pH was increased by addition of NaOH. The thermodynamic constants were obtained from refinement of the UV/Vis data by the commercial SPECFIT 32 software (Spectrum Software Associated). Their calculation was based on the spectral changes induced by addition of base. At $^{s}_{w}$pH = 2, the visible spectra of both complexes consist of $Cu^{II}$ d-d transitions at around 650 nm ($\varepsilon < 100\ M^{-1}\,cm^{-1}$), consistent with the phenol benzimidazolium complexes being the major species present at this $^{s}_{w}$pH. The shift of the $\lambda_{max}$ band that occurs when $CH_3CN$ is replaced by $CH_3CN/H_2O$ (1:1) suggests that the coordinating acetonitrile in $[Cu^{II}(H_2L^{H})]^{3+}$ and $[Cu^{II}(H_2L^{Me})]^{3+}$ is replaced by a water molecule from the solvent mixture. Increasing the $^{s}_{w}$pH to 5 results in the appearance of a phenolate-to-copper(II) CT in the 475–500 nm region, showing that the phenolate benzimidazolium complexes are formed. The first p$K_a$ values, 3.40 ± 0.01 and 3.55 ± 0.02 for the copper(II) complexes of $HL^{H}$ and $HL^{Me}$ respectively, are thus attributed to the deprotonation of the phenol group. Such values are remarkable, as they are much lower than those reported

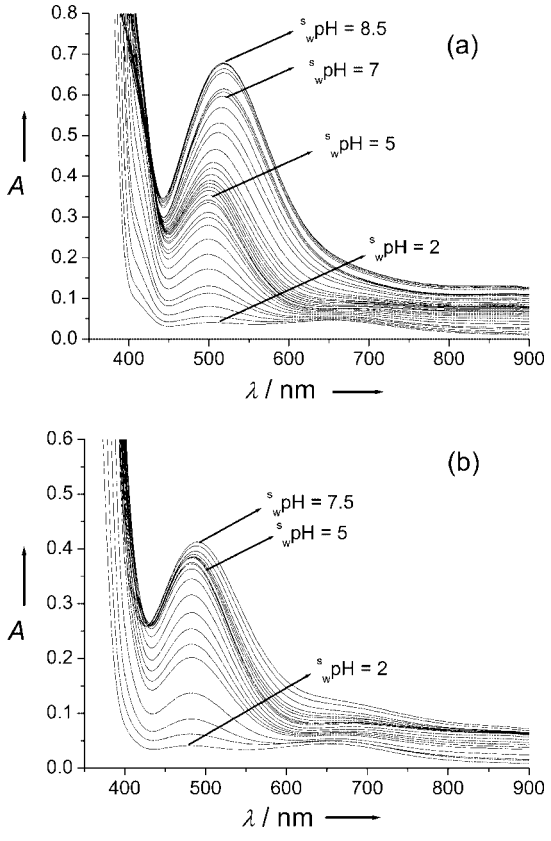


Figure 4. $^{s}_{w}$pH dependence of the electronic spectra of 0.1 mM $CH_3CN/H_2O$ (1:1) solutions of $[Cu^{II}(H_2L^{H})]^{3+}$ (a) and $[Cu^{II}(H_2L^{Me})]^{3+}$ (b). $^{s}_{w}$pH was increased by addition of NaOH, $T$ = 298 K, $l$ = 1.000 cm, $I$ = 0.1 M ($NaClO_4$).

 © 2006 Wiley-VCH Verlag GmbH & Co. KGaA, Weinheim 

for phenol copper(II) complexes of tripodal ligands (6.66–7.31),[50] and for GO itself (7.9).[53] This can be explained by the strong electron-withdrawing effect of the benzimidazolium (or *N*-methylbenzimidazolium) substituent that very efficiently stabilizes the phenolate form, and therefore lowers its p$K_a$. As a consequence, deprotonation of the phenol group occurs prior to deprotonation of the coordinated water molecule. This is in contrast with GO, for which deprotonation of the tyrosine occurs after deprotonation of the coordinated water molecule (in the absence of substrate). When the $^{s}_{w}$pH is raised to 7.5, a shift of the LMCT transition towards lower energy regions is observed, while the $\varepsilon$ value increases by a factor of 1.7 for the copper(II) complex of $HL^H$, and a factor of 1.1 for the $HL^{Me}$ complex. This structural evolution is close to that observed during addition of $NEt_3$ to neat acetonitrile solutions of $[Cu^{II}(HL^H)]^{2+}$ and $[Cu^{II}(HL^{Me})]^{2+}$. We therefore attribute these spectral changes to deprotonation of the benzimidazolium (or *N*-methylbenzimidazolium) group, rather than deprotonation of a coordinated water molecule. The corresponding deprotonation constants, 6.56 ± 0.02 for the copper(II) complex of $HL^H$ and 6.22 ± 0.06 for the $HL^{Me}$ complex are within the range of those reported for free benzimidazolium and *N*-methylbenzimidazolium (5.63 and 5.67 respectively).[54] Further increasing the $^{s}_{w}$pH results in the precipitation of the copper(II) complex of $HL^{Me}$. A shift of the $\lambda_{max}$ band is observed for the copper(II) complex of $HL^H$, which may be attributed to the deprotonation of a coordinated water molecule (p$K_a$ = 8.03 ± 0.10).

### Electrochemistry of the Copper(II) Complexes

The CV curves of $[Cu^{II}(H_2L^H)]^{3+}$ and $[Cu^{II}(H_2L^{Me})]^{3+}$ in $CH_3CN$ (0.1 M TBAP) at 298 K display an oxidation wave at $E_p^a$ = 1.01 and 0.95 V (referred to the $Fc/Fc^+$ system) respectively, attributed to the oxidation of the phenol moiety (Figure 5, c). It is irreversible, attesting to the primary oxidation products not being stable over the timescale of the measurement. Therefore, the redox processes will not be investigated further.

The CV curves of the phenolate complexes $[Cu^{II}(HL^H)]^{2+}$ and $[Cu^{II}(HL^{Me})]^{2+}$ in $CH_3CN$ display quasi reversible electrochemical signals centered at $E_{1/2}$ = 0.50 V ($I_p^a/I_p^c$ 2.5) and $E_{1/2}$ = 0.59 V vs. $Fc^+/Fc$ ($I_p^a/I_p^c$ = 5), respectively (Figure 5, b). Coulometric titrations reveal that one electron redox processes are occurring in both cases, suggesting that these signals correspond to the oxidation of the phenolate to give a phenoxyl radical (vide infra). The lower $I_p^a/I_p^c$ ratio obtained for $[Cu^{II}(HL^H)]^{2+}$ suggests that its oxidation product is more stable than the oxidation product of $[Cu^{II}(HL^{Me})]^{2+}$. Resonance effects may contribute to this, as the planarity between the phenolate ring and its *para* substituent is greater for $[Cu^{II}(HL^H)]^{2+}$ than for $[Cu^{II}(HL^{Me})]^{2+}$ in the solid state. The $E_{1/2}$ values obtained for $[Cu^{II}(HL^H)]^{2+}$ and $[Cu^{II}(HL^{Me})]^{2+}$ fall within the range for related copper(II) complexes in which the phenolate *para* substituent is either $NO_2$ or $CF_3$,[49,55] namely, an electron-withdrawing group.

Complexes $[Cu^{II}(L^H)]^+$ and $[Cu^{II}(L^{Me})]^+$ exhibit, in their CV curve, oxidation waves centered at $E_{1/2}$ = 0.23 V ($I_p^a/I_p^c$ = 1.6) and $E_{1/2}$ = 0.32 V vs. $Fc^+/Fc$ ($I_p^a/I_p^c$ = 3.9), respectively (Figure 5, a). As for $[Cu^{II}(HL^H)]^{2+}$ and $[Cu^{II}(HL^{Me})]^{2+}$, these signals correspond to the oxidation of the phenolate moieties to give phenoxyl radicals. The $I_p^c/I_p^a$ ratio, as well as the $E_{1/2}$ values, obtained for the *N*-methyl- or benzimidazolyl-phenolate complexes are lower than those found for the corresponding phenolate benzimidazolium (or *N*-methylbenzimidazolium) complexes. This reflects an increase in the stability of the oxidation products of the former complexes with respect to the latter. Deprotonation of the benzimidazolium (or *N*-methylbenzimidazolium) substituent makes the group less electron-withdrawing (inductive effect), and thus easier to be oxidized. These results nicely illustrate how an external perturbation (protonation) can influence the value of the phenoxyl/phenolate redox couple.

### One Electron Oxidized Copper(II) Complexes

Upon one electron electrochemical oxidation, the violet solutions of each copper(II) phenolate complexes turn blue.

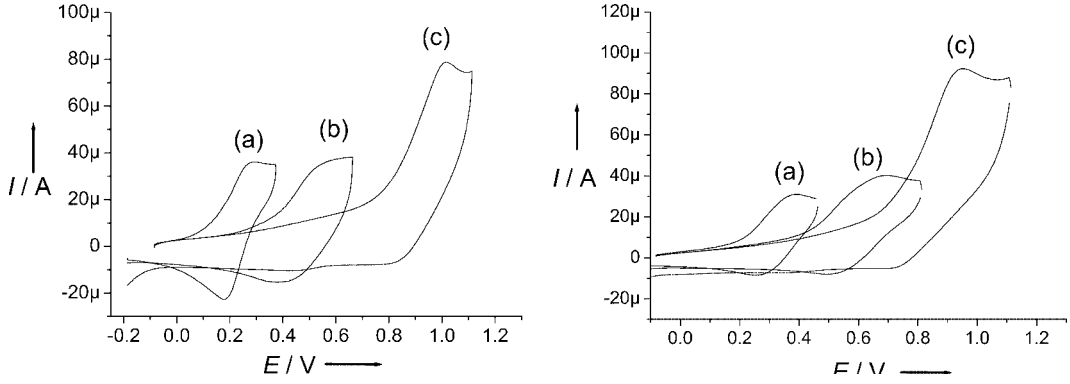


Figure 5. Cyclic voltammetry curves recorded on a vitrous carbon disc of 1 mM $CH_3CN$ (+0.1 M TBAP) solutions of, on the left: $[Cu^{II}(L^H)]^+$ (a), $[Cu^{II}(HL^H)]^{2+}$ (b), and $[Cu^{II}(H_2L^H)]^{3+}$ (c). On the right: $[Cu^{II}(L^{Me})]^+$ (a), $[Cu^{II}(HL^{Me})]^{2+}$ (b), and $[Cu^{II}(H_2L^{Me})]^{3+}$ (c). Scan rate 0.1 V $s^{-1}$, $T$ = 298 K, reference electrode $Fc^+/Fc$.

 © 2006 Wiley-VCH Verlag GmbH & Co. KGaA, Weinheim 

Two intense absorption bands at 400 and 435 nm and a lower intensity band at ca. 700 nm dominate the visible spectra, at 233 K, of the electrochemically generated $[Cu^{II}(L^{H})]^{\cdot 2+}$, $[Cu^{II}(HL^{H})]^{\cdot 3+}$ and $[Cu^{II}(HL^{Me})]^{\cdot 3+}$ complexes in $CH_3CN$ (Figure 6 and Figure 7).[56] Such bands, which have been previously reported for copper(II) phenoxyl complexes[57–59] and $[Cu^{II}(L^{tBu})]^{\cdot 2+}$,[49] are attributed to the π-π* transitions of the radical.[60–67]

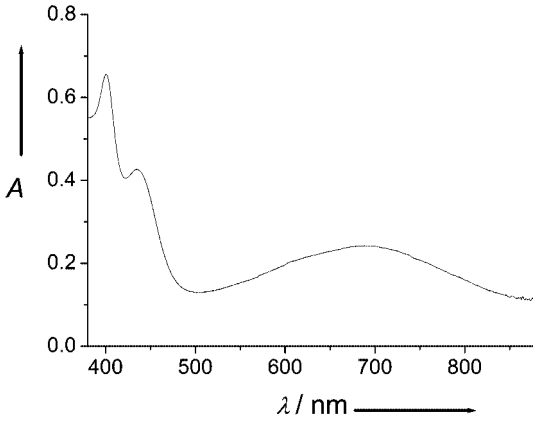


Figure 6. 233 K electronic spectra of a 0.1 mM $CH_3CN$ solution of $[Cu^{II}(L^{H})]^{\cdot 2+}$ ($l$ = 1.000 cm).

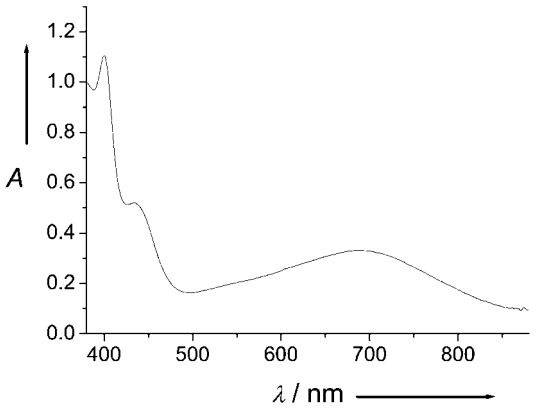


Figure 7. 233 K electronic spectra of a 0.1 mM $CH_3CN$ solution of $[Cu^{II}(HL^{H})]^{\cdot 3+}$ ($l$ = 1.000 cm).

The 4 K X-Band EPR spectra of the electrogenerated species $[Cu^{II}(L^{H})]^{\cdot 2+}$ and $[Cu^{II}(HL^{H})]^{\cdot 3+}$ in $CH_3CN$ show broad $\Delta M_S = \pm 1$ transitions at 250 and 390 mT. The associated $\Delta M_S = \pm 2$ signal is seen at 150 mT. This signal is split into four hyperfine lines separated by 8 mT (Figure 8), which are attributed to the interaction of the electronic spin with the nuclear spin of the copper(II) ($I$ = 3/2). This is clear evidence of ferromagnetic coupling between the spins of the radical and the copper(II). An additional mononuclear copper(II) signal, corresponding to degradation products, is also present in each EPR spectrum. $[Cu^{II}(L^{Me})]^{\cdot 2+}$ exhibits a weak transition at 160 mT, while $[Cu^{II}(HL^{Me})]^{\cdot 3+}$ was too unstable to be prepared in sufficient amounts to enable its EPR spectrum to be recorded.

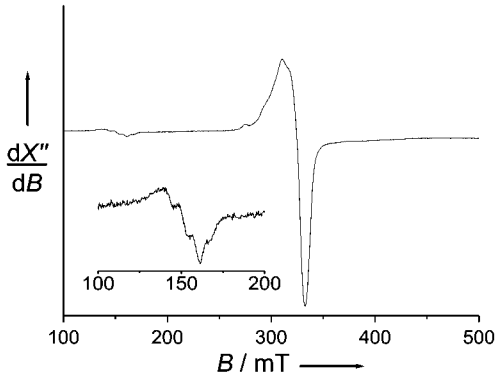


Figure 8. X-Band EPR spectra of a 1 mM $CH_3CN$ solution of $[Cu^{II}(L^{H})]^{\cdot 2+}$. Microwave frequency 4485 GHz, power 1 mW, mod. frequency 100 kHz, amp. 1.0 mT, $T$ = 4 K.

The temperature dependence of the UV/Vis spectrum of $[Cu^{II}(L^{Me})]^{\cdot 2+}$ precludes any investigation of its stability at 298 K, while $[Cu^{II}(HL^{Me})]^{\cdot 3+}$ was too unstable and degraded significantly even at 233 K. Complex $[Cu^{II}(L^{H})]^{\cdot 2+}$ has a decomposition rate constant $k_{decay}$ of 0.067 $min^{-1}$ ($t_{1/2}$ = 10.4 min at 298 K). This is 2.5 times weaker than that of $[Cu^{II}(L^{tBu})]^{\cdot 2+}$ ($k_{decay}$ = 0.155 $min^{-1}$), this is likely to be due to resonance stabilization in $[Cu^{II}(L^{H})]^{\cdot 2+}$. Moreover, $[Cu^{II}(L^{H})]^{+}$ exhibits an $E_{1/2}$ value (0.23 V vs. $Fc^{+}$/Fc) that is roughly similar to that of $[Cu^{II}(L^{F})]^{+}$ ($E_{1/2}$ = 0.20 V),[4] the structure of which differs from that of $[Cu^{II}(L^{H})]^{+}$ by the nature of phenolate *para* substituent, which is a fluorine atom. As the radical species $[Cu^{II}(L^{F})]^{\cdot 2+}$ decomposed during electrolysis at 233 K, $[Cu^{II}(L^{H})]^{\cdot 2+}$ it should be, in principle, too unstable to be characterized. This is not true, showing that charge delocalization over the benzimidazolium group contributes significantly to the chemical stability of the radical species $[Cu^{II}(L^{H})]^{\cdot 2+}$. This also shows that the usual correlation between the chemical stability of copper(II) phenoxyl radical species, and the potential values of the phenoxyl/phenolate redox couple, is not so evident when charge delocalization occurs. Complex $[Cu^{II}(HL^{H})]^{\cdot 3+}$ was much less stable than $[Cu^{II}(L^{H})]^{\cdot 2+}$ ($k_{decay}$ = 0.99 $min^{-1}$, $t_{1/2}$ = 0.7 min at 298 K), this is in agreement with the spectroscopic and electrochemical data. Protonation of benzimidazole, to produce a positively charged benzimidazolium group, makes it electron-withdrawing, which destabilizes the phenoxyl radical.

### Copper(II) Titration: Addition of 0 to 1 Molar Equivalent

The solution chemistry of each ligand has been studied in acetonitrile by increasing the ratio of copper(II) perchlorate to $HL^{H}$ and $HL^{Me}$. When one molar equiv. of copper(II) perchlorate is slowly added to an acetonitrile solution of $HL^{H}$, an absorption band appears gradually in the visible spectra at 526 nm (Figure 9), and EPR reveals the formation of a mononuclear copper(II) complex. These spectroscopic features well match those reported for the isolated copper(II) phenolate benzimidazolium species $[Cu^{II}(HL^{H})]^{2+}$. Likewise, the addition of one molar equiv.

 © 2006 Wiley-VCH Verlag GmbH & Co. KGaA, Weinheim 

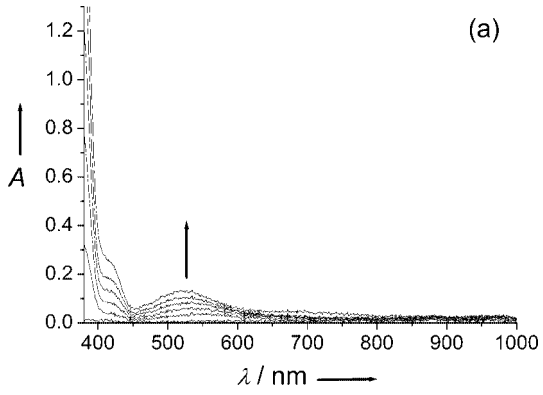


Figure 9. Titration of a 0.1 mM $CH_3CN$ solution of $HL^H$ against copper(II) perchlorate at 233 K: from 0 to 1 molar equiv. of copper (a), and from 1 to 2 molar equiv. of copper (b); arrows indicate spectral changes upon the addition of copper ($l$ = 1.000 cm).

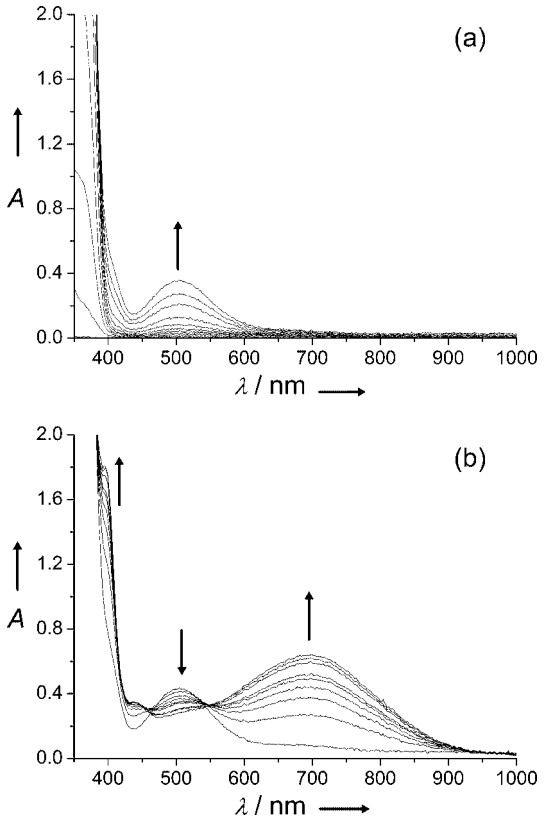


Figure 10. Titration of a 0.3 mM $CH_3CN$ solution of $HL^{Me}$ against copper(II) perchlorate at 233 K: from 0 to 1 molar equiv. of copper (a), and from 1 to 2 molar equiv. of copper (b); arrows indicate spectral changes upon the addition of copper ($l$ = 1.000 cm).

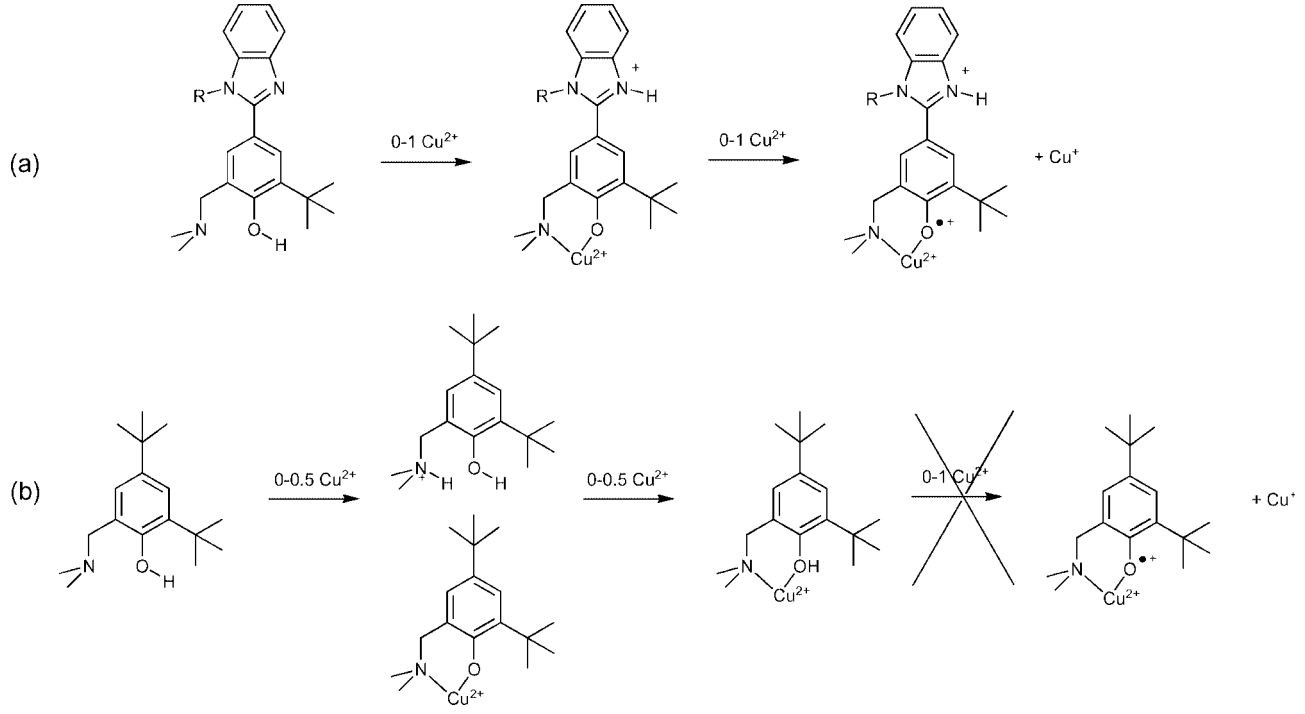


Scheme 3. Solution chemistry of $HL^{Me}$ and $HL^H$ (a), $HL^{tBu}$ (b), in the presence of copper(II) perchlorate in $CH_3CN$.

 © 2006 Wiley-VCH Verlag GmbH & Co. KGaA, Weinheim 

of copper(II) to $HL^{Me}$ affords the copper(II) phenolate *N*-methylbenzimidazolium complex $[Cu^{II}(HL^{Me})]^{2+}$ (Figure 10). Thus, the coordination of the ligands to copper(II) induces a transfer of the phenolic proton to the benzimidazole (or *N*-methylbenzimidazole) substituent (Scheme 3, a). This behavior is in sharp contrast with that of $HL^{tBu}$ (Scheme 3, b), which after addition of one molar equiv. of copper(II) affords the copper(II) phenol complex $[Cu^{II}(HL^{tBu})]^{2+}$.[50] Moreover, formation of this phenol complex was more complicated than the simple reaction between the ligand $HL^{tBu}$ and copper(II). As 0 to 0.5 molar equiv. of copper(II) perchlorate was added, a progressive increase in the phenolate to copper(II) CT transition was observed, showing that once the copper is chelated to by some of the available ligand in solution, the tertiary amine of the remaining free ligand deprotonates the weakly coordinated phenol (i.e. the $pK_a$ of the coordinated phenol is lower than that of the tertiary ammonium, Scheme 3, b). When 0.5 to one molar equiv. of copper(II) is added to $HL^{tBu}$, the spectrum of the copper(II) phenolate complex $[Cu^{II}(L^{tBu})]^{+}$ vanishes and is replaced by that of the copper(II) phenol complex $[Cu^{II}(HL^{tBu})]^{2+}$. Complexation of copper(II) to the free protonated ligand $H_2L^{tBu+}$ induces deprotonation of its tertiary ammonium group; the proton is transferred to the coordinated phenolate of $[Cu^{II}(L^{tBu})]^{+}$, affording the copper(II) phenol complex $[Cu^{II}(HL^{tBu})]^{2+}$ (Scheme 3, b).

Thus proton transfer, coupled to copper(II) complexation, occurs in all cases ($HL^{tBu}$, $HL^{H}$ and $HL^{Me}$). Nevertheless, a major difference exists between $HL^{tBu}$ and $HL^{H}$ (and $HL^{Me}$) namely, the endogenous base: proton transfer is managed either by the tertiary amine of $HL^{tBu}$, or by the benzimidazole moiety in $HL^{H}$ or $HL^{Me}$. In all these tripodal ligands, the tertiary amine is involved in copper(II) coordination. When the proton is transferred from the tertiary amine (ammonium form), it does not chelate the metal thus, a mixture of the protonated ligand and the copper(II) phenolate complex is obtained when 0.5 molar equiv. of copper(II) is added to $HLt^{Bu}$. The benzimidazolium group does not interfere with the complexation processes. Thus, when the proton is transferred from the benzimidazole (or *N*-methylbenzimidazole) group of $HL^{H}$ and $HL^{Me}$, all of the ligand in solution chelates to the metal, and no free ligand remains, even when only 0.5 molar equiv. of copper(II) is added to the ligand. The existence, and location, of the proton acceptor in the ligand is therefore of crucial importance in dictating the mechanism by which copper(II) is chelated by tripodal ligands.

### Copper(II) Titration: Addition of 1 to 2 Molar Equivalents

The acetonitrile solutions of $HL^{H}$ and $HL^{Me}$ were titrated against copper(II), at 233 K, and up to two molar equiv. of copper(II) was added. When one to two molar equiv. of copper(II) was added, the phenolate to copper(II) CT transition at 524 nm (and 508 nm) of $[Cu^{II}(HL^{H})]^{2+}$ (and $[Cu^{II}(HL^{Me})]^{2+}$) progressively decreases in intensity and then vanishes, while new intense transitions appear at around 400, 450 and 700 nm. The UV/Vis spectrum of the final species exhibits intense absorption bands at 401, 435 and 700 nm [396, 440 (shoulder) and 700 nm for $HL^{Me}$]. These features are similar to those of the electrogenerated $[Cu^{II}(HL^{H})]^{\cdot 3+}$ complex (and $[Cu^{II}(HL^{Me})]^{\cdot 3+}$). The copper(II) phenolate complexes $[Cu^{II}(HL^{H})]^{2+}$ and $[Cu^{II}(HL^{Me})]^{2+}$ are thus quantitatively oxidized by excess copper(II) to give the corresponding copper(II) phenoxyl complexes $[Cu^{II}(HL^{H})]^{\cdot 3+}$ and $[Cu^{II}(HL^{Me})]^{\cdot 3+}$, releasing free copper(I) according to Scheme 3 (a).[68]

When one molar equiv. of copper(II) was added to an acetonitrile solution of $HL^{tBu}$, the copper(II) phenol complex $[Cu^{II}(HL^{tBu})]^{2+}$ was obtained quantitatively. Continuing to add copper(II) results in the oxidation of a small amount of the $[Cu^{II}(HL^{tBu})]^{2+}$ complex (less than 8%) to give the radical species $[Cu^{II}(L^{tBu})]^{\cdot 2+}$, this is consistent with the oxidation potential of the phenol in $[Cu^{II}(HL^{tBu})]^{2+}$ being too high to allow it to be oxidized by copper(II) to produce the corresponding phenoxyl radical.[50]

After addition of one molar equiv. of copper(II) to $HL^{H}$ or $HL^{Me}$ deprotonation of the phenol occurs, induced by proton transfer to the benzimidazole or *N*-methylbenzimidazole substituent, which lowers its redox potential, making oxidation by exogenous copper(II) possible in the absence of exogenous base.[69] Deprotonation of the phenol group of $HL^{tBu}$ does not occur in the presence of one molar equiv. of copper(II), thus preventing its oxidation by excess copper(II).

On the other hand, if free copper(II) oxidizes the copper(II) phenolate complex, then one should expect the formation of a copper(II) phenoxyl complex at a copper(II)/ligand ratio lower than 1:1. This is not the case, showing that a comproportionation reaction consumes the radical once it is formed (as in the case of GO[70] and other $N_3O$ ligands[50]) according to Equation 1.

$$\text{copper(II) phenoxyl} + \text{copper(I)} \rightarrow 2\ \text{copper(II)}-\text{phenolate} \qquad (1)$$

## Conclusion

Herein we have reported a fine structural approach to the protonation/deprotonation sequence of the axial $Tyr_{495}$ in the GO active site. We have also provided evidence of a proton transfer reaction coupled to a copper(II) coordination process occurring in the ligands: in the presence of one molar equiv. of copper(II) the phenolic proton moves towards the *p*-benzimidazole (or *N*-methylbenzimidazole) substituent affording *p*-benzimidazolium phenolate complexes. In the presence of excess copper(II) (in absence of an exogenous base), a copper(II) phenoxyl radical is obtained, which was not observed for related ligands possessing a *p*-*tert*-butyl group. The existence and location of the proton acceptor (tertiary amine or benzimidazole) in the ligand is therefore of crucial importance in dictating the mechanism by which copper(II) is chelated, and influences the reactivity of the complex towards an exogenous oxidizer.

 © 2006 Wiley-VCH Verlag GmbH & Co. KGaA, Weinheim 

The control of the proton transfer and the metal coordination, are of prime importance in stabilizing phenoxyl radicals in proteins.[71–79] Recently, each phenomenon has been explored independently in biomimetic systems. This lead to the characterization of metal coordinated phenoxyl radicals,[16–50] or hydrogen bonded phenoxyl radicals generated by proton coupled to electron transfer.[80–83] Ligands $HL^H$ and $HL^{Me}$ are the first systems where both proton transfer and metal coordination occur simultaneously, contributing to the stabilization of the phenoxyl radical (by deprotonation, lowering of the redox potential by at least 0.35 V, metal coordination, and by resonance).

## Experimental Section

**General:** All chemicals were of reagent grade and used without purification. Microanalyses were performed by the Service Central d'Analyses du CNRS (Lyon, France).

Low-temperature visible spectra were recorded on a CARY 50 spectrophotometer equipped with a low temperature Hellma immersion probe (1.000 cm path length quartz cell). The temperature was controlled with a Lauda RK8 KS cryostat.

X-band EPR spectra were recorded on a BRUKER ESP 300E spectrometer equipped with a BRUKER nitrogen flow cryostat, and a BRUKER EMX spectrometer equipped with an ESR 900 helium flow cryostat (Oxford Instruments). Spectra were treated using the WINEPR software and simulated using the BRUKER SIMFONIA software.

Rate constants for the self-decomposition of the radical species were obtained spectrophotometrically. The absorbance decay at 450 nm (298 K) was fitted using the Biokine software (Bio Logic Co, Claix, France).

The cyclic and differential pulse voltammograms of each compound (1 mM) in $CH_3CN$, containing 0.1 M tetra-*n*-butylammonium perchlorate (TBAP) as the supporting electrolyte, were recorded on a CHI potentiostat at 298 K. The working electrode was a glassy carbon disc, and the secondary electrode was a Pt wire, and the reference electrode was 0.01 M $Ag/AgNO_3$. The potential of the regular ferrocenium/ferrocene ($Fc^+/Fc$) redox reaction, +0.087 V under our experimental conditions, was used as an internal reference. Electrolysis was performed at 233 K at a carbon felt electrode using a PAR 273 potentiostat.

**Crystal Structure Analysis:** For all structures, collected reflections were corrected for Lorentz and polarization effects, but not for absorption. The structures were solved by direct methods and refined using the TEXSAN software. All non-hydrogen atoms were refined with anisotropic thermal parameters. Hydrogen atoms were generated at idealized positions, and were modeled as riding on the carrier atoms, and refined with isotropic thermal parameters.

CCDC-259962, -259841, -275709 and -275881 contain the supplementary crystallographic data for this paper. These data can be obtained free of charge from The Cambridge Crystallographic Data Centre via www.ccdc.cam.ac.uk/data_request/cif.

**3-*tert*-Butyl-4-hydroxybenzaldehyde:** 2-*tert*-Butylphenol (20 g, 133 mmol) was dissolved in MeOH (80 mL), NaOH (80 g) was dissolved in water (80 mL) and added dropwise to the reaction mixture. Then $CHCl_3$ was added (during the course of 1 h) at 60 °C. The reaction mixture was stirred for 3 h, then cooled to 0 °C and hydrolyzed with 4 N HCl until the solution reached pH 5–6. The mixture was extracted with $CHCl_3$ and the combined organic layers were dried with $Na_2SO_4$ and then concentrated. Column chromatography on silica gel [ethyl acetate:pentane (1:20) was the eluent] yielded 3-*tert*-butyl-4-hydroxybenzaldehyde (24 g, 40%) as an orange solid. $^1H$ NMR (200 MHz, $CDCl_3$): $\delta$ = 1.44 (s, 9 H), 6.85–6.89 [d, $^3J_{H,H}$ = 8.2 Hz, 1 H], 7.62–7.67 [dd, $^3J_{H,H}$ = 8.2 Hz, $^4J_{H,H}$ = 1.7 Hz, 1 H], 7.84–7.85 [d, $^4J_{H,H}$ = 1.7 Hz, 1 H], 9.84 ppm (s, 1 H). $^{13}C$ NMR (75 MHz, $CDCl_3$): $\delta$ = 29.7 (t, 3C), 35.1 (q), 117.5 (s), 129.9 (q), 130.6 (s), 137,6 (q), 161.2 (q), 192.3 ppm (s). M.p. 125 °C. $C_{11}H_{14}O_2$ (178.23): calcd. C 74.13, H 7.92; found C 73.45, H 7.85.

**2-*tert*-Butyl-4-(1-methyl-1*H*-benzoimidazol-2-yl)phenol:** To 3-*tert*-Butyl-4-hydroxybenzaldehyde (1.04 g, 5.8 mmol) in MeOH (20 mL) was added *N*-methyl-1,2-phenylenediamine (0.709 g, 5.8 mmol) at 0 °C. The mixture was stirred for 0.5 h at 0 °C, and then for 3 h at room temperature. Benzofuroxane (0.795 g, 5.8 mmol) was dissolved in $CH_3CN$ (5 mL), and added to the reaction mixture at room temperature. The mixture was stirred for 12 h at 60 °C, then cooled to 0 °C, and 10% NaOH (10 mL) was added. The reaction was poured into 200 mL of water, and concentrated HCl was added to neutralize the solution. The brown precipitate was filtered, washed with cold water and $CHCl_3$, and then dried under vacuum. Yield: 50%. $^1H$ NMR (300 MHz, [D$_6$]DMSO): $\delta$ = 1.46 (s, 9 H), 3.89 (s, 3 H), 7.22–7.31 (m, 2 H), 7.54–7.60 (m, 2 H), 7.66–7.69 (m, 2 H), 10.00 ppm (s, 1 H). $^{13}C$ NMR (75 MHz, [D$_6$]DMSO): $\delta$ = 30.1 (t, 3C), 32.6 (t), 35.3 (q), 111.1 (s), 117.0 (s), 119.4 (s), 121.2 (q), 122.5 (s), 122.7 (s), 128.8 (s), 128.9 (s), 137.5 (q), 143.4 (q), 154.7 (q), 158.3 ppm (q). M.p. > 250 °C. MS (DCI, $NH_3$/isobutane) *m/z* (%): 280 (100) $[M+H]^+$. $C_{18}H_{20}N_2O$ (280.36): calcd. C 77.11, H 7.19, N 9.99; found C 75.40, H 7.21, N 9.76.

**$HL^{Me}$:** 2-*tert*-Butyl-4-(1-methyl-1*H*-benzoimidazol-2-yl)phenol (1.016 g, 3.6 mmol), bis(2-pyridylmethyl)amine (722 mg, 3.6 mmol) and formaldehyde (1.4 mL of a 37% aqueous solution) in EtOH/$H_2O$ (5:1, 100 mL) were refluxed together for 12 h. The reaction mixture was then extracted with ethyl acetate, dried with $Na_2SO_4$ and then concentrated. Column chromatography on silica gel [ethyl acetate/methanol (9:1) + 1% isopropylamine was the eluent] yielded $HL^{Me}$ (600 mg, 35%) as a pale orange solid. $^1H$ NMR (300 MHz, [D$_6$]DMSO): $\delta$ = 1.49 (s, 9 H), 3.89 (s, 3 H), 3.91 (s, 4 H), 3.95 (s, 2 H), 7.21–7.34 (m, 4 H), 7.42–7.44 (d, $^3J_{H,H}$ = 7.8 Hz, 2 H), 7.52–7.53 (d, $^4J_{H,H}$ = 2.0 Hz, 1 H), 7.56–7.60 (m, 1 H), 7.63–7.64 (d, $^4J_{H,H}$ = 2.0 Hz, 1 H), 7.65–7.68 (m, 1 H), 7.78–7.84 (m, $^3J_{H,H}$ = 4.7 Hz, $^4J_{H,H}$ = 1.7 Hz, 2 H), 8.59–8.60 (d, $^3J_{H,H}$ = 4.7 Hz, 2 H), 11.76 ppm (s, 1 H). $^{13}C$ NMR (75 MHz, [D$_6$]DMSO): $\delta$ = 32.6 (t), 35.4 (q), 57.2 (d), 59.2 (d), 111 (s), 119.4 (q), 120.5 (q), 122.5 (q), 122.7 (s), 123.4 (s, 2C), 124.0 (s, 2C), 128.1 (s), 129.8 (s), 136.8 (q), 137.5 (q), 137.7 (s, 2C), 149.7 (s, 2C), 154.6 (q), 158.4 ppm (q, 2C). MS (DCI, $NH_3$/isobutane) *m/z* (%): 492 (100) $[M+H]^+$. M.p. 150 °C. $C_{31}H_{33}N_5O$ (491.63): calcd. C 75.73, H 6.77, N 14.25; found C 75.65, H 7.01, N 14.19.

**$[Cu^{II}(HL^{Me})](ClO_4)_2$:** Ligand $HL^{Me}$ (132 mg, 0.269 mmol) was dissolved in $CH_3CN$ (10 mL) and $Cu(ClO_4)_2 \cdot 6H_2O$ (99 mg, 0.267 mmol) in $CH_3CN$ (2 mL) was then added dropwise. The solution was stirred for 15 min and then the volume was reduced to 2 mL. Single crystals of $[Cu^{II}(HL^{Me})](ClO_4)_2$ were obtained by slow diffusion of diisopropyl ether into the $CH_3CN$ solution (102 mg, yield: 68%). ESI MS (*m/z*): 553 $[M - H - (CH_3CN) - 2(ClO_4)]^+$. $C_{33}H_{36}Cl_2CuN_6O_9$ (795.13): calcd. C 49.85, H 4.56, N 10.57, Cu 7.99; found C 49.57, H 4.82, N 10.11, Cu 7.45.

**$[Cu^{II}(H_2L^{Me})](ClO_4)_3$:** Compound $[Cu^{II}(HL^{Me})](ClO_4)_2$ (23 mg, 0.029 mmol) was dissolved in $CH_3CN$ (1 mL), and $HClO_4$ (70%, 2.4 μL) was added. The solution was stirred for 5 min. Single crys-

 © 2006 Wiley-VCH Verlag GmbH & Co. KGaA, Weinheim 

tals of $[Cu^{II}(H_2L^{Me})](ClO_4)_3$ were obtained by slow diffusion of isopropyl ether into the $CH_3CN$ solution (18 mg, yield: 90%). ESI MS (*m*/*z*): 653 $[M - H - (CH_3CN) - 2(ClO_4)]^+$. $C_{33}H_{37}Cl_3CuN_6O_{13}$ (895.58): calcd. C 44.26, H 4.16, N 9.13, Cu 7.10; found C 44.18, H 4.13, N 9.13, Cu 6.88.

**4-(1*H*-Benzimidazol-2-yl)-2-*tert*-butylphenol:** To 3-*tert*-Butyl-4-hydroxybenzaldehyde (1.04 g, 5.8 mmol) in MeOH (20 mL) was added benzene-1,2-diamine (0.631 g, 5.8 mmol) at 0 °C. The mixture was stirred for 0.5 h at 0 °C, and then for 1 h at room temperature. Benzofuroxane (0.795 g, 5.8 mmol) was dissolved in $CH_3CN$ (5 mL), and added dropwise (over a 10 min period) to the reaction mixture. The mixture was stirred for 2 h at 60 °C, then cooled to 0 °C and then 10% NaOH (10 mL) was added. The reaction mixture was poured into 200 mL of water and concentrated HCl was added to neutralize the solution. The brown precipitate was filtered, washed with cold water and $CHCl_3$, and then dried under vacuum. Yield: 52%. $^1$H NMR (300 MHz, [D$_6$]DMSO): $\delta$ = 1.48 (s, 9 H), 6.95 (d, $J$ = 8.1 Hz, 1 H), 7.17 (dd, $^3J$ = 5.9 Hz, $^4J$ = 3.2 Hz, 2 H), 7.57 (dd, $^3J$ = 5.7 Hz, $^4J$ = 3.2 Hz, 2 H), 7.87 (dd, $^3J$ = 8.1 Hz, $^4J$ = 1.5 Hz, 1 H), 8.05 (d, $^4J$ = 1.5 Hz, 1 H), 9.94 (s, 1 H), 12.68 ppm (s, 1 H). $^{13}$C NMR (75 MHz, [D$_6$]DMSO): $\delta$ = 29.7 (t), 34.9 ($C_q$), 114.9 (CH), 116.8 (CH), 121.0 ($C_q$), 121.9 (CH), 125.6 (CH), 125.9 (CH), 136.2 ($C_q$), 139.7 ($C_q$), 152.6 ($C_q$), 158.2 ppm ($C_q$). M.p. > 250 °C. MS (DCI, $NH_3$/isobutane) *m*/*z* (%): 267 (100) $[M+H]^+$. $C_{17}H_{18}N_2O$ (266.34): calcd. C 76.66, H 6.81, N 10.52; found C 75.78, H 6.94, N 9.37.

**$HL^H$:** 2-*tert*-Butyl-4-(1*H*-benzoimidazol-2-yl)phenol (0.500 g, 1.88 mmol), bis(2-pyridylmethyl)amine (374 mg, 1.88 mmol) and formaldehyde (0.7 g of a 37% aqueous solution, 9.4 mmol) in EtOH/$H_2O$ (2:1, 100 mL) were refluxed together for 12 h. The reaction mixture was then extracted with ethyl acetate, washed with a saturated NaCl aqueous solution, dried with $Na_2SO_4$ and then concentrated. Column chromatography on silica gel [ethyl acetate/methanol (5:1)] yielded $HL^H$ (270 mg, 30%) as a beige solid. $^1$H NMR (300 MHz, [D$_6$]DMSO): $\delta$ = 1.50 (s, 9 H), 3.90 (s, 4 H), 3.94 (s, 2 H), 7.19 (dd, $^3J$ = 5.9 Hz, $^4J$ = 3.2 Hz, 2 H), 7.30 (d, $^3J$ = 6.5 Hz, 1 H), 7.32 (d, $^3J$ = 7.1 Hz, 1 H), 7.41 (d, $J$ = 7.8 Hz, 2 H), 7.50–7.62 (m, 2 H), 7.78 (td, $^3J$ = 7.6 Hz, $^4J$ = 1.6 Hz, 2 H), 7.87 (d, $^4J$ = 1.8 Hz, 1 H), 8.01 (d, $^4J$ = 1 Hz, 1 H, 8 Hz), 8.58 (d, $^3J$ = 4.0 Hz, 2 H), 11.73 (s, 1 H), 12.70 ppm (s, 1 H). $^{13}$C NMR (75 MHz, [D$_6$]DMSO): $\delta$ = 30.3 (*t*Bu), 35.6 ($C_q$), 57.6 ($CH_2$), 59.1 ($CH_2$Py), 121.0 ($C_q$), 122.4 (CH), 123.4 (CH), 123.9 (CH), 124.5 ($C_q$), 125.4 (CH), 127.6 (CH), 135.9 ($C_q$), 137.2 ($C_q$), 137.7 (CH), 144.9 ($C_q$), 149.7 (CH), 153.0 ($C_q$), 158.5 ($C_q$), 158.8 ppm ($C_q$). M.p. 200 °C. MS (DCI, $NH_3$/isobutane) *m*/*z* (%): 478 (100) $[M+H]^+$. $C_{30}H_{31}N_5O$ (477.60): calcd. C 75.44, H 6.54, N 14.66; found C 75.16, H 6.55, N 14.50.

**$[Cu^{II}(HL^H)](ClO_4)_2$:** $[Cu^{II}(HL^H)](ClO_4)_2$ was obtained in a similar way to $[Cu^{II}(HL^{Me})](ClO_4)_2$ by using $HL^H$ instead of $HL^{Me}$ (yield: 75%). ESI MS (*m*/*z*): 539 $[M - H - (CH_3CN) - 2(ClO_4)]^+$. $C_{32}H_{34}Cl_2CuN_6O_9{\cdot}H_2O{\cdot}CH_3CN$ (781.10): calcd. C 48.61, H 4.68, N 11.67, Cu 7.56; found C 47.92, H 4.51, N 11.68, Cu 7.50.

**$[Cu^{II}(H_2L^H)](ClO_4)_3$:** Complex $[Cu^{II}(H_2L^H)](ClO_4)_3$ was obtained in a similar way to $[Cu^{II}(H_2L^{Me})](ClO_4)_3$ by using $HL^H$ instead of $HL^{Me}$ (yield: 90%). ESI MS (*m*/*z*): 539 $[M - H - (CH_3CN) - 2(ClO_4)]^+$. $C_{32}H_{35}Cl_3CuN_6O_{13}$ (881.56): calcd. C 44.16, H 4.38, N 9.36, Cu 7.08; found C 44.51, H 4.35, N 9.70, Cu 6.75.

## Acknowledgments

The authors thank the Institute of Metals in Biology of Grenoble who provided facilities for performing the 4 K EPR studies, and Dr. Stephane Ménage for technical assistance with these experiments.

[1] D. J. Kosman, M. J. Ettinger, R. E. Weiner, E. J. Massaro, *Arch. Biochem. Biophys.* **1974**, *165*, 456.
[2] M. M. Whittaker, J. W. Whittaker, *J. Biol. Chem.* **1988**, *263*, 6074.
[3] M. M. Whittaker, J. W. Whittaker, *J. Biol. Chem.* **1990**, *265*, 9610.
[4] N. Ito, S. E. V. Phillips, C. Stevens, Z. B. Ogel, M. J. McPherson, J. N. Keen, K. D. S. Yadav, P. J. Knowles, *Nature* **1991**, *350*, 87.
[5] G. T. Babcock, M. K. El-Deeb, P. O. Sandusky, M. M. Whittaker, J. W. Whittaker, *J. Am. Chem. Soc.* **1992**, *114*, 3727.
[6] N. Ito, S. E. V. Phillips, K. D. S. Yadav, P. F. Knowles, *J. Mol. Biol.* **1994**, *238*, 794.
[7] R. Sayle, E. F. Milner-White, *Trends Biochem. Sci.* **1995**, *20*, 374.
[8] J. W. Whittaker, *Metal Ions in Biological Systems* (Eds.: H. Sigel, A. Sigel), Marcel Dekker, New York, **1994**, vol. 30, pp. 315–360.
[9] J. W. Whittaker, in *Advances in Protein Chemistry* (Eds.: F. M. Richards, D. S. Eisenberg, J. Kuriyan), Academic Press, Elsevier, **2002**, vol. 60, pp. 1–49.
[10] J. W. Whittaker, *Chem. Rev.* **2003**, *103*, 2347.
[11] M. S. Rogers, D. M. Dooley, *Curr. Opin. Chem. Biol.* **2003**, *7*, 189.
[12] M. S. Rogers, A. J. Baron, M. J. McPherson, P. F. Knowles, D. M. Dooley, *J. Am. Chem. Soc.* **2000**, *122*, 990.
[13] M. S. Rogers, D. M. Dooley, *Curr. Opin. Chem. Biol.* **2003**, *7*, 189.
[14] S. J. Firbank, M. S. Rogers, C. M. Wilmot, D. M. Dooley, M. A. Halcrow, P. F. Knowles, M. J. McPherson, S. E. V. Phillips, *Proc. Natl. Acad. Sci. USA* **2001**, *98*, 12932.
[15] M. M. Whittaker, J. W. Whittaker, *J. Biol. Chem.* **2003**, *278*, 22090.
[16] N. Kitajima, K. Whang, Y. Moro-oka, A. Uchida, Y. Sasada, *J. Chem. Soc., Chem. Commun.* **1986**, 1504.
[17] Y. Wang, T. D. P. Stack, *J. Am. Chem. Soc.* **1996**, *118*, 13097.
[18] D. Zurita, I. Gautier-Luneau, S. Ménage, J. L. Pierre, E. Saint-Aman, *J. Biol. Inorg. Chem.* **1997**, *2*, 46.
[19] A. Sokolowski, H. Leutbecher, T. Weyhermüller, R. Schnepf, E. Bothe, E. Bill, P. Hildenbrandt, K. Wieghardt, *J. Biol. Inorg. Chem.* **1997**, *2*, 444.
[20] J. A. Halfen, B. A. Jazdzewski, S. Mahapatra, L. M. Berreau, E. C. Wilkinson, L. Que Jr, W. B. Tolman, *J. Am. Chem. Soc.* **1997**, *119*, 8217.
[21] E. Saint-Aman, S. Ménage, J. L. Pierre, E. Defrancq, G. Gellon, *New J. Chem.* **1998**, *22*, 393.
[22] Y. Wang, J. L. DuBois, B. Hedman, K. O. Hodgson, T. D. P. Stack, *Science* **1998**, *279*, 537.
[23] P. Chaudhuri, M. Hess, U. Flörke, K. Wieghardt, *Angew. Chem. Int. Ed.* **1998**, *37*, 2217.
[24] M. Vaidyanathan, R. Viswanathan, M. Palaniandavar, T. Balasubramanian, P. Prabhaharan, P. T. Muthiah, *Inorg. Chem.* **1998**, *37*, 6418.
[25] P. Chaudhuri, M. Hess, J. Müller, K. Hildenbrandt, E. Bill, T. Weyhermüller, K. Wieghardt, *J. Am. Chem. Soc.* **1999**, *121*, 9599.
[26] E. Bill, J. Müller, T. Weyhermüller, K. Wieghardt, *Inorg. Chem.* **1999**, *38*, 5795.
[27] P. Chaudhuri, M. Hess, T. Weyhermüller, K. Wieghardt, *Angew. Chem. Int. Ed.* **1999**, *38*, 1095.
[28] S. Itoh, M. Taki, S. Takayama, S. Nagatomo, T. Kitagawa, N. Sakurada, R. Arakawa, S. Fukuzumi, *Angew. Chem. Int. Ed.* **1999**, *38*, 2774.
[29] Y. Shimazaki, S. Huth, A. Odani, O. Yamauchi, *Angew. Chem. Int. Ed.* **2000**, *39*, 1666.
[30] M. Taki, H. Kumei, S. Nagatomo, T. Kitagawa, S. Itoh, S. Fukuzumi, *Inorg. Chim. Acta* **2000**, *300–302*, 622.

 © 2006 Wiley-VCH Verlag GmbH & Co. KGaA, Weinheim 

[31] C. Ochs, F. E. Hahn, R. Fröhlich, *Eur. J. Inorg. Chem.* **2001**, 2427.
[32] M. Vaidyannathan, M. Palaniandavar, R. S. Gopalan, *Inorg. Chim. Acta* **2001**, *324*, 241.
[33] L. Benisvy, A. J. Blake, D. Collison, E. S. Davies, C. D. Garner, E. J. L. McInnes, J. McMaster, G. Whittaker, C. Wilson, *Chem. Commun.* **2001**, 1824.
[34] M. Vaidyanathan, M. Palaniandavar, R. S. Gopalan, *Inorg. Chim. Acta* **2001**, *324*, 241.
[35] F. Thomas, G. Gellon, I. Gautier-Luneau, E. Saint-Aman, J.-L. Pierre, *Angew. Chem. Int. Ed.* **2002**, *41*, 3047.
[36] M. Vaidyanathan, M. Palaniandavar, R. S. Gopalan, *Ind. J. Chem. A* **2003**, *42*, 2210.
[37] G. Klein, J. M. Robertus, M. Watanabee, R. C. Pratt, T. D. P. Stack, *Chem. Commun.* **2003**, 630.
[38] R. C. Pratt, T. D. P. Stack, *J. Am. Chem. Soc.* **2003**, *125*, 8716.
[39] A. Neves, A. dos Anjos, A. J. Bortoluzzi, B. Szpoganicz, E. W. Schwingel, A. S. Mangrich, *Inorg. Chim. Acta* **2003**, *356*, 41.
[40] O. Seneque, M. Campion, B. Douziech, M. Giorgi, Y. Le Mest, O. Reinaud, *Dalton Trans.* **2003**, 4216.
[41] F. Thomas, O. Jarjayes, C. Duboc, C. Philouze, E. Saint-Aman, J.-L. Pierre, *Dalton Trans.* **2004**, 2662.
[42] R. C. Pratt, T. D. P. Stack, *Inorg. Chem.* **2004**, *43*, 8030.
[43] M. Taki, H. Hattori, T. Osako, S. Nagatomo, M. Shiro, T. Kitagawa, S. Itoh, *Inorg. Chim. Acta* **2004**, *357*, 3369.
[44] T. K. Paine, T. Weyhermüller, K. Wieghardt, P. Chaudhuri, *Dalton Trans.* **2004**, 2092.
[45] P. Chaudhuri, K. Wieghardt, T. Weyhermüller, T. K. Paine, S. Mukherjee, C. Mukherjee, *Biol. Chem.* **2005**, *386*, 1023.
[46] A. Dos Anjos, A. J. Bortoluzzi, R. E. H. M. B. Osorio, R. A. Peralta, G. R. Friedermann, A. S. Mangrich, A. Neves, *Inorg. Chem. Commun.* **2005**, *8*, 249.
[47] E. Zueva, P. H. Walton, J. E. McGrady, *Dalton Trans.* **2006**, 159.
[48] A. K. Nairn, S. J. Archibald, R. Bhalla, B. C. Gilbert, E. J. MacLean, S. J. Teat, P. H. Walton, *Dalton Trans.* **2006**, 172.
[49] A. Philibert, F. Thomas, C. Philouze, S. Hamman, E. Saint-Aman, J.-L. Pierre, *Chem. Eur. J.* **2003**, *9*, 3803.
[50] F. Michel, F. Thomas, S. Hamman, E. Saint-Aman, C. Bucher, J.-L. Pierre, *Chem. Eur. J.* **2004**, *10*, 4115.
[51] C. Xie, P. M. Lahti, *Tetrahedron Lett.* **1999**, *40*, 4305.
[52] L. Benisvy, A. J. Blake, D. Collison, E. S. Davies, C. D. Garner, E. J. L. McInnes, J. McMaster, G. Whittaker, C. Wilson, *Dalton Trans.* **2003**, 1975.
[53] C. G. Saysell, T. Barna, C. D. Borman, A. J. Baron, M. J. McPherson, A. G. Sykes, *J. Biol. Inorg. Chem.* **1997**, *2*, 702.
[54] F. Michel, F. Thomas, S. Hamman, C. Philouze, E. Saint-Aman, J.-L. Pierre, unpublished results.
[55] UV/Vis data [$\lambda_{max}$ (nm) ($\varepsilon$ {$M^{-1}cm^{-1}$})] for $[Cu^{II}(L^{H})]^{\cdot 2+}$: 401 (6560), 435 (4270), 694 (2420); for $[Cu^{II}(HL^{H})]^{\cdot 3+}$: 400 (11044), 435 (5200), 689 (3310). Complex $[Cu^{II}(L^{Me})]^{\cdot 2+}$ was too unstable to allow accurate $\varepsilon$ values to be determined. The UV/Vis spectrum of $[Cu^{II}(L^{Me})]^{\cdot 2+}$ was found to be temperature-dependent (reversible process): the absorption bands at 395, 450 (shoulder) and 700 nm are only present at 298 K. Lowering the temperature to 233 K results in the disappearance of the lower energy absorption band, and changes in the 450 nm region. The same behavior is observed in the presence of excess pyridine (acting as an exogenous ligand, see ref.[4]). This is therefore not due to temperature dependent copper(II) coordination by the *p*-*N*-methylbenzimidazole moiety. Given the lack of additional information, more detailed discussion of this phenomenon would be premature.
[56] B. A. Jazdzewski, W. B. Tolman, *Coord. Chem. Rev.* **2000**, *200–202*, 633.
[57] S. Itoh, M. Taki, S. Fukuzumi, *Coord. Chem. Rev.* **2000**, *198*, 3.
[58] P. Chaudhuri, K. Wieghardt, *Prog. Inorg. Chem.* **2001**, *50*, 151.
[59] L. E. Kapinos, B. Song, H. Sigel, *Chem. Eur. J.* **1999**, *5*, 1794.
[60] R. Liu, K. Morokuma, A. M. Mebel, M. C. Lin, *J. Phys. Chem.* **1996**, *100*, 9314.
[61] A. Hinchliffe, R. E. Steinbank, M. A. Ali, *Theor. Chim. Acta* **1996**, *5*, 95.
[62] H. M. Chang, H. H. Jaffe, *Chem. Phys. Lett.* **1973**, *23*, 146.
[63] H. M. Chang, H. H. Jaffe, C. A. Masmandis, *J. Phys. Chem.* **1975**, *79*, 1118.
[64] J. Takahashi, T. Shida, *Bull. Chem. Soc. Jpn.* **1994**, *67*, 2038.
[65] J. Takahashi, T. Momose, T. Shida, *Bull. Chem. Soc. Jpn.* **1994**, *67*, 964.
[66] L. J. Johnston, N. Mathivanan, F. Negri, W. Siebrand, F. Zerbetto, *Can. J. Chem.* **1993**, *71*, 1655.
[67] J. G. Radziszewski, M. Gil, A. Gorski, J. Spanget-Larsen, J. Waluk, B. J. Mroz, *J. Chem. Phys.* **2001**, *115*, 9733.
[68] The thermodynamic feasibility of the reaction has been probed by recording the CV curve of $Cu(ClO_4)_2 \cdot 6H_2O$ in $CH_3CN$. The curve revealed a reduction peak at 0.32 V corresponding to the metal centered reduction wave of the hexaaquacopper(II). On the reverse scan, the oxidation peak is observed at a much higher value, 0.80 V, showing that a rearrangement in the metal coordination sphere occurs [this can be interpreted as the replacement of the water molecules by acetonitrile that stabilizes the copper(I) formal oxidation state]. The copper(II) ion is thus a strong oxidizer in acetonitrile, which can readily oxidize all of the copper(II) phenolate complexes ($[Cu^{II}(HL^{H})]^{2+}$ and $[Cu^{II}(HL^{Me})]^{2+}$) to the corresponding copper(II) phenoxyl radical complexes.
[69] When zero to one molar equiv. of copper(II) is added to acetonitrile solutions of $HL^{H}$, $HL^{Me}$ and $HL^{tBu}$, in the presence of $NEt_3$, the phenolate copper(II) complexes are obtained, whichever ligand is used (the exogenous base $NEt_3$ scavenges the phenolic proton). Addition of one to two molar equiv. of copper(II) results in the disappearance of the phenolate copper(II) complex (characterized by its phenolate to copper CT transition). The UV/Vis spectra, after the addition of two molar equiv. of copper(II), exhibit absorption bands at around 400, 435 and 700 nm for $HL^{H}$ and $HL^{Me}$, and 416 and 650 nm for $HL^{tBu}$. These features are similar to those of the electrogenerated $[Cu^{II}(L^{H})]^{\cdot 2+}$ and $[Cu^{II}(L^{tBu})]^{\cdot 2+}$ complexes, respectively. The copper(II) phenolate complexes are thus quantitatively oxidized by excess copper(II) to give the corresponding copper(II) phenoxyl complexes.
[70] C. Wright, A. G. Sykes, *J. Inorg. Biochem.* **2001**, *5*, 237.
[71] P. Nordlund, B.-M. Sjöberg, H. Eklund, *Nature* **1990**, *345*, 593.
[72] S. Un, M. Atta, M. Fontecave, A. W. Rutherford, *J. Am. Chem. Soc.* **1995**, *117*, 10713.
[73] P. P. Schmidt, K. K. Andersson, A.-L. Barra, L. Thelander, A. Graslünd, *J. Biol. Chem.* **1996**, *271*, 23615.
[74] P. J. Van Dam, J. P. Willems, P. P. Schmidt, S. Pötsch, A. L. Barra, W. R. Hagens, B. M. Hoffman, K. K. Andersson, A. Gräslund, *J. Am. Chem. Soc.* **1998**, *120*, 5080.
[75] B. A. Diner, D. A. Force, D. W. Randall, R. D. Britt, *Biochemistry* **1998**, *37*, 17931.
[76] J. Stubbe, W. A. van der Donk, *Chem. Rev.* **1998**, *98*, 705.
[77] P. Dorlet, A. W. Rutherford, S. Un, *Biochemistry* **2000**, *39*, 7826.
[78] Y.-N. Wang, L. A. Eriksson, *Int. J. Quantum Chem.* **2001**, *83*, 220.
[79] P. Faller, C. Goussias, A. W. Rutherford, S. Un, *Proc. Nat. Acad. Sc. USA* **2003**, *100*, 8732.
[80] T. Maki, Y. Araki, Y. Ishida, O. Onomura, Y. Matsumura, *J. Am. Chem. Soc.* **2001**, *123*, 3371.
[81] I. J. Rhile, J. M. Mayer, *J. Am. Chem. Soc.* **2004**, *126*, 12718.
[82] D. Kanamori, A. Furukawa, T.-A. Okamura, H. Yamamoto, N. Ueyama, *Org. Biomol. Chem.* **2005**, *3*, 1453.
[83] L. Benisvy, E. Bill, A. J. Blake, D. Collison, E. S. Davies, C. D. Garner, G. McArdle, E. J. L. McInnes, J. McMaster, S. H. K. Ross, C. Wilson, *Dalton Trans.* **2006**, 258.

Received: March 31, 2006
Published Online: August 3, 2006

 © 2006 Wiley-VCH Verlag GmbH & Co. KGaA, Weinheim 

DOI: 10.1002/ejic.200600287

# Highly Ordered Functional Organosilicas by Template-Directed Hydrolysis-Polycondensation of Chiral Camphorsulfonamide Precursors

**Benoît Gadenne,[a] Peter Hesemann,[a] Vivek Polshettiwar,[a] and Joël J. E. Moreau*[a]**

**Keywords:** Mesoporous materials / Organic-inorganic hybrid composites / Sol–gel processes / Supported catalysts / Template synthesis

Trialkoxysilylated camphorsulfonamides have been used for the synthesis of functional organosilicas in a template-directed hydrolysis-polycondensation with tetraethylorthosilicate (TEOS). The sol–gel transformation leading to the formation of highly ordered materials indicates that trialkoxysilylated camphorsulfonamides allow the synthesis of functional organosilicas with high structural regularity. This behaviour arises from the affinity of the chiral precursors towards the lyotropic phase of the ionic surfactants in the aqueous hydrolysis-polycondensation mixture.
(© Wiley-VCH Verlag GmbH & Co. KGaA, 69451 Weinheim, Germany, 2006)

## Introduction

Since the discovery of the template-directed synthesis of nanostructured silica by Kresge et al. in 1992,[1] these materials have attracted considerable interest due to the unique properties related to their specific morphology, namely high specific surface, high pore volume and narrow pore-size distribution on a mesoscopic scale. These features make these materials the candidates of choice for numerous applications, for example in the fields of catalysis, separation and sensing.

The incorporation of functional organic groups into nanostructured silica can be achieved either in two steps by post-grafting of silylated precursor molecules onto the surface of nanostructured silica or in one step by a template-directed one-pot hydrolysis-polycondensation of a silica precursor with a functional organosilane.[2,3] The two methodologies lead to organosilicas with different morphological features: although materials obtained by the post-grafting method are structurally better defined and hydrothermally more stable than samples obtained by the direct one-step method, they often suffer from inhomogeneous distribution of the functional groups on the support surface. Contrary to this, the one-step condensation procedure affords materials with a homogeneous distribution of the functional organic groups over the whole surface.[4] However, in most cases only low functionalisation degrees can be achieved following the one-step method. Low-structured materials are obtained when high molar fractions of functional organosilane or bulky silylated precursors are used.[5,6] The upper limit of preservation of structural ordering is often reached with 20 mol-% of added organosilane.[6] For this reason, the elaboration of methods that allow the incorporation of bulky functional groups within a highly structured mesoporous organosilica material is highly desirable.

Our current interest in the preparation of ordered organosilicas led us to explore the synthesis of nanostructured silica hybrids containing ionic species.[7] As an example, we achieved the immobilisation of bis-alkylated imidazolium species on a silica support by a template-directed hydrolysis-polycondensation procedure. Supported ionic liquid phases have attracted large interest in the last few years[8] as these materials that consist of an ionic layer that covers the whole surface of a solid support are promising systems for applications in catalysis,[9–12] separation[13] and chromatography.[14] We were interested in exploring whether functional precursor molecules bearing ionic substructures would allow us to enhance the structural regularity of the obtained functional materials in template directed sol–gel processes. We report here a new nanostructured organosilica containing ionic and non-ionic (+)-camphorsulfonamide substructures as these moieties have been shown to be efficient auxiliaries in asymmetric catalysis.[15,16]

## Results and Discussion

We first focused on the synthesis of functional organosilanes bearing camphor substructures. The synthesis of the trialkoxysilylated camphorsulfonamide precursors **1** and **3** is shown in Scheme 1. The precursor **1** was obtained by the reaction of (+)-camphorsulfonyl chloride with 3-aminopropyltriethoxysilane (Scheme 1, top). Compound **3**, which bears an ionic imidazolium substructure, was synthesised by

[a] UMR CNRS 5076, Architectures moléculaires et matériaux nanostructurés, Ecole Nationale Supérieure de Chimie de Montpellier,
34296 Montpellier Cedex 05, France
Fax: +33-467-14-72-12
E-mail: joel.moreau@enscm.fr

 © 2006 Wiley-VCH Verlag GmbH & Co. KGaA, Weinheim 

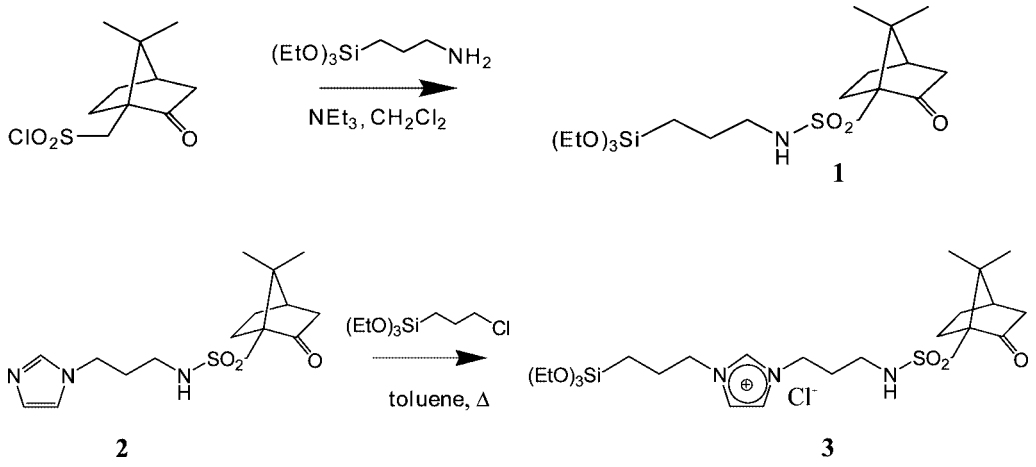


Scheme 1. Synthesis of the trialkoxysilylated camphorsulfonamides **1** (top) and **3** (bottom).

grafting 3-chloropropyltriethoxysilane to the camphorsulfonamide **2**[15] (Scheme 1, bottom). All reactions were quantitative, and the products could be used without further purification.

The synthesis of the organosilicas incorporating chiral camphorsulfonamide entities was then realised by a hydrolysis-polycondensation involving the chiral precursor **1** or **3** and tetraethoxysilane (TEOS; Scheme 2). All materials were prepared from alkaline mixtures containing TEOS, the trialkoxysilylated precursor **1** or **3**, water, ammonia and the surfactant hexadecylpyridinium chloride in the molar composition 0.9:0.1:114:8:0.12. We chose a pyridinium salt as template rather than an ammonium halide as the interaction between the imidazolium precursor **3** and pyridinium salts may be more favourable than that between imidazolium salts and surfactants based on ammonium substructures such as CTAB.[17] The resulting reaction mixture was heated to 80 °C for 48 h. The surfactant was then removed by washing in a Soxhlet apparatus and the materials were finally dried at 110 °C for 24 h.

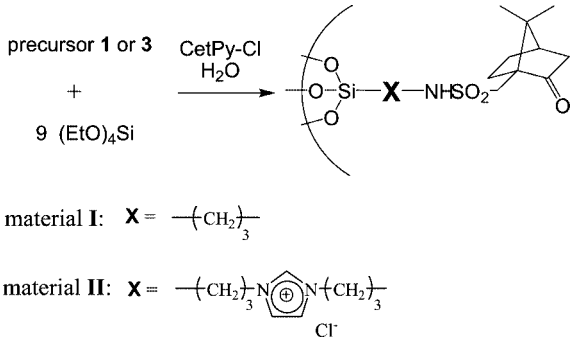


Scheme 2. Immobilisation of camphorsulfonamide species on the surface of mesoporous nanostructured silica.

Elemental analysis of the materials **I** and **II** indicated nearly complete incorporation of the organic precursors **1** and **3** into the organosilica materials during the sol–gel procedure. The incorporation of the organic entities within the silica network was also qualitatively monitored by FT-IR and $^{29}Si/^{13}C$-CP MAS NMR spectroscopy. The $^{29}Si$ CP-MAS NMR spectrum of material **I** is shown as an example in Figure 1. As reported for other functionalised mesoporous silica materials,[6] the spectrum shows the $T^3$ peak at $\delta$ = –65.8 ppm arising from the $RSiO_3$ substructures and the $Q^3$ and $Q^4$ peaks ($\delta$ = 101.4 and 109.6 ppm) which can be ascribed to $SiO_4$ substructures with different condensation degrees.

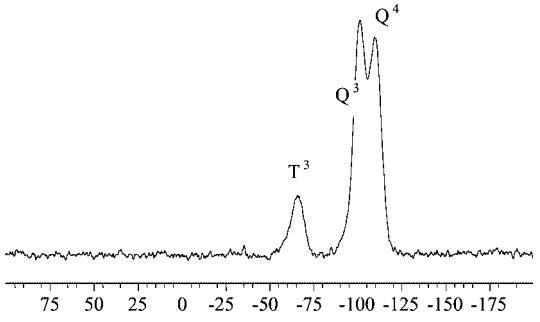


Figure 1. $^{29}Si$ CP MAS NMR spectrum of material **I**.

The morphological properties of materials **I** and **II** were investigated by XRD, TEM and nitrogen adsorption/desorption experiments. The XRD patterns of **I** and **II** are nearly identical and contain the (100), (110) and (200) peaks characteristic of hexagonal silica mesophases (Table 1). We have already obtained a material with a hexagonal architecture, although less regularly structured, using an ionic silylated dodecylimidazolium precursor.[7] The X-ray diffractograms of **I** and **II** are shown in Figure 2.

Table 1. XRD spacings of materials **I** and **II**.

| | *d* Spacings [nm] | | |
|---|---|---|---|
| | 100 | 110 | 200 |
| Material **I** | 4.00; | 2.31 | 2.00 |
| Material **II** | 4.00 | 2.30 | 1.99 |

The morphology of the materials was also studied by TEM. The TEM micrographs of **I** and **II** show a highly structured regular hexagonal array of two-dimensionally

 © 2006 Wiley-VCH Verlag GmbH & Co. KGaA, Weinheim 

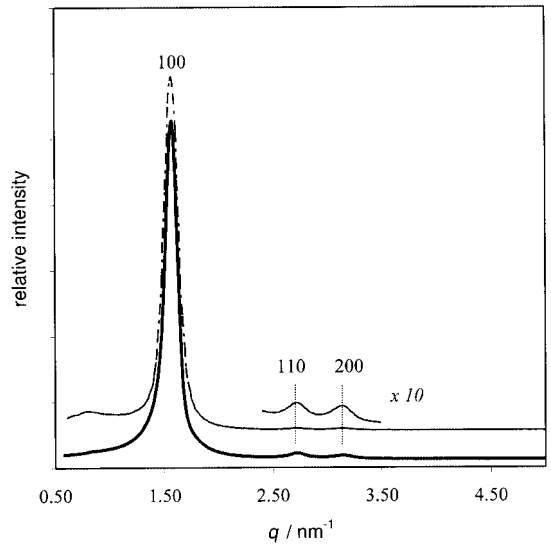


Figure 2. XRD patterns of the organosilica materials **I** (solid line) and **II** (dashed line).

aligned channels (Figure 3). In both cases, the distance between two pore centres was determined to be 4.0 nm, which corresponds to the (100) reflection in the XRD patterns.

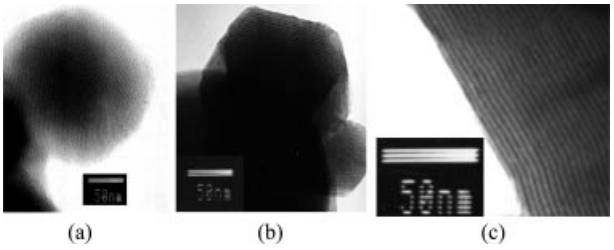


Figure 3. TEM micrographs of the functionalised organosilicas **I** (a) and **II** (b) along the (100) direction. (c) View along the (110) direction.

Thus, the TEM and XRD experiments give concordant results concerning the morphologies of materials **I** and **II**, which both appear as highly regularly structured solids with hexagonal symmetry. It has to be pointed out that the ionic substructure of precursor **3** does not have a significant effect on the structuration of the functionalised organosilica. The high structuration can rather be explained by the cosurfactant behaviour of the hydrolysed silylated precursors **1** and **3** in the basic aqueous media during the template-directed sol–gel procedure.

In a second experiment we studied the reduction of the carbonyl groups of the immobilised camphorsulfonamide entities in the porous material **II**. This reaction was performed with a suspension of sodium borohydride in methanol under reaction conditions identical to those reported for the reduction in homogeneous media.[15] This led to the formation of silica-supported borneol (material **III**). The reaction was monitored by FT-IR spectroscopy (disappearance of the absorption of the carbonyl group at $\tilde{\nu}$ = 1738 $cm^{-1}$). The ratio of the immobilized diastereoisomers could not be determined, but both borneol (*endo*) and isoborneol (*exo*) are probably formed. In solution, a 60:40 ratio has been reported (Scheme 3).[15]

Nitrogen adsorption/desorption experiments with materials **I**–**III** give information about the porosity and the pore volume of the samples. The isotherms of materials **I** and **II** reflect the formation of mesoporous silica hybrid materials with specific surface areas of 832 and 759 $m^2 g^{-1}$ and pore volumes of 0.52 and 0.49 $mL g^{-1}$, respectively. In both cases, the sorption curves show typical type-IV isotherms, thereby suggesting an ordered silica mesophase with pore diameters of 2.5 nm. The isotherm of material **II** shows a slight hysteresis loop due to capillary condensation of adsorbed nitrogen within the pores.[18] In contrast, material **III** shows a strongly reduced specific surface (82 $m^2 g^{-1}$), even after washing with acidic ethanol in a Soxhlet apparatus for three days. The reduced porosity of material **III** is probably due to the inclusion of borate ions within the pores during the reduction reaction. However, TEM and XRD experiments with material **III** confirm that the regular hexagonal structure of the silica framework is not affected. The sorption isotherms of materials **I**–**III** are presented in Figure 4.

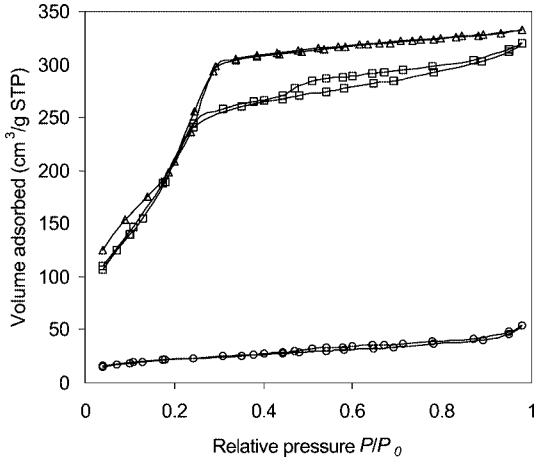


Figure 4. $N_2$ sorption curves of materials **I** (Δ), **II** (□) and **III** (○).

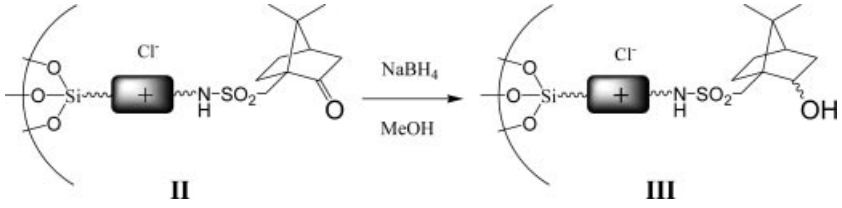


Scheme 3. Reduction of the immobilized camphorsulfonamide entities.

 © 2006 Wiley-VCH Verlag GmbH & Co. KGaA, Weinheim 

Table 2. Enantioselective addition of diethylzinc to benzaldehyde.[a]

| Entry | Used chiral auxiliary | Conversion[b] | *ee*[c] | Ref. |
|---|---|---|---|---|
| 1 | Material **II** | >99% | 3% | this study |
| 2 | 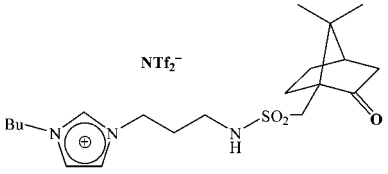 | >99% | 40% | [15] |
| 3 | Material **III** | >99% | 30% | this study |
| 4 | 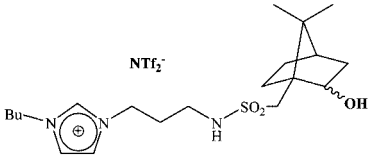 | >99% | 50% | [15] |
| 5 | Material **III**, second cycle | 95% | no selectivity detected | this study |

[a] General reaction conditions: benzaldehyde:ligand:Ti(O*i*Pr)$_4$:Et$_2$Zn = 1.0:0.1:1.1:1.2 (molar ratio), reaction time 18 h, reaction temperature 25 °C. [b] Determined by $^1$H NMR spectroscopy. [c] Determined by HPLC using a Daicel Chiralcel OD column.

### Heterogeneous Asymmetric Catalysis Using the Functional Organosilicas

The use of catalysts supported on mesoporous silica has been studied intensively.[19,20] Our interest in organic-inorganic hybrid materials as heterogeneous auxiliaries in asymmetric catalysis[21–23] led us to investigate materials **II** and **III**, which contain imidazolium substructures, as chiral auxiliaries in the asymmetric addition of diethylzinc to benzaldehyde. We also compared the catalytic properties of **II** and **III** with similar imidazolium salts bearing camphor or borneol substructures in homogeneous catalysis. The results of the utilisation of the various chiral auxiliaries in the addition of diethylzinc to benzaldehyde[24,25] (Scheme 4) are shown in Table 2.

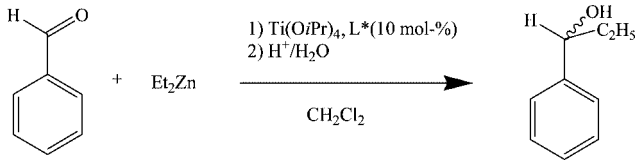


Scheme 4. Addition of diethylzinc to benzaldehyde.

Materials **II** and **III** act as catalytic auxiliaries and lead to the formation of 1-phenylpropanol in quantitative yield (entries 1 and 3) after hydrolytic work-up with hydrochloric acid (1 N). Despite its low porosity, material **III** shows a higher enantioselectivity than material **II**. However, the selectivities of both materials are lower than those obtained with the related imidazolium salts in homogeneous solution, thus indicating a limited complexation of the catalytic Ti$^{IV}$ species by the immobilised chiral camphorsulfonamide entities (entries 2 and 4). The reduced enantioselectivities obtained with silica-immobilised camphorsulfonamide ligands are probably due to the reaction being catalysed by Ti$^{IV}$ species in a nonchiral environment, for example by Ti(*i*OPr)$_4$ in homogeneous solution or by Ti$^{IV}$ species grafted onto the silica surface via Si–O–Ti bonds. Furthermore, material **III** appears to be of low recyclability. The second utilisation still gave high conversion, but no enantioselectivity was observed. We conclude therefore that the acidic work-up after the first reaction cycle strongly modifies the surface of the material by condensing oxidic Ti and Zn species, thus inhibiting the accessibility of the immobilised chiral ligand.

## Conclusion

We have shown the formation of highly ordered mesoporous silica with a hexagonal architecture containing chiral camphorsulfonamide substructures located in the pores. Both ionic and non-ionic precursors lead to the formation of highly structured materials with hexagonal symmetry. The high structuration of the materials can be explained by the high affinity of the silylated camphorsulfonamides towards the organised micellar phase of the surfactants in aqueous medium: the trialkoxysilylated camphorsulfonamides behave as co-surfactants and fit in the micellar arrangement of the hexadecylpyridinium chloride.[26] The ionic imidazolium substructure of precursor **3** does not show a significant effect during the template-directed hydrolysis polycondensation: material **II** does not show a higher structural regularity than material **I**. The utilisation of these functional organosilicas as chiral auxiliaries in asymmetric catalysis indicated inferior catalytic properties of the materials compared to related task-specific imidazolium salts in terms of selectivity and recyclability. These results are probably due to incomplete complexation of the titanium-based complexes to the camphorsulfonamide sites; considerable amounts of titanium may be linked to the silica support by covalent Si–O–Ti bonds.

To the best of our knowledge, material **II** is the first example of a chiral ionic substructure grafted onto a nano-

 © 2006 Wiley-VCH Verlag GmbH & Co. KGaA, Weinheim 

structured silica support. We believe that these highly porous functionalised materials may find applications in molecular recognition, in particular as chiral stationary phases in liquid chromatography.

## Experimental Section

**General:** All reactions were performed under nitrogen or argon using Schlenk-tube techniques when necessary. Elemental analyses were performed by the "Service Central de Microanalyse du CNRS" at Vernaison, France. Mass spectra were measured with a Jeol JMS-DX300 mass spectrometer. FT-IR spectra were recorded from KBr pellets or films with a Perkin–Elmer 1000 FT-IR spectrometer. $^1$H, $^{13}$C and $^{29}$Si liquid NMR spectra were recorded with a Bruker AC-250 spectrometer. $CDCl_3$ and [$D_6$]DMSO were used as NMR solvents. Chemical shifts are reported as $\delta$ values in ppm relative to TMS. $^{13}$C and $^{29}$Si CP MAS solid-state NMR spectra were recorded with a Bruker FT AM 400 FT-NMR spectrometer. Specific surface areas were determined by nitrogen adsorption/desorption experiments using a Micromeritics Gemini 2375 apparatus. TEM was performed with a Jeol 1200EX II electron microscope. X-ray diffraction measurements and data treatment were performed at the Groupe de Dynamique de Phases Condensées at the University of Montpellier 2. The X-ray diffraction experiments were carried out on solid powders in glass capillaries (1 mm diameter) in a transmission configuration. A copper rotating anode X-ray source (4 kW) with a multilayer focusing "Osmic" monochromator giving high flux ($10^8$ photons per second) and a pinhole collimation was employed. An "image plate" 2D detector was used, and the data obtained were radially averaged to yield the diffracted intensity as a function of the wave vector $q$. The diffracted intensity was corrected for exposure time, transmission and the background scattering arising from an empty capillary. The enantiomeric excess of 1-phenylpropanol was determined by chiral HPLC using a Waters 515 HPLC pump with a Waters 2487 UV detector and a Daicel Chiralcel OD column using a hexane/2-propanol mixture as eluent. All reagents were obtained from commercial sources and used without purification. In experiments requiring dry solvents, THF, toluene and diethyl ether were distilled from sodium/benzophenone, DMF was distilled from $CaH_2$, dichloromethane was distilled from $P_2O_5$ and alcohols were distilled from Mg. *C*-(7,7-Dimethyl-2-oxobicyclo[2.2.1]heptan-1-yl)-*N*-(3-imidazol-1-ylpropyl)-methanesulfonamide (**2**) was synthesised as described before.[15]

**Synthesis of the Trialkoxysilylated Precursors**

**1-(7,7-Dimethyl-2-oxobicyclo[2.2.1]heptan-1-yl)-*N*-[3-(triethoxysilyl)-propyl]methanesulfonamide (1):** (+)-Camphor-10-sulfonyl chloride (1 g, 4 mmol), (3-aminopropyl)triethoxysilane (0.9 g, 4 mmol) and triethylamine (0.45 g, 4.5 mmol) were stirred in dichloromethane (10 mL) at room temperature for 6 h. After completion, dichloromethane was evaporated and the resulting residue was extracted with diethyl ether. After evaporation of the solvent, the product was obtained as a colourless oil. Yield: 1.66 g (95%). $^1$H NMR ($CDCl_3$): $\delta$ = 0.68 (m, 2 H), 0.92, 1.04 (2 s, 6 H, 2×$CH_3$), 1.23 (t, $J$ = 7.1 Hz, 9 H), 1.4–1.5 (m, 1 H), 1.72 (m, 2 H), 1.85–2.45 (m, 6 H), 2.91 (d, $J$ = 14.6 Hz, 1 H), 3.17 (m, 2 H), 3.41 (d, $J$ = 14.6 Hz, 1 H), 3.83 (q, $J$ = 7.1 Hz, 6 H), 5.42 (broad t, 1 H) ppm. $^{13}$C NMR ($CDCl_3$): $\delta$ = 7.9, 18.6, 19.9, 20.2, 24.0, 26.7, 27.4, 43.1, 43.2, 46.4, 48.9, 49.6, 58.8, 59.4, 216.9 ppm. FT-IR (film): $\tilde{\nu}$ = 3288 cm$^{-1}$, 2973, 2888, 1746, 1330, 1147, 1079. HRMS [FAB+]: calcd. for $C_{19}H_{38}NO_6SSi$ [M + H]$^+$ 436.2189; found 436.2193.

**1-[3-(2-Hydroxy-7,7-dimethylbicyclo[2.2.1]hept-1-ylmethylsulfonylamino)propyl]-3-(3-triethoxysilyl)propyl-1*H*-imidazol-1-ium Chloride (3):** Under argon, 1 g (2.94 mmol) of **2** was dissolved in toluene (20 mL) and 3-chloropropyltriethoxysilane (0.71 g, 2.94 mmol) was added whilst stirring. The reaction mixture was heated to 80 °C during 48 h. After cooling to room temperature, the biphasic mixture was washed with diethyl ether (3×30 mL). Finally, the ether-insoluble layer was dried under reduced pressure. The product was obtained as a highly viscous yellow liquid. Yield: 1.60 g (94%). $^1$H NMR ($CDCl_3$): $\delta$ = 0.54 (m, 2 H), 0.84, 0.97 (2 s, 6 H, 2×$CH_3$), 1.15 (t, 9 = H, $J$ = 7.2 Hz), 1.38 (m, CH), 1.8–2.1 (m, 6 H, 3×$CH_2$), 2.29 (m, 4 H, 2×$CH_2$), 2.85 (d, $J$ = 15 Hz, 1 H), 3.11 (m, 2 H, $CH_2$), 3.33 (d, $J$ = 15 Hz, 1 H), 3.72 (q, $J$ = 7.2 Hz, 6 H), 4.17 (t, $J$ = 6.6 Hz, 2 H, $NCH_2$), 4.40 (t, $J$ = 6.8 Hz, 2 H), 6.40 (t, $J$ = 6.4 Hz, 1 H, NH), 7.68 (s, 2 H), 9.65 (s, 1 H) ppm. $^{13}$C NMR ($CDCl_3$): $\delta$ = 7.6, 14.4, 18.7, 20.0, 20.3, 20.7, 24.5, 26.1, 27.4, 30.7, 34.5, 40.2, 43.2, 47.6, 48.3, 52.4, 59.0, 122.3, 123.4, 137.0, 216.5 ppm. HRMS [FAB+]: calcd. for $C_{25}H_{46}N_3O_6SSi$ [M]$^+$ 544.2877; found 544.2859 (cation).

**Synthesis of the Materials:** Whilst stirring, the trialkoxysilylated precursor **1** or **3** was added to a solution of cetylpyridinium chloride in aqueous ammonia. The resulting mixture was vigorously stirred for 20 min at 30 °C. After this time, TEOS was added to the reaction mixture dropwise. The molar composition of the hydrolysis-polycondensation mixture was as follows: TEOS/**1**(**3**)/water/ammonia/hexadecylpyridinium chloride = 0.9:0.1:114:8:0.12. The resulting mixtures were heated to 80 °C for 48 h. The surfactant was removed by repeated washing with acidic ethanol and the materials were finally dried at 110 °C for 24 h.

**Material I:** $^{29}$Si CP MAS NMR: $\delta$ = –65.8, –101.5, –109.6 ppm. $^{13}$C CP MAS NMR: $\delta$ = 7.9, 18.1, 21.7–25.1, 42.6, 47.9, 58.7, 217.1 ppm. BET surface area: 832 m$^2$g$^{-1}$. FT-IR (KBr pellet): $\tilde{\nu}$ = 2969 cm$^{-1}$, 1640, 1224, 1067. Elemental analysis: C 15.83, H 2.87, N 1.56, S 2.73, Si 31.88.

**Material II:** $^{29}$Si CP MAS NMR: $\delta$ = –66.3, –101.0, –110.0 ppm. $^{13}$C CP MAS NMR: $\delta$ = 7.9, 21.9, 25.0, 42.9, 49.7, 58.3, 124.2, 133.7, 216.5 ppm. BET surface area: 759 m$^2$g$^{-1}$. FT-IR (KBr pellet): $\tilde{\nu}$ = 3452 cm$^{-1}$, 2973, 1738, 1636, 1225, 1146, 1071. Elemental analysis: C 18.23, H 3.20, N 3.26, S 2.50, Si 27.27.

**Material III:** The organosilica **II** (1.00 g) was suspended in methanol (10 mL) and cooled to 0 °C. Sodium borohydride (50 mg) was then added and the resulting mixture was stirred at this temperature for 2 h. The suspension was then filtered. The resulting residue was extracted in a Soxhlet apparatus with acidified ethanol for 72 h and finally dried at 110 °C for 24 h. Yield: 960 mg. $^{29}$Si CP MAS NMR: $\delta$ = –66.1, –100.0, –109.1 ppm. $^{13}$C CP MAS NMR: $\delta$ = 8.0, 19.0, 29.6, 45.5, 48.6, 49.8, 124.0, 134.0. BET surface area: 82 m$^2$g$^{-1}$. FT-IR (KBr pellet): $\tilde{\nu}$ = 3458 cm$^{-1}$, 2961, 1645, 1225, 1065. Elemental analysis: C 17.84, H 3.31, N 3.20, S 2.66, Si 26.73.

**General Procedure for the Addition of Diethylzinc to Benzaldehyde:** The functional organosilica was placed in a Schlenk tube and dried under vacuum at 100 °C dfor 1 h. After cooling to room temperature, dichloromethane (10 mL) and Ti(*i*OPr)$_4$ (313 mg, 1.1 mmol) were added to the solid. The resulting suspension was stirred at room temperature for 1 h. After this time, diethylzinc (1.2 mL of a 1 M solution in hexanes) was added and the mixture was stirred for another 15 min. Finally, after the addition of benzaldehyde (100 μL, 1 mmol), the suspension was stirred for 18 h at room temperature. The reaction mixture was then filtered and the residue was washed with dichloromethane. 1 mL of ethanol was added to the filtrate, which was completely hydrolysed by the addition of 15 mL of hydrochloric acid (1 N). Extraction of the solution with dichloromethane, drying and evaporation afforded the reaction products, which were analysed in order to determine the conversion

 © 2006 Wiley-VCH Verlag GmbH & Co. KGaA, Weinheim 

and the enantiomeric excess. The recovered organosilica was dried at 100 °C under reduced pressure.

## Acknowledgments

The authors thank Dr. P. Dieudonné for XRD measurements and fruitful discussions. V. P. gratefully acknowledges the French "Ministère de la Recherche" for a postdoctoral fellowship.

[1] C. T. Kresge, M. E. Leonowicz, W. J. Roth, J. C. Vartuli, J. S. Beck, *Nature* **1992**, *359*, 710.
[2] A. Stein, B. J. Melde, R. C. Schroeden, *Adv. Mater.* **2000**, *12*, 1403–1419.
[3] G. J. de A. A. Soler-Illia, C. Sanchez, B. Lebeau, J. Patarin, *Chem. Rev.* **2002**, *102*, 4093–4138.
[4] M. H. Lim, A. Stein, *Chem. Mater.* **1999**, *11*, 3285–3295.
[5] S. L. Burkett, S. D. Sims, S. Mann, *Chem. Commun.* **1996**, 1367–1368.
[6] C. E. Fowler, S. L. Burkett, S. Mann, *Chem. Commun.* **1997**, 1769–1770.
[7] B. Gadenne, P. Hesemann, J. J. E. Moreau, *Chem. Commun.* **2004**, 1768–1769.
[8] C. P. Mehnert, *Chem. Eur. J.* **2005**, *11*, 50–56.
[9] C. P. Mehnert, E. J. Mozeleski, R. A. Cook, *Chem. Commun.* **2002**, 3010–3011.
[10] C. P. Mehnert, R. A. Cook, N. C. Dispenziere, M. Afeworki, *J. Am. Chem. Soc.* **2002**, *124*, 12932–12933.
[11] H. Hagiwara, Y. Sugawara, T. Hoshi, T. Suzuki, *Org. Lett.* **2004**, *6*, 2325–2358.
[12] R. Ciriminna, P. Hesemann, J. J. E. Moreau, M. Carraro, S. Campestrini, M. Pagliaro, *Chem. Eur. J.* **2006**, *12*, 5220–5224.
[13] L. C. Branco, J. G. Crespo, C. A. M. Afonso, *Angew. Chem. Int. Ed.* **2002**, *41*, 2771.
[14] S.-J. Liu, F. Zhou, L. Zhao, X.-H. Xiao, X. Liu, S.-X. Jiang, *Chem. Lett.* **2004**, *33*, 496–497.
[15] B. Gadenne, P. Hesemann, J. J. E. Moreau, *Tetrahedron Lett.* **2004**, *45*, 8157–8160.
[16] D. J. Ramón, M. Yus, *Angew. Chem. Int. Ed.* **2004**, *43*, 284–287 and references cited therein.
[17] B. Lee, H.-J. Im, H. Luo, E. W. Hagaman, S. Dai, *Langmuir* **2005**, *21*, 5372–5376.
[18] M. Kruk, M. Jaroniec, *Chem. Mater.* **2001**, *13*, 3169–3183.
[19] D. Brunel, A. C. Blanc, A. Galarneau, F. Fajula, *Catal. Today* **2002**, *73*, 139–152 and references cited therein.
[20] A. Sayari, S. Hamoudi, *Chem. Mater.* **2001**, *13*, 3151–3168.
[21] A. Adima, J. J. E. Moreau, M. Wong Chi Man, *J. Mater. Chem.* **1997**, *7*, 2331–2333.
[22] P. Hesemann, J. J. E. Moreau, *Tetrahedron: Asymmetry* **2000**, *11*, 2183–2194.
[23] A. Brethon, J. J. E. Moreau, M. Wong Chi Man, *Tetrahedron: Asymmetry* **2004**, *15*, 495–502.
[24] P. J. Walsh, *Acc. Chem. Res.* **2003**, *36*, 739.
[25] L. Pu, *Chem. Rev.* **2001**, *101*, 757–824.
[26] L. Nicole, C. Boissière, D. Grosso, P. Hesemann, J. J. E. Moreau, C. Sanchez, *Chem. Commun.* **2004**, 2312–2313.

Received: March 31, 2006
Published Online: August 3, 2006

 © 2006 Wiley-VCH Verlag GmbH & Co. KGaA, Weinheim 

DOI: 10.1002/ejic.200600295

# Lanthanide(III) Double-Decker Complexes with Octaphenoxy- or Octathiophenoxyphthalocyaninato Ligands – Revealing the Electron-Withdrawing Nature of the Phenoxy and Thiophenoxy Groups in the Double-Decker Complexes

**Guifen Lu,[a] Ming Bai,[a] Renjie Li,[a] Xianxi Zhang,[a] Changqin Ma,[a] Pui-Chi Lo,[b] Dennis K. P. Ng,[b] and Jianzhuang Jiang*[a]**

**Keywords:** Phthalocyanine / Rare earth / Double-decker / Phenoxy group / Thiophenoxy group

A series of heteroleptic and homoleptic bis(phthalocyaninato) lanthanide(III) complexes, namely M(Pc)[Pc(OPh)$_8$], M[Pc(OPh)$_8$]$_2$, Eu(Pc)[Pc(SPh)$_8$], and Eu[Pc(SPh)$_8$]$_2$ [M = Eu, Ho, Lu; Pc = unsubstituted phthalocyaninate; Pc(OPh)$_8$ = 2,3,9,10,16,17,23,24-octaphenoxyphthalocyaninate; Pc(SPh)$_8$ = 2,3,9,10,16,17,23,24-octathiophenoxyphthalocyaninate] (**1**–**8**) have been prepared. The molecular structure of Eu[Pc(OPh)$_8$]$_2$ (**4**) has been determined by single-crystal X-ray diffraction analysis. All of the new sandwich compounds have been characterized with various spectroscopic methods. Their electrochemical characteristics show that the introduction of phenoxy or thiophenoxy groups onto the peripheral positions of the phthalocyaninato ligand makes the double-decker harder to oxidize and easier to reduce than the analogous compounds without the (thio)phenoxy group. Theoretical calculations, with the semi-empirical PM3 method, indicate that the change in the energy level of the frontier orbitals of these ligands induced by the electron-withdrawing substituents is responsible for these unusual electrochemical properties.
(© Wiley-VCH Verlag GmbH & Co. KGaA, 69451 Weinheim, Germany, 2006)

## Introduction

It is well established that bis(phthalocyaninato) metal complexes can serve as molecular materials for electronic devices such as semiconductors, visual displays, and field-effect transistors because of their intriguing electrical and optical properties.[1–3] As the bulk characteristics of molecular materials are closely related to the properties of individual molecules, various modifications have been made on these sandwich compounds with the goal to improve their performance as advanced materials. To facilitate the solution processing fabrication and formation of various mesophases and supramolecular structures, long alkyl chains, oxyethylene chains, or crown-ether units are usually added onto the peripheral or non-peripheral positions of the macrocyclic ligands.[1–3] However, to the best of our knowledge, there has been no report on double-decker complexes that contain phthalocyanine ligands substituted with eight bulky phenoxy groups at either the peripheral or non-peripheral positions. In this paper, we describe the synthesis, structure, spectroscopic, and electrochemical properties of a new series of eight homoleptic and heteroleptic lanthanide(III) complexes with octa-β-phenoxy or thiophenoxy phthalocyaninato ligands. Schematic structures of these compounds are shown in Figure 1.

It is worth noting that the electronic nature of the phenoxy and thiophenoxy groups has been a point of debate. They are usually regarded as an electron-donating group because of their similarity to the alkoxy or thioalkoxy groups,[4] but they can also act as an electron-withdrawing group depending on the nature of the group connected to these substituents.[5] In the present case, electrochemical studies showed that the introduction of eight phenoxy or thiophenoxy groups on the peripheral positions of the phthalocyaninato ligands slightly hinders the oxidation and facilitates the reduction of the resulting double-decker complexes. Similar results have also been previously observed for the metal-free 2(3),9(10),16(17),23(24)-tetraphenoxyphthalocyanine and 2,3,9,10,16,17,23,24-octaphenoxyphthalocyanine.[6] The results also revealed the electron-withdrawing nature of these substituents in the double-decker complexes. This was in agreement with the calculations on the frontier molecular orbitals of the metal-free phthalocyaninato ligands $H_2Pc$, $H_2Pc(OPh)_8$, and $H_2Pc(SPh)_8$.

[a] Department of Chemistry, Shandong University, Jinan 250100, China
Fax: +86-531-8856-5211
E-mail: jzjiang@sdu.edu.cn
[b] Department of Chemistry, The Chinese University of Hong Kong, Shatin, N.T., Hong Kong, China
Supporting information for this article is available on the WWW under http://www.eurjic.org or from the author.

 © 2006 Wiley-VCH Verlag GmbH & Co. KGaA, Weinheim 

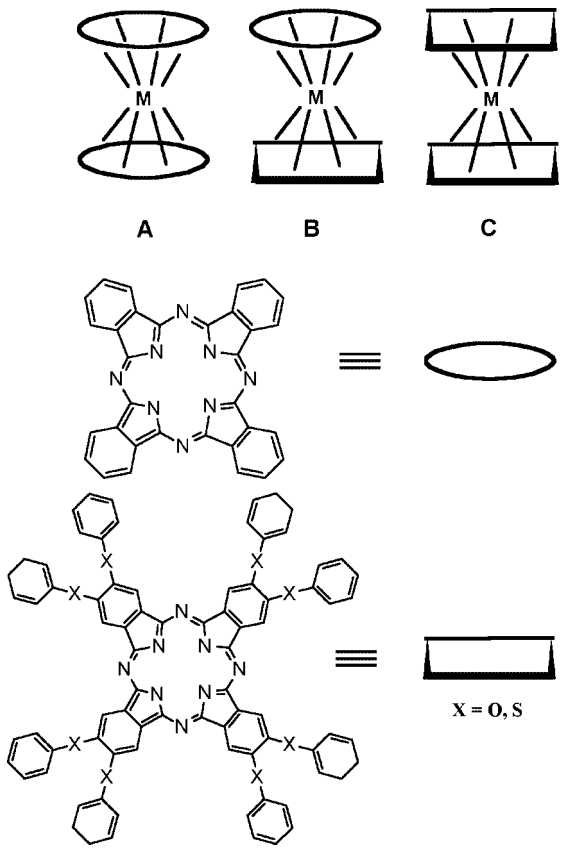


Figure 1. Schematic structures of bis(phthalocyaninato) lanthanide(III) complexes.

## Results and Discussion

### Synthesis

A substantial number of bis(phthalocyaninato)rare earth complexes have been synthesized and characterized.[1–3] A classical method for the preparation of homoleptic sandwich compounds involves the self-cyclic tetramerization of phthalonitriles in the presence of metal salts, whereas the heteroleptic analogues are usually prepared by the treatment of a rare earth acetate with two different lithium phthalocyaninates.[7–9] To facilitate the preparation and purification, in the present work, heteroleptic double-deckers M(Pc)[Pc(OPh)$_8$] (M = Eu, Ho, Lu) (**1**–**3**) and Eu(Pc)[Pc(SPh)$_8$] (**7**) were obtained by cyclic tetramerization of the corresponding disubstituted phthalonitriles with the half-sandwich compounds M(Pc)(acac) as the template in refluxing *n*-pentanol in the presence of 1,8-diazabicyclo[5.4.0]undec-7-ene (DBU).[10] It is worth mentioning that half-sandwich phthalocyaninato rare earth complexes M(Pc)(acac) were usually prepared by the reaction of M(acac)$_3$·*n*H$_2$O with Li$_2$Pc.[1b,1c] We found that M(Pc)(acac) could be easily synthesized and isolated by the treatment of M(acac)$_3$·*n*H$_2$O with phthalonitrile and DBU in *n*-pentanol at 100 °C for a short period of time (1.5 h). This method could also be applied to substituted phthalonitriles for the preparation of M[Pc(OPh)$_8$](acac) and Eu[Pc(SPh)$_8$](acac) complexes.

For the purpose of comparative studies, homoleptic analogues M[Pc(OPh)$_8$]$_2$ (M = Eu, Ho, Lu) (**4**–**6**) and Eu[Pc(SPh)$_8$]$_2$ (**8**) were also synthesized by the general cyclic tetramerization method.

### Spectroscopic Characterization

Satisfactory elemental analyses (Table 1) were obtained for both the heteroleptic and homoleptic double-decker complexes **1**–**8**, which had been repeatedly purified by column chromatography and recrystallization. These new sandwich compounds were also characterized with a range of spectroscopic methods. The MALDI-TOF mass spectra of **1**–**8** showed an intense cluster corresponding to the molecular ion (M$^+$); these data are also given in Table 1.

The electronic absorption data of this series of compounds were measured in CHCl$_3$ and are compiled in Table 2. Typical electronic absorption spectra of heteroleptic and homoleptic bis(phthalocyaninato)rare earth(III) complexes were observed for these newly prepared compounds, and the bands could therefore be assigned in a similar manner. Figure 2 displays the electronic absorption spectra of Eu(Pc)[Pc(OPh)$_8$] (**1**) and Eu[Pc(OPh)$_8$]$_2$ (**4**) as typical examples of the heteroleptic and homoleptic series, together with that of the unsubstituted Eu(Pc)$_2$. Compared with the unsubstituted analogues, almost all of the absorptions of M(Pc)[Pc(OPh)$_8$] (**1**–**3**) and Eu(Pc)[Pc(SPh)$_8$] (**7**) were redshifted when one Pc ring was replaced by the substituted ligand Pc(OPh)$_8$ or Pc(SPh)$_8$. Further redshifts were observed in the electronic absorption spectra of

Table 1. Analytical and mass spectroscopic data for double-decker complexes **1**–**8**.[a]

| Compound | M$^+$ [*m*/*z*][b] | Analysis [%] | | |
|---|---|---|---|---|
| | | C | H | N |
| Eu(Pc)[Pc(OPh)$_8$] (**1**) | 1913.5 (1913.4) | 69.79 (70.28) | 3.32 (3.38) | 11.72 (11.71) |
| Ho(Pc)[Pc(OPh)]$_8$ (**2**) | 1927.9 (1926.8) | 69.51 (69.29) | 3.50 (3.50) | 11.52 (11.44)[c] |
| Lu(Pc)[Pc(OPh)$_8$] (**3**) | 1937.8 (1936.8) | 67.45 (67.68) | 3.46 (3.26) | 11.25 (11.23)[c] |
| Eu[Pc(OPh)$_8$]$_2$ (**4**) | 2651.7 (2651.6) | 71.95 (72.49) | 3.77 (3.66) | 8.36 (8.47) |
| Ho[Pc(OPh)$_8$]$_2$ (**5**) | 2664.2 (2663.5) | 70.52 (70.79) | 3.71 (3.57) | 8.27 (8.23)[c] |
| Lu[Pc(OPh)$_8$]$_2$ (**6**) | 2674.2 (2673.6) | 71.87 (71.88) | 3.76 (3.62) | 8.48 (8.38)[c] |
| Eu(Pc)[Pc(SPh)$_8$] (**7**) | 2042.3 (2042.3) | 64.96 (65.06) | 3.27 (3.13) | 11.05(10.82)[c] |
| Eu[Pc(SPh)$_8$]$_2$ (**8**) | 2907.4 (2907.6) | 65.03 (64.97) | 3.48 (3.28) | 7.76 (7.55) |

[a] Calculated values given in parentheses. [b] By MALDI-TOF mass spectrometry. The value corresponds to the most abundant isotopic peak of the molecular ion (M$^+$). [c] For **2**·CH$_3$OH, **3**·1/2CHCl$_3$, **5**·1/2CHCl$_3$, **7**·1/4CHCl$_3$, and **8**·1/2CHCl$_3$.

 © 2006 Wiley-VCH Verlag GmbH & Co. KGaA, Weinheim 

Table 2. Electronic absorption data for double-decker complexes **1**–**8** in $CHCl_3$.

| Compound | $\lambda_{max}$ [nm] (log $\varepsilon$) | | | | | | | |
|---|---|---|---|---|---|---|---|---|
| Eu(Pc)[Pc(OPh)$_8$] (**1**) | 326 (5.15) | 350 (5.02) | 485 (4.54) | 609 (4.63) | 676 (5.27) | 909 (3.70) | 1399 (3.94) | 1612 (4.18) |
| Ho(Pc)[Pc(OPh)]$_8$ (**2**) | 323(5.11) | 349(4.99) | 472(4.50) | 604(4.59) | 669(5.31) | 917(3.76) | 1410(4.18) | 1609(3.93) |
| Lu(Pc)[Pc(OPh)$_8$] (**3**) | 321(5.11) | 347(5.02) | 466(4.52) | 600(4.57) | 665(5.34) | 913(3.85) | 1410(4.19) | 1526(3.82) |
| Eu[Pc(OPh)$_8$]$_2$ (**4**) | 331 (5.20) | 365 (5.17) | 500 (4.58) | 614 (4.76) | 681 (5.34) | 909 (3.79) | – | 1654 (4.05) |
| Ho[Pc(OPh)$_8$]$_2$ (**5**) | 328(5.13) | 362(5.14) | 492(4.53) | 608(4.68) | 674(5.33) | 917(3.81) | 1410(4.28) | 1617(4.07) |
| Lu[Pc(OPh)$_8$]$_2$ (**6**) | 326(5.15) | 361(5.18) | 484(4.58) | 605(4.69) | 670(5.39) | 911(3.92) | 1410(4.28) | 1526(4.01) |
| Eu(Pc)[Pc(SPh)$_8$] (**7**) | 327(5.08) | – | 452(4.54) | 624(4.68) | 694(5.25) | 924(3.62) | 1658(4.11) | 1858(3.87) |
| Eu[Pc(SPh)$_8$]$_2$ (**8**) | 311(5.12) | 341(5.09) | 450(4.72) | 646(4.88) | 715(5.23) | 949(3.71) | 1847(5.00) | 2030(4.12) |

M[Pc(OPh)$_8$]$_2$ (**4**–**6**) and Eu[Pc(SPh)$_8$]$_2$ (**8**) as a result of the replacement of the second Pc ring by Pc(OPh)$_8$ or Pc(SPh)$_8$ (Table 2). It is worth noting that in comparison with those of the alkoxy-substituted bis(phthalocyaninato)europium counterparts, namely Eu(Pc)[Pc(OC$_5$H$_{11}$)$_8$][10a] and Eu[Pc(OC$_5$H$_{11}$)$_8$]$_2$,[10d] a significant redshift takes place in the main absorption band in the near IR range of the thiophenoxy-substituted double-decker compounds **7** and **8**. In contrast, an insignificant shift was observed for the same band of phenoxy-substituted double-decker compounds **2** and **3**.

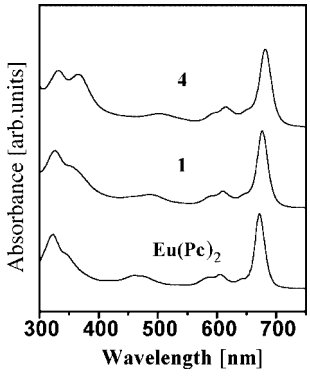


Figure 2. UV/Vis spectra of Eu(Pc)$_2$, Eu(Pc)[Pc(OPh)$_8$] (**1**), and Eu[Pc(OPh)$_8$]$_2$ (**4**) in $CHCl_3$.

IR spectroscopy is a very useful tool for the characterization of the phthalocyaninato ligand in sandwich tetrapyrrole complexes.[11] The IR spectra of **1**–**8** shows a medium-to-strong band in the range of 1317–1326 cm$^{-1}$, as observed for M(Pc)$_2$ (M = Eu, Ho, Lu), which is a diagnostic marker band for the phthalocyanine π-radical anions Pc$^{\bullet-}$, [Pc(OPh)$_8$]$^{\bullet-}$, and [Pc(SPh)$_8$]$^{\bullet-}$.

Upon the addition of hydrazine hydrate as a reducing agent,[12,13] well-resolved $^1$H NMR spectra were obtained for the reduced form of bis(phthalocyaninato)lanthanide(III) complexes **1**–**8**, in which both the macrocyclic ligands become diamagnetic dianions. Figure 3 shows the $^1$H NMR spectrum of the reduced form of **7**. For this heteroleptic compound, the non-peripheral and peripheral protons of the unsubstituted phthalocyaninato ligand resonate at $\delta$ = 11.08 and 9.09 ppm, respectively, as two relatively broad signals, whereas the non-peripheral protons of the substituted phthalocyanine ring resonate as a singlet at $\delta$ = 10.79 ppm. Three well-resolved signals at $\delta$ = 8.79–8.82 (doublet), 8.29–8.34 (triplet), and 8.07–8.12 (triplet) ppm in the ratio of 2:2:1 are shown for the thiophenoxy *ortho*, *meta*, and *para* protons, respectively. The observation of only one group of signals for the pairs of *ortho* and *meta* protons of the thiophenoxy group suggests that the thiophenoxy group is relatively free to rotate along the C$_{ipso}$–S bond in the double-decker complex under these conditions. Similar results were observed for phenoxy analogues **1**–**6**. This is in contrast to the restricted rotation of the aryl groups of *meso*-tetraarylporphyrinato ligands in double-decker complexes M(Por)(Ring) [Por = *meso*-tetrakis(4-chlorophenyl)porphyrinate (TClPP), *meso*-tetrakis(4-*tert*-butylphenyl)porphyrinate (TBPP); Ring = general phthalocyaninate (Pc′), general naphthalocyaninate (Nc′)].[12,14,15] This could be due to the lower steric hindrance of the additional *O*/*S* atom.

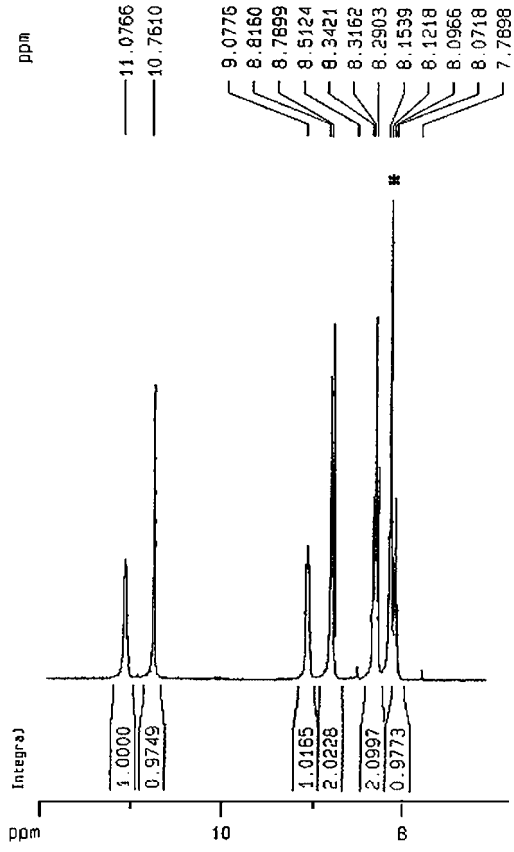


Figure 3. $^1$H NMR spectrum of the reduced form of Eu(Pc)[Pc(SPh)$_8$] (**7**) in $CDCl_3$/[D$_6$]DMSO (1:1) which contains ca. 1% hydrazine hydrate; * indicates residual $CHCl_3$.

 © 2006 Wiley-VCH Verlag GmbH & Co. KGaA, Weinheim 

### Structural Studies

Single crystals of Eu[Pc(OPh)$_8$]$_2$ (**4**) for X-ray diffraction analysis were obtained by the slow diffusion of MeOH into a THF solution of this compound. Unfortunately, the quality of the crystals was not high enough to obtain a suitable X-ray structure. Even when the data were collected at –150 °C, the $R_1$ value (0.1854) was still relatively high. This might be related to the disorder of the phenoxy groups. According to this set of data, the compound crystallizes in the orthorhombic system with eight double-decker molecules per unit cell. Figure S1 (Supporting Information) shows the molecular structure of **4** from two different perspectives. The europium center is octa-coordinated by the isoindole nitrogen atoms of the two octaphenoxyphthalocyaninato ligands with an average Eu–N bond length of 2.439 Å, and forms a square antiprism. The two $N_4$ mean planes are virtually parallel (dihedral angle = 0.4°) with a plane-to-plane separation of 2.851 Å with the europium atom lying in the center between the two ligands. In a similar structure to that of other bis(tetrapyrrole)rare earth double-decker complexes, such as Ce(Pc)(TPyP),[12] the two ligands are not planar and display a saucer shape. The extent of ligand deformation, as defined by the average dihedral angle $\varphi$ of the individual isoindole rings with respect to the corresponding $N_4$ mean plane, is 7.2°. The twist angle, which is defined as the rotation angle of one ring away from the eclipsed conformation of the two rings, is close to 45° for this complex; this shows that the two ligands are almost fully staggered. This staggered orientation probably acts to minimize the nonbonding interactions between the two substituted phthalocyanines.

### Electrochemical Properties

The electrochemical behavior of compounds **1**–**8** was examined by cyclic voltammetry (CV) and by differential pulse voltammetry (DPV), and the results are summarized in Table 3. For comparison, the data for the unsubstituted analogue Eu(Pc)$_2$ were also listed.[16] For all these complexes, one to two quasi reversible one-electron oxidation(s) and four to five quasi reversible one-electron reductions were revealed. The first oxidation and the first reduction processes involve the removal of an electron from and the addition of an electron to the singly occupied molecular orbital, respectively. Comparison of the first oxidation potentials and the first reduction potentials among the set M(Pc)$_2$, M(Pc)[Pc(OPh)$_8$], and M[Pc(OPh)$_8$]$_2$, and among the set Eu(Pc)$_2$, Eu(Pc)[Pc(SPh)$_8$], and Eu[Pc(SPh)$_8$]$_2$, reveals that the incorporation of the eight phenoxy or thiophenoxy groups on the phthalocyanine ring makes the compounds slightly harder to oxidize and easier to reduce than the analogous compounds without the (thio)phenoxy group. These results are in contrast to those found for alkoxy- or alkyl-substituted phthalocyanines, which clearly reveal the electron-withdrawing nature of these phenoxy and thiophenoxy substituents on the phthalocyaninato ligand.[16]

According to our calculations on the frontier molecular orbitals, with the semi-empirical PM3 method, the introduction of eight phenoxy or thiophenoxy groups on the peripheral positions of the phthalocyaninato ligand results in a decrease in the energy of the HOMO of the macrocycle ligand (Figure 4). As a result, these substituents at the peripheral positions of the phthalocyaninato ligand act mainly as electron-withdrawing groups and make this macrocyclic ligand harder to oxidize and easier to reduce.

On the basis of previous discussions, the interactions between the two rings of the monomer cause a splitting of their π-HOMO and π-LUMO, which results in a decrease in the energy of the HOMO and LUMO of the bis(phthalocyaninato)europium double-decker complexes.[16,17] This is supported by the experimental results. As shown in Table 3, the halfwave potentials for the first oxidation and reduction potentials (Oxd$_1$ and Red$_1$), which involve the HOMO of the double-decker complexes, are shifted in the more positive direction along with the increase in the number of Pc(OPh)$_8$ or Pc(SPh)$_8$ ligands from M(Pc)$_2$, M(Pc)[Pc(OPh)$_8$], to M[Pc(OPh)$_8$]$_2$ or from Eu(Pc)$_2$, Eu(Pc)[Pc(SPh)$_8$], to Eu[Pc(SPh)$_8$]$_2$, whereas the potentials for the second and third reductions, Red$_2$ and Red$_3$, which now involve the LUMO of these compounds, are also shifted in the positive direction in the same order.

The effect of the size of the rare earth metal is demonstrated, again, by the fact that the halfwave potentials for the first oxidation and for the first reduction of M(Pc)[Pc(OPh)$_8$] and M[Pc(OPh)$_8$]$_2$ are slightly shifted in the negative direction as the radius of the rare earth metal decreases in the order Eu, Ho, Lu (Table 3).[16]

Table 3. Halfwave redox potentials for double-decker complexes **1**–**8** in $CH_2Cl_2$ which contains 0.1 M [$NBu_4$][$ClO_4$].

| | $O_2$ | $O_1$ | $R_1$ | $R_2$ | $R_3$ | $R_4$ | $R_5$ | $\Delta E°_{1/2}$[b] |
|---|---|---|---|---|---|---|---|---|
| Eu(Pc)[Pc(OPh)$_8$] (**1**) | +1.61 | +0.63 | +0.20 | –1.00 | –1.31 | –1.67 | – | 0.43 |
| Ho(Pc)[Pc(OPh)]$_8$ (**2**) | – | +0.56 | +0.12 | –1.02 | –1.32 | –1.62 | –1.83[c] | 0.44 |
| Lu(Pc)[Pc(OPh)$_8$] (**3**) | +1.69 | +0.52 | +0.07 | –1.04 | –1.36 | –1.72 | – | 0.45 |
| Eu[Pc(OPh)$_8$]$_2$ (**4**) | +1.59 | +0.70 | +0.26 | –0.96 | –1.24 | –1.63 | – | 0.44 |
| Ho[Pc(OPh)$_8$]$_2$ (**5**) | +1.60 | +0.61 | +0.16 | –0.98 | –1.28 | –1.66 | – | 0.45 |
| Lu[Pc(OPh)$_8$]$_2$ (**6**) | +1.62 | +0.58 | +0.13 | –0.99 | –1.29 | –1.73 | – | 0.45 |
| Eu(Pc)$_2$[a] | +1.59 | +0.55 | +0.12 | –1.06 | –1.29 | –1.54[c] | –1.70[c] | 0.43 |
| Eu(Pc)[Pc(SPh)$_8$] (**7**) | +1.57 | +0.64 | +0.22 | –0.90 | –1.25 | –1.57 | –1.77[c] | 0.42 |
| Eu[Pc(SPh)$_8$]$_2$ (**8**) | +1.52 | +0.67 | +0.30 | –0.84 | –1.08 | –1.48[c] | –1.79[c] | 0.37 |

[a] Data taken from ref.[16]. [b] $\Delta E°_{1/2}$ is the potential difference between the first oxidation and the first reduction processes. [c] Recorded by DPV.

 © 2006 Wiley-VCH Verlag GmbH & Co. KGaA, Weinheim 

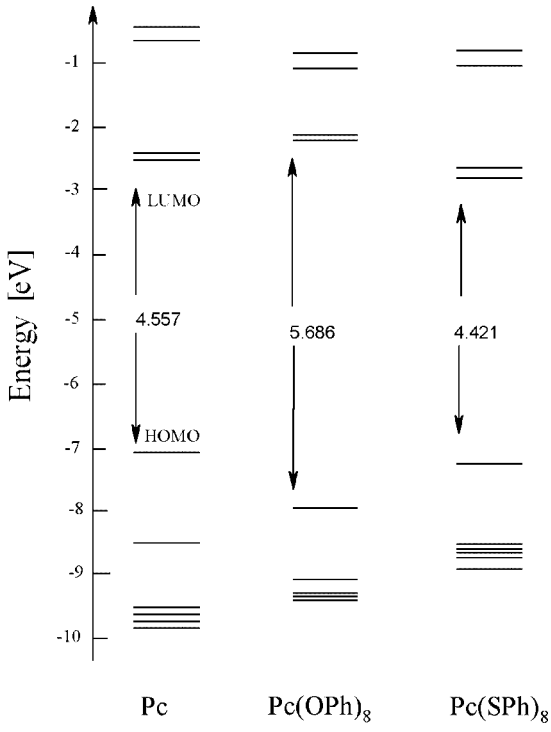


Figure 4. Partial energy diagram of $H_2Pc$, $H_2Pc(OPh)_8$, and $H_2Pc(SPh)_8$ obtained from theoretical calculations with the PM3 method.

## Conclusions

A series of lanthanide(III) double-decker complexes with the octaphenoxy- or octathiophenoxyphthalocyaninato ligand were synthesized and characterized. Their solution structures were investigated by $^1H$ NMR spectroscopy, which indicated that the phenoxy and thiophenoxy substituents are relatively free to rotate along the $C_{ipso}$–O or $C_{ipso}$–S bonds. Their electrochemical characteristics revealed that these substituents are electron-withdrawing when connected to the peripheral positions of the phthalocyanine ring. This conclusion was supported by the theoretical calculations on the energy levels of the frontier molecular orbitals of the corresponding phthalocyaninato ligands.

## Experimental Section

**General:** Hexanes and *n*-pentanol were distilled from anhydrous $CaCl_2$ and sodium, respectively. Phthalonitriles and the electrolyte $[Bu_4N][ClO_4]$ were recrystallized from toluene and acetone, respectively. Dichloromethane for voltammetric studies was freshly distilled from $CaH_2$ under a nitrogen atmosphere. Column chromatography was carried out on silica gel (Merck, Kieselgel 60, 70–230 mesh) with the indicated eluents. All other reagents and solvents were of reagent grade and used as received. The compounds $M(acac)_3{\cdot}nH_2O$,[18] 4,5-bis(phenoxy)phthalonitrile,[19] and 4,5-bis(thiophenoxy)phthalonitrile[19] were prepared according to the literature methods.

The UV/Vis and near-IR spectra were obtained with a Hitachi U-4100 spectrophotometer. IR spectra (KBr pellets) were recorded with a BIORAD FTS-165 spectrometer. MALDI-TOF mass spectra were recorded with a Bruker APEX47e ultra-high resolution Fourier transform ion cyclotron resonance (FT-ICR) mass spectrometer with α-cyano-4-hydroxycinnamic acid as the matrix. Elemental analyses were performed by the Institute of Chemistry, Chinese Academy of Sciences. $^1H$ NMR spectra were measured with a Bruker DPX 300 spectrometer in $CDCl_3$/[$D_6$]DMSO (1:1) in the presence of ca. 1% (by volume) hydrazine hydrate. Spectra were referenced internally with residual DMSO ($\delta$ = 2.49 ppm).

Electrochemical measurements were carried out with a BAS CV-50W voltammetric analyzer. The cell comprised inlets for a glassy carbon disk working electrode of 2.0 mm in diameter and a silver-wire counter electrode. The reference electrode was $Ag/Ag^+$, which was connected to the solution by a Luggin capillary whose tip was placed close to the working electrode. The electrode was corrected for junction potentials by being referenced internally to the ferrocenium/ferrocene ($Fe^+/Fe$) couple [$E_{1/2}$ ($Fe^+/Fe$) = 501 mV vs. SCE]. Typically, a 0.1 mol dm$^{-3}$ solution of $[Bu_4N][ClO_4]$ in $CH_2Cl_2$ containing 0.5 mmol dm$^{-3}$ of sample was purged with nitrogen for 10 min, the voltammograms were then recorded at ambient temperature. The scan rates were 20 and 10 mV s$^{-1}$ for CV and DPV, respectively.

The frontier molecular orbital energy calculations for unsubstituted and substituted phthalocyanines were carried out with the semi-empirical PM3 method.[20] The input structures of $H_2[Pc(OPh)_8]$ and $H_2[Pc(SPh)_8]$ were derived from the optimized geometry of metal free $H_2Pc$.[21] All calculations were carried out with the Gaussian98W program.[22]

**X-ray Crystallography:** Crystal data and details of data collection and structure refinement for **3** are given in Table S1 (Supporting Information). Data were collected with a Bruker SMART CCD diffractometer with an Mo-$K_\alpha$ sealed tube ($\lambda$ = 0.71073 Å) at –150 °C, with a $\omega$ scan mode and an increment of 0.3°. Preliminary unit cell parameters were obtained from 300 frames. Final unit cell parameters were derived by global refinements of reflections obtained from the integration of all the frame data. The collected frames were integrated with the preliminary cell-orientation matrix. The SMART software was used for collecting frames of data, indexing reflections and determination of lattice constants; SAINT-PLUS for integration of intensity of reflections and scaling;[23] SADABS for absorption correction;[24] and SHELXL for space group and structure determination, refinements, graphics and structure reporting.[25] All the H atoms in these compounds were obtained geometrically. These H atoms were included in the subsequent least-squares refinement as fixed contributors. The final refinement with anisotropic temperature factors for non-H atoms led to R = 0.1854 for compound **4**.

**General Procedure for the Preparation of Heteroleptic M(Pc)[Pc(OPh)$_8$] (1–3) and Eu(Pc)[Pc(SPh)$_8$] (7):** A mixture of $M(acac)_3{\cdot}nH_2O$ (93 mg, 0.20 mmol), phthalonitrile (102 mg, 0.80 mmol), and DBU (20 mg, 0.13 mmol) in *n*-pentanol (3 mL) was heated at 100 °C for 1.5 h under a slow stream of nitrogen to yield the half-sandwich compound M(Pc)(acac). The resulting blue solution was cooled to room temperature. The crude product was precipitated by the addition of hexanes into the solution and purified by chromatography with $CHCl_3$/MeOH (1:1) as the eluent (94 mg, 48%). The obtained product, M(Pc)(acac) (76 mg, 0.10 mmol), was mixed with DBU (20 mg, 0.13 mmol) and 4,5-bis(phenoxy)phthalonitrile (124 mg, 0.40 mmol) or 4,5-bis(thiophenoxy)phthalonitrile (137 mg, 0.40 mmol) in *n*-pentanol (3 mL), and the resulting mixture was heated at reflux for 8 h. The volatiles were removed under reduced pressure to afford a dark green residue which was chromatographed with $CHCl_3$/MeOH (9:1) as the

 © 2006 Wiley-VCH Verlag GmbH & Co. KGaA, Weinheim 

eluent. A small amount of metal-free phthalocyanine $H_2Pc(OPh)_8$ or $H_2Pc(SPh)_8$ was collected first, and then the heteroleptic product M(Pc)[Pc(OPh)$_8$] or Eu(Pc)[Pc(SPh)$_8$] was developed. Repeated chromatography followed by recrystallization from $CHCl_3$ and MeOH afforded pure M(Pc)[Pc(OPh)$_8$] (**1**–**3**) or Eu(Pc)[Pc(SPh)$_8$] (**7**) as a darkish-blue powder with a yield of ca. 30%. It is noteworthy that these heteroleptic double-decker complexes could also be prepared from the reaction of M[Pc(OPh)$_8$](acac) or M[Pc(SPh)$_8$](acac) with phthalonitrile by the same procedure.

**Eu(Pc)[Pc(OPh)$_8$] (1):** 56 mg, 28%. $^1$H NMR (300 MHz, $CDCl_3$/[D$_6$]DMSO): $\delta$ = 11.22–11.28 (m, 8 H, Pc-H), 10.67 (s, 8 H, Pc*-H), 9.00–9.06 (m, 8 H, Pc-H), 8.46 (d, $J$ = 7.8 Hz, 16 H, Ph-H$_o$), 8.22 (t, $J$ = 7.8 Hz, 16 H, Ph-H$_m$), 7.80 (t, $J$ = 7.8 Hz, 18 H, Ph-H$_p$) ppm.

**Ho(Pc)[Pc(OPh)$_8$] (2):** 53 mg, 26%. $^1$H NMR (300 MHz, $CDCl_3$/[D$_6$]DMSO): $\delta$ = 4.17 (s, 18 H, Ph-H$_p$), 3.85 (s, 16 H, Ph-H$_m$), 0.34 (s, 16 H, Ph-H$_o$), –1.71 (br. s, 8 H, Pc-H), –8.98 (br. s, 8 H, Pc-H or Pc*-H), –10.26 (br. s, 8 H, Pc-H or Pc*-H) ppm.

**Lu(Pc)[Pc(OPh)$_8$] (3):** 61 mg, 29%. $^1$H NMR (300 MHz, $CDCl_3$/[D$_6$]DMSO): $\delta$ = 9.02 (s, 8 H, Pc-H), 8.39 (s, 8 H, Pc*-H), 8.06 (s, 8 H, Pc-H), 7.74 (s, 16 H, Ph-H$_o$), 7.55 (s, 16 H, Ph-H$_m$), 7.43 (s, 18 H, Ph-H$_p$) ppm.

**Eu(Pc)[Pc(SPh)$_8$] (7):** 64 mg, 30%. $^1$H NMR (300 MHz, $CDCl_3$/[D$_6$]DMSO): $\delta$ = 11.08 (s, 8 H, Pc-H), 10.76 (s, 8 H, Pc*-H), 9.08 (s, 8 H, Pc-H), 8.82 (d, $J$ = 7.8 Hz, 16 H, Ph-H$_o$), 8.29 (t, $J$ = 7.6 Hz, 16 H, Ph-H$_m$), 8.12 (t, $J$ = 7.5 Hz, 18 H, Ph-H$_p$) ppm.

**General Procedure for the Preparation of Homoleptic M[Pc(OPh)$_8$]$_2$ (4–6) and Eu[Pc(SPh)$_8$]$_2$ (8):** A mixture of M(acac)$_3$·$n$H$_2$O (47 mg, 0.10 mmol), 4,5-bis(phenoxy)phthalonitrile (248 mg, 0.80 mmol) or 4,5-bis(thiophenoxy)phthalonitrile (274 mg, 0.80 mmol), and DBU (20 mg, 0.13 mmol) in *n*-pentanol (3 mL) was heated at reflux for 8 h under a slow stream of nitrogen. The volatiles were removed under reduced pressure to give a dark green residue, which was chromatographed with $CHCl_3$ as the eluent. Repeated chromatography followed by recrystallization from $CHCl_3$ and MeOH afforded M[Pc(OPh)$_8$]$_2$ (**4**–**6**) or Eu[Pc(SPh)$_8$]$_2$ (**8**) as darkish-blue crystals with the yield of ca. 40%.

**Eu[Pc(OPh)$_8$]$_2$ (4):** 127 mg,43%. $^1$H NMR (300 MHz, $CDCl_3$/[D$_6$]-DMSO): $\delta$ = 10.79 (s, 16 H, Pc*-H), 8.00 (d, $J$ = 7.8 Hz, 32 H, Ph-H$_o$), 7.75 (t, $J$ = 7.8 Hz, 32 H, Ph-H$_m$), 7.43 (t, $J$ = 7.8 Hz, 16 H, Ph-H$_p$) ppm.

**Ho[Pc(OPh)$_8$]$_2$ (5):** 119 mg, 40%. $^1$H NMR (300 MHz, $CDCl_3$/[D$_6$]DMSO): $\delta$ = 4.65 (s, 16 H, Ph-H$_p$), 4.39 (s, 32 H, Ph-H$_m$), 1.04 (s, 32 H, Ph-H$_o$), –9.74 (s, 16 H, Pc*-H) ppm.

**Lu[Pc(OPh)$_8$]$_2$ (6):** 107 mg, 36%. $^1$H NMR (300 MHz, $CDCl_3$/[D$_6$]DMSO): $\delta$ = 8.58 (s, 16 H, Pc*-H), 7.41 (t, $J$ = 7.7 Hz, 32 H, Ph-H$_o$), 7.19 (t, $J$ = 8.5 Hz, 32 H, Ph-H$_m$), 7.13 (s, 16 H, Ph-H$_p$) ppm.

**Eu[Pc(SPh)$_8$]$_2$ (8):** 135 mg, 42%. $^1$H NMR (300 MHz, $CDCl_3$/[D$_6$]DMSO): $\delta$ = 10.47 (s, 16 H, Pc*-H), 8.24 (d, $J$ = 7.8 Hz, 32 H, Ph-H$_o$), 7.83 (t, $J$ = 7.6 Hz, 32 H, Ph-H$_m$), 7.68 (t, $J$ = 7.3 Hz, 16 H, Ph-H$_p$) ppm.

**Supporting Information** (see footnote on the first page of this article): Molecular structure of Eu[Pc(OPh)$_8$]$_2$ (**4**) from two different perspectives for all non-hydrogen atoms and crystallographic data for Eu[Pc(OPh)$_8$]$_2$ (**4**).

## Acknowledgments

Financial support from the National Science Foundation of China (Grant No. 20325105, 20431010), National Ministry of Science and Technology of China (Grant No. 2001CB6105–07), Ministry of Education of China, Shandong University, and The Chinese University of Hong Kong is gratefully acknowledged.

[1] a) J. Jiang, K. Kasuga, D. P. Arnold in *Supramolecular Photo-Sensitive and Electro-Active Materials* (Ed.: H. S. Nalwa), Academic Press, New York, **2001**, pp. 113–210; b) D. K. P. Ng, J. Jiang, K. Kasuga, K. Machida in *Handbook on the Physics and Chemistry of Rare Earths* (Eds.: K. A. Gschneidner Jr, L. Eyring, G. H. Lander), Elsevier, Amsterdam, **2001**, pp. 611–654; c) R. Weiss, J. Fischer in *The Porphyrin Handbook* (Eds.: K. M. Kadish, K. M. Smith, R. Guilard), Academic Press, San Diego, **2003**, vol. 16, pp. 172–246; d) Y. Chen, W. Su, M. Bai, J. Jiang, X. Li, Y. Liu, L. Wang, S. Wang, *J. Am. Chem. Soc.* **2005**, *127*, 15700–15701.
[2] J. Jiang, W. Liu, D. P. Arnold, *J. Porphyrins Phthalocyanines* **2003**, *7*, 459–473.
[3] D. K. P. Ng, J. Jiang, *Chem. Soc. Rev.* **1997**, *26*, 433–442.
[4] a) K. H. Yew, H. J. Koh, H. W. Lee, I. Lee, *J. Chem. Soc., Perkin Trans. 2* **1995**, 2263–2268; b) T. Itoh, R. Noki, S. Simosato, I. Magara, S. Iwatsuki, *J. Polym. Sci., Part A: Polym. Chem.* **1995**, *33*, 1475–1485.
[5] U. Diefenbach, H. R. Allcock, *Inorg. Chem.* **1994**, *33*, 4562–4565.
[6] R. Li, X. Zhang, P. Zhu, D. K. P. Ng, N. Kobayashi, J. Jiang, *Inorg. Chem.* **2006**, *45*, 2327–2334.
[7] A. Pondaven, Y. Cozien, M. L′Her, *New J. Chem.* **1991**, *15*, 515–516.
[8] A. Pondaven, Y. Cozien, M. L′Her, *New J. Chem.* **1992**, *16*, 711–718.
[9] a) F. Guyon, A. Pondaven, P. Guenot, M. L′Her, *Inorg. Chem.* **1994**, *33*, 4787–4793; b) C. Cadiou, A. Pondaven, M. L′Her, P. Jéhan, P. Guenoy, *J. Org. Chem.* **1999**, *64*, 9046–9050; c) L. Gaimiche, F. Guyon, A. Pondaven, J.-Y. Moisan, M. L′Her, *J. Porphyrins Phthalocyanines* **2003**, *7*, 382–387.
[10] a) J. Jiang, W. Liu, W. Law, J. Lin, D. P. Arnold, *Inorg. Chim. Acta* **1998**, *268*, 141–144; b) J. Jiang, J. Xie, M. T. M. Choi, D. K. P. Ng, *J. Porphyrins Phthalocyanines* **1999**, *3*, 322–328; c) Y. Bian, R. Wang, J. Jiang, C.-H. Lee, J. Wang, D. K. P. Ng, *Chem. Commun.* **2003**, 1194–1195; d) J. Jiang, R. C. W. Liu, T. C. W. Mak, T. W. D. Chan, D. K. P. Ng, *Polyhedron* **1997**, *16*, 515–520.
[11] a) J. Jiang, D. P. Arnold, H. Yu, *Polyhedron* **1999**, *18*, 2129–2139; b) X. Sun, M. Bao, N. Pan, X. Cui, D. P. Arnold, J. Jiang, *Aust. J. Chem.* **2002**, *9*, 587–595; c) F. Lu, M. Bao, C. Ma, X. Zhang, D. P. Arnold, J. Jiang, *Spectrochim. Acta, Part A* **2003**, *59*, 3273–3286; d) M. Bao, N. Pan, C. Ma, D. P. Arnold, J. Jiang, *Vib. Spectrosc.* **2003**, *32*, 175–184; e) M. Bao, Y. Bian, L. Rintoul, R. Wang, D. P. Arnold, C. Ma, J. Jiang, *Vib. Spectrosc.* **2004**, *34*, 283–291; f) J. Jiang, M. L. Rintoul, D. P. Arnold, *Coord. Chem. Rev.* **2006**, *250*, 424–448.
[12] Y. Bian, J. Jiang, Y. Tao, M. T. M. Choi, R. Li, A. C. H. Ng, P. Zhu, N. Pan, X. Sun, D. P. Arnold, Z. Zhou, H.-W. Li, D. K. P. Ng, *J. Am. Chem. Soc.* **2003**, *125*, 12257–12267.
[13] J. Jiang, Y. Bian, F. Furuya, W. Liu, M. T. M. Choi, N. Kobayashi, H.-W. Li, Q. Yang, T. C. W. Mak, D. K. P. Ng, *Chem. Eur. J.* **2001**, *7*, 5059–5069.
[14] J. Jiang, W. Liu, K.-L. Cheng, K.-W. Poon, D. K. P. Ng, *Eur. J. Inorg. Chem.* **2001**, 413–417.
[15] F. Lu, X. Sun, R. Li, D. Liang, P. Zhu, X. Zhang, C.-F. Choi, D. K. P. Ng, T. Fukuda, N. Kobayashi, J. Jiang, *New J. Chem.* **2004**, *28*, 1116–1122.
[16] P. Zhu, F. Lu, N. Pan, D. P. Arnold, S. Zhang, J. Jiang, *Eur. J. Inorg. Chem.* **2004**, 510–517.
[17] a) E. Orti, J. L. Bredas, *J. Chem. Phys.* **1990**, *92*, 1228–1235; b) N. Ishikawa, *J. Porphyrins Phthalocyanines* **2001**, *5*, 87–101.
[18] J. G. Stites, C. N. McCarty, L. L. Quill, *J. Am. Chem. Soc.* **1948**, *70*, 3142–3143.
[19] D. Wohrle, M. Eskes, K. Shigehara, A. Yamada, *Synthesis* **1993**, 194–196.

 © 2006 Wiley-VCH Verlag GmbH & Co. KGaA, Weinheim 

[20] a) J. J. P. Stewart, *J. Comput. Chem.* **1989**, *10*, 209–220; b) J. J. P. Stewart, *J. Comput. Chem.* **1989**, *10*, 221–264.
[21] X. Zhang, Y. Zhang, J. Jiang, *J. Mol. Struct. THEOCHEM* **2004**, *673*, 103–108.
[22] M. J. Frisch et al., Gaussian-98, Revision A.9, Gaussian, Inc., Pittsburgh PA, 1998.
[23] SMART and SAINT for Windows NT Software Reference Manuals, Version 5.0, Bruker Analytical X-ray Systems, Madison, WI, **1997**.
[24] G. M. Sheldrick, SADABS – A Software for Empirical Absorption Correction, University of Göttingen, **1997**.
[25] SHELXL Reference Manual, Version 5.1, Bruker Analytical X-ray Systems, Madison, WI, **1997**.

Received: April 3, 2006
Published Online: August 1, 2006

 © 2006 Wiley-VCH Verlag GmbH & Co. KGaA, Weinheim 

DOI: 10.1002/ejic.200600306

# Syntheses, Structural, and Physical Studies of Basic $Cr^{III}$ and $Fe^{III}$ Benzilates and Benzoates: Evidence of Antisymmetric Exchange and Distributions of Isotropic and Antisymmetric Exchange Parameters

**Vassilios Psycharis,*[a] Catherine P. Raptopoulou,[a] Athanassios K. Boudalis,[a] Yiannis Sanakis,[a] Michael Fardis,[a] George Diamantopoulos,[a] and George Papavassiliou[a]**

*Dedicated to Professor Jean-Pierre Tuchagues on the occasion of his 65th birthday*

**Keywords:** Trinuclear oxo-centered chromium(III) and iron(III) complexes / Magnetic properties / Crystal structures / EPR spectroscopy / Mössbauer spectroscopy

The synthesis, crystal structures, spectroscopic and magnetic properties studies of four trinuclear oxo-centered carboxylate complexes are reported and discussed: $[Cr_3(\mu_3\text{-}O)\{O_2C(OH)Ph_2\}_6(H_2O)_3](NO_3)\cdot 2H_2O\cdot 3Me_2CO$ (**1**·$2H_2O$·$3Me_2CO$), $[Cr_3(\mu_3\text{-}O)(O_2CPh)_6(H_2O)_3](NO_3)\cdot 1.9MeCN\cdot 0.5H_2O$ (**2**·1.9MeCN·$0.5H_2O$), $[Fe_3(\mu_3\text{-}O)\{O_2C(OH)Ph_2\}_6(H_2O)_3](NO_3)\cdot 5.69H_2O$ (**3**·$5.69H_2O$), and $[Fe_3(\mu_3\text{-}O)(O_2CPh)_6(H_2O)_3](NO_3)\cdot 3MeCN$ (**4**·3MeCN). From a crystallographic point of view, the three metal ions form an isosceles triangle in **1** and **3** (benzilato complexes) and an almost equilateral one in **2** and **4** (benzoato complexes). Magnetic susceptibility measurements reveal metal-dependent isotropic exchange, for the $Cr^{III}$ clusters (**1**, **2**), with the "magnetic symmetry" resembling that of an almost equilateral triangle. For the $Fe^{III}$ clusters the "magnetic symmetry" resembles that of an isosceles triangle. Solid-state $^1H$ NMR studies for **1**, through the measurements of the temperature variation of the relaxation rate $1/T_1$, reveal that the first excited spin state with $S_T = 3/2$ is well above (ca. 30 $cm^{-1}$) the ground state with $S_T = 1/2$, consistent with the magnetic susceptibility data. Mössbauer spectroscopic studies give a larger quadrupole splitting, $\Delta E_Q$, value for **3** than for **4**, because of a larger charge asymmetry in **3** attributed to the different nature of the carboxylato ligands. EPR experiments at X-band reveal the presence of antisymmetric exchange within the $Cr^{III}$ clusters and distributions of both isotropic and antisymmetric exchange interactions. In the case of **2** the magnitude and distribution of these interactions are greater. EPR spectroscopy for **3** suggests weak interactions between neighboring units, which could be described assuming a dimer of trimers. For complex **4** the EPR spectra indicate a more complicated picture.

(© Wiley-VCH Verlag GmbH & Co. KGaA, 69451 Weinheim, Germany, 2006)

## Introduction

One of the reasons for the extensive study of trinuclear oxo-centered metal carboxylate assemblies (also known as "basic carboxylates") of the general formula $[M^{III}_3O(O_2CR)_6L_3]^+$ (M = 3d metal ion, L = monodentate terminal ligand) is that they serve as simple systems for the study of magnetic and electronic interactions between transition-metal ions.[1–5] Additional interest originates from the fact that they are used as precursors for the synthesis of higher nuclearity clusters exhibiting interesting magnetic properties.[6,7] Such clusters are also studied because they serve as models for the building blocks of polynuclear cores in proteins[8] and in the case of $Cr^{III}$ complexes, for their biological activity.[9]

Magnetic susceptibility studies have been performed for many "basic carboxylates",[3] and at least in the 200–300 K temperature range[1] they are well understood within the framework of the Heisenberg–Dirac–van Vleck (HDvV) isotropic spin Hamiltonian with antiferromagnetic interactions. Kambe[1] has interpreted the magnetic susceptibility data assuming that the exchange interactions within the triangle were all equal (equilateral model) or that one was different from the other two (isosceles model). The crystal structure for many trinuclear complexes reveals an equilateral configuration. Magnetostructural correlations suggest that the equilateral geometry would be appropriate for the description of the magnetic susceptibility data. However, even in highly symmetric cases the magnetic susceptibility measurements require the adoption of the isosceles configuration, in particular for the interpretation of the low-temperature properties of these systems.

The equilateral magnetic model leads to an energy-level diagram with a ground state consisting of two Kramers

[a] Institute of Materials Science, N.C.S.R. "Demokritos", 15310 Aghia Paraskevi, Athens, Greece

Supporting information for this article is available on the WWW under http://www.eurjic.org or from the author.

 InterScience © 2006 Wiley-VCH Verlag GmbH & Co. KGaA, Weinheim 

doublets. Lowering of the magnetic symmetry to the isosceles configuration indicated by the analysis of the magnetic susceptibility measurements has the consequence that these two doublets differ in energy. Experimental techniques such as heat capacity measurements[10] or inelastic neutron scattering[11,12] have confirmed the lift of the degeneracy of the ground state in consistency with a lower than equilateral geometry. In the case of $Fe^{III}$ complexes, Mössbauer spectroscopy at liquid helium temperatures and in the presence of external magnetic fields has led to the same conclusions; the spectra obtained could not be analyzed within the framework of equilateral configuration. Instead, the spectra were reproduced by assuming lower symmetry and in some cases a scalene configuration was considered more appropriate.[13]

In order to interpret the lifting of the ground-state fourfold degeneracy, a variety of models with different physical origins has been suggested. An early model introduced the concept of the magnetic Jahn–Teller effect, within which the ground state of the system, occupied at low temperatures, adopts an isosceles rather than an equilateral configuration.[14] An isotropic model involving dynamic distortions has been suggested[15] and the results are comparable to those obtained from Kambe's static isosceles model. Other models are based on Hamiltonians that include non-Heisenberg terms and retaining, or not, the $D_3$ symmetry of the cluster. These are biquadratic,[16] anisotropic,[16] and antisymmetric exchange.[2,4,5,17–23] Their appearance is generally associated with spin-orbit coupling and has been adequately described.[20]

Compelling evidence for the role of antisymmetric exchange in trinuclear clusters has been provided by EPR spectroscopy. Within the context of isotropic Heisenberg interactions the $S = 1/2$ ground state would give rise to EPR spectra characterized by the anisotropy of the intrinsic $g$-tensors of the single ions. In the case of $Cr^{III}$ and $Fe^{III}$ complexes this intrinsic anisotropy is small and spectra confined in a narrow region at $g \approx 1.9$–$2.0$ are expected. However, the observed spectra from many clusters exhibit significant $g$-anisotropy, and resonances with $g$ values significantly smaller ($g_{eff} < 1.7$) than those expected are observed.[18,19] Involvement of the antisymmetric exchange term has led to a successful interpretation of this behavior. Similarly, unexpectedly large anisotropies attributed to antisymmetric exchange have been recently observed in trinuclear $Cu^{II}$ complexes[24] and are also frequently encountered in $[3Fe4S]^{1+}$ clusters in proteins.[25]

In some cases analysis of the X-band EPR spectra suggests that, apart from the role of antisymmetric exchange, the role of distributions of the Heisenberg and non-Heisenberg exchange coupling parameters is also of special importance.[25–27] Such distributions have also been implied from Mössbauer studies in the case of $Fe^{III}$ complexes.[13,25,28] Inelastic neutron scattering studies with the spectral characteristics at low temperature have been explained assuming that more than one triangular complex with different degrees of symmetry-lowering are present in the structure.[12]

In the present work, we study the effect of metal and ligand variation ($Cr^{III}$ vs. $Fe^{III}$ and benzilates vs. benzoates) on the structural and electronic (magnetic, spectroscopic) characteristics of "basic metal carboxylates". We present the syntheses and studies of the basic benzilates and benzoates $[Cr_3(\mu_3\text{-}O)\{O_2C(OH)Ph_2\}_6(H_2O)_3](NO_3)\cdot 2H_2O\cdot 3Me_2CO$ (**1**·$2H_2O$·$3Me_2CO$), $[Cr_3(\mu_3\text{-}O)(O_2CPh)_6(H_2O)_3](NO_3)\cdot 1.9MeCN\cdot 0.5H_2O$ (**2**·1.9MeCN·$0.5H_2O$), $[Fe_3(\mu_3\text{-}O)\{O_2C(OH)Ph_2\}_6(H_2O)_3](NO_3)\cdot 5.69H_2O$ (**3**·$5.69H_2O$), and $[Fe_3(\mu_3\text{-}O)(O_2CPh)_6(H_2O)_3](NO_3)\cdot 3MeCN$ (**4**·3MeCN). In particular we present structural, magnetic and X-band EPR data for **1**–**4**, Mössbauer spectroscopic data for **3** and **4** and solid-state NMR spectroscopic data for **1**. This is a continuation of our work on $Cr^{III}$[26] and $Fe^{III}$[27,29–31] complexes exhibiting phenomena like spin frustration, antisymmetric exchange, and $J$-strain, studied with spectroscopic techniques such as EPR.

## Results and Discussion

### Syntheses

Most $Cr^{III}$ "basic carboxylate" complexes have in general been prepared by complicated synthetic routes yielding intractable solids or liquids.[3] $Fe^{III}$ "basic carboxylates" have been prepared by reaction of a $Fe^{III}$ salt with the appropriate sodium carboxylate in aqueous solutions, yielding amorphous solids. In any case, pure crystalline products could not be isolated without recrystallization from organic solvents. Thus, we have reacted $Cr^{III}$ and $Fe^{III}$ salts with the appropriate carboxylic acid or sodium salt directly in organic solvents and we have isolated the corresponding "basic carboxylates" in crystalline form following a straightforward and simple synthetic procedure.

The balanced chemical equations for the synthesis of the "basic benzilates" ($Cr^{III}$: **1**, $Fe^{III}$: **3**) and the "basic benzoates" ($Cr^{III}$: **2**, $Fe^{III}$: **4**) may be written in the forms of Equations (1) and (2) respectively. In every case it is assumed that $H_2O$ from the starting materials and/or the solvent is the source of the $O^{2-}$ ion.

$$3\,M(NO_3)_3\cdot 9\,H_2O + 6\,Ph_2C(OH)COOH \xrightarrow{Me_2CO\,(\mathbf{1}),\,CH_2Cl_2\,(\mathbf{3})} [M_3O\{O_2C(OH)Ph_2\}_6(H_2O)_3](NO_3) + 8\,HNO_3 + 23\,H_2O \quad M = Cr\,(\mathbf{1}),\,Fe\,(\mathbf{3}) \tag{1}$$

$$3\,M(NO_3)_3\cdot 9\,H_2O + 6\,PhCO_2Na \xrightarrow{MeCN\,(\mathbf{2},\mathbf{4})} [M_3O(PhCO_2)_6(H_2O)_3](NO_3) + 6\,NaNO_3 + 2\,HNO_3 + 23\,H_2O \quad M = Cr\,(\mathbf{2}),\,Fe\,(\mathbf{4}) \tag{2}$$

A point of synthetic interest is that for the carboxylates at hand, the use of the carboxylic acid (**1**/**3**) or the sodium carboxylate (**2**/**4**) have both led to the desired complexes.

 © 2006 Wiley-VCH Verlag GmbH & Co. KGaA, Weinheim 

Table 1. Selected bond lengths [Å] and angles [°] for **1**–**4**.[a]

| | 1 | 2 | 3 | 4 |
|---|---|---|---|---|
| M–$O_{oxo}$ | 1.904(3)–1.907(3) | 1.887(4)–1.899(4) | 1.893(6)–1.935(6) | 1.898(6)–1.908(7) |
| M–$O_{carboxylato}$ | 1.959(3)–1.990(3) | 1.947(4)–1.980(5) | 1.991(6)–2.036(7) | 1.977(8)–2.029(9) |
| M–$O_{H_2O}$ | 2.008(5)–2.024(5) | 2.025(5)–2.067(6) | 2.035(7)–2.133(6) | 2.082(8)–2.112(7) |
| M···M | 3.278(3)–3.314(3) | 3.276(4)–3.290(4) | 3.280(6)–3.333(6) | 3.290(8)–3.298(8) |
| M–$O_{oxo}$–M | 118.8(2)–120.9(2) | 119.3(2)–120.8(2) | 119.3(3)–121.1(3) | 119.6(4)–120.5(4) |

[a] M = Cr (**1**, **2**), Fe (**3**, **4**).

## Description of the Structures

### *General Remarks*

Compounds **1**–**4**, as members of the large family of "basic carboxylates" containing a central planar $[M_3(\mu_3\text{-}O)]^{7+}$ core and the carboxylato ligands, lie above and below this plane. The monodentate ligands are directed *trans* to the Fe–$O_{oxo}$ bonds. Their structural parameters are typical of "basic carboxylates" and will not be analyzed in detail. In the case of the benzilato complexes **1** and **3**, the triangles formed by the three metal ions are best described as isosceles, while in the benzoato complexes **2** and **4** the triangles formed are equilateral (within a few standard deviations). Selected bond lengths and angles for **1**–**4** are listed in Table 1, and the molecular structure of **1** is selectively shown in Figure 1. The most interesting feature in the structures of **1**–**4** is the presence of intermolecular interactions and the formation of 2D networks, which will be discussed in detail.

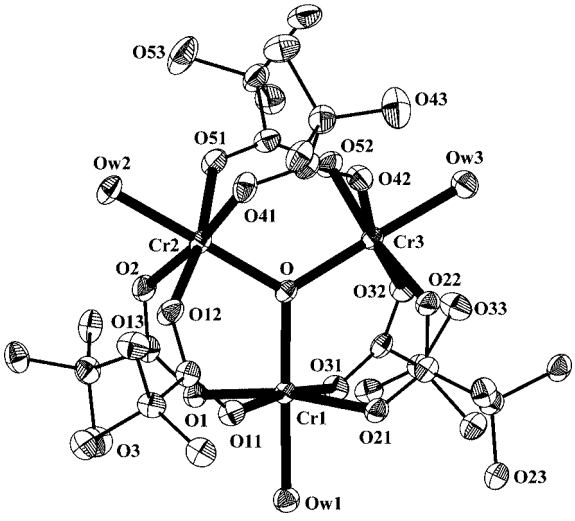


Figure 1. Partially labeled ORTEP plot of the cation of **1** with ellipsoids drawn at the 40% probability level. Only the *ipso* carbon atoms of the benzilato ligands are shown and hydrogen atoms have been omitted for clarity.

### *Lattice Structure of 1·2$H_2O$·3$Me_2CO$*

As shown in Figure 2, the cations of **1** are hydrogen-bonded through their aquo ligands [Ow(1), Ow(2) and Ow(3)] to the nitrate counterions and the solvate molecules [Ow(4), Ow(5) and acetone solvates]. In particular, the water solvate Ow(5) is the intermediate through which the trimers are connected to each other through the hydrogen bonds to Ow(2) and O(53) of one trimer [Ow(5)···O(w2) 2.642 Å, Ow(5)···O(53) 2.977 Å] and O(23) of a neighboring one [Ow(5)···O(23′) 2.809 Å (1 + *x*, *y*, *z*)] forming chains parallel to the *a* axis of the unit cell. The nitrate counterions link trimers belonging to neighboring chains resulting in the formation of layers extended along the *ab* plane [O(33)···O(62″) 3.001 Å (0.5 – *x*, –0.5 + *y*, 0.5 – *z*), Ow(3)···O(62″) 2.741 Å (0.5 – *x*, –0.5 + *y*, 0.5 – *z*), O(3)···O(61‴) 2.885 Å (*x*, –1 + *y*, *z*), Ow(1)···O(61‴) 2.659 Å (*x*, –1 + *y*, *z*)]. The three acetone and the second water solvate molecules are hydrogen-bonded to each other and to coordinated water molecules as well as to the hydroxy group of the benzilato ligands, thus further stabilizing the above-mentioned 2D network.

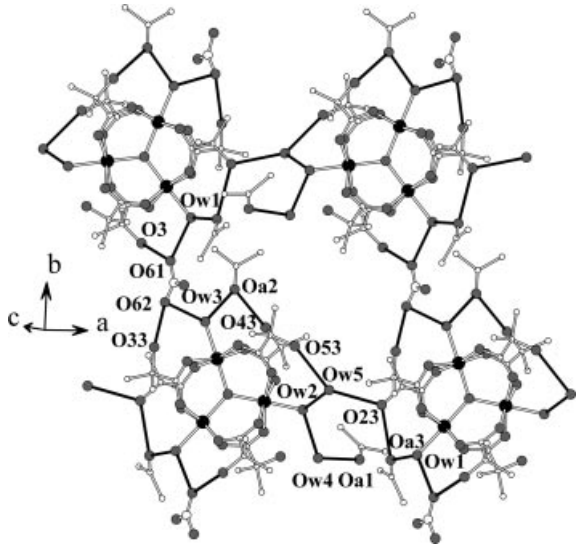


Figure 2. Plot of the 2D polymeric structure of **1** parallel to the *ab* plane. Hydrogen bonds are shown as thick black lines (only the *ipso* carbon atoms of the benzilato ligands are shown). Cr: black circles, O: dark gray, N: large open circles, C: small open circles.

### *Lattice Structure of 2·1.9MeCN·0.5$H_2O$*

The lattice structure of **2** due to hydrogen-bonding interactions is shown in Figure 3. The key feature is the presence of the nitrate counterion, which is hydrogen-bonded to the coordinated water molecules of three different trimers [O(61)···Ow(1′) 2.908 Å (–1 + *x*, *y*, *z*), O(62)···Ow(2″) 2.875 Å (*x*, –1 + *y*, *z*), O(63)···Ow(3) 2.901 Å]. Thus, a 2D network is formed that is parallel to the *ab* plane. The solvate molecules are hydrogen-bonded to each other and to coordinated water molecules but they do not contribute to

 © 2006 Wiley-VCH Verlag GmbH & Co. KGaA, Weinheim 

the formation of a further polymeric network (these interactions are not shown in Figure 3).

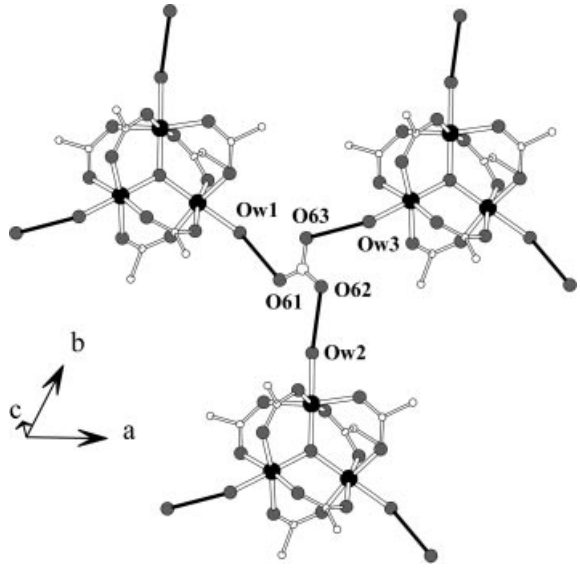


Figure 3. Plot of the 2D polymeric structure of **2** parallel to the *ab* plane. Hydrogen bonds are shown as thick black lines. (only the *ipso* carbon atoms of the benzoato ligands are shown). Cr: black circles, O: dark gray, N: large open circles, C: small open circles.

### *Lattice Structure of 3·5.69$H_2O$*

In the structure of **3**, the X-ray analysis could not reveal the hydrogen atoms of the aquo and benzilato ligands, thus only the intermolecular interactions will be considered for the formation of the lattice structure (Figure 4). Strong intermolecular interactions between O(53) of one trimer and O(13) and Ow(2) of a neighboring trimer [O(53)···O(13′) 2.917 Å (1.5 – *x*, 0.5 – *y*, 1 – *z*), O(53)···Ow(2′) 2.917 Å (1.5 – *x*, 0.5 – *y*, 1 – *z*)] are responsible for the formation of dimers of trimers. The presence of the nitrate counterions and the existence of strong intermolecular interactions [O(61)···Ow(1′′) 2.668 Å (–0.5 + *x*, 0.5 + *y*, *z*) and O(63)···Ow(3′′′) 2.612 Å (1 – *x*, *y*, 0.5 – *z*)] connects the dimers together and the final result is the formation of a 2D polymeric network parallel to the *bc* plane.

### *Lattice Structure of 4·3MeCN*

As in the case of **3**, the X-ray crystal structure analysis of **4** did not reveal the hydrogen atoms of the aquo ligands. Nevertheless, intermolecular interactions less than 3 Å with the nitrate counterions are considered as possible hydrogen-bonding interactions. In particular, the nitrate anions interact with three neighboring trimers [O(61)···Ow(3′) 2.890 Å (1 – *x*, –*y*, 1 – *z*), O(62)···Ow(1′′) 2.680 Å (0.5 – *x*, –0.5 + *y*, 1 – *z*), O(63)···Ow(2′′′) 2.798 Å (0.5 – *x*, 0.5 + *y*, 1 – *z*)], linking the trimers to form a 2D polymeric network parallel to the *ab* plane (Figure 5). The solvent molecules of crystallization also interact intermolecularly with the coordinated water molecules, but they do not contribute to a further development of the lattice structure (these interactions are not shown in Figure 5).

## Mössbauer Spectroscopy

Mössbauer spectra from solid powder samples of **3** and **4** were recorded at zero magnetic field in the 78–300 K temperature range. The spectra at 78 K are shown in Figure 6. Each compound gives rise to one doublet with the following values for the quadrupole interaction ($\Delta E_Q$) and the isomer shift ($\delta$): complex **3**, $\Delta E_Q$ = 0.65 mm s$^{-1}$, $\delta$ = 0.50 mm s$^{-1}$; complex **4**, $\Delta E_Q$ = 0.52 mm s$^{-1}$, $\delta$ = 0.52 mm s$^{-1}$. The values for the isomer shift are consistent with $Fe^{III}$ ($S$ = 5/2) in

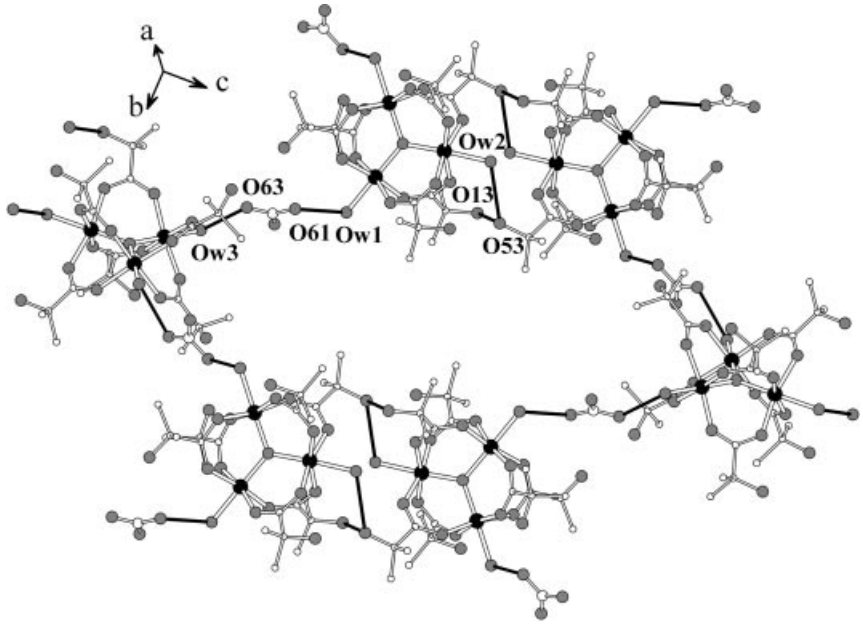


Figure 4. Plot of the 2D polymeric structure of **3** parallel to the *bc* plane. Hydrogen bonds are shown as thick black lines (only the *ipso* carbon atoms of the benzilato ligands are shown). Fe: black circles, O: dark gray, N: large open circles, C: small open circles.

 © 2006 Wiley-VCH Verlag GmbH & Co. KGaA, Weinheim 

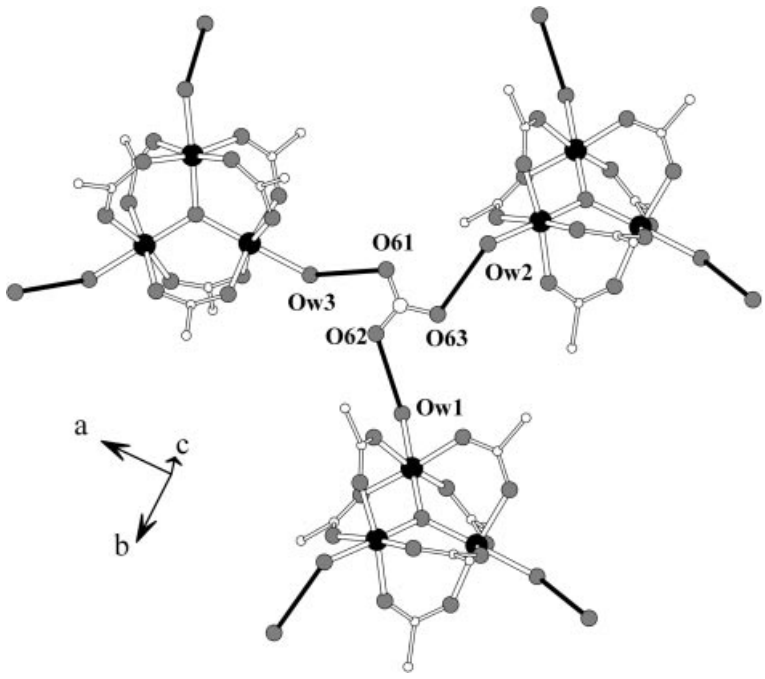


Figure 5. Plot of the 2D polymeric structure of **4** parallel to the *ab* plane. Hydrogen bonds are shown as thick black lines (only the *ipso* carbon atoms of the benzoato ligands are shown). Fe: black circles, O: dark gray, N: large open circles, C: small open circles.

an octahedral environment comprising O donors. The line widths are quite narrow (half width at half maximum 0.20 mm s$^{-1}$), indicating a homogeneous environment around the Fe$^{III}$ ions. Complex **3** is characterized by a larger value for $\Delta E_Q$ than complex **4**, indicating a larger electric field gradient (EFG) for the ferric sites for complex **3**. Inspection of the iron environments for the two compounds suggests that this larger EFG cannot be of geometrical origin; there are no systematic geometrical deviations between **3** and **4** for the ferric octahedra. The larger $\Delta E_Q$ for **3** may suggest, however, a larger charge asymmetry imposed by the different nature of the two carboxylates.

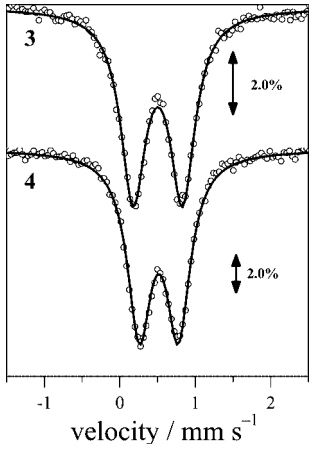


Figure 6. Zero-field Mössbauer spectra from solid powder samples of complexes **3** and **4** at 78 K.

## Magnetic Susceptibility Measurements

### *Cr$^{III}$ Complexes*

The $\chi_M T$ product at 300 K is 4.00 and 3.70 cm$^3$ mol$^{-1}$ K for **1** and **2** respectively, appreciably below the value anticipated for three noninteracting $S$ = 3/2 spins (5.61 cm$^3$ mol$^{-1}$ K), indicative of antiferromagnetic interactions (Figure 7). On cooling, this drops to 0.43 cm$^3$ mol$^{-1}$ K (for **1**) and 0.36 cm$^3$ mol$^{-1}$ K at 2 K (for **2**) not extrapolating to zero at 0 K, thus suggesting the existence of a paramagnetic impurity and/or a magnetic ground state. The $\chi_M$ versus $T$ plots show a gradual increase upon cooling, with a

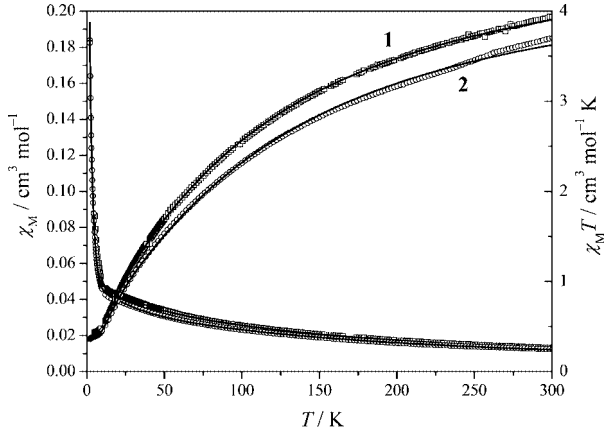


Figure 7. $\chi_M$ vs. $T$ and $\chi_M T$ vs. $T$ experimental data for complexes **1** (□) and **2** (○) and theoretical curves based on the Hamiltonian of Equation (4), using the parameters of solutions **1B** and **2B**, respectively.

 © 2006 Wiley-VCH Verlag GmbH & Co. KGaA, Weinheim 

more abrupt increase below 12 K, probably attributed to a paramagnetic impurity.

To fit the data, an initial model consisting of three equal $J$ values was considered, with the Hamiltonian being [Equation (3)]:

$$\hat{H} = -2J(\hat{S}_1\hat{S}_2 + \hat{S}_2\hat{S}_3 + \hat{S}_1\hat{S}_3) \quad (3)$$

where $S_i = 3/2$.

Assuming a small fraction of paramagnetic impurities, $\rho$, this model yielded satisfactory solutions with parameters $J = -10.3\ cm^{-1}$, $g = 1.87$, $\rho = 1.0\%$, and $R = 1.5\times10^{-5}$ for **1** (solution **1A**) and $J = -10.2\ cm^{-1}$, $g = 1.79$, $\rho = 0.8\%$, and $R = 3.8\times10^{-4}$ for **2** (solution **2A**). On further examining the system, a 2$J$ model was considered, in order to assess the validity of the previous results. The corresponding Hamiltonian was [Equation (4)]:

$$\hat{H} = -2[J(\hat{S}_1\hat{S}_2 + \hat{S}_1\hat{S}_3) + J'\hat{S}_2\hat{S}_3] \quad (4)$$

An examination of the parameter space for this model indicated the existence of two local minima (Figures S1 and S2, Supporting Information). On examining each, two solutions were obtained for complex **1**, with best-fit parameters $J = -10.6\ cm^{-1}$, $J' = -9.9\ cm^{-1}$, $g = 1.87$, $\rho = 0.98\%$, and $R = 1.3\times10^{-5}$ (**1B**) and $J = -10.1\ cm^{-1}$, $J' = -10.9\ cm^{-1}$, $g = 1.87$, $\rho = 0.98\%$, and $R = 1.3\times10^{-5}$ (**1C**). Similarly, two solutions were obtained for **2**, with best-fit parameters $J = -11.7\ cm^{-1}$, $J' = -9.6\ cm^{-1}$, $g = 1.82$, $\rho = 0.62\%$, and $R = 1.4\times10^{-4}$ (**2B**) and $J = -10.2\ cm^{-1}$, $J' = -12.9\ cm^{-1}$, $g = 1.82$, $\rho = 0.62\%$, and $R = 1.5\times10^{-4}$ (**2C**).

Solutions **1B**, **1C** and **2B**, **2C** are comparable in quality and only marginally better than solutions **1A** and **2A**, respectively. This small improvement of quality in the fits may stem from the fact that the isosceles model is more adequate, but might also be a result of overparametrization. This is further discussed below (see EPR Spectroscopy).

In order to further examine the validity of these results, the $M$ versus $H$ isotherms of **1** and **2** were measured and compared to the calculated ones, for each one of the solutions. In each case the magnetization isotherms were practically superimposable, and verified the data perfectly. Characteristic plots are shown in Figures S3 and S4 in the Supporting Information.

### *$Fe^{III}$ Complexes*

At 300 K the $\chi_M T$ product is 4.69 $cm^3\,mol^{-1}\,K$ for complex **3** and 3.67 $cm^3\,mol^{-1}\,K$ for complex **4**, significantly lower than the theoretically expected value for three noninteracting $S = 5/2$ spins (13.14 $cm^3\,mol^{-1}\,K$), indicating antiferromagnetic interactions (Figure 8). Upon cooling, the $\chi_M T$ product decreases without extrapolating to zero at 0 K, which also agrees with the interplay of antiferromagnetic interactions and a magnetic ground state.

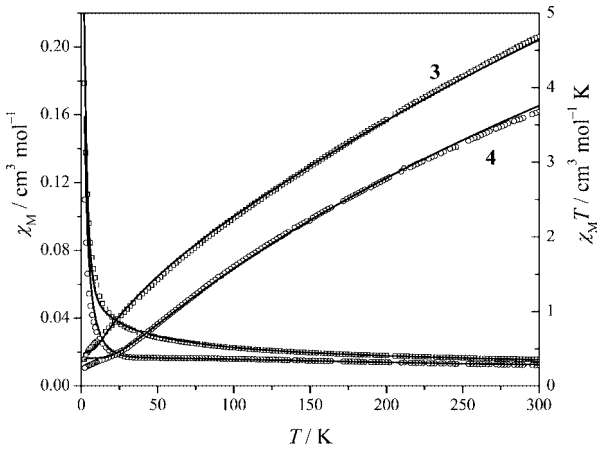


Figure 8. $\chi_M$ vs. $T$ and $\chi_M T$ vs. $T$ experimental data for complexes **3** (□) and **4** (○) and theoretical curves based on the Hamiltonian of Equation (4), using the parameters of solutions **3B** and **4C**, respectively.

Initial attempts to simulate the magnetic properties of complex **3** by considering a single $J$ interaction, viewing the complex as an equilateral triangle [Equation (3)], did not yield satisfactory results, so the Hamiltonian of Equation (4) was considered (with $S_i = 5/2$). From the fitting process two solutions of satisfactory quality were obtained, with a small amount of paramagnetic impurity, with their parameters being $J = -27.5\ cm^{-1}$, $J' = -20.5\ cm^{-1}$, $\rho = 0.36\%$, $g = 2.0$, and $R = 1.0\times10^{-3}$ (**3B**) and $J = -22.5\ cm^{-1}$, $J' = -32.6\ cm^{-1}$, $\rho = 0.35\%$, $g = 2.0$, and $R = 1.1\times10^{-3}$ (**3C**). These two solutions were also located on error contour-plots drawn for various values of $J$ versus $J'$ (Figure S7).

The above-mentioned solutions were further verified by simulations of the $M$ versus $H$ isotherm at 4 K (Figure S7). The experimental data were very well simulated using any set best-fit parameters, which yielded practically superimposable calculated curves.

The behavior of complex **4** could not be accounted for by this model in the low-temperature region, so fits were carried out between 300 and 14 K. These also yielded two solutions, with parameters $J = -34.9\ cm^{-1}$, $J' = -29.3\ cm^{-1}$, $\rho = 0$, $g = 2.0$, and $R = 2.7\times10^{-4}$ (**4B**) and $J = -31.0\ cm^{-1}$, $J' = -38.4\ cm^{-1}$, $\rho = 0$, $g = 2.0$, and $R = 1.7\times10^{-4}$ (**4C**), which were also located on error contour-plots for various $J$ versus $J'$ values (Table 2) (Figure S8). Below 14 K the experimental curve dropped below the theoretically calculated one. This was also evidenced from the magnetization curve, which at 2.5 is significantly lower than the one theoretically calculated based on the best-fit parameters (Figure S10).

Considering that exchange couplings are primarily mediated through the oxide ions,[32] the $J$ values for the $Fe^{III}$ complexes are very close to those derived by applying the formula proposed by Weihe and Güdel[33,34] using the Fe–O distances and the Fe–O–Fe bridging angles. Although for dinuclear $Cr^{III}$ compounds the exchange coupling depends on the same parameters (distances and bringing angles),[35] an analogous magnetostructural correlation scheme has not

 © 2006 Wiley-VCH Verlag GmbH & Co. KGaA, Weinheim 

Table 2. Exchange-coupling constants derived for complexes **1**–**4**.

| Best-fit solution | $J$ ($cm^{-1}$) | $J'$ ($cm^{-1}$) | $J_{av}$[a] ($cm^{-1}$) | $g$[b] |
|---|---|---|---|---|
| **1A** | –10.3 | | | 1.87 |
| **1B** | –10.6 | –9.9 | –10.4 | 1.87 |
| **1C** | –10.1 | –10.9 | –10.4 | 1.87 |
| **2A** | –10.2 | | | 1.79 |
| **2B** | –11.7 | –9.6 | –11.0 | 1.82 |
| **2C** | –10.2 | –12.9 | –11.1 | 1.82 |
| **3B** | –27.5 | –20.5 | –25.2 | **2.00** |
| **3C** | –22.5 | –32.6 | –25.9 | **2.00** |
| **4B** | –34.9 | –29.3 | –33.0 | **2.00** |
| **4C** | –31.0 | –38.4 | –33.5 | **2.00** |

[a] $J_{av} = (2J + J')/3$. [b] Values in bold were fixed during the fitting process.

yet been obtained for $Cr^{III}$ compounds[36] with nuclearity three and higher. The values obtained for the exchange parameters ($J$, $J'$) are very close to the corresponding values from similar trinuclear oxobridged $Cr^{III}$ and $Fe^{III}$ compounds.[3]

The ligands seem to have no discernible influence on the magnetic properties of the $Cr^{III}$-based complexes. On the contrary, in the case of $Fe^{III}$-based complexes the $J$ values are larger in the case of the benzoate ligand (**4**), as has also been observed in another series of trinuclear iron(III) carboxylate complexes.[37]

Although the number of examples presented herein is hardly sufficient to establish a valid correlation, we may still assume that there is some influence of the carboxylato ligand's electronic parameters on the magnitude of the exchange couplings. This influence should be secondary to that induced by the variation of structural parameters like M···M distances and M–O–M angles, but is probably not negligible. Such an influence has also been observed by Mössbauer spectroscopy, which reveals a larger (ca. 25%) quadrupole splitting for the ferric sites in **3** despite having very similar geometrical environments to the ferric sites in **4**.

In assessing the metal influence on the magnetic properties of the complexes, we first observe that couplings are stronger in iron(III) complexes than in their chromium(III) counterparts, by a factor of about 3. Secondly, we observe that, as in the case of "basic iron(III) carboxylates", "basic chromium(III) carboxylates" present two best-fit solutions of their magnetic susceptibility data within the isosceles model, one with $J > J'$ and one with $J < J'$. However, an important difference is that in the case of chromium(III) complexes these solutions are comparable in quality with the solution derived from the equilateral model ($J = J'$), whereas in the case of iron(III) complexes the latter model fails to satisfactorily reproduce the experimental data. Therefore, although the equilateral model may be insufficient to describe "basic chromium(III) carboxylates", other techniques (like EPR) are necessary to unambiguously prove this.

## Solid-State NMR

Solid-state NMR experiments in magnetic molecular clusters of transition-metal ions probe the magnetic excitations in the electronic spin system of the cluster. In particular, at low temperatures, $T_1$ spin-lattice relaxation measurements are quite sensitive to the low-lying energy levels of the system. The $^1H$ NMR spin-lattice relaxation time $T_1$ was measured at an applied magnetic field $H = 4.7$ T, between room and liquid-helium temperatures. The relaxation rate $1/T_1$ as a function of temperature is shown in Figure 9. At high temperatures the relaxation rate exhibits a weak temperature dependence, while below around 80 K an activated-type dependence is observed. The temperature dependence of $1/T_1$ measured for **1** is analogous to a previously studied trinuclear $Cr^{III}$ complex[26] and has a behavior that has been frequently encountered in previous $^1H$ NMR studies of molecular clusters that include transition-metal ions with low $S$ values, for example $S = 1/2$, 3/2.[38] The NMR $1/T_1$ relaxation data in clusters including metal ions with high $S$ values, such as $S = 5/2$, frequently exhibit a pronounced $1/T_1$ maximum at temperatures of the order of the exchange frequency $J$.[39,40] The absence of a maximum in clusters with metal ions having low $S$ values has not been adequately explained so far and is currently under investigation.

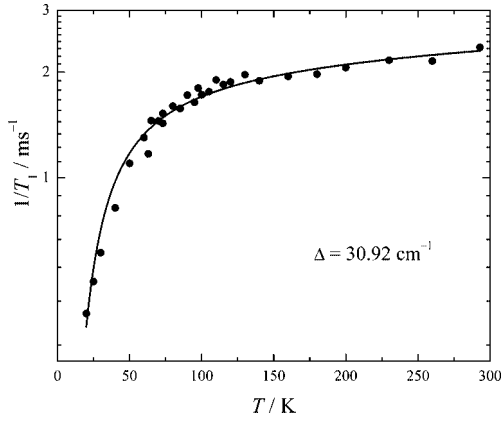


Figure 9. The relaxation rate $1/T_1$ as a function of temperature for **1**.

Using a two-level system and an Orbach-type activation process for the electronic excitation, we have been able to fit the experimental data considering an energy gap consistent with that obtained from the susceptibility data. In this model the NMR relaxation is caused by the local field fluctuations originating from the magnetic excitations from the ground state to the excited state, separated by the energy difference Δ. Assuming that the $Cr^{III}$ spin system remains in the ground state for an average time $\tau_0$ and in the excited state for a lifetime $\tau_1$, during which an effective transverse local field $h_\perp$ appears at the nuclear site, the relaxation rate is expressed as [Equation (5)]:[41]

 © 2006 Wiley-VCH Verlag GmbH & Co. KGaA, Weinheim 

$$\frac{1}{T_1} = (\gamma_N h_\perp)^2 \frac{\tau_1\tau_0}{(\tau_1+\tau_0)^2} \frac{\tau}{(\omega_N\tau)^2+1} \quad (5)$$

where

$$\frac{1}{\tau} = \frac{1}{\tau_0} + \frac{1}{\tau_1}$$

$\gamma_N$ is the proton gyromagnetic ratio, and $\omega_N$ is the Larmor angular frequency.

This model has been frequently employed for the nuclear magnetic relaxation in paramagnets.[38,42,43] For the excitation $1/\tau_0$, we may consider the sum of two processes [Equation (6)]:[44]

$$\frac{1}{\tau_0} = A_0 \coth\left(\frac{g\mu_B H}{2k_B T}\right) + B_0 \exp\left(-\frac{\Delta}{k_B T}\right) \quad (6)$$

The first term is a direct-type process, generally applicable at low temperatures, and the second term is an activation process of the Orbach type because of the presence of the energy level spacing $\Delta$ and is generally applicable at higher temperatures.

For the lifetime $\tau_1$ we consider a temperature-independent term [Equation (7)]:

$$1/\tau_1 = C_1 \quad (7)$$

Setting $\nu_N$ = 200.1 MHz ($H$ = 4.7 T), and using Equations (6) and (7), the experimental NMR points are fitted to Equation (5), shown as a solid line in Figure 13. The influence of the first term in Equation (6), the direct process, is quite small in the experimental determination of $\Delta$. We observe that the line describes the overall experimental features rather well. The value of $\Delta$ determined by the fitting is $\Delta$ = 30.92 $cm^{-1}$. According to the analysis of the magnetic susceptibility measurements for $Cr^{III}$ compounds presented in the previous paragraph, the ground state has $S_T$ = 1/2 (T for total) and the first excited state has $S_T$ = 3/2. For an equilateral exchange interaction model, which is the case (to a good approximation) for the $Cr^{III}$ compounds, $\Delta = 3J$[4] $\approx$ 30 $cm^{-1}$ (for $J \approx$ 10 $cm^{-1}$). Both values for the first excited multiple determined by the analysis of the susceptibility and NMR measurements are in good agreement.

## EPR Spectroscopy

EPR spectroscopy has been proven to be very useful in determining the magnetic properties of the ground state of trinuclear complexes.[2,4,5,17–23]

### *$Cr^{III}$ Complexes*

X-band EPR spectra from powder samples of **1** and **2** recorded at 4.2 K are shown in Figure 10. Both samples give rise to strong signals comprising an absorption peak at $g \approx$ 1.97–1.98 and broad features at higher magnetic fields (Figures 10, left and right). The magnetic susceptibility data indicate an $S_T$ = 1/2 ground state for complexes **1** and **2**. Indeed, the signals of Figure 10 are consistent with an isolated $S_T$ = 1/2 state. In coupled trimers, a relatively large anisotropy in the $g$ tensor for the $S_T$ = 1/2 ground state with a $g_\perp$ value significantly smaller than 2 is usually observed. This anisotropy is the result of antisymmetric exchange interaction [Equation (8)]:

$$\hat{H}_{AE} = \mathbf{d}(\hat{\mathbf{S}}_1 \times \hat{\mathbf{S}}_2 + \hat{\mathbf{S}}_2 \times \hat{\mathbf{S}}_3 + \hat{\mathbf{S}}_3 \times \hat{\mathbf{S}}_1) \quad (8)$$

In the framework of Hamiltonian (8), $g_\parallel \approx g_0$, where $g_0$ is the $g$ value for the $Cr^{III}$ metal ion. $g_\perp$ depends critically on the relationship between $d$ and $\Delta E$, where $\Delta E$ is the energy difference between the two lowest $S_T$ = 1/2 states. In the case of well-isolated $S_T$ = 1/2 doublets with respect to the higher $S$ = 3/2 states and small $d$ values, the dependence

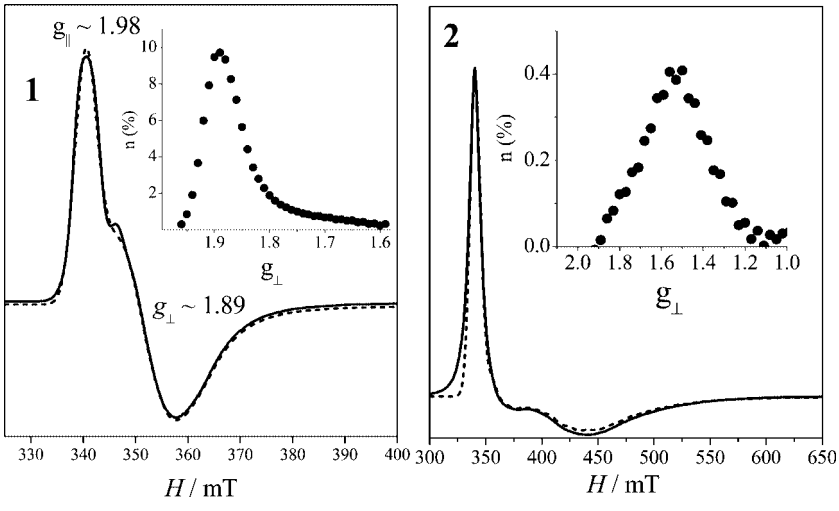


Figure 10. X-band EPR spectra in the high-field region from powdered samples from compounds **1** (left) and **2** (right) at 4.2 K. Dashed lines represent theoretical simulations as described in the text. Inset: Distribution of subspectra used to generate the simulations as described in the text. EPR conditions: microwave power 2.0 mW, mod. amplitude, 1.0 mT (left), 0.4 mT (right), microwave frequency 9.42 GHz.

 © 2006 Wiley-VCH Verlag GmbH & Co. KGaA, Weinheim 

of $g_\perp$ on these parameters is given analytically through the relationship [Equation (9)]:[19]

$$g_\perp = g_{0\perp}\left[1 - \frac{D^2}{\Delta E^2 - (h\nu)^2}\right]^{1/2} \quad (9)$$

$\Delta E$ stands for the separation of the lowest $S = 1/2$ doublets and is given by the relationship [Equation (10)]:

$$\Delta E = (\sigma^2 + D^2)^{1/2} \quad (10)$$

where $D = 4\sqrt{3d}$, and $\sigma = 4|J - J'|$.

From this model the characteristics of the spectra shown in Figure 10 can be understood. The absorption peak observed at $g \approx 1.97$–$1.98$ is attributed to the $g_\parallel$ component, whereas the broad derivative feature corresponds to $g_\perp$. Recently[26] we have observed similar EPR spectra in a $Cr^{III}$ complex similar to **2**. In order to reproduce the line shape of the spectra we follow the same procedure as in that case. Namely, we calculate a large number of axial spectra with $g_\parallel \approx 1.97$–$1.98$ and with smaller $g_\perp$ values, and then by a fitting routine we determine the distribution of the subspectra that reproduce the experimental one. The resulting simulations together with the distributions of the subspectra are shown in the insets in Figure 10.

In both cases the distribution profiles exhibit a maximum at certain $g$ values (1.90 for **1** and 1.53 for **2**). These values are considered as the $g_\perp$ for the $S = 1/2$ ground states. The crystal structure at room temperature revealed an isosceles configuration for **1** and an almost equilateral for **2**. The magnetic susceptibility measurements gave satisfactory results either with an equilateral ($J = J'$) or with an isosceles model ($J \neq J'$). An $S = 1/2$ EPR signal with an axial character cannot arise from a trinuclear system with $J = J'$, because in this case the transition probability corresponding to the $g_\parallel$ component vanishes.[5,13,18]

From the dependence of $g_\perp$ on the antisymmetric exchange parameter $|\mathbf{d}|$, the magnitude of the latter can be determined. For this, knowledge of $g_{0\perp}$ and $\Delta E$ is also required. For $Cr^{III}$ ($S = 3/2$) the intrinsic $\mathbf{g_0}$ tensor is slightly anisotropic with values $g_{0\parallel}$ and $g_{0\perp}$ smaller than 2 and in the 1.98–1.93 range. For the coupled system the $g_\parallel$ parameter does not depend on $|\mathbf{d}|$, therefore we can safely assume that $g_\parallel \equiv g_{0\parallel}$. For the perpendicular component we assume that $g_{0\perp}$ lies in the 1.98–1.93 region.

Although for the description of the magnetic susceptibility data we did not take into account the antisymmetric term, the determined values for $J$ and $J'$ can be used in order to estimate the separation, $\Delta E$ of the two lowest $S = 1/2$ states. We consider also that their average value $J_{av} = (2J + J')/3$ is valid as it satisfactorily reproduces the temperature dependence of the magnetic susceptibility. From Equation (9) and the given values for $\Delta E$ we determine the antisymmetric exchange parameter $|\mathbf{d}|$ for the two solutions (**1B**, **1C** and **2B**, **2C**). From these values we estimate that $|\mathbf{d}| \approx 0.10\ cm^{-1}$ for **1** and $|\mathbf{d}| \approx 1.1\ cm^{-1}$ for **2**. These values fall in the range reported for other carboxylato-bridged trinuclear complexes.[19] $|\mathbf{d}|$ is significantly larger for compound **2**, suggesting that the nature of the carboxylato-bridging ligands affects the magnitude of the antisymmetric exchange interaction.

From Equation (10) we find that $\sigma \approx 3\ cm^{-1}$ for **1** and $\sigma \approx 6\ cm^{-1}$ for **2**. This parameter depicts the splitting of the $S = 1/2$ doublets, which is due to the nonequivalence of the isotropic exchange parameters. We observe that incorporation of antisymmetric exchange through Equation (10) leads to a slightly smaller $\sigma$ compared with the one derived from a purely isotropic exchange Hamiltonian, which was considered in the analysis of the magnetic susceptibility data. From the relationship $\sigma = 4|J - J'|$ we see that the actual $J$ and $J'$ values should be slightly different from those derived from the analysis of the magnetic susceptibility data. This difference is too small to be discernible in the analysis of the temperature dependence of the magnetic susceptibility. Moreover, the magnitude of the antisymmetric exchange parameter $|\mathbf{d}|$ derived from the analysis of the EPR data is not expected to affect this analysis.

The parameter $\sigma$ can be taken as a measure for the lowering of the symmetry because for an equilateral triangle $\sigma = 0$. For compound **1** a non-zero value for $\sigma$ could be anticipated, as the room temperature crystal structure already reveals an isosceles configuration. On the contrary, compound **2** has an equilateral configuration at room temperature. Therefore the finite value of $\sigma$ for this compound (even larger than compound **1**) indicates a lowering of symmetry at low temperatures. The lowering of symmetry is one of the properties of trinuclear complexes that have been the subject of extensive studies during the last few decades, and from this point of view compound **2** belongs to this family of clusters.

The distribution of $g_\perp$ values required to reproduce the EPR spectra of Figure 10 is noteworthy. The distribution is more pronounced for compound **2**. From Equation (9) we observe that $g_\perp$ is extremely sensitive on the ratio $d/\Delta E$. A relatively small distribution on this parameter would lead to a large distribution of the $g$ values, resulting in a severely distorted axial EPR spectrum. This distribution may arise from structural inhomogeneities, resulting for instance from partial solvent loss. Alternatively, this behavior may be connected with the lowering of the symmetry discussed above. We note that, as $\Delta E$ depends on $\sigma$, a small distribution of the isotropic exchange constants would have a prominent effect. These constants are expected to depend on the geometrical characteristics of the clusters. It is probable, therefore, that upon cooling a multitude of geometric configurations are trapped, giving rise to slightly different sets of $J$ values, resulting eventually in a variety of $\sigma$ values. This effect would be more pronounced for compound **2** on going from the equilateral to isosceles configuration upon decrease of temperature.

As the temperature increases, new signals emerge in the lower-field region of the spectra, as shown in Figure 11. The temperature dependence of these signals indicates that they arise from excited states of a paramagnetic system. This is strong evidence against an assignment of these signals to mononuclear $Cr^{III}$ ($S = 3/2$) impurities.[46] On the other hand, they can be very well attributed to excited states with

 © 2006 Wiley-VCH Verlag GmbH & Co. KGaA, Weinheim 

$S > 1/2$ of the trimeric units, which are gradually populated as the temperature increases. The energy level with $S_T = 3/2$ is the most probable to generate these signals, because it is the first excited state with $S > 1/2$ for the system.

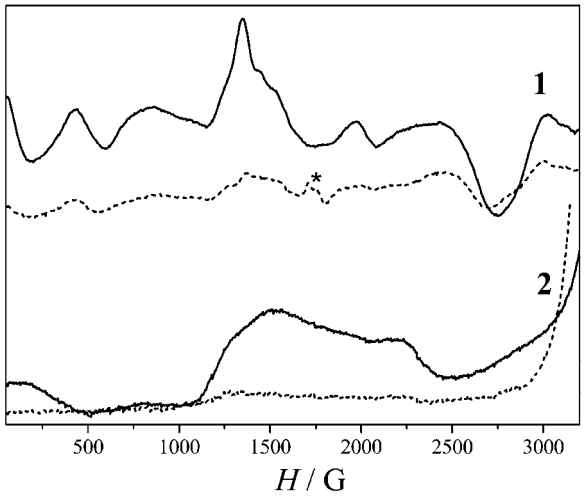


Figure 11. The low magnetic field region of EPR spectra from polycrystalline samples of **1** and **2** at 4.2 K (dotted lines) and 19 K (continuous lines). The asterisk * denotes a weak signal, which is attributed to impurities. EPR conditions: microwave power 2.0 mW, mod. amplitude 1.0 mT, microwave frequency 9.42 GHz.

For an equilateral triangle one has four states with $S_T = 3/2$ with the same energy. For $J \neq J'$ these states differ in energy leading to four separate quartets. Moreover, further splitting may be induced from non-Heisenberg interactions such as single-ion zero-field splitting, dipolar, and antisymmetric exchange. The analysis of the $S_T = 1/2$ signals from the ground state indicates that the magnitude of these interactions is too small to be discernible in the bulk magnetic susceptibility measurements; however they induce very complicated EPR spectra. As is clearly shown in Figure 11, the two complexes differ not only in the EPR spectra obtained from the $S_T = 1/2$ ground state, but also in the EPR spectra from the excited states.

### *$Fe^{III}$ Complexes*

The EPR spectrum recorded at 4.2 K from a polycrystalline sample of compound **3** is shown in Figure 12. Although the analysis of magnetic susceptibility measurements reveals that the ground state for compound **3** has $S_T = 1/2$, as in the case of compounds **1** and **2**, the EPR spectrum for this compound is different. Specifically, a very intense signal is observed at $g \approx 2.0$ and a number of weaker signals are recorded at lower values of the magnetic field. The signal recorded at $g = 2.0$ has a width of about 600 G, and comprises an absorption feature at $g \approx 2.18$, a derivative at $g \approx 1.98$, and a valley at 1.86. These signals are not explained by considering an isolated trinuclear complex as in the case of $Cr^{III}$-based **1** and **2** complexes. Recently, we have observed similar EPR spectra from powdered samples of another trinuclear complex and for their interpretation we suggested inter-trimer interactions leading to weakly coupled dimers of trinuclear units.[31] The crystal structure of **3** reveals intermolecular interactions leading to the formation of dimers of trinuclear centers. In order to reproduce the spectra we have employed the same model as in ref.[31] involving two weakly interacting $S_1 = S_2 = 1/2$ species in the framework of the spin Hamiltonian [Equation (11)]:[20]

$$\hat{H} = \hat{\mathbf{S}}_1\tilde{\mathbf{J}}_{12}\hat{\mathbf{S}}_2 + \hat{\mathbf{S}}_1\mathbf{g}_1\mathbf{B} + \hat{\mathbf{S}}_2\mathbf{g}_2\mathbf{B} \quad (11)$$

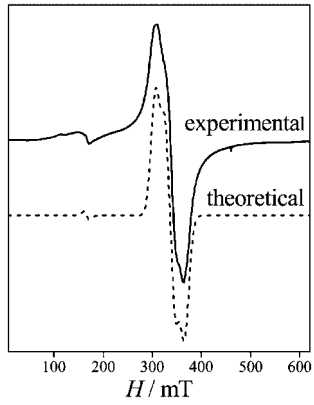


Figure 12. Experimental (solid) and theoretical (dotted) perpendicular-mode X-band EPR spectra from a powdered sample of **3** at 4.2 K. The simulation is obtained as described in the text using an intrinsic line width of 7 mT. EPR conditions: microwave power 2.0 mW, mod. amplitude 0.4 mT, microwave frequency 9.42 GHz.

The exchange interaction is represented by an anisotropic diagonal tensor $\tilde{\mathbf{J}}$. The distance between the trinuclear complexes in a dimer unit is relatively large and the isotropic exchange interaction is expected to be negligible. We find that the spectra are well reproduced for $\mathbf{J} = [0.04, 0.00, -0.04]$ $cm^{-1}$ with $g_1 = g_2 = 2.0$. The interaction of Equation (11) leads to a four-energy-level system.

Within this, manifold "half-field" transitions are expected at $g \approx 4.0$.[47] Indeed, such signals are observed in the EPR spectra of Figure 12. It could be argued that the signals in the $g \approx 4$ region arise from high-spin $Fe^{III}$ impurities which exhibit derivative signals at $g \approx 4.3$. In order to deduce whether the signals in the $g \approx 4.0$ region belong to the exchange coupled system of Equation (11) or arise from $Fe^{III}$ impurities, we have performed EPR spectroscopy in parallel mode (Figure 13). For a high-spin $Fe^{III}$ impurity with a zero-field splitting term $|D| \approx 1$–$2$ $cm^{-1}$, the $g \approx 4.3$ component has no contribution in parallel mode, as it arises from a Kramers doublet. The "half-field" transitions of a system described by Equation (11) involve non-Kramers doublets and the transition probability in parallel mode is finite. The existence of a signal at $g \approx 4.0$ in the parallel mode spectrum provides further evidence for an anisotropic exchange interaction between two neighboring $S = 1/2$ trimers.

The spectra are reproduced assuming isotropic $\mathbf{g}_i$ tensors with $g = 2.00$. From this point of view, complex **3** does not exhibit anisotropic $g$ tensors for the ground $S = 1/2$ state, unlike the Cr analogue complex **1**, for which anisotropic $S = 1/2$ signals are observed (Figure 10). Therefore, there is no indication for antisymmetric exchange in the case of **3**.

 © 2006 Wiley-VCH Verlag GmbH & Co. KGaA, Weinheim 

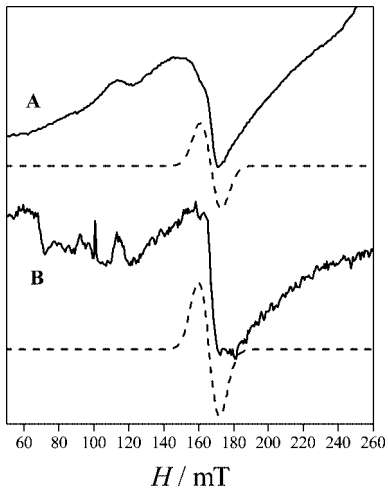


Figure 13. Experimental (solid) and theoretical (dotted) dual-mode X-band EPR spectra from powdered samples of **3** at 4.2 K. A: perpendicular mode; B: parallel mode. Simulations are obtained as described in the text. EPR conditions: A, as in Figure 11; B, microwave power 54 mW, mod. amplitude 0.4 mT, microwave frequency 9.36 GHz.

The anisotropic exchange interaction is mainly of dipolar origin. In the present case, the spin in each trimer delocalizes in three $Fe^{III}$ ions and the size of the triangles is of the same order of magnitude with the distance between the species. In such a case a point-dipole model is not a good approximation. We have observed similar EPR spectra from powdered samples of another trinuclear complex.[31]

Powdered samples from **4** gave rise to complicated EPR spectra at liquid helium temperatures extending several hundreds of mT. We have studied many samples exhibiting identical Mössbauer and IR spectra but each time their EPR spectra showed variations. A representative spectrum is shown in Figure S13. The X-band EPR spectra cannot be interpreted assuming isolated $S = 1/2$ species. The simplified model for intermolecular interactions, adopted in the case of **3**, does not apply to **4** either. Moreover, we note that the magnetic susceptibility data for liquid helium temperatures exhibited significant deviation from the isotropic exchange Hamiltonian [Equations (3) and (4)]. Therefore, it appears that more complicated magnetic interactions have to be taken into account in order to appropriately describe the low-temperature magnetic behavior of **4**.

## Conclusions

Structural, magnetic, and EPR spectroscopic studies have been carried out on two basic chromium(III) and two basic iron(III) carboxylates. In addition, solid-state $^1H$ NMR studies have been carried out on **1** and $^{57}Fe$ Mössbauer studies have been carried out on the ferric complexes **3** and **4**. This allowed us to examine the influence of ligand and metal variation on structural, magnetic, and spectroscopic properties.

From a structural viewpoint benzilato ligands induce a nearly isosceles geometry in **1** and **3**, whereas benzoato ligands induce a nearly equilateral geometry. However, these geometric characteristics are not reflected in the "magnetic symmetry" of the complexes; the magnetic susceptibility data of the chromium(III) complexes can be well described both by the equilateral or isosceles model, whereas those of the iron(III) complexes demand the use of the isosceles model. In the case of the isosceles model, two best-fit solutions are obtained for all complexes. Solid-state $^1H$ NMR studies on **1** reveal that the first excited state is well separated from the ground state and quantitatively confirm the magnetic susceptibility results.

Further information regarding the low-lying spin states of the trimers was obtained by X-band EPR spectroscopy. For **1** and **2** the EPR results favor the isosceles model at least at liquid helium temperatures and confirm the $S_T = 1/2$ ground state. In addition, in **1** and **2** the presence of antisymmetric exchange was revealed along with a distribution of the exchange parameters.

Concerning the iron(III) complexes, the EPR spectrum of **3** is influenced by intermolecular interactions of dipolar origin, whereas that of **4** is too complicated to be analyzed in detail. It is however concluded that antisymmetric exchange is not so important in **3**.

Another point of interest concerns the ligand-induced electronic effects on various magnetic and spectroscopic properties. In particular, it was observed that: (i) isotropic exchange couplings are stronger within benzoato complexes (**2**/**4**) than within benzilato complexes (**1**/**3**), (ii) the electric field gradient is larger for the ferric sites of the "basic iron(III) benzilate" (**3**) than for the sites of the "basic iron(III) benzoate" (**4**), and (iii) the magnitude of the antisymmetric exchange parameter **d** is about 10 times larger for **2** than for **1**.

These differences gain importance with the close structural resemblance of **1**/**2** and **3**/**4**, which does not allow for their simple geometric interpretation. Rather, we assume that electronic factors affect the exchange couplings (isotropic and antisymmetric) and EFG, although this point requires more elaborate studies. Weak intermolecular, metal-dependent interactions may complicate the analysis of the properties of the trinuclear units.

## Experimental Section

**Compound Preparations:** All manipulations were performed under aerobic conditions using materials as received (Aldrich Co). All chemicals and solvents were of reagent grade.

**$[Cr_3(\mu_3\text{-}O)\{O_2C(OH)Ph_2\}_6(H_2O)_3](NO_3)\cdot 2H_2O\cdot 3Me_2CO$ ($1\cdot 2H_2O\cdot 3Me_2CO$):** Solid benzilic acid (0.233 g, 1.01 mmol) was added to a refluxing green-purple solution of $Cr(NO_3)_3\cdot 9H_2O$ (0.204 g, 0.51 mmol) in $Me_2CO$ (15 mL). The reflux continued for 3 days, giving a green solution, which was layered with a mixture of $Et_2O$/*n*-hexane (1:1 v/v %) to afford X-ray-quality green crystals of **1**. The crystals were collected by filtration, and dried in vacuo. (Yield: 0.34 g, ca. 70%.) The resulting powder was analyzed as solvent-free. $C_{84}H_{72}Cr_3NO_{25}$ (1651.47): calcd. C 61.09, H 4.39, N 0.85; found C 60.15, H 4.32, N 0.80. Selected IR data: 3614 [$\nu$(OH)$_{free}$], 1636 [$\nu_{as}$(COO)], 1415 [$\nu_s$(COO)], 600 [$\nu_{as}(Cr_3O)$] $cm^{-1}$.

 © 2006 Wiley-VCH Verlag GmbH & Co. KGaA, Weinheim 

**$[Cr_3(\mu_3\text{-}O)(O_2CPh)_6(H_2O)_3](NO_3)\cdot 1.9MeCN\cdot 0.5H_2O$ (2·1.9MeCN·0.5$H_2O$):** Solid sodium benzoate (0.373 g, 2.58 mmol) was added to a refluxing green-purple solution of $Cr(NO_3)_3\cdot 9H_2O$ (0.517 g, 1.29 mmol) in MeCN (15 mL). The reflux continued for 2 h, giving a green solution, which upon slow evaporation afforded X-ray-quality green crystals of **2**. (Yield: 0.34 g, ca. 70%.) The crystals of **2** were collected by filtration and dried in vacuo. The resulting powder was analyzed as solvent-free. $C_{42}H_{36}Cr_3NO_{19}$ (1014.73): calcd. C 49.71, H 3.58, N 1.38; found C 48.90, H 3.44, N 1.29. Selected IR data: 1574 [$\nu_{as}$(COO)], 1421 [$\nu_s$(COO)], 620 [$\nu_{as}(Cr_3O)$] $cm^{-1}$.

**$[Fe_3(\mu_3\text{-}O)\{O_2C(OH)Ph_2\}_6(H_2O)_3](NO_3)\cdot 5.69H_2O$ (3·5.69$H_2O$):** Solid benzilic acid (0.228 g, 1.00 mmol) was added to a refluxing solution of $Fe(NO_3)_3\cdot 9H_2O$ (0.202 g, 0.50 mmol) in $CH_2Cl_2$ (20 mL). The color of the solution gradually turned from red to orange and the reflux continued for 2 h. The $NaNO_3$ that precipitated was filtered off and the orange filtrate was layered with *n*-hexane (1:1 v/v %). Orange crystals of **3** suitable for X-ray structure analysis were formed after one week. (Yield: 0.34 g, ca. 70%.) The crystals of **3** were collected by filtration and dried in vacuo. The resulting powder was analyzed as solvent-free. $C_{84}H_{72}Fe_3NO_{25}$ (1663.03): calcd. C 60.67, H 4.36, N 0.84; found C 59.86, H 4.28, N 0.80. Selected IR data: 3603 [$\nu$(OH)$_{free}$], 1612 [$\nu_{as}$(COO)], 1406 [$\nu_s$(COO)], 598 [$\nu_{as}(Fe_3O)$]$cm^{-1}$.

**$[Fe_3(\mu_3\text{-}O)(O_2CPh)_6(H_2O)_3](NO_3)\cdot 3MeCN$ (4·3MeCN):** Solid sodium benzoate (0.144 g, 1.00 mmol) was added to a refluxing solution of $Fe(NO_3)_3\cdot 9H_2O$ (0.202 g, 0.50 mmol) in MeCN (20 mL). The color of the solution gradually turned from red to orange and the reflux continued for 24 h. A white precipitate was filtered off and identified as $NaNO_3$ by FTIR spectroscopy. The orange filtrate was left for slow evaporation and after ca. 1 week, X-ray-quality orange crystals of **4** were formed. (Yield: 0.34 g, ca. 70%.) The crystals of **4** were collected by filtration and dried in vacuo. The resulting powder was analyzed as solvent-free. $C_{42}H_{36}Fe_3NO_{19}$ (1026.28): calcd. C 49.15, H 3.54, N 1.36; found C 48.30, H 3.22, N 1.27. Selected IR data: 1562 [$\nu_{as}$(COO)], 1410 [$\nu_s$(COO)], 573 [$\nu_{as}(Fe_3O)$] $cm^{-1}$.

**Physical Measurements:** Elemental analyses for carbon, hydrogen, and nitrogen were performed on a Perkin–Elmer 2400/*II* automatic analyzer. Infrared spectra were recorded as KBr pellets in the range 4000–500 $cm^{-1}$ with a Bruker Equinox 55/S FTIR spectrophotometer. EPR spectra were recorded with a Bruker ER 200D-SRC X-band spectrometer equipped with an Oxford ESR 9 cryostat in the 4.2–300 K temperature range, an NMR Gaussmeter, an Anritsu frequency counter, and a DM Bruker cavity. Simulations of the EPR spectra were done with home-written routines or software provided to us by Prof. Mike Hendrich, Dept. of Chemistry, Carnegie Mellon University, Pittsburgh, USA. Variable-temperature magnetic susceptibility measurements were carried out with polycrystalline samples of **1**–**4** in the 2.0–300 K temperature range using a Quantum Design MPMS SQUID susceptometer under magnetic fields of 0.1 T (for **1**, **2**) and 1.5 T (for **3**, **4**). Isothermal magnetization measurements were carried out over the 0–5 T magnetic field range. Diamagnetic corrections for the complexes were estimated from Pascal's constants. The calculation of the magnetic susceptibility was accomplished by analytical calculation of the energy levels associated with the spin Hamiltonian using Kambe's spin-coupling approach. Subsequent implementation of the van Vleck equation was done using a home-written routine. For the case of the equilateral model, an analytical expression can also be used.[48] Minimization was carried out with an adapted version of MINUIT.[49] The error factor $R$ is defined as $R = \sum(\chi_{exp} - \chi_{calc})^2/N\chi^2_{exp}$, where $N$ is the number of experimental points. Magnetization $M$ versus applied magnetic field $H$ isotherms were calculated from the best-fit parameters using MAGPACK.[50] Mössbauer spectra for **3** and **4** were recorded with a constant acceleration spectrometer using a $^{57}$Co (Rh) source at room temperature and a variable-temperature Oxford cryostat. The spectra were analyzed with home-written routines. Variable-temperature $^1$H-pulsed NMR experiments for **1** were performed at 4.7 T using a Bruker MSL200 spectrometer operating at 200.145 MHz. An Oxford 1200 CF continuous flow cryostat was employed for measurements in the range 5–300 K. $T_1$ spin-lattice relaxation times were measured using the standard spin-echo pulse sequence combined with the saturation recovery method.[51]

**X-ray Structure Determination:** Green prismatic crystals of **1** ($0.25\times0.35\times0.65$ mm) and **2** ($0.20\times0.30\times0.65$ mm), and orange prismatic crystals of **3** ($0.10\times0.25\times0.50$ mm) and **4** ($0.18\times0.28\times0.50$ mm) were mounted in capillaries with drops of mother liquid. Diffraction measurements were made on a Crystal Logic Dual Goniometer diffractometer using graphite-monochromated Mo-$K_\alpha$ radiation. Important crystal data and parameters for data collection are reported in Table 3. Unit cell dimensions were determined and refined by using the angular settings of 25 automatically centered reflections in the range $11° < 2\theta < 23°$. Intensity data were recorded using a $\theta$–$2\theta$ scan. Three standard reflections monitored every 97 reflections showed less than 3% intensity fluctuation and no decay. Lorentz, polarization, and psi-scan absorption corrections (for **2** and **3** only) were applied using Crystal Logic software. The structures were solved by direct methods using SHELXS-86[52] and refined by full-matrix least-squares techniques on $F^2$ with SHELXL-97.[53] In all cases, the crystals had poor diffraction ability (despite their sufficient size) and the data were collected in increasing $2\theta$ shells, and in each case the data collection was terminated when about 50% of the collected shell data were unobserved. Nevertheless, the quality of the collected data was adequate to establish the structure of the complexes. Further experimental crystallographic details for **1**: $2\theta_{max}$ = 43°, scan speed 1.3° $min^{-1}$; scan range 2.0 + $\alpha_{1\alpha2}$ separation; reflections collected/unique/used, 11108/10817 [$R_{int}$ = 0.0394]/10817; 1200 parameters refined; $(\Delta/\sigma)_{max}$ = 0.011; $(\Delta\rho)_{max}/(\Delta\rho)_{min}$ = 0.811/–0.352 e $Å^{-3}$; $R/R_w$ (for all data), 0.0813/0.1769. All non-hydrogen atoms were refined anisotropically. Hydrogen atoms on the phenyl rings were introduced at calculated positions as riding on bonded atoms; those on the hydroxide and coordinated water molecules were located by difference maps and were refined isotropically. No H atoms for the solvate molecules were included in the refinement. Further experimental crystallographic details for **2**: $2\theta_{max}$ = 45°, scan speed 2.5° $min^{-1}$; scan range 1.7 + $\alpha_{1\alpha2}$ separation; reflections collected/unique/used, 6522/6163 [$R_{int}$ = 0.0255]/6163; 667 parameters refined; $(\Delta/\sigma)_{max}$ = 0.019; $(\Delta\rho)_{max}/(\Delta\rho)_{min}$ = 0.762/–0.625 e $Å^{-3}$; $R/R_w$ (for all data), 0.0836/0.2175. All non-hydrogen atoms were refined anisotropically, except those of the solvate molecules, which were refined isotropically. Hydrogen atoms on the phenyl rings were introduced at calculated positions as riding on bonded atoms; those of the coordinated water molecules were located by difference maps and were refined isotropically. Further experimental crystallographic details for **3**: $2\theta_{max}$ = 42.1°, scan speed 1° $min^{-1}$; scan range 1.75 + $\alpha_{1\alpha2}$ separation; reflections collected/unique/used, 10064/9849 [$R_{int}$ = 0.0421]/9849; 1080 parameters refined; $(\Delta/\sigma)_{max}$ = 0.001; $(\Delta\rho)_{max}/(\Delta\rho)_{min}$ = 0.687/–0.424 e $Å^{-3}$; $R/R_w$ (for all data), 0.1449/0.2373. All non-hydrogen atoms were refined anisotropically, except those of some solvate water molecules that were found to be disordered and were refined isotropically with occupation factors summing one. Hydrogen atoms on the phenyl rings were introduced at calculated positions as riding on bonded atoms; the rest

 © 2006 Wiley-VCH Verlag GmbH & Co. KGaA, Weinheim 

Table 3. Crystallographic data for complexes **1**–**4**.

| | **1**·2H$_2$O·3Me$_2$CO | **2**·1.9MeCN·0.5H$_2$O | **3**·5.69H$_2$O | **4**·3MeCN |
|---|---|---|---|---|
| Formula | $C_{93}H_{94}Cr_3NO_{30}$ | $C_{45.8}H_{42.7}Cr_3N_{2.9}O_{19.5}$ | $C_{84}H_{83.38}Fe_3NO_{30.69}$ | $C_{48}H_{45}Fe_3N_4O_{19}$ |
| Formula mass | 1861.69 | 1101.73 | 1765.49 | 1149.43 |
| Space group | $P2_1/n$ | $P\bar{1}$ | $C2/c$ | $P2_1/a$ |
| $a$ [Å] | 13.647(6) | 11.433(7) | 32.52(2) | 21.33(2) |
| $b$ [Å] | 23.54(1) | 11.972(8) | 17.02(1) | 11.37(1) |
| $c$ [Å] | 29.52(1) | 21.76(1) | 35.44(3) | 22.40(2) |
| $\alpha$ [°] | | 84.20(2) | | |
| $\beta$ [°] | 90.47(2) | 87.47(2) | 106.49(2) | 95.42(4) |
| $\gamma$ [°] | | 64.36(2) | | |
| $V$ [Å$^3$] | 9481(7) | 2671(3) | 18803(2) | 5408(8) |
| $Z$ | 4 | 2 | 8 | 4 |
| $T$ [°C] | 298 | 298 | 298 | 298 |
| Radiation | Mo-$K_\alpha$ | Mo-$K_\alpha$ | Mo-$K_\alpha$ | Mo-$K_\alpha$ |
| $\rho_{calcd}$ [g cm$^{-3}$] | 1.304 | 1.370 | 1.247 | 1.412 |
| $\mu$ [mm$^{-1}$] | 0.416 | 0.673 | 0.532 | 0.869 |
| $R_1$ | 0.0573[a] | 0.0712[b] | 0.0795[c] | 0.0738[d] |
| $wR_2$ | 0.1561[a] | 0.2035[b] | 0.1943[c] | 0.1889[d] |

$w = 1/[\sigma^2(F_o^2) + (aP)^2 + bP]$ and $P = (\max(F_o^2,0) + 2F_c^2)/3$

$R_1 = \Sigma(|F_o| - |F_c|)/\Sigma(|F_o|)$ and $wR_2 = \{\Sigma[w(F_o^2 - F_c^2)^2]/\Sigma[w(F_o^2)^2]\}^{1/2}$

[a] $a = 0.0926$, $b = 18.5641$, for 8260 reflections with $I > 2\sigma(I)$. [b] $a = 0.1349$, $b = 4.3563$, for 5120 reflections with $I > 2\sigma(I)$. [c] $a = 0.1075$, $b = 111.5255$, for 5989 reflections with $I > 2\sigma(I)$. [d] $a = 0.1108$, $b = 34.2934$, for 3829 reflections with $I > 2\sigma(I)$.

were not included in the refinement. Further experimental crystallographic details for **4**: $2\theta_{max} = 45°$, scan speed 1° min$^{-1}$; scan range 1.6 + $\alpha_{1\alpha2}$ separation; reflections collected/unique/used, 5577/5407 [$R_{int}$ = 0.0442]/5407; 628 parameters refined; $(\Delta/\sigma)_{max}$ = 0.001; $(\Delta\rho)_{max}/(\Delta\rho)_{min}$ = 0.896/–0.556 e Å$^{-3}$; $R/R_w$ (for all data), 0.1198/0.2537. All non-hydrogen atoms were refined anisotropically, except those of the solvate MeCN, which were refined isotropically. Hydrogen atoms on the phenyl rings were introduced at calculated positions as riding on bonded atoms; the rest were not included in the refinement.

CCDC-603113 (for **1**), -603114 (for **2**), -603115 (for **3**), and -603116 (for **4**) contain the supplementary crystallographic data for this paper. These data can be obtained free of charge from The Cambridge Crystallographic Data Centre via www.ccdc.cam.ac.uk/data_request/cif.

**Supporting Information** (see footnote on the first page of this article): Tables S1, S2, S3, and S4 contain selected bond lengths and angles for compounds **1 2**, **3**, and **4** respectively. In Figures S1, S2, S7, and S8, error contour plots of $J$ versus $J'$, in Figures S3, S4, S9, and S10, $M$ versus $H$ isotherms at the appropriate temperature, and in Figures S5, S6, S11, and S12, the energy-level plots for the studied compounds are shown. Every figure of each one of the three groups of four figures given above corresponds to each one of the four studied compounds **1**, **2**, **3**, and **4** correspondingly. In Figure S13 the X-band EPR spectrum of a powdered sample of **4** is shown.

## Acknowledgments

The Greek General Secretariat of Research and Technology is acknowledged for supporting the present work within the frame of the Competitiveness EPAN 2000–2006, Centers of Excellence no. 25. A. K. B. thanks the Greek State Scholarship Foundation (IKY) for support through a postdoctoral grant. We also thank Dr. D. Stamopoulos for the magnetic measurements.

[1] K. Kambe, *J. Phys. Soc. Jpn.* **1950**, *5*, 48–51.
[2] V. A. Gaponenko, M. V. Eremin, Yu. V. Yablokov, *Sov. Phys. Solid State* **1973**, *15*, 909–913.
[3] R. D. Cannon, R. P. White, *Prog. Inorg. Chem.* **1988**, *36*, 195–298.
[4] M. Honda, *J. Phys. Soc. Jpn.* **1993**, *62*, 704–716.
[5] J. Y. Yoon, L. M. Mirica, T. Daniel, P. Stack, E. I. Solomon, *J. Am. Chem. Soc.* **2004**, *126*, 12586–12595.
[6] E. K. Brechin, Y. Yoo, M. Nakomo, J. C. Huffman, D. N. Hendrickson, G. Christou, *Chem. Commun.* **1999**, 783–784.
[7] D. Gatteschi, R. Sessoli, *Angew. Chem. Int. Ed.* **2003**, *42*, 268–297.
[8] S. Gorun, G. C. Papaefthymiou, R. B. Frankel, S. J. Lippard, *J. Am. Chem. Soc.* **1987**, *109*, 4244–4255.
[9] I. Mulyani, A. Levina, P. A. Lay, *Angew. Chem. Int. Ed.* **2004**, *43*, 4504–4507 and references cited therein.
[10] J. Wucher, J. D. Wasscher, *Physica* **1954**, *20*, 721–726.
[11] U. A. Jayasooriya, R. D. Cannon, R. P. White, G. J. Kearley, *Angew. Chem. Int. Ed. Engl.* **1989**, *28*, 930–931.
[12] F. E. Sowrey, C. Tilford, S. Wocadlo, C. E. Anson, A. K. Powell, S. M. Bennington, W. Montfrooij, U. Jayasooriya, R. D. Cannon, *J. Chem. Soc., Dalton Trans.* **2001**, 862–866 and references cited therein.
[13] M. Takano, *J. Phys. Soc. Jpn.* **1972**, *33*, 1312–1317.
[14] T. Murao, *Phys. Lett. A* **1974**, *49*, 33–35.
[15] D. H. Jones, J. R. Sams, R. C. Thomson, *J. Chem. Phys.* **1984**, *81*, 440–447.
[16] N. Uryu, S. A. Friedberg, *Phys. Rev.* **1965**, *140*, 1803–1811.
[17] B. S. Tsukerblat, M. I. Belinski, V. E. Fainzilberg, "Magnetochemistry and spectroscopy of transition metal exchange clusters", in *Soviet Scientific Reviews, Section B* (Chemistry) (Ed.: M. E. Vol'pin), Harwood, Amsterdam, **1987**, pp. 337–481.
[18] Y. V. Rakitin, Y. V. Yablokov, V. V. Zeletontsov, *J. Magn. Reson.* **1981**, *43*, 288–301.
[19] M. Honda, M. Morita, M. Date, *J. Phys. Soc. Jpn.* **1992**, *61*, 3773–3785.
[20] A. Bencini, D. Gatteschi, *EPR of Exchange Coupled Systems*, Springer Verlag, Heidelberg, Germany, **1990**.
[21] C. A. Bates, R. F. Jasper, *J. Phys. C: Solid State Phys.* **1971**, *4*, 2330–2340.
[22] B. S. Tsukerblat, M. I. Belinskii, A. V. Ablov, *Sov. Phys. Solid State (Engl. Transl.)* **1973**, *15*, 19–24.
[23] M. I. Belinskii, B. S. Tsukerblat, A. V. Ablov, *Molecules Molec. Phys.* **1974**, *28*, 283–291.

 © 2006 Wiley-VCH Verlag GmbH & Co. KGaA, Weinheim 

[24] X. M. Liu, M. P. de Miranda, E. J. L. McInnes, C. A. Kilner, M. A. Halcrow, *Dalton Trans.* **2004**, 59–64.
[25] Y. Sanakis, A. L. Macedo, I. Moura, J. I. G. Moura, V. Papaefthymiou, E. Münck, *J. Am. Chem. Soc.* **2000**, *122*, 11855–11863.
[26] A. Vlachos, V. Psycharis, C. P. Raptopoulou, N. Lalioti, Y. Sanakis, M. Fardis, M. Karayianni, G. Papavassiliou, A. Terzis, *Inorg. Chim. Acta* **2004**, *357*, 3162–3172.
[27] A. K. Boudalis, Y. Sanakis, F. Dahan, M. Hendrich, J.-P. Tuchagues, *Inorg. Chem.* **2006**, *45*, 443–453.
[28] C. Krebs, T. F. Henshaw, J. Cheek, B. H. Huynh, J. B. Broderick, *J. Am. Chem. Soc.* **2000**, *122*, 12497–12506.
[29] C. P. Raptopoulou, V. Tangoulis, V. Psycharis, *Inorg. Chem.* **2000**, *39*, 4452–4459.
[30] C. P. Raptopoulou, Y. Sanakis, A. K. Boudalis, V. Psycharis, *Polyhedron* **2005**, *24*, 711–721.
[31] A. K. Boudalis, Y. Sanakis, C. P. Raptopoulou, A. Terzis, J. P. Tuchagues, S. P. Perlepes, *Polyhedron* **2005**, *24*, 1540–1548.
[32] A. B. Blake, A. Yavari, W. E. Hatfield, C. N. Sethulekshmi, *J. Chem. Soc., Dalton Trans.* **1985**, 2509–2520.
[33] H. Weihe, H. U. Gudel, *J. Am. Chem. Soc.* **1997**, *119*, 6539–6543.
[34] C. Canada-Vilalta, T. A. O'Brien, E. K. Brechin, M. Pink, E. R. Davidson, G. Christou, *Inorg. Chem.* **2004**, *43*, 5505–5521.
[35] C. Wang, K. Fink, V. Staemmler, *Chem. Phys.* **1995**, *201*, 87–94.
[36] S. B. Mukkamala, R. Clerac, C. E. Anson, A. K. Powell, *Polyhedron* **2006**, *25*, 530–538.
[37] G. J. Long, W. T. Robinson, W. P. Tappmeyer, D. L. Bridges, *J. Chem. Soc., Dalton Trans.* **1973**, 573.
[38] M. Luban, F. Borsa, S. Bud'ko, P. Canfield, S. Jun, J. K. Jung, P. Kogerler, D. Mentrup, A. Muller, R. Modler, D. Procissi, B. J. Suh, M. Torikachvili, *Phys. Rev. B* **2002**, *66*, 4407.
[39] M. Fardis, G. Diamantopoulos, M. Karayianni, G. Papavassiliou, V. Tangoulis, A. Konsta, *Phys. Rev. B* **2001**, *65*, 14412 and references cited therein.
[40] D. Procissi, B. J. Suh, A. Lascialfari, F. Borsa, A. Caneschi, A. Cornia, *J. Appl. Phys.* **2002**, *91*, 7173–7175.
[41] G. E. G. Hardeman, N. J. Poulis, W. v. D. Lugt, *Physica (Utrecht)* **1956**, *22*, 48–56.
[42] T. Kohmoto, T. Goto, S. Maegawa, N. Fujiwara, Y. Fukuda, M. Kunitomo, M. Mekata, *Phys. Rev. B* **1994**, *49*, 6028–6039.
[43] T. Goto, T. Koshiba, T. Kubo, K. Agawa, *Phys. Rev. B* **2003**, *67*, 104408.
[44] A. Abragam, B. Bleaney, *Electron Paramagnetic Resonance of Transition Ions*, Clarendon, Oxford, **1970**.
[45] D. Rumbold, G. V. H. Wilson, *J. Phys. Chem. Solids* **1973**, *34*, 1887–1891.
[46] For the analysis of the magnetic susceptibility measurements, monomeric impurities of less than 1% were included for both complexes. At these concentrations these species would give rise to weak signals, which would decrease upon increase of temperature. Such a behavior was observed for a weak signal, denoted by an asterisk in Figure 11, most clearly seen in the spectrum recorded at 4.2 K.
[47] J. R. Pilbrow, *Transition Ion Electron Paramagnetic Resonance*, Clarendon Press, Oxford, **1990**.
[48] F. E. Mabbs, D. J. Machin, *Magnetism and Transition Metal Complexes*, Chapman and Hall, London, **1973**.
[49] *MINUIT Program*, a System for Function Minimization and Analysis of the Parameters Errors and Correlations: F. James, M. Roos, *Comput. Phys. Commun.* **1975**, *10*, 343–367.
[50] a) J. J. Borrás-Almenar, J. M. Clemente-Juan, E. Coronado, B. S. Tsukerblat, *Inorg. Chem.* **1999**, *38*, 6081–6088; b) J. J. Borrás-Almenar, J. M. Clemente-Juan, E. Coronado, B. S. Tsukerblat, *J. Comput. Chem.* **2001**, *22*, 985–991.
[51] E. Fukushima, S. B. W. Roeder, *Experimental Pulse NMR*, Addison-Wesley, Reading, MA, **1981**.
[52] G. M. Sheldrick, *SHELXS-86: Structure Solving Program*, University of Göttingen, Germany, **1986**.
[53] G. M. Sheldrick, *SHELXL-97: Crystal Structure Refinement*, University of Göttingen, Germany, **1997**.

Received: April 5, 2006
Published Online: August 2, 2006

 © 2006 Wiley-VCH Verlag GmbH & Co. KGaA, Weinheim 

DOI: 10.1002/ejic.200600407

# First Example of a Gold(I) *N*-Heterocyclic-Carbene-Based Initiator for the Bulk Ring-Opening Polymerization of L-Lactide

**Lipika Ray,[a] Vimal Katiyar,[a] Mustafa J. Raihan,[a] Hemant Nanavati,[a] Mobin M. Shaikh,[a] and Prasenjit Ghosh*[a]**

**Keywords:** Carbenes / Functionalized NHC / Ring-opening polymerization (ROP) / Organometallic catalysis / Silver–NHC complex / Gold–NHC complex

Synthesis, structure, and catalysis studies of two Au- and Ag-based initiators, namely, [3-(*N*-*tert*-butylacetamido)-1-(2-hydroxycyclohexyl)imidazol-2-ylidene]AuCl (**1c**) and [3-(*N*-*tert*-butylacetamido)-1-(2-hydroxycyclohexyl)imidazol-2-ylidene]AgCl (**1b**), for the bulk ring-opening polymerization of L-lactide are reported. Specifically, gold complex **1c** was obtained from silver complex **1b** by the transmetalation reaction with $(SMe_2)AuCl$. Silver complex **1b** was synthesized by the treatment of 3-(*N*-*tert*-butylacetamido)-1-(2-hydroxycyclohexyl)imidazolium chloride (**1a**) with $Ag_2O$. Compound **1a** was synthesized directly from the reaction of *N*-*tert*-butyl-2-chloroacetamide, cyclohexene oxide, and imidazole. The molecular structures of **1a**, **1b**, and **1c** have been determined by X-ray diffraction studies. The formation of neutral monomeric complexes with linear geometries at the metal centers was observed for both **1b** and **1c**. The Au and Ag complexes **1c** and **1b** successfully catalyzed the bulk ring-opening polymerization of L-lactide at elevated temperatures under solvent-free melt conditions to produce moderate to low molecular weight polylactide polymers with narrow molecular weight distributions.

(© Wiley-VCH Verlag GmbH & Co. KGaA, 69451 Weinheim, Germany, 2006)

## Introduction

The long-standing notion of gold being an expensive and unreactive coinage metal with limited utility is gradually changing. Various new applications of $Au^I$ complexes in pharmaceuticals,[1] chemical vapor depositions,[2] and in homogeneous catalysis[3] have been recently reported. Compared to the other coinage metals (i.e. Cu and Ag), Au has seen relatively few applications and poses a formidable challenge in utility-oriented research. Quite significantly, a recent report detailed the use of a $Au^I$ complex supported over a sterically demanding *N*-heterocyclic carbene (NHC) ligand as a catalyst for the ethyl diazoacetate-assisted carbene-transfer reaction;[3] this represents an important breakthrough in this field of chemistry and adds further promise to the use of gold in chemical catalysis. The growing utility of NHCs in homogeneous catalysis is now well-recognized, and a plethora of NHC-based catalysts have been developed in recent years for a wide variety of transformations, such as C–C coupling reactions,[4,5] olefin metatheses,[6] hydrogenations,[7,8] hydroformylations,[9] hydrosilylations,[10] CO-ethylene copolymerizations,[11] hydroboration[12] reactions, and so forth. Interestingly enough, despite the numerous NHC-transition metal complexes that exist, the Au–NHC complexes are surprisingly few in number and have seldomly been employed in catalysis.[13]

A growing number of new applications have appeared lately for the $Ag^I$–NHC counterparts however, and their catalytic utility has just begun to unfold.[14,15] Specifically, the $Ag^I$–NHC complexes have been found to be active catalysts for several chemical transformations, such as, ethyl diazoacetate (EDA)-assisted carbene-transfer reactions,[16] catalytic preparation of 1,2-bis(boronate) esters,[17] transesterification reactions, and ring-opening lactide polymerization reactions.[18] It is noteworthy that even though the applications of $Ag^I$–NHC complexes in chemical catalysis is a recent phenomenon, they are long-known for their use as transmetalation agents for the synthesis of other transition metal–NHC complexes.[14,15] Like its heavier congener, the Au analogue, biomedical applications, particularly with regard to antimicrobial activities, have recently been reported for $Ag^I$–NHC complexes.[19,20] Thus far, the popularity of Ag–NHC complexes can be ascribed to their broadly based applications, to their synthetic accessibility, and to their air and moisture stabilities, which make them user-friendly and hence convenient to handle.[14,15]

As the catalytic utility of Au–NHC complexes remains largely unexplored and that of the Ag–NHC complexes is just beginning to emerge, we became interested in the design of Au and Ag complexes for their potential application in homogeneous catalysis. In particular, we were interested in

[a] Department of Chemistry and Department of Chemical Engineering, Indian Institute of Technology Bombay,
Powai, Mumbai 400 076, India
Fax: +91-22-2572-3480
E-mail: pghosh@chem.iitb.ac.in

 © 2006 Wiley-VCH Verlag GmbH & Co. KGaA, Weinheim 

the design of Au–NHC and Ag–NHC based initiators for the ring-opening polymerization (ROP) of L-lactide. In this regard, we have recently reported a Ag–NHC complex as an initiator for the bulk ROP of L-lactide.[21] Although there exists a few reports on the use of $Ag^{I}$–NHC complexes for the ROP of L-lactides,[18,21] we are unaware of any such report in the case of the $Au^{I}$–NHC complexes.

Of late, the ROP of L-lactide has attracted considerable attention by virtue of its eco-friendliness. Not only is the polylactide polymer (PLA) biodegradable, but the lactide monomer can also be generated from renewable resources by a corn fermentation process or from agricultural starch wastes.[22,23] Because of their good mechanical properties and biocompatibility, PLAs have found wide utility in medical and pharmaceutical applications.[24,25] Various metals, such as Zn, Al, and Sn, have been extensively utilized for the synthesis of PLAs.[22a] The specific objective of our program is centered around the design of novel initiators for the bulk polymerization of L-lactides, which are often used for the large-scale production of PLAs. It is interesting to note that even though PLAs can be synthesized by both solution polymerization[26] and bulk polymerization,[27] solution polymerization suffers from certain disadvantages such as being susceptible to impurity levels and to various unwanted reactions, namely, racemization and transesterification, and hence is not conducive for the large-scale production of PLAs.[28] Our approach towards the design of initiators for bulk polymerization involved the utilization of functionalized NHCs as we rationalized that the presence of functional groups would enhance the solubility of the initiators in the monomer melt.

Here in this contribution, we disclose the first example of $Au^{I}$–NHC-based initiator **1c** along with $Ag^{I}$–NHC-based initiator **1b** for the bulk ROP of L-lactide (Figure 1). Specifically, both the gold and the silver complexes, namely, [3-(*N*-*tert*-butylacetamido)-1-(2-hydroxycyclohexyl)imidazol-2-ylidene]AuCl (**1c**) and [3-(*N*-*tert*-butylacetamido)-1-(2-hydroxycyclohexyl)imidazol-2-ylidene]AgCl (**1b**), effectively catalyze the ROP of L-lactide at elevated temperatures under solvent-free melt conditions to afford polylactide polymers of moderate to low molecular weights with narrow molecular weight distributions [Equation (1)]. We also disclose the synthesis and structural characterizations of both the Au (**1c**) and Ag (**1b**) complexes supported over a novel difunctionalized *N*-heterocyclic carbene ligand, 3-(*N*-*tert*-butylacetamido)-1-(2-hydroxycyclohexyl)imidazol-2-ylidene.

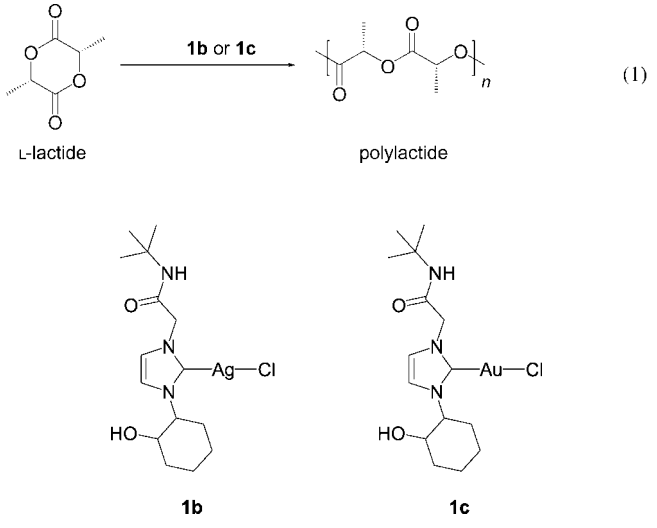


(1)

Figure 1. The complexes [3-(*N*-*tert*-butylacetamido)-1-(2-hydroxycyclohexyl)imidazol-2-ylidene]AgCl (**1b**) and [3-(*N*-*tert*-butylacetamido)-1-(2-hydroxycyclohexyl)imidazol-2-ylidene]AuCl (**1c**).

## Results and Discussion

A difunctionalized *N*-heterocyclic carbene ligand, 3-(*N*-*tert*-butylacetamido)-1-(2-hydroxycyclohexyl)imidazol-2-ylidene, with two functionalized imidazolyl *N*-substituents, a 2-hydroxycyclohexyl moiety and an *N*-*tert*-butylacetamido moiety, was synthesized by a modified procedure reported by Arnold and coworkers.[29] Specifically, the NHC precursor, 3-(*N*-*tert*-butylacetamido)-1-(2-hydroxycyclohexyl)imidazolium chloride (**1a**), was obtained from the direct reaction of *N*-*tert*-butyl-2-chloroacetamide, cyclohexene oxide, and imidazole in 96% yield (Scheme 1). The formation of imidazolium salt **1a** was confirmed by the appearance of the diagnostic (NC*H*N) resonance at $\delta$ = 9.31 ppm in the $^{1}$H NMR spectrum and the corresponding carbon resonance (N*C*HN) at $\delta$ = 136.3 ppm in the $^{13}$C NMR spectrum. The most interesting aspect of the $^{1}$H NMR spectrum is the diastereotopic nature of the two bridging methylene proton (-C$H_2$-) resonances which appear as two doublets at $\delta$ = 5.16 ppm and 4.96 ppm and display a geminal coupling between the two protons ($^{2}J_{H,H}$ = 15 Hz). For example, similar diastereotopic hydrogens for the bridging methylene moiety (-C$H_2$-) have been reported for Ir complexes with a 1-*n*-butyl-3-(2-pyridylmethyl)imidazol-2-ylidene ligand.[30] The carbonyl moiety (-*C*ONH-) appeared at $\delta$ = 163.8 ppm in the $^{13}$C NMR spectrum and at 1671 cm$^{-1}$ ($\nu_{co}$) in the infrared spectrum. In the electrospray mass spectrum the 3-(*N*-*tert*-butylacetamido)-1-(2-hydroxycyclohexyl)imidazolium cation appeared as a peak at *m*/*z* = 280 and was further substantiated by HRMS results.

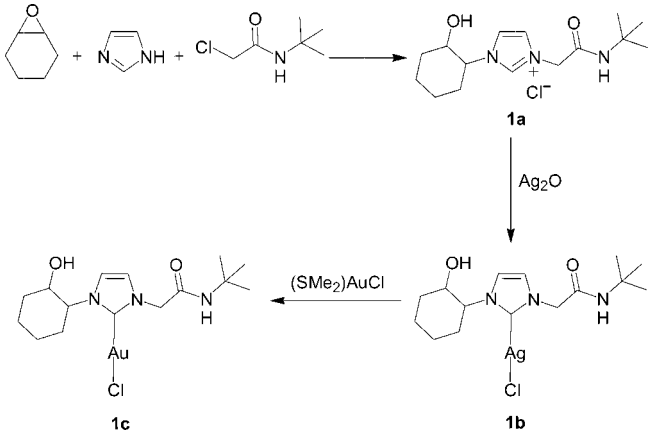


Scheme 1.

 © 2006 Wiley-VCH Verlag GmbH & Co. KGaA, Weinheim 

The imidazolium halide salt **1a** has been structurally characterized by X-ray diffraction studies (Figure 2). The N1–C9 and N2–C9 bond lengths are 1.326(6) Å and 1.314(6) Å, respectively, and the N2–C9–N1 angle is 107.9(5)° for **1a** and is comparable with other imidazolium halide salts. For example, in a CN-functionalized imidazolium salt, 1-$CH_2$CN-3-methylimidazolium chloride, the C–N bond lengths are 1.348(3) Å and 1.336(3) Å and the N–C–N angle is 107.6°.[31]

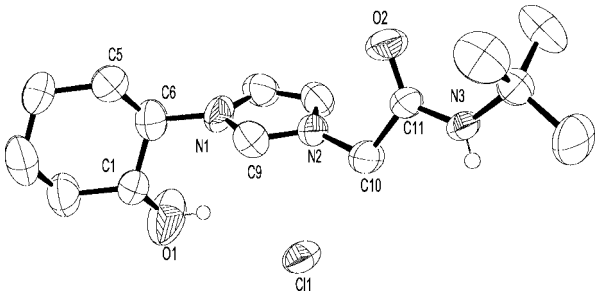


Figure 2. ORTEP drawing of **1a** with thermal ellipsoids drawn at 50% probability level. Selected bond lengths [Å] and angles [°]: N1–C9 1.326(6), N2–C9 1.314(6), N2–C9–N1 107.9(5).

The silver complex, [3-(*N*-*tert*-butylacetamido)-1-(2-hydroxycyclohexyl)imidazol-2-ylidene]AgCl (**1b**), was synthesized by the reaction of 3-(*N*-*tert*-butylacetamido)-1-(2-hydroxycyclohexyl)imidazolium chloride (**1a**) with $Ag_2O$ in dichloromethane at room temperature in 86% yield with the convenient methodology developed by Lin and coworkers.[32] The $^1$H NMR spectrum of **1b** confirmed the absence of the reactant imidazolium (NC*H*N) peak in the ca. 9 ppm region. The $^{13}$C NMR spectrum showed a new peak at $\delta$ = 181.6 ppm, which corresponds to the silver-bound carbene (N*C*N) resonance; the peak at $\delta$ = 136.3 ppm attributable to reactant **1a** (N*C*HN) was absent as a result of its deprotonation by $Ag_2O$ and is indicative of the formation of **1b**. The two diastereotopic protons of the bridging methylene (-C$H_2$-) group appeared shifted as two doublets at $\delta$ = 4.94 ppm ($^2J_{H,H}$ = 15 Hz) and 4.82 ppm ($^2J_{H,H}$ = 15 Hz), respectively, compared to that of **1a**. The carbon resonance of the bridging methylene (-*C*$H_2$-) group appeared at $\delta$ = 54.4 ppm in the $^{13}$C NMR spectrum. In the infrared spectrum, the amide carbonyl (-CONH-) appeared at 1673 cm$^{-1}$ while the hydroxy group appeared as a broad peak at 3302 cm$^{-1}$.

The definitive proof for the structure of **1b** came from X-ray diffraction studies (Figure 3), which revealed a neutral monomeric complex bearing a 1:1 (NHC ligand/metal) stoichiometry. The silver center of **1b** was found to be two-coordinate, displays a linear geometry [∠ C1–Ag1–Cl1 = 172.66(11)°], and is consistent with the most common geometry displayed by $d^{10}$ silver(I) ions.[33] The Ag–$C_{carb}$ (Ag1–C1 = 2.066(4) Å) bond length of **1b** is shorter than the sum of the individual covalent radii of Ag and C (2.111 Å),[34a] but is comparable to that observed in other related (NHC)AgCl-type complexes. For example, a Ag–$C_{carb}$ bond length of 2.056(7) Å was observed in the case of [1,3-*bis*(mesityl)imidazol-2-ylidene]AgCl,[35] while that of 2.098(2) Å was observed in another functionalized NHC complex, [1-(2-benzylideneamino-3,5-di-*tert*-butylbenzyl)-3-(*tert*-butyl)imidazol-2-ylidene]AgCl.[36] However, it is to be noted that the extent of π-backbonding in Group 11 metal–NHC (Cu, Au, Ag) complexes still remains a matter of debate with independent theoretical calculations carried out by Frenking[37] and Meyer,[38] who propose opposing views. In addition, a recent study by Cundari[39] concluded that a shortening of the metal–carbene bond up to 4% can be attributed to the change in hybridization state of the carbene carbon as a consequence of the enhanced *s*-character of the in-plane carbene lone pair σ-bonded to the metal in the metal–NHC complexes. The Ag1–Cl1 bond length of 2.3264(11) Å in **1b**, however, matches more closely with the sum of individual covalent radii of Ag and Cl (2.329 Å)[34a] and is in agreement with a single-bond character.

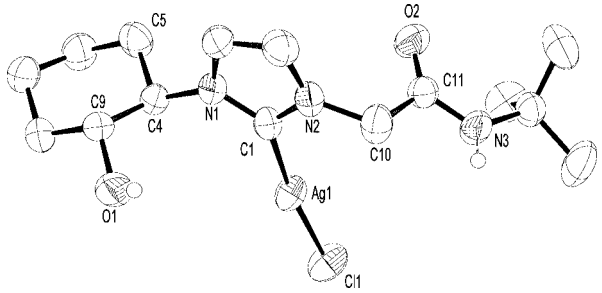


Figure 3. ORTEP drawing of **1b** with thermal ellipsoids drawn at 50% probability level. Selected bond lengths [Å] and angles [°]: Ag–C1 2.066(4), Ag–Cl1 2.3264(11), N1–C1 1.350(4), N2–C1 1.345(5), C1–Ag–Cl1 172.66(11), N2–C1–N1 110.9(3).

Another notable structural feature of **1b** is that both of the *N*-substituents, that is, the 2-hydroxycyclohexyl and the *N*-*tert*-butylacetamido moieties, are disposed *trans* to each other with respect to the plane that contains the central imidazole ring and the silver center. The 2-hydroxy cyclohexyl O atom (O1···Ag1 = 4.176 Å) and the *N*-*tert*-butylacetamido O atom (O2···Ag1 = 4.199 Å) are located equidistant from the central Ag atom but in approximately diagonally opposite directions (*trans* orientation). Furthermore, the 2-hydroxycyclohexyl and the *N*-*tert*-butylacetamido moieties are perpendicular to the imidazole ring where the dihedral angle is 111.2° (C9–C4–N1–C1) and 85.6° (C1–N2–C10–C11), respectively.

The treatment of silver complex **1b** with ($SMe_2$)AuCl yielded the gold complex, [3-(*N*-*tert*-butylacetamido)-1-(2-hydroxycyclohexyl)imidazol-2-ylidene]AuCl (**1c**), along with the precipitation of off-white AgCl in 77% yield. It is interesting to note that there are several methods available for the synthesis of Au–NHC complexes: (1) cleavage of electron-rich olefins,[40] (2) carbene transfer from Group 6 carbonyl complexes,[41] (3) reactions of azolium salts or free NHCs with $Au^I$ precursors,[42] (4) protonation or alkylation of gold azolyl complexes,[43] and (5) transmetalation by the reaction of $Ag^I$–NHC complexes with $Au^I$ precursors.[32] The popularity of the transmetalation method is primarily a result of the fact that the generation of free carbenes from the imidazolium salts with the use of strong bases often

 © 2006 Wiley-VCH Verlag GmbH & Co. KGaA, Weinheim 

promotes decomposition reactions, and also the generated free carbenes are often difficult to handle because of their air and moisture sensitivities.[13] The $^1$H NMR spectrum of **1c** shows two diastereotopic bridging methylene protons (-C$H_2$-) that appear as two sets of doublets at $\delta$ = 5.01 ppm ($^2J_{H,H}$ = 15 Hz) and 4.40 ppm ($^2J_{H,H}$ = 15 Hz). The Au-bound carbene (N*C*N) peak appears slightly shifted at $\delta$ = 170.2 ppm compared to the Ag-bound carbene (N*C*N) resonance at $\delta$ = 181.6 ppm in the $^{13}$C NMR spectrum. In the infrared spectrum, the carbonyl peak of the amido (-CONH-) moiety appears at 1676 cm$^{-1}$ while the cyclohexyl hydroxy peak appears at 3439 cm$^{-1}$.

The X-ray diffraction study revealed that the molecular structure of gold complex **1c** (Figure 4) is isomorphous with silver complex **1b**. The *N*-substituents, 2-hydroxycyclohexyl and *N*-*tert*-butylacetamido, were found to be perpendicular to the imidazole ring, and the dihedral angles between each of these two moieties and the imidazolium ring is 112.1(5)° (C9–C4–N2–C1) and 83.7(6)° (C11–C10–N1–C1), respectively. Notably, the 2-hydroxycyclohexyl O atom and the *N*-*tert*-butylacetamido O atom are disposed *trans* to each other with respect to the central imidazole ring and they also point away from the Au atom in diagonally opposite directions. The O1···Au1 (2-hydroxycyclohexyl O atom) and the O2···Au1 (*N*-*tert*-butylacetamido O atom) distances are 4.082 Å and 4.109 Å, respectively. Consistent with a shorter covalent radii of Au compared to Ag,[34] the Au1–C1 bond [1.969(5) Å] in **1c** was indeed shorter than the corresponding Ag1–Cl bond [2.066(4) Å] in **1b**. Another noticeable difference is that the N1–C1–N2 angle [105.2(4)°] in **1c** is slightly greater than the value seen in **1b** [104.3(3)°].

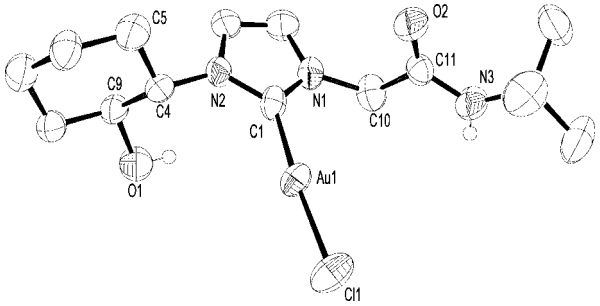


Figure 4. ORTEP drawing of **1c** with thermal ellipsoids drawn at 50% probability level. Selected bond lengths [Å] and angles [°]: Au–C1 1.969(5), Au–Cl1 2.2845(13), N1–C1 1.332(6), N2–C1 1.355(5), C1–Au–Cl1 175.30(15), N2–C1–N1 111.3(4).

It is worth noting that compared to the numerous Ag$^I$–NHC complexes that are known, the Au$^I$–NHC complexes are surprisingly few in number. Correspondingly, the structural diversity exhibited by Ag$^I$–NHC complexes are more varied and diverse[35,36,44,45] when compared to their gold counterparts,[46–48] which commonly exhibit neutral monomeric (NHC)AuX (X = halide) and cationic [(NHC)$_2$Au]$^+$ type structures.[13] In this regard, Nolan and coworkers[49] have recently reported a series of neutral monomeric gold complexes, [1,3-bis(R)imidazol-2-ylidene]AuCl (R = mesityl, 2,6-di-*i*-propylphenyl, cyclohexyl and adamentyl); the bond lengths and bond angles of which are comparable to that observed in **1c**.

Because of their synthetic ease and air and moisture stabilities, there is a growing emphasis on the catalytic utility of Au and Ag complexes of the (NHC)MX (M = Au, Ag, X = halide) type. Research in this area may facilitate their use as precursors in the preparation of other important compounds.

Quite significantly, both Au and Ag complexes **1c** and **1b** efficiently catalyze the bulk ROP of L-lactide under solvent-free melt conditions at elevated temperatures. To the best of our knowledge, **1c** represents the first example of a Au$^I$–NHC based initiator for the ROP of L-lactide. Even though there exists a report of solution polymerization[18] and a report of the bulk polymerization[21] of L-lactide by Ag$^I$–NHC complexes, we are not aware of any such polymerization by Au$^I$–NHC complexes. Bulk polymerization exhibits certain advantages over solution polymerization: (1) no solvent is required, (2) it is less vulnerable to impurity levels and unwanted side reactions, (3) it is often useful for the large-scale production of PLAs.[28]

Specifically, a typical polymerization experiment would involve the heating of L-lactide and the catalyst, **1b** or **1c**, for a given monomer to catalyst ratio in a sealed vessel under vacuum at a designated temperature for a specific period of time. Under these conditions, the reaction mixture would form a monomer melt in which the polymerization would occur. The variation of the [M]:[C] ratio (M = monomer, C = catalyst) showed that the maximum molecular weight in the case of **1b** (Entry 2: $M_n = 5.1 \cdot 10^3$, Table 1) as well as in **1c** (Entry 2: $M_n = 5.4 \cdot 10^3$, Table 2) were obtained at [M]:[C] ratio 100:1 for a 4 h run at 160 °C. The molecular weight distributions are almost similar for both catalysts **1b** (PDI = 1.10–1.53) and **1c** (PDI = 1.07–1.35). Interesting would be the comparison of the polymerization results of **1b** and **1c** with that of the other reported Au and Ag–NHC complexes. As we are unaware of any Au–NHC complex known for the ROP of L-lactide, such a comparison can only be drawn for the Ag–NHC complexes.[18,21] For example, for a cationic 2:1 (NHC ligand/metal) silver-NHC complex supported over a mono-functionalized NHC ligand re-

Table 1. Melt polymerization of L-lactide by **1b**.

| Entry | L-Lactide/**1b** ratio | Temp. [°C] | Time [h] | $M_n$ | Mw/$M_n$ | Conversion [%] |
|---|---|---|---|---|---|---|
| 1 | 50 | 160 | 4 | $3.6 \cdot 10^3$ | 1.39 | 98 |
| 2 | 100 | 160 | 4 | $5.1 \cdot 10^3$ | 1.23 | 93 |
| 3 | 150 | 160 | 4 | $4.9 \cdot 10^3$ | 1.24 | 86 |
| 4 | 200 | 160 | 4 | $4.8 \cdot 10^3$ | 1.16 | 67 |
| 5 | 250 | 160 | 4 | $4.5 \cdot 10^3$ | 1.14 | 53 |
| 6 | 300 | 160 | 4 | $4.1 \cdot 10^3$ | 1.13 | 42 |
| 7 | 100 | 120 | 4 | $4.2 \cdot 10^3$ | 1.10 | 78 |
| 8 | 100 | 140 | 4 | $4.9 \cdot 10^3$ | 1.17 | 96 |
| 9 | 100 | 180 | 4 | $4.9 \cdot 10^3$ | 1.31 | 96 |
| 10 | 100 | 160 | 1 | $3.0 \cdot 10^3$ | 1.19 | 67 |
| 11 | 100 | 160 | 2 | $4.0 \cdot 10^3$ | 1.25 | 92 |
| 12 | 100 | 160 | 3 | $4.4 \cdot 10^3$ | 1.20 | 95 |
| 13 | 100 | 160 | 6 | $5.1 \cdot 10^3$ | 1.29 | 98 |
| 14 | 100 | 160 | 8 | $4.6 \cdot 10^3$ | 1.53 | 99 |

 © 2006 Wiley-VCH Verlag GmbH & Co. KGaA, Weinheim 

cently reported by us[21] for the bulk polymerization of L-lactide under analogous melt conditions, higher molecular weight polymers were obtained as compared to that of **1b** and **1c**. However, it should be noted that in the present study neutral monomeric (NHC)MCl (M = Ag and Au) type complexes, supported over a different difunctionalized NHC ligand, were examined as initiators for lactide polymerizations.

Table 2. Melt polymerization of L-lactide by **1c**.

| Entry | L-Lactide/**1c** ratio | Temp. [°C] | Time [h] | $M_n$ | $Mw/M_n$ | Conversion [%] |
|---|---|---|---|---|---|---|
| 1 | 50 | 160 | 4 | $3.9\cdot10^3$ | 1.23 | 96 |
| 2 | 100 | 160 | 4 | $5.4\cdot10^3$ | 1.17 | 80 |
| 3 | 150 | 160 | 4 | $5.0\cdot10^3$ | 1.13 | 56 |
| 4 | 200 | 160 | 4 | $3.8\cdot10^3$ | 1.22 | 42 |
| 5 | 250 | 160 | 4 | $3.6\cdot10^3$ | 1.21 | 31 |
| 6 | 300 | 160 | 4 | $3.6\cdot10^3$ | 1.13 | 29 |
| 7 | 100 | 120 | 4 | $2.7\cdot10^3$ | 1.13 | 56 |
| 8 | 100 | 140 | 4 | $4.3\cdot10^3$ | 1.17 | 74 |
| 9 | 100 | 180 | 4 | $4.1\cdot10^3$ | 1.12 | 97 |
| 10 | 100 | 160 | 1 | $2.0\cdot10^3$ | 1.07 | 27 |
| 11 | 100 | 160 | 2 | $2.8\cdot10^3$ | 1.11 | 41 |
| 12 | 100 | 160 | 3 | $3.4\cdot10^3$ | 1.11 | 61 |
| 13 | 100 | 160 | 6 | $4.1\cdot10^3$ | 1.22 | 74 |
| 14 | 100 | 160 | 8 | $5.1\cdot10^3$ | 1.35 | 90 |

The time-dependence study showed that the average molecular weight ($M_n$) of the polymer increased with time for the first 6 h in the case of **1b** and for the first 4 h in the case of **1c**, after which it reached saturation. The temperature-dependence study was carried out in the range 120–180 °C and showed that for both **1b** and **1c** the molecular weight increased steadily with the temperature till 160 °C after which point it started to decrease. The decrease in molecular weight may be attributed to the depolymerization that takes place at higher temperatures. A similar decrease in the molecular weight at higher temperatures has been reported by Liao[27a] and by Albertson and Varma.[24] Detailed mechanistic studies are underway to establish the nature of the active species responsible for the catalysis. In this regard, it is worth mentioning that there have been reports of both metal-mediated polymerization[21] as well as carbene-mediated lactide polymerization.[52]

It is interesting to note that despite the fact that the Au–$C_{carb}$ bond energy (76.3 kcal/mol) is significantly stronger than the Ag–$C_{carb}$ bond energy (53.1 kcal/mol) in (NHC)-MCl (M = Ag and Au) complexes,[37] comparable polymer molecular weights were observed in the case of **1b** ($M_n$ = $3.0–5.1\cdot10^3$) and **1c** ($M_n$ = $2.0–5.4\cdot10^3$). At this juncture, it will be worthwhile to compare the activity of **1c**, with representative examples of other metal-based catalysts for the bulk ROP of L-lactide. For example, the zinc complexes of the picolyl carbene ligand, namely, ethyl zinc iodide·1-mesityl-3-picolylimidazol-2-ylidene adduct and its bis-ligand adduct gave PLAs with $M_n$ = $(6.1–20)\cdot10^3$, when the polymerization was carried out at 140 °C.[26b] The molecular weight distributions (PDI = 1.78–2.45) for PLAs obtained from these picolylcarbene-based zinc complexes are, however, higher as compared to that of **1b** or **1c**. Similarly, the Co, Ni, Cu, and Zn complexes of a Schiff base ligand derived from salicylidene and L-aspartic acid, also yielded PLAs with a viscosity average molecular weight in the order of $(4.86–11.1)\cdot10^3$ at 130 °C over a period of 24 h.[53] Furthermore, PLAs with a relatively narrow molecular weight distribution (PDI = 1.12–1.32) have been obtained with $M_n$ = $(1.93–2.3)\cdot10^4$ with the use of Red-Al as a catalyst in the temperature range of 110–135 °C.[27b] In addition, a series of titanatranes with varying ring sizes have been successfully employed to achieve molecular weights [$M_n$ = $(1.6–3.36)\cdot10^4$] with PDI in the range of 1.42–1.97 at 130 °C.[27c] Recently, various ferric alkoxides [$Fe(OR)_3$; R = Et, Pr, *i*Pr, Bu] have been reported for moderate molecular weight PLAs [$M_n$ = $(1.78–13.97)\cdot10^4$] with PDI = 1.60–1.98; however, the polymerization have been carried out up to 72 h at 130–150 °C.[27a] We believe that, as a first example of a Au-based initiator for the bulk polymerization of L-lactide, the Au–NHC complex **1c** would encourage further research in the utility of gold in this area.

## Conclusion

In summary, two new silver and gold complexes, namely, [3-(*N*-*tert*-butylacetamido)-1-(2-hydroxycyclohexyl)imidazol-2-ylidene]AgCl (**1b**) and [3-(*N*-*tert*-butylacetamido)-1-(2-hydroxycyclohexyl)imidazol-2-ylidene]AuCl (**1c**), supported over a difunctionalized *N*-heterocyclic carbene ligand have been synthesized. The **1a**, **1b**, and **1c** complexes have been structurally characterized by X-ray diffraction studies. The comparison of structures **1b** and **1c** show the formation of neutral monomeric complexes that have a 1:1 (NHC ligand/metal) stoichiometry. Notably, in neither structure **1b** nor structure **1c** was the chelation of the functionalized sidearms to the metals observed. This is in agreement with the two-coordinated $d^{10}$ configurations of the $Au^I$ and $Ag^I$ ions that prefer linear geometries. The gold and silver complexes **1c** and **1b** effectively catalyze the ROP of L-lactide under solvent-free melt conditions to produce the polylactide polymer of moderate to low molecular weight with a narrow molecular weight distribution. Gold complex **1c** represents the first example of a $Au^I$–NHC based initiator for the ROP of L-lactide.

## Experimental Section

**General Procedures:** All manipulations were carried out with a glove box and/or standard Schlenk techniques. Solvents were purified and degassed by standard procedures. $Ag_2O$ was purchased from SD-fine chemicals (India) and used without any further purification. $(SMe_2)AuCl$[50] and *N*-*tert*-butyl-2-chloroacetamide[51] were synthesized according to literature procedures. $^1H$- and $^{13}C\{^1H\}$ NMR spectra were recorded in $CDCl_3$ with a Varian 400 MHz NMR spectrometer. $^1H$ NMR peaks are labeled as singlet (s), doublet (d) and multiplet (m). Infrared spectra were recorded with a Perkin–Elmer Spectrum One FTIR spectrometer. Mass spectrometry measurements were performed with a Micromass Q-Tof spectrometer. Polymer molecular weights were determined with a Waters GPC (Waters 2414 RI Detector) and with PL-

 © 2006 Wiley-VCH Verlag GmbH & Co. KGaA, Weinheim 

gel, 5μ Mixed-D (2 × 300 mm) column, with polystyrene standards in chloroform, with a covered molecular weight range of l40 to $4{\cdot}10^5$. X-ray diffraction data for **1b** was collected with a NONIUS-MACH3 diffractometer and that of **1a** and **1c** was collected on Oxford diffraction XCALIBUR-S instrument. The crystal data collection and refinement parameters are summarized in Table 3. The structures were solved by direct methods and standard difference map techniques and were refined by full-matrix least-squares procedures on *F*2 with SHELXTL (Version 6.10). CCDC-606428 (**1a**), CCDC-606429 (**1b**), and CCDC-606427 (**1c**) contain the supplementary crystallographic data for this paper. These data can be obtained free of charge from The Cambridge Crystallographic Data Centre via www.ccdc.cam.ac.uk/data_request/cif.

Table 3. X-ray crystallographic data for **1a**, **1b** and **1c**.

| Compound | **1a** | **1b** | **1c** |
|---|---|---|---|
| Lattice | monoclinic | orthorhombic | orthorhombic |
| Formula | $C_{15}H_{26}ClN_3O_2$ | $C_{15}H_{25}AgClN_3O_2$ | $C_{15}H_{24}AuClN_3O_2$ |
| Formula weight | 315.84 | 422.70 | 510.79 |
| Space group | *P*21/*n* | *Pabc* | *Pcab* |
| *a* [Å] | 14.799(4) | 9.8760(11) | 9.879(2) |
| *b* [Å] | 5.648(5) | 19.0390(11) | 18.800(2) |
| *c* [Å] | 21.571(3) | 19.2450(12) | 19.391(3) |
| *α* [°] | 90.00 | 90.00 | 90.00 |
| *β* [°] | 105.802(15) | 90.00 | 90.00 |
| *γ* [°] | 90.00 | 90.00 | 90.00 |
| *V* [Å$^3$] | 1734.8(16) | 3618.6(5) | 3601.4(11) |
| *Z* | 4 | 8 | 8 |
| Temperature [K] | 293(2) | 293(2) | 293(2) |
| Radiation (*λ* [Å]) | 0.71073 | 0.71073 | 0.71073 |
| *ρ*(calcd.) [g cm$^{-3}$] | 1.209 | 1.884 | 1.884 |
| *μ*(Mo-$K_α$) [mm$^{-1}$] | 0.228 | 1.271 | 8.328 |
| *θ* max [°] | 32.2342 | 12.2000 | 2.99–30.16 |
| No. of data | 3051 | 3182 | 5309 |
| No. of parameters | 194 | 211 | 203 |
| $R_1$ | 0.0821 | 0.0320 | 0.0316 |
| $wR_2$ | 0.2143 | 0.0708 | 0.0560 |
| GOF | 1.102 | 0.964 | 0.827 |

**Synthesis of 3-(*N*-*tert*-Butylacetamido)-1-(2-hydroxycyclohexyl)-imidazolium Chloride (1a):** Cyclohexene oxide (0.656 g, 6.69 mmol) and imidazole (0.455 g, 6.69 mmol) were heated at 60 °C for 12 h and the resulting sticky brown solid was dissolved in acetonitrile (ca. 20 mL). *N*-*tert*-Butyl-2-chloroacetamide (1.00 g, 6.69 mmol) was added to the solution and the reaction mixture was heated at 90 °C for 2 h. A white precipitate was collected by filtration and was recrystallized from acetonitrile (ca. 10 mL) and dried under vacuum to give the product **1a** as a white solid (2.02 g, 96%). $^1$H NMR ($CDCl_3$, 400 MHz, 25 °C): $\delta$ = 9.31 (s, 1 H, NC*H*N), 8.19 (br., 1 H, N*H*), 7.44 (br., 2 H, NC*H*CHN), 5.16 (d, $^2J$ = 15 Hz, 1 H, C$H_2$), 4.96 (d, $^2J$ = 15 Hz, 1 H, C$H_2$), 4.12–4.00 (m, 1 H, $C_6H_{10}$), 3.62–3.56 (m, 1 H, $C_6H_{10}$), 2.12–1.98 (m, 4 H, $C_6H_{10}$), 1.78–1.68 (m, 4 H, $C_6H_{10}$), 1.30 [s, 9 H, C(C$H_3$)$_3$] ppm. $^{13}$C{$^1$H} NMR ($CDCl_3$, 100 MHz, 25 °C): $\delta$ = 163.8 (*C*O), 136.3 (N*C*HN), 123.1 (N*C*HCHN), 120.1 (NCH*C*HN), 51.8 (*C*H$_2$), 34.3 ($C_6H_{10}$), 31.2 ($C_6H_{10}$), 30.9 [*C*(CH$_3$)$_3$], 28.5 [C(*C*H$_3$)$_2$], 24.5 (2C, $C_6H_{10}$), 23.9 (2C, $C_6H_{10}$) ppm. IR (KBr): $\tilde{\nu}$ = 3213 (br, OH), 1671 (s, CO) cm$^{-1}$. LRMS (ES): *m*/*z* (%) = 280 [100, (NHC–Ligand)$^+$]. HRMS (ES): calcd. for (NHC–Ligand)$^+$ 280.2025; found 280.2022.

**Synthesis of [3-(*N*-*tert*-Butylacetamido)-1-(2-hydroxycyclohexyl)-imidazol-2-ylidene]AgCl (1b):** A mixture of 3-(*N*-*tert*-butylacetamido)-1-(2-hydroxycyclohexyl)imidazolium chloride **1a** (2.98 g, 9.53 mmol) and $Ag_2O$ (1.11 g, 4.77 mmol) in dichloromethane (ca. 25 mL) was stirred at room temperature for 6 h. The reaction mixture was filtered and the solvent was removed under vacuum to give the product **1b** as a white solid (3.46 g, 86%). $^1$H NMR ($CDCl_3$, 400 MHz, 25 °C): $\delta$ = 8.19 (br., 1 H, N*H*), 7.03 (br., 2 H, NC*H*CHN), 4.94 (d, $^2J$ = 15 Hz, 1 H, C$H_2$), 4.82 (d, $^2J$ = 15 Hz, 1 H, C$H_2$), 4.25–4.20 (m, 1 H, $C_6H_{10}$), 3.68–3.55 (m, 1 H, $C_6H_{10}$), 2.13–2.04 (m, 4 H, $C_6H_{10}$), 1.80–1.70 (m, 4 H, $C_6H_{10}$), 1.34 [s, 9 H, C(C$H_3$)$_3$] ppm. $^{13}$C{$^1$H} NMR ($CDCl_3$, 100 MHz, 25 °C): $\delta$ = 181.6 (N*C*N–Ag), 166.6 (*C*O), 123.0 (N*C*HCHN), 117.8 (NCH*C*HN), 54.4 (*C*H$_2$), 34.4 ($C_6H_{10}$), 32.9 ($C_6H_{10}$), 32.3 [*C*(CH$_3$)$_3$], 28.6 [C(*C*H$_3$)$_2$], 24.9 (2 C, $C_6H_{10}$), 24.4 (2 C, $C_6H_{10}$) ppm. IR (KBr): $\tilde{\nu}$ = 3302 (br, OH), 1673 (s, CO) cm$^{-1}$. LRMS (ES): *m*/*z* = 386 (NHC–Ag)$^+$, 667 (NHC)$_2$Ag]$^+$.

**Synthesis of [3-(*N*-*tert*-Butylacetamido)-1-(2-hydroxycyclohexyl)-imidazol-2-ylidene]AuCl (1c):** A mixture of [3-(*N*-*tert*-butylacetamido)-1-(2-hydroxycyclohexyl)imidazol-2-ylidene]AgCl **1b** (0.277 g, 0.651 mmol) and ($SMe_2$)AuCl (0.193 g, 0.651 mmol) in dichloromethane (ca. 15 mL) was stirred at room temperature for 6 h, when the formation of an off-white AgCl precipitate was observed. The reaction mixture was filtered and the solvent was removed under vacuum to obtain the product **1c** as a white solid (0.259 g, 77%). $^1$H NMR ($CDCl_3$, 400 MHz, 25 °C): $\delta$ = 9.12 (br., 1 H, N*H*), 7.12 (br., 1 H, NC*H*CHN), 6.93 (br., 1 H, NC*H*CHN), 5.01 (d, $^2J$ = 15 Hz, 1 H, C$H_2$), 4.40 (d, $^2J$ = 15 Hz, 1 H, C$H_2$), 4.35–4.29 (m, 1 H, $C_6H_{10}$), 3.76–3.70 (m, 1 H, $C_6H_{10}$), 2.07–2.01 (m, 4 H, $C_6H_{10}$), 1.80–1.67 (m, 4 H, $C_6H_{10}$), 1.30 [s, 9 H, C(C$H_3$)$_3$] ppm. $^{13}$C{$^1$H} NMR ($CDCl_3$, 100 MHz, 25 °C): $\delta$ = 170.2 (N*C*N–Au), 165.7 (*C*O), 123.6 (N*C*HCHN), 117.7 (NCH*C*HN), 54.4 (*C*H$_2$), 41.0 ($C_6H_{10}$), 34.0 ($C_6H_{10}$), 32.4 [*C*(CH$_3$)$_3$], 29.7 [C(*C*H$_3$)$_2$], 24.9 (2 C, $C_6H_{10}$), 24.3 (2 C, $C_6H_{10}$) ppm. IR (KBr): $\tilde{\nu}$ = 3439 (br, OH), 1676 (s, CO) cm$^{-1}$.

**Polymerization Experiments:** Bulk polymerizations of L-lactide were carried out in vacuo-sealed glass ampoules. Firstly, the glass ampoule was charged with monomer (L-lactide) and dried for a period of two hours under high vacuum at 50 °C. Subsequently, the catalyst (**1b** or **1c**) was then added with the monomer to catalyst ratio in the range of 50–300. The ampoule was sealed under high vacuum and immersed in an oil bath. Polymerizations were carried out in the temperature range 120–180 °C. After a predetermined time (1–8 h) the glass ampoule was removed and subsequently the molten reactive polymer mixture was cooled while the sealed ampoule was immersed in liquid nitrogen to stop the polymerization, and thereafter the samples were removed for analysis. The analyses were performed on the crude reaction mixture; no precipitation was executed in order to avoid fractionation of the sample.

## Acknowledgments

We thank the Department of Science and Technology (Grant No: SR/S1/IC-25/2003) for financial support of this research. We are grateful to the National Single Crystal X-ray Diffraction Facility at IIT Bombay, India, for the crystallographic results. LR thanks IIT Bombay, Mumbai, for a research fellowship.

[1] a) F. Caruso, M. Rossi, J. Tanski, C. Pettinari, F. Marchetti, *J. Med. Chem.* **2003**, *46*, 1737–1742; b) K. Nomiya, S. Yamamoto, R. Noguchi, H. Yokoyama, N. C. Kasuga, K. Ohyama, C. Kato, *J. Inorg. Biochem.* **2003**, *95*, 208–220; c) K. Nomiya, S. Takahashi, R. Noguchi, *J. Chem. Soc., Dalton Trans.* **2000**, 2091–2097; d) C. F. Shaw III, *Chem. Rev.* **1999**, *99*, 2589–2600.
[2] Y.-J. Chen, C.-T. Yeh, *J. Catal.* **2001**, *200*, 59–68.
[3] M. R. Fructos, T. R. Belderrain, P. de Frémont, N. M. Scott, S. P. Nolan, M. M. Díaz-Requejo, P. J. Pérez, *Angew. Chem. Int. Ed.* **2005**, *44*, 5284–5288.

 © 2006 Wiley-VCH Verlag GmbH & Co. KGaA, Weinheim 

[4] D. S. McGuinness, K. J. Cavell, *Organometallics* **2000**, *19*, 741–748.
[5] L. Xu, W. Chen, J. F. Bickley, A. Steiner, J. Xiao, *J. Organomet. Chem.* **2000**, *598*, 409–416.
[6] J. Huang, E. D. Stevens, S. P. Nolan, *Organometallics* **2000**, *19*, 1194–1197.
[7] For representative examples, see a) J. R. Miecznikowski, R. H. Crabtree, *Organometallics* **2004**, *23*, 629–631; b) S. Kuhl, R. Schneider, Y. Fort, *Organometallics* **2003**, *22*, 4184–4186; c) V. K. Dioumaev, D. J. Szalda, J. Hanson, J. A. Franz, R. M. Bullock, *Chem. Commun.* **2003**, 1670–1671; d) L. D. Vázquez-Serrano, B. T. Owens, J. M. Buriak, *Chem. Commun.* **2002**, 2518–2519; e) H. M. Lee, T. Jiang, E. D. Stevens, S. P. Nolan, *Organometallics* **2001**, *20*, 1255–1258; f) M. T. Powell, D.-R. Hou, M. C. Perry, X. Cui, K. Burgess, *J. Am. Chem. Soc.* **2001**, *123*, 8878–8879.
[8] M. Albrecht, J. R. Miecznikowski, A. Samuel, J. W. Faller, R. H. Crabtree, *Organometallics* **2002**, *21*, 3596–3604.
[9] H. Van Rensburg, R. P. Tooze, D. F. Foster, A. M. Z. Slawin, *Inorg. Chem.* **2004**, *43*, 2468–2470.
[10] For representative examples, see a) E. Mas-Marźa, M. Poyatos, M. Sanaú, E. Peris, *Inorg. Chem.* **2004**, *43*, 2213–2219; b) R. A. Diggle, S. A. Macgregor, M. M. Whittlesey, *Organometallics* **2004**, *23*, 1857–1865; c) H. Kaur, F. K. Zinn, E. D. Stevens, S. P. Nolan, *Organometallics* **2004**, *23*, 1157–1160; d) K. H. Park, S. Y. Kim, S. U. Son, Y. K. Chung, *Eur. J. Org. Chem.* **2003**, *22*, 4341–4345; e) W.-L. Duan, M. Shi, G.-B. Rong, *Chem. Commun.* **2003**, 2916–2917; f) I. E. Marko, S. Stérin, O. Buisine, G. Mignani, P. Branlard, B. Tinant, J.-P. Declercq, *Science* **2002**, *298*, 204–206; g) V. K. Dioumaev, R. M. Bullock, *Nature* **2003**, *424*, 530–532.
[11] M. G. Gardiner, W. A. Herrmann, C. P. Reisinger, J. Schwarz, M. Spiegler, *J. Organomet. Chem.* **1999**, *572*, 239–247.
[12] G. Grasa, Z. Moore, K. L. Martin, E. D. Stevens, S. P. Nolan, V. Paquet, H. Lebel, *J. Organomet. Chem.* **2002**, *658*, 126–131.
[13] For a recent review on Au–NHC complexes see I. J. B. Lin, C. S. Vasam, *Can. J. Chem.* **2005**, *83*, 812–825.
[14] J. C. Garrison, W. J. Youngs, *Chem. Rev.* **2005**, *105*, 3978–4008.
[15] P. L. Arnold, *Heteroat. Chem.* **2002**, *13*, 534–539.
[16] M. M. Díaz-Requejo, P. J. Pérez, *J. Organomet. Chem.* **2005**, *690*, 5441–5450.
[17] J. Ramírez, R. Corberán, M. Sanaú, E. Peris, E. Fernandez, *Chem. Commun.* **2005**, 3056–3058.
[18] A. C. Sentman, S. Csihony, R. M. Waymouth, J. L. Hedrick, *J. Org. Chem.* **2005**, *70*, 2391–2393.
[19] A. Melaiye, R. S. Simons, A. Milsted, F. Pingitore, C. Wesdemiotis, C. A. Tessier, W. J. Youngs, *J. Med. Chem.* **2004**, *47*, 973–977.
[20] A. Melaiye, Z. Sun, K. Hindi, A. Milsted, D. Ely, D. H. Reneker, C. A. Tessier, W. J. Youngs, *J. Am. Chem. Soc.* **2005**, *127*, 2285–2291.
[21] M. K. Samantaray, V. Katiyar, D. Roy, K. Pang, H. Nanavati, R. B. Sunoj, P. Ghosh, *Eur. J. Inorg. Chem.* **2006**, 2975–2984.
[22] a) O. Dechy-Cabaret, B. Martin-Vaca, D. Bourissou, *Chem. Rev.* **2004**, *104*, 6147–6176; b) B. J. O'Keefe, M. A. Hillmyer, W. B. Tolman, *J. Chem. Soc., Dalton Trans.* **2001**, 2215–2224.
[23] a) K. A. M. Thakur, R. T. Kean, E. S. Hall, J. J. Kolstad, E. J. Munson, *Macromolecules* **1998**, *31*, 1487–1494; b) K. A. M. Thakur, R. T. Kean, E. S. Hall, J. J. Kolstad, T. A. Lindgren, M. A. Doscotch, J. I. Siepmann, E. J. Munson, *Macromolecules* **1997**, *30*, 2422–2428.
[24] A.-C. Albertsson, I. K. Varma, *Biomacromolecules* **2003**, *4*, 1466–1486.
[25] a) M. Okada, *Prog. Polym. Sci.* **2002**, *27*, 87–133; b) H. R. Kriecheldorf, *Chemosphere* **2001**, *43*, 49–54.
[26] a) J. Ejfler, M. Kobylka, L. B. Jerzykiewicz, P. Sobota, *Dalton Trans.* **2005**, 2047–2050; b) T. R. Jensen, C. P. Schaller, M. A. Hillmyer, W. B. Tolman, *J. Organomet. Chem.* **2005**, *690*, 5881–5891; c) M. H. Chisholm, J. Gallucci, K. Phomphrai, *Chem. Commun.* **2003**, 48–49; d) C. K. Williams, L. E. Breyfogle, S. K. Choi, W. Nam, V. G. Young Jr, M. A. Hillmyer, W. B. Tolman, *J. Am. Chem. Soc.* **2003**, *125*, 11350–11359; e) M. Myers, E. F. Connor, T. Glauser, A. Möck, G. Nyce, J. L. Hedrick, *J. Polymer Sci., Part A: Polym. Chem.* **2002**, *40*, 844–851; f) B. M. Chamberlain, M. Cheng, D. R. Moore, T. M. Ovitt, E. B. Lobkovsky, G. W. Coates, *J. Am. Chem. Soc.* **2001**, *123*, 3229–3238; g) Ph. Dubios, N. Ropson, R. Jérôme, Ph. Teyssié, *Macromolecules* **1996**, *29*, 1965–1975.
[27] a) X. Wang, K. Liao, D. Quan, Q. Wu, *Macromolecules* **2005**, *38*, 4611–4617; b) H. Li, C. Wang, F. Bai, J. Yue, H.-G. Woo, *Organometallics* **2004**, *23*, 1411–1415; c) Y. Kim, J. G. Verkade, *Organometallics* **2002**, *21*, 2395–2399; d) .A. J. Nijenhuis, D. W. Grijpma, A. J. Pennings, *Macromolecules* **1992**, *25*, 6419–6424.
[28] D. Garlotta, *J. Polym. Environ.* **2001**, *9*, 63–84.
[29] P. L. Arnold, M. Rodden, K. M. Davis, A. C. Scarisbrick, A. J. Blake, C. Wilson, *Chem. Commun.* **2004**, 1612–1613.
[30] E. Mas-Marzá, M. Sanaú, E. Peris, *Inorg. Chem.* **2005**, *44*, 9961–9967.
[31] D. Zhao, Z. Fei, R. Scopelliti, P. J. Dyson, *Inorg. Chem.* **2004**, *43*, 2197–2205.
[32] H. M. J. Wang, I. J. B. Lin, *Organometallics* **1998**, *17*, 972–975.
[33] F. A. Cotton, G. Wilkinson, C. A. Murillo, M. Bochmann, M. *Advanced Inorganic Chemistry*, 6th ed. **1999**, p. 1085–1094.
[34] a) L. Pauling, *The Nature of the Chemical Bond*, 3rd ed.; Cornell University Press: Ithaca, NY, **1960**; p. 224–228, 256–258; b) U. M. Tripathi, A. Bauer, H. Schmidbaur, *J. Chem. Soc., Dalton Trans.* **1997**, 2865–2868.
[35] T. Ramnial, C. D. Abernethy, M. D. Spicer, I. D. Mckenzie, I. D. Gay, J. A. C. Clyburne, *Inorg. Chem.* **2003**, *42*, 1391–1393.
[36] A. A. D. Tulloch, A. A. Danopoulos, S. Winston, S. Kleinhenz, G. Eastham, *J. Chem. Soc., Dalton Trans.* **2000**, 4499–4506.
[37] D. Nemcsok, K. Wichmann, G. Frenking, *Organometallics* **2004**, *23*, 3640–3646.
[38] X. Hu, I. Castro-Rodriguez, K. Olsen, K. Meyer, *Organometallics* **2004**, *23*, 755–764.
[39] E. Baba, T. R. Cundari, I. Firkin, *Inorg. Chim. Acta* **2005**, *358*, 2867–2875.
[40] B. Cetinkaya, P. Dixneuf, M. F. Lappert, *J. Chem. Soc., Dalton Trans.* **1974**, 1827–1833.
[41] a) S.-T. Liu, K. R. Reddy, *Chem. Soc. Rev.* **1999**, *28*, 315–322; b) R.-Z. Ku, J.-C. Huang, J.-Y. Cho, F.-M. Kiang, K. R. Reddy, Y.-C. Chen, Y. K.-J. Lee, J.-H. Lee, G.-H. Lee, S.-M. Peng, S.-T. Liu, *Organometallics* **1999**, *18*, 2145–2154.
[42] K. M. Lee, C. K. Lee, I. J. B. Lin, *Angew. Chem. Int. Ed. Engl.* **1997**, *36*, 1850–1852.
[43] B. Bovio, S. Calogero, F. E. Wagner, A. Burini, B. R. Pietroni, *J. Organomet. Chem.* **1994**, *470*, 275–283.
[44] K. M. Lee, H. M. J. Wang, I. J. B. Lin, *J. Chem. Soc., Dalton Trans.* **2002**, 2852–2856.
[45] Q.-X. Liu, F.-B. Xu, Q.-S. Li, X.-S. Zeng, X.-B. Leng, Y. L. Chou, Z.-Z. Zhang, *Organometallics* **2003**, *22*, 309–314.
[46] V. J. Catalano, A. L. Moore, *Inorg. Chem.* **2005**, *44*, 6558–6566.
[47] H. M. J. Wang, C. S. Vasam, T. Y. R. Tsai, S.-H. Chen, H. H. Chang, I. J. B. Lin, *Organometallics* **2005**, *24*, 486–493.
[48] M. V. Baker, P. J. Barnard, S. J. Berners-Price, S. K. Brayshaw, J. L. Hickey, B. W. Skelton, A. H. White, *J. Organomet. Chem.* **2005**, *690*, 5625–5635.
[49] P. de Frémont, N. M. Scott, E. D. Stevens, S. P. Nolan, *Organometallics* **2005**, *24*, 2411–2418.
[50] M.-C. Brandys, M. C. Jennings, R. J. Puddephatt, *J. Chem. Soc., Dalton Trans.* **2000**, 4601–4606.
[51] M. P. Dave, J. M. Patel, N. A. Langalia, S. R. Shah, K. A. Thaker, *J. Indian Chem. Soc.* **1985**, *62*, 386–387.
[52] G. W. Nyce, T. Glauser, E. F. Connor, A. Mock, R. M. Waymouth, J. L. Hedrick, *J. Am. Chem. Soc.* **2003**, *125*, 3046–3056.
[53] J. Sun, W. Shi, D. Chen, C. Liang, *J. Appl. Polym. Sci.* **2002**, *86*, 3312–3315.

Received: May 3, 2006
Published Online: August 7, 2006

 © 2006 Wiley-VCH Verlag GmbH & Co. KGaA, Weinheim 

DOI: 10.1002/ejic.200600420

# A Comparative Study of the Optical and Electroluminescent Properties of $Eu^{III}$ Complexes with TTA and 2-(2′-Pyridyl)azoles: The Crystal Structure of $[Eu(TTA)_3(PBO)]$

**Li-Hua Gao,[a,b] Min Guan,[c] Ke-Zhi Wang,*[a] Lin-Pei Jin,[a] and Chun-Hui Huang[c]**

**Keywords:** X-ray diffraction / Luminescence / Chelates / N,O ligands / Lanthanides

Two $Eu^{III}$ mixed-ligand complexes, namely $[Eu(TTA)_3(PBO)]$ and $[Eu(TTA)_3(PBT)]$ [TTA = 1,1,1-trifluoro-3-(2-thenoyl)acetonato, PBO = 2-(2′-pyridyl)-1,3-benzoxazole, and PBT = 2-(2′-pyridyl)-1,3-benzothiazole], have been synthesized. $[Eu(TTA)_3(PBO)]$ has been structurally characterized by single-crystal X-ray diffraction analysis. The complex crystallizes in the monoclinic space group $C2/c$. The lattice parameters are $a$ = 41.346(4), $b$ = 10.0538(8), $c$ = 20.3793(16) Å, $\beta$ = 110.922(2)°, $Z$ = 8. The $Eu^{III}$ ion is eight-coordinate, with three bidentate $TTA^-$ anions and one bidentate N,O-chelated PBO molecule. A comparative study by UV and emission spectroscopy was carried out and electroluminescent properties of the related complexes $[Eu(TTA)_3(PBO)]$ and $[Eu(TTA)_3(PBT)]$ are reported as well.
(© Wiley-VCH Verlag GmbH & Co. KGaA, 69451 Weinheim, Germany, 2006)

## Introduction

$Eu^{III}$ complexes have attracted tremendous interest due to their highly monochromic red emission with large Stokes shifts and long emission lifetimes of up to a few milliseconds.[1] These materials have found widespread applications in chemical and earth sciences as well as bioinorganic chemistry, ranging from DNA binding properties to antibody labels in immunoassays.[1–3] A particularly important class of complexes is that of lanthanide β-diketonates, which have recently attracted attention in the development of new materials based on red, near-infrared, and white-light photo-conversion and switching/sensing molecular devices,[4] sol–gel glasses,[5] liquid crystals,[6] red-emitting electroluminescent devices,[7–9] supramolecular assemblies,[10] polymers,[11] and Langmuir–Blodgett (LB) and self-assembled ultrathin films.[12–14]

As far as $Eu^{III}$ β-diketonates developed for electroluminescent devices are concerned, [Eu(β-diketonate)$_3$L]-type complexes (L = bidentate neutral heterocyclic ligand) have played a very important role. It has been demonstrated that the introduction of L to replace the two coordinated water molecules in [Eu(β-diketonate)$_3$(H$_2$O)$_2$] is imperative to obtain vapor volatility for vacuum deposition film-based electroluminescent devices.[15] However, as almost all of the bidentate neutral heterocyclic ligands are α-diimines such as 2,2′-bipyridine (bpy), 1,10-phenanthroline (phen), or their substitutional derivatives, in addition to 2,2′-bipyridine *N*-oxide and 1,10-phenanthroline *N*-oxide,[16] novel types of complexes are limited.[1–8] We have reported a series of [Eu(β-diketonate)$_3$(α-diimine)]-type complexes for electroluminescent devices,[8] and introduced amphiphilic complexes of this kind into Langmuir–Blodgett films.[13] To promote rapid development of these research fields, it is important to develop novel examples of such complexes.

In addition to the great interest in functional metal complexes based on bpy and phen derivatives, structurally analogous 2-(2′-pyridyl)azoles such as 2-(2′-pyridyl)-1,3-benzoxazole (PBO), 2-(2′-pyridyl)-1,3-benzothiazole (PBT), and 2-(2′-pyridyl)benzimidazole (PBI), which are structurally similar to 2,2′-bipyridine or 1,10-phenanthroline *N*-oxide,[16] have attracted special attention for use in electroluminescent devices, as radiopharmaceuticals based on metal complexes of $[Re^{I}(CO)_3(L)X]$ (X = halide),[17] when attached to $Re^{V}O^{3+}$ and $Tc^{V}O^{3+}$ cores,[18] for complexation with $Ru^{II}$,[19] $Pt^{II}$,[20] $Rh^{III}$ and $Pd^{II}$,[20b] $Mo^{V}$,[21] $Sn^{II}$,[22] and $Co^{II}$, $Zn^{II}$ and $Cu^{II}$ etc.,[23] and because of their structural and physicochemical properties. We have reported the electroluminescence properties of $Eu^{III}$ complexes with PBI,[8c,8i] but so far little attention has been paid to lanthanide complexes with 2-(2′-pyridyl)azoles.[24] Here, we present a comparative study of the optical and electroluminescent

[a] Department of Chemistry, Beijing Normal University, Beijing 100875, P. R. China
Fax: +86-10-5880-2075
E-mail: kzwang@bnu.edu.cn
[b] School of Chemical and Environment Engineering, Beijing Technology and Business University, Beijing 100037, China
[c] State Key Laboratory of Rare Earth Materials Chemistry and Applications and the University of Hong Kong Joint Laboratory on Rare Earth Materials and Bioinorganic Chemistry, Peking University, Beijing 100871, P. R. China

 © 2006 Wiley-VCH Verlag GmbH & Co. KGaA, Weinheim 

cence properties of $Eu^{III}$ complexes of $[Eu(TTA)_3(L)]$ [TTA = 1,1,1-trifluoro-3-(2-thenoyl)acetonato; L = PBO, PBT, and PBI], and a single-crystal X-ray structural characterization of $[Eu(TTA)_3(PBO)]$.

## Results and Discussion

### Synthesis

2-(2′-Pyridyl)-1,3-benzoxazole (PBO), 2-(2′-pyridyl)-1,3-benzothiazole (PBT), and 2-(2′-pyridyl)benzimidazole (PBI), and their $Eu^{III}$ complexes $[Eu(TTA)_3(PBO)]$, $[Eu(TTA)_3(PBT)]$, and $[Eu(TTA)_3(PBI)]$ were prepared according to the reactions shown in Figure 1. The three 2-(2′-pyridyl)azoles were obtained by direct condensation of picolinic acid with 2-aminophenol, 2-aminothiophenol, and 1,2-phenylenediamine, respectively, in a 1:1 molar ratio in the presence of polyphosphoric acid,[25] although there have been reports of the synthesis of PBO based on the oxidation of the appropriate Schiff bases by $Ag_2O$[26a] and by the palladium-catalyzed carbonylation and condensation of aromatic halides and *o*-aminophenols.[27] Single crystals of PBT suitable for X-ray diffraction analysis were obtained by recrystallization from $CH_2Cl_2$/hexane; its structure and lattice parameters are consistent with those reported previously.[26b] The reaction of $[Eu(TTA)_3(H_2O)_2]$ with L (L = PBO, PBT and PBI) in a 1:1 molar ratio in refluxing ethanol for 1 h, and then washing of the filtered product with hot ethanol, yielded satisfactorily pure $[Eu(TTA)_3(L)]$. $[Eu(TTA)_3(PBO)]$ was also structurally characterized by single-crystal X-ray diffraction.

### Crystal Structure

A molecular view and the crystal packing of $[Eu(TTA)_3(PBO)]$ are shown in Figures 2 and 3, respectively; selected bond parameters are listed in Table 1. As expected, the PBO ligand coordinates to the $Eu^{III}$ ion in an unusual N,O-chelation mode. The complex crystallizes in the monoclinic space group $C2/c$ with lattice parameters $a$ = 41.346(4), $b$ = 10.0538(8), $c$ = 20.3793(16) Å, $\beta$ = 110.922(2)°, and $Z$ = 8. The complex is mononuclear and the $Eu^{III}$ ion is eight-coordinate, with six oxygen atoms of three bidentate $TTA^-$

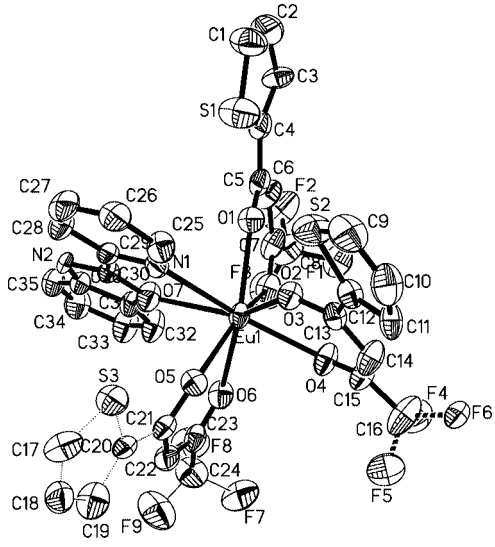


Figure 2. Asymmetric unit of $[Eu(TTA)_3(PBO)]$ with atom numbering scheme and thermal ellipsoids (30%).

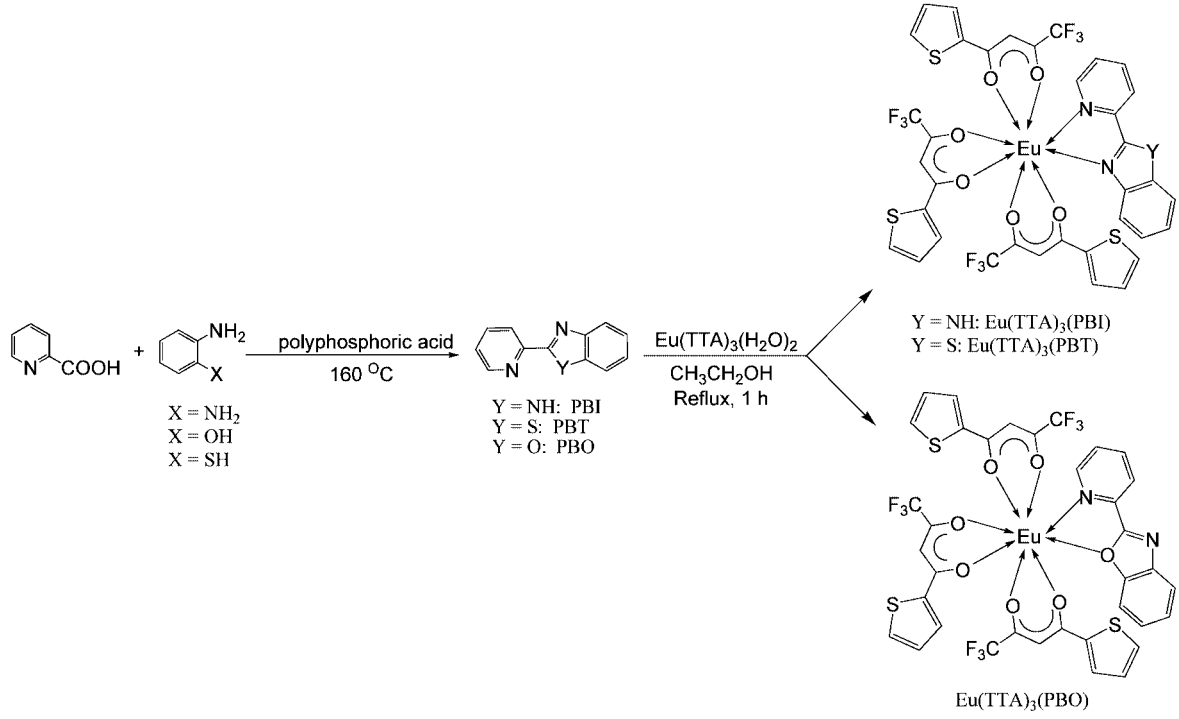


Figure 1. The synthetic routes to the $Eu^{III}$ complexes.

 © 2006 Wiley-VCH Verlag GmbH & Co. KGaA, Weinheim 

anions and one oxygen atom and one nitrogen atom of a bidentate PBO ligand. These atoms lie at the apices of a slightly distorted square antiprism. One of the two planes of the square antiprism is formed exclusively by oxygen atoms [O(1)–O(4)] and the other one by one nitrogen atom and three oxygen atoms [N(1) and O(5)–O(7)]. The two square planes are almost parallel to each other, as shown by the dihedral angle of 1.3°. The average bond lengths and angles of the $TTA^-$ ligands are similar to those reported for other TTA complexes.[28] The Eu–O bond lengths range from 2.33(2) to 2.58(2) Å, and the mean Eu–O(TTA) bond [2.36(2) Å] is 0.22 Å shorter than the average Eu–O(PBO) bond [2.58(2) Å], thus indicating that TTA has a stronger coordinating ability than PBO. The Eu−O bond in PBO of $[Eu(TTA)_3(PBO)]$, however, is stronger than the Eu−N bonds found in $[Eu(TTA)_3(PBO)]$, $[Eu(DBM)_3(pip)]$ (DBM = dibenzoylmethanato; pip = 2-phenylimidazo[4,5-*f*]1,10-phenanthroline),[8h] and $[Eu(DBM)_3(edapip)]$ {edapip = 3-ethyl-2-[4′-(dimethylamino)phenyl]imidazo[4,5-*f*]1,10-phenanthroline}.[8d] Interestingly, as shown in Figure 3, there is a π···π stacking interaction between two PBO molecular planes in two adjacent $[Eu(TTA)_3(PBO)]$ molecules, with an interplanar distance of 3.354(1) Å and a dihedral angle of 0° between them.

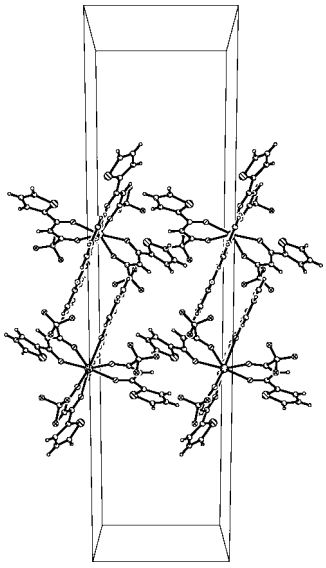

Figure 3. The molecular packing of $[Eu(TTA)_3(PBO)]$ along the *a*-axis. Hydrogen atoms have been omitted for clarity.

Table 1. Selected bond lengths [Å] and angles [°] for $[Eu(TTA)_3(PBO)]$.

| | | | |
|---|---|---|---|
| Eu(1)–O(1) | 2.33(2) | Eu(1)–O(2) | 2.38(2) |
| Eu(1)–O(3) | 2.38(2) | Eu(1)–O(4) | 2.33(2) |
| Eu(1)–O(5) | 2.36(2) | Eu(1)–O(6) | 2.38(2) |
| Eu(1)–O(7) | 2.58(2) | Eu(1)–N(1) | 2.68(2) |
| O(1)–Eu(1)–O(4) | 109.6(8) | O(1)–Eu(1)–O(5) | 135.2(7) |
| O(4)–Eu(1)–O(5) | 97.0(8) | O(1)–Eu(1)–O(6) | 147.3(8) |
| O(4)–Eu(1)–O(6) | 77.6(7) | O(5)–Eu(1)–O(6) | 72.1(8) |
| O(1)–Eu(1)–O(2) | 71.1(8) | O(4)–Eu(1)–O(2) | 80.0(8) |
| O(5)–Eu(1)–O(2) | 151.2(8) | O(6)–Eu(1)–O(2) | 79.3(8) |
| O(1)–Eu(1)–O(3) | 75.2(8) | O(4)–Eu(1)–O(3) | 71.4(7) |
| O(5)–Eu(1)–O(3) | 80.3(7) | O(6)–Eu(1)–O(3) | 135.2(8) |
| O(2)–Eu(1)–O(3) | 124.4(7) | O(1)–Eu(1)–O(7) | 85.9(8) |
| O(4)–Eu(1)–O(7) | 147.1(8) | O(5)–Eu(1)–O(7) | 90.7(8) |
| O(6)–Eu(1)–O(7) | 74.5(8) | O(2)–Eu(1)–O(7) | 78.1(8) |
| O(3)–Eu(1)–O(7) | 141.5(8) | O(1)–Eu(1)–N(1) | 69.4(7) |
| O(4)–Eu(1)–N(1) | 149.1(8) | O(5)–Eu(1)–N(1) | 69.3(8) |
| O(6)–Eu(1)–N(1) | 120.8(7) | O(2)–Eu(1)–N(1) | 125.4(8) |
| O(3)–Eu(1)–N(1) | 78.8(7) | O(7)–Eu(1)–N(1) | 63.0(8) |

## UV Spectra

The UV absorption spectrum of $[Eu(TTA)_3(PBO)]$ is compared with those of $[Eu(TTA)_3(H_2O)_2]$ and PBO in Figure 4. There is one principle π–π* absorption peak at 300 nm in the spectrum of PBO and two peaks at 266 and 338 nm in that of $[Eu(TTA)_3(H_2O)_2]$, while a new shoulder centered at 318 nm appears in the spectrum of $[Eu(TTA)_3(PBO)]$ in addition to one peak at 302 nm due to PBO and two peaks at 266 and 336 nm to $[Eu(TTA)_3(H_2O)_2]$, thus indicating the complexation of PBO to the $Eu(TTA)_3$ moiety.

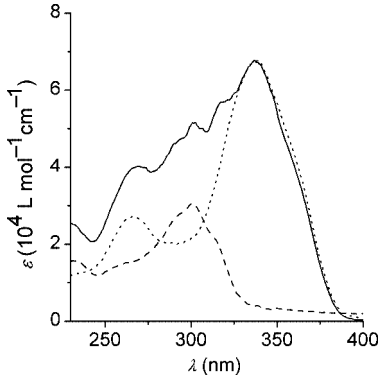


Figure 4. UV absorption spectra of PBO (dashed line), $[Eu(TTA)_3(H_2O)_2]$ (dotted line), and $[Eu(TTA)_3(PBO)]$ (solid line) in $CH_3CN$.

As shown in Figure 5, the complexation of PBT to $Eu(TTA)_3$ results in profound changes in the UV spectra: the π–π* absorption bands at 338 and 266 nm of $[Eu(TTA)_3(H_2O)_2]$ are blue-shifted to 330 and 251 nm, respec-

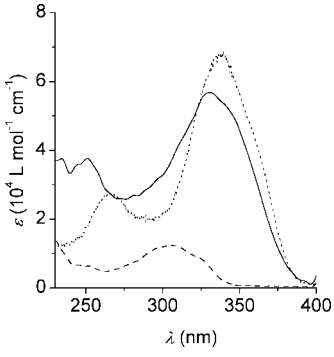


Figure 5. UV absorption spectra of PBT (dashed line), $[Eu(TTA)_3(H_2O)_2]$ (dotted line), and $[Eu(TTA)_3(PBT)]$ (solid line) in $CH_3CN$.

 © 2006 Wiley-VCH Verlag GmbH & Co. KGaA, Weinheim 

tively, for $[Eu(TTA)_3(PBT)]$ and the molar extinction coefficient for the former is decreased as the coordination reaction takes place. Furthermore, the broad band at 305 nm for PBT disappears in the spectrum of $[Eu(TTA)_3(PBT)]$.

In the spectrum of $[Eu(TTA)_3(PBI)]$ (Figure 6), the dominant absorption feature for $Eu(TTA)_3$ is also blue-shifted to 323 nm relative to $[Eu(TTA)_3(H_2O)_2]$; no absorption feature for PBI is observed (308 nm).

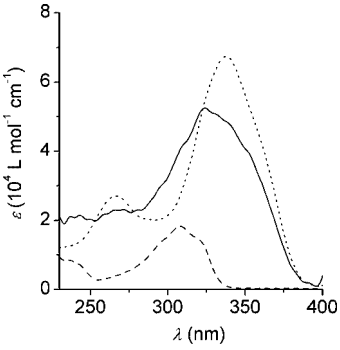


Figure 6. UV absorption spectra of PBI (dashed line), $[Eu(TTA)_3(H_2O)_2]$ (dotted line), and $[Eu(TTA)_3(PBI)]$ (solid line) in $CH_3CN$.

### Photo- and Electroluminescent Properties

The excitation spectra for PBO, PBT, and PBI in $CH_3CN$ show maximum excitation wavelengths at 300, 305, and 308 nm, respectively; these correspond well to their corresponding maximum UV absorption peaks. However, the excitation spectra for $[Eu(TTA)_3(PBO)]$, $[Eu(TTA)_3(PBT)]$, and $[Eu(TTA)_3(PBI)]$ in $CH_3CN$ show maximum excitation wavelengths at 341, 341, and 339 nm, respectively, which correspond well to the maximum UV absorption peak at 338 nm for $[Eu(TTA)_3(H_2O)_2]$, thus indicating that $TTA^-$ rather than neutral 2-(2′-pyridyl)azoles (PBO, PBT and PBI) is mainly involved in intramolecular energy transfer from the excited triplet of $TTA^{-}$* to the $^5D_0$ state of $Eu^{III}$.[1] The emission spectra of the three complexes show a similar pattern in the $Eu^{III}$ region, with sharp characteristic emission peaks at 595, 613, 654, and 702 nm due to $^5D_0 \rightarrow {}^7F_J$ ($J$ = 1, 2, 3, and 4) transitions, respectively, with the electric dipole transition ($^5D_0 \rightarrow {}^7F_2$) being the strongest. The emission quantum yields of $[Eu(TTA)_3(PBO)]$, $[Eu(TTA)_3(PBT)]$, and $[Eu(TTA)_3(PBI)]$ in $CH_3CN$ were determined to be 1.22-, 0.51-, and 0.54-times that of $[Eu(TTA)_3(H_2O)_2]$ in the same solvent, respectively.

By using *N*,*N*′-bis(3-methylphenyl)-*N*,*N*′-diphenyl-1,1′-biphenyl-4,4′-diamine (TPD) as hole-transporting material, 2,9-dimethyl-4,7-diphenyl-1,10-phenanthroline (BCP) as hole-blocking material, and tris(8-quinolinolato)aluminium ($Alq_3$) as electron-transporting material, we fabricated four-layer electroluminescence (EL) devices with the configuration ITO/TPD (20 nm)/$Eu^{III}$ complex (40 nm)/BCP (10 nm)/$Alq_3$ (40 nm)/$Mg_{0.9}$:$Ag_{0.1}$ (200 nm)/Ag (80 nm). Figure 7 shows the chemical structures of the materials and the configuration of the EL devices. As exemplified in Figure 8 for the electroluminescence spectrum of $[Eu(TTA)_3(PBO)]$, the two devices give similar features of an $Eu^{III}$ characteristic emission with good red-emitting purity centered at 613 nm, which corresponds to the $^5D_0 \rightarrow {}^7F_2$ transition. Figures 9 and 10 show current density/luminance/voltage curves for the devices ITO/TPD (20 nm)/$[Eu(TTA)_3(PBO)]$ (40 nm)/BCP (10 nm)/$Alq_3$ (40 nm)/$Mg_{0.9}$:$Ag_{0.1}$ (200 nm)/Ag (80 nm) and ITO/TPD (20 nm)/$[Eu(TTA)_3(PBT)]$ (40 nm)/BCP (10 nm)/$Alq_3$ (40 nm)/$Mg_{0.9}$:$Ag_{0.1}$ (200 nm)/Ag (80 nm), respectively. The $[Eu(TTA)_3(PBO)]$-based device has a turn-on voltage (the voltage at which the device gives a luminance of 1 cd m$^{-2}$) of about 10 V, which is comparable to the voltage of about 10.5 V for an $[Eu(TTA)_3(PBT)]$-based device. However, the maximum red-emitting brightness of 18 cd m$^{-2}$ achieved at 15 V and 4.3 mA cm$^{-2}$ for the $[Eu(TTA)_3(PBO)]$-based device is much lower than the value of 30 cd m$^{-2}$ observed at 15 V and 165 mA cm$^{-2}$ for an $[Eu(TTA)_3(PBT)]$-based device and much higher than the value of 0.43 cd m$^{-2}$ observed at 26 V and 1.6 mA cm$^{-2}$ for an $[Eu(TTA)_3(PBI)]$-based device;[8i] it is half that (36 cd m$^{-2}$) observed for an $[Eu(TTA)_3(HEPB)]$

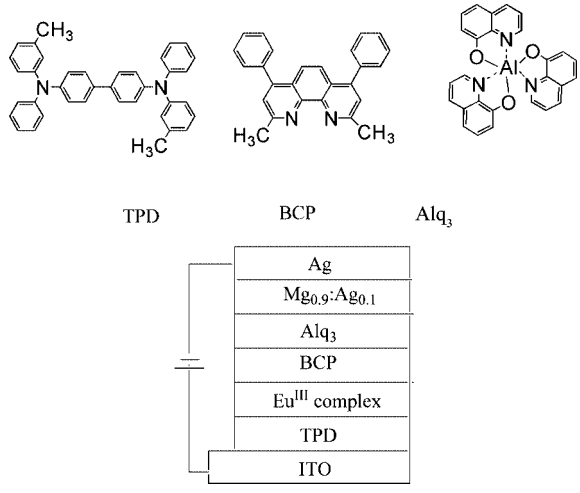


Figure 7. Chemical structures of the materials and the configuration of the EL device.

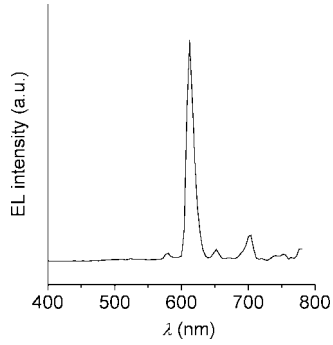


Figure 8. Electroluminescence spectrum of the $[Eu(TTA)_3(PBO)]$-based device ITO/TPD (20 nm)/$[Eu(TTA)_3(PBO)]$ (40 nm)/BCP (10 nm)/$Alq_3$ (40 nm)/$Mg_{0.9}$:$Ag_{0.1}$ (200 nm)/Ag (80 nm).

 © 2006 Wiley-VCH Verlag GmbH & Co. KGaA, Weinheim 

[EPBM = 1-ethyl-2-(2′-pyridyl)benzimidazole] based device.[8c] The poor EL performance observed for the $[Eu(TTA)_3(PBI)]$-based device is mainly attributed to the poor vacuum volatility of $[Eu(TTA)_3(PBI)]$ due to the presence of the strongly polar NH group on PBI.

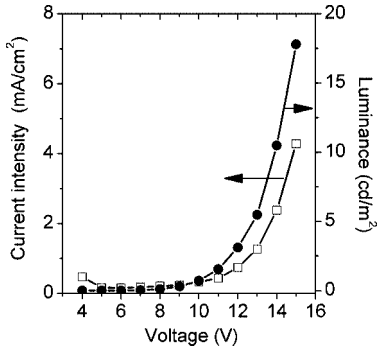


Figure 9. Current/voltage (*I*/*V*) and luminance/voltage (*L*/*V*) characteristics for the EL device ITO/TPD (20 nm)/$[Eu(TTA)_3(PBO)]$ (40 nm)/BCP (10 nm)/$Alq_3$ (40 nm)/$Mg_{0.9}$:$Ag_{0.1}$ (200 nm)/Ag (80 nm).

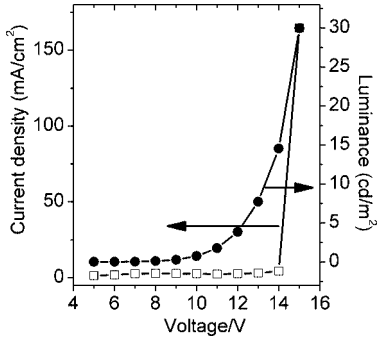


Figure 10. Current/voltage (*I*/*V*) and luminance/voltage (*L*/*V*) characteristics for EL device ITO/TPD (20 nm)/$[Eu(TTA)_3(PBT)]$ (40 nm)/BCP (10 nm)/$Alq_3$ (40 nm)/$Mg_{0.9}$:$Ag_{0.1}$ (200 nm)/Ag (80 nm).

## Conclusions

We have synthesized two $Eu^{III}$ mixed-ligand complexes with TTA and PBO or PBT. The N,O-bidentate coordination to $Eu^{III}$ by PBO in $[Eu(TTA)_3(PBO)]$ has been demonstrated by single-crystal X-ray diffraction. The N,N-Bidentate coordination to $Eu^{III}$ by PBT and PBI in $[Eu(TTA)_3(PBT)]$ and $[Eu(TTA)_3(PBI)]$ causes more evident changes in the UV spectra than in the N,O-bidentate coordinated $[Eu(TTA)_3(PBO)]$. However, the photoluminescence quantum yield of N,O-coordinated $[Eu(TTA)_3(PBO)]$ is the highest and follows the order: $[Eu(TTA)_3(PBO)] > [Eu(TTA)_3(PBI)] \approx [Eu(TTA)_3(PBT)]$. The maximum red-emitting EL brightness follows the order $[Eu(TTA)_3(PBT)] > [Eu(TTA)_3(PBO)] >> [Eu(TTA)_3(PBI)]$. The low brightness of only 0.43 cd m$^{-2}$ observed for the $[Eu(TTA)_3(PBI)]$-based EL device is most probably due to the poor vacuum volatility of $[Eu(TTA)_3(PBI)]$, since we noticed serious thermal decomposition during the vacuum deposition of $[Eu(TTA)_3(PBI)]$.

## Experimental Section

**Physical Measurements:** C, H, N elemental analyses were performed with a Vario EL elemental analyzer. IR spectra were measured with a Nicolet Avatar 360 FT-IR spectrometer as KBr disks. $^1$H NMR spectra were obtained with a Bruker DRX-500 spectrometer. UV absorption spectra were determined with a GBC Cintra 10e UV/Vis spectrophotometer. Emission spectra were recorded with a Shimadzu RF-5301PC spectrofluorimeter. The PL quantum yields of $CH_3CN$ solutions of the complexes were calculated using Equation (1),[29] where $\varphi_s$ and $\varphi_{std}$ are the quantum yields of unknown and standard $[Eu(TTA)_3(H_2O)_2]$, $A_s$ and $A_{std}$ ($< 0.1$) are the solution absorbance at the excitation wavelength, $I_s$ and $I_{std}$ are the integrated emission intensities, and $n_s$ and $n_{std}$ are the refractive indices of the solvents.

$$\varphi_s = \varphi_{std}(A_{std}/A_s)(I_s/I_{std})(n_s/n_{std})^2 \quad (1)$$

The EL devices were fabricated by sequentially depositing organic layers in one run under high vacuum ($<8\times10^4$ Pa) thermal evaporation onto a pre-cleaned indium/tin oxide glass substrate with a sheet resistance of 15 Ω/cm$^2$, which was kindly supplied by China Southern Glass Holding Co., Ltd as a gift. A shadow mask with 5-mm-diameter openings was used to define the cathode of a 200-nm thick $Mg_{0.9}$:$Ag_{0.1}$ alloy layer, with an 80-nm thick Ag cap. The thickness of the deposited layer and the evaporation speed of the individual materials were monitored in vacuo with quartz crystal monitors. The deposition rates were maintained to be 0.1–0.3 nm s$^{-1}$ for organic materials and 1.0–1.3 nm s$^{-1}$ for $Mg_{0.9}$:$Ag_{0.1}$ alloy. All electrical testing and optical measurements were performed under ambient conditions. The EL spectra were measured with a Spectrascan PR650 photometer. The current/voltage (*I*/*V*) and luminance/voltage (*L*/*V*) characteristics were measured with a computer-controlled Keithley 2400 Sourcemeter unit with a calibrated silicon diode.

**Materials:** $[Eu(TTA)_3(H_2O)_2]$[30] [TTA = 1,1,1-trifluoro-3-(2-thenoyl)acetonato] was prepared by a literature method. 2-(2′-Pyridyl)benzimidazole (PBI) and $[Eu(TTA)_3(PBI)]$ were synthesized as described previously.[8c,8i] The other materials were commercially available and were used without further purification.

**2-(2′-Pyridyl)-1,3-benzoxazole (PBO):** A mixture of powdered 2-picolinic acid (12.3 g, 0.1 mol), 2-aminophenol (10.9 g, 0.1 mol), and syrupy phosphoric acid (50 mL) was stirred at 160 °C for 4 h. The blue slurry was then poured into vigorously stirred cold water (500 mL). Aqueous ammonia was then added up to a pH of about 7. The resulting pink solid product was filtered off and recrystallized from $CH_2Cl_2$/hexane. Yield: 8.6 g (43.9%). $^1$H NMR (500 MHz, $CDCl_3$): $\delta$ = 8.86 (d, $J$ = 4.60 Hz, 1 H), 8.40 (d, $J$ = 7.90 Hz, 1 H), 7.94 (m, 1 H), 7.86 (m, 1 H), 7.71 (d, $J$ = 4.60 Hz, 1 H), 7.50 (m, 1 H), 7.44 (m, 2 H) ppm. IR (KBr): $\tilde{\nu}$ = 3058 (w), 1583 (m), 1552 (m), 1454 (vs), 1437 (s), 1347 (m), 1242 (m), 1076 (s), 809 (m), 742 (vs), 704 (m) cm$^{-1}$. $C_{12}H_8N_2O$ (196.21): calcd. C 73.50, H 4.10, N 14.30; found C 73.70, H 4.20, N 14.10.

**2-(2′-Pyridyl)-1,3-benzothiazole (PBT):** This was synthesized as described above for PBO except that 2-aminothiophenol was used instead of 2-aminophenol. Yield: 6.0 g (30.6%). $^1$H NMR (500 MHz, $CDCl_3$): $\delta$ = 8.72 (d, $J$ = 4.70 Hz, 1 H), 8.42 (d, $J$ = 7.91 Hz, 1 H), 8.13 (d, $J$ = 8.13 Hz, 1 H), 8.00 (d, $J$ = 7.94 Hz, 1 H), 7.89 (m, 1 H), 7.54 (m, 1 H), 7.44 (m, 2 H) ppm. IR (KBr): $\tilde{\nu}$

 © 2006 Wiley-VCH Verlag GmbH & Co. KGaA, Weinheim 

= 3052 (w), 1583 (m), 1562 (m), 1509 (m), 1456 (s), 1432 (vs), 1316 (s), 1292 (m), 1265 (m), 1233 (m), 996 (m), 978 (s), 783 (s), 758 (s), 739 (s), 725 (s), 618 (s) $cm^{-1}$. $C_{12}H_8N_2S$ (212.21): calcd. C 67.90, H 3.80, N 13.20; found C 68.00, H 3.85, N 13.15.

**[Eu(TTA)$_3$(PBO)]:** PBO (0.0785 g, 0.4 mmol) and [Eu(TTA)$_3$-($H_2O$)$_2$] (0.3408 g, 0.4 mmol) were refluxed in ethanol (10 mL) for 1 h. The solid product formed upon cooling was filtered off, washed with hot ethanol, and then vacuum-dried. Yield: 0.29 g (71.6%). UV ($CH_3CN$): $\lambda$ ($\varepsilon$) = 266 (4.03), 302 (5.18), 318 (5.70), 336 ($6.80\times10^4$ $M^{-1}cm^{-1}$) nm. IR (KBr): $\tilde{\nu}$ = 1598 (s), 1578 (m), 1541 (m), 1508 (w), 1463 (w), 1413 (m), 1359 (w), 1311 (s), 1250 (w), 1230 (w), 1189 (m), 1136 (s), 1085 (w), 1062 (w), 935 (w), 858 (w), 787 (m), 748 (m), 720 (m), 681 (w), 642 (w), 581 (w), 457 (vw) $cm^{-1}$. $C_{36}H_{20}EuF_9N_2O_7S_3$ (1011.7): calcd. C 42.74, H 1.99, N 2.77; found C 42.66, H 2.06, N 2.96.

**[Eu(TTA)$_3$(PBT)]:** This complex was synthesized as described above for [Eu(TTA)$_3$(PBO)] except that PBT was used instead of PBO. UV ($CH_3CN$): $\lambda$ ($\varepsilon$) = 234 (3.73), 251 (3.77), 330 ($5.69\times10^4$ $M^{-1}cm^{-1}$) nm. IR (KBr): $\tilde{\nu}$ = 1625 (m), 1598 (s), 1578 (m), 1540 (m), 1508 (w), 1464 (w), 1413 (m), 1357 (w), 1308 (s), 1248 (w), 1231 (w), 1187 (m), 1142 (s), 1083 (w), 1065 (m), 995 (w), 935 (w), 855 (w), 788 (m), 762 (w), 718 (m), 681 (w), 644 (m), 577 (m), 496 (vw), 461 (vw) $cm^{-1}$. $C_{36}H_{20}EuF_9N_2O_6S_4$ (1027.8): calcd. C 42.07, H 1.96, N 2.73; found C 41.77, H 2.11, N 2.76.

**X-ray Crystallographic Study:** Yellow single crystals with approximate dimensions suitable for X-ray structural analysis were obtained by recrystallization from $CH_2Cl_2$/$CH_3CN$. The data were collected at 294(2) K with a CCD area detector Bruker SMART 2000 X-ray diffractometer with graphite-monochromated Mo-$K_\alpha$ radiation ($\lambda$ = 0.71073 Å) in the $\omega$-2$\theta$ scan mode (2$\theta$ range: 5.52–52.48°). The coordinates of all non-hydrogen atoms and anisotropic thermal parameters were refined by full-matrix least squares. The data were processed with a Pentium PC using the Bruker SHELXTL software package.[16] Further details of the data collection and refinement are given in Table 2. CCDC-296449 contains the supplementary crystallographic data for this paper. These data can be obtained free of charge from The Cambridge Crystallographic Data Centre via www.ccdc.cam.ac.uk/data_request/cif.

Table 2. Principal crystallographic data and parameters of [Eu(TTA)$_3$(PBO)].

| | |
|---|---|
| Empirical formula | $C_{36}H_{20}EuF_9N_2O_7S_3$ |
| Formula mass | 1011.68 |
| Temp. [K] | 294(2) |
| Wavelength [Å] | 0.71073 |
| Crystal system | monoclinic |
| Space group | *C*2*c* |
| *a* [Å] | 41.346(4) |
| *b* [Å] | 10.0538(8) |
| *c* [Å] | 20.3793(16) |
| $\beta$ [°] | 110.922(2) |
| *V* [Å$^3$] | 7912.7(11) |
| *Z* | 8 |
| $D_{calcd.}$ [g cm$^{-3}$] | 1.698 |
| Absorption coefficient [mm$^{-1}$] | 1.835 |
| *F*(000) | 3984 |
| Crystal size [mm] | 0.16×0.14×0.10 |
| $\theta$ range [°] | 2.02–25.01 |
| No. of reflections collected | 19608 |
| No. of independent reflections | 6958 |
| No. of observed reflections [$I>2\sigma(I)$] | 5215 |
| No. of refined parameters | 652 |
| Largest peak/hole [e·Å$^{-3}$] | 0.765/–0.547 |
| Final $R_{int}$ [$I>2\sigma(I)$] | $R_1$ = 0.0363, $wR_2$ = 0.0911 |
| $R_{int}$ (all data)[a] | $R_1$ = 0.0570, $wR_2$ = 0.1095 |

[a] Structure was refined on $F_o^2$: $wR_2 = \{\Sigma[w(F_o^2 - F_c^2)^2]/\Sigma w(F_o^2)^2\}^{1/2}$, where $w^{-1} = [\Sigma(F_o^2) + (aP)^2 + bP]$ and $P = [\max(F_o^2,0) + 2F_c^2]/3$.

## Acknowledgments

We are grateful to the NSFC (20371008, 90401007, 20471004, and 20331010), and the Beijing Natural Science Foundation (2052008) for their financial support of this work.

[1] a) J.-C. G. Bünzli, G. R. Choppin, *Lanthanide Probes in Life, Chemical and Earth Sciences*, Elsevier, Amsterdam, **1989**, chapter 7; b) J.-C. G. Bünzli, *Acc. Chem. Res.* **2006**, *39*, 53–61; c) J.-C. G. Bünzli, C. Piguet, *Chem. Rev.* **2002**, *102*, 1897–1928; d) R. Pavithran, M. L. P. Reddy, S. A. Junior, R. O. Freire, G. B. Rocha, P. P. Lima, *Eur. J. Inorg. Chem.* **2005**, 4129–4137; e) J.-C. G. Bünzli, C. Piguet, *Chem. Soc. Rev.* **2005**, *34*, 1048–1077; f) C. Piguet, J.-C. G. Bünzli, *Chem. Soc. Rev.* **1999**, *28*, 347–358.

[2] P. B. Glover, P. R. Ashton, L. J. Childs, A. Rodger, M. Kercher, R. M. Williams, L. De Cola, Z. Pikramenou, *J. Am. Chem. Soc.* **2003**, *125*, 9918–9919.

[3] I. A. Hemmila, *Applications of Fluorescence in Immunoassays*, J. Wiley & Sons, New York, **1991**, vol. 117, Chemical Analysis Series.

[4] a) N. Shavaleev, L. P. Moorcraft, S. J. A. Pope, Z. R. Bell, S. Faulkner, M. D. Ward, *Chem. Commun.* **2003**, 1134–1135; b) H. Tsukube, S. Shinoda, *Chem. Rev.* **2002**, *102*, 2389–2403; c) P. Coppo, M. Duati, V. N. Kozhevnikov, J. W. Hofstraat, L. De Cola, *Angew. Chem. Int. Ed.* **2005**, *44*, 1806–1810; d) J. A. Fernandes, R. A. S. Ferreira, M. Pillinger, L. D. Carlos, I. S. Goncalves, P. J. A. Ribeiro-Claro, *Eur. J. Inorg. Chem.* **2004**, 3913–3919; e) T. Gunnlaugsson, J. P. Leonard, *Chem. Commun.* **2005**, 3114–3131.

[5] K. Binnemans, P. Lenaerts, K. Driesen, C. Gorller-Walrand, *J. Mater. Chem.* **2004**, *14*, 191–195.

[6] a) R. Van Deun, D. Moors, B. De Fre, K. Binnemans, *J. Mater. Chem.* **2003**, *13*, 1520–1522; b) L. N. Puntus, K. J. Schenk, J. C. G. Bünzli, *Eur. J. Inorg. Chem.* **2005**, 4739–4744.

[7] J. Kido, Y. Okamoto, *Chem. Rev.* **2002**, *102*, 2357–2368.

[8] a) M. Sun, H. Xin, K. Z. Wang, Y. A. Zhang, L. P. Jin, C. H. Huang, *Chem. Commun.* **2003**, 702–703; b) Z. Q. Bian, D. Q. Gao, K. Z. Wang, L. P. Jin, C. H. Huang, *Thin Solid Films* **2004**, *460*, 237–241; c) L. Huang, K. Z. Wang, C. H. Huang, F. Y. Li, Y. Y. Li, *J. Mater. Chem.* **2001**, *11*, 790–793; d) Z. Q. Bian, K. Z. Wang, L. P. Jin, *Polyhedron* **2002**, *21*, 313–319; e) H. Xin, M. Sun, K. Z. Wang, Y. A. Zhang, L. P. Jin, C. H. Huang, *Chem. Phys. Lett.* **2004**, *388*, 55–57; f) H. Xin, F. Y. Li, M. Guan, C. H. Huang, M. Sun, K. Z. Wang, Y. A. Zhang, L. P. Jin, *J. Appl. Phys.* **2003**, *94*, 4729–4731; g) K. Z. Wang, L. Huang, C. H. Huang, L. P. Jin, *Solid State Commun.* **2002**, *122*, 233–236; h) D. Q. Gao, Z. Q. Bian, K. Z. Wang, L. P. Jin, C. H. Huang, *J. Alloys Compd.* **2003**, *358*, 188–192; i) L. Huang, K. Z. Wang, C. H. Huang, D. Q. Gao, L. P. Jin, *Synth. Met.* **2002**, *128*, 241–245.

[9] a) H. Jang, C. H. Shin, B. J. Jung, D. H. Kim, H. K. Shim, Y. Do, *Eur. J. Inorg. Chem.* **2006**, 718–725; b) M. R. Robinson, M. B. O'Regan, G. C. Bazan, *Chem. Commun.* **2000**, 1645–1646; c) C. J. Liang, D. Zhao, Z. R. Hong, D. X. Zhao, X. Y. Liu, W. L. Liu, J. B. Peng, J. Q. Yu, C. S. Lee, S. T. Lee, *Appl. Phys. Lett.* **2000**, *76*, 67–69; d) C. Adachi, M. A. Baldo, S. R. Forrest, *J. Appl. Phys.* **2000**, *87*, 8049–8055.

[10] a) A. P. Bassett, S. W. Magennis, P. B. Glover, D. J. Lewis, N. Spencer, S. Parsons, R. M. Williams, L. D. Cola, Z. Pikramenou, *J. Am. Chem. Soc.* **2004**, *126*, 9413–9424; b) M. H. W. Lam, D. Y. K. Lee, S. S. M. Chiu, K. W. Man, W. T. Wong, *Eur. J. Inorg. Chem.* **2000**, 1483–1488.

 © 2006 Wiley-VCH Verlag GmbH & Co. KGaA, Weinheim 

[11] J. L. Bender, P. S. Corbin, C. L. Fraser, D. H. Metcalf, F. S. Richardson, E. L. Thomas, A. M. Urbas, *J. Am. Chem. Soc.* **2002**, *124*, 8526–8527.
[12] Y. L. Zhao, D. J. Zhou, C. H. Huang, L. B. Gan, L. M. Ying, X. S. Zhao, B. Zhang, Y. Ma, M. Xu, K. Wu, *Langmuir* **1998**, *14*, 417–422.
[13] a) K. Z. Wang, L. H. Gao, C. H. Huang, *J. Photochem. Photobiol. A: Chem.* **2003**, *156*, 39–43; b) D. J. Zhou, K. Z. Wang, C. H. Huang, G. X. Xu, L. G. Xu, T. K. Li, *Solid State Commun.* **1995**, *93*, 167–169; c) K. Z. Wang, V. W. W. Yam, C. H. Huang, *Solid State Commun.* **1998**, *107*, 249–252; d) L. H. Gao, K. Z. Wang, L. Cai, H. X. Zhang, L. P. Jin, C. H. Huang, H. J. Gao, *J. Phys. Chem. B* **2006**, *110*, 7402–7408.
[14] L. Zhang, H. G. Liu, R. J. Zhang, Y. D. Mu, D. J. Qian, X. S. Feng, *Colloids Surf. A* **2005**, *257–58*, 401–404.
[15] K. Z. Wang, L. J. Li, W. M. Liu, Z. Q. Xue, C. H. Huang, J. H. Lin, *Mater. Res. Bull.* **1996**, *31*, 993–998.
[16] X. H. Zhu, L. H. Wang, J. Ru, W. Huang, J. F. Fang, D. G. Ma, *J. Mater. Chem.* **2004**, *14*, 2732–2734.
[17] a) K. Z. Wang, L. Huang, L. H. Gao, L. P. Jin, C. H. Huang, *Inorg. Chem.* **2002**, *41*, 3353–3358; b) R. Czerwieniec, A. Kapturkiewicz, J. Lipkowski, J. Nowacki, *Inorg. Chim. Acta* **2005**, *358*, 2701–2710; c) X. Chen, F. J. Femia, J. B. Babich, J. Zubieta, *Inorg. Chim. Acta* **2001**, *314*, 91–96.
[18] S. Tzanopoulou, I. C. Pirmettis, G. Patsis, C. Raptopoulou, A. Terzis, M. Papadopoulos, M. Pelecanou, *Inorg. Chem.* **2006**, *45*, 902–909.
[19] a) N. Chanda, D. Paul, S. Kar, S. M. Mobin, A. Datta, V. G. Puranik, K. K. Rao, G. K. Lahiri, *Inorg. Chem.* **2005**, *44*, 3499–3511; b) N. Chanda, B. Sarkar, S. Kar, J. Fiedler, W. Kaim, G. K. Lahiri, *Inorg. Chem.* **2004**, *43*, 5128–5133; c) M. Maji, P. Sengupta, S. K. Chattopadhyay, G. Mostafa, C. H. Schwalbe, S. Ghosh, *J. Coord. Chem.* **2001**, *54*, 13–24.
[20] a) X. F. He, C. M. Vogels, A. Decken, S. A. Westcott, *Polyhedron* **2004**, *23*, 155–160; b) C. K. Choudhary, R. K. Choudhary, L. K. Mishra, *J. Indian Chem. Soc.* **2002**, *79*, 761–762.
[21] S. S. Mandal, P. C. Ghorai, S. Ray, H. K. Saha, *J. Indian Chem. Soc.* **1995**, *72*, 807–810.
[22] S. Hu, D. Shi, T. Huang, J. Wan, Z. Huang, J. Yang, C. Xu, *Inorg. Chim. Acta* **1990**, *173*, 1–4.
[23] a) P. S. K. Chia, L. F. Lindoy, S. E. Livingstone, *Inorg. Chim. Acta* **1968**, *2*, 459–462; b) L. F. Lindoy, S. E. Livingstone, *Inorg. Chim. Acta* **1968**, *2*, 119–126.
[24] For a paper dealing with the solid lanthanide(III) thiocyanate complexes $[Ln(NCS)_3(PBO)_2]\cdot nH_2O$, see: P. Hakur, V. Chakravortty, K. C. Dash, *Indian J. Chem. Sect. A* **1999**, *38*, 1223–1227.
[25] A. W. Addison, P. J. Burke, *J. Heterocycl. Chem.* **1981**, *18*, 803–805.
[26] a) J. Chang, K. Zhaob, S. Pana, *Tetrahedron Lett.* **2002**, *43*, 951–954; b) J. Gangopadhyay, S. Sengupta, S. Bhattacharyya, I. Chakraborty, A. Chakravorty, *Inorg. Chem.* **2002**, *41*, 2616–2622.
[27] R. J. Perry, B. D. Wilson, R. J. Miller, *J. Org. Chem.* **1992**, *57*, 2883–2887.
[28] a) K. Z. Wang, C. H. Huang, R. J. Wang, G. X. Xu, *Polyhedron* **1995**, *14*, 3669–3673; b) Y. Fukuda, A. Nakao, K. Hayashi, *J. Chem. Soc., Dalton Trans.* **2002**, 527–533.
[29] M. J. Han, L. H. Gao, Y. Y. Lu, K. Z. Wang, *J. Phys. Chem. B* **2006**, *110*, 2364–2371.
[30] L. R. Melby, N. J. Rose, E. Abramson, J. C. Caris, *J. Am. Chem. Soc.* **1964**, *86*, 5117–5125.

Received: May 8, 2006
Published Online: August 7, 2006

 © 2006 Wiley-VCH Verlag GmbH & Co. KGaA, Weinheim 

DOI: 10.1002/ejic.200600435

# Affinity of Polypyridines Towards $Cd^{II}$ and $Co^{II}$ Ions: a Thermodynamic and DFT Study

**Silvia Del Piero,[a] Plinio Di Bernardo,[b] Rosalisa Fedele,[a] Andrea Melchior,*[a] Pierluigi Polese,[a] and Marilena Tolazzi*[a]**

**Keywords:** Cadmium(II) / Cobalt(II) / Pyridine complexes / Thermodynamics / Density functional calculations

$Cd^{II}$ and $Co^{II}$ complex formation with pyridine (py), 2,2′-bipyridine (bipy), 2,2′6′,2′′-terpyridine (terpy), 2-(aminomethyl)pyridine (amp), and bis[(2-pyridyl)methyl]amine (dpma) was studied at 298 K in the aprotic solvent dimethyl sulfoxide (DMSO) and in an ionic medium set to 0.1 mol dm$^{-3}$ with $Et_4NClO_4$ in anaerobic conditions. Potentiometric, UV/Vis spectrophotometric, and calorimetric measurements were carried out to obtain the thermodynamic parameters of the systems investigated. Enthalpy-stabilized mononuclear $ML_j$ complexes are formed, whereas entropy changes counteract complex formation. These results are discussed in terms of different basicities, steric requirements, and solvation, of both the ligands and the resulting complexes. Density functional theory (DFT) calculations were carried out in order to obtain structural information and binding energies in vacuo. The DFT results are correlated with the solution studies.
(© Wiley-VCH Verlag GmbH & Co. KGaA, 69451 Weinheim, Germany, 2006)

## Introduction

In recent years, a variety of polyamine N-donor ligands have been investigated in water[1–7] and nonaqueous solvents[8–12] with the aim of studying the influence of basicity and steric effects on selectivity patterns in metal coordination. Examples of the attractive properties and applications of these ligands are their potential use as building blocks of sequestering agents for metals of environmental importance, such as Cd or Pb,[4] fluorescent chemosensors,[3e] catalysts,[3f] or models for small molecule carriers, as in $Cu^{I}$ or $Co^{II}$ dioxygen complexes.[13–18]

In this context, some of our published papers concerning the complexation of transition-metal ions like $Cd^{II}$ and $Co^{II}$[11] have shown that steric effects and N-methylation strongly influence not only the stoichiometry and nature of all metal ion complexes formed, but also the selectivity of these ligands toward metal ions. Systematic studies confirm that different N-alkylation of polyamines, or merely the substitution of only one amine with one alcohol group, causes important differences in the dioxygen affinity of $Co^{II}$ complexes:[11b,11e] this affinity greatly depends on the electron density at the central metal ion, which, in turn, is affected by the electron donor and steric properties of the coordinated ligands.

As an extension of previous works, we report here the results of research on quantifying the complexing ability of pyridine functions toward $Cd^{II}$ and $Co^{II}$ metal ions in DMSO. The $sp^2$ hybridized N can exert high ligand field strength, even though its basicity may be less significant than that of $sp^3$ hybridized nitrogens.[19–21] Moreover, their lower σ-donor ability, greater rigidity with respect to linear polyamines, and their ability to give rise to π backbonding makes them suitable to tune the electronic and steric effects that govern ligand affinity for metal ions.[22,23] Pyridine functions are often found in multifunctional compounds with desirable or predictable properties such as luminescence, electrochemical, or catalytic activity.[22,23]

The model ligands chosen were: pyridine (py), 2,2′-bipyridine (bipy), and 2,2′6′,2′′-terpyridine (terpy). In order to highlight the subtle interplays between steric and electronic effects, intermediate 2-(aminomethyl)pyridine (amp) and bis[(2-pyridyl)methyl]-amine (dpma) ligands were also studied. The latter possess potentially interesting and versatile ways of binding, and may also give rise to polymetallic complexes with luminescent properties or favor spin-crossover phenomena.[24–27]

The stability constants for $Cd^{II}$ were determined by direct potentiometric titration techniques, and UV/Vis spectroscopic measurements were employed for the $Co^{II}$ systems. Enthalpy values were obtained by direct calorimetric titration.

To obtain a gas-phase picture of metal–ligand interactions, the study was completed with calculations using den-

[a] Dipartimento di Scienze e Tecnologie Chimiche, Università di Udine,
Via Cotonificio 108, 33100 Udine, Italy
Fax: +39-0432-558803
E-mail: marilena.tolazzi@uniud.it
andrea.melchior@uniud.it
[b] Dipartimento di Scienze Chimiche, Università di Padova,
Via Marzolo 1, 35131 Padova, Italy
Supporting information for this article is available on the WWW under http://www.eurjic.org or from the author.

 © 2006 Wiley-VCH Verlag GmbH & Co. KGaA, Weinheim 

sity functional theory (DFT). DFT provides an excellent framework, yielding structural information and a number of chemical reactivity indices about ligands and their complexes, and gives results of quality comparable to those obtainable by correlated ab initio calculations. DFT has previously been used to study the influence of N-methylation on structural properties of transition-metal complexes with cyclic polyaza ligands[11g,28] and to describe the properties of polyamines, such as their basicity in both gas-phase[29] and solvent models.[30]

## Results

### Solution Thermodymamics

Computer treatment of the potentiometric, spectrophotometric, and calorimetric experimental data shows that the best fit is obtained when only mononuclear $ML_j$ species are considered. The overall stability constants and thermodynamic functions obtained, together with the corresponding limits of error, are listed in Table 1. For the $Co^{II}$–bipy system, stability constants in DMSO have been previously given[31] and are in good agreement with the data reported here.

For the $Co^{II}$–amp and –dpma systems, some experimental details must be given to explain why thermodynamic data for $Co^{II}$–amp are not reported. The color of the solutions turns from pink to deep blue as titration proceeds with both amp and dpma, as clearly shown in Figure 1, in which absorbances at increasing times are reported for the $Co^{II}$–dpma systems at $R_c = C_L/C_M$ (the total ligand-to-metal ratio) of 1. This spectral change had already been observed in basic aqueous solutions in the presence of $O_2$ and explained by catalytic oxidative dehydrogenation of the ligand, with the transformation of the amine to imine.[32,33] Evidently, this reaction also occurs in our case, although the concentrations of water and $O_2$ were very low in our experimental conditions. The Co–imine product was expected to be present in very low amounts; nevertheless, its very high molar extinction coefficients in the visible range prevented the use of d-d $Co^{II}$ bands to follow aminopyridine complexation. The rate of the undesired reaction was influenced by $C_L/C_M$: the lower this ratio, the slower the reaction. The inset in Figure 1 shows absorbance at 588 nm ($A_{588}$) as a function of time for various $R_c$. At a $C_L/C_M$

Table 1. Overall stability constants and thermodynamic functions for the reaction $M^{2+} + jL \rightleftharpoons ML_j^{2+}$ in DMSO at 298 K and $I$ = 0.1 mol dm$^{-3}$ (L = ligand) and in water.[34–38] Errors quoted correspond to three standard deviations.

| Ligand | Species | DMSO | | | | Water | | | |
|---|---|---|---|---|---|---|---|---|---|
| | | $\log\beta_j$ | $-\Delta G°_{\beta_j}$ [kJmol$^{-1}$] | $-\Delta H°_{\beta_j}$ [kJmol$^{-1}$] | $-T\Delta S°_{\beta_j}$ [kJmol$^{-1}$] | $\log\beta_j$ | $-\Delta G°_{\beta_j}$ [kJmol$^{-1}$] | $-\Delta H°_{\beta_j}$ [kJmol$^{-1}$] | $-T\Delta S°_{\beta_j}$ [kJmol$^{-1}$] |
| py | CoL | 0.7(0.3) | 4(1) | 24(5) | 20 | 1.16[a] | 6.62 | – | – |
| | $CoL_2$ | – | – | – | – | 2.93 | 10.10 | – | – |
| | CdL | – | – | – | – | 1.20[b] | 6.85 | – | – |
| | $CdL_2$ | – | – | – | – | 2.13 | 12.16 | – | – |
| | $CdL_3$ | – | – | – | – | 2.14 | 12.22 | – | – |
| 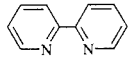 bipy | CoL | 3.86(0.1) | 22.0(0.6) | 29(1) | 7 | 6.06[c] | 34.01 | 34.33[c] | 0.32 |
| | $CoL_2$ | 7.35(0.1) | 41.9(1.1) | 52(1) | 10.1 | 11.42 | 64.10 | 63.64 | –0.46 |
| | $CoL_3$ | 8.66(0.2) | 49.4(1.1) | 67(1) | 17.6 | 16.02 | 89.92 | 89.18 | –0.74 |
| | CdL | 1.56(0.01) | 8.9(0.1) | 15.3(0.5) | 6.4 | 4.25[c] | 23.86 | 21.35[c] | –2.51 |
| | $CdL_2$ | 2.65(0.03) | 15.1(0.2) | 23(1) | 8.2 | 7.85 | 44.06 | 39.34 | –4.72 |
| | | | | | | 10.55 | 59.22 | 58.62 | –0.60 |
| 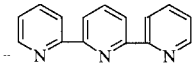 terpy | CoL | 5.56(0.15) | 31.0(0.9) | 33(1) | 2 | 8.4[d] | 47.95 | – | – |
| | $CoL_2$ | 10.52(0.15) | 60(1) | 63(1) | 3 | 18.3 | 104.46 | – | – |
| | CdL | 2.27(0.02) | 12.9(0.1) | 10.6(0.3) | –2.3 | 5.1[d] | 29.11 | – | – |
| | $CdL_2$ | 4.57(0.05) | 26.1(0.3) | 27.8(0.3) | 1.7 | – | – | – | – |
| 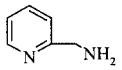 amp | CoL | – | – | – | – | 5.47[e] | 31.23 | 29.1[e] | –2.13 |
| | $CoL_2$ | – | – | – | – | 10.11 | 57.70 | 60.6 | 2.88 |
| | $CoL_3$ | – | – | – | – | 13.56 | 77.40 | 91.9 | 14.49 |
| | CdL | 4.12(0.01) | 23.5(0.2) | 32.6(0.5) | 9.1 | 4.38[f] | 25.01 | | |
| | $CdL_2$ | 7.79(0.01) | 44.4(0.4) | 65.0(0.5) | 20.6 | 8.30 | 47.40 | – | – |
| | $CdL_3$ | 10.47(0.01) | 59.7(0.6) | 103.6(0.6) | 43.8 | 11.33 | 64.70 | | |
| 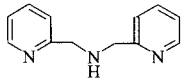 dpma | CoL | 6.2(0.3) | 35.4(0.1) | 49(1) | 14 | 8.05[g] | 45.18 | 36.2[g] | –8.98 |
| | $CoL_2$ | 11.2(0.6) | 63.9(0.2) | 86(2) | 23 | 13.85 | 77.74 | 68.2 | –9.54 |
| | CdL | 4.49(0.01) | 25.6(0.2) | 27.3(3) | 1.7 | 6.40[g] | 36.52 | 24.7 | –11.22 |
| | $CdL_2$ | 8.69(0.02) | 49.6(0.9) | 73 (0.7) | 23.4 | 11.76 | 67.11 | 57.7 | –8.31 |

[a] Ref.[34] [b] Ref.[35] [c] Ref.[36a,36b] [d] Ref.[37] [e] Ref.[38] [f] Ref.[36d] [g] Ref.[36c]

 © 2006 Wiley-VCH Verlag GmbH & Co. KGaA, Weinheim 

value ≤0.7, this process does not occur within a reasonable interval of time, sufficient to collect reliable spectrophotometric titration point data. This was not the case when amp was used, as this secondary reaction was much faster and also not prevented at very low $C_L/C_M$ ratios.

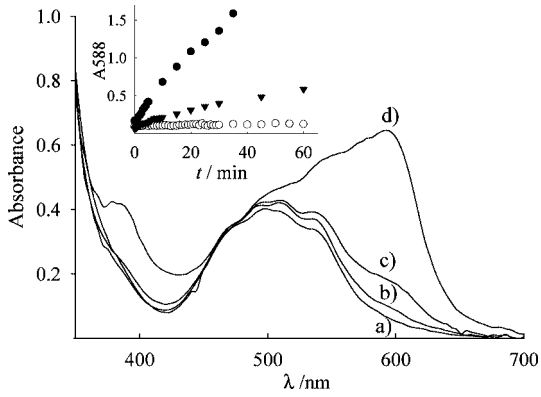


Figure 1. Spectral changes of a Co/dpma solution ($C_L/C_M$ = 1) at increasing times: a) 5 s; b) 30 s; c) 5 min; d) 75 min. Time evolution (small graph) of absorbance at $\lambda$ = 588 nm in case of different Co/dpma ratios: (○) $C_L/C_M$ = 0.7; (▼) $C_L/C_M$ = 1; (●) $C_L/C_M$ = 1.5.

Figure 2 and Figure 3 show $\Delta h_v$, the total molar enthalpy change, as a function of $R_c$ for $Cd^{2+}$- and $Co^{2+}$-ligand systems. The fit between experimental and calculated curves (full lines in the figures) is good, and their shapes are fully consistent with the information obtained from analysis of potentiometric and spectrophotometric data.

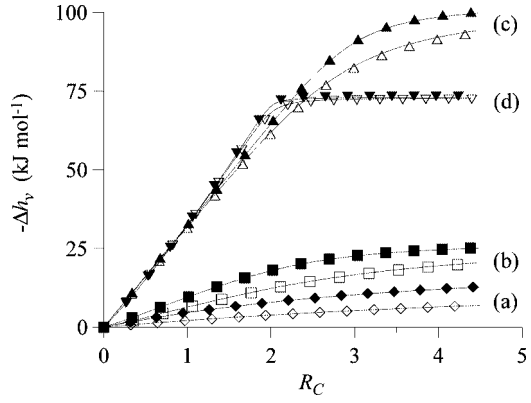


Figure 2. Total molar enthalpy changes $\Delta h_v$ as a function of $R_c$ = $C_L/C_M$ for $Cd^{II}$ complex formation in DMSO. (a) bipy, (◊) 5.05, (♦) 15.01 mmol dm$^{-3}$ in $Cd^{2+}$; (b) terpy, (□) 5.04, (■) 15.10 mmol dm$^{-3}$ in $Cd^{2+}$; (c) amp, (△) 4.98, (▲) 14.97 mmol dm$^{-3}$ in $Cd^{2+}$; (d) dpma, (▽) 5.07, (▼) 14.93 mmol dm$^{-3}$ in $Cd^{2+}$. Solid lines calculated from values of $\beta_j$ and $\Delta H°_{\beta j}$, Table 1.

Some considerations may be made: (*i*) differentiation of curves of the complexation of Cd with bipy and terpy at various $C_M$ indicates the formation of complexes of low stability; (*ii*) for Co with bipy, differentiation after $R_c$ = 1 is explained by the formation of a very stable mononuclear ML complex, followed by other $ML_j$ species of lower stability; (*iii*) the linear trend of the curve for the Co–terpy and –dpma systems up to $R_c$ = 2 and the absence of heat

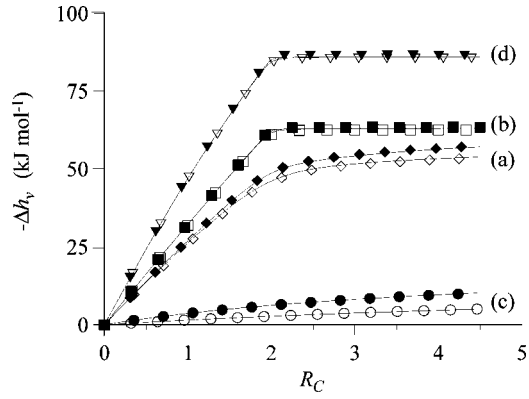


Figure 3. Total molar enthalpy changes $\Delta h_v$ as a function of $R_c$ = $C_L/C_M$ for $Co^{II}$ complex formation in DMSO. For (a), (b), and (d), see legend of Figure 2 for same (a), (b), and (d) systems. In this case, (c) refers to py, (○) 15.05, (●) 45.01 mmol dm$^{-3}$ in $Co^{2+}$.

evolving beyond this value are consistent with the formation of ML and $ML_2$ complexes of comparable stability; (*iv*) as regards Co–dpma, the presence of an equivalent point at exactly $R_c$ = 2 is in good agreement with the hypothesis that the secondary reaction is negligible from a calorimetric point of view.

Calorimetric data show that a very small thermal effect occurs between Cd and py, even at high metal concentrations ($C_M$ = 50 mmol dm$^{-3}$). For this reason, no $\Delta H°_{\beta j}$ are reported, and only a rough value of $\log\beta_1$ ($\log\beta_1$ = 0.5 ± 0.2) could be calculated from potentiometric measurements. A similar trend was found for $Co^{II}$, but the higher thermal effects due to metal–ligand interaction allow the calculation of reliable values for $\log\beta_1$ and $\Delta H°_{\beta 1}$ by treatment of calorimetric data.

For the sake of comparison, Table 1 lists the available stability constants and thermodynamic functions for complex formation in water.[34–38] The set of data presented are the most complete in the literature, independently of the fact that some of them[36] refer to 20 °C. The choice seems to be reasonable, as the stability constants available at 25 °C, for which enthalpy data are not given,[39,40] are very close to those reported at 20 °C.

## Computational Results

The M–N distances of complexes $[CdL]^{2+}$ and $[CoL]^{2+}$, whose geometries were optimized in vacuo, are listed in Table 2. A comprehensive list of bond lengths and angles is given as supporting information also for the free ligands (Supporting Information, Tables S1–S6): the results are in good agreement with experimental X-ray data.[41] To check the reliability of model chemistry in predicting the structural features of the compounds, the geometry of the structurally known[42] $[Co(terpy)_2]^{2+}$ was optimized (Supporting Information, Table S7) and also in this case the match between calculated and experimental data is good.

 © 2006 Wiley-VCH Verlag GmbH & Co. KGaA, Weinheim 

Table 2. M–N distances in Å.

| | 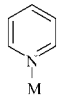 | 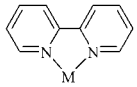 | 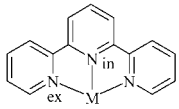 | |
|---|---|---|---|---|
| | $d_{M-N}$ | $d_{M-N}$ | $d_{M-Nin}$ | $d_{N-Nex}$ |
| $Co^{2+}$ | 1.782 | 1.853 | 1.871 | 1.936 |
| $Cd^{2+}$ | 2.169 | 2.205 | 2.205 | 2.267 |

In all cases, the M–N bond lengths appear to be shorter than in crystal structures;[41,43] this is of course due to the approximate models used and to the absence of other electrodonating ligands. The qualitative result of longer Cd–N distances of 0.33–0.39 Å with respect to Co–N is consistent with experimental structures, although in the last case the gap is in the range 0.18–0.31 Å. Table 3 lists total binding energies, $E_{bind}$, calculated for the formation of ML adducts. Energies for σ donation from the nitrogen lone pair to the metal, $E_{LP(N) \rightarrow M}$, calculated by using natural bond orbital (NBO) analysis,[44] are also listed in Table 3. In order to provide some indication of the role of π acceptor pyridine units in ligand–metal bonds, the NBO charges of the N atoms and metals in the compounds are calculated and listed in Table 4.

Table 3. Binding energies ($E_{bind}$) and strengths of N lone pair → metal interactions from NBO analysis ($E_{LP(N)\rightarrow M}$) in kJ mol$^{-1}$ for formation of $ML^{2+}$ complexes. $\Delta E = E^{Co^{2+}} - E^{Cd^{2+}}$.

| | $E_{bind}$ | | |
|---|---|---|---|
| | py | bipy | terpy |
| $Co^{2+}$ | –615.0 | –1007.9 | –1341.8 |
| $Cd^{2+}$ | –548.8 | –841.4 | –1090.7 |
| $\Delta E_{bind}$ | –66.3 | –166.5 | –251.1 |
| | $E_{LP(N)\rightarrow M}$ | | |
| $Co^{2+}$ | 205.1 | 317.5 | 455.7 |
| $Cd^{2+}$ | 193.1 | 292.8 | 412.0 |
| $\Delta E_{LP(N)\rightarrow M}$ | 12.0 | 24.7 | 43.7 |

Table 4. NBO charges on metals and N atoms in compounds.

| L | $Cd^{2+}$ | $Co^{2+}$ | $CdL^{2+}$ | $CoL^{2+}$ | $CdL^{2+}$ | $CoL^{2+}$ |
|---|---|---|---|---|---|---|
| | | | $N_{in}$ | | $N_{ex}$ | |
| py | 1.611 | 1.663 | –0.650 | –0.736 | – | – |
| bipy | 1.610 | 1.579 | –0.659 | –0.701 | – | – |
| terpy | 1.597 | 1.550 | –0.642 | –0.648 | –0.638 | –0.688 |

## Discussion

### General Remarks on Solvent Role

All complexes form in highly exothermic reactions, whereas entropy terms oppose reactions (Table 1), with the exception of the $Cd^{II}$–terpy system, for which a small positive entropy value was found. Negative enthalpy and entropy values are typical of reactions involving complexation of metal ions by neutral ligands in aprotic solvents.[8–12]

Pyridine complexes are characterized by higher stabilities in water than in DMSO: the trend is opposite to that found for simple primary and secondary aliphatic amines, in which the greater solvation of ligands in water through strong hydrogen bonds[45,46] overcomes the greater solvation[11a,47] of metal ions in DMSO. In the present case, the role of ligand solvation is evidently of minor importance, and the stability constants follow the trend expected on the basis of metal ion solvation. As regards amp and dpma, higher stability is still observed in water although it is much less marked. This higher stability in the case of dpma systems, for which all the thermodynamic functions are available in the two solvents, is essentially entropic in origin, as enthalpy terms are more favorable in DMSO. This indicates that the desolvation effects of the amino group, more important in water than in DMSO, play a major role in determining the stability trend in the two solvents.

### Pyridine Ligands

Pyridine shows a much lower affinity for $Cd^{2+}$ and $Co^{2+}$ ions with respect to monoamines ($\log K_1^{n\text{-butylamine}} = 2.6$ and 1.91 for Cd and Co, respectively):[11a,11b] this point is certainly due to the lower basicity of pyridine nitrogen when compared with amines in DMSO.[45,46] Steric effects may also be considered, as *ortho* hydrogens on pyridine rings produce steric hindrance once coordinated to a metal ion.[2]

The higher stabilities and more negative enthalpy and entropy data for the $Co^{II}$–bipy system, as compared with py, fit the formation of chelated complexes, although some steric strain, due to hydrogens in 3,3′-positions, occurs in the *cis*-conformer allowing coordination to metal ion.[2]

Certainly, the entry of the third bipy molecule causes unfavorable electronic and steric effects due to the other two ligands, and this explains the lower stability and enthalpy gain for the third complexation step. This fits crystallographic data, which show that, in the solid state, a distorted octahedron is formed by three bipy molecules around $Co^{II}$.[48]

When $[Co(terpy)]^{2+}$ (and $[Co(terpy)_2]^{2+}$) is formed, the ligand behaves as a terdentate: the low gain in the enthalpy term with respect to $[Co(bipy)]^{2+}$ complex formation ($\Delta\Delta H^{\circ}_{\beta_1}{}^{Co(terpy)\rightarrow Co(bipy)} = -4$ kJ mol$^{-1}$) is mainly due to extensive desolvation effects that come into play when this rigid terdentate ligand coordinates. This is confirmed by the low unfavorable entropy term associated with the same complexation step for the two ligands ($\Delta T\Delta S^{\circ}_{\beta_1}{}^{Co(terpy)\rightarrow Co(bipy)} = +5$ kJ mol$^{-1}$). Extra energy should also be considered for terpy rearrangement in the preorganized planar conformer with convergent nitrogen atoms. Lastly, strain is also produced by the resulting two fused five-membered chelate rings.

Analysis of thermodynamic data on $Cd^{2+}$ reactions suggests some preliminary considerations: (*i*) the positive in-

 © 2006 Wiley-VCH Verlag GmbH & Co. KGaA, Weinheim 

crease in the stability constants of $Co^{II}$ complexes on going from py to bipy and terpy (in both solvents) is not observable in the $Cd^{II}$ systems; (*ii*) the lower affinity for $Cd^{II}$ than for $Co^{II}$ is a peculiarity of all the pyridine ligands examined here. This effect is connected to the intrinsic nature of the ligands and the size of the metal ions, and not to the different solvation of central ions, as this was presumed to be larger for $Co^{II}$ than for $Cd^{II}$,[11c] which would give an opposite trend in stability.

The calculated M–N distances (Table 2) show that, in the gas phase, this higher affinity for $Co^{II}$ is also present: bond lengths are always longer for $Cd^{II}$– than for $Co^{II}$–pyridine systems, these differences being more marked for the less stable $M^{II}$–py complexes (0.387 Å longer in $Cd^{II}$–py than in $Co^{II}$–py). It is noteworthy that the difference in M–$N_{in}$ bond lengths calculated with DFT in $Cd^{II}$– and $Co^{II}$–terpy complexes (0.334 Å) is slightly higher than that of the M–$N_{ex}$ bond (0.331 Å): this is in agreement with previous studies which found that small cations are able to better interact with the central nitrogen, due to the steric constraint of this rigid ligand.[49]

As regards the binding energies (Table 3), the high values found (549–1542 kJ mol$^{-1}$) cannot be compared with experimental ones, as solvation effects were not taken into account in calculations. However, they are important because they show relative trends equal to those experimentally determined: even in this case, the affinity of pyridine ligands is higher for $Co^{II}$ than for $Cd^{II}$. Certainly, one of the main factors influencing this trend is the higher charge density on $Co^{II}$, which causes this smaller ion to be a harder acid than $Cd^{II}$.

The π backbonding does not appear to be important as far as these bipositive metal ions are concerned. In fact, the trend in total binding energies ($E_{bind}$ in Table 3) is parallel to that found in $E_{LP(N)\rightarrow M}$, that is σ donation plays a dominant role in ligand–metal bond stabilization. The calculated NBO charges on metal ions and nitrogens in the compounds (Table 4) give the same indications. The addition of π-acceptor units (from py to terpy) leads to a decrease in metal charges (and a simultaneous increase in N charges), showing that electron transfer mainly goes from the ligand to the metal by σ donation. An opposite trend in the positive metal charge was observed when the number of pyridine units was increased in complexes where π backbonding played an important role.[50]

The stability of $Co^{II}$ complexes increases much more than that of $Cd^{II}$ ones on going from bidentate bipy to terdentate terpy ($\Delta\Delta G^{\circ}_{Cd(terpy-bipy)}$ = 0.7; $\Delta\Delta G^{\circ}_{Co(terpy-bipy)}$ = 1.7). This indicates that, whereas the affinity of the ligands towards $Co^{II}$ becomes larger and larger on increasing the number of pyridine donors, the stability of $Cd^{II}$ complexes is not so affected by the increase of binding sites in the ligand. This is also confirmed by the total binding energy values (Table 3), which show that $\Delta E_{bind}$ (= $E_{bind}{}^{Co^{2+}}$ – $E_{bind}{}^{Cd^{2+}}$) increases on going from py to terpy, particularly for terpy, clearly indicating more marked selectivity for $Co^{2+}$.

The results of this terpy complexation with $Cd^{II}$ are difficult to explain solely by desolvation and steric effects, already discussed for $Co^{II}$. An attempt to explain these data is that the ligand behaves as a terdentate one, and this is achieved by structural rearrangement in the metal ion coordination sphere, giving rise to a pentacoordinate species. A certain misfit between the size of the large cadmium ion and the steric requirements of the ligand lies at the origin of this behavior. Also in the solid state, some preference for pentacoordination has already been highlighted in Cd–terpy compounds with crowded anions.[43a] Reaction enthalpies, lower for $[Cd(terpy)]^{2+}$ than for $[Cd(bipy)]^{2+}$, and especially the favorable entropy term for the formation of the terpyridyl complex, compared with the unfavorable entropy of formation of the bipyridyl complex, fit this hypothesis.

### Aminopyridine Ligands

The thermodynamic data, when compared with those obtained for mono- and bidentate aliphatic amines[11a,11b] and with py, suggest the involvement of all the N atoms in metal complex formation with amp and dpma. In order to support this hypothesis, some $^1H$ NMR spectra of solutions of $Cd^{II}$ and dpma at various $R_c$ values were recorded. In particular, the spectrum of $[Cd(dpma)_2]^{2+}$ in [D$_6$]DMSO solution (Figure S1, Supporting Information) shows that the multiplet centered at $\delta$ = 8.49 ppm in the free ligand, assigned to *ortho* pyridine protons, is shifted by 0.38 ppm ($\delta$ = 8.11 ppm) after complexation. This effect, together with the symmetric pattern of the given spectrum, reflects the binding of all pyridine nitrogens to $Cd^{II}$ atoms in complex formation. The weak, broad signal due to the proton of the secondary -NH- amino group is also shifted by about 2 ppm on complex formation (from about 3.2 to 5.1 ppm). Another proof of the coordination of the amino group of dpma comes from FTIR spectra, recorded for a DMSO solution with a dpma-to-cadmium ratio of 2, where no bands for free secondary amino groups (at 3305 cm$^{-1}$) can be detected, whereas only the band due to bonded amine (at 3192 cm$^{-1}$) was observed.

Amp complexes with Cd are characterized by much higher stabilities with respect to bipy ($\Delta\log\beta_1$ = 2.56 and $\Delta\log\beta_2$ = 5.14), especially as regards the second complexation step. This is mainly due to the higher affinity for metal ions of amines compared with pyridines in DMSO.[45,46] More favorable steric and solvational effects certainly also play an important role, as indicated by the large gain in stability produced when the more crowded $[Cd(amp)_2]^{2+}$ is formed. At the origin of this large stability gain, there is a considerable and favorable increase in enthalpy that largely overcomes the parallel unfavorable decrease in entropy. This may reflect greater solvation of amp complexes in which the hydrogens of amines bonded to the metal ion can organize the solvent molecules near the metal complex by forming hydrogen bonds. This explanation is also in agreement with the formation of $[Cd(amp)_3]^{2+}$, a stable M/L = 1:3 species, which is not formed by the more rigid and less solvent-ordering bipy with the cadmium ion. When the third com-

 © 2006 Wiley-VCH Verlag GmbH & Co. KGaA, Weinheim 

plexation step is examined, desolvation effects are already over, as indicated by the higher negative stepwise enthalpy and entropy values. The same trend in desolvation effects, to an even more marked extent, is observed when examining the second complexation step with dpma.

When a pyridine ring is added to amp, a trend similar to that found on going from bipy to terpy is obtained for $Cd^{II}$ amp and dpma complexation. The gain in stability is very small, due to a less unfavorable entropy term, whereas the $\Delta H°_{\beta_1}$ value is even less favorable than for amp: the enthalpy gain due to the additional $Cd–N_{py}$ bond is overcome by the enthalpy spent during desolvation. As dpma donor atoms are undoubtedly all bonded to $Cd^{II}$, this result clearly confirms the low affinity of the pyridine moiety for $Cd^{II}$, which is even more enhanced when more py units are part of a more complex structural frame, as in dpma (and terpy).

From another point of view, as regards differences in complex stability between one metal ion with terpy and dpma, it should be noted that the gain in stability is much more significant for $Cd^{II}$ ($\Delta\log\beta_1^{dpma–terpy} = 2.22$) than for $Co^{II}$ ($\Delta\log\beta_1^{dpma–terpy} = 0.64$), that is, the relative selectivity towards $Co^{II}$ is decreased. This evidences the great influence of structural constraints in governing metal–ligand affinity: substitution of the central pyridine unit with a flexible amino group relaxes ligand structural requirements and decreases the particular misfit cited for Cd–terpy systems. Obviously, as two pyridines are still inserted in the ligand frame, residual strains still occur, and also contribute to the low gain in stability with respect to the Cd–amp system (see above).

When comparing analogous bidentate and tridentate aliphatic ligands, such as primary ethylenediamine (en), diethylenetriamine (dien), and secondary *N*,*N*′-dimethylethylenediammine (dmen) and *N*,*N*′′-dimethyldiethylenetriamine (dmdien), much higher stability and exothermicity are found,[11c,11d,11e] due to the higher basicity of the aliphatic ligands. The opposite occurs with the corresponding tertiary *N*,*N*,*N*′,*N*′-tetramethylethylenediammine (tmen) and *N*,*N*,*N*,′*N*′,*N*′′-pentamethyldiethylenetriamine (pmdien) although the basicity order in DMSO is still $R_3N > py$.[45,46] In this case, steric hindrance due to the methyl groups of the ligands in the complexes evidently explains this reverse behavior.

### Dioxygen Affinity

Reversible dioxygen-binding properties were found for $[Co(bipy)(terpy)]^{2+}$ mixed complexes in nonaqueous low-coordinating media, such as acetonitrile or nitrobenzene, and μ-peroxo adducts were isolated.[51] In order to verify if oxygen binding also occurs in DMSO, $O_2$ was bubbled in solutions containing the mixed complex $[Co(terpy)(bipy)]^{2+}$ {the stability constant for the reaction $Co^{2+}$ + terpy + bipy ⇌ $[Co(terpy)(bipy)]^{2+}$ was also evaluated by spectrophotometric titration and its value was $\log K = 8.9(0.1)$}. No changes in UV/Vis spectra were observed in the range 300–650 nm, thus showing that no $O_2$ absorption occurred. Fitting the dissociative mechanism at the basis of dioxygen coordination,[52] higher activation energy is probably required for the bond breaking necessary for $O_2$ coordination, when the $[Co(terpy)(bipy)]^{2+}$ species is solvated by the more-coordinating solvent DMSO.

## Conclusions

Much lower affinities are shown by pyridine ligands for $Cd^{II}$ than for $Co^{II}$: this is due to the poorer acid properties of the former ion, confirmed by the calculated binding energies of the complex and by longer M–N lengths in $Cd^{2+}$ complexes. No important π backbonding seems to be involved as far as these bipositive metal ion–ligand systems are concerned, as evidenced by DFT calculations on model systems. This selectivity increases with the number of pyridine units in the ligands: when the larger $Cd^{II}$ with rigid planar terpy is considered, a misfit between ion size and ligand structural requirement is invoked to explain the results. This point is also confirmed by the huge gain in the stability of the $Cd^{II}$ complex when one py unit is substituted with an amino group in dpma. This extra stability, especially with respect to cobalt systems, is not explained only in terms of the higher σ-donor properties of the amino group, but also by taking into account the particular relaxation introduced into the Cd–ligand system when the central py is substituted with an aliphatic moiety. A comparison with data available in water shows that the desolvation effects of the amino group, more important in water than in DMSO, play a crucial role in determining the stability trend in the two solvents, especially for aminopyridine ligands.

## Experimental Section

**General Remarks:** Solvated salts, $Co(ClO_4)_2·6DMSO$ and $Cd(ClO_4)_2·6DMSO$, ligands, and solvents were prepared and purified as described previously.[11a,11b,11c] All experiments in anaerobic conditions were carried out at room temperature in a MB Braun 150 glovebox under a controlled atmosphere containing less than 1 ppm of water and less than 1 ppm of oxygen.

**Potentiometric Measurements:** In a typical titration, known volumes of ligand solutions ($50 < C°_L < 400$ mmol dm$^{-3}$) were added to $Cd^{II}$ solutions (20 mL) ($2 < C°_{Cd} < 20$ mmol dm$^{-3}$) at 298.1 ± 0.1 K. The equilibrium concentrations of cadmium(II), necessary to calculate stability constants, were obtained from the emf data of a galvanic cell similar to that reported previously.[11a] Emf data were ascertained with an Amel 338 pHmeter equipped with a Weiss WCD1001 Cd ion-selective electrode as working electrode and a Methrom 6.0718.000 silver electrode as reference. The Nernstian response of Cd electrodes was checked in the range $10^{-7} <$ metal $< 10^{-2}$ mmol dm$^{-3}$. Equilibrium was typically reached in 2–5 min. The Hyperquad[53] minimization program was used to calculate stability constants.

**Spectrophotometric Measurements:** UV/Vis spectra were recorded with a Varian Cary 50 spectrophotometer, using optic fiber probes connected directly with the cell inside the glovebox. The concentra-

 © 2006 Wiley-VCH Verlag GmbH & Co. KGaA, Weinheim 

tions of cobalt(II) and ligands were in the range $2 < C°_{Co} < 20$ mmol dm$^{-3}$ and $50 < C°_{L} < 400$ mmol dm$^{-3}$, respectively. Data were recorded over the wavelength range 300–650 nm. The absorption maximum for $Co(ClO_4)_2$ in DMSO occurs at 535 nm, with an extinction molar coefficient of $\varepsilon = 11.9$ mol$^{-1}$ dm$^3$ cm$^{-1}$.[11a] Maximum absorption of $CoL_j$ complexes is shifted to lower wavelengths (Supporting Information, Figure S2 as an example), in line with an increase in ligand field strength. In the case of dpma with $Co^{II}$, UV/Vis data were collected in the presence of $Cd^{II}$ as a competitive ion, in order to obtain more reliable values for the stability constants.

The absorbance data at about 20 different wavelengths in the range 450–550 nm were analyzed and the formation constants of $CoL_j$ complexes were determined, together with the molar extinction coefficients of the complexes at each relevant wavelength, using the Hyperquad program.[53] UV/Vis measurements for dioxygen uptake were carried out on similar apparatus by means of 1-cm optic fiber probes (Hellma) dipped directly into the reaction vessel.

**Calorimetric Measurements:** A Tronac model 87-558 precision calorimeter was employed to measure reaction heats. The calorimeter was checked by titration of tris(hydroxymethyl)aminomethane (Tham) with a standard solution of HCl in water. The experimental value of the neutralization heat of Tham was $\Delta H° = -47.59$ kJ mol$^{-1}$, in good agreement with the accepted value of $-47.53 \pm 0.13$ kJ mol$^{-1}$.[1]

Calorimetric titrations were performed at 298.00 ± 0.02 K by adding known volumes of ligand solutions ($50 < C°_{L} < 400$ mmol dm$^{-3}$) to 20 mL of metal (metal = $Cd^{II}$, $Co^{II}$) solutions ($2.00 < C°_{metal} < 50.0$ mmol dm$^{-3}$).

For each titration run, the experimental values of the total heat produced in the reaction vessel were calculated as a function of the added titrant. These values were corrected only for the dilution heat of the titrant, which was determined separately. The dilution heat of the titrate was found to be negligible in the metal concentration range used.

Quantity $\Delta h_v$, total heat per mole of metal ion, was defined and calculated by dividing the net reaction heat by the number of moles of metal ion in the calorimetric vessel. The Letagrop Kalle[54] least-squares computer program was used to calculate enthalpy changes.

**NMR Measurements:** $^1$H NMR spectra were recorded at 298 K with a Bruker AC-200 spectrometer. Measurements were performed on [$D_6$]DMSO solutions containing metal ions (ca. 30 mmol dm$^{-3}$) and the dpma ligand in the molar ratio $R_c = 1$ or 2. Analogous measurements were carried out on solutions containing only the ligand concerned.

**FTIR Spectroscopy:** FTIR spectra were obtained on a Bio-Rad FTS 40 spectrometer (maximum resolution 4 cm$^{-1}$; 16 scans). A cell with barium fluoride windows (thickness 25 μm) was used. Cells were filled, closed in a glovebox, and quickly transferred to the spectrometer. $C°_{Cd}$ and $C°_{L}$ in the DMSO solutions were about 50 mmol dm$^{-3}$.

**Computational Procedure:** DFT calculations on $ML^{2+}$ complexes (M = Co, Cd; L = py, bipy, terpy) were performed using Gaussian03[55] with the B3LYP three-parameter hybrid density functional.[56] For the $Co^{2+}$ complexes the unrestricted formalism was employed with three unpaired electrons ($S = 4$). The split valence basis set 6-31G(d) was employed for the atoms of the ligands, and a 3-21G basis was applied for the metal ions. The use of the small 3-21G basis set was due to the observation that sometimes the application of ECPs with $Co^{2+}$ gave convergence problems with open-shell SCF in DFT calculations. Nevertheless, the choice of this basis set for the metal ions does not affect the qualitative trend of the results.

All geometries were optimized by symmetry constraints. After optimization, equilibrium points were characterized by calculating vibrational frequencies, in order to confirm that they were local minima.

Binding energies were corrected for zero-point energy and basis set superposition error (BSSE) by the counterpoise correction ($E_{bind} = E_{ML^{2+}} - E_{M^{2+}} - E_L + E_{BSSE}$).[57] NBO analysis was performed by the NBO3.1 program included in Gaussian.

**Supporting Information** (see footnote on the first page of this article): Figure S1 shows $^1$H NMR spectra for the Cd–dmpa system in [$D_6$]DMSO. Figure S2 shows spectral changes, in terms of molar absorption of *j* species versus wavelengths, for the Co–bipy species. Tables S1–S7 list DFT-optimized distances and angles of py, bipy, and terpy, their ML (M = $Cd^{II}$, $Co^{II}$) and $Co(terpy)_2$ complexes, and the numbering scheme.


[1] a) R. M. Smith, A. E. Martell in *Critical Stability Constants*, Plenum Press, New York, **1989**, vol. 6, 2nd supplement; b) A. E. Martell, R. M. Smith, R. J. Motekaitis (Eds.), *Critically Selected Stability Constants of Metal Complexes Database*, version 5.0, **1998**.

[2] R. Hancock, A. E. Martell, *Chem. Rev.* **1989**, *89*, 1875–1914.

[3] a) A. Bencini, A. Bianchi, P. Paoletti, *Coord. Chem. Rev.* **1992**, *120*, 51–85b) G. Golub, H. Cohen, P. Paoletti, A. Bencini, D. Meyerstein, *J. Chem. Soc., Dalton Trans.* **1996**, 2055–2060; c) A. Bencini, A. Bianchi, P. Fornasari, C. Giorgi, P. Paoletti, B. Valtancoli, *Polyhedron* **2002**, *21*, 1329–1335; d) C. Bazzicalupi, A. Bencini, A. Bianchi, C. Duce, P. Fornasari, C. Giorgi, P. Paoletti, R. Pardini, M. R. Tinè, B. Valtancoli, *Dalton Trans.* **2004**, 463–469; e) A. Bencini, E. Berni, A. Bianchi, P. Fornasari, C. Giorgi, J. C. Lima, C. Lodeiro, M. J. Melo, J. S. de Melo, A. J. Parola, F. Pina, J. Pina, B. Valtancoli, *Dalton Trans.* **2004**, 2180–2187; f) K. Kervinen, H. Korpi, J. G. Mesu, F. Soulimani, T. Repo, B. Rieger, M. Leskela, B. M. Weckhuysen, *Eur. J. Inorg. Chem.* **2005**, *13*, 2591–2599.

[4] F. C. J. M. van Veggel, W. Verboom, D. N. Reinboudt, *Chem. Rev.* **1994**, *94*, 279–299.

[5] I. Bertini, L. Messori, G. Golub, H. Cohen, D. Meyerstein, *Inorg. Chim. Acta* **1995**, *235*, 5–8.

[6] G. Ma, A. Fisher, *Inorg. Chim. Acta* **2005**, *358*, 3165–3173.

[7] Y. Almo, E. Maimon, I. Zilbermann, M. Saphier, H. Cohen, D. Meyerstein, *Eur. J. Inorg. Chem.* **2005**, 4335–4340.

[8] S. Ahrland in *The Chemistry of Non-Aqueous Solvents* (Ed.: J. J. Lagowsky), Academic Press, New York, **1978**, vol. 5a and references therein.

[9] a) B. G. Cox, J. Garcia-Rosas, H. Schneider, *J. Am. Chem. Soc.* **1981**, *103*, 1384–1389; b) N. Heidari, A. Thaler, H. Schneider, B. G. Cox, *Inorg. Chim. Acta* **1998**, *279*, 186–191; c) A. Thaler, N. Heidari, B. G. Cox, H. Schneider, *Inorg. Chim. Acta* **1999**, *286*, 160–168.

[10] F. Arnaud-Neu, *Chem. Soc. Rev.* **1994**, *23*, 235–241.

[11] a) C. Comuzzi, M. Grespan, P. Polese, R. Portanova, M. Tolazzi, *Inorg. Chim. Acta* **2001**, *321*, 49–55; b) C. Comuzzi, M. Grespan, A. Melchior, R. Portanova, M. Tolazzi, *Eur. J. Inorg. Chem.* **2001**, 3087–3094; c) C. Comuzzi, A. Melchior, P. Polese, R. Portanova, M. Tolazzi, *Eur. J. Inorg. Chem.* **2002**, 2194–2201; d) C. Comuzzi, A. Melchior, P. Polese, R. Portanova, M. Tolazzi, *Eur. J. Inorg. Chem.* **2003**, 1948–1955; e) S. Del Piero, A. Melchior, P. Polese, R. Portanova, M. Tolazzi, *Dalton Trans.* **2004**, 1358–1365; f) S. Del Piero, L. Ghezzi, A. Melchior, M. R. Tiné, M. Tolazzi, *Helv. Chim. Acta* **2005**, *88*, 839–853; g) S. Del Piero, A. Melchior, R. Portanova, P. Polese, M. Tolazzi, *Eur. J. Inorg. Chem.* **2006**, 304–313.


 © 2006 Wiley-VCH Verlag GmbH & Co. KGaA, Weinheim 

[12] A. P. Cole, V. Mahadevan, L. M. Mirica, X. Ottenwaelder, T. D. P. Stack, *Inorg. Chem.* **2005**, *44*, 7345–7364.
[13] a) A. F. Martell, D. T. Sawyer, *Oxygen Complexes and Oxygen Activation by Transition Metals*, Plenum Press, New York, **1988**; b) G. McLendon, A. E. Martell, *J. Chem. Soc., Chem. Commm.* **1975**, 223–225.
[14] H. Sugimoto, T. Nagayama, S. Maruyama, S. Fujinami, Y. Yasuda, M. Suzuki, A. Uehara, *Bull. Chem. Soc. Jpn.* **1998**, *71*, 2267–2279.
[15] R. D. Jones, D. A. Summerville, F. Basolo, *Chem. Rev.* **1979**, *79*, 139–179.
[16] E. C. Niederhoffer, J. H. Timmons, A. Martell, *Chem. Rev.* **1984**, *84*, 137–203.
[17] L. I. Simandi in *Dioxygen Activation and Homogeneous Catalytic Oxidation*, Elsevier, Amsterdam, **1991**.
[18] A. Huber, L. Muller, H. Elias, R. Klement, M. Valko, *Eur. J. Inorg. Chem.* **2005**, *8*, 1459–1467.
[19] R. Ziessel, *Coord. Chem. Rev.* **2001**, *216–217*, 195–223.
[20] L. E. Karpinos, H. Sigel, *Inorg. Chim. Acta* **2002**, *337*, 131–142.
[21] R. D. Kohn, Z. Pan, M. I. Mahan, G. Kociok-Kohn, *Dalton Trans.* **2003**, 2269–2275.
[22] T. Ayers, S. Scott, J. Goins, N. Caylor, D. Hathcock, S. J. Slattery, D. L. Jameson, *Inorg. Chim. Acta* **2000**, *307*, 7–12.
[23] L. De Cola, L. Prodi, N. Zaccheroni, B. König, *Inorg. Chim. Acta* **2002**, *336*, 1–7.
[24] P. Comba, T. W. Hambley, *Molecular Modelling of Inorganic Coordination Compounds*, 2nd ed., Wiley-VCH, Weinheim, **2001**.
[25] R. Clerac, F. A. Cotton, K. R. Dunbar, T. Lu, C. A. Murillo, X. Wang, *J. Am. Chem. Soc.* **2000**, *122*, 2272–2278.
[26] H. A. Goodwin, *Top. Curr. Chem.* **2004**, *234*, 23–47.
[27] S. H. Rahaman, D. Bose, H. Chowdhury, G. Mustafa, H.-K. Fun, B. K. Ghost, *Polyhedron* **2005**, *24*, 1837–1844.
[28] L. F. Lindoy, T. Rambush, B. W. Skelton, A. H. White, *J. Chem. Soc., Dalton Trans.* **2001**, 1857–1862.
[29] a) B. Lakard, G. Herlem, B. Fahys, *J. Mol. Struct.: THEOCHEM* **2002**, *584*, 15–36; b) A. Baeten, F. De Proft, W. Langenaeker, P. Geerlings, *J. Mol. Struct.: THEOCHEM* **1994**, *306*, 203–221.
[30] B. Safi, K. Choho, F. De Proft, P. Geerlings, *Chem. Phys. Lett.* **1999**, *300*, 85–92.
[31] Y. Abe, G. Wada, *Bull. Chem. Soc. Jpn.* **1987**, *60*, 1936–1939.
[32] N. Y. Murakami Iha, M. A. de Almeida Azzelini, S. Utsuno, *Polyhedron* **1998**, *17*, 3379–3390.
[33] C. J. Raleigh, A. E. Martell, *Inorg. Chem.* **1985**, *24*, 142–148.
[34] A. Jehlickova, F. Vlacil, *Collect. Czech. Chem. Commun.* **1973**, *38*, 3395–3398.
[35] J. Esmel, G. Berthon, *Bull. Soc. Chim. Fr.* **1979**, *3–4*, 68–72.
[36] a) G. Anderegg, *Helv. Chim. Acta* **1963**, *46*, 2813–2822; b) G. Anderegg, *Helv. Chim. Acta* **1963**, *46*, 2397–2410; c) G. Anderegg, E. Hubmann, N. G. Podder, *Helv. Chim. Acta* **1977**, *60*, 123–140; d) G. Anderegg, *Helv. Chim. Acta* **1971**, *54*, 509–512.
[37] R. H. Holyer, C. D. Hubbard, S. F. A. Kettle, R. G. Wilkins, *Inorg. Chem.* **1966**, *5*, 622–625.
[38] E. G. Espana, F. Nurri, A. Sabatini, A. Vacca, *Gazz. Chim. Ital.* **1987**, *117*, 275–280.
[39] O. Goemine, Z. Eeckhaut, *Bull. Soc. Chim. Belg.* **1971**, *80*, 605–610.
[40] J. Rowary, J. Barger, J. Bunds, *Inorg. Chem.* **1968**, *7*, 1142–1145.
[41] E. Bartoszak-Adamska, R. Bregier-Jarzebowska, L. Lechoslaw Lomozik, *Polyhedron* **2002**, *21*, 739–744.
[42] a) C. A. Bessel, R. F. See, D. L. Jameson, M. R. Churchill, K. J. Takeuchi, *J. Chem. Soc., Dalton Trans.* **1992**, 3223–3228; b) H. Oshio, H. Spiering, V. Ksenofontov, F. Renz, P. Gutlich, *Inorg. Chem.* **2001**, *40*, 1143–1150.
[43] a) J. Pickardt, B. Staub, K. O. Schafer, *Z. Anorg. Allg. Chem.* **1999**, *625*, 1217–1224; b) G. J. Long, P. J. Clarke, *Inorg. Chem.* **1978**, *17*, 1394–1401; c) Q. Yang, Z.-D. Liu, H.-L. Zhu, M.-Y. Tan, *Acta Crystallogr., Sect. E: Struct. Rep. Online* **2004**, *60*, m1013–1014; d) D. Maspoch, D. Ruiz-Molina, K. Wurst, G. Vaughan, N. Domingo, J. Tejada, C. Rovira, J. Veciana, *Cryst. Eng. Commun.* **2004**, *6*, 573–578; e) M. Harvey, S. Baggio, R. Baggio, A. Mombru, *Acta Crystallogr., Sect. C: Cryst. Struct. Commun.* **1999**, *55*, 1457–1460.
[44] A. E. Reed, L. A. Curtiss, F. Weinhold, *Chem. Rev.* **1988**, *88*, 899–926.
[45] a) A. Mucci, R. Domain, R. L. Benoit, *Can. J. Chem.* **1980**, *58*, 953–958; b) M. R. Crampton, I. A. Robotham, *J. Chem. Res., Synop.* **1997**, 22–23.
[46] R. L. Benoit, M. J. Mackinnon, L. Bergeron, *Can. J. Chem.* **1981**, *59*, 1501–1504.
[47] C. Halidas, G. Heffer, Y. Marcus, *Chem. Rev.* **2000**, *100*, 819–852.
[48] D. J. Szalda, C. Creutz, D. Mahajan, N. Sutin, *Inorg. Chem.* **1983**, *22*, 2372–2379.
[49] C. Rabba, V. Mikhalko, J. P. Dognon, *Theor. Chem. Acc.* **2000**, *104*, 280–283.
[50] A. Hofmann, D. Jaganyi, O. Q. Munro, G. Liehr, R. van Eldik, *Inorg. Chem.* **2003**; *42*, 1688–1700.
[51] J. Glerup, P. A. Goodson, D. J. Hodgson, K. Michelsen, K. M. Nielsen, H. Weihe, *Inorg. Chem.* **1992**, *31*, 4611–4616.
[52] R. van Eldik, *Coord. Chem. Rev.* **1999**, *182*, 373–410.
[53] P. Gans, A. Sabatini, A. Vacca, *Talanta* **1996**, *43*, 1739–1753.
[54] R. Arnek, *Ark. Kemi* **1970**, *32*, 81–88.
[55] M. J. Frisch, G. W. Trucks, H. B. Schlegel, G. E. Scuseria, M. A. Robb, J. R. Cheeseman, J. A. Montgomery Jr, T. Vreven, K. N. Kudin, J. C. Burant, J. M. Millam, S. S. Iyengar, J. Tomasi, V. Barone, B. Mennucci, M. Cossi, G. Scalmani, N. Rega, G. A. Petersson, H. Nakatsuji, M. Hada, M. Ehara, K. Toyota, R. Fukuda, J. Hasegawa, M. Ishida, T. Nakajima, Y. Honda, O. Kitao, H. Nakai, M. Klene, X. Li, J. E. Knox, H. P. Hratchian, J. B. Cross, C. Adamo, J. Jaramillo, R. Gomperts, R. E. Stratmann, O. Yazyev, A. J. Austin, R. Cammi, C. Pomelli, J. W. Ochterski, P. Y. Ayala, K. Morokuma, G. A. Voth, P. Salvador, J. J. Dannenberg, V. G. Zakrzewski, S. Dapprich, A. D. Daniels, M. C. Strain, O. Farkas, D. K. Malick, A. D. Rabuck, K. Raghavachari, J. B. Foresman, J. V. Ortiz, Q. Cui, A. G. Baboul, S. Clifford, J. Cioslowski, B. B. Stefanov, G. Liu, A. Liashenko, P. Piskorz, I. Komaromi, R. L. Martin, D. J. Fox, T. Keith, M. A. Al-Laham, C. Y. Peng, A. Nanayakkara, M. Challacombe, P. M. W. Gill, B. Johnson, W. Chen, M. W. Wong, C. Gonzalez, J. A. Pople, *Gaussian03*, Revision B.03, Gaussian, Inc., Pittsburgh, PA, **2003**.
[56] a) A. D. Becke, *J. Chem. Phys.* **1993**, *98*, 1372–1377; b) C. Lee, W. Yang, R. G. Parr, *Phys. Rev. B* **1988**, *37*, 785–789.
[57] F. F. Boys, F. Bernardi, *Mol. Phys.* **1970**, *19*, 533–566.

Received: May 10, 2006
Published Online: August 1, 2006

 © 2006 Wiley-VCH Verlag GmbH & Co. KGaA, Weinheim 

DOI: 10.1002/ejic.200600453

# Synthesis and Characterization of [(1*R*,2*R*)-*trans*-Diaminocyclohexane]-platinum(II) Coordinated to Sulfur and Selenium Amino Acids

**Claudia Rothenburger,[a] Markus Galanski,*[b] Vladimir B. Arion,[b] Helmar Görls,[a] Wolfgang Weigand,*[a] and Bernhard K. Keppler*[b]**

*Dedicated to Prof. Peter Schuster on the occasion of his 65th birthday*

**Keywords:** Bioinorganic chemistry / Platinum / Amino acids / Sulfur / Selenium

Dichloro[(1*R*,2*R*)-*trans*-diaminocyclohexane]platinum(II) was activated with $Ag_2CO_3$ and then treated with (*S*)-methionine, *S*-methyl-(*S*)-cysteine, (*S*)-selenomethionine and *Se*-methyl-seleno-(*S*)-cysteine. The *N*,*S*- and *N*,*Se*-chelated platinum(II) species were isolated as hexafluorophosphate salts and characterized by multinuclear NMR spectroscopy, ESI-MS, IR, elemental analyses and, in the case of the (*S*)-methionine and (*S*)-selenomethionine complexes, by X-ray crystallography.

(© Wiley-VCH Verlag GmbH & Co. KGaA, 69451 Weinheim, Germany, 2006)

## Introduction

Modern anticancer chemotherapy makes use of a variety of drugs, including metal-based agents. Cisplatin, *cis*-diamminedichloroplatinum(II), is one of the most effective anticancer drugs known to date.[1] It is widely used in the treatment of several solid tumors, including metastatic testicular germ-cell cancer, which has become a curable disease in more than 90% of cases.[2] In order to overcome the severe toxic side-effects of cisplatin-based therapy (nephrotoxicity, neurotoxicity, nausea, and vomiting), the second-generation platinum drug carboplatin, diammine(1,1-cyclobutanedicarboxylato)platinum(II), has been developed and approved for worldwide clinical use.[3,4]

Synthetic variations in the coordinating ligands have led to platinum complexes with 1,2-diaminocyclohexane (DACH) ligands.[5] The most prominent representative of this new class of third-generation platinum complexes is oxaliplatin (Figure 1), which was found to be active in primarily cisplatin- and carboplatin-resistant cell lines and tumors.[6] Recently, oxaliplatin (Eloxatin) has been approved in more than 60 countries all over the world for the treatment of metastatic colorectal cancer, which is the second most frequent cause of cancer death in developed countries.[7]

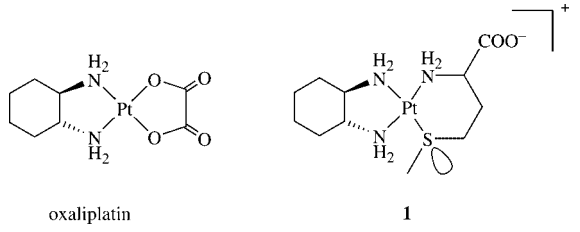


Figure 1. Chemical structures of oxaliplatin and of one of its metabolites (**1**) found in the plasma ultrafiltrate of cancer patients, both of which contain an (*S*)-methionine ligand.

It is widely accepted that cellular DNA is the crucial target for platinum anticancer drugs,[8] but how the drug reaches DNA is still puzzling. Platinum compounds display a high affinity for sulfur, in agreement with the hard/soft acid/base (HSAB) principle, therefore sulfur-containing biomolecules such as amino acids, peptides and proteins in the blood stream, the cytosol, and the nucleus should prevent anticancer platinum drugs from reaching the DNA.[9]

In plasma ultrafiltrate of rats and cancer patients treated with oxaliplatin, different kinds of metabolites, including those with (*S*)-methionine, have been detected in substantial amounts.[10,11] Whether these (*S*)-methionine species are produced from the organism just for detoxification and excretion purposes only, or themselves are involved in the anticancer process, is still a matter of some controversy. This is rather astonishing for a drug that is routinely used in

[a] Institut für Anorganische und Analytische Chemie, Friedrich-Schiller-Universität Jena,
August-Bebel-Strasse 2, 07743 Jena, Germany
Fax: +49-3641-948102
E-mail: c8wewo@uni-jena.de
[b] Institute of Inorganic Chemistry, University of Vienna,
Waehringer Strasse 42, 1090 Vienna, Austria
Fax: +43-1-4277-52680
E-mail: markus.galanski@univie.ac.at
bernhard.keppler@univie.ac.at

Supporting information for this article is available on the WWW under http://www.eurjic.org or from the author.

 © 2006 Wiley-VCH Verlag GmbH & Co. KGaA, Weinheim 

clinical practice and which has reached blockbuster status. Consequently, we have focused on finding an appropriate synthetic procedure for the synthesis of the (*S*)-methionine derivative, which has also been used and extended to other sulfur- and selenium-containing amino acids. Interestingly, it is worthwhile to mention that (*S*)-selenomethionine as well as *Se*-methylseleno-(*S*)-cysteine are currently being evaluated in preclinical[12] and clinical settings[13,14] as chemopreventive agents (also called cytoprotective or rescue agents). Therefore, syntheses of [(1*R*,2*R*)-*trans*-diaminocyclohexane]platinum(II) coordinated to (*S*)-selenomethionine and *Se*-methylseleno-(*S*)-cysteine are of great interest in order to provide these complexes for evaluation of their pharmacological properties in the future.

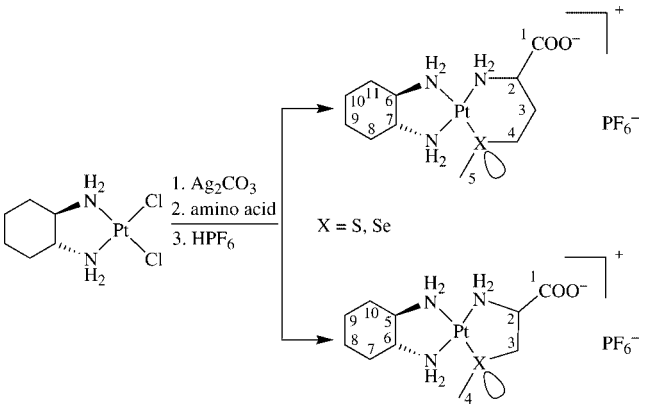


Figure 2. Syntheses of [(1*R*,2*R*)-*trans*-diaminocyclohexane]platinum(II) complexes containing (*S*)-methionine (**1**·$PF_6$), *S*-methyl-(*S*)-cysteine (**2**·$PF_6$), (*S*)-selenomethionine (**3**·$PF_6$), and *Se*-methylseleno-(*S*)-cysteine (**4**·$PF_6$) as amino acid ligands (stereochemistry at 2-C and X are omitted).

## Results and Discussion

There are several reports in the literature dealing with the characterization of complexes like **1** (Figure 1), but in nearly all cases the target complexes were synthesized in small amounts in an NMR tube without isolation. In only one case was the synthesis of **1** described based on several laborious isolation steps, including two HPLC separations.[15] Additionally, the yield was very low (1.2%). In the present work, synthesis of the amino acid platinum(II) complex [(1*R*,2*R*)-*trans*-diaminocyclohexane][(*S*)-methionine-$\kappa^2$*N*,*S*]platinum(II) (**1**·$PF_6$) started from $K_2PtCl_4$ and (1*R*,2*R*)-*trans*-diaminocyclohexane. The resulting complex dichloro[(1*R*,2*R*)-*trans*-diaminocyclohexane]platinum(II) was treated with silver carbonate in order to remove the chloro ligands (Figure 2). Direct addition of (*S*)-methionine to the activated platinum species afforded a yellow crude product after lyophilization. After dissolution and addition of aqueous $HPF_6$, the target compound **1**·$PF_6$ was isolated as a white solid in moderate yield. The decisive steps towards the improved preparation of **1** are the use of $Ag_2CO_3$ for the activation of the dichloro[(1*R*,2*R*)-*trans*-diaminocyclohexane]platinum(II) complex and the addition of aqueous $HPF_6$ to this raw product. $HPF_6$ efficiently removes the carbonate counterions, while $PF_6^-$ is known to be a beneficial partner in the crystallization process. The (*S*)-methionine complex **1**·$PF_6$ was intensively studied and characterized by $^1$H, $^{13}$C, $^{15}$N, $^{31}$P, and $^{195}$Pt NMR spectroscopy, X-ray diffraction analysis, elemental analysis, IR spectroscopy, and ESI MS.

The $^1$H NMR spectrum of **1**·$PF_6$, which was measured in $H_2O/D_2O$ (9:1), can be divided into three spectral regions (Figure 3). The signals deriving from the cyclohexane ring (6-H to 11-H) are found in the upfield region ($\delta$ = 1.0–2.3 ppm). The signals of the diastereotopic protons of the $CH_2$ groups display a marked splitting of up to nearly 0.8 ppm, as could be deduced from the $^1$H,$^{13}$C-COSY NMR spectrum. The 2-H, 3-H, and 4-H resonances of the coordinated (*S*)-methionine are found between $\delta$ = 2.1 and 3.5 ppm. All N*H* signals are detected most downfield ($\delta$ = 4.8–5.8 ppm) and are partly superimposed by the HDO resonance, which was suppressed by pre-saturation. Significant downfield shifts are observed for the signals of protons 4-H and 5-H. In uncoordinated (*S*)-methionine, 4-H and 5-H resonate at $\delta$ = 2.58 and 2.07 ppm, respectively. In the target complex, however, two sets of signals at $\delta$ = 2.87/2.94 (4-H) and 2.45/2.46 (5-H) ppm are detected. On the contrary, an upfield shift from $\delta$ = 3.80 ppm in the free ligand to $\delta$ = 3.35/3.44 ppm was found for the signal of the α-proton 2-H. Deconvolution of the $^1$H NMR spectrum in the region at $\delta \approx$ 2.45 ppm allowed us to estimate the ratio between the two sets of signals: under the experimental conditions (298 K), a ratio of 2:3 was found.

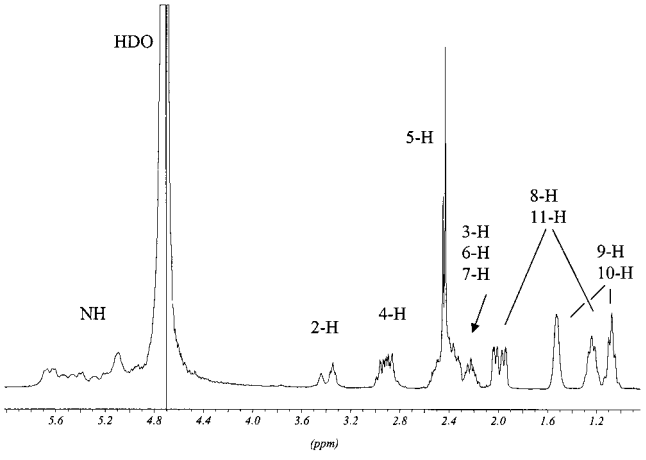


Figure 3. $^1$H NMR spectrum of **1**·$PF_6$ with the HDO signal suppressed by pre-saturation.

The coordination sphere around the central platinum ion could be determined on the basis of the $^{195}$Pt and $^{15}$N chemical shifts. The $^{195}$Pt NMR spectrum of **1**·$PF_6$ displays two signals at $\delta$ = –3313 and –3335 ppm for the two diastereoisomers (Figure 4), which is in accordance with a $PtN_3S$ configuration. Deconvolution and integration resulted in the same ratio of 2:3. For $PtN_3S$-type complexes, $^{195}$Pt chemical shifts in the range of $\delta$ = –3000 to –3300 ppm are expected,[16,17] whereas $PtN_2SO$ and $PtN_2S_2$ complexes

 © 2006 Wiley-VCH Verlag GmbH & Co. KGaA, Weinheim 

resonate in the region af $\delta \approx -2700$ and $-3700$ ppm,[18] respectively. Besides $^{195}$Pt NMR investigations, the $^{15}$N chemical shifts were used to characterize the structure of the platinum complexes. Two-dimensional $^{1}$H,$^{15}$N-correlated spectroscopy at natural abundance of the $^{15}$N nuclei (spin 1/2, 0.37% natural abundance) has proven to be a powerful tool since the $^{15}$N chemical shift of the nitrogen atom is diagnostic for ligands coordinated in *trans* position. Three $^{15}$N chemical shifts could be detected for **1**·$PF_6$: the $^{1}$H,$^{15}$N shift correlation peak at $\delta = -45$ ppm can be assigned to the 2-C*N*$H_2$ group of (*S*)-methionine *trans* to the nitrogen atom of the DACH ligand,[19] whereas the resonance at $\delta = -14$ ppm can be assigned to 7-C*N*$H_2$ *trans* to the nitrogen atom of the (*S*)-methionine ligand; the cross peak of 6-C*N*$H_2$ *trans* to the coordinated thioether group could be detected at $\delta = -4$ ppm.

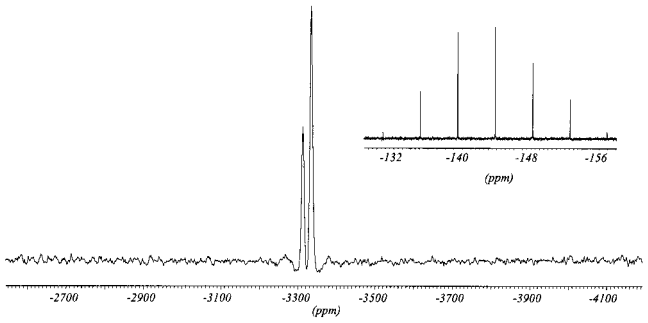


Figure 4. $^{195}$Pt and $^{31}$P (small inset) NMR spectra of **1**·$PF_6$.

The two sets of resonances for the (*S*)-methionine ligand in the $^{1}$H NMR spectrum as well as two $^{195}$Pt signals for **1**·$PF_6$ are a consequence of the coordination of (*S*)-methionine to the platinum(II) center through the sulfur and nitrogen atoms. As a result, another stereocenter which undergoes slow isomerization at the sulfur atom is formed. When the temperature was raised, the epimerization at the chiral sulfur center became faster, and at 333 K only one signal for the methyl protons 5-H was observed. This process was reversible (Figure S1, Supporting Information). In the case of the cyclohexane protons, the isomerization process seems to have no detectable influence on the proton signals. In the $^{13}$C NMR spectra of the free and coordinated (*S*)-methionine ligand, the resonances of the carbonyl carbon atom C-1 are found in close proximity at $\delta = 174.6$ and 176.3/176.8 ppm, respectively. However, a distinct downfield shift of the signal of the *S*-methyl group from $\delta = 14.3$ to 19.6/19.7 ppm was detected. These features are in accordance with an *N*,*S* coordination of (*S*)-methionine to the platinum(II) center as well. The hexafluorophosphate counterion signal appears at $\delta = -143.9$ ppm in the $^{31}$P NMR spectrum (Figure 4). Due to the coupling of the phosphorus nucleus with the six fluorine atoms, it appears as a septet with a coupling constant of 710 Hz.

X-ray diffraction quality single crystals were grown by slow concentration of a methanol solution of the complex. The structure of **1**·$PF_6$ consists of a complex cation **1** (Figure 5) and a complex anion $[PF_6]^-$, which interacts weakly through contacts of the type N−H···F (N1···F6 2.935, N2···F4 3.123, N2···F5 3.352, N2···F6 3.303 Å). The platinum(II) ion has a square-planar coordination geometry as it is chelated by two ligands: (1*R*,2*R*)-*trans*-diaminocyclohexane and (*S*)-methionine. (1*R*,2*R*)-*trans*-DACH acts as a neutral ligand and coordinates to the platinum(II) ion through nitrogen atoms N1 and N2 [Pt–N1 2.051(2), Pt–N2 2.051(2) Å]. These bond lengths are intermediate between those found in oxaliplatin [Pt−N1 2.06(2), Pt−N2 2.04(2) Å].[20] The second ligand, which is negatively charged due to the presence of the ionized carboxyl group, is bound to the platinum(II) ion through the nitrogen atom N3 and the thiomethyl sulfur atom S1. Coordination of the latter to the platinum(II) ion creates a new stereogenic center at the S atom, i.e. (*R*), in addition to the opposite configuration at atom C7. The Pt−N3 [2.062(2) Å] and Pt−S1 [2.2607(6) Å] bonds are markedly longer than the corresponding bonds in two independent molecules of dichloro[(*S*)-methionine-κ$^2$*N*,*S*)platinum(II)[21] [2.047(8), 2.029(8) and 2.246(2), 2.247(2) Å]. The deviation of the coordinated atoms from the mean plane through PtN1N2N3S1 does not exceed ±0.023 Å. The five-membered chelate ring has a distorted envelope conformation with a clear tendency towards a zigzag arrangement of C1 (+0.55 Å) and C6 (–0.14 Å). The torsion angle $\Theta_{N1–C1–C6–N2}$, which serves as a measure of the deviation of the chelate ring from planarity, is –54.3°. The cyclohexane ring adopts a chair conformation with the amino groups in equatorial positions.

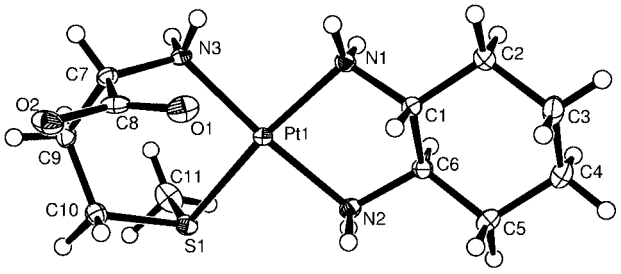


Figure 5. Structure of the cation in **1**·$PF_6$ with thermal ellipsoids at the 50% probability level. Selected bond lengths [Å] and angles [°]: Pt–N1 2.051(2), Pt–N2 2.051(2), Pt–N3 2.062(2), Pt–S1 2.2607(6), C10–S1 1.810(3), S1–C11 1.805(3), C8–O1 1.235(3), C8–O2 1.276(3); N1–Pt–N2 82.79(10), N3–Pt1–S1 95.35(7), C11–S1–C10–C9 –62.8, N3–C7–C8–O1 –2.2.

The six-membered metallocycle has a chair conformation, which is distorted because of the presence of heteroatoms. The methyl substituent at S1 and the $COO^-$ group are placed on opposite sides of the $PtN_3S$ plane. The orientation of the carboxylato group can be described by the torsion angle $\Theta_{N3–C7–C8–O1}$ (–2.2°). This angle is comparable with that observed on coordination of (*S*)-methionine to the palladium(II) ion in [$PdCl_2$(*S*-met)] (3.7°).[22]

The derivative **2**·$PF_6$, which contains an *S*-methyl-(*S*)-cysteine ligand, was synthesized in analogy to **1**·$PF_6$, thereby demonstrating the applicability of this reaction

 © 2006 Wiley-VCH Verlag GmbH & Co. KGaA, Weinheim 

pathway (Figure 2). Characterization was performed by elemental analysis, mass spectrometry, and IR, $^1$H, and $^{13}$C NMR spectroscopy. Besides the fact that one methylene unit is missing in **2**·$PF_6$, the $^1$H and $^{13}$C NMR spectra show a similar resonance pattern with respect to the (*S*)-methionine counterpart. The diastereoisomer ratio was found to be nearly 1:1. In **2**·$PF_6$, the proton signals are shifted to lower field in the amino acid ligand by 0.1 to 0.5 ppm. Comparison with the diastereoisomers of **1**·$PF_6$ revealed chemical shift differences smaller than 0.1 ppm. These differences are more pronounced in **2**·$PF_6$, with $\Delta\delta$ values of between 0.1 and 0.2 ppm. Remarkable $\Delta\delta$ values were observed especially in the case of the *S*-Me protons (**1**·$PF_6$: 0.01 ppm; **2**·$PF_6$: 0.1 ppm), thereby reflecting the change from the six-membered to the more strained five-membered platinacycle. The latter observation was also confirmed in the $^{13}$C NMR spectrum, in which the *S*-Me carbon resonances are found at $\delta$ = 19.6 and 19.7 ppm for **1**·$PF_6$ and at $\delta$ = 20.6 and 21.8 ppm for the *S*-methyl-(*S*)-cysteine analog **2**·$PF_6$.

As mentioned in the introduction, (*S*)-selenomethionine and *Se*-methylseleno-(*S*)-cysteine are currently being evaluated as cytoprotective agents during the treatment with platinum-based anticancer complexes. Administration of either selenium agent results in a decreased platinum-induced toxicity without affecting the tumor-inhibiting properties of the platinum complexes. In the case of cis- and carboplatin (two monodentate ammine ligands), in-depth NMR spectroscopic and ESI-MS studies have been performed.[23,24] These showed that one or both ammine ligands are released from the platinum center upon coordination of (*S*)-selenomethionine. It is widely accepted that such types of complexes are not further involved in the anticancer process.[24] In contrast, for oxaliplatin, which contains the bidentate DACH ligand, release of the coordinated diamine is not expected due to the chelate effect. Therefore, the anticancer-active [(1*R*,2*R*)-*trans*-diaminocyclohexane]-platinum(II) fragment will still remain intact, thus opening up the possibility to selectively synthesize these types of metabolites and study their pharmacological properties.

Synthesis of the (*S*)-selenomethionine complex **3**·$PF_6$ was performed in analogy to the (*S*)-methionine counterpart (Figure 2). A comparable peak pattern to **1**·$PF_6$ as well as analogous shift differences with respect to the uncoordinated ligand were observed in the $^1$H and $^{13}$C NMR spectra of **3**·$PF_6$. The signals of protons 4-H and 5-H are significantly shifted to lower field in the complex, whereas the signal of the 2-H protons displays an upfield shift (e.g. the methyl resonances in **3**·$PF_6$ at $\delta$ = 2.31 and 2.34 ppm occur in the free ligand at $\delta$ = 1.93 ppm). The $^{13}$C NMR resonances of **3**·$PF_6$ are equivalent to those observed for the (*S*)-methionine analog: the resonances for the carboxylate group in **3**·$PF_6$ appear at $\delta$ = 176.8 and 176.5 ppm and are slightly shifted in comparison to the free ligand ($\delta$ = 174.5 ppm); a distinct downfield shift of the signal of the *Se*-methyl group from $\delta$ = 3.6 ppm to $\delta$ = 11.7/11.6 ppm was also observed. The diastereoisomer ratio deduced from the $^1$H NMR spectrum by deconvolution and integration was 2:3, which is the same as for the (*S*)-methionine analog. Comparison of the $^1$H and $^{13}$C NMR spectra of the *Se*-methylseleno-(*S*)-cysteine complex **4**·$PF_6$ with those of **3**·$PF_6$ revealed the same pattern as described above for **1**·$PF_6$ and **2**·$PF_6$. The $^1$H chemical shift differences of the diastereoisomers (with respect to the amino acid ligand) were small in the case of **3**·$PF_6$ ($\Delta\delta < 0.05$ ppm), whereas the $\Delta\delta$ values of **4**·$PF_6$ were found to be between 0.05 and 0.16 ppm. This general behavior was also confirmed in the $^{13}$C NMR spectra, in which the *Se*-Me carbon atom resonates at $\delta$ = 11.7 and 11.6 ppm in the case of **3**·$PF_6$ and at $\delta$ = 12.6 and 13.5 ppm for the *Se*-methylseleno-(*S*)-cysteine analog **4**·$PF_6$. For the latter, a converted diastereoisomer ratio of 3:2 with respect to **3**·$PF_6$ was found. As explained above, $^{195}$Pt and $^{15}$N NMR resonances are very indicative of the coordination sphere around the platinum center. Both the $^{195}$Pt (Figure 6) and $^{15}$N chemical shifts of **3**·$PF_6$ [$^{195}$Pt NMR: $\delta$ = –3381, –3351 ppm; $^{15}$N NMR: $\delta$ = –48.0 (2-$CNH_2$), –18.0 (7-$CNH_2$), 3.5 (6-$CNH_2$) ppm] are similar to those observed for the (*S*)-methionine analog **1**·$PF_6$ ($^{195}$Pt NMR: $\delta$ = –3335, –3313 ppm;$^{15}$N NMR: $\delta$ = –45.2 (2-$CNH_2$), –14.0 (7-$CNH_2$), 4.0 (6-$CNH_2$) ppm] and are therefore in agreement with the structure presented in Figure 2.

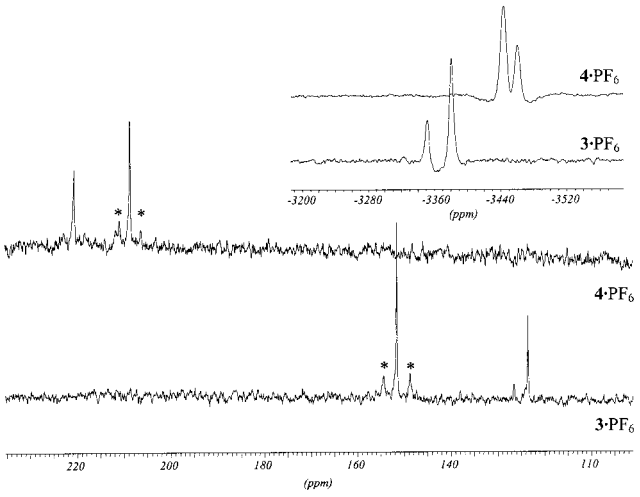


Figure 6. $^{77}$Se and $^{195}$Pt (small inset) NMR spectra of **3**·$PF_6$ and **4**·$PF_6$; $^{195}$Pt satellites are marked with asterisks. In the case of the less intense signals, $^{195}$Pt satellites could not unequivocally be detected.

From the analytical point of view, the selenium complexes offer an advantage since the selenium atom itself can be investigated by NMR spectroscopy ($^{77}$Se, spin 1/2, 7.6% natural abundance), thereby ultimately proving coordination of the selenium atom to the platinum center. Besides a remarkable downfield shift in comparison to the free ligand, coordination of the selenium atom is also reflected by the appearance of platinum satellites due to a $^1J_{^{77}Se,^{195}Pt}$ coupling (Figure 6).[25] In **3**·$PF_6$ and **4**·$PF_6$, the $^{77}$Se chemical shifts of the diastereoisomers appear at $\delta$ = 123.5/151.5 and 208.6/220.5 ppm, respectively; the uncoordinated amino acids resonate at $\delta$ = 84.8 and 51.2 ppm, respectively.

 © 2006 Wiley-VCH Verlag GmbH & Co. KGaA, Weinheim 

Coupling of $^{77}$Se with the $^{195}$Pt central ion in the (*S*)-selenomethionine complex **3**·$PF_6$ (435 Hz) is thereby significantly larger than in the *Se*-methylseleno-(*S*)-cysteine analog **4**·$PF_6$ (355 Hz).

Finally, the structure of **3**·$PF_6$ in the solid state was determined by X-ray crystallography. Single crystals were grown by slow concentration of a methanol solution of the complex. The structural motif of the complex cation **3** is very similar to that of complex **1**. Again, the methyl and carboxylate groups are positioned on opposite sides of the $PtN_3Se$ plane. However, it is worth noting that the Pt–Se distance [2.3777(10) Å] is more than 0.1 Å longer than the corresponding Pt–S distance in **1**. The Pt–Se bond length is comparable to that in dichloro[*O*-methyl-(*S*)-selenomethionine]platinum(II) [2.3697(8) Å].[26] Remarkably, the *Se*-methyl and COOMe groups lie on the same side of the $PtCl_2NSe$ plane in this complex (Figure 7).

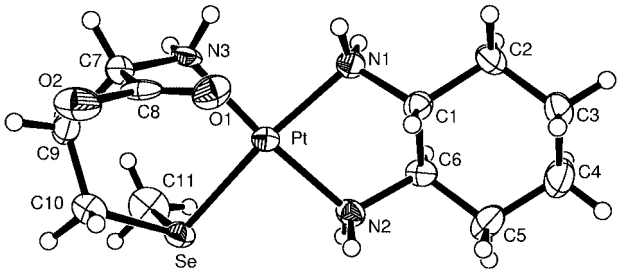


Figure 7. Structure of the cation in **3**·$PF_6$ with thermal ellipsoids at the 50% probability level. Selected bond lengths [Å] and angles [°]: Pt–N1 2.056(7), Pt–N2 2.061(7), Pt–N3 2.079(7), Pt–Se1 2.377(10), C10–Se1 1.948(9), Se1–C11 1.920(11), C8–O1 1.225(12), C8–O2 1.297(10); N1–Pt–N2 82.80(3), N3–Pt1–Se1 95.20(19), C11–Se1–C10–C9 –60.1, N3–C7–C8–O1 0.50.

## Conclusions

[(1*R*,2*R*)-*trans*-Diaminocyclohexane]platinum(II) complexes with coordinated (*S*)-methionine, *S*-methyl-(*S*)-cysteine, (*S*)-selenomethionine, and *Se*-methylseleno-(*S*)-cysteine ligands have been synthesized and characterized by multinuclear NMR spectroscopy, ESI-MS, IR spectroscopy, and elemental analysis. The (*S*)-methionine (**1**·$PF_6$) and (*S*)-selenomethionine (**3**·$PF_6$) complexes were also studied by X-ray crystallography. The synthetic procedure resulting in the (*S*)-methionine complex by activation of the dichloro[(1*R*,2*R*)-*trans*-diaminocyclohexane]platinum(II) species with $Ag_2CO_3$ and isolation of the resulting complex as its hexafluorophosphate salt can also be extended to other sulfur- and selenium-containing amino acids. This is of central interest since three out of the four complexes synthesized are metabolites in cancer patients treated with oxaliplatin. These metabolites can now be evaluated with respect to their pharmacological properties.

## Experimental Section

**General:** All chemicals and solvents used were obtained from commercial suppliers and were used as received. (*S*)-Methione was purchased from Roth and (*S*)-selenomethionine from Acros. *S*-Methyl-(*S*)-methionine, *Se*-methylseleno-(*S*)-cysteine, and $HPF_6$ (71% in water) were purchased from Fluka, and potassium tetrachloroplatinate(II) was obtained from Johnson Matthey. Dichloro[(1*R*,2*R*)-*trans*-diaminocyclohexane]platinum(II) was prepared according to a standard literature procedure.[27] The synthetic procedures were carried out in a light-protected environment in doubly distilled water and under argon using standard Schlenk-line techniques. Elemental analyses were performed by the microanalytical laboratory at the University of Vienna. $^1$H, $^{13}$C{$^1$H}, $^{31}$P{$^1$H}, $^1$H,$^1$H-COSY, $^1$H,$^{13}$C-COSY, $^1$H,$^{15}$N-COSY, $^{195}$Pt, and $^{77}$Se NMR spectra were recorded in $D_2O$ or $H_2O/D_2O$ (9:1) with a Bruker Avance DPX 400 instrument (UltraShield Magnet) using standard pulse programs at 400.13 ($^1$H), 162.0 ($^{31}$P), 100.63 ($^{13}$C), 85.99 ($^{195}$Pt), 76.32 ($^{77}$Se), and 40.55 ($^{15}$N) MHz. Two-dimensional spectra were measured in a gradient-enhanced mode. Chemical shifts were measured relative to the solvent peak ($\delta$ = 4.71 ppm), to external 85% $H_3PO_4$, to external $^{15}NH_4Cl$, to external $Ph_2Se_2$ at $\delta$ = 464 ppm, or to external $K_2[PtCl_4]$ at $\delta$ = –1630 ppm. Mass spectra (ESI-MS) were recorded with a Bruker ESQUIRE$_{3000}$ ion trap mass spectrometer. Infrared spectra (4000–400 cm$^{-1}$) were recorded in KBr pellets using a Perkin–Elmer FTIR instrument.

**(*SP*-4-3)-[(1*R*,2*R*)-*trans*-Diaminocyclohexane][(*S*)-methionine-κ$^2$*N*,*S*]platinum(II)·Hexafluorophosphate (1·$PF_6$):** Silver carbonate (355 mg, 1.29 mmol) was added in one portion to a suspension of dichloro[(1*R*,2*R*)-*trans*-diaminocyclohexane]platinum(II) (500 mg, 1.32 mmol) in 100 mL of water and the mixture was stirred at room temperature overnight. Silver chloride precipitated and was filtered off. (*S*)-Methionine (188 mg, 1.26 mmol) was then added to the bright-yellow solution and the mixture was stirred at room temperature for 8 h. Thereafter, the solution was lyophilized to give a slightly yellow crude product. The solid was dissolved in 5 mL of water in a 10-mL plastic vial and a solution of $HPF_6$ (146 μL, 1.26 mmol) in 1 mL of water was added. The mixture was lyophilized and the solid was washed with small portions of methanol. The target platinum(II) complex was obtained after filtration by removal of the solvent under reduced pressure and drying over $P_2O_5$. Yield: 380 mg (50%) [based on the amount of (*S*)-methionine]. $C_{11}H_{24}F_6N_3O_2PPtS$ (602.44): calcd. C 21.93, H 4.02, N 6.98, S 5.32; found C 21.62, H 4.05, N 6.76, S 5.30. ESI-MS (methanol): *m*/*z* = 457.3 [M$^+$]. FT-IR (KBr): $\tilde{\nu}$ = 3414 w (OH), 3080 w (NH), 1617 s (CO) cm$^{-1}$. Diastereoisomer 1: $^1$H NMR (400.13 MHz, $D_2O$): $\delta$ = 4.8–5.8 (m, 6 H, $NH_2$), 3.35 (m, 1 H, 2-H), 2.94 (m, 2 H, 4-H), 2.45 (m, 2 H, 6-H, 7-H), 2.44 (s, 3 H, 5-H), 2.23 (m, 2 H, 3-H), 2.00 (m, 2 H, 8-H, 11-H), 1.54 (m, 2 H, 9-H, 10-H), 1.25 (m, 2 H, 8-H, 11-H), 1.09 (m, 2 H, 9-H, 10-H) ppm. $^{13}$C NMR (100.63 MHz, $D_2O$): $\delta$ = 176.8 (1-C), 62.4 (6-C or 7-C), 61.0 (6-C or 7-C), 56.6 (2-C), 32.7 (2 C, 8-C, 11-C), 32.6 (4-C), 28.5 (3-C), 24.2 (2 C, 9-C, 10-C), 19.7 (5-C) ppm. $^{15}$N NMR (40.55 MHz, $H_2O/D_2O$): $\delta$ = 4.0 (6-$CNH_2$), –14.0 (7-$CNH_2$), –45.2 (2-$CNH_2$) ppm. $^{31}$P NMR (162.00 MHz, $D_2O$): $\delta$ = –143.9 (sept, $^1J_{P,F}$ = 710 Hz, $PF_6$) ppm. $^{195}$Pt NMR (85.99 MHz, $D_2O$): $\delta$ = –3335 ppm. Diastereoisomer 2: $^1$H NMR (400.13 MHz, $D_2O$): $\delta$ = 4.8–5.9 (m, 6 H, $NH_2$), 3.44 (m, 1 H, 2-H), 2.87 (m, 2 H, 4-H), 2.46 (m, 2 H, 6-H, 7-H), 2.45 (s, 3 H, 5-H), 2.33 (m, 2 H, 3-H), 2.00 (m, 2 H, 8-H, 11-H), 1.54 (m, 2 H, 9-H, 10-H), 1.25 (m, 2 H, 8-H, 11-H), 1.09 (m, 2 H, 9-H, 10-H) ppm. $^{13}$C NMR (100.63 MHz, $D_2O$): $\delta$ = 176.3 (1-C), 62.2 (6-C or 7-C), 61.4 (6-C or 7-C), 55.6 (2-C), 32.7 (2 C, 8-C, 11-C), 31.0 (4-C), 27.7 (3-C), 24.1 (2 C, 9-C, 10-C), 19.6 (5-C) ppm. $^{15}$N NMR (40.55 MHz, $H_2O/D_2O$): $\delta$ = 4.0 (6-$CNH_2$), –14.0 (7-$CNH_2$), –45.2 (2-$CNH_2$) ppm. $^{31}$P NMR (162.00 MHz, $D_2O$): $\delta$ = –143.9 (sept, $^1J_{P,F}$ = 710 Hz, $PF_6$) ppm. $^{195}$Pt NMR (85.99 MHz, $D_2O$): $\delta$ = –3313 ppm.

 © 2006 Wiley-VCH Verlag GmbH & Co. KGaA, Weinheim 

**(*SP*-4-3)-[(1*R*,2*R*)-*trans*-Diaminocyclohexane][*S*-methyl-(*S*)-cysteine-κ²*N*,*S*]platinum(II)·Hexafluorophosphate (2·$PF_6$):** Silver carbonate (238 mg, 0.86 mmol) was added in one portion to a suspension of dichloro[(1*R*,2*R*)-*trans*-diaminocyclohexane]platinum(II) (334 mg, 0.88 mmol) in 100 mL of water and the mixture was stirred at room temperature overnight. Silver chloride precipitated and was filtered off. *S*-Methyl-(*S*)-methionine (114 mg, 0.84 mmol) was then added to the bright-yellow solution and the mixture was stirred at room temperature for 8 h. Thereafter, the solution was lyophilized to give a slightly yellow crude product. The solid was dissolved in 2 mL of water in a 10-mL plastic vial and a solution of $HPF_6$ (98 μL, 0.84 mmol) in 1 mL of water was added. The mixture was lyophilized and the solid was washed with small portions of ethanol. The target platinum(II) complex was obtained after filtration by removal of the solvent under reduced pressure and drying over $P_2O_5$. Yield: 85 mg (17%) [based on the amount of *S*-methyl-(*S*)-cysteine]. $C_{10}H_{22}F_6N_3O_2PPtS$ (588.41): calcd. C 20.41, H 3.77, N 7.14, S 5.45; found C 20.85, H 3.97, N 7.04, S 5.51. ESI-MS (methanol): *m*/*z* = 443.3 [$M^+$]. FT-IR (KBr): $\tilde{\nu}$ = 3438 w (OH), 3224 w (NH), 1625 s (CO) $cm^{-1}$. Diastereoisomer 1: $^1H$ NMR (400.13 MHz, $D_2O$): $\delta$ = 5.0–6.1 (m, 6 H, $NH_2$), 3.68 (m, 1 H, 2-H), 2.92 (m, 2 H, 3-H), 2.58 (s, 3 H, 4-H), 2.43 (m, 2 H, 5-H, 6-H), 2.01 (m, 2 H, 7-H, 10-H), 1.54 (m, 2 H, 8-H, 9-H), 1.26 (m, 2 H, 7-H, 10-H), 1.09 (m, 2 H, 8-H, 9-H) ppm. $^{13}C$ NMR (100.63 MHz, $D_2O$): $\delta$ = 173.6 (1-C), 61.4 (2-C), 61.3 (2 C, 5-C, 6-C), 40.8 (3-C), 32.5 (2 C, 7-C, 10-C), 24.1 (2 C, 8-C, 9-C), 20.6 (4-C) ppm. Diastereoisomer 2: $^1H$ NMR (400.13 MHz, $D_2O$): $\delta$ = 5.0–6.1 (m, 6 H, $NH_2$), 3.48 (m, 1 H, 2-H), 3.06 (m, 2 H, 3-H), 2.48 (s, 3 H, 4-H), 2.43 (m, 2 H, 5-H, 6-H), 2.01 (m, 2 H, 7-H, 10-H), 1.54 (m, 2 H, 8-H, 9-H), 1.26 (m, 2 H, 7-H, 10-H), 1.09 (m, 2 H, 8-H, 9-H) ppm.$^{13}C$ NMR (100.63 MHz, $D_2O$): $\delta$ = 173.8 (1-C), 62.2 (2-C), 61.3 (2 C, 6-C, 7-C), 40.8 (3-C), 32.5 (2 C, 7-C, 10-C), 24.1 (2 C, 8-C, 9-C), 21.8 (4-C) ppm.

**(*SP*-4-3)-[(1*R*,2*R*)-*trans*-Diaminocyclohexane][(*S*)-selenomethionine-κ²*N*,*S*]platinum(II)·Hexafluorophosphate (3·$PF_6$):** Silver carbonate (404 mg, 1.46 mmol) was added in one portion to a suspension of dichloro[(1*R*,2*R*)-*trans*-diaminocyclohexane]platinum(II) (569 mg, 1.50 mmol) in 100 mL of water and the mixture was stirred at room temperature overnight. Silver chloride precipitated and was filtered off. (*S*)-Selenomethionine (283 mg, 1.44 mmol) was then added to the bright-yellow solution and the mixture was stirred at room temperature for 8 h. Thereafter, the solution was lyophilized to give a slightly yellow crude product. The solid was dissolved in 5 mL of water in a 10-mL plastic vial and a solution of $HPF_6$ (167 μL, 1.44 mmol) in 1 mL of water was added. The mixture was lyophilized and the solid was washed with small portions of methanol and ethanol. The target platinum(II) complex was obtained after filtration by removal of the solvent under reduced pressure and drying over $P_2O_5$. Yield: 232 mg (25%) [based on the amount of (*S*)-selenomethionine]. $C_{11}H_{24}F_6N_3O_2PPtSe$ (649.33): calcd. C 20.35, H 3.72, N 6.47; found C 19.79, H 3.83, N 6.25. ESI-MS (methanol): *m*/*z* = 504.3 [$M^+$]. FT-IR: $\tilde{\nu}$ = 3414 w (OH), 3080 w (NH), 1615 s (CO) $cm^{-1}$. Diastereoisomer 1: $^1H$ NMR (400.13 MHz, $D_2O$): $\delta$ = 4.9–5.7 (m, 6 H, $NH_2$), 3.39 (m, 1 H, 2-H), 2.91 (m, 2 H, 4-H), 2.42 (m, 2 H, 6-H, 7-H), 2.37 (m, 2 H, 3-H), 2.31 (s, 3 H, 5-H), 2.00 (m, 2 H, 8-H, 11-H), 1.53 (m, 2 H, 9-H, 10-H), 1.25 (m, 2 H, 8-H, 11-H), 1.09 (m, 2 H, 9-H, 10-H) ppm. $^{13}C$ NMR (100.63 MHz, $D_2O$): $\delta$ = 176.8 (1-C), 63.0 (6-C or 7-C), 60.6 (6-C or 7-C), 56.9 (2-C), 32.7 (2 C, 8-C, 11-C), 30.9 (3-C), 26.3 (4-C), 24.4 (9-C or 10-C), 24.1 (9-C or 10-C), 11.4 (5-C) ppm. $^{15}N$ NMR (40.55 MHz, $H_2O/D_2O$): $\delta$ = 3.5 (6-$CNH_2$), –18.0 (7-$CNH_2$), –48.0 (2-$CNH_2$) ppm. $^{31}P$ NMR (162.00 MHz, $D_2O$): $\delta$ = –141.2 (sept, $^1J_{P,F}$ = 709 Hz, $PF_6$) ppm. $^{77}Se$ NMR (76.32 MHz, $D_2O$): $\delta$ = 151.5 (s, $^1J_{Se,Pt}$ = 435 Hz) ppm. $^{195}Pt$ NMR (85.99 MHz, $D_2O$): $\delta$ = –3381 ppm. Diastereoisomer 2: $^1H$ NMR (400.13 MHz, $D_2O$): $\delta$ = 4.7–5.7 (m, 6 H, $NH_2$), 3.39 (m, 1 H, 2-H), 2.87 (m, 2 H, 4-H), 2.42 (m, 2 H, 6-H, 7-H), 2.35 (m, 2 H, 3-H), 2.34 (s, 3 H, 5-H), 2.00 (m, 2 H, 8-H, 11-H), 1.53 (m, 2 H, 9-H, 10-H), 1.25 (m, 2 H, 8-H, 11-H), 1.09 (m, 2 H, 9-H, 10-H) ppm. $^{13}C$ NMR (100.63 MHz, $D_2O$): $\delta$ = 176.5 (1-C), 62.8 (6-C or 7-C), 61.2 (6-C or 7-C), 56.1 (2-C), 32.6 (2 C, 8-C, 11-C), 29.5 (3-C), 24.4 (4-C), 24.2 (9-C or 10-C), 24.1 (9-C or 10-C), 11.4 (5-C) ppm. $^{15}N$ NMR (40.55 MHz, $H_2O/D_2O$): $\delta$ = 3.5 (6-$CNH_2$), –18.0 (7-$CNH_2$), –48.0 (2-$CNH_2$) ppm. $^{31}P$ NMR (162.00 MHz, $D_2O$): $\delta$ = –141.2 (sept, $^1J_{P,F}$ = 709 Hz, $PF_6$) ppm. $^{77}Se$ NMR (76.32 MHz, $D_2O$): $\delta$ = 123.5 (s, $^1J_{Se,Pt}$ not detectable) ppm. $^{195}Pt$ NMR (85.99 MHz, $D_2O$): $\delta$ = –3351 ppm.

**(*SP*-4-3)-[(1*R*,2*R*)-*trans*-Diaminocyclohexane][*Se*-methylseleno-(*S*)-cysteine-κ²*N*,*S*]platinum(II)·Hexafluorophosphate (4·$PF_6$):** Silver carbonate (400 mg, 1.45 mmol) was added in one portion to a suspension of dichloro[(1*R*,2*R*)-*trans*-diaminocyclohexane]platinum(II) (560 mg, 1.47 mmol) in 100 mL of water and the mixture was stirred at room temperature overnight. Silver chloride precipitated and was filtered off. *Se*-Methylseleno-(*S*)-cysteine (260 mg, 1.43 mmol) was added to the bright-yellow solution and the mixture was stirred at room temperature for 8 h. Thereafter, the solution was lyophilized to give a slightly yellow crude product. The solid was dissolved in 5 mL of water in a 10-mL plastic vial and a solution of $HPF_6$ (166 μL, 1.43 mmol) in 1 mL of water was added. The mixture was lyophilized and the solid was washed with small portions of methanol and ethanol. The target platinum(II) complex was obtained after filtration by removal of the solvent under reduced pressure and drying over $P_2O_5$. Yield: 152 mg (17%) [based on the amount of *Se*-methylseleno-(*S*)-cysteine]. $C_{10}H_{22}F_6N_3O_2PPtSe$ (635.30): calcd. C 18.91, H 3.49, N 6.61; found C 18.53, H 3.82, N 6.33. ESI-MS (methanol): *m*/*z* = 490.2 [$M^+$]. FT-IR: $\tilde{\nu}$ = 3418 w (OH), 3079 w (NH), 1622 s (CO) $cm^{-1}$. Diastereoisomer 1: $^1H$ NMR (400.13 MHz, $D_2O$): $\delta$ = 4.9–6.1 (m, 6 H, $NH_2$), 3.60 (m, 1 H, 2-H), 2.82 (m, 2 H, 3-H), 2.45 (s, 3 H, 4-H), 2.41 (m, 2 H, 5-H, 6-H), 2.02 (m, 2 H, 7-H, 10-H), 1.53 (m, 2 H, 8-H, 9-H), 1.26 (m, 2 H, 7-H, 10-H), 1.09 (m, 2 H, 8-H, 9-H) ppm. $^{13}C$ NMR (100.63 MHz, $D_2O$): $\delta$ = 174.0 (1-C), 62.9 (6-C or 7-C), 62.8 (2-C), 61.1 (5-C or 6-C), 32.7 (7-C or 10-C), 32.6 (7-C or 10-C), 32.0 (3-C), 24.3 (8-C or 9-C), 24.2 (8-C or 9-C), 12.6 (4-C) ppm. $^{15}N$ NMR (40.55 MHz, $H_2O/D_2O$): $\delta$ = 5.2 (6-$CNH_2$), 0.5 (7-$CNH_2$), –21.2 (2-$CNH_2$) ppm. $^{31}P$ NMR (162.00 MHz, $D_2O$): $\delta$ = –141.2 (sept, $^1J_{P,F}$ = 709 Hz, $PF_6$) ppm. $^{77}Se$ NMR (76.32 MHz, $D_2O$): $\delta$ = 208.6 (s, $^1J_{Se,Pt}$ = 355 Hz) ppm. $^{195}Pt$ NMR (85.99 MHz, $D_2O$): $\delta$ = –3444 ppm. Diastereoisomer 2: $^1H$ NMR (400.13 MHz, $D_2O$): $\delta$ = 4.9–6.1 (m, 6 H, $NH_2$), 3.65 (m, 1 H, 2-H), 2.98 (m, 2 H, 3-H), 2.41 (m, 2 H, 5-H, 6-H), 2.37 (s, 3 H, 4-H), 2.02 (m, 2 H, 7-H, 10-H), 1.53 (m, 2 H, 8-H, 9-H), 1.26 (m, 2 H, 7-H, 10-H), 1.09 (m, 2 H, 8-H, 9-H) ppm. $^{13}C$ NMR (100.63 MHz, $D_2O$): $\delta$ = 174.0 (1-C), 62.7 (6-C or 7-C), 62.6 (2-C), 61.0 (5-C or 6-C), 32.7 (7-C or 10-C), 32.6 (7-C or 10-C), 32.1 (3-C), 24.3 (8-C or 9-C), 24.1 (8-C or 9-C), 13.5 (4-C) ppm. $^{15}N$ NMR (40.55 MHz, $H_2O/D_2O$): $\delta$ = 5.2 (6-$CNH_2$), 0.5 (7-$CNH_2$), –21.2 (2-$CNH_2$) ppm. $^{31}P$ NMR (162.00 MHz, $D_2O$): $\delta$ = –141.2 (sept, $^1J_{P,F}$ = 709 Hz, $PF_6$) ppm. $^{77}Se$ NMR (76.32 MHz, $D_2O$): $\delta$ = 220.5 (s, $^1J_{Se,Pt}$ not detectable) ppm. $^{195}Pt$ NMR (85.99 MHz, $D_2O$): $\delta$ = –3461 ppm.

**Structure Determination:** X-ray diffraction measurements were performed with Nonius Kappa CCD diffractometers. Single crystals were positioned at 35 and 29.1 mm from the detector and 591 and 256 frames were measured, each for 20 s over a 1.5 and 1.0° scan width (for complexes **1**·$PF_6$ and **3**·$PF_6$, respectively). The data were processed using the Denzo-SMN software package.[28] Crystal data,

 © 2006 Wiley-VCH Verlag GmbH & Co. KGaA, Weinheim 

data collection parameters, and structure-refinement details for **1**·$PF_6$ and **3**·$PF_6$ are given in Table 1. The structures were solved by direct methods and refined by full-matrix least-squares techniques. Non-hydrogen atoms were refined with anisotropic displacement parameters. H atoms of **1**·$PF_6$ were located on difference Fourier maps and isotropically refined. All hydrogen atoms of **3**·$PF_6$ were included at calculated positions with fixed thermal parameters. Computer programs: structure solution: SHELXS-97;[29] refinement: SHELXL-97;[30] molecular diagrams: ORTEP;[31] computer: Pentium II; scattering factors.[32] CCDC-606533 (**1**·$PF_6$) and -606879 (**3**·$PF_6$) contain the supplementary crystallographic data for this paper. These data can be obtained free of charge from The Cambridge Crystallographic Data Centre via www.ccdc.cam.ac.uk/data_request/cif.

Table 1. Crystal data and details of data collection for **1**·$PF_6$ and **3**·$PF_6$.

| | **1**·$PF_6$ | **3**·$PF_6$ |
|---|---|---|
| Empirical formula | $C_{11}H_{24}F_6N_3O_2PPtS$ | $C_{11}H_{24}F_6N_3O_2PPtSe$ |
| Formula mass | 602.45 | 649.35 |
| Space group | $P2_12_12_1$ | $P2_12_12_1$ |
| $a$ [Å] | 6.5662(1) | 6.6369(4) |
| $b$ [Å] | 12.4846(1) | 12.5878(7) |
| $c$ [Å] | 22.1143(2) | 22.0958(16) |
| $V$ [Å$^3$] | 1812.85(4) | 1846.0(2) |
| $Z$ | 4 | 4 |
| $\lambda$ [Å] | 0.71073 | 0.71073 |
| $\rho_{calcd.}$ [g cm$^{-3}$] | 2.207 | 2.336 |
| Crystal size [mm] | 0.29 × 0.17 × 0.14 | 0.32 × 0.30 × 0.28 |
| $T$ [K] | 120 | 183 |
| $\mu$ [cm$^{-1}$] | 80.13 | 97.28 |
| Flack parameter | 0.006(4) | –0.017(14) |
| $R_1$[a] | 0.0127 | 0.043l |
| $wR_2$[b] | 0.0299 | 0.079 |
| GOF[c] | 1.110 | 1.030 |

[a] $R_1 = \Sigma||F_o| - |F_c||/\Sigma|F_o|$. [b] $wR_2 = \{\Sigma[w(F_o^2 - F_c^2)^2]/\Sigma[w(F_o^2)^2]\}^{1/2}$. [c] GOF = $\{\Sigma[w(F_o^2 - F_c^2)^2]/(n - p)\}^{1/2}$, where $n$ is the number of reflections and $p$ is the total number of parameters refined.

**Supporting Information** (see footnote on the first page of this article): Temperature-dependent $^1$H NMR spectra of **1**·$PF_6$.

## Acknowledgments

The support of the FWF (Fonds zur Förderung der wissenschaftlichen Forschung), the Austrian Council for Research and Technology Development, Faustus Forschung Translational Drug Development AG and COST (European Co-operation in the Field of Scientific and Technical Research) is gratefully acknowledged. C. R. is much obliged for financial support from COST for a research stay at the University of Vienna.

[1] *Cisplatin: Chemistry and Biochemistry of a Leading Anticancer Drug* (Ed.: B. Lippert), Verlag Helvetica Chimica Acta, Zürich, Switzerland, and Wiley-VCH, Weinheim, Germany, **1999**.
[2] M. A. Jakupec, M. Galanski, B. K. Keppler, *Rev. Physiol. Biochem. Pharmacol.* **2003**, *146*, 1–54.
[3] P. J. O'Dwyer, J. P. Stevenson, S. W. Johnson, *Drugs* **2000**, *59*, 19–27.
[4] M. Galanski, M. A. Jakupec, B. K. Keppler, *Curr. Med. Chem.* **2005**, *12*, 2075–2094.
[5] E. Wong, C. M. Giandomenico, *Chem. Rev.* **1999**, *99*, 2451–2466.
[6] M. Galanski, M. A. Jakupec, B. K. Keppler, in *Metal Compounds in Cancer Chemotherapy* (Eds.: J. M. Pérez, M. A. Fuertes, C. Alonso), Research Signpost, Kerala, **2005**, p. 155–185.
[7] J. Graham, M. Muhsin, P. Kirkpatrick, *Nat. Rev. Drug Discovery* **2004**, *3*, 11–12.
[8] E. R. Jamieson, S. J. Lippard, *Chem. Rev.* **1999**, *99*, 2467–2498.
[9] J. Reedijk, *Chem. Rev.* **1999**, *99*, 2499–2510.
[10] F. R. Luo, S. D. Wyrick, S. G. Chaney, *Cancer Chemother. Pharmacol.* **1999**, *44*, 19–28.
[11] M. A. Graham, G. F. Lockwood, D. Greenslade, S. Brienza, M. Bayssas, E. Gamelin, *Clin. Cancer Res.* **2000**, *6*, 1205–1218.
[12] M. Rao, M. N. A. Rao, *J. Pharm. Pharmacol.* **1998**, *50*, 687–691.
[13] M. Fakih, S. Cao, F. A. Durrani, Y. M. Rustum, *Clin. Colorectal Cancer* **2005**, *5*, 132–135.
[14] S. Cao, F. A. Durrani, Y. M. Rustum, *Clin. Cancer Res.* **2004**, *10*, 2561–2569.
[15] S. K. Mauldin, M. Plescia, F. A. Richard, S. D. Wyrick, R. D. Voyksner, S. G. Chaney, *Biochem. Pharmacol.* **1988**, *37*, 3321–3333.
[16] T. G. Appleton, J. W. Connor, J. R. Hall, *Inorg. Chem.* **1988**, *27*, 130–137.
[17] M. El-Khateeb, T. G. Appleton, L. R. Gahan, B. G. Charles, S. J. Berners-Price, A. Bolton, *J. Inorg. Biochem.* **1999**, *77*, 13–21.
[18] K. M. Williams, C. Rowan, J. Mitchell, *Inorg. Chem.* **2004**, *43*, 1190–1196.
[19] Y. Chen, Z. Guo, P. Murdoch, E. Zang, P. J. Sadler, *J. Chem. Soc., Dalton Trans.* **1998**, *9*, 1503–1508.
[20] M. A. Bruck, R. Bun, M. Noji, K. Inagaki, Y. Kidani, *Inorg. Chim. Acta* **1984**, *92*, 279–284.
[21] C. Wilson, M. L. Scudder, T. W. Hambley, H. C. Freeman, *Acta Crystallogr., Sect. C* **1992**, *48*, 1012–1015.
[22] A. Caubet, V. Moreno, E. Molins, C. Miravitlles, *J. Inorg. Biochem.* **1992**, *48*, 135–152.
[23] Q. Liu, J. Zhang, X. Ke, Y. Mei, L. Zhu, Z. Guo, *J. Chem. Soc., Dalton Trans.* **2001**, *6*, 911–916.
[24] Q. Liu, J. Lin, P. Jiang, J. Zhang, L. Zhu, Z. Guo, *Eur. J. Inorg. Chem.* **2002**, *8*, 2170–2178.
[25] J. A. Beaty, M. M. Jones, L. Ma, *Chem. Res. Toxicol.* **1992**, *5*, 647–653.
[26] M. Carland, B. F. Abrahams, T. Rede, J. Stephenson, V. Murray, W. A. Denny, W. D. McFadyen, *Inorg. Chim. Acta* **2006**, *359*, 3252–3256.
[27] M. Galanski, A. Yasemi, S. Slaby, M. A. Jakupec, V. B. Arion, M. Rausch, A. A. Nazarov, B. K. Keppler, *Eur. J. Med. Chem.* **2004**, *39*, 707–714.
[28] Z. Otwinowski, W. Minor, in *Methods in Enzymology*, vol. 276 ("Macromolecular Crystallography", part A) (Eds.: C. W. Carter Jr, R. M. Sweet), Academic Press, New York, **1997**, p. 307–326.
[29] G. M. Sheldrick, *SHELXS-97, Program for Crystal Structure Solution*, University Göttingen, Germany, **1997**.
[30] G. M. Sheldrick, *SHELXL-97, Program for Crystal Structure Refinement*, University Göttingen, Germany, **1997**.
[31] C. K. Johnson, Rep. ORNL-5138, OAK Ridge National Laboratory, OAK Ridge, TN, **1976**.
[32] *International Tables for X-ray Crystallography* (Ed.: A. J. C. Wilson), Kluwer Academic Press, Dordrecht, The Netherlands, **1992**, vol. C, Tables 4.2.6.8 and 6.1.1.4.

Received: May 15, 2006
Published Online: July 28, 2006

 © 2006 Wiley-VCH Verlag GmbH & Co. KGaA, Weinheim 

DOI: 10.1002/ejic.200600507

# $Co^{III}$ Complexes with Square-Planar $N_2S_2$- and $N_2(SO_2)_2$-Type Ligands as An Active Site Structural Model for Nitrile Hydratase – Biological Implications of an Amidate Coordination

**Takuma Yano,[a] Hidekazu Arii,[a] Syuhei Yamaguchi,[a] Yasuhiro Funahashi,[a] Koichiro Jitsukawa,[a] Tomohiro Ozawa,*[a] and Hideki Masuda*[a]**

**Keywords:** Nitrile hydratase / Cobalt / Amidate ligand / Electrophilic interactions / Lewis acids

In an attempt to understand the unique active site structure of nitrile hydratase, four $Co^{III}$ complexes with square-planar $N_2S_2$- or $N_2(SO_2)_2$-type donor sets, Na[$Co^{III}$(**L:$N_2S_2$**)] (**1**-Na), $PPh_4$[$Co^{III}$(**L:$N_2S_2$**)] (**1**-$PPh_4$), $PPh_4$[$Co^{III}$(**L:$N_2S_2$**)(*t*BuNC)$_2$] (**2**), and $PPh_4$[$Co^{III}${**L:$N_2(SO_2)_2$**}(*t*BuNC)$_2$] (**3**) were synthesized and characterized on the basis of electronic absorption spectroscopy, IR spectroscopy, cyclic voltammetry, and X-ray structural analysis. Both of the crystal structures of complexes **1**-Na and **1**-$PPh_4$ revealed a square planar structure with $N_2S_2$ donating atoms, and **2** exhibited an octahedral structure coordinated with two *tert*-butylisocyanide (*t*BuNC) molecules at the axial sites of complex **1**-$PPh_4$. Complex **3**, which showed an octahedral structure with sulfinate sulfur atoms equatorially coordinated to the center, was synthesized by the treatment of **2** with a suitable oxidant. The reduction potential values from $Co^{III}$ to $Co^{II}$ for complex **3** in solution demonstrated a larger positive shift when compared with those of complexes **1**-$PPh_4$ and **2**, which indicates that the oxygenation of the sulfur atoms increased the Lewis acidity of the $Co^{III}$ center. Interestingly, the coordination equilibrium, the C=O stretching frequency, and the redox potential for **1**-$PPh_4$ were all closely related to the acceptor number (AN) of the solvents. Furthermore, the coordination of monodentate *t*BuNC to the axial position of **1**-$PPh_4$ was dependent on the solvents used. These findings indicate that an electrophilic interaction between the carbonyl oxygen atoms and the solvent molecules control the Lewis acidity of the metal ion. On the other hand, such a solvent dependence was not detected in the S=O stretching frequency of sulfinates **3**. We have concluded that the increase in the redox potential/Lewis acidity of the metal center is a result of the oxygenation of sulfur, and that this increase is controlled by the interaction of the amidate carbonyl oxygen with the secondary coordination sphere. As demonstrated in previous mutation studies, this study suggests that the interaction of the nitrile hydratase active site with the functional groups from the peptide backbone is essential for the catalytic activity of the complex.

(© Wiley-VCH Verlag GmbH & Co. KGaA, 69451 Weinheim, Germany, 2006)

## Introduction

Nitrile Hydratase (NHase) is an enzyme that hydrates a nitrile compound to the corresponding amide. Because of its high conversion ability, this enzyme has been employed for the industrial production of acrylamide from acrylonitrile under mild conditions.[1] The NHases are largely classified into $Fe^{III}$-type and $Co^{III}$-type families.[2–4] *Rhodococcus rhodochrous* J1, which is a bacterium with the typical $Co^{III}$-type NHase, has been used to produce several kilotons of acrylamide per year.[3–5] The common amino acid sequence (C–**X**–**Y**–C–S–C) of the peptide in the $Fe^{III}$-type and the $Co^{III}$-type NHase has been proposed as the metal binding ligand on the basis of the similarity between the EXAFS and its pre-edge spectra[6,7] in addition to homology in significant amino acid sequences.[8]

Recent X-ray structure analysis of both NHase types revealed that the metal centers are surrounded by two amide nitrogen atoms and two cysteine sulfur atoms in the equatorial plane with a cysteine sulfur and an oxygen atom ($H_2O$ or $OH^-$), or a cysteine sulfur and a NO group, at the axial sites for the $Co^{III}$- or $Fe^{III}$-types, respectively.[9–12] Interestingly, two equatorially coordinated cysteine sulfur atoms are oxygenated to a sulfenate and a sulfinate, respectively, and the two nitrogen atoms contribute as an amidate ligand. Such a unique structure is very interesting in relation to its hydration mechanism in biological systems.

In such a hydration enzyme, a higher Lewis acidity of the metal center should be required, although M–$OH^-$ (or M–$OH_2$) or M–NCR are proposed as possible active intermediates. On the basis of the HSAB rule, the $N^-$ and $S^-$ ions employed in the enzymes may stabilize the higher oxidation state of the metal center, and the attached electron-withdrawing carbonyl group along with the sulfenyl and sulfinyl

[a] Graduate School of Engineering, Nagoya Institute of Technology,
Gokiso-cho, Showa-ku, Nagoya 466–8555, Japan
Fax: +81-52-735-5228
E-mail: masuda.hideki@nitech.ac.jp

Supporting information for this article is available on the WWW under http://www.eurjic.org or from the author.

 © 2006 Wiley-VCH Verlag GmbH & Co. KGaA, Weinheim 

oxygen atoms may reduce the electron density on the metal center to induce a higher acidity. It is quite apparent that both functional groups are very important for the enzymatic reaction. However, the use of the mutant Fe-type NHases that did not contain oxygenated sulfur atoms did not show any hydration reaction, which indicates that the oxygenated sulfur atoms are essential for the enzymatic activity.[13]Most studies that use model complexes have focused on the effect of the oxidation of sulfur. For example, several $Co^{III}$ and $Fe^{III}$ complexes with pentadentate ligands that contain an imine,[14] an amide,[15,16] or an amine[17] group and sulfur atoms have been synthesized and studied. Among them, Mascharak and coworkers[15a] have prepared the complex [Co(PyPS)(CN)] with the use of the amide-type ligand, which was easily replaced by a $H_2O$ molecule. The coordinated water molecule catalytically hydrated acetonitrile to acetamide at pH = 9.5. The addition of an oxidant to the solutions of the complexes afforded the corresponding sulfur-oxidized species.[15b] For the $Co^{III}$ mononuclear complex, the $Co^{III}$ species with a sulfinate was isolated. Hydration of acrylonitrile with this sulfonate–$Co^{III}$ complex proceeded three times faster than that of the complex with two unoxidized sulfur atoms even in acidic media (pH = 8.0). They concluded that the oxygenation of sulfur would make the acidity of the coordinated $H_2O$ molecule increase. Other groups have prepared and characterized the $Co^{III}$ and $Fe^{III}$ complexes with tetradentate planar ligands that contain two amide nitrogen atoms and two thiolate sulfur atoms in the same coordination environment as the NHase active sites,[18,19] and they also succeeded in the generation of sulfinate and sulfenate species by the oxidation of the coordinated sulfur atoms.[18a,18b,19a,19b] However, all of them showed octahedral structures with two monodentate ligands at the axial positions.[18a,18b,19a,19b] Recently, Artaud and coworkers reported that in the synthesis of the $N_2(SO_2)_2$-type $Co^{III}$ complex with a $CN^-$ ion at the apical position, the octahedral complex with a hydroxo ion at another axial position was derived.[20] Thus, the oxygenation of sulfur in the equatorial plane has been described to be one of the important factors that leads to an octahedral geometry.

Few have paid attention to the amidate group. However, a mutation study of Fe-containing NHase demonstrated that βR56K, whose Arg56 residue is replaced by lysine and coordinated to the sulfinate and sulfenate oxygen atoms through a hydrogen bond, demonstrated only ca. 1% of the reactivity of the native species.[21] For the βY68F mutant of the $Co^{III}$-type NHase, the enzymatic activity drastically decreased, although it was positioned at a distance from the active site.[22] Moreover, the OH group of tyrosine in βTyr68 is linked to the carbonyl oxygen of the active site through water molecules and the hydrogen bond network around βArg56. βArg56 is, itself, also connected to βTyr68. These facts indicate that the hydrogen-bonding interactions of the coordinating functional groups with the outer sphere strongly contribute to the appearance of the NHase activity. Therefore, we focused on the biological role of the amidate carbonyl group and synthesized two $Co^{III}$ complexes with $N_2S_2$-type ligands, *N*,*N*′-bis(2-mercapto-2-methylpropionyl)-1,3-diaminopropane ($H_4$**L**) and the corresponding sulfinic acid derivative [**L**:$N_2(SO_2)_2$; the two sulfur atoms of $H_4$**L** are oxygenated to sulfinates]. In order to evaluate the influence of the outer sphere, the coordination behaviors of the axial sites of the $Co^{III}$ complex with *tert*-butylisocyanide (*t*BuNC) were evaluated. Isocyanides such as isobutylisocyanide[23] and cyclohexylisocyanide[24] are often employed because of their well-known ability to act as coordinative monodentate ligands for NHase.

## Results and Discussion

### Crystal Structures of Na[Co(L:$N_2S_2$)]3$H_2O$ (1-Na), $PPh_4$[$Co^{III}$(L:$N_2S_2$)]$H_2O$ (1-$PPh_4$), $PPh_4$[$Co^{III}$(L:$N_2S_2$)$_2$-(*t*BuNC)$_2$] (2), and $PPh_4$[$Co^{III}${L:$N_2(SO_2)_2$}(*t*BuNC)$_2$]-EtOH (3)

The $N_2S_2$-type ligand, $H_4$**L**, which provides electron-donating atoms similar to the equatorial coordination environment of the NHase active center, was used for the construction of the model complexes. The $Co^{III}$ complex with **L**, Na[Co(**L**:$N_2S_2$)] (**1**-Na), was prepared by the air-oxidation of the corresponding $Co^{II}$ complex derived from the reaction of $CoCl_2$ and $H_4$**L** in DMF. Recrystallization of the compound from an acetonitrile/diethyl ether solution afforded a single crystal suitable for X-ray analysis, whose

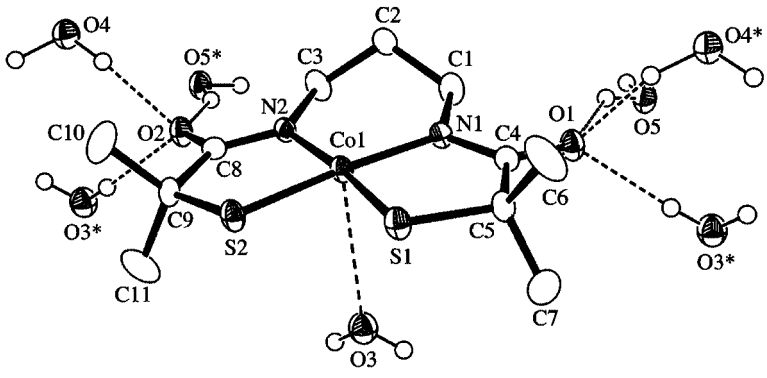


Figure 1. An ORTEP view of Na[Co(**L**:$N_2S_2$)] (**1**-Na) with solvated water molecules, which shows 50% probability ellipsoids. H atoms are omitted for clarity except for those of the water molecules.

 © 2006 Wiley-VCH Verlag GmbH & Co. KGaA, Weinheim 

crystal data and molecular structure are shown in Table 2 and Figure 1, respectively. Two $[Co^{III}(\mathbf{L}:N_2S_2)]^-$ and two $Na^+$ ions are included together with six water molecules in a unit cell (Figure S1). Selected bond lengths and angles are listed in Table 1. Complex **1**-Na has a square-planar geometry with $N_2S_2$ donor atoms as well as the equatorial coordination in the active site of NHase.[9–12] The bond lengths around the metal center [Co1–N1 = 1.919(3), Co1–N2 = 1.918(3), Co1–S1 = 2.141(1), Co1–S2 = 2.142(1) Å] are comparable to those of the $Co^{III}$ complexes with amide (Co–N = 1.86–1.90 Å) and thiolate coordinations (Co–S = 2.13–2.14 Å) that were previously reported.[18c,19c] Each carbonyl oxygen of the ligand **L** was significantly coordinated to three water molecules [$O_{carbonyl}\cdots O_{water}$ = 2.84–2.91 Å] in the crystal. Furthermore, one water molecule also weakly approaches the $Co^{III}$ ion with a bond length of 3.20 Å at the axial position, which is very similar to the case of Co-type NHase.[11]

One more $Co^{III}$ complex with **L**, $PPh_4[Co(\mathbf{L}:N_2S_2)]$ (**1**-$PPh_4$), was also prepared by the ion-exchange of **1**-Na in an aqueous solution of $PPh_4Cl$. Complex **1**-$PPh_4$ was obtained as a single crystal suitable for X-ray analysis, whose crystal data and molecular structure are shown in Table 2 and Figure 2, respectively. Four $[Co^{III}(\mathbf{L}:N_2S_2)]^-$ anions and four $PPh_4^+$ cations are included together with four water molecules in a unit cell (Figure S2). Selected bond lengths and angles are listed in Table 1. The molecular structure of complex **1**-$PPh_4$ was essentially the same as that of **1**-Na. The bond lengths around the metal center [Co1–N1 = 1.902(3), Co1–N2 = 1.896(3), Co1–S1 = 2.138(1), Co1–S2 = 2.144(1) Å] are in the range of those of the $Co^{III}$ complexes with amide (Co–N = 1.86–1.90 Å) and thiolate coordinations (Co–S = 2.13–2.14 Å) that were previously reported.[18c,19c] However, a detailed comparison of those of **1**-Na and **1**-$PPh_4$ indicated that the Co–N bonds of **1**-$PPh_4$ were significantly different from those of **1**-Na, although the Co–S bonds was almost the same as those of **1**-Na. This behavior is apparently influenced by the number of hydrogen bonds between water molecules and the amidate carbonyl oxygen atoms. The two carbonyl oxygen atoms of **1**-$PPh_4$ are hydrogen-bonded with one water molecule each. However, each carbonyl oxygen of **1**-Na is coordinated to three water molecules of a water–sodium cluster. The C=O [1.250(4), 1.243(4)], $C_{amide}$–N [1.341(4), 1.348(4)], and Co–N [1.902(3), 1.896(3)] bond lengths of **1**-$PPh_4$ with one water molecule for one carbonyl oxygen demonstrated significant alternations of shorter, longer, and shorter lengths in comparison with those of **1**-Na, C=O [1.263(4), 1,257(4)], $C_{amide}$–N [1.330(4), 1.332(3)], and Co–N [1.919(3), 1.918(3)], with three hydrogen bonds for each carbonyl oxygen. This alternation in bond lengths provides evidence for the fact that the amidate carbonyl oxygen is affected by the interaction of the secondary sphere.

An octahedral $Co^{III}$ complex, $PPh_4[Co^{III}(\mathbf{L}:N_2S_2)(t\text{BuNC})_2]$ (**2**), where two of the axial positions of **1** are occupied by *tert*-butylisocyanide (*t*BuNC) molecules, was also isolated from an ethanol solution that contained a large amount of *t*BuNC as a red-colored single-crystal suitable for X-ray analysis. Crystal data is listed in Table 2 and the ORTEP view of the anion moiety of **2** is shown in Figure 3. Four $[Co^{III}(\mathbf{L}:N_2S_2)(t\text{BuNC})_2]^-$ anions and four

Table 1. Selected bond lengths [Å] and angles [°] for Na[Co($\mathbf{L}:N_2S_2$)](**1**-Na) and $PPh_4[Co(\mathbf{L}:N_2S_2)]$(**1**-$PPh_4$) and $PPh_4$-$[Co(\mathbf{L}:N_2S_2)(t\text{BuNC})_2]$(**2**) and $PPh_4[Co\{\mathbf{L}:N_2(SO_2)_2\}(t\text{BuNC})_2]$-(**3**).[a]

| | | | |
|---|---|---|---|
| | **1**-Na | | |
| | Bond lengths [Å] | | |
| Co1–N1 | 1.919(3) | O1···O3 | 2.86 |
| Co1–N2 | 1.918(3) | O1···O4 | 2.91 |
| Co1–S1 | 2.141(1) | O1···O5 | 2.84 |
| Co1–S2 | 2.142(1) | O2···O3 | 2.86 |
| O1–C4 | 1.263(4) | O2···O4 | 2.91 |
| O2–C8 | 1.257(4) | O2···O5 | 2.84 |
| N1–C4 | 1.330(4) | | |
| N2–C8 | 1.332(3) | | |
| | Bond angles [°] | | |
| N1–Co1–N2 | 98.0(1) | S1–Co1–N2 | 173.99(9) |
| S1–Co1–S2 | 86.12(4) | S2–Co1–N1 | 173.96(9) |
| S1–Co1–N1 | 87.89(9) | S2–Co1–N2 | 87.92(9) |
| | **1**-$PPh_4$ | | |
| | Bond lengths [Å] | | |
| Co1–N1 | 1.902(3) | N1–C4 | 1.341(4) |
| Co1–N2 | 1.896(3) | N2–C8 | 1.348(4) |
| Co1–S1 | 2.138(1) | O1···O3 | 2.83 |
| Co1–S2 | 2.144(1) | O2···O3 | 2.82 |
| O1–C4 | 1.250(4) | | |
| O2–C8 | 1.243(4) | | |
| | Bond angles [°] | | |
| N1–Co1–N2 | 97.4(1) | S1–Co1–N2 | 174.07(9) |
| S1–Co1–S2 | 86.51(4) | S2–Co1–N1 | 171.07(9) |
| S1–Co1–N1 | 87.95(9) | S2–Co1–N2 | 88.50(9) |
| | **2** | | |
| | Bond lengths [Å] | | |
| Co1–N1 | 1.973(2) | O1–C3 | 1.258(3) |
| Co1–S1 | 2.2491(8) | N1–C3 | 1.318(3) |
| Co1–C7 | 1.844(3) | N2–C7 | 1.150(4) |
| | Bond angles [°] | | |
| N1–Co1–N1* | 99.7(1) | S1–Co1–N1* | 174.69(6) |
| S1–Co1–S1* | 89.12(4) | C7–Co1–C7* | 179.8(2) |
| S1–Co1–N1 | 85.57(6) | Co1–C7–N2 | 176.8(3) |
| | **3** | | |
| | Bond lengths [Å] | | |
| Co1–N1 | 1.996(2) | O1–C4 | 1.249(4) |
| Co1–N2 | 1.986(2) | O4–C8 | 1.252(3) |
| Co1–S1 | 2.1830(7) | N1–C4 | 1.320(3) |
| Co1–S2 | 2.1723(7) | N2–C8 | 1.322(3) |
| Co1–C12 | 1.874(3) | N2–C7 | 1.148(4) |
| Co1–C17 | 1.847(3) | N4–C17 | 1.148(3) |
| | | O1···O7 | 2.66 |
| | Bond angles [°] | | |
| N1–Co1–N2 | 97.64(8) | S2–Co1–N1 | 176.85(6) |
| S1–Co1–S2 | 93.07(3) | S2–Co1–N2 | 83.97(6) |
| S1–Co1–N1 | 85.25(6) | C12–Co1–C17 | 175.6(1) |
| S1–Co1–N2 | 176.70(6) | Co1–C12–N3 | 174.8(2) |
| | | Co1–C17–N4 | 174.4(2) |

[a] The atoms with and without * are related by a crystallographic mirror plane between each other.

 © 2006 Wiley-VCH Verlag GmbH & Co. KGaA, Weinheim 

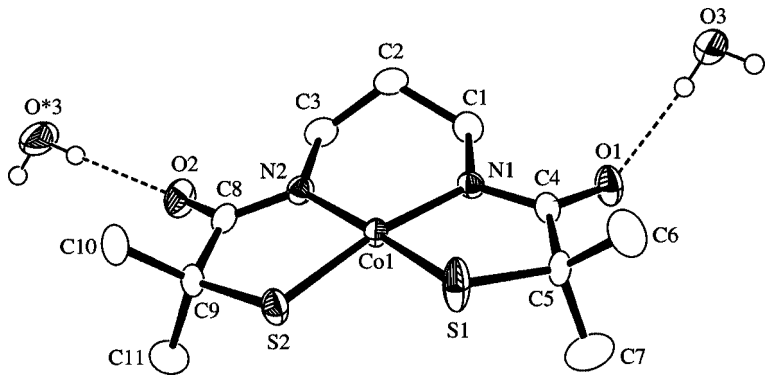


Figure 2. An ORTEP view of $[Co(\mathbf{L{:}N_2S_2})]^-$ anion part of complex **1** with solvated water molecules, which shows 50% probability ellipsoids. H atoms are omitted for clarity except for those of the water molecules.

$PPh_4^+$ cations are included in a unit cell. Selected bond lengths and angles are listed in Table 1. The *tert*-butyl group of the axial ligands and the propylene group of the equatorial ligand are disordered. The octahedral coordination formed by the axial binding of *t*BuNC ligands to **1** induces longer $Co–N_{amide}$ and Co–S bonds in comparison with those of **1**, although the average bond lengths of Co–S [2.2491(8) Å] and $Co–N_{amide}$ [1.973(2) Å] are within the range of those of the previously reported octahedral $Co^{III}$ complexes with thiols and/or amides (Co–S = 2.22–2.27 Å, Co–N = 1.91–2.00 Å).[18a,19a,19b,19d] The detailed examination of the bond lengths around the Co center indicate that the Co–N and Co–S bonds are clearly elongated in comparison with those of complexes **1**-$PPh_4$ and **1**-Na, which is explained by the coordination of the *t*BuNC molecules.

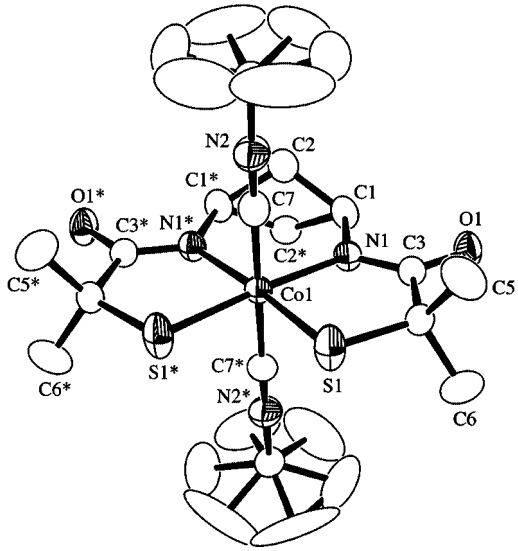


Figure 3. An ORTEP view of $[Co(\mathbf{L{:}N_2S_2})(t\text{BuNC})_2]^-$ anion part of complex **2**, which shows 50% probability ellipsoids.

Furthermore, treatment of complex **2** with 30% $H_2O_2$ according to a previously-reported procedure[19b] with some modifications successfully afforded the corresponding complex, $PPh_4[Co\{\mathbf{L{:}N_2(SO_2)_2}\}(t\text{BuNC})_2]$ (**3**), of which the two thiolate groups were oxygenated to sulfinates. The crystal data of a single crystal obtained from an EtOH/ether solution is listed in Table 2, and the molecular structure revealed the formation of complex **3**, as depicted in Figure 4. Selected bond lengths and angles are listed in Table 1. The bond lengths around the metal center [Co1–N1 = 1.996(2), Co1–N2 = 1.986(3), Co1–S1 = 2.1830(7), Co1–S2 = 2.1723(7) Å] lay within the range of those of the previously reported $Co^{III}$ complexes with amide and sulfinate groups (Co–N = 1.94–2.00 Å, Co–S = 2.21–2.23 Å).[18a,19b] The Co–N and Co–S bond lengths of **3** are longer than those of **1**-$PPh_4$ and **1**-Na, which is reasonably explained by the coordination of the *t*BuNC molecules. The oxygenation of sulfur in complexes **2** and **3** induced the lengthening of the Co–N bonds and the shortening of the Co–S bonds, although it did not influence the Co–C(*t*BuNC) bond lengths. The carbonyl oxygen atoms of the ligand $\mathbf{L{:}N_2(SO_2)_2}$ were also significantly coordinated to an ethanol molecule. Such a hydrogen bond was not found around the sulfinate oxygen atoms.

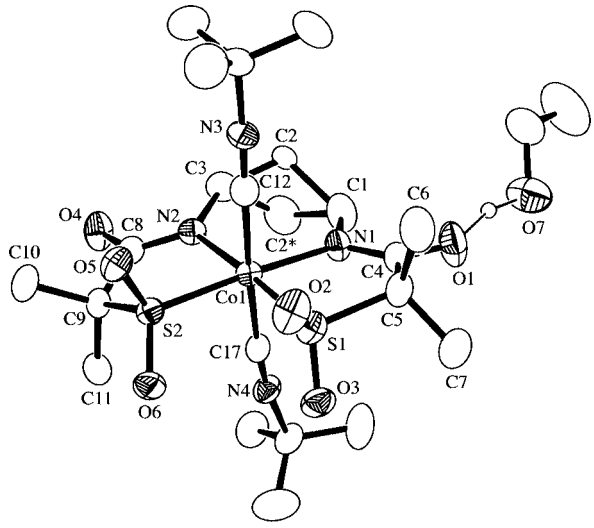


Figure 4. An ORTEP view of $[Co\{\mathbf{L{:}N_2(SO_2)_2}\}(t\text{BuNC})_2]^-$ anion part of complex **3**, which shows 50% probability ellipsoids. H atoms are omitted for clarity.

 © 2006 Wiley-VCH Verlag GmbH & Co. KGaA, Weinheim 

### Coordination Equilibrium of *t*BuNC to 1 in Solution

The electronic absorption spectrum of complex **1** showed a ligand-to-metal charge transfer (LMCT) band around 600 nm ($\varepsilon$ = 3800 $M^{-1}cm^{-1}$), which is characteristic of a square planar $Co^{III}$ complex with sulfur atoms.[18c,19c] The coordination behavior of the monodentate ligands at the axial positions of **1** was studied with anionic ligands, such as sodium phenolate, sodium thiophenolate, tetraethylammonium thiocyanate ($Et_4NSCN$), and tetraphenylphosphonium cyanide ($PPh_4CN$), and with neutral ligands, such as water, 4-phenylpyridine, and *tert*-butylisocyanide (*t*BuNC). Significant spectral changes were observed only when $PPh_4CN$ or *t*BuNC was added to a solution of **1** at ambient temperature. For $PPh_4CN$ and *t*BuNC, the absorption spectra had a change in the isosbestic point at 301 nm and 317 nm in EtOH, respectively (Figure S3). It is clear that both the monodentate ligands coordinate at the axial sites of **1**. In the case of *t*BuNC, such a spectral change in the isosbestic point of the LMCT band was also observed in other solvents, which indicates that the $Co^{III}$ complex reacted with *t*BuNC to form octahedral complex **2**.[18a,19c] Formation of the octahedral complex was also supported by the fact that the finally obtained spectrum was in good agreement with that of **2**. The axial coordination of *t*BuNC in complex **2** is also clear from the fact that complexes **1** and **2** show a paramagnetism and a diamagnetism, respectively, in their $^1H$ NMR spectra (Figure S4). It should be noted that the octahedral coordination of **2** was maintained without any release of the axial ligands in an aqueous solution, although the coordination of the ligands was not conserved in organic solvents (Figure S5). Therefore, we can conclude that the octahedral structure of complex **2** is maintained in water, which is comparable to the effect of the oxygenation of the sulfur atoms.

For the complete formation of octahedral species in acetone, the addition of a 1000-fold excess of *t*BuNC in methanol was required. The electrostatic effect on the metal center that is caused by the interaction between the coordinated amide groups and the solvent is best understood through the examination of the equilibrium experiment with complex **1** for the following reasons: (1) the sulfur atoms of the tetradentate ligand are not easily air-oxidized in the preparation of complex **1**; therefore, direct interactions of the oxygenated sulfinate oxygen atoms with the solvent molecules of the secondary coordination sphere can be eliminated, (2) the solvation of the neutral monodentate ligand *t*BuNC that is coordinated to the complex can be excluded, (3) the axial coordination of the ligands to the square-planar complex induces a higher lability of the complex. Therefore, we investigated the effect of solvents on the equilibrium constant ($K_s$) [Equation (1)].

$$[Co^{III}(\mathbf{L}{:}\mathbf{N_2S_2})]^- + 2\ t\text{BuNC} \overset{K}{\rightleftharpoons} [Co^{III}(\mathbf{L}{:}\mathbf{N_2S_2})(t\text{BuNC})_2]^- \quad (1)$$

With the use of the intensity change in the LMCT band (700 nm), the equilibrium constants for the reaction have been estimated. Equation (2) was derived on the basis of Equation (1) with material balances taken into account.

$$\log\{(A_0-A)/A\} = 2\log[C_{Bu}-\{2(A_0-A)/A_0\}C_{CoL}] + \log K_s \quad (2)$$

Here, $A_0$ and $A$ represent the absorption intensities of the $[Co^{III}(\mathbf{L}{:}\mathbf{N_2S_2})]^-$ solution and that of the mixed solution of $[Co^{III}(\mathbf{L}{:}\mathbf{N_2S_2})]^-$ and $[Co^{III}(\mathbf{L}{:}\mathbf{N_2S_2})(t\text{BuNC})_2]^-$, respectively. $C_{Bu}$ and $C_{CoL}$ are the total concentrations of *t*BuNC and the $[Co^{III}(\mathbf{L}{:}\mathbf{N_2S_2})]^-$ solutions, respectively. The relationship between the absorbance term of the complex versus the concentration term of added *t*BuNC was plotted according to Equation (1) and showed a linear relationship with a slope of 2, within experimental error. This indicates that two *t*BuNC molecules are coordinated to the $Co^{III}$ complex in all of the solvents. This result was also confirmed from the similarity in the absorption spectrum of **2** as described above. The equilibrium constant, $K_s$, clearly showed the solvent dependence (Table S1); they gradually decreased as follows: $H_2O$/MeOH (3:7) > $H_2O$/MeOH (1:9) > methanol > ethanol > 2-PrOH > dichloromethane > acetone. The constant, $K_s$, demonstrated a linear relationship only for the acceptor number (AN)[25–28] of solvents which is an index of electrophilicity[28,29] [Figure 5 (■)]. $K_s$ did not show this relationship for any other physical parameters such as a donor number[29,30] or a dielectric constant. This result indicates that an interaction of the electrophilic solvent with **1** makes the axial coordination of *t*BuNC easier.

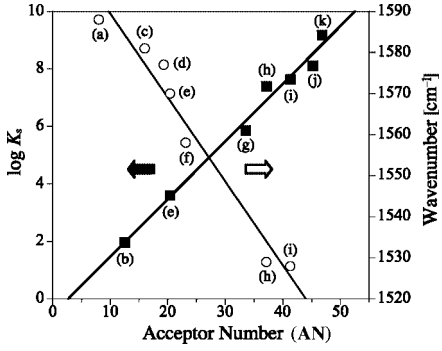


Figure 5. Plots of log$K_s$ values (■) and C=O stretching vibration values (○) for complex **1** versus ANs of organic solvents. (a) THF; (b) acetone; (c) DMF; (d) MeCN; (e) $CH_2Cl_2$; (f) $CHCl_3$; (g) 2-propanol; (h) EtOH; (i) MeOH; (j) $H_2O$/MeOH [1:9 (v/v)]; (k) $H_2O$/MeOH [3:7 (v/v)].

### Infrared Spectra of 1 and 3 in Organic Solvents

As described above, the coordination of *t*BuNC at the axial sites of **1** depends on the electrophilic solvents, whose solvent dependence should be considered to be caused by the interaction of complex **1** with the solvent molecules. The electron-rich carbonyl oxygen atoms of the ligand **L** can also interact with the electrophilic solvent. Therefore, IR spectra were obtained for **1** and **3** in order to identify the interaction site of the complexes with the solvent molecules.

 © 2006 Wiley-VCH Verlag GmbH & Co. KGaA, Weinheim 

The IR spectra of sample solutions without the $Co^{III}$ complex were measured as a base line. A difference spectrum between the solution of **1** and the base line was then adopted. Interestingly, the frequencies assigned to the stretching vibration of C=O are dependent on the solvents within the range of 1520–1590 $cm^{-1}$ as listed in Table S2. The C=O stretching vibrations are linearly dependent on the ANs as shown in Figure 5 (○), which suggests that the axial coordination is predominantly controlled by the interaction of the solvent molecules with the carbonyl oxygen atoms.

The solvent-dependent shift of the C=O stretching frequency was also observed for **3**, and the C=O stretching vibration for **3** (Table S3) showed a similar shift to that of **1**, as shown in Figure 6 (■). However, in the same solvents the absorption bands in **3** appeared in a higher energy region compared with those of **1**. An increase in the C=O bond strength of **3** compared with that of **1** induced a decrease in the Co–N bond strength, which may be explained in terms of the coordination saturation and strong *trans* influence of $SO_2$.[15c] On the other hand, remarkably, the stretching frequency of the S=O group, which is considered as another possible interaction site for the solvents, did not show any significant shift [Figure 6 (○), Table S4]. The vibration responsible for N≡C in **3** is also linearly dependent on the ANs of the solvents (Figure S6, Table S5). The linear relationship indicates that the interaction of the carbonyl oxygen atoms with the solvent molecules causes a change in the N≡C vibration, while the sulfinate oxygen did not show any interaction with the solvents as described above. The N≡C vibration showed a significantly higher energy shift with an increase in AN, which is similar to the case of the oxidized sulfur atoms.[18a] This result suggests that the attractive interaction of the carbonyl oxygen atoms with the solvent molecules causes an increase in the Lewis acidity of the $Co^{III}$ center.

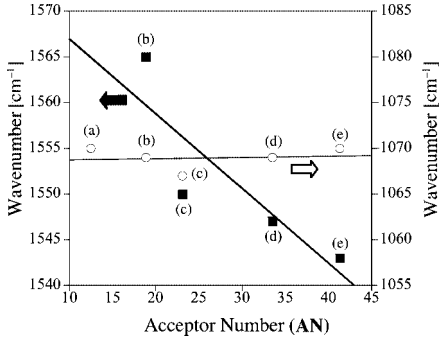


Figure 6. Plots of C=O (■) and S=O stretching vibration values (○) for complex **3** versus ANs of organic solvents. (a) Acetone; (b) MeCN; (c) $CHCl_3$; (d) 2-PrOH; (e) MeOH.

## Redox Behaviors of 1, 2 and 3 in Organic Solvents

The solvent dependence of the C=O stretching vibrations that appeared for complexes **1** and **3** must also influence the acidity of the metal center, so the electrochemical properties of the complexes was investigated with the use of cyclic voltammetry with an $Ag/Ag^+$ reference electrode. The voltammogram of **1** exhibited only one quasi reversible redox wave assignable to $Co^{III}/Co^{II}$ with $\Delta E \approx 100$ mV and $i_p/i_c \approx 1.0$ within the experimental potential range (–1.7 V to –1.1 V). The electrochemical parameters are listed in Table S5, in which the redox potentials have been standardized to the $Fc/Fc^+$ potential. The redox potential is high enough to maintain the Co center in the 3+ oxidation state and is consistent with those of previously reported $N_2S_2$-type Co complexes that contain two amidate nitrogen atoms and two sulfur atoms as coordinating atoms.[31–33] The redox potential in methanol is clearly much higher than that in acetone, which is in agreement with the tendencies for the equilibrium constant $K_s$ and the C=O stretching vibrations. The solvent dependence of the results led us to expect that the Lewis acidity of the $Co^{III}$ center could effectively be controlled by the interaction of **1** with the solvent molecules. The redox potential value ($E_{1/2}$) assignable to $Co^{III}/Co^{II}$ of **1**, as expected, exhibited a solvent dependency with a linear relation to the AN values of the solvents; that is, –1.12 V versus $Fc/Fc^+$ in MeOH (AN = 41.3) and –1.73 V in THF (AN = 8.0), respectively (Figure 7, Table S6). The redox potential values showed a significantly larger positive shift with an increase in AN, which suggests that the attractive interaction of the carbonyl oxygen atoms with the solvent molecules causes an increase in the Lewis acidity of the $Co^{III}$ center and promotes the axial coordination of a monodentate ligand. On the basis of such a linear relation, the ideal redox potential values of **1** in an aqueous solution (AN = 54.8) and in a noninteracting solvent (AN = 0) were estimated to be –0.93 and –1.89 V, respectively, which implies that the interaction of the amidate carbonyl group with the water molecules causes a shift in the redox potential for the $Co^{III}$ complex by ca. 1 V in comparison with that of a noninteracting solvent.

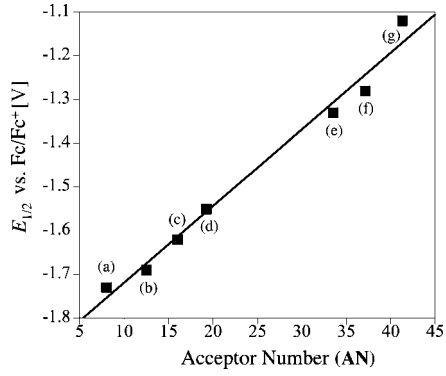


Figure 7. Plots of $E_{1/2}$ for complex **1** versus ANs of organic solvents. (a) THF; (b) acetone; (c) DMF; (d) MeCN; (e) 2-PrOH; (f) EtOH; (g) MeOH.

Furthermore, the reduction potential of complex **3** in MeOH was observed at –1.27 V and that of **2** in the presence of a large amount of *t*BuNC in a MeOH solution was detected at –2.18 V, which indicates that the oxygenation of the sulfur atoms raises the reduction potential of the $Co^{III}$

 © 2006 Wiley-VCH Verlag GmbH & Co. KGaA, Weinheim 

complex by ca. 0.9 V. The octahedral structure of complex **2** that is maintained in water is comparable to the effect of the oxygenation of the sulfur atoms. These findings indicate that the attractive interaction between the carbonyl oxygen atoms and the water molecules can control the Lewis acidity of the metal ion as well as the effect of the oxygenation of the sulfur atoms. Consequently, complex **2**, as described above, can maintain the octahedral structure in an aqueous solution (AN = 54.8) without the release of the axial ligands.

### Biological Implications

In the crystal structures of both the Co- and Fe-containing NHases,[9–12] the sulfenate and the sulfinate oxygen atoms interact with the arginine residue through hydrogen bonds as described above, and the amidate carbonyl oxygen atoms are coordinated to water molecules. Moreover, the water molecules form a hydrogen bonded network with other water molecules that starts from the tyrosyl oxygen (βTyr68 in $Co^{III}$-type NHases, Figure 8). It has recently been reported by Miyanaga et al. that the mutant of $Co^{III}$-type NHase, βY68F, where the hydrogen bonded network is destroyed by the replacement of tyrosine by phenylalanine, does not show significant hydratase function.[22] Miyanaga et al. have explained it on the basis of the crystal structures as follows: βTyr68 contributes to the capture of a substrate or an imidate intermediate through the hydrogen bonds.[22] With the consideration of this report[22] and our results, we can propose that a higher Lewis acidity of the central metal ion is required for the axial coordination of the ligands, which is important for the enzymatic reaction, and may finely be regulated by the hydrogen bonded network from tyrosine to the amidate oxygen atoms through water molecules. From the fact that the S=O group did not show an electrophilic interaction,[28,29] we can conclude that the sulfinate oxygen atoms do not contribute to the control of the Lewis acidity of the central metal. If the Lewis acidity of the central metal can be sensitively controlled by these hydrogen bonding interactions, the reaction will rapidly proceed and the reaction product will also be rapidly released from the central metal ion. In the crystal structures of **1**-$PPh_4$, **1**-Na, and **3** the carbonyl oxygen atoms of the ligands **L** and **L:$N_2(SO_2)_2$** are coordinated to water and ethanol molecules, respectively. Furthermore, as shown in the crystal structure of complex **1**-Na, three hydrogen bond interactions with three water molecules for each carbonyl oxygen influenced the Co–*N*–C–O bonding system. However, such an interaction was not found in the sulfinyl oxygen atoms of **3**, which may suggest that the sulfinyl oxygen groups do not significantly interact with the solvent molecules.

In conclusion, this paper describes that the hydration reaction in NHase is significantly controlled by the amidate groups as well as the oxygenated sulfur groups.

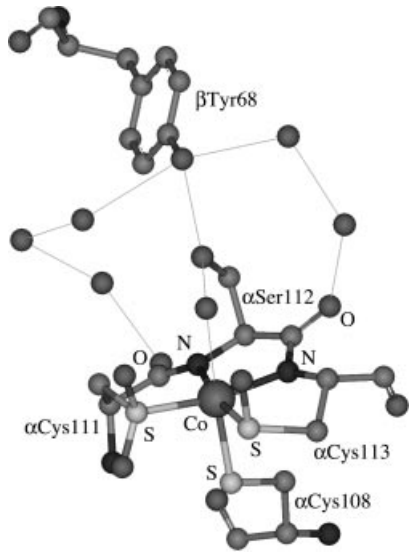


Figure 8. Hydrogen bonding networks near the active site of NHase: hydroxy oxygen of βTyr68 hydrogen-bonded to amide carbonyl oxygen atoms by water molecules.

## Experimental Section

**Reagents and Technique:** All manipulations were performed with Schlenk technique under an Ar atmosphere or in a glove box. Reagents in this study were purchased in reagent grade from Wako Pure Chemical Industries Ltd. or Tokyo Kasei Kogyo Co. Ltd. and used without further purification. Solvents in reagent grade were purchased from Wako Pure Chemical Industries Ltd. and Kanto Kagaku Co. Inc. and distilled twice prior to use.

**Synthesis of $H_4$L:** 2-benzylthio-2-methylpropionic acid chloride was synthesized as described previously.[34] The acid chloride (12.77 g, 50.00 mmol) was added dropwise to a THF solution containing 1,3-diaminopropane (1.85 g, 25.00 mmol) and triethylamine (5.06 g, 50.00 mmol). After filtration, a 1 M HCl aqueous solution was added to the filtrate and evaporated. Addition of diethyl ether to the concentrated solution afforded a white powder which was identified as an *S*-benzylated **L** by $^1$H NMR spectroscopy, whose powder (2.00 g, 4.36 mmol) was dissolved in THF (20 mL) and treated with liquid ammonia at –78 °C. To this solution was added sodium (1.91 g, 82.95 mmol), which was stirred vigorously for 30 min. After the excess ammonia was removed by evaporation at room temperature, the solution was adjusted to pH 3 with 1 M $KHSO_4$. The product was extracted with ethyl acetate and the solvent evaporated. $^1$H NMR (300 MHz, $CDCl_3$): $\delta$ = 1.63 (s, 12 H), 1.70 (m, 2 H), 2.29 (s, 2 H), 3.28 (q, 4 H), 7.83 (s, 2 H) ppm.

**Preparation of Na[Co(L:$N_2S_2$)] (1-Na) and $PPh_4$[Co(L:$N_2S_2$)] (1-$PPh_4$):** Na[Co(**L**:$N_2S_2$)] (**1**-Na) was prepared according to the literature with some modifications.[18,19] Recrystallization of the compound from acetonitrile/diethyl ether afforded a single crystal in atmosphere. Addition of $PPh_4Cl$ (269.4 mg, 0.72 mmol) to an aqueous solution (20 mL) of the sodium salt (256.3 mg, 0.72 mmol) afforded a single crystal of $PPh_4$[Co(**L**:$N_2S_2$)] (**1**-$PPh_4$). $C_{35}H_{40}CoN_2O_3PS_2$ (690.74): calcd. C 60.86, H 5.84, N 4.06; found C 60.93, H 5.77, N 4.03. Electronic absorption spectra ($CHCl_3$): $\lambda_{max}$ [$\varepsilon$ ($M^{-1}$ $cm^{-1}$)] = 312 (7300), 443 (sh), 640 (2600) nm.

**Preparation of $PPh_4$[Co(L:$N_2S_2$)(*t*BuNC)$_2$] (2):** Monodentate ligand, *t*BuNC, (200 μL, 1.76 mmol) was added to an acetonitrile solution (150 μL) containing $PPh_4$[Co(**L**:$N_2S_2$)] (3 mg,

 © 2006 Wiley-VCH Verlag GmbH & Co. KGaA, Weinheim 

$0.43 \cdot 10^{-2}$ mmol). A red crystal was isolated by the slow diffusion of diethyl ether into the solution at 0 °C. $C_{45}H_{56}CoN_4O_2PS_2$ (838.99): calcd. C 64.42, H 6.73, N 6.68; found C 64.14, H 6.60, N 6.47. Selected IR bands (KBr): $\tilde{\nu}$ = 2176 (s, CN), 1535 (s, CO) $cm^{-1}$. $^1H$ NMR (300 MHz,$D_2O$): $\delta$ = 1.36 (s, 12 H, $CH_3$), 1.49 (s, 18 H, *t*Bu), 1.75 (t, 2 H, $CH_2$), 3.79 (t, 4 H, $CH_2$), 7.72 (m, 20 H, Ph) ppm. Electronic absorption spectra ($H_2O$): $\lambda_{max}$ [$\varepsilon$ ($M^{-1}cm^{-1}$)] = 294 (12800), 360 (sh) nm.

**Preparation of $PPh_4$[Co{L:$N_2(SO_2)_2$}(*t*BuNC)$_2$] (3):** To an ethanol solution (1 mL) containing $PPh_4$[Co(**L:$N_2S_2$**)] (83 mg, 0.12 mmol) was added *t*BuNC (191 μL, 1.44 mmol). After the solution was stirred for 10 min, 30% $H_2O_2$ (0.62 mL, 5.45 mmol) was added dropwise to the ethanol solution at –10 °C. The solution was left to stand for 3 h at –10 °C. A crude compound was obtained by the addition of diethyl ether into the solution. Recrystallization of the compound from ethanol/diethyl ether afforded a single crystal suitable for X-ray analysis. $C_{47}H_{64}CoN_4O_8PS_2$ (967.07): calcd. C 58.37, H 6.67, N 5.79; found C 58.14, H 6.50, N 6.00. Selected IR bands (KBr) : $\tilde{\nu}$ = 2199 (s, CN), 1552 (s, CO), 1214 and 1071 (s, SO) $cm^{-1}$. $^1H$ NMR (300 MHz, [$D_6$]DMSO): 1.15 (s, 12 H, $CH_3$), 1.34 (s, 18 H, *t*Bu), 3.16 (t, 6 H, $CH_2$), 7.83 (m, 20 H, Ph) ppm. Electronic absorption spectrum (EtOH): $\lambda_{max}$ [$\varepsilon$ ($M^{-1}cm^{-1}$)] = 273 (9700), 313 (21400), 400 (sh) nm. ESI-MS ([$Co^{III}$(**L:$N_2(SO_2)_2$**)(*t*BuNC)$_2$]$^-$): *m*/*z* (%) = 563.

**X-ray Structural Analysis:** Crystals suitable for X-ray diffraction measurements were mounted on glass fibers. The diffraction data were collected with a Rigaku Mercury diffractometer using graphite-monochromated Mo-$K_\alpha$ radiation at –100 °C with the oscillation technique. Crystal data and experimental details are listed in Table 2. All structures were solved by a combination of direct methods and Fourier techniques. Non-hydrogen atoms were anisotropically refined by full-matrix least-squares calculations. Hydrogen atoms were included but not refined. Refinements were continued until all shifts were smaller than one-tenth of the standard deviations of the parameters involved. Atomic scattering factors and anomalous dispersion terms were taken from the International Tables for X-ray Crystallography.[35] All calculations were carried out with a Japan SGI workstation computer with the teXsan crystallographic software package.[36] CCDC-606977, CCDC-252730, CCDC-606976, and CCDC-281586 contain the supplementary crystallographic data for this paper. These data can be obtained free of charge from The Cambridge Crystallographic Data Centre via www.ccdc.cam.ac.uk/data_request/cif.

### Other Physical Measurements

Elemental analysis was performed with a Perkin–Elmer 2400II CHNS/O full-automatic analyzer. All mass spectra were acquired with a LCT mass spectrometer equipped with an ionspray interface (Micromass Limited, Manchester, UK). Instrument settings, data acquisition, and data processing were controlled by a computer with Windows NT operating system. Samples were introduced with a single syringe pump (KD scientific Inc., USA) fitted with Hamilton syringes (Hamilton Co, Reno, NE). The samples for all spectral measurements were prepared in MeCN or MeOH. $^1H$ NMR spectra were recorded with a Varian Gemini-300 FT-NMR instrument. Electronic absorption spectra were measured with a JASCO V-550 or V-570 spectrophotometer in the wavelength range of 900 – 250 nm. A match paired quartz cell was used with a 10 mm length. Infrared spectral measurements were carried out with a JASCO FT/IR 410 spectrophotometer. Solid samples were prepared with a pressure greater than 5 tons in KBr powder. Spectra in solution were measured with the use of a double-piled $CaF_2$ or KBr cell with 0.1 mm thick walls for the C=O and S=O stretching frequencies of the sulfinates. Differential spectra between the sample and the corresponding solvent were used to verify the spectral features. Electrochemical measurements were performed with a BAS BIOANALYTICAL Systems model CV-50W or with a ALS/CH Instruments Electrochemical Analyzer Model 600A. Pt electrodes were adopted as the working- and counter-electrode and an Ag/$Ag^+$ electrode was used as a reference. Cyclic voltammograms were collected in a glove box under an Ar atmosphere. The potential values were revised on the $Fc/Fc^+$ standard.

### Determination of Equilibrium Constants

Equilibrium constants were spectrophotometrically determined by means of spectral changes of **1** upon the addition of a suitable

Table 2. Crystallographic data and experimental details for Na[Co(**L:$N_2S_2$**)] (**1**-Na), $PPh_4$[Co(**L:$N_2S_2$**)] (**1**-$PPh_4$), $PPh_4$[Co(**L:$N_2S_2$**)(*t*BuNC)$_2$] (**2**) and $PPh_4$[Co{**L:$N_2(SO_2)_2$**}(*t*BuNC)$_2$] (**3**).

| | **1**-Na | **1**-$PPh_4$ | **2** | **3** |
|---|---|---|---|---|
| Empirical formula | $C_{11}H_{24}CoN_2O_5S_2Na$ | $C_{35}H_{40}CoO_3N_2PS_2$ | $C_{22.5}H_{28}Co_{0.5}ON_2P_{0.5}S$ | $C_{47}H_{62}CoO_7N_4PS_2$ |
| Formula mass | 410.36 | 690.74 | 419.49 | 949.06 |
| Crystal system | triclinic | monoclinic | tetragonal | monoclinic |
| Space group | $P\bar{1}$ (No. 2) | $P2_1/n$ (No. 14) | $P\bar{4}$ (No. 81) | $P2_1/a$ (No. 14) |
| *a* [Å] | 9.949(3) | 11.658(1) | 16.7400(7) | 10.4277(4) |
| *b* [Å] | 9.958(3) | 14.085(1) | | 33.484(1) |
| *c* [Å] | 10.156(3) | 20.977(2) | 7.8718(5) | 14.1350(5) |
| $\alpha$ [°] | 69.48(2) | | | |
| $\beta$ [°] | 69.54(2) | 100.159(4) | | 95.288 |
| $\gamma$ [°] | 74.05(2) | | | |
| *V* [$A^3$] | 869.5(5) | 3390.3(5) | 2205.9(2) | 4914.4(3) |
| *Z* | 2 | 4 | 4 | 4 |
| $D_{calcd.}$ [$g\,cm^{-3}$] | 1.567 | 1.353 | 1.263 | 1.283 |
| *F*(000) | 428.00 | 1448.00 | 888.00 | 2008.00 |
| $\mu$ [$cm^{-1}$] | 12.73 | 7.14 | 5.60 | 5.18 |
| $\lambda$ [Å] | 0.71070 | 0.71070 | 0.71070 | 0.17070 |
| *T* [K] | 173 | 173 | 173 | 173 |
| No. of refls. measured | 6948 | 27401 | 17735 | 37445 |
| No. of refls. used [$I > 2\sigma(I_0)$] | 2892 | 5649 | 4584 | 8175 |
| $R_1$[a]/$R_w$[b] | 0.041/0.117 | 0.049/0.102 | 0.040/0.110 | 0.051/0.13 |
| GOF | 1.05 | 1.08 | 1.12 | 1.11 |

 © 2006 Wiley-VCH Verlag GmbH & Co. KGaA, Weinheim 

amount of *t*BuNC. The concentration of complex **1** was kept constant at $5.00 \cdot 10^{-5}$ mol dm$^{-3}$.

**Supporting Information** (see footnote on the first page of this article):Crystal packing of **1**-Na with hydrogen bonding interactions (Figure S1), crystal packing of **1**-$PPh_4$ (Figure S2), representative UV/Vis spectral change of **1**-$PPh_4$ due to the addition of monodentate ligand (Figure S3), $^1$H NMR spectra of **1**-$PPh_4$ and **2** (Figure S4), UV/Vis spectra of **2** (Figure S5), plots of N≡C stretching vibration values for **3** versus ANs (Figure S6), tables of equilibrium constants, C=O stretching vibration values for **1** and **3**, S=O stretching vibration values for **3**, N≡C stretching vibration values for **3**, electrochemical parameters for **1** (Tables S1–S6) as PDF files.

## Acknowledgments

This work was supported partly by a Grant-in-Aid for Scientific Research from the Ministry of Education, Science, Sports, and Culture of Japan (H.M. and Y. F.) and supported in part by a grant from the NITECH 21st Century COE Program, to which our thanks are due. We also thank to Prof. Masafumi Odaka, Tokyo University of Agriculture and Technology, who kindly provided useful comments about our results.

[1] T. Nagasawa, H. Yamada, *Trends Biotechnol.* **1989**, *7*, 153–158.
[2] M. Kobayashi, S. Shimizu, *Nature Biotechnol.* **1998**, *16*, 733–736.
[3] H. Yamada, M. Kobayashi, *Biosci. Biotechnol. Biochem.* **1996**, *60*, 1391–1400.
[4] M. Kobayashi, T. Nagasawa, H. Yamada, *Trends Biotechnol.* **1992**, *10*, 402–408.
[5] T. Nagasawa, K. Ryuno, H. Yamada, *Experientia* **1989**, *45*, 1066–1070.
[6] B. A. Brennan, G. Alms, M. J. Nelson, L. T. Durney, R. C. Scarrow, *J. Am. Chem. Soc.* **1996**, *118*, 9194–9195.
[7] M. J. Nelson, H. Jin, I. M. Turner Jr, G. Grove, R. C. Scarrow, B. A. Brennan, L. Que Jr, *J. Am. Chem. Soc.* **1991**, *113*, 7072–7073.
[8] M. Kobayashi, M. Nishiyama, T. Nagasawa, S. Horinouchi, T. Beppu, H. Yamada, *Biochim. Biophys. Acta* **1991**, *1129*, 23–33.
[9] W. Haung, J. Jia, J. Cummings, M. Nelson, G. Schneider, Y. Lindqvist, *Structure* **1997**, *5*, 691–699.
[10] S. Nagashima, M. Nakasako, N. Domae, M. Tsujimura, K. Takio, M. Odaka, N. Kamiya, I. Endo, *Nat. Struct. Biol.* **1998**, *5*, 347–351.
[11] A. Miyanaga, S. Fushinobu, K. Ito, T. Wakagi, *Biochem. Biophys. Res. Commun.* **2001**, *288*, 1169–1174.
[12] S. Hourai, M. Miki, Y. Takashima, S. Mitsuda, K. Yanagi, *Biochem. Biophys. Res. Commun* **2003**, *312*, 340–345.
[13] T. Murakami, M. Nojiri, H. Nakayama, M. Odaka, M. Yohda, N. Dohmae, K. Takio, T. Nagamune, I. Endo, *Protein Science* **2000**, *9*, 1024–1030.
[14] a) J. J. Ellison, A. Nienstedt, S. C. Shoner, A. Basrnhart, J. A. Cowen, J. A. Kovacs, *J. Am. Chem. Soc.* **1998**, *120*, 5691–5700; b) J. Shearer, I. Y. Kung, S. Lovell, W. Kaminsky, J. A. Kovacs, *J. Am. Chem. Soc.* **2001**, *123*, 463–468; c) A. Dey, M. Chow, K. Taniguchi, P. Lugo-Mas, S. Davin, M. Maeda, J. A. Kovacs, M. Odaka, K. O. Hodgson, B. Hedman, E. I. Solomon, *J. Am. Chem. Soc.* **2006**, *128*, 533–541.
[15] a) J. C. Noveron, M. M. Olmstead, P. K. Mascharak, *J. Am. Chem. Soc.* **1999**, *121*, 3553–3554; b) L. A. Tyler, J. C. Noveron, M. M. Olmstead, P. K. Mascharak, *Inorg. Chem.* **2003**, *42*, 5751–5761; c) J. C. Noveron, M. M. Olmstead, P. K. Mascharak, *J. Am. Chem. Soc.* **2001**, *123*, 3247–3259.
[16] T. Ozawa, T. Ikeda, T. Yano, H. Arii, S. Yamaguchi, Y. Funahashi, K. Jitsukawa, H. Masuda, *Chem. Lett.* **2005**, *34*, 18–19.
[17] a) C. A. Grapperhaus, A. K. Patra, M. S. Mashuta, *Inorg. Chem.* **2002**, *41*, 1039–1041; b) C. A. Grapperhaus, M. Li, A. K. Patra, S. Poturovic, P. K. Kozlowski, M. Z. Zgierski, M. S. Mashuta, *Inorg. Chem.* **2003**, *42*, 4382–4388.
[18] a) M. Rat, R. A. de Sousa, J. Vaissermann, P. Leduc, D. Mansuy, I. Artaud, *J. Inorg. Biochem.* **2001**, *84*, 207–213; b) E. Galardon, M. Giorgi, I. Artaud, *Chem. Commun.* **2004**, 286–287; c) S. Chatel, M. Rat, S. Dijiols, P. Leduc, J. P. Tuchagues, D. Mansuy, I. Artaud, *J. Inorg. Biochem.* **2000**, *80*, 239–246; d) E. Bourles, R. A. de Sousa, E. Galardon, M. Giorgi, I. Artaud, *Angew. Chem. Int. Ed.* **2005**, *44*, 3526–3528.
[19] a) L. Heinrich, Y. Li, J. Vassermann, J.-C. Chottard, *Eur. J. Inorg. Chem.* **2001**, 1407–1409; b) L. Heinrich, A. Mary-Verla, Y. Li, J. Vassermann, J.-C. Chottard, *Eur. J. Inorg. Chem.* **2001**, 2203–2206; c) L. Heinrich, Y. Li, K. Provost, A. Michalowicz, J. Vassermann, J.-C. Chottard, *Inorg. Chim. Acta* **2001**, *318*, 117–126; d) L. Heinrich, A. Mary-Verla, J. Vassermann, J.-C. Chottard, Y. Li, *Inorg. Chim. Acta* **2004**, *357*, 117–126; e) L. Heinrich, Y. Li, J. Vassermann, G. Chottard, J.-C. Chottard, *Angew. Chem. Int. Ed.* **1999**, *38*, 6162–6165.
[20] M. Rat, R. A. de Sousa, A. Tomas, Y. Frapart, J.-P. Tuchagues, I. Artaud, *Eur. J. Inorg. Chem.* **2003**, *4*, 759–765.
[21] S. R. Piersma, M. Nojiri, M. Tsujimura, T. Noguchi, M. Odaka, M. Yohda, I. Endo, *J. Inorg. Biochem.* **2000**, *80*, 283–288.
[22] A. Miyanaga, S. Fushinobu, K. Ito, H. Shoun, T. Wakagi, *Eur. J. Biochem.* **2004**, *271*, 429–438.
[23] K. Taniguchi, M. Tsujimura, M. Odaka, T. Hirose, I. Endo, M. Maeda, *1st Joint Symposium on Biofunctional Chemistry and Biotechnology* **2003**, Oct. 12–13, Kumamoto University, Japan.
[24] H. Suzuki, M. Nojiri, N. Kamiya, T. Noguchi, *J. Biochem.* **2004**, *136*, 115–121.
[25] A. Taha, M. M. Mahmoud, *New J. Chem.* **2002**, *26*, 953–957.
[26] Q. Liu, D. Fang, J. Zheng, *Spectrochim. Acta, Part A* **2004**, *60*, 1453–1458.
[27] Q. Liu, X. Xu, W. Sang, *Spectrochim. Acta, Part A* **2003**, *59*, 471–475.
[28] H. Muta, K. Ishida, E. Tamaki, M. Satoh, *Polymer* **2003**, *43*, 103–110.
[29] R. W. Taft, N. J. Pienta, M. J. Kamlet, E. M. Arnett, *J. Org. Chem.* **1981**, *46*, 661–667.
[30] V. Gutmann, *Electrochim. Acta* **1976**, *21*, 661–670.
[31] S. Chatel, A.-S. Chauvin, J.-P. Tuchagues, P. Leduc, E. Bill, J.-C. Chotard, D. Mansuy, I. Artaud, *Inorg. Chim. Acta* **2002**, *336*, 19–28.
[32] T. J. Collins, *Acc. Chem. Res.* **1994**, *27*, 279–285.
[33] L. A. Tyler, M. M. Olmstead, P. K. Mascharak, *Inorg. Chem* **2001**, *40*, 5408–5414.
[34] G. Garminati, P. Galimrerti, M. Melandri, *Boll. Chim. Farm.* **1963**, *102*, 522–540.
[35] *International Tables for X-ray Crystallography* (Eds.: J. A. Ibers, W. C. Hamilton), Kynoch Press, Birmingham, U. K., **1974**, vol. IV.
[36] *Texsan, Crystal Structure Analysis Package*, Molecular Structure Corporation (1985), **1992**.

Received: May 15, 2006
Published Online: August 3, 2006

 © 2006 Wiley-VCH Verlag GmbH & Co. KGaA, Weinheim 

DOI: 10.1002/ejic.200600227

# Synthesis, Characterisation and Properties of *As*-Monohalogenated Dibenzoarsocines $S(C_6H_4S)_2AsHal$ (Hal = Cl, Br, I) – A Study of the Transannular Interaction S→As

**Simplicio González-Montiel,[a] Noemí Andrade-López,[a] and José G. Alvarado-Rodríguez*[a]**

**Keywords:** Arsenic complexes / Main group elements / Hypervalent compounds / Structure elucidation

Addition of $AsCl_3$ to $S(C_6H_4SH)_2$ in benzene solution leads to the formation of the stable compound $S(C_6H_4S)_2AsCl$ (**1**). The $S(C_6H_4S)_2AsHal$ [Hal = Br (**2**), I (**3**)] compounds have been synthesised by halogen exchange from **1** and the corresponding potassium halide. X-ray structure determinations of complexes **1**–**3** reveal that the arsenic atom acts as an acceptor atom exhibiting an intramolecular transannular interaction with the thioether-like sulfur atom. The geometry of the tetracoordinate As atom in the title compounds is described as distorted pseudo-trigonal-bipyramidal with a stereochemically active lone pair and 66–63 % trigonal-bipyramidal character. The transannular interaction influences the conformation of the dibenzotrithiarsocine system, adopting the central eight-membered ring with a boat–boat conformation and $C_s$ symmetry.

(© Wiley-VCH Verlag GmbH & Co. KGaA, 69451 Weinheim, Germany, 2006)

## Introduction

We have been interested in the coordination chemistry of dithio ligands that can increase the coordination number around an acidic Lewis atom A, where A is a heavy p-block element. Some of these ligands, in particular $D(CH_2CH_2S)_2^{2-}$ with the donor atom D = O, S and NR, are quite flexible and led to the atom A expanding its coordination number through an *intramolecular transannular* interaction D→A. In these metallocanes, the conformational diversity is very large.[1] In addition, in these compounds the interaction is a stabilising factor in comparison with the cyclooctane ring and can be envisaged as a tool for controlling stabilities and conformations. The strength of this interaction spans over a wide range. In some cases it is very strong; for example in arsocanes the cross-ring bond has been claimed as being responsible for the stabilisation of discrete arsenium cations.[2] On the other hand, the more constrained ligands of type **I** (Scheme 1) have been explored for several groups in the coordination chemistry of transitional metals as well as light p-block elements; in these type **II** complexes the transannular interaction can also take place.[3] In particular, we have studied some *Sb*-monohalogenated dibenzometallocines and we have shown by means of X-ray crystallographic and DFT studies the acidic behaviour of the antimony atom acting as a Lewis acceptor toward sulfur in the decreasing order I > Br > Cl. These results prompt us to expand our studies to arsenic, a lighter group 15 element.

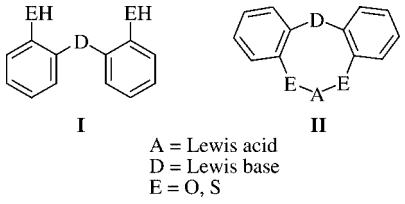


Scheme 1.

Here we report the synthesis and structural study of type **II** complexes with arsenic(III) as the acceptor atom. These compounds are good models for further understanding of the nature of the S→As interaction. After the description of the synthesis of dibenzoarsocines, IR and Raman spectra, mass spectra, NMR and X-ray crystallographic data are presented and discussed.

## Results and Discussion

### Synthesis of $S(C_6H_4S)_2AsHal$ (Hal = Cl, Br, I)

The ligand $S(C_6H_4SH)_2$ was prepared according to a reported method.[4] Treatment of $S(C_6H_4SH)_2$ with $AsCl_3$ in benzene yielded $S(C_6H_4S)_2AsCl$ (**1**) as colourless crystals (see Scheme 2). $S(C_6H_4S)_2AsBr$ (**2**) and $S(C_6H_4S)_2AsI$ (**3**) were obtained from a halogen-exchange reaction as reported for antimony complexes[3] between **1** and an excess of KBr/HBr or KI in hot benzene, respectively, yielding colourless crystals for **2** and pale yellow crystals for **3** (see

[a] Centro de Investigaciones Químicas, Universidad Autónoma del Estado de Hidalgo,
Km. 4,5 Carretera Pachuca-Tulancingo, Pachuca, Hidalgo C.P. 42076, México
Fax: +52-771-717-2000 ext. 6502
E-mail: galvarad@uaeh.reduaeh.mx


InterScience
© 2006 Wiley-VCH Verlag GmbH & Co. KGaA, Weinheim

Experimental Section for details). All complexes are air-stable, soluble in benzene and chloroform, and insoluble in pentane, hexane and 2-propanol.

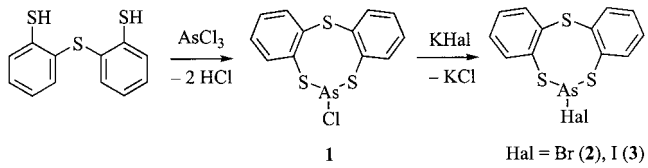


**1** Hal = Br (**2**), I (**3**)

Scheme 2.

## Vibrational Spectra

The Raman spectrum of each compound in the solid state was obtained for light scattered from the 1579.8 nm line of an argon ion laser. Under these conditions, compounds **1** and **2** experienced photodecomposition by the laser. The IR spectrum of each solid compound pressed on a CsI disk was collected in the 4000–200 $cm^{-1}$ range. The Raman spectrum of the iodo complex is shown in Figure 1.

Besides the expected benzene group bands, there are several bands below 400 $cm^{-1}$. In the 400–300 $cm^{-1}$ region we found two very intense bands assignable to the asymmetric and symmetric stretching vibration modes of the S–As–S group. In order to confirm the assignment of these bands, we compared these data with those exhibited by the antimony analogue complexes previously reported (see Scheme 3). The data are listed in Table 1. In the case of the arsenic complexes, the $\nu_{asym} - \nu_{sym}$ difference ($\Delta$) is $59 \pm 3$ $cm^{-1}$, whereas in antimony complexes with sulfur as the donor atom, $\Delta$ is $46 \pm 4$ $cm^{-1}$.

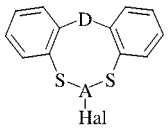


A = As, Sb

Scheme 3.

In the IR spectra of complexes **1** and **2** we assigned the 392 and 280 $cm^{-1}$ bands to the As–Cl and As–Br stretching bands, respectively.[5] In order to establish the presence of the As–I group frequency band, we used the Varshni ap-

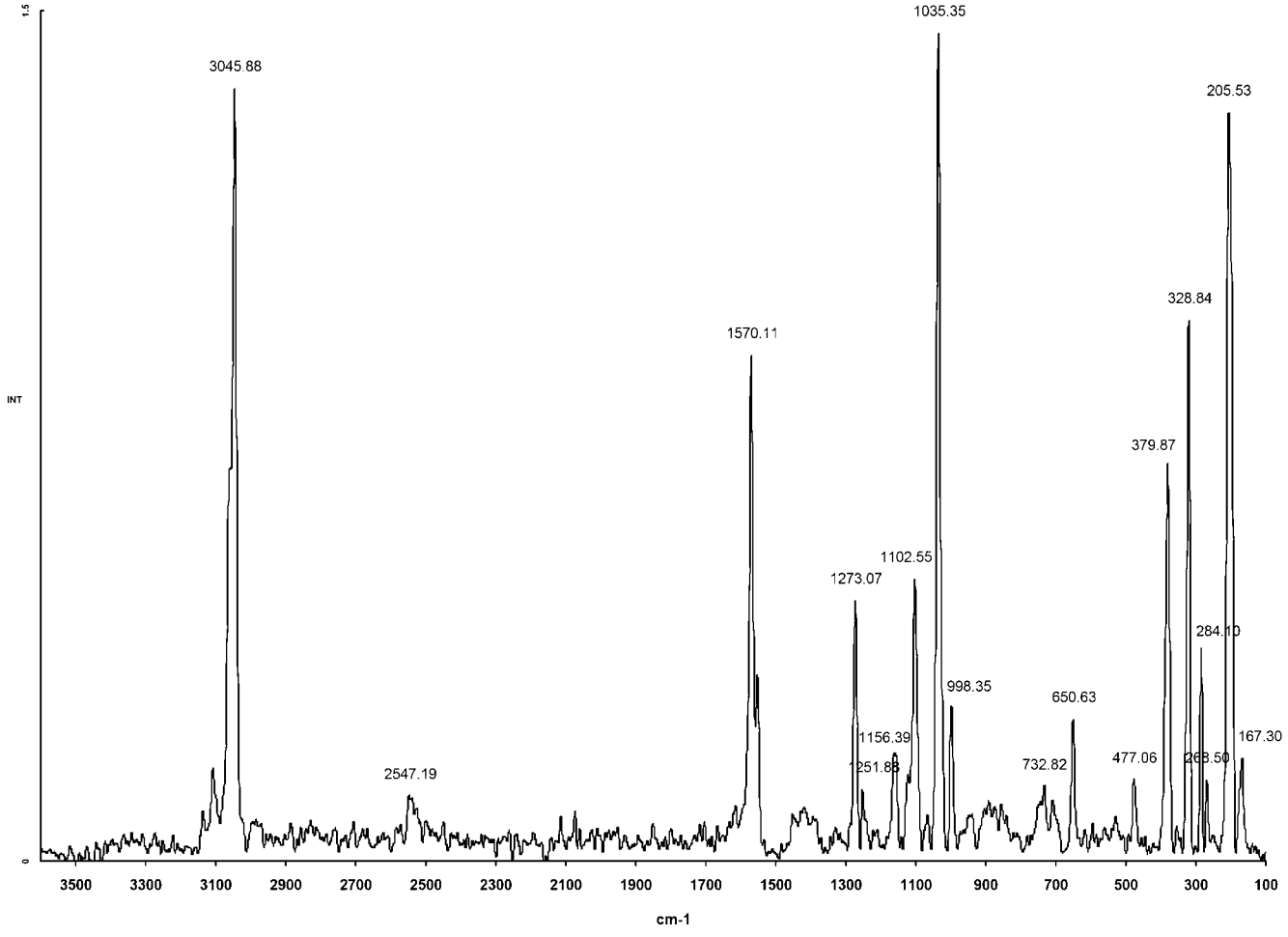


Figure 1. Raman spectra of $S(C_6H_4S)_2AsI$ (**3**).

 © 2006 Wiley-VCH Verlag GmbH & Co. KGaA, Weinheim 

Table 1. Stretching vibration frequencies of the S–A–S group [$cm^{-1}$] of $D(C_6H_4S)_2AHal$.

| D | A–Hal[a] | Spectroscopy | $\nu_{asym}$ | $\nu_{sym}$ | $\Delta$ ($\nu_{asym} - \nu_{sym}$) |
|---|---|---|---|---|---|
| S | As–Cl | IR | 380 | 326 | 54 |
| | | Raman | [b] | [b] | – |
| S | Sb–Cl | IR | 371 | 330 | 41 |
| | | Raman | 370 | 328 | 42 |
| S | As–Br | IR | 387 | 325 | 62 |
| | | Raman | [b] | [b] | – |
| S | Sb–Br | IR | 371 | 327 | 44 |
| | | Raman | 373 | 322 | 51 |
| S | As–I | IR | 380 | 320 | 60 |
| | | Raman | 380 | 321 | 59 |
| S | Sb–I | IR | 372 | 325 | 47 |
| | | Raman | 372 | 323 | 49 |
| O | Sb–Cl | IR | 369 | 316 | 53 |
| | | Raman | 370 | 311 | 59 |

[a] For the data of antimony complexes see ref.[3] [b] Not measured.

proach reported for a series of metallocanes containing As, Sb and Bi linked to halide ligands, in conjunction with the As–I bond length found in complex **3**.[6] By using this treatment, we calculated the stretching frequency at 172 $cm^{-1}$. However, we did not observe any significant band at this frequency. Therefore the intense band at 205 $cm^{-1}$ has been assigned to the As–I stretching frequency.[5] In this sense, Draeger et al. stated that the most intense bands in their series studied belong to the iodo complexes.[6] The vibrational data analysis has shown the usual tendency that the higher the mass of the halogen ligand, the lesser the frequency of the stretching As–Hal group band.

## Mass Spectra

The EI mass spectra were obtained at 70 eV. In **1** and **2** the molecular ion was observed as a low-intensity peak with the appropriate isotopic ratio; for **3** the molecular ion was not observed. In all cases the intense ion fragment in $m/z$ = 323 is assigned to the loss of the halogen atom in the compounds, yielding an $S(C_6H_4S)_2As$ tricyclic moiety, confirming the binding of arsenic to sulfur atoms and the stability of the dibenzotrithiarsocine system. In all the spectra there are peaks corresponding to the $S(C_6H_4S)_2$, $S(C_6H_4)S$ and $S(C_6H_4)_2$ fragments. No more peaks could be assigned.

## NMR Spectroscopy

The NMR spectra of the three complexes were recorded in $CDCl_3$ solution at room temperature and the chemical shifts are relative to TMS. The assignments of these complexes were made by two-dimensional heteronuclear and homonuclear correlation experiments (coloc and hetcor).

$^1H$ NMR spectra of complexes **1**–**3** each displayed four signals in an ABCD pattern (see Table 2, Scheme 4). In these spectra the disappearance of the signal of the SH proton at $\delta$ = 4.10 ppm indicated that the arsenic complexes were formed. In solution the two $S(C_6H_4SAs)$ halves are equivalent. In all complexes the signals of the protons 2-H, 3-H and 4-H are shifted towards high frequencies with respect to those of the free neutral ligand.[4]

Table 2. $^1H$ NMR chemical shift ($\delta$ values [ppm]) for **1**–**3**.

| | Hal | 1-H | 2-H | 3-H | 4-H |
|---|---|---|---|---|---|
| **1** | Cl | 7.53 | 7.29 | 7.21 | 7.56 |
| **2** | Br | 7.53 | 7.29 | 7.21 | 7.54 |
| **3** | I | 7.48 | 7.28 | 7.21 | 7.52 |

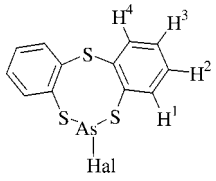


Scheme 4.

The $^{13}C$ NMR spectra of complexes **1**–**3** in $CDCl_3$ each show an important paramagnetic effect from the arsenic atom to the *ipso* carbon atom C-1a, causing chemical shift variations in the order of 8.6, 7.9 and 7.3 ppm at higher frequencies with respect to the free neutral ligand.[4] Similar shifts have been reported in dibenzostibocine analogues.[3] Another interesting feature was the observation of a small deshielding of the C-1a atom due to the increment of the electronegativity of the halogen ligand (see Table 3, Scheme 5).

Table 3. $^{13}C$ NMR chemical shift ($\delta$ values [ppm]) for **1**–**3**.

| | Hal | C-1 | C-1a | C-2 | C-3 | C-4 | C-4a |
|---|---|---|---|---|---|---|---|
| **1** | Cl | 134.7 | 143.6 | 130.0 | 127.7 | 130.9 | 131.7 |
| **2** | Br | 134.9 | 142.9 | 130.0 | 127.6 | 130.7 | 131.6 |
| **3** | I | 135.3 | 141.6 | 129.9 | 127.7 | 130.7 | 131.9 |

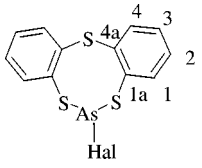


Scheme 5.

## X-ray Structures of Compounds 1–3

The structures in the crystalline solid state of all complexes were definitely determined by single-crystal X-ray diffraction analyses. The molecular structure drawings are depicted in Figure 2 and selected bond lengths, angles and torsion angles are given in Table 4. Compounds **1** and **3** crystallise with mirror symmetry in space groups $Pmn2_1$ and *Pnma*, respectively; the two $S(C_6H_4SAs)$ halves are related by a mirror plane containing the S2–As–Hal plane.

 © 2006 Wiley-VCH Verlag GmbH & Co. KGaA, Weinheim 

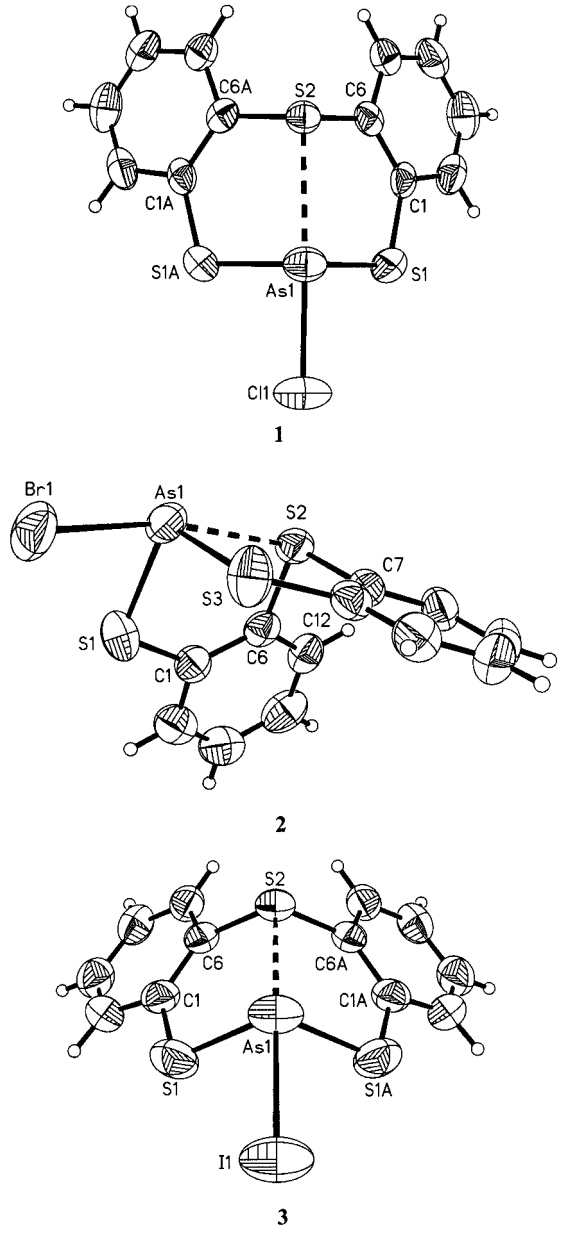


Figure 2. ORTEP diagrams of $S(C_6H_4S)_2AsCl$ (**1**), $S(C_6H_4S)_2AsBr$ (**2**) and $S(C_6H_4S)_2AsI$ (**3**) (50% probability ellipsoids).

In all complexes **1**, **2** and **3** the As–S distances are in good agreement with the covalent radii sum [$\Sigma r_{cov}$(As,S) = 2.22 Å][7] and with those reported in other heterocycles with arsenic–sulfur bonds.[8–19] The As–Hal distances (Hal = Cl, Br, I) are 5–7% longer than the corresponding covalent radii sum [($\Sigma r_{cov}$(As,Cl) = 2.19 Å; $\Sigma r_{cov}$(As,Br) = 2.34 Å; $\Sigma r_{cov}$(As,I) = 2.53 Å][5] and are similar to other distances in several heterocycles containing As–Hal bonds.[1,2,8,9,11,16,20,21] The angles around the arsenic atom can be divided in two sets. The larger angles are the endocyclic S–As–S ones, the largest found in the iodo complex [102.84(11), 103.22(9) and 104.30(7)° in **1**, **2** and **3**, respectively]. On the other hand, the angles involving the halogen atom are on average substantially smaller [87.00(8), 87.71(6) and 87.70(3)° in **1**, **2** and **3**, respectively]. At first glance, the local geometry of the tricoordinate arsenic atom could be described as pyramidal.

Table 4. Selected bond lengths [Å], angles and torsion angles [°] of $S(C_6H_4S)_2AsHal$.

| | **1** | **2** | **3** |
|---|---|---|---|
| Hal | Cl | Br | I |
| S2→As | 2.705(3) | 2.698(2) | 2.740(1) |
| As–S1 | 2.268(2) | 2.291(2) | 2.283(1) |
| As–S3 | – | 2.268(3) | – |
| As–Hal | 2.296(2) | 2.482(1) | 2.692(1) |
| S2–C6 | 1.789(6) | 1.801(8) | 1.786(4) |
| S2–C7 | – | 1.794(7) | – |
| S2→As–Hal | 166.4(1) | 168.36(6) | 166.96(3) |
| S1–As–Hal | 87.00(8) | 87.30(6) | 87.70(3) |
| S3–As–Hal | – | 88.12(6) | – |
| S1–As–S2 | 84.55(6) | 84.84(7) | 84.31(3) |
| S1–As–S1A | 102.8(1) | – | 104.30(7) |
| S1–As–S3 | – | 103.22(9) | – |
| C6–S2–C6a | 102.7(4) | – | 103.0(2) |
| C6–S2–C7 | – | 101.8(3) | – |
| C1–C6–S2–C6A | –104.3(5) | – | –104.7(3) |
| C1–S1–As–S1A | 85.8(2) | – | –84.7(1) |
| C1–C6–S2–C7 | – | 100.1(6) | – |
| C12–C7–S2–C6 | – | –102.9(7) | – |
| C1–S1–As–S3 | – | –83.9(3) | – |
| C12–S3–As–S1 | – | 83.4(3) | – |

In addition to the covalent bonds of the arsenic atom, a transannular interaction S2→As1 within the eight-membered rings was observed (see Figure 2). The S2→As1 bond lengths in **1**, **2** and **3** are 2.705(3), 2.698(2) and 2.740(1) Å, respectively, which are 22, 21 and 24% longer than the covalent radii sum of As and S but significantly shorter than the van der Waals radii sum [$\Sigma r_{vdW}$(As,S) = 3.65 Å],[7] prompting us to propose the existence of a secondary bonding.[22] These S2→As1 distances in **1**, **2** and **3** are significantly longer than those reported for the two crystallographic different cations in $[S(CH_2CH_2S)_2As][GaCl_4]$[2] [2.347(10) and 2.391(9) Å] and are similar to those reported for $S(CH_2CH_2S)_2AsCl$[9] [2.719(3) Å], $S(CH_2CH_2S)_2AsBr$[1] [2.70 Å], $S(CH_2CH_2S)_2AsI$[1] [2.77 Å], $[AsCl_3(9)aneS_3]$[20] [2.715(3) Å], $[AsBr_3\{MeS(CH_2)_2SMe\}]$[20] [2.725(3) Å] and $[AsI_3\{MeS(CH_2)_2SMe\}]$[20] [2.697(2) Å] for neutral tetra- and hexacoordinate arsenic complexes, but significantly shorter than those reported for $[AsCl_3(14)aneS_4]$[20] [2.8709(9) and 2.9655(9) Å] $[AsBr_3\{MeS(CH_2)_2SMe\}]$[20] [2.876(3) Å], $[AsI_3\{MeS(CH_2)_2SMe\}]$[20] [2.792(2) Å], $[S(CH_2CH_2S)_2AsS_2CN(CH_2CH)_2]$[1] [3.170(2) and 3.113(2) Å], $S(CH_2CH_2S)_2AsS_2CNEt_2$[12] [3.172(2) Å], $S(CH_2CH_2S)_2AsS_2PPh_2$[10] [2.881(4) Å], $S(CH_2CH_2S)_2AsS_2P(OMe)_2$[11] [2.911(1) Å] and $S(CH_2CH_2S)_2AsS_2P[OCH(Me)]_2CH_2$[1] [2.942(11) Å]. In the title compounds it can be clearly seen that the transannular interaction (S2→As1) decreases in the order Br > Cl > I with the shortest distance in the bromo compound. A similar phenomenon has been observed in the arsocanes.[1]

If the transannular interaction S→As is taken into account, the geometry of the coordination sphere of the arsenic atom can be described as pseudo-trigonal-bipyramidal, where the halogen and thioether-like sulfur atoms are in

 © 2006 Wiley-VCH Verlag GmbH & Co. KGaA, Weinheim 

Table 5. Comparison of S→As–Hal geometrical bond parameters, bond lengths [Å], bond angles [°], and % TBP and BO in **1**–**3** complexes.

| | Hal | S→As | S→As–Hal | % TBP | $\Delta d$[a] | BO[b] S→As |
|---|---|---|---|---|---|---|
| **1** | Cl | 2.705(3) | 166.4(1) | 66.1 | 0.485 | 0.207 |
| **2** | Br | 2.698(2) | 168.36(6) | 66.6 | 0.478 | 0.212 |
| **3** | I | 2.740(1) | 166.96(3) | 63.7 | 0.520 | 0.185 |

[a] Bond widening, $\Delta d = (d_{exp} - \Sigma r_{cov})$ according to standard bond lengths $d$(As,S) = 2.22 Å.[7] [b] Mode of calculation BO = $10^{-(1.41 \cdot \Delta d)}$.[26–28]

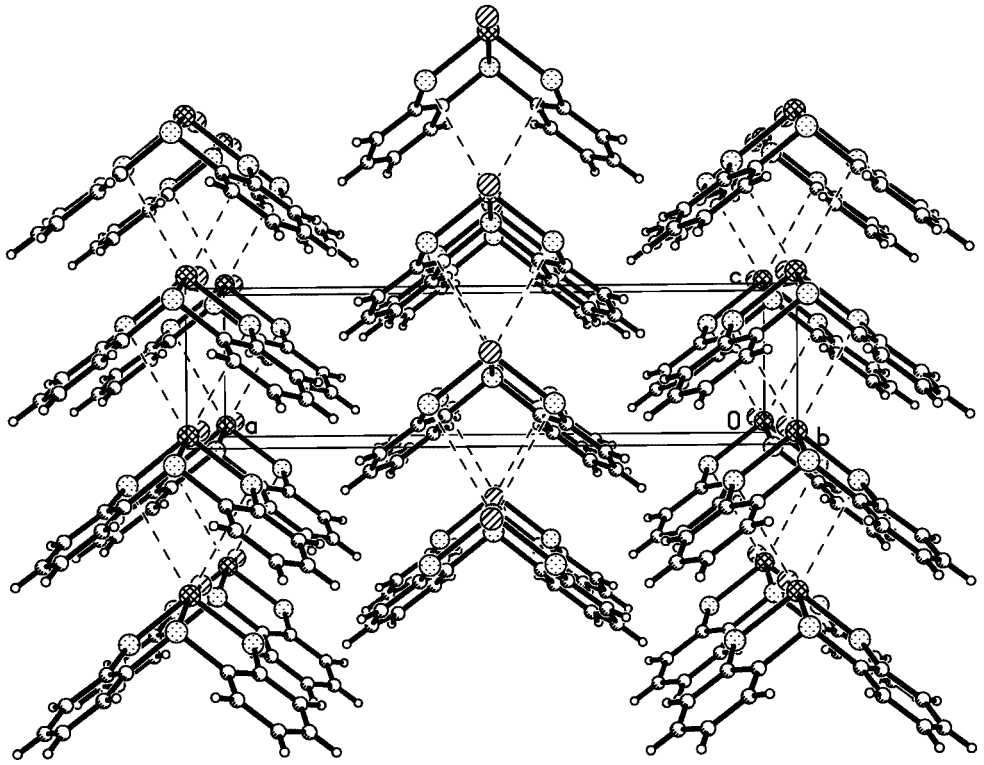


Figure 3. View of the As···S intermolecular interactions in the crystal structure of **1**.

axial positions; meanwhile the equatorial positions are occupied by the two thiolate-like sulfur atoms and the stereochemically active lone pair of the arsenic(III) atom.

The influence of the S→As interaction on the local geometry of the arsenic atom from pyramidal to trigonal-bipyramidal (TBP) can be evaluated. In this regard, we used the method of Holmes based upon donor–acceptor atom bond length.[23–25] Likewise, in order to establish the magnitude of the interaction, we calculated the Pauling-type bond order (BO) for all compounds.[26–28] The results are presented in Table 5. The displacement at geometry and bond order are related to bond lengths.

The percentages of TBP in the title compounds are slightly smaller than those reported for the antimony analogues, in spite of the smaller angles S→As–Hal to the ideal linear *trans* angle in comparison with the same S→Sb–Hal data. With regard to the BO, these values are relatively smaller than those observed for the trithiarsocanes $S(CH_2CH_2S)_2AsHal$ (Hal = Cl, Br, I) despite the apparent rigidity of the dibenzoarsocine system, and are also smaller than those calculated for the $S(C_6H_4S)_2SbHal$ analogues (0.308, 0.287 and 0.274 for Hal = I, Br and Cl, respectively).

The transannular interaction also influences the eight-membered ring conformation, which can be described as boat–boat ($C_s$ symmetry).[29] This conformation was also found in the iodo–antimony analogue with the shortest transannular interaction for that series and the arsenium cation $[S(CH_2CH_2S)_2As]^+$, which displays the largest BO in the series of arsocanes.

In the crystal the packing is mainly due to As···S intermolecular weak interactions, as is shown in Figure 3 for the chloro compound. These As···S distances are 3.602(2), 3.595(3)–3.662(3) and 3.711(2) Å for **1**, **2** and **3**, respectively; the increase in these distances can be ascribed to the increasing halogen atom sizes.

## Conclusions

In order to gain a better insight into the nature of the D→A interactions and their relation to the geometrical features in the dibenzometallocine systems containing heavier p-block elements, $S(C_6H_4S)_2AsHal$ compounds **1**–**3** have been synthesised and structurally fully characterised. All

 © 2006 Wiley-VCH Verlag GmbH & Co. KGaA, Weinheim 

compounds exhibit a pseudo-bipyramidal-trigonal local geometry of the arsenic atom with intramolecular weak As···S interactions in the crystal structure.

The title compounds exhibit a relatively strong S→As transannular interaction, where the distances are 21–23% longer than the covalent radii sum. All compounds have shown relatively high TBP displacement values, with Pauling-type bond orders similar to the more flexible arsocane systems. However, these BO values are smaller than those calculated for the antimony analogues, suggesting a much poorer Lewis acidity of $As^{III}$ in comparison to the heavier antimony atom.

## Experimental Section

**General Methods:** Unless noted otherwise, all reactions and operations were carried out under argon at room temperature with use of standard Schlenk techniques. Solvents were dried and distilled before use. Melting points were determined with a Melt-Temp II instrument and are uncorrected. Spectra were recorded with the following instruments. Mass spectra: EI, 70 eV, Hewlett Packard MS-598 mass spectrometer. Elemental analysis: Perkin–Elmer Series II CHNS/O Analyzer. IR spectra: 4000–400 $cm^{-1}$ range, Perkin–Elmer System 2000 FTIR spectrometer, as KBr pellets and 400–200 $cm^{-1}$ range, Bruker Tensor 27 spectrometer, as CsI pellets. Raman spectra: In the solid state, 4000–100 $cm^{-1}$ range, Perkin–Elmer Spectrum GX NIR FT-RAMAN spectrometer with 10–280 mW laser power and 4 $cm^{-1}$ resolution. NMR: Jeol Eclipse 400 spectrometer, residual protio-solvent signal used as reference for $^1H$ NMR spectra; $^{13}C\{^1H\}$ NMR spectra referenced through the solvent peaks; chemical shifts quoted on the $\delta$ scale (downfield shifts positive) relative to tetramethylsilane ($^1H$, $^{13}C\{^1H\}$); spectra recorded at 25 °C; $^1H$, 399.78 MHz; $^{13}C\{^1H\}$, 100.53 MHz. $AsCl_3$, KBr, HBr and KI were obtained commercially and used as received. $S(C_6H_4SH)_2$ was prepared as reported.[4]

**$S(C_6H_4S)_2AsCl$ (1):** $AsCl_3$ (1.38 g, 7.55 mmol) was added to a solution containing $S(C_6H_6SH)_2$ (1.76 g, 7.59 mmol) in benzene (25 mL). The yellow solution was stirred for 30 min, during which the colour changed to green, and then was refluxed for 24 h. The solution was cooled to room temperature and dried by means of a column of Celite and $Na_2SO_4$. Slow concentration of the benzene solution afforded colourless crystals of **1**, which were washed with hexanes (40 mL) and filtered by suction. Yield: 2.18 g (80%). M.p. 124–126 °C. MS (EI): *m*/*z* (%) = 358 (30) [$M^{\cdot+}$], 323 (70) [$M^{\cdot+}$ – Cl], 248 (10) [$S(C_6H_4S)_2^{\cdot+}$], 216 (100, base peak) [$S(C_6H_4S)^{\cdot+}$]. $C_{12}H_8AsClS_3$ (358.76): calcd. C 40.17, H 2.25; found C 40.29, H 2.28. $^1H$ NMR ($CDCl_3$): $\delta$ = 7.21 (ddd, $^3J_{3\text{-H},2\text{-H}} = {}^3J_{3\text{-H},4\text{-H}}$ = 7.68 Hz, $^4J_{3\text{-H},1\text{-H}}$ = 1.48 Hz, 2 H, 3-H), 7.29 (ddd, $^3J_{2\text{-H},1\text{-H}} = {}^3J_{2\text{-H},3\text{-H}}$ = 7.68 Hz, $^4J_{2\text{-H},4\text{-H}}$ = 1.48 Hz, 2 H, 2-H), 7.53 (dd, $^3J_{1\text{-H},2\text{-H}}$ = 7.68 Hz, $^4J_{1\text{-H},3\text{-H}}$ = 1.48 Hz, 2 H, 1-H), 7.56 (dd, $^3J_{4\text{-H},3\text{-H}}$ = 7.68 Hz, $^4J_{4\text{-H},2\text{-H}}$ = 1.48 Hz, 2 H, 4-H) ppm. $^{13}C\{^1H\}$ NMR ($CDCl_3$): $\delta$ = 127.7, 130.0, 130.9, 131.7, 134.7, 143.6 ppm. IR (KBr): $\tilde{\nu}$ = 3049, 1567, 1447, 1417, 1255, 1032, 732 $cm^{-1}$.

**$S(C_6H_4S)_2AsBr$ (2):** $S(C_6H_4S)_2AsCl$ (**1**, 200 mg, 0.56 mmol), KBr (400 mg, 3.32 mmol) and HBr (48%, 4 mL) were suspended in benzene (25 mL) and the mixture was refluxed for 24 h. The water was removed from the resulting colourless solution by means of a Dean–Stark trap. The yellow solution obtained was dried by means of a column of Celite and $Na_2SO_4$. Slow concentration of the benzene solution afforded colourless crystals of **2**, which were washed with hexanes (40 mL) and filtered by suction. Yield: 160 mg (71%). M.p. 138–140 °C. MS (EI): *m*/*z* (%) = 402 (7) [$M^{\cdot+}$], 323 (100, base peak) [$M^{\cdot+}$ – Br], 248 (20) [$S(C_6H_4S)_2^{\cdot+}$], 215 (30) [$S(C_6H_4S)^{\cdot+}$ – 1], 184. $C_{12}H_8AsBrS_3$ (403.22): calcd. C 35.74, H 2.00; found C 36.14, H 2.06. $^1H$ NMR ($CDCl_3$): $\delta$ = 7.21 (ddd, $^3J_{3\text{-H},2\text{-H}} = {}^3J_{3\text{-H},4\text{-H}}$ = 7.50 Hz, $^4J_{3\text{-H},1\text{-H}}$ = 1.48 Hz, 2 H, 3-H), 7.29 (ddd, $^3J_{2\text{-H},1\text{-H}} = {}^3J_{2\text{-H},3\text{-H}}$ = 7.50 Hz, $^4J_{2\text{-H},4\text{-H}}$ = 1.48 Hz, 2 H, 2-H), 7.53 (dd, $^3J_{1\text{-H},2\text{-H}}$ = 7.50 Hz, $^4J_{1\text{-H},3\text{-H}}$ = 1.48 Hz, 2 H, 1-H), 7.54 (dd, $^3J_{4\text{-H},3\text{-H}}$ = 7.50 Hz, $^4J_{4\text{-H},2\text{-H}}$ = 1.48 Hz, 2 H, 4-H) ppm. $^{13}C\{^1H\}$ NMR ($CDCl_3$): $\delta$ = 127.6, 130.0, 130.7, 131.6, 134.9, 142.9 ppm. IR (KBr): $\tilde{\nu}$ = 3042, 1551, 1444, 1415, 1252, 1033, 741 $cm^{-1}$.

**$S(C_6H_4S)_2AsI$ (3):** $S(C_6H_4S)_2AsCl$ (**1**, 200 mg, 0.56 mmol) and KI (550 mg, 3.32 mmol) were suspended in benzene (25 mL) and the mixture was refluxed for 24 h. The yellow solution obtained was dried by means of a column of Celite and $Na_2SO_4$. Slow concentration of the benzene solution afforded pale yellow crystals of **3**,

Table 6. Crystallographic data for compounds **1**–**3**.

| Compound | **1** | **2** | **3** |
|---|---|---|---|
| Empirical formula | $C_{12}H_8AsClS_3$ | $C_{12}H_8AsBrS_3$ | $C_{12}H_8AsIS_3$ |
| $M_r$ [g/mol] | 358.73 | 403.19 | 450.18 |
| Crystal size [mm] | 0.60 × 0.09 × 0.09 | 0.50 × 0.05 × 0.04 | 0.17 × 0.13 × 0.07 |
| Crystal system | orthorhombic | monoclinic | orthorhombic |
| Space group | *Pmn*$2_1$ | *P*$2_1$/*c* | *Pnma* |
| $\rho_{calcd.}$ [Mg/$m^3$] | 1.778 | 1.987 | 2.135 |
| *Z* | 2 | 4 | 4 |
| *a* [Å] | 17.306(5) | 4.5694(10) | 19.062(2) |
| *b* [Å] | 8.533(2) | 17.148(4) | 15.8609(17) |
| *c* [Å] | 4.5381(12) | 17.218(4) | 4.6332(5) |
| $\beta$ [°] | 90 | 92.167(6) | 90 |
| *V* [$Å^3$] | 670.1(3) | 1348.1(5) | 1400.8(3) |
| $\mu$ [$mm^{-1}$] | 3.175 | 5.922 | 5.051 |
| *F*(000) | 356 | 784 | 856 |
| Gof | 0.891 | 0.879 | 1.041 |
| Absorption correction | SADABS | SADABS | SADABS |
| Reflections collected | 4346 | 8046 | 16873 |
| Unique reflections, $R_{int}$ | 1310, 0.0752 | 2362, 0.0642 | 1570, 0.0509 |
| $R_1$, $wR_2$ [$I > 2\sigma(I)$] | 0.0470, 0.0854 | 0.0382, 0.0863 | 0.0347, 0.0868 |
| $R_1$, $wR_2$ (all data) | 0.0734, 0.0914 | 0.0875, 0.1236 | 0.0518, 0.0929 |
| Large residuals [e/$Å^3$] | 0.696/–0.345 | 0.538/–0.527 | 0.466/–0.598 |

 © 2006 Wiley-VCH Verlag GmbH & Co. KGaA, Weinheim 

which were washed with hexanes (40 mL) and filtered by suction. Yield: 250 mg (80%). M.p. 153–156 °C. MS (EI) *m*/*z* (%) = 323 (100, base peak) [$M^{+}$ – I], 248 (33) [$S(C_6H_4S)_2^{\cdot+}$], 215 (40) [$S(C_6H_4S)^{\cdot+}$ – 1]. $C_{12}H_8AsIS_3$ (450.22): calcd. C 32.01, H 1.79; found C 31.29, H 1.86. $^1$H NMR ($CDCl_3$): $\delta$ = 7.21 (ddd, $^3J_{3\text{-H},2\text{-H}} = {}^3J_{3\text{-H},4\text{-H}}$ = 7.48 Hz, $^4J_{3\text{-H},1\text{-H}}$ = 1.46 Hz, 2 H, 3-H), 7.28 (ddd, $^3J_{2\text{-H},1\text{-H}} = {}^3J_{2\text{-H},3\text{-H}}$ = 7.48 Hz, $^4J_{2\text{-H},4\text{-H}}$ = 1.46 Hz, 2 H, 2-H), 7.48 (dd, $^3J_{1\text{-H},2\text{-H}}$ = 7.48 Hz, $^4J_{1\text{-H},3\text{-H}}$ = 1.46 Hz, 2 H, 1-H), 7.52 (dd, $^3J_{4\text{-H},3\text{-H}}$ = 7.48 Hz, $^4J_{4\text{-H},2\text{-H}}$ = 1.46 Hz, 2 H, 4-H) ppm. $^{13}C\{^1H\}$ NMR ($CDCl_3$): $\delta$ = 127.7, 129.9, 130.7, 131.9, 135.3, 141.6 ppm. IR (KBr): $\tilde{\nu}$ = 3044, 1550, 1445, 1414, 1251, 1032, 751 $cm^{-1}$.

**X-ray Crystallography:** Suitable single crystals of all complexes were grown by slow concentration of benzene solutions. X-ray diffraction data on **1**–**3** were collected at room temperature with a CCD Smart 6000 diffractometer through the use of Mo-$K_\alpha$ radiation ($\lambda$ = 0.71073 Å, graphite monochromator). The data were integrated, scaled, sorted and averaged using the SMART software package. The structures were solved by direct methods, using SHELXTL NT Version 5.10 and refined by full-matrix least squares against $F^2$.[30] An empirical absorption correction based on the multiple measurement of equivalent reflections was applied by using the program SADABS.[31] The displacement parameters of non-hydrogen atoms were refined anisotropically. The positions of the hydrogen atoms were kept fixed with a common isotropic displacement parameter. Selected crystallographic data are given in Table 6. CCDC-600909 (**1**), -600910 (**2**) and -600911 (**3**) contain the supplementary crystallographic data for this paper. These data can be obtained free of charge from The Cambridge Crystallographic Data Centre via www.ccdc.cam.ac.uk/data_request/cif.

## Acknowledgments

J. G. A. R. fully acknowledges the financial support of the CONACyT (Project 44009) for these investigations and S. G. M. fully acknowledges a scholarship for supporting his studies. We wish to thank Dra. Verónica García Montalvo (UNAM) for the recording the IR and EI mass spectra and Mrs. Yolanda Marmolejo (UAEH) for the Raman spectra.

[1] For a review of metallocanes, see: R. Cea-Olivares, V. García Montalvo, M. M. Moya-Cabrera, *Coord. Chem. Rev.* **2005**, *249*, 859–872.
[2] N. Burford, T. M. Parks, P. K. Bakshi, T. S. Cameron, *Angew. Chem. Int. Ed. Engl.* **1994**, *33*, 1267–1268.
[3] For a brief review of several complexes, see: J. G. Alvarado-Rodríguez, N. Andrade-López, S. González Montiel, G. Merino, A. Vela, *Eur. J. Inorg. Chem.* **2003**, 3554–3562.
[4] D. Sellmann, D. Haussinger, *Eur. J. Inorg. Chem.* **1999**, 1715–1725.
[5] G. Sócrates, *Infrared and Raman Characteristic Group Frequencies – Tables and Charts*, 3rd ed., John Wiley and Sons, New York, USA, **2001**, p. 304.
[6] A. Zickgraf, E. Braeu, M. Draeger, *Spectrochim. Acta* **1998**, *54A*, 85–90.
[7] W. W. Porterfield, *Inorganic Chemistry: A Unified Approach*, 2nd ed., Academic Press, Inc., San Diego, California, **1993**, p. 214.
[8] M. Draeger, *Z. Anorg. Allg. Chem.* **1975**, *411*, 79–89.
[9] M. Draeger, *Chem. Ber.* **1974**, *107*, 2601–2611.
[10] M. A. Muñoz-Hernández, R. Cea-Olivares, G. Espinosa-Pérez, S. Hernández-Ortega, *J. Chem. Soc., Dalton Trans.* **1996**, 4135–4141.
[11] M.-A. Muñoz-Hernández, R. Cea-Olivares, S. Hernández-Ortega, *Inorg. Chim. Acta* **1996**, *253*, 31–37.
[12] R. Cea-Olivares, M. R. Estrada, G. Espinosa-Pérez, I. Haiduc, P. García y García, M. López-Cardoso, M. López-Vaca, *Main Group Chem.* **1995**, 159–164.
[13] N. Burford, T. M. Parks, B. W. Royan, B. Borecka, T. S. Cameron, J. F. Richardson, E. J. Gabe, R. Hynes, *J. Am. Chem. Soc.* **1992**, *114*, 8147–8153.
[14] A. W. Cordes, P. D. Gwinup, M. C. Malmstrom, *Inorg. Chem.* **1972**, *11*, 836–838.
[15] A. J. Di Maio, A. L. Rheingold, *Inorg. Chem.* **1990**, *29*, 798–804.
[16] R. Cea-Olivares, R. A. Toscano, M. López, P. García y García, *Heteroat. Chem.* **1993**, *4*, 313–317.
[17] O. M. Kekia, A. L. Rheingold, *Organometallics* **1998**, *17*, 726–730.
[18] A. T. Mohammed, V. Krug, U. Muller, *Z. Anorg. Allg. Chem.* **1988**, *557*, 91–97.
[19] J. M. Kisenyi, G. R. Willey, M. G. B. Drew, S. O. Wandiga, *J. Chem. Soc. Dalton Trans.* **1985**, 69–74.
[20] N. J. Hill, W. Levason, G. Reid, *Inorg. Chem.* **2002**, *41*, 2070–2076.
[21] A. J. Barton, N. J. Hill, W. Levason, G. Reid, *J. Am. Chem. Soc.* **2001**, *123*, 11801–11802.
[22] N. W. Alcock, *Adv. Inorg. Chem. Radiochem.* **1972**, *15*, 1–50.
[23] A. Chandrasekaran, P. Sood, R. O. Day, R. R. Holmes, *Inorg. Chem.* **1999**, *38*, 3369–3376.
[24] N. V. Timosheva, A. Chandrasekaran, R. O. Day, R. R. Holmes, *Inorg. Chem.* **1998**, *37*, 3862–3867.
[25] D. J. Sherlock, A. Chandrasekaran, R. O. Day, R. R. Holmes, *Inorg. Chem.* **1997**, *36*, 5082–5089.
[26] L. Pauling, *The Nature of the Chemical Bond*, 3rd ed., Cornell University Press, Ithaca, NY, **1960**, p. 239.
[27] U. Kolb, M. Beuter, M. Gerner, M. Draeger, *Organometallics* **1994**, *13*, 4413–4425.
[28] D. Britton, J. D. Dunitz, *J. Am. Chem. Soc.* **1981**, *103*, 2971–2979.
[29] T. Thompson, S. D. Pastor, G. Rihs, *Inorg. Chem.* **1999**, *38*, 4163–4467.
[30] *SHEXTL 5.10*, Bruker AXS, Inc., Madison, WI, USA, **1998**.
[31] *SADABS: Area-Detector Absorption Correction*, Siemens Industrial Automation, Inc., Madison, WI, **1996**.

Received: March 13, 2006
Published Online: August 1, 2006

 © 2006 Wiley-VCH Verlag GmbH & Co. KGaA, Weinheim 

DOI: 10.1002/ejic.200600347

# Product Diversity in the Reaction of [(norbornadiene){CpP(*i*Pr)$_2$}Rh] with Alkyl Iodides

**Esteban Ortega,[a] Nina Kleigrewe,[a] Gerald Kehr,[a] Gerhard Erker,*[a] and Roland Fröhlich[a]**

**Keywords:** Rhodium / Phosphonium salts / Dimetallic complexes / Cyclopentadienyl ligands / Phosphorus ylides

The reagents [(CpPR$_2$)Li] [R = *i*Pr (**2b**), cyclohexyl (**2c**)] react with [(nbd)RhCl] (nbd = norbornadiene) dimer [(**1a**)$_2$] to yield the respective mononuclear complexes [(nbd)Rh(CpPR$_2$)] (**3b**,**c**). Subsequent treatment of **3b** with a large excess of MeI led to the formation of the stable organometallic phosphonium salt [(nbd)Rh{CpP(*i*Pr)$_2$Me}]I (**4b**). The analogous reaction of **3b** with the slightly more bulky EtI or *n*PrI resulted in the formation of the dinuclear [μ-CpP(*i*Pr)$_2$]-bridged dirhodium complex [(nbd)Rh{CpP(*i*Pr)$_2$}Rh(nbd)I] (**5b**) and the corresponding ylides C$_5$H$_4$P(*i*Pr)$_2$R$^1$ [R$^1$ = Et (**6b**), *n*Pr (**6c**)]. The rhodium complexes **3b**, **4a** and **5b** were characterised by X-ray crystal-structure analyses.
(© Wiley-VCH Verlag GmbH & Co. KGaA, 69451 Weinheim, Germany, 2006)

## Introduction

[CpRh(L)$_n$] complexes have been of increasing interest lately due to some remarkable reactivities, for example their ability to catalyse selective C–H activation processes in conjunction with R$_2$B–BR$_2$ reagents.[1] It may be of interest to use Rh cyclopentadienides that bear functional groups at their Cp rings in order to potentially facilitate such currently high activation energy C–H cleavage reactions by precoordination of suitable substrates in a second coordination sphere around the catalytically active metal centre. For that reason, we have prepared a couple of (dialkylphosphanyl)-cyclopentadienyl-containing rhodium(I) complexes[2] and have encountered some unexpected features with regard to their reactions with alkyl iodides. This will be described and discussed in this article.

## Results and Discussion

### Synthetic Developments

The (diphenylphosphanyl)cyclopentadienide anion was prepared by treatment of CpLi with ClPPh$_2$ followed by deprotonation with *n*-butyllithium/hexane in toluene.[3] When we wanted to attach this simple functionalised ligand to an Rh(diene) framework, we encountered the same difficulties that had previously been observed by Poilblanc et al.[2] For example, treatment of the (nbd)RhCl (nbd = norbornadiene) dimer [(nbd)RhCl]$_2$ [(**1a**)$_2$][4] with [(CpPPh$_2$)Li] (**2a**) always resulted in the formation of a mixture of the desired mononuclear complex **3a** and its dinuclear adduct **5a** containing an unreacted monomeric (nbd)RhCl unit from the starting material (**1a**)$_2$. These two products could not be separated with sufficient ease, nor were we able to convert **5a** back to the desired **3a**, for example by treatment with additional **2a** (Scheme 1).

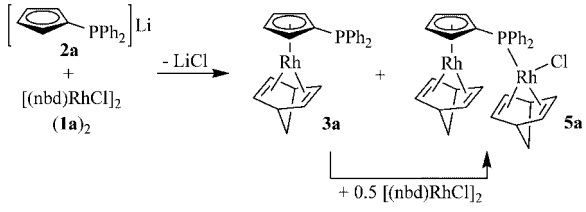


Scheme 1.

Therefore, we made a variety of changes in our synthetic scheme and slightly changed the substituents and reagents to eventually achieve a clean formation of mononuclear Rh$^I$ complexes of the desired type. The reagents [{CpP(*i*Pr)$_2$}Li] (**2b**) and [(CpPCy$_2$)Li] (**2c**; Cy = cyclohexyl) were prepared as described in the literature.[5,6] The reaction of [(nbd)-RhCl]$_2$ [(**1a**)$_2$] with **2b** was carried out in THF at room temperature. Removal of the solvent and extraction of the residue with pentane cleanly gave the mononuclear complex [(nbd)Rh{CpP(*i*Pr)$_2$}] (**3b**; 85% isolated yield). Complex **3b** was characterised by X-ray diffraction. Single crystals were obtained from pentane. The structure shows a typical disturbed trigonally planar coordination geometry around the rhodium atom made up by the pair of norbornadiene C=C double bonds [C=C(centroid)–Rh–C=C(centroid) = 70.7°] and the substituted Cp ring [Cp(centroid)–Rh–C=C(centroid) = 144.4° and 144.9°]. The norbornadiene ligand is almost symmetrically bonded to the metal atom through its

[a] Organisch-Chemisches Institut der Universität Münster, Corrensstrasse 40, 48149 Münster, Germany
E-mail: erker@uni-muenster.de

 © 2006 Wiley-VCH Verlag GmbH & Co. KGaA, Weinheim 

*endo* face [Rh–C14/C15 = 2.119(2), 2.127(2) Å; Rh–C18/C17 = 2.127(2), 2.135(2) Å]. The diisopropylphosphanyl-substituted Cp ring is rather uniformly $\eta^5$-coordinated to the rhodium atom, with Rh–C(Cp) distances being in a narrow range between 2.214(2) and 2.290(2) Å.[7] In the crystal, a metal complex conformation is found that has the bulky P(*i*Pr)$_2$ substituent rotated toward one side of the coordinated nbd ligand, with the C1–P vector almost bisecting the C15–Rh–C17 angle in the respective projection. The phosphorus centre in complex **3b** is three-coordinate and prochiral [C1–P–C7 = 103.1(1)°; C1–P–C6 = 99.7(1)°; C7–P–C6 = 101.9(1)°].

In solution, rotation around the Rh–Cp[P] vector is fast. Consequently, complex **3b** shows only one norbornene olefinic $^1$H NMR multiplet ($\delta$ = 3.24 ppm) representing four protons plus a signal for the two bridgehead hydrogen atoms ($\delta$ = 3.22 ppm). The methyl groups of the isopropyl substituents at the prochiral phosphorus atom are pairwise diastereotopic, as expected ($^{13}$C: $\delta$ = 19.7/20.4 ppm). The $^1$H NMR signals of the pairs of Cp hydrogen atoms are observed at $\delta$ = 4.93 (2 H) and 5.20 (2 H) ppm. The corresponding $^{31}$P NMR resonance of **3b** occurs at $\delta$ = –3.2 ppm.

The reaction of dimer (**1a**)$_2$ with [(CpPCy$_2$)Li] (**2c**) took place analogously. The product [(nbd)Rh(CpPCy$_2$)] (**3c**) was isolated in 68% yield. It was characterised spectroscopically and by C,H elemental analysis (for details see the Experimental Section and Scheme 2).

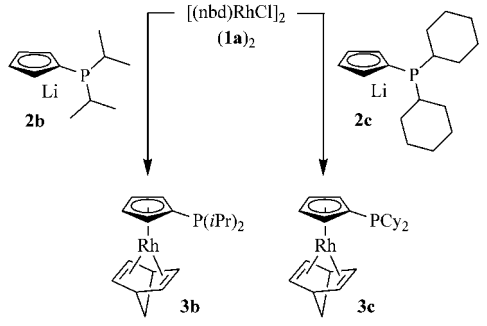


Scheme 2.

## Reactions with Alkyl Iodides

We expected that the CpPR$_2$ subunit in complex **3b**, for example, should show a typical reactivity pattern of a phosphorus nucleophile. Treatment with suitable alkyl electrophiles might, therefore, yield the respective quaternized phosphonium salts at the organometallic backbone. This was actually observed when we treated complex **3b** with methyl iodide. Treatment of **3b** with a large excess of MeI in pentane rapidly led to the formation of the organometallic phosphonium salt **4a** (Scheme 3), which precipitated from the solution and was obtained as a slightly beige-coloured solid in 92% yield.[8] Slow diffusion of pentane vapour into a solution of **3b** in dichloromethane gave single crystals that were suitable for an X-ray crystal structure analysis. The structure of phosphonium salt **4a** is very similar to that of phosphane complex **3b** as it features the same framework structure (see Figure 1 and Table 1). This similarity even extends to the overall characteristics of the favoured conformational orientation of the Cp[P] ring system. The C1–P bond in **4a** is shorter [1.767(5) Å] than in **3b** [1.822(2) Å] and the phosphorus centre is tetracoordinate (Figure 2).

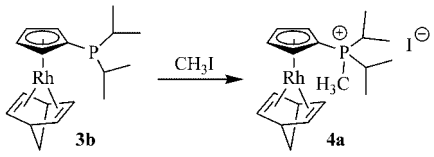


Scheme 3.

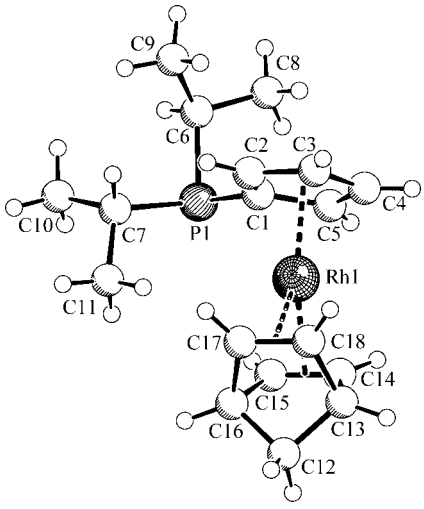


Figure 1. View of the molecular structure of [(nbd)Rh{CpP(*i*Pr)$_2$}] (**3b**).

Table 1. Comparison of selected structural parameters of complexes **3b**, **4a** and **5b**.[a]

| | **3b** | **4a** | **5b** (Rh1) | | **5b** (Rh2) |
|---|---|---|---|---|---|
| Rh–C1 | 2.290(2) | 2.276(5) | 2.291(3) | | |
| Rh–C2 | 2.281(2) | 2.256(5) | 2.216(3) | | |
| Rh–C3 | 2.252(2) | 2.268(6) | 2.256(3) | | |
| Rh–C4 | 2.261(2) | 2.249(6) | 2.256(3) | | |
| Rh–C5 | 2.214(2) | 2.291(5) | 2.248(3) | Rh2–I1 | 2.6624(4) |
| C1–P | 1.822(2) | 1.767(5) | 1.811(3) | Rh2–P1 | 2.2992(7) |
| Rh1–C14 | 2.119(2) | 2.129(6) | 2.118(3) | Rh2–C14b | 2.218(3) |
| Rh1–C15 | 2.127(2) | 2.122(5) | 2.126(3) | Rh2–C15b | 2.223(3) |
| Rh1–C17 | 2.135(2) | 2.122(5) | 2.125(3) | Rh2–C17b | 2.096(3) |
| Rh1–C18 | 2.127(2) | 2.133(5) | 2.105(3) | Rh2–C18b | 2.105(3) |
| C14–C15 | 1.409(4) | 1.396(9) | 1.404(4) | C14b-C15b | 1.361(4) |
| C17–C18 | 1.404(4) | 1.401(8) | 1.403(4) | C17b-C18b | 1.391(4) |

[a] Bond lengths [Å].

In solution, complex **4a** features a typical phosphonium-type $^{31}$P NMR chemical shift ($\delta$ = +35.1 ppm).[9,10] Again, the system is conformationally equilibrated in solution. The isopropyl methyl groups at the prochiral phosphorus atom are pairwise diastereotopic [$^{13}$C NMR: $\delta$ = 16.6/16.7 ($CH_3$), 22.8 (d, $^1J_{P,C}$ = 49.7 Hz, CH) ppm] and there is an additional $CH_3$ group bonded to the phosphorus centre [$^1$H NMR: $\delta$ = 2.24 ($^2J_{P,H}$ = 12.5 Hz) ppm; $^{13}$C NMR: $\delta$ = 4.3 ($^1J_{P,C}$ = 54.4 Hz) ppm].

 © 2006 Wiley-VCH Verlag GmbH & Co. KGaA, Weinheim 

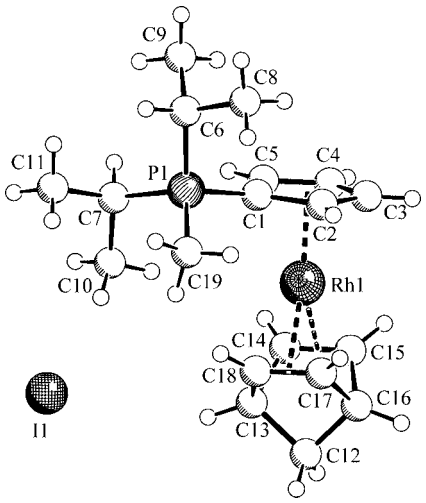


Figure 2. Molecular structure of [(nbd)Rh{CpP(*i*Pr)$_2$Me}]I (**4a**).

The reaction of complex **3b** with excess ethyl iodide under similar conditions gave a different reaction product. After removal of the volatiles in vacuo, we isolated the dinuclear [μ-CpP(*i*Pr)$_2$]-bridged dirhodium complex **5b** in good yield (86%; Scheme 4). This product was characterised spectroscopically, by C,H elemental analysis and by X-ray diffraction (single crystals were obtained from a pentane solution at –30 °C).

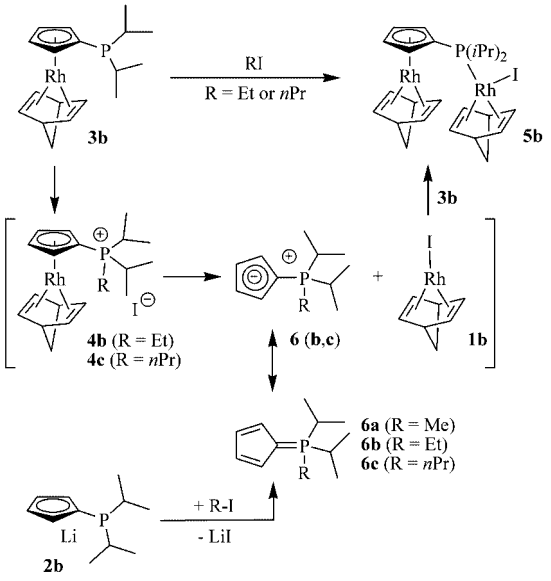


Scheme 4.

The X-ray crystal structure analysis of **5b** shows the presence of an [(nbd)Rh{CpP(*i*Pr)$_2$}] subunit that is structurally very similar to that found in **3b** or **4a** (see above and Table 1). The phosphorus atom of this unit coordinates to the Rh centre of an (nbd)RhI subunit. The norbornadiene ligand is again *endo*-coordinated through both its C=C double bonds. The rhodium centre Rh2 is distorted square-planar coordinated by this pair of C=C double bonds and P1 and I1 are *cis* to each other [Rh2–I1 = 2.6624(4), Rh2–P1 = 2.2992(7) Å; I1–Rh2–P1 = 95.76(2)°]. The resulting bond angle at the phosphorus atom (Rh2–P1–C1) is 119.24(9)° (Figure 3).

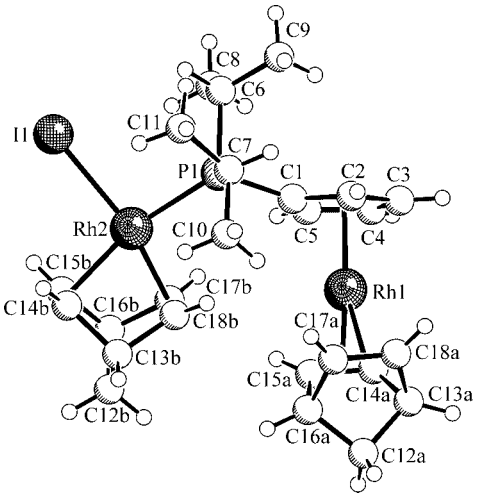


Figure 3. Molecular structure of complex **5b**.

In solution, there is again a rapid rotation around the Rh1–Cp[P] vector, resulting in the observation of a single $^1$H NMR =CH resonance [$\delta$ = 3.09 (4 H) ppm] for the nbd-1 ligand. In contrast, nbd-2, which is bonded to the distorted square planar Rh2 centre, exhibits a clearly differentiated pair of HC=CH $^1$H/$^{13}$C NMR features of the double bonds *cis* to I and *cis* to P1 [$^1$H NMR: $\delta$ = 3.83/5.36 (each 2 H) ppm; $^{13}$C NMR: $\delta$ = 51.0/78.4 ppm], respectively. Again, the isopropyl groups at the prochiral phosphorus atom are pairwise diastereotopic, as expected ($^1$H NMR: $\delta$ = 1.12/1.36 ppm; $^{13}$C NMR: $\delta$ = 19.7/20.1 ppm). The $^{31}$P NMR resonance of complex **5b** is located at $\delta$ = +40.1 ppm.

Although the complete mechanistic elucidation of the unexpected formation of the dinuclear product **5b** must await further detailed studies, we would like to propose a tentative scheme for the possible formation of this product. It may be assumed that the formation of the unexpected product **5b** might also be initiated by phosphonium salt formation. The resulting intermediates (**4b**, **4c**) seem not to be stable under the applied reaction conditions but rather undergo a nucleophilic displacement of the respective (C$_5$H$_4$)P(*i*Pr)$_2$R moiety (**6b**, **6c**) by iodide. Substitution of the Cp-phosphonium ylides **6b**, **6c** might be facilitated by their higher steric bulk as compared to the [P]-CH$_3$ derivative **6a** in **4a**. In the case of **4b** and **4c** the nucleophilic substitution reaction probably leads to the formation of the ethyl- or *n*-propyl-substituted phosphonium salts **6b** or **6c**, respectively, which must be assumed to be slightly more bulky than their methylphosphonium analogue **6a**. Apparently, the reaction in the cases **4b** and **4c**, in contrast to the more persistent **4a**, proceeds with cleavage of the Cp ligand bearing the bulky phosphonium substituent from the rhodium atom, with the possible formation of (nbd)RhI (**1b**). Under the applied reaction conditions, this monomeric species seems never to reach a high enough concentration to give rise to observable dimer formation, but is apparently

 © 2006 Wiley-VCH Verlag GmbH & Co. KGaA, Weinheim 

efficiently trapped by the neutral starting material **3b** to yield the $CpPR_2$-bridged dinuclear product **5b**.[5,11] We have only observed this unexpected reaction pathway in the case of treatment of **3b** with ethyl iodide or *n*-propyl iodide but so far not with methyl iodide, which only gave the organometallic phosphonium salt **4a** that is stable under the applied reaction conditions.

In order to further support the proposed reaction course, we treated **2b** with methyl iodide, ethyl iodide and *n*-propyl iodide. The corresponding trialkyl(Cp)phosphonium ylide products (**6a**–**c**) were isolated as pale-yellow solids and characterised spectroscopically. The resulting ylide **6a** features a $^{31}P$ NMR signal at $\delta$ = 24.7 ppm and a $^{13}C$ NMR resonance for the adjacent C1 ring carbon atom at $\delta$ = 74.0 ppm with a very characteristic $^1J_{P,C}$ coupling constant of 104 Hz [C=P(*i*Pr)$_2$Me].[12,13] The ethyl-substituted CpP(*i*Pr)$_2$Et ylide **6b** shows an analogous $^{13}C$ NMR feature at $\delta$ = 74.3 ppm ($^1J_{P,C}$ = 101 Hz). This signal was detected in the crude reaction mixture obtained by treatment of complex **2b** with ethyl iodide to eventually yield **5b**.

## Conclusions

The reaction of [(nbd){CpP(*i*Pr)$_2$}Rh] (**3b**) with simple alkyl iodides shows some remarkably different outcomes depending on the bulk of the alkyl group of the RI reagent used. The reaction with methyl iodide leads to the formation of a stable phosphonium salt **4a**, whereas the analogous reaction of **3b** with either EtI or *n*PrI rapidly results in the formation of the dinuclear product **5b**. The experimental characteristics of these reactions led us to assume that in the latter cases the corresponding phosphonium salts might also have been formed initially. However, these slightly more bulky systems seem to be unstable with regard to CpP(*i*Pr)$_2$R ylide dissociation,[14] a pathway that eventually leads to the formation of **5b**. For the less bulky [(nbd){CpP(*i*Pr)$_2$Me}Rh]I system this pathway seems not to be readily available under our typical reaction conditions. This specific alkyl group dependent behaviour makes the **3b** + RI reaction system a remarkable example of an observed borderline behaviour along a threshold determined by rather subtle differences in steric bulk.

## Experimental Section

**General:** All reactions involving air- or moisture-sensitive compounds were carried out under an inert gas using Schlenk-type glassware or in a glove box. Solvents were dried and distilled prior to use. The following instruments were used for physical characterisation of the compounds: Melting points: DSC 2010 TA-instruments; elemental analyses: Foss-Heraeus CHNO-Rapid; MS: Micromass Quattro LC-Z electrospray mass spectrometer; NMR: Bruker AC 200 P ($^1H$: 200 MHz; $^{13}C$: 50 MHz), ARX 400 ($^1H$: 400 MHz; $^{13}C$: 100 MHz), Varian 500 INOVA ($^1H$: 500 MHz; $^{13}C$: 125 MHz) or Varian UNITY plus 600 ($^1H$: 600 MHz; $^{13}C$: 151 MHz). The complex [(nbd)RhCl]$_2$ (**1a**)[4] and the reagents [{CpP(*i*Pr)$_2$}Li] (**2b**)[5] and [{CpPCy$_2$}Li] (**2c**)[5] were prepared according to literature procedures.

**X-ray Crystal-Structure Determinations:** Data sets were collected with a Nonius KappaCCD diffractometer equipped with a rotating anode generator. Programs used: data collection COLLECT (Nonius B.V., **1998**), data reduction Denzo-SMN (Z. Otwinowski, W. Minor, *Methods in Enzymology* **1997**, *276*, 307–326), absorption correction SORTAV (R. H. Blessing, *Acta Crystallogr., Sect. A* **1995**, *51*, 33–37; R. H. Blessing, *J. Appl. Crystallogr.* **1997**, *30*, 421–426) and Denzo (Z. Otwinowski, D. Borek, W. Majewski, W. Minor, *Acta Crystallogr., Sect. A* **2003**, *59*, 228–234), structure solution SHELXS-97 (G. M. Sheldrick, *Acta Crystallogr., Sect. A* **1990**, *46*, 467–473), structure refinement SHELXL-97 (G. M. Sheldrick, University of Göttingen, **1997**), graphics SCHAKAL (E. Keller, University of Freiburg, **1997**). CCDC-600987 to -600989 (for **3b**, **4a** and **5b**, respectively) contain the supplementary crystallographic data for this paper. These data can be obtained free of charge from The Cambridge Crystallographic Data Centre via www.ccdc.cam.ac.uk/data_request/cif.

**Reaction of [{CpP(*i*Pr)$_2$}Li] (2b) With [(nbd)RhCl]$_2$ [(1a)$_2$]. Formation of Complex 3b:** A solution of **2b** (94 mg, 0.50 mmol) in THF (3 mL) was added to a solution of (**1a**)$_2$ (115 mg, 0.25 mmol) in THF (3 mL) at ambient temperature and the suspension was stirred at room temperature overnight. Subsequently, the solvent was removed in vacuo and the crude product was extracted through Celite with pentane (4 mL) five times. Evaporation of the solvent yielded the rhodium complex **3b** as a yellow powder (160 mg, 0.43 mmol, 85%). Crystals suitable for X-ray crystal structure analysis were obtained by slow evaporation of the solvent from a concentrated pentane solution at ambient temperature. $^1H$ NMR (500 MHz, $C_6D_6$, 298 K): $\delta$ = 0.95 (t, $J$ = 1.5 Hz, 2 H, $CH_2^{nbd}$), 1.13 (dd, $J$ = 14.6, 7.1 Hz, 6 H, Me$^{iPr}$), 1.25 (dd, $J$ = 10.8, 6.8 Hz, 6 H, Me$^{iPr}$), 1.90 (dsept, $J$ = 7.0, 0.9 Hz, 2 H, CH$^{iPr}$), 3.22 (m, 2 H, CH$^{nbd}$), 3.24 (m, 4 H, =CH$^{nbd}$), 4.93 (m, 2 H, Cp), 5.20 (m, 2 H, Cp) ppm. $^{13}C\{^1H\}$ NMR (125 MHz, $C_6D_6$, 298 K): $\delta$ = 19.7 (d, $J$ = 9.3 Hz, Me$^{iPr}$), 20.4 (d, $J$ = 17.5 Hz, Me$^{iPr}$), 23.8 (d, $J$ = 12.8 Hz, CH$^{iPr}$), 30.5 (d, $J$ = 10.5 Hz, =CH$^{nbd}$), 47.0 (d, $J$ = 2.8 Hz, CH$^{nbd}$), 57.4 (d, $J$ = 7.0 Hz, $CH_2^{nbd}$), 86.3 (m, Cp), 89.0 (m, Cp), 94.7 (Cp; detected by $^1H/^{13}C$ ghmbc experiment) ppm. $^{31}P\{^1H\}$ NMR ($C_6D_6$, 81 MHz, 298 K): $\delta$ = –3.2 (s, P*i*Pr$_2$) ppm. $C_{18}H_{26}PRh$ (376.27): calcd. C 57.45, H 6.96; found C 57.49, H 6.92.

**X-ray Crystal Structure Analysis of 3b:** $C_{18}H_{26}PRh$, $M$ = 376.27, colourless crystal 0.30 × 0.30 × 0.05 mm, $a$ = 5.875(1), $b$ = 10.749(1), $c$ = 13.870(1) Å, $\alpha$ = 104.53(1), $\beta$ = 90.22(1), $\gamma$ = 93.37(1)°, $V$ = 846.3(2) Å$^3$, $\rho_{calcd.}$ = 1.477 g cm$^{-3}$, $\mu$ = 1.093 mm$^{-1}$, empirical absorption correction ($0.735 \leq T \leq 0.947$), $Z$ = 2, triclinic, space group $P\bar{1}$ (no. 2), $\lambda$ = 0.71073 Å, $T$ = 198 K, $\omega$- and $\varphi$-scans, 8037 reflections collected ($\pm h$, $\pm k$, $\pm l$), [(sin$\theta$)/$\lambda$] = 0.67 Å$^{-1}$, 4102 independent ($R_{int}$ = 0.034) and 3745 observed reflections [$I \geq 2\sigma(I)$], 185 refined parameters, $R$ = 0.027, $wR_2$ = 0.070, max. (min.) residual electron density 0.41 (–1.06) e Å$^{-3}$, hydrogen atoms calculated and refined as riding atoms.

**Reaction of [(CpPCy$_2$)Li] (2c) with [(nbd)Rhcl]$_2$ [(1a)$_2$]. Formation of Complex 3c:** According to the procedure described for the formation of **3b**, **3c** was obtained as a yellow powder (54 mg, 0.118 mmol, 68%) from **2c** (46 mg, 0.173 mmol) in THF (2 mL) and (**1a**)$_2$ (40 mg, 0.087 mmol) in THF (1 mL). The crude product was extracted three times through Celite with pentane (2 mL). $^1H$ NMR (400 MHz, $C_6D_6$, 298 K): $\delta$ = 0.97 (m, 2 H, $CH_2^{nbd}$), 1.11–1.47 (m, 12 H, Cy), 1.65 (dm, $J$ = 11.9 Hz, 2 H, Cy), 1.78 (dm, $J$ = 11.2 Hz, 2 H, Cy), 1.85 (m, 2 H, Cy), 1.93 (dm, $J$ = 11.7 Hz, 2 H, Cy), 2.31 (dm, $J$ = 11.7 Hz, 2 H, Cy), 3.25 (m, 4 H, =CH$^{nbd}$), 3.24 (m, 2 H, CH$^{nbd}$), 4.95 (m, 2 H, Cp), 5.18 (m, 2 H, Cp) ppm. $^{13}C\{^1H\}$ NMR (100.6 MHz, $C_6D_6$, 298 K): $\delta$ = 27.0 (s, Cy), 27.6

 © 2006 Wiley-VCH Verlag GmbH & Co. KGaA, Weinheim 

(d, $J$ = 7.8 Hz, Cy), 27.8 (d, $J$ = 11.5 Hz, Cy), 30.4 (broad d, $J$ = 10.6 Hz, Cy), 30.4 (d, $J$ = 8.7 Hz, Cy), 30.6 (d, $J$ = 15.2 Hz, =CH$^{nbd}$), 34.1 (d, $J$ = 12.8 Hz, Cy), 47.1 (d, $J$ = 2.1 Hz, CH$^{nbd}$), 57.4 (d, $J$ = 6.8 Hz, CH$_2^{nbd}$), 86.5 (m, Cp), 89.3 (dd, $J$ = 14.6, $J$ = 3.3 Hz, Cp), 95.1 (dd, $J$ = 23.5, $J$ = 4.6 Hz, Cp) ppm. $^{31}$P{$^1$H} NMR (121.5 MHz, $C_6D_6$, 298 K): $\delta$ = –11.2 (s, PCy$_2$) ppm. $C_{24}H_{34}$PRh (456.39): calcd. C 63.16, H 7.51; found C 63.55, H 7.62.

**Reaction of 3b with Methyl Iodide. Formation of the Organometallic Phosphonium Salt 4a:** A large excess of methyl iodide (0.25 mL, 4.00 mmol) was added to a solution of **3b** (35 mg; 0.09 mmol) in pentane (5 mL). Precipitation occurred immediately and the tawny suspension was stirred at ambient temperature for 2 h. The supernatant was removed by filtration in air and the resulting beige filter cake was washed carefully with pentane (1 mL). Subsequently, the residue was dried in vacuo and **4a** was obtained as a brown powder (44 mg, 0.085 mmol, 92%). Crystals suitable for X-ray crystal structure analysis were obtained by slow diffusion of pentane into a concentrated solution of **4a** in dichloromethane. $^1$H NMR (500 MHz, $CDCl_3$, 298 K): $\delta$ = 1.06 (t, $J$ = 1.6 Hz, 2 H, CH$_2^{nbd}$), 1.43 (dd, $J$ = 9.7, 7.1 Hz, 6 H, Me$^{i\mathrm{Pr}}$), 1.47 (dd, $J$ = 9.5, 7.1 Hz, 6 H, Me$^{i\mathrm{Pr}}$), 2.24 (d, $J$ = 12.5 Hz, 3 H, Me), 3.03 (m, 2 H, CH$^{i\mathrm{Pr}}$), 3.36 (broad s, 2 H, CH$^{nbd}$), 3.53 (m, 4 H, =CH$^{nbd}$), 5.19 (m, 2 H, Cp), 5.79 (m, 2 H, Cp) ppm. $^{13}$C{$^1$H} NMR (125 MHz, $CDCl_3$, 298 K): $\delta$ = 4.3 (d, $J$ = 54.4 Hz, Me), 16.6 (d, $J$ = 2.5 Hz, Me$^{i\mathrm{Pr}}$), 16.7 (d, $J$ = 2.9 Hz, Me$^{i\mathrm{Pr}}$), 22.8 (d, $J$ = 49.7 Hz, CH$^{i\mathrm{Pr}}$), 35.2 (d, $J$ = 10.1 Hz, =CH$^{nbd}$), 46.7 (d, $J$ = 2.6 Hz, CH$^{nbd}$), 58.4 (d, $J$ = 6.9 Hz, CH$_2^{nbd}$), 72.8 (dd, $J$ = 90.6, 6.0 Hz, Cp) 87.7 (dd, $J$ = 11.6, 4.2 Hz, Cp), 92.4 (dd, $J$ = 10.1, 3.7 Hz, Cp) ppm. $^{31}$P{$^1$H} NMR ($CDCl_3$, 121.5 MHz, 298 K): $\delta$ = 35.1 (s, P$i$Pr$_2$) ppm. MS (ESI): $m/z$ calcd. 391.105 [M–I]$^+$; found 391.00. $C_{19}H_{29}$IPRh (518.20): calcd. C 44.03, H 5.64; found C 43.94, H 5.50.

**X-ray Crystal-Structure Analysis of 4a:** $C_{19}H_{29}$IPRh·$CH_2Cl_2$, $M$ = 603.13, yellow crystal 0.30×0.10×0.03 mm, $a$ = 15.973(1), $b$ = 10.887(1), $c$ = 26.453(1) Å, $V$ = 4600.1(5) Å$^3$, $\rho_{calcd.}$ = 1.742 g cm$^{-3}$, $\mu$ = 2.389 mm$^{-1}$, empirical absorption correction (0.534 ≤ $T$ ≤ 0.932), $Z$ = 8, orthorhombic, space group $Pbca$ (no. 61), $\lambda$ = 0.71073 Å, $T$ = 198 K, $\omega$- and $\varphi$-scans, 22987 reflections collected (±$h$, ±$k$, ±$l$), [(sin$\theta$)/$\lambda$] = 0.66 Å$^{-1}$, 5470 independent ($R_{int}$ = 0.060) and 4556 observed reflections [$I \geq 2\sigma(I)$], 231 refined parameters, $R$ = 0.045, $wR_2$ = 0.146, max. (min.) residual electron density 1.75 (–0.82) e Å$^{-3}$ close to iodine, hydrogen atoms calculated and refined as riding atoms.

**Reaction of 3b with Ethyl Iodide. Formation of Complex 5b:** A large excess of ethyl iodide (0.25 mL, 3.10 mmol) was added to a solution of **3b** (30 mg; 0.08 mmol) in toluene (3 mL) at room temperature. After the reaction mixture had been stirred at ambient temperature overnight, all volatiles were removed in vacuo. The obtained yellow oil was washed twice with pentane (1 mL) and dried in vacuo. The pure product was obtained as a yellow solid (48 mg, 0.07 mmol, 86%). Crystals suitable for X-ray crystal structure analysis were obtained from a pentane solution at –30 °C. $^1$H NMR (600 MHz, $C_7D_8$, 298 K): $\delta$ = 0.90 (br., 2 H, CH$_2^{nbd1}$), 1.10/1.14 (each dm, $J$ = 8.5 Hz, each 1 H, CH$_2^{nbd2}$), 1.12 (dd, $J$ = 14.5, 7.1 Hz, 6 H, Me$^{i\mathrm{Pr}}$), 1.36 (dd, $J$ = 15.8, 7.0 Hz, 6 H, Me$^{i\mathrm{Pr}}$), 2.46 (dsept, $J$ = 7.9, 7.1 Hz, 2 H, CH$^{i\mathrm{Pr}}$), 3.09 (m, 4 H, =CH$^{nbd1}$), 3.08 (m, 2 H, CH$^{nbd1}$), 3.36 (br., 2 H, CH$^{nbd2}$), 3.83 (m, 2 H, =CH$^{nbd2}$), 4.41 (m, 2 H, Cp), 5.07 (m, 2 H, Cp), 5.36 (m, 2 H, =CH$^{nbd2}$) ppm. $^{13}$C{$^1$H} NMR (150 MHz, $C_7D_8$, 298 K): $\delta$ = 19.7 (Me$^{i\mathrm{Pr}}$), 20.1 (d, $J$ = 4.7 Hz, Me$^{i\mathrm{Pr}}$), 27.9 (d, $J$ = 24.1 Hz, CH$^{i\mathrm{Pr}}$), 31.9 (d, $J$ = 10.2 Hz, =CH$^{nbd1}$), 47.1 (d, $J$ = 2.4 Hz, CH$^{nbd1}$), 51.0 (dd, $J$ = 2.3, 1.6 Hz, CH$^{nbd2}$), 52.2 (d, $J$ = 11.7 Hz, =CH$^{nbd2}$), 57.7 (d, $J$ = 6.7 Hz, CH$_2^{nbd1}$), 65.1 (dd, $J$ = 4.9, 2.1 Hz, CH$_2^{nbd2}$), 78.4 (dd, $J$ = 11.4, 5.5 Hz, =CH$^{nbd2}$), 87.2 (dd, $J$ = 6.1, 4.2 Hz, Cp), 88.0 (dd, $J$ = 7.6, 3.9 Hz, Cp). 89.1 (Cp, detected by $^1$H/$^{13}$C ghmbc experiment) ppm. $^{31}$P{$^1$H} NMR (121.5 MHz, $C_6D_6$, 298 K): $\delta$ = 40.1 (d, $J$ = 163.4 Hz, P$i$Pr$_2$) ppm. $C_{25}H_{34}$IPRh$_2$ (698.23): calcd. C 43.00, H 4.91; found C 43.03, H 5.26.

**X-ray Crystal-Structure Analysis of 5b:** $C_{25}H_{34}$IPRh$_2$, $M$ = 698.21, red crystal 0.20×0.20×0.10 mm, $a$ = 10.097(1), $b$ = 17.498(1), $c$ = 13.770(1) Å, $\beta$ = 92.85(1)°, $V$ = 2429.8(2) Å$^3$, $\rho_{calcd.}$ = 1.909 g cm$^{-3}$, $\mu$ = 2.704 mm$^{-1}$, empirical absorption correction (0.614 ≤ $T$ ≤ 0.774), $Z$ = 4, monoclinic, space group $P2_1/n$ (no. 14), $\lambda$ = 0.71073 Å, $T$ = 198 K, $\omega$- and $\varphi$-scans, 16579 reflections collected (±$h$, ±$k$, ±$l$), [(sin$\theta$)/$\lambda$] = 0.67 Å$^{-1}$, 5968 independent ($R_{int}$ = 0.030) and 5230 observed reflections [$I \geq 2\sigma(I)$], 267 refined parameters, $R$ = 0.026, $wR_2$ = 0.059, max. residual electron density 1.47 (–1.62) e Å$^{-3}$ close to iodine, hydrogen atoms calculated and refined as riding atoms.

**Reaction of 3b with *n*-Propyl Iodide. Formation of Complexes 5b and 6c:** *n*-Propyl iodide (7.8 μL, 13.5 mg, 0.08 mmol) was added to a solution of **3b** (30 mg, 0.08 mmol) in $C_6D_6$ (1 mL) at room temperature. The reaction mixture was transferred into an NMR tube and the reaction was monitored by NMR spectroscopy.

**Reaction of [{CpP(*i*Pr)$_2$}Li] (2a) with Methyl Iodide. Generation of 6a:** Methyl iodide (99.30 μL, 227 mg, 1.60 mmol) was added to a solution of **2a** (300 mg, 1.60 mmol) in toluene (40 mL) at room temperature. After the reaction mixture had been stirred at ambient temperature overnight, all volatiles were removed in vacuo. The product was obtained as a bright yellow solid (310 mg, 0.94 mmol, 59%). M.p. 96 °C (DSC). $^1$H NMR [400 MHz, $C_6D_6$/TDF (4:1), 298 K]: $\delta$ = 6.66, 6.31 (each m, each 2 H, $C_5H_4$), 1.83 (dsept, $J_{H,H}$ = 6.8, $J_{P,H}$ = 10.0 Hz, 2 H, CH$^{i\mathrm{Pr}}$), 1.08 (d, $J_{P,H}$ = 12.0 Hz, 3 H, Me), 0.82 (dd, $J_{P,H}$ = 16.2, $J_{H,H}$ = 6.8 Hz, 6 H, Me$^{i\mathrm{Pr}}$), 0.70 (dd, $J_{P,H}$ = 15.8, $J_{H,H}$ = 6.8 Hz, 6 H, Me$^{i\mathrm{Pr}}$) ppm. $^{13}$C{$^1$H} NMR [100 MHz, $C_6D_6$/TDF (4:1), 298 K]: $\delta$ = 113.9 (d, $J$ = 16.3 Hz, $C_5H_4$), 113.3 (d, $J$ = 13.8 Hz, $C_5H_4$), 74.0 (d, $J$ = 104.2 Hz, C=P), 22.7 (d, $J$ = 52.9 Hz, CH$^{i\mathrm{Pr}}$), 15.6 (d, $J$ = 1.8 Hz, Me$^{i\mathrm{Pr}}$), 15.4 (d, $J$ = 2.1 Hz, Me$^{i\mathrm{Pr}}$), 0.6 (d, $J$ = 56.9 Hz, Me–P) ppm. $^{31}$P{$^1$H} NMR (81 MHz, $C_6D_6$, 298 K): $\delta$ = 24.7 (s, P$i$Pr$_2$) ppm. MS (ESI): $m/z$ calcd. 197.1459 [M + H]$^+$; found 197.1446. $C_{12}H_{21}$P·LiI (330.12): calcd. C 43.66, H 6.41; found C 42.61, H 6.52.

**Reaction of [{CpP(*i*Pr)$_2$}Li] (2a) with Ethyl Iodide. Generation of 6b:** According to the procedure described for the generation of **6a**, **6b** was obtained as a colourless powder (435 mg, 1.26 mmol, 79%) from the reaction of **2a** (300 mg, 1.60 mmol) with ethyl iodide (129 μL, 249 mg, 1.60 mmol) in toluene (40 mL). M.p. 144 °C (DSC). $^1$H NMR [600 MHz, $C_6D_6$/TDF (4:1), 298 K]: $\delta$ = 6.59, 6.28 (each m, each 2 H, $C_5H_4$), 1.99 (dsept, $J_{P,H}$ = 10.6, $J_{H,H}$ = 7.0 Hz, 2 H, CH$^{i\mathrm{Pr}}$), 1.77 (dq, $J_{P,H}$ = 12.7, $J_{H,H}$ = 7.7 Hz, 2 H, $CH_2$), 0.90 (dd, $J_{P,H}$ = 15.4, $J_{H,H}$ = 7.0 Hz, 6 H, Me$^{i\mathrm{Pr}}$), 0.86 (q, $J_{P,H}$ = $J_{H,H}$ = 7.7 Hz, 3 H, $CH_3$), 0.80 (dd, $J_{P,H}$ = 15.4, $J_{H,H}$ = 7.0 Hz, 6 H, Me$^{i\mathrm{Pr}}$) ppm. $^{13}$C{$^1$H} NMR (125 MHz, $C_6D_6$/TDF, 4:1, 298 K): $\delta$ = 113.7 (d, $J$ = 16.7 Hz, $C_5H_4$), 113.3 (d, $J$ = 13.3 Hz, $C_5H_4$), 73.1 (d, $J$ = 103.5 Hz, P=C), 22.0 (d, $J$ = 51.8 Hz, CH$^{i\mathrm{Pr}}$), 16.2 (d, $J$ = 1.8 Hz, Me$^{i\mathrm{Pr}}$), 16.0 (d, $J$ = 1.9 Hz, Me$^{i\mathrm{Pr}}$), 11.7 (d, $J$ = 52.9 Hz, $CH_2$), 7.5 (d, $J$ = 4.8 Hz, $CH_3$) ppm. $^{31}$P{$^1$H} NMR (81 MHz, $C_6D_6$, 298 K): $\delta$ = 24.7 (s, P$i$Pr$_2$) ppm. MS (ESI): $m/z$ calcd. 211.1616 [M + H]$^+$; found 211.1. $C_{13}H_{23}$P·LiI (344.15): calcd. C 45.37, H 6.74; found C 44.45, H 6.73.

**Reaction of [{CpP(*i*Pr)$_2$}Li] (2a) with *n*-Propyl Iodide. Generation of 6c:** According to the procedure described for the generation of **6a**, **6c** was obtained as a colourless powder (470 mg, 0.76 mmol, 82%) from the reaction of **2a** (300 mg, 1.60 mmol) with *n*-propyl

 © 2006 Wiley-VCH Verlag GmbH & Co. KGaA, Weinheim 

iodide (156.5 μL, 271 mg, 1.60 mmol) in toluene (40 mL). M.p. 101 °C (DSC). $^1$H NMR (600 MHz, $C_6D_6$/TDF (4:1), 298 K): $\delta$ = 6.67, 6.33 (each m, each 2 H, $C_5H_4$), 1.96 (dsept, $J_{P,H}$ = 10.8, $J_{H,H}$ = 7.2 Hz, 2 H, $CH^{iPr}$), 1.76 (m, 2 H, $PCH_2$), 1.32 (m, 2 H, $CH_2$), 0.90 (dd, $J_{P,H}$ = 15.8, $J_{H,H}$ = 7.2 Hz, 6 H, $Me^{iPr}$), 0.79 (dd, $J_{P,H}$ = 15.6, $J_{H,H}$ = 7.2 Hz, 6 H, $Me^{iPr}$), 0.76 (td, $J_{H,H}$ = 7.1, $J_{H,H}$ = 1.5 Hz, 3 H, $CH_3$) ppm. $^{13}C\{^1H\}$ NMR [125 MHz, $C_6D_6$/TDF (4:1), 298 K]: $\delta$ = 113.8 (d, $J$ = 16.6 Hz, $C_5H_4$), 113.4 (d, $J$ = 13.8 Hz, $C_5H_4$), 73.2 (d, $J$ = 102.3 Hz, P=C), 22.3 (d, $J$ = 52.3 Hz, $CH^{iPr}$), 20.9 (d, $J$ = 51.8 Hz, $PCH_2$), 17.1 (d, $J$ = 4.1 Hz, $CH_2$), 16.2 (d, $J$ = 2.1 Hz, $Me^{iPr}$), 16.0 (d, $J$ = 2.1 Hz, $Me^{iPr}$), 16.1 (d, $J$ = 15.3 Hz, $CH_3$) ppm. $^{31}P\{^1H\}$ NMR [81 MHz, $C_6D_6$/TDF (4:1), 298 K]: $\delta$ = 26.1 (s, P$i$Pr$_2$) ppm. MS (ESI): *m*/*z* calcd. 225.18 $[M + H]^+$; found 456.00 $[2M + H,Li]^+$. $C_{14}H_{25}P{\cdot}LiI$ (358.17): calcd. C 46.95, H 7.04; found C 47.24, H 7.34.

## Acknowledgments

Financial support from the Fonds der Chemischen Industrie and the Deutsche Forschungsgemeinschaft is gratefully acknowledged.

[1] H. Chen, S. Schlecht, T. C. Semple, J. F. Hartwig, *Science* **2000**, *287*, 1995–1997; J. F. Hartwig, K. S. Cook, M. Hapke, C. D. Incarvito, Y. Fan, C. E. Webster, M. B. Hall, *J. Am. Chem. Soc.* **2005**, *127*, 2538–2552.

[2] X. D. He, A. Maisonnat, F. Dahan, R. Poilblanc, *Organometallics* **1987**, *6*, 678–680; X. D. He, A. Maisonnat, F. Dahan, R. Poilblanc, *Organometallics* **1989**, *8*, 2618–2626.

[3] S. Barry, A. Kucht, H. Kucht, M. D. Rausch, *J. Organomet. Chem.* **1995**, *489*, 195–199; W. Tikkanen, Y. Fujita, J. L. Petersen, *Organometallics* **1986**, *5*, 888–894.

[4] E. W. Abel, M. A. Bennett, G. Wilkinson, *J. Chem. Soc.* **1959**, 3178–3182.

[5] C. Cornelissen, G. Erker, G. Kehr, R. Fröhlich, *Organometallics* **2005**, *24*, 214–225.

[6] J.-C. Hierso, A. Fihri, R. Amardeil, P. Meunier, H. Doucet, M. Santelli, V. V. Ivanov, *Org. Lett.* **2004**, *6*, 3473–3476; J.-C. Hierso, V. V. Ivanov, R. Amardeil, P. Richard, P. Meunier, *Chem. Lett.* **2004**, *33*, 1296–1297.

[7] A. G. Orpen, L. Brammer, F. H. Allen, O. Kennard, D. G. Watson, R. Tailor, *J. Chem. Soc., Dalton Trans.* **1989**, S1–S83.

[8] See, for comparison: G. Tresoldi, A. Recca, P. Finocchiaro, F. Faraone, *Inorg. Chem.* **1981**, *20*, 3103–3106.

[9] "Phosphorus-31 NMR Spectral Properties", in *Compound Characterisation and Structural Analysis* (Eds.: L. D. Quin, J. G. Verkade), VCH Publishers, New York **1994**.

[10] See also: C. Puke, G. Erker, N. C. Aust, E.-U. Würthwein, R. Fröhlich, *J. Am. Chem. Soc.* **1998**, *120*, 4863–4864; C. Puke, G. Erker, B. Wibbeling, R. Fröhlich, *Eur. J. Org. Chem.* **1999**, 1831–1841.

[11] C. P. Casey, R. M. Bullock, W. C. Fultz, A. L. Rheingold, *Organometallics* **1982**, *1*, 1591–1596; C. P. Casey, F. Nief, *Organometallics* **1985**, *4*, 1218–1220; M. Visseaux, A. Dormond, M. M. Kubicki, C. Moïse, D. Baudry, M. Ephritikhine, *J. Organomet. Chem.* **1992**, *433*, 95–106; B. Brumas, D. de Caro, F. Dahan, D. de Montauzon, R. Poilblanc, *Organometallics* **1993**, *12*, 1503–1505; B. Brumas, F. Dahan, D. de Montauzon, R. Poilblanc, *J. Organomet. Chem.* **1993**, *453*, C13–C15; L. Lettko, M. D. Rausch, *Organometallics* **2000**, *19*, 4060–4065; P. Le Gendre, P. Richard, C. Moïse, *J. Organomet. Chem.* **2000**, *605*, 151–156.

[12] L. J. Higham, P. G. Kelly, D. M. Corr, H. Müller-Bunz, B. J. Walker, D. G. Gilheany, *Chem. Commun.* **2004**, 684–685; S. Ito, H. Miyake, M. Yoshifuji, T. Höltzl, T. Vesprémi, *Chem. Eur. J.* **2005**, *11*, 5960–5965; F. Ramirez, S. Levy, *J. Am. Chem. Soc.* **1957**, *79*, 67–69; F. Ramirez, S. Levy, *J. Am. Chem. Soc.* **1957**, *79*, 6167–6172; H. L. Ammon, G. L. Wheeler, P. H. Watts Jr, *J. Am. Chem. Soc.* **1973**, *95*, 6158–6163.

[13] H. Schmidbaur, J. Jeong, A. Schier, W. Graf, D. L. Wilkinson, G. Müller, C. Krüger, *New J. Chem.* **1989**, *13*, 341–352. See also: *Phosphorus Ylides* (Ed.: O. I. Kolodiazhnyi), Wiley-VCH, Weinheim, **1999**.

[14] F. T. Lapido, G. K. Anderson, N. P. Rath, *Organometallics* **1994**, *13*, 4741–4745; W. Simanko, V. N. Sapunov, R. Schmid, K. Kirchner, *Organometallics* **1998**, *17*, 2391–2393; W. Simanko, W. Tesch, V. N. Sapunov, K. Mereiter, R. Schmid, K. Kirchner, *Organometallics* **1998**, *17*, 5674–5688.

Received: April 18, 2006
Published Online: August 3, 2006

 © 2006 Wiley-VCH Verlag GmbH & Co. KGaA, Weinheim 

EurJIC
European Journal of Inorganic Chemistry

Issue 19/2006

Pages 3777–3988

*Papers available ahead of print in Early View at www.interscience.wiley.com*

*Earliest available Table of Contents:*
*Automatically, free of charge by e-mail through*
*www.interscience.wiley.com/alerts*

## COVER PICTURE

**The cover picture shows** the Alhambra in Granada, the home town of the Spanish author of this paper. The Moors in their desert dreamt of palaces abundant with water, and that is why they built the Alhambra. Likewise, the water-soluble encapsulating pyrazolylborate ligand, shown as an (aqua)zinc complex set in one of Alhambra's gardens, is the realization of a long-standing dream of the Freiburg group, whose biomimetic zinc complex chemistry was previously confined by the hydrophobicity of the model complexes, typically the zinc hydroxide complex shown in the background. The abundance of red (carbonyl oxygen) and green (amide nitrogen) atoms in the foreground complex visualizes its hydrophilicity due to the carboxamide substituents on the tripod ligand. Details are discussed in the article by H. Vahrenkamp et al. on p. 3869 ff.

## MICROREVIEW

**Contents**

**3789** **F. Meyer***

Clues to Dimetallohydrolase Mechanisms from Studies on Pyrazolate-Based Bioinspired Dizinc Complexes – Experimental Evidence for a Functional $Zn-O_2H_3-Zn$ Motif

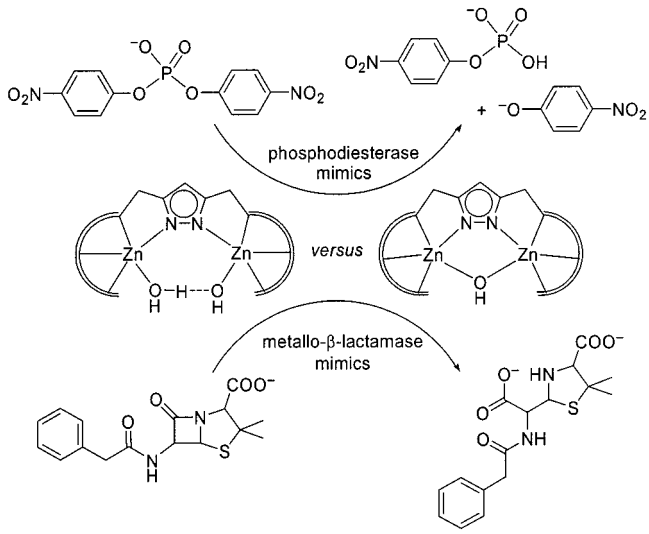


**Keywords:** Bioinorganic chemistry / Hydrolases / Metalloenzymes / Enzyme models / Zinc

 © 2006 Wiley-VCH Verlag GmbH & Co. KGaA, Weinheim 

**3801** **J. Arnhold, E. Monzani, P. G. Furtmüller, M. Zederbauer, L. Casella, C. Obinger***

Kinetics and Thermodynamics of Halide and Nitrite Oxidation by Mammalian Heme Peroxidases

**Keywords:** Bioinorganic chemistry / Peroxidases / Halides / Nitrites / Thermodynamics / Kinetics

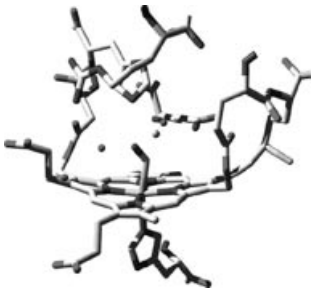

## SHORT COMMUNICATIONS

**3813** **D. Valigura,* J. Moncol, M. Korabik, Z. Púčeková, T. Lis, J. Mroziński, M. Melník**

New Dimeric Copper(II) Complex $[Cu(5\text{-}MeOsal)_2(\mu\text{-nia})(H_2O)]_2$ with Magnetic Exchange Interactions through H-Bonds

**Keywords:** Copper / Carboxylate ligands / Nicotinamide / Dimer / Structure / Magnetic properties

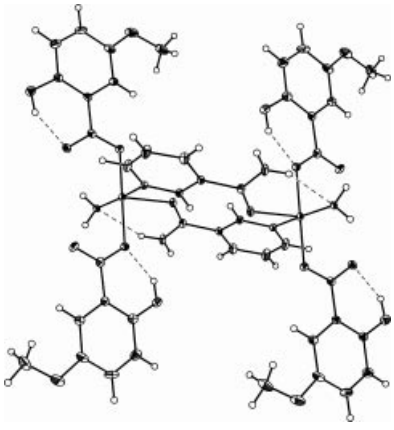

**3818** **M. Yang, G. Pang,* J. Li, L. Jiang, S. Feng***

Preparation of ZnO Nanowires in a Neutral Aqueous System: Concentration Effect on the Orientation Attachment Process

**Keywords:** Zinc oxide / Orientation attachment / Self-assembly / Nanostructures

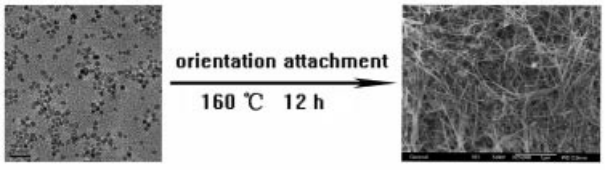


## FULL PAPERS

**3823** **M. González-Álvarez, G. Alzuet, L. del Castillo, J. Borrás,* M. Liu-González**

Genotoxic Potential of *N*-(Benzothiazolyl)-sulfonamide Copper(II) Complexes on Yeast Cells Transformed with YEGFP Expression Constructs Containing the RAD54 or RNR2 Promoter

**Keywords:** Copper complexes / DNA damage / Genotoxicity / yEGFP expression

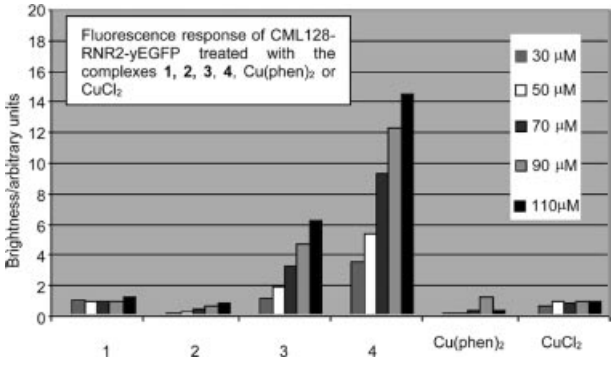


 © 2006 Wiley-VCH Verlag GmbH & Co. KGaA, Weinheim 

**3835** **L. Krippahl, P. N. Palma, I. Moura, J. J. G. Moura***

Modelling the Electron-Transfer Complex Between Aldehyde Oxidoreductase and Flavodoxin

**Keywords:** Bioinorganic chemistry / Electron transfer / Molybdenum / Enzyme models

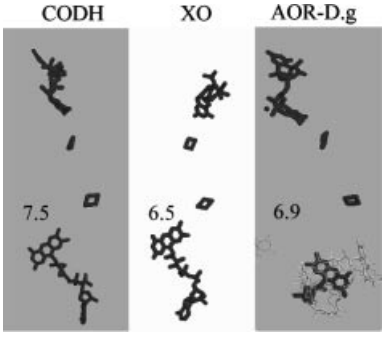


**3841** **F. B. Larsen, A. Boisen, K. J. Berry, B. Moubaraki, K. S. Murray, V. McKee, R. C. Scarrow, C. J. McKenzie***

Identification of the Dinuclear and Tetranuclear Air-Oxidized Products Derived from Labile Phenolate-Bridged Dimanganese(II) Pyridyl Chelate Compounds

**Keywords:** Manganese / O ligands / Chelates / Bond valence sum analysis / Oxidation

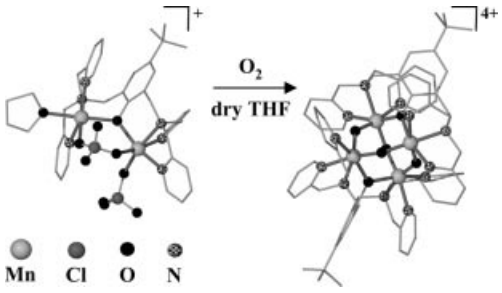


**3853** **S. Chaves, S. M. Marques, A. Cachudo, M. A. Esteves, M. A. Santos***

Zinc(II) Complexation Behaviour of Sulfonamide-Based Enzyme Inhibitors

**Keywords:** MMP inhibitors / Carbonic-anhydrase inhibitors / Hydroxamate / Hydroxypyrimidinone / Sulfonamido-based inhibitors / Sulfonamides

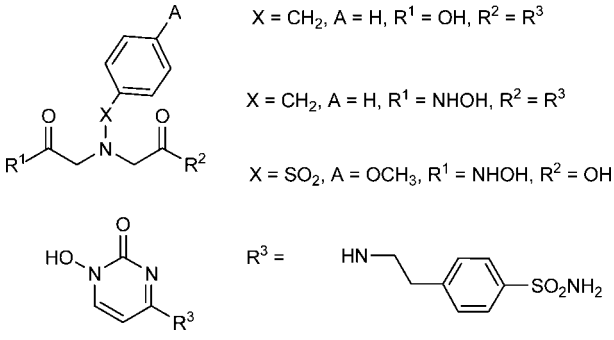


**3861** **T. E. de Jongh, A.-M. M. van Roon, M. Prudêncio, M. Ubbink, G. W. Canters***

Click Chemistry with an Active Site Variant of Azurin

**Keywords:** Metalloproteins / Protein structures / Zinc / Copper / Metal replacement

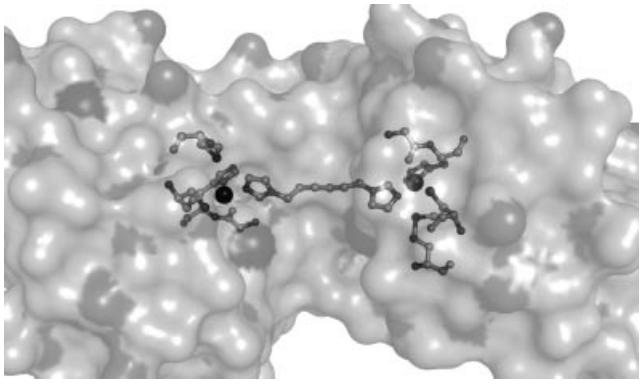

**3869** **C. Perez Olmo, K. Böhmerle, G. Steinfeld, H. Vahrenkamp***

New Polar Pyrazolylborate Ligands and Their Basic Zinc Complex Chemistry

**Keywords:** Tripod ligands / Pyrazolylborate ligands / Zinc complexes / Structure elucidation / Coordination modes

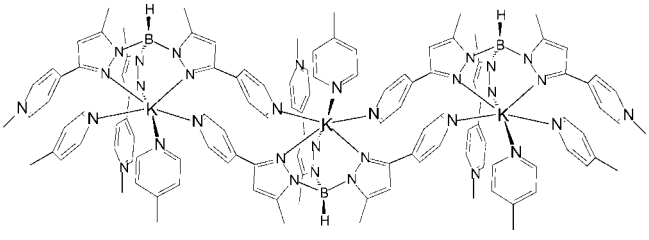

 © 2006 Wiley-VCH Verlag GmbH & Co. KGaA, Weinheim 

**3878** **A. Petitjean, F. Puntoriero, S. Campagna,* A. Juris, J.-M. Lehn***

Multicomponent Supramolecular Devices: Synthesis, Optical, and Electronic Properties of Bridged Bis-dirhodium and -diruthenium Complexes

**Keywords:** N ligands / Electronic coupling / Electrochemistry / Metal−metal interactions / Optical properties

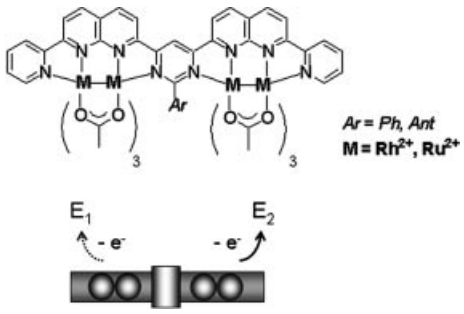


**3893** **F. Acha, M. A. Garralda,* R. Hernández, L. Ibarlucea, E. Pinilla, M. R. Torres, M. Zarandona**

Synthesis and Reactivity of New Mono- and Dinuclear Hydridoirida-β-diketones − The Formation and Characterization of a Dinuclear Tris-μ-acyliridium(III) Complex

**Keywords:** Iridium / Hydride ligands / Bridging ligands / P ligands

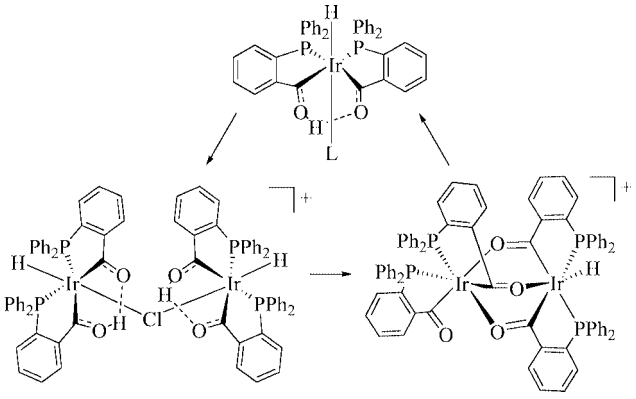

**3901** **S. W. Kohl, F. W. Heinemann, M. Hummert, H. Weißhoff, A. Grohmann***

Tetra- and Triphosphane Pyridine Podands and Their Cobalt(II) and Nickel(II) Complexes

**Keywords:** Cobalt / Nickel / N,P ligands

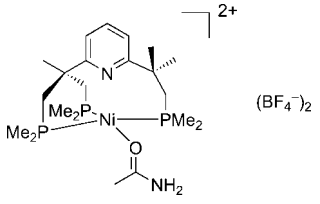


**3911** **C. Thoumazet, H. Grützmacher, B. Deschamps, L. Ricard, P. le Floch***

Testing Phosphanes in the Palladium-Catalysed Allylation of Secondary and Primary Amines

**Keywords:** Allylation / Amines / Catalysis / Palladium / Phosphorus

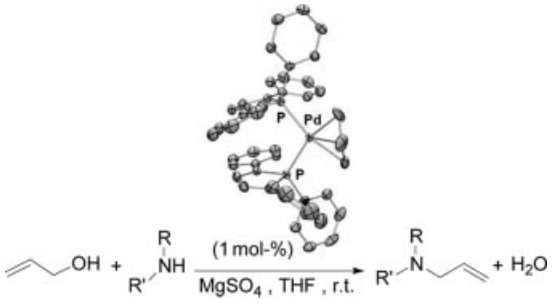


**3923** **P. P. Lima, S. A. Junior, O. L. Malta, L. D. Carlos, R. A. Sá Ferreira, R. Pavithran, M. L. P. Reddy***

Synthesis, Characterization, and Luminescence Properties of $Eu^{3+}$ 3-Phenyl-4-(4-toluoyl)-5-isoxazolonate Based Organic-Inorganic Hybrids

**Keywords:** Organic-inorganic hybrids / $Eu^{3+}$ / Heterocyclic β-diketonates / Synthesis / Characterization / Luminescence

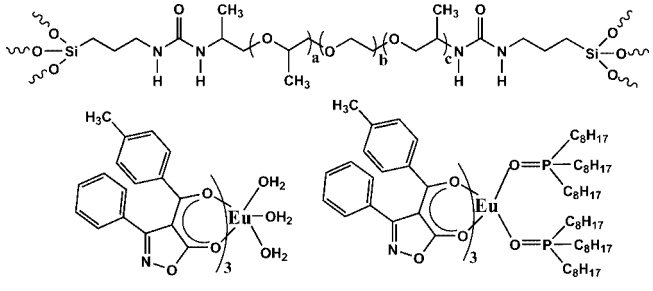


 © 2006 Wiley-VCH Verlag GmbH & Co. KGaA, Weinheim 

**3930** **J. Fielden, D.-L. Long, C. Evans, L. Cronin***

Metal-Dependent Formation of Mononuclear Complexes and $M_2L_2$ Mesocates with Schiff-Base Ligands

**Keywords:** Supramolecular chemistry / Schiff-base ligands / Coordination modes / Silver / Cadmium

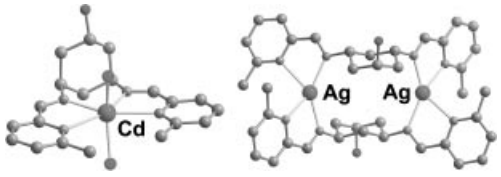


**3936** **S. Jana, R. Fröhlich, N. W. Mitzel***

Zinc Hydrazide and Zinc Alkoxide Hydrazide Cages with $Zn_4N_8$ and $Zn_4N_6O$ Cores − Cluster Isomerism as a Result of Subtle Changes in Ligand Size

**Keywords:** Zinc / Hydrazines / Cage compounds / Co-crystalline compounds / N ligands

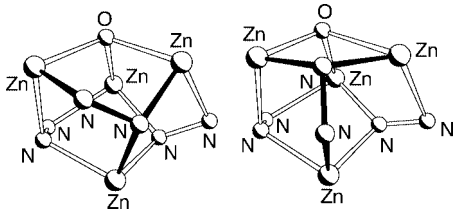


**3943** **F. Qu, G. Zhu,* H. Lin, J. Sun, D. Zhang, S. Li, S. Qiu***

Drug Self-Templated Synthesis of Ibuprofen/Mesoporous Silica for Sustained Release

**Keywords:** Template synthesis / Ibuprofen / Mesoporous materials / Silica

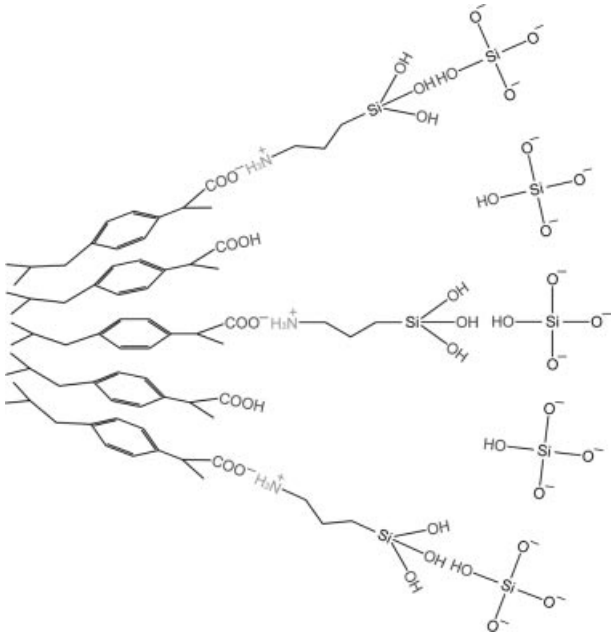


**3948** **H.-J. Frohn,* V. V. Bardin**

Organoethynylxenon(II) Tetrafluoroborates, $[RC{\equiv}CXe][BF_4]$ − The First Examples of Isolated Alkynylxenonium Salts: Preparation and Multi-NMR Characterisation

**Keywords:** Alkynes / Boranes / Xenon / NMR spectroscopy

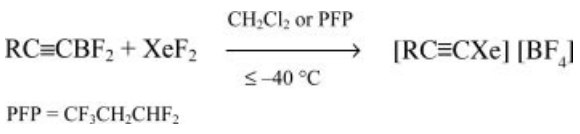


 © 2006 Wiley-VCH Verlag GmbH & Co. KGaA, Weinheim 

**3954** **S. K. Singh, M. Chandra, S. K. Dubey, D. S. Pandey***

Tuned Helical Array of $Rh^{III}/Ir^{III}$ Cp* Complexes with Polypyridyl Ligands

**Keywords:** Rhodium-Cp* / Iridium-Cp* / Polypyridyl ligands / Tuned helical / Weak interactions

**3962** **L.-N. Sun, J.-B. Yu, G.-L. Zheng, H.-J. Zhang,* Q.-G. Meng, C.-Y. Peng, L.-S. Fu, F.-Y. Liu, Y.-N. Yu**

Syntheses, Structures and Near-IR Luminescent Studies on Ternary Lanthanide ($Er^{III}$, $Ho^{III}$, $Yb^{III}$, $Nd^{III}$) Complexes Containing 4,4,5,5,6,6,6-Heptafluoro-1-(2-thienyl)hexane-1,3-dionate

**Keywords:** Lanthanides / Luminescence / Optical amplification

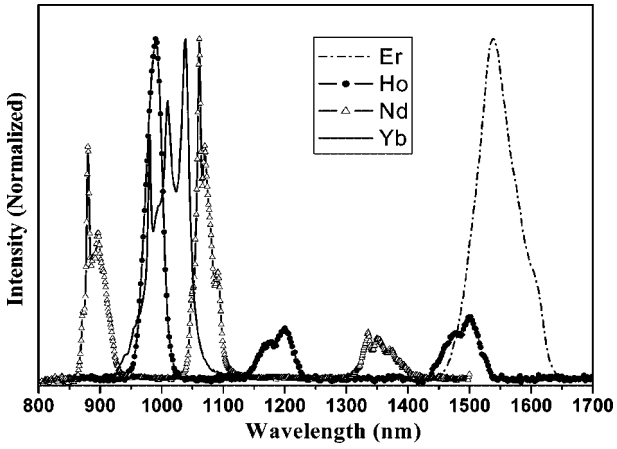


**3974** **C. López,* A. Caubet, S. Pérez, X. Solans, M. Font-Bardía, E. Molins**

Chiral Platinum(II) Compounds Containing Ferrocenyl Schiff Bases Acting as (N), $(N,O)^-$, $[C(sp^2,ferrocene),N]^-$ or $[C(sp^2,ferrocene),N,O]^{2-}$ Ligands

**Keywords:** Platinum / Ferrocene / Platinacycles / N ligands / N,O ligands

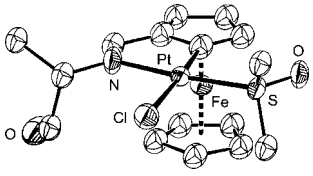

DOI: 10.1002/ejic.200600590

# Clues to Dimetallohydrolase Mechanisms from Studies on Pyrazolate-Based Bioinspired Dizinc Complexes – Experimental Evidence for a Functional $Zn–O_2H_3–Zn$ Motif

**Franc Meyer*[a]**

**Keywords:** Bioinorganic chemistry / Hydrolases / Metalloenzymes / Enzyme models / Zinc

Various hydrolytic metalloenzymes contain two adjacent zinc ions within their active site that work synergistically during substrate turnover. While structural biology, biochemical investigations, and quantum chemical calculations have provided much insight into those cocatalytic sites, crucial details of the catalytic mechanisms have remained under debate. Valuable contributions to further our understanding of the functional role of the zinc ions in a specific coordination environment can be obtained from the study of simple biomimetic synthetic complexes that emulate features of the natural systems. To this end, a series of highly preorganized pyrazolate-based dizinc complexes has been developed, which are particularly amenable to fine-tuning of the dimetallic core. These bioinspired dizinc complexes have made possible the investigation of systematic effects of factors such as the zinc–zinc separation on hydrolytic activity and substrate binding. The present microreview summarizes findings relevant to dimetallohydrolases that have been obtained from studies of the pyrazolate-based synthetic analogues, including experimental support for a functional role of the $Zn–O_2H_3–Zn$ motif and clues to the binding and hydrolytic cleavage of phosphodiester and β-lactam substrates.
(© Wiley-VCH Verlag GmbH & Co. KGaA, 69451 Weinheim, Germany, 2006)

## 1. Introduction

Numerous biological functions rely on enzymes that promote the hydrolytic cleavage of biological substrates such as phosphate esters, peptides or amides, and these enzymes often contain two or even three cooperating metal ions within their active site.[1–4] Although specific mechanisms are involved for the individual metalloenzymes, crucial roles of the metal ions are believed to comprise the generation of a hydroxide nucleophile at physiological pH by lowering the $pK_A$ of water, the Lewis acid activation and orientation of the substrate through metal coordination, as well as the stabilization of intermediates and leaving groups.[2,4,5] Since $Zn^{2+}$ is a strong Lewis acid with rapid ligand exchange and a flat coordination hypersurface that allows the coordination number und geometry to be changed easily, it fulfils all these requirements while, at the same time, lacking undesired redox activity.[6] Hence, zinc is found very often in hydrolytic enzymes, although other metals such as $Mg^{2+}$ or $Mn^{2+}$, or even $Ni^{2+}$ in urease may be preferred in certain cases.

[a] Institut für Anorganische Chemie, Georg-August-Universität Göttingen
Tammannstrasse 4, 37077 Göttingen, Germany
Fax: +49-551-393063
E-mail: franc.meyer@chemie.uni-goettingen.de

## 2. Oligozinc Hydrolases: Phosphatases, Metallo-β-lactamases, and Aminopeptidases as Examples

Prominent hydrolases that incorporate two proximate zinc ions include some metallo-β-lactamases,[7,8] several aminopeptidases,[9] phosphotriesterase,[10] and alkaline phosphatase.[11,12] Similarly, human phosphodiesterase features two divalent metal ions, at least one of which is $Zn^{2+}$ (the second is probably $Mg^{2+}$).[13,14] Enzymes that hydrolyze phosphodiesters are of prime importance to the manipula-

*Franc Meyer was born in 1965 in Hamburg and studied chemistry at RWTH Aachen. He earned his doctorate with Professor P. Paetzold in 1993 and was a postdoctoral fellow with Professor P. B. Armentrout in Salt Lake City until 1995. After his Habilitation with Professor G. Huttner in Heidelberg in 2000 and a visiting professorship at the University of Vienna he became full professor of inorganic chemistry at the Georg-August-University Göttingen in 2001. His research focuses on cooperative effects in bimetallic and multimetallic complexes, with particular interests in bioinorganic chemistry, bioinspired catalysis and magnetochemistry. His awards include a Dozentenstipendium from the Fonds der Chemischen Industrie and the Karl-Freudenberg prize of the Heidelberg Academy of Sciences and Humanities.*

 © 2006 Wiley-VCH Verlag GmbH & Co. KGaA, Weinheim 

tion of DNA and RNA because of their involvement in replication, transcription, recombination, and DNA repair. It is through the synergistic Lewis acid activation of the substrate, the nucleophile, and the leaving group in these processes that the $10^{16}$-fold rate enhancement can be achieved that is needed to hydrolyze DNA on the biological time scale.[3] A representative example illustrating the role of two active-site zinc ions in phosphoester hydrolysis is phosphotriesterase (PTE).[10] PTE efficiently degrades highly toxic organophosphate triesters by the proposed mechanism outlined in Scheme 1.[15] Similar to various other oligozinc enzymes, the crystallographically characterized form of PTE has a bridging O atom, which most likely is a bridging hydroxide in agreement with the experimental p*K*a value of 5.8.[16] It is assumed that the substrate enters the scene to replace a water at Zn2, followed by nucleophilic attack of the μ-OH onto the substrate-P and ejection of the leaving group. Proton transfer away from the active site, assisted by a nearby histidine residue, gives a phosphate anion which spans the two metal ions, and solvent molecules finally move in to regenerate the original state upon product release.

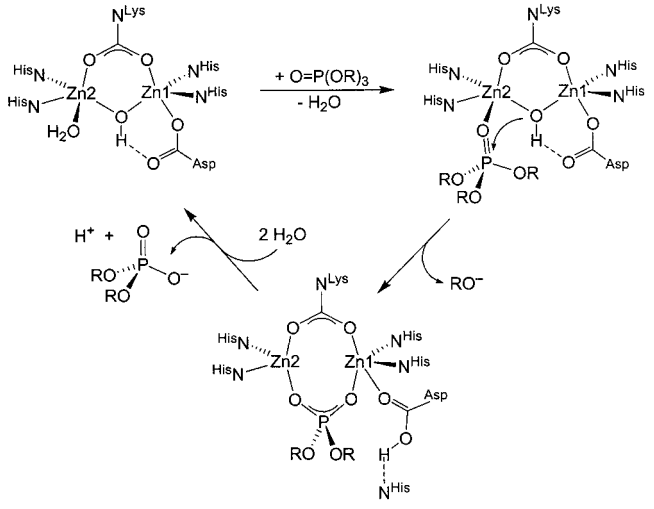


Scheme 1. Proposed mechanism of phosphotriesterase.[15]

Even more than two metal ions may be involved in phosphoester cleavage; an example is the P1 nuclease, which degrades single-stranded RNA and DNA into 5′-mononucleotides. P1 nuclease features a trinuclear zinc site sketched in Scheme 2, where a hydroxide bridging Zn1 and Zn2 is assumed to attack the phosphate substrate that binds to Zn3 in a bidentate fashion.[17]

Despite manifold investigations, details of the mode of action of these and other metallohydrolases remain controversial. One important aspect under debate is the identity and the exact binding mode of the nucleophile.[18,19] Since a hydroxide spanning two zinc ions has been detected crystallographically in the majority of dimetallohydrolases, this μ-OH is usually considered to be the active nucleophile. Computational evidence for a catalytic bridging hydroxide in a phosphodiesterase site has indeed been reported.[19] On the other hand, the hydroxide can be suspected to exhibit a rather low nucleophilicity in this tightly bridging form. It has thus been suggested in an alternative picture that a shift of the bridging hydroxide to a terminal position occurs upon substrate binding prior to attack on the coordinated substrate.[20] A similar scenario is also assumed for the dizinc-β-lactamase mechanism depicted in Scheme 3.

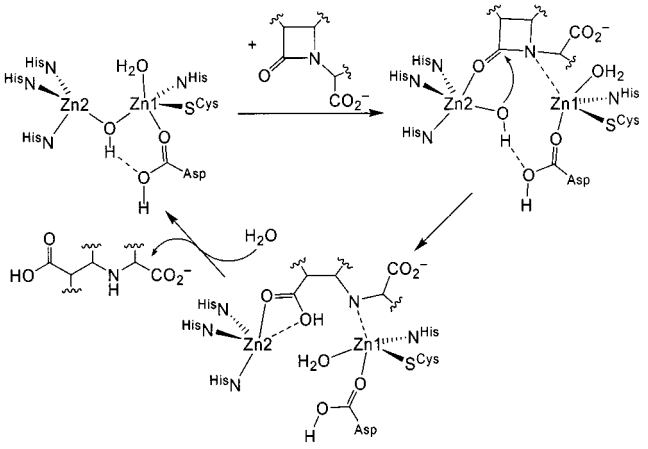


Scheme 3. Proposed simplified mode of action of dizinc metallo-β-lactamase CcrA from *B. fragilis*.[18,21]

β-Lactamases are enzymes that efficiently hydrolyze and cleave the four-membered ring of β-lactams.[22] This β-lactam motif is a crucial functionality in antibiotics derived from the penicillin, cephalosporin, and carbapenem families. Expression of β-lactamases capable of inactivating this motif and thus inactivating these drugs has become a standard bacterial defense mechanism. Among the four classes (A, B, C, and D),[23,24] of β-lactamases, enzymes of the most recently discovered class B depend on one or two zinc ions

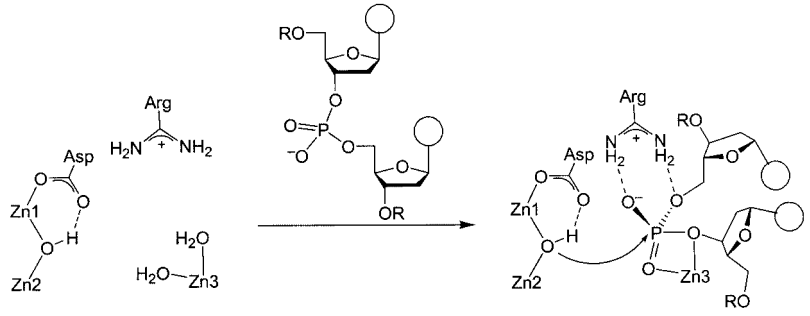

Scheme 2. Proposed mechanism of P1 nuclease.[17]

 © 2006 Wiley-VCH Verlag GmbH & Co. KGaA, Weinheim 

within their active site.[8,25] Unfortunately, clinically useful inhibitors are not yet available for those metallo-β-lactamases, in contrast to the serine-based β-lactamases of classes A, C, and D.[26] Bacterial resistance caused by metallo-β-lactamases now represents a serious clinical threat, and a spread of these enzymes to pathogenic bacteria has raised the concern of the biomedical community.[27] Current efforts thus focus on gathering a detailed picture of the mechanism of action within the active site of the metallo-β-lactamases,[8,28] which is not only of fundamental interest but may also contribute to the development of effective mechanism-based inhibitors.[29]

Molecular structures of several dizinc metallo-β-lactamases have been determined,[30–36] but mechanistic studies have concentrated on CcrA from *B. fragilis* and BcII from *B. cereus II*. While intimate details of the active-site structures vary, common features of dizinc metallo-β-lactamases comprise one tetrahedral {$(His)_3Zn(\mu\text{-}OH)$} motif (Zn2 in Scheme 3) in which the hydroxide serves as a bridge to the second zinc (Zn1). The latter is found in a distorted trigonal bipyramidal environment as a {$(His)(Asp)(X)Zn(H_2O)(\mu\text{-}OH)$} center, where X is His or Cys. From stopped-flow kinetic investigations in combination with theoretical studies, a mechanism has been postulated[18,21,37] that starts by docking the substrate to Zn2 by means of its ring carbonyl group. This polarizes the lactam unit and allows the N-atom to interact with Zn1, inducing conformational changes with rupture of the Zn–OH–Zn bridge and activation of the hydroxide for nucleophilic attack.[38] Zn1 then stabilizes the negative charge on the nitrogen leaving group, which is released upon rate-determining proton transfer.[18] Bringing in water from the medium finally regenerates the initial active-site state (Scheme 3).

Recent DFT, Hartree–Fock, and molecular dynamics studies have revealed a somewhat refined picture, suggesting that the active site can easily assume different conformations.[39] When the Asp residue is neutral, the dizinc core may readily interchange between a tightly bridged state **A** and a loosely bridged state **B** with changes of coordination number at Zn1 (Scheme 4). The more flexible state **B** can be described as an $O_2H_3$ unit between the two metal ions. Evidence for different active-site conformation is also available from experimental studies,[37] but details such as the protonation state of the Asp residue remain controversial.[40,41] It is obvious, however, that solid-state structures obtained crystallographically do not provide the whole story.

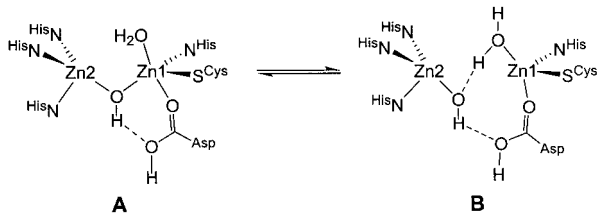


Scheme 4. Interconversion of tightly and loosely bridged active site forms of CcrA from *B. fragilis* as predicted by calculations.[39]

A Zn–(H)OHO(H)–Zn motif reminiscent of the situation in **B** has indeed been observed in bioinspired synthetic model complexes, and from those findings the bridging $O_2H_3$ unit has been proposed as a structural and possibly functional unit in oligozinc hydrolases.[42,43] Some further corroboration comes from a most recent DFT study on the dizinc active site of bovine lens leucine aminopeptidase (*bl*LAP).[44] This widespread enzyme preferably hydrolyzes the peptide bond of N-terminal leucine in a peptide chain and plays a central role in the degradation and modification of proteins.[9a,45,46] Most proposed catalytic mechanisms have assumed that the terminal amino group of the peptide binds to Zn2 and that the OH acts as the nucleophile,[46,47] but a QM/MM study predicted an unreasonably high calculated barrier for nucleophilic attack.[48] A more recent DFT study then demonstrated that an additional water molecule can be introduced by way of the water channel above Zn1 and may undergo facile insertion into the Zn–OH–Zn unit to result in an $O_2H_3$ bridge (Scheme 5). Since an additional water molecule may be spontaneously incorporated at Zn1, this scenario has been described as the formation of a water sluice in the *bl*LAP active site, providing a plausible mechanism for the continual generation of an active nucleophile (Scheme 5).[44]

In view of this accumulating body of evidence for the relevance of a bridging $O_2H_3$ in dizinc hydrolases, it appeared particularly desirable to experimentally test the hydrolytic efficiency of this motif relative to the related Zn–OH–Zn unit.

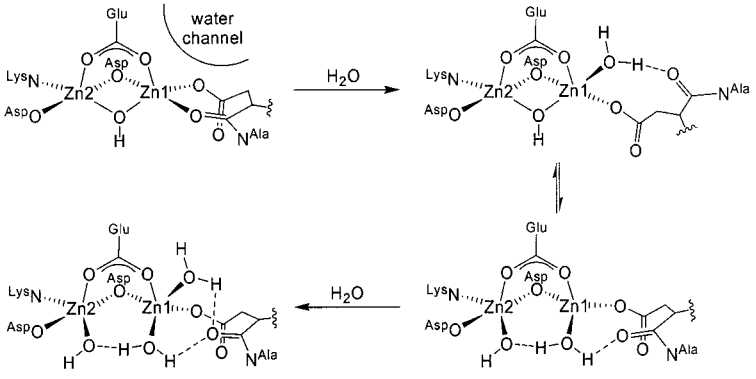


Scheme 5. Generation of a water sluice in the active site of *bl*LAP according to recent DFT calculations.[44]

 © 2006 Wiley-VCH Verlag GmbH & Co. KGaA, Weinheim 

## 3. Relevance of Synthetic Model Complexes

Synthetic hydrolase models have been very useful in providing information about basic functional principles and mechanistic aspects of enzyme action.[49,50] This is particularly true for the role of active-site metal ions in a specific biological donor environment, and most recent examples of hydrolase mimics even aim at elucidating second-sphere effects such as hydrogen-bonding patterns at metal-bound substrates.[51,52] As an advantage over their enzyme counterparts, small molecule synthetic analogues allow for easy systematic investigations of substituent effects, and it becomes possible to examine a variety of factors that influence reactivity.[50] Apart from the fundamental insights obtained from those biomimetic studies regarding structural, spectroscopic, and mechanistic features, there is hope that artificial nucleases for biomimetic hydrolysis of DNA or RNA will eventually lead to beneficial applications in biotechnology and medicine.[53] This has stimulated considerable efforts directed towards the development of well-designed metal complexes that mediate the hydrolytic cleavage of DNA or RNA or phosphodiester model substrates.[4,54,55] One should keep in mind, however, that no synthetic models have yet been developed that at the same time mimic all aspects of the natural enzymes, i.e., active-site structure, function and mechanism. As has been emphasized recently,[50] many structural models lack functional equivalence, while many functional models bear little structural resemblance to the enzyme active sites – a more elaborate combination of both properties in new synthetic compounds certainly is a demanding task. This is even more true for the emulation of additional factors provided by the protein matrix, such as regulation of activity, site-specific reactivity, and many more. These aspects are still far from being included in current model systems.

Successful strategies for obtaining (in a targeted manner) stable and well-defined di- and multinuclear complexes generally rely on compartmental ligand scaffolds that provide distinct binding pockets for the metal ions.[4,56] This may be achieved by incorporating proper donor sites within a single macrocyclic framework or by linking two (or more) individual ligand subunits by means of a more or less rigid spacer. The spacer itself may contain built-in donor atoms to reduce the flexibility and increase preorganization of the dinucleating scaffold; phenolate-based systems are certainly the most abundant among these. Attractive metal–metal distances usually range from 3 to 5 Å. This report will highlight a particular class of model complexes for di- and oligonuclear metallohydrolase active sites, where compartmental pyrazolate-based ligands are used as dinucleating scaffolds for nesting two metal ions (**C**).[57] The central pyrazolate unit is a reasonable compromise for mimicking bridging carboxylate donors that are widely found in nature but are difficult to incorporate into a polydentate compartmental ligand framework: just like a bridging carboxylate group, the pyrazolate provides a single negative charge and it supports a similar range of metal–metal distances.

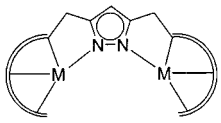


**C**

The scope of modulating electronic and geometric characteristics of the dimetallic core by varying the ligand side arms attached to the 3- and 5-positions of the heterocycle is an attractive option for this class of ligands. Important variations comprise the type and number of side-arm donor atoms as well as the lengths of the chelate arms (Scheme 6). While the former allows for the modification of the coordination numbers and electronic structures of the metal ions, the latter controls the properties of the dimetallic pocket, including the metal–metal distance.[58–63]

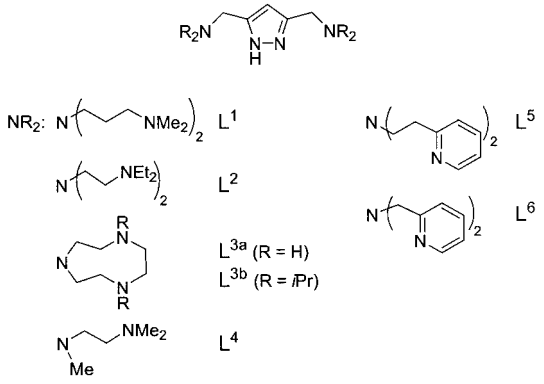


Scheme 6. Selection of dinucleating pyrazolate ligands.

The comparative experimental studies summarized in this microreview focus on dizinc complexes of ligands $L^1$–$L^6$ that provide two metal-ion-binding pockets each, either tridentate ($L^4$) or tetradentate ($L^1$–$L^3$, $L^5$, $L^6$). The primary intention behind this approach is to elucidate how the mutual arrangement of two metal ions determines their cooperative reactivity. It is not aimed at exactly reproducing any biological coordination environment, but emphasis is laid on the question how two (or more) metals may work in concert in order to bind and transform biorelevant substrates. Inter alia, studies on this assortment of ligands have provided experimental evidence for the less favorable reactivity of a tightly bridging hydroxide in the clamp of a dimetal site as compared with a more loosely bridging $O_2H_3$ unit. The results also reveal some general structure–activity correlations for bioinspired di- and oligozinc hydrolase mimics. In the long term, it is anticipated that such findings will contribute to the development of two-center catalysis not only in the biomimetic but also in a broader sense.

## 4. Zinc Coordination Chemistry of the Pyrazolate-Based Scaffolds

### (i) Dizinc Complexes with OH versus $O_2H_3$ Bridges

As outlined above, a dimetallic arrangement with a bridging $O_2H_3^-$ group can be described as a combination

 © 2006 Wiley-VCH Verlag GmbH & Co. KGaA, Weinheim 

of both a $Zn–OH_2$ and a Zn–OH function, and hence as a hydrated form of an active terminal Zn–OH. A comparative evaluation of the hydrolytic activity of a Zn–O(H)–Zn relative to that of a Zn–(H)OHO(H)–Zn species in synthetic model chemistry was achieved with the highly preorganized dizinc complexes **5** and **6** (Scheme 7), where the metal–metal separation is controlled by the lengths of the chelating side arms.[64] Complementing information was obtained from complexes **1** and **2** that are based on the related aliphatic ligand scaffolds, but in this case the system with long side arms (forming six-membered chelate rings in **1**) exhibits rather weak $Zn^{2+}$-binding capabilities in aqueous solution, which precludes any conclusive evaluation of its hydrolytic efficiency under the appropriate conditions.[65]

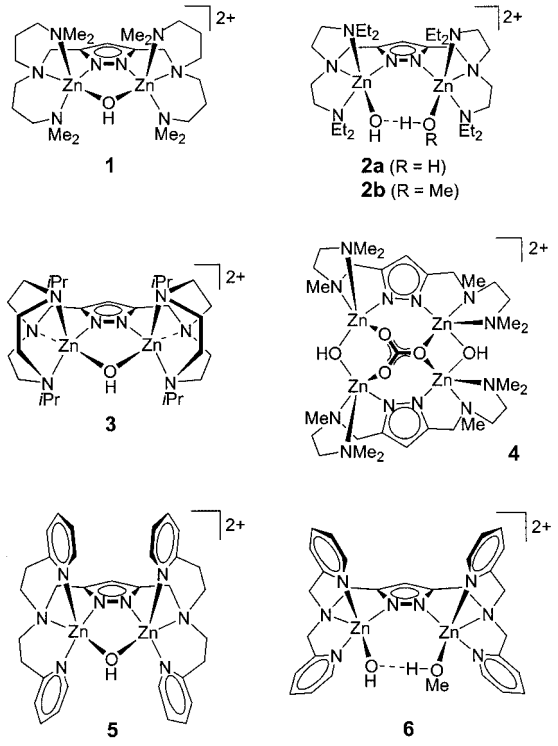


Scheme 7. Assortment of crystallographically characterized pyrazolate-based zinc complexes.[64,65]

In **1** and **5** the zinc ions may come rather close together (≈3.5 Å) and allow for a bridging position of a hydroxide coligand within the dimetallic pocket. In contrast, the shorter ligand side arms in **2a/b** and **6** pull the two zinc ions back and apart, thus enforcing much longer Zn···Zn distances (>4 Å). This prevents the small hydroxide from spanning the two metal ions and induces incorporation of an additional solvent molecule, water or MeOH, to give an $O_2H_3$ (**2a**) or $O_2H_2Me$ (**2b**, **6**) bridging unit, respectively. Differences in reactivity for these species are apparent, since in acetone solution **2a** gradually absorbs $CO_2$ from air to give a carbonato-bridged complex while **1** does not.[43] Stopped-flow studies on the dinickel(II) analogues of **2a/2b** have revealed that exchange of water and methanol in these complexes is very rapid with $k_{obs} > 10^3\ s^{-1}$ at room temperature.[66] The lability of the $Zn–H_3O_2–Zn$ bridge has been corroborated by extensive DFT calculations on the mechanism of the replacement of water by methanol in pyrazolate-based complexes of types **2** and **6** to successively give the Zn-bound HO–H–OMe and MeO–H–OMe functionalities (by an endothermic process).[67] The replacement can occur through two fundamentally different substitution mechanisms: an addition-elimination, controlled by the metal ions, and a direct exchange in which the metal ions serve as a template. Since the steric bulk and the stiffness of the ligands in **2a** and **6** prevent an easy expansion of the coordination sphere, only the direct exchange mechanism is possible for these systems. Nevertheless, barriers for the conversion of the HO–H–OH, HO–H–OMe, and MeO–H–OMe bridges are low enough (lower for **6** than for **2**) to enable a rapid equilibrium under experimental conditions. Comparing the different functionalities, the HO–H–OH form is clearly less nucleophilic than the methoxide form MeO–H–OMe, but the hydroxide in the mixed species HO–H–OMe is more nucleophilic than the methanol component.[67]

Fewer short side arms provided by the ligand in **4** allow for greater flexibility of the Zn···Zn distance and offer additional coordination sites for substrate binding. At neutral to basic pH, the dizinc complex **4′** formed in situ from $L^4$ and $Zn(ClO_4)_2$ was found to readily absorb $CO_2$ from air to give tetranuclear **4**, where two $\{L^4H_{-1}Zn_2\}$ subunits are linked by two hydroxide bridges and the resulting rectangle of four zinc ions is capped by a $\mu_4$-carbonate.[68]

Unexpectedly, a bridging hydroxide was detected crystallographically in **3**,[65] despite the short ligand side arms that were assumed to induce a situation similar to the corresponding dinickel(II) complex **2a**. This can be traced to the ability of zinc(II) to adopt a {4+1} coordination with two significantly elongated backside bonds between zinc and the bridgehead-N in **3**. However, the dinuclear scaffold in **3** appears to be somewhat strained and it is assumed that the bridging hydroxide in **3** more easily adopts a semibridging or even nonbridging position in solution than the tightly bound hydroxide in **1** and **5**. Unfortunately, no crystallographic information is yet available for $[L^{3a}Zn_2(OH)(H_2O)_x]^{2+}$.

### (ii) p$K_a$ of the Zn-Bound Water

While the X-ray crystallographic results provide structural insight for the various complexes, knowledge of the species distribution in aqueous solution is crucial for understanding their hydrolytic reactivity. Species distributions of ligands $L^1$–$L^6$ in the presence of $Zn^{2+}$ have been determined by potentiometric titrations and have revealed the existence of various mononuclear and dinuclear complexes depending on the pH, except for the case of $L^1$, where only mononuclear species are formed in the pH range 4–7 and precipitation of zinc hydroxide is observed at higher pH.[64,65,69,70] As expected, ligands that form six-membered chelate rings generally provide lower complex stability than the corresponding systems that form five-membered chelate

 © 2006 Wiley-VCH Verlag GmbH & Co. KGaA, Weinheim 

rings, and complexes with pyridyl-containing ($L^5$, $L^6$) or triazacyclononane-derived ligands ($L^{3a}$, $L^{3b}$) give more stable complexes than the corresponding open-chain aliphatic scaffolds ($L^1$, $L^2$, $L^4$). The species distribution diagram of $L^{3a}/Zn^{2+}$ differs somewhat from that of the system $L^{3b}/Zn^{2+}$, supporting a significant effect of the outer side-arm substituents.[65,70] For all ligands except $L^1$, the dominant species above pH ≈ 8 is $[(LH_{-2})Zn_2]^{2+}$, which most likely represents the complex structures **2a**, **3**, **5**, or **6** observed in the solid state. The species $[(LH_{-2})Zn_2]^{2+}$ is thus better described as $[(LH_{-1})Zn_2(OH)]^{2+}$ or $[(LH_{-1})Zn_2(O_2H_3)]^{2+}$. The $pK_A$ of the zinc-bound water can be extracted from the titration data, and values obtained for $[(LH_{-1})Zn_2(OH_2)_x]^{3+}$ (L = $L^2$ – $L^6$) are collected in Table 1.

Table 1. $pK_A$ values for the deprotonation of Zn-bound water in dizinc complexes $[(LH_{-1})Zn_2(OH_2)_x]^{3+}$ to give $[(LH_{-1})Zn_2(OH)(OH_2)_{x-1}]^{2+}$.[64,65,69,70]

| Species | $L^1$ | $L^2$ | $L^{3a}$ | $L^{3b}$ | $L^4$ | $L^5$ | $L^6$ |
|---|---|---|---|---|---|---|---|
| $pK_A$ | – | 7.57 | 8.29 | 8.04 | 7.66 | 7.96 | 7.60 |

All $pK_A$ values are clearly lower than the $pK_a$ of $[Zn(H_2O)_6]^{2+}$ (8.96)[71] and lower than most $pK_A$ values of zinc-bound water in five-coordinate mononuclear zinc complexes with tetradentate tripodal ligands. The $pK_A$ values 8.29, 8.04, and 7.96 for $[(L^{3a}H_{-1})Zn_2]^{3+}$, $[(L^{3b}H_{-1})Zn_2]^{3+}$, and $[(L^5H_{-1})Zn_2]^{3+}$, respectively, appear to be relatively high for bridging water in dinuclear zinc(II) complexes, which is often found to have $pK_a$ values below 8. However, a similar $pK_A$ of 8.0 for metal-bound water has been determined for the dizinc complex of the dinucleating ligand comprising two tacn subunits tethered by a bridging alkoxide.[72] The mononuclear complex $[(Me_3tacn)Zn(OH_2)_3]^{2+}$ ($Me_3tacn$ = 1,4,7-trimethyl-1,4,7-triazacyclononane) is much less acidic ($pK_A$ ≈ 10.8), which has to be attributed (at least in part) to its higher coordination number.[73] Comparison is more straightforward for the system $L^6/Zn^{2+}$, since $[(tpa)Zn(OH_2)]^{2+}$ {tpa = tris(pyridylmethyl)amine} can be viewed as a mononuclear analogue of $[(L^6H_{-1})Zn_2(OH_2)_x]^{3+}$.[60] The $pK_a$ of $[(tpa)Zn(OH_2)]^{2+}$ is 8.03,[74] clearly indicating a certain increase in acidity due to the dinuclear arrangement in **6** that induces formation of the $O_2H_3$ bridge.

As the most interesting result of these considerations, it should be noted that involvement in strong hydrogen bonding (such as in the $O_2H_3$ bridge) can cause an even more drastic decrease in the $pK_A$ of Zn-bound water than incorporation of the resulting hydroxide in a bridging position between two zinc ions, as is evident from a comparison of the values of $pK_A$ = 7.60 for $[(L^6H_{-1})Zn_2(OH_2)_x]^{3+}$ and $pK_A$ = 7.96 for $[(L^5H_{-1})Zn_2(OH_2)_x]^{3+}$.[64] The same holds true for the corresponding pyrazolate systems with aliphatic N-donor side arms, where $pK_A$ = 7.57 for $[(L^2H_{-1})Zn_2(OH_2)_x]^{3+}$, $pK_A$ = 8.29 for $[(L^{3a}H_{-1})Zn_2(OH_2)_x]^{3+}$, and $pK_A$ = 8.04 for $[(L^{3b}H_{-1})Zn_2(OH_2)_x]^{3+}$.[65,69,70] These findings clearly demonstrate that a bridging position of water (or the resulting hydroxide) is *not* required for sufficiently lowering its $pK_A$ to give a zinc-bound hydroxide at physiological pH, since this increase in acidity may well be achieved by the appropriate hydrogen-bonding pattern such as that found in the intramolecular $O_2H_3$ bridge.[64,65] Similar conclusions have also been reached for the influence of hydrogen bonding in mononuclear zinc hydroxide systems.[75] This observation supports the view that the $O_2H_3$ unit is an attractive structural and possibly functional motif in oligozinc enzyme chemistry.[42,43,64]

## 5. Models for Oligozinc Phosphatases

Despite the manifold studies on zinc-containing model phosphatases, there is still only limited knowledge about the intrinsic factors that govern hydrolytic activity and a lack of general structure–reactivity correlations.[72,76] The assortment of dizinc complexes described above appeared to be a promising set of systems for gaining further clues on the cooperative action of two proximate zinc atoms in biomimetic hydrolytic reactions.

### (i) Structure–Activity Correlations in Phosphate Diester Hydrolysis

Phosphatase activities of the various pyrazolate-based dizinc complexes have been evaluated in 1:1 DMSO/aqueous buffer (or pure water in the case of the $L^{3a}/Zn^{2+}$ system[77]), by using sodium bis(4-nitrophenyl) phosphate (sodium bnpp) as a test substrate (Scheme 8). Differences among the series of complexes gave valuable insights into structure–activity correlations and allowed for the experimental assessment of the hydrolytic efficiency of a bridging versus pseudo-terminal Zn-bound hydroxide.[64,65] Instead of crystallographically characterized **4**, dinuclear species $\{L^4H_{-1}Zn_2\}$ (**4′**) prepared in situ from $L^4$ and 2 equiv. $Zn(ClO_4)_2 \cdot 6H_2O$ was used without isolation of the complex in order to avoid any possible active-site inhibition by the carbonate.

Since **1** is not stable in aqueous solution, results for this complex are not meaningful. For all other systems (**2**, **3**, **4′**, **5**, **6**), the rate of BNPP hydrolysis was linearly dependent on complex concentration, in agreement with pyrazolate-based dizinc active species. Pseudo-first-order rate constants $k_{obs}$ (defined by $v_0 = k_{obs} \cdot [complex]_0$) at pH 8.28 are collected in Figure 1, showing drastic differences between the complexes. Except for **2**, inspection of the pH-depen-

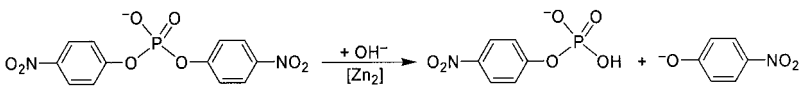


Scheme 8. Phosphodiesterase model reaction with BNPP test substrate.

 © 2006 Wiley-VCH Verlag GmbH & Co. KGaA, Weinheim 

dence of $k_{obs}$ revealed that the sigmoidal increase in hydrolysis rate at higher pH generally coincides with the formation of species $[LH_{-1}Zn_2(OH)(H_2O)_x]^{2+}$ featuring the Zn-bound hydroxide. This clearly established that deprotonation of the $Zn–OH_2$ function is required for hydrolytic activity, in accordance with findings for other phosphatase model systems. Only in the case of **2** did the species $[LH_{-1}Zn_2(OH)(H_2O)_x]^{2+}$ turn out to be inactive, which was interpreted in terms of a bidentate substrate binding within the dimetallic pocket that replaces the Zn-bound hydroxide and leaves no accessible coordination sites for activation of the water nucleophile (compare also results for phosphate ester binding summarized below).[65] Taking into account the individual species distributions and the predominance of the active species at the relevant pH, a more reliable comparison with reference to the true second-order rate constants $k_{bim}$ that included the percentage factor for the $[LH_{-1}Zn_2(OH)(H_2O)_x]^{2+}$ species at pH 8.28 is also given (Figure 1). Trends are qualitatively similar to those for the $k_{obs}$ values, with the order of activity **4′** > **6** > **5** > **3**.

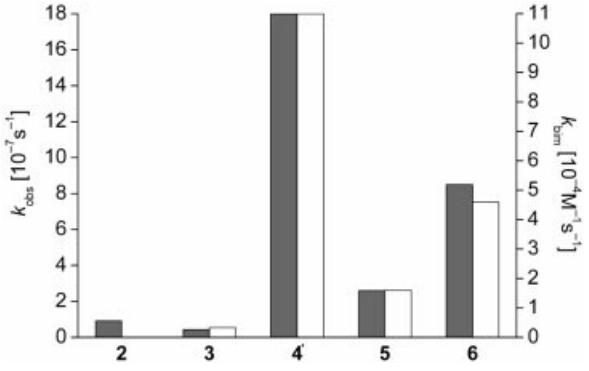


Figure 1. Comparison of rate constants $k_{obs}$ (dark) and $k_{bim}$ (light) for BNPP hydrolysis at pH 8.28 mediated by the different pyrazolate-based dizinc complexes.

Direct comparison of **5** and **6** proved most insightful and allowed us to draw valuable conclusions regarding the relative hydrolytic efficiencies of the Zn–OH–Zn and Zn–$O_2H_3$–Zn functions, since both **5** and **6** are fully stable under the experimental conditions and have closely related dimetallic core structures. The effect of substrate concentration on the initial hydrolysis rate suggested a substrate-binding pre-equilibrium, and a Michaelis–Menten type analysis gave almost identical $K_M$ values of 51 ± 5 mM and 56 ± 4 mM, but very distinct $k_{cat}$ values of $(0.49 \pm 0.04) \times 10^{-5}$ $s^{-1}$ and $(2.3 \pm 0.1) \times 10^{-5}$ $s^{-1}$ for **5** and **6**, respectively. Evidently, it is not the initial substrate binding, but the subsequent intrinsic reactivity at the dizinc core that makes the difference, leading to an almost fivefold higher hydrolytic activity for **6**. Although any further interpretation was hampered by the lack of structural information for the intermediate {complex–substrate} adducts, these data strongly support the view of the Zn–$O_2H_3$–Zn moiety as a favorable functional unit in dizinc enzyme chemistry.

After a single turnover, BNPP hydrolysis by any of the dizinc complexes **3**–**6** became much slower or even stopped completely. This has to be attributed to inhibition by the formed phosphate monoester (which is a much stronger ligand), and structural insight for the phosphate inhibited dizinc sites was obtained from isolated product-bound complexes (see below). In methanol, however, catalytic transesterification was observed to sequentially give the mixed diester methyl 4-nitrophenyl phosphate and dimethyl phosphate (dmp).[64] While the first transesterification step again occurred much faster when mediated by **6** as compared to **5**, the opposite was true for the second step. Apparently, complex **6** is intrinsically more active, but on the other hand, inhibition is also more pronounced for the system with the larger Zn···Zn distance. On the basis of structural insight for the two dizinc complexes with bound DMP as well as NMR studies, the differences in inhibition could be rationalized and traced to stronger DMP binding in the dimetallic clamp of **6**: while the larger Zn···Zn separation enforced by the ligand scaffold $L^6$ is perfectly suited to accommodate the bridging O–P–O moiety of DMP, ligand $L^5$ favors much shorter Zn···Zn distances.[64] Hence the pyrazolate-based dizinc arrangement in **5** has to be distorted drastically to host the DMP bridge (Figure 2), resulting in a much decreased DMP binding affinity. This may hint towards a suitable strategy to avoid the latent problem of product inhibition in synthetic dizinc hydrolase models.

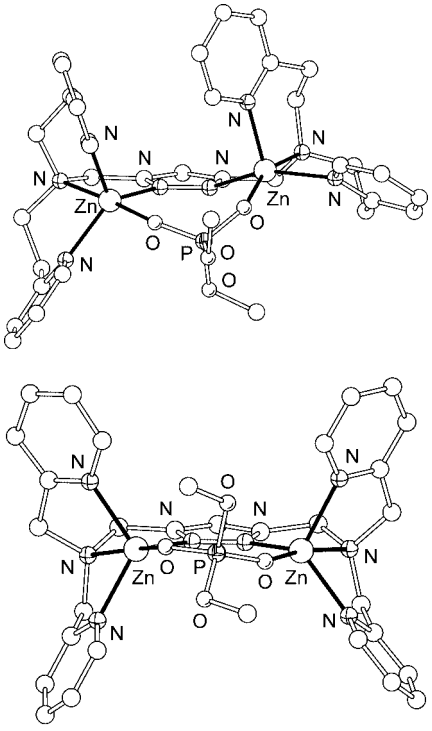


Figure 2. Molecular structures of $[L^5H_{-1}Zn_2(dmp)]^{2+}$ (top) and $[L^6H_{-1}Zn_2(dmp)]^{2+}$ (bottom) illustrating the much greater distortion of the dizinc scaffold in the former case.

As was also stated for the related complex $[L^{3a}H_{-1}Zn_2(OH)(H_2O)_x]^{2+}$,[77] it can be concluded that the pyrazolate-based dizinc complexes show many typical features of a metalloenzyme, such as formation of a substrate complex, activation of the substrate through coordination, preorganiza-

 © 2006 Wiley-VCH Verlag GmbH & Co. KGaA, Weinheim 

tion of the substrate and the nucleophile, and inhibition by the product.

### (ii) Dizinc Scaffolds with Bound Phosphate

The same *O*,*O*′-bridging DMP coordination mode shown in Figure 2 has been detected crystallographically in complexes $[L^2H_{-1}Zn_2(dmp)]^{2+}$, $[L^4H_{-1}Zn_2(dmp)(NO_3)_2]^{2+}$, $[L^5H_{-1}Zn_2(dmp)]^{2+}$, and $[L^6H_{-1}Zn_2(dmp)]^{2+}$, with Zn···Zn distances between 4.2 and 4.4 Å.[64,65] A similar binding mode was also observed for diphenyl phosphonate (dpp) in the related dicopper(II) complex $[L^{3a}H_{-1}Cu_2(dpp)]^{2+}$, while a $\mu_4$-κ*O*:κ*O*′:κ*O*′′:κ*O*′′′ phosphate was found in $[(L^{3a}H_{-1}Cu_2)_2(PO_4)]^{3+}$.[70] It should be noted that structures with bidentate bridging DMP are reminiscent of the proposed phosphate ester binding in the dizinc active sites of various metallohydrolases[78] and mimic a crucial intermediate in the phosphotriesterase mechanism (compare Scheme 1).[15]

ESI mass spectrometry confirmed the weak binding of BNPP, but significantly stronger coordination of the first hydrolysis product 4-nitrophenyl phosphate (npp), as well as of DMP. Active-site inhibition of the most active complex **4**′ by NPP was visualized in the structure of the complex $[(L^4H_{-1}Zn_2)_2(OH)_2(npp)]^{2+}$ (**7**; Scheme 9), where the NPP caps a rectangle of four zinc ions and blocks all accessible coordination sites.[65] Accordingly, only 0.5 equiv. BNPP is hydrolyzed per $\{L^4H_{-1}Zn_2\}$ (**4**′).

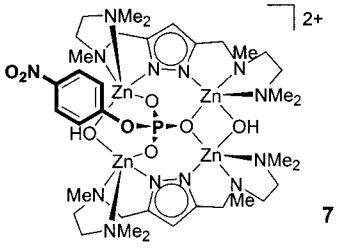


Scheme 9. Complex derived from inhibition of **4**′ by 4-nitrophenyl phosphate.[65]

## 6. Models for Dizinc Metallo-β-lactamases

Despite the extensive work on synthetic metallohydrolase models, very few studies have employed preorganized dinuclear zinc(II) complexes as functional mimics of metallo-β-lactamases.[79–81] Such model studies may contribute valuable insights into the mechanistic roles and cooperative effects of the proximate metal ions in that important class of enzymes and the identity of the active nucleophile. Furthermore, isolated adducts between synthetic dizinc scaffolds and β-lactam compounds or their ring-opened derivatives should provide clues to possible substrate binding modes.

### (i) Penicillin G Hydrolysis

Several pyrazolate-based dizinc complexes turned out to be active mediators for the hydrolytic cleavage of penicillin G. Following the time course of penicillin G hydrolysis promoted by **1**, **2a**, **5**, and **6** with in situ FTIR spectroscopy revealed drastic differences in activity (Scheme 10, Figure 3).[80]

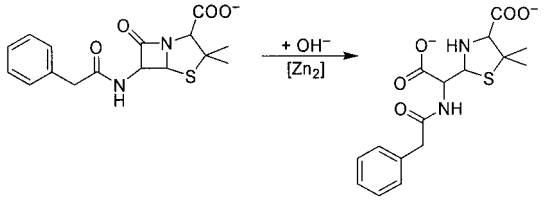


Scheme 10. Hydrolytic cleavage of penicillin G mediated by the dizinc complexes.

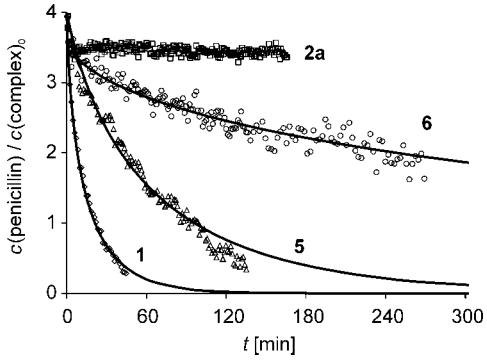


Figure 3. Time course of penicillin G hydrolysis in DMSO/water (9:1) in the presence of the different dizinc complexes.[80]

Unexpectedly, hydrolytic efficiency is much greater for systems **1** and **5**, which feature a shorter Zn···Zn separation and a bridging hydroxide in their resting state, while complex **2a** is not active at all, and **6** is still less efficient than free $Zn^{2+}$. Mass spectrometry in combination with NMR and IR spectroscopy indicated predominant coordination of the β-lactam antibiotics through their carboxylate group, whereas involvement of the β-lactam C=O in metal coordination could not be unambiguously deduced from the spectroscopic data, in agreement with findings for other dizinc metallo-β-lactamase model systems.[79] NMR experiments of the reaction mixtures suggested an explanation for the much greater hydrolytic activity of **1** and **5** relative to **2a** and **6**: after substrate binding through the carboxylate anchor with replacement of the Zn-bound hydroxide (compare the structure of **9** shown below), only in the case of the six-membered chelate rings in **1** and **5** do the labile side-arm N-donors tend to dissociate to generate an accessible coordination site and to allow for the binding and activation of the water nucleophile. In contrast, the five-membered chelate rings in **2a** and **5** impart much higher stability, rendering any detachment of the ligand side arms less likely. Hemilability of the longer side arms in related pyrazolate-based dimetal complexes could also be confirmed structurally in several cases.[59a,62a,80] These observations underline the necessity for the activation of both the substrate and the nucleophile through zinc coordination, which requires suitably designed dimetallic scaffolds that offer sufficient and properly oriented binding sites.

 © 2006 Wiley-VCH Verlag GmbH & Co. KGaA, Weinheim 

### (ii) Structural Characterization of Dizinc β-Lactam Adducts

Unfortunately, it was not possible to isolate any adduct between a dizinc complex and the penicillin substrate or its ring-opened product in crystalline form suitable for X-ray diffraction. In order to obtain structural insight into β-lactam binding at dizinc sites, we therefore turned to smaller substrate analogues featuring different levels of structural simplification as compared to penicillin. The most simple choice is 2-azetidinone, which is readily incorporated into the dimetallic pocket of some of the pyrazolate-based dizinc complexes, giving lactamide-bridged complexes such as **8** (Scheme 11).[82]

Comparison of the IR spectroscopic and metric characteristics of the N-deprotonated lactamide with those of free azetidinone,[83,84] and the β-lactamide subunit of a mononuclear $Tp^{Cum,Me}$Zn(β-lactamido) complex [Scheme 11; $Tp^{Cum,Me}$ = tris(3-cumyl-5-methylpyrazolyl)borate][85] was informative: in the latter system the β-lactamide is solely bound by its N atom to a single zinc ion, which reduces conjugation within the amide moiety and hence leads to lengthening of the C–N bond and a slight shortening of the C=O bond. Binding of a second zinc ion to the β-lactamide-O as observed in complex **8** reverses this trend, i.e. the C–N bond is shortened and the C=O bond is clearly elongated. In line with these structural findings, the β-lactam ν(C=O) stretch in $Tp^{Cum,Me}$Zn(β-lactamido) at 1709 $cm^{-1}$ is barely shifted from those of free 2-azetidinone, while the ν(C=O) vibration of **8** appears at much lower frequency. These findings underline the particular ability of highly preorganized dinuclear scaffolds to accommodate and polarize small substrate molecules within their dimetallic binding pocket, which is quite distinct from activation at a single metal ion.

2-Azetidinone is apparently unsuited as a model substrate with regard to penicillin binding at a dizinc site because coordination of the deprotonated β-lactam-*N* is undesired. N-substituted oxazetidinylacetate (oaa; Scheme 12) proved more appropriate, since that also incorporates the carboxylate group in an α position to the β-lactam-*N*. The carboxylate of penicillin G was identified spectroscopically as the primary anchoring group for substrate binding at the dizinc scaffolds, and the same applies to complexes of oaa, e.g. in structurally characterized **9**.[80]

Interestingly, additional coordination of the β-lactam-*O* does occur if the ligand scaffold provides fewer side arms and hence leaves accessible sites at the metal ion. The tetrametallic complex **10** represents the first system for which binding of a β-lactam-*O* has been verified crystallographically. The C=O bond in **10** is markedly lengthened relative to **9**, and the ν(C=O) stretch is found at a significantly lower frequency (Scheme 12). Such polarization is usually assumed to activate the amide moiety for nucleophilic attack.

While the structural findings confirm that for β-lactam antibiotics (or related β-lactam derivatives) binding of zinc to the carboxylate group is favored over binding to the β-lactam function, coordination of the β-lactam amide-O may still be induced under suitable circumstances or upon proper orientation of the substrate within the binding

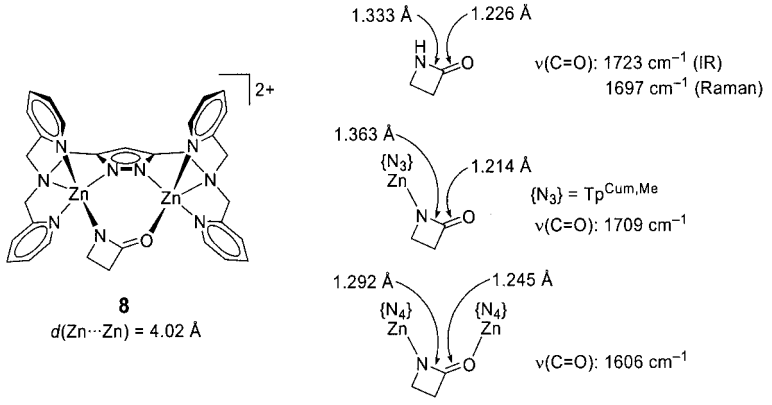


Scheme 11. (β-lactamido)zinc systems.

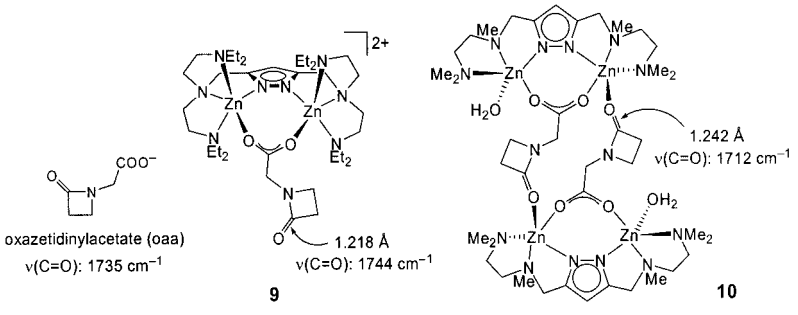


Scheme 12. Binding of oxazetidinylacetate (oaa).[80]

 © 2006 Wiley-VCH Verlag GmbH & Co. KGaA, Weinheim 

pocket, and this leads to significant changes of the internal geometry of the β-lactam moiety, which are likely to facilitate subsequent hydrolytic ring cleavage. It is plausible that electrostatics contributes significantly to the preferential binding of an anionic carboxylate to the highly charged pyrazolate-based dizinc scaffolds $\{LZn_2\}^{3+}$, but a lower positive charge of the dizinc arrangement or involvement of the carboxylate in interactions with positively charged protein residues or in strong hydrogen bonding within the enzyme active site may well alter the binding preference in favor of the neutral β-lactam amide moiety.

## Concluding Remarks

The studies summarized above demonstrate how the investigation of well-designed synthetic model complexes may afford clues to the understanding of substrate transformations at metalloenzyme active sites. The compartmental pyrazolate-based ligand scaffolds have the distinct advantage of easy tuning of essential parameters in the dimetallic core – such as the metal–metal separation – which have a decisive effect on reactivity. A bridging position of water (or the resulting hydroxide) between the two zinc ions is not required for sufficiently lowering its p$K_a$, but proper hydrogen bonding of the pseudo-terminal Zn–OH, such as the one in the $Zn–O_2H_3–Zn$ function, does the job and at the same time may result in higher nucleophilicity of the Zn-bound hydroxide. Comparative functional studies on the phosphodiesterase activity of an assortment of pyrazolate-based dizinc complexes provided experimental support for a possible functional role of the $Zn–O_2H_3–Zn$ motif and structural insight into phosphate ester binding at dimetal sites. Similarly, some structure–activity correlations could be deduced for penicillin hydrolysis at bioinspired dizinc sites, and first crystallographic evidence for coordination and activation of a β-lactam could be obtained. Future directions in the development of synthetic analogues of dizinc enzymes will comprise, inter alia, the incorporation of functional groups that emulate mechanistically important protein residues in the vicinity of the active site.

## Acknowledgments

Our work in the field of metallohydrolase models has been supported by the DFG, the German Academic Exchange Service (DAAD) and COST D21. Close collaborations with Dr. E. Farkas (Debrecen/Hungary) within the working group 0001 of the COST D21 program has been particularly beneficial for these studies.

[1] D. E. Wilcox, *Chem. Rev.* **1996**, *96*, 2435–2458.
[2] N. Sträter, W. N. Libscomb, T. Klabunde, B. Krebs, *Angew. Chem.* **1996**, *108*, 2159–2191; *Angew. Chem. Int. Ed. Engl.* **1996**, *35*, 2025–2055.
[3] N. C. Horton, J. J. Perona, *Nat. Struct. Biol.* **2001**, *8*, 290–293.
[4] J. Weston, *Chem. Rev.* **2005**, *105*, 2151–2174.
[5] J. A. Cowan, *Chem. Rev.* **1998**, *98*, 1067–1087.
[6] a) E. Kimura, T. Koike, *Adv. Inorg. Chem.* **1997**, *44*, 229–261; b) J. E. Coleman, *Curr. Opin. Chem. Biol.* **1998**, *2*, 222–234.
[7] a) N. O. Concha, B. A. Rasmussen, K. Bush, O. Herzberg, *Structure* **1996**, *4*, 823–836; b) Z. Wang, W. Fast, A. M. Valentine, S. Benkovic, *Curr. Opin. Chem. Biol.* **1999**, *3*, 614–622.
[8] J. A. Cricco, E. G. Orellano, R. M. Rasia, E. A. Ceccarelli, A. J. Vila, *Coord. Chem. Rev.* **1999**, *190–192*, 519–535.
[9] a) W. T. Lowther, B. W. Matthews, *Chem. Rev.* **2002**, *102*, 4581–4607; b) R. C. Holz, *Coord. Chem. Rev.* **2002**, *232*, 5–26; c) R. C. Holz, K. P. Bzymek, S. I. Swierczek, *Curr. Opin. Chem. Biol.* **2003**, *7*, 197–206.
[10] a) M. M. Benning, J. M. Kuo, F. M. Raushel, H. M. Holden, *Biochemistry* **1994**, *33*, 15001–15007; b) M. M. Benning, J. M. Kuo, F. M. Raushel, H. M. Holden, *Biochemistry* **1995**, *34*, 7973–7978; c) M. M. Benning, H. Shim, F. M. Raushel, H. M. Holden, *Biochemistry* **2001**, *40*, 2712–2722.
[11] E. E. Kim, H. W. Wyckoff, *J. Mol. Biol.* **1991**, *218*, 449–464.
[12] a) J. E. Coleman, *Annu. Rev. Biophys. Biomol. Struct.* **1992**, *21*, 441–483; b) K. M. Holtz, E. R. Kantrowitz, *FEBS Lett.* **1999**, *462*, 7–11; c) M. J. Jedrzejas, P. Setlow, *Chem. Rev.* **2001**, *101*, 607–618.
[13] R. X. Xu, A. M. Hassell, D. Vanderwall, M. H. Lambert, W. D. Holmes, M. A. Luther, W. J. Rocque, M. V. Milburn, Y. Zhao, H. Ke, R. T. Nolte, *Science* **2000**, *288*, 1822–1825.
[14] Q. Huai, J. Colicelli, H. Ke, *Biochemistry* **2003**, *42*, 13220–13226.
[15] a) S. D. Aubert, Y. Li, F. M. Raushel, *Biochemistry* **2004**, *43*, 5707–5715; b) M. L. Ortiz-Hernández, R. Quintero-Ramirez, A. A. Nava-Ocampo, A. M. Bello-Ramirez, *Fundam. Clin. Pharmacol.* **2003**, *17*, 717–723; c) S. B. Hong, F. M. Raushel, *Biochemistry* **1996**, *35*, 10904–10912.
[16] G. A. Omburo, J. M. Kuo, L. S. Mullins, F. M. Raushel, *J. Biol. Chem.* **1992**, *267*, 13278–13283.
[17] a) A. Volbeda, A. Lahm, F. Sakiyama, D. Suck, *EMBO J.* **1991**, *10*, 1607–1618; b) C. Romier, R. Dominguez, A. Lahm, O. Dahl, D. Suck, *Proteins: Struct., Funct., Bioinf.* **1998**, *32*, 414–424.
[18] Z. Wang, W. Fast, S. J. Benkovic, *Biochemistry* **1999**, *38*, 10013–10023.
[19] C.-G. Zhan, F. Zheng, *J. Am. Chem. Soc.* **2001**, *123*, 2835–2838.
[20] B. Bennett, R. C. Holz, *J. Am. Chem. Soc.* **1997**, *119*, 1923–1933.
[21] N. Díaz, D. Suárez, K. M. Merz Jr, *J. Am. Chem. Soc.* **2000**, *122*, 4197–4208.
[22] a) M. I. Page, *Acc. Chem. Res.* **1984**, *17*, 144–151; b) M. I. Page, A. P. Laws, *Chem. Commun.* **1998**, 1609–1617.
[23] K. Bush, G. A. Jacoby, A. E. Medeiros, *Antimicrob. Agents Chemother.* **1995**, *39*, 1211–1233.
[24] B. G. Hall, S. J. Salipante, M. Barlow, *J. Mol. Evol.* **2003**, *57*, 249–254.
[25] a) K. Bush, *Clin. Infect. Dis.* **1998**, *27*, 48–53; b) Z. Wang, W. Fast, A. M. Valentine, S. J. Benkovic, *Curr. Opin. Chem. Biol.* **1999**, *3*, 614–622; c) J. A. Cricco, A. J. Vila, *Curr. Pharm. Des.* **1999**, *5*, 915–927.
[26] a) H. C. Neu, *Science* **1992**, *257*, 1064–1072; b) U. Heinz, H. W. Adolph, *Cell. Mol. Life Sci.* **2004**, *61*, 2827–2839.
[27] a) D. J. Payne, *J. Med. Microbiol.* **1993**, *39*, 93–99; b) J. M. Frère, *Mol. Microbiol.* **1995**, *16*, 385–395; c) K. Bush, *Curr. Pharm. Des.* **1999**, *5*, 839–845; d) G. M. Rossolini, *Clin. Infect. Dis.* **2005**, *41*, 1557–1558.
[28] R. M. Rasia, A. J. Vila, *Biochemistry* **2002**, *41*, 1853–1860.
[29] J. Spencer, T. R. Walsh, *Angew. Chem.* **2006**, *118*, 1038–1042; *Angew. Chem. Int. Ed.* **2006**, *45*, 1022–1026.
[30] A. Carfi, S. Pares, E. Duée, M. Galleni, C. Duez, J. M. Frère, O. Dideberg, *EMBO J.* **1995**, *14*, 4914–4921.
[31] N. O. Concha, B. A. Rasmussen, K. Bush, O. Herzberg, *Structure* **1996**, *4*, 823–836.
[32] J. H. Ullah, T. R. Walsh, I. A. Taylor, D. C. Emery, C. S. Verma, S. J. Gamblin, J. Spencer, *J. Mol. Biol.* **1998**, *284*, 125–136.

 © 2006 Wiley-VCH Verlag GmbH & Co. KGaA, Weinheim 

[33] A. Carfi, E. Duée, M. Galleni, J. M. Frère, O. Dideberg, *Acta Crystallogr. Sect. D* **1998**, *54*, 313–323.
[34] S. M. Fabiane, M. K. Sohi, T. Wan, D. J. Payne, J. H. Bateson, T. Mitchell, B. J. Sutton, *Biochemistry* **1998**, *37*, 12404–12411.
[35] N. O. Concha, C. A. Janson, P. Rowling, S. Pearson, C. A. Cheever, B. P. Clarke, C. Lewis, M. Galleni, J. M. Frère, D. J. Payne, J. H. Bateson, S. S. Abdel-Meguid, *Biochemistry* **2000**, *39*, 4288–4298.
[36] I. García-Sáez, P. S. Mercuri, C. Papamicael, R. Kahn, J. M. Frère, M. Galleni, G. M. Rossolini, O. Dideberg, *J. Mol. Biol.* **2003**, *325*, 651–660.
[37] Z. Wang, S. J. Benkovic, *J. Biol. Chem.* **1998**, *273*, 22402–22408.
[38] D. Suárez, N. Díaz, K. M. Merz Jr, *J. Comput. Chem.* **2002**, *23*, 1587–1600.
[39] D. Suárez, E. N. Brothers, K. M. Merz Jr, *Biochemistry* **2002**, *41*, 6615–6630.
[40] M. Dal Peraro, A. J. Vila, P. Carloni, *Inorg. Chem.* **2003**, *42*, 4245–4247.
[41] M. Krauss, H. S. R. Gilson, N. Gresh, *J. Phys. Chem. B* **2001**, *105*, 8040–8049.
[42] M. Ruf, K. Weis, H. Vahrenkamp, *J. Am. Chem. Soc.* **1996**, *118*, 9288–9294.
[43] F. Meyer, P. Rutsch, *Chem. Commun.* **1998**, 1037–1038.
[44] S. Erhardt, E. Jaime, J. Weston, *J. Am. Chem. Soc.* **2005**, *127*, 3654–3655.
[45] A. Taylor, *FASEB J.* **1993**, *7*, 290–298.
[46] a) N. Sträter, W. N. Lipscomb, *Biochemistry* **1995**, *34*, 14792–14800; b) H. Kim, W. N. Lipscomb, *Proc. Natl. Acad. Sci. USA* **1993**, *90*, 5006–5010; c) S. K. Burley, P. R. David, R. M. Sweet, A. Taylor, W. N. Lipscomb, *J. Mol. Biol.* **1992**, *224*, 113–140; d) S. K. Burley, P. R. David, A. Taylor, W. N. Lipscomb, *Proc. Natl. Acad. Sci. USA* **1990**, *87*, 6878–6882.
[47] a) N. Sträter, W. N. Lipscomb, *Biochemistry* **1995**, *34*, 9200–9210; b) H. Kim, W. N. Lipscomb, *Biochemistry* **1993**, *32*, 8465–8478; c) H. Kim, S. K. Burley, W. N. Lipscomb, *J. Mol. Biol.* **1993**, *230*, 722–724.
[48] G. Schürer, A. H. C. Horn, T. Clark, *J. Phys. Chem. B* **2002**, *106*, 8815–8830.
[49] a) H. Vahrenkamp, *Acc. Chem. Res.* **1999**, *32*, 589–596; b) G. Parkin, *Chem. Commun.* **2000**, 1971–1985; c) E. Kimura, *Curr. Opin. Chem. Biol.* **2000**, *4*, 207–213.
[50] G. Parkin, *Chem. Rev.* **2004**, *104*, 699–767.
[51] a) G. Feng, J. C. Mareque-Rivas, N. H. Williams, *Chem. Commun.* **2006**, 1845–1847; b) G. Feng, J. C. Mareque-Rivas, R. T. Martin de Rosales, N. H. Williams, *J. Am. Chem. Soc.* **2005**, *127*, 13470–13471.
[52] A. S. Borovik, *Acc. Chem. Res.* **2005**, *38*, 54–61.
[53] a) E. L. Hegg, J.-N. Burstyn, *Coord. Chem. Rev.* **1998**, *173*, 133–165; b) R. C. Holz, K. P. Bzymek, S. I. Swierczek, *Curr. Opin. Chem. Biol.* **2003**, *7*, 197–206.
[54] a) M. W. Göbel, *Angew. Chem.* **1994**, *106*, 1201–1203; *Angew. Chem. Int. Ed. Engl.* **1994**, *33*, 1141–1143; b) R. Krämer, T. Gajda in "*Perspectives in Bioinorganic Chemistry*" **1999**, vol. 4, pp. 209–240; c) A. Blaskó, T. C. Bruice, *Acc. Chem. Res.* **1999**, *32*, 475–484; d) P. Molenveld, J. F. J. Engbersen, D. N. Reinhoudt, *Chem. Soc. Rev.* **2000**, *29*, 75–86; e) J. K. Bashkin, *Curr. Opin. Chem. Biol.* **1999**, *3*, 752–758; f) M. Rombach, C. Maurer, K. Weis, E. Keller, H. Vahrenkamp, *Chem. Eur. J.* **1999**, *5*, 1013–1027; g) E. Kimura, *Curr. Opin. Chem. Biol.* **2000**, *4*, 207–213; h) J. A. Cowan, *Curr. Opin. Chem. Biol.* **2001**, *5*, 634–642; i) M. Leivers, R. Breslow, *Bioorg. Chem.* **2001**, *29*, 345–356; j) F. Mancin, P. Scrimin, P. Tecilla, U. Tonellato, *Chem. Commun.* **2005**, 2540–2548.
[55] for some recent examples see: a) M. J. Young, J. Chin, *J. Am. Chem. Soc.* **1995**, *117*, 10577–10578; b) I. O. Fritsky, R. Ott, H. Pritzkow, R. Krämer, *Chem. Eur. J.* **2001**, *7*, 1221–1231; c) K. Worm, F. Chu, K. Matsumoto, M. D. Best, V. Lynch, E. V. Anslyn, *Chem. Eur. J.* **2003**, *9*, 741–747; d) M. Arca, A. Bencini, E. Berni, C. Caltagirone, F. A. Devillanova, F. Isaia, A. Garau, C. Giorgi, V. Lippolis, A. Perra, L. Tei, B. Valtancoli, *Inorg. Chem.* **2003**, *42*, 6929–6939; e) O. Iranzo, T. Elmer, J. P. Richard, J. R. Morrow, *Inorg. Chem.* **2003**, *42*, 7737–7746; f) M. Yashiro, H. Kaneiwa, K. Onaka, M. Komiyama, *Dalton Trans.* **2004**, 605–610; g) J. Aguilar, A. Bencini, E. Berni, A. Bianchi, E. Garćia-España, L. Gil, A. Mendoza, L. Ruiz-Ramírez, C. Soriano, *Eur. J. Inorg. Chem.* **2004**, 4061–4071; h) M. Yashiro, R. Kawahara, *J. Biol. Inorg. Chem.* **2004**, *9*, 914–921; i) H. Carlsson, M. Haukka, E. Nordlander, *Inorg. Chem.* **2004**, *43*, 5681–5687; j) J. Chen, X. Wang, Y. Zhu, J. Lin, X. Yang, Y. Li, Y. Lu, Z. Guo, *Inorg. Chem.* **2005**, *44*, 3422–3430; k) A. M. O'Donoghue, S. Y. Pyun, M.-Y. Yang, J. R. Morrow, J. P. Richard, *J. Am. Chem. Soc.* **2006**, *128*, 1615–1621.
[56] A. L. Gavrilova, B. Bosnich, *Chem. Rev.* **2004**, *104*, 349–383.
[57] J. Klingele, F. Meyer, *Coord. Chem. Rev.* submitted.
[58] F. Meyer, K. Heinze, B. Nuber, L. Zsolnai, *J. Chem. Soc., Dalton Trans.* **1998**, 207–214.
[59] a) J. Ackermann, F. Meyer, E. Kaifer, H. Pritzkow, *Chem. Eur. J.* **2002**, *8*, 247–258; b) J. Ackermann, F. Meyer, H. Pritzkow, *Z. Anorg. Allg. Chem.* **2004**, *630*, 2627–2631.
[60] J. Ackermann, F. Meyer, H. Pritzkow, *Inorg. Chim. Acta* **2004**, *357*, 3703–3711.
[61] M. Konrad, F. Meyer, K. Heinze, L. Zsolnai, *J. Chem. Soc., Dalton Trans.* **1998**, *199*–206.
[62] a) F. Meyer, A. Jacobi, B. Nuber, P. Rutsch, L. Zsolnai, *Inorg. Chem.* **1998**, *37*, 1213–1218; b) F. Meyer, E. Kaifer, P. Kircher, K. Heinze, H. Pritzkow, *Chem. Eur. J.* **1999**, *5*, 1617–1630; c) S. Buchler, F. Meyer, E. Kaifer, H. Pritzkow, *Inorg. Chim. Acta* **2002**, *337*, 371–386.
[63] T. A. Kaden, *Coord. Chem. Rev.* **1999**, *190–192*, 371–389.
[64] B. Bauer-Siebenlist, F. Meyer, E. Farkas, D. Vidovic, S. Dechert, *Chem. Eur. J.* **2005**, *11*, 4349–4360.
[65] B. Bauer-Siebenlist, F. Meyer, E. Farkas, D. Vidovic, J. A. Cuesta-Seijo, R. Herbst-Irmer, H. Pritzkow, *Inorg. Chem.* **2004**, *43*, 4189–4202.
[66] S. V. Kryatov, E. V. Rybak-Akimova, F. Meyer, H. Pritzkow, *Eur. J. Inorg. Chem.* **2003**, 1581–1590.
[67] E. Jaime, J. Weston, *Eur. J. Inorg. Chem.* **2006**, 793–801.
[68] B. Bauer-Siebenlist, F. Meyer, D. Vidovic, H. Pritzkow, *Z. Anorg. Allg. Chem.* **2003**, *629*, 2152–2156.
[69] L. Siegfried, T. A. Kaden, F. Meyer, P. Kircher, H. Pritzkow, *J. Chem. Soc., Dalton Trans.* **2001**, 2310–2315.
[70] M. Raidt, M. Neuburger, T. A. Kaden, *Dalton Trans.* **2003**, 1292–1298.
[71] L. H. Gade, *Koordinationschemie*, Wiley-VCH, Weinheim, **1998**, p. 436–442.
[72] O. Iranzo, A. Y. Kovalevsky, J. R. Morrow, J. P. Richard, *J. Am. Chem. Soc.* **2003**, *125*, 1988–1993.
[73] G. C. Silver, P. Gantzel, W. C. Trogler, *Inorg. Chem.* **1995**, *34*, 2487–2489.
[74] G. Anderegg, E. Hubmann, N. G. Podder, F. Wenk, *Helv. Chim. Acta* **1977**, *60*, 123–140.
[75] a) J. C. Mareque-Rivas, R. Prabaharan, R. T. Martín de Rosales, *Chem. Commun.* **2004**, 76–77; b) J. C. Mareque-Rivas, R. Prabaharan, S. Parsons, *Dalton Trans.* **2004**, 1648–1655.
[76] see for example: a) T. Koike, E. Kimura, *J. Am. Chem. Soc.* **1991**, *113*, 8935–8941; b) Y. Fujii, T. Itoh, K. Onodera, T. Tada, *Chem. Lett.* **1995**, 305–306; c) W. H. Chapman Jr, R. Breslow, *J. Am. Chem. Soc.* **1995**, *117*, 5462–5469; d) T. Itoh, Y. Fujii, T. Tada, Y. Yuzo, H. Hisada, *Bull. Chem. Soc. Jpn.* **1996**, *69*, 1265–1274; e) L. Bonfá, M. Gatos, F. Mancin, P. Tecilla, U. Tonellato, *Inorg. Chem.* **2003**, *42*, 3943–3949.
[77] C. Vichard, T. A. Kaden, *Inorg. Chim. Acta* **2002**, *337*, 173–180.
[78] examples for dizinc complexes with bridging phosphate esters: a) T. Tanase, J. W. Yun, S. J. Lippard, *Inorg. Chem.* **1996**, *35*, 3585–3594; b) C. Bazzicalupi, A. Bencini, A. Bianchi, V. Fusi, C. Giorgi, P. Paoletti, B. Valtancoli, D. Zanchi, *Inorg. Chem.* **1997**, *36*, 2784–2790; c) C. He, S. Lippard, *J. Am. Chem. Soc.* **2000**, *122*, 184–185; d) F. H. Fry, P. Jensen, C. M. Kepert, L. Spiccia, *Inorg. Chem.* **2003**, *42*, 5637–5644; e) E. Kinoshita, M.


 © 2006 Wiley-VCH Verlag GmbH & Co. KGaA, Weinheim 

Takahashi, H. Takeda, M. Shiro, T. Koike, *Dalton Trans.* **2004**, 1189–1193.
[79] a) N. V. Kaminskaia, B. Spingler, S. J. Lippard, *J. Am. Chem. Soc.* **2001**, *123*, 6555–6563; b) N. V. Kaminskaia, C. He, S. J. Lippard, *Inorg. Chem.* **2000**, *39*, 3365–3373; c) N. V. Kaminskaia, B. Spingler, S. L. Lippard, *J. Am. Chem. Soc.* **2000**, *122*, 6411–6422.
[80] B. Bauer-Siebenlist, S. Dechert, F. Meyer, *Chem. Eur. J.* **2005**, *11*, 5343–5352.
[81] Several groups have examined the hydrolysis or methanolysis of β-lactams by transitions metals salts including $Zn^{2+}$: a) M. I. Page, *Acc. Chem. Res.* **1984**, *17*, 144–151; b) A. A. M. García, P. G. Navarro, P. J. Martínez de las Parras, R. G. Ortiz, I. H. Blázquez, *Recent Res. Devel. Pure & Applied Anal. Chem.* **2002**, *4*, 89–106; c) P. J. Montoya-Pelaez, G. T. T. Gibson, A. A. Neverov, R. S. Brown, *Inorg. Chem.* **2003**, *42*, 8624–8632; d) N. Diaz, T. L. Sordo, D. Suárez, R. Méndez, J. Marin-Vallacorta, *New J. Chem.* **2004**, *28*, 15–25.
[82] F. Meyer, H. Pritzkow, *Eur. J. Inorg. Chem.* **2005**, 2346–2351.
[83] Q.-C. Yang, P. Seiler, J. D. Dunitz, *Acta Crystallogr., Sect. C* **1987**, *43*, 565–567.
[84] K. Hanai, Y. Maki, A. Kuwae, *Bull. Chem. Soc. Jpn.* **1985**, *58*, 1367–1375.
[85] H. Brombacher, H. Vahrenkamp, *Inorg. Chem.* **2004**, *43*, 6054–6060.

Received: June 22, 2006
Published Online: August 29, 2006

 © 2006 Wiley-VCH Verlag GmbH & Co. KGaA, Weinheim 

DOI: 10.1002/ejic.200600436

# Kinetics and Thermodynamics of Halide and Nitrite Oxidation by Mammalian Heme Peroxidases

**Jürgen Arnhold,[a] Enrico Monzani,[b] Paul G. Furtmüller,[c] Martina Zederbauer,[c] Luigi Casella,[b] and Christian Obinger*[c]**

**Keywords:** Bioinorganic chemistry / Peroxidases / Halides / Nitrites / Thermodynamics / Kinetics

The human heme peroxidases myeloperoxidase (MPO), eosinophil peroxidase (EPO) and lactoperoxidase (LPO) are able to oxidise (pseudo)halides and nitrite to reactive species that participate in host defence against foreign microorganisms as well as in immunomodulation and tissue degradation in certain pathologies. The heme in EPO and LPO is covalently linked to the apoprotein by two ester bonds, whereas in MPO it is additionally linked by a unique sulfonium ion bond to a methionine residue. As a consequence, the prosthetic group in MPO is significantly distorted from a planar conformation. These structural differences are reflected by distinct spectral and redox properties as well as reactivities toward chloride, bromide, iodide, thiocyanate and nitrite, which function as endogenous two- and one-electron donors for these enzymes in vivo. Standard reduction potentials at pH 7 have been determined for all redox couples involved in the halogenation and peroxidase cycle of MPO and LPO and partially of EPO. A detailed thermodynamic analysis of the formation of reactive halide species by MPO and EPO was also performed. Thus, for the first time, a comprehensive analysis of reactions catalysed by human heme peroxidases is presented that allows a better understanding of their role in physiological and pathophysiological processes.
(© Wiley-VCH Verlag GmbH & Co. KGaA, 69451 Weinheim, Germany, 2006)

## Heme Peroxidases

Peroxidases are iron-containing enzymes that have been used in a great number of analytical and technical applications[1] since they are able to catalyze one- and two-electron oxidation reactions of inorganic and organic compounds with hydrogen peroxide. Physiologically, these enzymes are not only responsible for protection against harmful side-effects of oxygen metabolism but are also involved in a variety of biosynthetic and degradative functions related to the consumption of hydrogen peroxide. Today we know, as result of gene and genome sequencing and increasing data deposited in protein data banks, of two heme-containing peroxidase superfamilies, namely the superfamily of plant, fungal and bacterial peroxidases[2] and the superfamily of animal peroxidases.[3] The physiological importance of these metalloenzymes is underlined by the fact that higher organisms often contain a high number of genes encoding peroxidases. For example, in *Arabidopsis thaliana*, the first plant for which the whole genome has been sequenced, 73 full-length genes encoding classical plant peroxidases[4] and several genes encoding so-called ascorbate peroxidases[5] have been identified in the genome. Moreover, the diversity in structure and function can be further increased by variations in gene transcription and translation resulting in the fact that one single gene can encode several multiple forms of a protein or enzyme.

In the human genome there are only four genes encoding for homologous heme peroxidases known as myeloperoxidase (MPO), eosinophil peroxidase (EPO), lactoperoxidase (LPO) and thyroid peroxidase (TPO), which are members of the animal peroxidase superfamily. MPO, EPO and LPO are functionally homologous enzymes closely involved in host defence. MPO is secreted at inflammatory sites from stimulated polymorphonuclear leukocytes and also monocytes,[6] while EPO is released from activated eosinophils.[7] LPO is found in mucosal surfaces and exocrine secretions such as milk, tears and saliva.[8] In contrast, TPO is involved in the biosynthesis of the thyroid gland hormones thyroxine and triiodothyronine.[9]

Closely related with the physiological role is the nature of the substrates oxidized by human peroxidases. These enzymes prefer small anionic molecules as electron donors, such as halides (chloride, bromide, iodide), thiocyanate and nitrite. The corresponding oxidation products, for example

[a] Institute of Medical Physics and Biophysics, University of Leipzig,
Leipzig, Germany
[b] Dipartimento di Chimica Generale, University of Pavia,
Pavia, Italy
[c] Department of Chemistry, Division in Biochemistry, BOKU – University of Natural Resources and Applied Life Sciences,
Vienna, Austria
Fax: +43-1-36006-6059
E-mail: christian.obinger@boku.ac.at

 © 2006 Wiley-VCH Verlag GmbH & Co. KGaA, Weinheim 

hypohalous acids or nitrogen dioxide, are responsible for killing microorganisms[6,10] or in iodination of tyrosine residues of thyroglobulin in hormone syntheses.[9] However, since many of these reaction products are (strong) halogenating and nitrating oxidants, they also contribute to tissue injury in certain inflammatory diseases.[11] Moreover, certain products of the halogenating activity of peroxidases are known to function as immunomodulators such as taurine chloramine[12] and hypothiocyanite.[13]

These functional features are closely related with the peculiar structural and redox properties of these heme proteins. Recently, the standard reduction potentials of the redox couple compound I/ferric enzyme for MPO, EPO and LPO, as well as compound II/ferric enzyme and compound I/compound II for MPO and LPO have been determined.[14–16] With this knowledge, it is now possible to relate much better data on (pseudo)halide and nitrite oxidation to the structural and functional properties of perox-

*Juergen Arnhold graduated from the Biophysical Department of the Biological Faculty of the Lomonossow State University Moscow in 1974. Since that time he has been working at the Institute of Medical Physics and Biophysics of the University of Leipzig, Germany, where he got his PhD degree in 1982 and habilitated in 1997. In 2003, he obtained the degree of an associate professor. His research interests concern the study of chemical processes during oxidative stress in biological systems, lipid peroxidation reactions, as well as chemistry and biochemistry of myeloperoxidase and other heme peroxidases. He is also a specialist for the physiology of neutrophilic granulocytes and oxidative damage of biomaterials during inflammation. Prof. Arnhold's studies have resulted in about 150 scientific publications.*

*Enrico Monzani was born in Locate Triulzi (Milano). He received his degree in Industrial Chemistry at the University of Milano in 1991 and his Ph.D degree in Chemistry at the University of Pavia in 1994. He did post-university training at the enzymology laboratory of the "Istituto di Ricerche Farmacologiche Mario Negri", Milano. From 1997 he obtained a permanent position as Research Associate in Inorganic Chemistry at the University of Pavia. His research interest is in the field of Bioinorganic chemistry, in particular on the structural and functional characterization of heme and copper proteins, covering both studies on the macromolecules and on the low molecular weight model systems.*

*Paul G. Furtmüller was born in 1965. He studied Biotechnology and Food Sciences at the University of Natural Resources and Applied Life Sciences in Vienna and obtained his M.Sc. degree in 1997. Then he reached his Ph.D. in Biochemistry in 2000 with Prof. Obinger at the same University, where he got in 2001 a position as a Research Assistant. During his Ph.D, in 1999, he was a Visiting Scientist at the University of Alberta with Prof. H. Brian Dunford, where he studied halide oxidation by myeloperoxidase. His main scientific interests are structure-function relationships of heme peroxidases.*

*Martina Zederbauer was born in Klagenfurt in 1967. After working as designer she studied Food Sciences and Biotechnology at the BOKU – University of Natural Resources and Applied Life Sciences in Vienna. At the moment she is finishing her PhD on "The Role of Heme to Protein Linkages in Catalysis of Human Myeloperoxidase".*

*Luigi Casella was born in Milano in 1947. He obtained his degree in Chemistry from the University of Milano in 1973. In the period 1978-1979 he was a postdoc with J.A. Ibers at Northwestern University, Evanston (USA) with a CNR-NATO fellowship. Since 1990 he is full professor of Inorganic Chemistry at the Faculty of Sciences of the University of Pavia. He has been the Chairperson of the European COST Chemistry Action D21 "Metalloenzymes and chemical biomimetics". His scientific interest is the chemistry of metal enzymes containing heme or copper cofactors involved in oxidative processes. He is the author of more than 150 papers in international chemical and biochemical journals and an international patent.*

*Christian Obinger was born in Salzburg in 1962. He obtained his degree in Chemistry and Biochemistry from the University of Vienna in 1988 and his Ph.D degree in 1992. In 1992 he obtained a position as research assistence at the Department of Chemistry at BOKU – University of Natural Resources and Applied Life Sciences. In 1995 he did postdoc training with Peter Nicholls at the Brock University in Canada and got his habilitation in 1999. He is associate professor in biochemistry and interested in the enzymology of iron- and copper-containing enzymes. He hosted two meetings on plant-type and mammalian peroxidases and was coordinator of a COST group within the Action D21 "Metalloenzymes and chemical biomimetics". He is the author of more than 90 papers in international journals.*

 © 2006 Wiley-VCH Verlag GmbH & Co. KGaA, Weinheim 

idases. This review summarises the present knowledge on halide and nitrite oxidation by MPO, EPO and LPO from the viewpoint of biophysical chemistry and compares their halogenation and nitration activity with respect to the modification of functional sites in proteins.

## Active Site of Mammalian Peroxidases

Among the mammalian peroxidases only the 3D structure of MPO is known. The structure of human MPO at 2.3 Å resolution was obtained and this structure has been refined at 1.8 Å, using X-ray data recorded at –180 °C.[17] Each half of dimeric MPO contains one iron, which is present as covalently bound heme. Besides differences in the overall structure, the mode of heme binding in animal peroxidases is the most significant structural difference to plant-type peroxidases, which have the heme not covalently attached to the protein. In MPO and other animal peroxidases, the methyl groups on pyrrole rings A and C of the protoporphyrin IX derivative are modified to allow formation of ester linkages with the carboxyl groups of Glu242 and Asp94. In addition, the β-carbon of the vinyl group on pyrrole ring A in MPO forms a covalent bond with the sulfur atom of Met243, giving rise to a sulfonium ion linkage (Figure 1, A).[17] The heme porphyrin ring is considerably distorted from planarity. Although pyrrole rings B and D are nearly coplanar, ring A and, to a lesser extent, ring C are tilted toward the distal side, resulting in a bow-shaped structure of the heme.

Unlike the two acidic residues, Met243 has no obvious equivalent in EPO, LPO or TPO,[18] although there is biochemical and biophysical evidence for a heme linkage through esters in EPO,[19] LPO[20] and TPO.[21] The uncommon manner of heme binding is responsible for the peculiar spectroscopic features[18] and redox properties of mammalian peroxidases. MPO has the largest red shift of the maximum of the Soret band in the visible spectrum among peroxidases and the highest values for standard reduction potentials of redox couples where compound I is involved. The MPO-specific sulfonium ion linkage could have the following roles: first, it serves as an electron-withdrawing substituent due to its positive charge, and, second, together with its neighbouring residue Glu242 (Figure 1, A), it appears to be responsible for the lower symmetry of the heme group and distortion from the planar conformation. The spectral properties of EPO, LPO and TPO are very similar, thereby underlining that they share an identical way of heme binding by two ester bonds.[18] All other active site residues, i.e. the proximal histidine (His336) and the heme distal site residues histidine (His95 in MPO), arginine (Arg239) and glutamine (Gln91; see Figure 1) are highly conserved in mammalian peroxidases. Moreover, the overall structure of the four representative proteins seems to be similar. There are only a small number of insertions/deletions and modelling suggests that almost all the regions corresponding to helices in MPO are well conserved in the other members of this protein superfamily.[18]

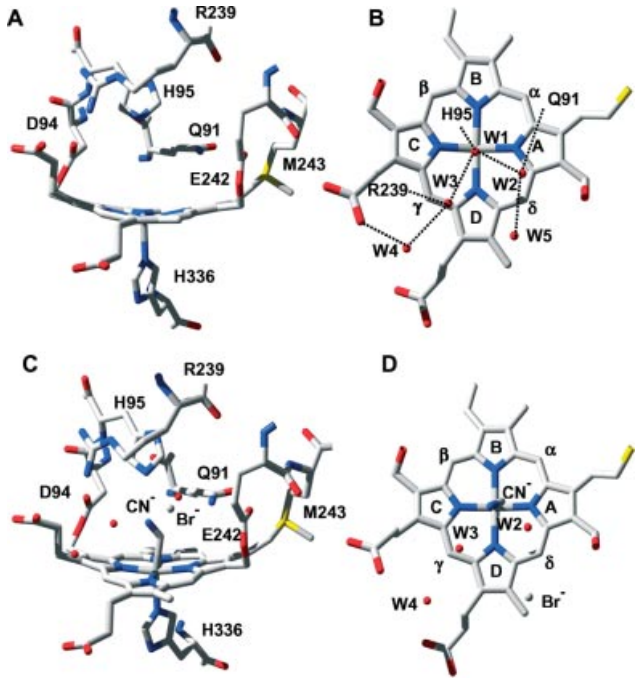


Figure 1. (A) The non-planar porphyrin ring in MPO and its covalent attachments to the protein through two ester bonds (Asp94 and Glu242) and one sulfonium linkage (Met243). The catalytic residues His95, Arg239 and Gln91 are also shown, the latter of which is important in halide binding. (B) The locations of the five water molecules in the distal heme cavity of ferric high-spin MPO. This figure was constructed using the coordinates deposited in the Protein Data Bank (accession code 1CXP). (C) The structure of the myeloperoxidase-cyanide-bromide double complex (MPO complexed with cyanide and bromide). The view in (D) is approximately normal to the heme plane. Please note that in the MPO–bromide complex the halide binds at W2, which is positioned above the δ-methine bridge carbon (i.e. the potential electron donation site of both nitrite and halides) between pyrrole rings A and D. This figure was constructed using the coordinates deposited in the Protein Data Bank (accession code 1D7W).

## Nitrite and Halide Binding

Cyanide and nitrite bind very tightly to the active site of mammalian peroxidases and convert the protein into a low-spin species. The pH dependency of cyanide binding resembles that of $H_2O_2$ in compound I formation (see below), since both require the deprotonated form of a group with a p$K_a$ of 4.0–4.3, which seems to be the distal histidine.[22–24] Following deprotonation of HCN by the distal histidine, the cyanide anion binds to the heme iron to produce an $S = 1/2$ low-spin complex. The crystal structure of the MPO–cyanide complex[25] shows that the orientation of the cyanide ion is determined by the formation of three hydrogen bonds between its nitrogen atom and the distal histidine as well as water molecules W2 and W3 (see C and D in Figure 1). Water W1 is displaced by cyanide and the heme iron moves about 0.2 Å into the plane of the heme during the transition of high-spin MPO to its low-spin form. No significant protein conformational changes are associated with cyanide binding.[25]

Similar to cyanide, nitrite binding converts ferric high-spin to low-spin MPO.[24,26] The structure of the MPO–

 © 2006 Wiley-VCH Verlag GmbH & Co. KGaA, Weinheim 

$NO_2^-$ complex is unknown. However, because of the large spectral changes, one would expect that nitrite also binds directly to $Fe^{III}$ through the nitrogen atom [Equation (1)], with $PorFe^{III}$–$NO_2^-$ being the peroxidase nitrite complex.

$$PorFe^{III} + NO_2^- \leftrightarrows PorFe^{III}–NO_2^- \quad (1)$$

The pH dependency of nitrite binding resembles that of halide binding to MPO (see below). In contrast to cyanide binding, nitrite and halide binding is favoured at acidic pH and needs protonation of the distal histidine. This is shown by a significant decrease of the dissociation constant of bound nitrite upon decreasing the pH from 7.0 (2.3 mM) to 5.0 (31 μM).[24] LPO shows a much reduced affinity toward nitrite, with a dissociation constant of about 45 mM at neutral pH.[28] From the pH dependence of $NO_2^-$[24] and chloride binding,[27] the p$K_a$ value of the distal histidine was found to be around 4.3.

Halides do not bind directly to the heme iron. The structure of the MPO–bromide complex[25] demonstrates that bromide binds at the position of water molecule W2 (Figure 1, B), which is hydrogen bonded to the amide nitrogen of Gln91. Bromide binding is accompanied by small shifts of the side-chains of His95 and the heme-ester-linked Glu242 as well as of water molecules W1 and W5. Possible electrostatic interactions occur between the bromide and water molecules W1 and W5, the Nε of His95 and the amide nitrogen of Gln 91.[25] The closest heme atom to the bromide is the δ-methylene bridge carbon between pyrrole rings A and D (Figure 1). Thus, halides are typical high-spin ligands in contrast to the low-spin ligands cyanide or nitrite. As a consequence, spectral changes upon halide binding are relatively small.[18]

## The Redox Couple Compound I/Native Enzyme

Hydrogen peroxide is known to convert resting ferric heme peroxidases ($PorFe^{III}$) into compound I ($^{\cdot+}PorFe^{IV}$=O),[29] which is a porphyrin π-cation radical with an oxygen atom coupled by a double bond to iron(IV) [Equation (2)].[30]

$$PorFe^{III} + H_2O_2 \rightarrow {}^{\cdot+}PorFe^{IV}=O + H_2O \quad (2)$$

In this redox reaction, the reduction of hydrogen peroxide to water is coupled with the oxidation of ferric heme. The oxidation and reduction steps of this redox reaction consist of the two half reactions (both written as reduction process) given in Equations (3) and (4).

$$^{\cdot+}PorFe^{IV}=O + 2e^- + 2H^+ \rightarrow PorFe^{III} + H_2O \quad (3)$$

$$H_2O_2 + 2e^- + 2H^+ \rightarrow 2H_2O \quad (4)$$

As the absorption of the Soret band of heme peroxidases shows a marked hypochromicity upon formation of compound I, it is possible to monitor this fast conversion by stopped-flow spectroscopy. By monitoring the resulting absorbance change at the wavelength for which the extinction coefficient of native enzyme and corresponding compound I are known, and taking into account the standard reduction potential, $E'°$, of 1.32 V at pH 7 for the redox couple $H_2O_2/2H_2O$,[31] equilibrium concentrations of all reactants and standard reduction potentials of the couples compound I/ferric enzyme have been determined for human heme peroxidases using the Nernst equation [Equation (5)] (Table 1). An alternative approach to generate compound I of peroxidases is the use of peroxyacetic acid, which is reduced to acetate and water. The redox couple peroxyacetic acid/acetate, $H_2O$ has a standard reduction potential of 1.14 V at pH 7.[16]

$$E' = E'^{o} + (RT/nF) \ln(a_{ox}/a_{red}) \quad (5)$$

Table 1. Standard reduction potentials ($E'°$) at pH 7 of all redox couples of the peroxidase cycle of human heme peroxidases.

| Redox couple | MPO | EPO | LPO |
|---|---|---|---|
| Compound I/native enzyme | 1.16 V[14] | 1.10 V[14] | 1.09 V[16] |
| Compound I/compound II | 1.35 V[37] | n.d.[a] | 1.14 V[16] |
| Compound II/native enzyme | 0.97 V[37] | n.d.[a] | 1.04 V[16] |

[a] n. d.: not determined.

In Equation (5) $E'$ is the reduction potential of any redox couple and $E'^{o}$ is the standard reduction potential that is referred to a concentration of 1 M or a pressure of 101.3 kPa in the case of gases. The gas constant $R$ is equal to 8.31 $JK^{-1}mol^{-1}$. The temperature $T$ is conventionally set to 298 K and $n$ represents the number of electrons transferred in a single reaction step by the redox couple. The Faraday constant $F$ is 96485 $A{\cdot}s\,mol^{-1}$ and $a_{ox}$ and $a_{red}$ are the activities of the oxidised and reduced species, respectively. This method has been applied since a direct electrochemical determination of the reduction potential of the compound I/native enzyme couple is not possible due to the very high instability of compound I.

The highest $E'°$ value for the compound I/ferric enzyme couple was found to be 1.16 ± 0.01 V for MPO[14] followed by EPO and LPO, with $E'°$ values of 1.10 ± 0.01 V[14] and 1.09 ± 0.01 V,[16] respectively. These differences are apparently caused by the mode of heme-to-protein linkages described above: only in MPO, in addition to the two ester linkages that are also present in EPO and LPO, is there the unique sulfonium ion linkage at Met243 (see A and C in Figure 1), which, besides its electron-withdrawing properties, will provoke an additional distortion of the prosthetic group with the consequence of a pronounced out-of-plane structure of the iron in the resting state.[17] This uncommon way of heme binding is also responsible for the red-shift of the Soret band in MPO (430 nm), EPO (413 nm) and LPO (412 nm) compared to proteins with a more coplanar heme such as ferric hemoglobin and horseradish peroxidase (HRP).[18] The critical role of Met243 in the heme–protein interaction is underlined by site-directed mutagenesis studies. Replacement of Met243 in mutant MPO strongly affects the physical properties, substrate binding, substrate specificity and substrate oxidation of the corresponding mutants.[32] In general, Met243 variants exhibit spectral and

 © 2006 Wiley-VCH Verlag GmbH & Co. KGaA, Weinheim 

catalytic properties similar to LPO and EPO, the heme of which is linked only by two ester bonds to the apoprotein.

## The Redox Couples Compound I/Compound II and Compound II/Ferric Enzyme

Compound I of heme peroxidases can be reduced by two consecutive one-electron steps to the ferric enzyme via the intermediate complex compound II [$PorFe^{IV}=O$], whereby numerous small molecular substrates, including aromatic amino acids, nitrite, indole derivatives and others, are oxidised by abstracting one electron.[24,33,34] For example, the generally accepted mechanism of nitrite oxidation involves the intermediates compound I and compound II [Equations (6) and (7)].

$$^{\cdot+}PorFe^{IV}=O + NO_2^- \rightarrow PorFe^{IV}=O + {}^{\cdot}NO_2 \quad (6)$$

$$PorFe^{IV}=O + NO_2^- + 2H^+ \rightarrow PorFe^{III} + {}^{\cdot}NO_2 + H_2O \quad (7)$$

These reactions, together with the oxidation of the ferric enzyme by hydrogen peroxide [Equation (2)], form the peroxidase cycle.

The oxidation of nitrite to nitrogen dioxide [$E'°({}^{\cdot}NO_2/NO_2^-) = 1.04$ V at pH 7][35] as well as of tyrosine to tyrosyl radical [$E'°$(tyrosyl radical/tyrosine) = 0.94 V at pH 7][36] has been used to convert compound II of MPO or LPO to the ferric enzyme and to calculate the standard reduction potentials of the redox couple compound II/ferric enzyme of these peroxidases (Table 1). Finally, the standard reduction potentials of the couple compound I/compound II have been calculated from the two other experimentally determined potentials of the peroxidase cycle (Table 1). Experimental details and calculations are described elsewhere.[15,16,37]

Significant differences were observed in the oxidation of indole derivatives by compound I and II of MPO and LPO. The rates of reduction of compound II to ferric peroxidase were similar, which is reflected by the fact that the standard reduction potentials of the redox couple compound II/ferric enzyme for MPO and LPO differ by only 0.07 V.[16,37] Higher differences, however, were found in one-electron substrate oxidation for reactions catalysed by compound I. The highest standard reduction potential of couple compound I/compound II ($1.35 \pm 0.01$ V at pH 7) was obtained for MPO.[37] The potential for this couple for LPO ($1.14 \pm 0.02$ V) is considerably lower,[16] and the corresponding potential for EPO is still unknown. As EPO exhibits more similarities to LPO than to MPO in its redox properties, it is assumed that the couple compound I/compound II of EPO has a similar $E'°$ value to LPO.

Thus, compound I of MPO is able to oxidise substrates with a reduction potential around 1.2 V and higher with sufficient rates,[38] thus underlining its extraordinary role in substrate oxidation during bacterial killing. A partial reduction of compound I of MPO to compound II is even observed in the presence of 250 mM hydrogen carbonate.[39] The redox couple $CO_3^{\cdot-}/HCO_3^-$ has a standard reduction potential at pH 7 equal to 1.78 V.[40] Assuming a very low concentration for the unstable carbonate radical, it follows from the Nernst equation [Equation (5)] that compound I of MPO is readily able to oxidise high concentrations of hydrogen carbonate.

The formation of isomeric compound I, where the radical function is transferred from the porphyrin ring to the protein moiety, is still under discussion.[18,41] The conversion from porphyryl to protein radical has been shown in MPO[42,43] and LPO[43] in the absence of good one- or two-electron donors. Apparently, this conversion can be neglected when considering the composition of the medium at inflammatory sites containing a high number of substrates being oxidised by peroxidases.

## Nitrite Oxidation by Mammalian Peroxidases

The oxidation of nitrite by its reaction with either compound I or compound II requires the formation of nitrogen dioxide [Equations (6) and (7)].[44] As has been demonstrated above, both compound I and compound II are able to perform the one-electron reaction of nitrite. Some of the rate constants for these reactions have been determined for mammalian peroxidases. Table 2 also includes, for comparative purpose, data for the plant model enzyme HRP.[44,45] Brück et al.[46] have reported that LPO compound I reacts with nitrite in a two-electron process to produce nitrate and the resting enzyme directly due to the lack of observation of the spectral features of compound II when compound I was mixed with nitrite in a stopped-flow apparatus. However, this could be due to the high rate of LPO compound II reduction by nitrite, which would prevent accumulation of compound II. Normally, the compound II spectrum dominates in a peroxidase cycle that consists of Equations (2), (6) and (7). In fact, with a sequential-mixing stopped-flow apparatus with millisecond mixing time, we have been able to observe the transient formation of LPO compound II (unpublished results) when compound I was mixed with nitrite. Unfortunately, the reaction rate constant for the reduction of EPO compound I by nitrite has not been obtained yet, although it is assumed to be much higher than that of compound II.[44k]

Table 2. Second-order rate constants for the reduction of the peroxidase intermediates by nitrite.

| Enzyme | Intermediate | pH | $k$ ($M^{-1}s^{-1}$) |
|---|---|---|---|
| LPO | compound I | 7.2 | $2.2 \times 10^7$ [46] |
| | compound II | 7.2 | $3.5 \times 10^5$ [46] |
| | compound II | 7.0 | $6.8 \times 10^4$ [16] |
| MPO | compound I | 7.0 | $(2.2 \pm 0.2) \times 10^6$ [24] |
| | compound II | 7.0 | $(5.5 \pm 0.1) \times 10^2$ [24] |
| | compound I | 5.0 | $(1.1 \pm 0.2) \times 10^7$ [24] |
| | compound II | 5.0 | $(8.9 \pm 0.6) \times 10^4$ [24] |
| EPO | compound II | 7.4 | $(5.6 \pm 0.2) \times 10^3$ [44k] |
| HRP | compound I | 6.93 | $6.7 \times 10^2$ [45a] |
| | compound II | 7.5 | $(6.6 \pm 0.4)$[44e] |
| | compound II | 7.0 | 13.3[45b] |

Generally, reduction of compound I [Equation (6)] is faster than that of compound II [Equation (7)], and this is

 © 2006 Wiley-VCH Verlag GmbH & Co. KGaA, Weinheim 

reflected by the higher redox potential for the compound I/compound II couple with respect to the compound II/native enzyme couple (Tables 1 and 2). Nevertheless, the same trend occurs with HRP (Table 2), which has a standard reduction potential of about 0.9 V for both redox intermediates.[47] This suggests that, besides the thermodynamic frame, kinetic aspects have to be taken into account. Considering Equations (6) and (7), according to the Marcus theory, there are significant differences in complexity. In compound I reduction the porphyrin cation radical has to be quenched; the rigid and highly delocalised aromatic skeleton of the macrocycle facilitates the electron transfer. In the case of MPO, it has been demonstrated that the δ-meso carbon of the porphyrin π-cation radical of compound I is most likely the electron donation site in compound I since it is located adjacent to the positively charged sulfonium ion linkage to the vinyl group attached to pyrrole ring A (Figure 1).[18,48] By contrast, reduction of the oxoiron(IV) species in compound II requires a more pronounced rearrangement; in fact, Equation (7) requires two protons for the formation of a water molecule from the oxoiron(IV) group. Furthermore, formation of the native enzyme includes a low-spin to high-spin shift that restores the out-of-plane disposition of $Fe^{III}$. The need for protons in compound II reduction by nitrite is also shown by the effect of pH on the reaction rates determined in the case of MPO (Table 2). Both reductions of compound I and compound II are controlled by an amino acid residue with a p$K_a$ value of $4.3 \pm 0.3$,[24] most likely the distal histidine, and the rates are higher at acidic pH. Reduction of compound I is approximately fivefold higher at pH 5 with respect to pH 7, whereas for compound II the ratio of the reaction rate constants at the two pH values increases by a factor of 160, thus indicating a much larger dependence on the proton concentration in the latter reaction.

## Redox Chemistry of (Pseudo)halide Oxidation by Peroxidases

Human heme peroxidases are unique among human enzymes in their ability to oxidise (pseudo)halides to (pseudo)hypohalous acids with concomitant reduction of compound I in a two-electron step to the ferric enzyme form. The overall reaction is given in Equation (8)

$$^{\cdot+}PorFe^{IV}{=}O + X^- + H^+ \rightarrow PorFe^{III} + HOX \quad (8)$$

where X denotes $Cl^-$, $Br^-$, $I^-$ or $SCN^-$. This redox process can be divided into two half-reactions, where the reduction of compound I [Equation (3)] is coupled with the (pseudo)halide oxidation ([Equation (9)], written as a reduction process.

$$XOH + 2e^- + H^+ \rightarrow X^- + H_2O \quad (9)$$

Standard reduction potentials for the redox couple XOH/$X^-$, $H_2O$ are given for pH 0 and pH 7 in Table 3. At pH 7, HOCl, HOBr and HOI exist predominantly in the undissociated form according to their p$K_a$ values (see also Table 3). Standard reduction potentials for HOCl, HOBr and HOI were originally described at pH 0. The reduction potentials of these couples decrease between pH 0 and pH 7 by about 0.03 V with increasing pH unit, as two electrons and one proton are involved in the corresponding half-reaction. Thus, the standard reduction potentials of the couples HOCl/$Cl^-$, $H_2O$, HOBr/$Br^-$, $H_2O$, and HOI/$I^-$, $H_2O$ are 1.28, 1.13 and 0.77 V, respectively, at pH 7. A further data set exists in the literature for these standard reduction potentials at pH 7;[31,49] they are about 0.20 V lower than those indicated in Table 3. These data were also originally determined from standard values at pH 0 by using, unfortunately, a wrong coefficient to consider the pH dependence.

Table 3. Standard reduction potentials [V] for two-electron oxidation of (pseudo)halides and p$K_a$ values of (pseudo)hypohalous acids.

| $X^-$ | p$K_a$ (HOX) | $E'°$(HOX/$X^-$, $H_2O$) pH 0 | pH 7 | $E'°$($X_2$/2 $X^-$) |
|---|---|---|---|---|
| $Cl^-$ | 7.53[50] | 1.49[51] | 1.28 | 1.39[52] |
| $Br^-$ | 8.8[53] | 1.33[54] | 1.13 | 1.09[55] |
| $I^-$ | 10.0[56] | 0.99[57] | 0.78 | 0.54[58] |
| $SCN^-$ | 5.3[59] | 0.82[a] | 0.56[a] | 0.72[a] |

[a] This work.

The standard reduction potential for the couple HOSCN/$SCN^-$, $H_2O$ can be calculated from the equilibrium constant of the following redox reaction [Equation (10)].

$$H_2O_2 + SCN^- \rightarrow OSCN^- + H_2O \quad (10)$$

An equilibrium constant of $3.7 \times 10^3$ $M^{-1}$ has been obtained for this reaction.[60] However, a critical re-evaluation yielded a totally different value of $5.65 \times 10^{25}$ $M^{-1}$.[61] With the latter value and $E'° = 1.32$ V at pH 7 for the couple $H_2O_2$/2 $H_2O$,[31] the unknown standard reduction potential for the couple $OSCN^-$/$SCN^-$, $H_2O$ can be determined to be 0.56 V at pH 7. With the p$K_a$ value of HOSCN (5.3),[59] a standard value of 0.82 V is obtained for this redox couple at pH 0.

Thus, the ease of oxidation of (pseudo)halide ions is the following: $SCN^- > I^- > Br^- > Cl^-$ (Table 3). In conversion of compound I to the ferric enzyme form by (pseudo)halide ions studied by rapid scan spectroscopy, the same order of sequence for the interacting (pseudo)halide has been obtained (Table 4). Only MPO compound I is able to react with chloride at pH 7.0 at reasonable rates.[42,62] It has been suggested that the experimental data for the interaction of chloride with compound I can be fitted best by a mechanism that includes a compound I–chloride complex.[62b] At low chloride concentration, the formation of the compound I–chloride complex is rate limiting, whereas at high chloride concentration its transition to ferric MPO and release of hypochlorous acid (HOCl) is rate controlling.[62b]

 © 2006 Wiley-VCH Verlag GmbH & Co. KGaA, Weinheim 

Table 4. Apparent second-order rate constants for the reactions between compound I of MPO, EPO and LPO with (pseudo)halide at pH 7 and 15 °C.

| | MPO[42] $\times 10^4$ ($M^{-1} s^{-1}$) | EPO[65] $\times 10^4$ ($M^{-1} s^{-1}$) | LPO[66] $\times 10^4$ ($M^{-1} s^{-1}$) |
|---|---|---|---|
| Chloride | 2.5 | 0.31 | – |
| Bromide | 110 | 1900 | 4.1 |
| Iodide | 720 | 9300 | 12000 |
| Thiocyanate | 960 | 10000 | 20000 |

At acidic pH compound I reduction is accelerated significantly, which is also reflected by an increase in the steady-state chlorination activity of MPO.[63] At pH 5 EPO compound I is also an oxidant of chloride (Table 4). At acidic pH, chloride binds to a protonated amino acid close to the ferryl oxygen since there is a halide-dependent change in the EPR spectrum at acidic pH.[64] Supported by the crystal structure of the MPO–bromide but not the MPO–cyanide–bromide double complex,[25] which can be regarded as a model of the compound I–halide complex, it is likely that the distal histidine, upon protonation, allows such direct interaction between chloride (but not bromide or iodide) and ferryl oxygen. In the native enzyme, bromide replaces water molecule W2, which is hydrogen bonded to the amide of Gln91 in the proximity of the Nε atom of His95 (Figure 1, B), but in the cyanide complex W2 is not displaced and bromide binds in place of W5, thereby preventing a direct H-bond interaction with protonated His95 (Figure 1, C and D).[25] Maybe the W2 site is inaccessible for larger anions like bromide or iodide when cyanide is bound to the iron. Although no crystallographic studies are available for chloride binding in the distal cavity of MPO, it is possible that the W2 position could accommodate this ion equally well in both native MPO and its cyanide complex, since chloride (1.81 Å) is significantly smaller than bromide (1.96 Å) or iodide (2.2 Å). The steric hindrance of $Br^-$ and $I^-$ to bind at the W2 position seems to be reflected by the fact that with increasing radii of the anionic substrates the increase of the rate of compound I reduction by the halide is less pronounced (Table 4).

It is important to note that EPO compound I is a much better oxidant of bromide, iodide and thiocyanate than MPO (Table 4),[65] which suggests some differences in substrate access and binding sites. LPO has been shown to have barely detectable activity with bromide at neutral pH but oxidizes iodide and thiocyanate very efficiently (Table 4).[66] Thus, in addition to redox thermodynamic properties, other factors such as anion size, anion binding and topological effects determine the effect of pH and substrate specificity of compound I reduction directly to ferric peroxidase.[18]

It has also been proposed that MPO is able to oxidise chloride to chlorine, bromide to bromine or to form the interhalogen bromine chloride (BrCl). The formation of $Cl_2$ and BrCl in myeloperoxidase-driven reactions and neutrophil suspensions has been reported in several publications.[67] In these cases, the reduction of compound I to the ferric enzyme [Equation (8)] would be coupled with halide oxidation by one of the following half-reactions [Equations (11), (12) and (13), all written as reduction process].

$$Cl_2 + 2e^- \rightarrow 2Cl^- \quad (11)$$

$$Br_2 + 2e^- \rightarrow 2Br^- \quad (12)$$

$$BrCl + 2e^- \rightarrow Br^- + Cl^- \quad (13)$$

The standard reduction potentials of the couples $Cl_2/2Cl^-$, $Br_2/2Br^-$ and $I_2/2I^-$ are given in Table 3. They are independent of pH. The redox couple $BrCl/Br^-$, $Cl^-$ has a standard reduction potential of 1.21 V.[68] Whether other halogenated oxidation products, including interhalogens, can result from (pseudo)halide oxidation by peroxidases is purely speculative. Due to the low iodide concentration (<1 μM[69]) in blood and most tissues (with the exception of the thyroid gland), iodide oxidation by MPO, EPO and LPO is of little importance. The redox chemistry of $SCN^-$ oxidation by peroxidases is rather complex. In addition to the formation of hypothiocyanite ($OSCN^-$), further oxidation products such as cyanate ($OCN^-$) and $(SCN)_2$ have been reported.[61,70] Hypothiocyanous acid (HOSCN) and $SCN^-$ are the hydrolysis products of $(SCN)_2$ with a hydrolysis constant of $5.7 \times 10^{-4}$ M².[61] From this constant and the values for the standard reduction potential of the couple $HOSCN/SCN^-$, $H_2O$ (Table 3), the unknown potential for the couple $(SCN)_2/2SCN^-$ (0.72 V) can be calculated.

In general, it follows from thermodynamic rules that the oxidation of a (pseudo)halide by compound I of peroxidases is only possible if the actual reduction potentials for (pseudo)halide oxidation [$E'(HOX/X^-, H_2O)$ or $E'(X_2/2X^-)$] are lower than the reduction potential for the reduction of compound I $E'$[compound I/PorFe$^{III}$] [Equations (14) and (15)].

$$E'(HOX/X^-, H_2O) < E'[\text{compound I/PorFe}^{III}] \quad (14)$$

$$E'(X_2/2X^-) < E'[\text{compound I/PorFe}^{III}] \quad (15)$$

The reduction potential of any redox couple depends on reactant concentrations and pH value and can be determined by means of the Nernst equation [Equation (5)]. As the redox couples involved in halide oxidation by peroxidases possess different dependencies on pH, certain pH threshold values depending on halide concentration exist for a given peroxidase − only below this pH threshold value is the halide oxidation thermodynamically favourable.[68] The reduction potential of the couple compound I/ferric enzyme declines by –0.059 V per increasing pH unit at neutral and slightly acidic pH values. The potential of the couple $HOX/X^-$, $H_2O$ is diminished by –0.0295 V per pH unit if the pH is lower than the p$K_a$ value of the corresponding hypohalous acid. At pH values higher than the p$K_a$ value, the slope will change by –0.059 V per pH unit. The redox couple $X_2/2X^-$ is independent of pH.

A selected example for the calculation of pH threshold values is presented for the formation of HOCl and HOBr by MPO and EPO assuming equimolar concentrations for compound I and the ferric enzyme form as well as concen-

 © 2006 Wiley-VCH Verlag GmbH & Co. KGaA, Weinheim 

trations of $10^{-6}$ M for HOCl, $10^{-1}$ M for $Cl^-$, $10^{-6}$ M for HOBr and $10^{-4}$ M for $Br^-$ (Figure 2). Under these conditions, clear pH thresholds are found for the formation of HOCl and HOBr by EPO at pH 5.75 and 7.6, respectively. The formation of HOBr by MPO would be possible at all pH values indicated in Figure 2, while the formation of HOCl is unlikely at pH values higher than 7.5. Both reduction potentials of both couples are nearly identical in this pH range. It is necessary to point out that these considerations are influenced by uncertainties about the knowledge of the real concentration values of all reactants.

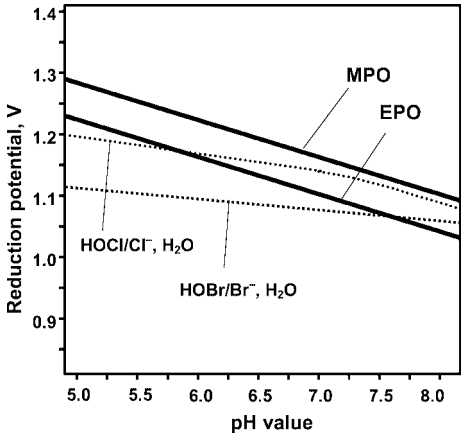


Figure 2. Selected example for the determination of pH threshold values below which the formation of HOBr or HOCl would be thermodynamically possible by the MPO (or EPO)-hydrogen peroxide-halide system. Reduction potentials of the redox couples compound I/ferric enzyme are given for MPO and EPO as a function of pH (solid lines) using equimolar concentrations of compound I and the ferric enzyme form. The reduction potentials of the couples $HOCl/Cl^-$, $H_2O$ and $HOBr/Br^-$, $H_2O$ (dotted lines) are indicated in the same pH range for $10^{-6}$ M HOCl, $10^{-1}$ M $Cl^-$, $10^{-6}$ M HOBr and $10^{-4}$ M $Br^-$.

Calculated pH thresholds for the chloride and bromide oxidation by MPO and EPO have been compared with experimentally determined pH threshold values for the formation of chloro- and bromohydrins from unsaturated phosphatidylcholines by these peroxidases at varying halide concentrations. This analysis revealed that chlorine, bromine and bromine chloride are the favoured chloride and bromide oxidation products by MPO, whereas hypochlorous and hypobromous acid will primarily be formed by EPO.[68]

The inability to induce MPO effects at 0.1 M $Cl^-$ and neutral pH values and the existence of certain pH threshold values by lowering the pH was also evidenced in other investigations on lipids, such as the formation of lysophospholipids from highly unsaturated phosphatidylcholines[71] or the accumulation of diene conjugates in low-density lipoproteins.[72] In contrast, when using taurine or monochlorodimedon as detection system, the chlorinating activity of MPO has been reported at neutral pH values up to pH 8.[73] Taurine is known to bind to MPO and be modified by the MPO–$H_2O_2$–$Cl^-$ system by so-called enzyme-bound hypochlorous acid but not by free HOCl, as revealed by kinetic studies at low pH.[74] Similarly, the chlorination of monochlorodimedon by chloroperoxidase occurs clearly by enzyme-bound HOCl.[75] Thus, the mechanism of chlorination of taurine and monochlorodimedon by MPO at neutral pH values remains unknown from the viewpoint of redox chemistry.

For MPO and chloride, it has been shown that chloride forms a reversible complex with compound I, the absorbance of which is in between those of compound I and native MPO.[62b] At pH 7 it was impossible to reconstitute the ferric enzyme form completely from compound I of MPO by adding chloride or bromide in the stopped-flow experiment.[42,74] Apparently, only the complex between compound I and $Cl^-$ or $Br^-$ was formed without inducing the halide oxidation; only at pH 5 did a complete reconstitution of ferric MPO from compound I take place.[28,76] How the addition of taurine facilitates the reconstitution of ferric MPO in halide oxidation at neutral pH values remains unknown.

## Protein Modification by Peroxidase Products

Reactive halide and nitrogen species produced by heme peroxidase contribute to the modification of functional sites of proteins and other biomolecules. Hypochlorous acid, hypobromous acid and nitrogen dioxide in particular have been investigated for their ability to induce post-translational modifications in proteins. As a result of the action of hypohalous acid, most of all, oxidation of sulfhydryl and methionine residues as well as halogenation of aromatic amino acid residues have been reported.[77] Although the chlorination of tyrosine residues in protein by the MPO–$H_2O_2$–$Cl^-$ system has been reported,[78] the formation of 3-chlorotyrosine is an unfavourable reaction for HOCl.[77a] Only 2% of HOCl produced by MPO or neutrophils is used to convert tyrosine residues in albumin to chlorotyrosines.[78a] A substantial bromination of tyrosine residues of albumin is observed at physiological concentrations of chloride and bromide at a pH higher than 7.[79]

Nitration of proteins is often observed during pathophysiological situations when oxidative and nitrative stress conditions are simultaneously produced and, in particular, both nitrite and hydrogen peroxide concentrations in cells increase.[80] The MPO–$H_2O_2$–nitrite system causes both nitration and nitrosylation of selected tyrosine and tryptophan residues in proteins, for example in human serum albumin.[79b] The most commonly detected marker of biological nitration is 3-nitrotyrosine, and different mechanisms, which are probably simultaneously active, have been proposed for its formation in vitro.[80e]

Nitrogen dioxide is derived from the one-electron oxidation of nitrite by compound I and compound II of heme peroxidases (see above). Dimerisation of two $^{\cdot}NO_2$ species in a reversible reaction generates $N_2O_4$, which forms symmetrical ($O_2N$–$NO_2$) and asymmetrical (ON–$NO_3$) tautomers that are able to produce nitrated and nitrosated tryptophan derivatives.[81]

Formation of 3-nitrotyrosine is also thought to occur by coupling of nitrogen dioxide with the phenoxy radical

 © 2006 Wiley-VCH Verlag GmbH & Co. KGaA, Weinheim 

[Equation (16)], which is also produced by one-electron oxidation of tyrosine residues in proteins mediated by the peroxidase intermediates compound I and compound II.

$$^{\cdot}NO_2 + Ph–O^{\cdot} \rightarrow O_2N–Ph–OH \quad (16)$$

Since the Tyr$^{\cdot}$/Tyr standard reduction potential at pH 7 is 0.94 V,[36] the phenoxy radical can be generated by oxidation of the phenol by both nitrogen dioxide or the peroxidase intermediates compound I and compound II.

Even though the dominant mechanism for nitration by peroxidases in the presence of nitrite and hydrogen peroxide considers the formation of nitrogen dioxide by the classical enzyme intermediates, several data show that another active species with chemical properties similar to those of peroxynitrite can be generated by mammalian peroxidases. This alternative species has been proposed for LPO based on kinetic analysis and product distribution in nitration/oxidation experiments of *p*-cyanophenol, phenylacetic acid[44d,44e] and tryptophan derivatives[44f] as mechanistic probes. For the enzymatic reactions, the importance of this second nitrating species becomes dominant as the nitrite concentration in solution increases. The generation of an oxidant species with the chemical properties of peroxynitrite by MPO and EPO in the presence of nitrite has been proposed in vivo, through the use of EPO- and MPO-knockout mice, from the detection of hydroxylated targets.[44h] It has been shown that while the major reacting nitrogen species generated by peroxidase catalysis is nitrogen dioxide, a further minor, but not negligible, contribution produces products typical of $ONOO^-$ reactivity.

The formation of the enzyme nitrating species with peroxynitrite reactivity can be explained by considering that, after coordination of nitrite to the iron, the nitrite adduct can undergo oxidation by hydrogen peroxide according to the following reaction [Equation (17)][44d–44f]

$$PorFe^{III}–NO_2^- + H_2O_2 \rightarrow PorFe^{III}–N(O)OO^- + H_2O \quad (17)$$

where the $PorFe^{III}–N(O)OO^-$ species is assumed to be an iron-bound peroxynitrite coordinated through the nitrogen donor atom. This assumption is based on its chemical properties and on the similarities between the spectral features of $PorFe^{III}–NO_2^-$ and the intermediate formed as a transient species upon treatment of LPO with hydrogen peroxide in the presence of an excess of nitrite.[44e]

The characterisation of this intermediate is complicated by its high reactivity, which causes a quick degradation by reaction with nearby amino acid residues of the protein. In addition, the lifetime of the heme-bound peroxynitrite may be reduced through the fast conversion to nitrate. In fact, the catalytic effect of heme complexes in the dismutation of (O-bound) peroxynitrite is well known,[82] and a similar activity can also be exerted with the N-bound species. For these reasons, the redox properties of the $PorFe^{III}–N(O)OO^-$ intermediate are not known. The species generated by LPO shares several reactivity features with free peroxynitrite, such as a certain preference to produce *N*-nitrosotryptophan rather than *N*-nitrotryptophan, and the capability of reacting with aromatic residues to give both nitration and hydroxylation of the ring.[44f] The latter activity indicates a strong oxidising property for $PorFe^{III}–N(O)OO^-$, although the relative relevance of the one-electron (radical) reactions with respect to the two-electron oxidations promoted by this species is still unclear. The lack of effect of $CO_2$ on the observed reactivity of the $PorFe^{III}–N(O)OO^-$ intermediate[44e] indicates that the reactivity is not, or is only partly, due to free peroxynitrite generated by the dissociation of the adduct; thus, the reactions observed occur within the protein active site and are due to the protein iron-bound peroxynitrite.

It has to be mentioned that MPO and EPO are strong cationic proteins with p$K_a$ values around 10. LPO, however, has a p$K_a$ value of about 7.5. The formation of complexes with acidic proteins is known for MPO. The binding and uptake of MPO to endothelial cells is mediated by MPO–albumin complexes.[83] After endocytosis by the endothelial, MPO becomes associated with fibronectin-rich fibrils.[84] Other proteins known to interact with myeloperoxidase are apoprotein A-1, ceruloplasmin and antitrypsin,[85] although the physiological meaning of these findings is unclear. Regarding the antimicrobial role of these enzymes, however, the combination of adhesion to pathogens with the biochemical capacity to generate strong oxidants seems to be a general strategy in unspecific immune defence that developed very early in evolution.

## Conclusion

Here we have demonstrated how the functional features of human peroxidases to use small anionic one- and two-electron donors are closely related with their peculiar structural and redox properties and how the corresponding products contribute to the modification of functional sites of proteins and other biomolecules. This knowledge will help in the rational design of new potent and specific inhibitors that will dampen inflammation without precipitating infectious diseases.

## Acknowledgments

This work was supported by the COST D21 Action "Metalloenzymes and Chemical Biomimetics", the Austrian Science Fund (project number P15660), the German Research Council (Postgraduate Training Programme "Mechanisms and Applications of Non-conventional Oxidation Reactions") and PRIN (Chemical processes and structural modifications in neurodegeneration) and FIRB (Protein folding and aggregation: Metal and biomolecules in protein conformational diseases) projects of the Italian MIUR.

[1] K. G. Paul, *Molecular and Physiological Aspects of Plant Peroxidases* (Eds.: H. Greppin, C. Penel, T. Gaspar), University of Geneva, Switzerland, **1986**, p. 1.
[2] K. G. Welinder, *Curr. Opin. Struct. Biol.* **1992**, *2*, 388–393.
[3] H. Daiyasu, H. Toh, *J. Mol. Evol.* **2000**, *51*, 433–445.
[4] K. G. Welinder, A. F. Justesen, V. H. Kjaersgard, R. B. Jensen, S. K. Rasmussen, H. M. Jespersen, L. Duroux, *Eur. J. Biochem.* **2002**, *269*, 6063–6081.

 © 2006 Wiley-VCH Verlag GmbH & Co. KGaA, Weinheim 

[5] H. M. Jespersen, I. V. Kjaersgard, L. Ostergaard, K. G. Welinder, *Biochem. J.* **1997**, *326*, 305–310.
[6] S. J. Klebanoff, *J. Leukocyte Biol.* **2005**, *77*, 598–625.
[7] G. J. Gleich, E. A. Ottesen, K. M. Leiferman, S. J. Ackerman, *Int. Arch. Allergy Appl. Immunol.* **1989**, *88*, 59–62.
[8] E. L. Thomas, P. M. Bozeman, D. B. Learn, *Peroxidases in Chemistry and Biology*, CRC Press, Boston, **1999**, pp. 123–143.
[9] A. Taurog, *Recent Prog. Horm. Res.* **1970**, *26*, 189–247.
[10] S. J. Klebanoff, *Peroxidases in Chemistry and Biology*, CRC Press, Boca Raton, Boston, **1991**, pp. 1–35.
[11] a) W. F. Reynolds, J. Rhees, D. Maciejewski, T. Paladino, H. Sieburg, R. A. Maki, E. Masliah, *Exp. Neurol.* **1999**, *155*, 31–41; b) C. Jolivalt, B. Leininger-Muller, R. Drozdz, J. W. Naskalski, G. Siest, *Neurosci. Lett.* **1996**, *210*, 61–64; c) A. Daugherty, J. L. Dunn, D. L. Rateri, J. W. Heinecke, *J. Clin. Invest.* **1994**, *94*, 437–444; d) E. Malle, G. Waeg, R. Schreiber, E. F. Grone, W. Sattler, H. J. Grone, *Eur. J. Biochem.* **2000**, *267*, 4495–4503.
[12] a) G. B. Schuller-Levis, E. Park, *FEMS Microbiol. Lett.* **2003**, *226*, 195–202; b) J. Marcinkiewicz, *Immunol. Lett.* **2003**, *89*, 187–193.
[13] J. Wang, S. A. Mahmud, J. A. Thompson, J. Geng, N. S. Key, A. Slungaard, *Blood* **2006**, *107*, 558–565.
[14] J. Arnhold, P. G. Furtmüller, G. Regelsberger, C. Obinger, *Eur. J. Biochem.* **2001**, *268*, 5142–5148.
[15] J. Arnhold, P. G. Furtmüller, C. Obinger, *Redox Rep.* **2003**, *8*, 179–186.
[16] P. G. Furtmüller, J. Arnhold, W. Jantschko, M. Zederbauer, C. Jakopitsch, C. Obinger, *J. Inorg. Biochem.* **2005**, *99*, 1220–1229.
[17] T. J. Fiedler, C. A. Davey, R. E. Fenna, *J. Biol. Chem.* **2000**, *275*, 11964–11971.
[18] P. G. Furtmüller, M. Zederbauer, W. Jantschko, J. Helm, M. Bogner, C. Jakopitsch, C. Obinger, *Arch. Biochem. Biophys.* **2006**, *445*, 199–213.
[19] C. Oxvig, A. R. Thomsen, M. T. Overgaard, E. S. Sorensen, P. Hojrup, M. J. Bjerrum, G. J. Gleich, L. Sottrup-Jensen, *J. Biol. Chem.* **1999**, *274*, 16953–16958.
[20] G. D. DePillis, S. Ozaki, J. M. Kuo, D. A. Maltby, P. R. Ortiz de Montellano, *J. Biol. Chem.* **1997**, *272*, 8857–8860.
[21] A. Taurog, *Biochimie* **1999**, *81*, 557–562.
[22] B. G. J. M. Bolscher, R. Wever, *Biochim. Biophys. Acta* **1984**, *788*, 1–10.
[23] M. Ikeda-Saito, *Biochemistry* **1987**, *26*, 4344–4349.
[24] U. Burner, P. G. Furtmüller, A. J. Kettle, W. H. Koppenol, C. Obinger, *J. Biol. Chem.* **2000**, *275*, 20597–20601.
[25] M. Blair-Johnson, T. Fiedler, R. Fenna, *Biochemistry* **2001**, *40*, 13990–13997.
[26] C. E. Cooper, E. Odell, *FEBS Lett.* **1992**, *314*, 58–60.
[27] M. Ikeda-Saito, *J. Biol. Chem.* **1985**, *260*, 11688–11696.
[28] E. Monzani, R. Roncone, M. Galliano, W. H. Koppenol, L. Casella, *Eur. J. Biochem.* **2004**, *271*, 895–906.
[29] L. A. Marquez, J. T. Huang, H. B. Dunford, *Biochemistry* **1994**, *33*, 1447–1454.
[30] D. Dolphin, R. H. Felton, *Acc. Chem. Res.* **1974**, *7*, 26.
[31] W. H. Koppenol, *Bioelectrochem. Bioenerg.* **1987**, *18*, 3–11.
[32] a) I. M. Kooter, N. Moguilevsky, A. Bollen, L. A. van der Veen, C. Otto, H. L. Dekker, R. Wever, *J. Biol. Chem.* **1999**, *274*, 26794–26802; b) S. Brogioni, A. Feis, M. P. Marzocchi, M. Zederbauer, P. G. Furtmüller, C. Obinger, G. Smulevich, *J. Raman Spectrosc.* **2006**, *37*, 263–276.
[33] W. Jantschko, P. G. Furtmüller, M. Allegra, M. A. Livrea, C. Jakopitsch, G. Regelsberger, C. Obinger, *Arch. Biochem. Biophys.* **2002**, *398*, 12–22.
[34] a) L. A. Marquez, H. B. Dunford, *J. Biol. Chem.* **1995**, *270*, 30434–30440; b) U. Burner, W. Jantschko, C. Obinger, *FEBS Lett.* **1999**, *443*, 290–296.
[35] D. M. Stanbury, *Adv. Inorg. Chem.* **1989**, *33*, 69–138.
[36] M. R. DeFilippis, C. P. Murthy, M. Faraggi, M. H. Klapper, *Biochemistry* **1989**, *28*, 4847–4853.
[37] P. G. Furtmüller, J. Arnhold, W. Jantschko, H. Pichler, C. Obinger, *Biochem. Biophys. Res. Commun.* **2003**, *301*, 551–557.
[38] W. Jantschko, P. G. Furtmüller, M. Zederbauer, K. Neugschwandtner, I. Lehner, C. Jakopitsch, J. Arnhold, C. Obinger, *Biochem. Pharmacol.* **2005**, *69*, 1149–1157.
[39] Unpublished results.
[40] O. Augusto, M. C. Bonini, A. M. Amanso, E. Linares, C. C. X. Santos, S. L. de Menezes, *Free Radical Biol. Med.* **2002**, *32*, 841–859.
[41] E. Ghibaudi, E. Laurenti, *Eur. J. Biochem.* **2003**, *270*, 4403–4412.
[42] P. G. Furtmüller, U. Burner, C. Obinger, *Biochemistry* **1998**, *37*, 17923–17930.
[43] a) O. M. Lardinois, K. F. Medzihradsky, P. R. Ortiz de Montellano, *J. Biol. Chem.* **1999**, *274*, 35441–35448; b) E. Monzani, A. L. Gatti, A. Profumo, L. Casella, M. Gullotti, *Biochemistry* **1997**, *36*, 1918–1926.
[44] a) A. Van der Vliet, J. P. Eiserich, B. Halliwell, C. E. Cross, *J. Biol. Chem.* **1997**, *272*, 7617–7625; b) J. B. Sampson, Y. Z. Ye, H. Rosen, J. S. Beckman, *Arch. Biochem. Biophys.* **1998**, *356*, 207–213; c) J. P. Eiserich, M. Hristova, C. E. Cross, A. D. Jones, B. A. Freeman, B. Halliwell, A. van der Vliet, *Nature* **1998**, *391*, 393–397; d) L. Casella, E. Monzani, R. Roncone, S. Nicolis, A. Sala, A. De Riso, *Environ. Health Perspect.* **2002**, *110*, 709–711; e) E. Monzani, R. Roncone, M. Galliano, W. H. Koppenol, L. Casella, *Eur. J. Biochem.* **2004**, *271*, 895–906; f) A. Sala, S. Nicolis, R. Roncone, E. Monzani, L. Casella, *Eur. J. Biochem.* **2004**, *271*, 2841–2852; g) R. Roncone, M. Barbieri, E. Monzani, L. Casella, *Coord. Chem. Rev.* **2006**, in press; h) M. L. Brennan, W. Wu, X. Fu, Z. Shen, W. Song, H. Frost, C. Vadseth, L. Narine, E. Lenkiewicz, M. T. Borchers, A. J. Lusis, J. J. Lee, N. A. Lee, H. M. Abu-Soud, H. Ischiropoulos, S. L. Hazen, *J. Biol. Chem.* **2002**, *277*, 17415–17427; i) D. Schmitt, Z. Shen, R. Zhang, S. M. Colles, W. Wu, R. G. Salomon, Y. Chen, G. M. Chisolm, S. L. Hazen, *Biochemistry* **1999**, *38*, 16904–16915; j) W. Wu, Y. Chen, S. L. Hazen, *J. Biol. Chem.* **1999**, *274*, 25933–25944; k) C. J. van Dalen, C. C. Winterbourn, A. J. Kettle, *Biochem. J.* **2006**, *394*, 707–713; l) C. J. van Dalen, C. C. Winterbourn, R. Senthilmohan, A. J. Kettle, *J. Biol. Chem.* **2000**, *275*, 11638–11644.
[45] a) R. Roman, H. B. Dunford, *Can. J. Chem.* **1973**, *51*, 588–596; b) L. Gebicka, *Acta Biochim. Pol.* **1999**, *46*, 919–927.
[46] T. B. Brück, R. J. Fielding, M. C. R. Symons, P. J. Harvey, *Eur. J. Biochem.* **2001**, *268*, 3214–3222.
[47] a) Y. Hayashi, I. Yamazaki, *J. Biol. Chem.* **1979**, *254*, 9101–9106; b) Z. S. Farhangrazi, M. E. Fossett, L. S. Powers, W. R. Ellis, *Biochemistry* **1995**, *34*, 2866–2871.
[48] M. Zederbauer, W. Jantschko, K. Neugschwandtner, C. Jakopitsch, N. Moguilevsky, C. Obinger, P. G. Furtmüller, *Biochemistry* **2005**, *44*, 6482–6491.
[49] a) W. H. Koppenol, J. Butler, *Adv. Free Radic. Biol. Med.* **1985**, *1*, 91–131; b) W. H. Koppenol, *FEBS Lett.* **1994**, *347*, 5–8.
[50] J. C. Morris, *J. Phys. Chem.* **1966**, *70*, 3798–3805.
[51] *Gmelins Handbuch der Anorganischen Chemie*, *Chlor*, 8th ed., Supplement A, Verlag Chemie, Weinheim, **1968**, p. 244.
[52] *Gmelins Handbuch der Anorganischen Chemie*, *Chlor*, 8th ed., Verlag Chemie, Weinheim, **1927**, p. 62.
[53] R. C. Troy, D. W. Margerum, *Inorg. Chem.* **1991**, *30*, 3538–3543.
[54] *Gmelins Handbuch der Anorganischen Chemie*, *Brom*, 8th ed., Verlag Chemie, Weinheim, **1931**, p. 290.
[55] *Gmelins Handbuch der Anorganischen Chemie*, *Brom*, 8th ed., Verlag Chemie, Weinheim, **1931**, p. 110.
[56] J. C. Wren, S. Paquette, S. Sunder, B. L. Ford, *Can. J. Chem.* **1986**, *64*, 2284–2296.
[57] *Handbook of Chemistry and Physics*, 56th ed., CRC Press, Cleveland, **1975**, p. D-142.
[58] A. Henglein, *Radiat. Phys. Chem.* **1980**, *15*, 151–157.
[59] E. L. Thomas, *Biochemistry* **1981**, *20*, 3273–3280.
[60] K. M. Pruitt, J. Tenevuo, B. Mansson-Rahemtulla, P. Harrington, D. C. Baldone, *Biochim. Biophys. Acta* **1986**, *870*, 385–391.

 © 2006 Wiley-VCH Verlag GmbH & Co. KGaA, Weinheim 

[61] J. J. Barnett, M. L. McKee, D. M. Stanbury, *Inorg. Chem.* **2004**, *43*, 5021–5033.
[62] a) L. A. Marquez, H. B. Dunford, *J. Biol. Chem.* **1994**, *269*, 7950–7956; b) P. G. Furtmüller, C. Obinger, Y. Hsuanyu, H. B. Dunford, *Eur. J. Biochem.* **2000**, *267*, 5858–5864.
[63] a) M. Ikeda-Saito, *J. Biol. Chem.* **1985**, *260*, 11688–11696; b) A. R. J. Bakkenist, J. E. G. De Boer, H. Plat, R. Wever, *Biochim. Biophys. Acta* **1980**, *613*, 337–348; c) M. Ikeda-Saito, C. Lee, K. Adachi, H. S. Eck, R. C. Prince, K. S. Booth, W. S. Caughey, S. Kimura, *J. Biol. Chem.* **1989**, *264*, 4550–4563; d) P. C. Andrews, N. I. Krinsky, *J. Biol. Chem.* **1982**, *257*, 13240–13245.
[64] H. C. Lee, K. S. Booth, W. S. Caughey, M. Ikeda-Saito, *Biochim. Biophys. Acta* **1991**, *1076*, 317–320.
[65] P. G. Furtmüller, U. Burner, G. Regelsberger, C. Obinger, *Biochemistry* **2000**, *39*, 15578–15584.
[66] P. G. Furtmüller, W. Jantschko, G. Regelsberger, C. Jakopitsch, J. Arnhold, C. Obinger, *Biochemistry* **2002**, *41*, 11895–11900.
[67] a) S. L. Hazen, F. F. Hsu, D. M. Mueller, J. R. Crowley, J. W. Heinecke, *J. Clin. Invest.* **1996**, *98*, 1283–1289; b) S. L. Hazen, F. F. Hsu, K. Duffin, J. W. Heinecke, *J. Biol. Chem.* **1996**, *271*, 23080–23088; c) J. P. Henderson, J. Byun, J. W. Heinecke, *J. Biol. Chem.* **1999**, *274*, 33440–33448; d) J. P. Henderson, J. Byun, M. V. Williams, D. M. Mueller, M. L. McCormick, J. W. Heinecke, *J. Biol. Chem.* **2001**, *276*, 7867–7875.
[68] H. Spalteholz, O. M. Panasenko, J. Arnhold, *Arch. Biochem. Biophys.* **2006**, *445*, 225–234.
[69] J. Holzbecher, D. E. Ryan, *Clin. Biochem.* **1980**, *13*, 277–278.
[70] M. Arlandson, T. Decker, V. A. Roongta, L. Banilla, K. H. Mayo, J. C. MacPherson, S. L. Hazen, A. Slungaard, *J. Biol. Chem.* **2001**, *276*, 215–224.
[71] O. M. Panasenko, H. Spalteholz, J. Schiller, J. Arnhold, *Free Radic. Biol. Med.* **2003**, *34*, 553–562.
[72] A. Jerlich, L. Horakova, J. S. Fabjan, A. Giessauf, G. Jürgens, R. J. Schaur, *Int. J. Clin. Lab. Res.* **1999**, *29*, 155–161.
[73] a) A. R. J. Bakkenist, J. E. G. de Boer, H. Plat, R. Wever, *Biochim. Biophys. Acta* **1980**, *613*, 337–348; b) C. C. Winterbourn, *Biochim. Biophys. Acta* **1985**, *840*, 204–210; c) K. W. M. Zuurbier, A. R. J. Bakkenist, R. Wever, A. O. Muijsers, *Biochim. Biophys. Acta* **1990**, *1037*, 140–146; d) A. J. Kettle, C. C. Winterbourn, *Methods Enzymol.* **1994**, *233*, 502–512.
[74] a) L. A. Marquez, H. B. Dunford, *J. Biol. Chem.* **1994**, *269*, 7950–7956; b) H. B. Dunford, *Redox Rep.* **2000**, *5*, 169–172.
[75] H. B. Dunford, A. M. Lambeir, M. A. Kashem, M. A. Pickard, *Arch. Biochem. Biophys.* **1987**, *252*, 292–302.
[76] P. G. Furtmüller, U. Burner, W. Jantschko, G. Regelsberger, C. Obinger, *Redox Rep.* **2000**, *5*, 173–178.
[77] a) D. I. Pattison, M. J. Davies, *Chem. Res. Toxicol.* **2001**, *14*, 1453–1464; b) C. L. Hawkins, D. I. Pattison, M. J. Davies, *Amino Acids* **2003**, *25*, 259–274; c) D. I. Pattison, M. J. Davies, *Biochemistry* **2004**, *43*, 4799–4809.
[78] a) A. J. Kettle, *FEBS Lett.* **1996**, *379*, 103–106; b) C. C. Winterbourn, A. J. Kettle, *Free Radic. Biol. Med.* **2000**, *29*, 403–409.
[79] a) R. Senthilmohan, A. J. Kettle, *Arch. Biochem. Biophys.* **2006**, *445*, 235–244; b) P. Salavei, H. Spalteholz, J. Arnhold, *Free Radic. Biol. Med.* **2006**, *40*, 515–525.
[80] a) J. S. Stamler, M. Feelisch, *Methods in Nitric Oxide Research* (Eds.: M. Feelisch, J. S. Stamler), Wiley, Chichester, UK., **1996**, p. 19.; b) F. Yamakura, K. Ikeda, *Nitric Oxide* **2006**, *4*, 152–161; c) M. M. Iravani, C. O. Haddon, S. Rose, P. Jenner, *Brain Res.* **2006**, *1067*, 256–262; d) X. Zhan, D. M. Desiderio, *Biochem. Biophys. Res. Commun.* **2004**, *325*, 1180–1186; e) H. Ischiropoulos, J. S. Beckman, *J. Clin. Invest.* **2003**, *111*, 163–169.
[81] A. Sala, S. Nicolis, R. Roncone, L. Casella, E. Monzani, *Eur. J. Biochem.* **2004**, *271*, 2841–2852.
[82] J. P. Crow, *Arch. Biochem. Biophys.* **1999**, *371*, 41–52.
[83] C. Tiruppathi, T. Naqvi, Y. Wu, S. M. Vogel, R. D. Minshall, A. B. Malik, *Proc. Natl. Acad. Sci. USA* **2004**, *101*, 7699–7704.
[84] S. Baldus, J. P. Eiserich, A. Mani, L. Castrom, M. Figueroa, P. Chumley, W. Ma, A. Tousson, R. White, D. C. Bullard, M.-L. Brennan, A. J. Lusis, K. P. Moore, B. A. Freeman, *J. Clin. Invest.* **2001**, *108*, 1759–1770.
[85] a) M. Segelmark, B. Persson, T. Hellmark, J. Wieslander, *Clin. Exp. Immunol.* **1997**, *108*, 167–174; b) C. Taggart, D. Cervantes-Laurean, G. Kim, N. G. McElvaney, N. Wehr, J. Moss, R. L. Levine, *J. Biol. Chem.* **2000**, *275*, 27258–27265; c) L. Zheng, M. Settle, G. Brubaker, D. Schmitt, S. L. Hazen, J. D. Smith, M. Kinter, *J. Biol. Chem.* **2005**, *280*, 38–47.

Received: May 10, 2006
Published Online: August 10, 2006

 © 2006 Wiley-VCH Verlag GmbH & Co. KGaA, Weinheim 

DOI: 10.1002/ejic.200600477

# New Dimeric Copper(II) Complex $[Cu(5\text{-}MeOsal)_2(\mu\text{-}nia)(H_2O)]_2$ with Magnetic Exchange Interactions through H-Bonds

**Dušan Valigura,*[a] Jan Moncol,[a] Maria Korabik,[b] Zuzana Púčeková,[a] Tadeusz Lis,[b] Jerzy Mroziński,[b] and Milan Melník[a]**

**Keywords:** Copper / Carboxylate ligands / Nicotinamide / Dimer / Structure / Magnetic properties

The synthesis and characterization (elemental analysis, IR, electronic and EPR spectra as well as magnetization measurements over the temperature range 1.8 K–300 K) of solid complex $[Cu(5\text{-}MeOsal)_2(\mu\text{-}nia)(H_2O)]_2$ (**1**; 5-MeOsal = 5-methoxysalicylate, nia = nicotinamide) is reported together with the crystal structure. In blue–green complex **1**, two $Cu(5\text{-}MeOsal)_2(H_2O)$ units are held together by a pair of bidentate nonchelating nicotinamide ligands, which form a $(CuNC_3O)_2$ ring. Each Cu atom adopts a distorted square-pyramidal geometry. The oxygen atoms from two unidentate 5-MeOsal anions occupy the *trans* position, a water molecule and the pyridine N atom of nicotinamide build the basal plane and a carboxamide O atom occupies the apical position. The separation between two Cu atoms within the centrosymmetric dimer is 6.940(2) Å. The dimeric units are self-assembled across a centre of symmetry by the formation of two pairs of strong hydrogen bonds, which create a one-dimensional polymeric structure with the interdimer Cu···Cu separation 4.901(2) Å. It is believed that these hydrogen bonds between the copper(II) atoms are responsible for the unique magnetic properties of compound **1**. The magnetic susceptibility of complex **1** exhibits a maximum at 6 K. A satisfactory explanation was found with the Bleaney–Bowers equation for Cu–Cu interaction through carboxylato groups and H-bond bridges ($2J = -6.83$ cm$^{-1}$). An additional molecular field correction that was used to characterize the interaction across the nia bridges is assumed to be extremely weak ($zJ' = -0.28$ cm$^{-1}$).
(© Wiley-VCH Verlag GmbH & Co. KGaA, 69451 Weinheim, Germany, 2006)

## Introduction

For quite some time, copper complexes with various organic ligands have been a subject of intense study because of their interesting properties which include biomedical activities. Nicotinamide (also known as a niacin derivative or vitamin $B_3$) is a nitrogen donor ligand that has been used in the treatment of various skin diseases (atopic eczema,[1,2] psoriasis and skin cancer[3–5]), and the biological activity of its copper complexes have also been studied.[6] In addition, the biological activity of different salicylic acid derivatives and their copper(II) complexes is well known.[7–10] Meanwhile, salicylatocopper(II) complexes that contain nicotinamide are rarely studied in spite of their possible structural diversities. There are only two examples (out of 26 known structures)[6,11] of polymeric copper(II) complexes where nicotinamide acts as a bridging ligand – $[Cu_2(CH_3COO)_4(\mu\text{-}nia)]_n$ and $\{[Cu(sacharinato)_2(\mu\text{-}nia)(H_2O)]\cdot H_2O\}_n$.

With the purpose to obtain and study the properties of all possible products that could be prepared by the reactions under study, we report the synthesis, structural characterisation and properties of the unusual dimeric complex $[Cu(5\text{-}MeOsal)_2(\mu\text{-}nia)(H_2O)]_2$ (**1**), which exhibits rare intradimer and/or interdimer interactions that result in magnetic properties that are of interest.

[a] Department of Inorganic Chemistry, Slovak Technical University,
Radlinského 9, 81237 Bratislava, Slovakia
Fax: +421-2-52493198
E-mail: dusan.valigura@stuba.sk
[b] Faculty of Chemistry, University of Wrocław,
50-383 Wrocław, Poland

## Results and Discussion

The molecular structure of **1** (Figure 1) consists of dimeric $[Cu(5\text{-}MeOsal)_2(\mu\text{-}nia)(H_2O)]_2$ molecules that are located at a centre of symmetry. Two equivalent $Cu(5\text{-}MeOsal)_2(H_2O)$ moieties are connected by a pair of bidentate nonchelating nicotinamide ligands, which creates a twelve-membered metallocyclic $(CuNC_3O)_2$ ring. Each Cu atom adopts a distorted square-pyramidal geometry with the oxygen atoms of two unidentate 5-MeOsal anions in the *trans* position [Cu–O12 = 1.945(2) Å]. A water molecule [Cu–O1W = 1.989(2) Å] and the pyridine N atom of nicotinamide [Cu–N1 = 2.030(3) Å] build the basal plane; a carboxamide O atom of the bridging nicotinamide assumes the apical position [Cu–O1 = 2.267(2) Å]. The copper atom is displaced from the basal plane towards the carboxamide O atom by 0.047(1) Å. The $\tau$ value[12] of 0.066 implies an almost perfect square-pyramidal geometry. The separation between Cu···Cu$^{i}$ ($1-x$, $1-y$, $1-z$) within the dimeric molecule is 6.940(2) Å(Figure 1). The amide H atoms of the apically coordinated carboxamide group are linked to the co-

 © 2006 Wiley-VCH Verlag GmbH & Co. KGaA, Weinheim 

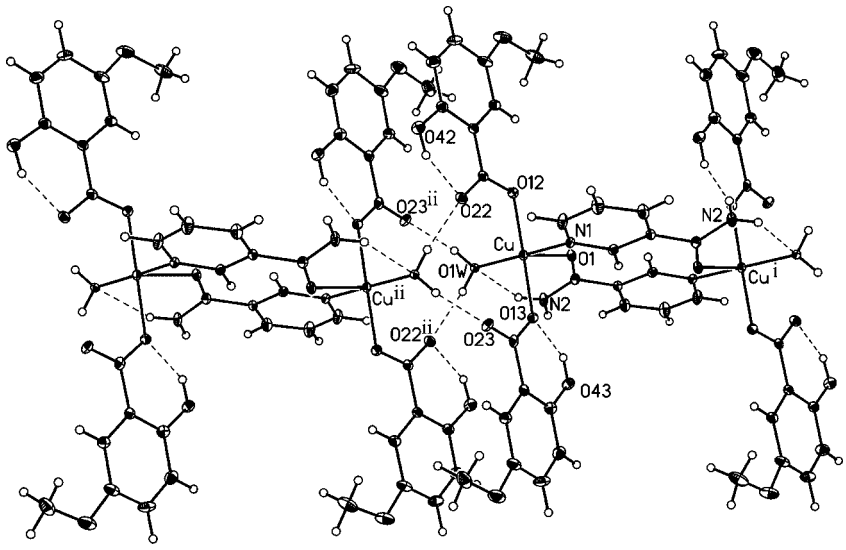


Figure 1. Perspective view of $[Cu(5\text{-}MeOsal)_2(\mu\text{-nia})(H_2O)]_2$, with the atom numbering scheme. Thermal ellipsoids are drawn at the 30% probability level. Selected bond lengths [Å] and angles [°]: Cu–O13 = 1.945(2), Cu–O12 = 1.952(2), Cu–N1 = 2.030(3), Cu–O1W = 1.989(2), Cu–O1 = 2.267(2), O13–Cu–O12 = 177.05(9), O1W–Cu–N1 = 173.09(10), O13–Cu–O1W = 87.35(9), O13–Cu–O1 = 86.67(9), O12–Cu–O1W = 90.27(9), O12–Cu–O1 = 91.73(9), O13–Cu–N1 = 92.14(10), O1W–Cu–O1 = 93.32(9), O12–Cu–N1 = 90.42(10), N1–Cu–O1 = 93.52(9), symmetry codes: (i) $1-x$, $1-y$, $1-z$, (ii) $1-x$, $-y$, $1-z$.

ordinated (in the equatorial position) water O atoms (O1W) by hydrogen bonds N2–H2A···O1W$^{i}$ ($1-x$, $1-y$, $1-z$) with interatomic distances N2···O1W$^{i}$ of 3.129(4) Å. These hydrogen bonds create six-membered metallocyclic rings ($CuO_2NCH$) and stabilize the molecular structure of the dimeric unit of **1**. The other short intramolecular hydrogen bonds are formed by the salicylato hydroxy H atoms (H43O and H42O) to the carboxylate O atoms (O13 and O22) and create six-membered cyclic rings ($O_2C_3H$) that stabilize the molecular structure as well.

The unusual dimeric structure of **1** prompted the study of its magnetic properties within the temperature range 1.8–300 K and the measurement of its EPR spectrum. The EPR spectrum (Figure 2) at room temperature is of axial symmetry and simulation of its shape[13] gave $g_{\perp}$ = 2.061 and $g_{\parallel}$ = 2.345 ($g_{av}$ = 2.156). When the temperature is decreased to –196 °C (liquid nitrogen), the spectrum becomes pseudo-isotropic in shape with $g$ = 2.133, and no information concerning the mutual interaction between the paramagnetic centres within the dimer could be drawn from these spectra (Figures 2 and 3).

Magnetization measurements showed that **1** exhibits maximum magnetic susceptibility at 6 K (Figure 3). The magnetic data of the complex were fit with the Bleaney–Bowers equation,[14] to characterize the intradimer interaction,

$$\chi_m = \frac{N\beta^2 g^2}{3kT}\left[1+\frac{1}{3}\exp\left(\frac{-2J}{kT}\right)\right]^{-1}$$

(where N is Avogadro's number, $g$ is the spectroscopic splitting factor, $\beta$ is the Bohr magneton, k is Boltzmann's con-

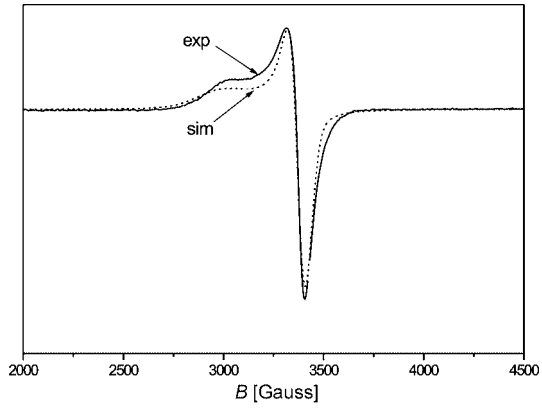


Figure 2. EPR spectrum of **1** at room temperature.

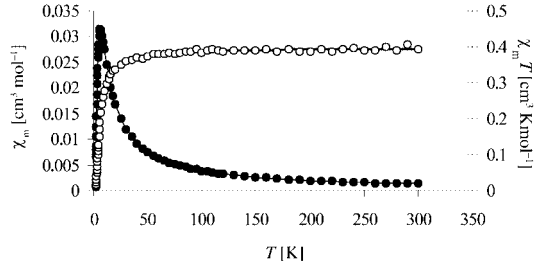


Figure 3. The plot of the $\chi_m$ and $\chi_m T$ product versus temperature [$\chi_m$ – the molar magnetic susceptibility calculated per one copper(II) centre]. The solid line was generated from the best-fit magnetic parameters.

 © 2006 Wiley-VCH Verlag GmbH & Co. KGaA, Weinheim 

stant and $J$ is the exchange parameter) together with the application of a molecular field model to the calculation of the present magnetic data of complex **1** to obtain characteristics of interdimer magnetic interactions.[15]

$$\chi_m^{corr} = \frac{\chi_m}{1 - \frac{2zJ'\chi_m}{Ng^2\beta^2}}$$

where $\chi_m$ is the molar susceptibility given by the Bleaney–Bowers equation, $zJ'$ is the molecular exchange parameter, $z$ is number of the nearest neighbours and $R$ is the agreement factor defined as

$$R = \sum_{i=1}^{n} \frac{(\chi_i^{exp}T - \chi_i^{calc}T)^2}{(\chi_i^{exp}T)^2}$$

Satisfactory least-squares fit to the experimental results was obtained for $g$ = 2.06, $2J$ = –6.83 cm$^{-1}$, $zJ'$ = –0.28 cm$^{-1}$, and $R$ = 9.99·10$^{-5}$. The small differences between the $g$ values obtained from the least-squares fit procedure and $g_{av}$ from the EPR spectra is often observed and can be attributed to the unresolved axial anisotropy of the EPR spectra and the fact that the $g$ values obtained from the magnetic data are only refined isotropically.[16]

This magnetic behaviour of **1** is surprising because the magnetic centres are bridged by a nicotinamide ligand (the shortest pathway covers a five-atom bridge) which includes the aromatic pyridine ring and the carboxamide side chain. The π-system of the pyridine ring is probably not the actual mode of interaction [the C31–C71 bond length of 1.506(4) Å is much longer than the average bond length of 1.385(4) Å within the pyridine ring]. The pyridine ring and the carboxamide group are not coplanar (ring plane to carboxamide group plane angle is 14.2°); thus, the structural data support the notion that there is no possibility for the π-system to be involved in the magnetic interaction. The σ-bonds involved in the intradimer magnetic interaction by nicotinamide ligands can be ruled out on the basis of our recently published results.[17] The 3-pyridylmethanol bridging ligand shows[17] the same number of σ-bonds and a very weak ferromagnetic interaction (Weiss constant $\Theta$ = +1.1 K). Consequently, the model for the magnetic interaction between the $Cu^{2+}$ ions within the dimeric molecule can be ruled out as well, and another interaction that is responsible for the magnetic properties of **1** should be found.

The strongest interdimer interactions are illustrated Figure 1 as a system of O–H···O hydrogen bonds between dimeric units of **1** that create a supramolecular chain of dimers along the $b$ axis with an interdimer copper-to-copper distance [distance Cu···Cu$^{ii}$ (1 – $x$, –$y$, 1 – $z$) of 4.901(2) Å] shorter than the distance Cu···Cu$^{i}$ within the dimeric units. The H atoms of the water molecules are linked to uncoordinated carboxyl O atoms (O12$^{ii}$ and O22$^{ii}$) of the neighbouring 5-methoxysalicylate anions by hydrogen bonds O1W–H1W···O22$^{ii}$ and O1W–H2W···O23$^{ii}$ (1 – $x$, –$y$, 1 – $z$) with interatomic distances O1W···O22$^{ii}$ of 2.695(3) Å and O1W···O23$^{ii}$ of 2.658(3) Å, respectively. The interdimer interactions could cause magnetic interactions because the pairs of $Cu^{2+}$ ions are, in this case, bridged by four carboxylato groups [similar to "paddle-wheel" copper(II) acetate structures], but one water molecule is inserted into each pair of carboxylato groups (Figure 4). This water molecule insertion into the bis-carboxylato bridge induces a greater distance between the polyhedra basal planes, a greater Cu···Cu distance and a longer path for the magnetic interaction compared with regular carboxylato dimers. This explanation needs further evidence based either on similar structures or the analysis of magnetic orbital interactions to be validated. Both of these topics are currently under investigation in our lab. Data which show that hydrogen bonds could cause antiferromagnetic interactions between copper(II) centres were found in literature,[18–22] but unfortunately most of the examples involve a completely different types of ligand.

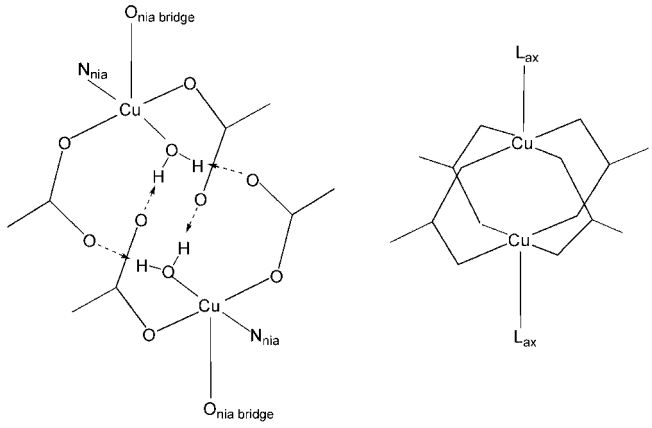


Figure 4. Schematic comparison of interdimer Cu···Cu interactions in **1** and in regular "paddle-wheel" carboxylatocopper(II) structures.

As mentioned above, the crystal structure of **1** can be compared with polymeric complexes[6,11] $[Cu_2(CH_3COO)_4(\mu\text{-nia})]_n$ and $\{[Cu(sacharinato)_2(\mu\text{-nia})(H_2O)]\cdot H_2O\}_n$ where each Cu atom has a square-pyramidal environment. In the former complex, the $Cu_2(CH_3COO)_4$ moieties form dimer units, and in the latter complex, the Cu(sacharinato)$_2$($H_2O$) units are connected by bidentate nonchelating nicotinamide ligands by N and O donor sites. The Cu–N (N atom of nia pyridine ring), Cu–O (O atom of carboxamide group of nia ligand) and finally Cu···Cu (neighbouring Cu atoms bridged by nia ligands) distances are 2.002, 2.315 and 7.547 Å, respectively, for $[Cu_2(CH_3COO)_4(\mu\text{-nia})]_n$, 2.158, 2.146 and 7.056 Å, respectively, for $\{[Cu(sacharinato)_2(\mu\text{-nia})(H_2O)]\cdot H_2O\}_n$ and 2.030(3), 2.268(2) and 6.939(2) Å, respectively, for complex **1**. The shorter Cu···Cu separation could be explained by a pair of nia bridging ligands and probably by additional hydrogen bond interaction with N–H···O (see above).

In $[CuCl_2(\mu\text{-denia})(denia)]_2$,[23] where a pair of denia ligands also serve as a bridge between two equivalent $CuCl_2$(denia) moieties, the Cu···Cu separation is about 0.762 Å longer than that found in **1**. The Cu–N (N atom of the pyridine ring of the bridging *N*,*N*-diethylnicotinamide molecule) of 2.012(3) Å compares well with the bond length Cu–N1 of complex $[Cu(5\text{-MeOsal})_2(\mu\text{-nia})(H_2O)]_2$, but Cu–

 © 2006 Wiley-VCH Verlag GmbH & Co. KGaA, Weinheim 

O (O atom from amide group of bridging *N*,*N*-diethylnicotinamide molecule) of 2.475(2) Å is about 0.207 Å longer than that found in **1**. These complexes, however, were not magnetically characterized.

## Conclusions

In conclusion, we have prepared and characterized a novel dimeric molecular complex that contains nicotinamide as a bridging ligand. These dimers are linked into a chain structure by strong hydrogen bonds that give interdimer copper-to-copper distances that are shorter than those found in intradimers. The nature of the bridging ligands (four carboxylic groups of salicylato anions) that are involved in the formation of the interdimer hydrogen bonds are probably the reason for the unusual magnetic behaviour of this dimeric substance.

## Experimental Section

**Materials:** All used chemicals were of analytical grade (Aldrich, or Sigma) and used without further purification.

**Physical Measurements:** Carbon, hydrogen and nitrogen elemental analyses were carried out with a CHNSO FlashEA 1112 (Thermo-Finnigan) elemental analyzer. The copper content of the complex was determined by the electrolysis of a water solution obtained by the mineralization of the sample in a mixture of sulfuric acid and potassium peroxodisulfate. Infrared spectra were measured with a Nicolet MAGNA 750 IR spectrometer with both KBr pellet and nujol suspension techniques for the 4000–400 $cm^{-1}$ region and a polyethylene pellet for the 400–100 $cm^{-1}$ region. Electronic spectra (190–1100 nm) of the complexes were measured in Nujol suspensions with a SPECORD 200 (Carl Zeiss Jena) spectrophotometer. Magnetization measurements in the temperature range of 1.8–300 K were carried out on powdered samples of the complexes with a magnetic field strength of 0.5 T and with a Quantum Design SQUID Magnetometer (type MPMS-XL5). Corrections for the diamagnetism of the constituting atoms were calculated with Pascal constants,[24] the value of $60 \cdot 10^{-6}$ $cm^3 mol^{-1}$ was used as the temperature-independent paramagnetism of the copper(II) ion. EPR spectra of the powdered samples were recorded at room temperature with a spectrometer Bruker ESP 300 operating at X-band equipped with an ER 035M Bruker NMR gaussmeter and a HP 5350B Hewlett Packard microwave frequency counter.

**Synthesis of 1:** Nicotinamide (122 mg, 1.0 mmol) was added to an ethanol solution (30 mL) of copper(II) acetate (200 mg, 1 mmol) while stirring. After several minutes, 5-methoxysalicylic acid (336 mg, 2 mmol) was added to the dark blue solution. The reaction mixture was stirred for a few days at ambient temperature. The blue–green powder product which precipitated from the solution was filtered off (150 mg, 56%), and the mother liquid was left to crystallize at ambient temperature. The dark blue–green crystals were separated and dried at ambient temperature. $C_{44}H_{44}Cu_2N_4O_{20}$ (1075.93): calcd C 49.03, H 4.30, Cu 11.79, N 5.19; found C 48.63, H 4.21, Cu 12.19, N 5.49. IR (KBr): $\tilde{\nu}$ = 1635 $\nu_{as}(COO^-)$, 1432 $\nu_s(COO^-)$ $cm^{-1}$. ES (Nujol): 244 (CT band), 323 (CT band), 671 (*d*←*d* band) nm.

**X-ray Structural Studies:** Data collection and cell refinement of complex **1** were carried out with a Kuma KM4-CCD difractometer with graphite monochromated Mo *Kα* radiation and the use of the *CrysAlis* software package.[25] Intensity data were corrected for Lorenz and polarization factors; absorption correction was applied as well. The structures of the complexes were solved by direct methods with *SHELXS-97*[26] and refined by the full-matrix least-squares procedure with *SHELXL-97*. Geometrical analyses were performed with *SHELXL-97*.[27] The structures were drawn with *XP* in *SHELXTL*.[28] Crystallographic data for $C_{44}H_{44}Cu_2N_4O_{20}$ (**1**): $M_r$ = 1075.93, dark green plate, 0.09 × 0.20 × 0.20 mm, monoclinic, *C*2/*c*, *a* = 21.805 (6), *b* = 11.735 (3), *c* = 17.585 (5) Å, *β* = 104.72 (3)°, *V* = 4352 (2) $Å^3$, *Z* = 4, $D_c$ = 1.642 $Mg \cdot m^{-3}$, $\mu$ = 1.07 $mm^{-1}$, *F*(000) = 2216, *T* = 100(2) K. Of the 15711 reflections, 5122 were unique ($R_{int}$ = 0.066), 3248 observed [$F_2 > 2.0\sigma(F^2)$], which refined to *R* = 0.058, *wR* = 0.091.

CCDC-603094 contains the supplementary crystallographic data for this paper. These data can be obtained free of charge from The Cambridge Crystallographic Data Centre via www.ccdc.cam.ac.uk/data_request/cif.

## Acknowledgments

We thank Scientific Grant Agency of the Ministry of Education of Slovak Republic and the Slovak Academy of Sciences (1/2452/05), Research and Development Support Agency (APVT-20–005504) and the Polish Ministry of Education and Science Grant No 1T09A 12430 for financial support.

[1] M. R. Namazi, *FASEB J.* **2003**, *17*, 1377–1379.
[2] G. M. Makara, G. M. Keseru, M. KajtarPeredy, W. K. Anderson, *J. Med. Chem.* **1996**, *39*, 1236–1242.
[3] P. Catz, W. Shinn, I. M. Kapetanovic, H. Kim, M. Kim, E. L. Jacobson, M. K. Jacobson, C. E. Green, *J. Chromatogr., B: Biomed. Appl.* **2005**, *829*, 123–155.
[4] H. L. Gensler, T. Williams, A. C. Huang, E. L. Jacobson, *Nutr. Cancer* **1999**, *34*, 36–41.
[5] H. L. Gensler, *Nutr. Cancer* **1997**, *29*, 157–162.
[6] B. Kozlevcar, I. Leban, I. Turel, P. Segedin, M. Petric, F. Pohleven, A. J. P. White, D. J. Williams, J. Sieler, *Polyhedron* **1999**, *18*, 755–762.
[7] T. Fujimori, S. Yamada, H. Yasui, H. Sakurai, Y. In, T. Ishida, *J. Biol. Inorg. Chem.* **2005**, *10*, 831–841.
[8] P. Lemoine, B. Viossat, G. Morgant, F. T. Grenaway, A. Tomas, N.-H. Dung, J. R. J. Sorenson, *J. Inorg. Biochem.* **2002**, *89*, 18–28.
[9] G. Morgant, N.-H. Dung, J.-C. Daran, B. Viossat, X. Labouze, M. Roch-Arveiller, F. T. Greenaway, W. Cordes, J. R. J. Sorenson, *J. Inorg. Biochem.* **2000**, *81*, 11–22.
[10] B. Viossat, J.-C. Daran, G. Savouret, G. Morgant, F. T. Greenaway, N.-H. Dung, V. A. Pham-Tran, J. R. J. Sorenson, *J. Inorg. Biochem.* **2003**, *96*, 375–385.
[11] S. Cakir, I. Bulut, K. Aoki, *J. Chem. Crystallogr.* **2003**, *33*, 875–884.
[12] A. W. Addison, T. N. Rao, J. Reedijk, J. Rija, G. C. Verchoors, *J. Chem. Soc. Dalton Trans.* **1984**, 1349–1356.
[13] R. T. Weber, WIN-EPR SimFonia, Software Version 1.2, User's Manual, EPR Division, Bruker Instruments, Inc., Billerica, **1995**.
[14] B. Bleaney, K. D. Bowers, *Proc. R. London, Ser. A* **1952**, *A214*, 451–465.
[15] O. Kahn, *Molecular Magnetism*, VCV Publishers, New York, **1993**.
[16] J. F. Berry, F. A. Cotton, P. Lei, C. A. Murillo, *Inorg. Chem.* **2003**, *42*, 377–382.
[17] P. Stachová, M. Korabik, M. Koman, M. Melník, J. Mrozinski, T. Glowiak, M. Mazúr, D. Valigura, *Inorg. Chim. Acta* **2006**, *359*, 1275–1281.

 © 2006 Wiley-VCH Verlag GmbH & Co. KGaA, Weinheim 

[18] J. A. Bertrand, F. T. Helm, *J. Am. Chem. Soc.* **1973**, *95*, 8184–8185.
[19] J. A. Bertrand, T. D. Black, P. G. Eller, F. T. Helm, R. Mahmood, *Inorg. Chem.* **1976**, *15*, 2965–2970.
[20] J. A. Bertrand, E. Fujita, D. G. VanDerveer, *Inorg. Chem.* **1980**, *19*, 2022–2028.
[21] N. Arulsamy, J. Glerup, D. J. Hodgson, *Inorg. Chem.* **1994**, *33*, 2066–2068.
[22] V. Tudor, V. Kravtsov, M. Julve, F. Lloret, Y. A. Simonov, J. Lipkowski, V. Buculei, M. Andruch, *Polyhedron* **2001**, *20*, 3033–3037.
[23] G. Davies, A. El-Toukhy, K. D. Onan, M. Veidis, *Inorg. Chim. Acta.* **1985**, *98*, 85–94.
[24] E. König, *Magnetic Properties of Coordination and Organometallic Transition Metal Compounds*, Springer, Berlin, **1996**.
[25] Oxford Diffraction, *CrysAlis CCD* and *CrysAlis RED* Versions 1.171, Oxford Diffraction Poland, Wrocław Poland, **2003**.
[26] G. M. Sheldrick, *Acta Crystallogr. Sect. A* **1990**, *46*, 467–473.
[27] G. M. Sheldrick, *SHELXL97*, University of Göttingen, Germany, **1997**.
[28] G. M. Sheldrick, *SHELXTL*, Version 5.1, Bruker AXS, Inc., Madison, Wisconsin, USA, **1998**.

Received: May 23, 2006
Published Online: August 24, 2006

 © 2006 Wiley-VCH Verlag GmbH & Co. KGaA, Weinheim 

DOI: 10.1002/ejic.200600369

# Preparation of ZnO Nanowires in a Neutral Aqueous System: Concentration Effect on the Orientation Attachment Process

Ming Yang,[a] Guangsheng Pang,*[a] Jixue Li,[a] Linfeng Jiang,[a] and Shouhua Feng*[a]

**Keywords:** Zinc oxide / Orientation attachment / Self-assembly / Nanostructures

ZnO nanowires with diameters in the range of 10 to 30 nm and lengths of ca. several micrometers are prepared with the use of ZnO nanoparticles as building blocks. The length and diameter of the ZnO nanowires can be controlled by the variation of the concentration of the nanoparticles in the orientation attachment process. A plausible mechanism for the concentration-controlled orientation attachment process is suggested.
(© Wiley-VCH Verlag GmbH & Co. KGaA, 69451 Weinheim, Germany, 2006)

## Introduction

The preparation of nanostructures with control of their size, shape, and crystalline structure has been one of the main objectives in the chemistry of nanomaterials.[1–5] Nanoparticles can be used as building blocks to obtain well-defined assemblies and superstructures, which can lead to novel and unique properties that are not found in the individual components.[6–7] Orientation attachment has attracted increased interest in recent years as a new means for the fabrication and self-organization of nanocrystalline materials.[8] Recent work has shown the universality of the orientation attachment in the formation and growth of nanocrystals.[9–14] To find a facile method that can precisely control the morphology of low dimensional nanostructures through the mastery of the orientation attachment process is still a challenge.

ZnO is an environmentally friendly transparent semiconductor with a large bandgap of 3.37 eV and it exhibits various distinct properties.[15–17] One-dimensional (1D) ZnO is a focused material, which allows it to possess excellent optical properties.[18] Various methods have been successfully utilized to synthesize 1D ZnO.[19–27] For the reported solution method, a basic environment is necessary to induce 1D growth of the ZnO particles in the nanoscale range.[14,24,27–32] Generally, the common formation mechanisms of 1D ZnO involve the vapor–liquid–solid (VLS) growth model,[26] and the Oswald ripening growth model.[27] The VLS process seems to be the most successful for the generation of 1D structures among all of the vapor-based methods. The Oswald ripening phenomenon is a classical crystal-growth method which describes the growth of the crystal in terms of the Gibbs-Thompson equation. The formation of ZnO nanorods on the basis of the orientation attachment process has only recently been demonstrated.[14] Other metal oxide (e.g. $TiO_2$ and CuO) nanorods have also been prepared by the orientation attachment of nanoparticles.[33–34] In this work, we provide an easy method for the preparation of ZnO nanowires in a neutral aqueous system by the careful control of the orientation attachment of the ZnO nanoparticles. A mechanism for the formation and growth of the low-dimensional nanostructure, which is critical to understand in order to achieve control over the morphology of the nanostructure, and the properties of the structure at the nanoscale level are discussed.

## Results and Discussion

Figure 1 shows the SEM image of 1D ZnO obtained by the hydrothermal treatment of ZnO colloidal nanoparticles at a concentration of 0.8 g/L. The ZnO nanowires are several micrometers in length and vary in diameter from 10 to 30 nm. The curvature of the wire implies that there is some flexibility in the backbone of the ZnO nanowires. Figure 1B shows the TEM image of an individual ZnO nanowire with a diameter of ca. 15 nm and a length of ca. 2.3 μm. The inset in Figure 1C displays the selected area electron diffraction (SAED) pattern of an individual ZnO nanowire. The SAED pattern reveals the single-crystalline nature of the ZnO nanowires. Figure 1D shows the HRTEM image of the ZnO nanowire that is shown in Figure 1C. The image indicates that the preferred direction of growth of the ZnO nanowires is [0001]. The morphology of 1D ZnO is strongly dependent on the concentration of the ZnO colloidal nanoparticles. When the concentration of the ZnO nanoparticles is increased to 4 g/L, ZnO nanorods with lengths that vary from 200 to 800 nm and diameters

[a] State Key Laboratory of Inorganic Synthesis and Preparative Chemistry, College of Chemistry, Jilin University, Changchun 130012, P. R. China
E-mail: shfeng@mail.jlu.edu.cn
panggs@jlu.edu.cn
Supporting information for this article is available on the WWW under http://www.eurjic.org or from the author.

 © 2006 Wiley-VCH Verlag GmbH & Co. KGaA, Weinheim 

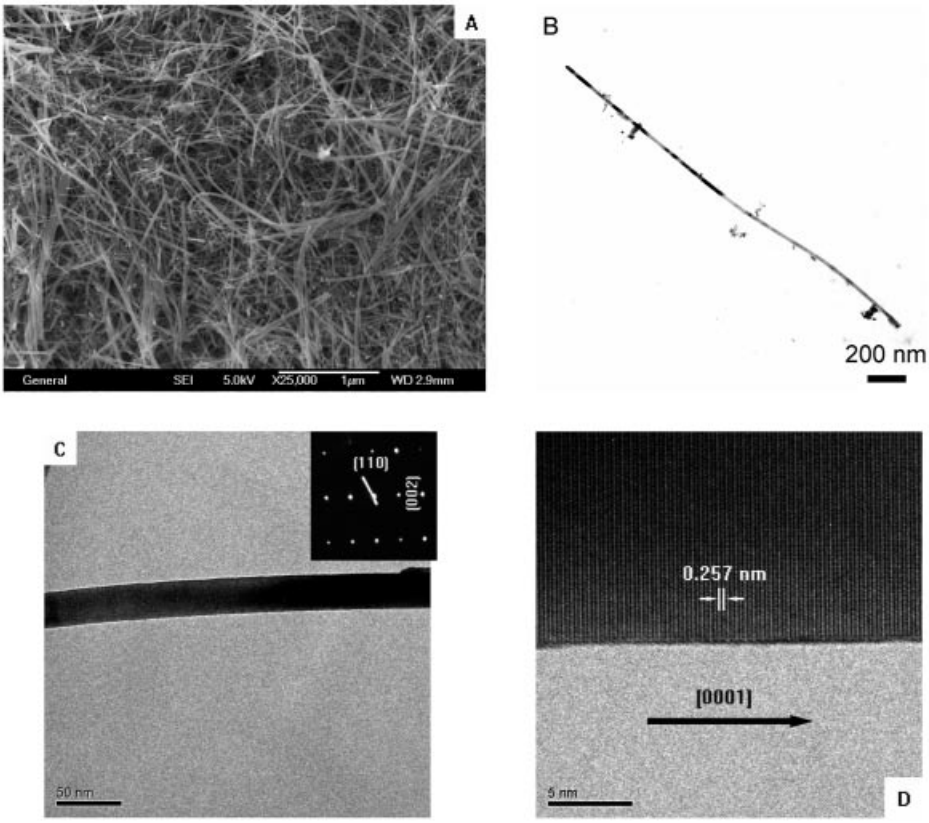


Figure 1. (A) SEM image of ZnO nanowires, (B) and (C) TEM images of ZnO nanowires (inset displays SAED pattern), (D) HRTEM of ZnO nanowires.

that vary from 20 to 40 nm are obtained (see Supporting Information). When the concentration is increased to 16 g/L, ZnO nanorods with smaller aspect ratios are obtained. The diameters of these nanorods vary from 30 to 50 nm and the lengths vary from 60 to 200 nm (see Supporting Information). The narrow distribution of the diameter of the ZnO nanowires is also indicated by the X-ray diffraction (XRD) line broadening. Figure 2 shows the XRD patterns for 1D ZnO obtained at different concentrations of the nanoparticles. All diffraction peaks can be well-indexed to hexagonal phase zinc oxide (JCPDC card No. 36–1451). The diameters estimated from the Debey-Scherrer formula on the basis of the full width of the peak at half-maximum height are 21.0 nm, 28.9 nm, and 48.2 nm obtained by the hydrothermal treatment of 0.8 g/L, 4.0 g/L, and 16.0 g/L ZnO colloidal nanoparticles, respectively. These values are consistent with the SEM observation.

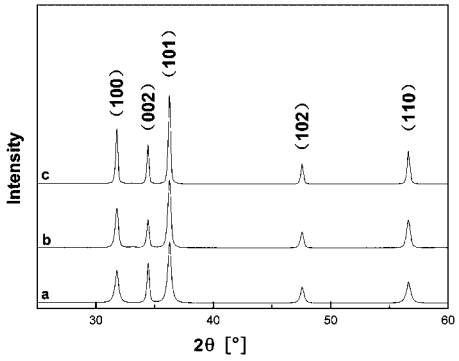


Figure 2. XRD patterns for 1D ZnO obtained by the hydrothermal treatment of (a) 0.8, (b) 4.0, and (c) 16.0 g/L ZnO colloids.

The orientation attachment of the ZnO nanoparticles in the preparation of the ZnO nanowires is observed after 1 h of hydrothermal treatment. Two primary nanoparticles attach to each other along the *c*-axis as shown in Figure 3A and Figure 3B. The nanoparticles may attach to each other along other axes as demonstrated by Pacholski and coworkers,[14] although we did not observe such a phenomenon. The orientation attachment is fundamentally driven by the high surface-energy (3.5 nm) of the ZnO nanoparticles. However, a decrease in the high surface-energy is observed upon the formation of 1D ZnO because there is a reduction in the surface-to-volume ratio. An important characteristic of ZnO is its polar surface. The oppositely charged ions produce positively charged Zn-(001) and negatively charged O-(00–1) polar surfaces, which results in a normal dipole moment and spontaneous polarization along the *c*-axis.[20] The electric dipole moments along the *c*-axis favor the orientation attachment in this direction. According to the model proposed by Penn,[35] the stability constant for the particle encounter complex ($K_{os}$) can be used to estimate the rate of crystal growth by the orientation attachment. High values of $K_{os}$ tend to favor the orientation attachment process. In a previous report,[14] a high concentration of the ZnO colloid was necessary to form

 © 2006 Wiley-VCH Verlag GmbH & Co. KGaA, Weinheim 

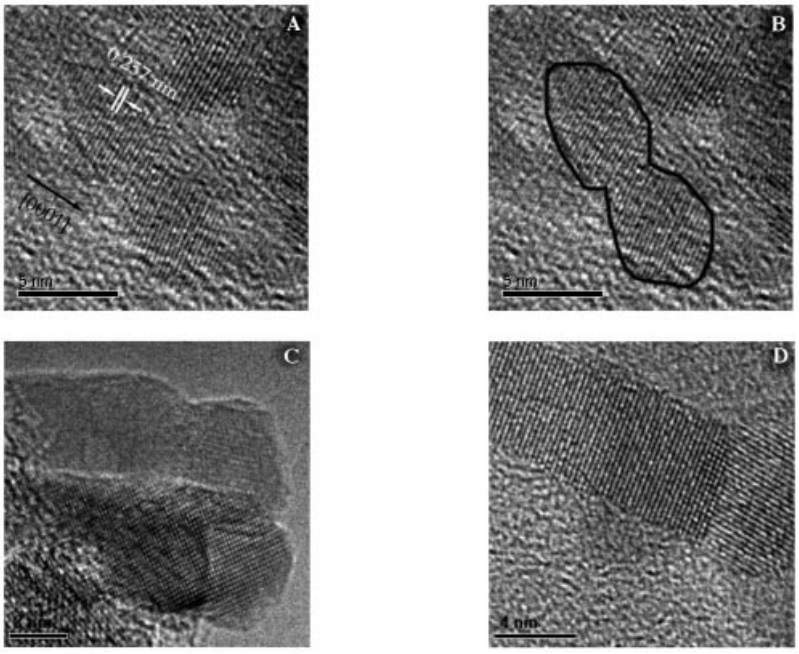


Figure 3. (A) and (B) HRTEM images of the orientation attachment of two ZnO nanoparticles, (C) and (D) HRTEM images of the fusion of "1D cores" and primary nanoparticles.

nanorods in a basic ethanol/water environment. Because ZnO nanoparticles are highly charged in the basic environment, an increase in the surface potential was observed. As the surface potential increased, the stability constant decreased. This means that the orientation attachment process was relatively slow in basic environments and a higher concentration of the nanoparticles was needed to accelerate it. In the neutral aqueous system we report here, the electrostatic repulsion from stabilizers such as $OH^-$ is avoided, which results in an overcompensation of the electric-dipole attractions between the nanoparticles. In other words, the value of $K_{os}$ is much larger in neutral aqueous solutions than it is in basic alcoholic solutions, which allows the orientation attachment of the nanoparticles to occur under much lower concentrations. Our results confirm that orientation attachment can occur at relatively low concentrations of the nanoparticles; in fact, this was found to occur at concentrations as low as 0.8 g/L (0.01 M), which is 10 times lower than the reported value.[14] However, there is also a critical concentration that must be met in order to produce 1D ZnO in neutral aqueous systems. If the concentration of the ZnO nanoparticles is less than 0.4 g/L, the orientation attachment of the ZnO nanoparticles is completely inhibited, and only ZnO nanoparticles that are larger in size relative to the starting nanoparticles are obtained.

Adjustments in the orientation attachment process can be realized by the variation of the concentration of the ZnO nanoparticles in the neutral aqueous system. At a certain concentration, there is a possibility that two primary particles collide and merge into a "1D (nanorod) core". These "1D cores" can continue to grow into nanorods or nanowires. Figure 3C and Figure 3D show that individual nanoparticles and "1D cores" can fuse together by the orientation attachment process, which results in additional 1D growth of the "1D cores". On the basis of our observations, we can speculate that the length of the nanowires can be influenced by the alteration of the number of viable "1D cores". The number of initially merged "1D cores" is related to the concentration of the nanoparticles. Large amounts of "1D cores" form when the concentration is high, whereas only small amounts of "1D cores" form when the concentration is low. In a certain colloidal stock, the number of ZnO nanoparticles is constant. If the number of "1D cores" was reduced, a greater share of nanoparticles would be available for continued 1D growth. It is understandable that fewer "1D cores" will result

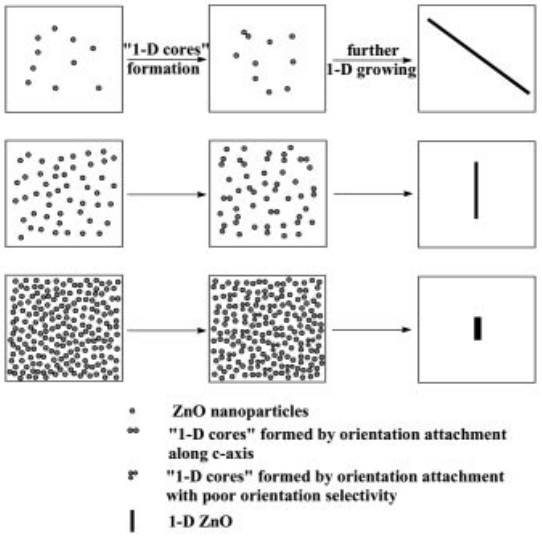


Scheme 1. Simplified illustration of the concentration-controlled orientation attachment process.

 © 2006 Wiley-VCH Verlag GmbH & Co. KGaA, Weinheim 

in an increase of the length of the nanorods. At the same time, if the concentration is high, the orientation attachment will occur with poor orientation selectivity and continued growth will result in ZnO nanorods with large diameters and small aspect ratios. Scheme 1 shows a simplified illustration of the concentration-controlled orientation attachment process. The irregular surface of the 1D ZnO nanostructures can be smoothed and should follow the conventional mechanism of dissolution and growth (Oswald ripening), which finally results in a single crystalline nanowire.

## Conclusions

In summary, ZnO nanowires have been obtained with the use of ZnO nanoparticles as building blocks by the concentration-controlled orientation attachment process in a neutral aqueous system. The concentration of the nanoparticles is found to influence the orientation attachment process, and therefore, the continued growth of the ZnO nanowires can be controlled. Our results suggest that the orientation attachment process is similar to the conventional crystal growth process if the nanoparticle colloid is viewed as an ion in solution.

## Experimental Section

**Physical Methods:** Powder X-ray diffraction (XRD) analysis was performed with a Rigaku D/MAX 2500/PC diffractometer with graphite-filtered Cu-$K_\alpha$ radiation. XRD data were collected over 25–60° with a step interval of 0.02° and a preset time of 1.2 s per step at room temperature. Scanning electron microscope (SEM) was performed with a JSM-6700F electron microscope. High resolution transmission electron microscope (HRTEM) was performed with a JEM-3010 electron microscope. The ZnO nanowires will break into shorter ZnO nanorods under strong ultrasonic treatment. If samples are to be observed by HRTEM, prolonged ultrasonic treatment of the samples should be avoided.

**Preparation of ZnO Nanoparticles:** ZnO nanoparticles are prepared by a conventional sol-gel method.[36–37] In a typical synthesis, zinc acetate dehydrate (2.195 g) is dissolved in ethanol (100 mL) and heated at reflux for 2 h. The solution is then cooled to room temperature and lithium hydroxide hydrate (0.588 g) is added. The suspension is then placed in an ultrasonic bath in order to solubilize the weakly soluble powder. After 30 min, the suspension is filtered through a glass fiber (0.1 μm) frit to remove the insoluble solids and then cyclohexane (300 mL) is added into the as-obtained ZnO colloids to precipitate the ZnO nanoparticles.

**Preparation of 1D ZnO:** Different amounts of ZnO nanoparticles (0.02 g, 0.10 g, 0.40 g) were dissolved in distilled water (25 mL) and then transferred to a 40-mL Teflon-lined stainless steel autoclave and heated at 160 °C for 12 h. The obtained precipitates were washed with distilled water and then dried at 60 °C for 2 h.

**Supporting Information** (see footnote on the first page of this article): SEM images of 1D ZnO obtained by hydrothermal treatment of 4.0 g/L and 16.0 g/L ZnO colloidal nanoparticles and TEM image of ZnO nanoparticles.

## Acknowledgments

This research was supported by the National Natural Science Foundation of China (No. 20371019 and 20121103).

[1] X. G. Peng, L. Manna, W. D. Yang, J. Wickham, E. Scher, A. Kadavanich, A. P. Alivisatos, *Nature* **2000**, *404*, 59–61.
[2] L. S. Li, J. Hu, W. Yang, A. P. Alivisatos, *Nano Lett.* **2001**, *1*, 349–351.
[3] Y. Sun, Y. Xia, *Science* **2002**, *298*, 2176–2179.
[4] C. Burda, X. Chen, R. Narayanan, M. A. El-sayed, *Chem. Rev.* **2005**, *105*, 1025–1102.
[5] J. H. Yu, J. Joo, H. M. Park, S.-I. Baik, Y. W. Kim, S. C. Kim, T. Hyeon, *J. Am. Chem. Soc.* **2005**, *127*, 5662–5670.
[6] L. S. Li, J. Walda, L. Manna, A. P. Alivisatos, *Nano Lett.* **2002**, *2*, 557–560.
[7] D. V. Talapin, E. V. Shevchenko, C. B. Murray, A. Kornowski, S. Forster, H. Weller, *J. Am. Chem. Soc.* **2004**, *126*, 12984–12988.
[8] R. L. Penn, J. F. Banfield, *Science* **1998**, *281*, 969–971.
[9] J. F. Banfield, S. A. Welch, H. Zhang, T. T. Ebert, R. L. Penn, *Science* **2000**, *289*, 751–754.
[10] P. Shen, W. H. Lee, *Nano Lett.* **2001**, *1*, 707–711.
[11] X. W. Lou, H. C. Zeng, *J. Am. Chem. Soc.* **2003**, *125*, 2697–2704.
[12] R. L. Penn, G. Oskam, T. J. Strathmann, P. C. Searson, A. T. Stone, D. R. Veblen, *J. Phys. Chem. B* **2001**,*105*, 2177–2182.
[13] J. T. Sampanthar, H. C. Zeng, *J. Am. Chem. Soc.* **2002**, *124*, 6668–6675.
[14] C. Pacholski, A. Kornowski, H. Weller, *Angew. Chem. Int. Ed.* **2002**, *41*, 1188–1191.
[15] J. C. Johnson, H. Yan, R. D. Schaller, L. H. Haber, R. J. Saykally, P. D. Yang, *J. Phys. Chem. B* **2001**, *105*, 11387–11390.
[16] Q. H. Li, Q. Wan, Y. J. Chen, T. H. Wang, H. B. Jia, D. P. Yu, *Appl. Phys. Lett.* **2004**, *85*, 636–638.
[17] I. Shalish, H. Temkin, V. Narayanamurti, *Phys. Rev. B* **2004**, *69*, 2454011–2454014.
[18] M. H. Huang, S. Mao, H. Feick, H. Q. Yan, Y. Y. Wu, H. Kind, E. Weber, R. Russo, P. D. Yang, *Science* **2001**, *292*, 1897–1899.
[19] Z. W. Pan, Z. R. Dai, Z. L. Wang, *Science* **2001**, *291*, 1947–1949.
[20] Z. L. Wang, X. Y. Kong, Y. Ding, P. Gao, W. L. Hughes, R. Yang, Y. Zhang, *Adv. Funct. Mater.* **2004**, *14*, 943–956.
[21] J.-J. Wu, S.-C. Liu, *Adv. Mater.* **2002**, *14*, 215–218.
[22] J.-J. Wu, S.-C. Liu, *Appl. Phys. Lett.* **2002**, *81*, 1312–1314.
[23] Y. W. Heo, V. Varadarajan, M. Kaufman, K. Kim, D. P. Norton, F. Ren, P. H. Fleming, *Appl. Phys. Lett.* **2002**, *81*, 3046–3048.
[24] L. E. Greene, M. Law, J. Goldberger, F. Kim, J. C. Johnson, Y. Zhang, R. J. Saykally, P. D. Yang, *Angew. Chem. Int. Ed.* **2003**, *42*, 3031–3034.
[25] Y. C. Kong, D. P. Yu, B. Zhang, W. Fang, S. Q. Feng, *Appl. Phys. Lett.* **2001**, *78*, 407–409.
[26] M. H. Huang, Y. Wu, H. Feick, N. Tran, E. Weber, P. D. Yang, *Adv. Mater.* **2001**, *13*, 113–116.
[27] B. Cheng, E. T. Samulski, *Chem. Commun.* **2004**, *8*, 986–987.
[28] L. Vayssieres, K. Keis, A. Hagfeldt, S.-E. Lindquist, *Chem. Mater.* **2001**, *13*, 4395–4398.
[29] L. Vayssieres, K. Keis, S.-E. Lindquist, A. Hagfeldt, *J. Phys. Chem. B* **2001**, *105*, 3350–3352.
[30] D. Li, Y. Wei, H. Liu, X. K. Wang, *Chem. Commun.* **2004**, *24*, 2856–2857.
[31] J. Zhang, L. D. Sun, J. L. Yin, H. L. Su, C. S. Liao, C. H. Yan, *Chem. Mater.* **2002**, *14*, 4172–4177.
[32] B. Liu, H. C. Zeng, *J. Am. Chem. Soc.* **2003**, *125*, 4430–4431.
[33] A. Chemseddine, T. Moritz, *Eur. J. Inorg. Chem.* **1999**, *2*, 235–245.

 © 2006 Wiley-VCH Verlag GmbH & Co. KGaA, Weinheim 

[34] J. Liu, X. Huang, Y. Li, K. M. Sulieman, X. He, F. Sun, *Cryst. Growth Des.* **2006**, *6*, 1690–1696.
[35] R. L. Penn, *J. Phys. Chem. B* **2004**, *108*, 12707–12712.
[36] L. Spanhel, M. A. Anderson, *J. Am. Chem. Soc.* **1991**, *113*, 2826–2833.
[37] E. A. Meulenkamp, *J. Phys. Chem. B* **1998**, *102*, 5566–5572.
Received: April 25, 2006
Published Online: August 28, 2006

 © 2006 Wiley-VCH Verlag GmbH & Co. KGaA, Weinheim 

DOI: 10.1002/ejic.200600305

# Genotoxic Potential of *N*-(Benzothiazolyl)sulfonamide Copper(II) Complexes on Yeast Cells Transformed with YEGFP Expression Constructs Containing the RAD54 or RNR2 Promoter

**Marta González-Álvarez,[a] Gloria Alzuet,[a] Lucas del Castillo,[b] Joaquín Borrás,*[a] and Malva Liu-González[c]**

**Keywords:** Copper complexes / DNA damage / Genotoxicity / yEGFP expression

Four ternary complexes $[Cu(L)_2(phen)]$ where L is an *N*-(benzothiazol-2-yl)sulfonamide derivative have been prepared and their ability to cleave DNA has been studied. The complexes were structurally characterized with the aid of single-crystal X-ray crystallography. Whereas the molecular structure of the $[Cu(L1)_2(phen)]$ (**1**) [HL1 = *N*-(6-chlorobenzothiazol-2-yl)benzenesulfonamide] and $[Cu(L3)_2(phen)]$ (**3**) [HL3 = *N*-(benzothiazol-2-yl)benzenesulfonamide] complexes can best be described as having a distorted square-planar geometry, that of the $[Cu(L4)_2(phen)]$ (**4**) [HL4 = *N*-(benzothiazol-2-yl)toluenesulfonamide] complex shows a strictly square-planar geometry. The $[Cu(L2)_2(phen)MeOH]$ (**2**) [HL2 = *N*-(6-chlorobenzothiazol-2-yl)toluenesulfonamide] complex displays an axially elongated square-pyramidal coordination geometry in which the phen ligand binds at the basal plane. Viscosity and fluorescence measurements indicated that $[Cu(L4)_2(phen)]$ (**4**) has a propensity for binding calf thymus DNA. The four complexes were found to be efficient chemical nucleases, with ascorbate/$H_2O_2$ activation giving rise to hydroxyl and superoxide radicals as active cleaving species. The nuclease activity of **4** is not only the highest of the four complexes, but also much higher than that of the copper–phenanthroline complex. The ability of the complexes to cleave DNA within cells has been tested by monitoring the expression of the yEGFP gene containing reporter plasmid. The significant induction of fluorescence by complex **4** indicates that it is able to cleave DNA inside the cell.
(© Wiley-VCH Verlag GmbH & Co. KGaA, 69451 Weinheim, Germany, 2006)

## Introduction

The mechanism of metal carcinogenesis has been widely studied since a number of metals are known to have carcinogenic potential. In 1986, for example, Kawanishi et al.[1] proposed the hypothesis that metal carcinogenesis involves the generation of endogenous reactive oxygen species (ROS). These same researchers subsequently reported that various carcinogenic metal compounds are capable of causing oxidative DNA damage in the presence of $H_2O_2$.[2–5] Indeed, metals are considered to act not only as carcinogens, but also as cocarcinogens that activate carcinogenic chemicals, since a large number of weak, nonmutagenic carcinogens have been found to act through metal-mediated oxidative DNA damage. Endogenous metals ions such as copper and iron seem to play a particularly important role in ROS generation from various carcinogens, which in turn leads to DNA damage. It has been shown, for example, that in phosphate buffer $Cu^{II}/H_2O_2$ induces DNA damage at the thymine and guanine positions by generating ROS.[6] Moreover, copper has a dual role in oxidative DNA damage: it generates ROS through autoxidation of carcinogens and also activates $H_2O_2$ to form a reactive $Cu^{I}$–hydroperoxo complex.

In recent years the interaction of transition metal complexes with nucleic acids has attracted attention because of their relevance in the development of new reagents for biotechnology and medical research. Interest in the rational design of novel transition metal complexes that bind and cleave duplex DNA with high sequence or structure selectivity has been especially keen. Indeed, there is already a considerable amount of literature that deals with the practical use of transition metal complexes as chemical nucleases. The redox activity of copper complexes of 1,10-phenanthroline as artificial nucleases, for instance, is well known.[7,8] Meunier et al.[9] even developed the Clip-Phen series containing two phen moieties linked through tethers in order to favor the stoichiometry of two phen units per copper. These authors showed that the DNA cleavage activity of copper Clip-Phen complexes increased dramatically in relation to that of the phen parent compound. They then went on to determine the cytostatic activity of these

[a] Departament de Química Inorgànica, Facultat de Farmàcia, Universitat de València,
Avda. Vicente Andrés Estellés s/n, 46100 Burjassot, Spain
Fax: +34-963544960
E-mail: Joaquin.Borras@uv.es
[b] Departament de Microbiologia i Ecologia, Facultat de Farmàcia, Universitat de València,
Avda. Vicente Andrés Estellés s/n, 46100 Burjassot, Spain
[c] SCSIE, RX. Universitat de València,
Dr. Moliner 50, 46100 Burjassot, Spain

 © 2006 Wiley-VCH Verlag GmbH & Co. KGaA, Weinheim 

complexes.[10] Our group has previously reported[11] several copper ternary complexes of *N*-substituted sulfonamides and phen with the ability to damage DNA in the presence of various reducing agents.

A great number of chemical substances are known to possess in vitro biocatalytic activity, emulating different enzymatic processes. Among these chemicals, copper-coordinated compounds have shown superoxide dismutase and/or DNAsa activities, depending on the type of ligand present. However, in vitro activity occurs under conditions that are usually not equivalent to the physiological environment in the cell. This is an important consideration in evaluating research in this field, as, in order to have any effect, the chemical product in question needs to penetrate within the cell itself. Once the substance is in the cytoplasm, the different mechanisms of cell detoxification can reduce or even prevent its activity, either through degradation or extrusion out of the cell or to intracellular compartments.

In the past, yeast has been used as a model for understanding physiological processes in superior eukaryotes and it is still considered to be an ideal organism for in vivo studies on the activity of biological compounds. Our group has used an *S. cerevisiae* strain deficient in superoxide dismutase for in vivo evaluation of the SOD-like activity of various copper complexes.[12,13] Induction of different yeast genes in response to exposure to DNA-damaging agents represents an important and promising approach for developing genotoxicity tests. Induction of RAD54 and RNR2, two promoters that control the expression of damage-inducible genes, has already been used successfully to evaluate DNA damage.[14–17] We have gone one step further and developed reporter plasmids that express the green fluorescent protein yEGFP gene.[18] The expression of this gene in cells containing the reporter plasmid in response to the exposure to DNA-damaging agents is thus monitored by noting the presence of its characteristic green fluorescence.

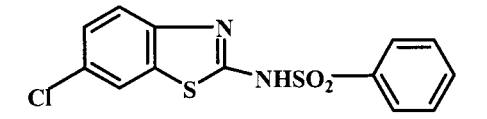


HL1

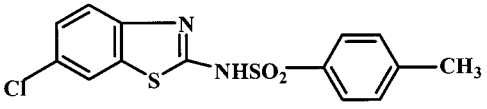


HL2

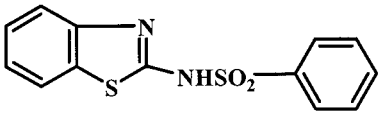


HL3

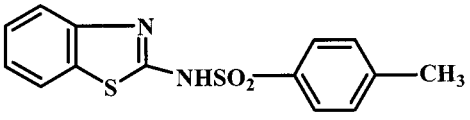


HL4

Scheme 1. *N*-(Benzothiazolyl)sulfonamide ligands.

In this paper we describe the synthesis, characterization, and biological activity assays of four copper ternary complexes with *N*-substituted sulfonamides and *o*-phenanthroline. The sulfonamide ligands selected for this study (Scheme 1) possess two main features that facilitate the synthesis of copper(II) complexes with nuclease activity; both a benzothiazole ring and an aromatic ring (benzene or toluene) able to intercalate between the DNA bases, as well as a sulfonamido group that can interact with DNA through hydrogen bonds. In addition, the benzenesulfonamido group has been suggested to be a functional element that facilitates various biological activities such as the inhibition of tumor cell growth.[19] The biological activity studies include evaluations of DNA binding ability, nuclease activity, and the ability to damage DNA in yeast cells transformed with yEGFP expression constructs containing either the RAD54 or the RNR2 promoter.

## Results and Discussion

### Spectroscopic and Structural Aspects

Ternary copper(II) complexes $[Cu(L)_2phen]$ (L = L1, L2, L3, and L4) were prepared and characterized with the aid of analytical, spectroscopic, and X-ray diffraction data.

All the complexes had the same infrared spectrum pattern, and the most significant feature was a shift of the characteristic band of the benzothiazole ring from 1550 $cm^{-1}$ in the free ligands to 1460 $cm^{-1}$ in the complexes. As for the sulfonamidato group, the bands assigned to $\nu(SO_2)_{as}$ and $\nu(SO_2)_s$ are shifted to slightly lower frequencies while the $\nu$(S–N) vibration appears at slightly higher frequencies than those of the uncoordinated ligands. In general, the IR spectra are similar to those observed for other copper *N*-sulfonamide derivatives[20,21] with the modifications noted above being mainly because of the ligand deprotonation at the sulfonamide group.

The diffuse reflectance spectra of complexes **1**, **3**, and **4** exhibit a d–d shoulder in the range of 652 to 671 nm while that of complex **2** shows two well-defined d–d bands at 543 and 702 nm. The room temperature magnetic moments of complexes **1** ($\mu_{eff}$ = 1.73 BM), **2** ($\mu_{eff}$ = 1.75 BM), **3** ($\mu_{eff}$ = 1.82 BM), and **4** ($\mu_{eff}$ = 1.77 BM) are consistent with the presence of a single unpaired electron. The EPR spectra of the complexes are axial with $g_{\|}$ ranging from 2.22 to 2.30 and $g_{\perp}$ around 2.05.

The complexes have been structurally characterized with the aid of single-crystal X-ray diffraction techniques. ORTEP drawings of the complexes, including the atomic numbering schemes, are shown in Figure 1, Figure 2, Figure 3, and Figure 4. Selected bond lengths and angles are listed in Table 1.

The crystal structures of compounds **1**, **3**, and **4** consist of a discrete monomeric copper(II) species surrounded by

 © 2006 Wiley-VCH Verlag GmbH & Co. KGaA, Weinheim 

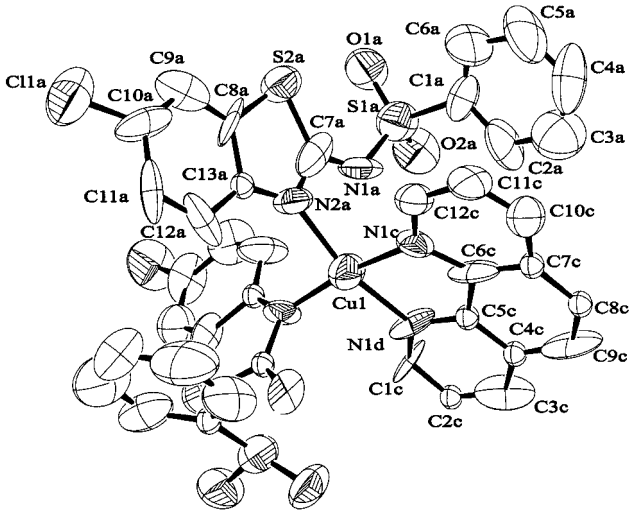


Figure 1. ORTEP drawing of the $[Cu(L1)_2(phen)]$ (**1**) complex.

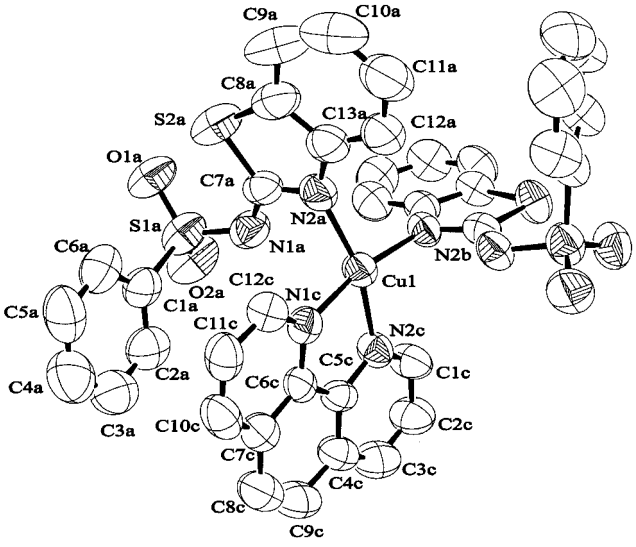


Figure 3. ORTEP drawing of the $[Cu(L3)_2(phen)]$ (**3**) complex.

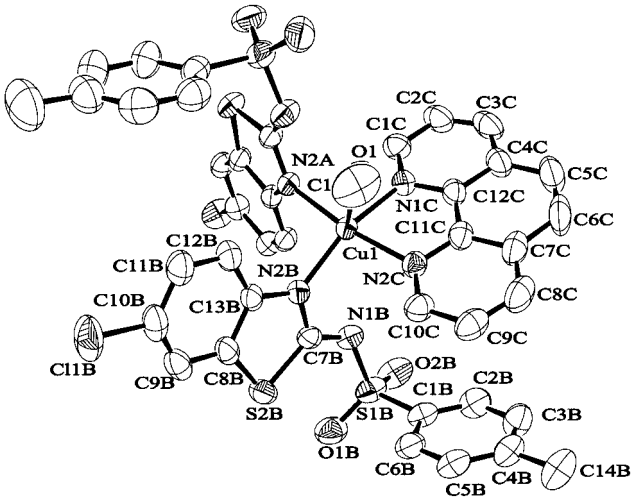


Figure 2. ORTEP drawing of the $[Cu(L2)_2(phen)MeOH]$ (**2**) complex.

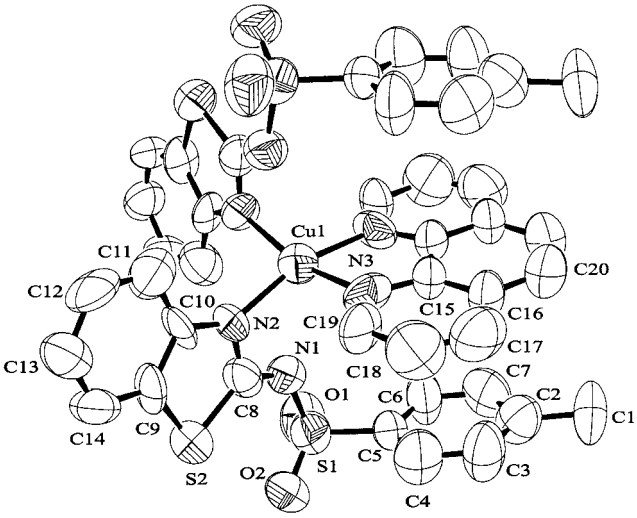


Figure 4. ORTEP drawing of the $[Cu(L4)_2(phen)]$ (**4**) complex.

Table 1. Selected bond lengths [Å] and angles [°] for $[Cu(L1)_2(phen)]$ (**1**), $[Cu(L2)_2(phen)MeOH]$ (**2**), $[Cu(L3)_2(phen)]$ (**3**), and $[Cu(L4)_2(phen)]$ (**4**).

| $[Cu(L1)_2(phen)]$ | | $[Cu(L2)_2(phen)MeOH]$ | | $[Cu(L3)_2(phen)]$ | | $[Cu(L4)_2(phen)]$ | |
|---|---|---|---|---|---|---|---|
| Cu(1)–N(2A) | 1.989(18) | Cu(1)–N(2B) | 1.983(2) | Cu(1)–N(2B) | 1.949(4) | Cu(1)–N(2)#1 | 1.954(15) |
| Cu(1)–N(2B) | 1.989(16) | Cu(1)–N(2A) | 2.018(2) | Cu(1)–N(2A) | 1.964(4) | Cu(1)–N(2) | 1.954(15) |
| Cu(1)–N(1C) | 2.027(12) | Cu(1)–N(1C) | 2.020(2) | Cu(1)–N(2C) | 2.006(4) | Cu(1)–N(3) | 1.989(14) |
| Cu(1)–N(1D) | 1.957(12) | Cu(1)–N(2C) | 2.036(2) | Cu(1)–N(1C) | 2.013(4) | Cu(1)–N(3)#1 | 1.989(13) |
| | | Cu(1)–O(1) | 2.353(3) | | | | |
| N(1D)–Cu(1)–N(2B) | 96.9(7) | N(2B)–Cu(1)–N(2A) | 94.32(9) | N(2B)–Cu(1)–N(2A) | 96.93(15) | N(2)#1–Cu(1)–N(2) | 94.2(6) |
| N(1D)–Cu(1)–N(2A) | 165.7(9) | N(2B)–Cu(1)–N(1C) | 159.55(10) | N(2B)–Cu(1)–N(2C) | 92.69(16) | N(2)#1–Cu(1)–N(3) | 162.7(7) |
| N(2B)–Cu(1)–N(2A) | 92.6(6) | N(2A)–Cu(1)–N(1C) | 91.05(10) | N(2A)–Cu(1)–N(2C) | 162.05(19) | N(2)–Cu(1)–N(3) | 95.8(10) |
| N(1D)–Cu(1)–N(1C) | 79.9(8) | N(2B)–Cu(1)–N(2C) | 93.98(10) | N(2B)–Cu(1)–N(1C) | 167.69(17) | N(3)–Cu(1)–N(3)#1 | 78.(2) |
| N(2B)–Cu(1)–N(1C) | 167.8(8) | N(2A)–Cu(1)–N(2C) | 171.67(10) | N(2A)–Cu(1)–N(1C) | 92.05(16) | N(1)–Cu(1)–N(2) | 58.57(3) |
| N(2A)–Cu(1)–N(1C) | 92.9(7) | N(1C)–Cu(1)–N(2C) | 81.35(10) | N(2C)–Cu(1)–N(1C) | 80.98(18) | N(1)–Cu(1)–N(3) | 91.39(3) |
| | | N(2B)–Cu(1)–O(1) | 107.03(11) | | | N(1)–Cu(1)–N(1)#1 | 159.03(5) |
| | | N(2A)–Cu(1)–O(1) | 98.82(9) | | | N(1)–Cu(1)–N(2)#1 | 105.88(3) |
| | | N(1C)–Cu(1)–O(1) | 91.57(11) | | | N(1)–Cu(1)–N(3)#1 | 104.96(2) |
| | | N(2C)–Cu(1)–O(1) | 78.09(9) | | | | |

 © 2006 Wiley-VCH Verlag GmbH & Co. KGaA, Weinheim 

four N atoms belonging to a phenanthroline molecule and two deprotonated *N*-sulfonamide ligands in a distorted square-planar geometry. In complexes **1** and **3** the tetrahedrality value of 15.51° and 18.79°, respectively, indicates that the copper ion adopts a distorted square-planar geometry.[22] The metal ion in complex **4** is located at an inversion symmetry center, hence its coordination polyhedron is strictly square planar. The Cu–N bond lengths lie in the range 1.949(4) to 2.027(12) Å, which are normal lengths for Cu–Nphen and Cu–N-benzothiazole coordination bonds.[11,13,23]

The copper(II) ion in complex **2** is five-coordinate with a distorted square-pyramidal geometry. The basal plane is defined by the benzothiazole N atoms of two deprotonated sulfonamide ligands and the two N atoms of a phenanthroline molecule. The Cu–N bond lengths are similar to those found in complexes **1**, **3**, and **4**. The oxygen atom of a coordinated methanol molecule occupies the axial position with a bond length of 2.353 Å. The changes in bond length are described by tetragonality ($T^5$); in this case, the tetragonality value of 0.85 fits into the range expected for square-pyramidal complexes with mixed nitrogen-oxygen ligands.[24] The in-plane angular distortion described by the ratio $\tau$ represents the percentage of trigonal distortion in a square-pyramidal geometry.[25] The $\tau$ value of 0.20 found here thus indicates the presence of a slight distortion.

The coordination mode of the sulfonamide as a monodentate ligand that binds through the benzothiazole N atom in complexes **1**, **2**, **3**, and **4** is the same as that usually found in other $Cu^{II}$ complexes with *N*-substituted sulfonamide analogs.[12,13,23]

## DNA Binding Properties

The mode of and propensity for binding of the complexes to calf thymus DNA (CT-DNA) has been studied with the aid of different techniques.

### *Viscosity Measurements*

Viscosity measurements were carried out on CT-DNA by varying the concentration of the complexes. Hydrodynamic measurements that are sensitive to length changes are regarded as the least ambiguous and the most critical tests of binding in solution. One classic intercalation model results in the lengthening of the DNA helix as the base pairs are separated to accommodate the binding ligand, thus leading to the increase of DNA viscosity. In contrast, complexes that bind exclusively in DNA grooves by means of partial and/or nonclassic intercalation under the same conditions typically cause either a less pronounced (positive or negative) or no change in DNA solution viscosity.[26] The results obtained with our compounds reveal that while complex **4** (Figure 5) interacts with DNA in a classic intercalative mode, the presence of complexes **1**, **2**, or **3** (data not shown) has no effect on the relative viscosity of CT-DNA. This indicates that the interaction of these complexes follows the general pattern of other complexes that bind in DNA grooves by either a partial or nonclassic intercalation.

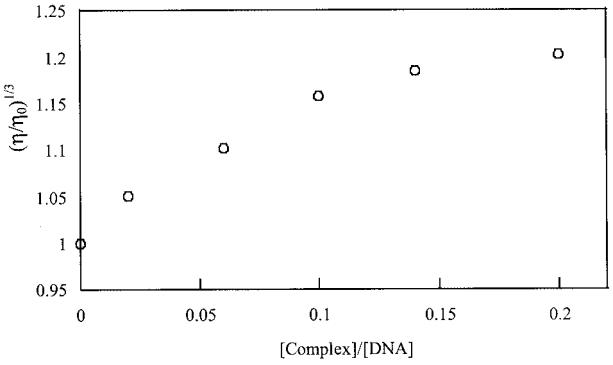


Figure 5. Effect of increasing amounts of the $[Cu(L4)_2(phen)]$ (**4**) complex on the relative viscosity of CT-DNA.

The different behavior exhibited by complex **4** may be attributable to its strictly square-planar geometry; in the other complexes, the distortion of the coordination polyhedron may prevent the intercalation between the bases of the DNA.

### *Effect of the Complexes on the Emission Spectra of the DNA-EB System*

To corroborate the findings from the viscometry results on the mode of DNA interaction, we carried out competitive ethidium bromide (EB) binding studies. Since EB shows a reduced emission intensity in buffers because of the quenching by the solvent molecules and a significantly enhanced intensity when bound to DNA, the emission intensity of this compound is often used as a spectroscopic probe.[27] Binding of the complexes to DNA decreases the emission intensity of EB and the extent of the emission intensity reduction actually gives a measure of the DNA binding propensity of the complexes in question. The results in Figure 6 (a) show that the fluorescence intensity of CT-DNA–EB decreases remarkably with the addition of complex **4**, which indicates that the complex binds to DNA, replacing the EB from the CT-DNA. Such a result is common in intercalative DNA interactions and is consistent with the results obtained from the viscosity measurements.

The fluorescence quenching of EB bound to DNA by complex **4** is in agreement with the classic linear Stern–Volmer equation[27]

$$I_{F0}/I_F = 1 + k_q[Q],$$

where $I_{F0}$ is the emission intensity in the absence of quencher, $I_F$ is the emission intensity in the presence of quencher, $k_q$ is the quenching constant, and $[Q]$ is the quencher concentration. This concordance can be observed by comparing the fluorescence quenching curve of $I_{F0}/I_F$ to the concentration of complex **4** (Figure 6, b). It may thus be concluded that complex **4** binds to DNA mainly by means of intercalation. The value of $K_{app}$ is $1.72 \times 10^6$ $M^{-1}$, which corresponds to the copper(II) complex concentration [Q] = 58.1 μM that causes a 50% quenching of the initial EB fluorescence. This finding suggests that the interaction of **4** with DNA is quite strong.

 © 2006 Wiley-VCH Verlag GmbH & Co. KGaA, Weinheim 

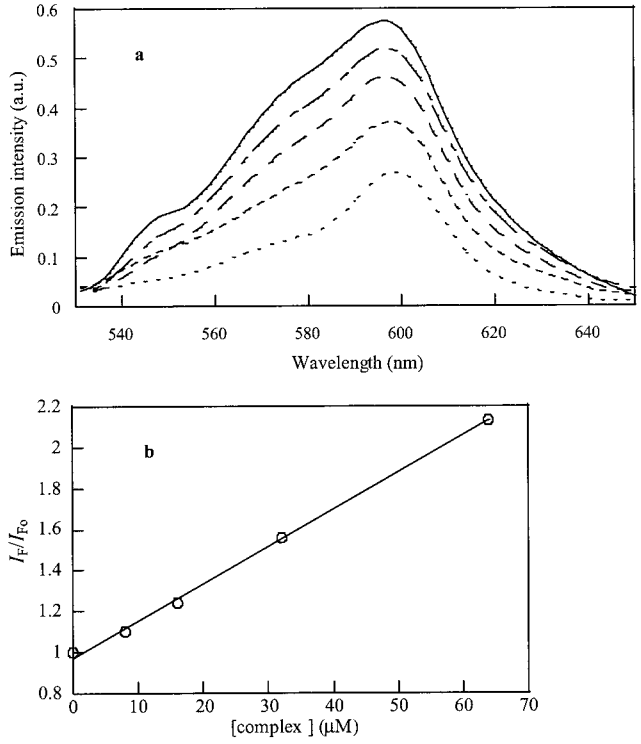


Figure 6. (a) Emission spectra of the DNA–EB system (100 μM CT-DNA base pairs and 10 μM ethidium bromide) $\lambda_{ex}$ = 500.0 nm $\lambda_{em}$ = 530–650 nm, in the absence (continuous line) and in the presence (discontinuous lines) of increasing amounts of complex **4** (0–64 μM). (b) Emission quenching of DNA–EB system upon addition of [Cu(L4)$_2$(phen)] (**4**).

The presence of complexes **1**, **2**, or **3** (data not shown) has no effect on the emission spectra of the DNA–EB system under the same conditions.

### *Thermal Denaturation Results*

The binding of complexes **1**–**4** to CT-DNA was then studied from the thermal denaturation profile of DNA. While complexes **1** and **2** produced no increase in the melting temperature ($T_m$) upon their addition to DNA (CT-DNA $T_m$ = 57 °C), complexes **3** and **4** increased the $T_m$ to 75 and 71 °C, respectively. These results suggest a groove binding for complexes **1** and **2** and intercalation for complexes **3** and **4**, thereby explaining the resulting increased duplex stabilization.[28]

The behavior of complex **3** is noteworthy, especially since the thermal denaturation experiments indicate that this compound can intercalate with DNA while fluorescence and viscosity results do not agree with this result. One possible explanation for the duplex stabilization that is effected by complex **3** is that specific hydrogen-bonding interactions are present between the *N*-(benzothiazolyl)sulfonamide ligands and the bases or phosphate backbone of the DNA. Another possibility is that deformations in the double-helix structure that occur upon binding of the complexes result in additional interstrand interactions.[29]

### pUC18 Cleavage

We then went on to study the activity of the complexes as chemical nucleases using supercoiled (SC) pUC18 DNA in cacodylate buffer (pH = 6.0) with ascorbate/$H_2O_2$ activation. The efficiency of the complexes has been compared with that of both copper salt and the bis(*o*-phenanthroline)-copper complex under the same conditions.

The results shown in Figure 7 indicate that the DNA cleavage activity order is **4** > **2** > **1** > **3**. The results also reveal that the DNA scission mediated by the compounds depends on complex concentration, with the cleavage being more efficient at higher concentrations.

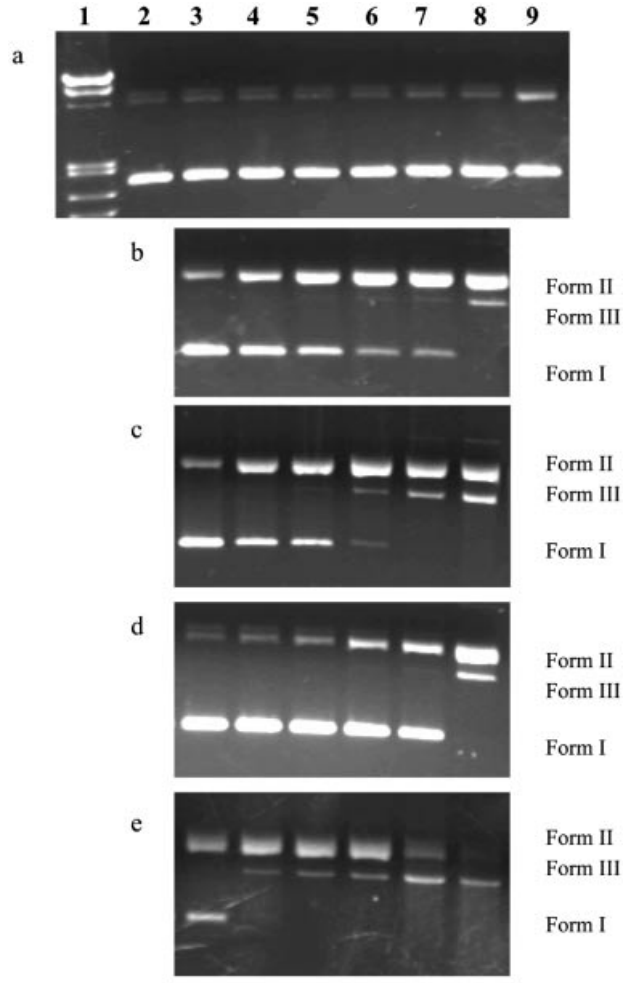


Figure 7. Agarose gel electrophoresis of pUC18 plasmid DNA treated with copper salt, the complexes, or bis(*o*-phenanthroline)-copper(II). [Ascorbate/$H_2O_2$]:[tested compound] = 1:1. Incubation time: 30 min (37 °C). (a) $CuSO_4$ (b) [Cu(L1)$_2$(phen)] (**1**) complex, (c) [Cu(L2)$_2$(phen)MeOH] (**2**) complex, (d) [Cu(L3)$_2$(phen)] (**3**) complex, (e) [Cu(L4)$_2$(phen)] (**4**) complex.
Lane 1: DNA/EcoRI + Hind III. Marker, 3; lane 2: supercoiled DNA; lane 3: copper salt (a) or complexes (b–e) 1.5 μM; lane 4: copper salt (a) or complexes (b–e) 3 μM; lane 5: copper salt (a) or complexes (b–e) 4.5 μM; lane 6: copper salt (a) or complexes (b–e) 6 μM; lane 7: copper salt (a) or complexes (b–e) 7.5 μM; lane 8: copper salt (a) or complexes (b–e) 9 μM; lane 9: [Cu(phen)$_2$]$^{2+}$ complex 9 μM.

 © 2006 Wiley-VCH Verlag GmbH & Co. KGaA, Weinheim 

Complexes **1** and **2** at 3 and 4.5 μM (see parts b and c in Figure 7, lanes 4 and 5) produced supercoiled DNA cleavage, which was transformed into circular DNA (Form II). Linearized DNA was not observed under these conditions. This latter finding suggests that cleavage may occur randomly over the DNA since a significant portion of the plasmid already appears to be converted to Form II without concurrent formation of Form III. For its part, Form III resulted from multiple cleavage of Form II and appeared only when full cleavage of Form I was practically achieved (Figure 7, part b, lane 8 and part c, lane 6).

At low concentrations of complex **3** (1.5, 3, and 4.5 μM, lanes 3, 4, and 5 in Figure 7, d) the plasmid remained supercoiled. In contrast to the reactivity of **1** and **2**, complex **3** was unable to mediate the conversion of supercoiled DNA (Form I) at 3 and 4.5 μM (Figure 7, part d, lanes 4 and 5). Upon increasing the concentration of **3** to 6 and 7.5 μM, the supercoiled DNA was partially transformed into open circular DNA (Figure 7, part d, lanes 6 and 7) whereas at 9 μM, DNA Form I was fully converted into Form II and Form III (Figure 7, part d, lane 8).

Complex **4** was the most reactive of the complexes (Figure 7, e), proving to be a very efficient chemical nuclease. At the very low concentration of 1.5 μM, the compound was capable of mediating the conversion of supercoiled DNA to its open circular form (lane 3 in Figure 7, e). In the concentration range from 3 to 6 μM, complex **4** induced complete degradation of the plasmid to yield the open circular and linear forms (Figure 7, part e, lanes 4–6) while at 7.5 μM, the supercoiled DNA was converted into Form II, Form III and small linear fragments that appeared as a smear on the gel (Figure 7, part e, lane 7). At a concentration of 9 μM, only the linear Form III and small linear fragments were observed (Figure 7, part e, lane 8). These products are inconsistent with a mechanism of concerted cleavage of both strains of the plasmid.

As no cleavage was found for $CuSO_4$ under the same conditions (lanes 3–8 of Figure 7, a), the DNA cleavage activity of the compounds can be ascribed to the cooperative effect between $Cu^{II}$ and its ligands.

Since our compounds contain *o*-phenanthroline as a ligand, we have compared their nucleolytic activity with that of bis(*o*-phenanthroline)copper complex, which is a well-known and very efficient chemical nuclease. A comparison of lane 8 of Figure 7, part b (**1**, 9 μM), part c (**2**, 9 μM), part d (**3**, 9 μM), and part e (**4**, 9 μM) with lane 9 of Figure 7 (a) ($[Cu(phen)_2]^{2+}$, 9 μM) clearly indicates that these complexes present considerably higher nuclease activity than the bis(*o*-phenanthroline)copper complex. Under these conditions, bis(*o*-phenanthroline)copper complex was only able to transform a small quantity of SC DNA into its open circular form while the complexes mediated the full conversion of the plasmid Form I to the Forms II and III, with complex **4** producing small linear fragments. It is thus clear that the presence of an *N*-sulfonamide ligand increases nuclease activity.

The existence of diffusible radical species in the nuclease mechanism can be inferred by monitoring the quenching of DNA cleavage in the presence of alternative H-atom donors, which should scavenge radicals (such as $OH^{\cdot}$) in solution. To this end, we included standard scavengers of reactive oxygen intermediates in the electrophoretic process (Figure 8).

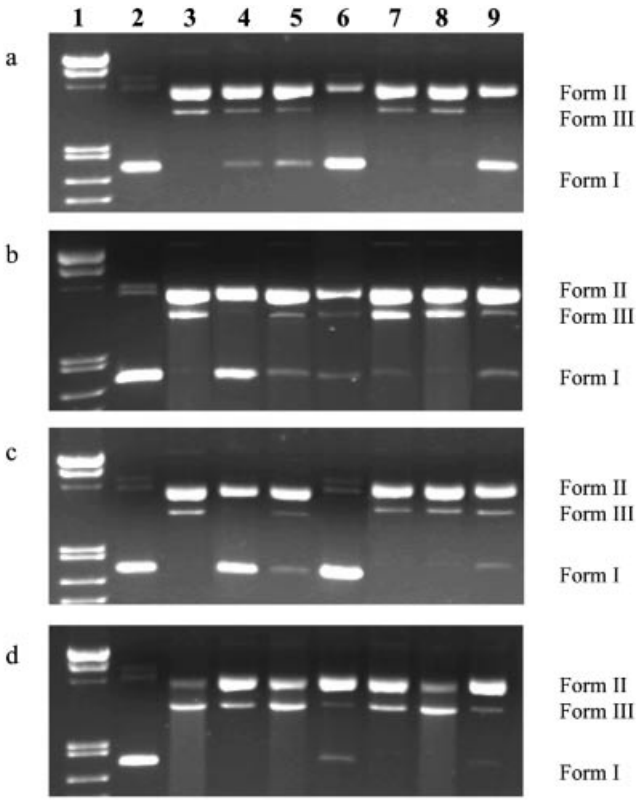


Figure 8. Agarose gel electrophoresis of pUC18 plasmid treated with 9 μM complexes and 9 μM ascorbate/$H_2O_2$ in the presence of potential inhibitors. Incubation time 30 min (37 °C). (a) $[Cu(L1)_2$-(phen)] (**1**) complex, (b) $[Cu(L2)_2$(phen)MeOH] (**2**) complex, (c) $[Cu(L3)_2$(phen)] (**3**) complex, (d) $[Cu(L4)_2$(phen)] (**4**) complex. Lane 1: DNA/EcoRI + Hind III. Marker, 3; lane 2: supercoiled DNA; lane 3: complex without inhibitors; lane 4: complex + DMSO (1 M); lane 5: complex + *tert*-butyl alcohol (1 M); lane 6: complex + $NaN_3$(100 mM); lane 7: complex + 2,2,6,6 tetramethyl-4-piperidone (100 mM); lane 8: complex + distamycin (8 μM); lane 9: complex + SOD (15 units).

The presence of the hydroxyl radical scavengers dmso and *tert*-butyl alcohol (lanes 4 and 5 of Figure 8a–d) significantly inhibited the chemical nuclease activity of the complexes. This suggests a cleavage pathway involving the formation of the reactive hydroxyl radical.

Sodium azide (lane 6 of Figure 8, a–d) inhibited DNA cleavage by the compounds to some extent, a finding that points to the participation of $^1O_2$ in the reaction. However, except in the case of **4**, 2,2,6,6-tetramethyl-4-piperidone, another singlet oxygen scavenger, had no observable effect on the cleavage reaction (lanes 7), which clearly contradicts the initial result. This may be resolved by taking into account that since the azide ion can act as a ligand of copper(II), inhibition of the nuclease reaction probably occurs not by radical quenching, but rather by blocking the coordination site on copper that is involved in radical formation. We can

 © 2006 Wiley-VCH Verlag GmbH & Co. KGaA, Weinheim 

thus conclude that $^1O_2$ is most likely not involved in the reaction.[30]

Lane 9 of Figure 8 (a–d) shows a significant reduction of the DNA cleavage of the complexes in the presence of the SOD enzyme, which indicates that $O_2^-$ is one of the reactive species that actually breaks the DNA.

In the presence of the minor groove binder distamycin (lanes 8), the complexes displayed no apparent inhibition of DNA damage. This suggests that there are no minor binding preferences for the complexes.[31]

The mechanism of the DNA strand scission of bis(*o*-phenanthroline)copper(II) in the presence of reducing agents indicates that upon its reduction, the copper(II) complex binds to DNA, thereby liberating a phenanthroline.[32] Hydrogen peroxide then forms a copper–oxene reactive species that attacks the C1–H of the D-ribose. However, for complexes **1**, **2**, **3**, and **4**, $OH^{\cdot}$ and $O_2^-$ are the active oxygen species involved in the reaction. The involvement of these ROS excludes the formation of a copper–oxene such as that proposed by Sigman for bis(*o*-phenanthroline)copper(II).[32]

Because of the presence of hydroxyl and superoxide radicals and taking into account that the complexes are not able per se to induce any effect on the double stranded DNA, but that the cleavage process can be induced with the addition of activating agents at very low concentrations, we propose that the DNA damage can occur either through a Fenton-type reaction:

$$Cu^{II}(L) + e^- \rightarrow Cu^{I}(L)$$

$$Cu^{I}(L) + H_2O_2 \rightarrow Cu^{II}(L) + OH^- + OH^{\cdot}$$

or a Haber–Weiss reaction:

$$Cu^{II}(L) + e^- \rightarrow Cu^{I}(L)$$

$$Cu^{I}(L) + O_2 \rightarrow Cu^{II}(L) + O_2^-$$

$$O_2^- + H_2O_2 \rightarrow O_2 + OH^- + OH^{\cdot}$$

The proposed mechanism for our compounds is similar to that for the related Cu–*N*-quinolinsulfonamide-*o*-phenanthroline complex.[11]

In summary, the four complexes are very efficient chemical nucleases at low concentrations and in the presence of a low concentration of $H_2O_2$/ascorbate. In particular, $[Cu(L4)_2(phen)]$ (**4**) is a promising compound with much higher activity than that exhibited by the paradigmatic bis(*o*-phenanthroline)copper(II) complex. The high efficiency of **4** is probably due to the fact that its intercalation binding to DNA permits ROS formation near the deoxyribose moiety. Studies with inhibiting reagents suggest that the cleavage mechanism for these compounds is different from that proposed by Sigman for the bis(*o*-phenanthroline)copper(II) complex.

## Genotoxicity Assay in Yeast Cells

### *Sensitivity of the RAD54-yEGFP and RNR2-yEGFP Reporter System to EMS at Different Incubation Times*

Previous studies have shown that the brightness of the fluorescence signal obtained from yeast strains carrying the RAD54-yEGFP promoter-reporter construct on the plasmid correlates with exposure to increasing concentrations of MMS (methyl methane sulfonate).[15] EMS (ethyl methane sulfonate) and MMS are alkylating agents that can act on DNA and lead to damage and mutagenesis. EMS is regularly used as the reference substance for assessing the mutagenic and DNA-damaging potential of chemicals.[14] In order to test the sensitivity of the various transformed

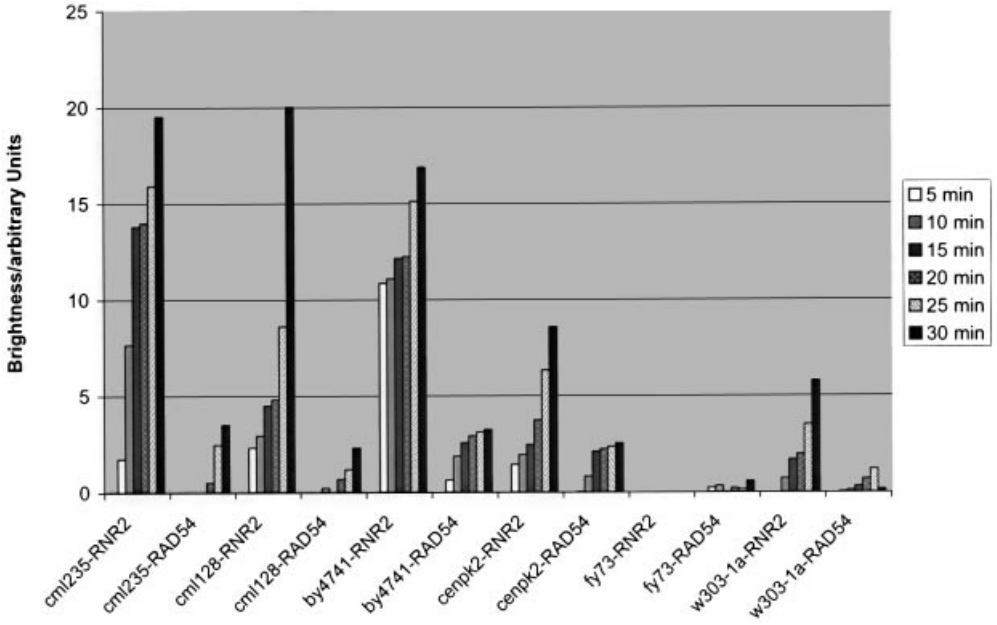


Figure 9. Comparison of EMS-dependent fluorescence in different *Saccharomyces cerevisiae* strains carrying the RAD54-yEGFP or the RNR2-yEGFP constructs. Intensity of the fluorescence signal is dependent on incubation time (0, 5, 10, 15, 20, 25, or 30 min; 0 min is represented as the background). The fluorescence signal displayed has been normalized for cell density.

 © 2006 Wiley-VCH Verlag GmbH & Co. KGaA, Weinheim 

strains to this paradigmatic mutagenic substance, we have performed fluorescence measurements in response to EMS treatment with yeast cell cultures carrying the RAD54-yEGFP or RNR2-yEGFP constructs. These assays have also been carried out with the aim of selecting the most sensitive transformed stain for subsequent evaluation of the genotoxicity of copper(II) complexes.

The results, shown in Figure 9, demonstrate that after treatment with EMS, only a weak increase in fluorescence is observed with the various RAD54-yEGFP constructions.

As an alternative sensor system, the RAD54 promoter was replaced by the promoter of the RNR2 gene. RNR2, a small subunit of ribonucleoside diphosphate reductase essential for the synthesis of nucleotide precursors, was shown to be induced by MMS treatment.[15] EMS was also able to induce measurable levels of yEGFP fluorescence driven by RNR2, where the fluorescence signal obtained with the RNR2 promoter was stronger than that observed with the RAD54 promoter. This result is consistent with data presented by Jelinsky and Samson[33] and Afanassiev et al.[14] The best results were obtained with the CML128-RNR2 strain, which was consequently chosen to test the ability of the copper compounds to cause DNA damage.

### *Sensitivity of the CML128-RNR2-yEGFP Reporter System to Copper Compounds at Different Concentrations*

The induction of a fluorescence signal driven by promoters that respond to DNA damage in the yeast *S. cerevisiae* provides a system to monitor the activity of substances that possess mutagenic potential at low concentrations. This method not only allows for the recognition of mutagenic agents that are able to produce DNA damage to living systems, but it can also be used to determine the biologically active concentrations of these substances, since the yeast system provides all the typical features of eucaryotic cell architecture and metabolism.

We thus tested the ability of compounds **1**, **2**, **3**, and **4**, previously shown to be strong DNA-cleaving agents, to induce a fluorescence signal in the selected CML128-RNR2-yEGFP system. The response obtained in the presence of $CuCl_2$ or $[Cu(phen)_2]^{2+}$ was studied for comparative purposes while EMS was used as a positive control. Figure 10 shows the intensity of the fluorescence signals induced by EMS, compounds **1**–**4**, and $CuCl_2$ and bis(*o*-phenanthroline)copper(II) over the system after 20 hours of incubation.

As can be seen in Figure 10, complexes **3** and **4** induced fluorescence. In particular, complex **4**, which had been found to be the most efficient chemical nuclease, showed a significant induction of the fluorescence reporter system, which indicates that this compound is able to produce DNA cleavage inside the cell. The signal was much stronger than that of complex **3**. Other substances that have been described in the literature as having induced fluorescence signals over similar systems include cisplatin (a strong DNA cleaving agent), camptothecin (an inhibitor of topoisomerase I), aphidicolin (an inhibitor of DNA polymerases α and δ), and actinomycin D (an intercalator that inhibits mainly transcription, but also replication to some extent).[14]

Complexes **1**, **2**, and bis(*o*-phenanthroline)copper(II), which possesses strong DNA cleaving activity, did not activate the RNR2 promoter-driven yEGFP expression Also, the results show that $CuCl_2$ was unable to induce a fluorescence signal. These negative results observed with complexes **1**, **2**, and bis(*o*-phenanthroline)copper(II), all of which are able to produce pUC18 DNA cleavage, could be because of enzymatic inactivation, lack of cell penetration, detoxification, or other specific properties of the yeast. Some substances known to have mutagenic or DNA-damaging potential, including psoralen, benzpyrene, tetracycline, colchicine, bleomycin, and mitomycin C, are unable to induce activity in similar systems.[14]

Because of the high genotoxic potential of **4**, our next task will be to evaluate the therapeutic use of this compound. With this aim, the potential antitumor activity of **4** will be tested on human tumor cell lines.

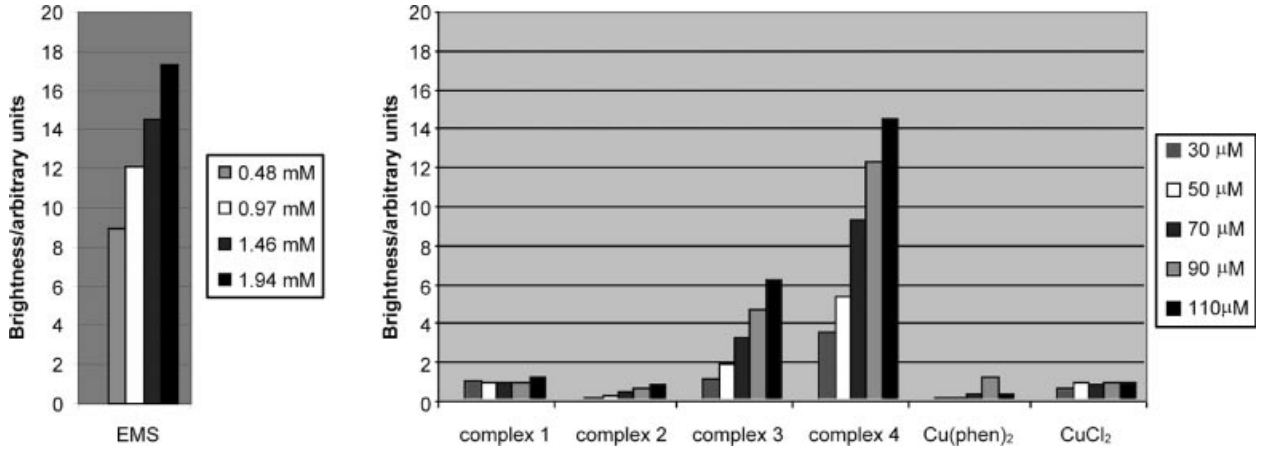


Figure 10. Fluorescence response profiles after treatment of CML128-RNR2-yEGFP with increasing concentrations of EMS, complexes **1**, **2**, **3**, or **4**, $[Cu(phen)_2]^{2+}$, or $CuCl_2$. Diagrams show the dose response of fluorescence after 20 h of incubation (0 M is represented as the background).

 © 2006 Wiley-VCH Verlag GmbH & Co. KGaA, Weinheim 

## Conclusions

Ternary copper(II) complexes with *N*-substituted sulfonamide ligands and *o*-phenanthroline have been prepared and structurally characterized with the aid of X-ray crystallography. The DNA cleavage activities of these complexes have been studied and compared with that of bis(*o*-phenanthroline)copper(II). All the complexes act as efficient chemical nucleases and their activities were found to be higher than that of the paradigmatic bis(*o*-phenanthroline)copper(II) complex. The most active cleaving agent was found to be $[Cu(L4)_2(phen)]$(**4**), which was able to mediate DNA scission at very low concentrations (1.5 μM) in the presence of low concentrations of activating agents. The significant activity of this complex can be ascribed to its efficient binding to DNA, as deduced from viscosity, fluorescence, and thermal denaturation studies. The sensitivity of the CML128-RNR2-yEGFP reporter system to copper compounds was tested to evaluate the genotoxic potential (i.e., the potential to inflict DNA damage) of the compounds at the cellular level. The significant induction of fluorescence by complex **4** indicated a high genotoxic potential for this compound. This fact makes **4** a very promising DNA damaging agent for further studies on human tumor cell lines.

## Experimental Section

**Materials:** Reagents and solvents were commercially available and were used without further purification. pUC18 was purchased from Roche Diagnostics. Calf thymus DNA (CT-DNA) was supplied by Sigma–Aldrich.

**Physical Methods:** Elemental analyses (C,H,N,S) were performed with a Carlo–Erba AAS instrument. IR spectra (KBr disks) were obtained with a Mattson satellite FT-IR in the range 4000–400 $cm^{-1}$. Fast atomic bombardment (FAB) mass spectra were obtained with a VG Autospec spectrometer with 3-nitrobenzyl alcohol as the matrix. Diffuse reflectance spectra (nujol mulls) of the complexes were carried out with a Shimadzu UV-2101 PC spectrophotometer. Electronic Paramagnetic Resonance (EPR) spectra were taken at the X-band frequency at room temperature with a Bruker ELEXSYS Spectrometer.

### Synthesis of the Ligands

***N*-(Benzothiazol-2-yl)benzenesulfonamide (HL3) and *N*-(Benzothiazol-2-yl)toluenesulfonamide (HL4):** A solution containing 2-aminobenzothiazole (1 g) and benzenesulfonyl chloride (2.5 g) or toluenesulfonyl chloride (2.5 g) in pyridine (6 mL) was heated at reflux for 1 h. The mixture was added to cold water (10 mL) and stirred for several minutes. The resulting solid was recrystallized from ethanol. After several weeks, slow evaporation of the filtrate gave rise to single crystals suitable for X-ray diffraction.

***N*-(Benzothiazol-2-yl)benzenesulfonamide (HL3):** Yield: 1.89 g, 98.9%. $C_{13}H_{10}N_2S_2O_2$ (290.35): calcd. C 53.77; H 3.47; N 9.65; S 20.08; found C 53.88; H 3.26; N 9.69; S 20.05. IR (KBr): $\tilde{\nu}$ = 1561 (thiazole); 1317–1304, 1146 $\nu(SO_2)$; 959 $\nu$(S–N) $cm^{-1}$. FAB: *m*/*z* = 291 [$M^+$]. UV: $\lambda_{max}$ = 309 (π→π*) nm.

***N*-(Benzothiazol-2-yl)toluenesulfonamide (HL4):** Yield: 1.88 g, 93.0%. $C_{14}H_{12}N_2S_2O_2$ (304.38): calcd. C 55.24; H 3.97; N 9.20; S 21.07; found C 55.11; H 3.97; N 9.26; S 21.14. IR (KBr): $\tilde{\nu}$ = 1560 (thiazole); 1314, 1146 $\nu(SO_2)$; 960 $\nu$(S–N) $cm^{-1}$. FAB: *m*/*z* = 305 [$M^+$]. UV: $\lambda_{max}$ = 302 (π→π*) nm.

***N*-(6-Chlorobenzothiazol-2-yl)benzenesulfonamide (HL1) and *N*-(6-Chlorobenzothiazol-2-yl)toluenesulfonamide (HL2):** These compounds were obtained and characterized as previously reported.[23,34]

### Synthesis of the Complexes

**$[Cu(L1)_2(phen)]$ (1), $[Cu(L2)_2(phen)MeOH]$ (2), $[Cu(L3)_2(phen)]$ (3), and $[Cu(L4)_2(phen)]$(4):** Aqueous NaOH (0.5 M, 2 mL) was added to a solution of the ligand (1 mmol) in methanol (40 mL). A suspension of $CuSO_4$ (0.5 mmol) and 1,10-phenanthroline monohydrate (0.5 mmol) in methanol was then added, and the resulting mixture was stirred for ca. 30 min at 40 °C. After cooling, the mixture was filtered to remove the precipitate that formed. Well-shaped crystals of **1**, **3**, and **4** were obtained from the filtrate by slow evaporation at room temperature for several months. Crystals of complex **2** were also formed, but they were not of sufficiently high quality for structural determination. Reaction in methanol by means of slow diffusion afforded good quality crystals of **2** after several days. Crystals of all the complexes were isolated by means of filtration, washed with MeOH, and dried under vacuum.

**Complex 1:** Yield: 0.142 g, 32%. $C_{38}H_{26}Cl_2CuS_4N_6O_4$: calcd. C 51.09, H 2.93, N 9.41, S 14.36; found C 51.15, H 2.96, N 9.39, S 14.28. IR (KBr): $\tilde{\nu}$ = 1465 (thiazole); 1279, 1129 $\nu(SO_2)$; 961 $\nu$(S–N) $cm^{-1}$. Solid UV/Vis: $\lambda_{max}$ = 355 (π→π*), 652 sh (d–d) nm.

**Complex 2:** Yield: 0.124 g, 26%. $C_{41}H_{32}Cl_2CuS_4N_6O_5$: calcd. C 51.76, H 3.39, N 8.83 S 13.48; found C 51.65, H 3.42, N 8.91 S 13.28. IR(KBr): $\tilde{\nu}$ = 1462 (thiazole); 1295, 1139 $\nu(SO_2)$; 968 $\nu$(S–N) $cm^{-1}$. Solid UV/Vis: $\lambda_{max}$ = 338 (π→π*), 543, 702 (d–d) nm.

**Complex 3:** Yield: 0.152 g, 37%. $C_{38}H_{26}CuS_4N_6O_4$: calcd. C 55.49, H 3.19 N 10.22 S 15.60; found C 55.32, H 3.15 N 10.10 S 15.67. IR (KBr): $\tilde{\nu}$ = 1432 (thiazole); 1276, 1144 $\nu(SO_2)$; 968 $\nu$(S–N) $cm^{-1}$. Solid UV/Vis: $\lambda_{max}$ = 371 (π→π*), 671 sh (d–d) nm.

**Complex 4:** Yield: 0.115 g, 27%. $C_{40}H_{30}CuS_4N_6O_4$: calcd. C 56.49 H 3.56 N 9.88 S 15.08. found C 56.53 H 3.42 N 9.88 S 15.08. IR(KBr): $\tilde{\nu}$ = 1489–1441 (thiazole); 1276, 1134 $\nu(SO_2)$; 967 $\nu$(S–N) $cm^{-1}$. Solid UV/Vis: $\lambda_{max}$ = 337 (π→π*), 665 sh (d–d) nm.

**X-ray Crystallography:** A green crystal measuring 0.04 × 0.04 × 0.08 mm (**1**), a blue crystal measuring 0.2 × 0.08 × 0.24 mm (**2**), a brown crystal measuring 0.04 × 0.1 × 0.2 mm (**3**), and a dark blue crystal measuring 0.14 × 0.12 × 0.08 mm (**4**), and either a triclinic space group $P\bar{1}$ (**1**) or a monoclinic space group *P*21/*c* (**2**, **3**, and **4**) (as determined from systematic absences) were used. Data collection was performed at 293 K with a Nonius Kappa-2000 single crystal diffractometer, with Cu-$K_\alpha$ radiation ($\lambda$ = 1.54184 Å) for complexes **1**, **3**, and **4** or with a Nonius Kappa CCD single crystal diffractometer with Mo-$K_\alpha$ radiation ($\lambda$ = 0.71073 Å) for complex **2**. The crystal-detector distance was fixed at 35 mm (**1**, **3**, and **4**) or 32.1 mm (**2**) and a total of 106 (**1**), 228 (**2**), 430 (**3**), and 91 (**4**) images were collected by means of the oscillation method, with a scan angle per frame of 2° (**1**, **3**, and **4**) or 1.7° (**2**) oscillation and 20 s (**1**), 15 s (**2**), 26 s (**3**), and 2 s (**4**) exposure time per image. The data collection was carried out and calculated with the program Collect.[35] Data reduction and cell refinements were performed with the programs HKL Denzo and Scalepack.[36]

Unit cell dimensions were determined from 295 (**1**), 10423 (**2**), 3916 (**3**), and 597 (**4**) reflections between $\theta$ = 0.999° and 39.973° (**1**),

 © 2006 Wiley-VCH Verlag GmbH & Co. KGaA, Weinheim 

0.998° and 28.7° (**2**), 0.999° and 63.691° (**3**), and 0.99° and 36.05° (**4**). Multiple observations were averaged: for complex **1** ($R_{merge}$ = 0.0000) this resulted in 1712 unique reflections of which 1189 were observed with $I > 2\sigma(I)$, for complex **2** ($R_{merge}$ = 0.030) this resulted in 10601 unique reflections of which 6891 were observed with $I > 2\sigma(I)$, for complex **3** ($R_{merge}$ = 0.0000) this resulted in 4086 unique reflections of which 2439 were observed with $I > 2\sigma(I)$, and for complex **4** ($R_{merge}$ = 0.0000) this resulted in 879 unique reflections of which 732 were observed with $I > 2\sigma(I)$. Final mosaicity was 0.35(**1**), 0.43 (**2**), 0.50 (**3**), and 0.509 (**4**). All data completeness was 74.2% (**1**), 98.2% (**2**), 84.0% (**3**), and 95.5% (**4**).

Crystal structures were solved by direct methods, either with the program SIR-97 (**1**, **2**, and **3**) or SHELXS-86 (**4**).[37] Anisotropic least-squares refinements were carried out with SHELXL-97.[38] All non-hydrogen atoms were anisotropically refined while hydrogen atoms were located geometrically. The final cycle of full-matrix least-squares refinement based on 1712 (**1**), 10601 (**2**), 4086 (**3**), and 879 (**4**) reflections and 494 (**1**), 536 (**2**), 561 (**3**), and 284 (**4**) parameters converged to a final value of $R_1$ [$F^2 > 2\sigma(F^2)$] = 0.052, $wR_2$ [$F^2 > 2\sigma(F^2)$] = 0.130, $R_1$ ($F^2$) = 0.082, $wR_2$ ($F^2$) = 0.150 for complex **1**; $R_1$ [$F^2 > 2\sigma(F^2)$] = 0.046, $wR_2$ [$F^2 > 2\sigma(F^2)$] = 0.127, $R_1$ ($F^2$) = 0.090, $wR_2$ ($F^2$) = 0.170 for complex **2**; $R_1$ [$F^2 > 2\sigma(F^2)$] = 0.044, $wR_2$ [$F^2 > 2\sigma(F^2)$] = 0.094, $R_1$ ($F^2$) = 0.092, $wR_2$ ($F^2$) = 0.112 for complex **3**; and $R_1$ [$F^2 > 2\sigma(F^2)$] = 0.036, $wR_2$ [$F^2 > 2\sigma(F^2)$] = 0.097, $R_1$ ($F^2$) = 0.045, $wR_2$ ($F^2$) = 0.105 for complex **4**. Final difference Fourier maps showed no peaks higher than 0.261 e/Å$^3$ nor deeper than –0.397 e/Å$^3$ for complex **1**, no peaks higher than 0.678 e/Å$^3$ to 1.06 Å to H14d nor deeper than 1.5 e/Å$^3$ to 0.85 Å to Cu for complex **2**, no peaks higher than 0.197 e/Å$^3$ to 1.14 Å to N1c nor deeper than –0.405 e/Å$^3$ to 0.98 to Cu1 for complex **3**, and no peaks higher than 0.411 e/Å$^3$ nor deeper than –0.167 e/Å$^3$ for complex **4**. Semi-empirical absorption correction was applied using the program XABS2[39] for complex **1**. Geometrical calculations were made with PARST.[40] The crystallographic plots were made with ORTEP.[41] A summary of crystallographic data of the complexes is given in Table 2.

The supplementary crystallographic data for this paper is contained in CCDC-299259, -299260, -299261, and -299262. These data can be obtained free of charge from The Cambridge Crystallographic Data Centre via www.ccdc.cam.ac.uk/data_request/cif.

**Metal Complexes–DNA Interactions**

**Viscosity Measurements:** Viscosity experiments were carried out with a Cannon 25 L97 viscosimeter immersed in a Julabo thermostatted water bath maintained at 25.0 ± 0.1 °C. Solutions of the complexes (1–10 μM) in cacodylate buffer (pH = 6.0) were added to a calf thymus DNA (50 μM base pairs) solution in cacodylate buffer. The flow times were measured with a digital stopwatch. The flow measurements were performed in triplicate. Data were presented as $(\eta/\eta_0)^{1/3}$ vs. the ratio of the concentration of complex and DNA, where $\eta$ is the viscosity of DNA in the presence of the complex and $\eta_0$ is the viscosity of DNA alone. Viscosity values were calculated from the observed flow time of a DNA-containing solution corrected from the flow time of buffer alone ($t_0$), $\eta = t - t_0$.

**Fluorescence Quenching of Ethidium Bromide Intercalated to DNA by Interaction of the Copper Complexes with DNA:** The fluorescence spectra were recorded with a JASCO FP-6200 spectrofluorimeter at room temperature. The experiments were conducted by adding copper(II) complex solutions at various concentrations (0–64 μM) to samples containing 100 μM calf thymus DNA base pairs and 10 μM ethidium bromide in cacodylate buffer (pH = 6.0). All the samples were excited at 500 nm and emission was recorded at 530–650 nm.

**Thermal Denaturation Experiments:** DNA-melting experiments were carried out by monitoring the absorbance (260 nm) of CT-DNA (100 μM base pairs) at different temperatures in the absence and presence of the complexes in a 4:1 DNA/complex ratio. Measurements were performed with an Agilent 8453 UV/Vis spectrophotometer equipped with a Peltier temperature controlled sample cell and driver (Agilent 89090A). The solution containing the ternary complex and CT-DNA in phosphate buffer (1 mM phosphate, 2 mM NaCl, pH = 7.2) was continuously stirred and heated with a rate of temperature increase of 1 °C/min. The temperature interval studied ranged from 25 to 90 °C.

**pUC18 DNA Cleavage:** A typical reaction for complexes was undertaken by mixing a cacodylate buffer (0.1 M, 7 μL, pH 6.0), pUC18 (1 μL, 0.25 μg/μL), a solution of the tested complex (6 μL) at increasing concentrations between 1.5 μM and 9 μM, ascorbate (3 μL), and a $H_2O_2$ (3 μL) twofold molar excess relative to the concentration of the complex in cacodylate buffer. The mixtures were allowed

Table 2. Crystal data and structure refinement for [Cu(L1)$_2$(phen)] (**1**), [Cu(L2)$_2$(phen)MeOH] (**2**), [Cu(L3)$_2$(phen)] (**3**), and [Cu(L4)$_2$-(phen)] (**4**).

| Compound | **1** | **2** | **3** | **4** |
|---|---|---|---|---|
| Empirical formula | $C_{38}H_{26}Cl_2CuN_6O_4S_4$ | $C_{41}H_{32}Cl_2CuN_6O_5S_4$ | $C_{38}H_{26}CuN_6O_4S_4$ | $C_{20}H_{15}Cu_{0.5}N_3O_2S_2$ |
| Formula mass [g/mol] | 893.33 | 958.41 | 822.43 | 425.24 |
| Crystal system | triclinic | monoclinic | monoclinic | monoclinic |
| Space group | $P\bar{1}$ | $P2_1/c$ | $P2_1/c$ | $P2_1/c$ |
| $a$ [Å] | 10.8510(9) | 17.4880(2) | 11.6840(3) | 12.0450(7) |
| $b$ [Å] | 11.4360(7) | 11.7090(2) | 18.0120(5) | 11.3450(6) |
| $c$ [Å] | 15.6000(12) | 20.5440(2) | 17.2570(3) | 17.8480(10) |
| $\alpha$ [°] | 86.714(3) | 90 | 90 | 90 |
| $\beta$ [°] | 81.697(3) | 95.7960(7) | 101.2430(11) | 126.072(3) |
| $\gamma$ [°] | 89.291(3) | 90 | 90 | 90 |
| $V$ [Å$^3$] | 1912.4(2) | 4185.23(10) | 3562.08(15) | 1971.34(19) |
| $Z$ | 2 | 4 | 4 | 4 |
| $\lambda$ [Å] | 1.54184 | 0.71073 | 1.54184 | 1.54184 |
| $\mu$ [mm$^{-1}$] | 4.551 | 0.903 | 3.485 | 3.167 |
| $\rho_{calcd.}$ [mg/m$^3$] | 1.551 | 1.521 | 1.534 | 1.433 |
| $T$ [K] | 293(2) | 293(2) | 293(2) | 293(2) |
| $R_1$ | 0.0523 | 0.0458 | 0.0437 | 0.0361 |
| $wR_2$ | 0.1304 | 0.1271 | 0.0941 | 0.0971 |

 © 2006 Wiley-VCH Verlag GmbH & Co. KGaA, Weinheim 

to stand for 30 min at 37 °C. After that, a quench buffer solution (3 μL) consisting of bromophenole blue (0.25%), xylene cyanole (0.25%), and glycerol (30%) were added. The solution was then subjected to electrophoresis on a 0.8% agarose gel in 0.5×TBE buffer (0.045 M Tris, 0.045 M boric acid, and 1 mM EDTA) containing 2 μL/100 mL of a solution of ethidium bromide (10 mg/mL) at 80 V for about 2 h. The gel was photographed on a capturing gel printer plus TDI.

To test for the presence of reactive oxygen species (ROS) generated during strand scission, various reactive oxygen intermediate scavengers were added to the reaction mixtures. The scavengers used were superoxide dismutase (15 units), DMSO (1 M), *tert*-butyl alcohol (1 M), sodium azide (100 mM), and 2,2,6,6-tetramethyl-4-piperidone (100 mM). An assay in the presence of the minor groove binder distamycin (8 μM) was also performed. Samples were treated as described above.

**Genotoxicity Assays**

**Construction of a Plasmid Containing yEGFP Under the Transcriptional Control of the RNR2 or RAD54 Promoter:** PCR was used to amplify the RNR2 and RAD54 promoters from genomic *Saccharomyces cerevisiae* DNA with the primers shown in Table 3. pUG35 plasmid was digested with Sal I and Sac I to remove the original promoter of yEGFP. The PCR products were digested with the same restriction enzymes and were ligated into the pUG35 to produce pUG35-RNR2 or pUG35-RAD54. The yeast strains used in this study, listed in Table 4, were grown on a YNB medium (1.68 g of YNB without aa and without salts, 5 g of ammonium sulfate, and 20 g of glucose per liter) with the required amino acids.

Table 3. Primers used in the construction of the RAD54-yRGFD or RNR2-yEGFD promoter-reporter plasmid.

| | |
|---|---|
| RAD54-3SAL | GGC CGT TCA CCG TCG ACT ATT CC |
| RAD54-5SAC | AAA ATA TTG AGC TCG AAG ATC TGT CC |
| RNR2-3SAL | GGA CAA TGC GTC GAC AGC AG |
| RNR2-5SAC | TAG CCA GAG CTC TGC ATT ACG C |

Table 4. Yeast strain used.

| Strain | Relevant genotype |
|---|---|
| BY4741 | MATa his3-δ1 leu2-δ0 met15-δ0 ura3-δ0 |
| CML235 | MATa his3-δ200 ura3-52 leu3-δ1 |
| W303-1A | MATa ura3-1 ade2-1 leu2-3,112 trp1-1 his3-11,15 |
| CML128 | MATa leu2-3,112 ura3-52 trp1-1 his4 can1r |
| CEN.PK2 | MATa/MATα ura3-52/ura3-52 trp1-289/trp1-289 leu2-3,112/leu2-3,112 his3δ1/his3δ1 |
| FY73 | MATα his3-Δ200, ura3-52 |
| Transformed reporter strains | |
| BY4741-RAD54 | BY4741 transformed with pUG35-RAD54 |
| CML235-RAD54 | CML235 transformed with pUG35-RAD54 |
| W303-1A-RAD54 | W303-1A transformed with pUG35-RAD54 |
| CML128-RAD54 | CML128 transformed with pUG35-RAD54 |
| CEN.PK2-RAD54 | CEN.PK2 transformed with pUG35-RAD54 |
| FY73-RAD54 | FY73 transformed with pUG35-RAD54 |
| BY4741-RNR2 | BY4741 transformed with pUG35-RNR2 |
| CML235-RNR2 | CML235 transformed with pUG35-RNR2 |
| W303-1A-RNR2 | W303-1A transformed with pUG35-RNR2 |
| CML128-RNR2 | CML128 transformed with pUG35-RNR2 |
| CEN.PK2-RNR2 | CEN.PK2 transformed with pUG35-RNR2 |
| FY73-RNR2 | FY73 transformed with pUG35-RNR2 |

**Sensitivity of the RAD54-yEGFP and RNR2-yEGFP Reporter Systems to EMS:** Liquid YNB (10 mL; 1.68 g of YNB without aa and without salts, 5 g of ammonium sulfate, and 20 g of glucose per liter) with the suitable requirements were inoculated into a fresh sample of the yeast strain to give approximately $1\times10^6$ cells/mL. The cultures were incubated overnight at 28 °C with vigorous shaking. The cultures were then washed twice in 50 mM potassium phosphate buffer (pH = 7.0) and resuspended in this buffer to a final concentration of $5\times10^7$ cells/mL. EMS (30 μL) was added to 1 mL of cells and incubated for 30 min at 30 °C. 100 μL samples were obtained at different times (0, 5, 10, 15, 20, 25, and 30 min) during the incubation. The EMS mutagenesis was stopped in each cell suspension by adding an equal volume of a freshly made 10% (w/v) filter-sterilized solution of sodium thiosulfate. The suspensions were then mixed well and centrifuged, after which the cells were collected and washed twice with sterile water. The cells were then inoculated in liquid medium and incubated at 28 °C for 20 h on an orbital shaker. For cell fluorescence measurements, the cell cultures were diluted (1:10 in sterile distilled water) and transferred directly to cuvettes. Samples with cell cultures with no mutagenic agents were taken as blanks. Fluorescence measurements were performed with a Jasco FP-6200 spectrofluorometer. The excitation and emission wavelengths were set to 488 and 511 nm, respectively, with a slit width of 10 nm. Fluorescence values were normalized for the absorption values of each cell. The normalized fluorescence values were then plotted against the substance concentration and incubation time. All calculations and plots were made with MS Excel.

**Evaluation of Genotoxicity Produced by the Complexes:** Single colonies of the selected transformed yeast strains grown on selective medium were used to inoculate 5 mL of medium and then grown to mid log phase (0.4 AU at 600 nm). The cells were resuspended in fresh medium to a final concentration of 0.1 AU. Solutions of EMS, the copper salt, or the test compounds at increasing concentrations were distributed in parallel. The tubes were incubated at 28 °C for 20 h on an orbital shaker at 120 rpm. Fluorescence measurements were performed as described above except that, in this case, the first measurement was taken at 0 h and repeated at 4, 16, and 20 h of incubation.

## Acknowledgments

J. B. and G. A. acknowledge financial support from the Spanish CICYT (CTQ2004-03735). M. G.-A. wishes to thank the city government of Valencia (Spain) for a Carmen and Severo Ochoa postdoctoral fellowship.

[1] S. Kawanishi, Y. Hiraku, M. Murata, S. Oikawa, *J. Biol. Chem.* **1986**, *261*, 5952–5958.
[2] S. Inoue, S. Kawanishi, *Cancer Res.* **1987**, *47*, 6522–6527.
[3] K. Yamamoto, S. Inoue, T. Yoshinaga, S. Kawanishi, *Chem. Res. Toxicol.* **1989**, *2*, 234–239.
[4] S. Kawanishi, S. Inoue, K. Yamamoto, *Carcinogenesis* **1989**, *10*, 2231–2235.
[5] S. Inoue, S. Kawanishi, *Biochem. Biophys. Res. Commun.* **1989**, *159*, 445–451.
[6] K. Yamamoto, S. Kawanishi, *J. Biol. Chem.* **1989**, *264*, 15435–15440.
[7] P. M. Doraiswamy, A. E. Finefrock, *Lancet Neurol.* **2004**, *3*, 431–434.
[8] K. J. Barnham, C. L. Masters, A. I. Bush, *Nat. Rev. Drug Discovery* **2004**, *3*, 205–214.
[9] M. Pitié, C. Boldron, H. Gortnitzka, C. Hemmert, B. Donnadieu, B. Meunier, *Eur. J. Inorg. Chem.* **2003**, 528–540.
[10] M. Pitié, A. Croisy, D. Carrez, C. Boldron, B. Meunier, *ChemBioChem* **2005**, *6*, 686–691.
[11] B. Macías, I. García, M. J. Villa, M. González-Álvarez, J. Borrás, A. Castiñeiras, *J. Inorg. Biochem.* **2003**, *96*, 367–374.

 © 2006 Wiley-VCH Verlag GmbH & Co. KGaA, Weinheim 

[12] M. González-Álvarez, G. Alzuet, J. Borrás, L. del Castillo Agudo, S. García-Granda, J. M. Montejo-Bernardo, *J. Biol. Inorg. Chem.* **2003**, *8*, 112–120.
[13] M. González-Álvarez, G. Alzuet, J. Borrás, L. del Castillo Agudo, S. García-Granda, J. M. Montejo-Bernardo, *Inorg. Chem.* **2005**, *44*, 9424–9433.
[14] V. Afanassiev, M. Sefton, T. Anantachaiyong, G. Barker, R. Walmsley, S. Wölfl, *Mutat. Res.* **2000**, *464*, 297–308.
[15] N. Billinton, M. G. Barker, C. E. Michel, A. N. Knight, W. D. Heyer, N. J. Goddard, P. R. Fielden, R. M. Walmsley, *Biosens. Bioelectron.* **1998**, *13*, 831–838.
[16] R. M. Walmsley, N. Billinton, W. D. Heyer, *Yeast* **1997**,*13*, 1535–1545.
[17] D. Averbeck, S. Averbeck, *Mutat. Res.* **1994**, *315*, 123–138.
[18] B. P. Cormack, G. Bertram, M. Egerton, N. A. R. Gow, S. Falkow, A. J. P. Brown, *Microbiology* **1997**, *143*, 303–311.
[19] Y.-H. Kim, K.-J. Shin, T. G. Lee, E. Kim, M.-S. Lee, S. H. Ryu, P.-G. Suh, *Biochem. Pharmacol.* **2005**, *69*, 1333–1341.
[20] R. Cejudo-Marín, G. Alzuet, S. Ferrer, J. Borrás, A. Castiñeiras, E. Monzani, L. Casella, *Inorg. Chem.* **2004**, *43*, 6805–6814.
[21] L. Gutiérrez, G. Alzuet, J. A. Real, J. Borrás, A. Castiñeiras, *Eur. J. Inorg. Chem.* **2002**, 2094–2102.
[22] L. P. Battaglia, A. Bonamartini-Corradi, G. Marcotrigiano, L. Menabue, G. C. Pellacani, *Inorg. Chem.* **1979**, *18*, 148–152.
[23] M. González-Álvarez, G. Alzuet, J. Borrás, L. del Castillo Agudo, S. García-Granda, J. M. Montejo-Bernardo, *J. Inorg. Biochem.* **2004**, *98*, 189–198.
[24] B. J. Hathaway, *Comprehensive Coordination Chemistry* (Eds.: R. D. Gillard, J. A. McCleverty), Pergamon, New York, **1987**, ch. 9, 535–591.
[25] W. Addison, T. N. Rao, J. Reedijk, J. van Rijn, G. C. Verschoor, *J. Chem. Soc., Dalton Trans.* **1984**, 1349–1356.
[26] J. Liu, T. Zhang, L. Qu, H. Zhou, Q. Zhang, J. Liangnian, *J. Inorg. Biochem.* **2002**, *91*, 269–276.
[27] Y. B. Zeng, N. Tang, W. S. Liu, N. Tang, *J. Inorg. Biochem.* **2003**, *97*, 258–264.
[28] S. Dhar, M. Nethaji, A. R. Chakravarty, *Inorg. Chem.* **2005**, *44*, 8876–8883.
[29] K.-L. Fu, P. M. Bradley, C. Turro, *Inorg. Chem.* **2003**, *42*, 878–884.
[30] M. González-Álvarez, G. Alzuet, J. Borrás, M. Pitié, B. Meunier, *J. Biol. Inorg. Chem.* **2003**, *8*, 644–652.
[31] N. Jiménez-Garrido, L. Perelló, R. Ortiz, G. Alzuet, M. González-Álvarez, E. Cantón, M. Liu-González, S. García-Granda, M. Pérez-Priede, *J. Inorg. Biochem.* **2005**, *99*, 677–689.
[32] D. S. Sigman, R. Landgraf, D. Perrin, M. L. Pearson, *Metal Ions in Biological Systems 33* (Eds.: A. Sigel, H. Sigel), Marcel Dekker Inc., New York, **1996**, pp. 485–523.
[33] S. A. Jelisnky, L. D. Samson, *Proc. Natl. Acad. Sci. USA*. **1999**, *96*, 1486–1491.
[34] M. González-Álvarez, G. Alzuet, J. Borrás, B. Macías, J. M. Montejo-Bernardo, S. García-Granda, *Z. Anorg. Allg. Chem.* **2003**, *629*, 239–243.
[35] COLLECT, B. V. Nonius, **1997–2000**.
[36] Z. Otwinowski, W. Minor, "Processing of X-ray Diffraction Data Collected in Oscillation Mode" in *Methods in Enzymology*, vol. 276 (Macromolecular Crystallography, Part A), Carter and Sweet, Academic Press, New York, **1997**, pp. 307–326.
[37] G. M. Sheldrick, SHELX-86, *Program for Crystal Structure Solution*, University of Göttingen, Germany, **1986**.
[38] G. M. Sheldrick, SHELX97, *Programs for Crystal Structure Analysis* (Release 97-2), University of Göttingen, Germany, **1997**.
[39] *XABS2*: S. Parkin, B. Moezzi, H. Hope, *J. Appl. Crystallogr.* **1995**, *28*, 53–56.
[40] *PARST*: a) M. Nardelli, *Comput. Chem.* **1983**, *7*, 95–97; b) M. Nardelli, *J. Appl. Crystallogr.* **1995**, *28*, 659.
[41] *ORTEP3 for Windows*: L. J. Farrugia, *J. Appl. Crystallogr.* **1997**, *30*, 565.

Received: April 5, 2006
Published Online: July 25, 2006

 © 2006 Wiley-VCH Verlag GmbH & Co. KGaA, Weinheim 

DOI: 10.1002/ejic.200600418

# Modelling the Electron-Transfer Complex Between Aldehyde Oxidoreductase and Flavodoxin

**Ludwig Krippahl,[a] P. Nuno Palma,[a][‡] Isabel Moura,[a] and José J. G. Moura*[b]**

**Keywords:** Bioinorganic chemistry / Electron transfer / Molybdenum / Enzyme models

Three-dimensional protein structures of the xanthine oxidase family show different solutions for the problem of transferring electrons between the flavin adenine dinucleotide (FAD) group and the molybdenum cofactor. In xanthine oxidase all the cofactors lie within domains of the same protein chain, whereas in CO dehydrogenase the Fe–S centres, FAD and Mo cofactors are enclosed in separate chains and the enzyme exists as a stable complex of all three. In aldehyde oxidoreductase, only Fe–S and Mo co-factors are present in a single protein chain. Flavodoxin is docked to aldehyde oxidoreductase to mimic the flavin component on the intramolecular electron transfer chain of aanthine oxidase and CO dehydrogenase and, remarkably, the main features of the electron-transfer pathway are observed.
(© Wiley-VCH Verlag GmbH & Co. KGaA, 69451 Weinheim, Germany, 2006)

## Introduction

Molybdenum and tungsten are found in a mononuclear form in the active site of a diverse group of enzymes that catalyze, in general, oxygen-atom transfer and are distinct from the nitrogenase enzyme that contains a complex FeSMo cluster. Mononuclear Mo-enzymes have been classified into three main groups, called the xanthine oxidase (XO), dimethyl sulfoxide reductase (DMSOR) and sulfite oxidase (SO) families.[1,2] The active site of these enzymes contains the metal atom coordinated to one or two pyranopterin molecules and to a variable number of ligands containing atoms such as oxygen (oxo, hydroxo, water, serine, and aspartic acid), sulfur (cysteines) and selenium (selenocysteines). Pyranopterin is an organic ligand that can be either in the monophosphate form or have a nucleotide molecule attached by a pyrophosphate link. In addition, these proteins may have other redox cofactors such as iron-sulfur (Fe–S) centres, hemes and flavin groups, which are involved in intra- and intermolecular electron-transfer processes.[1–3]

There are a few known crystal structures of molybdenum hydroxylases from the XO family. These include aldehyde oxidoreductase (AOR) from *Desulfovibrio gigas*,[4–6] xanthine oxidoreductase (XO) from *Bos taurus*[7] and Xanthine dehydrogenase (XDH) from *Rhodobacter capsulatus*.[8] There are also two known crystal structures of similar proteins containing Mo, namely CO dehydrogenase (CODH) from *Oligotropha carboxidovorans*, which catalyzes the oxidation of CO to $CO_2$ without cleavage of a C–H bond,[9,10] and 4-hydroxybenzoyl-CoA Reductase (4-HBCR) from *Thaurea aromatica*, which catalyzes reductive removal of an aromatic hydroxy group.[11,12]

Despite their similarity, these proteins show three different sequence arrangements for the active sites participating in electron transfer between the FAD group: the two [2Fe-2S] centres and the Molybdenum cofactor.[1,2,7–14] In general, all the cofactors in XO and XDH lie within domains of the same protein chain, although some exceptions are found in prokaryotic XDHs such as the one isolated from *Rhodobacter capasulatus.* In CODH and 4-HBCR, two [2Fe-2S] centres, one FAD and one Mo cofactor are enclosed in separate chains and the enzyme exists as a stable complex of all three. In AOR only the two [2Fe-2S] centres and Mo cofactor are present in a single and shorter polypeptide chain (Figure 1).

Although the arrangement of the 4-HBCR subunits containing the FAD group, the molybdenum cofactor and the two intermediary [2Fe-2S] centres is similar to that of CODH, 4-HBCR is significantly different from CODH. The gene sequences for the three subunits of 4-HBCR in *Rhodopseudomonas palustris*[15] and *T. aromatica*[13] reveal significant differences between these proteins, and 4-HBCR consists of three subunits of $(\alpha\beta\gamma)_2$ composition.[16,17] Each monomer contains a [4Fe-4S] centre[16] in addition to the prosthetic groups shared with CODH. The additional [4Fe-4S] centre is coordinated to conserved cysteinyl residues in a unique stretch of approximately 40 amino acids in the β subunit.[12,19] Nevertheless, for the purposes of this work the important features of 4-HBCR are shared with CODH,

[a] REQUIMTE-CQFB, Departamento de Química, Faculdade de Ciências e Tecnologia, Universidade Nova de Lisboa, 2829-516 Campus de Caparica, Portugal
[b] REQUIMTE-CQFB, Departamento de Química, Faculdade de Ciências e Tecnologia, Universidade Nova de Lisboa, 2829-516 Campus de Caparica, Portugal
Fax: +351-21-194-8550
E-mail: jose.moura@dq.fct.unl.pt
[‡] Present address: Laboratórios BIAL, Porto, Portugal

 © 2006 Wiley-VCH Verlag GmbH & Co. KGaA, Weinheim 

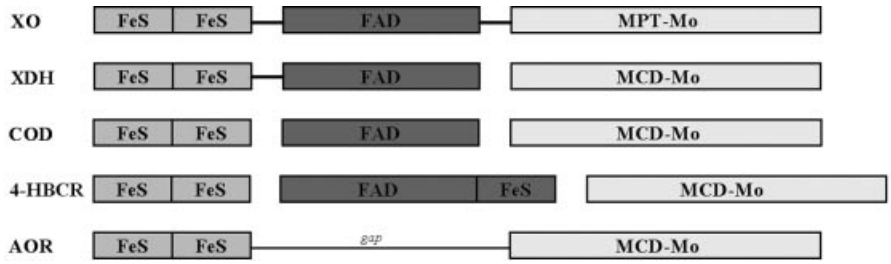


Figure 1. Schematic representation of the domain sequence for the three enzymes XO, CODH, 4-HBCR (that includes an extra elongation of the β-subunit that binds, in addition to the FAD moiety, the [4Fe-4S] center) and AOR (homologies among molybdenum hydroxylases). The FAD domain is absent in the *D. gigas* aldehyde oxidoreductase. In the *R. capsulatus* Xanthine dehydrogenase and the *Bos Taurus* XO, the iron-sulphur and flavin-binding portions of the protein constitute one subunit (XdhA), and the molybdenum-binding portion a second (XdhB). In the *O. carboxydovorans* CO dehydrogenase, the iron–sulphur centres are together in one subunit (CoxS), the flavin in a second (CoxM) and the molybdenum in a third subunit (CoxL). A comparison with the *R. capsulatus* XDH domain sequence is also included (a variation of the XO domain theme).

namely the electron-transfer pathway involving the FAD, the two [2Fe-2S] centres and the Mo cofactor.

The molybdenum [iron-sulfur] protein, first isolated from *Desulfovibrio gigas* (*Dg*AOR),[18] was later shown to mediate the electronic flow from salicylaldehyde to a suitable electron acceptor, and its 2,6-dichlorophenolindophenol (DCPIP)-dependent aldehyde oxidoreductase activity was studied in detail[19] using a wide range of aldehydes and analogues. A steady-state kinetic analysis ($K_M$ and $V_{max}$) was performed for acetaldehyde, propionaldehyde, benzaldehyde and salicylaldehyde in the presence of a suitable electron acceptor (DCPIP), and a simple Michaelis–Menten model was shown to be applicable as a first kinetic approach. Xanthine, purine, allopurinol and *N*1-methylnicotinamide (NMN), however, could not be utilized as enzyme substrates. DCPIP and ferricyanide were shown to be capable of cycling the electronic flow, whereas other cation and anion dyes [$O_2$ and $NAD(P)^+$] were not active in this process. This molybdenum hydroxylase was later shown to be part of an electron-transfer chain that is capable of linking the oxidation of aldehydes to the reduction of protons and involves flavodoxin.[20]

The FAD domain, which is present in XO and CODH but absent in AOR, and the evidence for in vitro electron transfer between AOR and flavodoxin, led to the reasonable assumption that flavodoxin can play the role of a reaction partner for AOR that replaces the missing domain. Our hypothesis was that the interaction between AOR and flavodoxin should mimic the arrangement of the domains or subunits of the other similar proteins, therefore to test this hypothesis we attempted to model the AOR-flavodoxin complex using the BiGGER docking algorithm.[21,22]

## Results and Discussion

Our hypothesis was thus that if flavodoxin assumed the role of the missing FAD domain, the complex of flavodoxin with AOR should be similar to the structures of CODH and XO, and should be consistent with the experimental data available.[20]

### The Nature of the Electron-Transfer Complex

The interaction between AOR and flavodoxin seems to be driven mostly by electrostatics, since both partners are highly charged and flavodoxins have high dipolar moments (approx. 400 Debye). Both AOR and flavodoxin are acidic, but the reaction rate of electron transfer, as measured using aldehydes as electron donor through AOR and following the formation of flavodoxin semiquinone state at 590 nm (Figure 2) (experimental conditions as in ref.[20]; see also caption to Figure 2), increased with increasing ionic strength up to 0.1 M. Although the strong ionic-strength dependency of the reaction kinetics for the electron transfer between AOR and flavodoxin from *D. gigas* indicates that the interaction is driven mostly by electrostatics, it was intriguing that the reaction rate increased with increasing ionic strength. However, the docking results (see below) helped to explain this observation and called our attention to the effect of ionic strength on the electrostatic field generated

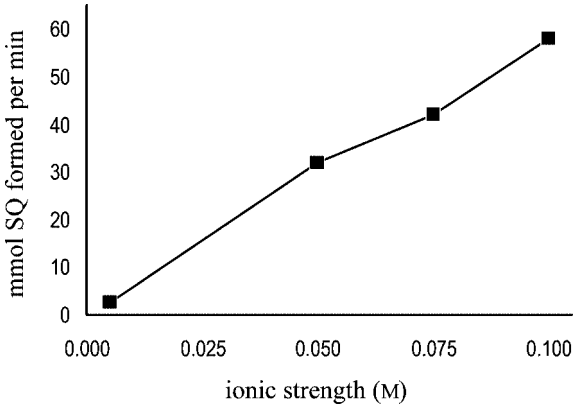


Figure 2. Dependency of the AOR-flavodoxin reaction rate on ionic strength. The reaction rate was measured by the formation of the semiquinone form of FAD, which was followed by spectroscopy at 590 nm. Anaerobic formation of flavodoxin semiquinone was followed at 580 nm, using benzaldehyde as electron donor, varying the media ionic strength (adjusted with NaCl). The experiments were conducted at 20 °C and pH 7.6 (Tris-HCl buffer). AOR was 2 μM, flavodoxin 24 μM and substrate 100 μM. General procedures as detailed indicated in ref.[20]

 © 2006 Wiley-VCH Verlag GmbH & Co. KGaA, Weinheim 

by AOR at the suggested interaction site, near the more exposed [2Fe-2S] moiety. Figure 3 shows the electrostatic field in this region at an ionic strength of 0.0, 0.1 and 0.5 M. The electrostatic field was calculated by solving the linearised Poisson–Boltzmann equation with a multi-grid finite difference solver,[23] with a grid resolution of 2 Å. The simplifying assumptions (equal concentrations and radii for positive and negative ions and linearisation of the hyperbolic sine term) and the finite difference solution limit the precision of the calculations, but this is not important for the qualitative result that explains the effects of ionic strength on this reaction. At higher ionic strength the overall negative charge of AOR has less influence near the positive patch surrounding the exposed [2Fe-2S] cluster, thus allowing a positive region of the field to project farther from the surface and possibly helping to guide the negatively charged flavodoxin. This explains both the reaction kinetics data and how these two strongly acidic proteins may interact despite their large negative charge.

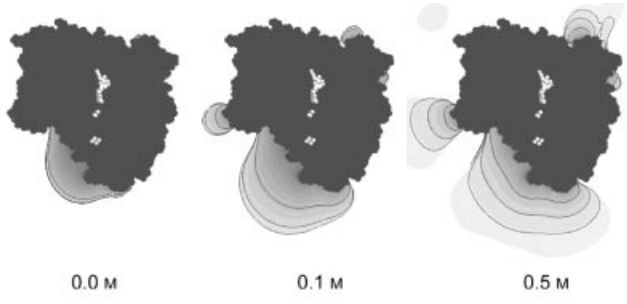


Figure 3. The three panels show the positive regions of the electrostatic field projected by AOR at 0.0, 0.1 and 0.5 M of ionic strength. The isopotential lines are for 0.1, 0.01 and 0.001 kcal mol. Only the positive regions of the electrostatic field are shown. The more exposed [2Fe-2S] cluster is shown on the lower part of each panel, and the projecting positive region of the field corresponds to the most likely docking site (Figure 4).

### AOR-Flavodoxin Complex: Docking Model

We used the BiGGER[21,22] docking algorithm both with the default soft docking parameters and with the hard docking option for all docking runs. The first stage of the docking algorithm was to select a set of 5000 solutions from all possible configurations and generate candidate complexes by shifting one of the partners relative to the other in steps of 1 Å of translation for each 15°-step in rotation. This exhaustive search generated billions of possibilities, most of which were excluded by eliminating excessive overlap and by keeping only those with the highest surface contact areas.

The soft docking algorithm[22] is a general docking algorithm applicable to cases ranging from tightly binding enzyme-inhibitor complexes to transient electron-transfer interactions, and so must take into account the effects of side-chain flexibility, which is potentially essential in strong interactions. This algorithm models side-chain flexibility implicitly by allowing some interatomic clashes involving selected regions of flexible side-chains at the surface of the protein. The downside is an increase in the fraction of incorrect models retained in those cases where side-chain flexibility is not a relevant factor. In such cases, which are common for weak interactions, the hard docking alternative tends to provide clearer results. Our approach was to use both alternatives to take advantage of the best features of each. Agreement between hard docking and soft docking results indicated that it was not necessary to account for side-chain conformation changes. In such cases we can use the hard docking results, which are generally clearer and easier to interpret. If the results of the two alternatives disagree, then we should use the soft docking models because this suggests side-chain conformation changes may be an important factor in the formation of the complex. In the case of the AOR-flavodoxin complex studied here, the results of hard docking agreed with those of soft docking − both approaches gave similar clusters of models among the highest ranking − so all results presented here are for hard docking. This agreement of the six different docking simulations, with different conditions and partners, shows the simulations to be reliable. Furthermore, in all cases there are structures with the configuration predicted by our hypothesis among the highest scoring models when ranked by the electrostatic interaction score.

The second stage of BiGGER is the ranking stage, in which the 5000 models are evaluated according to electrostatics, solvent exclusion, and surface complementarity and amino acid contacts. The global scoring function included in BiGGER is also designed for general applicability by combining these different factors to give a single score optimised to separate correct models from incorrect models over a broad range of complexes. This is the best option when no information is available regarding the interaction being studied. However, BiGGER also provides the hydrophobicity and electrostatic scores for those cases in which it is possible to estimate if the interaction is driven mainly by solvation effects or by electrostatics.[21,22] Since this was one such case, we chose to use the electrostatic score to rank the most likely models. Nevertheless, the global score also placed high scoring models in the same region (including the highest ranking model).

The choice of the electrostatic interaction score was dictated by experimental data on the ionic-strength dependency of the electron-transfer reaction between flavodoxin and AOR (both form *D. gigas*), and by the large charge of the partners, which suggested electrostatics to be the main driving force in this interaction. Furthermore, the docking simulations also suggested that the interaction between AOR and flavodoxin is strongly driven by electrostatics, since the electrostatic score value was high, with an estimated enthalpy for the electrostatic interaction of approximately 100 kcal mol$^{-1}$. This is an approximate value due to the fact that it is calculated from a simple Coulombic model and the docking models generated by BiGGER are not very precise as the translation search is in steps of 1 Å and the side-chain placement was not optimised for each model. However, these simplified calculations are the only practical

 © 2006 Wiley-VCH Verlag GmbH & Co. KGaA, Weinheim 

way of dealing with thousands of candidate models without excessive computational demands, and the results do not require precise energy estimates, as all six simulations were in agreement and the estimated energy contributed by electrostatics was one to two orders of magnitude greater than that for hydrophobicity. Overall, all the simulation results and experimental data agree that the interaction between these proteins is essentially due to electrostatics.

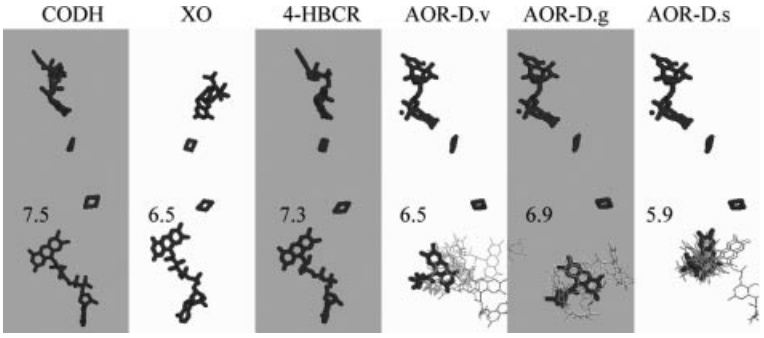


Figure 4. The relative positions of the FAD prosthetic groups for COD, XO, and 4-HBCR (first three panels) and the best models for the AOR-flavodoxin complex using the *D. vulgaris*, *D. gigas* and *D. salexigens* flavodoxins (last three panels). For the docking models the highest ranking configuration is shown in thick lines, and other high ranking configurations in thin lines. The numbers indicate the distances (in Å) between the cofactors. For the AOR-flavodixin complexes, the smallest distance of the fifteen highest ranking models is shown.

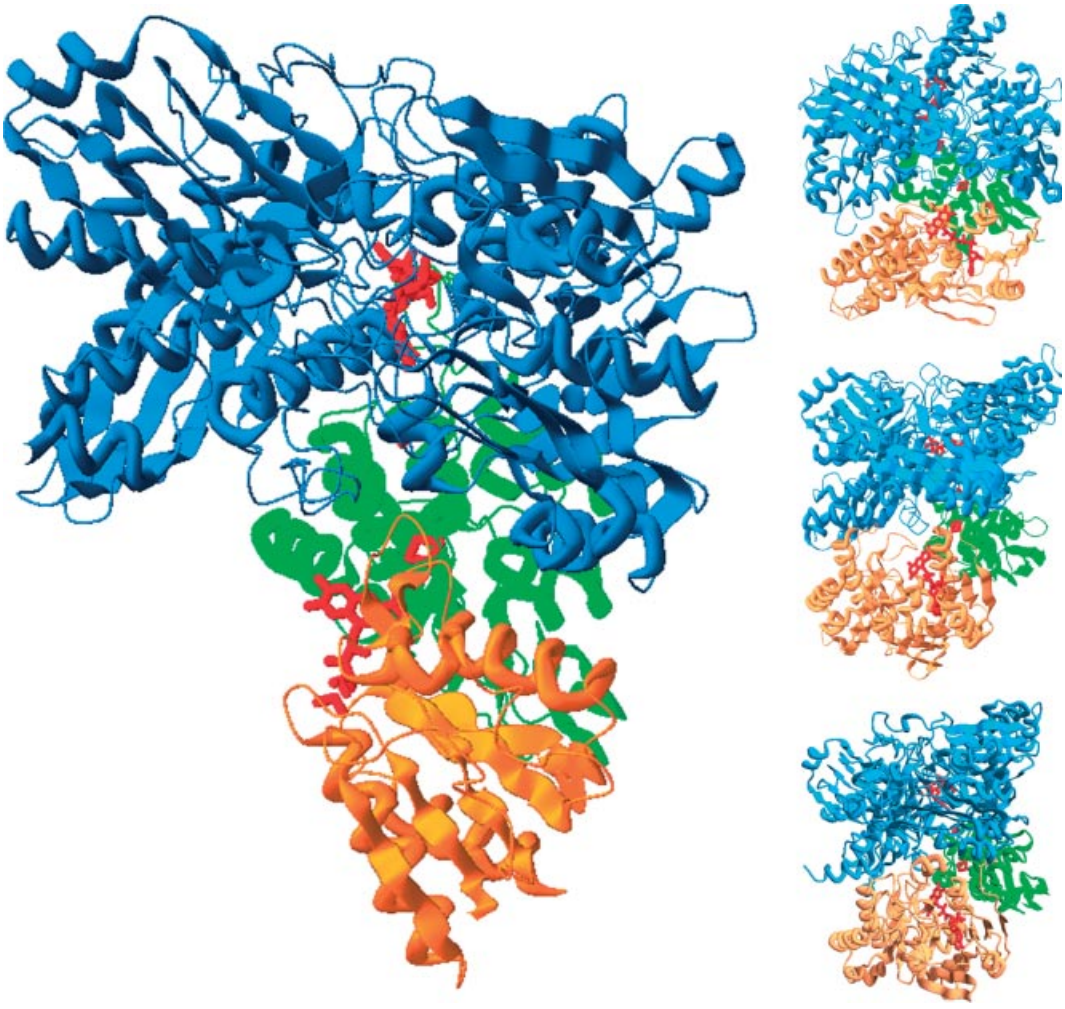

Figure 5. One possible docking configuration for *D. gigas* flavodoxin and AOR (left panel) compared with the structures of XO (top right), COD (centre right) and 4-HBCR (bottom right). The colours correspond to the sequence homology schemes shown in Figure 1, green for the FeS regions, orange for the FAD and flavodoxin, and blue for the MCD-Mo or MPT-Mo regions.

 © 2006 Wiley-VCH Verlag GmbH & Co. KGaA, Weinheim 

In short, all the docking results presented are for hard docking with electrostatic scoring. To model the complex between the flavodoxin and aldehyde oxidoreductase (AOR) from *Desulfovibrio gigas* we used the following structures:

– the X-ray structure for AOR (PDB code 1hlr, after correcting the transformation matrix to generate the dimer),[4,6]

– a homology model for the *D. gigas* flavodoxin using the Swiss-PROT sequence Q01095[24] and the structure from the *D. vulgaris* flavodoxin (PDB code 1fx1),[25]

– a homology model for the *D. salexigens* flavodoxin based on the *D. vulgaris* flavodoxin structure 1fx1,

– the *D. vulgaris* flavodoxin structure 1fx1.

Our goal was to model the *D. gigas* complex, although flavodoxins from *D. vulgaris* and *D. salexigens* also form productive complexes in vitro (unpublished data). Since the structure for the *D. gigas* flavodoxin was a model generated by homology, the other two − one a crystallographic structure and the other also a homology model − could be used to check the consistency of the results and verify that the *D. gigas* flavodoxin model was appropriate for our purposes. This was indeed the case, with the docking results for *D. salexigens* and *D. vulgaris* flavodoxin complexes being virtually identical to those obtained for the *D. gigas* flavodoxin.

We cannot give one unique model for the MOP-flavodoxin complex, and the interaction is most likely dynamic and cannot be represented by a single structure. However, these results indicate that flavodoxin interacts by docking near the exposed Fe–S cluster in a configuration resembling the structures of Xanthine oxidase (Figures 4 and 5). The distances between the FAD and [2Fe-2S] groups are similar in all three cases, with the shortest distance in the fifteen highest ranking models ranging between 6 and 7 Å, values similar to those of CODH, XO and 4-HBCR. Although not evident from the figure, in the models with the shortest distances among the highest ranking the dimethylbenzene part of the isoalloxazine ring is pointing towards the [2Fe-2S] centre in a manner analogous to CODH, XO and 4-HBCR. Despite this structural similarity, the contact surface of the flavodoxin in the AOR-flavodoxin models is less than half the contact surface of the FAD domain in XO. The contact surface area for flavodoxin, calculated with the DSSP program,[26] was no higher than 930 Å$^2$ (value for the model with largest surface contact among the highest ranking models), whereas the contact surface for the corresponding domain in XO is 2250 Å$^2$. This may explain why the XO complex is stable while AOR-flavodoxin is a transient complex.

## Conclusions

AOR was previously shown to be part of an electron-transfer chain comprising four different soluble proteins from *D. gigas*, namely:

AOR → flavodoxin → Cyt $c_3$ (4 hemes) → (NiFe) Hydrogenase

comprising a total of 11 discrete redox centres, which is capable of linking the oxidation of aldehydes to the reduction of protons to hydrogen and involves a flavodoxin-FMN semiquinone state.[22] The intramolecular electron-transfer process within AOR will follow, in the presence of substrate, the electron flow from Mo to the proximal [2Fe-2S] centre and then to the distal [2Fe-2S] centre and the redox partner, modelled here as flavodoxin.

Molybdenum hydroxylases (XO family) are a remarkable example of how biology finds a wide range of structural solutions to build up a required electron-transfer array of redox centres. Different arrangements of the building blocks (protein chains and domains) give rise to similar 3D placements of the redox cofactors participating in this optimised ET reaction. The docking results for the AOR-flavodoxin complex support the hypothesis of structural and functional equivalence to the active-site arrangements found in CODH and XO, and the smaller contact surface suggests an explanation for the AOR-flavodoxin complex being less stable than the otherwise similar XO.

This modular construction of complex enzymes by rearrangement of sub-domains and sub-units is a general observation. Superoxide reductases are also a good example,[27,28] but not unique. Relatively exposed sub-domains with characteristic structures that are recognized in simple electron-transfer proteins are, in most cases, used as docking sites for electron-transfer partners (i.e. ferredoxin folding in hydrogenase,[29] plant-type ferredoxin folding in AOR (see ref.[4] and this work) and Fd-NADPH reductase[30]).

A more complex situation was found for the structural homologue 4-HBCR,[12] which contains an additional iron-sulfur centre, whereby a low-potential ferredoxin serves as in vivo electron donor for the enzyme.[11,16] The redox potentials of the FAD$^{\cdot}$/FADH and $Mo^{V/IV}$ transitions are exceptionally low, thus making 4-HBCR the only member of the XO family whose function is to catalyze the reduction of the substrate and suggesting an inverted electron flow. But, even so, a conserved architecture is also maintained for the three key redox sites (Mo, 2 [2Fe-2S] centres and FAD).

## Acknowledgments

This work was supported by FCT-MCTES and COST D21-WG006.

[1] R. Hille, *Chem. Rev.* **1996**, *96*, 2757.
[2] C. D. Brondino, M. J. Romão, I. Moura, J. J. G. Moura, *Curr. Opin. Biol. Chem*. **2006**, in press.
[3] M. K. Johnson, D. C. Rees, M. W. Adams, *Chem. Rev.* **1996**, *96*, 2817.
[4] M. J. Romão, M. Archer, J. J. G. Moura, I. Moura, J. LeGall, R. Engh, M. Schneider, P. Hof, R. O. Duarte, R. Huber, *Science* **1995**, *270*, 1170.
[5] R. Huber, P. Hof, R. O. Duarte, J. J. G. Moura, I. Moura, M.-Y. Liu, J. LeGall, R. Hille, M. Archer, M. J. Romão, *Proc. Natl. Acad. Sci. USA* **1996**, *93*, 8846.
[6] J. M. Rebelo, J. M. Dias, R. Huber, J. J. G. Moura, M. J. Romão, *J. Biol. Inorg. Chem.* **2001**, *6*, 791.

 © 2006 Wiley-VCH Verlag GmbH & Co. KGaA, Weinheim 

[7] C. Enroth, B. T. Eger, K. Okamoto, T. Nishino, T. Nishino, E. F. Pai, *Proc. Natl. Acad. Sci. USA* **2000**, *97*, 10723.
[8] J. J. Truglio, K. Theis, S. Leimkühler, R. Rappa, K. V. Rajagopalan, C. Kisker, *Structure* **2002**, *10*, 115.
[9] H. Dobbek, L. Gremer, O. Meyer, R. Huber, *Proc. Natl. Acad. Sci. USA* **1999**, *96*, 8884.
[10] H. Dobbek, L. Gremer, L. Kiefersauer, R. Huber, O. Meyer, *Proc. Natl. Acad. Sci. USA* **1999**, *99*, 15971.
[11] K. Breese, G. Fuchs, *Eur. J. Biochem.* **1998**, *251*, 916.
[12] M. Unciuleac, E. Warkentin, C. C. Page, M. Boll, U. Ermler, *Structure* **2004**, *56*, 2249.
[13] R. Hille, *Arch. Biochem. Biophys.* **2005**, *433*, 107; R. Hille, *Eur. J. Inorg. Chem.* **2006**, 1913.
[14] K. Okamoto, K. Matsumoto, R. Hille, B. T. Eger, E. F. Pai, T. Nishino, *Proc. Natl. Acad. Sci. USA* **2004**, *101*, 793.
[15] J. Gibson, M. Dispensa, C. S. Harwood, *J. Bacteriol.* **1997**, *179*, 634.
[16] M. Boll, G. Fuchs, C. Meier, A. Trautwein, A. El Kasmi, S. W. Ragsdale, G. Buchanan, D. J. Lowe, *J. Biol. Chem.* **2001**, *276*, 47853.
[17] R. Brackmann, G. Fuchs, *Eur. J. Biochem.* **1993**, *213*, 563.
[18] J. J. G. Moura, A. V. Xavier, M. Bruschi, J. Le Gall, D. O. Hall, R. Cammack, *Biochem. Biophys. Res. Commun.* **1976**, *72*, 782.
[19] N. Turner, B. Barata, R. C. Bray, J. Deistung, J. LeGall, J. J. G. Moura, *Biochem. J.* **1987**, *243*, 755.
[20] B. A. Barata, J. LeGall, J. J. G. Moura, *Biochemistry* **1993**, *32*, 11559.
[21] P. N. Palma, L. Krippahl, J. E. Wampler, J. J. G. Moura, *Proteins: Struct., Function, Genetics* **2000**, *39*, 372.
[22] L. Krippahl, J. J. G. Moura, P. N. Palma, *Proteins: Struct., Funct., Genet.* **2003**, *52*, 19.
[23] I. Klapper, R. Hagstrom, R. Fine, K. Sharp, B. Honig, *Proteins* **1986**, *1*, 47.
[24] L. R. Helms, R. P. Swenson, *Biochim. Biophys. Acta* **1992**, *1131*, 325.
[25] K. D. Watenpaugh, L. C. Sieker, L. H. Jensen, J. Legall, M. Dubourdieu, *Proc. Natl. Acad. Sci. USA* **1972**, *69*, 3185.
[26] W. Kabsch, C. Sander, *Biopolymers* **1983**, *22*, 2577.
[27] C. Ascenso, F. Rusnak, I. Cabrito, M. J. Lima, S. Naylor, I. Moura, J. J. G. Moura, *J. Biol. Inorg. Chem.* **2000**, *5*, 720.
[28] T. Santos-Silva, J. Trincao, A. L. Carvalho, C. Bonifacio, F. Auchere, I. Moura, J. J. G. Moura, M. J. Romão, *Acta Crystallogr., Sect. F* **2005**, *61*, 967.
[29] X. Morelli, M. Czjzek, C. E. Hatchikian, O. Bornet, J. C. Fontecilla, P. N. Palma, J. J. G. Moura, F. Gurelesquin, *J. Biol. Chem.* **2000**, *275*, 23204.
[30] P. N. Palma, B. Lagoute, L. Krippahl, J. J. G. Moura, F. Guerlesquin, *FEBS Lett.* **2005**, *579*, 4585.

Received: May 7, 2006
Published Online: July 31, 2006

 © 2006 Wiley-VCH Verlag GmbH & Co. KGaA, Weinheim 

DOI: 10.1002/ejic.200600488

# Identification of the Dinuclear and Tetranuclear Air-Oxidized Products Derived from Labile Phenolate-Bridged Dimanganese(II) Pyridyl-Chelate Compounds

**Frank Bartnik Larsen,[a] Astrid Boisen,[a] Kevin J. Berry,[b] Boujemaa Moubaraki,[c] Keith S. Murray,[c] Vickie McKee,[d] Robert C. Scarrow,[e] and Christine J. McKenzie*[a]**

**Keywords:** Manganese / O ligands / Chelates / Bond valence sum analysis / Oxidation

Dioxygen-sensitive dinuclear manganese complexes of the phenoxo-hinged dinucleating ligand 2,6-bis{[*N*,*N*′-bis(2-picolyl)amino]methyl}-4-*tert*-butylphenolato (bpbp$^-$) containing exogenous labile THF, water and perchlorato ligands are described. The manganese(II) complexes $[Mn_2(bpbp)(ClO_4)_2(THF)]^+$ (**1**) and $[Mn_2(bpbp)(ClO_4)(H_2O)_2]^{2+}$ (**2**) have been isolated as the salts **1**·$ClO_4$·THF·$3H_2O$, **1**·$B(C_6H_5)_4$·4THF and **2**·$(ClO_4)_2$·$H_2O$. Complexes **1** and **2** are spontaneously oxidised in air in solution and the solid state. The reaction products of the air oxidation in THF, water and methanol solutions are labile dinuclear $Mn^{II}$–$Mn^{III}$, $Mn^{III}_2$ and $Mn^{III}$–$Mn^{IV}$ complexes containing water- and methanol-derived exogenous ligands. In addition, a $Mn_4$ complex has been isolated. Magnetic susceptibility data confirm the $Mn^{II}$–$Mn^{III}$ oxidation state assignment with an $S = 2/S = 5/2$ model with weak antiferromagnetic coupling ($J = -3.7$ cm$^{-1}$) in $[Mn_2(bpbp)(CH_3O)_2(H_2O)_2](ClO_4)_2$ [**3**·$(ClO_4)_2$]. A tetranuclear complex, $[Mn_4(O)_{4-n}(OH)_n(bpbp)_2](ClO_4)_4$ [$n$ = 1 or 2; **7**·$(ClO_4)_4$], recovered from THF shows a $Mn_4O_6$ adamantane-type core with the O bridges furnished by the two phenolato groups and four hydroxide/oxide bridges. We have arrived at two feasible formulations for the core metal oxidation states and oxo-bridge protonation states, namely $[Mn^{III}_4(O)_2(OH)_2(bpbp)_2]^{4+}$ and $[Mn^{III}_3Mn^{IV}(O)_3(OH)(bpbp)_2]^{4+}$, for **7**, on the basis of a bond valence sum analysis of the crystal structure, elemental analysis and XANES. Thus, complex **7** is at least two oxidation state levels lower than known complexes with the $Mn_4O_6$ adamantane core structure. The magnetism of **7** was fitted well to an $Mn^{III}_4$ three-*J* model. Complex cations related to **3** by homology, and to **7** by hydration/solvation, have been identified by ESI mass spectrometry. The $[Mn_2(bpbp)(OH)_2(H_2O)_2]^{2+}$ ion (**4**) present in aqueous solutions on dissolution of **1**·$ClO_4$·THF·$3H_2O$ in air or by simple dissolution of **3** in water-containing solvent is isoelectronic to **3**. In the presence of significant amounts of water the $Mn^{II}$–$Mn^{III}$ complexes **3** and **4** are susceptible to further metal oxidation and concomitant aquo ligand deprotonation to give ions assignable to $[Mn^{III/IV}_2(bpbp)O(OCH_3)_2(H_2O)]^{2+}$ (**5**) and $[Mn^{III}_2(bpbp)(OH)_3(H_2O)]^{2+}$ (**6**). ESI mass spectra of water or methanol solutions of **1**, **2**, **3** and **7** show predominantly an ion assignable to the oxide $[Mn_2(bpbp)(O)]^{2+}$ (**8**). Cation **8** is most likely not present in solution. Using mild source conditions and MS-MS techniques, the gas-phase fragmentation pathways to generate **8** have been mapped.
(© Wiley-VCH Verlag GmbH & Co. KGaA, 69451 Weinheim, Germany, 2006)

## Introduction

Dinuclear manganese compounds are of considerable interest due to their potential as catalysts for oxidation reactions in which hydrogen peroxide or, better, dioxygen are used as the terminal oxidant.[1] We have discovered that a dimanganese complex of the dinucleating ligand 2,6-bis{[*N*,*N*′-bis(2-picolyl)amino]methyl}-4-*tert*-butylphenolato (bpbp$^-$) (Scheme 1) promotes an $O_2$-dependent oxidative cleavage of ketones.[2] The product carboxylates from this reaction are trapped as bridging ligands in isolated $Mn^{II}$–$Mn^{III}$ complexes. For reactions in acetone this results in a mixture of three formate/actetate-bridged $Mn^{II}$–$Mn^{III}$ complexes $[Mn_2(bpbp)(RCO_2)(R'CO_2)](ClO_4)_2$ (R = R′ = H, R = H R′ = $CH_3$ and R = R′ = $CH_3$). $^{13}$C-Labelling experiments show that the one- and two-carbon fragments of the formate and acetate bridges, respectively, are derived from acetone. The putative reactive oxidizing species derived from the combination of the $[Mn_2(bpbp)]^{n+}$ core and dioxygen has not yet been identified for this system and the present study represents a further attempt to elucidate the oxygenation reaction mechanism. Here we report several species based on the $[Mn_2(bpbp)]^{n+}$ core containing water-,

[a] Department of Physics and Chemistry, University of Southern Denmark,
Odense Campus, 5230 Odense M, Denmark
Fax: +45-6615-8780
E-mail: chk@chem.sdu.dk
[b] Westernport Secondary College,
Hastings, Victoria 3915, Australia
[c] School of Chemistry, Building 23, Monash University,
Clayton, Victoria 3800, Australia
[d] Chemistry Department, Loughborough University,
Loughborough, UK
[e] Department of Chemistry, Haverford College,
370 Lancaster Ave., Haverford, PA 19041-1392, USA
Supporting information for this article is available on the WWW under http://www.eurjic.org or from the author.

 © 2006 Wiley-VCH Verlag GmbH & Co. KGaA, Weinheim 

methanol- and THF-derived ligands in the presence and absence of $O_2$.

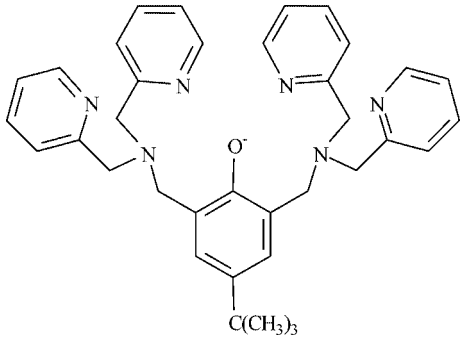

Scheme 1. 2,6-Bis{[*N*,*N*′-bis(2-picolyl)amino]methyl}-4-*tert*-butylphenolato ($bpbp^-$).

## Results and Discussion

### Air-Sensitive $Mn^{II}_2$ Complexes

The reaction of manganese(II) perchlorate with bpbpH in THF under an inert atmosphere gives a white compound formulated as $[Mn_2(bpbp)(ClO_4)_2(THF)](ClO_4)\cdot THF\cdot 3H_2O$ (**1**·$ClO_4$·THF·$3H_2O$). The cation was structurally characterised as its tetraphenylborate salt, $[Mn_2(bpbp)(ClO_4)_2(THF)][B(C_6H_5)_4]\cdot 4THF$ [**1**·$B(C_6H_5)_4$·4THF], which was obtained by recrystallisation of **1**·$ClO_4$·THF·$3H_2O$ in THF under $N_2$ in the presence of sodium tetraphenylborate. Recrystallisation of **1**·$ClO_4$·THF·$3H_2O$ in the noncoordinating solvent dichloromethane under $N_2$ resulted in replacement of the THF and terminal perchlorate ligands with adventitious water to give the complex $[Mn_2(bpbp)(ClO_4)(H_2O)_2](ClO_4)_2\cdot H_2O$ [**2**·$(ClO_4)_2$·$H_2O$].[2] The core structures of the $Mn^{II}_2$ complexes **1** and **2** are depicted in in Scheme 2 and the X-ray structures of cations **1** and **2** in Figure 1. Important bond lengths and angles are listed in Table 1. The metal coordination environments for each of the manganese ions in **1** and **2** are geometrically different. In the case of **1** this is further accentuated by the fact that the donor set on each metal ion is different. One of the tridentate 2,6-bis{[*N*,*N*′-bis(2-picolyl)amino]methyl} arms is coordinated in a facial mode while the other shows a meridional coordination geometry in both structures. The asymmetrical coordination of the bridging perchlorate is most pronounced in **2** [Mn1–O1 = 2.651(3) and Mn2–O2 = 2.334(2) Å] with a bond-length difference significantly larger than for **1** [Mn1–O7 = 2.185(18) and Mn2–O8 = 2.296(16) Å]. According to the Cambridge Crystallographic database,[3] these structures are the first reports of dimanganese complexes with a $\mu_2$-perchlorato-*O*,*O*′ bridge. Only one other example exists where a perchlorate bridges two

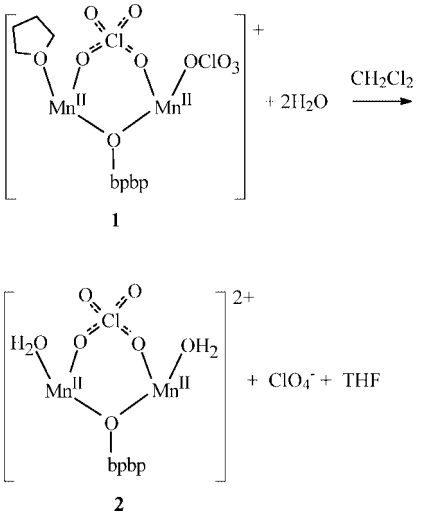

Scheme 2. Ligand-substitution reaction and core structure of the $Mn^{II}_2$ complexes **1** and **2**. For simplicity only the hinging donor O atom of the dinucleating ligand is shown. Not depicted are the three remaining N donors to each Mn ion from the heptadentate ligand.

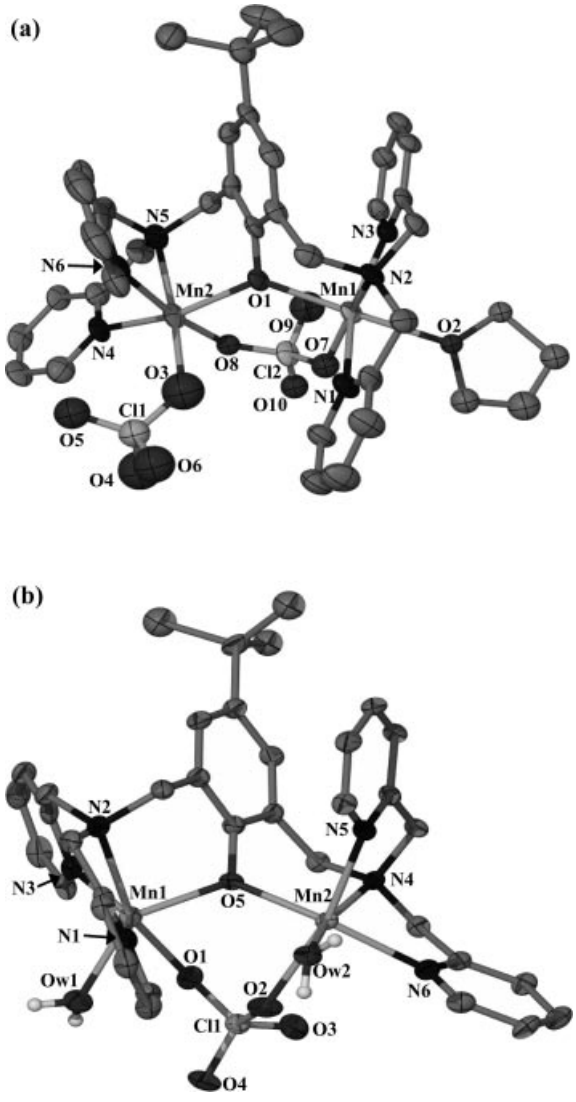

Figure 1. The X-ray crystal structures of the cations in **1** (a) and **2** (b). H atoms, except on the coordinated water molecules, have been omitted. The perchlorate counteranions and the THF molecules in **1** are modelled as disordered over two positions; only one orientation is shown.

 © 2006 Wiley-VCH Verlag GmbH & Co. KGaA, Weinheim 

Table 1. Selected bond lengths [Å] and angles [°] for **1** and **2**.

| | **1** | | **2** |
|---|---|---|---|
| Mn1–O1 | 2.135(5) | Mn1–O5 | 2.104(2) |
| Mn1–O2[a] | 2.284(16) | Mn1–Ow1 | 2.156(3) |
| Mn1–O7[a] | 2.185(18) | Mn1–O1 | 2.651(3) |
| Mn1–N1 | 2.212(7) | Mn1–N1 | 2.183(3) |
| Mn1–N2 | 2.259(6) | Mn1–N2 | 2.351(3) |
| Mn1–N3 | 2.204(6) | Mn1–N3 | 2.186(3) |
| Mn2–O1 | 2.130(5) | Mn2–O5 | 2.113(2) |
| Mn2–O3 | 2.213(16), 2.056(15) | Mn2–Ow2 | 2.123(3) |
| Mn2–O8[a] | 2.296(16) | Mn2–O2 | 2.334(2) |
| Mn2–N4 | 2.271(6) | Mn2–N6 | 2.239(3) |
| Mn2–N5 | 2.287(7) | Mn2–N4 | 2.295(3) |
| Mn2–N6 | 2.224(8) | Mn2–N5 | 2.248(3) |
| Mn1···Mn2 | 3.8620(17) | Mn1···Mn2 | 3.8044(7) |
| Mn1–O1–Mn2 | 129.8(3) | Mn1–O5–Mn2 | 128.91(10) |

[a] Bond lengths for the disordered bridging perchlorate and THF molecule in **1** are given as an average whenever the Mn–O bond lengths were not significantly different (bond difference less than $3\cdot\sqrt{[(\sigma_1)^2 + (\sigma_2)^2]}$).

manganese atoms, but in this case the perchlorate acts as a one-atom bridge ($\mu_2$-perchlorato-*O*,*O*).[4]

## Air Oxidation of the $Mn^{II}_2$ Complexes

Solutions of complexes **1** and **2** in water, methanol, acetone and THF darken within minutes on exposure to air. In acetone, this occurs with concomitant acetone oxidation.[2] The species we have now identified when air oxidation of **1** is carried out in water, methanol or THF are summarised in Scheme 3. The dinuclear, mixed-valence $Mn^{II}$–$Mn^{III}$ complex $[Mn_2(bpbp)(CH_3O)_2(H_2O)_2](ClO_4)_2$ [**3**·$(ClO_4)_2$] and the tetranuclear complex $[Mn_4(O)_{4-n}(OH)_n(bpbp)_2](ClO_4)_4$ ($n$ = 1 or 2) [**7**·$(ClO_4)_4$], were isolated from methanol and THF, respectively, as their perchlorate salts. Exposure of the salts of **1** and **2** as solid compounds to air results in them turning brown within hours. We have not determined the nature of this solid-state reaction.

## The Solid-State Characterisation

### *X-ray Structures*

The dark-green crystals obtained from the air oxidation of **1** in methanol are the mixed-valence $Mn^{II}$–$Mn^{III}$ complex **3**·$(ClO_4)_2$ (Figure 2). This complex is identical to the product of the methanol reaction of manganese perchlorate with bpbpH in air without isolating an intermediate $Mn^{II}$–$Mn^{II}$ complex.[5] The two exogenous H-bonded methoxo-aquo "bridging groups" span the metal ions. The complex is unsymmetrical and the valence trapping unambiguous: the two methoxide ligands are coordinated to the $Mn^{III}$ ion with an average $Mn^{III}$–O distance of 1.876 Å, while the two $Mn^{II}$–$OH_2$ distances are an average of 0.279 Å longer.

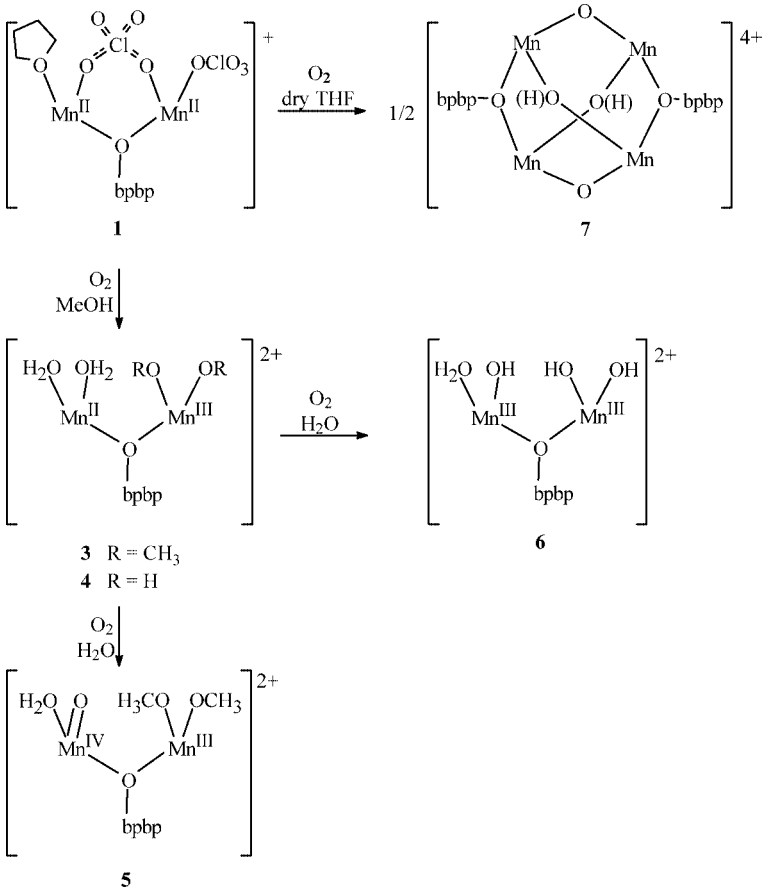


Scheme 3. The core structures of the starting compound **1** and the complexes isolated or identified by ESI MS.

 © 2006 Wiley-VCH Verlag GmbH & Co. KGaA, Weinheim 

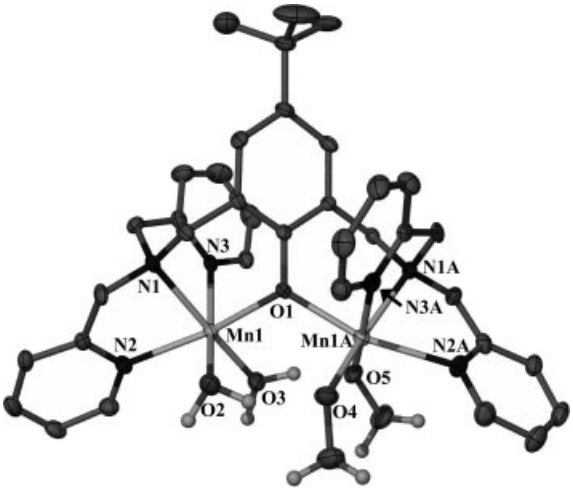


Figure 2. The X-ray crystal structure of the cation in **3**.

Solutions of **1** in THF turn dark in minutes and deposit brown-black solids in good yields over some hours. Addition of *tert*-butylhydrogen peroxide to the reaction results in an instant colour change and precipitation of a dark solid. The products isolated by these two synthetic routes give identical elemental analyses consistent with two $ClO_4^-$ ions per $[Mn_2(bpbp)]^{n+}$ unit. These products look to be amorphous and give no detectable powder XRD pattern. However, on one occasion crystals were obtained by the complete evaporation of the THF from a very dilute solution in a flask with a large surface area at the base. We have not been successful in growing better crystals under a variety of more appropriate conditions. The structure of these small ($0.20 \times 0.10 \times 0.02$ mm), weakly diffracting brown crystals was determined by synchrotron X-ray crystallography to be a tetranuclear, adamantane-type manganese complex [**7**·$(ClO_4)_4$; Figure 3]. The data are of low quality, although the core topology is clear. Bond lengths and angles are listed in Table 2. A definitive oxidation-state assignment cannot be made from the X-ray structure alone since the poor data quality precludes conclusive determination of the protonation state of the cation. The charge of the cation (4+) is without doubt, however, and the overall oxidation state can therefore in theory range from $Mn^{III}_2Mn^{IV}_2$ (only oxide bridges) down to $Mn^{II}_2Mn^{III}_2$ (only hydroxide bridges); lower oxidation-state assignments would require $H_2O$ as bridging ligand or protonation of the bridging phenolate, both of which are unfeasible.

We eliminated the lower oxidation-state formulations $[Mn^{II}Mn^{III}_3(O)(OH)_3(bpbp)_2]^{4+}$ and $[Mn^{II}_2Mn^{III}_2(OH)_4(bpbp)_2]^{4+}$ on the basis of a comparison of metric parameters with known compounds (see below). This leaves three possible assignments depending on the number of hydroxide bridges, namely $[Mn^{III}_4(O)_2(OH)_2(bpbp)_2]^{4+}$, $[Mn^{III}_3Mn^{IV}(O)_3(OH)(bpbp)_2]^{4+}$ and $[Mn^{III}_2Mn^{IV}_2(O)_4(bpbp)_2]^{4+}$. Notably, the structure of complex **7** is very similar to its $Fe^{III}_4$ counterpart $[(bpbp)_2Fe^{III}_4(\mu\text{-}O)_2(\mu\text{-}OH)_2](ClO_4)_4$,[6] thus implying that an isostructural **7** might also contain two hydroxide bridges and hence the same metal oxidation state, i.e. $Mn^{III}_4$. Both complexes have identical metal–$O_{phenoxo}$ distances [Fe–$O_{phenoxo}$ = 2.092(4), Mn–$O_{phenoxo}$ = 2.095(7) Å], although the average Fe–$O_{oxo/hydroxo}$ distance [1.893(5) Å] is slightly longer than

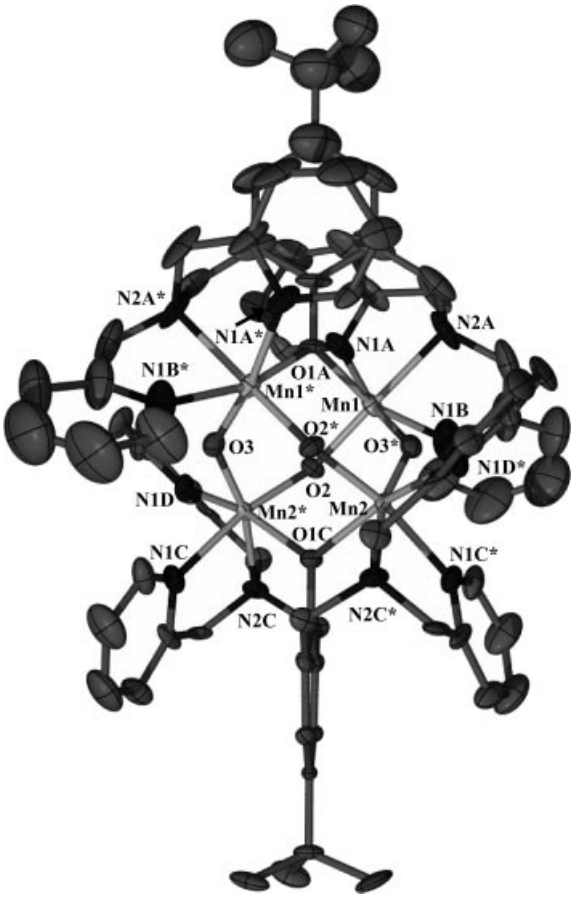


Figure 3. The X-ray crystal structure of the cation in **7**.

Table 2. Selected bond lengths [Å] and angles [°] for **7**. Symmetry transformations used to generate equivalent atoms as indicated by *: $-x$, $y$, $1/2 - z$.

| | | | |
|---|---|---|---|
| Mn1–Mn2* | 3.404(3) | Mn1–Mn1* | 3.664(5) |
| Mn1–Mn2 | 3.429(3) | Mn2–Mn2* | 3.648(4) |
| Mn1–O2 | 1.848(10) | Mn2–O3 | 1.818(11) |
| Mn1–O3* | 1.852(11) | Mn2–O2 | 1.864(11) |
| Mn1–O1A | 2.089(6) | Mn2–O1C | 2.100(7) |
| Mn1–N1A | 2.105(14) | Mn2–N1C | 2.119(14) |
| Mn1–N2A | 2.153(14) | Mn2–N2C | 2.149(14) |
| Mn1–N1B | 2.174(16) | Mn2–N1D | 2.215(12) |
| Mn1*–O1A–Mn1 | 122.6(6) | Mn1–O2–Mn2 | 135.0(6) |
| Mn2*–O1C–Mn2 | 120.6(6) | Mn2–O3–Mn1* | 136.1(6) |
| O2–Mn1–O3* | 98.1(5) | O3–Mn2–O2 | 99.3(5) |
| O2–Mn1–O1A | 99.1(4) | O3–Mn2–O1C | 100.0(4) |
| O3*–Mn1–O1A | 90.8(4) | O2–Mn2–O1C | 90.7(4) |
| O2–Mn1–N1A | 92.4(5) | O3–Mn2–N1C | 91.5(6) |
| O1A–Mn1–N1A | 85.5(5) | O1C–Mn2–N1C | 84.0(4) |
| O3*–Mn1–N2A | 90.7(6) | O2–Mn2–N2C | 90.9(5) |
| O1A–Mn1–N2A | 88.9(6) | O1C–Mn2–N2C | 89.0(4) |
| N1A–Mn1–N2A | 79.3(6) | N1C–Mn2–N2C | 79.1(6) |
| O2–Mn1–N1B | 96.7(6) | O3–Mn2–N1D | 96.0(5) |
| O3*–Mn1–N1B | 90.4(6) | O2–Mn2–N1D | 89.7(5) |
| N1A–Mn1–N1B | 90.4(7) | N1C–Mn2–N1D | 92.6(5) |
| N2A–Mn1–N1B | 74.9(7) | N2C–Mn2–N1D | 74.8(5) |

 © 2006 Wiley-VCH Verlag GmbH & Co. KGaA, Weinheim 

the equivalent distance in **7** [Mn–$O_{oxo/hydroxo}$ = 1.846(11) Å].

Jahn–Teller distortions are commonly observed in pseudo-octahedral high-spin $Mn^{III}$ ($d^4$) complexes; these distortions usually take the form of axial elongations or compressions. In the case of the manganese in complex **7**, the principal distortion is caused by the shorter bond lengths on one octahedral face due to the anionic oxygen-based ligands. In addition, there is an axial elongation in that the longest Mn–O bond is *trans* to the longest Mn–N bond. These effects are, however, too subtle to be used for oxidation,state assignment.

The majority of $Mn_4$ adamantane-type complexes with which **7** can be compared have been prepared using neutral tridentate capping ligands [e.g. 1,4,7-triazacyclononane, tris-(aminomethyl)ethane or *N*,*N*-bis(2-pyridylmethyl)ethylamine] and the oxygen atom bridging groups are all non-protonated oxides rather than hydroxides.[7,8] The strength of the $Mn^{IV}$–oxo bond typically yields robust adamantane $Mn^{IV}_4O_6$ cores with more or less unambiguous spectroscopic signatures. Two singly protonated[7d] complexes and two one-electron-reduced[7e,8] complexes derived from the $Mn^{IV}_4O_6$ core have been structurally characterised. Ligand-exchange reactions have furthermore yielded neutral bis-ligand complexes containing two *N*,*N*-bis(2-pyridylmethyl)-ethylamine ligands and two *N*-substituted iminodiacetate ligands.[7f] Typical geometrical parameters for these complexes are $Mn^{IV}$–O ≈ 1.80, $Mn^{IV}$–OH ≈ 1.95, $Mn^{III}$–O ≈ 1.83 Å and Mn–O–Mn ≈ 128–130°. Only small differences in the Mn–O bond length arise from reduction of $Mn^{IV}$ to $Mn^{III}$, while protonation induces significant changes. Only one other $Mn_4$ complex with an adamantane core incorporating bridging alkoxides/phenoxides as in **7** is known.[8] Armstrong and co-workers have shown that the mixed-valence complex $[(tphpn)_2Mn^{III}Mn^{IV}{}_3(\mu\text{-}O)_4](OTf)_2(ClO_4)_3$ [Htphpn = *N*,*N*,*N*′,*N*′-tetrakis(2-pyridylmethyl)-2-hydroxypropane-1,3-diamine] is formed by a core rearrangement induced by a one-electron oxidation of the $[\{(tphpn)Mn^{III}Mn^{IV}(\mu\text{-}O_2)\}_2]^{4+}$ dimer-of-dimers complex.[8] The complex contains four oxide and two alkoxide bridges and the average Mn–$O_{oxo}$ bond length is 1.805(8) Å, which corresponds well to a 3:1 mixture of $Mn^{IV}$ and $Mn^{III}$ with all oxide bridges. The analogous average Mn–$O_{oxo/hydroxo}$ bond length for **7** is 1.846(11) Å, which is slightly longer and therefore consistent with a lower average oxidation state in **7**.

### *Oxidation-State Assignment by Bond Valence Sum (BVS) Analysis*

To further assess the possible oxidation states of Mn in **7**, we employed Bond Valence Sum (BVS) analysis,[9] which uses all of the metal–ligand bond lengths to indicate the likely oxidation state. Each bond length is used to calculate a bond valence from the expression BV = exp[($r_0$ – $r_{MX}$)/0.37 Å], where $r_0$ depends on the identity of M and X. The traditional but cumbersome approach[9] to oxidation-state determination by BVS assumes that the $r_0$ values also depend on the oxidation state of M, and these $r_0$ values are selected so that, for complexes with unambiguous oxidation states, the BVS is approximately equal to the oxidation state. This approach requires a separate calculation for each possible oxidation state and is unsuited for mixed-valence complexes. An alternative, and simpler, approach[10] uses the BVS calculated with oxidation-state-independent $r_0$ but allows that it may deviate for some specific donors. For example, the parameters $r_0$(M–O) = 1.759, $r_0$(M–N) = 1.831 and $r_0$(M–S) = 2.151 Å can distinguish between complexes of high-spin iron(II) (BVS = 2.30 ± 0.14), high-spin iron(III) (BVS = 3.04 ± 0.12), and low-spin iron [BVS = 4.2 ± 0.3 for low-spin iron(II or III)].

Calculations of BVSs using data from mononuclear manganese complexes found in a search of the Cambridge Structural Database[3] indicate that the same $r_0$ parameters previously used for iron can be used to distinguish high-spin manganese oxidation states (Figure 4). The BVSs for mononuclear manganese complexes with oxidation states specified in the CSD name show a clear separation between manganese(II), (III) and (IV) complexes. About 5% of the "manganese(II)" complexes have BVSs greater than 2.5 (i.e. closer to values expected for $Mn^{III}$ or $Mn^{IV}$), but upon consulting the original literature these were found either to be misnamed in the CSD (NOTGUY, HOSTUE, WAQDEX, RULNER), oxidation-state ambiguous (SEVWOF), or likely intermediate-spin (HODTUP, MNPHCY02, TOGPEK) or low-spin (NTPOMN, NTPIPM10, LAHCUS, GOGBEJ, YEXWAZ, WEGQII, LIHBEJ) complexes. Excluding these from the manganese(II) data results in 279 complexes with BVS = 1.92 ± 0.17. Thus, we conclude that high-spin $Mn^{II}$, $Mn^{III}$ and $Mn^{IV}$ complexes have a BVS of approximately 1.9, 3.1 and 4.1 ± 0.2, respectively, when using the $r_0$ values previously used for iron complexes.

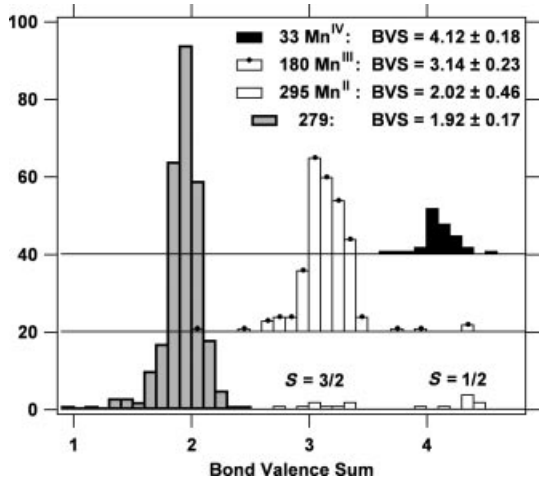


Figure 4. BVSs calculated from bond lengths in the Cambridge Structure Database (April 2001 release) for mononuclear manganese complexes (crystallographic $R < 0.10$) with only N, O and S coordination in which the oxidation state of the manganese (II, III or IV) is specified in the name field. BVS analyses in this paper use $r_0$ values of 1.759, 1.831 and 2.151 Å for Mn–O, Mn–N and Mn–S bonds, respectively.

 © 2006 Wiley-VCH Verlag GmbH & Co. KGaA, Weinheim 

Figure 5 shows that most binuclear manganese complexes in the CSD have BVSs that are within 0.2 of the average BVS expected from the assigned oxidation states. Most of the outliers shown in Figure 5 (those with CSD codes shown) can be explained as due to errors in oxidation state naming or differences in spin state, as explained in the figure caption.

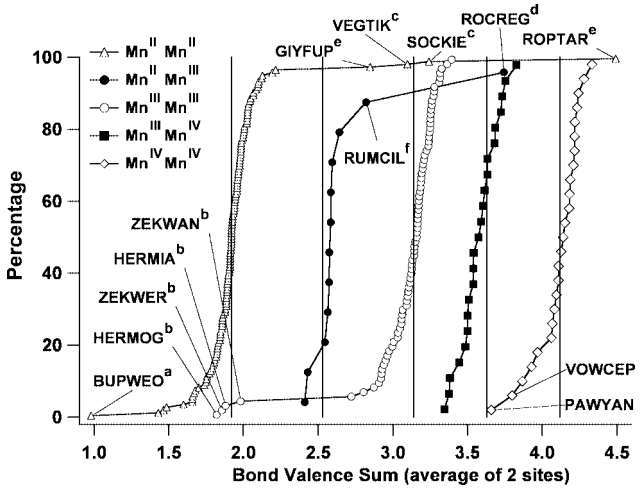


Figure 5. BVSs calculated for dinuclear manganese complexes where the oxidation states are specified by the name in the Cambridge Structure Database (April 2001 release) plotted vs. the percentile within each class. The five solid lines indicate, from left, the BVSs expected for (II,II), (II,III), (III,III), (III,IV) and (IV,IV) dinuclear complexes. CSD codes are indicated for structures with especially large deviations from the expected BVS. In most cases, the large deviations were explained upon inspection of the CSD record: (a) only 42% occupancy of manganese atoms; (b–d) misassigned oxidation states in name should be (b) $Mn^{II}Mn^{II}$, (c) $Mn^{III}Mn^{III}$ and (d) $Mn^{III}Mn^{IV}$; (e) probable low- or intermediate-spin $Mn^{III}$; ambiguous oxidation state due to presence of cobalt atom in cluster (assigned as $Co^{2+}$).

Using the same oxidation-state-independent $r_0$ values, the BVSs of the $Mn^{II}_2$ complexes **1**·$ClO_4$·THF·$3H_2O$ and **2**·$ClO_4$·$H_2O$ as well as the $Mn^{II}$–$Mn^{III}$ complex **3**·$(ClO_4)_2$ were calculated; they are listed in Table 3. There is excellent agreement with the values expected based on the data of Figures 4 and 5. From the BVSs of the individual Mn atoms of **3** it is clear that they are valence-trapped as a $Mn^{II}$ and $Mn^{III}$. The BVS of complex **7**·$(ClO_4)_4$, when compared to the values obtained by analysis of three X-ray structures of closely related $Mn^{III}Mn^{IV}_3$ and $Mn^{IV}_4$ adamantane core complexes, shows that **7** clearly has a much lower overall oxidation state. The average BVS (3.25) is equally consistent with a $Mn^{III}_4$ (expected $3.14 \pm 0.2$) or $Mn^{III}_3Mn^{IV}$ (expected $3.38 \pm 0.2$) core. The possibility of a $Mn^{III}_2Mn^{IV}_2$ dimer (expected BVS = $3.63 \pm 0.2$) is, however, much less likely.

### *Oxidation-State Assignment by XANES*

XANES of **1**·$ClO_4$·THF·$3H_2O$ and **7**·$(ClO_4)_4$ supports these oxidation-state assignments (see Figure 6). The edge energy, which we consider to be the energy at which the XANES spectrum intensity = 0.5, for **1**·$ClO_4$·THF·$3H_2O$ is almost identical to the energy recorded for $Mn^{II}(acac)_2$, thus confirming the oxidation-state assignment. The edge energy for **7**·$(ClO_4)_4$ is very close to that measured for $Mn^{III}(acac)_3$, thus indicating that the overall oxidation state of **7**·$(ClO_4)_4$ might be $Mn^{III}_4$. Furthermore, the edge energy is markedly lower than that found in the mixed-valent manganese(III,IV) complex $[tpa_2Mn_2O_2](ClO_4)_3$ [tpa = tris(2-pyridylmethyl)amine; lower by 1.5 eV] and the manganese(IV) complex $[(Me_3tacn)_2Mn_2O_3][PF_6]_2$ ($Me_3tacn$ = 1,4,7-trimethyl-1,4,7-triazacyclononane; lower by 3.0 eV). The large difference between the edge energy of **7**·$(ClO_4)_4$ and the mixed-valence tpa-manganese(III,IV) complex discounts a $Mn^{III}_2Mn^{IV}_2$ oxidation-state assignment for **7**·$(ClO_4)_4$. The difference in edge energy between a $Mn^{III}_3Mn^{IV}$ and a $Mn^{III}_4$ complex is, however, probably too small to be discerned by XANES, and these two oxidation-state assignments can therefore not be excluded for **7**·$(ClO_4)_4$.

Assignment of an oxidation state of $Mn^{III}_2Mn^{IV}_2$, and thus oxo bridges, for **7** has inherent problems due to its lack of solution stability, as indicated by the lack of Mn–O CT absorptions and $Mn_4$ ions in the ESI mass spectrum (see below). This contrasts with the data for the counterpart $Fe^{III}_4$ complex,[6] for which, for example, an ion assignable to the singly deprotonated species $[(bpbp)_2Fe^{III}_4(O)_3(\mu\text{-}OH)]^{3+}$ is easily observed. This is contradictory to the typical stability of oxo-bridged manganese complexes. The presence of hydroxo bridges, which typically are weaker than oxo bridges, can account for the instability of **7**·$(ClO_4)_4$ along with the fact that $Mn^{III}$–O bonds are believed to be more labile than $Mn^{IV}$–O bonds due to Jahn–Teller effects.[7e] Armstrong and co-workers have further shown that

Table 3. Values obtained for the oxidation state assignment from a BVS analysis of **1**, **2**, **3** and **7**.

| | BVS analysis for crystallographically unique Mn atoms | | | | Av. BVS | Oxidation state assignment | Theoretical av. BVS[a] |
|---|---|---|---|---|---|---|---|
| **1**·$ClO_4$·THF·$3H_2O$ | 1.84 | | 1.91 | | 1.87 | $Mn^{II}_2$ | $1.9 \pm 0.2$ |
| **2**·$ClO_4$·$H_2O$ | 1.96 | | 1.90 | | 1.93 | $Mn^{II}_2$ | $1.9 \pm 0.2$ |
| **3**·$(ClO_4)_2$[5] | 3.07 | | 2.02 | | 2.54 | $Mn^{II}Mn^{III}$ | $2.5 \pm 0.2$ |
| **7**·$(ClO_4)_4$ | 3.27 | | 3.24 | | 3.25 | $Mn^{III}_4$ | $3.1 \pm 0.2$ |
| | | | | | | ($Mn^{III}_3Mn^{IV}$) | ($3.4 \pm 0.2$) |
| $[Mn_4(\mu\text{-}O)_6(bpea)_4]^{4+}$ [7e] | 3.99 | 4.03 | 3.97 | 4.14 | 4.03 | $Mn^{IV}_4$ | $4.1 \pm 0.2$ |
| $[Mn_4(\mu\text{-}O)_6(bpea)_4]^{3+}$ [7e] | 4.01 | 4.05 | 3.66 | 3.89 | 3.90 | $Mn^{III}Mn^{IV}_3$ | $3.9 \pm 0.2$ |
| $[Mn_4(\mu\text{-}O)_4(tphpn)_4]^{5+}$ [8] | 4.06 | 3.80 | 4.13 | 3.69 | 3.92 | $Mn^{III}Mn^{IV}_3$ | $3.9 \pm 0.2$ |

[a] BVS values used: 1.9, 3.1 and $4.1 \pm 0.2$ for $Mn^{II}$, $Mn^{III}$ and $Mn^{IV}$ respectively. bpea = *N*′*N*-bis(2-pyridylmethyl)ethylamine; Htphpn = *N*,*N*,*N*′,*N*′-tetrakis(2-methylpyridyl)-2-hydroxypropanediamine. Bond lengths used for BVS analysis of **1**, **2** and **7** can be found in Tables 1 and 2; for structural data for the remaining complexes see the references given in brackets.

 © 2006 Wiley-VCH Verlag GmbH & Co. KGaA, Weinheim 

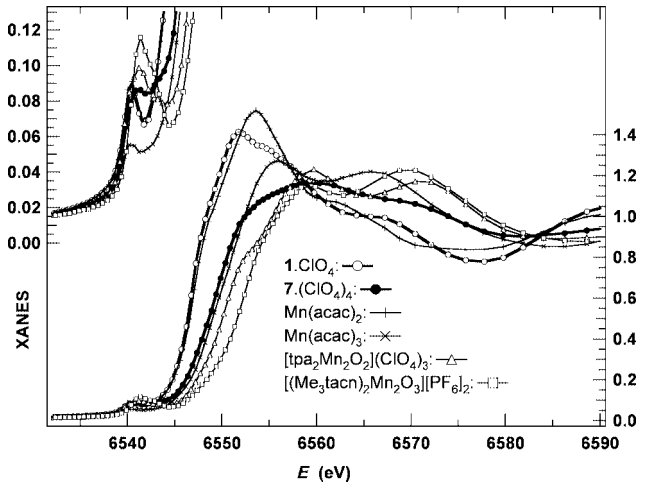


Figure 6. Comparison of Mn K-edge XANES spectra for **1**·$ClO_4$ and **7**·$(ClO_4)_4$ with those of $Mn^{II}$ and $Mn^{III}$ complexes of acetylacetonate (acac), a $Mn^{III}Mn^{IV}$ mixed-valence di-oxo-bridged complex of tris(2-pyridylmethyl)amine (tpa), and a $Mn^{IV}$ dimeric tri-oxo-bridged complex of 1,4,7-trimethyl-1,4,7-triazacyclononane ($Me_3tacn$).

the effective basicity of the oxo bridges in $[Mn_4O_6(bpea)_4]^{4+}$ increases by 17.5 orders of magnitude upon one-electron reduction.[7e] Thus, the presence of one or two hydroxo bridges in **7** is very feasible.

On the basis of the crystal structure (BVS analysis), elemental analysis and XANES of **7**·$(ClO_4)_4$, we therefore propose that the complex might be $[Mn_4(O)_{4-n}(OH)_n(bpbp)_2]^{4+}$ ($n$ = 1 or 2) and contain either three or four $Mn^{III}$ centres.

## The Structural Formulation of the Solution- and Gas-Phase Species Derived from Hydroxylic Solvents by Analysis of ESI Mass Spectra

Tractable products were not isolated after the air oxidation of **1** in water or in methanol containing significant amounts of water. Analyses of fragmentation pathways in ESI mass spectrometric studies of reaction solutions indicate that aqueous solutions contain the homologue of **3**, the $Mn^{II}$–$Mn^{III}$ $[Mn_2(bpbp)(OH)_2(H_2O)_2]^{2+}$ ion (**4**), and higher oxidation state $Mn^{III}_2$ and $Mn^{III/IV}_2$ solvent-derived species. The presence of methoxide vs. hydroxide most likely facilitates the isolation of **3**. Terminal methoxide ligands are more commonly characterised for $Mn^{III}$ and $Fe^{III}$ complexes than hydroxide ligands, presumably because proton-transfer interactions between the hydroxide ligand and solvent (non-coordinated) water are blocked. Mn compounds with terminal hydroxide ligands are usually characterised only when the hydroxide is found in cavities and other well-shielded environments.[11] A comparison of the ESI mass spectra of **3**·$(ClO_4)_2$ using both methanol and water as spray solvent is shown in Figure 7. Figure 7(a) and (e) show that similar spectra are obtained for **3**·$(ClO_4)_2$ in methanol and water, respectively, under standard source conditions. Through a series of Collision Activation Dissociation (CAD) experiments we were able to show that the ion at $m/z$ 348.8, which is observed as essentially the only species in both these mass spectra, can be assigned to the $Mn^{II}$–$Mn^{III}$ oxide $[Mn_2(bpbp)(O)]^{2+}$ (**8**). Cation **8** is, however, most likely *not* found solution. This ion corresponds to the loss of the mass equivalent of two water molecules and one dimethyl ether molecule from **3**, or the loss of the mass equivalent of three water molecules from **4**, to give **8**. The gas-phase fragmentation pathway to **8** could be mapped from spectra recorded using very mild source conditions [Figure 7(b) and (f)]. We assigned the higher oxidation state species $[Mn^{III}_2(bpbp)O(OH)_2]^{2+}$ ($m/z$ 357.2) and $[Mn^{III/IV}_2(bpbp)O(OH_2)(OCH_3)_2]^{2+}$ (**5**) ($m/z$ 388.7) to the ions generated from the water solutions under mild source conditions. Coordinated water ligands are retained by cations **3** and **4** in the spectra in Figure 7(b) and (f), which show also that methoxide ligands can be substituted by hydroxides. Assignments for the various ions are listed under the spectra. Only neutral species can be lost from cations in gas-phase CAD experiments: coordinated water loss is facile, and the mass equivalents of hydroxyl and methoxyl radicals and dimethyl ether can also be lost, ultimately to produce cation **8**. The pathways are delineated in the scheme under the spectra in Figure 7. We have previously noted the facile gas-phase formation of (sometimes novel) metal oxide ions from metal carbonates by loss of neutral $CO_2$.[12] The present cases showing mass losses equivalent to the neutral fragments $H_2O$, $CH_3OCH_3$, $HO^{\cdot}$ and $CH_3O^{\cdot}$ serve as another example.

## Magnetic Susceptibility

The magnetic susceptibility of **3**·$(ClO_4)_2$ was measured in the temperature range 4.2 to 300 K at an applied field of 1 T. The data are generally indicative of weak antiferromagnetic coupling occurring within $Mn^{II}/Mn^{III}$ pairs via the endogenous bridging phenolate group of $bpbp^-$. The strong H-bonding between the two aqua ligands of the $Mn^{II}$ and the two methoxide ligands of the $Mn^{III}$ may also contribute a superexchange pathway. Least-squares fitting of the susceptibility data to Heisenberg exchange models ($-2J\ S_1 \cdot S_2$) for $S$ = 5/2:4/2 pairs, assuming the $g$ values for $Mn^{II}$ and $Mn^{III}$, are the same and give the best fit parameters $g = 1.97 \pm 0.02$ and $J = -3.7 \pm 0.02\ cm^{-1}$. The experimental and calculated plots are shown in Figure 8. The $J$ value is similar to those found for other dinuclear $Mn^{II}$–$Mn^{III}$ μ-phenoxo complexes but does not agree with the structural correlation found by Latour et al.[13] for μ-phenoxo, bis-μ-carboxylato compounds, largely because the $Mn^{II}$–O and $Mn^{III}$–O(phenoxo) lengths are so similar in the present compound.

Magnetic susceptibility and variable-field magnetisation measurements on samples of the bulk materials of **7**·$(ClO_4)_4$ were also carried out. The plot of effective magnetic moment ($\mu_{eff}$) vs. temperature, measured in a field of 1 T, is shown in Figure 9, while the isothermal magnetisation data are given in Figure S1 (Supporting Information). A stronger magnetic coupling is evident from the overall

 © 2006 Wiley-VCH Verlag GmbH & Co. KGaA, Weinheim 

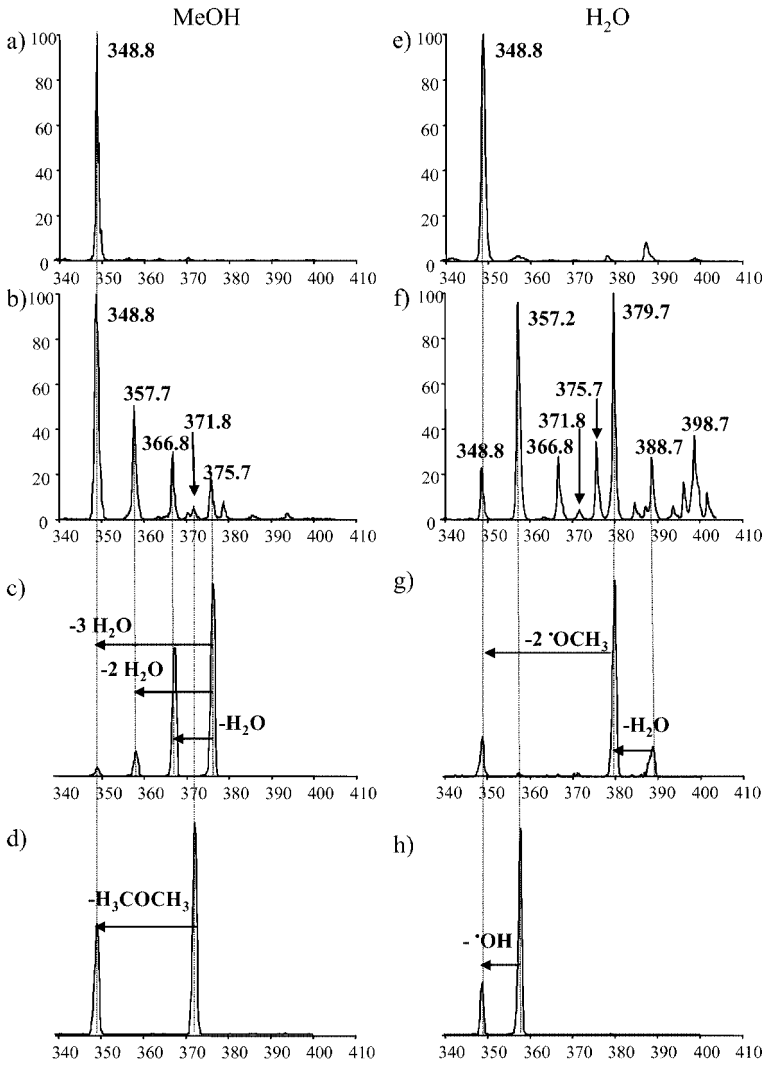


Figure 7. ESI mass spectra of **3**·$(ClO_4)_2$ in methanol (a and b) and in water (e and f). Spectra (a) and (e) were recorded with a tube lens potential of 100 V (normal source conditions); spectra (b) and (f) were recorded with a tube lens potential of 20 V (mild source conditions). Collision-Activated Dissociation (CAD) spectra (c, d and g, h) were recorded by mass selection from spectra (b) and (f), respectively. Mass selected for CAD: (c) *m*/*z* 375.7; (d) *m*/*z* 371.8; (g) *m*/*z* 388.7; (h) *m*/*z* 357.2. Peak assignment and CAD pathways are show below spectra.

 © 2006 Wiley-VCH Verlag GmbH & Co. KGaA, Weinheim 

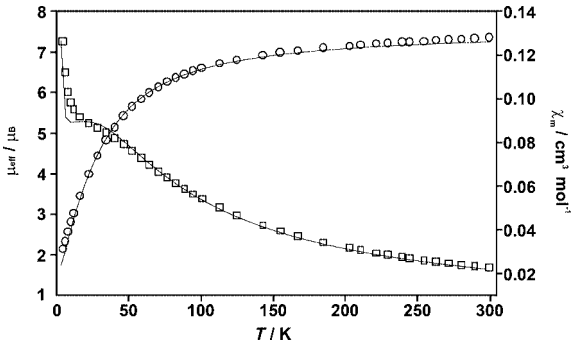


Figure 8. Plots of magnetic susceptibility () and moment (O) per molecule for complex **3**·$(ClO_4)_2$. The solid lines are the calculated values with the $S$ = 5/2:4/2 model and parameters given in the text.

lower magnetic moment per manganese ion in bulk samples of **7**·$(ClO_4)_4$ compared with **3**·$(ClO_4)_2$. This suggests a superexchange pathway that is more efficient than that in **3** and is consistent with the presence of oxo bridges, although in the absence of more a definitive oxidation state assignment from the X-ray crystal structure and XANES measurements a precise analysis cannot be made. We interpret the data as follows. At 300 K, a $\mu_{eff}$ value of 8.2 $\mu_B$ per $Mn_4$ is obtained, and this decreases gradually to reach 7.7 $\mu_B$ at 30 K, followed by a rapid decrease to reach 5.6 $\mu_B$ at 2 K, from where it continues to decrease. Four uncoupled $Mn^{III}$ $S$ = 2 centres would give a $\mu_{eff}$ of 9.8 $\mu_B$ ($g$ = 2.0), thus medium strength antiferromagnetic coupling is indicated. Except for the beginning of the region of rapid decrease (10–5 K), the $\mu_{eff}$ vs. temperature data can be fitted well to a three-$J$ ($S$ = 2) tetramer ($-2JS_1 \cdot S_2$) model[14] [for atoms Mn(1), Mn(2), Mn(3) and Mn(4), where Mn(3) is Mn(2′) and Mn(4) is Mn(1′) in Figure 3], with $g$ = 1.94 and $J_{12}$ = –8, $J_{13}$ = –38 and $J_{24}$ = 23 $cm^{-1}$. The $J_{13}$ and $J_{24}$ values could be positive or negative for a similar $J_{12}$ value to that shown (see Figure 9, dotted line). This is not the same as using a two-$J$ model with $J_{13} = J_{24}$ as such a model does not give a good fit of the data. Comparison of these $J$ values to those previously reported for $Mn^{III}$–O–$Mn^{III}$- (angular) and $Mn^{III}$–(OPh)–$Mn^{III}$-bridged systems unfortunately does not give an unambiguous assignment of the individual $J$ values to particular bridges in the adamantane core. This is because the $J$ values found for such bridges often overlap in size and are not as clearly defined as in analogous $Fe^{III}$ systems. In support of the fitting using three $J$ values, it should be noted that the best fit to the data for the isostructural, and possibly isovalent, $Fe^{III}_4$ complex was a three-$J$ value fit.[6] In that case they were readily assigned to the three types of bridge. The magnetisation isotherm for **7**·$(ClO_4)_4$, at 2 K (Figure S1), did not reach saturation in $M$ at the highest field of 5 T, but gave a value of 7.65 $\mu_B$, which is somewhere between $S$ = 3 and $S$ = 4 ground-state values. The best-fit parameter set, given above, gave a calculated $M$ value, at 2 K and 5 T, of 6.9 N$\mu_B$, which is less than the observed value. This discrepancy may be related to the heterogeneity of the sample used. The energy levels calculated from this parameter set show $S$ = 3 lower, but only by 4 $cm^{-1}$, than $S$ = 4, with other $S$ values greater than 100 $cm^{-1}$ above. It was also possible to obtain reasonable fits to the data of Figure 9 using a $Mn^{II}Mn^{III}Mn^{II}Mn^{III}$ model with spins {5/2, 2, 5/2, 2}, and a similar ground $S$ = 3 state and nearby $S$ = 4, but this formulation is unlikely in view of the XANES data.

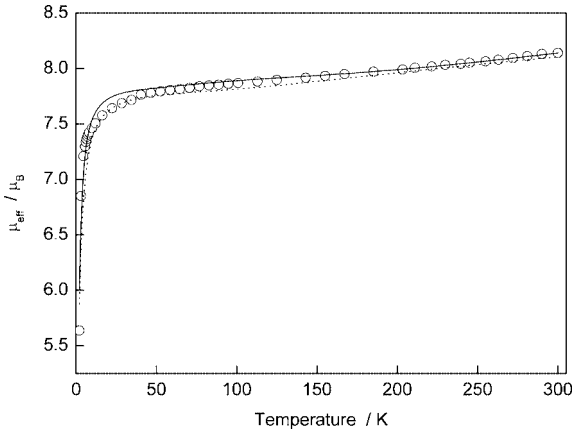


Figure 9. Plot of magnetic moment, $\mu_{eff}$, (open circles) vs. temperature, per $Mn_4$, for **7**·$(ClO_4)_4$. The solid line is that calculated using the parameters for the $Mn^{III}_4$ model, with $g$ = 1.94, $J_{12}$ = –8 $cm^{-1}$, $J_{13}$= –38 $cm^{-1}$ and $J_{24}$ = 23 $cm^{-1}$. The dotted line uses parameters, also for the $Mn^{III}_4$ model, with $g$ = 1.93, $J_{12}$ = –14 $cm^{-1}$, $J_{13}$ = 66 $cm^{-1}$ and $J_{24}$ = –67 $cm^{-1}$.

## Conclusions

Dioxygen-sensitive dimanganese(II) complexes of a pentadentate, phenoxide-hinged, dinucleating ligand with labile solvent-derived and perchlorate exogenous ligands have been structurally characterised. In previous work we have shown that the $[Mn^{II}_2(bpbp)]^{3+}$ cation can activate dioxygen in an as-yet-unknown mechanism to form an oxidant capable of oxidative ketone cleavage. Using other solvents we show here that reactions with $O_2$ yield a series of dinuclear $Mn^{II}$–$Mn^{III}$, $Mn^{III}_2$ and $Mn^{III}$–$Mn^{IV}$ complexes and one tetranuclear manganese complex. However, we cannot propose that any of these species is the pertinent $[Mn^{II}_2(bpbp)]^{3+}/O_2$-derived oxidant. The use of "anhydrous" conditions was crucial for obtaining the crystals of **1**, **2**, **3** and **7**. The structures of the solution species **4**, **5** and **6** have been predicted on the basis of the information provided by the crystal structures of the other members of the series and through a careful analysis of tandem MS experiments. The ESI MS studies indicate facile formation of a gas-phase oxide species **8**. Without the analysis of MS/MS under mild source conditions here, and knowledge of the solid-state structures of the precursors, such a species might otherwise have been mistaken as being present in solution.

The range of oxidation states attainable for an adamantane $Mn_4O_6$ core has been extended to a lower oxidation state in complex **7**. By comparison with known oxo-bridged, tetramanganese adamantane core complexes, as well as the use of BVS analysis and XANES measurements, the overall oxidation state of complex **7** has been narrowed

 © 2006 Wiley-VCH Verlag GmbH & Co. KGaA, Weinheim 

down to two possible assignments – $[Mn^{III}_4(O)_2(OH)_2(bpbp)_2]^{4+}$ and $[Mn^{III}_3Mn^{IV}(O)_3(OH)(bpbp)_2]^{4+}$. The difficulty in obtaining solution spectroscopic data, and thus further oxidation-state evidence, can be attributed to the expected reactivity of the $Mn^{III}$–OH–$Mn^{III}$ moieties and serve as further circumstantial evidence that **7** is not the oxide–phenoxide-bridged $Mn^{III}_2Mn^{IV}_2$ species $[Mn_4(O)_4(bpbp)_2](ClO_4)_4$. Although no definitive assignment can be made, **7** still represents the lowest overall oxidation state for a structurally characterised tetranuclear manganese complex with an adamantane core – it is either two or three oxidation levels lower, for example, than $[(tphpn)_2Mn^{III}Mn^{IV}_3(\mu\text{-}O)_4](OTf)_2(ClO_4)_3$.[8] Based on the very small differences of the metric parameters of **7** with the higher oxidation state $Mn_4O_6$ adamantane core compounds in the literature, it can be envisaged that a relatively wide range of oxidation and protonation states may be accessible for $Mn_4O_6$ adamantane core systems without a major structural deformation. A study of the redox chemistry of **7** and its reduced/oxidised and protonated/deprotonated counterparts would be particularly interesting with respect to modelling biological water and oxygen metabolism reactions. This has so far proved impossible in our hands due to solution instability.

## Experimental Section

Elemental analyses were performed at the Chemistry Department II at Copenhagen University, Denmark, and Atlantic Microlab, Inc., Norcross, Georgia 30091, USA. UV/Vis spectra were recorded with a Shimadzu UV-3100 spectrophotometer. ESI mass spectra were obtained using a Finnigan TSQ 700 triple quadrupole instrument equipped with a Finnigan API source in the nanoelectrospray mode. 2,6-Bis{[bis(2-pyridylmethyl)amino]methyl}-4-*tert*-butylphenol (bpbpH),[15] $[tpa_2Mn_2O_2](ClO_4)_3$ [tpa = tris(2-pyridylmethyl)amine],[16] and $[(Me_3tacn)_2Mn_2O_3][PF_6]_2$[7b] were synthesised following literature procedures. $Mn(acac)_2$ and $Mn(acac)_3$ were purchased from Aldrich Chemical company.

***CAUTION!*** *Although no problems were encountered in the preparation of the perchlorate salt, suitable care should be taken when handling such potentially hazardous compounds.*

**$[Mn_2(bpbp)(ClO_4)_2(THF)](ClO_4)\cdot THF\cdot 3H_2O$ ($1\cdot ClO_4\cdot THF\cdot 3H_2O$):** Triethylamine (28.8 μL, 0.21 mmol) was added to a solution of bpbpH (119.2 mg, 0.21 mmol) in degassed THF (3 mL). $Mn(ClO_4)_2\cdot 6H_2O$ (150.1 mg, 0.42 mmol) was then added to give a clear, colourless solution. Air-sensitive white microcrystals of the product deposited over 24 h. Yield: 230.8 mg (92%). $C_{40}H_{47}Cl_3Mn_2N_6O_{14}\cdot C_4H_8O\cdot 3H_2O$: calcd. C 44.85, H 5.22, N 7.13, Cl 9.03; found C 44.89, H 5.16, N 7.15, Cl 9.29. ESI MS ($CH_3CN$): *m*/*z* (%) 390.1 (100) $[(bpbp)Mn_2(ClO_4)]^{2+}$, 879.2 (50) $[(bpbp)Mn_2(ClO_4)_2]^{+}$.

**$[Mn_2(bpbp)(ClO_4)_2(THF)][B(C_6H_5)_4]\cdot 4THF$ ($1\cdot B(C_6H_5)_4\cdot 4THF$):** $1\cdot ClO_4\cdot THF\cdot 3H_2O$ and approx. 4 equiv. of $NaB(C_6H_5)_4$ were dissolved in degassed THF. Slow evaporation under $N_2$ gave very air-sensitive crystals as colourless blocks after a few days.

**$[Mn_2(bpbp)(ClO_4)(H_2O)_2](ClO_4)_2\cdot H_2O$ ($2\cdot (ClO_4)_2\cdot H_2O$):** A solution of $1\cdot ClO_4\cdot THF\cdot 3H_2O$ in degassed $CH_2Cl_2$ (approx. 50 ppm $H_2O$) was allowed to evaporate under $N_2$. Air-sensitive crystals formed as colourless blocks overnight.

**$[Mn_2(bpbp)(OCH_3)_2(H_2O)_2](ClO_4)_2$ ($3\cdot (ClO_4)_2$):** Triethylamine (113 mg, 1.11 mmol) was added to a pale-green solution of $Mn(ClO_4)_2\cdot 6H_2O$ (862 mg, 2.38 mmol) and bpbpH (599 mg, 1.05 mmol) in methanol (14 mL). The initially colourless solution changed to red brown. Dark-purple crystals of the product deposited over 24 h. Yield: 320 mg (31%). $C_{38}H_{49}Cl_2Mn_2N_6O_{13}$: calcd. C 46.64, H 5.05, N 8.59, Cl 7.25; found C 45.79, H 5.10, N 8.68, Cl 7.36. ESI MS (mild source conditions, $CH_3OH$): *m*/*z* (%) 348.8 (100) $[(bpbp)Mn_2O]^{2+}$, 357.7 (50) $[(bpbp)Mn_2(OH)_2]^{2+}$, 366.8 (30) $[(bpbp)Mn_2(OH)_2(H_2O)]^{2+}$, 371.8 (5) $[(bpbp)Mn_2(OCH_3)_2]^{2+}$, 375.7 (20) $(bpbp)Mn_2(OH)_2(H_2O)_2]^{2+}$. UV/Vis ($CH_3OH$): $\lambda_{max}$, ($\varepsilon$) = 309 nm (17200 L mol$^{-1}$ cm$^{-1}$), 258 (4560).

Alternatively, recrystallisation of $1\cdot ClO_4\cdot THF\cdot 3H_2O$ from dry MeOH in air gave $3\cdot (ClO_4)_2$.

**$[Mn_4(O)_2(OH)_2(bpbp)_2](ClO_4)_4$ ($7\cdot (ClO_4)_4$):** A solution of $1\cdot ClO_4\cdot THF\cdot 3H_2O$ (25 mg, 0.021 mmol) in dry THF (50 mL) was treated with 2 equiv. of *tert*-butylhydrogen peroxide (6 M in decane). The solution turned black. The mixture was allowed to stand in an open flask until dryness and the very small brown crystals used for the structural analysis were recovered. All other preparations of this material resulted in dark amorphous powders which give no XRPD pattern. Thus, the homogeneity of the bulk sample of this compound is not clear despite the fact that elemental analyses are consistent with the proposed formulation. $C_{72}H_{80}Cl_4Mn_4N_{12}O_{22}$: calcd. C 47.33, H 4.41, N 9.2, Cl 7.76; found (average) C 46.99, H 4.36, N 9.15, Cl 7.50.

**X-ray Crystallography:** Analysis of $1\cdot B(C_6H_5)_4\cdot 4THF$ was done at 180(2) K on a Bruker Nonius X8-APEXII instrument at the University of Southern Denmark. The structure was solved by direct methods and refined against all $F^2$ data using software incorporated in WinGX ver. 1.70.[17] The geometry of all solvent THF molecules was restrained and each THF molecule was refined with one isotropic displacement parameter. The O-position of one solvent THF could not be determined. Two of the remaining solvent THF molecules as well as the coordinated THF and the perchlorates were all refined with isotropic displacement parameters as disordered over two positions with equal occupancy, except for the position of the non-bridging perchlorate, which was refined with 33/66% occupancy. The chloride in the bridging perchlorate as well as all remaining non-hydrogen atoms were refined with anisotropic atomic displacement parameters, and hydrogen atoms bonded to carbon were inserted at calculated positions using a riding model. Crystals of $7\cdot (ClO_4)_4$ were too weakly diffracting for data collection using a standard laboratory sealed-tube source and so the data were collected at 150 K at Station 9.8 of the Synchrotron Radiation Source at Daresbury.[18] The structure was solved by direct methods and refined by full-matrix least-squares on $F^2$ using the SHELXTL package.[19] The cation has a twofold axis passing through the two phenolic oxygen atoms, there is disorder of the two *tert*-butyl groups and in one of the perchlorate anions these were both modelled with equal occupancy of two positions. All non-hydrogen atoms were refined with anisotropic atomic displacement parameters and hydrogen atoms bonded to carbon were inserted at calculated positions using a riding model; hydrogen atoms bonded to oxygen were not located and were not included in the model. Since the crystals were formed by complete evaporation of a reaction mixture, the high *R*-value might be ascribed to crystal defects caused by solvent loss. Voids remain in the structure ($4\times 204$ Å$^3$ per unit cell) but because of the weak diffraction data SQUEEZE[20] could not be used to estimate the electron density and it can therefore not be excluded that diffuse solvent molecules are located in these voids. Data collection and structure refinement details are summarised in Table 4.

 © 2006 Wiley-VCH Verlag GmbH & Co. KGaA, Weinheim 

CCDC-613204 (for **1·ClO$_4$·THF·3H$_2$O**) and -613205 [for **7·(ClO$_4$)$_4$**] contain the supplementary crystallographic data for this paper. These data can be obtained free of charge from The Cambridge Crystallographic Data Centre via www.ccdc.cam.ac.uk/data_request/cif.

Table 4. Crystallographic details.

| | **1**·B(C$_6$H$_5$)$_4$·4THF | **7**·(ClO$_4$)$_4$ |
|---|---|---|
| Empirical formula | $C_{80}H_{99}BCl_2Mn_2N_6O_{14}$ | $C_{72}H_{80}Cl_4Mn_4N_{12}O_{22}$ |
| $M_r$ | 1560.24 | 1827.04 |
| $\lambda$ [Å] | 0.71073 | 0.69410 |
| Crystal system | triclinic | monoclinic |
| Space group | $P\bar{1}$ | $C2/c$ |
| $Z$ | 2 | 4 |
| $a$ [Å] | 13.346(2) | 16.427(4) |
| $b$ [Å] | 14.490(3) | 24.404(4) |
| $c$ [Å] | 21.206(4) | 20.902(4) |
| $\alpha$ [°] | 78.589(7) | 90 |
| $\beta$ [°] | 86.275(7) | 93.402(6) |
| $\gamma$ [°] | 79.374(7) | 90 |
| $U$ [Å$^3$] | 3949.2(12) | 8365(3) |
| Crystal size [mm] | 0.40 × 0.16 × 0.08 | 0.20 × 0.10 × 0.02 |
| Crystal colour | colourless | brown |
| $T$ [K] | 180(2) | 150(2) |
| $\rho_{calcd.}$ [g cm$^{-3}$] | 1.312 | 1.451 |
| $\mu$(Mo-$K_\alpha$) [mm$^{-1}$] | 0.454 | 0.795 |
| $F$(000) | 1644 | 3760 |
| $T_{min}$, $T_{max}$ | 0.8394, 0.9646 | |
| $\theta_{min}$, $\theta_{max}$ [°] | 3.52 to 21.96 | 2.34 to 25.00 |
| Completeness to $\theta_{max}$ | 0.988 | 0.995 |
| Data collected | 33507 | 30596 |
| Unique data | 9530 | 7868 |
| $R_{int}$ | 0.0953 | 0.1404 |
| Observed data [$I > 2\sigma(I)$] | 5547 | 6145 |
| Parameters, restraints | 834, 92 | 590, 727 |
| Goof, $S$ | 1.037 | 1.236 |
| $R_1$, $wR_2$ [$I > 2\sigma(I)$] | 0.0907, 0.2447 | 0.2156, 0.4303 |
| $R_1$, $wR_2$ [all data] | 0.1552, 0.2957 | 0.2424, 0.4415 |
| $\rho_{min}$, $\rho_{max}$ [e Å$^{-3}$] | 0.755, –0.673 | 1.480, –1.712 |

**Magnetochemistry:** A Quantum Design MPMS5 Squid magnetometer was used to obtain magnetic susceptibility in a field of 1 T. Samples with a mass of about 20 mg were contained in a calibrated gelatine capsule which was held in the centre of a plastic drinking straw fixed to the sample oval. The instrument was calibrated by use of a standard palladium sample supplied by Quantum Design Inc. Magnetisation isotherms (2–20 K and 0–5 T fields) were obtained on a sample of **7**·(ClO$_4$)$_4$ dispersed in a Vaseline mull in order to prevent torquing of crystallites and production of anomalous data.

**XANES:** Complexes were diluted with boron nitride and data were obtained in fluorescence mode on beamlines X9B or X18 of the National Synchrotron Light Source, using the inflection point of a Mn foil spectrum at 6539.0 eV as the energy calibration. The general procedures for obtaining XANES spectra (which are normalised to the edge height) from the fluorescence data were similar to those used previously for iron and cobalt compounds.[10,21]

**Supporting Information** (see footnote on the first page of this article): Isothermal magnetisation data for **7**·(ClO$_4$)$_4$.

## Acknowledgments

Support from the Danish Technical and Natural Science Research Council (grant, 26-02-0192), DANSYNC and COST project no. D21/0010/01 is gratefully acknowledged. V.M. is grateful to the EPSRC for access to Station 9.8 of the SRS at Daresbury. X-ray beam time for the EXAFS and XANES study was provided at beam lines X9B and X18B through the General Users Program of the National Synchrotron Light Source, which is supported by the US Department of Energy, Divisions of Materials Science and Chemical Science (DOE contract number DE-AC02-76CH00016). K.S.M. thanks the Australian Research Council for support for the magnetic studies.

[1] a) R. Hage, J. Kerschner, *Trends Inorg. Chem.* **1998**, *5*, 145–159; b) K. F. Sibbons, K. Shastri, M. Watkinson, *Dalton Trans.* **2005**, 645–661.
[2] K. B. Jensen, E. Johansen, F. B. Larsen, C. J. McKenzie, *Inorg. Chem.* **2004**, *43*, 3801–3803.
[3] F. H. Allen, *Acta Crystallogr. Sect. B* **2002**, *58*, 380–388.
[4] S. Brooker, V. McKee, T. Metcalfe, *Inorg. Chim. Acta* **1996**, *246*, 171–179.
[5] A. Boisen, A. Hazell, C. J. McKenzie, *Chem. Commun.* **2001**, 2136–2137.
[6] M. Ghiladi, F. B. Larsen, C. J. McKenzie, I. Søtofte, J.-P. Tuchagues, *Dalton Trans.* **2005**, 1687–1692.
[7] a) K. Wieghardt, U. Bossek, W. Gebert, *Angew. Chem. Int. Ed. Engl.* **1983**, *22*, 328–329; b) K. Wieghardt, U. Bossek, B. Nuber, J. Weiss, J. Bonvoisin, M. Corbella, S. E. Vitols, J. J. Girerd, *J. Am. Chem. Soc.* **1988**, *110*, 7398–7411; c) C. E. Dubé, D. W. Wright, W. H. Armstrong, *J. Am. Chem. Soc.* **1996**, *118*, 10910–10911; d) K. S. Hagen, T. D. Westmoreland, M. J. Scott, W. H. Armstrong, *J. Am. Chem. Soc.* **1989**, *111*, 1907–1909; e) C. E. Dube, D. W. Wright, S. Pal, P. J. Bonitatebus Jr, W. H. Armstrong, *J. Am. Chem. Soc.* **1998**, *120*, 3704–3716; f) C. E. Dubé, S. Mukhopadhyay, P. J. Bonitatebus Jr, R. J. Staples, W. H. Armstrong, *Inorg. Chem.* **2005**, *44*, 5161–5175.
[8] S. Mukhopadhyay, H. J. Mok, R. J. Staples, W. H. Armstrong, *J. Am. Chem. Soc.* **2004**, *126*, 9202–9204.
[9] I. D. Brown, D. Altermatt, *Acta Crystallogr. Sect. B* **1985**, *41*, 244–247.
[10] R. C. Scarrow, B. A. Brennan, J. G. Cummings, H. Jin, D. J. Duong, J. Kindt, M. J. Nelson, *Biochemistry* **1996**, *35*, 10078–10088.
[11] a) D. M. Eichhorn, W. A. Armstrong, *J. Chem. Soc., Chem. Commun.* **1992**, 85–87; b) Z. Shirin, V. G. Young Jr, A. S. Borovik, *Chem. Commun.* **1997**, 1967–1968; c) S. Pal, M. K. Chan, W. H. Armstrong, *J. Am. Chem. Soc.* **1992**, *114*, 6398–6406; d) T.-S. Lai, H.-L. Kwong, C.-M. Che, S.-M. Peng, *Chem. Commun.* **1997**, 2373–2374; e) Z. Shirin, B. S. Hammes, V. G. Young Jr, A. S. Borovik, *J. Am. Chem. Soc.* **2000**, *122*, 1836–1837; f) S. Pal, W. H. Armstrong, *Inorg. Chem.* **1992**, *31*, 5417–5423; g) T. J. Hubin, J. M. McCormick, N. W. Alcock, D. H. Busch, *Inorg. Chem.* **2001**, *40*, 435–444; h) M. Corbella, R. Costa, J. Ribas, P. H. Fries, J.-M. Latour, L. Öhrstrom, X. Solans, V. Rodriguez, *Inorg. Chem.* **1996**, *35*, 1857–1865.
[12] a) P. Dalgaard, C. J. McKenzie, *J. Mass Spectrom.* **1999**, *34*, 1033–1039; b) Y. Dussart, C. Harding, P. Dalgaard, C. McKenzie, R. Kadirvelraj, V. McKee, J. Nelson, *J. Chem. Soc., Dalton Trans.* **2002**, 1704–1713.
[13] L. Dubois, D.-F. Xiang, X.-S. Tan, J. Pécaut, P. Jones, S. Baudron, L. Le Pape, J.-M. Latour, C. Baffert, S. Chardon-Noblat, M.-N. Collomb, A. Deronzier, *Inorg. Chem.* **2003**, *42*, 750–760 and references cited therein for $J$ values for related $Mn^{II}Mn^{III}$ complexes. The $J$ value is similar to that of related bis-carboxylate-bridged $Mn^{II}$–$Mn^{III}$ systems.
[14] K. S. Murray, *Adv. Inorg. Chem.* **1995**, *43*, 261–358.
[15] M. Ghiladi, C. J. McKenzie, A. Meier, A. K. Powell, J. Ulstrup, S. Wocaldo, *J. Chem. Soc., Dalton Trans.* **1997**, 4011–4018.
[16] D. K. Towle, C. A. Botsford, D. J. Hodgson, *Inorg. Chim. Acta* **1988**, *141*, 167–168.
[17] L. J. Farrugia, *J. Appl. Crystallogr.* **1999**, *32*, 837–838.

 © 2006 Wiley-VCH Verlag GmbH & Co. KGaA, Weinheim 

[18] R. J. Cernik, W. Clegg, C. R. A. Catlow, G. Bushnell-Wye, J. V. Flaherty, G. N. Greaves, M. Hamichi, I. Burrows, D. J. Taylor, S. J. Teat, *J. Synchrotron Radiat.* **1997**, *4*, 279–286.
[19] G. M. Sheldrick, SHELXTL version 5.1, Bruker AXS, Madison, Wisconsin, USA **1997**.
[20] A. L. Spek, *J. Appl. Crystallogr.* **2003**, *36*, 7–13.
[21] K. M. Padden, J. F. Krebs, K. T. Trafford, G. P. Yap, A. H. Rheingold, A. S. Borovik, R. C. Scarrow, *Chem. Mater.* **2001**, *13*, 4305–4313.

Received: May 25, 2006
Published Online: August 7, 2006

 © 2006 Wiley-VCH Verlag GmbH & Co. KGaA, Weinheim 

DOI: 10.1002/ejic.200600443

# Zinc(II) Complexation Behaviour of Sulfonamide-Based Enzyme Inhibitors

**Sílvia Chaves,[a] Sérgio M. Marques,[a] Anabela Cachudo,[b] M. Alexandra Esteves,[b] and M. Amélia Santos*[a]**

**Keywords:** MMP inhibitors / Carbonic-anhydrase inhibitors / Hydroxamate / Hydroxypyrimidinone / Sulfonamido-based inhibitors / Sulfonamides

Sulfonamide derivatives containing extrafunctional groups, such as hydroxamic acids, hydroxypyrimidinones and carboxylic acids, have been recently identified as inhibitors towards several zinc-containing enzymes, such as the matrix metalloproteinases (MMPs) and/or carbonic anhydrases (CAs). Since these inhibitors are supposed to bind the zinc ion at the active site, it was decided to study the zinc(II) complexation with a set of representative compounds in order to identify the most probable coordination modes and to find eventual relationships with the inhibitory properties. These studies were performed in aqueous solution, by potentiometry and $^1$H NMR spectroscopy, and in the solid phase, by infrared spectroscopy. The solution equilibrium studies indicate that these compounds present similar affinity for zinc (pZn ≈ 6). Under stoichiometric conditions, the formation of 1:1 metal complex species involves a preferential (*O*,*O*) coordination via the hydroxamic or hydroxypyrimidinone moieties, while the coordination via the sulfonamide groups could mainly be achieved under zinc excess conditions.

(© Wiley-VCH Verlag GmbH & Co. KGaA, 69451 Weinheim, Germany, 2006)

## 1. Introduction

Matrix metalloproteinases (MMPs) and some carbonic anhydrase (CA) isoenzymes are known to be involved in carcinogenesis and tumour invasion processes.[1–3] Therefore, both types of zinc-containing enzymes became the targets for drug design and specific inhibitors for each type of enzymes are well known. In particular, many inhibitors of CAs containing aromatic/heteroaromatic sulfonamides have been used in the treatment of several diseases; concerning the MMP inhibitors, hydroxamate derivatives have been widely developed as possible anti-tumour/metastatic agents.[1,4]

Since these two families of inhibitors bind the zinc at the enzyme active sites, efforts have already been made to explore connections between CA and MMP inhibitors and eventual "cross-reactivity" or synergic effects.[5,6] Following the current trend of exploring potential dual inhibitors for those metalloenzymes,[7] we have recently identified a set of potent enzyme inhibitors,[8,9] some of them containing sulfonamide moieties inserted in diverse scaffolds bearing the usual zinc-binding groups in matrix metalloproteinase inhibitors (MMPi), namely: carboxylic and primary hydroxamic groups as well as, more recently, the hydroxypyrimidinones (heterocyclic hydroxamic acids).[10]

Direct comparison of the previously described compounds showed a clear trend towards an increased inhibitory activity of the sulfonamide derivatives. In the absence of X-ray structures of the enzyme-inhibitor adducts, some modelling studies have already been performed to simulate the inhibition of some MMPs and to aid the understanding of those results.[8] Aimed at shedding some extra light on the rationalization of the enzyme inhibition results, a set of four representative compounds ($H_iL^n$, $n$ = 1–4, see Scheme 1) was selected and their Zn complexation behaviour was studied to identify the 1:1 zinc-binding mode preferences of the diverse bifunctional compounds, in order to establish eventual zinc-binding affinity/inhibitory activity relationships. Results with some model compounds (e.g. $H_2L^5$ and $HL^6$) were also analysed for comparison purposes.

The zinc complexation studies were mainly performed in aqueous solution, using potentiometric and $^1$H NMR spectroscopic methods, although a brief analysis of solid zinc complexes was also carried out by infrared spectroscopy.

[a] Centro de Química Estrutural, Complexo I, Instituto Superior Técnico,
Av. Rovisco Pais, 1049-001 Lisboa, Portugal
Fax: +351-21-8464455
E-mail: masantos@ist.utl.pt
[b] INETI, Departamento de Tecnologia de Indústrias Químicas, Estrada do Paço do Lumiar, 1649-038 Lisboa, Portugal

Supporting information for this article is available on the WWW under http://www.eurjic.org or from the author.

 © 2006 Wiley-VCH Verlag GmbH & Co. KGaA, Weinheim 

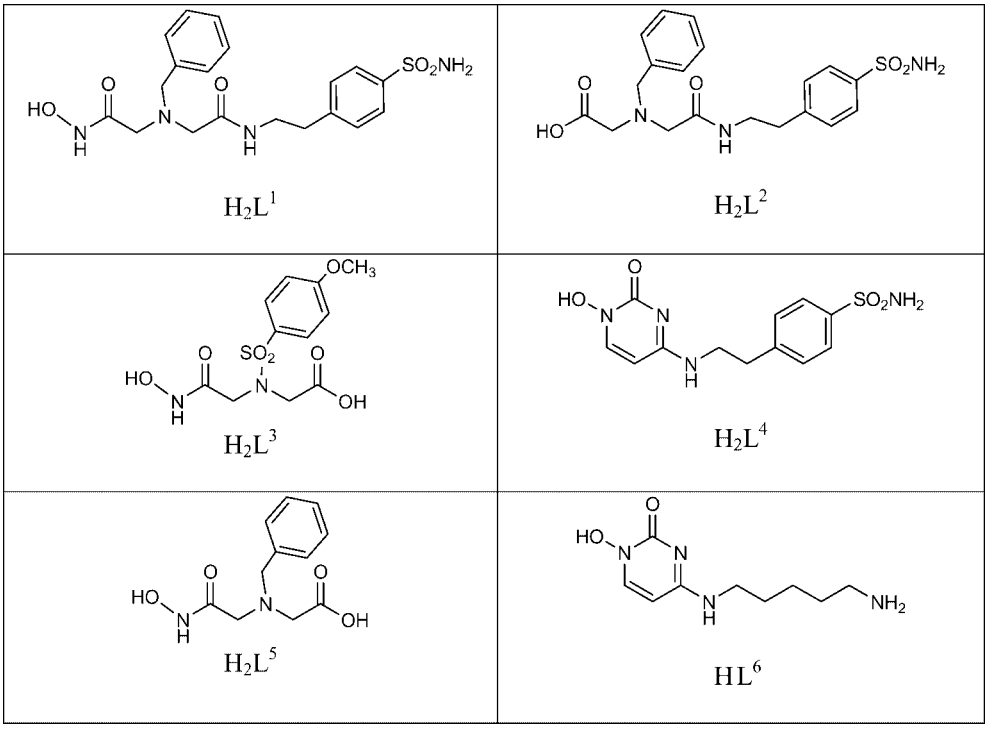


Scheme 1.

## 2. Results and Discussion

### 2.1. Acid Base Properties of the Ligands

The fully protonated form of the ligands under study has three ($H_2L^n$, $n$ = 1, 2, 4) or two ($H_2L^3$) dissociable protons. The determination of the corresponding protonation constants was mainly performed by potentiometry but, for $H_2L^2$, $\log K_3$ (<2) was calculated by $^1$H NMR spectroscopy. Table 1 shows the stepwise protonation constants ($\log K_i$) calculated for the sulfonamide derivatives under study ($H_2L^n$, $n$ = 1–4) and also the values previously determined for $H_2L^5$ and $HL^6$ (used for comparison purposes).

$^1$H NMR titration was also used to determine the protonation sequence for compounds containing a primary sulfonamide group ($H_2L^n$, $n$ = 1, 2, 4). In fact, for $H_2L^1$ and $H_2L^4$, the protonation sequence is more difficult to predict than for the remaining compounds, because both the sulfonamide anions and the hydroxamate hydroxy groups are protonated at nearby high pH ranges. $H_2L^2$ was also analysed by $^1$H NMR titration due to its analogy to $H_2L^1$, to aid the discussion of the coordination modes for the corresponding zinc complexes. Analysis of the titration curve profiles (Figure 1) suggests that, for ligands $H_2L^1$ and $H_2L^2$, the sulfonamide anion ($SO_2NH^-$) is the first group to be protonated. In fact, for both ligands, at pD ca. 10–11, peaks 1, 5 and 6 are downfield shifted. Regarding $H_2L^1$, the chemical shift profiles of the nonlabile protons nearby the sulfonamide group, indicate that the protonation successively occurs on the hydroxamate group (downfield shifts of peaks 3 and 4 at pD ≈ 8.5) and the *N*-amine group (at pD ca. 2 large deshielding effect on peaks 2, 3, 4).

Table 1. Stepwise protonation constants ($\log K_i$) of $H_iL^n$ ($i$ = 1, 2, $n$ = 1–6) as well as the global formation constants ($\log\beta$) of the corresponding $Zn^{2+}$ complexes ($I$ = 0.1 M KCl, $t$ = 25.0±0.1 °C).

| Ligand | $H_iL$ $\log K_i$ | Protonated centre | $Zn_mH_hL_l$ $(m,h,l)$ $\log\beta$ |
|---|---|---|---|
| $H_2L^1$ | 10.28(2) | [b] | (1,1,1) 15.14(5) |
| | 8.75(3) | [b] | (1,2,2) 30.09(7) |
| | 3.21(4) | amine | |
| pZn[a] | | | 6.04 |
| $H_2L^2$ | 9.64(1) | sulfonamide | (1,1,1) 13.52(2) |
| | 5.86(2) | amine | (1,2,2) 26.61(6) |
| | 1.8(1)[c] | carboxylate | |
| pZn | | | 6.05 |
| $H_2L^3$ | 8.47(1) | hydroxamate | (1,0,1) 4.96(1) |
| | 2.99(2) | carboxylate | (1,0,2) 8.68(3) |
| pZn | | | 6.05 |
| $H_2L^4$ [d] | 10.16(1) | sulfonamide | (1,1,1) 14.74(3) |
| | 7.09(2) | hydroxamate | (1,2,2) 28.95(4) |
| | 2.90(2) | *N*-imine | |
| pZn | | | 6.12 |
| $H_2L^5$ [e] | 9.11(3) | hydroxamate | (1,0,1) 6.63(5) |
| | 5.75(5) | amine | (1,1,1) 12.84(4) |
| | 1.6 | carboxylate | (1,0,2) 11.06(7) |
| | | | (1,1,2) 18.6(1) |
| | | | (1,2,2) 24.51(5) |
| pZn | | | 6.27 |
| $HL^6$ [d] | 10.45(1) | amine | (1,1,1) 15.30(1) |
| | 7.11(2) | hydroxamate | (1,2,2) 29.59(2) |
| | 2.99(3) | *N*-imine | |
| pZn | | | 6.18 |

[a] pZn is defined as –log[Zn] calculated for $C_L/C_M$ = 10, $C_M$ = $10^{-6}$ M at pH 7.4. [b] Overlap of the protonation processes of hydroxamate and sulfonamidate groups. [c] Determined by $^1$H NMR titration. [d] In 5% DMSO solution. [e] Ref.[12]

 © 2006 Wiley-VCH Verlag GmbH & Co. KGaA, Weinheim 

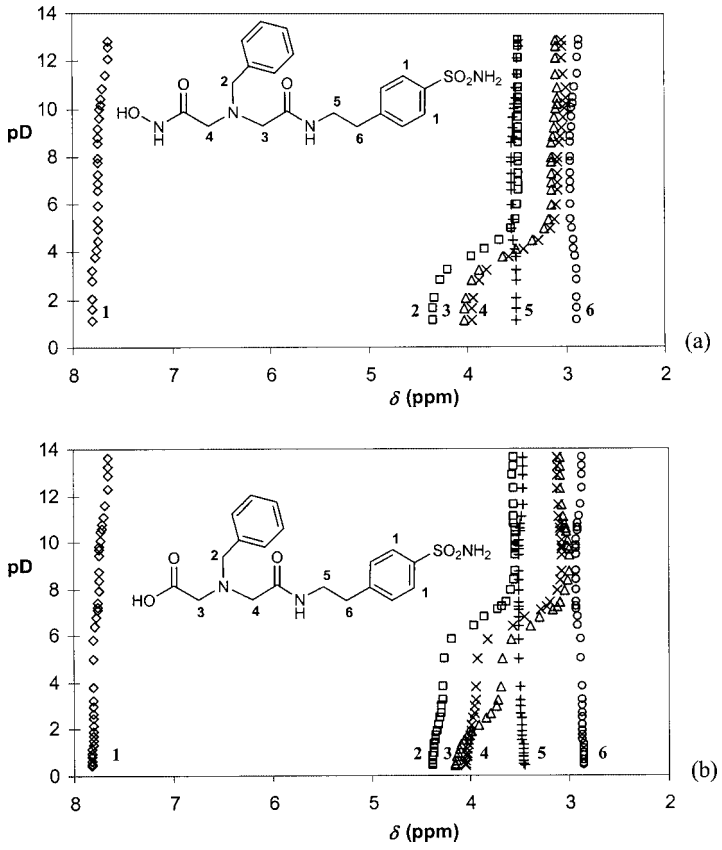


Figure 1. $^1$H NMR titration curves of (a) $H_2L^1$ and (b) $H_2L^2$.

For $H_2L^2$, Figure 1, b) illustrates that the second and third protonation occur in the *N*-amine (large downfield shifts of peaks 2, 3 and 4 at pD ≈ 5) and carboxylate (at pD ≈ 1 large downfield shift of peak 3) groups, respectively.

Concerning the hydroxypyrimidinone derivative, $H_2L^4$, Figure 2 shows the following protonation sequence: sulfonamide group (at pD ca. 11 downfield shift of peaks 2 and 3); hydroxy group (downfield shift of peaks 1 and 4 at pD ca. 7); *N*-imine group (downfield shift of all peaks at pD ca. 2). As found for the $HL^6$ analogue,[11] all the protons feel the protonation of the *N*-imine group, probably due to the enamine-imine equilibrium.

A brief analysis of the protonation constants summarized in Table 1 indicates that the $\log K_1$ (9.6, 10.2) values of ligands $H_2L^n$ ($n$ = 2, 4) should be attributed to the protonation of the sulfonamide group. The lower value of $\log K_1$ found for $H_2L^2$, as compared to $H_2L^1$, is probably due to an electron donation effect that maybe slightly higher for the hydroxamate than the carboxylate group. The values calculated for the hydroxamate protonation constants of ligands $H_2L^1$ ($\log K_2$ = 8.75) and $H_2L^3$ ($\log K_1$ = 8.47) are also slightly lower than the previously calculated value for $H_2L^5$ ($\log K_1$ = 9.11[12]) due to a possible cumulative effect of the carboxylate group on the stabilisation of the $H_2L^5$ protonated form through a bifurcated hydrogen bond network with the *N*-amine. For $H_2L^1$, the protonation processes of the hydroxamate and the sulfonamidate groups seem to overlap and so the corresponding values of $\log K_1$ and $\log K_2$ presented in Table 1 cannot be accurately assigned to each individual group.

Regarding the acid-base properties of the hydroxypyrimidinone derivatives, the protonation constants calculated for $H_2L^4$ and $HL^6$ present very similar values, namely for the hydroxy ($\log K_2$ 7.09 and 7.11) and the *N*-imine groups ($\log K_3$ 2.90 and 2.99). The fact that the amine group of $H_2L^1$ ($\log K_3$ = 3.21) presents a lower basicity than those of $H_2L^2$ ($\log K_2$ = 5.86) and $H_2L^5$ ($\log K_2$ = 5.75) must be due to the presence of the adjacent negatively charged carboxylate groups in $H_2L^2$ and $H_2L^5$, which stabilise the formation of the positively charged ammonium group. Finally, analysis of the protonation constants obtained for the carboxylate groups shows that lower values were obtained for $H_2L^2$ ($\log K_3$ = 1.76) and $H_2L^5$ ($\log K_3$ = 1.6), than for $H_2L^3$ ($\log K_2$ = 2.99); that difference can be rationalized in terms of an extra stabilization of the conjugate base due to the electrostatic interaction between the positively charged amine and the negatively charged carboxylate groups, as well as to hydrogen bonding interaction between the ammonium proton and the carboxylate, involving 5-member ring intermediates.

 © 2006 Wiley-VCH Verlag GmbH & Co. KGaA, Weinheim 

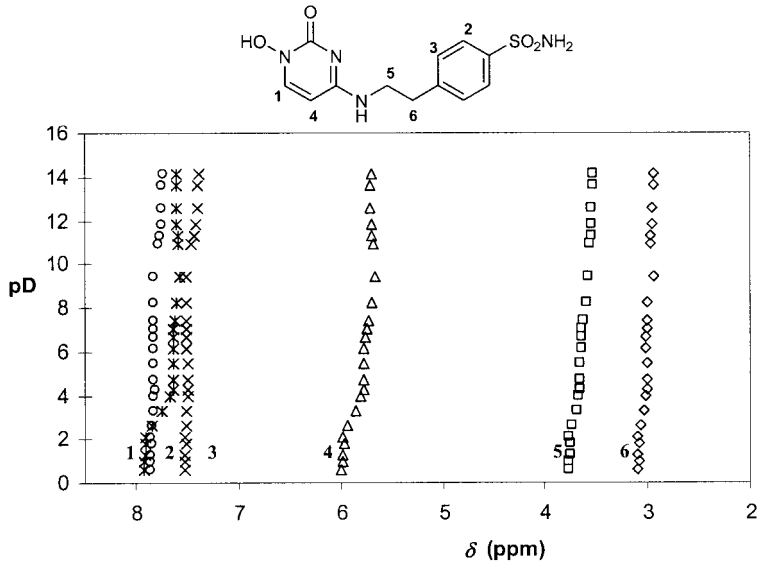


Figure 2. $^1$H NMR titration curves of $H_2L^4$.

### 2.2. Zinc Complexation Studies

In this study, the chelating ability of four sulfonamide derivatives towards $Zn^{II}$ in aqueous solution was evaluated. Although the sulfonamides, in their neutral form, are expected to be poor ligands due to the withdrawal of electron density from the nitrogen atom onto the electronegative oxygen atoms, if this *N*-atom has a dissociable proton, the electron-withdrawing effect increases its acidity making the sulfonamide anions effective sigma-donor ligands.

The global formation constants of the $H_iL^n$ ($n$ = 1–4) zinc complexes were determined by potentiometry at conditions of 1:1, 1:2 and 2:1 metal-to-ligand molar ratios and they are collected in Table 1, together with the reported values for two analogues ($H_2L^5$ and $HL^6$).

Figure 3 shows representative potentiometric titration curves for one of the ligands ($H_2L^1$), alone and in the presence of $Zn^{II}$. Analysis of the titration curve profiles (Figure 3) indicates the noninvolvement of the *N*-amine group in the zinc coordination and that the hydroxamic acid deprotonation feels the presence of the metal ion. For pH values above 6.5–7.0, precipitation occurred and the potentiometric titrations were stopped.

Regarding the other ligands under study, the potentiometric titration curves also showed the noninvolvement of specific groups in the coordination to the $Zn^{II}$ ion, namely: the carboxylate group for $H_2L^3$ and the *N*-imine group for $H_2L^4$. In the case of $H_2L^2$, the potentiometric curves cannot give information about the involvement of the carboxylate group in the zinc coordination since the determined value of $\log K_3$ is extremely low ($<2$).

Aimed at getting some further information about coordination modes, $^1$H NMR titrations of solutions containing the systems $Zn^{II}/H_2L^n$ ($n$ = 1, 2, 4) were performed and the corresponding titration curves compared to those of the respective ligand alone. However, for some of those solution zinc systems, precipitation occurred due to the eventual formation of neutral zinc complexes, namely: for $H_2L^1$ (at pH above 7), for $H_2L^2$ (at pH ca. 4.5–9) and for $H_2L^4$ (at pH 6–10). Therefore, conclusions can be only drawn for pH ranges outside the precipitation zone. $^1$H NMR studies of the $Zn^{II}$ complexes ($C_L/C_M$ = 1) with $H_2L^n$ ($n$ = 2, 4) suggested the noninterference of the sulfonamide group in the coordination mode of these complexes, which is in accordance with the formation of more soluble zinc-hydroxo species for high pH values. In fact, the NMR titration curves of the ligands and respective zinc complexes are superimposed at pD > 11. In the case of $H_2L^1$, it is possible to confirm the noninvolvement of the amine group in the zinc coordination (Figure S1 in the Supporting Information). Moreover, the binding of compounds $H_2L^1$ and $H_2L^4$ to $Zn^{II}$, via the two oxygen atoms of the hydroxamic moiety, was also somehow supported by the absence of significant modifications of the $^1$H NMR spectrum of these ligands due to the presence of the metal ion.[13]

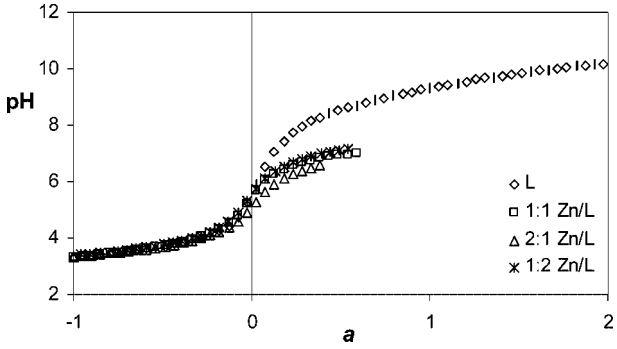


Figure 3. Potentiometric titration curves of $H_2L^1$ and 1:1, 2:1 and 1:2 $Zn^{II}/H_2L^1$ systems ($C_L$ = 0.67 mM).

Analysis of Table 1, containing the results of the solution complexation studies of the diverse compounds ($H_2L^n$, $n$ = 1–4) with $Zn^{II}$, indicates the existence of 1:1 (ZnHL and ZnL) and 1:2 ($ZnH_2L_2$ and $ZnL_2$) complex species in the

 © 2006 Wiley-VCH Verlag GmbH & Co. KGaA, Weinheim 

adopted equilibrium model. As expected, the $Zn^{II}$ complexes with typical (*O*,*O*) hydroxamate coordination, as those formed with $H_2L^1$, $H_2L^4$ and HL[6], have analogous $\log\beta_{MHL}$ and $\log\beta_{MH_2L_2}$ values. For the complexes with $H_2L^1$ or $H_2L^4$, the sulfonamide groups are protonated and the net charges are +1 and 0 for the MHL and the $MH_2L_2$ species, respectively. The speciation at different pH conditions for the zinc binary systems under study ($H_2L^n$, $n$ = 1–4) is illustrated in Figure S2 of the Supporting Information.

Concerning $H_2L^2$, the NMR spectral changes with pD showed the noninvolvement of the sulfonamide group in the metal coordination, in agreement with the potentiometric results that indicated a coordination via amine group. The carboxylate group may also be coordinated to zinc, although the estimated value of $\log\beta_{ZnL}$ (ca. 3.6, $\log\beta_{ZnHL} - \log K_1$) is lower than the reported one for glycine (4.96 with α-aminocarboxylate coordination mode[14]) probably due to the electron-withdrawing effect of the amide group in its vicinity. With regard to $H_2L^3$, a comparative analysis of the potentiometric curve profiles of the ligand, alone and in the presence of $Zn^{II}$, showed a superimposition of the two curves in the buffer region corresponding to the deprotonation of the carboxylic group, thus indicating that the carboxylate group is not in the coordination sphere of the metal ion, according to our expectations. Furthermore, the global formation constants calculated for the zinc complexes with this ligand ($\log\beta_{ZnL}$ = 4.96 and $\log\beta_{ZnL_2}$ = 8.68) are quite similar to the reported values for the corresponding complexes with glycinehydroxamic acid (5.38, 10.07[15]), thus suggesting that for $H_2L^3$ the complexation with zinc should also involve a (*O*,*O*) hydroxamate coordination mode (the small differences found for the stability constants of those two ligands are ascribed to the electron-withdrawing effect of the sulfonamide group). So, the coordination mode for the 1:1 zinc complex with $H_2L^3$ is different from that previously presented for $H_2L^5$ (see Figure 4), in which the species ZnL evidenced an (*N*,*N*,*O*) coordination type with the involvement of the hydroxamate-*N* atom, but also the amine-*N* atom and the carboxylate group.[12]

To make a comparative analysis of the affinity of the studied compounds towards $Zn^{II}$, the corresponding pM values at the physiological pH (pM = –log[M], $C_L/C_M$ = 10 and $C_L = 10^{-5}$ M, pH = 7.4) were calculated, in order to account for the distinct proton concentration dependence of the compounds. Table 1 shows that, in spite of the possible different coordination modes, all the compounds present quite similar affinity for zinc (pZn ≈ 6).

The infrared (IR) spectra of the solid-state samples for the ligands $H_2L^n$ ($n$ = 1–4) and their corresponding zinc species were also performed to aid the identification of the metal coordination modes, namely the eventual involvement of the sulfonamide group. IR data for the ligands and respective zinc species are listed in Table 2 with provisional assignments of the selected vibrational modes.

The IR spectra of ligands $H_2L^n$ ($n$ = 1, 2, 4) present two bands (near 1330 and 1160 $cm^{-1}$), attributable to the asymmetric (as) and symmetric (sy) S=O stretching (st) frequencies; the spectra of the corresponding zinc complexes

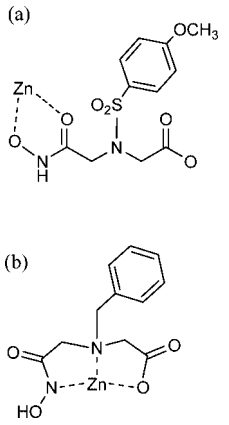


Figure 4. Proposed structures for 1:1 $Zn^{II}$ complexes with the following ligands: (a) $H_2L^3$ and (b) $H_2L^5$[12] (charges and coordinated water molecules are omitted).

show these bands with lower intensity and two new bands appear at lower wave numbers (1260 and 1130 $cm^{-1}$), the intensity of which increases with $Zn^{II}$ excess, namely from 1:1 to 2:1 (M:L) stoichiometric conditions (see Figure 5). The blue shifts of these IR bands, upon complexation,[16] suggest the involvement of the sulfonamide group on the zinc complexation, at least in the solid phase, for the compounds $H_2L^n$ ($n$ = 1, 2, 4).

On the contrary, the IR spectra obtained for $H_2L^3$ and the corresponding zinc complex reveal that the sulfonamide group is not coordinated to the metal ion, even in conditions of metal ion excess, since there is no shift of the S=O stretching frequencies (see Table 2).

The spectra of $H_2L^n$ ($n$ = 1, 3) also present a strong band near 1650 $cm^{-1}$, which should be attributed to the C=O st of the amide groups; upon zinc complexation, this band is shifted to lower wave numbers, thus suggesting that the coordination of these ligands to $Zn^{II}$ occurs via the hydroxamate group. The corresponding C=O st band for the hydroxypyrimidinone derivative ($H_2L^4$) appears at a higher wave number (1722 $cm^{-1}$) than the primary hydroxamic acids, caused by the higher double character of this carbonyl group, and it is considerably shifted to lower energy upon complexation with zinc, thus giving support to the expected hydroxypyrimidinone (*O*,*O*) coordination mode.

Moreover, in the IR spectra of compounds containing carboxylate groups, besides the strong C=O st band corresponding to the amide groups, it is also possible to identify two bands near 1630 $cm^{-1}$ ($COO^-$ st, very strong) and 920 $cm^{-1}$ ($COO^-$ bending $\delta$). For the systems containing $H_2L^2$, upon complexation, these two bands shifted to lower wave numbers, which is consistent with the participation of the carboxylate group in the zinc coordination. Nevertheless, for the $H_2L^3$ spectra, there is a broad band at 1628 $cm^{-1}$, probably arising from overlapping of C=O st (amide) and $COO^-$ st (carboxylate), which upon complexation presents only a slight shift to lower wave numbers. Although this feature cannot give much help to the elucidation of the group involved in the coordination (hydroxamate or carboxylate), the fact that no shift was observed

 © 2006 Wiley-VCH Verlag GmbH & Co. KGaA, Weinheim 

Table 2. Infrared spectroscopic data of compounds $H_iL^n$ ($n$ = 1–4) and respective zinc(II) species ($C_M/C_L$ = 2).

| Systems | Vibrational spectra $\nu$ [cm$^{-1}$] S=O as st | S=O sy st | C=O st amide | $COO^-$ as st | $COO^-$ δ |
|---|---|---|---|---|---|
| $H_2L^1$ | 1334 | 1162 | 1653 | – | – |
| (2:1) $Zn^{2+}/H_2L^1$ | 1259 | 1138 | 1641 | | |
| $H_2L^2$ | 1334 | 1160 | 1660 | 1633 | 912 |
| (2:1) $Zn^{2+}/H_2L^2$ | 1265 | 1136 | 1639 | 1605 | 858 |
| $H_2L^3$ | 1346 | 1151 | 1628 | 1628 | 943 |
| (2:1) $Zn^{2+}/H_2L^3$ | 1342 | 1151 | 1616 | 1616 | 945 |
| $H_2L^4$ | 1306 | 1167 | 1722 | – | – |
| (2:1) $Zn^{2+}/H_2L^4$ | 1261 | 1136 | 1634 | | |

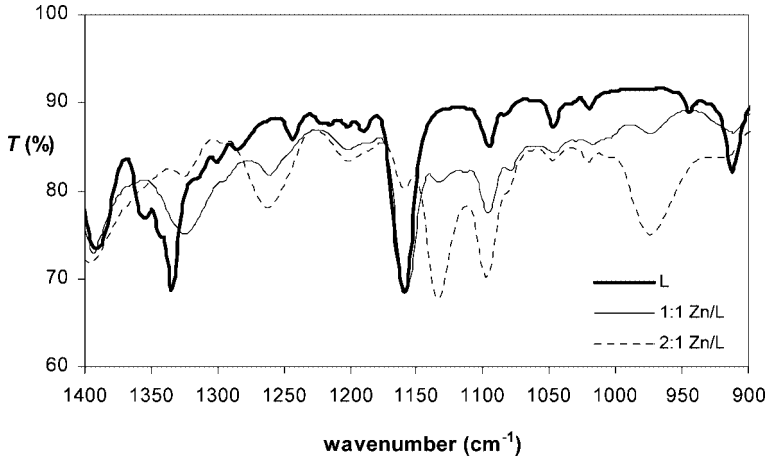


Figure 5. IR spectra of $H_2L^2$ and corresponding 1:1 and 2:1 $Zn^{II}/H_2L^2$ systems in KBr pellets.

for the $COO^-$ bending band, supports the noninvolvement of the carboxylate group in the coordination to the metal ion.

Therefore, the solid-state IR data corroborate the coordination modes found in the solution studies for all the ligands and indicate that for the zinc $H_2L^2$ complex the carboxylate group may be also involved in the metal coordination. Furthermore, it also illustrated the existence of coordination via the sulfonamide group in conditions of metal ion excess.

Previous studies of the compounds $H_2L^n$ ($n$ = 1–6) as MMP and CA inhibitors showed that the sulfonamide derivatives present, in general, a much higher activity against these metalloenzymes than the corresponding non-sulfonamide analogues. In fact, from all the compounds under study, enzyme inhibition ($IC_{50}$) of nanomolar order was only detected for the primary sulfonamide derivatives ($H_2L^1$, $H_2L^2$, $H_2L^4$), against CA I and CA II, and the secondary sulfonamide derivative ($H_2L^3$) against MMP-2, MMP-7 and MMP-9.[8,9] However, the present complexation studies reveal that, in aqueous solution, the sulfonamide group does not seem to be involved in the zinc-coordination. Therefore, since the primary sulfonamides are believed to bind the zinc active site of CAs,[4] the difference between the in vivo and the aqueous solution behaviour should be due to the inaccessibility of the active site to the stronger binding moieties. Concerning the secondary sulfonamide derivative ($H_2L^3$), its high inhibitory activity can be rationalized in terms of extra-functional interactions between the sulfonyl groups and specific amino-acid residues, namely through hydrogen bonds and lipophilic interactions at the active site of the metalloenzymes, as suggested by molecular simulation.[8]

## 3. Conclusions

The complexation equilibrium studies of four sulfonamide derivatives ($H_2L^n$, $n$ = 1–4), already known for their inhibitory activity towards zinc-containing enzymes, show that they have similar affinity for zinc (pZn ≈ 6). The solution and solid infrared studies proved that the 1:1 complexes with ligands $H_2L^n$ ($n$ = 1, 3, 4) present ($O,O$) hydroxamate coordination mode, while the zinc complex with $H_2L^2$ seems to involve both the $N$-amine and the carboxylate groups. Moreover, the infrared studies of the solid complexes indicate that the metal coordination via the sulfonamide groups can mainly occur under conditions of zinc excess. Therefore, the considerable improvements observed in the enzyme inhibitory activity of these sulfonamide-containing compounds, as compared to the non-sulfonamide derivatives, does not seem to be determined by their zinc coordination mode but by extra-binding or specific stereochemical requirements for the accommodation of the inhibitor into the enzyme active site.

 © 2006 Wiley-VCH Verlag GmbH & Co. KGaA, Weinheim 

## 4. Experimental Section

### 4.1. Materials and General Information

The synthesis of the compounds has already been reported or is in the process of being published, namely the hydroxamic/acetic acid derivatives[8,9,12]: 2-(*N*-{[2-(4-sulfamoylphenyl)ethyl-carbamoyl]methyl}-*N*-benzyl-amino)acetohydroxamic acid ($H_2L^1$), 2-(*N*-{[2-(4-sulfamoylphenyl)ethylcarbamoyl]methyl}-*N*-benzylamino)acetic acid ($H_2L^2$), *N*-[(hydroxycarbamoyl)methyl]-*N*-(4-methoxyphenylsulfonyl)aminoacetic acid ($H_2L^3$), *N*-{(hydroxycarbamoyl)methyl}-*N*-benzylaminoacetic acid ($H_2L^5$), and the hydroxy-pyrimidinone derivatives:[10,11] 4-(2-(4-sulfamoylphenyl)-ethylamino)-1-hydroxy-2(1*H*)-pyrimidinone ($H_2L^4$) and 4-(5-aminopentylamino)-1-hydroxy-2(1*H*)-pyrimidinone ($HL^6$).

All $^1$H NMR spectra were recorded with a Varian Unity 300 MHz spectrometer at probe temperature. Chemical shifts are reported in ppm ($\delta$) from internal reference DSS (sodium 3-trimethylsilyl-[$D_4$]-propionate). The pD values were adjusted with DCl or $CO_2$-free KOD, by using a ThermoORION model 420 instrument fitted with a combined Mettler Toledo U402-M3 S7/200 microelectrode. The IR spectra were performed with a FTS3000MX Bio-Rad spectrophotometer.

### 4.2. Potentiometric Titrations

**Solutions:** The $ZnCl_2$ (0.0156 M) solution from Merck was standardized by titration with $K_2H_2EDTA$ (EDTA = ethylenediaminetetraacetic acid). The titrant (KOH) was prepared from a carbonate-free commercial concentrate (Titrisol) and standardized by titration with a solution of potassium hydrogen phthalate, being discarded whenever the percentage of carbonate (Gran's method[17]) was higher than 0.5% of the total amount of base.

**Measurements:** The equipment used was as previously described.[18] All the potentiometric titrations were performed at 25.0 ± 0.1 °C and ionic strength ($I$) 0.10 M KCl, the atmospheric $CO_2$ being excluded from the cell by passing purified $N_2$ across the top of the experimental solution. Because of the low water-solubility of $H_2L^4$, this compound and $HL^6$ were studied in a 5% DMSO aqueous medium. For these studies, the calibration procedure was analogous to that in an aqueous medium, but in a 5% DMSO/95% water solvent mixture, and the same procedure was adopted for the parent ligand $HL^6$.

The cell ligand concentrations, in the absence and in the presence of the metal ion, at different stoichiometric conditions (1:1, 1:2 and 2:1 molar ratios), were ca. $(6.0–7.0)\times10^{-4}$ M, except for $H_2L^3$ ($C_L = 1\cdot10^{-3}$ M). The measurement of the electromotive force of the cell allowed the calculation of $[H^+]$[19] and the determined value of $K_w$ used in the computations was $10^{-13.76}$ and $10^{-13.74}$ for the water and 5% DMSO studies, respectively.

**Calculation of Equilibrium Constants:** The stepwise protonation constants, $K_i = [H_iL]/[H_{i-1}L][H]$, and the overall zinc complex stability constants, $\beta_{Zn_mH_hL_l} = [Zn_mH_hL_l]/[Zn]^m[H]^h[L]^l$, were calculated by fitting analysis of the potentiometric titration curves of the ligand in the absence and in the presence of the zinc ion, respectively, with the HYPERQUAD 2003 program.[20] The stability constants determined in aqueous medium for the $Zn^{2+}$ hydrolytic species[21] were included in all the equilibrium models proposed for the metal complex systems and the species distribution curves were plotted with the HYSS program.[20] The quoted errors are the standard deviations of the overall stability constants given by the program for the input data. The $K_i$ standard deviations were determined by the normal propagation rules and do not represent the total experimental errors.

### 4.3. $^1$H NMR Titrations

**Measurements:** $^1$H NMR titrations of solutions containing $H_2L^n$ ($n$ = 1, 2, 4, $C_L \approx 10$ mM) or of the corresponding $Zn^{II}/H_2L^n$, 1:1 systems were performed in NMR tubes. The adopted medium was $D_2O$ and 1:4 DMSO/$D_2O$ solutions for ligands $H_2L^n$, with $n$ = 1, 2 and $n$ = 4, respectively. The pH* value corresponds to the reading of the pH meter calibrated with the aqueous buffers (pH 4 and 7) and it was adjusted with DCl or $CO_2$-free KOD. The final pD values are determined from the equation pD = pH* + 0.40.[22]

**Calculation of Equilibrium Constants:** The $\log K_3^D$ value for $H_2L^2$ was calculated by fitting analysis of the experimental data, using the PSEQUAD program[23] and then that value determined in $D_2O$ was converted into the corresponding value in $H_2O$ by the equation $pK^D = 0.32 + 1.044\ pK^H$.[24]

### 4.4. IR Measurements

The solid-state IR spectra of the compounds $H_2L^n$ ($n$ = 1–4) and related zinc species were performed as KBr pellets. The complexes were prepared by adding to the ligand solution the corresponding amount of 0.0156 M $ZnCl_2$ standard solution, in order to obtain a 1:1 or 2:1 metal-to-ligand molar ratio. In the cases of $H_2L^1$, $H_2L^2$ and $H_2L^4$, 1 M HCl solution was added to enhance the solubility. Afterwards, the pH was raised (6–8) with 0.5 M KOH solution until precipitation occurred; the solid was filtered and dried before recording the IR spectra.

**Supporting Information** (see also the footnote on the first page of this article): Figure S1 containing the $^1$H NMR titration curves of $H_2L^1$ and 1:1 $Zn^{II}/H_2L^1$ systems and Figure S2 containing species distribution diagrams for the 1:2 $Zn^{2+}$-to-ligand systems with ligands $H_2L^n$ ($n$ = 1–4).

## Acknowledgments

The authors thank Portuguese Fundação para a Ciência e Tecnologia (FCT) (SFRH/BD/10714/2002) and the European COST-D21-001 project program for financial support.

[1] C. M. Overall, O. Kleifeld, *Nat. Rev. Cancer* **2006**, *6*, 227–239.
[2] C. T. Supuran, A. Scozzafava, "Matrix Metalloproteinases (MMPs)" in *Proteinase and Peptidase Inhibition: Recent Potential Targets for Drug Development* (Eds.: H. J. Smith, C. Simons), Taylor & Francis, London, New York, **2002**, p. 35–61.
[3] E. Svastova, A. Hulikova, M. Rafajova, M. Zat'ovicova, A. Gibadulinova, A. Casini, A. Cecchi, A. Scozzafava, C. T. Supuran, J. Pastorek, S. Pastorekova, *FEBS Lett.* **2004**, *577*, 439–445.
[4] C. T. Supuran, A. Casini, A. Scozzafava, *Med. Res. Rev.* **2003**, *23*, 535–558.
[5] A. Scozzafava, C. T. Supuran, *J. Med. Chem.* **2000**, *43*, 3677–3678.
[6] A. Casini, A. Scozzafava, A. Mastrolorenzo, C. T. Supuran, *Curr. Cancer Drug Targets* **2002**, *2*, 55–75.
[7] R. Morphy, Z. Rankovic, *J. Med. Chem.* **2005**, *48*, 6523–6543.
[8] M. A. Santos, S. M. Marques, T. Tuccinardi, P. Carelli, L. Panelli, A. Rossello, *Bioorg. Med. Chem.*, in press.
[9] M. A. Santos, S. M. Marques, D. Vullo, A. Innocenti, A. Scozzafava, C. T. Supuran, unpublished results.
[10] M. A. Esteves, A. Cachudo, C. Ribeiro, S. Chaves, A. Rossello, M. A. Santos, *Metal Ions in Biology and Medicine*, John Libbey Eurotext, **2006**, vol. 9, p. 35–39.
[11] M. A. Esteves, A. Cachudo, S. Chaves, M. A. Santos, *Eur. J. Inorg. Chem.* **2005**, 597–605.
[12] S. Chaves, S. Marques, M. A. Santos, *J. Inorg. Biochem.* **2003**, *97*, 345–353.

 © 2006 Wiley-VCH Verlag GmbH & Co. KGaA, Weinheim 

[13] B. Kurzak, H. Kozlowski, P. Decock, *J. Inorg. Biochem.* **1991**, *41*, 71–78.
[14] R. M. Smith, A. E. Martell, *Critical Stability Constants*, Plenum, New York, **1989**, vol. 6, p. 2.
[15] E. B. Paniago, S. Carvalho, *Inorg. Chim. Acta* **1987**, *136*, 159–163.
[16] G. Socrates, *Infrared and Raman Characteristic Group Frequencies, Tables and Charts*, John Wiley & Sons, Chichester, **2001**; W. P. Griffith, S. I. Mostafa, *Polyhedron* **1992**, *11*, 2997–3005.
[17] F. J. C. Rossotti, H. Rossotti, *J. Chem. Educ.* **1965**, *42*, 375–378.
[18] S. Chaves, S. Marques, L. Gano, M. A. Santos, *J. Inorg. Biochem.* **2003**, *97*, 161–172.
[19] M. A. Santos, M. Gil, S. Marques, L. Gano, G. Cantinho, S. Chaves, *J. Inorg. Biochem.* **2002**, *92*, 43–54.
[20] P. Gans, A. Sabatini, A. Vacca, *Talanta* **1996**, *43*, 1739–1753.
[21] R. M. Smith, A. E. Martell, *Critical Stability Constants*, Plenum, New York, **1976**, vol. 4, p. 9.
[22] A. K. Covington, M. Paabo, R. A. Robinson, R. G. Bates, *Anal. Chem.* **1968**, *40*, 700–706.
[23] L. Zékány, I. Nagypál, G. Peintler, *PSEQUAD* 501, **2001**.
[24] R. Delgado, J. J. R. Fraústo da Silva, M. T. S. Amorim, M. F. Cabral, S. Chaves, J. Costa, *Anal. Chim. Acta* **1991**, *245*, 271–282.

Received: May 11, 2006
Published Online: July 25, 2006

 © 2006 Wiley-VCH Verlag GmbH & Co. KGaA, Weinheim 

DOI: 10.1002/ejic.200600574

# Click Chemistry with an Active Site Variant of Azurin

**Thyra E. de Jongh,[a] Anne-Marie M. van Roon,[a][‡] Miguel Prudêncio,[a][‡‡] Marcellus Ubbink,[a] and Gerard W. Canters*[a]**

**Keywords:** Metalloproteins / Protein structures / Zinc / Copper / Metal replacement

The active site of the blue copper protein azurin (Azu) from *Pseudomonas aeruginosa* consists of a Cu ion immobilized by bonds to four amino acid side chains. The protein assists in electron transfer *in vivo*. Replacement of Cu-ligand His117 by a Gly makes the Cu site accessible for exogenous ligands. Incubation of the H117G Azu with *n*-alkane linkers carrying imidazole groups at opposite ends leads to the formation of noncovalently linked Azu dimers. The active site of H117G Azu is vulnerable to Cu-catalyzed oxidative attack. Replacement of $Cu^{II}$ by $Zn^{II}$ leads to stable dimers, whose structures have been determined by X-ray diffraction. These structures are reported here. The similarity in the structure of the active site between the wild type (*wt*) Zn-Azu and the dimer is remarkable in light of the different relation of the coordinating imidazole to the protein framework (covalently attached vs. exogenous origin, respectively). The part of the "ligand loop" running from amino acid 116 to 121 has acquired increased flexibility in the mutant. The connected subunits have adopted an unexpected orientation relative to each other.

(© Wiley-VCH Verlag GmbH & Co. KGaA, 69451 Weinheim, Germany, 2006)

## Introduction

When applied to proteins, "click" chemistry can provide decisively new insight in structure and function. Click chemistry refers to the technique by which a side chain or a prosthetic group is removed from a protein framework, either chemically or by site-directed mutagenesis, and the resulting gap is filled by exogenous compounds. In this way, modified flavins or heme groups have been inserted into the apo forms of flavoproteins and heme proteins.[1–3] It allows the modification of active sites of enzymes in a simple and straightforward manner. When the prosthetic group is extended with a linker ("hot wire"), click chemistry can also allow for the connection of the active site of an enzyme to a partner molecule or to an electrode.

In copper-containing proteins, the active site consists of one or more Cu ions that are immobilized in the protein through coordinate bonds to side chains. By replacing one of these side chains by a small amino acid (Gly or Ala), the Cu centre becomes directly accessible for exogenous ligands. The technique has been successfully applied to the active site of blue copper proteins and to the type-1 site of the Cu-containing nitrite reductase.[4,5]

[a] Leiden Institute of Chemistry, Leiden University, Gorlaeus Laboratories
Einsteinweg 55, P. O. Box 9502, 2300 RA Leiden, The Netherlands
Fax: +31-71-527-4349
E-mail: canters@chem.leidenuniv.nl
[‡] Current address: MRC Laboratory of Molecular Biology, Hills Road, Cambridge CB2 2QH, United Kingdom
[‡‡]Current address: Unidade de Malária, Instituto de Medicina Molecular, Faculdade de Medicina de Lisboa, Av. Prof. Egas Moniz, 1649-028 Lisbon, Portugal

In the case of the small blue copper protein azurin (Azu) from *Pseudomonas aeruginosa*, His117 has been subjected to such modification. In Azu the Cu is bound by the Sγ and Sδ atoms of Cys112 and Met121, respectively, and the Nδ atoms of the residues His46 and His117. There is also a weak interaction with the backbone carbonyl of Gly45.[6] Azu is an electron-transfer protein, possibly involved in oxidative stress response.[7] With many electron-transfer proteins, a small part of the prosthetic group (flavin in the case of flavodoxins or heme in the case of cytochromes, for instance) or the active centre (the Fe-S cluster in ferredoxins or the Cu site in cupredoxins, for instance) is directly accessible from the outside. In Azu this part of the structure is formed by the Cu-ligand His117. It protrudes through the protein surface at a shallow depression in the so-called hydrophobic patch. His117 provides for electronic coupling with the Cu and, presumably, represents the site where physiological partners dock.[8,9]

Replacement of His117 by a Gly results in a slightly destabilized form of the protein with a Cu site that has been classified as Type-2 with spectral characteristics (EPR, UV/Vis) that clearly differ from the native protein but revert to those of the native protein upon incubation with imidazole.[4,10,11] So far, attempts to determine the structure of this Azu variant by crystallography failed because the destabilized Cu site appears vulnerable to $Cu^{2+}$ catalyzed oxidative attack by oxygen, which converts the Cys112 sulfur into a sulfonate.[12] NMR studies showed an increased mobility of the ligand loop (running from Cys112 to Met121) on which His117 is located.[13] Click chemistry can enable the formation of protein multimers by using multifunc-

 © 2006 Wiley-VCH Verlag GmbH & Co. KGaA, Weinheim InterScience 

tional linkers. It has, for instance, been shown that the incubation of H117G Azu with 1,ω-di(imidazol-1-yl)-*n*-alkane linkers leads to formation of dimers when butane, pentane and hexane are employed as the alkane moiety.[14]

In principle, the Cu-catalyzed oxidative modification of the Cu site in H117G Azu should be avoidable by substituting the Cu by the redox-inactive Zn. It is known that in the small blue copper proteins this substitution leads to minimal distortion of the native structure and of the active site in particular, the changes in the latter being limited to a shortening of the $M^{2+}$–Gly45 carbonyl bond and an elongation of the $M^{2+}$–Sδ(Met121) bond.[15]

Here we report on the preparation and characterization of the 1,5-di(imidazol-1-yl)pentane (1,5-dip) and 1,6-di(imidazol-1-yl)hexane (1,6-dih) linked dimers of Zn-H117G Azu. The results provide insight into the structural and dynamic properties of the H117G Azu variant. In particular, they give an unexpected perspective on the mobility of the ligand loop in native and H117G Azu.

## Results

### Dimerization of Zn-H117G Azurin

As Zn-H117G Azu is colourless, coordination of the imidazole-based linkers can not be followed by the green-to-blue optical transition that occurs upon coordination of

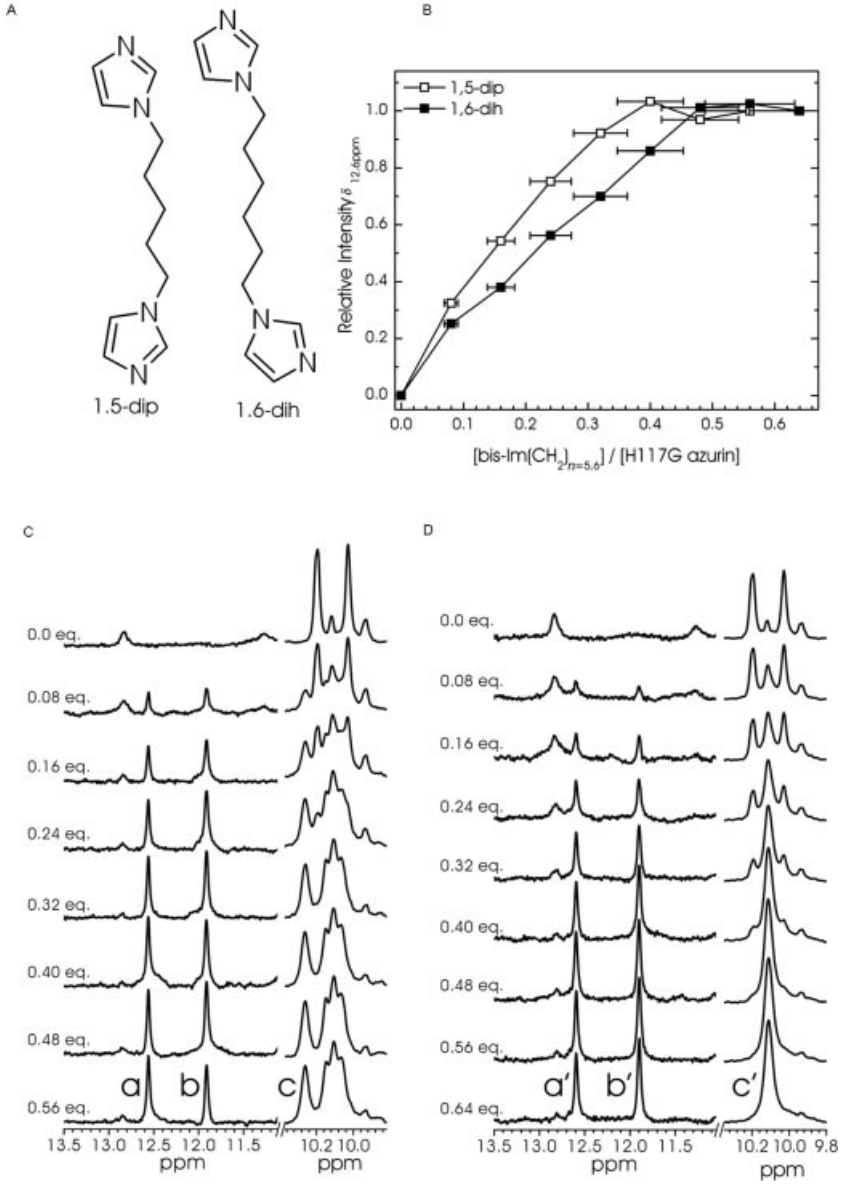


Figure 1. Titration of Zn-H117G Azu with linkers 1,5-dip and 1,6-dih (A): (B) Relative averaged intensity of resonance a [1,5-dip (□)] and resonance a′ [1,6-dih (■)] of Zn-H117G at increasing ratios of linker to protein (see also panels C and D). (C) and (D): High-field regions of the $^1$H NMR spectra of 1 mM Zn-H117G Azu upon titration with 1,5-dip (C) or 1,6-dih (D), at pH 6.5 and 305 K for different molar equivalents of linker to Zn-H117G Azu.

 © 2006 Wiley-VCH Verlag GmbH & Co. KGaA, Weinheim 

imidazole to $Cu^{II}$-H117G Azurin.[4,10] Instead, ligand binding was monitored by $^1H$ NMR spectroscopy. Addition of 0.7 molar equiv. of 1,5-dip or 1,6-dih to apo-H117G Azu had no discernible effect on the $^1H$ NMR spectrum (not shown), whereas subsequent addition of a slight molar excess of $Zn(SO_4)_2$ to the sample led to the occurrence of several new protein resonances in the downfield region of the spectrum (Figure 1C, D). This demonstrates the formation of a new species for which Zn is required. The new species exhibits a 3–4 Hz increase in line width corresponding to a 40–60% increase in $T_2^{-1}$. As the latter varies proportionally with the rotational correlation time, $\tau_c$, the increase in line width reflects an increase in $\tau_c$. While doubling of the molecular weight should be accompanied with a doubling of $\tau_c$ for a spherical molecule, the smaller increase may reflect the nonspherical shape of the dimer. The line broadening and the appearance of new resonances confirm the formation of $Zn^{II}$-His117Gly Azu dimers noncovalently linked by di(imidazolyl)alkanes.

To check the stoichiometry, samples of Zn-H117G Azu were titrated with 1,5-dip and 1,6-dih. The NMR spectra are shown in Figure 1C and Figure 1D. In the course of the 1,5-dip titration, the signals at 12.56, 11.91 and 10.26 ppm (Figure 1C: signals a, b and c) grew, while the peaks around 10.1 ppm, consisting of a number of partially overlapping signals, changed shape. Similar observations were made for signals at 12.59, 11.90 and 10.11 ppm (Figure 1D: signals a′, b′ and c′) in the case of the 1,6-dih titration. In the latter case, signal c′ almost completely overlaps with the signals clustered around 10.1 ppm. The average intensities of signals a and a′ as a function of the added amount of linker are shown in Figure 1B. The signal intensities depend on the equilibria L + A ⇄ LA and LA + A ⇄ ALA, with dissociation constants $K_1$ and $K_2$, respectively. Reliable determinations of $K_1$ and $K_2$ require concentrations of the reactants at which there is substantial dissociation. Since $K_1$ and $K_2$ are expected to be in the micromolar range,[14] and NMR measurements require millimolar quantities for the titrations, no accurate $K$ values could be extracted from Figure 1B. What the data do demonstrate is that the equivalence point in the titration is reached at an [L]/[A] ratio of about 1:2, confirming that one linker molecule associates with two Azu molecules. (The accuracy of the data points in Figure 1B is limited by an uncertainty in the linker concentration and the inherent inaccuracy of the peak intensities caused by line-width variations in the NMR spectra. This explains why the equivalence points are not reached at exactly [L]/[A] = 1:2.)

### Crystal Structure of (Zn-H117G)$_2$-1,6-dih Azurin

From diffraction data collected at 100 K, the crystal structure of (Zn-H117G)$_2$-1,6-dih Azu was solved to 2.85 Å resolution (Table 3). Data collected at room temperature showed that the resolution is directly limited by the quality of the crystals and is not affected by the freezing process. The asymmetric unit contains a total of four protein molecules arranged as a pair of dimers (Figure 2), reminiscent of the molecular arrangement observed in crystals of *wt* Azurin.[16] Each of the molecules within the dimer is aligned with its long axis roughly parallel to the 1,6-dih linker. The intramolecular Zn-to-Zn distance amounts to 16.1 Å. The four molecules within the asymmetric unit are superimposable with an RMSD of 0.4 Å for the Cα trace of the entire protein backbone, which diminishes to 0.2 Å when the loop region between residues 116 and 120 is excluded, indicating a well conserved core structure. The Cα trace of Zn-H117G Azu, averaged over all four molecules in the asymmetric unit, is superimposable with *wt* Zn-Azu within 1.1 Å which diminishes to 0.5 Å when residues 116–120 are ignored. The structural details of the metal site are reported in Table 1.

Table 1. Bond lengths and angles between ligands and the metal centre (M) in structures of Azu (*P. aeruginosa*).[a]

| Bond lengths [Å] | $Cu^{I}$-*wt* (1E5Y, 2.0 Å) | $Cu^{II}$-*wt* (4AZU, 1.9 Å) | $Zn^{II}$-*wt* (1E67, 2.14 Å) | Zn-H117G-1,6-dih (2.85 Å) |
|---|---|---|---|---|
| Gly45–M | 3.02 (0.06) | 2.76 (0.49) | 2.32 (0.07) | 1.99 (0.01) |
| His46–M | 2.14 (0.07) | 2.29 (0.29) | 2.07 (0.04) | 2.06 (0.02) |
| Cys112–M | 2.29 (0.01) | 2.24 (0.04) | 2.30 (0.02) | 2.34 (0.01) |
| Met121–M | 3.25 (0.06) | 3.15 (0.05) | 3.38 (0.07) | 3.51 (0.15) |
| His117/Linker–M | 2.10 (0.07) | 2.01 (0.05) | 2.01 (0.03) | 2.07 (0.01) |
| Bond angles [°] | | | | |
| Sγ112–M–Nδ46 | 133 (2) | 132 (3) | 128 (3) | 136 (1) |
| Sγ112–M–Nδ117/Linker | 122 (1) | 122 (2) | 121 (1) | 98 (13) |
| Sγ112–M–Sδ121 | 113 (1) | 110 (1) | 103 (1) | 99 (2) |
| Nδ46–M–Sδ121 | 72 (1) | 77 (3) | 70 (2) | 67 (2) |
| Nδ46–M–Nδ117/Linker | 105 (2) | 105 (2) | 110 (3) | 118 (10) |
| Sδ121–M–Nδ117/Linker | 91 (4) | 87 (2) | 83 (1) | 81 (2) |
| O45–M–Nδ46 | 75 (1) | 74 (3) | 84 (1) | 89 (4) |
| O45–M–Sδ121 | 145 (1) | 148 (2) | 152 (2) | 152 (3) |
| O45–M–Nδ117/Linker | 87 (2) | 89 (1) | 98 (2) | 102 (4) |
| O45–M–Sγ112 | 99 (1) | 105 (10) | 101 (1) | 107 (1) |
| $N_2S$–M distance [Å] | 0.09 (0.01) | 0.06 (0.07) | – 0.16 (0.04) | – 0.32 (0.08) |

[a] The bond lengths and angles were obtained by averaging over all the molecules within the asymmetric unit. Numbers between brackets indicate standard deviations.

 © 2006 Wiley-VCH Verlag GmbH & Co. KGaA, Weinheim 

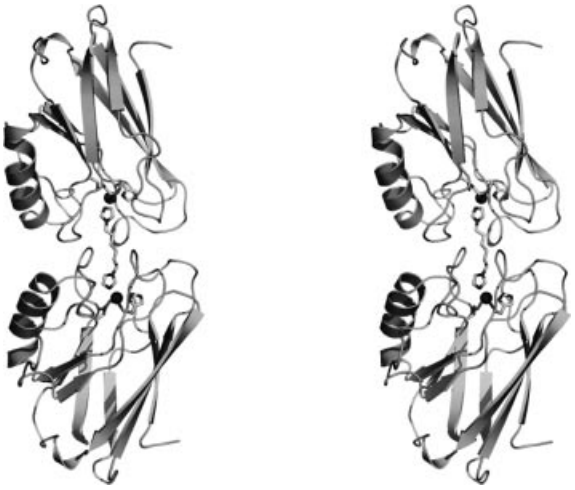

Figure 2. Stereo view of the $(Zn\text{-}H117G)_2$-1,6-dih Azu dimer. The side chains of residues G45, H46, C112, and M121 as well as the 1,6-dih linker are shown as sticks while both zinc atoms are depicted as spheres.

## Discussion

### Metal Site Structure

Although the limited resolution of the structure of the H117G dimer reported here requires caution with the interpretation of the data, averaging over all of the molecules within the asymmetric unit permits us to compare the structural characteristics of the metal site with those in *wt* $Cu^{II}$- and $Zn^{II}$-Azu (Table 1). The main structural difference between the $Cu^{II}$ and $Zn^{II}$ sites in *wt* Azu relates to the decrease in the distance between the metal and the carbonyl of Gly45 and the concomitant increase in the metal–Sδ(Met121) distance when Cu is substituted by Zn. Clearly, the "hard" Zn ion is pulled over from the "soft" sulfur ligand to the "harder" oxygen ligand so that the Zn ion ends up at the other side of the $N_2S$ plane as compared with the Cu ion. A similar observation applies for *wt* Zn-H117G Azurin.[15] The extent to which the structural details of the Zn site in the dimer seem to reproduce those of the *wt* Zn-Azu is remarkable, despite the fact that the imidazole ring is not covalently attached to the protein framework in the dimer. In particular, the positions of the three hard ligands His46, Ser112, and His117/Linker which together form a near-equatorial plane are well conserved. The two axial ligands Met121 and Gly45 show slightly larger deviations relative to *wt* Zn-Azu. They form weak coordinate bonds to the Zn ion and have more positional freedom.

### NMR Titration

The NMR titration data (Figure 1) clearly demonstrate that the $Zn^{II}$-H117G Azu does bind the bifunctional linkers used for this study. The signals used to follow the titration have not been assigned. In native *wt* $Cu^{I}$ Azu there are seven distinct high-field signals in the range of from 9.60 to 11.30 ppm.[27] They derive from the backbone amide protons of Asn38, Asn47, Thr52, Ile87, Thr113, Phe114 and Ser118. Three of these stand out because they occur at very high chemical shift positions: 11.30 (N38), 10.58 (N47) and 10.48 (F114) ppm. Those of N47 and F114, in the *wt* structure, form a H-bridge with the Sγ of the Cys112 metal ligand; their chemical shifts to some extent reflect the charge distribution over the metal site. The amide proton of Asn38 forms a H-bridge with the carboxyl group of Asp11 which is located in the interface of the $Zn^{II}$-H117G Azu-dimer. One expects these three signals to stand out in the spectrum of the dimer as well, but a definitive identification of the high-field signals a–c and a′–c′ must await a detailed assignment of the spectrum. The low-intensity resonances at 10.14 and 9.96 ppm derive from an apo-Azu impurity.

### Ligand Loop Dynamics

Although the overall protein structure of each of the subunits is very similar to *wt* Zn-Azu, the loop on which residues 116 to 119 are located has adopted different conformations in each of the four subunits in the asymmetric unit (Figure 3A). They all have relatively high B factors indicative of increased flexibility (Figure 3B) This flexibility is understandable, given that in H117G Azu the loop is comprised of a series of small, flexible amino acids (Gly-Gly-Ser-Ala) and is consistent with the finding by Jeuken et al. that for $Cu^{I}$-H117G Azu the residues 116–120 display increased backbone dynamics in solution relative to *wt* Azu.[13]

It is interesting to note that the complete ligand loop runs from Cys112 to Met121 but that only the part running from residues 116–119 shows enhanced disorder. Apparently residues 112–115 are sufficiently strongly anchored to the protein framework to keep them fixed in the structure even when His117 is replaced by a Gly. Of the residues 116–119 in the *wt* structure, only the side chain of His117 is anchored to the protein structure, namely through a bond of the imidazole ring to the Cu. Yet, this is not what keeps His117 in place because in apo-Azu this loop retains its native conformation.[17] It is found that some of the ligand loop residues of $Zn^{II}$-H117G Azu occur in the disallowed regions of the Ramachandran plot (Figure 4). These dihedral angles have become accessible to the protein only because the His117 has been replaced by a Gly. It is therefore impossible for the ligand loop in *wt* Azu to adopt a configuration as seen here. To what extent the flexibility of the ligand loop in Azu differs from those in other blue copper proteins like plastocyanin, pseudoazurin and amicyanin remains to be seen.

### Interface Packing and Solvation

It is of interest to compare the relative orientation of the Azu monomers in the $(Zn\text{-}H117G)_2$-1,6-dih Azu structure with what has been observed for *wt* Azu. For *wt* Azu, the α-helices of the two monomers are situated on opposite sides of the dimer (Figure 5). Covalent dimers of Azu, in

 © 2006 Wiley-VCH Verlag GmbH & Co. KGaA, Weinheim 

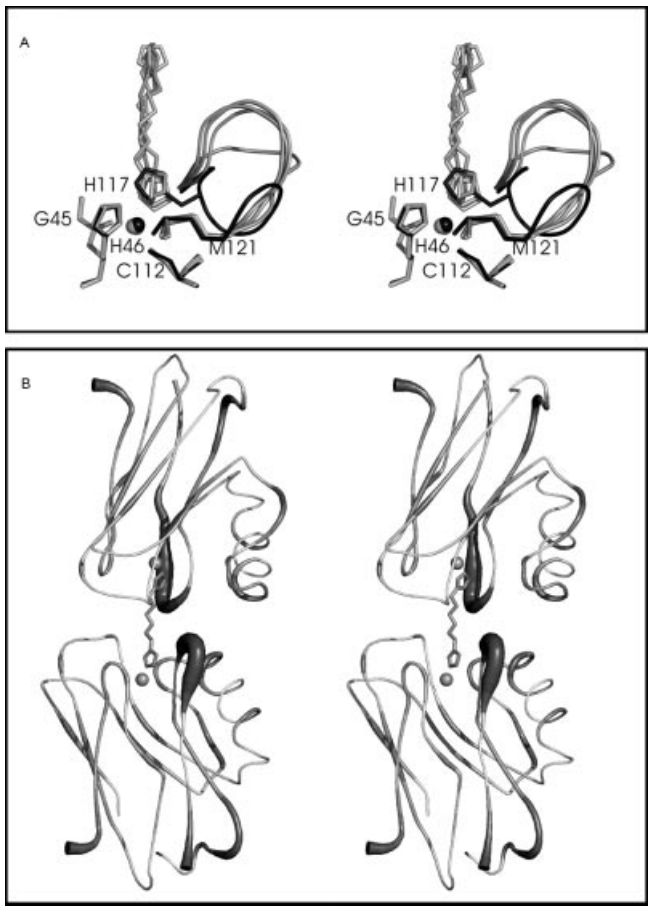


Figure 3. Representation of structural data. (A) Stereo view of residues G45, H46, C112, H/G117 and M121 of each of the monomeric subunits of (Zn-H117G)$_2$-1,6-dih Azu (grey) in the asymmetric unit, superimposed on the structure of Zn-*wt* Azu (black). The ligand loops between residues 115–121 are shown in cartoon representation; the zinc atoms are shown as spheres. Labels correspond to the ligands of *wt* Azu. (B) Stereo image of one of the dimers of (Zn-H117G)$_2$-1,6-dih Azu observed in the asymmetric unit. Darker shading and larger tube diameter indicate increased B factors. The 1,6-dih linker is shown in stick representation; the zinc atoms are shown as spheres. The dimer shown has the most flexible ligand loops of the two dimers found within the asymmetric unit.

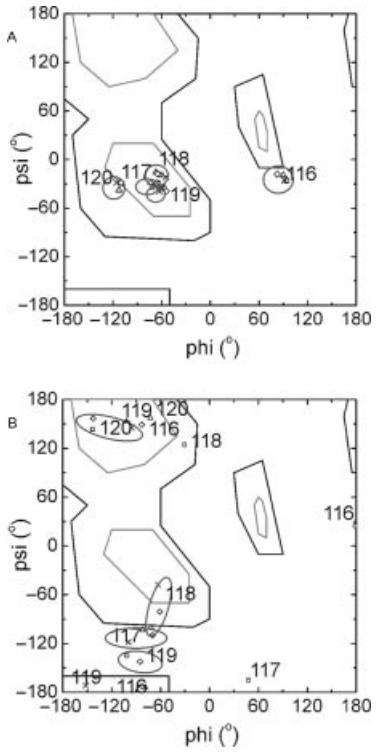


Figure 4. Ramachandran plots of the loop residues 116-120 of (A) Zn-*wt* Azu and (B) (Zn-H117G)$_2$-1,6-dih Azu. Different symbols are used to represent the individual amino acid chains within the asymmetric unit.

Figure 5. Cartoon representations of (Zn-H117G)$_2$-1,6-dih Azu (left) and the crystal packing of Zn-*wt* Azu (right); the α-helical regions are shown in dark grey. The zinc atoms are shown as large spheres (black). Hydrogen-bonded water molecules in the protein interface of *wt* Azu are shown as small spheres (light grey).

which the Azu moieties are connected through a bis(maleimidomethyl) ether (BMME) linker also have a tendency to adopt this orientation.[18] In contrast, the structure of the noncovalent dimer of (Zn-H117G)$_2$-1,6-dih Azu, in which the metal ions are connected with the linker through coordinate Zn-imidazole bonds, has both α-helices on the same side (Figure 5). Somewhat similar orientations have been observed for the C112D and F114A mutants of Azu (1AG0 and 1AZN, respectively).[19,20]

Although the interface area in the dimer is largely retained, its solvent accessibility is slightly larger than that in the structures of *wt* Azu or the BMME-linked N42C Azu-dimer, both of which display the classical hydrophobic interaction packing (Table 2).[16,18,21] A disulfide-linked N42C Azu dimer does not fit in this comparison and is a separate case: its *intra*-dimer interface is very small (ca. 360 Å$^2$) since two monomers are rotated around the C42–C42 disulfide bond as compared with the *wt* packing. The *inter*-dimer interface is sizeable but smaller than in the *wt* case. The decrease in interface for the (Zn-H117G)$_2$-1,6-dih Azu, however, although not large, is significant and is related to

 © 2006 Wiley-VCH Verlag GmbH & Co. KGaA, Weinheim 

Table 2. Solvent accessibility and interface area in azurin dimers.

| | Accessible surface area [Å$^2$] per monomer Free[a] | Complex[b] | Interface area [Å$^2$] |
|---|---|---|---|
| *wt* (1E5Y) *inter* | 6579 | 6066 | 1026 |
| N42C-BMME (1JVL) *intra* | 6547 | 6050 | 995 |
| N42C-disulfide bridged (1JVO) *intra* | 6524 | 6343 | 363 |
| N42C-disulfide bridged (1JVO) *inter*[c] | 6524 | 6033 | 983 |
| (Zn-H117G)$_2$-1,6-dih *intra* | 6687 | 6205 | 964 |

[a] The coordinate file used for the calculation contained a single monomer; additional monomers were removed from the asymmetric unit. [b] The coordinate files used for the calculation were edited to contain only the molecules that share the contact surface under consideration. [c] Numbers correspond to the intermolecular interface between two different dimers in the asymmetric unit.

the packing of the monomers. From previous experiments on H117G Azu it was concluded that 1,5-dip gives optimal packing of the Azu monomers and that 1,6-dih Azu is slightly too long to let monomers approach as close as in the *wt* case.[14] The increase in metal-to-metal distance in the Zn-H117G Azu dimer (16.1 Å *vs.* 14.9 Å in *wt* Azu[16]) is in line with this conclusion. A slightly larger distance between the two Azu halves in the dimer would also mean a smaller contact area, in agreement with the data in Table 2.

The findings reported here and in the preceding discussion show that the packing of two Azu molecules with their hydrophobic patches together is thermodynamically favourable. Previous experiments have shown that the gain in free energy when two Azu molecules associate is 2.1 kcal/mol.[14] The present data show that Azu molecules prefer to pack with their hydrophobic patches opposite to each other, but that the precise mutual orientation of the monomers may vary and probably depends on small variations in the free energy of association caused by small adjustments in the van der Waals energy, remote charge effects and the precise configuration of hydrogen bridges across the interface.

## Conclusions

Site-directed mutagenesis of the copper ligand H117 of the blue copper protein Azu (*P. aeruginosa*) creates a solvent-exposed aperture in the protein, which can accommodate a variety of ligands, thereby permitting "hotwiring" of the protein. Incubation of the H117G variant with bifunctional linkers like the 1,ω-di(imidazol-1-yl)-*n*-alkanes allows the formation of Azu dimers noncovalently linked by the functionalized alkanes. The (Zn-H117G)$_2$-1,6-dih Azu dimer was crystallized and its structure was solved to 2.85 Å resolution. Relative to *wt* Azu, H117G Azu shows increased flexibility in the loop region between residues 116–120, surrounding the site of mutation. The displacement of this loop from the protein interior may facilitate the coordination of larger exogenous ligands. The structure represents a type of dimer in which the proteins have adopted a relative orientation distinct from those previously reported for dimers of Azu.

## Experimental Section

**Protein Expression and Isolation:** Apo-H117G Azu was produced and purified as described previously. The concentration of apoprotein was determined from the absorbance at 280 nm ($\varepsilon_{280}$ = 9.1 ± 0.1 mM$^{-1}$ cm$^{-1}$) recorded at room temperature (r.t.) on a Perkin–Elmer lambda 18 spectrophotometer.

**Linkers:** The bifunctional ligands (Figure 1A) 1,5-di(imidazol-1-yl)pentane and 1,6-di(imidazol-1-yl)hexane were synthesized as previously reported.[14] Purity and integrity of the samples after prolonged storage was confirmed by $^1$H NMR and working solutions of 6 mM were prepared in MilliQ grade water.

**NMR Spectroscopy:** All $^1$H NMR spectra were recorded with a Bruker Avance DMX 600 MHz spectrometer at 304 K with a spectral width of 12.98 ppm in 4 K memory by using a Watergate-filtered pulse sequence. Free induction decays were Fourier transformed by using a squared sine window function. All samples were prepared in potassium phosphate ($KP_i$), pH 6.5 buffer (20 mM) supplemented with 6% $D_2O$ for locking of the signal. The binding of 1,6-dih to Zn-H117G Azu was assessed by addition of linker (0.7 equiv.) to a solution of apo-H117G Azu (0.5 mM). After recording of the $^1$H NMR spectrum, $Zn(SO_4)_2$ (2 equiv.) was added, and the sample was incubated at r.t. for ca. 10 min allowing coordination of the linker to the reconstituted protein. The effects of coordination of 1,6-dih or 1,5-dip on the $^1$H NMR spectra of Zn-H117G Azu were compared by titration of protein (1 mM) in $KP_i$, (20 mM, pH 6.5) with either of the linkers. Zn-H117G Azu was prepared by incubating a solution of the apoprotein at the desired concentration with $ZnSO_4$ (1.2 equiv.) for 10 min at r.t. This solution was used as prepared.

**Crystallization and X-ray Data Collection:** A solution of apo-H117G Azu (10 mg/mL) in Tris-HCl (10 mM, pH 7.5) was incubated with $ZnCl_2$ (1.3 equiv.) for 2 h at r.t. Excess $ZnCl_2$ was removed by ultracentrifugation (Centricon, MWCO 10,000). The sample was then incubated with either 1,5-dip (0.6 equiv.) or 1,6-dih (0.6 equiv.). Prior to crystallization the samples were filtered through a low-protein-binding, 0.22-μm filter (Millipore). Crystals of (Zn-H117G)$_2$-1,6-dih were obtained by sitting drop vapour diffusion at 295 K by using equal volumes of protein and reservoir solution. Crystals suitable for X-ray crystallography appeared within 3 d, from protein solution (1 μL) mixed with reservoir solution (1 μL) containing Tris-HCl (100 mM, pH 8.56) and 20% (w/v) polyethylene glycol (PEG) 8000. No crystals were obtained for (Zn-H117G)$_2$-1,5-dip. X-ray diffraction data of (Zn-H117G)$_2$-1,6-dih were collected on an in-house beam by using a MAR345 Image Plate detector. A crystal was mounted in a cryo-loop (Hampton Research) and passed quickly through a cryo-protectant solution

 © 2006 Wiley-VCH Verlag GmbH & Co. KGaA, Weinheim 

containing 20% glycerol, followed by flash-freezing in a nitrogen gas stream at 100 K. A data set was collected to 2.85 Å resolution. All collected data were indexed, integrated and scaled with HKL2000.[22] Data collection and refinement statistics can be found in Table 3.

Table 3. X-ray diffraction data collection, refinement and model statistics.

| | |
|---|---|
| **Data collection** | |
| Space group | *P*1 |
| Unit cell parameters $a \times b \times c$ [Å] | 42.66 × 49.72 × 66.07 |
| Resolution [Å][a] | 25–2.85 (2.9–2.85) |
| Measured reflections | 28364 |
| Unique reflections | 11979 |
| Completeness (%) | 88.2 |
| $R_{merge}$[b] (%) | 8.7 (34.1) |
| Average *I*/sigma (*I*) | 9.36 (1.83) |
| **Refinement statistics** | |
| *R*-factor (%) | 19.2 (32.5) |
| Free *R*-factor (%) | 23.3 (44.7) |
| Average total B-value protein [Å$^2$] | 30.5 |
| **Model statistics** | |
| Number of TLS groups | 4 |
| Number of monomers in the asymmetric unit | 4 |
| Number of protein residues | 512 |
| Number of solvent molecules | 3 |
| Number of Zn ions | 4 |
| Number of ligands | 2 |
| **Ramachandran plot (%)** | |
| Most favoured region | 89.5 |
| Additionally favoured region | 10.2 |
| Generally favoured region | 0.2 |
| Disallowed region | 0.1 |
| **R.m.s. deviation from ideality** | |
| Bond lengths [Å] | 0.013 |
| Bond angles [°] | 1.070 |

[a] Values of reflections recorded in the highest resolution shell are shown in parentheses. [b] $R_{merge} = \Sigma_o(|I-<I>|)/\Sigma(I)$ (scalepack output). The coordinates have been deposited in the Protein Data Bank under accession code 2IWE.

**Structure Determination and Refinement:** The structure of (Zn-H117G)$_2$-1,6-dih was solved by molecular replacement by using the program Molrep[23] from the CCP4 program suite[24] by employing the structure of Zn-*wt* Azu (PDB entry 1E67)[15] as a search model. A solution was obtained with an *R* factor of 39.7% and a correlation coefficient of 58.8. After several rounds of rigid-body and restrained refinement with Refmac5,[25] the mutated amino acids were built in manually with Xtalview,[26] followed by automatic solvent building with ARP/wARP.[27] Upon inspection of an $F_o - F_c$ difference density map, a double conformation of the main chain running from residue G116 to M121 of molecule A could be modelled and refined, leading to an improvement of $R_{free}$. Extra density was also observed for this flexible loop in the three other molecules present in the asymmetric unit but was considered too weak to build any amino acids. Final refinement by using tight NCS restraints between residues 1 to 114 of each protein chain and refinement of translation, liberation and screw (TLS) parameters[28] resulted in a model with an *R* factor of 19.2% ($R_{free}$ 23.3%). The quality of the model was checked by PROCHECK[29] and WHATIF[30] (see Table 3). The coordinates and structure factors have been deposited in the Protein Data Bank under accession code 2IWE. Figure 2, Figure 3 and Figure 5 were made in PyMOL 0.98.[31] Figure 3 was generated with the help of the color_b.py script for colouring according to B factor (http://adelie.biochem.queensu.ca/~rlc/).

**Solvent Accessibility and Interface Areas:** The solvent-accessible surface area (ASA) was calculated by using the program NACCESS 2.1.1 with a probe radius of 1.4 Å. The interface area was defined as the sum of the ASAs of the individual proteins minus the ASA of the complex.


[1] I. Hamachi, S. Shinkai, *Eur. J. Org. Chem.* **1999**, 539–549.
[2] T. Hayashi, Y. Hitomi, T. Takimura, A. Tomokuni, T. Mizutani, Y. Hisaeda, H. Ogoshi, *Coord. Chem. Rev.* **1999**, *192*, 961–974.
[3] A. Riklin, E. Katz, I. Willner, A. Stocker, A. F. Buckmann, *Nature* **1995**, *376*, 672–675.
[4] T. den Blaauwen, M. van de Kamp, G. W. Canters, *J. Am. Chem. Soc.* **1991**, *113*, 5050–5052.
[5] H. J. Wijma, M. J. Boulanger, A. Molon, M. Fittipaldi, M. Huber, M. E. P. Murphy, M. P. Verbeet, G. W. Canters, *Biochemistry* **2003**, *42*, 4075–4083.
[6] H. Nar, A. Messerschmidt, R. Huber, M. van de Kamp, G. W. Canters, *J. Mol. Biol.* **1991**, *218*, 427–447.
[7] E. Vijgenboom, J. E. Busch, G. W. Canters, *Microbiology* **1997**, *143*, 2853–2863.
[8] M. van de Kamp, M. C. Silvestrini, M. Brunori, J. van Beeumen, F. C. Hali, G. W. Canters, *Eur. J. Biochem.* **1990**, *194*, 109–118.
[9] M. van de Kamp, R. Floris, F. C. Hali, G. W. Canters, *J. Am. Chem. Soc.* **1990**, *112*, 907–908.
[10] T. den Blaauwen, G. W. Canters, *J. Am. Chem. Soc.* **1993**, *115*, 1121–1129.
[11] T. den Blaauwen, C. W. G. Hoitink, G. W. Canters, J. Han, T. M. Loehr, J. Sanders-Loehr, *Biochemistry* **1993**, *32*, 12455–12464.
[12] C. Hammann, G. van Pouderoyen, H. Nar, F. X. G. Ruth, A. Messerschmidt, R. Huber, T. den Blaauwen, G. W. Canters, *J. Mol. Biol.* **1997**, *266*, 357–366.
[13] L. J. C. Jeuken, M. Ubbink, J. H. Bitter, P. van Vliet, W. Meyer-Klaucke, G. W. Canters, *J. Mol. Biol.* **2000**, *299*, 737–755.
[14] G. van Pouderoyen, T. den Blaauwen, J. Reedijk, G. W. Canters, *Biochemistry* **1996**, *35*, 13205–13211.
[15] H. Nar, R. Huber, A. Messerschmidt, A. C. Filippou, M. Barth, M. Jaquinod, M. van de Kamp, G. W. Canters, *Eur. J. Biochem.* **1992**, *205*, 1123–1129.
[16] H. Nar, A. Messerschmidt, R. Huber, M. van de Kamp, G. W. Canters, *J. Mol. Biol.* **1991**, *221*, 765–772.
[17] H. Nar, A. Messerschmidt, R. Huber, M. van de Kamp, G. W. Canters, *Febs Lett.* **1992**, *306*, 119–124.
[18] I. M. C. van Amsterdam, M. Ubbink, O. Einsle, A. Messerschmidt, A. Merli, D. Cavazzini, G. L. Rossi, G. W. Canters, *Nat. Struct. Biol.* **2002**, *9*, 48–52.
[19] S. Faham, T. J. Mizoguchi, E. T. Adman, H. B. Gray, J. H. Richards, D. C. Rees, *J. Biol. Inorg. Chem.* **1997**, *2*, 464–469.
[20] L. C. Tsai, L. Sjolin, V. Langer, T. Pascher, H. Nar, *Acta Crystallogr., Sect. D* **1995**, *51*, 168–176.
[21] I. M. C. van Amsterdam, M. Ubbink, L. J. C. Jeuken, M. P. Verbeet, O. Einsle, A. Messerschmidt, G. W. Canters, *Chem. Eur. J.* **2001**, *7*, 2398–2406.
[22] Z. Otwinowski, W. Minor, *Methods Enzymol.* **1997**, *276*, 307–326.
[23] A. Vagin, A. Teplyakov, *J. Appl. Crystallogr.* **1997**, *30*, 1022–1025.
[24] S. Bailey, *Acta Crystallogr., Sect. D* **1994**, *50*, 760–763.
[25] G. N. Murshudov, A. A. Vagin, E. J. Dodson, *Acta Crystallogr., Sect. D* **1997**, *53*, 240–255.
[26] D. E. McRee, *J. Struct. Biol.* **1999**, *125*, 156–165.


 © 2006 Wiley-VCH Verlag GmbH & Co. KGaA, Weinheim 

[27] V. S. Lamzin, K. S. Wilson, *Acta Crystallogr., Sect. D* **1993**, *49*, 129–147.
[28] M. D. Winn, M. N. Isupov, G. N. Murshudov, *Acta Crystallogr., Sect. D* **2001**, *57*, 122–133.
[29] R. A. Laskowski, M. W. MacArthur, D. S. Moss, J. M. Thornton, *J. Appl. Crystallogr.* **1993**, *26*, 283–291.
[30] G. Vriend, *J. Mol. Graph.* **1990**, *8*, 52–56.
[31] W. L. DeLano, *The PyMOL Molecular Graphics System* (http://www.pymol.org), San Carlos, CA, USA **2002**.
Received: June 19, 2006
Published Online: September 5, 2006

 © 2006 Wiley-VCH Verlag GmbH & Co. KGaA, Weinheim 

DOI: 10.1002/ejic.200600382

# New Polar Pyrazolylborate Ligands and Their Basic Zinc Complex Chemistry

**Cristina Pérez Olmo,[a] Karin Böhmerle,[a] Gunther Steinfeld,[a] and Heinrich Vahrenkamp*[a]**

**Keywords:** Tripod ligands / Pyrazolylborate ligands / Zinc complexes / Structure elucidation / Coordination modes

By refinement of Trofimenko's procedures, four new tris(pyrazolyl)borate (Tp) ligands bearing pyridyl and carboxamide substituents at the 3-positions of the pyrazole rings, were obtained. Two of them were identified by structure determinations of their potassium salts. Their coordinative properties were explored by preparing Tp*Zn-X complexes, with X = Cl, Br, I, $NO_3$, OAc, phenolate, thiophenolate and diorganophosphate, including the cationic complexes $[Tp^*Zn{\cdot}L]^+$ with L = methanol and pyrazole. From the spectra and structure determinations of these complexes it has become evident that the polar Tp* ligands favor coordination numbers higher than four for zinc, either by inducing bidentate coordination of the coligands X and L, using the carboxamide oxygen atoms for coordination, or by linking two Tp*Zn-X units through the pyridyl nitrogen atoms. As a result, the structural chemistry of these complexes is quite varied, and includes coordination dimers and polymers.

(© Wiley-VCH Verlag GmbH & Co. KGaA, 69451 Weinheim, Germany, 2006)

## Introduction

Trofimenko's tris(pyrazolyl)borate (Tp) ligands[1] have been the key to success in biomimetic zinc complex chemistry, in our own hands[2] as well as in those of our competitors,[3] as evidenced by Parkin's recent review.[4] One reason for this is the ease by which their structures can be varied, for example, by attaching various substituents at the 3- and 5-positions of their pyrazole rings. The substituents at the 3-positions create and control the protective pocket around the zinc ion, which is the "active center" of the enzyme model. Substituents as small as methyl groups at the 5-positions protect the B–N bonds, preventing hydrolytic self-destruction of the ligands due to the presence of zinc ions.

Until now most of the 3-substituted Tp ligands bear nonpolar, i.e. mostly hydrocarbon, substituents. This is due to the fact that most functional organic groups do not survive the reaction conditions during the Tp ligand synthesis that occurs in the presence of $KBH_4$ at 150–200 °C. The advantage of the nonpolar $Tp^{R,Me}$ ligands (with Me at the 5-positions and the variable R at the 3-positions) is that they can be relied upon to form tetrahedral zinc complexes including $Tp^{R,Me}$Zn-OH the essential enzyme model, and that the resultant ligand pocket around the zinc ion stabilizes many kinds of reaction products that model the intermediates of the zinc enzyme catalyzed processes.[2–4] Their disadvantage is that these "intermediates" form such stable zinc complexes that so far the $Tp^{R,Me}$Zn-OH species could not be used for catalytic processes, and that both the potassium salts and the zinc complexes of the Tp ligands are not soluble in water, thereby severely hampering their suitability as enzyme models.

Until now only a few attempts have been made to overcome these limitations. We have attached 3-pyridyl substituents to Tp ligands and studied their zinc complex chemistry,[5–7] and Ward did the same with 2-pyridyl groups.[8,9] Carrano reported Tp ligands with carboxylic ester and carboxamide substituents and a number of zinc complexes thereof;[10,11] unfortunately this work could not be reproduced by us.[12] In our eyes the most promising approach has been reported recently by Trofimenko and involved pyrrolidinocarbonyl substituents,[13] which have not yet been exploited in zinc complex chemistry. Insofar as zinc complexes of these Tp ligands with polar substituents have been studied, it was found that the benefit of their enhanced polarity comes along with a liability: the coordination number of zinc goes up to five or six, either by using the substituents' donor groups for coordination, or by the attachment of additional donor ligands.

In this paper we describe some attempts by our group to improve this situation. Our plan was to develop pyrazolylborate ligands whose polar substituents have a reduced tendency to coordinate to the zinc ion in the complex, but support the solubility of their zinc complexes in protic media by having the potential to form hydrogen-bonding interactions. The latter condition led to the choice of pyridyl and amide functionalities, and the former required these donor groups to point away from the metal ion, or to be sterically hindered. We succeeded in preparing four new ligands, **L$^1$**–**L$^4$** (Scheme 1). This paper demonstrates their suitability for

[a] Institut für Anorganische und Analytische Chemie der Universität Freiburg,
Albertstr. 21, 79104 Freiburg, Germany
Fax: +49-761-203-6001
E-mail: vahrenka@uni-freiburg.de

 © 2006 Wiley-VCH Verlag GmbH & Co. KGaA, Weinheim 

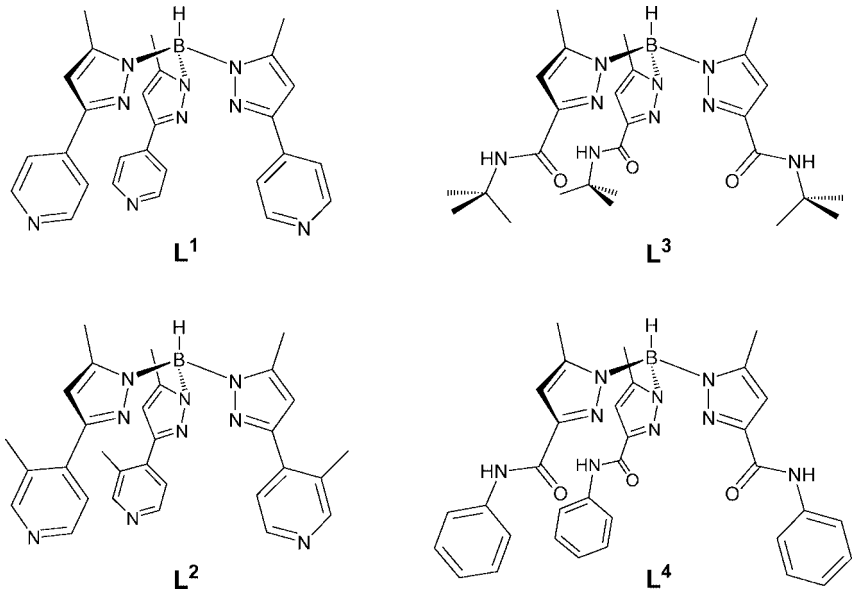


Scheme 1.

basic zinc complex chemistry. Their use for enzyme modeling will be the subject of a subsequent publication. It should be mentioned that the ligand hydridotris[3-(4′-pyridyl)pyrazolyl]borate, which is a relative of **L¹**, has recently been obtained and used in some complexes by Ward.[14]

## Results and Discussion

### Ligands L¹–L⁴

All four ligands were prepared according to Trofimenko's method, i.e. by heating the appropriate pyrazole with $KBH_4$. In case of **L¹** and **L²** the most cumbersome part of this synthesis was the preparation of the substituted pyrazoles, via the corresponding β-diketones, by previously reported procedures.[15–18] The best yields for the potassium salts of **L¹** and **L²** were obtained by heating $KBH_4$ with 4 equiv. of the pyrazole to 200 °C without solvent. In this way K**L¹** and K**L²** were obtained as colorless crystalline materials in yields of 40–50%. These compounds are insoluble in hydrocarbons, diethyl ether and chloroform, but soluble in DMSO, acetonitrile, methanol and water/methanol mixtures. The ligand K**L¹** possesses a rare property for pyrazolylborates in that it is, as expected, soluble in water.

The crystallinity of K**L¹** allowed its structure to be determined by X-ray diffraction. Figure 1 shows that the ligand **L¹** acts as a tripodal donor towards the potassium ion; however, the sideways coordination of the pyrazole nitrogen atoms N3 and N6 is weak. In addition, all the pyridyl nitrogen atoms are attached to different potassium ions. If one counts N3 and N6 as being coordinated at a single position, the potassium ions have a reasonably perfect octahedral coordination.

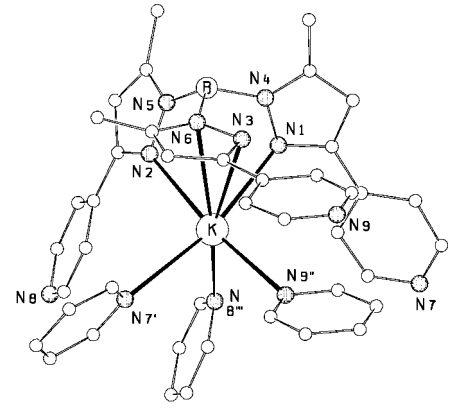


Figure 1. Coordination of the potassium ions in K**L¹**. Bond lengths [Å]: K–N1 2.897(3), K–N2 2.810(3), K–N3 3.022(3), K–N6 2.954(3), K–N7′ 3.152(4), K–N8′′′ 2.869(3), K–N9′′ 2.802(4).

Crystalline K**L¹** is a 3D coordination polymer. A substructure of this polymer is displayed in Scheme 2, showing that the pairwise coordination of the pyridyl nitrogen atoms to neighboring potassium ions creates a chain-like array. The third remaining pyridyl nitrogen atom of each **L¹** ligand is used to build the 3D network. In general, the structure of K**L¹** resembles the structures of our K**L** compounds, with **L** being 3-pyridyl-substituted pyrazolylborates.[5]

The preparation of the carboxamide-substituted ligands **L³** and **L⁴** was even more time-consuming than for **L¹** and **L²**. One reason for this was the multistep syntheses required for the preparation of the corresponding pyrazoles via diketopiperazines,[19–22] as outlined by Trofimenko.[13] Secondly, the unavoidable non-stoichiometric compositions of the $KBH_4$/pyrazole reaction mixtures resulted in purification problems for the K**L** products. As for **L¹** and **L²**, the pyrazoles had to be provided in excess during the reactions with $KBH_4$ in order to obtain reaction mixtures from which

 © 2006 Wiley-VCH Verlag GmbH & Co. KGaA, Weinheim 

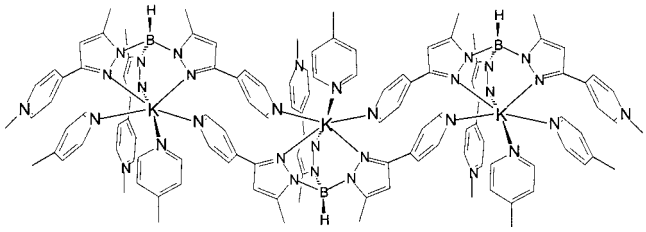

Scheme 2.

the desired ligands could be isolated. Again, these reactions were performed without solvent, this time at temperatures around 150–160 °C. After the purification procedures, only K**L**$^4$ could be obtained free from byproducts. One reason for the problems experienced in purifying K**L**$^3$ is its high solubility,·K**L**$^3$ is soluble in chloroform and more polar organic solvents,·K**L**$^4$ is insoluble in chloroform and acetonitrile, but soluble in alcohols. Both compounds are soluble in alcohol/water mixtures, but not in water.

While K**L**$^3$ could be identified, in the presence of its pyrazole, by its spectra, it had to be converted into the zinc halide complexes **2a** and **2b** (see below) to enable crystallographic proof of the **L**$^3$ structure to be obtained, and to generate a starting material so its zinc complex chemistry could be investigated. In contrast, K**L**$^4$ could be crystallized and subjected to structure determination by X-ray diffraction. The solvated crystals contain one K**L**$^4$ unit, one water molecule, and 2.5 methanol molecules per asymmetric unit. The solvent molecules are severely disordered, so their positions in the coordination sphere of the potassium ion are ill-defined. In Figure 2 the water molecule, and the methanol molecule with the highest occupancy factor located near the potassium ion, are included in the drawing. While it is meaningless to discuss the coordination geometry of the metal ion, the binding of the pyrazolylborate ligand to the potassium ion is neatly defined. Unlike in K**L**$^1$, it coordinates in the established tripodal fashion. In addition, two of its three carboxamide substituents use their oxygen atoms for coordination to two different neighboring potassium ions, thereby making **L**$^4$ a pentadentate ligand.

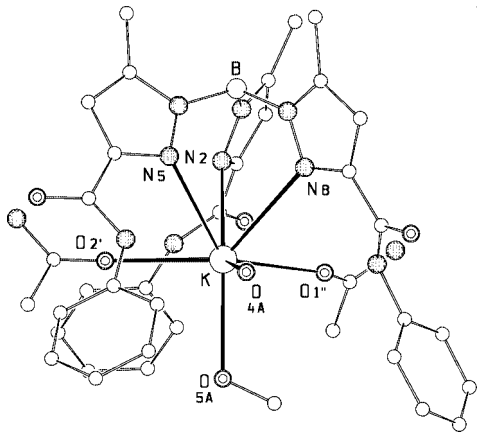


Figure 2. Coordination of the potassium ions in K**L**$^4$. Bond lengths [Å]: K–N2 2.802(2), K–N5 3.122(2), K–N8 3.040(2), K–O1′′ 2.860(2), K–O2′ 2.822(2), K–O4a 2.707(3), K–O5a 2.762(4).

Like in K**L**$^1$, the linking of neighboring complex units in K**L**$^4$ occurs in a pairwise manner, resulting in a chain-like array, as shown in Scheme 3. Unlike in K**L**$^1$, there are no further links to create a 3D network, as the third carbonyl oxygen atom of each **L**$^1$ unit remains uncoordinated.

### Zinc Complexes of L$^1$

The coordinative properties of the new pyridyl-substituted Tp ligands were explored by preparing some zinc complexes of **L**$^1$. Thus, the halide complexes **1a**–**1c** resulted from the reaction of K**L**$^1$ and the corresponding zinc halides. Their $^1$H-NMR spectra in DMSO solution show split resonances for the pyrazolyl as well as the pyridyl protons, with intensity ratios between 2:1 and 5:1, and their ν(BH) IR bands in KBr are also split. This indicates different coordination modes for the "arms" of the **L**$^1$ tripod, and possibly different coordination modes for different tripods, the simplest explanation for which is oligomerization, which was found in almost all the crystal structures reported in this paper. **1a**–**1c** did not yield suitable crystals for analysis, and therefore could not be used to verify this hypothesis.

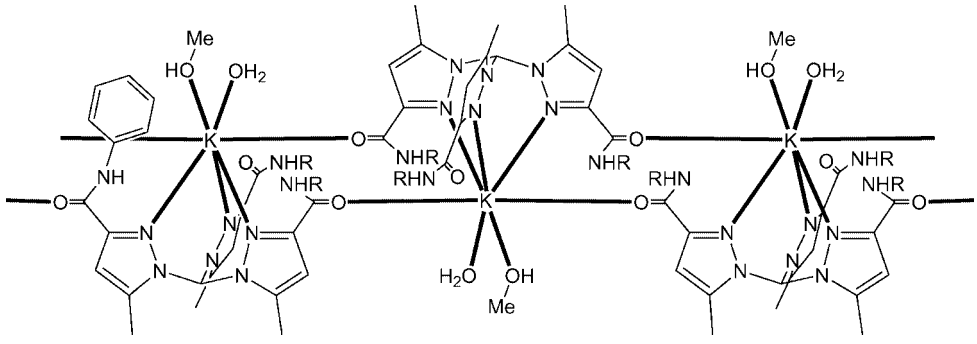

Scheme 3.

 © 2006 Wiley-VCH Verlag GmbH & Co. KGaA, Weinheim 

$\mathbf{L^1}$Zn-Cl **1a** $\mathbf{L^1}$Zn-Br **1b** $\mathbf{L^1}$Zn-I **1c**

The reactions between K$\mathbf{L^1}$ and zinc acetate or zinc nitrate led to complexes **1d** and **1e**. While the $^1$H-NMR spectrum of **1d** is simple, indicating the monomeric nature of the complex, the spectrum of **1e** shows split resonances, just like those seen in the spectra of complexes **1b** and **1c**, with intensity ratios of 5:1, pointing to an as yet unidentified oligomeric state being present in solution.

$\mathbf{L^1}$Zn-OCOCH$_3$ **1d** $\mathbf{L^1}$Zn-ONO$_2$ **1e**

The solid-state nature of both **1d** and **1e** could be determined by X-ray methods. Complex **1d** is a monomer containing a semi-bidentate acetate ligand, see Figure 3. Its zinc coordination sphere offers no unusual features compared to the many (pyrazolylborate)zinc carboxylate structures in the Cambridge Structural Database. However, this makes **1d** an exception among the zinc complexes of $\mathbf{L^1}$.

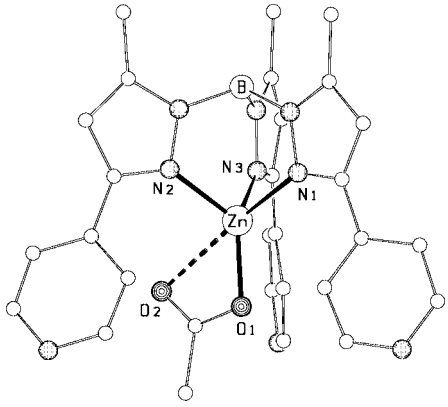


Figure 3. Molecular structure of **1d**. Bond lengths [Å]: Zn–N1 2.108(3), Zn(N2) 2.018(3), Zn–N3 2.018(3), Zn–O1 1.919(3), Zn–O2 2.534(3).

The nitrate complex **1e** is a 1D coordination polymer. Figure 4 shows the coordination sphere for one of the zinc ions in this polymer. Ligand $\mathbf{L^1}$ is nicely tripodal and the nitrate is symmetrically bound in a bidentate manner. One of the pyridyl nitrogen atoms coordinates to a neighboring zinc ion. This results in an octahedral coordination environment for the zinc ion, albeit a quite distorted one. The polymer chains comprise a zig-zag array of $\mathbf{L^1}$ZnONO$_2$ units linked by the pyridyl substituents.

The *p*-nitrophenolate complex **1f** and the bis(*p*-nitrophenyl)phosphate complex **1g** were prepared. It was thought that they would result from the hydrolytic cleavages of *p*-nitrophenyl acetate and tris(*p*-nitrophenyl)phosphate, reactions which were to be performed in subsequent studies with suitable $\mathbf{L^1}$ZnX compounds. For their unambiguous identification they were prepared from K$\mathbf{L^1}$, zinc perchlorate, and *p*-nitrophenolate and bis(*p*-nitrophenyl)phosphate, respectively.

The syntheses of **1f** and **1g** did not yield crystals suitable for structure determinations, and **1g** could not be obtained in an analytically pure form. Their $^1$H-NMR spectra show

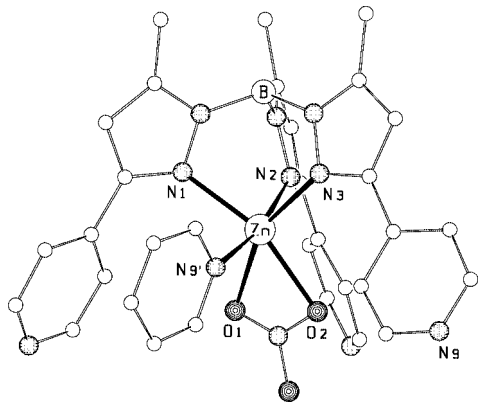


Figure 4. Monomeric fragment of polymeric **1e**. Bond lengths [Å]: Zn–N1 2.126(3), Zn–N2 2.263(3), Zn–N3 2.102(3), Zn–O1 2.189(3), Zn–O2 2.200(3), Zn-N9′ 2.250(3).

$\mathbf{L^1}$Zn-ONit **1f** $\mathbf{L^1}$Zn-OPO(ONit)$_2$ **1g**

no splitting of the pyrazolyl or pyridyl resonances, thereby indicating a monomeric structure. This was also the case for the corresponding zinc complexes with the 3-pyridyl-substituted Tp ligands. Of these, the nitrophenolate is a pyridyl-bridged dimer,[23] while the phosphate is a hydrated monomer with five-coordinate zinc ions.[24] The structures of **1f** and **1g** may be similar to either of these. Complex **1f** is precipitated with one water molecule per formula unit.

Finally, an attempt was made to obtain a zinc perchlorate complex of $\mathbf{L^1}$. To achieve this purpose, K$\mathbf{L^1}$ was treated with $Zn(ClO_4)_2$ in a dichloromethane/methanol solution. However, it became apparent that methanol is a better ligand for zinc than perchlorate, and the methanol complex **1h** was obtained. In the case of the related sulfur-containing tripod ligands, there is precedence for the preferred coordination of alcohol and perchlorate ligands.[25,26]

[$\mathbf{L^1}$Zn(CH$_3$OH)] ClO$_4$ **1h**

The $^1$H-NMR spectrum of **1h**, just like the spectra for several other complexes of **1**, displays a splitting of the pyrazolyl and pyridyl resonances with intensity ratios of 1:5,

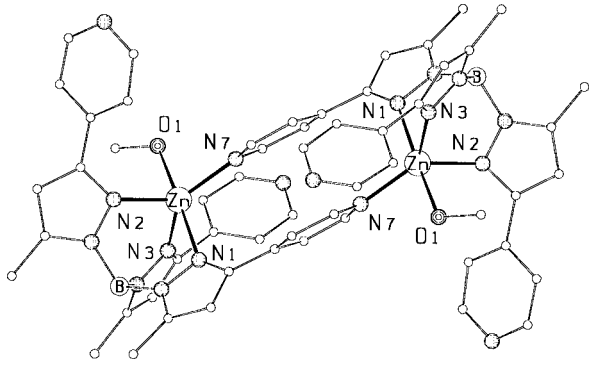


Figure 5. Structure of the dimeric cations of **1h**. Bond lengths [Å]: Zn–N1 2.210(2), Zn–N2 2.047(2), Zn–N3 2.047(2), Zn–O1 2.185(2), Zn–N7′ 2.034(2).

 © 2006 Wiley-VCH Verlag GmbH & Co. KGaA, Weinheim 

indicating the presence in solution of a complex with an unknown mode of oligomerization. In the solid state **1h** is dimeric, with the two complex units being held together by a pair of bridging pyridine rings that lie across a center of symmetry, see Figure 5. This type of coordination with trigonal-bipyramidal zinc ions has precedence in the zinc complexes of the 3-pyridyl-substituted Tp ligands.[6] The methanol ligand in **1h** is positioned on the axis of the trigonal bipyramid. It is linked by a hydrogen bond to a pyridyl nitrogen atom of a neighboring complex unit, such that a pairwise linkage across a center of symmetry exists. In this way a zig-zag array of complex units is seen in the solid state, that are bridged by pairs of pyridine donors and hydrogen bonds in an alternating fashion.

### Zinc Complexes of $L^3$ and $L^4$

As mentioned above, ligand $\mathbf{L^3}$ had to be converted into a zinc halide complex in order to have a clean starting material for the synthesis of the $\mathbf{L^3}$Zn complexes. This was done by treating the crude reaction product, K$\mathbf{L^3}$, with zinc chloride and bromide, leading to **2a** and **2b**. Likewise, K$\mathbf{L^4}$ was easily converted with zinc chloride to yield **3a**. All three halide complexes show a rather low solubility, even in dichloromethane and methanol. This points to an oligomeric nature, but their $^1$H-NMR spectra are simple, and thus yield no further information.

$\mathbf{L^3}$Zn-Cl **2a** $\mathbf{L^3}$Zn-Br **2b** $\mathbf{L^4}$Zn-Cl **3a**

The zinc nitrate complex of $\mathbf{L^3}$, **2c**, was prepared from **2b** and silver nitrate. The treatment of **2c** with potassium acetate yielded **2d**. The two corresponding complexes of $\mathbf{L^4}$, **3b** and **3c**, were synthesized in a more direct fashion from K$\mathbf{L^4}$ and the zinc salts. All four of these complexes are noticeably more soluble than the halide complexes, indicating a monomeric or dimeric nature, as observed for **1d** and **1h**. Only in case of **3c** did the $^1$H-NMR spectrum yield structural information, as it showed split signals for the methyl groups of the pyrazole with a 2:1 intensity ratio. The simplest explanation for this is that dimerization has occurred with a pair of bridging carboxamide substituents. However, this must remain a speculative structural assignment until the structural chemistry of the zinc complexes of $\mathbf{L^3}$ and $\mathbf{L^4}$ can be based on a sufficient number of X-ray structure determinations.

$\mathbf{L^3}$Zn-$ONO_2$ **2c** $\mathbf{L^3}$Zn-$OCOCH_3$ **2d**
$\mathbf{L^4}$Zn-$ONO_2$ **3b** $\mathbf{L^4}$Zn-$OCOCH_3$ **3c**

As noted above, the *p*-nitrophenolate complex **2e** and the *p*-nitrothiophenolate complex **2f** were prepared in order to have reference materials for their identification in product mixtures during subsequent studies of zinc-catalyzed hydrolytic ester cleavage reactions. Compounds **2e** and **2f** resulted from the reaction between **2b**, KOH, and the corresponding phenols (as yellow powders). Complex **2e** was not obtained analytically pure. Again, little information could be gathered concerning their structures. They are more soluble in solvents of low polarity than the other complexes of $\mathbf{L^3}$ and $\mathbf{L^4}$, and hence may be monomeric.

$\mathbf{L^3}$Zn-ONit **2e** $\mathbf{L^3}$Zn-SNit **2f**

As for $\mathbf{L^1}$, a simple reaction of $\mathbf{L^3}$ aimed at preparing a perchlorate complex did not yield the desired product, but instead a solvated cationic zinc complex of $\mathbf{L^3}$ was produced. Treating the raw product K$\mathbf{L^3}$, which contains considerable amounts of 3-*tert*-butylcarboxamido-5-methylpyrazole (Pz*), with zinc perchlorate in dichloromethane/methanol produced a small amount of the pyrazole complex **2g**, which could be identified by its spectra.

[$\mathbf{L^3}$Zn(Pz*)] $ClO_4$ **2g**

Unlike the other complexes of $\mathbf{L^3}$ and $\mathbf{L^4}$, **2g** was produced as crystals suitable for X-ray structure determination. The result is displayed in Figure 6. Complex **2g** is mononuclear. Ligand $\mathbf{L^3}$ is coordinated to the zinc ion in the normal tripodal fashion, with the notable detail that all three carboxamide oxygen atoms are pointing towards the zinc ion. The pyrazole coligand is bidentate and produces a five-membered O,N chelate ring. Thereby **2g** resembles the large number of TpZn chelate complexes which are frequently discussed as models for enzyme-inhibitor complexes.[27,28] The coordination of the zinc ion can be described as reasonably close to trigonal-bipyramidal, with N8 and O4 on the axis forming the long Zn–X bonds. Additional rigidity in the structure comes from a hydrogen bond between the NH group of the pyrazole coligand and one carboxamide oxygen atom. Thus, the structure of **2g** has yielded two valuable pieces of information with respect to the subsequent use of ligands like $\mathbf{L^3}$ and $\mathbf{L^4}$ for modeling zinc enzymes: firstly, these ligands can form mononuclear zinc complexes and secondly, the carboxamide functional groups can show polar interactions and hydrogen bonding at, or near, the zinc center.

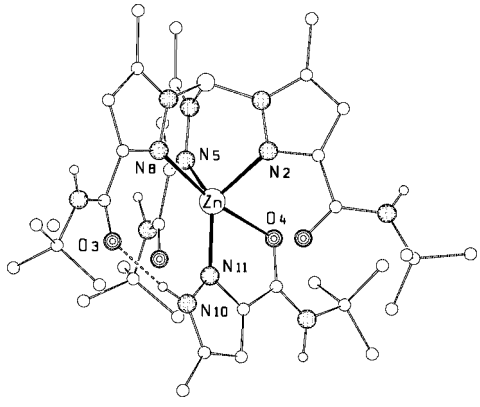


Figure 6. Molecular structure of complex **2g**. Bond lengths [Å]: Zn–N2 2.036(5), Zn–N5 2.036(5), Zn–N8 2.269(5), Zn–N11 1.979(5), Zn–O4 2.312(4), N10···O3 2.602(6).

 © 2006 Wiley-VCH Verlag GmbH & Co. KGaA, Weinheim 

## Conclusions

The four new pyrazolylborate ligands described in this paper have been found to have conventional properties (i.e. they coordinate to the zinc ion in the tripodal fashion) as well as novel features that qualify them for a biomimetic zinc complex chemistry (i.e. they contain further donor functional groups, they allow for variable metal coordination numbers, they engage in various kinds of hydrogen bonds, and they form complexes which are soluble in water-containing solvents or even in pure water). Just like the previously described Tp ligands with 3-pyridyl substituents they allow, or more accurately they enforce, coordination numbers higher than four for zinc. The well-established term "tetrahedral enforcer", which qualifies many Tp ligands, does not hold for **L**$^{1}$–**L**$^{4}$.

Variability in coordination numbers and geometries, as seen for the zinc complexes described herein, is a prerequisite for catalytic activity. This, together with the increased solubility in water-containing solvents, indicates that zinc complexes of **L**$^{1}$–**L**$^{4}$ with coordinated water or hydroxide, or with labile coligands X, should qualify as new, or better, models for, hydrolytic zinc enzymes. In this context, the carboxamide-substituted ligands **L**$^{3}$ and **L**$^{4}$ deserve special attention. Their CO–NH functionality mimics the peptide environment of the zinc ion in an enzyme in terms of its hydrogen-bonding ability, as well as in its polarity and donor quality. We therefore believe that the carboxamide-substituted pyrazolylborates should lead to significant advancements in enzyme modeling with zinc complexes, and once again Swiatoslaw Trofimenko has to be praised for being the first person to prepare such ligands.

## Experimental Section

**General:** For general working and measuring procedures see ref.[29] Zinc salts and organic starting materials were obtained commercially.

**Pyrazoles:** The synthesis of the two pyrazoles needed for the synthesis of **L**$^{1}$ and **L**$^{2}$ started with the Claisen condensation of acetone with ethyl isonicotinate (commercially available) and ethyl 2-methylisonicotinate[15] to yield the corresponding diketones.[16] Their reaction with hydrazine hydrate, as previously described,[17,18] resulted in 5-methyl-3-(4′-pyridyl)pyrazole and 5-methyl-3-[4′-(6′-methyl)pyridyl]pyrazole in good yields. The two pyrazoles needed for the synthesis of **L**$^{3}$ and **L**$^{4}$ were obtained from the same intermediate, 2,7-dimethyldipyrazolo[1,5-*a*;1′,5′-*a*′]pyrazine-4,9-dione, which was synthesized according to literature procedures.[13,19–22] Treatment of this with *tert*-butylamine or aniline in refluxing toluene, as previously described,[13,22] resulted in 3-(*tert*-butylcarboxamido)-5-methylpyrazole and 3-(phenylcarboxamido)-5-methylpyrazole, respectively, in very good yields.

### Tripod Ligands

**KL**$^{1}$**:** A mixture of 6.28 g (39.44 mmol) of 5-methyl-3-(4′-pyridyl)-pyrazole and 532 mg (9.86 mmol) of $KBH_4$ was stirred in a three-necked 100-mL flask equipped with an immersing thermometer. The temperature was slowly increased to 200 °C over a period of 30 min. At 140–160 °C, the mixture melted and the gas evolution became brisk. The melt was stirred continuously at 200 °C until it started to turn brown (ca. 3 h) and then slowly cooled to room temperature. The resulting glassy residue was carefully powdered and refluxed in 100 mL of toluene for 30 min, in order to remove unreacted pyrazole impurities. The mixture was filtered while hot, and the light brown residue was washed 3 times with 5 mL of boiling toluene and once with 5 mL of petroleum ether (30–50 °C). Recrystallization from 50 mL of acetonitrile at –20 °C yielded 2.59 g (50%) of K**L**$^{1}$ as colorless crystals, m.p. 328 °C. $C_{27}H_{25}BKN_9$ (525.46): calcd. C 61.72, H 4.80, N 23.99; found C 61.23, H 4.85, N 23.87. $^1$H NMR ([D$_6$]DMSO): $\delta$ = 2.02 [s, 9 H, Me(pz)], 6.44 [s, 3 H, H(pz)], 7.58 (dd, $J$ = 4.5 and 1.5 Hz, 6 H, Py), 8.42 (dd, $J$ = 4.5 and 1.5 Hz, 6 H, Py) ppm. IR (KBr): $\tilde{\nu}$ = 2446 m (BH), 1605 vs (Py) cm$^{-1}$.

**KL**$^{2}$**:** 5-Methyl-3-[4′-(6′-methyl)pyridyl]pyrazole (2.66 g, 15.35 mmol), and 207 mg (3.84 mmol) of $KBH_4$ were mixed by stirring in a three-necked 50-mL flask equipped with an immersing thermometer. The temperature was slowly increased to 200 °C over a period of 30 min. The melt was continuously stirred at 200 °C until it started to turn brown (ca. 3 h) and then slowly cooled to room temperature. The resulting glassy residue was carefully powdered and refluxed in 50 mL of toluene for 30 min, in order to remove unreacted pyrazole impurities. The mixture was filtered while hot, and the light brown residue was washed 3 times with 5 mL of boiling toluene and once with 5 mL of petroleum ether (30–50 °C). Recrystallization from 50 mL of undried acetonitrile at –20 °C yielded 871 mg (40%) of K**L**$^{2}$ as colorless crystals, m.p. 319 °C (dec.). $C_{30}H_{31}BKN_9{\cdot}H_2O$ (567.54 + 18.02): calcd. C 61.54, H 5.68, N 21.53; found C 61.05, H 5.76, N 21.33. $^1$H NMR ([D$_6$]DMSO): $\delta$ = 1.99 [s, 9 H, Me(pz)], 2.41 [s, 9 H, Me(py)], 6.41 [s, 3 H, H(pz)], 7.38 (d, $J$ = 5.1 Hz, 3 H, Py), 7.45 (s, 3 H, Py), 8.28 (d, $J$ = 5.1 Hz, 3 H, Py) ppm. IR (KBr): $\tilde{\nu}$ = 2486 m (BH), 1612 vs (Py) cm$^{-1}$.

**KL**$^{3}$**:** 3-(*tert*-butylcarboxamido)-5-methylpyrazole (3.03 g, 16.65 mmol), and 0.28 g (5.08 mmol) of $KBH_4$ were mixed by stirring in a 100-mL three-necked flask equipped with an immersing thermometer, and slowly heated until melting, which occurred at 130 °C. The temperature was raised to 160 °C over a period of 2 h, after which time the gas evolution ceased. After cooling, the solid residue was carefully powdered and stirred in chloroform overnight. Then the suspension was filtered and the filtrate concentrated to dryness, leaving behind 2.34 g of a colorless mixture of K**L**$^{3}$ and the unreacted pyrazole. According to NMR analysis, the mixture contained 1.78 g (59%) of K**L**$^{3}$. Attempts at further purification resulted in increasing the amount of impurities present. $^1$H NMR of K**L**$^{3}$ ($CD_3OD$): $\delta$ = 1.38 (s, 27 H, *t*Bu), 2.05 [s, 9 H, Me(pz)], 6.39 [s, 3 H, H(pz)] ppm. IR of K**L**$^{3}$ (KBr): $\tilde{\nu}$ = 3396 m (NH), 2444 m (BH), 1652 vs (CO) cm$^{-1}$.

**KL**$^{4}$**:** A mixture of 3.29 g (16.35 mmol) of 3-methyl-5-(phenylcarboxyamido)pyrazole and 221 mg (4.09 mmol) of $KBH_4$ was stirred in a three-necked 50-mL flask equipped with an immersing thermometer. The temperature was slowly increased to 150 °C over a period of 30 min, at which point the mixture melted. The melt was continuously stirred at 150 °C until no more hydrogen was evolved (ca. 2 h), and then heated to 160 °C over a period of 30 min. It was then cooled to room temperature. The resulting glassy residue was carefully powdered and refluxed in 30 mL of acetonitrile for 30 min in order to remove unreacted pyrazole impurities. The mixture was filtered while hot, and the residue was washed 3 times with 5 mL of boiling acetonitrile and once with 2 mL of water. Recrystallization from 40 mL of methanol/dichloromethane (1:2) at –20 °C yielded 300 mg (11%) of K**L**$^{4}$ as large crystals, m.p. 250 °C. $C_{33}H_{31}BKN_9O_3{\cdot}H_2O$ (651.58 + 18.02): calcd. C 59.19, H 4.97, N 18.83; found C 59.43, H 5.14, N 18.44. $^1$H NMR ([D$_6$]DMSO): $\delta$

 © 2006 Wiley-VCH Verlag GmbH & Co. KGaA, Weinheim 

= 2.01 [s, 9 H, Me(pz)], 6.46 [s, 3 H, H(pz)], 7.01 (m, 3 H, Ph), 7.27 (m, 6 H, Ph), 7.64 (d, $J$ = 7.6 Hz, 6 H, Ph), 9.25 (s, 3 H, NH) ppm. IR (KBr): $\tilde{\nu}$ = 3365 s (NH), 2470 m (BH), 1653 vs. (CO) $cm^{-1}$.

**Zinc Complexes of $L^1$**

**1a:** A solution of 46 mg (0.33 mmol) of $ZnCl_2$ in 5 mL of methanol was added dropwise to a solution of 160 mg (0.30 mmol) of $KL^1$ in 20 mL of methanol/dichloromethane (1:1) over a period of 5 min. After 6 h of stirring, a small amount of a cloudy precipitate was removed by filtration, and the clear filtrate was slowly concentrated at room temperature to yield, after 2 d, 116 mg (65%) of **1a** as colorless needles, m.p. 238 °C. $C_{27}H_{25}BClN_9Zn{\cdot}1.5H_2O$ (587.21 + 27.02): calcd. C 52.80, H 4.59, N 20.52; found C 52.63, H 4.48, N 20.66. $^1$H NMR ([D$_6$]DMSO): $\delta$ = 2.02 [s, 6 H, Me(pz)], 2.54 [s, 3 H, Me(pz)], 6.44 [s, 2 H, H(pz)], 6.65 [s, 1 H, H(pz)], 7.58 (d, $J$ = 6.0 Hz, 4 H, Py), 7.70 (d, $J$ = 5.5 Hz, 2 H, Py), 8.41 (d, $J$ = 6.0 Hz, 4 H, Py), 8.59 (d, $J$ = 6.0 Hz, 2 H, Py) ppm. IR (KBr): $\tilde{\nu}$ = 2553 and 2496 w (BH), 1619 s (Py) $cm^{-1}$.

**1b:** A solution of 150 mg (0.67 mmol) of $ZnBr_2$ in 10 mL of methanol/dichloromethane (1:1) was added dropwise to a stirred solution of 318 mg (0.61 mmol) of $KL^1$ in 20 mL of methanol/dichloromethane (1:1) over a period of 30 min. A white solid precipitated immediately, but the mixture was allowed to react for 6 h. Then the solvent was removed in vacuo and the residue was dissolved in chloroform/methanol (90:10) under reflux. After storage at 5 °C for 2 d, a precipitate of **1b**, 298 mg (78%), as colorless needles formed, m.p. 252 °C. $C_{27}H_{25}BBrN_9Zn$ (631.66): calcd. C 51.34, H 3.99, N 19.96; found C 50.77, H 4.11, N 19.53. $^1$H NMR ([D$_6$]DMSO): $\delta$ = 2.07 [s, 1.5 H, Me(pz)], 2.53 [s, 7.5 H, Me(pz)], 6.46 [s, 0.5 H, H(pz)], 6.63 [s, 2.5 H, H(pz)], 7.61 (m, 6 H, Py), 8.42 (d, $J$ = 5.3 Hz, 1 H, Py), 8.62 (d, $J$ = 4.9 Hz, 5 H, Py) ppm. IR (KBr): $\tilde{\nu}$ = 2557 and 2499 w (BH), 1621 vs (Py) $cm^{-1}$.

**1c:** The preparation of **1c** was analogous to that of **1b**, but with $ZnI_2$ (127 mg, 0.40 mmol) in place of $ZnBr_2$. Recrystallization from chloroform/methanol (90:10) at 5 °C yielded 184 mg (75%) of **1c** as colorless needles, m.p. 226 °C. $C_{27}H_{25}BIN_9Zn$ (678.66): calcd. C 47.78, H 3.71, N 18.57; found C 47.09, H 3.83, N 19.00. $^1$H NMR ([D$_6$]DMSO): $\delta$ = 2.00 [s, 1.5 H, Me(pz)], 2.54 [s, 7.5 H, Me(pz)], 6.46 [s, 0.5 H, H(pz)], 6.63 [s, 2.5 H, H(pz)], 7.56 (m, 6 H, Py), 8.41 (d, $J$ = 6.0 Hz, 1 H, Py), 8.72 (dd, J = 4.6 Hz and 1.4 Hz, 5 H, Py) ppm. IR (KBr): $\tilde{\nu}$ = 2557 and 2491 w (BH), 1617 s (Py) $cm^{-1}$.

**1d:** A solution of 174 mg (0.79 mmol) of $Zn(OAc)_2{\cdot}2H_2O$ in 5 mL of methanol was added dropwise to a solution of 379 mg (0.72 mmol) of $KL^1$ in 20 mL of methanol/dichloromethane (1:1) over a period of 5 min. After 6 h of stirring, a small amount of a cloudy precipitate was removed by filtration, and the clear filtrate was concentrated to dryness in vacuo. Recrystallization from 15 mL of methanol at 5 °C yielded 401 mg (91%) of **1d** as large colorless crystals, m.p. 242 °C. $C_{29}H_{28}BN_9O_2Zn$ (610.80): calcd. C 57.03, H 4.62, N 20.64; found C 56.49, H 4.82, N 20.42. $^1$H NMR ([D$_6$]-DMSO): $\delta$ = 1.51 (s, 3 H, Ac), 2.56 [s, 9 H, Me(pz)], 6.64 [s, 3 H, H(pz)], 7.60 (dd, J = 4.6 and 1.4 Hz, 6 H, Py), 8.60 (d, $J$ = 6.0 Hz, 6 H, Py) ppm. IR(KBr): $\tilde{\nu}$ = 2558 m (BH), 1608 vs (Py) $cm^{-1}$.

**1e:** A solution of 146 mg (0.49 mmol) of $Zn(NO_3)_2{\cdot}6H_2O$ in 5 mL of methanol was added dropwise to a solution of 234 mg (0.45 mmol) of $KL^1$ in 20 mL of methanol over a period of 5 min. A white solid precipitated immediately, but the mixture was stirred for 6 h. Then the solvent was removed in vacuo and the residue was dissolved in chloroform/methanol (90:10) under reflux. After storage at 5 °C for 5 d, a precipitate of **1e**, 188 mg (69%), as colorless crystals formed, m.p. 210 °C (dec.). $C_{27}H_{25}BN_{10}O_3Zn{\cdot}H_2O$ (613.76 + 18.02): calcd. C 51.33, H 4.31, N 22.17; found C 51.47, H 4.01, N 22.05. $^1$H NMR ([D$_6$]DMSO): $\delta$ = 2.01 [s, 1.5 H, Me(pz)], 2.55 [s, 7.5 H, Me(pz)], 6.45 [s, 0.5 H, H(pz)], 6.62 [s, 2.5 H, H(pz)], 7.56 (m, 6 H, Py), 8.41 (d, $J$ = 5.7 Hz, 1 H, Py), 8.72 (d, $J$ = 5.9 Hz, 5 H, Py). IR(KBr): $\tilde{\nu}$ = 2550 m (BH), 1613 s (Py) cm.

**1f:** To a stirred mixture of 266 mg (0.50 mmol) of $KL^1$ and 207 mg (0.55 mmol) of $Zn(ClO_4)_2{\cdot}6H_2O$ in 30 mL of methanol/dichloromethane/water (1:1:0.5) at 0 °C was added a solution of 42 mg (0.75 mmol) of KOH in methanol/dichloromethane (1:1). After 1 h of stirring at 0 °C, a solution of 68 mg (0.49 mmol) of *p*-nitrophenol in 5 mL of methanol was added. After 6 h of stirring and subsequent filtration, all volatiles were removed in vacuo, and the residue was recrystallized from 15 mL of methanol/dichloromethane (1:2) at –20 °C, yielding 314 mg (93%) of **1f** as a light yellow powder, m.p. 254 °C (dec.). $C_{33}H_{29}BN_{10}O_3Zn{\cdot}H_2O$ (689.86 + 18.02): calcd. C 55.99, H 4.41, N 19.79; found C 56.15, H 4.42, N 19.74. $^1$H NMR ($CDCl_3$): $\delta$ = 1.66 (br. s, 2 H, $H_2O$), 2.62 [s, 9 H, Me(pz)], 5.88 (d, $J$ = 9.1 Hz, 2 H, Ph), 6.43 [s, 3 H, H(pz)], 7.51 (m, 8 H, Py, Ph), 8.41 (dd, J = 4.5 and 1.4 Hz, 6 H, Py) ppm. IR (KBr): $\tilde{\nu}$ = 2559 w (BH), 1607 s (Py), 1584 s and 1304 vs (NO) $cm^{-1}$.

**1g:** The method for the preparation of **1g** is like the synthetic procedure for **1f**. The reaction mixture contained 266 mg (0.50 mmol) of $KL^1$, 207 mg (0.55 mmol) of $Zn(ClO_4)_2{\cdot}6H_2O$, 42 mg (0.75 mmol) of KOH, and 183 mg (0.54 mmol) of bis(*p*-nitrophenyl)phosphoric acid in 35 mL of methanol/dichloromethane (2:1) at 0 °C. After 2 h of stirring and subsequent filtration, all volatiles were removed in vacuo and the raw product was suspended in 5 mL of chloroform. The suspension was filtered again and the filtrate concentrated to dryness, leaving behind 134 mg (31%) of impure **1g** as a light yellow powder, m.p. 231 °C. Attempts at purification by recrystallization were unsuccessful. $^1$H NMR ($CDCl_3$): $\delta$ = 2.60 [s, 9 H, Me(pz)], 6.40 [s, 3 H, H(pz)], 6.85 (d, $J$ = 8.9 Hz, 4 H, Ph), 7.52 (d, $J$ = 5.9 Hz, 6 H, Py), 7.98 (d, $J$ = 9.1 Hz, 4 H, Ph), 8.61 (d, $J$ = 5.7 Hz, 6 H, Py) ppm. IR (KBr): $\tilde{\nu}$ = 2566 w (BH), 1621 s (Py), 1591 s and 1346 vs (NO) $cm^{-1}$.

**1h:** Compound $KL^1$, 210 mg (0.40 mmol), was dissolved in 30 mL of methanol/dichloromethane (1:1), and a solution of 163 mg (0.44 mmol) of $Zn(ClO_4)_2{\cdot}6H_2O$ in 5 mL methanol was added dropwise over a period of 10 min. A slurry of $KClO_4$ precipitated immediately. This was filtered off and the clear filtrate was stirred for 6 h. After this time, a large amount of colorless solid had precipitated. This precipitate was filtered off and dried in vacuo to yield 180 mg (66%) of **1h** as a colorless powder, m.p. 284 °C. The mother liquor was concentrated in vacuo to ca. 20 mL and kept at 5 °C overnight to yield 10 mg (4%) of **1h** as X-ray quality crystals. $C_{28}H_{29}BClN_9O_5Zn{\cdot}H_2O$ (683.25 + 18.02): calcd. C 47.96, H 4.46, N 17.98; found C 47.75, H 4.36, N 17.60. $^1$H NMR ([D$_6$]DMSO): $\delta$ = 2.01 [s, 1.5 H, Me(pz)], 2.55 [s, 7.5 H, Me(pz)], 3.34 (s, 3 H, MeOH), 6.45 [s, 0.5 H, H(pz)], 6.62 [s, 2.5 H, H(pz)], 7.56 (m, 6 H, Py), 8.41 (d, $J$ = 5.9 Hz, 1 H, Py), 8.73 (d, $J$ = 5.9 Hz, 5 H, Py) ppm. IR (KBr): $\tilde{\nu}$ = 3572 m (OH), 3428 bs ($H_2O$), 2574 m (BH), 1623 s (Py), 1094 vs (ClO) $cm^{-1}$.

**Zinc Complexes of $L^3$ and $L^4$**

**2a:** To a stirred solution of 1.59 g of impure $KL^3$ (ca. 2.0 mmol of $KL^3$) in 10 mL of methanol was added dropwise a solution of 0.44 g (3.2 mmol) of $ZnCl_2$ in 3 mL of methanol. After 4 h of stirring, the volume was reduced to 3 mL in vacuo. The precipitate was filtered off and washed with 5 mL of water. After drying in vacuo, it was suspended in 4 mL of THF and 1 mL of methanol. The remaining precipitate was filtered off and dried in vacuo, yielding 430 mg (27%) of **2a** as a colorless powder, m.p. 278 °C. $C_{27}H_{48}BClN_9O_3Zn{\cdot}0.5H_2O$ (653.35 + 9.01): calcd. C 48.96, H 6.70, N 19.03; found C 48.80, H

 © 2006 Wiley-VCH Verlag GmbH & Co. KGaA, Weinheim 

6.74, N 18.86. $^1$H NMR ($CD_3OD$): $\delta$ = 1.48 (s, 27 H, *t*Bu), 2.46 [s, 9 H, Me(pz)], 6.54 [s, 3 H, H(pz)] ppm. IR (KBr): $\tilde{\nu}$ = 3398 m (NH), 2505 w (BH), 1648 vs and 1605 vs (CO) cm$^{-1}$.

**2b:** The method of synthesis for **2b** is like the procedure for the preparation of **2a**. From 1.97 g (ca. 2.5 mmol) of **KL$^3$** and 0.90 g (4.03 mmol) of $ZnBr_2$, 650 mg (38%) of **2b** was obtained as a colorless powder, m.p. 260 °C. $C_{27}H_{48}BBrN_{10}O_6Zn{\cdot}1.5H_2O$ (679.80 + 27.03): calcd. C 44.74, H 6.40, N 17.39; found C 44.94, H 6.22, N 17.39. $^1$H NMR ($CD_3OD$): $\delta$ = 1.48 (s, 27 H, *t*Bu), 2.46 [s, 9 H, Me(pz)], 6.55 [s, 3 H, H(pz)] ppm. IR(KBr): $\tilde{\nu}$ = 3397 w (NH), 2500 w (BH), 1650 vs and 1605 vs (CO) cm$^{-1}$.

**3a:** A solution of 22 mg (0.16 mmol) of $ZnCl_2$ in 2 mL of methanol was added dropwise to a solution of 96 mg (0.15 mmol) of **KL$^4$** in 10 mL of methanol/dichloromethane (1:1). After 3 h of stirring, a small amount of cloudy precipitate was removed by filtration, and the clear filtrate was slowly concentrated at room temperature to yield after 1 d 91 mg (87%) of **3a** as colorless needles, m.p. 216 °C. $C_{33}H_{31}BClN_9O_3Zn{\cdot}H_2O$ (713.32 + 18.02): calcd. C 54.20, H 4.55, N 17.05; found C 53.74, H 4.66, N 17.05. $^1$H NMR ($CDCl_3$): $\delta$ = 1.57 (br. s, 2 H, $H_2O$), 2.53 [s, 9 H, Me(pz)], 6.80 [s, 3 H, H(pz)], 7.14 [m, 3 H, Ph], 7.33 (m, 6 H, Ph), 7.74 (d, *J* = 7.8 Hz, 6 H, Ph), 8.89 (s, 3 H, NH) ppm. IR (KBr): $\tilde{\nu}$ = 3315 s (NH), 2511 w (BH), 1648 vs and 1598 vs (CO) cm$^{-1}$.

**2c:** A solution of 30 mg (0.19 mmol) of $AgNO_3$ in 2 mL of methanol was slowly added dropwise to a stirred solution of 0.13 g (0.19 mmol) of **2b** in 15 mL of methanol at 0 °C. After 30 min, the precipitate was filtered off and the filtrate concentrated to dryness, leaving behind 100 mg (77%) of **2c** as a colorless hygroscopic powder, m.p. 190 °C (dec.). $C_{27}H_{48}BN_9O_3Zn{\cdot}2H_2O$ (679.90 + 36.04): calcd. C 45.30, H 6.62, N 19.56; found C 45.34, H 6.68, N 19.08. $^1$H NMR ($CD_3OD$): $\delta$ = 1.48 (s, 27 H, *t*Bu), 2.46 [s, 9 H, Me(pz)], 6.55 [s, 3 H, H(pz)] ppm. IR (KBr): $\tilde{\nu}$ = 3294 m (NH), 2557 w (BH), 1642 s and 1608 s (CO) cm$^{-1}$.

**2d:** A solution of 8 mg (0.08 mmol) of KOAc in 1 mL of methanol was added dropwise to a stirred solution of 50 mg (0.07 mmol) of **2c** in 4 mL of dichloromethane. After 2 h of stirring, the precipitate was filtered off and the filtrate concentrated to dryness. The residue was washed with 1 mL of water and dried in vacuo, leaving behind 35 mg (74%) of **2d** as a colorless powder, m.p. 188 °C. $C_{29}H_{46}BN_9O_5Zn{\cdot}2H_2O$ (676.94 + 36.04): calcd. C 48.85, H 7.07, N 17.68; found C 48.96, H 7.12, N 17.40. $^1$H NMR ($CD_3OD$): $\delta$ = 1.47 (s, 27 H, *t*Bu), 1.90 (s, 3 H, OAc), 2.46 [s, 9 H, Me(pz)], 6.54 [s, 3 H, H(pz)] ppm. IR (KBr): $\tilde{\nu}$ = 3293 w (NH), 2559 w (BH), 1648 vs and 1605 s (CO) cm$^{-1}$.

**3b:** A solution of 50 mg (0.17 mmol) of $Zn(NO_3)_2{\cdot}6H_2O$ in 5 mL of methanol was added dropwise to a solution of 100 mg (0.15 mmol) of **KL$^4$** in 10 mL of methanol. After 3 h of stirring, a small amount of cloudy precipitate was removed by filtration, and the clear filtrate was concentrated to dryness in vacuo. Recrystallization from 10 mL of methanol/dichloromethane (1:1) at 5 °C yielded 87 mg (77%) of **3b** as a white powder, m.p. 190 °C. $C_{33}H_{31}BN_{10}O_6Zn$ (739.87): calcd. C 53.57, H 4.22, N 18.93; found C 52.93, H 4.31, N 19.01. $^1$H NMR($CDCl_3$): $\delta$ = 2.39 [s, 9 H, Me(pz)], 6.54 [s, 3 H, H(pz)], 6.76 (m, 9 H, Ph), 7.03 (d, *J* = 8.2 Hz, 6 H, Ph), 9.80 (s, 3 H, NH) ppm. IR (KBr): $\tilde{\nu}$ = 3282 m (NH), 2566 w (BH), 1648 s and 1601 s (CO) cm$^{-1}$.

**3c:** A solution of 35 mg (0.16 mmol) of $Zn(OAc)_2{\cdot}2H_2O$ in 2 mL of methanol was added dropwise to a solution of 94 mg (0.14 mmol) of **KL$^4$** in 10 mL of methanol/dichloromethane (2:1). After 3 h of stirring, a small amount of cloudy precipitate was removed by filtration, and the clear filtrate was slowly concentrated at room temperature to yield after 1 d 93 mg (88%) of **3c** as colorless crystals, m.p. 216 °C. $C_{35}H_{34}BN_9O_5Zn$ (736.91): calcd. C 57.05, H 4.65, N 17.11; found C 56.29, H 4.75, N 16.84. $^1$H NMR ($CDCl_3$): $\delta$ = 1.75 (s, 3 H, OAc), 2.39 [s, 3 H, Me(pz)], 2.52 [s, 6 H, Me(pz)], 6.69 [m, 5 H, H(pz) + Ph], 7.08 (m, 6 H, Ph), 7.28 (m, 4 H, Ph), 7.67 (d, *J* = 7.6 Hz, 4 H, Ph), 8.95 (br. s, 1 H, NH) ppm. IR (KBr): $\tilde{\nu}$ = 3307 m (NH), 2573 w (BH), 1650 s and 1600 s (CO) cm$^{-1}$.

**2e:** A solution of 11 mg (0.15 mmol) of *p*-nitrophenol in 2 mL of methanol was deprotonated by the addition of a solution of 9 mg (0.16 mmol) of KOH in 1 mL of methanol. This intensive yellow solution was added to a solution of 0.11 g (0.15 mmol) of **2b** in 12 mL of methanol. After 3 h, the clear solution was concentrated under vacuum until the first turbidity appeared, at this time the solution had been reduced to 3 mL. Addition of 3 mL of dichloromethane caused a pale yellow precipitate to form. After filtration, the filtrate was concentrated to dryness. A yellow-brown powder (68 mg) remained, which consisted mainly of **2e**, but could not be purified by recrystallization. $^1$H NMR ($CDCl_3$): $\delta$ = 1.37 (s, 27 H, *t*Bu), 2.44 [s, 9 H, Me(pz)], 6.36 [s, 3 H, H(pz)], 6.55 (s, 1 H, NH), 6.65 (d, *J* = 9.0 Hz, 2 H, Ph), 7.96 (d, *J* = 9.0 Hz, 2 H, Ph) ppm. IR (KBr): $\tilde{\nu}$ = 3332 w (NH), 2559 w (BH), 1647 s and 1606 s (CO) cm$^{-1}$.

**2f:** The procedure for the preparation of **2f** is like the method for the synthesis of **2e**. From 20 mg (0.13 mmol) of *p*-nitrothiophenol, 8 mg (0.14 mmol) of KOH, and 0.09 g (0.13 mmol) of **2b**, 67 mg (67%) of **2f** resulted. Recrystallization from benzene/dichloromethane reduced this amount to 18 mg (18%) of pure **2f**, m.p. 234 °C. $C_{33}H_{47}BN_{10}O_5SZn$ (772.05): calcd. C 51.34, H 6.13, N 18.14; found C 51.08, H 6.20, N 17.90. $^1$H NMR ($CD_3OD$): $\delta$ = 1.35 (s, 27 H, *t*Bu), 2.44 [s, 9 H, Me(pz)], 6.50 [s, 3 H, H(pz)], 7.29 (d, *J* = 8.9 Hz, 2 H, Ph), 7.68 (d, *J* = 8.9 Hz, 2 H, Ph) ppm. IR (KBr): $\tilde{\nu}$ = 3305 m (NH), 2482 w (BH), 1645 s and 1604 vs (CO) cm$^{-1}$.

**2g:** A solution of 1.89 g (5.08 mmol) of $Zn(ClO_4)_2{\cdot}6H_2O$ in 3 mL of methanol was added to a stirred solution of 2.57 g of raw **KL$^3$** contaminated with 3-(*tert*-butylcarboxamido)-5-methylpyrazole (ca. 2.7 mmol of **KL$^3$**) in 10 mL of dichloromethane. After 2 h of stirring, the precipitate was filtered off and the filtrate was concentrated to dryness. The residue was dissolved in 5 mL of dichloromethane/methanol (20:1) and the mixture subjected to slow concentration. After one week, 140 mg (6%) of **2g** had precipitated as colorless crystals, m.p. 250 °C. $C_{36}H_{58}BClN_{12}O_8Zn{\cdot}CH_3OH$ (898.57 + 32.04): calcd. C 47.75, H 6.71, N 18.06; found C 47.37, H 6.67, N 18.04. $^1$H NMR ($CD_3OD$): $\delta$ = 1.40 [s, 9 H, *t*Bu(Pz*)], 1.45 (s, 27 H, *t*Bu), 2.34 [s, 3 H, Me(Pz*)], 2.48 [s, 9 H, Me(pz)], 6.55 [s, 4 H, H(Pz*) and H(pz)] ppm. IR (KBr): $\tilde{\nu}$ = 3397 (m, NH), 3356 m (NH), 2561 w (BH), 1676 s and 1647 vs and 1557 vs (CO), 1076 vs (ClO) cm$^{-1}$.

**Structure Determinations:**[30] Crystals were obtained by the slow evaporation of solvents: acetonitrile for **KL$^1$**, dichloromethane/methanol for **KL$^2$** and **1h**, methanol for **1d**, chloroform/methanol for **1e** and anhydrous dichloromethane for **2g**. In those cases where the crystals contained solvent, care had to be taken to avoid solvent loss. Diffraction data were recorded at room temperature for **KL$^2$** and **2g**, and at –50 °C for **KL$^1$**, **1d**, **1e** and **1h** with a Bruker Smart CCD diffractometer. The datasets for **KL$^1$**, **KL$^2$**, **1h** and **2g** were subjected to an empirical absorption correction (SADABS).[31] The structures were solved with direct methods and refined anisotropically using the SHELX program suite.[31] Serious disorder problems concerning the cocrystallized solvent molecules hampered the refinements of **KL$^2$** and **1h**. In the case of **1h** we had to resort to using Spek's SQUEEZE program, which includes the total electron

 © 2006 Wiley-VCH Verlag GmbH & Co. KGaA, Weinheim 

Table 1. Crystallographic details.

| | **KL[1]** | **KL[4]** | **1d** | **1e** | **1h** | **2 g** |
|---|---|---|---|---|---|---|
| Empirical formula | $C_{27}H_{25}BKN_9 \cdot CH_3CN$ | $C_{33}H_{31}BKN_9O_3 \cdot H_2O \cdot 2.5CH_3OH$ | $C_{29}H_{28}BN_9O_2Zn \cdot CH_3OH$ | $C_{27}H_{25}BN_{10}O_3Zn$ | $C_{28}H_{29}BClN_9O_5Zn$ | $C_{36}H_{58}BClN_{12}O_8Zn \cdot 2CH_2Cl_2$ |
| Formula mass | 566.51 | 749.71 | 642.84 | 613.75 | 683.25 | 1068.45 |
| Crystal size [mm] | 0.2×0.15×0.1 | 0.15×0.2×0.3 | 0.25×0.15×0.05 | 0.1×0.15×0.2 | 0.3×0.2×0.1 | 0.15×0.15×0.25 |
| Space group | $P2_1/c$ | $P\bar{1}$ | $P2_1/c$ | $P2_1/n$ | $P\bar{1}$ | $Pbca$ |
| Z | 4 | 2 | 4 | 4 | 2 | 8 |
| $a$ [Å] | 11.375(2) | 13.211(2) | 12.936(4) | 9.918(3) | 10.838(2) | 18.560(2) |
| $b$ [Å] | 16.015(3) | 13.332(2) | 16.933(6) | 9.280(3) | 12.544(2) | 22.349(3) |
| $c$ [Å] | 16.499(3) | 13.378(2) | 16.460(4) | 29.539(8) | 16.023(3) | 25.651(3) |
| $\alpha$ [°] | 90 | 105.313(2) | 90 | 90 | 90.583(3) | 90 |
| $\beta$ [°] | 103.399(3) | 102.689(2) | 120.67(2) | 97.220(4) | 101.794(3) | 90 |
| $\gamma$ [°] | 90 | 114.741(2) | 90 | 90 | 94.111(3) | 90 |
| $V$ [Å$^3$] | 2924(1) | 1911.8(4) | 3101(2) | 2697(1) | 2126.3(6) | 10640(2) |
| $d$(calcd.) [g·cm$^{-3}$] | 1.29 | 1.28 | 1.38 | 1.51 | 1.07 | 1.33 |
| $\mu$(Mo-$K_\alpha$) [mm$^{-1}$] | 0.22 | 0.20 | 0.84 | 0.96 | 0.68 | 0.77 |
| $hkl$ range | $h$: –15 to 8 | $h$: –17 to 16 | $h$: –17 to 17 | $h$: –13 to 12 | $h$: –14 to 14 | $h$: –8 to 25 |
| | $k$: –20 to 22 | $k$: –17 to 17 | $k$: –22 to 22 | $k$: –12 to 12 | $k$: –16 to 16 | $k$: –24 to 30 |
| | $l$: –20 to 23 | $l$: –17 to 18 | $l$: –22 to 21 | $l$: –38 to 39 | $l$: –21 to 21 | $l$: –34 to 20 |
| Refl. measd. | 19542 | 17246 | 28041 | 22184 | 18887 | 38586 |
| Indep. refl. | 8052 | 8887 | 7663 | 6429 | 9849 | 13078 |
| Obsd. refl. [$I > 2\sigma(I)$] | 3088 | 4891 | 3942 | 3589 | 5623 | 3502 |
| Parameters | 371 | 525 | 403 | 379 | 438 | 602 |
| Refl. refined | 8052 | 8887 | 7663 | 6429 | 9849 | 13078 |
| $R_1$ (obsd. refl.) | 0.068 | 0.055 | 0.058 | 0.053 | 0.053 | 0.070 |
| $wR_2$ (all refl.) | 0.238 | 0.172 | 0.174 | 0.158 | 0.156 | 0.236 |
| Resid. electron dens. [e/Å$^{-3}$] | +0.4/–0.4 | +0.7/–0.5 | +0.7/–0.7 | +0.6/–0.8 | +1.0/–0.4 | +0.9/–0.8 |

density, but not the specific atomic positions in the refinement.[32] Drawings were produced with SCHAKAL.[33] Table 1 lists the crystallographic details.

## Acknowledgments

This work was supported by the Deutsche Forschungsgemeinschaft and by the Fonds der Chemischen Industrie. We are indebted to Mrs. P. Klose for help in the laboratory, to Dr. H. Brombacher for help with the structure determinations and to B. Benkmil and Dr. J. Maldonado for assistance.

[1] S. Trofimenko, *Scorpionates*, Imperial College Press, London, **1999**.
[2] H. Vahrenkamp, *Acc. Chem. Res.* **1999**, *32*, 589–596.
[3] G. Parkin, *Adv. Inorg. Chem.* **1995**, *42*, 291–393.
[4] G. Parkin, *Chem. Rev.* **2004**, *104*, 699–767.
[5] K. Weis, H. Vahrenkamp, *Inorg. Chem.* **1997**, *36*, 5589–5591.
[6] K. Weis, H. Vahrenkamp, *Inorg. Chem.* **1997**, *36*, 5592–5596.
[7] M. Ruf, K. Weis, H. Vahrenkamp, *J. Am. Chem. Soc.* **1996**, *118*, 9288–9294.
[8] A. J. Amoroso, A. M. Cargill Thompson, J. C. Jeffery, P. L. Jones, J. A. McCleverty, M. D. Ward, *J. Chem. Soc., Chem. Commun.* **1994**, 2751–2752.
[9] a) P. L. Jones, A. J. Amoroso, J. C. Jeffery, J. A. McCleverty, E. Psillakis, L. Rees, M. D. Ward, *Inorg. Chem.* **1997**, *36*, 10–18; b) R. L. Paul, A. J. Amoroso, P. L. Jones, S. M. Couchman, Z. R. Reeves, L. H. Rees, J. C. Jeffery, J. A. McCleverty, M. D. Ward, *J. Chem. Soc., Dalton Trans.* **1999**, 1563–1568.
[10] B. S. Hammes, X. M. Luo, M. W. Carrano, C. J. Carrano, *Inorg. Chim. Acta* **2002**, *341*, 33–38.
[11] Z. Shirin, C. J. Carrano, *Polyhedron* **2004**, *23*, 239–244.
[12] C. Pérez Olmo, H. Vahrenkamp, Results unpublished.
[13] A. L. Rheingold, C. D. Incarvito, S. Trofimenko, *J. Chem. Soc., Dalton Trans.* **2000**, 1233–1234.
[14] H. Adams, S. R. Batten, G. M. Davies, M. B. Duriska, J. C. Jeffery, P. Jensen, J. Lu, G. R. Motson, S. J. Coles, M. B. Hursthouse, M. D. Ward, *Dalton Trans.* **2005**, 1910–1923.
[15] O. Efimovsky, P. Rumpf, *Bull. Soc. Chim. Fr.* **1954**, 648–649.
[16] F. W. Swamer, C. R. Hauser, *J. Am. Chem. Soc.* **1950**, *72*, 1352–1356.
[17] G. A. C. Gough, H. King, *J. Chem. Soc.* **1933**, 350–351.
[18] J. Elguero, R. Jaquier, *Bull. Soc. Chim. Fr.* **1966**, 2832–2845.
[19] C. S. Marvel, E. E. Dreger, *Org. Synth., Coll. Vol.* **1941**, *1*, 238.
[20] K. Dewar, *J. Chem. Soc.* **1945**, 114–117.
[21] K. Seki, J. Isegawa, M. Fukuda, M. Ohki, *Chem. Pharm. Bull.* **1984**, *32*, 1568–1577.
[22] C. Musante, *Gazz. Chim. Ital.* **1945**, *75*, 121–123.
[23] K. Weis, Dissertation, University of Freiburg, **1997**.
[24] K. Weis, M. Rombach, M. Ruf, H. Vahrenkamp, *Eur. J. Inorg. Chem.* **1998**, 263–270.
[25] M. Shu, R. Walz, B. Wu, J. Seebacher, H. Vahrenkamp, *Eur. J. Inorg. Chem.* **2003**, 2502–2511.
[26] M. M. Ibrahim, M. Shu, H. Vahrenkamp, *Eur. J. Inorg. Chem.* **2005**, 1388–1397.
[27] M. Ruf, K. Weis, I. Brasack, H. Vahrenkamp, *Inorg. Chim. Acta* **1996**, *250*, 271–281.
[28] D. T. Puerta, S. M. Cohen, *Inorg. Chem.* **2003**, *42*, 3423–3430.
[29] M. Förster, R. Burth, A. K. Powell, T. Eiche, H. Vahrenkamp, *Chem. Ber.* **1993**, *126*, 2643–2648.
[30] CCDC-604241 (for **KL[1]**), -604242 (**KL[2]**), -604243 (for **1d**), -604244 (for **1e**), -604245 (for **1h**) and -604246 (for **2g**) contain the supplementary crystallographic data for this paper. These data can be obtained free of charge from The Cambridge Crystallographic Data Centre via www.ccdc.cam.ac.uk/data_request/cif.
[31] G. M. Sheldrick, *SHELXTL program package for the Bruker Smart CCD diffractometer*, version 5.1, Universität Göttingen, **2002**.
[32] A. L. Spek, *J. Appl. Crystallogr.* **2003**, *36*, 7–13.
[33] E. Keller, *SCHAKAL for Windows*, University of Freiburg, **2002**.

Received: April 27, 2006
Published Online: July 13, 2006

 © 2006 Wiley-VCH Verlag GmbH & Co. KGaA, Weinheim 

DOI: 10.1002/ejic.200600466

# Multicomponent Supramolecular Devices: Synthesis, Optical, and Electronic Properties of Bridged Bis-dirhodium and -diruthenium Complexes

**Anne Petitjean,[a][‡] Fausto Puntoriero,[b] Sebastiano Campagna,*[b] Alberto Juris,[c] and Jean-Marie Lehn*[a]**

*Dedicated to Professor Vincenzo Balzani*

**Keywords:** N ligands / Electronic coupling / Electrochemistry / Metal–metal interactions / Optical properties

Four ruthenium- and rhodium-based metal–metal-bonded multicomponent systems have been synthesized, and their absorption, redox, spectroelectrochemical and structural properties have been studied. The absorption spectra of the four bis-dimetallic compounds $M_2LM_2$, where L is a bridging ligand and M is rhodium or ruthenium, exhibit very strong bands in the UV, visible and, for the diruthenium species, near-IR region. The low-energy absorption bands are assigned to charge-transfer transitions involving a metal–metal bonding orbital as the donor and an orbital centered on the bis-tetradentate aromatic ligands as the acceptor (metal–metal to ligand charge transfer, $M_2LCT$). Each compound exhibits reversible bridging-ligand-centered reductions at mild potentials and several reversible oxidation processes. The oxidation signals of the two equivalent dimetallic centers of each bis-dimetallic compound are split, with the splitting – a measure of the electronic coupling – depending on both the metal and bridging ligand. The mixed-valence species of the dirhodium species was investigated, and the electronic coupling matrix element calculated from the experimental intervalence band parameters for one of them (86 $cm^{-1}$) indicates a significant inter-component electronic interaction which compares well with good electron conducting anionic bridges such as cyanides. Although none of these compounds is luminescent, the $M_2LCT$ excited state of one of the bis-dirhodium complexes is relatively long-lived (about 6 μs) in degassed acetonitrile at room temperature. The results presented here are promising for the development of linear poly-dimetallic complexes built on longer naphthyridine-based strands, with significant long-range electronic coupling and molecular-wire-like behavior.

(© Wiley-VCH Verlag GmbH & Co. KGaA, 69451 Weinheim, Germany, 2006)

## Introduction

Since the discovery of mixed-valence complexes by Creutz and Taube[1] over 30 years ago, architectures including several redox centers of the same[2] or different[3] nature and capable of exhibiting inter-component electronic interaction have been the center of much attention. Due to their rich redox properties, transition metal ions connected by a bridging spacer have been the focus of much work in this field, although recent examples have also proved the tremendous potential of organic redox-active species connected through bridging transition metal complexes.[4] A variety of systems connecting mononuclear metal ions have been explored, where the spacer is itself a ligand[1,5] or where spacer and ligands are decoupled and involve single bonds[6] and multiple bonds (alkynyl for 1D,[7] 2D,[7b,7c] and 3D[7c] architectures; alkenyl,[5b] cumulenes,[7a,8] aryl[5b,7b,7d,9a,9b]). These systems may incorporate other inert[10a] or labile[7b,10b] complexes and have the electronic communication between the two sites modulated by pH,[11] light,[12a,12b] or auxiliary ligands.[13] The field has more recently been extended to metal–metal-bonded redox units because they themselves can include multiple bonds,[14] similar to carbon-based units but energetically more accessible, and may therefore play the role of a conductor. The dissymmetry around the metal sites allows for testing of the communication along the metal–metal bond through axial ligands and spacers similar to their mononuclear counter-

[a] ISIS, Université Louis Pasteur, CNRS UMR 7006, B. P. 70028, 67083 Strasbourg, France
Fax: +33-3-90245140
E-mail: lehn@isis.u-strasbg.fr
[b] Dipartimento di Chimica Inorganica, Chimica Analitica e Chimica Fisica, Università di Messina, Via Sperone 31, 96166 Villaggio S. Agata, Messina, Italy
Fax: +39-090-393-756
E-mail: campagna@unime.it
[c] Dipartimento di Chimica "G. Ciamician", Università di Bologna, Via F. Selmi 2, 40126 Bologna, Italy
Fax: +39-051-209-9456
E-mail: alberto.juris@unibo.it
[‡] Present address: Department of Chemistry, Queen's University, 90 Bader Lane, Kingston ON, K7L 3N6, Canada
Supporting information for this article is available on the WWW under http://www.eurjic.org or from the author.

 © 2006 Wiley-VCH Verlag GmbH & Co. KGaA, Weinheim 

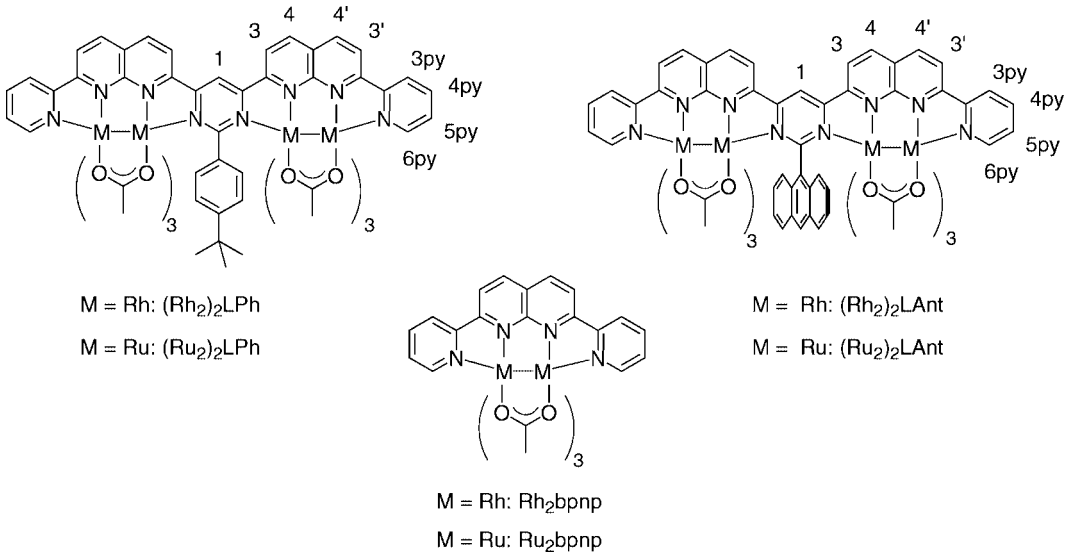


Figure 1. Formulae and abbreviation of the complexes. Numbering is related to the discussion of the $^1$H NMR spectroscopic data.

parts (e.g., triple bonds[15] and double bonds[16]), but also successfully along the equatorial direction.[17]

We report here the synthesis and characterization, absorption spectra, redox behavior, and spectroelectrochemistry of four bi-component systems in which each "component" or subunit is made of a metal–metal-bonded dimetallic site (Figure 1). The excited-state properties of one such species are also investigated. As we will see later, each dimetallic site can indeed be viewed as a single component of a "dinuclear" system from a redox viewpoint.

## Results and Discussion

### Synthesis

#### *Ligands*

The naphthyridine-based ligands 2-(4-*tert*-butylphenyl)-4,6-bis(7-pyridin-2-yl[1,8]naphthyridin-2-yl)pyrimidine (LPh) and 2-anthracen-9-yl-4,6-bis(7-pyridin-2-yl[1,8]naphthyridin-2-yl)pyrimidine (LAnt) were obtained by a Friedländer condensation methodology applied to a pyrimidine scaffold, in a very similar fashion as previously reported[18] (Schemes 1 and 2). Two synthetic routes were used to access the central pyrimidine unit. In the case of the 4-*tert*-butylphenyl substituent leading to LPh (Scheme 1), the pyrimidine ring was built by condensation of the corresponding amidine **2**, resulting from ammonia addition to the corresponding nitrile **1**, with diethyl malonate. The obtained dihydroxypyrimidine **3** was then chlorinated with a combination of phosphoryl chloride and *N*,*N*-dimethylaniline to yield the dichloropyrimidine **4**Ph. The 9-anthracenyl-substituted dichloropyrimidine **4**Ant, on the other hand, was prepared directly from unsubstituted 4,6-dichloropyrimidine by deprotonation at the 2-position, reaction with 9-bromoanthracene, and oxidation with DDQ, as published earlier (Scheme 2).[19] The dichloropyrimidines **4**Ph and **4**Ant were then coupled with 1-(tri-*n*-butylstannyl)-1-vinyl ethyl ether[20] and submitted to acidic hydrolysis to yield the corresponding diketones **5**Ph and **5**Ant, ready for Friedländer condensation. Once again, different routes were used for the butyl- and anthracenyl-substituted ligands. The butyl-substituted ligand was obtained by two consecutive Friedländer condensations: a base-catalyzed condensation with 4-aminopyrimidine-5-carboxaldehyde[21] yielded pyrimidine-ended intermediate **6**Ph, which was then converted into the bis(aminocarbaldehyde) **7**Ph under acidic conditions. The latter was then condensed with commercially available 2-acetylpyridine to yield the final ligand LPh. Bis(ketone) **5**Ant, on the other hand, was directly condensed with 6-amino-2,2′-bipyridinyl-5-carbaldehyde (**9**) to yield ligand LAnt. Compound **9** was also synthesized by Friedländer condensation of 2-acetylpyridine and 4-aminopyrimidine-5-carboxaldehyde (**8**) followed by acidic hydrolysis. LAnt displays the fluorescence emission typical of anthracene derivatives.

#### *Metal Complexes*

Both dirhodium complexes were obtained by treatment of a suspension of the ligand with commercially available dirhodium tetraacetate in methanol in the presence of two equivalents of protons (1 equiv. per acetate bridge to be substituted).[22a] Heating a suspension of the ligand with the mixed-valence complex $[Ru_2(OAc)_4Cl]$[23] in methanol yielded the desired diruthenium(II) complexes without additional reductant.[22b] All complexes were isolated as their hexafluorophosphate salts.

### Characterization

#### *$^1$H NMR Spectroscopy*

The diamagnetic dirhodium(II) complexes show a simple set of signals, thus revealing that the $C_2$ symmetry of the ligands is maintained in the complexes and therefore that

 © 2006 Wiley-VCH Verlag GmbH & Co. KGaA, Weinheim 

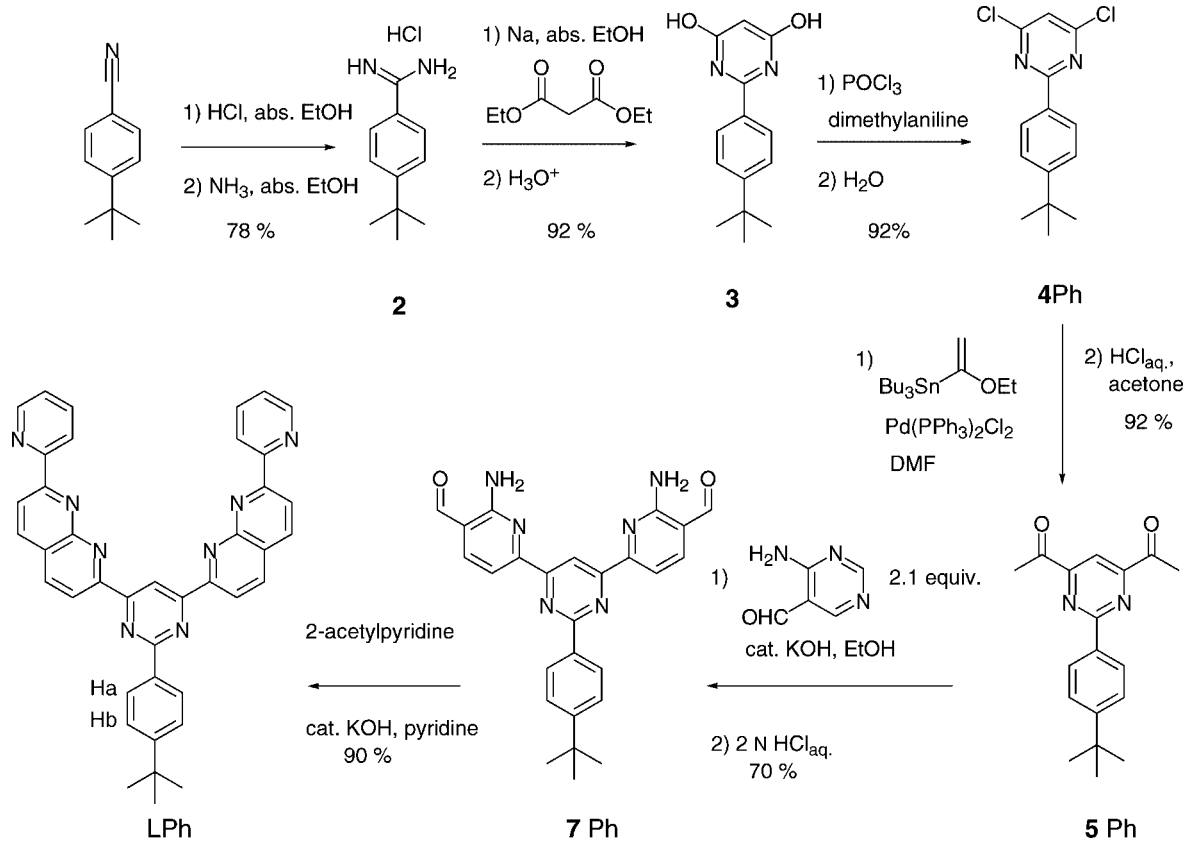


Scheme 1. Synthesis of LPh (numbering relates to the discussion of the $^1$H NMR spectroscopic data).

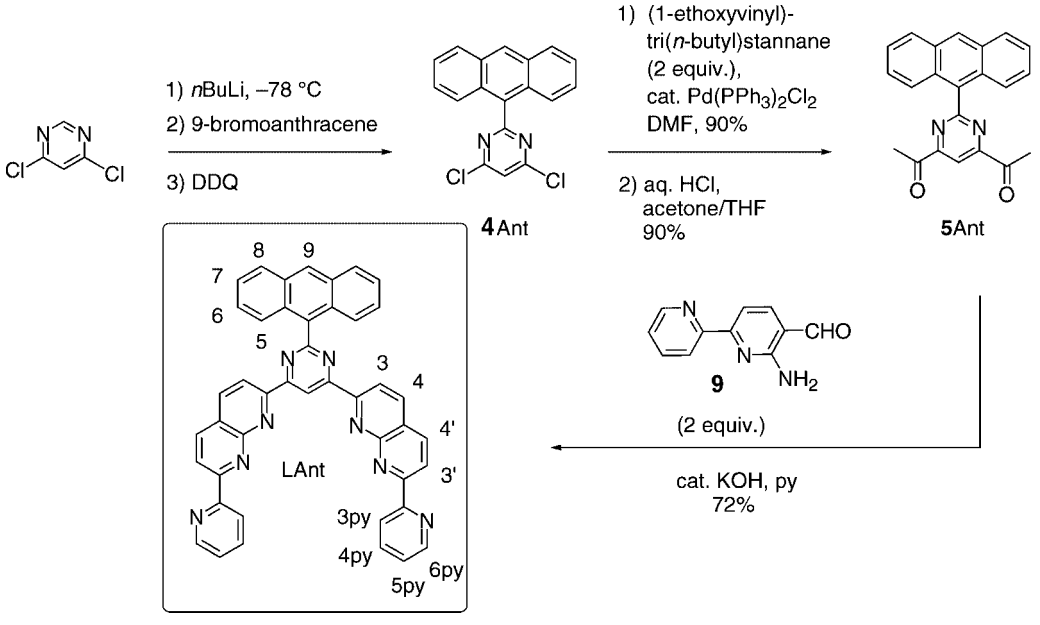


Scheme 2. Synthesis of LAnt (numbering relates to the discussion of the $^1$H NMR spectroscopic data).

both dinuclear binding sites are occupied (in agreement with elemental analysis and mass spectrometry measurements). The two sets of signals from the acetate ligands confirm the dissymmetry introduced by a single L ligand (two different signals for the 12 equatorial and the six axial $CH_3$ acetate protons). The six axial acetate protons are shielded due to the ring effect provided by the anthracene moiety, thua confirming the involvement of the pyrimidine nitrogen atoms in the coordination of the $Rh_2$ units and the rotation of the C–C bonds between the heteroaryl units compared to the initial ligands. Although the spectra of free ligands and metal complexes were recorded in different solvents

 © 2006 Wiley-VCH Verlag GmbH & Co. KGaA, Weinheim 

Table 1. Chemical shifts [ppm] of the protons in ligands LPh and LAnt (in $CDCl_3$) and their dirhodium complexes (in $CD_3CN$).

| Compound | H1 | H3 | H3′ | H3py | H4 | H4′ | H4py | H5py | H6py | Ha | Hb | *t*Bu |
|---|---|---|---|---|---|---|---|---|---|---|---|---|
| LPh | 10.06 | 8.81–9.0 | | | 8.42 | 8.47 | 7.97 | 7.43 | 8.8 | 8.73 | 7.64 | 1.44 |
| $[(Rh_2)_2LPh]$ | 9.71 | 8.8–9.0 | | | | | 8.58 | 8.29 | 9.67 | 9.24 | 7.75 | 1.49 |

| Compound | H1 | H3 | H3′ | H3py | H4 | H4′ | H4py | H5py | H6py | H5 | H6 | H7 | H8 | H9 |
|---|---|---|---|---|---|---|---|---|---|---|---|---|---|---|
| LAnt | 10.3 | 8.7–8.85 | | 9.03 | 8.3–8.4 | | 7.99 | 7.4–7.6 | 8.7–8.9 | 7.88 | 7.4–7.6 | | 8.14 | 8.67 |
| $[(Rh_2)_2LAnt]$ | 10.1 | 9.47 | | 8.8–9.1 | 8.8–9.1 | | 8.52 | 8.2–8.3 | 9.50 | 7.92 | 7.31, 7.47 | | 8.2–8.3 | 8.8–9.1 |

and therefore the chemical shifts cannot be accurately compared (cf. *t*Bu signal as a probe of solvent effect), the introduction of the $Rh_2$ units has a significant deshielding effect on the protons *para* to the nitrogen atoms of the bound heterocycles (ca. +0.5 ppm for H4, H4′and H4py; Table 1) and on the pyridine protons. The substituents on the pyrimidine ring also undergo a downfield shift due to the proximity of the acetate ligands (ca. +0.5 ppm for Ha in LPh and ca. +0.2 ppm for H9 in LAnt).

The diruthenium(II) complexes are paramagnetic, as expected for the distribution of the 12 d-electrons of the two ruthenium(II) centers in a $\sigma^2\pi^4\delta^2\delta^{*2}\pi^{*2}$ configuration. The $^1H$ NMR spectra nevertheless show well-defined peaks ranging from $\delta$ = –50 to 80 ppm (Figure 2) whose number is in accordance with the expected symmetry.

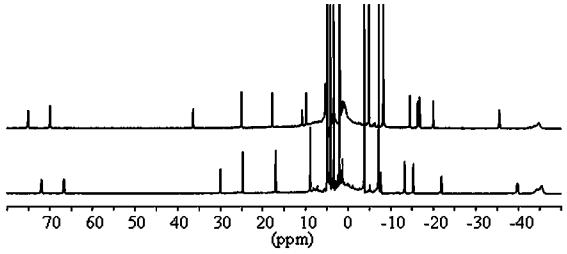


Figure 2. $^1H$ NMR spectra of the paramagnetic complexes $[(Ru_2)_2LAnt]^{2+}$ (top) and $[(Ru_2)_2LPh]^{2+}$ (bottom) ($CD_3CN$, 200 MHz, 25 °C).

### *X-ray Structure Determination*

Single-crystal X-ray analysis of $[(Rh_2)_2LPh]$[24] confirmed the anticipated structure of the bis-dirhodium complex (Figure 3). All nitrogen sites are bound to the rhodium centers. The distance between the two rhodium centers (2.40 Å) is the same as that found in the parent $[Rh_2bpnp]^+$ complex [$Rh_2$ is $Rh_2(OAc)_3$ and bpnp is bis(pyridyl)naphthyridine],[22a] as are the distances involving the coordinated

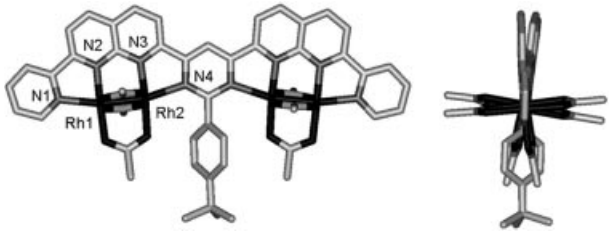


Figure 3. Solid-state structure of $[(Rh_2)_2LPh]$[24] showing the alignment of the two bis-dirhodium units bridged by the central pyridimine (hydrogen atoms, solvent, and counter anions have been omitted for clarity).

naphthyridines [Rh(1)–N(2) 2.00 and Rh(2)–N(3) 1.98 Å]. As anticipated by the difference in basicity, the strong coordinative contribution of the pyridine [Rh(1)–N(1) 2.16 Å] stands in contrast to the weaker binding of the pyrimidine ring [Rh(2)–N(4) 2.31 Å]. Overall, the quasi-planar, crescent-shaped ligand[25] holds the two bis-dirhodium metallic units in a linear alignment that is bridged by the central pyrimidine and slightly bent by the coordination-induced pinching of the subunits.

### *IR Spectra*

The IR spectra of all complexes show many common features (number and location of bands), which is further evidence for their similar functional and structural environments as well as identical symmetry.

### *Absorption Spectra*

All complexes are deeply colored. The optical properties are represented in Figure 4 and reported in Table 2, together with those of the simple $[M_2bpnp]^+$ dimetallic complexes reported earlier by other groups[22a,22b] (M = $Ru^{II}$ or $Rh^{II}$; these complexes were synthesized again for comparison purposes). The absorption spectra are very rich, as expected because of the presence of several chromophoric units. The spectra of all the complexes exhibit an intense absorption feature between 320 and 400 nm. This feature should therefore receive contribution from spin-allowed π–π* transitions involving the common L bridging ligand. In $[(Rh_2)_2LAnt]$ and $[(Ru_2)_2LAnt]$, the spin-allowed, anthracene-centered $^1L_a$ transitions are expected within the same wavelength range,[26c,27,28] and their contribution is clear when looking at the vibrational progression appearing in the spectra of both species. For these latter species, the very intense absorption band around 254 nm can be straightforwardly assigned to the $^1B_a$ transition of the anthryl subunits.[26c,27,28]

As far as the visible absorption is concerned, the lowest-energy band of the rhodium species is attributed to a charge-transfer transition from each dirhodium subunit (most likely from a π* orbital extending over the two metal centers) to the bridging ligand. Such a transition is a form of metal–metal to ligand charge transfer ($M_2LCT$) transition because of the strong interaction between the metal–metal-bonded units of each component. The red shift of the lowest-energy absorption band in the present compounds {$\lambda_{max}$ = 622 and 634 nm for $[(Rh_2)_2LPh]$ and $[(Rh_2)_2LAnt]$, respectively} compared to that of the parent species $[Rh_2bpnp]$ ($\lambda_{max}$ = 578 nm) supports the CT assignment, since in the dicomponent species the LUMO of the polypyr-

 © 2006 Wiley-VCH Verlag GmbH & Co. KGaA, Weinheim 

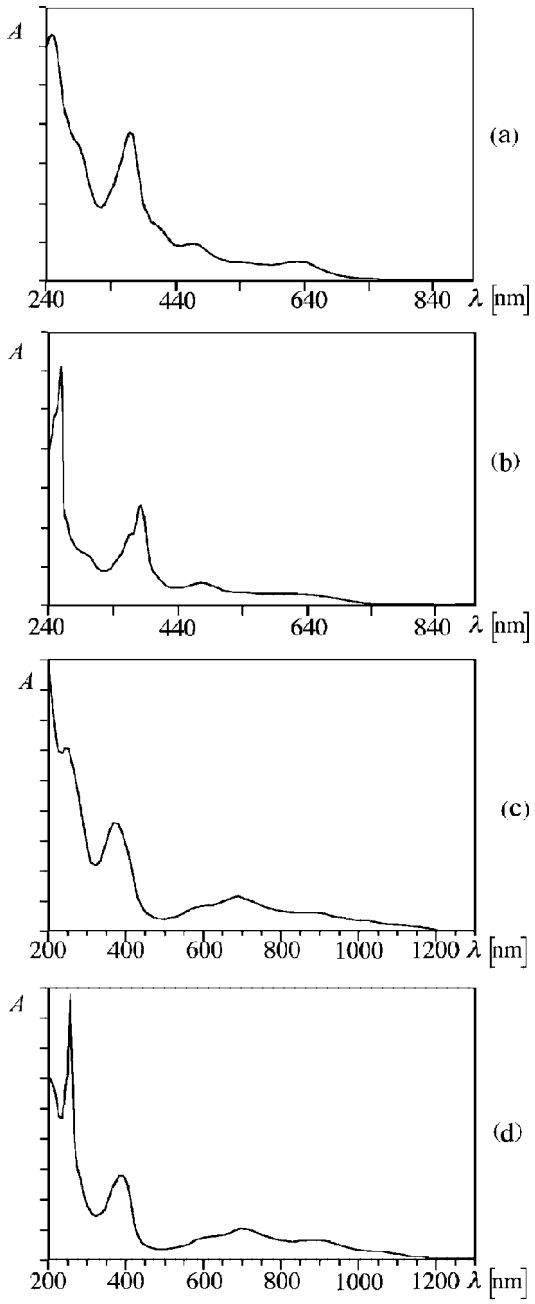


Figure 4. Absorption spectra of $[(Rh_2)LPh(Rh_2)]$ (a), $[(Rh_2)$-$LAnt(Rh_2)]$ (b), $[(Ru_2)LPh(Ru_2)]$ (c), and $[(Ru_2)LAnt(Ru_2)]$ (d) in acetonitrile solution.

idine-type bridging ligand (i.e., the acceptor orbital of the CT transition) is lower in energy than the LUMO of bpnp (see below).

For the ruthenium compounds, the absorption bands, which have a similar origin to those of the rhodium analogues, are displaced to lower energies than the rhodium species, with the lowest-energy band in the near-IR region (Figure 4). This is also in agreement with a $M_2LCT$ assignment, since the metal-based HOMOs of the ruthenium compounds are higher in energy than those of the corresponding rhodium species (see redox behavior).

## Redox Behavior

The four bis-dimetallic species investigated here exhibit a rich redox behavior. Figure 5 shows the cyclic voltammograms of the compounds and Table 3 reports the main redox data, together with data relative to the free ligands (bpnp and LPh) and parent $[Rh_2bpnp]^+$ complex for comparison. To better evidence the bi-component nature of the studied compounds, these latter are labeled $(M_2)L(M_2)$ instead of $(M_2)_2L$ (M = Rh or Ru; L = LPh or LAnt) in this paragraph.

As already discussed,[24] the easier reduction of the LPh ligand compared to the bpnp ligand ($\Delta E_{1/2}^{\text{first-red}} = -0.28$ V) is mirrored by the reduction properties of the complexes, with $[(Rh_2)LPh(Rh_2)]$ being easier to reduce than $[Rh_2bpnp]^+$ ($\Delta E_{1/2}^{\text{first-red}} = -0.43$ V). This observation is in accordance with earlier work describing the LUMO of $[Rh_2(acetate)_3L]^+$ complexes (L = chelating pyridine/naphthyridine-type ligand) as being mainly ligand-based.[29] Substituting a pyridine for a more easily reduced pyrimidine yields a new ligand and its derived complexes with less negative reduction potentials. The lowering of the LUMO of polypyridyl-type ligands upon complexation has also already been observed.[26b] Such considerations allow us to assign the reduction potential of all the bis-dimetallic complexes studied here to bridging-ligand-based processes.

Table 3 also indicates that both bis-dirhodium complexes are easier to reduce than their bis-diruthenium counterparts (ca. 0.1 V difference). This may be due to an enhanced π back-donation in the bis-diruthenium complexes, which have metal-centered HOMOs of higher energy (see below).

Table 2. Absorption data in $CH_3CN$ at room temperature.

| | $\lambda_{max}$ [nm] ($\log_{10}\varepsilon$ [$M^{-1}cm^{-1}$]) | | | | | | | | | | | |
|---|---|---|---|---|---|---|---|---|---|---|---|---|
| $[Rh_2bpnp]\cdot PF_6$ | 248 | | 283 | 346 | 363 | 408 sh | 440 sh | 540 sh | 578 | | | |
| | (4.69) | | (4.33) | (4.46) | (4.63) | (3.34) | (3.08) | (3.40) | (3.52) | | | |
| $[(Rh_2)LPh(Rh_2)]\cdot 2PF_6$ | 250 | | 292 | 347 sh | 371 | 412 sh | 468 | 543 | 622 | | | |
| | (4.9) | | (4.6) | (4.5) | (4.6) | (4.2) | (4.0) | (3.7) | (3.7) | | | |
| $[(Rh_2)Ant(Rh_2)]\cdot 2PF_6$ | 248 | 254 | 295 | 347 sh | 364 | 382 | 478 | 545 | 634 | | | |
| | (3.1) | (5.2) | (4.5) | (4.5) | (4.6) | (4.8) | (4.1) | (3.8) | (3.8) | | | |
| $[Ru_2bpnp]\cdot PF_6$ | 246 | 274 | 287 | 351 | | | 440 sh | 520 sh | 586 sh | 612 | 729 | 917 |
| | (4.5) | (4.4) | (4.3) | (4.5) | | | (3.35) | (3.4) | (3.6) | (3.7) | (3.8) | (3.2) |
| $[(Ru_2)LPh(Ru_2)]\cdot 2PF_6$ | 248 | 270 sh | | 370 | | | 400 sh | 600 | 695 | | | |
| | (4.8) | (4.6) | | (4.6) | | | (4.4) | (4.0) | (4.2) | | | |
| $[(Ru_2)LAnt(Ru_2)]\cdot 2PF_6$ | 254 | | | 369 | | | 387 (4.6) | 602 | 701 | | | |
| | (4.7) | | | (4.5) | | | | (4.0) | (4.2) | | | |

 © 2006 Wiley-VCH Verlag GmbH & Co. KGaA, Weinheim 

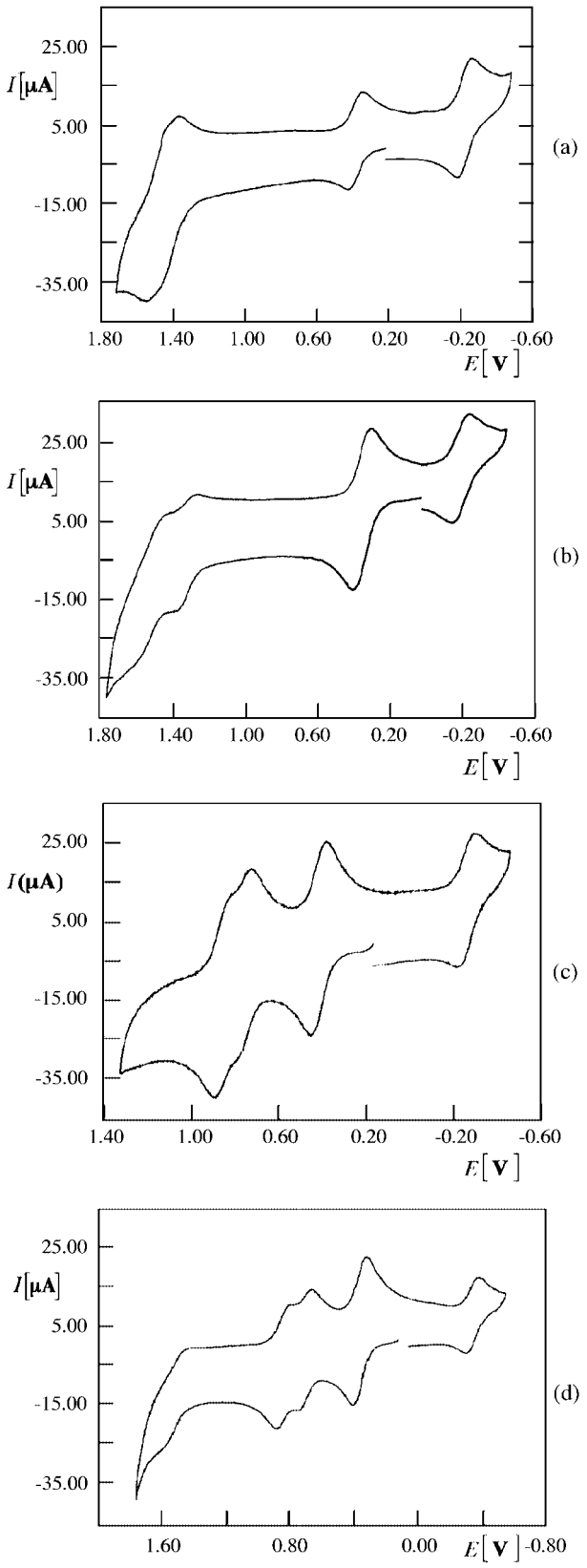


Figure 5. Cyclic voltammograms (vs. SCE) of the four complexes $[(Rh_2)LPh(Rh_2)]$ (a), $[(Rh_2)LAnt(Rh_2)]$ (b), $[(Ru_2)LPh(Ru_2)]$ (c), and $[(Ru_2)LAnt(Ru_2)]$ (d) in acetonitrile at room temperature. Scanning rate: 500 mV $s^{-1}$. The process at about 0.4 V is the ferrocene oxidation, used as an internal reference.

Table 3. Half-wave potentials (vs. SCE) for the oxidation and first reduction of the four bis-dimetallic complexes and of reference species in acetonitrile at room temperature (0.5 mM, 0.05 M $NBu_4ClO_4$). Number of exchanged electrons in square brackets. The processes are reversible unless otherwise stated.

| Compound | Oxidation, $E_{1/2}$ [V] vs. *SCE* | Reduction, $E_{1/2}$ [V] vs. SCE |
|---|---|---|
| bpnp[a] | no oxidation at V < +1.80 | –1.64 [1] |
| LPh[a] | no oxidation at V < +1.80 | –1.36 [1] |
| $[Rh_2bpnp]$[a] | +1.30 [1] | –0.64 [1] |
| $[(Rh_2)LPh(Rh_2)]$ | +1.43 [1], +1.50 [1] | –0.21 [1][b] |
| $[(Rh_2)LAnt(Rh_2)]$ | +1.32 [1], +1.53 [2][c] | –0.18 [1][b] |
| $[(Ru_2)LPh(Ru_2)]$ | +0.76 [1], +0.85 [1] | –0.31 [1][b] |
| $[(Ru_2)LAnt(Ru_2)]$ | +0.73 [1], +0.86 [1], +1.51 [1][c] | –0.30 [1][b] |

[a] Data taken from ref.[24] For the free ligands, the solvent is dichloromethane and the reported values were obtained at 0 °C. [b] Further reduction processes take place for all the complexes but they are ill-behaved and will not be discussed here. [c] Irreversible process.

The contribution of the diruthenium unit to the LUMO destabilization thus results in a more negative reduction potential.

Several oxidation waves are observed for all complexes, as evidenced by the cyclovoltammograms reported in Figure 5. $[(Rh_2)LPh(Rh_2)]$ shows two very close oxidation waves (resolved by differential voltammetry), each of which corresponds to a one-electron oxidation and is related to the sequential removal of one electron from each $Rh_2$ unit. Therefore, the first oxidation process leads to the mixed-valence, bi-component system $[(Rh_2^{5+})LPh(Rh_2^{4+})]$, whereas $[(Rh_2^{5+})LPh(Rh_2^{5+})]$ is obtained upon further oxidation. The first one-electron oxidation of $[(Rh_2)LAnt(Rh_2)]$ is followed by a two-electron irreversible oxidation at 1.53 V. To assign the various processes occurring in this latter compound to specific subunits, it is useful to consider that an irreversible oxidation at +1.51 V is observed for $[(Ru_2)LAnt(Ru_2)]$ (attributed to oxidation of the anthryl center, see below) and the second oxidation of the dimetallic subunit of $[(Rh_2)LPh(Rh_2)]$ occurs at +1.50 V (see above). It is therefore likely that the first oxidation process of $[(Rh_2)LAnt(Rh_2)]$ corresponds to the oxidation of one bimetallic subunit and the subsequent irreversible bi-electronic oxidation involves both the one-electron oxidation of the second $Rh_2$ unit and the irreversible oxidation of the anthracene unit.

Both the bis-diruthenium complexes are much easier to oxidize than their bis-dirhodium counterparts. This indicates that the HOMOs are higher in energy for the diruthenium centers than for the dirhodium ones. Once again, two consecutive one-electron oxidations occur for the bis-ruthenium species (Table 3, Figure 5), which are assigned to the consecutive oxidation of the interacting dimetallic subunits. The additional irreversible oxidation at 1.51 V in $[(Ru_2)LAnt(Ru_2)]$, mentioned above, is attributed to the anthracene oxidation.

### Intercomponent Interactions

The observation of two distinct oxidation potentials for the two $M_2$ units in $[(M_2)LPh(M_2)]$ and $[(M_2)LAnt(M_2)]$

 © 2006 Wiley-VCH Verlag GmbH & Co. KGaA, Weinheim 

suggests that a non-negligible electronic interaction exists between the two metal–metal-bonded dimetallic subunits of the four complexes. Actually, the difference between the two oxidation potentials is a function of the degree of interaction between the two redox centers.[30] The splittings between the first two oxidation waves reported in Table 4 show that [(Ru$_2$)LPh(Ru$_2$)] displays a slightly greater degree of electronic interaction than its bis-dirhodium counterpart (for the LAnt series, overlap between the second metal-based oxidation and the anthracene-based irreversible oxidation in [(Rh$_2$)LAnt(Rh$_2$)] makes the comparison meaningless). To rationalize such a difference, it is useful to recall that, beside Coulombic factors, which are expected to be identical for both the dirhodium and diruthenium compounds studied here, contribution to the electronic interaction can be related to the separation between the energetic levels of the HOMOs, which are centered on the metallic unit, and the LUMO, which is centered on the bridging ligand, assuming that an effective mechanism for inter-component electronic interaction is superexchange via an electron-transfer pathway involving the bridging ligands.[30] Hence, on the basis of the Koopman theorem, which approximates the energy of the orbitals to the redox potential values, a smaller difference between first oxidation and reduction potentials corresponds to a larger inter-component interaction. From the redox data in Table 3, the HOMOs of the bis-diruthenium compounds are located at higher energy than those of the bis-dirhodium species, and this justifies why the interaction is larger in the former compounds (the effect on the HOMO is only partially compensated by a reversed effect on the LUMO).

As highlighted in Table 4, it also appears that the anthracene-derived ligand promotes a larger electronic coupling than the 4-*tert*-butylphenyl-substituted ligand: the half-potential difference for [(Ru$_2$)LAnt(Ru$_2$)] is 0.13 V, compared with 0.09 V for [(Ru$_2$)LPh(Ru$_2$)], and, although the potential of the metal-based oxidation of [(Rh$_2$)LAnt(Rh$_2$)] is not known exactly, the same appears also to be valid for the dirhodium couple of complexes. Comparison between the redox properties of the bis-dimetallic compounds studied here with those of closely related dinuclear complexes in which each component is made by a Ru$^{II}$ polypyridine subunit[26b–26d] reveals striking similarities. The structure of the naphthyridine-based ligands LPh and LAnt is indeed derived from that of the pyridine-based parents L′Ph and L′Ant, which accommodate mononuclear ruthenium(II) complexes (see Table 4, right, for the structure of the Ru$^{II}$ complexes). Interestingly, the enhancement of the electronic interaction provided by the anthracene pyrimidine substituent in the bis-dimetallic complexes and the "classic" dinuclear Ru$^{II}$ polypyridine complexes[26b–26d] is the same (0.04 V), thus suggesting that similar processes could be occurring.

Two main contributions can explain the anthracene effect. On the one hand, the anthracene moiety moves the electronic levels of the bridging ligand to lower energies, as also suggested by the reduction potentials {[(Rh$_2$)-LAnt(Rh$_2$)] is easier to reduce than [(Rh$_2$)LPh(Rh$_2$)], see Table 3, with the reduction mainly based on the bridging ligand}, probably because the anthryl substituent can contribute to a better delocalization of the added electron. As a consequence, the LUMO–HOMO gap becomes smaller and the interaction is enhanced. However, according to this mechanism, the effect on the HOMO(s) should be negligible, but this is not the case, since the data in Table 3 indicate that on passing from the LPh to the LAnt series the HOMOs are even more affected than the LUMO by the presence of the anthracene group. On the other hand, the anthracene moiety may contribute to the electronic coupling between the redox sites by opening a new pathway for superexchange, for example by mediating a through-space interaction involving anthracene-based orbitals. The redox data indeed indicate that the anthracene-based HOMO is close in energy to the metal-centered orbitals, so that a hole-transfer pathway involving the anthracene HOMO is quite possible. It is likely that both contributions come into play. This situation is schematized in Figure 6.

Table 4. Differences in half-wave potentials between the first two one-electron oxidations of the four bis-dimetallic complexes and the two related ruthenium-based bis-mononuclear analogues (the structure of the latter is presented on the right).

| Complex | $E_{1/2}^{ox2} - E_{1/2}^{ox1}$ | |
|---|---|---|
| (Rh$_2$)LPh(Rh$_2$) | 0.07 V[a] | 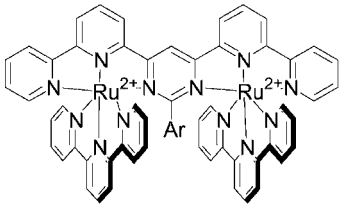 |
| (Rh$_2$)LAnt(Rh$_2$) | n.d.[b] | |
| (Ru$_2$)LPh(Ru$_2$) | 0.09 V[a] | |
| (Ru$_2$)$_2$LAnt(Ru$_2$) | 0.13 V[a] | |
| (Ru)L'Ph(Ru)·4 PF$_6$ | 0.13 V[c] | (Ru)L'Ph(Ru)·4 PF$_6$ Ar = Ph |
| (Ru)L'Ant(Ru)·4 PF$_6$ | 0.17 V[c] | (Ru)L'Ant(Ru)·4 PF$_6$ Ar = 9-Ant |

[a] In acetonitrile. [b] Not determined due to overlap of the second oxidation signal with the anthracene peak. [c] DMF.

 © 2006 Wiley-VCH Verlag GmbH & Co. KGaA, Weinheim 

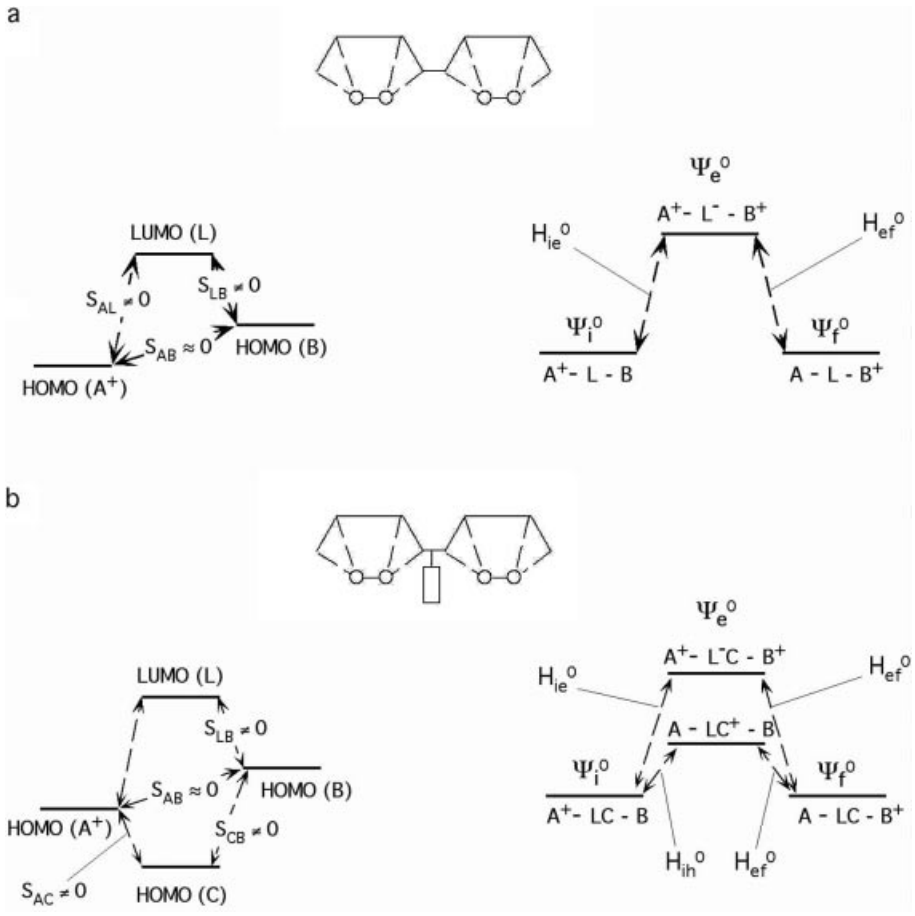


Figure 6. Schematic representation of the interaction between the subunits. In the scheme, A and B represent the dimetallic subunits, with one of them oxidized (so the mixed-valence species is considered, for clarity). (a) refers to species with LPh as the bridge and (b) to LAnt as the bridging ligand. Orbital interactions are shown on the left and interactions between states are represented on the right. In (b), the anthracene (identified as "C") HOMO contributes to the overall coupling; the bridge is here labeled LC on the "state" diagram to highlight the contribution of anthracene. S indicates overlap integrals, Ψ the wavefunctions of the various states, and H the electron coupling matrix elements. The superscript 0 indicates zero-order quantities (i.e. quantities that derive from pure, localized electronic configurations). The subscripts i, f, e, and h indicate the initial, final, electron- and hole-transfer states, respectively (these latter two are "virtual" states).[30]

The electronic information gathered through the electrochemical (and electronic absorption) studies reported above is summarized in Scheme 3. In both the metal–metal-bonded dirhodium and diruthenium complexes, the LUMO–HOMO gap is reduced on going from the bpnp-based "mononuclear" to the LPh- and LAnt-based "dinuclear" complexes, mainly due to a significant LUMO lowering (LUMO centered on the ligand where a pyridine is substituted by a pyrimidine, plus bimetallic coordination of the second chelating site). An additional gap reduction is caused by changing the substitution of the pyrimidine substituent from a phenyl to an anthryl moiety, which results in a small further decrease of the LUMO energy and an increase of the HOMO level.

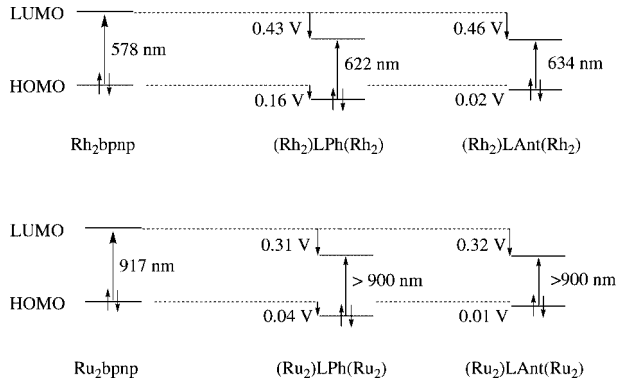


Scheme 3. Compared electronic levels of the one and two dimetallic site complexes of rhodium and ruthenium.

### Spectroelectrochemistry

The splitting of the oxidation processes of the four bis-dimetallic compounds, which indicates a relatively high stability of the mixed-valence species with respect to the isovalent forms,[31] prompted us to investigate the properties of their mixed-valence compounds in more detail by performing spectroelectrochemistry experiments. However, results were poor for the ruthenium complexes: featureless absorption spectra were obtained, probably due to the very

 © 2006 Wiley-VCH Verlag GmbH & Co. KGaA, Weinheim 

broad and unresolved absorption spectra of the starting compounds (see Figure 4), particularly in the otherwise diagnostic visible and near-IR region. For this reason, our discussion will be limited to [($Rh_2$)LPh($Rh_2$)] and [($Rh_2$)-LAnt($Rh_2$)].

Figure 7 shows the changes in the absorption spectrum of [($Rh_2$)LPh($Rh_2$)] on applying increasingly positive potentials. At the beginning (potential: +1.45 V), a slight increase of absorption in the range 680–900 nm occurs, with simultaneous decrease of the absorption of the $M_2$LCT band at about 640 nm. A slight absorption decrease of the 350-nm band also takes place, with formation of a new absorption in the range 380–450 nm. The absorption feature in the red is attributed to an intervalence transfer (IT) transition from the $Rh_2^{4+}$ subunit to the $Rh_2^{5+}$ component of the mixed-valence "dinuclear" [($Rh_2^{5+}$)LPh($Rh_2^{4+}$)] species obtained upon first oxidation, whereas the decrease of the $M_2$LCT band is a consequence of the disappearance of one of the donor orbitals of the corresponding CT transition. The changes in the 340–440-nm region are probably the consequence of an asymmetry of the coordination sites of the otherwise symmetric bridge induced by the mixed-valence nature of the species. On increasing the applied potential, a new process starts, as indicated by the isosbestic points at about 440 and 345 nm (not visible in Figure 7, where only a limited numbers of spectra are shown for clarity): the IT band disappears, as does the $M_2$LCT band, and the ligand-centered bands continue to change. The final spectrum is constant upon successive increase of applied potential, and the initial spectrum is recovered when the potential is eliminated, in agreement with the reversibility of the oxidation processes.

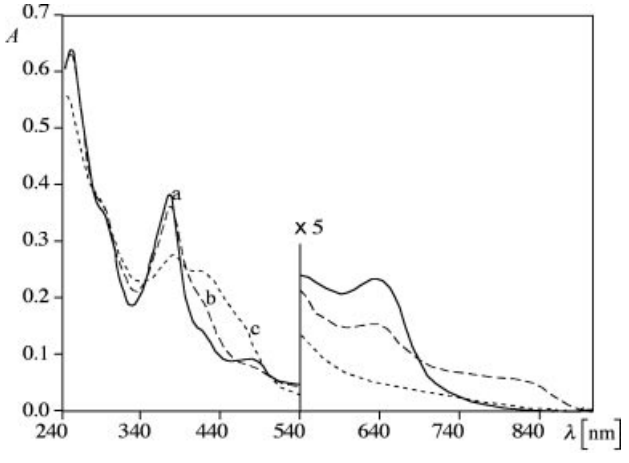


Figure 7. Changes in the absorption spectrum of [($Rh_2$)LPh($Rh_2$)] in acetonitrile on applying positive potentials: (a) starting spectrum; (b) applied voltage of +1.45 V; (c) applied voltage of +1.60 V.

Figure 8 shows the changes of the absorption spectrum of [($Rh_2$)LAnt($Rh_2$)] upon oxidation at relatively mild potentials. In this case, probably due to the increased separation between the two oxidation potentials (Table 4), it is possible to follow the first oxidation process in more detail, as evidenced by the several isosbestic (or quasi-isosbestic) points. Indeed, Figure 8 only shows changes related to the first oxidation process: as for the former compound, a new absorption (assigned to the IT transition) appears in the 680–900-nm region even for [($Rh_2$)LAnt($Rh_2$)], with concomitant decrease of the $M_2$LCT band and changes in the 330–450-nm ligand-centered region. Removing the applied potential leads back to the starting spectrum quantitatively, whereas the increase of the positive applied potential leads to the disappearance of both IT and $M_2$LCT bands and further changes in the ligand-centered region (not shown) also in this case.

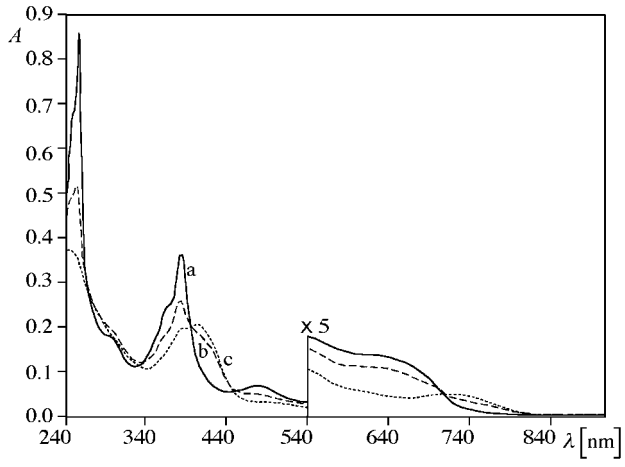


Figure 8. Changes in the absorption spectrum of [($Rh_2$)LAnt($Rh_2$)] in acetonitrile on applying positive potentials: (a) starting spectrum; (b) applied voltage of +1.40 V; (c) applied voltage of +1.55 V.

The possibility of following the formation and disappearance of the IT band in [($Rh_2$)LAnt($Rh_2$)] allowed us to calculate the electronic interaction parameters from Equation (1).[32]

$$\varepsilon_{max} = (2380\ r^2/E_{op}\ \Delta\nu^{1/2})\ H_{AB}^2 \quad (1)$$

According to Hush,[32] Equation (1) correlates the optical inter-valence transfer band with the magnitude of the electronic coupling matrix element between the two subunits A and B (in the present case, the $Ru_2^{4+}$ subunits), $H_{AB}$, $\varepsilon_{max}$ is the maximum molar absorption coefficient of the IT band, $E_{op}$ and $\Delta\nu$ are the band maximum energy and half-width (in $cm^{-1}$), respectively, and $r$ is the inter-component distance (in Å). For [($Rh_2$)LAnt($Rh_2$)], $\varepsilon_{max}$ is 1900 $M^{-1}cm^{-1}$, $E_{op}$ is 13700 $cm^{-1}$, $\Delta\nu$ is 3000 $cm^{-1}$, and $r$ is 9.0 Å ($r$ is taken as the center-to-center distance). By using the above experimental parameters, a value of 86 $cm^{-1}$ is calculated for $H_{AB}$. This value compares well with the electronic coupling matrix elements of dinuclear $Ru^{II}$ polypyridine complexes bridged by good electron coupling mediator spacers such as cyanide ligands,[33] thus confirming the significant inter-component interaction mediated by the LAnt bridge.

## Excited-State Properties

None of the four bis-dimetallic compounds studied here (including the two species containing the LAnt ligand,

 © 2006 Wiley-VCH Verlag GmbH & Co. KGaA, Weinheim 

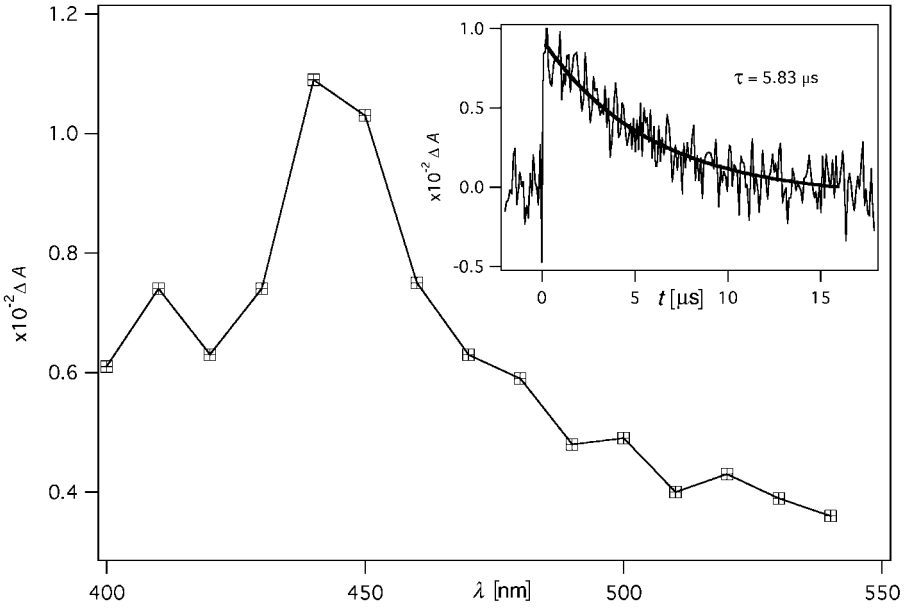


Figure 9. Transient absorption spectrum and (inset) decay of [($Rh_2$)LPh($Rh_2$)] in acetonitrile. Excitation wavelength: 532 nm.

which shows the typical anthracene fluorescence when not coordinated to metals) exhibits any luminescence, either at room temperature or at 77 K. This agrees with the excited-state properties of metal–metal-bonded acetate species, which are known to deactivate by nonradiative transitions.[34] However, it has recently been reported[35] that dirhodium compounds of this class, although nonluminescent, can exhibit lifetimes on the microsecond timescale and can therefore be easily involved in bimolecular photoinduced electron- and energy-transfer processes. This is the case, for example, for the complexes [$Rh_2(O_2CCH_3)_4(L)_2$] (L = $CH_3OH$, tetrahydrofuran, triphenylphosphane, pyridine).[35] However, the nature of the long-lived excited state was not clarified.

The similarity between the dirhodium complexes reported to exhibit the long-lived excited state[35] and the bis-dimetallic species studied here prompted us to perform nanosecond transient absorption spectroscopy (in degassed acetonitrile at room temperature) on the present systems. With our nanosecond-limited equipment, no transient spectrum could be recorded for [($Rh_2$)LAnt($Rh_2$)], [($Ru_2$)-LAnt($Ru_2$)], or [($Ru_2$)LPh($Ru_2$)]. This suggests that the excited states of these latter species decay faster than the laser flash (10 ns). On the contrary, a clear absorption feature appeared in the transient absorption spectrum of [($Rh_2$)-LPh($Rh_2$)]. This transient absorption exhibits a broad maximum around 440 nm that extends over a large part of the visible region (Figure 9). It resembles the absorption spectrum of the *reduced* [($Rh_2$)LPh($Rh_2$)], so it can be assigned to the absorption of the radical anion of the bridging ligand, in agreement with the $M_2$LCT assignment of the lowest-energy excited state for the complex.

The transient spectrum of [($Rh_2$)LPh($Rh_2$)] disappears with a monoexponential decay, yielding a lifetime of 5.8 μs, the same timescale reported for the excited state of other metal–metal-bonded dirhodium complexes.[35] The reason for the absence of such long excited-state lifetimes in the other compounds studied here could be the nature of the metal (for the diruthenium species, for which the $M_2$LCT state is probably so low in energy that nonradiative transitions are very fast) and the presence of the anthracene moiety {for [($Rh_2$)LAnt($Rh_2$)]; the anthracene moiety could introduce other low-lying excited states, such as an anthracene-to-bridging ligand CT level, which can accelerate the decay to the ground state}. Nevertheless, the relatively long-lived excited state of [($Rh_2$)LPh($Rh_2$)] indicates that this class of compounds also has a good potential to be involved in processes based on light as the energy input.

## Conclusion

The naphthyridine-based ligands reported here are able to accommodate two sets of dimetallic redox active units that show electronic communication with one another. Bis-dirhodium and bis-diruthenium complexes of similar structure have been synthesized and characterized. Among the two families of species, electronic communication is stronger in the diruthenium complexes than in their dirhodium counterparts and is further enhanced by the replacement of the phenyl group born by the bridging pyrimidine with an anthryl moiety. The positive effect of the anthracene substituent on the electronic communication between dimetallic units is similar to that observed earlier with analogous mononuclear ruthenium complexes and is proposed to be mainly due to the involvement of an anthracene-based HOMO in the interaction mechanism. Moreover, one of the compounds exhibits a long-lived (microsecond timescale) excited state. The results presented here are promising for the development of poly-dimetallic complexes built on

 © 2006 Wiley-VCH Verlag GmbH & Co. KGaA, Weinheim 

longer naphthyridine-based strands. Furthermore, the replacement of the bridging pyrimidine by a pyrazine group should lead to a linear (not curved) structure with stronger electronic coupling between subunits, as is the case in mononuclear bi-component complexes.[26e] The introduction of dimetallic units characterized by single metal–metal (such as the those described here) but also by multiple metal–metal bonds (e.g., $Mo_2$, $Re_2$) in larger ligands is currently in progress to extend the work on mononuclear ruthenium racks[26] towards nanoscale molecular wires.[36]

## Experimental Section

**Materials and Methods:** All reagents were used as received. Dry solvents (dichloromethane, toluene, THF) were distilled over drying agents (calcium hydride, Na, Na/benzophenone, respectively) under argon. 4-Amino-5-cyanopyrimidine,[37] 4-aminopyrimidine-5-carboxaldehyde,[21] (1-ethoxyvinyl)tri(*n*-butyl)stannane,[20] 2-(anthracen-9-yl)-4,6-dichloropyrimidine,[26b] and tetra-μ-acetodiruthenium(II,III) chloride $[Ru_2(OAc)_4Cl]$[23] were prepared according to published protocols. $^1H$ and $^{13}C$ NMR spectra were recorded with a Bruker AC 200 (200 and 50 MHz respectively) at 25 °C. Electronic and luminescence spectra were recorded with a Varian CARY 13e and an AMINCO Bowman Series 2 spectrometer, respectively, in the reported spectroscopic grade solvents. Mass spectrometry was performed at the Laboratoire de Spectrométrie de masse Bio-organique (LSMBO, Strasbourg, France) and elemental analyses at the elemental analysis service, Louis Pasteur University (Strasbourg, France). IR spectra: (f) = weak, (F) = strong, (m) = medium.

The electrochemical equipment and methods have been described previously.[26e] Absorption spectroscopy in the near-IR region were recorded with a JASCO V570 spectrophotometer. For spectroelectrochemical measurements, the latter spectrophotometer was used in connection with an EG&G 273A potentiostat. Nanosecond transient absorption experiments were performed in argon-purged acetonitrile solutions. A Continuum Surelite SLI-10 Nd:YAG laser was used to excite the sample with 10-ns pulses at 355 nm. The monitoring beam was supplied by a Xe arc lamp, and the signal was detected by a red-sensitive photodiode after passing through a high radiance monochromator. Differential absorption spectra were recorded point-by-point, while kinetic measurements were made at a fixed wavelength. Sixty four individual laser shots were averaged to improve the reliability of each acquisition. The signals were stored and analyzed on a dedicated PC.

**7-(Pyridin-2-yl)pyrido[2,3-*d*]pyrimidine (8):** Two drops of 10% methanolic sodium hydroxide were added to a hot solution of 4-aminopyrimidine-5-carboxaldehyde[21] (198 mg, 1.61 mmol) and 2-acetylpyridine (220 mg, 1.82 mmol, 1.13 equiv.) in 23 mL of absolute ethanol. The solution was then refluxed for 4 h under argon and concentrated in vacuo. The residue was recrystallized from ethanol to yield 229 mg of an off-white solid (68%, m.p. 205 °C). $^1H$ NMR ($CDCl_3$): $\delta$ = 9.57 (s, 1 H), 9.50 (s, 1 H), 8.92 (d, $^3J$ = 8.5 Hz, 1 H), 8.88 (d, $^3J$ = 7.9 Hz, 1 H), 8.8 (br. d, 1 H), 8.44 (d, $^3J$ = 8.5 Hz, 1 H), 7.93 (td, $^3J$ = 7.9, $^4J$ = 1.7 Hz, 1 H), 7.45 (m, 1 H) ppm. FAB+: *m*/*z* 209.1 [$MH^+$]. $C_{12}H_8N_4$ (208.22) + 0.025 $CHCl_3$: calcd. C 68.38, H 3.83, N 26.53; found C 68.42, H 3.85, N 26.53.

**6-Amino-2,2′-bipyridinyl-5-carbaldehyde (9):** A solution of 7-(pyridin-2-yl)pyrido[2,3-*d*]pyrimidine (229 mg, 1.1 mmol) in 2 N aqueous hydrochloric acid (80 mL) was refluxed for 2.5 h and then cooled in ice. The solution was neutralized with concentrated aqueous ammonia (pH ca. 8–9), extracted with ethyl acetate (3 × 50 mL), and the combined organic layers were dried ($Na_2SO_4$), concentrated, and the brown residue purified by column chromatography (basic alumina, $CH_2Cl_2$/EtOAc) to give 180 mg (82%) of the desired amino aldehyde as a yellow powder (m.p. 143 °C). $^1H$ NMR ($CDCl_3$): $\delta$ = 9.90 (s, 1 H), 8.70 (br. d, $^3J$ = 4.3 Hz, 1 H), 8.36 (d, $^3J$ = 8.0 Hz, 1 H), 7.94 (d, $^3J$ = 7.9 Hz, 1 H), 7.85 (d, $^3J$ = 7.7 Hz, 1 H), 7.81 (br. t, $^3J$ = 8.0 Hz, 1 H), 7.33 (ddd, $^3J_{5',4'}$ = 7.5, $^3J_{5',6'}$ = 4.8, $^4J_{5',3'}$ = 1.4 Hz, 1 H) ppm. $^{13}C$ NMR ($CDCl_3$): $\delta$ = 192.3, 160.2, 158.0, 155.1, 149.3, 145.0, 136.8, 124.5, 122.1, 113.8, 110.6 ppm. FAB+: *m*/*z* 200.1 [$MH^+$]. $C_{11}H_9N_3O$ (199.21) + 0.064 EtOAc: calcd. C 66.00, H 4.68, N 20.51, O 8.81; found C 66.00, H 4.62, N 20.50.

**2,7-Dipyridin-2-yl[1,8]naphthyridine (bpnp):** Two drops of a 10% methanolic potassium hydroxide solution were added to a hot solution of 6-amino-2,2′-bipyridinyl-5-carbaldehyde (**3**; 75 mg, $3.76 \times 10^{-4}$ mol) and 2-acetylpyridine (51 mg, $4.21 \times 10^{-4}$ mol, 1.1 equiv.) in absolute ethanol (15 mL). The solution was further refluxed for 6 h under dinitrogen. The solvent was evaporated and the solid taken up in dichloromethane (35 mL) and washed with water (10 mL). The aqueous layer was extracted with dichloromethane (5 mL) and the combined organic layers washed with brine (15 mL), dried ($Na_2SO_4$), filtered, concentrated, purified by column chromatography (basic $Al_2O_3$, $CH_2Cl_2$), and washed with acetone and diethyl ether to yield an off-white solid (88 mg, 82%). $^1H$ NMR ($CDCl_3$): $\delta$ = 8.89 (d, $^3J$ = 8.0 Hz, 2 H), 8.75 (d, $^3J$ = 8.5 Hz, 2 H), 8.8 (m, 2 H), 8.36 (d, $^3J$ = 8.5 Hz, 2 H), 7.92 (td, $^3J$ = 7.7, $^4J$ = 1.7 Hz, 2 H), 7.41 (ddd, $^3J$ = 7.5, $^3J$ = 4.8, $^4J$ = 1.0 Hz, 2 H) ppm.

**4-*tert*-Butylbenzamidine Hydrochloride (2):**[38] Gaseous hydrogen chloride was bubbled into a solution of 4-*tert*-butylbenzonitrile (**1**; 15.94 g, 0.10 mol) in a mixture of dry benzene (25 mL) and absolute ethanol (20 mL) until saturation was attained. The solution was stirred for an hour and left to stand at room temperature for three days. The solution was then concentrated to half its volume in vacuo until white crystals appeared. The flask was cooled in ice and diethyl ether was added. The white solid was then filtered and washed with diethyl ether (3 × 15 mL) and dried in vacuo. It was then suspended in absolute ethanol (40 mL) and 60 mL of ammonia-saturated ethanol was added. A white precipitate formed immediately and the reaction mixture was stirred for a day and left to stand for four days. The white suspension was filtered and the filtrate concentrated in vacuo. The solid residue was then collected and washed with diethyl ether and dried in vacuo to yield 16.71 g [78%; m.p. 155 °C (dec.)] of the desired amidine hydrochloride as a white solid. $^1H$ NMR ([D$_6$]DMSO): $\delta$ = 9.5 (br. s, 2 H), 9.3 (br. s, 2 H), 7.85 (d, $^3J$ = 8.6 Hz, 2 H), 7.62 (d, $^3J$ = 8.6 Hz, 2 H), 1.30 (s, 9 H) ppm. $^{13}C$ NMR ([D$_6$]DMSO): $\delta$ = 165.4, 156.9, 127.9, 125.7, 124.9, 34.8, 30.6 ppm. IR (KBr): $\tilde{\nu}$ = 3061 (F), 1674 (m), 1486 (m), 852 (f), 734 (f), 674 (f), 557 (f), 210 (m) $cm^{-1}$. FAB+: *m*/*z* 177.2 $[C_{11}H_{17}N_2]^+$. $C_{11}H_{17}ClN_2$ (212.72): calcd. C 62.11, H 8.06, N 13.17; found C 62.20, H 7.92, N 13.14.

**2-(4-*tert*-Butylphenyl)-4,6-dihydroxypyrimidine (3):**[39] A freshly prepared solution of sodium methoxide (6.6 g sodium in 75 mL absolute methanol) was added dropwise, at room temperature, to a suspension of 4-*tert*-butylbenzamidine hydrochloride (16.71 g, 79 mmol) and diethyl malonate (12.8 mL, 84 mmol, 1.07 equiv.) in absolute ethanol (150 mL). The mixture was refluxed under dinitrogen for 7 h. The volatile solvents were removed and the pinkish residue taken up in water (120 mL) and acidified to pH 3–4 with concentrated hydrochloric acid (ca. 20 mL). The pale-yellow precipitate was filtered and washed with water (2 × 20 mL), dried in

 © 2006 Wiley-VCH Verlag GmbH & Co. KGaA, Weinheim 

air and in vacuo to yield 18.4 g of 2-(4-*tert*-butylphenyl)-4,6-dihydroxypyrimidine [92%, m.p. > 260 °C (dec.)]. $^1$H NMR ([D$_6$]-DMSO): $\delta$ = 8.8 (br. s, 1 H), 8.05 (d, $^3J$ = 8.5 Hz, 2 H), 7.54 (d, $^3J$ = 8.6 Hz, 2 H), 5.32 (s, 1 H), 1.31 (s, 9 H) ppm. $^{13}$C NMR ([D$_6$]-DMSO): $\delta$ = 167.3, 157.2, 154.6, 129.3, 127.5, 125.3, 88.1, 34.6, 30.8 ppm. IR (KBr): $\tilde{\nu}$ = 2962 (m), 1637 (F), 1325 (m), 1268 (m), 1197 (f), 844 (f), 520 (f) cm$^{-1}$. FAB+: *m*/*z* 245.2 [MH$^+$]. $C_{14}H_{16}N_2O_2$ (244.29): calcd. C 68.83, H 6.60, N 11.47, O 13.10; found C 68.79, H 6.60, N 11.33.

**2-(4-*tert*-Butylphenyl)-4,6-dichloropyrimidine (4Ph):**[39] Phosphoryl chloride (21 mL, 0.23 mol, 5.3 equiv.) was added dropwise followed by 2-(4-*tert*-butylphenyl)-4,6-dihydroxypyrimidine (10.34 g, 42.3 mmol) portionwise to *N*,*N*-dimethylaniline (9.2 mL, 73 mmol, 1.7 equiv.) at room temperature under argon. The brown mixture was allowed to warm up whereupon it turned reddish. The mixture was refluxed for 1.25 h, then allowed to cool and cautiously poured onto ice (ca. 80 g). The pinkish solid was filtered, washed with water until the filtrate was colorless, dried in air and in vacuo, and purified by flash chromatography ($SiO_2$; hexane/$CH_2Cl_2$, 80:6 to 40:7) to yield 21.6 g of a crystalline white solid (92%, m.p. 93 °C). $^1$H NMR ($CDCl_3$): $\delta$ = 8.35 (d, $^3J$ = 8.6 Hz, 2 H), 7.51 (d, $^3J$ = 8.7 Hz, 2 H), 7.22 (s, 1 H), 1.37 (s, 9 H, $CH_3$) ppm. $^{13}$C NMR ($CDCl_3$): $\delta$ = 165.9, 162.0, 156.0, 132.3, 128.8, 125.8, 118.4, 35.1, 31.3 ppm. $R_f$ ($SiO_2$; hexane/$CH_2Cl_2$, 2.0:0.3) = 0.47. IR (KBr): $\tilde{\nu}$ = 2964 (f), 1551 (F), 1519 (F), 1387 (m), 1248 (f), 1097 (f), 830 (m), 642 (f), 218 (F) cm$^{-1}$. FAB+: *m*/*z* 281.1 [MH$^+$]. $C_{14}H_{14}Cl_2N_2$ (280.05): calcd. C 59.96, H 5.04, N 10.05, Cl 25.31; found C 59.91, H 5.02, N 9.85.

**1-[6-Acetyl-2-(4-*tert*-butylphenyl)pyrimidin-4-yl]ethyl Ketone (5Ph):**[20] Dichlorobis(triphenylphosphane)palladium(II) (450 mg) was added to a solution of 2-(4-*tert*-butylphenyl)-4,6-dichloropyrimidine (**4Ph**; 6.0 g, 21,3 mmol) and (1-ethoxyvinyl)tri(*n*-butyl)-stannane[20] (17.68 g, 49 mmol, 2.3 equiv.) in dry DMF (90 mL). The solution was heated at 80 °C under argon for 12 h. At room temperature, the black solution was poured into an aqueous solution of potassium fluoride (20 g KF in 200 mL of water). The brown precipitate was filtered and washed with diethyl ether (300 mL and 4 × 80 mL). The organic layer was washed with brine (6 × 40 mL), dried ($Na_2SO_4$), filtered, and concentrated. The resulting beige solid was purified by flash chromatography ($SiO_2$; hexane/diethyl ether, 95:5) to yield 7.22 g of the bis(vinyl) ether as a pale-yellow solid (97%). The latter (5.11 g, 14.5 mmol) was dissolved in acetone (80 mL), 2 N aqueous HCl (15 mL) was added, and the solution stirred at room temperature for 6 h. The volatile solvent was removed and the white residual solid taken up in dichloromethane (200 mL) and washed with an aqueous saturated solution of sodium hydrogen carbonate (60 mL). The aqueous layer was extracted with dichloromethane (3 × 20 mL) and the combined organic layers dried ($Na_2SO_4$), filtered, concentrated, and purified by flash chromatography ($SiO_2$; hexane/$CH_2Cl_2$, 1.0:2.0) to yield the desired bis-acetylated arylchloropyrimidine (4.1 g, 95%, m.p. 136 °C). $^1$H NMR ($CDCl_3$): $\delta$ = 8.50 (d, $^3J$ = 8.6 Hz, 2 H), 8.25 (s, 1 H), 7.58 (d, $^3J$ = 8.6 Hz, 2 H), 2.83 (s, 6 H), 1.40 (s, 9 H) ppm. $^{13}$C NMR ($CDCl_3$): $\delta$ = 199.2, 165.4, 161.4, 155.4, 133.6, 128.4, 125.9, 110.5, 35.1, 31.3, 25.8 ppm. $R_f$ ($SiO_2$; hexane/$CH_2Cl_2$, 1.0:2.0) = 0.30. IR (KBr): $\tilde{\nu}$ = 2963 (m), 1712 (F), 1551 (F), 1419 (F), 1355 (F), 1239 (F), 1182 (F), 854 (m), 790 (m), 565 (m), 210 (F) cm$^{-1}$. FAB+: *m*/*z* 297.4 [MH$^+$]. $C_{18}H_{20}N_2O_2$ (296.36): calcd. C 72.94, H 6.81, N 9.46, O 10.8; found C 72.84, H 6.79, N 9.61.

**4,6-Bis(2-amino-3-formylpyridyl)-2-(4-*tert*-butylphenyl)pyrimidine (7Ph):**[40] Five drops of a 10% methanolic potassium hydroxide solution were added to a solution of 1-[6-acetyl-2-(4-*tert*-butylphenyl)pyrimidin-4-yl] ethyl ketone (**5Ph**; 1.00 g, 3.41 mmol) and 4-aminopyrimidine-5-carboxaldehyde (890 mg, 7.23 mmol, 2.1 equiv.) in absolute ethanol (100 mL) at reflux under argon. The solution rapidly turned brown and a beige precipitate appeared. The mixture was refluxed for 8 h, cooled to room temperature, and the precipitate was centrifuged and dried in vacuo. It was then suspended in 2 N aqueous HCl (340 mL) and vigorously stirred at reflux for 5 h. At room temperature, the mixture was neutralized with concentrated ammonia. The orange suspension was filtered, washed with water (2 × 15 mL), dried in vacuo, and purified by flash chromatography ($SiO_2$; $CH_2Cl_2$/EtOAc, 400:15 to 400:40) to yield the desired bis(aminoaldehyde) [1.1 g, 70%, m.p. > 260 °C (dec.)] as a yellow solid. A sample was recrystallized from dichloromethane/hexane for analysis. $^1$H NMR ($CDCl_3$): $\delta$ = 9.99 (s, 2 H), 9.11 (s, 1 H), 8.60 (d, $^3J$ = 8.5 Hz, 2 H), 8.16 (d, $^3J$ = 7.4 Hz, 2 H), 8.01 (d, $^3J$ = 7.6 Hz, 2 H), 7.59 (br. s), 7.59 (d, $^3J$ = 8.5 Hz, 2 H), 6.86 (br. s, 4 H), 1.43 (s, 9 H) ppm. $^{13}$C NMR ([D$_6$]DMSO): $\delta$ = 193.4, 163.3, 163.0, 157.8, 157.0, 153.9, 146.2, 134.1, 127.9, 125.5, 114.6, 111.8, 110.0, 34.6, 30.9 ppm. $R_f$ ($SiO_2$; $CH_2Cl_2$/EtOAc, 2.0:0.3) = 0.46. IR (KBr): $\tilde{\nu}$ = 3349 (m), 2961 (m), 1671 (m), 1619 (m), 1581 (m), 1534 (F), 1379 (m), 1211 (m), 795 (m), 210 (F) cm$^{-1}$. FAB+: *m*/*z* 453.0 [MH$^+$]. $C_{26}H_{24}N_6O_2$ (452.51) + 0.37hexane: calcd. C 69.97, H 6.07, N 17.35, O 6.61; found C 69.97, H 6.07, N 16.53.

**2-(4-*tert*-Butylphenyl)-4,6-bis(7-pyridin-2-yl[1,8]naphthyridin-2-yl)-pyrimidine (LPh):** Two drops of a 10% methanolic potassium hydroxide solution were added to a hot solution of bis(aminoaldehyde) **7**Ph (150 mg, $3.31 \times 10^{-4}$ mol) and 2-acetylpyridine (103 mg, $8.5 \times 10^{-4}$ mol, 2.6 equiv.) in pyridine (26 mL) and the solution stirred at 75 °C for 22 h. The solvent was removed in vacuo and the solid taken up in chloroform (60 mL), which was successively washed with water (20 mL), brine (15 mL), dried ($Na_2SO_4$), filtered, and concentrated. The residue was washed with acetone to yield an off-white solid (184 mg, 90%; m.p. > 260 °C), which was recrystallized from chloroform and acetone and then purified by flash chromatography ($SiO_2$; $CH_2Cl_2$/$CH_3OH$, 1.0:0.1). $^1$H NMR ($CDCl_3$): $\delta$ = 10.06 (s, 1 H), 9.0 (br. d, $^3J$ = 8.4 Hz, 4 H), 8.81 (d, $^3J$ = 8.4 Hz, 2 H), 8.8 (m, 2 H), 8.73 (d, $^3J$ = 8.5 Hz, 2 H), 8.47 (d, $^3J$ = 8.5 Hz, 2 H), 8.42 (d, $^3J$ = 8.6 Hz, 2 H), 7.97 (td, $^3J$ = 7.7, $^4J$ = 1.8 Hz, 2 H), 7.64 (d, $^3J$ = 8.5 Hz, 2 H), 7.43 (ddd, $^3J$ = 7.5, $^3J$ = 4.8, $^3J$ = 1.1 Hz, 2 H), 1.44 (s, 9 H) ppm. IR (KBr): $\tilde{\nu}$ = 1604 (F), 1525 (F), 1469 (f), 1427 (m), 1371 (f), 862 (f), 792 (m), 409 (f) cm$^{-1}$. FAB+: *m*/*z* 623.1 [MH$^+$], 645.3 [MNa$^+$]. $C_{40}H_{30}N_8$ (622.72) + 0.32 $CHCl_3$: calcd. C 74.55, H 4.70, N 17.30; found C 74.49, H 4.83, N 17.09. UV/Vis ($CH_2Cl_2$): $\lambda_{max}$ (log$\varepsilon$) = 253 nm (4.95), 273 (sh, 4.8), 293 (sh, 4.6), 331 (sh, 4.4), 344 (4.56), 363 (4.48).

**1-[6-Acetyl-2-(anthracen-9-yl)pyrimidin-4-yl]ethyl Ketone (5Ant):** 2-Anthracen-9-yl-4,6-dichloropyrimidine **4Ant** (986 mg, 3.03 mmol)[26b] and 1-(tri-*n*-butylstannyl)-1-vinyl ethyl ether (2.40 g, 6.66 mmol, 2.2 equiv.) were suspended in 15 mL of DMF. After purging three times with argon, dichlorobis(triphenylphosphane)-palladium(II) (64 mg, $9.1 \times 10^{-5}$ mol, 0.03 equiv.) was added and the mixture heated to 80 °C under argon for 12 h whilst being protected from light. The solvent was removed in vacuo and the brown residue taken up in dichloromethane (50 mL) and washed with water (3 × 40 mL). The organic layer was dried ($Na_2SO_4$), filtered, concentrated, and purified by flash chromatography ($SiO_2$; hexane/$CH_2Cl_2$, 1.0:1.0) to yield 1.078 g of the desired bis(vinyl ether) as a yellow solid (90%). $^1$H NMR ($CDCl_3$): $\delta$ = 8.55 (s, 1 H), 8.05 (s, 1 H), 8.05 (d, $^3J$ = 8.3 Hz, 2 H), 7.70 (d, $^3J$ = 8.6 Hz, 2 H), 7.3–7.6 (m, 4 H), 5.66 (d, $^2J$ = 2.0 Hz, 2 H), 4.49 (d, $^2J$ = 2.0 Hz, 2 H), 4.05 (q, $^3J$ = 7.0 Hz, 4 H), 1.52 (t, $^3J$ = 7.0 Hz, 6 H) ppm. $^{13}$C

 © 2006 Wiley-VCH Verlag GmbH & Co. KGaA, Weinheim 

NMR ($CDCl_3$): $\delta$ = 165.5, 162.1, 157.1, 134.2, 131.5, 129.9, 128.4, 128.0, 126.1, 125.9, 125.1, 108.2, 88.5, 63.8, 14.5 ppm. $R_f$ ($SiO_2$; hexane/$CH_2Cl_2$, 1.0:1.0) = 0.40.

2 N Hydrochloric acid (6 mL) was added to a mixture of this bis(vinyl ether) in acetone/THF (25/10 mL) and the mixture stirred at room temperature for 12 h. The volatiles were evaporated and the residue taken up in dichloromethane (50 mL) and washed with an aqueous saturated sodium hydrogen carbonate solution (2 × 10 mL). The combined aqueous layers were extracted with dichloromethane (2 × 10 mL), and the combined organic layers dried ($Na_2SO_4$), filtered, concentrated, and purified by flash chromatography ($SiO_2$; hexane/$CH_2Cl_2$, 1.0:2.0) to yield 828 mg of a yellow solid [90%; m.p. 228 °C (dec.)], which was recrystallized from chloroform/diethyl ether. $^1$H NMR ($CDCl_3$): $\delta$ = 8.66 (s, 1 H), 8.57 (s, 1 H), 8.12 (d, $^3J$ = 8.4 Hz, 2 H), 7.4–7.6 (m, 6 H), 2.72 (s, 6 H) ppm. $^{13}$C NMR ($CDCl_3$): $\delta$ = 199.0, 168.0, 161.6, 132.3, 131.3, 129.9, 129.1, 128.8, 126.6, 125.4, 125.1, 111.2, 25.9 ppm. $R_f$ ($SiO_2$; hexane/$CH_2Cl_2$, 1.0:2.0) = 0.36. EI-MS: *m/z* 340.3 [M$^-$], 297.3 [M – $COCH_3$]$^-$, 255.3 [M – 2 $COCH_3$]$^-$. $C_{22}H_{16}N_2O_2$ (340.37) + 0.075 $CH_2Cl_2$: calcd. C 76.46, H 4.69, N 8.08, O 9.23; found C 76.50, H 4.62, N 8.06.

**2-(Anthracen-9-yl)-4,6-bis(7-pyridin-2-yl[1,8]naphthyridin-2-yl)pyrimidine (LAnt):** One drop of a 10% methanolic potassium hydroxide solution was added to a hot solution (65 °C) of the diketone **5Ant** (45 mg, $1.32 \times 10^{-4}$ mol) and 6-amino-2,2′-bipyridinyl-5-carbaldehyde (54 mg, $2.71 \times 10^{-4}$ mol, 2.05 equiv.) in pyridine (10 mL). The solution was stirred at this temperature for 11 h. The solvent was then removed in vacuo and the solid taken up in dichloromethane (40 mL), washed with water (10 then 15 mL), dried ($Na_2SO_4$), filtered, and concentrated. The crude was purified by column chromatography (basic alumina) and recrystallized by diffusion of acetone into a concentrated chloroform solution to yield a pale-yellow solid (63 mg, 72%, m.p. > 260 °C). $^1$H NMR ($CDCl_3$): $\delta$ = 10.3 (s, 1 H), 9.03 (d, $^3J$ = 7.9 Hz, 2 H), 8.7–8.85 (m, $^3J$ = 8.4 Hz, 6 H), 8.67 (s, 1 H), 8.39 (d, $^3J$ = 9.1 Hz, 2 H), 8.34 (d, $^3J$ = 8.7 Hz, 2 H), 8.14 (br. d, $^3J$ = 7,6 Hz, 2 H), 7.99 (td, $^3J$ = 7.8, $^4J$ = 1.8 Hz, 2 H), 7.88 (br. d, $^3J$ = 8.6 Hz, 2 H), 7.4–7.6 (m, 6 H) ppm. $^{13}$C NMR ($CDCl_3$): $\delta$ = 164.7, 164.6, 160.3, 158.0, 157.3, 155.6, 149.2, 138.1, 137.7, 137.2, 131.6, 130.1, 128.6, 128.0, 127.8, 126.3, 125.3, 124.8, 123.9, 123.0, 121.1, 120.9, 120.7, 114.7 ppm. IR (KBr): $\tilde{\nu}$ = 1601 (F), 1523 (F), 1467 (f), 1426 (m), 1379 (f), 865 (f), 783 (m), 739 (f), 413 (f) cm$^{-1}$. FAB+: *m/z* 667.3 [MH$^+$]. $C_{44}H_{26}N_8$ (666.73) + 0.90 $CHCl_3$: calcd. C 72.55, H 3.63, N 15.18; found C 72.61, H 3.57, N 15.18. UV/Vis ($CH_2Cl_2$): $\lambda_{max}$ (log $\varepsilon$) = 250 nm (sh, 5.0), 256 (5.14), 275 (sh, 4.5), 320 (sh, 4.1), 333 (sh, 4.3), 347 (4.46), 363 (4.47), 385 (3.88). Fluorescence ($CH_2Cl_2$): $\lambda_{max}$ (emission) = 331, 356, 376 (sh) nm.

**[{(CH$_3$COO)$_3$Rh$_2$}$_2$LPh](PF$_6$)$_2$ [(Rh$_2$)$_2$LPh]:**[22a] 1.0 N Aqueous hydrochloric acid (66 μL, $6.6 \times 10^{-5}$ mol, 2.0 equiv.) was added to a suspension of ligand LPh (20.5 mg, $3.29 \times 10^{-5}$ mol) and dirhodium tetraacetate (29.9 mg, $6.6 \times 10^{-5}$ mol, 2.0 equiv.) in methanol (7 mL) under argon and the mixture was heated to 50 °C for 12 h. The deep green solution was filtered and ammonium hexafluorophosphate (51 mg, $3.1 \times 10^{-4}$ mol, 9.5 equiv.) in water (1 mL) was added. The solvent was then evaporated and diethyl ether allowed to diffuse into a concentrated solution of the residue in acetonitrile. The precipitate was filtered and washed with water and diethyl ether to yield a deep green solid (47 mg, 85%, m.p. > 260 °C). $^1$H NMR ($CD_3CN$): $\delta$ = 9.71 (s, 1 H), 9.67 (br. d, $^3J$ = 4.4 Hz, 2 H), 9.24 (d, $^3J$ = 8.8 Hz, 2 H), 8.8–9.0 (m, 10 H), 8.58 (td, $^3J$ = 8.0, $^4J$ = 1.5 Hz, 2 H), 8.29 (dd, $^3J$ = 7.5, $^3J$ = 4.7 Hz, 2 H), 7.75 (d, $^3J$ = 8.8 Hz, 2 H), 1.49 (s, 15 H), 1.27 (s, 12 H) ppm. IR (KBr): $\tilde{\nu}$ = 3450 (F), 1604 (f), 1564 (F), 1437 (f), 1158 (f), 1021 (f), 846 (F), 705 (f), 560 (f), 405 (m) cm$^{-1}$. ES-MS ($CH_3CN$, 100 V): *m/z* 694.0 [(Rh$_2$)$_2$LPh]$^{2+}$, 1532.8 [(Rh$_2$)$_2$LPh, PF$_6$]$^+$. UV/Vis ($CH_3CN$): $\lambda_{max}$ (log $\varepsilon$) = 250 nm (4.9), 292 (4.6), 347 (sh, 4.5), 371 (4.6), 412 (sh, 4.2), 468 (4.0), 543 (3.7), 622 (3.7). $E_{1/2}$ (V vs. SCE, $CH_2Cl_2$, 0 °C): –1.72 (rev.), –1.41 (rev.), –1.20 (rev.), –0.60 (rev.), –0.22 (rev.), 1.46 (rev.).

**[{(CH$_3$COO)$_3$Rh$_2$}$_2$LAnt](PF$_6$)$_2$ [(Rh$_2$)$_2$LAnt]:**[22a] The same protocol as above starting from ligand LAnt yielded a brown-green product with a similar yield after precipitation of the hexafluorophosphate salt from a methanolic solution. (m.p. > 260 °C) $^1$H NMR ($CD_3CN$): $\delta$ = 10.13 (s, 1 H), 9.50 (br. d, $^3J$ = 5 Hz, 2 H), 9.47 (d, $^3J$ = 8.8 Hz, 2 H), 8.8–9.1 (m, 9 H), 8.52 (td, $^3J$ = 7.7, $^4J$ = 1,4 Hz, 2 H), 8.2–8.3 (m, 4 H), 7.92 (d, $^3J$ = 8.4 Hz, 2 H), 7.47 (br. t, $^3J$ = 8.4 Hz, 2 H), 7.31 (br. t, $^3J$ = 7.3 Hz, 2 H), 1.33 (s, 6 H), 1.21 (s, 12 H) ppm. IR (KBr): $\tilde{\nu}$ = 3450 (F), 1605 (f), 1565 (F), 1437 (m), 1414 (m), 1154 (f), 1017 (f), 845 (F), 704 (f), 559 (f), 406 (m) cm$^{-1}$. ES-MS ($CH_3CN$, 20 V): *m/z* 716.0 [(Rh$_2$)$_2$LAnt]$^{2+}$, 1576.9 [(Rh$_2$)$_2$LAnt, PF$_6$]$^+$. $C_{56}H_{44}F_{12}N_8O_{12}P_2Rh_4 \cdot 2.6\ CH_3OH$: calcd. C 38.98, H 3.04, N 6.21; found C 39.24, H 3.05, N 6.65. UV/Vis ($CH_3CN$): $\lambda_{max}$ (log $\varepsilon$) = 248 nm (3.1), 254 (5.2), 295 (4.5), 347 (sh, 4.5), 364 (4.6), 382 (4.8), 478 (4.1), 545 (3.8), 634 (3.8). $E_{1/2}$ (V vs. SCE, $CH_3CN$, 25 °C): –0.30 (rev.), 0.73 (rev.), 0.86 (rev.), 1.51 (irrev.).

**[{(CH$_3$COO)$_3$Ru$_2$}$_2$LPh](PF$_6$)$_2$ [(Ru$_2$)$_2$LPh]:**[22b] A suspension of ligand LPh (14 mg, $2.25 \times 10^{-5}$ mol) and [$Ru_2(CH_3COO)_4Cl$] (21.8 mg, $4.60 \times 10^{-5}$ mol, 2.05 equiv.) in methanol (5 mL) was heated at 50 °C under argon for 48 h. After cooling to room temperature, the hexafluorophosphate salt was precipitated by addition of ammonium hexafluorophosphate (38 mg in 1 mL of degassed water, $2.33 \times 10^{-4}$ mol, 10 equiv.). The solid was washed with methanol and diethyl ether and dried in vacuo to yield 28 mg of a dark blue paramagnetic powder (75%; m.p. > 260 °C). $^1$H NMR ($CD_3OD$, before addition of $NH_4PF_6$): $\delta$ = 72.0, 66.7, 29.9, 25.7, 16.9, 8.8, 4.1, 2.0, 1.25, –3.8, –7.3, –13.3, –15.4, –22.0, –39.8 ppm. IR (KBr): $\tilde{\nu}$ = 3450 (F), 1593 (f), 1536 (m), 1437 (F), 1329 (f), 1197 (f), 1018 (f), 843 (F), 777 (f), 691 (f), 558 (f), 407 (m) cm$^{-1}$. ES-MS ($CH_3CN$): *m/z* 691.0 [(Ru$_2$)$_2$LPh]$^{2+}$, 1527 [(Ru$_2$)$_2$LPh, PF$_6$]$^+$, 460.4 [(Ru$_2$)$_2$LPh]$^{3+}$. $C_{52}H_{48}F_{12}N_8O_{12}P_2Ru_4 \cdot 2.65\ H_2O$: calcd. C 36.33, H 3.13, N 6.52; found C 36.33, H 3.26, N 6.59. UV/Vis ($CH_3CN$): $\lambda_{max}$ (log $\varepsilon$) = 248 nm (4.8), 270 (sh, 4.6), 370 (4.6), 400 (sh, 4.4), 600 (4.0), 695 (4.2). $E_{1/2}$ (V vs. SCE, degassed $CH_3CN$, 25 °C): –0.31 (rev.), 0.76 (rev.), 0.85 (rev.).

**[{(CH$_3$COO)$_3$Ru$_2$}$_2$LAnt](PF$_6$)$_2$ [(Ru$_2$)$_2$LAnt]:**[22b] A suspension of ligand LAnt (19.6 mg, $2.94 \times 10^{-5}$ mol) and [$Ru_2(OAc)_4Cl$] (30.2 mg, $6.37 \times 10^{-5}$ mol, 2.17 equiv.) in degassed methanol (6.5 mL) was heated at 50 °C under argon for 44 h. After cooling to room temperature, the hexafluorophosphate salt was precipitated by addition of ammonium hexafluorophosphate (53 mg in 1.3 mL of degassed water, $3.25 \times 10^{-4}$ mol, 11 equiv.). The solid was washed with methanol and diethyl ether, and dried in vacuo to yield 40 mg of a deep blue paramagnetic compound (79%; m.p. > 260 °C). $^1$H NMR ($CD_3OD$, before addition of $NH_4PF_6$): $\delta$ = 75.1, 69.8, 29.9, 36.3, 25.0, 17.7, 10.7, 9.8, 5.3, 2.0, –5.0, –8.3, –14.5, –16.5, –16.9, –20.0, –35.6 ppm. IR (KBr): $\tilde{\nu}$ = 3448 (F), 1630 (f), 1597 (f), 1535 (m), 1437 (F), 1329 (f), 1266 (f), 1213 (f), 844 (F), 776 (f), 691 (m), 559 (f), 406 (f) cm$^{-1}$. ES-MS ($CH_3CN$, 20 V): *m/z* 713.1 [(Ru$_2$)$_2$LAnt]$^{2+}$, 1570 [(Ru$_2$)$_2$LAnt, PF$_6$]$^+$, 475.3 [(Ru$_2$)$_2$LAnt]$^{3+}$. $C_{56}H_{44}F_{12}N_8O_{12}P_2Ru_4 \cdot 2.2\ H_2O$: calcd. C 38.33, H 2.78, N 6.39; found C 38.33, H 2.92, N 6.37. UV/Vis ($CH_3CN$): $\lambda_{max}$ (log $\varepsilon$) = 254 nm (4.7), 369 (4.5), 387 (4.6), 602 (4.0), 701 (4.2). $E_{1/2}$ (V vs. SCE, degassed $CH_3CN$, 25 °C): –0.30 (rev.), 0.73 (rev.), 0.86 (rev.), 1.51 (irrev.).

**Supporting Information** (see also the footnote on the first page of this article): Figures S1 and S2 show differential pulse voltammog-

 © 2006 Wiley-VCH Verlag GmbH & Co. KGaA, Weinheim 

rams of complexes [($Rh_2$)LPh($Rh_2$)] and [($Ru_2$)LPh($Ru_2$)], respectively, in acetonitrile.

## Acknowledgments

A. P. acknowledges the support the French ministère de l'Éducation Nationale, de la Recherche et de la Technologie for a PhD fellowship. The Italian team thanks the University of Bologna ("Funds for selected topics") and the University of Messina for financial support.

[1] a) C. Creutz, H. Taube, *J. Am. Chem. Soc.* **1969**, *91*, 3988–3989; b) C. Creutz, H. Taube, *J. Am. Chem. Soc.* **1973**, *95*, 1086–1094.

[2] a) V. Balzani, A. Juris, M. Venturi, S. Campagna, S. Serroni, *Chem. Rev.* **1996**, *96*, 759–833; b) D. Astruc, *Acc. Chem. Res.* **1997**, *30*, 383–391; c) M. Marcaccio, F. Paolucci, C. Paradisi, S. Roffia, C. Fontanesi, L. J. Yellowlees, S. Serroni, S. Campagna, G. Denti, V. Balzani, *J. Am. Chem. Soc.* **1999**, *121*, 10081–10091.

[3] a) J.-P. Sauvage, J.-P. Collin, J.-C. Chambron, S. Guillerez, C. Coudret, V. Balzani, F. Barigelletti, L. De Cola, L. Flamigni, *Chem. Rev.* **1994**, *94*, 993–1019; b) L. De Cola, P. Belser, *Coord. Chem. Rev.* **1998**, *177*, 301–346; c) A. Ceccon, S. Santi, L. Orian, A. Bisello, *Coord. Chem. Rev.* **2004**, *248*, 683–724.

[4] a) K. Lee, H. Song, B. Kim, J. T. Park, S. Park, M.-G. Choi, *J. Am. Chem. Soc.* **2002**, *124*, 2872–2873; b) K. Lee, Y. J. Choi, Y.-J. Cho, C. Y. Lee, H. Song, Y. S. Lee, J. T. Park, *J. Am. Chem. Soc.* **2004**, *126*, 9837–9844; c) P. H. Dinolfo, M. E. Williams, C. L. Stern, J. T. Hupp, *J. Am. Chem. Soc.* **2004**, *126*, 12989–13001.

[5] a) H. Vahrenkamp, A. Geiß, G. N. Richardson, *J. Chem. Soc., Dalton Trans.* **1997**, 3643–3651; b) W. Kaim, A. Klein, M. Glöckle, *Acc. Chem. Res.* **2000**, *33*, 755–763 and references cited therein; c) K. D. Demadis, C. M. Hartshorn, T. J. Meyer, *Chem. Rev.* **2001**, *101*, 2655–2683 and references cited therein.

[6] J. A. Mc Cleverty, M. D. Ward, *Acc. Chem. Res.* **1998**, *31*, 842–851 and references cited therein.

[7] a) B. Hong, *Comments Inorg. Chem.* **1999**, *20*, 177–207; b) R. Ziessel, M. Hissler, A. El-Ghayoury, A. Harriman, *Coord. Chem. Rev.* **1998**, *178–180*, 1251–1298; c) F. Fabrizi de Biani, M. Corsini, P. Zanello, H. Yao, M. E. Bluhm, R. N. Grimes, *J. Am. Chem. Soc.* **2004**, *126*, 11360–11369; d) Y. Hoshino, *Platinum Met. Rev.* **2001**, *45*, 2–11.

[8] N. Mantovani, M. Brugnati, L. Gonsalvi, E. Grigiotti, F. Laschi, L. Marvelli, A. Peruzzini, G. Reginato, R. Rossi, P. Zanello, *Organometallics* **2005**, *24*, 405–418.

[9] a) R. C. Rocha, H. E. Toma, *Inorg. Chim. Acta* **2000**, *310*, 65–80; b) Y. Hoshino, T. Suzuki, H. Umeda, *Inorg. Chim. Acta* **1996**, *245*, 87–90.

[10] a) T. Sheng, H. Vahrenkamp, *Eur. J. Inorg. Chem.* **2004**, 1198–1203; b) M. Heitzmann, J.-C. Moutet, J. Pécaut, O. Reynes, G. Royal, E. Saint-Aman, G. Serratrice, *Eur. J. Inorg. Chem.* **2003**, 3767–3773.

[11] C. Di Pietro, S. Serroni, S. Campagna, M. T. Gandolfi, R. Ballardini, S. Fanni, W. R. Browne, J. G. Vos, *Inorg. Chem.* **2002**, *41*, 2871–2878.

[12] a) G. Giuffrida, G. Calogero, V. Ricevuto, S. Campagna, *Inorg. Chem.* **1995**, *34*, 1957; b) S. Encinas, F. Barigelletti, A. M. Barthram, M. D. Ward, S. Campagna, *Chem. Commun.* **2001**, *3*, 277–278.

[13] G. García-Herbosa, N. G. Connelly, A. Muñoz, J. V. Cuevas, A. G. Orpen, S. D. Politzer, *Organometallics* **2001**, *20*, 3223–3229.

[14] a) F. A. Cotton, *Chem. Soc. Rev.* **1975**, *4*, 27–53; b) *Multiple Bonds between Metal Atoms*, 3rd ed. (Eds.: F. A. Cotton, C. A. Murillo, R. A. Walton), Springer Science and Business Media, **2005**.

[15] Y. Shi, G. T. Yee, G. Wang, T. Ren, *J. Am. Chem. Soc.* **2004**, *126*, 10552–10553.

[16] a) D. Osella, R. Rossetti, C. Nevi, M. Ravera, M. Moretta, J. Fiedler, L. Pospísil, E. Samuel, *Organometallics* **1997**, *16*, 695–700; b) K.-T. Wong, J.-M. Lehn, S.-M. Peng, G.-H. Lee, *Chem. Commun.* **2000**, 2259–2260.

[17] a) R. H. Cayton, M. H. Chisholm, J. C. Huffman, E. B. Lobkovsky, *J. Am. Chem. Soc.* **1991**, *113*, 8709–87324; b) F. A. Cotton, C. Y. Liu, C. A. Murillo, D. Villagrán, X. Wang, *J. Am. Chem. Soc.* **2004**, *126*, 14822–14831; c) B. E. Bursten, M. H. Chisholm, J. S. D'Acchioli, *Inorg. Chem.* **2005**, *44*, 5571–5579; d) M. H. Chisholm, A. M. Macintosh, *Chem. Rev.* **2005**, *105*, 2949–2976.

[18] A. Petitjean, L. A. Cuccia, J.-M. Lehn, H. Nierengarten, M. Schmutz, *Angew. Chem. Int. Ed.* **2002**, *41*, 1195–1198.

[19] G. S. Hanan, U. S. Schubert, D. Volmer, E. Rivière, J.-M. Lehn, N. Kyritsakas, J. Fischer, *Can. J. Chem.* **1997**, *75*, 169–182.

[20] L. A. Cuccia, E. Ruiz, J.-M. Lehn, J.-C. Homo, M. Schmutz, *Chem. Eur. J.* **2002**, *8*, 3448–3467.

[21] H. Bredereck, G. Simchen, H. Traut, *Chem. Ber.* **1967**, *100*, 3664–3670.

[22] a) W. R. Tikkanen, E. Binamira-Soriaga, W. Kaska, P. C. Ford, *Inorg. Chem.* **1984**, *23*, 141–146; b) E. Binamira-Soriaga, N. L. Keder, W. Kaska, *Inorg. Chem.* **1990**, *29*, 3167–3171.

[23] R. W. Mitchell, A. Spencer, G. Wilkinson, *J. Chem. Soc., Dalton Trans.* **1973**, 846–854.

[24] A. Petitjean, J.-M. Lehn, R. G. Khoury, A. DeCian, N. Kyritsakas, *C. R. Chimie* **2002**, *5*, 337–340.

[25] Weak repulsive steric interactions between protons H1 and H3 prevent the ligand from being perfectly planar, which explains the 11° angle observed between the two naphthyridine planes.

[26] a) G. S. Hanan, C. R. Arana, J.-M. Lehn, G. Baum, D. Fenske, *Angew. Chem. Int. Ed. Engl.* **1995**, *34*, 1122–1124; b) G. S. Hanan, C. R. Arena, J.-M. Lehn, G. Baum, D. Fenske, *Chem. Eur. J.* **1996**, *2*, 1292–1302; c) A. Credi, V. Balzani, S. Campagna, G. S. Hanan, C. R. Arana, J.-M. Lehn, *Chem. Phys. Lett.* **1995**, *243*, 102–107; d) P. Ceroni, A. Credi, V. Balzani, S. Campagna, G. S. Hanan, C. R. Arana, J.-M. Lehn, *Eur. J. Inorg. Chem.* **1999**, *9*, 1409–1414; e) A.-M. Stadler, F. Puntoriero, S. Campagna, N. Kyritsakas, R. Welter, J.-M. Lehn, *Chem. Eur. J.* **2005**, *11*, 3997–4009; f) J. Ramirez, M. Stadler, A. DeCian, J.-M. Lehn, work in progress.

[27] a) M. Klessinger and J. Michl, *Excited States and Photochemistry of Organic Molecules*, VCH, New York, **1995**; b) *Handbook of Photochemistry*, 3rd Edition, Revised and Expanded (Eds.: M. Montalti, A. Credi, L. Prodi, M. T. Gandolfi), CRC Press, **2005**.

[28] B. Maubert, N. D. McClenaghan, M. T. Indelli, S. Campagna, *J. Phys. Chem. A* **2003**, *107*, 447–455, and refs. therein.

[29] J. L. Bear, L. K. Chau, M. Y. Chavan, F. Lefoulon, R. P. Thummel, K. M. Kadish, *Inorg. Chem.* **1986**, *25*, 1514–1516.

[30] G. Giuffrida, S. Campagna, *Coord. Chem. Rev.* **1994**, *135–136*, 517–531 and references cited therein.

[31] a) C. Creutz, *Progr. Inorg. Chem.* **1983**, *30*, 1–73; b) B. S. Brunschwig, C. Creutz, N. Sutin, *Chem. Soc. Rev.* **2002**, *31*, 168–184.

[32] a) N. S. Hush, *Prog. Inorg. Chem.* **1967**, *8*, 391–444; b) V. Balzani, F. Scandola, *Supramolecular Photochemistry*, E. Horwood, Chichester, **1991**, chapter 3.

[33] C. A. Bignozzi, R. Argazzi, C. Chiorboli, F. Scandola, R. B. Dyer, J. R. Schoonover, T. J. Meyer, *Inorg. Chem.* **1994**, *33*, 1652–1659.

[34] D. M. Roundhill, *Photochemistry and Photophysics of Metal Complexes*, Plenum, New York, **1994**.

[35] P. M. Bradley, B. E. Bursten, C. Turro, *Inorg. Chem.* **2001**, *40*, 1376–1379.

[36] a) A. Harriman, R. Ziessel, *Coord. Chem. Rev.* **1998**, *171*, 331–339; b) F. Paul, C. Lapinte, *Coord. Chem. Rev.* **1998**, *178–180*, 431–509; c) J. M. Tour, *Acc. Chem. Res.* **2000**, *33*, 791–804; d) C. M. Lieber, *Sci. Amer.* **2001**, *285*, 58–65; e) N. Robertson,

 © 2006 Wiley-VCH Verlag GmbH & Co. KGaA, Weinheim 

C. A. McGowan, *Chem. Soc. Rev.* **2003**, *32*, 96–103; f) A. C. Benniston, *Chem. Soc. Rev.* **2004**, *33*, 573–578; g) T. Ren, *Organometallics* **2005**, *24*, 4854–4870; h) S. Flores-Torres, G. R. Hutchinson, L. J. Soltzberg, H. D. Abruña, *J. Am. Chem. Soc.* **2006**, *128*, 1513–1522.
[37] K. R. Huffman, F. C. Schaefer, G. A. Peters, *J. Org. Chem.* **1962**, *27*, 551–558.
[38] H. von Schubert, H. Zaschke, *J. Prakt. Chem.* **1970**, *312*, 494–506.
[39] K. von Burdeska, H. Fuhrer, G. Kabas, A. E. Siegrist, *Helv. Chim. Acta* **1981**, *64*, 113–152.
[40] G. Evens, P. Caluwe, *J. Org. Chem.* **1975**, *40*, 1438–1439.
Received: May 19, 2006
Published Online: August 15, 2006

 © 2006 Wiley-VCH Verlag GmbH & Co. KGaA, Weinheim 

DOI: 10.1002/ejic.200600458

# Synthesis and Reactivity of New Mono- and Dinuclear Hydridoirida-β-diketones – The Formation and Characterization of a Dinuclear Tris-μ-acyliridium(III) Complex

**Francisco Acha,[a] María A. Garralda,*[a] Ricardo Hernández,[a] Lourdes Ibarlucea,[a] Elena Pinilla,[b] M. Rosario Torres,[b] and Malkoa Zarandona[a]**

*Dedicated to Professor Victor Riera on the occasion of his retirement*

**Keywords:** Iridium / Hydride ligands / Bridging ligands / P ligands

The hydridoirida-β-diketone [IrH{[$PPh_2$(*o*-$C_6H_4CO$)]$_2$H}Cl] (**1**) reacts with silver salts of potentially coordinating anions such as tosylate ($^-$OTs) or triflate ($^-$OTf) to afford the mononuclear neutral derivatives [IrH{[$PPh_2$(*o*-$C_6H_4CO$)]$_2$H}(X)] [X = OTs (**2**), OTf (**3**)]. In acetone solution the triflate anion in **3** is displaced by the solvent to afford the cationic complex [IrH{[$PPh_2$(*o*-$C_6H_4CO$)]$_2$H}(acetone)]OTf (**4**), which is stable only in acetone solution. The reaction of **1** with halide scavengers containing less coordinating anions such as $PF_6^-$ or $BF_4^-$ results in the formation of cationic compounds [{IrH[{$PPh_2$(*o*-$C_6H_4CO$)}$_2$H]}$_2$(μ-Cl)]A [A = $BF_4$ (**5**), $PF_6$ (**6**)] containing a dinuclear species with a single chlorine atom bridging two hydridoirida-β-diketone fragments. Both fragments are magnetically non-equivalent and the acylphosphane groups in each hydridoirida-β-diketone fragment are chemically equivalent. This species undergoes a fluxional process in solution, with $\Delta H^{\ddagger}$ = 7.8 ± 0.4 kcal mol$^{-1}$ and $\Delta S^{\ddagger}$ = –10.9 ± 0.5 eu. A combination of rotation around the Ir–Cl bonds and variation of the Ir–Cl–Ir angle is suggested to be responsible for the fluxionality. Complex **5** reacts further with $AgBF_4$ to undergo chloride abstraction along with hydrogen loss and deprotonation to give the cationic dinuclear complex [$Ir_2$H{$PPh_2$(*o*-$C_6H_4CO$)}{μ-$PPh_2$(*o*-$C_6H_4CO$)}$_3$]$BF_4$ (**7**), which contains an acylphosphane chelate along with three acylphosphane bridging ligands and a single hydrido ligand. Bubbling of HCl through an MeOH solution of **7** gives **1**, thus making the loss of hydride, enolic protons and chloride from complex **1** a reversible process. All the complexes were fully characterized spectroscopically. Single-crystal X-ray diffraction analysis was performed on complexes **5** and **7**.
(© Wiley-VCH Verlag GmbH & Co. KGaA, 69451 Weinheim, Germany, 2006)

## Introduction

Metalla-β-diketones can be considered as enol tautomers of neutral β-diketones in which the methine group has been substituted by a transition metal organometallic moiety. Therefore, they may also be understood as acyl(hydroxycarbene) complexes that are stabilized by an intramolecular hydrogen bond between the acyl and the hydroxycarbene moiety (see Scheme 1). Hydroxycarbene complexes, for which a tautomeric equilibrium with the acyl hydrides has been reported,[1] have been proposed as important intermediates in CO reduction reactions[2] or in alkene hydrocarbonylation reactions to produce alcohols.[3] Metalla-β-diketones were synthesized for the first time by Lukehart et al. by the protonation of diacylmetalate anions [$L_x$M(COR)(COR′)]$^-$ (M = Mo, W, Mn, Re, Fe, Os).[4] Rhena-β-diketones can be deprotonated by transition metal complexes containing basic ligands to give rhena-β-diketonate derivatives of $Cu^{II}$, $Fe^{II}$, $Cr^{III}$ and $Zn^{II}$.[5] More recently, Steinborn et al. have reported mono- and dinuclear platina-β-diketones obtained by the reaction of hexachloroplatinic acid with alkynes or by the reaction of diacylhydridoplatinum(IV) complexes with $TlPF_6$.[6] Partial deprotonation of the dinuclear derivatives with amines affords platina-β-diketonates of platina-β-diketones.[7] The reaction of [Ir(Cl)(H)-{$PPh_2$(*o*-$C_6H_4CO$)}(cod)] (cod = 1,5-cyclooctadiene) with $PPh_2$(*o*-$C_6H_4CHO$) in protic solvents has allowed the preparation of the first hydridoirida-β-diketone [IrH{[$PPh_2$(*o*-$C_6H_4CO$)]$_2$H}Cl].[8] Cationic mononuclear hydridoirida-β-

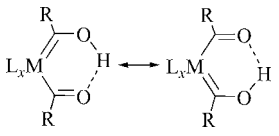

Scheme 1.

[a] Facultad de Química de San Sebastián, Universidad del País Vasco,
Apdo. 1072, 20080 San Sebastián, Spain
E-mail: mariaangeles.garralda@ehu.es
[b] Departamento de Química Inorgánica, Laboratorio de Difracción de Rayos X, Facultad de Ciencias Químicas,
Universidad Complutense, 28040 Madrid, Spain

 © 2006 Wiley-VCH Verlag GmbH & Co. KGaA, Weinheim 

diketones $[IrH\{[PPh_2(o\text{-}C_6H_4CO)]_2H\}(L)]^+$ may undergo reversible deprotonation/protonation reactions, and their reaction with amines affords neutral diacylhydridoiridium(III) derivatives.[9]

We report now on the preparation of new hydridoirida-β-diketones, including novel dinuclear species, and on the deprotonation of the latter to afford a dinuclear tris-μ-acyliridium(III) complex.

## Results and Discussion

The hydridoirida-β-diketone $[IrH\{[PPh_2(o\text{-}C_6H_4CO)]_2H\}Cl]$ (**1**) reacts with silver salts of potentially coordinating anions such as tosylate ($^-$OTs) or triflate ($^-$OTf) to afford the neutral complexes $[IrH\{[PPh_2(o\text{-}C_6H_4CO)]_2H\}(X)]$ [X = OTs (**2**), OTf (**3**)] with loss of AgCl, as shown in Scheme 2. The IR spectrum of **3** indicates the presence of the coordinated triflate anion, as shown by the presence of a ν(SO) absorption at 1317 cm$^{-1}$, which is shifted to higher wavenumbers with respect to the free anion (1270 cm$^{-1}$) upon coordination, as expected.[10] The IR spectrum of **2** contains a ν(SO) absorption at 1259 cm$^{-1}$, which is also shifted towards higher wavenumbers with respect to the silver tosylate (1205 cm$^{-1}$).[11] The FAB mass spectra show the corresponding $[M - X]^+$ peak, as expected for mononuclear complexes. Both the ν(Ir–H) absorptions (2224 cm$^{-1}$ for **2** and 2264 cm$^{-1}$ for **3**) at rather high wavenumber and the hydride resonances ($\delta$ = –24.24 ppm for **2** and –25.89 ppm for **3**) at rather high field are in accordance with a hydrido ligand being *trans* to the bonded oxygen atom of the anion.[8] The σ-donor strength of O-coordinated anions is among the smallest and this is reflected in the *trans* effect.[12] The NMR spectroscopic data for both **2** and **3** indicate the presence of two equivalent acylphosphane fragments. The $^{31}P\{^1H\}$ NMR spectra show singlets at $\delta \approx 30$ ppm and the $^{13}C\{^1H\}$ NMR spectrum of **2** shows a doublet at $\delta$ = 256.9 ppm, in the range expected for irida-β-diketones with acyl(hydroxycarbene) character, with a large $J_{P,C}$ coupling constant of 102 Hz due to the acyl groups being *trans* to the phosphorus atoms. The $^1H$ NMR spectra show the hydride resonances as triplets due to a $J_{P,H}$ coupling of about 12 Hz, which agrees with the hydride being *cis* to both phosphane ligands, and sharp, low-field singlets at $\delta$ = 22.72 ppm for **2** and 22.69 ppm for **3**, which support the presence of fairly strong O···H···O hydrogen bonds and the existence of irida-β-diketones containing a formally tetradentate PCCP ligand.[8,9]

Complex **2** behaves as nonelectrolyte in acetone solution, whereas acetone solutions of **3** show conductivity values expected for 1:1 electrolytes.[13] This indicates that in acetone solution the tosylate group remains bonded to the iridium ion while the triflate anion is easily displaced by the solvent to afford the cationic complex $[IrH\{[PPh_2(o\text{-}C_6H_4CO)]_2H\}(acetone)]OTf$ (**4**), as shown in Scheme 2. To confirm this assumption, we recorded the NMR spectra of both complexes in [D$_6$]acetone solution. The $^1H$ NMR spectrum of **2** in [D$_6$]acetone is almost the same as that in $CDCl_3$, with the hydride resonance at $\delta$ = –24.03 (t, $J_{P,H}$ = 13.25 Hz) ppm, while the $^1H$ NMR spectrum of **3** shows two hydride resonances in a 6:1 ratio according to the integrals. The most abundant signal – that of the hydride at $\delta$ = –24.59 (t, $J_{P,H}$ = 12.80 Hz) ppm – is due to **4** and appears at lower field (ca. 1 ppm) than that of **3**, which appears at $\delta$ = –25.74 (t, $J_{P,H}$ = 13.25 Hz) ppm in $CDCl_3$. Attempts to obtain the acetone complex **4** proved unsuccessful and only resulted in the isolation of complex **3**.

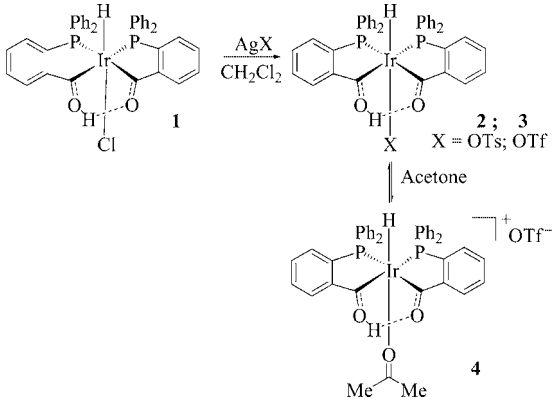


Scheme 2.

The reaction of $[IrH\{[PPh_2(o\text{-}C_6H_4CO)]_2H\}Cl]$ (**1**) with halide scavengers containing noncoordinating anions such as $Et_3OPF_6$, $Et_3OBF_4$ or $AgBF_4$ and using Ir/scavenger ratios of 2:1 results in the abstraction of only one half of the chlorine atoms in the starting material and the formation of the compounds $[\{IrH[\{PPh_2(o\text{-}C_6H_4CO)\}_2H]\}_2(\mu\text{-}Cl)]A$ [A = $BF_4$ (**5**), $PF_6$ (**6**)], which contain a cationic dinuclear species with a single chlorine atom bridging two hydridoirida-β-diketone fragments (see *i* in Scheme 3). The spectroscopic data for the cation in compounds **5** and **6** are the same. Compounds **5** and **6** show a ν(Ir–H) absorption and a hydride resonance that agree with a hydride ligand being *trans* to a chlorine atom, and a sharp, low-field singlet at $\delta$ = 22.66 ppm that supports the presence of an O···H···O

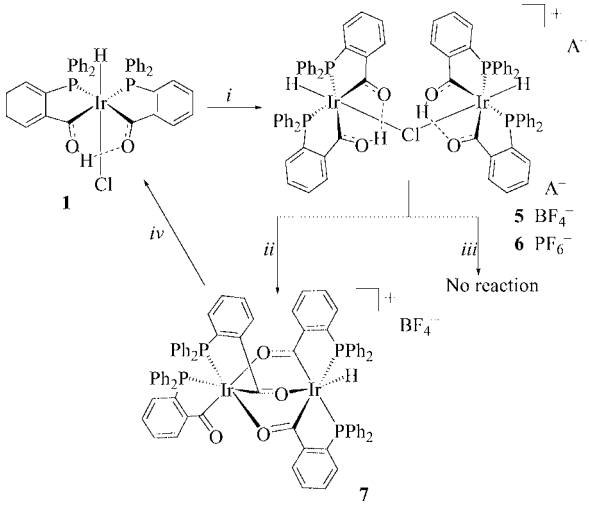


Scheme 3. *i*: $AgBF_4$, $Et_3OBF_4$ or $Et_3OPF_6$ in $CH_2Cl_2$; *ii*: $AgBF_4$ in $CH_2Cl_2$; *iii*: $Et_3OBF_4$ or $Et_3OPF_6$ in $CH_2Cl_2$; *iv*: HCl in MeOH.

 © 2006 Wiley-VCH Verlag GmbH & Co. KGaA, Weinheim 

fragment. They behave as 1:1 electrolytes in acetone solution and the FAB spectrum of **6** shows the $[M]^+$ peak at $m/z$ = 1581, as expected for such a dinuclear species.

In order to ascertain the structure shown in Scheme 3, a single-crystal X-ray diffraction study of compound **5** was undertaken. Selected bond lengths and angles, including the enolic hydrogen bond, are listed in Table 1. The crystal structure consists of discrete, cationic dinuclear units formed by pseudo-octahedral Ir moieties sharing the position occupied by the chloro ligand and $BF_4^-$ anions. An ORTEP view of the cation is given in Figure 1. Both bridging Ir–Cl distances in **5** are equal within experimental error and are, as expected, significantly longer [2.539(3) Å] than the terminal Ir–Cl distance in **1** [2.485(3) Å].[8] As far as we are aware, there is only one precedent of a dinuclear iridium complex containing a single chlorine bridge, which is *trans* to an $SiR_2R'$ group.[14] The Ir–Cl distances in **5** are shorter than those found in this previously reported complex and this difference may reflect the expected stronger structural *trans* influence of $SiR_3$ groups than of hydrido ligands.[15] The coordination around both Ir atoms is pseudo-octahedral with distortions of the type usually observed in hydrido complexes (maximal deviation from ideal angles of 19° and 16° for Ir1 and Ir2, respectively). The Ir1–Ir2 distance (4.609 Å) and the Ir1–Cl1–Ir2 angle [130.3(1)°] exclude any Ir–Ir interaction. This angle is similar to those reported for related octahedral rhodium [138.15(7)°] or molybdenum [134.0(1)°] complexes containing a single chlorine bridge between two metal atoms.[16] The best least-squares equatorial planes (P1, P2, C20, C1) and (P3, P4, C39, C58) of the Ir atoms form a dihedral angle of 54.1(2)°, in accordance with the Ir1–Cl1–Ir2 angle. There are some differences between both moieties. For example, the average Ir–P distances are slightly longer [by 0.023(3) Å] in the Ir1 moiety and the relative disposition of the pseudo-octahedra is eclipsed with a slight torsion angle of 26.71°. These facts mean a breaking of the $C_2$ symmetry around the chlorine atom for the whole structure and the twofold axis is only

Table 1. Selected bond lengths [Å] and angles [°] for Complex **5**.

| | | | |
|---|---|---|---|
| Ir1–P1 | 2.372(3) | Ir2–P3 | 2.336(3) |
| Ir1–P2 | 2.364(3) | Ir2–P4 | 2.354(3) |
| Ir1–C1 | 2.01(1) | Ir2–C58 | 2.01(1) |
| Ir1–C20 | 2.05(1) | Ir2–C39 | 2.03(1) |
| Ir1–H1A | 1.417 | Ir2–H1B | 1.420 |
| Ir1–Cl(1) | 2.535(3) | Ir2–Cl(1) | 2.544(3) |
| C1–O1 | 1.31(1) | C39–O3 | 1.27(1) |
| C20–O2 | 1.28(1) | C58–O4 | 1.27(1) |
| O2–H2A | 1.16 | O3–H2B | 1.19 |
| O1–H2A | 1.27 | O4–H2B | 1.33 |
| O2···-O1 | 2.39(1) | O4···-O3 | 2.42(1) |
| C1–Ir1–C20 | 91.7(5) | C39–Ir2–C58 | 90.3(5) |
| C1–Ir1–P1 | 81.5(4) | C39–Ir2–P3 | 83.7(4) |
| C20–Ir1–P1 | 168.8(3) | C58–Ir2–P3 | 173.9(4) |
| C1–Ir1–P2 | 172.8(4) | C39–Ir2–P4 | 164.3(4) |
| C20–Ir1–P2 | 81.6(4) | C58–Ir2–P4 | 82.2(4) |
| P1–Ir1–P2 | 104.7(1) | P3–Ir2–P4 | 103.6(1) |
| C1–Ir1–Cl(1) | 89.0(3) | C39–Ir2–Cl(1) | 98.9(3) |
| C20–Ir1–Cl(1) | 92.4(3) | C58–Ir2–Cl(1) | 88.7(3) |
| P1–Ir1–Cl(1) | 96.4(1) | P3–Ir2–Cl(1) | 92.8(1) |
| P2–Ir1–Cl(1) | 94.0(1) | P4–Ir2–Cl(1) | 94.7(1) |
| C1–Ir1–H1A | 104.6 | C39–Ir2–H1B | 77.0 |
| C20–Ir1–H1A | 83.1 | C58–Ir2–H1B | 102.0 |
| P1–Ir1–H1A | 90.0 | P3–Ir2–H1B | 76.1 |
| P2–Ir1–H1A | 71.9 | P4–Ir2–H1B | 91.1 |
| Cl(1)–Ir1–H1A | 165.7 | Cl(1)–Ir2–H1B | 168.4 |
| O2–H2A–O1 | 159.0 | O3–H2B–O4 | 147.4 |
| Ir1–Cl(1)–Ir2 | 130.3(1) | | |

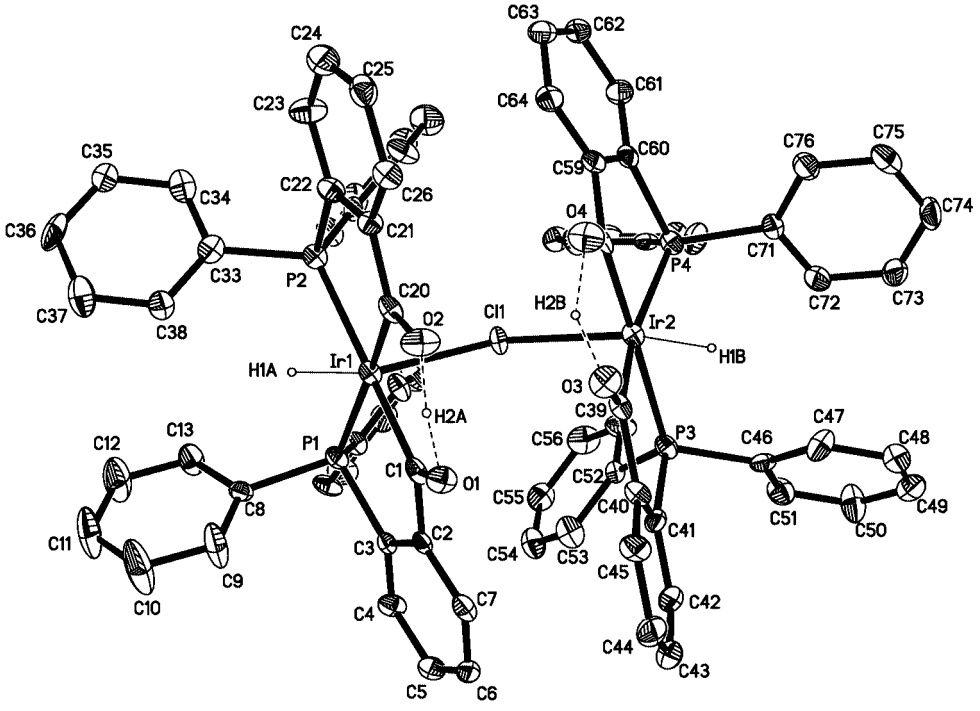


Figure 1. ORTEP view of the cation in **5** showing the atomic numbering (20% probability ellipsoids) and the intramolecular hydrogen bonds. The hydrogen atoms, except for the four shown, and the labels of some carbon atoms have been omitted for clarity.

 © 2006 Wiley-VCH Verlag GmbH & Co. KGaA, Weinheim 

kept for the Ir cores. The C=O distances, which are in the range 1.27–1.31 Å, are similar to those found in monomeric irida-β-diketones. The O···O distances and O–H–O angles are in accordance with a strong enolic character for the hydrogen bond and agree with those reported for other irida-β-diketones.[8,9]

In keeping with the crystal structure, the $^{31}P\{^1H\}$ NMR spectra of **5** and **6** show two singlets at $\delta$ = 30.7 and 18.3 ppm, respectively, at 203 K, and in the $^{13}C\{^1H\}$ NMR spectra two doublets at $\delta$ = 257.6 ($J_{P,C}$ = 101 Hz) and 255.6 ppm ($J_{P,C}$ = 103 Hz) are observed. The $^1H$ NMR spectra contain a triplet at $\delta$ = –23.17 ($J_{P,H}$ = 14.6) ppm and a singlet at $\delta$ = 22.66 ppm. Such a pattern is consistent with the nonequivalence of the hydridoirida-β-diketone fragments connected through the chlorine bridge, the equivalence of the acylphosphane groups in each hydridoirida-β-diketone fragment, and the NMR parameters of the hydride ions and of the enolic protons of both fragments being equal. Inspection of the $^{31}P\{^1H\}$ NMR spectra at various temperatures shows that on raising the temperature the singlets broaden and coalesce at 253 K, giving rise to a broad resonance centered at $\delta$ = 25 ppm at room temperature (see Figure 2). On the other hand, at room temperature the $^{13}C\{^1H\}$ NMR spectra show only a doublet at $\delta$ = 256.5 ($J_{P,C}$ = 101 Hz) ppm due to the bonded acyl groups. The $^1H$ NMR spectra remain unaltered in the whole temperature range. From line-shape analysis[17] of the variable-temperature $^{31}P\{^1H\}$ NMR spectra of complex **5**, the activation parameters $\Delta H^{\ddagger}$ = 7.8 ± 0.4 kcal mol$^{-1}$ and $\Delta S^{\ddagger}$ = –10.9 ± 0.5 cal K$^{-1}$ mol$^{-1}$ have been determined. The entropy of activation is indicative of an intramolecular rearrangement process.[18] A combination of rotation around the Ir–Cl bonds, which is restricted at low temperatures due to the presence of the phenyl groups, and variation of the Ir–Cl–Ir angle may account for the observed fluxional behavior.

Complex **5** reacts further with $AgBF_4$ to give complex **7**, which contains three acylphosphane bridging groups (see *ii* in Scheme 3). Compound **7** shows an IR stretch at 1628 cm$^{-1}$ due to the terminal acyl group and a strong stretch at 1525 cm$^{-1}$ assigned to the bridging acyl groups. It behaves as 1:1 electrolyte in acetone solution and the FAB spectrum shows the $[M]^+$ peak at $m/z$ = 1543, as expected for such a dinuclear species. At 223 K, the NMR spectra of **7** are consistent with the structure shown in Scheme 3. The $^1H$ NMR spectrum shows only one resonance at high field ($\delta$ = –23.24 ppm) as a doublet of doublets, with a $J_{P,H}$ coupling of about 18 Hz, due to the presence of one hydrido ligand *cis* to two nonequivalent phosphorus atoms. The formation of three bridging acyl groups breaks the equivalence of the acylphosphane fragments present in the starting material **5**. The $^{31}P\{^1H\}$ NMR spectrum consists of two sets of doublets due to the presence of four nonequivalent acylphosphane fragments, two per iridium atom, and the $J_{P,P}$ coupling constants agree with both phosphorus atoms bonded to the same iridium atom being mutually *cis*. The $^{13}C\{^1H\}$ NMR spectrum contains a singlet at $\delta$ = 209.1 ppm due to the terminal acyl group and three resonances at $\delta$ = 266.5 (d), 264.8 (d), and 257.5 (d) ppm,

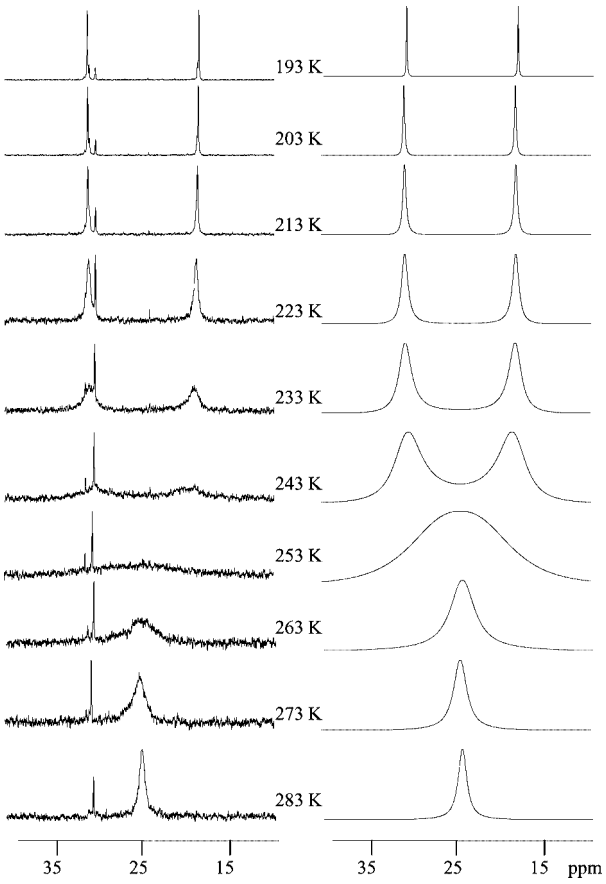


Figure 2. Variable-temperature $^{31}P\{^1H\}$ NMR spectra of **5**; experimental in $CD_2Cl_2$ (left) and calculated (right).

respectively, with high $J_{P,C}$ coupling constants of about 95 Hz, due to three acyl groups *trans* to phosphorus atoms. The rather low field of the latter suggests the bridging nature and significant carbene-like character for all three acyl groups.[19–21] Inspection of the NMR spectra at variable temperature shows that on raising the temperature the doublet of doublets due to the hydrido ligand collapses into a triplet at $\delta$ = –23.23 ($J_{P,H}$ = 18.3 Hz) ppm. The $^{31}P\{^1H\}$ resonances at lower field ($\delta$ = 23 and 21 ppm) show a marked chemical shift temperature dependence such that $\Delta\delta$ decreases as the temperature increases and the AX system observed at low temperature becomes an AB system centered at $\delta$ = 22.3 ppm. The two chemical shifts coincide at room temperature, and above this temperature they exchange position. This behavior has also been reported for monomeric $Ir^{III}$ complexes.[22] Over the whole temperature range, the corresponding $J_{P,P}$ value, the $^{31}P\{^1H\}$ resonances at higher field, and the $^{13}C\{^1H\}$ resonances remain unchanged. A $\{^1H,^{31}P\}$ HSQC experiment at room temperature shows that the hydrido ligand is coupled to the $^{31}P$ AB system at $\delta$ = 22 ppm.

Acyl groups are well known as bridging ligands towards transition metals, although their behavior as such in iridium homodinuclear complexes is scarce,[21] and the acylphosphane chelating ligand *o*-$PPh_2(C_6H_4CO)$ has been reported to behave as a bridging acyl group only in ruthenium or

 © 2006 Wiley-VCH Verlag GmbH & Co. KGaA, Weinheim 

osmium clusters.[23] We have succeeded in isolating complex **7** as single crystals suitable for X-ray diffraction. To the best of our knowledge no structural report on dinuclear transition metal complexes with three bridging acyl groups has been published, although a crystallographic study of a triacetylrhenate complex of boron has been reported.[24] The crystal structure of **7** shows the presence of dinuclear cations and $BF_4^-$ anions packed within normal van der Waals interaction distances. Two crystallographically independent cations and anions were identified in the structural determination, namely A and B. No significant differences are observed in the molecular geometries of both. Selected bond lengths and angles are listed in Table 2, and Figure 3 shows a molecular drawing of the cation A. The dinuclear cation consists of two pseudo-octahedral iridium(III) moieties, assuming that the hydrido ligand occupies the sixth coordination site on Ir1A, with three bridging acyl groups. Two of the corresponding carbon atoms are bonded to the iridium atom coordinated to the hydrido ligand such that the coordination around Ir1 is similar to that of the parent hydridoirida-β-diketone **5**. The hydrido ligand is *trans* to the oxygen atom in **7** instead of to the chlorine atom in **5** and the two oxygen atoms are bonded to the iridium atom in **7** instead of to a proton in **5**. Ir2 is bonded to two oxygen atoms and one carbon atom of the bridging acyl groups and six-coordination is attained with two phosphane groups and one terminal acyl group. The Ir–P distances in the Ir1A moiety and the Ir2A–P3A distance are equivalent [average of 2.354(4) Å] and longer than the Ir2A–P4A distance of 2.242(4) Å as a consequence of the weaker structural *trans* influence of the oxygen atom *trans* to P4 than that of an acyl carbon atom *trans* to P1, P2, and P3. The Ir–O distances [2.23(1), 2.19(1), and 2.12(1) Å for Ir1A–O4A, Ir2A–O1A, and Ir2A–O2A, respectively] reflect the *trans* influence being strongest for the hydrido ligand, similar or slightly weaker for the acyl carbon atom, and weaker for the phosphorus atom. Bridging acyl groups can be described by acyl↔oxycarbene resonance structures and this is reflected by shorter M–C and longer C–O bond lengths than in terminal acyl ligands.[19–21] In spite of the oxycarbene character of the bridging acyl groups suggested by $^{13}C$ NMR spectroscopy, the Ir–C and C–O distances for the bridging groups in complex **7** [average of 2.03(2) and 1.23(2) Å, respectively] are similar to the Ir2A–C39A [1.97(2) Å] and the C39A–O3A [1.26(2) Å] distances of the terminal acyl ligand. These fea-

Table 2. Selected bond lengths [Å] and angles [°] for complex **7**.

| | | | |
|---|---|---|---|
| Ir1A–P1A | 2.345(4) | Ir2A–P3A | 2.363(4) |
| Ir1A–P2A | 2.353(4) | Ir2A–P4A | 2.242(4) |
| Ir1A–O4A | 2.23(1) | Ir2A–O1A | 2.185(8) |
| | | Ir2A–O2A | 2.123(8) |
| Ir1A–C1A | 2.03(1) | Ir2A–C39A | 1.97(2) |
| Ir1A–C20A | 2.02(1) | Ir2A–C58A | 2.05(2) |
| C1A–O1A | 1.23(1) | C39A–O3A | 1.26(2) |
| C20A–O2A | 1.25(1) | C58A–O4A | 1.21(2) |
| | | | |
| C1A–Ir1A–P1A | 80.9(4) | C39A–Ir2A–P3A | 83.2(5) |
| C1A–Ir1A–P2A | 167.6(4) | C39A–Ir2A–P4A | 93.2(5) |
| C20A–Ir1A–P2A | 80.2(4) | P4A–Ir2A–P3A | 102.4(2) |
| C20A–Ir1A–P1A | 172.3(4) | O1A–Ir2A–P4A | 94.0(2) |
| C20A–Ir1A–C1A | 91.7(6) | C58A–Ir2A–P3A | 173.2(4) |
| P1A–Ir1A–P2A | 106.7(1) | C58A–Ir2A–P4A | 80.6(4) |
| O1A–C1A–Ir1A | 128(1) | O2A–Ir2A–P4A | 172.5(3) |
| O2A–C20A–Ir1A | 127(1) | O2A–Ir2A–O1A | 86.0(3) |
| C58A–O4A–Ir1A | 121(1) | C1A–O1A–Ir2A | 120.1(9) |
| C39A–Ir2A–O1A | 172.9(5) | C20A–O2A–Ir2A | 124.3(8) |
| C39A–Ir2A–O2A | 86.9(5) | O4A–C58A–Ir2A | 128(1) |

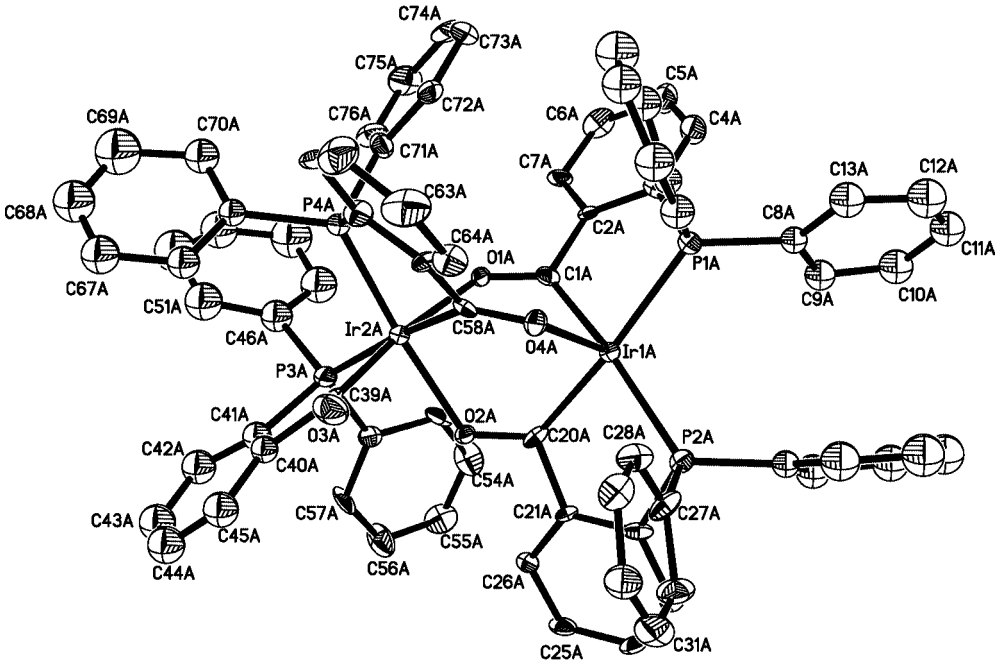


Figure 3. ORTEP view of the cation A in complex **7** showing the atomic numbering (20% probability ellipsoids). The hydrogen atoms and the labels of some carbon atoms have been omitted for clarity.

 © 2006 Wiley-VCH Verlag GmbH & Co. KGaA, Weinheim 

tures may be related to the fact that the terminal acyl ligand is *trans* to the oxygen atom, which has a weak *trans* influence, while the carbon atoms of the bridging ligands are *trans* to the phosphorus atoms, and/or to the acyl resonance structure being a stronger contributor than the oxycarbene resonance structure to the ground-state structure, as suggested for related iridium(III) complexes.[22]

The reaction of **5** with $AgBF_4$ to give **7** is a complex transformation and its mechanism is not yet totally clear. Complex **5** contains two hydrido ligands and also two enolic protons along with a chlorine atom, while complex **7** contains only one hydrido ligand; this means release of one Cl and three H atoms. Attempts to abstract the chloride ion from complexes **5** or **6** by using $Et_3OBF_4$ or $Et_3OPF_6$ proved unsuccessful (see *iii* in Scheme 3) and this indicates that the silver salt promotes a reaction path that is not available for other halide scavengers. It is known that metathesis reactions of silver salts may lead to the formation of different adducts that can involve silver coordination to the iridium atom,[25] or formation of a halide bridge between both metal atoms.[26] In our case, replacement of the enolic protons by silver ions, similar to that observed in pyrazolyliridium complexes,[27] can also be considered. Cationic acyl(hydroxycarbene)platinum(II) complexes can be obtained by the reaction of diacylhalohydridoplatinum(IV) complexes with $TlPF_6$ and may involve an intermolecular deprotonation/protonation reaction.[28] We believe that the silver salt is responsible for the abstraction of the chloride ion and one proton, while evolution of $H_2$, formed by combination of one hydride ion and one proton, occurs.

Bubbling of HCl through an MeOH solution of **7** gives **1** (see *iv* in Scheme 3). This result shows that the loss of hydrido ligands, enolic protons, and chloride ions in complex **1** can be reversed; this observation has potential interest in studies directed toward catalytic ionic hydrogenation.[29]

## Conclusions

Neutral, mononuclear hydridoirida-β-diketones containing labile anions have been prepared that can be used to afford mononuclear, cationic hydridoirida-β-diketones. Fluxional, dinuclear, cationic hydridoirida-β-diketones containing a single chloride bridge can be obtained upon treatment with a halide abstractor. Silver salts may afford an asymmetric, dinuclear iridium complex with three acylphosphane bridging ligands. The starting material can be recovered by addition of HCl. The loss and recovery of hydride ions and protons could be relevant to studies of catalytic processes such as ionic hydrogenation.

## Experimental Section

**General Procedures:** The preparation of the metal complexes was carried out at room temperature under nitrogen by using standard Schlenk techniques. [IrH{[$PPh_2$(*o*-$C_6H_4CO$)]$_2$H}Cl] (**1**) was prepared as reported previously.[8] Microanalysis were carried out with a Leco CHNS-932 microanalyser. Conductivities were measured in acetone solution with a Metrohm 712 conductimeter. IR spectra were recorded with a Nicolet FTIR 510 spectrophotometer in the range 4000–400 $cm^{-1}$ using KBr pellets. NMR spectra were recorded with Bruker Avance DPX 300 or Bruker Avance 500 spectrometers. $^1H$ and $^{13}C\{^1H\}$ (TMS internal standard), $^{31}P\{^1H\}$ ($H_3PO_4$ external standard) and 2D spectra were measured for $CDCl_3$, $CD_2Cl_2$, or [$D_6$]acetone solutions. Mass spectra were recorded with a VG Autospec, by the liquid secondary ion (LSI) technique using nitrobenzyl alcohol as matrix and a cesium gun (Universidad de Zaragoza).

**Preparation of [IrH{[$PPh_2$(*o*-$C_6H_4CO$)]$_2$H}(OTs)] (2):** AgOTs (42 mg, 0.150 mmol) was added to a dichloromethane solution of **1** (60 mg, 0.075 mmol). After stirring for 24 h, the silver salts were filtered off. Addition of diethyl ether to the solution gave a yellow precipitate, which was filtered off, washed with diethyl ether, and vacuum-dried (yield: 50 mg, 70%). IR (KBr): $\tilde{\nu}$ = 2224 (w) [ν(IrH)], 1632(s) [ν(C=O)], 1259(s) [ν(SO)] $cm^{-1}$. $^1H$ NMR ($CDCl_3$): $\delta$ = –24.24 (t, $J_{P,H}$ = 12.24 Hz, 1 H, HIr), 2.19 (s, 3 H, $CH_3$), 22.72 (s, 1 H, OHO) ppm. $^{13}C\{^1H\}$ NMR ($CDCl_3$): $\delta$ = 256.9 (d, $J_{P,C}$ = 102 Hz, CO), 21.2 (s, $CH_3$) ppm. $^{31}P\{^1H\}$ NMR ($CDCl_3$): $\delta$ = 29.9 (s) ppm. FAB MS: calcd. for $C_{45}H_{37}IrO_5P_2S$ 944, found 773 [M – OTs]$^+$. $C_{45}H_{37}IrO_5P_2S{\cdot}0.25CH_2Cl_2$ (965.25): calcd. C 56.31, H 3.92, S 3.32; found C 56.18, H 3.89, S 3.44.

**Preparation of [IrH{[$PPh_2$(*o*-$C_6H_4CO$)]$_2$H}(OTf)] (3):** AgOTf (38 mg, 0.150 mmol) was added to a dichloromethane solution of **1** (60 mg, 0.075 mmol). After stirring for 30 min, the silver salts were filtered off. Addition of diethyl ether to the solution gave a yellow precipitate, which was filtered off, washed with diethyl ether, and vacuum-dried (yield: 47 mg, 68%). IR (KBr): $\tilde{\nu}$ = 2264 (w) [ν(IrH)], 1628 (s) [ν(C=O)], 1317 (s) [ν(SO)] $cm^{-1}$. $\Lambda_M$ = 116 $\Omega^{-1}cm^2mol^{-1}$. $^1H$ NMR ($CDCl_3$): $\delta$ = –25.89 (t, $J_{P,H}$ = 12.86 Hz, 1 H, HIr), 22.69 (s, 1 H, OHO) ppm. $^{31}P\{^1H\}$ NMR ($CDCl_3$): $\delta$ = 31.21 (s) ppm. FAB MS: calcd. for $C_{39}H_{30}F_3IrO_5P_2S$ 922; found 773 [M – OTf]$^+$. $C_{39}H_{30}F_3IrO_5P_2S$ (921.89): calcd. C 50.81, H 3.28, S 3.48; found C 50.74, H 3.57, S 3.45.

**Preparation of [{IrH[{$PPh_2$(*o*-$C_6H_4CO$)}$_2$H]}$_2$(μ-Cl)]A [A = $BF_4$ (5), $PF_6$ (6)]:** $Et_3OPF_6$ (9.42 mg, 0.038 mmol) or $Et_3OBF_4$ (7.22 mg, 0.038 mmol) was added to a dichloromethane solution of **1** (60 mg, 0.075 mmol). After stirring for 60 min, addition of diethyl ether to the solution gave a yellow precipitate, which was filtered off, washed with diethyl ether, and vacuum-dried. IR (KBr): $\tilde{\nu}$ = 2221 (m) [ν(IrH)], 1629 (s) [ν(C=O)] $cm^{-1}$. $^1H$ NMR ($CD_2Cl_2$, 203 K): $\delta$ = –23.17 (t, $J_{P,H}$ = 14.2 Hz, 1 H, HIr), 22.66 (s, 1 H, OHO) ppm. $^{13}C\{^1H\}$ NMR ($CD_2Cl_2$, 203 K): $\delta$ = 257.6 (d, $J_{P,C}$ = 101 Hz, CO), 255.6 (d, $J_{P,C}$ = 103 Hz, CO) ppm. $^{31}P\{^1H\}$ NMR ($CD_2Cl_2$, 203 K): $\delta$ = 30.7 (s), 18.3 (s) ppm. FAB MS: calcd. for $C_{76}H_{60}ClO_4P_4Ir_2$ 1581; found 1581 [M]$^+$. **Data for 5:** Yield: 42 mg (68%). $\Lambda_M$ = 147 $\Omega^{-1}cm^2mol^{-1}$. $C_{76}H_{60}BClF_4Ir_2O_4P_4$ (1667.9): calcd. C 54.73, H 3.63; found C 54.61, H 3.57. **Data for 6:** Yield: 48 mg (73%). $\Lambda_M$ = 179 $\Omega^{-1}cm^2mol^{-1}$. $C_{76}H_{60}ClF_6Ir_2O_4P_5{\cdot}0.5CH_2Cl_2$ (1768.5): calcd. C 51.96, H 3.48; found C 52.03, H 3.23.

**Preparation of [$Ir_2$H{$PPh_2$(*o*-$C_6H_4CO$)}{μ-$PPh_2$(*o*-$C_6H_4CO$)}$_3$]$BF_4$ (7):** To a dichloromethane solution of **5** (125 mg, 0.075 mmol) was added $AgBF_4$ (29.1 mg, 0.15 mmol). After stirring for 30 min, the silver salts were filtered. Addition of diethyl ether to the solution gave a yellow precipitate that was filtered off, washed with diethyl ether and vacuum-dried (yield: 68 mg, 53%). IR (KBr): $\tilde{\nu}$ = 2189 (w), [ν(IrH)], 1628 (s), 1525 (s) [ν(C=O)] $cm^{-1}$. $\Lambda_M$ = 152 $\Omega^{-1}cm^2mol^{-1}$. $^1H$ NMR ($CDCl_3$, 223 K): $\delta$ = –23.24 (dd, $J_{P,H}$ = 19.2 and 18.3 Hz, 1 H, HIr) ppm. $^{31}P\{^1H\}$ NMR ($CDCl_3$, 223 K): $\delta$ = 23.6 and 21.2 (d, $J_{P,P}$ = 12 Hz), 20.1 and 14.2 (d, $J_{P,P}$

 © 2006 Wiley-VCH Verlag GmbH & Co. KGaA, Weinheim 

Table 3. Crystal and refinement fata for **5** and **7**.

| | **5** | **7** |
|---|---|---|
| Empirical formula | $[C_{76}H_{60}Cl_1O_4P_4Ir_2]BF_4 \cdot 1/2CH_2Cl_2$ | $[C_{76}H_{56}F_3O_4P_4Ir_2]BF_4$ |
| $M_r$ | 1710.24 | 1628.3 |
| Crystal system | monoclinic | monoclinic |
| Space group | $P2_1/c$ | $P2_1/n$ |
| $a$ [Å] | 14.3279(7) | 15.583(1) |
| $b$ [Å] | 36.606(2) | 36.688(2) |
| $c$ [Å] | 13.235(7) | 23.299(2) |
| $\beta$ [°] | 97.062(1) | 94.954(2) |
| $V$ [Å$^3$] | 6888.6(6) | 13271(2) |
| $Z$ | 4 | 8 |
| $D_{calcd.}$ [g cm$^{-3}$] | 1.649 | 1.630 |
| $\mu$ [mm$^{-1}$] | 4.091 | 4.165 |
| $F$(000) | 3364 | 6392 |
| $\theta$ [°] | 1.11–25.0 | 1.04–25.0 |
| Data collected | (–17, –42, –14) to (15, 43, 15) | (–18, –40, –26) to (18, 43, 27) |
| No. of reflns. collected | 36113 | 102296 |
| No. of ind. reflns. | 12105 ($R_{int}$ = 0.1195) | 23299 ($R_{int}$ = 0.1700) |
| Completeness to $\theta$ | 99.8% | 99.6% |
| Data/restraints/parameters | 12105/6/616 | 23299/8/1279 |
| $R$[a] [$I > 2\sigma(I)$] | 0.0585 (6212 obsd. reflect.) | 0.0553 (8848 obsd. reflect.) |
| $R_{wF}$[b] (all data) | 0.16000 | 0.1306 |

[a] $\Sigma||F_o| - |F_c||/\Sigma|F_o|$. [b] $\{\Sigma[w(F_o^2 - F_c^2)^2]/\Sigma[w(F_o^2)^2]\}^{1/2}$.

= 8 Hz) ppm. $^{13}C\{^1H\}$ NMR ($CDCl_3$, 223 K): $\delta$ = 266.5 (d, $J_{P,C}$ = 91 Hz, CO), 264.5 (d, $J_{P,C}$ = 89 Hz, CO), 257.5 (d, $J_{P,C}$ = 101 Hz, CO) 209.1 (s, CO) ppm. FAB MS: calcd. for $C_{76}H_{57}O_4P_4Ir_2$ 1543; found 1543 $[M]^+$. $C_{76}H_{57}BF_4O_4P_4Ir_2 \cdot CH_2Cl_2$ (1714.37): calcd. C 53.95, H 3.47; found C 53.65, H 3.61.

**Reaction of $[Ir_2H\{PPh_2(o\text{-}C_6H_4CO)\}\{\mu\text{-}PPh_2(o\text{-}C_6H_4CO)\}_3]BF_4$ (7) with HCl:** HCl gas was bubbled at room temperature through a methanol solution of **7** (30 mg, 0.018 mmol) for 30 min, upon which a small amount of precipitate was formed. The solvent was evaporated and the residue analyzed by NMR spectroscopy. According to the spectra, the solid contained mainly complex **1**.

**X-ray Structure Determination of 5 and 7:** Yellow prismatic single crystals of **5** and needles of **7** suitable for X-ray diffraction were successfully grown by slow diffusion of diethyl ether into dichloromethane or methanol solutions, respectively. Data collection was carried out at room temperature on a Bruker Smart CCD diffractometer, using graphite-monochromated Mo-$K_\alpha$ radiation ($\lambda$ = 0.71073 Å), operating at 50 kV and 20 mA. In both cases, data were collected over a hemisphere of the reciprocal space by combination of three exposure sets. Each exposure of 10 s covered 0.3° in $\omega$. The first 100 frames were recollected at the end of the data collection to monitor crystal decay after X-ray exposition; no appreciable drop in the intensities was observed. A summary of the fundamental crystal data for the crystals is given in Table 3. The structures were solved by direct methods and conventional Fourier techniques. The refinement was done by full-matrix least squares on $F^2$ for **5** and by blocked full-matrix least squares on $F^2$ for **7**.[30] Anisotropic parameters were used in the last cycles of refinement for all non-H atoms, with some exceptions. The $BF_4^-$ anions in both compounds were refined by three isotropic cycles and in subsequent cycles their thermal parameters were kept constant while their coordinates were refined with geometric restraints and a variable common B–F distance. For **7**, the carbon atoms of some phenyl rings were refined isotropically. After the last cycles of refinement, the Fourier difference of **5** showed some residual electronic density. This was assigned to one half solvent $CH_2Cl_2$. The carbon and chlorine atoms were treated like the $BF_4^-$ anions, i.e. three isotropic cycles and geometrical restraints. All hydrogen atoms were calculated at geometrical positions and refined as riding on their respective carbon atoms, except the hydride atoms (H1A, H1B) and the enolic hydrogen atoms (H2A, H2B) for **5**, which were found in a difference Fourier synthesis and their coordinates and thermal parameters fixed. For **7**, it was impossible to locate the hydride ions. These features led to $R1$ factors of 0.0585 (6212 reflections observed) and 0.0553 (8848 reflections observed) for **5** and **7**, respectively. The largest residual peaks in the final difference map (1.54 and 1.62 e Å$^{-3}$, respectively) were found in the vicinity of the fluorine atoms of the $BF_4^-$ groups in both compounds. CCDC-606708 (**5**) and -606709 (**7**) contain the supplementary crystallographic data for this paper. These data can be obtained free of charge from The Cambridge Crystallographic Data Center via www.ccdc.cam.ac.uk/datarequest/cif.

## Acknowledgments

Partial financial support by MCYT (project BQU2002-0129), UPV, and the Diputación Foral de Guipuzcoa is gratefully acknowledged.

[1] C. P. Casey, C. J. Czerwinski, K. A. Fusie, R. K. Hayashi, *J. Am. Chem. Soc.* **1997**, *119*, 3971–3978.
[2] *Applied Homogeneous Catalysis with Organometallic Compounds* (Eds.: B. Cornils, W. A. Herrmann), VCH, Weinheim, **1996**.
[3] a) M. Solà, T. Ziegler, *Organometallics* **1996**, *15*, 2611–2618; b) P. Cheliatsidou, D. F. S. White, D. J. Cole-Hamilton, *Dalton Trans.* **2004**, 3425–3427.
[4] a) C. M. Lukehart, *Acc. Chem. Res.* **1981**, *14*, 109–116; b) C. M. Lukehart, *Adv. Organomet. Chem.* **1986**, *25*, 45–71.
[5] C. M. Lukehart, G. P. Torrence, *Inorg. Chem.* **1979**, *18*, 3150–3155.
[6] D. Steinborn, *Dalton Trans.* **2005**, 2664–2671.
[7] a) D. Steinborn, M. Gerish, F. W. Heinemann, C. Bruhn, *Chem. Commun.* **1997**, 843–844; b) M. Gerish, C. Bruhn, A. Porzel, D. Steinborn, *Eur. J. Inorg. Chem.* **1998**, 1655–1659.
[8] M. A. Garralda, R. Hernández, L. Ibarlucea, E. Pinilla, M. R. Torres, *Organometallics* **2003**, *22*, 3600–3603.

 © 2006 Wiley-VCH Verlag GmbH & Co. KGaA, Weinheim 

[9] F. Acha, M. A. Garralda, L. Ibarlucea, E. Pinilla, M. R. Torres, *Inorg. Chem.* **2005**, *44*, 9084–9091.
[10] G. A. Lawrance, *Chem. Rev.* **1986**, *86*, 17–33.
[11] R. Schibli, R. Alberto, U. Abram, S. Abram, A. Egli, P. A. Schubiger, T. A. Kade, *Inorg. Chem.* **1998**, *37*, 3509–3516.
[12] a) B. Olgemöller, W. Beck, *Inorg. Chem.* **1983**, *22*, 997–998; b) W. Beck, K. Sünkel, *Chem. Rev.* **1988**, *88*, 1405–1421.
[13] W. J. Geary, *Coord. Chem. Rev.* **1971**, *7*, 81–122.
[14] M. Stradiotto, K. L. Fudjala, T. D. Tilley, *Chem. Commun.* **2001**, 1200–1201.
[15] T. G. Appleton, H. C. Clark, L. E. Manzer, *Coord. Chem. Rev.* **1973**, *10*, 335–422.
[16] a) D. Cuervo, J. Díez, M. P. Gamasa, J. Gimeno, *Organometallics* **2005**, *24*, 2224–2232; b) M. D. Curtis, N. A. Fatinos, *J. Organomet. Chem.* **1984**, *272*, 43–54.
[17] P. H. M. Budzelaar, *gNMR Software*, version 5.0, Adept Scientific plc, Letchworth, UK, **2004**.
[18] G. J. H. Buisman, L. A. van der Veen, P. C. J. Kamer, P. W. N. M. van Leeuwen, *Organometallics* **1997**, *16*, 5681–5687.
[19] R. Shafiq, K. W. Kramarz, R. Eisenberg, *Inorg. Chim. Acta* **1993**, *213*, 111–119.
[20] B. D. Roswell, R. McDonald, M. Cowie, *Organometallics* **2004**, *23*, 3873–3883.
[21] J. M. O'Connor, R. Merwin, A. L. Rheingold, M. L. Adams, *Organometallics* **1995**, *14*, 2102–2105.
[22] C. Bianchini, E. Farnetti, M. Graziani, G. Nardin, A. Vacca, F. Zanobini, *J. Am. Chem. Soc.* **1990**, *112*, 9190–9197.
[23] a) C. J. Adams, M. I. Bruce, O. Kühl, B. W. Skelton, A. H. White, *J. Organomet. Chem.* **1993**, *445*, C6–C9; b) C. J. Adams, M. I. Bruce, P. A. Duckworth, P. A. Humphrey, O. Kühl, E. R. T. Tiekink, W. R. Cullen, P. Braunstein, S. Coco, B. W. Skelton, A. H. White, *J. Organomet. Chem.* **1994**, *467*, 251–281.
[24] C. M. Lukehart, L. J. Warfield, *Inorg. Chim. Acta* **1980**, *41*, 105–111.
[25] D. J. Liston, C. A. Reed, C. W. Eigenbrot, W. R. Scheidt, *Inorg. Chem.* **1987**, *26*, 2740–2741.
[26] D. Carmona, F. Viguri, F. J. Lahoz, L. A. Oro, *Inorg. Chem.* **2002**, *41*, 2385–2388.
[27] D. Carmona, L. A. Oro, M. P. Lamata, M. L. Jimeno, J. Elguero, A. Belguise, Ph. Lux, *Inorg. Chem.* **1994**, *33*, 2196–2203.
[28] D. Steinborn, M. Gerish, C. Bruhn, J. A. Davies, *Inorg. Chem.* **1999**, *38*, 680–683.
[29] R. M. Bullock, *Chem. Eur. J.* **2004**, *10*, 2366–2374.
[30] G. M. Sheldrick, *SHELX-97, Program for Crystal Structure Determination*; University of Göttingen, Germany, **1997**.

Received: May 16, 2006
Published Online: August 7, 2006

 © 2006 Wiley-VCH Verlag GmbH & Co. KGaA, Weinheim 

DOI: 10.1002/ejic.200600530

# Tetra- and Triphosphane Pyridine Podands and Their Cobalt(II) and Nickel(II) Complexes

**Stephan W. Kohl,[a] Frank W. Heinemann,[b] Markus Hummert,[a] Hardy Weißhoff,[c] and Andreas Grohmann*[a]**

*Dedicated to Professor Robert Weiß on the occasion of his 65th birthday*

**Keywords:** Cobalt / Nickel / N,P ligands

The reaction of the 2,6-diethylpyridine-derived tetraphosphane ligand $C_5H_3N[CMe(CH_2PMe_2)_2]_2$ (**1**$_{Me}$) with nickel(II) or cobalt(II) perchlorate or tetrafluoroborate in methanol produces complexes of approximate square-pyramidal geometry ($NP_4$ coordination). The nickel complexes are diamagnetic, with NMR spectral features ($^{31}P$) that reflect a tetrahedral distortion of diametrically opposite phosphorus donors; this is also found in the solid state. In terms of bond lengths and angles, all complexes differ significantly from their analogues containing the phenyl-substituted ligand $C_5H_3N[CMe(CH_2PPh_2)_2]_2$. The ligand **1**$_{Me}$ is readily and completely oxidised to the corresponding tetrakis(phosphane oxide) upon reaction with NO. Slow oxidation of the cobalt(II) tetrafluoroborate complex of **1**$_{Me}$ with aerobic oxygen in acetonitrile produces a trinuclear cobalt complex containing two equivalents of partially oxidised ligand ($C_2$-symmetrical; donor set: $[PMe_2]_2[P(O)Me_2]_2$). Four phosphane oxide oxygen atoms coordinate the central cobalt(II) ion in tetrahedral fashion, whereas the lateral cobalt(II) ions are in a square-pyramidal environment provided by two $PMe_2$ donors and three acetonitrile ligands in each case. The reaction of the cobalt(II) perchlorate complex of **1**$_{Me}$ with carbon monoxide gives an octahedral, 19-valence-electron dicarbonyl complex in which one of the dimethylphosphanyl groups is uncoordinated. A structural relative of **1**$_{Me}$, $C_5H_3N[CMe(CH_2PMe_2)_2][CMe_2(CH_2PMe_2)]$ (**2**), which contains one fewer dimethylphosphanyl donor, can be prepared in a straightforward manner from 2-ethyl-6-isopropylpyridine in a four-stage process. In a series of mononuclear nickel(II) complexes, **2** employs only its three phosphane donors which, together with a monodentate ligand (acetonitrile, acetamide, or bromide), provide a tetragonal coordination environment for the metal ion which is intermediate between square planar and tetrahedral. The acetamide complex is generated from the acetonitrile complex by slow hydrolysis of the coordinated ligand. Full spectroscopic details for the complexes, as well as X-ray structure analyses, are reported.

(© Wiley-VCH Verlag GmbH & Co. KGaA, 69451 Weinheim, Germany, 2006)

## Introduction

Phosphanes are the workhorse ligands of transition metal chemistry due to their variability in terms of steric demand and electronic properties. Both factors, which are mutually dependent, may be controlled within wide limits, depending on the bulk of substituents and the σ-donor/π-acceptor balance they impart to the donor atom. The major application of phosphane complexes is in catalysis, where the phosphane-coordinated metal ion is the mediator of the desired reaction.[1] It is mainly for the mechanistic implications in catalysis that the reactivity, or lack thereof, of coordinated tertiary phosphanes themselves (e.g., metallation of C–H or C–P bonds) has become a focus of investigation.[2]

Within this context, we have extended our study of tetrapodal pentadentate ligands[3] to include tetraphosphane pyridine ligands (general formula: **1**). We are especially interested in *mono*nuclear complexes of these ligands in which the "coordination cap" focuses the properties of several $PR_2$ donors on a single metal ion M. Such coordination modules can bind an additional monodentate ligand, L, to form complexes of pseudo-octahedral geometry. Previous reports have described the diphenylphosphanyl derivative **1**$_{Ph}$, whose steric bulk causes the metal centres to be largely inert with respect to further coordination (e.g., $M = Co^{II}$, $L = O_2$),[4] and iron(II) complexes of the dimethylphosphanyl derivative (**1**$_{Me}$), which undergo unusual P–C bond breaking and re-forming reactions, depending on the nature of

[a] Technische Universität Berlin, Institut für Chemie, Sekretariat C2,
Straße des 17. Juni 135, 10623 Berlin, Germany
Fax: +49-30-3142-2935,
E-mail: andreas.grohmann@chem.tu-berlin.de
[b] Universität Erlangen-Nürnberg, Institut für Anorganische Chemie,
Egerlandstraße 1, 91058 Erlangen, Germany
[c] Humboldt-Universität zu Berlin, Institut für Chemie,
Brook-Taylor-Str. 2, 12489 Berlin, Germany

 © 2006 Wiley-VCH Verlag GmbH & Co. KGaA, Weinheim 

the solvent (nucleophilic/non-nucleophilic), the anion, and other conditions.[5] The present contribution summarises coordination chemistry aspects of this ligand with respect to nickel(II) and cobalt(II), and introduces a structural relative having only three $PMe_2$-substituted "tentacles" (**2**).

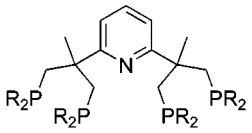

**1**

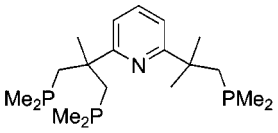

**2**

R = Ph: $\mathbf{1}_{Ph}$; R = Me: $\mathbf{1}_{Me}$

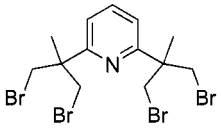

**3**

## Results and Discussion

The tetraphosphane $\mathbf{1}_{Me}$ {systematic name: 2,6-bis[1,3-bis(dimethylphosphanyl)-2-methylpropan-2-yl]pyridine; "py($PMe_2$)$_4$"} may be prepared in good yield (>80%) from the reaction of the corresponding tetrabromide $C_5H_3N[CMe(CH_2Br)_2]_2$ (**3**)[4] with four equivalents of $LiPMe_2$[6] in diethyl ether.[5] The yield of this reaction increases considerably with the purity of the halogenated precursor. Whereas **3** had previously been obtained as an oil or waxy solid, which reflected the presence of minor impurities introduced during the multi-stage synthesis, we have recently been able to obtain **3** in its crystalline form. The compound crystallises solvent-free in the space group *Pbca*, with no crystallographically imposed molecular symmetry ($C_1$; Figure 1). One of the 1,3-dibromo-2-methylprop-2-yl chains (involving Br3, Br4) adopts a "*syn*-pentane arrangement", whereas the other has a more random orientation, also with respect to the pyridine ring. The bond distances and angles are unexceptional.[7]

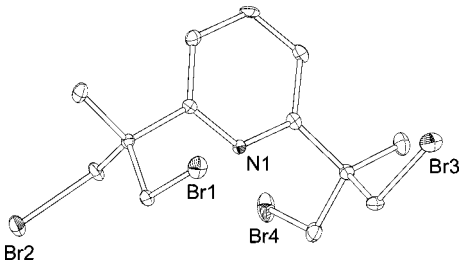


Figure 1. Structure of the tetrabromide **3**.

Compound $\mathbf{1}_{Me}$, which is obtained as a colourless oil, has the expected spectroscopic signature ($^1H$, $^{13}C$, $^{31}P$), suggesting $C_{2v}$ symmetry in solution. Upon mixing methanol solutions of equimolar amounts of $\mathbf{1}_{Me}$ and the hexahydrate salts of nickel(II) or cobalt(II) perchlorate or tetrafluoroborate at room temperature, complex formation is spontaneous, as judged by the immediate appearance of a deep red or brown colour. The reaction mixtures soon begin to deposit microcrystalline precipitates which, upon filtration and drying, analyse for the respective $LMX_2$ complexes [L = $\mathbf{1}_{Me}$, M = $Ni^{II}$, X = $ClO_4$ (**4**) or $BF_4$ (**5**); M = $Co^{II}$, X = $ClO_4$ (**6**) or $BF_4$ (**7**); see Equation (1), Scheme 1, and Exp. Sect.].

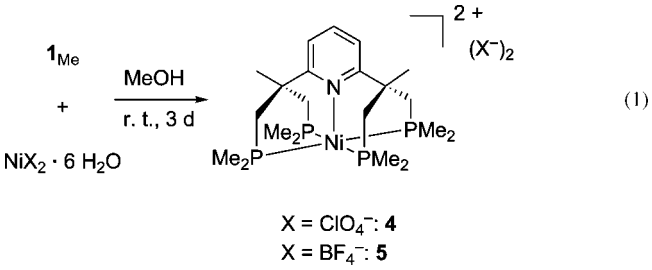


(1)

In the IR spectra of **4**–**7**, there is no indication for the coordination (if weak) of the perchlorate or tetrafluoroborate counterions, which would lead to a splitting of the respective anion bands owing to the reduction of local symmetry from $T_d$ to $C_{3v}$.[8] The nickel complexes **4** and **5** are diamagnetic, with well-resolved and very similar NMR spectra. In the $^1H$ NMR spectra, the pyridine protons appear as an $AB_2$ spin system (triplet/doublet), and in the $^{13}C$ spectra there are three signals for the pyridine carbon atoms. These features and others, taken together, suggest

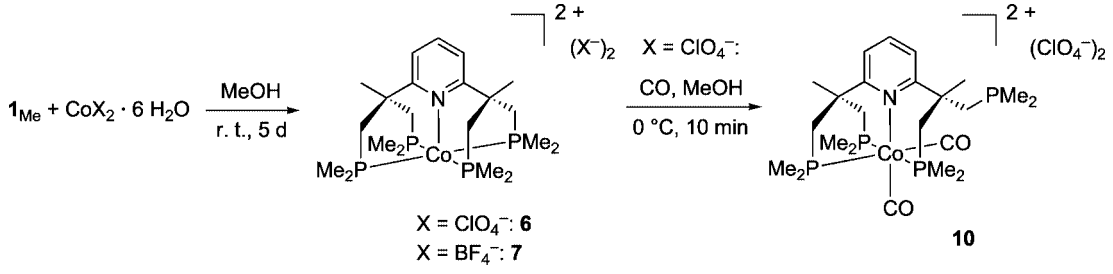


Scheme 1. Preparation of the cobalt complexes **6** and **7**, and reaction of **6** with CO to form **10**.

 © 2006 Wiley-VCH Verlag GmbH & Co. KGaA, Weinheim 

largely symmetrical (i.e., to a first approximation, square pyramidal) coordination of the ligand. The proton-decoupled $^{31}P$ NMR spectra ([$D_3$]acetonitrile) contain two signals for the four ligand P atoms, at $\delta$ = –13 ppm and –15 ppm, thus indicating a tetragonal distortion of the basal ligands (two diametrically opposite P donor atoms above and two below the $NiP_4$ best plane) in solution. This structural feature persists in the solid state in both the nickel(II) and the cobalt(II) complex. Figures 2 and 3 show the crystal structures of the cations in **4**·$CHCl_3$ and **7**·MeOH, respectively (the cation structure of **5**·MeOH is very similar; see deposited crystallographic data).

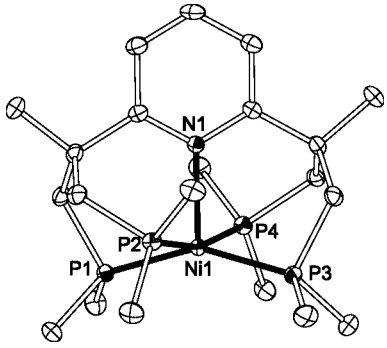


Figure 2. Structure of the dication in the nickel(II) complex **4**·$CHCl_3$ (perchlorate salt).

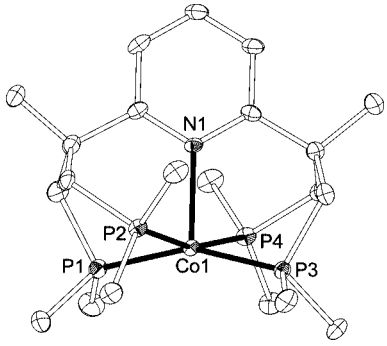


Figure 3. Structure of the dication in the cobalt(II) complex **7**·MeOH (tetrafluoroborate salt).

The bond lengths (see Table 1) involving the central ions in **4** and **7** are markedly shorter than in the structures of the phenyl-substituted ligand $\mathbf{1}_{Ph}$.[4] Whereas the metal–nitrogen distance is approximately 2.13 Å in both **4** and **7**, it is 2.28 and 2.19 Å in the nickel(II) and cobalt(II) complexes of $\mathbf{1}_{Ph}$, respectively, and whereas the metal–phosphorus distances in **4** and **7** vary around 2.20 Å within a relatively narrow range, the range is much wider (2.23–2.33 Å) in the corresponding complexes of $\mathbf{1}_{Ph}$. The N–M–P and P–M–P angles of the two sets of complexes vary accordingly. These differences reflect the considerable decrease in steric bulk of the ligand periphery upon going from $\mathbf{1}_{Ph}$ to $\mathbf{1}_{Me}$.

Table 1. Selected bond distances [Å] and angles [°] in **4**·$CHCl_3$ and **7**·MeOH (standard deviations in parentheses). The structural parameters of **5**·MeOH are very similar (see CCDC data).

| Distance or angle | **4**·$CHCl_3$ | **7**·MeOH |
|---|---|---|
| M1–N1 | 2.138(4) | 2.131(4) |
| M1–P1 | 2.1806(13) | 2.2261(15) |
| M1–P2 | 2.2018(13) | 2.2119(15) |
| M1–P3 | 2.1797(13) | 2.2177(14) |
| M1–P4 | 2.1900(15) | 2.2203(14) |
| N1–M1–P1 | 104.34(10) | 101.70(12) |
| N1–M1–P2 | 82.12(10) | 81.54(13) |
| N1–M1–P3 | 104.72(11) | 101.65(12) |
| N1–M1–P4 | 82.45(10) | 81.77(13) |
| P1–M1–P2 | 89.59(5) | 88.86(6) |
| P2–M1–P3 | 94.58(5) | 93.31(6) |
| P3–M1–P4 | 89.26(5) | 89.72(6) |
| P4–M1–P1 | 94.30(5) | 94.84(6) |
| P1–M1–P3 | 150.94(5) | 156.62(6) |
| P2–M1–P4 | 164.57(6) | 163.31(6) |

Steric factors, in addition to electronic ones, can also be expected to play a major role in determining the readiness with which the polyphosphane is oxidised. Whereas $\mathbf{1}_{Ph}$ does not react with nitrogen monoxide at 0 °C,[4] the reaction of $\mathbf{1}_{Me}$ under the same conditions is quantitative after a few minutes, giving the tetrakis(phosphane oxide) **8** as a white microcrystalline material [Equation (2)]. Similar to the reaction of $\mathbf{1}_{Ph}$ under more forcing conditions, the reaction proceeds with concomitant formation of $N_2O$. The P=O stretching vibration appears as a strong band in the IR spectrum (KBr disc) at 1161 $cm^{-1}$, and the $^{31}P$ chemical shift of the $RP(O)Me_2$ functions is $\delta$ = 44.95 ppm (s), similar to the values reported for $P(O)Me_3$ ($\delta$ =36.2 or 41.0 ppm).[9] The ligand properties of **8** are as yet unstudied. No oxidation of the ligand is observed when the nickel(II) complexes **4** or **5** are treated with NO under identical conditions.

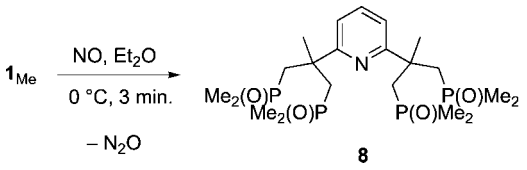


(2)

Whereas the cobalt(II) complexes $[\mathbf{1}_{Ph}Co]X_2$ (X = $ClO_4$, $BF_4$) were found to be unreactive towards aerobic oxygen,[4] preliminary results indicate that the methyl derivative $[\mathbf{1}_{Me}Co](BF_4)_2$ (**7**) does react to a minor extent, albeit with partial oxidation of the ligand and not with spontaneous formation of cobalt(III), as might initially be expected. While the processes involved require further study, we have been able to isolate (in very small amount) and characterise one oxidation product (**9**) structurally: it is the acetonitrile solvate of a trinuclear complex in which two symmetry-related molecular halves, each made up of a cobalt(II) ion and a partially oxidised ligand, hinge upon a central cobalt ion which is also in the +II oxidation state (space group *C*2/*c*; the central cobalt ion lies on a crystallographic twofold rotation axis). The overall charge of the trinuclear complex

 © 2006 Wiley-VCH Verlag GmbH & Co. KGaA, Weinheim 

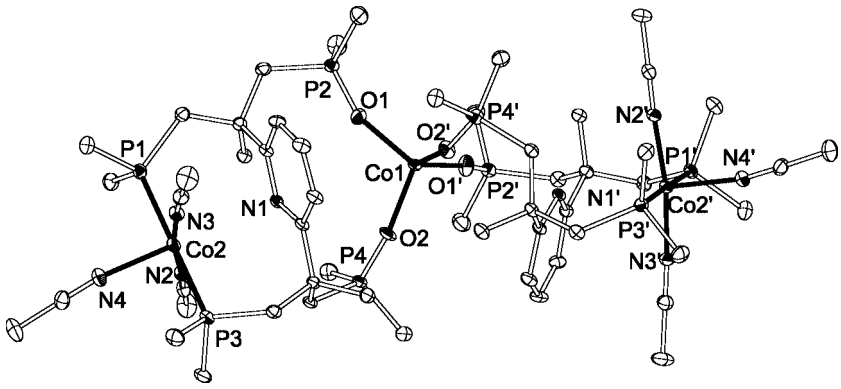


Figure 4. Structure of the hexacation in **9**·2$CH_3CN$ (tetrafluoroborate salt).

is balanced by six tetrafluoroborate anions [Figure 4, composition: $C_{54}H_{100}Co_3N_8O_4P_8(BF_4)_6$·2$CH_3CN$]. The donor set of the chelate ligand is $(PMe_2)_2(P[O]Me_2)_2$, with the pyridine nitrogen atom remaining uncoordinated. The pairs of $P[O]Me_2$ donors in either ligand coordinate the central cobalt ion in a tetrahedral fashion, while the remaining pair of $PMe_2$ donors in each ligand coordinates an additional cobalt ion in a *trans* arrangement. These lateral cobalt(II) ions have three additional acetonitrile ligands, and thus approximate a square-pyramidal coordination geometry, with Co–P bond lengths slightly longer (at 2.27 Å; Table 2) than in **7**. The 1,3-didentate ligand side-arms each contain one $PMe_2$ and one $P[O]Me_2$ donor and are homochiral, thereby reducing the symmetry from $C_{2v}$ in **1** to $C_2$ in the partially oxidised tetrapodal ligand (Figure 5). The formation of **9** parallels, to a certain extent, the partial oxidation of the triphos ligand, $MeC(CH_2PPh_2)_3$, upon reaction of its cobalt(II) complex with aerobic oxygen, as described by Huttner et al.[10]

The pentacoordinate cobalt(II) complexes are 17-valence-electron species, and the coordination of an additional ligand is therefore possible in principle. We studied the behaviour of methanol solutions of the perchlorate salt **6** towards carbon monoxide (see Exp. Sect.), and obtained a well-defined product which, by elemental analysis and based on its IR spectroscopic and MS data, is a dicarbonylcobalt(II) complex in which one phosphane donor has become decoordinated, as shown in Scheme 1. In addition to two very strong bands for CO stretching vibrations (at 1988 and 1937 $cm^{-1}$), there is a prominent band at 875 $cm^{-1}$ due to the P–C rocking deformation vibration of an uncoordinated dimethylphosphanyl group.[11] Further, the mass spectrum (MALDI-TOF) has three prominent peaks associated with the parent ion {546 (28) $[M - H]^+$, 430 (100) $[M - H - Co - 2CO]^+$, 273.5 (18) $[M]^{2+}$}, thus supporting the assignment of **10** as a 19-valence-electron, dicarbonylcobalt(II) complex of the pyridine-based tetraphosphane ligand. However, a 17-valence-electron species with an uncoordinated pyridine nitrogen atom is also possible.

There is a certain degree of similarity between the coordination mode adopted by the tetrapodal ligand in compound **10**, where it coordinates through an $NP_3$ donor subset, and the coordination mode adopted by a P–C bond

Table 2. Selected bond distances [Å] and angles [°] in **9**·2$CH_3CN$ (standard deviations in parentheses).

| Distance or angle | **9**·2$CH_3CN$ |
|---|---|
| Co1–O1 | 1.924(3) |
| Co1–O2 | 1.924(3) |
| P2–O1 | 1.503(3) |
| P4–O2 | 1.507(3) |
| Co2–P1 | 2.2741(12) |
| Co2–P3 | 2.2655(12) |
| Co2–N2 | 1.899(3) |
| Co2–N3 | 2.100(4) |
| Co2–N4 | 1.899(3) |
| O1–Co1–O2 | 109.56(13) |
| O1′–Co1–O2′ | 109.56(13) |
| O1–Co1–O2′ | 107.23(14) |
| O2–Co1–O2′ | 106.02(19) |
| P2–O1–Co1 | 158.7(5) |
| P4–O2–Co1 | 155.2(2) |
| P1–Co2–P3 | 178.41(5) |
| P1–Co2–N2 | 90.26(11) |
| P1–Co2–N3 | 90.62(11) |
| P1–Co2–N4 | 90.69(11) |
| P3–Co2–N2 | 91.30(11) |
| P3–Co2–N3 | 87.79(11) |
| P3–Co2–N4 | 89.63(11) |

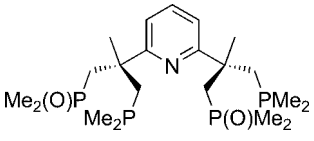


Figure 5. The partially oxidised, $C_2$-symmetrical tetrapodal ligand in **9**·2$CH_3CN$.

activated form of the same ligand in an iron(II) complex, where the donor set is likewise $NP_3$, augmented by a carbanionic methylene group which results from methanol-induced nucleophilic cleavage of one of the dimethylphosphanyl moieties.[5] For this reason, we decided to synthesise a structural relative (**2**) of the tetraphosphane ligand $\mathbf{1}_{Me}$, which can formally be derived from it by replacing one of the dimethylphosphanyl substituents by a hydrogen atom. The synthetic protocol is summarised in Scheme 2. It starts from 2-ethyl-6-isopropylpyridine, which is exhaustively hydroxymethylated in the reactive α-carbon positions by reaction with aqueous formaldehyde in an autoclave at elevated

 © 2006 Wiley-VCH Verlag GmbH & Co. KGaA, Weinheim 

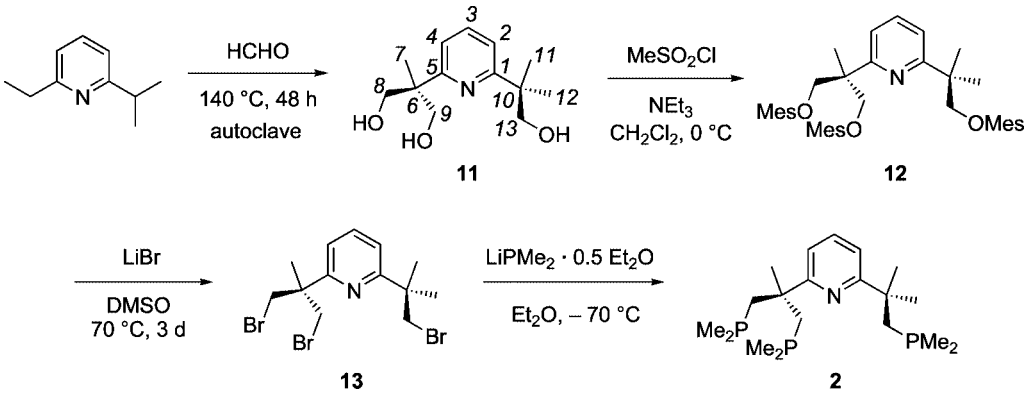


Scheme 2. Preparation of the tripodal tetradentate ligand **2**.

temperature. The trialcohol **11** is then successively transformed into the mesylate **12**, the bromide **13** and, upon treatment with lithium dimethylphosphide according to a procedure described by Karsch et al.,[6] into the triphosphane **2**. The intermediacy of the tribromide **13** is mandatory, as we found the mesylate, in a manner similar to the tosylated derivative, does not react cleanly with dimethylphosphide.

The reaction of **2** with $Ni(BF_4)_2{\cdot}6H_2O$ in anhydrous acetonitrile initially gives the $CH_3CN$-coordinated complex **14** (Scheme 3); when reaction mixtures are allowed to stand for several days, solvate water initiates hydrolysis of the coordinated, and hence activated, nitrile,[12] to give the acetamide complex **15**. Freshly prepared nitrile complex **14** is transformed into the bromo complex **16** upon treatment with lithium bromide in methanol (Scheme 3). In every one of the complexes **14**–**16**, the chelate ligand **2** is tridentate, with an uncoordinated pyridine nitrogen atom, and there is one additional monodentate ligand (acetonitrile, acetamide or bromide). The solid-state structures (Figures 6, 7 and 8, respectively) show the nickel ion in a coordination geometry intermediate between square planar and tetrahedral, with varying degrees of distortion. The following discussion applies to all three complexes, with complex **14** singled out for reference.

The exocyclic methyl substituents (**14**: C13, C14) are in different stereochemical environments, which makes the complex topologically chiral. It is diamagnetic in acetonitrile solution, as may be inferred from its fully assigned NMR spectra (see Exp. Sect. and Figure 6 for the numbering scheme used). Significantly, in solution at ambient temperature and on the NMR timescale, the cation has $C_s$ symmetry, as indicated by the equivalence of the phosphanyl substituents P1 and P2, the methyl groups C13/14 (radiating from the quaternary carbon atom C2) and the methyl substituents C11/12 on P3. We are currently investigating whether or not the implied stereochemical flexibility of the P3-substituted ligand arm can be "frozen" in solution by

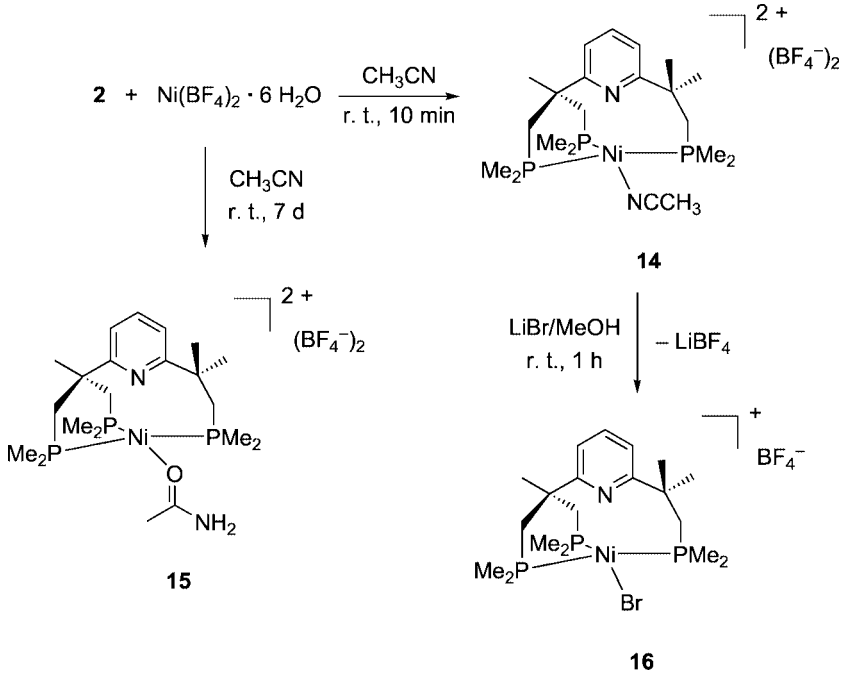


Scheme 3. Nickel(II) complexes of the tripodal ligand **2**.

 © 2006 Wiley-VCH Verlag GmbH & Co. KGaA, Weinheim 

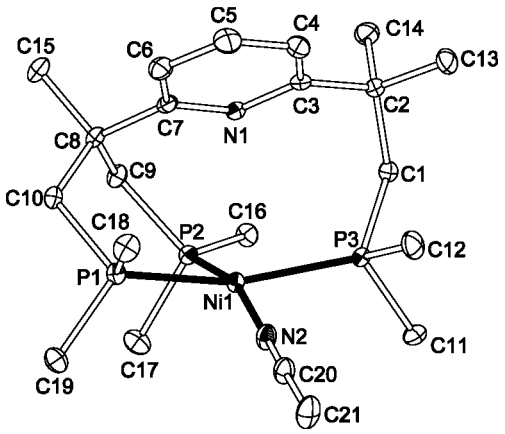


Figure 6. Structure of the dication in **14** (tetrafluoroborate salt).

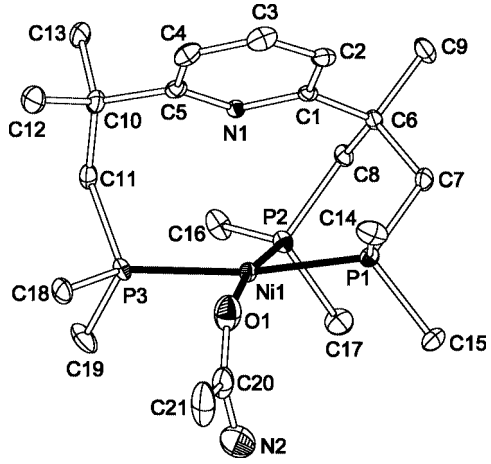


Figure 7. Structure of the dication in **15** (tetrafluoroborate salt).

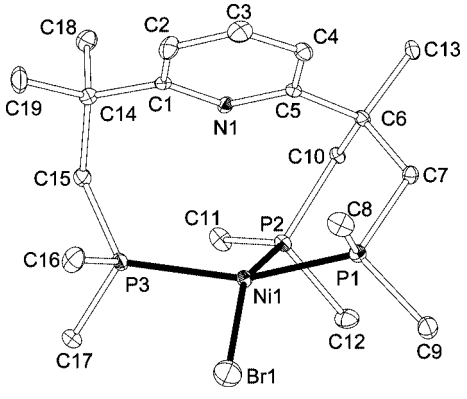


Figure 8. Structure of the dication in **16** (tetrafluoroborate salt).

forcing the pyridine nitrogen atom to coordinate to the central metal: this would cause the newly formed –N1–C3–C2–C1–P3–M– chelate ring to adopt a boat conformation, which would force either the methyl group C13 or the methyl group C14 into closer proximity to the metal and thus make C2 a stereogenic centre, as in structurally related iron(II) complexes.[5] The nickel–phosphorus bond lengths are within the normal range (Table 3), with the bond *trans* to the monodentate ligand being the shortest in each complex. This resembles the situation in a structurally related chloro complex of the phenyl-substituted tetrapodal ligand $\mathbf{1}_{Ph}$,[4] in which one phosphane arm, in addition to the pyridine nitrogen atom, is uncoordinated. The non-bonded distances between nickel(II) and the pyridine nitrogen atom are similar in complexes **14**–**16**, ranging from 2.9 to 3.1 Å (Table 3).

Table 3. Selected bond distances [Å] and angles [°] in **14**, **15** and **16** (standard deviations in parentheses).

| Distance or angle | **14** | **15** | **16** |
|---|---|---|---|
| Ni1–P1 | 2.2345(7) | 2.2302(10) | 2.2128(16) |
| Ni1–P2 | 2.1808(7) | 2.1926(10) | 2.1492(15) |
| Ni1–P3 | 2.2437(7) | 2.2208(10) | 2.2409(16) |
| Ni1–N2 (O1) (Br1) | 1.890(2) | 1.919(3) | 2.3088(10) |
| Ni1···N1 | 3.010(2) | 2.869(3) | 3.128 (10) |
| N2–C20 | 1.132(3) | – | – |
| O1–C20 | – | 1.272(5) | – |
| P1–Ni1–P2 | 89.82(3) | 89.35(4) | 89.72(6) |
| P2–Ni1–P3 | 98.12(3) | 96.39(4) | 99.33(6) |
| P3–Ni1–N2 (O1), (Br1) | 89.31(7) | 88.78(9) | 92.83(5) |
| P1–Ni1–N2 (O1), (Br1) | 88.07(7) | 86.88(10) | 90.58(5) |
| P3–Ni1–P1 | 161.23(3) | 168.70(4) | 155.30(6) |
| P2–Ni1–N2 (O1), (Br1) | 162.29(7) | 170.82(11) | 149.77(6) |
| Ni1–N2–C20 | 179.1(2) | – | – |
| Ni1–O1–C20 | – | 129.6(3) | – |
| N2–C20–C21 | 178.6(3) | – | – |
| O1–C20–C21 | – | 122.8(5) | – |

## Conclusions

Approximately square-pyramidal nickel(II) and cobalt(II) complexes are obtained with the pyridine-derived tetraphosphane ligand $C_5H_3N[CMe(CH_2PMe_2)_2]_2$ ($\mathbf{1}_{Me}$), its $NP_4$ donor set being fully employed in coordination. The formal replacement of one dimethylphosphanyl group in $\mathbf{1}_{Me}$ by a hydrogen atom gives the new ligand $C_5H_3N[CMe(CH_2PMe_2)_2][CMe_2(CH_2PMe_2)]$ (**2**) which, in a series of nickel(II) complexes, acts as a chelating triphosphane, with no involvement of the pyridine nitrogen atom in coordination. Instead, two ten-membered chelate rings are formed. This contrasts sharply with the situation in a series of iron(II) complexes,[5] where **2**, formed in situ by cleavage of one of the $PMe_2$ substituents in $\mathbf{1}_{Me}$, coordinates through its complete $NP_3$ donor set. This forces one of the $CMe_2$ methyl substituents into close proximity to the metal and allows it to act as an agostic two-electron donor.

## Experimental Section

***CAUTION!*** The perchlorate complexes **4** and **6** (and possibly also **10**) are explosive in the solid state. They explode when put under mechanical stress (e.g., upon tapping with a metal spatula). They are to be prepared in quantities not exceeding 150 mg, and the utmost care is to be exercised in their handling.

**Materials and Instrumentation:** Unless noted otherwise, all reactions were carried out at room temperature in dried solvents under dry dinitrogen, using standard Schlenk techniques. $\mathbf{1}_{Me}$ and **3** were

 © 2006 Wiley-VCH Verlag GmbH & Co. KGaA, Weinheim 

prepared as described in the literature.[5] $Co(BF_4)_2{\cdot}6H_2O$, $Co(ClO_4)_2{\cdot}6H_2O$, $Ni(BF_4)_2{\cdot}6H_2O$, and $Ni(ClO_4)_2{\cdot}6H_2O$ were purchased from Aldrich and used without further purification. Carbon monoxide (99.997%) and nitrogen monoxide (99.99%) were purchased from Air Liquide, and 2-ethyl-6-isopropylpyridine was purchased from Alfa Aesar. The IR spectra of solids were measured using KBr disks. IR spectra were assigned on the basis of literature data.[11] Spectroscopic data were obtained using the following instruments: IR spectroscopy: Nicolet Magna System 750; mass spectrometry: Varian 311A, Bruker Daltonics Esquire 3000+ and Voyager-DE Biospectrometry Workstation, PerSeptive Biosystems; NMR spectroscopy: Bruker ARX 200 and Bruker ARX 400. Signs of coupling constants in the $^1H$, $^{13}C$, $^{19}F$, and $^{31}P$ spectra were not determined. The atom numbering (superscripts) used for NMR assignments of compounds **2** and **11**–**13** follows the numbering scheme adopted for compound **11** (Scheme 2). The atom numbering (superscripts) used for NMR assignments of compounds **14** and **16** follows the labelling of the X-ray crystal structure of the compounds (Figures 6 and 8, respectively). Elemental analyses were carried out using a Thermo Finnigan, Flash EA, 1112 Series analyser.

**Preparation of 2:** A solution of **13** (1.2 g, 2.7 mmol) in diethyl ether (25 mL) was added from a dropping funnel over a period of 1 h at –70 °C to a suspension of $LiPMe_2{\cdot}0.5Et_2O$ (1.0 g, 9.5 mmol) in diethyl ether (20 mL). The mixture was warmed to room temperature overnight. The colour changed from brown to red, and all solid dissolved. After distilling off the solvent, the yellow residue was treated with pentane (25 mL) and filtered. The light-yellow solution was dried to yield a colourless oil (0.8 g, 83%). EI-MS (70 eV): *m/z* (%) 356 (100) $[M - CH_3]^+$. $^1H$ NMR (200 MHz, [D$_8$]-THF, 25 °C, TMS): $\delta$ = 7.53 (t, $^3J_{H,H}$ = 7.8 Hz, 1 H, *H*$^3$), 7.15 (d, $^3J_{H,H}$ = 7.9 Hz, 1 H, *H*$^2$), 7.13 (d, $^3J_{H,H}$ = 7.9 Hz, 1 H, *H*$^4$), 2.14–1.86 (ddd, AB, $^2J_{H,H}$ = 10.7, $^2J_{P,H}$ = 3.5 Hz, 4 H, *H*$^{8,9}$), 1.87 (d, $^2J_{P,H}$ = 3.4 Hz, 2 H, *H*$^{13}$), 1.57 (s, 3 H, *H*$^7$), 1.44 (s, 6 H, *H*$^{11,12}$), 0.85–0.63 (3 × d, $^2J_{P,H}$ = 3.2 Hz 18 H, PC*H*$_3$) ppm. $^{13}C\{^1H\}$ NMR (50.32 MHz, [D$_8$]THF, 25 °C, TMS): $\delta$ = 167.47 (s, 1 C, *C*$^1$), 165.83 (s, 1 C, *C*$^5$), 136.81 (s, 1 C, *C*$^3$), 118.17 (s, 1 C, *C*$^2$), 117.48 (s, 1 C, *C*$^4$), 49.50 (m, 3 C, *C*$^{8,9,13}$), 44.73 (t, 1 C, *C*$^6$), 41.59 (d, 1 C, *C*$^{10}$), 29.63 (m, 2 C, *C*$^{11,12}$), 26.48 (m, 1 C, *C*$^7$), 16.18 (m, 6 C, P*C*H$_3$) ppm. $^{31}P\{^1H\}$ NMR (80.95 MHz, [D$_8$]THF, 25 °C, 85% $H_3PO_4$): $\delta$ = –61.84 [s, 1 × *P*(Me$_2$)], –62.06 [s, 2 × *P*(Me$_2$)] ppm.

**Preparation of 4:** A solution of $Ni(ClO_4)_2{\cdot}6H_2O$ (87 mg, 0.239 mmol) in methanol (2.0 mL) was added over a period of 10 min at room temperature with stirring to a solution of **1** (103 mg, 0.239 mmol) in methanol (1.5 mL). The colour of the solution changed immediately from green to red, and a red microcrystalline precipitate began to form. After three days of continued stirring, the product was filtered off, washed with methanol (3 × 1.0 mL) and dried in vacuo to yield a red solid (148 mg, 90%). $C_{21}H_{41}Cl_2NNiO_8P_4$ (689.05): calcd. C 36.60, H 6.00, N 2.03; found C 36.92, H 5.81, N 1.97. IR (KBr): $\tilde{\nu}$ = 2977 m, 2922 m, 1572 m, 1454 s, 1424 m, 1300 m, 1091 vs ($ClO_4^-$), 944 s, 918 s, 622 s cm$^{-1}$. MALDI-TOF MS: *m/z* (%) 490 (100) $[(py\{PMe_2\}_4)Ni]^+$. $^1H$ NMR (200 MHz, [D$_3$]acetonitrile, 25 °C, TMS): $\delta$ = 8.11 (t, $^3J_{H,H}$ = 7.9 Hz, 1 H, *para-H*), 7.88 (d, $^3J_{H,H}$ = 8.0 Hz, 2 H, *meta-H*), 2.37–2.29 (m, 8 H, C*H*$_2$), 1.83 (s, 6 H, C*H*$_3$), 1.74 (m, 24 H, PC*H*$_3$) ppm. $^{13}C\{^1H\}$ NMR (50.32 MHz, [D$_3$]acetonitrile, 25 °C, TMS): $\delta$ = 165.68 (s, 2 C, *ortho-C*), 141.89 (s, 1 C, *para-C*), 125.26 (s, 2 C, *meta-C*), 44.79 (s, 2 C, *C*CH$_2$), 36.72 (m, 4 C, *C*H$_2$), 33.07 (m, 2 C, *C*H$_3$), 16.72 (m, 8 C, P*C*H$_3$) ppm. $^{31}P\{^1H\}$ NMR (80.95 MHz, [D$_3$]acetonitrile, 25 °C, 85% $H_3PO_4$): $\delta$ = –13.16 [m, 2 × *P*(Me$_2$)], –14.97 [m, 2 × *P*(Me$_2$)] ppm.

**Compound 5:** The procedure is similar to the preparation of compound **4** but with $Ni(BF_4)_2{\cdot}6H_2O$ (114 mg, 0.336 mmol) and **1** (145 mg, 0.336 mmol). Complex **5** was isolated as a red microcrystalline solid; yield: 203 mg (91%). $C_{21}H_{41}B_2F_8NNiP_4$ (663.75): calcd. C 38.00, H 6.23, N 2.11; found C 37.71, H 5.85, N 2.11. IR (KBr): $\tilde{\nu}$ = 2978 m, 2929 m, 1575 m, 1453 s, 1425 m, 1306 m, 1055 vs ($BF_4^-$), 946 s, 916 s, 520 m cm$^{-1}$. MALDI-TOF MS: *m/z* (%) 490 (100) $[(py\{PMe_2\}_4)Ni]^+$. $^1H$ NMR (200 MHz, [D$_3$]acetonitrile, 25 °C, TMS): $\delta$ = 8.12 (t, $^3J_{H,H}$ = 7.9 Hz, 1 H, *para-H*), 7.88 (d, $^3J_{H,H}$ = 8.0 Hz, 2 H, *meta-H*), 2.38–2.30 (m, 8 H, C*H*$_2$), 1.81 (s, 6 H, C*H*$_3$), 1.71 (m, 24 H, PC*H*$_3$) ppm. $^{13}C\{^1H\}$ NMR (50.32 MHz, [D$_3$]acetonitrile, 25 °C, TMS): $\delta$ = 165.65 (s, 2 C, *ortho-C*), 141.91 (s, 1 C, *para-C*), 125.27 (s, 2 C, *meta-C*), 44.80 (s, 2 C, *C*CH$_2$), 36.71 (m, 4 C, *C*H$_2$), 33.11 (m, 2 C, *C*H$_3$), 16.73 (m, 8 C, P*C*H$_3$) ppm. $^{19}F\{^1H\}$ NMR (188.31 MHz, [D$_3$]acetonitrile, 25 °C, $CFCl_3$): $\delta$ = –147.88 (s, 4 F, $BF_4^-$) ppm. $^{31}P\{^1H\}$ NMR (80.95 MHz, [D$_3$]acetonitrile, 25 °C, 85% $H_3PO_4$): $\delta$ = –13.15 [m, 2 × *P*(Me$_2$)], –14.99 [m, 2 × *P*(Me$_2$)] ppm.

**Compound 6:** The procedure is similar to the preparation of compound **4** but with $Co(ClO_4)_2{\cdot}6H_2O$ (55 mg, 0.15 mmol) and **1** (65 mg, 0.15 mmol). The reaction mixture changed colour from pink to brown and gave an olive-green microcrystalline precipitate; reaction time: five days. The product is an olive-green microcrystalline solid. Yield: 90 mg (87%). $C_{21}H_{41}Cl_2CoNO_8P_4$ (689.29): calcd. C 36.59, H 6.00, N 2.03; found C 36.82, H 6.02, N 2.02. IR (KBr): $\tilde{\nu}$ = 2978 m, 2923 m, 1573 m, 1453 s, 1424 m, 1299 m, 1089 vs ($ClO_4^-$), 944 s, 918 s, 622 s cm$^{-1}$. MALDI-TOF MS: *m/z* (%) 490 (80) $[(py\{PMe_2\}_4)Co]^+$, 430 (100) $[M - H - Co]^+$.

**Compound 7:** The procedure is similar to the preparation of compound **4** but with $Co(BF_4)_2{\cdot}6H_2O$ (328 mg, 0.962 mmol) in methanol (4.0 mL) and **1** (415 mg, 0.962 mmol) in methanol (5.0 mL); addition time: 20 min at room temperature; observed colours as for compound **6**; reaction time: five days. The product is an olive-green microcrystalline solid. Yield: 543 mg (85%). $C_{21}H_{41}B_2CoF_8NP_4$ (663.99): calcd. C 37.99, H 6.22, N 2.11; found C 37.84, H 6.03, N 2.00. IR (KBr): $\tilde{\nu}$ = 2975 m, 2924 m, 1574 m, 1454 s, 1426 m, 1300 m, 1054 vs ($BF_4^-$), 945 s, 919 s, 520 s cm$^{-1}$. MALDI-TOF MS: *m/z* (%) 490 (81) $[(py\{PMe_2\}_4)Co]^+$, 430 (100) $[M - H - Co]^+$. $^{31}P\{^1H\}$ NMR (80.95 MHz, [D$_4$]methanol, 25 °C, 85% $H_3PO_4$): $\delta$ = 48.12 [br., 4 × *P*(Me$_2$)] ppm.

**Preparation of 8:** Nitrogen monoxide was bubbled through a solution of **1** (110 mg, 0.255 mmol) in diethyl ether (8.0 mL) at approximately 0 °C for three minutes. A white microcrystalline powder precipitated, which was filtered off and washed with diethyl ether (3 × 2.5 mL) to yield a white solid (124 mg, 98%). $C_{21}H_{41}NO_4P_4$ (495.45): calcd. C 50.91, H 8.34, N 2.83; found C 50.71, H 8.25, N 2.78. IR (KBr): $\tilde{\nu}$ = 2978 m, 2911 m, 1653 m, 1574 m, 1457 s, 1420 m, 1384 s, 1295 s, 1161 vs (P=O), 941 s, 875 s, 745 m cm$^{-1}$. EI-MS (70 eV): *m/z* (%) 494 (100) $[M - H]^+$. $^1H$ NMR (200 MHz, [D$_3$]-acetonitrile, 25 °C, TMS): $\delta$ = 7.78 (t, $^3J_{H,H}$ = 7.5 Hz, 1 H, *para-H*), 7.44 (d, $^3J_{H,H}$ = 7.6 Hz, 2 H, *meta-H*), 2.69–2.61 (dd, AB, $^2J_{H,H}$ = 6.0 Hz, 8 H, C*H*$_2$), 1.86 (s, 6 H, CC*H*$_3$), 1.35–1.28 (2 d, $^2J_{P,H}$ = 2.4 Hz, 24 H, PC*H*$_3$) ppm. $^{31}P\{^1H\}$ NMR (80.95 MHz, [D$_3$] acetonitrile, 25 °C, 85% $H_3PO_4$): $\delta$ = 44.95 [s, 4 × *P*(O)Me$_2$] ppm.

**Preparation of 9:** A solution of **7** (160 mg, 0.241 mmol) in acetonitrile (3.0 mL) was refluxed in air for five minutes, then placed in a Dewar vessel filled with hot water (80 °C), and the complete setup cooled to 2 °C in a refrigerator. This produced a few single crystals of **9**·2CH$_3$CN within 7 d. Due to lack of material, the crystals were characterised solely by X-ray crystallography.

**Preparation of 10:** A brownish solution of 6 (105 mg, 0.152 mmol) in methanol (6.0 mL) was cooled in an ice bath, and a stream of

 © 2006 Wiley-VCH Verlag GmbH & Co. KGaA, Weinheim 

carbon monoxide was passed through the solution for five seconds. The colour of the solution darkened, and stirring was continued for a further ten minutes. The solvent was then evaporated, and the residue washed with a 1:2 mixture of methanol and diethyl ether (3 × 1.5 mL) to yield a brown solid (61 mg, 54%). $C_{23}H_{41}Cl_2CoNO_{10}P_4$ (745.31): calcd. C 37.06, H 5.54, N 1.88; found C 36.82, H 5.66, N 1.98. IR (KBr): $\tilde{\nu}$ = 2983 m, 2921 m, 1988 vs (CO), 1937 vs (CO), 1575 s, 1453 s, 1422 s, 1300 s, 1093 vs ($ClO_4^-$), 944 s (P–C, coordinated), 917 s (P–C, coordinated), 875 s (P–C, uncoordinated), 623 vs $cm^{-1}$. MALDI-TOF MS: *m/z* (%) 546 (28) $[M - H]^+$, 430 (100) $[M - H - Co - 2CO]^+$, 273.5 (18) $[M]^{2+}$.

**Preparation of 11:** An autoclave (volume: 2.1 L) was charged with 2-ethyl-6-isopropylpyridine (50 g, 0.33 mol) and an aqueous formaldehyde solution (37%, stabilised with 10% methanol; 250 mL, 3.30 mol) and the mixture heated to 140 °C for 48 h. After cooling to room temperature, the pressure was released and the solvent evaporated. The yellow oily residue was then heated to 100 °C for 24 h to remove excess formaldehyde. The residue was dissolved in trichloromethane (250 mL) and extracted with water (20 × 70 mL). The aqueous phase was separated, water removed on a rotary evaporator, and the remaining syrupy material dried for a further two days in vacuo at a temperature of 95 °C to yield a white solid, which was purified by washing with diethyl ether (27.7 g, 35%). $C_{13}H_{21}NO_3$ (239.31): calcd. C 65.25, H 8.84, N 5.75; found C 64.97, H 8.80, N 5.67. IR (KBr): $\tilde{\nu}$ = 3299 vs (OH), 2961 vs, 2873 vs, 1577 vs, 1461 vs, 1409 m,1042 vs, 1027 vs, 756 s $cm^{-1}$. EI-MS (70 eV): *m/z* (%) 239 (100) $[M]^+$. $^1$H NMR (400 MHz, [D$_1$]trichloromethane, 25 °C, TMS): $\delta$ = 7.66 (t, $^3J_{H,H}$ = 7.9 Hz, 1 H, $H^3$), 7.20 (d, $^3J_{H,H}$ = 8.0 Hz, 1 H, $H^2$), 7.17 (d, $^3J_{H,H}$ = 8.0 Hz, 1 H, $H^4$), 4.14 (br., 3 H, O$H$), 3.92–3.75 (dd, AB, $^2J_{H,H}$ = 11.2 Hz, 4 H, $H^{8,9}$), 3.66 (s, 2 H, $H^{13}$), 1.29 (s, 6 H, $H^{11,12}$), 1.17 (s, 3 H, $H^7$) ppm. $^{13}$C{$^1$H} NMR (100.64 MHz, [D$_1$]trichloromethane, 25 °C, TMS): $\delta$ = 165.23 (s, 1 C, $C^1$), 163.27 (s, 1 C, $C^5$), 137.56 (s, 1 C, $C^3$), 118.95 (s, 1 C, $C^2$), 118.66 (s, 1 C, $C^4$), 71.83 (s, 1 C, $C^{13}$), 69.38 (s, 2 C, $C^{8,9}$), 45.97 (s, 1 C, $C^6$), 42.01 (s, 1 C, $C^{10}$), 24.95 (s, 2 C, $C^{11,12}$), 19.89 (s, 1 C, $C^7$) ppm.

**Preparation of 12:** A solution of **11** (11.0 g, 0.046 mol) and triethylamine (29.2 mL, 0.207 mol) in dichloromethane (200 mL) was cooled to –2 °C, and a solution of methanesulfonyl chloride (12.8 mL, 0.166 mol) in dichloromethane (50 mL) added dropwise, taking care that the temperature did not exceed +2 °C. The resulting suspension was warmed to room temperature and stirred for one hour. The reaction product was washed successively with hydrochloric acid (1 N, 1 × 50 mL), water (1 × 50 mL), sodium carbonate solution (1 × 50 mL), brine (1 × 50 mL) and finally again with water (1 × 50 mL). After drying over $Na_2SO_4$ and evaporating the solvent, the residue was dried in vacuo to yield the product as a colourless oil (20.3 g, 93%). IR (KBr): $\tilde{\nu}$ = 3029 vs, 2976 vs, 2941 vs, 1578 vs, 1352 vs, 1172 vs, 958 vs, 528 vs $cm^{-1}$. EI-MS (70 eV): *m/z* (%) 394 (100) $[M - CH_3SO_2]^+$. $^1$H NMR (200 MHz, [D$_1$]trichloromethane, 25 °C, TMS): $\delta$ = 7.70 (t, $^3J_{H,H}$ = 8.0 Hz, 1 H, $H^3$), 7.27 (d, $^3J_{H,H}$ = 7.9 Hz, 1 H, $H^2$), 7.21 (d, $^3J_{H,H}$ = 7.9 Hz, 1 H, $H^4$), 4.63–4.52 (dd, AB, $^2J_{H,H}$ = 8.8 Hz, 4 H, $H^{8,9}$), 4.47 (s, 2 H, $H^{13}$), 2.96 (s, 6 H, $SO_2$-C$H_3$), 2.86 (s, 3 H, $SO_2$-C$H_3$), 1.50 (s, 3 H, $H^7$), 1.41 (s, 6 H, $H^{11,12}$) ppm. $^{13}$C{$^1$H} NMR (50.32 MHz, [D$_1$]trichloromethane, 25 °C, TMS): $\delta$ = 163.36 (s, 1 C, $C^1$), 158.42 (s, 1 C, $C^5$), 137.56 (s, 1 C, $C^3$), 119.13 (s, 1 C, $C^2$), 118.86 (s, 1 C, $C^4$), 77.64 (s, 1 C, $C^{13}$), 72.74 (s, 2 C, $C^{8,9}$), 45.14 (s, 1 C, $C^6$), 41.35 (s, 1 C, $C^{10}$), 36.84 (s, 2 C, $SO_2CH_3$), 36.74 (s, 1 C, $SO_2CH_3$), 24.57 (s, 2 C, $C^{11,12}$), 19.16 (s, 1 C, $C^7$) ppm.

**Preparation of 13:** Compound **12** (6.27 g, 0.013 mol) was dissolved in anhydrous dimethyl sulfoxide (150 mL) and heated to 70 °C. Vigorously dried (vacuo, 100 °C, 3 d) lithium bromide (5.17 g, 0.059 mol) was then added in one portion, and the solution stirred for two days at 70 °C. After cooling to room temperature, water (200 mL) was added, and the mixture stirred for 30 min. The milky solution was extracted with diethyl ether (7 × 70 mL), and the combined ether extracts washed with water (3 × 50 mL) to remove residual dimethyl sulfoxide. The organic phase was separated, dried with $Na_2SO_4$, and the solvent evaporated to give an oily, crude product. Column chromatography ($SiO_2$, 0.060–0.200 mm, pore diameter ca. 6 nm) using a combination of ethyl acetate and hexane (3:1) as eluent yielded the product as a colourless oil (3.1 g, 56%). IR (KBr): $\tilde{\nu}$ = 2969 vs, 2870 m, 1576 vs, 1458 vs, 1423 m, 1247 vs, 750 s $cm^{-1}$. EI-MS (70 eV): *m/z* (%) 416 (32) $[M - CH_3]^+$, 414 (98) $[M - CH_3]^+$, 412 (100) $[M - CH_3]^+$, 410 (34) $[M - CH_3]^+$. $^1$H NMR (200 MHz, [D$_1$]trichloromethane, 25 °C, TMS): $\delta$ = 7.66 (t, $^3J_{H,H}$ = 7.9 Hz, 1 H, $H^3$), 7.23 (d, $^3J_{H,H}$ = 7.9 Hz, 1 H, $H^2$), 7.18 (d, $^3J_{H,H}$ = 7.9 Hz, 1 H, $H^4$), 4.00–3.86 (dd, AB, $^2J_{H,H}$ = 10.0 Hz, 4 H, $H^{8,9}$), 3.80 (s, 2 H, $H^{13}$), 1.63 (s, 3 H, $H^7$), 1.49 (s, 6 H, $H^{11,12}$) ppm. $^{13}$C{$^1$H} NMR (50.32 MHz, [D$_1$]trichloromethane, 25 °C, TMS): $\delta$ = 164.07 (s, 1 C, $C^1$), 160.04 (s, 1 C, $C^5$), 137.07 (s, 1 C, $C^3$), 118.48 (s, 1 C, $C^2$), 118.36 (s, 1 C, $C^4$), 46.01 (s, 2 C, $C^{10,13}$), 42.10 (s, 3 C, $C^{6,8,9}$), 26.63 (s, 2 C, $C^{11,12}$), 23.09 (s, 1 C, $C^7$) ppm.

**Preparation of 14:** A solution of $Ni(BF_4)_2{\cdot}6H_2O$ (311 mg, 0.915 mmol) in acetonitrile (3.5 mL) was added over a period of 10 min at room temperature to a solution of **2** (340 mg, 0.915 mmol) in acetonitrile (2.5 mL). The solution changed colour immediately from green to red, and was stirred overnight. Diffusion of diethyl ether into this solution produced a red crystalline solid within 3 d. The product was filtered off and washed with diethyl ether (3 × 1.5 mL) to yield red crystals (442 mg, 75%). $C_{21}H_{39}B_2F_8N_2NiP_3$ (644.78): calcd. C 39.12, H 6.10, N 4.34; found C 39.09, H 6.19, N 4.30. IR (KBr): $\tilde{\nu}$ = 2970 s, 2932 s, 2292 m (CN), 1574 vs, 1426 vs, 1296 s, 1056 vs ($BF_4^-$), 948 vs, 920 vs, 520 s $cm^{-1}$. ESI-MS: *m/z* (%) 236 (100) $[M]^{2+}$. $^1$H NMR (400 MHz, [D$_3$]acetonitrile, 25 °C, TMS): $\delta$ = 7.88 (t, $^3J_{H,H}$ = 7.3 Hz, 1 H, $H^5$), 7.53 (d, $^3J_{H,H}$ = 7.2 Hz, 1 H, $H^6$), 7.52 (d, $^3J_{H,H}$ = 7.2 Hz, 1 H, $H^4$), 2.50–2.00 (2 × m, 4 H, C$H_2^{9,10}$), 2.46 (s, 2 H, C$H_2^1$), 1.96 (s, 3 H, C$H_3^{21}$), 1.53–1.50 (m, 6 H, PC$H_3^{16,18}$), 1.51 (s, 3 H, C$H_3^{15}$), 1.46–1.43 (m, 6 H, PC$H_3^{17,19}$), 1.45 (2 × s, 6 H, C$H_3^{13,14}$), 1.26–1.22 (m, 6 H, PC$H_3^{11,12}$) ppm. $^{13}$C{$^1$H} NMR (100.64 MHz, [D$_3$]acetonitrile, 25 °C, TMS): $\delta$ = 166.78 (s, 1 C, $C^3$), 162.87 (s, 1 C, $C^7$), 139.79 (s, 1 C, $C^5$), 122.26 (s, 1 C, $C^4$), 121.22 (s, 1 C, $C^6$), 43.80 (s, 1 C, $C^8$), 42.25 (s, 1 C, $C^2$), 41.38 (d, $^1J_{P,C}$ = 23.3 Hz, 1 C, $C^1$), 37.69 (m, 2 C, $C^{9,10}$), 32.86 (s, 2 C, $C^{13,14}$), 32.13 (s, 1 C, $C^{15}$), 16.66 (m, 2 C, P$CH_3^{11,12}$), 15.62 (m, 4 C, P$CH_3^{16-19}$), 1.75 (s, 1 C, $C^{21}$) ppm. $^{19}$F{$^1$H} NMR (188.31 MHz, [D$_3$]acetonitrile, 25 °C, $CFCl_3$): $\delta$ = –147.90 (s, 4 F, $BF_4^-$) ppm. $^{31}$P{$^1$H} NMR (80.95 MHz, [D$_3$]acetonitrile, 25 °C, 85% $H_3PO_4$): $\delta$ = –3.53 (d, $^2J_{P,P}$ = 70.5 Hz, 2 P, $P^{2,1}$), –8.64 (t, $^2J_{P,P}$ = 70.5 Hz, 1 P, $P^3$) ppm.

**Preparation of 15:** Prepared similar to **14**, from $Ni(BF_4)_2{\cdot}6H_2O$ (150 mg, 0.441 mmol); solvent: acetonitrile (3.0 mL); addition time: 10 min at room temperature; **2**: 190 mg, 0.512 mmol; solvent: acetonitrile (2.0 mL); observed colours as for compound **14**; reaction time: seven days; appearance of product: orange blocks. $C_{21}H_{41}B_2F_8N_2NiOP_3$ (662.79): calcd. C 38.06, H 6.24, N 4.23; found C 38.29, H 6.39, N 4.34. ESI-MS: *m/z* (%) 245 (100) $[M]^{2+}$.

**Preparation of 16:** A solution of **14** (115 mg, 0.178 mmol) and LiBr (16 mg, 0.18 mol) in methanol (4.5 mL) was stirred at room temperature for 1 h. The solvent was evaporated, the residual red solid dried in vacuo, stirred in diethyl ether (10 mL) for 10 min, the mixture filtered, and the remaining solid dried again in vacuo. Dif-

 © 2006 Wiley-VCH Verlag GmbH & Co. KGaA, Weinheim 

fusion of diethyl ether into a saturated solution of **16** in methanol produced a red microcrystalline solid, as well as single crystals, within 4 d. The single crystals were separated, and the polycrystalline material filtered off and washed with diethyl ether (3 × 1.0 mL) to yield a red solid (85 mg, 80%). $C_{19}H_{36}BBrF_4NNiP_3$ (596.83): calcd. C 38.24, H 6.08, N 2.35; found C 38.20, H 6.06, N 2.30. $^1H$

Table 4. Selected crystallographic data for **3**, **4**·$CHCl_3$, **7**·MeOH, **9**·2$CH_3CN$, **14**, **15** and **16**.

| | **3** | **4**·$CHCl_3$ | **7**·MeOH | **9**·2$CH_3CN$ |
|---|---|---|---|---|
| Formula | $C_{13}H_{17}Br_4N$ | $C_{22}H_{42}Cl_5NNiO_8P_4$ | $C_{22}H_{45}B_2CoF_8NOP_4$ | $C_{58}H_{106}B_6Co_3F_{24}N_{10}O_4P_8$ |
| $M_r$ [g mol$^{-1}$] | 506.92 | 808.41 | 696.04 | 1952.94 |
| Size [mm$^3$] | 0.20 × 0.19 × 0.17 | 0.60 × 0.18 × 0.12 | 0.50 × 0.25 × 0.20 | 0.62 × 0.40 × 0.18 |
| Colour | colourless | red | green | violet |
| $F$ (000) | 1936 | 3344 | 1772 | 4012 |
| Crystal system | orthorhombic | orthorhombic | orthorhombic | monoclinic |
| Space group | *Pbca* (no. 61) | *Pna*2$_1$ (no. 33) | *Pna*2$_1$ (no. 33) | *C*2/*c* (no. 15) |
| $a$ [Å] | 11.2917(18) | 21.794(4) | 22.6555(6) | 23.5131(9) |
| $b$ [Å] | 14.011(3) | 9.583(2) | 11.5947(3) | 11.0384(3) |
| $c$ [Å] | 20.701(4) | 32.694(5) | 11.8607(3) | 34.8349(11) |
| $\beta$ [°] | 90 | 90 | 90 | 99.759(2) |
| $V$ [Å$^3$] | 3275.2(10) | 6828.0(2) | 3115.6(1) | 8910.5(5) |
| $Z$ | 8 | 8 | 4 | 4 |
| $\rho_{calc}$ [g cm$^{-3}$] | 2.056 | 1.573 | 1.854 | 1.456 |
| $\mu$ [mm$^{-1}$] | 9.814 | 1.190 | 0.877 | 0.792 |
| Abs. correction | multi-scan | psi-scan | SADABS | SADABS |
| Temperature [K] | 173(2) | 180(2) | 293(2) | 293(2) |
| $T_{max}/T_{min}$ | 0.286/0.244 | 0.870/0.535 | 0.879/0.603 | 0.871/0.639 |
| Scan | ω and ψ | ω and ψ | ω and ψ | ω and ψ |
| 2$\Theta$ range [°] | 6.1–51.6 | 3.9–48.2 | 3.6–50.0 | 3.5–50.0 |
| Measured reflections | 10034 | 38301 | 19062 | 27646 |
| Unique reflections | 2663 | 10555 | 5290 | 7838 |
| Obsd. reflections[a] | 2077 | 8292 | 4561 | 5704 |
| Refined parameters | 165 | 761 | 380 | 657 |
| $wR2$ (all data)[b] | 0.0637 | 0.0634 | 0.1277 | 0.1426 |
| $R1$ (obs. data)[c] | 0.0375 | 0.0340 | 0.0525 | 0.0566 |
| $\rho_{fin}$ (max./min.) [e Å$^{-3}$] | 0.623/–0.491 | 0.654/–0.440 | 0.588/–0.511 | 0.609/–0.770 |
| Weighting scheme[d] | $k$ = 0.0289/$l$ = 3.5634 | $k$ = 0.0267/$l$ = 0.0000 | $k$ = 0.0654/$l$ = 4.5591 | $k$ = 0.0584/$l$ = 16.9833 |
| Abs. struct. parameter | – | 0.448(12) | 0.00(2) | – |

| | **14** | **15** | **16** |
|---|---|---|---|
| Formula | $C_{21}H_{39}B_2F_8N_2NiP_3$ | $C_{21}H_{41}B_2F_8N_2NiOP_3$ | $C_{19}H_{36}BBrF_4NNiP_3$ |
| $M_r$ [g mol$^{-1}$] | 644.78 | 662.80 | 596.83 |
| Size [mm$^3$] | 0.72 × 0.67 × 0.55 | 0.25 × 0.17 × 0.14 | 0.09 × 0.09 × 0.08 |
| Colour | yellow | orange | red |
| $F$ (000) | 2672 | 2752 | 1224 |
| Crystal system | orthorhombic | monoclinic | monoclinic |
| Space group | *Pbca* (no. 61) | *P*2$_1$/*n* (no. 14) | *P*2$_1$/*c* (no. 14) |
| $a$ [Å] | 13.391(3) | 19.419(2) | 12.6633(14) |
| $b$ [Å] | 18.763(3) | 15.591(1) | 11.845(4) |
| $c$ [Å] | 23.050(3) | 21.099(2) | 16.986(2) |
| $\beta$ [°] | 90 | 109.981(5) | 96.337(10) |
| $V$ [Å$^3$] | 5791.4(18) | 6003.4(9) | 2532.4(9) |
| $Z$ | 8 | 8 | 4 |
| $\rho_{calc}$ [g cm$^{-3}$] | 1.479 | 1.467 | 1.565 |
| $\mu$ [mm$^{-1}$] | 0.902 | 0.875 | 2.570 |
| Abs. correction | psi-scan | SADABS | multi-scan |
| Temperature [K] | 150(2) | 100(2) | 173(2) |
| $T_{max}/T_{min}$ | 0.637/0.563 | 0.880/0.745 | 0.821/0.802 |
| Scan | ω and ψ | ω and ψ | ω and ψ |
| 2$\Theta$ range [°] | 3.5–51.9 | 6.8–54.2 | 5.9–57.2 |
| Measured reflections | 15298 | 87231 | 13028 |
| Unique reflections | 5672 | 13166 | 3647 |
| Obsd. reflections[a] | 4501 | 9307 | 5505 |
| Refined parameters | 345 | 1006 | 281 |
| $wR2$ (all data)[b] | 0.0888 | 0.1278 | 0.1783 |
| $R1$ (obs. data)[c] | 0.0332 | 0.0482 | 0.0550 |
| $\rho_{fin}$ (max./min.) [e Å$^{-3}$] | 0.564/–0.657 | 0.812/–0.687 | 0.987/–1.979 |
| Weighting scheme[d] | $k$ = 0.0425/$l$ = 4.4217 | $k$ = 0.0415/$l$ = 16.7211 | $k$ = 0.1003/$l$ = 1.1743 |
| Abs. struct. parameter | – | – | – |

[a] With $F_o \geq 4\sigma(F)$. [b] $wR2 = (\{\Sigma[w(F_o^2 - F_c^2)^2]\}/\{\Sigma[w(F_o^2)^2]\})^{0.5}$. [c] $R1 = \Sigma||F_o| - |F_c||/\Sigma|F_o|$ for $F_o > 4\sigma(F)$. [d] $w = 1/[\sigma^2(F_o^2) + (k \cdot P)^2 + l \cdot P]$ and $P = (F_o^2 + 2F_c^2)/3$.

 © 2006 Wiley-VCH Verlag GmbH & Co. KGaA, Weinheim 

NMR (400 MHz, [D$_4$]methanol, 25 °C, TMS): $\delta$ = 8.16 (t, $^3J_{H,H}$ = 7.3 Hz, 1 H, $H^3$), 7.83 (d, $^3J_{H,H}$ = 7.3 Hz, 1 H, $H^4$), 7.81 (d, $^3J_{H,H}$ = 7.3 Hz, 1 H, $H^2$), 2.39–1.90 (2×m, 4 H, C$H_2^{7,10}$), 2.28 (s, 2 H, C$H_2^{15}$), 1.87 (s, 3 H, C$H_3^{13}$), 1.81 (s, 6 H, C$H_3^{18,19}$), 1.72–1.65 (m, 6 H, PC$H_3^{8,11}$), 1.59–1.53 (m, 6 H, PC$H_3^{9,12}$), 0.74–0.69 (m, 6 H, PC$H_3^{16,17}$) ppm. $^{13}$C{$^1$H} NMR (100.64 MHz, [D$_4$]methanol, 25 °C, TMS): $\delta$ = 168.52 (s, 1 C, $C^1$), 167.97 (s, 1 C, $C^5$), 143.09 (s, 1 C, $C^3$), 124.86 (s, 1 C, $C^2$), 123.79 (s, 1 C, $C^4$), 43.58 (s, 1 C, $C^6$), 42.75 (s, 1 C, C$^{14}$), 38.68 (m, 1 C, $C^{15}$), 38.24 (m, 2 C, $C^{7,10}$), 32.52 (s, 2 C, $C^{18,19}$), 31.16 (s, 1 C, $C^{13}$), 15.44 (m, 2 C, P$C$H$_3^{16,17}$), 14.38 (m, 4 C, P$C$H$_3^{8,9,11,12}$) ppm. $^{19}$F{$^1$H} NMR (188.31 MHz, [D$_4$]-methanol, 25 °C, CFCl$_3$): $\delta$ = –147.92 (s, 4 F, B$F_4^-$) ppm. $^{31}$P{$^1$H} NMR (80.95 MHz, [D$_4$]methanol, 25 °C, 85% H$_3$PO$_4$): $\delta$ = 3.00 (d, $^2J_{P,P}$ = 83.6 Hz, 2 P, $P^{2,1}$), –0.90 (t, $^2J_{P,P}$ = 83.6 Hz, 1 P, $P^3$) ppm.

**X-ray Crystallography for Compounds 3, 4, 5, 7, 9, 14, 15 and 16:** Colourless single crystals of "pyBr$_4$" (**3**) formed upon keeping the oily product under oil pump vacuum for three weeks. Red single crystals of [(py{PMe$_2$}$_4$)Ni](ClO$_4$)$_2$·CHCl$_3$ (**4**·CHCl$_3$) were obtained within 10 d by isothermal diffusion of diethyl ether into a saturated solution of the reaction product in chloroform. Red crystals of [(py{PMe$_2$}$_4$)Ni](BF$_4$)$_2$·MeOH (**5**·MeOH) and green crystals of [(py{PMe$_2$}$_4$)Co](BF$_4$)$_2$·MeOH (**7**·MeOH) were similarly obtained by isothermal diffusion of diethyl ether into a saturated solution of the reaction product in methanol within a few days. Violet blocks of [{(py{PMe$_2$}$_2${OPMe$_2$}$_2${CH$_3$CN}$_3$)Co}$_2$Co](BF$_4$)$_6$·2CH$_3$CN (**9**·2 CH$_3$CN) formed after a solution of the reaction product in acetonitrile had been saturated hot and subsequently cooled to 2 °C. Single crystals of [(py{PMe$_2$}$_3$CH$_3$CN)Ni](BF$_4$)$_2$ (yellow, **14**), [(py{PMe$_2$}$_3$CH$_3$CONH$_2$)Ni](BF$_4$)$_2$ (orange, **15**) and [(py{PMe$_2$}$_3$Br)Ni](BF$_4$) (red, **16**) were obtained by isothermal diffusion of diethyl ether into an acetonitrile (**14** and **15**) or a methanol (**16**) solution. Crystal data for compounds **3**, **4**·CHCl$_3$, **5**·MeOH, **9**·2 CH$_3$CN, **14**, **15** and **16** are given in Table 4, and selected distances and angles are listed in Tables 1–3. Structures are presented in Figures 1–8. Compounds **4**, **5** and **7** are isostructural. Intensity data for **4**·CHCl$_3$ and **14** were collected on a Stoe Stadi 4 diffractometer; data for **5**·MeOH, **7**·MeOH and **9**·2 CH$_3$CN were collected on a SMART CCD diffractometer; data for **15** were collected on a Bruker-Nonius KappaCCD diffractometer and data for **3** and **16** on a Oxford Diffraction Xcalibur S Sapphire diffractometer using Mo-$K_a$ radiation ($\lambda$ = 0.71073 Å, graphite monochromator) in all cases. The structures were solved by direct methods using SHELXS-97[13] or SIR 97[14] and were refined on $F^2$ using SHELXL-97.[15] All non-hydrogen atoms were refined anisotropically. Hydrogen atoms were placed in calculated positions using a riding model. SADABS[16] was used to perform area detector scaling absorption corrections, as applicable (Table 4). The absolute structure in non-centrosymmetric space groups was determined with SHELXL-97 according to Flack.[13] The geometrical features of the structures were analysed using the DIAMOND programme.[17]

CCDC-608569 (for **3**), -608571 (for **4**·CHCl$_3$), -608566 (for **5**·MeOH), -608567 (for **7**·MeOH), -608568 (for **9**·2 CH$_3$CN), -608564 (for **14**), -608565 (for **15**) and -608570 (for **16**) contain the supplementary crystallographic data. These data can be obtained free of charge from The Cambridge Crystallographic Data Centre via www.ccdc.cam.ac.uk/data_request/cif.

## Acknowledgments

Financial support of this work by the Deutsche Forschungsgemeinschaft (SPP 1118) is gratefully acknowledged. We are indebted to Dr. Ziemer (Humboldt-Universität zu Berlin) for the structural characterisation of compounds **4** and **14**.

[1] a) *Applied Homogeneous Catalysis with Organometallic Compounds*, vol. 1 (Eds.: B. Cornils, W. A. Herrmann), VCH, Weinheim, **1996**; b) G. W. Parshall, S. D. Ittel, *Homogeneous Catalysis*, 2nd ed., Wiley, New York, **1992**.
[2] M. E. van der Bloom, D. Milstein, *Chem. Rev.* **2003**, *103*, 1759.
[3] A. Grohmann, *Adv. Inorg. Chem.* **2004**, *56*, 179.
[4] C. Zimmermann, F. W. Heinemann, A. Grohmann, *Eur. J. Inorg. Chem.* **2005**, 3506.
[5] S. W. Kohl, F. W. Heinemann, M. Hummert, W. Bauer, A. Grohmann, *Chem. Eur. J.* **2006**, *12*, 4313.
[6] H. H. Karsch, A. Appelt, *Z. Naturforsch., Teil B* **1983**, *38*, 1399.
[7] P. Klaboe, B. Klewe, K. Martinsen, C. J. Nielsen, D. L. Powell, D. J. Stubbles, *J. Mol. Struct.* **1986**, *140*, 1.
[8] C. Dietz, F. W. Heinemann, J. Kuhnigk, C. Krüger, M. Gerdan, A. X. Trautwein, A. Grohmann, *Eur. J. Inorg. Chem.* **1998**, 1041.
[9] S. Berger, S. Braun, H.-O. Kalinowski, *NMR-Spektroskopie von Nichtmetallen*, vol. 3, $^{31}$P-NMR-Spektroskopie, Thieme, Stuttgart, **1993**, p. 53.
[10] K. Heinze, G. Huttner, L. Zsolnai, *Chem. Ber./Recueil* **1997**, *130*, 1393.
[11] G. Socrates, *Infrared Characteristic Group Frequencies*, 2nd ed., Wiley, New York, **1994**.
[12] E. C. Constable, *Metals and Ligand Reactivity*, VCH, Weinheim, **1996**, p. 65.
[13] G. M. Sheldrick, *SHELXS-97 Program for the Solution of Crystal Structures*, University of Göttingen, Germany, **1990**.
[14] A. Altomare, M. C. Burla, M. Camalli, G. L. Cascarano, C. Giacovazzo, A. Guagliardi, A. G. G. Moliterni, G. Polidori, R. Spagna, *J. Appl. Crystallogr.* **1999**, *32*, 115.
[15] G. M. Sheldrick, *SHELXL-97 Program for the Refinement of Crystal Structures*, University of Göttingen, Germany, **1997**.
[16] H. D. Flack, *Acta Crystallogr., Sect. A* **1983**, *39*, 876; G. Bernardinelli, H. D. Flack, *Acta Crystallogr., Sect. A* **1985**, *41*, 500.
[17] G. M. Sheldrick, *SADABS Program for Empirical Absorption Correction of Area Detector Data*, University of Göttingen, Germany, **1996**.

Received: June 7, 2006
Published Online: August 10, 2006

 © 2006 Wiley-VCH Verlag GmbH & Co. KGaA, Weinheim 

DOI: 10.1002/ejic.200600592

# Testing Phosphanes in the Palladium-Catalysed Allylation of Secondary and Primary Amines

Claire Thoumazet,[a] Hansjörg Grützmacher,[b] Bernard Deschamps,[a] Louis Ricard,[a] and Pascal le Floch*[a]

**Keywords:** Allylation / Amines / Catalysis / Palladium / Phosphorus

The electronic nature of the ligand plays a crucial role in the palladium-catalysed allylation of amines with allylic alcohols. The better the ligand is as a π acceptor, the more active the catalyst. Experiments with a series with mono- and bidentate ligands featuring phosphanes and phospholes applied in the catalytic allylation of aniline clearly demonstrate this. Bolstered by DFT calculations, we have devised a new efficient catalyst for this process which carries the strong π acceptor 1,2,5-triphenylphosphole as a ligand.

(© Wiley-VCH Verlag GmbH & Co. KGaA, 69451 Weinheim, Germany, 2006)

## Introduction

Carbon–nitrogen bond formation is a major challenge in organic synthesis for the preparation of nitrogen containing molecules of biological and physiological interest.[1] Among various metal promoted catalytic processes, the Tsuji–Trost[1a,2] coupling reaction involving the reaction of a nucleophile with a transient allyl palladium complex proves to be one of the most straightforward routes towards allylamines. Various nucleophiles and protected allylic alcohols can be employed and this reaction usually proceeds with good conversion under mild conditions.[3] However, as in other allylic alkylation processes, the presence of a good leaving group such as carboxylate, carbonate, phosphate or other related derivatives on the allylic moiety is a prerequisite in most cases in order to obtain sufficient activity. From a practical, economical and environmental point of view an interesting goal consists of directly using allylic alcohols as alkylating agents.[4] This approach has been explored by Tamaru as well as Ozawa and Yoshifuji in 2002. Tamaru et al. showed that classical palladium(0) complexes, such as $Pd(PPh_3)_4$ and $Pd(OAc)_2/PnBu_3$, could be employed as catalysts for the allylation of primary and secondary amines using a variable amount of $BEt_3$ (between 0.3 and 2.4 equiv.) as a cocatalyst. The group of Ozawa demonstrated that DPCB Pd(allyl) complexes (DPCB stands for diphosphanylidenecyclobutene ligands) efficiently catalyse the coupling between aniline derivatives and allylic alcohols in the presence of $MgSO_4$ as a water scavenger to afford the corresponding allylamines in good yields (Scheme 1).[4a–4d] Recently, we showed that allyl palladium complexes of mixed bidentate P-S ligands featuring a phosphabarrelene moiety and a diphosphanyl sulfide pendant arm are efficient catalysts for the bis(allylation) of primary amines under mild conditions.[5]

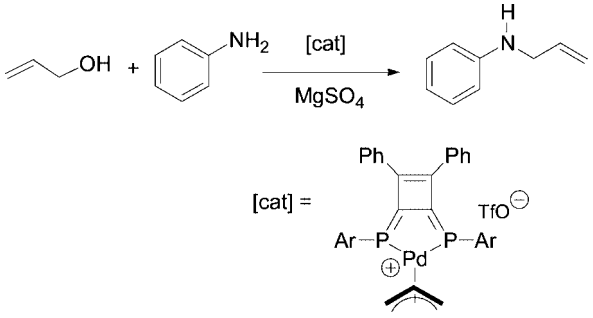


Scheme 1. Allylation of primary amines by DPCB based complexes.

Though the mechanism of this new catalytic process has not been explored in detail, the experimental results suggest that the π accepting capacity of the ligand likely plays a decisive role in the outcome of the reaction. That is, the stronger the π accepting capacity, the faster the process. In this article we report on the use of mono- and bidentate ligands in this allylation process and show through DFT calculations that the electronic nature of the phosphane indeed plays a crucial role. As will be seen, these studies led

[a] Laboratoire "Hétéroéléments et Coordination" UMR CNRS 7653, École Polytechnique,
91128 Palaiseau Cedex, France
Fax: +33-1-69-33-39-90
E-mail: lefloch@poly.polytechnique.fr
[b] Department of Chemistry and Applied Biosciences (D-CHAB), ETH Hönggerberg,
Wolfgang-Pauli Str., 8093 Zürich, Switzerland
Fax: +41-1-633-10.32
E-mail: gruetzmacher@inorg.chem.eth.ch
Supporting information for this article is available on the WWW under http://www.eurjic.org or from the author.

 © 2006 Wiley-VCH Verlag GmbH & Co. KGaA, Weinheim 

us to devise a new efficient catalyst featuring the easily available 1,2,5-triphenylphosphole[6] as a ligand.

## Results and Discussion

### Synthesis of Complexes

All experiments were carried out using cationic palladium(allyl) complexes as precursors. As neutral donor ligands, various acyclic and cyclic phosphanes and one 1,4-diazabutadiene ligand **1** (Ar = 2,6-diisopropylbenzene) were tested as models for N–N chelating ligands (see Scheme 2 for a representation of all ligands employed in this study). The classical triphenylphosphane ligand **2** was used as a reference and its activity was compared with that of chelating ligands such as dppe **3** [dppe = 1,2-bis(diphenylphosphanyl)ethane] and dppp **4** [dppp = 1,3-bis(diphenylphosphanyl)propane] to assess the importance of the chelate effect. Furthermore, a series of phosphole based ligands was investigated including the readily available 1,2,5-triphenylphosphole **5** and the phenyldibenzophosphole **6**[7] as well as the chelate ligands **7** and **8**[8] which are the phospholyl counterparts of dppe and dppp, respectively. To complete this series, we extended our study to the 1-dibenzotropylidene-*P*-dibenzophosphole **9**, a ligand which has already proved to be very efficient in the Suzuki–Miyaura cross coupling process allowing the synthesis of arylboronic esters.[9] Note that it was shown previously that this highly rigid phosphane alkene (PAL) acts as a firmly binding bis(chelate) because of its well preorganised concave shaped binding site.

All cationic palladium complexes were conventionally prepared by treating equimolar amounts of the ligand with the $[PdCl(allyl)]_2$ dimer in dichloromethane at room temperature. After stirring for 5 min, the formation of the complexes $[Pd(allyl)(L_2)]Cl$ ($L_2$ = two monodentate ligands or one bidentate ligand) was verified by $^{31}P$ NMR spectroscopy (see the experimental section for $^{31}P$ NMR spectroscopic data of the intermediary complexes). Subsequently, a silver salt AgX (X = OTf or $NTf_2$; Tf = $-SO_3CF_3$) was added to exchange the chloride thereby affording the expected cationic complexes **10a**–**17a** (X = OTf) or **10b**–**17b** (X = $NTf_2$) (see Scheme 3). Complexes **10a**,**b** were isolated as orange powders in excellent yields and their structures are in accord with by NMR spectroscopy and elemental analysis. Complex **10a** was also structurally characterised (X-ray crystal structure given in the available supplementary material). Complexes **11a**,**b** were characterised by NMR spectroscopy and elemental analyses and their NMR spectroscopic data were compared with those reported in the literature for the $[Pd(PPh_3)_2(allyl)][X]$ complexes.[10] The dppe and dppp complexes **12a**,**b**, and **13a**,**b** as well as the phosphole derivatives **14a**,**b** and **15a**,**b** were synthesised by following the same experimental procedure and isolated as colourless or pale-yellow powders (fully characterised by NMR spectroscopy and elemental analyses). X-ray analyses of single-crystals of complexes **11a** (not reported in this paper), **12b** and **13a** (given in the available supplementary material) and of the phosphole complexes **14a** and **15a** were performed to elucidate their structures. The structures of the latter are presented in Figure 1 and Figure 2, respectively. Information concerning the data col-

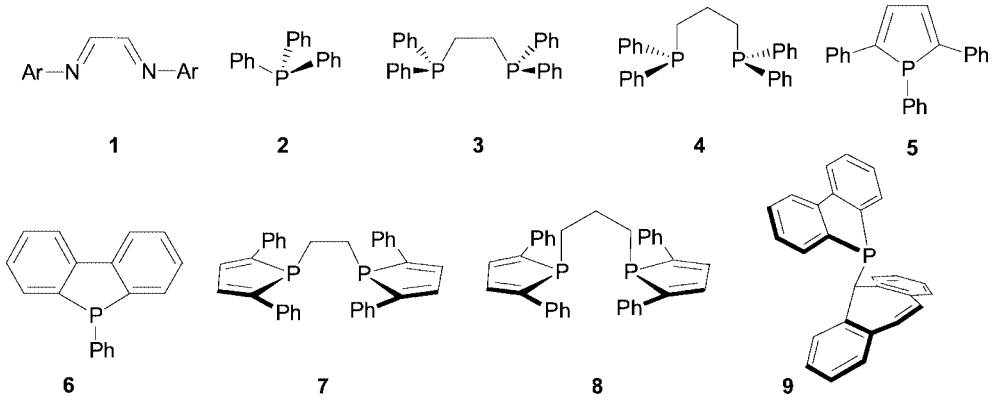


Scheme 2. Ligands used in this study.

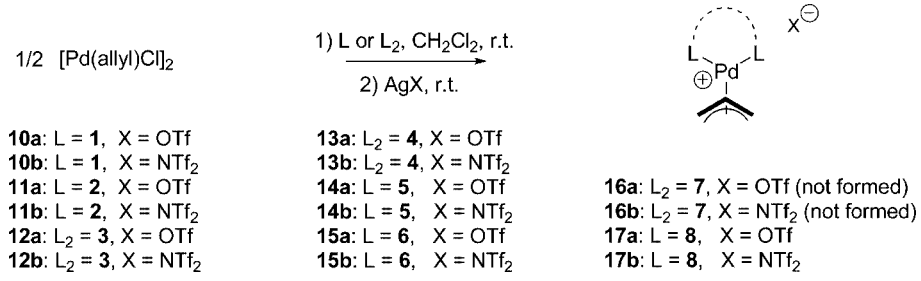


Scheme 3. Synthesis of cationic complexes **10**–**17a**,**b**.

 © 2006 Wiley-VCH Verlag GmbH & Co. KGaA, Weinheim 

lection and refinement are given in Table 9 for both complexes. Selected bond lengths (Å) and angles (°) are listed in Table 1 (complex **14a**) and Table 2 (complex **15a**), respectively.

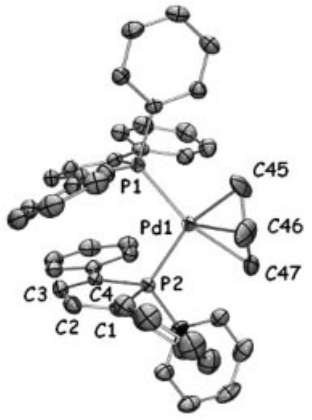


Figure 1. A view of one molecule of complex **14a**.

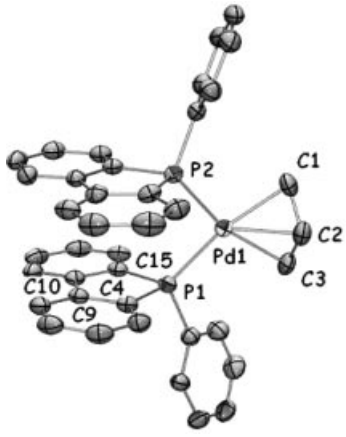


Figure 2. A view of one molecule of complex **15a**.

Table 1. Selected bond lengths [Å] and bond angles [°] for complex **14a**.

| | | | |
|---|---|---|---|
| P1–Pd1 | 2.3066(6) | C2–C3 | 1.437(4) |
| P2–Pd1 | 2.3254(6) | C3–C4 | 1.360(3) |
| Pd1–C45 | 2.143(2) | C4–P2 | 1.818(2) |
| Pd1–C46 | 2.141(3) | P1–Pd1–P2 | 102.4(2) |
| Pd1–C47 | 2.202(3) | C45–C46–C47 | 123.7(3) |
| P2–C1 | 1.812(2) | C4–P2–C1 | 107.6(2) |
| C1–C2 | 1.348(3) | P1–Pd1–C45 | 130.2(1) |

Table 2. Selected bond lengths [Å] and bond angles [°] for complex **15a**.

| | | | |
|---|---|---|---|
| P1–Pd1 | 2.3096(7) | C9–C10 | 1.465(4) |
| P2–Pd1 | 2.2882(7) | C10–C15 | 1.398(4) |
| Pd1–C1 | 2.190(3) | C15–P1 | 1.824(3) |
| Pd1–C2 | 2.176(3) | P1–Pd1–P2 | 99.13(2) |
| Pd1–C3 | 2.164(3) | C1–C2–C3 | 121.0(3) |
| P2–C4 | 1.804(3) | C15–P1–C4 | 91.2(1) |
| C4–C9 | 1.405(4) | P1–Pd1–C3 | 67.5(1) |

As displayed in Figure 1, complex **14a** adopts the expected square-planar geometry. The two phenyl rings of the phosphole ligands point in opposite directions in order to minimise the steric congestion with the second phosphole ligand. No stacking interactions between the two phosphole rings or their phenyl substituents can be observed. The P1–Pd1 and P2–Pd1 bond lengths at 2.307(1) Å and 2.325(1) Å are comparable with the corresponding Pd–P bonds in the $PPh_3$ complex (**11a**) [2.311(1) Å and 2.339(1) Å]. Similarly, the Pd–$C_{allyl}$ bonds (see Table 1) fall in the same range as those of the $PPh_3$ complex [2.153(2), 2.174(4) and 2.236(8) Å]. Note that in the 1,4-diazabutadiene complex **10a**, the Pd–$C_{allyl}$ bonds [2.107(3), 2.122(2) and 2.114(3) Å] are significantly shorter than in the two phosphole complexes indicating a stronger bond between the Pd atom and the allyl group.

The structure of **15a** is different and π stacking between the planar dibenzophosphole ligands can be observed (distance between the two planes: 3.66 Å). Other metric parameters are close to those recorded for the structures of complexes **11a** and **14a**. The bidentate ligands **7** and **8** have already been synthesised by Neibecker et al. following the classical procedure which consists of treating the 2,5-diphenylphospholide anion with 1,2-dibromoethane and 1,3-dibromopropane.[8] Complexes **17a**,**b** were straightforwardly formed and isolated as dark-red powders and their identities were ascertained by NMR spectroscopic studies and elemental analyses (see Scheme 3). On the contrary, the synthesis of complexes **16a**,**b** failed. Whatever the experimental conditions used, each attempt led to the formation of dark solids that could not be dissolved in common organic solvents and despite many efforts, the insoluble materials could not be characterised.

The synthesis of complexes **19a**,**b** took a slightly different reaction pathway. Specifically, the reaction of ligand **9** with $[Pd(allyl)Cl]_2$ did not yield a cationic complex with chloride as the counter-anion but the neutral species **18** which results from the breaking of the dimer, the chloride ligand remaining coordinated to the palladium centre (see Scheme 4). Complex **18** was characterised by $^{31}P$ NMR spectroscopy and its structure determined by an X-ray diffraction study.

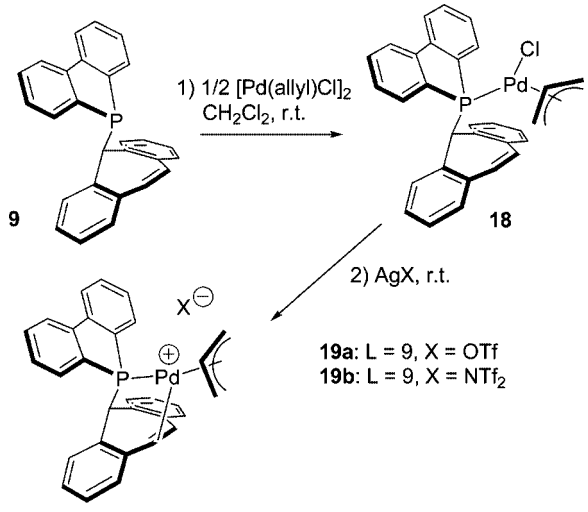


Scheme 4. Synthesis of cationic complexes **18** and **19a**,**b**.

 © 2006 Wiley-VCH Verlag GmbH & Co. KGaA, Weinheim 

Figure 3 shows the result and selected bond lengths and angles are listed in Table 3. The structure of complex **18** shows that the 1-dibenzotropylidene-*P*-dibenzophosphole is coordinated to the metal centre by means of the phosphorus atom only, the C=$C_{trop}$ unit remaining uncoordinated. In order to minimise repulsive steric interactions, the tropylidene and the allyl fragment point in opposite directions with respect to the central plane through the Pd atom.

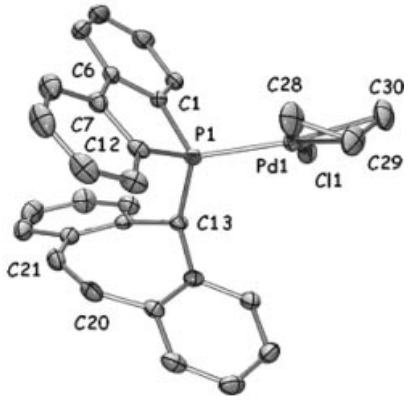


Figure 3. A view of one molecule of complex **18**.

Table 3. Selected bond lengths [Å] and bond angles [°] for complex **18**.

| | | | |
|---|---|---|---|
| P1–Pd1 | 2.2822(6) | Pd1–C29 | 2.170(4) |
| P1–C1 | 1.813(2) | Pd1–C30 | 2.215(4) |
| C1–C6 | 1.407(3) | Pd1–Cl1 | 2.3767(7) |
| C6–C7 | 1.466(3) | C20–C21 | 1.337(4) |
| C7–C12 | 1.403(3) | C28–C29–C30 | 120.5(7) |
| C12–P1 | 1.811(2) | C1–P1–C12 | 91.6(1) |
| P1–C13 | 1.875(2) | P1–Pd1–C28 | 96.7(2) |
| Pd1–C28 | 2.104(5) | P1–Pd1–C30 | 164.0(2) |

Treatment with one equivalent of AgX (X = OTf, $NTf_2$) yielded the expected cationic species **19a**,**b** which were isolated as very stable colourless powders (see Scheme 4). The coordination of the double bond to the metal was ascertained by NMR studies and is also seen in the solid-state structure of complex **19b** (Figure 4). Selected bonding parameters are listed in Table 4. Details concerning the crystal data collection and refinement are given in Table 9.

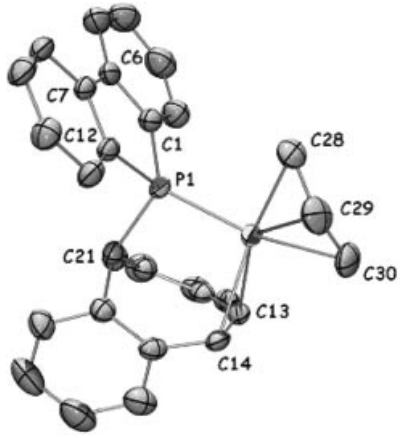


Figure 4. A view of one molecule of complex **19b**.

Table 4. Selected bond lengths [Å] and bond angles [°] for complex **19b**.

| | | | |
|---|---|---|---|
| P1–Pd1 | 2.272(1) | Pd1–C30 | 2.214(4) |
| P1–C1 | 1.815(4) | Pd1–C13 | 2.306(3) |
| C1–C6 | 1.406(5) | Pd1–C14 | 2.293(3) |
| C6–C7 | 1.468(6) | C13–C14 | 1.380(6) |
| C7–C12 | 1.415(5) | C28–C29–C30 | 120.2(5) |
| C12–P1 | 1.788(4) | C1–P1–C12 | 92.1(2) |
| P1–C21 | 1.866(4) | C13–Pd1–C14 | 34.9(1) |
| Pd1–C28 | 2.135(4) | P1–Pd1–C28 | 99.0(1) |
| Pd1–C29 | 2.166(4) | P1–Pd1–C30 | 165.9(1) |

The metric parameters of complex **19b** are comparable with those found in complex **15a**. The C=$C_{trop}$ bond length of the tropylidene unit [1.380(6) Å] is slightly lengthened when compared with the uncoordinated C=$C_{trop}$ bond in **18** indicating π back donation from the metal fragment to the ligand.

## Catalytic Experiments

Having all these complexes at hand, we investigated their performance in catalytic allylic aminations. The allylation of aniline was chosen as a model reaction (Scheme 5). All experiments were carried under the same experimental conditions, that is, in THF or toluene at room temperature with $MgSO_4$ as a water scavenger using 1 mol-% of catalyst, two equiv. of aniline and one equiv. of allylic alcohol. These conditions are similar to those used by Ozawa et al. during their studies with the above mentioned DPCB complexes. The use of two equiv. of aniline disfavours the formation of the bis(allylation) derivatives.

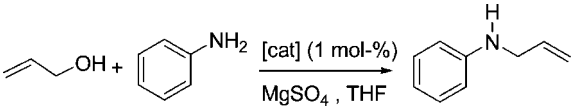


Scheme 5. Catalytic coupling of allyl alcohol with aniline using palladium allyl complexes **10a**,**b**–**19a**,**b** as catalyst precursors.

A first series of experiments showed that the use of toluene or THF as solvent had no influence and gave similar results. Therefore, all subsequent experiments were performed in THF. As shown in Table 5, only catalysts **11a**,**b**, **14a**,**b**, **15a**,**b** and **19b** gave a complete or nearly complete conversion (80 to 100%) after a reaction time of 24 h. In the experiments with **11a**,**b**–**17a**,**b**, the nature of counteranion did not have a significant influence on the catalytic performance. However, under the reaction conditions used in these experiments, a strong influence was seen with complexes **19a**,**b**, where the triflate derivative **19a** gave only a 20% conversion (vide supra).

 © 2006 Wiley-VCH Verlag GmbH & Co. KGaA, Weinheim 

Table 5. Conversion in the catalytic coupling of allyl alcohol with aniline using palladium allyl complexes **10a**,**b**–**19a**,**b** as catalyst precursors. (n.t. = not tested).

| Catalyst | 24 h | 1 h | Catalyst | 24 h | 1 h |
|---|---|---|---|---|---|
| **10a** | 0% | n.t. | 14a | 100% | 72% |
| **10b** | 0% | n.t. | 14b | 100% | 100% |
| **11a** | 100% | 47% | 15a | 100% | 52% |
| **11b** | 80% | 27% | 15b | 85% | 34% |
| **12a** | 20% | n.t. | 17a | 73% | 18% |
| **12b** | 5% | n.t. | 17b | 69% | 13% |
| **13a** | 5% | n.t. | 19a | 20% | n.t. |
| **13b** | 2% | n.t. | 19b | 98% | 30% |

Hard σ donor ligands such as the diazadiene ligand in complexes **10a**,**b** are not suited to the Pd-catalysed allylation of aniline and no conversion was achieved. Complexes such as **12a**,**b** and **13a**,**b** with bidentate ligands also showed very low activities with conversions not exceeding 20%. The chelate complexes **17a**,**b** carrying the bis(phosphole) ligand **8** gave better results but no complete conversion was observed after 24 h.

In a second series of experiments, the most active catalysts were selected and the reaction was stopped after 1 h. As the results in Table 5 show, catalyst **14b** proved to be the most active (complete conversion) and, as previously observed with **19a**,**b**, this complex with the $NTf_2$ counteranion was more active than its triflate counterpart **14a** (72%). However, complete conversion with **14a** was achieved after 2 h. The second best catalyst in terms of efficiency is the dibenzophosphole based complex **15a** which afforded a conversion of 52%. In this case, the $NTf_2$ derivative **15b** was less active (34%). The triphenylphosphane complex **11a** (47% of conversion) ranks in third place. Among the complexes which showed substantial conversion after 1 h reaction time, complex **19b** was the least efficient catalyst (30%). Note that in all these experiments the addition of $MgSO_4$ is not necessary and the absence of this water scavenger resulted only in a small decrease in the conversion yields (about 10%).

Having identified **14b** as an efficient catalyst, some additional experiments were also conducted with a lower loading of catalyst (0.5 and 0.1 mol-%) and by varying the substitution scheme of the allyl alcohol. These results are presented in Scheme 6. Longer reaction times or heating were needed to achieve a nearly complete conversion when a low loading of the catalyst was used (7 h at room temp. with 0.5 mol-% of catalyst and 5 h at 70 °C with 0.1 mol-% of catalyst). Methylallyl alcohol and *trans*-crotyl alcohol were also used as substrates. Introduction of a methyl group at the alpha position of the alcohol resulted in a significant decrease in the catalytic activity and, after 24 h at room temp., only 40% of the substrate was converted. As previously observed by Ozawa and Yoshifuji, introduction of a methyl group at the β position (*trans*-crotyl alcohol) leads to a mixture of $SN_2$ and $SN_2'$ products in a 71:12 ratio.

To complete this study, we then focused our efforts on the bis(allylation) of primary amines as well as on the monoallylation of secondary amines. This latter transformation is known, in particular, to be much more difficult to achieve.[4c–4d,5] For the bis(allylation) process, catalyst **14b** (1 mol-%) was treated with one equiv. of amine and two or three equiv. of the allylic alcohol in THF at room temperature with $MgSO_4$. With two equiv. of alcohol a nearly complete conversion was obtained after 39 h of stirring [92% of bis(allylation), 8% of monoallylation]. With three equiv. a complete conversion could be obtained after 14 h of reaction (see Scheme 7).

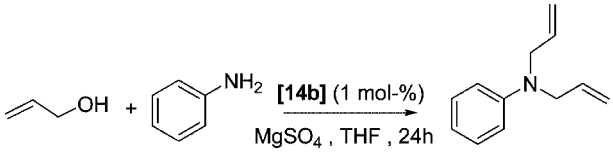


Scheme 7. Bis(allylation) of primary amines with catalyst **14b**.

Experiments to test the activity of **14b** in the allylation of secondary amines were conducted with 1 mol-% of catalyst, one equiv. of amine and two equiv. of allyl alcohol in THF (at room temperature and 50 °C) in the presence of $MgSO_4$. Three amines were tested: morpholine, dibenzylamine and *N*-methylaniline. A complete conversion was obtained after 24 h of heating at 50 °C with morpholine and *N*-methylaniline as substrates. Note that **14b** is therewith the most efficient catalyst reported to date for this transformation.[5] All the results are summarised in Table 6.

The results from the catalyses clearly demonstrate that the electronic nature of the phosphane plays a crucial role for the activity. As previously observed, strong π acceptor ligands lead to higher TON (TON = turn over numbers). Because diarylalkyl-substituted phosphanes such as dppe, dppp and ligand **8** show weaker π accepting capacities than triaryl phosphanes, the better performance of $[Pd(C_3H_5)(PPh_3)_2][X]$ **11a**,**b** can be explained. However, the

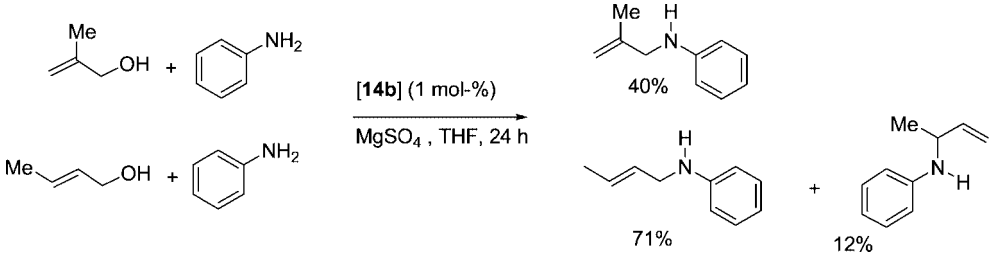


Scheme 6. Reaction of aniline with methyl alcohol and *trans*-crotyl alcohol catalysed by complex **14b**.

 © 2006 Wiley-VCH Verlag GmbH & Co. KGaA, Weinheim 

Table 6. Conversion in the catalytic coupling of allyl alcohol with secondary amines with **14b** as a catalyst precursor.

| Secondary amines | Temperature | Conversion |
|---|---|---|
| *N*-Methylaniline | room temp. | 100% |
| Morpholine | room temp. | 28% |
| Morpholine | 50 °C | 100% |
| Dibenzylamine | room temp. | 11% |
| Dibenzylamine | 50 °C | 44% |

explanation of the especially high activity of catalyst precursor **14** with the 2,5-diphenylphosphanylphosphole **5** as ligand as compared with **15** with the dibenzophosphole derivative **6** is less straightforward and requires a better understanding of the electronic nature of the ligands. Consequently, a DFT study was carried out.

### DFT Calculations

Calculations were carried out at the B3PW91/6-31G* level of theory using the Gaussian 03 set of programs. Views of the two calculated structures are shown in Figure 5 and selected bond lengths and angles are listed in Table 7. The agreement between the calculated and experimentally found bonding parameters[11] is satisfactory. Because of the nonplanarity of the phosphorus atom, phospholes are weakly aromatic.[12] The aromaticity of phospholes has been the subject of many debates and several factors determine the degree of aromaticity, such as the substitution pattern at the carbon atoms, the pyramidalisation of the coordination sphere at phosphorus and, most importantly, the nature of the substituent at phosphorus which determines the amplitude of the overlap between the π system of the $C_4$-butadienyl fragment and the P–R bond. This has been recently demonstrated with a series of 1-R–P substituted phospholes.[13] Both **5** and **6** carry a phenyl group as the substituent, hence the degree of deviation $\varphi$ of the P–C bond from the ring plane can be used in first approximation as an indicator. Thus **5** ($\varphi$ = 68°) would show a higher degree of aromaticity than **6** ($\varphi$ = 72°). The significantly lower inversion barrier at the phosphorus atom for **5** (16.9 kcal mol$^{-1}$) than in **6** (26.2 kcal mol$^{-1}$) supports this conclusion (see the supporting information for a presentation and structure parameters of the transition states of the inversions calculated at the same level of theory). Two explanations can be proposed to rationalise the weaker inversion barrier in phosphole **5**. First one may propose that the higher barrier for **6** is the result of significant overlap between the σ-P–R bond and the π system of the butadienyl fragment (negative hyperconjugation) which stabilises the ground state of this less aromatic ring system. Note that the inversion barrier for triphenylphosphane **2** was found to be equivalent to that of **6**, that is 26.2 kcal mol$^{-1}$. A second possibility is to consider that in the transition state the phosphole **5** is more aromatic than **6** since in this fused system the π electrons are delocalised into the two neighbouring six-membered aromatic rings.[14] To confirm our findings further, the nucleus independent chemical shifts (NICS) were calculated for both phospholes and their transition states (noted **TS5** and **TS6**, respectively). There is a good relationship between the NICS and other aromaticity criteria in phospholes and the more negative the NICS the higher the aromatic character.[15] NICS calculations were performed with the optimised structures at the RHF/6-311+G** level of theory (measured at 1 Å above the plane defined by the ring, opposite to the substituent at phosphorus). Table 8 shows that phosphole **5** is more aromatic than **6**. Not surprisingly, the presence of two fused benzene rings in **6** decreases the aromatic character of the central phosphole nucleus. A similar phenomenon has already been reported by Schleyer in the case of other fused structures such as phenanthrene.[15b] In **6**, the NICS value of the peripheral benzene rings (–10.3) is higher than that calculated for benzene (–8.4) using the same method and basis set. NICS calculations were also performed on the two transitions states **TS5**

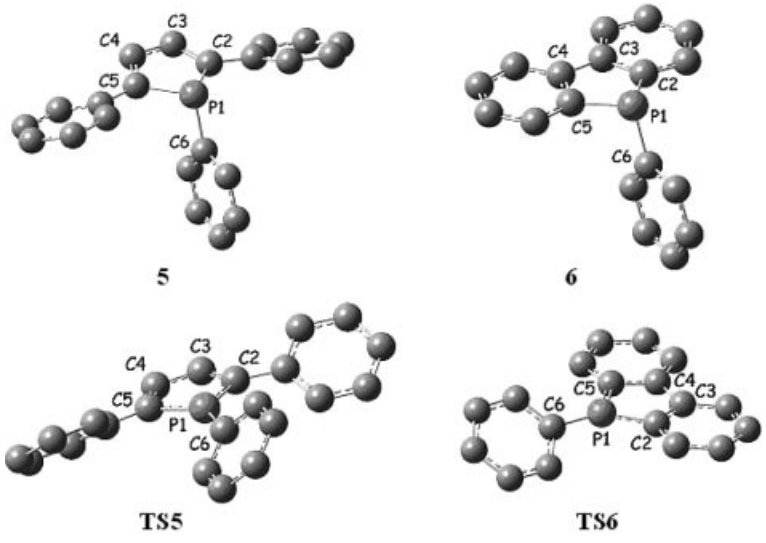


Figure 5. Views of the optimised geometries of the two ligands **5** and **6** and **TS5** and **TS6** (hydrogens have been excluded).

 © 2006 Wiley-VCH Verlag GmbH & Co. KGaA, Weinheim 

and **TS6**, the structures of which are also presented in Figure 5. Both transition states are, as expected, more aromatic than their respective precursors but the differences between the NICS values are insignificant (NICS for **TS5**: –9.0; NICS for **TS6** = –8.9), that is, the degree of aromaticity of the transition states is not the determining factor (see Scheme 8).

Table 7. A comparison between calculated and experimental bond lengths [Å] and angles [°] for ligands **5** and **6**.

| | **5** theoretical | **5**[11a] experimental | **6** theoretical | **6**[11b] experimental |
|---|---|---|---|---|
| P1–C2 | 1.822 | 1.822 | 1.832 | 1.812 |
| C2–C3 | 1.368 | 1.348 | 1.412 | 1.385 |
| C3–C4 | 1.441 | 1.440 | 1.469 | 1.465 |
| P1–C6 | 1.839 | 1.822 | 1.848 | 1.841 |
| C3–C2 | 114.8 | 116.1 | 110.0 | 110.2 |
| P1–C5 | 1.821 | 1.822 | 1.832 | 1.818 |

Table 8. Sum of the bond angles around the P atoms, Σ° (P), deviation $\varphi$ of the P–C bond out the $PC_4$ plane in the calculated structures of ligands **5** and **6**. NICS values and data from CDA calculations for complexes **I**, **II** and **III**. *b* and *d* values are expressed in electrons and *d*/*b* and *b*/*d*+*b* ratios are given in percent.

| Ligands and complexes | **5** | **6** | **I** | **II** | **III** |
|---|---|---|---|---|---|
| Σ° (P) | 302 | 296 | | | |
| $\varphi$° | 68 | 72 | | | |
| NICS (1 Å) | – 4.3 | – 2.1 | | | |
| donation (d) | | | 0.437 | 0.406 | 0.420 |
| back-donation (b) | | | 0.065 | 0.086 | 0.067 |
| *d*/*b* | | | 6.7 | 4.7 | 6.3 |
| *d*/*d*+*b* | | | 13 | 17.5 | 13.7 |
| *r* | | | – 0.341 | – 0.331 | – 0.331 |
| $\Delta$ | | | – 0.010 | – 0.009 | – 0.009 |

The binding properties of **5** and **6** towards transition metal fragments were estimated by means of a charge decomposition analysis (CDA) as developed by Frenking et al.[16] For simplicity, and in order to allow comparison with previous work, we chose, as models, the $Ni(CO)_3$ complexes **I**, **II** and **III** with triphenylphosphane **2**, triphenylphosphole **5** and dibenzophosphole **6** as ligands, respectively (Figure 6).

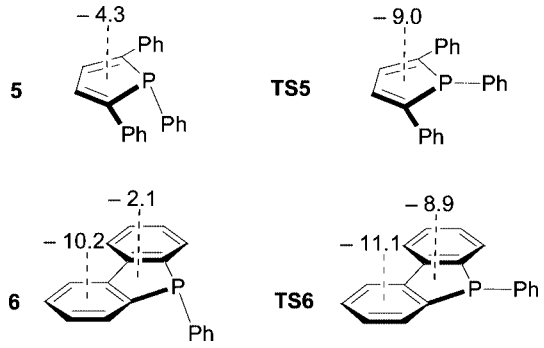


Scheme 8. NICS values calculated at the RHF/6-311+G** level of theory (measured at 1 Å above the plane defined by the ring, opposite to the substituent at phosphorus) for **5**, **6**, **TS5** and **TS6**.

Results of this CDA analysis are presented in Table 8, further details are given in the experimental section. The small residual term ($\Delta$) in all complexes shows that the electron density has been adequately partitioned into the repulsive term, *r*, and L→M donor, *d*, as well as the M→L back-donating terms, *b*. Hence, the discussion of the data from the CDA is meaningful.

The data given in Table 8 show that the ligands $PPh_3$ and dibenzophosphole **6** have similar electronic properties, that is, they have similar donation/back-donation ratios, *d*/*b*, of about 6.5. The triphenylphosphole **5** is a better acceptor, its *d*/*b* ratio is significantly smaller (4.7).

Inspection of the MO's involved in the bonding in complexes **II** (HOMO-12 and HOMO-2, see Figure 7) and **III** (HOMO-11 and HOMO-2) revealed that, as expected, the most significant contribution to the bonding comes from the orbital which describes the lone pair at phosphorus, i.e. the HOMO-1 in **5** and the HOMO in **6**. On the other hand, the π back donation mainly results from the combination of a filled orbital of the $Ni(CO)_3$ fragment with the LUMO+7 of **5** and **6** (σ* orbitals).

In summary, the results from the DFT calculations fully support the idea that the π accepting capacity of the ligand governs the catalytic activity of the palladium complexes prepared from them: while $[Pd(C_3H_6)(PPh_3)_2]X$ **10a**,**b** and $[Pd(C_3H_6)(\mathbf{6})]X$ **15a**,**b** perform similarly, $[Pd(C_3H_3)(\mathbf{5})]$ **14a**,**b** stands out with its exceptional activity.

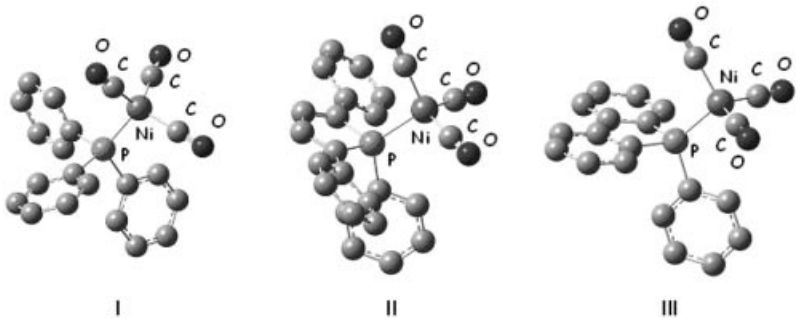


Figure 6. Views of the optimised geometries of the complexes **I**, **II** and **III** (hydrogen atoms have been excluded).

 © 2006 Wiley-VCH Verlag GmbH & Co. KGaA, Weinheim 

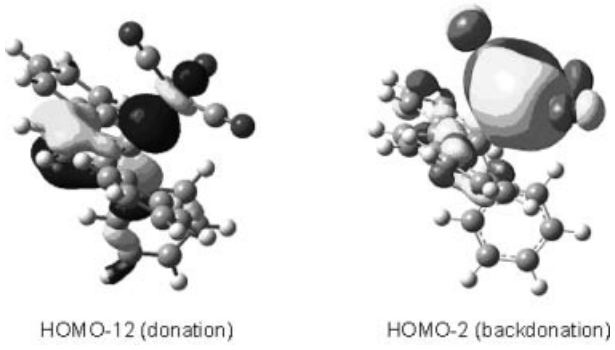


Figure 7. Views of the two MO's which describe the bonding in complex **II**.

## Conclusions

The performance of a series of catalysts with different phosphane ligands and one complex with a diazabutadiene ligand was evaluated in the palladium catalysed allylation of primary and secondary amines. In this way, a new efficient catalyst carrying the 1,2,5-triphenylphosphole **5** as a ligand (complexes **14a**,**b**) was found which enables these coupling reactions under mild conditions. DFT calculations enabled a comparison of the electronic structures of the ligands which gave the most active catalysts and, in combination with calculations on simple model complexes, strongly support the proposition that the best catalysts are obtained with π accepting ligands. Further studies will now focus on a systematic investigation of other strong π acceptor ligands, especially suitably substituted phospholes and phosphanes. Though significant progress has been achieved through this study, the influence of the ligands and their related complexes on the mechanistic pathway has yet to be precisely assessed as well as details on the stereochemical course of the reaction. DFT calculations aimed at determining the whole catalytic cycle of this important transformation are currently underway and will be presented in due course.

## Experimental Section

**General Remarks:** All reactions were routinely performed under an inert atmosphere of argon or nitrogen by using Schlenk and glovebox techniques and dry deoxygenated solvents. Dry THF and hexanes were obtained by distillation from Na/benzophenone. Dry dichloromethane was distilled from $P_2O_5$, dry toluene from Na and dry acetonitrile from $CaH_2$. NMR spectra were recorded on a Bruker Avance 300 spectrometer operating at 300 MHz for $^1H$, 75.5 MHz for $^{13}C$ and 121.5 MHz for $^{31}P$. Solvent peaks were used as internal references relative to $Me_4Si$ for $^1H$ and $^{13}C$ chemical shifts (ppm). $^{31}P$ chemical shifts are relative to an 85% $H_3PO_4$ external reference and coupling constants are expressed in Hertz. Abbreviations used: b broad, s singlet, d doublet, t triplet, m multiplet, p pentuplet, sext sextuplet, sept septuplet, v virtual. Elemental analyses were performed by the Service d'analyse du CNRS at Gif sur Yvette, France. $[Pd(COD)Cl_2]$,[17] *P*-phenyldibenzophosphole (**6**),[7] (dibenzo[*a*,*d*]cyclohepten-5-yl)dibenzophosphole (**9**),[9] triphenylphosphole (**5**),[6] diazadiene (**1**)[18] and (2,5-diphenylphosphol-1-yl)alkanes **7** and **8**[8] were prepared according to literature procedures. All other reagents and chemicals were obtained commercially and used as received. The GC yields were determined on a Varian Star 3400 gas chromatograph equipped with a CHROMPACK column (column type: WCOT FUSED SILICA, stationary phase: CP-SIL 5 CB).

**Theoretical Methods:** The calculations were performed with the GAUSSIAN 03 series of programs.[19] The geometries of compounds **2** and **5** and **6** were optimised by using the B3PW91 functional.[20] The standard 6-31G* basis set was used for all atoms (H, C and P). NICS calculations were performed at the RHF/6-311+G** level of theory using geometries calculated at the RB3PW91/6-31G* level of theory. The $Ni(CO)_3$ complexes **I**, **II** and **III** were calculated with the B3PW91 functional using the 6-31+G** basis set for P atoms, the 6-31G** basis set for the carbonyl groups and the 6-31G basis set for the H and C atoms. The basis set for the metal was that associated with the pseudo potential, with a standard double-ζ LANL2DZ contraction. In each case, harmonic frequencies were calculated at the same level of theory to characterise the stationary points and to determine the zero-point energies (ZPE). Intrinsic reaction coordinate calculations (IRC) were performed to ensure that transition states were found for the inversion at the phosphorus atoms in the structures of **5** and **6**. All optimised structures reported here have only positive eigenvalues of the Hessian matrix, i.e they are minima on the potential energy surface. Inspection of ligand to metal donor-acceptor interactions were performed using the charge-decomposition analysis (CDA). In the CDA method the (canonical, natural or Kohn–Sham) molecular orbitals of the complex are expressed in terms of MO's of appropriately chosen fragments. In the cases studied, the Kohn–Sham orbitals of the calculations are formed in the CDA procedure as a linear combination of the MO's of the phosphorus ligands **2**, **5** and **6** and those of the remaining $[Ni(CO)_3]$ fragment. In all cases, the ligands and the metal fragments were computed in the geometry of the complex. The orbital contributions are divided into four parts: (i) the mixing of the occupied MO's of the ligand and the unoccupied MO's of the metal fragment. This value (noted *d*) represents the L→M donation; (ii) the mixing of the unoccupied MO's of the ligand and the occupied MO's of the metal fragment. This value (noted *b*) accounts for the M→L back donation; (iii) the mixing of the occupied MO's of the ligand and the occupied MOs of the metal fragment. This term (noted *r*), which describes the repulsive polarisation between the ligand and metal fragment, is negative because electronic charge is removed from the overlapping area of the occupied orbitals; (iv) the residual term ($\Delta$) which results from the mixing of the unoccupied MO's of the two respective fragments. Usually this term is very close to zero for closed-shell interactions. This value constitutes an important probe for determining whether the bonding studied can be really classified as a donor-acceptor interaction following the Dewar–Chatt–Duncansson model. Important deviations from $\Delta = 0$ imply that the bond studied is more conventionally described as a normal covalent bond between two open shell fragments. A more detailed presentation of the CDA method and the interpretation of the results can be found in the literature. Compositions of molecular orbitals, overlap populations between molecular fragments, bond orders and density-of-states spectra were calculated by using the AOMix program developed by I. Gorelski (version 6.23).[21]

**X-ray Structure Data:** Nonius KappaCCD diffractometer, $\varphi$ and $\omega$ scans, Mo-$K_\alpha$ radiation ($\lambda = 0.71073$ Å), graphite monochromator, $T = 150$ K, structure solution with SIR97,[22] refinement against $F^2$ in SHELXL97[23] with anisotropic thermal parameters for all non-hydrogen atoms, calculated hydrogen positions with riding isotropic thermal parameters (Table 9).

 © 2006 Wiley-VCH Verlag GmbH & Co. KGaA, Weinheim 

Table 9. Crystal data for complexes **14a**, **15a**, **18** and **19b**.

| | **14a** | **15a** | **18** | **19b** |
|---|---|---|---|---|
| Empirical formula | $C_{47}H_{39}P_2Pd$, $CF_3O_3S$, $CH_2Cl_2$ | $C_{39}H_{31}P_2Pd$, $CF_3O_3S$ | $C_{30}H_{23}ClPPd$ | $C_{30}H_{24}PPd$, $C_2F_6NO_4S_2$ |
| Molecular mass [g mol$^{-1}$] | 1006.12 | 817.05 | 556.30 | 802.05 |
| Crystal size [mm] | 0.20 × 0.18 × 0.18 | 0.23 × 0.20 × 0.03 | 0.20 × 0.18 × 0.18 | 0.22 × 0.16 × 0.16 |
| Crystal colour and shape | yellow block | light yellow plate | yellow plate | colourless block |
| Crystal system | monoclinic | monoclinic | monoclinic | monoclinic |
| Temperature [K] | 150.0(1) | 150.0(1) | 150.0(1) | 150.0(1) |
| Space group | $P2_1/n$ | $P2_1$ | $P2_1$ | $P2_1/c$ |
| $a$ [Å] | 12.2870(10) | 11.6440(10) | 9.4010(10) | 44.9220(10) |
| $b$ [Å] | 22.1630(10) | 11.8720(10) | 13.9750(10) | 14.9800(10) |
| $c$ [Å] | 16.1300(10) | 13.8110(10) | 10.0440(10) | 18.8280(10) |
| $\beta$ [°] | 93.9700(10) | 110.7300(10) | 115.3000(10) | 97.6100(10) |
| $V$ [Å$^3$] | 4381.9(5) | 1785.6(3) | 1193.00(19) | 12558.4(11) |
| Z | 4 | 2 | 2 | 16 |
| Density (calculated) [g cm$^{-3}$] | 1.525 | 1.520 | 1.549 | 1.697 |
| Absorbtion coefficient [mm$^{-1}$] | 0.722 | 0.722 | 0.974 | 0.851 |
| $F$(000) | 2048 | 828 | 562 | 6431 |
| $\theta$ max [°] | 30.03 | 27.45 | 30.03 | 27.48 |
| Reflections collected [$I \geq 2\sigma(I)$] | 21134 | 8000 | 5637 | 45074 |
| Independent reflections | 12788 [$R_{int}$ = 0.0208] | 8000 [$R_{int}$ = 0.0000] | 5637 [$R_{int}$ = 0.0000] | 26730 [$R_{int}$ = 0.0164] |
| Data/restraints/parameters | 9168/16/550 | 7463/16/466 | 5344/17/309 | 20798/13/1558 |
| Gof on $F^2$ | 1.039 | 1.024 | 1.055 | 1.042 |
| $R$(F), $R_w(F^2)$ [$I \geq 2\sigma(I)$] | 0.0439, 0.1281 | 0.0293, 0.0730 | 0.0252, 0.0636 | 0.0503, 0.1609 |
| Largest diff peak/hole [e Å$^{-3}$] | 1.549(0.092)/ –0.986(0.092) | 0.633(0.057)/ –0.637(0.057) | 0.509(0.067)/ –0.626(0.067) | 2.068(0.110)/ –0.757(0.110) |

CCDC-294689 to -294695 contain the crystallographic data for the structures reported in this paper and have been deposited with the Cambridge Crystallographic Data Centre. Copies of these data can be obtained free of charge from The Cambridge Crystallographic Data Centre via www.ccdc.cam.ac.uk/data_request/cif.

**Synthesis of Complexes 10a,b [Pd(1)($\eta_3$-$C_3H_5$)][X]:** To a solution of glyoxal-bis(2,6-diisopropylphenyl)imine (100 mg, 0.26 mmol) in dichloromethane (2 mL) was added $[Pd(allyl)Cl]_2$ (48.6 mg, 0.13 mmol). After 5 min stirring, the silver salt AgX (0.26 mmol, **10a**: 68.2 mg, **10b**: 99.3 mg) was added and the pale-yellow solution became orange. Filtration of AgCl on celite followed by evaporation of the dichloromethane yielded the complexes as orange powders in very good yields (**10a**: 97%, 170 mg; **10b**: 98%, 201 mg). Single-crystals of **10a** were obtained by slow diffusion of hexanes into a solution of the complex in chloroform at room temperature. $^1$H NMR ($CDCl_3$, 25 °C): $\delta$ = 1.32 (m, 24 H, CHC$H_3$), 3.03 (m, 2 H, C$H$CH$_3$), 3.17 (vd, AA′BB′C, Σ $J$ = 12.8 Hz, 2 H, $CH_{allyl}$), 3.25 (m, 2 H, C$H$CH$_3$), 3.59 (vd, AA′BB′C, Σ $J$ = 7.0 Hz, 2 H, $CH_{allyl}$), 5.56 (tt, $J$ = 7.0 and 12.8 Hz Hz, 1 H, $CH_{allyl}$), 7.26–7.40 (m, 6 H, $m$-Ph), 8.61 (s, 2 H, C$H$=N) ppm. $^{13}$C NMR ($CDCl_3$, 25 °C): $\delta$ = 23.0 (CH$C$H$_3$), 23.7 ($C$H=N), 28.9 ($C$HCH$_3$), 65.1 ($CH_{2allyl}$), 120.1 ($CH_{allyl}$), 124.1–128.8 ($m$-Ph), 138.1 ($o$-Ph), 146.1 ($ipso$-Ph), 170.0 ($p$-Ph) ppm. $C_{30}H_{41}F_3N_2O_3PdS$ (673.14): calcd. C 53.53, H 6.14; found C 53.28, H 6.12.

**Synthesis of Complexes 12a,b [Pd(3)($\eta_3$-$C_3H_5$)][X]:** To a solution of 1,2-bis(diphenylphosphanyl)ethane (100 mg, 0.25 mmol) in dichloromethane (2 mL) was added $[Pd(allyl)Cl]_2$ (0.13 mmol, 45.9 mg). After stirring for 5 min, the formation of a bidentate complex was confirmed by $^{31}$P NMR ($\delta$ = 51.2 ppm). The silver salt AgX was then added (0.25 mmol, **12a**: 64.5 mg, **12b**: 93.9 mg). Filtration of AgCl on celite followed by evaporation of the dichloromethane yielded the complexes as white powders in very good yields (**12a**: 98%, 170 mg; **12b**: 98%, 200 mg). Single-crystals of **12b** were obtained by slow diffusion of hexanes into a solution of the complex in dichloromethane at room temperature. $^{31}$P NMR ($CDCl_3$, 25 °C): $\delta$ = 51.4 ppm. $^1$H NMR ($CDCl_3$, 25 °C): $\delta$ = 2.70 (m, $A_2A'_2XX'$, Σ $J$ = 99.5 Hz, 4 H, C$H_2$PPh$_2$), 3.39 (vddd, AA′BB′CXX′, Σ$J$ = 24.8 Hz, 2 H, $CH_{allyl}$), 4.86 (m, AA′BB′CXX′, Σ $J$ = 12.4 Hz, 2 H, $CH_{allyl}$), 5.81 (vtt, $AB_2C_2X_2$, Σ $J$ = 42.5 Hz, 1 H, $CH_{allyl}$), 7.43–7.60 (m, 20 H, Ph) ppm. $^{13}$C NMR ($CDCl_3$, 25 °C): $\delta$ = 27.5 (vt, AXX′, Σ $J$ = 46.0 Hz, $CH_2$PPh), 71.4 (vt, AXX′, Σ $J$ = 33.2 Hz, $CH_{2allyl}$), 123.6 (vt, AXX′, Σ $J$ = 12.2 Hz, $CH_{allyl}$), 129.9–132.8 (Ph) ppm. $C_{31}H_{29}F_6NO_4P_2PdS_2$ (826.1): calcd. C 45.07, H 3.54; found C 44.85, H 3.53.

**Synthesis of Complexes 13a,b [Pd(4)($\eta_3$-$C_3H_5$)][X]:** To a solution of 1,2-bis(diphenylphosphanyl)propane (100 mg, 0.24 mmol) in dichloromethane (2 mL) was added $[Pd(allyl)Cl]_2$ (0.12 mmol, 44.5 mg). After 5 min stirring, the formation of a bidentate complex was confirmed by $^{31}$P NMR ($\delta$ = 6.3 ppm). The silver salt AgX was then added (0.24 mmol, **13a**: 61.7 mg, **13b**: 89.8 mg). Filtration of AgCl on celite followed by evaporation of the dichloromethane yielded the complexes as white powders in very good yields (**13a**: 96%, 165 mg; **13b**: 95%, 190 mg). Single-crystals of **13a** were obtained by slow diffusion of hexanes into a solution of the complex in dichloromethane at room temperature. $^{31}$P NMR ($CDCl_3$, 25 °C): $\delta$ = 6.8 ppm. $^1$H NMR ($CDCl_3$, 25 °C): $\delta$ = 2.00 (m, $A_2M_4X_2$, Σ $J$ = 147.7 Hz, 2 H, C$H_2$CH$_2$PPh$_2$), 2.76 (m, $A_2A'_2M_2XX'$, Σ $J$ = 87.4 Hz, 4 H, CH$_2$C$H_2$PPH$_2$), 3.28 (vddd, AA′BB′CXX′, Σ $J$ = 25.6 Hz, 2 H, $CH_{allyl}$), 3.95 (vddd, AA′BB′CXX′, Σ $J$ = 13.5 Hz, 2 H, $CH_{allyl}$), 5.7 (vtt, $AB_2C_2X_2$, Σ $J$ = 42.2 Hz, 1 H, $CH_{allyl}$), 7.31–7.48 (m, 20 H, Ph) ppm. $^{13}$C NMR ($CDCl_3$, 25 °C): $\delta$ = 18.7 (s, $C$H$_2$CH$_2$PPh$_2$), 25.3 (vt, AXX′, Σ $J$ = 30.7 Hz, CH$_2$C$H_2$PPh$_2$), 73.7 (vt, AXX′, Σ $J$ = 32.5 Hz, $CH_{2allyl}$), 123.0 (vt, AXX′, Σ $J$ = 12.4 Hz, $CH_{allyl}$), 128.9–132.8 (Ph) ppm. $C_{31}H_{31}F_3O_3P_2PdS$ (709.0): calcd. C 52.51, H 4.41; found C 52.35, H 4.40.

**Synthesis of Complexes 14a,b [Pd(5)($\eta_3$-$C_3H_5$)][X]:** To a solution of $[Pd(allyl)Cl]_2$ (0.16 mmol, 58.6 mg) in dichloromethane (2 mL) was added triphenylphosphole (0.32 mmol, 100 mg). The formation of the monophosphole complex was confirmed by $^{31}$P NMR ($\delta$ = 20.9 ppm). A second equiv. of triphenylphosphole (0.32 mmol, 100 mg) was added and after 5 min stirring, the formation of the

 © 2006 Wiley-VCH Verlag GmbH & Co. KGaA, Weinheim 

bis(phosphole) complex was confirmed by $^{31}P$ NMR ($\delta$ = 11.0 ppm). The chloride was then abstracted with a silver salt AgX (0.32 mmol, **14a**: 83 mg, **14b**: 120 mg). Filtration of AgCl on celite followed by evaporation of the dichloromethane yielded the complexes as yellow powders in very good yields (**14a**: 98%, 280 mg; **14b**: 95%, 325 mg). Single-crystals of **14a** were obtained by slow diffusion of hexanes into a solution of the complex in dichloromethane at room temperature. $^{31}P$ NMR ($CD_2Cl_2$, 25 °C): $\delta$ = 22.7 ppm. $^1H$ NMR ($CD_2Cl_2$, 25 °C): $\delta$ = 3.61 (vdd, AA′BB′CXX′, $\Sigma J$ = 22.5 Hz, 2 H, $CH_{allyl}$), 4.61 (vdd, AA′BB′CXX′, $\Sigma J$ = 9.5 Hz, 2 H, $CH_{allyl}$), 5.75 (vsept, $AB_2C_2X_2$, $\Sigma J$ = 41.9 Hz, 1 H, $CH_{allyl}$), 6.88 (m, $A_2A'_2XX'$, $\Sigma J$ = 68.9 Hz, 4 H, $H_\beta$), 7.03–7.32 (m, 30 H, $H_{Ph}$) ppm. $^{13}C$ NMR ($CD_2Cl_2$, 25 °C): $\delta$ = 80.1 (vt, AXX′, $\Sigma J$ = 25.8 Hz, $CH_{2allyl}$), 122.8 (vt, AXX′, $\Sigma J$ = 9.9 Hz, $CH_{allyl}$), 126.7 (vt, AXX′, $\Sigma J$ = 7.5 Hz, $CH_{Ph}$), 127.0 (vt, AXX′, $\Sigma J$ = 7.4 Hz, $CH_{Ph}$), 129.0 (s, $CH_{Ph}$), 129.1 (s, $CH_{Ph}$), 129.2 (s, $CH_{Ph}$), 129.6 (vt, AXX′, $\Sigma J$ = 10.9 Hz, $CH_{Ph}$), 131.9 (s, $CH_{Ph}$), 132.4 (vt, AXX′, $\Sigma J$ = 11.6 Hz, $C_{Ph}$), 133.1 (vt, AXX′, $\Sigma J$ = 14.4 Hz, $C_{Ph}$), 133.2 (vt, AXX′, $\Sigma J$ = 14.4 Hz, $C_{Ph}$), 135.0 (vt, AXX′, $\Sigma J$ = 13.5 Hz, $CH_\beta$), 135.4 (vt, AXX′, $\Sigma J$ = 13.4 Hz, $CH_\beta$), 142.6 (m, $\Sigma J$ = 121.7 Hz, Cα) ppm. $C_{48}H_{39}F_3O_3P_2PdS$ (921.3): calcd. C 62.58, H 4.27; found C 62.18, H 4.25.

**Synthesis of Complexes 15a,b [Pd(6)($\eta_3$-$C_3H_5$)][X]:** To a solution of $[Pd(allyl)Cl]_2$ (0.14 mmol, 50 mg) in dichloromethane (2 mL) was added the 1-phenyl dibenzophosphole (0.27 mmol, 71 mg). The formation the monophosphole complex was confirmed by $^{31}P$ NMR ($\delta$ = 15.8 ppm). A second equiv. of 1-phenyl dibenzophosphole (0.27 mmol, 71 mg) was added and after 5 min stirring, the formation of the bis(phosphole) complex was confirmed by $^{31}P$ NMR ($\delta$ = 11.9 ppm). The chloride was then abstracted with a silver salt AgX (0.27 mmol, **15a**: 70 mg, **15b**: 102 mg). Filtration of AgCl on celite followed by evaporation of the dichloromethane yielded the complexes as pale yellow powders in very good yields (**15a**: 98%, 217 mg; **15b**: 97%, 245 mg). Single-crystals of **15a** were obtained by slow diffusion of hexanes into a solution of the complex in dichloromethane at room temperature. $^{31}P$ NMR ($CD_2Cl_2$, 25 °C): $\delta$ = 13.9 ppm. $^1H$ NMR ($CD_2Cl_2$, 25 °C): $\delta$ = 3.84 (br. s, 4 H, $CH_{allyl}$), 5.71 (vq, $AB_2C_2X_2$, $\Sigma J$ = 41.9 Hz, 1 H, $CH_{allyl}$), 7.68–7.21 (m, 26 H, Ph) ppm. $^{13}C$ NMR ($CD_2Cl_2$, 25 °C): $\delta$ = 74.23 (br. s, $CH_{2allyl}$), 121.0 (br. s, $CH_{allyl}$), 122.2 (d, $J_{PH}$ = 5.0 Hz, $CH_{Ph}$), 129.1 (d, $J_{PH}$ = 11.2 Hz, $CH_{Ph}$), 129.3 (d, $J_{PH}$ = 12.3 Hz, $CH_{Ph}$), 131.1 (br. s, $CH_{Ph}$), 131.3 (s, $CH_{Ph}$), 131.6 (vt, AXX′, $\Sigma J$ = 11.9 Hz, $CH_{Ph}$), 142.7 (d, $J_{PH}$ = 8.7 Hz, $C_{Ph}$) ppm. $C_{40}H_{31}F_3O_3P_2PdS$ (817.1): calcd. C 58.80, H 3.82; found C 58.57, H 3.82.

**Synthesis of Complexes 17a,b [Pd(8)($\eta_3$-$C_3H_5$)][X]:** To a solution of bis(2,5-diphenylphosphol-1-yl)propane (100 mg, 0.20 mmol) in dichloromethane (2 mL) was added $[Pd(allyl)Cl]_2$ (0.10 mmol, 35.7 mg). After 15 min stirring, the silver salt AgX was added (0.10 mmol, **17a**: 50.2 mg, **17b**: 73 mg) and the formation of the complexes were confirmed by $^{31}P$ NMR ($\delta$ = 9.0 ppm). Filtration of AgCl on celite followed by evaporation of the dichloromethane yielded the complexes as dark-red powders in very good yields (**17a**: 95%, 150 mg; **17b**: 96%, 174 mg). $^{31}P$ NMR ($CDCl_3$, 25 °C): $\delta$ = 9.0 ppm. $^1H$ NMR ($CDCl_3$, 25 °C): $\delta$ = 2.24 [m, 6 H, $P(CH_2)_3P$], 3.19 (vdt, AA′BB′CXX′, $\Sigma J$ = 23.5 Hz, 2 H, $CH_{allyl}$), 4.17 (vd AA′BB′CXX′, $\Sigma J$ = 7.0 Hz, 2 H, $CH_{allyl}$), 5.58 (vsept, $AB_2C_2X_2$, $\Sigma J$ = 41.1 Hz, 1 H, $CH_{allyl}$), 7.15–7.45 (m, 24 H, Ph and $H_\beta$) ppm. $^{13}C$ NMR ($CDCl_3$, 25 °C): $\delta$ = 19.1 (vt, AXX′, $\Sigma J$ = 29.4 Hz, $CH_2CH_2P$), 20.3 (s, $CH_2CH_2P$), 75.3 (vt, AXX′, $\Sigma J$ = 25.6 Hz, $CH_{2allyl}$), 121.9 (vt, AXX′, $\Sigma J$ = 9.1 Hz, $CH_{allyl}$), 126.3 (m, $CH_{Ph}$), 128.0 (s, $CH_{Ph}$), 128.7 (vd, $\Sigma J$ = 10.1 Hz, $CH_{Ph}$), 132.5 (vt, AXX′, $\Sigma J$ = 14.6, $C_{Ph}$), 132.9 (vt, AXX′, $\Sigma J$ = 14.6, $C_{Ph}$), 134.9 (vt, AXX′, $\Sigma J$ = 14.6 Hz, $CH_\beta$), 135.6 (vt, AXX′, $\Sigma J$ = 14.8 Hz, $CH_\beta$), 144.9 (m, $\Sigma J$ = 86.7 Hz, Cα) ppm. $C_{41}H_{35}F_3O_3P_2PdS$ (833.2): calcd. C 59.11, H 4.23; found C 58.88, H 4.22.

**Synthesis of Complexes 19a,b [Pd(9)($\eta_3$-$C_3H_5$)][X]:** To a solution of ligand (100 mg, 0.27 mmol) in dichloromethane (2 mL) was added $[Pd(allyl)Cl]_2$ (0.13 mmol, 48.8 mg). After stirring for 5 min, the formation of the intermediate complex **18** was confirmed by $^{31}P$ NMR ($\delta$ = 49.5 ppm) and single-crystals of **18** were grown by slow diffusion of hexanes into a solution in dichloromethane at room temperature. The chloride was then abstracted with a silver salt AgX (0.27 mmol, **19a**: 68.6 mg, **19b** 100 mg). Filtration of AgCl on celite followed by evaporation of the dichloromethane yielded the complexes as white powders in very good yields (**19a**: 97%, 175 mg; **19b**: 96%, 205 mg). Single-crystals of **19b** were obtained by slow diffusion of hexanes into a solution of the complex in dichloromethane at room temperature.

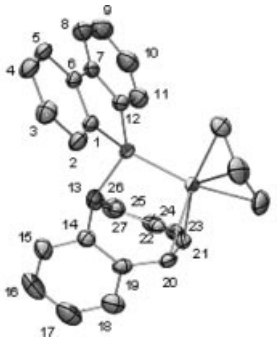

$^{31}P$ NMR ($CD_2Cl_2$): $\delta$ = 55.8 ppm. $^1H$ NMR ($CD_2Cl_2$): $\delta$ = 3.25 (m, 2 H, $CH_{allyl}$), 4.10 (vdd, ABCDEX, $\Sigma J$ = 23.4 Hz, 1 H, $CH_{allyl}$), 4.62 (d, $J_{PH}$ = 15.8 Hz, 1 H, $H^{13}$), 5.43 (vt, ABCDEX, $\Sigma J$ = 13.6 Hz, 1 H, $CH_{allyl}$), 5.77 (vsept, ABCDEX, $\Sigma J$ = 41.9 Hz, 1 H, $CH_{allyl}$), 6.08 (dd, $J_{H,H}$ = 7.5, $J_{P,H}$ = 7.5 Hz, 2 H, $H^5$–$H^8$), 7.01 (m, $\Sigma J$ = 10.5 Hz, 2 H, $H^{15}$–$H^{26}$), 7.15 (m, $\Sigma J$ = 21.3 Hz, 2 H, $H^3$–$H^{10}$), 7.53 (m, 6 H, $H^{17}$–$H^{24}$, $H^{16}$–$H^{25}$ and $H^4$–$H^9$), 7.66 (s, 2 H, $H^{20}$–$H^{21}$), 7.72 (m, $\Sigma J$ = 8.9 Hz, 2 H, $H^{18}$–$H^{23}$), 7.95 (m, $\Sigma J$ = 9.6 Hz, 2 H, $H^2$–$H^{11}$) ppm. $^{13}C$ NMR ($CD_2Cl_2$, 25 °C): $\delta$ = 54.8 (d, $J_{P,C}$ = 14.2 Hz, $C^{13}$), 66.0 (s, $CH_{2allyl}$), 85.9 (d, $J_{PC}$ = 24.7 Hz, $CH_{2allyl}$), 104.3 (s, $C^{20}$–$C^{21}$), 122.3 (d, $J_{P,C}$ = 6.1 Hz, $C^2$–$C^{11}$), 124.9 (d, $J_{P,C}$ = 5.3 Hz, $C^3$–$C^{10}$), 129.0 (d, $J_{P,C}$ = 10.5 Hz $C^{15}$–$C^{26}$), 129.5 (d, $J_{P,C}$ = 2.4 Hz, $C^4$–$C^9$), 130.8 (d, $J_{P,C}$ = 22.2 Hz, $C^5$–$C^8$), 130.9 (d, $J_{P,C}$ = 2.7 Hz, $C^{16}$–$C^{25}$), 131.8 (d, $J_{P,C}$ = 45.9 Hz, $C^1$–$C^{12}$), 131.9 (d, $J_{P,C}$ = 4.5 Hz, $C^{18}$–$C^{23}$), 132.9 (d, $J_{P,C}$ = 2.1 Hz, $C^{17}$–$C^{24}$), 133.5 (d, $J_{P,C}$ = 9.2 Hz, $C^{14}$–$C^{27}$), 135.3 (d, $J_{P,C}$ = 2.8 Hz, $C^{19}$–$C^{22}$), 142.8 (d, $J_{P,C}$ = 9.6 Hz, $C^6$–$C^7$) ppm, missing $CH_{allyl}$. $C_{32}H_{24}F_6NO_4PPdS_2$ (802.1): calcd. C 47.92, H 3.02; found C 47.57, H 3.01.

**General Procedure for Catalytic Reactions:** The catalyst (1 mol-%) was placed in a Schlenck tube with $MgSO_4$ (0.25 g) and THF (1 mL). The Schlenck tube was then filled with aniline (182 μL, 2 mmol) and allyl alcohol (68 μL, 1 mmol). The mixture was stirred at room temperature and the progress of the reaction was monitored by GC. The mixture was filtered to remove the $MgSO_4$ and the solvent evaporated in vacuo. The product was then isolated by column chromatography on alumina (hexanes).

***N*-(2-Propenyl)aniline:** See ref.[4a]

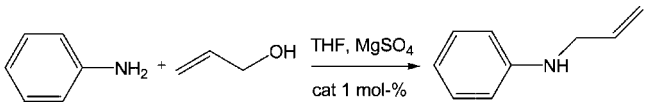


 © 2006 Wiley-VCH Verlag GmbH & Co. KGaA, Weinheim 

***N*,*N*-Bis(2-propenyl)aniline:** See ref.[4a]

**(*E*)- and (*Z*)-*N*-(2-Butenyl)aniline and *N*-(1-Methyl-2-propenyl)aniline:** See ref.[4a]

***N*-(2-Propenyl)morpholine:** See ref.[5]

***N*-(2-Propenyl)dibenzylamine:** See ref.[5]

***N*-(2-Propenyl)methylaniline:** See ref.[5]

***N*-(2-Methyl-2-propenyl)aniline:** $^1$H NMR ($CDCl_3$): $\delta$ = 1.80 (s, 3 H, H$^4$), 3.69 (s, 2 H, H$^1$), 4.02 (br. s, 1 H, NH), 4.89 (d, $J$ = 1.0 Hz, 1 H, H$^3$), 4.97 (d, $J$ = 1.0 Hz, 1 H, H$^3$), 6.63 (AA′BB′C, $\Sigma J$ = 8.5 Hz, 2 H, *m*-Ph), 6.71 (tt, $AB_2C_2$, $\Sigma J$ = 16.8 Hz, 1 H, *p*-Ph), 7.18 (AA′BB′C, $\Sigma J$ = 15.9 Hz, 2 H, *o*-Ph) ppm. $^{13}$C NMR ($CDCl_3$, 25 °C): $\delta$ = 20.6 (s, C$^4$), 50.1 (s, C$^1$), 111.1 (s, C$^3$), 113.0 (s, *m*-Ph), 117.5 (s, *p*-Ph), 129.3 (s, *o*-Ph), 142.8 (s, C$^2$), 148.2 (s, *ipso*-Ph) ppm.

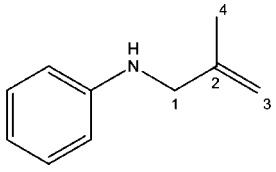


**Supporting Information Available** (see footnote on the first page of this article): ORTEP views and Crystallographic data for **10a**, **12b** and **13a** and optimised geometries and frequencies for compounds **5** and **6**, and for the transition states of the inversion of **5** and **6** and for the nickel complexes **I**, **II** and **III.**

## Acknowledgments

The authors thank the CNRS (Centre National de la Recherche Scientifique) and the École Polytechnique for the financial support of this work, the ETH Hönggerberg (Zürich, Switzerland) and IDRIS (Orsay, Paris XI) for the allowance of computer time.

[1] a) B. M. Trost, *Chem. Pharm. Bull.* **2002**, *50*, 1–14; b) M. Johannsen, K. A. Jorgensen, *Chem. Rev.* **1998**, *98*, 1689–1708; c) B. M. Trost, D. L. Van Vranken, C. Bingel, *J. Am. Chem. Soc.* **1992**, *114*, 9327–9343; d) B. M. Trost, in: *Advances in Natural Product Chemistry* (Ed.: Atta-Ur-Rahman), Harwood Academic Publishers, Harwood, **1992**, pp. 19–34; e) S. A. Godleski, in: *Comprehensive Organic Synthesis*, vol. 4 (Eds.: B. M. Trost, I. Fleming), Pergamon Press, New York, **1991**, pp. 585–661.

[2] a) B. M. Trost, D. L. Van Vranken, *Chem. Rev.* **1996**, *96*, 395–422; b) B. M. Trost, F. D. Toste, A. B. Pinkerton, *Chem. Rev.* **2001**, *101*, 2067–2096; c) S. A. Godleski, in: *Comprehensive Organic Synthesis*, vol. 4, chapter 3.3 (Eds.: B. M. Trost, I. Fleming, M. F. Semmelhack), Pergamon Press, Oxford, **1990**; d) J. A. Davis, in: *Comprehensive Organometallic Chemistry II*, vol. 9 (Eds.: E. W. Abel, F. G. A. Stone, G. Wilkinson), Pergamon, Oxford, **1995**, p. 291; e) J. Tsuji, *Transition Metal Reagents and Catalysts*, Wiley, New York, **2000**; f) B. M. Trost, *Science* **1991**, *254*, 1471; g) B. M. Trost, *Angew. Chem. Int. Ed. Engl.* **1995**, *34*, 259–281.

[3] a) J. C. Hierso, A. Fihri, R. Amardeil, P. Meunier, H. Doucet, M. Santelli, *Tetrahedron* **2005**, *61*, 9759–9766; b) M. Feuerstein, D. Laurenti, H. Doucet, M. Santelli, *Tetrahedron Lett.* **2001**, *42*, 2313–2315; c) J. Tsuji, *Palladium Reagents and Catalysis: Innovations in Organic Synthesis* Wiley, Chichester, **1995**, p. 292; d) T. Ohmura, J. F. Hartwig, *J. Am. Chem. Soc.* **2002**, *124*, 15164–15165; e) T. Ohmura, J. F. Hartwig, *J. Am. Chem. Soc.* **2003**, *125*, 3426–3427; f) R. Kuwano, K. I. Uchida, Y. Ito, *Org. Lett.* **2003**, *5*, 2177–2179.

[4] a) F. Ozawa, H. Okamoto, S. Kawagishi, S. Yamamoto, T. Minami, M. Yoshifuji, *J. Am. Chem. Soc.* **2002**, *124*, 10968–10969; b) F. Ozawa, T. Ishiyama, S. Yamamoto, S. Kawagishi, H. Murakami, M. Yoshifuji, *Organometallics* **2004**, *23*, 1698–1707; c) H. Bricout, J.-F. Carpentier, A. Mortreux, *J. Mol. Catal. A* **1998**, *136*, 243–251; d) M. Kimura, M. Futamata, K. Shibata, Y. Tamaru, *Chem. Commun.* **2003**, 234–235; e) M. Sakaibara, A. Ogawa, *Tetrahedron Lett.* **1994**, *35*, 8013–8014; f) S. C. Yang, Y. C. Tsai, *Organometallics* **2001**, *20*, 763–770; g) Y. Tamaru, *J. Organomet. Chem.* **1999**, *576*, 215–231.

[5] O. Piechaczyk, M. Doux, L. Ricard, P. Le Floch, *Organometallics* **2005**, *24*, 1204–1213.

[6] For the synthesis see B. Lukas, R. M. G. Roberts, J. Silver, A. S. Wells, *J. Organomet. Chem.* **1983**, *256*, 103–110. For applications in catalysis see: a) C. Bergounhou, D. Neibecker, R. Réau, *J. Chem. Soc., Chem. Commun.* **1988**, 1370–1372; b) D. Neibecker, R. Réau, S. Lecolier, *J. Org. Chem.* **1989**, *54*, 5208–5210; c) D. Neibecker, R. Réau, *J. Mol. Catal.* **1989**, *50*, 153–163; d) D. Neibecker, R. Réau, *New J. Chem.* **1991**, *15*, 279–281; e) A. Polo, C. Claver, S. Castillon, A. Ruiz, J. C. Bayon, J. Real, C. Mealli, D. Masi, *Organometallics* **1992**, *11*, 3525–3533; f) L. M. Wilkes, J. H. Nelson, L. B. McCusker, K. Seff, F. Mathey, *Inorg. Chem.* **1983**, *22*, 2476–2485.

[7] S. Affandi, R. L. Green, B. T. Hsieh, M. S. Holt, J. H. Nelson, *Synth. React. Inorg. Met. Org. Chem.* **1987**, *17*, 307–318.

[8] S. Bousquet, J. J. Brunet, T. Courcet, D. Neibecker, *Phosphorus Sulfur Silicon Relat. Elem.* **1998**, *142*, 117–124.

[9] C. Thoumazet, L. Ricard, H. Grutzmacher, P. Le Floch, *Chem. Commun.* **2005**, 1592–1594.

[10] a) S. Ogoshi, M. Morita, H. Kurosawa, *J. Am. Chem. Soc.* **2003**, *125*, 9020–9021; b) S. Ogoshi, K. Tsutsumi, H. Kurosawa, *J. Organomet. Chem.* **1995**, *493*, C19–C21; c) M. W. Baize, P. W. Blosser, V. Plantevin, D. G. Schimpff, J. C. Gallucci, A. Wojcicki, *Organometallics* **1996**, *15*, 164–173.

[11] a) W. P. Ozbirn, R. A. Jacobson, J. C. Clardy, *J. Chem. Soc., Chem. Commun.* **1971**, 1062; b) E. C. Alyea, G. Ferguson, J. F. Gallagher, *Acta Crystallogr., Sect. C* **1992**, *48*, 959–961.

[12] F. Mathey, *Phosphorus-Carbon Heterocyclic Chemistry: The Rise of a New Domain*, chapter 4, Pergamon Press, Amsterdam, **2001**, p. 219.

[13] E. Mattmann, F. Mathey, A. Sevin, G. Frison, *J. Org. Chem.* **2002**, *67*, 1208–1213.

[14] W. Egan, R. Tang, G. Zon, K. Mislow, *J. Am. Chem. Soc.* **1971**, *93*, 6205–6216.

[15] a) A. Dransfeld, L. Nyulaszi, P. v. R. Schleyer, *Inorg. Chem.* **1998**, *37*, 4413–4420; b) P. v. R. Schleyer, C. Maerker, A. Dransfeld, H. J. Jiao, N. Hommes, *J. Am. Chem. Soc.* **1996**, *118*, 6317–6318; c) L. Nyulaszi, *Chem. Rev.* **2001**, *101*, 1229–1246; d) M. K. Cyranski, T. M. Krygowski, A. R. Katritzky, P. v. R. Schleyer, *J. Org. Chem.* **2002**, *67*, 1333–1338; e) P. Schleyer, *Chem. Rev.* **2001**, *101*, 1115–1117.

[16] G. Frenking, N. Frölich, *Chem. Rev.* **2000**, *100*, 717–774.

[17] D. Drew, J. R. Doyle, in: *Inorganic Syntheses*, vol. 28 (Ed.: R. J. Angelici), **1990**, pp. 348–349.

[18] M. Zettlitzer, H. tom Dieck, E. T. K. Haupt, L. Stamp, *Chem. Ber.* **1986**, *119*, 1868–1875.

[19] Gaussian 03 Revision C.02, M. J. Frisch, G. W. Trucks, H. B. Schlegel, G. E. Scuseria, M. A. Robb, J. R. Cheeseman, J. A. Montgomery Jr, T. Vreven, K. N. Kudin, J. C. Burant, J. M. Millam, S. S. Iyengar, J. Tomasi, V. Barone, B. Mennucci, M. Cossi, G. Scalmani, N. Rega, G. A. Petersson, H. Nakatsuji, M. Hada, M. Ehara, K. Toyota, R. Fukuda, J. Hasegawa, M. Ishida, T. Nakajima, Y. Honda, O. Kitao, H. Nakai, M. Klene, X. Li, J. E. Knox, H. P. Hratchian, J. B. Cross, V. Bakken, C. Adamo, J. Jaramillo, R. Gomperts, R. E. Stratmann, O. Yazyev, A. J. Austin, R. Cammi, C. Pomelli, J. W. Ochterski, P. Y. Ayala, K. Morokuma, G. A. Voth, P. Salvador, J. J. Dannenberg, V. G. Zakrzewski, S. Dapprich, A. D. Daniels, M. C. Strain, O. Farkas, D. K. Malick, A. D. Rabuck, K. Raghavachari, J. B. Foresman, J. V. Ortiz, Q. Cui, A. G. Baboul, S. Clif-

 © 2006 Wiley-VCH Verlag GmbH & Co. KGaA, Weinheim 

ford, J. Cioslowski, B. B. Stefanov, G. Liu, A. Liashenko, P. Piskorz, I. Komaromi, R. L. Martin, D. J. Fox, T. Keith, M. A. Al-Laham, C. Y. Peng, A. Nanayakkara, M. Challacombe, P. M. W. Gill, B. Johnson, W. Chen, M. W. Wong, C. Gonzalez, and J. A. Pople, Gaussian, Inc., Wallingford CT, **2004**.

[20] a) A. D. J. Becke, *J. Phys. Chem.* **1993**, *98*, 5648–5662; b) J. P. Perdew, Y. Wang, *Phys. Rev. B* **1992**, *45*, 13244–13249.

[21] a) S. I. Gorelsky, *AOMIX: Program for Molecular Orbital Analysis*, *http://www.sg-chem.net/*, York University: Toronto, Canada, **1997**; b) S. I. Gorelsky, *J. Organomet. Chem.* **2001**, *635*, 187–196.

[22] A. Altomare, M. C. Burla, M. Camalli, G. Cascarano, C. Giacovazzo, A. Guagliardi, A. G. G. Moliterni, G. Polidori, R. Spagna, *SIR97, An Integrated Package of Computer Programs for the Solution and Refinement of Crystal Structures using Single Crystal Data*.

[23] G. M. Sheldrick, *SHELXL-97*, University of Göttingen, Göttingen, Germany, **1997**.

Received: January 17, 2006
Published Online: August 7, 2006

 © 2006 Wiley-VCH Verlag GmbH & Co. KGaA, Weinheim 

DOI: 10.1002/ejic.200600268

# Synthesis, Characterization, and Luminescence Properties of $Eu^{3+}$ 3-Phenyl-4-(4-toluoyl)-5-isoxazolonate Based Organic-Inorganic Hybrids

**Patricia P. Lima,[a,b] Severino A. Junior,[a] Oscar L. Malta,[a] Luis D. Carlos,[b] Rute A. Sá Ferreira,[b] Rani Pavithran,[c] and M. L. P. Reddy*[c]**

**Keywords:** Organic-inorganic hybrids / $Eu^{3+}$ / Heterocyclic β-diketonates / Synthesis / Characterization / Luminescence

Organic-inorganic hybrids incorporating $Eu(TPI)_3{\cdot}3H_2O$ or $Eu(TPI)_3{\cdot}2TOPO$ [where TPI and TOPO stand for 3-phenyl-4-(4-toluoyl)-5-isoxazolone and tri-*n*-octylphosphane oxide, respectively] were synthesized either by acetic acid solvolysis or a conventional hydrolysis sol-gel route. The host framework of these materials, named as di-ureasil, consists of a siliceous skeleton grafted, through urea cross-linkages, to both ends of poly(ethylene oxide) chains. The resulting $Eu^{3+}$-based di-ureasils were characterized by X-ray diffraction and Fourier transform mid-IR, $^{29}Si$ and $^{13}C$ NMR, and photoluminescence spectroscopy. The room-temperature photoluminescence (PL) spectra of the $Eu^{3+}$-based di-ureasils display the typical $Eu^{3+}$ red emission, assigned to transitions between the first excited state ($^5D_0$) and the ground multiplet ($^7F_{0-4}$). Enhanced $^5D_0$ quantum efficiency ($\eta$ = 13 % vs. 32 %) and a longer lifetime ($\tau$ = 0.30 vs. 0.42 ms) was noticed for the hybrid incorporating the $Eu(TPI)_3{\cdot}3H_2O$ complex, compared with the undoped complex. The enhancement is explained by the coordination ability of the organic counter part of the host structure, which is strong enough to displace the water molecules of the $Eu(TPI)_3{\cdot}3H_2O$ complex from the $Eu^{3+}$ neighborhood in the hybrids. On the other hand, a decrease in the $^5D_0$ quantum efficiency ($\eta$ = 76 % vs. 61 %) and lifetime ($\tau$ = 0.98 vs. 0.75 ms) was noticed for the hybrid incorporating the $Eu(TPI)_3{\cdot}2TOPO$ complex, relative to the undoped complex, probably because of an increase in the nonradiative transition probability.

(© Wiley-VCH Verlag GmbH & Co. KGaA, 69451 Weinheim, Germany, 2006)

## Introduction

Lanthanide complexes with organic ligands are of great interest for a wide range of photonic applications, such as tuneable lasers, optical fibres for telecommunications, components of emitting layers in multilayer organic light-emitting diodes (OLEDs), and light conversion molecular devices (LCMDs).[1–5] The β-diketone ligand is one of the most important "antenna" from which the energy can be effectively transferred to lanthanide ions for high harvest emissions.[4] Despite lanthanide β-diketonate complexes being characterized by a highly efficient light emission under UV excitation they have not been employed so far as tuneable solid-state lasers or phosphor devices essentially because of their low thermal and photochemical stability and poor mechanical properties.[6] Furthermore, lanthanide β-diketonate chelates are usually isolated as hydrates in which two or three water molecules are included in the first coordination sphere of the central metal ion, quenching the emission from the activation of nonradiative decay paths.[4,7–8]

One of the strategies adopted in recent years to simultaneously improve the thermal stability, mechanical properties, and light-emission properties of lanthanide β-diketonate complexes is to incorporate these complexes into sol-gel-derived organic-inorganic hybrids.[9–13] The main interest of the organic-inorganic hybrid concept basically derives from the possibility of tailoring the properties of novel multifunctional advanced materials through the combination, at the nanosize level, of the organic and inorganic components in one single material.[14,15] Among the sol-gel-derived structures proposed so far, a family of interesting lanthanide-based hybrid compounds have been reported.[16] The host matrix, termed as di-ureasil, comprises poly(ethylene oxide) (PEO) chains of variable length grafted to both ends to a siliceous backbone through urea cross linkages. These xerogels, which are easily produced as thin, elastomeric and highly transparent monoliths, may withstand a large amount of guest dopants. When doped with trivalent lanthanide ions like $Nd^{3+}$, $Eu^{3+}$, and $Tb^{3+}$ the di-ureasils display remarkable emission properties. Besides a broad long-lived emission covering the whole visible range of the electromagnetic spectrum, the di-ureasils exhibit the typical intra-4f narrow line emission in the green ($Tb^{3+}$),[17] red ($Eu^{3+}$),[18–20] and even in the near infrared ($Nd^{3+}$) region,[21] thus opening new prospects for their applications.

[a] Departamento de Quimica Fundamental – UFPE, 50670-901 Recife, PE, Brazil
[b] Departamento de Fisica, CICECO, Universidade Aveiro, 3810-193 Aveiro, Portugal
[c] Chemical Sciences and Technology Division, Regional Research Laboratory (CSIR), Thiruvananthapuram 695019, India
E-mail: mlpreddy@yahoo.co.uk

 © 2006 Wiley-VCH Verlag GmbH & Co. KGaA, Weinheim 

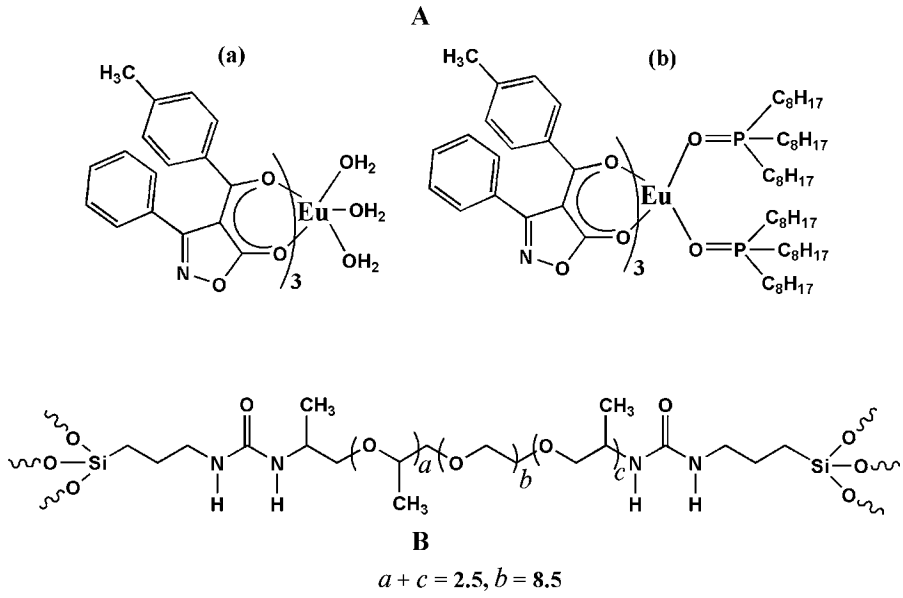


Figure 1. A: Chemical structure of (a) $Eu(TPI)_3{\cdot}3H_2O$ (**1**) and (b) $Eu(TPI)_3{\cdot}2TOPO$ (**2**); B: d-U(600) di-ureasil hybrid.

A significant part of the research strategy in the field involves the encapsulation of lanthanide organic complexes with β-diketonates, aromatic carboxylic acids and heterocyclic ligands in sol-gel-derived matrices. These complexes can be embedded in the matrix by using the ligands covalently grafted to the framework or by anchoring the lanthanide ion to specific functional groups of the hybrid matrix. Recently, $Eu^{3+}$ β-diketonate complexes have been successfully incorporated into organic-inorganic hybrids and their photophysical properties have been investigated.[9–11] Nevertheless, the incorporation of heterocyclic β-diketonate complexes, namely $Eu^{3+}$ 4-acyl-3-phenyl-5-isoxazolonate complexes, into organic-inorganic hybrids has not been attempted to date.

In this paper, heterocyclic β-diketone $Eu^{3+}$ complexes with the molecular formulae $Eu(TPI)_3{\cdot}3H_2O$ and $Eu(TPI)_3{\cdot}2TOPO$ [where TPI = 3-phenyl-4-(4-toluoyl)-5-isoxazolone and TOPO = tri-*n*-octylphosphane oxide], recently introduced as light conversion molecular devices by Reddy et al.,[22] were incorporated into di-ureasil organic-inorganic hybrids (Figure 1) by conventional hydrolysis and acetic acid solvolysis. The photoluminescence (in excitation and emission modes), the $^5D_0$ quantum efficiency, and lifetime of the di-ureasil hybrids were investigated and compared with those of the precursor complexes.

## Results and Discussion

The synthesis procedures and characterization of the complexes $Eu(TPI)_3{\cdot}3H_2O$ (**1**) and $Eu(TPI)_3{\cdot}2TOPO$ (**2**) (Figure 1A) are detailed in our earlier publication.[22] The complexes **1** and **2** were incorporated into the di-ureasil host by acetic acid solvolysis according to the procedure described elsewhere.[10] Complex **2** was also incorporated into di-ureasil by a conventional hydrolysis sol-gel route.[10] Figure 1B illustrates the structure of the undoped hybrid matrix.

### Powder X-ray Diffraction (XRD)

The X-ray diffraction patterns of d-U(600)-**1**-AA [$Eu(TPI)_3{\cdot}3H_2O$ (**1**) incorporated into the d-U(600) di-ureasil by acetic acid (AA) solvolysis], d-U(600)-**2**-AA [$Eu(TPI)_3{\cdot}2TOPO$ (**2**) incorporated into the d-U(600) di-ureasil by acetic acid (AA) solvolysis], and d-U(600)-**2** [$Eu(TPI)_3{\cdot}2TOPO$ (**2**) incorporated into the d-U(600) di-ureasil by conventional hydrolysis] are shown in Figure 2. The patterns display a main peak centered at ca. 21.0–21.7° associated with ordering within the siloxane domains. The second-order peak appears as a broad weak hump around 38–46°. The structural unit distance, calculated using the Bragg law, is approximately 4.07–4.21 Å. These results are similar to those reported for carboxylic acid solvolysis derived undoped hybrids.[14] These data reveal that the $Eu^{3+}$-based hy-

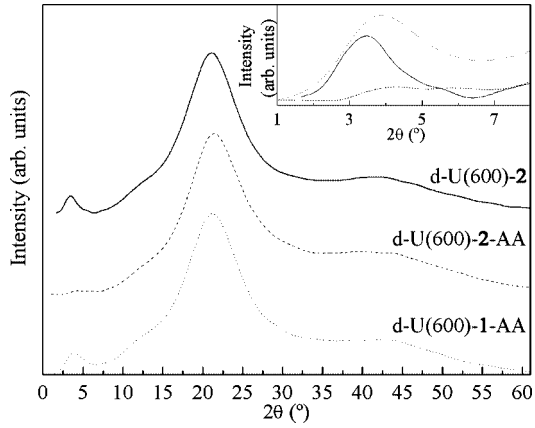


Figure 2. XRD patterns of the $Eu^{3+}$-based di-ureasil hybrids.

 © 2006 Wiley-VCH Verlag GmbH & Co. KGaA, Weinheim 

brids are highly amorphous. The peak appearing at lower angles in the XRD patterns, at ca. 3.5 and 5.2° (inset of Figure 1), has been assigned to interparticle scattering interference between siliceous domains[23] located at the ends of the polymer chain and spatially correlated at a mean distance of 25 ± 1 Å, for d-U(600)-**1**-AA, 28 ± 1 Å, for d-U(600)-**2**, and 19 ± 1 Å, for d-U(600)-**2**-AA. The different values calculated for the hybrids incorporating complex **2** indicate that the synthesis methods induce significant differences in the hybrid structure.

### Fourier-Transform Infrared Spectroscopy (FT-IR)

The FT-IR spectra of d-U(600)-**1**-AA, d-U(600)-**2**-AA, and d-U(600)-**2** are shown in Figure 3. The shoulder at ca. 920 $cm^{-1}$ provides evidence that in the di-ureasils the PEO chains attain complete disorder. Compared with the undoped di-ureasil,[24] the intensity of the shoulder shows a very slight decrease, indicating a very weak interaction between the polymer and the complex.[10] The bands at 1324 $cm^{-1}$ are characteristic of the amorphous state.[10] The 1354 $cm^{-1}$ bands, ascribed to the $CH_2$ wagging vibrations, are clearly seen in the spectra. It is known that the νCO mode of PEO is an excellent tool to probe the changes that the polymer chains of the hybrids undergo upon incorporation of the guest compounds. The fact that peaks at about 1110 $cm^{-1}$, characteristic of noncoordinated oxyethylene moieties,[24] are almost unchanged in the spectra of the $Eu^{3+}$-based di-ureasils suggests that the PEO chains of the host materials persist in an uncomplexed state.

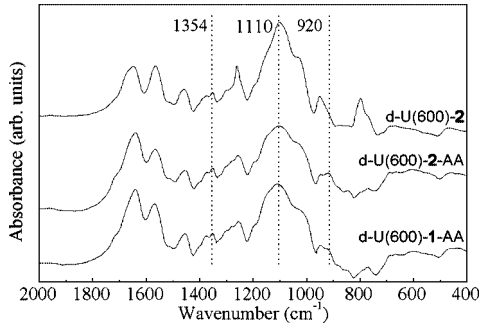


Figure 3. FTIR spectra of the $Eu^{3+}$-based di-ureasil hybrids.

In order to study in detail the vibrations of the urea groups, spectral deconvolutions to the so-called "amide I" (1800–1600 $cm^{-1}$) and "amide II" (1600–1500 $cm^{-1}$) regions were carried out using Gaussian band shapes, as reported elsewhere.[14,24] Three components were isolated for the "amide I" band at 1700, 1672, and 1647 $cm^{-1}$. According to the literature,[19,24] the former two components are ascribed to the vibrations of urea–polyether hydrogen-bonded structures, whereas the last one is ascribed to the strong self-associated hydrogen-bonded urea–urea associations. For the $Eu^{3+}$-doped di-ureasils, besides the three mentioned peaks, a new peak appears at 1619–1625 $cm^{-1}$, indicating an effective interaction between the $Eu^{3+}$ ions and the carbonyl oxygen atoms of the urea cross-links. While for the hybrids incorporating complex **1** this result suggests the probable substitution of the water molecules in the $Eu^{3+}$ coordination sphere, for those with complex **2** an interaction between the $Eu^{3+}$ ions and the urea cross-links through the carbonyl groups should occur. In addition, the absence of an individual band at ca. 1750 $cm^{-1}$ in all the spectra indicates that neither C=O nor N–H groups from urea cross-linkages are left free in the hybrid materials.[10] The "amide II" mode is a mixed contribution of the N–H in-plane bending, C–N stretching, and C–C stretching vibrations, peaking, for all the samples, at ca. 1565 $cm^{-1}$.

### NMR Spectra

The $^{29}Si$ MAS NMR spectra of d-U(600)-**1**-AA and d-U(600)-**2**-AA exhibit broad signals characteristic of $T_1$, $T_2$, and $T_3$ units (Figure 4). These sites are labeled using the conventional $T_n$ notation, where $n$ ($n$ = 1, 2, 3) is the number of Si-bridging oxygen atoms. The absence of $T_0$ indicates that, although the polycondensations are not, in most cases, complete, no precursor is left unreacted. The $T_2$ and $T_3$ environments (at $\delta \approx -58$ and –66 ppm, respectively) are clearly dominant, showing the presence of two main types of local structures: $(SiO)_2Si(CH_2)_3OH$ and $(SiO)_3Si(CH_2)_3$. The very weak shoulder displayed in these hybrids at $\delta \approx 51.5$ and 53.1 ppm, for d-U(600)-**1**-AA and d-U(600)-**2**-AA, respectively, is ascribed to $T_1$ sites. The condensation degree $c$ (Table 1), was calculated using the expression $c = 1/3(\%T_1 + 2\%T_2 + 3\%T_3)$. Compared with the undoped sample[14] the condensation degree decreases, suggesting that there are some interactions between the complex and the matrix (urea cross-links) and that the relatively larger molecular size for the complex sterically prevents the polycondensation process and results in the lower condensation degree.

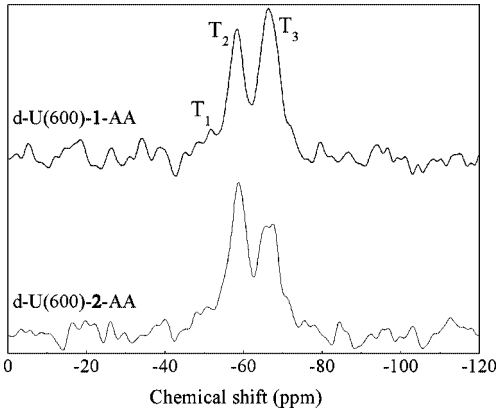


Figure 4. $^{29}$ Si MAS NMR spectra of the $Eu^{3+}$-based di-ureasil hybrids prepared by solvolysis.

The $^{13}C$ CP MAS NMR spectra of d-U(600)-**1**-AA and d-U(600)-**2**-AA display a peak at $\delta$ = 70.6 ppm, attributed to $-(OCH_2CH_2)-$, whereas the shoulder at about 75.0 ppm originates from the main-chain carbons of propylene oxide.

 © 2006 Wiley-VCH Verlag GmbH & Co. KGaA, Weinheim 

Table 1. $^{29}Si$ NMR chemical shifts (ppm), population of different $T_n$ ($n$ = 1, 2, 3) species (%), and degree of condensation (%), $c$, of d-U(600)-AA, d-U(600)-**1**-AA, and d-U(600)-**2**-AA.

| Hybrids | $T_1$ | $T_2$ | $T_3$ | $c$ |
|---|---|---|---|---|
| d-U(600)-AA | –55.5(11) | –58.9(28) | –66.9(61) | 83[10] |
| d-U(600)-**1**-AA | –51.5(19.3) | –58.2(25.4) | –66.5(55.3) | 75.3 |
| d-U(600)-**2**-AA | –53.1(26.8) | –58.6(27.9) | –66.6(45.3) | 72.8 |

The peaks at ca. 46 and 24 ppm are characteristic of the $(CH_2)_3$ aliphatic chains. The signal at $\delta$ = 18.5 ppm is assigned to different $CH_3$ groups of the polymer chains, while the shoulder at $\delta$ = 17.4 ppm is ascribed to the ethoxy groups of the carbon atoms. The weak peak at $\delta \approx 159$ ppm is associated with the C=O groups of the urea linkages,[25,26] supporting the interaction between the complex and the hybrid matrix, in agreement with the results obtained from FT-IR spectroscopy. These results are similar to those reported elsewhere.[10]

## Photoluminescence

Figures 5A and B compare the room-temperature excitation spectra (monitored around the peak of the intense $^5D_0 \rightarrow {}^7F_2$ transition) of complexes **1** and **2** with those of d-U(600)-**1**-AA, d-U(600)-**2**-AA, and d-U(600)-**2**. While the spectrum of complex **1** is dominated by the intra-4f$^6$ lines corresponding to the $^7F_{0-1} \rightarrow {}^5D_{1-2}$ transitions, the spectrum of complex **2** displays an intense broad band, with three main components at ca. 298, 330, and 400 nm, ascribed to the ligand levels. For the latter complex the relative intensity of the intra-4f$^6$ lines is weaker than the absorption of the organic ligands, indicating that luminescence sensitization from the ligand excitation is more efficient than the direct intra-4f$^6$ absorption. Moreover, in that complex the $Eu^{3+}$ ions are excited over a much larger wavelength range (240–440 nm) than that observed for complex **1** (310–440 nm). The spectra of the $Eu^{3+}$-based di-ureasils are blueshifted with respect to that of the two complexes presenting mainly a broad band (260–450 nm) peaking around 375 nm and related to the ligand levels and to the hybrid host emitting centers. This reinforces that the complex incorporation of the d-U(600) host changes the $Eu^{3+}$ surroundings. As illustrated for complex **2** in Figure 5B, the synthesis route used to incorporate the complexes leads to slight differences in the $Eu^{3+}$ excitation paths, as reported for analogous $Eu^{3+}$-based di-ureasil hybrids.[10] It is worth noting that the efficiency of the sensitized process in the hybrids is almost constant over a very broad UV/Vis spectral region (250–450 nm). Moreover, the absence of $Eu^{3+}$ intra-4f$^6$ lines in the excitation spectra of the hybrids strongly suggests that the metal ions are essentially excited by an efficient sensitized process rather than by direct population of the intra-4f$^6$ levels (the di-ureasil host contributes to enhancing the $Eu^{3+}$ sensitization process).

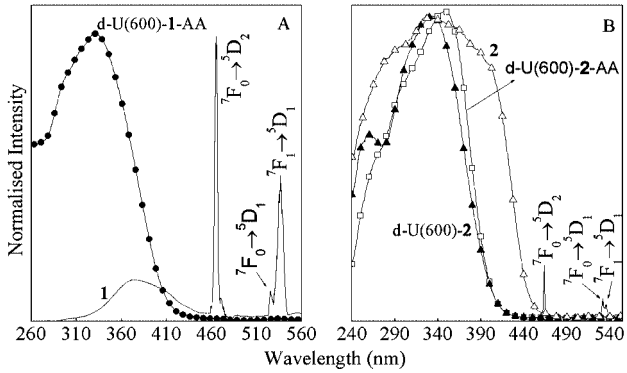


Figure 5. Room-temperature excitation spectra (monitored around 610–614 nm) of (A) complex **1** (solid line), d-U(600)-**1**-AA (solid circles) and of (B) complex **2** (open triangles), d-U(600)-**2**-AA (solid triangles), d-U(600)-**2** (open squares).

Figures 6 and 7 show the room-temperature emission spectra of the two complexes and the corresponding $Eu^{3+}$-based di-ureasils. The spectra display the characteristic sharp peaks of the $Eu^{3+}$ $^5D_0 \rightarrow {}^7F_{0-4}$ transitions (575–725 nm) being dominated by the hypersensitive $^5D_0 \rightarrow {}^7F_2$ lines, which point to a highly polarizable chemical environment around the $Eu^{3+}$ ion.[11,13] The detection of a single $^5D_0 \rightarrow {}^7F_0$ transition for all the samples investigated (Figure 6 and Figure 7B), with a typical full-width at half-maximum (fwhm) value of ca. 20 cm$^{-1}$, suggests the presence of a single $Eu^{3+}$ chemical environment. The detection of that line, the local-field splitting of the $^7F_{1,2}$ levels in the 3 and 4 Stark components (Figure 6, Figure 7C and D) and the higher intensity of the $^5D_0 \rightarrow {}^7F_2$ transition indicate that the $Eu^{3+}$ local coordination site has a low symmetry without an inversion center. For the two complexes, no emission arising from the ligand triplet levels is detected, pointing to an efficient ligand-to-$Eu^{3+}$ energy transfer. On the other hand, the emission spectra of the hybrids display a very-low-intensity band in the blue-green region, as illustrated in the inset of Figure 6 for d-U(600)-**1**-AA. This band has been as-

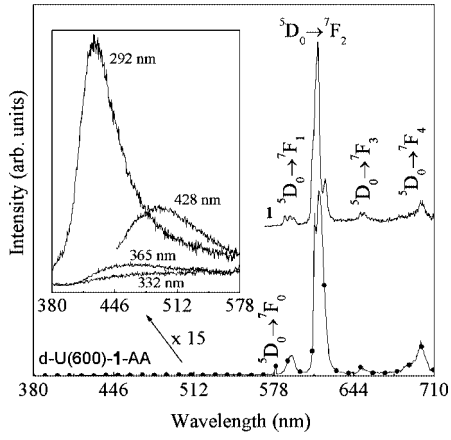


Figure 6. Room-temperature emission spectra of complex **1** (solid line) and d-U(600)-**1**-AA (solid circles), excited at 341 and 332 nm, respectively. The inset shows the magnification of the low-wavelength side of the emission spectra of d-U(600)-**1**-AA for different excitation wavelengths between 292 and 428 nm.

 © 2006 Wiley-VCH Verlag GmbH & Co. KGaA, Weinheim 

cribed to the hybrid host emission originated from donor–acceptor pair recombination occurring in the NH groups of the urea linkages and in the siliceous nanodomains.[27–30] The negligible intensity of this emission clearly suggests the presence of active energy transfer channels between the emitting centers of the hybrid and the $Eu^{3+}$ ions, a claim that is in agreement with the suggested interaction between the $Eu^{3+}$ ions and the urea cross-links through the carbonyl groups. Comparing the emission spectra of d-U(600)-**2**-AA and d-U(600)-**2** (Figure 7), changes were observed in the energy peak values, fwhm of each line, and number of Stark components, suggesting that the two different synthesis methods affect the $Eu^{3+}$ first coordination sphere, as already noticed in the excitation spectra.

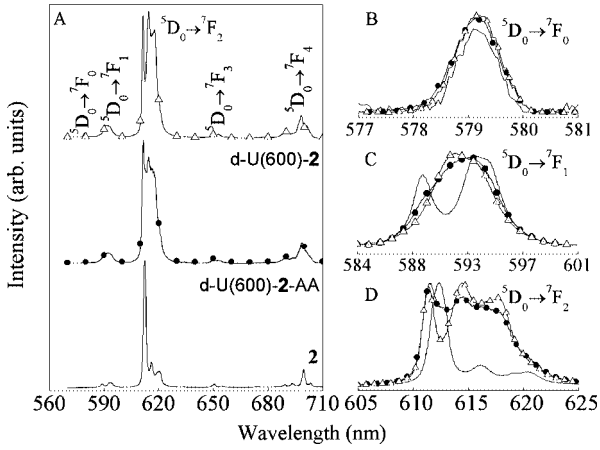


Figure 7. A: Room-temperature emission spectra of (a) complex **2**, d-U(600)-**2**-AA (solid circles) and d-U(600)-**2** (open triangles); the excitation wavelengths are 339 nm for d-U(600)-**2**, 348 nm for d-U(600)-**2**-AA and 327 nm for complex **2**. B, C, D: Details of the $^5D_0\rightarrow{}^7F_{0-2}$ transitions.

The Judd–Ofelt theory is a useful tool for analyzing f–f electronic transitions.[31] Interaction parameters of ligand fields are given by the Judd–Ofelt parameters, $\Omega\lambda$ (where $\lambda$ = 2, 4, and 6). In particular, $\Omega_2$ is more sensitive to the symmetry and sequence of ligand fields. To produce faster $Eu^{3+}$ radiation rates, antisymmetrical $Eu^{3+}$ complexes with larger $\Omega_2$ parameters need to be designed. The experimental $\Omega_2$ and $\Omega_4$ intensity parameters were determined from the emission spectra given in Figures 6 and 7 by using the $^5D_0\rightarrow{}^7F_2$ and $^5D_0\rightarrow{}^7F_4$ electronic transitions, respectively, and by expressing the emission intensity $I_J = \hbar\omega_{J0}A_{RAD}(J)$-$N(^5D_0)$ in terms of the area under the emission curve. Here, $\hbar\omega_{J0}$ is the transition energy and $N$ is the population of the $^5D_0$ level. The radiative emission rates, $A_{RAD}(J)$, are given by [Equation (1)],[32] where $e$ is the electronic charge, $\omega$ the angular frequency of the transition, $\hbar$ the Planck's constant over $2\pi$, $c$ the velocity of light, $\chi$ the Lorentz local field correction term given by $n(n^2+2)^2/9$, where $n$ is the refraction index, and $\langle {}^7F_J\|U^{(\lambda)}\|{}^5D_0\rangle^2$ is a squared reduced matrix element whose values are 0.0032 and 0.0023, for $J$ = 2 and 4, respectively.[33]

$$A_{RAD} = \frac{4e^2\omega^3}{3\hbar c^3}\chi\sum_{\lambda}\Omega_\lambda\left\langle {}^7F_J\left\|U^{(\lambda)}\right\|{}^5D_0\right\rangle^2\frac{1}{2J+1} \quad (1)$$

The magnetic dipole allowed $^5D_0\rightarrow{}^7F_1$ transition was taken as the reference,[13,32] in vacuo $A_{RAD}(^5D_0\rightarrow{}^7F_1)$ = 14.65 $s^{-1}$.[31] An average index of refraction equal to 1.5[34] was considered leading to $A_{RAD}(^5D_0\rightarrow{}^7F_1) \approx 50\ s^{-1}$.[13] The $\Omega_6$ parameter was not determined since the $^5D_0\rightarrow{}^7F_{5,6}$ transitions could not be experimentally detected. Table 2 lists the $\Omega_2$ and $\Omega_4$ intensity parameters estimated for complexes **1** and **2** and corresponding hybrids. A point to be noted is the relatively high values of the $\Omega_2$ parameter. This might be interpreted as being a consequence of the hypersensitive behavior of the $^5D_0\rightarrow{}^7F_2$ transition.[35] The dynamic coupling mechanism is, therefore, dominant, indicating that the $Eu^{3+}$ ion is in a highly polarizable chemical environment.

Table 2. Experimental intensity parameters ($\Omega_2$ and $\Omega_4$), radiative decay rates, $A_{RAD}$, nonradiative decay rates, $A_{NRAD}$, $^5D_0$ lifetimes, $\tau$, and quantum efficiency, $\eta$, for the complex and hybrids. The parameters' errors are estimated within 5–10%.

| Compounds | $\Omega_2$ $\times10^{-20}$ [$cm^2$] | $\Omega_4$ $\times10^{-20}$ [$cm^2$] | $A_{RAD}$ [$s^{-1}$] | $A_{NRAD}$ [$s^{-1}$] | $\tau$ [ms] | $\eta$ [%] |
|---|---|---|---|---|---|---|
| Complex **1**[22] | 8.1 | 5.8 | 381 | 2952 | 0.30 | 13 |
| d-U(600)-**1**-AA | 19.3 | 8.2 | 751 | 1630 | 0.42 | 32 |
| Complex **2**[22] | 20.7 | 6.4 | 773 | 242 | 0.98 | 76 |
| d-U(600)-**2** | 19.8 | 8.0 | 765 | 822 | 0.63 | 48 |
| d-U(600)-**2**-AA | 21.1 | 8.6 | 813 | 520 | 0.75 | 61 |

The $^5D_0$ lifetime values ($\tau$) were determined by fitting the emission decay profiles to a mono-exponential function, Table 2. The shorter $^5D_0$ lifetime of complex **1**, relative to that of complex **2**, is associated with the nonradiative decay channel from the vibronic coupling with water molecules.[22] While the lifetime of the d-U(600)-**1**-AA hybrid increases around 40%, relative to that of complex **1**, the incorporation of complex **2** into the hybrid host induces a decrease of the $^5D_0$ lifetime between 24 and 36%, depending on the synthesis route. On the basis of the emission spectra and the lifetime measurements, and considering that only nonradiative and radiative processes are essentially involved in the depopulation of the $^5D_0$ state, we can estimate the emission quantum efficiency of the $^5D_0$ excited state ($\eta$) as [Equation (2)], where $A_{RAD}$ is obtained by summing the radiative rates $A_{0J}$ for each $^5D_0\rightarrow{}^7F_{0-4}$ transition[31] and the nonradiative rates, $A_{NRAD}$, are calculated from the experimental decay rates [Equation (3)].

$$\eta = \frac{A_{RAD}}{A_{RAD} + A_{NRAD}} \quad (2)$$

$$\frac{1}{\tau} = A_{RAD} + A_{NRAD} \quad (3)$$

Table 2 lists the $A_{RAD}$, $A_{NRAD}$, and $\eta$ for the complexes and hybrids. The nonradiative rate of d-U(600)-**1**-AA decreases by ca. 55%, relative to that of complex **1**, causing

 © 2006 Wiley-VCH Verlag GmbH & Co. KGaA, Weinheim 

an enhancement in the emission quantum efficiency ($\eta$ = 32%) in comparison with complex **1** ($\eta$ = 13%[22]). This result is in agreement with the suggested interaction between the hybrid host and the $Eu^{3+}$ ions through the oxygen atom of the carbonyl group, replacing water molecules present in the precursor complex. The lower $^5D_0$ quantum efficiency found for the hybrid prepared by the conventional sol-gel route, relative to that prepared by solvolysis, is mainly because of an increase in $A_{NRAD}$, meaning that a more efficient nonradiative channel involving the first excited triplet state exists in the former di-ureasil. These results indicate that the substitution of the water molecules in the $Eu^{3+}$ coordination sphere of complex **1** by two TOPO molecules induces a higher $^5D_0$ emission quantum efficiency relative to the interaction with the oxygen atoms of the carbonyl groups from the d-U(600) host.

## Conclusions

Di-ureasil organic-inorganic hybrids incorporating $Eu(TPI)_3{\cdot}3H_2O$ or $Eu(TPI)_3{\cdot}2TOPO$ complexes were prepared either by acetic acid solvolysis or by conventional hydrolysis. XRD and FT-IR, $^{29}Si$ and $^{13}C$ MAS NMR spectroscopic results demonstrate an effective interaction between the $Eu^{3+}$ 3-phenyl-4-(4-toluoyl)-5-isoxazolonate complex and carbonyl groups of the urea linkages. The PL spectra of these di-ureasil organic-inorganic hybrids display the characteristic $Eu^{3+}$ $^5D_0 \rightarrow {}^7F_{0-4}$ transitions. The broad emission typical of amine-functionalized hybrids has negligible intensity pointing to the activation of energy channels between the emitting centers of the hybrid host and the $Eu^{3+}$ ions. The high values obtained for the experimental 4f–4f $\Omega_2$ intensity parameters suggest that the dynamic coupling mechanism is quite operative in these compounds. The incorporation of complex **1** into the d-U(600) host enhanced the $^5D_0$ quantum efficiency and lifetime because of the coordination ability of the organic counterpart of the host structure to displace water molecules from the complex coordination sphere. A suitable choice of ligands that better sensitize the $Eu^{3+}$ emission together with a fine control of the synthesis process definitely endorse the design of nanohybrids with better emission performance.

## Experimental Section

**Materials and Synthesis:** The synthesis procedures of the complexes $Eu(TPI)_3{\cdot}3H_2O$ and $Eu(TPI)_3{\cdot}2TOPO$ and their characterizations are described in a recent publication.[22] The diamine α,ω-diamine-poly(oxyethylene-co-oxypropylene) with a molecular weight of about 600 a.m.u., corresponding to approximately 8.5 ($OCH_2CH_2$) repeat units and commercially designated as Jeffamine ED-600® (Fluka), was dried with molecular sieves (4 Å, 1.6 mm pellets, Aldrich) before use. ICPTES (3-isocyanatopropyltriethoxysilane, 95%, Fluka) and acetic acid (AA, 99.7%, Aldrich) were used without further purification. Tetrahydrofuran (THF) and absolute ethanol were dried with molecular sieves at room temperature before use. The synthesis of the di-ureasils has already been described in detail elsewhere.[14] The first stage of the synthesis involved the reaction in THF of the isocyanate group of the alkoxysilane precursor ICPTES with the terminal amine groups of the doubly functional diamine to form a urea cross-linked organic-inorganic hybrid precursor, so-called ureapropyltriethoxysilane [d-UPTES(600)]. In the second step, complexes were incorporated into the hybrid host by dissolving an appropriate amount of these complexes in ethanol and chloroform. A typical synthetic procedure was as follows.

**Step 1. Synthesis of the Di-ureasil Precursor d-UPTES(600):** Jeffamine ED-600® (1.0 mL, 1.75 mmol) was dissolved in dried THF (5.0 mL) in a flask in a fume hood. ICPTES (0.91 mL, 3.5 mmol) was then added to this solution whilst stirring. The molar ratio of Jeffamine ED-600/ICPTES was 1:2. The flask was sealed and the solution was stirred at room temperature under $N_2$ for 24 h.

**Step 2. Synthesis of the Di-ureasils Incorporating $Eu(TPI)_3{\cdot}3H_2O$ and $Eu(TPI)_3{\cdot}2TOPO$ Complexes by the Conventional Sol-Gel Method or the Carboxylic Acid Solvolysis Process:** The THF in the precursor solution was evaporated under vacuum, and a transparent precursor d-UPTES(600) oil was thus obtained. For the synthesis of the hybrids by the conventional sol–gel method, the $Eu(TPI)_3{\cdot}2TOPO$ complex (0.0116 mmol) was dissolved in $CH_3CH_2OH$ (0.82 mL, 14.04 mmol), and then chloroform (0.5 mL) and HCl at pH = 2 (0.096 mL, 5.34 mmol) were added to this solution. The molar ratio of ICPTES/$CH_3CH_2OH$/$H_2O$ is 1:4:3. Finally, this mixed solution was added to the precursor whilst stirring in air at room temperature. The solution was further stirred for 24 h. For the synthesis of hybrids by acetic acid solvolysis, the $Eu(TPI)_3{\cdot}3H_2O$ and $Eu(TPI)_3{\cdot}2TOPO$ complexes (0.0116 mmol) were dissolved in $CH_3CH_2OH$ (0.82 mL, 14.04 mmol) and chloroform (0.5 mL) was added to this solution. The mixture was added to the precursor. Finally, AA (0.60 mL) was added whilst stirring under $N_2$ at room temperature, and the mixture was stirred for 24 h.

**Experimental Techniques:** Mid-IR spectra were recorded at room temperature using a MATTSON 7000 FTIR Spectrometer. The spectra were collected over the range 4000–400 $cm^{-1}$ by averaging 64 scans at a maximum resolution of 4 $cm^{-1}$. The compounds were finely ground (about 2 mg), mixed with approximately 175 mg of dried potassium bromide (Merck, spectroscopic grade) and pressed into pellets. Consecutive spectra were recorded until reproducible results were obtained. X-ray diffraction patterns were recorded using a Philips X'Pert MPD Powder X-ray diffractometer system. The powders were exposed to Cu-$K_\alpha$ radiation ($\lambda$ = 1.54 A°) at room temperature in a $2\theta$ range (scattering angle) between 1 and 70°. The xerogel samples, analyzed as films, were not submitted to any thermal pre-treatment. $^{29}Si$ magic-angle spinning (MAS) and $^{13}C$ cross-polarization (CP) MAS NMR spectra were recorded with a Bruker Avance 400 (9.4 T) spectrometer at 79.49 and 100.62 MHz, respectively. $^{29}Si$ MAS NMR spectra were recorded with 2 μs (equivalent to 30°) rf pulses, a recycle delay of 60 s and at a 5.0 kHz spinning rate. $^{13}C$ CP/MAS NMR spectra were recorded with a 4 μs $^1H$ 90° pulse, 2 ms contact time, a recycle delay of 4 s, and at a spinning rate of 8 kHz. Chemical shifts are quoted in ppm from tetramethylsilane (TMS). The emission, PL, excitation, and PLE spectra and the lifetimes were measured at room temperature with a modular double grating excitation spectrofluorimeter with a TRIAX 320 emission monochromator (Fluorolog-3, Jobin Yvon-Spex), coupled to an R928 Hamamatsu photomultiplier, using the front face acquisition mode. All the photoluminescence spectra were corrected for optical and detection spectral responses.

 © 2006 Wiley-VCH Verlag GmbH & Co. KGaA, Weinheim 

## Acknowledgments

The authors would like to acknowledge the financial support from the Defence Research and Development Organization India, the FCT (Portuguese Agency, POCTI/P/CTM/46780/02), CAPES and CNPq (Brazilian Agencies), and the RENAMI project (Brazilian Molecular and Interfaces Nanotechnology Network). The authors also wish to thank Prof. T. K. Chandrashekar, Director, Regional Research Laboratory, Trivandrum, India and Prof. C. K. Jayasanker, S. V. University, Tirupathi, India for their constant encouragement and valuable discussions.

[1] J. Kido, Y. Okamoto, *Chem. Rev.* **2002**, *102*, 2357–2368.
[2] J. C. G. Bunzli, C. Piguet, *Chem. Soc. Rev.* **2005**, *34*, 1048–1077.
[3] J. C. G. Bunzli, C. Piguet, *Chem. Rev.* **2002**, *102*, 1897–1928.
[4] G. F. de Sa, O. L. Malta, C. de Mello Donega, A. M. Simas, R. L. Longo, P. A. Santa-Cruz, E. F. da Silva Jr, *Coord. Chem. Rev.* **2000**, *196*, 165–195.
[5] D. Parker, *Coord. Chem. Rev.* **2000**, *205*, 109–130.
[6] K. Binnemans, in *Handbook on the Physics and Chemistry of Rare Earths* (Eds: A. Gschneidner Jr, J. C. G. Bunzli, V. K. Pecharsky), Elsevier, Amsterdam, **2005**, vol. 35, pp.107–272.
[7] R. Pavithran, N. S. Saleesh Kumar, S. Biju, M. L. P. Reddy, S. Alves Jr, R. O. Freire, *Inorg. Chem.* **2006**, *45*, 2184–2192.
[8] H. Xin, M. Shi, X. C. Gao, Y. Y. Huang, Z. L. Gong, D. B. Nie, H. Cao, Z. Q. Bian, F. Y. Li, C. H. Huang, *J. Phys. Chem. B* **2004**, *108*, 10796–10800.
[9] C. Molina, K. Dahmouche, Y. Messaddeq, S. J. L. Ribeiro, M. A. P. Silva, V. de Zea Bermudez, L. D. Carlos, *J. Lumin.* **2003**, *104*, 93–101.
[10] L. Fu, R. A. Sá Ferreira, N. J. O. Silva, J. A. Fernandes, P. Ribeiro-Claro, I. S. Gonçalves, V. de Zea Bermudez, L. D. Carlos, *J. Mater. Chem.* **2005**, *15*, 3117–3125.
[11] P. P. Lima, R. A. S. Ferreira, R. O. Freire, F. A. A. Paz, L. Fu, S. Alves Jr, L. D. Carlos, O. L. Malta, *ChemPhysChem* **2006**, *7*, 735–746.
[12] M. M. Silva, V. de Zea Bermudez, L. D. Carlos, A. Almeida, M. J. Smith, *J. Mater. Chem.* **1999**, *9*, 1735–1740.
[13] L. D. Carlos, Y. Messaddeq, H. M. Brito, R. A. Sá Ferreira, V. de Zea Bermudez, S. J. L. Ribeiro, *Adv. Mater.* **2000**, *12*, 594–598.
[14] L. S. Fu, R. A. Sá Ferreira, N. J. O. Silva, L. D. Carlos, V. de Zea Bermudez, J. Rocha, *Chem. Mater.* **2004**, *16*, 1507–1516.
[15] C. Sanchez, F. Ribot, B. Lebeau, *J. Mater. Chem.* **1999**, *9*, 35–44.
[16] L. D. Carlos, V. de Zea Bermudez, M. C. Duarte, M. M. Silva, C. J. Silva, M. J. Smith, M. Assuncao, L. Alcacer, in: *Physics and Chemistry of Luminescent Materials* (Eds: C. Ronda, T. Welker) VI, Electrochemical Society Proceedings, San Francisco, **1998**, vol. 97-29, p. 352.
[17] V. Bekiari, P. Lianos, P. Judeinstein, *Chem. Phys. Lett.* **1999**, *307*, 310–316.
[18] L. D. Carlos, R. A. Sá Ferreira, V. de Zea Bermudez, C. Molina, L. A. Bueno, S. J. L. Ribeiro, *Phys. Rev. B* **1999**, *60*, 10042–10053.
[19] V. de Zea Bermudez, R. A. Sá Ferreira, L. D. Carlos, C. Molina, K. Dahmouche, S. J. L. Ribeiro, *J. Phys. Chem. B* **2001**, *105*, 3378–3386.
[20] M. M. Silva, V. de Zea Bermudez, L. D. Carlos, A. Almeida, M. J. Smith, *J. Mater. Chem.* **1999**, *9*, 1735–1740.
[21] M. C. Gonçalves, N. J. O. Silva, V. de Zea Bermudez, R. A. Sá Ferreira, L. D. Carlos, K. Dahmouche, C. V. Santilli, D. Ostrovskii, I. C. Correia Vilela, A. F. Craievich, *J. Phys. Chem. B* **2005**, *109*, 20093–20104.
[22] R. Pavithran, M. L. P. Reddy, S. Alves Jr, R. O. Freire, G. B. Rocha, P. P. Lima, *Eur. J. Inorg. Chem.* **2005**, *20*, 4129–4137.
[23] K. Dahmouche, L. D. Carlos, V. De Zea Bermudez, R. A. Sá Ferreira, C. V. Santilli, A. F. Craievich, *J. Mater. Chem.* **2001**, *11*, 3249–3257.
[24] V. de Zea Bermudez, L. D. Carlos, L. Alcácer, *Chem. Mater.* **1999**, *11*, 569–580.
[25] A. C. Franville, R. Mahiou, D. Zambon, J. C. Cousseins, *Solid State Sci.* **2001**, *3*, 211–222.
[26] M. C. Gonçalves, V. de Zea Bermudez, R. A. Sá Ferreira, L. D. Carlos, D. Ostrovskii, J. Rocha, *Chem. Mater.* **2004**, *16*, 2530–2543.
[27] L. D. Carlos, V. de Zea Bermudez, R. A. Sá Ferreira, L. Marques, M. Assuncao, *Chem. Mater.* **1999**, *11*, 581–588.
[28] L. D. Carlos, R. A. Sá Ferreira, V. de Zea Bermudez, in: *Handbook of Organic-Inorganic Hybrid Materials and Nanocomposites* (Eds: H. S. Nalwa), American Scientific Publishers, Morth Lewis Way, California, **2004**, vol. 1, chapter 9, p. 353.
[29] L. D. Carlos, R. A. Sá Ferreira, V. de Zea Bermudez, S. J. L. Ribeiro, *Adv. Funct. Mater.* **2001**, *11*, 111–115.
[30] L. D. Carlos, R. A. Sá Ferreira, R. N. Pereira, M. Assunção, V. de Zea Bermudez, *J. Phys. Chem. B* **2004**, *108*, 14924–14932.
[31] M. H. V. Werts, R. T. F. Jukes, J. W. Verhoeven, *Phys. Chem. Chem. Phys.* **2002**, *4*, 1542–1548.
[32] O. L. Malta, M. A. C. dos Santos, L. C. Thompson, N. K. Ito, *J. Lumin.* **1996**, *69*, 77–84.
[33] W. T. Carnall, H. M. Crosswhite, "Energy Levels, Structure and Transition Probabilities of the Trivalent Lanthanides", in: $LaF_3$, Argonne National Laboratory, Illinois, **1977**.
[34] C. Molina, P. J. Moreira, R. R. Gonçalves, R. A. Sá Ferreira, Y. Messaddeq, S. J. L. Ribeiro, O. Soppera, A. P. Leite, P. V. S. Marques, V. de Zea Bermudez, L. D. Carlos, *J. Mater. Chem.* **2005**, *15*, 3937–3945.
[35] R. D. Peacock, *Struct. Bonding (Berlin)* **1975**, *22*, 83–121.

Received: March 28, 2006
Published Online: August 7, 2006

 © 2006 Wiley-VCH Verlag GmbH & Co. KGaA, Weinheim 

DOI: 10.1002/ejic.200600367

# Metal-Dependent Formation of Mononuclear Complexes and $M_2L_2$ Mesocates with Schiff-Base Ligands

John Fielden,[a] De-Liang Long,[a] Cameron Evans,[a] and Leroy Cronin*[a]

**Keywords:** Supramolecular chemistry / Schiff-base ligands / Coordination modes / Silver / Cadmium

The coordination chemistry of the tetradentate pyridyl N-donor ligands *r*-1-hydroxy-*t*-3,*t*-5-bis{[(2-pyridinyl)methylene]amino}cyclohexane (DDOP) and *r*-1-hydroxy-*t*-3,*t*-5-bis{[(*E*)-(6-methyl-2-pyridinyl)methylene]amino}cyclohexane (DDMOP) has been investigated with the $d^{10}$ metal centres silver(I) and cadmium(II). These conformationally flexible ligands offer two coordination modes; either a mononucleating tetradentate coordination pocket or a bridging bis(bidentate) chelate. Hence, reaction with $Cd^{II}$ produced six-coordinate mononuclear complexes whose compositions were determined by X-ray crystallography as $[Cd(DDOP)(NO_3)_2]$ (**1**) and $[Cd(DDMOP)(Cl)_2]$·MeOH (**2**), while $Ag^I$ led to the four-coordinate dinuclear mesocate structures $[\{Ag(DDOP)\}_2](CF_3SO_3)_2$ (**3**) and $[\{Ag(DDMOP)\}_2](CF_3SO_3)_2$·0.5MeOH (**4**). It is thought that the mononuclear, octahedral complexes in the case of zinc(II) and cadmium(II) result from the energetic stabilisation gained through two extra coordinate bonds, while in the case of silver(I) the lower propensity of the metal centre for six-coordination causes the ligand to retain its energetically preferred dinucleating conformation and to form the mesocates.

(© Wiley-VCH Verlag GmbH & Co. KGaA, 69451 Weinheim, Germany, 2006)

## Introduction

Control over the nuclearity and shape of coordination complexes has been a vital topic in inorganic chemistry for decades, most particularly since the emergence of supramolecular chemistry in the late 1970s, and provides the key to future development of designed functional materials.[1–3] Through careful choice of ligand topology, numerous research groups have been able to control formation of oligomeric and polymeric structures; for example the formation of double- and triple-stranded helicates/mesocates,[4–6] molecular squares and boxes,[7,8] and infinite inorganic grids.[9,10] Such chemistry often relies on the use of large, rigid aromatic N-donor sets, for example the various bi- and terpyridines, linked by spacers whose shape and rigidity (or relative flexibility) determines the type of complex. Schiff-base derivatisation of aliphatic amines or anilines with pyridinecarbaldehydes provides an attractive route to aromatic N-donor ligands, due to the relative synthetic ease of this transformation and the availability of many different parent amines.[11]

Recent work in our laboratory has focused on the synthesis and coordination behaviour of the small, cyclohexane-based aliphatic amino ligands *r*-1,*t*-3,*t*-5-triaminocyclohexane (TACH)[12–14] and *t*-3,*t*-5-diamino-*r*-1-hydroxycyclohexane (DAHC).[15–17] While becoming rigid upon coordination due to conformational locking of the cyclohexane backbone, these ligands offer two coordination modes; either bridging with the *cis*-diamino donor set in the equatorial plane, or bidentate chelating upon "ring-flip" to the bis(axial) conformation. Derivatisation of the amine groups of these ligands with Schiff bases allows the synthesis of pyridyl N-donor ligands which, like their parent amines, possess two distinct coordination modes. Such ligands may form complexes with different nuclearity according to the coordination preferences of the metal centre.[18,19] Herein, we describe mono- and dinuclear coordination complexes of the DAHC Schiff-base derivatives *r*-1-hydroxy-*t*-3,*t*-5-bis{[(2-pyridinyl)methylene]amino}cyclohexane (DDOP) and *r*-1-hydroxy-*t*-3,*t*-5-bis{[(*E*)-(6-methyl-2-pyridinyl)methylene]amino}cyclohexane (DDMOP) with the $d^{10}$ transition-metal ions $Cd^{II}$ and $Ag^I$.

## Results and Discussion

### Overview

DDOP and DDMOP were synthesised from DAHC by a simple Schiff-base derivatisation using the appropriate pyridinecarbaldeyhyde, yielding a more highly pre-organised ligand with a tetradentate [or bis(bidentate)] donor set. The aromatic rings increase the system's rigidity, strengthening the hand of the ligand and reducing the influence of anions, solvent and metal centres on the outcome of the complexation. Furthermore, they provide a hydrophobic surface capable of participating in π-stacking or other van der Waals interactions.

[a] WestCHEM, Department of Chemistry, University of Glasgow, Joseph Black Building,
University Avenue, Glasgow, G12 8QQ, United Kingdom
E-mail: L.Cronin@chem.gla.ac.uk

 © 2006 Wiley-VCH Verlag GmbH & Co. KGaA, Weinheim 

Despite the rigidity of the donor set, the conformational flexibility of the cyclohexane backbone gives these ligands two possible coordination modes (Scheme 1); either as a dinucleating, bis(bidentate) chelator, or a bis(axial) tetradentate mononucleating conformation. Both coordination modes are observed in this study, the dinuclear compounds being formed with silver(I) and mononuclear, ring-flipped compounds occurring with cadmium(II). The ligands direct the formation of $M_2L_2$ mesocate structures when in their bis(equatorial) conformation, since the two $N_2$ donor sets are suitably oriented to bind to one side of the metal–metal axis, and the angle of approximately 105° between the planes of the aromatic rings provides an effective corner piece. Consequently, formation of dinuclear complexes is favoured by four-coordinate, tetrahedral metal centres whose ca. 90° twist angle provides a good geometric match for the bis(equatorial) ligand. Mononuclear species are favoured by coordination to octahedral metal centres, whose equatorial sites can accept the planar $N_4$ donor set of the bis(axial) ligand, with their axial sites being occupied by solvent molecules or counterions. Formation of the two types of complexes is described by the balanced equations below, which summarise the reaction of two metal centres with two ligands:

Dinuclear complex:

$2\ MX_2{\cdot}nH_2O + 2\ L \rightarrow M_2L_2^{4+} + 4\ X^- + 2n\ H_2O$; $(2n + 5)$ species, 8 coordinate bonds.

Mononuclear complex:

$2\ MX_2{\cdot}nH_2O + 2\ L \rightarrow 2\ MLX_2 + 2n\ H_2O$; $(2n + 2)$ species, 12 coordinate bonds.

For silver(I) and cadmium(II), which can access both tetrahedral and octahedral coordination geometries, the two reactions are in competition with each other. It can be seen from the larger number of species formed that four-coordinate $M_2L_2$ structures are favoured due to entropic factors; furthermore, the bis(equatorial) ligand conformation observed in such complexes is more energetically favourable due to reduced steric clash between the imine arms and the cyclohexane ring. However, the extra coordination bonds formed in the mononuclear case means that these complexes are favoured by enthalpy.

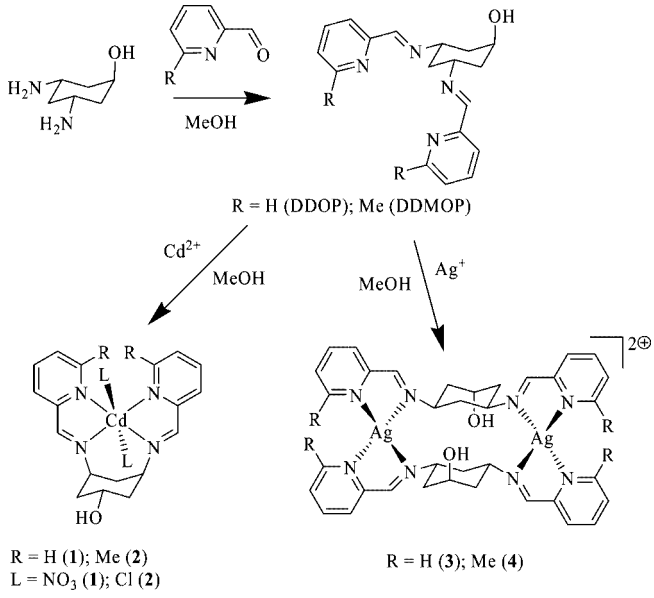


Scheme 1. Parent amine DAHC, and mono- and dinuclear species formed by complexation of its Schiff-base derivatives DDOP and DDMOP.

## Cadmium(II) Complexes

Cadmium(II) complexes of DDOP and DDMOP were prepared in moderately low yields by reaction with cadmium(II) salts (nitrate or chloride) in methanol, followed by crystallisation by diffusion of diethyl ether. This yielded the (DDOP)bis(nitrato)cadmium complex [Cd(DDOP)-$(NO_3)_2$] (**1**), and the (DDMOP)bis(chlorido)cadmium complex [Cd(DDMOP)$Cl_2$]·MeOH (**2**) (the DDMOP complex would not crystallise with the nitrato ligand). In both, the $N_4$ ligand acts as a tetradentate chelator in the equatorial plane, while the chlorido or nitrato ligands occupy the axial coordination sites (Figure 1). However, interestingly, the asymmetric unit of **1** contains two crystallographically independent complexes, which appear to be associated with each other through a slipped π-stacking interaction with a centroid-to-centroid distance of around 3.80 Å.

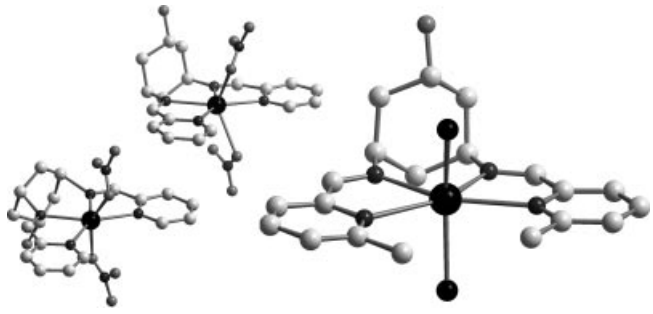

Figure 1. The two [Cd(DDOP)$(NO_3)_2$] complexes in the asymmetric unit of **1** (left) and the complex in [Cd(DDMOP)$(Cl)_2$]·MeOH (**2**). C: light grey; N: dark grey; O: medium grey; Cl: small black spheres; Cd: large black spheres; H: omitted.

Curiously, the pair of complexes in **1** differs quite noticeably in its Cd–O bond lengths; Cd2 has longer bonds to the oxygen atoms, and shorter bonds to the equatorial nitrogen atoms (Table 1). The size of the cadmium cation causes the pyridyl arms of the ligand to open from their idealised parallel alignment, as indicated by longer coordination bonds to the pyridyl nitrogen atoms, and also by an N–Cd–N angle that is much larger between the pyridyl nitrogen atoms than the imino nitrogen atoms. This effect is more dramatic in **2**, where replacement of hydrogen with a methyl group at the 6-position of the pyridyl ring forces the imine arms to open wider to accommodate the increased steric demand (Figure 1). Bond lengths to the axial chlorido ligands are comparable to the axial Cd2–O bond lengths in compound **1**. In solution, $^1$H NMR spectroscopy ($CD_3OD$) reveals the ring-flipped structure of these complexes, as shown by the

 © 2006 Wiley-VCH Verlag GmbH & Co. KGaA, Weinheim 

Table 1. Selected bond lengths [Å] and angles [°] in [Cd(DDMOP)$(NO_3)_2$] (**1**) and [Cd(DDMOP)$Cl_2$]·MeOH (**2**). $L_{eq}$ = $NO_3$ or Cl.

| | Compound **1**, Cd1 | Compound **1**, Cd2 | Compound **2** |
|---|---|---|---|
| $Cd–N_{im}$ | 2.316(13), 2.327(13) | 2.316(13), 2.321(13) | 2.376(2), 2.415(2) |
| $Cd–N_{py}$ | 2.349(11), 2.372(12) | 2.332(11), 2.354(14) | 2.499(2), 2.600(2) |
| $N_{py}–Cd–N_{py}$ | 132.4(4) | 132.9(4) | 139.97(8) |
| $N_{im}–Cd–N_{im}$ | 82.9(4) | 83.8(5) | 82.97(8) |
| $Cd–L_{eq}$ | 2.381(13), 2.475(17) | 2.50(3), 2.506(14) | 2.500(1), 2.530(1) |
| $L_{eq}–Cd–L_{eq}$ | 164.3(6) | 153.4(5) | 139.97(8) |

multiplicities of the cyclohexane protons which provide an excellent conformational probe. Identical NMR spectra were obtained by directly dissolving the ligand and a small excess of the cadmium salt in $CD_3OD$, indicating that the low yields are due to inefficient crystallisation, rather than formation of other architectures. Furthermore, coordination to Cd is indicated by satellites resulting from coupling of the imine protons to the $I$ = 1/2 isotopes $^{111}Cd$ and $^{113}Cd$ (combined abundance = 25%).

The differing shapes and hydrogen-bonding properties of the chlorido and nitrato ligands result in contrasting extended structures for the two compounds. In **1** there are alternating layers of the two crystallographically independent complexes (Figure 2), in which they associate in chains parallel to the crystallographic *c*-axis through hydrogen-bonding interactions between the nitrato ligands and the DDOP alcohol groups (2.976 Å in the Cd1 layer). However, in the Cd2 layers the nitrato–hydroxy distance (3.126 Å) is longer than the sum of the van der Waals radii. Association of the layers appears to occur by the π-stacking interactions observed in the asymmetric unit. In **2**, the [Cd(DDMOP)-$Cl_2$] units are arranged in hydrogen-bonded chains parallel to the crystallographic *b*-axis (Figure 2). To generate the chains, one chlorido ligand accepts a hydrogen bond from the DDMOP alcohol group (3.195 Å) of the next complex, and the other chlorido ligand accepts a hydrogen bond from an included methanol molecule (3.140 Å). The pyridyl–pyridyl separations observed are too large to suggest any significant contributions from π-stacking.

To investigate the influence of temperature on these complexations, reactions were also performed at –94 °C, –78 °C, and in refluxing *n*-propanol (97 °C). It was anticipated that low temperatures might reduce the conformational flexibility of the ligand, encouraging formation of dinuclear aggregates on kinetic grounds, while higher temperatures would increase the influence of entropy, again favouring dinuclear species. However, $^1H$ NMR revealed that mononuclear species still result under these conditions.

### Silver(I) Complexes

In contrast to cadmium(II), complexation of DDOP and DDMOP with silver(I) results in the formation of $M_2L_2$ mesocates, synthesised in analogous fashion to the cadmium complexes by reaction with silver(I) triflate. The $M_2L_2^{2+}$ complex cations are formed by two ligands in the bis(equatorial) conformation, linked by two Ag(1) centres with distorted pseudo-tetrahedral geometries (Figure 3). These dinuclear structures occur because the octahedral coordination mode is less accessible for silver(I) than cadmium(II), and because nonplanar geometries are favoured by four-coordinate silver atoms.[18] Furthermore, the bis-(equatorial) coordination mode is more favourable for the ligand as it minimises steric clashes between the pyridyl and cyclohexane rings. $^1H$ NMR ($CD_3OD$) reveals the $M_2L_2$ form of the complexes upon dissolution, and while coupling of the imine protons to the silver ion ($I$ = 1/2) is only observed in **4**, the change in chemical shift relative to uncomplexed ligand suggests that **3** does not dissociate. Identical spectra obtained simply by mixing the silver salt and ligand in $CD_3OD$ suggest that the low yield obtained for **3** is due

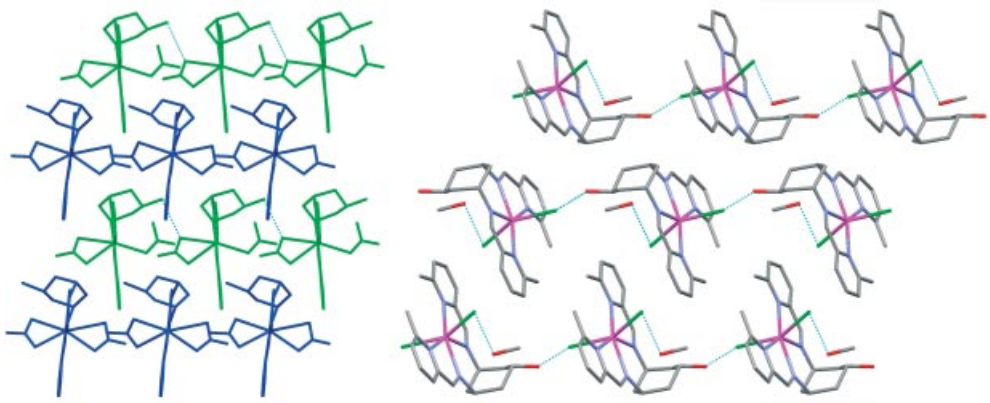

Figure 2. Crystal packing and hydrogen bonding in [Cd(DDOP)$(NO_3)_2$] (**1**, left) and [Cd(DDMOP)$Cl_2$]·MeOH (**2**, right). In **1**, Cd1 complexes are green and Cd2 blue; colour scheme in **2**: C grey; N blue; O red; Cl green; Cd purple; H omitted. Hydrogen bonds are shown as bright blue dotted lines.

 © 2006 Wiley-VCH Verlag GmbH & Co. KGaA, Weinheim 

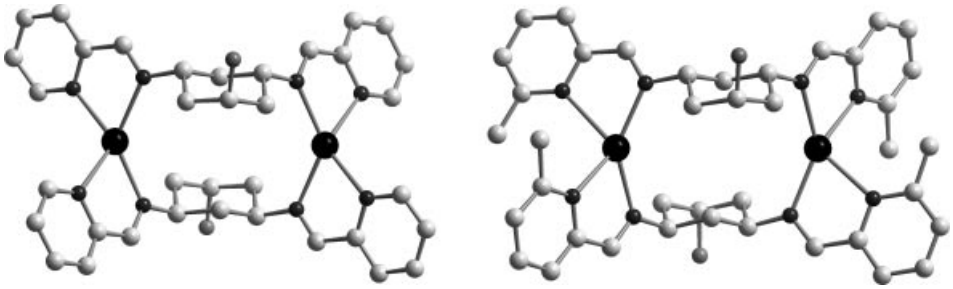

Figure 3. Complex cations in $[\{Ag(DDOP)\}_2](CF_3SO_3)_2$ (**3**) and $[\{Ag(DDMOP)\}_2](CF_3SO_3)_2 \cdot 0.5MeOH$ (**4**). Ag black, C light grey; N dark grey; O medium grey; H omitted.

Table 2. Bond lengths [Å] and angles [°] in $[\{Ag(DDOP)\}_2](CF_3SO_3)_2$ (**3**) and $[\{Ag(DDMOP)\}_2](CF_3SO_3)_2 \cdot 0.5MeOH$ (**4**).

| | Compound **3** | Compound **4** |
|---|---|---|
| Ag(1)–N | 2.236(4), 2.290(4), 2.342(5), 2.438(5) | 2.241(5), 2.250(4), 2.410(5), 2.427(5) |
| Ag(2)–N | N/A | 2.209(4), 2.287(4), 2.357(5), 2.549(5) |
| N–Ag(1)–N | 133.18(15), 141.50(19), 73.05(17), 72.40(16), 127.99(16), 117.00(17) | 141.72(17), 139.35(16), 72.17(16), 73.02(17), 129.48(16), 103.35(17) |
| N–Ag(2)–N | N/A | 140.93(17), 138.44(16), 72.31(17), 71.42(16), 134.37(15), 103.34(16) |

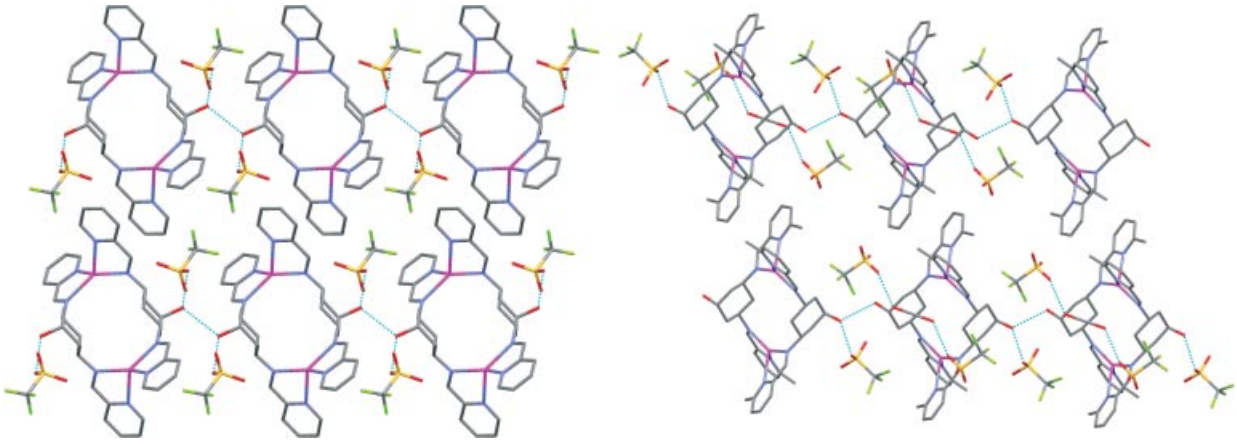

Figure 4. Crystal packing in $[\{Ag(DDOP)\}_2](CF_3SO_3)_2$ (**3**, left) and $[\{Ag(DDMOP)\}_2](CF_3SO_3)_2$ (**4**, right). S yellow; F light yellow; Ag purple; C grey; N blue; O red; H omitted. Disordered atoms are omitted for clarity. Hydrogen-bonded interactions shown by blue dotted line.

to inefficient crystallisation rather than formation of other architectures.

In both complexes, the coordination geometry around the silver atoms is substantially distorted from the tetrahedral ideal, as shown by the wide range of bond lengths and angles in Table 2. Most importantly, the twist angle between the two donor sets of each tetrahedron, ideally 90°, is around 79.5° in **3**, and 68° and 71.5° at the two crystallographically independent silver centres in **4**, compensating for the >100° corner piece provided by the ligands.

Both complexes pack in one-dimensional chains of hydrogen-bonded complex cations and counterions (Figure 4). In **3**, these chains propagate parallel to a line bisecting the crystallographic *bc* plane through the origin, with each DDOP alcohol group donating a bifurcated hydrogen bond to one triflate counterion (3.011 Å) and the alcohol group of the next cation (2.886 Å) in the chain. Edge–face contacts of around 3.73 Å suggest a contribution from C–H–π interactions,[20] although there do not appear to be any face–face π–π interactions. In the DDMOP complex **4** the chains run parallel to the crystallographic *a*-axis, with the cations connected by hydrogen bonds between their alcohol groups (2.818 Å), while one of the two triflate anions per formula unit also accepts a hydrogen bond from a DDMOP alcohol group (2.775 Å). The second triflate counterion is disordered and interacts with disordered methanol molecules (2.696 Å), but not the cations. It appears that slipped face-to-face π-stacking interactions may control the association of the hydrogen-bonded chains, with a number of C–C contacts in the range of 3.45–3.92 Å.

## Conclusions

A series of closed-shell transition-metal complexes of two novel Schiff-base ligands have been synthesised and charac-

 © 2006 Wiley-VCH Verlag GmbH & Co. KGaA, Weinheim 

terised in the solid and solution states. These ligands offer two possible coordination modes, and while mononuclear complexes are preferred with cadmium(II), $M_2L_2$ mesocates form with silver(I). This preference for mononuclear complexes with cadmium(II) prevails over a wide temperature range and is due to the greater ability of $Cd^{II}$ to accept six-coordinate environments, and the consequent gain in stability through formation of two extra coordinate bonds to solvent molecules or counterions. Further investigation will be carried out into the possibility of using the conformational "switch" as a sensor.

## Experimental Section

**Materials, Methods and Instrumentation:** The ligands DDOP and DDMOP were synthesised by reaction of *t*-3,*t*-5-diamino-*r*-1-hydroxycylcohexane with 2-pyridinecarbaldehyde or 6-methyl-2-pyridinecarbaldehyde.[16] All other reagents and solvents were purchased (Fisher/Lancaster/Riedel-de Haën/Aldrich) as AR grade and used without further purification. Deuterated solvents were obtained from Aldrich. All complexations were performed under ambient conditions. IR spectra were measured with a Jasco FTIR-410 spectrometer and $^1$H NMR measurements were performed at room temperature with Bruker DPX-400 and Avance-400 spectrometers. X-ray diffraction data were collected with a Nonius Kappa-CCD diffractometer with Mo-$K_\alpha$ radiation ($\lambda$ = 0.7107 Å) and a graphite monochromator.

**Preparation of [Cd(DDOP)(NO$_3$)$_2$] (1):** DDOP (0.070 g, 0.226 mmol) was dissolved in methanol (20 mL). $Cd(NO_3)_2{\cdot}4H_2O$ (0.105 g, 0.340 mmol) was added in methanol (5 mL) and the solution stirred for 5 h, before the volume was reduced to ca. 3 mL in vacuo. A white solid was removed by filtration and the solution was set for crystallisation by $Et_2O$ diffusion. After 24 h, clear and colourless crystals of **1** were observed (0.030 g, 0.0551 mmol, 23.8% yield). $^1$H NMR (400 MHz, $CD_3OD$): $\delta$ = 9.01 (d, 2 H, 2Ar*H*), 8.81 [m (s with satellites from coupling to $I$ = 1/2 Cd isotopes $^{111}$Cd and $^{113}$Cd, combined abundance 25%), 2 H, 2 *H*C=N], 8.33 (pseudo-td, 2 H, 2 Ar*H*), 8.03 (d, 2 H, 2 Ar*H*), 7.94 (m, 2 H, 2 Ar*H*), 4.51 (m, 2 H, 2 *H*C–N), 4.39 (tt, 1 H, *H*COH), 2.34–2.14 (m, 4 H, 3 $H_{eq}$CH, $H_{ax}$CH), 2.01 (pseudo-td, 2 H, 2 $H_{ax}$CH) ppm. IR (KBr disc): $\tilde{\nu}$ = 3431 s, 3062 w, 2933 m, 1651 m, 1595 s, 1423 s, 1296 vs cm$^{-1}$. $C_{18}H_{20}CdN_6O_7$ (544.80): calcd. C 39.68, H 3.70, N 15.43; found C 39.39, H 3.72, N 15.18.

**Preparation of [Cd(DDMOP)(Cl)$_2$]·MeOH (2):** DDMOP (0.070 g, 0.208 mmol) was dissolved in methanol (20 mL). $CdCl_2{\cdot}2.5H_2O$ (0.047 g, 0.210 mmol) was added in methanol (5 mL), and the solution stirred overnight, before the volume was reduced to ca 4.5 mL in vacuo. A white solid was removed by filtration and after 24 h, clear, colourless crystals of **2** were produced by diffusion of diethyl ether into the methanolic solution (0.027 g, 0.0489 mmol, 23.5% yield). $^1$H NMR (400 MHz, $CD_3OD$): $\delta$ = 8.73 [m (s with satellites from coupling to 25% abundace $I$ = 1/2 Cd isotopes), 2 H, 2 *H*C=N], 8.08 (pseudo-t, 2 H, 2 Ar*H*), 7.74 (d, 2 H, 2 Ar*H*), 7.67 (d, 2 H, 2 Ar*H*), 4.68 (tt, 1 H, *H*COH), 4.44 (m, 2 H, 2 *H*CN), 3.03 (s, 6 H, 2 $H_3$CAr), 2.36–2.13 (m, 4 H, 3 $H_{eq}$CH, $H_{ax}$CH), 1.98 (pseudo-td, 2 H, 2 $H_{ax}$CH) ppm. IR (KBr disc): $\tilde{\nu}$ = 3404 s, 2923 m, 1647 s, 1591 s, 1458 s, 1256 m, 1163 m, 1129 m 1002 m, 808 s cm$^{-1}$. $C_{21}H_{28}CdCl_2N_4O_2$ (551.79): calcd. C 45.71, H 5.11, N 10.15; found C 45.40, H 4.74, N 10.09.

**Preparation of [{Ag(DDOP)}$_2$](CF$_3$SO$_3$)$_2$ (3):** DDOP (0.070 g, 0.226 mmol) was dissolved in methanol (20 mL). AgOTf (0.0875 g, 0.339 mmol) was added in methanol (5 mL) and the solution stirred in the dark for 48 h, before the volume was reduced to ca 4 mL in vacuo. After a few minutes, the formation of very small crystals was observed. The solution was filtered and set to crystallise by $Et_2O$ diffusion. Within 24 h, small, colourless cubic or rectangular crystals of **3** were observed (0.0411 g, 0.0364 mmol, 16.1% yield). $^1$H NMR (400 MHz, $CD_3OD$): $\delta$ = 8.91 (s, 4 H, 4 *H*C=N), 8.39 (d, 4 H, 4 Ar*H*), 8.16 (pseudo-td, 4 H, 4 Ar*H*), 7.92 (d, 4 H, 4 Ar*H*), 7.17 (m, 4 H, 4 Ar*H*), 4.45 (m, 4 H, 4 *H*CN), 4.29 (m, 2 H, 2 *H*COH), 2.13 (m, 8 H, 6 $H_{eq}$CH, 2 $H_{ax}$CH), 1.84 (m, 4 H, 4 $H_{ax}$CH) ppm. IR (KBr disc): $\tilde{\nu}$ = 3429 s, 2924 m, 1645 m, 1593 s, 1441 m, 1281 vs, 1255 vs, 1555 s, 1030 s cm$^{-1}$. $C_{38}H_{40}Ag_2F_6N_8O_8S_2$ (1130.63): calcd. C 40.37, H 3.57, N 9.91; found C 40.29, H 3.40, N 9.79.

**[{Ag(DDMOP)}$_2$](CF$_3$SO$_3$)$_2$·0.5MeOH (4):** DDMOP (0.070 g, 0.208 mmol) was dissolved in methanol (20 mL). AgOTf (0.0802 g, 0.310 mmol) was added in methanol (5 mL) and the solution stirred in the dark for 48 h, before the volume was reduced to ca 3 mL in vacuo. After a few minutes, the formation of very small crystals was observed. The solution was filtered and set to crystal-

Table 3. Crystallographic data for **1**–**4**.[a]

| | **1** | **2** | **3** | **4** |
|---|---|---|---|---|
| Empirical formula | $C_{18}H_{20}CdN_6O_7$ | $C_{21}H_{28}CdCl_2N_4O_2$ | $C_{38}H_{40}Ag_2F_6N_8O_8S_2$ | $C_{42.5}H_{48}Ag_2F_6N_8O_{8.5}S_2$ |
| $F_w$ | 544.80 | 551.77 | 1130.63 | 1200.75 |
| Crystal system | monoclinic | triclinic | triclinic | triclinic |
| $a$ [Å] | 12.1888(4) | 8.9466(3) | 9.0415(7) | 12.2018(3) |
| $b$ [Å] | 11.9874(4) | 9.3958(3) | 11.3901(7) | 15.6356(5) |
| $c$ [Å] | 14.0365(5) | 14.0929(5) | 12.2172(8) | 15.8170(5) |
| $\alpha$ [°] | 90 | 76.769(2) | 95.435(4) | 61.247(1) |
| $\beta$ [°] | 91.604(2) | 85.356(2) | 93.135(3) | 70.358(2) |
| $\gamma$ [°] | 90 | 76.842(2) | 110.024(3) | 87.980(2) |
| Space group | *Pc* | *P*$\bar{1}$ | *P*$\bar{1}$ | *P*$\bar{1}$ |
| $V$ [Å$^3$] | 2050.10(12) | 1122.41(7) | 1171.68(14) | 2462.21(13) |
| $Z$ | 4 | 2 | 1 | 2 |
| $\rho_{calcd.}$ [g cm$^{-3}$] | 1.765 | 1.633 | 1.602 | 1.620 |
| $\mu$ [mm$^{-1}$] | 1.121 | 1.236 | 1.005 | 0.962 |
| $T$ [K] | 150(2) | 150(2) | 293(2) | 150(2) |
| No. observations | 20922 (3815 unique) | 21739 (4400 unique) | 22306 (6684 unique) | 37421 (9610 unique) |
| Residuals $R$, $R_w$ | 0.0624, 0.1634 | 0.0294, 0.0698 | 0.0750, 0.2047 | 0.0659, 0.1722 |

[a] $R_1 = \Sigma||F_o|-|F_c||/\Sigma|F_o|$. $wR_2 = \{\Sigma[w(F_o^2-F_c^2)^2]/\Sigma[w(F_o^2)^2]\}^{1/2}$.

 © 2006 Wiley-VCH Verlag GmbH & Co. KGaA, Weinheim 

lise by $Et_2O$ diffusion. Within 24 h, small, colourless cubic or rectangular crystals of **4** were observed (0.0744 g, 0.0620 mmol, 59.5% yield). $^1$H NMR (400 MHz, $CD_3OD$): $\delta$ = 8.90 (d, 4 H, 4 *H*C=N, d due to coupling with $I$ = 1/2 Ag), 8.03 (pseudo-t, 4 H, 4 Ar*H*), 7.74 (d, 4 H, 4 Ar*H*), 7.58 (d, 4 H, 4 Ar*H*), 4.48 (m, 4 H, 4 *H*CN), 4.32 (m, 2 H, 2 *H*COH), 2.26–2.01 (m, 8 H, 6 $H_{eq}$CH, 2 $H_{ax}$CH), 2.20 (s, 12 H, 4 $H_3$CAr), 1.90 (m, 4 H, 4 $H_{ax}$CH) ppm. IR (KBr disc): $\tilde{\nu}$ = 3423 s, 2920 m, 1642 m, 1592 s, 1458 m, 1278 vs, 1261 vs, 1030 s cm$^{-1}$. $C_{42}H_{48}Ag_2F_6N_8O_8S_2$ (1186.74, losing solvent): calcd. C 42.58, H 3.91, N 9.46; found C 42.51, H 4.01, N 9.27.

**Single-Crystal Structure Determination:** Suitable single crystals of **1**–**4** were mounted on the end of a thin glass fibre using Fomblin oil. X-ray diffraction intensity data were measured at 150 or 293 K with a Nonius Kappa-CCD diffractometer [$\lambda$(Mo-$K_\alpha$) = 0.7107 Å]. Structure solution and refinement for **1**–**4** were carried out with SHELXS-97[21] and SHELXL-97[22] using WinGX.[23] Corrections for incident and diffracted beam absorption effects were applied using empirical[24] or numerical methods.[25] Compound **1** crystallised in the space group *Pc* and compounds **2**, **3** and **4** in $P\bar{1}$, as determined by systematic absences in the intensity data, intensity statistics and the successful solution and refinement of the structures. All structures were solved by a combination of direct methods and difference Fourier syntheses and refined against $F^2$ by the full-matrix least-squares technique. Crystal data, data collection parameters and refinement statistics for **1**–**4** are listed in Table 3. CCDC-605439 to -605442 contain the supplementary crystallographic data for this paper. These data can be obtained free of charge from The Cambridge Crystallographic Data Centre via www.ccdc.cam.ac.uk/data_request/cif.

## Acknowledgments

J. F. would like to thank the EPSRC, and D. L. the Leverhulme Trust, for funding.

[1] J.-M. Lehn, *Pure Appl. Chem.* **1978**, *50*, 871–892.
[2] S. Leininger, B. Olenyuk, P. J. Stang, *Chem. Rev.* **2000**, *100*, 853–908.
[3] M. Fujita, K. Umemoto, M. Yoshizawa, N. Fujita, T. Kusukawa, K. Biradha, *Chem. Commun.* **2001**, 509–518.
[4] M. Albrecht, *Chem. Rev.* **2001**, *101*, 3457–3498.
[5] J. M. Lehn, A. Rigualt, *Angew. Chem. Int. Ed. Engl.* **1988**, *27*, 1095–1097.
[6] J. Xu, T. J. Parac, K. N. Raymond, *Angew. Chem. Int. Ed.* **1999**, *38*, 2878–2882.
[7] M. Fujita, J. Yazaki, K. Ogura, *J. Am. Chem. Soc.* **1990**, *112*, 5645–5647.
[8] M. Yoshizawa, Y. Takeyama, T. Kusukawa, M. Fujita, *Angew. Chem. Int. Ed.* **2002**, *41*, 1347–1349.
[9] M. J. Zaworotko, *Angew. Chem. Int. Ed.* **2000**, *39*, 3052–3054.
[10] O. M. Yaghi, M. O'Keeffe, N. W. Ockwig, H. K. Chae, M. Eddaoudi, J. Kim, *Nature* **2003**, *423*, 705–714.
[11] M. J. Hannon, C. L. Painting, A. Jackson, J. Hamblin, W. Errington, *Chem. Commun.* **1997**, 1807–1808.
[12] G. Seeber, D.-L. Long, B. M. Kariuki, L. Cronin, *Dalton Trans.* **2003**, 4498–4504.
[13] G. Seeber, A. L. Pickering, D.-L. Long, L. Cronin, *Chem. Commun.* **2003**, 2002–2003.
[14] G. Seeber, P. Kögerler, B. M. Kariuki, L. Cronin, *Chem. Commun.* **2004**, 1580–1581.
[15] J. Fielden, D.-L. Long, L. Cronin, *Chem. Commun.* **2004**, 2156–2157.
[16] J. Fielden, J. Sprott, L. Cronin, *New J. Chem.* **2005**, *29*, 1152–1158.
[17] J. Fielden, J. Sprott, D.-L. Long, P. Kögerler, L. Cronin, *Inorg. Chem.* **2006**, *45*, 2886 –2895.
[18] G. C. van Stein, H. van der Poel, G. van Koten, A. L. Spek, A. J. M. Duisenberg, P. S. Pregosin, *J. Chem. Soc. Chem. Commun.* **1980**, 1016–1017.
[19] G. K. Patra, I. Goldberg, *New J. Chem.* **2003**, *27*, 1124–1131.
[20] C. Janiak, *J. Chem. Soc. Dalton Trans.* **2000**, 3885–3896.
[21] G. M. Sheldrick, *Acta Crystallogr. Sect. A* **1990**, *46*, 467–473.
[22] G. M. Sheldrick, *Programs for Crystal Structure Analysis*, release 97-2, University of Göttingen, Germany, **1998**.
[23] L. J. Farrugia, *J. Appl. Crystallogr.* **1999**, *32*, 837–838.
[24] R. H. Blessing, *Acta Crystallogr. Sect. A* **1995**, *51*, 33–38.
[25] P. Coppens, L. Leiserowitz, D. Rabinovich, *Acta Crystallogr.* **1965**, *18*, 1035–1038.

Received: April 25, 2006
Published Online: August 7, 2006

 © 2006 Wiley-VCH Verlag GmbH & Co. KGaA, Weinheim 

DOI: 10.1002/ejic.200600129

# Zinc Hydrazide and Zinc Alkoxide Hydrazide Cages with $Zn_4N_8$ and $Zn_4N_6O$ Cores – Cluster Isomerism as a Result of Subtle Changes in Ligand Size

**Surajit Jana,[a] Roland Fröhlich,[b] and Norbert W. Mitzel*[a]**

**Keywords:** Zinc / Hydrazines / Cage compounds / Cocrystalline compounds / N ligands

The hydrazide cluster $[(i\text{PrZn})_4(NHNMe_2)_4]$ (**1**) was synthesised by the reaction of diisopropylzinc with *N*,*N*-dimethylhydrazine and was characterised by $^1H$- and $^{13}C$ NMR and IR spectroscopy, mass spectrometry, elemental analysis and X-ray crystallography. This compound forms asymmetric aggregates containing $Zn_4N_8$ cores. The Zn atoms in these aggregates are arranged in topological tetrahedra in which the triangular faces are bridged by $NHNMe_2$ substituents. Each NH group is connected to two Zn atoms and each $NMe_2$ group to one Zn atom. Alkoxide clusters were prepared in one-pot syntheses by treating diisopropylzinc solutions with mixtures of *N*,*N*-dimethylhydrazine and ROH (R = Et, *i*Pr). The resulting compounds have the formula $[(i\text{PrZn})_4(NHNMe_2)_3(OR)]$ [R = Et (**3**), *i*Pr(**4**)] and contain $Zn_4N_6O$ cages, such that one $NHNMe_2$ in **1** is replaced by one alkoxide group. Two different aggregation modes were found for these $Zn_4N_6O$ cages. In compound **3**, one Zn atom is bound to two $NMe_2$ groups and one NH group. The other three Zn atoms each have three bonds to NH groups and one dative bond to an $NMe_2$ group. The cage consists of one four-membered and one six-membered ring as well as four five-membered rings. In compound **4**, the fourth zinc atom is exclusively bonded to three anionic NH functions in such a way that the rings in the cage are all five-membered. Compounds **3** and **4** were characterised by NMR spectroscopy and single-crystal X-ray diffraction. Hydrazide hydroxide clusters were also obtained through the reaction of a diisopropylzinc solution with *N*,*N*-dimethylhydrazine and a small amount of water. The structure of the resulting cocrystalline material, $[(i\text{PrZn})_4(NHNMe_2)_4]\cdot[(i\text{PrZn})_4(NHNMe_2)_3(OH)]$ (**2**), was also confirmed by X-ray diffraction. The hydroxide cluster in **2** contains a $Zn_4N_6O$ cage, with a similar aggregation mode to that of **4**.

(© Wiley-VCH Verlag GmbH & Co. KGaA, 69451 Weinheim, Germany, 2006)

## Introduction

The great variety of the chemistry of group 13 metal hydrazides has recently been reviewed by Uhl.[1] Such metal hydrazides can be employed as single-source precursors for the generation of metal nitrides[2] by CVD methods, although they have been applied in this context less frequently than metal amides.[3] The compounds reported include simple dimers like $[(Me_2Al\text{-}\mu\text{-}NHNMe_2)_2]$,[4] trimers like $[(Me_2Ga\text{-}\mu\text{-}NHNMe_2)_3]$[5] or more complex ladder-type aggregates such as $[Al_4(NHNMe_2)_8(NNMe_2)_2]$.[6] The different aggregation modes in such metal hydrazides originate from the presence of two directly connected inequivalent donor sites. Scheme 1 shows some examples of typical bridging modes realised in various metal hydrazides.

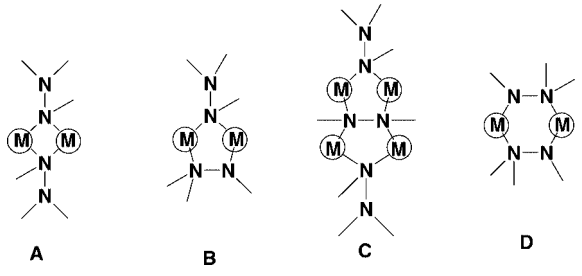


Scheme 1.

A few of these hydrazides also show β-donor bonding leading to three-membered AlNN units.[7a–7e] The reaction between hydrazine, $N_2H_4$, and $GaMe_3$ affords a singular bicyclic compound, $[(Me_2Ga)_4(N_2H_2)(NHNH_2)_2]$,[8] in which two five-membered heterocycles are connected by a common N–N bond and also have N–$NH_2$ groups in exocyclic positions as in type C. A high degree of coordinative flexibility has also recently been documented for the related hydroxylamides in organoaluminium and -gallium chemistry; examples of the corresponding four-, five- and six-membered ring isomers have been reported.[9]

[a] Institut für Anorganische und Analytische Chemie and NRW Graduate School of Chemistry, Westfälische Wilhelms-Universität Münster,
Corrensstrasse 30, 48149 Münster, Germany
Fax: +49-251-8336007
E-mail: Mitzel@uni-muenster.de
[b] Organisch-chemisches Institut, Westfälische Wilhelms-Universität Münster,
Corrensstrasse 40, 48149 Münster, Germany

 © 2006 Wiley-VCH Verlag GmbH & Co. KGaA, Weinheim 

On the basis of these results, it seems surprising that a corresponding organometallic chemistry with group 12 elements, in particular with zinc, which neighbours gallium, has not been extensively established so far. Zinc alkoxides are a well-established class of compounds.[10] They include homoleptic compounds,[10b] alkylzinc alkoxide clusters,[10c] and the zinc siloxide clusters, which have been described as early as 1960 by Schmidbaur and co-workers[10d,10e] and have recently been investigated by Driess and co-workers, who uncovered new varieties of aggregation and interesting thermolysis behaviour.[10f–10h] The only known hydrazide of zinc was $[Zn(N_2H_3)_2]$,[11] but this compound is quite cumbersome to synthesise and furthermore has the disadvantage of containing the $N_2H_3$ group, which exhibits a considerable explosion hazard. In our recent work, we have synthesised the first organometallic zinc hydrazide clusters of the type $[(RZn)_4(NHNMe_2)_4]$ (R = Me, Et) and their alkoxide and hydrazide hydroxide derivatives.[12] Hydrazides of other divalent metal ions have been described, examples include the magnesium hydrazides $\{Mg[NPhN(SiMe_3)_2]_2\}$ and $\{Mg[N(SiMe_3)NMe_2]_2\}$[13] and the beryllium hydrazide $[Be(NMeNMe_2)_2]$.[14] The results of these investigations can be compared with the better established chemistry of the alkali metal hydrazides, in particular that of lithium, which has a large variety of structural motifs.[15–21]

The driving force for preparing these zinc hydrazides and their oxygen derivatives is to explore their aggregation chemistry and behaviour in pyrolysis. Zinc oxide is a widely used semiconductor as it has a wide bandgap. The substitution of oxide by nitride in zinc-based materials such as ZnO would result in a *p*-type semiconductor, which was so far only realised with Ga codoping or by treatment with active nitrogen or with nitrogen oxides such as $N_2O$.[22a–22c] However, these substitution processes show poor reproducibility. The synthesis of such materials by using a molecular precursor route has not been tried to date, probably because of the restricted number of readily accessible thermolabile Zn/N precursor compounds.

In this contribution, we report the synthesis of new organozinc hydrazides and derivatives thereof in which hydrazide units are replaced by hydroxide or alkoxide units. This will be the starting point for the exploration of a new class of compounds, which could possibly be used as molecular precursors for new materials.

## Results and Discussion

### Isopropylzinc Hydrazide

The reaction of diisopropylzinc with *N*,*N*-dimethylhydrazine gives the hydrazide $[(i\text{PrZn})_4(NHNMe_2)_4]$ (**1**) in moderate yield (Scheme 2). It is soluble in all hydrocarbons and ethers and is easily purified by crystallisation. Compound **1** melts at 228–229 °C.

Hydrazide **1** was formed by combining $i\text{Pr}_2\text{Zn}$ and $H_2NNMe_2$ in a 1:1 ratio and was characterised by NMR spectroscopy and elemental analysis. The presence of tetrameric aggregates was proven by mass spectroscopy; the highest mass found was that of the tetramer minus one isopropyl group. Two bands at 3150 and 3174 $cm^{-1}$ in the IR spectrum proved the presence of NH functions. The $^1H$- and $^{13}C$ NMR spectra in $CDCl_3$ solution indicated the absence of molecular symmetry in the tetramer, as all four hydrazide methyl groups and all four isopropyl groups at zinc gave individual sets of signals. However, it is impossible to prove the formation of a single aggregation type solely from these data. Therefore, analysis by X-ray diffraction was performed on colourless single crystals of **1**, grown by storing an *n*-hexane solution of the compound at –26 °C for several days.

Compound **1** exhibits an unusual $M_4N_8$ cage structure which is $C_1$ symmetric (Figure 1). The topology is related to that of $[(MeGa)_4(NHNPh)_4]$, which contains a $Ga_4N_8$ cage and a dianionic ligand compensating for the formal double charge of the cationic unit $MeGa^{2+}$.[23] There is also a structural resemblance to the zinc oximate $[(MeZn)_4(ONCMe_2)_4]$, which also has a $Zn_4N_4O_4$ core,[24] but has oxygen as the primary binding atom. Furthermore, the structure is similar to the dimethyl- and diethylhydrazides $[(RZn)_4(NHNMe_2)_4]$ (R = Me, Et) recently reported by us.[12]

In compound **1**, all the zinc and nitrogen atoms have coordination number four. There are altogether six rings, two of which are six-membered ($Zn_2N_4$) and four are five-membered ($Zn_2N_3$). The zinc atoms in **1** span a topological tetrahedron, each one of whose four triangular faces are capped by a hydrazide ligand. Each hydrazide unit forms two bonds to zinc atoms from its NH group and one dative bond from its $NMe_2$ group. The distribution of these types of bonds is uneven: Zn1 has three bonds to NH units, Zn2

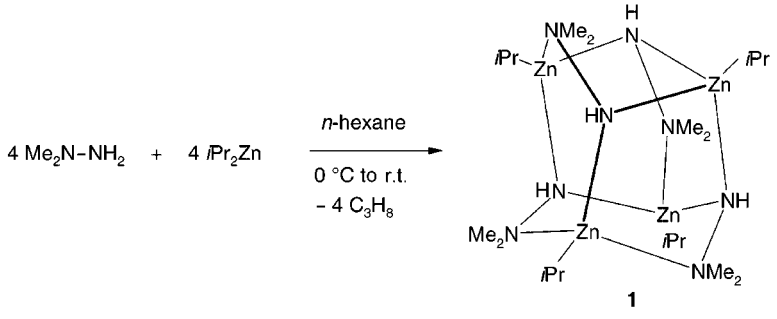


Scheme 2.

 © 2006 Wiley-VCH Verlag GmbH & Co. KGaA, Weinheim 

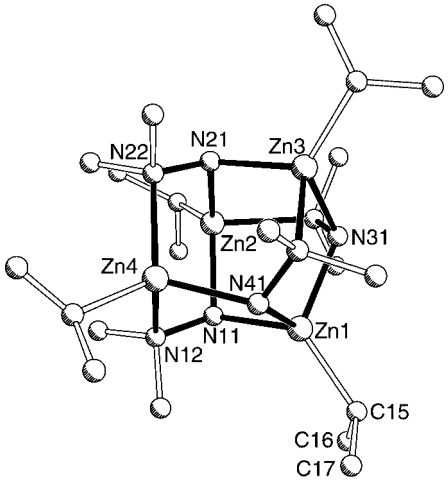


Figure 1. Molecular structure of $[(i\text{PrZn})_4(\text{NHNMe}_2)_4]$ (**1**) as determined by X-ray crystallography. Hydrogen atoms are omitted for clarity.

and Zn3 have two to NH units and one to an $NMe_2$ group, and finally Zn4 has one bond to an NH unit and two to $NMe_2$ groups. The bonds from the Zn atoms to the formally anionic NH groups are shorter by more than 0.1 Å than those to the $NMe_2$ groups. Table 1 lists selected geometric parameters for **1**.

Table 1. Selected bond lengths [Å] and angles [°] for $[(i\text{PrZn})_4(\text{NHNMe}_2)_4]$ (**1**) as determined by X-ray crystallography.

| Bond lengths | | Angles | |
|---|---|---|---|
| Zn1–C15 | 2.011(8) | C15–Zn1–N11 | 122.0(3) |
| Zn1–N11 | 2.094(6) | C15–Zn1–N31 | 120.8(3) |
| Zn1–N31 | 2.066(6) | C25–Zn2–N21 | 124.5(4) |
| Zn1–N41 | 2.064(7) | Zn1–N11–Zn2 | 106.4(3) |
| Zn2–N11 | 2.039(7) | Zn1–N11–N12 | 110.7(3) |
| Zn2–N21 | 2.059(8) | Zn2–N32–C33 | 109.2(6) |
| Zn2–N32 | 2.150(6) | N11–Zn1–N31 | 95.5(2) |
| N11–N12 | 1.436(9) | N31–Zn1–N41 | 97.6(3) |

### Isopropylzinc Hydrazide Hydroxide

We have previously reported the formation of the mixed hydrazide hydroxide clusters $[(\text{MeZn})_4(\text{NHNMe}_2)_3(\text{OH})]$ and $[(\text{EtZn})_4(\text{NHNMe}_2)_3(\text{OH})]$[12] from the one-pot reaction between dimethyl- or diethylzinc, *N*,*N*-dimethylhydrazine and water. By carrying out the reaction under similar conditions, but with diisopropylzinc as the organometallic component, we expected to obtain $[(i\text{PrZn})_4(\text{NHNMe}_2)_3(\text{OH})]$. Unexpectedly, the cocrystalline compound $[(i\text{PrZn})_4(\text{NHNMe}_2)_4]\cdot[(i\text{PrZn})_4(\text{NHNMe}_2)_3(\text{OH})]$ (**2**) (Scheme 3) formed and was characterised by single-crystal X-ray diffraction. The presence of the OH group was also confirmed by IR spectroscopy. In the $^1$H NMR spectrum, we could find three sets of signals for the hydrogen atoms at the isopropyl groups. Adding larger amounts of water to the mixture of diisopropylzinc and *N*,*N*-dimethylhydrazine leads to the formation of complicated mixtures of compounds and insoluble precipitates, which could not be separated or identified.

Compound **2** is very soluble in *n*-hexane and in ethereal solvents. Single crystals were obtained by cooling an *n*-hexane solution of **2** for several days at –26 °C.

The crystals of **2** adopt the monoclinic space group $P2_1/c$ and comprise $M_4N_8$ and $M_4N_6O$ cores (Figure 2). Selected geometric parameters for **2** are listed in Table 2.

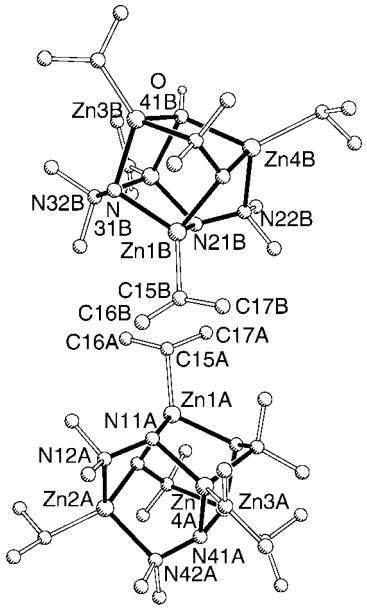


Figure 2. Molecular structure of the cocrystalline compound $[(i\text{PrZn})_4(\text{NHNMe}_2)_4]\cdot[(i\text{PrZn})_4(\text{NHNMe}_2)_3(\text{OH})]$ (**2**) as determined by X-ray crystallography. Hydrogen atoms except the one bound to oxygen are omitted for clarity.

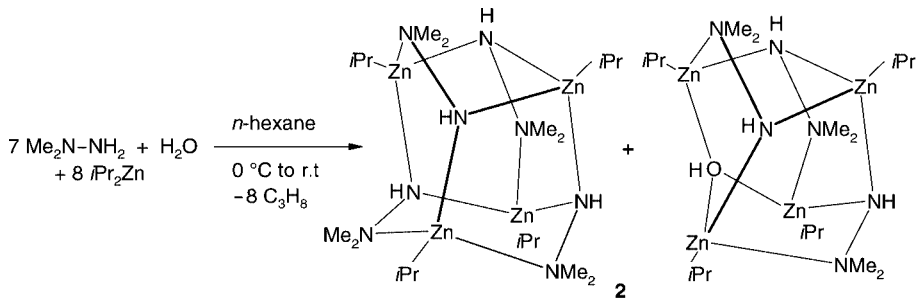


Scheme 3.

 © 2006 Wiley-VCH Verlag GmbH & Co. KGaA, Weinheim 

Table 2. Selected bond lengths [Å] and angles [°] for $[(i\text{PrZn})_4(\text{NHNMe}_2)_4]\cdot[(i\text{PrZn})_4(\text{NHNMe}_2)_3(\text{OH})]$ (**2**) as determined by X-ray crystallography. Each Zn cage appears as a separate column.

| $[(i\text{PrZn})_4(\text{NHNMe}_2)_4]$ | | $[(i\text{PrZn})_4(\text{NHNMe}_2)_3(\text{OH})]$ | |
|---|---|---|---|
| Zn1A-C15A | 2.014(7) | Zn1B-C15B | 2.000(15) |
| Zn1A-N21A | 2.081(6) | Zn1B-N21B | 2.080(9) |
| Zn1A-N11A | 2.073(6) | Zn1B-N31B | 2.082(9) |
| Zn1A-N31A | 2.083(5) | Zn2B-C25B | 2.012(15) |
| Zn2A-C25A | 2.014(9) | Zn2B-N21B | 2.025(8) |
| Zn2A-N21A | 2.048(6) | Zn2B-N12B | 2.150(6) |
| Zn2A-N12A | 2.139(8) | N11B-N12B | 1.444(11) |
| N11A-N12A | 1.472(9) | O41B-Zn2B | 2.226(11) |
| C15A-Zn1A-N21A | 121.0(3) | O41B-Zn3B | 2.175(12) |
| C15A-Zn1A-N11A | 122.4(3) | C15B-Zn1B-N11B | 118.1(6) |
| C15A-Zn1A-N31A | 118.3(3) | C15B-Zn1B-N31B | 122.9(8) |
| N21A-Zn1A-N11A | 94.9(3) | N21B-Zn1B-N11B | 96.5(4) |
| N21A-Zn1A-N31A | 98.0(2) | N21B-Zn1B-N31B | 95.8(4) |
| N11A-Zn1A-N31A | 96.5(2) | Zn1B-N21B-Zn2B | 104.4(4) |
| Zn1A-N21A-Zn2A | 108.9(3) | Zn1B-N21B-N22B | 109.2(7) |
| Zn1A-N21A-N22A | 110.1(4) | Zn2B-O41B-Zn3B | 98.7(6) |

### Isopropylzinc Monoalkoxide Trihydrazide

In order to obtain zinc alkoxide hydrazide compounds, we combined dialkylzinc solutions, alcohol and hydrazine in one-pot syntheses. To achieve the formation of monoalkoxide clusters, a diisopropylzinc/hydrazine/alcohol ratio of 4:2.4:2 was employed (Scheme 4). From this mixture we obtained the compounds $[(i\text{PrZn})_4(\text{NHNMe}_2)_3(\text{OR})]$ [R = Et (**3**), *i*Pr(**4**)]. In an earlier publication, we mentioned the formation of similar products by alcoholysis of the pure hydrazides with dimethyl- and diethylzinc units.[12]

The $^1$H and $^{13}$C NMR spectra of **3** and **4** show one set of alcoholate signals and three sets of signals for the hydrogen atoms at isopropyl groups. The integration ratio gives a zinc alkyl/hydrazide/alkoxide stoichiometry of 4:3:1. The IR spectra show bands corresponding to NH stretching modes. The highest peak in the mass spectrum corresponds to the mass of the molecular cations minus the mass of the alkyl group attached to the O atom. Compounds **3** and **4** melt at 195 °C and 223 °C, respectively. They are soluble in hydrocarbons and ethereal solvents.

The structures of **3** and **4** were obtained by single-crystal X-ray diffraction (Figure 3 and Figure 4). The compounds crystallise in the monoclinic space groups $P2_1/n$ and $P2_1/c$, respectively, from *n*-hexane solutions upon cooling to –26 °C for several days.

The quality of the diffraction data for compound **3** was poor, mainly because of the conformational flexibility of the isopropyl groups, as we frequently observe in this area of chemistry. Therefore, the structural data, which we provide here for the purpose of comparison, should not be overinterpreted.

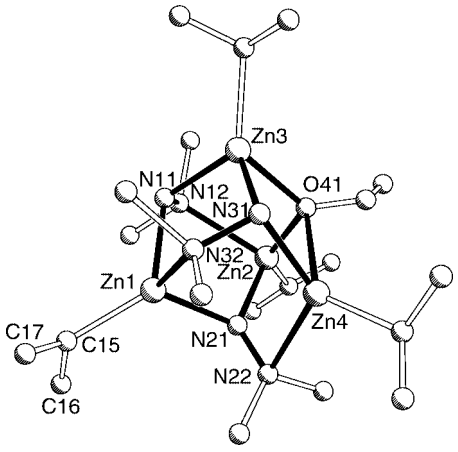


Figure 3. Molecular structure of $[(i\text{PrZn})_4(\text{NHNMe}_2)_3(\text{OEt})]$ (**3**) as determined by X-ray crystallography. Hydrogen atoms are omitted for clarity. Selected bond lengths [Å] and angles [°]: Zn1–N21 2.040(12), Zn1–N11 2.057(11), Zn1–N32 2.17(2), Zn2–N21 2.001(12), Zn2–N12 2.199(12), O41–Zn2 2.018(15), O41–Zn3 1.989(18), O41–Zn4 2.34(3); C15–Zn1–N21 122.3(9), C15–Zn1–N11 123.7(10), C15–Zn1–N32 119.1(8), N21–Zn1–N11 94.3(5), N11–Zn1–N32 88.7(8), Zn1–N21–N22 123.1(11), O41–Zn3–N11 91.0(5), Zn2–O41–Zn3 111.9(7).

Both **3** and **4** contain $Zn_4N_6O$ cores in their molecular structures. We found two different types of aggregation mode in the crystal cores of **3** and **4**. In **3**, the three zinc atoms that are connected to oxygen form one bond to an anionic NH unit and one dative bond to an $NMe_2$ group. The fourth zinc atom is bound to one NH unit and forms two dative bonds to $NMe_2$ groups. Therefore, compound **3**

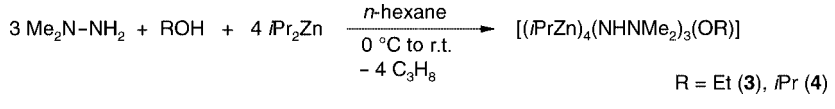


Scheme 4.

 © 2006 Wiley-VCH Verlag GmbH & Co. KGaA, Weinheim 

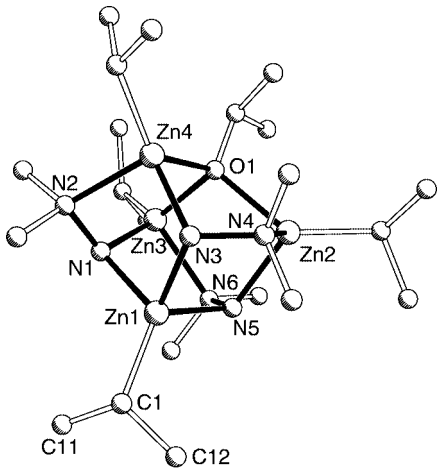


Figure 4. Molecular structure of one of the two independent molecules of $[(i\text{PrZn})_4(\text{NHNMe}_2)_3(\text{O}i\text{Pr})]$ (**4**) as determined by X-ray crystallography. Hydrogen atoms are omitted for clarity. Selected bond lengths [Å] and angles [°]: Zn1–C1 2.016(7), Zn1–N1 2.067(6), Zn2–N5 2.041(5), Zn2–N4 2.150(6), O1–Zn2 2.117(5), O1–Zn4 2.142(6); C1–Zn1–N1 121.3(3), N1–Zn1–N5 94.8(2), N1–Zn1–N3 92.9(3), Zn1–N1–Zn3 107.6(3), O1–Zn3–N1 92.2(3), Zn2–O1–Zn3 108.0(2).

forms one four-membered $Zn_2NO$ and one six-membered $Zn_2N_4$ ring as well as two five-membered $Zn_2N_3$ and two five-membered $Zn_2N_2O$ rings. By contrast, in compound **4**, the fourth zinc atom, which is not connected to the oxygen atom, bonds to three anionic NH units, allowing all six rings to be five-membered (Figure 5). This shows that subtle changes in the sizes of the oxygen substituents can lead to substantial variations in the cage structure of such aggregates. On the other hand, these results indicate that such different cage constitutions vary only slightly in energy.

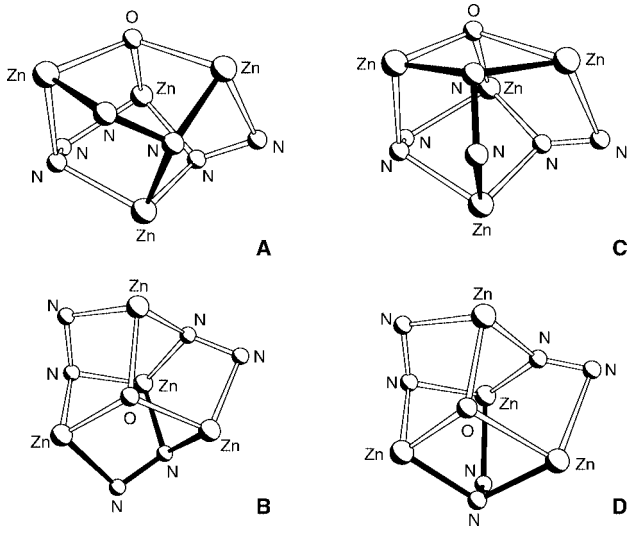


Figure 5. Illustration of the possible aggregation isomers of one of the hydrazide units at the common core structure $Zn_4(\text{NHNMe}_2)_2(\text{OR})$ in $[(i\text{PrZn})_4(\text{NHNMe}_2)_3(\text{OEt})]$ (**3**, **C** and **D**) and $[(i\text{Pr}_2\text{Zn})_4(\text{NHNMe}_2)_3(\text{O}i\text{Pr})]$ (**4**, **A** and **B**). Only the two different $Zn_4N_6O$ cores are shown in two views rotated by about 90°. The structures of the common $Zn(N_2)_2(O)$ cores of the $Zn_4(\text{NHNMe}_2)_2(\text{OR})$ units are shown in hollow lines, the orientation of the $N_2$ unit of the $\text{NHNMe}_2$ group and its connection to the rest of the structure are shown in filled lines.

## Experimental Section

**General Considerations:** All manipulations of air-sensitive compounds were carried out under a dry nitrogen atmosphere with standard Schlenk and high-vacuum techniques by using double manifolds or in a glovebox operated under argon. Solvents were purified and dried by standard methods immediately prior to use. *N*,*N*-Dimethylhydrazine was purchased from Aldrich Chemical Company and dried by distillation from $CaH_2$ under dry nitrogen. Diisopropylzinc was synthesised according to a literature procedure.[25] $^1$H and $^{13}$C NMR spectra were recorded with a Varian Inova-300, 400, 500 or a Varian Unity Plus 600 spectrometer in $CDCl_3$ which was dried with activated molecular sieves. $^1$H- and $^{13}$C assignments were confirmed when necessary by use of two-dimensional $^1$H–$^1$H and $^{13}$C–$^1$H correlation NMR experiments. All spectra were recorded at 25 °C and referenced internally to residual protiosolvent ($^1$H) or solvent ($^{13}$C) resonances. Chemical shifts are quoted in ppm and coupling constants in Hz. A Nonius Kappa-CCD ($\lambda$ = 0.71073 Å) (for compounds **1**, **2** and **3**) or a Bruker Smart CCD X-ray diffractometer ($\lambda$ = 1.54184 Å) (for compound **4**) was used to collect the scattering intensities for single-crystal X-ray diffraction experiments. IR spectra were measured with a Bruker IFS (103 V) by using KBr pellets prepared in the glovebox.

**$[(i\text{PrZn})_4(\text{NHNMe}_2)_4]$ (1):** $i\text{Pr}_2\text{Zn}$ (8.00 mL of a 2.5 M solution in *n*-hexane/diethyl ether; 20.0 mmol) was added dropwise with a syringe to a stirred solution of $H_2\text{NNMe}_2$ (2.30 mL, 30.0 mmol) in *n*-hexane (20 mL) at 0 °C. The reaction mixture was gradually warmed to room temp. and stirred for 6 h. Solvents were removed under reduced pressure The residue was then dissolved in *n*-hexane and filtered. The clear, colourless filtrate was stored at –26 °C to afford colourless, plate-like crystals.

Yield: 63% (2.11 g, 3.14 mmol). M.p. 228–229 °C. $^1$H NMR (400 MHz): $\delta$ = 0.07 [sept, $^3J_{\text{H,H}}$ = 7.7 Hz, 1 H, ZnC*H*], 0.14–0.30 [m, 2 H, ZnC*H*], 0.37 [sept, $^3J_{\text{H,H}}$ = 7.7 Hz, 1 H, ZnC*H*], 1.13–1.25 [m, 24 H, $\text{ZnCH}(\text{C}H_3)_2$], 2.06, 2.09, 2.12 [s, 4 H, N-*H*], 2.23–2.77 [m, 24 H, $\text{N}(\text{C}H_3)_2$] ppm. $^{13}$C{$^1$H} NMR (125.7 MHz): $\delta$ = 10.22, 11.07, 11.32, 11.69 [Zn*C*H], 24.73, 24.89, 25.15, 25.31, 25.33, 25.50, 25.59, 25.73 [$\text{ZnCH}(C\text{H}_3)_2$], 53.87, 54.76, 55.14, 55.64, 56.51, 56.83, 57.14, 57.89 [$\text{N}(C\text{H}_3)_2$] ppm. $C_{20}H_{56}N_8Zn_4$ (670.24): calcd. C 35.83, H 8.42, N 16.72; found C 35.75, H 8.21, N 16.38. EI-MS [*m*/*z* (%)]: 627 (100), $[\text{M}^+-\text{C}_3\text{H}_7]$, 567 (53), $[\text{M}^+-\text{C}_3\text{H}_7-(\text{NHNMe}_2)]$, 459 (78), $[\text{M}^+-2\ \text{C}_3\text{H}_7-(\text{NHNMe}_2)]$. IR (KBr): $\tilde{\nu}$ = 3150, 3174 (w, N–H), 2867 (vs), 2821 (vs), 2693 (w), 1465(vs) 1161 (s), 994 (s) 951 (s), 820 (vs), 571 (s) cm$^{-1}$.

**$[(i\text{PrZn})_4(\text{NHNMe}_2)_4]\cdot[(i\text{PrZn})_4(\text{NHNMe}_2)_3(\text{OH})]$ (2):** $i\text{Pr}_2\text{Zn}$ (4.00 mL, 2.5 M in *n*-hexane/diethyl ether, 10.0 mmol) was added dropwise with a syringe to a stirred solution of $H_2\text{NNMe}_2$ (0.60 mL, 7.83 mmol) in *n*-hexane (10 mL) at 0 °C. Water (0.07 mL, 3.88 mmol) was added dropwise with a syringe. The reaction mixture was gradually warmed to room temp. and stirred for 6 h. After removal of the solvent under reduced pressure, the residue was dissolved in *n*-hexane and filtered. Colourless crystals of **2** were obtained by storing an *n*-hexane solution of **2** at –26 °C.

Yield: 62% (1.00 g, 1.54 mmol). M.p. 263–264 °C (decomp.). $^1$H NMR (300 MHz): $\delta$ = 0.21 [sept, $^3J_{\text{H,H}}$ = 7.6 Hz, 1 H, ZnC*H*-$(\text{CH}_3)_2$], 0.44 [sept, $^3J_{\text{H,H}}$ = 7.6 Hz, 1 H, $\text{ZnC}H(\text{CH}_3)_2$], 0.83 [sept, $^3J_{\text{H,H}}$ = 7.5 Hz, 2 H, $\text{ZnC}H(\text{CH}_3)_2$], 1.09–1.29 [m, 24 H, $\text{ZnCH}(\text{C}H_3)_2$], 2.06–2.78 [m, 21 H, N-*H*, $\text{N}(\text{C}H_3)_2$] ppm. $^{13}$C{$^1$H}

 © 2006 Wiley-VCH Verlag GmbH & Co. KGaA, Weinheim 

NMR (125.7 MHz): $\delta$ = 11.14, 11.35, 11.60, 11.96, 13.41 [Zn*C*H], 23.74, 25.07, 25.26, 25.68, 25.78, 25.91, 27.63 [ZnCH(*C*$H_3$)$_2$], 53.78, 54.15, 55.39, 55.94, 56.78, 57.11, 57.44, 58.16 [N(*C*$H_3$)$_2$] ppm. EI-MS [*m*/*z* (%)]: 627 (100), [$M^+ - C_3H_7$]. IR (KBr): $\tilde{\nu}$ = 3323 (w, O–H), 3147 (w, N–H), 2928 (s), 2863 (vs), 2815 (s), 1451 (vs) 1159 (s), 987 (s) 951 (s), 813 (vs) cm$^{-1}$.

**[(*i*PrZn)$_4$(NHNMe$_2$)$_3$(OEt)] (3):** *i*Pr$_2$Zn (8.00 mL of 2.5 M in *n*-hexane/diethyl ether; 20.0 mmol) was added dropwise with a syringe to a stirred solution of $H_2NNMe_2$ (0.92 mL, 12.0 mmol) and EtOH (0.58 mL, 9.96 mmol) in *n*-hexane (20 mL) at 0 °C. The reaction mixture was gradually warmed to room temp. and stirred for 4 h. After removal of the solvent under reduced pressure, the residue was dissolved in *n*-hexane and filtered. The clear, colourless filtrate was stored at –26 °C to afford colourless crystals of **3**.

Yield: 49% (1.60 g, 2.44 mmol). M.p. 195–196 °C. $^1$H NMR (300 MHz): $\delta$ = 0.50 [sept, $^3J_{H,H}$ = 7.6 Hz, 1 H, ZnC*H*(CH$_3$)$_2$], 0.64 [sept, $^3J_{H,H}$ = 7.6 Hz, 2 H, ZnC*H*(CH$_3$)$_2$], 0.79 [sept, $^3J_{H,H}$ = 7.5 Hz, 1 H, ZnC*H*(CH$_3$)$_2$], 1.12–1.28 [m, 24 H, ZnCH(C*H*$_3$)$_2$], 1.30 [t, $^3J_{H,H}$ = 7.0 Hz, 3 H, OCH$_2$C*H*$_3$], 2.04, 2.10 [s, 3 H, N-*H*], 2.32–2.70 [m, 18 H, N(C*H*$_3$)$_2$], 3.93 [q, $^3J_{H,H}$ = 7.0 Hz, 2 H, OC*H*$_2$CH$_3$] ppm. $^{13}$C{$^1$H} NMR (75 MHz): $\delta$ = 10.62, 11.81, 12.04, 12.35 [Zn*C*H], 20.98 [OCH$_2$*C*H$_3$], 23.94, 24.02, 24.25, 24.95, 24.74, 24.87, 24.92, 25.15 [ZnCH(*C*H$_3$)$_2$], 53.76, 54.14, 54.37, 54.62, 55.18, 55.46 [N(*C*H$_3$)$_2$], 63.49 [O*C*H$_2$CH$_3$] ppm. IR (KBr): $\tilde{\nu}$ = 3174 (w, N–H), 2865 (vs), 2816 (s), 2700 (w), 1159 (s), 874 (vs) cm$^{-1}$. $C_{20}H_{54}N_6OZn_4$ (654.19): calcd. C 36.72, H 8.01, N 12.85; found C 36.36, H 8.21, N 12.64.

**[(*i*PrZn)$_4$(NHNMe$_2$)$_3$(O*i*Pr)] (4):** *i*Pr$_2$Zn (6.00 mL of 2.5 M in *n*-hexane/diethyl ether; 15.0 mmol) was added dropwise with a syringe to a stirred solution of $H_2NNMe_2$ (0.77 mL, 10.06 mmol) and *i*PrOH (0.45 mL, 7.02 mmol) in *n*-hexane (10 mL) at 0 °C. The reaction mixture was gradually warmed to room temp. and stirred for 4 h. The solvents were removed under reduced pressure, the residue was dissolved in *n*-hexane and filtered. The clear, colourless filtrate was stored at –26 °C to afford colourless crystals of **4**.

Yield: 52% (1.30 g, 1.94 mmol). M.p. 223–224 °C. $^1$H NMR (500 MHz): $\delta$ = 0.31 [sept, $^3J_{H,H}$ = 7.5 Hz, 1 H, ZnC*H*(CH$_3$)$_2$], 0.43 [sept, $^3J_{H,H}$ = 7.5 Hz, 2 H, ZnC*H*(CH$_3$)$_2$], 0.52 [sept, $^3J_{H,H}$ = 7.5 Hz, 1 H, ZnC*H*(CH$_3$)$_2$], 1.15–1.19 [m, 6 H, OCH(C*H*$_3$)$_2$], 1.20–1.32 [m, 24 H, ZnCH(C*H*$_3$)$_2$], 1.91, 1.94, 2.01 [s, 3 H, N-*H*], 2.27–2.70 [m, 18 H, N(C*H*$_3$)$_2$], 4.17 [sep, 1 H, OC*H*(CH$_3$)$_2$] ppm. $^{13}$C{$^1$H} NMR (125.7 MHz): $\delta$ = 11.10, 13.38, 13.68 [Zn*C*H-(CH$_3$)$_2$], 24.35, 24.37, 24.69, 24.72, 24.91, 24.93 [ZnCH(*C*H$_3$)$_2$], 25.43, 25.50 [OCH(*C*H$_3$)$_2$], 54.17, 54.36, 54.46, 54.83, 54.86, 54.95 [N(*C*H$_3$)$_2$], 68.53 [O*C*H(CH$_3$)$_2$] ppm. EI-MS [*m*/*z* (%)]: 627 (100), [$M^+ - C_3H_7$], 459 (99), [$M^+ - C_3H_7 - C_3H_7ZnOC_3H_7$]. IR (KBr): $\tilde{\nu}$ = 3168 (w, N–H), 2867 (vs), 2829 (vs), 1459 (vs), 1377 (s), 1163 (s), 1114 (s), 996 (s), 939 (s), 817 (vs), 787 (s), 570 (s) cm$^{-1}$. $C_{21}H_{56}N_6OZn_4$ (670.24): calcd. C 37.63, H 8.42, N 12.54; found C 37.41, H 8.44, N 12.39.

**Crystal Structures:** Crystals of compounds **1**, **2** and **3** were selected and prepared under perfluoropolyether and mounted in a drop of this solution onto the glass fibre tip of the goniometer head. The crystallographic data sets for compounds **1**, **2** and **3** were collected with a Nonius Kappa CCD diffractometer; the data set for **4** was collected with a Bruker Smart CCD diffractometer. The structures were solved by direct methods and refined with the full-matrix least-squares procedure (SHELXTL[26]) against $F^2$. Details of the crystal data and refinements are provided in Table 3. The generation of good quality crystals of this class of substance has proven very difficult previously,[12] probably because of the ball-shaped structure of the tetrameric or pseudotetrameric aggregates. Despite the limited accuracy of the geometry parameters which could be achieved with the crystalline materials, the crystal structure determination results give valuable information regarding the constitution of the cluster-like aggregates.

One of the two independent molecules in the crystal of **4** is less well defined than the other. In this molecule, two isopropyl groups were refined as a split model to give abundances for the major disorder components of 0.54 and 0.87. Furthermore, two N–N bonds [N(1)–N(2) and N(9)–N(10)] in this molecule were restrained

Table 3. Crystal and refinement data for the compounds **1**, **2**, **3** and **4**.

| | **1** | **2** | **3** | **4** |
|---|---|---|---|---|
| Formula | $C_{20}H_{56}N_8Zn4$ | $(C_{20}H_{56}N_8Zn_4)\cdot(C_{18}H_{50}N_6OZn_4)$ | $C_{20}H_{54}N_6OZn_4$ | $C_{21}H_{56}N_6OZn_4$ |
| $M_r$ | 670.21 | 1298.32 | 656.17 | 670.20 |
| Crystal system | monoclinic | monoclinic | monoclinic | monoclinic |
| *a* [Å] | 15.978(1) | 18.191(1) | 13.898(1) | 17.651(1) |
| *b* [Å] | 12.006(1) | 19.247(1) | 13.515(1) | 19.763(1) |
| *c* [Å] | 16.607(1) | 19.101(1) | 16.714(1) | 18.286(1) |
| $\alpha$ [°] | 90 | 90 | 90 | 90 |
| $\beta$ [°] | 101.30(1) | 110.58(1) | 100.60(1) | 105.29(1) |
| $\gamma$ [°] | 90 | 90 | 90 | 90 |
| *V* [Å$^3$] | 3124.0(4) | 6260.9(6) | 3085.8(4) | 6152.9(3) |
| *T* [°C] | –75 | –75 | –75 | –153 |
| Space group | $P2_1/n$ | $P2_1/c$ | $P2_1/n$ | $P2_1/c$ |
| *Z* | 4 | 4 | 4 | 8 |
| $\rho_{calcd.}$ [g·cm$^{-3}$] | 1.425 | 1.377 | 1.412 | 1.447 |
| Crystal size [mm] | 0.50×0.50×0.35 | 0.40×0.25×0.10 | 0.60×0.25×0.15 | 0.40×0.18×0.06 |
| $\lambda$ [Å] | 0.71073 | 0.71073 | 0.71073 | 1.54184 |
| $\mu$ [mm$^{-1}$] | 3.055 | 3.047 | 3.092 | 3.696 |
| $Refl_{collected}$ | 18372 | 36365 | 14219 | 33862 |
| $Refl_{unique}$ | 7442 | 11015 | 3991 | 11349 |
| $R_{int}$ | 0.043 | 0.062 | 0.051 | 0.063 |
| $R_1$/w$R_2$ [$I > 2\sigma(I)$] | 0.079/0.219 | 0.069/0.185 | 0.098/0.279 | 0.082/0.204 |
| $R_1$/w$R_2$ (all data) | 0.130/0.255 | 0.137/0.222 | 0.131/0.319 | 0.125/0.230 |
| $\Delta\rho_{fin}$ [e·Å$^{-3}$] | 2.18/–1.37 | 1.28/–1.15 | 0.85/–0.55 | 4.06/–1.12 |
| CCDC number | 292691 | 292692 | 292693 | 292694 |

 © 2006 Wiley-VCH Verlag GmbH & Co. KGaA, Weinheim 

to a length of 1.46 (1) Å and the bonds Zn(4)–N(2) and Zn(7)–N(10) to a length of 2.13(1) Å as they tended to refine to inappropriate values. All the distances (bonding and non-bonding) in the disordered isopropyl groups containing C(7) and C(8) were restrained to the average geometry values for the isopropyl groups in the other, better defined molecule. Crystallographic data (excluding structure factors) for the structures reported in this paper have been forwarded to the Cambridge Crystallographic Data Centre as supplementary publications. The deposition numbers are listed in the last line of Table 3. These data can be obtained free of charge from The Cambridge Crystallographic Data Centre via www.ccdc.cam.ac.uk/data_request/cif.

## Acknowledgments

We are grateful to the NRW Graduate School of Chemistry at Münster (GSC-MS) for a PhD stipend for S.J. The authors would like to thank Dr. F. Rogel for collecting the X-ray data set of **4**, Dr. K. Bergander for recording the NMR spectroscopic data and M. Ullrich for providing diisopropylzinc solutions and for helpful discussions.

[1] W. Uhl, "Aluminium and Gallium Hydrazides" in *Structure and Bonding, Volume 105: Group 13 Chemistry III* (Eds.: H. W. Roesky, D. A. Atwood), Springer-Verlag, Berlin, **2003**, p. 41–66.
[2] D. A. Neumayer, J. G. Ekerdt, *Chem. Mater.* **1996**, *8*, 9–25.
[3] A selection of references for metal amides as precursors for nitride materials: a) A. P. Purdy, *Inorg. Chem.* **1994**, *33*, 282–286; b) D. V. Baxter, M. H. Chisholm, G. J. Gama, V. F. Distasi, A. L. Hector, I. P. Parkin, *Chem. Mater.* **1996**, *8*, 1222–1228; c) S. A. Rushworth, J. R. Brown, D. J. Houlton, A. C. Jones, V. Robert, J. S. Roberts, G. W. Critchlow, *Adv. Mater. for Optics and Electronics* **1996**, *6*, 119–126; d) R. Fix, R. G. Gordon, D. M. Hoffman, *Chem. Mater.* **1993**, *5*, 614–619; e) J. Khanderi, D. Rische, H. W. Becker, R. A. Fischer, *J. Mater. Chem.* **2004**, *14*, 3210–3214.
[4] Y. Kim, J. H. Kim, J. E. Park, H. Song, J. T. Park, *J. Organomet. Chem.* **1997**, *545–546*, 99–103.
[5] D. A. Neumayer, A. H. Cowley, A. Decken, R. A. Jones, V. Lakhotia, J. G. Eckerdt, *Inorg. Chem.* **1995**, *34*, 4698–4700.
[6] J. S. Silverman, C. D. Abernethy, R. A. Jones, A. H. Cowley, *Chem. Commun.* **1999**, 1645.
[7] a) W. Uhl, J. Molter, B. Neumüller, *Chem. Eur. J.* **2001**, *7*, 1510; b) W. Uhl, J. Molter, R. Koch, *Eur. J. Inorg. Chem.* **1999**, 2021; c) W. Uhl, J. Molter, R. Koch, *Eur. J. Inorg. Chem.* **2000**, 2255; d) W. Uhl, J. Molter, B. Neumüller, *Organometallics* **2000**, *19*, 4422; e) W. Uhl, J. Molter, B. Neumüller, *Inorg. Chem.* **2001**, *40*, 2011.
[8] H. Nöth, T. Seifert, *Eur. J. Inorg. Chem.* **2002**, 602.
[9] N. W. Mitzel, C. Lustig, M. Woski, *Dalton Trans.* **2004**, 397.
[10] a) D. C. Bradley, R. C. Mehrotra, I. P. Rothwell, A. Singh, *Alkoxo and Aryloxo Derivatives of Metals*, Academic Press, San Diego, **2001**; b) S. C. Goel, M. Y. Chiang, W. E. Buhro, *Inorg. Chem.* **1990**, *29*, 4646; c) H. M. M. Shearer, C. B. Spenser, *Chem. Commun. (London)* **1966**, 194; d) F. Schindler, H. Schmidbaur, U. Krüger, *Angew. Chem.* **1965**, *77*, 865; *Angew. Chem. Int. Ed. Engl.* **1965**, *4*, 876; e) F. Schindler, H. Schmidbaur, *Angew. Chem.* **1967**, *79*, 697; *Angew. Chem. Int. Ed. Engl.* **1967**, *6*, 683–694; f) M. Driess, K. Merz, S. Rell, *Eur. J. Inorg. Chem.* **2000**, 2517; g) J. Hambrock, S. Rabe, K. Merz, A. Birkner, A. Wohlfart, R. A. Fischer, M. Driess, *J. Mater. Chem.* **2003**, *13*, 1731; h) K. Merz, H. M. Hu, S. Rell, M. Driess, *Eur. J. Inorg. Chem.* **2003**, 51.
[11] a) B. Fröhling, G. Kreiner, H. Jacobs, *Z. Anorg. Allg. Chem.* **1999**, *625*, 211; b) J. Goubeau, U. Kull, *Z. Anorg. Allg. Chem.* **1962**, *316*, 182.
[12] S. Jana, R. Fröhlich, N. W. Mitzel, *Chem. Eur. J.* **2006**, *12*, 592.
[13] H. Sachdev, *Eur. J. Inorg. Chem.* **2002**, 2681.
[14] N. R. Fetter, *Can. J. Chem.* **1964**, *42*, 861.
[15] C. Drost, C. Jäger, S. Freitag, U. Klingebiel, M. Noltemeyer, G. M. Sheldrick, *Chem. Ber.* **1994**, *127*, 845.
[16] U. Klingebiel, S. Dielkus, C. Drost, R. Herbst-Irmer, *Angew. Chem.* **1993**, *105*, 1689; *Angew. Chem. Int. Ed. Engl.* **1993**, *32*, 1625.
[17] H. Nöth, H. Sachdev, M. Schmidt, H. Schwenk, *Chem. Ber.* **1995**, *128*, 105.
[18] B. Gemünd, H. Nöth, H. Sachdev, M. Schmidt, *Chem. Ber.* **1996**, *129*, 1335.
[19] J. Knizek, I. Krossing, H. Nöth, T. Seifert, *Chem. Ber./Recueil* **1997**, *130*, 1053.
[20] N. Metzler, H. Nöth, H. Sachdev, *Angew. Chem.* **1994**, *106*, 1837; *Angew. Chem. Int. Ed. Engl.* **1994**, *33*, 1746.
[21] K. Bode, U. Klingebiel, M. Noltemeyer, H. Witte-Abel, *Z. Anorg. Allg. Chem.* **1995**, *621*, 500.
[22] a) M. Joseph, H. Tabata, T. Kawai, *Jpn. J. Appl. Phys.* **1999**, *38*, L1205; b) T. Yamamoto, H. Katayama-Yoshida, *Jpn. J. Appl. Phys.* **1999**, *38*, L166; c) T. Dietl, H. Ohno, F. Matsukura, J. Cibert, D. Ferrand, *Science* **2000**, *287*, 1019.
[23] D. W. Peters, M. P. Power, E. D. Burret, J. Arnold, *Chem. Commun.* **1998**, 753.
[24] N. A. Bell, H. M. M. Shearer, C. B. Spencer, *Acta Crystallogr. Sect. C* **1984**, *40*, 613.
[25] A. Boudier, C. Darcel, F. Flachsmann, L. Micouin, M. Oestreich, P. Knochel, *Chem. Eur. J.* **2000**, *6*, 2748.
[26] a) *SHELXTL 6.10*, Bruker-AXS X-ray Instrumentation Inc. Madison, WI, **2000**; b) G. M. Sheldrick, *SHELXL-93: Program for Crystal Structure Refinement*, Universität Göttingen, Göttingen, Germany, **1993**.

Received: February 15, 2006
Published Online: August 24, 2006

 © 2006 Wiley-VCH Verlag GmbH & Co. KGaA, Weinheim 

DOI: 10.1002/ejic.200501035

# Drug Self-Templated Synthesis of Ibuprofen/Mesoporous Silica for Sustained Release

Fengyu Qu,[a,b] Guangshan Zhu,*[a] Huiming Lin,[a] Jinyu Sun,[a] Daliang Zhang,[a] Shougui Li,[a] and Shilun Qiu*[a]

**Keywords:** Template synthesis / Ibuprofen / Mesoporous materials / Silica

The synthesis of Ibuprofen/mesoporous silica has been achieved by a drug self-templated one-step co-condensation process. The drug template of Ibuprofen, a co-template of 3-aminopropyltriethoxysilane (APTES), and tetraethoxysiliane (TEOS) were self-assembled into Ibuprofen/mesoporous silica in a neutral aqueous reaction system. This drug/mesoporous silica was characterized by powder XRD diffraction, FTIR spectroscopy, $N_2$ adsorption/desorption, TEM, and $^{29}Si$/MAS and $^{13}C$/MAS NMR spectroscopy. The Ibuprofen/mesoporous silica system gives a well-sustained release profile.
(© Wiley-VCH Verlag GmbH & Co. KGaA, 69451 Weinheim, Germany, 2006)

## Introduction

Over the past three decades there has been rapid growth in sustained/controlled drug delivery in the field of modern medication and pharmaceuticals since sustained/controlled release can bring both therapeutic and commercial value to health-care products.[1] Among a wide number of materials, micelles, liposomes, and polymeric and co-polymeric nanoparticles are widely employed as drug carriers for sustained/controlled delivery. Recently, a new application of mesoporous silica as a drug-delivery system has been explored,[2] and there is now growing interest in the use of mesoporous silica as a sustained/controlled drug delivery system due to its several attractive features, such as stable uniform mesoporous structure, high surface area, tunable pore sizes with narrow distributions, well-defined surface properties,[1,3] nontoxic nature,[4] and good biocompatibility.[5–7] Several research groups have reported on the design of mesoporous silica-based carriers for sustained/controlled drug-delivery systems.[1–3,6,8–12]

Up to now, the loading of drugs into the channel of mesoporous silica was mainly post-synthesis, that is, the mesoporous silica carrier was synthesized first followed by storage of the drug molecules. The post-synthesis introduction of drug molecules has been achieved by two general strategies: (i) by physical adsorption of drug molecules in the pure mesoporous silica[2,5,8,10,12] or by an acid-base interaction of the drug molecules with amine-supported mesoporous silica,[1,3] or (ii) by anchoring the drug molecules with modified mesoporous silica by covalent attachment to form a pro-drug with release potential.[11]

Ibuprofen is frequently employed as a model drug for sustained/controlled delivery owing to its suitable molecule size of about $1.0 \times 0.5$ nm,[2] good pharmacological activity, and short biological half-life (2 h).[13]

Here, we propose a novel approach to encapsulating Ibuprofen in the channels of mesoporous silica by a one-step, drug self-templating technique. The Ibuprofen/mesoporous silica sample was characterized by powder XRD diffraction, FTIR spectroscopy, $N_2$ adsorption/desorption, TEM, and $^{29}Si$/MAS and $^{13}C$/MAS NMR spectroscopy. Drug-release profiles have also been determined.

## Results and Discussion

Figure 1 schematically illustrates the one-step, drug self-templated synthesis of our mesoporous silica drug-carrier system. The synthesis is based on $S^-N^+–I^-$ template pathways,[14–16] where $S^-$ denotes the anionic drug template and $N^+$ and $I^-$ represent the protonated amine group and negatively charged silane group, respectively. The formation mechanism is thought to be controlled by the electrostatic interaction between the negatively charged carboxylic headgroup of the drug template (Ibuprofen) and the protonated amine group of the organoalkoxysilane (APTES). Condensation occurs preferentially at the alkoxysilane sites in APTES to onset the formation of the silicate framework. Meanwhile, drug molecules are encapsulated in the channels of the mesoporous silicate to finally give the drug-encapsulated Ibu/MS system.

The XRD pattern of Ibu/MS shows only one reflection (see Supporting Information Figure S1), with a *d*-spacing of

[a] State Key Laboratory of Inorganic Synthesis and Preparative and Chemistry, Jilin University, Changchun 130023, China
[b] Chemistry Department of Harbin Normal University, Harbin, 150080, China
Fax: +86-431-516-8331
E-mail: zhugs@mail.jlu.edu.cn
sqiu@mail.jlu.edu.cn
Supporting information for this article is available on the WWW under http://www.eurjic.org or from the author.

 © 2006 Wiley-VCH Verlag GmbH & Co. KGaA, Weinheim 

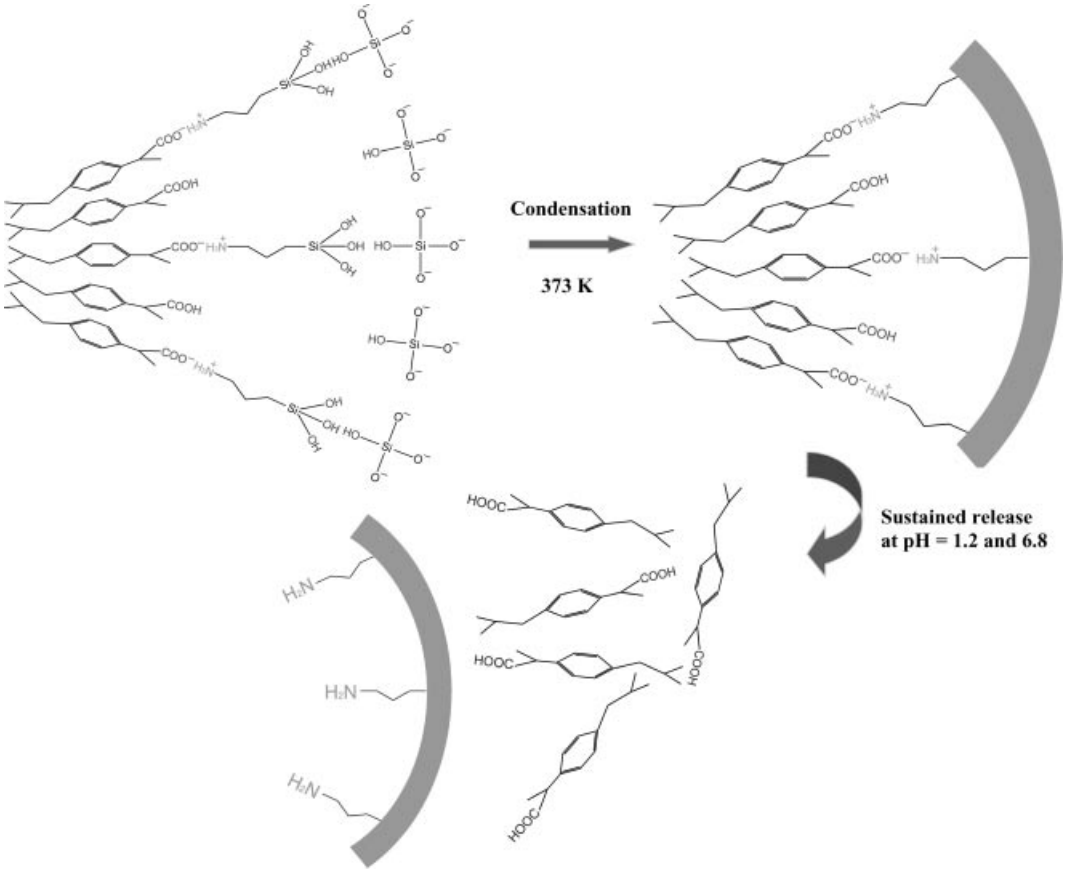


Figure 1. The one-step, drug self-templated synthesis of Ibu/MS system and sustained release.

4.28 nm. The TEM image confirms that the Ibu/MS sample possesses an ordered mesoporous structure (Figure 2). Furthermore, the characteristic mesoporous system was also confirmed by nitrogen adsorption/desorption measurements (shown in Figure 3), which revealed that the samples possess a high specific surface area of 1262 $m^2 g^{-1}$, a large pore volume of 0.66 $cm^3 g^{-1}$, and an average pore size of 2.08 nm. It can be seen that a well-defined step occurs in the adsorption curve at a relative pressure, $P/P_o$, of 0.2–0.3, which indicates the filling of framework-confined mesopores.[17] This isotherm can be classified as type IV.[18]

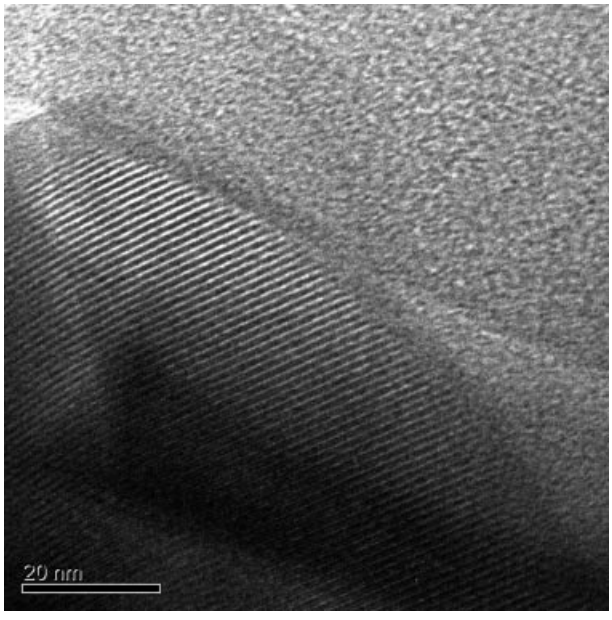


Figure 2. TEM image of Ibu/MS.

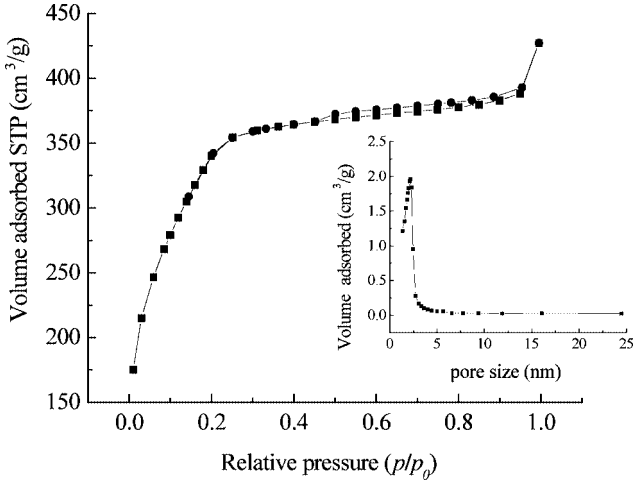


Figure 3. Nitrogen adsorption/desorption isotherm and pore-size distribution of Ibu/MS.

 © 2006 Wiley-VCH Verlag GmbH & Co. KGaA, Weinheim 

The FT IR spectra of Ibuprofen show that the band corresponding to a free carboxylic acid (1723 $cm^{-1}$) has changed to a carboxylate one (1463 and 1637 $cm^{-1}$) in the Ibu/MS sample (see Supporting Information, Figure S2), which suggests $COO^{-}\cdots N^{+}$ bonding between Ibuprofen and the co-template (APTES).[1,3,8,19] In addition, bands for the quaternary carbon atom of Ibuprofen at 1463 and 1519 $cm^{-1}$ and bands for C–$H_x$ of APTES at 2919 and 2962 $cm^{-1}$ can be clearly seen in the Ibu/MS system.[20] These observations show that Ibuprofen and APTES are involved in the formation of the mesoporous phase.

Figure 4 (part A) shows a typical $^{29}Si$/MAS NMR spectrum for the Ibu/MS sample. In addition to the free hydroxy group ($Q_3$) at $\delta$ = –110 ppm and cross-linked silicon atoms ($Q_4$), a new peak group appears between $\delta$ = –50 and –80 ppm in Ibu/MS, which is assigned to the Si atoms covalently bound to organic groups {$T_2$ [$(SiO)_2Si(OH)CSi$] and $T_3$ [$(SiO)_3SiCSi$], respectively}.[21–23]

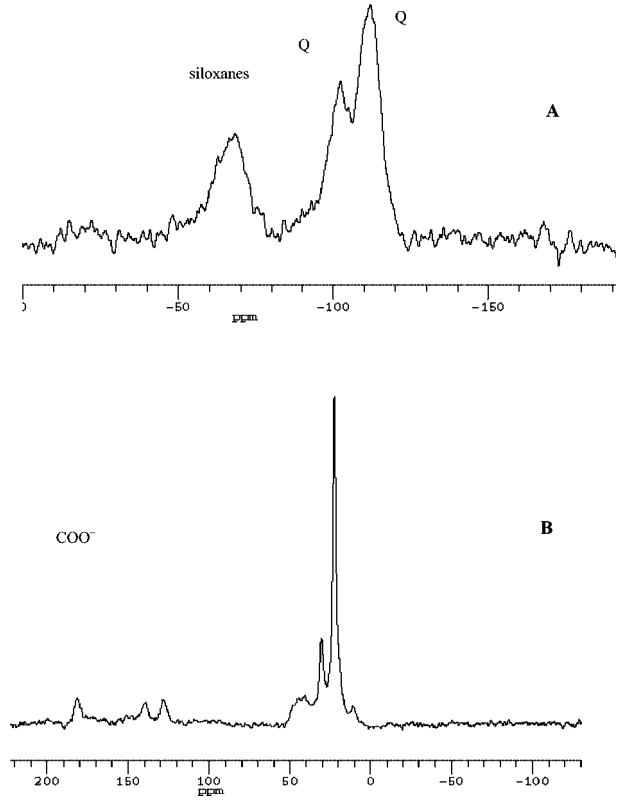


Figure 4. NMR spectra of Ibu/MS: (A) $^{29}Si$/MAS NMR spectrum; (B) solid-state $^{13}C$/MAS NMR spectrum.

The $^{13}C$/MAS NMR spectrum of Ibu/MS is shown in part B of Figure 4. The peaks of $-CH_2CH_3$ at $\delta$ = 58 and 14 ppm of pure APTES have disappeared in the Ibu/MS system due to the condensation of APTES with TEOS, which is consistent with $^{29}Si$ MAS/NMR observations. Furthermore, the peak of the carboxylic acid group of pure Ibuprofen at $\delta$ = 183.22 ppm is shifted slightly to a higher shielding of $\delta$ = 181.16 ppm in the Ibu/MS system due to the shift of a proton from the carboxylic acid to the amine. These NMR spectra are in agreement with the results of the FT IR spectra, which further confirms the $COO^{-}$-$N^{+}$ interaction between Ibuprofen and the co-template, as well as the encapsulation of Ibuprofen in the channels of the mesoporous silica.

The loading of ibuprofen in the Ibu/MS sample is about 24%, as determined from the drug released ($M_\infty$) at infinite time. Since Ibuprofen is mainly adsorbed in the stomach and proximal intestine, the release profiles of Ibu/MS in simulated gastric and proximal intestine were determined; the cumulative release rates are shown in Figure 5. This diagram clearly proves that both systems exhibit sustained-release profiles. Only 8.61 wt.-% of Ibuprofen is released within 2 h, and it takes nearly 12 and 45 h to reach 45.06 and 95.2 wt.-% of drug released in simulated gastric fluid, respectively. The release rate in simulated proximal intestine fluid is higher than that in the simulated gastric fluid. Thus, 13.95 wt.-% of Ibuprofen is released within 2 h, 52.22 wt.-% of the drug is released in 12 h, and drug release is finished in 45 h. The difference of release profiles should be mainly due to the different solubility of Ibuprofen at different pH values. Additionally, the integrity of the drug molecules is maintained upon their release from the mesoporous silica (see Supporting Information, Figure S5).

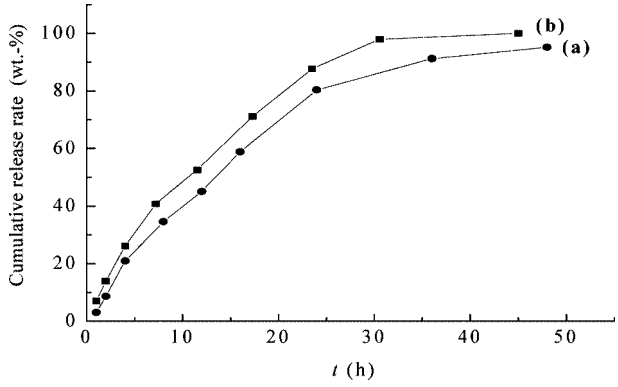


Figure 5. Cumulative release rates of Ibuprofen in simulated (a) stomach and (b) proximal intestinal fluid.

For comparison, MCM-41 was functionalized with APTES and the release kinetics were studied (see Supporting Information, Figure S6). It can be seen that this system shows a faster initial release rate than the Ibu/MS system, with 17.5 wt.-% of Ibuprofen released within 2 h and 55.56 wt.-% of the drug released in 12 h.

In order to investigate the release behavior of Ibuprofen, the drug-release kinetics were analyzed with the Korsmeyer–Peppas model.[24,25] This model often deviates from Fick's law and follows an anomalous behavior that follows the exponential model $M_t/M_\infty = kt^n$, where $M_t$ is the drug released at time $t$, $M_\infty$ is the quantity of drug released at infinite time, $k$ is the kinetic constant, and $n$ is the release exponent, which characterizes the drug-transport mechanism. When $n$ = 0.5, the drug diffusion and release from the matrix follow Fick's law and drug initial release is slower, while for $1 > n > 0.5$ it follows an anomalous non-Fick-type transport and drug initial release is faster than that of $n$ = 0.5. A relatively larger initial drug release is essential for sustained/controlled drug release. The ln(frac-

 © 2006 Wiley-VCH Verlag GmbH & Co. KGaA, Weinheim 

tional release of Ibuprofen) is plotted as a function of ln(time) with the data up to 45 h. The exponent for the Ibu/MS system is 0.763 and 0.876 at pH 1.2 and 6.8, respectively (Table 1), which suggests that Ibuprofen release from this system follows an anomalous non-Fick-type transport behavior.

Table 1. The Korsmeyer–Peppas model fit of Ibuprofen release.

| Samples | Release medium | $\ln(M_t/M_\infty)$ vs. $\ln t$ | $n$ | R |
|---|---|---|---|---|
| Ibu/MS | pH 1.2 | $y = 0.763x - 2.519$ | 0.763 | 0.9949 |
| Ibu/MS | pH 6.8 | $y = 0.876x - 3.094$ | 0.876 | 0.9775 |

## Conclusions

In summary, we have achieved a novel and effective method that uses a drug in a one-step template synthesis that leads to an Ibu/mesoporous silica system. The reported Ibu/MS system possesses an ordered mesoporous structure and gives a well-sustained release profile. The release mechanism follows an anomalous non-Fick-type behavior. This new drug/mesoporous silica synthesis technique is likely find applications in the encapsulation of drugs, fragrances, nanoparticles, and (bio)macromolecules inside mesoporous silica systems.

## Experimental Section

**Materials:** (3-Aminopropyl)triethoxysilane (APTES, Aldrich), tetraethoxysilane (TEOS, Tiantai Co., Tianjin), and Ibuprofen (Ibu, Tianzunzezhong, Chemical Co., Nanjing) were used as received.

**Synthesis of Ibuprofen/Mesoporous Silica System:** In a typical procedure, 0.11 g of Ibu was first dissolved in a mixture of 0.1 g of APTES and 0.5 mL of distilled water by stirring until a clear solution had formed. Then, 1.01 g of TEOS was added with continuous stirring for 24 h at room temperature. The pH value of the final gel was about 7. This white gel was sealed in a Teflon-lined stainless-steel autoclave and heated at 323 K for 8 h, followed by further heating at 373 K overnight under static conditions. The white precipitate obtained was filtered and washed extensively. The as-synthesized sample was air-dried at room temperature for 48 h.

**Characterization:** Powder XRD diffraction data were collected on a SIEMENS D5005 diffractometer with Cu-$K_\alpha$ radiation at 40 kV and 30 mA. Nitrogen adsorption/desorption was measured with a Micromeritics ASAP 2010 M sorptometer. Before measurement, the samples was calcined at 723 K for 5 h, degassed at 373 K for 12 h, and the measurements were carried out at 77 K. Specific surface areas and pore-size distributions were calculated using the Brunauer–Emmett–Teller (BET) and Barrett–Joyner–Halenda (BJH) models from the adsorption branches, respectively. Solid-state/MAS NMR spectra were recorded on a Varian infinity plus 400 spectrometer. $^{29}$Si/MAS NMR: resonance frequency: 79.41 MHz; spinning frequency: 4.00 kHz; pulse delay: 10.00 s; pulse width: 30°; $^{13}$C/MAS NMR: resonance frequency: 100.52 MHz; contact time: 1.00 min; spin rate: 3.33 kHz. UV/Vis spectra were recorded with a UV-2450 visible spectrophotometer from Shimadzu. An FT-IR spectrometer (JASCOFT/IR-420) was used to record infrared spectra of the samples by the KBr method. Powder materials were pressed into a tungsten mesh grid and installed in an in situ FTIR transmission cell; the samples were outgassed in a vacuum system with a residual pressure of less than $3 \times 10^{-4}$ Torr at ambient temperature. TEM images were recorded with a JEOL 3010 at an acceleration voltage of 300 kV.

**Drug Release:** After the Ibu/MS sample has been compressed into tablet with a diameter of 10 mm and a thickness of 0.5 mm, the release rate was obtained by soaking the sample tablets (150 mg) in 500 mL of simulated gastric and proximal intestinal fluid (pH 1.2 HCl and pH 6.8 buffer solution), respectively, at a temperature of 310 K. At predetermined time intervals, 3-mL samples were withdrawn and immediately replaced with an equal volume of dissolution medium to keep the volume constant. These samples were filtered (0.45 μm), diluted, then the Ibuprofen contents were analyzed at 222 nm using a UV/Vis spectrophotometer.

**Supporting Information** (see footnote on the first page of this article): Figure S1 shows the powder X-ray diffraction spectra of Ibu/MS, which confirms the mesoporous structure. Figure S2 shows the FTIR spectra of (a) pure Ibuprofen and (b) Ibu/MS. Figure S3 shows the $^{13}$C/MAS NMR spectrum of neat APTES. Figure S4 shows the $^{13}$C/MAS NMR spectrum of neat Ibuprofen, which may give information that ibuprofen and APTES may be involved in the formation of the mesoporous structure. Figure S5 shows the UV/Vis spectra of (a) neat Ibuprofen and (b) Ibuprofen released from the Ibu/MS system. Figure S6 shows the cumulative release rates of Ibuprofen from functionalized MCM-41 in simulated fluid. Figure S7 shows SEM images of the Ibu/MS sample.

## Acknowledgments

This work was supported by the National Natural Science Foundation of China (grant nos. 20571030, 20531030 and 20371020), and the State Basic Research Project (2006CB806100).

[1] S.-W. Song, K. Hidajat, S. Kawi, *Langmuir* **2005**, *21*, 9568–9575.
[2] M. Vallet-Regí, A. Rámila, R. P. Del Real, J. Pérez-Pariente, *Chem. Mater.* **2001**, *13*, 308–311.
[3] B. Muñoz, A. Rámila, J. Pérez-Pariente, I. Díaz, M. Vallet-Regí, *Chem. Mater.* **2003**, *15*, 500–503.
[4] C. Tourné-Péteilh, D. A. Lerner, C. Charnay, L. Nicole, S. Begu, J. M. Devoisselle, *ChemPhysChem* **2003**, *4*, 281–286.
[5] Y. L. Cheng, T. G. Brian, M. J. Dusan, J. Ksenija, X. Shu, J. Srdija, S. Y. L. Victor, *J. Am. Chem. Soc.* **2003**, *125*, 4451–4459.
[6] D. R. Radu, Y. L. Cheng, K. Jeftinija, E. W. Rowe, S. Jeftinija, V. S.-Y. Lin, *J. Am. Chem. Soc.* **2004**, *126*, 13216–13217.
[7] C. Barbé, J. Bartlett, L. Kong, K. Finnie, H. Q. Lin, M. Larkin, S. Calleja, A. Bush, G. Calleja, *Adv. Mater.* **2004**, *16*, 1959–1966.
[8] A. Rámilia, B. Muńoz, J. Pérez-Pariente, M. Vallet-Regí, *J. Sol-Gel Sci. Technol.* **2003**, *26*, 1199–1202.
[9] P. Horcajada, A. Rámila, J. Pérez Pariente, M. Vallet-Regí, *Microporous Mesoporous Mater.* **2004**, *68*, 105–109.
[10] J. Andersson, J. Rosenholm, S. Areva, M. Lindén, *Chem. Mater.* **2004**, *16*, 4160–4167.
[11] C. Tourné-Péteih, D. Brunel, S. Bégu, B. Chiche, F. Fajula, D. A. Lerner, J. M. Devoissele, *New J. Chem.* **2003**, *27*, 1415–1418.
[12] A. L. Doadrio, E. M. B. Sousa, J. C. Doadrio, J. Pérez Pariente, I. Izquierdo-Barba, M. Vallet-Regí, *J. Controlled Release* **2004**, *97*, 125–132.

 © 2006 Wiley-VCH Verlag GmbH & Co. KGaA, Weinheim 

[13] F. Highton, *The Pharmaceutics of Ibuprofen*, in *Ibuprofen. A Critical Bibliographic Review* (Ed.: K. D. Rainsford), Taylor and Francis, London, **1999**, pp. 53.
[14] S. N. Che, A. E. Garcia-Bennett, T. Yokoi, K. Sakamoto, H. Kunieda, O. Terasaki, T. Tatsumi, *Nat. Mater.* **2003**, *2*, 801–805.
[15] S. N. Che, Z. Liu, T. Ohsuna, K. Sakamoto, O. Terasaki, T. Tatsumi, *Nature* **2004**, *429*, 281–284.
[16] E. Alfonso, A. E. Garcia-Bennett, O. Terasaki, S. N. Che, T. Tatsumi, *Chem. Mater.* **2004**, *16*, 813–821.
[17] P. T. Tanev, T. J. Pinnavaia, *Chem. Mater.* **1996**, *8*, 2068–2079.
[18] M. Grün, K. K. Unger, A. Matsumoto, K. Tsutsumi, *Microporous Mesoporous Mater.* **1999**, *27*, 207–216.
[19] A. Matsumoto, K. Tsutsumi, K. Schumacher, K. K. Unger, *Langmuir* **2002**, *18*, 4014–4019.
[20] H. L. Li, A. P. Fu, D. S. Xu, G. L. Guo, L. L. Gui, Y. Q. Tang, *Langmuir* **2002**, *18*, 3198–3202.
[21] A. S. M. Chong, X. S. Zhao, *J. Phys. Chem. B* **2003**, *107*, 12650–12657.
[22] D. W. Sindorf, G. E. Maciel, *J. Am. Chem. Soc.* **1983**, *105*, 3767–3776.
[23] L. Ekkehard, S. Theodor, A. Friedrich, H. A. Mayer, *Angew. Chem. Int. Ed.* **1999**, *38*, 2154–2174.
[24] T. Higuchi, *J. Pharm. Sci.* **1961**, *50*, 874–875.
[25] T. Higuchi, *J. Pharm. Sci.* **1963**, *52*, 1145–1149.

Received: November 19, 2005
Published Online: August 18, 2006

 © 2006 Wiley-VCH Verlag GmbH & Co. KGaA, Weinheim 

DOI: 10.1002/ejic.200600366

# Organoethynylxenon(II) Tetrafluoroborates, [RC≡CXe][$BF_4$] – The First Examples of Isolated Alkynylxenonium Salts: Preparation and Multi-NMR Characterisation

**Hermann-Josef Frohn*[a] and Vadim V. Bardin[b]**

**Keywords:** Alkynes / Boranes / Xenon / NMR spectroscopy

The perfluorinated organoethynylxenon(II) salts, [RC≡CXe][$BF_4$] [R = $CF_3$, $C_3F_7$, $(CF_3)_2CF$, *cis*-, *trans*-$CF_3CF$=CF, $C_6F_5$], were prepared by the reaction of $XeF_2$ with the corresponding perfluoroorganoethynyldifluoroboranes, RC≡$CBF_2$, in 1,1,1,3,3-pentafluoropropane (PFP) or $CH_2Cl_2$ at –60 to –40 °C and isolated in 30–98 % yield. Similarly, the non-fluorinated organoethynylxenon(II) salts [$C_4H_9$C≡CXe][$BF_4$] and [$(CH_3)_3$CC≡CXe][$BF_4$] were obtained in 20 to 40 % yield. All [RC≡CXe][$BF_4$] salts are soluble in anhydrous HF (aHF) and the salts with R = $C_4H_9$ or R = $(CH_3)_3$C display sufficient solubility in the weakly coordinating solvents $CH_2Cl_2$ and PFP. The xenonium salts [RC≡CXe][$BF_4$] were unambiguously characterised by their $^1$H-, $^{11}$B-, $^{13}$C-, $^{19}$F-, and $^{129}$Xe NMR spectra in solution.
(© Wiley-VCH Verlag GmbH & Co. KGaA, 69451 Weinheim, Germany, 2006)

## Introduction

The preparative chemistry of organoxenon compounds was established in 1989 with the synthesis of pentafluorophenylxenon(II) salts, [$C_6F_5$Xe][Y], obtained by the reaction of $XeF_2$ with $(C_6F_5)_3$B.[1,2] In the subsequent years xenonium salts, [RXe][Y], with different types of organo groups in the cation (R = substituted phenyl, polyfluorocycloalk-1-enyl) as well as arylxenon(II) molecules ArXeX (X = F, Cl, $O_2CC_6F_5$, CN, $C_6F_5$) and the first example of a Xe(IV)–C compound, [$C_6F_5XeF_2$][$BF_4$], were investigated. The achievements made in the first decade of xenon–carbon chemistry are compiled in some reviews published in 1999–2002.[3] In the following years reactivities of arylxenon(II) salts,[4,5] of diarylxenon ArXeAr′,[6] and the preparation and reactivity of a series of acyclic polyfluoroalk-1-enylxenon(II) salts [RCF=CR′Xe][$BF_4$][7–9] were reported. In 2004 Naumann et al. observed RC≡CXeF molecules (R = Me, Bu, Ph) in the fluoride-catalysed reaction of $XeF_2$ and $Me_3$SiC≡CR. The authors reported a significant decomposition of RC≡CXeF in solution above –60 °C.[10]

In 1992, Zhdankin et al. published a short communication on the salt [*t*BuC≡CXe][$BF_4$] obtained by the reaction of Li[*t*BuC≡$CBF_3$] with $BF_3$ and $XeF_2$ in $CH_2Cl_2$ (Scheme 1).[11] This salt, which could not be isolated because of its decomposition at –30 °C, was characterised by $^1$H-, $^{11}$B-, $^{13}$C-, and $^{129}$Xe NMR spectroscopy at –40 °C, by IR spectroscopy at 0 °C, and by the alkynylation of $PPh_3$ to [*t*BuC≡C$PPh_3$][$BF_4$] at –78 °C.

In the analogous reactions of $XeF_2$ with alkynylsilanes, RC≡$CSiMe_3$ (R = Et, Pr, *t*Bu, and $Me_3$Si), and $BF_3$·$OEt_2$ in $CD_2Cl_2$ at –45 °C, the authors reported no multi-NMR spectroscopic data of the desired products, the xenonium salts. Each reaction solution was only characterised by a singlet in the $^{129}$Xe NMR spectrum. No $^{129}$Xe resonances were found in the spectra of the reaction solutions for R = H, Me, Ph, $CF_3$, 4-$CH_3C_6H_4SO_2$, $(i$Pr$)_3$Si, $PhMe_2$Si.[11]

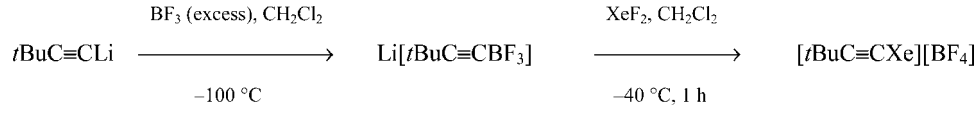


Scheme 1.

We published a preliminarily report of the first isolation of an alkynylxenon(II) salt in 2003 when we succeeded in preparing trifluoropropynylxenon(II) tetrafluoroborate [$CF_3$C≡CXe][$BF_4$].[12] We employed the previously developed approach to polyfluorinated arylxenon(II) and alk-1-enylxenon(II) salts: the reaction of xenon difluoride with

[a] Department of Chemistry, Inorganic Chemistry, University Duisburg-Essen,
Lotharstr. 1, 47048 Duisburg, Germany
Fax: +49-203-379-2231
E-mail: frohn@uni-duisburg.de
[b] N. N. Vorozhtsov Novosibirsk Institute of Organic Chemistry, SB RAS,
Acad. Lavrentjev Ave. 9, 630090 Novosibirsk, Russia
E-mail: bardin@nioch.nsc.ru
Supporting information for this article is available on the WWW under http://www.eurjic.org or from the author.

 © 2006 Wiley-VCH Verlag GmbH & Co. KGaA, Weinheim 

polyfluoroorganoboron difluoride in the appropriate solvent.[3b] This preparative method allowed for the isolation of the new salt as a pure product and opened the possibility of extensive and unambiguous characterisation. Subsequently, we extended this preparative method to a representative series of alkynylxenon(II) salts, $[RC{\equiv}CXe][BF_4]$, where R represents any alkyl chain, a perfluoroalkyl group, a perfluoroalk-1-enyl group or a perfluoroaryl group.

## Results and Discussion

The addition of $XeF_2$ to the solution of either trifluoropropynyldifluoroborane (**1a**) or heptafluoropent-1-ynyldifluoroborane (**2a**) in PFP[13] at –40 to –55 °C was accompanied by the precipitation of trifluoropropynylxenon(II) tetrafluoroborate (**1b**) or heptafluoropent-1-ynylxenon(II) tetrafluoroborate (**2b**), respectively. Both salts are insoluble in PFP and form white solids. After decantation of the mother liquors and removal of the residual volatiles in vacuo, alkynylxenon salts **1b** and **2b** were isolated in 60–90% yield (Scheme 2).

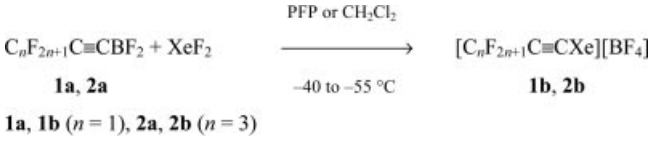


Scheme 2.

In a similar way, the reaction of heptafluoro-3-methylbut-1-ynyldifluoroborane (**3a**) with $XeF_2$ gave heptafluoro-3-methylbut-1-ynylxenon(II) tetrafluoroborate (**3b**) in 82% yield (Scheme 3).

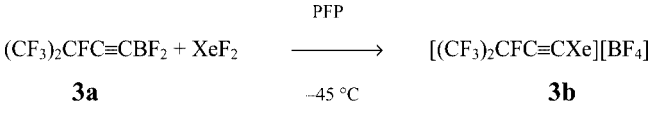


Scheme 3.

The replacement of the perfluorinated alkyl group at C-2 of boranes **1a**, **2a**, and **3a** by the pentafluoropropenyl or pentafluorophenyl group did not affect the course of the reaction. Both pentafluoropent-3-en-1-ynyldifluoroboranes (*cis*-**4a**) and (*trans*-**4a**) and pentafluorophenylethynyldifluoroborane (**5a**) were successfully converted into pentafluoropent-3-en-1-ynylxenon(II) tetrafluoroborates (*cis*-**4b**) and (*trans*-**4b**) and pentafluorophenylethynylxenon(II) tetrafluoroborate (**5b**), respectively. No addition of fluorine to the double bond in the perfluorinated propenyl or phenyl moiety of **4a** or **5a** occurred. The ratio *cis*-**4b**/*trans*-**4b** = 1:2 was equal to that in the parent boranes **4a** (Scheme 4).

To complete the investigations of xenon difluoride with alkynyldifluoroboranes, we studied the reaction of $XeF_2$ with boranes that contained a hydrocarbon alkynyl chain. $XeF_2$ was treated with hex-1-ynyldifluoroborane (**6a**) and 3,3-dimethylbut-1-ynyldifluoroborane (**7a**) under the conditions mentioned above and formed hex-1-ynylxenon(II) tetrafluoroborate (**6b**) and 3,3-dimethylbut-1-ynylxenon(II) tetrafluoroborate (**7b**), respectively (Scheme 5). Surprisingly, these salts are significantly soluble in PFP even below –40 °C. Salt **6b** is more soluble than salt **7b**. Thus, under comparable reaction conditions in PFP at –50 °C, **6b** remained in solution whereas half of isomer **7b** precipitated. When borane **6a** reacted with $XeF_2$ in $CH_2Cl_2$ at –65 °C solely a solution of **6b** was obtained.

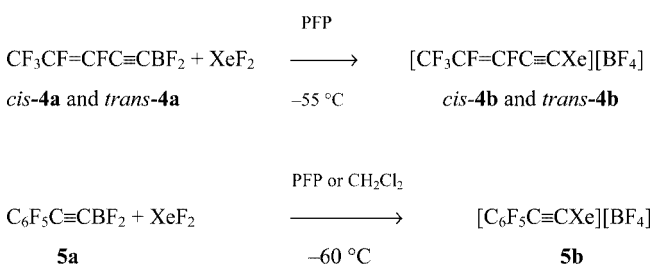


Scheme 4.

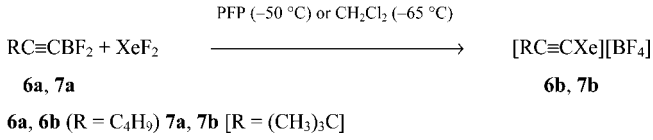


Scheme 5.

In contrast to the reaction of alk-1-enyldifluoroboranes, $RCF{=}CFBF_2$, with $XeF_2$,[7] neither the alk-1-enyltrifluoroborate anions, $[RCF{=}CFBF_3]^-$, nor their fluorination products, $[XBF_3]^-$ (X = RCF=CF, $RCF_2CF_2$), were observed.

The results demonstrate the easy xenodeborylation (replacement of the three-coordinate boron atom by xenon) of both non-fluorinated organoethynyldifluoroboranes and perfluoroorganoethynyldifluoroboranes, $RC{\equiv}CBF_2$, in reactions with xenon difluoride. Significant differences between the present reactions and the previously studied reactions of $XeF_2$ with alk-1-enyldifluoroboranes are their insensitivity to the type of R group attached to C-2 of the multiple C–C bond. It is worth mentioning that in the reactions of hydrocarbon alk-1-enyldifluoroboranes with $XeF_2$ no xenonium salts were obtained. Thus under the same reaction conditions as those of alkynyldifluoroboranes, *cis*- and *trans*-hex-1-enyldifluoroboranes, $C_4H_9CH{=}CHBF_2$, only gave complex mixtures but no hexenylxenon compounds.[7]

The novel alkynylxenon(II) compounds **1b**–**5b** were isolated as white solids at low temperatures (<–40 °C). When warmed from –40 °C the solutions took on a brown colouration, and at 20 °C the conversion into dark liquids took place within a few minutes (**4b**, **5b**) or a few hours (**1b**–**3b**). Salts **1b**–**5b** are very soluble in aHF and insoluble in PFP and $CH_2Cl_2$. A characteristic property of solutions of **1b**–**5b** in aHF is their longer lifetime at room temperature than that of the salts themselves in the solid state. In detail, no decomposition of perfluoroalkynylxenon tetrafluoroborates **1b**–**3b** was detected in aHF solutions within 20–24 h. The salts **4b** and **5b**, which contain the unsaturated perfluoro groups R = $CF_3CF{=}CF$ and R = $C_6F_5$, respectively, at C–

 © 2006 Wiley-VCH Verlag GmbH & Co. KGaA, Weinheim 

2, decomposed much faster than **1b**–**3b**. Salt **5b** totally decomposed in aHF at –40 °C within 1 h, whereas the total decomposition of **4b** in aHF at 22–24 °C took ca. 4 h. The complete decomposition of pure solids **4b** and **5b** at 20 °C led to the formation of brown materials, insoluble in aHF, which consisted of non-volatile complex mixtures ($^{19}$F NMR).

Hex-1-ynylxenon(II) tetrafluoroborate **6b** and its isomer **7b** were isolated as brownish powders (probably contaminated with impurities) which were easily liquefied above –40 °C (cf.[11]). Solutions or suspensions of these salts in either PFP or $CH_2Cl_2$ decomposed in a manner similar to that of the salts in the solid state. Surprisingly, solutions of **6b** and **7b** in aHF are stable at 22–25 °C for more than 12 h. After 22 h, 38% of **6b** and 80% of **7b** still remained unchanged. Finally the complete decomposition led to tar.

Salts **1b**–**7b** were unambiguously characterised by multi-NMR spectroscopy. The $^{19}$F NMR spectra of fluoroorganoethynylxenon(II) tetrafluoroborates **1b**–**5b** in aHF displayed signals for the fluoroorgano groups and for the $[BF_4]^-$ anion (at approximately $\delta$ = –148 ppm) with the expected integrations. Long-range couplings $J_{^{19}F,^{129}Xe}$ were observed in the spectra of both isomers of $[CF_3CF{=}CFC{\equiv}CXe][BF_4]$. The signal for F-4 at $\delta$ = –128.2 ppm (*cis*-**4b**) and F-3 at $\delta$ = –149.3 ppm (*trans*-**4b**) displayed $^{129}$Xe satellites ($^5J_{F\text{-}4,Xe}$ = 17 Hz and $^4J_{F\text{-}3,Xe}$ = 6 Hz, respectively) in accordance with the natural abundance of the $^{129}$Xe isotope of 26%. The assignment of the coupling $^4J_{F\text{-}3,Xe}$ = 8 Hz in the $^{19}$F NMR spectrum of $[(CF_3)_2CFC{\equiv}CXe][BF_4]$ was confirmed in a $^{19}F\{^{19}F(CF_3)\}$ homodecoupling NMR experiment. In the $^{19}$F NMR spectrum of salts with unbranched perfluoroalkyl R groups, as in **1b** (signal for the $CF_3$ group at $\delta$ = –52.5 ppm, $\tau_{1/2}$ = 1.5 Hz) or **2b** [$^{19}F\{^{19}F(CF_3)\}$ spectrum of the $CF_3CF_2CF_2$ group] such couplings were not observed. For comparison, in the case of *cis*-perfluoroalk-1-enylxenonium salts, larger $^4J_{F\text{-}3,Xe}$ couplings are known. In the spectra of [*cis*-$YCF_2CF{=}CFXe][BF_4]$, $^4J_{F\text{-}3,Xe}$ = 40 Hz (Y = F) and $^4J_{F\text{-}3,Xe}$ = 56 Hz (Y = $CF_3$) were measured.[7]

The $^{129}$Xe NMR signals of salts $[RC{\equiv}CXe][BF_4]$ **1b**–**5b** in aHF at –60 °C are singlets located between $\delta$ = –3600 and –3662 ppm (Table 1). The influence of the type of the perfluorinated R group in $[RC{\equiv}CXe]^+$ on the $^{129}$Xe NMR chemical shifts is demonstrated by the remarkably high-frequency shift (deshielding) of the xenon atom parallel to the replacement of fluorine atoms in $[CF_3C{\equiv}CXe]^+$ by perfluoroalkyl groups: $\delta(^{129}Xe)$ = –3636 ppm ($R_F{=}CF_3$) < –3609 ppm ($R_F{=}CF_3CF_2CF_2$) < –3600 ppm [$R_F$ = $(CF_3)_2CF$]. Furthermore, there is yet a very small but still experimentally detectable distinction in the $^{129}$Xe NMR chemical shifts caused by configurational distinctions at C-4 as shown in the case of the isomeric cations [*cis*-$CF_3CF{=}CFC{\equiv}CXe]^+$ ($\delta$ = –3613.2 ppm) and [*trans*-$CF_3CF{=}CFC{\equiv}CXe]^+$ ($\delta$ = –3613.4 ppm).

Solutions of the salts $[C_4H_9C{\equiv}CXe][BF_4]$ and $[(CH_3)_3CC{\equiv}CXe][BF_4]$ in aHF (–60 °C) displayed the most shielded xenon nuclei in the series of alkynylxenonium salts with $^{129}$Xe resonances at $\delta$ = –3775 ppm and $\delta$ = –3781 ppm, respectively (Table 1).

The $^{13}$C NMR spectra of $[RC{\equiv}CXe][BF_4]$ are of particular interest because they should allow a direct and unambiguous proof of the C–Xe bond in alkynylxenon(II) salts. To our surprise, the resonances C-1 are located at unusually low frequencies between 8 and –24 ppm. The shielding of C-1 in aHF solutions of alkynylxenon(II) salts bearing either hydrocarbon or perfluoroalkyl groups increases in the same order as the shielding of the xenon atom, e.g. from R = $(CF_3)_2CF$ to R = $(CH_3)_3C$ (Table 1). Salts **4b** and **5b** with unsaturated perfluoro R groups attached to C-2 possess the most deshielded C-1, which is probably the result of a π-electron interaction of the $CF_3CF{=}CF$ group or the $C_6F_5$ group with the C≡C triple bond. The $^{13}$C NMR spectra for C-1 of the cations $[RC{\equiv}CXe]^+$ contains satellites from the $^{13}$C–$^{129}$Xe coupling, which increases from ca. $^1J_{C\text{-}1,Xe}$ = 265 Hz [R = $C_4H_9$, $(CH_3)_3C$] to $^1J_{C\text{-}1,Xe}$ = 308 Hz (R = $C_6F_5$) to approximately $^1J_{C\text{-}1,Xe}$ = 345 Hz (R = perfluoroalkyl). An opposite course of couplings is found for $^2J_{C\text{-}2,Xe}$. In addition, it is worth mentioning that the chemi-

Table 1. $^{129}$Xe and selected $^{13}$C NMR spectroscopic data for $[RC{\equiv}CXe][BF_4]$.

| R | Solvent | $T$ [°C] | $\delta$(Xe) [ppm] | $\delta$(C-1) [ppm] | $^1J_{C\text{-}1,Xe}$ [Hz] | $\delta$(C-2) [ppm] | $^2J_{C\text{-}2,Xe}$ [Hz] |
|---|---|---|---|---|---|---|---|
| $(CH_3)_3C$ | aHF | –60 | –3781 | –23.7 | 267 | 107.0 | 76 |
| $(CH_3)_3C$ | PFP | –60 | –3773 | | | | |
| $(CH_3)_3C$ | $CH_2Cl_2$ | –40 | –3719 | –15.7 | [a] | 105.7 | [a] |
| $(CH_3)_3C$[11] | $CDCl_3$ | –40 | –3631 | 26.9 | 120 | 105.2 | 79 |
| $C_4H_9$ | aHF | –30 | –3783 | –24.0 | 264 | 101.6 | 69 |
| | | –60 | –3775 | | | | |
| $C_4H_9$ | PFP | –60 | –3762 | –21.2 | 279 | 99.3 | 73 |
| $C_4H_9$ | $CH_2Cl_2$ | –60 | –3698 | –16.7 | 288 | 98.7 | 75 |
| $C_6F_5$ | aHF | –60 | –3662 | 0.6 | 308 | 81.0 | 62 |
| $CF_3$ | aHF | –60 | –3636 | –5.2 | 343 | 81.2 | 69 |
| *cis*-$CF_3CF{=}CF$ | aHF | –60 | –3613.2 | 6.9 | [a] | 79.8 | 64 |
| *trans*-$CF_3CF{=}CF$ | aHF | –60 | –3613.4 | 7.9 | 332 | 79.8 | 64 |
| $C_3F_7$ | aHF | –20 | –3619 | –0.7 | 349 | 80.9 | 70 |
| $(CF_3)_2CF$ | aHF | –20 | –3610 | –0.5 | 343 | 80.4 | 68 |
| | | | (–3601)[b] | | | | |

[a] The coupling $^{13}$C–$^{129}$Xe was not observed because of the low intensity of the parent signal. [b] Extrapolated to –60 °C from the equation: $\Delta\delta(^{129}Xe)/\Delta T$ = –0.22 ppm $K^{-1}$.[20]

 © 2006 Wiley-VCH Verlag GmbH & Co. KGaA, Weinheim 

cal shift values for C-2 in the above series show an opposite trend to that of C-1 and diminish from $\delta$ = 107 ppm to approximately $\delta$ = 80 ppm.

In contrast to **1b**–**5b**, the salts $[C_4H_9C{\equiv}CXe][BF_4]$ and $[(CH_3)_3CC{\equiv}CXe][BF_4]$ are soluble in weakly coordinating solvents such as $CH_2Cl_2$ and PFP and do not decompose in these solutions below –60 °C over the course of several weeks. The $^{129}$Xe resonances of **6b** and **7b** in PFP are similar to those in aHF but are slightly shifted by (9–13 ppm) to higher frequencies. In contrast, the NMR spectra of **6b** and **7b** in $CH_2Cl_2$ display significant distinctions relative to those in aHF. Thus, in $CH_2Cl_2$ the $^{129}$Xe NMR spectra show signals that are shifted by 67 ppm (**7b**) and 77 ppm (**6b**) to higher frequencies. In the $^{13}$C NMR spectra of both salts, the resonance for C-1 is even shifted by 8 ppm into the same direction, whereas the resonance for C-2 moves by 2 ppm in the opposite direction. The position of the resonance for the $[BF_4]^-$ anion in the $^{19}$F NMR spectra of **6b** and **7b** is shifted to $\delta = -144 \pm 1$ ppm in $CH_2Cl_2$ and to $\delta = -140 \pm 1$ ppm in PFP. For comparison, solutions of $[Bu_4N][BF_4]$ in aHF (–20 °C), $CH_2Cl_2$ (24 °C) and PFP (–10 °C) display the $^{19}$F NMR signal at $\delta$ = –148.3, –151.8 and –148.4 ppm, respectively. The deshielding of the signal for the anion in the $^{19}$F NMR spectra of the solutions of salts **6b** and **7b** in $CH_2Cl_2$ and PFP is attributed to a significant cation–anion interaction (borderline description as contact or tight ion pair). This is in contrast to their behaviour in aHF solutions where the salts exist as solvent-shared ion pairs. The solvation of $[BF_4]^-$ in aHF can be described as the protonation of the fluorine terminus by the superacid aHF or by the formation of a hydrogen bridge between $[BF_4]^-$ and the fluorine atom of the HF molecule. Recently the related phenomena have been reported for solutions of (aryl)(pentafluorophenyl)iodonium tetrafluoroborates[14] and (pentafluorophenyl)(perfluoroalkenyl)iodonium tetrafluoroborates[15] in $CH_2Cl_2$ and aHF.

Finally, we have to mention that some of the NMR spectroscopic data of salt **7b** presented here differ (see Table 1) from those reported for the product solution obtained in accordance with Scheme 1.[11]

## Experimental Section

The NMR spectra were recorded with an AVANCE 300 Bruker spectrometer. The chemical shifts are referenced to TMS ($^1$H, $^{13}$C), $BF_3{\cdot}OEt_2/CDCl_3$ (15% v/v) ($^{11}$B), $CCl_3F$ ($^{19}$F) [with $C_6F_6$ as a secondary reference, $\delta$ = –162.9 ppm], and $XeOF_4$ ($^{129}$Xe) [with $XeF_2$ as a secondary reference, $XeF_2$/MeCN/24 °C (c→0), $\delta$ = –1813.28 ppm].[16] The multiplicities of the $^{13}$C- and $^{19}$F NMR signals caused by couplings with the $^{129}$Xe nucleus (satellites) are denoted by (*). The composition of the reaction mixtures and the yields of the products were determined by NMR spectroscopy by using the internal quantitative standard 1,1,2-trichlorotrifluoroethane.

1,1,1,3,3-Pentafluoropropane (Honeywell), 1,1,2-trichlorotrifluoroethane (Merck) were used as supplied. Dichloromethane (Fluka) was purified and dried by standard procedures.[17] Anhydrous hydrogen fluoride was stored over $CoF_3$. Solutions of organoethynyldifluoroboranes **1a**–**7a** were prepared from the corresponding potassium organoethynyltrifluoroborate salts.[18] All manipulations with organoethynyldifluoroboranes, organoethynylxenon(II) salts and anhydrous HF were performed in FEP (block copolymer of tetrafluoroethylene and hexafluoropropylene) equipment under an atmosphere of dry argon.

**Trifluoropropynylxenon(II) Tetrafluoroborate, $[CF_3C{\equiv}CXe][BF_4]$, (1b):** A solution of $CF_3C{\equiv}CBF_2$ (0.45 mmol) in PFP (1.5 mL) was cooled to –47 °C, and xenon difluoride (83 mg, 0.49 mmol) was added in one portion. Within a few minutes, a white suspension was formed which was stirred at –45 °C for an additional 1.5 h before all volatiles were removed in vacuo at –45 °C to give **1b** (82 mg, 59%). Similarly, salt **1b** (123 mg, 57%) was prepared in $CH_2Cl_2$ (4.8 mL) at –55 °C from $CF_3C{\equiv}CBF_2$ (0.80 mmol) and xenon difluoride (120 mg, 0.71 mmol).

**1b:** $^{11}$B NMR (96.29 MHz, aHF, –20 °C): $\delta$ = –2.4 (s, $[BF_4]^-$) ppm. $^{13}$C{$^{19}$F} NMR (75.46 MHz, aHF, –20 °C): $\delta$ = 112.2 (C-3), 80.5 (d*, $^2J_{C,Xe}$ = 69 Hz, C-2), –5.2 (d*, $^1J_{C,Xe}$ = 345 Hz, C-1) ppm. $^{19}$F NMR (282.40 MHz, aHF, –20 °C): $\delta$ = –52.5 (s, 3 F, $CF_3$), –148.0 (s, 4 F, $[BF_4]^-$) ppm.

**Heptafluoropent-1-ynylxenon(II) Tetrafluoroborate, $[C_3F_7C{\equiv}CXe][BF_4]$, (2b):** A solution of $C_3F_7C{\equiv}CBF_2$ (0.66 mmol) in PFP (1.5 mL) was cooled to –40 °C, and xenon difluoride (99 mg, 0.58 mmol) was added in one portion. The resulting white suspension was stirred at –40 °C for 2 h before the volatiles were removed in vacuo (0.13 hPa) at –40 °C to give **2b** (237 mg, 98%).

**2b:** $^{11}$B NMR (96.29 MHz, aHF, –20 °C): $\delta$ = –1.3 (s, $[BF_4]^-$) ppm. $^{13}$C{$^{19}$F} NMR (75.46 MHz, aHF, –20 °C): $\delta$ = 117.5 (C-5), 107.9 and 106.9 (C-3 and C-4), 80.9 (d*, $^2J_{C,Xe}$ = 70 Hz, C-2), –0.7 (d*, $^1J_{C,Xe}$ = 349 Hz, C-1) ppm. $^{19}$F NMR (282.40 MHz, aHF, –20 °C): $\delta$ = –78.6 (t, $^4J_{F,F}$ = 9 Hz, 3 F, F-5), –101.1 (t, $^3J_{F,F}$ = 3 Hz, q, $^4J_{F,F}$ = 9 Hz, 2 F, F-3), –124.2 (t, $^3J_{F,F}$ = 3 Hz, 2 F, F-4), –147.2 (s, 4 F, $[BF_4]^-$) ppm.

**Heptafluoro-3-methylbut-1-ynylxenon(II) Tetrafluoroborate, $[(CF_3)_2CFC{\equiv}CXe][BF_4]$, (3b):** A solution of $(CF_3)_2CFC{\equiv}CBF_2$ (0.73 mmol) in PFP (2 mL) was cooled to –45 °C before solid xenon difluoride (128 mg, 0.75 mmol) was added in one portion. Within a few minutes, a white suspension was formed which was stirred at –40 °C for an additional 1.5 h. The mother liquor was decanted, and the residue was washed with cold (–40 °C) PFP (1 mL). After drying in vacuo (0.13 hPa) at –40 °C, salt **3b** (207 mg, 69%) was obtained. The mother liquor contained borane **3a** (0.16 mmol) along with traces of $(CF_3)_2CFC{\equiv}CH$ and unknown products ($^{19}$F NMR).

**3b:** $^{11}$B NMR (96.29 MHz, aHF, –20 °C): $\delta$ = –1.3 (s, $[BF_4]^-$) ppm. $^{13}$C{$^{19}$F} NMR (75.46 MHz, aHF, –20 °C): $\delta$ = 118.8 ($CF_3$), 85.9 (C-3), 80.4 (d*, $^2J_{C,Xe}$ = 68 Hz, C-2), –0.5 (d*, $^1J_{C,Xe}$ = 343 Hz, C-1) ppm. $^{19}$F NMR (282.40 MHz, aHF, –20 °C): $\delta$ = –74.0 (d, $^3J_{F,F}$ = 10 Hz, 6 F, $CF_3$), –170.9 ($^3J_{F,F}$ = 10 Hz, d*, $^4J_{F,Xe}$ = 8 Hz, septet, 1 F, F-3), –147.6 (s, 4 F, $[BF_4]^-$) ppm.

**Pentafluoropent-3-en-1-ynylxenon(II) Tetrafluoroborate, $[CF_3CF{=}CFC{\equiv}CXe][BF_4]$, (4b):** A solution of $CF_3CF{=}CFC{\equiv}CBF_2$ (0.50 mmol) (*cis*/*trans* = 1:2) in PFP (2 mL) was cooled to –55 °C, and solid xenon difluoride (84 mg, 0.50 mmol) was added in one portion. Within a few minutes, a white suspension was formed which was stirred at –55 °C for an additional 1 h. After centrifugation at –78 °C, the mother liquor was decanted at –60 °C, the residue was washed with cold (–60 °C) PFP (2 mL) and dried in vacuo at –55 °C to give **4b** (130 mg, 70%).

***cis*-4b:** $^{11}$B NMR (96.29 MHz, aHF, –20 °C): $\delta$ = –1.3 (s, $[BF_4]^-$) ppm. $^{13}$C{$^{19}$F} NMR (75.46 MHz, aHF, –60 °C): $\delta$ = 150.3 and

 © 2006 Wiley-VCH Verlag GmbH & Co. KGaA, Weinheim 

135.1 (C-3 and C-4), 119.5 (C-5), 79.8 (d*, $^2J_{C,Xe}$ = 64 Hz, C-2), 6.9 (C-1) (the signal was too low in intensity to detect $^1J_{C,Xe}$) ppm. $^{19}$F NMR (282.40 MHz, aHF, –60 °C): $\delta$ = –68.1 (d, $^3J_{F,F}$ = 12 Hz, d, $^4J_{F,F}$ = 6 Hz, 3 F, F-5), –128.2 (d, q, $^3J_{F,F}$ = 12 Hz, $^3J_{F,F}$ = 3 Hz, d*, $^5J_{F,Xe}$ = 17 Hz, 1 F, F-4), –134.4 (d, $^3J_{F,F}$ = 3 Hz, q, $^4J_{F,F}$ = 6 Hz, 1 F, F-3), –147.5 (s, 4 F, [B$F_4$]$^-$) ppm.

***trans*-4b:** $^{11}$B NMR (96.29 MHz, aHF, –20 °C): $\delta$ = –1.3 (s, [*B*$F_4$]$^-$) ppm. $^{13}$C{$^{19}$F} NMR (75.46 MHz, aHF, –60 °C): $\delta$ = 148.0 and 133.2 (C-3 and C-4), 116.3 (C-5), 79.8 (d*, $^2J_{C,Xe}$ = 64 Hz, C-2), 7.9 (d*, $^1J_{C,Xe}$ = 332 Hz, C-1) ppm. $^{19}$F NMR (282.40 MHz, aHF, –60 °C): $\delta$ = –67.9 (d, $^3J_{F,F}$ = 7 Hz, d, $^4J_{F,F}$ = 18 Hz, 3 F, F-5), –150.0 (d, $^3J_{F,F}$ = 139 Hz, q, $^3J_{F,F}$ = 7 Hz, 1 F, F-4), –149.3 (d, $^3J_{F,F}$ = 139 Hz, q, $^4J_{F,F}$ = 18 Hz, d*, $^4J_{F,Xe}$ = 6 Hz, 1 F, F-3), –147.5 (s, 4 F, [B$F_4$]$^-$) ppm.

**Pentafluorophenylethynylxenon(II) Tetrafluoroborate, [$C_6F_5C{\equiv}CXe$][$BF_4$], (5b)**

**A:** A solution of $C_6F_5C{\equiv}CBF_2$ (0.34 mmol) in PFP (0.9 mL) was cooled to –55 °C, and xenon difluoride (50 mg, 0.29 mmol) was added in one portion. The resulting suspension was stirred at –50 to –55 °C for 1 h. After centrifugation at –78 °C the brown mother liquor was decanted at –45 °C. The residue was dried in vacuo (0.13 hPa) at –45 °C, and pale brownish **5b** was obtained (37 mg, 31%). The dissolution in aHF at –40 °C was accompanied by decomposition of **5b**. Total decomposition occurred within 30–50 min ($^{19}$F and $^{129}$Xe NMR).

**B:** A solution of $C_6F_5C{\equiv}CBF_2$ (0.26 mmol) in $CH_2Cl_2$ (1.5 mL) was cooled to –60 °C and xenon difluoride (38 mg, 0.22 mmol) was added in one portion. The white suspension was stirred at –60 °C for 1 h, and subsequently **5b** (0.15 mmol, 68%) ($^{19}$F NMR) was extracted with cold (–65 °C) aHF (0.5 mL).

**5b:** $^{11}$B NMR (96.29 MHz, aHF, –60 °C): $\delta$ = –1.7 (q, $^1J_{B,F}$ = 11 Hz, [*B*$F_4$]$^-$) ppm. $^{13}$C{$^{19}$F} NMR (75.46 MHz, aHF, –60 °C): $\delta$ = 149.5, 145.7, 137.9, 95.2 (C-2,6, C-4, C-3,5, and C-*ipso*, $C_6F_5$), 81.0 (d*, $^2J_{C,Xe}$ = 62 Hz, C-2), 0.6 (d*, $^1J_{C,Xe}$ = 308 Hz, C-1) ppm. $^{19}$F NMR (282.40 MHz, aHF, –60 °C): $\delta$ = –131.7 (m, 2 F, F-*ortho*), –142.4 (t, $^3J_{F,F}$ = 19 Hz, t, $^4J_{F,F}$ = 6 Hz, 1 F, F-*para*), –159.0 (m, 2 F, F-*meta*), –148.1 (s, 4 F, [B$F_4$]$^-$) ppm.

The solution of **5b** in aHF obtained as described under *B* showed no significant decomposition at –60 °C over 13 h ($^{19}$F-, $^{129}$Xe NMR), but when the temperature was raised above –30 °C, **5b** quickly decomposed to give mainly *cis*-$C_6F_5CF{=}CHF$.[19]

***cis*-$C_6F_5CF^2{=}CHF^1$:** $^1$H NMR (300.13 MHz, $CDCl_3$, 24 °C): $\delta$ = 6.80 (d, $^2J_{H,F\text{-}1}$ = 71 Hz, d, $^3J_{H,F\text{-}2}$ = 16 Hz) ppm. $^{19}$F NMR (282.40 MHz, $CDCl_3$, 24 °C): $\delta$ = –135.9 (d, $^3J_{F,H}$ = 16 Hz, d, $^3J_{F,F}$ = 15 Hz, t, $^4J_{F,F\text{-}ortho}$ = 15 Hz, 1 F, F-2), –138.0 (m, 2 F, F-*ortho*), –149.1 (d, $^2J_{F,H}$ = 71 Hz, d, $^3J_{F,F}$ = 15 Hz, t, $^5J_{F,F\text{-}ortho}$ = 5, d, $^7J_{F,F\text{-}para}$ = 3 Hz, 1 F, F-1), –149.8 (t, $^3J_{F,F}$ = 21 Hz, 1 F, F-*para*), –160.4 (m, 2 F, F-*meta*) ppm.

**Hex-1-ynylxenon(II) Tetrafluoroborate, [$C_4H_9C{\equiv}CXe$][$BF_4$], (6b)**

**A:** A solution of $C_4H_9C{\equiv}CBF_2$ (0.25 mmol) in $CH_2Cl_2$ (0.6 mL) was cooled to –70 °C and added in one portion to the cold (–70 °C) suspension of xenon difluoride (60 mg, 0.35 mmol) in $CH_2Cl_2$ (0.2 mL). The dark reaction mixture was stirred at –65 to –70 °C for 1 h. The $^1$H- and $^{19}$F NMR spectra showed the quantitative conversion of **6a** into **6b**.

**6b:** $^1$H NMR (300.13 MHz, $CH_2Cl_2$, –60 °C): $\delta$ = 2.59 (t, $^3J_{H,H}$ = 7 Hz, 2 H, 3-H), 1.55 (t, $^3J_{H,H}$ = 7 Hz, t, $^3J_{H,H}$ = 7 Hz, 2 H, 4-H), 1.35 (t, $^3J_{H,H}$ = 7 Hz, q, $^3J_{H,H}$ = 7 Hz, 2 H, 5-H), 0.87 (t, $^3J_{H,H}$ = 7 Hz, 3 H, 6-H) ppm. $^{11}$B NMR (96.29 MHz, $CH_2Cl_2$, –60 °C): $\delta$ = –1.4 (s, [*B*$F_4$]$^-$) ppm. $^{13}$C{$^1$H} NMR (75.46 MHz, $CH_2Cl_2$, –60 °C): $\delta$ = 98.7 (d*, $^2J_{C,Xe}$ = 75 Hz, C-2), 28.7, 21.8, 20.5 (C-3, C-4, C-5), 13.4 (C-6), –16.7 (d*, $^1J_{C,Xe}$ = 288 Hz, C-1) ppm. $^{19}$F NMR (282.40 MHz, $CH_2Cl_2$, –60 °C): $\delta$ = –143.0 (s, [B$F_4$]$^-$) ppm.

aHF (0.4 mL) was added to a solution of **6b** in $CH_2Cl_2$ and stirred at –45 °C for 10 min before the acidic phase was decanted.

**6b:** $^1$H NMR (300.13 MHz, aHF, –30 °C): $\delta$ = 2.68 (t, $^3J_{H,H}$ = 7 Hz, 2 H, 3-H), 1.66 (t, $^3J_{H,H}$ = 7 Hz, t, $^3J_{H,H}$ = 7 Hz, 2 H, 4-H), 1.46 (t, $^3J_{H,H}$ = 7 Hz, q, $^3J_{H,H}$ = 7 Hz, 2 H, H-5), 0.95 (t, $^3J_{H,H}$ = 7 Hz, 3 H, 6-H) ppm. $^{11}$B NMR (96.29 MHz, aHF, –30 °C): $\delta$ = –1.2 (s, [*B*$F_4$]$^-$) ppm. $^{13}$C{$^1$H} NMR (75.46 MHz, aHF, –30 °C): $\delta$ = 101.6 (d*, $^2J_{C,Xe}$ = 69 Hz, C-2), 29.0, 21.9, 20.1 (C-3, C-4, C-5), 12.0 (C-6), –24.0 (d*, $^1J_{C,Xe}$ = 264 Hz, C-1) ppm. $^{19}$F NMR (282.40 MHz, aHF, –30 °C): $\delta$ = –147.8 (s, [B$F_4$]$^-$) ppm.

**B:** A solution of $C_4H_9C{\equiv}CBF_2$ (0.25 mmol) in PFP (0.7 mL) was cooled to –70 °C and added in one portion to the cold (–70 °C) suspension of xenon difluoride (54 mg, 0.32 mmol) in PFP (0.2 mL). The brown reaction mixture was stirred at –65 °C for 1 h. The NMR spectra of the suspension showed the total conversion of **6a** and the formation of **6b** in >25% yield.

**6b:** $^1$H NMR (300.13 MHz, PFP, –60 °C): $\delta$ = 1.58 (m, 2 H, 4-H), 1.42 (m, 2 H, 5-H), 0.91 (t, $^3J_{H,H}$ = 7 Hz, 3 H, 6-H) ppm (the signal for 3-H overlapped with the resonance of PFP at 2.6 ppm). $^{11}$B NMR (96.29 MHz, PFP, –60 °C): $\delta$ = –0.1 (s, [*B*$F_4$]$^-$) ppm. $^{13}$C{$^1$H} NMR (75.46 MHz, PFP, –60 °C): $\delta$ = 99.3 (d*, $^2J_{C,Xe}$ = 73 Hz, C-2), 28.5, 21.4, 19.6 (C-3, C-4, C-5), 12.1 (C-6), –21.2 (d*, $^1J_{C,Xe}$ = 279 Hz, C-1) ppm. $^{19}$F NMR (282.40 MHz, PFP, –60 °C): $\delta$ = –140.7 (s, [B$F_4$]$^-$) ppm. No changes were found in a solution of **6b** in $CH_2Cl_2$ after storage at –70 °C over 5 months. When **6b** was stored as aHF solution at 22 °C the content of **6b** was reduced from 95–100% (after 2 h) to 38% (after 22 h) to 10% (after 46 h).

**3,3-Dimethylbut-1-ynylxenon(II) Tetrafluoroborate, [$(CH_3)_3$-$CC{\equiv}CXe$][$BF_4$], (7b)**

**A:** A cold (–60 °C) solution of $(CH_3)_3CC{\equiv}CBF_2$ (0.44 mmol) in PFP (1.7 mL) was added in one portion to the cold (–60 °C) stirred suspension of xenon difluoride (69 mg, 0.40 mmol) in PFP (0.1 mL). After 2 h, the reaction mixture was centrifuged at –78 °C and subsequently the brown mother liquor was decanted at –65 °C. The precipitate was dried at –60 °C in vacuo to give **7b** (37 mg, 0.12 mmol). The mother liquor still contained borane **7a** (0.05 mmol) along with product **7b** (0.15 mmol) ($^1$H-, $^{11}$B-, $^{19}$F NMR).

**7b:** $^1$H NMR (300.13 MHz, PFP, –50 °C): $\delta$ = 1.30 (s, C$H_3$) ppm. $^{11}$B NMR (96.29 MHz, PFP, –50 °C): $\delta$ = –1.4 (s, [*B*$F_4$]$^-$) ppm. $^{19}$F NMR (282.40 MHz, PFP, –50 °C): $\delta$ = –138.9 (s, [*B*$F_4$]$^-$) ppm.

**7b:** $^1$H NMR (300.13 MHz, aHF, –60 °C): $\delta$ = 1.26 (s, C$H_3$) ppm. $^{11}$B NMR (96.29 MHz, aHF, –50 °C): $\delta$ = –1.2 (quintet, $^1J_{B,F}$ = 10 Hz, [B$F_4$]$^-$) ppm. $^{13}$C{$^1$H} NMR (75.46 MHz, aHF, –60 °C): $\delta$ = 107.0 (d*, $^2J_{C,Xe}$ = 76 Hz, C-2), 30.9 (C-3), 27.6 (*C*$H_3$), –23.7 (d*, $^1J_{C,Xe}$ = 267 Hz, C-1) ppm. $^{19}$F NMR (282.40 MHz, aHF, –50 °C): $\delta$ = –148.0 (s, [B$F_4$]$^-$) ppm.

**B:** When a solution of **7b** in PFP was warmed to 20 °C, it became dark, and a black precipitate was formed within 5–10 min. The decomposition of the colourless solution of **7b** in aHF proceeded slowly at 20 °C and led to a dark colouration. The intensity of the $^{129}$Xe NMR signal was also reduced to 80% (after 24 h) and then to 11% (after 44 h).

**7b:** $^1$H NMR (300.13 MHz, $CH_2Cl_2$, –60 °C): $\delta$ = 1.28 (s, C$H_3$) ppm. $^{11}$B NMR (96.29 MHz, $CH_2Cl_2$, –60 °C): $\delta$ = –1.4 (s, [*B*$F_4$]$^-$) ppm. $^{13}$C{$^1$H} NMR (75.46 MHz, $CH_2Cl_2$, –40 °C): $\delta$ = 105.7 (C-

 © 2006 Wiley-VCH Verlag GmbH & Co. KGaA, Weinheim 

2), 30.4 (C-3), 28.9 ($CH_3$), –15.7 (C-1) ppm. $^{19}F$ NMR (282.40 MHz, $CH_2Cl_2$, –60 °C): $\delta$ = –144.7 (s, $[BF_4]^-$) ppm.

**Supporting Information** (see also the footnote on the first page of this article): Multi-NMR spectra of the [RC≡CXe][$BF_4$] salts.

## Acknowledgments

We gratefully acknowledge financial support from the Deutsche Forschungsgemeinschaft, the Russian Foundation for Basic Research (Grant 04–03–04002 NNIO_a) and the Fonds der Chemischen Industrie. We thank Honeywell Specialty Chemicals Seelze GmbH for the generous donation of chemicals.

[1] D. Naumann, W. Tyrra, *J. Chem. Soc., Chem. Commun.* **1989**, 47–50.
[2] H.-J. Frohn, S. Jakobs, *J. Chem. Soc., Chem. Commun.* **1989**, 625–627.
[3] a) J. H. Holloway, E. G. Hope, *Adv. Inorg. Chem.* **1999**, *46*, 51–100; b) H.-J. Frohn, V. V. Bardin, *Organometallics* **2001**, *20*, 4750–4762; c) V. K. Brel, N. Sh. Pirkuliev, N. S. Zefirov, *Russ. Chem. Rev.* **2001**, *70*, 231–264; d) W. Tyrra, D. Naumann, "Organoxenon Compounds" in *Inorganic Chemistry Highlights*, (Eds.: G. Meyer, D. Naumann, L. Wesemann), VCH, Weinheim, **2002**, p. 297–317.
[4] Yu. L. Yagupolskii, W. Tyrra, R. Gnann, N. Maggiarosa, D. Naumann, *J. Fluorine Chem.* **2002**, *113*, 143–146.
[5] J. Helber, H.-J. Frohn, A. Klose, Th. Scholten, *Arkivoc* **2003**, 71–82; http://www.arkat-usa.org/ark/journal/2003/Varvoglis/AV-682A/682.pdf
[6] H.-J. Frohn, M. Theissen, *J. Fluorine Chem.* **2004**, *125*, 981–988.
[7] H.-J. Frohn, N. Yu. Adonin, V. V. Bardin, *Z. Anorg. Allg. Chem.* **2003**, *629*, 2499–2508.
[8] H.-J. Frohn, V. V. Bardin, *Z. Anorg. Allg. Chem.* **2003**, *629*, 2465–2469.
[9] H.-J. Frohn, V. V. Bardin, *Z. Anorg. Allg. Chem.* **2004**, *630*, 1022–1024.
[10] H. Schmidt, H. Scherer, W. Tyrra, J. Hahn, D. Naumann, *Inorg. Chem.* **2004**, *43*, 1837–1839.
[11] V. V. Zhdankin, P. J. Stang, N. S. Zefirov, *J. Chem. Soc., Chem. Commun.* **1992**, 578–579.
[12] H.-J. Frohn, V. V. Bardin, *Chem. Commun.* **2003**, 2352–2353.
[13] The choice of an appropriate solvent for the reaction of $XeF_2$ with highly acidic organodifluoroboranes was discussed in ref.[7]
[14] F. Bailly, P. Barthen, H.-J. Frohn, M. Koeckerling, *Z. Anorg. Allg. Chem.* **2000**, *626*, 2419–2427.
[15] A. Abo-Amer, N. Yu. Adonin, V. V. Bardin, P. Fritzen, H.-J. Frohn, Ch. Steinberg, *J. Fluorine Chem.* **2004**, *125*, 1771–1778.
[16] G. A. Schumacher, G. J. Schrobilgen, *Inorg. Chem.* **1984**; *23*, 2923–2929.
[17] D. D. Perrin, W. L. F. Armarego (Eds.), *Purification of Laboratory Chemicals*, 3rd ed., Pergamon Press, Oxford, **1980**.
[18] a) V. V. Bardin, N. Yu. Adonin, H.-J. Frohn, *Organometallics* **2005**, *24*, 5311–5317; b) V. V. Bardin, N. Yu. Adonin, H.-J. Frohn, manuscript in preparation.
[19] A. E. Pedler, J. C. Tatlow, A. J. Uff, *Tetrahedron* **1969**, *25*, 1597–1601.
[20] V. V. Bardin, H.-J. Frohn, *Magn. Res. Chem*, accepted for publication.

Received: April 24, 2006
Published Online: August 7, 2006

 © 2006 Wiley-VCH Verlag GmbH & Co. KGaA, Weinheim 

DOI: 10.1002/ejic.200600355

# Tuned Helical Array of $Rh^{III}/Ir^{III}$ Cp* Complexes with Polypyridyl Ligands

Sanjay K. Singh,[a] Manish Chandra,[a] Santosh K. Dubey,[a] and Daya S. Pandey*[a]

**Keywords:** Rhodium-Cp* / Iridium-Cp* / Polypyridyl ligands / Tuned helical / Weak interactions

Reactions of the chloro-bridged dimeric complexes $[\{(\eta^5\text{-}C_5Me_5)M(\mu\text{-}Cl)Cl\}_2]$ (M = Rh, Ir) with the polypyridyl ligands 2,3-di(2-pyridyl)pyrazine (dpp) and 2,4,6-tri(2-pyridyl)-1,3,5-triazine (tptz) in the presence of ammonium tetrafluoroborate gave the mononuclear complexes $[(\eta^5\text{-}C_5Me_5)MCl(\kappa^2\text{-}dpp)]BF_4$ [M = Rh (**1**), Ir (**2**)] and $[(\eta^5\text{-}C_5Me_5)MCl(\kappa^2\text{-}tptz)]BF_4$ [M = Rh (**3**), Ir (**4**)]. The complexes have been characterised by elemental analysis, FAB-MS, ESMS, IR, NMR, electronic and emission spectroscopic studies and the molecular structures of **1**, **2** and **3** have been crystallographically determined. Structural studies on the complexes revealed the presence of helical superstructures resulting from C–H···X (X = N, F, Cl and π) interactions.

(© Wiley-VCH Verlag GmbH & Co. KGaA, 69451 Weinheim, Germany, 2006)

## Introduction

The chemistry and photophysical properties of the $Rh^{III}$ and $Ir^{III}$ complexes of polypyridyl ligands and substituted cyclopentadienyl group are well documented.[1] Since their discovery in 1968 the pentamethylcyclopentadienyl complexes $[\{(\eta^5\text{-}C_5Me_5)M(\mu\text{-}Cl)Cl\}_2]$ (M = Rh, Ir) have attracted the attention of many research groups because of their potential as precursors and uses as hydride transfer catalysts.[2] The complexes undergo a rich variety of chemical transformations via the intermediacy of chloro bridge cleavage reactions leading to the formation of a series of interesting neutral and cationic mononuclear complexes.[3] Despite extensive studies on the complexes $[\{(\eta^5\text{-}C_5Me_5)M(\mu\text{-}Cl)Cl\}_2]$ (M = Rh, Ir), their reactivity with potential bridging ligands, viz. 2,3-di(2-pyridyl)pyrazine (dpp) and 2,4,6-tri(2-pyridyl)-1,3,5-triazine, has yet to be explored. Furthermore, the construction of self-assembled structures has attracted increasing scientific attention.[4,5] A properly designed building block with a metal ion defines the morphology of coordination networks and huge supramolecular architectures.[4] The use of forces such as hydrogen bonding and weak interactions as a powerful tool for self-assembling is widely accepted. The introduction of helices into artificial systems (as in supramolecular chemistry) has increased the number of intensive investigations by chemists for many years.[4,5]

During past few years we have become interested in this area and, in continuation of our studies in this direction, we have examined the reactivity of the polypyridyl ligands 2,3-di(2-pyridyl)pyrazine and 2,4,6-tri(2-pyridyl)-1,3,5-triazine with the chloro-bridged complexes $[\{(\eta^5\text{-}C_5Me_5)M(\mu\text{-}Cl)Cl\}_2]$ (M = Rh, Ir) under varying reaction conditions.[6–7] We present herein, reproducible syntheses and spectroscopic properties of the complexes $[(\eta^5\text{-}C_5Me_5)MCl(\kappa^2\text{-}dpp)]BF_4$ [M = Rh (**1**), Ir (**2**)] and $[(\eta^5\text{-}C_5Me_5)MCl(\kappa^2\text{-}tptz)]BF_4$ [M = Rh (**3**), Ir (**4**)]. We also describe the crystal and molecular structures of the representative dpp and tptz complexes $[(\eta^5\text{-}C_5Me_5)Rh(\kappa^2\text{-}dpp)]BF_4$ **1**, $[(\eta^5\text{-}C_5Me_5)Ir(\kappa^2\text{-}dpp)]BF_4$ **2** and $[(\eta^5\text{-}C_5Me_5)RhCl(\kappa^2\text{-}tptz)]BF_4$ **3** as well as our results from studies of weak interaction in these complexes.

## Results and Discussion

### Synthesis and Characterisation

The reactions of the chloro-bridged dimeric complexes $[\{(\eta^5\text{-}C_5Me_5)M(\mu\text{-}Cl)Cl\}_2]$ (M = Rh, Ir) with an excess of the polypyridyl ligands 2,3-di(2-pyridyl)pyrazine and 2,4,6-tri(2-pyridyl)-1,3,5-triazine in methanol afforded cationic mononuclear complexes in reasonably good yields (Scheme 1). The complexes were isolated as their tetrafluoroborate salts $[(\eta^5\text{-}C_5Me_5)RhCl(\kappa^2\text{-}dpp)]BF_4$ (**1**), $[(\eta^5\text{-}C_5Me_5)RhCl(\kappa^2\text{-}tptz)]BF_4$ (**2**), $[(\eta^5\text{-}C_5Me_5)IrCl(\kappa^2\text{-}dpp)]BF_4$ (**3**) and $[(\eta^5\text{-}C_5Me_5)IrCl(\kappa^2\text{-}tptz)]BF_4$ (**4**).

The cationic orange-red crystalline compounds with high melting temperatures were isolated as air-stable, nonhygroscopic solids. The complexes are soluble in methanol, acetone, dichloromethane, chloroform, acetonitrile, dimethylformamide and dimethylsuphoxide but insoluble in petroleum ether and diethyl ether. They form air sensitive solutions in acetonitrile, dimethyl sulfoxide and dimethylformamide and turn brownish-black after a couple of hours. The structural identities and homogeneity of **1**–**4** were estab-

[a] Department of Chemistry, Faculty of Science, Banaras Hindu University,
Varanasi 221005 (U. P.), India
E-mail: dspbhu@bhu.ac.in
dsprewa@yahoo.com

 InterScience © 2006 Wiley-VCH Verlag GmbH & Co. KGaA, Weinheim 

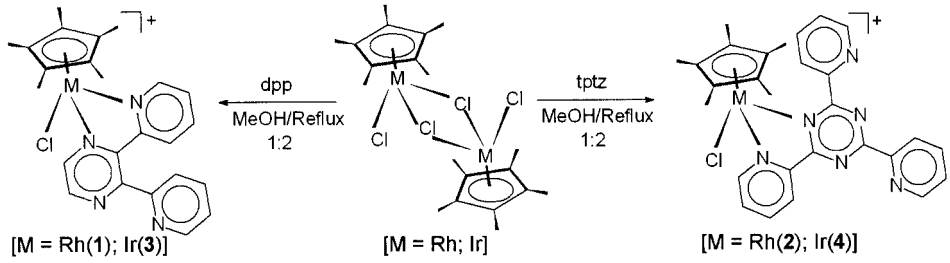


Scheme 1.

lished by analytical techniques, the results of which are consistent with their proposed formulations. Further information regarding compositions was obtained from FAB-mass spectrometry. FAB-mass spectrometric data (reported in the Exp. Sect.) of **1**–**4** are consistent with their respective formulations. $^1$H NMR spectroscopic data in $CDCl_3$ for **1**–**4** are reported in the experimental section and representative spectra for $[(\eta^5\text{-}C_5Me_5)RhCl(\kappa^2\text{-dpp})]BF_4$ (**1**) in $CDCl_3$ are shown in Figure 1. The $^1$H NMR spectrum of **1** exhibits distinct resonances at $\delta$ = 7.14 (d, $J$ = 6.0 Hz, 1 H), 7.60 (dd, $J$ = 4.5 Hz, 1 H), 7.78 (t, $J$ = 2.9 Hz, 2 H), 8.08 (d, $J$ = 3.9 Hz, 2 H), 8.64 (d, $J$ = 4.5 Hz, 1 H), 8.89 (t, $J$ = 3.3 Hz, 1 H), 9.00 (d, $J$ = 2.7 Hz, 1 H) and 9.07 (d, $J$ = 2.7 Hz, 1 H) ppm corresponding to the pyrazyl and pyridyl protons of 2,3-di(2-pyridyl)pyrazine (dpp). The $\eta^5$-Cp* protons resonate as a singlet at $\delta$ = 1.80 ppm. The positions and integrated intensities of the various resonances corroborate well with the formulation of **1**. The $^1$H NMR spectrum of the complex $[(\eta^5\text{-}C_5Me_5)RhCl(\kappa^2\text{-tptz})]BF_4$ **2** exhibits signals at $\delta$ = 7.61 (t, $J$ = 7.2 Hz, 2 H), 7.95 (t, $J$ = 5.4 Hz, 2 H), 8.03 (m, 2 H), 8.22 (t, $J$ = 7.8 Hz, 1 H), 8.95 (m, 4 H) and 9.19 (d, $J$ = 7.8 Hz, 1 H) ppm assignable to the pyridyl protons of the coordinated tptz ligand and a singlet at $\delta$ = 1.79 ppm corresponding to $\eta^5$-Cp* protons. A similar trend was observed in the resonances of the analogous iridium complexes **3** and **4**.

Comparative absorption spectra of **1**–**4** recorded in dichloromethane are shown in Figure 2a. Transitions in the 327–455 nm region can be assigned to $M_{d\pi}\rightarrow L_{\pi}^*$ metal to ligand charge-transfer bands (MLCT) and higher energy transitions at ca. 280 nm to the intra-ligand $\pi$–$\pi$* transition. The absorption bands for the rhodium complexes **1** and **2** are blue shifted relative to those of the iridium(III) counterpart. The complexes were found to be luminescent at room temperature in dichloromethane. Emission spectra of **1** and **2** are shown in Figure 2b. Upon excitation at their respective excitation bands (in parentheses) the complexes exhibit moderate green-yellow to yellow-orange luminescence [449 nm (396 nm) for **1**; 427 nm (351 nm) for **2**; 475 nm (415 nm) for **3** and 469 nm (347 nm) for **4**]. The resultant emissions correspond to $[M_{d\pi}\rightarrow L_{\pi}^*]$ $^3$MLCT transitions for the polypyridyl ligand since the MCp*Cl moiety does not emit. The Rh–dpp, **1** and Ir–dpp, **3** complexes exhibit analogous emission spectra suggesting $M_{d\pi}\rightarrow dpp_{\pi}^*$ as a common transition origin. This view is further strengthened by a significantly red shifted emission band for the iridium complexes compared with the analogous rhodium complex. This is in keeping with the fact that the $d_{\pi}$ orbitals of $Rh^{III}$ are more stable than those of $Ir^{III}$. Rigidity and the delocalisation factor of the acceptor ligand play an appreciable role in the overall photophysical properties of the complexes because they decrease the extent of structural changes in the excited state which in turn decreases the nonradiative decay and stabilises the $^3$MLCT based excited state. The analogous Rh–tppz, **2** and Ir–tppz, **4** complexes exhibit equally intense emissions as the respective dpp complexes. These emissions, however, are blue shifted, much broader and less distinct. These results may be better viewed as a consequence of more delocalisation and rigidity of the framework in the coordinated dpp than in tptz.

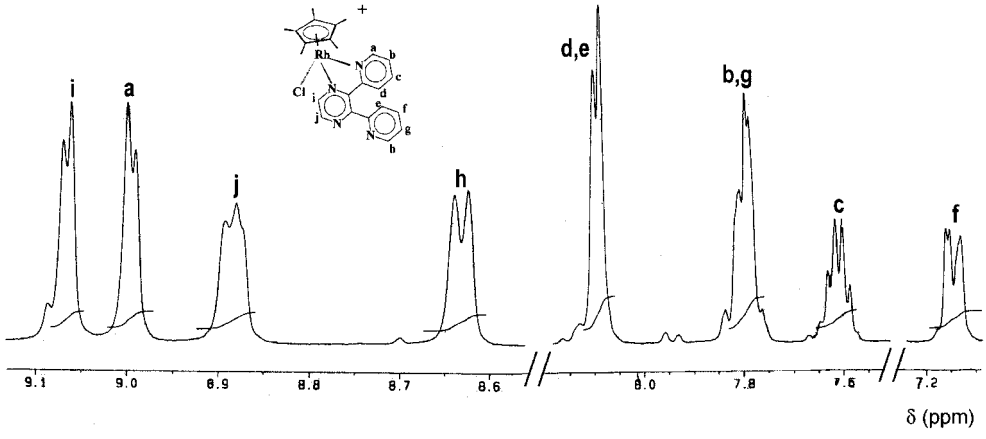


Figure 1. $^1$H NMR spectra of **1** in $CDCl_3$.

 © 2006 Wiley-VCH Verlag GmbH & Co. KGaA, Weinheim 

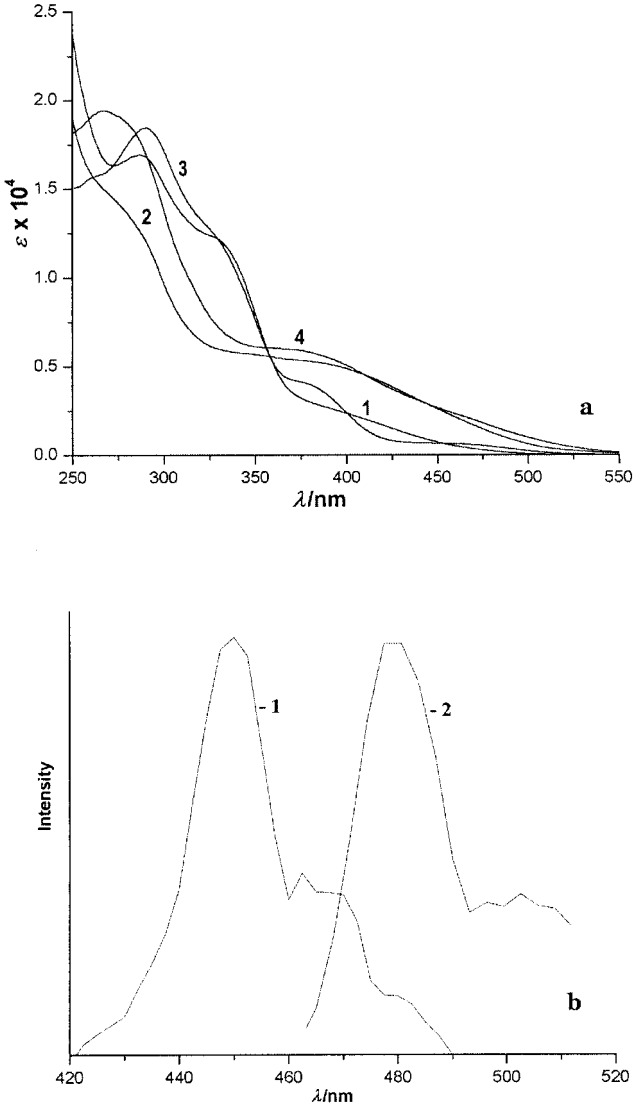


Figure 2. (a) Electronic spectra of **1**, **2**, **3** and **4**; (b) emission spectra of **1** ($\lambda_{ex}$ = 396 nm) and **2** ($\lambda_{ex}$ = 351 nm) in dichloromethane.

### *Solid-State Characterisation of 1, 2 and 3*

Suitable crystals with distinct morphologies of **1**, **2**·$CH_2Cl_2$, and **3**·0.5$H_2O$ were grown from dichloromethane and petroleum ether (40–60°) by diffusion. ORTEP[8] depictions, including atom-numbering schemes of the cations of **1**, **2** and **3** are shown in Figure 3 with selected bond lengths and bond angles listed in Table 1. Complexes **1** and **3** crystallise in the monoclinic space groups $P2_1$ and $P2_1/n$, respectively, while **2** crystallises in the orthorhombic $P2_12_12_1$ space group. Two crystallographically independent molecules can be observed in the unit cell of **1**, the only major difference between them being the orientation and a lengthening of the Rh–Cl and Ru–N bonds in one molecule. The solid-state structures of **1** and **3** are analogous, each metal centre is coordinated to a pyridyl nitrogen, a pyrazyl nitrogen, a chlorine ligand and an $\eta^5$-coordinated Cp* group. In **2**, the Rh metal centre is coordinated to N(1) and N(2) from the tptz ligand, the chlorine ligand Cl(1) and the $\eta^5$ Cp* group. Considering the Cp* as a single coordination site, the overall coordination geometry about the metal centres in the complexes **1**, **2** and **3** is pseudo-octahedral or typical piano stool geometry. Average $M–C_{Cp^*}$ distances in **1** (two asymmetric units), **2** and **3** are 2.141 Å [range 2.114(18)–2.19(2) Å; Rh–$C_{ct}$ 1.759 Å], 2.179 Å [range 2.135(19)–2.231(19) Å; Rh–$C_{ct}$ 1.817 Å], 2.154 Å [range 2.127(10)–2.184(12) Å; Rh–$C_{ct}$ 1.776 Å] and 2.169 Å [range 2.154(10)–2.190(10) Å; Ir–$C_{ct}$ 1.795 Å], respectively.[9,10a] The C–C bond lengths within the Cp* ring and the C–$CH_3$ bond lengths are normal. The M–Cl distances in **1**, **2** and **3** are normal [Rh–Cl 2.378(5), 2.403(6) Å **1**; 2.408(3) Å **2** and Ir–Cl 2.395(3) Å **3**].[9a,10] The Rh–N bond lengths in **1** and **2** are all within reported values.[9a,10,13] The Ir–N distances are comparable with those in related Cp*Ir complexes.[3c,3d,9a] The angles N–M–N and N–M–Cl (M = Rh, Ir) are as expected for all the complexes. The molecular structures of **1** and **3** show that the coordinated pyridyl ring and pyrazine ring deviate slightly from planarity [9(2)°, 10(2)° **1** and 9(2)° **3**] while the uncoordinated pyridyl ring is inclined at an angle of ca. 44° with respect to the coordinated pyrazine ring plane [44(2)°, 42(3)° **1** and 44.6(15)° **3**]. However, in the free dpp ligand, the dihedral angles between the pyrazine and pyridyl rings are 42.2°.[11] The pyrazyl rings in both the **1** and **3** are planer with a deviation of ca. 8°. In **2**, upon coordination with the metal centre rhodium in the $\kappa^2$-mode, the tptz ligand loses its planarity. The coordinated pyridyl ring subtends an angle of 11.9(13)° with respect to central triazine ring whereas the uncoordinated pyridyl rings are inclined from the central triazine ring by 9.6(14)° for the N(1)–C(5) ring and 34.6(14)° for the N(6)–C(14) ring. The average C–C($C_5Me_5$) bond lengths in the Cp* group are 1.415 Å and 1.438 Å in **1**, 1.432 Å in **2** and 1.443 Å in **3** and the exterior C($C_5Me_5$)–C($C_5Me_5$) average bond lengths are 1.482 Å and 1.500 Å in **1**, 1.479 Å in **2** and 1.493 Å in **3**.[12]

Weak interaction studies on the isostructural complexes **1**, **2** and **3** revealed the presence of supramolecular helical self-assembled architectures with their individual peculiarities (Figure 4). Various intra- and intermolecular C–H···X (X = F, Cl, N, and π) weak interactions are involved in stabilising the helical superstructures of the complexes **1**–**3**.[4,5,13] Determinant intermolecular interactions D–H···A–X ($d$ = H···A, $D$ = D–H···A, $\theta$ = D–H···A, $\varphi$ H···A–X and $\omega$ = D–H···A–X) which stabilise the helical superstructures are listed in Table 2. A distorted circular void space can be visualised for the complexes when viewed parallel to the $a$ axis as depicted in Figure 5. A correlation between the pitch length and void size has been established. The helical superstructures for all the complexes involve two molecular residues in each coil though a steady contraction of the void space may be observed upon moving from **1** to **3**. The observed pitches are 7.639, 11.354 and 15.186 Å for **1**, **2** and **3**, respectively. Furthermore, it was observed that as the pitches of the helical superstructures show an increase of almost 50% (ca. 7.5 Å) and the diameter of the void spaces decrease by ca. 8.0 Å (80%) (diameters of the void space are ca. 10.0 Å in **1**, ca. 5.0 Å in **2** and ca. 2.0 Å in **3** as

 © 2006 Wiley-VCH Verlag GmbH & Co. KGaA, Weinheim 

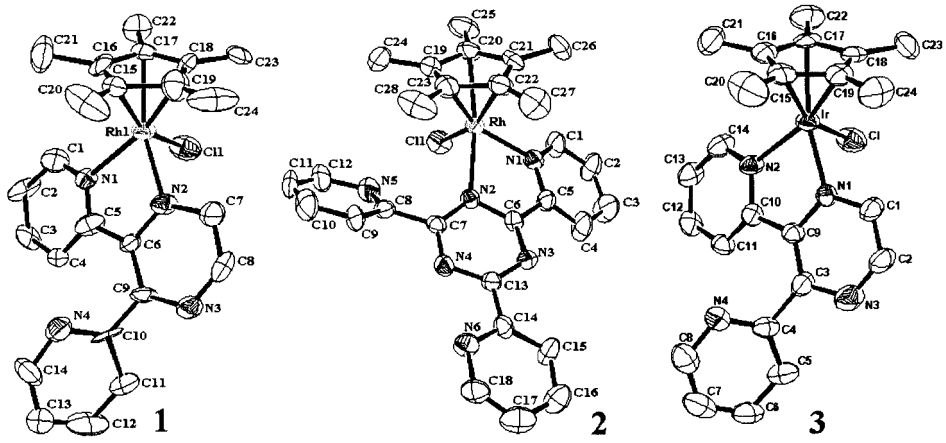


Figure 3. ORTEP view of **1**, **2** and **3**.

Table 1. Selected bond length [Å], bond angles [°] and torsion angles [°] in **1**, **2** and **3**.

| **1** | | **2** | **3** |
|---|---|---|---|
| Rh(1)–N(1) 2141(14) | Rh(2)–N(5) 2.049(13) | Rh–N(1) 2.114(8) | Ir–N(1) 2.090(8) |
| Rh(1)–N(2) 2.084(14) | Rh(2)–N(6) 2.106(16) | Rh–N(2) 2.191(7) | Ir–N(2) 2.074(8) |
| Rh(1)–Cl(1) 2.403(6) | Rh(2)–Cl(2) 2.378(5) | Rh–Cl(1) 2.378(5) | Ir–Cl 2.395(3) |
| Rh(1)–Ct 1.759 | Rh(2)–Ct 1.817 | Rh–Ct 1.776 | Ir–Ct 1.795 |
| Rh(1)–Cav 2.141 | Rh(2)–Cav 2.179 | Rh–Cav 2.154 | Ir–Cav 2.1694 |
| N(1)–Rh(1)–N(2) 74.9(5) | N(5)–Rh(2)–N(6) 77.2(6) | N(1)–Rh–N(2) 76.3(3) | N(1)–Ir–N(2) 75.6(3) |
| N(1)–Rh(1)–Cl(1) 85.7(4) | N(5)–Rh(2)–Cl(2) 86.9(5) | N(1)–Rh–Cl 96.4(2) | N(1)–Ir–Cl 84.9(2) |
| N(2)–Rh(1)–Cl(1) 86.6(5) | N(6)–Rh(2)–Cl(2) 86.3(5) | N(2)–Rh–Cl 85.8(3) | N(2)–Ir–Cl 84.7(3) |
| N(1)–C(5)–C(6)–N(2) 10(2) | N(5)–C(29)–C(30)–N(6) 9(2) | N(1)–C(5)–C(6)–N(2) 11.9(13) | N(1)–C(5)–C(6)–N(2) 9(12) |
| N(2)–C(7)–C(8)–N(3) 0(3) | N(6)–C(31)–C(32)–N(7) 16(4) | N(2)–C(7)–C(8)–N(5) 34.6(14) | N(2)–C(7)–C(8)–N(3) 9(2) |
| N(3)–C(9)–C(10)–N(4) 44(2) | N(7)–C(33)–C(34)–N(8) 140.5(16) | N(4)–C(13)–C(14)–N(6) 9.6(14) | N(3)–C(9)–C(10)–N(4) 136.3(11) |

shown in Figure 5).[14] Thus it is noteworthy to mention here that *the pitch size is inversely proportional to the diameter of the void space in the helical superstructure.* Though no guest molecules are included in the void spaces of the helical frameworks in any of the complexes they are, however, prospective hosts for guest inclusion.

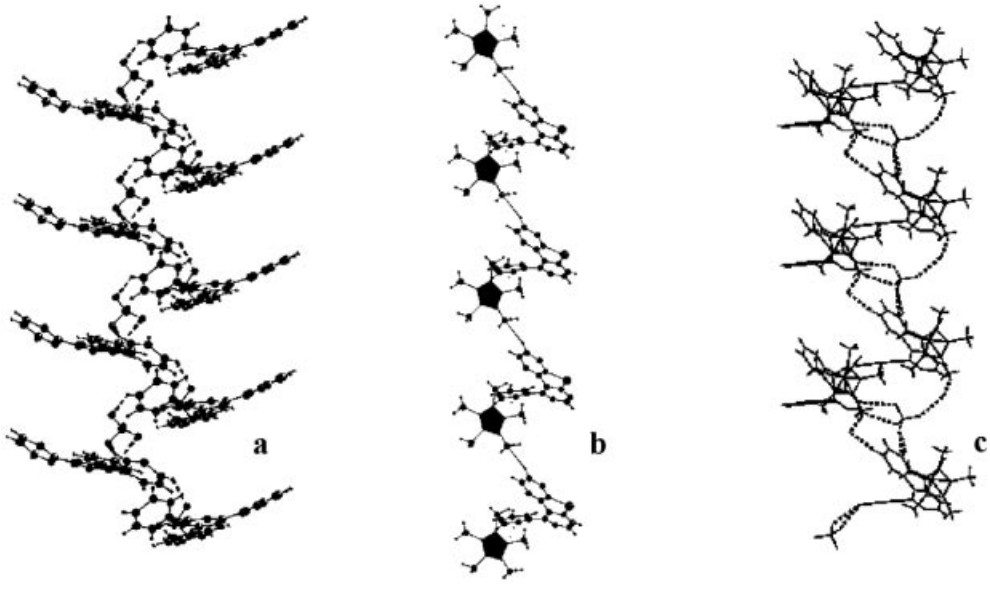


Figure 4. Helical arrangements of **1** (a) (*P*-type), **2** (b) (*M*-type) and **3** (c) (*M*-type).

 © 2006 Wiley-VCH Verlag GmbH & Co. KGaA, Weinheim 

Table 2. Hydrogen bond parameters for **1**, **2** and **3**.

| D–H···A–X | *d* H···A [Å] | *D* D···A [Å] | θ D–H···A [°] | φ H···A–X [°] | ω D–H···A–X [°] |
|---|---|---|---|---|---|
| **1** | | | | | |
| C1–H1···F7–B2[a] | 2.53 | 3.26 | 135.5 | 149.0 | 161.7 |
| C13–H13···F7–B2[b] | 2.55 | 3.25 | 132.9 | 129.5 | 0.2 |
| C8–H8···π | 2.85 | 3.37 | 116.2 | – | – |
| C46–H46A···π | 2.87 | 3.71 | 145.9 | – | – |
| **2** | | | | | |
| C1–H1···Cl3–C29[c] | 2.58 | 3.40 | 146.8 | 119.9 | 37.7 |
| C11–H11···Cl3–C29[d] | 2.34 | 3.04 | 132.4 | 125.5 | 41.5 |
| **3** | | | | | |
| C7–H7···F2–B[e] | 2.43 | 3.20 | 140.1 | 119.4 | 88.9 |
| C1–H1···F1–B[f] | 2.39 | 3.13 | 137.1 | 149.3 | 164.1 |
| C23–H23A···N4[g] | 2.58 | 3.43 | 148.3 | – | – |

[a] $-x + {}^1/_2, y + {}^1/_2, -z + {}^1/_2$. [b] $x + 1, y, z + 1$. [c] $x - {}^1/_2, -y + {}^3/_2, -z$. [d] $-x + 1, y + {}^1/_2, -z + {}^1/_2$. [e] $-x + {}^3/_2, y - {}^1/_2, -z + {}^1/_2$. [f] $-x + 1, -y + 1, -z + 1$. [g] $x - {}^1/_2, -y + {}^1/_2, z - {}^1/_2$.

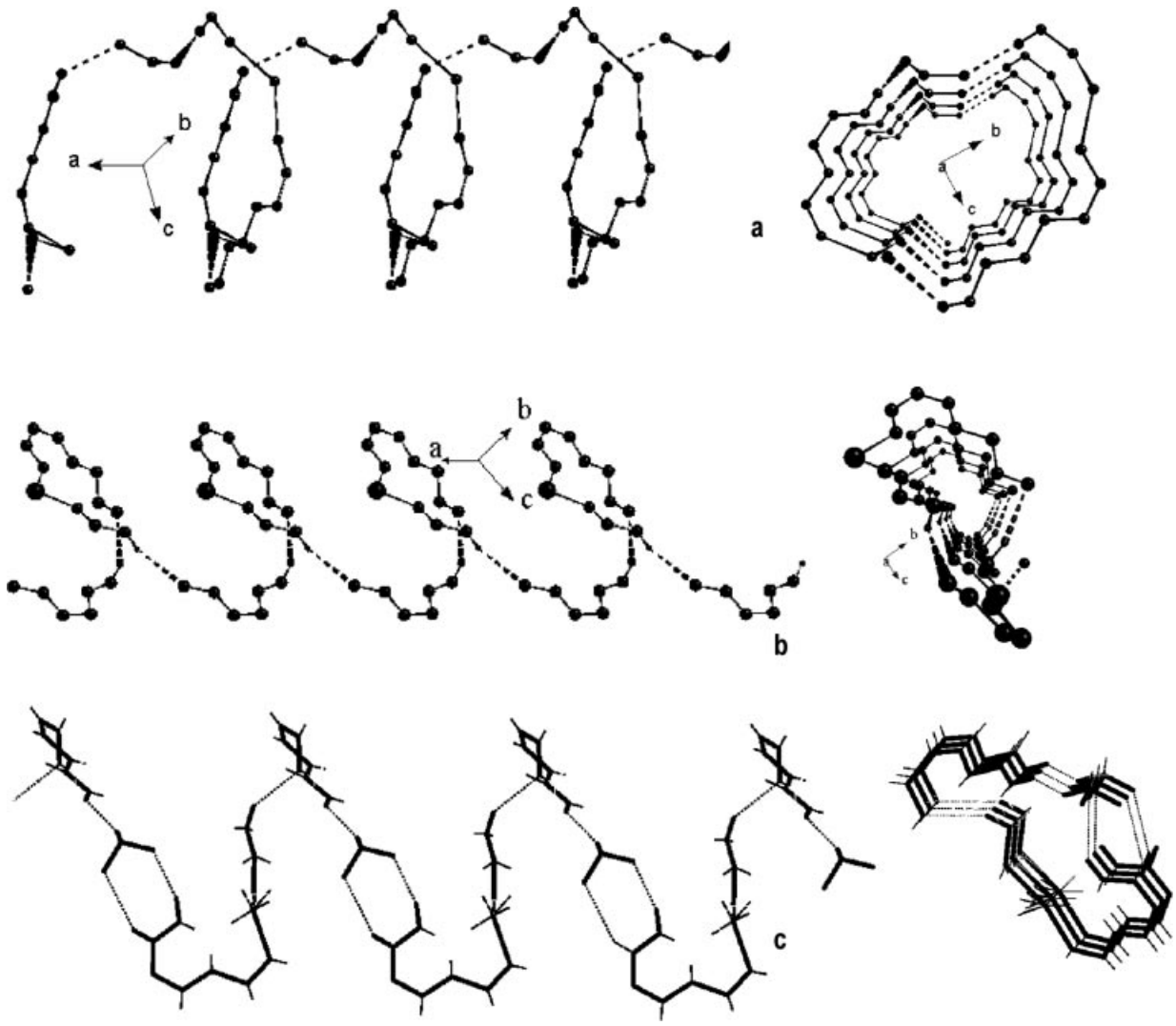


Figure 5. Helical superstructure with circular cavity for **1** (a), **2** (b) and **3** (c).

 © 2006 Wiley-VCH Verlag GmbH & Co. KGaA, Weinheim 

## Conclusions

In this work we have presented four new cationic mononuclear rhodium(III) and iridium(III) complexes $[(\eta^5\text{-}C_5Me_5)MCl(\kappa^2\text{-}L)]BF_4$ (M = Rh, L = dpp **1**, tptz **2** and M = Ir, L = dpp **3**, tptz **4**) and have described spectroscopic properties and molecular structures of three representative complexes. Due to the presence of uncoordinated pendant donor sites, these have the potential to behave as *synthons* or *metallo-ligands* and could find applications in the synthesis of $[(\eta^5\text{-}C_5Me_5)MCl]$ (M = Rh, Ir) containing homo- or heterobimetallic complexes. We have also illustrated here an approach towards the organisation of 3D helices, which are stabilised by weak interactions in the crystalline state. Furthermore, a noteworthy relationship between the pitches and the diameters of the void space in the helical superstructures has been observed.

## Experimental Section

**General:** Analytical grade chemicals were used throughout. Solvents were dried and distilled prior to use following standard literature procedures. 2,3-di(2-pyridyl)pyrazine, 2,4,6-tri(2-pyridyl)-1,3,5-triazine, pentamethylcyclopentadiene, ammonium tetrafluoroborate, hydrated rhodium(III) chloride and iridium(III) chloride (all from Aldrich) were used as received. The precursor complexes $[\{(\eta^5\text{-}C_5Me_5)M(\mu\text{-}Cl)Cl\}_2]$ (M = Rh, Ir) were prepared by literature procedures.[15] Elemental analyses on the complexes were performed by the Microanalytical Laboratory, Sophisticated Analytical Instrument Facility, Central Drug Research Institute, Lucknow. Electronic and emission spectra in dichloromethane were obtained on a Shimadzu UV-1601 and a Perkin–Elmer-LS 55 luminescence spectrometer, respectively. Infrared spectra were recorded on a Perkin–Elmer-577 spectrophotometer. $^1H$ NMR spectra in $CDCl_3$, using tetramethylsilane as an internal reference, were recorded at room temperature on a Bruker-DRX 300 NMR machine. FAB mass spectra were obtained on a JEOL SX 102/DA-6000 mass spectrometer system using xenon as the FAB gas (6 kV, 10 mA). The accelerating voltage was 10 kV and spectra were recorded at room temperature using *m*-nitrobenzyl alcohol as the matrix.

**Synthesis of $[(\eta^5\text{-}C_5Me_5)RhCl(\kappa^2\text{-}dpp)]BF_4$ (1):** A suspension of $[\{(\eta^5\text{-}C_5Me_5)Rh(\mu\text{-}Cl)Cl\}_2]$ (0.618 g, 1.0 mmol) in methanol (30 mL) was treated with 2,3-di(2-pyridyl)pyrazine (0.468 g, 2.0 mmol) and stirred at room temperature. The precursor complex slowly dissolved resulting in an orange-red solution. The resultant solution was further stirred at room temperature for about 4 h and then filtered through celite to remove any solid residue. To the filtrate was added a saturated methanolic solution of $NH_4BF_4$ (10 mL) and the resultant solution was left for slow crystallization in the refrigerator at ca. 4 °C. After a couple of days, a shiny crystalline product appeared which was separated by filtration, washed with methanol (2×10 mL), diethyl ether (2×10 mL) and dried in vacuo. Red-brown solid, yield 0.363 g (61%). $C_{24}H_{25}BClF_4N_4Rh$ (594.65): calcd. C 48.47, H 4.23, N 9.42; found C 48.21, H 4.35, N 9.24. IR (nujol): $\tilde{\nu}$ = 1079 $cm^{-1}$ (B–F). $^1H$ NMR ($CDCl_3$, 300 MHz): $\delta$ = 1.80 (s, 15 H, $C_5Me_5$), 7.14 (d, $J$ = 6.0 Hz, 1 H), 7.60 (dd, $J$ = 4.5 Hz, 1 H), 7.78 (t, $J$ = 2.9 Hz, 2 H), 8.08 (d, $J$ = 3.9 Hz, 2 H), 8.64 (d, $J$ = 4.5 Hz, 1 H), 8.89 (t, $J$ = 3.3 Hz, 1 H), 9.00 (d, $J$ = 2.7 Hz, 1 H), 9.07 (d, $J$ = 2.7 Hz, 1 H). FAB-MS: $m/z$ = 507 $[M]^+$, 472 $[M - Cl]^{2+}$, 237 $[M - Cl - dpp]^{2+}$. UV/Vis: $\lambda_{max}$ ($\varepsilon$, $dm^3\,mol^{-1}\,cm^{-1}$) = 396 ($2.4\times10^3$), 328 ($1.2\times10^4$), 286 ($1.7\times10^4$), 237 ($3.3\times10^4$) nm.

**Synthesis of $[(\eta^5\text{-}C_5Me_5)RhCl(\kappa^2\text{-}tptz)]BF_4$ (2):** This was prepared from $[\{(\eta^5\text{-}C_5Me_5)Rh(\mu\text{-}Cl)Cl\}_2]$ (0.618 g, 1.0 mmol) in methanol following the above procedure for **1** but using tptz (0.624 g, 2.0 mmol) in place of dpp. Bright yellow solid, yield 0.417 g (62%). $C_{28}H_{27}BClF_4N_6Rh$ (673.72): calcd. C 49.92, H 4.04, N 12.47; found C 49.97, H 3.98, N 12.31. IR (nujol): $\tilde{\nu}$ = 1083 $cm^{-1}$ (B–F). $^1H$ NMR ($CDCl_3$, 300 MHz): $\delta$ = 1.79 (s, 15 H, $C_5Me_5$), 7.61 (t, $J$ = 7.2 Hz, 2 H), 7.95 (t, $J$ = 5.4 Hz, 2 H), 8.03 (m, 2 H), 8.22 (t, $J$ = 7.8 Hz, 1 H), 8.95 (m, 4 H), 9.19 (d, $J$ = 7.8 Hz, 1 H). FAB-MS: $m/z$ = 585 $[M]^+$, 550 $[M - Cl]^{2+}$, 238 $[M - Cl - tptz]^{2+}$. UV/Vis: $\lambda_{max}$ ($\varepsilon$, $dm^3\,mol^{-1}\,cm^{-1}$) = 370 ($5.4\times10^3$), 273 ($1.5\times10^4$), 235 ($2.7\times10^4$) nm.

**Synthesis of $[(\eta^5\text{-}C_5Me_5)IrCl(\kappa^2\text{-}dpp)]BF_4$ (3):** This was prepared by following the same procedure as for **1** but using $[\{(\eta^5\text{-}C_5Me_5)Ir(\mu\text{-}Cl)Cl\}_2]$ (0.796 g, 1.0 mmol) in methanol (30 mL) and 2,3-di(2-pyridyl)pyrazine (0.468 g, 2.0 mmol). Yellow-orange solid, yield 0.451 g (66%). $C_{24}H_{25}BClF_4N_4Ir$ (683.94): calcd. C 42.11, H 3.65, N 8.19; found C 42.20, H 3.50, N 8.26. IR (nujol): $\tilde{\nu}$ = 1081 $cm^{-1}$ (B–F). $^1H$ NMR ($CDCl_3$, 300 MHz): $\delta$ = 1.75 (s, 15 H, $C_5Me_5$), 7.20 (d, $J$ = 3.2 Hz, 1 H), 7.58 (t, $J$ = 5.9 Hz, 1 H), 7.76 (t, $J$ = 4.1 Hz, 2 H), 8.11 (m, 2 H), 8.66 (d, $J$ = 4.3 Hz, 1 H), 8.79 (t, $J$ = 3.3 Hz, 1 H), 8.93 (d, $J$ = 3.2 Hz, 1 H), 9.08 (d, $J$ = 3.1 Hz, 1 H). FAB-MS: $m/z$ = 596 $[M]^+$, 560 $[M - Cl]^{2+}$, 326 $[M - Cl - dpp]^{2+}$.

Table 3. Crystallographic data and refinement parameters for **1**, **2** and **3**.

| | **1** | **2**·$CH_2Cl_2$ | **3**·0.5$H_20$ |
|---|---|---|---|
| Formula | $C_{24}H_{25}BClF_4N_4Rh$ | $C_{29}H_{29}BCl_3F_4N_6Rh$ | $C_{24}H_{27}BClF_4IrN_4O0.5$ |
| Formula weight | 594.65 | 757.65 | 693.96 |
| Crystal system | monoclinic | orthorhombic | monoclinic |
| Space group | $P2_1$ | $P2_12_12_1$ | $P2_1/n$ |
| $a$ [Å] | 11.354(3) | 7.6390(10) | 11.3600(8) |
| $b$ [Å] | 15.797(3) | 19.6490(10) | 15.8850(12) |
| $c$ [Å] | 15.019(5) | 21.5380(10) | 15.0970(15) |
| $\beta$ [°] | 111.88(2) | 90.00 | 111.618(7) |
| $V$ [$Å^3$] | 2499.9(11) | 3232.8(5) | 2532.7(4) |
| $Z$ | 4 | 4 | 4 |
| $D_{calcd.}$ [$mg\,m^{-3}$] | 1.580 | 1.557 | 1.820 |
| Radiation ($\lambda$ [Å]) | Mo-$K_\alpha$ (0.71073) | Cu-$K_\alpha$ (1.54180) | Mo-$K_\alpha$ (0.70930) |
| Reflections: | | | |
| Collected/unique | 4783/4557 | 3259/3259 | 4654/4417 |
| $R_1$, $wR_2$ [$I > \sigma(I)$] | 0.0487, 0.1525 | 0.0713, 0.1989 | 0.0550, 0.1366 |
| GOF | 1.335 | 1.245 | 1.010 |

 © 2006 Wiley-VCH Verlag GmbH & Co. KGaA, Weinheim 

UV/Vis: $\lambda_{max}$ ($\varepsilon$, $dm^3 mol^{-1} cm^{-1}$) = 452 ($6.3 \times 10^2$), 380 ($4.0 \times 10^3$), 326 ($1.2 \times 10^4$), 290 ($1.8 \times 10^4$), 233 ($1.9 \times 10^4$) nm.

**Synthesis of [($\eta^5$-$C_5Me_5$)IrCl($\kappa^2$-tptz)]$BF_4$ (4):** This was prepared following the above procedure for **3** but using tptz (0.624 g, 2.0 mmol) in place of dpp. Red-brown solid, yield 0.480 g (63%). $C_{28}H_{27}BClF_4N_6Ir$ (763.02): calcd. C 44.09, H 3.54, N 11.02; found C 44.15, H 3.68, N 11.10. IR (nujol): $\tilde{\nu}$ = 1084 $cm^{-1}$ (B–F). $^1H$ NMR ($CDCl_3$, 300 MHz): $\delta$ = 1.69 (s, 15 H, $C_5Me_5$), 7.68 (t, $J$ = 7.1 Hz, 2 H), 7.91 (t, $J$ = 5.5 Hz, 2 H), 8.10 (m, 2 H), 8.27 (t, $J$ = 7.5 Hz, 1 H), 9.01 (m, 4 H), 9.23 (d, $J$ = 7.6 Hz, 1 H). FAB-MS: $m/z$ = 675 $[M]^+$, 639 $\{M - Cl\}^{2+}$, 327 $[M - Cl - tptz]^{2+}$. UV/Vis: $\lambda_{max}$ ($\varepsilon$, $dm^3 mol^{-1} cm^{-1}$) = 455 ($2.5 \times 10^3$), 366 ($6.0 \times 10^3$), 265 ($1.9 \times 10^4$), 233 ($2.2 \times 10^4$) nm.

**X-ray Crystallography:** Suitable crystals of **1**, **2** and **3** for X-ray crystallographic studies were obtained from $CH_2Cl_2$/petroleum ether by diffusion. X-ray data for **1** and **3** were collected on an automatic Enraf–Nonius MACH 3 diffractometer using graphite-monochromated Mo-$K_\alpha$ radiation at 293(2) K. For **2**, X-ray data were collected at 293(2) K on an Enraf–Nonius CAD-4 diffractometer using monochromated Cu-$K_\alpha$ radiation, $\lambda$ = 1.54180 Å. The structures were solved by direct methods and refined by using MAXUS-99 and SHELX-97.[16] The non-hydrogen atoms had anisotropically refined thermal parameters. All hydrogen atoms were geometrically fixed and were refined using a riding model. The computer program PLATON was used for analysing the interactions and stacking distances.[16] All the pertinent crystallographic data are listed in Table 3.

CCDC-604770 to -604772 contain the supplementary crystallographic data for this paper. These data can be obtained free of charge from The Cambridge Crystallographic Data Centre via www.ccdc.cam.ac.uk/data_request/cif.

## Acknowledgments

Financial support from Department of Science and Technology, New Delhi, is gratefully acknowledged. We also thank The Head, RSIC, Central Drug Research Institute, Lucknow, for providing analytical and spectroscopic facilities. Special thanks are due to the Head, A. P. S. University, Rewa (M.P.), the Head of the Department of Chemistry, Faculty of Science, Banaras Hindu University, Varanasi, for extending laboratory facilities and Prof. T. P. Singh, Head, Department of Biophysics, AIIMS, New Delhi, for providing single-crystal X-ray facilities.

[1] a) H. Werner, M. Steinmetz, K. Peters, G. H. Schnering, *Eur. J. Inorg. Chem.* **1998**, 1605; b) M. C. DeRosa, P. J. Mosher, G. P. A. Yap, K.-S. Focsaneanu, R. J. Crutchley, C. E. B. Evans, *Inorg. Chem.* **2003**, *42*, 4864; c) K. K.-W. Lo, C.-K. Chung, T. K.-M. Lee, L.-H. Lui, K. H.-K. Tsang, N. Zhu, *Inorg. Chem.* **2003**, *42*, 6886; d) S. Park, Y. Choi, H. Han, S. H. Yang, S. Chang, *Chem. Commun.* **2003**, 1936; e) K. K.-W. Lo, C.-K. Li, K.-W. Lau, N. Zhu, *Dalton Trans.* **2003**, 4682; f) D. Drommi, F. Faraone, G. Francio, *Organometallics* **2002**, *21*, 761; g) R. Zurawinski, B. Donnadieu, M. Mikolajczyk, R. Chauvin, *Organometallics* **2003**, *22*, 4810; h) P. Marcazzan, B. O. Patrick, B. R. James, *Organometallics* **2003**, *22*, 1177; i) D. Noveski, T. Braun, M. Schultz, B. Neumann, H.-G. Stammier, *Dalton Trans.* **2003**, 4075.

[2] a) J. W. Kang, K. Mosley, P. M. Maitlis, *Chem. Commun. (London)* **1968**, 1304; b) J. W. Kang, K. Mosley, P. M. Maitlis, *J. Am. Chem. Soc.* **1969**, *91*, 5970; c) J. W. Kang, P. M. Maitlis, *J. Am. Chem. Soc.* **1968**, *90*, 3259; d) P. M. Maitlis, *J. Organomet. Chem.* **1995**, *500*, 239; e) P. M. Maitlis, *Acc. Chem. Res.* **1978**, *11*, 301; f) C. M. Hagen, J. A. Widegren, P. M. Maitlis, R. G. Finke, *J. Am. Chem. Soc.* **2005**, *127*, 4423; g) G. D. Williams, C. E. Wade, M. Wills, *Chem. Commun.* **2005**, 4735.

[3] a) D. Herebian, W. S. Sheldrick, *J. Chem. Soc., Dalton Trans.* **2002**, 966; b) M.-L. Lehaire, R. Scopelliti, L. Herdeis, K. Polborn, P. Mayer, K. Severin, *Inorg. Chem.* **2004**, *43*, 1609; c) A. Buryak, K. Severin, *J. Am. Chem. Soc.* **2005**, *127*, 3700; d) C. Pettinari, R. Pettinari, M. Fianchini, F. Marchetti, B. W. Skeleton, A. H. White, *Inorg. Chem.* **2005**, *44*, 7933; e) J.-Q. Wang, C.-X. Ren, G.-X. Jin, *Chem. Commun.* **2005**, 4738; f) W. Kaim, S. Berger, S. Greulich, R. Reinhardt, J. Fiedler, *J. Organomet. Chem.* **1999**, *582*, 153; g) R. P. Hughes, D. C. Lindner, L. M. Liable-Sands, A. L. Rheingold, *Organometallics* **2001**, *20*, 363.

[4] a) J.-P. Zhang, Y.-Y. Lin, X.-C. Huang, X.-M. Chen, *Inorg. Chem.* **2005**, *44*, 3146; b) G. R. Desiraju, *J. Chem. Soc., Dalton Trans.* **2000**, 3745; c) X.-Q. Lu, J. J. Jiang, C.-L. Chen, B.-S. Kang, C.-Y. Su, *Inorg. Chem.* **2005**, *44*, 4515; d) H. Yin, G. I. Lee, H. S. Park, G. A. Payne, J. M. Rodriguez, S. M. Sebti, A. D. Hamilton, *Angew. Chem. Int. Ed.* **2005**, *44*, 2707; e) Y. Wang, J. Yu, M. Guo, R. Xu, *Angew. Chem. Int. Ed.* **2003**, *42*, 4089; f) K. Biradha, C. Seward, M. J. Zaworotko, *Angew. Chem. Int. Ed.* **1999**, *38*, 492; g) J. H. K. K. Hirschberg, L. Brunsveld, A. Ramzi, J. A. J. M. Vekemans, R. P. Sijbesma, E. W. Meijer, *Nature* **2000**, *407*, 167.

[5] a) C. Piguet, G. Bernardinelli, G. Hopfgartner, *Chem. Rev.* **1997**, *97*, 2005; b) C.-Y. Su, Y.-P. Lai, C.-L. Chem, F. Lissner, B.-S. Kang, W. Kaim, *Angew. Chem. Int. Ed.* **2002**, *41*, 3371; c) D. L. Reger, R. F. Semeniuc, V. Rassolov, M. D. Smith, *Inorg. Chem.* **2004**, *43*, 537; d) S. K. Singh, M. Chandra, D. S. Pandey, M. C. Puerta, P. Valerga, *J. Organomet. Chem.* **2004**, *689*, 3612; e) S. K. Singh, S. Sharma, M. Chandra, D. S. Pandey, *J. Organomet. Chem.* **2005**, *690*, 3105; f) X. Meng, Y. Song, H. Hou, H. Han, B. Xiao, Y. Fan, Y. Zhu, *Inorg. Chem.* **2004**, *43*, 3528.

[6] a) A. Singh, N. Singh, D. S. Pandey, *J. Organomet. Chem.* **2002**, *642*, 48; b) S. K. Singh, M. Trivedi, M. Chandra, A. N. Sahay, D. S. Pandey, *Inorg. Chem.* **2004**, *43*, 8600; c) S. K. Singh, M. Chandra, D. S. Pandey, *J. Organomet. Chem.* **2004**, *689*, 2073; d) A. Singh, S. K. Singh, M. Trivedi, D. S. Pandey, *J. Organomet. Chem.* **2005**, *690*, 4243; e) S. K. Singh, M. Trivedi, M. Chandra, D. S. Pandey, *J. Organomet. Chem.* **2005**, *690*, 647.

[7] a) G. Albano, P. Belser, C. Dual, *Inorg. Chem.* **2001**, *40*, 1408; b) R. Bhattacharya, R. S. Drago, K. A. Abboud, *Inorg. Chem.* **1997**, *36*, 2913; c) D. J. Chesnut, A. Kusnetzow, R. R. Birgeard, J. Zubieta, *Inorg. Chem.* **1999**, *38*, 2663; d) A. Klein, V. Kasack, R. Reinhardt, S. Torsten, T. Scheiring, S. Zalis, J. Fiedler, W. Kaim, *J. Chem. Soc., Dalton Trans.* **1999**, 575; e) J.-D. Lee, L. M. Vrana, E. R. Bullock, K. J. Brewer, *Inorg. Chem.* **1998**, *37*, 3575; f) C. Ceroni, F. Paolucci, S. Roffia, S. Serroni, S. Campagna, A. J. Bard, *Inorg. Chem.* **1998**, *37*, 2829.

[8] L. J. Farrugia, *J. Appl. Crystallogr.* **1997**, *30*, 565.

[9] a) D. L. Davies, O. Al-Duaij, J. Fawcett, M. Giardiello, S. T. Hilton, D. R. Russell, *Dalton Trans.* **2003**, 4132; b) H. Amouri, C. Guyard-Duhayon, J. Vaissermann, *Inorg. Chem.* **2002**, *41*, 397.

[10] a) T. Scheiring, J. Fiedler, W. Kaim, *Organometallics* **2001**, *20*, 1437; b) H. Aneetha, P. S. Zacharias, B. Srinivas, G. H. Lee, Y. Wong, *Polyhedron* **1999**, *18*, 299.

[11] a) N.-T. Huang, W. T. Pennington, J. D. Peterson, *Acta Crystallogr., Sect. C* **1991**, *47*, 2011; b) A. Escuer, R. Vicente, T. Comas, J. Ribas, M. Gomez, X. Solans, D. Gatteschi, C. Zanchini, *Inorg. Chim. Acta* **1991**, *181*, 51; c) E. Brauns, W. Sumner, J. A. Clark, S. M. Molnar, Y. Kawanishi, K. J. Brewer, *Inorg. Chem.* **1997**, *36*, 2861.

[12] P. Paul, B. Tyagi, A. K. Bilakhia, D. Parthsarthi, M. M. Bhadbhade, E. Suresh, G. Ramchandraiah, *Inorg. Chem.* **1998**, *37*, 5733.

[13] a) P. Gagngopadhyay, T. P. Radhakrishnan, *Angew. Chem. Int. Ed.* **2001**, *40*, 2451; b) J.-M. Lehn, *Supramolecular Chemistry,*

 © 2006 Wiley-VCH Verlag GmbH & Co. KGaA, Weinheim 

*Concept and Prospectives*: VCH: Weinheim, **1995**; c) G. R. Desiraju, *Acc. Chem. Res.* **2002**, *35*, 565; d) H. Suezawa, T. Yoshida, S. Ishihara, Y. Umezawa, M. Nishio, *Cryst. Eng. Comm* **2003**, *5*, 514.

[14] a) X.-D. Chen, T. C. W. Mak, *Dalton Trans.* **2005**, 3646; b) R. Custelcean, M. D. Ward, *Angew. Chem. Int. Ed.* **2002**, *41*, 1724; c) S. K. Ghosh, P. K. Bharadwaj, *Inorg. Chem.* **2004**, *43*, 2293; d) M. J. Hannon, C. L. Pointing, N. W. Alcock, *Chem. Commun.* **1999**, 2023; e) S. R. Halper, S. M. Cohen, *Angew. Chem. Int. Ed.* **2004**, *43*, 2385; f) O.-S. Jung, Y. J. Kim, Y.-A. Lee, J. K. Park, H. K. Chae, *J. Am. Chem. Soc.* **2000**, *122*, 9921; g) L. Yi, X. Yang, T. Lu, P. Cheng, *Cryst. Growth Des.* **2005**, *5*, 1215.

[15] a) D. D. Perrin, W. L. F. Armango, D. R. Perrin, *Purification of Laboratory Chemicals*, Pergamon, Oxford, U. K., **1986**; b) B. L. Booth, R. N. Haszeldine, M. Hill, *J. Chem. Soc. A* **1969**, 1299; c) C. White, A. Yates, P. M. Maitilis, *Inorg. Synth.* **1992**, *29*, 228.

[16] a) S. Mackay, W. Dong, C. Edwards, A. Henderson, C. Gilmox, N. Stewart, K. Shankland, A. Donald, University of Glasgow, Scotland, **1999**; b) G. M. Sheldrick, SHELX-97: *Programme for the solution and refinement of crystal structures*, University of Göttingen: Germany, **1997**; c) A. L. Spek, *Acta Crystallogr., Sect. A* **1990**, *46*, C31.

Received: April 20, 2006
Published Online: August 7, 2006

 © 2006 Wiley-VCH Verlag GmbH & Co. KGaA, Weinheim 

DOI: 10.1002/ejic.200600334

# Syntheses, Structures and Near-IR Luminescent Studies on Ternary Lanthanide ($Er^{III}$, $Ho^{III}$, $Yb^{III}$, $Nd^{III}$) Complexes Containing 4,4,5,5,6,6,6-Heptafluoro-1-(2-thienyl)hexane-1,3-dionate

**Li-Ning Sun,[a,b,c] Jiang-Bo Yu,[a] Guo-Li Zheng,[a,c] Hong-Jie Zhang,*[a] Qing-Guo Meng,[a] Chun-Yun Peng,[a] Lian-She Fu,[a] Feng-Yi Liu,[a] and Ying-Ning Yu[a]**

**Keywords:** Lanthanides / Luminescence / Optical amplification

The ligand Hhfth [4,4,5,5,6,6,6-heptafluoro-1-(2-thienyl)hexane-1,3-dione], which contains a heptafluoropropyl group, has been used to synthesize several new ternary lanthanide complexes (Ln = Er, Ho, Yb, Nd) in which the synergistic ligand is 1,10-phenanthroline (phen) or 2,2′-bipyridine (bipy). The two series of complexes are [Ln(hfth)$_3$phen] [abbreviated as (Ln)**1**, where Ln = Er, Ho, Yb] and [Ln(hfth)$_3$bipy] [abbreviated as (Ln)**2**, where Ln = Er, Ho, Yb, Nd]. Members of the two series have been structurally characterized. The growth morphology, diffuse reflectance (DR) spectra, thermogravimetric analyses, and photophysical studies of these complexes are described in detail. After ligand-mediated excitation of the complexes, they all show the characteristic near-infrared (NIR) luminescence of the corresponding $Ln^{3+}$ ions (Ln = Er, Ho, Yb, Nd). This is attributed to efficient energy transfer from the ligands to the central $Ln^{3+}$ ions, i.e. an antenna effect. The heptafluorinated substituent in the main hfth sensitizer serves to reduce the degree of vibrational quenching. With these NIR-luminescent lanthanide complexes, the luminescent spectral region from 1300 to 1600 nm, which is of particular interest for telecommunication applications, can be covered completely.
(© Wiley-VCH Verlag GmbH & Co. KGaA, 69451 Weinheim, Germany, 2006)

## Introduction

There has been increasing interest in the use of near-infrared (NIR) light, which is one of the best strategies to obtain high-resolution pictures of deep tissues as NIR light diffracts much less than visible light [diffraction is proportional to $1/(\lambda)^{SP}$, SP = scattering power].[1] Recently, the lanthanide ions that are emissive in the NIR region of the spectrum (800–1700 nm), such as $Yb^{III}$, $Nd^{III}$, $Ho^{III}$, and $Er^{III}$, have received much attention. Interest in the photophysical properties of these lanthanide ions mainly stems from the following three points. First, the $Yb^{3+}$ ion emission occurs in the NIR region (approximately 1000 nm) where biological tissues and fluids (e.g. blood) are relatively transparent, thus the development of $Yb^{3+}$ ion luminescence for various analytical and chemosensor applications is promising. Second, Nd-containing systems have been regarded as the most popular infrared luminescent materials for application in laser systems (the basis of the common 1064-nm laser). Third, two telecommunication windows for amplification are commonly used for long-distance communication, one at 1.3 μm using Nd emission and the other at 1.5 μm using Er or Ho emission.[2]

However, the low optical cross-section due to the forbidden nature of the 4f→4f transitions of these NIR-luminescence lanthanide ions results in inefficient direct excitation.[3] Since the discovery that energy transfer from the triplet state of an organic ligand can efficiently sensitize the emissive states of lanthanide ions,[4] there has been considerable effort devoted to designing ligands that optimize this energy transfer and thus give efficient lanthanide luminescence. β-Diketones are most commonly used for the complexation of lanthanide ions. Because of their potential applications, tris- and tetrakis(β-diketonato)lanthanides(III) are the most widely studied complexes of the 4f-element series.[5] In addition, noncharged ligands like 1,10-phenanthroline (phen) or 2,2′-bipyridine (bipy) can serve as the synergistic agent, since an important issue in the design of NIR-emitting lanthanide complexes is to prevent water molecules from binding to the lanthanide ions. Sensitizer-functionalized $Eu^{3+}$ and $Tb^{3+}$ complexes have already been applied as long-lasting luminescent probes in time-resolved fluoroimmunoassays,[6] whereas sensitizer-functionalized complexes of the NIR-emitting lanthanide ions $Er^{3+}$, $Yb^{3+}$, $Nd^{3+}$, and especially $Ho^{3+}$, are less well studied. These com-

[a] Key Laboratory of Rare Earth Chemistry and Physics, Changchun Institute of Applied Chemistry, Chinese Academy of Sciences,
Changchun, 130022, P. R. China
Fax: +86-431-5262127
E-mail: hongjie@ns.ciac.jl.cn
[b] State Key Laboratory of Structural Chemistry, Fujian Institute of Research on the Structure of Matter, Chinese Academy of Sciences,
Fuzhou, 350002, P. R. China
[c] Graduate School of the Chinese Academy of Sciences,
Beijing, P. R. China
Supporting information for this article is available on the WWW under http://www.eurjic.org or from the author.

 © 2006 Wiley-VCH Verlag GmbH & Co. KGaA, Weinheim 

plexes are very promising not only for application in fluoroimmunoassays, but also for use in laser systems and for amplification of light.[2]

It is well established that the NIR-emitting $Ln^{3+}$ ions are particularly prone to vibrational deactivation. Species containing high-energy oscillators, such as C–H and O–H bonds (typically found in the ligand), are able to quench the metal excited states nonradiatively, thereby leading to lower luminescence intensities and shorter excited-state lifetimes. The replacement of C–H bonds with C–F bonds is important in the syntheses of lanthanide complexes with efficient photoemission properties.[5,7] According to the literature reported previously, the replacement of C–H bonds in a β-diketone ligand with lower-energy C–F oscillators is able to lower the vibration energy of the ligand, which decreases the energy loss caused by ligand vibration and enhances the emission intensity of the lanthanide ion.[8] Due to the heavy-atom effect,[7e] which facilitates intersystem crossing, the lanthanide-centered luminescent properties are enhanced.[9] It has been reported that the fluorescence quantum yield of a europium(III) complex increases with more fluorinated alkyl groups on the β-diketonate ligand.[5,8c] More fluorinated β-diketones form more stable ternary complexes with Lewis bases in organic solvents.[7f] In this work, the β-diketone ligand Hhfth [4,4,5,5,6,6,6-heptafluoro-1-(2-thienyl)hexane-1,3-dione], which contains a long perfluoroalkyl chain, is used as the main sensitizer for synthesizing new NIR-emitting lanthanide complexes.

In this context, and in connection with our interest in photoluminescence and electroluminescence,[2a,8a,9,10] we are interested in studying the crystal structures and luminescence properties of lanthanide complexes. Herein, we report the syntheses and structures of new sensitizer-functionalized NIR-luminescence complexes [$Ln(hfth)_3phen$] [abbreviated as (Ln)**1**, where Ln = Er, Ho, Yb] and [$Ln(hfth)_3bipy$] [abbreviated as (Ln)**2**, where Ln = Er, Ho, Yb, Nd], which contain the hfth ligand with a heptafluoropropyl group (see Figure S1, Supporting Information). The properties of these complexes were investigated using diffuse reflectance (DR) spectra and thermogravimetric analyses, and the photophysical properties were studied in detail and compared with those of the [$Ln(hfth)_3(H_2O)_2$] complexes.

## Results and Discussion

### Design and Preparation of Complexes (Ln)1 and (Ln)2

The molar ratio of the lanthanide ion and the β-diketonate investigated was determined to be 1:3 or 1:4. Three possible types of lanthanide complexes can be designed depending on the ratio:[11,12] (1) When the ratio is 1:3, a simple tris(complex) can be obtained with three hfth ligands coordinated to one lanthanide ion. However, the six oxygen atoms from three hfth ligands are not sufficient to complete the coordination number requirement of a lanthanide ion (typically 8 or 9). Thus, the tris(complex) usually contains water or other solvent molecules in the first coordination sphere, which is disadvantageous for obtaining high luminescence intensity. (2) When a metal/ligand ratio of 1:4 is used, the tetrakis(complex) can be obtained. Although the tetrakis(complexes) usually show much higher luminescence intensity, the disadvantage is that a single positively charged counterion is needed to assure the electrical neutrality of the complex. This is problematic in the design of electroluminescent devices for charged species. The above two types leave us with the third option. (3) In addition to a metal/ligand ratio of 1:3, a Lewis base such as phen or bipy is added to give a Lewis base adduct of the tris(complex). The function of phen or bipy is to saturate the coordination sphere of the lanthanide ion and also to absorb excitation energy that can be transferred to the excited states of the lanthanide ion.

It is well known that the positions of the luminescence bands in the spectrum are characteristic for a specific lanthanide ion. This means that the given organic ligands that are capable of coordinating with different lanthanide ions can serve various applications operating at different wavelengths simply by changing the central lanthanide ion (in our case Ln = Er, Ho, Yb, Nd).

### Crystal Structures

The structure of the lanthanide complex is essential to understand the energy transfer from the coordinated ligands to the central lanthanide ion. Therefore, a considerable number of these complexes with various β-diketonates have been structurally characterized by X-ray crystallography since the 1970s. In the present work, the single-crystal X-ray diffraction studies revealed isostructural crystals (orthorhombic, $Z = 8$) for complexes (Ln)**1** and (Ln)**2** whose crystals fall in the same *Pbca* space group. Thus, only the structures of (Er)**1** and (Yb)**2** will be described in detail as examples.

The crystal structure of (Er)**1**, with the numbering scheme, is displayed in Figure 1a. Analysis of the crystal structure indicates that the central $Er^{3+}$ ion is eight-coordinate, with six oxygen atoms from three hfth ligands and two nitrogen atoms from the phen ligand. From the coordination angles, the coordination geometry may be described as a square antiprism, one of the two most stable eight-coordinate polyhedra (shown in Figure 1b). The crystal structure of (Yb)**2** (Figure 2a) is similar. The coordination number of the central $Yb^{3+}$ ion is also eight, with six oxygen atoms from three hfth ligands and two nitrogen atoms from the bipy ligand. The coordination polyhedron can also be regarded as a square antiprism (see Figure 2b). For these two complexes, the Ln–O bonds adjacent to the thienyl ring are slightly longer than the others, which is probably due to the inductive effect of the fluorine atoms on the alkyl chain. In the β-diketone rings of the lanthanide complexes, all of the average distances for the C–C and C–O bonds are shorter than a single bond but longer than a double bond. This can be explained by the fact that there is conjugation between the thienyl ring and the coordinated β-diketonate, which

 © 2006 Wiley-VCH Verlag GmbH & Co. KGaA, Weinheim 

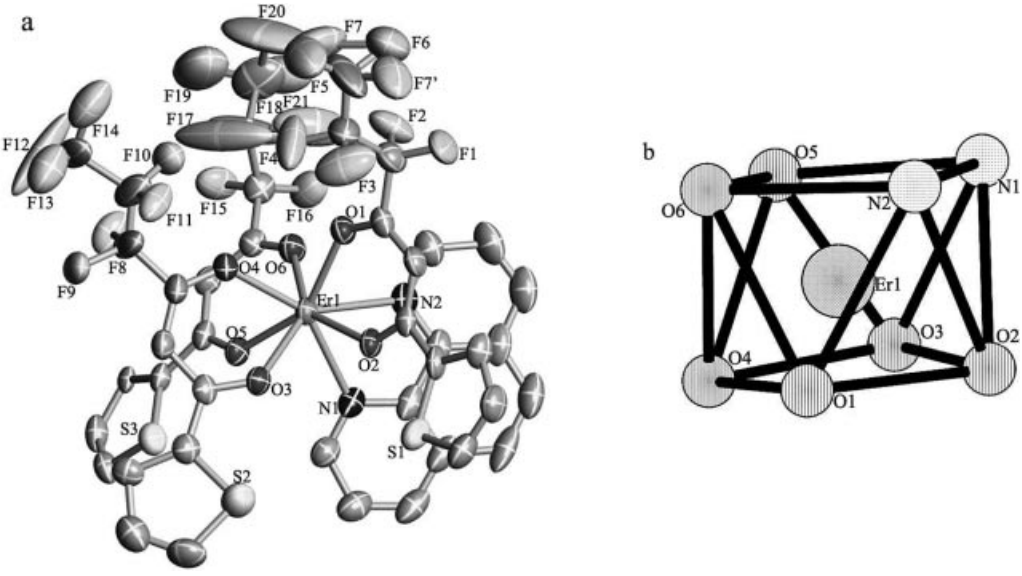


Figure 1. (a) ORTEP plot for (Er)**1** with ellipsoids drawn at the 30% probability level. Hydrogen atoms have been omitted for clarity. (b) Coordination polyhedron of the $Er^{III}$ ion.

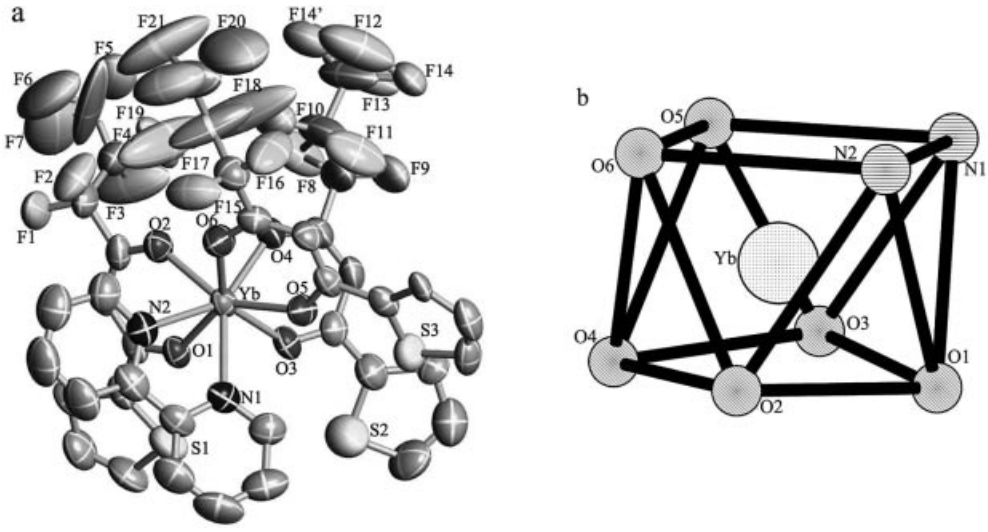


Figure 2. ORTEP plot for (Yb)**2** with ellipsoids drawn at the 30% probability level. Hydrogen atoms have been omitted for clarity.

leads to the delocalization of electron density of the coordinated β-diketonate chelate ring. However, the C–C bond lengths near the fluorine atoms are close to that of a C=C bond, which is due to the inductive effect of the fluorine atoms.[13] The central $Ln^{3+}$ ion is completely surrounded by the bulky anionic ligand hfth and the synergistic ligands phen [for (Ln)**1**] or bipy [for (Ln)**2**], and this encapsulated structure therefore meets the structural requirements of a lanthanide luminescent sensor[14] by protecting the metal ion from vibrational coupling and increasing the light absorption cross-section by the "antenna effect".

The average Ln–O and Ln–N bond lengths in the crystals are shown in Table 1, where it can be seen that the average Ln–O and Ln–N bond lengths decrease from Ho to Yb [for (Ln)**1**] and from Nd to Yb [for (Ln)**2**] due to the so-called "lanthanide contraction". It can also be seen that the cell volume contracts by about 3.81% for (Ln)**1** when the lanthanide ion changes from Ho to Yb and about 1.58% for (Ln)**2** when the lanthanide ion changes from Nd to Yb.

Table 1. Average Ln–O and Ln–N bond lengths [Å] for (Ln)**1** and (Ln)**2**.

| | (Ho)**1** | (Er)**1** | (Yb)**1** | (Nd)**2** | (Ho)**2** | (Yb)**2** |
|---|---|---|---|---|---|---|
| Ln–O | 2.310 | 2.296 | 2.276 | 2.393 | 2.311 | 2.279 |
| Ln–N | 2.551 | 2.520 | 2.501 | 2.633 | 2.532 | 2.492 |

## Observed Growth Morphology

Of the single crystals obtained, all the (Ln)**1** crystals show a regular, diamond-like shape whereas the shape of the (Ln)**2** crystals is irregular. We are not sure about the

 © 2006 Wiley-VCH Verlag GmbH & Co. KGaA, Weinheim 

reason for this phenomenon, although we think that it may be due to the different molecular structures of phen and bipy. All atoms of the phen molecule are in the same conjugate area, yet those of the bipy molecule are not. Microscope pictures of a single crystal of (Er)**1** with a diamond shape are shown in Figure 3 to illustrate the growth morphology that is representative for crystals of (Ln)**1** but not for those of (Ln)**2**. A schematic sketch of each crystal selected is shown in Figure 3 (right), which reveals the growth habit of the crystals.

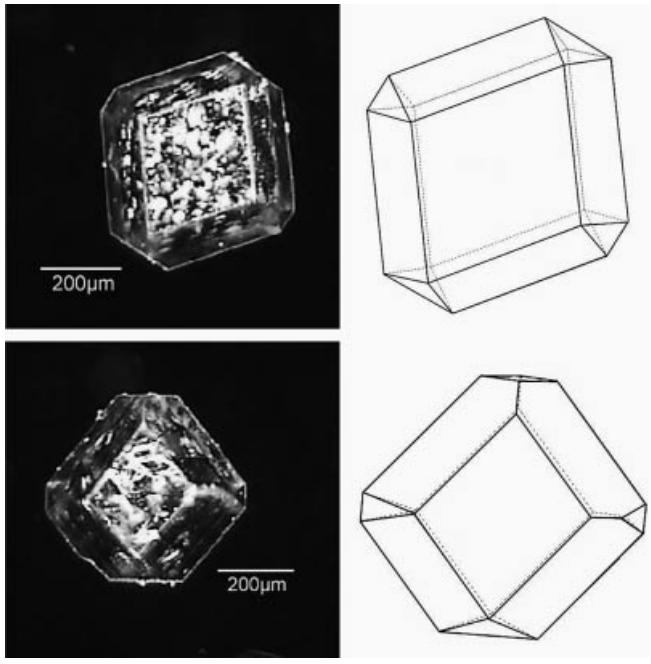


Figure 3. Microscope images and corresponding sketches of the (Er)**1** crystals grown from the ethanol/acetone mother liquor.

## DR Spectra

The DR Spectra of (Ln)**1** and (Ln)**2** (Ln = Er, Ho, Yb, Nd) are shown in Figure 4. In the UV region of the DR curves (200–400 nm), all broad absorption bands are observed and can be assigned to electronic transitions from the ground-state level $S_0$ to the excited level $S_1$ of the organic ligands. In the region above 400 nm in these figures, each absorption band corresponds to a characteristic transition between two spin-orbit coupling levels of the lanthanide ion (see the insets of Figure 4). Based on the energy level scheme of each ion, these bands can be assigned to the transitions from the ground levels $^4I_{15/2}$, $^5I_8$, $^2F_{7/2}$, and $^4I_{9/2}$ to the higher energy levels for the erbium, holmium, ytterbium, and neodymium complexes, respectively.[15–17]

## Photophysical Properties

In 1942, Weissman reported that lanthanide luminescence can be improved by using an intramolecular energy transfer, the so-called "antenna effect".[4a] Because the intraconfigurational f↔f transitions are forbidden, absorption of the lanthanide(III) is very weak. In most cases, one can use the excitation of strongly absorbing ligands followed by energy transfer to promote the lanthanide ion to the emitting state.[18] Each of the lanthanide ions used in the course of this work is known to exhibit one or more spectral emission bands in the 800–1700 nm region. Thus, to provide a clear understanding of the photophysics and luminescence properties of these new series of lanthanide complexes, the excitation and emission spectra of each complex as well as the absorption spectra of the ligands were characterized and discussed in detail.

The excitation spectra of (Ln)**1** and (Ln)**2** (Ln = Er, Ho, Yb, Nd) and the absorption spectra of the ligands (phen,[2a] Hhfth, and bipy) were obtained (Figure S2, Supporting Information). As is clearly visible in this figure, there are overlaps between the excitation band of each lanthanide complex and the absorption bands of Hhfth and phen (or Hhfth and bipy), which indicates the typical sensitization of the $Ln^{3+}$ ions by the two organic ligands[19] and thus confirms that the $Ln^{3+}$ ions are surrounded by hfth and phen (or hfth and bipy) in the complexes.[3a,20] It is also worth noting that the overlap between the absorption band of Hhfth and the lanthanide excitation band is larger than that between the absorption band of phen (or bipy) and the excitation band, which suggests that the antenna effect of the hfth ligand is more efficient than that of the synergistic ligand (phen or bipy). Thus, it is reasonable to deduce that the intramolecular energy transfer in the lanthanide complexes mainly occurs between the hfth ligand and the $Ln^{3+}$ ions.[13]

The emission studies were carried out in the NIR region on all of these complexes upon excitation of the ligand absorption bands, followed by NIR emission for the $Er^{3+}$, $Ho^{3+}$, $Yb^{3+}$, and $Nd^{3+}$ complexes where the synergistic ligand is phen or bipy. Using identical experimental settings (slit width, integration time, excitation wavelength, sampling interval), the direct comparison of the emission intensity of the NIR luminescence for the same lanthanide ion with different synergistic ligands was investigated.

### *Erbium*

As is shown in Figure S2, the excitation spectra of the (Er)**1** and (Er)**2** complexes were obtained by monitoring the characteristic emission of the $Er^{3+}$ ion at 1541 nm. In the excitation spectra, a broad band ranging from 260 to 435 nm for (Er)**1** and a broad band from 235 to 430 nm for the (Er)**2** complex are observed. The two broad bands can be assigned to the absorption of the organic ligands, which is in agreement with the DR spectra mentioned above (Figure 4a). Some small bands, originating from f–f absorption transitions of the $Er^{3+}$ ion, are also observed in the excitation spectra of the two complexes. They correspond to the energy transitions $^4I_{15/2}\rightarrow{}^4F_{7/2}$ [492 nm for (Er)**1** and 486 nm for (Er)**2**] and $^4I_{15/2}\rightarrow{}^2H_{11/2}$ [528 nm for (Er)**1** and 524 nm for (Er)**2**], which is also in agreement with the DR spectra (Figure 4a).

Excitation of the ligand absorption bands at 397 nm resulted in the emission spectra (Figure 5) of the two Er complexes. For (Er)**1** and (Er)**2**, the emission bands cover large

 © 2006 Wiley-VCH Verlag GmbH & Co. KGaA, Weinheim 

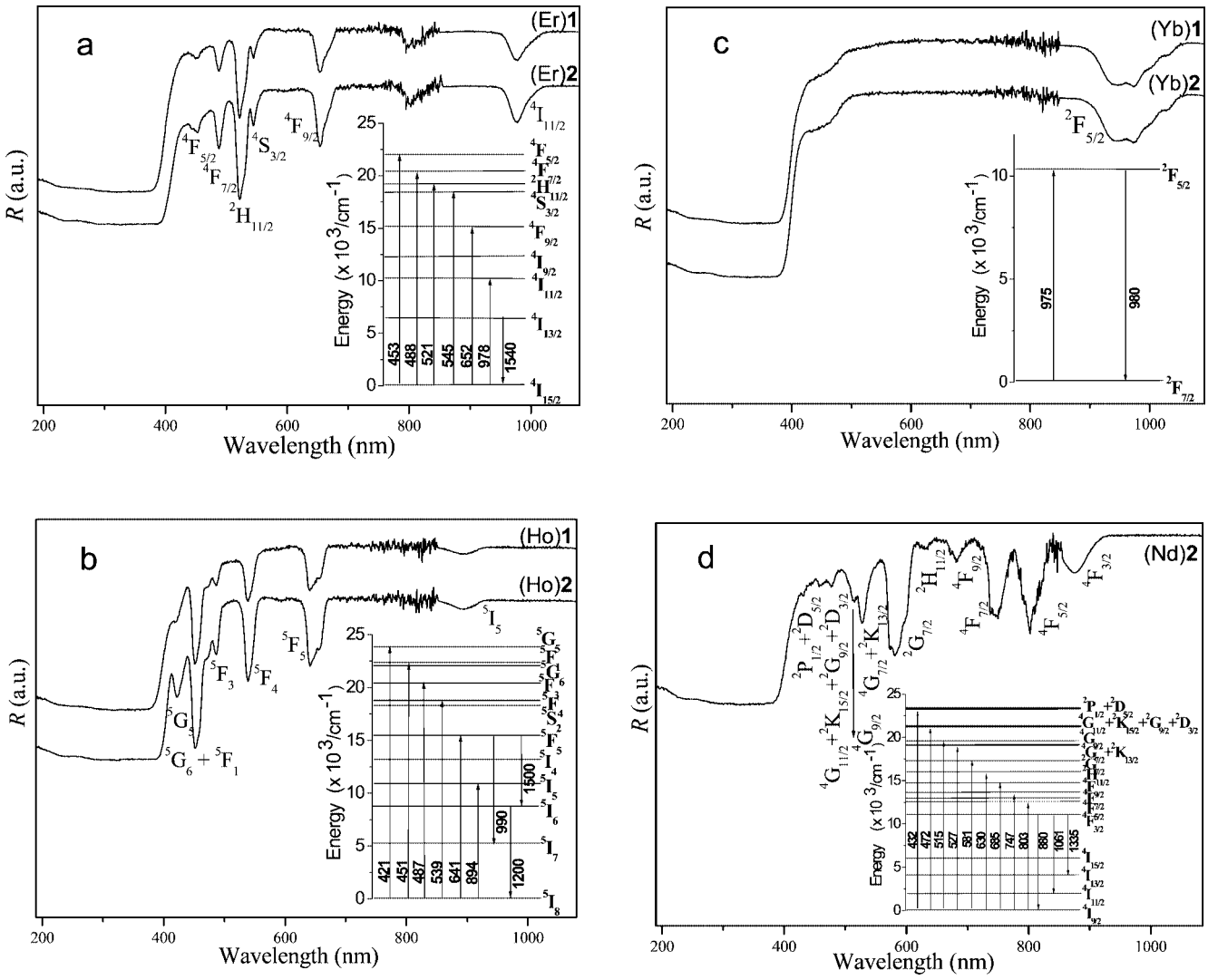


Figure 4. DR spectra of (Er)**1** and (Er)**2** (a), (Ho)**1** and (Ho)**2** (b), (Yb)**1** and (Yb)**2** (c), and (Nd)**2** (d). The insets show the energy level diagrams of $Er^{3+}$, $Ho^{3+}$, $Yb^{3+}$, and $Nd^{3+}$. The transitions of the bands [nm] are indicated by arrows.

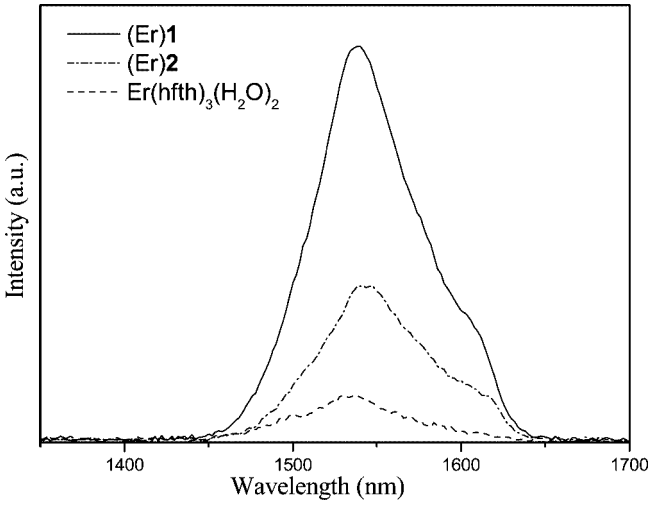


Figure 5. Emission spectra ($\lambda_{ex}$ = 397 nm) of (Er)**1**, (Er)**2**, and $[Er(hfth)_3(H_2O)_2]$ (in the solid state as powder) at room temperature.

spectrum ranges extending from 1414 to 1664 nm and from 1448 to 1656 nm, respectively, with the emission maxima both located at 1540 nm. The emission obtained is attributed to the transition from the first excited state ($^4I_{13/2}$) to the ground state ($^4I_{15/2}$) of the partially filled 4f shell of the $Er^{3+}$ ion (see the inset of Figure 4a). The erbium complexes are especially interesting for application in optical amplification because the transition around 1540 nm is in the right position for the third telecommunication window. To enable a wide-gain bandwidth for optical amplification, a broad emission band is desirable.[2d,21] The full widths at half maximum (FWHM) of the $^4I_{13/2} \rightarrow {}^4I_{15/2}$ transition for the (Er)**1** and (Er)**2** complexes are 76 and 74 nm, respectively, which enable a wide-gain bandwidth for optical amplification.[22]

### *Holmium*

In the excitation spectra of (Ho)**1** and (Ho)**2** (Figure S2), the broad excitation bands in the UV region are both observed, which can be attributed to the absorption of the

 © 2006 Wiley-VCH Verlag GmbH & Co. KGaA, Weinheim 

ligands. The excitation edge of the ligands overlaps some absorption bands corresponding to the characteristic transitions of the $Ho^{3+}$ ion. These f–f transitions correspond to $^5I_8 \rightarrow {}^5G_4 + {}^3F_7$ (389 nm), $^5I_8 \rightarrow {}^5G_5$ (421 nm), $^5I_8 \rightarrow {}^5G_6 + {}^5F_1$ (453 nm), and $^5I_8 \rightarrow {}^5F_3$ (488 nm), which are in agreement with those of the DR spectra discussed above (Figure 4b).

Of importance is the observation of less frequently investigated NIR luminescence in holmium complexes.[1b,2e,23] The emission spectra of (Ho)**1** and (Ho)**2**, after ligand-mediated excitation at 397 nm, are shown in Figure 6. Both luminescence spectra consist of three bands at 990, 1200, and 1500 nm, which are attributed to the $^5F_5 \rightarrow {}^5I_7$, $^5I_6 \rightarrow {}^5I_8$, and $^5F_5 \rightarrow {}^5I_6$ transitions, respectively. For (Ho)**1** and (Ho)**2**, the intensity sequence of the bands is $I(^5F_5 \rightarrow {}^5I_7) > I(^5F_5 \rightarrow {}^5I_6) > I(^5I_6 \rightarrow {}^5I_8)$. As is shown in the energy diagram of the $Ho^{3+}$ ion (inset of Figure 4b), the $^5I_7 \rightarrow {}^5I_8$ transition (>1900 nm) exceeds the measurement range of our detector. Since the optimum energy difference favors efficient ligand-to-ion energy transfer, it is supposed that the $^5F_4$, $^5S_2$, and $^5F_5$ levels are the main acceptor levels, and the excited electrons on the $^5F_5$ and $^5I_6$ levels could partially come from the relaxation of the upper levels followed by the transitions to the lower levels to give the NIR emission of the $Ho^{3+}$ ion.[2e] Among these obtained NIR emissions, the 1500-nm emission is particularly attractive for its good agreement with the efficient working window of a quartz fiber. For the (Ho)**1** complex, the 1500-nm emission, which covers from 1420 to 1550 nm, may be due to the Stark splitting of the $^5F_5$ and $^5I_6$ levels, providing a satisfying waveband for the wavelength division multiplexing technology in optical communications.[2e] The FWHM of this emission is 62 nm, which is a broad bandwidth for the potential application of the optical communication systems.

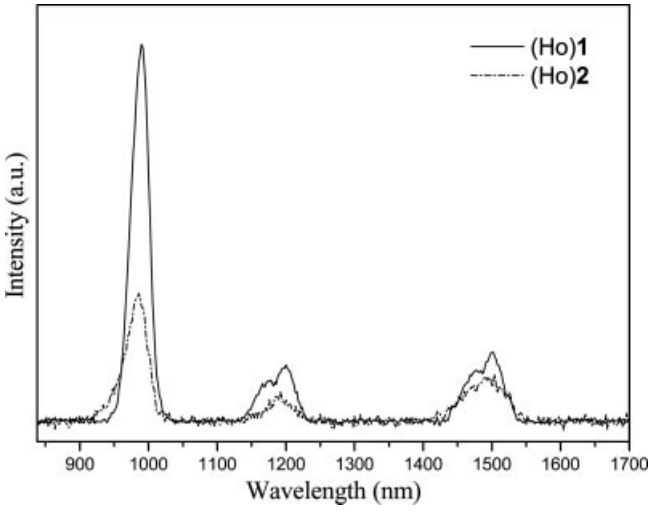


Figure 6. Emission spectra ($\lambda_{ex}$ = 397 nm) of (Ho)**1** and (Ho)**2** (in the solid state as powder) at room temperature.

### *Ytterbium*

The excitation spectra of (Yb)**1** and (Yb)**2** were obtained by monitoring the characteristic emission of the $Yb^{3+}$ ion at 980 nm (Figure S2). The excitation spectra are dominated by a broad band ranging from 200 to 500 nm for both complexes. These two broad bands can be assigned to the absorption of the organic ligands and are in agreement with those in the DR spectra (Figure 4c). The emission spectra of the two complexes (Figure 7), after ligand-mediated excitation at 397 nm, clearly show the characteristic emission bands of the $Yb^{3+}$ ion at 980 nm, which are assigned to the $^2F_{5/2} \rightarrow {}^2F_{7/2}$ transition. It should be noted that the $Yb^{3+}$ ion emission in the two complexes is not a single sharp band but an envelope of bands arising at the lower energy side (1009 and 1038 nm) of the primary 980-nm emission band. A similar splitting has been reported previously.[24–26] According to the literature, these bands arise from the $M_J$ splitting of the emitting and/or fundamental state as a consequence of ligand-field effects.[26]

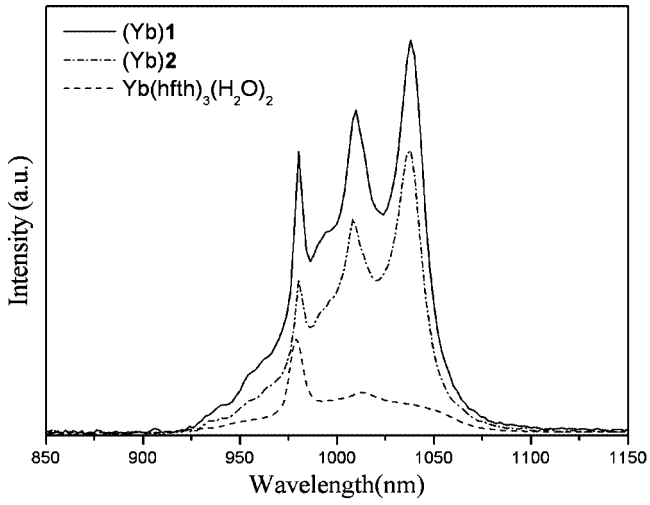


Figure 7. Emission spectra ($\lambda_{ex}$ = 397 nm) of (Yb)**1**, (Yb)**2**, and $[Yb(hfth)_3(H_2O)_2]$ (in the solid state as powder) at room temperature.

The $Yb^{3+}$ ion plays an important role in laser emission because of its very simple f–f energy level structure: besides the $^2F_{7/2}$ ground multiplet, there is only the $^2F_{5/2}$ excited multiplet at around 10000 $cm^{-1}$. There is no excited-state absorption on reducing the effective laser cross-section, no up-conversion, no concentration quenching, and no absorption in the visible range. The intense $Yb^{3+}$ ion absorption lines are well suited for laser diode pumping in this range and the smaller Stokes shift (about 650 $cm^{-1}$) between absorption and emission reduces the thermal loading of the material during laser operation.[27] These properties of the $Yb^{3+}$ ion and the obtained high intensity emission make these Yb complexes very important for various photonic applications in ionic crystals and glasses.[28] In addition, the relative transparency of human tissue at approximately 1000 nm suggests that in vivo luminescent probes operating at this wavelength (Yb-based emission) could have diagnostic value.[29]

### *Neodymium*

In the excitation spectrum of (Nd)**2** ($\lambda_{em}$ = 1061 nm), a broad band ranging from 260 to 498 nm due to the absorp-

 © 2006 Wiley-VCH Verlag GmbH & Co. KGaA, Weinheim 

tion of the organic ligands superimposed with some excitation bands originating from the characteristic absorption transition of the $Nd^{3+}$ ion is observed (Figure S2). These f–f transitions correspond to $^4I_{9/2}\rightarrow{}^2P_{1/2} + {}^2D_{5/2}$ (432 nm), $^4I_{9/2}\rightarrow{}^4G_{11/2} + {}^2K_{15/2} + {}^2G_{9/2} + {}^2D_{3/2}$ (474 nm), $^4I_{9/2}\rightarrow{}^4G_{9/2}$ (515 nm), and $^4I_{9/2}\rightarrow{}^2K_{13/2} + {}^4G_{7/2}$ (529 nm) of the $Nd^{3+}$ ion, which are well in agreement with those of the DR spectrum (Figure 4d). It should be noted that these absorption transitions are much weaker than that of the ligands, which proves that luminescence sensitization by excitation of the ligands is much more efficient than direct excitation of the absorption levels of the $Nd^{3+}$ ion.

The excitation of the Nd complex by strongly absorbing ligands ($\lambda_{ex}$ = 397 nm) is quite feasible, as expected based on the energy level of the triplet state, which is higher than the Nd luminescent excited state $^4F_{3/2}$ (11527 $cm^{-1}$). The emission spectrum of the Nd complex (Figure 8) consists of three bands at $\lambda$ = 880, 1061, and 1335 nm, which are attributed to the f–f transitions $^4F_{3/2}\rightarrow{}^4I_{9/2}$, $^4F_{3/2}\rightarrow{}^4I_{11/2}$, and $^4F_{3/2}\rightarrow{}^4I_{13/2}$, respectively. Some crystal-field fine structure can be observed, which is an indication that the $Nd^{3+}$ ion occupies well-defined crystallographic sites in the complex.[23] Among the three emission bands of the Nd complex, the intensity of the transition at 1061 nm is the strongest and is potentially applicable for laser emission. The fine structure of the 1335-nm band of the complex offers the opportunity to develop new materials suitable for optical amplifiers operating at 1.3 μm.[30]

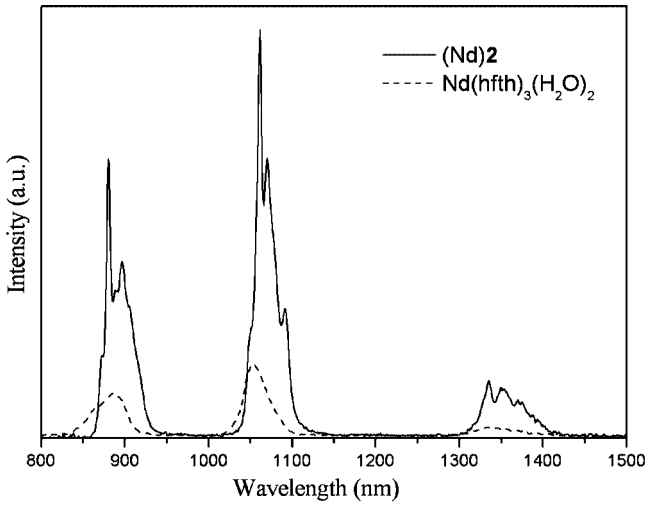


Figure 8. Emission spectra ($\lambda_{ex}$ = 397 nm) of (Nd)**2** and [Nd(hfth)$_3$(H$_2$O)$_2$] (in solid state as powder) at room temperature.

Upon excitation of the ligand absorption band (397 nm), these lanthanide complexes all show the characteristic NIR luminescence of $Ln^{3+}$ ions. The NIR luminescence obtained in this study shows that the ligands shield the lanthanide ions well from their surroundings and transfer energy from their triplet states to the $Ln^{3+}$ ions efficiently.[31–34] Because no direct excitation of the lanthanide moiety occurs at the excitation wavelength (397 nm), the observed NIR emission signals only arise by sensitization of the lanthanide ions by the ligands.

Many authors have reported the influence of water on the intensity of $Eu^{III}$ luminescence.[35] In fact, the NIR luminescence is even more sensitive to water than the visible luminescence. As shown in Figures 5, 7, and 8, respectively, an obvious decrease of the NIR-emission intensity for [Ln(hfth)$_3$(H$_2$O)$_2$] (Ln = Er, Yb, Nd) is detected when compared to the intensity of the corresponding (Ln)**1** or (Ln)**2** complex. This is probably related to the replacement of solvent molecules (ethanol or water) by phen or bipy in the $Ln^{III}$ coordination sphere, which could depress nonradiative deactivation pathways through vibrational quenching.[36] These results suggest that the introduction of a second ligand instead of water molecules is able to increase the efficiency of energy transfer from the ligands to the central metal ions, thus resulting in an improvement in the emission intensity. In the meantime, it is worth noting that the relative emission intensity of (Ln)**1** is stronger than that of (Ln)**2** (Ln = Er, Ho, Yb). Basically, in the lanthanide complexes the ligands may sensitize the $Ln^{3+}$ ion by energy transfer, and the probability of energy transfer is strongly influenced by the energy difference between the energy donor and acceptor.[37] The triplet-state energy level of bipy was measured and calculated to be 23095 $cm^{-1}$ from the shortest-wavelength phosphorescence band of the phosphorescence spectrum for [Gd(bipy)$_3$Cl$_2$] (Figure S3, Supporting Information), in which the fine-structure is observed. We have measured the triplet energy states of the phen[38] and Hhfth[10c] ligands to be 22173 and 20400 $cm^{-1}$, respectively. So, the energy difference between the phen ligand and the Hhfth ligand is smaller than that between the bipy ligand and the Hhfth ligand. The phen ligand may transfer energy to hfth more efficiently and accordingly afford a stronger sensitization of the $Ln^{3+}$ ion emission.[35a,39] In addition, all the C and N atoms of the phen molecule are located in the same conjugate area, yet those of the bipy molecule are not. It is therefore concluded that the presence of a rigid planar structure in the complex causes a higher intensity of the sensitized luminescence because such a structure allows a better energy transfer.[5] Therefore, the combination of phen and hfth ligands may sensitize the $Ln^{3+}$ ion more efficiently, followed by the stronger NIR luminescence of the $Ln^{3+}$ ion.

The luminescence decay curves obtained from time-resolved luminescence experiments could be fitted monoexponentially, thus confirming that the chemical environment of the $Ln^{3+}$ ion is uniform in the materials.[20,40] The corresponding lifetimes of the lanthanide excited states are shown in Table 2. Due to the weakness of the signal and the limitations of our equipment, no reliable decay time could be measured for the Ho complexes. The quantum yields of the lanthanide-centered luminescence in these complexes were determined by taking [Yb(tta)$_3$phen] (tta = thenoyltrifluoroacetonate) as standard. The quantum yields ($Q$) of these complex samples (S) were calculated by using the following equation,[24c,41] where $n$ is the refractive index

 © 2006 Wiley-VCH Verlag GmbH & Co. KGaA, Weinheim 

of the solvent, $I$ is the wavelength-integrated area of the corrected emission spectrum, and $A$ is the absorbance value at the excitation wavelength.

$$Q_S = \frac{n_S^2 I_S A_R}{n_R^2 A_S I_R} Q_R$$

Table 2. Emission properties for the different NIR-emitting lanthanide complexes.

| Complex | Transition | $\lambda_{em}$ [nm] | $\tau$ [μs][a] | $Q_S$ [%][b] |
|---|---|---|---|---|
| (Er)**1** | $^4I_{13/2}\rightarrow{}^4I_{15/2}$ | 1541 | 2.73 | 0.019 |
| (Er)**2** | $^4I_{13/2}\rightarrow{}^4I_{15/2}$ | 1541 | 2.27 | 0.014 |
| (Yb)**1** | $^2F_{5/2}\rightarrow{}^2F_{7/2}$ | 980 | 14.7 | 1.28 |
| (Yb)**2** | $^2F_{5/2}\rightarrow{}^2F_{7/2}$ | 980 | 13.8 | 1.24 |
| $Yb(hfth)_3(H_2O)_2$ | $^2F_{5/2}\rightarrow{}^2F_{7/2}$ | 980 | 0.97 | 0.37 |
| (Nd)**2** | $^4F_{3/2}\rightarrow{}^4I_{11/2}$ | 1061 | 1.27 | 0.072 |
| $Nd(hfth)_3(H_2O)_2$ | $^4F_{3/2}\rightarrow{}^4I_{11/2}$ | 1065 | 0.15 | 0.0085 |

[a] Luminescence lifetimes in the solid state. [b] Quantum yields of the solution of these complexes in toluene. The excitation wavelength is 355 nm.

The quantum yield of the reference (R), [Yb(tta)$_3$phen] in toluene solution ($n$ = 1.4964), was taken as $Q_R$ = 1.1%.[42] Then, the quantum yields of the solution of these complexes in toluene were obtained (Table 2). It can be seen that the quantum yields of these complexes in toluene increase in the order (Ln)**1** > (Ln)**2**, which agrees well with the corresponding lengthening of the emission lifetime. This correlation further shows that the combination of hfth and phen ligands may sensitize the $Ln^{3+}$ ion more efficiently than the combination of hfth and bipy ligands. It should also be noted that the emission lifetimes and quantum yields for the Yb and Nd complexes investigated are considerably longer than those of the corresponding [Ln(hfth)$_3$(H$_2$O)$_2$] complexes, probably because the two water ligands (containing four potentially quenching O–H oscillators) have been replaced by phen or bipy, in which most of the C–H oscillators are remote from the metal center.

The luminescence lifetimes and quantum yield values obtained are in line with, or a little higher than, other recently published results on NIR-luminescent lanthanide complexes.[36,42,43] High-frequency oscillators, such as C–H vibrations in the ligand, can provide a very efficient nonradiative pathway for relaxation of the luminescent state of the NIR-emitting lanthanide ions by vibronic coupling, since it can be effectively mediated by the ubiquitous molecular vibrations. It would appear that the heptafluorinated substituent in the main sensitizer hfth serves to reduce the degree of vibrational quenching, which, in turn, probably leads to a slightly longer lived $Ln^{3+}$ ion excited state. There still exists one C–H bond in the β-diketonate chelate ring of the complex, however, and this results in the main nonradiative factor. Suppression of such vibrational excitation in the system requires deuteration of the C–H bonds or replacement of C–H bonds with C–F bonds in the ligand.[7g] In addition, improvement of the spectral overlap of the NIR-emitting $Ln^{3+}$ ion and the antenna and optimization of the luminescence quantum yield could be achieved by incorporating antenna chromophores with lower lying triplet states. This ligand feature is particularly important in the design of NIR-emitting lanthanide complexes.

### Thermogravimetric Analyses

The TGA-DTA analyses of all the (Ln)**1** and (Ln)**2** complexes were carried out. The TGA diagrams of (Ln)**1** and (Ln)**2** are similar, and all reveal two main weight losses. (Yb)**1** and (Nd)**2** are given as examples in Figure 9. For (Yb)**1**, the analysis show that the melting point is 207.04 °C. The first weight loss of 74.02% is close to the calculated value (73.23%) corresponding to the loss of the hfth ligands and the second weight loss of 12.57% corresponds to the loss of the phen ligand (calculated: 13.65%). For (Nd)**2**, the analysis displays a first weight loss of 74.22% corresponding to the loss of hfth ligands (calculated: 76.23%) and a second weight loss of 12.23% corresponding to the loss of the bipy ligand (calculated: 12.33%). The final residues for (Yb)**1** and (Nd)**2** are composed of $Yb_2O_3$ and $Nd_2O_3$, respectively. The analyses show that the melting points of the (Ln)**1** and (Ln)**2** complexes are between 200 and 215 °C, and the decomposition temperatures are higher than 350 °C. These results suggest that these complexes have good thermal stability. This may be due to the heptafluorinated substituent in the ligand, as we and other authors have reported that a fluorinated substituent in a ligand leads to an improved thermal and oxidative stability and increases

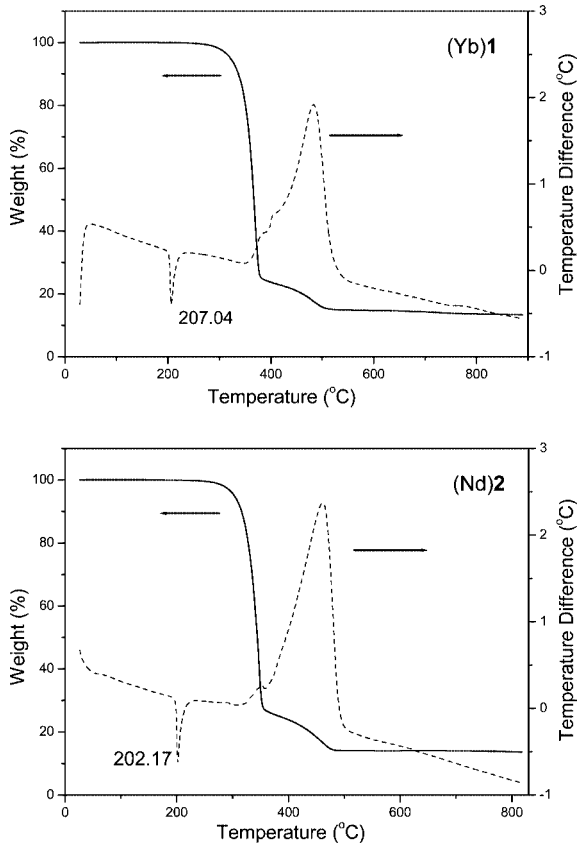


Figure 9. TGA (−) and DTA (---) curves of (Yb)**1** and (Nd)**2**.

 © 2006 Wiley-VCH Verlag GmbH & Co. KGaA, Weinheim 

the volatility of the complex.[9,10c,44] The improved thermal stability and volatility result in good film-forming ability, which facilitates the fabrication of electroluminescent devices.

## Conclusions

Based on the ligand hfth, seven new ternary lanthanide complexes (Ln)**1** (Ln = Er, Ho, Yb) and (Ln)**2** (Ln = Er, Ho, Yb, Nd) have been synthesized. Their single-crystal X-ray diffraction analyses [except (Er)**2**], growth morphology, DR spectra, optical properties, and TGA-DTA analyses have been reported. We have demonstrated the characteristic NIR luminescence of the corresponding lanthanide complexes upon excitation of the ligand absorption bands, mediated by the sensitizing effect of the ligands in the complexes, known as the antenna effect. The broadband emission at 1540 nm for the Er complexes, 1500 nm for the Ho complexes, and the fine structure at 1335 nm for the Nd complex offer the opportunities to develop new materials suitable for optical amplifiers operating at 1.5 and 1.3 μm, the two telecommunications windows. The heptafluorinated substituent in the main sensitizer hfth serves to reduce the degree of vibrational quenching. In addition, improvement of the spectral overlap of the NIR-emitting $Ln^{3+}$ ion and the antenna and optimization of the luminescence quantum yield could be achieved by incorporating antenna chromophores with lower lying triplet states. This ligand feature is particularly important in the design of NIR-emitting lanthanide complexes and further work is in process. Furthermore, the above results are pertinent to the application of these complexes in NIR electroluminescent devices. In ongoing work, we are exploring the properties of electroluminescent devices fabricated using these lanthanide complexes as the active materials.

## Experimental Section

**Materials:** Ytterbium oxide ($Yb_2O_3$, 99.99%), neodymium oxide ($Nd_2O_3$, 99.99%), holmium oxide ($Ho_2O_3$, 99.99%), erbium oxide ($Er_2O_3$, 99.99%), and gadolinium oxide ($Gd_2O_3$, 99.99%) were purchased from Yue Long Chemical Plant (Shanghai, China). Sodium metal (≥98%, A. R.), 1,10-phenanthroline monohydrate (phen·$H_2O$, 99%, A. R.), and 2,2′-bipyridine (≥99.5%, A. R.) were bought from Beijing Fine Chemical Co. (Beijing, China). Hhfth was purchased from Acros Organics Co. (Geel, Belgium) and Htta (2-thenoyltrifluoroacetone) from Aldrich. All these reagents were used directly without further purification. The toluene solvent was dried by a standard procedure (with Na/benzophenone), distilled under nitrogen, and kept over molecular sieves. The $LnCl_3$ (Ln = Er, Ho, Yb, Nd, Gd) ethanol solution was prepared as follows: the rare earth oxide ($Ln_2O_3$) was dissolved in concentrated hydrochloric acid (HCl) and the surplus HCl was removed by evaporation. The residue was diluted with anhydrous ethanol. The concentration of the rare earth ion was measured by titration with a standard EDTA (ethylenediaminetetraacetic acid) aqueous solution.

**Instrumentation:** The CHN elemental analyses were carried out with a VarioEL analyzer. The DR measurements were performed with a Hitachi U-4100 spectrophotometer. The UV/Vis absorption spectra (solutions of Hhfth and bipy in ethanol; solutions of the investigated complexes in toluene) were recorded with a TU-1901 spectrophotometer. The excitation and emission spectra were measured with an Edinburgh Analytical Instruments FLS920 equipped with a laser diode (LD) from the PicoQuant Company as the light source. The time-resolved measurements for the Yb and Nd complexes were performed with an Edinburgh Analytical Instruments FLS920 equipped with a 397-nm picosecond laser diode (LD) from the PicoQuant Company and for Er complexes with an Edinburgh Combined Fluorescence Lifetime and Steady State Spectrometer FLS920 equipped with a μF900 lamp ($\lambda_{ex}$ = 397 nm). Freshly collected (Er)**1** crystals were mounted on the glass and were observed and recorded with an infrared microscope (HYPERION 3000) from German Bruker Company. All measurements were performed at room temp. The low-temperature phosphorescence spectrum of the $Gd^{3+}$ complex was measured with a Hitachi F-4500 spectrophotometer at liquid nitrogen temperature (77 K). The TGA-DTA analyses were measured with an SDT 2960 Simultaneous DSC-TGA of American TA Instruments, with a heating rate of 10 °C min$^{-1}$.

**Synthesis of the (Ln)1 Complexes (Ln = Er, Ho, Yb):** Hhfth (190 μL, 0.9 mmol) and phen·$H_2O$ (0.0595 g, 0.3 mmol) were dissolved in a suitable volume of anhydrous ethanol. Then, an appropriate amount of 1.0 M sodium hydroxide solution was added dropwise to the solution to adjust the pH value to approximately 7. $LnCl_3$ ethanol solution (0.3 mmol), prepared separately, was then added dropwise to this mixture with stirring. The mixture was heated to reflux and kept at 78 °C for 6 h, and then cooled to the room temperature. The precipitates were collected by filtration, washed with water and ethanol, and dried at 70 °C under vacuum overnight. The lanthanide complex was recrystallized from an ethanol/acetone mixture. Pink (for erbium), pale-yellow (for ytterbium), or yellow crystals (for holmium) suitable for X-ray single-crystal structural determination were grown from the mother liquor at room temp.

**Synthesis of the (Ln)2 Complexes (Ln = Er, Ho, Yb, Nd):** The procedure used to prepare the (Ln)**2** was the same as that used for the (Ln)**1** complex expect that bipy (0.0469 g, 0.3 mmol) was dissolved in anhydrous ethanol instead of phen·$H_2O$ (0.0595 g, 0.3 mmol). The (Ln)**2** complex obtained was also recrystallized from an ethanol/acetone mixture. Lilac (for neodymium), pale-yellow (for ytterbium), or yellow crystals (for holmium) suitable for X-ray single-crystal structural determination were grown from the mother liquor at room temp. The purity of the compounds was verified by CHN elemental analysis (Table S1, Supporting Information).

**Synthesis of the [Ln(hfth)$_3$(H$_2$O)$_2$] Complexes (Ln = Er, Ho, Yb, Nd):** An appropriate amount of 1.0 M sodium hydroxide solution was added dropwise to an Hhfth (190 μL, 0.9 mmol) ethanol solution whilst stirring to adjust the pH value to approximately 7. The $LnCl_3$ ethanol solution (0.3 mmol) was added dropwise to this mixture with stirring. Then, an appropriate amount of water was added and the mixture was heated to reflux and kept at 60 °C for 6 h. The rest of the procedure was similar to that used for the (Ln)**1** complex. All complexes were found to be dihydrates.

**Synthesis of [Gd(bipy)$_3$Cl$_2$]:** At room temperature, 1.5 mmol of bipy was dissolved in a suitable volume of anhydrous ethanol. Then, 0.5 mmol of a $GdCl_3$ ethanol solution was added whilst stirring and the solution was heated under reflux for 2 h. The white powder was filtered and washed with ethanol. The resulting complex was dried at 60 °C under vacuum overnight.

**Synthesis of [Yb(tta)$_3$phen]:** This complex was synthesized according to a published method.[45]

 © 2006 Wiley-VCH Verlag GmbH & Co. KGaA, Weinheim 

Table 3. Crystal data and structure refinement for (Ln)**1** and (Ln)**2** [except (Er)**2**].

| | (Ho)**1** | (Er)**1** | (Yb)**1** | (Nd)**2** | (Ho)**2** | (Yb)**2** |
|---|---|---|---|---|---|---|
| Empirical formula | $C_{42}H_{20}F_{21}HoN_2O_6S_3$ | $C_{42}H_{20}ErF_{21}N_2O_6S_3$ | $C_{42}H_{20}F_{21}N_2O_6S_3Yb$ | $C_{40}H_{20}F_{21}N_2NdO_6S_3$ | $C_{40}H_{20}F_{21}HoN_2O_6S_3$ | $C_{40}H_{20}F_{21}N_2O_6S_3Yb$ |
| Formula mass | 1308.71 | 1311.04 | 1316.82 | 1264.00 | 1284.69 | 1292.80 |
| $T$ [K] | 293(2) | 187(2) | 187(2) | 187(2) | 187(2) | 187(2) |
| $\lambda$ [Å] | 0.71073 | 0.71073 | 0.71073 | 0.71073 | 0.71073 | 0.71073 |
| Crystal system | orthorhombic | orthorhombic | orthorhombic | orthorhombic | orthorhombic | orthorhombic |
| Space group | *Pbca* | *Pbca* | *Pbca* | *Pbca* | *Pbca* | *Pbca* |
| $a$ [Å] | 20.9790(5) | 20.6146(9) | 20.6224(9) | 19.9666(12) | 19.8709(7) | 19.8161(9) |
| $b$ [Å] | 18.3620(5) | 18.0507(8) | 18.0173(8) | 18.4175(11) | 18.1779(6) | 18.0740(8) |
| $c$ [Å] | 25.5920(5) | 25.5197(12) | 25.5224(11) | 25.3703(15) | 25.5521(9) | 25.6376(11) |
| $\alpha$ [°] | 90 | 90 | 90 | 90 | 90 | 90 |
| $\beta$ [°] | 90 | 90 | 90 | 90 | 90 | 90 |
| $\gamma$ [°] | 90 | 90 | 90 | 90 | 90 | 90 |
| $V$ [Å$^3$] | 9858.4(6) | 9496.1(7) | 9483.1(7) | 9329.5(10) | 9229.7(6) | 9182.3(7) |
| $Z$ | 8 | 8 | 8 | 8 | 8 | 8 |
| $D_{calcd.}$ [mg m$^{-3}$] | 1.763 | 1.834 | 1.845 | 1.800 | 1.849 | 1.870 |
| Abs. coeff. [mm$^{-1}$] | 1.859 | 2.031 | 2.236 | 1.379 | 1.984 | 2.307 |
| $F$(000) | 5104 | 5112 | 5128 | 4952 | 5008 | 5032 |
| Crystal size [mm] | 0.53×0.34×0.19 | 0.33×0.27×0.17 | 0.35×0.29×0.14 | 0.33×0.12×0.05 | 0.25×0.27×0.15 | 0.26×0.16×0.10 |
| $\theta$ range [°] | 1.59 to 28.29 | 1.70 to 26.03 | 1.70 to 26.04 | 1.61 to 25.08 | 1.59 to 26.05 | 1.59 to 28.65 |
| Reflns collected | 59772 | 51450 | 51480 | 46137 | 50058 | 55491 |
| Ind. reflns ($R_{int}$) | 11819 (0.0447) | 9368 (0.0601) | 9342 (0.0213) | 8274 (0.1044) | 9118 (0.0445) | 11192 (0.0876) |
| Refinement method | full-matrix least squares on $F^2$ | | | | | |
| Data/restraints/parameters | 11819/26/631 | 9368/4/685 | 9342/56/638 | 8274/37/505 | 9118/24/667 | 11192/23/667 |
| GOF on $F^2$ | 1.038 | 1.061 | 1.012 | 1.037 | 1.023 | 0.931 |
| $R_1$ [$I > 2\sigma(I)$] | 0.0713 | 0.0554 | 0.0679 | 0.1240 | 0.0553 | 0.0568 |
| $wR_2$ [$I > 2\sigma(I)$] | 0.2404 | 0.1631 | 0.1952 | 0.3134 | 0.1611 | 0.1428 |
| $R_1$ (all data) | 0.1217 | 0.0727 | 0.0777 | 0.1831 | 0.0783 | 0.1043 |
| $wR_2$ (all data) | 0.2734 | 0.1754 | 0.2050 | 0.3579 | 0.1769 | 0.1643 |

**Single-Crystal X-ray Diffraction Study:** X-ray data for the selected crystal mounted on a glass fiber were collected with a CCD area detector with graphite-monochromated Mo-$K_\alpha$ radiation. Reflections were collected with a Bruker SMART APEX detector and processed with SAINT from Bruker. Data were corrected for Lorentz and polarization effects. The structure was solved by direct methods and expanded using Fourier techniques. The non-hydrogen atoms [for (Yb)**1** except F3–F7, F17–F21; for (Nd)**2** except F atoms] were refined anisotropically. The hydrogen atoms were included using a riding model. All calculations were performed using the SHELXL-97 crystallographic software package.[46] For the crystallographic data some $R$ values are high, and for the ORTEP plots some of the ellipsoids of some fluorine atoms have a very irregular shape. These problems could be due to the poor X-ray data and disorder of the fluorine atoms. Crystallographic data and structural refinements for compounds (Ln)**1** and (Ln)**2** are summarized in Table 3. CCDC-266576 [for (Ho)**2**], -266577 [for (Ho)**1**], -266578 [for (Er)**1**], -266579 [for (Yb)**2**], -266816 [for (Yb)**1**], and -266983 [for (Nd)**2**] contain the supplementary crystallographic data for this paper. These data can be obtained free of charge from The Cambridge Crystallographic Data Centre via www.ccdc.cam.ac.uk/data_request/cif.

**Supporting Information** (see footnote on the first page of this article): Molecular structures of the complexes (Ln)**1** and (Ln)**2** (Figure S1), excitation spectra of (Ln)**1** and (Ln)**2** complexes (Ln = Er, Ho, Yb, Nd) and absorption spectra of the ligands (phen, Hhfth and bipy) (Figure S2), phosphorescence spectrum of $[Gd(bipy)_3Cl_2]$ (Figure S3), results of elemental analyses of complexes (Ln)**1** and (Ln)**2** (Table S1).

## Acknowledgments

This work was supported by the National Natural Science Foundation of China (grant nos. 20372060, 20131010, 20490210, 20340420326) and financial aid from MOST of China ("973" Program, no. 2006CB601103). We are grateful to Dr. E. Ma and Prof. J. G. Mao of the Fujian Institute of Research on the Structure of Matter, Chinese Academy of Sciences, and Prof. Q. Su and Dr. L. Feng of Sun Yat-sen University for assistance with the fluorescence measurements. We also thank Dr. D. M. Wang and Dr. Y. J. Zhang (Changchun Institute of Applied Chemistry) for their help with the microscope pictures of the crystals.

[1] a) S. Kim, Y. T. Lim, E. G. Soltesz, A. M. De Grand, J. Lee, A. Nakayama, J. A. Parker, T. Mihaljevic, R. G. Laurence, D. M. Dor, L. H. Cohn, M. G. Bawendi, J. V. Frangioni, *Nat. Biotechnol.* **2004**, *22*, 93–97; b) J. Zhang, P. D. Badger, S. J. Geib, S. Petoud, *Angew. Chem. Int. Ed.* **2005**, *44*, 2508–2512.

[2] a) L. N. Sun, H. J. Zhang, Q. G. Meng, F. Y. Liu, L. S. Fu, C. Y. Peng, J. B. Yu, G. L. Zheng, S. B. Wang, *J. Phys. Chem. B* **2005**, *109*, 6174–6182; b) T. J. Foley, B. S. Harrison, A. S. Knefely, K. A. Abboud, J. R. Reynolds, K. S. Schanze, J. M. Boncella, *Inorg. Chem.* **2003**, *42*, 5023–5032; c) W. D. Horrocks Jr, J. P. Bolender, W. D. Smith, R. M. Supkowski, *J. Am. Chem. Soc.* **1997**, *119*, 5972–5973; d) M. P. O. Wolbers, F. C. J. M. van Veggel, B. H. M. Snellink-Ruël, J. W. Hofstraat, F. A. J. Geurts, D. N. Reinhoudt, *J. Chem. Soc., Perkin Trans. 2* **1998**, 2141–2150; e) F. X. Zang, W. L. Li, Z. R. Hong, H. Z. Wei, M. T. Li, X. Y. Sun, C. S. Lee, *Appl. Phys. Lett.* **2004**, *84*, 5115–5117; f) G. A. Casay, D. B. Shealy, G. Patonay, *Near-*

 © 2006 Wiley-VCH Verlag GmbH & Co. KGaA, Weinheim 

*Infrared Fluorescence Probes*, Plenum Press, New York, London, **1994**, vol, 4, p. 183–222; g) L. H. Slooff, A. Polman, M. P. Oude Wolbers, F. C. J. M. van Veggel, D. N. Reinhoudt, J. W. Hofstraat, *J. Appl. Phys.* **1997**, *83*, 497–503; h) M. H. V. Werts, J. W. Hofstraat, F. A. J. Geurts, J. W. Verhoeven, *Chem. Phys. Lett.* **1997**, *276*, 196–201.

[3] a) M. Kawa, J. M. J. Fréchet, *Chem. Mater.* **1998**, *10*, 286–296; b) C. Piguet, J.-C. G. Bünzli, G. Bernardinelli, G. Hopfgartner, A. F. Williams, *J. Am. Chem. Soc.* **1993**, *115*, 8197–8206.

[4] a) S. I. Weissman, *J. Chem. Phys.* **1942**, *10*, 214–217; b) G. A. Crosby, R. E. Whan, J. J. Freeman, *J. Phys. Chem.* **1962**, *66*, 2493–2499.

[5] K. Binnemans, in *Handbook on the Physics and Chemistry of Rare Earths* (Eds.: K. A. Gschneidner Jr, J.-C. G. Bünzli, V. K. Pecharsky), Elsevier, Amsterdam, **2005**, vol. 35, chapter 225, p. 107–272.

[6] I. K. Hemmilä, *Applications of Fluorescence in Immunoassays*, Wiley and Sons, New York, **1991**.

[7] a) G. Mancino, A. J. Ferguson, A. Beeby, N. J. Long, T. S. Jones, *J. Am. Chem. Soc.* **2005**, *127*, 524–525; b) G. E. Buono-Core, H. Li, B. Marciniak, *Coord. Chem. Rev.* **1990**, *99*, 55–87; c) J. H. Melman, T. J. Emge, J. G. Brennan, *Inorg. Chem.* **2001**, *40*, 1078–1081; d) Y. Hasegawa, T. Ohkubo, K. Sogabe, Y. Kawamura, Y. Wada, N. Nakashima, S. Yanagida, *Angew. Chem. Int. Ed.* **2000**, *39*, 357–360; e) J.-C. G. Bünzli, C. Piguet, *Chem. Soc. Rev.* **2005**, *34*, 1048–1077; f) A.-S. Chauvin, F. Gumy, I. Matsubayashi, Y. Hasegawa, J.-C. G. Bünzli, *Eur. J. Inorg. Chem.* **2006**, 473–480; g) S. Yanagida, Y. Hasegawa, K. Murakoshi, Y. Wada, N. Nakashima, T. Yamanaka, *Coord. Chem. Rev.* **1998**, *171*, 461–480.

[8] a) Y. X. Zheng, J. Lin, Y. J. Liang, Q. Lin, Y. N. Yu, Q. G. Meng, Y. H. Zhou, S. B. Wang, H. Y. Wang, H. J. Zhang, *J. Mater. Chem.* **2001**, *11*, 2615–2619; b) Y. Hasegawa, Y. Kimura, K. Murakoshi, Y. Wada, J. H. Kim, N. Nakashima, T. Yamanaka, S. Yanagida, *J. Phys. Chem.* **1996**, *100*, 10201–10205; c) J. L. Yuan, K. Matsumoto, *Anal. Sci.* **1996**, *12*, 31–36.

[9] J. B. Yu, L. Zhou, H. J. Zhang, Y. X. Zheng, H. R. Li, R. P. Deng, Z. P. Peng, Z. F. Li, *Inorg. Chem.* **2005**, *44*, 1611–1618.

[10] a) L. N. Sun, H. J. Zhang, L. S. Fu, F. Y. Liu, Q. G. Meng, C. Y. Peng, J. B. Yu, *Adv. Funct. Mater.* **2005**, *15*, 1041–1048; b) Y. X. Zheng, Y. H. Zhou, J. B. Yu, Y. N. Yu, H. J. Zhang, W. P. Gillin, *J. Phys. D: Appl. Phys.* **2004**, *37*, 531–534; c) Y. X. Zheng, L. S. Fu, Y. H. Zhou, J. B. Yu, Y. N. Yu, S. B. Wang, H. J. Zhang, *J. Mater. Chem.* **2002**, *12*, 919–923; d) L. N. Sun, H. J. Zhang, L. S. Fu, F. Y. Liu, Q. G. Meng, C. Y. Peng, J. B. Yu, S. B. Wang, *J. Rare Earths* **2004**, *22*, 812–815.

[11] a) R. Van Deun, D. Moors, B. De Fré, K. Binnemans, *J. Mater. Chem.* **2003**, *13*, 1520–1522; b) R. Van Deun, P. Fias, P. Nockemann, A. Schepers, T. N. Parac-Vogt, K. Van Hecke, L. Van Meervelt, K. Binnemans, *Inorg. Chem.* **2004**, *43*, 8461–8469.

[12] a) C. Tedeschi, J. Azéma, H. Gornitzka, P. Tisnès, C. Picard, *Dalton Trans.* **2003**, 1738–1745; b) J. A. Fernandes, R. A. Sá Ferreira, M. Pillinger, L. D. Carlos, I. S. Gonçalves, P. J. A. Ribeiro-Claro, *Eur. J. Inorg. Chem.* **2004**, 3913–3919.

[13] J. B. Yu, H. J. Zhang, L. S. Fu, R. P. Deng, L. Zhou, H. R. Li, F. Y. Liu, H. L. Fu, *Inorg. Chem. Commun.* **2003**, *6*, 852–854.

[14] J.-C. G. Bünzli, P. Froidevaux, C. Piguet, *New J. Chem.* **1995**, *19*, 661–668.

[15] a) M. Benatsou, B. Capoen, M. Bouazaoui, W. Tchana, J. P. Vilcot, *Appl. Phys. Lett.* **1997**, *71*, 428–430; b) V. V. Filippov, P. P. Pershukevich, V. V. Kuznetsova, V. S. Homenko, *J. Lumin.* **2002**, *99*, 185–195; c) J. A. Capobianco, F. Vetrone, J. C. Boyer, A. Speghini, M. Bettinelli, *J. Phys. Chem. B* **2002**, *106*, 1181–1187.

[16] a) K. Binnemans, H. De Leebeeck, C. Görller-Walrand, J. L. Adam, *Chem. Phys. Lett.* **1999**, *303*, 76–80; b) F. S. Liu, Q. L. Liu, J. K. Liang, J. Luo, L. T. Yang, G. B. Song, Y. Zhang, L. X. Wang, J. N. Yao, G. H. Rao, *J. Lumin.* **2005**, *111*, 61–68; c) M. Malinowski, Z. Frukacz, M. Szuflińska, A. Wnuk, M. Kaczkan, *J. Alloys Compd.* **2000**, *300–301*, 389–394.

[17] a) W. T. Carnall, P. R. Fields, K. Rajnak, *J. Chem. Phys.* **1968**, *49*, 4424–4442; b) G. F. Wang, W. Z. Chen, Z. B. Li, Z. S. Hu, *Phys. Rev. B* **1999**, *60*, 15469–15471; c) H. D. Jiang, J. Y. Wang, H. J. Zhang, X. B. Hu, H. Liu, *J. Appl. Phys.* **2002**, *92*, 3647–3650; d) V. Mehta, G. Aka, A. L. Dawar, A. Mansingh, *Opt. Mater.* **1999**, *12*, 53–63.

[18] a) K. Driesen, P. Nockemann, K. Binnemans, *Chem. Phys. Lett.* **2004**, *395*, 306–310; b) C. L. Maupin, R. S. Dickins, L. G. Govenlock, C. E. Mathieu, D. Parker, J. A. G. Williams, J. P. Riehl, *J. Phys. Chem. A* **2000**, *104*, 6709–6717.

[19] a) V. Bekiari, P. Lianos, *Adv. Mater.* **1998**, *10*, 1455–1458; b) N. Sabbatini, A. Mecati, M. Guardigli, V. Balzani, J. M. Lehn, R. Zeissel, R. Ungaro, *J. Lumin.* **1991**, *48–49*, 463–468; c) N. Sabbatini, M. Guardigli, J. M. Lehn, *Coord. Chem. Rev.* **1993**, *123*, 201; d) K. Driesen, R. Van Deun, C. Görller-Walrand, K. Binnemans, *Chem. Mater.* **2004**, *16*, 1531–1535.

[20] H. R. Li, J. Lin, H. J. Zhang, L. S. Fu, Q. G. Meng, S. B. Wang, *Chem. Mater.* **2002**, *14*, 3651–3655.

[21] R. Van Deun, P. Nockemann, C. Görller-Walrand, K. Binnemans, *Chem. Phys. Lett.* **2004**, *397*, 447–450.

[22] a) O. H. Park, S. Y. Seo, J. I. Jung, J. Y. Bae, B. S. Bae, *J. Mater. Res.* **2003**, *18*, 1039–1042; b) O. H. Park, S. Y. Seo, B. S. Bae, J. H. Shin, *Appl. Phys. Lett.* **2003**, *82*, 2787–2789.

[23] J. W. Stouwdam, F. C. J. M. van Veggel, *Nano Lett.* **2002**, *2*, 733–737.

[24] a) P. Lenaerts, K. Driesen, R. Van Deun, K. Binnemans, *Chem. Mater.* **2005**, *17*, 2148–2154; b) M. P. Tsvirko, G. F. Stelmakh, V. E. Pyatosin, K. N. Solovyov, T. F. Kachura, *Chem. Phys. Lett.* **1980**, *73*, 80–83; c) S. Quici, M. Cavazzini, G. Marzanni, G. Accorsi, N. Armaroli, B. Ventura, F. Barigelletti, *Inorg. Chem.* **2005**, *44*, 529–537.

[25] W. G. Perkins, G. A. Crosby, *J. Chem. Phys.* **1965**, *42*, 407–414.

[26] F. R. G. e Silva, O. L. Malta, C. Reinhard, H.-U. Güdel, C. Piguet, J. E. Moser, J.-C. G. Bünzli, *J. Chem. Phys. A* **2002**, *106*, 1670–1677.

[27] G. Boulon, A. Collombet, A. Brenier, M. T. Cohen-Adad, A. Yoshikawa, K. Lebbou, J. H. Lee, T. Fukuda, *Adv. Funct. Mater.* **2001**, *11*, 263–270.

[28] C. Reinhard, H. U. Güdel, *Inorg. Chem.* **2002**, *41*, 1048–1055.

[29] G. M. Davies, R. J. Aarons, G. R. Motson, J. C. Jeffery, H. Adams, S. Faulkner, M. D. Ward, *Dalton Trans.* **2004**, 1136–1144.

[30] a) S. I. Klink, P. O. Alink, L. Grave, F. G. A. Peters, J. W. Hofstraat, F. Geurts, F. C. J. M. van Veggel, *J. Chem. Soc., Perkin Trans. 2* **2001**, 363–372; b) W. P.-W. Lai, W.-T. Wong, *New J. Chem.* **2000**, *24*, 943–944.

[31] A. Beeby, S. Faulkner, D. Parker, J. A. G. Williams, *J. Chem. Soc., Perkin Trans. 2* **2001**, 1268–1273.

[32] N. Sabbatini, M. T. Indelli, M. T. Gandolfi, V. Balzani, *J. Phys. Chem.* **1982**, *86*, 3585–3591.

[33] O. L. Malta, F. R. G. e Silva, *Spectrochim. Acta Part A* **1998**, *54*, 1593–1599.

[34] F. R. G. e Silva, O. L. Malta, *J. Alloys Compd.* **1997**, *250*, 427–430.

[35] a) S. T. Frey, M. L. Gong, W. D. Horrocks Jr, *Inorg. Chem.* **1994**, *33*, 3229–3234; b) Y. X. Zheng, J. Lin, Y. J. Liang, Y. N. Yu, Y. H. Zhou, C. Guo, S. B. Wang, H. J. Zhang, *J. Alloys Compd.* **2002**, *336*, 114–118; c) Y. Haas, G. Stein, *J. Phys. Chem.* **1971**, *75*, 3677–3681; d) P. C. R. Soares-Santos, H. I. S. Nogueira, V. Félix, M. G. B. Drew, R. A. Sá Ferreira, L. D. Carlos, T. Trindade, *Chem. Mater.* **2003**, *15*, 100–108.

[36] N. M. Shavaleev, G. Accorsi, D. Virgili, Z. R. Bell, T. Lazarides, G. Calogero, N. Armaroli, M. D. Ward, *Inorg. Chem.* **2005**, *44*, 61–72.

[37] G. A. Crosby, R. E. Whan, R. M. Alire, *J. Chem. Phys.* **1961**, *34*, 743–748.

[38] C. Y. Peng, H. J. Zhang, J. B. Yu, Q. G. Meng, L. S. Fu, H. R. Li, L. N. Sun, X. M. Guo, *J. Phys. Chem. B* **2005**, *109*, 15278–15287.

 © 2006 Wiley-VCH Verlag GmbH & Co. KGaA, Weinheim 

[39] Y. T. Yang, Q. D. Su, G. W. Zhao, *Spectrochim. Acta Part A* **1999**, *55*, 1527–1533.
[40] H. R. Li, J. Lin, H. J. Zhang, H. C. Li, L. S. Fu, Q. G. Meng, *Chem. Commun.* **2001**, 1212–1213.
[41] M. H. V. Werts, R. T. F. Jukes, J. W. Verhoeven, *Phys. Chem. Chem. Phys.* **2002**, *4*, 1542–1548.
[42] L. N. Puntus, K. J. Schenk, J.-C. G. Bünzli, *Eur. J. Inorg. Chem.* **2005**, 4739–4744.
[43] a) N. M. Shavaleev, S. J. A. Pope, Z. R. Bell, S. Faulkner, M. D. Ward, *Dalton Trans.* **2003**, 808–814; b) M. H. V. Werts, J. W. Verhoeven, J. W. Hofstraat, *J. Chem. Soc., Perkin Trans. 2* **2000**, 433–439.
[44] a) V. V. Grushin, N. Herron, D. D. LeCloux, W. J. Marshall, V. A. Petrov, Y. Wang, *Chem. Commun.* **2001**, 1494–1495; b) M. A. Omary, M. A. Rawashdeh-Omary, H. V. K. Diyabalanage, H. V. R. Dias, *Inorg. Chem.* **2003**, *42*, 8612–8614; c) I. R. Lasker, T.-M. Chen, *Chem. Mater.* **2004**, *16*, 111–117; d) H. V. R. Dias, W. Jin, *Inorg. Chem.* **1996**, *35*, 3687–3694; e) M. Becht, T. Gerfin, K. H. Dahmen, *Chem. Mater.* **1993**, *5*, 137–144.
[45] L. R. Melby, N. J. Rose, E. Abramson, J. C. Caris, *J. Am. Chem. Soc.* **1964**, *86*, 5117–5125.
[46] M. D. Regulacio, N. Tomson, S. L. Stoll, *Chem. Mater.* **2005**, *17*, 3114–3121.

Received: April 13, 2006
Published Online: August 7, 2006

 © 2006 Wiley-VCH Verlag GmbH & Co. KGaA, Weinheim 

DOI: 10.1002/ejic.200600179

# Chiral Platinum(II) Compounds Containing Ferrocenyl Schiff Bases Acting as (N), $(N,O)^-$, $[C(sp^2,ferrocene),N]^-$ or $[C(sp^2,ferrocene),N,O]^{2-}$ Ligands

**Concepción López,*[a] Amparo Caubet,[a] Sonia Pérez,[a] Xavier Solans,[b] Mercè Font-Bardía,[b] and Elies Molins[c]**

**Keywords:** Platinum / Ferrocene / Platinacycles / N ligands / N,O ligands

A study of the reactions of the following ferrocenyl Schiff bases: ($S_C$)-(+)-[FcCH=NCH($R^1$)$CH_2$OH] {Fc = ($\eta^5$-$C_5H_5$)-Fe($\eta^5$-$C_5H_4$), $R^1$ = Me (**1a**) or $CHMe_2$ (**1b**)} with *cis*-[$PtCl_2$(dmso)$_2$] under different experimental conditions is reported. This study enabled the isolation and characterisation of the enantiomerically pure platinum(II) complexes *trans*-($S_C$)-[Pt{FcCH=NCH($R^1$)$CH_2$OH}$Cl_2$(dmso)] {$R^1$ = Me (**2a**) or $CHMe_2$ (**2b**)} and *cis*-($S_C$)-[Pt{FcCH=NCH($R^1$)-$CH_2$OH}$Cl_2$(dmso)] {$R^1$ = Me (**3a**) or $CHMe_2$ (**3b**)} as well as four isomeric forms of ($S_C$)-[Pt{FcCH=N–CH($R^1$)-$CH_2$O}Cl(dmso)] {$R^1$ = Me or $CHMe_2$} (**4**–**7a**,**b**). These isomers differ in the conformation of the imine {*anti*-(*E*) (in **4** and **6**) or *syn*-(*Z*) (in **5** and **7**)} or in the relative arrangement of the nitrogen and the dmso group {*trans* (in **4** and **5**) or *cis* (in **6** and **7**)}. Imines **1** behave as a N-donor ligand in **2** and **3** and as a $(N,O)^-$ group in **4**–**7**. We also prepared the diastereomers {($S_p$,$S_C$) and ($R_p$,$S_C$)} of the platinacycles [Pt{[($\eta^5$-$C_5H_3$)CH=NCH($R^1$)$CH_2$OH]Fe($\eta^5$-$C_5H_5$)}Cl(dmso)] {**8** and **9**; $R^1$ = Me ($S_p$,$S_C$) (**8a**) and ($R_p$,$S_C$) (**9a**) or $R^1$ = $CHMe_2$ ($S_p$,$S_C$) (**8b**) and ($R_p$,$S_C$) (**9b**)}, [Pt{[($\eta^5$-$C_5H_3$)CH=NCH($R^1$)$CH_2$O]-Fe($\eta^5$-$C_5H_5$)}(dmso)] {**10** and **11**; $R^1$ = Me ($S_p$,$S_C$) (**10a**) and ($R_p$,$S_C$) (**11a**) or $R^1$ = $CHMe_2$ ($S_p$,$S_C$) (**10b**) and ($R_p$,$S_C$) (**11b**)} and [Pt{[($\eta^5$-$C_5H_3$)CH=NCH($R^1$)$CH_2$OH]Fe($\eta^5$-$C_5H_5$)}Cl-($PPh_3$)] {**12** and **13**; $R^1$ = Me ($S_p$,$S_C$) (**12a**) and ($R_p$,$S_C$) (**13a**) or $R^1$ = $CHMe_2$ ($S_p$,$S_C$) (**12b**) and ($R_p$,$S_C$) (**13b**)}, containing a $[C(sp^2,ferrocene),N]^-$ (in **8**, **9**, **12** and **13**) or a $[C(sp^2,ferrocene),N,O]^{2-}$ (in **10** and **11**) group. The X-ray crystal structures of **1b**·$H_2O$, **3b**, **7b**·$CH_2Cl_2$·1/2$H_2O$ and **9a** are also reported. Our study allows the elucidation of the factors affecting the preferential formation of a given platinum(II) complex.

(© Wiley-VCH Verlag GmbH & Co. KGaA, 69451 Weinheim, Germany, 2006)

## Introduction

Palladium(II) and platinum(II) complexes containing chiral ligands attract great interest because of their potential applications in different fields.[1–11] It is well known that compounds of this kind are useful in homogeneous catalysis[3–4] and as chiral derivatising agents,[5] as reagents to determine enantio- or diastereomeric excesses of organic substrates,[6] or even due to their antitumoral activity.[1c,7] Of the examples reported, those having a bidentate $[C(sp^2,aryl),N]^-$ group are particularly relevant.[1,3,6,8–11] The utility of chiral pallada- and platinacycles in asymmetric catalytic processes[8] including asymmetric Claisen rearrangements[10] is well documented. Notably, Leung et al.[11] have recently described the first example of a platinacycle that promotes the asymmetric [4+2] Diels–Alder reaction between diphenylvinylphosphane and *N*-(diphenylphosphanyl)pyrrole.

On the other hand, palladium(II) complexes containing (N), (N,E), $(C,N)^-$ or $(C,N,E)^-$ (E = N′, S or P) ferrocenyl ligands have attracted great interest in recent years,[12–17] mainly because of their applications in homogeneous catalysis[16] or in organometallic synthesis.[17] Platinum(II) analogues are less common[18,19] but some of these also exhibit antitumoral activity against cisplatin-resistant cells.[19] Despite *a*) the wide variety of chiral ferrocene derivatives reported so far, *b*) the prochiral nature of the ferrocenyl unit in the metallation process[20] and *c*) the interest in chiral palladium(II) and platinum(II) complexes containing ferrocenyl units, only a few enantio- or diastereomerically pure palladacycles with a σ[Pd–$C(sp^2$,ferrocene)] bond are described,[21,22] and the platinum(II) derivatives are less common.[23] Cycloplatination of [$FcCH_2NMe_2$] (**I**) or [Fc-$C(R^1)$=$NR^2$] (**II**) {Fc = ($\eta^5$-$C_5H_5$)Fe($\eta^5$-$C_5H_4$), $R^1$ = H, Me or Ph, and $R^2$ = OH, $(CH_2)_3NMe_2$ or phenyl groups} led to the enantiomers $R_p$ and $S_p$.[24] Ryabov et al.[23] have re-

[a] Departament de Química Inorgànica, Facultat de Química, Universitat de Barcelona,
Martí i Franquès 1–11, 08028 Barcelona, Spain
Fax: +34-934907725
E-mail: conchi.lopez@qi.ub.es
[b] Departament de Cristal·lografia, Mineralogia i Dipòsits Minerals, Facultat de Geologia,
Martí i Franquès s/n, 08028 Barcelona, Spain
[c] Institut de Ciència de Materials de Barcelona (ICMAB-CSIC), Campus de la Universitat Autònoma de Barcelona,
08913 Bellaterra, Spain

Supporting information for this article is available on the WWW under http://www.eurjic.org or from the author.

 © 2006 Wiley-VCH Verlag GmbH & Co. KGaA, Weinheim 

ported the synthesis of the diastereomers ($R_p$,$S_S$) and ($S_p$,$S_S$) of [Pt{[($\eta^5$-$C_5H_3$)$CH_2NMe_2$]Fe($\eta^5$-$C_5H_5$)}Cl-{S(O)Me($C_6H_4$-4Me)}].

In view of these facts and as a part of a project directed towards the preparation of chiral platinum(II) compounds with potentially bi- or tridentate ligands, we prepared the enantiomerically pure ferrocenyl Schiff bases: ($S_C$)-(+)-[FcCH=NCH($R^1$)$CH_2$OH] (**1**) {$R^1$ = Me (**1a**) or $CHMe_2$ (**1b**)} (Scheme 1) and studied their reactivity with *cis*-[$PtCl_2$(dmso)$_2$]. We then *a*) evaluated the potential coordination abilities of these ligands to platinum(II), *b*) achieved a variety of enantio- and diastereomerically pure platinum(II) complexes and *c*) established the best experimental conditions required to achieve the desired chiral platinum(II) compounds. A preliminary account in this field has recently been reported.[25]

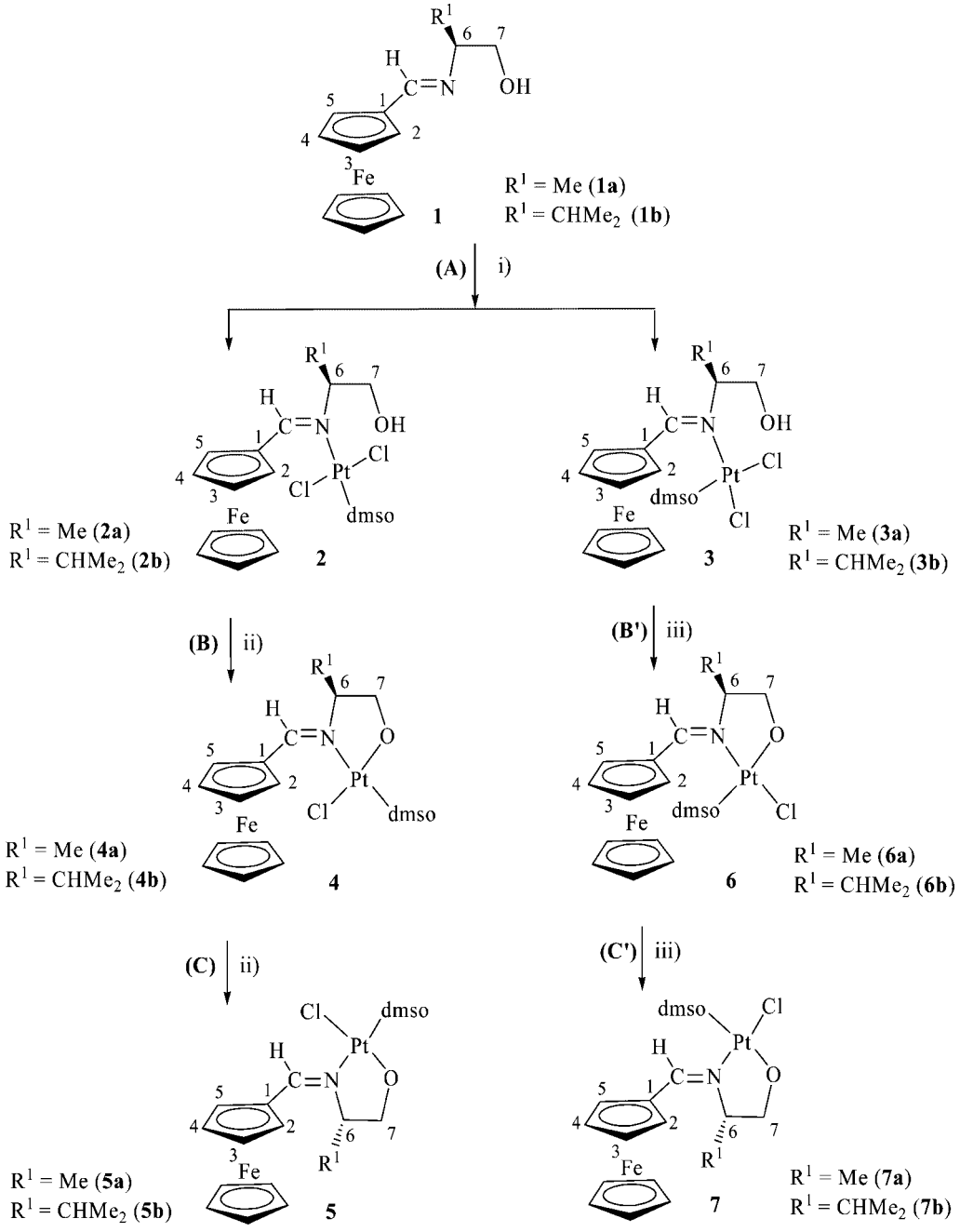


Scheme 1. *i*) Equimolar amount of *cis*-[$PtCl_2$(dmso)$_2$] in refluxing methanol for 4 h followed by $SiO_2$ column chromatography (see text). *ii*) Addition of NaOD (in [$D_4$]methanol) to a solution of **2** or **4** in chloroform. For molar ratios NaOD/**2** = 1 compounds **4** were the major components. The complete conversion of **2** (or **4**) into **5** requires molar ratios NaOD/**2** = 1.8. The formation of **5a** was achieved at room temperature, but that of **5b** required the reaction mixture to be warmed up at 333 K for 1.5 h (see text). *iii*) The method used was identical to that of (*ii*), but because of the small amount of compounds **3** available the intermediate species **6** were detected by NMR but they were not isolated using this procedure. A more effective method to achieve compounds **7** is presented in the text.

 © 2006 Wiley-VCH Verlag GmbH & Co. KGaA, Weinheim 

## Results and Discussion

### The Ligands

The ferrocenyl Schiff bases ($S_C$)-(+)-[FcCH=NCH($R^1$)-$CH_2OH$] {$R^1$ = Me (**1a**) or $CHMe_2$ (**1b**)} were prepared following the procedure described for [FcCH=$NR^2$] with $R^2$ = phenyl, benzyl groups.[26] This method consists in the reaction of equimolar amounts of ferrocenecarboxaldehyde (FcCHO) and the amine under reflux using a Dean–Stark apparatus. When ($S_C$)-(+)-$H_2$NCH($R^1$)$CH_2OH$ ($R^1$ = Me or $CHMe_2$) was used, the process yielded **1a** and **1b**, respectively. Elemental analyses of **1a** and **1b**[27] agreed with those expected for [FcCH=N–CH(Me)$CH_2OH$] and [FcCH=NCH($CHMe_2$)$CH_2OH$]·$H_2O$, respectively and NMR spectra suggested, according to the literature,[26] that they adopted the *anti*-(*E*) conformation in solution. The crystal structure of **1b**·$H_2O$ (Figure 1) consists of equimolar amounts of [FcCH=NCH($CHMe_2$)-$CH_2OH$] and $H_2O$ molecules. The >C=N- bond length [1.172(11) Å] is slightly shorter than the values reported for [FcC($R^3$)=$NR^2$] ($R^3$ = H, Me or Ph and $R^2$ = phenyl, benzyl or naphthyl substituents),[26,28] the imine moiety forms an angle of 4.80(9)° with the $C_5H_4$ ring and the value of the torsion angle C(10)–C(11)–N–C(12) [176.6(11)°] is consistent with the *anti*-(*E*) conformation.

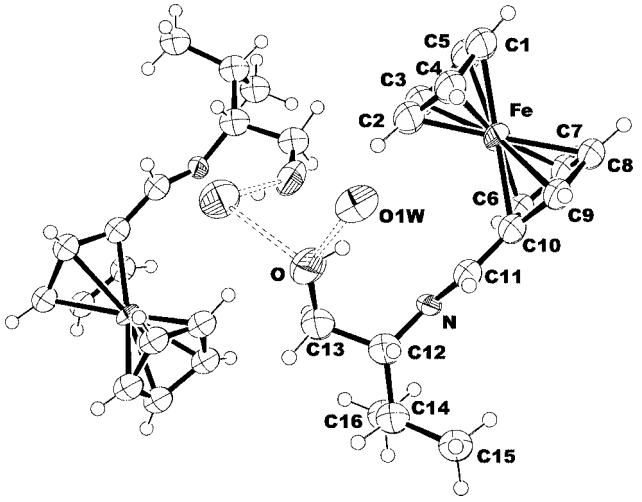


Figure 1. Molecular structure and atom labelling scheme for ($S_C$)-(+)-[FcCH=NCH($CHMe_2$)$CH_2OH$] (**1b**)·$H_2O$ showing the H–O···H interactions. Selected bond lengths (Å) and angles (°): O–C(13) 1.523(13), N–C(11) 1.172(11), N–C(12) 1.396(9), C(10)–C(11) 1.365(9), C(12)–C(13) 1.520(9), C(12)–C(14) 1.523(12), C(14)–C(15) 1.544(10), C(14)–C(16) 1.373(13), C(6)–C(10)–C(11) 117.3(4), C(9)–C(10)–C(11) 132.7(4), C(11)–N–C(12) 134.5(12), N–C(11)–C(10) 144.4(17), N–C(12)–C(13) 113.3(6), N–C(12)–C(14) 121.2(10), C(13)–C(12)–C(14) 115.9(7), C(12)–C(13)–O 112.7(8), C(16)–C(14)–C(12) 102.3(10), C(16)–C(14)–C(15) 119.1(10), C(12)–C(14)–C(15) 110.4(8).

Bond lengths and angles of the Fc moiety agree with those reported for most ferrocene derivatives,[29] and the two pentagonal rings are planar and nearly parallel {tilt angle = 3.6(5)°}, deviating by about 7.35° from the ideal eclipsed conformation. In the crystal, the distance between the hydrogen of the O–H group of the ligand and the oxygen of the water molecule, O(1W), is 2.696(13) Å and the O–H···O bond angle is 113.98°, thus suggesting a weak O–H(10)···O(1W) intermolecular interaction.

### Platinum(II) Compounds

In a first attempt to evaluate the potential coordination abilities of the ferrocenyl Schiff bases **1** to platinum(II), their reactivity with *cis*-[$PtCl_2$(dmso)$_2$] under different experimental conditions was studied. Because of the variety of products isolated, the most representative results obtained are in Table 1 and Scheme 1.

When **1a** (or **1b**) was treated with *cis*-[$PtCl_2$(dmso)$_2$] in refluxing methanol for 4 h, two compounds were isolated {Table 1, entries ***Ia*** and ***Ib*** and Scheme 1, step (A)}. One of these was identified as FcCHO. The $^1$H NMR spectrum of the crude materials showed the typical resonances of this product. This suggests that it hydrolyses during the reaction with residual water in the solvent. Examples of a partial hydrolysis of related Schiff bases induced by the presence of palladium(II) or platinum(II) salts have been reported in the literature.[24c,30] The first portions of the second band gave [Pt{FcCH=NCH($R^1$)$CH_2OH$}$Cl_2$(dmso)] {$R^1$ = Me (**2a**) or $CHMe_2$ (**2b**)} and the remaining ones produced orange solids containing **2a** (or **2b**) and traces of an additional isomer (**3a** and **3b**, respectively). Longer refluxing periods (6 h) did not substantially improve the molar ratios **2a/3a** and **2b/3b** (1.00:0.10 and 1.00:0.11, respectively).

Previous $^1$H NMR spectroscopic studies of platinum(II) and palladium(II) complexes derived from imines have shown that the chemical shift of the methinic proton is indicative of the conformation of the ligand.[24b,26,30–35] If the imine is in the *syn*-(*Z*) form in the complexes, the signal of the imine proton is shifted downfield relative to the free ligand because of the paramagnetic anisotropy of the metal,[34] which is close to this proton. In contrast, for compounds where the imine is in the *anti*-(*E*) form the resonance of the methinic proton is high-field shifted. The comparison of $^1$H NMR spectra of **2** and **3** with those of their parent ligands **1** indicated that in **2a**, **3a**, **2b** and **3b** the ligands had the *anti*-(*E*) conformation and {$^1$H-$^1$H}-NOESY spectra confirmed this result. Fractional crystallisation of the solids containing the isomeric forms enabled the isolation of small amounts of **3a** and **3b** and highly enriched (about 98%) **2a** and **2b**. Characterisation data of **2**–**3a**,**b**[27] agreed with the formulas presented in Scheme 1.

The crystal structure of **3b** consists of discrete molecules of [Pt{FcCH=NCH($CHMe_2$)$CH_2OH$}$Cl_2$(dmso)] separated by van der Waals contacts (Figure 2). The platinum(II) is in a slightly distorted square-planar environment bound to the imine nitrogen, the sulfur of the S(O)$Me_2$ ligand and two chlorines {Cl(1) and Cl(2)}. The Pt–S bond length [2.194(4) Å] agrees with the values reported for other platinum(II) complexes with dimethyl sulfoxide.[12,24,29,35] The chloro ligands are in a *cis* arrangement and the value of the torsion angle C(1)–C(11)–N(12)–C(13) [179.6(14)°] is consistent with an *anti*-(*E*) conformation. Because of the

 © 2006 Wiley-VCH Verlag GmbH & Co. KGaA, Weinheim 

Table 1. Summary of the experimental conditions [reagents, solvents, temperature ($T$) and reaction periods ($t$)] used in the studies of the reactivity of **1** with *cis*-[$PtCl_2(dmso)_2$], which is abbreviated as [Pt], or of some of the platinum(II) complexes together with the products isolated in these reactions.

| Entry | Reagent (molar ratio) | Solvent | $T$ [K] | $t$ | Final products[a] (molar ratios) |
|---|---|---|---|---|---|
| ***Ia*** | **1a** and [Pt] (1:1) | MeOH | reflux | 4 h | **2a** and **3a** [b] |
| ***Ib*** | **1b** and [Pt] (1:1) | MeOH | reflux | 4 h | **2b** and **3b** (1.00:0.05) |
| ***IIa*** | **2a** and NaOD (1:1) | $CDCl_3$/MeOD | 298 | 5 min | **4a** |
| ***IIb*** | **2b** and NaOD (1:1) | $CDCl_3$/MeOD | 298 | 5 min | **4b** |
| ***IIIa*** | **2a** and NaOD (1:1.8) | $CDCl_3$/MeOD | 298 | 5 min | **5a** |
| ***IIIb*** | **2b** and NaOD (1:1.8) | $CDCl_3$/MeOD | 333 | 1.5 h | **5b** |
| ***IVa*** | **2a** and NaOAc (1:2) | MeOH/toluene[c] | reflux | 72 h | **8a** and **9a** (1:1) |
| ***IVb*** | **2b** and NaOAc (1:2) | MeOH/toluene[c] | reflux | 72 h | **8b** and **9b** (1:1) |
| ***Va*** | **1a**, [Pt] and NaOAc (1:1:2) | MeOH/toluene[c] | reflux | 72 h | **8a** and **9a** (1:1) |
| ***Vb*** | **1b**, [Pt] and NaOAc (1:1:2) | MeOH/toluene[c] | reflux | 72 h | **8b** and **9b** (1:1) |
| ***VIa*** | **8a** (or **8b**) and NaOD[d] (1:1) | $CHCl_3$/MeOH[d] | 298 | | **10a** (or **10b**) |
| ***VIb*** | **9a** (or **9b**) and NaOD[d] (1:1) | $CHCl_3$/MeOH[d] | 298 | | **11a** (or **11b**) |

[a] In entries ***Ia,b*** and ***IV–Va,b*** small amounts of FcCHO were also isolated as a byproduct. $^1$H NMR spectra of the crude materials obtained also showed the presence of this aldehyde, thus suggesting that the formation of FcCHO takes place during the reaction because of residual water in the solvent and that it is not a byproduct generated in the course of the work-up of the column. [b] The presence of a small amount of **3a** (about 5 mg) was detected. [c] A (1:4) mixture. [d] Saturated solution of NaOD in [$D_4$]methanol.

similarity between the NMR spectroscopic data[27] of **3a** and **3b** we assumed that the environment of the platinum(II) in **3a** is the same as in **3b** and consequently, in **2a** and **2b** the two $Cl^-$ ligands would be in a *trans* arrangement.

On the other hand, the presence of the OH group in the dangling arm of **2** and **3** prompted us to study whether the addition of a base could induce the deprotonation of the OH group and the formation of enantiomerically pure platinum(II) complexes containing imines **1** acting as bidentate $(N,O)^-$ ligands. In a first attempt to achieve this aim, the reactions of **2a** (in $CDCl_3$) with NaOD dissolved in methanol (in molar ratios NaOD/**2a** varying from 0.2 to 1.8) were studied on an NMR scale {Scheme 1, steps (B) and (C)}. The results showed that, for molar ratios smaller than 0.4, **2a** and a new platinum(II) complex (**4a**) coexisted in solution. As can be easily seen in Figure 3, the proportion **2a**/**4a** decreased as the molar ratio NaOD/**2a** increased and for a NaOD/**2a** ratio of 1 (Table 1, entry ***IIa***) the major product was **4a** and only traces of **2a** and of a new byproduct (hereafter referred to as **5a**) were detected. NMR studies revealed that in **4a** the ligand adopted the *anti*-(*E*) conformation and behaved as a $(N,O)^-$ bidentate ligand. In view of the characterisation data available,[27] for **4a** we postulate the chemical formula depicted in Scheme 1. An increase of the NaOD/**2a** molar ratio (up to 1.8) reduced the relative abundance of **2a** and **4a** compared with that of **5a** and the complete conversion of **2a** into **5a** was achieved

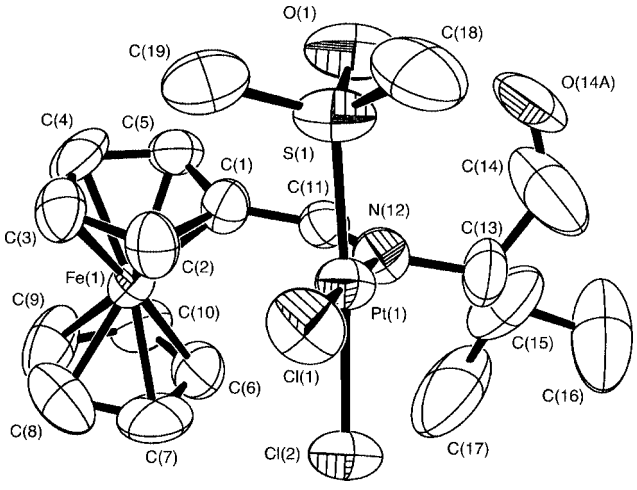


Figure 2. ORTEP plot of *cis*-($S_C$)-[Pt{FcCH=NCH(CHMe$_2$)-CH$_2$OH}Cl$_2$(dmso)] (**3b**). Thermal ellipsoids at 50% probability; hydrogen atoms have been omitted for clarity. Selected bond lengths (Å) and angles (°): Pt(1)–Cl(1) 2.294(4), Pt(1)–Cl(2) 2.306(4), Pt(1)–N(12) 2.041(11), Pt(1)–S(1) 2.194(4), C(1)–C(11) 1.431(18), C(11)–N(12) 1.322(16), N(12)–C(13) 1.496(19), C(13)–C(14) 1.45(3), C(14)–O(14A) 1.26(4), C(13)–C(15) 1.46(3), C(15)–C(16) 1.58(4), C(15)–C(17) 1.583(5), Cl(1)–Pt(1)–Cl(2) 89.75(16), Cl(1)–Pt(1)–S(1) 90.71(18), S(1)–Pt(1)–N(12) 91.1(4), N(12)–Pt(1)–Cl(2) 88.6(4), C(1)–C(11)–N(12) 128.9(12), C(11)–N(12)–C(13) 118.1(16), N(12)–C(13)–C(14) 114.2(19), N(12)–C(13)–C(15) 118.1(16).

 © 2006 Wiley-VCH Verlag GmbH & Co. KGaA, Weinheim 

using NaOD/**2a** = 1.8 {Table 1, entry ***IIIa*** and Scheme 1, step (C)}. Similar results were obtained when these experiments were performed using **2b** (Table 1, entries ***IIb***–***IIIb***),[36] showing the formation of an intermediate complex **4b**, which could be partially transformed into **5b** upon the addition of NaOD {Scheme 1, steps (B) and (C)}. The reaction **4b** → **5b** at 298 K was slower than the process **4a** → **5a**, but it could be accelerated by warming at 333 K. Characterisation data of **5**[27] were consistent with those expected for the isomeric form of [Pt{FcCH=NCH($R^1$)$CH_2$O}-Cl(dmso)] {$R^1$ = Me (**5a**) or $CHMe_2$ (**5b**)} that contains a $(N,O)^-$ bidentate imine [in a *syn*-(*Z*) conformation] and a *trans* arrangement between the oxygen and the $Cl^-$ ligand.

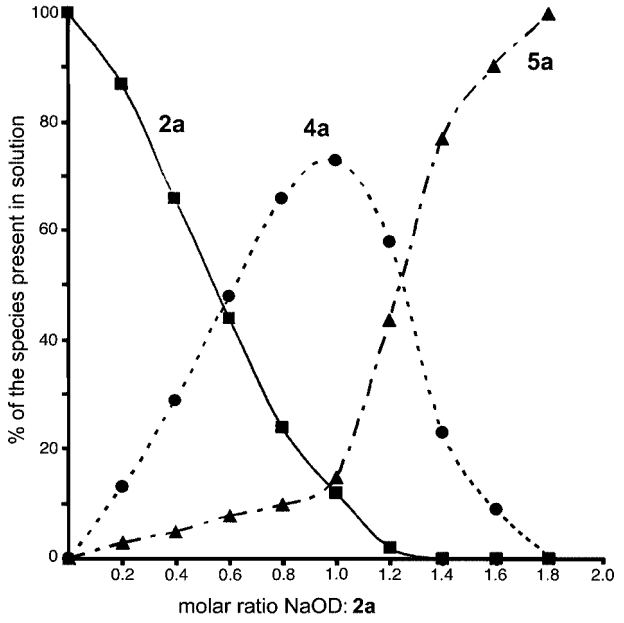


Figure 3. Graphic plot showing the dependence of the relative abundance (in %) of compounds **2a** (squares), **4a** (circles) and **5a** (triangles) on the molar ratios NaOD/**2a**.

The different ease with which **4a** and **4b** undergo the *anti*-(*E*) → *syn*-(*Z*) isomerisation of the ligand could be attributed to the different bulk of the substituents (Me or $CHMe_2$) on the stereogenic carbon.

All these findings suggest that: *a*) NaOD promotes the conversions of **2a** into **4a** and **5a** (or of **2b** into **4b** and **5b**) and *b*) these reactions proceed in two consecutive steps: the formation of the five-membered chelate ring, followed by the *anti*-(*E*) → *syn*-(*Z*) isomerisation of the imine.

In order to evaluate the potential reversibility of these reactions, the action of DCl on **5a** (or **5b**) was also studied. In all cases FcCHO was isolated as the major product and only traces of **2a** (or **2b**) could be detected by $^1$H NMR spectroscopy. This suggests that: *a*) the hydrolysis of the coordinating ligand was promoted in acidic media and *b*) the transformations **5a** → **2a** and **5b** → **2b** were not feasible under these experimental conditions.

Similarly, the reaction of **3a** (or **3b**) with NaOD gave **7a** (or **7b**) {Scheme 1, steps (B′) and (C′)}. However, the effectiveness of this procedure is limited because of the small amounts of **3a** or **3b** available from experiments ***Ia***,***b***. In these reactions, evidence of the formation of intermediate species (**6a** and **6b**, in Scheme 1) was also detected by NMR spectroscopy.

Compounds **7** could be isolated in a higher yield using an alternative path that consists in the treatment of equimolar amounts of the corresponding ligand, *cis*-[$PtCl_2$(dmso)$_2$] and NaOAc in refluxing methanol for 72 h.[37] These reactions lead to mixtures of FcCHO and the platinum(II) complexes **2**, **3**, **5** and **7** (in molar ratios **2a/3a/5a/7a** = 0.51:0.40:0.02:1.00 and **2b/3b/5b/7b** = 0.41:0.20:0.26:1.00). Characterisation data of **7**[27] agreed with the proposed formulae and complex **7b**·$CH_2Cl_2$·1/2$H_2O$ was also characterised by X-ray diffraction.

The crystal structure is formed by molecules of [Pt{FcCH=NCH($CHMe_2$)$CH_2$O}Cl(dmso)] (Figure 4), $CH_2Cl_2$ and $H_2O$ in a 1:1:0.5 molar ratio. In the heterodimetallic molecules, the platinum(II) is bound to a chloride, the sulfur of the dmso ligand, the nitrogen and the oxygen of ligand **1b** in a slightly distorted square-planar environment. Bond lengths and angles around the platinum(II) agreed with those of related compounds containing similar cores.[29] The values of the Cl(1)–Pt–O(14) bond angle [85.5(6)°] indicate a *cis* arrangement between the Cl(1) and the oxygen of the ligand and consequently the $S_{(dmso)}$ and N atoms occupy adjacent positions of the coordination plane. The metallacycle has an envelope-like conformation in which the C(13) atom deviates by about 0.667 Å (towards the $Fe^{II}$ atom) from the mean plane. The ligand adopts the *syn*-(*Z*) form, the >C=N– group is not included in the five-membered chelate ring and the C(11)–N(12) bond length is similar to those of other platinum(II) compounds containing ferrocenyl or organic imines.[24b,24c,29,30,35]

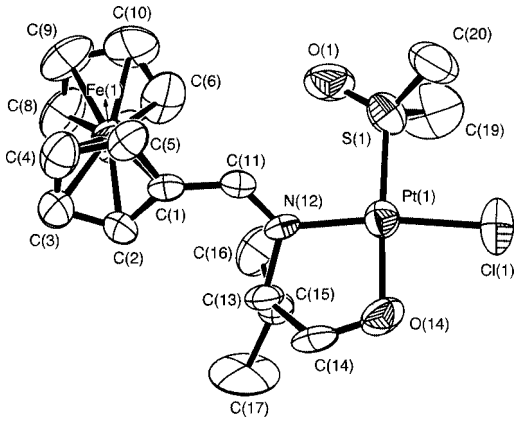


Figure 4. ORTEP plot of ($S_C$)-[Pt{FcCH=NCH($CHMe_2$)-$CH_2$O}Cl(dmso)] (**7b**). Thermal ellipsoids at 50% probability; hydrogen atoms have been omitted for clarity. Selected bond lengths (Å) and angles (°): Pt(1)–Cl(1) 2.310(7), Pt(1)–S(1) 2.194(8), Pt(1)–N(12) 2.013(18), Pt(1)–O(14) 1.956(19), C(1)–C(11) 1.44(3), C(11)–N(12) 1.28(3), C(14)–O(14) 1.42(4), C(13)–C(15) 1.45(4), C(15)–C(16) 1.56(4), C(15)–C(17) 1.60(4), N(12)–Pt(1)–O(14) 96.5(5), O(14)–Pt(1)–Cl(1) 85.5(6), Cl(1)–Pt(1)–S(1) 92.4(3), S(1)–Pt(1)–N(12) 96.8(5), Pt(1)–O(14)–C(14) 109.4(15).

More interesting were the results obtained when compounds **2** were treated with sodium acetate (in a molar ratio $AcO^-$:**2** = 2) in a toluene/methanol (4:1) mixture under re-

 © 2006 Wiley-VCH Verlag GmbH & Co. KGaA, Weinheim 

flux for 72 h {Scheme 2, step (A) and Table 1, entries ***IVa*** and ***IVb***}. These reactions gave FcCHO and purple solids whose elemental analyses[27] were consistent with those expected for the platinacycles [Pt{[($\eta^5$-$C_5H_3$)CH=NCH($R^1$)-$CH_2OH$]Fe($\eta^5$-$C_5H_5$)}Cl(dmso)] and their $^1$H NMR spectra showed two sets of superimposed signals of identical intensity. These platinum(II) complexes arise from the activation of the σ[C($sp^2$,ferrocene)–H] bond and because of the prochiral nature of the ferrocenyl moiety in process,[1a,20,21,22b,23,24] the duplicity of the signals detected in their NMR spectra could be attributed to the presence of diastereomers of [Pt{[($\eta^5$-$C_5H_3$)CH=NCH($R^1$)$CH_2OH$] Fe($\eta^5$-$C_5H_5$)}Cl(dmso)] {**8** and **9**; $R^1$ = Me ($S_p$,$S_C$) (**8a**) and ($R_p$,$S_C$) (**9a**) or $R^1$ = $CHMe_2$ ($S_p$,$S_C$) (**8b**) and ($R_p$,$S_C$) (**9b**)}. Their characterisation data[27] and the crystal structures of two of these compounds (**8b** and **9a**) (see below) confirmed this result.

Compounds **8** and **9** could also be isolated when a mixture of the corresponding ligand **1**, *cis*-[$PtCl_2(dmso)_2$] and NaOAc (in a 1:1:2 molar ratio) was dissolved in a toluene/methanol (4:1) mixture and refluxed for 72 h {Scheme 2, step (B) and Table 1, entries ***Va*** and ***Vb***}. This is an alternative and more effective path to achieve compounds **8**–**9a**,**b** (with slightly higher yields and in shorter times) than that shown in entries ***IVa*** and ***IVb*** and Scheme 2, step (A).

The two diastereomers of [Pt{[($\eta^5$-$C_5H_3$)CH=NCH($R^1$)-$CH_2OH$]Fe($\eta^5$-$C_5H_5$)}Cl(dmso)] {**8** and **9**; $R^1$ = Me ($S_p$,$S_C$) (**8a**) and ($R_p$,$S_C$) (**9a**) or $R^1$ = $CHMe_2$ ($S_p$,$S_C$) (**8b**) and ($R_p$,$S_C$) (**9b**)} were separated and characterised.[27] The crystal structure of **8b** was reported in a preliminary communication[25] and that of **9a** consists of two nonequivalent molecules (**I** and **II**) of [Pt{[($\eta^5$-$C_5H_3$)CH=NCH(Me)$CH_2OH$]-Fe($\eta^5$-$C_5H_5$)}Cl(dmso)] (Figure 5) separated by van der Waals contacts. In molecules **I** and **II**, the platinum(II) atom is bound to a chlorine {Cl(1) or Cl(1A)}, the sulfur {S(1) or S(1A)} of the dmso ligand, the nitrogen {N(1) or N(1A)} and the carbon atoms {C(6) (in **I**) or C(6A) (in **II**)}. This results in a slightly distorted square-planar environment. Bond lengths around the platinum(II) atom are similar to those of other platinacycles with "Pt(C,N)-$ClS_{(dmso)}$" cores.[12,18,29] The values of the bond angles Cl(1)–Pt(1)–N(1) and Cl(1A)–Pt(1A)–N(1A) {91.7(8)° and 95.2(9)°, respectively} indicate that the $Cl^-$ and the N are in a *cis* arrangement. The platinacycles are nearly planar and the large separation between the $Fe^{II}$ and the $Pt^{II}$ atoms precludes the existence of any direct interaction between them.

The main difference between molecules **I** and **II** arises from the relative orientation of the pendant OH arm. The values of the torsion angles O(2)–C(14)–C(12)–C(13) and

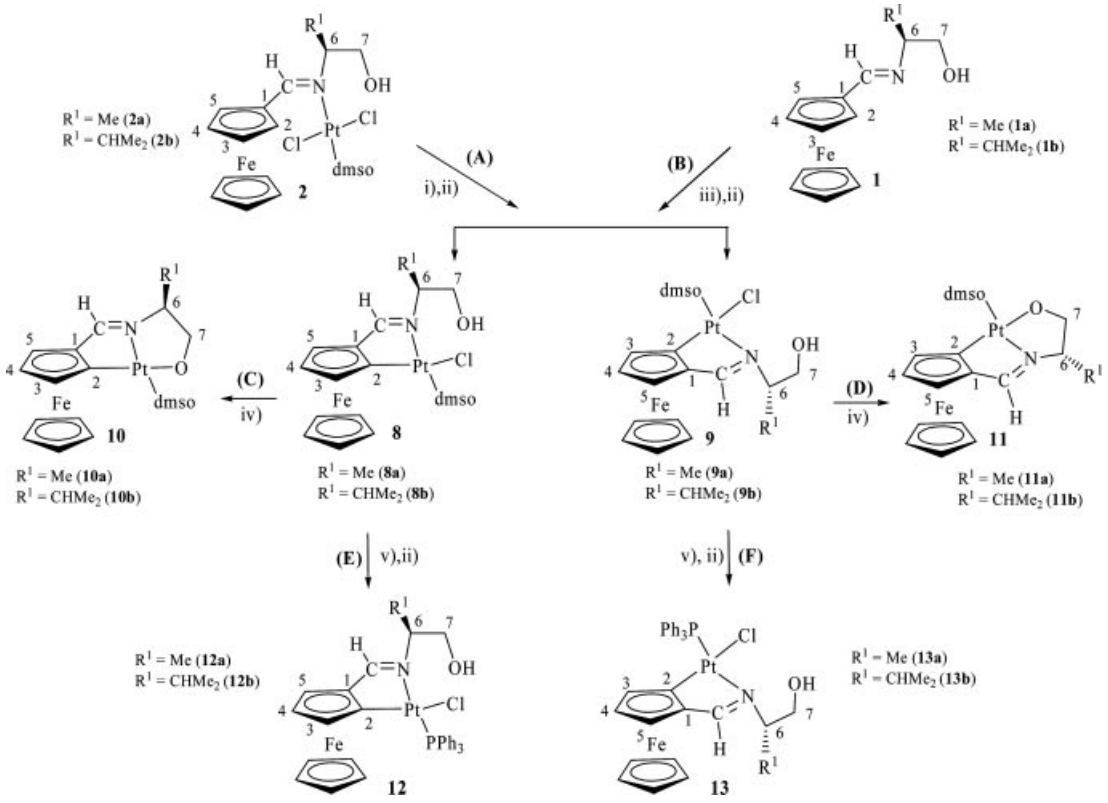


Scheme 2. *i*) In toluene, addition of NaOAc (in a NaOAc:**2** molar ratio of 2) dissolved in methanol followed by a reflux of the reaction mixture for 72 h (see text). *ii*) $SiO_2$ column chromatography. *iii*) *cis*-[$PtCl_2(dmso)_2$] and NaOAc in a molar ratio **1**/$Pt^{II}$/NaOAc = 1:1:2 in a toluene/methanol (4:1) mixture under reflux for 72 h (see text). *iv*) Addition of the stoichiometric amount of NaOD dissolved in methanol. *v*) In benzene followed by the addition of the equimolar amount of $PPh_3$ and stirring at 343 K for 1 h.

 © 2006 Wiley-VCH Verlag GmbH & Co. KGaA, Weinheim 

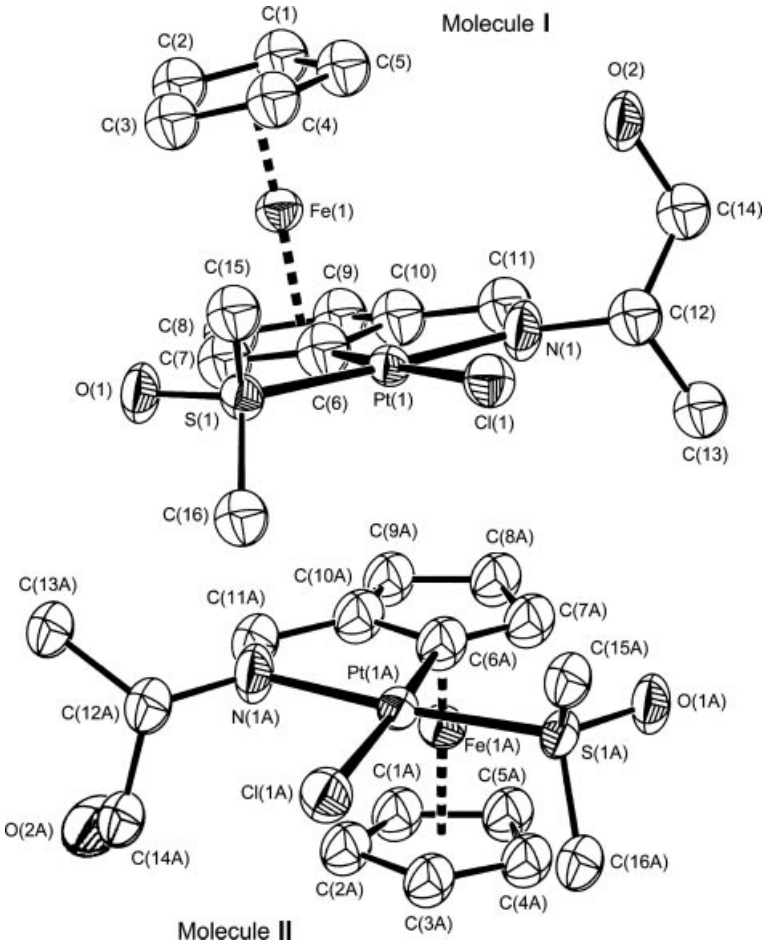


Figure 5. ORTEP plot of ($R_p$,$S_C$)-(+)-[Pt{[($\eta^5$-$C_5H_3$)CH=NCH(Me)$CH_2$OH]Fe($\eta^5$-$C_5H_5$)}Cl(dmso)] (**9a**). Thermal ellipsoids at 50% probability; hydrogen atoms have been omitted for clarity. Selected bond lengths (Å) and angles (°): Pt(1)–C(6) 2.01(3), Pt(1)–N(1) 2.05(2), Pt(1)–S(1) 2.214(2), Pt(1)–Cl(1) 2.427(8), C(10)–C(11) 1.40(4), N(1)–C(11) 1.26(3), N(1)–C(12) 1.50(2), O(2)–C(14) 1.40(3), Pt(1A)–C(6A) 2.03(3), Pt(1A)–N(1A) 2.01(3), Pt(1A)–S(1A) 2.197(8), C(10A)–C(11A) 1.46(4), N(1A)–C(11A) 1.24(4), N(1A)–C(12A) 1.51(4), O(2A)–C(14A) 1.42(3), C(6)–Pt(1)–N(1) 81.5(12), C(6)–Pt(1)–S(1) 97.8(10), N(1)–Pt(1)–Cl(1) 91.7(8), S(1)–Pt(1)–Cl(1) 89.0(3), C(6A)–Pt(1A)–N(1A) 78.6(12), C(6A)–Pt(1A)–S(1A) 95.9(9), N(1A)–Pt(1A)–Cl(1A) 95.2(9), S(1A)–Pt(1A)–Cl(1A) 90.4(3).

O(2A)–C(14A)–C(12A)–C(13A) are 174(2)° and 61(3)°; as a consequence of this arrangement the separation between the $Fe^{II}$ and the oxygen of the OH group in **I** is greater than in **II**.

The formation of platinacycles of general formula [Pt(C,N)Cl(dmso)] {$(C,N)^-$ = cyclometallated imine (L)} from [Pt(L)$Cl_2$(dmso)] requires a proper orientation between the σ(C–H) bond to be activated and the platinum(II)[1a,38] and the release of one of the $Cl^-$ ligands. The formation of a nearly equimolar ratio of **8** and **9** can be explained assuming a free rotation around the $C_{ipso}$–$C_{imine}$ bond of **2a** or **2b**. A similar argument has been used for the cyclopallada- or cycloplatination of several 1,1′-ferrocenyldiimines or diamines.[39]

In order to explore the coordinating ability of the oxygen to the platinum(II) and the potential hemilability[40] of the σ(Pt–O) bond, solutions of **8a**, **8b**, **9a** or **9b** were treated separately with the equimolar amount of NaOD. In all cases, the corresponding diastereomer of [Pt{[($\eta^5$-$C_5H_3$)-CH=NCH($R^1$)$CH_2$O]Fe($\eta^5$-$C_5H_5$)}(dmso)][27] {**10** and **11**; $R^1$ = Me ($S_p$,$S_C$) (**10a**) and ($R_p$,$S_C$) (**11a**) or $R^1$ = $CHMe_2$ ($S_p$,$S_C$) (**10b**) and ($R_p$,$S_C$) (**11b**)} {Scheme 2, steps (C) and (D)} was isolated. These compounds arise from the activation of the σ(O–H) bond. In their $^1$H NMR spectra the signal due to the imine proton exhibited the typical satellites due to the coupling with the $^{195}$Pt nucleus and appeared at higher fields than for the parent complex. Besides, the resonance of the $^{13}$C nuclei of the "$>CHCH_2$–" moiety shifted downfield. These findings suggested, in keeping with the bibliography,[41] a $(C,N,O)^{2-}$ mode of binding of the ligand.

Solutions of **10** and **11** (in $CDCl_3$) changed with time and after 3 days the spectra revealed the coexistence of the pairs (**8** and **10**) or (**9** and **11**) (molar ratios **8a/10a** = 1.1, **9a/11a** = 1.0, **8b/10b** = 1.5 and **9b/11b** = 0.9). The addition of DCl to solutions of **10** (or **11**) gave **8** (or **9**) and subsequent cycles exposing **8** or **9** to acidic and basic conditions showed that the transformations **8** ↔ **10** and **9** ↔ **11** were reproducible and robust, enabling these systems to function as a simple molecular switch.[42] Therefore, the deproton-

 © 2006 Wiley-VCH Verlag GmbH & Co. KGaA, Weinheim 

ation of the OH group by the action of a base and the subsequent intramolecular replacement of the adjacent chloride moiety can be easily tuned by manipulating the acidity/basicity of the media. Examples of diastereomerically pure metallacycles exhibiting this behaviour are still unknown.

Finally, and in order to elucidate the potential utility of the platinacycles [Pt{[($\eta^5$-$C_5H_3$)CH=NCH($R^1$)$CH_2$OH]-Fe($\eta^5$-$C_5H_5$)}Cl(dmso)] (**8** and **9**) as precursors for the synthesis of other diastereomerically pure platinum(II) derivatives, we studied the reactions of **8**–**9a**,**b** with $PPh_3$. In all cases, the platinacycles [Pt{[($\eta^5$-$C_5H_3$)CH=NCH($R^1$)-$CH_2$OH]Fe($\eta^5$-$C_5H_5$)}Cl($PPh_3$)] {**12**–**13**; $R^1$ = Me ($S_p$,$S_C$) (**12a**) and ($R_p$,$S_C$) (**13a**) or $CHMe_2$ ($S_p$,$S_C$) (**12b**) and ($R_p$,$S_C$) (**13b**)} {Scheme 2, steps (E) and (F)} were isolated. $^{31}P\{^1H\}$ and $^{195}Pt\{^1H\}$ NMR spectroscopic data[27] for **12**–**13** were consistent with those reported for other platinacycles containing a cyclometallated Schiff base,[24b,24c,43] in which the phosphane and the metallated carbon are in a *cis* arrangement, in good agreement with the *transphobia effect*.[44]

In summary, the results presented have allowed us to establish the best experimental conditions to selectively control the mode of binding {(N), $(N,O)^-$, [C($sp^2$,ferrocene),N]$^-$ or [C($sp^2$,ferrocene),N,O]$^{2-}$} of ligands **1** to platinum(II). For each one of the ligands, three different pairs of enantiomerically pure complexes (**2**–**7a**,**b**) are isolated. These compounds differ in the mode of binding of the ferrocenyl ligand {N-donor group (in **2** and **3**) or a monoanionic $(N,O)^-$ group (in **4**–**7**)}, or in the relative arrangement between: *a*) the monodentate ligands bound to platinum(II) (in **2** and **3**), *b*) these groups and the two heteroatoms of the ferrocenyl Schiff base (in **4**–**7**) or *c*) the conformation of the ligand *anti*-(*E*) (in **4** and **6**) or *syn*-(*Z*) (in **5** and **7**). Moreover, these studies also enable the isolation of the diastereomerically pure platinacycles: [Pt{[($\eta^5$-$C_5H_3$)-CH=NCH($R^1$)$CH_2$OH]Fe($\eta^5$-$C_5H_5$)}Cl(L)] {L = dmso (**8** and **9**) or $PPh_3$ (**12** and **13**)} and [Pt{[($\eta^5$-$C_5H_3$)-CH=NCH($R^1$)$CH_2$O]Fe($\eta^5$-$C_5H_5$)}(dmso)] (in **10** and **11**) {with a [C($sp^2$,ferrocene),N]$^-$ or [C($sp^2$,ferrocene),N,O]$^{2-}$ ligand, respectively}. As far as we know, chiral ligands exhibiting such interesting and versatile modes of binding to transition metals and, in particular, to platinum(II) have not been described so far.

The studies undertaken also showed the outstanding reactivity of compounds **2** and their utility for the preparation of a wide variety of chiral platinum(II) complexes by: *a*) activation of the σ(O–H) to give **4** {which may be transformed into **5** by the subsequent isomerisation *anti*-(*E*) → *syn*-(*Z*) of the coordinated Schiff base, Scheme 1, steps (B) and (C)} or *b*) the cycloplatination of the ferrocenyl unit {Scheme 2, step (A)} to give the diastereomers **8** and **9**. In the presence of NaOH, **8** (or **9**) evolve to the chiral derivatives **10** (or **11**) with a [C($sp^2$,ferrocene),N,O]$^{2-}$ ligand {Scheme 2, steps (C) and (D)}. Moreover, the reactivity of **2** through pathways (B) and (A) in Scheme 1 and Scheme 2, respectively, can be easily controlled by the appropriate selection of the reagent (NaOH or NaOAc) and the solvent. The use of equimolar amounts of NaOH and MeOH as solvent promotes the formation of the coordination compounds with $(N,O)^-$ bidentate ligands (**4**), while larger excesses induce the *anti*-(*E*) → *syn*-(*Z*) isomerisation of the ligands giving **5**. The replacement of NaOH by NaOAc and the decrease of the polarity of the reaction media promotes the activation of the σ[C($sp^2$,ferrocene)–H] bond, giving the platinacycles **8** and **9**, which can be easily transformed into [Pt{[($\eta^5$-$C_5H_3$)CH=NCH($R^1$)$CH_2$O]Fe($\eta^5$-$C_5H_5$)}(dmso)] (**10** and **11**) {with a [C($sp^2$,ferrocene),N,O]$^{2-}$ ligand}. Platinacycles **8**–**13** are especially attractive as they may be used as starting materials for the synthesis of a wide variety of diastereomerically pure platinum(II) compounds, or even platinum(IV) derivatives (through oxidative addition reactions). Furthermore, the results presented have demonstrated that the interconversion between the pairs of the corresponding diastereomerically pure platinacycles (**8** and **10** or **9** and **11**) can be viewed as an acid–base controlled molecular switch.[42] These transformations modify the hapticity of the ligand and are particularly relevant in view of the potential utility of **8**–**11** in homogeneous catalysis. Moreover, the environments around the platinum(II) in **2**, **3**, **8** and **9** are similar to those of [Pt{[($\eta^5$-$C_5H_3$)$CH_2$N$Me_2$]-Fe($\eta^5$-$C_5H_5$)}Cl(dmso)] or [Pt{Fc$CH_2$N$Me_2$}$Cl_2$(dmso)],[19] which exhibit antitumoral activity, and consequently they are also interesting from this point of view.

Finally, preliminary results reveal that the procedures described here can also be extended to other imino-alcohols derived from **1** by the replacement of the ferrocenyl group by a phenyl {i.e. ($S_C$)-$C_6H_5$CH=NCH($R^1$)$CH_2$OH with $R^1$ = Me or $CHMe_2$}. Thus, these studies constitute an initial step toward further research focused on the synthesis and the study of the properties and potential applications of a wide variety of novel enantio- or diastereomerically pure platinum complexes.

## Experimental Section

**Materials:** *cis*-[$PtCl_2$(dmso)$_2$] was prepared as described.[45] Ferrocenecarboxaldehyde, ($S_C$)-(+)-$H_2$NCH($R^1$)$CH_2$OH {$R^1$ = Me or $CHMe_2$} and the remaining reagents were obtained from Aldrich and used as received. The methanol was HPLC grade,[46] and the remaining solvents used, except benzene, were dried and distilled before use.[47]

**Instrumentation:** Elemental analyses were carried out at the Serveis Cientifico-Tècnics (University of Barcelona) and Servei de Recursos Cientifics i Tècnics (University Rovira i Virgili, Tarragona). Infrared spectra were obtained with a Nicolet Impact 400 instrument using KBr discs. Proton and the two-dimensional NMR [{$^1$H-$^1$H}-(COSY) and (NOESY) and the {$^1$H-$^{13}$C}-(HSQC) and (HMBC)] experiments were run at 500 MHz with either Varian 500 or Bruker Avance 500DMX instruments. Except where quoted, the solvent used for the $^1$H NMR experiments was $CDCl_3$ (99.9%) and $SiMe_4$ was the internal reference. $^{195}Pt\{^1H\}$ NMR spectra as well as $^{31}P\{^1H\}$ NMR spectra were recorded with a Bruker-250DXR instrument using $CDCl_3$ (99.9%) as solvent and referenced to $H_2[PtCl_6]$ [$\delta^{195}Pt\{H_2[PtCl_6]\}$ = 0.0 ppm] and $P(OMe)_3$ [$\delta^{31}P\{P(OMe)_3\}$ = 140.17 ppm], respectively. In all cases the chemical shifts ($\delta$) are given in ppm and the coupling constants ($J$) in Hz.

 © 2006 Wiley-VCH Verlag GmbH & Co. KGaA, Weinheim 

Table 2. Crystal data and details of the refinement of the crystal structures of **1b**·$H_2O$, **3b**, **7b**·$CH_2Cl_2$·1/2$H_2O$ and **9a**.

| | **1b**·$H_2O$ | **3b** | **7b**·$CH_2Cl_2$·1/2$H_2O$ | **9a** |
|---|---|---|---|---|
| Crystal system | monoclinic | orthorhombic | monoclinic | orthorhombic |
| Space group | $P2_1$ (no. 4) | $P2_12_12_1$ (no. 19) | $P2_1$ (no. 4) | $P2_12_12_1$ (no.19) |
| $a$ [Å] | 10.749(6) | 10.157(4) | 10.368(3) | 9.893(5) |
| $b$ [Å] | 6.048(8) | 14.356(5) | 9.259(3) | 16.054(9) |
| $c$ [Å] | 12.411(9) | 15.448(6) | 14.587(3) | 23.633(5) |
| $\beta$ [°] | 99.80(6) | 90.0 | 101.74(3) | 90.0 |
| $Z$ | 2 | 4 | 2 | 8 |
| $T$ [K] | 293(2) | 294(2) | 294(2) | 293(2) |
| No. reflections collected | 2514 | 6528 | 2563 | 4780 |
| No. reflections observed | 855 | 4520 | 1999 | 1918 |
| $R$ indices [$I > 2\sigma(I)$] | $R_1$ = 0.0426, $wR_2$ = 0.0902 | $R_1$ = 0.0644, $wR_2$ = 0.1679 | $R_1$ = 0.0665, $wR_2$ = 0.1829 | $R_1$ = 0.0480, $wR_2$ = 0.0665 |
| $R$ indices (all data) | $R_1$ = 0.2394, $wR_2$ = 0.1393 | $R_1$ = 0.1036, $wR_2$ = 0.1959 | $R_1$ = 0.1030, $wR_2$ = 0.2044 | $R_1$ = 0.2410, $wR_2$ = 0.0993 |
| Max. and min. diff. density [e $A^{-3}$] | 0.42 and –0.99 | 4.69 and –3.41 | 1.79 and –1.61 | 0.19 and –0.11 |
| Flack coefficient[a] | 0.10(6) | –0.008(19) | 0.00(3) | –0.004(18) |

[a] Data from ref.[51]

The optical rotations were determined in $CH_2Cl_2$ at 293 K using a Perkin–Elmer 241 MC polarimeter and the concentration used is specified in the characterisation section of each compound. Mass spectra ($FAB^+$) were obtained with a VG-Quattro Fisions instrument using 3-nitrobenzylalcohol (NBA) as matrix.

**Crystallography:** A prismatic crystal of **1b**·$H_2O$ (orange, 0.2×0.1×0.1 mm), **3b** (orange, 0.59×0.16×0.14 mm), **7b**·$CH_2Cl_2$·1/2$H_2O$ (red, 0.53×0.12×0.12 mm) or **9a** (purple, 0.2×0.1×0.1 mm) was selected and mounted on an Enraf–Nonius CAD4 diffractometer. Unit-cell parameters (Table 2) were determined from automatic centring of 25 reflections {in the ranges: 12° < $\Theta$ < 21° (for **1b**·$H_2O$ and **9a**), 8.3° < $\Theta$ < 15.4°(for **3b**) and 8.73° < $\Theta$ < 17.9° (for **7b**·$CH_2Cl_2$·1/2$H_2O$)} and refined by the full-matrix least-squares method. For **3b**, **7b**·$CH_2Cl_2$·1/2$H_2O$ and **9a** Lorentz polarisation corrections and absorption corrections were made.

The structures were solved by direct methods using the SHELXS computer program[48] and refined by the full-matrix least-squares method with the SHELX97 or SHELX93 computer programs.[49] The function minimised was $\Sigma w||F_o|^2 - |F_c|^2|^2$, where $w = [\sigma^2(I) + (0.0434P)^2]^{-1}$ (for **1b**·$H_2O$), $[\sigma^2(I) + (0.1070P)^2 + 9.0330P]^{-1}$ (for **3b**), $[\sigma^2(I) + (0.1467P)^2]^{-1}$ (for **7b**·$CH_2Cl_2$·1/2$H_2O$) and $[\sigma^2(I) + (0.0132P)^2]^{-1}$ (for **9a**) and $P = (|F_o|^2 + 2|F_c|^2)/3$; scattering factors were taken from the literature.[50] The chirality of the structures was determined by the Flack coefficient.[51]

CCDC-299520 to -2999523 contain the supplementary crystallographic data for this paper. These data can be obtained free of charge from The Cambridge Crystallographic Data Centre via www.ccdc.cam.ac.uk/data_request/cif.

**Supporting Information** (see also the footnote on the first page of this article): Experimental procedures for the preparation of all the compounds and their characterisation data; graphical plot of the relative abundance of the species present on solution when **2b** was treated with NaOD (Figure S1).

## Acknowledgments

This work was supported by the Ministerio de Ciencia y Tecnología of Spain and by the Generalitat de Catalunya (projects BQU2003-00906, BQU2002-00601 and 2001-SRG-00054, respectively) and FEDER funds.

[1] a) J. Dupont, C. S. Consorti, J. Spencer, *Chem. Rev.* **2005**, *105*, 2527–2572; b) V. I. Sokolov, *Chirality and Optical Activity in Organometallic Compounds*, Gordon and Breach, London, UK, **1990**; c) E. Wong, C. M. Giandomenico, *Chem. Rev.* **1999**, *99*, 2451–2466; d) T. W. Hambley, *Coord. Chem. Rev.* **1997**, *166*, 181–223; e) I. Omae, *Coord. Chem. Rev.* **2004**, *248*, 995–1023.

[2] For a general overview of the latest advances on chiral palladium(II) and platinum(II) compounds, see for instance: a) G. Du, A. Ellern, L. K. Woo, *Inorg. Chem.* **2003**, *42*, 873–877; b) L. Diez, P. Espinet, J. A. Miguel, M. B. Ros, *J. Mater. Chem.* **2002**, *12*, 3694–3695; c) H. Hamaskima, D. Hotta, M. Sodeaka, *J. Am. Chem. Soc.* **2002**, *124*, 11240–11241; d) A. Ikeda, H. Udzu, Z. Zhong, S. Shinkai, S. Sakamoto, K. Yamaguchi, *J. Am. Chem. Soc.* **2001**, *123*, 3872–3877; e) V. P. Munk, C. I. Diakos, B. A. Messerle, R. R. Fenton, T. W. Hambley, *Chem. Eur. J.* **2002**, *8*, 5486–5493; f) J. Bravo, C. Cativela, J. E. Chaves, R. Navarro, E. P. Urriolabeitia, *Inorg. Chem.* **2003**, *42*, 1006–1013.

[3] a) I. Omae, *Applications of Organometallic Compounds*, John Wiley, Chichester, UK, **1998**; b) P. W. Jolly, G. Wilke, W. A. Kermann, B. Cornils (Eds.), *Applied Homogeneous Catalysis with Organometallic Compounds*, VCH, Weinheim, Germany, **1996**.

[4] For the latest applications of these compounds in homogeneous catalysis, see for instance: a) S. F. Kirsch, L. E. Overman, M. P. Watson, *J. Org. Chem.* **2004**, *69*, 8101–8104; b) K. Ito, Y. Imahayashi, T. Kuroda, S. Eno, B. Saito, T. Katsuki, *Tetrahedron Lett.* **2004**, *45*, 7277–7281; c) D. Franco, M. Gómez, F. Jiménez, G. Muller, M. Rocamora, M. A. Maestro, J. Mahía, *Organometallics* **2004**, *23*, 3197–3209; d) T. J. Brunker, J. R. Moncarz, D. J. Glueck, L. N. Zakharov, J. A. Golen, A. L. Rheingold, *Organometallics* **2004**, *23*, 2228–2230; e) P. Dotta, P. G. A. Kumar, P. S. Pregosin, A. Albinati, S. Rizzato, *Organometallics* **2004**, *23*, 2295–2304.

[5] G. Uccello-Barretta, R. Bernardini, F. Balzano, P. Salvadori, *Chirality* **2002**, *14*, 484–489.

[6] a) S. B. Wild, *Coord. Chem. Rev.* **1997**, *166*, 291–311 and references cited therein; b) G. He, K. F. Mok, P. H. Leung, *Organometallics* **1999**, *18*, 4027–4031.

[7] a) C. Sacht, M. S. Datt, S. Otto, A. Roodt, *J. Chem. Soc., Dalton Trans.* **2000**, 727–733; b) T. W. Failes, M. D. Hall, T. W. Hambley, *Dalton Trans.* **2003**, *8*, 1596–1600.

[8] a) M. Albrecht, G. van Koten, *Angew. Chem. Int. Ed.* **2001**, *40*, 3750–3781; b) J. Dupont, M. Pfeffer, J. Spencer, *Eur. J. Inorg.*

 © 2006 Wiley-VCH Verlag GmbH & Co. KGaA, Weinheim 

*Chem.* **2001**, 1917–1927; c) R. B. Bedford, *Chem. Commun.* **2003**, 1787–1796.

[9] a) C. Anderson, M. Crespo, F. D. Rochon, *J. Organomet. Chem.* **2001**, *631*, 164–174; b) R. Wünch, G. Bosl, C. Robl, W. Weigand, *J. Organomet. Chem.* **2001**, *621*, 352–358; c) C. Cativela, L. R. Falvello, J. C. Ginés, R. Navarro, E. P. Urriolabeitia, *New J. Chem.* **2001**, *25*, 334–352.

[10] a) T. K. Hollis, L. E. Overman, *Tetrahedron Lett.* **1997**, *38*, 8837–8840; b) P. X. Liu, K. F. Mok, J. J. Vittal, P. H. Leung, *Organometallics* **2000**, *19*, 3722–3729.

[11] W. C. Yeo, J. J. Vittal, L. L. Koh, G. K. Tan, P. H. Leung, *Organometallics* **2004**, *23*, 3474–3482.

[12] Y. Wu, S. Huo, J. Gong, X. Cui, L. Ding, K. Ding, C. Du, Y. Liu, M. Song, *J. Organomet. Chem.* **2001**, *637–639*, 27–46 and references cited therein.

[13] For recent reports concerning cyclopalladated complexes with (N) or [C(sp$^2$,ferrocene),N]$^-$ ligands, see for instance: C. López, R. Bosque, J. Arias, E. Evangelio, X. Solans, M. Font-Bardía, *J. Organomet. Chem.* **2004**, *672*, 34–42 and references cited therein.

[14] For palladacycles with tridentate [C(sp$^2$,ferrocene),N,E]$^-$ (E = N′ or O) ligands: a) S. Pérez, C. López, A. Caubet, A. Pawełczyk, X. Solans, M. Font-Bardía, *Organometallics* **2003**, *22*, 2396–2408; b) C. López, A. Caubet, S. Pérez, X. Solans, M. Font-Bardía, *J. Organomet. Chem.* **2002**, *651*, 105–113; c) C. J. Isaac, C. Price, B. R. Horrocks, A. Houlton, M. R. J. Elsegood, W. Clegg, *J. Organomet. Chem.* **2000**, *598*, 248–253.

[15] Latest contributions on palladium and platinum(II) complexes with a [C(sp$^2$,ferrocene),N,S]$^-$ ligand: a) S. Pérez, C. López, A. Caubet, R. Bosque, X. Solans, M. Font-Bardía, A. Roig, E. Molins, *Organometallics* **2004**, *23*, 224–236; b) C. López, S. Pérez, X. Solans, M. Font-Bardía, *J. Organomet. Chem.* **2005**, *690*, 228–243.

[16] Y. Wu, J. Hou, H. Yun, C. Cui, R. Yuan, *J. Organomet. Chem.* **2001**, *637–639*, 793–795.

[17] a) M. Pfeffer, J. P. Sutter, A. de Cian, J. Fischer, *Organometallics* **1993**, *12*, 1167–1173; b) G. Zhao, Q. G. Wang, T. C. W. Mak, *J. Organomet. Chem.* **1999**, *574*, 311–317; c) M. Benito, C. López, X. Morvan, X. Solans, M. Font-Bardía, *J. Chem. Soc., Dalton Trans.* **2000**, 4470–4478; d) R. Bosque, M. Benito, C. López, *New J. Chem.* **2001**, *25*, 827–853; e) C. López, A. Caubet, X. Solans, M. Font-Bardía, *J. Organomet. Chem.* **2000**, *598*, 87–102.

[18] P. R. R. Ranatunge-Bandarage, N. W. Duffy, S. M. Johnston, B. H. Robinson, J. Simpson, *Organometallics* **1994**, *13*, 511–521 and references cited therein.

[19] R. W. Wason, K. McGrouther, P. R. R. Ranatunge-Bandarage, B. H. Robinson, J. Simpson, *Appl. Organomet. Chem.* **1999**, *13*, 163–174.

[20] A. Togni, T. Hayashi, *Ferrocenes, Homogeneous Catalysis, Organic Synthesis and Materials Science*, VCH, Weinheim, Germany, **1995**.

[21] a) G. Zhao, Q. G. Wang, T. C. W. Mak, *Tetrahedron: Asymmetry* **1998**, *9*, 2253–2257; b) M. Benito, C. López, X. Solans, M. Font-Bardía, *Tetrahedron: Asymmetry* **1998**, *9*, 4219–4238; c) C. López, R. Bosque, D. Sainz, X. Solans, M. Font-Bardía, *Organometallics* **1997**, *16*, 3261–3266.

[22] Recent contributions in this field: a) A. Moyano, M. Rosol, R. M. Moreno, C. López, M. A. Maestro, *Angew. Chem. Int. Ed.* **2005**, *44*, 1865–1869; b) C. E. Anderson, Y. Donde, C. J. Douglas, L. E. Overman, *J. Org. Chem.* **2005**, *70*, 648–657.

[23] A. D. Ryabov, I. M. Panyashkina, V. A. Polyakov, J. A. K. Howard, L. G. Kuz′mina, M. S. Datt, C. Sacht, *Organometallics* **1998**, *17*, 3615–3618.

[24] a) A. D. Ryabov, G. M. Kazankov, I. M. Panyashkina, O. G. Grozovsky, O. G. Dyachenko, V. A. Polyakov, L. G. Kuz'mina, *J. Chem. Soc., Dalton Trans.* **1997**, 4385–4391; b) Y. J. Wu, L. Ding, H. X. Wang, Y. H. Liu, H. Z. Yuan, X. A. Mao, *J. Organomet. Chem.* **1997**, *535*, 49–58; c) S. Pérez, C. López, A. Caubet, X. Solans, M. Font-Bardía, *New J. Chem.* **2003**, *27*, 975–982.

[25] C. López, A. Caubet, S. Pérez, X. Solans, M. Font-Bardía, *Chem. Commun.* **2004**, 540–541.

[26] a) C. López, J. Sales, R. Zquiak, X. Solans, *J. Chem. Soc., Dalton Trans.* **1992**, 2321–2328; b) R. Bosque, C. López, J. Sales, X. Solans, M. Font-Bardía, *J. Chem. Soc., Dalton Trans.* **1994**, 735–745.

[27] Characterisation data are provided in the Supporting Information.

[28] C. López, R. Bosque, X. Solans, M. Font-Bardía, *New J. Chem.* **1996**, *20*, 1285–1292.

[29] T. H. Allen, *Acta Crystallogr., Sect. B: Struct. Sci.* **2002**, *58*, 380–388.

[30] a) J. Bravo, C. Cativela, R. Navarro, E. P. Urriolabeitia, *J. Organomet. Chem.* **2002**, *650*, 157–172; b) A. Caubet, C. López, X. Solans, M. Font-Bardía, *J. Organomet. Chem.* **2003**, *669*, 164–171.

[31] Y. J. Wu, X. L. Cui, C. X. Du, W. L. Wang, R. Y. Guo, R. F. Chen, *J. Chem. Soc., Dalton Trans.* **1998**, 3727–3730.

[32] A. Caubet, C. López, R. Bosque, X. Solans, M. Font-Bardía, *J. Organomet. Chem.* **1999**, *577*, 292–304.

[33] a) J. Albert, M. Gómez, J. Granell, J. Sales, X. Solans, *Organometallics* **1990**, *9*, 1405–1413; b) J. Albert, R. M. Ceder, M. Gómez, J. Granell, J. Sales, *Organometallics* **1992**, *11*, 1536–1536.

[34] R. G. Miller, R. D. Stauffer, D. R. Fahey, D. R. Pernell, *J. Am. Chem. Soc.* **1970**, *92*, 1511–1521.

[35] a) M. Crespo, M. Font-Bardía, J. Granell, M. Martínez, X. Solans, *Dalton Trans.* **2003**, 3763–3769; b) M. Crespo, J. Granell, X. Solans, M. Font-Bardía, *J. Organomet. Chem.* **2003**, *681*, 143–149.

[36] The variations of the composition of the solutions obtained from **2b** upon the addition of NaOD [in NaOD/**2b** molar ratios varying from 0.2 to 1.8] are presented in the Supporting Material (Figure S1).

[37] Shorter reaction periods produced a considerable decrease of the relative abundance of compounds **7**. In particular, after 27 h of reflux the molar ratios **2a/3a/5a/7a** and **2b/3b/5b/7b** were 0.38:0.18:1.00:0.43 and 0.30:0.23:1.00:0.39, respectively.

[38] a) I. Omae, *Coord. Chem. Rev.* **1976**, *18*, 327–352; b) A. D. Ryabov, *Chem. Rev.* **1990**, *90*, 403–424; c) V. V. Dunina, O. A. Zalevskaya, V. M. Potatov, *Russ. Chem. Rev.* **1988**, *57*, 250–260.

[39] a) R. Bosque, C. López, X. Solans, M. Font-Bardía, *Organometallics* **1999**, *18*, 1267–1274; b) Y. J. Wu, Y. H. Liu, L. Yang, Q. X. Zhu, *Polyhedron* **1997**, *16*, 335–339; c) L. Ding, D. P. Zou, Y. J. Wu, *Polyhedron* **1998**, *17*, 2511–2516.

[40] a) A. Bader, E. Lindner, *Coord. Chem. Rev.* **1991**, *108*, 27–110; b) C. S. Stone, D. Weinberger, C. A. Mirkin, *Prog. Inorg. Chem.* **1999**, *48*, 233–350.

[41] C. López, A. Caubet, S. Pérez, X. Solans, M. Font-Bardía, *J. Organomet. Chem.* **2003**, *681*, 82–90.

[42] For a general overview on molecular devices see for instance the special issue devoted to "Molecular Machines" published in *Acc. Chem. Res.* **2001**, *34*.

[43] X. Riera, A. Caubet, C. López, V. Moreno, X. Solans, M. Font-Bardía, *Organometallics* **2000**, *19*, 1384–1390.

[44] J. Vicente, J. A. Abad, E. Martínez-Viviente, P. G. Jones, *Organometallics* **2002**, *21*, 4454–4467 and references cited therein.

[45] J. H. Price, A. N. Williamson, F. R. Schram, B. Wayland, *Inorg. Chem.* **1972**, *11*, 1280–1286.

[46] The success of the preparations of compounds **2**–**11a,b** is strongly dependent on the quality of the methanol used. The presence of small amounts of water induces the formation of large amounts of FcCHO and reduces the yields. Thus, the use of MeOH (HPLC grade) is strongly required.

[47] D. D. Perrin, W. L. F. Amarego, *Purification of Laboratory Chemicals*, 4th ed., Butterworth-Heinemann, Oxford, UK, **1996**.

 © 2006 Wiley-VCH Verlag GmbH & Co. KGaA, Weinheim 

[48] G. M. Sheldrick, *SHELXS. A computer program for determination of crystal structures*, University of Göttingen, Germany, **1997**.
[49] a) G. M. Sheldrick, *SHELX93. A computer program for determination of crystal structures*, University of Göttingen, Germany, **1994**; b) *SHELX97. A computer program for determination of crystal structures*, University of Göttingen, Germany, **1997**.
[50] *International Table of X-ray Crystallography*, The Kynoch Press, Birmingham, UK, **1974**, vol. IV, pp. 99–100 and 149.
[51] H. D. Flack, *Acta Crystallogr., Sect. A: Found. Crystallogr.* **1983**, *39*, 876–888.

Received: February 28, 2006
Published Online: August 7, 2006

 © 2006 Wiley-VCH Verlag GmbH & Co. KGaA, Weinheim 

EurJIC
European Journal of Inorganic Chemistry

Issue 20/2006

Pages 3989–4192

*Papers available ahead of print in Early View at www.interscience.wiley.com*

*Earliest available Table of Contents:*
*Automatically, free of charge by e-mail through*
*www.interscience.wiley.com/alerts*

## COVER PICTURE

**The cover picture shows** an organoruthenium antimetastasis compound, superimposed over a Sudoku puzzle, representing the challenge of discovering new anticancer drugs and elucidating their mechanisms of action. One needs to uncover pieces of information which are interrelated, and eventually, the complete "picture" is revealed. In this review, we describe the extent to which the picture has been revealed for ruthenium-based drugs, which are currently growing in interest as a result of recent successes in clinical trials. The emphasis is directed towards classifying the vast array of ruthenium compounds already evaluated in vitro and in vivo against primary and secondary cancers within the context of their probable target. It is hoped that on the basis of the picture presented here more of this intriguing puzzle will be revealed soon. Details are presented in the Microreview by W. H. Ang and P. J. Dyson on p. 4003 ff.

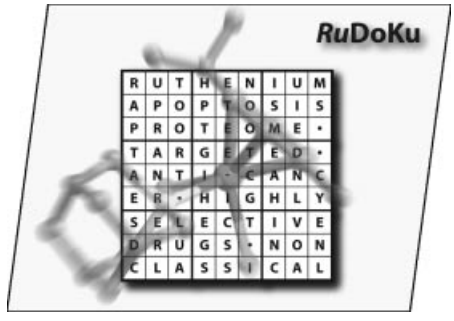


## MICROREVIEW

**Contents**

**4003** **W. H. Ang, P. J. Dyson***

Classical and Non-Classical Ruthenium-Based Anticancer Drugs: Towards Targeted Chemotherapy

**Keywords:** Ruthenium / Anticancer drugs / Targeted chemotherapy / DNA binding / Antimetastasis drugs

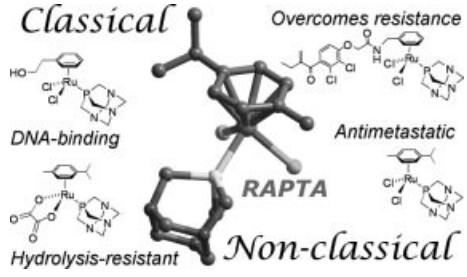


 © 2006 Wiley-VCH Verlag GmbH & Co. KGaA, Weinheim 

# SHORT COMMUNICATIONS


**4019** **L. Barišić, V. Rapić, N. Metzler-Nolte***

Incorporation of the Unnatural Organometallic Amino Acid 1′-Aminoferrocene-1-carboxylic Acid (Fca) into Oligopeptides by a Combination of Fmoc and Boc Solid-Phase Synthetic Methods

**Keywords:** Bioorganometallic chemistry / Ferrocene / Peptides / Solid-phase peptide synthesis / Unnatural amino acids

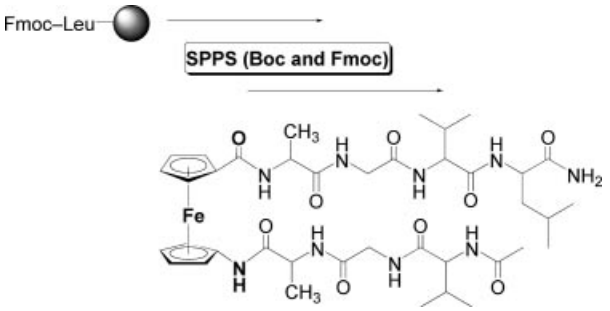


**4022** **S. Giuffrida, G. Ventimiglia, F. L. Callari, S. Sortino***

Straightforward Light-Driven Synthesis of Ultrasmall, Water-Soluble Monolayer-Protected Platinum Nanoparticles

**Keywords:** Platinum / Nanoparticles / Monolayers / Carboxylates / Light

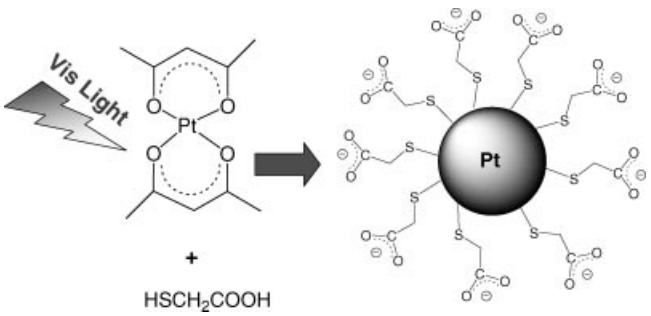


**4026** **M. G. B. Drew, D. Parui, S. De, J. P. Naskar, D. Datta***

An Eight-Coordinate Mononuclear Double Helical Complex

**Keywords:** Cadmium / Single helicate / Double helicate / N ligands / Seven-coordinate complexes / Eight-coordinate complexes

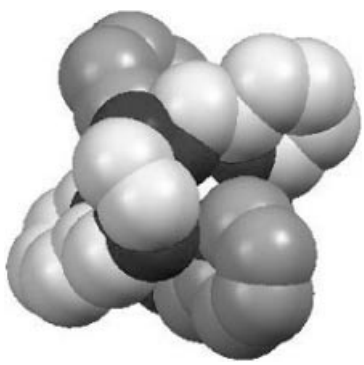

**4029** **S. Singh, A. Pal, H. W. Roesky,* R. Herbst-Irmer**

Adducts of $Cp_3Ln$ with LGa(Me)OH, Syntheses and X-ray Crystal Structures of LGa(Me)-HO→$LnCp_3$ {Ln = Sm, Nd, Yb; L = $HC[C(Me)N(2,6\text{-}iPr_2C_6H_3)]_2$}

**Keywords:** Adducts / Hydroxides / Gallium / Heterodimetallic compounds / Lanthanides

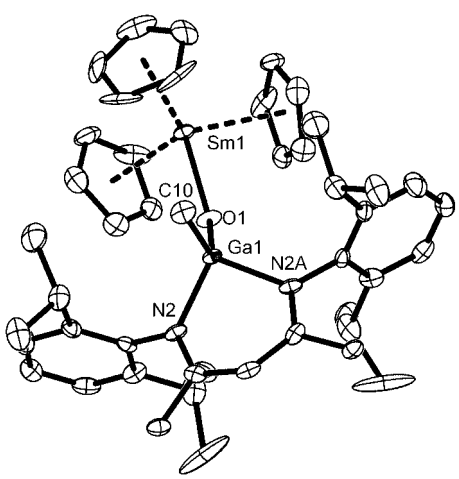



 © 2006 Wiley-VCH Verlag GmbH & Co. KGaA, Weinheim 

**4033** **A. Decken, F. A. LeBlanc, J. Passmore,* X. Wang**

Cyclodimethylsiloxane $(Me_2SiO)_m$ ($m$ = 3−6) Ring Transformations on Reactions with $AgSbF_6$; Crystal Structure of $Ag(Me_2SiO)_7SbF_6$

**Keywords:** Cyclodimethylsiloxane / Host−guest systems / Silver / Silicon ethers / Ring transformation / Hexafluoroantimonate

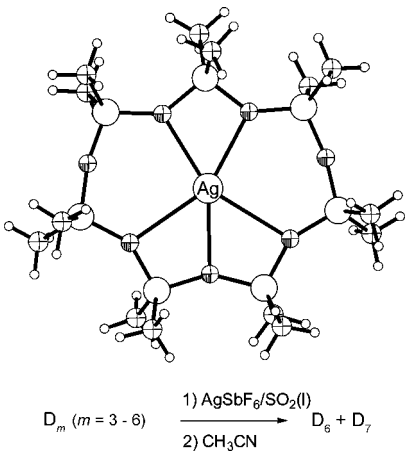


**4037** **E. Martin, D. L. Hughes, S. J. Lancaster***

The Remarkable Solvent-Dependent Crystallization of the Mono- and Bis(4-pyrrol-1-ylbenzonitrile) Adducts of Bis(pentafluorophenyl)zinc

**Keywords:** Crystal structure / Zinc / Pentafluorophenyl group / Nitrile adduct / Intermolecular interaction / Arene coordination

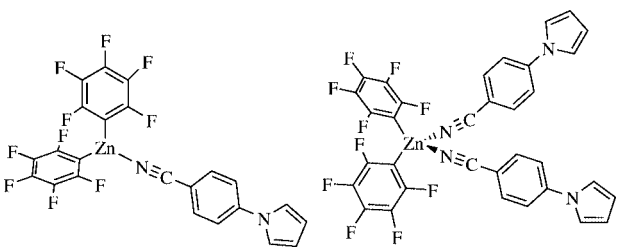


## FULL PAPERS

**4043** **K. Kano,* H. Kitagishi, Y. Sone, N. Nakazawa, M. Kodera**

Redox Behavior of a Manganese Porphyrin Complexed with Per-*O*-methylated β-Cyclodextrin in Aqueous Solution

**Keywords:** Macrocyclic ligands / Manganese / Redox chemistry / Cyclodextrins / Electrochemistry

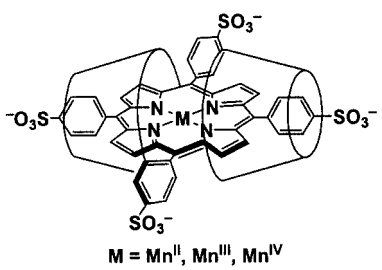


**4054** **K. K.-W. Lo,* J. S.-Y. Lau, D. K.-K. Lo, L. T.-L. Lo**

Luminescent, Cyclometalated Iridium(III) Polypyridine Complexes Containing a Thiourea Moiety: Synthesis, Characterization, Photophysics, Electrochemistry and Anion-Binding Properties

**Keywords:** Fluorescence spectroscopy / Iridium / Luminescence / N ligands / Sensors

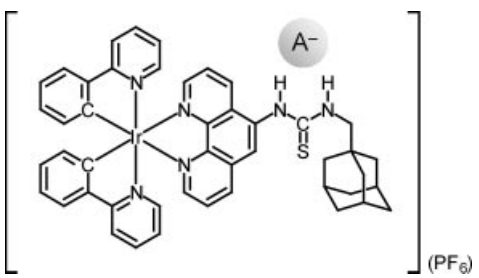


 © 2006 Wiley-VCH Verlag GmbH & Co. KGaA, Weinheim 

**4063** **R. Puchta, R. Meier, N. J. R. van Eikema Hommes, R. van Eldik***

Quantum Chemical Analysis of the Enantiomerisation Mechanism of Complexes of the Type $[M^{II}(XU)_4]F^+$ (M = Pt, Pd, Ni; X = S, Se, Te; U = urea)

**Keywords:** Enantiomers / Density functional calculations / Metal complexes

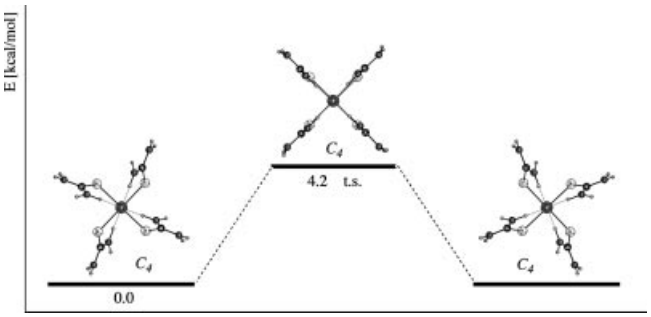


**4068** **N. Merle, C. G. Frost, G. Kociok-Köhn, M. C. Willis, A. S. Weller***

Chelating Phosphane−Boranes as Hemilabile Ligands − Synthesis of $[Mn(CO)_3(\eta^2\text{-}H_3B\cdot dppm)][BAr^F{}_4]$ and $[Mn(CO)_4(\eta^1\text{-}H_3B\cdot dppm)][BAr^F{}_4]$

**Keywords:** Boranes / Catalysis / Hemilabile ligands / Manganese / Phosphanes

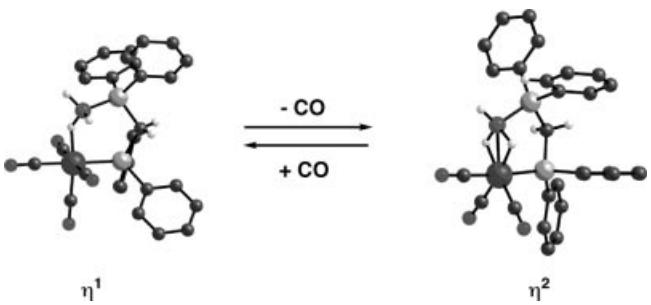


**4074** **L. A. Kushch,* L. S. Kurochkina, E. B. Yagubskii, G. V. Shilov, S. M. Aldoshin, V. A. Emel'yanov, Y. N. Shvachko, V. S. Mironov, D. Schaniel, T. Woike, C. Carbonera, C. Mathonière**

Bifunctional Materials Based on the Photochromic Cation $[RuNO(NH_3)_5]^{3+}$ with Paramagnetic Metal Complex Anions

**Keywords:** Photochromism / Magnetic properties / Mononitrosyl ruthenium complexes / Paramagnetic metal complexes

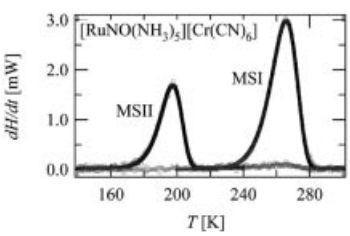


**4086** **D. Mandal, B. D. Gupta***

Cobaloximes with Pyrazine and Their Dimetallic Complexes

**Keywords:** Cobaloximes / Cyclic voltammetry / X-ray structure / Helical structures

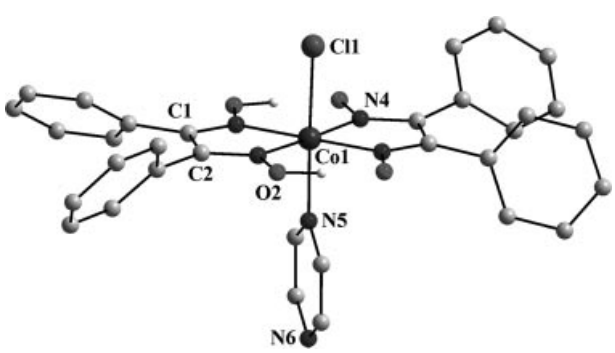


 © 2006 Wiley-VCH Verlag GmbH & Co. KGaA, Weinheim 

**4096** **P. N. Martinho, S. Quintal, P. J. Costa, S. Losi, V. Félix, M. C. Gimeno, A. Laguna, M. G. B. Drew, P. Zanello, M. J. Calhorda***

New Polynuclear Mo−Fe Complexes with Ferrocenylamidobenzimidazole Ligands

**Keywords:** $Mo^{II}$ complexes / Ferrocenyl ligands / Polynuclear complexes / DFT calculations / Electrochemistry

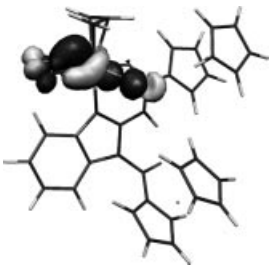

**4104** **G. Paolucci,* M. Vignola, A. Zanella, V. Bertolasi, E. Polo,* S. Sostero**

Substituted Ring-Fused Yttrium Derivatives − X-ray Crystal Structures of $[(L'YCl_2{\cdot}THF)_2LiCl{\cdot}2THF]$ and $[\{L'YCl(OH)\}_6{\cdot}2THF]$ (L′ = 2-Phenyl-4,5,6,7,8-hexahydroazulenyl)

**Keywords:** Yttrium / Fused-ring systems / Olefin polymerization

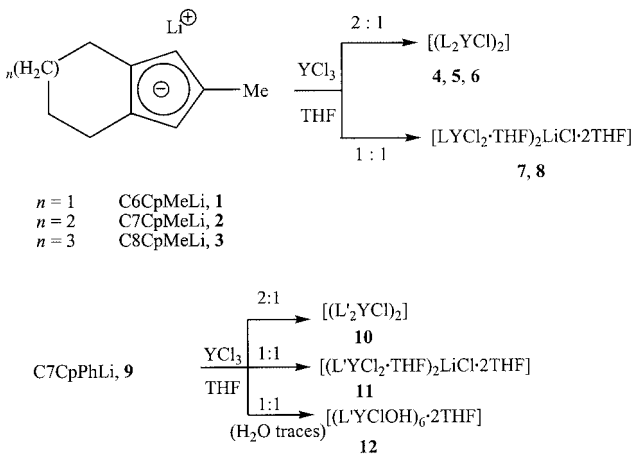


**4111** **B. Dutta, B. Adhikary, U. Flörke, K. Nag***

Controlled Synthesis of 3d−4d Heterobimetallic Complexes of a Symmetrical Tetraiminodiphenolate Macrocycle − Structural, Spectroscopic, and Redox Properties

**Keywords:** Heterobimetallic complexes / Macrocyclic complexes / Palladium / Rhodium / 3d metals(II)

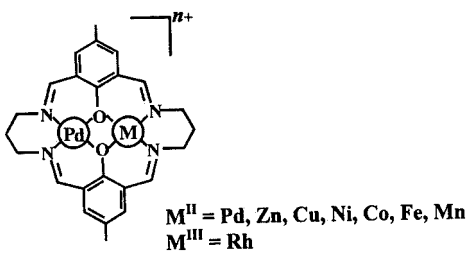


**4123** **H. Li, G.-S. Zhu,* X.-D. Guo, F.-X. Sun, H. Ren, Y. Chen, S.-L. Qiu***

Synthesis, Structure, and Magnetism of a Highly Thermally Stable Microporous Metal Organodiphosphonate with Reversible Dehydration/Rehydration Behavior

**Keywords:** Organic−inorganic hybrid composites / Organophosphonates / Thermal stability / Dehydration/rehydration behavior / Microporous materials

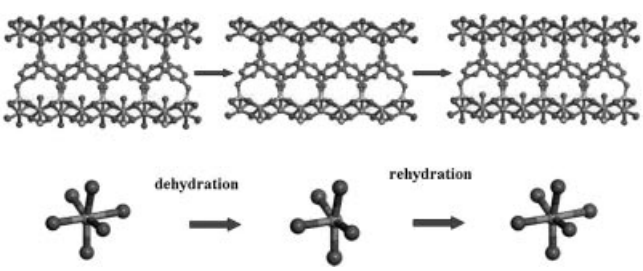


 © 2006 Wiley-VCH Verlag GmbH & Co. KGaA, Weinheim 

**4129** **V. Chandrasekhar,* R. Boomishankar, K. Gopal, P. Sasikumar, P. Singh, A. Steiner, S. Zacchini**

Synthesis, Structure and Reactivity of Hydrated and Dehydrated Organotin Cations

**Keywords:** Organotin cations / Organooxotin / Organostannoxane / Acetylation / Transacetylation

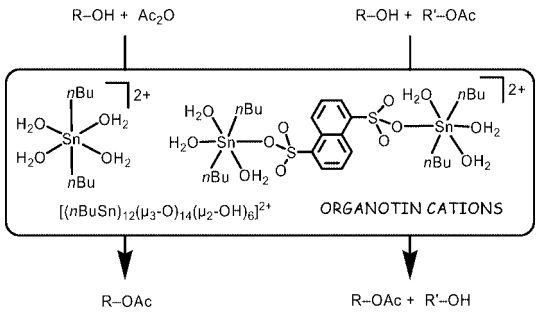


**4137** **S. Pavlik, M. Puchberger, K. Mereiter, K. Kirchner***

Synthesis and Reactivity of the $Ru^{III}$ Complexes $[RuTp(PR_3)Cl_2]$ − Precursors for RuTp Dihydrogen Complexes

**Keywords:** Ruthenium / N ligands / Dihydrogen complexes

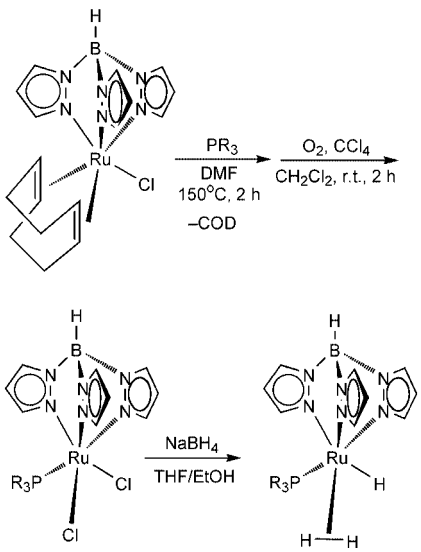


**4143** **X.-M. Shang, J.-Z. Wu,* Q.-S. Li***

New Coordination Modes of Substituted Benzohydroxamic Acid with Dialkyltin(IV): Structural Diversity through Ligand Isomerization

**Keywords:** Coordination modes / Organotin / Hydroxamic / Hydroximic / Isomerization

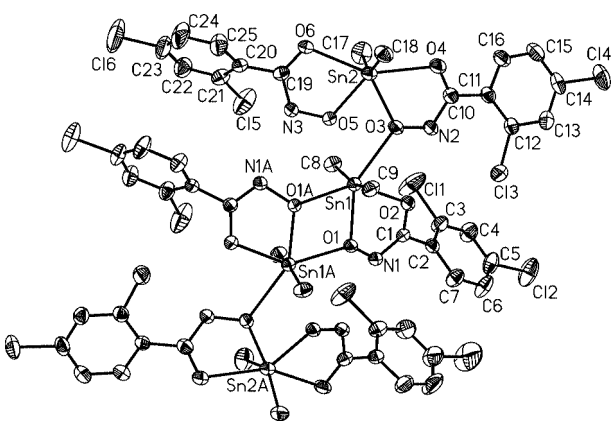

 © 2006 Wiley-VCH Verlag GmbH & Co. KGaA, Weinheim 

**4151** **R. Sasikala,* V. Sudarsan, S. K. Kulshreshtha**

Studies on the Interaction of Vanadia with Modified Silica Supports and Catalytic Activity for Oxidative Dehydrogenation of Propane: Effect of Support Modification by $Al^{3+}$, $Zr^{4+}$ or $Y^{3+}$

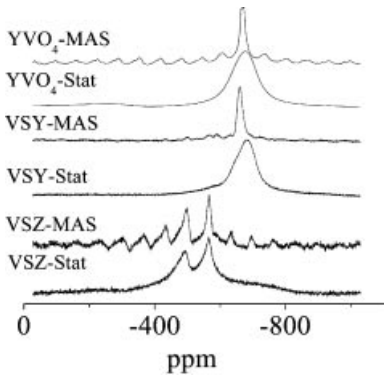


**Keywords:** Supported catalysts / Vanadia-support interaction / IR spectroscopy / Heterogeneous catalysis

**4157** **D. Stein, A. Dransfeld, M. Flock, H. Rüegger, H. Grützmacher***

Lithium Oligophosphanediides in the Li/$PhPCl_2$ System

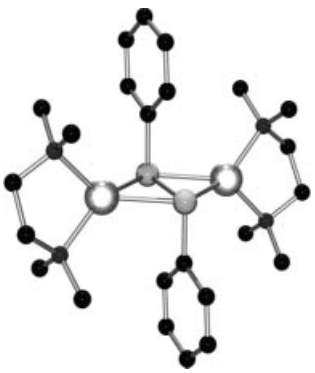

**Keywords:** Alkali metals / Dianions / Ion pairs / NMR spectroscopy / Phosphorus / Reduction

**4168** **M. Velázquez,* A. Ferrier, O. Pérez, S. Péchev, P. Gravereau, J.-P. Chaminade, R. Moncorgé**

A Cationic Order-Disorder Phase Transition in $KPb_2Cl_5$

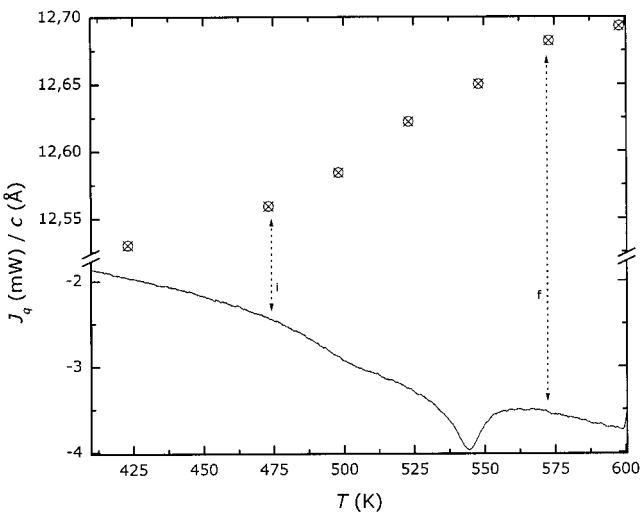


**Keywords:** Halides / Solid-state structures / Structure elucidation / Phase transitions / Thermodynamics

**4179** **W. Guan, G.-C. Yang, L.-K. Yan, Z.-M. Su***

How Do the Different Defect Structures and Element Substitutions Affect the Nonlinear Optical Properties of Lacunary Keggin Polyoxometalates? A DFT Study

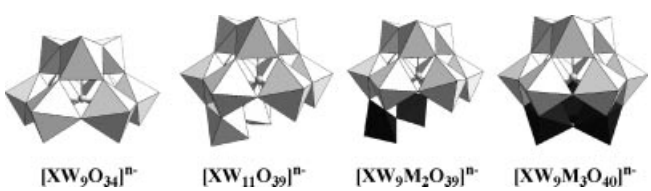


**Keywords:** Polyoxometalates / Nonlinear optics / Lacunary species / Tungsten / Density functional theory

 © 2006 Wiley-VCH Verlag GmbH & Co. KGaA, Weinheim 

**4184** **D. F. Weng, X. J. Zheng,* L. P. Jin***

Assembly and Upconversion Properties of Lanthanide Coordination Polymers Based on Hexanuclear Building Blocks with ($\mu_3$-OH) Bridges

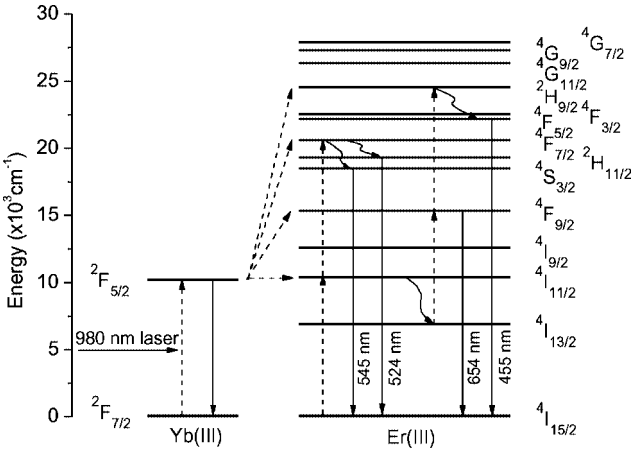


**Keywords:** Hydroxido clusters / Lanthanide coordination polymers / Codoped complexes / Upconversion properties

DOI: 10.1002/ejic.200600723

# Classical and Non-Classical Ruthenium-Based Anticancer Drugs: Towards Targeted Chemotherapy

**Wee Han Ang[a] and Paul J. Dyson*[a]**

**Keywords:** Ruthenium / Anticancer drugs / Targeted chemotherapy / DNA binding / Antimetastasis drugs

Ruthenium-based anticancer chemotherapies are making significant advances in clinical trials. Until recently, the focus has been on coordination complexes, and mechanisms such as "activation by reduction" and "transferrin-targeted delivery" have been proposed to account for the excellent cytotoxicity and low general toxicity of these complexes. More recently organoruthenium compounds, which to some extent appear not to follow the established rules, have started to be investigated. Despite such differences, similar activities between certain coordination and organometallic compounds suggest similar modes of action are present. DNA, the classic target, is believed to be the dominant mechanism for cytotoxicity with certain ruthenium drugs, while with others, non-classical targets are thought to be more important. In this article we describe these features and show how both ruthenium coordination complexes and organoruthenium compounds represent an ideal scaffold for further drug design and optimisation.
(© Wiley-VCH Verlag GmbH & Co. KGaA, 69451 Weinheim, Germany, 2006)

## Introduction

The landmark discovery of the antitumoural properties of *cis*-diamminedichloroplatinum(II) (*cisplatin*), by Rosenberg in 1965, heralded a new era of anticancer research based on metallopharmaceuticals.[1] To date, cisplatin and its analogues are some of the most effective chemotherapeutic agents in clinical use (see Figure 1), often as the first line of treatment in testicular and ovarian cancers.[2,3] However, they are not without their problems. In particular, their high toxicity and incidence of drug resistance, acquired or intrinsic, remain the main challenges in their clinical application.[4] These limitations have provided the motivation for alternative chemotherapeutic strategies. For example, *satraplatin* is a platinum(IV) prodrug, that could be orally administered, and is reduced by intracellular biomolecules to yield cytotoxic platinum(II) moieties once inside the cell.[5] Platinum(IV) compounds with functionalised ligands have also been harnessed to defeat glutathione-S-transferase-mediated drug resistance, to target estrogen receptor-positive breast cancer and as a pro-drug for photo-chemotherapy (see Figure 1).[6] There are also a number of platinum(II) compounds that target aspects of cancer cells to enhance uptake and improve selectivity.[7] At the same time, the search for effective anticancer compounds based on other metal centres has intensified. In particular, anticancer drugs based on ruthenium have gained significant prominence.

Ruthenium is an attractive alternative to platinum: besides the rich synthetic chemistry, ruthenium has a range of oxidation states ($Ru^{II}$, $Ru^{III}$ and $Ru^{IV}$) accessible under physiological conditions, which is unique among the platinum-group metals.[8] This feature is significant since the activities of most metal-based anticancer drugs are dependent on their oxidation states. In addition, ruthenium compounds are known to be less toxic than their platinum counterparts.[8–10] This is believed to be due to the ability of ruthenium to mimic iron in the binding to biological molecules, such as albumin and transferrin, although plati-

[a] Institut des Sciences et Ingénierie Chimiques, Ecole Polytechnique Fédérale de Lausanne (EPFL),
1015 Lausanne, Switzerland
E-mail: paul.dyson@epfl.ch

*Paul Dyson (left) is the director of the Laboratory of Organometallic and Medicinal Chemistry (since 2002) at the Swiss Federal Institute of Technology in Lausanne (EPFL). Previously he was based in the UK conducting research at the University of York, Imperial College and the Universities of Edinburgh and Cambridge.*

*Wee Han Ang (right) obtained his BSc(Hons) First Class in Chemistry at the Imperial College of Science, Technology and Medicine, London. He joined the Swiss Federal Institute of Technology in Lausanne (EPFL) in 2003 with a Roche Research Fellowship. He is currently completing his PhD in Paul Dyson's research group, focussing on developing strategies to overcome drug resistance in platinum and ruthenium-based anticancer compounds.*

 © 2006 Wiley-VCH Verlag GmbH & Co. KGaA, Weinheim 

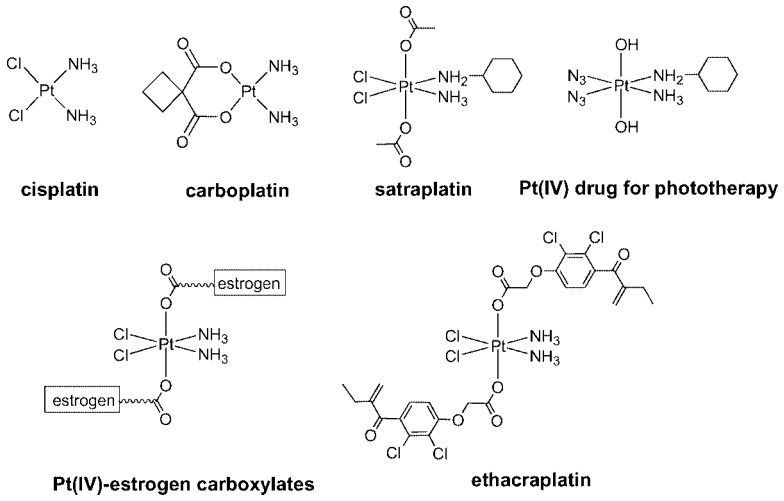


Figure 1. Clinical and preclinical platinum-based anticancer drugs.

num drugs can also bind to these proteins. Since rapidly dividing cells, such as cancer cells, have a greater demand for iron, transferrin receptors are over-expressed, thereby allowing ruthenium-based drugs to be more effectively delivered to cancer cells.[9,10] In addition, the "activation by reduction" mechanism could also account for the lower general toxicity of some ruthenium compounds.[9] Two ruthenium-based anticancer drugs, namely NAMI-A and KP1019 (see Figure 2), have successfully completed phase 1 clinical trials and are scheduled to enter phase 2 trials in the near future.[11–13]

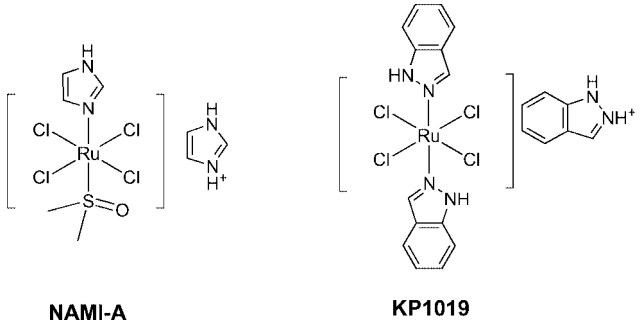


Figure 2. Ruthenium-based anticancer drugs under clinical evaluation.

In the past two decades, a new approach to treating cancer, known as targeted therapy, has started to take root.[14] The new strategy involves targeting cellular signalling pathways of cancer cells, yielding highly effective cancer treatments with much reduced severe side effects.[14,15] A few of them, e.g. Imatinib mesylate and Erlotinib hydrochloride (see Figure 3), have demonstrated such potential that their approval processes were fast-tracked by the US Food and Drug Administration. Eventually, targeted therapies could become mainstream as the first line therapeutic options, replacing existing classical anticancer drugs such as 5-fluorouracil and cisplatin. It is therefore worthwhile to consider if the existing approaches being used to develop ruthenium-based anticancer drugs are adequate.

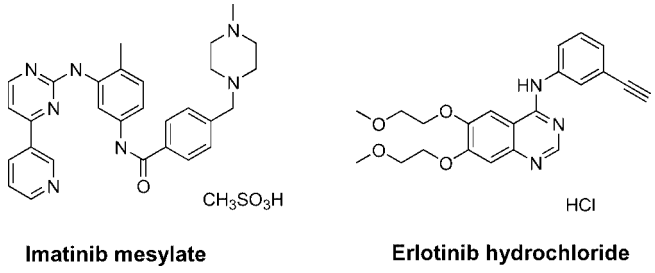


Figure 3. Drugs for targeted therapy in clinical use.

## Classical versus Targeted Chemotherapy

Classical (or conventional) chemotherapy, which originated in the 1950s, refers to drugs interfering with replication and mitotic processes of tumour cells.[14] Historically, these were the main "target" of chemotherapy, since cancer biology was not well established at that time and little was known about the causes of cancer and its mechanism, so the general therapeutic strategy was largely premised on the fact that cancer cells replicate their DNA more frequently than normal cells and hence are more susceptible to DNA damage. Examples of cytotoxic substances include alkylating agents, mitosis inhibitors and topoisomerase inhibitors. In recent years, with the advent of molecular oncology, the study of cancer at the molecular level has been made possible.[14] The discovery of receptors and growth factors, such as epidermal growth factor receptor (EGFR), vascular endothelial growth factor (VEGF), cyclin-dependent kinases (CDK) that are upregulated in cancer cells, provides new "targets" for cancer therapy.[15,16] Whereas the strategy of classical chemotherapy relies on damaging cancerous cells more than normal cells, targeted therapies are far more specific and their toxicity profile more manageable. Important classes of target therapeutic agents include monoclonal antibodies that interfere with the activities of EGFR, VEGF or proteasome, small molecule inhibitors of the tyrosine ki-

 © 2006 Wiley-VCH Verlag GmbH & Co. KGaA, Weinheim 

nase receptor (which includes EGFR), as well as immunotherapeutic agents that trigger an immune response against CD20 antigens.[15,17]

The main drawback of classical chemotherapy strategies is that by blocking the metabolism of rapidly dividing malignant cells, it inadvertently inflicts damage on healthy cells that divide frequently, such as hair follicles, bone marrow and cells lining of the gastrointestinal tract. Consequently, there are associated side effects, such as hair loss, anaemia and neutropenia, that are often severe and limit the treatment options.[18] In contrast, targeted therapies focus on specific cellular signalling pathways on which the cancer cells depend for growth, proliferation, metastasis and angiogenesis, and are therefore much more selective.[15] It is of no doubt that the centre of efforts in anticancer research has shifted towards the latter approach, and while targeted therapies are still in their infancy, they offer considerable potential.[14,16]

Despite the potential of targeted therapies, classical chemotherapeutic drugs, like cisplatin, remain the most effective and widely available drugs in use. This is because classical chemotherapeutic approaches target the most fundamental aspect of cancer cells, their rapidly dividing nature, whereas targeted approaches are contingent on discovering unique and specific features of particular cancer cells. As it stands, most targeted therapeutic drugs are only effective in fairly specific types of cancer, e.g. Imatinib mesylate for chronic myelogenous leukaemia, Erlotinib for advanced non-small cell lung cancer, etc. This limits their applicability and most common cancers cannot be treated with "targeted" chemotherapeutic agents, although this is expected to change in the future.

In recent years, ruthenium-based drug research appears to be moving away from classical approaches into the realm of "non-classical" ruthenium-based drugs. It is useful to take stock of the developments so far, drawing on the lessons learnt with respect to drug design and development. In this review, we explore the major classes of classical and non-classical ruthenium-based drugs and highlight the principal and emerging development strategies.

## Classical Ruthenium Anticancer Drugs

### *Polypyridyl-Ru-Complexes*

Polypyridyl-Ru systems have been exploited extensively as molecular DNA probes, given their photoluminescence properties and the ability of polypyridyl ligands to intercalate DNA. The large, rigid, multidentate polypyridyl ligands confer shape and chirality to the ruthenium complexes that could be exploited to achieve customised DNA-binding properties. This has provided the motivation to develop polypyridyl-Ru complexes as DNA-targeting anticancer agents, and a large number of these complexes have been screened for anticancer activity. Typical polypyridyl ring ligands include 2,2′-bipyridine (bpy), 1,10-phenanthroline (phen) and 2,2′:6′2′′-terpyridine (terpy) as they are commercially available and readily form stable complexes with ruthenium (see Figure 4). Some of the earliest polypyridyl-Ru complexes studied for potential anticancer properties include *cis*-[Ru(bpy)$_2$Cl$_2$] (both Δ and Λ enantiomers) and *mer*-[Ru(terpy)Cl$_3$]. In vitro, *mer*-[Ru(terpy)Cl$_3$] was significantly more cytotoxic (L1210, HeLa) than both enantiomers of *cis*-[Ru(bpy)$_2$Cl$_2$], which matches the in vivo data (BALB/c × C$_{57}$BL/6 female mice).[19] This trend correlates to the ability of *mer*-[Ru(terpy)Cl$_3$] to form DNA-interstrand crosslinks, whereas the inactive *cis*-[Ru(bpy)$_2$Cl$_2$] appears to exhibit no such interactions.[19,20] There have also been numerous examples of polypyridyl-Ru complexes comprising one or more [Ru(bpy)$_2$L]$^{2+}$ or [Ru(phen)$_2$L]$^{2+}$ units [where L = derivatised quinolines, 2,6-(2′-benzyimidazolyl)pyridine/chalcone, aryldiazo-β-diketonate, 4-substituted thiosemicarbazides, 4-substituted thiopicolinanalides, 2-phenylazoimidazole, etc.] in an attempt to improve the DNA-intercalating ability of the complex.[21] However, it is not clear if there has been any serious attempt to advance these compounds into clinical trials. A series of DNA-binding ruthenium(II) complexes with tetradentate cyclam rings and varying DNA-intercalating quinonediimide ligands were studied in vitro (KB-3–1, KB-V1). It was noted that cytotoxicity was linked to the ability of the quinonediimide ligands to intercalate, although the IC$_{50}$ values were considered too high to be of interest.[22] Reedijk et al. reported an example of a NO-containing polypyridyl-Ru complex that readily liberates NO upon irradiation under a mercury lamp and that could potentially be applied in phototherapy.[23] The complex *cis*-(Cl,Cl)-[Ru$^{II}$(terpy)(NO)Cl$_2$]Cl exhibited good cytotoxicity towards A2780 human ovarian carcinoma cell lines, significantly higher than that of *mer*-[Ru(terpy)Cl$_3$], cisplatin or carboplatin, although their activity under irradiation was not reported. Harding et al. reported the synthesis of ruthenium analogues of streptonigrin, a DNA-targeting antitumour antibiotic.[24] On the basis of structural activity studies, the investigators identified the key structures responsible for their activity and synthesised quinolinide and bipyridine ligands to mimic the active sites. Subsequent dicarbonyl(dichloro)ruthenium(II) complexes [Ru(CO)$_2$Cl$_2$L] (where L = quinolinide and bipyridine mimics of streptonigrin) were prepared, although it appears that no further in vitro studies were undertaken. More recently,

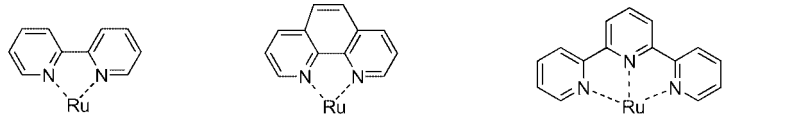


Figure 4. Polypyridyl ligands used in ruthenium anticancer complexes.

 © 2006 Wiley-VCH Verlag GmbH & Co. KGaA, Weinheim 

a heteronuclear (Pt, Ru) complex, comprising a Ru(terpy) moiety, with a highly flexible bridging chain was developed (see Figure 5).[25] The Pt end was designed to bind directly to DNA, leaving the Ru(terpy) end to intercalate, thereby providing additional anchor support. Ultimately, this type of hybrid complex could provide the basis for customised DNA-targeting agents that could form long-range DNA adducts.

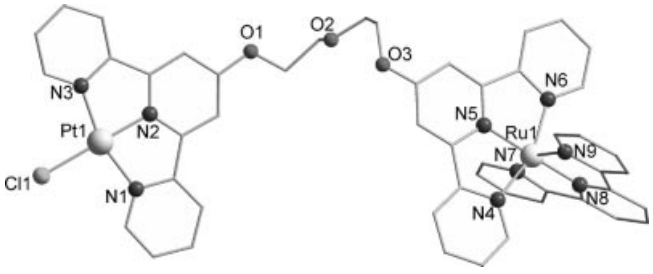


Figure 5. Ball and stick representation of a heteronuclear (Pt, Ru) complex that potentially coordinates *and* intercalates DNA.

### *Ru-Polyaminocarboxylate Complexes*

The use of polyaminocarboxylate (pac) ligands in metallopharmaceutical applications is of growing interest not only because of their ability to bind strongly with metal centres but also because their amino and carboxylate binding entities are akin to those in biological systems.[26] One of the earlier pac-Ru complexes evaluated for anticancer activity is the highly water-soluble dichloro(1,2-propylenediaminetetraacetate)ruthenium(III), Ru(pdta)$Cl_2$ (see Figure 6), which demonstrated antitumoural activity in vivo (EAT, L1210, P388, MX-1, M5076) with low systemic toxicity.[27] The presence of the two chloride ligands in the *cis*-conformation was found to be an important feature of its biological activity; under physiological conditions, the chlorides rapidly hydrolyse.[28] Ru(pdta)$Cl_2$ was found to alter the DNA conformation in pHV14 DNA and inhibit DNA lysis by restriction enzymes.[29] The structurally similar K[$Ru^{III}$(eddp)$Cl_2$] complex (where eddp = ethylenediamine-*N*,*N*-di-3-propionate) also displayed cytotoxicity in vitro (HeLa, BT-20, HT-29) and was found to induce DNA cleavage.[30] A related compound, $K_2$[$Ru^{III}$(dmgly)$Cl_4$] (where dmgly = *N*,*N*′-dimethylglycine), was reported to be cytotoxic towards the murine C6 astrocytoma cell line but not towards primary rat astrocytes, further demonstrating the selective toxicity of ruthenium complexes towards cancer cells.[31] Another class of pac-Ru complexes that has been extensively studied, K[$Ru^{III}$(pac)Cl], contains ethylenediaminetetraacetatic acid and its derivatives as the pac ligands (see Figure 6).[26,32] Like Ru(pdta)$Cl_2$, these complexes also rapidly hydrolyse to yield Ru(pac)($H_2O$) species at low pH. In vitro cytotoxicity against tumour cell lines (MCF-7, NCI-H460, SF-268) showed K[$Ru^{III}$(pdta)Cl] and K[$Ru^{III}$(edta)Cl] to be more efficacious inhibitors of cell growth, presumably because of their higher reactivity towards nucleotides.[26,32,33] In addition, several of these complexes were found to be effective NO scavengers and protease inhibitors, thus they could be used to treat various diseases or serve as antiviral agents.[34]

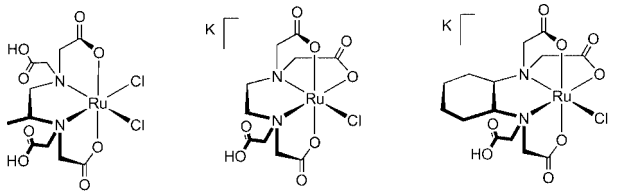


Figure 6. Examples of Ru-pac complexes investigated for anticancer activity (cdta = cyclohexane-1,2-*trans*-diamine-*N*,*N*,*N*′,*N*′-tetraacetate).

### *Dimethyl Sulfoxide-Ru Complexes*

As early as 1988, *cis*- and *trans*-Ru(DMSO)$_4X_2$ (where X = Br, Cl) were screened for antitumour activity (C75B1/BD2F1 female mice with lung carcinoma) and *trans*-Ru(DMSO)$_4Cl_2$ was 20-fold more active against metastasis than its *cis* counterpart (see Figure 7).[35,36] In leukaemic mice, the complexes were able to prolong the lifespan of the host without affecting the number of tumour cells.[35,37] No further development of *cis*- and *trans*-Ru(DMSO)$_4Cl_2$ was reported, presumably in favour of NAMI-A which was found to be a strong antimetastatic agent by the same investigators. However, analogues of *cis*- and *trans*-Ru(DMSO)$_4Cl_2$ containing chelating DMSO ligands such as bis(methylsulfinyl)ethane, bis(ethylsulfinyl)ethane (BESE), bis(propylsulfinyl)ethane and bis(methylsulfinyl)propane have since been reported and studied in vitro (CHO).[38] The compounds were found to be non-cytotoxic under aerobic and hypoxic conditions, despite accumulating significantly within the cellular DNA. *cis*-Ru(DMSO)$_4Cl_2$, in particular, has been used as a synthon for numerous compounds such as *cis*,*cis*,*trans*-Ru$L_2$(DMSO)$_2Cl_2$ (where L corresponds to cytotoxic nitrofurylsemicarbazone ligands), although the conjugated products did not offer improved cytotoxicity (MCF-7, TK-10, HT-29).[39] Similarly, complexes with derivatised DMSO, *cis*,*cis*,*trans*-Ru$L_2$("DMSO")$_2Cl_2$ and *cis*-Ru("DMSO")$_2$(mal)$_2$ type compounds (where L = metroidazole and mal = maltol or ethylmaltol), show no advantageous improvement in cytotoxicity (MDA-MB-435S).[40] *cis*-Ru(DMSO)$_4Cl_2$ has been used to prepare heterodinuclear Pt–Ru compounds crosslinked by 1,4-diaminobutane, i.e. [{*cis*,*fac*-Ru$Cl_2$-(DMSO)$_3$}($NH_2(CH_2)_4NH_2$){*cis*-Pt($NH_3$)$Cl_2$}], with a view to develop a compound that could crosslink DNA–DNA or DNA–protein structures (see Figure 7).[41] On the basis of DNA-binding studies, it was demonstrated that the heterodinuclear compound could form specific DNA lesions that could cross-link proteins to DNA, but its sensitivity to light and rapid hydrolysis prevented further evaluation.[25,42] More recently, both *cis*- and *trans*-Ru(DMSO)$_4Cl_2$ were investigated for their phototoxicity under UVA illumination.[43] Both complexes exhibited photodependent cytotoxicity against human and murine mela-

 © 2006 Wiley-VCH Verlag GmbH & Co. KGaA, Weinheim 

noma cell lines (SK-MEL 188, S91) – the *trans* isomer was more photocytotoxic. In addition, their reactivity towards oligonucleotides was found to be greatly accelerated through a photochemical pathway when irradiated by UVA.

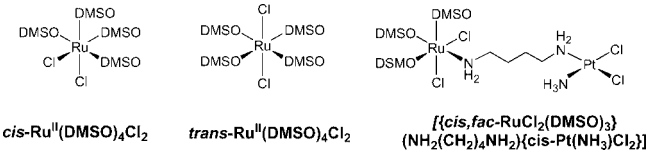


Figure 7. Examples of DMSO–ruthenium compounds evaluated for antitumour activity.

### *Ruthenium Arylazopyridine Complexes*

Arylazopyridine ruthenium(II) complexes, $Ru(azpy)_2Cl_2$ (where azpy = 2-phenylazopyridine), represent a class of well-characterised anticancer compounds with a strong structural dependency. Although these complexes can exist in up to five different isomeric forms, arising from the lack of a twofold symmetry axis, only three have been reported, namely the α, β and γ isomers, and their structures unequivocally established by X-ray crystallography (see Figure 8).[44,45] The structural characteristics have a significant impact on the efficacy of the compounds as cytotoxic agents. Reedijk et al. reported that the high cytotoxicities of the α and γ isomers in vitro (A498, EVSA-T, H226, IGROV, MCF-7, WIDR, M19) were comparable to those of cisplatin and 5-fluorouracil and is about 10-fold higher than that of the corresponding β isomer. This result is surprising since the α and β isomers are structurally similar and differ only in the orientation of the azpy ligand.[45,46] The addition of methyl groups to either the pyridine or phenyl moiety, as in $Ru(tazpy)_2Cl_2$ and $Ru(mazpy)_2Cl_2$ (tazpy = *o*-tolylazopyridine and mazpy = 4-methyl-2-phenylazopyridine), did not alter the trend, validating the structure–activity relationship of the isomers on cytotoxicity.[46] DFT calculations suggest that the ability of the $Ru(mazpy)_2Cl_2$ isomers to intercalate to DNA decreases from γ > α > β isoforms on the basis of the geometric and electronic factors, which correlates with the observed cytotoxicity.[47] The γ isomer has the most preferential geometric arrangement of the mazpy ligand for DNA intercalation, as well as the lowest LUMO energy level and smallest HOMO–LUMO energy gap. Accordingly, it is the most reactive towards DNA. A mixed ligand analogue, *cis*-Ru(bpy)(azpy)$Cl_2$, which is structurally similar to α-$Ru(azpy)_2Cl_2$, was found to be 2–10 fold more cytotoxic in vitro (A498, EVSA-T, H226, IGROV, MCF-7, WIDR, M19) than *cis*-$Ru(bpy)_2Cl_2$ but much less cytotoxic (>50-fold) than either α- or β-$Ru(azpy)_2Cl_2$.[48] The replacement of the chloride ligands with a 2,2′-bipyridine group, as in $[Ru(bpy)_n(azpy)_{3-n}](PF_6)_2$, also did not offer any significant advantage over the parent α-$Ru(azpy)_2Cl_2$.[49] Some water-soluble derivatives of the α isoform, where the chloride ligands are replaced by bridging carboxylate ligands, e.g. oxalate, malonate or 1,1-cyclobutanedicarboxylate, overcome one of the main limitation of these complexes.[50] Although the compounds are 5–10 fold less cytotoxic than α-$Ru(azpy)_2Cl_2$ (A2780, A2780cisR) and slightly less cytotoxic than cisplatin, its cytotoxicity is comparable to that of carboplatin (see Figure 9). Another water-soluble derivative $[NEt_4]_2[Ru(sazpy)_2Cl_2]$ (where sazpy = 2-phenylazopyridine-5-sulfonate), which contains a sulfonate functionality on the azpy group,[51] was >100-fold less cytotoxic (A2780, A2780cisR) than α-$Ru(azpy)_2Cl_2$. More recently, dinuclear analogues with bridging azpy ligands, comprising two azpy units joined at the *para* position of the phenyl rings by a bridging methylene group, have been reported.[52] The supramolecular complexes each contain two $Ru(azpy)_2Cl_2$ moieties arranged in either the α or γ isoforms. Three isomers have been isolated that contain either α/α-, α/γ- or γ/γ- "$Ru(azpy)_2Cl_2$" units and their structures have been confirmed by X-ray crystallography (see Figure 9). The α/γ and γ/γ isomers were tested in vitro on cancer and non-tumourgenic cell lines (T47D, HBL-100) with the γ/γ isoform exhibiting the highest cytotoxicity – >30-fold higher than that of cisplatin.

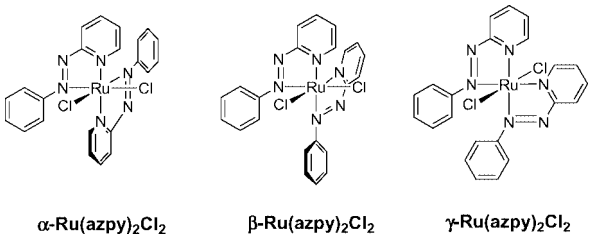


Figure 8. Different isomeric forms of $Ru(azpy)_2Cl_2$ complexes.

### *Organometallic Arene–Ruthenium-Complexes*

Organometallic ruthenium complexes bearing $\eta^6$-arene ligands have been investigated extensively as potential anticancer drug candidates. One of the earlier examples is ($\eta^6$-benzene)Ru(DMSO)$Cl_2$ (see Figure 10), which has been shown to strongly inhibit topoisomerase II activity by cleavage complex formation.[53] The authors suggested that the ruthenium complex interacts with DNA and forms cross-links with topoisomerase II. The complex exhibited antiproliferative activity in vitro (Crit-2), but it is inconclusive if there is a direct link to its ability to inhibit topoisomerase II activity. Arene–ruthenium complexes containing BESE, which is essentially a bidentate "DMSO" ligand, have been tested in vitro (MDA-MB-435s), but their cytotoxicities were more than 5-fold higher than that of cisplatin, and no further investigation was reported.[54] In contrast, monofunctional $Ru^{II}$ complexes of the type $[(\eta^6\text{-arene})Ru(en)X]^+$ (where en = ethylenediammine or its derivatives and X = halide) exhibit high cytotoxicity in vitro (A2780, A2780cisR, A2780adr, HT29, Panc-1, NX02), comparable to that of cisplatin, that is dependent on the arene ligand (see Figure 10).[55] Large arene ligands, such as biphenyl and tetrahydroanthracene, improved the cytotoxicity of the drug. Replacement of the en ligand with bpy or tmeda (*N*,*N*,*N*′,*N*′-tetramethylethylenediamine) resulted in complexes with poor cytotoxicity.[56] Extensive oligonucleotide studies have been carried out and $[(\eta^6\text{-cymene})Ru(en)X]^+$ have been found to preferentially bind to guanine bases to

 © 2006 Wiley-VCH Verlag GmbH & Co. KGaA, Weinheim 

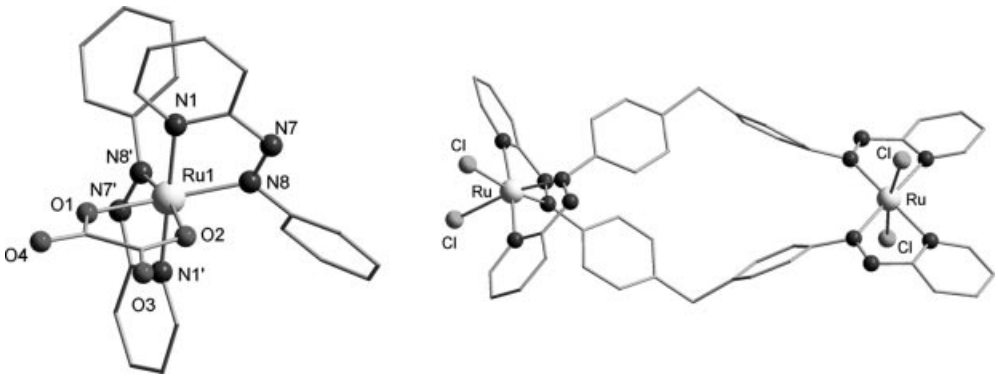


Figure 9. Ball and stick representation of derivatives of α-Ru(azpy)$_2$Cl$_2$. Unlabelled spheres represent N atoms.

form monofunctional DNA adducts.[57] This was supported by NMR spectroscopic studies that suggest that the binding of the [(η$^6$-arene)Ru(en)X]$^+$ moiety to guanine is enhanced through H-bonding interactions between the en ligand and the exocylic oxygen atom (i.e. C$^6$–O) on the guanine nucleotide.[58] In contrast, binding to adenine is weakened because of steric interactions between the en ligand and the exocyclic amino groups (i.e. C$^6$–NH$_2$),[58] whereas (η$^6$-cymene)-Ru(acac)Cl (where acac = acetylacetonate) [see Figure 10] binds to both adenine and guanine bases – the authors noted that these results could lead to compounds designed to target specific DNA nucleotides.[59] With large arene rings systems, e.g. dihydroanthracene and tetrahydroanthracene, binding of [(η$^6$-arene)Ru(en)X]$^+$ complexes to nucleotide bases was promoted by hydrophobic arene–purine base π–π stacking interactions, which could explain the enhanced cytotoxicity of those derivatives.[60] There was also evidence of dynamic chiral recognition of ethylguanine by the diastereomers of [(η$^6$-biphenyl)Ru(Et-en)Cl]$^+$, realizing the concept of induced-fit recognition of DNA by chiral derivatives of ruthenium complexes.[61]

## Non-Classical Ruthenium Anticancer Drugs

### *Antimetastatic NAMI-A Type Complexes*

Imidazolium *trans*-[tetrachloro(DMSO)(imidazole)ruthenate(III)] H$_2$im[*trans*-RuCl$_4$-(DMSO)Him], more commonly known as NAMI-A (see Figure 11), was the first ruthenium-based anticancer drug to enter clinical trials – as

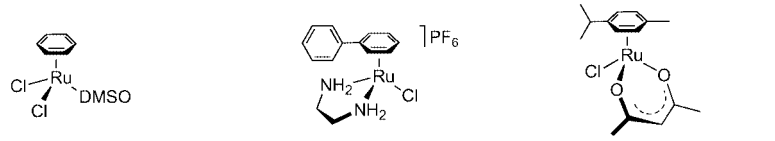


Figure 10. Examples of organometallic (η$^6$-arene) ruthenium anticancer drugs.

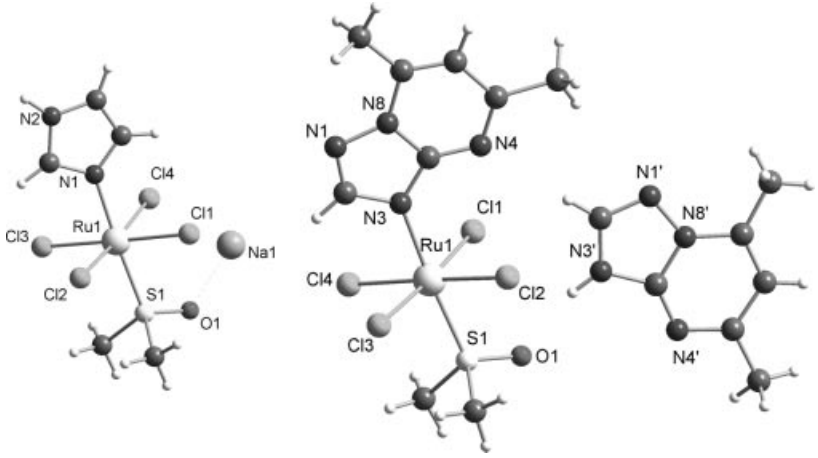


Figure 11. Ball and stick representation of NAMI-A precursor, Na[*trans*-RuCl$_4$–(DMSO)Him] (left) and Hdmtp[*trans*-RuCl$_4$-(DMSO)dmtp] (right).

 © 2006 Wiley-VCH Verlag GmbH & Co. KGaA, Weinheim 

a drug candidate against non-small cell lung cancer (NSCLC).[62] Compared to other transition-metal-based drugs such as cisplatin, NAMI-A is unique. In vitro, it is virtually devoid of cytotoxicity, while in vivo, it inhibits lung metastases formation and reduces metastases weight without affecting the primary tumour,[63] in contrast to platinum-based drugs which typically exhibit strong growth inhibition on primary tumours. Indeed, both in vitro and in vivo data appear to exclude DNA as the primary target, in line with the observation that the binding of NAMI-A to DNA is much weaker than that of platinum complexes.[63–65] Instead, strong binding to serum proteins is observed and the drug could potentially exploit receptor-mediated delivery by transferrin for selective delivery to cancer cells.[66] There is strong evidence linking the antimetastatic behaviour to the lack of cytotoxicity in vitro, cell-cycle changes corresponding to cell arrest in the premitotic $G_2$-M phase and inhibition of Matrigel invasion, which could constitute an in vitro screening strategy for ruthenium complexes with similar properties.[67] Phase 1 clinical trials showed that the drug was well-tolerated in patients, reversible blister formation is the dose-limiting toxicity.[12] Several NAMI-A analogues have been studied for potential antimetastatic activity as a means to ascertain the structure–activity relationships in this class of compounds. NAMI-A derivatives [*mer*-$RuCl_3$(DMSO)(acv)($H_2O$)] and [*mer*-$RuCl_3$(DMSO)(acv)-(MeOH)] and [*trans*-$RuCl_4$(DMSO) guaH] (where acv = acyclovir and gua = guanine) exhibited low cytotoxicity in vitro (TS/A), similar to NAMI-A.[68] Analogues with the dmtp ligand (where dmtp = 5,7-dimethyl[1,2,4]triazolo[1,5-*a*]pyridmidine) were also investigated and found to be slightly cytotoxic in vitro (TS/A, KB, B16-F10).[69] In particular, Hdmtp[*trans*-$RuCl_4$(DMSO) dmtp] exhibited a similar in vivo profile to NAMI-A (CBA mice with MCa carcinoma), strongly inhibiting lung metastases formation without significantly affecting the primary tumours (see Figure 11).[69] This trend has also been replicated in NAMI-A analogues with pyrazine, pyrazole and bidentate *N*-heterocyclic ligands, e.g. 4,4′-bipyridine, 1,2-bis(4,4′-pyridyl)ethane, suggesting that the imidazole fragment is not an essential feature for the antimetastatic property of NAMI-A.[70]

### *Exploiting the Transferrin Delivery Mechanism*

Indazolium *trans*-[tetrachlorobis(1*H*-indazole)ruthenate-(III)] $H_2$in[*trans*-$RuCl_4(Hin)_2$], KP1019 (see Figure 12), the only other ruthenium drug presently undergoing clinical evaluation, contains two indazole ligands in the *trans* conformation (whereas in NAMI-A the imidazole ligand is *trans* to a DMSO moiety). Unlike NAMI-A, KP1019 is significantly cytotoxic in vitro against colorectal cell lines (SW480, HT29) by induction of apoptosis.[71] There is also evidence of P-glycoprotein (Pgp) mediated drug resistance to KP1019, although other multidrug resistance (MDR) associated proteins (MRP1, BCRP and LRP) did not affect its activity significantly.[72] The drug was evaluated in vivo against autochthonous colorectal tumours in rats and was found to be highly effective in reducing tumour growth (superior to 5-fluorouracil, the most effective drug in clinical use against colorectal cancer).[11] In contrast, cisplatin was inactive in the in vivo model. The activity of KP1019 is attributed, at least in part, to transferrin-mediated drug transport, with KP1019 binding strongly to transferrin in the iron-binding pockets.[73] Indeed, its imidazolium analogue, which binds more weakly to transferrin, is taken up less effectively by transferrin and is also less cytotoxic in vitro.[71] Another possible mechanism in play is that the drug is activated by reduction, from $Ru^{III}$ to $Ru^{II}$, selectively in hypoxic tumour tissue by endogenous bioreductants such as glutathione. It appears that KP1019 induces apoptosis in colorectal cell lines predominantly by the intrinsic mitochondria pathway and that DNA could be a target, although studies have shown that the DNA lesions formed by KP1019 is different to that by cisplatin.[11,74] In phase 1 clinical trials, the drug was well-tolerated, and five out of six patients treated achieved disease stabilisation.[11,13] A large number of KP1019 analogues, comprising different types and numbers of *N*-heterocyclic rings, have been reported.[75,76] Notably, it was found that increasing the number of indazole ligands, as in *trans*-$Ru^{II}Cl_2(Hin)_4$ and [*trans*-$Ru^{II}Cl_2(Hin)_4$]Cl, improved the in vitro cytotoxicity significantly (CH1, SW480).[76] This was correlated with the increased cellular uptake and a higher reduction potential of the homologues, in line with the "activation by reduction" hypothesis.

### *Ruthenium-Based Selective Estrogen Receptor Modulators*

Selective estrogen receptor modulators (SERMs), such as tamoxifen (see Figure 13), are a class of drug that have been successfully used to treat hormone-dependent (ER-positive) breast cancer, i.e. which express the estrogen receptor ERα. At the same time, there is no satisfactory therapeutic treatment for hormone-independent (ER-negative) breast tumours that contain another estrogen receptor ERβ, which accounts for about one-third of breast cancer cases. Jaouen et al. have developed a series of hydroxytamoxifen derivatives comprising ferrocene (hydroxyferrocifen) (see Figure 13), and other potentially cytotoxic organometallic fragments of rhodium, manganese, titanium and rhenium have been reported, representing a strategy to defeat breast tumours which contain both ERα and ERβ receptors.[77] Hydroxytamoxifen analogues containing organometallic ruthenocenes and their biological evaluation in vitro (MCF7, MDA-MB231) have also been reported.[78] Although the hydroxytamoxifen-Ru complexes (see Figure 13) were found to bind strongly to both ERα and ERβ, unlike hydroxyferrocifen, hydroxytamoxifen-Ru exhibits no cytotoxic effect towards ER-negative breast cancer cell lines, possibly because of the increased stability of the ruthenium fragment compared to the iron analogue with respect to oxidation, and thus would not offer any therapeutic advantage over existing treatment options. Nonetheless, the authors noted that the hydroxytamoxifen-Ru complexes could be suitable for radioimaging of tumour cells using either of two γ-emitting Ru isotopes, $^{97}$Ru and $^{103}$Ru.[78]

 © 2006 Wiley-VCH Verlag GmbH & Co. KGaA, Weinheim 

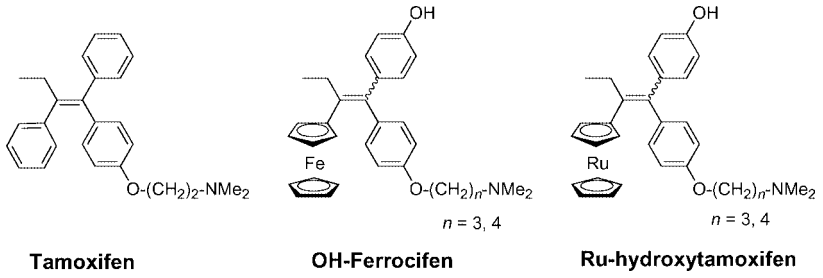


Figure 13. Derivatives of tamoxifen.

### *Ruthenium Ketoconazole Complexes*

Ketoconazole (KTZ) and clotrimazole (CTZ) are azole compounds that were originally developed as antifungal agents. They also exhibit anticancer properties and ketoconazole in particular is being used in the clinic as a second-line agent for hormone-refractory prostate cancer. Ketoconazole-ruthenium $Ru(KTZ)_2Cl_2$ and clotrimazole-ruthenium $Ru(CTZ)_2Cl_2$ complexes were originally developed to treat tropical diseases,[79] but more recently, they have been evaluated for anticancer activity. In vitro, $Ru(KTZ)_2Cl_2$ and $Ru(CTZ)_2Cl_2$ were found to be more effective inhibitors of cell growth proliferation (C8161) than the parent ligands KTZ and CTZ.[80] The effects of $Ru(KTZ)_2Cl_2$ on various cell signalling pathways were investigated. In particular, it was observed that A431 spheroids, known to overexpress EGF-R and to be resistant to either $Ru(KTZ)_2Cl_2$ or C225 *anti*-hEGF-R monoclonal antibody (MAb), were susceptible towards a combination treatment of $Ru(KTZ)_2Cl_2$ and the C225 antibody. C225 is an experimental monoclonal antibody presently under clinical evaluation as a targeted therapeutic agent against EGFR-expressing metastatic colorectal cancer. The authors suggested that $Ru(KTZ)_2Cl_2$ could potentially be used to enhance other targeted therapeutic treatment methods.[80]

### *Ruthenium-Based Protein Kinase Inhibitors*

The three-dimensional structure of many biomolecules is complicated and their syntheses are often difficult given the need to maintain specific conformity and spatial orientation. With a view to develop synthetic compounds with superior biological activity, Meggers et al. reported an organometallic ruthenium complex that mimics the shape of a known protein kinase inhibitor, staurosporine (see Figure 14).[81,82] The strategy exploits the relative ease of synthesising ruthenium moieties of a specific spatial conformation to mimic aspects of an inhibitor not easily accessible using purely organic scaffolds.[81,83,84] The authors further demonstrated the superior binding of the ruthenium mimic to Pim-1, a protein kinase, and reported co-crystallisation of the protein with the ruthenium complex.[81] This provides a basis for the development of further transition-metal-based enzyme inhibitors and could lead to new types of organometallic-targeted therapeutic agents.

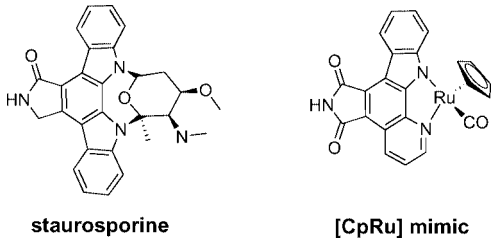


Figure 14. Staurosporine and an organometallic ruthenium mimic.

### Arene PTA Ruthenium(II) (RAPTA) Complexes

The RAPTA compounds comprise a class of organometallic ruthenium(II) complexes with a monodentate 1,3,5-triaza-7-phosphatricyclo[3.3.1.1]decane (pta) ligand and a $\eta^6$-arene ligand. The compounds are readily synthesised in two steps: the first step involves the reaction of $C_6$-dienes,

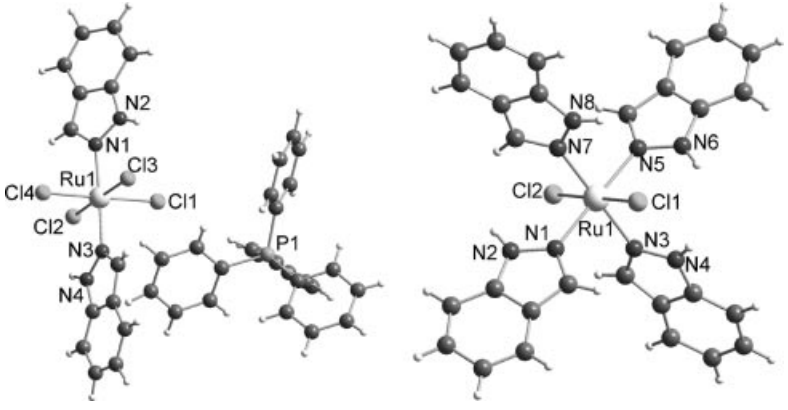


Figure 12. Ball and stick representation of $PPh_4[trans\text{-}RuCl_4(Hin)_2]$ (left) and $trans\text{-}Ru^{II}Cl_2(Hin)_4$ (right).

 © 2006 Wiley-VCH Verlag GmbH & Co. KGaA, Weinheim 

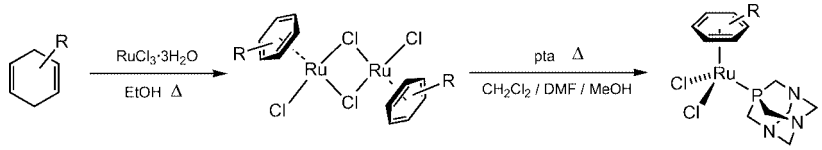


Scheme 1. General synthesis of RAPTA complexes.

typically derived using Birch reduction of the desired arene, with hydrated $Ru^{III}Cl_3$ to yield dimeric $[(\eta^6\text{-arene})Ru^{II}Cl_2]_2$.[85] In the second step, 2 equiv. pta are added to $[(\eta^6\text{-arene})RuCl_2]_2$ in organic solvents to yield the desired RAPTA complex (see Scheme 1). The reaction is thermodynamically favoured and proceeds in high yield. Alternatively, ligand exchange using the arene-labile complex $[(\eta^6\text{-}PhCO_2Et)RuCl_2]_2$ can be carried out for arene ligands that cannot be readily reduced by Birch reduction, such as benzocrown ethers, but yields are lower.[86] In comparison to typical phosphane ligands, pta is relatively compact and sterically undemanding, with a cone angle of 103° (c.f. $PPh_3$ 143° and $PMe_3$ 134°).[87] As such, RAPTA compounds are generally air-stable complexes with good thermodynamic stability. The pta ligand can also be readily derivatised to form acetylated species, e.g. 3,7-diacetyl-1,3,7-triaza-5-phosphabicyclo[3.3.1]nonane (pta-Ac) or methylated species (pta-$Me^+$), further expanding the scope of possible RAPTA compounds.[87] Importantly, the presence of the phosphorus atom makes the characterisation of RAPTA compounds by $^{31}P$ NMR spectroscopy fairly straightforward. RAPTA is also unusual in comparison with other phosphane ruthenium complexes in that it is not only soluble in polar organic solvents, but also in water. The prototype $[(\eta^6\text{-cymene})Ru^{II}(pta)Cl_2]$, RAPTA-C, has been central to biological evaluation and is the reference compound from which other RAPTA compounds are developed (see Figure 15). Two key approaches have thus been adopted. The first is centred on evolving RAPTA into an effective drug that is highly selective towards tumour cells with a low systemic toxicity. In vitro evaluation and oligonucleotide-binding studies supplemented by computational studies were undertaken, with a view that DNA is a possible target, as with most transition-metal-based anticancer drugs. The second approach is aimed at discovering "non-classical" chemotherapeutic applications for RAPTA complexes and to study drug interactions at the proteome level. Early on, specific protein binding interactions were detected with RAPTA, which could be the basis for new therapeutic targets beyond DNA. Furthermore, the remarkably similar in vivo activity of RAPTA-T and NAMI-A suggests that they could respond to similar targets.[10] The development of complementary proteomic techniques as well as rational drug design for RAPTA complexes has been carried out. On the basis of these two approaches, more than 20 RAPTA complexes of the general formula (arene)$Ru^{II}$(pta)$X_2$, where X = Cl, Br, I, SCN or bridging carboxylate ligands, have so far been synthesised and studied (see Scheme 2). In addition, RAPTA analogues containing other organometallic fragments, namely [CpRu], [Cp*Ru], [Cp*Rh] and [CyOs] have also been studied.[88]

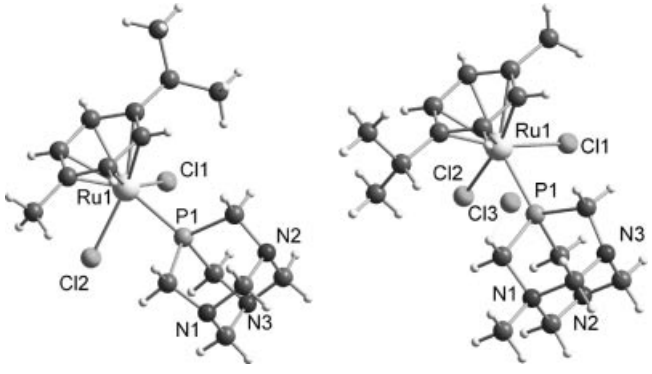


Figure 15. Ball and stick representation of RAPTA-C **1** (left), RAPTA($Me^+$)-C **14** (right).

### *Evolution of RAPTA Complexes: Hybrid Classical / Non-Classical Compounds*

The motivation to study RAPTA complexes as potential anticancer drugs came from the observation that RAPTA-C **1** induces pH-dependent DNA damage against *E Coli* pBR322 DNA plasmids, with a significant retardation of the migration of the supercoiled DNA at pH <7.0 because of unwinding of the DNA as a result of drug interactions.[89] This provided a means to target cancer cells, since they generally exhibit lower pH as a result of metabolic changes, partly because of accelerated cell division. Binding studies using calf thymus DNA further suggested that RAPTA-C stabilises the DNA upon binding (see Figure 16), with a significant increase in the melting temperature of the DNA-RAPTA-C adduct.[90] This suggests that the reaction between DNA and RAPTA-C could be thermodynamically driven and thus highly favourable. However, the RAPTA complexes do not show selective binding to DNA in vitro, proteins and RNA appear to be the main intracellular targets.[91]

The reactivity of RAPTA complexes towards single-strand oligonucleotides, studied by ESI-MS, shows that RAPTA-C **1** and its methylated analogue RAPTA($Me^+$)-C **14** bind to the 14-mer oligomer (5′-ATACATGGTACATA-3′) across a range of pH values and concentrations, irrevocably with the loss of the chloride and arene ligands, while the pta ligand remains intact.[92] Although the purine bases could, in principle, offer heterocyclic aromatic rings for an arene-type π-bonding mode with the ruthenium centre, DFT calculations revealed that such binding would be unlikely, and it is more probable that the interaction is based on multiple coordinative N-donor bonds, such binding only possible with RNAs.[92]

 © 2006 Wiley-VCH Verlag GmbH & Co. KGaA, Weinheim 

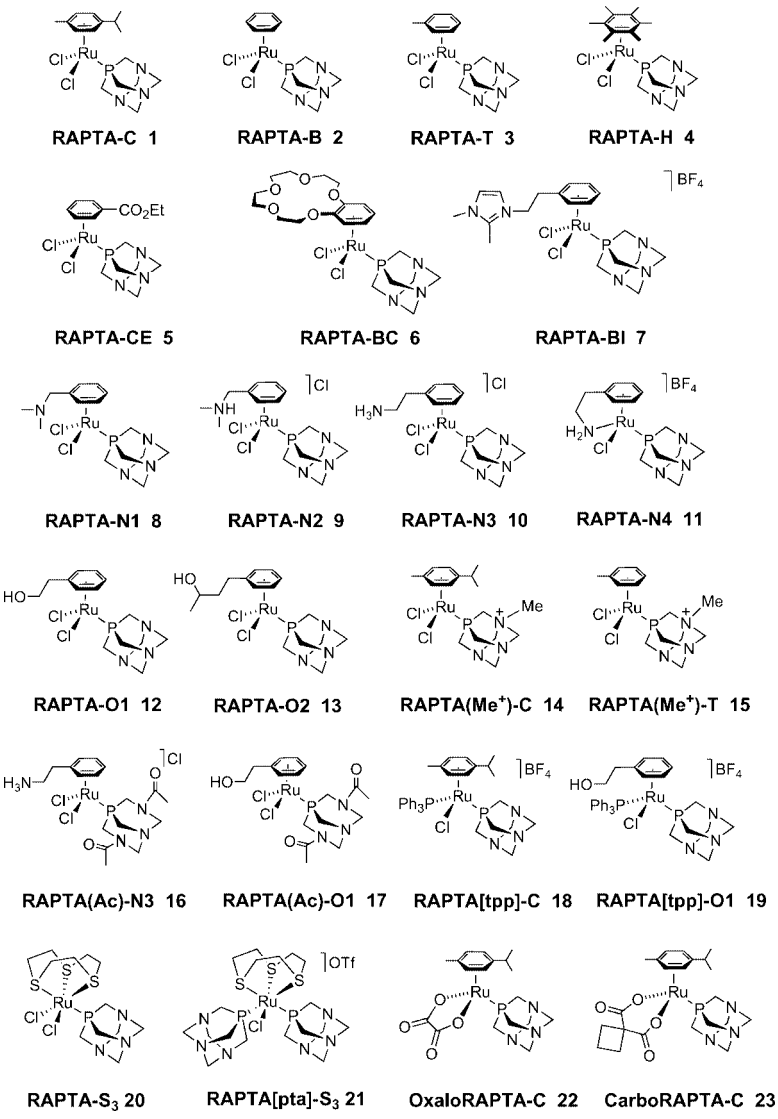


Scheme 2. Family of RAPTA complexes.

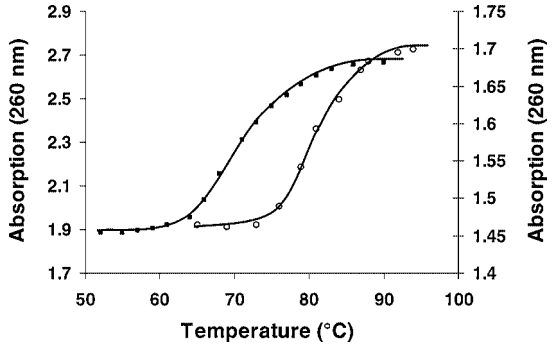


Figure 16. DNA melting curves of calf thymus DNA alone (■) and calf thymus DNA with RAPTA-C (1:1 ratio) (○), buffer: 10 mM phosphate buffer and 50 mM $NaClO_4$.

The cytotoxicity of the RAPTA complexes is generally very low, at least in both TS/A murine adenocarinoma and non-tumourgenic HBL-100 human mammary cell lines in comparison to cisplatin (see Table 1).[90] However, the lead RAPTA complexes **1**–**3** exhibit selective cytotoxicity towards the TS/A cancer cell lines relative to HBL-100, which provided early indication that the complexes are benign towards healthy cells. This is important since high systemic toxicity is associated with the drastic side-effects of cisplatin and related drugs and limits the amount of drug that can be administered. Similarly, NAMI-A is non-cytotoxic to both TS/A and HBL-100 cell lines up to 1 mM concentration. The pta fragment appears to play a significant part in determining this selectivity. When pta was replaced with pta-$Me^+$, as in **14** and **15** (see Figure 15), selectivity was lost and the compounds were equally toxic in both the cancerous and non-tumourgenic cell lines.[90] This coincides with the hypothesis that RAPTA compounds derived their cytotoxic activity through the protonation of its pta ligand under hypoxic pH conditions,[89] although such a process is deemed unlikely given the low p$K_a$ of the coordinated pta moiety.

 © 2006 Wiley-VCH Verlag GmbH & Co. KGaA, Weinheim 

Table 1. $IC_{50}$ values of RAPTA complexes on TS/A and HBL100 cell lines[a] and ruthenium uptake in TS/A cells.[b]

| Complex | | Aromatic | pta | Anion | $IC_{50}$ (TS/A) [μM] | $IC_{50}$ (HBL-100) [μM] | Selectivity Index | Intracellular RAPTA [μg/$10^6$ cells] | Intracellular RAPTA [$\times10^{-4}$ M] |
|---|---|---|---|---|---|---|---|---|---|
| | | Fragment | Fragment | | | | | | |
| RAPTA-C | **1** | cymene | pta | – | 507 | >1000 | >2.0 | 0.12±0.02 | 2.55±0.06 |
| RAPTA-B | **2** | benzene | pta | – | 231 | >1000 | >4.3 | 0.13±0.02 | 3.26±0.04 |
| RAPTA-T | **3** | toluene | pta | – | 74 | >1000 | >13.5 | 0.16±0.02 | 2.9±0.3 |
| RAPTA-H | **4** | hexamethylbenzene | pta | – | 199[d] | >300[d] | >1.5 | 0.15±0.01 | 3.16±0.27 |
| RAPTA-CE | **5** | ethyl benzoate | pta | – | 103[d] | >300[d] | >2.9 | 3.40±0.41 | 54.67±6.66 |
| RAPTA-BC | **6** | benzo-15-crown-5 | pta | – | 159[d] | >300[d] | >1.9 | 0.28±0.02 | 4.63±0.35 |
| RAPTA-BI | **7** | 2,3-dimethyl-1-(2-phenylethyl)-1*H*-imidazolium·$BF_4$ | pta | $BF_4^-$ | 66[d] | >300[d] | >4.5 | 0.19±0.04 | 3.03±0.67 |
| RAPTA-N1 | **8** | *N*,*N*′-dimethylbenzylamine | pta | – | 458 | 813 | 1.8 | 0.04±0.004 | 0.95±0.09 |
| RAPTA-N2 | **9** | *N*,*N*′-dimethylbenzylamine·HCl | pta | $Cl^-$ | 449 | 603 | 1.3 | 0.10±0.02 | 2.02±0.38 |
| RAPTA-N3 | **10** | benzylamine·HCl | pta | $Cl^-$ | 820 | 666 | 0.8 | 0.05±0.005 | 1.05±0.09 |
| RAPTA-N4 | **11** | benzylamine·HCl | pta | $BF_4^-$ | >1000 | 612 | <0.6 | 0.06±0.01 | 1.14±0.21 |
| RAPTA-O1 | **12** | 2-phenylethanol | pta | – | 570 | 778 | 1.4 | 0.06±0.01 | 1.33±0.20 |
| RAPTA-O2 | **13** | 1-phenylbutan-3-ol | pta | – | 505 | 891 | 1.8 | 0.07±0.01 | 1.46±0.30 |
| RAPTA($Me^+$)-C | **14** | cymene | pta-$Me^+$ | $Cl^-$ | >300 | 246 | <0.8 | – | – |
| RAPTA($Me^+$)-T | **15** | toluene | pta-$Me^+$ | $Cl^-$ | 110 | 77 | 0.7 | 0.33±0.08 | 5.9±1.4 |
| RAPTA(Ac)-N3 | **16** | benzylamine·HCl | pta-Ac | $Cl^-$ | >1000 | >1000 | 1.0 | 0.05±0.01 | 0.81±0.19 |
| RAPTA(Ac)-O1 | **17** | 2-phenylethanol | pta-Ac | – | 538 | 715 | 1.3 | 0.07±0.006 | 1.39±0.12 |
| RAPTA[tpp]-C | **18** | cymene | pta, $PPh_3$ | $BF_4^-$ | >100[c] | 37[c] | <0.4 | – | – |
| RAPTA[tpp]-O1 | **19** | 2-phenylethanol | pta, $PPh_3$ | $BF_4^-$ | 124 | 82 | 0.7 | – | – |
| RAPTA-$S_3$ | **20** | [9]$anes_3$ | pta | – | 650 | 738 | 1.1 | – | – |
| RAPTA[pta]-$S_3$ | **21** | [9]$anes_3$ | 2× pta | $OTf^-$ | 388 | >1000 | >2.6 | – | – |

[a] 72 h exposure at a maximum concentration of 1000 μM, unless otherwise stated. Cell growth inhibition was determined using the MTT assay. [b] 24 h exposure at concentration of 100 μM. Ru levels determined using GF-AAS. [c] Compounds were tested in medium containing 1.0% DMSO, at a maximum concentration of 100 μM. [d] Compounds were tested up to a maximum concentration of 300 μM.

The aromatic fragment is significant, to a certain degree, in influencing the drug uptake and in vitro activity. The presence of the ester group significantly improved the drug uptake in RAPTA-CE **5**, with a corresponding improvement in cytotoxicity against TS/A cells. Upon entering the cells, endogenous esterases could cleave the ester bond, thereby retaining the charged species within the cell walls.[90] Addition of functional groups such as benzocrown and an imidazolium moiety appeared to improve cytotoxicity towards TS/A, but not to a significant degree to warrant further studies.[90] RAPTA complexes with H-bonding groups attached to the arene ring (complexes **8**–**13**, **16**, **17** in Scheme 2) were developed and found to be generally more reactive than lead compounds **1**–**3** with respect to oligonucleotide binding.[93] However, in vitro, they are not only less cytotoxic towards TS/A cells but also less selective between the cell lines. This correlated with drug uptake studies on TS/A cells which showed that the uptake of these complexes decreased, presumably because of the incorporation of the hydrophilic H-bonding substituents. The addition of the hydrophobic triphenylphosphane (tpp) ligand in RAPTA complexes **18** and **19** reversed the trend. The complexes were found to be cytotoxic towards both cell lines, hence poorly selective, presumably because of increased drug uptake (see Figure 17).[94] The replacement of the aromatic fragment with a [9]ane$S_3$ ligand, RAPTA-$S_3$ **20**, results in only a slight decrease in selectivity and cytotoxicity, alluding to the fact that the aromatic fragment may not be an essential feature for in vitro activity and could be effectively replaced by another face-capping ligand with low steric demand (see Figure 17).[95] Interestingly, RAPTA[pta]-$S_3$ **21**, with [9]ane$S_3$ and two pta ligands, shows good selectivity and cytotoxicity towards TS/A cells, comparable to that of **1** and **2**. RAPTA analogues are presently being evaluated.

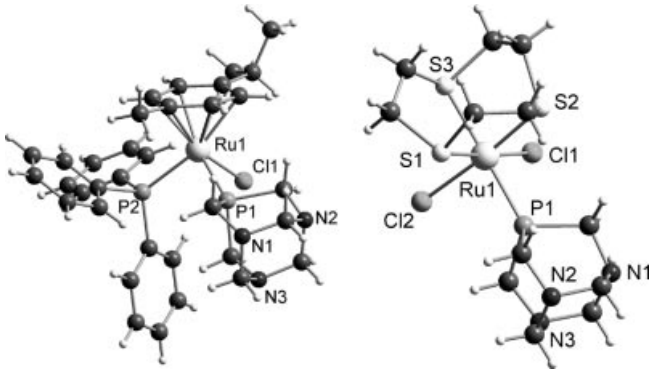


Figure 17. Ball and stick representation of RAPTA[tpp]-C **18** (left) and RAPTA-$S_3$ **20** (right); the $BF_4$ anion on **18** was omitted for clarity.

One of the potential issues with regard to eventual clinical application is the behaviour of drugs in water. Second-generation cisplatin drugs with oxalate and 1,1-cyclobutane-dicarboxylate ligands have been developed to improve the stability and solubility of the platinum complexes in water.[2] RAPTA complexes are prone to hydrolysis and would have to be administered in saline to suppress the cleavage of the chloride ligands. With a view to develop drugs that could resist hydrolysis in aqueous media, RAPTA complexes **22** and **23**, bearing chelating carboxylate ligands instead of the two chloride ligands, have been

 © 2006 Wiley-VCH Verlag GmbH & Co. KGaA, Weinheim 

developed (see Figure 18).[96] They were found to be kinetically more stable than **1**, and essentially, retained the carboxylate ligand in aqueous solution. Preliminary investigations show that these derivatives exhibit the same order of cytotoxicity in vitro (A549, T47D, MCF7, HT29) as **1** and exhibit similar oligonucleotide binding characteristics, hence proving to be a possible replacement for RAPTA-C in clinical studies.[96]

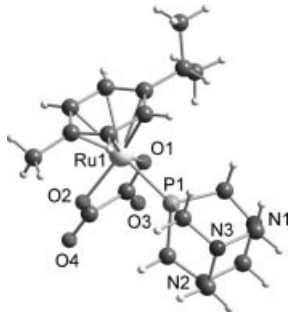


Figure 18. Ball and stick representation of OxaloRAPTA-C **22**.

As a strategy to enhance drug efficacy, the next generation of RAPTA complexes should be more "targeted". Such complexes could have multiple modes of activity, functionalised to achieve specific, desirable outcomes. As proof of concept, RAPTA complexes designed to inhibit Glutathione-S-Transferases (GST), a cytosolic detoxification enzyme associated with drug resistance, have been developed (see Figure 19.).[97] GST catalyses the conjugation of intracellular xenobiotics with glutathione, which is then expelled from cells by the GS-export pump. RAPTA complexes conjugated through the arene ring to ethacrynic acid, a known inhibitor of GST enzymes, were found to be effective GST inhibitors with significantly increased cytotoxic activity, i.e. showing comparable cytotoxicity to that of cisplatin in cell lines known to contain elevated levels of GST (A549, HT29, T47D). Other potential enzyme targets are presently being investigated.

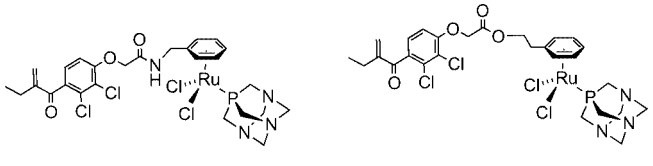

**24** **25**

Figure 19. RAPTA complexes designed to defeat GST-mediated drug resistance.

### *Beyond the Classical Approach: RAPTA as Antimetastatic Agents*

Despite the differences in oxidation state and ligand sphere, the striking semblance of RAPTA complexes to NAMI-A in vitro, primarily their low toxicity towards non-tumourgenic HBL-100, prompted the investigation of the lead RAPTA complexes **1**, **2** and **3** for potential antimetastatic activity.[90] In vivo experiments on MCa mammary carcinoma in CBA mice were used to evaluate the effects of the drugs i.p. on primary tumour growth and lung metastases formation. Firstly, it was found the lead RAPTA complexes were well tolerated by the mice at very high doses, consistent with in vitro data. Secondly, a low sustained treatment regime of RAPTA-C at 4× 100 mg/kg/day resulted in significant reduction in both lung metastases weight and number in treated mice whilst leaving the primarily tumour unaffected. In fact, under this regime 40% of the mice were completely free from metastases at the end of the treatment. This phenomenon was replicated in RAPTA-B and RAPTA-T under various treatment regime conditions and at 3× 80 mg/kg/day, RAPTA-T was able to reduce lung metastases in treated mice by 75%.[91] This result is comparable to that of NAMI-A which typically at 6× 35 mg/kg/day, reduces lung metastases by 71–90% and metastases number by 40–60%. Accordingly, there is no corresponding activity on the primary tumour. While the RAPTA complexes displayed marginally less antimetastatic activity than NAMI-A, it is much less toxic to mice and can potentially be administered at much higher dosage.

It is therefore apparent that the antimetastatic behaviour is not unique to NAMI-A, but applicable to other classes of ruthenium complexes. In the case of the well-studied NAMI-A, it is apparent that DNA is not the target, and more likely, activity is a consequence of drug–protein interactions. Therefore, a proteomic-based analytical approach based on 2-D PAGE and laser-ablation inductively-coupled mass spectrometry (ICP-MS) is being developed to identify the specific proteins interacting with ruthenium-based drugs.[98,99] The analytical technique utilises well-established methods in protein separation and exploits the high sensitivity of ICP-MS instruments in detecting non-endogenous transition-metal isotopes (in the order of parts per billion). While the technique is still under development, it has been used effectively to identify drug–protein interactions in human blood plasma, and was used to identify the main protein target of cisplatin in bacteria using 1D PAGE.[99,100]

At the same time, with a view to rationally develop other ruthenium-based antimetastatic agents, a new class of imidazole ($\eta^6$-arene)ruthenium complexes of the general formula [($\eta^6$-arene)$Ru^{II}Cl_2$(imid)], [($\eta^6$-arene)$Ru^{II}$Cl$(imid)_2$]X or [($\eta^6$-arene)$Ru^{II}(imid)_3]X_2$ (where imid = imidazolium ligand, X = Cl, $BF_4$, $BPh_4$, 15 examples) have been prepared, combining the unique structural aspects of NAMI-A and the "piano-stool" arene ruthenium(II) complexes.[101] The derived complexes exhibit similar cytotoxicity with RAPTA complexes in vitro (TS/A, HBL-100) and several of the complexes exhibit selectivity towards cancer cells. Specifically, [($\eta^6$-cymene)$Ru^{II}$Cl(vinylimid)$_2$]Cl **26** and [($\eta^6$-benzene)$Ru^{II}(mimid)_3](BF_4)_2$ **27** have been identified for further in vivo experiments (see Figure 20).[101] Further derivatisation of the imidazolium moiety, to yield antimetastatic ruthenium complexes conjugated to ethacrynic acid and other inhibitors of multidrug resistance-associated enzymes, is also being carried out.[97]

 © 2006 Wiley-VCH Verlag GmbH & Co. KGaA, Weinheim 

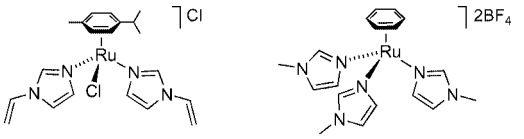


**26** **27**

Figure 20. New class of RAPTA-NAMI antimetastatic drug candidates.

## Outlook - Towards Targeted Chemotherapy

Drug discovery and evaluation strategies for ruthenium-based anticancer complexes rely largely on the classical approach of screening for biological activity using specific in vitro or in vivo models, identifying potential drug candidates, deriving structure–activity relationships and thereafter cycles of structural modifications and testing for improved drug efficacy. These tests are "result-oriented", especially those based on the effect of the drug on cell viability, and reveal immediately the inhibitory effect of the drug on cell growth proliferation. However, even if potential drugs are identified, to establish directly the drug mechanism is not trivial, especially where there is no target definition in the drug design, and investigators often rely on peripheral experiments in order to rationalise drug behaviour. It is therefore fortunate that ruthenium, and indeed other transition metals not endogenous to biological systems, can be detected using ICP-MS to high levels of sensitivity. Analytical methods based on ICP-MS could therefore directly establish the fate of ruthenium drugs once administered. Keppler et al. employed capillary electrophoresis and size exclusion chromatography techniques, coupled to ICP-MS, to determine drug–protein binding of ruthenium drugs in human blood plasma, and much is now known about metal-drug plasma-protein interactions.[102] We have demonstrated the efficacy of proteomic methods in protein separation on polyacrylamide gels, in conjunction with laser-ablation ICP-MS, to establish drug–protein interactions in the human plasma and from cell samples.[98,100] The ultimate goal is to create a map of drug–protein interactions in the proteome of a cancer cell line after treatment with ruthenium drugs. This is important not only in establishing the mechanism of drug activity, but also as a way of identifying areas in the proteome on which ruthenium drugs could target, and hence towards a more systematic way of developing non-classical ruthenium drugs.

It is debatable whether the inhibition of cell growth proliferation or cytotoxicity should continue to be the predominant "measure of success" for ruthenium-based anticancer drugs. Many ruthenium drugs are known for their low systemic toxicity as compared to established platinum-based drugs. If cytotoxicity is the sole determinant, it is unlikely that ruthenium drugs would offer significant therapeutic advantages. Instead, attributes like cancer-cell selectivity or low systemic toxicity need to be incorporated into drug evaluation, which would focus preclinical drug development towards highly selective ruthenium drugs of low toxicity. Furthermore, existing cytotoxicity assays ignore other aspects of ruthenium drugs that would have greater therapeutic scope. Indeed, NAMI-A failed the in vitro evaluation using the NCI's protocol against a 60-panel cell lines and would have been omitted for further evaluation if the conventional method of drug screening were strictly followed.[98] Sava et al. demonstrated the antimetastatic potential of ruthenium-based drugs, and we have subsequently shown that this attribute is not confined to NAMI-A, while Keppler et al. has exploited known ruthenium–transferrin interactions for drug delivery.[11,63,64] Clearly, more suitable models for testing ruthenium drugs are needed but it is imperative that these testing methods exploit the unique biological profile of ruthenium.[10]

A relatively uncharted area that holds much potential for the application of ruthenium-based drugs is combination therapy. An example is the ketoconazole ruthenium complex which is found to potentiate A431 cells overexpressing EGF-R to C225 MAb treatment, although the mechanism is not fully understood.[80] More recently, in vivo experiments (CBA mice with MCa carcinoma) showed that the combination treatment of NAMI-A and cisplatin led to a synergistic enhancement in the inhibition of metastases formation and growth of primary tumour in mice, as compared to the treatment of NAMI-A or cisplatin alone. At the same time, the increase in toxicity was additive, which was anticipated since both drugs are based on transition-metal centres and discharged mainly by renal excretion.[98] Such a strategy would be extremely attractive but would be dependent on finding other unique applications of ruthenium drugs, such as the antimetastatic behaviour of NAMI-A, which is beyond the scope of existing therapies.

Beyond developing better ways to augment existing drug discovery strategies, Meggers et al. have demonstrated the viability of organometallic ruthenium-based protein-kinase inhibitors, in a strategy that employs chiral ruthenium moieties surrounded by stable inert ligands as a spatial replacement for the carbohydrate moiety which is difficult to synthesise. In this way, the ruthenium centre plays a relatively minor role in determining biological activity and serves more as a connector for other ligands which provides the shape and conformation.[81,83] The sheer range of possible ligands of different shapes and sizes gives a high degree of synthetic flexibility, but it would not be unreasonable to replace the ruthenium by other transition metals and those which occur in living systems may prove preferable. The possibility of ruthenium clusters extending the scope of this approach could also be worth considering, especially since clusters have already been shown to have pharmacological potential.[103] Another approach would be to modify existing receptor and inhibitor molecules, e.g. in the approaches taken by Jaouen et al. in the design of SERMs and by our group in the development of multifunctional RAPTA complexes.[78,97] Nonetheless, developing ruthenium complexes for target therapies would invariably involve structural biology in the design phase of the receptor/inhibitor molecule. Designing the receptor/inhibitor molecule around the ruthenium scaffold in the beginning, rather

 © 2006 Wiley-VCH Verlag GmbH & Co. KGaA, Weinheim 

than in retrospect, could lead to viable ruthenium drugs with well-defined and predictable modes of activity.

It is clear that with two ruthenium compounds proceeding through clinical trials, combined with the limited number of platinum drugs that have entered the clinic since the discovery of cisplatin and putative drugs based on other transition metals being withdrawn from clinical trials, ruthenium systems hold great potential. With the new strategies outlined in this review, it is likely that we will witness increased research efforts in this domain.

## Acknowledgments

The authors would like to thank the Swiss National Science Foundation, la Ligue Suisse Contre le Cancer and the Roche Research Foundation for their financial support.

[1] V. H. Mansour, B. Rosenberg, L. Vancamp, J. E. Trosko, *Nature* **1969**, *222*, 385–386.
[2] T. Boulikas, M. Vougiouka, *Oncol. Rep.* **2003**, *10*, 1663–1682.
[3] A. Pasini, F. Zunino, *Angew. Chem. Int. Ed. Engl.* **1987**, *26*, 615–624.
[4] a) E. Wong, C. M. Giandomenico, *Chem. Rev.* **1999**, *99*, 2451–2466; b) M. Galanski, M. A. Jakupec, B. K. Keppler, *Curr. Med. Chem.* **2005**, *12*, 2075–2094.
[5] S. Vouillamoz-Lorenz, T. Buclin, F. Lejeune, J. Bauer, S. Leyvraz, L. A. Decosterd, *Anticancer Res.* **2003**, *23*, 2757–2765.
[6] a) W. H. Ang, I. Khalaila, C. S. Allardyce, L. Juilleratt-Jeanneret, P. J. Dyson, *J. Am. Chem. Soc.* **2005**, *127*, 1382–1383; b) W. H. Ang, S. Pilet, R. Scopelliti, F. Bussy, L. Juilleratt-Jeanneret, P. J. Dyson, *J. Med. Chem.* **2005**, *48*, 8060–8069; c) K. R. Barnes, A. Kutikov, S. J. Lippard, *Chem. Biol.* **2004**, *11*, 557–564; d) P. Muller, B. Schroder, J. A. Parkinson, N. A. Kratochwil, R. A. Coxall, A. Parkin, S. Parsons, P. J. Sadler, *Angew. Chem. Int. Ed.* **2003**, *42*, 335–339.
[7] a) L. Cerasino, F. P. Intini, J. Kobe, E. de Clercq, G. Natile, *Inorg. Chim. Acta* **2003**, *344*, 174–182; b) C. Descôteaux, J. Provencher-Mandeville, I. Mathieu, V. Perron, E. Asselin, G. Bérube, S. K. Mandal, *Bioorg. Med. Chem. Lett.* **2003**, *13*, 3927–3931; c) B. B. Hasinoff, X. Wu, Y. W. Yang, *J. Inorg. Biochem.* **2004**, *98*, 616–624.
[8] a) C. S. Allardyce, P. J. Dyson, *Platinum Met. Rev.* **2001**, *45*, 62–69; b) I. Kostova, *Curr. Med. Chem.* **2006**, *13*, 1085–1107.
[9] a) C. S. Allardyce, A. Dorcier, C. Scolaro, P. J. Dyson, *Appl. Organomet. Chem.* **2005**, *19*, 1–10; b) M. Galanski, V. B. Arion, M. A. Jakupec, B. K. Keppler, *Curr. Pharm. Des.* **2003**, *9*, 2078–2089.
[10] P. J. Dyson, G. Sava, *Dalton Trans.* **2006**, 1929–1933.
[11] C. G. Hartinger, S. Zorbas-Seifried, M. A. Jakupec, B. Kynast, H. Zorbas, B. K. Keppler, *J. Inorg. Biochem.* **2006**, *100*, 891–904.
[12] J. M. Rademaker-Lakhai, D. Van Den Bongard, D. Pluim, J. H. Beijnen, J. H. M. Schellens, *Clin. Cancer Res.* **2004**, *10*, 3717–3727.
[13] M. A. Jakupec, V. B. Arion, S. Kapitza, E. Reisner, A. Eichinger, M. Pongratz, B. Marian, N. Graf v. Keyserlingk, B. K. Keppler, *Int. J. Clin. Pharmacol. Ther.* **2005**, *43*, 595–596.
[14] H. Varmus, *Science* **2006**, *312*, 1162–1165.
[15] J. S. Sebolt-Leopold, J. M. English, *Nature* **2006**, *441*, 457–462.
[16] R. M. Schultz, In *Advances in Targeted Cancer Therapy* (Eds.: P. L. Herrling, A. Matter); Birkhäuser: **2005**.
[17] a) A. L. Goldberg, K. Rock, *Nat. Med.* **2002**, *8*, 338–340; b) A. Gschwind, O. M. Fischer, A. Ullrich, *Nat. Rev. Cancer* **2004**, *4*, 361–370.
[18] P. Kay, *Semin. Oncol. Nurs.* **2006**, *22*, 1–4.
[19] O. Novakova, J. Kasparkova, O. Vrana, P. M. Vanvliet, J. Reedijk, V. Brabec, *Biochemistry* **1995**, *34*, 12369–12378.
[20] P. M. Vanvliet, S. M. S. Toekimin, J. G. Haasnoot, J. Reedijk, O. Novakova, O. Vrana, V. Brabec, *Inorg. Chim. Acta* **1995**, *231*, 57–64.
[21] a) U. K. Mazumder, M. Gupta, A. Bera, S. Bhattacharya, S. Karki, L. Manikandan, S. Patra, *Indian J. Chem. Sect. A* **2003**, *42*, 313–317; b) U. K. Mazumder, M. Gupta, S. Bhattacharya, S. S. Karki, S. Rathinasamy, S. Thangavel, *J. Enzyme Inhib. Med. Chem.* **2004**, *19*, 185–192; c) U. K. Mazumder, M. Gupta, S. S. Karki, S. Bhattacharya, S. Rathinasamy, T. Sivakumar, *Bioorg. Med. Chem.* **2005**, *13*, 5766–5773; d) U. K. Mazumder, M. Gupta, S. S. Karki, S. Bhattacharya, S. Rathinasamy, S. Thangavel, *Chem. Pharm. Bull.* **2004**, *52*, 178–185; e) L. Mishra, R. Sinha, H. Itokawa, K. F. Bastow, Y. Tachibana, Y. Nakanishi, N. Kilgore, K. H. Lee, *Bioorg. Med. Chem.* **2001**, *9*, 1667–1671; f) L. Mishra, A. K. Yadaw, S. Bhattacharya, S. K. Dubey, *J. Inorg. Biochem.* **2005**, *99*, 1113–1118.
[22] H. L. Chan, H. C. Liu, B. L. C. Tzeng, Y. S. Y. You, S. M. Peng, M. S. Yang, C. M. Che, *Inorg. Chem.* **2002**, *41*, 3161–3171.
[23] K. Karidi, A. Garoufis, A. Tsipis, N. Hadjiliadis, H. den Dulk, J. Reedijk, *Dalton Trans.* **2005**, 1176–1187.
[24] P. I. Anderberg, M. M. Harding, I. J. Luck, P. Turner, *Inorg. Chem.* **2002**, *41*, 1365–1371.
[25] K. van der Schilden, F. Garcia, H. Kooijman, A. L. Spek, J. G. Haasnoot, J. Reedijk, *Angew. Chem. Int. Ed.* **2004**, *43*, 5668–5670.
[26] D. Chatterjee, A. Mitra, G. De, *Platinum Met. Rev.* **2006**, *50*, 2–12.
[27] R. Vilaplana, M. Romero, M. Quiros, J. Salas, F. Gonzalez Vilchez, *Met.-Based Drugs* **1995**, *2*, 211–219.
[28] F. Gonzalez Vilchez, R. Vilaplana, G. Blasco, L. Messori, *J. Inorg. Biochem.* **1998**, *71*, 45–51.
[29] E. Gallori, C. Vettori, E. Alessio, F. G. Vilchez, R. Vilaplana, P. Orioli, A. Casini, L. Messori, *Arch. Biochem. Biophys.* **2000**, *376*, 156–162.
[30] S. R. Grguric-Sipka, R. A. Vilaplana, J. M. Perez, M. A. Fuertes, C. Alonso, Y. Alvarez, T. J. Sabo, F. Gonzalez-Vilchez, *J. Inorg. Biochem.* **2003**, *97*, 215–220.
[31] V. Djinovic, M. Momcilovic, S. Gruric-Sipka, V. Trajkovic, M. M. Stojkovic, D. Miljkovic, T. Sabo, *J. Inorg. Biochem.* **2004**, *98*, 2168–2173.
[32] D. Chatterjee, A. Mitra, M. S. A. Hamza, R. van Eldik, *J. Chem. Soc., Dalton Trans.* **2002**, 962–965.
[33] D. Chatterjee, A. Sengupta, A. Mitra, S. Basak, *Inorg. Chim. Acta* **2005**, *358*, 2954–2959.
[34] a) D. Chatterjee, M. S. A. Hamza, M. M. Shoukry, A. Mitra, S. Deshmukh, R. van Eldik, *Dalton Trans.* **2003**, 203–209; b) D. Chatterjee, A. Mitra, A. Sengupta, P. Saha, M. Chatterjee, *Inorg. Chim. Acta* **2006**, *359*, 2285–2290; c) D. Chatterjee, A. Sengupta, A. Mitra, S. Basak, R. Bhattacharya, D. Bhattacharyya, *J. Coord. Chem.* **2005**, *58*, 1703–1711.
[35] E. Alessio, G. Mestroni, G. Nardin, W. M. Attia, M. Calligaris, G. Sava, S. Zorzet, *Inorg. Chem.* **1988**, *27*, 4099–4106.
[36] G. Sava, S. Pacor, S. Zorzet, E. Alessio, G. Mestroni, *Pharmacol. Res.* **1989**, *21*, 617–628.
[37] M. Coluccia, G. Sava, F. Loseto, A. Nassi, A. Boccarelli, D. Giordano, E. Alessio, G. Mestroni, *Eur. J. Cancer* **1993**, *29A*, 1873–1879.
[38] D. T. T. Yapp, S. J. Rettig, B. R. James, K. A. Skov, *Inorg. Chem.* **1997**, *36*, 5635–5641.
[39] E. Cabrera, H. Cerecetto, M. Gonzalez, D. Gambino, P. Noblia, L. Otero, B. Parajon-Costa, A. Anzellotti, R. Sanchez-Delgado, A. Azqueta, A. L. de Cerain, A. Monge, *Eur. J. Med. Chem.* **2004**, *39*, 377–382.
[40] A. Wu, D. C. Kennedy, B. O. Patrick, B. R. James, *Inorg. Chem.* **2003**, *42*, 7579–7586.
[41] Y. Qu, N. Farrell, *Inorg. Chem.* **1995**, *34*, 3573–3576.

 © 2006 Wiley-VCH Verlag GmbH & Co. KGaA, Weinheim 

[42] B. Van Houten, S. Illenye, Y. Qu, N. Farrell, *Biochemistry* **1993**, *32*, 11794–11801.
[43] M. Brindell, E. Kulis, S. K. C. Elmroth, K. Urbanska, G. Stochel, *J. Med. Chem.* **2005**, *48*, 7298–7304.
[44] a) A. Seal, S. Ray, *Acta Crystallogr., Sect. C* **1984**, *40*, 929–932; b) R. A. Krause, K. Krause, *Inorg. Chem.* **1980**, *19*, 2600–2603.
[45] A. H. Velders, H. Kooijman, A. L. Spek, J. G. Haasnoot, D. de Vos, J. Reedijk, *Inorg. Chem.* **2000**, *39*, 2966–2967.
[46] A. C. G. Hotze, S. E. Caspers, D. De Vos, H. Kooijman, A. L. Spek, A. Flamigni, M. Bacac, G. Sava, J. G. Haasnoot, J. Reedijk, *J. Biol. Inorg. Chem.* **2004**, *9*, 354–364.
[47] J. C. Chen, J. Li, L. Qian, K. C. Zheng, *J. Mol. Struct. (THEOCHEM)* **2005**, *728*, 93–101.
[48] A. C. G. Hotze, E. P. L. van der Geer, S. E. Caspers, H. Kooijman, A. L. Spek, J. G. Haasnoot, J. Reedijk, *Inorg. Chem.* **2004**, *43*, 4935–4943.
[49] A. C. G. Hotze, E. P. L. Van Der Geer, H. Kooijman, A. L. Spek, J. G. Haasnoot, J. Reedijk, *Eur. J. Inorg. Chem.* **2005**, 2648–2657.
[50] A. C. G. Hotze, M. Bacac, A. H. Velders, B. A. J. Jansen, H. Kooijman, A. L. Spek, J. G. Haasnoot, J. Reedijk, *J. Med. Chem.* **2003**, *46*, 1743–1750.
[51] A. C. G. Hotze, H. Kooijman, A. L. Spek, J. G. Haasnoot, J. Reedijk, *New J. Chem.* **2004**, *28*, 565–569.
[52] A. C. G. Hotze, B. M. Kariuki, M. J. Hannon, *Angew. Chem. Int. Ed.* **2006**, *45*, 4839–4842.
[53] Y. N. V. Gopal, N. Konuru, A. K. Kondapi, *Arch. Biochem. Biophys.* **2002**, *401*, 53–62.
[54] L. A. Huxham, E. L. S. Cheu, B. O. Patrick, B. R. James, *Inorg. Chim. Acta* **2003**, *352*, 238–246.
[55] a) Y. K. Yan, M. Melchart, A. Habtemariam, P. J. Sadler, *Chem. Commun.* **2005**, 4764–4776; b) A. F. A. Peacock, A. Habtemariam, R. Fernandez, V. Walland, F. P. A. Fabbiani, S. Parsons, R. E. Aird, D. I. Jodrell, P. J. Sadler, *J. Am. Chem. Soc.* **2006**, *128*, 1739–1748.
[56] R. E. Morris, R. E. Aird, P. Del Socorro Murdoch, H. Chen, J. Cummings, N. D. Hughes, S. Parsons, A. Parkin, G. Boyd, D. I. Jodrell, P. J. Sadler, *J. Med. Chem.* **2001**, *44*, 3616–3621.
[57] O. Novakova, H. Chen, O. Vrana, A. Rodger, P. J. Sadler, V. Brabec, *Biochemistry* **2003**, *42*, 11544–11554.
[58] H. Chen, J. A. Parkinson, R. E. Morris, P. J. Sadler, *J. Am. Chem. Soc.* **2003**, *125*, 173–186.
[59] R. Fernandez, M. Melchart, A. Habtemariam, S. Parsons, P. J. Sadler, *Chem. Eur. J.* **2004**, *10*, 5173–5179.
[60] H. Chen, J. A. Parkinson, S. Parsons, R. A. Coxall, R. O. Gould, P. J. Sadler, *J. Am. Chem. Soc.* **2002**, *124*, 3064–3082.
[61] H. Chen, J. A. Parkinson, O. Novakova, J. Bella, F. Wang, A. Dawson, R. Gould, S. Parsons, V. Brabec, P. J. Sadler, *Proc. Natl. Acad. Sci. USA* **2003**, *100*, 14623–14628.
[62] E. Alessio, G. Mestroni, A. Bergamo, G. Sava, *Curr. Top. Med. Chem.* **2004**, *4*, 1525–1535.
[63] M. Cocchietto, S. Zorzet, A. Sorc, G. Sava, *Invest. New Drugs* **2003**, *21*, 55–62.
[64] F. Frausin, M. Cocchietto, A. Bergamo, V. Searcia, A. Furlani, G. Sava, *Cancer Chemother. Pharmacol.* **2002**, *50*, 405–411.
[65] M. Ravera, S. Baracco, C. Cassino, D. Colangelo, G. Bagni, G. Sava, D. Osella, *J. Inorg. Biochem.* **2004**, *98*, 984–990.
[66] A. Bergamo, L. Messori, F. Piccioli, M. Cocchietto, G. Sava, *Invest. New Drugs* **2003**, *21*, 401–411.
[67] S. Zorzet, A. Bergamo, M. Cocchietto, A. Sorc, B. Gava, E. Alessio, E. Iengo, G. Sava, *J. Pharmacol. Exp. Ther.* **2000**, *295*, 927–933.
[68] I. Turel, M. Pecanac, A. Golobic, E. Alessio, B. Serli, A. Bergamo, G. Sava, *J. Inorg. Biochem.* **2004**, *98*, 393–401.
[69] A. H. Velders, A. Bergamo, E. Alessio, E. Zangrando, J. G. Haasnoot, C. Casarsa, M. Cocchietto, S. Zorzet, G. Sava, *J. Med. Chem.* **2004**, *47*, 1110–1121.
[70] a) E. Alessio, E. Iengo, S. Zorzet, A. Bergamo, M. Coluccia, A. Boccarelli, G. Sava, *J. Inorg. Biochem.* **2000**, *79*, 173–177; b) A. Bergamo, G. Stocco, C. Casarsa, M. Cocchietto, E. Alessio, B. Serli, S. Zorzet, G. Sava, *Int. J. Oncol.* **2004**, *24*, 373–379; c) A. Bergamo, G. Stocco, B. Gava, M. Cocchietto, E. Alessio, B. Serli, E. Iengo, G. Sava, *J. Pharmacol. Exp. Ther.* **2003**, *305*, 725–732.
[71] S. Kapitza, M. Pongratz, M. A. Jakupec, P. Heffeter, W. Berger, L. Lackinger, B. K. Keppler, B. Marian, *J. Cancer Res. Clin. Oncol.* **2005**, *131*, 101–110.
[72] P. Heffeter, M. Pongratz, E. Steiner, P. Chiba, M. A. Jakupec, L. Elbling, B. Marian, W. Korner, F. Sevelda, M. Micksche, B. K. Keppler, W. Berger, *J. Pharmacol. Exp. Ther.* **2005**, *312*, 281–289.
[73] a) C. G. Hartinger, S. Hann, G. Koellensperger, M. Sulyok, M. Groessl, A. R. Timerbaev, A. V. Rudnev, G. Stingeder, B. K. Keppler, *Int. J. Clin. Pharmacol. Ther.* **2005**, *43*, 583–585; b) F. Piccioli, S. Sabatini, L. Messori, P. Orioli, C. G. Hartinger, B. K. Keppler, *J. Inorg. Biochem.* **2004**, *98*, 1135–1142; c) M. Pongratz, P. Schluga, M. A. Jakupec, V. B. Arion, C. G. Hartinger, G. Allmaier, B. K. Keppler, *J. Anal. At. Spectrom.* **2004**, *19*, 46–51.
[74] J. Malina, O. Novakova, B. K. Keppler, E. Alessio, V. Brabec, *J. Biol. Inorg. Chem.* **2001**, *6*, 435–445.
[75] a) V. Arion, A. Eichinger, M. Jakupec, B. K. Keppler, *J. Inorg. Biochem.* **2001**, *86*, 129–129; b) E. Reisner, V. B. Arion, A. Eichinger, N. Kandler, G. Giester, A. J. L. Pombeiro, B. K. Keppler, *Inorg. Chem.* **2005**, *44*, 6704–6716; c) E. Reisner, V. B. Arion, M. Fatima, C. G. da Silva, R. Lichtenecker, A. Eichinger, B. K. Keppler, V. Y. Kukushkin, A. J. L. Pombeiro, *Inorg. Chem.* **2004**, *43*, 7083–7093.
[76] M. A. Jakupec, E. Reisner, A. Eichinger, M. Pongratz, V. B. Arion, M. Galanski, C. G. Hartinger, B. K. Keppler, *J. Med. Chem.* **2005**, *48*, 2831–2837.
[77] a) A. Vessieres, S. Top, W. Beck, E. Hillard, G. Jaouen, *Dalton Trans.* **2006**, 529–541; b) S. Top, A. Vessieres, G. Jaouen, R. H. Fish, *Organometallics* **2006**, *25*, 3293–3296.
[78] P. Pigeon, S. Top, A. Vessieres, M. Huche, E. A. Hillard, E. Salomon, G. Jaouen, *J. Med. Chem.* **2005**, *48*, 2814–2821.
[79] a) M. Navarro, T. Lehmann, E. J. Cisneros-Fajardo, A. Fuentes, R. A. Sanchez-Delgado, P. Silva, J. A. Urbina, *Polyhedron* **2000**, *19*, 2319–2325; b) R. A. Sanchezdelgado, K. Lazardi, L. Rincon, J. A. Urbina, A. J. Hubert, A. N. Noels, *J. Med. Chem.* **1993**, *36*, 2041–2043; c) R. A. Sanchez-Delgado, M. Navarro, K. Lazardi, R. Atencio, M. Capparelli, F. Vargas, J. A. Urbina, A. Bouillez, A. F. Noels, D. Masi, *Inorg. Chim. Acta* **1998**, *276*, 528–540.
[80] M. S. Rieber, A. Anzellotti, R. A. Sanchez-Delgado, M. Rieber, *Int. J. Cancer* **2004**, *112*, 376–384.
[81] J. E. Debreczeni, A. N. Bullock, G. E. Atilla, D. S. Williams, H. Bregman, S. Knapp, E. Meggers, *Angew. Chem. Int. Ed.* **2006**, *45*, 1580–1585.
[82] L. Zhang, P. Carroll, E. Meggers, *Org. Lett.* **2004**, *6*, 521–523.
[83] H. Bregman, P. J. Carroll, E. Meggers, *J. Am. Chem. Soc.* **2006**, *128*, 877–884.
[84] D. S. Williams, G. E. Atilla, H. Bregman, A. Arzoumanian, P. S. Klein, E. Meggers, *Angew. Chem. Int. Ed.* **2005**, *44*, 1984–1987.
[85] M. A. Bennett, A. K. Smith, *J. Chem. Soc., Dalton Trans.* **1974**, 233–241.
[86] T. J. Geldbach, M. R. H. Brown, R. Scopelliti, P. J. Dyson, *J. Organomet. Chem.* **2005**, *690*, 5055–5065.
[87] A. D. Phillips, L. Gonsalvi, A. Rornerosa, F. Vizza, M. Peruzzini, *Coord. Chem. Rev.* **2004**, *248*, 955–993.
[88] a) D. N. Akbayeva, L. Gonsalvi, W. Oberhauser, M. Peruzzini, F. Vizza, P. Bruggeller, A. Romerosa, G. Sava, A. Bergamo, *Chem. Commun.* **2003**, 264–265; b) A. Dorcier, W. H. Ang, S. Bolaño, L. Gonsalvi, L. Juillerat-Jeannerat, G. Laurenczy, M. Peruzzini, A. D. Phillips, F. Zanobini, P. J. Dyson, *Organometallics* **2006**, *25*, 4090–4096.
[89] C. S. Allardyce, P. J. Dyson, D. J. Ellis, S. L. Heath, *Chem. Commun.* **2001**, 1396–1397.

 © 2006 Wiley-VCH Verlag GmbH & Co. KGaA, Weinheim 

[90] C. Scolaro, A. Bergamo, L. Brescacin, R. Delfino, M. Cocchietto, G. Laurenczy, T. J. Geldbach, G. Sava, P. J. Dyson, *J. Med. Chem.* **2005**, *48*, 4161–4171.
[91] A. Bergamo, C. Scolaro, G. Sava, P. J. Dyson, unpublished results.
[92] A. Dorcier, P. J. Dyson, C. Gossens, U. Rothlisberger, R. Scopelliti, I. Tavernelli, *Organometallics* **2005**, *24*, 2114–2123.
[93] C. Scolaro, T. J. Geldbach, S. Rochat, A. Dorcier, C. Gossens, A. Bergamo, M. Cocchietto, I. Tavernelli, G. Sava, U. Rothlisberger, P. J. Dyson, *Organometallics* **2006**, *25*, 756–765.
[94] A. B. Chaplin, C. Scolaro, P. J. Dyson, unpublished results.
[95] B. Serli, E. Zangrando, T. Gianferrara, C. Scolaro, P. J. Dyson, A. Bergamo, E. Alessio, *Eur. J. Inorg. Chem.* **2005**, 3423–3434.
[96] W. H. Ang, E. Daldini, C. Scolaro, R. Scopelliti, L. Juillerat-Jeannerat, P. J. Dyson, *Inorg. Chem.* **2006**, in press.
[97] W. H. Ang, P. J. Dyson, unpublished results.
[98] I. Khailaila, A. Bergamo, F. Bussy, G. Sava, P. J. Dyson, *Int. J. Oncol.* **2006**, *29*, 261–268.
[99] C. S. Allardyce, P. J. Dyson, F. R. Abou-Shakra, H. Birtwistle, J. Coffey, *Chem. Commun.* **2001**, 2708–2709.
[100] C. S. Allardyce, P. J. Dyson, D. J. Ellis, P. A. Salter, R. Scopelliti, *J. Organomet. Chem.* **2003**, *668*, 35–42.
[101] C. Vock, C. Scolaro, A. D. Phillips, R. Scopelliti, G. Sava, P. J. Dyson, *J. Med. Chem.* **2006**, *49*, 5552–5561.
[102] a) A. R. Timerbaev, C. G. Hartinger, S. S. Aleksenko, B. K. Keppler, *Chem. Rev.* **2006**, *106*, 2224–2248; b) K. Polec-Pawlak, J. K. Abramski, O. Semenova, C. G. Hartinger, A. R. Timerbaev, B. K. Keppler, M. Jarosz, *Electrophoresis* **2006**, *27*, 1128–1135; c) J. Szpunar, A. Makarov, T. Pieper, B. K. Keppler, R. Lobinski, *Anal. Chim. Acta* **1999**, *387*, 135–144; d) A. R. Timerbaev, A. V. Rudnev, O. Semenova, C. G. Hartinger, B. K. Keppler, *Anal. Biochem.* **2005**, *341*, 326–333.
[103] a) C. S. Allardyce, P. J. Dyson, *J. Cluster Sci.* **2001**, *12*, 563–569; b) E. Rosenberg, F. Spada, K. Sugden, B. Martin, L. Milone, R. Gobetto, A. Viale, J. Fiedler, *J. Organomet. Chem.* **2003**, *668*, 51–58.

Received: August 2, 2006
Published Online: ■

 © 2006 Wiley-VCH Verlag GmbH & Co. KGaA, Weinheim 

DOI: 10.1002/ejic.200600534

# Incorporation of the Unnatural Organometallic Amino Acid 1′-Aminoferrocene-1-carboxylic Acid (Fca) into Oligopeptides by a Combination of Fmoc and Boc Solid-Phase Synthetic Methods

**Lidija Barišić,[a] Vladimir Rapić,[a] and Nils Metzler-Nolte*[b][‡]**

**Keywords:** Bioorganometallic chemistry / Ferrocene / Peptides / Solid-phase peptide synthesis / Unnatural amino acids

The organometallic amino acid 1′-aminoferrocene-1-carboxylic acid (Fca) was incorporated internally into a peptide sequence by solid-phase methods combining natural Fmoc-protected amino acids and Boc-Fca-OH to give the pentapeptide Boc-Fca-Ala-Gly-Val-Leu-$NH_2$ (**2**) and the octapeptide Ac-Val-Gly-Ala-Fca-Ala-Gly-Val-Leu-$NH_2$ (**3**). Compound **3** was found to have a helically ordered structure by NMR and CD spectroscopy, which is stabilized by intramolecular hydrogen bonding in an antiparallel β-sheet-like arrangement.
(© Wiley-VCH Verlag GmbH & Co. KGaA, 69451 Weinheim, Germany, 2006)

Turn structures are ubiquitous secondary structural elements in proteins that have become important targets in medicinal chemistry.[1–4] Metal complexes, in particular ferrocene, may serve as turn mimetics in peptides.[5] The use of ferrocene-1,1′-dicarboxylic acid as a turn inducer was described by several groups, particularly those of Herrick, Hirao and Kraatz.[6–14] Ferrocene derivatives bearing *parallel* podand peptide strands were shown to induce helically ordered structures which are controlled by strong intramolecular hydrogen bonds as shown in the solid state by X-ray crystallography studies as well as in solution by IR, $^1$H NMR and CD spectroscopy.[7–10,15,16]

In previous work we investigated the role of 1′-aminoferrocene-1-carboxylic acid (Fca) as a turn mimetic in the tetrapeptide Boc-Ala-Fca-Ala-Ala-OMe (**1**) which contains *antiparallel* peptide strands stabilized by two intramolecular hydrogen bonds in both, solution and solid phases (Scheme 1).[17] All derivatives of ferrocene-1,1′-dicarboxylic acid and Fca so far were prepared by stepwise synthesis in solution. Solid-phase peptide synthesis (SPPS) using orthogonal protecting groups and linkers is the standard method for the synthesis of small to medium-sized peptides. Twenty years ago, a few papers were published dealing with the application of SPPS to metallocenes. Ferrocenylalanine (Fer) and cymantrenylalanine (Cym) were incorporated into biologically active peptides (enkephalin, bradykinin and substance P). Most work was carrid out on enkephalin which was transformed into [Fer$^4$,Leu$^5$] or [Cym$^4$,Leu$^5$] analogues by replacement of the phenylalanine side chain (Phe$^4$) with Fer or Cym, thus preserving the aromatic character of this residue.[18–21] It is worth to mention SPPS of a "ferrocenophanic" conformationally constrained analogue of substance P.[22] Very recently, SPPS of *N*-terminated cobaltocenium-NLS peptides[23] and metallocenoyl (M = Fe, Co) tripeptides[24] with antibacterial activity were described by one of us. In all peptides described up to the present day, the organometallic group is part of the side chain or linked to the *N*-terminus. We therefore set out to incorporate a metallocene such as Fca into the peptide backbone by SPPS. In this paper we describe for the first time an SPPS procedure for constitutive insertion of a ferrocene derivative into the peptide chain back bone.

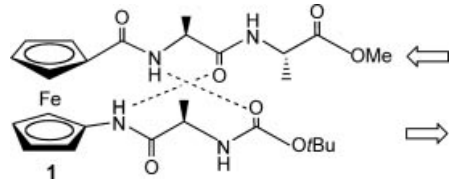


Scheme 1. The antiparallel orientation of peptide strands in tetrapeptide **1** is induced by the unnatural amino acid 1′-aminoferrocene-1-carboxylic acid (Fca) and stabilized by intramolecular hydrogen bonds.

In recent years, the fluorenylmethoxycarbonyl (Fmoc) group has largely replaced the original Merrifield *tert*-butoxycarbonyl (Boc) group as the temporary *N*-terminal protecting group because it may be easily removed under mild basic conditions. Boc removal, on the other hand, requires strong acid which is incompatible with sensitive com-

[a] Faculty of Food Technology and Biotechnology, University of Zagreb,
Pierottijeva 6, 10000 Zagreb, Croatia
[b] Institut für Pharmazie und Molekulare Biotechnologie, Universität Heidelberg,
Im Neuenheimer Feld 364, 69120 Heidelberg, Germany
[‡] New address: Department of Chemistry, University of Bochum, Universitätsstraße 150, 44801 Bochum, Germany, Fax: +49-234-32-14378, E-mail: Nils.Metzler-Nolte@rub.de
Supporting information for this article is available on the WWW under http://www.eurjic.org or from the author.

 © 2006 Wiley-VCH Verlag GmbH & Co. KGaA, Weinheim 

pounds, for instance some organometallic complexes.[25,26] For this reason, we originally planned to synthesize Fca-containing oligopeptides according to the standard Fmoc approach.[27] However, *N*-Fmoc-Fca-terminated oligopeptides turned out to be very unstable. Therefore, a combination of Boc-Fca-OH and Fmoc-Aaa-OH had to be chosen, thereby reintroducing the classical Merrifield method to the synthesis of Fca-containing peptides by solid-phase synthesis.

Pentapeptide **2** was obtained by standard Fmoc SPPS, starting from Fmoc-Leu loaded TentaGel S resin with the base-labile HMB linker, Fmoc-Val-OH, Fmoc-Gly-OH and Fmoc-Ala-OH.[27] Subsequent coupling to Boc-Fca-OH, cleavage from the resin by concentrated ammonia in methanol and thin layer chromatography (TLC) purification gave Boc-Fca-Ala-Gly-Val-Leu-$NH_2$ (**2**) (Scheme 2).

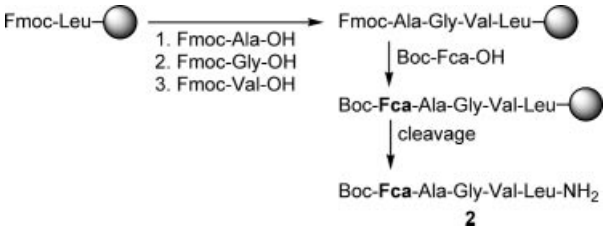


Scheme 2. Solid-phase synthesis of the Fca-containing pentapeptide **2**.

Octapeptide **3** was prepared starting from pentapeptide **2** attached to the solid support. The temporary Boc-protecting group masking the α-amino group of Fca was removed by gaseous HCl in $CH_2Cl_2$ during 1 h. The resulting ammonium salt was converted by the action of 10% $NEt_3/CH_2Cl_2$ into the corresponding amino species which was coupled with Fmoc-Ala-OH, Fmoc-Gly-OH and Ac-Val-OH to give octapeptide Ac-Val-Gly-Ala-Fca-Ala-Gly-Val-Leu-$NH_2$ (**3**) (Scheme 3). The product was cleaved from the resin by concd. $NH_3$ in MeOH and purified by TLC. The yields of both compounds after TLC purification (14% for **2** and 23% for **3**, respectively) were in the expected range for SPPS procedures, given that no effort was made for optimization in these initial experiments. The purity of both peptides **2** and **3** was confirmed by analytical HPLC (see Supporting Information).

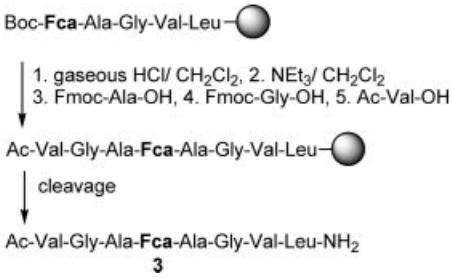


Scheme 3. Solid-phase synthesis of octapeptide **3** with the organometallic amino acid Fca incorporated internally.

Evidence for the proposed composition of **2** and **3** was obtained from ESI-MS where peaks at $m/z$ = 1391.7 $[2 \times M + Na]^+$ (**2**) and $m/z$ = 876.5 $[M + Na]^+$ (**3**) were observed. The $^1H$ NMR spectra confirmed the proposed structures, too. Due to the limited solubility of the metallocene peptides, all spectra were measured in $[D_6]$DMSO (approx. 10 mM), which competes as a hydrogen-bond acceptor. First of all, the correct number of amide proton signals confirms the number of amino acids, i.e. six for **2** and nine for **3**, both including the *C*-terminal amide with the intensity of 2 H. Upon closer inspection, the $^1H$ NMR spectrum of **2** shows two signals at $\delta > 8$ ppm, whereas **3** has five amide signals at $\delta > 8$ ppm. Intermolecular hydrogen bonding is unlikely to occur in DMSO at mM concentrations. Thus, these signals are indicative of relatively strong intramolecular hydrogen bonds between the peptide strands.[14] From this analysis it follows for **2** that a structure similar to the one in Scheme 1, but with a Boc group on the ferrocene amide moiety, is stabilized by only two hydrogen bonds, one being between Gly-NH and the Boc group carbonyl oxygen atom. Much stronger stabilization prevails in **3**, with about five intramolecular hydrogen bonds. This situation is indeed similar to an antiparallel β-sheet-like protein structure.

CD spectra (in DMSO) were recorded in order to further elucidate the hydrogen bonding situation (Figure 1). The strong Cotton effect in the CD spectrum of octapeptide **3** at about 480 nm is evidence for a chiral conformation at the ferrocene core, similar to our results on the tetrapeptide **1**. The strong intramolecular hydrogen bonding is retained even in DMSO, which confirms our NMR analysis above. A positive signal, as observed for **3**, correlates with a (*P*)-helical arrangement as shown by Hirao[9,10] and by us.[14,17] Compound **2** lacks one pendant peptide strand and, as explained above, the secondary structure is far less stabilized. Consequently, the absence of a Cotton effect in the CD spectrum of **2** may be readily explained by the lack of strong intramolecular hydrogen bonding.

In conclusion, we have prepared and characterized two peptides containing the organometallic amino acid Fca as part of the backbone by SPPS, namely pentapeptide **2** and octapeptide **3**. Our method is unique because it combines Fmoc and Boc procedures. The total decomposition of Fmoc-Fca-Ala-Gly-Val-Leu-resin upon removal of the protecting group led us to terminate this peptide with Boc-Fca which is a convenient intermediate either for further elongation of the peptide chain by Fmoc-protected amino acids to yield **3** or for its successfully cleavage from the resin (for **2**). The target molecules of previously reported SPPS with metallocenes were: (*i*) bioconjugates obtained by replacement of one or two Phe "internal" subunits by metallocenylalanine or (metallocene-1,1′-diyl)bis(alanine),[18–22] (*ii*) *N*-metallocenoyl terminated peptide sequences.[23,24] In this paper, we show that it is possible to incorporate the unnatural ferrocene amino acid Fca into the peptide backbone by SPPS. To this end, a suitable combination of Fmoc and Boc SPPS strategies, which are usually seen as orthogonal, had to be adopted. The two cyclopentadienyl rings in ferrocene may rotate almost freely against each other. This gives ferrocene-based turn mimetics a unique degree of structural flexibility compared to all known organic systems. Indeed, we obtained evidence for an antiparallel β-

 © 2006 Wiley-VCH Verlag GmbH & Co. KGaA, Weinheim 

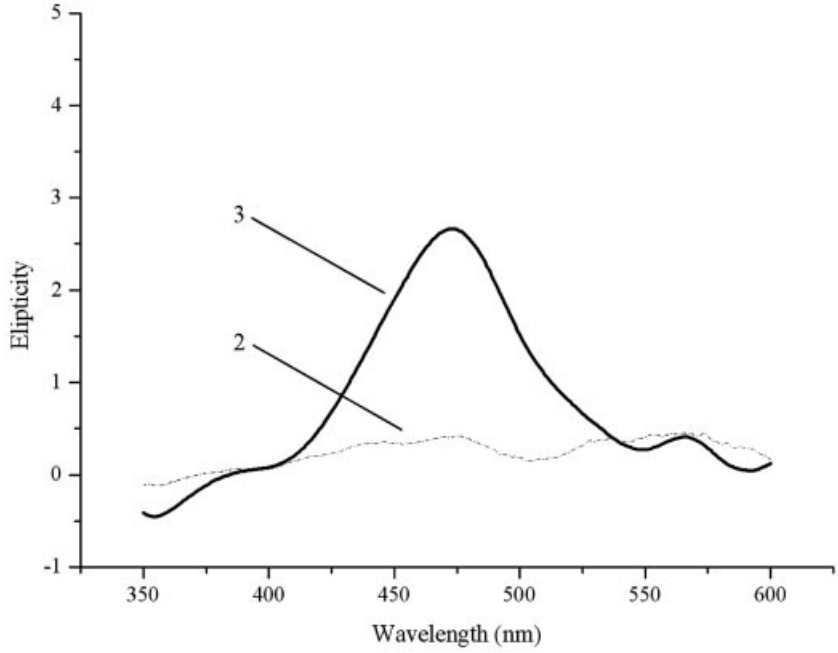


Figure 1. CD spectra of **2** and **3** (1 mM in DMSO).

sheet-like arrangement for the first time with an organometallic turn inducer. Further work in our groups will explore the possibilities inherent in such biomimetic organometallic systems.[28–31]

**Supporting Information** (see footnote on the first page of this article): Synthetic details and spectroscopic data including HPLCs for compounds **2** and **3**.

## Acknowledgments

We thank the Ministry of Science, Education and Sport of Croatia for support through a grant. Financial support by the DAAD (fellowship to L. B.) and help from S. I. Kirin for the SPPS is gratefully acknowledged.

[1] G. Hölzemann, *Kontakte (Darmstadt)* **1991**, (1), 3–13.
[2] G. Hölzemann, *Kontakte (Darmstadt)* **1991**, (2), 55–64.
[3] D. Obrecht, M. Altorfer, J. A. Robinson, *Adv. Med. Chem.* **1999**, *4*, 1–68.
[4] K. S. Kee, S. D. S. Jois, *Curr. Pharm. Des.* **2003**, *9*, 1209–1224.
[5] D. R. van Staveren, N. Metzler-Nolte, *Chem. Rev.* **2004**, *104*, 5931–5985.
[6] R. S. Herrick, R. M. Jarret, T. P. Curran, D. R. Dragoli, M. B. Flaherty, S. E. Lindyberg, R. A. Slate, L. C. Thornton, *Tetrahedron Lett.* **1996**, *37*, 5289–5292.
[7] A. Nomoto, T. Moriuchi, S. Yamazaki, A. Ogawa, T. Hirao, *Chem. Commun.* **1998**, 1963–1964.
[8] T. Moriuchi, A. Nomoto, K. Yoshida, T. Hirao, *J. Organomet. Chem.* **1999**, *589*, 50–58.
[9] T. Moriuchi, A. Nomoto, K. Yoshida, T. Hirao, *Organometallics* **2001**, *20*, 1008–1013.
[10] T. Moriuchi, A. Nomoto, K. Yoshida, A. Ogawa, T. Hirao, *J. Am. Chem. Soc.* **2001**, *123*, 68–75.
[11] Y. Xu, P. Saweczko, H.-B. Kraatz, *J. Organomet. Chem.* **2001**, *637–639*, 335–342.
[12] H.-B. Kraatz, M. Galka, *Metal Ions Biol. Syst.* **2001**, *38*, 385–409.
[13] M. Oberhoff, L. Duda, J. Karl, R. Mohr, G. Erker, R. Fröhlich, M. Grehl, *Organometallics* **1996**, *15*, 4005–4011.
[14] S. I. Kirin, H.-B. Kraatz, N. Metzler-Nolte, *Chem. Soc. Rev.* **2006**, *35*, 348–354.
[15] T. Moriuchi, T. Hirao, *Chem. Soc. Rev.* **2004**, *33*, 294–301.
[16] D. R. van Staveren, T. Weyhermüller, N. Metzler-Nolte, *Dalton Trans.* **2003**, 210–220.
[17] L. Barišić, M. Dropučić, V. Rapić, H. Pritzkow, S. I. Kirin, N. Metzler-Nolte, *Chem. Commun.* **2004**, 2004–2005.
[18] E. Cuingnet, C. Sergheraert, A. Tartar, *J. Organomet. Chem.* **1980**, *195*, 325–329.
[19] J. C. Brunet, E. Cuingnet, H. Gras, P. Marcincal, A. Mocz, C. Sergheraert, A. Tartar, *J. Organomet. Chem.* **1981**, *216*, 73–77.
[20] E. Cuingnet, M. Dautrevaux, C. Sergheraert, A. Tartar, *Eur. J. Med. Chem.* **1982**, *17*, 203–206.
[21] P. Hublau, C. Sergheraert, L. Ballester, M. Dautrevaux, *Eur. J. Med. Chem.* **1983**, *18*, 131–133.
[22] S. Maričić, A. Ritzén, U. Berg, T. Frejd, *Tetrahedron* **2001**, *57*, 5623–6529.
[23] F. Noor, A. Wüstholz, R. Kinscherf, N. Metzler-Nolte, *Angew. Chem. Int. Ed.* **2005**, *44*, 2429–2432.
[24] J. T. Chantson, M. V. V. Falzacappa, S. Crovella, N. Metzler-Nolte, *J. Organomet. Chem.* **2005**, *690*, 4564–4572.
[25] D. R. van Staveren, E. Bothe, T. Weyhermüller, N. Metzler-Nolte, *Eur. J. Inorg. Chem.* **2002**, *6*, 1518–1529.
[26] D. R. van Staveren, N. Metzler-Nolte, *Chem. Commun.* **2002**, 1406–1407.
[27] *Fmoc Solid Phase Peptide Synthesis* (Eds.: W. C. Chan, P. D.White), Oxford University Press, Oxford, **2000**.
[28] L. Barišić, V. Rapić, H. Pritzkow, G. Pavlović, I. Nemet, *J. Organomet. Chem.* **2003**, *682*, 131–142.
[29] L. Barišić, M. Čakić, K. A. Mahmoud, Y. Liu, H.-B. Kraatz, H. Pritzkow, S. I. Kirin, N. Metzler-Nolte, V. Rapić, *Chem. Eur. J.* **2006**, *12*, 4965–4980.
[30] S. I. Kirin, D. Wissenbach, N. Metzler-Nolte, *New J. Chem.* **2005**, *29*, 1168–1173.
[31] S. I. Kirin, U. Schatzschneider, X. de Hatten, T. Weyhermüller, N. Metzler-Nolte, *J. Organomet. Chem.* **2006**, *691*, 3451–3457.

Received: June 8, 2006
Published Online: September 5, 2006

 © 2006 Wiley-VCH Verlag GmbH & Co. KGaA, Weinheim 

DOI: 10.1002/ejic.200600610

# Straightforward Light-Driven Synthesis of Ultrasmall, Water-Soluble Monolayer-Protected Platinum Nanoparticles

**Salvatore Giuffrida,[a] Giorgio Ventimiglia,[b] Fiorella L. Callari,[a] and Salvatore Sortino*[a]**

**Keywords:** Platinum / Nanoparticles / Monolayers / Carboxylates / Light

A facile synthetic methodology to obtain, in one-step, ultrasmall (ca. 1 nm) and water-soluble carboxylate-terminated platinum nanoparticles is reported. It involves visible light as a reaction trigger and platinum acetylacetonate and thioglycolic acid as the only chemical reactants. These nanoparticles are stable for weeks and can be easily transferred into organic solvents such as toluene, chloroform or dichloromethane by using the cationic surfactant tetraoctylammonium bromide as the phase-transfer agent. To the best of our knowledge, they are among *the smallest* water-soluble platinum nanoparticles prepared to date and represent the *first example* of preparation of thiol-protected platinum nanoparticles exclusively driven by light.

(© Wiley-VCH Verlag GmbH & Co. KGaA, 69451 Weinheim, Germany, 2006)

## Introduction

Metal nanoparticles are continuing to draw a great deal of attention by interdisciplinary areas of the scientific community due to their exciting optical, electronic, magnetic and catalytic properties.[1] Potential applications of metal nanoparticles span indeed from molecular electronics and optoelectronics to medicine and biology.[2] The modification of metal nanoparticles with monolayers of thiol derivatives, has been proven to be an appropriate strategy to achieve monolayer-protected clusters which are air-stable, isolable and dispersible in organic solvents.[3] In contrast to the large number of reports focused on the preparation of thiol-capped gold nanoparticles, only limited examples have addressed the synthesis of thiol-protected platinum nanoparticles.[4–7] The interest on these hybrid nanostructures is strongly motivated not only by their well-established catalytic activity, but also by their biomedical relevance. Furthermore, as these nanoparticles are characterized by negligible plasmon absorption into the visible region,[8] they represent ideal platforms for the fabrication of hybrid optical nanodevices by self-assembling of functional chromogenic units.[9] Many practical applications necessitate platinum nanoparticles to be dispersible in water with preservation of their physicochemical properties over long time.[10] In this regard, Chen and Kimura have shown simple synthetic protocols to prepare water-soluble platinum nanoparticles, with diameters ranging from 2.5 to 4.7 nm, capped with mercaptosuccinic acid and involving the chemical reduction of water-soluble platinum salts.[7]

Herein we report a facile synthetic methodology to obtain ultrasmall (ca. 1 nm), water-soluble and stable platinum nanoparticles, implying visible light as a reaction trigger and platinum acetylacetonate, $Pt(acac)_2$, and thioglycolic acid (TA) as the only chemical reactants.

## Results and Discussion

Differently to β-diketonate complexes with metals such as Cu, Ni, and Pd, $Pt(acac)_2$ undergoes photodecomposition with comparable efficiency upon irradiation with both UV and Vis light due to the absence of low-lying d,d states which deactivate the reactive π,π* state.[11] In hydrogen-donating solvents $Pt(acac)_2$ undergoes efficient photodegradation to yield colloidal platinum and β-diketones.[11a] The main steps for this photoprocess are recalled in Scheme 1 for the sake of clarity. They involve the homolytic cleavage of the metal–ligand bond followed by hydrogen abstraction by the ligand-centered radical.

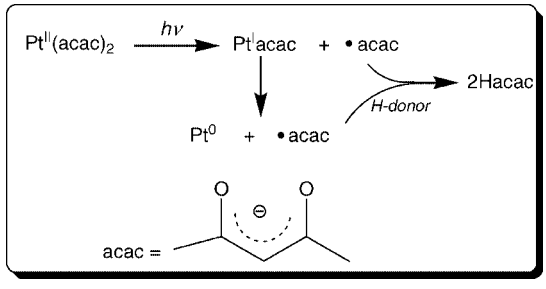


Scheme 1. General photodecomposition mechaism of $Pt(acac)_2$ in the presence of hydrogen donors.

[a] Dipartimento di Scienze Chimiche, Università di Catania, 95125 Catania, Italy
Fax: +39-095-580138
E-mail: ssortino@unict.it
[b] LoC R&D, Microfluidic Division – CPG STMicroelectronics, 95121 Catania, Italy

 © 2006 Wiley-VCH Verlag GmbH & Co. KGaA, Weinheim 

We have recently demonstrated that colloidal platinum can also be obtained in water medium by irradiation of $Pt(acac)_2$ caged in a β-cyclodextrin cavity acting as suitable host and excellent hydrogen donor.[12] Accordingly, when $Pt(acac)_2$ is irradiated in acetonitrile, which is not a hydrogen donor, the photodecomposition is negligible and does not lead to the formation of platinum colloids. On these grounds, we irradiated with visible light an acetonitrile solution of $Pt(acac)_2$ in the presence of TA. The role of TA is expected to be twofold. In fact, it is a good hydrogen donor (the hydrogen atom bound to the sulfur atom is highly reactive towards free radicals) and represents a suited capping agent to obtain platinum nanoparticles with negatively charged surface due to the presence of carboxylate groups. The almost colorless solution turned yellow upon irradiation. As shown in Figure 1, the disappearance of the $Pt(acac)_2$ absorption was accompanied by the appearance of the typical absorption band of Hacac (see dotted spectrum, for comparison) and a structureless absorption extending up to the visible region, attributed to colloidal platinum. The quantum yield for the photochemical reaction (see Experimental Section) was $\Phi = 0.02 \pm 0.005$.

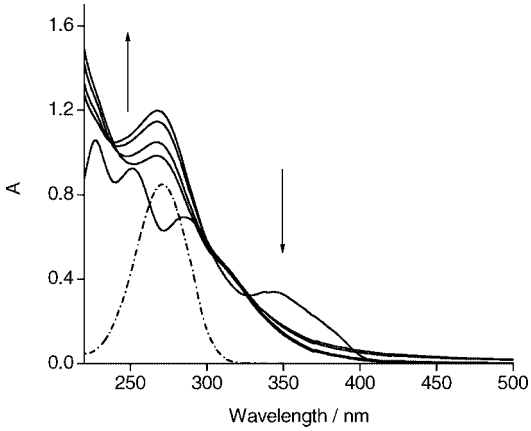


Figure 1. Absorption spectral changes observed upon 0, 8, 16, 40, 50 min of light irradiation of a 0.5 mM acetonitrile solution of $Pt(acac)_2$ in the presence of 1 mM TA. The dotted line shows the absorption spectrum of Hacac in acetonitrile. The arrows indicate the direction of the spectral evolution with time. Cell pathlength 1 mm.

A control experiment carried out with an acetonitrile solution of Hacac provided unambiguous evidence for the quantitative release of the ligand from $Pt(acac)_2$ upon irradiation. As Hacac does not absorb the exciting light, it is not photodecomposed during the course of the photoreaction and thus, can be easily removed from the reaction mixture by drying the irradiated solution under vacuum at 70 °C for 1 h. The dried sample was very soluble in water at pH = 8 but not at pH = 2, according to the presence of the ionizable carboxylic groups bound to the metal surface. This pH dependence allowed the removal of the unbound TA through few cycles of redispersion/centrifugation at pH = 2. The absence of free TA in the supernatant was verified by ESI-MS. At last, the precipitate was solubilized in water at pH = 8 and the absorption spectrum was recorded. As shown in Figure 2A, the spectrum obtained does not show any detectable absorption associated to Hacac but is exclusively characterized by a structureless absorption extending into the visible region which is in full agreement with the spectra reported in the literature for other platinum nanoparticles.[4a,7,8a,8b] High-resolution transmission electron microscopy (HRTEM) on this sample (Figure 2B) shows that the platinum nanoparticles are quite well dispersed and are characterized by an average diameter of $(1.0 \pm 0.3)$ nm. The FFT analysis (inset Figure 2B) reveals that the nanoparticles are single crystals with fcc structure.

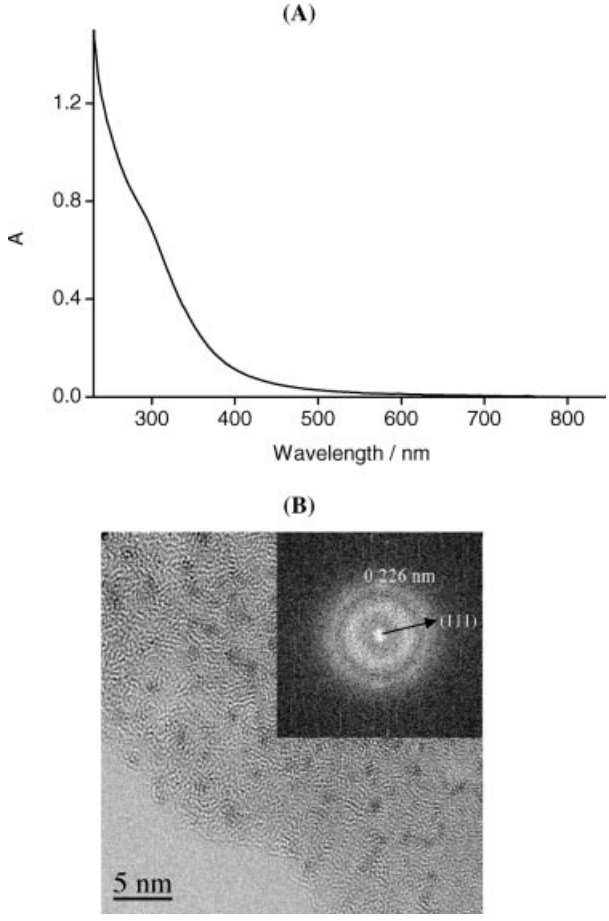


Figure 2. (A) Absorption spectrum in water solution at pH = 8, cell pathlength 1 mm and (B) HRTEM micrograph of the TA-modified platinum nanoparticles. The inset shows the FFT analysis showing an fcc packing arrangement.

Elemental analysis conducted on the sample gave the following results: C 4.65, H 0.42, Na 4.48, O 6.40, Pt 74.49, S 6.33. The atomic ratio of C/H/O/S/Na is 1.94:2.15:2.05:1.01:1. This result provides evidence for the chemisorption of TA through the mercapto termination as well as for the existence of the carboxylate form ($C_2H_2O_2SNa$).

These colloidal nanoparticles exhibited good air stability. Indeed, they remained dispersed in water for several weeks with no relevant aggregation, as evidenced by the negligible variation of the absorption spectrum and the particle size noted after this period of aging.

 © 2006 Wiley-VCH Verlag GmbH & Co. KGaA, Weinheim 

Interestingly, the monolayer-protected nanoparticles can be easily transferred into organic solvents such as toluene, chloroform or dichloromethane by using the cationic surfactant tetraoctylammonium bromide (TOAB) as the phase-transfer agent. Figure 3A shows representative images of the aqueous solution of the TA-modified platinum nanoparticles before (left) and after (right) shaking with dichloromethane containing 0.1 M TOAB. The color change between the aqueous and organic phase clearly indicates that a complete phase transfer is achieved. It is also noteworthy that the phase transfer occurs without any aggregation as suggested by the negligible variation of the surface plasmon absorption after the nanoparticles transfer into the organic phase (Figure 3B).[13] In fact, particle aggregation would have led to significant broadening of the plasmon absorption.[15] These transference experiments provide a further confirmation that the platinum nanoparticles are negatively charged due to the presence of the carboxylate moieties. Pure electrostatic interaction between these functional groups and the positively charged TOAB has indeed pointed out by Chen and Kimura in the case of modified platinum and gold nanoparticles.[7,16]

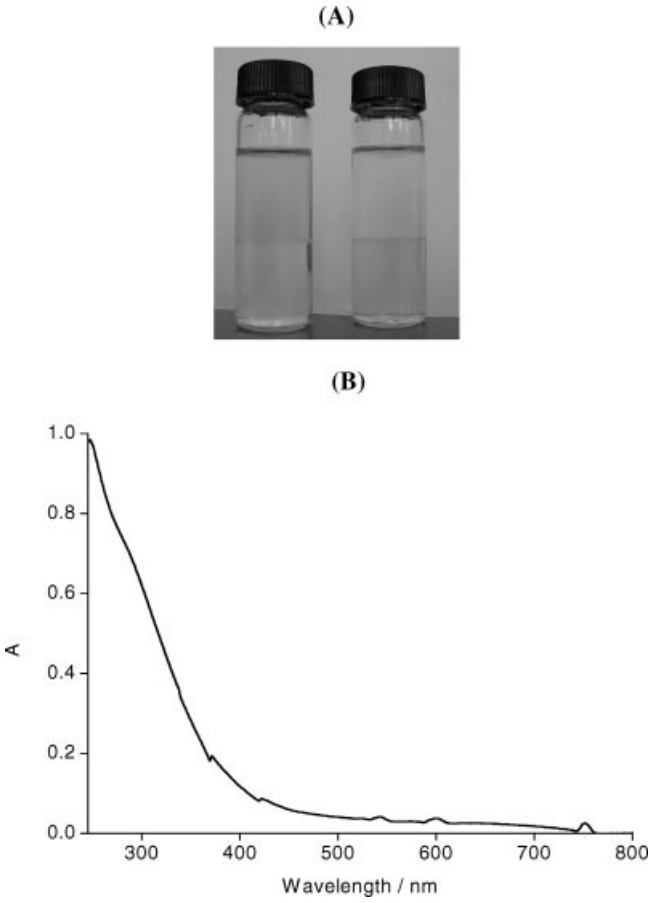


Figure 3. (A) Photograph of the TA-modified platinum nanoparticles in water at pH = 8 before (left) and after (right) shaking with a dichloromethane solution containing 0.1 M TOAB. (B) Absorption spectrum of the TA-modified platinum nanoparticles after transferring in dichloromethane. Cell pathlength 1 mm.

As shown in Scheme 1, the release of the free ligand involves hydrogen abstraction reaction by the ligand-centered radical. Since the occurrence of such a process from acetonitrile is, of course, out of question because thermodynamically not favored, it is reasonable to conceive that the acac˙ radical leads to the formation of Hacac by abstraction of the –SH hydrogen atom, according to the high reactivity of thiols towards free radicals.[17]

## Conclusions

The photochemical methodology pictorially sketched in Scheme 2 is very simple, and effective to produce ultrasmall, water-soluble and stable platinum nanoparticles in a single step. To the best of our knowledge, they are among *the smallest* water-soluble platinum nanoparticles prepared to date and represent the *first example* of preparation of thiol-protected platinum nanoparticles exclusively driven by light. The advantage offered by the light radiation as a reaction trigger is twofold. Firstly, the use of visible excitation produced by conventional lamps with moderate light intensity is environmentally friendly and cheap in contrast to the use of toxic chemicals and sophisticated laser sources. Secondly, the light radiation allows to produce a large number of atoms homogeneously and instantaneously, exerting a key function in the nucleation, growth and dispersion of the nanoparticles. In view of their small sizes and the well-known role of the carboxylic moiety in the formation of self-assembled supramolecular architectures,[18] these carboxylate-terminated platinum nanoparticles might be intriguing candidates for potential biological applications and building-up of two- and three-dimensional self-assembled nanocomposite devices.

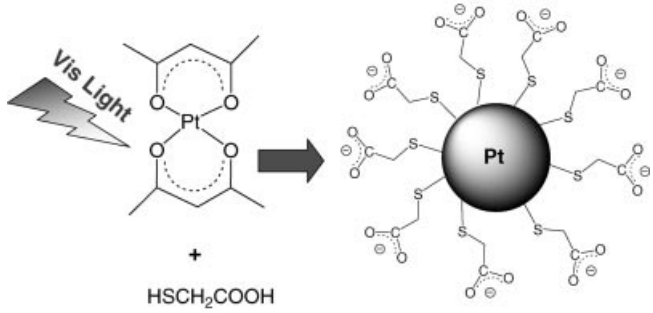


Scheme 2. Pictorial view illustrating the single-step formation of the monolayer-protected platinum nanoparticles.

## Experimental Section

All reagents were obtained from Sigma–Aldrich and used as received. The solvents used were of analytical and spectrophotometric grade. All glassware used was immersed in piraña solution (70:30 $H_2SO_4/H_2O_2$) at 70 °C for 1 h. ***Warning:*** *piraña solution should be handled with caution!* Next, the glassware was rinsed with large amounts of high-purity water and dried. Water was purified through a Millipore Milli-Q system. Irradiation was carried out under a continuous argon flux in a 10 mm quartz cuvette with

 © 2006 Wiley-VCH Verlag GmbH & Co. KGaA, Weinheim 

3 mL capacity using a Rayonet photochemical reactor equipped with 16 RPR lamps with an emission in the 380–480 nm range with a maximum at 420 nm. The incident photon flux on the sample was ca. $10^{16}$ quanta $s^{-1}$. The total irradiation time was 50 min, the concentrations of $Pt(acac)_2$ and TA were 0.5 mM and 1 mM, respectively. The photodecomposition quantum yield for the $Pt(acac)_2$ complex was determined spectrophotometrically by using the following equation: $\Phi = \Delta[C]V/\Delta t I_0 F$, where $\Delta[C]/\Delta t$ is the rate of disappearance of the platinum complex, $V$ is the volume of the irradiated solution, $I_0$ is the intensity of the incident photons and $F$ is the fraction of the photons absorbed by the platinum complex. Absorption spectra were recorded with a Jasco V-560 spectrophotometer. ESI mass spectra were recorded with an Agilent 1100 series ESI/MSD spectrometer. Experimental conditions were as follows: capillary voltage, 3.5 kV; fragmentor, 100 V; source temperature, 350 °C; drying gas, $N_2$ (10 L/min); carrier solvent, methanol (0.4 mL/min). HRTEM images were obtained by means of an FEG JEM 2010F instrument with a field emission gun operating at 200 kV. The electro-optical configuration guarantees ultrahigh spatial resolution (0.19 nm). This microscope is equipped with the GIF (Gatan Image Filter) apparatus which allows to realize images filtered to narrow windows of the electron energy loss spectrum. Elemental analyses were conducted by means of standard techniques.

## Acknowledgments

We thank Mr. C. Bongiorno of the IMM-IMETEM-CNR (Catania) for his precious technical assistance in the TEM measurements.

[1] H. G. Craighead, *Science* **2000**, *290*, 1532–1536; A. C. Templeton, W. P. Wuelfing, R. W. Murray, *Acc. Chem. Res.* **2000**, *33*, 27–36; G. Schmid, *Chem. Rev.* **1992**, *92*, 1709–1727.

[2] V. L. Colvin, M. C. Schlamp, A. P. Alivisatos, *Nature* **1994**, *370*, 354–357; A. Roucoux, J. Schulz, H. Patin, *Chem. Rev.* **2002**, *102*, 3757–3778.

[3] M. Brust, M. Walker, D. Bethell, D. J. Schiffrin, R. Whyman, *J. Chem. Soc. Chem. Commun.* **1994**, 801–802; X. M. Li, J. Huskens, D. N. Reinhoudt, *J. Mater. Chem.* **2004**, *14*, 2954–2971; M. C. Daniel, D. Astruc, *Chem. Rev.* **2004**, *104*, 293–346; P. K. Sudeep, B. I. Ipe, K. G. Thomas, M. V. George, S. Barazzouk, S. Hotchandani, P. V. Kamat, *Nano Lett.* **2002**, *2*, 29–35; X. M. Zhao, Y. N. Xia, G. M. Whitesides, *J. Mater. Chem.* **1997**, *7*, 1069–1074; A. K. Boal, V. M. Rotello, *J. Am. Chem. Soc.* **2000**, *122*, 734–735; D. C. Hone, P. I. Walker, R. Evans-Gowing, S. FitzGerald, A. Beeby, I. Chabrier, M. J. Cook, D. A. Russell, *Langmuir* **2002**, *18*, 2985–2987; M. C. Daniel, J. Ruiz, S. Nlate, J. Palumbo, J. C. Blais, D. Astruc, *Chem. Commun.* **2001**, 2000–2001.

[4] a) C. Yee, M. Scotti, A. Ulman, H. White, M. Rafailovich, J. Sokolov, *Langmuir* **1999**, *15*, 4314–4316; b) S. E. Eklund, D. E. Cliffel, *Langmuir* **2004**, *20*, 6012–6018; c) K.-S. Kim, D. Demberelnyamba, H. Lee, *Langmuir* **2004**, *20*, 556–560.

[5] a) J. Alvarez, J. Liu, E. Román, A. Kaifer, *Chem. Commun.* **2000**, 1151–1152; b) W. Tu, K. Takai, K. Fukui, A. Miyazaki, T. Enoki, *J. Phys. Chem. B* **2003**, *107*, 10134–10140.

[6] a) S. Chen, R. W. Murray, *Langmuir* **1999**, *15*, 682–689; b) J. Yang, J. Y. Lee, T. C. Deivaraj, H.-P. Too, *Langmuir* **2003**, *19*, 10361–10365.

[7] S. Chen, K. Kimura, *J. Phys. Chem. B* **2001**, *105*, 5397–5403.

[8] The most intense plasmon absorption of platinum nanoparticles falls in the UV region;[4,7,8a,8b] a) C. Chen, M. Akashi, *Langmuir* **1997**, *13*, 6465–6472; b) J. A. Creighton, D. G. Eadon, *J. Chem. Soc. Faraday Trans.* **1991**, *87*, 3881–3891.

[9] S. Sortino, S. Di Bella, S. Conoci, S. Petralia, M. Tomasulo, E. J. Pacsial, F. M. Raymo, *Adv. Mater.* **2005**, *17*, 1390–1393; S. Sortino, S. Petralia, S. Conoci, S. Di Bella, *J. Mater. Chem.* **2004**, *14*, 811–813; S. Sortino, S. Petralia, S. Conoci, S. Di Bella, *J. Am. Chem. Soc.* **2003**, *125*, 1122–1123; S. Conoci, S. Petralia, P. Samorì, F. M. Raymo, S. Di Bella, S. Sortino, *Adv. Funct. Mater.*, DOI: 10.1002/adfm.200500110.

[10] D. I. Gittings, F. Caruso, *Angew. Chem. Int. Ed.* **2001**, *40*, 3001–3004; L. N. Lewis, *Chem. Rev.* **1993**, *93*, 2693–2730; J. H. Fendler, *Nanoparticles and Nanostructured Films*, Wiley, Weinheim, **1998**.

[11] a) F. D. Lewis, A. M. Miller, G. D. Salvi, *Inorg. Chem.* **1995**, *34*, 3173–3181; b) H. D. Gafney, R. L. Lintvedt, *J. Am. Chem. Soc.* **1971**, *93*, 1623–1628; c) S. Giuffrida, G. G. Condorelli, L. L. Costanzo, I. Fragalà, G. Ventimiglia, G. Vecchio, *Chem. Mater.* **2004**, *16*, 1260–1266.

[12] S. Giuffrida, G. Ventimiglia, S. Petralia, S. Conoci, S. Sortino, *Inorg. Chem.* **2006**, *45*, 508–510.

[13] The slight difference observed in the plasmon absorption could be attributable to change in the refractive index of the solvent.[14]

[14] P. Mulvaney, L. M. Liz-Marzan, M. Giersig, T. Ung, *J. Mater. Chem.* **2000**, *10*, 1259–1270.

[15] P. Mulvaney, *Langmuir* **1996**, *12*, 788–800.

[16] S. Chen, K. Kimura, *Langmuir* **1999**, *15*, 1075–1082.

[17] At this point it is unclear if the sulfur-centered radicals generated upon hydrogen abstraction (i) directly bind to the naked platinum surface, (ii) dimerize to disulfides which at last chemisorb to the metal serface, or (iii) both.

[18] See, for example: G. Decher, in: *Comprehensive Supramolecular Chemistry* (Eds.: J. P. Sauvage, M. W. Hosseini), Elsevier Science, Oxford, **1996**, vol. 9, pp. 1154–1196.

Received: June 28, 2006
Published Online: September 5, 2006

 © 2006 Wiley-VCH Verlag GmbH & Co. KGaA, Weinheim 

DOI: 10.1002/ejic.200600617

# An Eight-Coordinate Mononuclear Double Helical Complex

**Michael G. B. Drew,[a] Debarati Parui,[b] Senjuti De,[b] Jnan P. Naskar,[b] and Dipankar Datta*[b]**

**Keywords:** Cadmium / Single helicate / Double helicate / N ligands / Seven-coordinate complexes / Eight-coordinate complexes

From the reaction of $Cd(CH_3COO)_2{\cdot}2H_2O$ with the 1:2 condensate (L) of benzil dihydrazone and 2-acetylpyridine, $[CdL(CH_3COO)(H_2O)]PF_6{\cdot}3H_2O$ (**1**) is isolated by adding $NH_4PF_6$. L reacts with $Cd(ClO_4)_2{\cdot}xH_2O$ to yield $[CdL_2](ClO_4)_2{\cdot}0.5H_2O$ (**2**). The yellowish complexes **1** and **2** are characterized by NMR and single-crystal X-ray diffraction. **1** is found to be a seven-coordinate single helical complex having a $Cd^{II}N_4O_3$ core and homoleptic **2** an eight-coordinate double helical complex with a $Cd^{II}N_8$ core.

(© Wiley-VCH Verlag GmbH & Co. KGaA, 69451 Weinheim, Germany, 2006)

## Introduction

Many naturally occurring molecules are helical.[1] But synthetic helical organic molecules like [*n*]helicenes[2] are rare. These are achieved only through designed synthesis.[3,4] Non-helical organic molecules containing suitable hetero donor atoms can give rise to helical topology when they bind to many metal ions because of the coordination properties of the metal ions.[1,5,6] This has been an important area of research in metallo-organic chemistry in recent times. Metallo-organic helices, commonly, can be single, double, or triple. A single helical complex may contain a single metal ion or multiple metal ions. But for multiple helical complexes, it seems that at least two metal ions in combination with an at least tetradentate ligand are necessary. So far, only one example of a mononuclear triple helical complex is known where the metal ion is nine-coordinate $La^{III}$ and the helicand is tridentate.[7] To date there is no example of a mononuclear double helical inorganic complex. Herein we report such a complex. The metal ion in our case is $Cd^{II}$ and the ligand is a tetradentate N donor.

## Results and Discussion

The ligand L we used is helical. It is a 1:2 condensate of benzil dihydrazone and 2-acetylpyridine.[8] In the area of inorganic helices, others have been using non-helical ligands. But for quite some time, we have been engaged in generating helical topologies by using ligands which are themselves helical.[9,10] The helical twist in L is brought about by the N=C(Ph)–C(Ph)=N torsion angle which is 85.9(5)° in the solid state.[11]

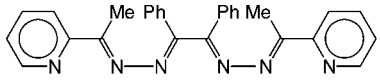


ligand L

Reaction of $Cd(CH_3COO)_2{\cdot}2H_2O$ with L in an equimolar ratio in methanol at room temperature and subsequent addition of a stoichiometric amount of $NH_4PF_6$ gives $[CdL(CH_3COO)(H_2O)]PF_6{\cdot}3H_2O$ (**1**) in 65% yield. From the reaction of $Cd(ClO_4)_2{\cdot}xH_2O$ and L in an equimolar ratio in methanol at room temperature, $[CdL_2](ClO_4)_2{\cdot}0.5H_2O$ (**2**) is isolated in 20% yield. The yield of **2** increased to 60% when the Cd/L ratio was 1:2. Both complexes **1** and **2** have a faint yellow colour.

The X-ray crystal structures of **1** and **2** have been determined. The structure of the cation of **1** is shown in Figure 1 together with the atomic numbering scheme. The metal atom is bonded to four nitrogen atoms of the tetradentate ligand L, two oxygen atoms of an acetate group at 2.354(9), 2.396(10) Å and a water molecule at 2.342(7) Å. The bond lengths to the four nitrogen atoms of L are 2.390(7) Å to N(11), 2.411(7) Å to N(18), 2.428(6) Å to N(23), and 2.405(7) Å to N(30), thus the distances to the pyridine nitrogen atoms are slightly shorter. The conformation of the ligand is described by the N=C(Ph)–C(Ph)=N torsion angle which is 75.4(1)°. The geometry of the coordination sphere can be described as a capped trigonal prism with the water molecule O(100) capping the face of N(11), N(23), N(30), and O(52) but this is severely distorted by the small bite of the acetate group. The Cd atom in **1** is seven-coordinate; but in the homoleptic complex **2**, its coordination sphere expands to

[a] School of Chemistry, University of Reading, Whiteknights, Reading RG6 6AD, UK
[b] Department of Inorganic Chemistry, Indian Association for the Cultivation of Science, Calcutta 700032, India
E-mail: icdd@mahendra.iacs.res.in

 InterScience © 2006 Wiley-VCH Verlag GmbH & Co. KGaA, Weinheim 

eight to accommodate two ligands. The structure of the cation of **2** is shown in Figure 2 together with the atomic numbering scheme. The geometry is a distorted dodecahedron in which the pyridine nitrogen atoms N(11), N(30), N(41), N(60) form one plane (r.m.s. deviation 0.01 Å) and the acyclic nitrogen atoms N(18), N(23), N(48), N(53) (r.m.s. deviation 0.30 Å) the other plane, the two planes intersecting at 85.8°. In this structure there is a much greater variation in Cd–N bond lengths, no doubt because of steric crowding in the metal coordination sphere. For one of the ligands, distances are Cd(1)–N(11) 2.422(4), Cd(1)–N(18) 2.504(4), Cd(1)–N(223) 2.495(4), and Cd(1)–N(30) 2.414(4) Å showing a regular pattern in which the bonds to the acyclic nitrogen atoms are longer than the bonds to the pyridine nitrogen atoms. However, the distances to the other ligand are more irregular with Cd(1)–N(41) 2.506(4), Cd(1)–N(48) 2.596(4), Cd(1)–N(53) 2.513(4), and Cd(1)–N(60) 2.460(4) Å. The conformations of the ligands are the same as that found in **1**; the N=C(Ph)–C(Ph)=N torsion angle in the two independent ligand moieties are 73.6 and 77.7 °, respectively. Complexes **1** and **2** contain seven-membered chelate ring(s).

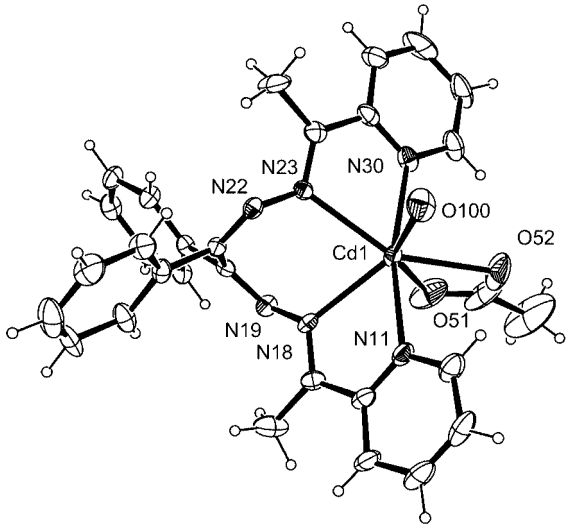


Figure 1. The structure of the cation in **1** with ellipsoids at 25% probability. The hydrogen atoms on the water molecule were not located. Selected bond lengths [Å] and angles [°]: Cd1–O100 2.342(7), Cd1–O51 2.354(9), Cd1–N11 2.390(7), Cd1–O52 2.396(10), Cd1–N30 2.405(7), Cd1–N18 2.411(7), Cd1–N23 2.428(6); O100–Cd1–O51 144.9(4), O100–Cd1–N11 88.4(3), O51–Cd1–N11 93.2(3), O100–Cd1–O52 90.7(5), O51–Cd1–O52 54.9(5), N11–Cd1–O52 83.6(3), O100–Cd1–N30 85.2(3), O51–Cd1–N30 85.3(3), N11–Cd1–N30 166.5(3), O52–Cd1–N30 84.6(3), O100–Cd1–N18 126.9(3), O51–Cd1–N18 85.0(4), N11–Cd1–N18 66.5(2), O52–Cd1–N18 128.7(4), N30–Cd1–N18 126.6(2), O100–Cd1–N23 81.6(3), O51–Cd1–N23 125.0(4), N11–Cd1–N23 123.0(2), O52–Cd1–N23 151.7(3), N30–Cd1–N23 67.8(3), N18–Cd1–N23 75.8(2).

The topologies of the complexes **1** and **2** are helical which can be discerned better from their space-filling models shown in Figure 3. Complex **1** is a mononuclear single helix. Many examples of such mononuclear single helices are known,[5,6] but very few with Cd.[12,13] Complex **2** is a mononuclear double helical complex which is unprecedented in its coordination chemistry. Though similar experimental conditions were used for obtaining complexes **1** and **2**, their compositions are different. We believe this difference is due to the difference in the coordinating ability of the anions. Since acetate is much more coordinating in nature than perchlorate, the presence of acetate gives rise to a heteroleptic complex such as **1**. At present we are engaged in studying the effect of the anion on the nature of the product of our synthetic method. Starting with $Cd(NO_3)_2{\cdot}4H_2O$, it seems that we obtain a single helical complex of composition $CdL(NO_3)_2{\cdot}H_2O$.

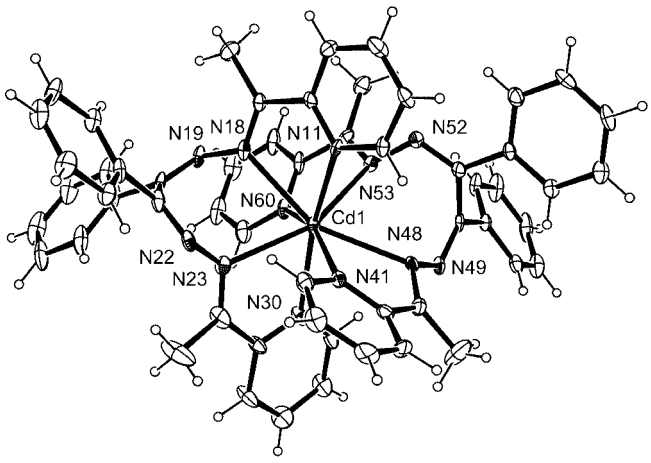


Figure 2. The structure of the cation in **2** with ellipsoids at 25% probability. Selected bond lengths [Å] and angles [°]: Cd1–N11 2.422(4), Cd1–N18 2.504(4), Cd1–N23 2.495(4), Cd1–N30 2.414(4), Cd1–N41 2.506(4), Cd1–N48 2.596(4), Cd1–N53 2.513(4), Cd1–N60 2.460(4); N30–Cd1–N11 160.2(1), N30–Cd1–N60 79.1(1), N11–Cd1–N60 120.7(1), N30–Cd1–N23 66.9(1), N11–Cd1–N23 108.8(1), N60–Cd1–N23 93.7(1), N30–Cd1–N18 127.2(1), N11–Cd1–N18 64.7(1), N60–Cd1–N18 73.1(1), N23–Cd1–N18 71.1(1), N30–Cd1–N41 80.3(1), N11–Cd1–N41 79.9(1), N60–Cd1–N41 159.4(1), N23–Cd1–N41 77.0(1), N18–Cd1–N41 119.6(1), N30–Cd1–N53 118.9(1), N11–Cd1–N53 73.9(1), N60–Cd1–N53 64.7(1), N23–Cd1–N53 153.9(1), N18–Cd1–N53 88.0(1), N41–Cd1–N53 128.1(1), N30–Cd1–N48 78.5(1), N11–Cd1–N48 92.4(1), N60–Cd1–N48 112.5(1), N23–Cd1–N48 131.5(1), N18–Cd1–N48 153.9(1), N41–Cd1–N48 64.1(1), N53–Cd1–N48 73.0(1).

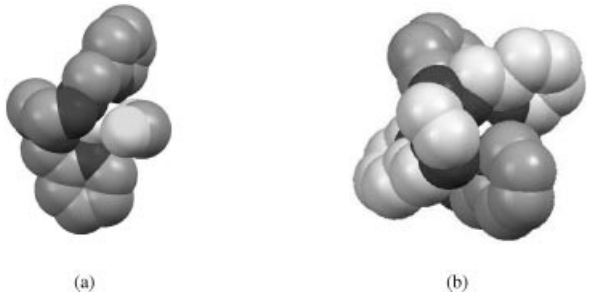


Figure 3. Space-filling models of the cations in **1** (a) and **2** (b) showing the helical nature of the complexes. The methyl and phenyl groups, and H atoms are removed for clarity. Code: (a) C, dark grey; N, black; O, light grey; Cd, white; (b) in one of the ligand strands C is dark grey and in the other light grey, the others are the same as in (a).

Since compounds **1** and **2** are helical, enantiomers are expected. Complex **1** crystallises in the non-centrosymmetric space group *Cc* and twinned refinement gave no evi-

 © 2006 Wiley-VCH Verlag GmbH & Co. KGaA, Weinheim 

dence for a twin being present, so the structure can be considered as non-racemic in the individual single crystals. On the other hand, complex **2** crystallises in the centrosymmetric space group *Pbca* and therefore represents a racemic mixture in the solid state.

Bidentate ligands cannot afford a mononuclear helix. However, they can form at least dinuclear helicates by bridging two metal ions.[14] From the example of the $La^{III}$ compound of Renaud et al.,[7] it is clear that, to generate a mononuclear helical metal complex, the minimum denticity of the helicand (ligand) has to be three. Now, with some imagination it can be realized that with a six-coordinate metal ion, which can give rise to an octahedral geometry, a tridentate ligand will never yield a mononuclear double helix. This is the reason why so far a mononuclear double helical complex has never been found with a six-coordinate metal ion. So the next choice is a tetradentate ligand with an eight-coordinate metal ion. Both the conditions are fulfilled in complex **2**.

## Experimental Section

**General:** L was synthesised as reported earlier.[8] Microanalyses were performed with a Perkin–Elmer 2400II elemental analyser. FT-IR spectra (KBr) were recorded with a Shimadzu FTIR-8400S spectrometer, UV/Vis spectra in $CH_2Cl_2$ with a Shimadzu UV-160A spectrophotometer and 300 MHz NMR spectra in $CD_2Cl_2$ (reference: TMS) with a Bruker DPX300 spectrometer.

**Synthesis of $[CdL(CH_3COO)(H_2O)]PF_6\cdot 3H_2O$ (1):** $Cd(CH_3COO)_2\cdot 2H_2O$ (0.13 g, 0.5 mmol), dissolved in methanol (5 mL), was added to a methanolic (20 mL) solution of the ligand L (0.22 g, 0.5 mmol), synthesised by a procedure previously published.[8] After stirring the resulting light-yellow solution for 30 min, a methanolic solution (5 mL) of $NH_4PF_6$ (0.84 g, 0.5 mmol) was added and the mixture left for the solvent to evaporate. When the volume was ca. 5 mL, the deposited yellow crystals were filtered off and found to be suitable for X-ray diffraction. Yield: 0.27 g (65%). $C_{30}H_{35}CdF_6N_6O_6P$ (833.01): calcd. C 43.23, H 4.24, N 10.09; found C 43.33, H 4.12, N 10.19. FTIR (KBr): $\tilde{\nu}$ = 839 (vs) [$\nu(PF_6)$] $cm^{-1}$. UV/Vis: $\lambda_{max}$ ($\varepsilon_{max}$) = 219 ($6.2\cdot10^4$), 265 ($2.5\cdot10^4$), 310 ($2.8\cdot10^4$ $M^{-1}cm^{-1}$) nm. $^1H$ NMR: $\delta$ = 2.03 (s, methyl of acetate), 2.51 (s, methyl of L), 7.11–8.01 (aromatic protons) ppm.

**Synthesis of $[CdL_2](ClO_4)_2\cdot 0.5H_2O$ (2):** $Cd(ClO_4)_2\cdot xH_2O$ (0.15 g, 0.5 mmol), dissolved in methanol (5 mL), was added to a methanolic (35 mL) solution of L (0.44 g, 1 mmol) and the mixture stirred for 2 h (a white crystalline compound started appearing within 15 min). Then the precipitate was filtered, washed with petroleum ether (5 mL) and dried in air. Yield: 0.36 g (60%). Single crystals were grown by direct diffusion of *n*-hexane into a moderately concentrated solution of the complex in dichloromethane. $C_{56}H_{49}CdCl_2N_{12}O_{8.5}$ (1208.36): calcd. C 55.29, H 4.08, N 13.52; found C 55.41, H 4.12, N 13.78. FTIR (KBr): $\tilde{\nu}$ = 1089 (vs), 623 (s) [$\nu(ClO_4)$] $cm^{-1}$. UV/Vis: $\lambda_{max}$ ($\varepsilon_{max}$) = 265 ($8.6\cdot10^4$), 305 ($8.8\cdot10^4$ $M^{-1}cm^{-1}$) nm. $^1H$ NMR: $\delta$ = 2.52 (s, methyl protons), 7.12–8.03 (aromatic protons) ppm.

**X-ray Crystallography:** Crystal Data for **1**: $C_{30}H_{35}CdF_6N_6O_6P$, $M$ = 833.01, monoclinic, space group *Cc*, $Z$ = 4, $a$ = 19.74(2), $b$ = 11.304(14), $c$ = 17.277(19) Å, $\beta$ = 100.59(1)°, $V$ = 3790(8) $Å^3$, $d_{calcd.}$ = 1.460 $gcm^{-3}$. Crystal data for **2**: $C_{56}H_{48}$ Cd $Cl_2$ $N_{12}$ $O_{8.50}$, $M$ = 1208.36, orthorhombic, space group *Pbca*, $Z$ = 8, $a$ = 16.2318(7), $b$ = 21.0442(10), $c$ = 32.2236(14) Å, $V$ = 11007(1) $Å^3$, $d_{calcd.}$ = 1.458 $gcm^{-3}$. Data for **1** were collected with a Marresearch Image Plate system at 293 K using Mo-$K_\alpha$ radiation. The crystal was positioned at 70 mm from the Image Plate. 95 frames were measured at 2° intervals with a counting time of 2 min. Data reduction was carried out using the XDS program[15] to give 5256 independent reflections. Data for **2** were collected with an Oxford Instruments X-Calibur CCD system at 150 K using Mo-$K_\alpha$ radiation. The crystal was positioned at 50 mm from the CCD. 321 frames were measured with a counting time of 10 s. Data reduction was carried out using the Crysalis program[16] to give 16192 independent reflections. Both structures were solved using Shelxs97.[17] The non-hydrogen atoms were refined with anisotropic thermal parameters. The hydrogen atoms bonded to carbon atoms were included in geometric positions and given thermal parameters equivalent to 1.2 times those of the atom to which they are attached. Absorption corrections were carried out using the DIFABS program[18] for **1** and the ABSPACK program[19] for **2**. The structures were refined on $F^2$ using Shelxl97 to give $R1$ = 0.0525, $wR2$ = 0.1382 (for **1**) and $R1$ = 0.0964, $wR2$ = 0.1239 (for **2**) using 4786 (for **1**) and 9503 (for **2**) reflections with $I > 2\sigma(I)$. CCDC-611911 (for **1**) and -611912 (for **2**) contain the supplementary crystallographic data for this paper. These data can be obtained free of charge from The Cambridge Crystallographic Data Centre via www.ccdc.cam.ac.uk/data_request/cif.

## Acknowledgments

We thank EPSRC and the University of Reading for funds for the Image Plate and X-Calibur systems.

[1] V. G. Machado, P. N. W. Baxter, J.-M. Lehn, *J. Braz. Chem. Soc.* **2001**, *12*, 431–462.
[2] A. Urbano, *Angew. Chem. Int. Ed.* **2003**, *42*, 3986–3989.
[3] J. C. Nelson, J. G. Saven, J. S. Moore, P. G. Wolynes, *Science* **1997**, *277*, 1793–1796.
[4] V. Berl, I. Huc, R. G. Khoury, M. J. Krische, J.-M. Lehn, *Nature* **2000**, *407*, 720–723.
[5] C. Piguet, *Chem. Rev.* **1997**, *97*, 2005–2062.
[6] M. A. Albrecht, *Chem. Rev.* **2001**, *101*, 3457–3497.
[7] F. Renaud, C. Piguet, G. Bernardinelli, J. C. G. Bunzli, G. Hopfgartner, *Chem. Eur. J.* **1997**, *3*, 1646–1659.
[8] P. K. Pal, S. Chowdhury, M. G. B. Drew, D. Datta, *New J. Chem.* **2000**, *24*, 931–933.
[9] S. Chowdhury, P. B. Iveson, M. G. B. Drew, D. A. Tocher, D. Datta, *New J. Chem.* **2003**, *27*, 193–196.
[10] S. Chowdhury, M. G. B. Drew, D. Datta, *Indian J. Chem. Sect A* **2004**, *43*, 51–55.
[11] S. Chowdhury, Ph. D. Thesis, Jadavpur University, India, **2002**.
[12] W. Dai, H. Hu, X. Wei, S. Zhu, D. Wang, K. Yu, N. K. Dalley, X. Kou, *Polyhedron* **1997**, *16*, 2059–2065.
[13] C. R. Rice, C. J. Baylies, L. P. Harding, J. C. Jeffery, R. L. Paul, M. D. Ward, *Polyhedron* **2003**, *22*, 755–762.
[14] G. K. Patra, I. Goldberg, S. K. Chowdhury, B. C. Maiti, A. Sarkar, P. R. Bangal, S. Chakravorti, N. Chattopadhyay, D. A. Tocher, M. G. B. Drew, G. Mostafa, S. Chowdhury, D. Datta, *New J. Chem.* **2001**, *25*, 1371–1373.
[15] W. Kabsch, *J. Appl. Crystallogr.* **1988**, *21*, 916–921.
[16] *Crysalis*, v. 1, Oxford Diffraction, Ltd., Oxford, UK, **2005**.
[17] G. M. Sheldrick, *Shelxs-97*, *Shelxl-97*, University of Göttingen, Göttingen, Germany, **1997**.
[18] N. Walker, D. Stuart, *Acta Crystallogr., Sect. A* **1983**, *39*, 158–166.
[19] *ABSPACK*, Oxford Diffraction, Ltd., Oxford, UK, **2005**.

Received: June 30, 2006
Published Online: September 5, 2006

 © 2006 Wiley-VCH Verlag GmbH & Co. KGaA, Weinheim 

DOI: 10.1002/ejic.200600650

# Adducts of $Cp_3Ln$ with LGa(Me)OH, Syntheses and X-ray Crystal Structures of $LGa(Me)HO{\rightarrow}LnCp_3$ {Ln = Sm, Nd, Yb; L = $HC[C(Me)N(2,6\text{-}iPr_2C_6H_3)]_2$}

**Sanjay Singh,[a] Aritra Pal,[a] Herbert W. Roesky,*[a] and Regine Herbst-Irmer[a]**

**Keywords:** Adducts / Hydroxides / Gallium / Heterodimetallic compounds / Lanthanides

Various heterodimetallic (gallium-lanthanide) compounds have been prepared by the reaction of LGa(Me)OH (**2**) with $Cp_3Ln$. Thus, the adducts $LGa(Me)HO{\rightarrow}LnCp_3$ (Ln = Sm, **3**; Nd, **4**; Yb, **5**) were obtained and characterized by IR spectroscopy and elemental analyses. The single-crystal X-ray structures of **3** and **4** are also reported.
(© Wiley-VCH Verlag GmbH & Co. KGaA, 69451 Weinheim, Germany, 2006)

## Introduction

Due to our long-standing interest in the syntheses of molecular main group hydroxides, we have successfully assembled several novel hydroxido complexes.[1–4] Among these, soluble group 13 hydroxides of aluminum[5] are of special interest in view of their utilization in the syntheses of alumoxanes[6] and other heterodimetallic compounds of potential applications.[7–10] The toluene/liquid ammonia two-phase hydrolysis[5] or the hydrolysis in the presence of N-heterocyclic carbenes, as an HCl scavenger,[8] are genuine routes to prepare these molecules. According to the latter method, we have assembled the methylgallium hydroxide (Scheme 1) and have also utilized it as a synthon to prepare new heterodimetallic compounds. Thus, the reaction of the gallium hydroxide LGa(Me)OH (**2**) with $Cp_2ZrMe_2$ gave the Ga–Zr mixed oxide LGa(Me)–O–Zr(Me)$Cp_2$.[11] Also, the reaction of LAl(Me)OH (**1**) with $Cp_3Ln$ (Ln = Yb, Er, Dy) led to the formation of various aluminum–lanthanide mixed oxides (Scheme 2).[9]

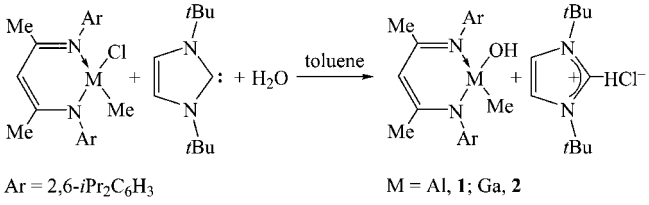


Scheme 1.

This new area of research that combines both main group and lanthanide elements to constitute a novel class

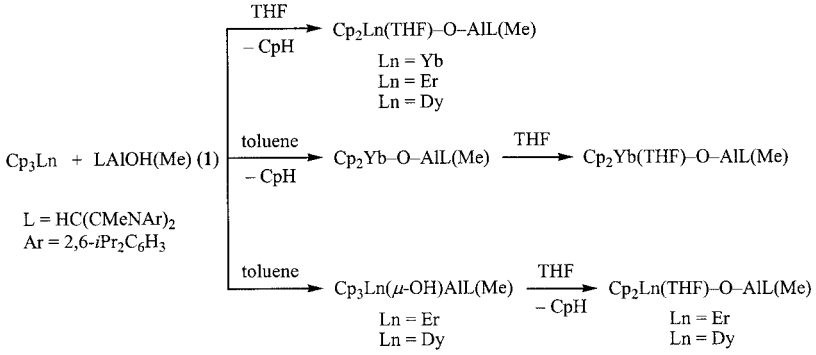


Scheme 2.

of heterodimetallic species started with the work of Mehrotra and co-workers who reported in the late 1970s the isopropoxides of gallium and lanthanides (La, Pr, Nd, Sm, Gd, Ho and Er), $[Ln\{Ga(OiPr)_4\}_3]$, by the reaction of either

[a] Institut für Anorganische Chemie der Georg-August-Universität Göttingen,
Tammannstrasse 4, 37077 Göttingen, Germany
Fax: +49-551-393373
E-mail: hroesky@gwdg.de

 © 2006 Wiley-VCH Verlag GmbH & Co. KGaA, Weinheim 

lanthanide chlorides with potassium gallium isopropoxides or by the reaction of lanthanide isopropoxides with gallium isopropoxides.[12,13] However, none of these compounds were structurally characterized and to the best of our knowledge there has been no other attempt to prepare mixed metal oxides or hydroxides of gallium with lanthanide atoms. It is to be noted that heterodimetallic compounds containing aluminum and lanthanides are well known but the corresponding gallium compounds are very rare. Our main aim in this area is to prepare mixed metal gallium–lanthanide compounds connected by an oxygen atom. Therefore, we report herein the synthesis and structural characterization of various Ga–Ln metal hydroxides by the reaction of LGa(Me)OH with $Cp_3Ln$ (Ln = Sm, Nd, Yb). Moreover, the reactivity of LGa(Me)OH is also compared with its aluminum analogue LAl(Me)OH.

## Results and Discussion

Reaction of LGa(Me)OH (**2**) with 1 equiv. of $Cp_3Ln$ was carried out in toluene at room temperature to afford the adducts LGa(Me)(μ-OH)Ln$Cp_3$ (Ln = Sm, **3**; Nd, **4**; Yb, **5**) (Scheme 3) in good yields. Compounds **3** and **5** are stable yellow solids and **3** melts at 275 °C whereas **5** melts with decomposition at 275 °C. Compound **4** is a blue-green solid that melts with decomposition at 254 °C. As observed in the IR spectrum of the adducts **3**, **4** and **5**, elimination of CpH did not occur and the (μ-OH) stretching frequency was observed at 3592, 3591, and 3609 $cm^{-1}$ respectively. These frequencies are redshifted when compared to that of LGa(Me)OH (**2**) observed at 3676 $cm^{-1}$, which also confirms that the hydroxide group bridges between the Ga and Ln atom. This is in contrast to the reaction of the corresponding aluminum hydroxide LAl(Me)OH (**1**) with $Cp_3Ln$ where the elimination of CpH occurred (Scheme 2). This indicates that the proton of LGa(Me)OH (**2**) is less acidic than that of LAl(Me)OH (**1**).[9]

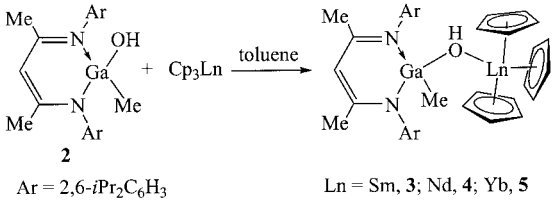


Scheme 3.

Single crystals of **3** and **4** were obtained from a toluene solution. Figures 1 and 2 show the structures of **3** and **4**, respectively. Both **3** and **4** are isomorphous and crystallize in the monoclinic space group $P2_1/m$ with half of a molecule in the asymmetric unit. The lanthanide ions possess a pseudotetrahedral geometry surrounded by three cyclopentadienyl rings and an oxygen atom. The Ga atom forms a distorted tetrahedron with two nitrogen atoms of the β-diketiminato ligand, one carbon atom of the methyl group and an oxygen atom of the hydroxy bridge. The hydrogen atom of the bridging hydroxido group [O(1)] in compound **3** cannot be located in the electron density map, probably due to the refinement against non-merohedrally twinned data. However, its presence was confirmed by the infrared spectrum and also due to the presence of three cyclopentadienyl rings connected to the samarium atom.

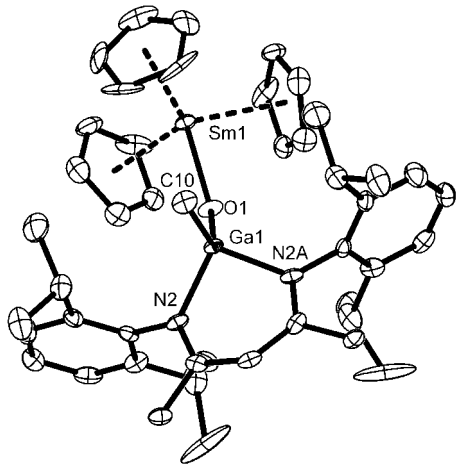


Figure 1. Molecular structure of LGa(Me)(μ-OH)Sm$Cp_3$ (**3**). Thermal ellipsoids are shown at 50% probabilities. Hydrogen atoms are omitted for clarity.

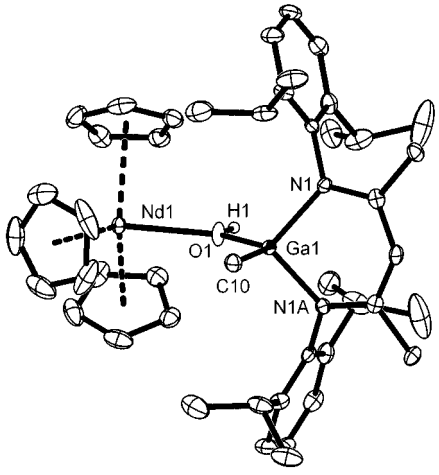


Figure 2. Molecular structure of LGa(Me)(μ-OH)Nd$Cp_3$ (**4**). Thermal ellipsoids are shown at 50% probabilities. Hydrogen atoms (except that at the oxygen atom) are omitted for clarity.

The Ga(1)–O(1) bond in compounds **3** [1.862(7) Å] and **4** [1.851(3) Å] is longer than that found in LGa(Me)OH [1.831(1) Å]. This elongation is expected due to coordination of the hydroxy group to the other metal atoms in **3** and **4**. The Sm(1)–O(1) bond of 2.465(7) Å is significantly shorter than that of the corresponding aluminum compound LAl(Me)(μ-OH)Sm$Cp_3$ [2.500(4) Å][9] but longer than that of $[Cp^*_2Sm(\mu\text{-}O_2CSPh)]_2$ [2.328(2) Å].[14] The Nd(1)–O(1) bond of 2.479(3) Å is longer than the bridging Nd–O bond in $Nd_5O(OiPr)_{13}$ [2.304(12)–2.345(11) Å] and significantly longer than the terminal Nd–O bonds [2.082(11)–2.123(11) Å].[15] The Ga(1)–O(1)–Sm(1)/Nd(1) core is bent with an angle of 149.3(4)° (**3**)/149.7(2)° (**4**)

 © 2006 Wiley-VCH Verlag GmbH & Co. KGaA, Weinheim 

which is comparable to that of LAl(Me)(μ-OH)SmCp$_3$ [151.9(2)°] (Table 1).

Table 1. Selected bond lengths [Å] and angles [°] of **3** and **4**.

| **3** | | **4** | |
|---|---|---|---|
| Ga(1)–C(10) | 1.971(2) | Ga(1)–C(10) | 1.961(5) |
| Ga(1)–O(1) | 1.862(7) | Ga(1)–O(1) | 1.851(3) |
| Ga(1)–N(2) | 1.963(7) | Ga(1)–N(1) | 1.956(3) |
| Sm(1)–O(1) | 2.465(7) | Nd(1)–O(1) | 2.479(3) |
| Ga(1)–O(1)–Sm(1) | 149.3(4) | Ga(1)–O(1)–Nd(1) | 149.7(2) |
| O(1)–Ga(1)–N(2) | 108.1(2) | O(1)–Ga(1)–N(1) | 108.4(2) |
| N(2A)–Ga(1)–N(2) | 95.4(4) | N(1)–Ga(1)–N(1A) | 95.68(2) |
| N(2)–Ga(1)–C(10) | 114.0(3) | N(1)–Ga(1)–C(10) | 114.1(2) |

## Conclusion

We have attempted to synthesize heterodimetallic compounds containing gallium and lanthanide elements. The adducts thus obtained represent rare examples for such a system. We anticipate that further reaction of LGa(Me)OH with other suitable lanthanide precursors may allow the formation of heterodimetallic gallium–lanthanide oxides. Such studies are underway in our laboratory.

## Experimental Section

**General:** All manipulations were performed under dry and oxygen-free $N_2$ or Ar using Schlenk-line and glove-box techniques. Solvents were purified according to conventional procedures and were freshly distilled prior to use. LGa(Me)OH,[11] Cp$_3$Yb,[16] and Cp$_3$Nd[16] were synthesized according to literature procedures. Cp$_3$Sm was purchased from Aldrich and used without further purification.

**Synthesis of LGa(Me)(μ-OH)SmCp$_3$ (3):** Toluene (40 mL) was added to a mixture of LGa(Me)OH (0.52 g, 1.00 mmol) and Cp$_3$Sm (0.35 g, 1.00 mmol) at room temperature. The mixture was stirred overnight when the color of the mixture slowly turned to yellow from orange. After removal of all volatiles in vacuo, toluene (60 mL) was added and the mixture was heated to 80 °C and filtered while hot. The clear yellow filtrate was kept at room temperature to afford yellow crystals of **3** (0.58 g), another crop of yellow crystals was obtained from the mother liquor (0.17 g). Total crystal yield (0.75 g, 87%). M.p. 275 °C. $C_{45}H_{60}GaN_2OSm$ (865.05): calcd. C 62.48, H 6.99, N 3.24; found C 62.17, H 6.80, N 3.22. EI-MS: *m*/*z* (%) = 504 (72) [M$^+$ – Me – Cp$_3$Sm]. IR (Nujol): $\tilde{\nu}$ = 3592, 1521, 1442, 1384, 1311, 1255, 1204, 1176, 1105, 1013, 967, 941, 867, 801, 772, 755, 725, 587, 557, 442 cm$^{-1}$.

**Synthesis of LGa(Me)(μ-OH)NdCp$_3$ (4):** Toluene (45 mL) was added to a mixture of LGa(Me)OH (0.26 g, 0.50 mmol) and Cp$_3$Nd (0.17 g, 0.50 mmol) at room temperature. The mixture was stirred overnight when the color of the mixture slowly turned to light blue-green. After removal of all volatiles in vacuo, toluene (40 mL) was added to the residue. The mixture was heated to 90 °C and filtered while hot. The clear light blue-green filtrate was kept at room temperature to afford greenish crystals of **4**. Crystal yield (0.38 g, 88%). M.p. 254 °C (decomp.). $C_{45}H_{60}GaN_2NdO$ (858.93): calcd. C 62.92, H 7.04, N 3.26; found C 62.69, H 7.13, N 3.22. EI-MS: *m*/*z* (%) = 792 (2) [M$^+$ – CpH], 503 (24) [M$^+$ – Me – Cp$_3$Nd]. IR (Nujol): $\tilde{\nu}$ = 3591, 1553, 1521, 1463, 1440, 1378, 1311, 1258, 1204, 1177, 1106, 963, 942, 868, 801, 784, 770, 953, 725, 587, 557, 442 cm$^{-1}$.

**Synthesis of LGa(Me)(μ-OH)YbCp$_3$ (5):** Toluene (40 mL) was added to a mixture of LGa(Me)OH (0.26 g, 0.50 mmol) and Cp$_3$Yb (0.18 g, 0.50 mmol) at room temperature. The mixture was stirred overnight when the color of the mixture slowly turned to orange-

Table 2. Crystallographic data for the structural analyses of compounds **3** and **4**.

| Compound | **3** | **4** |
|---|---|---|
| Empirical formula | $C_{45}H_{60}GaN_2OSm$ | $C_{45}H_{60}GaN_2NdO$ |
| Formula mass | 865.01 | 858.91 |
| *T* [K] | 100(2) | 100(2) |
| Crystal system | monoclinic | monoclinic |
| Space group | $P2_1/m$ | $P2_1/m$ |
| *a* [Å] | 10.219(2) | 10.223(3) |
| *b* [Å] | 19.616(3) | 19.588(3) |
| *c* [Å] | 10.586(2) | 10.594(2) |
| *β* [°] | 109.23(3) | 109.26(2) |
| *V* [Å$^3$] | 2003.6(6) | 2002.7(6) |
| *Z* | 2 | 2 |
| *D*(calcd.) [g·cm$^{-3}$] | 1.434(2) | 1.424(2) |
| $\mu$(Cu-$K_\alpha$) [mm$^{-1}$] | 11.971 | 10.858 |
| *F*(000) | 890 | 886 |
| *θ* range [°] | 4.42 to 59.05 | 4.42 to 58.98 |
| Index range | $-11 \le h \le 10$ | $-11 \le h \le 10$ |
| | $0 \le k \le 21$ | $0 \le k \le 21$ |
| | $0 \le l \le 11$ | $0 \le l \le 11$ |
| Reflections collected | 18619 | 18407 |
| Independent reflections | 2951 | 3414 |
| Refinement method | full-matrix least squares on $F^2$ | full-matrix least squares on $F^2$ |
| Data/restraints/parameters | 2951/0/241 | 3414/2/248 |
| $R_1$, $wR_2$ [$I > 2\sigma(I)$][a] | 0.0521, 0.1192 | 0.0234, 0.0591 |
| $R_1$, $wR_2$ (all data)[a] | 0.0528, 0.1197 | 0.0236, 0.0592 |
| *S* | 1.077 | 1.147 |
| $\Delta\rho$(min), $\Delta\rho$(max) [e·Å$^3$] | 1.141, –1.077 | 0.651, –0.414 |

[a] $R_1 = \Sigma||F_o| - |F_c||/\Sigma|F_o|$. $wR_2 = [\Sigma w(|F_o^2| - |F_c^2|)^2/\Sigma w|F_o^2|^2]^{1/2}$.

 © 2006 Wiley-VCH Verlag GmbH & Co. KGaA, Weinheim 

yellow from green. After removal of all volatiles in vacuo, toluene (45 mL) was added and the mixture was heated to 90 °C and filtered while hot. The clear orange-yellow filtrate was kept at room temperature to afford yellow crystals of **5**. Crystal yield (0.37 g, 91%). M.p. 275 °C (decomp.). $C_{45}H_{60}GaN_2OYb$ (887.73): calcd. C 60.88, H 6.81, N 3.16; found C 60.79, H 6.86, N 3.20. EI-MS: *m*/*z* (%) = 726 (50) [$M^+$ – 2 Cp – 2 Me], 711 (60) [$M^+$ – 2 Cp – 3 Me]. IR (Nujol): $\tilde{\nu}$ = 3609, 1552, 1524, 1440, 1398, 1315, 1261, 1177, 1106, 1015, 940, 832, 817, 797, 760, 643, 555, 444 $cm^{-1}$.

**X-ray Structure Determination of 3 and 4:** A suitable crystal of **3** and **4** was mounted on a glass fibre and coated with paraffin oil. Data for **3** and **4** were obtained with a Bruker three-circle diffractometer equipped with a SMART 6000 CCD detector using mirror-monochromated Cu-$K_\alpha$ radiation ($\lambda$ = 1.54178 Å). Data of both structures were non-merohedrally twinned. The twin operation in both cases is a twofold axis along the reciprocal axis 001. The fractional contribution of the minor domain refined to 0.475(2) (**3**) and 0.495(1) (**4**). The structures were solved by direct methods using SHELXS-97[17] and refined against $F^2$ on all data by full-matrix least squares with SHELXL-97.[18] All non-hydrogen atoms were refined anisotropically. Atom scattering factors (including anomalous scattering) were taken from the "International Tables for X-ray Crystallography".[19] Hydrogen atoms connected to carbon atoms were included at geometrically calculated positions and refined using a riding model. The hydrogen atom of the OH group could be located in **4** in the electron density map and was refined with distance restraints (Table 2). CCDC-614180 (**3**) and -614181 (**4**) contain the supplementary crystallographic data for this paper. These data can be obtained free of charge from The Cambridge Crystallographic Data Centre via www.ccdc.cam.ac.uk/data_request/cif.

## Acknowledgments

This work was supported by the Deutsche Forschungsgemeinschaft and the Göttinger Akademie der Wissenschaften. S. S. thanks the Graduiertenkolleg 782 for a fellowship.

[1] H. W. Roesky, S. Singh, V. Jancik, V. Chandrasekhar, *Acc. Chem. Res.* **2004**, *37*, 969–981.
[2] J. Janssen, J. Magull, H. W. Roesky, *Angew. Chem. Int. Ed.* **2002**, *41*, 1365–1367.
[3] L. W. Pineda, V. Jancik, H. W. Roesky, D. Neculai, A. M. Neculai, *Angew. Chem. Int. Ed.* **2004**, *43*, 1419–1421.
[4] V. Jancik, L. W. Pineda, J. Pinkas, H. W. Roesky, D. Neculai, A. M. Neculai, R. Herbst-Irmer, *Angew. Chem. Int. Ed.* **2004**, *43*, 2142–2145.
[5] G. Bai, Y. Peng, H. W. Roesky, J. Li, H.-G. Schmidt, M. Noltemeyer, *Angew. Chem. Int. Ed.* **2003**, *42*, 1132–1135.
[6] G. Bai, H. W. Roesky, J. Li, M. Noltemeyer, H.-G. Schmidt, *Angew. Chem. Int. Ed.* **2003**, *42*, 5502–5506.
[7] S. Singh, S. S. Kumar, V. Chandrasekhar, H.-J. Ahn, M. Biadene, H. W. Roesky, N. S. Hosmane, M. Noltemeyer, H.-G. Schmidt, *Angew. Chem. Int. Ed.* **2004**, *43*, 4940–4943.
[8] H. W. Roesky, G. Bai, V. Jancik, S. Singh, European Patent, **2005** PCT/EP, **2005**/002741, Int. Pat. Classification. C07F17/00.
[9] J. Chai, V. Jancik, S. Singh, H. Zhu, C. He, H. W. Roesky, H.-G. Schmidt, M. Noltemeyer, N. S. Hosmane, *J. Am. Chem. Soc.* **2005**, *127*, 7251.
[10] G. Bai, S. Singh, H. W. Roesky, M. Noltemeyer, H.-G. Schmidt, *J. Am. Chem. Soc.* **2005**, *127*, 3449–3455.
[11] S. Singh, V. Jancik, H. W. Roesky, R. Herbst-Irmer, *Inorg. Chem.* **2006**, *45*, 949–951.
[12] R. C. Mehrotra, M. M. Agarwal, *Synth. Inorg. Met.-Org. Chem.* **1973**, *3*, 407–414.
[13] R. C. Mehrotra, M. M. Agarwal, U. D. Tripathi, S. R. Bindal, *Proc. Rare Earth Res. Conf., 7th* **1969**, *2*, 759–770.
[14] W. J. Evans, K. A. Miller, J. W. Ziller, *Inorg. Chem.* **2006**, *45*, 424–429.
[15] M. Kritikos, M. Moustiakimov, M. Wijk, G. Westin, *J. Chem. Soc., Dalton Trans.* **2001**, 1931.
[16] W. A. Herrmann, *Synthetic Methods of Organometallic and Inorganic Chemistry*, vol. 6 (Ed.: F. T. Edelmann), Georg Thieme Verlag, Stuttgart, **1997**, p. 85–89.
[17] SHELXS-97, Program for Structure Solution: G. M. Sheldrick, *Acta Crystallogr. Sec. Sect. A* **1990**, *46*, 467–473.
[18] G. M. Sheldrick, *SHELXL-97, Program for Crystal Structure Refinement*, University of Göttingen, Göttingen, Germany, **1997**.
[19] *International Tables for Crystallography*, vol. C (Ed.: A. C. J. Wilson), Kluwer Academic Publishers, Dordrecht, **1992**, Tables 4.2.6.8 and 6.1.1.4.

Received: July 11, 2006
Published Online: September 5, 2006

 © 2006 Wiley-VCH Verlag GmbH & Co. KGaA, Weinheim 

DOI: 10.1002/ejic.200600659

# Cyclodimethylsiloxane $(Me_2SiO)_m$ ($m$ = 3–6) Ring Transformations on Reactions with $AgSbF_6$; Crystal Structure of $Ag(Me_2SiO)_7SbF_6$

**Andreas Decken,[a] Francis Arthur LeBlanc,[a] Jack Passmore,*[a] and Xinping Wang[a]**

**Keywords:** Cyclodimethylsiloxane / Host–guest systems / Silver / Silicon ethers / Ring transformation / Hexafluoroantimonate / Pseudo crown ethers / Lewis bases

The reaction of $D_m$ (D = $Me_2SiO$, $m$ = 3–6) with silver hexafluoroantimonate in liquid $SO_2$ affords a mixture of $AgD_nSbF_6$ ($n$ = 6–8) complexes. Upon the addition of $CH_3CN$, $Ag^+$-directed ring transformations are effected, which allows for the isolation of neat $D_n$ ($n$ = 6–8). The $AgD_n^+$ cations are rare examples of Lewis acid donor complexes of silicon ethers and $Ag^+$ oxygen donor complexes, and their isolation implies that numerous metal cation cyclosiloxanes can be prepared from readily available starting materials.

(© Wiley-VCH Verlag GmbH & Co. KGaA, 69451 Weinheim, Germany, 2006)

We recently reported the preparation of $Li^+$-cyclodimethylsiloxane host–guest cations directly from their components[1] and provided rare examples of silicon ethers behaving as Lewis bases as shown in Equation (1). Their structures imply that cyclodimethylsiloxanes ($D_5$ and $D_6$, D = $Me_2SiO$) act as pseudo crown ethers. Apart from alkali metal cations ($Li^+$ and $K^+$[2]) with large anions, no other examples of a metal-cation–siloxane adduct have been reported. Metal-cation–siloxane salt formation is favored by large anions, which minimizes the unfavorable lattice-energy changes. Therefore, the question as to whether the formation of the complexes could be extended to the use of commercially available salts with smaller anions as the starting materials remains. The $Ag^+$ cation is regarded as a soft Lewis acid[3] and has a low affinity to oxygen donor ligands.[4] Nevertheless, we report below the first examples of the transition-metal-cation–siloxane $SbF_6^-$ salts of $AgD_n^+$ ($n$ = 6–8) formed by the reactions of $D_m$ ($m$ = 3–6) with $AgSbF_6$ in liquid $SO_2$. Unlike the Li[Al] case, transformation of the siloxane rings occur with $Ag^+$ acting as a template for the formation of the most thermodynamically stable metal-cation–cyclodimethylsiloxane complex. The formation of macrocyclic ethers by the reaction of $AgAsF_6$ with $(CH_2O)_3$ or ethylene oxide was described by Roesky and his coworkers.[5] However, no similar ring transformation reactions of cyclodimethylsiloxanes under mild conditions have been previously reported.[6] Ring-opening polymerization of $D_m$ ($m$ = 3–6) has been widely investigated, and these results are also of interest in this context.

$$\mathrm{Li[Al]} + \mathrm{D}_m \xrightarrow[\text{r.t.}]{\mathrm{CH_2Cl_2}} \mathrm{LiD}_m\mathrm{[Al]} \quad (1)$$

$$\mathrm{[Al]} = \mathrm{Al(OC(CF_3)_3)_4},\ m = 5 \text{ or } 6;\quad = \mathrm{Al(OC(CF_3)_2Ph)_4},\ m = 6$$

The reaction of excess $AgSbF_6$ with $D_5$ (1.4:1) in liquid $SO_2$ affords a colorless, highly hygroscopic solubilized product. When a saturated $SO_2$ solution of the product is cooled, a colorless crystalline material is afforded. Several single-crystals were identified by X-ray diffraction analysis as $AgD_7SbF_6$. However, the mass spectrum of the material showed fragments which can be attributed to $(D_6 - Me)^+$ and $(D_7 - Me)^+$. This implies that the crystalline material was a mixture of $AgD_7SbF_6$ and $AgD_6SbF_6$. Addition of a large excess of $CH_3CN$ to the solubilized product led to a two-phase liquid. GC–MS analysis of the upper oily phase showed three main components: $D_6$, $D_7$ (3.4:1), and $D_8$ (Figure 1). The amount of $D_8$ present in the sample was very small in comparison with that of $D_6$ and $D_7$ (Figure 1c),[7] but its presence implies that a small amount of $AgD_8SbF_6$ was part of the mixture. The composition of the product was further confirmed by in situ $^{29}Si\{^1H\}$ NMR (Figure 1a) of the reaction of $AgSbF_6$ with $D_5$ (1.5:1). Three peaks (–13.585 [$AgD_7^+$], –14.187 [$AgD_6^+$], –12.83 ppm [$AgD_8^+$]) in a molar ratio of $AgD_7^+/AgD_6^+/AgD_8^+$ = 3.7:1:0.2 were found in the spectrum, which is consistent with the GC results ($D_7/D_6$ = 3.4:1). The change in the intensity of the peaks in the $^{29}Si\{^1H\}$ NMR spectrum with temperature implies that an equilibrium in liquid $SO_2$ exists: $2AgD_7^+ \rightleftarrows AgD_6^+ + AgD_8^+$ (Supporting Information, Figure S2.3). The $^{29}Si\{^1H\}$ NMR spectrum (in $SO_2$, Figure 1b) of the solution obtained after the addition of an excess amount of $CH_3CN$ showed $D_7$ (–23.09 ppm) and $D_6$

[a] Department of Chemistry, University of New Brunswick
Fredericton, NB E3B 6E2, Canada
Fax: +1-506-453-4981
E-mail: passmore@unb.ca

Supporting information for this article is available on the WWW under http://www.eurjic.org or from the author.

 © 2006 Wiley-VCH Verlag GmbH & Co. KGaA, Weinheim 

(–22.42 ppm) with traces of $D_4$ (–20.67 ppm) and $D_5$ (–21.89 ppm).[8] The reaction of $AgSbF_6$ with $D_5$ leads to the ring transformation of $D_5$ to $D_6$, and $D_7$ can be expressed as shown in Scheme 1. The separate reactions of excess $AgSbF_6$ with $D_3$, $D_4$, and $D_6$ gave similar results (Supporting Information, Figure S2.4). Thus, these $AgD_n^+$ ($n$ = 6–8) cations are intermediates in cyclosiloxane ring transformations. The $AgD_nSbF_6$ complexes slowly decompose in $SO_2$ solutions to afford $Me_2SiF_2$, $(MeFSi)_2O$, $Me_2SiFOMe_2SiOSiFMe_2$, and $(Me_2SiFOMe_2SiF)_2O$ (Supporting Information, Figure S2.5).[9]

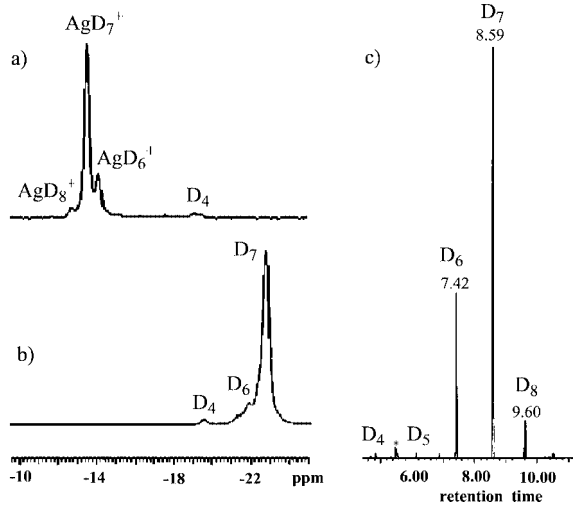


Figure 1. a) In situ $^{29}Si\{^1H\}$ NMR spectrum of the reaction of $AgSbF_6$ + $D_5$ (1.5:1) in liquid $SO_2$; b) in situ $^{29}Si\{^1H\}$ NMR spectrum after the addition of excess $CH_3CN$ into the $AgSbF_6$ + $D_5$ (1.5:1) mixture in liquid $SO_2$; c) GC of the oily phase upon the addition of $CH_3CN$ onto the solid product of the $AgSbF_6$ + $D_5$ (1.4:1) mixture in liquid $SO_2$ (The peak marked with * is due to an unidentified siloxane chain or rearranged siloxane ring).

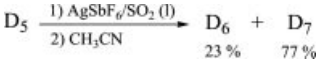


Scheme 1.

The solid-state structure[10] of $AgD_7SbF_6$ (Figure 2) shows discrete $AgD_7^+$ cations and $SbF_6^-$ anions connected by four weak Ag–F contacts {4×[2.785(2) Å, 0.070 v.u.]}[11] which forms a chain along the *c*-axis (Figure 2c). The Ag atom coordinates with five oxygen atoms from $D_7$; three of these interactions are strong {Ag–O1 2.489(2) Å, 0.174 v.u.; 2×[Ag–O4 2.553(1) Å, 0.146 v.u.]} in comparison with the Ag–O distances in $[(CH_2O)_6Ag_2]^{2+}$ and $Ag(12\text{-crown-}4)_2^+$ {6× [2.458(5) Å, 0.188 v.u.] and 8×[2.57(1) Å, 0.137 v.u.]}. Two of the Ag–O2 contacts are weak {2×[2.811(1) Å, 0.073 v.u.]}. There are no significant contacts between the Ag and the O3 atoms {2×[3.601(1) Å, 0.0086 v. u.]}. The sum of the bond valences (0.909 v.u.) of all the Ag–O contacts [0.174 + (0.146×2) + (0.073×2) + (0.0086×2) = 0.629 v.u.] and the Ag–F contacts (0.070×4 = 0.280 v.u.) correspond to one positive charge on Ag. The $Si_7O_7$ framework and the Ag atom are approximately planar, and the $AgD_7^+$ has an overall crystallographic $C_{2v}$ symmetry.[12] This is different from the approximate $D_{7h}$ symmetry found for $KD_7^+$ where $K^+$ is coplanar with the ring and interacts with all seven oxygen atoms of the cyclosiloxane ring. Near-planar pentadentate silver(I) complexes have been reported,[13] but this coordination mode is not common for silver(I) complexes. These complexes usually adopt a linear or octahedral coordination geometry.[4] The oxygen atoms that are not bonded to silver have Si–O bond lengths of 1.608 (2) Å (average), which is significantly shorter than the Si–O bond lengths for the oxygen atoms [1.636(1) Å, average] that are bonded to silver. This is similar to the situation for $LiD_6^+$. The average Si–O–Si angle at the coordinated O atoms, 144.1(1)°, is much smaller than that at the noncoordinated O atoms, 166.9(1)°. To the best of our knowledge, this Si–O–Si angle [166.9(1)°] is the largest reported among the Si–O–Si angles in cyclodimethylsiloxane. The nature of the bonding in $AgD_7^+$ is likely similar to that previously described in $LiD_6^+$, the differences are currently under investigation.

Some of the steps in a tentative $Ag^+$-directed ring transformation process are shown in Scheme 2. Coordination of $Ag^+$ to $D_m$ lengthens and weakens the Si–O bond and induces a higher positive charge on silicon. Abstraction of $F^-$ from $SbF_6^-$ [fluoride ion affinity of $SbF_5$ (g) = 514 or 503 kJ·mol$^{-1}$][14] is therefore promoted and is driven by the formation of the Si–F bond (bond enthalpy of Si–F = 582 kJ·mol$^{-1}$),[15] which leads to the formation of the $FSiMe_2(OSiMe_2)_{m-2}OSiMe_2O^-$ anion. This anion can react further with $D_m$ or $AgD_n^+$, which can lead to larger chain anions. These chain anions can then attack the silicon atoms to afford the most thermodynamically favored $AgD_n^+$ species (e.g. $AgD_7^+$ is more stable than $AgD_6^+$ [$Ag^+$ (g) + 1.4 $D_5$ (g) → $AgD_7^+$ (g), $\Delta H$ = –439 kJ·mol$^{-1}$; $Ag^+$ (g) + 1.2 $D_5$ (g) → $AgD_6^+$ (g), $\Delta H$ = –414 kJ·mol$^{-1}$].[16] The changes in the intensities of the $AgD_n^+$ ($n$ = 6–8) signals with temperature in the $^{29}Si\{^1H\}$ NMR spectra (Supporting Information, Figure S2.3) imply that the system is in thermodynamic equilibrium. A cation-induced ring-opening mechanism has been established for base-initiated cyclodimethylsiloxane ring-opening polymerization. Alkali metal cyclodimethylsiloxane adducts are proposed as the intermediates; the mechanism is supported by the structure of $AgD_7^+$ and the detection of $AgD_n^+$ ($n$ = 6–8) in this study.

This work implies that numerous salts of metal cyclodimethylsiloxane complexes can be prepared from commercially available starting materials. Cyclosiloxanes are believed to act as pseudo crown ethers. The work also suggests that other polycyclosiloxanes may be prepared if the metal cation is tailored in size. The size and nature of the anion, along with related ring transformations (e.g. cyclophosphazenes), may also be affected by $AgSbF_6$ or related salts.

 © 2006 Wiley-VCH Verlag GmbH & Co. KGaA, Weinheim 

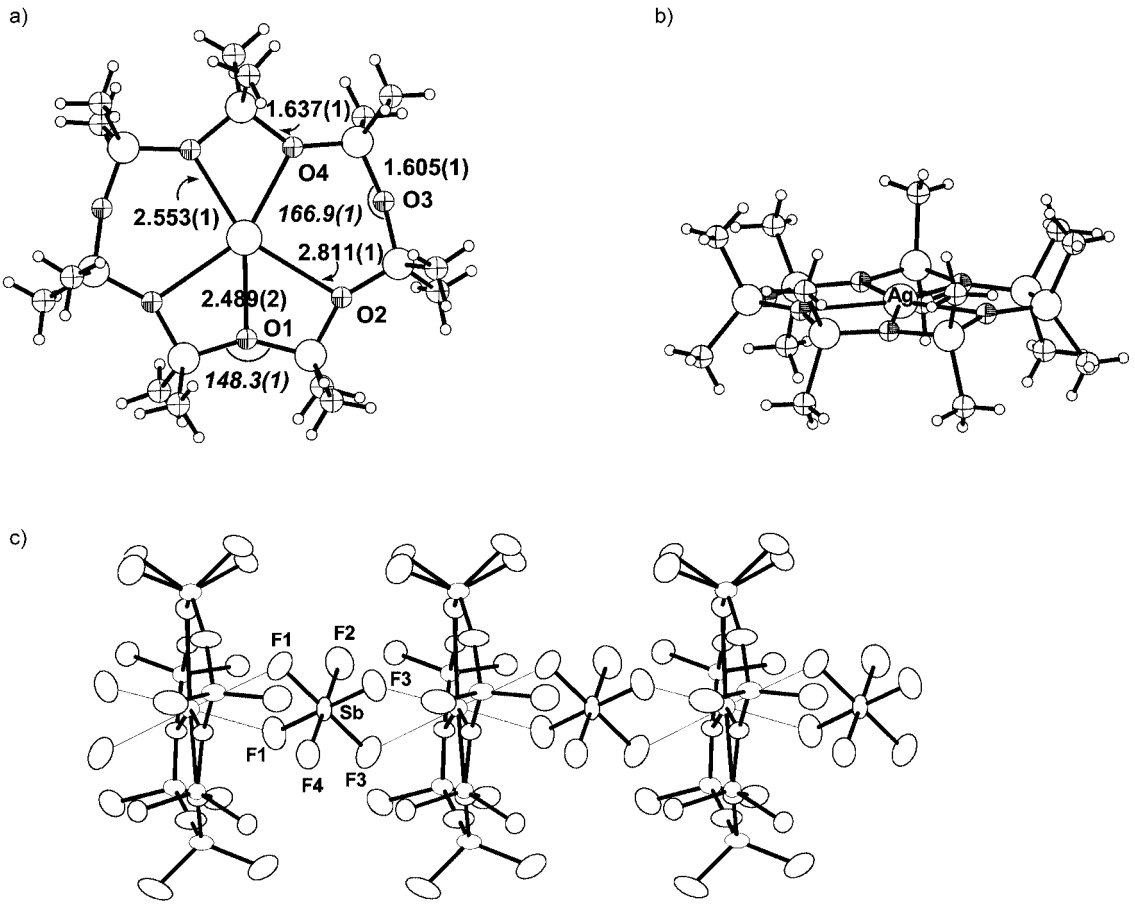


Figure 2. a) A top-view of $AgD_7^+$(bond length [Å], bond angle [°]); b) a side-view of $AgD_7^+$; c) a view of $AgD_7SbF_6$ along the *c*-axis (bond valences were unlined and hydrogen atoms were omitted for clarity).

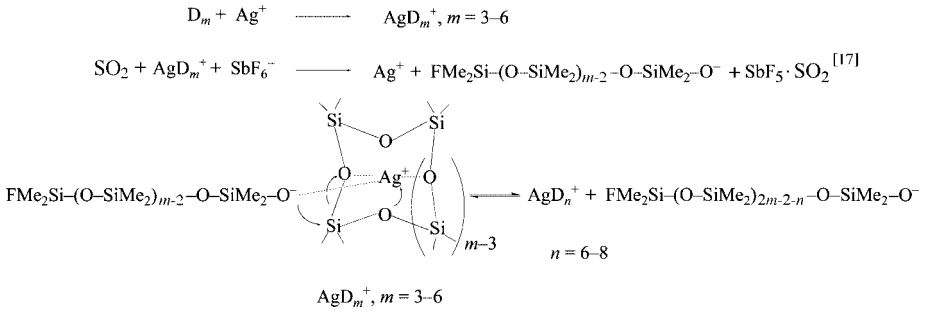


Scheme 2.

## Experimental Section

**Reaction of $AgSbF_6$ with $D_5$ (mole ratio $AgSbF_6/D_5$ = 1.4:1) To Afford Single-Crystals of $AgD_7SbF_6$:** $AgSbF_6$ (1.237 g, 3.6 mmol) in one tube (OD 1.5 cm) of a two-tube (Pyrex), two-valve (Teflon in glass) vessel with an incorporated medium frit was treated with $(Me_2SiO)_5$ (1 mL, 2.58 mmol). The vessel was cooled in liquid $N_2$ and degassed. $SO_2$ (7 mL) was distilled onto the mixture, and the reaction was warmed to room temperature. A small amount of colorless precipitate was then observed over a clear solution. This mixture was stirred overnight at 5 °C and then filtered. Removal of the volatiles afforded a colorless solubilized product (1.863 g) and a very small amount of colorless insoluble product. Insoluble product: IR (KBr, Nujol Mull, room temp.): $\tilde{\nu}$ = 3488 (wb), 2921 (s), 1613 (w), 1458 (s), 1377 (s), 1264 (s), 1061 (sb), 897 (s), 809 (s), 667 (s), 632 (m), 476 (m) $cm^{-1}$. Scanning electron microscopy-energy dispersive angle X-ray (SEM-EDAX) analysis showed that the insoluble product probably contained $SiO_2$, $Sb_2O_3$, $SbF_3 \cdot SbF_5$, and AgF. The solubilized product that was obtained in similar reactions was used in the following workups: i) *Crystallization*: $SO_2$ (about 8 g) was added to the solubilized products (1.65 g) in a two-tube vessel. The resulting solution was concentrated until saturation and then cooled to 5 °C overnight, to afford a colorless crystalline product. The vessel was cooled to –78 °C and one valve opened. Crystals were quickly picked out of the solution with a miniature nickel spoon.[18] Single-crystals suitable for X-ray diffraction were coated with paratone-N oil, mounted with a glass fiber, and frozen in liquid nitrogen while mounted on the goniometer. The crystalline product was collected in dry box (0.375 g, 23%). M.p: 150 °C (decomp.). IR (KBr, neat, room temp.): $\tilde{\nu}$ = 2959 (m), 2903 (w), 1605

 © 2006 Wiley-VCH Verlag GmbH & Co. KGaA, Weinheim 

(wb), 1446 (wb), 1412 (w), 1377 (w), 1262 (s), 1056 (vs), 859 (m), 799 (vs), 701 (m), 658 (s, $SbF_6^-$), 536 (w), 506 (w), 382 (s, $SbF_6^-$) $cm^{-1}$. EI-MS (60 ev): *m/z* (%) = 503 (25) $[D_7 – 15]^+$, 429 (12) $[D_6 – 15]^+$. ii) *Displacement*: $CH_3CN$ (3 mL) was condensed onto the solubilized product (2 g) in a 10 mm-NMR tube glass-blown onto a valve (Teflon in glass) to afford a two-layer solution. The upper layer of oily liquid was removed by syringe (0.6 mL). GC–MS: *m/z* (%) = 429 (21) $[D_6 – 15]^+$, 503 (100) $[D_7 – 15]^+$, 429 (21) $[D_6 – 15]^+$, 577 (9) $[D_8 – 15]^+$. GC-FID: % = 23 ($D_6$), 77 ($D_7$).

**In situ NMR Reaction of $AgSbF_6$ with $D_5$ (1.5:1):** $SO_2$ (4 mL) was condensed onto $AgSbF_6$ (2.018 g, 5.87 mmol) and $D_5$ (1.5 mL, 3.87 mmol) in a 10 mm NMR tube described above and sonicated in ice water for 0.5 h to afford a colorless solution over a small amount of colorless precipitate. $^{29}Si\{^1H\}$ NMR (79.4 MHz, $SO_2$, 25 °C): $\delta$ = –14.187 (s, $AgD_6^+$), –13.585 (s, $AgD_7^+$), –12.83 (s, $AgD_8^+$) ppm. $^{29}Si\{^1H\}$ NMR (79.4 MHz, $SO_2$, 5 °C):$\delta$ = –14.106 (s, $AgD_6^+$), –13.502 (s, $AgD_7^+$), –12.01 (s, $AgD_8^+$) ppm. $^{29}Si\{^1H\}$ NMR (79.4 MHz, $SO_2$, –5 °C): $\delta$ = –14.03 (s, shoulder, $AgD_6^+$), –13.456 (s, $AgD_7^+$), –12.02 (s, $AgD_8^+$) ppm. $^{29}Si\{^1H\}$ NMR (79.4 MHz, $SO_2$, –15 °C): $\delta$ = –13.403 (br. s, $AgD_7^+$) ppm. $^{29}Si\{^1H\}$ NMR (79.4 MHz, $SO_2$, –40 °C): $\delta$ = –13.547 (s, $AgD_7^+$), –12.379 (s, $AgD_8^+$) ppm. $^{29}Si\{^1H\}$ NMR (79.4 MHz, $SO_2$, –70 °C): $\delta$ = –13.315 (s, $AgD_7^+$), –12.196 (s, $AgD_8^+$) ppm. $^1H$ NMR (400 MHz, $SO_2$, 25 °C): $\delta$ = 0.225 (s, $SiMe_2$) ppm; $^{13}C\{^1H\}$ (100 MHz, $SO_2$, 25 °C): $\delta$ = 0.414 (s, $SiMe_2$) ppm. $CH_3CN$ (ca. 1.5 mL) was then condensed into this solution and sonicated in ice water for 1 h. $^{29}Si\{^1H\}$ NMR (79.4 MHz, $SO_2$/$CH_3CN$, 25 °C): $\delta$ = –23.093 (s, $D_7$), –22.415 (s, $D_6$), –21.90 (s, $D_5$), –20.668 (s, $D_4$) ppm. $^1H$ NMR (400 MHz, $SO_2$, 25 °C): $\delta$ = 1.350 (s, $CH_3CN$), –0.693 (s, $SiMe_2$) ppm; $^{13}C\{^1H\}$ (100 MHz, $SO_2$, 25 °C): $\delta$ = 119.027 (s, $CH_3{}^{13}CN$), 1.586 (m, $^{13}CH_3CN$ and $SiMe_2$) ppm.

**Supporting Information** (see footnote on the first page of this article): General experimental techniques, in situ $^{29}Si$ NMR reactions of $AgSbF_6$ with $D_m$ (*m* = 3, 4, and 6) in liquid $SO_2$, FT-IR, MS, and $^{29}Si\{^1H\}$ NMR spectra, and full details of the crystal structure of $AgD_7SbF_6$ as well as a comparison with $KD_7^+$.

## Acknowledgements

Acknowledgement is made to NSERC (Canada) for financial support of this research.

[1] A. Decken, J. Passmore, X. Wang, *Angew. Chem. Int. Ed.* **2006**, *45*, 2773; *Angew. Chem.* **2006**, *118*, 2839.

[2] The $K^+$ complexes were formed in reactions involving silicon grease in unspecified yields: a) M. R. Churchill, C. H. Lake, S. H. Chao, J. O. T. Beachley, *J. Chem. Soc. Chem. Commun.* **1993**, 1577; b) C. Eaborn, P. B. Hitchcock, K. Izod, J. D. Smith, *Angew. Chem. Int. Ed. Engl.* **1995**, *34*, 2679; *Angew. Chem.* **1995**, *107*, 2936.

[3] R. G. Pearson, *J. Am. Chem. Soc.* **1963**, *85*, 3533.

[4] F. A. Cotton, G. Wilkinson, *Advanced Inorganic Chemistry*, Wiley, New York, **1997**.

[5] a) H. W. Roesky, E. Peymann, J. Schimkowiak, M. Noltemeyer, W. Pinkert, G. M. Sheldrick, *J. Chem. Soc. Chem. Commun.* **1983**, 981; b) P. G. Jones, T. Gries, H. Grützmacher, H. W. Roesky, J. Schimkowiak, G. M. Sheldrick, *Angew. Chem. Int. Ed. Engl.* **1984**, *23*, 376; *Angew. Chem.* **1984**, *96*, 357.

[6] $D_3$ was converted into higher cyclodimethylsiloxane rings ($D_m$, *m* = 4–7) catalyzed by $Li_2PdCl_4$ + $CuCl_2$ at 120 °C, see I. S. Akhrem, N. M. Chistovalova, E. I. Mysov, M. E. Vol'pin, *Bull. Acad. Sci. USSR Div. Chem. Sci.* **1978**, *27*, 1396.

[7] Calibrated by GC-FID. $D_8$ ring was detected by GC but not by GC-FID likely because of the low concentration.

[8] $D_8$ ring was not detected likely because of the low concentration and its signals overlapped with those of $D_7$. $^{29}Si\{^1H\}$ NMR [79.4 MHz, $SO_2$]: $\delta$ = –19.64 ($D_4$), –21.67 ($D_5$), –22.69 ($D_6$) ppm, this work. For $^{29}Si\{^1H\}$ NMR (19.87 MHz, $C_6D_6$): $\delta$ = –9.88 ($D_3$), –23.03 ($D_7$),–22.98 ($D_8$) ppm, see D. J. Burton, R. K. Harris, K. Dodgson, C. J. Pellow, J. A. Semlyen, *Polym. Commun.* **1983**, *9*, 278.

[9] a) O. Farooq, *J. Organomet. Chem.* **2000**, *613*, 239; b) A. M. Filippov, V. N. Bochkarev, *Zhurnal Obshchei Khimii* **1990**, *60*, 861.

[10] X-ray structure determination of $AgD_7SbF_6$: Bruker AXS P4/SMART 1000 diffractometer with graphite monochrometer, $T$ = 173 ± 1 K. Unit cell determination: absorption correction by SADABS, direct methods, refinement with SHELXTL 6.14. Space group = $P21/m$, $a$ = 7.4272(6) Å, $b$ = 20.8687(16) Å, $c$ = 11.4437(9) Å, $\beta$ = 102.484(1)°, $V$ = 1731.8(2) $Å^3$, $Z$ = 2, $D_{calc}$ = 1.654 $Mg/m^3$, $2\theta_{max}$ = 55.0°, reflections: 12112 collected, 3995 independent, 823 parameters, $R1$ ($I > 2\theta$) = 0.0206, $R1$ (all data) = 0.0272. CCDC-610025 contains the supplementary crystallographic data for this paper. These data can be obtained free of charge from The Cambridge Crystallographic Data Centre via www.ccdc.cam.ac.uk/data_request/cif.

[11] The bond valences *s* (in valence units v.u.) are defined as $s = \exp[(R_o – R)/B]$, where $R$ is the observed distance, $R_o$ is the covalent bond length of the bond (bond order = 1; for Ag–F, $R_o$ = 1.80 Å; for Ag–O, $R_o$ = 1.84 Å), and $B$ is an empirical parameter set to 0.37. a) I. D. Brown in *Structure and Bonding in Crystals*, vol. 2 (Eds.: M. O'Keefe, A. Navrotsky), Academic Press, London, **1981**; b) I. D. Brown, *The Chemical Bond in Inorganic Chemistry – The Bond Valence Model*, Oxford University Press, Oxford, **2002**.

[12] A plane defined by O1, O3, and O4; O2 [0.284(4) Å] and Ag [0.096(2) Å] are above the plane.

[13] a) S. M. Nelson, S. G. McFall, *J. Chem. Soc. Chem. Comm.* **1977**, 370; b) E. C. Constable, M. G. B. Drew, G. Forsyth, M. D. Ward, *J. Chem. Soc. Chem. Comm.* **1988**, 1450.

[14] a) H. D. B. Jenkins, I. Krossing, J. Passmore, I. Raabe, *J. Fluorine Chem.* **2004**, *125*, 1585; b) K. O. Christe, D. A. Dixon, D. McLemore, W. W. Wilson, J. A. Sheehy, J. A. Boatz, *J. Fluorine Chem.* **2000**, *101*, 151.

[15] C. E. Housecroft, A. G. Sharpe, *Inorganic Chemistry*, Prentice Hall, **2001**, p. 285.

[16] Calculated at B3LYP/3-21G//HF/3-21G level. *Gaussian 03, Revision C.02*. M. J. Frisch, G. W. Trucks, H. B. Schlegel, G. E. Scuseria, M. A. Robb, J. R. Cheeseman, J. A. Montgomery Jr, T. Vreven, K. N. Kudin, J. C. Burant, J. M. Millam, S. S. Iyengar, J. Tomasi, V. Barone, B. Mennucci, M. Cossi, G. Scalmani, N. Rega, G. A. Petersson, H. Nakatsuji, M. Hada, M. Ehara, K. Toyota, R. Fukuda, J. Hasegawa, M. Ishida, T. Nakajima, Y. Honda, O. Kitao, H. Nakai, M. Klene, X. Li, J. E. Knox, H. P. Hratchian, J. B. Cross, V. Bakken, C. Adamo, J. Jaramillo, R. Gomperts, R. E. Stratmann, O. Yazyev, A. J. Austin, R. Cammi, C. Pomelli, J. W. Ochterski, P. Y. Ayala, K. Morokuma, G. A. Voth, P. Salvador, J. J. Dannenberg, V. G. Zakrzewski, S. Dapprich, A. D. Daniels, M. C. Strain, O. Farkas, D. K. Malick, A. D. Rabuck, K. Raghavachari, J. B. Foresman, J. V. Ortiz, Q. Cui, A. G. Baboul, S. Clifford, J. Cioslowski, B. B. Stefanov, G. Liu, A. Liashenko, P. Piskorz, I. Komaromi, R. L. Martin, D. J. Fox, T. Keith, M. A. Al-Laham, C. Y. Peng, A. Nanayakkara, M. Challacombe, P. M. W. Gill, B. Johnson, W. Chen, M. W. Wong, C. Gonzalez, J. A. Pople, Gaussian, Inc., Wallingford CT, **2004**.

[17] R. Minkwitz, W. Molsbeck, H. Preut, *Z. Naturforsch. B* **1989**, *44*, 1581.

[18] J. Beck, F. Steden, A. Reich, H. Fölsing, *Z. Anorg. Allg. Chem.* **2003**, *629*, 1073.

Received: June 6, 2006
Published Online: August 31, 2006

 © 2006 Wiley-VCH Verlag GmbH & Co. KGaA, Weinheim 

DOI: 10.1002/ejic.200600671

# The Remarkable Solvent-Dependent Crystallization of the Mono- and Bis(4-pyrrol-1-ylbenzonitrile) Adducts of Bis(pentafluorophenyl)zinc

**Eddy Martin,[a] David L. Hughes,[a] and Simon J. Lancaster*[a]**

**Keywords:** Crystal structure / Zinc / Pentafluorophenyl group / Nitrile adduct / Intermolecular interaction / Arene coordination

Treatment of a toluene solution of $Zn(C_6F_5)_2$ with *p*-$C_4H_4N$–$C_6H_4CN$ yields (*p*-$C_4H_4N$–$C_6H_4CN)_2Zn(C_6F_5)_2$, which has been structurally characterised following recrystallization from 1,2-difluorobenzene by single-crystal X-ray diffraction and possesses the expected distorted tetrahedral molecular geometry. However, crystallization from dichloromethane yields a trigonal planar complex with only one *p*-$C_4H_4N$–$C_6H_4CN$ ligand. The three-coordinate complex forms an intermolecular dimer in the solid state through a cooperative combination of zinc–arene, offset homoaromatic and dipole–dipole interactions.

(© Wiley-VCH Verlag GmbH & Co. KGaA, 69451 Weinheim, Germany, 2006)

The coordination chemistry of zinc continues to enjoy healthy academic interest spurred by diverse applications in biology,[1] materials[2–4] and catalysis.[5–6] The characteristic properties of zinc are the predominance of the redox-resistant zinc(II) oxidation state, flexible coordination number and geometry, and Lewis acidity of its complexes. Four- to six-coordinate complexes of zinc are most common but there are many examples of two-coordinate zinc centres, particularly with amide, silyl and alkyl donors.[1] In contrast, mononuclear trigonal-planar complexes of zinc are relatively rare, but can be favoured through steric factors[7,8] or the combination of sterics and electrostatics as is the case for the $[Zn(C_6F_5)_3]^-$ anion.[9]

To date, all structurally characterised neutral adducts of the form $ZnX_2L_n$, where X is Cl, Br, I or the pseudohalide $C_6F_5$, and L is a monodentate Lewis base, have been shown to adopt essentially tetrahedral geometries where *n* is 2.[1,10] As part of our continuing investigations into the supramolecular architectures of bis(pentafluorophenyl)zinc complexes, we have structurally characterised a series of $(nitrile)_2Zn(C_6F_5)_2$ adducts.[11] We report here the unexpected isolation of the mono(nitrile) adduct (*p*-$C_4H_4N$–$C_6H_4CN)Zn(C_6F_5)_2$ and compare its solid-state structure to that of the bis(nitrile) (*p*-$C_4H_4N$–$C_6H_4CN)_2Zn(C_6F_5)_2$.

In the solid-state structure of the donor-free form of $Zn(C_6F_5)_2$ (**1**), the essentially linear geometry is perturbed only by a weak intermolecular C–F···Zn interaction.[12] Compound **1** is most conveniently prepared by the exchange between $ZnEt_2$ and $B(C_6F_5)_3$ in an aromatic solvent, from which it crystallizes with 1 equiv. of the arene.[13] The solid-state structure of the $\eta^2$-bonded toluene adduct $(MeC_6H_5)Zn(C_6F_5)_2$ (**2**) has very recently been determined.[14] This weakly bound toluene ligand can be readily displaced by Lewis bases. For example, we find that treatment of a toluene solution of **1** with 2 equiv. of the nitrogen donor ligands $tBuNH_2$, $Me_2NH$, $(PhCH_2)_2NH$, *cyclo*-$C_4H_8NH$, pyridine or benzonitrile followed by removal of toluene under reduced pressure and recrystallisation from a dichloromethane and light petroleum solvent mixture gives X-ray quality single crystals. In all but the instance discussed herein, complexes of the form $L_2Zn(C_6F_5)_2$ with distorted tetrahedral zinc environments are obtained.[11,15]

Treatment of a toluene solution of **1** with 2 equiv. of 4-(pyrrol-1-yl)benzonitrile followed by solvent removal yields a crude white solid. Subsequent crystallization from a dichloromethane and light petroleum solvent mixture at –28 °C yielded crystals (Scheme 1), which were determined by X-ray crystallography to be the mono(nitrile) complex (*p*-$C_4H_4N$–$C_6H_4CN)Zn(C_6F_5)_2$ (**3**) (Figure 1). This result was unexpected and initially assumed to be a consequence of a mistake in the reaction stoichiometry. However, despite taking great care over the reagent ratios, crystallization from dichloromethane consistently gave compound **3**. Employing identical preparative conditions but attempting crystallisation from toluene instead of dichloromethane yielded small colourless crystals that gave a different unit cell from those of **3** but did not diffract strongly enough for a full structure determination. Larger crystals, with an identical cell to those from toluene, were grown from a 1,2-difluorobenzene and light petroleum solvent mixture at +2 °C. Crystallographic analysis of this sample revealed it

[a] Wolfson Materials and Catalysis Centre, School of Chemical Sciences and Pharmacy, University of East Anglia, Norwich, NR4 7TJ, UK
Fax: +44-1603-592003
E-mail: S.Lancaster@uea.ac.uk

Supporting information for this article is available on the WWW under http://www.eurjic.org or from the author.

 © 2006 Wiley-VCH Verlag GmbH & Co. KGaA, Weinheim 

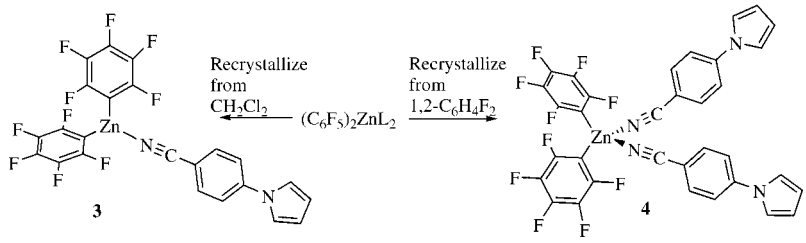


Scheme 1.

to be the bis(nitrile) adduct ($p$-$C_4H_4N$–$C_6H_4CN)_2Zn(C_6F_5)_2$ (**4**) (Figure 2). It therefore seems likely that the expected bis(nitrile) adduct is initially formed in the reaction but that recrystallization from dichloromethane yields the mono(nitrile) adduct.

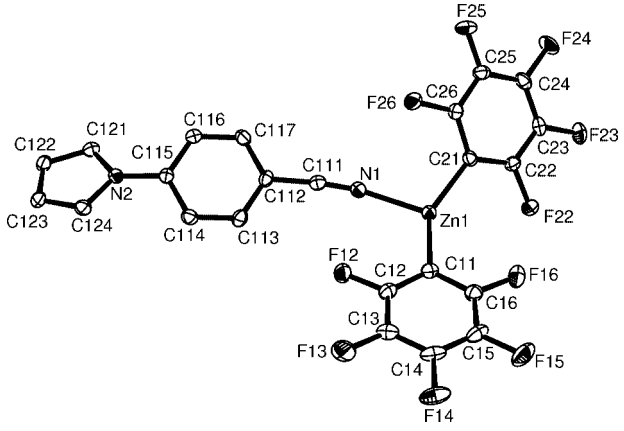


Figure 1. ORTEP representation of the molecular structure of **3** with 30% displacement ellipsoids. The hydrogen atoms have been omitted for clarity. Selected bond lengths [Å] and angles [°]; e.s.d.s are in parentheses: Zn(1)–N(1) 2.094(4), Zn(1)–C(11) 1.983(4), Zn(1)–C(21) 1.981(4), C(111)–N(1) 1.147(6), C(111)–C(112) 1.436(6), C(115)–N(2) 1.411(5); C(21)–Zn(1)–C(11) 140.1(2), C(21)–Zn(1)–N(1) 106.4(2), C(11)–Zn(1)–N(1) 108.2(2), C(111)–N(1)–Zn(1) 165.9(4), C(112)–C(111)–N(1) 174.7(5).

Complex **3** is best described as trigonal-planar, the sum of the angles about the Zn atom is 354.6° and the Zn atom is only 0.258(3) Å removed from the plane defined by C(11), C(21), and N(1). The greater steric requirement of the Zn–$C_6F_5$ groups explains the somewhat larger C–Zn–C vs. C–Zn–N angles. Scheme 2 shows the only other structurally characterised neutral nitrogen-ligated trigonal-planar zinc complexes we are aware of and in each case the neutral nitrogen donor is part of a bidentate ligand. The Zn–N distances for the neutral $sp^2$ benzimidazole and imine donors were 2.067(4), 2.089(2) 1.9805(23), and 1.962(2) Å for **I**, **II**, **III**, and **IV**, respectively. Some of these are somewhat shorter than the 2.094(4) Å found for **3**.[7,8] The average Zn–C bond length [1.982(1) Å, for **3**] is 0.03 Å less than that in $[Zn(C_6F_5)_3]^-$, which presumably reflects the combination of reduced steric congestion and electrostatic repulsion.[9] The dihedral angle between the aromatic planes in the coordinated nitrile ligand in **3** is 23.2(2)°.

The zinc center of the bis(nitrile) adduct **4** has an asymmetrically distorted tetrahedral coordination sphere. The 123.55(6)° C(11)–Zn–C(21) angle and the Zn–C(21) and Zn–C(11) bond lengths at 2.021(2) and 2.029(2) Å, respectively, lie well within the range observed for four-coordinate amine adducts of $Zn(C_6F_5)_2$. The average dative Zn–N bonding distance of 2.09 Å is similar to those observed for $(RR'R''N)_2Zn(C_6F_5)_2$ (2.09–2.16 Å),[11] and only slightly longer than those found in $(MeCN)_2ZnCl_2$ (2.05 Å) and $(MeCN)_2ZnI_2$ (2.04 Å).[16,17] We ascribe the differences between the Zn–N distances and the dihedral angles between the aromatic rings in the ligand bonded through N(11) [2.0660(14) Å and 6.22(7)°] compared to that containing N(21) [2.1206(15) Å and 26.71(7)°] to subtle crystal packing effects. There are no other significant structural differences between the two ligands. The N(11)–Zn–N(21) angle [95.75(6)°] is somewhat smaller than those observed in the $(RR'R''N)_2Zn(C_6F_5)_2$ series, doubtless as a consequence of the modest cone angle of the nitrile ligand, and is comparable to the N–Zn–N angles in $(MeCN)_2ZnCl_2$ and $(MeCN)_2ZnI_2$.[18] There is no evidence for the sort of steric congestion that would favour a three-coordinate complex.

Multinuclear NMR investigations of amine adducts of bis(pentafluorophenyl)zinc have previously indicated solution-phase equilibria involving rapid exchange of free and coordinated amine [Equation (1)]. Addition of further equivalents of amine produced a movement in the observed $^1H$ chemical shifts towards the values for the free amine, but very little change to the $^{19}F$ resonances of the Zn–$C_6F_5$ groups, which we interpreted as the equilibrium strongly favouring the four-coordinate complex.[11] This is consistent with simple thermodynamic considerations favouring the four-coordinate adduct in which two dative bonds have been formed. Regardless of the position of the solution equilibrium, the four-coordinate complexes had invariably been observed to crystallize preferentially until the isolation of **3**.

For comparison we conducted a variable-temperature $^1H$ and $^{19}F$ NMR study of complex **4** (an analogous study with complex **3** was not possible because of its poor solubility in toluene). The $^{19}F$ MMR spectrum of a [$D_8$]toluene solution barely changed on cooling from 20 to –60 °C. In contrast,

 © 2006 Wiley-VCH Verlag GmbH & Co. KGaA, Weinheim 

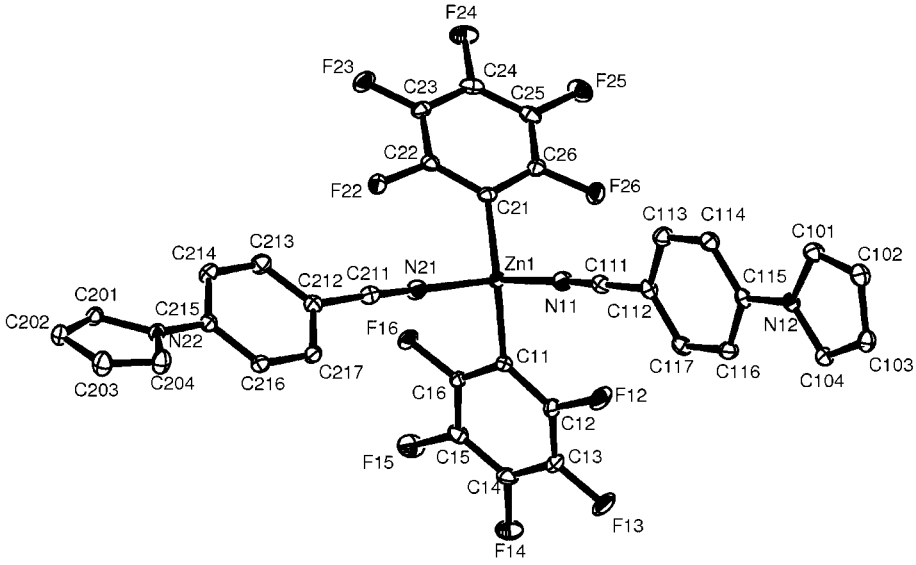


Figure 2. ORTEP representation of the molecular structure of **4** with 30% displacement ellipsoids. The hydrogen atoms have been omitted for clarity. Selected bond lengths [Å] and angles [°]; e.s.d.s are in parentheses: Zn(1)–N(11) 2.0660(14), Zn(1)–N(21) 2.1206(15), Zn(1)–C(21) 2.0209(15), Zn(1)–C(11) 2.0292(16), C(111)–N(11) 1.139(2), C(111)–C(112) 1.437(2), C(115)–N(12) 1.409(2), C(211)–N(21) 1.143(2), C(211)–C(212) 1.437(2), C(215)–N(22) 1.412(2); C(21)–Zn(1)–C(11) 123.55(6), C(21)–Zn(1)–N(11) 114.80(6), C(11)–Zn(1)–N(11) 107.92(6), C(21)–Zn(1)–N(21) 105.58(6), C(11)–Zn(1)–N(21) 104.96(6), N(11)–Zn(1)–N(21) 95.75(6), Zn(1)–N(11)–C(111) 175.60(14), N(11)–C(111)–C(112) 179.4(2), Zn(1)–N(21)–C(211) 174.76(14), N(21)–C(211)–C(212) 176.54(17).

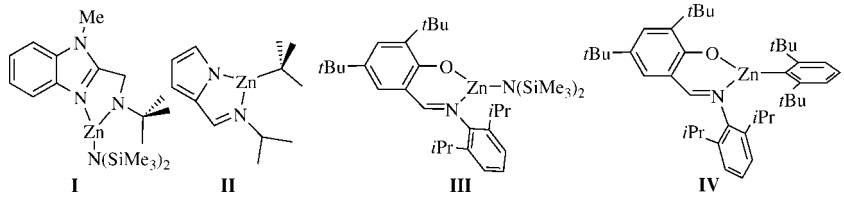


Scheme 2.

the chemical shifts of the $^1$H resonances exhibited significant temperature dependence (Supporting Information). However, there was no sign of decoalescence down to –60 °C and therefore no indication for the position of this equilibrium (1).

$$(C_6F_5)_2ZnL + L \rightleftharpoons (C_6F_5)_2ZnL_2 \quad (1)$$

Analysis of the crystal packing for complex **3** suggests a possible explanation for its preferential crystallisation. In the solid state, molecules of **3** are closely paired about centres of symmetry (Figure 3), in such a fashion that the *p*-$C_4H_4N$–$C_6H_4CN$ ligand of one molecule runs parallel and in the opposite direction to that of the associated molecule. As well as counter-aligning the two ligand dipoles, this arrangement also leads to an offset homoaryl interaction between the phenyl rings. The centroid···centroid distance is 3.71 Å and the centroid–plane separation is 3.37 Å. The supramolecular motif in which hydroaromatics form offset pairs or stacks has been well documented.[19,20] Nevertheless, we believe that two short zinc–pyrrole ring contacts are most significant in directing this intermolecular pairing. The Zn–C(122′) distance is 2.73 Å, which is well within the sum of the van der Waals radii (ca. 3.1 Å), while the distances to C(121′) and C(123′) are in excess of 3 Å. The Zn···π interaction in **3** is evidently weaker than those reported for $(C_6F_4\text{-}2\text{-}C_6F_5)_2Zn$·(toluene) in which there is a close [2.524(3) Å] contact to one arene carbon atom, and for **2** in which two contacts of 2.784(2) and 2.685(2) Å were found.[14] It is, however, strikingly similar to the Zn···π interaction observed in the solid-state structure of **II**, which also forms an intermolecular dimer with a 2.715(3) Å contact between the zinc atom and the carbon atom in the 3-position of the pyrrolyl ring.[7c]

We propose that this intermolecular association yields a species which is significantly less soluble in dichloromethane than complex **4**, and crystallizes out, thereby driving the equilibrium to the "three-coordinate" complex. In 1,2-difluorobenzene solution presumably either the formation of the intermolecular dimer is inhibited or perhaps more likely it is no longer significantly less soluble than the four-coordinate adduct **4**.

In summary, during the course of a structural survey of bis(nitrile) adducts of bis(pentafluorophenyl)zinc, an unusual and surprising example of a three-coordinate complex, (*p*-$C_4H_4N$–$C_6H_4CN$)$Zn(C_6F_5)_2$, was isolated from dichloromethane solution and structurally characterised.

 © 2006 Wiley-VCH Verlag GmbH & Co. KGaA, Weinheim 

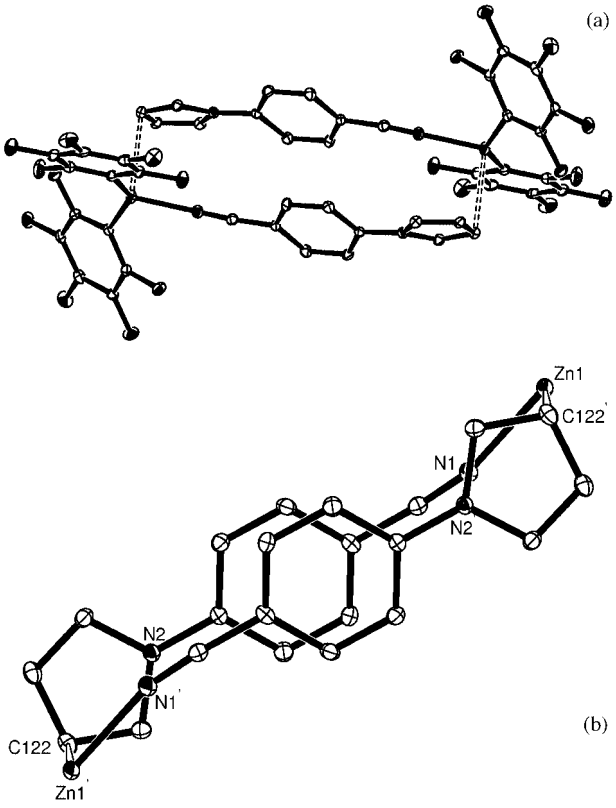


Figure 3. ORTEP representations of (a) the intermolecular dimer of **3** and (b) the alignment of the two interacting fragments projected on to the plane of the $C_6$ ring (the displacement ellipsoids are at 30% probability and the hydrogen atoms have been omitted for clarity).

The driving force for its crystallization is thought to be intermolecular dimerisation predominantly through Zn···π interactions.

## Experimental Section

**General:** All experimental procedures were conducted using standard Schlenk techniques under anhydrous and anaerobic conditions. [21] The toluene adduct of bis(pentafluorophenyl)zinc was prepared according to a literature procedure.[13] 4-(Pyrrol-1-yl)benzonitrile was prepared from 4-aminobenzonitrile and 2,5-dimethoxytetrahydrofuran in refluxing acetic acid according to a modified literature procedure.[22] $^1$H and $^{19}$F NMR chemical shifts are referenced to the residual solvents and $CFCl_3$ respectively.

**(*p*-$C_4H_4N$–$C_6H_4CN$)Zn($C_6F_5$)$_2$ (3):** A solution of ($MeC_6H_5$)-Zn($C_6F_5$)$_2$ (0.44 g, 0.9 mmol) in toluene (10 mL) was treated with *p*-$C_4H_4N$–$C_6H_4CN$ (0.3 g, 1.8 mmol). The reaction mixture was stirred for 30 min before being filtered to separate a small amount of solid material. The volatiles were removed under reduced pressure and the residue was purified by crystallisation from a mixture of dichloromethane and light petroleum at –28 °C to afford colourless crystals of **3** (0.30 g, 0.52 mmol, 58%). Crystals suitable for single-crystal X-ray diffraction required a further recrystallization step. $C_{23}H_8F_{10}N_2Zn$ (567.69): calcd. C 48.66, H 1.42, N 4.93; found C 47.92, H 1.24, N 5.30. $^1$H NMR (300 MHz, $CD_2Cl_2$): $\delta$ = 7.76 (d, $^3J_{H\text{-}H}$ = 8.1 Hz, 2 H, Ar), 7.54 (d, $^3J_{H\text{-}H}$ = 8.7 Hz, 2 H, Ar), 7.19 (t, $^3J_{H\text{-}H}$ = 2.1 Hz, 2 H, Pyr), 6.41 (t, $^3J_{H\text{-}H}$ = 2.1 Hz, 2 H, Pyr) ppm. $^{19}$F NMR (282 MHz, $CD_2Cl_2$): $\delta$ = –162.79 to –162.81 (m, 4 F, *o*-*F*), –157.06 (t, $^3J_{F\text{-}F}$ = 19.8 Hz, 2 F, *p*-*F*), –118.99 to –118.78 (m, 4 F, *m*-*F*) ppm.

**(*p*-$C_4H_4N$–$C_6H_4CN$)$_2$Zn($C_6F_5$)$_2$ (4):** Compound **4** was prepared according to precisely the same experimental method prior to crystallization as compound **3**. The crude solid was crystallised from a mixture of 1,2-difluorobenzene and light petroleum at +2 °C affording colourless crystals of **4** (0.65 g, 0.88 mmol, 98%) suitable for X-ray analysis. $C_{34}H_{16}F_{10}N_4Zn$ (735.89): calcd. C 55.49, H 2.19 N 7.61; found C 54.94, H 2.14, N 7.91. $^1$H NMR (300 MHz, $CDCl_3$): $\delta$ = 6.41 (t, $^3J_{H\text{-}H}$ = 2.1 Hz, 2 H) 7.19 (t, $^3J_{H\text{-}H}$ = 2.1 Hz, 2 H), 7.56 (d, $^3J_{H\text{-}H}$ = 8.7 Hz, 2 H), 7.82 (d, $^3J_{H\text{-}H}$ = 8.7 Hz, 2 H) ppm. $^{19}$F NMR (282 MHz, $CDCl_3$): $\delta$ = –163.6 to –163.4 (m, 4 F, *o*-*F*), –158.7 (t, $^3J_{F\text{-}F}$ = 17 Hz, 2 F, *p*-*F*), –119.0 (d, $^3J_{F\text{-}F}$ = 18 Hz, 4 F, *m*-*F*) ppm.

**X-ray Analyses:** Intensity data for crystals of **3** and **4** were collected with an Oxford Diffraction Xcalibur-3 CCD diffractometer with Mo-$K_\alpha$ radiation ($\lambda$ = 0.71073 Å) and graphite monochromator. Data were processed using the CrysAlis-CCD and -RED programs.[23] The structures were determined by direct methods in SHELXS and refined using full-matrix least squares with SHELXL.[24] The non-hydrogen atoms were refined with anisotropic thermal parameters. Hydrogen atoms were included in idealised positions and their $U_{iso}$ values were set to ride on the $U_{eq}$ values of the parent carbon atoms. Scattering factors for neutral atoms were taken from ref.[25] The analysis process was run through WinGX.[26] CCDC-615024 (**3**) and -615025 (**4**) contain the supplementary crystallographic data. These data can be obtained free of charge from The Cambridge Crystallographic Data Centre via www.ccdc.cam.ac.uk/data_request/cif.

**Crystal Structure and Refinement Data for 3:** $C_{23}H_8F_{10}N_2Zn$, $F_W$ = 567.7 g·mol$^{-1}$; monoclinic, $P2_1/c$, $a$ = 6.8993(3), $b$ = 20.4167(8), $c$ = 14.2444(16) Å, $\beta$ = 93.691(6)°, $V$ = 2002.3(3) Å$^3$, $Z$ = 4, $T$ = 140(1) K, $\rho_{calcd.}$ = 1.883 Mg/m$^3$, $\mu$(Mo-$K_\alpha$) = 1.335 mm$^{-1}$, $F$(000) = 1120; colourless prism 0.35 × 0.30 × 0.15 mm. The total number of reflections, recorded to $\theta_{max}$ = 27.5°, was 25382, of which 4550 were unique ($R_{int}$ = 0.041); 3803 were "observed" with $I > 2\sigma_I$. Final $R$ factors: $wR_2$ = 0.132 and $R_1$ = 0.066 for all 4550 reflections weighted, $w = [\sigma^2(F_o^2) + 11.38\ P]^{-1}$ where $P = (F_o^2 + 2F_c^2)/3$; for the "observed" data only, $R_1$ = 0.055. Largest residual electron density 1.69 e·Å$^{-3}$, located close to C(123).

**Crystal Structure and Refinement Data for 4:** $C_{34}H_{16}F_{10}N_4Zn$, $F_W$ = 735.9 g·mol$^{-1}$; triclinic, $P\bar{1}$, $a$ = 8.0378(5), $b$ = 14.0455(7), $c$ = 14.5510(9) Å, $\alpha$ = 114.357(6), $\beta$ = 91.807(5), $\gamma$ = 97.603(5)°, $V$ = 1476.60(15) Å$^3$, $Z$ = 2, $T$ = 140(1) K, $\rho_{calcd.}$ = 1.655 Mg/m$^3$, $\mu$(Mo-$K_\alpha$) = 0.928 mm$^{-1}$, $F$(000) = 736; colourless prism 0.59 × 0.33 × 0.30 mm. The total number of reflections, recorded to $\theta_{max}$ = 25°, was 16139, of which 5174 were unique ($R_{int}$ = 0.022); 4726 were "observed" with $I > 2\sigma_I$. Final $R$ factors: $wR_2$ = 0.063 and $R_1$ = 0.026 for all 5174 reflections weighted, $w = [\sigma^2(F_o^2) + (0.0338P)^2 + 0.589P]^{-1}$ where $P = (F_o^2 + 2F_c^2)/3$; for the "observed" data only, $R_1$ = 0.023. Largest residual electron density 0.36 e·Å$^{-3}$, located close to Zn(1).

**Supporting Information** (see footnote on the first page of this article): Figure showing the temperature dependence of the $^1$H NMR chemical shifts of a [$D_8$]toluene solution of complex **4**.

## Acknowledgments

E. M. wishes to thank UEA for a PhD scholarship and Oxford Diffraction Ltd. for a CASE award. We are grateful for support from the Engineering and Physical Sciences Research Council.

 © 2006 Wiley-VCH Verlag GmbH & Co. KGaA, Weinheim 

[1] S. J. Archibald, *Comprehensive Coordination Chemistry II*, Elsevier-Pergamon, Oxford, **2004**, vol. 6, p. 1148.
[2] a) O. R. Evans, W. Lin, *Acc. Chem. Res.* **2002**, *35*, 511; b) O. Maury, H. Le Bozec, *Acc. Chem. Res.* **2005**, *38*, 691.
[3] M. Eddaoudi, J. Kim, N. Rosi, D. Vodak, J. Wachter, M. O'Keeffe, O. M. Yaghi, *Science* **2002**, *295*, 469.
[4] A. Erxleben, *Coord. Chem. Rev.* **2003**, *246*, 203.
[5] M. Cheng, E. B. Lobkovsky, G. W. Coates, *J. Am. Chem. Soc.* **1998**, *120*, 11018.
[6] B. M. Chamberlain, M. Cheng, D. R. Moore, T. M. Ovitt, E. B. Lobkovsky, G. W. Coates, *J. Am. Chem. Soc.* **2001**, *123*, 3229.
[7] a) M. S. Chinn, J. Chen, *Inorg. Chem.* **1995**, *34*, 6080; b) M. H. Chisholm, J. C. Gallucci, H. Zhen, *Inorg. Chem.* **2001**, *40*, 5051; c) J. Lewiński, M. Dranka, I. Kraszewska, W. Sliwiński, I. Justyniak, *Chem. Commun.* **2005**, 4935.
[8] For an oxygen-ligated three coordinate dialkylzinc compound, see: H.-J. Gais, G. Bülow, G. Ranbe, *J. Am. Chem. Soc.* **1993**, *115*, 7215.
[9] S. Garratt, A. Guerrero, D. L. Hughes, M. Bochmann, *Angew. Chem. Int. Ed.* **2004**, *43*, 2166.
[10] a) M. Weidenbruch, M. Herrndorf, A. Schäfer, S. Pohl, W. Saak, *J. Organomet. Chem.* **1989**, *361*, 139; b) V. W. Day, D. H. Campbell, C. J. Michejd, *J. Chem. Soc. Chem. Commun.* **1975**, 118.
[11] A. J. Mountford, S. J. Lan caster, S. J. Coles, P. N. Horton, D. L. Hughes, M. B. Hursthouse, M. E. Light, *Organometallics* **2006**, *25*, 3837.
[12] Y. Sun, W. E. Piers, M. Parvez, *Can. J. Chem.* **1998**, *76*, 513.
[13] D. A. Walker, T. J. Woodman, D. L. Hughes, M. Bochmann, *Organometallics* **2001**, *20*, 3772.
[14] A. Guerrero, E. Martin, D. L. Hughes, N. Kaltsoyannis, M. Bochmann, *Organometallics* **2006**, *25*, 3311.
[15] E. Martin, C. Spendley, A. Mountford, D. L. Hughes, S. J. Coles, P. N. Horton and M. B. Hursthouse, manuscript in preparation.
[16] V. K. Bel'sky, N. R. Streltsova, B. M. Bulychev, P. A. Storozhenko, L. V. Ivankina, A. I. Gorbuvnov, *Inorg. Chim. Acta* **1989**, *164*, 211.
[17] F. Raubacher, F. Weller, *Z. Kristallogr.* **1996**, *211*, 576.
[18] The intermolecular interactions in molecule **4** and a series of pyridine- and benzonitrile-derived adducts will be discussed in ref.[15]
[19] S. Lorenzo, G. R. Lewis, I. Dance, *New J. Chem.* **2000**, *24*, 295.
[20] C. A. Hunter, J. K. M. Sanders, *J. Am. Chem. Soc.* **1990**, *112*, 5525.
[21] For further details on experimental methodology, see ref.[11]
[22] I. Sanchez, M. D. Pujol, *Tetrahedron* **1999**, *55*, 5593.
[23] Programs CrysAlis-CCD and -RED, Oxford Diffraction Ltd., Abingdon, UK, **2005**.
[24] G. M. Sheldrick, *SHELX-97, Programs for crystal structure determination (SHELXS) and refinement (SHELXL)*, University of Göttingen, Germany, **1997**.
[25] *International Tables for X-ray Crystallography*, Kluwer Academic Publishers, Dordrecht, **1992**, vol. C, p. 500, 219 and 193.
[26] L. J. Farrugia, *J. Appl. Crystallogr.* **1999**, *32*, 837.

Received: July 18, 2006
Published Online: September 12, 2006

 © 2006 Wiley-VCH Verlag GmbH & Co. KGaA, Weinheim 

DOI: 10.1002/ejic.200600336

# Redox Behavior of a Manganese Porphyrin Complexed with Per-*O*-methylated β-Cyclodextrin in Aqueous Solution

**Koji Kano,*[a] Hiroaki Kitagishi,[a] Yumiko Sone,[a] Nami Nakazawa,[a] and Masahito Kodera[a]**

**Keywords:** Macrocyclic ligands / Manganese / Redox chemistry / Cyclodextrins / Electrochemistry

[5,10,15,20-Tetrakis(*p*-sulfonatophenyl)porphyrinato]-manganese(III) in its diaqua form $[(H_2O)_2Mn^{III}(tpps)]$ forms a complex with heptakis(2,3,6-tri-*O*-methyl)-β-cyclodextrin (TMe-β-CD) to afford a stable 2:1 host–guest inclusion complex whose binding constants, $K_1$ and $K_2$, in phosphate buffer at pH 7.0 and 25 °C are $8.1 \times 10^5$ and $2.8 \times 10^4$ $M^{-1}$, respectively. $[(H_2O)_2Mn^{III}(tpps)]$ dissociates into the monohydroxo complex $[(H_2O)(OH^-)Mn^{III}(tpps)]$ above pH 11 ($pK_a$ = 11.9) when incorporated into the TMe-β-CD cavities. The $pK_a$ value of $[(H_2O)_2Mn^{III}(tpps)]$ in the absence of TMe-β-CD is 12.4, which suggests that the monohydroxo form without a net charge on the central porphyrin is stabilized by complexation with TMe-β-CD. In an aqueous alkaline solution of TMe-β-CD, $[(H_2O)(OH^-)Mn^{III}(tpps)]$ is autoreduced to $[(H_2O)Mn^{II}(tpps)]$ by an electron transfer from bound $OH^-$ to $Mn^{III}$. TMe-β-CD stabilizes the low-valent $[(H_2O)Mn^{II}(tpps)]$. For example, the rate of autoxidation of $[(H_2O)Mn^{II}(tpps)]$ in the presence of TMe-β-CD at pH 7.0 was reduced by a factor of $2.8 \times 10^4$ as compared with the rate without TMe-β-CD. The redox potentials ($E_{1/2}$) of [Mn(tpps)] were measured by spectroelectrochemical methods. The $E_{1/2}$ values in phosphate buffer at pH 7.0 in the absence and the presence of TMe-β-CD are –211 and –108 mV (vs. NHE), respectively. TMe-β-CD causes a positive shift of $E_{1/2}$, which indicates the stabilization of low-valent $[(H_2O)Mn^{II}(tpps)]$ by TMe-β-CD against autoxidation. These electrochemical data, as well as the thermodynamic ones, give the $K_1K_2$ values for complexation of $[(H_2O)Mn^{II}(tpps)]$ with TMe-β-CD to be $1.2 \times 10^{12}$ $M^{-2}$, while that for $[(H_2O)_2Mn^{III}(tpps)]$ is $2.3 \times 10^{10}$ $M^{-2}$.

(© Wiley-VCH Verlag GmbH & Co. KGaA, 69451 Weinheim, Germany, 2006)

## Introduction

Although manganese porphyrins (MnPor) are not known to be prosthetic groups of metalloproteins, they have widely been utilized as functional models of metalloproteins such as the manganese-stabilizing protein in photosynthesis II,[1] cytochrome P450,[2] superoxide dismutases,[3] catalases,[4] and peroxidases.[5] MnPors have many advantages when it comes to mimicking the functions of metalloproteins. For example, they have poor ability to form μ-oxo dimers[6] and to bind inorganic anions[7] and have a high ability to resist degradation of their ligands and to take various high-valent metal states.[8] The modeling of cytochrome P450 function using MnPor is a typical example. The formation of an $Fe^{IV}$=O cation radical, the so-called "compound I", has not been proved in artificial systems, although such a high-valent iron-oxo complex has been assumed as a dominant intermediate in oxygenation catalyzed by cytochrome P450.[9] Meanwhile, a high-valent $Mn^{V}$=O porphyrin complex has been verified spectroscopically when a porphyrin ligand has positively charged pyridinium substituents at the *meso* positions of the porphyrin.[10] The $Mn^{V}$=O complex is a reactive intermediate in the epoxidation of alkenes by *m*-CPBA. $Mn^{V}$=O corrole with a Mn out-of-plane orientation is more stable than the corresponding porphyrin complex with a Mn in-plane orientation.[8d,11] MnPors have mainly been utilized as substitutes of heme and/or hemin.

Since the prominent function of a metalloprotein is apparently dominated by its prosthetic group, the main interest of chemists tends to be focused on the chemical behavior of this group. In general, however, a protein surrounding the prosthetic group plays an essential role in its biological activity. Therefore, construction of a model system involving functions of both the protein and prosthetic group is a very important subject in biomimetic chemistry.[12] There are various kinds of hemoproteins in nature. In spite of a common prosthetic group (heme), each hemoprotein shows different functions. A typical example of the inherent characteristics is the oxidation-reduction potentials of hemoproteins (see Supporting Information).[13] Although myoglobin (Mb), hemoglobin (Hb), and peroxidases have a common

[a] Department of Molecular Science and Technology, Faculty of Engineering, Doshisha University,
Kyotanabe, Kyoto 610-0321, Japan
Fax: +81-774-65-6845
E-mail: kkano@mail.doshisha.ac.jp

Supporting information for this article is available on the WWW under http://www.eurjic.org or from the author.

 © 2006 Wiley-VCH Verlag GmbH & Co. KGaA, Weinheim 

core structure composed of an iron center and an imidazole moiety as an axial monoligand, their redox potentials differ. The redox potentials of Mb (+50 mV vs. NHE) and Hb (+170 mV) are positive, meaning low reactivity in autoxidation of heme to hemin, with these proteins having particular affinity for dioxygen binding. On the other hand, cytochrome c peroxidase has a redox potential of –194 mV. The redox potential of cytochrome P450cam with cysteine as an axial ligand is –300 mV. Hemoproteins with negative redox potentials tend to form high-valent iron complexes as active intermediates in their enzymatic reactions. The protein surrounding an iron center regulates the redox potential and hence the functions of the hemoprotein.

In the present study, we focused on the effects of incorporation of [5,10,15,20-tetrakis(*p*-sulfonatophenyl)porphyrinato]manganese [Mn(tpps)] by heptakis(2,3,6-tri-*O*-methyl)-β-cyclodextrin (TMe-β-CD) on the redox behavior of [Mn(tpps)] in aqueous solution. We,[14] as well as Tonellato et al.,[15] have reported the extremely strong ability of TMe-β-CD to include water-soluble porphyrins to afford *trans*-type 2:1 host–guest complexes. Previously, we interpreted the novel ability of TMe-β-CD to include the water-soluble porphyrins in terms of induced-fit-type inclusion by TMe-β-CD, whose cavity is transformable because of the absence of intramolecular hydrogen bonding.[14d] Recently, we also found metMb-mimetic functions of a 2:1 complex of TMe-β-CD and [$Fe^{III}$(tpps)], which shows selective binding of inorganic anions in aqueous solution.[16] In advance of our study, Lawrence and co-workers reported their pioneering work on a hemoprotein mimic composed of a cationic ferric porphyrin and heptakis(2,6-di-*O*-methyl)-β-cyclodextrin (2,6-DMe-β-CD).[17] These results led us to prepare a Mb model that works in aqueous solution.[18] Since the 1970s, many Mb models have been proposed.[19] Typically, these models have bulky substituents at the *meso* positions of tetraphenylporphyrin to prevent μ-oxo dimer formation. Although those model compounds whose ferrous center is coordinated by a base such as imidazole or pyridine bind dioxygen in absolute organic solvents, no dioxygen adducts are formed if the system contains a trace amount of water. Recently, we succeeded in preparing a Mb model (hemoCD) in aqueous solution that is composed of an *O*-methylated β-cyclodextrin dimer containing a pyridine linker and [$Fe^{II}$(tpps)].[18] HemoCD binds dioxygen in aqueous solution ($P_{1/2}^{O_2}$ = 16.9 Torr and $t_{1/2}$ = 30 h in pH 7.0 phosphate buffer at 25 °C). In this model system, tight encapsulation of [$Fe^{II}$(tpps)] by two *O*-methylated β-cyclodextrin moieties is essential to stabilize [$Fe^{II}$(tpps)] and to bind dioxygen. As an extension of this work, we decided to study the redox behavior of a manganese porphyrin complexed with TMe-β-CD. In the present study, we tried to obtain information about the effects of TMe-β-CD on the stabilization of the low-valent manganese complex [$(H_2O)Mn^{II}$(tpps)]. In order to prepare a good functional model of Mb and/or Hb, the system should be designed to stabilize $Fe^{II}$Por, which is labile in a homogeneous aerobic solution, by using an artificial protein such as cyclodextrin. Control of the redox potential of a metalloporphyrin by an artificial protein is essential to develop a new artificial and functional metalloprotein. The present study might contribute to these subjects.

## Results and Discussion

### Complexation of [$Mn^{II}$(tpps)], [$Mn^{III}$(tpps)], and [$Mn^{IV}$(tpps)] with TMe-β-CD

At first, complexation of [$Mn^{III}$(tpps)] with TMe-β-CD was studied by means of UV/Vis spectroscopy and isothermal titration calorimetry (ITC). Figure 1 shows the UV/Vis spectral changes of [$(H_2O)_2Mn^{III}$(tpps)] in 0.05 M phosphate buffer at pH 7.0 upon addition of TMe-β-CD. The Soret band at 466 nm is shifted to shorter wavelength and increases in intensity with increasing concentration of TMe-β-CD. Three titration curves obtained by monitoring the absorbances at three different wavelengths were fitted simultaneously by a set of binding constants ($K_1$ and $K_2$) using a nonlinear least-squares method (Figure 1, b).[14b]

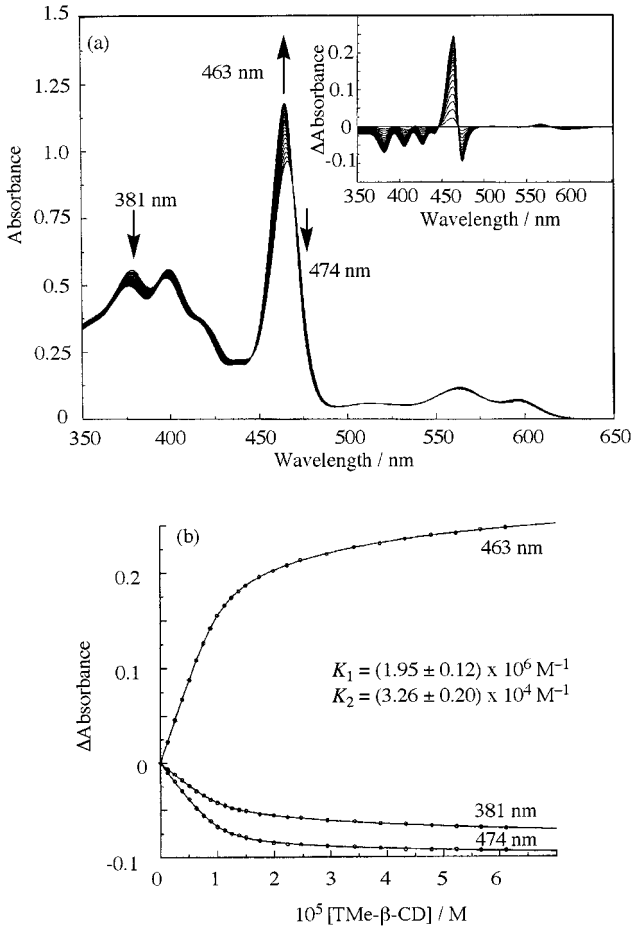


Figure 1. UV/Vis spectral changes of [$(H_2O)_2Mn^{III}$(tpps)] ($1.0 \times 10^{-5}$ M) in 0.05 M phosphate buffer at pH 7.0 upon addition of TMe-β-CD at 25 °C (a) and the plots of the changes in absorbances of [$(H_2O)_2Mn^{III}$(tpps)] vs. [TMe-β-CD] (b). The solid lines are the best fit of the data to an equation for the simultaneous 1:1 and 1:2 complexation.

 © 2006 Wiley-VCH Verlag GmbH & Co. KGaA, Weinheim 

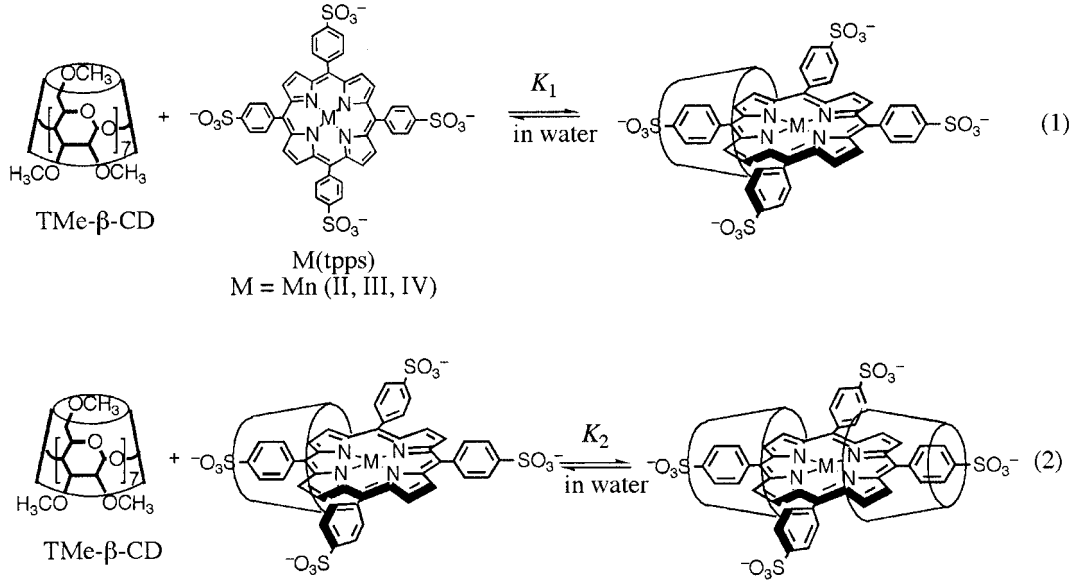


Figure 2. Complexation of MnPor with TMe-β-CD in aqueous solution.

Table 1. Binding constants and thermodynamic parameters for complexation of M(tpps) (M = $Mn^{II}$, $Mn^{III}$, $Mn^{IV}$ and $Fe^{III}$) in aqueous solution at 25 °C.

| M(tpps) | Method | $10^{-6}\cdot K_1$ [$M^{-1}$] | $10^{-4}\cdot K_2$ [$M^{-1}$] | $\Delta H^0_1$ [kJ mol$^{-1}$] | $\Delta S^0_1$ [mol$^{-1}$ K$^{-1}$] | $\Delta H^0_2$ [kJ mol$^{-1}$] | $\Delta S^0_2$ [J mol$^{-1}$ K$^{-1}$] | Ref. |
|---|---|---|---|---|---|---|---|---|
| $Mn^{III}$ | UV[a] | 2.0 ± 0.1 | 3.3 ± 0.2 | – | – | – | – | this work |
| $Mn^{III}$ | ITC[a] | 0.81 ± 0.13 | 2.8 ± 0.2 | –49 ± 1 | –50 ± 3 | –22 ± 1 | 11 ± 2 | this work |
| $Fe^{III}$ | ITC[b] | 1.3 ± 0.1 | 6.3 ± 0.4 | –49 ± 1 | –47 ± 1 | –12 ± 1 | 53 ± 1 | [16] |
| $Mn^{II}$ | UV, ITC[c] | too large | too large | – | – | – | – | this work |
| $Mn^{IV}$ | ITC[d] | 0.34 ± 0.11 | 7.5 ± 1.3 | –25 ± 1 | 21 ± 6 | –6 ± 1 | 73 ± 4 | this work |

[a] In 0.05 M phosphate buffer at pH 7.0. [b] In 0.1 M succinic acid buffer at pH 4.0. [c] In 0.05 M phosphate buffer at pH 7.0. The measurement was carried out in the presence of excess $Na_2S_2O_4$. [d] In 1.0 M aqueous NaOH solution. [($OH^-$)$Mn^{IV}$(tpps)] was prepared by oxidation of [$(H_2O)_2Mn^{III}$(tpps)] with three equivalents of $K_3[Fe(CN)_6]$.

The titration curves were well-fitted by a theoretical equation for 2:1 host–guest complexation. The $K_1$ and $K_2$ values (Figure 2) were determined to be $(2.0 \pm 0.1) \times 10^6$ and $(3.3 \pm 0.2) \times 10^4$ $M^{-1}$, respectively (Table 1).

We decided to check the accuracy of the binding constants by a different method (ITC). ITC simultaneously provides the thermodynamic parameters for complexation of [$(H_2O)_2Mn^{III}$(tpps)] with TMe-β-CD. The isothermal calorimetric titration curve obtained by the addition of TMe-β-CD to the [$(H_2O)_2Mn^{III}$(tpps)] solution at pH 7.0 is shown in Figure 3. The titration curve was analyzed by an equation for 2:1 host–guest complex formation; the results are summarized in Table 1. The $K_1$ and $K_2$ values from ITC are somewhat smaller than those from UV/Vis spectroscopy; the reasons for this are not clear. However, both methods clearly indicate that $K_1$ is larger than $K_2$. Since tpps is a dianionic ligand, a positive charge remains at the center of [$(H_2O)_2Mn^{III}$(tpps)]. Capping of such a polar metal center by two hydrophobic cyclodextrin cavities seems to be inadequate compared with the 1:1 complexation where half of the metalloporphyrin is exposed to the bulk aqueous phase. This might be the reason why $K_1$ is larger than $K_2$. Such an assumption is supported by the thermodynamic parameters for complexation. Both enthalpy ($\Delta H_1{}^0$) and entropy changes ($\Delta S_1{}^0$) for the 1:1 complexation are negative and large, thereby suggesting the contribution of a van der Waals interaction to the 1:1 complex formation as a main binding force. The negative and large value of $\Delta S_1{}^0$ is ascribed to the restriction of free rotation of the sulfonatophenyl groups at the 10- and 20-positions of the porphyrin due to inclusion of a sulfonatophenyl group at the 5-position. The complexation of the 1:1 complex with TMe-β-CD to form a 2:1 complex is accompanied by a positive $\Delta S_2{}^0$. From this observation we assume that dehydration which is needed for further complexation supports the formation of the 2:1 complex.

As mentioned below, [$Mn^{III}$(tpps)] exists in a diaqua form [$(H_2O)_2Mn^{III}$(tpps)] in aqueous solution at pH 7.0. Under the same conditions, the ferric porphyrin [$Fe^{III}$(tpps)] forms a μ-oxo dimer in the absence of TMe-β-CD. Since the apparent p$K_a$ value for the equilibrium between [$(H_2O)_2Fe^{III}$(tpps)] and the μ-oxo dimer is 6.4,[20] the $K_1$ and $K_2$ values for [$(H_2O)_2Fe^{III}$(tpps)] in aqueous solution below pH 5 seem to be meaningful to compare with those for [$(H_2O)_2Mn^{III}$(tpps)]. The binding constants and the thermodynamic parameters for [$(H_2O)_2Fe^{III}$(tpps)] at pH 4.0 are shown in Table 1.[16] A similar behavior has been observed in the complexation of [$(H_2O)_2Fe^{III}$(tpps)] with

 © 2006 Wiley-VCH Verlag GmbH & Co. KGaA, Weinheim 

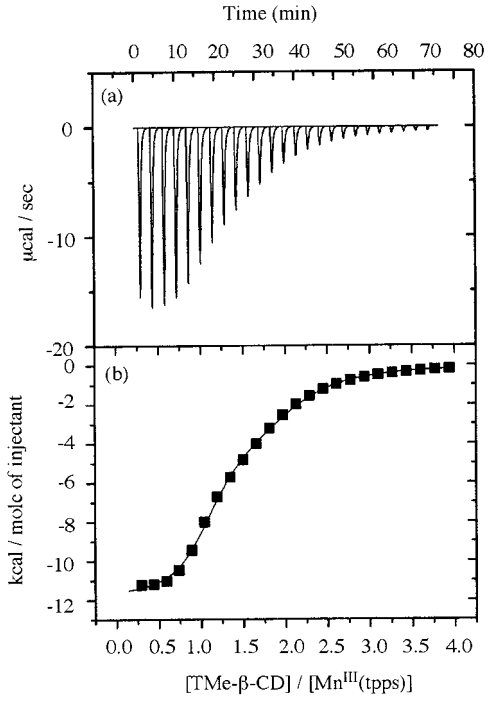


Figure 3. Calorimetric titration of $[(H_2O)_2Mn^{III}(tpps)]$ ($2.28 \times 10^{-4}$) with 25 aliquots (10 μL each) of TMe-β-CD ($4.79 \times 10^{-3}$ M) in 0.05 M phosphate buffer at pH 7.0 and 25 °C. The solid line represents the best fit of the experimental data to the 1:2 Sequential Binding Sites Model in the ORIGIN software.

TMe-β-CD, although the $\Delta S^0$ value for $[(H_2O)_2Fe^{III}(tpps)]$ is much larger than that for $[(H_2O)_2Mn^{III}(tpps)]$.

$[(H_2O)_2Mn^{III}(tpps)]$ is easily reduced to $[(H_2O)Mn^{II}(tpps)]$ by sodium dithionite ($Na_2S_2O_4$). The UV/Vis spectral changes of $[(H_2O)Mn^{II}(tpps)]$ in pH 7.0 phosphate buffer containing an excess amount of $Na_2S_2O_4$ were monitored as a function of the concentration of TMe-β-CD (see Supporting Information). The spectral change was clearly saturated upon addition of two equivalents of TMe-β-CD, thus indicating the formation of an extremely stable 2:1 host–guest complex. Binding constants and thermodynamic parameters for $[(H_2O)Mn^{II}(tpps)]$ could not be determined by either UV/Vis spectroscopy or ITC because of the too-large $K$ values, although the $K_1K_2$ value was estimated (vide infra). Since the net charge at the center of $[(H_2O)Mn^{II}(tpps)]$ is zero, the encapsulation of $[(H_2O)Mn^{II}(tpps)]$ by two TMe-β-CD molecules seems to proceed satisfactorily from the viewpoint of polarity matching between the host and the guest.

$[Mn^{III}(tpps)]$ was oxidized to $[Mn^{IV}(tpps)]$ in 1.0 M aqueous NaOH solution upon addition of $K_3[Fe(CN)_6]$.[21] A strongly basic solution is needed to stabilize the high-valent $Mn^{IV}$ state by coordination of $OH^-$ to $Mn^{IV}$. In the presence of an excess amount of TMe-β-CD, the second-order rate constant ($k_{ox}$) for oxidation of $[(H_2O)(OH^-)Mn^{III}(tpps)]$ to $[(OH^-)_nMn^{IV}(tpps)]$ ($n$ = 1 or 2) was determined to be 50.1 $M^{-1}s^{-1}$ at 25 °C (Figure 4). Harriman et al. have determined the $k_{ox}$ value for the same oxidation in the absence of TMe-β-CD to be $1.08 \times 10^5$ $M^{-1}s^{-1}$.[21] It is clear that encapsulation of $[(H_2O)(OH^-)Mn^{III}(tpps)]$ by two TMe-β-CD molecules markedly depresses the oxidation by the polar ferricyanide ion. In other words, the TMe-β-CD molecules provide a very hydrophobic environment around the center of $[(H_2O)(OH^-)Mn^{III}(tpps)]$ that isolates it from the aqueous bulk phase.

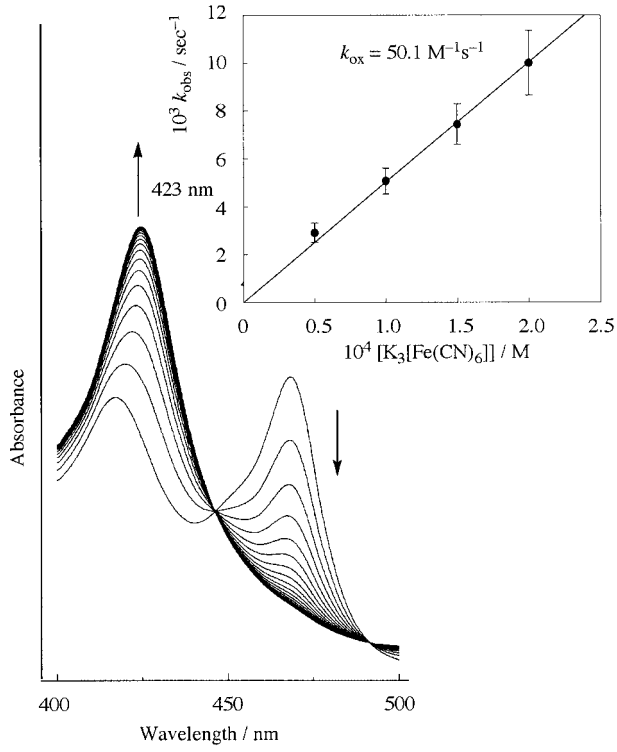


Figure 4. UV/Vis spectral changes of $(H_2O)(OH^-)Mn^{III}(tpps)$ ($1.0 \times 10^{-5}$ M) to $[(OH^-)Mn^{IV}(tpps)]$ in 1.0 M aqueous NaOH solution containing TMe-β-CD ($2.0 \times 10^{-4}$ M) upon addition of $K_3[Fe(CN)_6]$ ($1.0 \times 10^{-4}$ M) at 25 °C and the dependence of the pseudo first-order rate constant ($k_{obs}$) for the oxidation of $(H_2O)(OH^-)Mn^{III}(tpps)$ to $[(OH^-)Mn^{IV}(tpps)]$ on the concentration of $K_3[Fe(CN)_6]$ to determine the second-order rate constant ($k_{ox}$).

The $K_1$ and $K_2$ values for complexation of $[(OH^-)_nMn^{IV}(tpps)]$ with TMe-β-CD were determined in 1.0 M aqueous NaOH solution by ITC (see Supporting Information). The results are shown in Table 1. To the best of our knowledge, the axial ligation of $[Mn^{IV}(tpps)]$ in aqueous NaOH solution has not been clarified. If $[Mn^{IV}(tpps)]$ exists as $[(OH^-)Mn^{IV}(tpps)]$, the net charge at the center of the porphyrin is +1, the same as that of $[(H_2O)_2Mn^{III}(tpps)]$. The $K_1$ and $K_2$ values for $[(OH^-)_nMn^{IV}(tpps)]$ in aqueous NaOH solution are not much different from those of $[(H_2O)_2Mn^{III}(tpps)]$ at pH 7.0. However, the thermodynamic parameters for $[(OH^-)Mn^{IV}(tpps)]$ differ markedly from those for $[(H_2O)_2Mn^{III}(tpps)]$. The entropy change for the 1:1 complexation of $[(OH^-)_nMn^{IV}(tpps)]$ is positive while that of $[(H_2O)_2Mn^{III}(tpps)]$ is negative and large. The entropy change for the second complexation of $[(OH^-)_nMn^{IV}(tpps)]$ is also larger than that of $[(H_2O)_2Mn^{III}(tpps)]$. It is assumed that the high-valent $Mn^{IV}$ porphyrin gathers a larger amount of water molecules to its metal center than

 © 2006 Wiley-VCH Verlag GmbH & Co. KGaA, Weinheim 

the $Mn^{III}$ porphyrin. It is interesting that complexation of high-valent $[(OH^-)_nMn^{IV}(tpps)]$ is entropically favorable due to extended dehydration while it is enthalpically unfavorable due to weak hydrophobic effect. Complexation promoted by extended dehydration is commonly observed in cyclodextrin chemistry.[22] The difference between the thermodynamic parameters of $[(OH^-)_nMn^{IV}(tpps)]$ and $[(H_2O)_2Mn^{III}(tpps)]$ might be ascribed to the difference in the net charges of the manganese porphyrins. In other words, there is a possibility of $[(OH^-)_2Mn^{IV}(tpps)]$ rather than $[(OH^-)Mn^{IV}(tpps)]$. The axial ligation of $[Mn^{IV}(tpps)]$ in aqueous alkaline solution could not be clarified from the present study.

### pH Titration

$[Mn^{III}(tpps)]$ exists as a diaqua form in aqueous solution at neutral pH.[6a] An increase in pH up to 11 did not cause any UV/Vis spectral change for $[(H_2O)_2Mn^{III}(tpps)]$ ($\lambda_{max}$ = 465 nm) in aqueous solution containing TMe-β-CD. However, the absorption spectrum changes markedly above pH 11 (Figure 5) and the pH-titration curve gave a p$K_a$ of 11.9. Since the isosbestic points are observed clearly, there should only be an equilibrium in the pH range between 2.5 and 13.5. The most reasonable process is the acid dissociation of $[(H_2O)_2Mn^{III}(tpps)]$ to $[(H_2O)(OH^-)Mn^{III}(tpps)]$. In the absence of TMe-β-CD, the p$K_a$ value was determined to be 12.4, somewhat lower than that of the $[(H_2O)_2Mn^{III}$-(tpps)]/TMe-β-CD complex. Such a result means that $[(H_2O)(OH^-)Mn^{III}(tpps)]$ is stabilized by complexation with TMe-β-CD. Harriman et al. have reported two p$K_a$ values (8.6 and 11.6) for $[Mn^{III}(tpps)]$ in aqueous solution without cyclodextrin.[6a] However, we could not observe the equilibrium corresponding to p$K_a$ 8.6. It should be noted that a weak absorption band was observed at 433 nm in the higher pH region. The absorption maximum of this band is in good agreement with that of $[(H_2O)Mn^{II}(tpps)]$. This band did not affect the isosbestic points, which suggests only an equilibrium in this system. Such a contradiction might be ascribed to the formation of only a small amount of $[(H_2O)Mn^{II}(tpps)]$.

### Autoreduction of $[Mn^{III}(tpps)]$ in Aqueous Alkaline Solution

Figure 6 shows the absorption spectral changes of $[(H_2O)(OH^-)Mn^{III}(tpps)]$ in 1.0 M aqueous NaOH solution containing TMe-β-CD at 50 °C under a nitrogen atmosphere. The absorbance at 463 nm due to $[(H_2O)(OH^-)$-$Mn^{III}(tpps)]$ gradually decreases and a band with a peak at 434 nm, which is ascribed to $[(H_2O)Mn^{II}(tpps)]$, appears. $[(H_2O)(OH^-)Mn^{III}(tpps)]$ is autoreduced to $[(H_2O)Mn^{II}$-(tpps)] in aqueous alkaline solution under anaerobic conditions. Since such an autoreduction occurs only in aqueous alkaline solution, the $OH^-$ ion must participate in this reduction. Clear isosbestic points indicate the quantitative nature of this reaction. Arasasingham and Bruice have reported that [5,10,15,20-tetrakis(2,4,6-trimethylphenyl)porphyrinato]manganese(III) $[Mn^{III}(tmp)]$ is reduced to $[Mn^{II}$-(tmp)] in $CH_3CN$ containing methanolic tetrabutylammonium hydroxide.[23] Jeon et al. have also studied the autoreduction of [5,10,15,20-tetrakis(2,6-dichlorophenyl)porphyrinato]manganese(III) $[Mn^{III}(tcp)]$ in $CH_3CN$ containing aqueous tetraethyl hydroxide.[24] Both groups reported the formation of five-coordinate $[(L)Mn^{II}Por]$ complexess (L: solvent; $\lambda_{max}$ = 436–437 nm) via $[(L)(OH^-)Mn^{III}Por]$ and/or $[(L)(CH_3O^-)Mn^{III}Por]$. As a next step, ligand exchange of $[(L)Mn^{II}Por]$ to $[(OH^-)Mn^{II}Por]$ ($\lambda_{max}$ = 444–445 nm) proceeds. The former group assumed further conversion of

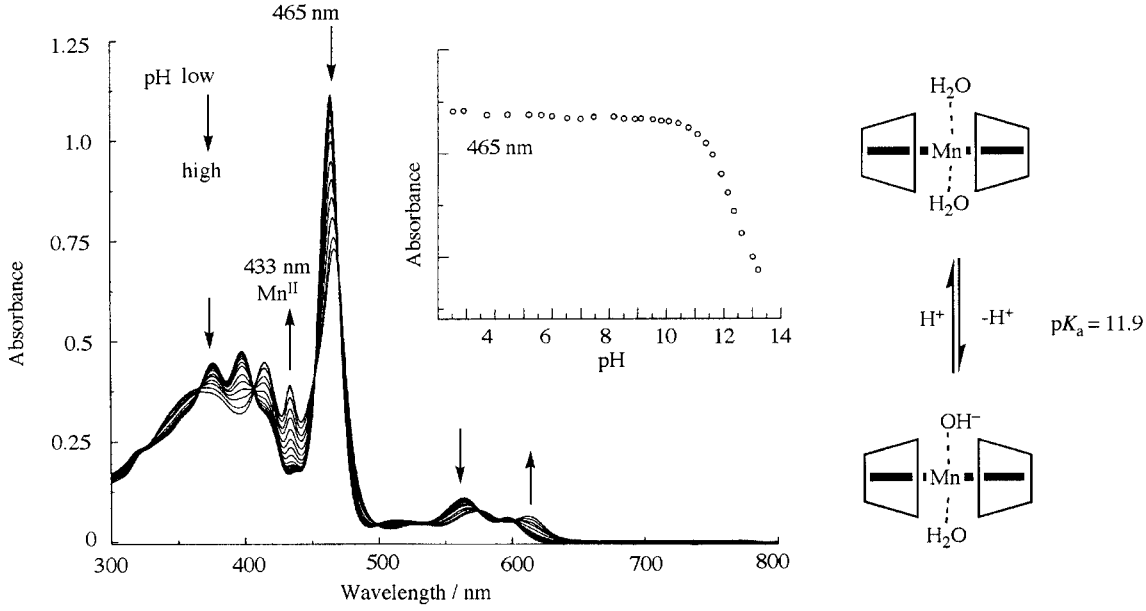


Figure 5. UV/Vis spectral changes of $Mn^{III}(tpps)$ ($1.0\times10^{-5}$ M) in aqueous TMe-β-CD ($1.0\times10^{-3}$ M) solution in the presence of 0.1 M $NaClO_4$ as a function of pH.

 © 2006 Wiley-VCH Verlag GmbH & Co. KGaA, Weinheim 

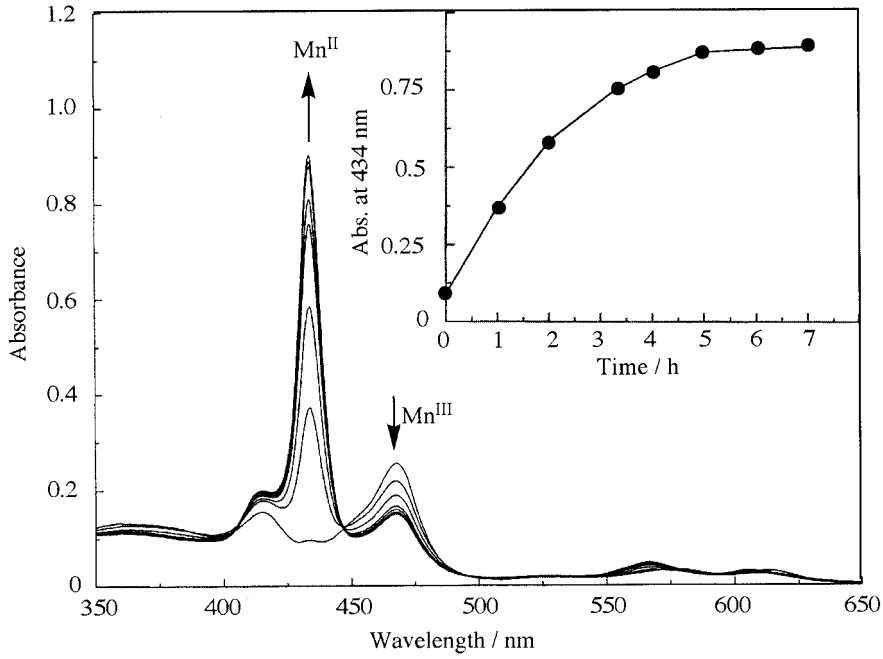


Figure 6. Progressive UV/Vis spectral changes of $[(H_2O)(OH^-)Mn^{III}(tpps)]$ ($5.0\times10^{-6}$ M) to $[(H_2O)Mn^{II}(tpps)]$ in 1.0 M aqueous NaOH solution containing TMe-β-CD ($1.0\times10^{-4}$ M) at 50 °C under $N_2$. Inset: time course in absorbance at 434 nm due to $[(H_2O)Mn^{II}(tpps)]$.

$[(OH^-)Mn^{II}(tmp)]$ to a mixture of $[(OH^-)_2Mn^{III}(tmp)]$, $[(OH^-)(CH_3O^-)Mn^{III}(tmp)]$, and $[(CH_3O^-)_2Mn^{III}(tmp)]$ with absorption maxima at 412 and 448 nm, although the mechanism was not clarified.[23] The present system is simpler than the systems in $CH_3CN$. Only autoreduction of $[(H_2O)(OH^-)Mn^{III}(tpps)]$ to $[(H_2O)Mn^{II}(tpps)]$ occurs in 1.0 M aqueous NaOH solution containing TMe-β-CD at 50 °C. We measured the pH-dependent absorption spectral change of $[(H_2O)Mn^{II}(tpps)]$ complexed with TMe-β-CD and could not find any spectral change in the pH range between 3.0 and 13.5, therefore no equilibrium exists between $[(H_2O)Mn^{II}(tpps)]$ and $[(OH^-)Mn^{II}(tpps)]$ under the present conditions. In the absence of TMe-β-CD, no autoreduction occurred in 1.0 M aqueous NaOH solution. Although we did not study the mechanism of the autoreduction in detail, one-electron transfer from bound $OH^-$ to the $Mn^{III}$ center might occur, as demonstrated by Sawyer and co-workers, who found that the oxidation potentials of $OH^-$ and a phenoxide ion in $CH_3CN$ shift to less positive potentials upon coordination to $[Mn^{III}Por]$.[25] As a preliminary experiment, we measured the ESI mass spectrum (positive mode) of the $CHCl_3$ extract of a reaction mixture obtained by heating a mixture of TMe-β-CD ($1\times10^{-3}$ M) in 1.0 M aqueous NaOH solution containing $[(H_2O)(OH^-)Mn^{III}(tpps)]$ ($5\times10^{-4}$ M) at 70 °C for 16 h. The molecular ion peaks were observed at *m/z* 1438.6, 1452.6, 1468.6, and 1550.6, which correspond to $[(TMe\text{-}β\text{-}CD - OCH_3 + OH + Na)^+$; calcd. 1438.2], $[(TMe\text{-}β\text{-}CD + Na)^+$; calcd. 1452.5], $[(TMe\text{-}β\text{-}CD + K)^+$; calcd. 1468.6], and $[(TMe\text{-}β\text{-}CD + CHCl_3 + H)^+$; calcd. 1550.9], respectively (see Supporting Information). These results strongly suggest that generated $^{\cdot}OH$ radical reacts with TMe-β-CD leading to replacement of an $OCH_3$ group of TMe-β-CD with an OH group.

### Stabilization of Low-Valent $[(H_2O)Mn^{II}(tpps)]$ by TMe-β-CD

As shown in Figure 5, the autoreduction occurs even under aerobic conditions if TMe-β-CD is present in the system. We therefore studied the effects of TMe-β-CD on stabilization of $[(H_2O)Mn^{II}(tpps)]$. Oxidation of $[(H_2O)Mn^{II}(tpps)]$ was carried out by bubbling oxygen through asolution of $[(H_2O)Mn^{II}(tpps)]$, which was prepared by the reaction of $[(H_2O)_2Mn^{III}(tpps)]$ with $Na_2S_2O_4$ in phosphate buffer at pH 7.0. In the absence of TMe-β-CD, $[(H_2O)Mn^{II}(tpps)]$ ($\lambda_{max}$ = 432 nm) was oxidized at once to $[(H_2O)_2Mn^{III}(tpps)]$ ($\lambda_{max}$ = 466 nm) immediately after $S_2O_4^{2-}$ disappeared upon oxidation with $O_2$ (Supporting Information). In the presence of TMe-β-CD, however, the autoxidation of $[(H_2O)Mn^{II}(tpps)]$ to $[(H_2O)_2Mn^{III}(tpps)]$ occurs gradually (Figure 7), thus indicating that low-valent $[(H_2O)Mn^{II}(tpps)]$ is stabilized against autoxidation by complexation with TMe-β-CD.

The pseudo-first-order rate constants for autoxidation of $[(H_2O)Mn^{II}(tpps)]$ ($1.7\times10^{-6}$ M) in 0.05 M phosphate buffer containing TMe-β-CD ($3.4\times10^{-5}$ M) at pH 7.0 and 25 °C were determined as a function of partial dioxygen pressure (see Supporting Information). The second-order rate constant ($k$) for the autoxidation was determined to be 5.4 $M^{-1}s^{-1}$. In the absence of TMe-β-CD, the second-order rate constant has been reported to be $1.5\times10^5$ $M^{-1}s^{-1}$.[26] Encapsulation of $[(H_2O)Mn^{II}(tpps)]$ by two TMe-β-CD molecules drastically depresses the autoxidation. Such a phenomenon is quite similar to the effect of globin on the stabilization of a ferrous porphyrin (heme) against autoxidation.

 © 2006 Wiley-VCH Verlag GmbH & Co. KGaA, Weinheim 

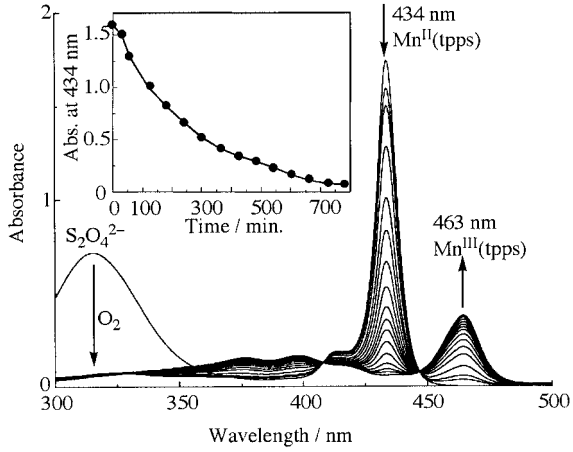


Figure 7. UV/Vis spectral changes of $[(H_2O)Mn^{II}(tpps)]$ ($5.0\times10^{-6}$ M) in 0.05 M phosphate buffer at pH 7.0 and 25 °C in the presence of TMe-β-CD ($1.0\times10^{-4}$ M) after bubbling $O_2$ gas through the solution. $[(H_2O)Mn^{II}(tpps)]$ was prepared by the reduction of $[(H_2O)_2Mn^{III}(tpps)]$ with an excess amount of $Na_2S_2O_4$. Inset: The time course in absorbance at 434 nm due to $[(H_2O)Mn^{II}(tpps)]$ after $O_2$ bubbling.

There are two plausible mechanisms for autoxidation of $[(H_2O)Mn^{II}Por]$ (Figure 8). Mechanism 1 is an outer-sphere electron-transfer mechanism where the electron transfer occurs intermolecularly. Mechanism 2 is similar to the mechanism proposed for autoxidation of oxy-myoglobin[27] and its model oxy-hemoCD.[18b] Dioxygen complexes of $Mn^{II}$ porphyrin complexes are known to be formed in organic solvents at low temperature.[28] To the best of our knowledge, the dioxygen adduct of $Mn^{II}$Por has not been detected at ambient temperature, meaning that the dioxygen adduct of $Mn^{II}$ porphyrin is very unstable. In Mechanism 2, the rate-determining step of the autoxidation must be the ligand-exchange step of $[(H_2O)Mn^{II}Por]$ to $[(O_2)Mn^{II}Por]$ because the autoxidation obeys second-order kinetics. In our previous work, we determined the rate constant for dioxygen association to the iron(II) center of hemoCD to be $4.7\times10^7$ $M^{-1}s^{-1}$.[18b] The penetration of dioxygen into the cleft formed by the *O*-methylated β-cyclodextrin dimer is extremely fast. The cleft of hemoCD should be much less labile than the present case, where the cleft is formed intermolecularly by two TMe-β-CD molecules. The less labile nature of hemoCD is ascribed to the lower mobility of the cyclodextrin moieties linked to each other by a covalent bond and to ligation of the pyridine moiety involved in the linker to the $Fe^{II}$ center. On the basis of these considerations, mechanism 2 can be excluded. In other words, $[(H_2O)Mn^{II}(tpps)]$ seems to be oxidized by an outer-sphere electron-transfer mechanism (mechanism 1). Since the penetration of dioxygen into the cleft formed by two TMe-β-CD molecules is expected to be a fast process, the marked stabilization of $[(H_2O)Mn^{II}(tpps)]$ by the TMe-β-CD molecules is not ascribed to the encapsulation effect due to tight blocking of the $Mn^{II}$ center. One possibility that explains the stabilization of low-valent $[(H_2O)Mn^{II}(tpps)]$ is alteration of the redox potential of [Mn(tpps)] upon inclusion into the TMe-β-CD cavities. We therefore measured the redox potentials of [Mn(tpps)] in the absence and presence of TMe-β-CD.

## Redox Potential of $[(H_2O)_2Mn^{III}(tpps)]$

At first, cyclic voltammetry (CV) was applied to determine the $Mn^{III}$-$Mn^{II}$ redox potential of $[(H_2O)_2Mn^{III}$-(tpps)]. In the absence of TMe-β-CD, CV provided a redox potential, $E_{1/2}$, of –410 mV (vs. Ag/AgCl) in 0.05 M phosphate buffer at pH 7.0 containing 0.1 M $Na_2SO_4$ as supporting electrolyte (see Supporting Information). In the presence of TMe-β-CD, however, no redox peak appeared because the metal center of $[(H_2O)_2Mn^{III}(tpps)]$ is blocked by two TMe-β-CD molecules. It has been shown that an electrode reaction is strictly inhibited by inclusion of a sample in cyclodextrin.[29] Ribo et al. measured the cyclic voltammograms of $Mn^{III}$(tpps) complexed with cyclodextrins such as α-cyclodextrin and 2-hydroxypropyl-β-cyclodextrin.[6b] They assumed the electrode reactions of the Mn(tpps)-cyclodextrin complexes adsorbed on the electrode. We were unable to observe any redox peak when TMe-β-CD, a stronger host for water-soluble porphyrins, was added to the system, therefore we decided to use a spectroelectrochemical method, which is the established method to determine the redox potential of metalloenzymes as well as metal complexes,[30] to study the electrochemistry of the Mn(tpps)/TMe-β-CD complex.

The Nernst equation [Equation (1)] applied to an electrode reaction is

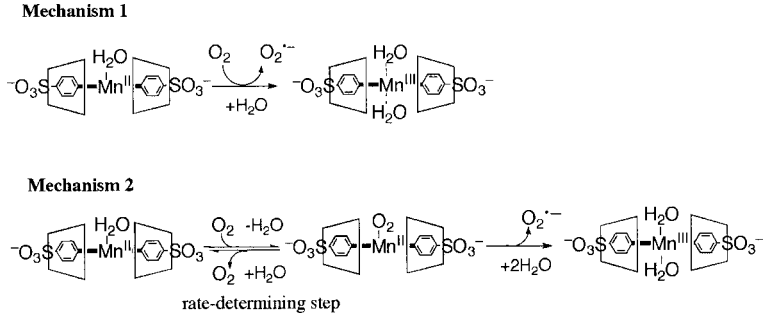


Figure 8. Plausible mechanisms for autoxidation of $[(H_2O)Mn^{II}(tpps)]$ complexed with TMe-β-CD.

 © 2006 Wiley-VCH Verlag GmbH & Co. KGaA, Weinheim 

$$E = E_{1/2} + [(RT)/(nF)]\ln(a_{Ox}/a_{Red}) \quad (1)$$

where $E$ and $E_{1/2}$ are the actual potential and the standard redox potential, respectively, and $a_{Ox}$ and $a_{Red}$ are the chemical activities of the chemical species on the oxidized and reduced electrodes, respectively. $R$, $T$, and $F$ are the gas constant, the absolute temperature, and the Faraday constant, respectively. Equation (1) can be transformed into Equation (2), which is the equation for a one-electron redox reaction at 25 °C applicable to a spectroelectrochemical measurement.

$$E = E_{1/2} + 0.05914\log[(A_{Red} - A)/(A - A_{Ox})] \quad (2)$$

where $A$ is the experimentally observed absorbance of a sample at $E$ and a certain wavelength and $A_{Red}$ and $A_{Ox}$ are the absorbances of the reduced and oxidized species, respectively, at the same wavelength. In order to accelerate the electrode reaction, 9,10-anthraquinone-2-sulfonate ($E_{1/2}$ = –442 mV vs. Ag/AgCl)[31] was used as an electron mediator. The UV/Vis spectral changes of [Mn(tpps)] in phosphate buffer containing 0.1 M $Na_2SO_4$ as a function of applied potential ($E$ = –200 to –475 mV vs. Ag/AgCl) are shown in Figure 9. The spectral changes as a function of $E$ indicate the existence of only equilibrium between $[(H_2O)_2Mn^{III}(tpps)]$ and $(H_2O)Mn^{II}(tpps)$. From the Nernst plot, the $E_{1/2}$ value for the $Mn^{III}$-$Mn^{II}$ redox of the Mn(tpps)/TMe-β-CD complex was determined to be –320 ± 3 mV at pH 7.0 and 25 °C. A similar spectroelectrochemical titration provided an $E_{1/2}$ value of –423 ± 8 mV for [Mn(tpps)] in phosphate buffer (pH 7.0) without TMe-β-CD (see Supporting Information). Interestingly, complexation of [Mn(tpps)] with TMe-β-CD causes a positive shift of $E_{1/2}$ by about 100 mV, which suggests stabilization of low-valent $[(H_2O)Mn^{II}(tpps)]$ against autoxidation by TMe-β-CD. The free-energy change ($\Delta G^0$) during a redox reaction can be evaluated from Equation (3).

$$\Delta G^0 = -nFE_{1/2} \quad (3)$$

The free-energy changes for the equilibria shown in Figure 10 were calculated from the $E_{1/2}$ values and the binding constants for complexation of $[(H_2O)_2Mn^{III}(tpps)]$ and TMe-β-CD. The $\Delta G^0$ value for the redox reaction of [Mn(tpps)] in the presence of TMe-β-CD is 10 kJ mol$^{-1}$, while that for the system in the absence of TMe-β-CD is 20 kJ mol$^{-1}$. From the thermodynamic and electrochemical data, the $K_1K_2$ value for the complexation of $[(H_2O)Mn^{II}$-(tpps)] with TMe-β-CD to form a 2:1 host–guest complex can be calculated to be $1.2\times10^{12}$ M$^{-2}$. In the case of $[(H_2O)_2Mn^{III}(tpps)]$, the $K_1K_2$ value is $2.3\times10^{10}$ M$^{-2}$. It is clear that a positive net charge remaining on the center of $[(H_2O)_2Mn^{III}(tpps)]$ greatly destabilizes the 2:1 host–guest complex.

Although we also measured the $Mn^{III}$-$Mn^{IV}$ redox potentials in aqueous alkaline solutions with and without TMe-β-CD, we could not obtain reliable data to compare the redox potential of the Mn(tpps)/TMe-β-CD complex with that of free [Mn(tpps)] (see Supporting Information).

## Conclusions

The present study leads to the following conclusions:
(1) The 1:2 inclusion complex of $[(H_2O)Mn^{II}(tpps)]$ and TMe-β-CD is much more stable than that of $[(H_2O)_2Mn^{III}$-(tpps)] and TMe-β-CD. Destabilization of $[(H_2O)_2Mn^{III}$-(tpps)]/TMe-β-CD is ascribed to a positive net charge remaining on the center of the metalloporphyrin;
(2) $[(H_2O)(OH^-)Mn^{III}(tpps)]$ in aqueous alkaline solution containing TMe-β-CD gradually changes to $[(H_2O)Mn^{II}$-

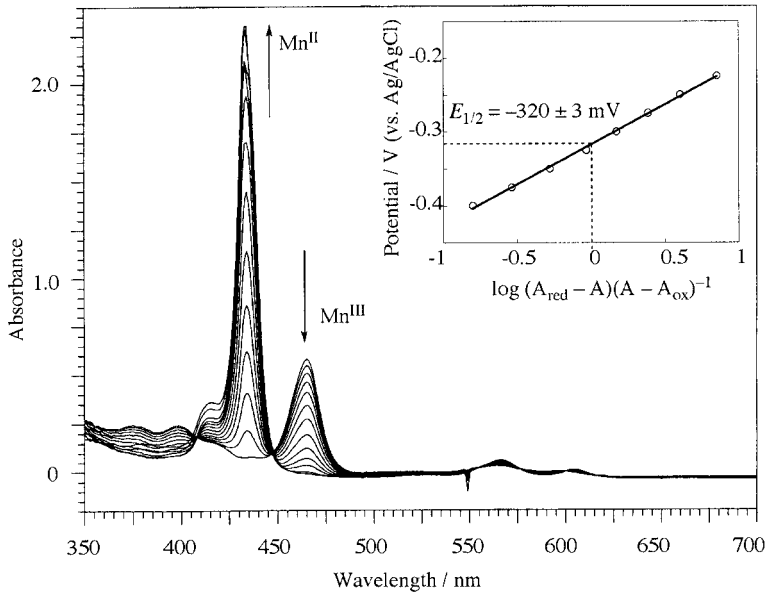


Figure 9. UV/Vis spectral changes of [Mn(tpps)] ($5.0\times10^{-5}$ M) in 0.05 M phosphate buffer containing $5.0\times10^{-4}$ M TMe-β-CD and 0.1 M $Na_2SO_4$ at various applied potentials ($E$ = –200 to –475 mV vs. Ag/AgCl) during the spectroelectrochemical titration at pH 7.0 and 25 °C. Inset: the Nernst plot obtained from the spectral changes at 463 nm.

 © 2006 Wiley-VCH Verlag GmbH & Co. KGaA, Weinheim 

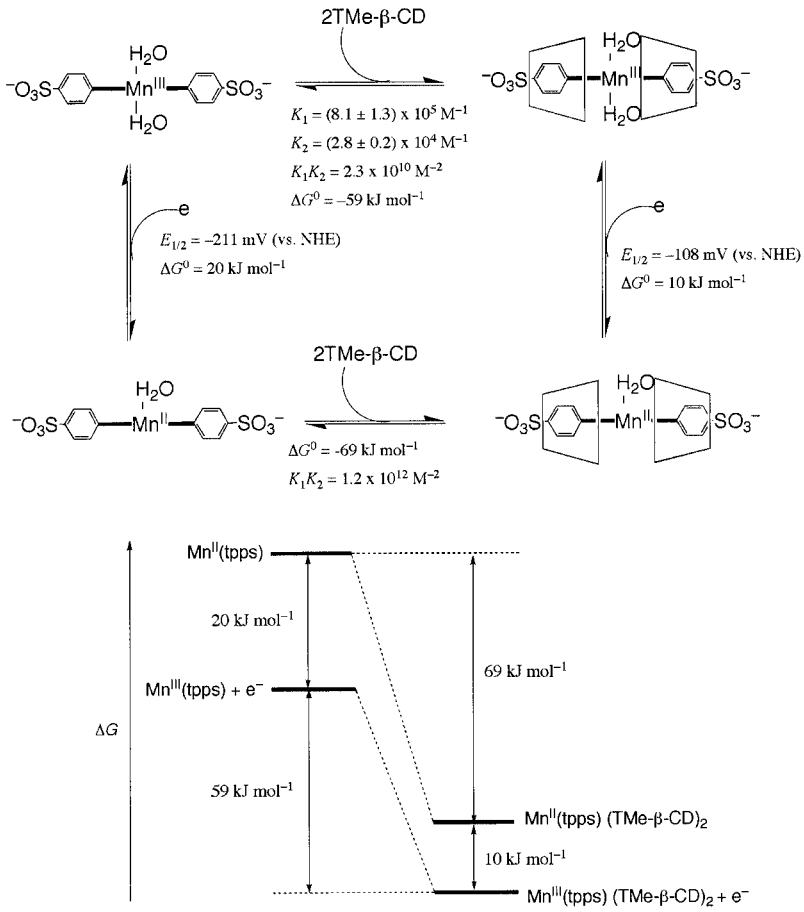


Figure 10. Free-energy changes for the equilibria of the Mn(tpps)/TMe-β-CD system in aqueous solution at pH 7.0 and 25 °C.

(tpps)] through a one-electron transfer from bound $OH^-$ to $Mn^{III}$. Formation of low-valent [$(H_2O)Mn^{II}$(tpps)] is detectable even under aerobic conditions because of marked stabilization due to incorporation of [$(H_2O)Mn^{II}$(tpps)] into the TMe-β-CD cavities;

(3) The redox potentials of [Mn(tpps)] in pH 7.0 phosphate buffer are –211 and –108 mV (vs. NHE) in the absence and the presence of TMe-β-CD, respectively. [$(H_2O)Mn^{II}$(tpps)] is stabilized against autoxidation by complexation with TMe-β-CD, which mimics the function of proteins in biological systems.

## Experimental Section

**Materials:** [5,10,15,20-Tetrakis(*p*-sulfonatophenyl)porphyrinato]-manganese(III) chloride in an acidic form (Frontier Scientific), TMe-β-CD (Nacalai), and anthraquinone-2-sulfonate sodium salt (Nacalai) were purchased and used as received. On the basis of the extinction coefficient of [$(H_2O)_2Mn^{III}$(tpps)] ($\varepsilon_{466} = 9.5 \times 10^4$), the purchased manganese porphyrin was determined to be the hexahydrate. Water was purified with a Millipore Simpak 1 apparatus. Pure $O_2$ (99.999%) and pure $N_2$ (99.999%) gases were purchased from Sumitomo Seika Chemicals.

**Measurements:** UV/Vis spectra were recorded with a Shimadzu UV-2450 spectrophotometer with a thermostatted cell holder. The pH values were measured with a Horiba pH meter M-12. Determination of the binding constants for the complexation of [Mn(tpps)] with TMe-β-CD was performed from the UV/Vis spectral titrations according to a published method.[14b,16] Microcalorimetric measurements were carried out using a Microcal Isothermal Titration Calorimeter VP-ITC. The titration curve obtained was analyzed using the Sequential Binding Sites Model for 2:1 host–guest complexation in the ORIGIN software program.[32]

Mixed $O_2$ gases with various partial pressures in $N_2$ were prepared with a KOFLOC GM-4B gas-mixing apparatus.

Cyclic voltammetry was carried out with a BAS CV-50W electrochemical analyzer. A gold working electrode, a platinum counter electrode, and a Ag/AgCl (3 M NaCl) reference electrode were utilized in a single-component cell. The working electrode was polished with 0.05-μm alumina and washed with pure water prior to use. The measurements were carried out under a $N_2$ atmosphere.

The spectroelectrochemical measurements were carried out using an optically transparent thin-layer electrode cell (BAS, optical length: 0.5 mm). A working platinum mesh electrode ($7 \times 8 \times 0.2\ mm^3$, 80 mesh) was immersed in the cell. A platinum wire and Ag/AgCl (3 M NaCl) were used as the counter and reference electrodes, respectively. The potential was controlled by a potentiostat system (ALS1100A electrochemical analyzer, BAS). The UV/Vis spectra during electronic reduction were recorded with a Shimadzu Multispec-1500 spectrometer with a thermostatted cell holder. Anthraquinone-2-sulfonate was used to mediate electron transfer between the Mn(tpps)/TMe-β-CD complex and the working electrode. The measurements were carried out at 25 °C under

 © 2006 Wiley-VCH Verlag GmbH & Co. KGaA, Weinheim 

$N_2$. The UV/Vis spectral changes at various applied potentials were analyzed by using a Nernst equation to determine the redox potential between $Mn^{II}$(tpps) and $Mn^{III}$(tpps).[31,33]

**Supporting Information** (see also the footnote on the first page of this article): Redox potentials of hemoproteins (Table S1), UV/Vis spectral changes of [$(H_2O)Mn^{II}$(tpps)] as a function of [TMe-β-CD] (Figure S1), ITC for complexation of [$(OH^-)_nMn^{IV}$(tpps)] with TMe-β-CD (Figure S2), ESI mass spectrum of a reaction mixture of [$(H_2O)Mn^{II}$(tpps)] and TMe-β-CD in aqueous alkaline solution (Figure S3), UV/Vis spectra of [$(H_2O)Mn^{II}$(tpps)] and its oxidized product in phosphate buffer without TMe-β-CD (Figure S4), plot of the pseudo-first-order rate constant for autoxidation of [$(H_2O)Mn^{II}$(tpps)] in phosphate buffer with TMe-β-CD vs. [$O_2$] (Figure S5), CVs. of [Mn(tpps)] in phosphate buffer with and without TMe-β-CD (Figure S6), spectroelectrochemical data of [Mn(tpps)] in phosphate buffer without TMe-β-CD (Figure S7), and $Mn^{III}$-$Mn^{IV}$ redox behavior of [Mn(tpps)] in aqueous alkaline solutions with and without TMe-β-CD.

## Acknowledgments

This study was supported by Grants-in-Aid for Scientific Research B (nos. 14340224 and 17350074) and on Scientific Research for Priority Area (no. 16041243) from the Ministry of Education, Culture, Sports, Science and Technology, Japan.

[1] Y. Naruta, M. Sasayama, T. Sasaki, *Angew. Chem.* **1994**, *106*, 1964–1965; *Angew. Chem. Int. Ed. Engl.* **1994**, *33*, 1839–1841.
[2] a) H. Zhou, J. T. Groves, *J. Porphyrins Phthalocyanines* **2004**, *8*, 125–140; b) J. Yang, B. Gabriele, S. Belvedere, Y. Huang, R. Breslow, *J. Org. Chem.* **2002**, *67*, 5057–5067; c) R. Breslow, *Chem. Rec.* **2001**, *1*, 3–11; d) Z. Fang, R. Breslow, *Org. Lett.* **2006**, *8*, 251–254.
[3] a) V. L. Pecoraro, M. J. Baldwin, A. Gelasco, *Chem. Rev.* **1994**, *94*, 807–826; b) I. Batinic-Haberle, I. Spasojevic, P. Hambright, L. Benov, A. L. Crumbliss, I. Fridovich, *Inorg. Chem.* **1999**, *38*, 4011–4022.
[4] a) V. L. Pecoraro, M. J. Baldwin, A. Gelasco, *Chem. Rev.* **1994**, *94*, 807–826; b) N. N. Gerasimchuk, A. Gerges, T. Clifford, A. Danby, K. Bowman-James, *Inorg. Chem.* **1999**, *38*, 5633–5636.
[5] R. Weiss, V. Bulach, A. Gold, J. Terner, A. X. Trauwein, *J. Biol. Inorg. Chem.* **2001**, *6*, 831–845.
[6] a) A. Harriman, G. Porter, *J. Chem. Soc., Faraday Trans. 2* **1979**, *75*, 1532–1542; b) O. Ramirez-Gutierrez, J. Claret, J. M. Ribo, *J. Porphyrins Phthalocyanines* **2005**, *9*, 368–376; c) S.-P. Chen, D. Ejeh, D. Levermore, H. Griffith, Y. Bullen, C. M. Hosten, P. Hambright, *J. Phys. Chem. B* **1998**, *102*, 9101–9108.
[7] S. L. Kelly, K. M. Kadish, *Inorg. Chem.* **1982**, *21*, 3631–3639.
[8] a) I. Tabushi, N. Koga, *J. Am. Chem. Soc.* **1979**, *101*, 6456–6458; b) P. Bhyrappa, J. K. Young, J. S. Moore, K. S. Suslik, *J. Am. Chem. Soc.* **1996**, *118*, 5708–5711; c) Y. Shimazaki, T. Nagano, H. Takesue, B.-H. Ye, F. Tani, Y. Naruta, *Angew. Chem.* **2004**, *116*, 100–102; *Angew. Chem. Int. Ed.* **2004**, *43*, 98–100; d) S. P. de Visser, F. Ogliaro, Z. Gross, S. Shaik, *Chem. Eur. J.* **2001**, *7*, 4954–4960; e) R. Weiss, V. Bulach, A. Gold, J. Terner, A. X. Trautwein, *J. Biol. Inorg. Chem.* **2001**, *6*, 831–845.
[9] a) Y. Watanabe, *J. Biol. Inorg. Chem.* **2001**, *6*, 846–856; b) S. Shaik, S. P. de Visser, D. Kumar, *J. Biol. Inorg. Chem.* **2004**, *9*, 661–668; c) S. Jin, T. A. Bryson, J. H. Dawson, *J. Biol. Inorg. Chem.* **2004**, *9*, 644–653; d) C. Jung, V. Schünemann, F. Lendzian, *Biochem. Biophys. Res. Commun.* **2005**, *338*, 355–364; e) M. Newcomb, R. E. P. Chandrasena, *Biochem. Biophys. Res. Commun.* **2005**, *338*, 394–403.
[10] a) J. T. Groves, J. Lee, S. S. Marla, *J. Am. Chem. Soc.* **1997**, *119*, 6269–6273; b) N. Jin, J. T. Groves, *J. Am. Chem. Soc.* **1999**, *121*, 2923–2924.
[11] a) Z. Gross, G. Golubkov, L. Simkhovich, *Angew. Chem.* **2000**, *112*, 4211–4213; *Angew. Chem. Int. Ed.* **2000**, *39*, 4045–4047; b) S. P. de Visser, F. Ogliaro, Z. Gross, S. Shaik, *Chem. Eur. J.* **2001**, *7*, 4954–4960.
[12] Y. Murakami, J. Kikuchi, Y. Hisaeda, O. Hayashida, *Chem. Rev.* **1996**, *96*, 721–758.
[13] J. A. Cowan, *Inorganic Biochemistry: An Introduction*, 2nd ed., Wiley-VCH, New York, **1997**.
[14] a) K. Kano, N. Tanaka, H. Minamizono, Y. Kawakita, *Chem. Lett.* **1996**, 925–926; b) K. Kano, R. Nishiyabu, T. Asada, Y. Kuroda, *J. Am. Chem. Soc.* **2002**, *124*, 9937–9944; c) K. Kano, R. Nishiyabu, T. Yamazaki, I. Yamazaki, *J. Am. Chem. Soc.* **2003**, *125*, 10625–10634; d) K. Kano, R. Nishiyabu, R. Doi, *J. Org. Chem.* **2005**, *70*, 3667–3673.
[15] T. Carofiglio, R. Fornasier, V. Lacchini, C. Rosso, U. Tonellato, *Tetrahedron Lett.* **1996**, *37*, 8019–8022.
[16] K. Kano, H. Kitagishi, S. Tamura, A. Yamada, *J. Am. Chem. Soc.* **2004**, *126*, 15202–15210.
[17] D. L. Dick, T. V. S. Rao, D. Sukumaran, D. S. Lawrence, *J. Am. Chem. Soc.* **1992**, *114*, 2664–2669.
[18] a) K. Kano, H. Kitagishi, M. Kodera, S. Hirota, *Angew. Chem.* **2005**, *117*, 439–442; *Angew. Chem. Int. Ed.* **2005**, *44*, 435–438; b) K. Kano, H. Kitagishi, C. Dagallier, M. Kodera, T. Matsuo, T. Hayashi, Y. Hisaeda, S. Hirota, *Inorg. Chem.* **2006**, *45*, 4448–4460; c) K. Kano, H. Kitagishi, S. Tanaka, *J. Incl. Phenom. Macrocycl. Chem.*, DOI: 10.1007/S10847-006-9063-8.
[19] a) J. P. Collman, *Acc. Chem. Res.* **1977**, *10*, 265–272; b) T. G. Traylor, *Acc. Chem. Res.* **1981**, *14*, 102–109; c) M. Momenteau, C. A. Reed, *Chem. Rev.* **1994**, *94*, 659–698; d) J. P. Collman, R. Boulatov, C. J. Sunderland, L. Fu, *Chem. Rev.* **2004**, *104*, 561–588.
[20] S. Mosseri, J. C. Mialocq, B. Perly, P. Hambright, *J. Phys. Chem.* **1991**, *95*, 4659–4663.
[21] N. Carnieri, A. Harriman, G. Porter, *J. Chem. Soc., Dalton Trans.* **1982**, 931–938.
[22] a) K. Kano, T. Kitae, Y. Shimofuri, N. Tanaka, Y. Mineta, *Chem. Eur. J.* **2000**, *6*, 2705–2713; b) K. Kano, H. Hasegawa, *J. Am. Chem. Soc.* **2001**, *123*, 10616–10627.
[23] R. D. Arasasingham, T. C. Bruice, *Inorg. Chem.* **1990**, *29*, 1422–1427.
[24] S. Jeon, H. K. Lee, Y.-K. Choi, *Bull. Korean Chem. Soc.* **1996**, *17*, 929–934.
[25] a) P. K. S. Tsang, P. Cofré, D. T. Sawyer, *Inorg. Chem.* **1987**, *26*, 3604–3609; b) D. T. Sawyer, J. L. Roberts Jr, *Acc. Chem. Res.* **1988**, *21*, 469–476.
[26] I. A. Duncan, A. Harriman, G. Porter, *J. Chem. Soc., Faraday Trans. 2* **1980**, *76*, 1415–1428.
[27] K. Shikama, *Chem. Rev.* **1998**, *98*, 1357–1373.
[28] a) C. J. Weschler, B. M. Hoffman, F. Basolo, *J. Am. Chem. Soc.* **1975**, *97*, 5278–5280; b) B. M. Hoffman, T. Szymanski, T. G. Brown, F. Basolo, *J. Am. Chem. Soc.* **1978**, *100*, 7253–7259; c) R. D. Jones, D. A. Summerville, F. Basolo, *J. Am. Chem. Soc.* **1978**, *100*, 4416–4424; d) A. Weselucha-Birczynska, L. M. Proniewicz, K. Bajdor, K. Nakamoto, *J. Raman Spectrosc.* **1991**, *22*, 315–319.
[29] a) T. Matsue, D. H. Evans, T. Osa, N. Kobayashi, *J. Am. Chem. Soc.* **1985**, *107*, 3411–3417; b) A. Mirzoian, A. E. Kaifer, *Chem. Eur. J.* **1997**, *3*, 1052–1058.
[30] For example: a) K. M. Kadish, J. Shao, Z. Ou, R. Zhan, F. Burdet, J.-M. Barbe, P. Gros Claude, R. Guilard, *Inorg. Chem.* **2005**, *44*, 9023–9038; b) X. Zhao, N. Yeung, Z. Wang, Z. Guo, Y. Lu, *Biochemistry* **2005**, *44*, 1210–1214.
[31] a) L. S. Reid, V. T. Taniguchi, H. B. Gray, A. G. Mauk, *J. Am. Chem. Soc.* **1982**, *104*, 7516–7519; b) T. Matsuo, H. Dejima, S. Hirota, D. Murata, H. Sato, T. Ikegami, H. Hori, Y. Hisaeda, T. Hayashi, *J. Am. Chem. Soc.* **2004**, *126*, 16007–16017.

 © 2006 Wiley-VCH Verlag GmbH & Co. KGaA, Weinheim 

[32] *ITC Data Analysis in Origin - Tutorial Guide*, MicroCal, Northampton, **1998**; pp. 76–78.
[33] a) J. A. Zahn, D. M. Arciero, A. B. Hooper, A. A. Dispirito, *Eur. J. Biochem.* **1996**, *240*, 684–691; b) D. P. Hildebrand, H. Tang, Y. Luo, C. L. Hunter, M. Smith, G. D. Brayer, A. G. Mauk, *J. Am. Chem. Soc.* **1996**, *118*, 12909–12915; c) H. Sawai, N. Kawada, K. Yoshizato, H. Nakajima, S. Aono, Y. Shiro, *Biochemistry* **2003**, *42*, 5133–5142.

Received: April 14, 2006
Published Online: August 7, 2006

 © 2006 Wiley-VCH Verlag GmbH & Co. KGaA, Weinheim 

DOI: 10.1002/ejic.200600428

# Luminescent Cyclometalated Iridium(III) Polypyridine Complexes Containing a Thiourea Moiety: Synthesis, Characterization, Photophysics, Electrochemistry and Anion-Binding Properties

**Kenneth Kam-Wing Lo,*[a] Jason Shing-Yip Lau,[a] David Ka-Kit Lo,[a] and Larry Tso-Lun Lo[a]**

**Keywords:** Fluorescence spectroscopy / Iridium / Luminescence / N ligands / Sensors

A series of new luminescent cyclometalated iridium(III) polypyridine thiourea complexes $[Ir(N\text{-}C)_2(N\text{-}N)](PF_6)$ [HN-C = 2-phenylpyridine (Hppy), N-N = *N*-ethyl-*N*′-1,10-phenanthrolin-5-yl thiourea (phen-TU-Et) (**1a**), *N*-phenyl-*N*′-1,10-phenanthrolin-5-yl thiourea (phen-TU-Ph) (**1b**), *N*-(1-adamantanemethyl)-*N*′-1,10-phenanthrolin-5-yl thiourea (phen-TU-MeA) (**1c**); HN-C = 7,8-benzoquinoline (Hbzq), N-N = phen-TU-Et (**2a**), phen-TU-Ph (**2b**), phen-TU-MeA (**2c**); HN-C = 2-phenylquinoline (Hpq), N-N = phen-TU-Et (**3a**), phen-TU-Ph (**3b**), phen-TU-MeA (**3c**)] have been synthesized and characterized. The photophysical and electrochemical properties of these complexes have been investigated. On the basis of the photophysical and electrochemical data, the nature of the emissive states has been assigned. The thiourea moieties of the complexes allow them to act as receptors for anions; the binding of $OAc^-$, $F^-$, and $H_2PO_4^-$ to the complexes has been investigated by emission titrations.

(© Wiley-VCH Verlag GmbH & Co. KGaA, 69451 Weinheim, Germany, 2006)

## Introduction

Recognition of anions is an interesting area of research because of the important roles of anions in industrial and biological processes and environmental science. Hydrogen-bonding interactions have been commonly used in the development of artificial anion receptors;[1–9] for example, traditional amide-based receptors have been employed as hydrogen-bond donors to bind various anions.[1–5] Recently, the thiourea moiety has attracted much attention because of its specific binding of $F^-$ and oxyanions such as $OAc^-$ and $H_2PO_4^-$.[6–9] It has been attached to various organic chromophores and fluorophores to produce effective anion sensors.[6–8]

The photophysics and photochemistry of luminescent iridium(III) polypyridine complexes have attracted much attention recently.[10–25] This interest originates from the successful use of these complexes as dopants in the fabrication of light-emitting diode devices.[16a,16e] Some luminescent iridium(III) polypyridine complexes have been developed as luminescent sensors for various analytes, including oxygen,[11c] proton,[17a] and alkali and alkaline-earth metal cations.[23d] However, the use of luminescent iridium(III) polypyridine complexes as anion sensors is very limited.[17b] With our recent interest in using luminescent iridium(III) polypyridine complexes as biological labeling reagents and probes,[25] we envisage that incorporation of a thiourea moiety into these complexes can afford a new anion-sensory system. Herein, we report the synthesis, characterization, photophysics, and electrochemistry of a series of new luminescent cyclometalated iridium(III) polypyridine thiourea complexes $[Ir(N\text{-}C)_2(N\text{-}N)](PF_6)$ [HN-C = 2-phenylpyridine (Hppy), N-N = *N*-ethyl-*N*′-1,10-phenanthrolin-5-yl thiourea (phen-TU-Et) (**1a**), *N*-phenyl-*N*′-1,10-phenanthrolin-5-yl thiourea (phen-TU-Ph) (**1b**), *N*-(1-adamantanemethyl)-*N*′-1,10-phenanthrolin-5-yl thiourea (phen-TU-MeA) (**1c**); HN-C = 7,8-benzoquinoline (Hbzq), N-N = phen-TU-Et (**2a**), phen-TU-Ph (**2b**), phen-TU-MeA (**2c**); HN-C = 2-phenylquinoline (Hpq), N-N = phen-TU-Et (**3a**), phen-TU-Ph (**3b**), phen-TU-MeA (**3c**)] (Scheme 1). The emission and electrochemical properties of these complexes have been compared to those of their amine and isothiocyanate counterparts $[Ir(N\text{-}C)_2(N\text{-}N)](PF_6)$ [HN-C = Hppy, N-N = 5-amino-1,10-phenanthroline (phen-$NH_2$) (**1d**), 5-isothiocyanato-1,10-phenanthroline (phen-ITC) (**1e**); HN-C = Hbzq, N-N = phen-$NH_2$ (**2d**), phen-ITC (**2e**); HN-C = Hpq, N-N = phen-$NH_2$ (**3d**), phen-ITC (**3e**)] (Scheme 1).[25a,25c] The binding of anions including $OAc^-$, $F^-$, and $H_2PO_4^-$ to the thiourea complexes has been investigated by emission titrations.

[a] Department of Biology and Chemistry,
City University of Hong Kong,
Tat Chee Avenue, Kowloon, Hong Kong, P. R. China
Fax: +852-2788-7406
E-mail: bhkenlo@cityu.edu.hk

 © 2006 Wiley-VCH Verlag GmbH & Co. KGaA, Weinheim 

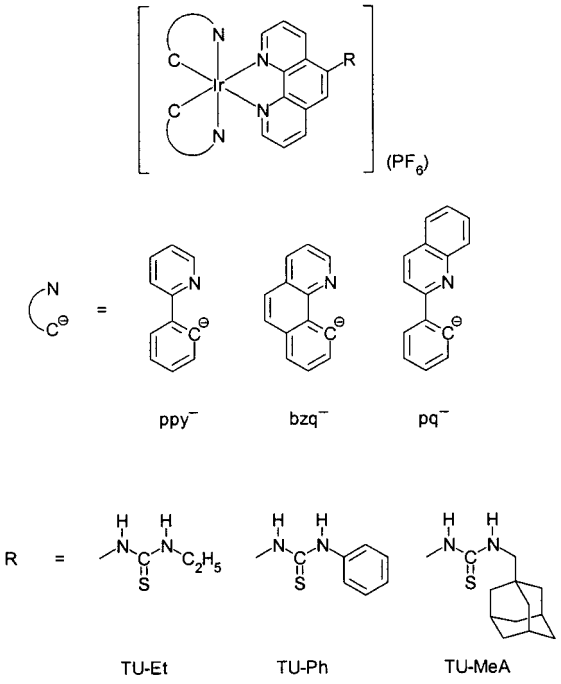


N-C⁻ = ppy⁻; R = TU-Et (**1a**), TU-Ph (**1b**), TU-MeA (**1c**), $NH_2$ (**1d**), NCS (**1e**)

N-C⁻ = bzq⁻; R = TU-Et (**2a**), TU-Ph (**2b**), TU-MeA (**2c**), $NH_2$ (**2d**), NCS (**2e**)

N-C⁻ = pq⁻; R = TU-Et (**3a**), TU-Ph (**3b**), TU-MeA (**3c**), $NH_2$ (**3d**), NCS (**3e**)

Scheme 1. Structures of the iridium(III) polypyridine complexes.

## Results and Discussion

### Synthesis

The isothiocyanate group of $[Ir(N\text{-}C)_2(phen\text{-}ITC)](PF_6)$ reacts readily with primary amines to form thiourea linkages. We have used these luminescent complexes as labeling reagents for amine-containing biological molecules.[25a,25c] All the cyclometalated iridium(III) thiourea complexes in the current work were prepared by the reaction of $[Ir(N\text{-}C)_2(phen\text{-}ITC)](PF_6)$ with the corresponding amines. To investigate the effects of the substituent of the thiourea moiety on the photophysical, electrochemical, and anion-binding properties of the target complexes, we have employed an electron-donating ethyl group and an electron-withdrawing phenyl ring as the substituents. Additionally, a relatively bulky 1-adamantanemethyl unit has also been employed. All the iridium(III) thiourea complexes were characterized by $^1H$ NMR spectroscopy, positive-ion ESI-MS, IR spectroscopy, and gave satisfactory microanalysis.

### Electronic Absorption and Emission

The electronic absorption spectroscopic data of the iridium(III) thiourea complexes are listed in Table 1. The electronic absorption spectra of complexes **1a**, **2a**, and **3a** in $CH_2Cl_2$ are shown in Figure 1. All the complexes showed intense spin-allowed intra-ligand ($^1$IL) ($\pi\rightarrow\pi^*$) (N-N and N-C⁻) absorption bands at around 252–348 nm ($\varepsilon$ of the order of $10^4\ M^{-1}cm^{-1}$) and spin-allowed metal-to-ligand charge-transfer ($^1$MLCT) [$d\pi(Ir)\rightarrow\pi^*$(N-N and N-C⁻)] absorption shoulders at around 370–521 nm. Similar to related cyclometalated iridium(III) polypyridine systems,[10–16,17a,17c–17e,18–24] spin-forbidden $^3$MLCT [$d\pi(Ir)\rightarrow\pi^*$(N-N and N-C⁻)] absorption tailing was also observed in a lower-energy region (ca. 518–550 nm) due to spin-orbital coupling associated with the iridium(III) center. It is noteworthy that the absorption data of the complexes with the same cyclometalating ligand but different substituents on the thiourea moiety (i.e. ethyl, phenyl or 1-adamantanemethyl) are very similar, thus indicating that these substituents do not substantially affect the energy levels of the $\pi^*$ orbitals of the diimine ligands.

Table 1. Electronic absorption spectroscopic data of the iridium(III) polypyridine thiourea complexes at 298 K.

| Complex | Medium | $\lambda_{abs}$ [nm] ($\varepsilon$ [$M^{-1}cm^{-1}$]) |
|---|---|---|
| **1a** | $CH_2Cl_2$ | 255 (71500), 266 sh (65785), 278 sh (49880), 333 sh (16710), 380 sh (9615), 466 sh (1155) |
| | $CH_3CN$ | 252 (70060), 266 sh (59590), 279 sh (43780), 332 sh (16520), 375 sh (9100), 465 sh (1205) |
| **1b** | $CH_2Cl_2$ | 254 (68330), 266 (66960), 282 sh (50175), 332 sh (18330), 375 sh (11605), 463 sh (1550) |
| | $CH_3CN$ | 253 (62645), 266 sh (59160), 284 sh (42560), 332 sh (16390), 375 sh (10140), 463 sh (1405) |
| **1c** | $CH_2Cl_2$ | 256 (62640), 268 sh (57860), 332 sh (16890), 370 sh (10950), 464 sh (1855) |
| | $CH_3CN$ | 253 (64400), 268 sh (55870), 332 sh (16440), 370 sh (10210), 464 sh (1817) |
| **2a** | $CH_2Cl_2$ | 257 (60335), 282 sh (32620), 328 (20330), 405 sh (6355) |
| | $CH_3CN$ | 254 (55390), 277 sh (31940), 326 (19420), 408 sh (5500) |
| **2b** | $CH_2Cl_2$ | 257 (51405), 284 sh (29295), 330 (17935), 403 sh (5490) |
| | $CH_3CN$ | 254 (56525), 280 sh (35375), 323 (21390), 408 sh (5720) |
| **2c** | $CH_2Cl_2$ | 256 (72380), 284 sh (37600), 328 (24410), 410 sh (7040) |
| | $CH_3CN$ | 253 (74020), 280 sh (39225), 325 (25525), 408 sh (6975) |
| **3a** | $CH_2Cl_2$ | 262 sh (58600), 273 (62095), 333 (29025), 348 sh (26165), 433 (6915), 519 sh (655) |
| | $CH_3CN$ | 262 sh (62475), 274 (65435), 332 (27140), 346 sh (24660), 427 (6650), 520 sh (685) |
| **3b** | $CH_2Cl_2$ | 262 (60590), 284 sh (55450), 333 (26340), 347 sh (23070), 436 (5590), 518 sh (510) |
| | $CH_3CN$ | 262 (61690), 280 sh (57675), 331 (26275), 348 sh (22535), 432 (5725), 521 sh (550) |
| **3c** | $CH_2Cl_2$ | 263 (69450), 280 sh (63150), 334 (30505), 346 sh (26895), 436 (6700), 520 sh (705) |
| | $CH_3CN$ | 262 (68875), 280 sh (61795), 334 (29170), 348 sh (25115), 432 (6430), 520 sh (720) |

Upon irradiation, all the iridium(III) thiourea complexes displayed intense and long-lived green to orange luminescence under ambient conditions and in low-temperature alcohol glass. The emission data of these complexes and their amine (**1d**–**3d**) and isothiocyanate (**1e**–**3e**) counterparts are summarized in Table 2. The emission spectra of

 © 2006 Wiley-VCH Verlag GmbH & Co. KGaA, Weinheim 

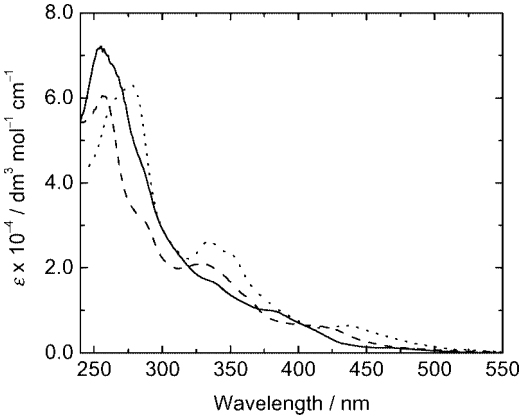


Figure 1. Electronic absorption spectra of complexes **1a** (—) **2a** (---), and **3a** (···) in $CH_2Cl_2$ at 298 K.

complexes **1a**, **2a**, and **3a** in degassed $CH_2Cl_2$ at 298 K and in alcohol glass at 77 K are shown in Figures 2, 3, and 4, respectively. The emission of the ppy⁻ (**1a**–**1c**) and bzq⁻ (**2a**–**2c**) thiourea complexes occurred at a lower energy with a shorter excited-state lifetime and lower emission quantum yield in more polar $CH_3CN$ than in less polar $CH_2Cl_2$ (Table 2). These findings suggest that the emissive states bear a high parentage of triplet MLCT [dπ(Ir)→π*(N-N)] character.[10,11b–11f,13a,14a,15,16,17c–17e,19a,20–24,25a,25c,25d,25f] This assignment is supported by the observations that the iridium(III) thiourea complexes emitted at lower energy than complexes **1d** and **2d**, which contain an electron-donating amine group on the diimine ligand, and at higher energy than complexes **1e** and **2e**, which contain an electron-withdrawing isothiocyanate group on the diimine ligand. Interestingly, in fluid solutions at 298 K the emission spectra of all the pq⁻ complexes **3a**–**3c** showed very similar structural features, with an emission maximum at around 558–563 nm and a shoulder at around 584–588 nm (Table 2 and Figure 4). The independence of the nature of the diimine ligands on the emission behavior is further reflected by the fact that the phen-$NH_2$ complex **3d** and the phen-ITC complex **3e** also exhibited very similar emission energies (Table 2). The excited-state lifetimes of the pq⁻ thiourea complexes varied from around 3.11 to 1.27 μs and are much longer than those of their ppy⁻ and bzq⁻ counterparts. On the basis of these observations, we propose that the emissive states of these pq⁻ complexes are essentially triplet IL (π→π*) (pq⁻) in nature, perhaps with mixing of some $^3$MLCT [dπ(Ir)→π*(pq⁻)] character. Similar $^3$IL emission has been observed for related iridium(III) pq⁻ systems.[25c,25d]

Upon cooling to 77 K, the emission bands of the ppy⁻ (**1a**–**1c**) and bzq⁻ (**2a**–**2c**) thiourea complexes showed large hypsochromic shifts (Table 2, Figure 2 and Figure 3), which is a typical feature of common iridium(III) $^3$MLCT emitters.[10a,10c,11b,11c,11e,11f,13a,14b,15,16b–16e,17c,19a,20a,21,22,25a,25c,25d,25f] Bi-exponential emission decays were observed; the longer- and shorter-lived counterparts are ascribed to $^3$MLCT excited states involving the cyclometalating and di-

Table 2. Photophysical data of the iridium(III) polypyridine complexes.

| Complex | Medium ($T$ [K]) | $\lambda_{em}$ [nm] | $\tau_o$ [μs] | $\Phi$ |
|---|---|---|---|---|
| **1a** | $CH_2Cl_2$ (298) | 584 | 0.81 | 0.32 |
| | $CH_3CN$ (298) | 587 | 0.34 | 0.12 |
| | glass[a] (77) | 516, 540 sh | 49.93 (9%), 5.73 (91%) | |
| **1b** | $CH_2Cl_2$ (298) | 577 | 0.97 | 0.13 |
| | $CH_3CN$ (298) | 588 | 0.47 | 0.068 |
| | glass[a] (77) | 531 | 49.54 (9%), 5.48 (91%) | |
| **1c** | $CH_2Cl_2$ (298) | 585 | 0.98 | 0.11 |
| | $CH_3CN$ (298) | 593 | 0.43 | 0.032 |
| | glass[a] (77) | 522, 553 sh | 49.38 (10%), 5.50 (90%) | |
| **1d**[b] | $CH_2Cl_2$ (298) | 564 | 9.52 | 0.43 |
| | $CH_3CN$ (298) | 568 | 11.38 | 0.079 |
| | glass[a] (77) | 560 (max), 602, 658 sh | 286.21 | |
| **1e**[b] | $CH_2Cl_2$ (298) | 598 | 0.77 | 0.29 |
| | $CH_3CN$ (298) | 608 | 0.41 | 0.079 |
| | glass[a] (77) | 512 (max), 552, 594 sh | 93.52 (32%), 14.58 (68%) | |
| **2a** | $CH_2Cl_2$ (298) | 581 | 1.13 | 0.20 |
| | $CH_3CN$ (298) | 590 | 0.45 | 0.039 |
| | glass[a] (77) | 520 (max), 539, 574 sh | 48.04 (21%), 4.82 (79%) | |
| **2b** | $CH_2Cl_2$ (298) | 580 | 1.11 | 0.15 |
| | $CH_3CN$ (298) | 588 | 0.56 | 0.041 |
| | glass[a] (77) | 505, 540 (max), 575 sh | 47.79 (28%), 4.78 (72%) | |
| **2c** | $CH_2Cl_2$ (298) | 587 | 0.87 | 0.13 |
| | $CH_3CN$ (298) | 593 | 0.37 | 0.040 |
| | glass[a] (77) | 508 sh, 520 (max), 539 | 47.64 (30%), 5.30 (70%) | |
| **2d**[b] | $CH_2Cl_2$ (298) | 568 | 6.65 | 0.26 |
| | $CH_3CN$ (298) | 567 | 25.02 | 0.015 |
| | glass[a] (77) | 506 sh, 562 (max), 606, 666 sh | 260.30 | |
| **2e**[b] | $CH_2Cl_2$ (298) | 597 | 0.67 | 0.12 |
| | $CH_3CN$ (298) | 607 | 0.32 | 0.046 |
| | glass[a] (77) | 511 (max), 553, 600 sh | 51.83 (23%), 4.48 (77%) | |
| **3a** | $CH_2Cl_2$ (298) | 558, 587 sh | 3.11 | 0.44 |
| | $CH_3CN$ (298) | 561, 584 sh | 2.58 | 0.11 |
| | glass[a] (77) | 545 (max), 587, 640 sh | 6.10 | |
| **3b** | $CH_2Cl_2$ (298) | 558, 584 sh | 2.64 | 0.44 |
| | $CH_3CN$ (298) | 563, 588 sh | 2.31 | 0.21 |
| | glass[a] (77) | 544 (max), 587, 631 sh | 6.65 | |
| **3c** | $CH_2Cl_2$ (298) | 562, 587 sh | 2.06 | 0.28 |
| | $CH_3CN$ (298) | 562, 587 sh | 1.27 | 0.22 |
| | glass[a] (77) | 545 (max), 587, 632 sh | 6.07 | |
| **3d**[b] | $CH_2Cl_2$ (298) | 555, 599 sh | 4.07 | 0.36 |
| | $CH_3CN$ (298) | 559, 599 sh | 5.99 | 0.17 |
| | glass[a] (77) | 540 sh, 570, 615 sh, 681 sh | 389.15 | |
| **3e**[b] | $CH_2Cl_2$ (298) | 560, 599 sh | 1.50 | 0.25 |
| | $CH_3CN$ (298) | 559, 599 sh | 1.13 | 0.17 |
| | glass[a] (77) | 540 (max), 582, 626 sh | 4.96 | |

[a] EtOH/MeOH (4:1, v/v). [b] From ref.[25c]

 © 2006 Wiley-VCH Verlag GmbH & Co. KGaA, Weinheim 

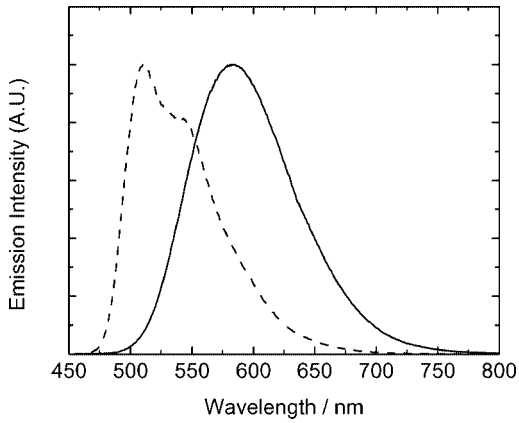


Figure 2. Emission spectra of complex **1a** in $CH_2Cl_2$ at 298 K (—) and in EtOH/MeOH (4:1, v/v) at 77 K (---).

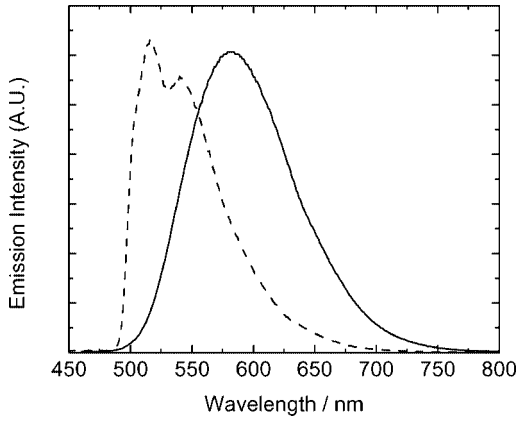


Figure 3. Emission spectra of complex **2a** in $CH_2Cl_2$ at 298 K (—) and in EtOH/MeOH (4:1, v/v) at 77 K (---).

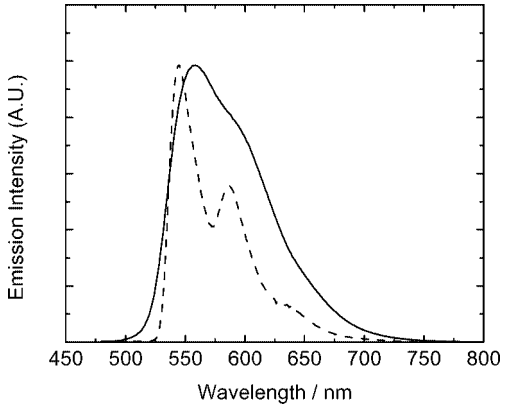


Figure 4. Emission spectra of complex **3a** in $CH_2Cl_2$ at 298 K (—) and in EtOH/MeOH (4:1, v/v) at 77 K (---).

imine ligands, respectively.[10,13a] On the contrary, the emission bands of the $pq^-$ thiourea complexes **3a**–**3c** only showed small blue shifts upon cooling to 77 K (Table 2 and Figure 4). The complexes displayed very similar and vibronically structured emission spectra with an excited-state lifetime of about 6 μs in alcohol glass at 77 K. It is conceivable that the nature of the emissive states is essentially $^3$IL ($\pi\rightarrow\pi^*$) ($pq^-$), probably mixed with some $^3$MLCT [$d\pi(Ir)\rightarrow\pi^*(pq^-)$] character.

It is important to note that the emission properties of these cyclometalated iridium(III) polypyridine complexes are sensitive to the substituents on the diimine ligands. In most cases, the emission energies of the complexes follow the order: phen-$NH_2$ > phen-thiourea > phen-ITC, which is indicative of the involvement of $^3$MLCT [$d\pi(Ir)\rightarrow\pi^*$(N-N)] character in the emissive states. On the contrary, variation of the substituent of the thiourea moiety does not result in any substantial difference of the emission properties of the thiourea complexes (Table 2). It appears that the thiourea bridge does not facilitate electronic communication and its substituent cannot profoundly perturb the electronic structures of the diimine ligand and the iridium(III) complex.

## Electrochemistry

The electrochemical properties of the iridium(III) thiourea complexes have been studied by cyclic voltammetry. The electrochemical data of these complexes and the phen-$NH_2$ and phen-ITC analogs are listed in Table 3. All the iridium(III) thiourea complexes showed an irreversible wave at about +1.08 to +1.19 V vs. SCE, which is assigned to the oxidation of the thiourea groups because similar waves are absent in the cyclic voltammograms of the phen-$NH_2$ and phen-ITC complexes (Table 3). An additional quasi-reversible oxidation couple appeared at about +1.21 to +1.31 V, attributable to the metal-centered $Ir^{IV/III}$ oxidation.[10a,10c,11–13,14a,15b,15c,19a,19b,23a,24b,24c,25] The lower reversibility of these couples compared to that of typical iridium(III) polypyridine complexes could be a result of the irreversible thiourea-based oxidation that occurred at lower potentials. The iridium(III) thiourea complexes exhibited the first reduction waves at about –1.32 to –1.37 V vs. SCE. These waves are assigned to the reduction of the diimine ligands. This assignment agrees with the find-

Table 3. Electrochemical data of the iridium(III) polypyridine complexes in $CH_3CN$ (0.1 M TBAP) at 298 K (glassy-carbon working electrode; sweep rate: 100 mV $s^{-1}$; all potentials vs. SCE).

| Complex | Oxidation, $E_{1/2}$ or $E_a$ [V] | Reduction, $E_{1/2}$ or $E_c$ [V] |
|---|---|---|
| **1a** | +1.12,[a] +1.27[b] | –1.36,[a] –1.61,[b] –2.30[a] |
| **1b** | +1.19,[a] +1.27[b] | –1.34,[a] –1.57,[b] –2.28[a] |
| **1c** | +1.12,[a] +1.26[b] | –1.36,[a] –1.61,[b] –2.45[a] |
| **1d**[c] | +1.27[a] | –1.45,[a] –2.24,[b] –2.53[a] |
| **1e**[c] | +1.27 | –1.21,[a] –1.48, –1.98,[a] –2.43[a] |
| **2a** | +1.08,[a] +1.21[b] | –1.36,[a] –2.10,[b] –2.34[a] |
| **2b** | +1.13,[a] +1.21[b] | –1.36,[a] –1.61,[b] –2.08,[a] –2.32[a] |
| **2c** | +1.09,[a] +1.21[b] | –1.34,[a] –1.63,[b] –2.08,[a] –2.32[a] |
| **2d**[c] | +1.13[b] | –1.42,[b] –1.69,[b] –2.00,[a] –2.29[a] |
| **2e**[c] | +1.15 | –1.20,[a] –1.47,[a] –2.08,[a] –2.37[a] |
| **3a** | +1.13,[a] +1.31[b] | –1.37,[a] –1.90,[a] –2.27[a] |
| **3b** | +1.14,[a] +1.30[b] | –1.37,[a] –1.56,[b] –1.90,[a] –2.04,[a] –2.24[a] |
| **3c** | +1.12,[a] +1.27[b] | –1.32,[a] –1.58,[b] –1.88,[a] –2.04,[a] –2.27[a] |
| **3d**[c] | +1.25[a] | –1.45, –1.75,[b] –1.99,[b] –2.35[b] |
| **3e**[c] | +1.28 | –1.20,[a] –1.45,[b] –1.87,[b] –2.56[a] |

[a] Irreversible waves. [b] Quasi-reversible couples. [c] From ref.[25c]

 © 2006 Wiley-VCH Verlag GmbH & Co. KGaA, Weinheim 

ings that the potentials of these waves are less negative than those of the phen-$NH_2$ (ca. –1.42 to –1.45 V) and more negative than the phen-ITC analogs (ca. –1.20 to –1.21 V) due to the electron-donating and -withdrawing properties of the amine and isothiocyanate groups, respectively. Whilst most diimine-based reductions of cyclometalated iridium(III) polypyridine complexes are reversible in nature (see references cited above), the irreversibility of these waves suggests the possible involvement of thiourea in the reduction process. Again, variation of the substituent of the thiourea moiety does not cause much difference in the reduction potentials of these complexes (Table 3), thus confirming that the π* orbitals of the diimine ligand are not strongly affected by the substituents on the other side of the thiourea linkage. Other irreversible and distorted waves appeared at lower potentials; these are assigned to reduction of the cyclometalating ligands.

### Anion-Binding Properties

Since the $OAc^-$, $F^-$, and $H_2PO_4^-$ ions are well known to bind to thiourea,[6–9] we have studied their binding to the iridium(III) thiourea complexes. The absorption spectra of the complexes did not exhibit any changes in the presence of these three ions. It is therefore likely that the binding does not significantly alter the π* energy levels of the diimine ligands and hence the energies of the $^1$IL and $^1$MLCT transitions. Emission titrations have been performed to study the anion-binding properties of the complexes. As an example, the luminescence spectral traces for complex **3c** in $CH_3CN$ upon addition of $OAc^-$, $F^-$, and $H_2PO_4^-$ ions are illustrated in Figures 5(a), 6(a), and 7(a), respectively. The emission intensities of all the iridium(III) thiourea complexes in the current work were reduced in the presence of these three anions. These findings are attributed to binding of the anions to the thiourea moieties because no changes were observed for the control complexes $[Ir(N\text{-}C)_2(phen)](PF_6)$ ($N\text{-}C^-$ = $ppy^-$, $bzq^-$, $pq^-$).[26] It is worth mentioning that the emission energies of the thiourea complexes were not altered upon the binding events, thereby suggesting that the uptake of the anions by the thiourea moieties did not increase the π* levels of the diimine ligands. To a certain extent, this is in agreement with the independence of the emission properties of the complexes on the substituents of the thiourea moieties (see above). We tentatively ascribe the observed emission quenching to a more efficient nonradiative deactivation pathway. Similar anion-induced emission quenching has also been observed in the luminescent rhenium(I) polypyridine thiourea complexes that we reported previously.[9]

Treatment of the emission titration data of all the iridium(III) thiourea complexes and the three anions using a 1:1 binding model gave satisfactory fits.[27] Plots of $I_o/(I_o - I_x)$ vs. $[A^-]^{-1}$ ($A^-$ = $OAc^-$, $F^-$, $H_2PO_4^-$) for complex **3c** and the corresponding theoretical fits are shown in Figures 5(b), 6(b), and 7(b), respectively. The $\log K_s$ values for the binding of all the iridium(III) thiourea complexes and the three

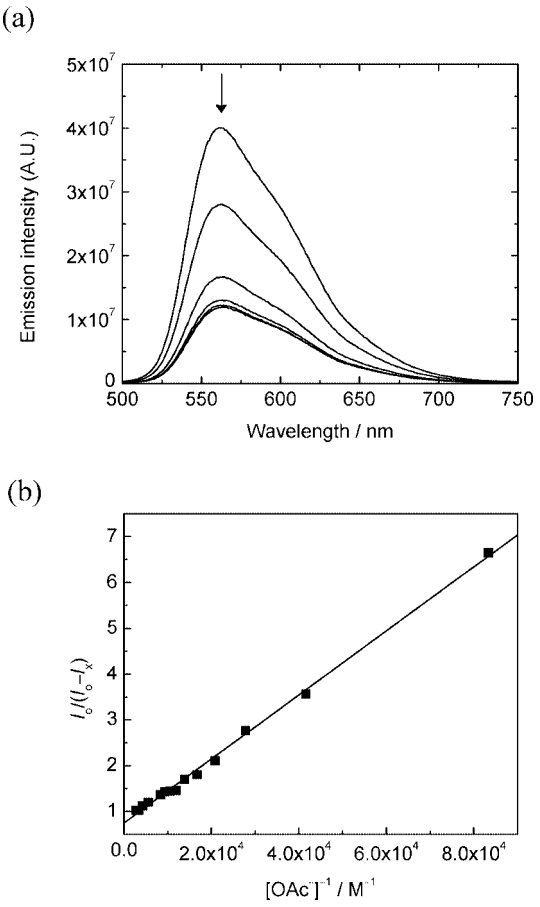


Figure 5. (a) Luminescence spectral traces of complex **3c** (120 μM) in $CH_3CN$ (0.1 M TBAP) upon addition of $OAc^-$ at 298 K. The concentrations of $OAc^-$ were 0, 24, 48, 72, 96, and 120 μM, respectively. (b) A plot of $I_o/(I_o - I_x)$ vs. $[OAc^-]^{-1}$ (■) and the theoretical fit on the basis of a 1:1 binding stoichiometry (—).

anions in $CH_3CN$ have been determined from the fitting (Table 4). The $\log K_s$ values for the binding of $OAc^-$ range from 4.03 to 4.35 and are larger than those for $F^-$ (from 3.13 to 3.73) and $H_2PO_4^-$ (from 3.12 to 3.68). Importantly, variation of the cyclometalating ligands and the substituents of the thiourea moieties did not lead to any noticeable difference in the anion-binding properties of the complexes. The minor role of the cyclometalating ligands on the anion-binding behavior is reasonable. However, the use of various thiourea substituents of different electronic and structural properties was expected to affect the anion-binding affinities of the complexes. Our experimental results indicate, however, that these effects are minimal. A possible reason is that these thiourea substituents can only control the electronic density of one of the two NH groups of the thiourea moiety, and that the bulky adamantane unit does not hamper the binding properties owing to the flexible methylene linkage. Overall, the iridium(III) thiourea complexes revealed a stronger affinity for $OAc^-$ than for the $F^-$ and $H_2PO_4^-$ ions (Table 4). A similar trend has been observed for a related naphthalimide-thiourea conjugate [$\log K_s$ = 4.47 ($OAc^-$), 3.80 ($F^-$), 3.48 ($H_2PO_4^-$) in DMSO][8f] and a

 © 2006 Wiley-VCH Verlag GmbH & Co. KGaA, Weinheim 

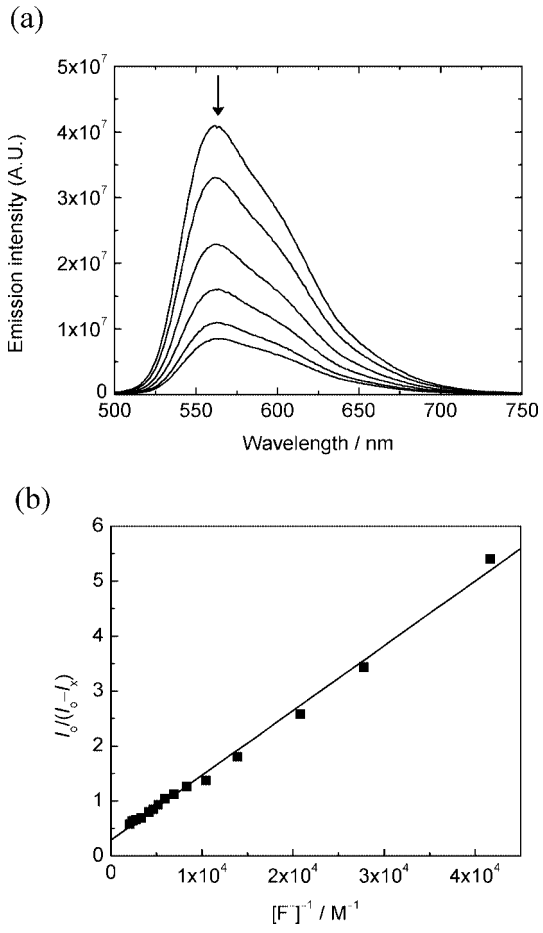


Figure 6. (a) Luminescence spectral traces of complex **3c** (120 μM) in $CH_3CN$ (0.1 M TBAP) upon addition of $F^-$ at 298 K. The concentrations of $F^-$ were 0, 24, 48, 72, 96, and 120 μM, respectively. (b) A plot of $I_o/(I_o - I_x)$ vs. $[F^-]^{-1}$ (■) and the theoretical fit on the basis of a 1:1 binding stoichiometry (—).

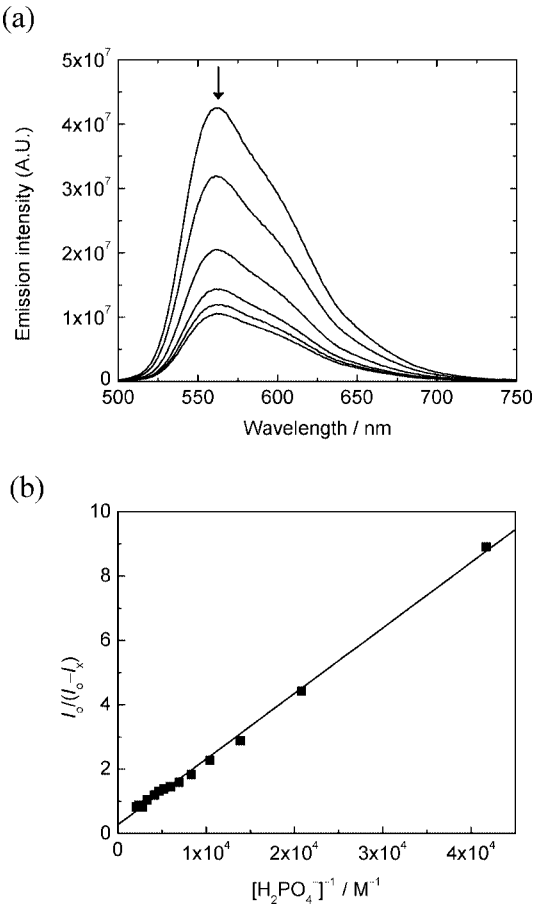


Figure 7. (a) Luminescence spectral traces of complex **3c** (120 μM) in $CH_3CN$ (0.1 M TBAP) upon addition of $H_2PO_4^-$ at 298 K. The concentrations of $H_2PO_4^-$ were 0, 24, 48, 72, 96, and 120 μM, respectively. (b) A plot of $I_o/(I_o - I_x)$ vs. $[H_2PO_4^-]^{-1}$ (■) and the theoretical fit on the basis of a 1:1 binding stoichiometry (—).

rhenium(I) polypyridine anthraquinone thiourea complex [$\log K_s$ = 4.61 ($OAc^-$), 3.66 ($F^-$), 3.70 ($H_2PO_4^-$) in $CH_3CN$].[9] It is likely that this preferential binding of $OAc^-$ ion is associated with the basicity of the anions [$pK_a$ = 4.75 (HOAc), 3.45 (HF), 2.12 ($H_3PO_4$) in aqueous solution at 298 K].[28] The binding affinities of the iridium(III) thiourea complexes to $F^-$ and $H_2PO_4^-$ are very similar. The geometry of the anions appears to contribute strongly to the stabilities of the receptor–anion adducts,[29] with the trigonal $OAc^-$ and tetrahedral $H_2PO_4^-$ ions fitting the trigonal planar shape of the thiourea unit better than the spherical $F^-$ ion. Thus, it is likely that the binding affinities of the iridium(III) thiourea complexes to $OAc^-$, $F^-$, and $H_2PO_4^-$ are a combined effect of the basicity and molecular geometry of the guest ions.

Table 4. $\log K_s$ values for the binding of anions by the iridium(III) polypyridine thiourea complexes in $CH_3CN$ (0.1 M TBAP) at 298 K.

| Complex | $OAc^-$ | $F^-$ | $H_2PO_4^-$ |
|---|---|---|---|
| **1a** | 4.02 | 3.13 | 3.34 |
| **1b** | 4.35 | 3.12 | 3.46 |
| **1c** | 4.03 | 3.16 | 3.16 |
| **2a** | 4.17 | 3.14 | 3.45 |
| **2b** | 4.19 | 3.73 | 3.68 |
| **2c** | 4.16 | 3.24 | 3.26 |
| **3a** | 4.03 | 3.18 | 3.13 |
| **3b** | 4.10 | 3.23 | 3.12 |
| **3c** | 4.03 | 3.38 | 3.14 |

## Conclusions

This paper describes the synthesis, characterization, photophysics, electrochemistry, and anion-binding properties of a series of new luminescent cyclometalated iridium(III) polypyridine thiourea complexes. The emission intensities of all the complexes were reduced upon addition of anions $OAc^-$, $F^-$, and $H_2PO_4^-$. The binding stoichiometries were determined to be 1:1 in all cases, and the $\log K_s$ values ranged from 3.12 to 4.35. The binding affinity of the iridium(III) thiourea complexes for $OAc^-$ was higher than those for $F^-$ and $H_2PO_4^-$, which is a combined effect of the

 © 2006 Wiley-VCH Verlag GmbH & Co. KGaA, Weinheim 

basicity and molecular geometry of the anions. Interestingly, the substituents of the thiourea moieties did not affect the photophysical, electrochemical, and anion-binding properties of the complexes, probably due to insufficient communication between these substituents and the diimine ligand. Nevertheless, these thiourea complexes are the first systematic design of specific anion receptors derived from luminescent cyclometalated iridium(III) polypyridine complexes. The development of related luminescent transition metal complexes as anion receptors is in progress.

## Experimental Section

**Materials and Reagents:** All solvents were of analytical grade and were purified according to published procedures.[30] Ethylamine (2 M in THF) (International Laboratory), aniline (Aldrich), 1-adamantanemethylamine (International Laboratory), tetra-*n*-butylammonium acetate (TBAOAc; Aldrich), tetra-*n*-butylammonium fluoride (TBAF; Acros), and tetra-*n*-butylammonium dihydrogen phosphate ($TBAH_2PO_4$; Aldrich) were used without purification. Tetra-*n*-butylammonium hexafluorophosphate (TBAP; Aldrich) was recrystallized from hot ethanol twice and dried in vacuo at 110 °C before use.

**Synthesis:** A mixture of $[Ir(N\text{-}C)_2(phen\text{-}ITC)](PF_6)$ (HN-C = Hppy, Hbzq, Hpq; 0.12 mmol)[25c] and the corresponding amine (ethylamine, aniline, 1-adamantanemethylamine; 0.12 mmol) in acetone (30 mL) was stirred at room temperature under an inert atmosphere of nitrogen in the dark for 12 h. Recrystallization of the products from a mixture of acetone and diethyl ether gave air-stable orange-yellow crystals.

**$[Ir(ppy)_2(phen\text{-}TU\text{-}Et)](PF_6)$ (1a):** Yield: 93 mg (84%). $^1$H NMR (300 MHz, [D$_6$]acetone, 298 K, relative to TMS): $\delta$ = 9.37 (s, 1 H, phen-N*H*), 8.86 (t, *J* = 8.4 Hz, 2 H, 6-H of pyridyl ring of ppy$^-$), 8.47 (s, 1 H, 6-H of phen), 8.45 (dd, *J* = 5.0 and 1.2 Hz, 1 H, 2-H of phen), 8.38 (dd, *J* = 5.0 and 1.5 Hz, 1 H, 9-H of phen), 8.25 (d, *J* = 8.2 Hz, 2 H, 3-H of pyridyl ring of ppy$^-$), 8.10–8.02 (m, 2 H, 3-H and 8-H of phen), 7.96–7.89 (m, 4 H, 4-H of pyridyl ring and 3-H of phenyl ring of ppy$^-$), 7.81 (t, *J* = 4.9 Hz, 1 H, Et-N*H*), 7.72 (d, *J* = 5.0 Hz, 1 H, 7-H of phen), 7.65 (d, *J* = 5.9 Hz, 1 H, 4-H of phen), 7.11–6.94 (m, 6 H, 5-H of pyridyl ring and 4-H and 5-H of phenyl ring of ppy$^-$), 6.45 (d, *J* = 7.6 Hz, 2 H, 6-H of phenyl ring of ppy$^-$), 3.72–3.63 (m, 2 H, C*H*$_2$CH$_3$), 1.21 ppm (t, *J* = 6.2 Hz, 3 H, CH$_2$C*H*$_3$). IR (KBr): $\tilde{\nu}$ = 3367 (m, N–H), 1269 (m, C=S), 844 (s, $PF_6^-$) cm$^{-1}$. Positive-ion ESI-MS: ion cluster at *m*/*z* 783 [*M*]$^+$. $C_{37}H_{30}F_6IrN_6PS\cdot 0.5\,H_2O$ (936.94): calcd. C 47.43, H 3.33, N 8.97; found C 47.43, H 3.27, N 8.98.

**$[Ir(ppy)_2(phen\text{-}TU\text{-}Ph)](PF_6)$ (1b):** Yield: 88 mg (75%). $^1$H NMR (300 MHz, [D$_6$]acetone, 298 K, relative to TMS): $\delta$ = 10.43 (s, 1 H, phen-N*H*), 10.31 (s, 1 H, Ph-N*H*), 9.11 (d, *J* = 8.2 Hz, 1 H, 6-H of pyridyl ring of ppy$^-$), 8.81 (d, *J* = 8.5 Hz, 1 H, 6-H of pyridyl ring of ppy$^-$), 8.55 (s, 1 H, 6-H of phen), 8.42 (d, *J* = 5.0 Hz, 1 H, 2-H of phen), 8.37 (d, *J* = 5.0 Hz, 1 H, 9-H of phen), 8.24 (d, *J* = 8.2 Hz, 2 H, 3-H of pyridyl ring of ppy$^-$), 8.06–7.99 (m, 2 H, 3-H and 8-H of phen), 7.95–7.88 (m, 4 H, 4-H of pyridyl ring and 3-H of phenyl ring of ppy$^-$), 7.73–7.67 (m, 4 H, 4-H and 7-H of phen and 2-H and 6-H of Ph), 7.38 (t, *J* = 7.6 Hz, 2 H, 3-H and 5-H of Ph), 7.20 (t, *J* = 7.0 Hz, 1 H, 4-H of Ph), 7.10–6.94 (m, 6 H, 5-H of pyridyl ring and 4-H and 5-H of phenyl ring of ppy$^-$), 6.45 ppm (d, *J* = 6.7 Hz, 2 H, 6-H of phenyl ring of ppy$^-$). IR (KBr): $\tilde{\nu}$ = 3374 (m, N–H), 1268 (m, C=S), 844 (s, $PF_6^-$) cm$^{-1}$. Positive-ion ESI-MS: ion cluster at *m*/*z* 829 [*M*]$^+$. $C_{41}H_{30}F_6IrN_6PS\cdot H_2O$ (994.00): calcd. C 49.54, H 3.24, N 8.45; found C 49.78, H 3.49, N 8.25.

**$[Ir(ppy)_2(phen\text{-}TU\text{-}MeA)](PF_6)$ (1c):** Yield: 89 mg (77%). $^1$H NMR (300 MHz, [D$_6$]acetone, 298 K, relative to TMS): $\delta$ = 9.44 (s, 1 H, phen-N*H*), 8.86 (dd, *J* = 8.8 and 5.6 Hz, 2 H, 6-H of pyridyl ring of ppy$^-$), 8.52 (s, 1 H, 6-H of phen), 8.45 (d, *J* = 4.4 Hz, 1 H, 2-H of phen), 8.38 (d, *J* = 4.4 Hz, 1 H, 9-H of phen), 8.25 (d, *J* = 8.2 Hz, 2 H, 3-H of pyridyl ring of ppy$^-$), 8.10–8.01 (m, 2 H, 3-H and 8-H of phen), 7.99–7.89 (m, 4 H, 4-H of pyridyl ring and 3-H of phenyl ring of ppy$^-$), 7.73–7.63 (m, 3 H, 4-H and 7-H of phen and CH$_2$-N*H*), 7.11–6.95 (m, 6 H, 5-H of pyridyl ring and 4-H and 5-H of phenyl ring of ppy$^-$), 6.45 (d, *J* = 7.3 Hz, 2 H, 6-H of phenyl ring of ppy$^-$), 2.83 (s, 2 H, C*H*$_2$NH), 1.97 (s, 3 H, CH of adamantane), 1.76–1.61 ppm (m, 12 H, CH$_2$ of adamantane). IR (KBr): $\tilde{\nu}$ = 3387 (m, N–H), 1266 (m, C=S), 844 (s, $PF_6^-$) cm$^{-1}$. Positive-ion ESI-MS: ion cluster at *m*/*z* 903 [*M*]$^+$. $C_{46}H_{42}F_6IrN_6PS$ (1048.1): calcd. C 52.71, H 4.04, N 8.02; found C 52.58, H 3.98, N 8.25.

**$[Ir(bzq)_2(phen\text{-}TU\text{-}Et)](PF_6)$ (2a):** Yield: 75 mg (64%). $^1$H NMR (300 MHz, [D$_6$]acetone, 298 K, relative to TMS): $\delta$ = 10.66 (s, 1 H, phen-N*H*), 9.19 (d, *J* = 5.9 Hz, 1 H, 2-H of phen), 8.95 (s, 1 H, Et-N*H*), 8.71 (d, *J* = 7.6 Hz, 2 H, 6-H and 9-H of phen), 8.50 (d, *J* = 6.7 Hz, 2 H, 4-H of bzq$^-$), 8.39 (d, *J* = 5.3 Hz, 1 H, 4-H of phen), 8.29 (d, *J* = 4.4 Hz, 1 H, 7-H of phen), 8.16 (d, *J* = 4.1 Hz, 2 H, 2-H of bzq$^-$), 8.00 (d, *J* = 8.8 Hz, 2 H, 6-H of bzq$^-$), 7.92–7.86 (m, 4 H, 5-H of bzq$^-$ and 3-H and 8-H of phen), 7.59 (d, *J* = 7.9 Hz, 2 H, 7-H of bzq$^-$), 7.46 (t, *J* = 5.3 Hz, 2 H, 3-H of bzq$^-$), 7.23 (t, *J* = 7.3 Hz, 2 H, 8-H of bzq$^-$), 6.47 (d, *J* = 6.5 Hz, 2 H, 9-H of bzq$^-$), 3.65–3.63 (m, 2 H, C*H*$_2$CH$_3$), 1.29–1.20 ppm (m, 3 H, CH$_2$C*H*$_3$). IR (KBr): $\tilde{\nu}$ = 3365 (m, N–H), 1266 (m, C=S), 847 (s, $PF_6^-$) cm$^{-1}$. Positive-ion ESI-MS: ion cluster at *m*/*z* 831 [*M*]$^+$. $C_{41}H_{30}F_6IrN_6PS\cdot H_2O$ (994.00): calcd. C 49.54, H 3.24, N 8.45; found C 49.44, H 3.24, N 8.17.

**$[Ir(bzq)_2(phen\text{-}TU\text{-}Ph)](PF_6)$ (2b):** Yield: 86 mg (70%). $^1$H NMR (300 MHz, [D$_6$]acetone, 298 K, relative to TMS): $\delta$ = 9.88 (s, 1 H, phen-N*H*), 9.77 (s, 1 H, Ph-N*H*), 8.99 (d, *J* = 7.6 Hz, 1 H, 2-H of phen), 8.83 (d, *J* = 7.9 Hz, 1 H, 9-H of phen), 8.52 (d, *J* = 7.3 Hz, 2 H, 4-H of bzq$^-$), 8.47 (s, 1 H, 6-H of phen), 8.43 (d, *J* = 5.0 Hz, 1 H, 4-H of phen), 8.37 (d, *J* = 4.1 Hz, 1 H, 7-H of phen), 8.19 (d, *J* = 4.4 Hz, 1 H, 2-H of bzq$^-$), 8.11 (d, *J* = 5.6 Hz, 1 H, 2-H of bzq$^-$), 8.03–7.86 (m, 7 H, 2-H, 3-H and 8-H of phen and 5-H and 6-H of bzq$^-$), 7.66–7.59 (m, 4 H, 2-H and 6-H of Ph and 7-H of bzq$^-$), 7.50–7.38 (m, 4 H, 3-H and 5-H of Ph and 3-H of bzq$^-$), 7.24 (t, *J* = 7.6 Hz, 3 H, 4-H of Ph and 8-H of bzq$^-$), 6.48 ppm (d, *J* = 7.3 Hz, 2 H, 9-H of bzq$^-$). IR (KBr): $\tilde{\nu}$ = 3395 (m, N–H), 1262 (m, C=S), 847 (s, $PF_6^-$) cm$^{-1}$. Positive-ion ESI-MS: ion cluster at *m*/*z* 879 [*M*]$^+$. $C_{45}H_{30}F_6IrN_6PS\cdot 0.5\,H_2O$ (1033.0): calcd. C 52.32, H 3.02, N 8.14; found C 52.19, H 3.28, N 8.08.

**$[Ir(bzq)_2(phen\text{-}TU\text{-}MeA)](PF_6)$ (2c):** Yield: 95 mg (72%). $^1$H NMR (300 MHz, [D$_6$]acetone, 298 K, relative to TMS): $\delta$ = 10.80 (s, 1 H, phen-N*H*), 9.24 (d, *J* = 6.7 Hz, 1 H, 2-H of phen), 8.83 (s, 1 H, CH$_2$-N*H*), 8.77 (s, 1 H, 6-H of phen), 8.69 (d, *J* = 6.5 Hz, 1 H, 9-H of phen), 8.51 (dd, *J* = 3.5 and 7.3 Hz, 2 H, 4-H of bzq$^-$), 8.40 (d, *J* = 3.8 Hz, 1 H, 4-H of phen), 8.30 (d, *J* = 5.0 Hz, 1 H, 7-H of phen), 8.16 (t, *J* = 4.5 Hz, 2 H, 2-H of bzq$^-$), 8.01 (dd, *J* = 7.0 and 1.8 Hz, 2 H, 6-H of bzq$^-$), 7.94–7.86 (m, 4 H, 3-H and 8-H of phen and 5-H of bzq$^-$), 7.60 (d, *J* = 7.6 Hz, 2 H, 7-H of bzq$^-$), 7.46 (dd, *J* = 5.0 and 2.6 Hz, 2 H, 3-H of bzq$^-$), 7.24 (t, *J* = 7.6 Hz, 2 H, 8-H of bzq$^-$), 6.48 (d, *J* = 7.3 Hz, 2 H, 9-H of bzq$^-$), 2.83 (s, 2

 © 2006 Wiley-VCH Verlag GmbH & Co. KGaA, Weinheim 

H, C$H_2$NH), 1.97 (s, 3 H, CH of adamantane), 1.68–1.67 ppm (m, 12 H, $CH_2$ of adamantane). IR (KBr): $\tilde{\nu}$ = 3439 (m, N–H), 1266 (m, C=S), 847 (s, $PF_6^-$) $cm^{-1}$. Positive-ion ESI-MS: ion cluster at *m/z* 950 $[M]^+$. $C_{50}H_{42}F_6IrN_6PS$ (1096.2): calcd. C 54.79, H 3.86, N 7.67; found C 54.99, H 3.99, N 7.92.

**[Ir(pq)$_2$(phen-TU-Et)](PF$_6$) (3a):** Yield: 86 mg (70%). $^1$H NMR (300 MHz, [D$_6$]acetone, 298 K, relative to TMS): $\delta$ = 9.24 (s, 1 H, phen-N*H*), 9.03 (d, *J* = 7.8 Hz, 1 H, 2-H of phen), 8.75–8.65 (m, 3 H, 3-H, 8-H and 9-H of phen), 8.58–8.46 (m, 5 H, 4-H, 6-H and 7-H of phen and 3-H of quinolinyl ring of pq$^-$), 8.31 (d, *J* = 7.6 Hz, 1 H, 5-H of quinolinyl ring of pq$^-$), 8.15–7.96 (m, 2 H, 4-H of quinolinyl ring of pq$^-$), 7.89 (s, 1 H, Et-N*H*), 7.81 (d, *J* = 6.7 Hz, 2 H, 8-H of quinolinyl ring of pq$^-$), 7.41–7.21 (m, 6 H, 6-H and 7-H of quinolinyl ring and 3-H of phenyl ring of pq$^-$), 6.95–6.86 (m, 4 H, 4-H and 5-H of phenyl ring of pq$^-$), 6.68 (d, *J* = 7.9 Hz, 2 H, 6-H of phenyl ring of pq$^-$), 3.62–3.58 (m, 2 H, C$H_2$CH$_3$), 1.32 ppm (t, *J* = 7.2 Hz, 3 H, CH$_2$C$H_3$). IR (KBr): $\tilde{\nu}$ = 3387 (m, N–H), 1288 (m, C=S), 846 (s, $PF_6^-$) $cm^{-1}$. Positive-ion ESI-MS: ion cluster at *m/z* 882 $[M]^+$. $C_{45}H_{34}F_6IrN_6PS{\cdot}H_2O$ (1046.1): calcd. C 51.67, H 3.47, N 8.03; found C 51.58, H 3.27, N 8.24.

**[Ir(pq)$_2$(phen-TU-Ph)](PF$_6$) (3b):** Yield: 96 mg (74%). $^1$H NMR (300 MHz, [D$_6$]acetone, 298 K, relative to TMS): $\delta$ = 10.35 (s, 1 H, phen-N*H*), 10.06 (s, 1 H, Ph-N*H*), 8.95 (d, *J* = 8.5 Hz, 1 H, 2-H of phen), 8.72–8.63 (m, 3 H, 3-H, 8-H and 9-H of phen), 8.58–8.46 (m, 4 H, 4-H and 7-H of phen and 3-H of quinolinyl ring of pq$^-$), 8.31 (dd, *J* = 7.8 and 3.2 Hz, 2 H, 5-H of quinolinyl ring of pq$^-$), 8.22 (s, 1 H, 6-H of phen), 8.06–7.99 (m, 2 H, 4-H of quinolinyl ring of pq$^-$), 7.80 (t, *J* = 6.9 Hz, 2 H, 2-H and 6-H of Ph), 7.65 (d, *J* = 8.8 Hz, 2 H, 8-H of quinolinyl ring of pq$^-$), 7.41–7.13 (m, 9 H, 3-H, 4-H and 5-H of Ph and 6-H and 7-H of quinolinyl ring and 3-H of phenyl ring of pq$^-$), 6.94–6.84 (m, 4 H, 4-H and 5-H of phenyl ring of pq$^-$), 6.69 ppm (d, *J* = 7.6 Hz, 2 H, 6-H of phenyl ring of pq$^-$). IR (KBr): $\tilde{\nu}$ = 3351 (m, N–H), 1288 (m, C=S), 845 (s, $PF_6^-$) $cm^{-1}$. Positive-ion ESI-MS: ion cluster at *m/z* 931 $[M]^+$. $C_{49}H_{34}F_6IrN_6PS{\cdot}1.5\,H_2O$ (1103.12): calcd. C 53.35, H 3.38, N 7.62; found C 53.25, H 3.44, N 7.78.

**[Ir(pq)$_2$(phen-TU-MeA)](PF$_6$) (3c):** Yield: 106 mg (77%). $^1$H NMR (300 MHz, [D$_6$]acetone, 298 K, relative to TMS): $\delta$ = 10.87 (s, 1 H, phen-N*H*), 9.20 (d, *J* = 8.2 Hz, 1 H, 2-H of phen), 9.00 (s, 1 H, CH$_2$-N*H*), 8.68 (d, *J* = 4.4 Hz, 1 H, 9-H of phen), 8.60–8.53 (m, 5 H, 3-H, 6-H and 8-H of phen and 3-H of quinolinyl ring of pq$^-$), 8.48–8.44 (m, 2 H, 4-H and 7-H of phen), 8.30 (d, *J* = 8.2 Hz, 2 H, 5-H of quinolinyl ring of pq$^-$), 7.98–7.93 (m, 2 H, 4-H of quinolinyl ring of pq$^-$), 7.78 (d, *J* = 8.2 Hz, 2 H, 8-H of quinolinyl ring of pq$^-$), 7.38–7.20 (m, 6 H, 6-H and 7-H of quinolinyl ring and 3-H of phenyl ring of pq$^-$), 6.92–6.85 (m, 4 H, 4-H and 5-H of phenyl ring of pq$^-$), 6.68 (dd, *J* = 7.6 and 2.3 Hz, 2 H, 6-H of phenyl ring of pq$^-$), 2.83 (s, 2 H, C$H_2$NH), 1.90 (s, 3 H, CH of adamantane), 1.70–1.62 ppm (m, 12 H, $CH_2$ of adamantane). IR (KBr): $\tilde{\nu}$ = 3410 (m, N–H), 1288 (m, C=S), 846 (s, $PF_6^-$) $cm^{-1}$. Positive-ion ESI-MS: ion cluster at *m/z* 1002 $[M]^+$. $C_{54}H_{46}F_6IrN_6PS{\cdot}0.5\,H_2O$ (1157.26): calcd. C 56.05, H 4.09, N 7.26; found C 56.26, H 4.38, N 7.38.

**Instrumentation and Methods:** Equipment for characterization and photophysical and electrochemical studies has been described previously.[25c] Luminescence quantum yields were measured by the optically dilute method[31] using an aerated aqueous solution of $[Ru(bpy)_3]Cl_2$ ($\Phi$ = 0.028)[32] as the standard solution.

**Anion-Binding Studies:** Steady-state emission spectral titrations were used to determine the binding constants. A supporting electrolyte (0.1 M TBAP) was present in the titration solutions to maintain a constant ionic strength. The binding constant, $K_s$, of the anion $A^-$ to the receptor Ir for the following equilibrium

$$\mathrm{Ir} + \mathrm{A}^- \overset{K_s}{\rightleftharpoons} \mathrm{Ir\text{-}A}^-$$

was obtained by fitting the experimental data to Equation (1)[27]

$$\frac{I_o}{I_o - I_x} = \left(\frac{I_o}{I_o - I_\infty}\right)\left(\frac{1}{K_s[A^-]} + 1\right) \quad (1)$$

where $I_o$ is the emission intensity of the receptor only, $I_x$ is the emission intensity of the receptor in the presence of the anion at a concentration [$A^-$], and $I_\infty$ is the limiting emission intensity.

## Acknowledgments

We thank City University of Hong Kong for financial support (Project Number 7001797). J. S.-Y. L. acknowledges the receipt of a Postgraduate Studentship and a Research Tuition Scholarship, both administered by the City University of Hong Kong.

[1] a) P. D. Beer, P. A. Gale, G. Z. Chen, *Coord. Chem. Rev.* **1999**, *185–186*, 3–36; b) P. D. Beer, J. Cadman, *Coord. Chem. Rev.* **2000**, *205*, 131–155; c) P. D. Beer, P. A. Gale, *Angew. Chem. Int. Ed.* **2001**, *40*, 486–516; d) P. D. Beer, E. J. Hayes, *Coord. Chem. Rev.* **2003**, *240*, 167–189.
[2] P. A. Gale, *Coord. Chem. Rev.* **2001**, *213*, 79–128.
[3] K. Choi, A. D. Hamilton, *Coord. Chem. Rev.* **2003**, *240*, 101–110.
[4] R. Martínez, F. Scancenón, *Chem. Rev.* **2003**, *103*, 4419–4476.
[5] A. Bianchi, K. Bowman-James, E. García-España, *Supramolecular Chemistry of Anions*, John Wiley & Sons, New York, **1997**.
[6] a) D. H. Lee, H. Y. Lee, J.-I. Hong, *Chem. Commun.* **2001**, 1188–1189; b) D. H. Lee, H. Y. Lee, J.-I. Hong, *Tetrahedron Lett.* **2002**, *43*, 7273–7276; c) D. H. Lee, J. H. Im, J.-H. Lee, J.-I. Hong, *Tetrahedron Lett.* **2002**, *43*, 9637–9640.
[7] a) R. Kato, S. Nishizawa, T. Hayashita, N. Teramae, *Tetrahedron Lett.* **2001**, *42*, 5053–5056; b) L.-H. Wei, Y.-B. He, J.-L. Wu, L.-Z. Meng, X. Yang, *Supramol. Chem.* **2004**, *16*, 561–567; c) L. Nie, Z. Li, J. Han, X. Zhang, R. Yang, W.-X. Liu, F.-Y. Wu, J.-W. Xie, Y.-F. Zhao, Y.-B. Jiang, *J. Org. Chem.* **2004**, *69*, 6449–6454; d) V. Amendola, D. Esteban-Gómez, L. Fabbrizzi, M. Licchelli, E. Monzani, F. Sancenón, *Inorg. Chem.* **2005**, *44*, 8690–8698; e) D. A. Jose, D. K. Kumar, B. Ganguly, A. Das, *Tetrahedron Lett.* **2005**, *46*, 5343–5346; f) T. Gunnlaugsson, P. E. Kruger, P. Jensen, J. Tierney, H. D. P. Ali, G. M. Hussey, *J. Org. Chem.* **2005**, *70*, 10875–10878.
[8] a) S. Nishizawa, H. Kaneda, T. Uchida, N. Teramae, *J. Chem. Soc., Perkin Trans. 2* **1998**, 2325–2327; b) Y. Kubo, M. Tsukahara, S. Ishihara, S. Tokita, *Chem. Commun.* **2000**, 653–654; c) S.-i. Sasaki, D. Citterio, S. Ozawa, K. Suzuki, *J. Chem. Soc., Perkin Trans. 2* **2001**, 2309–2313; d) T. Gunnlaugsson, A. P. Davis, M. Glynn, *Chem. Commun.* **2001**, 2556–2557; e) F.-Y. Wu, Z. Li, Z.-C. Wen, N. Zhou, Y.-F. Zhao, Y.-B. Jiang, *Org. Lett.* **2002**, *4*, 3203–3205; f) J.-L. Wu, Y.-B. He, L.-H. Wei, S.-Y. Liu, L.-Z. Meng, L. Hu, *Supramol. Chem.* **2004**, *16*, 353–359.
[9] K. K.-W. Lo, J. S.-Y. Lau, V. W.-Y. Fong, N. Zhu, *Organometallics* **2004**, *23*, 1098–1106.
[10] a) F. O. Garces, K. A. King, R. J. Watts, *Inorg. Chem.* **1988**, *27*, 3464–3471; b) A. P. Wilde, R. J. Watts, *J. Phys. Chem.* **1991**, *95*,

 © 2006 Wiley-VCH Verlag GmbH & Co. KGaA, Weinheim 

622–629; c) A. P. Wilde, K. A. King, R. J. Watts, *J. Phys. Chem.* **1991**, *95*, 629–634.
[11] a) S. Serroni, A. Juris, S. Campagna, M. Venturi, G. Denti, V. Balzani, *J. Am. Chem. Soc.* **1994**, *116*, 9086–9091; b) G. Calogero, G. Giuffrida, S. Serroni, V. Ricevuto, S. Campagna, *Inorg. Chem.* **1995**, *34*, 541–545; c) G. Di Marco, M. Lanza, A. Mamo, I. Stefio, C. Di Petro, G. Romeo, S. Campagna, *Anal. Chem.* **1998**, *70*, 5019–5023; d) F. Neve, A. Crispini, S. Campagna, S. Serroni, *Inorg. Chem.* **1999**, *38*, 2250–2258; e) P. M. Griffiths, F. Loiseau, F. Puntoriero, S. Serroni, S. Campagna, *Chem. Commun.* **2000**, 2297–2298; f) F. Neve, M. La Deda, A. Crispini, A. Bellusci, F. Puntoriero, S. Campagna, *Organometallics* **2004**, *23*, 5856–5863.
[12] a) M. Polson, S. Fracasso, V. Bertolasi, M. Ravaglia, F. Scandola, *Inorg. Chem.* **2004**, *43*, 1950–1956; b) M. Polson, M. Ravaglia, S. Fracasso, M. Garavelli, F. Scandola, *Inorg. Chem.* **2005**, *44*, 1282–1289.
[13] a) P. Didier, I. Ortmans, A. Kirsch-De Mesmaeker, R. J. Watts, *Inorg. Chem.* **1993**, *32*, 5239–5245; b) I. Ortmans, P. Didier, A. Kirsch-De Mesmaeker, *Inorg. Chem.* **1995**, *34*, 3695–3704.
[14] a) I. M. Dixon, J.-P. Collin, J.-P. Sauvage, L. Flamigni, S. Encinas, F. Barigelletti, *Chem. Soc. Rev.* **2000**, *29*, 385–391; b) E. Baranoff, I. M. Dixon, J.-P. Collin, J.-P. Sauvage, B. Ventura, L. Flamigni, *Inorg. Chem.* **2004**, *43*, 3057–3066; c) L. Flamigni, B. Ventura, F. Barigelletti, E. Baranoff, J.-P. Collin, J.-P. Sauvage, *Eur. J. Inorg. Chem.* **2005**, 1312–1318.
[15] a) M. G. Colombo, H. U. Güdel, *Inorg. Chem.* **1993**, *32*, 3081–3087; b) M. G. Colombo, A. Hauser, H. U. Güdel, *Inorg. Chem.* **1993**, *32*, 3088–3092; c) M. G. Colombo, T. C. Brunold, T. Riedener, H. U. Güdel, M. Förtsch, H.-B. Bürgi, *Inorg. Chem.* **1994**, *33*, 545–550.
[16] a) S. Lamansky, P. Djurovich, D. Murphy, F. Abdel-Razzaq, H.-E. Lee, C. Adachi, P. E. Burrows, S. R. Forrest, M. E. Thompson, *J. Am. Chem. Soc.* **2001**, *123*, 4304–4312; b) A. B. Tamayo, B. D. Alleyne, P. I. Djurovich, S. Lamansky, I. Tsyba, N. N. Ho, R. Bau, M. E. Thompson, *J. Am. Chem. Soc.* **2003**, *125*, 7377–7387; c) J. Li, P. I. Djurovich, B. D. Alleyne, M. Yousufuddin, N. N. Ho, J. C. Thomas, J. C. Peters, R. Bau, M. E. Thompson, *Inorg. Chem.* **2005**, *44*, 1713–1727; d) T. Sajoto, P. I. Djurovich, A. Tamayo, M. Yousufuddin, R. Bau, M. E. Thompson, *Inorg. Chem.* **2005**, *44*, 7992–8003; e) A. B. Tamayo, S. Garon, T. Sajoto, P. I. Djurovich, I. M. Tsyba, R. Bau, M. E. Thompson, *Inorg. Chem.* **2005**, *44*, 8723–8732.
[17] a) M. Licini, J. A. G. Williams, *Chem. Commun.* **1999**, 1943–1944; b) W. Goodall, J. A. G. Williams, *J. Chem. Soc., Dalton Trans.* **2000**, 2893–2895; c) W. Leslie, A. S. Batsanov, J. A. K. Howard, J. A. G. Williams, *Dalton Trans.* **2004**, 623–631; d) W. Leslie, R. A. Poole, P. R. Murray, L. J. Yellowlees, A. Beeby, J. A. G. Williams, *Polyhedron* **2004**, *23*, 2769–2777; e) A. J. S. Bexon, J. A. G. Williams, *C. R. Chimie* **2005**, *8*, 1326–1335.
[18] N. P. Ayala, C. M. Flynn, L. Sacksteder, J. N. Demas, B. A. DeGraff, *J. Am. Chem. Soc.* **1990**, *112*, 3837–3844.
[19] a) J. H. van Diemen, J. G. Haasnoot, R. Hage, E. Müller, J. Reedijk, *Inorg. Chim. Acta* **1991**, *181*, 245–251; b) J. H. van Diemen, R. Hage, J. G. Haasnoot, H. E. B. Lempers, J. Reedijk, J. G. Vos, L. De Cola, F. Barigelletti, V. Balzani, *Inorg. Chem.* **1992**, *31*, 3518–3522.
[20] a) E. A. Plummer, J. W. Hofstraat, L. De Cola, *Dalton Trans.* **2003**, 2080–2084; b) P. Coppo, E. A. Plummer, L. De Cola, *Chem. Commun.* **2004**, 1774–1775; c) P. Coppo, M. Duati, V. N. Kozhevnikov, J. W. Hofstraat, L. De Cola, *Angew. Chem. Int. Ed.* **2005**, *44*, 1806–1810.
[21] a) M. Maestri, V. Balzani, C. Deuschel-Cornioley, A. von Zelewsky, *Adv. Photochem.* **1992**, *17*, 1–68; b) C. Schaffner-Hamann, A. von Zelewsky, A. Barbieri, F. Barigelletti, G. Muller, J. P. Riehl, A. Neels, *J. Am. Chem. Soc.* **2004**, *126*, 9339–9348.
[22] T. Yutaka, S. Obara, S. Ogawa, K. Nozaki, N. Ikeda, T. Ohno, Y. Ishii, K. Sakai, M. Haga, *Inorg. Chem.* **2005**, *44*, 4737–4746.
[23] a) F.-M. Hwang, H.-Y. Chen, P.-S. Chen, C.-S. Liu, Y. Chi, C.-F. Shu, F.-L. Wu, P.-T. Chou, S.-M. Peng, G.-H. Lee, *Inorg. Chem.* **2005**, *44*, 1344–1353; b) H.-C. Li, P.-T. Chou, Y.-H. Hu, Y.-M. Cheng, R.-S. Liu, *Organometallics* **2005**, *24*, 1329–1335; c) J.-M. Hsieh, M.-L. Ho, P.-W. Wu, P.-T. Chou, T.-T. Tsai, Y. Chi, *Chem. Commun.* **2006**, 615–617; d) M.-L. Ho, F.-M. Hwang, P.-N. Chen, Y.-H. Hu, Y.-M. Cheng, K.-S. Chen, G.-H. Lee, Y. Chi, P.-T. Chou, *Org. Biomol. Chem.* **2006**, *4*, 98–103.
[24] a) E. Holder, V. Marin, M. A. R. Meier, U. S. Schubert, *Macromol. Rapid Commun.* **2004**, *25*, 1491–1496; b) E. Holder, V. Marin, A. Alexeev, U. S. Schubert, *J. Polym. Sci. A: Polym. Chem.* **2005**, *43*, 2765–2776; c) E. Holder, V. Marin, D. Kozodaev, M. A. R. Meier, B. G. G. Lohmeijer, U. S. Schubert, *Macromol. Chem. Phys.* **2005**, *206*, 989–997.
[25] a) K. K.-W. Lo, D. C.-M. Ng, C.-K. Chung, *Organometallics* **2001**, *20*, 4999–5001; b) K. K.-W. Lo, C.-K. Chung, N. Zhu, *Chem. Eur. J.* **2003**, *9*, 475–483; c) K. K.-W. Lo, C.-K. Chung, T. K.-M. Lee, L.-H. Lui, H.-K. Tsang, N. Zhu, *Inorg. Chem.* **2003**, *42*, 6886–6897; d) K. K.-W. Lo, J. S.-W. Chan, L.-H. Lui, C.-K. Chung, *Organometallics* **2004**, *23*, 3108–3116; e) K. K.-W. Lo, C.-K. Li, J. S.-Y. Lau, *Organometallics* **2005**, *24*, 4594–4601; f) K. K.-W. Lo, C.-K. Chung, N. Zhu, *Chem. Eur. J.* **2006**, *12*, 1500–1512.
[26] a) The possibility that the change is due to deprotonation[26b] of the thiourea protons is excluded by $^1$H NMR studies using acetone or DMSO as solvents. For example, in the presence of $OAc^-$ or $F^-$, ([Ir] = 0.01 M, [anion$^-$] = 0.05 M), the resonance signals of the thiourea protons of complex **1a** disappeared[26b] and those of 6-H of the phen-TU-R ligands were shifted to lower field, from about $\delta$ = 8.47 to 8.80 ppm. These changes are typical of hydrogen-bonding interactions between the thiourea protons and the anions, see: b) V. Amendola, D. Esteban-Gómez, L. Fabbrizzi, M. Licchelli, *Acc. Chem. Res.* **2006**, *39*, 343–353; c) F. M. Pfeffer, A. M. Buschgens, N. W. Barnett, T. Gunnlaugsson, P. E. Kruger, *Tetrahedron Lett.* **2005**, *46*, 6579–6584.
[27] H. A. Benesi, J. H. Hildebrand, *J. Am. Chem. Soc.* **1949**, *71*, 2703–2707.
[28] D. R. Lide, *CRC Handbook of Chemistry and Physics* 73rd Edition; CRC Press, Boca Raton, Florida, USA, **1993**.
[29] P. D. Beer, P. A. Gale, D. K. Smith, *Supramolecular Chemistry*, Oxford University Press, Oxford, **1999**, p. 31.
[30] D. D. Perrin, W. L. F. Armarego, *Purification of Laboratory Chemicals*, Pergamon, Oxford, **1997**.
[31] J. N. Demas, G. A. Crosby, *J. Phys. Chem.* **1971**, *75*, 991–1024.
[32] K. Nakamaru, *Bull. Chem. Soc. Jpn.* **1982**, *55*, 2697–2705.

Received: May 9, 2006
Published Online: August 7, 2006

 © 2006 Wiley-VCH Verlag GmbH & Co. KGaA, Weinheim 

DOI: 10.1002/ejic.200600483

# Quantum Chemical Analysis of the Enantiomerisation Mechanism of Complexes of the Type $[M^{II}(XU)_4]F^+$ (M = Pt, Pd, Ni; X = S, Se, Te; U = urea)

**Ralph Puchta,[a,b] Roland Meier,[a] Nico J. R. van Eikema Hommes,[b] and Rudi van Eldik*[a]**

**Keywords:** Enantiomers / Density functional calculations / Metal complexes

The enantiomerisation pathway for $\{[Pt(thiourea)_4]\}F^+$ [a model for the $C_4$-symmetric $[Pt(SU)_4]SiF_6$ (SU = thiourea) complex] and derivatives is explored by density functional theory (B3LYP/LANL2DZp) und the activation barrier for the one-step process from $C_4$ to $C_4'$ via a $C_4$ transition state is computed. The substitution of $Pt^{2+}$ by $Pd^{2+}$ and $Ni^{2+}$ and the exchange of selenourea and tellurourea increase the barrier. ($\{[Pt(thiourea)_4]\}F^+$: 4.2 kcal/mol, $\{[Pd(thiourea)_4]\}F^+$: 4.5 kcal/mol, $\{[Ni(thiourea)_4]\}F^+$: 7.6 kcal/mol, $\{[Pt(selenourea)_4]\}F^+$: 5.3 kcal/mol, $\{[Pt(tellurourea)_4]\}F^+$: 8.8 kcal/mol).

(© Wiley-VCH Verlag GmbH & Co. KGaA, 69451 Weinheim, Germany, 2006)

## Introduction

Besides the common use of platinum complexes as catalysts in industrial processes,[1–4] $Pt^{II}$ complexes deliver the most common anti-tumour drugs for certain types of cancer.[5] Intracellular thiols are known to play an important role in the metabolism of Pt anti-tumour drugs because of their participation in trapping the drug.[6] Also, thiols can influence renal toxicity and can be involved in other side-effects.[7] Thiourea (SU) is one of the best-known nucleophiles for $Pt^{II}$ complexes[8,9] and is commonly used in the investigation of ligand-substitution reactions in coordination chemistry. Hence, thiourea can very easily displace other ligands from the metal centre in $Pt^{II}$ complexes, including S-bonded ligands such as L-cysteine in $[Pt(terpy)(S\text{-}cys)]^+$.[10] The strong binding ability of S-donor nucleophiles can also be applied to reverse unwanted side-effects in chemotherapy.[11,12] It has been demonstrated that thiourea could restore the biological activity of Pt-loaded DNA.[13] Thiourea and other sulfur-containing compounds have been applied as emergency or protective agents in order to reduce the toxicity of platinum anti-tumour complexes.[14–16] The protective effect of these compounds is either to prevent or to reverse the formation of Pt–S adducts of proteins.

As shown in Figure 1, thiourea is able to coordinate in different ways to the $Pt^{II}$ centre depending on the packing forces and H-bonding networks in different solid $[Pt(SU)_4]^{2+}$ salts,[17,18] which is controlled by the selected counter anions. There is current interest in the design of selective receptors for anions,[19,20] held together by either electrostatic or hydrogen-bonding-based forces.[21,22] Even though thiourea seems to show an inherently flexible coordination of the $S{=}C(NH_2)_2$ branches to the platinum centre, the IOIO conformation has until recently been known as the only isomer of $[Pt(SU)_4]^{2+}$, based on the structure of $[Pt(SU)_4]Cl_2$.[17,18,23] In contrast, $[Pd(SU)_4]Cl_2$ and $[Pd(SU)_4]I_2$ show the IIOO conformer.[23,24] While investigating the effects of solvent[25] and dicarboxylates[26] on the structure of $[Pt(SU)_4]^{2+}$, Gale et al. isolated IIOO as a new conformer. By serendipity they were able to build a molecular capsule from two $[Pt(SU)_4]^{2+}$ moieties in the OOOO conformer complexing endohedrally to a $Cl^-$ ion. This molecular capsule is stabilised by a hydrogen-bonded corset of croconates. In a recent study, we were able to show that all

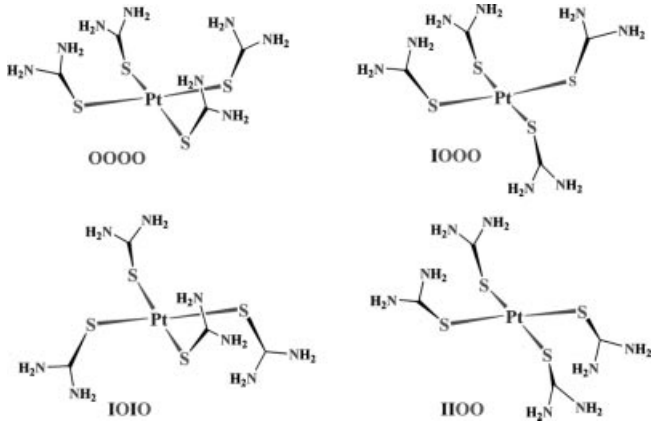


Figure 1. The four possible conformers of $[Pt(SU)_4]^{2+}$.

[a] Institute for Inorganic Chemistry, University of Erlangen-Nürnberg,
Egerlandstr. 1, 91058 Erlangen, Germany
vaneldik@chemie.uni-erlangen.de
[b] Computer Chemistry Center, University of Erlangen-Nürnberg,
Nägelsbachstr. 25, 91052 Erlangen, Germany

 © 2006 Wiley-VCH Verlag GmbH & Co. KGaA, Weinheim 

four possible conformers (see Figure 1) of the $[Pt(SU)_4]^{2+}$ unit can be realised in the solid state by nothing more than a systematic tuning of the molecular structure by the hydrogen-bonding ability of the counter anion.[27] The chiral $C_4$-symmetric (four SU moieties up) was realised in $[Pt(SU)_4]SiF_6$, where four $NH_2$ groups interact with the $SiF_6^{2-}$ ion (see Figure 2).

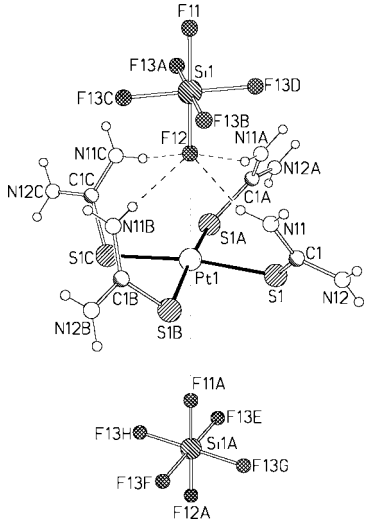


Figure 2. Conformation and H-bonding in $[Pt(SU)_4]SiF_6$ (OOOO).[27]

The H-bonds of the $NH_2$ protons formed with adjacent acceptors usually lead to the formation of clusters bearing interesting host–guest motifs.[28] The H-bonds formed by the $NH_2$ protons are especially important in terms of the motivation for the current study. We recently studied a larger number of $[Pt(SU)_4]X_2$ salts (X = $S_2O_6^{2-}$, $SiF_6^{2-}$, $ClO_4^-$, $CF_3SO_3^-$, $I^-$, $BPh_4^-$, etc.),[29] and found that the relatively strong N–H···X interactions in the case of X = one $F^-$ of the $SiF_6^{2-}$ anion in $[Pt(SU)_4]SiF_6 \cdot 0.25H_2O$ drives the $[Pt(SU)_4]^{2+}$ cation into the OOOO conformation (see Scheme 1). An analogous arrangement to that shown in Scheme 1 was recently also found by Gale et al. for the salt where X = $Cl^-$.[30,31]

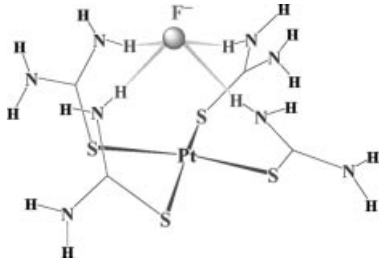


Scheme 1. View of the N–H···$F^-$ interactions in the $\{[Pt(SU)_4]F\}^+$ unit of $[Pt(SU)_4]SiF_6 \cdot 0.25H_2O$.

In these $[Pt(SU)_4]X$ units, six-membered proton chelate rings of the type Pt–S–C–N–H···X are formed. As found so far,[30] these four rings give rise (in the solid state) to either λλλλ or δδδδ chiral patterns (cf. Scheme 2).

Scheme 2. Enantiomers of the $\{[Pt(SU)_4]F\}^+$ unit based on the difference in ring chirality.

The question that we want to answer in the present study concerns the mechanistic details of the interconversion between the enantiomers shown in Scheme 2. On the basis of the well-known flexibility of the Pt–S bond, one would expect a nondissociative enantiomerisation mechanism, but the nature of this pathway is so far completely unknown. In order to simplify our computational studies, the $SiF_6^{2-}$ counterion was replaced by a simple $F^-$ ion leading to the $C_4$ model units $\{[Pt(SU)_4]F\}^+$ (see Scheme 2). In order to learn more about the influence of the metal centre and the donor atoms coordinated to the metal ion, we extended our investigation of the enantiomerisation mechanism to $[Ni(SU)_4]F^+$ and $[Pd(SU)_4]F^+$, and also to the $Pt^{II}$ complexes of the heavier analogue, viz. selenourea (SeU) and tellurourea (TeU).

## Results and Discussion

Two alternative pathways seem to be possible for the enantiomerisation of the $\{[Pt(SU)_4]F\}^+$ entity shown in Scheme 2, viz. a dissociative or a nondissociative mechanism. Bond breakage would imply either cleavage of the Pt–S bond or rupture of the N–H···F H-bond. The nondissociative alternative is ruled out based on the strength of both the Pt–S bond and the N–H···F interactions.

The $\{[Pt(SU)_4]F\}^+$ unit can be considered to be a {3}-cryptand consisting of one metal bridgehead, one fluorine bridgehead and four *pseudo bidentate* SU ligands (one S-donor and one NH-hydrogen-bond donor, see Figure 3). Therefore, $\{[Pt(SU)_4]F\}^+$ can be regarded as a special cryptand, viz. a mixed {3}-metalla-halide-cryptand.

The nondissociative enantiomerisation can either proceed by a fully chiral pathway, in line with Mislow's paradoxon,[29,30] or via a nonchiral transition state of higher symmetry. In the present study, our DFT calculations clearly show that the twisted quadratic prismatic enantiomers with $C_4$ symmetry, containing four puckered semi-chelate rings of opposite chirality (λλλλ vs. δδδδ), are linked by a single-step, all-chiral enantiomerisation path (see Figure 4). In contrast to other enantiomerisation processes,[31] all ground and transition states have the same point group $C_4$.

The complexes in the present study contain ligands with puckered six-membered pseudo-chelate rings, where enantiomerisation involves flipping of these rings (cf. Figure 5).

 © 2006 Wiley-VCH Verlag GmbH & Co. KGaA, Weinheim 

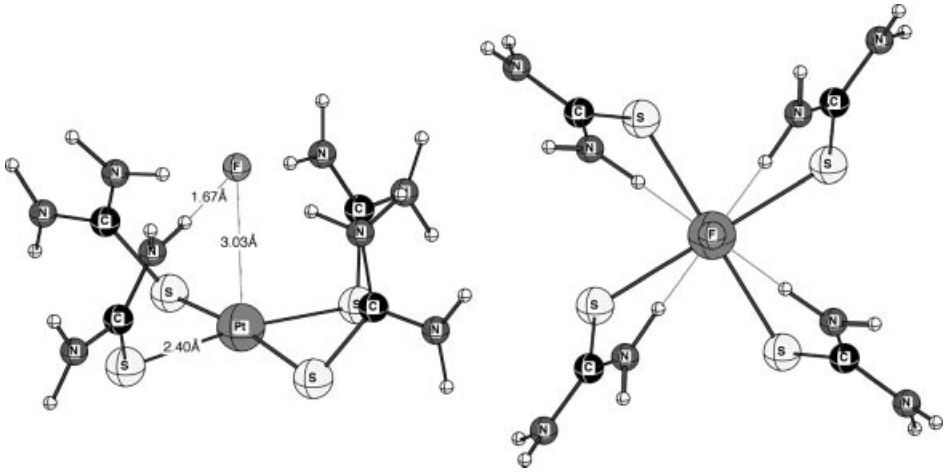


Figure 3. Calculated (RB3LYP/LANL2DZp) structure of $\{[Pt(SU)_4]F\}^+$.

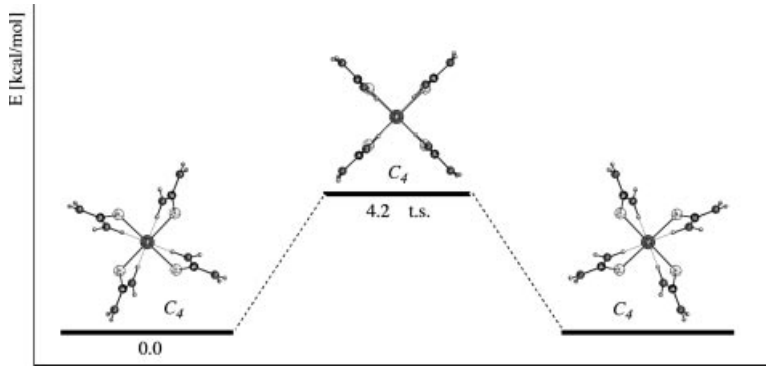


Figure 4. Calculated (RB3LYP/LANL2DZp) enantiomerisation pathway for $[Pt(SU)_4]F^+$.

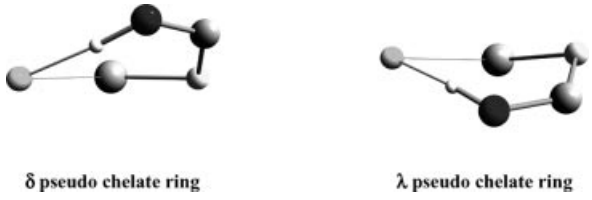


Figure 5. Comparison of the enantiomeric pseudo proton chelate rings belonging to the enantiomers shown in Scheme 2.

It is well known that the six-membered all-$sp^3$ carbon ring of cyclohexane can undergo ring inversion in a three-step process at room temperature. In contrast to $C_6H_{12}$, $\{[Pt(SU)_4]F\}^+$ and related complexes contain chelate rings with atoms linked by different types of bonding interactions and a type of hybridisation that differs from cyclohexane. These features seem to account for the unexpected single-step isomerisation pathway found in the present case. Despite extensive searches, no alternative isomerisation pathways could be found.

On the basis of planar six-membered rings in the transition state, one would expect an achiral $C_{4v}$ structure. This was computed to be a higher order saddle point (five imaginary frequencies), since the symmetry in the transition is diminished by the slightly pyramidal $NH_2$ groups of the XU ligands.

The activation barrier for enantiomerisation of the three $\{[M(SU)_4]F\}^+$ (M = $Ni^{2+}$, $Pd^{2+}$, $Pt^{2+}$) cations decreases from $Ni^{2+}$ to $Pd^{2+}$ and $Pt^{2+}$ to ca. 60% (see Table 1). Except for the obvious differences in the $M^{II}$–S bonds, the structural parameters of the three complexes, describing the ground and transition states, are essentially the same. On going from the ground state to the transition state, the $M^{II}$–S bonds are elongated somewhat, while the $M^{2+}\cdots F$ distances are slightly shortened and the twist angles [M–S···N–F] are reduced to a tenth of the value (see Table 2). The elongation of the $M^{II}$–S bond is most pronounced in the case of $Ni^{2+}$; we expect this to be the main reason for the higher activation barrier.

Table 1. Calculated (RB3LYP/LANL2DZp) energy barriers for the enantiomerisation of complexes of the type $[M(XU)_4]F^+$.[a]

| $[M(XU)_4]F^+$ | $[Ni(SU)_4]F^+$ | $[Pd(SU)_4]F^+$ | $[Pt(SU)_4]F^+$ | $[Pt(SeU)_4]F^+$ | $[Pt(TeU)_4]F^+$ |
|---|---|---|---|---|---|
| [kcal/mol] | 7.6 | 4.5 | 4.2 | 5.3 | 8.8 |

[a] SU = thiourea, SeU = selenourea, TeU = tellurourea.

In contrast to the straightforward results for $[M(SU)_4]F^+$, a variation of the donor atom type in the thiourea ligands from S to Se and Te reveals a more complex picture. Here the activation barrier increases on going to the heavier chalcogens. Whereas the transition from SU to SeU is ac-

 © 2006 Wiley-VCH Verlag GmbH & Co. KGaA, Weinheim 

Table 2. Calculated (RB3LYP/LANL2DZp) data for $[M(XU)_4]F^+$.[a]

| $[M(XU)_4]F^+$ | Ground state | | | | | Transition state | | | | |
|---|---|---|---|---|---|---|---|---|---|---|
| | PG | M–donor [Å] | F–$H_{NH2}$ [Å] | F···M [Å] | [F–D···N–M] [°] | PG | M–donor [Å] | F–$H_{NH2}$ [Å] | F···M [Å] | [M–D···N–M] [°] |
| $[Ni(SU)_4]F^+$ | $C_4$ | 2.30 | 1.69 | 2.60 | 24.6 | $C_4$ | 2.33 | 1.67 | 2.55 | 2.3 |
| $[Pd(SU)_4]F^+$ | $C_4$ | 2.42 | 1.68 | 2.85 | 24.5 | $C_4$ | 2.43 | 1.67 | 2.79 | 2.3 |
| $[Pt(SU)_4]F^+$ | $C_4$ | 2.40 | 1.67 | 3.03 | 25.2 | $C_4$ | 2.41 | 1.66 | 3.01 | 2.5 |
| $[Pt(SeU)_4]F^+$ | $C_4$ | 2.51 | 1.67 | 3.05 | 26.3 | $C_4$ | 2.53 | 1.66 | 3.03 | 1.0 |
| $[Pt(TeU)_4]F^+$ | $C_4$ | 2.67 | 1.69 | 3.13 | 27.4 | $C_1$ | 2.70 | 1.68 | 3.07 | –5.3, 9.3, 7.4, –10.2 |

[a] SU = thiourea, SeU = selenourea, TeU = tellurourea.

companied by only a moderate increase in the barrier (4.2 and 5.3 kcal/mol, respectively), the barrier for TeU is almost twice as high (8.8 kcal/mol) compared to that for SU. This can obviously be attributed to the metalloid character of Te, as shown by the change in the Natural Population Analysis (NPA) charges for the platinum centre and the S, Se and Te atoms, respectively (see Table 3).[32]

Table 3. Calculated NPA charges (RB3LYP/LANL2DZp) for $Pt^{2+}$ and the coordinating donor atom of XU.[a]

| $[Pt(XU)_4]F^+$ | $[Pt(SU)_4]F^+$ | $[Pt(SeU)_4]F^+$ | $[Pt(TeU)_4]F^+$ |
|---|---|---|---|
| NPA charge of $Pt^{2+}$ | +0.2 | ±0.0 | –0.2 |
| NPA charge of donor (X) | –0.1 | ±0.0 | +0.2 |

[a] SU = thiourea, SeU = selenourea, TeU = tellurourea.

The $Pt^{2+}$–X bond lengths and the Pt···F distances increase in the expected range. The F···$H_{NH2}$ distances show no significant differences, neither in the ground state, nor in the transition state. The constant F···$H_{NH2}$ distances lead in the case of $\{[Pt(TeU)_4]F\}^+$ to a $C_1$ transition state, since the arms of the tellurourea cage have to be more twisted than in all other cases. Again, the $M^{2+}$–chalcogen bonds are slightly extended in the transition state, whereas the Pt···F distance is now somewhat reduced.

## Conclusions

We have shown that the enantiomerisation of $[M(TU)_4F]^+$ and related model complexes of this type do not require cleavage of the $M^{2+}$–chalcogen bonds nor the rupture of the N–H···X bond. Instead, a pathway with a chiral transition structure with four planar rings was found. The activation barrier is lowered by 60% along the series $[Ni(SU)_4]F^+$, $[Pd(SU)_4]F^+$ and $[Pt(SU)_4]F^+$. In the series $[Pt(SU)_4]F^+$, $[Pt(SeU)_4]F^+$ and $[Pt(TeU)_4]F^+$, the activation barrier increases slightly on going from the SU to the SeU derivatives, but doubles in the case of $[Pt(TeU)_4]F^+$.

## Quantum Chemical Methods

We performed hybrid density functional calculations using the B3LYP functional[33a–33c] and the LANL2DZ basis set with effective core potentials,[33d–33g] augmented with polarisation functions on non-hydrogen atoms.[33h] The performance of this level (denoted as B3LYP/LANL2DZp) has been documented by us and others.[34] Structures were characterised as minima, transition structures, or higher-order saddle points by computation of vibrational frequencies. Relative energies were corrected for zero point vibrational energy. The GAUSSIAN suite of programs was used.[35]

## Acknowledgments

The authors gratefully acknowledge financial support from the Deutsche Forschungsgemeinschaft within SFB 583 ("Redox-active Metal Complexes"). We thank Dr. W. Schiessl for stimulating discussions, Prof. Tim Clark for support and the Regionales Rechenzentrum Erlangen (RRZE) for a generous allotment of computer time.

[1] V. I. Okafor, N. J. Coville, *South Afr. J. Sci.* **1999**, *95*, 503–508.
[2] V. Dragutan, I. Dragutan, A. T. Balaban, *Platinum Met. Rev.* **2000**, *44*, 58–66.
[3] V. Dragutan, I. Dragutan, A. T. Balaban, *Platinum Met. Rev.* **2000**, *44*, 112–118.
[4] V. Dragutan, I. Dragutan, A. T. Balaban, *Platinum Met. Rev.* **2000**, *44*, 168–172.
[5] B. Lippert (Ed.), *Cisplatin: Chemistry and Biochemistry of a Leading Anticancer Drug*, Wiley-VCH, Weinheim, **1999**.
[6] P. M. Takahara, C. A. Frederick, S. J. Lippard, *J. Am. Chem. Soc.* **1996**, *118*, 12309–12321.
[7] N. Farrell in *Transition Metal Complexes as Drugs and Chemotherapeutic Agents* (Eds.: R. Ugo, B. R. James), Kluwer, Dordrecht, The Netherlands, **1989**.
[8] Ž. D. Bugarčić, G. Liehr, R. van Eldik, *J. Chem. Soc. Dalton Trans.* **2002**, 282–2830.
[9] D. Jaganyi, A. Hofmann, R. van Eldik, *Angew. Chem. Int. Ed.* **2001**, *40*, 1680–1683.
[10] Ž. D. Bugarčić, F. W. Heinemann, R. van Eldik, *Dalton Trans.* **2004**, 279–286.
[11] J. M. Berry, C. Jacobs, B. Sikic, J. Halsey, R. F. Borch, *J. Clin. Oncol.* **1990**, *8*, 1585–1590.
[12] M. Treskes, U. Holwerda, L. G. J. Nijtmans, H. M. Pinedo, W. J. F. van der Vijgh, *Cancer Chemoth. Pharm.* **1992**, *29*, 467–470.
[13] J. Filipski, K. W. Kohn, R. Prather, W. M. Bonner, *Science* **1979**, *204*, 181–183.
[14] R. F. Ozols, B. J. Corden, J. Collins, R. C. Young in *Platinum Coordination Complexes in Cancer Chemotherapy* (Eds.: M. P. Hacker, E. B. Douple, I. H. Krakoff), Martinus Nijhoff, Boston, **1984**, p. 321.
[15] J. H. Burchenal, K. Kalaher, K. Dew, L. Lokys, G. Gale, *Biochimie* **1978**, *60*, 961–965.
[16] J. Reedijk, *Chem. Rev.* **1999**, *99*, 2499–2510.
[17] R. L. Girling, K. K. Chatterjee, E. L. Amma, *Inorg. Chim. Acta* **1973**, *7*, 557–562.
[18] J. Arpalahti, B. Lippert, H. Schoellhorn, U. Thewalt, *Inorg. Chim. Acta* **1988**, *153*, 51–55.
[19] P. D. Beer, P. A. Gale, *Angew. Chem. Int. Ed.* **2001**, *40*, 486–516.
[20] C. R. Bondy, P. A. Gale, S. J. Loeb, *J. Supramol. Chem.* **2003**, *2*, 93–96.

 © 2006 Wiley-VCH Verlag GmbH & Co. KGaA, Weinheim 

[21] J. Calvo, J. S. Casas, E. Garcia-Martinez, Y. Parajo, A. Sanchez-Gonzalez, J. Sordo, *Z. Anorg. Allg. Chem.* **2004**, *630*, 215–216.
[22] V. Amendola, M. Boiocchi, L. Fabbrizzi, A. Palchetti, *Chem. Eur. J.* **2005**, *11*, 5648–5660.
[23] L. Fuks, N. Sadlej-Sosnowska, K. Samochocka, W. Starosta, *J. Mol. Struct.* **2005**, *740*, 229–235.
[24] G. De Munno, B. Gabriele, G. Salerno, *Inorg. Chim. Acta* **1995**, *234*, 181–183.
[25] P. A. Gale, M. E. Light, R. Quesada, *Polyhedron* **2006**, *25*, 901–909.
[26] P. A. Gale, M. E. Light, R. Quesada, *Chem. Commun.* **2005**, 5864–5866.
[27] W. Schiessl, R. Puchta, Ž. D. Bugarčić, F. W. Heinemann, R. van Eldik, *Inorg. Chem.*, submitted.
[28] T. C. Mak, Q. Li, *Adv. Mol. Struct. Res.* **1998**, *4*, 151–225.
[29] K. Mislow, *Science* **1954**, *120*, 232–233; K. Mislow, *J. Am. Chem. Soc.* **1955**, *77*, 6712–6713.
[30] M. Mauksch, P. v. R. Schleyer, *Angew. Chem. Int. Ed. Engl.* **1997**, *36*, 1856–1868; M. Mauksch, P. v. R. Schleyer, *Angew. Chem.* **1997**, *109*, 1976–1979.
[31] R. Puchta, N. J. R. van Eikema Hommes, R. Meier, R. van Eldik, *Dalton Trans.* **2006**, 3392–3395.
[32] The inclusion of solvent effects by IPCM calculations was not possible throughout because of technical problems. For $[Pd(SU)_4]F^+$, for example, we obtained a similar value of 5.2 kcal/mol.
[33] a) A. D. Becke, *J. Phys. Chem.* **1993**, *97*, 5648–5652; b) C. Lee, W. Yang, R. G. Parr, *Phys. Rev. B* **1988**, *37*, 785–789; c) P. J. Stephens, F. J. Devlin, C. F. Chabalowski, M. J. Frisch, *J. Phys. Chem.* **1994**, *98*, 11623–11627; d) T. H. Dunning Jr, P. J. Hay, *Mod. Theor. Chem.* **1976**, *3*, 1–28; e) P. J. Hay, W. R. Wadt, *J. Chem. Phys.* **1985**, *82*, 270–283; f) P. J. Hay, W. R. Wadt, *J. Chem. Phys.* **1985**, *82*, 284–298; g) P. J. Hay, W. R. Wadt, *J. Chem. Phys.* **1985**, *82*, 299–310; h) S. Huzinaga (Ed.), *Gaussian Basis Sets for Molecular Calculations*, Elsevier, Amsterdam, **1984**.
[34] See for example S. Klaus, H. Neumann, H. Jiao, A. Jacobi von Wangelin, D. Gördes, D. Strübing, S. Hübner, M. Hately, C. Weckbecker, K. Huthmacher, T. Riermeier, M. Beller, *J. Organomet. Chem.* **2004**, *689*, 3685–3700; R. W. Saalfrank, Ch. Deutscher, H. Maid, A. M. Ako, S. Sperner, T. Nakajima, W. Bauer, F. Hampel, B. A. Heß, N. J. R. van Eikema Hommes, R. Puchta, F. W. Heinemann, *Chem. Eur. J.* **2004**, *10*, 1899–1905; P. Illner, A. Zahl, R. Puchta, N. J. R. van Eikema Hommes, P. Wasserscheid, R. van Eldik, *J. Organomet. Chem.* **2005**, *690*, 3567–3576; A. Scheurer, H. Maid, F. Hampel, R. W. Saalfrank, L. Toupet, P. Mosset, R. Puchta, N. J. R. van Eikema Hommes, *Eur. J. Org. Chem.* **2005**, 2566–2574; M. Galle, R. Puchta, N. J. R. van Eikema Hommes, R. van Eldik, *Z. Phys. Chem.* **2006**, *220*, 511–523, and literature cited therein.
[35] M. J. Frisch, G. W. Trucks, H. B. Schlegel, G. E. Scuseria, M. A. Robb, J. R. Cheeseman, J. A. Montgomery Jr, T. Vreven, K. N. Kudin, J. C. Burant, J. M. Millam, S. S. Iyengar, J. Tomasi, V. Barone, B. Mennucci, M. Cossi, G. Scalmani, N. Rega, G. A. Petersson, H. Nakatsuji, M. Hada, M. Ehara, K. Toyota, R. Fukuda, J. Hasegawa, M. Ishida, T. Nakajima, Y. Honda, O. Kitao, H. Nakai, M. Klene, X. Li, J. E. Knox, H. P. Hratchian, J. B. Cross, V. Bakken, C. Adamo, J. Jaramillo, R. Gomperts, R. E. Stratmann, O. Yazyev, A. J. Austin, R. Cammi, C. Pomelli, J. W. Ochterski, P. Y. Ayala, K. Morokuma, G. A. Voth, P. Salvador, J. J. Dannenberg, V. G. Zakrzewski, S. Dapprich, A. D. Daniels, M. C. Strain, O. Farkas, D. K. Malick, A. D. Rabuck, K. Raghavachari, J. B. Foresman, J. V. Ortiz, Q. Cui, A. G. Baboul, S. Clifford, J. Cioslowski, B. B. Stefanov, G. Liu, A. Liashenko, P. Piskorz, I. Komaromi, R. L. Martin, D. J. Fox, T. Keith, M. A. Al-Laham, C. Y. Peng, A. Nanayakkara, M. Challacombe, P. M. W. Gill, B. Johnson, W. Chen, M. W. Wong, C. Gonzalez, J. A. Pople, *Gaussian 03*, Revision C.02, Gaussian, Inc., Wallingford, CT, **2004**.

Received: May 24, 2006
Published Online: August 10, 2006

 © 2006 Wiley-VCH Verlag GmbH & Co. KGaA, Weinheim 

DOI: 10.1002/ejic.200600526

# Chelating Phosphane–Boranes as Hemilabile Ligands – Synthesis of $[Mn(CO)_3(\eta^2\text{-}H_3B{\cdot}dppm)][BAr^F{}_4]$ and $[Mn(CO)_4(\eta^1\text{-}H_3B{\cdot}dppm)][BAr^F{}_4]$

**Nicolas Merle,[a] Christopher G. Frost,[a] Gabriele Kociok-Köhn,[a] Michael C. Willis,[a] and Andrew S. Weller*[a]**

**Keywords:** Boranes / Catalysis / Hemilabile ligands / Manganese / Phosphanes

Manganese complexes bearing the chelating phosphane–borane ligand $H_3B{\cdot}$dppm [dppm = bis(diphenylphosphanyl)-methane] have been prepared. Addition of $H_3B{\cdot}$dppm to $Mn(CO)_5Br$ using $Na[BAr^F{}_4]$ as a halide-abstracting reagent affords $[Mn(CO)_3(\eta^2\text{-}H_3B{\cdot}dppm)][BAr^F{}_4]$ (**1**). This reacts with CO to open the bidentate borane to afford $[Mn(CO)_4(\eta^1\text{-}H_3B{\cdot}dppm)][BAr^F{}_4]$ (**2**) in which the borane is now bound in a monodentate manner. The CO addition is reversible, and placing **2** under vacuum (hours) regenerates **1** quantitatively, demonstrating that the chelating phosphane–boranes can act as hemilabile ligands. The complexes **1** and **2** have been fully characterised by NMR spectroscopy and X-ray crystallography.

(© Wiley-VCH Verlag GmbH & Co. KGaA, 69451 Weinheim, Germany, 2006)

## Introduction

Reactions catalysed by Lewis acid transition metal fragments invariably rely on the generation of a vacant site on a cationic metal centre. Often this is generated by dissociation of a weakly bound ligand (e.g. solvent)[1] or anion.[2] An alternative mechanism – when a suitable ligand set is available – is one that involves a hemilabile ligand,[3–5] in which one donor atom in a chelate ligand has the ability to reversibly decoordinate in a catalytic cycle to reveal a coordinatively unsaturated metal centre. The design of hemilabile ligands is often based on ligands in which one end is a phosphane (which binds strongly) and the other a more weakly ligating group that can move away to generate a vacant site (Scheme 1). Examples of the weakly binding group include phosphane oxides,[6] sulfides,[7,8] and ether groups.[9] As pointed out nearly 30 years ago by Marks,[10] $[BH_4]^-$ can also potentially be a hemilabile ligand, by moving from $\eta^2$- to $\eta^1$-coordination modes (Scheme 1), thus generating the vacant site needed for substrate coordination. Examples of borohydride acting in this way are rare however, as on addition of ligand L loss of $H_3B{\cdot}$L often occurs with the concomitant generation of a metal hydride.[11,12] A recently reported observation of $\eta^2$- to $\eta^1$-borohydride hemilability comes from the addition of Lewis base (e.g. $PMe_2Ph$) to $Ru(PMe_2Ph)_2H(CO)(\eta^2\text{-}BH_4)$ to afford $Ru(PMe_2Ph)_3H(CO)(\eta^1\text{-}BH_4)$, although at temperatures above 300 K $H_3B{\cdot}PMe_2Ph$ is irreversibly lost to generate $Ru(PMe_2Ph)_3H_2(CO)$.[13]

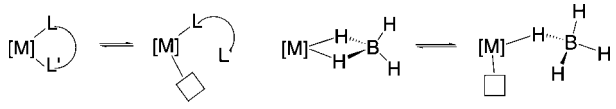


Scheme 1.

One way of preventing borane loss would be to include the borohydride ligand in a chelate ring, allowing this potentially useful $\eta^2$- to $\eta^1$-transformation to occur without decomposition. Others[14,15] and we[16–18] have recently reported on the coordination chemistry of chelating phosphane–boranes $XH_2B{\cdot}$dppm (X = H, Cl, dppm = $PPh_2CH_2PPh_2$) in which one end of the ligand is valence-isoelectronic with borohydride while the other provides a firm phosphane anchor to the metal centre. These ligands show promise for hemilabile behaviour as the cationic complexes $[RuCp^*(\eta^2\text{-}XH_2B{\cdot}dppm)][Y]$ [X = H (**I**), Cl (**II**); Cp* = $\eta^5\text{-}C_5Me_5$; Y = $BAr^F{}_4$; $PF_6$] react with Lewis bases (CO, $PMe_3$) to open the borane from $\eta^2$ to $\eta^1$, thus forming $[RuCp^*(L)(\eta^1\text{-}XH_2B{\cdot}dppm)]^+$ (Scheme 2).[16,18] With these strong ligands the reaction is not reversible, and the ligand cannot be removed. The $\eta^2$-precursors **I** and **II** can thus be considered as being operationally unsaturated, effectively acting as a source of a reactive cationic 16-electron $\{RuCp^*(\eta^1\text{-}XH_2B{\cdot}dppm)\}^+$ fragment. The lack of borane loss on reaction with Lewis bases can be contrasted both with borohydride complexes, as discussed earlier, and also complexes of the monodentate phosphane–boranes developed by Shimoi, such as $MnCp^*(CO)_2(\eta^1\text{-}H_3B{\cdot}PMe_3)$, which react with weak Lewis bases to displace the borane.[19–21]

[a] Department of Chemistry, University of Bath,
Bath, BA2 7AY, UK
Fax: +44-1225-386231
E-mail: a.s.weller@bath.ac.uk


InterScience
© 2006 Wiley-VCH Verlag GmbH & Co. KGaA, Weinheim

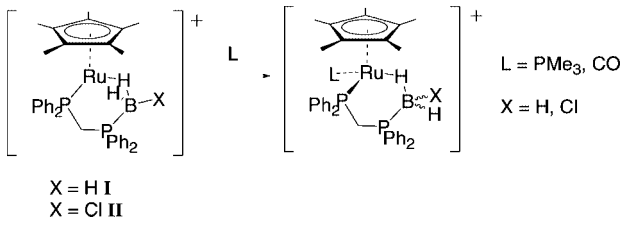


Scheme 2.

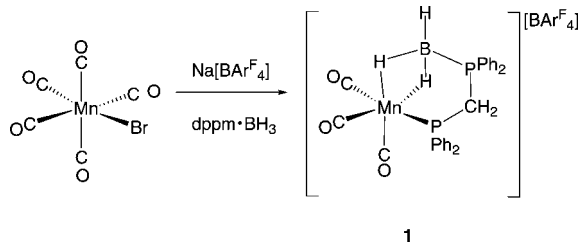


Scheme 3.

We report here the synthesis of some new cationic manganese complexes with the $H_3B$·dppm ligand. In these complexes the phosphane–borane opens and closes reversibly (i.e. shows true hemilabile behaviour) on the addition/removal of carbon monoxide.

## Results

Treatment of $Mn(CO)_5Br$ with $H_3B$·dppm using $Na[BAr^F_4]$ as a halide-abstracting reagent results in the isolation of analytically pure (46% yield) $[Mn(CO)_3(\eta^2\text{-}H_3B{\cdot}dppm)][BAr^F_4]$ (**1**) (Scheme 3). The equivalent reactions with $ClH_2B$·dppm or $BrH_2B$·dppm[18] only resulted in mixtures of intractable products. Complex **1** has been fully characterised by NMR spectroscopy and X-ray crystallography, which all show that the chelating phosphane–borane adopts a bidentate ($\eta^2$) bridging mode of the $BH_3$ group. Figure 1 shows the solid-state structure of **1**.

The $BH_3$ fragment binds to the manganese atom through two B–H–Mn 3-centre-2-electron interactions. The hydrogen atoms associated with the $BH_3$ group were located in the final difference map and freely refined. Within the limits of confidence associated with the location of hydrides by X-ray crystallography the two hydrogen atoms that bridge to the metal atom have B–H bonds that can be considered longer than that to the terminal hydride [B1–H1a 1.07(3) Å, B1–H1b 1.30(4) Å, B1–H1c 1.24(3) Å], consistent with the 3c–2e bond description. The Mn–B distance is short [2.146(4) Å] mirroring that observed in the ruthenium complexes **I** and **II**,[16,18] being slightly longer than that found in three-coordinate boryl complexes of Mn such as $(CO)_5MnB(O_2C_6H_4)$ [2.108(6) Å][22] and comparable with the σ-borane complex $Mn(\eta^5\text{-}C_5H_4Me)(CO)_2(HB\{O_2C_4Me_4\})$ [2.149(2) Å].[23] It is significantly shorter than in the four-coordinate boryl complex $Mn(CO)_4(PMe_2Ph)(BH_2{\cdot}PMe_3)$ [2.314(2) Å] for which an $[Mn(CO)_4(PMe_2Ph)]^-$-$[BH_2(PMe_3)]^+$ bonding description is suggested.[19] A similar short distance is observed in $[Cr(CO)_4(\eta^2\text{-}BH_4)][PPN]$

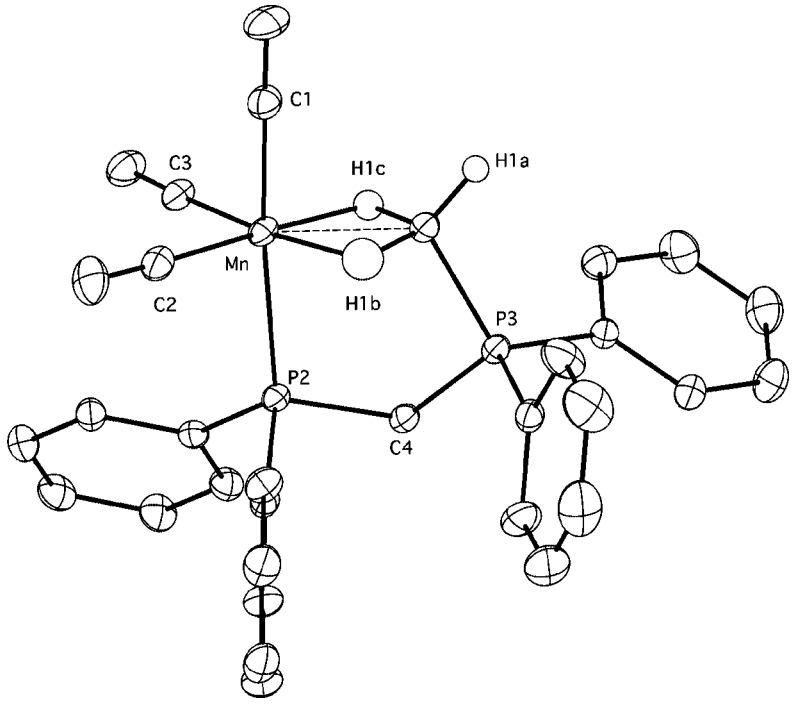


Figure 1. Solid-state structure of complex **1**. Thermal ellipsoids are shown at the 50% probability level; hydrogen atoms are omitted apart form those associated with the boron atom.

 © 2006 Wiley-VCH Verlag GmbH & Co. KGaA, Weinheim 

[2.29(1) Å] which is valence-isoelectronic with **1**.[24] As for **I** and **II**,[16,18] this interaction in **1** is best described as being like borohydride and not a dihydridoboryl complex, as the B–Mn–H and H–Mn–H angles are far more compressed than expected for a complex with two hydrides and a boryl ligand.[25] As expected for a relatively weakly bound $BH_3$ group, the M–C bond lengths associated with the carbonyl ligands *trans* to the bridging hydrides [Mn–C2 1.803(4) Å and Mn–C3 1.817(4) Å] are shorter than that *trans* to the phosphane group [Mn–C1 1.849(4) Å].

In solution, the $^{11}B$ NMR spectrum of **1** demonstrates the Mn···B interaction by a significant downfield shift of the signal of the $H_3B$·dppm ligand on coordination, from $\delta$ = –37.1 ppm in the free ligand to $\delta$ = 16.7 ppm ($\Delta\delta$ = +53.8 ppm) in **1**, consistent with $\eta^2$-coordination of the borane and a significant M···B interaction. In the $^1H\{^{11}B\}$ NMR spectrum two signals observed at $\delta$ = –9.08 (2 H) ppm and $\delta$ = 4.99 (1 H) ppm are assigned to the bridging and terminal BH groups, respectively, indicating that exchange between the terminal and bridging hydrides does not occur at room temperature. The methylene backbone in the dppm group is observed as an integral 2 H doublet of doublets, indicating time-averaged $C_s$ symmetry in solution. The $^{31}P\{^1H\}$ NMR spectrum displays two peaks, a sharp doublet at $\delta$ = 73.7 ppm and a broad signal as $\delta$ = 15.6 ppm, the latter assigned to the boron-bound phosphorus atom. Other spectroscopic data are also in full accord with the solid-state structure.

Addition of CO (1 atm) to **1** results in the rapid formation of the tetracarbonyl complex $[Mn(CO)_4(\eta^1\text{-}H_3B\cdot dppm)][BAr^F{}_4]$ (**2**) and the opening of the phosphane–borane ligand form $\eta^2$ to $\eta^1$ (Scheme 4). The NMR spectroscopic data for **2** are very similar to those for the isoelectronic complex $Cr(CO)_4(\eta^1\text{-}H_3B\cdot dppm)$ (**III**).[16] A diagnostic high-field chemical shift change for the $BH_3$ signal in the $^{11}B\{^1H\}$ NMR spectrum to $\delta$ = –37.5 ppm (similar to the free ligand[16,26]) indicates the $\eta^1$-binding mode and loss of a significant M···B interaction. In the $^1H$ NMR spectrum, the $BH_3$ group is observed as a quadrupolar, broadened integral 3 H signal at $\delta$ = –3.74 ppm, which sharpens on decoupling of $^{11}B$. The observation of one integral 3 H $BH_3$ signal at room temperature shows that the $BH_3$ group is rapidly spinning around the P–B bond at this temperature, exchanging terminal and bridging hydrides. Consistent with this fluxional process, the methylene group on the dppm ligand is observed as an integral 2 H doublet of doublets. In **III** this fluxional process also occurs but cannot be frozen out at low temperature. For **2**, cooling to 190 K ($CD_2Cl_2$) results in the observation of two broad signals in the ratio 2:1 at $\delta$ = 1.99 (fwhm = 160 Hz) ppm and $\delta$ = –15.52 (fwhm = 250 Hz) ppm in the $^1H\{^{11}B\}$ NMR spectrum, assigned to the terminal and bridging hydrides, respectively, showing that the exchange process has been halted. This difference between neutral **III** and cationic **2** can be attributed to the increased electrostatic attraction between the cationic manganese centre and the polarised $H^{\delta-}$–$B^{\delta+}$ group. At low temperature, the methylene protons for **2** are observed as a single integral 2 H broadened peak (fwhm = 50 Hz) centred at $\delta$ = 3.5 ppm in the $^1H\{^{11}B\}$ NMR spectrum, suggesting $C_s$ symmetry for the molecule at low temperature. In the solid-state structure (see below) the molecule adopts $C_1$ symmetry, resulting in the methylene protons and the B–H protons being all inequivalent, contrary to the observation of just two signals for the B–H protons and one for the methylene group. However, due to the broadness of these signals at 190 K and the inherent difficulty associated with reliably integrating such broad signals, it is not possible to say whether inequivalent environments are present for each group, or instead if a low-energy libration of the bridging hydride around the Mn–B vector is occurring to make both the dppm methylene and $BH_2$ protons each equivalent.

The solid-state structure of **2** shows an $\eta^1$-binding mode for the phosphane–borane ligand, which forms a δ-agostic Mn–H–B interaction (Figure 2). The structural metrics are similar to those already discussed for **III**,[16] as expected for this isoelectronic pair and are consistent with a relatively weak δ-agostic Mn–H–B interaction [Mn···H 1.71(3) Å, Mn···B 2.748(3) Å]. Notably the Mn···B bond is long – being similar to that calculated for $[Mn(CO)_4(PH_3)(\eta^1\text{-}H_3B\cdot PMe_3)]^+$ [2.780 Å][19] and slightly shorter than observed for neutral $Cr(CO)_5(\eta^1\text{-}H_3B\cdot PMe_3)$ [2.79(1) Å].[21] The Mn–H–B angle of 134(2)° means that the molecule does not have $C_s$ symmetry in the solid state, in contrast to the solution NMR spectroscopic data (vide supra). This angle is far more open than those observed in **1** [viz. 91(1), 93(1)°], consistent with move from didentate to monodentate coordination modes. The carbonyl ligand *trans* to the weakly bound $H_3B$ group has the shortest Mn–C distance, as expected. The Mn···H distance in **2** is significantly shorter than that found in γ-agostic complex $[Mn(CO)_3(PCy_3)_2][BAr^F{}_4]$ [2.01(9) Å],[27] in part a consequence of the polarised Bδ⁺···Hδ⁻ group interacting with the cationic metal centre.

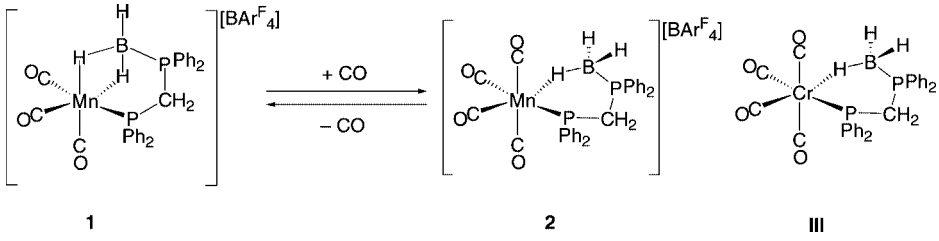


Scheme 4.

 © 2006 Wiley-VCH Verlag GmbH & Co. KGaA, Weinheim 

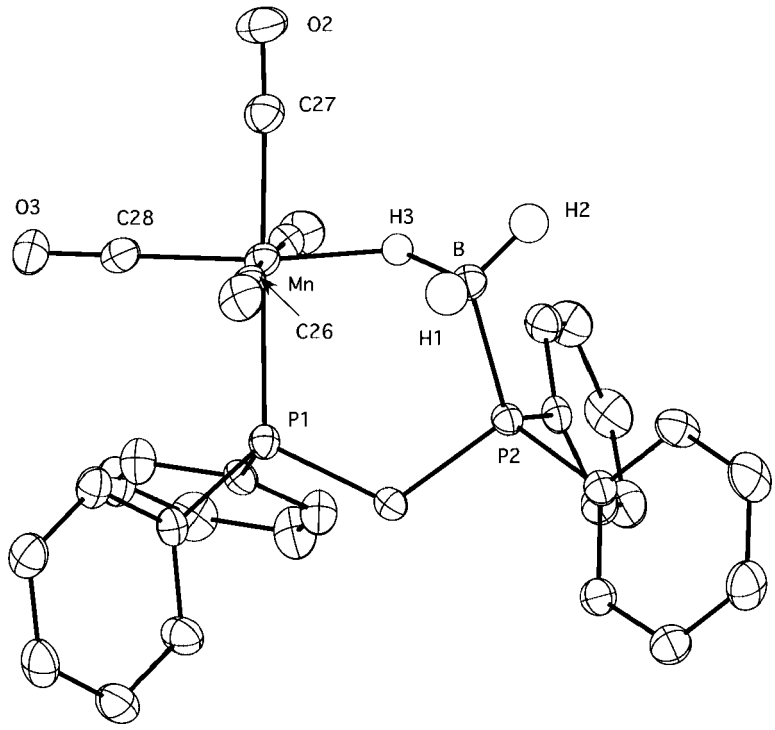


Figure 2. Solid-state structure of complex **2**. Thermal ellipsoids are shown at the 50% probability level; hydrogen atoms are omitted apart form those associated with the boron atom.

The addition of CO to **2** is reversible. Placing **2** under a dynamic vacuum (minutes) or under argon (days) regenerates **1** quantitatively in both the solid state and solution. For this reason, crystals of **2** are best obtained under CO and good microanalytical data could not be obtained. Addition of Lewis bases other than CO to **2** (MeCN, $PR_3$) resulted in decomposition. Addition of the weaker Lewis base $H_2$ did not displace the borane, and addition of $D_2$ did not result in H/D exchange. This is contrary to complexes **I** and **II** in which H/D exchange occurs, via a putative dihydride intermediate that results from the opening of the borane to $\eta^1$.[16,18] Presumably, the cationic $\{Mn(CO)_3\}^+$ fragment is reluctant to undergo oxidative addition of $H_2$ and thus no H/D exchange is observed in **1**.

Interestingly, the complex isoelectronic with **2**, $Mn(CO)_5(\eta^1\text{-}BH_4)$, has only been briefly reported as a possible intermediate in the formation of $Mn_3(CO)_{10}(BH_3)_3H$ from $Al[BH_4]$ and $Mn(CO)_5Br$,[28] while the borohydride complex equivalent to **1**, $Mn(CO)_4(\eta^2\text{-}BH_4)$, has not been reported apart from a calculated structure.[29] Related complexes with monodentate phosphanes such as $[Mn(CO)_4(PMe_2Ph)(\eta^1\text{-}H_3B{\cdot}PMe_3)][BAr^F{}_4]$[19] and $MnCp^*(CO)_2(\eta^2\text{-}H_3B{\cdot}PMe_3)$[20] are also unstable in solution. The stability of **2** is doubtlessly associated with the chelate ring, as we have commented on previously.[16]

## Conclusions

As with our earlier studies,[16,18] the results we report here show that the chelating phosphane–borane ligand $H_3B{\cdot}$dppm can open from $\eta^2$ to $\eta^1$ on addition of Lewis bases. For $[Mn(CO)_3(\eta^1\text{-}H_3B{\cdot}dppm)][BAr^F{}_4]$ this opening is reversible, and this observation of hemilabile behaviour suggests that, with suitable systems and substrates, they have the potential for application in catalysis.

## Experimental Section

**General:** All manipulations were carried out under argon, using standard Schlenk-line and glove-box techniques, unless otherwise stated. Glassware was pre-dried in an oven at 130 °C and flamed with a blowtorch under vacuum prior to use. Solvents were dried with activated alumina, copper or molecular sieves columns by using an MBraun solvent purification system and stored under slight vacuum in ampoules equipped with Young's taps. $CD_2Cl_2$ was distilled under vacuum from $CaH_2$. $Mn(CO)_5Br$,[30] $Na[BAr^F{}_4]$[31] and $H_3B{\cdot}$dppm[26] were prepared according to published routes. All other chemicals were used as received from Aldrich and Strem. Microanalyses were performed by Elemental Microanalysis Ltd, Devon, UK.

**NMR Spectroscopy:** $^1H$, $^1H\{^{11}B\}$, $^{11}B\{^1H\}$, $^{11}B$ and $^{31}P\{^1H\}$ NMR spectra were recorded with Bruker Avance 300 MHz or 400 MHz spectrometers. Resonances were referenced to residual hydrogen from the solvent for $^1H$ and $^1H\{^{11}B\}$ NMR spectra ($CD_2Cl_2$: $\delta$ = 5.30 ppm). $^{11}B$, $^{11}B\{^1H\}$ and $^{31}P\{^1H\}$ spectra were referenced against $BF_3{\cdot}OEt_2$ (external) and 85%% $H_3PO_4$ (external), respectively. Values are quoted in ppm. Coupling constants are quoted in Hz.

**X-ray Crystallography:** The crystal structure data for compounds **1** and **2** were collected with a Nonius KappaCCD diffractometer (Tables 1 and 2). Structure solution, followed by full-matrix least-squares refinement was performed using the SHELX suite of programs throughout.[32] Hydrogen atoms were included at calculated

 © 2006 Wiley-VCH Verlag GmbH & Co. KGaA, Weinheim 

Table 1. Details of crystallographic data collection and refinement for complexes **1** and **2**.

| Compound | **1** | **2** |
|---|---|---|
| Empirical formula | $C_{60}H_{37}B_2F_{24}MnO_3P_2$ | $C_{61}H_{37}B_2F_{24}MnO_4P_2 \cdot 0.35CH_2Cl_2 \cdot 0.65\ C_5H_{12}$ |
| $M_r$ [g mol$^{1}$] | 1400.40 | 1505.02 |
| Crystal size [mm] | 0.70 × 0.40 × 0.30 | 0.35 × 0.28 × 0.23 |
| Crystal colour | orange | yellow |
| Crystal system | monoclinic | orthorhombic |
| Space group | *C*2/*c* | *Pbca* |
| *a* [Å] | 25.4630(3) | 13.3490(2) |
| *b* [Å] | 12.37800(10) | 26.4730(5) |
| *c* [Å] | 38.1190(4) | 38.1720(7) |
| *β* [°] | 91.98 | 90 |
| *V* [Å$^3$] | 12007.2(2) | 13489.5(4) |
| Z | 8 | 8 |
| $D_{calcd.}$ [g cm$^{-3}$] | 1.549 | 1.482 |
| *μ* [mm$^{-1}$] | 0.393 | 0.383 |
| *F*(000) | 5616 | 6064 |
| *T* [K] | 150(2) | 150(2) |
| *λ* [Å] | 0.71073 | 0.71073 |
| *Θ* range [°] | 3.22 to 28.68 | 3.53 to 28.26 |
| Reflections collected | 34057 | 52244 |
| Data/parameters | 10178/913 | 14338/936 |
| Goodness-of-fit on $F^2$ | 1.078 | 1.020 |
| Final *R* indices [$I > 2\sigma(I)$] | $R_1$ = 0.0602, $wR_2$ = 0.1308 | $R_1$ = 0.0515, $wR_2$ = 0.1154 |
| Largest diff. peak/hole [e·Å$^{-3}$] | 0.588/–0.670 | 0.532/–0.416 |

Table 2. Selected bond lengths [Å] and angles [°] for complexes **1** and **2**.

| Compound **1** | | | | | |
|---|---|---|---|---|---|
| Mn–C(1) | 1.849(4) | Mn–C(2) | 1.803(4) | Mn–C(3) | 1.817(4) |
| Mn–B(1) | 2.146(4) | Mn–P(2) | 2.3428(9) | B(1)–P(1) | 1.944(4) |
| Mn–H(1B) | 1.68(4) | Mn–H(1C) | 1.69(3) | B(1)–H(1A) | 1.07(3) |
| B(1)–H(1B) | 1.30(4) | B(1)–H(1C) | 1.24(3) | | |
| C(2)–Mn–B(1) | 129.67(15) | C(3)–Mn–B(1) | 139.74(16) | C(1)–Mn–B(1) | 87.24(15) |
| B(1)–Mn–H(1C) | 35(1) | B(1)–Mn–H(1B) | 37(1) | H(1B)–Mn–H(1C) | 72(2) |
| Compound **2** | | | | | |
| Mn–C(26) | 1.883(3) | Mn–C(27) | 1.868(3) | Mn–C(28) | 1.816(3) |
| Mn–C(29) | 1.871(3) | Mn–P(1) | 2.3321(8) | B(1)–P(2) | 1.929(3) |
| Mn–H(1) | 1.71(3) | B–H(1) | 1.08(3) | B–H(2) | 1.05(3) |
| B–H(3) | 1.26(3) | Mn–B(1) | 2.748(3) | B–H(3)–Mn | 134(2) |

positions throughout apart from those associated with the borane which were located in the final Fourier difference map and refined without constraints. For complex **2** two, partial occupancy, solvent molecules ($CH_2Cl_2$ and pentane) were included in the refinement. CCDC-284481 (**1**) and -284482 (**2**) contain the supplementary crystallographic data for this paper. These data can be obtained free of charge from The Cambridge Crystallographic Data Centre via www.ccdc.cam.ac.uk/data_request/cif.

**[(CO)$_3$Mn(η$^2$-BH$_3$·dppm)][BAr$^F_4$] (1):** $NaBAr^F_4$ (0.267 g, 0.301 mmol) was dissolved in 10 mL of diethyl ether and added to a mixture of $(CO)_5MnBr$ (0.083 g, 0.301 mmol) and dppm·$BH_3$ (0.120 g, 0.301 mmol) in 20 mL of $CH_2Cl_2$. The solution was stirred for 2 d with regular degassing of the solution to remove the released CO. The reaction mixture was filtered to remove the insoluble NaBr to give an orange solution. Solvent was removed in vacuo to leave an orange solid. Crystals suitable for an X-ray diffraction study were grown by dissolving the solid in a minimum of $CH_2Cl_2$ and layering with pentane to yield orange crystals (0.183 g, 46% yield). $^1H\{^{11}B\}$ NMR ($CD_2Cl_2$): *δ* = 7.79–7.24 (m, 32 H, Ph, $BAr_4^F$), 4.99 (s, 1 H, B*H*), 2.90 [dd, *J*(PH) = 10.5 Hz, *J*($P_{(BH3)}$H) = 12.5 Hz, 2 H, C*H*$_2$], –9.08 [br. d, *J*(PH) = 6 Hz, 2 H, B*H*$_2$] ppm. $^{31}P\{^1H\}$ ($CD_2Cl_2$): *δ* = 73.7 [d, *J*(PP) = 102.1 Hz, 1 P, *P*Ph$_2$], 15.6 (br., 1 P, *P*BH$_3$) ppm. $^{11}B\{^1H\}$ NMR ($CD_2Cl_2$): *δ* = 16.7 (br. s, 1 B, *B*H$_3$), –5.9 (s, 1 B, $BAr^F_4$). $C_{60}H_{37}B_2F_{24}MnP_2$ (1400): calcd. C 51.46, H 2.66; found C 51.60, H 2.74. IR (KBr): $\tilde{\nu}_{max}$ = 2519 (m, BH), 2070 (s, CO), 2010 (s, CO), 1975 (s, CO) cm$^{-1}$.

**[(CO)$_4$Mn(η$^1$-BH$_3$·dppm)][BAr$^F_4$] (2):** A $CH_2Cl_2$ solution of [(CO)$_3$Mn(η$^2$-BH$_3$·dppm)][$BAr^F_4$] (0.100 g, 0.074 mmol) was stirred under CO for 15 min to give a yellow solution. The compound loses a carbonyl group in vacuo to give **2**. Crystals suitable for an X-ray diffraction study were grown by layering the CO-saturated $CH_2Cl_2$ solution with CO-saturated pentane to yield yellow crystals. $^1H$ NMR ($CD_2Cl_2$): *δ* = 7.78–7.30 (m, 32 H, Ph, $BAr_4^F$), 3.54 [dd, *J*(PH) = 11.5 Hz, *J*($P_{(BH3)}$H) = 11.9 Hz, 2 H, C*H*$_2$], –3.74 [br., *J*(BH) 61.4 Hz, 3 H, B*H*$_3$]. Selected $^1H\{^{11}B\}$ NMR ($CD_2Cl_2$) data: *δ* = –3.74 [br. d, *J*(PH) = 8 Hz, 3 H, B*H*$_3$] ppm. $^{31}P\{^1H\}$ NMR ($CD_2Cl_2$): *δ* = 55.2 [d, 1 P, *J*(PP) = 54.7 Hz, *P*Ph$_2$], 16.0 (br., 1 P, *P*BH$_3$) ppm. $^{11}B\{^1H\}$ NMR ($CD_2Cl_2$): *δ* = –5.9 (s, 1 B, $BAr_4^F$), –37.5 (br. s, 1 B, *B*H$_3$) ppm. IR (KBr): $\tilde{\nu}_{max}$ = 2498 (m, BH), 2440 (m, BH) 2112 (s, CO), 2053 (s, CO), 2028 (s, CO), 2000 (s, CO) cm$^{-1}$. Selected low-temperature NMR spectroscopic data (190 K): $^1H\{^{11}B\}$ NMR ($CD_2Cl_2$): *δ* = 3.50 (br., 2 H, $CH_2$), 1.99 (v br., 2 H, B*H*), –15.52 (br., 1 H, B*H*) ppm.

 © 2006 Wiley-VCH Verlag GmbH & Co. KGaA, Weinheim 

## Acknowledgments

The EPSRC (GR/R90475/01) and the Royal Society are thanked for support.

[1] R. H. Crabtree, *The Organometallic Chemistry of the Transition Elements*, Wiley, New York, **2001**.
[2] A. Macchioni, *Chem. Rev.* **2005**, *105*, 2039.
[3] P. Braunstein, F. Naud, *Angew. Chem. Int. Ed.* **2001**, *40*, 680.
[4] P. Espinet, K. Soulantica, *Coord. Chem. Rev.* **1999**, *195*, 499.
[5] C. S. Slone, D. A. Weinberger, C. A. Mirkin, *Prog. Inorg. Chem.* **1999**, *48*, 233.
[6] V. V. Grushin, *Chem. Rev.* **2004**, *104*, 1629.
[7] a) J. W. Faller, J. C. Wilt, J. Parr, *Org. Lett.* **2004**, *6*, 1301; b) J. W. Faller, J. Lloret-Fillol, J. Parr, *New J. Chem.* **2002**, *26*, 883.
[8] C. J. Chapman, C. G. Frost, M. P. Gill-Carey, G. Kociok-Köhn, M. F. Mahon, A. S. Weller, M. C. Willis, *Tetrahedron: Asymmetry* **2003**, *14*, 705.
[9] B. J. Holliday, P. A. Ulmann, C. A. Mirkin, C. L. Stern, *Organometallics* **2004**, *23*, 1671.
[10] T. J. Marks, J. R. Kolb, *Chem. Rev.* **1977**, *77*, 263.
[11] S. C. P. Joseph, F. G. N. Cloke, C. J. Cardin, P. B. Hitchcock, *Organometallics* **1995**, *14*, 3566.
[12] R. J. Hamilton, C. G. Leong, G. Bigman, M. Miskolzie, S. H. Bergens, *J. Am. Chem. Soc.* **2005**, *127*, 4152.
[13] B. Chamberlain, S. B. Duckett, J. P. Lowe, R. J. Mawby, J. C. Stott, *Dalton Trans.* **2003**, 2603.
[14] R. Macias, N. P. Rath, L. Barton, *Angew. Chem. Int. Ed.* **1999**, *38*, 162.
[15] O. Volkov, R. Macías, N. P. Rath, L. Barton, *Inorg. Chem.* **2002**, *41*, 5837.
[16] N. Merle, G. Koicok-Köhn, M. F. Mahon, G. D. Ruggerio, C. G. Frost, A. S. Weller, M. C. Willis, *Dalton Trans.* **2004**, 3883.
[17] M. Ingleson, N. J. Patmore, G. D. Ruggiero, C. G. Frost, M. F. Mahon, M. C. Willis, A. S. Weller, *Organometallics* **2001**, *20*, 4434.
[18] N. Merle, C. G. Frost, G. Kociok-Kohn, M. C. Willis, A. S. Weller, *J. Organomet. Chem.* **2005**, *690*, 2829.
[19] T. Yasue, K. Kawano, M. Shimoi, *Angew. Chem. Int. Ed.* **2003**, *42*, 1727.
[20] T. Kakizawa, K. Kawano, M. Shimoi, *Organometallics* **2001**, *20*, 3211.
[21] M. Shimoi, S. Nagai, M. Ichikawa, K. Kawano, Y. Katoh, M. Uruichi, H. Ogino, *J. Am. Chem. Soc.* **1999**, *121*, 11704.
[22] K. M. Waltz, C. N. Muhoro, J. F. Hartwig, *Organometallics* **1999**, *18*, 3383.
[23] S. Schlecht, J. F. Hartwig, *J. Am. Chem. Soc.* **2000**, *122*, 9435.
[24] M. Y. Darensbourg, R. Bau, M. W. Marks, R. R. Burch Jr, J. C. Deaton, S. Slater, *J. Am. Chem. Soc.* **1982**, *104*, 6961.
[25] J. F. Hartwig, S. R. De Gala, *J. Am. Chem. Soc.* **1994**, *116*, 3661.
[26] D. R. Martin, C. M. Merkel, J. P. Ruiz, *Inorg. Chim. Acta* **1986**, *115*, L29.
[27] A. Toupadakis, G. J. Kubas, W. A. King, B. L. Scott, J. Huhmann-Vincent, *Organometallics* **1998**, *17*, 5315.
[28] P. H. Bird, M. G. H. Wallbridge, *J. Chem. Soc. Chem. Commun.* **1968**, 687.
[29] Y. Oishi, T. A. Albright, *Polyhedron* **1995**, *14*, 2603.
[30] M. H. Quick, R. J. Angelici, *Inorg. Synth.* **1979**, *19*, 160.
[31] W. E. Buschmann, J. S. Miller, *Inorg. Synth.* **2002**, *33*, 85.
[32] G. M. Sheldrick, *SHELX-97, A Computer Program for Refinement of Crystal Structures*, University of Göttingen, Germany, **1997**.

Received: June 6, 2006
Published Online: August 10, 2006

 © 2006 Wiley-VCH Verlag GmbH & Co. KGaA, Weinheim 

DOI: 10.1002/ejic.200600271

# Bifunctional Materials Based on the Photochromic Cation $[RuNO(NH_3)_5]^{3+}$ with Paramagnetic Metal Complex Anions

**Lyudmila A. Kushch,*[a] Lyudmila S. Kurochkina,[a] Eduard B. Yagubskii,[a] Gennadii V. Shilov,[a] Sergei M. Aldoshin,[a] Vyacheslav A. Emel'yanov,[b] Yurii N. Shvachko,[c] Vladimir S. Mironov,[d] Dominik Schaniel,[e] Theo Woike,[e] Chiara Carbonera,[f] and Corine Mathonière[f]**

**Keywords:** Photochromism / Magnetic properties / Mononitrosyl ruthenium complexes / Paramagnetic metal complexes

The synthesis of a series of compounds containing the photochromic mononitrosyl cation, $[RuNO(NH_3)_5]^{3+}$ and metal complex paramagnetic anions $[M(CN)_6]^{3-}$ [M = Cr (**1**), Fe(**2**)], $[M(ox)_3]^{3-}$ [M = Cr(**3**), Fe(**4**)] and $[CrNO(CN)_5]^{3-}$ (**5**) is reported. The crystal structures of the salts **1** and **3** are discussed. In contrast to **1** and **3** which exhibit reversible photochromic properties, illumination of **2** and **4** results in an irreversible photochemical reaction and compound **5** is not photochromic at all. The magnetic properties of **1** and **3** have been investigated and complex **1** shows a weak reversible increase in the value of $\chi_M T$ under light irradiation at low temperature.
(© Wiley-VCH Verlag GmbH & Co. KGaA, 69451 Weinheim, Germany, 2006)

## Introduction

Over the last decade new types of molecular based magnets, namely functionalised magnets with combined magnetic and optical properties, have been studied extensively.[1–4] Current research in this field is focused not only on the improvement of magnetic properties but also on the search for unusual properties which have not been realised in magnets so far. In 1996, low-temperature photoinduced magnetisation was discovered in the prussian blue analogue $K_{0.2}Co_{1.4}[Fe(CN)_6]\cdot 6.9H_2O$.[1] The design of such bifunctionalised molecular materials with reversible modifications of their magnetic properties makes it possible to control magnetic properties by an external stimulus (light) and this opens up the possibility for technical applications in displays, information and energy storage devices and sensors.[5]

Up to now several strategies exist, using different types of light-sensitive building blocks, for producing the photomagnetic effect in molecular compounds combining magnetic and optical properties.[5] One of the approaches uses anionic photochromic mononitrosyl complexes of transition metals as light-sensitive units in the synthesis of bifunctionalised magnetic materials. This was successfully shown with $Ni[FeNO(CN)_5]$. The nitroprusside anion is diamagnetic but exhibits a photoinduced transition to two extremely long-lived metastable states, MSI and MSII, by irradiation with light in the blue-green spectroscopic range (350–580 nm) at temperatures below 180 K.[6,7] In $Ni[FeNO(CN)_5]$, randomly aligned neighbouring $Ni^{II}$ spins with $S = 1$ are ordered after excitation to MSI via two antiferromagnetically coupled spins formed by charge transfer from the Fe atom to the NO ligand. These spins induce magnetic coupling between the neighbouring Ni cations followed by the formation of a magnetic cluster with $S = 5$.[2a,2c]

Recently, it has been found that cationic mononitrosyl Ru complexes also exhibit photochromic properties. Like the anionic mononitrosyl complexes, the cationic Ru species exhibit two long-lived metastable states. MSI can be generated by light irradiation in the blue-green spectroscopic range (350–580 nm), while MSII can be obtained by subsequent illumination in the blue-green and infrared spectroscopic ranges (e.g. 1064 nm). In these Ru complexes, the metastable states have higher decay temperatures (up to +20 °C for MSI and up to –45 °C for MSII).[8–10]

It was of interest to use the photochromic mononitrosyl Ru cation as a light-sensitive building block for synthesising bimetallic compounds with paramagnetic anions.[11] Here we report the preparation, structures, photochromic and magnetic properties of bimetallic complexes containing the

[a] Institute of Problems of Chemical Physics, RAS, MD142432 Chernogolovka, Russia
E-mail: lkushch@icp.ac.ru
[b] Institute of Inorganic Chemistry, Siberian Division of RAS, 630090 Novosibirsk, Russia
[c] Institute of Metal Physics Ural Division, RAS, GSP-170, 620219 Ekaterinburg, Russia
[d] A.V. Shubnikov Institute of Crystallography, RAS, 117333 Moscow, Russia
[e] Institut für Mineralogie, Universität zu Köln, Zülpicherstrasse 49b, 50674 Köln, Germany
[f] Groupe des Sciences Moléculaires, University of Bordeaux 1, Institut de Chimie de la Matière Condensée de Bordeaux, UPR CNRS 9048, 33608 Pessac Cedex, France

 © 2006 Wiley-VCH Verlag GmbH & Co. KGaA, Weinheim 

photochromic cation $[RuNO(NH_3)_5]^{3+}$ and the paramagnetic metal complex anions $[M(CN)_6]^{3-}$, [M = Cr(**1**), Fe(**2**)], $[M(ox)_3]^{3-}$ [M = Cr(**3**), Fe(**4**)] and $[CrNO(CN)_5]^{3-}$(**5**). The influence of light on the magnetic properties of $[Ru(NH_3)_5NO][Cr(CN)_6]$ has been studied. A weak increase in the value of $\chi_M T$ under light irradiation at low temperature has been observed.

## Results and Discussion

### Synthesis and Structural Characterisation

The following series of salts, comprised of the mononitrosyl photochromic cation of $[RuNO(NH_3)_5]$ and paramagnetic anions, was synthesised by metathesis in water: $[RuNO(NH_3)_5][Cr(CN)_6]$ (**1**), $[RuNO(NH_3)_5][Fe(CN)_6]$ (**2**), $[RuNO(NH_3)_5][Cr(ox)_3]\cdot 3H_2O$ (**3**), $[RuNO(NH_3)_5][Fe(ox)_3]\cdot xH_2O$ ($x \approx 3$) (**4**) and $[RuNO(NH_3)_5][CrNO(CN)_5]$ (**5**).

The crystal structures of **1**–**5** were investigated. Compound **2** is isostructural with **1** whereas **4** is not isostructural with **3**. The complete structural solutions of **2**, **4** and **5** are currently in progress. The main crystallographic data for **1** and **3** are presented in Table 1 and the crystal structure of **1** has been briefly published in ref.[11] The structure is formed from two independent structural units, i.e. $[RuNO(NH_3)_5]^{3+}$ and $[Cr(CN)_6]^{3-}$. The Ru and Cr atoms lie on a threefold axis and alternate along the *c* axis (Figure 1). There are numerous N···N contacts [2.93–3.23(2) Å] between the CN ligands of the anion and the $NH_3$ ligands of the cation. The occurrence of the N···N contacts is apparently due to the existence of C–N···H–N hydrogen bonds between complex components. The cations and anions located on the same threefold axis are coupled to each other by three hydrogen bonds. However, each cation and anion pair is linked by hydrogen bonds with three neighbouring cations and anions located on neighbouring threefold axes. It should be noted that the anion and cation from a pair are always linked with the cation and anion from different pairs, which results in the formation of a 3D network of hydrogen bonds in the crystal.

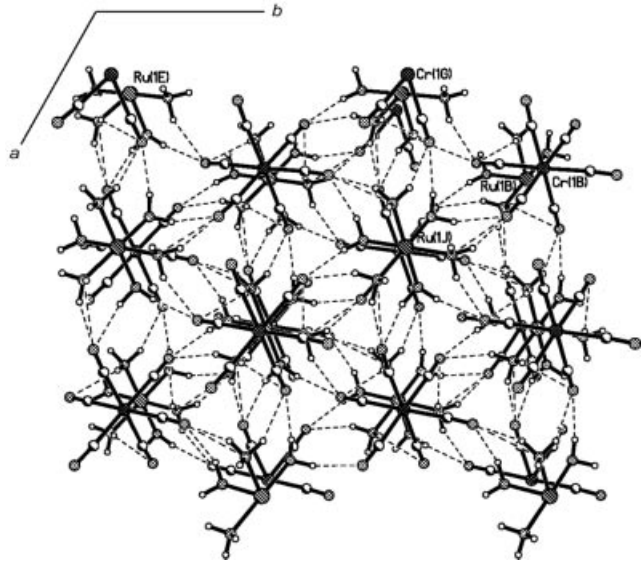


Figure 1. Projection of the crystal structure of **1** on the *ab* plane.

It should be especially emphasised that some anomalies can be observed in the structure of **1**: (a) the Ru–N–O linkage in the $[RuNO(NH_3)_5]^{3+}$ cations is bent (ca. 155°) and

Table 1. Crystal data and structure refinement for **1** and **3**.

| Compound | $[RuNO(NH_3)_5][Cr(CN)_6]$(**1**) | $[RuNO(NH_3)_5][Cr(C_2O_4)_3]\cdot 3H_2O$(**3**) |
|---|---|---|
| Formula | $C_6H_{15}CrN_{12}ORu$ | $C_6H_{21}CrN_6O_{16}Ru$ |
| *F*w | 424.37 | 586.36 |
| Temp. [K] | 293(2) | 293(2) |
| Radiation $\lambda$ [Å] | 0.71069 | 0.71069 |
| Crystal size [mm] | 0.08×0.1×0.35 | 0.15×0.15×0.50 |
| Crystal system | hexagonal | hexagonal |
| Space group | *R*3 | $P\bar{3}1c$ |
| *a* [Å] | 11.224(2) | 12.613(2) |
| *b* [Å] | 11.224(2) | 12.613(2) |
| *c* [Å] | 10.957(2) | 20.652(4) |
| $\alpha$ [°] | 90 | 90 |
| $\beta$ [°] | 90 | 90 |
| $\gamma$ [°] | 120 | 120 |
| *V* [Å$^3$] | 1195.4(4) | 2845.3(8) |
| *Z* | 3 | 6 |
| $\rho_{calcd.}$ [g cm$^{-3}$] | 1.768 | 1.864 |
| $\mu$, [cm$^{-1}$] | 1.643 | 1.442 |
| Reflections collected | 1926 | 7491 |
| Independent reflections | 1244 | 2534 |
| [$I > 2\sigma I$] | 681 | 2009 |
| $\theta$ range [°] | 2.80–40.08 | 1.86–30.10 |
| GOOF | 0.928 | 0.906 |
| *R* | 0.1151 | 0.0588 |
| $R_1$ | 0.0377 | 0.0491 |
| $wR_2$ | 0.1009 | 0.1009 |
| abs. structure Flack | –0.29(16) | – |

 © 2006 Wiley-VCH Verlag GmbH & Co. KGaA, Weinheim 

(b) the Cr–C distances differ considerably (ca. 0.1 Å) in the $[Cr(CN)_6]^{3-}$ hexacyano anion. This deserves a special comment. In the ground state of mononitrosyl $Ru^{II}$ complexes such as $[RuNO(NH_3)_5]Cl_3 \cdot H_2O$,[13,24] $Na_2[RuNO(CN)_5]$,[14] $K_2[RuNOCl_5]$[21] and $K_2[RuNOBr_5]$[22] containing the positively charged $(NO)^+$ ligand, the M–N–O group is normally linear although a strongly bent M–N–O geometry (ca. 90°) may be observed in the photoexcited metastable MSII state in some of these complexes. Related six-coordinate iron(II), osmium(II) and some other mononitrosyl complexes such as $[Ni(NO)(\eta^5\text{-Cp})]$ show similar behaviour.[13] However, in complexes with a neutral NO ligand the M–N–O group is often strongly bent even in the ground state.[13,15,16] This is due to the role of the antibonding π*(NO) orbital of the NO ligand. According to the classification scheme of Feltham and Enemark,[17] the M–N–O bond angle in transition-metal nitrosyl complexes is defined by a total number of electrons, *n*, in the metal ion M and the π*(NO) orbital. For six-coordinate (pseudo-octahedral) mononitrosyl complexes, the M–N–O angle is 180 ± 10° for $n \leq 6$, 145 ± 10° for $n = 7$ and 125 ± 10° for $n = 8$. These data are consistent with quantum chemical calculations.[18,19]

The nonlinear ground-state geometry of the Ru–N–O group in $[RuNO(NH_3)_5]^{3+}$ is unusual since a study of the optical properties of **1** showed the NO group to be positively charged ($\tilde{\nu}_{NO}$ = 1947 and 1914 $cm^{-1}$). On closer inspection, however, this can naturally be rationalised in terms of attractive coulombic interactions between $NO^+$ and $CN^-$ groups (having opposite electrical charges) combined with the specific crystal structure of **1**, as illustrated in Figure 2. In the room-temperature crystal structure of **1**, the nitrosyl groups are statistically disordered in three equivalent positions. Therefore, the occupancy in the refined structure was assumed to be equal to ⅓ for the NO ligand and ⅔ for the corresponding $NH_3$ groups. However, regardless of the specific location of the $NO^+$ group in the "frozen rotation" configuration of the $[RuNO(NH_3)_5]^{3+}$ cations, the positively charged nitrosyl group (N1c and O1c atoms, Figure 2) is always in contact with five negatively charged cyano groups from three $[Cr(CN)_6]^{3-}$ anions, Figure 2. The environment of the O1c atom is symmetric enough: five contacts form a square bipyramid (contacts of the O1c atom with N4o, N3s, N4c, N4w, and N3g atoms, shown in solid grey lines). The resultant coulombic force is directed towards the N3g atom (black downward arrow). The environment of the nitrogen N1c atom of the nitrosyl group is less symmetric and consists of two short contacts [N1c–N3s 3.00(2) Å and N1c–N4o 3.09(2) Å] and two long contacts [N1c–N4w 3.58(2) Å and N1c–N4c 3.57(2) Å black lines]. The fifth contact (with the N3g atom) is absent. Since the positive electrical charge of the nitrosyl group is preferentially concentrated on the N1c atom (due to lower electronegativity), this atom is attracted to the two nitrogen atoms of two cyano groups with short contacts (N1c–N3s and N1c–N4o, two thin arrows, Figure 2). The resultant coulombic force should be directed approximately to the midpoint of the N3s–N4o line (this force is shown with a bold and long black arrow in Figure 2). As a consequence, two coulombic forces at O1c and N1c make a torsional moment which bends the Ru1c–N1c–O1c bond. Note that at such short distances (3.0–3.5 Å), attractive coulombic interactions are quite strong (ca. 2–4 eV, depending on effective charges on the actual atoms) resulting in such a pronounced distortion in the Ru–N–O bond angle (ca. 25°). Note that

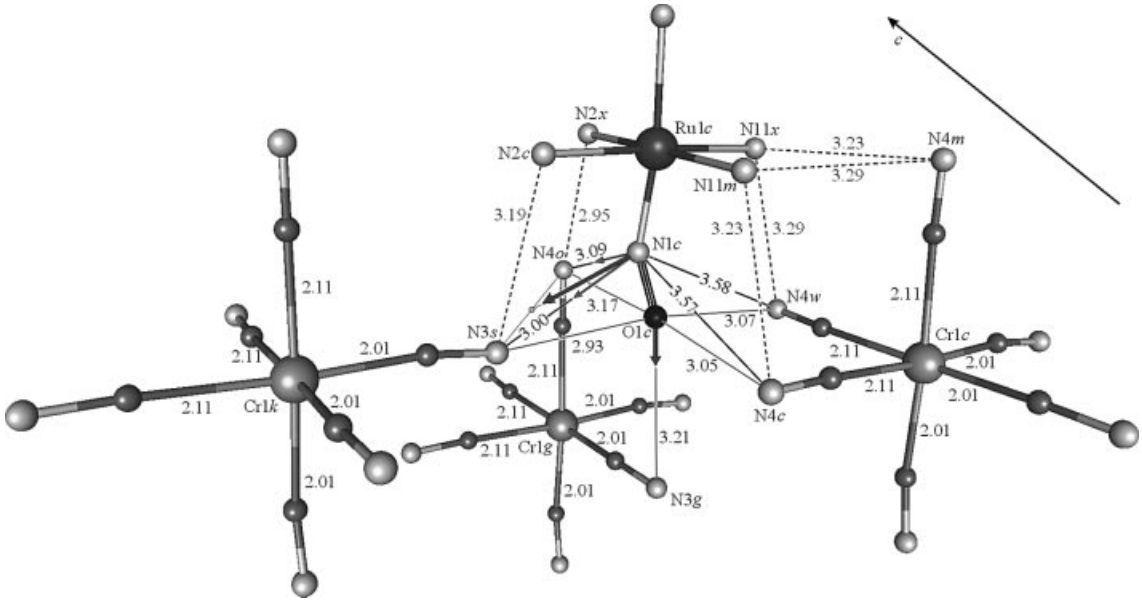


Figure 2. Immediate environment of the nitrosyl group (O1c and N1c atoms) in the 'frozen' orientation of the $[RuNO(NH_3)_5]^{3+}$ cation is drawn in perspective. The coulombic forces acting on the N1c and O1c atoms of the nitrosyl group are shown by arrows. Some of the H···N hydrogen bonds between H atoms of the $NH_3$ ligands of the $[RuNO(NH_3)_5]^{3+}$ cations and N atoms of the cyano groups of the $[Cr(CN)_6]^{3-}$ anions are shown with grey dashed lines as contacts between the N atoms of $NH_3$ ligand (N2c, N2x, N11m, and N11x, hydrogen atoms are not shown) with N atoms of the cyano groups (N4o, N3s, N4c, N4w, and N4m). Short (2.01 Å) and long (2.11 Å) Cr–C bonds of the $[Cr(CN)_6]^{3-}$ anions are indicated (the errors in length bonds do not exceed 0.02 Å).

 © 2006 Wiley-VCH Verlag GmbH & Co. KGaA, Weinheim 

the azimuthal orientation of the Ru1c–N1c–O1c plane is consistent with local geometry conditions for the coulombic forces shown in Figure 2. Therefore, despite rather limited accuracy in the refinement of the N–O position in the X-ray analysis of **1**, these arguments strongly support the existence of a bent Ru–N–O geometry. Furthermore a similar bent Ru–N–O ground-state structure (ca. 160°) was previously observed in the molecular compound $(BETS)_2[RuNOBr_5]$.[20] This anomaly was explained by the change in the effective charge on the nitrosyl ligand due to partial transfer of electron density from the organic BETS molecules. However, similar to the case of **1**, this can also be rationalised in terms of attractive coulombic attractions between the $NO^+$ group and the S centre of the BETS molecules and with $Br^-$ ligands of neighbouring $[RuNOBr_5]^{2-}$ anions. Interestingly, in the related complex $(BETS)_2[RuNOCl_5]$, the Ru–N–O group is almost linear (178°). This could be due to the differences in the specific geometry of $Ru–NO^+\cdots X^-$ contacts (distances, bond angles) in $(BETS)_2[RuNOX_5]$ (X = Cl, Br) which have different crystal structures. In the case of X = Br, the $NO^+–X^-$ attractive interactions seem to be stronger than in the case of X = Cl. Qualitatively, this is consistent with the fact that in the compound with X = Br the $NO^+$ group occupies only one crystallographic position, while in compound with X = Cl the $NO^+$ group is disordered between two positions. In contrast to $(BETS)_2[RuNOX_5]$ compounds, the Ru–N–O bond angles are almost linear in the precursor compounds $K_2[RuNOBr_5]$ and $K_2[RuNOCl_5]$, i.e. 174.4(1)° for X = Br and 176.7(5)° for X = Cl.[21,22] These observations indicate that in some molecular compounds with $[RuNOX_5]^{2-}$ building blocks, external interactions can strongly affect the Ru–N–O bond angle. This effect is sensitive to the specific crystal structure.

The second anomaly is associated with the distortion of the octahedral $Cr(CN)_6^{3-}$ anion. The Cr–CN bonds are essentially different, three of them are 2.01(1) Å and the other three are 2.11(1) Å (Figure 2). The C(2)–Cr(1)–C(2) angles are 87.3(2)° and the C(1)–Cr(1)–C(1) angles are 92.3(2)° (Figure 3). The origin of this structural anomaly in the $[Cr(CN)_6]^{3-}$ anions is less evident. In contrast to the case of the nitrosyl group, the immediate environment of the CN group can vary depending on the specific orientation of the $NO^+$ groups in the closest $[RuNO(NH_3)_5]^{3+}$ cations. These may rotate about the $C_3$ axis by 120° and many local configurations are therefore possible. An example of the local crystal structure around the $CN^-$ group is shown in Figure 3. The cyano group (N3 and C1 atoms in Figure 3) is involved in several $CN\cdots NH_3$ and $NO^+\cdots CN^-$ contacts with $[RuNO(NH_3)_5]^{3+}$ cations lying in the same Ru–Cr–Ru chain (running along the *c* axis, Figure 3) and in the neighbouring chains. Within each specific Ru–Cr–Ru chain, the cyano groups in contact with $NO^+$ groups (such as C2–N4 and C2b–N4b cyano groups in Figure 3) have considerably longer Cr–C bonds [2.11(1) Å] compared with those [2.01(1) Å] for cyano groups in contact only with $NH_3$ ligands (such as the C1–N3 and C1a–N3a cyano groups in Figure 3). This is unusual because in many molecular compounds containing $[Cr(CN)_6]^{3-}$, the octahedra are slightly distorted with the Cr–C distances fluctuating typically around 2.06 ± 0.03 Å.[23] Therefore, a pronounced difference in the Cr–C bond lengths indicates a strong perturbing effect of the $CN\cdots H(NH_3)$ hydrogen bonds and $NO^+\cdots CN^-$ coulombic attractions (they are comparable in magnitude). This implies that the actual "frozen" structure of the $[Cr(CN)_6]^{3-}$ anions can be considerably different from the statistically averaged crystallographic structure of $C_{3v}$ symmetry. In particular, some of the Cr–C bonds to the CN groups in contact with the $NO^+$ ligand of $[RuNO(NH_3)_5]^{3+}$ are even longer than 2.11 Å. Similarly, some of the Cr–C bonds of CN groups in contact with the $NH_3$ ligand may be shorter than 2.01 Å. This can cause a large zero-field splitting of the $^4A_{2g}$ ground spin state of the $[Cr(CN)_6]^{3-}$ anion (see below).

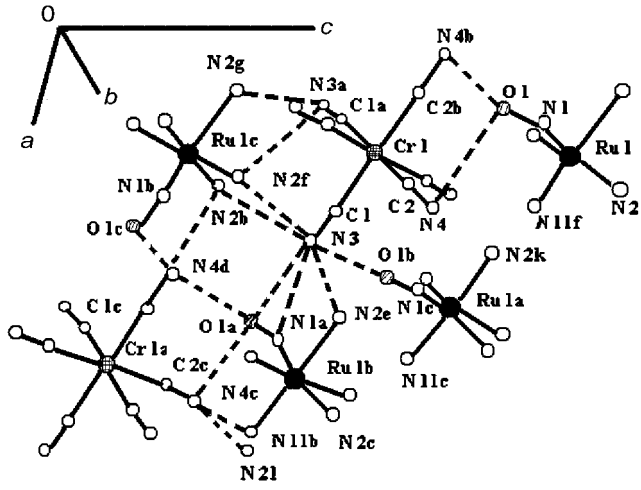


Figure 3. Fragment of the crystal structure of **1**. The threefold axes run through Ru(1), Cr(1), Ru(1c) and Cr(1a), Ru(1b), Ru(1a). The dotted lines show N···N and N···O contacts between CN ligands of the anions and $NH_3$ and NO ligands of the cations. The hydrogen atoms have been omitted for clarity.

An X-ray analysis of **3** showed that the crystal structure is formed from two types of $[RuNO(NH_3)_5]$ cations, $[Cr(ox)_3]$ anions and two types of water molecules. In two of the six $[Ru(1)NO(NH_3)_5]$ cations (Ru1) arranged in the unit cell, the NO group is disordered over six positions and in the other four $[Ru(2)NO(NH_3)]$ cations (Ru2) it is disordered over three positions (Figure 4, a). The Ru–N–O angle in Ru1 is 170(3)°, while in Ru2 it is equal to 178.5(2)°. Other valence angles and bond lengths in both types of cation are close to those found in **1** and $[RuNO(NH_3)_5]Cl_3\cdot H_2O$.[24] In two $[Cr(1)(C_2O_4)_3]$ (Cr1) anions all six Cr(1)–(O1) distances are 1.986(2) Å, while in four $[Cr(2)(C_2O_4)_3]$ (Cr2) groups the Cr–O distances are somewhat longer, namely, 2.017(2) and 2.013(2) Å. There are two different water molecules in the structure: one of them is in a general position (O7) and the other one is in a special position (O8). The water molecule (O8) is orientationally disordered. There are many shortened N···O and O···O contacts between cations, anions and water molecules. As in **1**, the occurrence of short N···O and O···O contacts is apparently due to the existence of

 © 2006 Wiley-VCH Verlag GmbH & Co. KGaA, Weinheim 

a net of N–H···O, N–O···O and O–H···O hydrogen bonds between the components of the complex (Figure 4, a and b). Ru1 cations are linked to Cr1 anions by five hydrogen bonds [intermolecular N(1)···O(1) contacts of 2.89(2) Å]. Instead of a sixth hydrogen bond, a shortened van der Waals O(11)···O(1) contact equal to 2.74(2) Å can be observed. A shorter contact O(11)···O(21) [2.47(2) Å] can be observed between the Ru1 and Ru2 cations (Figure 4, a). The Ru2 cations are linked by N(3)–H···O(2) hydrogen bonds with the Cr1 anion and intermolecular N(3)–H···O(2) contacts of 2.87(2) Å. The Cr1 and Cr2 anions are linked to each other by O(7) water molecules along the *c*

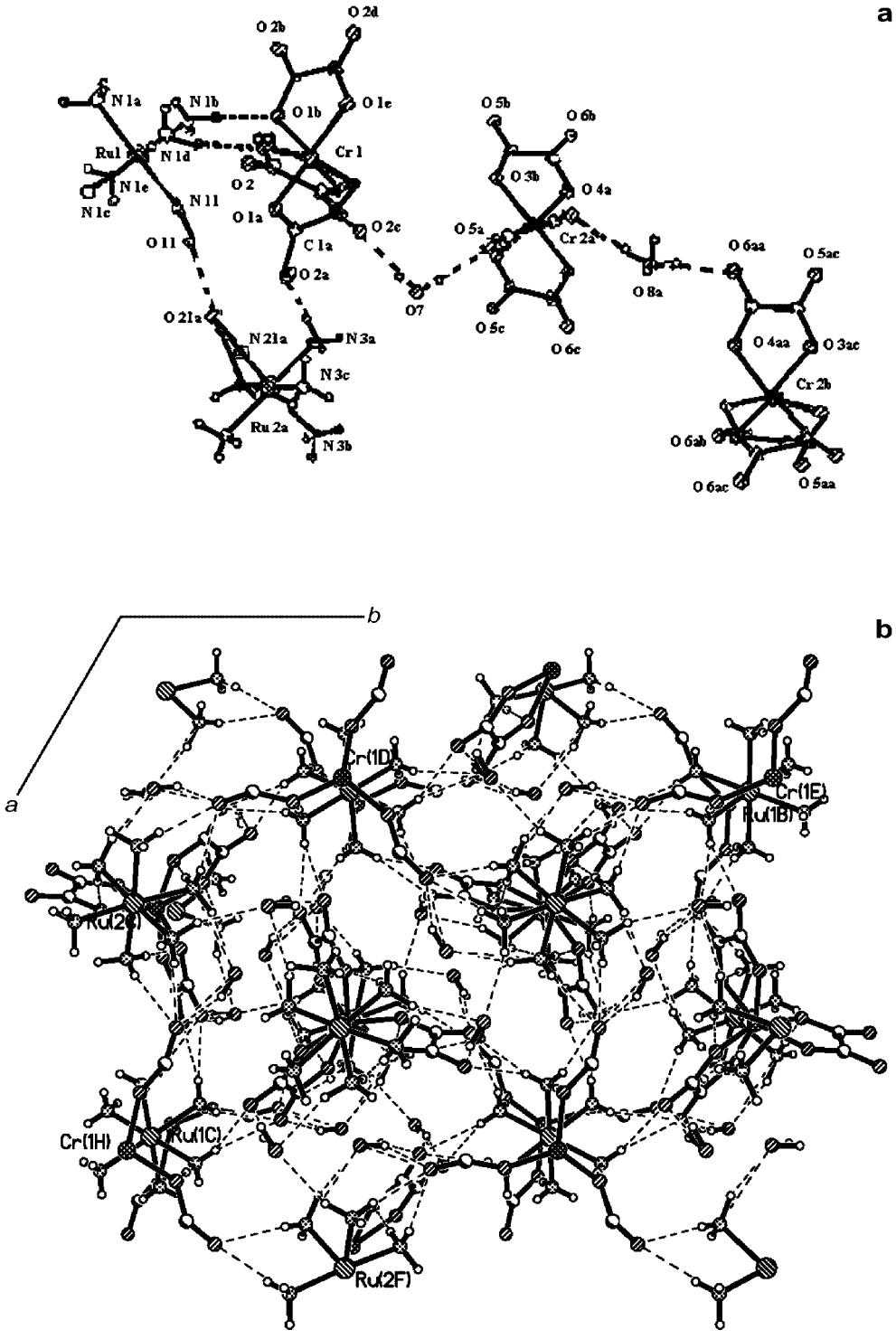


Figure 4. a) Fragment of the crystal structure of **3**. The dotted lines show O···N and O···O contacts between oxalate ligands of the anions and $NH_3$ and NO ligands of the cations and water molecules. The *c* axis runs parallel to the line connecting Ru(1) and Cr(1). b) Projection of crystal structure of **3** on the *ab* plane.

 © 2006 Wiley-VCH Verlag GmbH & Co. KGaA, Weinheim 

axis [intermolecular O(2)···O(7) and O(7)···O(5) contacts of 2.86(2) Å and 2.95(2) Å, respectively]. The O(8) water molecule links Cr2 [O(8)···O(6)–2.88(2) Å] anions in the same direction (Figure 4, a). It should be noted that the carboxyl oxygen atoms of the Cr2 anions do not participate in the formation of the hydrogen bonds, which is distinct from Cr1. This is probably the reason for the distinction between the Cr–O bond lengths in the Cr1 and Cr2 anions.

### Differential Scanning Calorimetry

The photochromic properties of compounds **1**–**5** were investigated by differential scanning calorimetry (DSC). This technique has already been used to detect the existence of metastable states in complexes containing the nitroprusside anion[25,26] and some ruthenium mononitrosyl anionic[27,28] and cationic complexes.[29] With DSC we can determine the amount of energy, which heats the lattice during the thermal decay of metastable states. In contrast to mononitrosyl anionic complexes of transition metals, one exothermal peak was detected in **1** and **3** after their illumination with blue light (Figure 5).

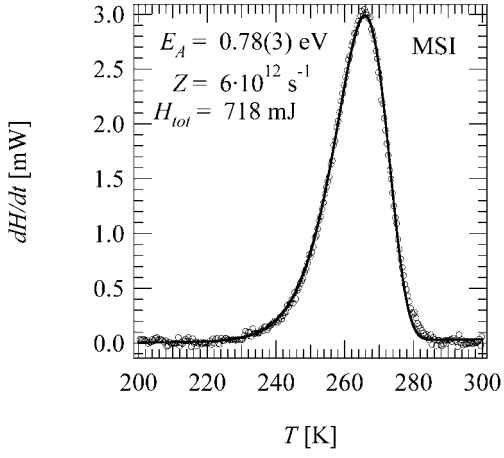


Figure 5. Thermal decay spectra ($q$ = 5 K min$^{-1}$) of $[RuNO(NH_3)_5][Cr(CN)_6]$ after irradiation at 120 K with $\lambda$ = 434 nm for MSI.

The appearance of the exothermal heatflow is associated with the transition of a photochromic cation from the metastable MSI state to the ground state (GS). The temperatures of the peak maxima observed in the spectra of these complexes are very close to that of $[RuNO(NH_3)_5]Cl_3{\cdot}H_2O$ (ca. 260 K).[30] It should be noted that the intensity of the DSC signal in **3** was essentially lower than that in **1**. Since the area under the heatflow curve is proportional to the number density of cations in the metastable state, this is evidence of a low population in **3**. This is possibly due to a small penetration depth of light into the "oxalate" complex crystals, which are deep-brown in colour in contrast to the light-orange crystals of **1**.

It is known that the illumination of anionic photochromic complexes by NIR light (1064 nm) transforms MSI to MSII. Recently, it was shown that subsequent irradiation of $[RuNO(NH_3)_5]Cl_3{\cdot}H_2O$ by light with wavelengths of 400–500 nm and 1000–1200 nm transfers MSI into MSII. The decay of MSII occurs at 220 K.[30] By irradiation of **1** in a manner completely analogous to $[RuNO(NH_3)_5]Cl_3{\cdot}H_2O$ this second metastable state was also detected (Figure 6).

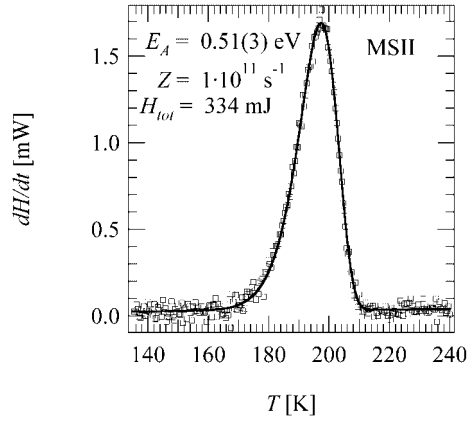


Figure 6. Thermal decay spectra ($q$ = 5 K min$^{-1}$) of $[RuNO(NH_3)_5][Cr(CN)_5]$ after irradiation at 120 K with $\lambda$ = 434 nm and $\lambda$ = 1064 nm for MSII.

It should be noted that the decay temperature of MSII in **1** ($T_d$ = 195 K) is 25 K lower than in the starting complex $[RuNO(NH_3)_5]Cl_3{\cdot}H_2O$ ($T_d$ = 220 K). A possible explanation for this significant temperature reduction may be given by the structural peculiarities presented in Figure 2 and discussed above in terms of coulombic interactions. The generation of the metastable states implies that these attractive forces are overcome or at least neutralised. This may occur by means of the charge transfer from the ground state to the light-induced intermediate state π*(NO), in which the new charge distribution of the NO ligand reduces the attractive forces. During the lifetime of this intermediate state, the motion of the NO ligand is quasi-free and is finally stabilised in the new relaxed electron density distribution of the NO ligand. The same arguments apply to the generation of MSI. The key feature which allows the rotation of the NO ligand is the new charge configuration in the intermediate π*(NO) state in order to overcome the coulombic interactions. Otherwise no rotation could occur and the metastable states would not be occupied.

Since the decay of the metastable states is mono-exponential over time under isothermal conditions, the depopulation processes are first-order reactions and can be conveniently described by the Arrhenius law (see Exp. Sect.). In the present case, a fit of the experimental data allowed us to evaluate the activation energy ($E_a$) and the frequency factor ($Z$) for MSI and MSII in **1**. We obtained $E_a$ = 0.78(3) and 0.51(3) eV, and $Z = 6\times10^{12}$ and $5\times10^{11}$ s$^{-1}$ for MSI and MSII, respectively. The error in the frequency factor is one order of magnitude due to the small temperature range of the measurements. These high activation energies are within the range of those determined for $[RuNO(NH_3)_5]Cl_3{\cdot}H_2O$ [$E_a$ = 0.73(3) eV, $E_a$ = 0.66(3) eV; $Z = 1\times10^{12}$ s$^{-1}$, $Z = 1\times10^{12}$ s$^{-1}$][31] and account for the stability of the induced metastable states at low temperature.

 © 2006 Wiley-VCH Verlag GmbH & Co. KGaA, Weinheim 

Complexes **2**, **4** and **5** have also been investigated by the DSC method. In contrast to **1** and **3**, which exhibit reversible photochromic properties, the illumination of **2** and 4, both of which are comprised of $[Fe(CN)_6]^{3-}$ and $[Fe(ox)_3]^{3-}$ anions, results in an irreversible photochemical reaction related to a partial reduction of $Fe^{3+}$ to $Fe^{2+}$. The IR spectrum of a photoproduct of **2** shows a new band near 2044 $cm^{-1}$ attributed to valence vibrations of the $CN^-$ group bound to $Fe^{2+}$.

The DSC signal was not observed in **5** with the $[CrNO(CN)_5]^{3-}$ anion. Possibly, the X-ray analysis of the crystal structure of **5** clarifies the reason for the absence of photochromic properties. Thus, the study of the photochromic properties of **1**–**5** shows that the nature of the paramagnetic metal complex anion strongly affects the photochromism of mononitrosyl Ru complexes.

### Magnetic Properties

Figure 7 shows the temperature dependence of the reciprocal paramagnetic susceptibility, $\chi_P^{-1}$, for $[RuNO(NH_3)_5][Cr(ox)_3]\cdot 3H_2O$. The measurements were carried out at Field Cooling (FC) and $B = 10000$ G. A fit with the Curie–Weiss law, $\chi_P = C/(T - \Theta)$, with $C = 1.98$ emu K $mol^{-1}$ and $\Theta = 0.26$ K is in good agreement with experiment down to 1.8 K. The low-temperature part of the curve is depicted in the inset. Figure 8 shows the temperature evolution of $\chi_P^{-1}$ for $[RuNO(NH_3)_5][Cr(CN)_6]$ obtained under similar experimental conditions. The data are well described by the Curie–Weiss law with $C = 1.86$ emu K $mol^{-1}$ and $\Theta = 0.18$ K. Several experimental points at $T < 5$ K shown on the inset slightly deviate from the fitting curve. At 300 K $\chi_P$ values for **1** and **3** are equal to $6.07 \times 10^{-3}$ and $6.25 \times 10^{-3}$ emu $mol^{-1}$, respectively. A positive $\Theta$ value is usually indicative of ferromagnetic correlations, though for $S \geq 1$ such small values of $\Theta$ might also come from the zero-field splitting of the ground spin state, $D$. For a system of noninteracting spins with zero-field splitting, the average molar paramagnetic susceptibility $\chi_P$ shows an effective Weiss temperature $\Theta$ at $T > |D|/\kappa$ (due to interplay of perpendicular and parallel components). At $T < |D|/\kappa$, $\chi_P^{-1}$ deviates from the Curie–Weiss law. The Curie constants $C$ for both complexes are very close to 1.88 emu K $mol^{-1}$, which is characteristic of noninteracting $S = 3/2$ spins. Thus, the paramagnetism of both complexes can be attributed to the $Cr^{3+}$ spin system. No indications of the presence of a paramagnetic $Ru^{III}$ ($S = 1/2$) oxidation state were found. The temperature behaviour of $\mu_{eff}$ for both complexes [where $\mu_{eff} = (3\kappa\chi_P T/\mu_0 N_A)^{1/2} = 2.828(\chi_P T)^{1/2}$] is presented Figure 9. The magnetic moment $\mu_{eff}$ of both complexes is little affected in the temperature range from 300 K to 5 K. Below 5 K, $\mu_{eff}$ of $[RuNO(NH_3)_5][Cr(CN)_6]$ reveals a pronounced decrease from 3.83 to 2.91 $\mu_B$ (at 1.99 K) whereas $\mu_{eff}$ of $[RuNO(NH_3)_5][Cr(ox)_3]\cdot 3H_2O$ remains nearly constant. In Figure 10 the magnetisation data in terms of magnetic moment $M$ in Bohr magnetons ($N_{A\mu B}$) are plotted against the reduced variable $B/T$ (in T/K). The diamagnetic response of the gel capsule has been subtracted. Samples of **1** and **3** were frozen in fields of 3 T and 5 T, respectively. Experimental points were obtained by decreasing the field to 0 at constant temperatures of 2.00 K and 1.83 K. Maximum values are 2.70 (5 T) and 2.20 (3 T), respectively. The field dependence for $[RuNO(NH_3)_5][Cr(ox)_3]\cdot 3H_2O$ is consistent with the model of noninteracting spins. A solid line corresponds to the Brillouin function with $S = 3/2$ and $g = 2.080$. The enhanced $g$ value might be due to the ligand field splitting effect. The low-temperature behaviour of $[Cr(CN)_6]^{3-}$ anions in **1** is quite unusual and cannot be explained in terms of the Brillouin function. At higher fields ($B > 5000$ G) the effective spin value of the $Cr^{3+}$ ions in the ground state is considerably smaller than $S = 3/2$. On the other hand, at lower fields ($B < 5000$ G), the abrupt approach of $M$ to its maximum value is reminiscent of magnet behaviour. These peculiarities rapidly disappear at $T \geq 5$ K.

This anomalous magnetic behaviour of **1** below 5 K can be related to the zero-field splitting of the $^4A_{2g}$ ground spin state ($S = 3/2$) of $Cr^{3+}$ ions. In distorted $[Cr(CN)_6]^{3-}$ com-

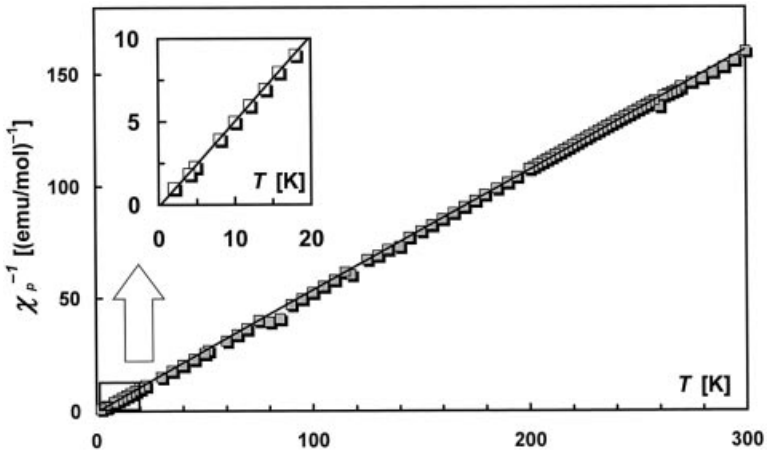


Figure 7. Temperature dependence of the reciprocal paramagnetic susceptibility, $\chi_p^{-1}$(T), at 10 kG for $[RuNO(NH_3)_5][Cr(ox)_3]\cdot 3H_2O$. The inset shows the low temperature segment following the Curie–Weiss law with $C = 1.98$ emu K $mol^{-1}$ and $\Theta = 0.26$ K.

 © 2006 Wiley-VCH Verlag GmbH & Co. KGaA, Weinheim 

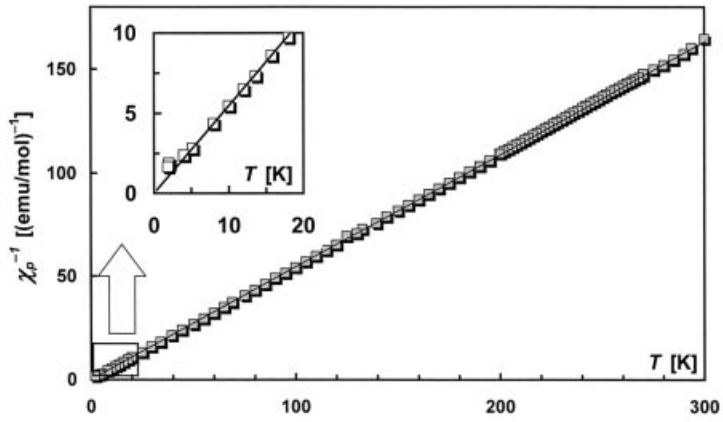


Figure 8. Temperature dependence of the reciprocal paramagnetic susceptibility, $\chi_p^{-1}(T)$, at 10 kG for $[RuNO(NH_3)_5][Cr(CN)_6]$. The inset shows the low temperature segment following the Curie–Weiss law with $C = 1.86$ emu K mol$^{-1}$ and $\Theta = 0.18$ K.

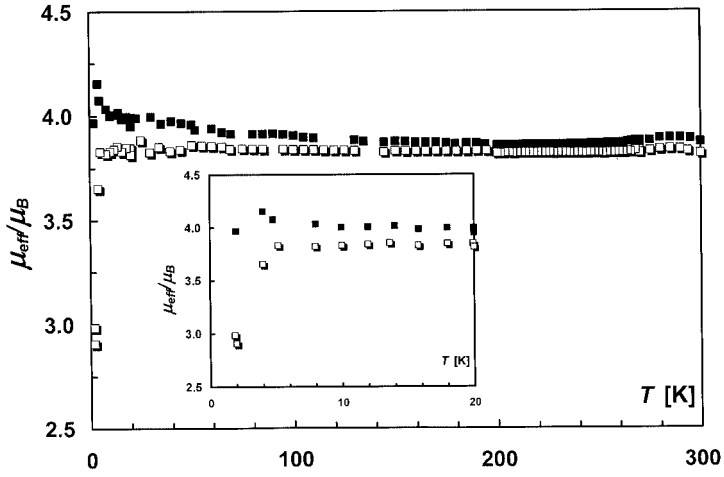


Figure 9. Temperature dependence of the effective magnetic moments of $[RuNO(NH_3)_5][Cr(ox)_3]\cdot 3H_2O$ (filled squares) and $[RuNO(NH_3)_5][Cr(CN)_6]$ (open squares) microcrystals measured at cooling, $B = 10$ kG. The insert shows the low temperature segment.

plexes, the spin-orbit interaction combined with the low-symmetry crystal-field component splits the $^4A_{2g}$ ground spin state into two Kramers doublets separated by a gap of $2D$ zero-field splitting energy. As a result, at low temperatures ($kT < 2D$) the effective magnetic moment drops (from 3.83 to 2.91 $\mu_B$, Figure 9) due to preferential thermal population of the lower Kramers doublet. In this case, the low-temperature limit of the effective magnetic moment $\mu_{eff}$ of $[Cr(CN)_6]^{3-}$ can be calculated as $\mu_{eff}^2 = g_{av}^2\mu_B^2 S(S+1)$, where $S = 1/2$, $g_{av}^2 = (g_1^2 + g_2^2 + g_3^2)/3$ and $g_1$, $g_2$ and $g_3$ refer to the anisotropic $g$-tensor of the effective spin ($S = 1/2$) associated with the lower Kramers doublet of the split $^4A_{2g}$ ground state. Though the $g_1$, $g_2$, $g_3$ $g$-tensor components of the lower Kramers doublet can vary considerably for different distortions of $[Cr(CN)_6]^{3-}$ cyano complexes (typically, $g_1 = 1.97$, $g_2 = 3.78$, $g_3 = 4.08$ and $g_1 = 1.24$, $g_2 = 1.59$, $g_3 = 5.55$), the $g_{av}$ value is insensitive to the specific type of distortion ($g_{av} \approx 3.40$). Thus we obtained $\mu_{eff} = 2.95$ $\mu_B$ for the low-temperature magnetic moment of $[Cr(CN)_6]^{3-}$, which is remarkably close to the measured value of 2.91 $\mu_B$ (at 1.99 K, Figure 9). This is also consistent with the low-temperature field dependence of magnetisation in which the saturated magnetic moment of **1** is considerably smaller that that of **2**, Figure 10.

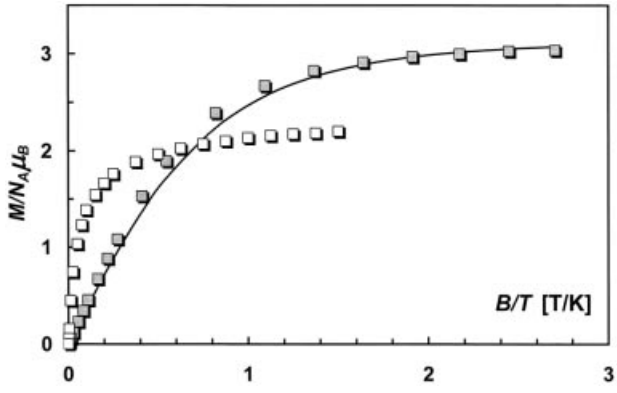


Figure 10. Field dependences of the magnetisation, $M/N_{A\mu B}$, of $[RuNO(NH_3)_5][Cr(ox)_3]\cdot 3H_2O$ (filled squares) and $[RuNO(NH_3)_5][Cr(CN)_6]$ (open squares) microcrystals at 1.83 K and 2.00 K, respectively. Measurements were carried out by decreasing the field down to 0 after field cooling at 50 kG and 30 kG, respectively. The solid curve denotes fitting by the Brillouin function with $S = 3/2$ and $g = 2.0800$. The experimental points are depicted with a normalised OX scale of $B/T$, unit G K$^{-1}$.

 © 2006 Wiley-VCH Verlag GmbH & Co. KGaA, Weinheim 

The zero-field splitting of $[Cr(CN)_6]^{3-}$ in **1** is approximately of the order $2D/k \approx 5$ K ($2D \approx 3$ cm$^{-1}$), as can be estimated from the onset of the drop of the magnetic moment of **1** (ca. 5 K, Figure 9). In most of $Cr^{III}$ complexes (and $Cr^{3+}$ ions doped in host lattices), the zero-field splitting of the $^4A_{2g}$ state is within 1 cm$^{-1}$. However, in some cases $2D$ can be considerably larger. This is especially true for complexes with ligands producing strong crystal-field splittings, such as cyanide ligands in $[Cr(CN)_6]^{3-}$ (in which the crystal-field splitting energy is as large as 26600 cm$^{-1}$ [32]). It is important to note that the $2D$ splitting is sensitive to the strength of π-type metal–ligand interactions, which are especially strong for $CN^-$ ligands.[33] Qualitative estimates of the $2D$ value (in terms of angular-overlap model calculations taking into account spin-orbit interaction, see ref.[34] for detail) indicate that for some hypothetical distortions of $[Cr(CN)_6]^{3-}$ complexes corresponding to the "frozen" crystal structure of **1** (Figure 2), the zero field splitting can reach a value of 3 cm$^{-1}$ or even more.

On the other hand, an alternative explanation for the low-temperature magnetic behaviour of **1** in terms of through-space exchange interactions between paramagnetic $[Cr(CN)_6]^{3-}$ anions seems not to be reasonable since exchange interactions in **1** are expected to be very weak. This is evidenced from the fact that exchange interactions between $Cr^{3+}$ ions involved in bulk and well-isolated complexes are generally quite small.[35,36] Thus, exchange interactions between isolated $[Cr(CN)_6]^{3-}$ complexes in a closely related compound $[Co(NH_3)_5(H_2O)]$ $[Cr(CN)_6]$ were found to be as small as $J = -0.03$ cm$^{-1}$.[35] A similar strength to the exchange interactions between $[Cr(NH_3)_6]^{3+}$ complexes can be found in $[Cr(NH_3)_6](ClO_4)_2Br{\cdot}CsBr$.[36] More detailed information on the low-temperature magnetic properties of $[RuNO(NH_3)_5][Cr(CN)_6]$ could be obtained from direct EPR and magnetic measurements for single crystals. Unfortunately, in contrast to the case of $[Co(NH_3)_5(H_2O)][Cr(CN)_6]$,[35] the sizes of the crystals of **1** obtained in our experiments were still too small for such measurements. The absence of these anomalies in the oxalate complexes **2** is consistent with a smaller zero-field splitting in $Cr(ox)_3$, ($2D \approx 0.9$ cm$^{-1}$ ≈ 1.3 K.[37]).

Further information can be obtained from AC susceptibility measurements. The field dependences of the in-phase ($\chi'_M$) and out-of-phase ($\chi''_M$) AC susceptibility of $[RuNO(NH_3)_5][Cr(ox)_3]{\cdot}3H_2O$ and $[RuNO(NH_3)_5]$-$[Cr(CN)_6]$ are shown in Figure 11. We have not observed a maximum of $\chi'_M$ in the temperature dependences and this could be associated with the Curie constant. This indicates the absence of long-range order. However, the field dependences of $\chi''_M$ for $[RuNO(NH_3)_5][Cr(CN)_6]$ demonstrate a pronounced maximum of $3.46 \times 10^{-2}$ emu mol$^{-1}$ at 5200 G (note, that the $X$ scale in Figure 11 is nonlinear). Similarly, $\chi'_M$ demonstrates an abrupt decrease in the same field range, $1500 < B < 23000$ G. Such behaviour is not typical of usual paramagnetic insulators. $[RuNO(NH_3)_5][Cr(ox)_3]{\cdot}3H_2O$ exhibits similar behaviour but with a much smaller out-of-phase susceptibility of $5.08 \times 10^{-3}$ emu mol$^{-1}$ at 5200 G. Taking into account spin dynamics, the experimental data presented in Figure 9 and Figure 10 can be interpreted as indicative of short-range magnetic ordering in both hexacyanide and oxalate complexes. This could not be explained in terms of the single-ion zero-field splitting effects only. Such behaviour for **1** is most likely due to weak exchange interactions between $[Cr(CN)_6]^{3-}$anions (which are expected to be of order 0.03 cm$^{-1}$, as is the case in $[Co(NH_3)_5(H_2O)]$-$[Cr(CN)_6]$[35]) combined with a rather strong (> 1 cm$^{-1}$) zero-field splitting of the $^4A_{2g}$ ground state and a statistical disorder of strongly distorted $[Cr(CN)_6]^{3-}$ cyano complexes (caused by the $NO^+$–$CN^-$ coulombic interactions discussed above). In this case, magnetic interactions between strongly anisotropic ground Kramers doublets (effective spin $S = 1/2$) of $Cr^{3+}$ ions can differ considerably from the conventional

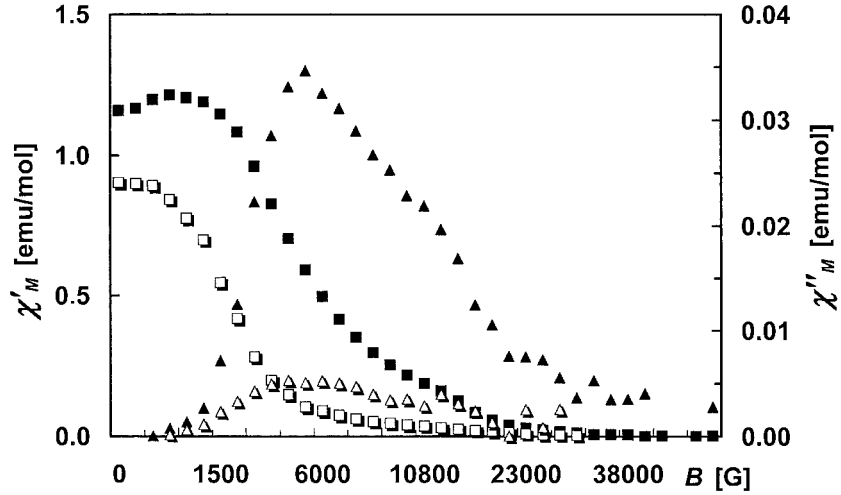


Figure 11. Field dependences of the AC magnetic susceptibilities of $[RuNO(NH_3)_5][Cr(ox)_3]{\cdot}3H_2O$ (open squares, open triangles) and $[RuNO(NH_3)_5][Cr(CN)_6]$ (filled squares, filled triangles) microcrystals measured at 1.81 K and 2.00 K, respectively. Solid squares denote the in-phase susceptibility, $\chi'_M$, (filled and open symbols respectively, left axis) and solid triangles denote the out-of-phase susceptibility, $\chi''_M$, (filled and open symbols respectively, right axis). The $x$ axis has a nonlinear scale.

 © 2006 Wiley-VCH Verlag GmbH & Co. KGaA, Weinheim 

isotropic (Heisenberg) spin-spin coupling model [which is typical of the spin-only ($S = {}^3/_2$) $^4A_{2g}$ state of $Cr^{3+}$ ions with a small zero-field splitting]. Interestingly, it has been found that the magnetic behaviour of a related compound $[Co(NH_3)_5(H_2O)][Cr(CN)_6]$ is compatible with the anisotropic Ising-type exchange interaction with $J = -0.18\ cm^{-1}$.[35] This value is consistent in magnitude with the paramagnetic Curie parameter $\Theta = 0.18$ K obtained for compound **1**. In principle, at low temperatures, this can lead to a spin-glass spin structure with strong local magnetic correlations caused by strongly anisotropic spin coupling. This might be responsible for the complicated low-temperature dynamic magnetic properties of **1** observed in our AC experiments. In contrast, AC magnetic characteristics of the oxalate compound are more compatible with the paramagnetic $S = {}^3/_2$ spin system with a small zero-field splitting. Further experiments on the AC susceptibility are in progress.

From the DSC experiments presented above one can conclude that the photochromic effect in $[RuNO(NH_3)_5][Cr(CN)_6]$ is stronger than that in $[RuNO(NH_3)_5][Cr(ox)_3]\cdot 3H_2O$. This result correlates with low-temperature magnetic measurements, according to which $Cr^{3+}$ spins in hexacyanide complexes demonstrate a more pronounced dissipation to the lattice reservoir. This is generally consistent with a larger zero-field splitting of the $S = {}^3/_2$ ground spin state in $[Cr(CN)_6]^{3-}$ complexes, which provides a more efficient spin-lattice coupling.

### Photomagnetic Properties

We measured the magnetic properties of **1** at 10 K and 5000 Oe while irradiating with blue light. Figure 12 shows the result of this photomagnetic experiment. Before irradiation, the $\chi_M T$ value was 1.89 emu mol$^{-1}$ K. When the laser was switched on, thermal heating caused the sudden decrease of the magnetic signal, which then increased continuously until a plateau was reached after 8 h of light irradiation. When the laser was switched off, a sudden increase of the magnetic signal was observed due to the cessation of the thermal heating caused by the laser irradiation. The $\chi_M T$ value in the dark after the illumination was found to be 1.91 emu mol$^{-1}$ K. Hence the light induces an increase of only 1% in the magnetic signal of compound **1**. This small effect is real and fully reversible, as was demonstrated by anneling the material at 300 K and then cooling again to 5 K whereby the original $\chi_M T$ value of 1.89 emu mol$^{-1}$ K was measured again. The observation of such a weak photomagnetic effect is not really surprising, despite the fact that at 5 K the compound is in a photoexcited state. This may be interpreted as follows: the low-temperature metastable state is diamagnetic due to the $4d^6$ low-spin configuration of $RuNO(NH_3)_5$. In the irradiated compound, the NO ligand is rotated by about 180° from Ru–N–O (GS) to Ru–O–N (MSI). Hence, the coupling through hydrogen bonds to the paramagnetic $[Cr(CN)_6]$ anions changes with respect to the ground state as the attractive coulombic forces between the inverted NO (in MSI) and the $CN^-$ differ from those between $NO^+$ and $CN^-$ in GS. This indirect change of the electron density distribution in $[Cr(CN)_6]$ is the reason for the weak variation in the $\chi_M T$ value.

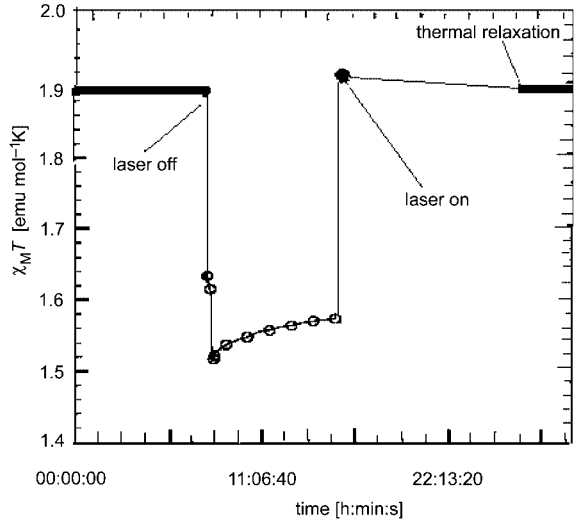


Figure 12. The time dependence of $\chi_M$T before, during and after irradiation at 406–415 nm ($P_{eff}$ = 10 mW cm$^{-2}$). The abrupt decreases are due to thermal effects when the laser is switched on.

## Conclusions

The use of the photochromic mononitrosyl $[RuNO(NH_3)_5]^{3+}$ cation complex as a light sensitive building block for the preparation of functionalised paramagnets led to five new compounds: $[RuNO(NH_3)_5][Cr(CN)_6]$(**1**), $[RuNO(NH_3)_5][Fe(CN)_6]$(**2**), $[RuNO(NH_3)_5][Cr(ox)_3]\cdot 3H_2O$(**3**), $[RuNO(NH_3)_5][Fe(ox)_3]\cdot 3H_2O$(**4**) and $[RuNO(NH_3)_5][CrNO(CN)_5]$(**5**). The crystal structures of **1** and **3** are characterised by the presence of 3D networks of hydrogen bonds due to numerous N···N or N···O contacts between the CN (**1**) or ox (**3**) ligands of the anions and $NH_3$ ligands of the cations. The study of the photochromic properties of **1**–**5** showed that the anion's nature strongly affects the photochromism of the mononitrosyl Ru complex. In contrast to **1** and **3**, which exhibit reversible photochromic properties, the irradiation of **2** and **4** results in an irreversible photochemical reaction. Compound **5** composed of $[CrNO(CN)_5]^{3-}$ anions shows no photochromic behaviour. The study of the magnetic properties has shown that the paramagnetism of the complexes **1** and **3** is due to the $Cr^{3+}$ spin system. No indications of the presence of a paramagnetic $Ru^{III}$ oxidation state were found. The magnetic moment $\mu_{eff}$ of both complexes hardly changes in the temperature range from 300 K to 5 K. Below 5 K the $\mu_{eff}$ of $[RuNO(NH_3)_5][Cr(CN)_6]$ shows a pronounced decrease from 3.83 to 2.91 $\mu_B$ (at 1.99 K) whereas the $\mu_{eff}$ of $[RuNO(NH_3)_5][Cr(ox)_3]\cdot 3H_2O$ remains nearly constant. The field dependence of magnetisation for $[RuNO(NH_3)_5][Cr(ox)_3]\cdot 3H_2O$ is consistent with the model of noninteracting spins while the low-temperature behaviour of the field dependence of **1** is unusual and can not be explained

 © 2006 Wiley-VCH Verlag GmbH & Co. KGaA, Weinheim 

in terms of the Brillouin function. The anomalous magnetic behaviour of **1** below 5 K is due to both the zero-field splitting of the $S = {}^3/_2$ ground spin state of the $Cr^{3+}$ ions and a weak exchange interaction between $[Cr(CN)_6]^{3-}$ anions. A weak reversible increase in the $\chi_M T$ value of **1** under light irradiation at low temperature has been observed.

## Experimental Section

**Materials:** Chemicals: $H_2C_2O_4$, $FeCl_3$ (anhydrous), $K_3[M(CN)_6]$ (M = Cr, Fe), $K_3[Cr(ox)_3]$ and $(NH_4)_3[Fe(ox)_3]$ were used as purchased.

### Syntheses

**$[RuNO(NH_3)_5]Cl_3{\cdot}H_2O$:** $[Ru(NH_3)_6]Cl_2$ (0.548 g, 2 mmol) synthesised as described in ref.[12] was dissolved in water (10 mL). 1 M HCl (10 mL) was added to the solution and then $NaNO_2$ (0.138 g, 2 mmol) was added in portions with continuous stirring. The resultant solution was heated in a water bath until intense gas evolution stopped. More $NaNO_2$ (0.069 g, 1 mmol) was then added to the cooled solution, which was then heated in a water bath until intense gas evolution stopped, concentrated to 10 mL, cooled and filtered from the $[RuNO(NH_3)_4Cl]Cl_2$ precipitate. The mother liquor was concentrated to ca. 2–3 mL, cooled and the $[RuNO(NH_3)_5]Cl_3{\cdot}H_2O$ precipitate was separated. The product was dissolved in 0.1 M HCl (4–5 mL), filtered from the $[RuNO(NH_3)_4Cl]Cl_2$ impurity and re-precipitated by addition of 96% ethanol (15–20 mL) to the mother liquor. The yield of purified $[RuNO(NH_3)_5]Cl_3{\cdot}H_2O$ was 516 mg (80%). $H_{17}N_6Cl_3O_2Ru$ (340.5): calcd. H 4.99, N 24.67, Cl 31.28; found H 4.98, N 24.09, Cl 31.21. IR: $\tilde{\nu}$ = 3432 ($NH_3$), 1928, 1913 (NO) $cm^{-1}$.

**$[RuNO(NH_3)_5][Cr(CN)_6]$ (1):** An aqueous solution (10 mL) of $K_3[Cr(CN)_6]$ (0.0487 g, 0.15 mmol) was added to an aqueous solution (5 mL) of $[RuNO(NH_3)_5]Cl_3H_2O$ (0.0511 g, 0.15 mmol). The yellow solution was allowed to stand for 2 d in the dark to form yellow-orange crystals. The crystals were collected by filter suction, washed with water and dried in vacuo over blue silica. The yield was 41.2 mg (65%). $C_6H_{15}N_{12}ORuCr$ (424): calcd. H 3.54, C 16.98, N 39.62; found H 3.50, C 17.03, N 39.98. IR: $\tilde{\nu}$ = 3432 ($NH_3$), 2199, 2127 (CN), 1947, 1914 (NO) $cm^{-1}$. Single crystals of quality suitable for X-ray diffraction analysis were selected from the synthetic sample.

**$[RuNO(NH_3)_5][Fe(CN)_6]$ (2):** The complex was prepared as a yellow powder in a similar way to the synthesis of **1** except that $K_3[Fe(CN)_6]$ was used instead of $K_3[Cr(CN)_6]$. The precipitate was formed immediately after mixing the solutions. The powder was collected by filter suction, washed with water and dried in vacuo over blue silica. The yield was 41.6 mg (65%). $C_6H_{15}N_{12}ORuFe$ (428.1): calcd. H 3.53, C 16.82, N 39.24; found H 3.80, C 17.03, N 39.17. IR: $\tilde{\nu}$ = 3449 ($NH_3$), 2112 (CN), 1944 (NO) $cm^{-1}$. Single crystals of quality suitable for X-ray diffraction were obtained by diffusion of the starting aqueous solutions into agar gel over 1.5 months.

**$[RuNO(NH_3)_5][Cr(ox)_3]{\cdot}3H_2O$ (3):** The compound was obtained as black hexagonal crystals in a synthesis similar to that of **1** except that $K_3[Cr(ox)_3]$ was used instead of $K_3[Cr(CN)_6]$. The yield was 86.8 mg (85%). $C_6H_{21}N_6O_{22}RuCr$ (682): calcd. H 3.58, C 12.29, N 14.33; found H 3.65, C 12.45, N 14.45. IR: $\tilde{\nu}$ = 3450 ($NH_3$), 1701 (C=O), 1918 and 1937 (NO) $cm^{-1}$. Single crystals of quality suitable for X-ray diffraction were selected from the synthetic sample.

**$[RuNO(NH_3)_5][Fe(ox)_3]{\cdot}xH_2O$($x \approx 3$) (4):** The complex was obtained as a yellow-orange powder in a synthesis similar to that used for **3** except that $(NH_4)_3[Fe(ox)_3]$ was used instead of $K_3[Cr(ox)_3]$. The precipitate was formed immediately after mixing the solutions. The yield was 80.1 mg (78%). $C_6H_{21}N_6O_{22}RuFe$ (686): calcd. H 3.56, C 12.20, N 14.24; found H 3.68, C 12.50, N 14.69. IR: $\tilde{\nu}$ = 3450 ($NH_3$), 1679 (C=O), 1914 (NO) $cm^{-1}$. Single crystals of quality suitable for X-ray diffraction analysis were prepared as follows: an aqueous solution (5 mL) of oxalic acid (0.27 g, 0.3 mmol) was added dropwise to a solution (5 mL) of $FeCl_3$ (anhydrous, 0.0163 g, 0.1 mmol) and an aqueous solution (5 mL) of $[RuNO(NH_3)_5]Cl_3{\cdot}H_2O$ (0.0341 g, 0.1 mmol) was then added. The yellow-orange solution was allowed to stand for 3 weeks in the dark to allow the formation of yellow-orange hexagonal crystals.

**$[RuNO(NH_3)_5][CrNO(CN)_5]$ (5):** An aqueous solution (5 mL) of $[RuNO(NH_3)_5]Cl_3{\cdot}H_2O$ was mixed with a solution of $K_3[CrNO(CN)_5]$ (1:1 equal molar ratio) and a powder precipitated. The yield was 51.2 mg (80%). $C_5H_{15}N_{12}O_2RuCr$ (428): calcd. H 3.15, C 14.02, N 39.24; found H 3.25, C 14.65, N 38.94. IR: $\tilde{\nu}$ = 3449 and 3440 ($NH_3$), 2118 (CN), 1936 (NO) $cm^{-1}$. Single crystals of quality suitable for X-ray diffraction were obtained by diffusion of the starting aqueous solutions into agar gel over 1.5 months.

### Physical Measurements.

**Spectra:** Infrared spectra were recorded with a Perkin–Elmer spectrometer BX-2 in KBr pellets in the 4000-400 $cm^{-1}$ region.

**Crystallographic Data Collection and Structure Determination:** Single crystals of **1** and **3** were mounted on an automatic four-circle KUMA DIFFRACTION diffractometer equipped with a graphite-monochromated Mo-$K_\alpha$ radiation source [$\omega/2\theta$ scanning, 2($\theta$) max = 80°]. The crystal structures were solved by direct methods using the SHELX-97[38] program package.The positions of hydrogen atoms were found evenly from the difference Fourier syntheses. The structures were refined in an anisotropic approximation excluding hydrogen atoms. The positions of the latter were refined in an isotropic approximation. The positions of N and O (NO) were determined from the difference Fourier synthesis. Since the position of N is a weighted average value between those of N ($NH_3$) and N (NO), it was used as a basic value in the refinement. The structures were refined using the restrained bond lengths by considering the occupancies of the positions of $NH_3$ and NO: Ru1–N1 1.75(0.03) Å, Ru1–N11 2.13(0.01) Å, N1–O1 1.22(0.01) Å. Crystallographic data are summarized in Table 1.

CCDC-602209 and -602210 (for compounds **1** and **3**) contain the supplementary crystallographic data for this paper. These data can be obtained free of charge from The Cambridge Crystallographic Data Centre via www.ccdc.cam.ac.uk/data_request/cif.

**Differential Scanning Calorimetry (DSC):** DSC measurements were performed using a modified differential scanning calorimeter (Mettler DSC 30, TA 3000) equipped with two quartz windows inside and outside the cryostat. The absolute calibration of enthalpy $H$ and temperature $T$ was controlled by measuring the phase-transition of In, Hg, pentane and $KH_2PO_4$. During illumination, the sample was kept at 120 K in a dry nitrogen atmosphere and subsequently heated at a constant heating rate $q = dT/dt = 5$ K/min. The exothermal heatflow is the time derivative of the enthalpy $H$. To obtain only the contribution of enthalpy of the metastable states, the enthalpy of the nonirradiated sample was subtracted from that of the irradiated one. The residual enthalpy was evaluated by fitting to the Arrhenius law modified for dynamic measurements.[10]

$$dH/dt = H_{tot}Z{\cdot}\exp[-\{(Z/q)\ {}_{T_0}\textstyle\int^{T}\exp(-E_A/k_BT) + (E_A/k_BT)\}]$$

 © 2006 Wiley-VCH Verlag GmbH & Co. KGaA, Weinheim 

($Z$ = frequency factor, $E_A$ = activation energy, $k_B$ = Boltzmann constant)

As a light source for generating MSI we used a metal-vapour lamp (HMI 575 Osram) filtered by dichroitic and interference filters to the spectroscopic range of 420–460 nm with the maximum at 434 nm. The intensity was 180 mW cm$^{-2}$. The irradiation time was 3 h which yielded an integrated flux of $Q$ = 1944 J cm$^{-2}$ on the sample. For the generation of MSII the samples were irradiated as described above and then irradiated with a Nd-YAG laser (1064 nm). The intensity was 138 mW cm$^{-2}$. The irradiation time was 0.5 h yielding an integrated flux of $Q$ = 250 J cm$^{-2}$.

**Magnetic and Photomagnetic Studies:** The temperature and magnetic field dependences of the molar paramagnetic susceptibility, $\chi_P$, magnetic moment in Bohr magnetons, $M/N_{A\mu B}$, effective magnetic moment, $\mu_{eff}/\mu_B$, and the in-phase ($\chi'_M$) and out-of-phase ($\chi''_M$) AC susceptibility of **1** and **3** were measured with a commercial SQUID magnetometer MPMS "Quantum Design". The temperature range was 1.8–300 K and the maximum magnetic field attained $B$ = 5.0 T. AC susceptibility measurements were carried out at 80 Hz with modulation field amplitude of 4 G. Randomly oriented microcrystals of a typical weight of ca. 10 mg were put into a gel capsule. Typical cooling rates were 2 K min$^{-1}$ for 300 K > $T$ >200 K, 4 K min$^{-1}$ for 200 K > $T$ > 15 K and 1 K min$^{-1}$ below 15 K. The background signal of a capsule was diamagnetic within the entire temperature range, not exceeding 16% (at 300 K) and 0.1% (at 1.98 K) of the sample signal. This was subtracted from the total signal. For field dependences, the signal from an empty capsule did not exceed 0.06%. The paramagnetic susceptibility was also corrected by taking into account the magnetic contributions of the ligands.

The photomagnetic experiments for **1** were performed with a $Kr^+$ laser coupled through an optical fibre directed into the SQUID cavity of the magnetometer working in the dc mode (MPMS-5S "Quantum Design"). Powdered samples of **1** were mounted on a sample holder as thin layers (weight 0.83 mg) to avoid surface effects during illumination. The mass was estimated based on the considering that at 5 K, the magnetisation after irradiation follows a Brillouin function for an $S$ = $^3/_2$ spin. With this method and calculating a molecular weight at 424.37 g, the estimated mass of the sample is 0.83 mg. The samples were irradiated continuously over 8 hours using the multiline 406–415 nm under a magnetic field of 5 kOe at 10 K. The effective power of the light on the sample was measured to ca. 10 mW cm$^{-2}$. Magnetic properties ($\chi_M T$) were recorded before and after irradiation, in each case the light being turned off to avoid thermal inhomogeneities.[10]

## Acknowledgments

We are grateful for the financial support of an RFBR grant No. 06-03-32433, the programme of RAS "Multifunctional materials", RAS grant No. 05-03-32384, NSH-1380.2003.2 and the DFG (Wo618/5-1).

[1] O. Sato, T. Iyoda, A. Fujishimi, K. Hashimoto, *Science* **1996**, *272*, 704.
[2] a) Z.-Z. Gu, O. Sato, T. Iyoda, K. Hashimoto, A. Fujishima, *J. Phys. Chem.* **1996**, *100*, 18289; b) Z.-Z. Gu, O. Sato, T. Iyoda, K. Hashimoto, A. Fujishima, *Mol. Cryst. Liq. Cryst.* **1996**, *286*, 147; c) Z.-Z. Gu, O. Sato, T. Iyoda, K. Hashimoto, A. Fujishima, *Chem. Mater.* **1997**, *9*, 1092.
[3] S. Ohkoshi, K. Hashimoto, *J. Am. Chem. Soc.* **1999**, *121*, 10591.
[4] a) O. Sato, Y. Einaga, A. Fujishima, K. Hashimoto, *Inorg. Chem.* **1999**, *38*, 4405; b) D. A. Pejakovich, J. L. Manson, J. S. Miller, A. J. Epstein, *Phys. Rev. Lett.* **2000**, *85*, 1994; c) A. Goujon, O. Roubeau, F. Varret, A. Dolbecq, A. Bleuzen, M. Verdaguer, *Eur. Phys. J.* **2000**, *B14*, 115.
[5] P. Gütlich, Y. Garcia, T. Woike, *Coord. Chem. Rev.* **2001**, *219–221*, 839.
[6] T. Hauser, V. Oestreich, H. D. Rohrweck, *Z. Phys. A* **1977**, *280*, 17.
[7] Th. Woike, W. Krasser, P. S. Bechthold, S. Haussühl, *Phys. Rev. Lett.* **1984**, *53*, 1767.
[8] P. Coppens, D. Fomichev, M. D. Carducci, K. J. Culp, *J. Chem. Soc. Dalton Trans.* **1998**, 865.
[9] Y. Morioka, A. Ishikawa, H. Tomizawa, E. Miki, *J. Chem. Soc. Dalton Trans.* **2000**, 781.
[10] D. Schaniel, Th. Woike, B. Delley, C. Boskovic, D. Biner, W. Krämer, H.-U. Güdel, *Phys. Chem. Chem. Phys.* **2005**, *7*, 1164.
[11] L. A. Kushch, L. S. Plotnikova, Yu. N. Shvachko, V. A. Emel′yanov, E. B. Yagubskii, G. V. Shilov, S. M. Aldoshin, *J. Phys. IV Fr.* **2004**, *114*, 459.
[12] F. M. Lever, A. R. Powell, *J. Chem. Soc. (A)* **1969**, *9*, 1477.
[13] P. Coppens, I. Novozhilova, A. Kovalevsky, *Chem. Rev.* **2002**, *102*, 861.
[14] J. A. Olabe, L. A. Gentil, G. Rigotti, A. Navaza, *Inorg. Chem.* **1984**, *23*, 4297.
[15] D. Schaniel, Th. Woike, J. Schrefer, V. Petrichek, *Phys. Rev. B* **2005**, *71*, 174112.
[16] E. A. Bruker, J. S. Olson, M. Ikeda-Saito, G. N. Phillips, *J. Proteins: Struct. Function, Genetics* **1998**, *30*, 352.
[17] R. Feltham, J. Enemark, in *Topics in Inorganic and Organometallic Stereochemistry* (Ed.: G. Geoffroy), Wiley-VCH, New York, USA, **1981**, 155–215.
[18] S. I. Gorelsky, A. B. P. Lever, *Int. J. Quant. Chem.* **2000**, *80*, 636.
[19] S. C. Da Silva, D. W. Franco, *Spectrochim. Acta Part A* **1999**, *55*, 1515.
[20] M. E. Sanchez, M. L. Doublet, C. Faulmann, I. Malfant, P. Cassoux, L. A. Kushch, E. B. Yagubskii, *Eur. J. Inorg. Chem.* **2001**, 2797.
[21] J. T. Veal, D. J. Hodgson, *Inorg. Chem.* **1972**, *11*, 1420.
[22] Y. N. Mikhailov, A. S. Kanishcheva, A. A. Svetlov, *Zh. Neorg. Khim.* **1989**, *34*, 2803.
[23] H. J. Choi, J. J. Sokol, J. R. Long, *Inorg. Chem.* **2004**, *43*, 1606.
[24] F. Bottomley, *J. Chem. Soc. Dalton Trans.* **1997**, 1600.
[25] T. Woike, W. Krasser, H. Zöllner, W. Kirchner, S. Z. Haussühl, *Phys. D* **1993**, *351*, 25.
[26] H. Zöllner, W. Krasser, Th. Woike, *Chem. Phys. Lett.* **1989**, *161*, 497.
[27] T. Woike, H. Zöllner, W. Krasser, S. Haussühl, *Solid State Comm.* **1990**, *73*, 149.
[28] T. Woike, S. Haussühl, *Solid State Comm.* **1993**, *86*, 333.
[29] K. Ookubo, Y. Morioka, H. Tomizawa, E. J. Miki, *Mol. Struct.* **1996**, *379*, 241.
[30] D. Schaniel, T. Woike, C. Boskovich, H.-U. Güdel, *Chem. Phys. Lett.* **2004**, *390*, 347.
[31] D. Schaniel, T. Woike, L. Tsankov, M. Imlau, *Thermochim. Acta* **2005**, *429*, 19.
[32] B. N. Figgis, P. A. Reynolds, *Inorg. Chem.* **1985**, *24*, 1864.
[33] L. E. Mohrmann, B. B. Garrett, *Inorg. Chem.* **1974**, *13*, 357.
[34] D. Gatteschi, L. Sorace, *Solid State Chem.* **2001**, *159*, 253.
[35] P. A. Reynolds, C. D. Delfs, B. N. Figgis, B. Moubaraki, K. S. Murray, *Austr. J. Chem.* **1992**, *45*, 1899.
[36] R. D. Chirico, R. L. Carlin, *Inorg. Chem.* **1980**, *19*, 3031.
[37] L. S. Singer, *J. Chem. Phys.* **1955**, *23*, 379.
[38] G. M. Sheldrick, *SHELX97, Program for Crystal Structure Refinement*, University of Göttingen, Germany, **1997**

Received: March 28, 2006
Published Online: August 21, 2006

 © 2006 Wiley-VCH Verlag GmbH & Co. KGaA, Weinheim 

DOI: 10.1002/ejic.200600280

# Cobaloximes with Pyrazine and Their Dimetallic Complexes

**Debaprasad Mandal[a] and Bhagwan D. Gupta*[a]**

**Keywords:** Cobaloximes / Cyclic voltammetry / X-ray structure / Helical structures

Mono- and dinuclear cobaloximes with inorganic anions and pyrazine (Pz) as a base/bridging ligand were synthesized and characterized by $^1H$, $^{13}C$, UV/Vis and IR spectroscopy and X-ray structure analysis. Mononuclear complexes $XCo(dioxime)_2Pz$ were used as precursors for building homo- and heterodimetallic complexes. The X-ray crystal structures of $ClCo(dmgH)_2Pz$, $ClCo(dpgH)_2Pz$, $[Co(dpgH)_2(NO_2)_2]Na$, and $[Co(dmgH)_2(NO_2)_2]_2[Ag]_2{\cdot}H_2O$ are reported. $[Co(dmgH)_2(NO_2)_2]_2[Ag]_2{\cdot}H_2O$ shows two $Ag^I$ ions in different environments: one is in tetrahedral, whereas the other is in capped trigonal coordination and the metal-organic framework in this molecule shows helical structure. A cyclic voltammetry study in $[XCo(dioxime)_2]_2$-μ-Pz and $XCo(dioxime)_2Pz$ [dioxime = dmgH (dimethylglyoximato), dpgH (diphenylglyoximato)] is reported. The reduction, $Co^{III}$ to $Co^{II}$ and $Co^{II}$ to $Co^{I}$, is found to be more difficult in $[XCo(dpgH)_2]_2$-μ-Pz than in $XCo(dpgH)_2Pz$. The CV data have been interpreted in terms of cobalt anisotropy.
(© Wiley-VCH Verlag GmbH & Co. KGaA, 69451 Weinheim, Germany, 2006)

## Introduction

Organocobaloximes, initially proposed as models of the $B_{12}$ coenzyme, have now acquired an independent research field because of their rich coordination chemistry and potential application in organic synthesis.[1] The variation in the N–Co–C bond properties, including its strength, has been described not only in terms of the *trans* influence of the axial neutral base but also of the steric and electronic properties of the alkyl group.[2,3] The influence of the equatorial ligands on the axial ligands (*cis* influence) in dioximates, Costa's model, and iminates (cobalt complexes with tetradentate Schiff bases) has been previously reported.[2] Such studies are limited in cobaloximes.[4,5] In recent years the description of spectroscopic data and structure-property relationships and their correlation to Co–C bonds have been most emphasized.[6] We have shown that spectral correlations are much better understood in terms of field effect; the model takes into account the total effect of cobalt anisotropy of the $[Co(dioxime)_2]^+$ metallabicycle (electron-withdrawing power) and the ring current arising from the delocalization of electron density throughout the $[Co(dioxime)_2]^+$ metallabicycle.[5,7]

Ligand-bridged complexes are of interest in view of their role as reaction intermediates in inner-sphere electron-transfer processes[8] and pyrazine has been extensively used as a bridging ligand. Although a number of examples of the pyrazine-bridged mixed-valence homo- and heterodimetallic complexes of Ru, Fe, and Co are known,[9] there are few in cobaloxime chemistry.[10–12] A mixing of two cobalt centers with electron delocalization by pyrazine has been observed in the recently reported pyrazine-bridged organodicobaloximes, $[RCo(dioxime)_2]_2$-μ-Pz.[11,12]

Among the electrochemical studies on cobaloximes only few describe a correlation to related cobalt complexes to show the mutual *cis* and *trans* influence.[13] Recent work has shown that the reduction potential depends upon both the axial and equatorial ligands.[5,7,14] CV data have been rationalized in terms of cobalt anisotropy and this in turn is affected by the axial ligands; the effect is more distinct when the axial ligand is an inorganic group/atom.[5,7] A single peak with a very high reduction potential is observed in $[RCo(dioxime)_2]_2$-μ-Pz, which points to electron delocalization and also shows that the dicobaloximes are more difficult to reduce than the corresponding monocobaloximes.[12]

In general, the inorganic cobaloximes $XCo(dioxime)_2B$ (B = neutral base) give a better CV curve than organocobaloximes.[5,7] Also, the changes in NMR chemical shifts in the inorganic complexes are much more marked than in organocobaloximes and these are more effectively rationalized with the field effect.[4c,5,7,15]

It is therefore interesting and useful to study the pyrazine-bridged dinuclear inorganic cobaloximes, $[XCo(dioxime)_2]_2$-μ-Pz. The spectral and CV data in these dinuclear complexes should complement the reported data in $[RCo(dioxime)_2]_2$-μ-Pz. It would also be useful to compare the data with the corresponding mononuclear cobaloximes, $XCo(dioxime)_2Pz$.

The aim of the present study is (a) to synthesize $[XCo(dioxime)_2]_2$-μ-Pz, $XCo(dioxime)_2Pz$, and $XCo(dioxime)_2$-

[a] Department of Chemistry, Indian Institute of Technology, Kanpur 208016, India
Fax: +91-512-2597436
E-mail: bdg@iitk.ac.in
Supporting information for this article is available on the WWW under http://www.eurjic.org or from the author.

 © 2006 Wiley-VCH Verlag GmbH & Co. KGaA, Weinheim 

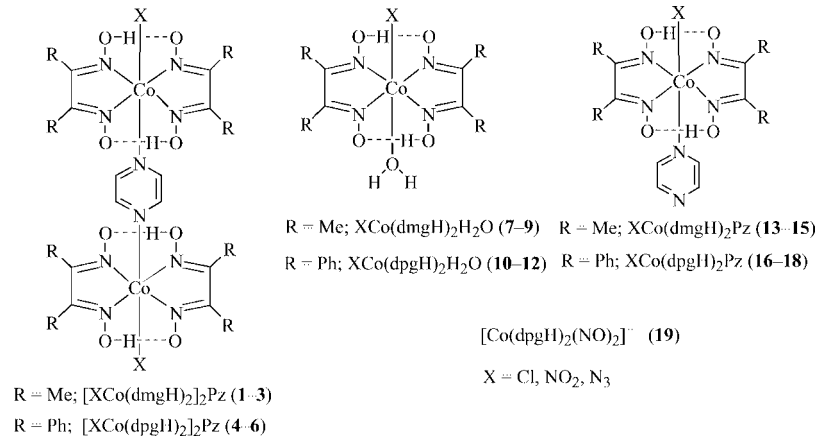


Scheme 1. Cobaloximes.

Pz–M [M = $Cu^{I}$, $Ag^{I}$], (b) to verify the validity of our recently proposed field effect model in the interpretation of spectroscopic data in these complexes, and (c) to perform a CV study (Scheme 1).

## Results and Discussion

### Synthesis

The synthesis of complexes **1** and **4** was easy; an addition of pyrazine to the corresponding aqua complex ClCo(dioxime)$_2$H$_2$O in a 1:2 molar ratio afforded the corresponding dicobaloxime.

Two possibilities were considered for the preparation of complexes **2**, **3** and **5**, **6**:

(a) We have recently synthesized XCo(dioxime)$_2$Py (X = $NO_2$, $N_3$) complexes by the nucleophilic substitution of the chlorido ligand in ClCo(dioxime)$_2$Py.[5,7,15,16] An obvious choice was to follow the same route. However, the reaction of $NaN_3$ or $NaNO_2$ with [ClCo(dpgH)$_2$]$_2$-μ-Pz (**4**) did not give the desired compound, but instead a $Co^{III}$ complex was isolated that was sparingly soluble in chloroform and dichloromethane but soluble in methanol/water and acetone/water. The $^1$H NMR in [D$_6$]DMSO showed the absence of a pyrazine peak. It indicated the presence of a salt (discussed later).

(b) The same procedure as used in the preparation of **1** and **4** was followed. The dicobaloximes were formed in good yield. However, this procedure required the preparation of the corresponding aqua complexes, XCo(dioxime)$_2$-H$_2$O (**8**, **9**, **11**, **12**).[17] These were prepared from the corresponding aqua(chlorido)cobaloximes (**7** or **10**) by the nucleophilic substitution of the chlorido ligand. Any change in concentration or use of excess NaX led to the formation of a salt along with the desired product. The salt was identical to the product obtained earlier in the reaction of [ClCo(dpgH)$_2$]$_2$-μ-Pz (**4**) with $NaNO_2$ and was identified as [Co(dpgH)$_2$(NO$_2$)$_2$]$^-$ by X-ray crystallography (**19**). López et al. have reported a similar type of salt formation in the reaction of ClCo(dioxime)$_2$B with excess KCN.[18]

XCo(dioxime)$_2$Pz (**13**–**18**) were prepared by the reaction of the corresponding aqua complexes **7**–**12** with pyrazine in a 1:1 ratio by slow evaporation of the solvent. These were the only products formed in dilute solution, but in a concentrated solution the precipitation of the dinuclear product (**1** or **4**) occurred and no mononuclear product was formed. Also a rapid evaporation of the solvent resulted in the formation of a dinuclear complex.

### Spectroscopy: Characterization of the Complexes

The $^1$H NMR spectra of **1**–**6** and **13**–**18** are easily assigned based on the chemical shifts. The signals are assigned according to their relative intensities and are consistent with the related dioxime compounds previously described.[11] Complexes **1**–**3** are sparingly soluble in most organic solvents and it took more than 1000 scans to obtain a reasonable $^1$H NMR spectrum in $CDCl_3$. The $^1$H values are given in Table 1.

All four protons in the unligated pyrazine are equivalent and appear as a singlet at $\delta$ = 8.59 ppm. The ligated pyrazine in **4**–**6** appears as a singlet which is shifted downfield as compared to that of free pyrazine. On the other hand, pyrazine appears as two doublets in **13**–**18**; the one that is more upfield is assigned to the protons that are in close proximity to the cobaloxime moiety. The ring current of the metallabicycle affects these protons.[5,7] Hence, their signals are more downfield in **16**–**18** than in **13**–**15** because of the lower ring current in the dpgH complexes. $^1$H NMR spectroscopy in the region $\delta$ = 7.5–9.0 ppm can easily differentiate between the di- and mononuclear complexes; pyrazine appears as a singlet in the former and as two doublets in the latter.

### Spectral Studies

#### *NMR*

In the earlier NMR study on cobaloximes XCo(dioxime)$_2$Py (dioxime = dmgH, dpgH), $Py_\alpha$ and $Py_\gamma$ were

 © 2006 Wiley-VCH Verlag GmbH & Co. KGaA, Weinheim 

Table 1. $^1$H NMR and yield.

| No. | O–H···O | Pz | dmgH | dpgH/others | Yield (%) |
|---|---|---|---|---|---|
| **1** | – | 8.09 | 2.45 | – | 89 |
| **2** | – | 8.16 | 2.42 | – | 70 |
| **3** | – | 8.18 | 2.45 | – | 75 |
| **4** | 18.52 | 8.66 | – | 7.82 (d), 7.77 (t), 7.32 (t), 7.18–7.33 (m) | 49 |
| **5** | 18.48 | 8.74 | – | 7.13–7.29 | 48 |
| **6** | 18.36 | 8.63 | – | 7.14–7.26 (m) | 58 |
| **13** | – | 8.33 (d)<br>8.50 (d) | 2.42 | – | 60 |
| **14** | – | 8.35 (d)<br>8.57 (d) | 2.35 | – | 58 |
| **15** | 17.93 | 8.38 (d)<br>8.55 (d) | 2.42 | – | 58 |
| **16**[a] | 18.57 | 8.61 (d)<br>8.64 (d) | – | 7.05–7.28 (m) | 80 |
| **17** | 18.39 | 8.66 (d)<br>8.72 (d) | – | 7.16–7.34 (m) | 70 |
| **18** | 18.41 | 8.60 (d)<br>8.62 (d) | – | 7.16–7.32 (m) | 65 |
| **19**[b,c] | 18.47 | – | – | 7.24–7.44 (m) | |

[a] $^{13}$C NMR: δ = 154.05, 147.31, 145.46, 129.92, 129.80, 129.31, 128.01 ppm. [b] Recorded in [$D_6$]DMSO. [c] $[Co(dpgH)_2(N_3)_2]^-$ ([$D_6$]-DMSO): $^1$H NMR: δ = 18.59, 7.41 (d, 4 H), 7.39 (d, 8 H), 7.27–7.24 (dd, 8 H) ppm; $^{13}$C NMR: δ = 151.5, 130.0, 128.7, 127.5 ppm.

found to be the most affected by a change in X.[5,15] The cobaloximes **13**–**18** are very similar to pyridine complexes except that pyridine is replaced by pyrazine (p$K_a$ of Pz 1.1,[19] Py 5.3[20]). Also, the spectral studies of pyrazine-bridged alkyl- (and benzyl-) dicobaloximes have already been reported from our laboratory.[11,12] Therefore, rather than going into the details about the spectroscopic data and *cis*/*trans* influence study in the present systems, we want to highlight only the salient points.

The coordination shift[21] $\Delta\delta^1$H of the $Pz_\alpha$ signal in **13**–**18** is very close to the coordination shift $\Delta\delta^1$H of the $Py_\alpha$ signal in the corresponding pyridine complexes, indicating further the similarity in the two systems (Table ST2). As $H_\alpha$ is affected by the dioxime ring current and cobalt anisotropy, its signal appears more upfield in the dmgH complexes than that of the dpgH complexes in both pyridine and pyrazine complexes.[4a,11,12] One of the major differences found in the pyridine and pyrazine complexes is the coordination shift of the β-hydrogen signal. It is almost unaltered in the pyrazine complexes, whereas it was shifted downfield (by 0.2–0.3 ppm) in the corresponding pyridine complexes. This is due to the presence of a nitrogen atom instead of a carbon atom at the sixth position in pyrazine. The cobalt anisotropy is less in the pyrazine complexes because of its lower p$K_a$ value and hence it compensates for the β-hydrogen signal downfield shift.

In the $[(R/X)Co(dioxime)_2]_2$-μ-Pz complexes, $Pz_\alpha$ is affected by the ring current and the cobalt anisotropy of the two metallabicycles (the factors ring current and cobalt anisotropy work in opposite directions: the $Pz_\alpha$ signal is shifted upfield by the ring current and downfield by the cobalt anisotropy) as compared to one in $(R/X)Co(dioxime)_2Pz$, therefore $\Delta\delta$ of the $Pz_\alpha$ signals should be much larger or even doubled in the former. It is found to be –0.2 to –0.3 ppm in **13**–**15** and –0.4 to –0.5 ppm in **1**–**3**; however, the difference is unexpectedly small in the corresponding dpgH complexes (compare **4**–**6** and **16**–**18** with $Pz_\alpha$ in free pyrazine). This is because of the higher cobalt anisotropy of dpgH, which completely compensates for the upfield shift due to the ring current. Similar compensation is also observed in the mono(pyrazine) complexes (compare **13**–**15** with **16**–**18**) as well as in the pyridine complexes $XCo(dioxime)_2Py$, viz. $\Delta\delta$ of the $Py_\alpha$ signals in the dmgH complexes is around –0.3 ppm, whereas it is close to zero in the dpgH complexes.

The pyrazine signals in $[RCo(dioxime)_2]_2$-μ-Pz were found to be shifted downfield in the dpgH complexes and upfield in the dmgH complexes as compared to the unligated pyrazine.[11,12] A similar trend is observed in the inorganic complexes **1**–**6** and $\Delta\delta$ of the $Pz_\alpha$ signals in $[RCo(dioxime)_2]_2$-μ-Pz complexes is larger than that in **1**–**6** because of the higher *trans* effect of the R group with respect to the X.

### *UV/Vis*

Three bands, a strong band at 263 nm corresponding to the Co→dioxime metal-to-ligand charge transfer (MLCT) and two shoulders around 313 and 330 nm (Co→Pz), are observed in **16**. A similar spectrum is obtained in **4** except that the intensity of the band corresponding to Co→Pz is significantly increased. This is expected because of the additive factor of the two identical chromophoric groups in the dinuclear complexes. A similar result is found in the dmgH complexes (see Table 2).

In general, organo-cobaloximes exist largely as pentacoordinate species in coordinating solvents like methanol and as hexacoordinate species in chloroform or dichloromethane.[4a,22] Pyrazine-bridged alkyldicobaloximes show similar behavior to the alkyl(pyridine)cobaloximes.[11] The base-on/base-off behavior of organocobaloximes has generally been studied by titration with the base, and the inference is made from the change in shape of the Co–C CT band with the

 © 2006 Wiley-VCH Verlag GmbH & Co. KGaA, Weinheim 

Table 2. UV/Vis and IR data.

| Compound | UV/Vis: $\lambda_{max}$ [nm] | | | IR: $\tilde{\nu}$ [cm$^{-1}$] | | | |
|---|---|---|---|---|---|---|---|
| | Co→dioxime (MLCT) | Co→Pz (shoulder) | Co→Pz (shoulder) | O–H···O | C=N | N–O | N–O′ |
| **1** | 224 (sh), 250 (4.32) | 292 (3.77) | 312 (3.76) | 3417.6 (br.) | 1563.7 | 1242.9 | 1091.4 |
| **4** | 220 (3.71), 258 (4.36) | 292 (4.21) | 325 (4.30) | 3433.0 (br.) | 1530.4 | 1288.5 | 1139.8 |
| **13** | 256 (4.35) | 290 (3.74) | 308 (3.69) | 3530.0<br>3446.7 | 1574.9 | 1239.9 | 1094.1 |
| **16** | 263 (4.46) | 313 (4.09) | 330 (4.04) | 3459.8<br>3421.2 | 1531.5 | 1285.6 | 1136.9 |
| **13**·$Cu^{I}PF_6$ | 230 (4.91), 259 (4.52) | | | 3443.5, 1566.4, 1239.3, 1092.3, 845 | | | |
| $[Co(dpgH)_2(N_3)_2]^-$ | – | | | 3438.7, 2025.3, 1383.3, 1136.5 | | | |

gradual addition of base to the cobaloxime. It has, however, not been possible to obtain a similar information in the present inorganic cobaloximes, because the phenomenon can be monitored by the Co→dioxime MLCT band only and this occurs at the same position as in the pyrazine case.

*Titration with $Cu^{I}BF_4$ Salt*

The titration of $Cu^+$ with a solution of **13** in dichloromethane was monitored by UV/Vis spectroscopy at 233 and 259 nm. The absorbance of the solution increased until 0.5 equiv. of $Cu^+$ was added (see Figure 1). No spectral change was observed after the addition of 0.5–1.0 equiv. of $Cu^+$. This suggests that there is a 2:1 complexation with $Cu^+$. Job's plot also suggests a 2:1 complexation (Figure S14).

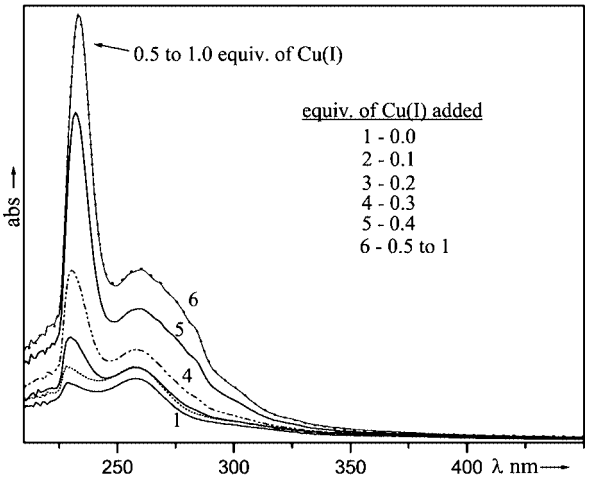


Figure 1. $Cu^+$ addition to a solution of $[ClCo(dmgH)_2Pz]$ (**13**). The $Cu^+$ saturation point is at 0.5 mol-equiv. $[ClCo(dmgH)_2Pz] = 1\times10^{-5}$ M (1 mL). $[Cu^+] = 1\times10^{-5}$ M (0.1–1.0 mL).

***IR***

All IR spectra were recorded as solid samples on KBr pellets and are tabulated in Table 3. The mononuclear and pyrazine-bridged dicobaloximes can be distinguished by IR spectroscopy; the O–H···O peak is a sharp doublet in monocobaloximes, whereas it is a broad singlet in the case of dicobaloximes. The O–H···O and C=N peaks appear at lower frequency in dpgH complexes as compared to dmgH complexes because of the higher cobalt anisotropy and lower electron density in the dpgH complexes. The $Cu^{I}PF_6$-bridged complex gives an IR spectrum identical to that of dicobaloxime **1** along with a distinct sharp peak at 845 cm$^{-1}$ for $PF_6^-$ (Figures S16 and S17).

**Cyclic Voltammetry**

The cyclic voltammogram (CV) of a cobaloxime shows three types of redox couples: $Co^{III}/Co^{II}$, $Co^{II}/Co^{I}$, and $Co^{IV}/Co^{III}$. Organo-cobaloximes, in general, give poor CVs and most of the time the $Co^{III}/Co^{II}$ redox couple is not visible. On the other hand, inorganic cobaloximes show relatively better CVs and all the redox couples are prominent. Two common solvents used for the study are dichloromethane and acetonitrile. We have preferred to use dichloromethane because of the higher solubility of the cobaloximes. The cyclic voltammogram of **13** (Figure 2A) shows an irreversible wave in the reductive half at –0.47 V corresponding to $Co^{III}/Co^{II}$ and a quasireversible wave at –1.08 V corresponding to $Co^{II}/Co^{I}$. [Interestingly, a CV of **13** recorded in acetonitrile gives a much better plot in which all the peaks are prominent and show the reversible nature (Figure 2B).] In comparison, **16** (Figure 2C) is much more easily reduced, with values at –0.32 and –0.73 V, respectively. In the oxidation half corresponding to $Co^{IV}/Co^{III}$, **13** and **16** show one reversible wave at +1.25 and 1.38 V, respectively. The CV data are very similar to those of the corresponding pyridine analogues except that the reduction potential values are low and the oxidation halves are high (see Table 3). This agrees well with the p$K_a$ of pyridine and pyrazine.

The CV data for both the oxidative and reductive halves can be rationalized on the basis of the cobalt anisotropy. The higher the cobalt anisotropy, the lower the reduction potential and the higher is the oxidation potential.[5,7] A comparison of the data in **13** with those in **16** shows that the reduction is easier and the oxidation is more difficult in **16** because of the higher cobalt anisotropy in dpgH complexes than in dmgH complexes. We have made a similar observation in the gH, dpgH, mestgH, and mixed dioxime complexes.[5,7,15] In view of this it is quite likely that the cobalt anisotropy may be the major factor responsible for the reduction/oxidation process.

We could not record the CV for **1** because of its insolubility in most organic solvents. The CV graph for **4** has three peaks; $Co^{IV}/Co^{III}$ is prominent but $Co^{III}/Co^{II}$ and $Co^{II}/Co^{I}$

 © 2006 Wiley-VCH Verlag GmbH & Co. KGaA, Weinheim 

Table 3. CV data in dichloromethane and $TBAPF_6$ at 0.2 V $s^{-1}$ at 25 °C.

| No. | $Co^{III}/Co^{II}$ | | | | | $Co^{II}/Co^{I}$ | | | | | $Co^{IV}/Co^{III}$ | | | | |
|---|---|---|---|---|---|---|---|---|---|---|---|---|---|---|---|
| | $E_{1/2}$ ($\Delta E_p$)[a] [V] ([mV]) | $E_{1/2}$[b] [V] | $i_{pc}$ [μA] | $i_{pa}$ [μA] | $i_{pa}/i_{pc}$ | $E_{1/2}$ ($\Delta E_p$)[a] [V] ([mV]) | $E_{1/2}$[b] [V] | $i_{pc}$ [μA] | $i_{pa}$ [μA] | $i_{pa}/i_{pc}$ | $E_{1/2}$ ($\Delta E_p$)[a] [V] ([mV]) | $E_{1/2}$[b] [V] | $i_{pc}$ [μA] | $i_{pa}$ [μA] | $i_{pa}/i_{pc}$ |
| **4** | –0.88[c] | –1.39 | 0.1 | – | – | –1.10[c] | –1.61 | 0.4 | – | – | 1.33 (220) | 0.82 | 0.2 | 8 | 40.0 |
| **13** | –0.47[c] | –0.98 | 15 | – | – | –1.08 (320) | –1.59 | 21 | 10.7 | 0.5 | 1.25 (280) | 0.74 | 26.8 | 31.2 | 1.2 |
| **13**[d] | –0.22 (130) | –0.73 | 6.1 | 6.3 | 1.0 | –1.01 (80) | –1.52 | 11.5 | 11.5 | 1.0 | 1.20 (107) | 0.69 | 9.5 | 10.0 | 1.0 |
| **16** | –0.32[c] | –0.83 | 11.2 | – | – | –0.73 (180) | –1.24 | 19.0 | 12.7 | 0.64 | 1.38 (120) | 0.87 | 22.3 | 23.6 | 1.1 |
| $ClCo(dmgH)_2Py$ | –0.66[c] | –1.17 | | | | –1.12 (200) | –1.63 | | | | 1.20 (190) | 0.69 | | | |
| $ClCo(dpgH)_2Py$ | –0.29 (490) | –0.80 | | | | –0.82 (260) | –1.33 | | | | 1.33 (150) | 0.82 | | | |

[a] vs. Ag/AgCl. [b] vs. $Fc/Fc^+$. [c] Values refer to $E_{pc}$. [d] Value is in $CH_3CN$.

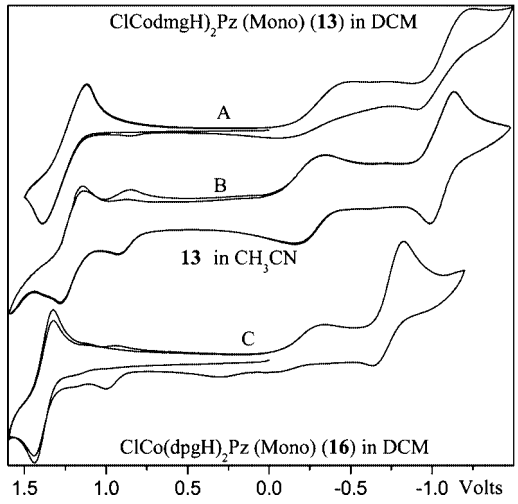


Figure 2. Cyclic voltammograms of **13** in dichloromethane (DCM) (A), in $CH_3CN$ (B), and **16** in DCM (C) with 0.1 M ($nBu_4N$)$PF_6$ as supporting electrolyte at 0.2 V $s^{-1}$ at 25 °C.

are not; however, the differential pulse voltammogram (DPV) clearly shows reduction. The pyrazine-bridged benzyl dpgH complex, $[PhCH_2Co(dpgH)_2]_2Pz$, also showed a poor CV in the reduction half.[12] The $Co^{III}/Co^{II}$ and $Co^{II}/Co^{I}$ values in **4** are –0.88 and –1.10 V, respectively. The $Co^{II}/Co^{I}$ reduction potential is much lower than the corresponding value in $[PhCH_2Co(dpgH)_2]_2Pz$ (–1.41 V). This is expected because of the higher cobalt anisotropy in **4**. Similarly, the oxidation potential $Co^{IV}/Co^{III}$ is higher (+1.33 V) in **4** than in $[PhCH_2Co(dpgH)_2]_2Pz$ (+1.12 V).

## X-ray Crystallographic Studies

### *Description of Structures 13 and 16*

The "diamond" diagrams of molecular structures **13** and **16** along with selected numbering schemes are shown in Figures 3 and 4, respectively. Selected bond lengths, bond angles, and structural parameters are given in Table 4. The crystal structure of **13** contains two molecules in its asymmetric unit. As there is a structural variation, they are numbered as **13-I** and **13-II** and the crystal data are given separately (Table 4).[23] Cobalt is in a distorted octahedral geometry with four nitrogen atoms of the dioxime in the equatorial plane and pyrazine and Cl axially coordinated. The cobalt atom deviates +0.013 and +0.028 Å from the mean equatorial $CoN_4$ plane toward the neutral pyrazine ligand in **13-I** and **13-II**, respectively, while the deviation is –0.016 Å in **16**. The positive sign means the deviation is towards the axial base group.[2]

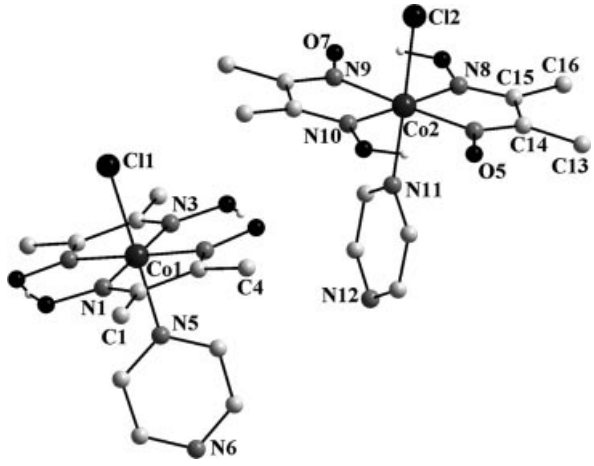


Figure 3. Molecular structure of $ClCo(dmgH)_2Pz$ (**13-I** and **13-II**) with two molecules in the asymmetric unit. The hydrogen atoms of the C–H bonds are omitted for clarity.

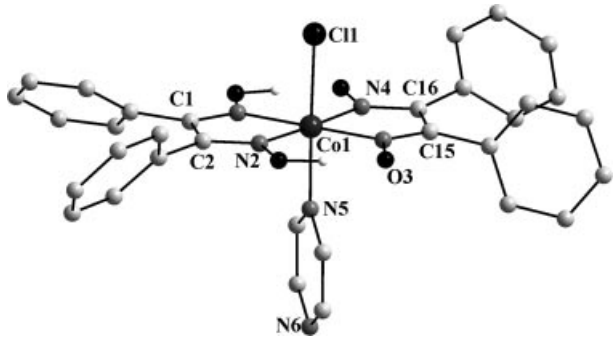


Figure 4. Molecular structure of $ClCo(dpgH)_2Pz$ (**16**). The hydrogen atoms of the C–H bonds are omitted for clarity.

The Co–Cl [2.2332(9), 2.2262(10), and 2.2185(10) Å] and Co–N5 [1.958(3), 1.967(3), and 1.961(3) Å] bond lengths in **13-I**, **13-II**, and **16** are very similar to their those of the corresponding $ClCo(dioxime)_2Py$ cobaloximes (dioxime = dmgH or dpgH). This indicates that the bond length does not change with a slight difference in the *cis* or *trans* influence.[2a,5] However, the Co–Cl [2.252(1) Å] and Co–N5 [1.981(3) Å] bonds are significantly longer in ClCbl.[24]

 © 2006 Wiley-VCH Verlag GmbH & Co. KGaA, Weinheim 

Table 4. Selected bond lengths, bond angles, and structural data.

| | **13** | | **16** | **16**·2DCM | **19** | $[Co(dmgH)_2(NO_2)_2]_2Ag_2$[a] |
|---|---|---|---|---|---|---|
| | Co1 | Co2 | | | | |
| Co–Cl [Å] | 2.2332(9) | 2.2262(10) | 2.2185(10) | 2.2174(10) | | |
| Co–N(ax) [Å] | 1.958(3) | 1.967(3) | 1.961(3) | 1.963(3) | 1.943(3), 1.948(4) | 1.937, 1.940; 1.940, 1.940 |
| X–Co–N5 [°] | 179.12 | 178.11 | 177.62(9) | 179.15(9) | 180 | 177.0, 180 |
| *d* [Å] | +0.013 | +0.028 | –0.016 | +0.054 | 0.0 | 0 |
| *α* [°] | 4.14 | 1.04 | 1.62 | 11.38 | ca. 0 | 0 |
| *τ* [°] | 81.34 | 72.63 | 86.38 | 82.60 | 90, 0 | ca. 90 |

[a] Ag1–O8 2.426(6), Ag1–O10 2.428(6), Ag2–O3 2.548 (6), Ag2–O6 2.352(6), Ag2–O11 2.698(5), Ag2–O12 2.383(6), Ag2–O13 2.337(5) Å.

The pyrazine ring is almost parallel to the dioxime C–C bonds and the twist angles (*τ*)[25a] are 81.34, 72.63, and 86.38° in **13-I**, **13-II**, and **16**, respectively. The butterfly bending angle (*α*)[25b] in **13-I** and **13-II** is 4.14 and 1.04°, respectively, while it is 1.62° in **16**.

When **16** is crystallized with dichloromethane, the single-crystal analysis shows two dichloromethane molecules in the unit cell and its molecular structure differs from **16** (Figure S22). The Co–Cl and Co–N bond lengths are 2.2174(10) and 1.963(3) Å and comparable to the values in **16**; however, *α* (11.38°) and *d* (+0.054 Å) are larger and the twist angle is smaller (82.60°). These changes are the results of crystal packing forces due to the extensive H-bonding and π-interaction.

### *Description of Structure 19*

The characterization of **19** by X-ray analysis shows it to be $[Co(dpgH)_2(NO_2)_2]Na$ (Figure 5). An extensive hydrogen-bonding network results in large solvent-accessible voids of about 211 Å$^3$.

The crystal structure contains two cobaloxime molecules in its asymmetric unit and has two $Na^+$ as counter cations. The two cobaloxime molecules are structural isomers and differ only in their orientation of the $NO_2$ group; one is above the dioxime unit [with a Co–$N_{ax}$ distance of 1.943(3)] and the other is above the O–H···O unit [Co–$N_{ax}$ distance 1.948(4) Å]. Of the two units, one has a positional disorder of the $NO_2$ group attached to Co2. The Co–$NO_2$ distances are comparable to those of $NO_2$Cbl [1.942(6) Å][24] and $[Co(dmgH)_2(NO_2)_2]^-$ [1.945(3) Å][26] indicates no *cis* influence.

### *Description of the Structure of $[Co(dmgH)_2(NO_2)_2]_2$-$[Ag]_2$·$H_2O$*

The molecular structure shows the silver atoms in two distinct environments: a pseudo-four-coordinate and a pseudo-five-coordinate arrangement are displayed. A "diamond" picture of the unique portion of this structure is shown in Figure 6. Two cobaloxime units are repeated in three dimensions, linked by bridging Ag atoms, to form a 3D coordination polymer. The two silver atoms are in different coordination spheres: one is in a tetrahedral environment and the other is in a capped trigonal environment, as demonstrated in Figure 7.

We see two crystallographically inequivalent silver centers arranged linearly, whose differences arise from the binding mode of Ag. Ag1 is in a tetrahedral environment bridged by four oxygen atoms; two sets of symmetry-equivalent oxygen atoms are present. One set belongs to two nitro groups and the other set to two dioxime units. The Ag1–O bond lengths are 2.426(6) and 2.428(6) Å, respectively.

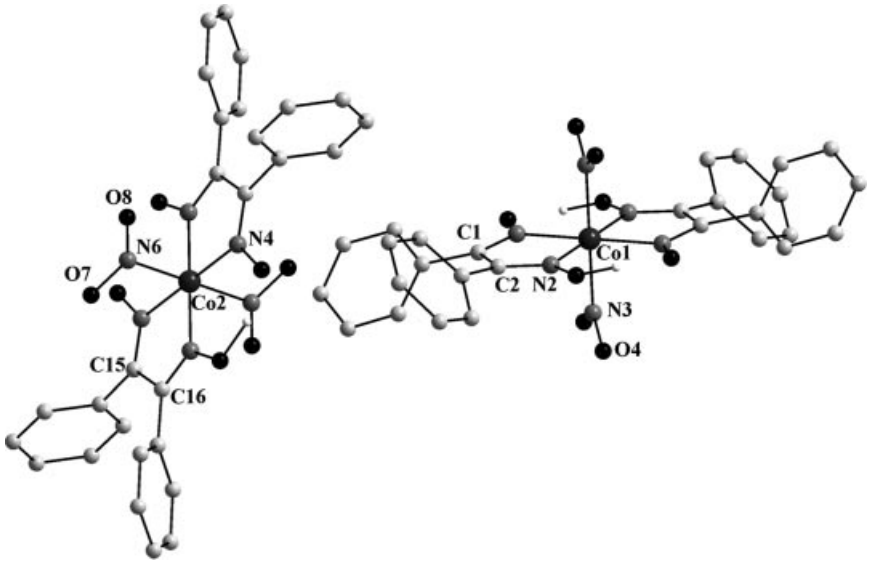


Figure 5. Molecular structure of $[Co(dpgH)_2(NO_2)_2]Na$ (**19**). Counter cations and hydrogen atoms of the C–H bonds are omitted for clarity.

 © 2006 Wiley-VCH Verlag GmbH & Co. KGaA, Weinheim 

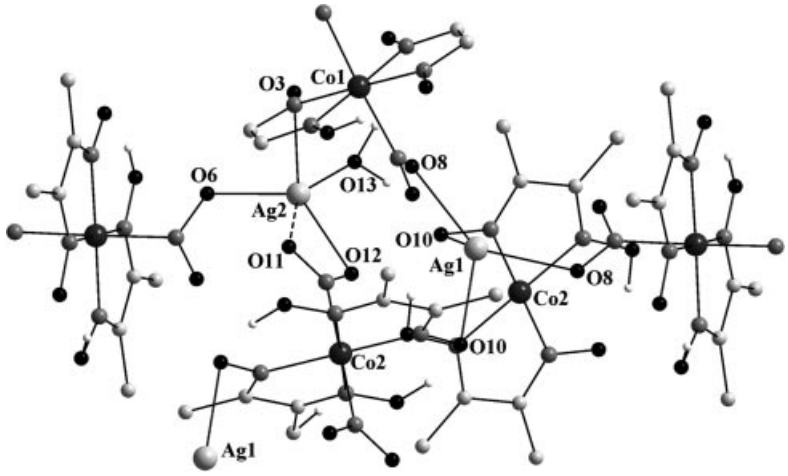


Figure 6. Molecular structure of $[Co(dmgH)_2(NO_2)_2]_2[Ag]_2{\cdot}H_2O$.

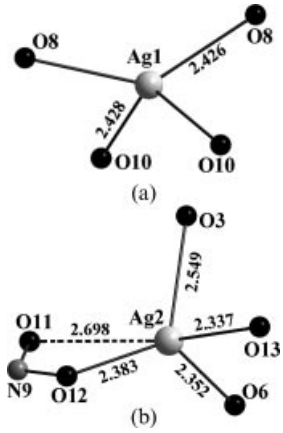


Figure 7. Ag1 and Ag2 coordination environment in $[Co(dmgH)_2(NO_2)_2]_2[Ag]_2{\cdot}H_2O$.

Ag2 has a (3+1) capped trigonal coordination sphere with four oxygen atoms. Three short bonds [Ag2–O6 2.352(6), Ag2–O12 2.383(6), Ag2–O13 2.337(5) Å] with bridging $NO_2$ groups and a water molecule form the trigonal geometry (slightly deviated from the planar geometry). The longer bond Ag2–O3 [2.548(6) Å] is with the dioxime oxygen atom; O11 acts like a chelating atom and has a weak interaction with Ag2 at a distance of 2.698(6) Å to generate a five-member silver-containing ring.[27]

In the solid state, these tetrahedral building blocks and cobaloxime units are linked together by the oxygen atom of the coordinated nitro group into a novel 2D helical structure along the *a*-axis. A right-handed helix present in the crystal structure is shown in Figure 8a. The helix is formed through four Ag–O bonding interactions (O8–Ag1–O8 and O6–Ag2–O12) along the $2_1$ screw axis (Figure 8b). Only one of the oxygen atoms of each nitro group takes part in the formation of the helix. Each coil of the helix contains six cobaloxime residues and six Ag atoms and the distance between the coils is 42.91(1) Å. Also it shows a 2D metal-organic framework (Figure S23) and an infinite zigzag coordination polymer (Figure S24).

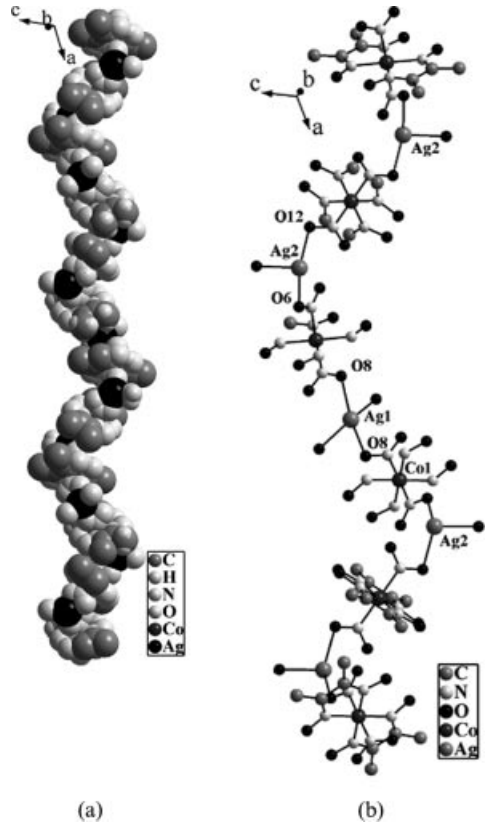


Figure 8. (a) Space-filling view of the right-handed helix of $[Co(dmgH)_2(NO_2)_2]_2[Ag]_2{\cdot}H_2O$. (b) 2D helical assembly along the *a*-axis. Some of the atoms have been omitted for clarity.

## Conclusions

Procedures were developed for the synthesis of mono- and dinuclear inorganic cobaloximes with pyrazine. The changes observed in NMR and CV are much more prominent than in organocobaloximes and these are more effectively rationalized with the field effect, a model proposed recently by us. Electron delocalization throughout the two metallabicycles through pyrazine is observed in the NMR

 © 2006 Wiley-VCH Verlag GmbH & Co. KGaA, Weinheim 

and CV studies. $[XCo(dioxime)_2]_2$-μ-Pz complexes are more difficult to reduce than $XCo(dioxime)_2Pz$. Mononuclear pyrazine complexes behave similarly to the corresponding pyridine complexes. $[Co(dmgH)_2(NO_2)_2]_2[Ag]_2{\cdot}H_2O$ shows two $Ag^I$ ions in different environments: one is tetrahedral whereas the other is in a capped trigonal coordination, and the metal-organic framework in this molecule shows helical structure.

## Experimental Section

**General:** Cobalt chloride hexahydrate, dimethylglyoxime (SD Fine Chemicals, India), and pyrazine (Aldrich Chemical Company) were used as received. Diphenylglyoxime (Lancaster Chemicals) was washed with methanol before use. Silica gel (100–200 mesh) and distilled solvents were used in all chromatographic separations. $ClCo(dmgH)_2H_2O$,[28] $ClCo(dpgH)_2H_2O$,[29] $ClCo(dmgH)_2Pz$,[18] and $ClCo(dpgH)_2Pz$[18] were prepared according to the literature procedure. $^1H$ and $^{13}C$ NMR spectra were recorded with a JEOL JNM LA 400 FT NMR spectrometer (400 MHz for $^1H$ and 100 MHz for $^{13}C$) in $CDCl_3$ solution with TMS as internal standard. NMR spectroscopic data are reported in ppm. UV/Vis spectra were recorded with a JASCO V-570 spectrophotometer in dichloromethane (dry) and methanol (dry) at 298 K. IR spectra were recorded with KBr pellets in the range 4000–650 $cm^{-1}$ using a Vertex-70 Bruker Spectrophotometer. Elemental analysis was carried out at the Regional Sophisticated Instrumentation Center, Lucknow (see Table ST1). Cyclic voltammetry measurements were carried out using a BAS Epsilon Electrochemical workstation with platinum working electrode, Ag/AgCl reference electrode (3 M KCl), and a platinum wire counter electrode. All the measurements were performed in 0.1 M $nBu_4N(PF_6)$ in dichloromethane (dry) at a concentration of 1 mM of each complex. In addition, in a separate series of experiments, an internal reference system (ferrocene/ferrocenium ion) was used. Under the conditions used, the reversible $Fc/Fc^+$ potential occurred at 0.51 V versus the Ag/AgCl electrode.

**X-ray Structural Determination and Refinement:** Orange crystals were obtained by slow evaporation of the solvent {acetone/hexane for **13** and **16**; chloroform/methanol/hexane for **19**; dichloromethane/acetone for $[Co(dmgH)_2(NO_2)_2]_2[Ag]_2{\cdot}H_2O$}. Single-crystal X-ray data were collected at 100 K with a Bruker SMART APEX CCD diffractometer using graphite-monochromated Mo-$K_\alpha$ radiation ($\lambda$ = 0.71073 Å). The linear absorption coefficients, scattering factors for the atoms, and the anomalous dispersion corrections were taken from the *International Tables for X-ray Crystallography*.[30a] The data integration and reduction were processed with SAINT[31] software. An empirical absorption correction was applied to the collected reflections with SADABS[32] using XPREP.[33] All the structures were solved by direct methods using SIR-97[34] and were refined on $F^2$ by the full-matrix least-squares technique using the SHELXL-97[30b] program package. All non-hydrogen atoms were refined anisotropically in all the structures. The hydrogen atoms of the OH group of oxime were located on difference Fourier maps and were constrained to those difference Fourier map positions. The hydrogen atom positions or thermal parameters were not refined but were included in the structure factor calculations. The pertinent crystal data and refinement parameters are compiled in Table 5. CCDC-299539, -299540, -299541, -299543, and -299544 contain the supplementary crystallographic data for this paper. These data can be obtained free of charge from The Cambridge Crystallographic Data Centre via www.ccdc.cam.ac.uk/data_request/cif.

**Synthesis**

**$[ClCo(dmgH)_2]_2$-μ-Pz (1):** Pyrazine (0.14 mmol, 0.01 g), dissolved in acetone (1 mL), was added to a clear brown solution of

Table 5. Crystal data and structure refinement details.

| | **13** | **16** | **19** | $[Co(dmgH)_2(NO_2)_2]Ag$ |
|---|---|---|---|---|
| Empirical formula | $(C_{12}H_{18}Cl_1Co_1N_6O_4)_2$ | $C_{32}H_{26}Cl_1Co_1N_6O_4$ | $C_{29}H_{24}Co_1N_6Na_{1.5}O_{14}$ | $C_{24}H_{46}Ag_3Co_3N_{18}O_{26}$ |
| Formula mass | 809.41 | 652.97 | 773.96 | 1503.19 |
| $T$ [K] | 100(2) | 100(2) | 100(2) | 100(2) |
| Crystal system | monoclinic | monoclinic | triclinic | monoclinic |
| Space group | $P2_1/c$ | $P2_1/c$ | $P\bar{1}$ | $C2/c$ |
| $a$ [Å] | 10.0217(7) | 9.953(7) | 9.6382(10) | 23.6052(24) |
| $b$ [Å] | 21.7874(16) | 24.6908(16) | 12.9620(13) | 15.5292(17) |
| $c$ [Å] | 15.5993(11) | 11.8723(8) | 16.5136(17) | 14.3357(15) |
| $\alpha$ [°] | 90 | 90 | 73.438(2) | 90 |
| $\beta$ [°] | 107.352(10) | 102.212(10) | 83.668(2) | 115.993(2) |
| $\gamma$ [°] | 90 | 90 | 75.135(2) | 90 |
| $V$ [Å$^3$] | 3251.0(4) | 2852(2) | 1909.7(3) | 4723.4(8) |
| $Z$ | 4 | 2 | 2 | 4 |
| $\rho_{calcd.}$ [mg m$^{-3}$] | 1.654 | 1.521 | 1.346 | 2.114 |
| $\mu$ [mm$^{-1}$] | 1.251 | 0.746 | 0.535 | 2.355 |
| $F$ (000) | 1664 | 1344 | 791 | 2984 |
| Crystal size [mm] | 0.31 × 0.23 × 0.21 | 0.32 × 0.25 × 0.21 | 0.26 × 0.19 × 0.16 | 0.32 × 0.17 × 0.12 |
| Index ranges | $-8 \le h \le 13$, $-28 \le k \le 28$, $-20 \le l \le 19$ | $-12 \le h \le 13$, $-32 \le k \le 31$, $-15 \le l \le 9$ | $-12 \le h \le 10$, $-17 \le k \le 15$, $-19 \le l \le 21$ | $-23 \le h \le 31$, $-20 \le k \le 14$, $-18 \le l \le 19$ |
| Reflections collected | 20450 | 18797 | 12682 | 15455 |
| Independent reflections | 7392 | 7024 | 9048 | 5832 |
| Gof on $F^2$ | 1.046 | 1.101 | 1.056 | 1.116 |
| Final $R$ indices | $R_1$ = 0.0510 | $R_1$ = 0.0528 | $R_1$ = 0.0866 | $R_1$ = 0.0650 |
| $[I > 2\sigma(I)]$ | $wR_2$ = 0.1137 | $wR_2$ = 0.1070 | $wR_2$ = 0.2173 | $wR_2$ = 0.1188 |
| $R$ indices (all data) | $R_1$ = 0.0748 | $R_1$ = 0.0787 | $R_1$ = 0.1119 | $R_1$ = 0.1007 |
| | $wR_2$ = 0.1273 | $wR_2$ = 0.1414 | $wR_2$ = 0.2449 | $wR_2$ = 0.1522 |
| Data/restraints/parameters | 7392/0/441 | 7024/0/397 | 9048/0/488 | 5832/0/342 |

 © 2006 Wiley-VCH Verlag GmbH & Co. KGaA, Weinheim 

$ClCo(dmgH)_2H_2O$ (**7**) (0.29 mmol, 0.10 g in 10 mL of MeOH). An immediate precipitation occurred. The solution was stirred for several hours to ensure complete precipitation. The yellow precipitate was filtered, washed with acetone, and dried in vacuo over phosphorus pentoxide. Yield 0.091 g (89%) with respect to pyrazine.

**$[ClCo(dpgH)_2]_2$-μ-Pz (4):** The same procedure as in **1** was used except that $ClCo(dpgH)_2H_2O$ (**10**) (0.20 g, 0.34 mmol) was dissolved in acetone (2 mL) and methanol (1 mL). Yield 0.096 g (49%) with respect to pyrazine.

**$[XCo(dioxime)_2]_2$-μ-Pz (2, 3, 5, 6). (a):** A solution of $NaNO_2$ (0.03 g, 0.43 mmol) in water (2 mL) was added to a refluxing suspension of **4** (0.53 g, 0.43 mmol) in methanol (30 mL). The reaction mixture was further refluxed for 0.5 h. The solvent was evaporated to 2–5 mL. The product isolated was a salt and did not contain the pyrazine unit. **(b):** The complexes were prepared from the corresponding aqua complexes according to the method outlined for **1** and **4** (Scheme 2).

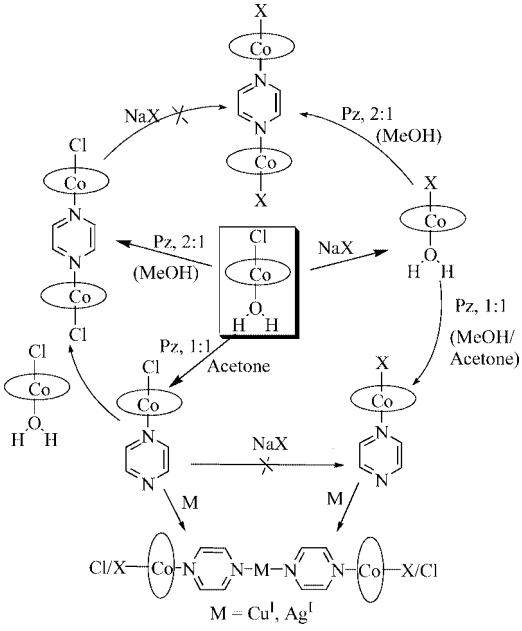


Scheme 2.

**$XCo(dmgH)_2H_2O$ (8, 9):**[35] These compounds were synthesized by the nucleophilic substitution of the chlorido ligand by $X^-$ in $ClCo(dmgH)_2H_2O$ (**7**). In a typical experiment, a solution of $NaNO_2$ (0.03 g, 0.43 mmol) in water (2 mL) was added to a refluxing suspension of $ClCo(dmgH)_2H_2O$ (**7**) (0.15 g, 0.43 mmol) in methanol (30 mL). The reaction mixture was further refluxed for 0.5 h. The solvent was evaporated to 2–5 mL and a sufficient amount of water was added to precipitate the compound; the precipitate was filtered and dried over phosphorus pentoxide. Yield (0.12 g, 77%).

**$XCo(dpgH)_2H_2O$ (11, 12):** The same procedure as outlined for $XCo(dmgH)_2H_2O$ was used. Two products, a salt and the desired compound **11**, were formed. The salt was identified as $[Co(dpgH)_2(NO_2)_2]^-$ by X-ray crystallography (**19**). However, when a dilute solution of $NaNO_2$ (0.03 g, in 10 mL) was treated with $ClCo(dpgH)_2H_2O$ (**10**) (0.25 g, 0.43 mmol) in methanol/acetone (1:1, 30 mL) (**11**), the desired product was formed exclusively. Yield (0.145 g, 71%).

**$XCo(dmgH)_2Pz$ (13–15):** Pyrazine (0.084 g, 1.05 mmol) dissolved in acetone (5 mL) was added to a clear brown solution of $N_3Co(dmgH)_2H_2O$ (0.34 g, 1.00 mmol) in acetone (70 mL). The solution was stirred for 1 h and kept aside for slow evaporation of the solvent. The needle-shaped brown crystals, formed after 2–3 d, were filtered and air-dried. Yield 60%. **(a):** When acetone was less than 70 mL, an immediate precipitation occurred and the compound identified was the dinuclear complex **3** (see above). **(b):** The use of methanol always led to the formation of a mixture of mono- and dinuclear complexes.

**$XCo(dpgH)_2Pz$ (16–18):** These were prepared from the corresponding aqua complexes according to the method outlined for **13**–**15**. Yield 80%.

**Heterodimetallic Complexes**

**Reaction of $Cu^IX$ (X = $BF_4$, $PF_6$, $ClO_4$) with $ClCo(dmgH)_2Pz$:** When $CuBF_4$ was added dropwise to $ClCo(dmgH)_2Pz$ (**13**) (both taken in dry dichloromethane), a dark red precipitate formed, which was completely insoluble in dichloromethane. (A similar kind of precipitation occurred with other $Cu^I$ salts also.) The precipitate dissolved instantaneously upon the addition of 2–3 drops of acetonitrile and the color changed to yellow. The precipitate was totally insoluble in most noncoordinating solvents and hence it could not be characterized by CV, NMR spectroscopy, or crystallographic studies.

**Reaction of $Ag^I(PF_6)$ with $XCo(dmgH)_2Pz$:** The addition of $Ag^I$ to **13** or **16** in dichloromethane/acetone immediately formed a white precipitate of AgCl, whereas the addition of an acetone solution of $AgPF_6$ to **14** gave an orange-yellow precipitate. In an effort to grow a single crystal by the layering process, most of the salt precipitated from the solution but a few orange crystals appeared on the inside wall of the tube. X-ray analysis of one of these crystals showed it to be $[Co(dmgH)_2(NO_2)_2][Ag]_2H_2O$. The complex may have formed during the crystallization process or because of a small impurity of $[Co(dmgH)_2(NO_2)_2]Na$ in **14**. However, this compound can be reproduced with addition of an $AgPF_6$ solution to $[Co(dmgH)_2(NO_2)_2]Na$ salt in acetone.

**Attempted Synthesis of Mixed Dicobaloximes $ClCo(dmgH)_2$-Pz-$Co(dpgH)_2Cl$ (20):** The synthesis of **20** turned out to be unexpectedly complicated. The procedure used in the synthesis of **1**–**6** did not afford the required product, for example the reaction of **10** with **13** (1:1) or the reaction of **7** with **16** (1:1) in chloroform formed **4** instead of the desired complex (**20**). The same reactions in acetone/methanol afforded **1** as the exclusive product. It is very difficult to offer any conclusive evidence for the formation of **4** or **1**. It is, however, possible that **4** is thermodynamically the more stable product and arises from the intermediate $ClCo(dpgH)_2$-Pz-$Co(dmgH)_2Cl$, a kinetically controlled product. [We have, however, not been able to isolate this compound, even at low temperatures (see Scheme S1).] Similarly, all efforts to synthesize other combinations like $ClCo(dmgH)_2$-Pz-$Co(dpgH)_2$*n*Pr and $MeCo(dmgH)_2$-Pz-$Co(dpgH)_2Cl$ also failed, although many procedures were tried (see Supporting Information).

**Supporting Information** (see footnote on the first page of this article): Representative figures of UV/Vis, IR, NMR spectra, and X-ray metal-organic framework for the subject compounds.

## Acknowledgments

We thank the CSIR [01(1949)/04/EMR-II] New Delhi, India, for financial support.

[1] a) B. Giese, *Radicals in Organic Synthesis: Formation of Carbon–Carbon Bonds*, Pergamon Press, Oxford, UK, **1986**; b) R.

 © 2006 Wiley-VCH Verlag GmbH & Co. KGaA, Weinheim 

Scheffold, G. Rytez, L. Walder in *Transition Metals in Organic Synthesis* (Ed.: S. Scheffold), Wiley, Chichester, UK, **1983**, vol. 3; c) B. P. Branchaud, G. F. Friestad, "Vitamin B12", in *Encyclopedia of Reagents for Organic Synthesis* (Ed.: L. A. Paquette), John Wiley & Sons, Chichester, West Sussex, **1995**, pp. 5511; d) M. E. Welker, *Curr. Org. Chem.* **2001**, *5*, 785–807; e) M. Tada, *Rev. Heteroat. Chem.* **1999**, *20*, 97–144; f) Y. L. Nishikubo, B. P. Branchaud, *J. Am. Chem. Soc.* **1999**, *121*, 10924–10927; g) C. J. Tucker, M. E. Welker, C. S. Day, M. W. Wright, *Organometallics* **2004**, *23*, 2257–2262; h) M. W. Wright, M. E. Welker, *J. Org. Chem.* **1996**, *61*, 133–141; i) T. Brown, A. Dronsfield, A. Jablonski, A. S. Wilkinson, *Tetrahedron Lett.* **1996**, *37*, 5413–5416; j) G. B. Gill, G. Pattenden, G. A. Roan, *Tetrahedron Lett.* **1996**, *37*, 9369–9372; k) B. D. Gupta, V. Vijaikanth, *J. Organomet. Chem.* **2004**, *689*, 1102–1109 and references therein; l) A. A. Gridnev, S. D. Ittel, *Chem. Rev.* **2001**, *101*, 3611–3659; m) M. W. Wright, T. L. Smalley, M. E. Welker, A. L. Rheingold, *J. Am. Chem. Soc.* **1994**, *116*, 6777–6791; n) T. L. Smalley, M. W. Wright, S. A. Garmon, M. E. Welker, A. L. Rheingold, *Organometallics* **1993**, *12*, 998–1000; o) B. P. Branchaud, Y. L. Choi, *Tetrahedron Lett.* **1988**, *29*, 6037–6038; p) R. R. Pidaparthi, M. E. Welker, C. S. Day, *Organometallics* **2006**, *25*, 974–981; q) X. Hu, B. M. Cossairt, B. S. Brunschwig, N. S. Lewis, J. C. Peters, *Chem. Commun.* **2005**, 4723–4725; r) M. Razavet, V. Artero, M. Fontecave, *Inorg. Chem.* **2005**, *44*, 4786–4795.

[2] a) L. Randaccio, *Comments Inorg. Chem.* **1999**, *21*, 327–376; b) L. Randaccio, N. Bresciani-Pahor, E. Zangrando, L. G. Marzilli, *Chem. Soc. Rev.* **1989**, *18*, 225–250.

[3] a) M. S. A. Hamza, A. Felluga, L. Randaccio, G. Tauzher, R. van Eldik, *Dalton Trans.* **2004**, 287–291; b) N. Bresciani-Pahor, L. Randaccio, E. Zangrando, M. F. Summers Jr, J. H. Ramsden, P. A. Marzilli, L. G. Marzilli, *Organometallics* **1985**, *4*, 2086–2089.

[4] a) B. D. Gupta, K. Qanungo, *J. Organomet. Chem.* **1997**, *543*, 125–134; b) B. D. Gupta, V. Singh, R. Yamuna, T. Barclay, W. Cordes, *Organometallics* **2003**, *22*, 2670–2678; c) B. D. Gupta, K. Qanungo, T. Barclay, W. Cordes, *J. Organomet. Chem.* **1998**, *560*, 155–161.

[5] D. Mandal, B. D. Gupta, *Organometallics* **2005**, *24*, 1501–1510.

[6] a) K. L. Brown, S. Satyanarayana, *J. Am. Chem. Soc.* **1992**, *114*, 5674–5684; b) L. Randaccio, S. Geremia, E. Zangrando, C. Ebert, *Inorg. Chem.* **1994**, *33*, 4641–4650; c) R. S. Drago, *J. Organomet. Chem.* **1996**, *512*, 61–68.

[7] R. Yamuna, B. D. Gupta, D. Mandal, *Organometallics* **2006**, *25*, 706–714.

[8] a) V. Balzani, A. Juris, M. Venturi, S. Campagna, S. Serroni, *Chem. Rev.* **1996**, *96*, 759–833, and references cited therein; b) A. Haim, *Acc. Chem. Res.* **1975**, *8*, 264–272.

[9] a) C. Creutz, H. Taube, *J. Am. Chem. Soc.* **1973**, *95*, 1086–1094; b) J. T. Hupp, Y. Dong, *Inorg. Chem.* **1994**, *33*, 4421–4424; c) A. Yeh, A. Haim, *J. Am. Chem. Soc.* **1985**, *107*, 369–376; d) K. J. Pfenning, L. Lee, H. D. Wohlers, J. D. Petersen, *Inorg. Chem.* **1982**, *21*, 2477–2482; e) J. M. Malin, D. A. Ryan, T. V. O'Halloran, *J. Am. Chem. Soc.* **1978**, *100*, 2097–2102.

[10] a) A. W. Herlinger, T. L. Brown, *J. Am. Chem. Soc.* **1972**, *94*, 388–393; b) A. W. Herlinger, K. Ramakrishna, *Polyhedron* **1985**, *4*, 551–561.

[11] B. D. Gupta, K. Qanungo, *J. Organomet. Chem.* **1998**, *557*, 243–249.

[12] D. Mandal, B. D. Gupta, *J. Organomet. Chem.* **2005**, *690*, 3746–3754.

[13] C. Tavagnacco, G. Balducci, G. Costa, K. Täschler, W. von Philipsborn, *Helv. Chim. Acta* **1990**, *73*, 1469–1480.

[14] B. D. Gupta, V. Vijaykanth, V. Singh, *Organometallics* **2004**, *23*, 2069–2079.

[15] B. D. Gupta, R. Yamuna, V. Singh, U. Tewari, *Organometallics* **2003**, *22*, 226–232.

[16] a) B. D. Gupta, K. Qanungo, R. Yamuna, A. Pandey, U. Tewari, V. Singh, V. Vijaikanth, T. Barclay, W. Cordes, *J. Organomet. Chem.* **2000**, *608*, 106–114; b) B. D. Gupta, U. Tewari, T. Barclay, W. Cordes, *J. Organomet. Chem.* **2001**, *629*, 83–92.

[17] It is worth noting that the procedure typically used for the preparation of $RCo(dioxime)_2H_2O$ from the corresponding pyridine complex by Dowex ($H^+$ form) has failed in the inorganic complexes.[11] This might be because pyridine is much less labile because of the poor *trans* effect of X as compared to R.

[18] C. López, S. Alvarez, X. Solans, M. Font-Altaba, *Inorg. Chem.* **1986**, *25*, 2962–2969.

[19] D. A. Keyworth, *J. Org. Chem.* **1959**, *24*, 1355.

[20] H. C. Brown, D. H. McDaniel, O. Hafliger, in *Determination of Organic Structures by Physical Methods* (Eds.: E. A. Braude, F. C. Nachod), Academic Press, New York, **1955**, pp. 567–662.

[21] Coordination shift $\Delta\delta = [\delta(\text{complex}) - \delta(\text{free base})]$.

[22] K. L. Brown, D. Lyles, M. Penencovici, R. G. Kallen, *J. Am. Chem. Soc.* **1975**, *97*, 7338–7346.

[23] J. W. Steed, *CrystEngComm* **2003**, *5*, 169–179.

[24] G. Garau, S. Geremia, L. G. Marzilli, G. Nardin, L. Randaccio, G. Tauzher, *Acta Crystallogr., Sect. B: Struct. Sci.* **2003**, *59*, 51–59.

[25] a) The twist angle ($\tau$) is the angle between the pyrazine plane and one virtual plane, which is formed by considering the middle point of the C–C bond of two oxime units that pass through the cobalt atom and the pyrazine nitrogen atom. b) The butterfly bending angle ($\alpha$) is the dihedral angle between two dioxime planes.

[26] A. I. Shkurpelo, Yu. A. Simonov, *Izv. Akad. Nauk Mold. SSR, Ser. Fiz.-Tekh. Mat. Nauk* **1979**, 46–52.

[27] Y.-B. Dong, X. Zhao, R.-Q. Huang, M. D. Smith, H.-C. zur Loye, *Inorg. Chem.* **2004**, *43*, 5603–5612.

[28] N. Yamazaki, Y. Hohokabe, *Bull. Chem. Soc. Jpn.* **1971**, *44*, 63–69.

[29] C. López, S. Alvarez, M. Font-Bardia, X. Solans, *J. Organomet. Chem.* **1991**, *414*, 245–259.

[30] a) *International Tables for X-ray Crystallography*, Kynoch Press, Birmingham, England, **1974**, vol. IV; b) G. M. Sheldrick, *SHELXL-97, Program for Crystal Structure Refinement*, University of Göttingen, Göttingen, Germany, **1997**.

[31] *SAINT+*, 6.02 ed., Bruker AXS, Madison, WI, **1999**.

[32] G. M. Sheldrick, *SADABS, Empirical Absorption Correction Program*, University of Göttingen, Göttingen, Germany, **1997**.

[33] *XPREP*, 5.1 ed., Siemens Industrial Automation Inc., Madison, WI, **1995**.

[34] A. Altomare, M. C. Burla, M. Camalli, G. L. Cascarano, C. Giacovazzo, A. Guagliardi, A. G. G. Moliterni, G. Polidori, R. Spagna, *J. Appl. Crystallogr.* **1999**, *32*, 115–119.

[35] a) U. Englert, A. Fischer, A. Gammersbach, *Struct. Chem.* **1995**, *6*, 115–119; b) U. Englert, J. Strähle, *Gazz. Chim. Ital.* **1988**, *118*, 845–855; c) Z.-Y. Dong, X.-W. Liu, X.-Q. Wang, R.-J. Wang, G.-Q. Shen, *Acta Crystallogr., Sect. E: Struct. Rep. Online* **2003**, *59*, m260–m262.

Received: March 30, 2006
Published Online: August 11, 2006

 © 2006 Wiley-VCH Verlag GmbH & Co. KGaA, Weinheim 

DOI: 10.1002/ejic.200600296

# New Polynuclear Mo–Fe Complexes with Ferrocenylamidobenzimidazole Ligands

**Paulo N. Martinho,[a,b] Susana Quintal,[a,b] Paulo J. Costa,[a,b] Serena Losi,[c] Vitor Félix,[d] M. Concepción Gimeno,[e] Antonio Laguna,[e] Michael G. B. Drew,[f] Piero Zanello,[c] and Maria José Calhorda*[a,b]**

**Keywords:** $Mo^{II}$ complexes / Ferrocenyl ligands / Polynuclear complexes / DFT calculations / Electrochemistry

The reaction between $[Mo(\eta^3\text{-}C_3H_5)(CO)_2(NCMe)_2Br]$ (**1**) and the ferrocenylamidobenzimidazole ligands $FcCO(NH_2benzim)$ (**L1**) and $(FcCO)_2(NHbenzim)$ (**L2**) led to a binuclear (**2**) and a trinuclear (**3**) Mo–Fe complex, respectively. The single-crystal X-ray structure of $[Mo(\eta^3\text{-}C_3H_5)(CO)_2(L2)Br]$ [L2 = $\{[(\eta^5\text{-}C_5H_5)Fe(\eta^5\text{-}C_5H_4CO)]_2$(2-NH-benzimidazolyl)$\}$] shows that **L2** is coordinated to the *endo* $Mo(\eta^3\text{-}C_3H_5)(CO)_2$ group in a $\kappa^2$-N,O-bidentate chelating fashion whereas the $Mo^{II}$ centre displays a pseudooctahedral environment with Br occupying an equatorial position. Complex **2** was formulated as $[Mo(\eta^3\text{-}C_3H_5)(CO)_2(L1)Br]$ on the basis of a combination of spectroscopic data, elemental analysis, conductivity and DFT calculations. **L1** acts as a $\kappa^2$-*N*,*N*-bidentate ligand. In both **L1** and **L2**, the HOMOs are mainly localised on iron while the C=O bond(s) contribute to the LUMO(s) and the next highest energy orbitals are Fe–allyl antibonding orbitals. When the ligands bind to $Mo(\eta^3\text{-}C_3H_5)(CO)_2Br$, the greatest difference is that Mo becomes the strongest contributor to the HOMO. Electrochemical studies show that, in complex **2**, no electronic interaction exists between the two ferrocenyl ligands and that the first electron has been removed from the $Mo^{II}$-centred HOMO.
(© Wiley-VCH Verlag GmbH & Co. KGaA, 69451 Weinheim, Germany, 2006)

## Introduction

Polynuclear complexes containing molybdenum and iron have received much attention as possible models for the site active metal centre(s) in nitrogenases.[1] In particular, organometallic ligands derived from ferrocene, with one or both the cyclopentadienyl rings properly functionalised with suitable substituents, represent an easy and successful way of designing polynuclear species able to mimic molecules featuring different biological functions or material science properties.[2] Common routes start either from ferrocene carbonyl chloride and an amine, elimination of HCl affording the desired product, or from lithiated ferrocene.[3] Interestingly, both ferrocenium and some ferrocenylalkyl benzimidazoles have been shown to exhibit antitumor properties.[4] A large amount of chemistry has been developed around the ferrocenyl amides, arising from the special biological properties characteristic of amino acids and peptides.[5] Ferrocene labelled amino acids have thus been synthesised,[6] their complexation behaviour towards other metal centres studied[7] and other properties[8] and applications, namely as sensors, investigated.[9] We recently described the synthesis of two new ferrocenylamidobenzimidazole ligands, $FcCO(NH_2benzim)$ (**L1**) and $(FcCO)_2$-(NHbenzim) (**L2**).[10] In this work, we studied their activity as ligands towards the $Mo^{II}$ complex $[Mo(\eta^3\text{-}C_3H_5)(CO)_2(NCMe)_2X]$ (X = halide), **1**,[11] following our interest in the reactivity and properties of $Mo^{II}$ systems.[12,13] Complex **1** has been used as a synthetic precursor for obtaining several types of derivatives, some of which have proved to be suitable catalysts for, among other things, polymerisation of dienes or in organic synthesis for allylic alkylations.[14,15] The complex of **L2** was structurally characterised by single-crystal X-ray diffraction and the other complex by spectroscopic studies. Their redox properties were studied by electrochemical techniques and DFT calculations[16] were carried out to interpret the behaviour upon oxidation and to assign the molecular structure of the complex with **L1**.

[a] Instituto de Tecnologia Química e Biológica (ITQB), Av. da República, EAN,
2781-901 Oeiras, Portugal
[b] Departamento de Química e Bioquímica, Faculdade de Ciências da Universidade de Lisboa,
1749-016 Lisboa, Portugal
E-mail: mjc@fc.ul.pt
[c] Dipartimento di Chimica dell'Università di Siena,
Via Aldo Moro, 53100 Siena, Italy
[d] Departamento de Química, CICECO, Universidade de Aveiro,
3810-193 Aveiro, Portugal
[e] Departamento de Química Inorgánica, Instituto de Ciencia de Materials de Aragón, Universidad de Zaragoza-CSIC,
50009 Zaragoza, Spain
[f] School of Chemistry, University of Reading,
Whiteknights, Reading, RG6 6AD, UK

## Results and Discussion

### Chemical Studies

The coupling reaction between FcCOCl [Fc = $(\eta^5\text{-}C_5H_5)$-$Fe(\eta^5\text{-}C_5H_4)$] and 2-aminobenzimidazole, $[NH_2(benzimH)]$,

 © 2006 Wiley-VCH Verlag GmbH & Co. KGaA, Weinheim 

in 1:1 and 2:1 ratios led to the ligands FcCO(NH$_2$benzim) (**L1**) and (FcCO)$_2$(NHbenzim) (**L2**)[10] shown in Scheme 1.

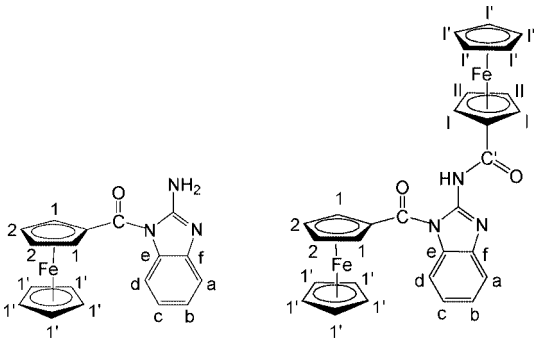

**L1** **L2**

Scheme 1.

[Mo($\eta^3$-C$_3$H$_5$)(CO)$_2$(NCMe)$_2$Br], **1**, reacted with the ferrocenyl ligand **L1** in a 1:1 ratio affording, by means of substitution of the acetonitrile ligands, a new complex assigned as [Mo($\eta^3$-C$_3$H$_5$)(CO)$_2$(L1)Br] (**2**) from elemental analysis and spectroscopic data.

The infrared spectrum of **2** shows two very strong bands at 1933 and 1839 cm$^{-1}$, assigned to the two C≡O stretching modes typical of the carbonyl groups and shifted by 16 and 12 cm$^{-1}$ relative to those in the precursor complex **1**. The $\nu_{C=O}$ stretching frequency can be observed at 1675 cm$^{-1}$ which is essentially the same value as observed in the free ligand (1678 cm$^{-1}$) suggesting that the carbonyl group does not coordinate to the metal centre. In contrast, both the N–H asymmetric stretches of the NH$_2$ group and the C–NH$_2$ stretch are shifted to lower frequencies, from 3415 cm$^{-1}$ to 3392 cm$^{-1}$ and from 1304 cm$^{-1}$ to 1296 cm$^{-1}$, respectively. These changes indicate that the NH$_2$ amino group may be coordinated to the molybdenum. The bands assigned to the ferrocenyl subunits appear at 3101 ($\nu_{C-H}$), 1419 ($\nu_{C-C}$), 1107 (asymmetric ring breathing), 1002 $(\delta_{C-H})_{\|}$, 822 $(\pi_{C-H})_{\perp}$, 490 $(\delta_{Fe-Cp})_a$ and 438 cm$^{-1}$ ($\nu_{Fe-Cp}$), i.e. almost in the same positions as in the free ligand which are 3087 ($\nu_{C-H}$), 1450 ($\nu_{C-C}$), 1105 (asymmetric ring breathing), 1000 $(\delta_{C-H})_{\|}$, 823 $(\pi_{C-H})_{\perp}$, 494 $(\delta_{Fe-Cp})_a$ and 440 cm$^{-1}$ ($\nu_{Fe-Cp}$).[17]

The signals in the room temperature $^1$H NMR spectra of **2** and **3** in [D$_7$]DMF are too broad to be resolved. At room temperature, free rotation across the amide bonds leads to the interconversion between different rotamers of **2** and **3**, with proton resonances occurring on the same time scale. The temperature dependence of the variable hydrogen bonding networks present in the complexes, as seen in the crystal structure of **3** (below), has been reported for several related complexes and explains this behaviour.[6d–f,8] Upon decreasing the temperature to 253 K, the broad signals merge to very well defined signals.

At 253 K, one broad signal at $\delta$ = 7.95 ppm can be clearly assigned to the two NH$_2$ protons. This signal is downfield relative to that in the free ligand ($\delta$ =6.45 ppm), in agreement with the proposed coordination of the NH$_2$ group to molybdenum.

The Ha, Hb, Hd and Hc protons of the benzimidazole fragment in complex **2** can be seen in the aromatic region at 7.32 (doublet), 7.17 (triplet), 7.08 (doublet) and 6.98 ppm (triplet), respectively. In the free ligand **L1**, they appear at 7.29 (doublet, Ha), 7.06 (Hb), 6.93 (doublet, Hd) and 6.81 ppm (triplet, Hc). The deviations are quite small since these protons are not close to any atom likely to bind to the metal.

The signals of the ferrocenyl unit appear as multiplets (H1, H2 at 5.00, 4.79 ppm) and as a singlet (H1′ at $\delta$ = 4.38 ppm), close to the values for the free ligand (two multiplets at 4.89 and 4.53 ppm, and one at $\delta$ = 4.22 ppm). The upfield signals at 3.51 (multiplet), 3.30 and 1.18 ppm (doublets) can be assigned, respectively, to the H$_{meso}$, H$_{syn}$ and H$_{anti}$ protons of the allyl fragment. Despite the low global symmetry of the complexes, the signals reflect the local *C*s symmetry of the ferrocenyl ligands. There is no evidence in the NMR spectra for coordinated acetonitrile, suggesting that the two nitrile ligands in the precursor **1** are replaced by **L1**. The methyl signals at $\delta$ = 2.19 ppm in the $^1$H NMR and 1.34 ppm in the $^{13}$C NMR spectrum may be assigned to uncoordinated acetonitrile. The low molar conductivity ($\Lambda$M = 4.8 $\Omega^{-1}$ cm$^2$ mol$^{-1}$ in dmf) is characteristic of a neutral complex which is expected when two nitriles are lost but not when the bromide and one nitrile are lost. Both the IR and the NMR spectroscopic results thus suggest the coordination of the **L1** ligand in a $\kappa^2$-*N*,*N*-bidentate mode in [Mo($\eta^3$-C$_3$H$_5$)(CO)$_2$(L1)Br] (**2**). DFT calculations provided more information on the preferred geometry (see below).

The precursor complex [Mo($\eta^3$-C$_3$H$_5$)(CO)$_2$(NCMe)$_2$Br], **1**, also reacted with the ligand **L2** to give [Mo($\eta^3$-C$_3$H$_5$)(CO)$_2$(L2)Br], **3**, by substitution of the two acetonitrile ligands, as confirmed by single-crystal X-ray diffraction (see below). The infrared spectrum of **3** shows two very strong bands at 1927 and 1830 cm$^{-1}$, characteristic of the $\nu_{C\equiv O}$ stretching frequencies of the carbonyl groups. Two other very strong bands, at 1704 and 1655 cm$^{-1}$, can be assigned to C=O stretches. In the free ligand, only one very intense band was observed at 1678 cm$^{-1}$. The large shift of one band to lower frequency (1655 cm$^{-1}$) in the complex suggests coordination of one C=O group to molybdenum whereas the other frequency (1704 cm$^{-1}$) can be assigned to the uncoordinated C=O. The bands assigned to the ferrocenyl subunits appear at 3073 ($\nu_{C-H}$), 1434 ($\nu_{C-C}$), 1107 (asymmetric ring breathing), 1002 $(\delta_{C-H})_{\|}$, 827 $(\pi_{C-H})_{\perp}$ and 495 $(\delta_{Fe-Cp})_a$, approximately in the same positions as in the free ligand.

The $^1$H NMR spectrum of **3** at 253 K shows one broad signal at $\delta$ = 9.10 ppm assigned to one NH proton as well as four signals in the aromatic region at 8.54, 7.75, 7.53 and 7.39 ppm assigned to the Ha, Hb, Hd and Hc protons of the benzimidazole fragment of **L2**. The H1, H2, and H1′ signals of one ferrocenyl unit appear at $\delta$ = 4.73, 4.46 and 4.23 ppm with those of the other at $\delta$ = 5.13, 4.91 and 4.44 ppm, respectively. The H$_{meso}$, H$_{syn}$ and H$_{anti}$ protons of the allyl fragment can be observed at $\delta$ = 3.76, 3.30 and 1.18 ppm, respectively. Unfortunately, the $^{13}$C{$^1$H} NMR

 © 2006 Wiley-VCH Verlag GmbH & Co. KGaA, Weinheim 

spectrum was not of sufficient quality for making assignments.

### Crystallography

The X-ray diffraction study of the $Mo^{II}$ complex **3** showed that its crystal structure consists of discrete molecules of $[Mo(\eta^3\text{-}C_3H_5)(CO)_2(L2)Br]$ and disordered $CH_2Cl_2$ solvent molecules. The chlorine atoms occupy two alternative tetrahedral positions with identical statistical occupancies. Selected bond lengths and angles are given in Table 1.

Table 1. Selected bond lengths [Å] and angles [°] in the molybdenum coordination sphere.

| | | | |
|---|---|---|---|
| Mo–C(100) | 1.934(7) | Mo–C(200) | 1.964(8) |
| Mo–N(11) | 2.223(5) | Mo–O(34) | 2.225(4) |
| Mo–Br | 2.7169(9) | | |
| C(100)–Mo–C(200) | 81.9(3) | C(100)–Mo–N(11) | 97.4(2) |
| C(200)–Mo–N(11) | 88.4(2) | C(100)–Mo–O(34) | 174.1(2) |
| C(200)–Mo–O(34) | 100.5(2) | N(11)–Mo–O(34) | 77.4(2) |
| C(100)–Mo–Br | 93.8(2) | C(200)–Mo–Br | 168.1(2) |
| N(11)–Mo–Br | 81.2(1) | O(34)–Mo–Br | 82.84(1) |

The molecular structure of **3** presented in Figure 1 shows the molybdenum centre to have a pseudo octahedral coordination environment with the centroid of the $\eta^3$-allyl ligand and two carbonyl ligands assuming a *fac* arrangement. The **L2** ligand is coordinated in a $\kappa^2$-N,O-bidentate chelating fashion with the oxygen atom [O(34)] from a carbonyl group and the N donor atom from the benzimidazole ring occupying equatorial and axial coordination positions, respectively. The Mo–N and Mo–O distances are 2.223(5) and 2.225(4) Å, respectively, leading to a N–Mo–O bite angle of 77.4(2)° for the six-membered chelating ring. The metal coordination sphere is completed by a bromine atom in the equatorial position with a Mo–Br distance of 2.7169(9) Å. This gives rise to the axial isomer depicted in Scheme 2. In addition, in the solid-state, the $\eta^3$-allyl ligand adopts an *endo* conformation while the Cp rings of both ferrocenyl subunits display almost eclipsed conformations.

Comparable geometric arrangements with the donor atoms adopting the same spatial disposition around the molybdenum centre have been found for related $Mo^{II}(\eta^3\text{-}C_3H_5)$ complexes.[12,13] To the best of our knowledge, the X-ray structure determination reported here represents the first evidence for the formation of a molybdenum derivative of $(FcCO)_2(NHbenzim)$. The two carbonyl groups from the ligand **L2** adopt a *trans* configuration with the free carbonyl slightly twisted by 79.7(2)° relative to plane of the benzimidazole ring. This arrangement is stabilised by an intramolecular hydrogen bond between the oxygen atom O(20) of the free carbonyl group and the nitrogen atom N(32) from the chelating ring (N–H···O 2.08 Å, 127.0°). The distance between the two iron centres is 7.372(1) Å while the Mo is separated from the iron centres at distances of 5.666(1) and 7.051(1) Å, respectively. These long distances indicate that there is no through-space electronic communication between the three metal centres.

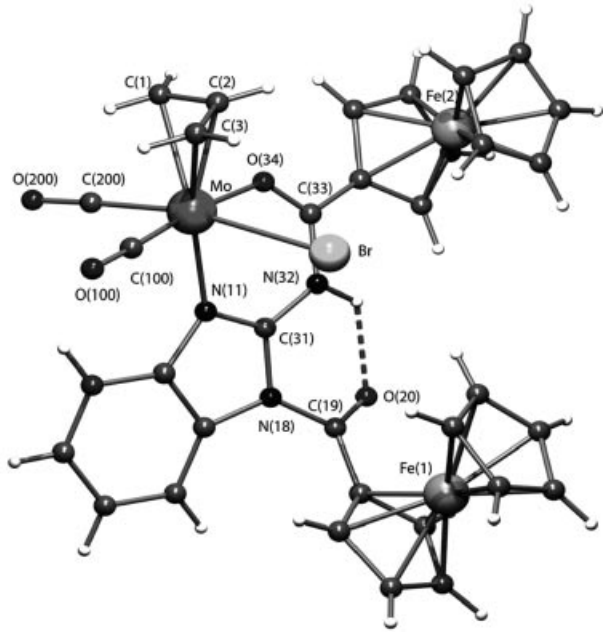


Figure 1. Molecular diagram showing the overall structure of $[Mo(\eta^3\text{-}C_3H_5)(CO)_2(L2)Br]$ (**3**) with the atomic notation scheme used. The labels for the aromatic atoms have been omitted for clarity.

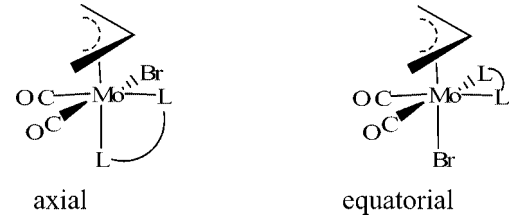


Scheme 2.

### DFT Calculations

$[Mo(\eta^3\text{-}C_3H_5)(CO)_2(L1)Br]$ (**2**) can exist as one of two isomers, axial or equatorial (Scheme 2).

DFT[16] calculations (ADF program;[18] see section Computational Details) were performed in order to find the most stable isomer of **2**. The axial isomer (Figure 2) was found to be more stable by 3.2 kcal mol$^{-1}$. The four-membered ring motif has been found in many related Mo complexes.[19]

The second feature addressed by the DFT calculations was the nature of the frontier orbitals of the ligands **L1** and **L2** and of complexes **2** and **3** in order to further support the electrochemical results described below. The HOMO, LUMO and LUMO+1 of **L1** are shown in Figure 3.

The HOMO and the next levels with lower energy are strongly localised on Fe, as is characteristic of ferrocenes and they represent the orbitals derived from the $t_{2g}$ set of this pseudo octahedral structure of a $d^6$ species. The LUMO is mainly the $\pi^*$ orbital of the C=O group while the L+1 orbital is the antibonding Fe–Cp combination involving $x^2–y^2$ and Cp $\pi^*$.

 © 2006 Wiley-VCH Verlag GmbH & Co. KGaA, Weinheim 

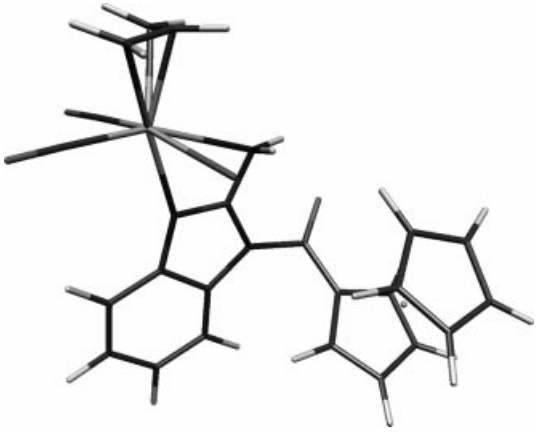

Figure 2. Molekel[20] 3D representation of the structure of the axial isomer of complex **2**, [Mo($\eta^3$-$C_3H_5$)$(CO)_2$(L1)Br].

$(FcCO)_2$(NHbenzim) (**L2**) has two ferrocenyl groups hanging from the benzimidazole unit. The frontier orbitals are comparable with those of **L1** but their number is double. The HOMO is the analogue of the HOMO of **L1**, localised on one Fc unit, while the H-1 is the same but localised on the second ferrocenyl. The LUMO also has a large contribution of the C=O π* orbital. The Fe–Cp antibonding levels appear at higher energies.

When the ligands bind to the $Mo^{II}$ centre a question about the nature of the HOMO arises, namely, is it localised on Mo or does it remain on Fe? In most known compounds, the higher occupied MOs are Fe orbitals, therefore enabling multiple applications of ferrocenyl derivatives as probes, although there are examples of the opposite behaviour.[21] The most relevant frontier orbitals of complex **2** are depicted in Figure 4.

The HOMO is strongly localised on the $Mo(CO)_2$ fragment, being Mo–C bonding, while the iron based orbitals start at H-1 and continue below. The LUMO is mostly the C=O π* orbital with some Fe contribution.

The same electronic structure can be observed for complex **3** with the HOMO located on $Mo(CO)_2$ and having some contribution from Br. The H-1 is more delocalised with participation of Mo, CO, Br and Fe. H-2 to H-6 are iron d orbitals as in Figure 3 (left). H-7 and H-8, despite a small Fe contribution, are essentially localised on the bromine atom. The LUMO and L+1 are again based on the two C=O π* orbitals, with different proportions of each. Both in the ligands and in their molybdenum complexes, the frontier orbitals are mostly localised on one of the metal atoms.

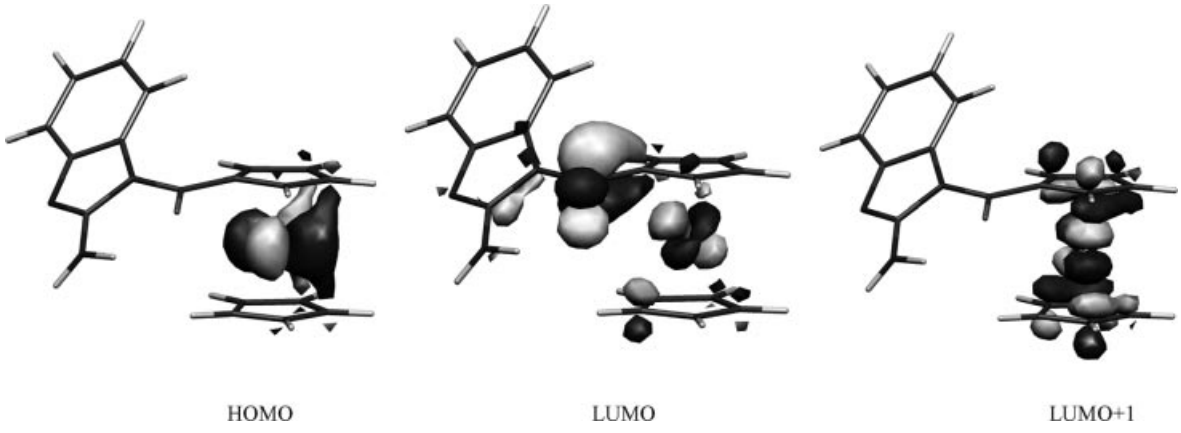


Figure 3. Molekel[20] 3D representation of the HOMO (left), LUMO (centre) and LUMO+1 (right) of FcCO($NH_2$benzim) (**L1**).

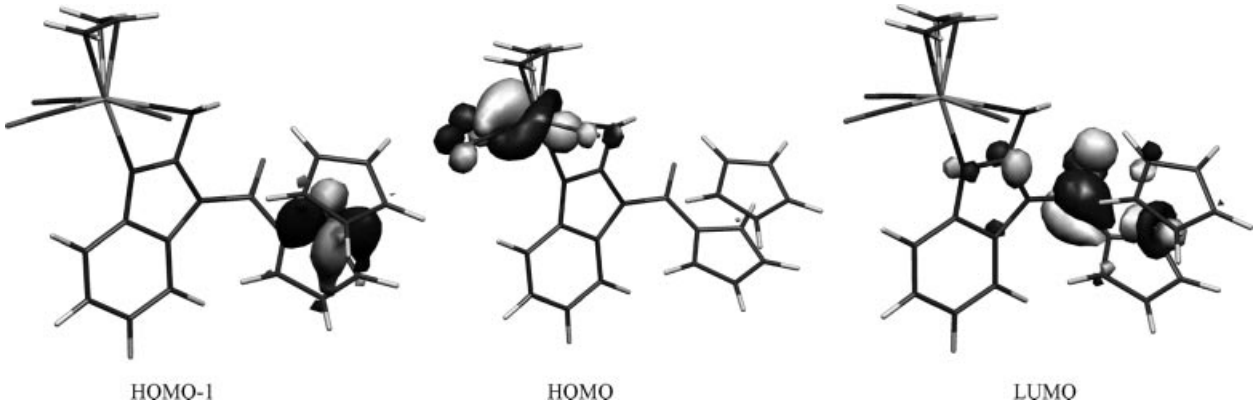


Figure 4. Molekel[20] 3D representation of the HOMO-1 (left), HOMO (centre) and LUMO (right) of [Mo($\eta^3$-$C_3H_5$)$(CO)_2$(L1)Br], **2**.

 © 2006 Wiley-VCH Verlag GmbH & Co. KGaA, Weinheim 

**Electrochemistry**

As deducible from Figure 5, the ferrocene/ferrocenium oxidation exhibited by ligand **L1** is accompanied by chemical complications.

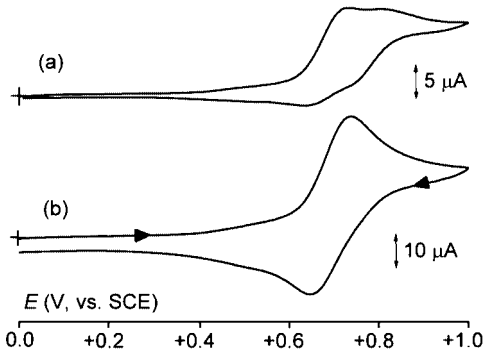


Figure 5. Cyclic voltammetric responses recorded at a platinum electrode in a $CH_2Cl_2$ solution of **L1** ($0.8\times10^{-3}$ mol dm$^{-3}$). $[NBu_4][PF_6]$ (0.2 mol dm$^{-3}$) supporting electrolyte. Scan rates: (a) 0.02 V s$^{-1}$; (b) 0.2 V s$^{-1}$.

In fact, at very low scan rates two almost overlapping anodic processes appear, which merge in a single process at higher scan rates. In confirmation of the chemical complications following the expected one-electron oxidation, controlled potential coulometric measurements ($E_w$ = +0.9 V) indicated that two electrons *per* molecule are consumed. Even if the closeness of the two processes makes difficult a detailed analysis of the overall process at low scan rates, it is conceivable that the original one-electron oxidation leads to a primary species which converts slowly to a new oxidisable species (ECE mechanism).[22]

It is hence not unexpected that the Mo complex **2**, which further contains the redox-active centres $Mo^{II}$ and $Br^-$, might afford a more complicated voltammetric pattern, Figure 6. As a matter of fact, three anodic steps can be detected, namely A, B and C. Unfortunately, any attempt to determine the precise number of electrons involved in each step by controlled potential coulometry failed, probably because of both their closeness and the underlying complex electron-transfer mechanisms.

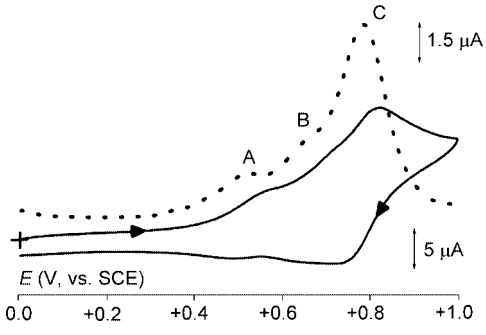


Figure 6. Cyclic (—) and Osteryoung square wave (···) voltammetric responses recorded at a platinum electrode in a $CH_2Cl_2$ solution of **2** ($0.7\times10^{-3}$ mol dm$^{-3}$). $[NBu_4][PF_6]$ (0.2 mol dm$^{-3}$) supporting electrolyte. Scan rates: (—) 0.2 V s$^{-1}$; (···) 0.1 V s$^{-1}$.

Based on the good extent of chemical reversibility, the most anodic process C can therefore be somewhat naïvely assigned to the ferrocene/ferrocenium oxidation, whereas the process B can be tentatively assigned to the oxidation of the bromide coligand. However, since under the same experimental conditions the free $Br^-$ ion affords two substantially irreversible oxidations[23] ($E_p$ = +0.71 V and +0.94 V, respectively), a contribution to peak C from the second bromide oxidation cannot be ruled out. Finally, in agreement with either the previous findings[24] or the above theoretical calculations, the anodic process A, which also looks likely to exhibit partial chemical reversibility, can be assigned to the $Mo^{II}/Mo^{III}$ couple.

As illustrated in Figure 7, a qualitatively similar situation is exhibited by the diferrocenyl couple **L2/3**.

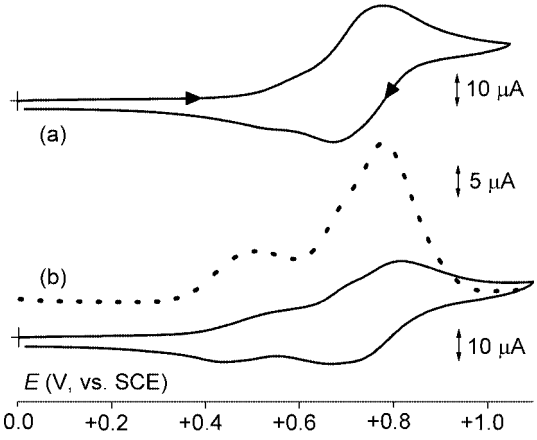


Figure 7. Cyclic (—) and Osteryoung square wave (···) voltammetric responses recorded at a platinum electrode in $CH_2Cl_2$ solutions of: (a) **L2** ($0.7\times10^{-3}$ mol dm$^{-3}$); (b) **3** ($0.6\times10^{-3}$ mol dm$^{-3}$). $[NBu_4][PF_6]$ (0.2 mol dm$^{-3}$) supporting electrolyte. Scan rates: (—) 0.2 V s$^{-1}$; (···) 0.1 V s$^{-1}$.

Controlled potential coulometric measurements corresponding to the anodic process of **L2** indicate that more than the expected two electrons *per* molecule are consumed (a low level of the electrolytic current still persists even after the consumption of 3.2 electrons per molecule). In this case, however, the final cyclic voltammetric control simply shows partial re-reduction of the oxidised product, which means that the chemical complication could be only due to slow regeneration of the original product likely triggered by traces of water present in the nominally anhydrous solvent. Such a drawback is not unusual in exhaustive electrolysis carried out at relatively high potential values.

It can be noted that the rather rounded peaks exhibited by **L2** give evidence for the postulation that the two ferrocenyl subunits are substantially electronically independent from each other. In turn, as deduced by crystal data, the insertion of the Mo fragment does not modify such electronic interactions.

Table 2 lists the formal electrode potentials for the oxidation of the ferrocenyl fragment in the two series of compounds.

 © 2006 Wiley-VCH Verlag GmbH & Co. KGaA, Weinheim 

Table 2. Formal electrode potentials (V, vs. the SCE), peak-to-peak separations (mV) and current ratios for the ferrocene/ferrocenium ion oxidation processes in the couples **L1/2** and **L2/3** in $CH_2Cl_2$ solution.

| Complex | $E°'$ | $\Delta E_p$ [a] | $i_{pc}/i_{pa}$ [a] |
|---|---|---|---|
| **L1** | +0.69 | 70 | 0.86 |
| **2** | +0.78 | 70 | [b] |
| **L2** | +0.72 [c] | 93 | 0.80 |
| **3** | +0.76 [c] | 96 | [b] |
| $Fe(C_5H_5)_2/[Fe(C_5H_5)_2]^+$ | +0.39 | 76 | 1.0 |

[a] Measured at 0.1 $V s^{-1}$. [b] Difficult to determine because of close-spaced preceding processes (see text). [c] Nominal two-electron process; from OSWV.

It should be noted that the electron-withdrawing effect exerted by the Mo fragment with respect to the sandwich ligands is, as expected, almost halved on passing from the diferrocenyl to the monoferrocenyl complexes.

## Conclusions

The two new ferrocenylamidobenzimidazole ligands $FcCO(NH_2benzim)$ (**L1**) and $(FcCO)_2(NHbenzim)$ (**L2**) react with $[Mo(\eta^3\text{-}C_3H_5)(CO)_2(NCMe)_2Br]$ to afford two polynuclear Mo–Fe complexes. Complex **3**, with the **L2** ligand was structurally characterised by single-crystal X-ray diffraction. The axial isomer was formed and **L2** was coordinated in a $\kappa^2$-N,O-bidentate mode using the benzimidazole nitrogen and the closest carbonyl oxygen as donor atoms. The N–H···O hydrogen bond to the second carbonyl of **L2**, already present in the free ligand, was preserved. A combination of spectroscopic data, elemental analysis, conductivity and DFT calculations led us to formulate complex **2** as $[Mo(\eta^3\text{-}C_3H_5)(CO)_2(L1)Br]$ with **L1** coordinating in the neutral form using both the benzimidazole and the $NH_2$ nitrogen atoms thereby resulting in the most stable axial isomer. The occupied frontier orbitals of the ligands were based on iron, with a LUMO located on the C=O bond(s) and the LUMO+1 being Fe–allyl antibonding. Coordination of the ferrocenyl ligands to Mo leads to Mo based HOMOs, the Fe orbitals coming next and the unoccupied levels being similar to those in the free ligands. In agreement with crystal data and theoretical calculations, electrochemistry shows that in complex **2** no electronic interaction exists between the two ferrocenyl ligands and the first electron is removed from the $Mo^{II}$-centred HOMO.

## Experimental Section

### Chemical Studies

Commercially available reagents and all solvents were purchased from standard chemical suppliers. Solvents were dried using common procedures. The syntheses of the molybdenum complexes were carried out under nitrogen using Schlenk tube techniques. The complex $[Mo(\eta^3\text{-}C_3H_5)(CO)_2(NCCH_3)_2Br]$ was synthesised according to literature procedures.[5] The ligands **L1** and **L2** were prepared as described in the literature.[10] Infrared spectra were measured on a Mattson 7000 FT spectrometer. Samples were run as KBr pellets. NMR spectra were recorded on a Bruker Avance-400 spectrometer in $[D_7]$DMF. Electronic spectra were recorded with a UNICAM model UV-4 spectrophotometer. Materials and apparatus for electrochemistry have been described elsewhere.[25] Elemental analyses were carried out at ITQB.

**Preparation of $[Mo(\eta^3\text{-}C_3H_5)(CO)_2(L1)Br]$ (2):** To a yellow solution of $[Mo(\eta^3\text{-}C_3H_5)(CO)_2(NCCH_3)_2Br]$ (0.177 g, 0.5 mmol) in dichloromethane (10 mL) was added **L1** (0.173 g, 0.5 mmol). The dark-red solution obtained was stirred at room temperature for 3 h. Addition of *n*-hexane resulted in the formation of red solid which was filtered, washed with *n*-hexane and dried under vacuum. Unsuccessful attempts to grow crystals suitable for X-ray diffraction were carried out by vapour diffusion of diethyl ether into a solution of the complex in $CH_2Cl_2$. Yield 0.274 g (78%). Elemental analysis for $\mathbf{2}\cdot CH_3CN\cdot 0.5CH_2Cl_2$ ($C_{25.5}H_{24}BrClFeMoN_4O_3$) (701.64): calcd. C 43.65, H 3.45, N 7.98; found C 44.12, H 3.51, N 7.73. $^1$H NMR (400 MHz, $[D_7]$DMF, 253 K): $\delta$ = 7.95 (br., $NH_2$), 7.32 (d, 1 H, Ha), 7.17 (t, 1 H, Hb), 7.08 (d, 1 H, Hd), 6.98 (t, 1 H, Hc), 5.23 ($CH_2Cl_2$, 1 H), 5.00 (br., 2 H, H1), 4.79 (br., 2 H, H2), 4.38 (br., 5 H, H1′), 3.51 (m, 1 H, $H_{meso}$), 3.30 (d, 2 H, $H_{syn}$), 2.19 (s, $CH_3CN$), 1.18 (d, 2 H, $H_{anti}$) ppm. $^{13}$C NMR (100.6 MHz, $[D_7]$DMF, 253 K): $\delta$ = 123.7 (Cb), 120.3 (Cc), 114.7 (Ca), 112.5 (Cd), 75.2 ($H_{meso}$), 73.1 (C2), 72.3 (C1), 70.9 (C1′), 57.6 ($C_{anti/syn}$), 1.34 ($CH_3CN$) ppm. UV/Vis ($CH_2Cl_2$): $\lambda$ = 482 nm, $\varepsilon$ = 1377 $cm^{-1} mol^{-1} dm^3$.

**Preparation of $[Mo(\eta^3\text{-}C_3H_5)(CO)_2(L2)Br]$ (3):** To a yellow solution of $[Mo(\eta^3\text{-}C_3H_5)(CO)_2(NCCH_3)_2Br]$ (0.177 g, 0.5 mmol) in dichloromethane was added **L2** (0.278 g, 0.5 mmol). The dark-red solution formed was stirred at room temperature for 30 min. Addition of *n*-hexane resulted in the formation of a red solid which was filtered, washed with *n*-hexane and dried under vacuum. Yield 0.382 g (66%). Elemental analysis for $\mathbf{3}\cdot 3CH_2Cl_2\cdot 2CH_3CN$ ($C_{41}H_{40}N_5O_4Cl_6Fe_2BrMo$) (1167.05): calcd. C 42.20, H 3.45, N 6.00; found C 41.73, H 3.26, N 6.00. $^1$H NMR (400 MHz, $[D_7]$DMF, 253 K): $\delta$ = 9.10 (br., NH), 8.54 (d, 1 H, Ha), 7.75 (m, 1 H, Hb), 7.53 (d, 1 H, Hd), 7.39 (t, 1 H, Hc), 5.91 ($CH_2Cl_2$, 6 H), 5.13 (br., 2 H, HI), 4.91 (br., 2 H, HII), 4.73 (m, 2 H, H1), 4.46 (m, 2 H, H2), 4.44 (s, 5 H, HI′), 4.23 (s, 5 H, H1′), 3.76 (m, 1 H, $H_{meso}$), 3.30 (d, 2 H, $H_{syn}$), 2.12 ($CH_3CN$, 6 H), 1.18 (d, 2 H, $H_{anti}$) ppm. UV/Vis ($CH_2Cl_2$): $\lambda$ = 482 nm, $\varepsilon$ = 3750 $cm^{-1} mol^{-1} dm^3$.

### Crystallography

Red single-crystals of $[Mo(\eta^3\text{-}C_3H_5)(CO)_2(L2)Br]$ (**3**) of suitable quality for X-ray diffraction were obtained by vapour diffusion of *n*-hexane into a solution of the complex in $CH_2Cl_2$.

**Crystal Data:** $C_{35}H_{30}BrCl_2Fe_2MoN_3$, $M_r$ = 915.07; monoclinic, space group $P2_1/n$, $Z$ = 4, $a$ = 15.784(17), $b$ = 12.632(14), $c$ = 18.170(21) Å, $\beta$ = 105.33(1)°, $V$ = 3494(7), $Z$ = 4, $\rho$(calc) = 1.740 $Mg m^{-3}$, $\mu$(Mo-$K_\alpha$) = 2.512 $mm^{-1}$. X-ray data were collected at room temperature on a MAR research plate system using graphite monochromated Mo-$K_\alpha$ radiation ($\lambda$ = 0.71073 Å) at Reading University. The crystals were positioned at 70 mm from the image plate. 95 frames were taken at 2° intervals using an appropriate counting time. Data analysis was performed with the XDS program.[26] Intensities were corrected for absorption effects using the DIFABS program.[27] 21894 reflections were collected and merged to 6467 unique reflections giving an $R_{int}$ of 0.0449. The structure was solved by direct methods and by subsequent difference Fourier syntheses and refined by full-matrix least-squares on $F^2$ using the SHELX-97 system programs.[28] The $CH_2Cl_2$ solvent molecule was found to be disordered over two positions and the two chlorine atoms were refined in two alternative tetrahedral positions with occupancy factors of 1 – $x$ and $x$, $x$ being equal to 0.657(9). In addition, the C–Cl distances were constrained at 1.778 Å. Aniso-

 © 2006 Wiley-VCH Verlag GmbH & Co. KGaA, Weinheim 

tropic thermal parameters were used for the remaining non-hydrogen atoms. The hydrogen atoms bonded to the carbon and nitrogen atoms were included in the refinement in calculated positions with isotropic parameters equivalent to 1.2 times those of the atom to which they are attached. The protons and the hydrogen atoms were not located from the Fourier difference maps and their positions were not included in the refinement. The residual electronic density ranging from –1.157 to 1.480 e Å$^{-3}$ was within expected values. The final refinement of 433 parameters converged to final $R$ and $R_w$ indices $R_1 = 0.0664$ and $wR_2 = 0.1217$ for 5705 reflections with $I > 2\sigma(I)$ and $R_1 = 0.0767$ and $wR_2 = 0.1257$ for all 6467 *hkl* data. Molecular diagrams presented were drawn with the PLATON graphical package software.[29]

CCDC-603243 contains the supplementary crystallographic data for this paper. These data can be obtained free of charge from The Cambridge Crystallographic Data Centre via www.ccdc.cam.ac.uk/data_request/cif.

**Computational Details**

Density functional calculations[16] were carried out with the Amsterdam Density Functional program (ADF2005).[18] Gradient corrected geometry optimisations,[30] without any symmetry constraints, were performed using the Local Density Approximation of the correlation energy (Vosko, Wilk and Nusair's)[31] and the Generalised Gradient Approximation (Becke Perdew[32,33] exchange and correlation corrections).

A triple-ζ Slater-type orbital (STO) basis set augmented by one polarisation function was used for Mo, Fe, N, O, C and H. A frozen core approximation was used to treat the core electrons: (1s) for N, C and O; ([1–2]s, 2p) for Fe and ([1–3]s, [2–3]p, 3d) for Mo. The calculations were carried out on the crystal structure described above for complex **3** and the structure of L1[10] without any modifications. Geometries for **L2** and complex **2** were based on these structures.

## Acknowledgments

We thank FCT for grant POCI/QUIM/58925/2004. PJC acknowledges FCT for grant (SFRH/BD/10535/2002) and SQ for grant (SFRH/BPD/11463/2002). MJC and MCG acknowledge the Acção Integrada Luso-Espanhola (CRUP). PZ gratefully acknowledges the financial support from the University of Siena (PAR 2005). The University of Reading and the EPSRC are thanked for funds for the Image Plate system. MCG and AL thank the Ministerio de Educación y Ciencia (no. CTQ2004-05495-C02-01). We acknowledge the elemental analysis service at the Instituto de Tecnologia Química e Biológica, UNL, Oeiras, Portugal.

[1] J. J. R. Fraústo da Silva, R. J. P. Williams, *The Biological Chemistry of the Elements*, Clarendon Press, Oxford, **1991**.

[2] a) A. Togni, T. Hayashi, *Ferrocenes. Homogeneous Catalysis, Organic Synthesis and Materials Science* (Eds.: A. Togni, T. Hayashi), VCH, Weinheim, **1995**; b) A. Togni, *Metallocenes* (Eds.: A. Togni, R. L. Halterman), Wiley-VCH, Weinheim, **1998**.

[3] a) E. M. Barranco, O. Crespo, M. C. Gimeno, A. Laguna, *Inorg. Chem.* **2000**, *39*, 680; b) S. Canales, O. Crespo, A. Fortea, M. C. Gimeno, P. G. Jones, A. Laguna, *J. Chem. Soc., Dalton Trans.* **2002**, 2250; c) Y. F. Yuan, J. T. Wang, M. C. Gimeno, A. Laguna, P. G. Jones, *Inorg. Chim. Acta* **2001**, *324*, 309; d) E. M. Barranco, O. Crespo, M. C. Gimeno, P. G. Jones, A. Laguna, *J. Chem. Soc., Dalton Trans.* **2001**, 2523.

[4] a) H. Tamura, M. Miwa, *Chem. Lett.* **1997**, 1177; b) D. Osella, M. Ferrali, P. Zanello, F. Laschi, M. Fontani, C. Nervi, G. Cavigiolo, *Inorg. Chim. Acta* **2000**, *306*, 42; c) L. V. Popova, V. N. Babin, Y. A. Beleusov, Y. S. Nekrasov, A. E. Snegireva, N. P. Borodina, G. M. Shaposhnikova, O. B. Bychenko, P. M. Raevskii, M. N. Morozova, A. I. Ilyna, K. G. Shitkov, *Appl. Organomet. Chem.* **1993**, *7*, 85; d) L. V. Snegur, A. A. Simenel, Y. S. Nekrasov, E. A. Morozova, Z. A. Starikova, S. M. Peregudova, Y. V. Kuzmenko, V. N. Babin, L. A. Ostrovskaya, N. V. Bluchterova, M. M. Fomina, *J. Organomet. Chem.* **2004**, *689*, 2473; e) V. N. Babin, P. M. Raevskii, K. G. Snchitkov, L. V. Snegur, Y. S. Nekrasov, *Mendeleev Chem. J.* **1995**, 39.

[5] D. R. van Staveren, N. Metzler-Nolte, *Chem. Rev.* **2004**, *104*, 5931.

[6] a) S. I. Kirin, D. Wissenbach, N. Metzler-Nolte, *New J. Chem.* **2005**, *29*, 1168; b) O. Brosh, T. Weyhermüller, N. Metzler-Nolte, *Inorg. Chem.* **1999**, *38*, 5308; c) X. Hatten, T. Weyhermüller, N. Metzler-Nolte, *J. Organomet. Chem.* **2004**, *689*, 4856; d) A. Hess, O. Brosh, T. Weyhermüller, N. Metzler-Nolte, *J. Organomet. Chem.* **1999**, *589*, 75; e) S. Chowdhury, K. A. Mahmoud, G. Schatte, H.-B. Kraatz, *Org. Biomol. Chem.* **2005**, *3*, 3018; f) F. E. Appoh, T. C. Sutherland, H.-B. Kraatz, *J. Organomet. Chem.* **2004**, *689*, 4669.

[7] a) F. E. Appoh, T. C. Sutherland, H.-B. Kraatz, *J. Organomet. Chem.* **2005**, *690*, 1209; b) O. Brosh, T. Weyhermüller, N. Metzler-Nolte, *Eur. J. Inorg. Chem.* **2000**, 323.

[8] a) K. Heinze, M. Beckmann, *Eur. J. Inorg. Chem.* **2004**, 2974; b) K. Heinze, M. Beckmann, *Eur. J. Inorg. Chem.* **2005**, 3450.

[9] a) H. Shinoara, T. Kusaka, E. Yokota, R. Monden, M. Sisido, *Sens. Actuators B* **2000**, *65*, 144; b) C. Suksai, P. Leeladee, D. Jainuknan, T. Tuntulani, N. Muangsin, O. Chailapakul, P. Kongsaeree, C. Pakavatchai, *Tetrahedron Lett.* **2005**, *46*, 2765; c) A. Berduque, G. Herzog, Y. E. Watson, D. W. M. Arrigan, O. Reynes, G. Royal, E. Saint-Aman, *Electroanalysis* **2005**, *17*, 392; d) H. Miyaji, G. Gasser, S. J. Green, Y. Molard, S. M. Strawbridge, J. H. R. Tucker, *Chem. Commun.* **2005**, 5355.

[10] M. J. Calhorda, P. J. Costa, P. N. Martinho, M. C. Gimeno, A. Laguna, S. Quintal, M. D. Villacampa, *J. Organomet. Chem.* (article accepted).

[11] a) H. Tom Dieck, H. Friedel, *J. Organomet. Chem.* **1968**, *14*, 375; b) R. G. Hayter, *J. Organomet. Chem.* **1967**, *13*, P1; c) P. K. Baker, *Adv. Organomet. Chem.* **1996**, *40*, 45 and references cited therein.

[12] J. R. Ascenso, C. G. de Azevedo, M. J. Calhorda, M. A. A. F. de C. T. Carrondo, P. Costa, A. R. Dias, M. G. B. Drew, V. Félix, A. M. Galvão, C. C. Romão, *J. Organomet. Chem.* **2001**, *632*, 197.

[13] P. M. F. J. Costa, M. Mora, M. J. Calhorda, V. Félix, P. Ferreira, M. G. B. Drew, H. Wadepohl, *J. Organomet. Chem.* **2003**, *687*, 57.

[14] a) F. Dewans, J. Dewailly, J. Meunier- Piret, P. Piret, *J. Organomet. Chem.* **1974**, *76*, 53; b) F. Dewans, E. Goldenberg, *Brevet d'Invention, Inst. Int. Prop. Indust.* **1972**, 2.120.573.

[15] a) B. M. Trost, M. J. Lautens, *Organometallics* **1983**, *2*, 1687; b) B. M. Trost, M. J. Lautens, *J. Am. Chem. Soc.* **1982**, *104*, 5543; c) B. M. Trost, M. J. Lautens, *J. Am. Chem. Soc.* **1982**, *105*, 3343; d) B. M. Trost, M.-H. Hung, *J. Am. Chem. Soc.* **1983**, *105*, 7757.

[16] R. G. Parr, W. Yang, *Density Functional Theory of Atoms and Molecules*, Oxford, University Press, New York, **1989**.

[17] L. Phillips, A. R. Lacey, M. K. Cooper, *J. Chem. Soc., Dalton Trans.* **1988**, 1383.

[18] a) G. te Velde, F. M. Bickelhaupt, S. J. A. van Gisbergen, C. Fonseca Guerra, E. J. Baerends, J. G. Snijders, T. Ziegler, *J. Comput. Chem.* **2001**, *22*, 931; b) C. Fonseca Guerra, J. G. Snijders, G. te Velde, E. J. Baerends, *Theor. Chem. Acc.* **1998**, *99*, 391; c) ADF2005.01, SCM, Theoretical Chemistry, Vrije Universiteit, Amsterdam, The Netherlands.

[19] For instance AMDTMO, AXEGUF, BZATMO, CAPKIN, CAPKOT, DINRAT10, DOLDIR, EBEGIC, FAKBID, GIPTEE, JIDMAK, JOHNAV, NEKFUE, NEKGAL, VAT-

 © 2006 Wiley-VCH Verlag GmbH & Co. KGaA, Weinheim 

WUU, from the CSD: F. H. Allen, *Acta Crystallogr., Sect. B* **2002**, *58*, 380.
[20] S. Portmann, H. P. Lüthi, *Chimia* **2000**, *54*, 766.
[21] T. Avilés, A. Dinis, J. O. Gonçalves, V. Félix, M. J. Calhorda, Â. Prazeres, M. G. B. Drew, H. Alves, R. T. Henriques, V. da Gama, P. Zanello, M. Fontani, *J. Chem. Soc., Dalton Trans.* **2002**, 4595.
[22] P. Zanello, *Inorganic Electrochemistry. Theory, Practice and Application*, RSC, United Kingdom, **2003**.
[23] G. Dryhurst, P. J. Elving, *Anal. Chem.* **1967**, *39*, 606.
[24] F. Fabrizi de Biani, F. Jäkle, M. Spiegler, M. Wagner, P. Zanello, *Inorg. Chem.* **1997**, *36*, 2103.
[25] E. Stulz, J. K. M. Sanders, M. Montalti, L. Prodi, N. Zaccheroni, F. Fabrizi de Biani, E. Grigiotti, P. Zanello, *Inorg. Chem.* **2002**, *41*, 5269.
[26] W. Kabsch, *J. Appl. Crystallogr.* **1988**, *21*, 916.
[27] DIFABS: N. Walker, D. Stuart, *Acta Crystallogr., Sect. A* **1983**, *39*, 158.
[28] G. M. Sheldrick, *SHELX-97*, University of Göttingen, Germany, **1997**.
[29] A. L. Spek, *PLATON*, *A Multipurpose Crystallographic Tool*, Utrecht University, Utrecht, The Netherlands, **1999**.
[30] a) L. Versluis, T. Ziegler, *J. Chem. Phys.* **1988**, *88*, 322; b) L. Fan, T. J. Ziegler, *Chem. Phys.* **1991**, *95*, 7401.
[31] S. H. Vosko, L. Wilk, M. Nusair, *Can. J. Phys.* **1980**, *58*, 1200.
[32] A. D. Becke, *Phys. Rev. A* **1988**, *38*, 3098
[33] J. P. Perdew, *Phys. Rev. B* **1986**, *33*, 8822.

Received: April 3, 2006
Published Online: August 10, 2006

 © 2006 Wiley-VCH Verlag GmbH & Co. KGaA, Weinheim 

DOI: 10.1002/ejic.200600399

# Substituted Ring-Fused Yttrium Derivatives – X-ray Crystal Structures of $[(L'YCl_2{\cdot}THF)_2LiCl{\cdot}2THF]$ and $[\{L'YCl(OH)\}_6{\cdot}2THF]$ (L′ = 2-Phenyl-4,5,6,7,8-hexahydroazulenyl)

**Gino Paolucci,*[a] Manuela Vignola,[a] Alessandra Zanella,[a] Valerio Bertolasi,[b] Eleonora Polo,*[c] and Silvana Sostero[c]**

**Keywords:** Yttrium / Fused-ring systems / Olefin polymerization

The reaction of lithium salts of ring-fused ligands (L), where the ring fused to the cyclopentadienyl moiety is a saturated one (six, seven, or eight carbon atoms), with $YCl_3$ in THF in 2:1 and 1:1 molar ratios affords complexes of formula $[L_2YCl]_2$ and $[(LYCl_2{\cdot}THF)_2LiCl{\cdot}2THF]$, respectively. Here we report the synthesis, spectroscopic characterization, and X-ray crystal structure of $[(L'YCl_2{\cdot}THF)_2LiCl{\cdot}2THF]$ (L′ = 2-phenyl-4,5,6,7,8-hexahydroazulenyl), together with the crystal structure of the hexameric species $[\{L'YCl(OH)\}_6{\cdot}2THF]$, which was quite unexpectedly isolated during the attempted crystallization of the latter complex and is probably formed by partial hydrolysis of that complex. The activity of the new complexes towards ethylene and 1-hexene polymerization reactions was also tested.
(© Wiley-VCH Verlag GmbH & Co. KGaA, 69451 Weinheim, Germany, 2006)

## Introduction

The chemistry of group 3 organometallics has undergone a spectacular growth in the past two decades.[1] Besides their activity as catalysts and reagents for a number of reactions,[2] they are also reckoned to be excellent models[3] and very active catalysts for Ziegler–Natta polymerizations of olefins, often without the aid of activators or co-catalysts.

Lanthanide chemistry has been dominated mainly by cyclopentadienyl complexes[4] because this family of ligands allows a wide range of modifications of the environment at the metal center through simple variation of the substitution pattern. Despite the interesting results thus far obtained, their high sensitivity to air and moisture, polar solvents,[5] and reagents[5,6] makes their application on an industrial scale still quite difficult. Furthermore, lanthanides with unsubstituted cyclopentadienyl ligands are almost insoluble in hydrocarbon solvents and usually show low activity.[7] Due to the delicate balance required in the ligand substitution pattern, it is advisable to find a family of cyclopentadienyl ligands provided with a more versatile structure and also capable of imparting higher stability and better solubility in most common organic solvents. In the framework of our research for metallocenes suitable for application in homogeneous catalysis, we have recently[8] synthesized several froup 4 ring-fused metallocenes where the ring (six, seven, or eight carbon atoms) fused to the cyclopentadienyl moiety is a saturated one. Besides their higher solubility, stability, and resistance to hydrolysis in comparison with the corresponding unsaturated counterparts, these complexes proved to be interesting polymerization catalysts,[9] since their particular structure introduces a conformational flexibility that can be finely tuned by varying the size of the cycloalkyl-ring and by introducing different substituents on the cyclopentadienyl ring. Here, we report the reactions of some ligands of this family with yttrium trichloride in 1:1 and 2:1 molar ratios as a test for lanthanides to check if they can produce more stable and soluble complexes for catalytic applications.

[a] Dipartimento di Chimica, Università Ca'Foscari di Venezia, Dorsoduro 2137, 30123 Venezia, Italy
E-mail: paolucci@unive.it
[b] Centro di Strutturistica Diffrattometrica and Dipartimento di Chimica, Università di Ferrara, 44100 Ferrara, Italy
Fax: +39-053-224-0709
E-mail: m38@unife.it
[c] C.N.R.I.S.O.F., sez. Ferrara, Dipartimento di Chimica, Università di Ferrara, Ferrara, Italy
Fax: +39-053-224-0709
E-mail: tr3@unife.it
Supporting information for this article is available on the WWW under http://www.eurjic.org or from the author.

## Results and Discussion

### Synthesis and Characterization of Yttrium Complexes

The lithium salts (C6CpMe)Li (**1**; HL = 2-methyl-4,5,6,7-tetrahydro-1*H*-indene), (C7CpMe)Li (**2**; HL = 2-methyl-1,4,5,6,7,8-hexahydroazulene, and (C8CpMe)Li (**3**; HL = 2-methyl-4,5,6,7,8,9-hexahydro-1*H*-cyclopenta[8]annulene, prepared according to the literature procedures,[9a] were treated with $YCl_3$ in a 2:1 molar ratio to afford the corresponding complexes $[L_2YCl]_2$ with L = C6CpMe (**4**),

 © 2006 Wiley-VCH Verlag GmbH & Co. KGaA, Weinheim 

C7CpMe (**5**), and C8CpMe (**6**), and in a 1:1 ratio to give the complexes $[(LYCl_2{\cdot}THF)_2LiCl{\cdot}2THF]$ with L = C7CpMe (**7**) and C8CpMe (**8**); see Scheme 1.

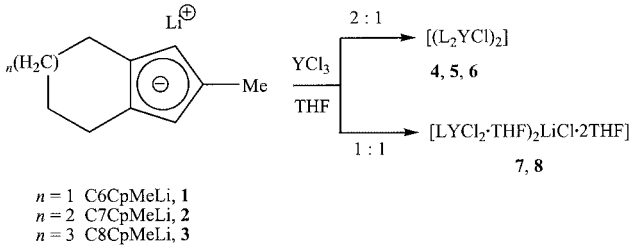


Scheme 1. Synthesis of the 2-methyl-substituted complexes.

The resulting complexes, which were isolated as dusty solids by precipitation with *n*-hexane from toluene or $CH_2Cl_2$ solutions, are also completely soluble in diethyl ether and THF. Analytical (elemental analyses and MS data) and NMR ($^1H$ and $^{13}C$; assignments by HMQC and HMBC experiments) data were consistent with the given formulations.

## Crystal Structures

Crystals of complexes **4**, **6**, **7**, and **8** were obtained by slow evaporation of concentrated $CH_2Cl_2$ solutions, but, despite repeated attempts, they were not suitable for X-ray analysis. This difficulty in obtaining ordered structures is probably due both to the flexibility of the saturated ring and to the small size of the methyl group. Only complex **5** gave crystals suitable for X-ray diffraction, but they did not withstand the treatment (Fomblin F06206R or dehydrated Nujol) necessary to protect them from air and moisture during X-ray data acquisition.

Since the reactivity, stability, and solubility of lanthanide compounds are highly dependent on the steric hindrance of the ligand preventing oligomer formation, we decided to substitute the methyl group in the 2-position of the ligands for a phenyl group in order to obtain more ordered crystals. We chose the ligand with a saturated ring of seven carbon atoms since it was the only one that gave acceptable crystals for **5** and **7**. Treatment of lithium 2-phenyl-1,4,5,6,7,8-hexahydroazulenyl (L′, **9**)[9b] with $YCl_3$ in a 2:1 or 1:1 molar ratio, afforded complexes $[(L'_2YCl)_2]$ (**10**) and $[(L'YCl_2{\cdot}THF)_2LiCl{\cdot}2THF]$ (**11**), respectively (Scheme 2).

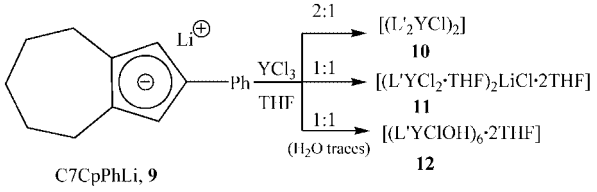


Scheme 2. Synthesis of the 2-phenyl-substituted complexes.

Crystals suitable for X-ray diffractometry studies were obtained only in the case of complex **11**. While attempts to protect the crystals with Fomblin failed, the use of anhydrous Nujol allowed X-ray data collection at 150 K; this confirmed the analytical and NMR spectroscopic data, which correspond to a complex of formula $[(L'YCl_2{\cdot}THF)_2LiCl{\cdot}2THF]$ (L′ = C7CpPh; Figure 1).

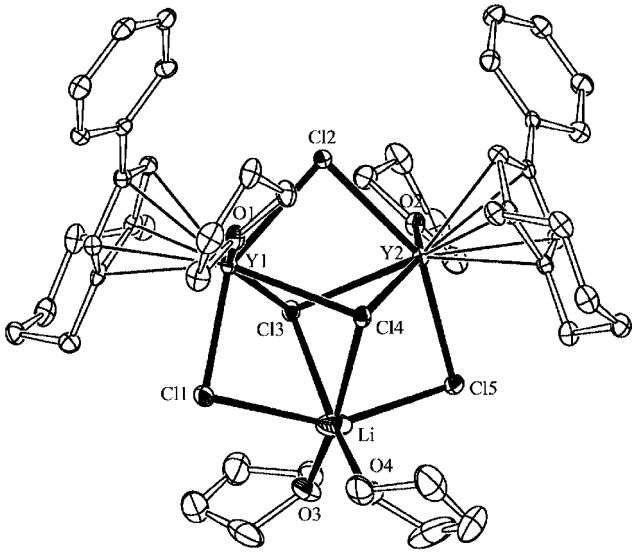


Figure 1. ORTEP[10] view of complex **11** displaying the thermal ellipsoids at 30% probability. The hydrogen atoms have been omitted for sake of clarity.

The structure (Figure 1, and Tables S1 and S2 in the Supporting Information) consists of a trimetallic complex where two atoms of yttrium and one atom of lithium, in a distorted octahedral coordination, are bridged by three μ-Cl (Cl1, Cl2, and Cl5) and two $\mu_3$-Cl (Cl3 and Cl4) anions. Each Y atom is coordinated to four chloride ions, an $\eta^5$-cyclopentadienyl ring of the 2-phenyl-1,4,5,6,7,8-hexahydroazulenyl ligand, and a molecule of THF, while the lithium cation is coordinated to four Cl ions (Cl1, Cl3, Cl4, and Cl5) and two molecules of THF. The six Y–C1 bonds involved in the formation of Y–Cl–Y bridges display distances in the range 2.677(1)–2.860(1) Å (2.77 Å on average), and are slightly longer than those observed in dimeric bis[(μ-Cl)$Y^{III}$(cyclopentadienyl)] complexes (2.66–2.70 Å).[11–13] This Y–Cl lengthening can be justified by the presence of a μ-Cl bridge between yttrium atoms and two $\mu_3$-Cl bridges which involve all three metal centers. The remaining μ-Cl1 and μ-Cl5 chlorides connecting yttrium atoms with lithium display shorter Y–Cl distances of 2.607(2) and 2.627(1) Å, in agreement with those found in the range 2.62–2.65 Å in similar Y–Cl–Li fragments.[14,15]

During our attempts to finding the appropriate crystallization solvents for complex **11**, in one crop we isolated several crystals stable to Fomblin treatment which allowed crystal data collection. Quite unexpectedly, they turned out to be the partial hydrolysis product of **11**, most probably caused by slight traces of water in the crystallization solvent. The results of the fast X-ray data collection at 120 K revealed the structure of an organometallic yttrium cluster, namely $[\{L'YCl(OH)\}_6{\cdot}2THF]$ (**12**; Figure 2 and Tables S3 and S4 in the Supporting Information). It is well known

 © 2006 Wiley-VCH Verlag GmbH & Co. KGaA, Weinheim 

that hydrolysis and oxidation reactions are a common mode of decomposition for organometallic complexes of yttrium and the f elements, giving in most cases organometallic species containing M–OH or M–O–O–M bonds.[16–18]

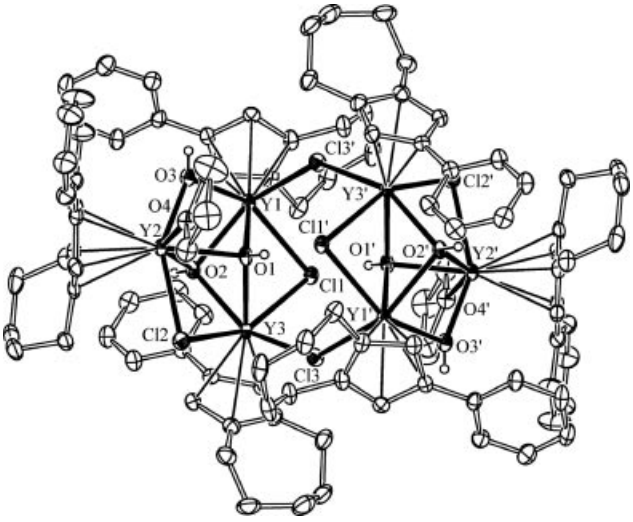


Figure 2. ORTEP view of complex **12** displaying the thermal ellipsoids at 30% probability. The hydrogen atoms have been omitted for sake of clarity.

The $^1$H NMR spectrum of crystals of complex **12** is quite similar to that of **11** except for the presence of a very broad singlet at $\delta$ = 2.73 ppm that can be attributed to the OH group. The IR spectrum in $CH_2Cl_2$ solution shows an OH stretch at 3540 cm$^1$.

Complex **12** is a hexamer where two trimetallic clusters of yttrium atoms are held together, around a center of symmetry, by two μ-Cl3 chlorides between Y1 and Y3 (Figure 3). In each trimer the yttrium atoms are surrounded by an $\eta^5$-bonded cyclopentadienyl ring belonging to a 2-phenyl-1,4,5,6,7,8-hexahydroazulenyl ligand and bridged by chloride and hydroxy groups. In particular, the three Cl1, Cl2, and O3H anions span the three edges of the triangles formed with the Y atoms, while the $\mu_3$-O1H and $\mu_3$-O2H hydroxy groups triply bridge above and below the triangle formed by the yttrium atoms. The sixfold coordination around Y2 is completed by the oxygen atom of a THF molecule.

Accordingly, the overall geometry about each yttrium atom can be described as a distorted octahedral coordination. The Y–(μ-Cl) distances (2.66–2.74 Å) are in agreement with those observed in dimeric bis[(μ-Cl)Y$^{III}$(cyclopentadienyl)] complexes. Furthermore, as observed in other compounds,[16–19] the Y–(μ-OH) distances of 2.230(6) and 2.216(4) Å for Y1–O3 and Y2–O3, respectively, are shorter than those of Y–($\mu_3$-OH), which are in the range 2.34–2.43 Å. In both complexes the Y–Cp(cyclopentadienyl centroid) bond length (2.37–2.40 Å) and the Y–O(THF) distance of 2.338(6) Å are in accordance with the respective values observed in other cyclopentadienylyttrium derivatives.[20–23]

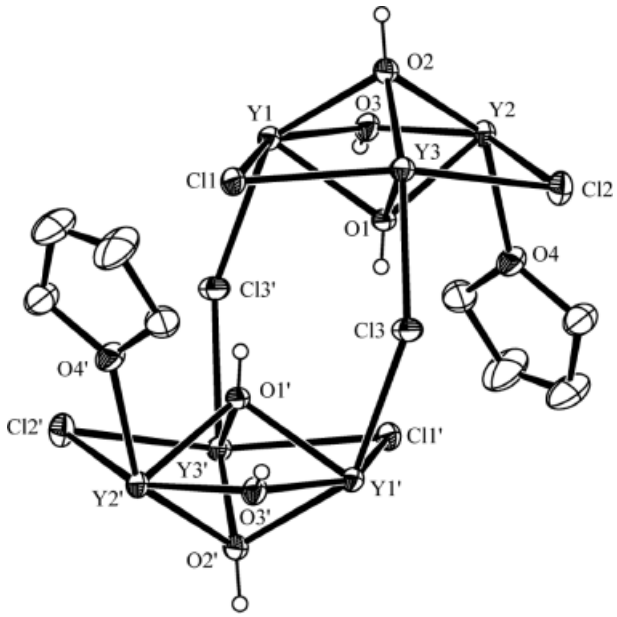


Figure 3. Diagram of the metal, halogen, and hydroxy framework of complex **12**, including the coordinated THF molecules.

## Polymerization Studies

We have examined the activity of the new yttrium complexes, with MAO as co-catalyst, as a preliminary test for their polymerization activity. It is known[2] that organolanthanide complexes often do not require a co-catalyst or an activator to show high activity, but they must be previously converted into the corresponding sterically demanding alkyl derivatives [(trimethylsilyl)methyl or bis(trimethylsilyl)-methyl], to prevent β-alkyl elimination, and as intermediates to the more unstable, but much more active, hydrides.

The bis(cyclopentadienyl) complexes **4**, **5**, **6**, and **10** did not show any activity towards ethene polymerization, while the mono(cyclopentadienyl) complexes **7** and **11**, which have a more open coordination sphere around the metal center, show a moderate activity (Table 1). This result can be interpreted by taking into account the fact that only a limited number of mono(cyclopentadienyl) half-sandwich rare-earth complexes of the type [($\eta^5$-$C_5R_5$)Ln$X_2$(L)$_n$] have been synthesized, and their catalytic performance is often hampered by "ate complex" formation with concomitant alkali metal salt incorporation.[24] We also noticed some differences between the polymers obtained with the methyl-substituted (**7**) and phenyl-substituted (**11**) derivatives. While with the methyl-substituted complex **7**, after the usual work-up, a single fraction of highly linear polyethylene was produced (single peak at $\delta$ = 27.7 ppm in the $^{13}$C NMR spectrum), with the phenyl-substituted complex **11** the yield was almost twice as high but the solid consisted of two fractions, the first (43%) of which is similar to the polymer isolated with the catalyst **7** and the second (57%) of which contains a mixture of oligomers. Apparently this different behavior can be attributed to the influence of the substituent in the ancillary ligand. It is likely that the methyl group, which exerts a symmetrical steric hindrance around the

 © 2006 Wiley-VCH Verlag GmbH & Co. KGaA, Weinheim 

metal center, produces a more homogeneous material than the phenyl with its different space occupancy. We also tried the polymerization of a more sterically demanding monomer, 1-hexene, but we could not get any polymer. In structurally similar achiral lanthanocenes,[2e,25] which are also inactive towards 1-alkene polymerization, this negative result has been attributed to the formation of stable $\eta^3$-allyl type complexes.[26]

Table 1. Results of ethane and 1-hexene polymerizations.

| Complex | Monomer | Activity[a] | Oligomers [%] |
|---|---|---|---|
| **4**, **5**, **6**, **10** | ethene[b] | – | – |
| **7** | ethene[b] | 820 | 7 |
| **11** | ethene[b] | 1650 | 57 |
| **7** | 1-hexene[c] | – | – |
| **11** | 1-hexene[c] | – | – |

[a] $g_{Pol}(mmol_Y\,h\,atm)^{-1}$. [b] Reaction conditions: toluene: 100 mL, [Y] = $8\times10^{-6}$ M, [MAO]/[Y] = 1100, $t_{rxn}$ = 24 h, room temp. [c] Reaction conditions: toluene: 100 mL, [Y] = $8\times10^{-6}$ M, [MAO]/[Y] = 1875, $t_{rxn}$ = 24 h, room temp.

## Conclusions

Novel unbridged bicyclic yttrium complexes containing six-, seven-, and eight-membered saturated rings fused to a cyclopentadienyl moiety substituted in position 2 ($CH_3$, Ph) have been synthesized with 2:1 and 1:1 ligand/metal ratios, and fully characterized. Unlike their analogous cyclopentadienyl derivatives, these complexes are very soluble in most common organic solvents but are highly sensitive to air and moisture. The crystal structure of complex **11** shows its dimeric nature, thus confirming that the high coordinative unsaturation of the monomer in the absence of high steric hindrance favors the formation of dimeric yttrium species. Quite unexpectedly, we have been able to isolate and fully characterize the hexameric yttrium organometallic cluster **12**, which is probably formed by the reaction of **11** with traces of water in the crystallization solvent. The yttriocenes **4**, **5**, **6**, and **10**, in combination with MAO as cocatalyst, are inactive in the polymerization of ethylene and 1-hexene, while complexes **7** and **11** show a low reactivity towards ethene polymerization and are also inactive towards 1-hexene. These unsatisfactory results can be attributed to the probably dimeric nature of the complexes, which is maintained after MAO activation, thus preventing access of the olefin to the reactive center due to steric hindrance. Further studies are necessary to modify the chloro complexes (i.e., by substitution with bulky alkyl groups) in order to produce monomeric yttrium species, which should be more efficient polymerization catalysts.

## Experimental Section

**General procedures:** All manipulations were carried out under an oxygen- and moisture-free atmosphere in a Braun MB 200 GII glove box. All solvents were thoroughly deoxygenated and dehydrated under argon by refluxing and distillation over a suitable drying agent (*n*-hexane, toluene, and THF over Na or K/benzophenone ketyl; $CH_2Cl_2$, $CD_2Cl_2$, and $CDCl_3$ over $CaH_2$; $C_6D_5N$ over KOH). $YCl_3$ (Aldrich) was used as received. Nujol (Aldrich) was degassed and dehydrated by reflux over potassium. Fomblin (ABCR) F06206R, viscosity 1600cSt, was degassed prior to use. The ligands C6CpMeH,[8] C6CpMeLi (**1**),[8] C7CpMeH,[8] C8CpMeH,[8] and C7CpPhH[9a] were prepared according to literature methods. Microanalyses were performed at the Istituto di Chimica Inorganica e delle Superfici, CNR, Padova. The Li contents of the complexes were determined by ICP using an ICP-MS Agilent 7500 apparatus. Mass spectra were recorded with a Finnigan Trace MS equipped with a probe for the direct introduction of the sample (EI = 70 eV, $T_{probe}$ = 120–150 °C). $^1H$ and $^{13}C$ NMR spectra were obtained for $CDCl_3$ or $CD_2Cl_2$ solutions with a Bruker AMX 300 spectrometer operating at 300 and 100.61 MHz, respectively. 2D-Heterocorrelated COSY experiments (HMQC and HMBC) allowed the identification of all $^1H$ and $^{13}C$ resonances.

**Lithium Salts of the Ligands. General Synthetic Procedure:** The starting diene (14 mmol) was suspended in *n*-hexane at –80 °C. *n*-Butyllithium (14 mmol) was then added dropwise, whilst stirring, and the solution was slowly allowed to reach room temperature (about 4 h) and stirred overnight. The lithium salt that separated from the solution was isolated by centrifugation, washed several times with *n*-hexane, and dried under vacuum to give a dusty solid.

**2-Methyl-1,4,5,6,7,8-hexahydroazulenyllithium (2):** White solid. Yield: 1.94 g (90%). $^1H$ NMR ([D$_5$]pyridine): $\delta$ = 1.73–1.94 (m, 6 H, C-CH$_2$-C$H_2$-), 2.43 (s, 3 H, C$H_3$), 2.85 (br. s, 4 H, -C-C$H_2$-CH$_2$-), 5.86 (s, 2 H, -C*H*-,Cp) ppm.

**2-Methyl-4,5,6,7,8,9-hexahydro-1*H*-cyclopenta[8]annulenyllithium (3):** White solid. Yield: 2.22 g (88%). $^1H$ NMR ([D$_5$]pyridine): $\delta$ = 1.57–1.74 (m, 8 H, C-CH-C$H_2$-), 2.41 (s, 3 H, C$H_3$), 2.68–2.74 (m, 4 H, -C-C$H_2$-CH$_2$-), 5.86 (s, 2 H, -C*H*-, Cp) ppm.

**2-Phenyl-1,4,5,6,7,8-hexahydroazulenyllithium (9):** Pink-white solid. Yield 1.82 g (60%). $^1H$ NMR ([D$_5$]pyridine): $\delta$ = 1.47–1.65 (m, 6 H, C-CH-C$H_2$-), 2.48 (m, 4 H, -C-C$H_2$-CH$_2$-), 6.11 (s, 2 H, -C*H*-, Cp), 6.50 (t, $^3J_{H,H}$ = 7.7 Hz, 1 H, *meta*-C$_5$H$_6$), 6.90 (t, $^3J_{H,H}$ = 7.7 Hz, 2 H, *para*-C$_5$H$_6$), 7.42 (d, $^3J_{H,H}$ = 7.6 Hz, 2 H, *ortho*-C$_5$H$_6$) ppm.

**Yttrium Complexes. General Synthetic Procedure:** $YCl_3$ (1.0 mmol) was dissolved in warm THF (30 mL) and cooled to room temperature. A solution of the lithium salt (2.0 or 1.0 mmol) dissolved in THF (20 mL) was then added with vigorous stirring at room temperature, and the reaction mixture stirred overnight. The solvent was then removed under reduced pressure, the residue washed with dichloromethane (3 × 10 mL), and separated from LiCl, when necessary, by centrifugation. The yellow solution was concentrated (to about 10 mL) and left at –25 °C for several days to give microcrystals.

**Bis[(μ-chloro){bis[η$^5$-(2-methyl-4,5,6,7-tetrahydro-1*H*-indenyl)]-yttrium}] (4):** Yellow solid. Yield: 0.508 g (65%). $C_{40}H_{52}Cl_2Y_2$ (781.57): calcd. C 61.47, H 6.71, Cl 9.07; found C 61.05, H 6.95, Cl 8.90. $^1H$ NMR ($CDCl_3$): $\delta$ = 1.65–1.80 (m, 8 H, C-CH$_2$-C$H_2$-), 2.05 (s, 6 H, C$H_3$), 2.50–2.90 (m, 8 H, -C-C$H_2$-CH$_2$-), 5.90 (s, 4 H, -C*H*-, Cp) ppm. $^{13}C$ NMR ($CDCl_3$): $\delta$ = 14.9 (*C*H$_3$), 29.9 (-C-CH$_2$-*C*H$_2$-), 33.1(-C-*C*H$_2$-CH$_2$-), 114.6 (-*C*H, Cp), 125.7 (-*C*-CH$_3$), 132.8 (-CH$_2$-*C*=CH-, Cp) ppm. MS ($T_{probe}$ = 120 °C): *m*/*z* (%) 766 (18) [M$^{+\cdot}$ – CH$_3$]$^+$, 751 (22) [M$^{+\cdot}$ – 2CH$_3$]$^+$, 746 (12) [M$^{+\cdot}$ – Cl]$^+$, 731 (10) [M$^{+\cdot}$ – CH$_3$ – Cl]$^+$.

**Bis[(μ-chloro){bis[η$^5$-(2-methyl-1,4,5,6,7,8-hexahydroazulenyl)]-yttrium}] (5):** Yellow solid. Yield: 0.611 g (73%). $C_{44}H_{60}Cl_2Y_2$ (837.68): calcd. C 63.09, H 7.22, Cl 8.46; found C 62.75, H 6.95, Cl 8.65. $^1H$ NMR ($CDCl_3$): $\delta$ = 1.35–1.70 (m, 8 H, C-CH$_2$-C$H_2$-

 © 2006 Wiley-VCH Verlag GmbH & Co. KGaA, Weinheim 

$CH_2$-), 1.70–1.95 (m, 4 H, C-$CH_2$-$CH_2$-C$H_2$-), 2.08 (s, 6 H, C$H_3$), 2.50–2.90 (m, 8 H, -C-C$H_2$-$CH_2$-$CH_2$-), 5.95 (s, 4 H, -C*H*-, Cp) ppm. $^{13}$C NMR ($CDCl_3$): $\delta$ = 14.9 (*C*$H_3$), 29.9 (-C-$CH_2$-*C*$H_2$-$CH_2$-), 31.6 (-C-*C*$H_2$-$CH_2$-$CH_2$-), 33.2 (C-$CH_2$-$CH_2$-*C*$H_2$), 114.4 (-*C*H, Cp), 120.3 (-*C*-$CH_3$), 129.8 (-$CH_2$-*C*=CH-, Cp) ppm. MS ($T_{probe}$ = 120 °C): *m/z* (%) 837 (1) $[M]^{+\cdot}$, 822 (21) $[M^{+\cdot} - CH_3]^+$, 807 (25) $[M^{+\cdot} - 2CH_3]^+$, 802 (15) $[M^{+\cdot} - Cl]^+$, 690 (42) $[C_{33}H_{45}Cl_2Y_2]^+$, 403 (44) $[C_{21}H_{27}ClY]^+$, 388 (100) $[C_{20}H_{24}ClY]^+$, 368 (37) $[C_{21}H_{27}Y]^+$.

**Bis[(μ-chloro){bis[η$^5$-(2-methyl-4,5,6,7,8,9-hexahydro-1*H*-cyclopenta[8]annulenyl)]yttrium}] (6):** Yellow solid. Yield: 0.590 g (66%). $C_{48}H_{68}Cl_2Y_2$ (893.78): calcd. C 64.50, H 7.67, Cl 7.93; found C 64.15, H 7.25, Cl 7.80. $^1$H NMR ($CDCl_3$): $\delta$ = 1.10–1.25 (m, 12 H, -C$H_2$-), 1.25–1.50 (m, 4 H, -C$H_2$-), 2.00 (s, 6 H, C$H_3$), 2.30–2.45 (m, 4 H, -C-C$H_2$-$CH_2$-), 2.55–2.75 (m, 4 H, -C-C$H_2$-$CH_2$-), 5.95 (s, 4 H, s, 4 H, -C*H*-, Cp) ppm. $^{13}$C NMR ($CDCl_3$): $\delta$ = 14.9 (*C*$H_3$), 26.3 (C-$CH_2$-*C*$H_2$–$CH_2$-), 27.4 (-C-*C*$H_2$-$CH_2$-$CH_2$-), 33.4 (C-$CH_2$-$CH_2$-*C*$H_2$), 112.3 (-*C*H, Cp), 122.0 (-*C*-$CH_3$), 128.3 (-$CH_2$-*C*=CH-, Cp) ppm. MS ($T_{probe}$ = 10 °C): 893 (3) $[M]^{+\cdot}$, 878 (27) $[M^{+\cdot} - CH_3]^+$, 863 (31) $[M^{+\cdot} - 2CH_3]^+$, 858 (15) $[M^{+\cdot} - Cl]^+$, 446 (8) $[C_{24}H_{34}ClY]^+$, 431 (100) $[C_{23}H_{31}ClY]^+$, 416 (65) $[C_{22}H_{28}ClY]^+$, 396 (37) $[C_{23}H_{31}Y]^+$.

**Complex 7:** Yellowish solid. Yield: 0.803 g (85%). $C_{38}H_{62}Cl_5LiO_4Y_2$ (944.92): calcd. C 48.30, H 6.61, Cl 18.76, Li 0.73; found C 47.95, H 6.55, Cl 18.45, Li 0.80. $^1$H NMR ($CDCl_3$): $\delta$ = 1.25–1.95 (m, 12 H, -C$H_2$-), 1.90 (br. s, 16 H, THF), 2.00 (s, 6 H, C$H_3$), 2.45–2.80 (m, 8 H, -C-C$H_2$-$CH_2$-), 3.80 (br. s, 16 H, THF), 5.95 (s, 4 H, -C*H*-, Cp) ppm.

**Complex 8:** Yellow solid. Yield: 0.807 g (83%). $C_{40}H_{66}Cl_5O_4LiY_2$ (972.96): calcd. C 49.38, H 6.84, Cl 18.22, Li 0.71; found C 49.15, H 6.75, Cl 18.45, Li 0.80. $^1$H NMR ($CDCl_3$): $\delta$ = 1.10–1.85 (m, 16 H, -C$H_2$-), 1.98 (br. s, 16 H, THF), 2.05 (s, 6 H, C$H_3$), 2.10–2.65 (m, 8 H, -C-C$H_2$-$CH_2$-), 4.04 (br. s, 16 H, THF), 5.72 (s, 4 H, -C*H*-, Cp) ppm. $^{13}$C NMR ($CDCl_3$): $\delta$ = 16.28 (*C*$H_3$), 25.81 (THF), 26.47 (-C-$CH_2$-C$H_2$-$CH_2$-), 27.71 (-C-*C*$H_2$-$CH_2$-$CH_2$-), 33.33 (C-$CH_2$-$CH_2$-*C*$H_2$-), 71.02 (THF), 114.16 (-*C*H, Cp), 123.0 (-*C*–$CH_3$), 129.91 (-$CH_2$-*C*=CH-, Cp) ppm.

**Bis[(μ-chloro){bis[η$^5$-(2-phenyl-1,4,5,6,7,8-hexahydroazulenyl)]-yttrium}] (10):** Deep-yellow solid. Yield: 0.847 g (78%). $C_{64}H_{68}Cl_2Y_2$ (1085.9): calcd. C 70.78, H 6.31, Cl 6.53; found C 70.45, H 6.15, Cl 6.75. $^1$H NMR ($CD_2Cl_2$): $\delta$ = 1.12–2.10 (m, 12 H, -C$H_2$-), 2.25–2.85 (m, 8 H, -C-C$H_2$-$CH_2$-$CH_2$-), 6.14 (s, 4 H, -C*H*-, Cp), 7.12 (t, $^3J_{H,H}$ = 7.23 Hz, 2 H, *para*-$C_5H_6$), 7.33 (t, $^3J_{H,H}$ = 7.62 Hz, 4 H, 4 H, *meta*-$C_5H_6$), 7.46 (d, $^3J_{H,H}$ = 7.23, 4 H, *ortho*-$C_5H_6$) ppm. MS ($T_{probe}$ = 120 °C): *m/z* (%) 1085 (1) $[M]^{+\cdot}$, 877 (44) $[C_{48}H_{51}Cl_2Y_2]^+$, 667 (2) $[C_{32}H_{34}Cl_2Y_2]^+$, 543 (1) $[C_{32}H_{34}ClY]^+$, 528 (100) $[C_{31}H_{31}ClY]^+$, 493 (28) $[C_{31}H_{31}Y]^+$, 298 (1) $[C_{16}H_{16}Y]^+$, 210 (20) $[C_{16}H_{18}]^+$.

**Complex 11:** Deep-yellow solid. Yield: 0.823 g (77%). $C_{48}H_{66}Cl_5LiO_4Y_2$ (1069.05): calcd. C 53.93, H 6.22, Cl 16.58, Li 0.65; found C 54.10, H 6.05, Cl 16.80, Li 0.70. $^1$H NMR ($CD_2Cl_2$): $\delta$ = 1.65 (m, 8 H, C-$CH_2$-C$H_2$-$CH_2$-), 1.78 (m, 4 H, C-$CH_2$-$CH_2$-C$H_2$-), 1.89 (br. s, 16 H, THF), 2.40–2.53 (m, 8 H, -C-C$H_2$-$CH_2$-$CH_2$-), 3.99 (br. s, 16 H, THF), 6.65 (s, 4 H, -C*H*-, Cp), 7.11 (t, $^3J_{H,H}$ = 7.3 Hz, 2 H, *para*-$C_5H_6$), 7.27 (t, $^3J_{H,H}$ = 7.3 Hz, 4 H, *meta*-$C_5H_6$), 7.43 (d, $^3J_{H,H}$ = 7.3 Hz, 4 H, *ortho*-$C_5H_6$) ppm. $^{13}$C NMR ($CD_2Cl_2$): $\delta$ = 25.7 (THF), 28.3 (-C-$CH_2$-*C*$H_2$-$CH_2$-), 28.4 (-C-$CH_2$-*C*$H_2$-$CH_2$-), 30.1 (-C-*C*$H_2$-$CH_2$-$CH_2$-), 30.7 (-C-*C*$H_2$-$CH_2$-$CH_2$-), 31.9 (-C-$CH_2$-$CH_2$-*C*$H_2$-), 70.4 (THF), 124.7 (*ortho*-$C_5H_6$), 126.1 (*para*-$C_5H_6$), 128.7 (*meta*-$C_5H_6$), 133.0 (-*C*H, Cp), 142.0 (*ipso*-$C_5H_6$), 142.8 (-*C*–$C_5H_6$), 143.6 (-$CH_2$-*C*=CH-, Cp) ppm. Crystals suitable for X-ray analysis were obtained from a very concentrated $CH_2Cl_2$ solution after four days at –26 °C.

**Complex 12:** Yellow solid, $C_{104}H_{108}Cl_6O_8Y_6$ (2232.12): calcd. C 55.96, H 5.73, Cl 9.53; found C 55.80, H 5.60, Cl 9.40. IR ($CH_2Cl_2$): $\tilde{\nu}$ = 3540 cm$^{-1}$. $^1$H NMR ($CD_2Cl_2$): $\delta$ = 1.55–1.71 (m, 8 H, C-$CH_2$-C$H_2$-$CH_2$-), 1.71–1.83 (m, 4 H, C-$CH_2$-$CH_2$-C$H_2$-), 1.89 (br. s, 2.7 H, THF), 2.37–2.55 (m, 8 H, -C-C$H_2$-$CH_2$-$CH_2$-), 2.73 (br. s, 1 H, OH), 3.97 (br. s, 2.7 H, THF), 6.66 (s, 4 H, -C*H*-, Cp), 7.12 (t, $^3J_{H,H}$ = 7.0 Hz, 2 H, *para*-$C_5H_6$), 7.27 (t, $^3J_{H,H}$ = 7.0 Hz, 4 H, *meta*-$C_5H_6$), 7.44 (d, $^3J_{H,H}$ = 7.0 Hz, 4 H, *ortho*-$C_5H_6$) ppm.

**X-ray Crystallographic Structure Determinations for 11 and 12:** The crystal data for compounds **11** and **12** (Table 2) were collected at 120 and 150 K, respectively, using a Nonius Kappa CCD diffractometer with graphite-monochromated Mo-$K_\alpha$ radiation. The data sets were integrated with the Denzo-SMN package[27] and corrected for Lorentz, polarization, and absorption (SORTAV[28]) effects. The structures were solved by direct methods (SIR97[29]) and refined using full-matrix least-squares with all non-hydrogen atoms anisotropic and hydrogens included at calculated positions as riding on their carrier atoms. All calculations were performed using SHELXL97[30] and PARST[31] implemented in WINGX[32] system of programs.

Table 2. Crystal data for complexes **11** and **12**.

| Compound | **11** | **12** |
|---|---|---|
| Formula | $C_{48}H_{66}Cl_5LiO_4Y_2$ | $C_{104}H_{108}Cl_6O_8Y_6$ |
| *MW* | 1069.02 | 2520.56 |
| Space group | $P2_12_12_1$ | $P\bar{1}$ |
| Crystal system | orthorhombic | triclinic |
| *a* [Å] | 11.6874(3) | 14.0415(3) |
| *b* [Å] | 19.9579(5) | 14.4971(3) |
| *c* [Å] | 21.3214(4) | 15.4855(5) |
| *α* [°] | 90 | 76.886(1) |
| *β* [°] | 90 | 86.128(1) |
| *γ* [°] | 90 | 65.722(2) |
| *T* [K] | 120 | 150 |
| *Z* | 4 | 1 |
| $D_c$ [g cm$^{-3}$] | 1.428 | 1.496 |
| *F*(000) | 2200 | 1286 |
| $\mu$(Mo-$K_\alpha$) [cm$^{-1}$] | 26.313 | 33.940 |
| Measured reflections | 29098 | 42244 |
| Unique reflections | 9657 | 12718 |
| $R_{int}$ | 0.101 | 0.050 |
| Obs. reflns [$I \geq 2\sigma(I)$] | 7677 | 9484 |
| $\Theta_{min}$, $\Theta_{max}$ [°] | 2.85–26.00 | 4.00–27.50 |
| *hkl* ranges | –13,14; –24,24; –26,26 | –18,18; –16,18; –19,20 |
| $R(F^2)$(obs. reflns.) | 0.0537 | 0.0701 |
| $wR(F^2)$ (all reflns.) | 0.0961 | 0.1781 |
| No. variables | 541 | 625 |
| Goodness of fit | 1.054 | 1.218 |
| $\rho_{min}$, $\rho_{max}$ [e Å$^{-3}$] | –0.686, 0.379 | –0.750, 1.180 |

CCDC-297382 (for **11**) and -297383 (for **12**) contain the supplementary crystallographic data for this paper. These data can be obtained free of charge from The Cambridge Crystallographic Data Centre via www.ccdc.cam.ac.uk/data_request/cif.

**Supporting Information** (see also the footnote on the first page of this article): Selected interatomic distances and angles are given in Tables S1–S4.

**General Polymerization Conditions:** All manipulations of air- and/or moisture-sensitive materials were carried out under inert atmosphere using either a dual vacuum/nitrogen line and standard Schlenk techniques or in a dry-box under nitrogen atmosphere

 © 2006 Wiley-VCH Verlag GmbH & Co. KGaA, Weinheim 

(<10 ppm oxygen, <20 ppm water). MAO (Witco, 10 wt.-% solution in toluene) was used after drying in vacuo (5 h, 50 °C, 0.1 mbar) to remove the solvent and unreacted $AlMe_3$, and was stored under nitrogen. Nitrogen and ethylene were purified by passage through columns of BASF RS-11 (Fluka) and Linde 4-Å molecular sieves. 1-Hexene was deoxygenated and dehydrated under nitrogen by refluxing and distillation over $LiAlH_4$, and stored under nitrogen.

**Ethylene Polymerizations:** A 250-mL glass reactor equipped with a magnetic stirrer was charged with anhydrous toluene (100 mL) and MAO (8.8 mmol) from a syringe. Ethylene was then added until saturation. The polymerization was started by adding a solution of the catalyst (**7** or **11**) (8 μmol; [Al]/[Y] ratio: 1100) in toluene (5 mL) with a syringe under ethylene pressure. After 24 h the reaction was terminated by addition of a small amount of ethanol, and the polymer was precipitated by pouring the whole reaction mixture into ethanol (600 mL) to which concentrated hydrochloric acid (5 mL) had been added. The organic phase was separated, washed with $NaHCO_3$ saturated solution, deionized water, and dried with $MgSO_4$. After filtration, the solvent was evaporated under reduced pressure and the last traces of toluene were eliminated by azeotropic distillation with absolute ethanol (three times). Absolute ethanol was added again and the polymer was collected by filtration, washed with absolute ethanol, and dried overnight under vacuum at 70 °C. If oligomers were produced (as with catalyst **7**), they were retrieved as an oily residue after evaporation of the ethanol from the filtered solution, extraction with pentane, and evaporation of the solvent.

**1-Hexene Polymerizations:** A 250-mL glass reactor equipped with a magnetic stirrer was charged with anhydrous toluene (100 mL), 1-hexene (1 mol/L), and MAO (15 mmol). The polymerization was started by adding a solution of the catalyst (**7** or **11**) (8 μmol; [Al]/[Y] ratio: 1875) in toluene (5 mL) with a syringe under nitrogen pressure. After 24 h the polymerization was quenched by adding a small amount of ethanol. The contents of the reactor were poured into a conical flask, and a solution of concentrated HCl in ethanol (200 mL; 15% by volume) was added. After 30 min stirring, the mixture was transferred into a separating funnel, the organic phase was separated, washed once with $NaHCO_3$ saturated solution, twice with deionized water, and dried with $MgSO_4$. After filtration, the solvent was removed under reduced pressure. No polymer was obtained.

## Acknowledgments

The authors warmly thank Dr. F. Forlini of ISMAC-C.N.R. (Milano, Italy) for performing the polymerization tests. This work was funded by the MURST PRIN-2004 (prot. 2004030307_3).

[1] a) W. J. Evans, *Polyhedron* **1987**, *6*, 803–835; b) C. J. Schaverien, *Adv. Organomet. Chem.* **1994**, *36*, 283–362; c) F. T. Edelmann, in *Comprehensive Organometallic Chemistry* (Eds.: E. W. Abel, F. G. A. Stone, G. Wilkinson, M. F. Lappert), Pergamon, Oxford, **1995**, vol. 4; d) H. Schumann, J. A. Meese-Marktscheffel, L. Esser, *Chem. Rev.* **1995**, *95*, 865–986; e) G. A. Molander, J. A. C. Romero, *Chem. Rev.* **2002**, *102*, 2161–2186; f) R. Anwander, in *Applied Homogeneous Catalysis with Organometallic Compounds* (Eds.: B. Cornils, W. A. Herrmann), VCH, Weinheim, **1996**, vol. 2, p. 866; g) *Lanthanides: Chemistry and Use in Organic Synthesis* (Ed.: S. Kobayashi), Springer, Berlin, **1999**.

[2] a) T. R. Jensen, J. J. O'Donnel III, T. J. Marks, *Organometallics* **2004**, *23*, 740–754; b) M. Nishiura, Z. Hou, *J. Mol. Catal. A* **2004**, *213*, 101–106; c) Z. Hou, Y. Wakatsuki, *Coord. Chem. Rev.* **2002**, *231*, 1–22 and references cited therein; d) G. Lanza, I. L. Fragalà, T. J. Marks, *Organometallics* **2002**, *21*, 5594–5612; e) G. Jeske, H. Lauke, H. Mauermann, P. N. Swepston, H. Schumann, T. J. Marks, *J. Am. Chem. Soc.* **1985**, *107*, 8091–8103.

[3] a) P. L. Watson, *J. Am. Chem. Soc.* **1982**, *104*, 337–339; b) P. L. Watson, G. W. Parshall, *Acc. Chem. Res.* **1985**, *18*, 51–56.

[4] J. Okuda, T. Eberle, in *Metallocenes* (Eds.: A. Togni, R. L. Halterman), Wiley-VCH, Weinheim, Germany, **1998**; vol. 1, p. 415.

[5] a) P. L. Watson, *J. Chem. Soc., Chem. Commun.* **1983**, 276–277; b) W. J. Evans, L. R. Chamberlain, T. A. Ulibarri, J. W. Ziller, *J. Am. Chem. Soc.* **1988**, *110*, 6423–6432; c) B. J. Deelman, M. Booij, A. Meetsma, J. H. Teuben, H. Kooijman, A. L. Spek, *Organometallics* **1995**, *14*, 2306–2317.

[6] W. E. Piers, P. J. Shapiro, E. E. Bunel, J. E. Bercaw, *Synlett* **1990**, 74–84.

[7] a) J. L. Namy, P. Girard, H. B. Kagan, P. E. Caro, *Nouv. J. Chim.* **1981**, *5*, 479–484; b) R. E. Maginn, S. Manastyrskyj, M. Dubeck, *J. Am. Chem. Soc.* **1963**, *85*, 672; c) W. J. Evans, J. H. Meadows, W. E. Hunter, J. L. Atwood, *J. Am. Chem. Soc.* **1984**, *106*, 1291–1300.

[8] E. Polo, R. M. Bellabarba, G. Prini, O. Traverso, M. L. H. Green, *J. Organomet. Chem.* **1999**, *577*, 211–218.

[9] a) E. Polo, S. Losio, F. Forlini, P. Locatelli, A. Provasoli, M. C. Sacchi, *Macromol. Chem. Phys.* **2002**, *203*, 1859–1865; b) E. Polo, A. Barbieri, S. Sostero, M. L. H. Green, *Eur. J. Inorg. Chem.* **2002**, 405–409; c) E. Polo, A. Barbieri, O. Traverso, *Eur. J. Inorg. Chem.* **2003**, 324–330; d) E. Polo, A. Barbieri, O. Traverso, *New J. Chem.* **2004**, *28*, 652–656; e) E. Polo, F. Forlini, P. Locatelli, M. C. Sacchi, *Macromol. Chem. Phys. Macrom. Symp.* **2004**, *213*, 89–99; f) E. Polo, S. Losio, G. Zecchi, F. Bertini, M. C. Sacchi, *Macromol. Rapid. Commun.* **2004**, *25*, 1845–1850; g) S. Losio, G. Zecchi, F. Bertini, M. C. Sacchi, V. Bertolasi, E. Polo, *Macromolecules* **2005**, *38*, 7231–7240; h) M. C. Sacchi, I. Tritto, F. Bertini, S. Losio, G. Zecchi, E. Polo, *Kinet. Catal.* **2006**, *47*, 268–273.

[10] M. N. Burdett, C. K. Johnson, *ORTEP III, Report ORNL6895*, Oak Ridge National Laboratory, Oak Ridge, TN, **1996**.

[11] W. J. Evans, M. S. Sollberger, J. S. Shreeve, J. M. Olofson, J. H. Hain Jr, J. W. Ziller, *Inorg. Chem.* **1992**, *31*, 2492–2501.

[12] R. Broussier, G. Delmas, P. Perron, B. Gautheron, J. L. Petersen, *J. Organomet. Chem.* **1996**, *511*, 185–192.

[13] H. Schumann, H. Heim, J. Damtschuk, S. H. Mühle, *Organometallics* **2003**, *22*, 118–128.

[14] W. E. Evans, T. J. Boyle, J. W. Ziller, *Inorg. Chem.* **1992**, *31*, 1120–1122.

[15] H. Schumann, J. Loebel, J. Pickardt, C. Qian, Z. Xie, *Organometallics* **1991**, *10*, 215–219.

[16] W. E. Damrau, G. Paolucci, J. Zanon, E. Siebel, R. D. Fischer, *Inorg. Chem. Commun.* **1998**, *1*, 424–426.

[17] H. Schumann, F. H. Görlitz, F. E. Hahn, J. Pickardt, C. Qian, Z. Xie, *Z. Anorg. Allg. Chem.* **1992**, *609*, 131.

[18] W. J. Evans, M. A. Hozbor, S. G. Bott, G. H. Robinson, J. L. Atwood, *Inorg. Chem.* **1988**, *27*, 1990–1993.

[19] E. H. Barash, P. S. Coan, E. B. Lobkovsky, W. E. Streib, K. G. Coulton, *Inorg. Chem.* **1993**, *32*, 497–501.

[20] H. Schumann, H. Heim, J. Damtschuk, S. H. Mühle, *Organometallics* **2002**, *21*, 3323–3334.

[21] R. A. L. Gendron, D. J. Berg, P. Shao, T. Barclay, *Organometallics* **2001**, *20*, 4279–4286.

[22] K. C. Hultzsch, P. Voth, K. Beckerle, T. P. Spaniol, J. Okuda, *Organometallics* **2000**, *19*, 228–243.

[23] E. Ihara, S. Yoshioka, M. Furo, K. Katsura, H. Yasuda, S. Mohri, N. Kanehisa, Y. Kai, *Organometallics* **2001**, *20*, 1752–1761.

[24] a) P. J. Shapiro, E. Bunel, W. P. Schaefer, J. E. Bercaw, *Organometallics* **1990**, *9*, 867869; b) P. J. Shapiro, W. D. Cotter, W. P. Schaefer, J. A. Labinger, J. E. Bercaw, *J. Am. Chem. Soc.* **1994**,

 © 2006 Wiley-VCH Verlag GmbH & Co. KGaA, Weinheim 

*116*, 46234640; c) C. J. Schaverien, *Organometallics* **1994**, *13*, 6982; d) I. Albrecht, H. Schumann, *J. Organomet. Chem.* **1986**, *310*, C29; e) H. Schumann, I. Albrecht, J. Pickardt, E. Hahn, *J. Organomet. Chem.* **1984**, *276*, C5.

[25] a) G. Jeske, L. E. Schock, P. N. Swepston, H. Schumann, T. J. Marks, *J. Am. Chem. Soc.* **1985**, *107*, 81038110; b) W. J. Evans, T. A. Ulibarri, J. W. Ziller, *J. Am. Chem. Soc.* **1990**, *112*, 2314–2324.

[26] a) C. P. Casey, T.-Y. Lee, J. A. Tunge, D. W. Carpenetti II, *J. Am. Chem. Soc.* **2001**, *123*, 210763; b) C. P. Casey, J. F. Klein, M. A. Fagan, *J. Am. Chem. Soc.* **2000**, *122*, 4320–4330; c) C. P. Casey, S. L. HallenBeck, J. M. Wright, C. R. Landis, *J. Am. Chem. Soc.* **1997**, *119*, 9680–9690.

[27] Z. Otwinowski, W. Minor, in *Methods in Enzymology* (Eds.: C. W. Carter, R. M. Sweet), vol. 276, part A, Academic Press, London, **1997**, 307–326.

[28] R. H. Blessing, *Acta Crystallogr. Sect. A* **1995**, *51*, 33–38.

[29] SIR97: A. Altomare, M. C. Burla, M. Camalli, G. L. Cascarano, C. Giacovazzo, A. Guagliardi, A. G. Moliterni, G. Polidori, R. Spagna, *J. Appl. Crystallogr.* **1999**, *32*, 115–119.

[30] G. M. Sheldrick, *SHELX97, Program for Crystal Structure Refinement*, University of Göttingen, Germany, **1997**.

[31] M. Nardelli, *J. Appl. Crystallogr.* **1995**, *28*, 659–661.

[32] L. J. Farrugia, *J. Appl. Crystallogr.* **1999**, *32*, 837–838.

Received: May 2, 2006
Published Online: August 11, 2006

 © 2006 Wiley-VCH Verlag GmbH & Co. KGaA, Weinheim 

DOI: 10.1002/ejic.200600403

# Controlled Synthesis of 3d–4d Heterobimetallic Complexes of a Symmetrical Tetraiminodiphenolate Macrocycle – Structural, Spectroscopic, and Redox Properties

**Bula Dutta,[a] Bibhutosh Adhikary,[b] Ulrich Flörke,[c] and Kamalaksha Nag*[a]**

**Keywords:** Heterobimetallic complexes / Macrocyclic complexes / Palladium / Rhodium / 3d metals(II)

The mononuclear complexes $[Rh(LH_2)Cl_2](ClO_4)\cdot 3H_2O$ (**1**) and $[Pd(LH_2)](ClO_4)_2$ (**2**) of the tetraiminodiphenolate macrocycle $L^{2-}$ have been synthesized by the transmetallation reaction between $[Pb(LH_2)](ClO_4)_2$, and $RhCl_3\cdot xH_2O$ and $Na_2[PdCl_4]$, respectively. In these compounds, the uncoordinated imino nitrogen atoms are protonated and are hydrogen bonded to the phenolate oxygen atoms to stabilize them against hydrolytic cleavage. Using these mononuclear complexes, the following heterodinuclear complexes: $[Rh^{III}Cl_2(L)Pd^{II}](X)$ [X = $ClO_4$ (**3**), $PF_6$ (**4**)], $[Pd^{II}(L)M^{II}(H_2O)_2](ClO_4)_2$ [M = Mn (**5**), Fe (**6**), Co (**7**), Ni (**8**)], $[Pd^{II}(L)M^{II}](ClO_4)_2$ [M = Cu (**9**), Zn (**10**)]; and the dipalladium(II) complex $[Pd_2L](ClO_4)_2$ (**11**) have been synthesized. The crystal structure determined for $[RhCl_2(L)Pd](PF_6)$ (**4**) shows an axially elongated octahedral geometry for $Rh^{III}$ and a square-planar geometry for $Pd^{II}$. In $[Pd^{II}(L)Cu^{II}](ClO_4)_2$ (**9**), both the metal ions lie in the flat plane of the macrocyclic ligand and they are positionally disordered with equal occupancies. The $Cu^{II}$ center has an apically elongated square-pyramidal geometry due to the weak perturbation by an oxygen atom of a perchlorate anion. Complexes **2**, **10**, and **11** on excitation at 400 nm exhibit luminescence at room temperature at 505, 437, and 443 nm, respectively. Spectrofluorimetric titrations of $[Pd^{II}(LH_2)]^{2+}$ with the acetate salts of zinc(II) and palladium(II) have shown that the formation of $[Pd(L)Zn]^{2+}$ and $[Pd_2L]^{2+}$ complex species are accompanied by blue shift of luminescence with increased and reduced emission intensities, respectively. The hyperfine-shifted $^1H$ NMR spectral features of the paramagnetic compounds **7**–**9** have been analyzed by determining their longitudinal ($T_1$) and transverse ($T_2$) relaxation times. Cyclic and square-wave voltammetric measurements have been carried out for complexes **7**–**9** in acetonitrile. For complexes **8** and **9**, reversible one-electron reduction occurs with $E_{1/2}$ = –0.10 V for $Pd^{II}Cu^{II}/Pd^{II}Cu^{I}$ and –0.80 V for $Pd^{II}Ni^{II}/Pd^{II}Ni^{I}$ versus Ag/AgCl. Complex **7** undergoes irreversible reduction for cobalt(II) at –0.78 V.

(© Wiley-VCH Verlag GmbH & Co. KGaA, 69451 Weinheim, Germany, 2006)

## Introduction

Over the past three decades extensive studies have been made on the chemistry of the phenolate-bridged tetraiminodiphenol macrocyclic complexes[1–17] derived from the symmetrical ligand $L^{2-}$ (**I**). The focus of interest in complexes of this sort has been to study the implications of cooperative metal–metal interactions that are manifested in spin-exchange couplings,[6–15] redox activities,[4,8,9a,11] and bimetallic reactivities.[9b,16]

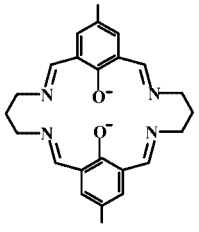

**I** ($L^{2-}$)

There is considerable interest in involving heterobimetallic complexes in catalytic reactions by way of dual activation of substrates.[18–20] Heterobimetallic complexes also have distinct potentiality to act as precursors for producing bimetallic nanoparticles, especially those containing platinum metals and first-row transition metals.[21] The synthesis of heterobimetallic complexes where the two metal ions are held in close proximity by a bridging ligand is a nontrivial problem, particularly when the ligand is symmetrical in nature. The most common problem in such cases is either the preferential formation of a particular homodinuclear complex species or the statistical formation of a mixture of two products. Clearly, the development of a controlled synthetic route for the generation of heterobimetallic complexes is an important task. We have introduced a controlled systematic route to synthesize bimetallic systems of the symmetric

[a] Department of Inorganic Chemistry, Indian Association for the Cultivation of Science,
Jadavpur, Kolkata 700 032, India
E-mail: ickn@iacs.res.in
[b] Department of Chemistry, Bengal Engineering and Science University,
Shibpur, Howrah 711 103, India
[c] Anorganische und Analytische Chemie, Universität Paderborn, 33098 Paderborn, Germany

Supporting information for this article is available on the WWW under http://www.eurjic.org or from the author.

 © 2006 Wiley-VCH Verlag GmbH & Co. KGaA, Weinheim 

macrocyclic ligand $L^{2-}$ incorporating 4d–3d metal ions. Herein we report the synthesis, structures, and spectroscopic properties of the mononuclear complexes $[M(LH_2)]^{n+}$ ($M = Rh^{III}$, $Pd^{II}$; $n = 3$, 2) and the heterodinuclear complexes $[RhCl_2(L)Pd]^+$ and $[Pd(L)M]^{2+}$ ($M = Mn^{II}$, $Fe^{II}$, $Co^{II}$, $Ni^{II}$, $Cu^{II}$, $Zn^{II}$). The X-ray crystal structures of two heterodinuclear complexes $[RhCl_2(L)Pd](PF_6)$ and $[Pd(L)Cu](ClO_4)_2$ have been determined. Paramagnetic proton NMR studies have provided information about the influence of electron spins on the hyperfine-shifted spectral patterns of $[Pd(L)M^{II}]^{2+}$ (M = Fe, Co, Ni, Cu) complexes.

## Results and Discussion

### Syntheses

The synthesis of heterobimetallic complexes involving 3d–4d metal ions and the symmetrical compartmental macrocyclic ligand $L^{2-}$ would ideally require mononuclear precursor complexes in which one compartment of the ligand is metal-free. However, for the ligand $L^{2-}$ such mononuclear complexes are generally not obtainable.[1,2,5,16b] It has been reported[22] that metal-directed macrocyclization usually does not take place with nonlabile platinum metals. Indeed, we have failed to produce mononuclear or dinuclear complexes of palladium(II) and rhodium(III) of $L^{2-}$ through a [2+2] condensation reaction between 2,6-diformyl-4-methylphenol and 1,3-diaminopropane in the presence of $Na_2[PdCl_4]$ or $RhCl_3{\cdot}xH_2O$. In both cases, a mixture of reaction products was obtained which consisted of, inter alia, amine aldehyde condensed oligomers, metal diamine complexes, and $[Pd_2L']$ or $[RhL'(H_2O)Cl]$ where $H_2L'$ is the [2+1] Schiff base of 2,6-diformyl-4-methylphenol and 1,3-diaminopropane.

To obviate this problem, sometime back we reported the synthesis of a mononuclear lead(II) complex, $[Pb(LH_2)](ClO_4)_2$,[23] by reacting 1 equiv. of lead perchlorate with 2 equiv. each of 2,6-diformyl-4-methylphenol and 1,3-diaminopropane in the presence of acetic acid. In this complex, $LH_2$ represents the macrocycle in the zwitterionic form in which the two uncoordinated imine nitrogens are protonated and are hydrogen-bonded to the metal-bound phenolate oxygens. The utility of $[Pb(LH_2)](ClO_4)_2$ as a precursor to obtain other mononuclear complexes has been demonstrated by us[24] by isolating complexes $[M^{III}(LH_2)(H_2O)Cl](ClO_4)_2{\cdot}nH_2O$ of trivalent labile metal ions such as aluminum, gallium, and indium.

As shown in Scheme 1, the metathetical reaction involving stoichiometric amounts of $[Pb(LH_2)](ClO_4)_2$ and $RhCl_3{\cdot}xH_2O$ or $Na_2[PdCl_4]$ and excess $NaClO_4$ leads to the formation of $[Rh(LH_2)Cl_2](ClO_4){\cdot}3H_2O$ (**1**) and $[Pd(LH_2)](ClO_4)_2$ (**2**). The driving force for the reaction is precipitation of $PbCl_2$ and occupation of its vacant site by rhodium(III) or palladium(II). The palladium(II) complex (**2**), on reaction with a stoichiometric amount of a 3d metal perchlorate $M(ClO_4)_2{\cdot}6H_2O$ (M = Mn, Fe, Co, Ni, Cu, Zn)

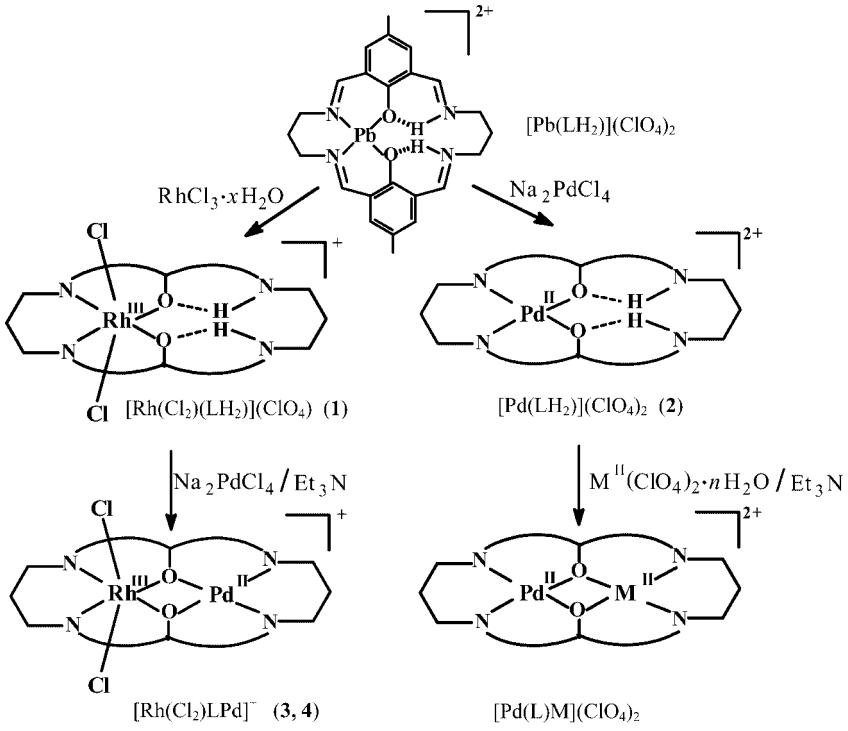


Scheme 1.

 © 2006 Wiley-VCH Verlag GmbH & Co. KGaA, Weinheim 

and triethylamine, affords the heterodinuclear complexes $[Pd(L)M(H_2O)_2](ClO_4)_2$ (**5**–**8**, Mn–Ni), $[Pd(L)Cu](ClO_4)_2$ (**9**), and $[Pd(L)Zn(H_2O)](ClO_4)_2{\cdot}H_2O$ (**10**). If the above reaction is carried out with $Na_2[PdCl_4]$ and $NaClO_4$, the homodinuclear complex $[Pd_2L](ClO_4)_2$ (**11**) is obtained. In contrast to **2**, the reaction of $[RhCl_2(LH_2)](ClO_4){\cdot}3H_2O$ (**1**) with the above-mentioned metal perchlorates, however, failed to produce the desired $[RhCl_2(L)M(H_2O)_n]^+$-type complexes. On the other hand, when **1** is reacted with $Na_2[PdCl_4]$ and triethylamine in the presence of $NaClO_4$ or $NH_4[PF_6]$ the mixed-metal $[RhCl_2(L)Pd](ClO_4)/(PF_6)$ complexes **3**, **4** are readily obtained. This indicates that the *trans* axial chloride ions of **1** sterically inhibit the entry of a second metal ion into the ligand compartment if the coordination number of the incoming metal ion exceeds four. In the case of palladium(II), no difficulty is encountered in obtaining $[RhCl_2(L)Pd]^+$ because of the square-planar geometry of the palladium center.

It needs to be mentioned at this stage that the dipalladium(II) complex $[Pd_2L](BF_4)_2$ has been prepared earlier[16a] by reacting the macrocyclic ligand salt $[H_4L](BF_4)_2$ with palladium(II) chloride or acetate in acetonitrile in the presence of a 10-fold excess of triethylamine. The X-ray crystal structure of this compound has been reported.[16a] Further, the heterodinuclear complex $[PdLNi(CH_3CN)_2](ClO_4)_2$ has been previously synthesized[25] by reacting the much earlier reported mononuclear nickel(II) complex $[Ni(H_2L)](ClO_4)_2{\cdot}H_2O$[1] with palladium(II) acetate in acetonitrile. This compound has also been structurally characterized.[25] We note that the proton NMR spectra reported for $[PdLNi(CH_3CN)_2]^{2+}$ in $CD_3OD$ are similar to those of $[PdLNi(H_2O)_2]^{2+}$ in $CD_3CN$ obtained in this study.

## Crystal Structures

### *[Rh(Cl$_2$)(L)Pd]PF$_6$ (4)*

The structural analysis of complex **4** revealed the presence of the core cation $[Pd(L)RhCl_2]^+$ and one hexafluorophosphate anion. An ORTEP representation of the cation $[Pd(L)RhCl_2]^+$ is shown in Figure 1 and selected interatomic distances and angles are listed in Table 1.

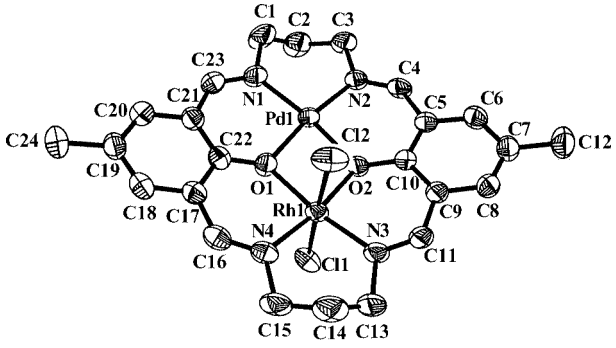


Figure 1. ORTEP representation of the $[Pd(L)Rh(Cl_2)]^+$ cation of complex **4** at the 50% probability level. H atoms omitted.

The structure of the cation of **4** consists of one palladium(II) and one rhodium(III) center bridged by the two phenolate oxygens O(1) and O(2) and they are separated by a distance of 3.150(1) Å. The dihedral angle between the two phenyl rings is 22.76(1)°, indicating significant deviation of the macrocycle from the planarity. For the Pd(1) center the basal plane is provided by the atoms O(1), O(2), N(1), and N(2) [Pd(1)–O(1) 2.022(2) Å, Pd(1)–O(2) 2.024(2) Å, Pd(1)–N(1) 1.980(3) Å, and Pd(1)–N(2) 1.990(3) Å]. These donor atoms are deviated from the mean plane by not more than ±0.010(1) Å and the Pd(1) center lies below the plane by 0.009(1) Å. The Rh(1) center is bonded to the phenolate oxygen atoms O(1) [Rh(1)–O(1) 2.056(2) Å] and O(2) [Rh(1)–O(2) 2.062(2) Å], and the imine nitrogen atoms N(3) [Rh(1)–N(3) 1.984(3) Å] and N(4) [Rh(1)–N(4) 2.001(3) Å]. The mean plane is formed by O(1), O(2), N(3), and N(4) atoms in which the deviations of the donor atoms do not exceed ±0.004(1) Å. The *trans* axial Cl(1) and Cl(2) atoms are placed above and below the metal plane to complete

Table 1. Selected bond lengths [Å] and angles [°] for $[RhCl_2(L)Pd](PF_6)$ (**4**).

| | | | |
|---|---|---|---|
| Pd(1)–N(1) | 1.980(3) | Rh(1)–N(3) | 1.984(3) |
| Pd(1)–N(2) | 1.990(3) | Rh(1)–N(4) | 2.001(3) |
| Pd(1)–O(1) | 2.022(2) | Rh(1)–O(1) | 2.056(2) |
| Pd(1)–O(2) | 2.024(2) | Rh(1)–O(2) | 2.062(2) |
| | | Rh(1)–Cl(1) | 2.3395(13) |
| | | Rh(1)–Cl(1) | 2.3065(13) |
| N(1)–Pd(1)–N(2) | 95.78(12) | N(3)–Rh(1)–N(4) | 96.86(13) |
| N(1)–Pd(1)–O(1) | 92.43(11) | N(3)–Rh(1)–O(1) | 170.34(11) |
| N(2)–Pd(1)–O(1) | 171.71(11) | N(4)–Rh(1)–O(1) | 92.79(12) |
| N(1)–Pd(1)–O(2) | 171.82(11) | N(3)–Rh(1)–O(2) | 92.63(11) |
| N(2)–Pd(1)–O(2) | 92.40(11) | N(4)–Rh(1)–O(2) | 170.51(11) |
| O(1)–Pd(1)–O(2) | 79.39(10) | O(1)–Rh(1)–O(2) | 77.72(9) |
| | | N(3)–Rh(1)–Cl(2) | 89.58(10) |
| Pd(1)–O(1)–Rh(1) | 101.12(11) | N(4)–Rh(1)–Cl(2) | 91.10(10) |
| Pd(1)–O(2)–Rh(1) | 100.88(10) | N(3)–Rh(1)–Cl(1) | 89.06(10) |
| | | N(4)–Rh(1)–Cl(1) | 90.43(10) |
| | | O(1)–Rh(1)–Cl(2) | 89.82(9) |
| | | O(2)–Rh(1)–Cl(2) | 88.97(8) |
| | | O(1)–Rh(1)–Cl(1) | 91.29(9) |
| | | O(2)–Rh(1)–Cl(1) | 89.72(8) |
| | | Cl(2)–Rh(1)–Cl(1) | 178.07(4) |

 © 2006 Wiley-VCH Verlag GmbH & Co. KGaA, Weinheim 

the octahedron. The two Rh–Cl distances [Rh(1)–Cl(1) 2.339(1) Å and Rh(1)–Cl(2) 2.306(1) Å] are almost the same, albeit rather long. The Cl(2)–Rh(1)–Cl(1) angle [178.07(4)°] is practically linear. The displacement of Rh(1) from the least-square plane is only 0.003(1) Å.

### *[Pd(L)Cu](ClO$_4$)$_2$ (9)*

Compound **9** is comprised of the cation $[Pd(L)Cu]^{2+}$ and two perchlorate anions. The ORTEP view of the cation is shown in Figure 2. The relevant bond lengths and angles are given in Table 2. The $[Pd(L)Cu]^{2+}$ cation lies on a crystallographic inversion center and thus the $M_2O_2$ ring is planar with M = Pd and Cu centers disordered over both sites (site occupation factor 0.5). The two metal centers are bridged by the two phenolate oxygens O(1) and O(1A) and they are separated by a distance of 3.083(1) Å. The basal plane for either of the metal atoms is formed by the $N_2O_2$ donor atoms and the average metal–donor atom distances are M(1)–O(1) 1.965(4) Å, M(1)–O(1)#1 1.998(4) Å, M(1)–N(1) 1.997(5) Å, and M(1)–N(2) 1.971(6) Å. The deviation of the constituent $N_2O_2$ atoms from the mean plane is 0.024(1) Å and both the metal centers are equally displaced in opposite directions from the mean plane by 0.031(1) Å. The $[Pd(L)Cu]^{2+}$ cation is not perfectly flat, as the atoms C(2) and C(2A) are significantly off [0.62(1) Å] the mean cation plane. Moreover, the perchlorate anions are heavily disordered. The distance between the Cu center and a perchlorate oxygen O(14) is 2.54 Å. This Cu···O distance is not unusual for an apical perchlorate donor on otherwise square-planar copper(II).

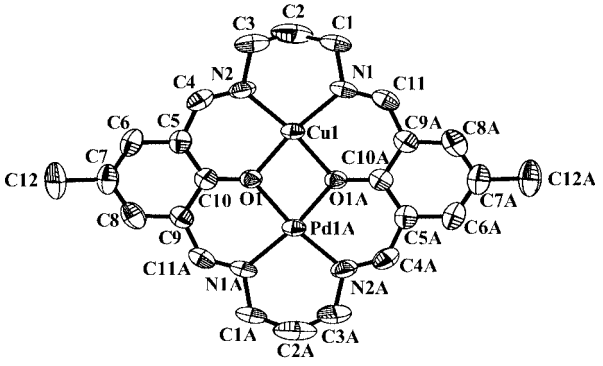


Figure 2. ORTEP representation of the $[Pd(L)Cu]^{2+}$ of complex **9** at the 50% probability level. H atoms omitted. "A" labels indicate symmetry-related atoms (–*x*, –*y* + 1, –*z* + 1).

It should be noted that 0.5:0.5 disorder of the palladium(II) and copper(II) centers over two sites might as well indicate that **9** is a 1:1 mixture of $[Pd_2L](ClO_4)_2$ and $[Cu_2L](ClO_4)_2$ rather than the mixed-metal complex $[Pd(L)Cu](ClO_4)_2$. However, it will be seen in the next section that the mass spectrum of **9** provides clear evidence that it is a truly heterodinuclear complex.

In this context it would be relevant to consider the crystal structures reported for the homodinuclear complexes of palladium(II) and copper(II). In $[Pd_2L](BF_4)_2 \cdot 2CH_3NO_2$,[16a] the average Pd–O, Pd–N, and Pd···Pd distances are 2.015(1), 1.987(6), and 3.1511(6) Å, respectively. The structure determined for the dicopper(II) complex $\{[Cu_2L(H_2O)_2(ClO_4)_2][Cu_2L(H_2O)_2](ClO_4)_2\}$[12b] showed the presence of two different complex units in the unit cell. In one of these units, the dicopper(II) centers are pseudo-octahedral because of *trans* axial coordination by the oxygen atoms of perchlorate and water and the relevant bond lengths are Cu–O 1.985(6) Å, Cu–N 1.956(8) Å, Cu–O(perchlorate) 2.589(10) Å, Cu–O(water) 2.451(9) Å, and Cu···Cu 3.091(3) Å. In the second unit, the copper(II) centers have square-pyramidal geometry with the following bond lengths: Cu–O 1.970(6) Å, Cu–N 1.965(9) Å, Cu–O(water) 2.451(6) Å, and Cu···Cu 3.096(3) Å. Further, in the first unit the copper center is displaced from the equatorial mean plane by only 0.019(4) Å, while in the second unit this displacement, 0.083(6) Å, is greater. A comparison of the structural geometries of the metal centers and the metrical parameters of **9** with the dipalladium(II) and dicopper(II) systems clearly reveals that **9** is a discrete compound.

Table 2. Selected bond lengths [Å] and angles [°] for [Pd(L)Cu](-ClO$_4$)$_2$ (**9**).

| | |
|---|---|
| M(1)–O(1) | 1.965(4) |
| M(1)–O(1)# | 1.998(4) |
| M(1)–N(1) | 1.997(5) |
| M(1)–N(2) | 1.971(6) |
| M···M | 3.0831(1) |
| O(1)–M(1)–N(2) | 92.2(2) |
| O(1)–M(1)–N(1) | 170.5(2) |
| N(1)–M(1)–N(2) | 96.5(2) |
| O(1)–M(1)–O(1)# | 77.86(19) |
| N(2)–M(1)–O(1)# | 170.3(2) |
| N(1)–M(1)–O(1)# | 92.7(2) |
| C(11)–N(1)–M(1) | 122.8(4) |
| C(1)–N(1)–M(1) | 122.9(5) |
| C(4)–N(2)–M(1) | 123.3(5) |
| C(3)–N(2)–M(1) | 120.4(6) |

### Mass Spectra

The electrospray ionization mass spectra (ESI positive) of complexes **1**–**11**, except for **5**, have been measured using their acetonitrile solutions (about $10^{-4}$ mol·dm$^{-3}$). The mononuclear complex **1** shows two peaks due to the cations $[Rh^{III}(Cl_2)(LH_2)]^+$ and $[Rh^{III}(Cl)(ClO_4)(LH_2)]^+$, whereas compound **2** shows peaks due to the cations $[Pd^{II}(LH_2)(ClO_4)]^+$ and $[Pd^{II}(LH_2)]^{2+}$. The heterodinuclear $Rh^{III}Pd^{II}$ compounds **3** and **4** show only a single peak due to the $[Rh^{III}(Cl_2)(L)Pd^{II}]^+$ cation.

For the heterodinuclear $Pd^{II}M^{II}$ complexes (M = Fe, Co, Ni, Cu, Zn) and the homodinuclear $Pd^{II}Pd^{II}$ complex similar spectral features have been observed. These are characterized by the occurrence of two types of positively charged species: $[Pd^{II}(L)M^{II}(ClO_4)]^+$ and $[Pd^{II}(L)M^{II}]^{2+}$, of which the doubly positive-charged ion forms the base peak. Figure 3 shows the cluster of peaks observed for the two types of molecular cations of **7** along with their corresponding simulated spectral patterns. It may be noted that the

 © 2006 Wiley-VCH Verlag GmbH & Co. KGaA, Weinheim 

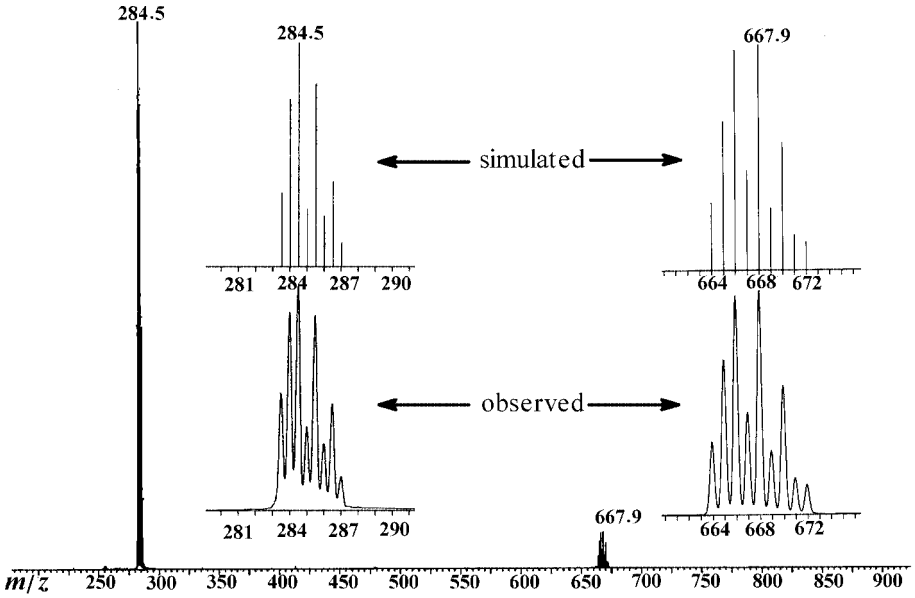


Figure 3. Electrospray ionization mass spectra (ESI-MS+) of $[Pd^{II}(L)Co^{II}](ClO_4)_2$ (**7**) in acetonitrile. Simulated isotropic spectral patterns are compared with the observed major positively charged cationic species.

number of peaks, *m*/*z* values, and the relative peak heights observed for the cations $[Pd^{II}(L)Co^{II}(ClO_4)]^+$ and $[Pd(L)Co]^{2+}$ are in excellent agreement with the calculated spectral patterns obtained by taking into consideration the relative abundances of the isotopes of the constituent elements.

The mass spectrum of the complex $[Pd(L)Cu](ClO_4)_2$ (**9**) has been of particular interest in this context because, as already noted, the X-ray structure of this compound raised the possibility of considering it as a mixture of $[Pd_2L](ClO_4)_2$ and $[Cu_2L](ClO_4)_2$. The spectrum of **9** (shown in Figure S1) depicts the presence of peaks only due to $[Pd(L)Cu(ClO_4)]^+$ with *m*/*z* = 671.9 (10%) and $[Pd(L)Cu]^{2+}$ with *m*/*z* = 287.5 (100%). The observed and calculated isotopic abundance ratio patterns of the positively charged species (see Figure S1, supporting information) are in excellent agreement with each other. Further, the total absence of peaks due to $[Pd_2(L)(ClO_4)]^+$ (715), $[Cu_2(L)(ClO_4)]^+$ (629), $[Pd_2(L)]^{2+}$ (309), and $[Cu_2(L)]^{2+}$ (265) rules out the possibility of **9** as a mixture of the two homodinuclear complexes.

## Infrared Spectra

The IR spectroscopic data of complexes **1**–**11** are given in the Exp. Sect. The $\nu_{C=N}$ stretching vibrations of all the complexes lie between 1650 and 1630 $cm^{-1}$. For the mononuclear complexes **1**, **2** the $\nu_{C=N}$ vibration is observed at 1650 $cm^{-1}$, while for the dinuclear complexes **3**–**11** this band is shifted to lower energy, 1635–1630 $cm^{-1}$. In the mononuclear complexes, a weak band is observed at about 3150 $cm^{-1}$ due to the protonated imine ($\nu_{NH}$), which is hydrogen-bonded to the phenolate oxygen. As expected, this band is not observed in the dinuclear complexes.

## Electronic Spectra

The electronic spectroscopic data for complexes **1**–**11** are listed in Table 3. The mononuclear complexes $[Rh(LH_2)Cl_2](ClO_4)\cdot 3H_2O$ (**1**) and $[Pd(LH_2)](ClO_4)_2$ (**2**) exhibit similar absorption spectral features with a relatively broad band around 406 nm and two intense bands around 260 nm and 220 nm. The latter two bands are due to intraligand charge transfer transitions, whereas the first one seems to be due to ligand (phenolate) to metal charge transfer (LMCT) transition. The spectral patterns observed for the heterodinuclear $Rh^{III}Pd^{II}$ complexes are again similar to those of **1** and **2**, although the LMCT band is shifted to 385 nm.

The heterodinuclear diamagnetic $Pd^{II}M$ (M = Zn, Pd) complexes **10**, **11** also exhibit spectral features as above (Table 3). Significant spectral changes occur when $M^{II}$ is a transition-metal ion. For example, the absorption spectrum of the $Pd^{II}Co^{II}$ complex (**7**) (Figure S2) shows three bands at 970 nm (16 $dm^3\cdot mol^{-1}\cdot cm^{-1}$), 375 nm (36400 $dm^3\cdot mol^{-1}\cdot cm^{-1}$) and 256 nm (177600 $dm^3\cdot mol^{-1}\cdot cm^{-1}$). While the band observed at 375 nm is due to the LMCT transition, the band at 970 nm is assignable to $^4T_{1g}$ (F) $\rightarrow$ $^4T_{2g}$ transition of high-spin $Co^{II}$ center in an octahedral environment. In the $Pd^{II}Ni^{II}$ complex **8**, in addition to the two bands in the UV region (378 and 260 nm), two more bands are observed in the visible (550 nm) and in the near-IR region (985 nm). Figure S3 shows the absorption spectrum of complex **8** in acetonitrile. The bands observed at 985 nm (8 $dm^3\cdot mol^{-1}\cdot cm^{-1}$) and 550 nm (17 $dm^3\cdot mol^{-1}\cdot cm^{-1}$) are due to $^3A_{2g} \rightarrow {}^3T_{2g}$ and $^3A_{2g} \rightarrow {}^3T_{1g}$ (P) transitions of the six-coordinate nickel(II) center. We note that a third band expected for $^3A_{2g} \rightarrow {}^3T_{1g}$ transition is not observed. The $Pd^{II}Cu^{II}$ complex **9** exhibits a single d–d band at 700 nm (39.9 $dm^3\cdot mol^{-1}\cdot cm^{-1}$) in addition to the bands at

 © 2006 Wiley-VCH Verlag GmbH & Co. KGaA, Weinheim 

Table 3. Absorption and emission spectroscopic data for complexes **1**–**11**.[a]

| | Absorption | Emission | |
|---|---|---|---|
| | $\lambda_{max}$ [nm] ($\varepsilon$ [dm$^3$·mol$^{-1}$·cm$^{-1}$]) | $\lambda_{max}$ [nm] | $\varphi$ |
| **1** | 409 (24700), 266 (129800), 221 (190500) | | |
| **2** | 407 (26300), 261 (144500), 222 (176000) | 505 | 0.012 |
| **3** | 385 (27800), 261 (131000), 223 (183900) | | |
| **4** | 385 (27800), 261 (131000), 223 (183900) | | |
| **5** | 372 (32000), 261 (167000) | | |
| **6** | 374 (34200), 259 (163200) | | |
| **7** | 970 (16), 375 (36400), 256 (177600) | | |
| **8** | 985 (8), 550 (17), 378 (32500), 259 (157000) | | |
| **9** | 700 (40), 375 (34200), 258 (162000) | | |
| **10** | 406 (22400), 259 (166700), 219 (189700) | 437 | 0.033 |
| **11** | 398 (21200), 264 (100900), 219 (179500) | 443 | 0.005 |

[a] In acetonitrile.

375 and 258 nm (Figure S4). No d–d bands could be observed for the $Pd^{II}Mn^{II}$ and $Pd^{II}Fe^{II}$ complexes **5** and **6**, respectively.

### Luminescence Spectra

The luminescence spectra of the mononuclear palladium complex **2**, the heterodinuclear $Pd^{II}Zn^{II}$ complex **10**, and the dipalladium(II) complex **11** were measured in acetonitrile solution at room temperature. Table 3 summarizes the emission spectral characteristics of the complexes, including their quantum yields. The mononuclear $Pd^{II}$ complex on excitation at 400 nm exhibits a luminescence peak at 505 nm. In the $Pd^{II}Zn^{II}$ complex **10**, the luminescence peak is blue-shifted to 437 nm with increased intensity. On the other hand, for the dipalladium(II) complex **11**, considerable diminution of emission intensity occurs for the luminescence peak observed at 443 nm.

Spectrofluorimetric titrations carried out by adding incremental amounts of an acetonitrile solution of $Zn(OAc)_2·2H_2O$ to a solution of **2** containing 2 equiv. of sodium acetate in the same solvent, leading to the formation of **10**, is shown in Figure 4. The emission band of **2** at 505 nm ($\lambda_{ex}$ = 400 nm) progressively gets quenched with the addition of zinc(II), whereas a new band appearing at 437 nm due to the formation of **10** progressively increases. The growth of the emission band at 437 nm was monitored as a function of the concentration of zinc acetate added. The inset in Figure 4 shows that the luminescence intensity reached its maximum when 1 equiv. of $Zn(OAc)_2·2H_2O$ was added.

A similar observation has been made for the spectrofluorimetric titration of **2** with palladium acetate (Figure 5). With the incremental addition of palladium acetate the band at 505 nm decreases, giving rise to a new band at 443 nm corresponding to the formation of the dipalladium complex **11**. Again, the growth of the 443 nm band was complete when 1 equiv. of palladium acetate was added. It has been established from additional measurements that the presence of 2 equiv. of sodium acetate is essential for the completion of the reactions. For instance, when titrations were carried out without adding sodium acetate, 2 equiv. of

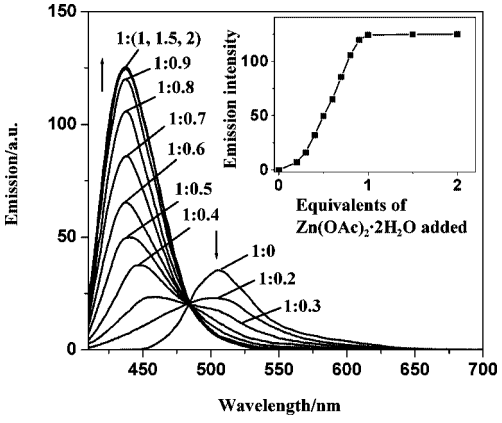


Figure 4. Spectrofluorimetric titration of a mixture of $[Pd(LH_2)][ClO_4]_2$ (**2**) ($1\times10^{-5}$ mol·dm$^{-3}$) and NaOAc ($2\times10^{-5}$ mol·dm$^{-3}$) with $Zn(OAc)_2·2H_2O$ in acetonitrile. The excitation wavelength used was 400 nm. The inset shows the variation of luminescence intensity with the number of equivalents of $Zn(OAc)_2·2H_2O$ added.

$M(OAc)_2$ were required for the completion of the reactions. Clearly, the role of the excess acetate is to provide a buffer effect to the liberated acetic acid in Reaction (1).

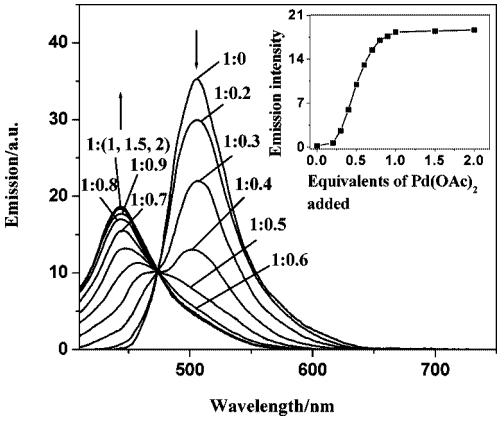


Figure 5. Spectrofluorimetric titration of a mixture of $[Pd(LH_2)][ClO_4]_2$ (**2**) ($1\times10^{-5}$ mol·dm$^{-3}$) and NaOAc ($2\times10^{-5}$ mol·dm$^{-3}$) with $Pd(OAc)_2$ in acetonitrile. The excitation wavelength used was 400 nm. The inset shows the variation of luminescence intensity with the number of equivalents of $Pd(OAc)_2$ added.

 © 2006 Wiley-VCH Verlag GmbH & Co. KGaA, Weinheim 

$$[Pd(LH_2)]^{2+} + M(OAc)_2 \rightleftharpoons [Pd(L)M]^{2+} + 2\ HOAc \quad (1)$$

In this context, it may be mentioned that relative to $[PdLZn]^{2+}$ the luminescence intensity of $[Zn_2L]^{2+}$ is seven times stronger.[26]

## Proton NMR Spectra

Proton NMR spectroscopic studies were carried out for the diamagnetic complexes **1**–**4**, **10**, **11** in $(CD_3)_2SO$ and for the paramagnetic complexes **6**–**9** in $CD_3CN$. The observed chemical shifts along with the spectral assignments are given in the Experimental Section.

The spectral features exhibited by the mononuclear $Rh^{III}$ complex **1** and $Pd^{II}$ complex **2** are quite similar. The hydrogen-bonded protonated imine N–H···O is observed as a broad singlet at $\delta$ = 12.44 ppm for **1** and 12.22 ppm for **2**. Complex **1** exhibits a doublet for the N=CH resonance in the metal-free compartment at $\delta$ = 8.75 ppm ($J$ = 14.8 Hz, 2 H), because of *trans* coupling between the NH and CH protons; however, for complex **2** this is observed as a singlet at $\delta$ = 8.80 ppm. The N=CH resonance in the metal-containing part appears as a singlet at $\delta$ = 8.06 ppm (for **1**) and 8.11 ppm (for **2**). The occurrence of the doublet at $\delta$ = 8.75 ppm in **1** can be alternatively argued as being due to the coupling of the CH=N proton with $^{103}Rh$ ($I$ = 1/2). However, we have recently reported[27] that in the $[Ln(LH_2)(NO_3)_3]$-type diamagnetic lanthanide (La, Lu, and Y) complexes the CH=N resonances are observed as a doublet between 8.73 and 8.80 ppm and a singlet between 8.20 and 8.30 ppm. Significantly, while $^{89}Y$ (100%) is a spin 1/2 nucleus, neither La nor Lu have a $I$ = 1/2 isotope, albeit for all three compounds the chemical shifts and splitting patterns are similar. It, therefore, appears more reasonable to us to conclude that the doublet arises because of *trans* coupling with the N–H proton. In the heterodinuclear $Rh^{III}Pd^{II}$ complexes **3**/**4**, the protons on the Rh-containing site are more shielded than the protons on the Pd-containing site, whereas in the $Pd^{II}Zn^{II}$ complex **10** the protons on the Pd site are more shielded than those on the Zn-containing site.

Studies on the paramagnetic $^1H$ NMR spectroscopic behavior of the heterodinuclear complexes **6**–**9** were carried out in $CD_3CN$ solution. The $Pd^{II}Mn^{II}$ complex **5** could not be investigated as it readily decomposes in solution. The spectroscopic data for complexes **6**–**9** are given in the Experimental Section. In paramagnetic compounds, hyperfine-shifted resonances are observed due to interactions between nuclear spin and unpaired electron spins, in addition to the normal diamagnetic nuclear spin interactions. Electron and nuclear spin interactions occurring through bonds give rise to contact shift, while those occurring through space interactions give rise to dipolar or pseudocontact shift. Dipolar shift depends on the magnetic anisotropy of the system and the position in space of a given proton. The contribution of contact shift decreases rapidly with the increase of the number of bonds connecting the proton with the paramagnetic center. However, when the unpaired electron spin is delocalized the interaction remains significant for protons many bonds away from the metal center. For assignment of signals in paramagnetic compounds, measurement of longitudinal relaxation times ($T_1$) and transverse relaxation times ($T_2$) are particularly important. $T_1$ correlates proximity of proton to paramagnetic center, while $T_2 = 1/\pi(\text{fwh})$, where fwh is full width of a signal at its half-height, correlates line width to proximity of a proton to the paramagnetic site. Closer proximity of a proton to the metal center gives rise to shorter $T_1$ and broader line width.[28]

Figure 6 and Figure 7 show the $^1H$ NMR spectra of $Pd^{II}Co^{II}$ (**7**) and $Pd^{II}Ni^{II}$ (**8**) compounds, while the spectrum of $Pd^{II}Cu^{II}$ (**9**) is available as supporting information (Figure S5). The assignments of signals given in Table 4 (numbering scheme for protons is shown in Scheme 2) have been made from $T_1$ values, line widths, and integration of protons. The M···H distances ($R_{M\cdots H}$) have been estimated by using the relation $R_{M\cdots H} = R_{ref}(T_1/T_{ref})^{1/6}$, where $R_{ref}$ and $T_{ref}$ are the reference values and in the present case the 4-methyl group is treated as the reference. As compared in Table 4, there is good agreement between the $R_{M\cdots H}$ values

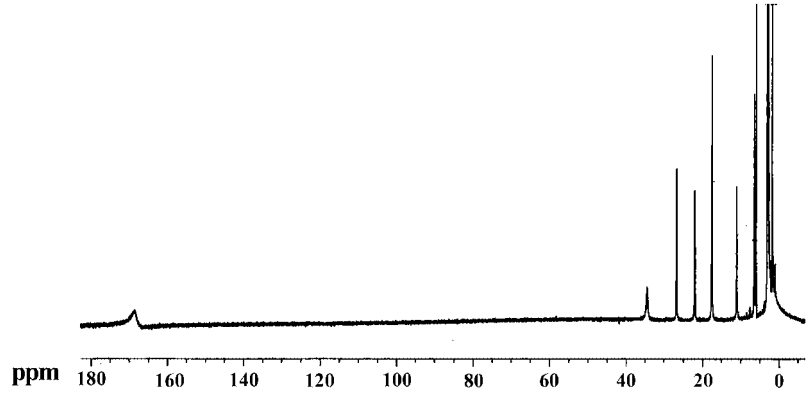


Figure 6. $^1H$ NMR spectrum of $[Pd^{II}LCo^{II}(H_2O)_2](ClO_4)_2$ (**7**) in $CD_3CN$.

 © 2006 Wiley-VCH Verlag GmbH & Co. KGaA, Weinheim 

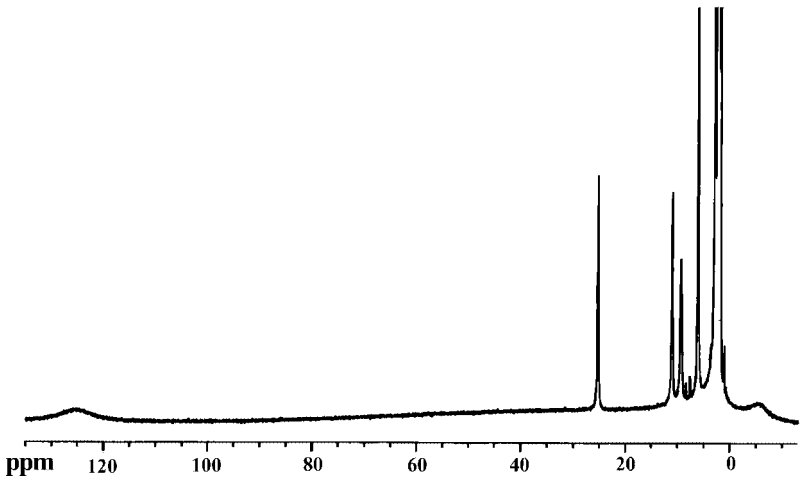


Figure 7. $^1$H NMR spectrum of $[Pd^{II}LNi^{II}(H_2O)_2](ClO_4)_2$ (**8**) in $CD_3CN$.

Table 4. Peak positions, $T_1$ and $T_2$ values, proximity of H's to M, and assignments for compounds **7**–**9**.

| | $Pd^{II}Co^{II}$ (**7**) | | | | | $Pd^{II}Ni^{II}$ (**8**) | | | | | $Pd^{II}Cu^{II}$ (**9**) | | | | |
|---|---|---|---|---|---|---|---|---|---|---|---|---|---|---|---|
| Assign ment | δ [ppm] | $T_1$ [ms] | $T_2$[a] [ms] | $R_{Co\cdots H}$ [Å] X-ray | soln.[b] | δ [ppm] | $T_1$ [ms] | $T_2$[a] [ms] | $R_{Ni\cdots H}$ [Å][25] X-ray | soln.[b] | δ [ppm] | $T_1$ [ms] | $T_2$[a] [ms] | $R_{Cu\cdots H}$ [Å] X-ray | soln.[b] |
| a | 6.09 | 11.53* | 26.20 | 7.46* | | 2.96 | 10.90* | 21.23 | 7.46* | | 3.08 | 14.05* | 17.69 | 7.47* | |
| b | 22.08 | 4.19 | 8.84 | | 6.30 | 11.15 | 4.02 | 4.89 | 6.31 | 6.32 | 7.50 | 4.85 | 3.74 | 6.25 | 6.26 |
| b′ | 11.09 | 1.28 | 7.96 | | 5.17 | 9.42 | 1.25 | 3.31 | 5.18 | 5.20 | 22.64 | 1.66 | 0.29 | 5.18 | 5.23 |
| c | 26.73 | 2.55 | 9.80 | | 5.80 | 25.53 | 2.68 | 5.13 | 5.88 | 5.90 | 7.96 | 3.29 | 6.63 | 5.81 | 5.86 |
| c′ | — | | | | | — | | | 3.71 | | — | | | 3.72 | |
| d | 17.60 | 5.59 | 8.85 | | 6.61 | 6.14 | 4.92 | 5.68 | 6.49 | 6.53 | 5.19 | 6.81 | 5.52 | 6.49 | 6.62 |
| d′ | 168.3 | — | 0.5 | | — | 128.10 | — | 0.14 | 3.78 | — | — | | | 3.81 | |
| e | 6.58 | 9.88 | 13.26 | | 7.27 | 2.60 | 9.65 | 6.92 | 7.34 | 7.30 | 1.21 | 12.04 | 8.84 | 7.11 | 7.28 |
| e′ | 34.46 | — | 2.27 | | — | –5.0 | — | 0.27 | 3.15 | — | –12.0 | — | 0.27 | 3.21 | — |

[a] $T_2 = 1/\pi$(fwh), fwh is full width at half height. [b] In solution, calculated $R_{M\cdots H} = R_{ref}(T_1/T_{ref})^{1/6}$, where $R_{ref}$ and $T_{ref}$ are reference (*) values.

obtained by the NMR method and those obtained from the X-ray structure determinations of the compounds $Pd^{II}Ni^{II}$ (**8**)[25] and $Pd^{II}Cu^{II}$ (**9**). The $Pd^{II}Co^{II}$ compound **7** may be considered as isostructural with the $Pd^{II}Ni^{II}$ compound **8** and on that basis the Co···H distances obtained from $T_1$ measurements are in good agreement with the Ni···H distances obtained from the X-ray structure.

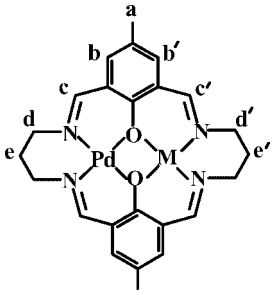


Scheme 2.

## Electrochemistry

The electrochemical properties of complexes **7**–**9** have been studied in acetonitrile using platinum and glassy carbon electrodes. Figure 8 (a) shows the cyclic voltammogram and square-wave voltammogram of $Pd^{II}Cu^{II}$ complex **9**, which undergoes one electron reduction of copper(II). The redox potential ($E_{1/2}$) of the $Pd^{II}Cu^{II}/Pd^{II}Cu^{I}$ couple, as obtained from CV, is –108 mV and the peak-to-peak separation is 60 mV versus Ag/AgCl. The $E_{1/2}$ obtained from square-wave voltammetry is –104 mV. In the potential range 0–1.5 V, an irreversible oxidation occurs for the $Pd^{II}Cu^{II}$

 © 2006 Wiley-VCH Verlag GmbH & Co. KGaA, Weinheim 

compound at 760 mV, which, however, is not observed for the $Pd^{II}Ni^{II}$ and $Pd^{II}Co^{II}$ complexes. It appears that this oxidation is not due to the formation of the ligand-based phenoxide radical because a similar observation has not been made for compounds **7** and **8**. As oxidation to the $Pd^{III}$ state seems unlikely, the formation of $Pd^{II}Cu^{III}$ species appears to be more plausible. As shown in Figure 8 (b), the $Pd^{II}Ni^{II}$ complex **8** also undergoes near-reversible reduction with $E_{1/2}$ = –803 mV for the couple $Pd^{II}Ni^{II}/Pd^{II}Ni^{I}$ and $\Delta E_p$ = 74 mV. In contrast, the $Pd^{II}Co^{II}$ complex **7** undergoes irreversible reduction for $Co^{II}$ at $E_{p,c}$ = –780 mV.

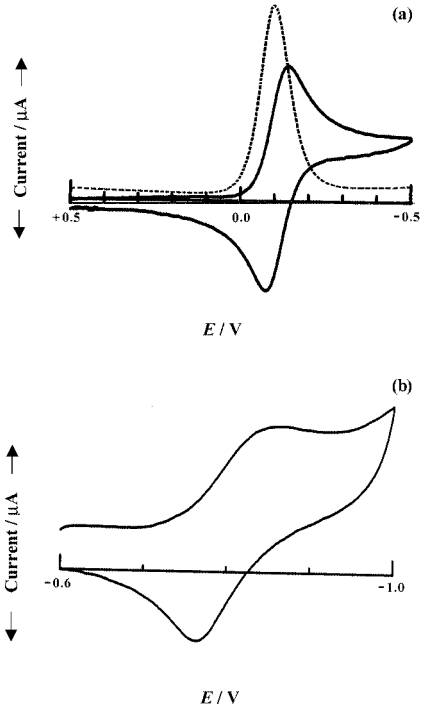


Figure 8. (a) Cyclic and square-wave voltammogram of $[Pd^{II}LCu^{II}](ClO_4)_2$ (**9**) and (b) cyclic voltammogram of $[Pd^{II}LNi^{II}(H_2O)_2](ClO_4)_2$ (**8**) in acetonitrile.

## Conclusions

Using $[Pb(LH_2)](ClO_4)_2$ as the precursor macrocyclic complex, mononuclear $[Pd(LH_2)_2](ClO_4)_2$ and $[Rh(LH_2)Cl_2](ClO_4)\cdot 3H_2O$ complexes have been prepared, which in turn have been used to produce 4d–3d heterobimetallic complexes, viz. $[Pd(L)M(H_2O)_2](ClO_4)_2$ (M = Mn, Fe, Co, Ni), $[Pd(L)Cu](ClO_4)_2$, and $[Pd(L)Zn(H_2O)](ClO_4)_2\cdot H_2O$ as well as $[RhCl_2(L)Pd](PF_6)$ and $[Pd_2L](ClO_4)_2$. The crystal structures of the $Rh^{III}Pd^{II}$ and $Pd^{II}Cu^{II}$ complexes have been determined. Proton NMR spectroscopic measurements have been carried out for the paramagnetic compounds and M···H (ligand proton) distances estimated from the relaxation time ($T_1$) values agreed fairly well with those obtained from X-ray studies. The mononuclear palladium(II) complex, which exhibits photoluminescence, during titration with $Pd(OAc)_2$ undergoes blue-shift of $\lambda_{em}$ and diminution of luminescence intensity because of the formation of the $[Pd_2L]^{2+}$ complex. On the other hand, the formation of $[Pd(L)Zn]^{2+}$ species, although it leads to a similar blue-shift of $\lambda_{em}$, is accompanied by augmentation of luminescence intensity. The $Pd^{II}Cu^{II}$ complex undergoes facile reversible electrochemical reduction to $Pd^{II}Cu^{I}$ with $E_{1/2}$ = –106 mV and irreversible oxidation to $Pd^{III}Cu^{II}$ at $E_{p,a}$ = 760 mV. The $Pd^{II}Ni^{II}$ complex also undergoes one-electron reversible reduction to $Pd^{II}Ni^{I}$ with $E_{1/2}$ = –803 mV, although no oxidation occurs up to +1.5 V. The redox behavior of the $Pd^{II}Co^{II}$ complex in the positive potential range (0 to +1.5 V) is again featureless, albeit reduction of the $Co^{II}$ center takes place irreversibly at $E_{p,c}$ = –780 mV.

## Experimental Section

**Materials:** Reagent grade chemicals obtained from commercial sources were used as received. Solvents were purified and dried according to standard methods.[29] 2,6-Diformyl-4-methylphenol was prepared according to the literature method.[30] The precursor complex $[Pb(LH_2)](ClO_4)_2$ was synthesized as reported earlier.[23]

**Preparation of the Complexes**

***CAUTION:*** All the perchlorate salts reported in this study are potentially explosive and therefore should be handled with care.

**Mononuclear Complexes $[Rh(LH_2)Cl_2](ClO_4)\cdot 3H_2O$ (1), $[Pd(LH_2)](ClO_4)_2$ (2):** A methanol solution (10 mL) of the metal chloride salts $RhCl_3\cdot xH_2O$ or $Na_2[PdCl_4]$ (1 mmol) and an acetonitrile solution (10 mL) of $NaClO_4\cdot xH_2O$ (550 mg, 4 mmol) were added to a boiling acetonitrile solution (50 mL) of $[Pb(LH_2)](ClO_4)_2$ (810 mg, 1 mmol). The color of the solution changed from yellow to wine red (for Rh) or orange (for Pd). The solution was refluxed for 12 h. After removal of the precipitated $PbCl_2$ by filtration, the filtrate was concentrated on a water bath to a volume of about 20 mL. The yellow or orange crystalline products that deposited on standing were collected by filtration and washed with methanol and diethyl ether.

**$[Rh(LH_2)Cl_2](ClO_4)\cdot 3H_2O$ (1):** Orange crystalline compound. Yield: 450 mg (62%). MS (ESI+ in $CH_3CN$): *m*/*z* = 577 $[Rh(Cl_2)(LH_2)]^+$ (100%), 641 $[Rh(Cl)(ClO_4)(LH_2)]^+$ (50%). $^1H$ NMR [300 MHz, $(CD_3)_2SO$, 25 °C]: $\delta$ = 12.44 (s, 2 H, N–H···O), 8.75 (d, $J$ = 14.8 Hz, 2 H, CH=N, metal-free site), 8.06 (s, 2 H, CH=N, metal-containing site), 7.57 (s, 2 H, Ar, metal-free site), 7.44 (s, 2 H, Ar, metal-containing site), 4.10 (s, 4 H, α-$CH_2$, metal-free site), 4.02 (s, 4 H, α-$CH_2$, metal-containing site), 2.21 (s, 6 H, $CH_3$), 2.09 (m, 4 H, β-$CH_2$) ppm. IR (KBr [$cm^{-1}$]): $\tilde{\nu}$ = 3459 br, 3147 w, 3080 w, 2919 w, 1650 s, 1550 s, 1469 m, 1445 m, 1357 m, 1279 m, 1237 m, 1122 s, 1084 s, 870 w, 823 w, 769 w, 628 m, 561 w, 487 w. $C_{24}H_{34}Cl_3N_4O_9Rh$ (731.82): calcd. C 39.39, H 4.68, N 7.66; found C 39.09, H 4.58, N 7.71.

**$[Pd(LH_2)](ClO_4)_2$ (2):** Yellow crystalline compound. Yield: 510 mg (72%). MS (ESI+ in $CH_3CN$): *m*/*z* = 611 $[Pd(LH_2)(ClO_4)]^+$ (10%), 256 $[Pd(LH_2)]^{2+}$ (100%). $^1H$ NMR [300 MHz, $(CD_3)_2SO$, 25 °C]: $\delta$ = 12.23 (s, 2 H, N–H···O), 8.80 (s, 2 H, CH=N, metal-free site), 8.11 (s, 2 H, CH=N, metal-containing site), 7.78 (s, 2 H, Ar, metal-free site), 7.63 (s, 2 H, Ar, metal-containing site), 3.98 (s, 4 H, α-$CH_2$, metal-free site), 3.85 (s, 4 H, α-$CH_2$, metal-containing site), 2.27 (s, 6 H, $CH_3$), 2.10 (s, 4 H, β-$CH_2$) ppm. IR (KBr [$cm^{-1}$]): $\tilde{\nu}$ = 3449 br, 3143 w, 3078 w, 2921 w, 1650 s, 1552 s, 1477 m, 1450 m, 1351 m, 1291 w, 1236 w, 1233 w, 1217 w, 1082 s, 1014 s, 861 w, 822 m, 624 m, 519 w. $C_{24}H_{28}Cl_2N_4O_{10}Pd$ (709.83): calcd. C 40.61, H 3.98, N 7.89; found C 40.52, H 4.05, N 7.87.

 © 2006 Wiley-VCH Verlag GmbH & Co. KGaA, Weinheim 

**$[RhCl_2(L)Pd](ClO_4)\cdot 0.5H_2O$ (3):** A methanol solution (15 mL) of $Na_2[PdCl_4]$ and an acetonitrile solution (15 mL) of triethylamine (40 mg, 0.4 mmol) were slowly added to an acetonitrile solution (15 mL) of compound **1** (150 mg, 0.2 mmol) with stirring. The resulting orange solution was refluxed for 4 h after which it was filtered. The filtrate was concentrated on a water bath to a volume of about 10 mL and then slowly cooled to room temperature. On standing for several hours a crystalline red-orange compound deposited, which was filtered and washed with methanol and diethyl ether. Yield: 110 mg (69%). MS (ESI+ in $CH_3CN$): *m*/*z* = 682.9 $[Rh(Cl_2)(L)Pd]^+$ (100%). $^1H$ NMR [300 MHz, $(CD_3)_2SO$, 25 °C]: $\delta$ = 8.19 (s, 2 H, CH=N, Pd site), 8.13 (s, 2 H, CH=N, Rh site), 7.65 (s, 2 H, Ar, Pd site), 7.62 (s, 2 H, Ar, Rh site), 3.94 (s, 4 H, α-$CH_2$, Pd site), 3.74 (s, 4 H, α-$CH_2$, Rh site), 2.27 (s, 6 H, $CH_3$), 2.07 (s, 4 H, β-$CH_2$) ppm. IR (KBr [$cm^{-1}$]): $\tilde{\nu}$ = 3422 br, 3065 w, 2924 w, 2866 w, 1630 s, 1569 s, 1468 m, 1435 m, 1367 w, 1330 s, 1279 m, 1248 m, 1089 s, 950 w, 833 m, 754 m, 624 m, 520 w, 439 w. $C_{24}H_{27}Cl_3N_4O_{6.5}PdRh$ (790.98): calcd. C 36.44, H 3.44, N 7.08; found C 36.52, H 3.69, N 6.86.

**$[RhCl_2(L)Pd](PF_6)$ (4):** Solid ammonium hexafluorophosphate (150 mg) was added to an acetonitrile solution (15 mL) of compound **3** (60 mg, 0.07 mmol), and the orange solution turned to red-orange. The solution was filtered and the filtrate was slowly concentrated on a hot plate. The product that deposited as red-orange crystals was collected by filtration. Crystals suitable for X-ray diffraction studies were obtained by diffusing diethyl ether into an acetonitrile solution of the compound. Yield: 40 mg (72%). MS (ESI+ in $CH_3CN$): *m*/*z* = 682.9 $[Rh(Cl_2)(L)Pd]^+$ (100%). IR (KBr [$cm^{-1}$]): $\tilde{\nu}$ = 2942 w, 1629 s, 1571 s, 1469 m, 1433 m, 1330 m, 1277 w, 1247 m, 1198 w, 1117 m, 958 w, 839 s, 753 m, 646 w, 555 m, 518 m, 407 w. $C_{24}H_{26}Cl_2F_6N_4O_2PPdRh$ (827.69): calcd. C 34.82, H 3.17, N 6.77; found C 34.96, H 3.26, N 6.64. The $^1H$ NMR spectrum of **4** is identical to that of **3**.

**Heterodinuclear $[Pd^{II}(L)M^{II}(H_2O)_n](ClO_4)_2$ [M = Mn, Fe, Co, Ni, Cu, Zn] Complexes (5–10):** A generalized procedure for preparing these complexes is given. An acetonitrile solution (15 mL) of $M(ClO_4)_2\cdot 6H_2O$ ($M = Mn^{II}$, $Fe^{II}$, $Co^{II}$, $Ni^{II}$, $Zn^{II}$) was added to an acetonitrile solution (30 mL) of compound **2** (140 mg, 0.2 mmol). The resulting solution was then slowly treated with an acetonitrile solution (15 mL) of triethylamine (40 mg, 0.4 mmol). After refluxing the solution for 2 h, it was concentrated on a water bath to a volume of about 10 mL. Preparation of the $Pd^{II}Mn^{II}$, $Pd^{II}Fe^{II}$, and $Pd^{II}Co^{II}$ complexes was carried out under nitrogen. The product that deposited in crystalline form on keeping the solution at room temperature was collected by filtration and washed with methanol and diethyl ether.

**$[Pd(L)Mn(H_2O)_2](ClO_4)_2$ (5):** Light orange crystalline compound. Yield: 110 mg (73%). Satisfactory mass spectrum could not be obtained. IR (KBr [$cm^{-1}$]): $\tilde{\nu}$ = 3410 br, 2929 m, 2851 w, 1633 s, 1563 s, 1459 w, 1434 m, 1412 m, 1324 m, 1114 s, 1087 s, 966 w, 825 s, 759 w, 622 m, 561 w, 501 w. $C_{24}H_{30}Cl_2MnN_4O_{12}Pd$ (798.98): calcd. C 36.09, H 3.79, N 7.01; found C 36.17, H 3.79, N 7.09.

**$[Pd(L)Fe(H_2O)_2](ClO_4)_2$ (6):** Red-brown crystalline compound. Yield: 100 mg (67%). MS (ESI+ in $CH_3CN$): *m*/*z* = 662.9 $[Pd(L)Fe(ClO_4)]^+$ (9%) and 283 $[Pd(L)Fe]^{2+}$ (100%). $^1H$ NMR (300 MHz, $CD_3CN$, 25 °C): $\delta$ = 80.21 (4 H), 35.84 (2 H), 20.83 (2 H), 10.90 (2 H), 7.91 (2 H), 4.44 (2 H), 4.22 (2 H), 3.79 (6 H), 1.23 (2 H) ppm. IR (KBr [$cm^{-1}$]): $\tilde{\nu}$ = 3456 br, 3169 w, 2921 w, 2856 w, 1635 s, 1566 s, 1440 m, 1413 w, 1317 m, 1277 m, 1243 w, 1196 w, 1106 s, 959 w, 924 w, 821 m, 755 w, 622 m, 519 w. $C_{24}H_{30}Cl_2FeN_4O_{12}Pd$ (799.69): calcd. C 36.05, H 3.78, N 7.01; found C 36.29, H 3.78, N 7.10.

**$[Pd(L)Co(H_2O)_2](ClO_4)_2$ (7):** Red-orange crystalline compound. Yield: 120 mg (75%). MS (ESI+ in $CH_3CN$): *m*/*z* = 667.9 $[Pd(L)Co(ClO_4)]^+$ (11%) and 284.5 $[Pd(L)Co]^{2+}$ (100%). $^1H$ NMR (300 MHz, $CD_3CN$, 25 °C): $\delta$ = 168.31 (4 H), 34.46 (2 H), 26.73 (2 H), 22.07 (2 H), 17.6 (4 H), 11.09 (2 H), 6.58 (2 H), 6.09 (6 H) ppm. IR (KBr [$cm^{-1}$]): $\tilde{\nu}$ = 3433 br, 2923 w, 2852 w, 1634 s, 1563 s, 1555 m, 1461 w, 1438 m, 1412 m, 1326 s, 1279 w, 1242 w, 1195 w, 1114 s, 1087 s, 966 w, 922 w, 823 m, 759 w, 624 m, 519 w. $C_{24}H_{30}Cl_2CoN_4O_{12}Pd$ (802.78): calcd. C 35.91, H 3.77, N 6.98; found C 35.84, H 3.72, N 7.04.

**$[Pd(L)Ni(H_2O)_2](ClO_4)_2$ (8):** Light green crystalline compound. Yield: 120 mg (75%). MS (ESI+ in $CH_3CN$): *m*/*z* = 666.9 $[Pd(L)Ni(ClO_4)]^+$ (8%) and 285 $[Pd(L)Ni]^{2+}$ (100%). $^1H$ NMR (300 MHz, $CD_3CN$, 25 °C): $\delta$ = 128.10 (4 H), 25.53 (2 H), 11.15 (2 H), 9.42 (2 H), 6.14 (4 H), 2.96 (6 H), 2.60 (2 H), –5.00 (2 H) ppm. IR (KBr [$cm^{-1}$]): $\tilde{\nu}$ = 3428 br, 2909 w, 2851 w, 1643 s, 1618 s, 1565 s, 1461 m, 1438 m, 1413 m, 1326 s, 1283 m, 1243 w, 1195 w, 1121 s, 1092 sh, 1052 sh, 965 w, 922 w, 823 m, 760 w, 621 m, 520 w. $C_{24}H_{30}Cl_2N_4NiO_{12}Pd$ (800.54): calcd. C 36.01, H 3.78, N 6.99; found C 35.99, H 3.85, N 6.81.

**$[Pd(L)Cu](ClO_4)_2$ (9):** Deep green crystalline compound. Yield: 130 mg (86%). MS (ESI+ in $CH_3CN$): *m*/*z* = 671.9 $[Pd(L)Cu(ClO_4)]^+$ (10%) and 287.5 $[Pd(L)Cu]^{2+}$ (100%). $^1H$ NMR (300 MHz, $CD_3CN$, 25 °C): $\delta$ = 22.64 (2 H), 7.96 (2 H), 7.50 (2 H), 5.19 (4 H), 3.08 (6 H), 1.21 (2 H), –12.00 (2 H) ppm. IR (KBr [$cm^{-1}$]): $\tilde{\nu}$ = 2922 w, 2859 w, 1632 s, 1572 s, 1468 w, 1436 m, 1419 m, 1326 s, 1283 m, 1245 m, 1198 m, 1094 s, 961 w, 935 w, 826 m, 756 m, 620 m, 518 w. $C_{24}H_{26}Cl_2CuN_4O_{10}Pd$ (771.36): calcd. C 37.37, H 3.39, N 7.26; found C 37.37, H 3.27, N 7.42.

**$[Pd(L)Zn(H_2O)](ClO_4)_2\cdot H_2O$ (10):** Yellow crystalline compound. Yield: 110 mg (69%). MS (ESI+ in $CH_3CN$): *m*/*z* = 672.9 $[Pd(L)Zn(ClO_4)]^+$ (12%) and 288 $[Pd(L)Zn]^{2+}$ (100%). $^1H$ NMR [300 MHz, $(CD_3)_2SO$, 25 °C]: $\delta$ = 8.45 (s, 2 H, CH=N, Zn site), 8.10 (s, 2 H, CH=N, Pd site), 7.49 (s, 2 H, Ar, Zn site), 7.46 (s, 2 H, Ar, Pd site), 3.94 (s, 4 H, α-$CH_2$, Zn site), 3.82 (s, 4 H, α-$CH_2$, Pd site), 2.26 (s, 6 H, $CH_3$), 2.06 (s, 4 H, β-$CH_2$) ppm. IR (KBr [$cm^{-1}$]): $\tilde{\nu}$ = 3410 br, 2927 m, 2866 w, 1637 s, 1564 s, 1439 m, 1414 m, 1366 w, 1280 m, 1243 m, 1197 w, 1087 s, 969 w, 937 w, 890 w, 825 m, 761 m, 627 m, 572 w, 506 w. $C_{24}H_{30}Cl_2N_4O_{12}PdZn$ (809.23): calcd. C 35.62, H 3.74, N 6.92; found C 35.80, H 3.78, N 7.01.

**Homodinuclear $[Pd(L)Pd](ClO_4)_2$ Complex (11):** A methanol solution (15 mL) of $Na_2[PdCl_4]$ (60 mg, 0.2 mmol) and an acetonitrile solution (5 mL) of triethylamine (40 mg, 0.4 mmol) were added successively to an acetonitrile solution (30 $cm^3$) of $[Pd(LH_2)](ClO_4)_2$ (140 mg, 0.2 mmol). The mixture was refluxed for 2 h, during which time NaCl was precipitated and removed by filtration. $NaClO_4$ (50 mg) was added to the filtrate and the volume of the solution was reduced to about 15 mL on a rotary evaporator. After filtration, the filtrate was kept on a hot plate for slow evaporation and eventually orange crystals were deposited. The product was collected by filtration and washed with cold methanol and diethyl ether. Yield: 120 mg (75%). MS (ESI+ in $CH_3CN$): *m*/*z* = 714.9 $[Pd(L)Pd(ClO_4)]^+$ (8%) and 309 $[Pd(L)Pd]^{2+}$ (100%). $^1H$ NMR [300 MHz, $(CD_3)_2SO$, 25 °C]: $\delta$ = 8.16 (s, 4 H, CH=N), 7.77 (s, 4 H, Ar), 3.68 (s, 8 H, α-$CH_2$), 2.30 (s, 6 H, $CH_3$), 2.03 (s, 4 H, β-$CH_2$) ppm. IR (KBr [$cm^{-1}$]): $\tilde{\nu}$ = 2930 w, 2848 w, 1625 s, 1571 s, 1469 m, 1329 s, 1283 w, 1246 w, 1097 m, 1087 s, 955 m, 879 w, 838 m, 751 m, 620 m, 512 w. $C_{24}H_{26}Cl_2N_4O_{10}Pd_2$ (814.23): calcd. C 35.40, H 3.22, N 6.88; found C 35.59, H 3.18, N 6.91.

**Physical Measurements:** Elemental C, H, and N analyses were performed with a Perkin–Elmer 2400II elemental analyzer. The $^1H$

 © 2006 Wiley-VCH Verlag GmbH & Co. KGaA, Weinheim 

NMR (300 MHz) spectra were performed in $CD_3CN$ (for **6**–**9**) and $(CD_3)_2SO$ solutions (for **1**–**4**, **10**, **11**) with a Bruker Avance DPX-300 spectrometer. Longitudinal relaxation times ($T_1$) were measured by the inversion recovery method. IR spectra were recorded using KBr disks with a FTIR Nexus Nicolet spectrometer using KBr disks. The electronic spectra of **1**–**11** in acetonitrile were measured in the range 250–1100 nm using Perkin–Elmer Lambda 950 spectrophotometer. Emission spectral measurements were carried out with a Perkin–Elmer LS55 luminescence spectrometer with $10^{-5}$ mol·dm$^{-3}$ acetonitrile solutions. Emission quantum yields ($\varphi$) were measured at room temperature in acetonitrile solution relative to perylene as the standard.[31] The quantum yields were calculated using the relation[32]

$$\varphi = \varphi_{std}(A_{std}/A)(I/I_{std})(\eta^2/\eta^2_{std})$$

where $A$, $I$, and $\eta$ refer to absorbance, integrated emission intensity, and solution refractive index, respectively. Electrospray ionization mass spectra (ESI-MS) of compounds **1**–**11** were measured in acetonitrile with a Micromass Qtof YA263 mass spectrometer. The electrochemical measurements were carried out with a BAS 100B electrochemistry system using a three-electrode assembly comprising a Pt or glassy carbon working electrode, Pt auxiliary electrode, and an aqueous Ag/AgCl reference electrode. The measurements (CV) were carried out at 25 °C under nitrogen in acetonitrile solution of complexes **7**–**9** (about 1 mmol·dm$^{-3}$) with tetraethylammonium perchlorate (TEAP) (0.1 mol·dm$^{-3}$) as the supporting electrolyte. The reference electrode was separated from the bulk electrolyte by a salt bridge containing 0.1 mmol·dm$^{-3}$ TEAP in acetonitrile/water (1:1). The potentials measured were automatically compensated for the iR drop and under this condition the ferrocene/ferrocenium couple occurred at 430 mV.

**X-ray Crystallography:** The crystal structure analyses were carried out for compounds **4** and **9**, whose intensity data were collected at 293 K and 203 K, respectively with a Bruker AXS P4 diffractometer using graphite-monochromated Mo-$K_\alpha$ radiation ($\lambda$ = 0.71073 Å). Crystal data and details of structure determinations are summarized in Table 5. The intensity data were corrected for Lorentz polarization effects and semiempirical absorption corrections were made from $\psi$-scans. The structures were solved by direct and Fourier methods and refined by full-matrix least-squares based on $F^2$ using SHELXTL.[33] The non-hydrogen atoms were refined anisotropically, while the hydrogen atoms were placed at the geometrically calculated positions with fixed isotropic thermal parameters.

Table 5. Crystallographic data for $[RhCl_2(L)Pd][PF_6]$ (**4**) and $[Pd(L)Cu](ClO_4)_2$ (**9**).

| | **4** | **9** |
|---|---|---|
| Empirical formula | $C_{24}H_{26}Cl_2F_6N_4O_2PdRh$ | $C_{24}H_{26}Cl_2CuN_4O_{10}Pd$ |
| Formula mass | 827.67 | 770.92 |
| Crystal size [mm] | 0.42×0.32×0.24 | 0.58×0.52×0.40 |
| Crystal system | monoclinic | monoclinic |
| Space group | $P2_1/c$ | $P2_1/n$ |
| $a$ [Å] | 12.583(5) | 7.2680(19) |
| $b$ [Å] | 17.446(2) | 8.9890(13) |
| $c$ [Å] | 13.867(3) | 20.738(5) |
| $\alpha$ [°] | 90 | 90 |
| $\beta$ [°] | 109.16(2) | 92.30(2) |
| $\gamma$ [°] | 90 | 90 |
| $V$ [Å$^3$] | 2875.5(13) | 1353.8(5) |
| $Z$ | 4 | 2 |
| $D$ [g·cm$^{-3}$] | 1.912 | 1.892 |
| $T$ [K] | 293(2) | 203(2) |
| $\lambda$ [Å] | 0.71073 | 0.71073 |
| $\mu$ [mm$^{-1}$] | 1.511 | 1.713 |
| Measured/observed reflections | 7944/6577 | 4316/3110 |
| Parameters refined | 371 | 187 |
| Final $R$ indices | $R_1$[a] = 0.0331, | $R_1$[a] = 0.0591, |
| [$I > 2\sigma(I)$] | $wR_2$[b] = 0.0735 | $wR_2$[b] = 0.1779 |
| $R$ indices | $R_1$ = 0.0505, | $R_1$ = 0.0761, |
| (all data) | $wR_2$ = 0.0830 | $wR_2$ = 0.1825 |

[a] $R_1(F) = \Sigma||F_o| - |F_c||/\Sigma|F_o|$. [b] $wR_2(F^2) = [\Sigma w(F_o^2 - F_c^2)^2/\Sigma w(F_o^2)^2]^{1/2}$.

CCDC-293271 and -293272 contain the supplementary crystallographic data for this paper. These data can be obtained free of charge from The Cambridge Crystallographic Data Centre via www.ccdc.cam.ac.uk/data_request/cif.

**Supporting Information** (see footnote on the first page of this article): Electrospray ionization mass spectra (ESI-MS+) of $[Pd^{II}(L)Cu^{II}](ClO_4)_2$ (**9**) in acetonitrile (Figure S1), absorption spectrum of compounds **7**–**9** (Figures S2–S4), and $^1$H NMR spectrum of **9** in $CD_3CN$ (Figure S5).


[1] N. H. Pilkington, R. Robson, *Aust. J. Chem.* **1970**, *23*, 2225–2236.

[2] a) H. Okawa, S. Kida, *Inorg. Nucl. Chem. Lett.* **1971**, *7*, 751–754; b) H. Okawa, S. Kida, *Bull. Chem. Soc. Jpn.* **1972**, *45*, 1759–1770.

[3] a) B. F. Hoskins, G. A. Williams, *Aust. J. Chem.* **1975**, *28*, 2607–2614; b) B. F. Hoskins, N. J. McLeod, H. A. Schaap, *Aust. J. Chem.* **1976**, *29*, 515–521.

[4] A. N. Addision, *Inorg. Nucl. Chem. Lett.* **1976**, *12*, 899–903.

[5] a) R. R. Gagne, C. A. Koval, T. J. Smith, *J. Am. Chem. Soc.* **1977**, *99*, 8367–8368; b) R. R. Gagne, C. A. Koval, T. J. Smith, M. C. Cimolino, *J. Am. Chem. Soc.* **1979**, *101*, 4571–4580.

[6] a) C. L. Spiro, S. E. Lambert, T. J. Smith, E. N. Duesler, R. R. Gagne, D. N. Hendrickson, *Inorg. Chem.* **1981**, *20*, 1229–1237; b) R. C. Long, D. N. Hendrickson, *J. Am. Chem. Soc.* **1983**, *105*, 1513–1521.

[7] a) S. K. Mandal, K. Nag, *J. Chem. Soc., Dalton Trans.* **1983**, 2429–2434; b) S. K. Mandal, K. Nag, *J. Chem. Soc., Dalton Trans.* **1984**, 2141–2149; c) S. K. Mandal, B. Adhikary, K. Nag, *J. Chem. Soc., Dalton Trans.* **1986**, 1175–1180.

[8] a) S. K. Mandal, L. K. Thompson, K. Nag, J.-P. Charland, E. J. Gabe, *Inorg. Chem.* **1987**, *26*, 1391–1395; b) S. K. Mandal, L. K. Thompson, K. Nag, J.-P. Charland, E. J. Gabe, *Can. J. Chem.* **1987**, *65*, 2815–2823; c) S. K. Mandal, L. K. Thompson, M. J. Newlands, E. J. Gabe, K. Nag, *Inorg. Chem.* **1990**, *29*, 1324–1327.

[9] a) P. Zanello, S. Tamburini, P. A. Vigato, G. A. Mazzocchin, *Coord. Chem. Rev.* **1987**, *77*, 165–273; b) P. A. Vigato, S. Tamburini, D. E. Fenton, *Coord. Chem. Rev.* **1990**, *106*, 25–170; c) P. Guerriero, S. Tamburini, P. A. Vigato, *Coord. Chem. Rev.* **1995**, *139*, 17–243.

[10] F. Lacroix, O. Kahn, F. L. Theobald, J. Leory, C. Wakselman, *Inorg. Chim. Acta* **1988**, *142*, 129–134.

[11] a) K. Brychcy, K. Dragger, K.-J. Jens, M. Tilset, U. Behrens, *Chem. Ber.* **1994**, *127*, 465–476; b) K. Brychcy, K.-J. Jens, M. Tilset, U. Behrens, *Chem. Ber.* **1994**, *127*, 991–995; c) K. Brychcy, K. Dragger, K.-J. Jens, M. Tilset, U. Behrens, *Chem. Ber.* **1994**, *127*, 1817–1826.

[12] a) L. K. Thompson, S. K. Mandal, S. S. Tandon, J. N. Bridson, M. K. Park, *Inorg. Chem.* **1996**, *35*, 3117–3125; b) S. K. Mandal, L. K. Thompson, M. J. Newlands, E. J. Gabe, *Inorg. Chem.* **1989**, *28*, 3707–3713.

[13] a) K. K. Nanda, L. K. Thompson, J. N. Bridson, K. Nag, *J. Chem. Soc., Chem. Commun.* **1994**, 1337–1338; b) K. K. Nanda, R. Das, L. K. Thompson, K. Venkatsubramanian, P. Paul, K. Nag, *Inorg. Chem.* **1994**, *33*, 1188–1193; c) K. K. Nanda, R. Das, L. K. Thompson, K. Venkatsubramanian, K.


 © 2006 Wiley-VCH Verlag GmbH & Co. KGaA, Weinheim 

Nag, *Inorg. Chem.* **1994**, *33*, 5934–5939; d) S. K. Dutta, R. Werner, U. Flörke, S. Mohanta, K. K. Nanda, W. Haase, K. Nag, *Inorg. Chem.* **1996**, *35*, 2292–2300; e) S. Mohanta, K. K. Nanda, L. K. Thompson, U. Flörke, K. Nag, *Inorg. Chem.* **1998**, *37*, 1465–1472.
[14] B. Bosnich, *Inorg. Chem.* **1999**, *38*, 2554–2562 and references cited therein.
[15] a) A. Asokan, B. Verghese, P. T. Manoharan, *Inorg. Chem.* **1999**, *38*, 4393–4399; b) S. Mohanta, B. Adhikary, S. Baitalik, K. Nag, *New J. Chem.* **2001**, *25*, 1466–1471.
[16] a) A. J. Atkins, A. J. Blake, M. Schröder, *J. Chem. Soc., Chem. Commun.* **1993**, 353–355; b) A. J. Atkins, D. Black, A. J. Blake, A. Marin-Becerra, S. Parsons, L. Rez-Ramirez, M. Schröder, *Chem. Commun.* **1996**, 457–464 and references cited therein; c) D. Black, A. J. Blake, R. L. Finn, L. F. Lindoy, A. Nezhdali, G. Rougnaghi, P. A. Tasker, M. Schröder, *Chem. Commun.* **2002**, 340–341.
[17] P. A. Vigato, S. Tamburini, *Coord. Chem. Rev.* **2004**, *248*, 1717–2128.
[18] N. Wheatley, P. Kalk, *Chem. Rev.* **1999**, *99*, 3379–3420.
[19] K. Severin, *Chem. Eur. J.* **2002**, *8*, 1514–1518.
[20] D. Karshtedt, A. T. Bell, T. D. Tilley, *Organometallics* **2003**, *22*, 2855–2861.
[21] a) R. W. J. Scott, A. K. Datye, R. M. Crooks, *J. Am. Chem. Soc.* **2003**, *125*, 3708–3709; b) Y. Mizukoshi, T. Fujimoto, Y. Nagata, R. Oshima, Y. Maeda, *J. Phys. Chem. B* **2000**, *104*, 6028–6032; c) R. W. J. Scott, O. M. Wilson, R. M. Crooks, *Chem. Mater.* **2004**, *16*, 5682–5688; d) R. W. J. Scott, O. M. Wilson, S. K. Oh, E. A. Kenik, R. M. Crooks, *J. Am. Chem. Soc.* **2004**, *126*, 15583–15591; e) R. W. J. Scott, C. Sivadinarayana, O. M. Wilson, Z. Yan, D. W. Goodman, R. M. Crooks, *J. Am. Chem. Soc.* **2005**, *127*, 1380–1381.
[22] A. J. Blake, T. I. Hyde, R. S. E. Smith, M. Schröder, *J. Chem. Soc., Chem. Commun.* **1986**, 334–336.
[23] B. Dutta, B. Adhikary, P. Bag, U. Flörke, K. Nag, *J. Chem. Soc., Dalton Trans.* **2002**, 2760–2767.
[24] B. Dutta, P. Bag, K. Nag, *New J. Chem.* **2005**, *29*, 1182–1188.
[25] P. Starynowicz, J. Lisowski, *Chem. Commun.* **1999**, 769–770.
[26] B. Dutta, P. Bag, U. Flörke, K. Nag, *Inorg. Chem.* **2005**, *44*, 147–157.
[27] P. Bag, U. Flörke, K. Nag, *Dalton Trans.* **2006**, 3236–3248.
[28] a) I. Bertini, P. Turano, A. Vila, *Chem. Rev.* **1993**, *93*, 2833–2932; b) I. Bertini, C. Luchinat, *NMR of Paramagnetic Substances*, Elsevier, Amsterdam, **1996**.
[29] D. D. Perrin, W. L. Armarego, D. R. Perrin, *Purification of Laboratory Chemicals*, 2nd ed., Pergamon, Oxford, **1980**.
[30] a) R. R. Gagne, C. L. Spiro, T. J. Smith, C. A. Hamann, W. R. Thies, A. K. Shiemke, *J. Am. Chem. Soc.* **1981**, *103*, 4073–4081; b) F. Ullmann, K. Brittner, *Ber. Dtsch. Chem. Ges.* **1909**, *42*, 2539–2548.
[31] H. Du, R. A. Fuh, J. Li, A. Corkan, J. S. Lindsay, *Photochem. Photobiol.* **1998**, *68*, 141–142.
[32] J. Van Houten, R. J. Watts, *J. Am. Chem. Soc.* **1976**, *98*, 4853–4858.
[33] Bruker, *SHELXTL* (Version 6.10), Bruker AXS Inc., Madison, WI, USA, **2002**.

Received: May 3, 2006
Published Online: August 21, 2006

 © 2006 Wiley-VCH Verlag GmbH & Co. KGaA, Weinheim 

DOI: 10.1002/ejic.200600465

# Synthesis, Structure, and Magnetism of a Highly Thermally Stable Microporous Metal Organodiphosphonate with Reversible Dehydration/Rehydration Behavior

**Hua Li,[a] Guang-shan Zhu,*[a] Xiao-dan Guo,[a] Fu-xing Sun,[a] Hao Ren,[a] Yan Chen,[a] and Shi-lun Qiu*[a]**

**Keywords:** Organic–inorganic hybrid composites / Organophosphonates / Thermal stability / Dehydration/rehydration behavior / Microporous materials

The synthesis and crystal structure of a novel organic–inorganic hybrid material $Co_2(H_2O)_2[O_3PCH_2(C_6H_4)CH_2PO_3]$ is described. It crystallizes in the orthorhombic space group *Pca*2(1) [*a* = 9.6214(19), *b* = 5.6855(11), *c* = 21.725(4) Å, *V* = 1188.4(4) Å$^3$], which consists of two-dimensional cobalt–oxygen inorganic layers pillared by *p*-xylylenediphosphonate to form a three-dimensional framework, which has 10.850 × 5.687 Å channels running along the *b*-axis. The material is exceptionally stable, even when heated up to 500 °C in air. More interestingly, the framework components display a reversible dehydration/rehydration behavior. There is an antiferromagnetic interaction between the cobalt ions.
(© Wiley-VCH Verlag GmbH & Co. KGaA, 69451 Weinheim, Germany, 2006)

## Introduction

Organic–inorganic hybrid materials have received considerable interest because of their potential ability to incorporate an organic functionality within a robust framework and promising applications in adsorbents, optical materials, magnets, catalysts, and so forth.[1–4] One such group of hybrid materials that has attracted much attention is the metal phosphonate/diphosphonate family, which exhibits great possibilities for application in the areas of sensors, charge and energy storage, biotechnology, and so forth.[5–8] As one hydroxy group (OH) of the phosphonic acid can be replaced by other organic groups, the organic diphosphonic acid has a greater advantage in the synthesis of open-framework compounds than phosphonic acid. The structure and functionality of these materials can be rationally designed by controlling the organic portion of organodiphosphonate ligands ($[O_3P–R–PO_3]^{4–}$, R = organic unit). The combination of organodiphosphonate ligands with metal ions is expected to lead to new three-dimensional structures with open frameworks and unique properties.[9–11] Not only do these ligands form materials with progressively longer organic chains to expand the pore size or contain organic functional groups to present both metal and organic species to guest molecules within the pores,[12,13] but they are also desirable in their pillared framework with clearly different organic and inorganic parts. Investigations of di-, tri-, and tetravalent metal phosphonates in recent years have yielded exciting structural diversity with interesting properties.[14–16]

Because the metal polyhedra are bridged by phosphonic tetrahedra to form two-dimensional layers, many $M^{II}(RPO_3)\cdot H_2O$ compounds are two-dimensional structures, with the metal/$PO_3$ layer arrangement and the adsorption behavior of some dehydrated layered phosphates reported in the literature.[17–21] The hydrothermal method has proved to be a promising technique in the preparation of highly stable and infinite metal–ligand frameworks.[22,23] The organophosphorus compound *p*-xylylenediphosphonate, which possesses much longer chains and a more rigid framework, has been used successfully in the hydrothermal synthesis of diphosphonates. Ferey et al. solved the structure of the copper diphosphonate $Cu_2(H_2O)_2[O_3PCH_2(C_6H_4)CH_2PO_3]$ by powder X-ray diffraction to reveal that it was built up from inorganic layers covalently linked by the organic chains.[24] The inorganic layers are constructed by the dimers of edge-sharing $CuO_4(H_2O)$ square pyramids and the $PO_3C$ tetrahedron. Harvey et al. have reported $Ga_2[O_3PCH_2(C_6H_4)CH_2PO_3](H_2O)_2F_2$, containing linear chains of corner-sharing $GaO_4F_2$ octahedra connected by diphosphonate groups to form two-dimensional framework structures.[12] *meta*-Xylylenediphosphonic acid has been used instead of the *para* isomer, leading to a layered compound.[25]

However, frameworks of organic–inorganic hybrid materials showing simultaneously permanent porosity and high

[a] State Key Laboratory of Inorganic Synthesis & Preparative Chemistry, Jilin University,
Changchun 130012, China
Fax: +86-431-5168331
E-mail: zhugs@mail.jlu.edu.cn
sqiu@mail.jlu.edu.cn
Supporting information for this article is available on the WWW under http://www.eurjic.org or from the author.

 © 2006 Wiley-VCH Verlag GmbH & Co. KGaA, Weinheim 

thermal stability are extremely rare.[26,27] The inability of these materials to support a stable framework at higher temperatures or after removing guest molecules has hindered further application in many fields.[28] So the application of diphosphonates is still quite limited relative to that of zeolites or aluminophosphates, despite the extensive studies. Generally, they are thermally unstable when compared with inorganic phosphates and most of them are destroyed at high temperature (>300 °C).

Some diphosphonates containing coordinated water and showing dehydration behavior have been reported, but their dehydration behaviors are diverse. The copper ethylenediphosphonate loses water irreversibly from the metal center, resulting in the collapse of the structure.[29] The aluminum and gallium diphosphonates lose water in two stages: first the water residing within channels and subsequently the water from positions coordinated to metal cations, and the latter stage leads to loss of crystallinity.[30,31] The aluminum and vanadium ethylenediphosphonates show reversible dehydration/rehydration behavior without losing their crystallinity and may therefore have potential applications as adsorbents, sensors, and catalysts, but such diphosphonates are still not very common.[32,33]

We have successfully synthesized a novel three-dimensional cobalt diphosphonate $Co_2(H_2O)_2[O_3PCH_2(C_6H_4)$-$CH_2PO_3]$ with two-dimensional infinite cobalt–oxygen inorganic layers pillared by an organophosphorus *p*-xylylenediphosphonate. The compound is exceptionally stable even when heated up to 500 °C in air. More interestingly, the framework components display a reversible dehydration/rehydration behavior.

## Results and Discussion

### Description of Crystal Structure

Single-crystal X-ray analysis shows that the compound is a 3D structure that possesses 2D infinite cobalt–oxygen inorganic layers pillared by the P–$CH_2$–$C_6H_4$–$CH_2$–P group. As shown in Figure 1, the asymmetric unit contains two crystallographically independent cobalt atoms, one *p*-xylylenediphosphonate ligand, and two water molecules. Each of the cobalt atoms is located in an octahedral coordination environment with five oxygen atoms (O1, O2, O3, O4, O5 for Co1; O1, O2A, O3A, O4A, O8 for Co2) from the *p*-xylylenediphosphonate ligand, and one oxygen atom (O6 for Co1; O7 for Co2) from the water molecule.

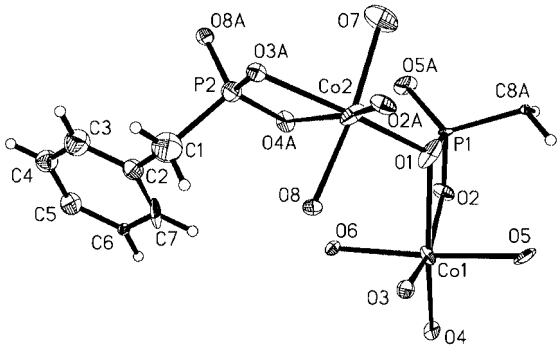


Figure 1. Thermal ellipsoid plot showing an asymmetric unit of $Co_2(H_2O)_2[O_3PCH_2(C_6H_4)CH_2PO_3]$.

The compound crystallizes in the orthorhombic space group *Pca*2(1). Interestingly, the structure consists of infinite inorganic layers of corner-sharing $CoO_6$ octahedra, which is totally different from other reported metal phosphonates using *p*-xylylenediphosphonate as the ligand.[24] The coordination between the cobalt atoms and the $PO_3$ groups in the compound is similar to that found in $Mn(C_6H_5PO_3)\cdot H_2O$[17] or $Zn(C_6H_5PO_3)\cdot H_2O$,[20] but these are 2D layered structures and the former is a 3D pillared

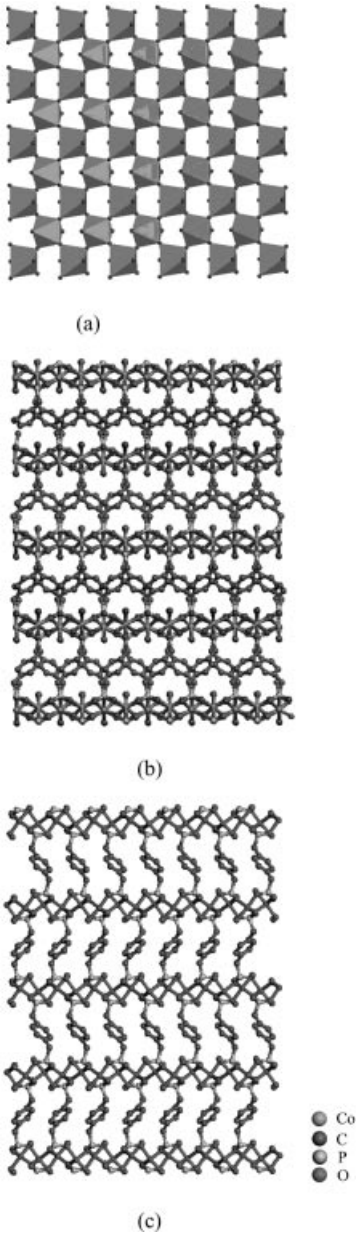


Figure 2. (a) The view of the Co–O layers of $Co_2(H_2O)_2$-$[O_3PCH_2(C_6H_4)CH_2PO_3]$ in the [001] plane. (b) A ball-and-stick representation of the structure viewed along the [100] and (c) [010] directions. Hydrogen atoms are omitted for clarity.

 © 2006 Wiley-VCH Verlag GmbH & Co. KGaA, Weinheim 

layered structure. As shown in Figure 2a, such a compound is a rare example of a hybrid metal oxide containing an infinite 2D –M–O–M–O– net framework.[34] The adjacent cobalt–oxygen layers are interconnected to each other through the organic part of *p*-xylylenediphosphonate, P–$CH_2$–$C_6H_4$–$CH_2$–P, to produce a 3D structure (Figure 2b). The pillars can connect the inner layers of the Co–O network and, thus, further stabilize the structure. As presented in Figure 2b, The *p*-xylylenediphosphonate groups link the inorganic octahedral layers in the fashion of an alternately left and right arrangement along the [100] direction. As indicated in Figure 2c, the framework along the [010] direction contains a 10.850 Å [Co1–Co1] × 5.687 Å [C3–C3] one-dimensional channel system. The overall structure may be described in terms of alternating inorganic infinite metal oxygen layers and organic pillars (P–$CH_2$–$C_6H_4$–$CH_2$–P). To the best of our knowledge, inorganic metal oxygen layers pillared by organophosphorus groups with the in situ hydrothermal method have not been reported so far.

## Thermal Stability

The thermal stability of the sample has been studied by using TGA and XRD at different temperatures. Thermogravimetric analysis (TGA) of the compound (Figure 3) showed that the first weight loss of 8.61% from 200 to 500 °C corresponds to the loss of two coordinated water molecules (calculated: 8.66%). The decomposition of the compound starts above 500 °C, which is in good agreement with the TGA of the calcined sample, except for the absence of the first weight loss, indicating that the coordinated water had already been removed during calcination (Figure S1). Considering the thermal stability of the compound, X-ray powder diffraction (PXRD) studies are performed for the as-synthesized sample and the samples heated at 350 °C, 400 °C, and 500 °C. Figure 4 presents X-ray diffraction (XRD) patterns simulated from single-crystal X-ray diffraction data as well as those of the as-synthesized sample, the calcined samples, and the rehydrated sample. The XRD pattern of the as-synthesized sample fits well with the simulated one, indicating that the sample is a pure phase. The XRD patterns for the calcined samples (Figure 4c, d, e) are similar to that of the as-synthesized sample (Figure 4b). The very intense peaks, (002) and (004), located at two Bragg angles $2\theta$ of 8.06° and 16.3°, are always maintained after calcination and rehydration, indicating that the structure of 2D cobalt–oxygen pillared by organophosphate does not collapse after the removal of the coordinated water molecules and that the calcined sample retains high crystallinity and pure phase. It is quite surprising that the compound could maintain its structure even when heated up to 500 °C, which is extremely rare in organophosphates and suggests that the compound can preserve its rigid and stable framework at high temperature. It is also clear that the dehydration of the water lattice is reversible (Figure 4f).

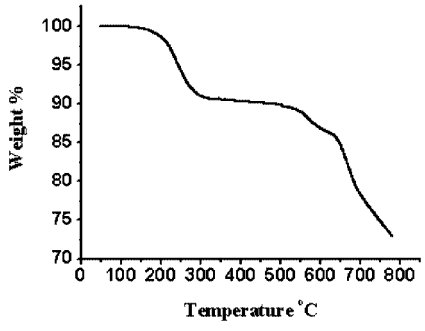


Figure 3. TGA curves of the sample.

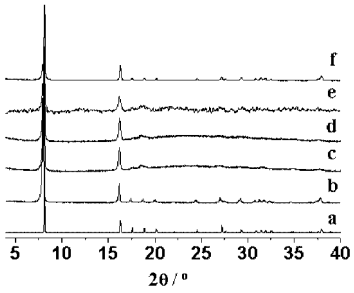


Figure 4. Simulated powder X-ray diffraction patterns of the single-crystal crystallography data (a), as-synthesized sample (b), dehydrated sample after calcination at 350 °C (c), 400 °C (d), 500 °C (e), and rehydrated sample after calcination at 350 °C (f).

## Dehydration/Rehydration Properties

Interestingly, it was found that the color of the crystals changed from pink to blue when they were heated at 350 °C for 2 h, while optical microscopy showed that they maintained their transparency and morphology (Figure 5a). Because of the difference in the crystal field splitting energy between the octahedral field and the square-pyramidal field,[35] the observed color of the compound containing octahedrally coordinated cobalt ions is pink, while that of the compound containing square-pyramidally coordinated cobalt is blue. Therefore, accompanying the change of color from pink to blue, the coordination environment of the cobalt ion is changed from octahedral to square-pyramidal.

For a deep understanding of how the structure of the compound changes with temperature and how it undergoes a reversible dehydration/rehydration process, it is instructive to simulate the distorted square-pyramidal coordination geometry of the cobalt atom in the dehydrated compound (Figure 5b). Notably, all the coordinated water can be removed from the structure at 350 °C within 2 h without loss of framework periodicity. The coordinated water is removed and diffuses out along the [100] direction, which is confirmed by the observation that some partly dehydrated crystals presented different colors after being calcined at 300 °C for 2 h: pink at the central part and blue at the two ends of the crystal (Figure 5c). Therefore, without sufficient time or higher temperature, the central part could not be fully dehydrated. More significantly, the crystals can be fully rehydrated when they are immersed in water for several hours. Thus, the rehydration process is accompanied by a return

 © 2006 Wiley-VCH Verlag GmbH & Co. KGaA, Weinheim 

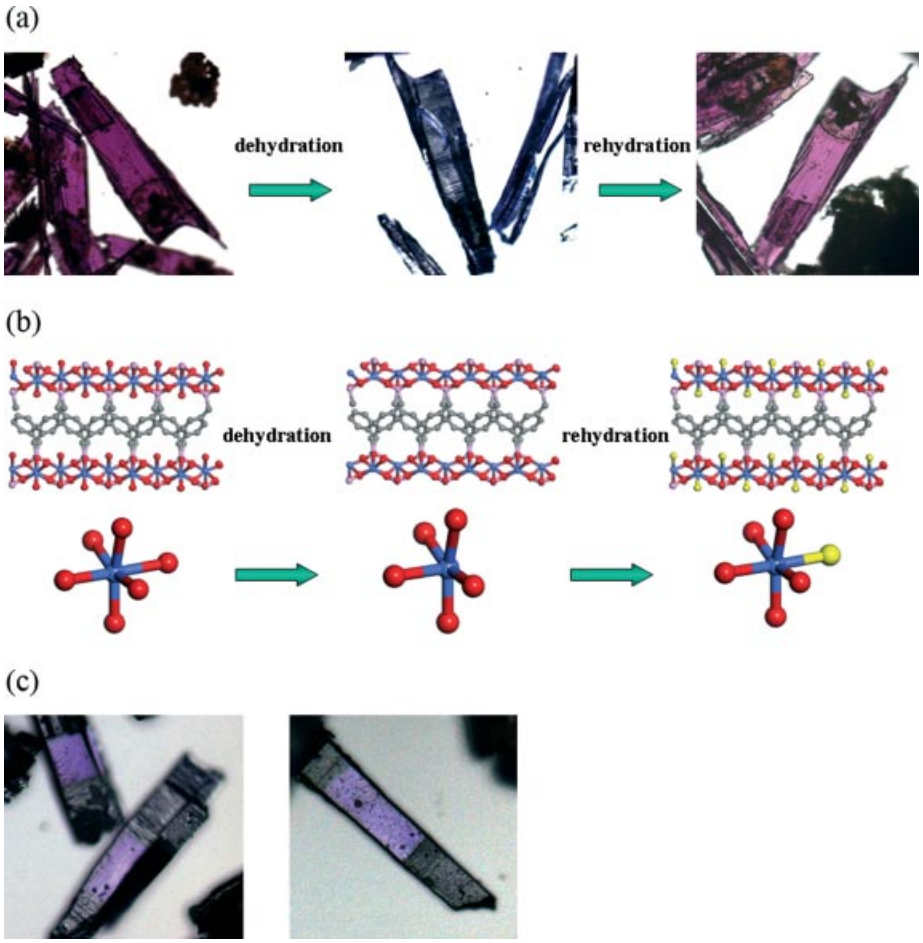


Figure 5. Pictorial representation of the dehydration/rehydration process and the partly dehydrated crystals. The pink crystals turned blue after dehydration, then changed back to pink after rehydration (a). Correspondingly, the cobalt coordination environment changed from octahedral to square pyramidal, and finally returned to octahedral (b). The partly dehydrated crystals are pink at the center and blue at the two ends (c).

of the original pink color (Figure 5a). The XRD pattern of the rehydrated sample (Figure 4f) indicates that a high degree of crystallinity is retained after water is resorbed.

### Water Sorption Properties

The phenomenon of dehydration/rehydration in the microporous frameworks and the thermal stability encouraged us to try to create the micropores after removing the coordinated and guest water molecules. The calcined compound was evacuated under reduced pressure ($1 \times 10^{-5}$ Torr) until no more weight loss occurred at 150 °C, and then it was exposed to water vapor. As shown in Figure S2, type I behavior is observed in the water adsorption isotherm of the sample in the range $P/P_0$ = 0–0.7. At saturation, the amount of water sorbed is 87.6 mg g$^{-1}$, which is equivalent to the adsorption of about eight water molecules per formula unit. Therefore, the pore volume is estimated to be approximately 0.09 mL g$^{-1}$ by the water adsorption isotherm.

### IR Spectrum

This dehydration process can be further confirmed by IR spectroscopy (Figure 6). The IR spectrum of the as-synthesized sample (Figure 6a) presents broad peaks at 3494 cm$^{-1}$

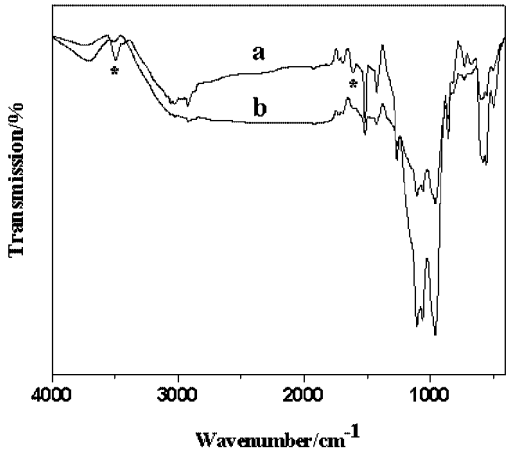


Figure 6. IR spectrum of the sample (a) and of the sample after calcination at 350 °C (b).

 © 2006 Wiley-VCH Verlag GmbH & Co. KGaA, Weinheim 

corresponding to the stretching of water molecules and a sharp peak at 1618 $cm^{-1}$ corresponding to the bending vibration of coordinated water. After calcination at 350 °C for 2 h, the two types of peaks mentioned above decreased in size significantly (Figure 6b). The main structure peaks could correspondingly be observed in the spectrum of the calcined sample as compared to the as-synthesized sample, indicating that the main framework of the compound is retained after calcination.

### Magnetic Properties

The temperature-dependent (4–300 K) magnetic susceptibility of the compound is shown in Figure 7. Between 4 and 300 K, $\chi_m$ continuously increases with decreasing temperature and achieves a maximum of 0.115 $cm^3 mol^{-1}$ at 8.99 K. In the $1/\chi_m$ versus $T$ plot, the susceptibility can be fitted to the Curie–Weiss law with $C = 6.87\ cm^3 K mol^{-1}$. The Weiss temperature, $\theta = -50.97$ K, indicates that antiferromagnetic interactions exist between the metallic Co centers.

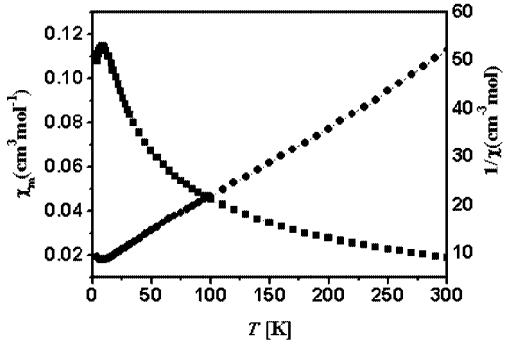


Figure 7. $\chi_m$ vs. $T$ and $1/\chi_m$ vs. $T$ plots of $Co_2(H_2O)_2[O_3PCH_2(C_6H_4)CH_2PO_3]$.

## Conclusions

A cobalt diphosphonate with micropores has been synthesized by a hydrothermal method. The structure was solved by single-crystal X-ray diffraction and found to be constructed of infinite cobalt oxygen layers pillared by *p*-xylylenediphosphonate groups. The compound is stable up to 500 °C, illustrating the exceptional stability of the framework. The more important feature is that it undergoes a reversible dehydration/rehydration process driven by temperature, which can be detected by changes in crystal color. This is a rare example of a metal diphosphonate framework that has a "defect" site with incomplete coordination, which can be created without loss of framework architecture. Such defect sites in compounds can result in changes in physical properties, such as color, and are expected to show shape-selective adsorption behavior for small molecules and could be potentially used as sensors, adsorbents, catalysts and so forth.

Currently, we are carrying out investigations into the ability of dehydrated compounds to absorb molecules other than water. Efforts toward the preparation of new hybrid materials containing other transition metals based on this type of ligand are underway.

## Experimental Section

**General Remarks:** All chemicals purchased were of reagent grade or better and were used without further purification. The elemental analyses were carried out with a Perkin–Elmer 240C elemental analyzer. TGA (thermal gravimetric analyses) were performed under nitrogen with a heating rate of 10 °C $min^{-1}$ by using a Perkin–Elmer TGA 7 thermogravimetric analyzer. XRD was performed with a Siemens D5005 diffractometer with Cu-$K_\alpha$ radiation, 40 kV, 35 mA at a scanning rate of 0.3°$min^{-1}$ ($2\theta$). The IR spectra were recorded (400–4000 $cm^{-1}$ region) with a Nicolet Impact 410 FTIR spectrometer by using KBr pellets.

**Synthesis of $Co_2(H_2O)_2[O_3PCH_2(C_6H_4)CH_2PO_3]$:** As a typical preparation procedure, a mixture of tetraethyl *p*-xylylenediphosphonate (0.03 mmol) and $Co(NO_3)_2{\cdot}4H_2O$ (0.03 mmol) was suspended in deionized water (8 mL) and cyclohexanol (2 mL), and then triethylamine (0.1 mL) was added while stirring to adjust the pH value of the mixture. The mixture (pH ≈ 6) was sealed in a 15-mL Teflon-lined autoclave after being stirred for 60 min. Upon being heated at 160 °C for 2 d, the autoclaved mixture was naturally cooled to room temperature. The pink crystals were collected, washed with deionized water, and dried at room temperature. The compound was stable in air and insoluble in water and common organic solvents. $C_8H_{12}Co_2O_8P_2$: calcd. C 23.10, H 2.90, Co 28.33, P 14.89; found C 23.40, H 3.34, Co 28.03, P 14.20.

**X-ray Crystallographic Study:** The intensity data were collected with a Smart CCD diffractometer with graphite-monochromated Mo-$K_\alpha$ ($\lambda = 0.71073$ Å) radiation at 293 K in the $\omega$-scan mode. An empirical absorption correction was applied to the data by using the SADABS program.[36] The structures were solved by direct methods. All non-hydrogen atoms were refined anisotropically. Hydrogen atoms were fixed at calculated positions and refined by using a riding mode. All calculations were performed with the SHELXTL program.[37] The crystallographic data are summarized in Table 1, and the selected bond lengths and bond angles of the compound are listed in Table 2. CCDC-608190 for $Co_2(H_2O)_2[O_3PCH_2(C_6H_4)CH_2PO_3]$ contains the supplementary crystallographic data for this paper. These data can be obtained free of charge from The Cambridge Crystallographic Data Centre via www.ccdc.cam.ac.uk/data_request/cif.

Table 1. Crystallographic data for the compound.

| | |
|---|---|
| Empirical formula | $C_8H_{12}Co_2O_8P_2$ |
| Formula mass | 415.98 |
| Crystal system | orthorhombic |
| Space group | *Pca*2(1) |
| *a* [Å] | 9.6214(19) |
| *b* [Å] | 5.6855(11) |
| *c* [Å] | 21.725(4) |
| *V* [Å$^3$] | 1188.4(4) |
| *Z* | 4 |
| $\rho_{calcd.}$ [g $cm^{-3}$] | 0.2325 |
| $\mu$ [$mm^{-1}$] | 3.096 |
| $R^{[a]}$ [$I > 20\sigma(I)$] | 0.0582 |
| $R_w^{[b]}$ | 0.1316 |

[a] $R = \Sigma||F_o| - |F_c||/\Sigma|F_o|$. [b] $R_w = [\Sigma w(F_o^2 - F_c^2)/\Sigma w(F_o^2)^2]^{1/2}$.

 © 2006 Wiley-VCH Verlag GmbH & Co. KGaA, Weinheim 

Table 2. Selected bond lengths [Å] and angles [°] for the compound.[a]

| | | | |
|---|---|---|---|
| Co1–O1 | 2.275(5) | Co1–O2 | 2.088(4) |
| Co1–O3 | 2.012(5) | Co1–O4 | 2.046(5) |
| Co1–O5 | 2.102(5) | Co1–O6 | 2.156(5) |
| Co2–O1 | 2.095(5) | Co2–O2A | 2.068(5) |
| Co2–O3B | 2.192(5) | Co2–O4C | 2.342(5) |
| Co2–O7 | 2.150(6) | Co2–O8 | 2.082(5) |
| | | | |
| O2–Co1–O1 | 66.62(17) | O3–Co1–O1 | 90.39(19) |
| O4–Co1–O1 | 164.72(17) | O5–Co1–O1 | 85.12(18) |
| O6–Co1–O1 | 91.72(18) | O3–Co1–O2 | 156.82(18) |
| O4–Co1–O2 | 98.12(19) | O5–Co1–O2 | 87.81(18) |
| O3–Co1–O4 | 104.9(2) | O3–Co1–O5 | 93.41(19) |
| O4–Co1–O5 | 93.80(19) | O2–Co1–O6 | 88.51(18) |
| O3–Co1–O6 | 89.24(18) | O4–Co1–O6 | 88.55(18) |
| O5–Co1–O6 | 175.88(19) | O2A–Co2–O1 | 104.95(19) |
| O2A–Co2–O3B | 93.05(19) | O1–Co2–O3B | 162.00(18) |
| O7–Co2–O3B | 85.9(2) | O8–Co2–O3B | 88.13(19) |
| O1–Co2–O4C | 95.89(19) | O3B–Co2–O4C | 66.36(17) |
| O7–Co2–O4C | 90.5(2) | O8–Co2–O4C | 83.67(18) |
| O2A–Co2–O4C | 157.89(16) | O1–Co2–O7 | 91.6(2) |
| O2A–Co2–O7 | 96.12(19) | O8–Co2–O7 | 173.0(2) |
| O1–Co2–O8 | 92.99(19) | O2A–Co2–O8 | 87.87(17) |

[a] Symmetry transformations used to generate equivalent atoms: A: $x$, $y-1$, $z$; B: $x-1/2$, $-y$, $z$; C: $x-1/2$, $-y+1$, $z$.

**Water Sorption Isotherm:** Water sorption isotherm studies were performed by measuring the increase in weight at equilibrium as a function of relative pressure. The weight of the sample was measured by a CAHN 2000 electrobalance and the adsorbate ($H_2O$) was added incrementally and manually.

**Supporting Information** (see footnote on the first page of this article): Figure S1, TGA curves of the compound after being calcined at 350 °C, and Figure S2, water sorption isotherm for the dehydrated compound, are available.

## Acknowledgments

This work was funded by the State Basic Research Project (No. 2006CB806100) and the National Nature Science Foundation of China (Grant nos. 20571030, 20531030 and 20371020).

[1] A. Clearfield, *Progress in Inorganic Chemistry* (Ed.: K. D. Karlin), John Wiley & Sons, New York, **1998**, vol. 47, p. 371.
[2] a) D. Deniaud, G. A. Spyroulias, J. F. Bartoli, P. Battioni, D. Mansuy, C. Pinel, F. Odobel, B. Bujoli, *New J. Chem.* **1998**, *22*, 901–905; b) S. M. Zakeeruddin, M. K. Nazeeruddin, P. Pechy, F. P. Rotzinger, R. Humphry-Baker, K. Kalyanasundaram, M. Graltzel, *Inorg. Chem.* **1997**, *36*, 5937–5946.
[3] C. Maillet, P. Janvier, M. Pipelier, T. Praveen, Y. Andres, B. Bujoli, *Chem. Mater.* **2001**, *13*, 2879–2884.
[4] D. Deniaud, B. Schollorn, D. Mansuy, J. Rouxel, P. Battioni, B. Bujoli, *Chem. Mater.* **1995**, *7*, 995–1000.
[5] a) K. Maeda, Y. Kiyozumi, F. Mizukami, *J. Phys. Chem. B* **1997**, *101*, 4402–4412; b) L. C. Brousseau III, T. E. Mallouk, *Anal. Chem.* **1997**, *69*, 679–687; c) L. C. Brousseau III, D. J. Aurentz, A. J. Benesi, T. E. Mallouk, *Anal. Chem.* **1997**, *69*, 688–694.
[6] G. Alberti, M. Casciola, *Solid State Ion.* **1997**, *97*, 177–186.
[7] L. A. Vermeulen, M. E. Thompson, *Nature* **1992**, *358*, 656–658.
[8] B. Bujoli, S. M. Lane, G. Nonglaton, M. Pipelier, J. Léger, D. R. Talham, C. Tellier, *Chem. Eur. J.* **2005**, *11*, 1980–1988.
[9] T. Asefa, M. J. MacLachlan, N. Coombs, G. A. Ozin, *Nature* **1999**, *402*, 867–871.
[10] M. A. Said, H. W. Roesky, C. Rennekamp, M. Andruh, H. Schmidt, M. Noltemeyer, *Angew. Chem. Int. Ed.* **1999**, *38*, 661–664.
[11] V. A. Russell, C. C. Evans, W. Li, M. D. Ward, *Science* **1997**, *276*, 575–579.
[12] H. G. Harvey, A. C. Herve, H. C. Hailes, M. P. Attfield, *Chem. Mater.* **2004**, *16*, 3756–3766.
[13] W. F. Yan, E. W. Hagaman, S. Dai, *Chem. Mater.* **2004**, *16*, 5182–5186.
[14] D. K. Cao, Y. Z. Li, L. M. Zheng, *Inorg. Chem.* **2005**, *44*, 2984–2985.
[15] H. G. Harvey, S. J. Teat, M. P. Attfield, *J. Mater. Chem.* **2000**, *10*, 2632–2633.
[16] A. Subbiah, D. Pyle, A. Rowland, J. Huang, R. A. Narayanan, P. Thiyagarajan, J. Zon, A. Clearfield, *J. Am. Chem. Soc.* **2005**, *127*, 10826–10827.
[17] G. Cao, H. Lee, V. M. Lynch, T. E. Mallouk, *Inorg. Chem.* **1988**, *27*, 2781–2785.
[18] G. Cao, T. E. Mallouk, *Inorg. Chem.* **1991**, *30*, 1434–1438.
[19] K. J. Frink, R. C. Wang, J. L. Colbn, A. Clearfield, *Inorg. Chem.* **1991**, *30*, 1438–1441.
[20] K. J. Martin, P. J. Squattrito, A. Clearfield, *Inorg. Chim. Acta* **1989**, *155*, 7–9.
[21] A. Clearfield, *Curr. Opin. Solid State Mater. Sci.* **2002**, *6*, 495–506.
[22] A. Rujiwatra, C. J. Kepert, J. B. Claridge, M. J. Rosseinsky, H. Kumagai, M. Kurmoo, *J. Am. Chem. Soc.* **2001**, *123*, 10584–10594.
[23] D. Kong, A. Clearfield, *Chem. Commun.* **2005**, 1005–1006.
[24] D. Riou, F. Beler, C. Serre, M. Nogues, D. Vichard, G. Ferey, *Int. J. Inorg. Mater.* **2000**, *2*, 29–33.
[25] V. Penicaud, D. Massiot, G. Gelbard, F. Odobel, B. Bujoli, *J. Mol. Struct.* **1998**, *470*, 31–38.
[26] T. M. Reineke, M. Eddaoudi, M. Fehr, D. Kelley, O. M. Yaghi, *J. Am. Chem. Soc.* **1999**, *121*, 1651–1657.
[27] E. Y. Lee, S. Y. Jang, M. P. Suh, *J. Am. Chem. Soc.* **2005**, *127*, 6374–6381.
[28] H. Li, M. Eddaoudi, M. O'Keefe, O. M. Yaghi, *Nature* **1999**, *402*, 276–279.
[29] D. M. Poojary, B. L. Zhang, A. Clearfield, *J. Am. Chem. Soc.* **1997**, *119*, 12550–12559.
[30] H. G. Harvey, S. J. Teat, M. P. Attfield, *J. Mater. Chem.* **2000**, *10*, 2632–2633.
[31] H. G. Harvey, J. Hu, M. P. Attfield, *Chem. Mater.* **2003**, *15*, 179–188.
[32] R. N. Devi, P. Wormald, P. A. Cox, P. A. Wright, *Chem. Mater.* **2004**, *16*, 2229–2237.
[33] K. O. Kongshaug, D. Riou, *J. Chem. Soc., Dalton Trans.* **2002**, 4152–4155.
[34] P. J. Hagrman, R. L. LaDuca, H. J. Koo, R. Rarig, R. C. Haushalter, M. H. Whangbo, J. Zubieta, *Inorg. Chem.* **2000**, *39*, 4311–4317.
[35] F. A. Cotton, G. Wilkinson, *Advanced Inorganic Chemistry*, John Wiley & Sons, Inc., New York, **1972**, pp. 593–619.
[36] G. M. Sheldrick, *SADABS, Program for Empirical Absorption Correction for Area Detector Data*, University of Göttingen, Göttingen, **1996**.
[37] G. M. Sheldrick, *SHELXS 97, Program for Crystal Structure Refinement*, University of Göttingen, Göttingen, **1997**.

Received: May 19, 2006
Published Online: August 15, 2006

 © 2006 Wiley-VCH Verlag GmbH & Co. KGaA, Weinheim 

DOI: 10.1002/ejic.200600468

# Synthesis, Structure and Reactivity of Hydrated and Dehydrated Organotin Cations

**Vadapalli Chandrasekhar,*[a] Ramamoorthy Boomishankar,[a] Kandasamy Gopal,[a] Palani Sasikumar,[a] Puja Singh,[a] Alexander Steiner,[b] and Stefano Zacchini[b]**

**Keywords:** Organotin cations / Organooxotin / Organostannoxane / Acetylation / Transacetylation

Monomeric organotin dications $\{[n\mathrm{Bu_2Sn(H_2O)_4}]^{2+}\cdot 2\mathrm{C_6H_5SO_3^-}\}$ and $\{[n\mathrm{Bu_2Sn(H_2O)_4}]^{2+}\cdot 1,5\text{-}\mathrm{C_{10}H_6(SO_3^-)_2}\}$ have been synthesized by the reaction of $[n\mathrm{Bu_2SnO}]_n$ and the corresponding arylsulfonic acid. Dodecanuclear organooxotin macrocations $\{[(n\mathrm{BuSn})_{12}(\mu_3\text{-}\mathrm{O})_{14}(\mu_2\text{-}\mathrm{OH})_6]^{2+}\cdot 2\mathrm{RSO_3^-}\}$ (R = $\mathrm{C_6H_5}$; 2,5-$\mathrm{Me_2C_6H_3}$) have been synthesized by the reaction of *n*BuSn(O)(OH) and the corresponding arylsulfonic acid. The X-ray crystal structure of one of the dodecanuclear cages is reported. These organotin cations have been shown to be effective catalysts in acetylation and transacetylation reactions.

(© Wiley-VCH Verlag GmbH & Co. KGaA, 69451 Weinheim, Germany, 2006)

## Introduction

Organotin oxides $[(\mathrm{R_3Sn})_2\mathrm{O}; (\mathrm{R_2SnO})_n]$, hydroxides $[\mathrm{R_3SnOH}]$ and oxide hydroxides $[\{\mathrm{RSn(O)OH}\}_n]$ are important precursors for the synthesis of a large number of organotin compounds.[1] These precursors are the eventual hydrolysis products of the corresponding organotin halides. Initial hydrolysis of organotin halides leads to the formation of hydrated organotin cations.[2] Inspite of their apparent simplicity there have been very few reports on the isolation of such species in the solid state.[3] In most cases, dehydrated hydroxide-bridged compounds[4a] or oxo-bridged ladders[4b] are the products. In preliminary communications we have recently reported that arylsulfonic acids are effective in stabilizing $\{[n\mathrm{Bu_2Sn(H_2O)_4}]^{2+}\cdot 2\ 2,5\text{-}\mathrm{Me_2C_6H_3SO_3^-}\}$ (**1**)[5a] and $\{[n\mathrm{Bu_2Sn(H_2O)_3}]_2[\mu\text{-}1,5\text{-}\mathrm{C_{10}H_6(SO_3)_2}]\}^{2+}\cdot 1,5\text{-}\mathrm{C_{10}H_6(SO_3^-)_2}$ (**2**).[5b] Herein we report the general applicability of this synthetic procedure. Accordingly, the hydrated organotin cations, $\{[n\mathrm{Bu_2Sn(H_2O)_4}]^{2+}\cdot[x\mathrm{Y}]^{2-}\}$, where $x = 2$, $\mathrm{Y} = \mathrm{C_6H_5SO_3}$ (**3**); $x = 1$, $\mathrm{Y} = 1,5\text{-}\mathrm{C_{10}H_6(SO_3)_2}$ (**4**) have been prepared and characterized. Attempts to prepare hydrated monoorganotin cations resulted in the macromeric dodecanuclear organooxotin cages (*foot-ball cages*), $\{[(n\mathrm{BuSn})_{12}(\mu_3\text{-}\mathrm{O})_{14}(\mu_2\text{-}\mathrm{OH})_6]^{2+}\cdot 2\mathrm{RSO_3^-}\}$, where R = $\mathrm{C_6H_5}$ (**5**); 2,5-$\mathrm{Me_2C_6H_3}$ (**6**). The X-ray crystal structure of **6** is reported and compared with other members of this structural type. In view of the interest in neutral and cationic organotin compounds in esterification and transesterification reactions we have explored the catalytic activity of **1**–**6** towards acetylation of alcohols and phenols.

[a] Department of Chemistry, Indian Institute of Technology, Kanpur,
Kanpur 208 016, India
Fax: +91-512-2590007 / 2597436
E-mail: vc@iitk.ac.in
[b] The Donnan and Robinson Laboratories, Department of Chemistry, University of Liverpool,
Liverpool L697ZD, U.K.

## Results and Discussion

### Synthesis of Organotin Cations

The synthesis of the organotin cations has been accomplished in high yields by the reaction of an organotin oxide with an arylsulfonic acid. The work-up of the reaction mixture and subsequent crystallization in open air allows the isolation of the compounds **1**–**4**. All of these organotin cations are air-stable solids. Compounds **3** and **4** are prepared by a reaction of the polymeric $[n\mathrm{Bu_2SnO}]_n$ with the corresponding sulfonic acids (Scheme 1). This procedure is similar to that reported by us recently for the synthesis of **1** (Scheme 1).[5a] Compound **2**, which contains two tin units bridged by a disulfonate, is synthesized by the dealkylation reaction involving a 1:1 reaction of $(n\mathrm{Bu_3Sn})_2\mathrm{O}$ with naphthalene-1,5-disulfonic acid.[5b] The dodecanuclear organooxotin cages **5** and **6** are assembled by the reaction of *n*-butylstannonic acid, *n*BuSn(O)(OH) with the corresponding sulfonic acids (Scheme 2).[6]

### Solution Studies

All of these compounds have been characterized by analytical and spectroscopic techniques (see experimental section). Consistent with the above formulation; conductivity studies on **3** and **4** revealed that these compounds are 1:2 electrolytes. While the specific and molar conductivities of **3** are 1811 $\mu\mathrm{S\,cm^{-1}}$ and 300 $\mathrm{S\,cm^2\,mol^{-1}}$ (3 mmol/L in

 © 2006 Wiley-VCH Verlag GmbH & Co. KGaA, Weinheim 

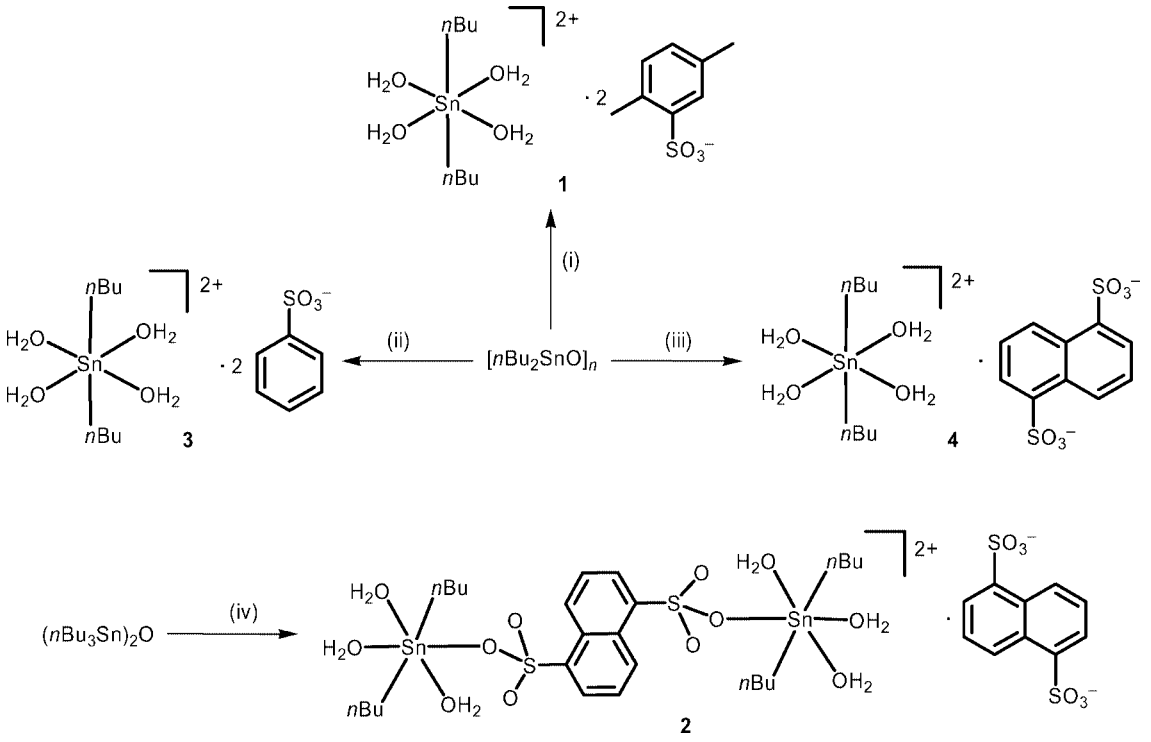


Scheme 1. Synthesis of diorganotin cations **1**–**4**. (i) 2 2,5-$Me_2C_6H_3SO_3H$, toluene, reflux, 8 h. (ii) 2 $C_6H_5SO_3H$, toluene, reflux, 8 h. (iii) 1,5-$C_{10}H_6(SO_3H)_2$, toluene, reflux, 8 h. (iv) 2 1,5-$C_{10}H_6(SO_3H)_2$, toluene, reflux, 6 h.

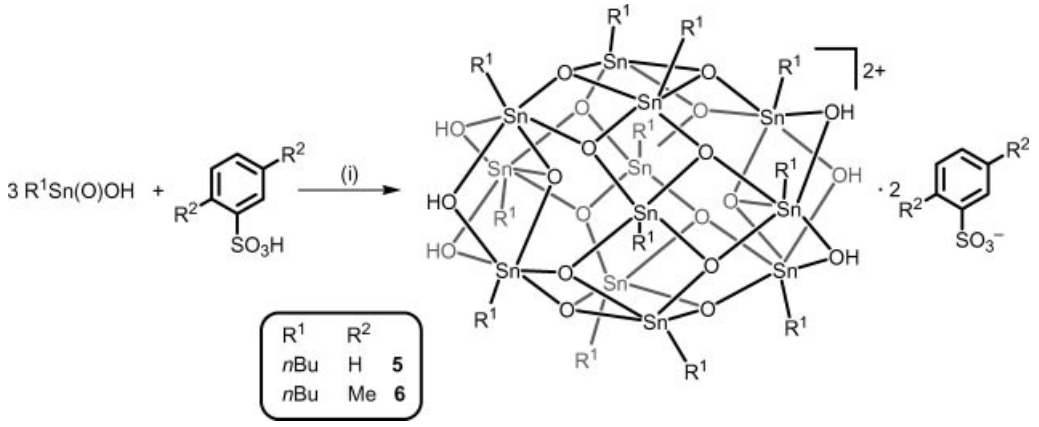


Scheme 2. Synthesis of monoorganotin macrocations **5** and **6**. (i) toluene, reflux, 72 h.

$CH_3OH$), **4** has a specific conductivity of 898 $\mu S\,cm^{-1}$ and a molar conductivity of 150 $S\,cm^2\,mol^{-1}$ (3 mmol/L in DMF) (Table 1). The increased ionic conductivity of **3** when compared to **1** [specific conductivity 946 $\mu S\,cm^{-1}$; molar conductivity 158 $S\,cm^2\,mol^{-1}$ (3 mmol/L in $CH_3OH$)][5a] and **4** is attributed to the increased acidic nature of **3** which arises due to the benzenesulfonate ligand. The $^{119}Sn$ NMR spectra of **3** and **4** show a single resonance at –360.6 and –384.9 ppm, respectively (Table 1), which are comparable to that observed for **1** (a single resonance at $\delta$ = –360.0 ppm)[5a] which is characteristic of a $C_2O_4$ environment around tin atoms.[1b]

The solution ionic conductivity measurement on **2** shows that the observed specific and molar conductivities are 2257 $\mu S\,cm^{-1}$ and 376 $S\,cm^2\,mol^{-1}$ (3 mmol/L in $CH_3OH$), respectively. These values suggest that in solution **2** does not exist as a 1:2 electrolyte but presumably undergoes an unsymmetrical disproportionation of the tin–sulfonate oxygen bond and thereby producing different kinds of cationic species. Support for such a hypothesis also comes from the $^{119}Sn$ NMR chemical shifts of the compound **2**. $^{119}Sn$ NMR spectrum of a [$D_6$]DMSO solution of **2** shows two resonances at –385.7 and 8.3 ppm (Table 1). Whereas, the signal at $\delta$ = –385.7 ppm corresponds to the six-coordinate

 © 2006 Wiley-VCH Verlag GmbH & Co. KGaA, Weinheim 

Table 1. Solution studies of some of the selected organotin compounds.

| Entry | Compound | Specific conductivity [$\mu S\,cm^{-1}$] | Molar conductivity [$S\,cm^2\,mol^{-1}$] | $^{119}Sn$ NMR [$\delta$, ppm] | Ref. |
|---|---|---|---|---|---|
| 1 | $\{n\mathrm{Bu_2Sn(\mu\text{-}OH)(H_2O)(O_3SCF_3)}\}_2$ | 870[a] | 43.5[a] | –203.2[h] (–209.7[i]) | [3c] |
| 2 | $\{[t\mathrm{Bu_2Sn(\mu\text{-}OH)(H_2O)}]^+\cdot\mathrm{CF_3SO_3^-}\}_2$ | 994[a] | 49.7[a] | –249.7[h] (–249.6[i]) | [3c] |
| 3 | $\{[(2\text{-}\mathrm{C_6H_5}\text{–}\mathrm{C_4H_8})_2\mathrm{Sn(\mu\text{-}OH)(H_2O)}]^+\cdot\mathrm{CF_3SO_3^-}\}_2$ | 805[a] | 40.0[a] | –188.4[i] | [3d] |
| 4 | **1** | 946[b] | 158[b] | –360.04[j] | [5a] |
| 5 | **3** | 1811[b] | 300[b] | –360.61[j] | this work |
| 6 | **4** | 898[c] | 150[c] | –384.91[k] | this work |
| 7 | **2** | 2257[b] | 376[b] | –385.7, +8.3[k] | this work |
| 8 | **5** | 1503[b] | 250[b] | –284.28, –463.8[l] | this work |
| 9 | **6** | 971[b] | 162[b] | –283.97, –462.77[l] | this work |
| 10 | $[\mathrm{Me_2Sn(H_2O)_2(OPPh_3)_2}]^{2+}\cdot 2\mathrm{CF_3SO_3^-}$ | 714[d] | – | –296.4[l] (–343.9[i]) | [3e] |
| 11 | $[n\mathrm{Bu_2Sn(H_2O)_2(OPPh_3)_2}]^{2+}\cdot 2\mathrm{CF_3SO_3^-}$ | 705[d] | – | –302.1[l] (–363.5[i]) | [3e] |
| 12 | *foot-ball cage*[n] | 5[e] 200[f]–1210[g] | – | –282.8, –461.8[m] | [6] |

[a] 10 mmol/L in $CH_3CN$. [b] 3 mmol/L in $CH_3OH$. [c] 3 mmol/L in DMF. [d] 3.3 mmol/L in $CH_3CN$. [e] 5 mmol/L in $CD_2Cl_2$ (for pure $CD_2Cl_2$, 5 $\mu Scm^{-1}$). [f] 5 mmol/L in DMSO. [g] 50 mmol/L in DMSO. [h] [$D_6$]acetone. [i] $CD_3CN$. [j] $CD_3OD$. [k] [$D_6$]DMSO. [l] $CDCl_3$. [m] $CD_2Cl_2$. [n] Anion: 2 4-$MeC_6H_4SO_3^-$.

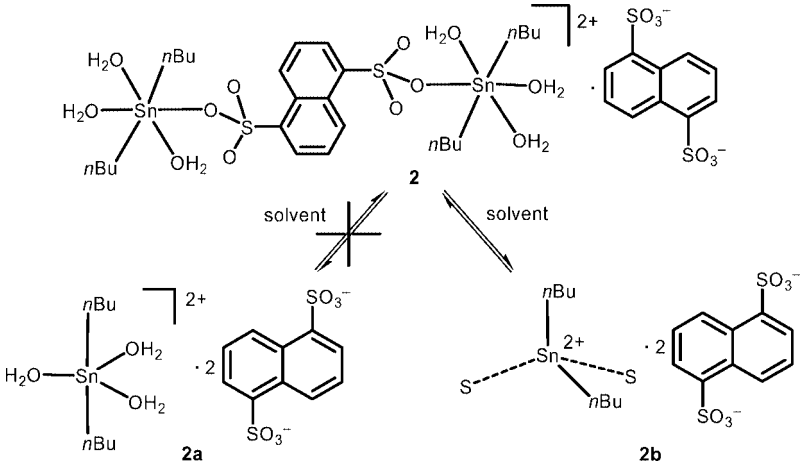


Scheme 3. Solution equilibrium exhibited by the cation **2**. S: more polar solvents ($CH_3OH$ or [$D_6$]DMSO).

$C_2O_4$ environment around tin, the value of +8.3 ppm is quite unusual for a diorganotin oxo species and could be attributed to a tetracoordinate tin containing two coordinated DMSO molecules.[7] If a very dilute solution is used only the signal at +8.3 ppm is seen. This could presumably due to the highly polar nature of the solvent DMSO which displaces all the ligated (water and sulfonate) groups of tin and thereby producing a $[n\mathrm{Bu_2Sn(DMSO)_2}]^{2+}$ species **2b** (Scheme 3).

The conductivity values of **5** and **6** suggest that these compounds are 1:2 electrolytes in solution. While the observed specific and molar conductivities of **5** are 1503 $\mu S\,cm^{-1}$ and 250 $S\,cm^2\,mol^{-1}$ (3 mmol/L in $CH_3OH$), the respective values observed for **6** are 971 $\mu S\,cm^{-1}$ and 162 $S\,cm^2\,mol^{-1}$ (3 mmol/L in $CH_3OH$), respectively (Table 1). The $^{119}Sn$ NMR spectra of **5** and **6** show two resonances around –280 and –460 ppm. The chemical shift value of $\delta$ = –280 ppm is characteristic of the five-coordinate tin situated at the equator of the molecule whereas the signal at $\delta$ = –460 ppm is due to the presence of six-coordinate tins at the poles.[6]

## Molecular Structure

Whereas the molecular structures of **1** and **2** have been determined previously,[5] that of **6** is reported here. The molecular structure of **6**·2(dioxane) is shown in Figure 1 (a). The macrocation is composed of a centrosymmetric $[(n\mathrm{BuSn})_{12}(\mu_3\text{-}O)_{14}(\mu_2\text{-}OH)_6]^{2+}$ moiety with the asymmetric unit possessing two symmetry-related "*half molecules*". The structure of this cationic tin cage was described previously by the use of anions such as chloride,[8a] hydroxide[8b] or phosphinate.[8c] There has been one report on the structure of this macrocation where *p*-toluenesulfonate is the counter anion.[6] The structure of the macrocation in **6** is like a *"football"* consisting of twelve tin atoms which are linked by $\mu_3$-oxo and $\mu_2$-hydroxo bridges. All the *n*-butyl chains situated on the tin atom are pointing outside the cage core. The bonding parameters found in this cage are given in Table 2 and are comparable with the literature values.[6,8] The structure of the molecule can be understood as follows. Among the twelve tin atoms present in the molecule, six are situated at the two poles of the cage and the remaining six

 © 2006 Wiley-VCH Verlag GmbH & Co. KGaA, Weinheim 

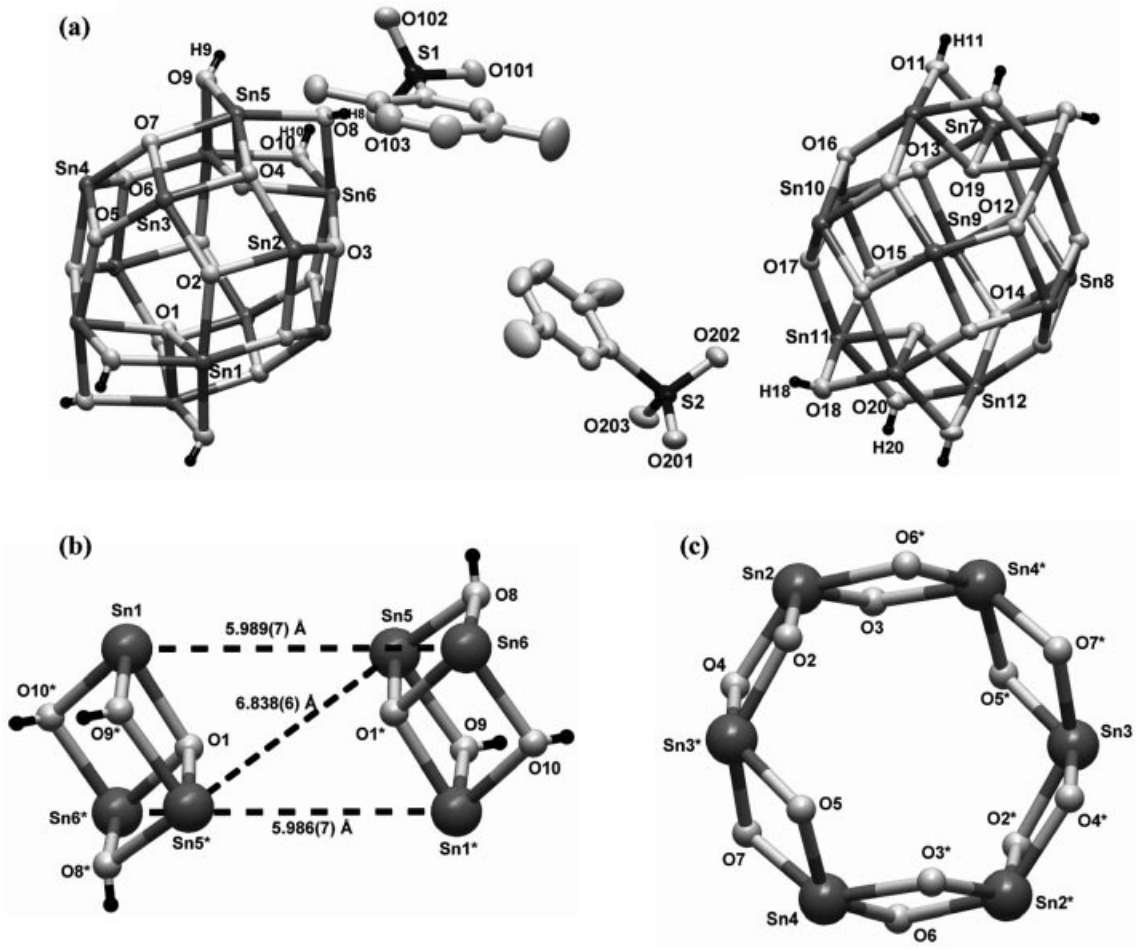


Figure 1. (a) View of the two molecules of **6** present in its asymmetric unit (at 50% ellipsoidal probability level). The unlabeled atoms are symmetric counterparts of the labeled atoms. All the *n*-butyl groups on tin atoms along with their protons and protons in the sulfonate moieties are removed. (b) View of the two *poles* consist of two trimeric O-capped subunits of $Sn_3(\mu_3\text{-}O)(\mu_2\text{-}OH)_3$. (c) View of the *equator* is spanned by a hexameric oxotin cycle $Sn_6(\mu_3\text{-}O)_{12}$.

Table 2. Comparison of (bond) distances in the core structures of selected monoorgano oxotin cages.

| Compound | Average Sn–O($\mu_3$) [Å] | Average Sn–OH($\mu_2$) [Å] | Average Sn–O(X) [Å] | Average Sn···Sn[c] [Å] | Inter pole [O($\mu_3$)···O($\mu_3$)] [Å] | Ref. |
|---|---|---|---|---|---|---|
| *Foot-ball cage* **6**[a] | 2.087(4)[f]<br>2.117(4)[g]<br>2.059(4)[h] | 2.110(5) | – | 6.366(5) | 3.955(5) | this work |
| | 2.086(4)[i]<br>2.112(4)[j]<br>2.063(4)[k] | 2.109(4) | – | 6.386(6) | 3.938(4) | |
| *Foot-ball cage*[b] | 2.080(2)[f]<br>2.115(2)[g]<br>2.057(8)[h] | 2.119(2) | – | 6.379(3) | 3.984(2) | [6] |
| *Foot-ball cage*[c] | 2.091(7)[f]<br>2.054(8)[g]<br>2.140(8)[h] | 2.096(8) | – | 6.331(6) | 3.899(6) | [8b] |
| *Foot-ball cage*[d] | 2.117(2)[f]<br>2.098(2)[g]<br>2.060(2)[h] | 2.142(2) | – | 6.373(3) | 3.996(3) | [8a] |
| *O-Capped cluster* | 2.075(5) | 2.128(6) | 2.122(6), X = P | – | – | [9b] |
| *Double O-capped cluster* | 2.065(3) | 2.172(2) | 2.072(2), X = P | 6.337(1)[l] | 3.778(4) | [9a] |
| *Drum* | 2.101(5) | – | 2.155(5), X = C | – | – | [9c] |

[a] Two crystallographically independent molecules are present; anion: two 2,5-$Me_2C_6H_3SO_3^-$. [b] Anion: two 4-$MeC_6H_4SO_3^-$. [c] Anion: two $OH^-$. [d] Anion: two $Cl^-$. [e] Average distance between the diametrically opposite tin atoms present in the equator. [f] Sn is bonded with $\mu_3$-capped oxygen (O-capped) in the poles. [g] Pole tin atoms bonded with $\mu_3$-oxygens which are part of the equator. [h] Equator tin atoms bonded with $\mu_3$-oxygens which are part of the equator. [i] Sn is bonded with $\mu_3$-capped oxygen (O-capped) in the poles. [j] Pole tin atoms bonded with $\mu_3$-oxygens which are part of the equator. [k] Equator tin atoms bonded with $\mu_3$-oxygens which are part of the equator. [l] Average distance between the diametrically opposite phosphorus atoms present in the equator.

 © 2006 Wiley-VCH Verlag GmbH & Co. KGaA, Weinheim 

tin atoms occupy the equator of the cage. The poles consist of two trimeric *O-capped* subunits of $[(n\text{BuSn})_3(\mu_3\text{-O})(\mu_2\text{-OH})_3]$ (Figure 1, b).[9a] Within these subunits the tin atoms are hexa-coordinate and possess bridging oxo and hydroxo groups.

The shorter and longer Sn···Sn distances between the two poles are given in Figure 1 (b). The equator of the cage is spanned by a hexameric cycle $[(n\text{BuSn})_6(\mu_2\text{-O})_{12}]$ (Figure 1, c).[9a] In this sub-unit the tins are five-coordinate and are nearly square pyramidal. This hexameric cycle is stitched by means of six distannoxane motifs ($Sn_2O_2$) with the average diameter of the cycle being 6.366(5) Å. Thus, it is possible to envisage the construction of the cage by capping each side of the hexameric cycle by the two trimeric tin units.

## Supramolecular Assembly

In compound **6**, two molecules of the 2,5-dimethylbenzenesulfonate anion interact with three hydroxy groups at the poles through intermolecular O–H···O hydrogen bonding to generate a one-dimensional chain structure (Figure 2). The bonding parameters involved in these hydrogen bonds point to the fact that these are essentially strong hydrogen bonds. Hydrogen-bonding interactions among these cages have resulted in the formation of two different rings; a seven-membered $Sn_2O_4S$ ring and a 12-membered $Sn_2O_8S_2$ ring. The average O···O distance observed in this molecule is 2.72 Å and are comparable with the *p*-toluenesulfonate derivative.[6] The distance between two such polymeric sheets is 11.11 Å. Ribot et al. have utilized a similar type of cage as versatile nanobuilding blocks for the design of tin-based organic–inorganic hybrid materials.[10]

## Catalysis

In solution all the organotin cations behave as 1:2 electrolytes (Table 1). In view of their anticipated Lewis acidity, these compounds were tested as catalysts for acetylation of alcohols. All the organotin cations are very effective in the acetylation reactions of alcohols (Table 3 and Table 4). These reactions are completed much faster than those catalyzed by neutral tetraorganodistannoxanes.[11] Thus, acetylation of menthol (**7d**) and cholesterol (**7e**) are completed only in 15 min (Table 3; Entries 19–25 and 26–32). Interestingly, inspite of low positive charge, the macrocations **5** and **6** are also reasonably effective although the reaction times are slightly longer.[3d] The dications **1** and **3** are the most effective, in keeping with their increased Lewis acidity.

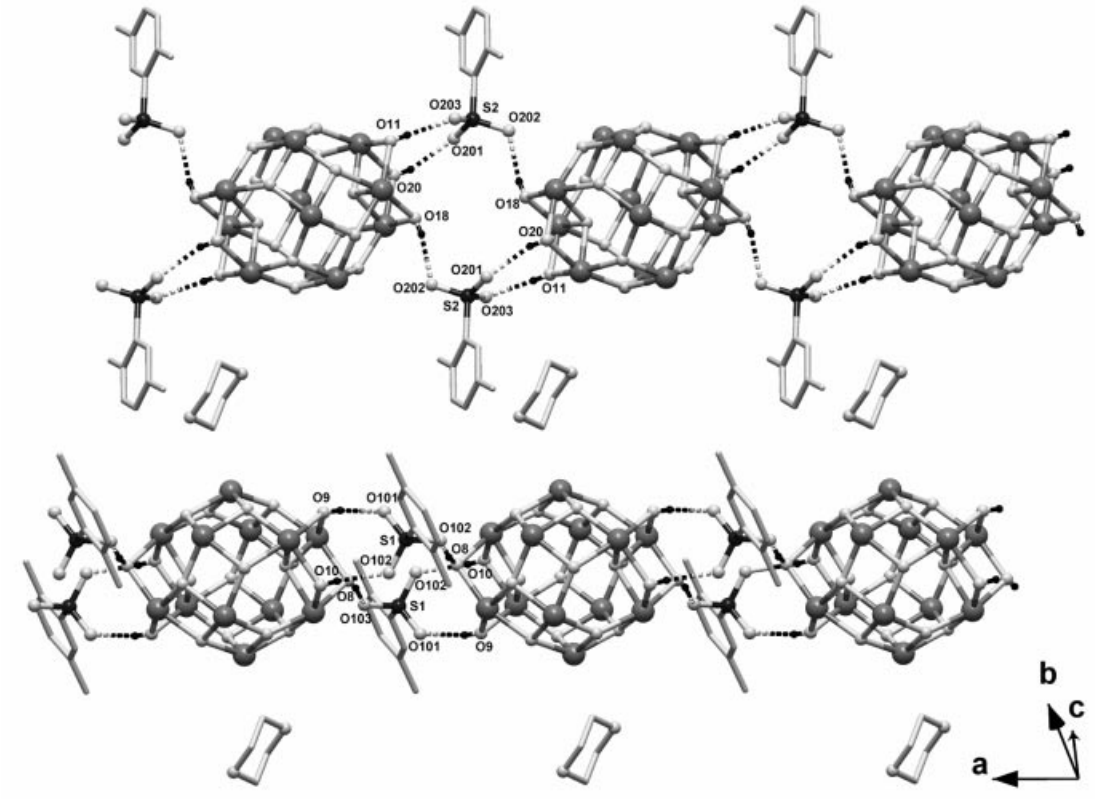


Figure 2. O–H···O hydrogen-bond-mediated one-dimensional supramolecular assembly in compound **6**. All the *n*-butyl groups on tin atoms along with their protons and protons in the sulfonate moieties are removed. Bonding parameters for hydrogen bonding are: O8–H8 0.701(1), H8···O103 2.027(2), O8···O103 2.701(1) Å, O8–H8···O103 161.45(3)°; O9–H9 0.680(4), H9···O101 2.104(3), O9···O101 2.757(3) Å, O9–H9···O101 161.21(4)°; O10–H10 0.688(2), H10···O102 2.043(4), O10···O102 2.725(5) Å, O10–H10···O102 171.22(1)°; O11–H11 0.696(6), H11···O203 1.985(4), O11···O203 2.681(8) Å, O11–H11···O203 178.18(5)°; O18–H18 0.696(1), H18···O202 2.053(3), O18···O202 2.736(8) Å, O18–H18···O202 167.44(1)°; O20–H20 0.690(1), H20···O201 2.058(3), O20···O202 2.721(5) Å, O20–H20···O201 161.45(2)°.

 © 2006 Wiley-VCH Verlag GmbH & Co. KGaA, Weinheim 

Thus, even 0.05 mol-% of **1** is sufficient to drive the reaction to completion (Table 3; Entries 2 and 10). In all instances, just 0.2 mol-% of the organotin catalyst is sufficient for the completion of acetylation.

Table 3. Acetylation of alcohols catalyzed by organotin cations.[a]

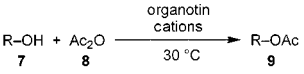


| Entry | Substrate | Catalyst | Cat. conc. (mol-%) | Reaction time (min) | Yield (%)[b] |
|---|---|---|---|---|---|
| 1 | 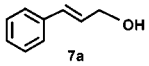 7a | 1 | 0.1 | 140 | 96[c] |
| 2 | | 1 | 0.05 | 145 | 98[c] |
| 3 | | 1 | 0.2 | 120 | 97 |
| 4 | | 3 | 0.2 | 70 | 91 |
| 5 | | 4 | 0.2 | 30 | 96 |
| 6 | | 2 | 0.2 | 40 | 98 |
| 7 | | 5 | 0.2 | 105 | 96 |
| 8 | | 6 | 0.2 | 110 | 99 |
| 9 | 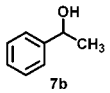 7b | 1 | 0.1 | 140 | 95[c] |
| 10 | | 1 | 0.05 | 240 | 90[c] |
| 11 | | 1 | 0.2 | 90 | 96 |
| 12 | | 3 | 0.2 | 25 | 94 |
| 13 | | 4 | 0.2 | 90 | 94 |
| 14 | | 2 | 0.2 | 35 | 97 |
| 15 | | 5 | 0.2 | 150 | 95 |
| 16 | | 6 | 0.2 | 150 | 95 |
| 17 | 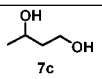 7c | 1 | 0.1 | 40 | 92[d] |
| 18 | | 1 | 0.2 | 30 | 99[d] |
| 19 | 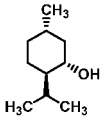 7d | 1 | 0.1 | 60 | 90 |
| 20 | | 1 | 0.2 | 60 | 93 |
| 21 | | 3 | 0.2 | 15 | 97 |
| 22 | | 4 | 0.2 | 15 | 98 |
| 23 | | 2 | 0.2 | 15 | 94 |
| 24 | | 5 | 0.2 | 15 | 96 |
| 25 | | 6 | 0.2 | 45 | 95 |
| 26 | 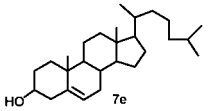 7e | 1 | 0.2 | 60 | 99 |
| 27 | | 1 | 0.4 | 40 | 99 |
| 28 | | 3 | 0.2 | 15 | 97 |
| 29 | | 4 | 0.2 | 20 | 98 |
| 30 | | 2 | 0.2 | 20 | 98 |
| 31 | | 5 | 0.2 | 25 | 100 |
| 32 | | 6 | 0.2 | 10 | 99 |

[a] Reaction conditions: R–OH (1 mmol); $Ac_2O$ (1 mL); catalyst (mol-%); room temp. [b] Isolated yield. [c] See ref.[5a] [d] Product: diester.

Acetylation of phenols is also catalyzed quiet readily by the dications **1** and **3**. β-Naphthol (**7h**) is acetylated in the presence of **3** in nearly 55 min (Table 4; Entry 17). The reactions catalyzed by dinuclear and dodecanuclear organotin cations **2**, **5** and **6** require longer times (Table 4; Entries 5–7, 12–14 and 19–21). However, as before only 0.2 mol-% of the catalyst is required for completion of the reaction.

In order to assess if the organotin cations can be used for transacetylation reactions, two test cases were examined, using the reaction of the alcohols **7a** and **7b** with vinyl acetate (**10**) (Table 5). Transacetylation was completed in all cases quantitatively, although higher catalyst loadings were

Table 4. Acetylation of phenols catalyzed by organotin cations.[a]

| Entry | Substrate | Catalyst | Cat. conc. (mol-%) | Reaction time (min) | Yield (%)[b] |
|---|---|---|---|---|---|
| 1 | 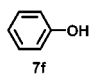 7f | 1 | 0.1 | 145 | 83[c] |
| 2 | | 1 | 0.2 | 140 | 93[c] |
| 3 | | 3 | 0.2 | 150 | 93 |
| 4 | | 4 | 0.2 | 165 | 92 |
| 5 | | 2 | 0.2 | 3000 | 35 |
| 6 | | 5 | 0.2 | 3600 | 36 |
| 7 | | 6 | 0.2 | 5760 | 80 |
| 8 | 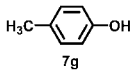 7g | 1 | 0.1 | 70 | 85[c] |
| 9 | | 1 | 0.2 | 50 | 98[c] |
| 10 | | 3 | 0.2 | 60 | 99 |
| 11 | | 4 | 0.2 | 90 | 97 |
| 12 | | 2 | 0.2 | 120 | 92 |
| 13 | | 5 | 0.2 | 290 | 97 |
| 14 | | 6 | 0.2 | 1140 | 93 |
| 15 | 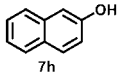 7h | 1 | 0.1 | 360 | 98 |
| 16 | | 1 | 0.2 | 180 | 99 |
| 17 | | 3 | 0.2 | 55 | 98 |
| 18 | | 4 | 0.2 | 80 | 96 |
| 19 | | 2 | 0.2 | 240 | 99 |
| 20 | | 5 | 0.2 | 360 | 99 |
| 21 | | 6 | 0.2 | 480 | 99 |

[a] For reaction Scheme, see Table 3; Reaction conditions: R–OH (1 mmol); $Ac_2O$ (1 mL); catalyst (mol-%); room temp. [b] Isolated yield. [c] See ref.[5a]

required (1 mol-%). Interestingly the dodecanuclear macrocations (**5** and **6**) are as effective as the mononuclear dications (**1**, **3** and **4**).

Table 5. Transacetylation reactions using organotin cations.[a]

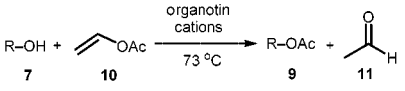


| Entry | Substrate | Catalyst | Cat. conc. (mol-%) | Reaction time (h) | Yield (%)[b] |
|---|---|---|---|---|---|
| 1 | 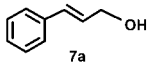 7a | 1 | 1 | 8 | 95 |
| 2 | | 3 | 1 | 7 | 94 |
| 3 | | 4 | 1 | 9 | 91 |
| 4 | | 2 | 1 | 4 | 99 |
| 5 | | 5 | 1 | 6 | 96 |
| 6 | | 6 | 1 | 4.5 | 99 |
| 7 | 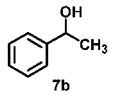 7b | 1 | 1 | 7 | 96 |
| 8 | | 3 | 1 | 8 | 94 |
| 9 | | 4 | 1 | 5.5 | 96 |
| 10 | | 2 | 1 | 6 | 99 |
| 11 | | 5 | 1 | 7 | 99 |
| 12 | | 6 | 1 | 5.5 | 97 |

[a] Reaction conditions: R–OH (1 mmol); vinyl acetate (10 mmol); catalyst (1 mol-%); 75 °C. [b] Isolated yield.

## Conclusions

In summary, we report a series of organotin cations with varying nuclearity and charge and have shown their efficacy in acetylation and in transacetylation reactions. All of the

 © 2006 Wiley-VCH Verlag GmbH & Co. KGaA, Weinheim 

organotin cations are air-stable solids that can be prepared in excellent yields in a one-step synthesis, thus making them as potentially useful reagents.

## Experimental Section

**General Remarks:** Solvents were dried with sodium benzophenone ketyl and were collected from the still at the time of reaction. $(n\mathrm{Bu_3Sn})_2O$, $[n\mathrm{Bu_2SnO}]_n$, *n*BuSn(O)(OH), 1,5-$C_{10}H_6(SO_3H)_2{\cdot}4H_2O$ (Aldrich), L-menthol (Lancaster), cholesterol (Acro chemicals), cinnamyl alcohol (Fluka), $C_6H_5SO_3H$ (75% w/w water solution), phenol, *p*-cresol, acetic anhydride, vinyl acetate and β-naphthol (sd-fine, India) were purchased and used as such without any further purification. 2,5-$Me_2C_6H_3SO_3H$,[12] 1-phenylethanol,[12] 1,3-diphenyl-2-propen-1-ol[12] and organotin cations **1**[5a] and **2**[5b] were prepared by literature methods. Melting points were measured with a JSGW melting point apparatus and are uncorrected. Elemental analyses were carried out with a Thermoquest CE instruments model EA/110 CHNS-O elemental analyzer. Infrared spectra were recorded in dichloromethane solution as well as neat liquid or as KBr pellets with a FT-IR Bruker-Vector Model. $^1$H and $^{119}$Sn NMR spectra were obtained with a JEOL-JNM LAMBDA 400 model spectrometer using $CDCl_3$, $CD_3OD$ and $(CD_3)_2SO$ solutions with shifts referenced to tetramethylsilane (for $^1$H NMR) and tetramethyltin (for $^{119}$Sn NMR), respectively. $^{119}$Sn NMR spectra were recorded under broad-band decoupled conditions. Conductivity measurements were done with a Century Digital Conductivity Meter Model CC-601.

**Synthesis of $[n\mathrm{Bu_2Sn(H_2O)_4}]^{2+}{\cdot}2\mathrm{C_6H_5SO_3^-}$ (3):** A mixture of $[n\mathrm{Bu_2SnO}]_n$ (0.42 g, 1.68 mmol) and $C_6H_5SO_3H$ (75% w/w water solution) (0.70 g, 3.34 mmol) in toluene (60 mL) was heated under reflux for 8 h using a Dean–Stark apparatus to remove the water formed in the reaction by azeotropic distillation. A white puffy solid formed in the reaction was filtered by a sintered funnel (G-4), dried (in air) and identified as **3** (0.87 g, 87% yield). M.p. 270 °C (dec.). $C_{20}H_{36}O_{10}S_2Sn$ (619.33): calcd. C 38.78, H 5.85; found C 37.94, H 5.61. IR (KBr, cm$^{-1}$): $\tilde{\nu}$ = 3420 (br., $H_2O$), 1251 (s, $SO_3$ assym. str.), 1192 (s, $SO_3$ assym. str.), 1070 (s, $SO_3$ sym. str.), 1022 (s, $SO_3$ ionic) and 624 (m, C–S). $^1$H NMR (400 MHz, $CD_3OD$, ppm): $\delta$ = 0.83 (t, $J$ = 7.31 Hz, 6 H, butyl C$H_3$), 1.25 (q, $J$ = 7.31 Hz, 4 H, Sn–C$H_2$), 1.58–1.64 (m, 4 H, butyl C$H_2$), 1.75–1.80 (m, 4 H, butyl C$H_2$), 7.43–7.51 (m, 6 H, aromatic) and 7.82–7.85 (m, 4 H, aromatic). $^{119}$Sn NMR (150 MHz, $CD_3OD$, ppm): $\delta$ = –360.61 (s).

**Synthesis of $[n\mathrm{Bu_2Sn(H_2O)_4}]^{2+}{\cdot}1,5\text{-}\mathrm{C_{10}H_6(SO_3^-)_2}$ (4):** A mixture of $[n\mathrm{Bu_2SnO}]_n$ (0.30 g, 1.20 mmol) and 1,5-$C_{10}H_6(SO_3H)_2{\cdot}4H_2O$ (0.43 g, 1.20 mmol) was taken in toluene (60 mL) and heated under reflux for 8 h using a Dean–Stark apparatus to remove the water formed in the reaction by azeotropic distillation. A white solid formed in the reaction was filtered by a sintered funnel (G-4) and dried (in air) to obtain **4** in good yield (0.66 g, 93% yield). M.p. > 280 °C (dec.). $C_{18}H_{32}O_{10}S_2Sn$ (591.91): calcd. C 36.56, H 5.45; found C 36.29, H 5.19. IR (KBr, cm$^{-1}$): $\tilde{\nu}$ = 3454 (br., $H_2O$), 1206 (s, $SO_3$ assym. str.), 1161 (s, $SO_3$ assym. str.), 1044 (s, $SO_3$ ionic) and 613 (s, C–S). $^1$H NMR (400 MHz, [D$_6$]DMSO, ppm): $\delta$ = 0.86 (t, $J$ = 7.2 Hz, 6 H, butyl C$H_3$), 1.28 (q, $J$ = 7.2 Hz, 4 H, Sn–C$H_2$), 1.47–1.49 (m, 8 H, butyl C$H_2$C$H_2$), 7.44 (t, $J$ = 7.2 Hz, 2 H, aromatic), 7.95 (d, $J$ = 6.8 Hz, 2 H, aromatic) and 8.86 (d, $J$ = 8.4 Hz, 2 H, aromatic). $^{119}$Sn NMR (150 MHz, [D$_6$]DMSO, ppm): –384.91(s).

**Synthesis of $[(n\mathrm{BuSn})_{12}(\mu_3\text{-}O)_{14}(\mu_2\text{-}OH)_6]^{2+}{\cdot}2\mathrm{C_6H_5SO_3^-}$ (5):** A mixture of *n*BuSn(O)(OH) (1.80 g, 8.62 mmol) and $C_6H_5SO_3H$ (75% w/w water solution) (0.45 g, 2.87 mmol) in toluene (150 mL) was heated under reflux for 72 h using a Dean–Stark apparatus to remove the water formed in the reaction by azeotropic distillation. The reaction mixture was cooled and filtered through a sintered funnel (G-4) and the clear filtrate was evaporated in vacuo to yield **5** as a white amorphous solid (1.88 g, 95% yield). M.p. 196 °C. $C_{60}H_{124}O_{26}S_2Sn_{12}$ (2750.26): calcd. C 26.20, H 4.54; found C 26.09, H 4.24. IR (KBr, cm$^{-1}$): $\tilde{\nu}$ = 3214 (br., OH), 1258 (s, $SO_3$ assym. str.), 1194 (s, $SO_3$ assym. str.), 1126 (s, $SO_3$ sym. str.), 1035 (s, $SO_3$ ionic) and 618 (m, C–S). $^1$H NMR (400 MHz, $CDCl_3$, ppm): $\delta$ = 0.79–0.89 (m, 36 H, butyl C$H_3$), 1.05–1.69 (m, 72 H, Sn–C$H_2$C$H_2$C$H_2$) and 6.88–7.79 (m, 10 H, aromatic). $^{119}$Sn NMR (150 MHz, $CDCl_3$, ppm): $\delta$ = –284.28 [s, $^2J(^{117/119}\mathrm{Sn}{-}^{13}\mathrm{C})$ = 204, 208 Hz] and –463.8 [s, $^2J(^{117/119}\mathrm{Sn}{-}^{13}\mathrm{C})$ = 204 Hz].

**Synthesis of $[(n\mathrm{BuSn})_{12}(\mu_3\text{-}O)_{14}(\mu_2\text{-}OH)_6]^{2+}{\cdot}2$ 2,5-$\mathrm{Me_2C_6H_3SO_3^-}$ (6):** A mixture of *n*BuSn(O)(OH) (3.36 g, 16.10 mmol) and 2,5-$Me_2C_6H_3SO_3H$ (1.0 g, 5.37 mmol) in toluene (150 mL) was heated under reflux for 72 h using a Dean–Stark apparatus to remove the water formed in the reaction by azeotropic distillation. The reaction mixture was cooled and filtered through a sintered funnel (G-4) and the clear filtrate was evaporated in vacuo to yield **6** as a white amorphous solid (3.62 g, 96% yield). Crystals suitable for single-crystal X-ray diffraction were obtained by recrystallizing compound **6** in dioxane with 0.5% water. M.p. 158 °C. $C_{64}H_{132}O_{26}S_2Sn_{12}$ (2806.39): calcd. C 27.39, H 4.74; found C 26.97, H 4.85. IR (KBr, cm$^{-1}$): $\tilde{\nu}$ = 3198 (br., OH), 1193 (s, $SO_3$ assym. str.), 1195 (s, $SO_3$ assym. str.), 1088 (s, $SO_3$ sym. str.), 1021 (s, $SO_3$ ionic) and 616 (m, C–S). $^1$H NMR (400 MHz, $CDCl_3$, ppm): $\delta$ = 0.80 (t, $J$ = 7.32 Hz, 18 H, butyl C$H_3$), $\delta$ = 0.88 (t, $J$ = 7.36 Hz, 18 H, butyl C$H_3$), 1.19–1.32 (m, 24 H, Sn–C$H_2$), 1.38–1.70 (m, 48 H, butyl C$H_2$C$H_2$), 2.23 (s, 6 H, Ar–C$H_3$), 2.55 (s, 6 H, Ar–C$H_3$), 7.00 (s, 2 H, aromatic), 7.09 (s, 2 H, aromatic) and 7.69 (s, 2 H, aromatic). $^{119}$Sn NMR (150 MHz, $CDCl_3$, ppm): $\delta$ = –283.97 [s, $^2J(^{117/119}\mathrm{Sn}{-}^{13}\mathrm{C})$ = 204, 207 Hz] and –462.77 [s, $^2J(^{117/119}\mathrm{Sn}{-}^{13}\mathrm{C})$ = 205 Hz].

**General Procedure for Acetylation of Alcohols and Phenols:**[5a] A mixture of the alcohol or phenol (**7a**–**h**) (1 mmol), acetic anhydride (**8**) (1 mL) and catalytic amount (mol%) of the organotin catalyst **1**–**6** were stirred at room temperature. The progress of the reaction was monitored by TLC. At the end of the reaction excess acetic anhydride was removed in vacuo. The residual portion was dissolved in minimum amount of dichloromethane and filtered through a short column (in some cases the compound was eluted with ethyl acetate and hexane) to yield the corresponding acetate **9a**–**h**. All the acetates were characterized by $^1$H NMR spectra and compared with authentic samples.

**General Procedure for trans-Acetylation Reactions:** A mixture of alcohol (**7a**–**b**) (1 mmol), vinyl acetate (**10**) (10 mmol) and catalytic amount (1 mol%) of the tin catalyst **1**–**6** were refluxed at 75 °C. The progress of the reaction was monitored by TLC. After the reaction was complete, excess vinyl acetate was evaporated and the residue was subjected to column chromatography on silica gel to give acetates **9a**–**b** in good yields. All the acetates were characterized by $^1$H NMR spectra and compared with authentic samples.

**X-ray Crystallographic Study:** Colorless block-like crystal of **6** suitable for single-crystal X-ray diffraction was loaded on a Bruker AXS Smart Apex CCD diffractometer. The details pertaining to the data collection and refinement for **6** are as follows: size 0.4 × 0.4 × 0.3 mm$^3$; empirical formula $C_{66}H_{136}O_{27}S_2Sn_{12}$; $M_w$ = 2850.15; triclinic; space group $P\bar{1}$; $a$ = 12.6693(11) Å; $b$ = 16.4765(14) Å; $c$ = 24.8100(2) Å; $\alpha$ = 77.131(2)°; $\beta$ = 86.091(2)°; $\gamma$ = 69.637(2)°; $V$ = 4733.1(7) Å$^3$; $Z$ = 2; $T$ = 150(2) K; $D_{calcd.}$ = 2.000 Mg·m$^{-3}$; Mo-

 © 2006 Wiley-VCH Verlag GmbH & Co. KGaA, Weinheim 

$K_\alpha$ radiation; $\theta$ range 1.35 to 25.03°; 24859 reflections collected, 16441 independent reflections ($R_{int}$ = 0.0180); $R_1$ = 0.0271, $wR_2$ = 0.0688 [for $I > 2\sigma(I)$]; $R_1$ = 0.0314, $wR_2$ = 0.0715 (for all data); GOF = 1.015. The maximum and minimum electron densities are 0.964 and –0.727 e·Å$^{-3}$, respectively. The structure was solved by direct methods using SHELXS-97 and refined by full-matrix least-squares on $F^2$ using SHELXL-97.[13] The hydrogen atoms attached to oxygen atoms in the hydroxy groups were located from the difference map and their position were refined. All other hydrogen atoms were included in idealized positions, and a riding model was used. Non-hydrogen atoms were refined with anisotropic displacement parameters. A 1,4-dioxane molecule was also present in the asymmetric unit of **6** as a solvate.

CCDC-296001 contains the supplementary crystallographic data for this paper. These data can be obtained free of charge from The Cambridge Crystallographic Data Centre via www.ccdc.cam.ac.uk/data_request/cif. Figure 1 and 2 and its bonding parameters were obtained from DIAMOND 3.0 software package.[14]

## Acknowledgments

We are thankful to the DST, India, for financial support. K. G., P. S. and P. S. gratefully acknowledge the CSIR, New Delhi, India, for Research Fellowships. A. S. and S. Z. thank the EPSRC of the U. K. for financial support.

[1] a) R. R. Holmes, *Acc. Chem. Res.* **1989**, *22*, 190–197; b) V. Chandrasekhar, S. Nagendran, V. Baskar, *Coord. Chem. Rev.* **2002**, *235*, 1–52; c) V. Chandrasekhar, K. Gopal, P. Sasikumar, R. Thirumoorthi, *Coord. Chem. Rev.* **2005**, *249*, 1745–1765.

[2] a) E. G. Rochow, D. Seyferth, *J. Am. Chem. Soc.* **1953**, *75*, 2877–2878; b) R. S. Tobias, M. Yasuda, *Can. J. Chem.* **1964**, *42*, 781–789.

[3] a) M. Wada, R. Okawara, *J. Organomet. Chem.* **1965**, *4*, 487–488; b) I. Hippel, P. G. Jones, A. Blaschette, *J. Organomet. Chem.* **1993**, *448*, 63–67; c) K. Sakamoto, Y. Hamada, H. Akashi, A. Orita, J. Otera, *Organometallics* **1999**, *18*, 3555–3557; d) K. Sakamoto, H. Ikeda, H. Akashi, T. Fukuyama, A. Orita, J. Otera, *Organometallics* **2000**, *19*, 3242–3248; e) J. Beckmann, D. Dakternieks, A. Duthie, C. Mitchell, *Dalton Trans.* **2003**, 3258–3263.

[4] a) R. R. Holmes, S. Shafieezad, V. Chandrasekhar, J. M. Holmes, R. O. Day, *J. Am. Chem. Soc.* **1988**, *110*, 1174–1180; b) J. F. Vollano, R. O. Day, R. R. Holmes, *Organometallics* **1984**, *3*, 745–750.

[5] a) V. Chandrasekhar, R. Boomishankar, S. Singh, A. Steiner, S. Zacchini, *Organometallics* **2002**, *21*, 4575–4577; b) V. Chandrasekhar, R. Boomishankar, A. Steiner, J. F. Bickley, *Organometallics* **2002**, *22*, 3342–3344.

[6] C. Eychenne-Baron, F. Ribot, N. Steunou, C. Sanchez, F. Fayon, M. Biesemans, J. C. Martins, R. Willem, *Organometallics* **2000**, *19*, 1940–1949.

[7] a) P. G. Harrison, in: *Chemistry of Tin* (Eds.: P. G. Harrison), Blackie, Chapman & Hall, New York, **1989**, p. 60; b) D. L. An, Z. Peng, A. Orita, A. Kurita, S. Man-e, K. Ohkubo, X. Li, S. Fukuzumi, J. Otera, *Chem. Eur. J.* **2006**, *12*, 1642–1647.

[8] a) D. Dakternieks, H. Zhu, E. R. T. Tiekink, R. Colton, *J. Organomet. Chem.* **1994**, *476*, 33–40; b) F. Banse, F. Ribot, P. Tolédano, J. Maquet, C. Sanchez, *Inorg. Chem.* **1995**, *34*, 6371–6379; c) F. Ribot, C. Sanchez, R. Willem, J. C. Martins, M. Biesemans, *Inorg. Chem.* **1998**, *37*, 911–917.

[9] a) V. Chandrasekhar, V. Baskar, J. J. Vittal, *J. Am. Chem. Soc.* **2003**, *125*, 2392–2393; b) R. O. Day, J. M. Holmes, V. Chandrasekhar, R. R. Holmes, *J. Am. Chem. Soc.* **1987**, *109*, 940–941; c) R. O. Day, V. Chandrasekhar, K. C. K. Swamy, J. M. Holmes, S. D. Burton, R. R. Holmes, *Inorg. Chem.* **1988**, *27*, 2887–2893.

[10] F. Ribot, A. Lafuma, C. Eychenne-Baron, C. Sanchez, *Adv. Mater.* **2002**, *14*, 1496–1499.

[11] a) A. Orita, A. Mitsutome, J. Otera, *J. Org. Chem.* **1998**, *63*, 2420–2421; b) A. Orita, K. Sakamoto, Y. Hamada, A. Mitsutome, J. Otera, *Tetrahedron* **1999**, *55*, 2899–2910; c) J. Otera, N. Dan-oh, H. Nozaki, *J. Chem. Soc. Chem. Commun.* **1991**, 1742–1745; d) B. Jousseaume, C. Laporte, M.-C. Rascle, T. Toupance, *Chem. Commun.* **2003**, 1428–1429; e) S. Durand, K. Sakamoto, T. Fukuyama, A. Orita, J. Otera, A. Duthie, D. Dakternieks, M. Schulte, K. Jurkschat, *Organometallics* **2000**, *19*, 3220–3223.

[12] B. S. Furniss, A. J. Hannaford, P. W. G. Smith, A. R. Tatchell, *Vogel's Text book of Practical Organic Chemistry*, 5th ed., ELBS and Longman, London, **1989**.

[13] G. M. Scheldrick, SHELXL-97, *Program for Crystal Structure Analysis* (release 97-2), University of Göttingen, Göttingin, Germany, **1998**.

[14] *DIAMOND* version 3.0, Crystal Impact GbR, Bonn, Germany, **2004**.

Received: May 19, 2006
Published Online: August 10, 2006

 © 2006 Wiley-VCH Verlag GmbH & Co. KGaA, Weinheim 

DOI: 10.1002/ejic.200600503

# Synthesis and Reactivity of the $Ru^{III}$ Complexes $[RuTp(PR_3)Cl_2]$ − Precursors for RuTp Dihydrogen Complexes

**Sonja Pavlik,[a] Michael Puchberger,[b] Kurt Mereiter,[c] and Karl Kirchner*[a]**

**Keywords:** Ruthenium / N ligands / Dihydrogen complexes

The air-sensitive DMF-containing intermediate $[RuTp(PR_3)(Cl)(DMF)]$ is formed by refluxing a DMF solution of $[RuTp(COD)Cl]$ (**1**) in the presence of at least 1 equiv. of $PR_3$ ($PR_3$ = $PPh_3$, $PPh_2iPr$, $PiPr_3$, and $PCy_3$). On exposure to air in the presence of $CCl_4$, this complex is readily converted into the respective $Ru^{III}$ complexes $[RuTp(PR_3)Cl_2]$ (**2a–d**). These compounds are air-stable, readily accessible, permit easy variations as far as the electronic and steric properties of the $PR_3$ co-ligands are concerned, and are reducible to a variety of $Ru^{II}Tp$ complexes. Treatment of **2** with $NaBH_4$ affords dihydrogen compounds of the type $[RuTp(PR_3)(H)(\eta^2\text{-}H_2)]$. Reduction of **2** can also be accomplished with Zn in the presence of $CH_3CN$ and pyridine, which affords the diamagnetic $Ru^{II}$ compounds $[RuTp(PR_3)(CH_3CN)_2]^+$ (**4a–c**) and $[RuTp(PR_3)(py)Cl]$ (**5**). X-ray structures of representative complexes are presented.
(© Wiley-VCH Verlag GmbH & Co. KGaA, 69451 Weinheim, Germany, 2006)

## Introduction

In our continuing systematic studies of the chemistry of ruthenium trispyrazolylborate (Tp) complexes[1] we have shown that $[RuTp(PCy_3)(Cl)(DMF)]$ reacts with MeOH or EtOH in the presence of air to afford the $Ru^{III}$ alkoxide complexes $[RuTp(PCy_3)(Cl)(OR)]$ (R = Me, Et).[2] The formation of alkoxy compounds was restricted to very basic phosphanes, however, and failed, for instance, in the case of $PPh_3$. Nevertheless, these complexes turned out to be very useful precursors for a couple of new $Ru^{II}$ complexes of the types $[RuTp(PCy_3)(Cl)L]$ [L = $CH_3CN$, pyridine, CO, $P(OMe)_3$, $PMe_3$] and $[RuTp(PCy_3)(Cl)(=C=CHR)]$ (R = Ph, COOEt, $SiMe_3$, *n*Bu). In the present contribution, we sought a synthetic route to obtain alternative $Ru^{III}Tp$ precursors that are both air-stable, readily accessible, reducible to $Ru^{II}Tp$ complexes, and permit easy variations as far as the $PR_3$ co-ligands are concerned. We report here the synthesis, characterization, and reactivity of the dichloro $Ru^{III}$ complexes $[RuTp(PR_3)Cl_2]$ ($PR_3$ = $PPh_3$, $PPh_2iPr$, $PiPr_3$, $PCy_3$). These compounds turned out to be valuable precursors for dihydrogen complexes of the type $[RuTp(PR_3)(H)(\eta^2\text{-}H_2)]$ as well as other complexes containing the $[RuTp(PR_3)]^+$ fragment.

[a] Institute of Applied Synthetic Chemistry, Vienna University of Technology,
Getreidemarkt 9, 1060 Vienna, Austria
Fax: +43-1-58801-16399
E-mail: kkirch@mail.zserv.tuwien.ac.at
[b] Institute of Materials Chemistry, Vienna University of Technology,
Getreidemarkt 9, 1060 Vienna, Austria
[c] Institute of Chemical Technologies and Analytics, Vienna University of Technology,
Getreidemarkt 9, 1060 Vienna, Austria

## Results and Discussion

The synthesis of $[RuTp(PR_3)Cl_2]$ ($PR_3$ = $PPh_3$, $PPh_2iPr$, $PiPr_3$, and $PCy_3$; **2a–d**) was performed as a one-pot reaction by refluxing a DMF solution of $[RuTp(COD)Cl]$ (**1**) in the presence of $PR_3$ (≥ 1 equiv.) to yield the air-sensitive DMF intermediate $[RuTp(PR_3)(Cl)(DMF)]$. On exposure to air in the presence of $CCl_4$, this complex is readily converted to afford, on workup, **2a–d** in 77–88% isolated yields (Scheme 1). No attempts were made to isolate the $[RuTp(PR_3)(Cl)(DMF)]$ intermediate in this reaction sequence. It should be noted, however, that the $PPh_3$ and $PPyr_3$ (Pyr = pyrrolyl) compounds $[RuTp(PPh_3)(Cl)(DMF)]$ and $[RuTp(PPyr_3)(Cl)(DMF)]$ have recently been isolated and even crystallographically characterized.[3] Complexes **2a–d** are thermally robust orange solids that are stable to air both in the solid state and in solution. They are very soluble in most common organic solvents such as $CH_2Cl_2$, THF, or toluene. All complexes were characterized by elemental analysis. The NMR spectra suffer from severe line broadening due to the paramagnetic nature of these complexes. The measured magnetic moments, $\mu_{eff}$, of **2a–2d** were determined at 295 K to be 1.89, 1.99, 1.90, and 1.40 $\mu_B$, respectively, consistent with a $d^5$ ($Ru^{III}$) low-spin configuration with one unpaired electron. To further probe the electronic structure of **2a–d**, we examined their redox behavior by cyclic voltammetry. All four complexes display only one oxidation-reduction wave with $E_{1/2}$ values vs. NHE of 0.31 ($PPh_3$), 0.24 ($PPh_2iPr$), 0.16 ($PiPr_3$), and 0.12 V ($PCy_3$). These values correlate roughly with the increasing electron σ-donating abilities and decreasing π-accepting properties of the tertiary phosphanes, i.e., the relative stability of the $Ru^{III}$ complexes follows the order $PPh_3$

 © 2006 Wiley-VCH Verlag GmbH & Co. KGaA, Weinheim 

$<$ $PPh_2iPr$ $<$ $PiPr_3$ $\approx$ $PCy_3$. Incidentally, the $E_{1/2}$ values decrease with increasing cone angles of the tertiary phosphane ligands.

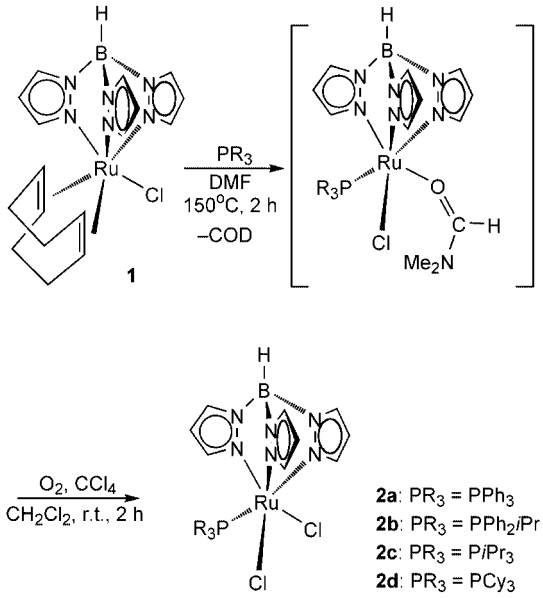


Scheme 1.

The molecular structures of **2a**, **2b**, and **2d** are depicted in Figures 1, 2, and 3, respectively; selected bond lengths are reported in the captions. The coordination geometry of these complexes is approximately octahedral, and the bond lengths and angles in these three complexes are relatively uniform. Mean bond lengths for the three complexes are: Ru–Cl = 2.337(8) Å, Ru–N = 2.071(6) Å for N(2) and N(4), and Ru–N(6) = 2.112(4) Å; N(6) is *trans* to the phosphane, which exerts a *trans* effect, as shown by the Ru–N mean bond length elongation of 0.041 Å in comparison to the other Tp nitrogen atoms. The Ru–P bond lengths increase gradually from 2.364 Å in **2a** via 2.380 in **2b** to 2.417 Å in **2d**; this correlates with the electrochemical data. Another point of interest is the conformation of the $PPh_3$ ligand in **2a**, which instead of the frequent rotor (or propeller) has an irregular conformation, as can be shown by the Ru–P–

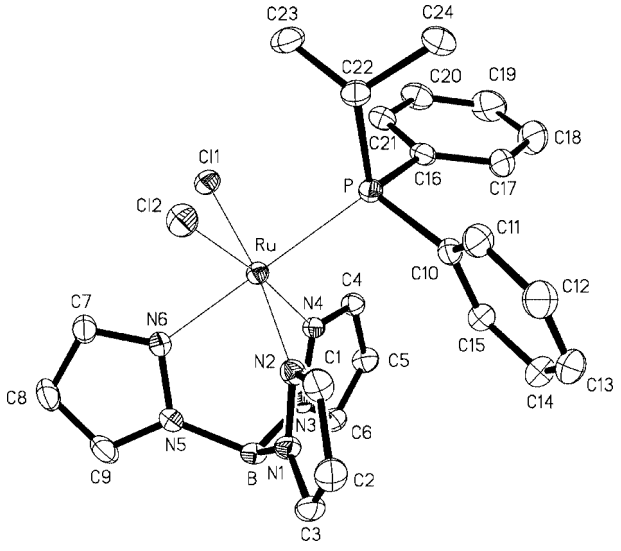


Figure 2. Structural view of $[RuTp(PPh_2iPr)Cl_2]$ (**2b**) showing 20% thermal ellipsoids (hydrogen atoms omitted for clarity). Selected bond lengths [Å] and angles [°]: Ru–N(2) 2.073(2), Ru–N(4) 2.077(2), Ru–N(6) 2.115(2), Ru–P 2.3796(7), Ru–Cl(1) 2.3442(8), Ru–Cl(2) 2.3311(8); P–Ru–Cl(1) 92.92(3), P–Ru–Cl(2) 90.62(3), Cl(1)–Ru–Cl(2) 93.00(3).

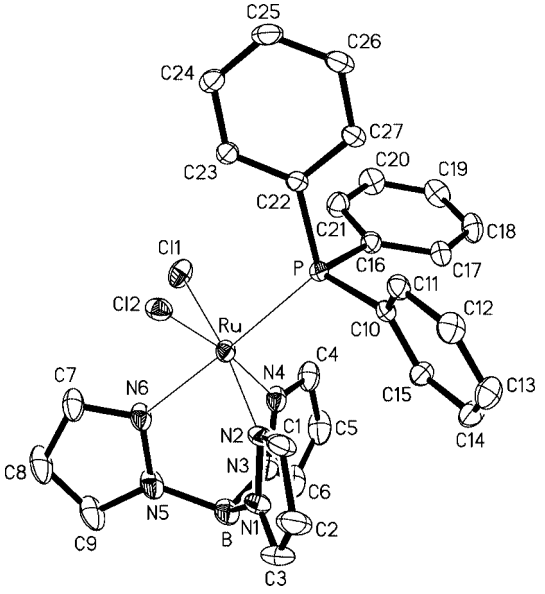


Figure 1. Structural view of $[RuTp(PPh_3)Cl_2]$ (**2a**) showing 30% thermal ellipsoids (hydrogen atoms omitted for clarity). Selected bond lengths [Å] and angles [°]: Ru–N(2) 2.079(2), Ru–N(4) 2.069(2), Ru–N(6) 2.106(2), Ru–P 2.3642(6), Ru–Cl(1) 2.3236(6), Ru–Cl(2) 2.3368(6); P–Ru–Cl(1) 90.08(2), P–Ru–Cl(2) 90.28(2), Cl(1)–Ru–Cl(2) 95.80(2).

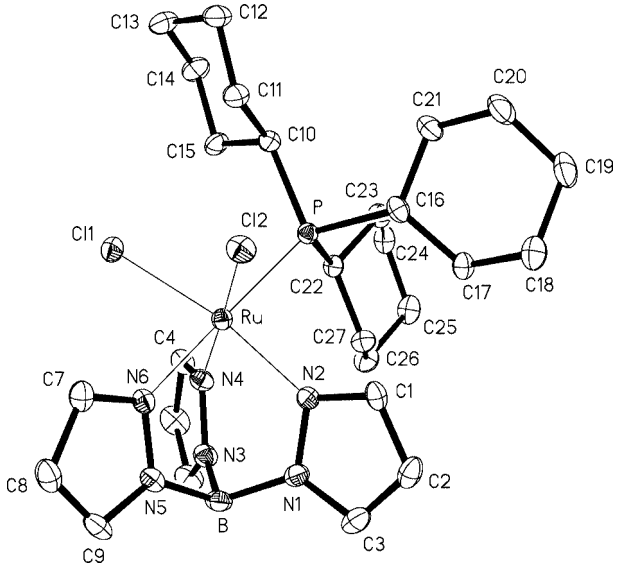


Figure 3. Structural view of $[RuTp(PCy_3)Cl_2]\cdot CH_2ClCH_2Cl$ (**2d**·$CH_2ClCH_2Cl$) showing 40% thermal ellipsoids (hydrogen and $CH_2ClCH_2Cl$ atoms omitted for clarity). Selected bond lengths [Å] and angles [°]: Ru–N(2) 2.065(2), Ru–N(4) 2.063(2), Ru–N(6) 2.114(2), Ru–P 2.4168(8), Ru–Cl(1) 2.3459(8), Ru–Cl(2) 2.3433(8), P–Ru–Cl(1) 95.36(3); P–Ru–Cl(2) 89.11(3), Cl(1)–Ru–Cl(2) 92.79(3).

 © 2006 Wiley-VCH Verlag GmbH & Co. KGaA, Weinheim 

$C_{ipso}$–C torsion angles of 63.6°, 66.8°, and –19.9° for phenyl rings C(10)–C(15), C(16)–C(21), and C(22)–C(27),[4] whereas the $PPh_3$ orientation relative to the $RuTpCl_2$ moiety is defined by an angle of 0.2° for N(2)–Ru–P–C(10). These data suggest that the phenyl ring C(22)–C(27) is in an approximately bisecting orientation and fits with C(23)–H(23) in between the two chlorine atoms (Figure 1). It is interesting to note that this appears to be a preferred configuration rather than merely a packing effect as the crystal structures of two solvates of **2a**, one with $ClCH_2CH_2Cl$ and one with $Et_2O$, have essentially the same complex conformation although they crystallize in entirely different lattices ($ClCH_2CH_2Cl$ solvate: orthorhombic, space group $P2_12_12_1$; $Et_2O$ solvate: triclinic, space group $P\bar{1}$).

Complexes **2** turned out to be useful reagents for the preparation of dihydrogen compounds of the types [RuTp(PR$_3$)(H)($\eta^2$-H$_2$)]. Thus, treatment of **2a**–**d** with $NaBH_4$ affords the diamagnetic $Ru^{II}$ compounds [RuTp(PR$_3$)(H)($\eta^2$-H$_2$)] (**3a**–**d**) in high yields (Scheme 2). All these compounds are thermally robust solids that slowly decompose in the presence of air both in the solid state and in solution. Characterization was accomplished by elemental analysis as well as $^1$H, $^{13}$C{$^1$H}, and $^{31}$P{$^1$H} NMR spectroscopy. Complexes **3a**–**d** show a doublet resonance for the hydride signal at all accessible temperatures in the range $\delta$ = –9.31 to –10.53 ppm (Table 1). The integration ratios toward the other ligands are in agreement with the presence of three metal-bound hydrogen atoms in all complexes. The presence of a dihydrogen ligand in **3b**–**d** is confirmed by the small $T_{1min}$ for the hydride signal, as shown in Table 1. Measurement of the relaxation time $T_{1min}$ has been reported previously for **3a**.[5] Irreversible isomerization to the ruthenium(IV) trihydride form [RuTp(PR$_3$)(H)$_3$] has not been observed, at variance with what commonly happens in related CpRu or Cp*Ru systems.[6]

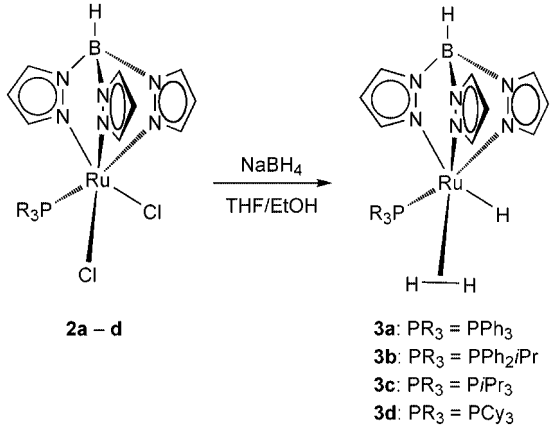


Scheme 2.

Table 1. Selected spectroscopic properties of complexes [RuTp(PR$_3$)(H)($\eta^2$-H$_2$)] **3a**–**d**.

| | $^1$H NMR $\delta$ [ppm] | $^2J_{H,P}$ [Hz] | $^{31}$P{$^1$H} NMR $\delta$ [ppm] | $T_{1min}$ [ms] | $T$ [K] |
|---|---|---|---|---|---|
| **3a** | –9.31 | 18.1 | 75.4 | 34[a] (400 MHz) | 216 |
| **3b** | –9.68 | 18.2 | 82.4 | 41 (300 MHz) | 235 |
| **3c** | –10.53 | 18.1 | 82.2 | 24 (300 MHz) | 200 |
| **3d** | –10.41 | 17.6 | 76.5 | 27 (300 MHz) | 227 |

[a] Ref.[5]

It should be noted that this type of dihydrogen complex has also been prepared by different methods utilizing precursors such as [Ru(PCy$_3$)$_2$(H)$_2$HI],[7] [RuTp(PPh$_3$)(CH$_3$CN)H],[5] [RuTp(P*i*Pr$_2$Me)(CH$_3$CN)Cl],[8] and [RuTp*(COD)H].[9]

Reduction of complexes **2** can also be accomplished with Zn in the presence of suitable ligands. Thus, treatment of **2** with Zn in neat $CH_3CN$ affords the cationic diamagnetic $Ru^{II}$ compounds [RuTp(PR$_3$)(CH$_3$CN)$_2$]$^+$ (**4a**–**c**) with either $ZnCl_4^{2-}$ as counterion or, if the reaction is performed in the presence of $NaBPh_4$, with $BPh_4^-$ as counterion (Scheme 3). Similarly, reduction of **2** in the presence of pyridine (5 equiv.) yields the neutral complex [RuTp(PR$_3$)(py)Cl] (**5**). It is noteworthy that if **2** is refluxed in neat pyridine for 2 h, clean reduction to **5** also takes place in the absence of Zn powder. It was not possible to obtain the cationic bispyridine complex [RuTp(PR$_3$)(py)$_2$]$^+$ under these reaction conditions. Compounds **4** and **5** are thermally robust solids that are stable to air both in the solid state and in solution. Characterization was accomplished by elemental analysis and $^1$H, $^{13}$C{$^1$H}, and $^{31}$P{$^1$H} NMR spectroscopy; no unusual features were observed.

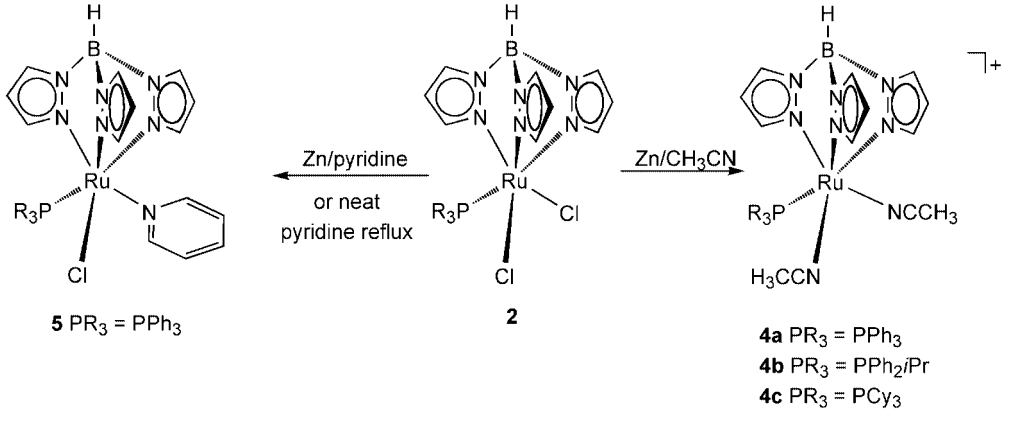


Scheme 3.

 © 2006 Wiley-VCH Verlag GmbH & Co. KGaA, Weinheim 

The structures of $[RuTp(PPh_2iPr)(CH_3CN)_2]_2(ZnCl_4)$ (**4b**) and $[RuTp(PPh_3)(py)Cl]$ (**5**) were determined by X-ray crystallography. The molecular structures are depicted in Figures 4 and 5, respectively; important bond lengths are reported in the caption. Complex **4b** is closely related in terms of stereochemistry and ligand disposition to complex **2b**, including the *trans* influence of the phosphane on the Ru–N(6) bond (Figure 4). Complex **5** is remarkable in having $PPh_3$ with a very regular propeller-like conformation, as can be seen by the three Ru–P–$C_{ipso}$–C torsion angles of –46.3°, –47.4°, and –54.1°. With this conformation and N(2)–Ru–P–C(10), the phenyl rings C(10)–C(15) and C(16)–C(21) exhibit stabilizing intramolecular π-π stacking interactions with one pyrazole and the pyridine ring.

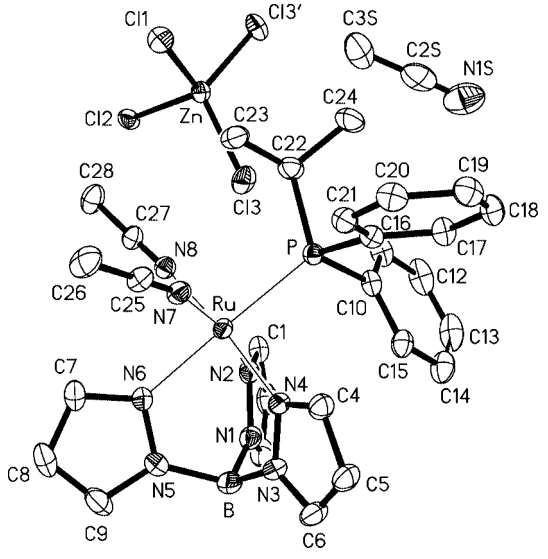


Figure 4. Structural view of $[RuTp(PPh_2iPr)(CH_3CN)_2]_2[ZnCl_4]\cdot CH_3CN$ (**4b**·$CH_3CN$) showing 30% thermal ellipsoids (hydrogen atoms omitted for clarity). Selected bond lengths [Å] and angles [°]: Ru–N(2) 2.064(2), Ru–N(4) 2.078(2), Ru–N(6) 2.113(2), Ru–P 2.3234(5), Ru–N(7) 2.028(8), Ru–N(8) 2.029(2), Zn–Cl(1) 2.258(1), Zn–Cl(2) 2.290(1), Zn–Cl(3) 2.307(1), Zn–Cl(3′) 2.238(2); P–Ru–N(7) 96.37(5), P–Ru–N(8) 92.90(4), N(7)–Ru–N(8) 90.54(6).

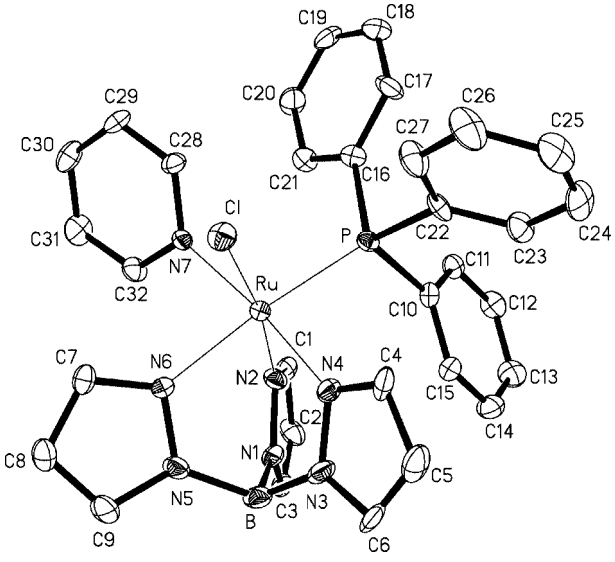


Figure 5. Structural view of $[RuTp(PPh_3)(py)(Cl)]\cdot$solv (**5**·solv) showing 30% thermal ellipsoids (hydrogen atoms omitted for clarity). Selected bond lengths [Å] and angles [°]: Ru–N(2) 2.072(6), Ru–N(4) 2.063(7), Ru–N(6) 2.111(5), Ru–P 2.294(2), Ru–Cl 2.428(2), Ru–N(7) 2.080(7); P–Ru–Cl 98.44(6), P–Ru–N(7) 96.7(2), Cl–Ru–N(7) 86.2(2).

In summary, we have described a facile synthesis of a series air-stable dichloro $Ru^{III}$ complexes of the type $[RuTp(PR_3)Cl_2]$. These compounds are readily reduced to $Ru^{II}$ complexes containing the $[RuTp(PR_3)]^+$ fragment. The use of $NaBH_4$ as reducing agent gives the dihydrogen complexes $[RuTp(PR_3)(H)(\eta^2\text{-}H_2)]$, while with Zn in the presence of $CH_3CN$ and pyridine, respectively, complexes $[RuTp(PR_3)(CH_3CN)_2]^+$ and $[RuTp(PR_3)(py)Cl]$ are obtained.

## Experimental Section

**General:** All manipulations were performed under an inert atmosphere of purified argon by using Schlenk techniques. All chemicals were standard reagent grade and used without further purification. The solvents were purified according to standard procedures.[10] The deuterated solvents were purchased from Aldrich and dried with 4-Å molecular sieves. [RuTp(COD)Cl] (**1**) was prepared according to the literature method.[11] $^1H$, $^{13}C\{^1H\}$, and $^{31}P\{^1H\}$ NMR spectra were recorded with Bruker Avance-250, -300, and -400 spectrometers and are referenced to $SiMe_4$ and $H_3PO_4$ (85%), respectively.

**$[RuTp(PPh_3)Cl_2]$ (2a):** A suspension of **1** (150 mg, 0.33 mmol) and $PPh_3$ (89.1 mg, 0.34 mmol) in DMF (4 mL) was heated at reflux for 2 h. After removal of the solvent, the remaining residue was dissolved in $CH_2Cl_2$ and $CCl_4$ (2 mL) was added. After stirring of the solution for 2 h at room temperature, the volume of the solution was reduced to about 1 mL and the product was precipitated by addition of $Et_2O$ and petroleum ether. The residue was collected on a glass-frit, washed with $Et_2O$, and dried in vacuo. Yield: 183 mg (86%). $C_{27}H_{25}BCl_2N_6PRu$ (647.30): calcd. C 50.10, H 3.89, N 12.98; found C 50.21, H 3.91, N 12.41. $\mu_{eff}$ = 1.89 $\mu_B$.

**$[RuTp(PPh_2iPr)Cl_2]$ (2b):** This complex was prepared analogously to **2a** using **1** (150 mg, 0.33 mmol) and $PPh_2iPr$ (77.6 mg, 0.34 mmol) as starting materials. Yield: 174 mg (88%). $C_{24}H_{27}BCl_2N_6PRu$ (613.28): calcd. C 47.00, H 4.44, N 13.70; found C 47.11, H 4.35, N 13.88. $\mu_{eff}$ = 1.99 $\mu_B$.

**$[RuTp(PiPr_3)Cl_2]$ (2c):** This complex was prepared analogously to **2a** using **1** (150 mg, 0.33 mmol) and $PiPr_3$ (64.9 μL, 0.34 mmol) as starting materials. Yield: 156 mg (87%). $C_{18}H_{31}BCl_2N_6PRu$ (545.24): calcd. C 39.65, H 5.73, N 15.41; found C 39.55, H 5.40, N 15.53. $\mu_{eff}$ = 1.99 $\mu_B$.

**$[RuTp(PCy_3)Cl_2]$ (2d):** This complex was prepared analogously to **2a** using **1** (150 mg, 0.33 mmol) and $PCy_3$ (95.3 mg, 0.34 mmol) as starting materials. Yield: 169 mg (77%). $C_{27}H_{43}BCl_2N_6PRu$ (665.44): calcd. C 48.73, H 6.51, N 12.63; found C 48.60, H 6.91, N 12.70. $\mu_{eff}$ = 1.40 $\mu_B$.

**$[RuTpH(H_2)(PPh_3)]$ (3a):** $NaBH_4$ (28 mg, 0.75 mmol) was added to a solution of **2a** (100 mg, 0.15 mmol) in THF (5 mL) and EtOH (1 mL) and the reaction mixture was stirred at room temperature for 2 h. The solution was then evaporated to dryness and the residue was redissolved in THF. Insoluble materials were removed by filtration and the solution was again evaporated to dryness to yield

 © 2006 Wiley-VCH Verlag GmbH & Co. KGaA, Weinheim 

a white solid, which was dried under vacuum. Yield: 84 mg (97%). $C_{27}H_{28}BN_6PRu$ (579.41): calcd. C 55.97, H 4.87, N 14.50; found C 56.10, H 4.76, N 14.60. $^1$H NMR ($C_6D_6$, 20 °C): $\delta$ = 7.70–7.51 (m, 7 H, Ph, Tp), 7.25–7.18 (m, 2 H, Tp), 7.15–6.99 (m, 12 H, Ph, Tp), 5.93–5.79 (m, 3 H, Tp), –9.31 (d, $^2J_{H,P}$ = 18.1 Hz, 3 H, H, H$_2$) ppm. $^{31}$P{$^1$H} NMR ($C_6D_6$, 20 °C): $\delta$ = 75.4 ppm.

**[RuTpH(H$_2$)(PPh$_2$*i*Pr)] (3b):** This complex was prepared analogously to **3a** using **2b** (100 mg, 0.16 mmol) and $NaBH_4$ (31 mg, 0.82 mmol) as starting materials. Yield: 76 mg (87%). $C_{24}H_{30}BN_6PRu$ (545.40): calcd. C 52.85, H 5.54, N 15.41; found C 52.77, H 5.49, N 15.50. $^1$H NMR ($C_6D_6$, 20 °C): $\delta$ = 7.71–7.46 (m, 6 H, Tp), 7.20–6.86 (m, 10 H, Ph), 5.95–5.69 (m, 3 H, Tp), 2.24–2.03 (m, 1 H, CH), 1.24 (dd, $^3J_{H,P}$ = 14.1, $^3J_{H,H}$ = 7.0 Hz, 6 H, $CH_3$), –9.68 ppm (d, $^2J_{H,P}$ = 18.1 Hz, 3 H, H,H$_2$); $T_{1min}$: 41 ms (–38 °C, [D$_8$]toluene, 300 MHz). $^{31}$P{$^1$H} NMR ($C_6D_6$, 20 °C): $\delta$ = 82.4 ppm.

**[RuTpH(H$_2$)(P*i*Pr$_3$)] (3c):** This complex was prepared analogously to **3a** using **2c** (100 mg, 0.18 mmol) and $NaBH_4$ (34 mg, 0.90 mmol) as starting materials. Yield: 71 mg (83%). $C_{18}H_{34}BN_6PRu$ (477.36): calcd. C 45.29, H 7.18, N 17.61; found C 45.17, H 7.23, N 17.69. $^1$H NMR ($C_6D_6$, 20 °C): $\delta$ = 8.13–7.40 (m, 6 H, Tp), 6.25–5.82 (m, 3 H, Tp), 2.12–1.88 (m, 3 H, CH), 1.09 (dd, $^3J_{H,P}$ = 12.6, $^3J_{H,H}$ = 7.1 Hz, 18 H, $CH_3$), –10.53 ppm (d, $^2J_{H,P}$ = 18.1 Hz, 3 H, H, H$_2$); $T_{1min}$: 24 ms (–73 °C, $CD_2Cl_2$, 300 MHz). $^{31}$P{$^1$H} NMR ($C_6D_6$, 20 °C): $\delta$ = 82.2 ppm.

**[RuTpH(H$_2$)(PCy$_3$)] (3d):** This complex was prepared analogously to **3a** using **2d** (100 mg, 0.15 mmol) and $NaBH_4$ (28 mg, 0.75 mmol) as starting materials. Yield: 80 mg (89%). $C_{27}H_{46}BN_6PRu$ (597.55): calcd. C 54.27, H 7.76, N 14.06; found C 54.20, H 7.69, N 14.00. $^1$H NMR ($C_6D_6$, 20 °C): $\delta$ = 8.16–7.49 (m, 6 H, Tp), 6.32–5.86 (m, 3 H, Tp), 3.60–3.36 (m, 3 H, CH), 2.12–0.95 (m, 30 H), –10.41 ppm (d, $^2J_{H,P}$ = 17.6 Hz, 3 H, H, H$_2$); $T_{1min}$: 27 ms (–46 °C, $CD_2Cl_2$, 300 MHz). $^{31}$P{$^1$H} NMR ($C_6D_6$, 20 °C): $\delta$ = 76.5 ppm.

**[RuTp(PPh$_3$)(CH$_3$CN)$_2$]$_2$(ZnCl$_4$) (4a):** Zn powder (98 mg, 1.5 mmol) was added to a solution of **2a** (100 mg, 0.15 mmol) in acetonitrile and the reaction mixture was stirred at room temperature for 2 h. Insoluble materials were then removed by filtration. The volume of the solution was then reduced to about 1 mL and the product was precipitated by addition of $Et_2O$. The pale-yellow residue was collected on a glass frit, washed with $Et_2O$, and dried under vacuum. Yield: 174 mg (76%) $C_{62}H_{62}B_2Cl_4N_{16}P_2Ru_2Zn$ (1524.2): calcd. C 48.86, H 4.10, N 14.70; found C 48.75, H 4.02, N 14.78. $^1$H NMR ($CD_3CN$, 20 °C): $\delta$ = 8.12–8.04 (m, 1 H, Tp), 7.93–7.80 (m, 3 H, Tp), 7.59–7.44 (m, 3 H, Ph), 7.43–7.33 (m, 6 H, Ph), 7.23–7.04 (m, 6 H, Ph), 6.85–6.74 (m, 2 H, Tp), 6.44–6.36 (m, 1 H, Tp), 6.04–5.93 (m, 2 H, Tp), 2.33 (s, 6 H, C*H*$_3$CN) ppm. $^{13}$C{$^1$H} NMR ($CD_3CN$, 20 °C): $\delta$ = 146.8–127.0 (Ph, Tp), 125.8 ($CH_3CN$), 107.8 (d, $J_{C,P}$ = 1.5 Hz, Tp), 107.4 (Tp), 104.8 (Tp), 5.1 ($CH_3CN$) ppm. $^{31}$P{$^1$H} NMR ($CD_3CN$, 20 °C): $\delta$ = 51.9 ppm.

**[RuTp(PPh$_2$*i*Pr)(CH$_3$CN)$_2$]$_2$(ZnCl$_4$) (4b):** This complex was prepared analogously to **4a** using **2b** (100 mg, 0.16 mmol) and zinc powder as starting materials. Yield: 156 mg (67%). $C_{56}H_{66}B_2Cl_4N_{16}P_2Ru_2Zn$ (1456.14): calcd. C 46.19, H 4.57, N 15.39; found C 46.23, H 4.61, N 15.42. $^1$H NMR ($CD_3CN$, 20 °C): $\delta$ = 8.08–7.95 (m, 1 H, Tp), 7.83–7.64 (m, 3 H, Tp), 7.48–6.97 (m, 10 H, Ph), 6.89–6.82 (m, 1 H, Tp), 6.41–6.30 (m, 1 H, Tp), 5.96–5.80 (m, 2 H, Tp), 3.30–3.06 (m, 1 H, CH), 2.51 (6 H, C*H*$_3$CN), 1.33 (dd, $^3J_{H,P}$ = 14.5, $^3J_{H,H}$ = 6.9 Hz, 6 H, $CH_3$) ppm. $^{13}$C{$^1$H} NMR ($CD_3CN$, 20 °C): $\delta$ = 154.0–127.4 (Ph, Tp), 126.3 ($CH_3CN$), 106.3 (d, $J_{C,P}$ = 3.1 Hz, Tp), 106.3 (Tp), 25.4 (CH), 18.3 ($CH_3$), 4.0 ($CH_3CN$) ppm. $^{31}$P{$^1$H} NMR ($CD_3CN$, 20 °C): $\delta$ = 54.3 ppm.

**[RuTp(PCy$_3$)(CH$_3$CN)$_2$]BPh$_4$ (4c):** $NaBPh_4$ (56.6 mg, 0.165 mmol) and Zn powder (98 mg, 1.5 mmol) were added to a solution of **2d** (100 mg, 0.15 mmol) in acetonitrile and the reaction mixture was stirred at room temperature for 2 h. Insoluble materials were removed by filtration. The volume of the solution was then reduced to about 1 mL and the product was precipitated by addition of $Et_2O$. The pale-yellow residue was collected on a glass frit, washed with $Et_2O$, and dried in vacuo. Yield: 126 mg (89%). $C_{51}H_{63}B_2N_8PRu$ (941.78): calcd. C 65.04, H 6.74, N 11.90; found C 64.97, H 6.78, N 11.89. $^1$H NMR ($CD_3CN$, 20 °C): $\delta$ = 7.91–7.79 (m, 3 H, Tp), 7.78–7.70 (m, 1 H, Tp), 7.67–7.55 (m, 2 H, Tp), 7.38–7.14 (m, 8 H, Ph), 7.09–6.92 (m, 8 H, Ph), 6.90–6.74 (m, 4 H, Ph), 6.37–6.22 (m, 3 H, Tp), 2.43 (6 H, C*H*$_3$CN), 2.26–2.05 (m, 3 H, Cy), 1.82–1.56 (m, 18 H, Cy), 1.54–1.32 (m, 4 H, Cy), 1.31–1.02 (m, 8 H, Cy) ppm. $^{13}$C{$^1$H} NMR ($CD_3CN$, 20 °C): $\delta$ = 146.1–121.7 (Ph, Tp, $CH_3CN$), 106.5 (Tp), 106.2 (d, $J_{C,P}$ = 2.1 Hz, Tp), 34.6 (d, $^1J_{C,P}$ = 18.6 Hz, CH), 29.1 ($CH_2$), 27.4 (d, $J_{C,P}$ = 9.7 Hz, $CH_2$), 26.3 ($CH_2$), 3.9 ($CH_3CN$) ppm. $^{31}$P{$^1$H} NMR ($CD_3CN$, 20 °C): $\delta$ = 38.8 ppm.

**[RuTp(PPh$_3$)(py)Cl] (5). Method (a):** Pyridine (63 μL, 0.75 mmol) and Zn powder (98 mg, 1.5 mmol) were added to a solution of **2a** (100 mg, 0.15 mmol) in toluene, and the reaction mixture was stirred at room temperature for 1 h. Insoluble materials were removed by filtration. The volume of the solution was then reduced to about 1 mL and the product was precipitated by addition of $Et_2O$ and petroleum ether. The yellow residue was collected on a glass frit, washed with $Et_2O$ and petroleum ether, and dried under vacuum. Yield: 102 mg (98%).

**Method (b):** A solution of **2a** (100 mg, 0.15 mmol) in pyridine (5 mL) was heated at reflux for 2 h. The volume of the solution was then reduced to about 1 mL and the product was precipitated by addition of $Et_2O$ and petroleum ether. The yellow residue was collected on a glass frit, washed with petroleum ether, and dried under vacuum. Yield: 98 mg (95%). $C_{32}H_{30}BClN_7PRu$ (691.11): calcd. C 55.63, H 4.38, N 14.19; found C 55.70, H 4.48, N 14.23. $^1$H NMR ($CD_2Cl_2$, 20 °C): $\delta$ = 8.78 (d, $J_{H,H}$ = 8.8 Hz, 2 H, py), 7.99 (t, $J_{H,H}$ = 7.7 Hz, 1 H, py), 7.89–6.73 (m, 22 H, Ph, Tp, py), 6.63 (d, $J_{H,H}$ = 1.7 Hz, 1 H, Tp), 6.18–6.12 (m, 1 H, Tp), 5.92 (dd, $^1J_{H,H}$ = 2.2, $^2J_{H,H}$ = 2.3 Hz, 1 H, Tp), 5.80 (dd, $^1J_{H,H}$ = 2.3, $^2J_{H,H}$ = 2.3 Hz, 1 H, Tp) ppm. $^{13}$C{$^1$H} NMR ($CD_2Cl_2$, 20 °C): $\delta$ = 156.4 (py), 146.4 (Tp), 141.9 (Tp), 140.1 (Tp), 137.5–127.5 (Ph, Tp, py), 125.5 (py), 105.8 (Tp), 105.4 (Tp) ppm. $^{31}$P{$^1$H} NMR ($CD_2Cl_2$, 20 °C): $\delta$ = 54.7 ppm.

**X-ray Structure Determination:** Crystals of **2a**, **2b**, **4b**·$CH_3CN$, and **5**·solv were obtained by diffusion of $Et_2O$ or pentane into solutions in $CH_2Cl_2$ (**2a**, **2b**, **5**) or $CH_3CN$ (**4b**). Crystals of **2d**·$CH_2ClCH_2Cl$ were obtained by solvent evaporation. Crystal data and experimental details are given in Table 2. X-ray data were collected on a Bruker Smart CCD area detector diffractometer using graphite-monochromated Mo-$K_\alpha$ radiation ($\lambda$ = 0.71073 Å) and 0.3° $\omega$-scan frames covering either hemispheres or complete spheres of the reciprocal space. Corrections for absorption, $\lambda$/2 effects, and crystal decay were applied.[12] The structures were solved by direct methods using the program SHELXS-97.[13] Structure refinement on $F^2$ was carried out with the program SHELXL-97.[4] All non-hydrogen atoms were refined anisotropically. Hydrogen atoms were inserted in idealized positions and were refined as riding on the atoms to which they are bonded. Solvent disorder (**2d**·$CH_2ClCH_2Cl$, **4b**·$CH_3CN$) and anion disorder (**4b**·$CH_3CN$) was taken into account. The disordered solvent in **5**·solv (a mixture of $CH_2Cl_2$ and $Et_2O$) was squeezed with the program PARST.[14]

CCDC-609376 (for **2a**), -609377 (for **2b**), -609378 (for **2d**·$CH_2ClCH_2Cl$), -609379 (for **4b**·$CH_3CN$), and -609380 (for

 © 2006 Wiley-VCH Verlag GmbH & Co. KGaA, Weinheim 

Table 2. Details for the crystal structure determinations of complexes [RuTp(PPh$_3$)Cl$_2$] (**2a**), [RuTp(PPh$_2$*i*Pr)Cl$_2$] (**2b**), [RuTp(PCy$_3$)Cl$_2$]·CH$_2$ClCH$_2$Cl (**2d**·CH$_2$ClCH$_2$Cl), [RuTp(PPh$_2$*i*Pr)(CH$_3$CN)$_2$]$_2$[ZnCl$_4$]·CH$_3$CN (**4b**·CH$_3$CN), and [RuTp(PPh$_3$)(py)(Cl)]·solv (**5**·solv).

| | **2a** | **2b** | **2d**·CH$_2$ClCH$_2$Cl | **4b**·CH$_3$CN | **5**·solv[a] |
|---|---|---|---|---|---|
| Formula | $C_{27}H_{25}BCl_2N_6PRu$ | $C_{24}H_{27}BCl_2N_6PRu$ | $C_{29}H_{47}BCl_4N_6PRu$ | $C_{58}H_{69}B_2Cl_4N_{17}P_2Ru_2Zn$ | $C_{32}H_{30}BClN_7PRu$ |
| *Fw* | 647.28 | 613.27 | 764.38 | 1497.17 | 690.93 |
| Crystal size [mm] | 0.58 × 0.31 × 0.21 | 0.33 × 0.32 × 0.14 | 0.24 × 0.12 × 0.06 | 0.40 × 0.30 × 0.25 | 0.45 × 0.18 × 0.08 |
| Space group | $P2_1/c$ (no. 14) | $P2_1/c$ (no. 14) | $P2_1/n$ (no. 14) | $C2/c$ (no. 15) | $P2_1/n$ (no. 14) |
| *a* [Å] | 10.3997(4) | 9.2269(5) | 17.9316(10) | 24.7471(12) | 10.892(3) |
| *b* [Å] | 19.9941(9) | 29.8909(17) | 8.8672(5) | 18.9497(9) | 30.243(7) |
| *c* [Å] | 13.2929(6) | 10.0220(6) | 23.4699(13) | 18.7346(9) | 11.008(3) |
| *β* [°] | 93.397(1) | 104.133(1) | 111.056(1) | 129.629(1) | 99.425(5) |
| *V* [Å$^3$] | 2759.2(2) | 2680.4(3) | 3482.6(3) | 6766.6(6) | 3577.3(15) |
| *Z* | 4 | 4 | 4 | 4 | 4 |
| $\rho_{calcd.}$ [g cm$^{-3}$] | 1.558 | 1.520 | 1.458 | 1.470 | 1.283 |
| *T* [K] | 173(2) | 297(2) | 173(2) | 173(2) | 173(2) |
| $\mu$ [mm$^{-1}$] (Mo-$K_\alpha$) | 0.849 | 0.869 | 0.833 | 1.048 | 0.588 |
| *F*(000) | 1308 | 1244 | 1580 | 3048 | 1408 |
| $\theta_{max}$ [deg] | 30 | 27 | 27 | 30 | 25 |
| Reflections measd. | 27878 | 24434 | 37555 | 34395 | 11091 |
| Unique reflections | 8034 | 5830 | 7579 | 9766 | 5517 |
| Refl. with $I > 2\sigma(I)$ | 6739 | 4951 | 5554 | 8010 | 3657 |
| Parameters | 344 | 316 | 386 | 433 | 388 |
| $R_1$ [$I > 2\sigma(I)$][b] | 0.0390 | 0.0363 | 0.0396 | 0.0322 | 0.0829 |
| $R_1$ (all data) | 0.0510 | 0.0462 | 0.0664 | 0.0430 | 0.1250 |
| $wR_2$ (all data) | 0.0848 | 0.0787 | 0.0844 | 0.0871 | 0.1912 |
| Diff. Fourier peaks, min./max. [e Å$^{-3}$] | –1.10/0.62 | –0.35/0.28 | –0.58/0.66 | –0.53/0.77 | –1.08/1.32 |

[a] Disordered solvent ($CH_2Cl_2$/$Et_2O$) squeezed with program PARST. Chemical formula and derived quantities given without solvent content. [b] $R_1 = \Sigma||F_o| - |F_c||/\Sigma|F_o|$; $wR_2 = [\Sigma\{w(F_o^2 - F_c^2)^2\}/\Sigma\{w(F_o^2)^2\}]^{1/2}$.

**5**·solv) contain the supplementary crystallographic data for this paper. These data can be obtained free of charge from The Cambridge Crystallographic Data Centre via www.ccdc.cam.ac.uk/data_request/cif.

**Electrochemical Studies:** Cyclic voltammograms were measured in a three-electrode cell using a 0.2-mm-diameter glassy carbon working electrode, a platinum auxiliary electrode, and a Ag|Ag$^+$ reference electrode containing 0.1 M $AgNO_3$, the potential of which was corrected using an internal standard redox couple of ferrocenium/ferrocene. Measurements were performed at room temperature using an EG & G PARC 273A potentiostat/galvanostat. Deaeration of solutions was accomplished by passing a stream of argon through the solution for 5 min prior to the measurement and then maintaining a blanket atmosphere of argon over the solution during the measurement. The potentials were measured in 0.15 M [*n*Bu$_4$N][BF$_4$]/CH$_3$CN, using FeCp$_2$ ($E_{1/2}$ = +0.69 V vs. NHE) as internal standard and are quoted relative to NHE.

**Magnetic Measurements:** For the determination of the magnetic susceptibility, the powdered complex was pressed into pellets. VT magnetic susceptibility measurements of the complex were performed with a superconductivity interferometer device (SQUID) in external fields of up to 3 T, within the temperature range 4.2–300 K.

## Acknowledgments

Financial support by the "Fonds zur Förderung der wissenschaftlichen Forschung" is gratefully acknowledged (project no. P16600-N11). We thank G. Hilscher for the measurements of the magnetic moments and C. Kowol for carrying out the electrochemical studies.

[1] C. Slugovc, R. Schmid, K. Kirchner, *Coord. Chem. Rev.* **1999**, *185–186*, 109.
[2] C. Gemel, G. Kickelbick, R. Schmid, K. Kirchner, *J. Chem. Soc., Dalton Trans.* **1997**, 2119.
[3] a) C. Slugovc, V. N. Sapunov, P. Wiede, K. Mereiter, R. Schmid, K. Kirchner, *J. Chem. Soc., Dalton Trans.* **1997**, 4209; b) C. Slugovc, K. Kirchner, K. Mereiter, *Acta Crystallogr., Sect. E* **2006**, *62*, m1356.
[4] I. Dance, M. Scudder, *J. Chem. Soc., Dalton Trans.* **2000**, 1579.
[5] Y.-Z. Chen, W. C. Chan, C. P. Lau, H. S. Chu, H. L. Lee, G. Jia, *Organometallics* **1997**, *16*, 1241.
[6] a) H. Suzuki, D. H. Lee, N. Oshima, Y. Moro-oka, *J. Organomet. Chem.* **1986**, *317*, C45; b) S. G. Davies, S. D. Moon, S. J. Simpson, *J. Chem. Soc., Chem. Commun.* **1983**, 1278.
[7] M. A. Halcrow, B. Chaudret, S. Trofimenko, *J. Chem. Soc., Chem. Commun.* **1993**, *5*, 465.
[8] M. A. Tenorio, M. J. Tenorio, M. C. Puerta, P. Valerga, *J. Chem. Soc., Dalton Trans.* **1998**, 3601.
[9] B. Moreno, S. Sabo-Etienne, B. Chaudret, A. Rodriguez, F. Jalon, S. Trofimenko, *J. Am. Chem. Soc.* **1995**, *117*, 7441.
[10] D. D. Perrin, W. L. F. Armarego, *Purification of Laboratory Chemicals*, 3rd ed.; Pergamon: New York, **1988**.
[11] C. Gemel, G. Trimmel, C. Slugovc, S. Kremel, K. Mereiter, R. Schmid, K. Kirchner, *Organometallics* **1996**, *15*, 3998.
[12] Bruker programs: *SMART*, version 5.629; *SAINT*, version 6.45; *SADABS*, version 2.10; *SHELXTL*, version 6.1 (Bruker AXS Inc., Madison, WI, **2003**).
[13] G. M. Sheldrick, *SHELX97*: Program System for Crystal Structure Determination; University of Göttingen, Germany, **1997**.
[14] A. L. Spek, *PLATON*: A Multipurpose Crystallographic Tool; University of Utrecht, The Netherlands, **2003**.

Received: May 30, 2006
Published Online: August 10, 2006

 © 2006 Wiley-VCH Verlag GmbH & Co. KGaA, Weinheim 

DOI: 10.1002/ejic.200600546

# New Coordination Modes of Substituted Benzohydroxamic Acid with Dialkyltin(IV): Structural Diversity through Ligand Isomerization

**Xian-mei Shang,[a,b] Ji-zhou Wu,*[b] and Qing-shan Li*[a,b]**

**Keywords:** Coordination modes / Organotin / Hydroxamic / Hydroximic / Isomerization

When $R_2SnCl_2$ (R = Me, *n*Bu) reacted with substituted benzohydroxamic acid (substituent = 4-F; 2,4-$Cl_2$; 2,5-$F_2$) and potassium hydroxide in aqueous methanol solution, two types of condensation products could be obtained, depending on the molar ratio $R_2SnCl_2$/RCONHOH/KOH. When a 1:1:2 molar ratio was used, 1:1 alkyltin hydroxamates $\{(n\text{-}C_4H_9)_2Sn[4\text{-}FC_6H_4C(O)NO]\}_n$ (**1**) and $\{(CH_3)_2Sn[2,5\text{-}F_2C_6H_3C(O)NO]\}_n$ (**2**) were formed. When a 1:2:2 ratio was used, another two unexpected 2:3 alkyltin hydroxamates, $\{(CH_3)_4Sn_2[(2,4\text{-}Cl_2C_6H_3C(O)NHO)_2][2,4\text{-}Cl_2C_6H_3C(O)NO]\}_n$ (**3**) and $\{(n\text{-}C_4H_9)_4Sn_2[(4\text{-}FC_6H_4C(O)NHO)_2][4\text{-}FC_6H_4C(O)NO]\}_n$ (**4**), were obtained. All these complexes were characterized by elemental analysis, IR, $^1H$, $^{13}C$, $^{119}Sn$ NMR spectra and X-ray diffraction analysis. The results indicated overall (*Z*)-iminol coordination mode in the hydroximic tautomeric form for **1** and **2**, and keto-iminol mixed-coordination mode including both in (*Z*)-hydroxamic and -hydroximic tautomeric forms for **3** and **4**.

(© Wiley-VCH Verlag GmbH & Co. KGaA, 69451 Weinheim, Germany, 2006)

## Introduction

Hydroxamic acids (HAs) have attracted considerable attention recently as supporting ligands in organometallic chemistry and biology because of their tautomerization,[1] and potential as therapeutics agents.[2] The biological importance and different conformation of HAs may make their organometallic derivatives exert a subtle influence on their medicinal applications. In principle, each of the two oxygen atoms of the hydroxamato ligand is capable of acting as a coordination site, and the bonding modes are flexible. Moreover, tautomers of HAs assume different conformations or configurations, as indicated in Scheme 1. The HAs preferentially adopt the (*Z*) configurations when binding with metal ions to form a complex, either through the hydroxamic acid form or the hydroximic acid form. In addition, it is well documented by both theoretical[3] and experimental studies that the hydroxamic form is the dominant one in free acids[4] or metal hydroxamates.[5]

Despite these attractive features, studies on the coordination modes of the complexes possessing hydroxamic ligands are still relatively scarce. According to the literature,[6] the complexes of hydroxamic derivatives with metal formed O,O five-membered chelate rings in most cases, and the ligands were usually in the hydroxamic form rather than hydroximic form. To the best of our knowledge, the complexes in which ligands are only in the hydroximic form are rarely observed, and indeed, a case with the ligands coordinated to the metal center both in the hydroxamic and hydroximic forms in the same complex has not yet been reported.

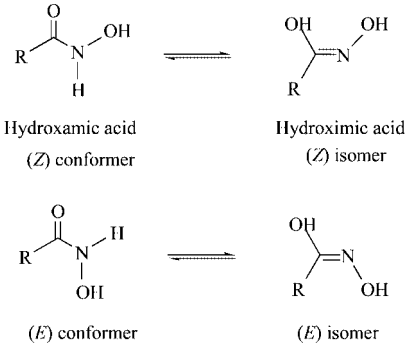


Scheme 1. Isomers of hydroxamic acids.

On the other hand, in contrast to the extensive chemistry of transition-metal hydroxamato complexes,[7,8] little is known about the hydroxamato organotin(IV) complexes,[9] especially their coordination modes. The synthesis and structure of 1:2 diorganotin(IV)/hydroxamato complexes have been previously reported by our group,[10,11] which provides a novel coordination mode for hydroxamato diorganotin(IV) complexes. To obtain a deeper insight into the influence of the ligand and to further explore structural diversity, in this work, an extension of the work on the 1:2 diorganotin(IV)/hydroxamato complexes was carried out, and four unusual complexes containing the (*Z*) isomer hydroximic ligand were obtained, presenting novel 1:1 and 2:3 organotin(IV)/hydroxamato complexes with hydroximic ligands. Furthermore, the reaction of substituted benzohydroxamic acid with dialkyltin(IV) compounds, leading to

[a] School of Pharmaceutical Science, Shanxi Medical University, Taiyuan 030001, P. R. China
[b] School of Pharmaceutical Science, Tongji Medical College, Huazhong University of Science and Technology, 13 Hangkong Road, Wuhan 430030, P. R. China

 © 2006 Wiley-VCH Verlag GmbH & Co. KGaA, Weinheim 

the formation of these special organotin(IV) complexes with hydroximato ligands, is also discussed.

## Results and Discussion

### Reaction of Dialkyltin Dichloride with Substituted Benzohydroxamic Acid

To obtain a deeper insight into the coordination of hydroxamic acid to the tin center, the reaction of dialkyltin dichloride with substituted benzohydroxamic acid was studied. It was found that the reaction of dialkyltin dichloride ($Bu_2SnCl_2$ and $Me_2SnCl_2$) with substituted benzohydroxamic acid and potassium hydroxide at a 1:1:2 ratio in methanol/water gave 1:1 dialkyltin hydroxamates $\{(n\text{-}C_4H_9)_2Sn[4\text{-}FC_6H_4(O)C{=}NO]\}_n$ (**1**) and $\{(CH_3)_2Sn[2,5\text{-}2F\text{-}C_6H_3C(O)NO]\}_n$ (**2**). When a 1:2:2 ratio was used, another two unexpected 2:3 alkyltin hydroxamates, $\{(CH_3)_4Sn_2[(2,4\text{-}Cl_2C_6H_3C(O)NHO)_2][2,4\text{-}Cl_2C_6H_3C(O)NO]\}_n$ (**3**) and $\{(n\text{-}C_4H_9)_4Sn_2[(4\text{-}FC_6H_4C(O)NHO)_2][4\text{-}FC_6H_4C(O)NO]\}_n$ (**4**), were obtained. All of these complexes contain chelating hydroximic acid ligands [(*Z*) isomer], which is obviously different from well-known dialkyltin hydroxamates. Although the reactions of metal ions with hydroxamic acid have been studied extensively, most of them form 1:2 complexes containing hydroxamic acid ligands [(*Z*) conformer], and very little is reported on complexes containing hydroximic acid ligands [(*Z*) isomer]. Presumably, complexes **1**, **2**, **3**, and **4** could result from the tautomerism of the hydroxamic acid ligand, as shown in Scheme 1. The present observation might be attributed to three favorable factors: (1) the alkaline reaction conditions might make the equilibrium (as shown in Scheme 1) move from hydroxamic acid [(*Z*) conformer] toward hydroximic acid [(*Z*) isomer] easily, and thus, the hydrogen atom linked to the nitrogen atom could migrate to the oxygen atom of the carbonyl group; then the ratio of hydroximic acid in the keto-iminol tautomerism equilibrium would be raised in this way, resulting in these complexes with new coordinated modes; (2) the strong electron-withdrawing nature of F or Cl may enhance the 1,3-migratory aptitude of the hydrogen atom in the hydroxamic acid ligands; (3) it is also conceivable that a hydroxamic acid in the (*E*) conformation could also give the observed products, as any energy requirement for isomerism to the (*Z*) form would be compensated for by the favorable energetics associated with the formation of a stable five-membered chelate ring (i.e. chelate effect).

### Syntheses and Characterizations of 1 and 2

When dialkyltin dichloride ($Bu_2SnCl_2$; $Me_2SnCl_2$) reacts with substituted benzohydroxamic acid (substituent = 4-F; 2,5-$F_2$) and potassium hydroxide, 1:1 condensation products **1** and **2** can be obtained (Scheme 2). In the IR spectra for the two complexes, a remarkable difference is the complete disappearance of the stretching vibration bands of N–H in contrast to their free ligands. This unambiguously confirms that these ligands are coordinated to the tin atoms through the hydroximic form. The characteristic absorptions at both 1661–1610 $cm^{-1}$ in the spectra of **1** and **2** indicate the presence of a C=N group.[12–15] For **1**, the Bu–Sn–Bu angle of 129° calculated from the equation of Holeček and Lyčka[16] is very close to the value of 130.1(4)° found by X-ray analysis (Table 1). The Me–Sn–Me angle for **2** in solution calculated from the equation of Lockhart and Manders[17] is 128°, also close to the 131.45(19)° observed in the solid state (Table 2). The $^{119}Sn$ NMR spectroscopic data show only one signal at $\delta \approx -124.8$ ppm for **1** and $\delta \approx -129.9$ ppm for **2**, indicating a typical five-coordinate species,[16] which was further confirmed by single-crystal X-ray analysis.

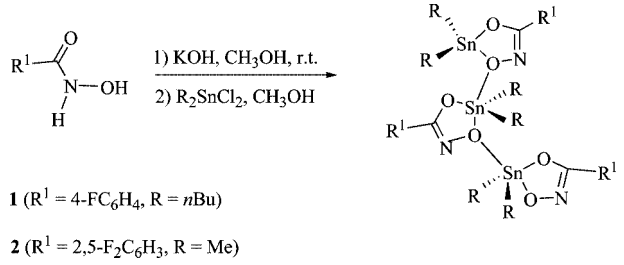


**1** ($R^1$ = 4-$FC_6H_4$, R = *n*Bu)

**2** ($R^1$ = 2,5-$F_2C_6H_3$, R = Me)

Scheme 2.

Reaction of dialkyltin dichloride ($Me_2SnCl_2$; $Bu_2SnCl_2$) with substituted benzohydroxamic acid (substituent = 2,4-$Cl_2$; 4-F) in 1:2 stoichiometry yields 2:3 condensation products **3** and **4** (Scheme 3). In their free ligands, a strong band near 3207 $cm^{-1}$ is observed, assigned to be the $\nu$(NH) absorption, which is shifted to higher frequency (near 3290 $cm^{-1}$) in the two complexes. This shows that the NH group is retained in the two complexes. In the $^1H$ NMR spectra of complex **3**, two single resonances for the proton in the –NH–O– group are observed at $\delta$ = 9.21 and 10.56 ppm, indicating that the proton of the –NH–O– group exists in complex **3**, and confirming the ligand coordinates to the tin atom in the keto (hydroxamato) form.

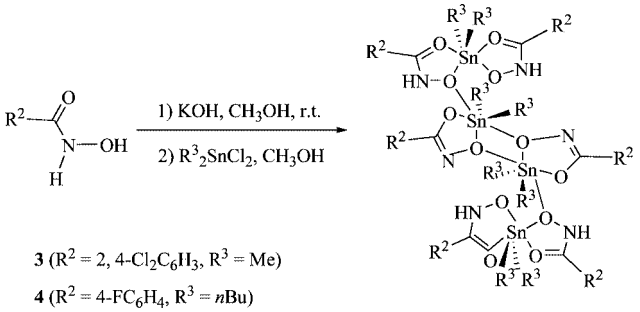


**3** ($R^2$ = 2, 4-$Cl_2C_6H_3$, $R^3$ = Me)

**4** ($R^2$ = 4-$FC_6H_4$, $R^3$ = *n*Bu)

Scheme 3.

The $^{119}Sn$ NMR spectroscopic data show two signals at $\delta \approx -222.6$ and –221.0 ppm for **3** ($\delta \approx -217.4$, –216.6 ppm for **4**), indicating the presence of two different tin sites in solution, which has been confirmed in the solid state for **3** and **4**. The $\delta(^{119}Sn)$ values of compounds **3** and **4** belong in the range of six-coordinate compounds.[16,18] In complexes

 © 2006 Wiley-VCH Verlag GmbH & Co. KGaA, Weinheim 

**3** and **4**, the ligands are also coordinated to the tin atom in the iminol (hydroximato) form, which was verified by X-ray crystal diffraction technique and is discussed below.

### Crystal Structures of Complexes 1 and 2

Selected bond lengths and angles of complexes **1** and **2** are listed in Tables 1 and 2, respectively. The molecular structures of the two complexes are shown in Figures 1 and 2 for a single chain based on the one-dimensional oxygen-bridged dialkyltin(IV) complex. The substituted benzohydroximic ligands are found to be chelated to the Sn atom through the carbonyl O atom and the hydroxy O atom, and Sn–O bond lengths are 2.065(6) and 2.191(5) Å for **1**, and 2.064(2) and 2.155(2) Å for **2**. The $Sn^{IV}$ atoms are bonded to two alkyl groups, and the C(8)–Sn1–C(12) linkage for **1** [C(8)–Sn1–C(9) for **2**] is not linear, having an angle of 130.1(4)° for **1** [131.45(19)° for **2**]. All these Sn–C and Sn–O bond lengths and also all bond angles around the Sn center are typical values compared with other diorganotin(IV) complexes.[19,20]

However, the endocyclic C–N and C–O bond lengths are special in contrast with those of well-known 1:2 diorganotin hydroxamates. The bond length C(7)–N(1) in complex **1** is 1.237(9) Å, and is significantly shorter than the values in the known 1:2 complexes [the average C–N distance of 1.32 Å is comparable to the corresponding distance in diorganotin(IV) hydroxamates]. Moreover, no hydrogen atom is at the N1 position, suggesting that the C–N bond in complex **1** is a typical double bond.[21] Meanwhile, the bond length C(7)–O(1) in complex **1** is 1.378(9) Å, and is significantly longer than the typical value of C=O [the average C=O distance of 1.25 Å is comparable to the corresponding distance in diorganotin(IV) hydroxamates],[22] which shows the C–O bond in the complex should be a typical single bond. The bonding mode is in good agreement with hydroximic acid [(*Z*) isomer]. From the above analysis it could be concluded that the ligand is coordinated to the tin(IV) atom in the hydroximic acid form, and complex **1** is a hydroximate rather than a hydroxamate.

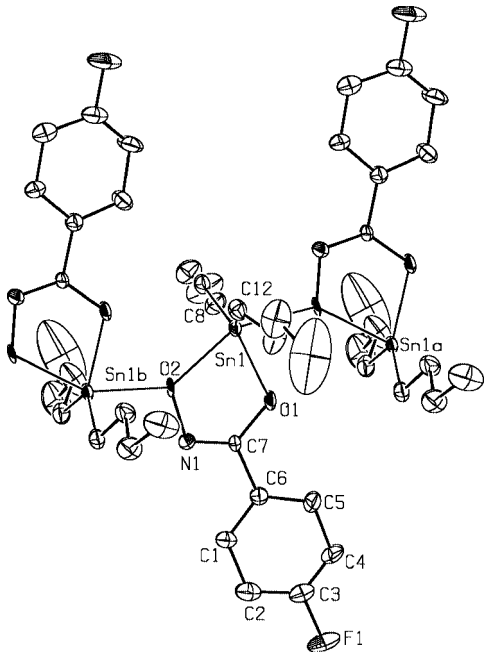


Figure 1. Diagram of a section of polymeric **1**. Hydrogen atoms are omitted for clarity.

For complex **2**, the overall structure (Figure 2, Table 2) is similar to that of complex **1**. The $Sn^{4+}$ ion is bonded with two $CH_3$ groups and one substituted benzohydroximic ligand. The coordination number of the Sn atom is 5. The complex has no unusual distances or angles in the $Me_2Sn$ unit.

Like complex **1**, the bond length C(7)–N(1) in complex **2** is 1.286(5) Å, and is significantly shorter than those values in the known 1:2 complexes.[11] Consistently, the average C(7)–O(2) distance [1.318(4) Å] of complex **2** is significantly

Table 1. Selected bond lengths [Å] and angles [°] for **1**. Symmetry operators: #1: $-x + 2, y + 1/2, -z + 1/2$; #2: $-x + 2, y - 1/2, -z + 1/2$.

| | | | |
|---|---|---|---|
| O(1)–Sn(1) | 2.065(6) | C(7)–N(1) | 1.237(9) |
| O(2)–Sn(1) | 2.191(5) | C(7)–O(1) | 1.378(9) |
| O(2)–Sn(1)#1 | 2.134(4) | N(1)–O(2) | 1.428(8) |
| Sn(1)–O(2)#2 | 1.512(14) | C(8)–Sn(1) | 2.085(10) |
| C(8)–Sn(1)–C(12) | 130.1(4) | O(1)–Sn(1)–C(12) | 114.2(4) |
| O(1)–Sn(1)–C(8) | 115.7(3) | O(1)–Sn(1)–O(2)#2 | 76.4(2) |
| C(8)–Sn(1)–O(2)#2 | 96.3(3) | C(12)–Sn(1)–O(2)#2 | 95.3(3) |
| O(1)–Sn(1)–O(2) | 75.0(2) | C(8)–Sn(1)–O(2) | 96.0(3) |
| C(12)–Sn(1)–O(2) | 96.3(3) | O(2)#2–Sn(1)–O(2) | 151.45(9) |

Table 2. Selected bond lengths [Å] and angles [°] for **2**. Symmetry operators: #1: $-x + 1, y - 1/2, z + 1/2$; #2: $-x + 1, y + 1/2, -z + 1/2$.

| | | | |
|---|---|---|---|
| Sn(1)–O(1) | 2.155(2) | C(7)–N(1) | 1.286(5) |
| Sn(1)–O(2) | 2.064(2) | C(7)–O(2) | 1.318(4) |
| Sn(1)–O(1)#1 | 2.151(2) | N(1)–O(1) | 1.430(4) |
| O(1)–Sn(1)#2 | 2.151(2) | Sn(1)–C(8) | 2.097(4) |
| C(8)–Sn(1)–C(9) | 131.45(19) | C(9)–Sn(1)–O(1)#1 | 95.40(15) |
| O(2)–Sn(1)–C(8) | 111.39(16) | O(2)–Sn(1)–O(1) | 74.03(9) |
| O(2)–Sn(1)–C(9) | 117.15(15) | C(8)–Sn(1)–O(1) | 98.71(14) |
| O(2)–Sn(1)–O(1)#1 | 76.97(9) | C(9)–Sn(1)–O(1) | 94.63(15) |
| C(8)–Sn(1)–O(1)#1 | 95.00(13) | O(1)#1–Sn(1)–O(1) | 150.78(5) |

 © 2006 Wiley-VCH Verlag GmbH & Co. KGaA, Weinheim 

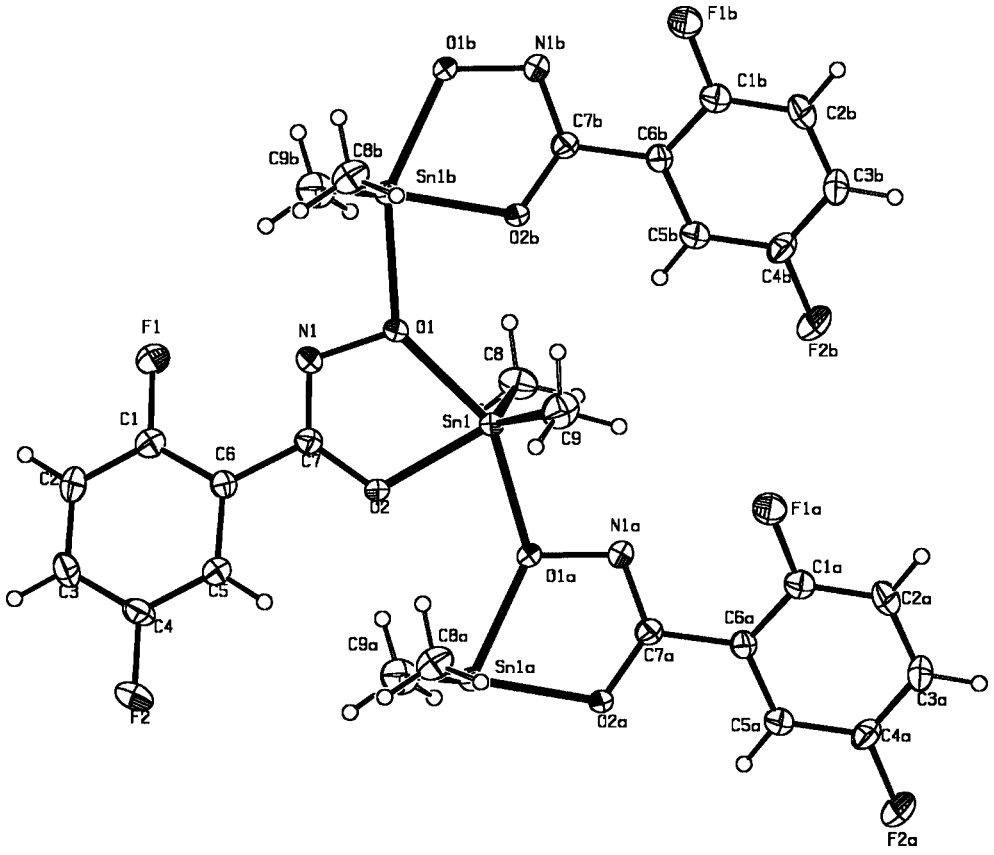


Figure 2. ORTEP drawing of a section of polymeric **2** with atomic numbering scheme.

longer than the corresponding distance of C=O, indicating the C–O bond in complex **2** should be a typical single bond. These data show that the ligand is coordinated to the tin(IV) atom in the hydroximic acid form and the coordination mode of complex **2** is similar to that of complex **1**.

### Crystal Structures of Complexes 3 and 4

The molecular structures of **3** and **4** are shown in Figures 3 and 4, respectively. Selected bond lengths and angles for complexes **3** and **4** are listed in Tables 3 and 4, respec-

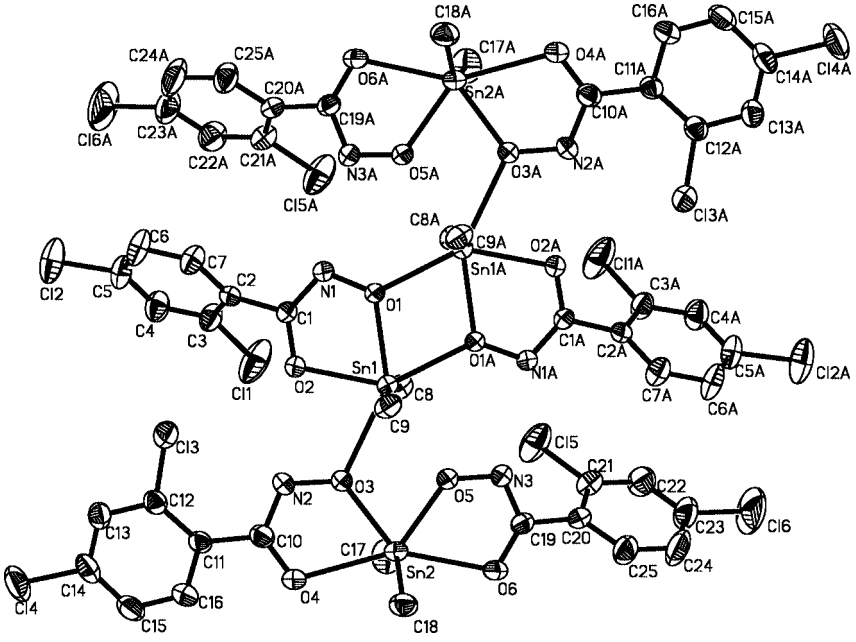


Figure 3. Diagram of the dimeric repeating units in polymeric **3**. Hydrogen atoms are omitted for clarity.

 © 2006 Wiley-VCH Verlag GmbH & Co. KGaA, Weinheim 

tively. The crystal structure of the two compounds consists of one-dimensional linear chains in which $Me_4Sn_2[(2,4\text{-}Cl_2C_6H_3C(O)NHO)_2][2,4\text{-}Cl_2C_6H_3C(O)NO]$ or $(n\text{-}C_4H_9)_4Sn_2\{[4\text{-}FC_6H_4C(O)NHO]_2\}[4\text{-}FC_6H_4C(O)NO]$ units are sequentially bridged by the oxygen atom of the N–O bond in the ligands and contain a central planar $Sn_2O_2$ four-membered ring. The ligands in the two complexes have been combined with dialkyltin(IV), forming many five-membered heterometallacycles. However, the number and configuration of the ligand bonded to a different Sn atom are obviously not consistent with each other. Only one ligand is coordinated to Sn1 through the hydroximic form, while the other two ligands are coordinated to Sn2 through the hydroxamic form. In contrast to the behavior observed for the 1:2 or 1:1 diorganotin hydroxamate complexes, both **3** and **4** are 2:3 condensation products with an unusual coordinating mode.

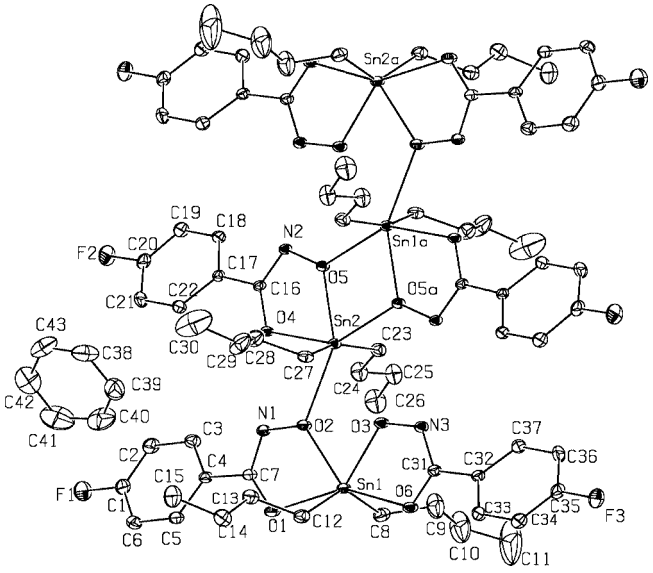


Figure 4. Diagram of the dimeric repeating units in polymeric **4**. Hydrogen atoms are omitted for clarity.

In complex **3**, the bond lengths N(2)–C(10) and N(3)–C(19) are 1.314(6) and 1.314(5) Å respectively. The distances are in the range of a typical single bond, and nearly equivalent N(2)–C(10) and N(3)–C(19) bond lengths suggest two similar hydroxamate ligands attached to the same Sn2 atom. Bond lengths C(10)–O(4) and C(19)–O(6) are 1.247(6) and 1.255(5) Å, respectively, which are in the expected range for C=O bond interaction with obvious double and donor-bond character. The bonding mode of the ligand is well in agreement with the (*Z*) conformer of hydroxamic acid, indicating that ligands are coordinated to Sn2 through the hydroxamic ligand [(*Z*) conformer] form.

Complex **4** is similar to complex **3** in molecular structure. The bond lengths N(1)–C(7) and N(3)–C(31) are 1.323(5) and 1.311(5) Å, respectively, indicating the distances are in the range of a typical single bond in diorganotin(IV) hydroxamates. The slight difference in the bond lengths N(1)–C(7) and N(3)–C(31) may be a result of the existence of solvent molecules (benzene). Bond lengths C(7)–O(1) and C(31)–O(6) are 1.241(5) and 1.255(5) Å, respectively, which are in the expected range for the C=O bond. The bonding mode of the ligand is in good agreement with the (*Z*) conformer of hydroxamic acid, indicating that the ligands are coordinated to Sn1 through the hydroxamic ligand [(*Z*) conformer] form.

Characteristically, the distance between the central carbon atom and the coordinated oxygen atom, C(1)–O(2), is 1.305(5) Å in complex **3** {the C(16)–O(4) distance [1.307(4) Å] in complex **4**}, significantly longer than that of the expected C=O double bond in typical diorganotin(IV) hydroxamates, indicating a typical single bond. Concurrently, the relatively short N(1)–C(1) [1.280(5) Å] bond in complex **3** and N(2)–C(16) [1.302(5) Å] bond in complex **4** exist in the same ligand and no hydrogen atom is at the nitrogen atom, indicating a C=N double bond. The ligand-bonding mode is consistent with hydroximic acid [(*Z*) isomer], indicating the ligand is coordinated to Sn1 in complex **3** (Sn2 in complex **4**) in the hydroximic ligand [(*Z*) isomer] form.

Table 3. Selected bond lengths [Å] and angles [°] for **3**. Symmetry operator: #1: $-x, y, -z + 1/2$.

| | | | |
|---|---|---|---|
| Sn(1)–C(9) | 2.097(5) | N(1)–C(1) | 1.280(5) |
| Sn(1)–C(8) | 2.100(5) | N(1)–O(1) | 1.422(4) |
| Sn(1)–O(1) | 2.167(3) | N(2)–C(10) | 1.314(6) |
| Sn(1)–O(2) | 2.190(3) | N(2)–O(3) | 1.381(5) |
| Sn(1)–O(1)#1 | 2.274(3) | N(3)–C(19) | 1.314(5) |
| Sn(1)–O(3) | 2.450(3) | N(3)–O(5) | 1.381(4) |
| Sn(2)–C(18) | 2.095(5) | O(2)–C(1) | 1.305(5) |
| Sn(2)–C(17) | 2.105(5) | O(4)–C(10) | 1.247(6) |
| Sn(2)–O(3) | 2.109(3) | O(6)–C(19) | 1.255(5) |
| C(9)–Sn(1)–C(8) | 163.48(19) | C(18)–Sn(2)–O(3) | 108.87(18) |
| C(9)–Sn(1)–O(1) | 95.54(16) | C(17)–Sn(2)–O(3) | 101.7(2) |
| C(8)–Sn(1)–O(1) | 99.78(15) | C(18)–Sn(2)–O(5) | 101.99(17) |
| C(9)–Sn(1)–O(2) | 98.94(17) | C(17)–Sn(2)–O(5) | 110.8(2) |
| O(1)–Sn(1)–O(2) | 71.72(11) | C(18)–Sn(2)–O(6) | 89.25(17) |
| C(9)–Sn(1)–O(1)#1 | 88.95(17) | C(17)–Sn(2)–O(6) | 82.62(19) |
| C(8)–Sn(1)–O(1)#1 | 90.24(16) | O(3)–Sn(2)–O(6) | 139.41(11) |
| O(2)–Sn(1)–O(1)#1 | 142.31(11) | C(18)–Sn(2)–O(4) | 85.51(17) |
| C(8)–Sn(1)–O(3) | 88.23(16) | O(3)–Sn(2)–O(4) | 68.37(12) |
| O(2)–Sn(1)–O(3) | 75.54(11) | O(6)–Sn(2)–O(4) | 151.28(11) |

 © 2006 Wiley-VCH Verlag GmbH & Co. KGaA, Weinheim 

Table 4. Selected bond lengths [Å] and angles [°] for **4**. Symmetry operator: #1: $-x + 1, -y + 2, -z + 1$.

| | | | |
|---|---|---|---|
| Sn(1)–C(12) | 2.109(5) | N(1)–C(7) | 1.323(5) |
| Sn(1)–C(8) | 2.111(5) | N(1)–O(2) | 1.379(4) |
| Sn(1)–O(1) | 2.492(3) | N(2)–C(16) | 1.302(5) |
| Sn(1)–O(2) | 2.130(3) | N(2)–O(5) | 1.434(4) |
| Sn(1)–O(3) | 2.137(3) | N(3)–C(31) | 1.311(5) |
| Sn(1)–O(6) | 2.353(3) | N(3)–O(3) | 1.363(4) |
| Sn(2)–C(27) | 2.110(4) | O(1)–C(7) | 1.241(5) |
| Sn(2)–C(23) | 2.112(5) | O(4)–C(16) | 1.307(4) |
| Sn(2)–O(4) | 2.167(3) | C(31)–O(6) | 1.255(5) |
| C(12)–Sn(1)–C(8) | 138.4(2) | C(27)–Sn(2)–C(23) | 161.25(18) |
| C(12)–Sn(1)–O(2) | 103.17(16) | C(27)–Sn(2)–O(5) | 97.45(14) |
| C(8)–Sn(1)–O(2) | 107.81(17) | C(23)–Sn(2)–O(5) | 98.38(15) |
| C(12)–Sn(1)–O(3) | 112.64(17) | O(5)–Sn(2)–O(4) | 72.66(9) |
| O(2)–Sn(1)–O(3) | 68.75(10) | O(4)–Sn(2)–O(5)#1 | 141.74(9) |
| C(12)–Sn(1)–O(6) | 84.36(15) | C(27)–Sn(2)–O(2) | 85.07(14) |
| C(8)–Sn(1)–O(6) | 90.49(17) | C(23)–Sn(2)–O(2) | 86.91(15) |
| O(2)–Sn(1)–O(6) | 138.10(10) | O(5)–Sn(2)–O(2) | 147.69(9) |

Based on the above studies, it could be concluded that a keto-iminol mixed-coordination mode including both hydroxamic and hydroximic tautomeric forms existed for complexes **3** and **4**.

## Conclusion

Under alkaline condition, dialkyltin dichloride ($Bu_2SnCl_2$; $Me_2SnCl_2$) and substituted benzohydroxamic acid (substituent = 4-F; 2,4-$Cl_2$; 2,5-$F_2$) in aqueous methanol solution form two types of condensation products: 1:1 dialkyltin hydroxamate complexes (**1** and **2**) and unexpected 2:3 alkyltin hydroxamate complexes (**3** and **4**). All of them have been verified by spectral methods and X-ray single-crystal diffraction analysis. The present results demonstrate that all of these alkyltin hydroxamates contain hydroximic ligands [(*Z*) isomer], presenting two kinds of new coordination modes. Concurrently, dialkyltin hydroxamate complexes exhibit structural diversity through the isomerism of hydroxamic ligand, which develops the coordination chemistry of diorganotin hydroxamic complexes. So far, the result proves that diorganotin complexes containing substituted hydroxamate ligands could take on three different coordination modes. Namely, ligands of the diorganotin complexes are only in hydroxamic form [(*Z*) conformer], or only in hydroximate form [(*Z*) isomer] or in both hydroxamate form and hydroximate form [(*Z*) conformer and (*Z*) isomer], forming diversiform hydroxamate complexes.

## Experimental Section

**Materials and Methods:** Dibutyltin(IV) dichloride, ethyl 4-fluorobenzoate, ethyl 2,5-difluorobenzoate, and 2,4-dichlorobenzoic acid were purchased from Aldrich and used as received. The other reagents were of analytical grade. 4-Fluorobenzohydroxamic acid, 2,5-difluorobenzohydroxamic acid, and 2,4-dichlorobenzohydroxamic acid were prepared according to reported methods.[23] Elemental analyses were performed with a PE-2400-II elemental analyzer. IR spectra in the range 4000–400 $cm^{-1}$ were recorded with a Perkin–Elmer FTIR spectrophotometer as KBr discs. $^1H$, $^{13}C$, and $^{119}Sn$ NMR spectra were recorded with a Varian INOVA 600 spectrometer (600.0 MHz for $^1H$, 150.8 MHz for $^{13}C$, 223.6 MHz for $^{119}Sn$) at ambient temperature [$\delta$ values in ppm relative to $Me_4Si$ ($^1H$, $^{13}C$) or $Me_4Sn$ ($^{119}Sn$)].

**Synthesis of $\{(n\text{-}C_4H_9)_2Sn[4\text{-}FC_6H_4(O)C{=}NO]\}_n$ (1):** Dibutyltin dichloride (0.304 g, 1.0 mmol) in methanol (10 mL) was added dropwise to an aqueous methanol solution (water/methanol, 1:3, v/v, 30 mL) of 4-fluorobenzohydroxamic acid (0.150 g, 1.0 mmol) and KOH (0.112 g, 2.0 mmol). The solution was stirred under $N_2$ at room temperature overnight. Water (30 mL) was added to form a white precipitate, which was separated by filtration. The white solid was then recrystallized from methanol/water. Colorless sheet-shaped crystals of **1** were slowly formed at room temperature. Yield: 0.12 g, 32%. M.p. 176–178 °C. $C_{15}H_{22}FNO_2Sn$ (385.69): calcd. C 46.67, H 5.74, N 3.63; found C 46.48, H 5.85, N 3.56. IR (KBr): $\tilde{\nu}$ = 1661 s, 1601 s (CO/NC), 913 s (N–O), 587 w (Sn–C), 531 s (Sn–O) $cm^{-1}$. $^1H$ NMR ($CDCl_3$): $\delta$ = 7.12–7.70 (m, 4 H, $C_6H_4$), 1.64 [m, $^2J$(Sn,H) = 76 Hz, 4 H, 2 $CH^1_2$], 1.52 (m, 4 H, 2 $CH^2_2$), 1.37 (m, 4 H, 2 $C^3H_2$), 0.79 (t, $J$ = 7.2 Hz, 6 H, 2 $C^4H_3$) ppm. $^{13}C$ NMR ($CDCl_3$): $\delta$ = 164.2 (CO), 161.4, 131.4, 127.6, 115.4 and 114.9 ($C_{arom}$), 27.3 [$^1J$($^{119}Sn$,$^{13}C$) = 537 Hz, $CH_2$–Sn], 23.7 [$^2J$($^{119}Sn$,$^{13}C$) = 40 Hz, $CH_2CH_2Sn$], 26.1 [$^3J$($^{119}Sn$,$^{13}C$) = 138 Hz, $CH_2CH_2CH_2Sn$], 14.0 (R–Sn) ppm. $^{119}Sn$ NMR ($CDCl_3$): $\delta$ = –124.8 ppm.

**Synthesis of $\{(CH_3)_2Sn[2,5\text{-}F_2C_6H_3(O)C{=}NO]\}_n$ (2):** Dimethyltin dichloride (0.220 g, 1.0 mmol) in methanol (10 mL) was added dropwise to an aqueous methanol solution (water/methanol, 1:3, v/v, 30 mL) of 2,5-difluorobenzohydroxamic acid (0.173 g, 1.0 mmol) and KOH (0.112 g, 2.0 mmol). The solution was stirred under $N_2$ at room temperature overnight. Water (30 mL) was added to form a white precipitate, which was separated by filtration. The white solid was then recrystallized from methanol/water. Colorless sheet-shaped crystals of **2** were slowly formed at room temperature. Yield: 0.10 g, 28.2%. M.p. 262 °C dec. $C_9H_9F_2NO_2Sn$ (319.86): calcd. C 33.79, H 2.84, N 4.38; found C 33.52, H 2.96, N 4.29. IR (KBr): $\tilde{\nu}$ = 1665 s, 1616 s (CO/NC), 926 s (N–O), 586 w (Sn–C), 528 s (Sn–O) $cm^{-1}$. $^1H$ NMR ($CDCl_3$): $\delta$ = 7.70–7.16 (m, 3 H, $C_6H_3$), 0.89 [s, $^2J$(Sn,H) = 79 Hz, 6 H, 2 $CH_3$, R–Sn] ppm. $^{13}C$ NMR ($CDCl_3$): $\delta$ = 165.0 (CO), 163.4, 162.6, 132.3, 127.4 and 115.7 ($C_{arom}$), 6.6 [$^1J$($^{119}Sn$,$^{13}C$) = 584 Hz, $CH_3$, R–Sn] ppm. $^{119}Sn$ NMR ($CDCl_3$): $\delta$ = –129.9 ppm.

**Synthesis of $\{(CH_3)_4Sn_2[(2,4\text{-}Cl_2C_6H_3C(O)NHO)_2][2,4\text{-}Cl_2C_6H_3(O)C{=}NO]\}_n$ (3):** Dimethyltin dichloride (0.220 g, 1.0 mmol) was

 © 2006 Wiley-VCH Verlag GmbH & Co. KGaA, Weinheim 

Table 5. Crystal and data collection parameters of complexes **1**–**4**.

| | **1** | **2** | **3** | **4** |
|---|---|---|---|---|
| Empirical formula | $C_{15}H_{22}FNO_2Sn$ | $C_9H_9F_2NO_2Sn$ | $C_{50}H_{54}Cl_{12}N_6O_{12}Sn_4$ | $C_{86}H_{112}F_6N_6O_{12}Sn_4$ |
| Formula mass | 385.69 | 319.86 | 1829.83 | 2010.58 |
| Crystal system | monoclinic | orthorhombic | monoclinic | triclinic |
| Space group | *P*2(1)/c | *P*2(1)2(1)2(1) | *C*2/c | $P\bar{1}$ |
| *a* [Å] | 10.3740(17) | 6.7490(8) | 22.5882(18) | 13.6579(12) |
| *b* [Å] | 7.8608(13) | 7.7636(9) | 19.8408(16) | 14.1315(13) |
| *c* [Å] | 22.078(4) | 20.754(2) | 16.2922(13) | 14.3894(13) |
| *α* [°] | 90 | 90 | 90 | 110.0320(10) |
| *β* [°] | 102.119(3) | 90 | 115.1810(10) | 94.206(2) |
| *γ* [°] | 90 | 90 | 90 | 114.0800(10) |
| Volume [Å$^3$] | 1760.3(5) | 1079.0(2) | 6607.8(9) | 2307.5(4) |
| *Z* | 4 | 4 | 4 | 1 |
| $D_{calcd.}$ [Mg/m$^3$] | 1.457 | 1.969 | 1.833 | 1.447 |
| Absorption coefficient [mm$^{-1}$] | 1.462 | 2.375 | 2.039 | 1.140 |
| *F*(000) | 776 | 616 | 3552 | 1020 |
| Crystal size [mm] | 0.20 × 0.10 × 0.06 | 0.12 × 0.06 × 0.01 | 0.20 × 0.20 × 0.20 | 0.20 × 0.10 × 0.10 |
| Total no. of reflections measured | 16283 | 12746 | 34228 | 26012 |
| No. of unique reflections | 3113 | 2580 | 6506 | 9990 |
| *R*(int) | 0.1624 | 0.0755 | 0.0832 | 0.0853 |
| Max./min. transmission | 0.9174/0.7587 | 0.9766/0.7637 | 0.6859/0.6859 | 0.8945/0.8040 |
| No. of data/restraints/parameters | 3113/2/184 | 2580/0/138 | 6506/0/383 | 9990/2/518 |
| Goodness-of-fit on $F^2$ | 0.953 | 1.029 | 0.956 | 0.945 |
| Final *R* indices [$I > 2\sigma(I)$] | $R_1$ = 0.0664<br>$wR_2$ = 0.1248 | $R_1$ = 0.0295<br>$wR_2$ = 0.0557 | $R_1$ = 0.0436<br>$wR_2$ = 0.0985 | $R_1$ = 0.0461<br>$wR_2$ = 0.0976 |
| *R* indices (all data) | $R_1$ = 0.1196<br>$wR_2$ = 0.1390 | $R_1$ = 0.0313<br>$wR_2$ = 0.0561 | $R_1$ = 0.0572<br>$wR_2$ = 0.1023 | $R_1$ = 0.0737<br>$wR_2$ = 0.1133 |
| Largest diff. peak/hole [e/Å$^3$] | 0.860/–0.686 | 0.637/–0.670 | 0.942/–0.582 | 1.599/–0.606 |

added dropwise to an aqueous methanol solution (water/methanol, 1:4, v/v, 30 mL) of 2,4-dichlorobenzohydroxamic acid (0.412 g, 2.0 mmol) and KOH (0.112 g, 2.0 mmol). The solution was stirred under $N_2$ at room temperature overnight. Water (30 mL) was added to form a white precipitate, which was separated by filtration. The white solid was then recrystallized from methanol/benzene. Colorless block-shaped crystals of **3** were slowly formed at room temperature. Yield: 0.12 g, 26.3%. M.p. 188 °C (dec). $C_{50}H_{54}Cl_{12}N_6O_{12}Sn_4$ (1829.83): calcd. C 32.79, H 2.97, N 4.59; found C 32.62, H 3.01, N 4.55. IR (KBr): $\tilde{\nu}$ = 3290 s (N–H), 1591 s, 1569 s (CO/NC), 918 s (N–O), 575 s, 477 m (Sn–C), 541 s (Sn–O) cm$^{-1}$. $^1$H NMR ($CDCl_3$): $\delta$ = 10.56 (s, H, N–H), 9.21 (s, H, N–H), 7.81–7.27 (m, 6 H, 2 $C_6H_3$), 1.25 [s, $^2J$(Sn,$^1$H) = 91 Hz, 2 $CH_3$, R–Sn], 0.94 [d, $^2J$(Sn,H) = 77 Hz, 4 $CH_3$, R–Sn] ppm. $^{13}$C NMR ($CDCl_3$): $\delta$ = 164.2, 162.7 (CO), 158.4, 157.2, 131.1, 113.3, 111.1 and 103.3 ($C_{arom}$), 5.3 [$^1J$($^{119}$Sn,$^{13}$C) = 717 Hz, $CH_3$, R–Sn] and 6.9 [$^1J$($^{119}$Sn,$^{13}$C) = 845 Hz, $CH_3$, R–Sn] ppm. $^{119}$Sn NMR ($CDCl_3$): $\delta$ = –222.6, –221.0 ppm.

**Synthesis of {$(C_4H_9)_4Sn_2$[(4-$FC_6H_4C(O)NHO)_2$][4-$FC_6H_4$(O)-C=NO]}$_n$ (4):** Dibutyltin dichloride (0.304 g, 1.0 mmol) in methanol (10 mL) was added dropwise to an aqueous methanol solution (30 mL) of 4-fluorobenzohydroxamic acid (0.310 g, 2.0 mmol) and KOH (0.112 g, 2.0 mmol). The solution was stirred under $N_2$ at room temperature overnight. Water (30 mL) was added to form a white precipitate, which was separated by filtration. The white solid was then recrystallized from methanol/benzene. Colorless block-shaped crystals of **4** were slowly formed at room temperature. Yield: 0.26 g, 56%. M.p. 160–161 °C. $C_{86}H_{112}F_6N_6O_{12}Sn_4$ (2010.58): calcd. C 51.33, H 5.57, N 4.18; found C 51.20, H 5.71, N 4.03. IR (KBr): $\tilde{\nu}$ = 3287 s (N–H), 2956 (Bu), 1617 s, 1559 s (CO/NC), 904 s (N–O), 579 s, 471 m (Sn–C), 579 s (Sn–O) cm$^{-1}$. $^1$H NMR ($CDCl_3$): $\delta$ = 7.68–6.94 (m, 16 H, 4 $C_6H_4$), 1.67–1.62 (m, 8 H, 4 $CH^2{}_2CH^1{}_2$), 1.35–1.34 (m, 8 H, 4 $C^3H_2$), 0.92–0.84 (t, *J* = 7.2 Hz, 12 H, 4 $C^4H_3$) ppm. $^{13}$C NMR ($CDCl_3$): $\delta$ = 165.5, 164.1 (CO), 163.9, 161.9, 133.9, 130.7, 128.8, 126.1, 120.4, 115.7 and 114.9 ($C_{arom}$), 28.5 [$^1J$($^{119}$Sn,$^{13}$C) = 701 Hz, $CH^1{}_2$, R–Sn] and 27.4 [$^1J$($^{119}$Sn,$^{13}$C) = 830 Hz, $CH^1{}_2$, R–Sn], 26.6, 23.2, 13.9–13.7 (R–Sn) ppm. $^{119}$Sn NMR ($CDCl_3$): $\delta$ = –217.4, –216.6 ppm.

**X-ray Data Collection, Structure Determination, and Refinement:** Suitable single crystals of the four complexes were mounted in glass capillaries for X-ray structural analysis. Diffraction data were collected with a Bruker SMART CCD diffractometer with Mo-$K_\alpha$ ($\lambda$ = 0.71073 Å) radiation at room temperature. During the intensity data collection, no significant decay was observed. The intensities were collected for Lorentz-polarization effects and empirical absorption with the SADABS program. The structures were solved by direct methods using the SHELXL-97 program. All non-hydrogen atoms were found from difference Fourier syntheses. The H atoms were included in calculated positions with isotropic thermal parameters related to those of the supporting carbon atoms but were not included in the refinement. All calculations were performed using the Bruker Smart program.[24] A summary of the crystallographic data and selected experimental information are given in Table 5. CCDC-610570, -610571, -610572, and -610573 contain the supplementary crystallographic data for this paper. These data can be obtained free of charge from The Cambridge Crystallographic Data Centre via www.ccdc.cam.ac.uk/data_request/cif.

## Acknowledgments

Financial support from the Program for New Century Excellent Talents at the University of China (No. NCET-04-0258), from the Science and Technology Commission of Shanxi Province of China (No. 051105-2), and from the Education Commission of Shanxi Province of China (No. 200413) is gratefully acknowledged.

 © 2006 Wiley-VCH Verlag GmbH & Co. KGaA, Weinheim 

[1] a) L. R. Scolnick, A. M. Clements, J. Liao, L. Crenshaw, M. Hellberg, J. May, T. R. Deam, D. W. Christianson, *J. Am. Chem. Soc.* **1997**, *119*, 850–851; b) J. Schraml, *Appl. Organomet. Chem.* **2000**, *14*, 604–610; c) J. Schraml, L. Soukupova, V. Blechta, J. Karban, I. Cisarova, *J. Organomet. Chem.* **2001**, *628*, 81–91; d) T. V. Surova, A. N. Enyashin, *J. Struct. Chem.* **2003**, *44*, 297–300; e) J. Schraml, M. Tkadlecova, S. Pataridis, L. Soukupova, V. Blechta, J. Oithova, O. Exner, *Magn. Reson. Chem.* **2005**, *43*, 535–542.

[2] a) K. Tsukamoto, H. Itakura, K. Sato, K. Fukuyama, S. Miura, S. Takahashi, H. Ikezawa, T. Hosoya, *Biochemistry* **1999**, *38*, 12558–12568; b) E. C. O'Brien, E. Farkas, M. J. Gil, D. Fitzgerald, A. Castineras, K. B. Nolan, *J. Inorg. Biochem.* **2000**, *79*, 47–51; c) G. Bardos, K. Moricz, L. Jaszlits, G. Rabloczky, K. Tory, I. Racz, S. Bernath, B. Sumegi, B. Farkas, B. Literati-Nagy, P. Literati-Nagy, *Toxicol. Appl. Pharmacol.* **2003**, *190*, 9–16; d) M. Barbarić, S. Uršić, V. Pilepić, B. Zorc, A. Hergold-Brundić, A. Nagl, M. Gradiša, K. Pavelić, R. Snoeck, G. Andrei, J. Balzarini, E. D. Clercq, M. Mintas, *J. Med. Chem.* **2005**, *48*, 884–887.

[3] a) J. E1 Yazal, Y. P. Pang, *J. Phys. Chem. B* **2000**, *104*, 6499–6504; b) J. E1 Yazal, Y. P. Pang, *J. Phys. Chem. A* **1999**, *103*, 8346–8350; c) M. Remko, J. Sefcikova, *THEOCHEM* **2000**, *528*, 287–296.

[4] a) L. Salmon, E. Prost, C. Merienne, R. Hardre, G. Morgant, *Carbohydr. Res.* **2001**, *335*, 195–204; b) Y. Hoshino, N. Murase, M. Oishi, H. Yamamoto, *Bull. Chem. Soc. Jpn.* **2000**, *73*, 1653–1658; c) A. Henriksen, D. J. Schuller, K. Meno, K. G. Welinder, A. T. Smith, M. Gajhede, *Biochemistry* **1998**, *37*, 8054–8060.

[5] a) M. D. Santana, G. Garcia, J. Perez, E. Molins, G. Lopez, *Inorg. Chem.* **2001**, *40*, 5701–5703; b) J. Swiatek-Kozlowska, I. O. Fritsky, A. Dobosz, A. Karaczyn, N. M. Dudarenko, T. Yu. Sliva, E. Gumienna-Kontecka, L. Jerzykiewicz, *J. Chem. Soc., Dalton Trans.* **2000**, 4064–4068; c) W. Chen, S. Gao, S. X. Liu, *Acta Crystallogr., Sect. C: Cryst. Struct. Commun.* **1999**, *55*, 531–533; d) D. Gaynor, Z. A. Starikova, W. Haase, K. B. Nolan, *J. Chem. Soc., Dalton Trans.* **2001**, 1578–1581.

[6] a) D. A. Brown, D. McKeith, W. K. Glass, *Inorg. Chim. Acta* **1979**, *35*, 5–10; b) C. K. Narula, V. D. Gupta, *Indian J. Chem.* **1980**, *19A*, 1095–1098; c) D. C. Fisher, S. J. Barclay-Peet, C. A. Balfe, K. N. Raymond, *Inorg. Chem.* **1989**, *28*, 4399–4406; d) S. H. Hosseini, A. A. Entezami, *J. Appl. Polym. Sci.* **2003**, *90*, 63–71.

[7] a) K. V. Luzyanin, V. Y. Kukushkin, M. L. Kuznetsov, D. A. Garnovskii, M. Haukka, A. J. L. Pombeiro, *Inorg. Chem.* **2002**, *41*, 2981–2986; b) J. H. Bell, R. F. Pratt, *Inorg. Chem.* **2002**, *41*, 2747–2753; c) S. X. Liu, S. Gao, *Inorg. Chim. Acta* **1998**, *282*, 149–154; d) D. A. Brown, K. M. Herlihy, S. K. O'Shea, *Inorg. Chem.* **1999**, *38*, 5198–5202.

[8] G. A. Brewer, E. Sinn, *Inorg. Chem.* **1981**, *20*, 1823–1830.

[9] a) C. Y. Wong, J. D. Woollins, *Coord. Chem. Rev.* **1994**, *130*, 175–241; b) M. K. Das, S. De, *J. Organomet. Chem.* **1995**, *495*, 177–184; c) T. V. Drovetskaia, N. S. Yashina, T. V. Leonova, V. S. Petrosyan, J. Lorberth, S. Wocadlo, W. Massa, J. Pebler, *J. Organomet. Chem.* **1996**, *507*, 201–205.

[10] Q. Li, M. Fátima, C. G. da Silva, A. J. L. Pombeiro, *Chem. Eur. J.* **2004**, *10*, 1456–1462.

[11] a) Q. Li, M. Fátima, C. G. da Silva, J. Zhao, A. J. L. Pombeiro, *J. Organomet. Chem.* **2004**, *689*, 4584–4591; b) X. Shang, Q. Li, J. Wu, *J. Organomet. Chem.* **2005**, *690*, 3997–4000.

[12] D. K. Rastogi, S. K. Dua, V. B. Rana, S. K. Shni, *J. Inorg. Nucl. Chem.* **1978**, *40*, 323–1326.

[13] a) V. Yu. Kukushkin, A. J. L. Pombeiro, *Inorg. Chem.* **2000**, *39*, 216–225; b) V. Yu. Kukushkin, T. B. Pakhomava, Yu. N. Kukushkin, R. Herrmann, G. Wagner, A. J. L. Pombeiro, *Inorg. Chem.* **1998**, *37*, 6511–6517.

[14] a) F. Tao, X. F. Chen, Z. H. Wang, G. Q. Xu, *J. Phys. Chem. B* **2002**, *106*, 3890–3895; b) F. Tao, X. F. Chen, Z. H. Wang, G. Q. Xu, *J. Am. Chem. Soc.* **2002**, *124*, 7170–7180.

[15] a) N. Shirota, S. Yagi, M. Taniguchi, E. Hashimoto, *J. Vac. Sci. Technol. A* **2000**, *18*, 2578–2580; b) H. G. Huang, C. L. Xiang, Y. S. Ning, J. Y. Huang, G. S. Ang, G. Q. Xu, *J. Phys. Chem. B* **2005**, *109*, 19296–19300.

[16] J. Holeček, M. Nádvorník, K. Handlíř, A. Lyčka, *J. Organomet. Chem.* **1986**, *315*, 299–308.

[17] T. P. Lockhart, W. F. Manders, *J. Am. Chem. Soc.* **1987**, *109*, 7015–7020.

[18] W. F. Howard, R. W. Crecely, W. H. Nelson, *Inorg. Chem.* **1985**, *24*, 2204–2208.

[19] a) J. Beckmann, K. Jurkschat, *Coord. Chem. Rev.* **2001**, *215*, 267–300; b) L. Pellerito, L. Nagy, *Coord. Chem. Rev.* **2002**, *224*, 111–150.

[20] a) M. Gielen, *Coord. Chem. Rev.* **1996**, *151*, 41–51; b) M. Gielen, *Appl. Organomet. Chem.* **2002**, *16*, 481–494; c) M. Gielen, M. Biesemans, R. Willem, *Appl. Organomet. Chem.* **2005**, *19*, 440–450.

[21] F. H. Allen, O. Kennard, D. G. Watson, L. Brammer, A. G. Orpen, R. Taylor, *J. Chem. Soc., Perkin Trans. 2* **1987**, S1–S19.

[22] D. A. Garnovskii, M. F. C. Guedes da Silva, T. B. Pakhomova, G. Wagner, M. T. Duarte, J. J. R. Frausto da Silva, A. J. L. Pombeiro, V. Y. Kukushkin, *Inorg. Chim. Acta* **2000**, *300–302*, 499–504.

[23] a) B. Chatterjee, *Coord. Chem. Rev.* **1978**, *26*, 281–303; b) B. V. Riet, G. L. Wampler, H. L. Elford, *J. Med. Chem.* **1979**, *22*, 589–592; c) J. H. Zhao, T. G. Liang, Q. S. Li, A. J. L. Pombeiro, *Chin. Chem. Lett.* **2003**, *14*, 840–843.

[24] G. M. Sheldrick, *SHELXTL-97, Program for X-ray Crystal Structure Solution and Refinement*, University of Göttingen, Germany, **1997**.

Received: June 13, 2006
Published Online: August 21, 2006

 © 2006 Wiley-VCH Verlag GmbH & Co. KGaA, Weinheim 

DOI: 10.1002/ejic.200600555

# Studies on the Interaction of Vanadia with Modified Silica Supports and Catalytic Activity for Oxidative Dehydrogenation of Propane: Effect of Support Modification by $Al^{3+}$, $Zr^{4+}$ or $Y^{3+}$

**Rajamma Sasikala,*[a] Vasanth Sudarsan,[a] and Shailendra K. Kulshreshtha[a]**

**Keywords:** Supported catalysts / Vanadia-support interaction / IR spectroscopy / Heterogeneous catalysis

Detailed structural studies of vanadia supported on $SiO_2$ and modified $SiO_2$ ($Si_{0.8}M_{0.2}O_{2\pm\delta}$ where M = $Al^{3+}$, $Zr^{4+}$ and $Y^{3+}$) were carried out using different techniques such as powder XRD, IR spectroscopy and $^{29}Si$, $^{27}Al$ and $^{51}V$ MAS NMR spectroscopy. All samples except vanadia impregnated on $Zr^{4+}$ or $Y^{3+}$ modified $SiO_2$ existed as amorphous phases. A crystalline phase of $ZrO_2$ was seen in $Zr^{4+}$ modified $SiO_2$ and $YVO_4$ was seen in $Y^{3+}$ modified $SiO_2$ after vanadia impregnation. Based on $^{29}Si$ MAS NMR and IR spectroscopic studies it was concluded that substitution of $Si^{4+}$ by M results in the breakage of the Si–O–Si network and formation of silicon structural units with Si–O–M type linkages. Unlike all other modified $SiO_2$, the silicon structural units remained unaffected in $Al^{3+}$ modified $SiO_2$ before and after vanadia impregnation. A profound change in the interaction of vanadia with the support was observed when the $SiO_2$ support was modified with different cations and in all cases the $V^{5+}$ preferentially interacted with the substituted cations. Two types of vanadia species, viz. the octahedral and tetrahedral $V^{5+}$, were present in vanadia impregnated silica and $Al^{3+}$ modified silica but the amount of tetrahedral $V^{5+}$ was more in the latter. In $Zr^{4+}$ modified silica, $V^{5+}$ was present in a crystalline environment which is the $V^{5+}$ dissolved in the $ZrO_2$ phase. Vanadia impregnated on $Y^{3+}$ modified silica exhibited very little chemical shift anisotropy indicating a symmetric environment around $V^{5+}$ in $YVO_4$. The catalytic activity for the selective oxidation of propane to propene was tested on these supported catalysts. Vanadia supported on $Zr^{4+}$ modified silica showed maximum selectivity whereas vanadia on silica and $Al^{3+}$ modified silica showed comparable selectivity for propene formation. Vanadia on $Y^{3+}$ modified silica did not show the formation of propene at all.
(© Wiley-VCH Verlag GmbH & Co. KGaA, 69451 Weinheim, Germany, 2006)

## Introduction

Supported vanadia catalysts are widely used for selective oxidation of hydrocarbons[1–4] and for the reduction of $NO_x$ by ammonia.[5,6] It is well known that the catalytic activity of vanadia catalysts varies with the supporting oxides. The reason for the observed change in the catalytic activity has been attributed to a vanadia-support interaction, which varies with the nature of the support. Different factors influencing the interaction are the acidity of the support, the concentration of vanadia as well as pretreatment conditions etc.[7–10] Thus, different types of vanadia species exist on different supports such as isolated tetrahedral vanadium ions, polymeric species, 2D layers of vanadium oxide or $V_2O_5$ crystallites.[11–15] It has been demonstrated that isolated vanadia species possessing $VO_4$ coordination predominate at low surface coverage of vanadia whereas at higher surface coverage both isolated and polymerised species may be observed on the surface of the support. A monolayer of vanadia is formed on the support when the surface coverage is 7–8 V atoms per $nm^2$.[2,16] However, in the case of $V_2O_5$ supported on $SiO_2$, only isolated vanadia species may be observed on the surface and the maximum attainable surface coverage is less than 3 V atoms per $nm^2$. Hence it is of interest to modify the $SiO_2$ support by partial substitution of $Si^{4+}$ by $Al^{3+}$, $Zr^{4+}$ or $Y^{3+}$ and to see whether the support modification improves the dispersion of vanadia on the surface and also to study the structure of the resultant vanadia species. Because the catalytic activity and turnover frequency of a reaction changes with the type of $VO_x$ species, which in turn depends on the nature of support, it is useful to study the interaction of vanadia with this modified support. To the best of our knowledge, the variation of the nature of the interaction of vanadia with the silica support when it is modified with different cations has not been reported so far.

In the present work $SiO_2$ was modified by partial substitution of the $Si^{4+}$ by $Al^{3+}$, $Zr^{4+}$ or $Y^{3+}$ and vanadia was loaded on these supports as well as on $SiO_2$. All supports and vanadia impregnated supports were investigated by various spectroscopic and diffraction techniques such as powder XRD, infrared and NMR spectroscopy to see whether there would be any change in the interaction of vanadia with the modified silica support compared with the

[a] Chemistry Division, Bhabha Atomic Research Centre, Trombay, Mumbai 400085, India
Fax: +91-22-25505151
E-mail: sasikala@magnum.barc.ernet.in

 © 2006 Wiley-VCH Verlag GmbH & Co. KGaA, Weinheim 

unmodified one. The activity of these supported vanadia materials as catalysts for the oxidative dehydrogenation of propane to propene has been examined in order to deduce the dependence of the product selectivity on the type of surface vanadia species.

## Results and Discussion

Figure 1 shows the powder XRD patterns of $SiO_2$, VS, SA, VSA, SZ, VSZ, SY and VSY ($Si_{0.8}M_{0.2}O_{2\pm\delta}$, M = $Al^{3+}$, $Zr^{4+}$ and $Y^{3+}$ represented as SA, SZ and SY, respectively). It can be seen from the figure that the XRD patterns of $SiO_2$, VS, SA, VSA, SZ and SY oxides show broad peaks centred around 22°, which is characteristic of amorphous silica. However, after vanadia impregnation, samples VSZ and VSY exhibited crystalline phases. The VSZ sample exhibits a pattern with three peaks centred around 30.3, 50.2 and 59.9°, which can be matched with the tetragonal phase of $ZrO_2$ (JCPDS card no. 17-0923). The presence of this phase was further confirmed from the XRD pattern of the sample heated at 650 °C for 18 h. This clearly showed peaks corresponding to the tetragonal phase of $ZrO_2$. It is known that $V_2O_5$ stabilises the tetragonal phase of $ZrO_2$.[2] The XRD pattern of VSY indicates a crystalline phase, the peak positions of which were found to be matching those of $YVO_4$. The three most intense peaks seen at 25.0, 33.6 and 49.8° are due to the $YVO_4$ phase (JCPDS card no. 17–0341). Table 1 gives the total surface area of $SiO_2$, all modified silica supports before and after vanadia impregnation and the amount of vanadia on these supports (% $V_2O_5$ on the support by weight, wt.-%). The surface area was found to decrease with vanadia impregnation and this is in agreement with the previous report.[12]

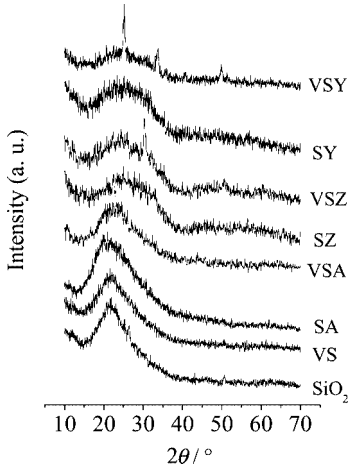


Figure 1. Powder X-ray diffraction patterns of $SiO_2$, modified silica samples and vanadia impregnated samples.

Since the XRD patterns of these samples indicate poor crystallinity, it was not possible to ascertain whether the $Al^{3+}$, $Zr^{4+}$ and $Y^{3+}$ cations had really substituted the $Si^{4+}$ sites. Since $^{29}Si$ NMR spectroscopy can give information regarding the local coordination of $Si^{4+}$ and Si–O–Si bonding in $SiO_2$, MAS NMR spectra of these samples were recorded. Figure 2 shows the $^{29}Si$ MAS NMR spectra of $SiO_2$, the modified silica support and modified supports impregnated with vanadia. For the $SiO_2$ and VS samples, a clear asymmetry was observed in their spectra indicating that more than one type of silicon structural unit ($Q^n$, where "$n$" represents the number of $SiO_4$ tetrahedra attached to $Si^{4+}$) is present in these samples. The peaks of all modified supports and vanadia containing supports are broad and showed varying amounts of asymmetry indicating the presence of different types of $Q^n$ structural units within them.

Table 1. Total surface area and wt.-% of $V_2O_5$ on different supports.

| Support | wt.-% $V_2O_5$ on the support | Surface area [$m^2 g^{-1}$] |
|---|---|---|
| $SiO_2$ | – | 73 |
| VS | 9.7 | 69 |
| SA | – | 72 |
| VSA | 9.7 | 47 |
| SZ | – | 173 |
| VSZ | 8.0 | 128 |
| SY | – | 125 |
| VSY | 8.0 | 75 |

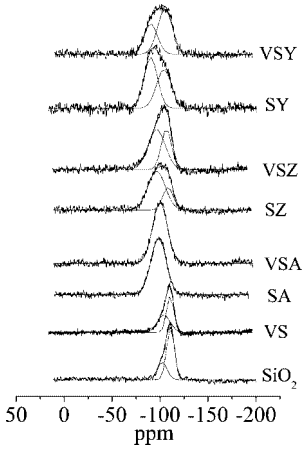


Figure 2. Deconvoluted $^{29}Si$ MAS NMR spectra of $SiO_2$, modified silica samples and vanadia impregnated samples.

However, the spectra of the SA and VSA samples are identical, with a peak maximum around –99 ppm indicating that no significant change occurs in the vicinity of the $SiO_4$ tetrahedra upon vanadia impregnation. A downfield shift seen in the spectra of SA and VSA with respect to $SiO_2$ indicates that $Al^{3+}$ units have substituted $Si^{4+}$ ion thereby forming an Si–Al mixed oxide.

In order to characterise the different structural units in detail, all spectra except those of SA and VSA were deconvoluted based on a Guassian fit and it was found that these patterns mainly consist of $Q^4$ and $Q^3$ structural units of silicon. The peak positions of the $Q^4$ and $Q^3$ units and their relative ratios are given in Table 2. It can be seen that the ratio of $Q^3$ to $Q^4$ is more for VS than that for $SiO_2$ indicating that $V^{5+}$ modifies the Si–O–Si network. Similarly, the ratio of $Q^3$ to $Q^4$ is more in all modified supports compared with in $SiO_2$ indicating that incorporation of $Al^{3+}$, $Zr^{4+}$ or

 © 2006 Wiley-VCH Verlag GmbH & Co. KGaA, Weinheim 

$Y^{3+}$ in silica results in the breakage of Si–O–Si linkages. The spectra of SA and VSA could be satisfactorily fitted only as a single Gaussian peak with a peak maximum around –99 ppm characteristic of $Q^3$ structural units. This establishes that $V^{5+}$ has no direct interaction with silicon structural units in the alumino-silicate network. Had there been any direct interaction between the silicon and vanadium structural units, this would have been reflected in the relative concentration of $Q^n$ structural units and their chemical shift values but this was not observed in the present study. It was observed, however, that a downfield shift occurs for the peaks corresponding to the $Q^4$ and $Q^3$ structural units in the spectra of modified silica supports compared with that of $SiO_2$ (see Table 2) and this has been attributed to the decreased Si–O–Si chain length brought about by the modification.

Table 2. Fitted peak positions of $Q^4$ and $Q^3$ units present in different samples and their relative ratios.

| Sample | Chemical shift [ppm] $Q^4$ | $Q^3$ | $Q^3/(Q^4+Q^3)$ |
|---|---|---|---|
| $SiO_2$ | –110·9 | –102.0 | 0.29 |
| VS | –110·6 | –103.9 | 0.46 |
| SA | – | –99.0 | ≈ 1.0 |
| VSA | – | –99.9 | ≈ 1.0 |
| SZ | –108.0 | –96.0 | 0.73 |
| VSZ | –106.7 | –96.5 | 0.65 |
| SY | –104.1 | –90.4 | 0.54 |
| VSY | –105.2 | –90.5 | 0.38 |

To obtain more information regarding the silicon structural units attached to OH groups in these samples, $^1H \rightarrow ^{29}Si$ cross polarisation (CP) MAS NMR spectra were recorded and these are shown in Figure 3. A comparison of a single pulse spectrum and a CPMAS NMR spectrum of pure $SiO_2$ reveals that even in unmodified $SiO_2$, $Q^3$ and $Q^2$ structural units exist in the form of Si–OH linkages.

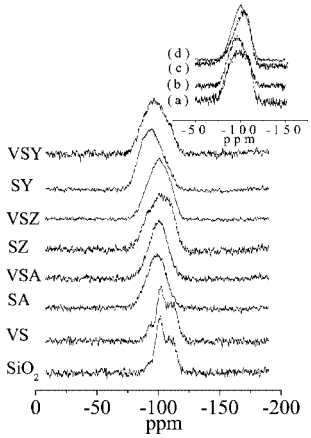


Figure 3. $^1H \rightarrow ^{29}Si$ CP MAS NMR spectra of $SiO_2$, modified silica samples and vanadia impregnated samples. Inset shows the $^{29}Si$ single pulse and CP MAS NMR spectra, respectively, for VSY (a and b) and VSZ (c and d).

A careful observation of the VS sample revealed a slight increase in the intensity of the peak corresponding to the $Q^2$ structural unit and this can be attributed to the breakage of Si–O–Si linkages brought about by the vanadia incorporation in silica. Unlike the single pulse spectra of these samples, the peak corresponding to the $Q^2$ unit can be clearly seen here due to the sensitivity of the technique to the OH groups attached to the silica structural units. The spectra of SA and VSA obtained from single pulse experiments and CP MAS experiments are exactly identical and can be superimposed over one another. This observation once again suggests that vanadia incorporation does not bring about any change in the vicinity of the $SiO_4$ tetrahedra and hence vanadia probably interacts with the $Al^{3+}$ of the support. For the SZ and SY samples, the spectra resulting from single pulse and CP MAS spectroscopy are identical, demonstrating that no Si–OH linkages are created by $Zr^{4+}$ or $Y^{3+}$ incorporation in silica. However for the VSZ and VSY samples, the CP MAS spectra showed a slightly different line shape with a downfield shift of the peak maxima over a range of 5–6 ppm compared with that obtained from single pulse experiments (see inset in Figure 3). This can be attributed to the formation of Si–OH ($Q^3$ type) linkages brought about by the removal of $Zr^{4+}/Y^{3+}$ from the VSZ/VSY samples to form $ZrO_2$ and $YVO_4$, respectively.

The $^{27}Al$ NMR spectra of SA and VSA are shown in Figure 4. A single peak with a chemical shift of 53 ppm with a comparable line shape can be seen indicating that $Al^{3+}$ is in a tetrahedral coordination environment before and after vanadia impregnation. Since there is no $Al^{3+}$ present in an octahedral coordination mode, it can be concluded that the $\gamma$-$Al_2O_3$ phase is not present in these samples. Due to the quadrupolar nature of the $Al^{3+}$ ion, it is less sensitive to the changes in the chemical environment brought about by vanadium incorporation and hence no change in the line shape is to be expected for the VSA sample and such is the case.

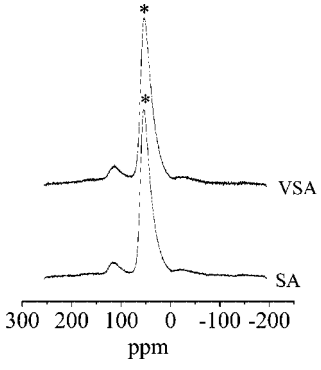


Figure 4. $^{27}Al$ MAS NMR spectra of SA and VSA samples (the peak marked with an asterisk is the isotropic peak).

The IR spectra of all modified silica samples with and without vanadia impregnation are shown in Figure 5. It can be seen that the spectra of all silica containing samples are somewhat similar to the spectrum of $SiO_2$. However, some subtle changes can be observed in the spectra of modified silica samples upon closer observation. The IR spectrum of $V_2O_5$ shows three prominent bands at 472, 810 and

 © 2006 Wiley-VCH Verlag GmbH & Co. KGaA, Weinheim 

1020 $cm^{-1}$. The band at 1020 $cm^{-1}$ corresponds to the unshared V=O stretching vibration and the bands located around 810, 472 and 364 $cm^{-1}$ can be assigned to the vibrations of the bound oxygen which are shared by two vanadium atoms.[17,18] The IR spectrum of silica mainly shows three broad bands centred at 1091, 808 and 470 $cm^{-1}$ which can be assigned to the Si–O stretching (antisymmetric stretching of the type ←Si O→ ←Si), Si stretching (symmetric stretching mode of type ←Si O Si→) and Si–O–Si bending of the characteristic groups, respectively.[19,20] Since the peak positions of both $V_2O_5$ and $SiO_2$ are close, they overlap and hence IR bands due to $V_2O_5$ cannot be seen in vanadia impregnated samples. In all substituted silica samples, it can be seen that the band around 1091 $cm^{-1}$ shifts to a slightly lower frequency compared with that in pure $SiO_2$. This is due to the substitution of some of the $Si^{4+}$ centres by bigger cations which form M–O bonds (M = $Al^{3+}$, $Zr^{4+}$ and $Y^{3+}$). This results in a softening of the Si–O bond. A similar effect has been observed for the Si stretching band located around 808 $cm^{-1}$. A downward frequency shift of the V–O stretch in $V_2O_5$–$MoO_3$ has been reported by Hirata et al.[21] due to the softening of this bond arising from the replacement of $V^{V}$ by $V^{IV}$ in this mixed oxide. The IR spectra of reduced $V_2O_5$ also show a similar effect in the V=O stretching vibration due to the $V^{IV}$ species, the ionic radius of which is larger than $V^{V}$.[17] In the case of the SZ and SY samples, it can be seen that the band around 1091 $cm^{-1}$ is very broad compared with that in $SiO_2$ and this is due to the distortion of the Si–O–Si bond brought about by the substitution. However, in the case of VSZ and VSY, a shift in this band to a slightly higher frequency can be observed. This high frequency shift can be attributed to the formation of $ZrO_2$ and $YVO_4$ compounds in SZ and SY, respectively, resulting from the removal of $Zr^{4+}$or $Y^{3+}$ from the silica structure. This observation is in accord with the $^{29}Si$ MAS NMR spectroscopic results. A weak narrow band around 1630 $cm^{-1}$ present in the IR patterns of all samples except $V_2O_5$ arises due to the bending vibrations of the OH groups attached to silicon.

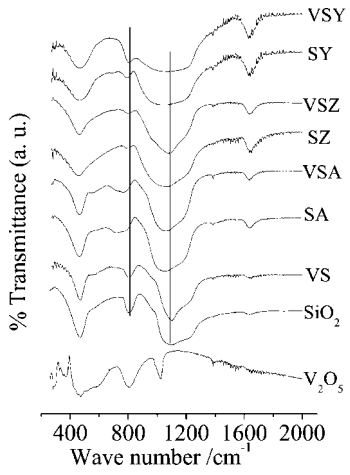


Figure 5. IR spectra of $V_2O_5$, $SiO_2$, modified silica samples and vanadia impregnated samples.

$^{51}V$ solid state NMR spectroscopy can give a clear understanding of the state of $V^{5+}$ species on different supports and many such studies have identified different vanadia species such as tetrahedrally or octahedrally coordinated $V^{5+}$ or vanadia crystallites on various supports.[22–28] Figure 6 shows the $^{51}V$ static and MAS NMR spectra of $V_2O_5$, VS and VSA. The static pattern of $V_2O_5$ is similar to that reported in the literature indicating a distorted octahedrally coordinated $V^{5+}$ ion with axial symmetry. The MAS NMR spectrum shows an isotropic peak at $\delta$ = –614 ppm with a side band pattern typical of this compound. The static spectrum of VS was found to be different from that of $V_2O_5$. It consists of two peaks with maxima around –380 and –597 ppm which are similar to those for the "a" (octahedral) and "b" (tetrahedral) type $V^{5+}$ species reported by Eckert and Wachs.[22] The MAS NMR spectrum of this sample consists of an extensive side band pattern superimposed over a weak broad peak. The extensive side band patterns have been attributed to the presence of bulk-like $V_2O_5$ or a precursor of $V_2O_5$[22,24] in which vanadium is in a distorted octahedral configuration. The weak broad background arises from the vanadium species existing in the tetrahedral configuration. Hence it can be concluded that both octahedral and tetrahedral $V^{5+}$ are present in this sample. The static spectrum of VSA also showed a similar pattern to that of VS with two peaks centred around –340 and –590 ppm showing the presence of both octahedral and tetrahedral $V^{5+}$. Unlike the MAS NMR spectrum of VS, the spectrum of the VSA sample clearly showed a side band pattern similar to that of bulk-like $V_2O_5$ superimposed over a broad peak characteristic of tetrahedral $V^{5+}$ species. From these results it can be inferred that the dispersion of vanadia is better on SA than on $SiO_2$. The static and MAS NMR spectra of VSZ, VSY and $YVO_4$ are shown in Figure 7. The static spectrum of VSZ shows two narrow peaks around –495 and –566 ppm having line widths significantly less than those of VS and VSA. The MAS NMR pattern for this sample is characterised by a sharp isotropic peak at $\delta$ = –566 ppm along with a number of side bands. Both static and MAS NMR spectroscopic results thus suggest that $V^{5+}$ structural units exist in a highly crystalline environment. However, the XRD pattern revealed that the only crystalline phase present in the sample is $ZrO_2$. Thus, based on the XRD and NMR results, it can be inferred that in the VSZ sample, the $V^{5+}$ species are dissolved in the $ZrO_2$ phase. The static spectrum of VSY showed a narrow peak (peak maximum at $\delta$ = –682 ppm), which suggests that $V^{5+}$ species exist in a symmetric environment and hence exhibit very little chemical shift anisotropy. Since the VSY sample showed a crystalline phase of $YVO_4$ in its XRD pattern, the NMR spectrum of $YVO_4$ was also recorded and is shown in Figure 7. Both the static and MAS NMR spectra of $YVO_4$ are similar to that of VSY. The MAS spectrum of $YVO_4$ showed an isotropic peak at –673ppm, which is very close to that of the VSY sample. Hence the peak seen at $\delta$ = –663 ppm for VSY can be assigned to the $YVO_4$ phase. Thus, $^{51}V$ NMR spectroscopy gives clear evidence for a different type of interaction between vanadia and modified

 © 2006 Wiley-VCH Verlag GmbH & Co. KGaA, Weinheim 

silica compared with unmodified silica. Based on the $^{29}Si$, $^{27}Al$ and $^{51}V$ NMR results it can be concluded that $V^{5+}$ selectively interacts with the substituted cations and not $Si^{4+}$. This conclusion is in agreement with the observation of Gao and Wachs[29] who reported a preferential interaction of V cations with Ti, Zr or Al on multilayered metal oxide catalysts such as $V_2O_5/MO/SiO_2$ where M = $Ti^{4+}$, $Zr^{4+}$ or $Al^{3+}$. Similarly, a preferential interaction of $Cr^{n+}$ with alumina compared with silica has been reported where the $Cr^{n+}$ is adsorbed as a chromate ion.[30]

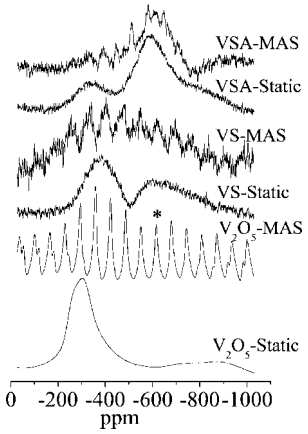


Figure 6. $^{51}V$ static and MAS NMR spectra of $V_2O_5$, VS and VSA (the peak marked with an asterisk is the isotropic peak).

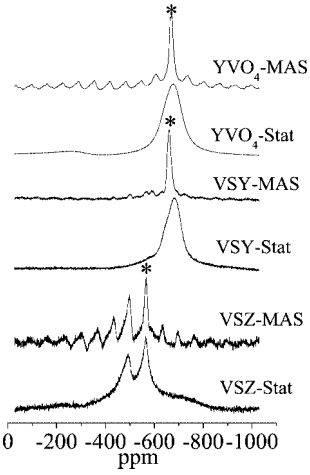


Figure 7. $^{51}V$ static and MAS NMR spectra of VSZ, VSY and $YVO_4$ samples (the peak marked with an asterisk is the isotropic peak).

The results of catalytic tests performed on these supported catalysts for the selective oxidation of propane to propene are summarised in Table 3. The products formed during the reactions were mainly propene and $CO_2$. Small quantities of $CH_4$ and $C_2H_4$ were detected and the selectivity for these products was around 1%. CO, if formed during the reaction, was not analysed. It can be seen from Table 3 that the catalytic activity and selectivity of vanadia varies as the silica support is modified with different cations. VSZ showed maximum selectivity for propene formation whereas VSY gave no propene formation at all. Though the $C_3H_8$ conversion was highest for VS, its selectivity for propene formation was less when compared with VSZ. The selectivity of VSA for catalytic propene formation was comparable with that of VS. These results clearly demonstrate that the product selectivity and catalytic activity depend significantly on the type of vanadia species, which in turn depends on the cations used for the modification of the silica support. The relatively low value of propene selectivity observed for these catalysts could be due to the low flow rate of the reactants. It has been reported that low flow rates result in an increased residence time of the reactants on the catalysts which can lead to the formation of $CO_x$ species from the secondary oxidation of $C_3H_6$ as observed in the present study.[2]

Table 3. Percentage conversion and selectivity data for oxidative dehydrogenation of propane for various $V_2O_5$ supported catalysts at 550 °C.

| No. | Catalyst | $C_3H_8$ conversion [%] | $C_3H_6$ selectivity [%] |
|---|---|---|---|
| 1 | VS | 51 | 14 |
| 2 | VSA | 34 | 12 |
| 3 | VSZ | 36 | 23 |
| 4 | VSY | 26 | – |

The salient feature of this study is that the interaction of vanadia with the support varies when the $SiO_2$ is modified by substitution of just 20% of the $Si^{4+}$ by different cations. This change in the interaction of vanadia with the modified support has a significant impact on its catalytic activity and selectivity for the oxidative dehydrogenation of propane to propene.

## Conclusions

The interaction of vanadia with silica supports varies as the silica is modified with cations such as $Al^{3+}$, $Zr^{4+}$or $Y^{3+}$. A preferential interaction of $V^{5+}$ with $Al^{3+}$, $Zr^{4+}$or $Y^{3+}$ cations present in $SiO_2$ occurs in these samples. Vanadia present on unmodified $SiO_2$ contains two types of $V^{5+}$ species which are tetrahedrally and octahedrally coordinated. Bulk-like $V_2O_5$ with a distorted octahedral configuration is the predominant species on unmodified $SiO_2$ whereas on $Al^{3+}$ modified $SiO_2$, both tetrahedral and octahedral $V^{5+}$ species can be clearly seen. On $Zr^{4+}$ modified silica, $V^{5+}$ becomes dissolved in the $ZrO_2$ phase. On $Y^{3+}$ modified silica, vanadia reacts with $Y^{3+}$ forming the $YVO_4$ phase. Catalytic tests conducted for the oxidative dehydrogenation of propane indicated that the catalytic activity and selectivity of vanadia varies with support modification. This is due to the presence of different types of surface vanadia species on these catalysts formed by the selective interaction of $V^{5+}$ with the cations present in modified silica.

## Experimental Section

Samples of $Si_{0\cdot8}M_{0\cdot2}O_{2\pm\delta}$ (M = $Al^{3+}$, $Zr^{4+}$ and $Y^{3+}$ represented as SA, SZ and SY, respectively, in the text) were prepared by the

 © 2006 Wiley-VCH Verlag GmbH & Co. KGaA, Weinheim 

coprecipitation technique. Aqueous solutions of aluminium nitrate, zirconium oxychloride and yttrium nitrate were used for the preparation of the SA, SZ and SY samples. Each of these solutions, with the required ratio of cations, was mixed thoroughly with sodium silicate solution and precipitated using ammonia solution (pH ≈ 8). The precipitates, after filtering, were washed thoroughly and dried in an oven for nearly 10 h. This was followed by calcination in air at 500 °C for 2 h. Unmodified $SiO_2$ was prepared by adding ammonia to an aqueous solution of sodium silicate, followed by a similar washing and heating procedure mentioned above. Vanadia was impregnated on these supports (6 atom-% of V) by an impregnation technique. $SiO_2$ and modified $SiO_2$ were kept in contact with an aqueous solution of ammonium vanadate and were then dried on a hot plate with constant stirring followed by heating in air at 500 °C for 2 h (vanadia impregnated on $SiO_2$, SA, SZ and SY are represented as VS, VSA, VSZ and VSY, respectively, in the text). The surface areas of these samples were measured using the BET technique with nitrogen as the adsorbing gas. Since a second phase of $YVO_4$ was seen in the VSY sample, $YVO_4$ was prepared for comparison purposes. $YVO_4$ was prepared by mixing ammonium vanadate and yttrium oxide thoroughly in the correct stiochiometric ratio and heating in air at 800 °C for 6 h. $V_2O_5$ obtained from Fluka was used for recording NMR and IR spectra.

Powder X-ray diffraction patterns of these samples were recorded using a Philips PW1820-X-ray diffractometer coupled with a PW 1729 generator, which was operated at 30 kV and 20 mA. A graphite crystal monochromator was used for generating monochromatic Cu-$K_\alpha$ radiation. IR spectra were recorded as KBr pellets using a Bomem MB102 FTIR machine having a range of 200–4000 $cm^{-1}$. NMR spectra were recorded with a Bruker Avance DPX 300 spectrometer at basic frequencies of 78.206, 59.6214 and 78.9005 MHz for $^{27}Al$, $^{29}Si$ and $^{51}V$, respectively. Spectra were recorded using 7 mm zirconia rotors packed with the sample. Different spinning speeds of 5 kHz, 4 kHz and 3 kHz were employed to identify the isotropic peaks. A typical 90° pulse duration for recording $^{27}Al$ NMR spectra was 3.5 μs and a delay time of 5 s was used. $^{51}V$ MAS spectra were recorded with a 90° pulse duration of 3.5 μs and a delay time of 4 s. Experiments were also carried out by varying the 90° pulse duration from 1 μs to 3 μs with a view to establishing any line distortion brought about by the satellite transitions of the quadrupolar $^{51}V$ nuclei. However, it was observed that the line shapes were unaffected by the different pulse durations. For recording $^{29}Si$ MAS NMR spectra, a 90° pulse duration of 4.0 μs and a delay time of 5 s were employed. Delay times were varied from 5 s to 20 s to see whether there would be any change in the line shape of the spectra since the $^{29}Si$ nucleus has a long relaxation time. For $^{1}H \rightarrow ^{29}Si$ cross polarisation (CP) MAS NMR experiments, a contact time of 5 μs and delay time of 6 s were employed. Around 4000 scans were recorded for each sample in order to obtain NMR patters with reasonable signal to noise ratios. All $^{29}Si$, $^{27}Al$ and $^{51}V$ NMR chemical shifts are expressed with respect to tetramethylsilane, aqueous $[Al(H_2O)_6]^{3+}$ and $VOCl_3$, respectively.

A preliminary test of the catalytic activity of these supported catalysts for the selective oxidation of propane to propene was carried out in a tubular quartz reactor of 25 cm length and 0.7 cm internal diameter using a fixed bed. A quantity of 200 mg of catalyst was used for each experiment and the reactant gas mixture had a composition of $C_3H_8$:$O_2$:He as 1.06:1.09:97.85 (by volume). The reaction was studied at 550 °C using a continuous flow method with a flow rate of 20 $cm^3\,min^{-1}$ of the reactant mixture. The effluent gas mixture was analysed online by an automatic gas sampling valve connected to a gas chromatograph (CIC, GC2011) equipped with a porapak Q column and a thermal conductivity detector. The hydrocarbons formed were also analysed in an FID mode using a porapak R column.

[1] B. M. Weckhuysen, D. E. Keller, *Catal. Today* **2003**, *78*, 25.
[2] A. Khodakov, B. Olthof, A. T. Bell, E. Iglesia, *J. Catal.* **1999**, *181*, 205.
[3] G. G. Cortez, M. A. Banares, *J. Catal.* **2002**, *20*, 197.
[4] I. E. Wachs, Y. Chen, J. M. Jehng, L. E. B. Briand, T. Tanaka, *Catal. Today* **2003**, *78*, 13.
[5] N. Y. Topsoe, H. Topsoe, J. A. Dumesic, *J. Catal.* **1995**, *151*, 226.
[6] Z. Zhu, Z. Liu, S. Liu, H. Niu, *Appl. Catal. B: Environ.* **1999**, *23*, L229.
[7] F. Klose, M. Joshi, C. Hamel, A. S. Morgenstern, *Appl. Catal. A: General* **2004**, *260*, 101.
[8] G. Martra, F. Arena, S. Coluccia, F. Frusteri, A. Parmaliana, *Catal. Today* **2000**, *63*, 197.
[9] S. Xie, E. Iglesia, A. T. Bell, *Langmuir* **2000**, *16*, 7162.
[10] B. Olthof, A. Khodakov, A. T. Bell, E. Iglesia, *J. Phys. Chem. B J. Phys. Chem.* **2000**, *104*, 1516.
[11] F. Chiker, J. Ph. Nogier, J. L. Bonardet, *Catal. Today* **2003**, *78*, 139.
[12] X. Gao, S. R. Bare, B. M. Weckhuysen, I. E. Wachs, *J. Phys. Chem. B J. Phys. Chem.* **1998**, *102*, 10842.
[13] M. Baltes, P. V. D. Voort, B. M. Weckhuysen, R. R. Rao, G. Catana, R. A. Schoonheydt, E. F. Vansant, *Phys. Chem. Chem. Phys.* **2000**, *2*, 2673.
[14] E. P. Reddy, R. S. Varma, *J. Catal.* **2004**, *221*, 93.
[15] X. Gao, I. E. Wachs, *J. Catal.* **2000**, *192*, 18.
[16] G. Deo, I. E. Wachs, *J. Catal.* **1994**, *146*, 323.
[17] I. L. Botto, M. B. Vassallo, E. J. Baran, G. Minelli, *Mat. Chem. Phys.* **1997**, *50*, 267.
[18] L. Abello, E. Hussan, Y. Repelin, G. Lucazeau, *J. Solid State Chem.* **1985**, *56*, 379.
[19] E. R. Lippincott, A. V. Valkenburg, C. E. Weir, E. N. Bunting, *J. Res. Natl. Bur. Stand.* **1958**, *61*, 61.
[20] F. Boccussi, D. Coluccia, C. Morterra, A. Zecchina, *J. Phys. Chem.* **1978**, *82*, 1298.
[21] T. Hirata, H. Y. Zhu, *J. Phys.: Condens. Matter.* **1992**, *4*, 7377.
[22] H. Eckert, I. E. Wachs, *J. Phys. Chem.* **1989**, *93*, 6796.
[23] O. B. Lapina, V. M. Mastikhin, A. A. Shubin, V. N. Krasilnikov, K. I. Zamaraev, *Prog. NMR Spectrosc.* **1992**, *24*, 457.
[24] T. Blasco, J. M. L. Nieto, *Colloid Surf. A* **1996**, *11*, 5187.
[25] N. Das, H. Eckert, H. Hu, I. E. Wachs, J. F. Walzer, F. J. Feher, *J. Phys. Chem.* **1993**, *97*, 8240.
[26] C. B. Wang, G. I. Deo, I. E. Wachs, *J. Catal.* **1998**, *178*, 640.
[27] J. M. Miller, L. J. Lakshmi, *Appl. Catal. A: General* **2000**, *190*, 197.
[28] J. H. Kwak, J. E. Herrera, J. Z. Hu, Y. Wang, C. H. F. Peden, *Appl. Catal. A: General* **2006**, *300*, 109.
[29] X. Gao, I. E. Wachs, *Top. Catal.* **2002**, *18*, 243.
[30] B. M. Weckhuysen, B. Schoofs, R. A. Schoonheydt, *J. Chem. Soc., Faraday Trans.* **1997**, *93*, 2117.

Received: June 15, 2006
Published Online: August 7, 2006

 © 2006 Wiley-VCH Verlag GmbH & Co. KGaA, Weinheim 

DOI: 10.1002/ejic.200600571

# Lithium Oligophosphanediides in the Li/$PhPCl_2$ System

**Daniel Stein,[a] Alk Dransfeld,[b] Michaela Flock,[b] Heinz Rüegger,[a] and Hansjörg Grützmacher*[a]**

**Keywords:** Alkali metals / Dianions / Ion pairs / NMR spectroscopy / Phosphorus / Reduction

Optimized conditions for the selective synthesis of $[Li_2(P_nPh_n)(tmeda)_x]$ ($n$ = 2, 3, 4) have been developed. X-ray diffraction with single crystals show $[Li_2(P_2Ph_2)(tmeda)_2]$ and $[Li_2(P_4Ph_4)(tmeda)_2]$ to be ion triples, while for $n$ = 3 the ion pair $[Li(tmeda)_2]^+[Li(P_3Ph_3)(tmeda)]^-$ is observed. NMR experiments support the assumption that these structures are retained in solution. Structural differences between the lithium and the corresponding sodium compounds, $[Na_2(P_nPh_n)(tmeda)_x]$, can be partially rationalized using the electrostatic stabilization parameters, ESP = $\Sigma(1/r_{M^+,M^+}) + \Sigma(1/r_{P^-,P^-}) - \Sigma(1/r_{M^+,P^-})$; M = Li, Na.

(© Wiley-VCH Verlag GmbH & Co. KGaA, 69451 Weinheim, Germany, 2006)

## Introduction

Dichlorophenylphosphane ($PhPCl_2$; also known as phenylphosphonous acid dichloride) is a versatile starting material in organophosphorus chemistry that is produced on a large scale from $PCl_3$ and benzene.[1] Its reductive dehalogenation reaction with alkali metals (M) to give cyclic oligo(phenyl)phosphanes, $(PhP)_n$ ($n$ = 3–6) has been investigated.[2a–2j] Further reaction of $(PhP)_n$ with strongly reducing metals (M = Li, Na, or K) leads to reductive bond cleavage (RBC) and formation of alkali metal *catena*-oligophosphane-α,ω-diides, $[M_2(P_nPh_n)(solv)_x]$.[2a,2b,3] In their pioneering work, Caulton[3a] and Baudler[3b,3c] were able to obtain some structural information about the dimetal 1,2,3-triphenyltriphosphane-1,3-diides $[M_2(P_3Ph_3)(solv)_x]$ and the 1,2,3,4-tetraphenyltetraphosphane-1,4-diides $[M_2(P_4Ph_4)(solv)_x]$ from $^{31}P$ NMR spectroscopy in solution. Recently, Hey-Hawkins et al.[4] and ourselves[5a–5c] have succeeded in the crystallization of various sodium *catena*-oligophosphane-α,ω-diides, namely 1,2-diphenyldiphosphane-1,2-diide $[Na_6(P_2Ph_2)_3(dme)_3]$ (**I**),[5a] 1,2,3-triphenyltriphosphane-1,3-diide $[Na_2(P_3Ph_3)(tmeda)_3]$ (**II**),[5a] and the 1,2,3,4-tetraphenyltetraphosphane-1,4-diides $[Na_2(P_4Ph_4)(tmeda)_2]$ (**IIIa**),[5a] $[Na_2(P_4Ph_4)(dme)_3]$ (**IIIb**),[5a] $[Na_2(P_4Ph_4)(thf)_4(tmu)]$ (**IIIc**),[5b] and $[Na_2(P_4Ph_4)(thf)_5]$ (**IIId**) (tmeda = tetramethylethylenediamine, tmu = tetramethylurea), which can be isolated from the $PhPCl_2$/Na system in organic solvents.[4] Figure 1 summarizes these results.

Compound **I** consists of a $[Na(dme)_3]^+$ cation and the cluster anion $[Na_5(P_2Ph_2)_3(dme)_3]^-$ (see Figure 1a for a schematic representation and Figure 1b for a space-filling model). The structure of **II** is shown in Figure 1 (c and d), parts e and f show the structure of **IIIa** as a representative of all $[M_2(P_4Ph_4)(solv)_n]$ compounds. A solvent molecule acts as bridging ligand L (L = dme, tmu, or thf) between the two $Na^+$ ions in **IIIb**–**d**. In the schematic pictures of the structures of **I**, **II**, and **III**, a plus sign is placed at the position of the sodium cations and a minus sign at the terminal phosphorus centers of the dianionic $(P_nPh_n)^{2-}$ chains. Compounds **II** and **III** are classical *ion triples* (two cations, one dianion). The cluster anion in **I** may be viewed as a cyclic trimer of a corner-sharing ion triple that is additionally capped by two sodium cations on the top and bottom of the central hexagonal $P_6$ prism. With the structural parameters of these ionic aggregates, the electrostatic stabilization parameter (ESP) given by Equation (1) was calculated. The resulting data are listed in Table 1.

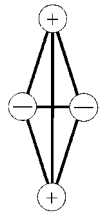

$$\mathrm{ESP} = \sum \frac{1}{r_{+,-}} + \sum \frac{1}{r_{-,-}} - \sum \frac{1}{r_{+,}} \quad (1)$$

The ESP was introduced by Streitwieser Jr. to account for the amazingly high stability of ion triples in carbanion chemistry[6] and is simply the sum of the repulsive interactions between like charges, expressed by $(1/r_{+,+})$ and

[a] Department of Chemistry and Applied Biosciences, HCI, ETH Hönggerberg,
8093 Zürich, Switzerland,
Fax: +41-1-632-1032
E-mail: gruetzmacher@inorg.chem.ethz.ch
[b] Institut für Anorganische Chemie der TU Graz,
8010 Graz, Austria
E-mail: alk.dransfeld@tugraz.at

Supporting information for this article is available on the WWW under http://www.eurjic.org or from the author.

 © 2006 Wiley-VCH Verlag GmbH & Co. KGaA, Weinheim 

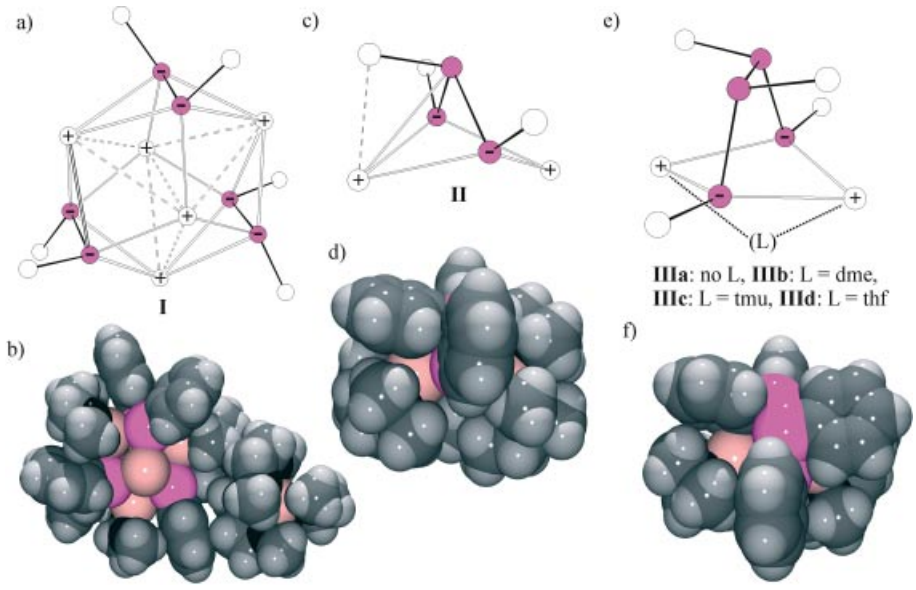


Figure 1. Schematic representations and space-filling plots of $[Na_5(P_2Ph_2)_3]^-$ (a, b), $[Na_2(P_3Ph_3)]$ (c, d), and $[Na_2(P_4Ph_4)(L)]$ (e, f).

Table 1. Repulsive interactions $r(Na^+Na^+)$ and $r(P^-P^-)$ [Å] and attractive interactions $r(Na^+P^-)$ [Å] and the resulting ESPs [$Å^{-1}$] for **I**, **II**, and **IIIa**–**c**. L indicates a bridging dme or tmu ligand between the $Na^+$ ions.

| | $[Na_5(P_2Ph_2)_3]^-$ **I** | $[Na_2(P_3Ph_3)]$ **II** | $[Na_2(P_4Ph_4)]$ **IIIa** | $[Na_2(P_4Ph_4)L]$ **IIIb** | $[Na_2(P_4Ph_4)L]$ **IIIc** |
|---|---|---|---|---|---|
| $r(Na^+Na^+)$ | 3.669(7) × 6 | 4.781(1) | 4.587(5) | 3.519(6) | 3.491(4) |
| | 3.96(1) × 1 | | | | |
| | 5.35(1) × 3 | | | | |
| $r(P^-P^-)$ | 2.20(1) × 3 | 3.146(1) | 3.406(3) | 3.947(4) | 3.475(2) |
| | 4.66(1) × 6 | | | | |
| | 5.10(1) × 6 | | | | |
| $r(Na^+P^-)$ | 3.063(6) × 6 | 2.968(1) | 2.848(4) | 2.916(6) | 2.974(2) × 2 |
| | 3.158(7) × 6 | 2.966(1) | 2.885(4) | 2.933(6) | 2.918(2) × 2 |
| | 2.831(5) × 6 | 3.106(1) | 2.829(4) | 2.960(6) | |
| | 4.092(7) × 6 | 3.097(1) | 2.972(5) | 2.849(6) | |
| ESP | –1.17 | –0.79 | –0.87 | –0.84 | –0.77 |

$(1/r_{-,-})$, minus the sum of attractive interactions, expressed by $(1/r_{+,-})$. Despite the fact that the ESP treats the ions simply as point charges and completely neglects steric interactions and solvation energies, it can be used to interpret the stability of ion pairs qualitatively. For example, the high negative ESP value for **I** explains why the structure of this cluster is also maintained in solution.[5a] The ESP also indicates that ion pairs with the $(P_3Ph_3)^{2-}$ dianion like **II** may be labile because of the rather short P1···P3 distance (ca. 3.15 Å) and the significantly longer Na–P distances. These are caused by repulsive steric interactions between the phenyl groups, especially the one at the central phosphorus atom, and the solvent molecules coordinated to $Na^+$. In structures with the $(P_4Ph_4)^{2-}$ dianion, the steric encumbrance is less pronounced and the $Na^+$–$P^-$ distances are shorter, which leads to more negative ESPs.

Only in **IIIc**, which contains a bridging tmu molecule and a strongly folded $Na_2P_2$ ring, is the $Na^+$–$Na^+$ distance more than 1 Å shorter than in **IIIa** (no bridging L); as a result the electrostatic stabilization is slightly less than that of **II**.

The motivation for this work was i) to find reliable conditions for the synthesis and isolation of the dilithium(*catena*-oligophosphane-α,ω-diides) $[Li_2(P_nPh_n)(solv)_x]$ (here and further on $x$ stands for an unspecified number of solvent molecules), ii) to determine their solid-state structures, and iii) to make, whenever possible, proposals for their behavior in solution. We focused on the isolation of compounds with tmeda as co-ligand for $Li^+$ in order to obtain a set of comparable compounds.

## Results and Discussion

### Syntheses

The syntheses that worked best in our hands and gave good yields of pure isolated and crystalline material are outlined in Scheme 1. In a reductive bond cleavage (RBC) reaction, pentaphenylcyclopentaphosphane (**1**)[2i] was treated with an excess of lithium powder in THF. The resulting orange-red solution showed only one signal at $\delta$ =

 © 2006 Wiley-VCH Verlag GmbH & Co. KGaA, Weinheim 

–102.9 ppm in the $^{31}$P NMR spectrum, thus indicating the formation of the $P_2^{2-}$ dianion. The primary product, $[Li_2(P_2Ph_2)(thf)_x]$ (**2′**) was obtained as red powder after evaporation of the solvent. Subsequent recrystallization of **2′** from hot toluene/tmeda (2:1 by vol.) gave red crystals of $[Li_2(P_2Ph_2)(tmeda)_2]$ (**2**).

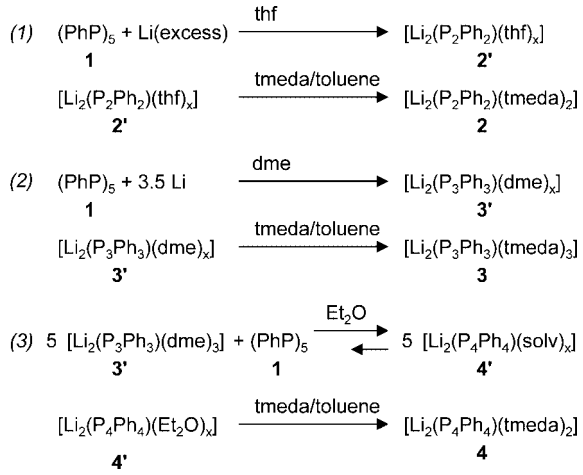


Scheme 1. Syntheses of isolable dilithium(*catena*-oligophosphane-α,ω-diides), $[Li_2(P_nPh_n)(tmeda)_m]$ **2** ($n$ = 2, $m$ = 2), **3** ($n$ = 3, $m$ = 3), and **4** ($n$ = 4, $m$ = 2).

The best synthesis for dilithium 1,2,3-triphenyltriphosphane-1,3-diide (**3**) was found to be the reaction of $(PhP)_5$ with a stoichiometric amount of lithium in dme as reaction medium. In this solvent, the product $[Li_2(P_3Ph_3)(dme)_x]$ (**3′**) precipitates directly from the reaction mixture as a bright-orange powder in good yield (about 70%). The content of dme ($x$ = 2–3) was estimated by NMR spectroscopy. Subsequently, **3′** was dissolved in a 5:1 mixture of toluene and tmeda and this solution was concentrated to dryness under high vacuum to remove all volatiles, especially dme; the resulting yellow powder was recrystallized at 7 °C from toluene to give yellow crystals of the composition $[Li_2(P_3Ph_3)(tmeda)_3]$ (**3**).

The best method for the synthesis of pure dilithium 1,2,3,4-tetraphenyltetraphosphane-1,4-diide (**4**) turned out to be the stoichiometric reaction of **3′** with $(PhP)_5$ (**1**) in diethyl ether. After removal of all volatiles under vacuum, the resulting orange powder (**4′**) of composition $[Li_2(P_4Ph_4)(solv)_x]$ (solv = $Et_2O$, dme) was dissolved in a 10:3 mixture of toluene and tmeda, again concentrated to dryness under vacuum, and then recrystallized from methyl *tert*-butyl ether (mtbe) to give slightly yellow crystals of the composition $[Li_2(P_4Ph_4)(tmeda)_2]$ (**4**). Attempts to synthesize **4′** or **4** by a direct RBC reaction of **1** with the corresponding amount of lithium gave a lower yield (<50%).

## Structures

The structures of the dilithium *catena*-oligophosphane-α,ω-diides $[Li_2(P_nPh_n)]$ ($n$ = 2–4) were investigated by X-ray diffraction studies. All compounds contain tmeda molecules as co-ligands bonded to the lithium ions. The $Li^+Li^+$, $P^-P^-$, and $Li^+P^-$ distances in **2**, **3**, and **4** are listed in Table 2.

The centrosymmetric structure of **2** (Figure 2) can be viewed as the archetypical structure of an ion triple with two formal negative charges in the α-position of the dianion. The P–P distance [2.244(3) Å] is slightly longer than the comparable one in the sodium compound [2.20(1) Å]. The main structural difference resides in the orientation of the phenyl rings, which are in a *trans* arrangement in **2** while they take a gauche conformation in the cluster anion $[Na_5(P_2Ph_2)_3]^-$ of **I** (the C–P–P–C torsion angle is about –72°[5a]). The Ph–P–P–Ph moiety in **2** is planar. As a result of the short attractive $Li^+$–$P^-$ interactions, the ESP for **2** (–0.94 Å$^{-1}$) is considerably more negative than the ESP (–0.72 Å$^{-1}$) for a hypothetical $[Na_2(P_2Ph_2)]$ ion triple with a structure analogous to that of **2** (an Na–P distance of 2.98 Å, which is the average of the data listed in Table 1, is assumed).

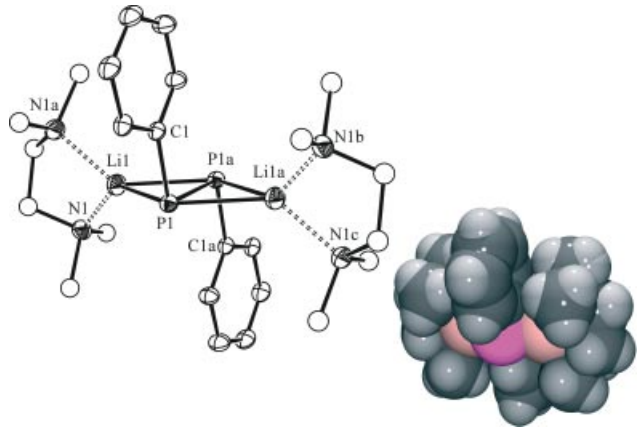


Figure 2. Structure of **2**. Selected distances [Å] and angles [°]: P1–P1 2.244(3), Li–P1 2.483(1), P1–C1 1.820(1), Li–N1 2.077(1); C1–P1–P1 98.66(2), C1–P1–Li 93.90(1), Li–P1–Li 126.28(3); torsion angles: Li–P1–LiA–P1A 0.0, P1A–P1–C1–C2 0.0, C1–P1–P1A–C1A 180.0.

In the solid state, **3** forms an *ion pair* composed of a $[Li(tmeda)_2]^+$ cation and an anionic *ion double*, namely $[Li(P_3Ph_3)(tmeda)]^-$. Only one lithium ion coordinates to the terminal phosphorus atoms P1 and P3 and, as expected for steric reasons, the coordination occurs from the opposite site to the central phenyl group at P2. The distance between the two terminal phosphorus atoms P1 and P3 in **2** is about 0.2 Å longer (the P–P–P angle is about 8° larger)

Table 2. Selected distances [Å] and the resulting ESPs for **2**–**4**.

| | $[Li_2(P_2Ph_2)(tmeda)_2]$ | $[Li(tmeda)_2]^+[Li(P_3Ph_3)(tmeda)]^-$ | $[Li_2(P_4Ph_4)(tmeda)_2]$ |
|---|---|---|---|
| $r(Li^+Li^+)$ | 4.430(2) | – | 3.967(2) |
| $r(P^-P^-)$ | 2.244(3) | 3.347(1) | 3.229(2) |
| $r(Li^+P^-)$ | 2.483(1)×4 | 2.499(7), 2.525(7) | 2.618(4)×2, 2.653(4)×2 |
| ESP | –0.94 | –0.50 | –0.96 |

 © 2006 Wiley-VCH Verlag GmbH & Co. KGaA, Weinheim 

than in the neutral ion triple $[Na_2(P_3Ph_3)(tmeda)_3]$ (**II**), where two sodium ions coordinate to P1 and P3. The only other known triphosphanediide is found in the highly unstable ion pair $[Na(NH_3)_5]^+[Na(P_3H_3)(NH_3)_3]^-$, which contains the anionic ion double $[Na(P_3H_3)(NH_3)_3]^-$.[7] An even longer $P^-$–$P^-$ distance (3.67 Å) and larger P–P–P angle (113.4°) is observed in this compound. An increase of the $P^-$–$P^-$ distance will help to diminish the repulsive interactions in the ion doubles which, evidently, have less negative ESPs than the ion triples because of the long and hence less stabilizing Na–P distances {–0.79 $Å^{-1}$ for $[Na_2(P_3Ph_3)(tmeda)_3]$ **II**, –0.50 for $[Li(P_3Ph_3)(tmeda)]^-$, and only –0.37 for $[Na(P_3H_3)]^-$}. This loss of stabilizing electrostatic energy in the anionic ion doubles is compensated for by the solvation energy of the counter cations. Because these are much higher for lithium than for sodium,[8,9] the formation of an ion pair in the case of **3** and the formation of an ion triple for the sodium compound **II** is easily understood (Figure 3). Note that in the other ion pair, $[Na(NH_3)_5]^+[Na(P_3H_3)(NH_3)_3]^-$, the smaller size of the ammonia ligand compared to tmeda allows a higher coordination number at the sodium cations and a better solvation. Hence, the loss of ESP on going from the ion triple to the ion double can be compensated.

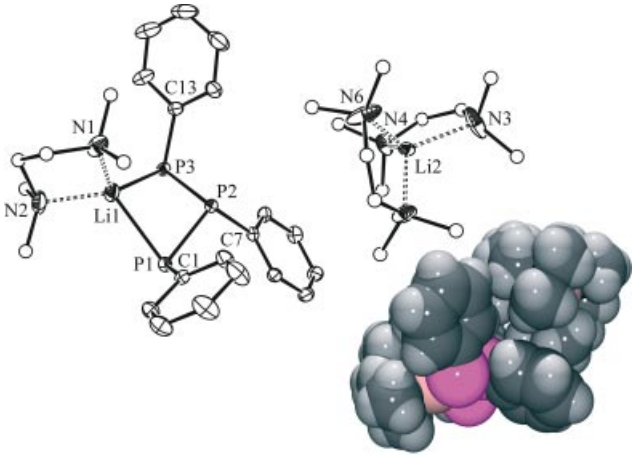


Figure 3. Structure of **3**. Selected distances [Å] and angles [°]: P1–P2 2.179(1), P2–P3 2.177(1), P1–C1 1.814(3), P2–C7 1.847(3), P3–C13 1.819(4), P1–Li1 2.493(7), P3–Li1 2.525(6), P1–P3 3.347(1), P1–P2–P3 100.02(5), P1–Li1–P3 83.37(2), C1–P1–P2 103.7(1), C7–P2–P3 105.8(1), C7–P2–P1 104.0(1), C13–P3–P2 102.8(1); torsion angles: C1–P1–P2–C7 106.7(2), C1–P1–P2–P3 40.9(2), C7–P2–P3–C13 112.9(2), C13–P3–P2–P1 139.3(1), Li1–P1–P2–C7 150.1(2), Li1–P3–P2–C7 148.2(2).

Finally, the structure of **4** was investigated. This compound has a composition very close to the corresponding sodium compound **IIIa** (both contain two tmeda molecules) and the solid-state structures are also very similar (Figure 4). Compounds **4** and **IIIa** are obtained as racemic mixtures and form ion triples in which the $P_4$ chain has either an (*R*,*R*)- or an (*S*,*S*)-configuration. Note the highly distorted coordination spheres around the lithium atoms and their contacts to the *ipso*-carbon atoms of the central phenyl rings. Both features are also observed in the sodium compound. However, due to the short $Li^+$–$P^-$ distances, the ESP for this ion triple is rather high (–0.96 $Å^{-1}$).

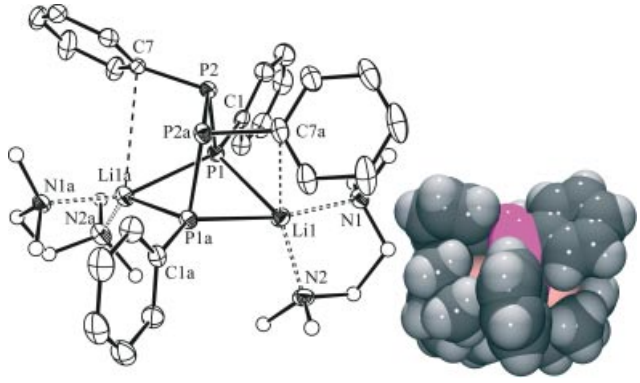


Figure 4. Structure of **4**. Selected distances [Å] and angles [°]: Li–P1 2.618(4), Li–P1A 2.652(4), Li–N1 2.144(4), Li–N2 2.095(5), P1–P2 2.167(1), P1–C1 1.832(2), P2–P2A 2.190(1), P2–C7 1.851(2); P1–Li–P1A 75.6(1), C1–P1–P2 102.26(9), P1–P2–P2A 103.37(2), P1–P2–C7 105.55(9), P2–P2A–C7A 99.70(8); torsion angles: P1–P2–P2A–P1A –13.3(1), C1–P1–P2–P2A –160.33(8), C1–P1–P2–C7 95.4(1), Li1–P1–P2–P2A –39.2(1), Li1A–P1A–P2A–P2 58.8(1).

The P–P distances for the $(P_2Ph_2)^{2-}$, $(P_3Ph_3)^{2-}$, and $(P_4Ph_4)^{2-}$ dianions are very similar in the lithium and sodium compounds. In the dianions of **2** and **I**, the P–P distance is greater than 2.2 Å, whereas in the dianions in **3** and **II** it is below 2.2 Å. The terminal P–P bonds in the $(P_4Ph_4)^{2-}$ dianions in **4** and **IIIa**–**d** are very slightly shorter (ca. 2.17 Å) than the central P–P bond (ca. 2.20 Å). The bonds between the formally negatively charged terminal phosphorus centers and the *ipso*-carbon atoms of the phenyl rings are a little shorter (by ca. 0.04 Å) in all compounds than the P–$C_{ipso}$ bonds at the central phosphorus atoms. This observation may be taken as an indication of some delocalization of the negative charges into the phenyl groups, although this effect is small compared to amides.[10]

## NMR Spectra

The compound $[Li_2(P_2Ph_2)(tmeda)_2]$ (**2**) is sparingly soluble in hydrocarbons but sufficiently soluble in $[D_8]$thf to obtain $^1H$, $^{13}C$, $^{31}P$, and $^7Li$ NMR spectra. All data correspond quite closely with those observed for the sodium cluster anion $[Na_5(P_2Ph_2)_3(dme)_3]^-$ in **I**. The *ipso*-$^{13}C$ carbon resonances of the phenyl groups are observed at $\delta$ = 162.2 ppm ($\delta$ = 160.7 ppm in **I**) and the $^{31}P$ NMR shifts also vary little ($\delta$ = –102.9 ppm in **2**, $\delta$ = –106.4 ppm in **I**). Unfortunately, the $^{31}P$-$^7Li$ couplings could not be resolved in the $^7Li$ NMR spectrum (broad signal at $\delta$ = 0.6 ppm). However, in view of the large loss of electrostatic stabilization energy upon dissociation of the ion triple into the ion pair $[Li(solv)_x][Li(P_2Ph_2)(solv)_y]$, we believe that the structure of **2** is retained in solution.

A $[D_8]$toluene solution of the salt $[Li(tmeda)_2]^+$-$[Li(P_3Ph_3)(tmeda)]^-$ (**3**) shows an $AM_2$ spin system with two multiplets centered at $\delta_A(^{31}P)$ = –52.3 ppm and $\delta_M(^{31}P)$ = –71.5 ppm. From a simulation of the spectrum, the coup-

 © 2006 Wiley-VCH Verlag GmbH & Co. KGaA, Weinheim 

ling constant $^1J_{A,M} \approx 224$ Hz was obtained. These data are very different from those for the sodium compound $[Na_2(P_3Ph_3)(tmeda)_3]$ (**II**), which shows an eight-line $AB_2$ spin system with $\delta_A = -54.0$ and $\delta_B = -56.7$ ppm ($^1J_{A,B}$ = 242 Hz). This finding indicates that different species containing the $P_3Ph_3$ unit are present in solution. The $^7$Li NMR spectrum in [D$_8$]toluene at low temperature confirms this assumption: two signals are observed, one broad singlet at $\delta = 10.5$ ppm for the $[Li(tmeda)_2]^+$ cation and one broad multiplet at $\delta = 11.4$ ppm for the $[Li(P_3Ph_3)(tmeda)]^-$ anion, that is, **3** exists as an ion pair in solution, as observed in the solid state. That we could not resolve the $^{31}$P-$^7$Li coupling is probably due to dynamic processes involving exchange of the Li-coordinated solvent molecules. On the contrary, the very different $^{31}$P NMR chemical shifts for the sodium compound indicate that this forms an intact ion triple in solution.

The tetraphosphanediide $[Li_2(P_4Ph_4)(tmeda)_2]$ (**4**) is sufficiently soluble in [D$_8$]toluene to allow NMR measurements. At room temperature, ill-resolved multiplets at $\delta$ = –35 to –39 ppm and very broad signals at about $\delta \approx -76$ and $\delta \approx -95$ ppm are observed. At low temperature (248 K), two species (**4** and **4′′**) are observed in a 100:80 ratio in the $^{31}$P NMR spectrum (see Figure 5, a). The major compound **4** shows two multiplets of an $AA'BB'X_2$ spin system in the $^{31}$P NMR spectrum with chemical shifts at

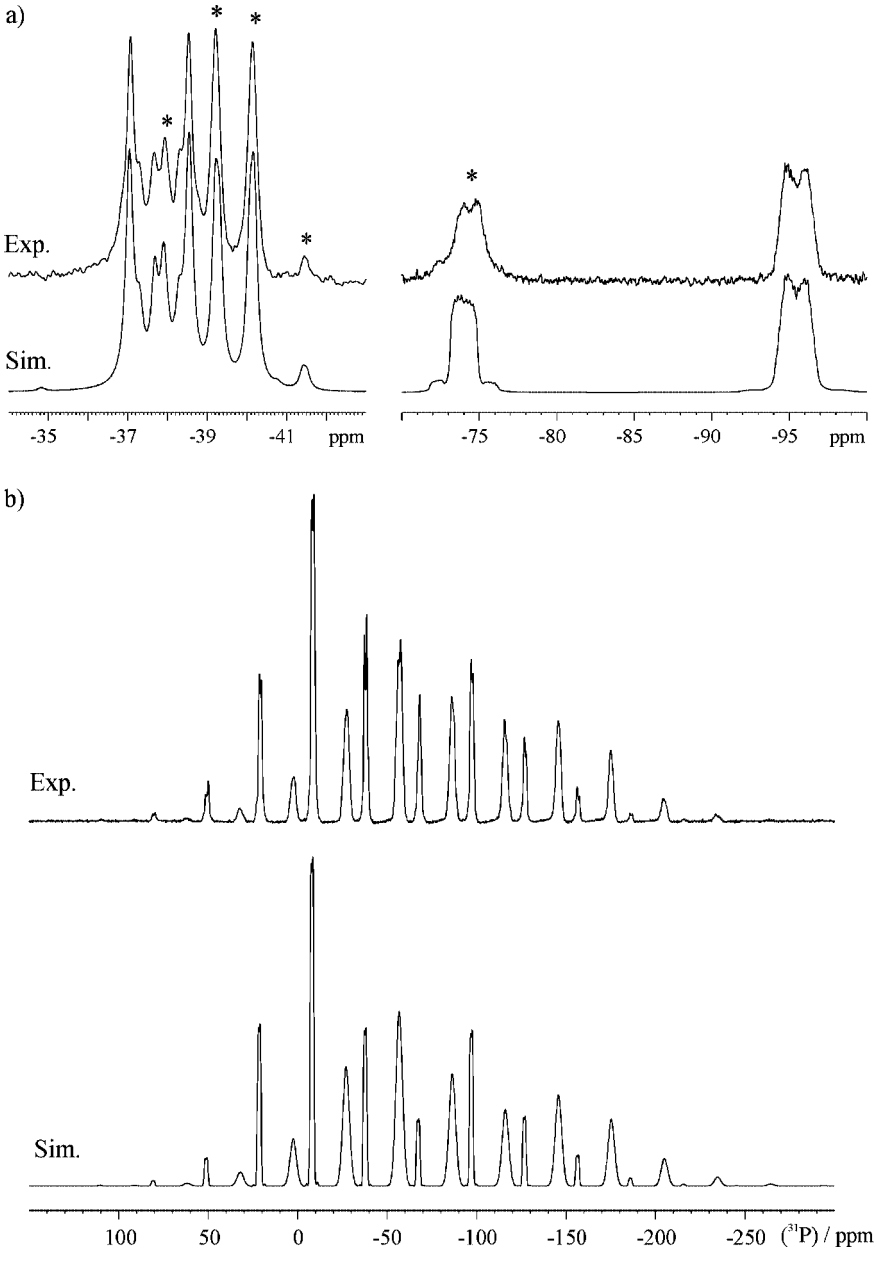


Figure 5. a) Experimental and simulated $^{31}$P NMR spectra of $[Li_2(P_4Ph_4)(tmeda)_2]$ (**4**) and **4′′** (marked with asterisks) in toluene solution at $T$ = 248 K. Chemical shifts and coupling constants are given in Table 3. b) $^{31}$P CMAS spectrum of $[Li_2(P_4Ph_4)(tmeda)_2]$ (**4**). Top: experimental spectrum at 6000 Hz rotation frequency. Bottom: simulated spectrum with: $P^{2,3}$: $\delta_{iso} = -38.0$, $\delta_{11} = 33$, $\delta_{22} = 13$, $\delta_{33} = -159$ ppm; $P^{1,4}$: $\delta_{iso} = -86.3$, $\delta_{11} = 20$, $\delta_{22} = -62$, $\delta_{33} = -217$ ppm.

 © 2006 Wiley-VCH Verlag GmbH & Co. KGaA, Weinheim 

$\delta$ = –38.0 for $P^{2,3}$ and $\delta$ = –95.1 ppm for $P^{1,4}$. The X part is observed in the $^7$Li NMR spectrum, where a slightly broadened triplet at $\delta$ = 10.9 ppm is observed ($^1J_{Li,P}$ = 37 Hz).

The resonances of the protons in the *para*-position of the phenyl rings are sharp, whereas those of the *ortho*- and *meta*-protons are broadened at low temperature. This is probably due to hindered rotation of the phenyl groups in **4**. This species corresponds to the ion triple with a structure close to that observed in the solid state.

This is further bolstered by the solid-state $^{31}$P CPMAS spectrum of **4** (Figure 5, b). Only one species is present in the isolated crystalline material. The observation of only two isotropic chemical shifts ($\delta_{iso}$ = –38.0 and –86.3 ppm for the central and terminal P spins, respectively) is in agreement with the crystallographic $C_2$ symmetry of the ion triple **4** (see Figure 4). The principal elements of the chemical shift tensor, $\delta_{11}$ = 33, $\delta_{22}$ = 13, $\delta_{33}$ = –159 and $\delta_{11}$ = 20, $\delta_{22}$ = –62, $\delta_{33}$ = –217 ppm were obtained by a Herzfeld–Berger[11] analysis of the intensities of the spinning side-bands and refined by spectral simulation using the SIMPSON package.[12] It should be noted that the fine structure observed in the resonances shown in Figure 5 (b) is a consequence of orientation-dependent cross-terms involving the scalar and dipolar coupling and the chemical shift interactions and depends significantly on the frequency of magic angle spinning.[13] For the purpose of spectral simulation, phosphorus–phosphorus scalar coupling constants were taken into account as their isotropic solution values (Table 3) but were not refined, and coupling to the lithium isotopes was accounted for by processing with an appropriate Gaussian line-shape function.

It is interesting to note that while the isotropic chemical shifts of the central phosphorus atoms ($\delta_{iso}$ = –38.0 ppm) are equal, those of the terminal ones differ ($\delta_{iso}$ = –86.3 and –95.1 ppm in the solid state and solution, respectively). As there is no doubt about the constitution of **4** − in both cases the compound exists as the ion triple − we assume a slightly different conformation in solution, which might be due to loss of the Li–$C_{ipso}$ interaction present in the solid phase.

The other species (**4′′**) observed in [$D_8$]toluene solution at 248 K also shows an AA′BB′X spin system (marked with asterisks in Figure 5a) with chemical shifts at $\delta$ = –39.7 ppm for $P^{2,3}$ and a broad resonance at $\delta$ = –74.4 ppm for $P^{1,4}$ in the $^{31}$P NMR spectrum. For this species, no signal could be found in the $^7$Li NMR spectrum.

## Computations

Recently, Kaupp et al. have calculated the dependence of the $J_{P,P}$ coupling constants for the conformations **A** and **B** of the $P_4$ chain based on the experimentally known $M_2(P_4R_4)$ structures (Figure 6).[14] The coupling constants given in Table 3 depend on the alignment of nonbonding electron pairs at the phosphorus centers. In **A**, which has a small P–P–P–P torsion angle $\varphi$, the couplings follow the order $J_{1,4}$ (>300 Hz) >> $J_{1,3}/J_{2,4}$ (11–35 Hz), whereas in **B**,

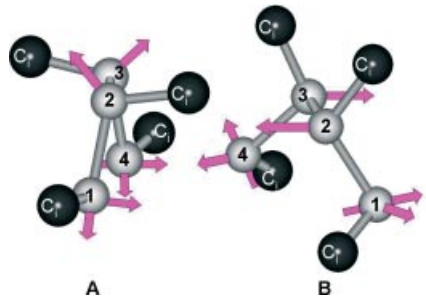


Figure 6. Conformations of the $P_4$ chains in tetraphosphanediides of type **A** {found in all $[M_2(P_4Ph_4)(solv)_x]$ with M = Li, Na, and $[Na_2(P_4tBu_4)(thf)_4]$} and **B** {observed in $[M_2(P_4Mes_4)(thf)_x]$ M = Na, $x$ = 4; M = K, $x$ = 6}. The *ipso* carbons of the aryl groups are indicated as $C_i$ and the nonbonding electron pairs at the phosphorus centers are shown as magenta-colored arrows.

Table 3. Experimentally derived $^{31}$P–$^{31}$P coupling constants [Hz] of the $P^1$–$P^2$–$P^3$–$P^4$ chain in **IIIa**,[5a] $[Na_2(P_4tBu_4)(thf)_4]$,[4] $[Na_2(P_4Mes_4)(thf)_4]$,[4] **4**, and **4′′**. The computed,[a] geometric, and magnetic properties for $Li_2(P_4H_4)_{opt}$,[b] $Na_2(P_4H_4)_{opt}$,[b] $Li_2(P_4Ph_4)(tmeda)_{2,cry,trunc}$,[c] and the $Li_2(tmeda)_1(P_4Ph_4)_{opt,trunc}$[c] isomers **A** and **B** are also given.

| Entry | | Type | $P^1$–$P^2$/$P^3$–$P^4$ [d] | $^1J_{1,2}/^1J_{3,4}$ | $P^2$–$P^3$ | $^1J_{2,3}$ | $\varphi$ | $J_{1,3}/J_{2,4}$ | $P^1\cdots P^4$ | $J_{1,4}$ |
|---|---|---|---|---|---|---|---|---|---|---|
| Experimental | | | | | | | | | | |
| 1 | $[Na_2(P_4Ph_4)(tmeda)_2]$ (**IIIa**) | A | 2.160 | –322 | 2.185 | –306 | 20.3 | –11 | 3.406 | 310 |
| 2 | $[Na_2(P_4tBu_4)(thf)_4]$ | A | 2.169 | –341 | 2.222 | –306 | 8.8 | –13 | 3.615 | 201 |
| 3 | $[Na_2(P_4Mes_4)(thf)_4]$ | B | 2.165 | –310 | 2.261 | –118 | 72.7 | 120 | 4.247 | 3 |
| 4 | $[Li_2(P_4Ph_4)(tmeda)_2]$ (**4**) | A | 2.166 | –271 | 2.190 | –268 | 13.3 | –35 | 3.229 | 310 |
| 5 | **4′′** | | | –266 | | –15 | | 67 | | 280 |
| Calculated | | | | | | | | | | |
| 6 | $[Na_2(P_4H_4)]_{opt}$[b] | A | 2.251 | –200 | 2.248 | –229 | 25.7 | –26 | 3.644 | 292 |
| 7 | $[Na_2(P_4Ph_4)(thf)_{2.5}]_{cry,trunc}$[14] | A | 2.166 | –304 | 2.207 | –323 | 32.1 | –21 | 3.486 | 432 |
| 8 | $[Li_2(P_4H_4)]_{opt}$[b] | A | 2.248 | –190 | 2.252 | –204 | 24.3 | –22 | 3.414 | 320 |
| 9 | $[Li_2(P_4Ph_4)(tmeda)_2]_{cry,trunc}$[a] | A | 2.166 | –267 | 2.190 | –321 | 13.3 | –29 | 3.229 | 529 |
| 10 | $Li_2(tmeda)_1(P_4Ph_4)_{opt,trunc;}$ Isomer **A** [c] | | 2.215/2.231 | –270/–259 | 2.254 | –323 | 23.6 | –27/–20 | 3.364 | 417 |
| 11 | $Li_2(tmeda)_1(P_4Ph_4)_{opt,trunc;}$ Isomer **B**[c] | | 2.213 | –305 | 2.262 | –317 | 38.3 | –25 | 3.451 | 323 |

[a] Coupling constants in Hz calculated at GIAO/B3LYP/6-311+G**//B3LYP/6-31G*.[15] [b] opt = properties of B3LYP/6-31G*-optimized structure. [c] trunc = truncated geometry; the NMR properties are calculated for the molecule where phenyl groups have been replaced by H atoms at a standard P–H distance of 1.427 Å and solvent molecules (tmeda) are omitted. [d] $P^1$–$P^2$ = $P^3$–$P^4$ if only one distance and $^1J_{1,2}$ = $^1J_{3,4}$ and $J_{1,3}$ = $J_{2,4}$ if only one coupling is given.

 © 2006 Wiley-VCH Verlag GmbH & Co. KGaA, Weinheim 

which has a large angle (>70°), a poor 1,4 alignment of the lone pairs causes the inverse ordering $J_{1,4}$ (<5 Hz) << $J_{1,3}$/$J_{2,4}$ (>100 Hz).

We performed the following computations:[15] i) $^{31}$P chemical shifts were calculated at the GIAO/B3LYP/6-31G* level for a number of structural isomers of molecules of the general formula [$Li_2(P_4Ph_4)(tmeda)_n$] ($n$ = 0, 1, 2). The values obtained for [$Li_2(P_4Ph_4)(tmeda)_2$] (**4**) with the structure observed in the crystal and with the optimized structure (B3LYP/6-31G*), denoted as $\mathbf{4}_{cry}$ and $\mathbf{4}_{opt}$, respectively, are $\delta$ = –108 ($\mathbf{4}_{cry}$, terminal), –52 ($\mathbf{4}_{cry}$, inner), –70 ($\mathbf{4}_{opt}$, terminal), and –17 ppm ($\mathbf{4}_{opt}$, inner), respectively. The chemical shift difference, $\Delta\delta$, between the terminal and the inner backbone $^{31}$P nuclei is rather constant (–53 ppm relaxed and –56 ppm crystal geometry). The calculated data reproduce the experimental ones satisfactorily, which means that the chosen theoretical level is sufficient; ii) for comparison, the structures of the simple molecules [$Li_2(P_4H_4)$] and [$Na(P_4H_4)$] were optimized at the B3LYP/6-31G* level; iii) the $^{31}$P–$^{31}$P coupling constants were calculated for model compounds in which the structure of the $M_2P_4$ core of the complete [$Li_2(P_4Ph_4)(tmeda)_n$] was maintained but the phenyl groups were replaced by hydrogen atoms and the tmeda molecules omitted. These truncated geometries are denoted as [$Li_2(P_4Ph_4)(tmeda)_n$]$_{trunc}$.

Table 3 lists the P–P coupling constants for the sodium tetraphosphanediides [$Na_2(P_4Ph_4)(tmeda)_2$] (**IIIa**),[5a] [$Na_2(P_4Ph_4)(thf)_5$] (**IIId**),[5] [$Na_2(P_4tBu_4)(thf)_4$],[4] and the lithium tetraphosphanediides **4** and **4′** as obtained by simulating the experimental spectra. The calculated data for $Li_2(P_4H_4)_{opt}$, $Na_2(P_4H_4)_{opt}$, [$Li_2(P_4Ph_4)(tmeda)_2$]$_{cry,trunc}$, and the isomers **A** and **B** of $Li_2(tmeda)(P_4Ph_4)_{opt,trunc}$ are given for comparison. We have also included the data of [$Na_2(P_4Ph_4)(thf)_{2.5}$]$_{cry,trunc}$ reported by Kaupp et al.[14]

The experimental data listed for compounds of structure type **A** show that the one-bond P–P couplings $^1J_{1,2}$ = $^1J_{3,4}$ are somewhat smaller for M = Li (entries 4, 5) than for M = Na (entries 1–3) and this trend is reproduced with the calculated model structures (entries 6–9). The $P^{1,2}$–$P^{3,4}$ bonds in the optimized models [$M_2(P_4H_4)$]$_{opt}$ (M = Li, Na) are longer than in the truncated structures [$M_2(P_4H_4)$]$_{trunc}$ and consequently the $^1J$ couplings are smaller. The $^1J_{2,3}$ coupling is influenced by both the $P^2$–$P^3$ distance and also by the dihedral angle $\varphi$. In compounds with structure **B** (entry 3), where $\varphi$ is large, the $^1J_{2,3}$ coupling is rather small. As expected, the couplings $J_{1,3}$ = $J_{2,4}$ in the dilithium tetraphosphanediide [$Li_2(P_4Ph_4)(tmeda)_2$] (**4**) are in the range of the disodium compounds with the same structure type **A** and are smaller (entry 4) than for compounds with structure type **B** (entry 3). The $J_{1,4}$ coupling shows a dependency on the $P^1\cdots P^4$ distance and on the dihedral angle $\varphi$. At longer distances (>3.6 Å), $J_{1,4}$ decreases (compare entries 2 with entries 1 and 4). To some extent, this is also reflected by the calculations (compare entries 6 with 7 and 8 with 9). Especially small values for $J_{1,4}$ are observed for large torsion angles $\varphi$ (entry 3). In agreement with the experiment, the calculated coupling constants for [$Na_2(P_4H_4)$]$_{opt}$ and [$Li_2(P_4H_4)$]$_{opt}$ show only little differences. Nevertheless, the difference $\Delta\delta$ = $\delta(P^1,P^4)$ – $\delta(P^2,P^3)$ between the calculated chemical shifts of the terminal and internal $^{31}$P nuclei is strongly dependent on the alkali cation and significantly larger for Na [$Na_2(P_4H_4)$: $\Delta\delta$ = –176 ppm, with $\delta(P^1,P^4)$ = –232 and $\delta(P^2,P^3)$ = –56 ppm; $Li_2(P_4H_4)$: $\Delta\delta$ = –137 ppm, with $\delta(P^1,P^4)$ = –241 and $\delta(P^2,P^3)$ = –104 ppm]. It is noteworthy that the shifts of the atoms directly attached to the different cations are less affected than the remote phosphorus centers. Although much less pronounced, this is reflected by the experimental data {[$Na_2(P_4Ph_4)(tmeda)_2$] (**IIIa**): $\Delta\delta$ = –64.2 ppm with $\delta(P^1,P^4)$ = –89.1 and $\delta(P^2,P^3)$ = –24.9 ppm; [$Li_2(P_4Ph_4)(tmeda)_2$] (**4**): $\Delta\delta$ = –57.1 ppm, with $\delta(P^1,P^4)$ = –95.1 and $\delta(P^2,P^3)$ = –38.0 ppm}.

With respect to a possible structure for the second species **4′′** in solutions of **4**, the data in Table 3 give some hints: the slightly smaller $J_{1,4}$ and the positive $J_{1,3}$ = $J_{2,4}$ indicate that the conformation of the $P_4$ chain in **4′′** has a P–P–P–P torsion angle $\varphi$ that is significantly larger than in **4** (>> 20°). The very small $^1J_{2,3}$ indicates that the $P^2$–$P^3$ bond may also be elongated. The fact that broadened $^{31}$P NMR signals for the terminal phosphorus nuclei $P^1$, $P^4$ are observed and no $^7$Li signal could be recorded even at low temperatures point to fast exchange processes. For the sodium compound, we have suggested previously the equilibrium [$Na_2(P_4Ph_4)(thf)_x$] ⇆ [$Na(thf)_y$]$^+$ + [$Na(P_4Ph_4)(thf)_z$]$^-$, (with $\delta_1$ = –73.3, $\delta_2$ = –30.8, $\delta_3$ = –16.8, and $\delta_4$ = –70.4 ppm and $^1J_{1,2}$ = 340, $^1J_{2,3}$ = 340, $^1J_{3,4}$ = 274, and $J_{2,4}$ = 148 Hz for the [$Na(P_4Ph_4)(thf)_z$]$^-$ anion).[5] A computational search of possible structures for a [$Li(P_4Ph_4)(thf)_z$]$^-$ anion only gave species with an almost co-planar $P_4$ chain and at least one significantly high-frequency-shifted resonance for an *internal* phosphorus nucleus (>39 ppm). This finding is not compatible with the experimental results, which show that the chemical shifts of the external $^{31}$P nuclei in **4** and **4′′** are quite different. In view of the rather high ESP, it seems likely that **4′′** also has the structure of an ion triple with a strongly distorted $P_4$ chain. We therefore inspected various possible structures for **4′′** that contain only one tmeda molecule as co-ligand to lithium (Scheme 2).

Two isomers were found: isomer **A**, with a chelating tmeda molecule binding to only one Li ion in a $\kappa^2$-fashion, and isomer **B**, where the tmeda molecule bridges the two lithium ions in a $\mu_2$-$\kappa^1$,$\kappa^1$-fashion. Isomer **A** is about 3 kcal mol$^{-1}$ more stable than isomer **B**. The calculated (gas-phase) energies, $\Delta H_r$, for the dissociation of one tmeda from **4** are in a reasonable range (21–24 kcal mol$^{-1}$; Scheme 2) to allow this process in solution. This idea is supported by measuring the diffusion coefficients of the $(P_4Ph_4)^{2-}$-containing species ($0.26746\times10^{-9}$ m$^2$ s$^{-1}$) and the tmeda molecules ($0.29214\times10^{-9}$ m$^2$ s$^{-1}$) by pulsed field gradient NMR techniques.[16] The significantly larger diffusion coefficient (ca. 10%) for the tmeda molecules is compatible with the dissociation process, [$Li_2(P_4Ph_4)(tmeda)_2$] ⇆ [$Li_2(P_4Ph_4)$-(tmeda)] + tmeda, where, on average, three tmeda molecule are coordinated and one tmeda molecule is free.

Indeed, the P–P–P–P torsion angle $\varphi$ in **A** (23.6°) and especially **B** (38.3°) is somewhat larger than that observed in crystals (13.3°) and calculated (12°) for **4**. For isomer **A**,

 © 2006 Wiley-VCH Verlag GmbH & Co. KGaA, Weinheim 

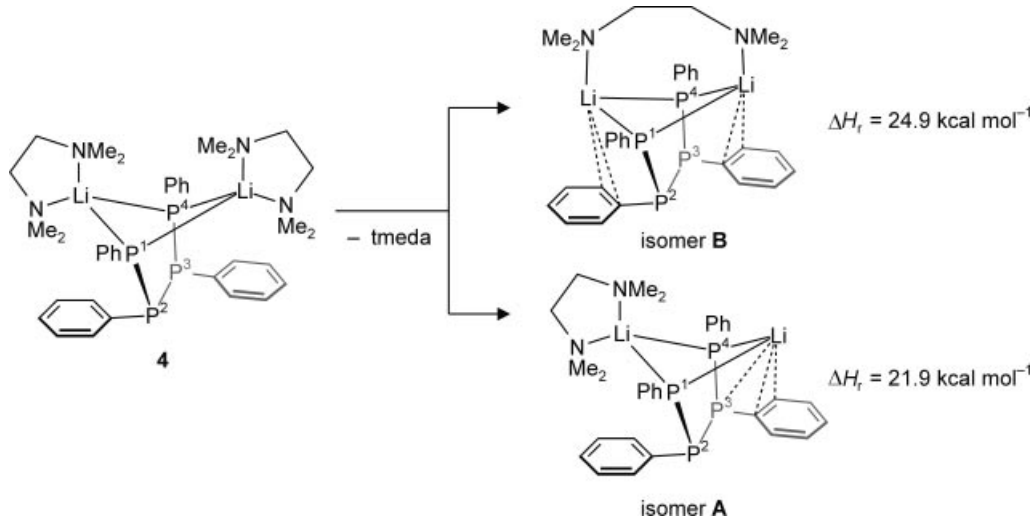


Scheme 2. Computed reaction enthalpies for the dissociation $[Li_2(P_4Ph_4)(tmeda)_2] \rightarrow [Li_2(P_4Ph_4)(tmeda)] + tmeda$.

the predicted $^{31}P$ chemical shifts are: $P^1$: $\delta$ = –74.03 ppm; $P^2$: $\delta$ = 6.87 ppm; $P^3$: $\delta$ = –28.52 ppm; $P^4$: $\delta$ = –30.06 ppm; and for the more symmetric isomer **B**: $P^1$,$P^4$: $\delta$ = –55 ppm; $P^2$,$P^3$: $\delta$ = 7 ppm. Considering that the equilibrium shown in Scheme 2 is likely to be fast on the NMR timescale, the chemical shift difference ($\Delta\delta$ = –42 ppm) between the averages of the chemical shifts for the external and internal $^{31}P$ nuclei, ½($P^1$ + $P^4$) = –53 ppm and ½($P^2$ + $P^3$) = –11 ppm, in isomer **A** fits better the experimental data for **4**′′ ($\Delta\delta$ = –34.7 ppm) than isomer **B** ($\Delta\delta$ = –62 ppm). However, the agreement between the calculated and experimental $^{31}P$–$^{31}P$ couplings is very poor (see Table 3) and at this point we cannot draw any definitive conclusion about the exact nature of **4**′′.

## Conclusions

Optimized conditions for the selective syntheses of dilithium (*catena*-oligophosphane-α,ω-diides) $[Li_2(P_nPh_n)(solv)_x]$ have bee developed and the species with solv = tmeda and $n$ = 2, 3, and 4 have been isolated as crystalline materials and structurally characterized. The compounds $[Li_2(P_2Ph_2)(tmeda)_2]$ and $[Li_2(P_4Ph_4)(tmeda)_2]$ form centrosymmetric genuine ion triples in the solid state and very probably also in solution. The lithium salt of the triphosphanediide behaves differently and is an ion pair, $[Li(tmeda)_2]^+[Li(P_3Ph_3)(tmeda)]^-$, in the solid and in solution. On average, the Li–P bonds (average of Li–P distances listed in Table 2: 2.55 Å) are 15% shorter than the Na–P distances (av. 2.98 Å) in comparable sodium oligophosphane-α,ω-diides (see Table 1). As a consequence, the electrostatic stabilization parameters, ESPs, of the lithium phosphanediides are significantly larger. Within its limits, this very simple model, which involves placing point charges at the positions of the cations and terminal phosphorus centers and neglecting all solvation energies and steric interactions, can be used to rationalize why $Li_2(P_2Ph_2)$ forms a simple ion triple while the sodium analogue forms a larger aggregate. Also, the fact that $[Na_2(P_3Ph_3)(solv)_x]$ forms an intact ion triple but the lithium analogue readily dissociates into an ion pair is expected. Specifically, the large drop of the ESP when going from the ion triple $[Na_2(P_3Ph_3)]$ (–0.79) to a hypothetical ion pair $[Na]^+$-$[Na(P_3Ph_3)]^-$ (ESP = –0.35; calculated with Na–P = 2.98 Å, P–P = 3.14 Å) cannot be overcompensated by the solvation of the dissociated $Na^+$ cation in an organic solvent. Further studies will concentrate on the question of whether these different aggregates also have different reactivity.

## Experimental Section

**General Techniques:** All manipulations were performed under argon. All solvents were dried and purified using standard procedures and were freshly distilled under argon from sodium/benzophenone (THF, toluene, tmeda, dme, mtbe) or from sodium/diglyme/benzophenone (*n*-hexane) prior to use. Air sensitive compounds were stored and weighed in a glove box (Braun MB 150 B-G system) and reactions on small scale were performed directly in the glove box.

NMR Spectra were measured on Bruker AVANCE 500, 400, 300, and 250 systems. The chemical shifts ($\delta$) are measured according to IUPAC[17] and expressed in ppm relative to TMS ($^1H$, $^{13}C$), LiCl ($^7Li$), and $H_3PO_4$ ($^{31}P$). No satisfactory elemental analysis could be obtained due to the high air and moisture sensitivity of the compounds.

**Solid State NMR:** $^{31}P$ CP-MAS solid-state NMR spectra were acquired at room temperature on a Bruker Avance instrument operating at a $^1H$ Larmor frequency of 500 MHz. Conventional cross-polarization and magic-angle-spinning techniques were implemented using 4-mm rotors, with which rotational frequencies of more than 11 kHz were achieved. The $^{13}C$ carboxylate resonance of α-glycine appeared at $\delta$ = 176.0 ppm. As a consequence, referencing of all isotopes could be achieved as for the solution NMR using the unified Ξ scale.[17] Chemical shifts are expressed relative to $H_3PO_4$.

**X-ray Crystallographic Investigations and Crystal Data:** Data collection for the X-ray structure determinations were performed on

 © 2006 Wiley-VCH Verlag GmbH & Co. KGaA, Weinheim 

a Bruker SMART Apex diffractometer system with CCD area detector by using graphite-monochromated Mo-$K_\alpha$ (0.71073 Å) radiation and a low-temperature device. Crystals of $[Li_2(P_2Ph_2)(tmeda)_2]$ (**2**) suitable for X-ray diffraction were obtained by crystallization of a saturated toluene/tmeda solution at ambient temperature. Those of $[Li(tmeda)_2]^+[Li(P_3Ph_3)(tmeda)]^-$ (**3**) were grown from a toluene solution at 7 °C and of $[Li_2(P_4Ph_4)(tmeda)_2]$ (**4**) from a saturated mtbe solution at ambient temperature. In order to avoid quality degradation the single crystals were mounted in paraffin oil on top of a glass fiber and then brought into the cold nitrogen stream of a low-temperature device so that the oil solidified. All calculations were performed with SHELXTL (ver. 6.12) and SHELXL-97 (G.M. Sheldrick, Göttingen, 1997). The structures were solved by direct methods and successive interpretation of the difference Fourier maps, followed by full-matrix least-squares refinement (against $F^2$). Moreover, an empirical absorption correction using SADABS (ver. 2.03) was applied to all structures. All non-hydrogen atoms were refined anisotropically in the X-ray structures of $[Li_2(P_2Ph_2)(tmeda)_2]$ (**2**) and $[Li_2(P_4Ph_4)(tmeda)_2]$ (**4**), whereas the tmeda ligand in $[Li(tmeda)_2]^+[Li(P_3Ph_3)(tmeda)]^-$ (**3**) was refined isotropically. The ethylene bridge of the tmeda ligand is highly disordered on two positions and a large number (17) of restraints had to be used to achieve a satisfactory w$R$2 value. The contribution of the hydrogen atoms, in their calculated positions, was included in the refinement using a riding model for the X-ray structures of $[Li(tmeda)_2]^+[Li(P_3Ph_3)(tmeda)]^-$ (**3**) and $[Li_2(P_4Ph_4)(tmeda)_2]$ (**4**). Some hydrogen atoms of $[Li_2(P_2Ph_2)(tmeda)_2]$ (**2**) could be located in the Fourier difference map and hence were refined freely. The disordering in this molecule, which is caused by a flip of the Li–P–P–Li plane by 48° with respect to the Li–Li vector, was fixed using the bond lengths of the main structure, resulting in a large number (12) of restraints. The contribution of the hydrogen atoms of the disordered part was included by using a riding model. Upon convergence, the final Fourier difference map of all structures showed no significant peaks. Relevant data concerning crystallographic data, data collection, and refinement details are summarized in Table 4.

CCDC-280997 to -280999 (for **2**–**4**, respectively) contain the supplementary crystallographic data for this paper. These data can be obtained free of charge from The Cambridge Crystallographic Data Centre via www.ccdc.cam.ac.uk/data_request/cif

**Computational Methods:** Geometries were ab initio optimized[15] at the B3LYP/6-31G* level unless otherwise stated. Chemical shifts and nuclear spin-spin coupling constants were obtained for these geometries and truncated moieties by the GIAO/B3LYP/6-31G* method. The $^{31}$P chemical shift of $PH_3$ ($\delta$ = 586 ppm) was calculated using a B3LYP/6-31G* structure at the GIAO/B3LYP/6-31G* level and set to –240 ppm vs. $H_3PO_4$ as the reference shift for all computed structures.

**Synthesis of $[Li_2(P_2Ph_2)(tmeda)_2]$ (2):** Lithium sand (39 mg, 5.62 mmol, 6 equivalents) and ($P_5Ph_5$) (500 mg, 0.925 mmol, 1 equiv.) were stirred for 24 h in THF (10 mL). The remaining lithium sand was filtered off and the solvent of the deep red filtrate was removed under high vacuum. The orange red powder was suspended in hot toluene (10 mL) and filtered off. The red powder was recrystallized from a hot mixture of toluene (4 mL) and tmeda (2 mL) and, on cooling to ambient temperature, the product separated as red crystals (673 mg, 63%). Red, very air-sensitive single crystals of $[Li_2(P_2Ph_2)(tmeda)_2]$ were obtained by storing a saturated toluene/tmeda solution at ambient temperature. $[Li_2(P_2Ph_2)(tmeda)_2]$ ($C_{24}H_{42}Li_2N_4P_2$, M = 462.45 g mol$^{-1}$): M.p. 151–153 °C (single crystal, uncorrected). $^1$H NMR (500.23 MHz, [D$_8$]THF, 25 °C): $\delta$ = 2.18 [s, 8 H, $CH_{3(TMEDA)}$], 2.34 [s, 24 H, $CH_{2(TMEDA)}$], 6.33 (m, 2 H, *p*-H), 6.62 (m, 4 H, *m*-H), 7.26 ppm (m, 4 H, *o*-H). $^7$Li NMR (194.4 MHz, DME/[D$_8$]toluene, 25 °C): $\delta$ = 0.6 ppm [s (br.)]. $^{13}$C NMR (125.8 MHz, [D$_8$]THF, 25 °C): $\delta$ = 46.7 [s, $CH_{3(TMEDA)}$], 59.4 [s, $CH_{2(TMEDA)}$], 117.5 [s (br.), 4-C in Ph], 126.7 [t, ($^3J_{C,P}$ + $^4J_{C,P}$) = 2.4 Hz, 3,5-C in Ph], 131.0 [t, ($^2J_{C,P}$ + $^3J_{C,P}$) = 12.2 Hz, 2,6-C in Ph], 162.2 ppm [t, ($^1J_{C,P}$ + $^2J_{C,P}$) = 34.8 Hz, 1-C in Ph]. $^{31}$P NMR (202.5 MHz, [D$_8$]THF, 25 °C): $\delta$ = –102.9 ppm (s).

**Synthesis of $[Li(tmeda)_2]^+[Li(P_3Ph_3)(tmeda)]^-$ (3):** Lithium sand (45 mg, 6.47 mmol; 3.5 equiv.) and ($P_5Ph_5$) (1.00 g, 1.85 mmol; 1 equiv) were stirred for 24 h in dme (10 mL). The orange precipitate was filtered off, washed with dme (2 mL), and dried in high vacuum. The light orange powder was dissolved in a mixture of toluene (5 mL) and tmeda (1 mL). The solvent was removed under

Table 4. Crystallographic data for compounds **2**, **3**, and **4**.

| Compound | $[Li_2(P_2Ph_2)(tmeda)_2]$ (**2**) | $[Li(tmeda)_2]^+$ $[Li(P_3Ph_3)(tmeda)]^-$ (**3**) | $[Li_2(P_4Ph_4)(tmeda)_2]$ (**4**) |
|---|---|---|---|
| Empirical formula | $C_{24}H_{42}Li_2N_4P_2$ | $C_{36}H_{63}Li_2N_6P_3$ | $C_{36}H_{52}Li_2N_4P_4$ |
| $M$ | 462.44 | 686.71 | 678.58 |
| Crystal system | monoclinic | monoclinic | monoclinic |
| Space group | $C_2/m$ (no. 12) | $P2_1/c$ (no. 14) | $C_2/c$ (no. 15) |
| $a$ [Å] | 12.192(1) | 13.283(1) | 10.299(1) |
| $b$ [Å] | 14.059(1) | 17.535(1) | 17.644(1) |
| $c$ [Å] | 8.335(1) | 18.331(1) | 21.464(1) |
| $\beta$ [°] | 101.905(2) | 99.828(2) | 93.412(2) |
| $V$ [Å$^3$] | 1398.2(1) | 4207.2(4) | 3893.4(5) |
| $\mu$ [mm$^{-1}$] | 0. 172 | 0.172 | 0.223 |
| $D_{calcd.}$ [g cm$^{-3}$] | 1.098 | 1.084 | 1.158 |
| Crystal dimensions [mm] | 0.52 × 0.45 × 0.34 | 0.24 × 0.13 × 0.05 | 0.14 × 0.13 × 0.10 |
| $Z$ | 2 | 4 | 4 |
| $T$ [K] | 100 | 100 | 200 |
| $2\theta_{max}$ [°] | 104.30 | 52.90 | 52.74 |
| Reflections measured | 22784 | 37854 | 14022 |
| Reflections unique | 8099 ($R_{int}$ = 0.0191) | 8646 ($R_{int}$ = 0.0781) | 3975 ($R_{int}$ = 0.0505) |
| Parameters/restraints | 184/12 | 377/17 | 212/0 |
| $R1$ [$I \geq 2\sigma(I)$] | 0.0411 | 0.0968 | 0.0594 |
| $wR2$ (all data) | 0.1260 | 0.2233 | 0.1391 |
| Max./min. resid. e$^-$ dens. [e Å$^{-3}$] | 1.035/–0.449 | 0.930/–0.747 | 0.355/–0.181 |

 © 2006 Wiley-VCH Verlag GmbH & Co. KGaA, Weinheim 

high vacuum to give a yellow powder (1.525 g, 72%). Yellow, very air-sensitive single crystals of $[Li(tmeda)_2]^+[Li(P_3Ph_3)(tmeda)]^-$ were obtained by storing a saturated toluene solution for several days at 7 °C. $[Li(tmeda)_2]^+[Li(P_3Ph_3)(tmeda)]^-$ ($C_{36}H_{63}Li_2N_6P_3$, $M$ = 686.73 g mol$^{-1}$): M.p. 166 °C (single crystal, uncorrected). $^1$H NMR (300.1 MHz, [D$_8$]toluene, 25 °C): $\delta$ = 1.92 [s (br.), 12 H, $CH_{2(TMEDA)}$], 2.03 [s (br.), 36 H, $CH_{3(TMEDA)}$], 6.87 (m, 1 H, *p*-H in Ph at $P_A$), 6.89 (m, 2 H, *p*-H in Ph at $P_M$), 6.97 (m, 2 H, *m*-H in Ph at $P_A$), 7.20 (m, 4 H, *m*-H in Ph at $P_M$), 8.04 (m, 4 H, *o*-H in Ph at $P_M$), 8.18 ppm (m, 2 H, *o*-H in Ph at $P_A$). $^7$Li NMR (194.4 MHz, [D$_8$]toluene, –73 °C): $\delta$ = 11.4 [m (br.)], 10.5 ppm [s (br.)]. $^{13}$C NMR (75.5 MHz, [D$_8$]toluene, 25 °C): $\delta$ = 45.9 [s, $CH_{3(TMEDA)}$], 57.2 [s, $CH_{2(TMEDA)}$], 120.0 (s, 4-C in Ph at $P_M$), 124.8 (s, 4-C in Ph at $P_A$), 127.4 (m, 3,5-C in Ph at $P_A$), 128.1 (m, 3,5-C in Ph at $P_M$), 130.0 (m, 2,6-C in Ph at $P_M$), 131.0 (m, 2,6-C in Ph at $P_A$), 155.8 (m, 1-C in Ph at $P_M$), 159.1 ppm (m, 1-C in Ph at $P_A$). Multiplets in the $^{13}$C NMR spectra represent the X part of an AMM′X spin system. $^{31}$P NMR (101.3 MHz, [D$_8$]toluene, 25 °C): $\delta$ = –52.3 [m, $^1J_{P(M),P(A)}$ = 223.8 Hz, A part of an $AM_2$ spin system, $P_A$], –71.5 ppm [m, $^1J_{P(M),P(A)}$ = 223.8 Hz, M part of an AMM′ spin system, $P_{(M+M')}$].

**Synthesis of $[Li_2(P_4Ph_4)(tmeda)_2]$ (4):** $[Li_2(P_3Ph_3)(dme)_x]$ (**3′**; 892 mg, 1.466 mmol, 5 equiv., $x$ = 3) and ($P_5Ph_5$) (158 mg, 0.242 mmol, 1 equiv.) were suspended in $Et_2O$ (30 mL). The yellow suspension was stirred for 24 h. The almost clear yellow solution was filtered through a Teflon filter. The solvent was removed under high vacuum and the obtained orange powder was dissolved in a mixture of toluene (10 mL) and tmeda (3 mL). The solvent was removed under high vacuum to give a yellow powder (865 mg, 87%). Slightly yellow, very air-sensitive single crystals of $[Li_2(P_4Ph_4)(tmeda)_2]$ were obtained by storing a saturated mtbe solution for several days at ambient temperature. $[Li_2(P_4Ph_4)(tmeda)_2]$ ($C_{36}H_{52}Li_2N_4P_4$, M = 678.6 g mol$^{-1}$): M.p. 174 °C (single crystals, uncorrected). $^1$H NMR (500.2 MHz, [D$_8$]toluene, 25 °C): $\delta$ = 1.76 [s (br.), 8 H, $CH_{2(TMEDA)}$], 1.95 [s (br.), 24 H, $CH_{3(TMEDA)}$], 6.86 (m, 2 H, *p*-H in Ph at $P_A$), 7.02 (m, 2 H, *p*-H in Ph at $P_B$), 7.09 (m, 4 H, *m*-H in Ph at $P_A$), 7.14 (m, 4 H, *m*-H in Ph at $P_B$), 7.72 (m, 4 H, *o*-H in Ph at $P_A$), 8.22 ppm (m, 4 H, *o*-H in Ph at $P_B$). $^7$Li NMR (194.4 MHz, [D$_8$]toluene, –25 °C): $\delta$ = 10.9 ppm (t, $^1J_{Li,P}$ = 37.3 Hz, 2 Li) ppm. $^{13}$C NMR (125.8 MHz, [D$_8$]toluene, 25 °C): $\delta$ = 46.1 [s, $CH_{3(TMEDA)}$], 56.8 [s, $CH_{2(TMEDA)}$], 120.6 (s, 4-C in Ph at $P_A$), 125.7 (s, 4-C in Ph at $P_B$), 127.5 (s, 3,5-C in Ph at $P_A$), 127.6 (s, 3,5-C in Ph at $P_B$), 130.2 (m, 2,6-C in Ph at $P_A$), 133.9 (m, 2,6-C in Ph at $P_B$), 148.3 [m (br), 1-C in Ph at $P_B$], 154.3 ppm [m (br.), 1-C in Ph at $P_A$]. Multiplets in the $^{13}$C NMR spectra represent the X part of an AA′BB′X spin system. $^{31}$P NMR (202.5 MHz, [D$_8$]toluene, 25 °C): $\delta$ = –2.3 [m, $(PPh)_5$], –36.8 (br., $[Li_2(P_4Ph_4)(tmeda)_2]$), –53.3 (m, $[Li_2(P_3Ph_3)(tmeda)_3]$), –73.0 (m, $[Li_2(P_3Ph_3)(tmeda)_3]$), –76.0 (br., $[Li_2(P_4Ph_4)(tmeda)_2]$), –95.4 (br., $[Li_2(P_4Ph_4)(tmeda)_2]$) ppm. $^{31}$P NMR (202.5 MHz, [D$_8$]toluene, –25 °C): $\delta$ = –38.0 (m, B part of an AA′BB′$X_2$ spin system, $P_B$ [**4**]), –39.7 (m, B part of an AA′BB′X spin system, $P_B$ [**4′′**]), –74.4 (m, A part of an AA′BB′X spin system, $P_A$ [**4′′**]), –95.1 ppm (m, A part of an AA′BB′$X_2$ spin system, $P_A$ [**4**]); ratio **4**/**4′′** = 100:81. $^{31}$P{$^1$H} CPMAS (202.5 MHz, 25 °C): $\delta_{iso}$ = –38, $\delta_{11} \approx 50$, $\delta_{22} \approx -10$, $\delta_{33} \approx -155$ (B part); $\delta_{iso}$ = –87, $\delta_{11} \approx 0$, $\delta_{22} \approx -55$, $\delta_{33} \approx -205$ ppm (A part). $^7$Li NMR (194.4 MHz, [D$_8$]toluene, –25 °C): $\delta$ = 10.9 ppm (t, $^1J_{Li,P}$ = 37.3 Hz, 2 Li).

**Supporting Information** (see footnote on the first page of this article): Plots of the $^{13}$C NMR spectra of compounds **2**, **3**, and **4** and details of the simulation of the $^{31}$P CP-MAS spectrum with the SIMPSON package.

## Acknowledgments

This work was supported by Ciba Speciality Chemicals and the ETH Zürich.

[1] Z.-W. Wang, Li-S. Wang, *Green Chem.* **2003**, *5*, 737.
[2] Reviews: a) K. Issleib, *Z. Chem.* **1962**, *2*, 163; b) M. Baudler, K. Glinka, *Chem. Rev.* **1993**, *93*, 1623. The formation of cyclic oligophosphanes is described from $PhPCl_2$/Li in: c) P. R. Bloomfield, K. Parvin, *Chem. Ind.* **1959**, 541; from $PhPCl_2$/Na: d) F. Pass, H. Schindlbauer, *Monatsh. Chem.* **1959**, *90*, 148; e) L. Horner, P. Beck, H. Hoffmann, *Chem. Ber.* **1959**, *92*, 2088; f) W. Kuchen, H. Buchwald, *Chem. Ber.* **1958**, *91*, 2296; from $PhPCl_2$/Mg: g) W. A. Henderson, M. Epstein, F. S. Seichter, *J. Am. Chem. Soc.* **1963**, *85*, 2462; h) A. Hinke, W. Kuchen, *Chem. Ber.* **1983**, *116*, 3003; from $PhPCl_2$/Zn: i) M. Scherer, D. Stein, F. Breher, J. Geier, H. Schönberg, H. Grützmacher, *Z. Anorg. Allg. Chem.* **2005**, *631*, 2770; j) H. Grützmacher, J. Geier, H. Schönberg, M. Scherer, D. Stein, S. Boulmaâz, WO2004/050668.
[3] $[M_2(P_nPh_n)]$, M = Li–Cs, $n$ = 3, 4: a) P. R. Hoffman, K. G. Caulton, *J. Am. Chem. Soc.* **1975**, *97*, 6370; b) M. Baudler, D. Koch, *Z. Anorg. Allg. Chem.* **1976**, *425*, 227; $[M_2(P_3Ph_3)]$, M = Na, K: c) M. Baudler, D. Koch, E. Tolls, K. M. Diedrich, B. Kloth, *Z. Anorg. Allg. Chem.* **1976**, *420*, 146; $[Na_2(P_2Ph_2)]$: d) J. W. B. Reesor, G. F. Wright, *J. Org. Chem.* **1957**, *22*, 385; $[Li_2(P_2Ph_2)]$ and $[K_2(P_2Ph_2)]$: e) K. Issleib, K. Krech, *Chem. Ber.* **1966**, *99*, 1310; $PhPNa_2$ has been assumed to be a by-product in the reaction of $(PhP)_n$ with sodium: f) W. Kuchen, H. Buchwald, *Chem. Ber.* **1958**, *91*, 2296; $[Na_2(tBu_3Si–P–P=P–P–SitBu_3)]$: g) N. Wiberg, A. Wörner, K. Karaghiosoff, D. Fenske, *Chem. Ber./Recueil* **1997**, *130*, 135.
[4] R. Wolf, A. Schisler, P. Lönnecke, C. Jones, E. Hey-Hawkins, *Eur. J. Inorg. Chem.* **2004**, 3277.
[5] a) J. Geier, H. Rüegger, M. Wörle, H. Grützmacher, *Angew. Chem.* **2003**, *115*, 4081; *Angew. Chem. Int. Ed.* **2003**, *42*, 3951; b) J. Geier, J. Harmer, H. Grützmacher, *Angew. Chem.* **2004**, *116*, 4185–4189; *Angew. Chem. Int. Ed.* **2004**, *43*, 4093–4097c) D. Stein, J. Geier, H. Schönberg, H. Grützmacher, *Chimia* **2005**, *59*, 119.
[6] A. Streitwieser Jr, *Acc. Chem. Res.* **1984**, *17*, 353.
[7] N. Korber, J. Aschenbrenner, *J. Chem. Soc., Dalton Trans.* **2001**, 1165.
[8] Compare, for example, the molar enthalpy of solution for LiCl (–37.03 kJ mol$^{-1}$) and NaCl (3.88 kJ mol$^{-1}$).
[9] H. Bock, C. Nather, Z. Havlas, A. John, C. Arad, *Angew. Chem.* **1994**, *106*, 931; *Angew. Chem. Int. Ed. Engl.* **1994**, *33*, 875.
[10] For the structure of [K(18-C-6)][NHPh] see: P. B. Hitchcock, A. V. Khvostov, M. F. Lappert, A. V. Protchenko, *J. Organomet. Chem.* **2002**, *647*, 198 and references cited therein.
[11] J. Herzfeld, A. E. Berger, *J. Chem. Phys.* **1980**, *73*, 6021.
[12] M. Bak, J. T. Rasmussen, J. C. Nielsen, *J. Magn. Reson.* **2000**, *147*, 296.
[13] G. Wu, B. Sun, R. E. Wasylishen, R. G. Griffin, *J. Magn. Reson.* **1997**, *124*, 366.
[14] M. Kaupp, A. Patrakov, R. Reviakine, O. L. Malkina, *Chem. Eur. J.* **2005**, *11*, 2773.
[15] M. J. Frisch, G. W. Trucks, H. B. Schlegel, G. E. Scuseria, M. A. Robb, J. R. Cheeseman, J. A. Montgomery Jr, T. Vreven, K. N. Kudin, J. C. Burant, J. M. Millam, S. S. Iyengar, J. Tomasi, V. Barone, B. Mennucci, M. Cossi, G. Scalmani, N. Rega, G. A. Petersson, H. Nakatsuji, M. Hada, M. Ehara, K. Toyota, R. Fukuda, J. Hasegawa, M. Ishida, T. Nakajima, Y. Honda, O. Kitao, H. Nakai, M. Klene, X. Li, J. E. Knox, H. P. Hratchian, J. B. Cross, C. Adamo, J. Jaramillo, R. Gomperts, R. E. Stratmann, O. Yazyev, A. J. Austin, R. Cammi, C. Pomelli, J. W. Ochterski, P. Y. Ayala, K. Morokuma, G. A. Voth, P. Salvador, J. J. Dannenberg, V. G. Zakrzewski, S. Dapprich, A. D.

 © 2006 Wiley-VCH Verlag GmbH & Co. KGaA, Weinheim 

Daniels, M. C. Strain, O. Farkas, D. K. Malick, A. D. Rabuck, K. Raghavachari, J. B. Foresman, J. V. Ortiz, Q. Cui, A. G. Baboul, S. Clifford, J. Cioslowski, B. B. Stefanov, G. Liu, A. Liashenko, P. Piskorz, I. Komaromi, R. L. Martin, D. J. Fox, T. Keith, M. A. Al-Laham, C. Y. Peng, A. Nanayakkara, M. Challacombe, P. M. W. Gill, B. Johnson, W. Chen, M. W. Wong, C. Gonzalez, J. A. Pople, *Gaussian 03*, revision C.02, Gaussian, Inc., Wallingford CT, **2004**.

[16] M. Valentini, H. Rüegger, P. S. Pregosin, *Helv. Chim. Acta* **2001**, *84*, 2833.

[17] R. K. Harris, E. D. Becker, S. M. Cabral de Menezes, R. Goodfellow, P. Granger, *Pure Appl. Chem.* **2001**, *73*, 1795.

Received: April 26, 2006
Published Online: August 18, 2006

 © 2006 Wiley-VCH Verlag GmbH & Co. KGaA, Weinheim 

DOI: 10.1002/ejic.200600337

# A Cationic Order-Disorder Phase Transition in $KPb_2Cl_5$

Matias Velázquez,*[a] Alban Ferrier,[a] Olivier Pérez,[b] Stanislas Péchev,[c] Pierre Gravereau,[c] Jean-Pierre Chaminade,[c] and Richard Moncorgé[a]

**Keywords:** Halides / Solid-state structures / Structure elucidation / Phase transitions / Thermodynamics

The phase transition occurring at $T_t$ = 528 K in the natural mineral and synthetic laser host compound $KPb_2Cl_5$ has been characterized by means of both single-crystal X-ray diffraction (XRD) as a function of temperature and differential scanning calorimetry (DSC). The $K^+$ and $Pb^{2+}$(2) cations order on passing from the high-temperature orthorhombic phase (space group *Pmcn*; $a$ = 8.951, $b$ = 8.015, $c$ = 12.683 Å, $Z$ = 4 at 623 K) to the low-temperature monoclinic one (space group $P2_1/c$; $a$ = 8.849, $b$ = 7.918, $c$ = 12.472 Å, $\beta$ = 90.11°, $Z$ = 4, at room temperature), leading to a group-subgroup first-order phase transition displaying moderately fast kinetics and low entropy production upon thermal cycling around $T_t$. The positional entropy calculated from our crystal structure models corresponds to the transition entropy measured by DSC within the experimental error, and amounts to about 0.34 $R$. The driving force for the phase transition, $A \leq 22\ J\,mol^{-1}$, remains negligible with respect to both the thermal energy at $T_t$ ($RT_t \approx 4.4\ kJ\,mol^{-1}$) and the transition latent heat ($\Delta H \approx 790\ J\,mol^{-1}$), thereby suggesting that this phase transition is a close-to-equilibrium process.
(© Wiley-VCH Verlag GmbH & Co. KGaA, 69451 Weinheim, Germany, 2006)

## Introduction

$KPb_2Cl_5$ is a chloride[1] that has been known for a long time but has recently triggered a substantial body of literature because of its use as a host crystal for optical amplifiers in near- and middle-infrared solid-state lasers.[2] In this realm of applications, the growth of centimeter-sized high-quality single crystals is of paramount importance for several reasons. Firstly, it allows for the investigations of the intrinsic optical performances (grain boundaries and other microstructural defects can introduce passive losses within the laser cavity). Secondly, it permits the characterization of the anisotropy of these optical properties (absorption and emission cross-sections, for instance, can depend on the relative orientation of the electric field with respect to the optical axis of the crystal). Thirdly, it provides a means of concentrating a sufficiently large number of optically active ions with virtually no diffusion mobility within a cubic-centimeter-sized volume (with respect to gas lasers) to ensure optical amplification. In other respects, $KPb_2Cl_5$ occurs as a natural mineral named "challacolloite"[3] that readily forms in the flue dusts of steelmaking plants[4] and in the high-temperature fumarole gases of the Kudryavyi (Iturup Island, Kuril Islands), Vesuvius (Italy), and Satsuma–Iwojima (Japan) volcanoes.[3,5] Until now, the main crystal-growth method for elaborating pure and rare-earth-doped $KPb_2Cl_5$ single crystals has been the Bridgman–Stockbarger one: at least 20 different single crystals have been successfully elaborated by this method.[6–10] Powder X-ray diffraction (XRD) carried out at room temperature has established that $KPb_2Cl_5$ adopts the $NH_4Pb_2Cl_5$ structural type,[11] and a recent accurate refinement of single-crystal XRD data firmly confirmed this crystal structure.[12] Although several researchers have evoked the likelihood of a phase transition undergone by the crystals between the melting point and room temperature,[7,13] it is only recently that it was characterized by differential scanning calorimetry (DSC) and found to display a low entropy production per thermal cycle around $T_t$ = 528.15 K.[10] In this paper we present a combined crystallographic and thermodynamic analysis of the phase transition in $KPb_2Cl_5$ by means of single-crystal XRD as a function of temperature and DSC experiments which supplement the ones previously undertaken. We demonstrate that it corresponds to a close-to-equilibrium cationic order-disorder group-subgroup first-order transition that displays moderately fast kinetics.

[a] Centre Interdisciplinaire de Recherche Ions Lasers, UMR 6637 CNRS/CEA/ENSICaen/Université de Caen,
6 Boulevard du Maréchal Juin, 14050 Caen cedex 04, France
Fax: +33-2-31452557
E-mail: matias.velazquez@ensicaen.fr
[b] Laboratoire de Cristallographie et Sciences des Matériaux, UMR 6508 CNRS/Université de Caen,
6 Boulevard du Maréchal Juin, 14050 Caen cedex 04, France
[c] Institut de Chimie de la Matière Condensée de Bordeaux, UPR 9048 CNRS,
87 Avenue du Docteur Albert Schweitzer, 33608 Pessac, France

## Results and Discussion

### Crystallographic Aspects

Both the room- and high-temperature structures consist of edge-sharing $Pb^{2+}$(1) monocapped octahedra that form

 InterScience © 2006 Wiley-VCH Verlag GmbH & Co. KGaA, Weinheim 

infinite chains along [100] (Figures 1 and 2). These are isolated from each other but surrounded by, and joined to, six $K^+/Pb^{2+}(2)$ face-sharing bicapped trigonal prism-based chains that also extend along the [100] direction (Figures 1 and 3). The $K^+$ and $Pb^{2+}(2)$ cations alternate in the room-temperature phase but are disordered in the high-temperature phase. The $K^+/Pb^{2+}(2)$ chains arrange in a pseudo-hexagonal network in the $(\bar{b}\bar{c})$ planes that contain the $Pb^{2+}(1)$ chains (Figure 4). Along [010], the $K^+/Pb^{2+}(2)$ polyhedra share one of their triangular faces, which gives rise to corrugated chains [with a 128.8° angle between three successive $K^+$ or $Pb^{2+}(2)$ cations] that are linked to each other by a Cl(5)–Cl(5) edge every three polyhedra (Figures 4 and 5). The $Pb^{2+}(1)$ monocapped octahedra share all their vertices but not more than one edge simultaneously with a neighboring $K^+$ and/or $Pb^{2+}(2)$ polyhedra. The two equatorial edges that are not linked to the $Pb^{2+}(1)$ polyhedra, along the [100] direction, are unshared. The three edges defining the triangular face at the opposite side from the capped face, as well as all the faces of the $Pb^{2+}(1)$ polyhedra, also remain unshared. In Figure 6 (a), the pseudo-quadrilateral face on the capped side has in common its four edges with the neighboring two $K^+$ and two $Pb^{2+}(2)$ polyhedra, which block the view of it. The rise in symmetry in the high-temperature phase stems from the fact that the $K^+$ and $Pb^{2+}(2)$ cations become equivalent, much like the (8d) $K^+$ cations do in $K_2PrCl_5$, which adopts the *Pnma* space group.[14] Hence, a mirror plane appears at 1/4,*y*,*z*, on which the $Pb^{2+}(1)$ cations are located (Figure 6). The 153.75° angle between the successive $Pb^{2+}(1)$ cations is virtually unaffected (155.6° at 623 K) by cationic ordering in the neighboring $K^+/Pb^{2+}(2)$ chains, whereas in the latter chains the angle between two consecutive $K^+$ and $Pb^{2+}(2)$ cations passes from 170.9° at room temperature to 180° at 623 K. Some of the structural parameters are quite sensitive to the phase transition. The analysis of the behavior of the unit-cell parameters (Figure 7) and of the diagonal coefficients of the anisotropic atomic displacement parameters (ADPs, presented in Figure 8) as a function of temperature is not devoid of interest for understanding the phase-transition mechanism. While the *a* and *b* parameters show a linear dependency on temperature from 293 to 573 K, the *c* parameter shows two breaks of slope at about 473 and 573 K, which provide clear evidence for the phase transition since they correspond to the initial and final peak temperatures in the $C_p$ vs. $T$[10] and $J_q$ vs. $T$ curves (Figure 9). The

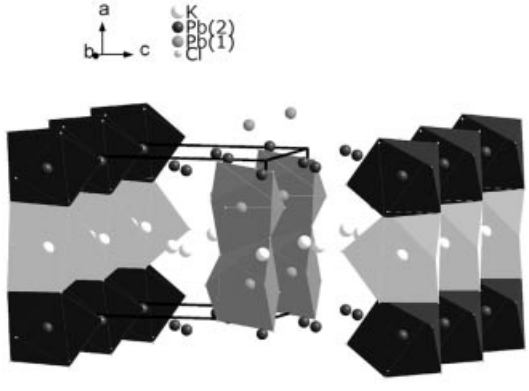


Figure 1. Simplified view of the $KPb_2Cl_5$ crystal structure at room temperature ($P2_1/c$) showing the two kinds of chains running along [100]: the ordered $K^+/Pb^{2+}(2)$ one and the $Pb^{2+}(1)$ one. In the high-temperature phase, the $K^+$ and $Pb^{2+}(2)$ cations become crystallographically equivalent and a cationic disorder appears in the $K^+/Pb^{2+}(2)$ chains over a length typically of 10–1000 Å (see text).

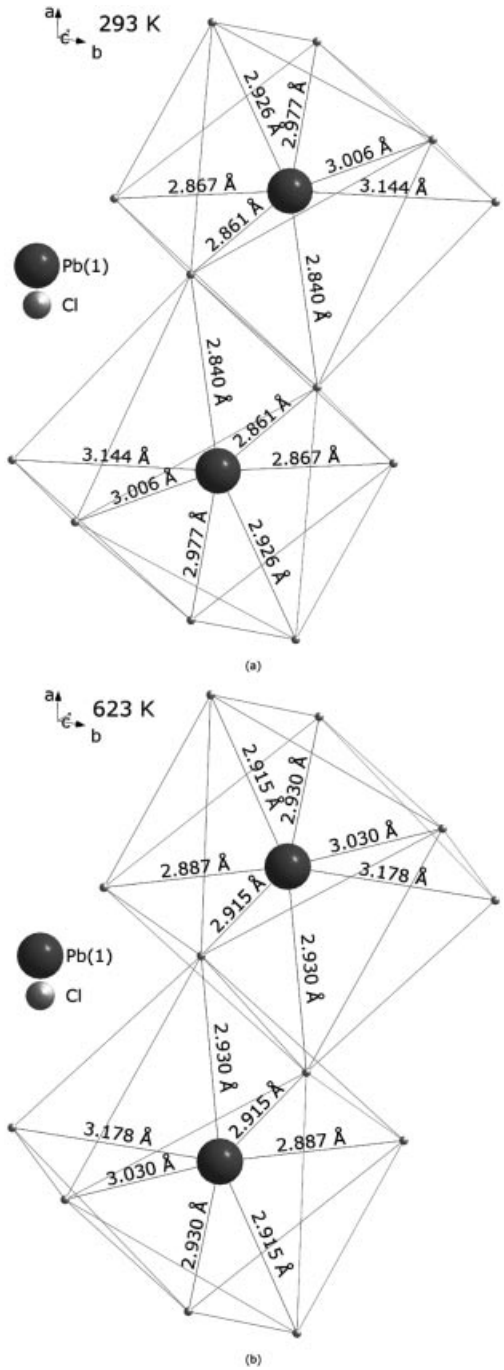


Figure 2. (a) Sketch of the $Pb^{2+}(1)$ chains in the room-temperature phase along [100]; (b) sketch of the $Pb^{2+}(1)$ chains at 623 K (*Pmcn* phase) along [100]. Both views show the edge-sharing of the monocapped octahedra.

 © 2006 Wiley-VCH Verlag GmbH & Co. KGaA, Weinheim 

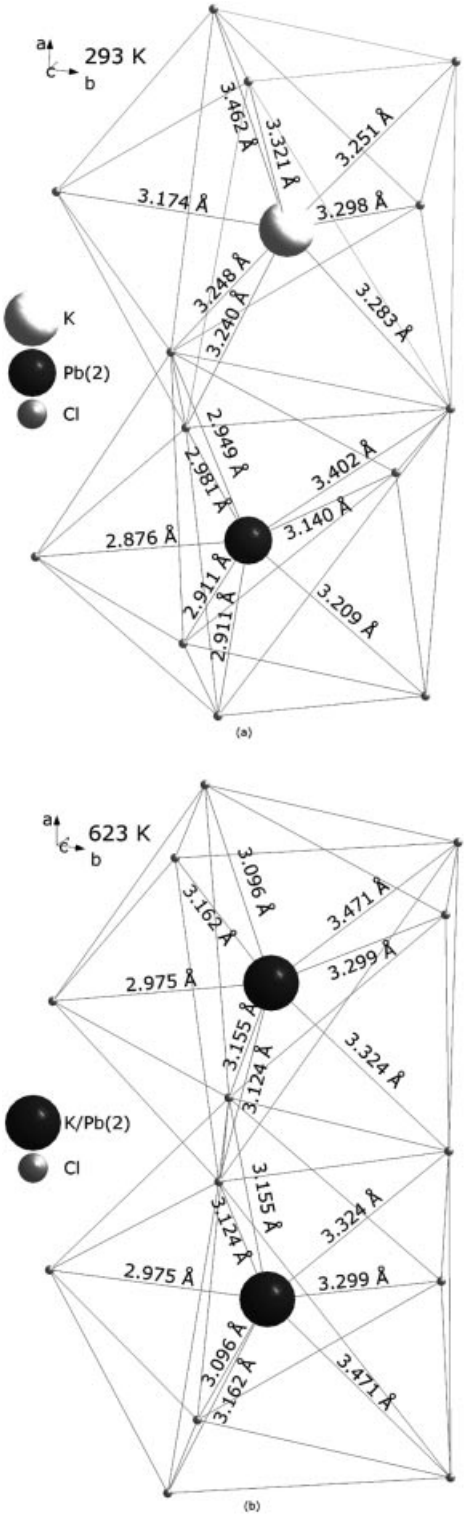


Figure 3. (a) Sketch of the ordered $K^+/Pb^{2+}(2)$ chains in the room-temperature phase along [100]; (b) sketch of the disordered $K^+/Pb^{2+}(2)$ chains at 623 K (*Pmcn* phase) along [100]. Both views show the triangular face-sharing of the bicapped trigonal prisms.

mean lattice-expansion coefficients are: $\frac{1}{a(293\text{ K})}\frac{da}{dT} \approx 38.6\times10^{-6}\text{ K}^{-1}$ (293–598 K), $\frac{1}{b(293\text{ K})}\frac{db}{dT} \approx 42.6\times10^{-6}\text{ K}^{-1}$ (293–598 K) and $\frac{1}{c(293\text{ K})}\frac{dc}{dT} \approx 39.3\times10^{-6}\text{ K}^{-1}$ (293–473 K). Although the lattice parameters' thermal expansion is not strictly equal to the thermal expansion tensor diagonal elements,[15] it provides a sufficiently accurate estimate of the latter quantities. Worthy of note is the patent decrease in the *c* parameter upon cooling, from 573 to 473 K $-\frac{1}{c(473\text{ K})}\frac{dc}{dT} \approx 97.9\times10^{-6}\text{ K}^{-1}$ − which suggests that in this temperature range the thermal stress may be substantial and also that a very slow cooling under an extremely flat temperature profile should be applied to the crystal to prevent the generation of dislocations in too large a concentration. The relative difference in unit cell volume between 293 K and the *Pmcn* phase at 623 K is about –3.9%. This anisotropic increase in lattice thermal expansion upon heating might be attributed to a larger density of weaker bonds along [001] than along the [100] and [010] directions. The $K^+$ and $Pb^{2+}$ chloride polyhedral framework along [001] does not imply any single face-sharing, unlike along the [100] and [010] directions; however, the highest rises in $U_{ii}$ values in the vicinity of the transition temperature occur along [100]. Analysis of the ADPs (Figure 8) supplies information about the possible diffusion paths for the $K^+$ and $Pb^{2+}(2)$ cations at high temperature. The doubling of the ADPs undergone by both $K^+$ and $Pb^{2+}(2)$ along the [100], [010] and [001] directions at the transition outlines the three-dimensional character of the diffusion of these two species. Moreover, the isotropy of the lattice thermal expansion up to 473 K, in conjunction with the interchain connections in the ($\vec{b}\vec{c}$) plane also indicate that the $KPb_2Cl_5$ structure possesses a good deal of three-dimensional character notwithstanding the existence of both ordered $K^+/Pb^{2+}(2)$ and $Pb^{2+}(1)$ chains in the room-temperature phase. The increase in the ADPs of the $Pb^{2+}(1)$ cations proves to be less marked than that of both $K^+$ and $Pb^{2+}(2)$. $Cl^-(1)$ shows a net rise in $U_{33}$ between 473 and 548 K whereas in the other directions the thermal evolution of its ADPs seems regular. $Cl^-(2)$, but above all $Cl^-(5)$ and $Cl^-(3)$, displays a sharp increase in the displacement parameter along [100]. From the knowledge of the structure, three possible K/Pb(2) microscopic jumps can be conjectured: one along the [100] direction through the $Cl^-(3)$–$Cl^-(5)$–$Cl^-(2)$ triangular face, another one along [010] through the $Cl^-(1)$–$Cl^-(2)$–$Cl^-(3)$ triangular face (Figure 5) and the last one along [001] through the $Cl^-(5)$–$Cl^-(5)$ edge mentioned previously. The anisotropy of the ADPs' elongation [Figure 8 (b)] observed for $Cl^-(1)$ and $Cl^-(5)$ suggests a possible diffusion path along [001]. Indeed, this elongation occurs along [100] for $Cl^-(5)$, i.e. perpendicularly to the jump direction, and along [001] for $Cl^-(1)$, as sketched in Figure 5. Although these features are consistent with $K^+/Pb^{2+}(2)$ cation diffusion along the [001] direction, they are still speculative and call for a detailed energy-landscape calculation. Figure 10 illustrates how an XRD experiment can evidence the temperature spreading over about 100 K[10] of the phase transition: the *hk0* ($h + k = 2n + 1$) reflections observed at

 © 2006 Wiley-VCH Verlag GmbH & Co. KGaA, Weinheim 

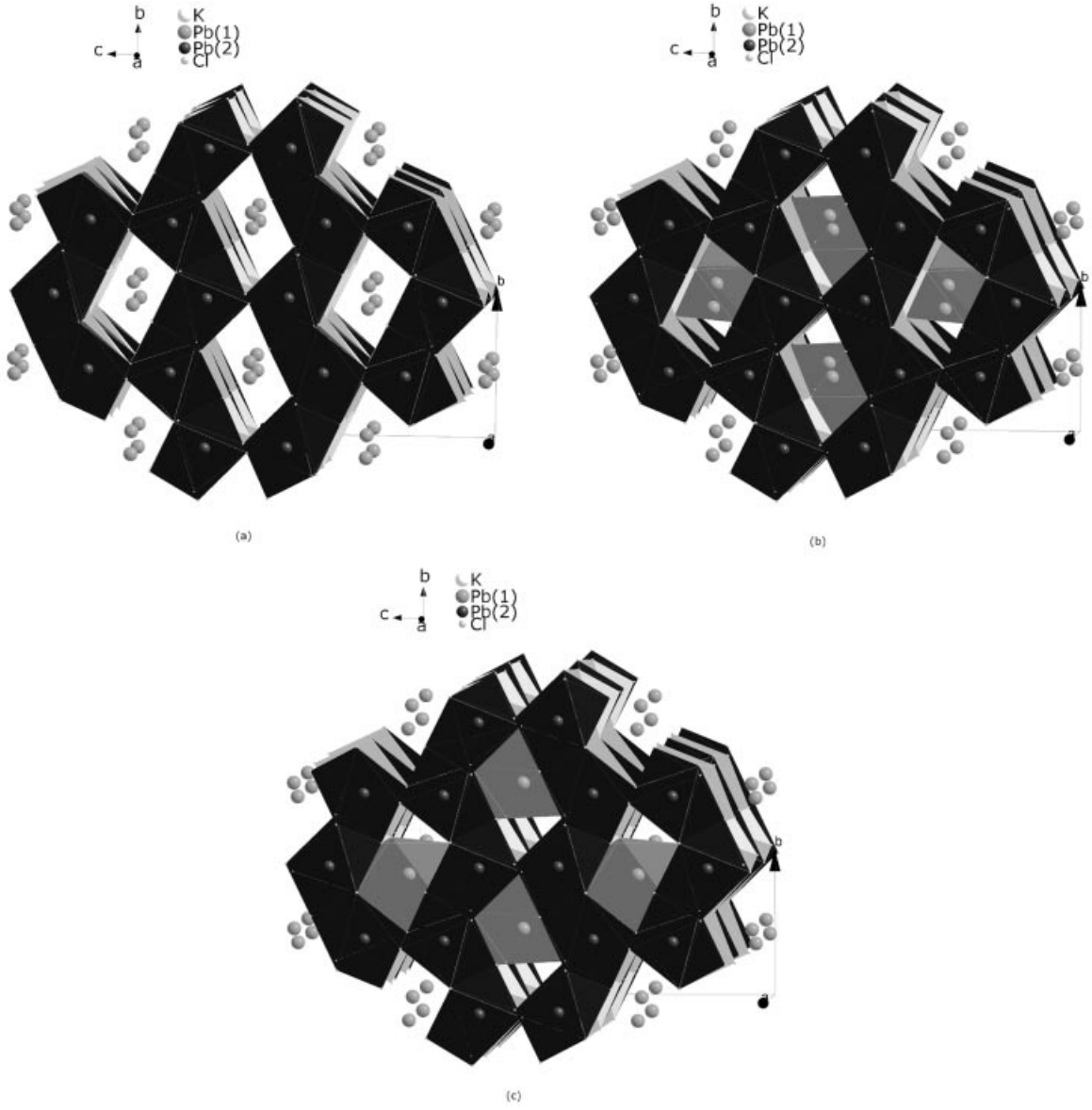


Figure 4. View of the $KPb_2Cl_5$ crystal structure at room temperature ($P2_1/c$) along [100] showing how the ordered $K^+/Pb^{2+}(2)$ chains share common edges in the ($\vec{b}\vec{c}$) planes to form a pseudo-hexagonal channel containing the $Pb^{2+}(1)$ chains: (a) without $Pb^{2+}(1)$ monocapped octahedra sketched; (b) with one $Pb^{2+}(1)$ monocapped octahedron drawn; (c) with the closest neighbor of the $Pb^{2+}(1)$ monocapped octahedron sketched in (b) drawn. These figures illustrate the zig-zag chains formed by the $Pb^{2+}(1)$ monocapped octahedra consistently with the 153.75° angle between three successive $Pb^{2+}(1)$ cations.

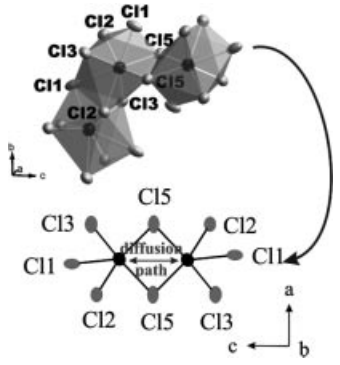


Figure 5. Speculative diffusion path for the $K^+$ and $Pb^{2+}(2)$ cations in $KPb_2Cl_5$ as deduced from the anisotropy of the $Cl^-$ anions' thermal vibrations.

293 and 473 K transform, at first, at 548 K, into diffuse scattering and then vanish at 623 K. The occurrence of diffuse scattering is likely to be due to the $K^+/Pb^{2+}(2)$ cationic diffusion.

### Structure of Rare-Earth Defects

Figures 6 (a) and (b) portray views of the $Pb^{2+}(1)$ polyhedron and chains that may prove useful when considering the local structure of the rare-earth defects that are liable to form when introduced within this compound to produce laser emission in the near- and middle-infrared wavelength range. In a recent work, we pointed out that the most expected rare-earth defects can be expressed in the Kröger–Vink notation as $RE^{\cdot}_{Pb} - V'_K$, $RE^{\cdot}_{Pb} - K'_{Pb}$, $RE^{\cdot\cdot}_K - V''_{Pb}$,

 © 2006 Wiley-VCH Verlag GmbH & Co. KGaA, Weinheim 

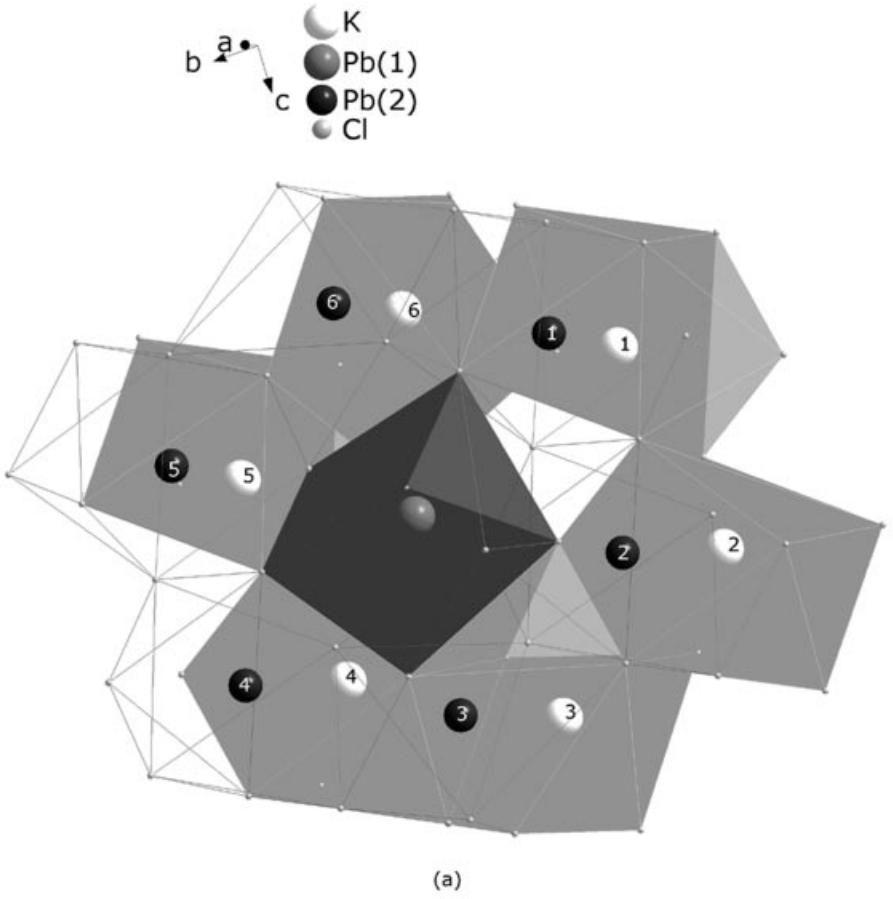


(a)

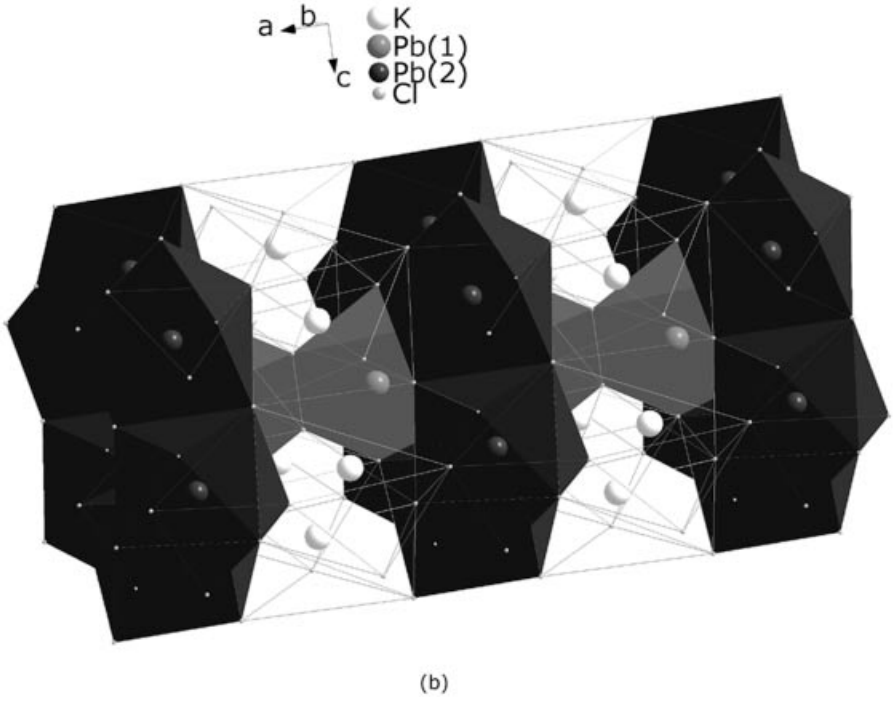


(b)

Figure 6. (a) Simplified view of the $Pb^{2+}(1)$ monocapped octahedron surrounded by six $K^+$ and $Pb^{2+}(2)$ polyhedra in the ($\bar{b}c$) planes; (b) simplified view of the isolated $Pb^{2+}(1)$ chains surrounded by six ordered $K^+/Pb^{2+}(2)$ chains in the room-temperature $P2_1/c$ phase. The labeling of the $K^+$ and $Pb^{2+}(2)$ sites indicates that they are symmetrically non-equivalent with respect to the $Pb^{2+}(1)$ sites.

 © 2006 Wiley-VCH Verlag GmbH & Co. KGaA, Weinheim 

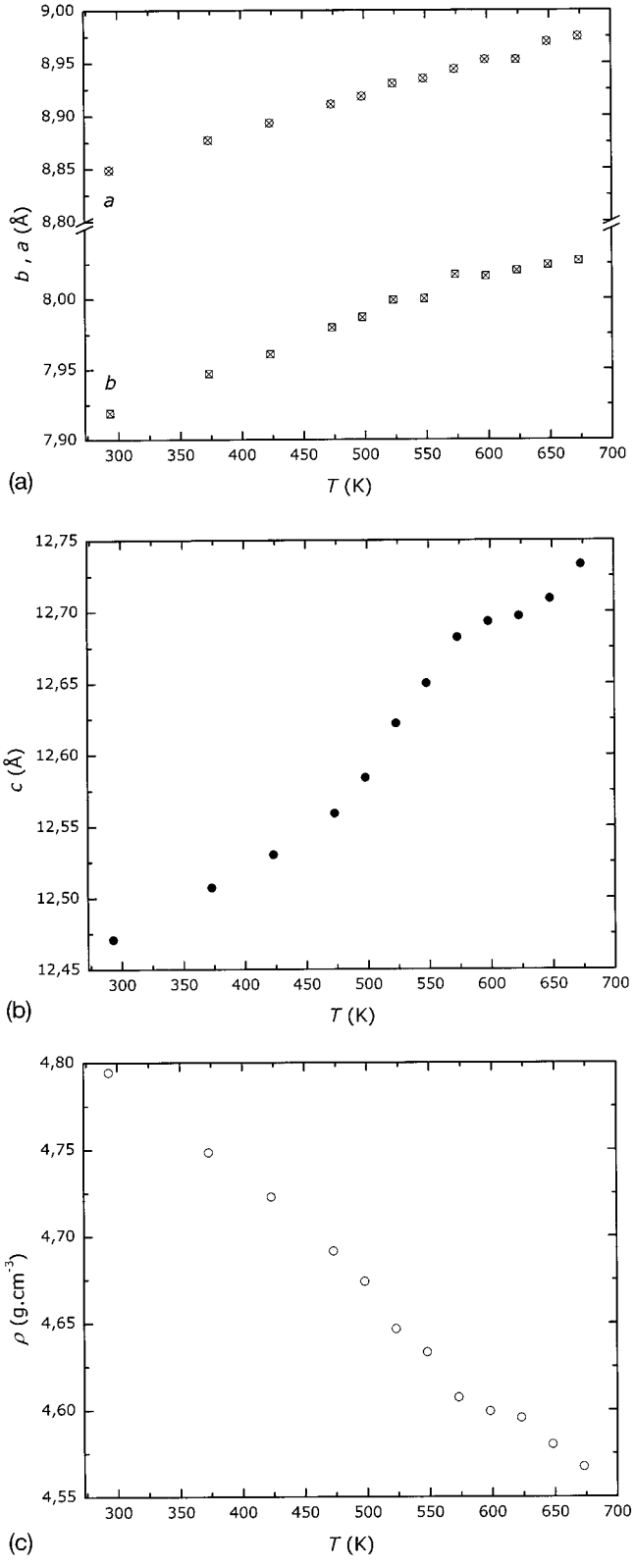


Figure 7. (a), (b) Thermal dependence of the $KPb_2Cl_5$ lattice parameters; (c) $KPb_2Cl_5$ "X-ray" volumic mass.

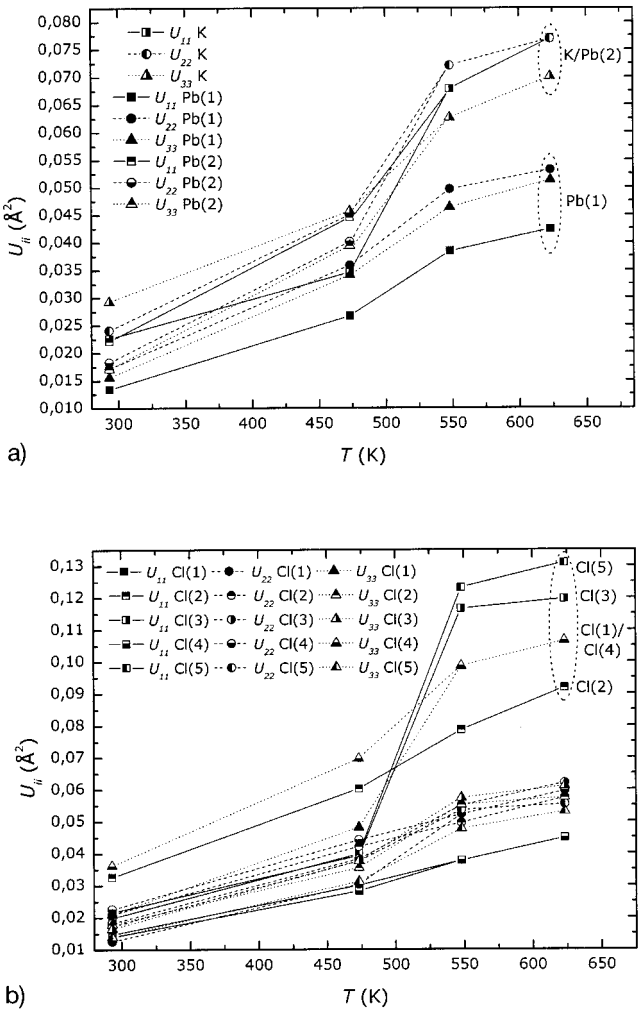


Figure 8. Refined diagonal elements of the anisotropic atomic displacement parameters for (a) the $K^+$ and $Pb^{2+}$ cations and (b) the $Cl^-$ anions in $KPb_2Cl_5$ at selected temperatures.

$RE^{\cdot}_{K} + 2V'_{K}$ and $2RE^{\cdot}_{Pb} + V''_{Pb}$. Let us now describe the situation more precisely by restricting our counting to nearest neighbors. There are six possible ways of forming each of the $RE^{\cdot}_{Pb(1)} - V'_{K}$, $RE^{\cdot}_{Pb(1)} - K'_{Pb(2)}$ and $RE^{\cdot}_{K} - V''_{Pb(1)}$ defects as the absence of symmetry elements makes all the nearest $K^+$ and $Pb^{2+}(2)$ neighbors symmetrically non-equivalent with respect to the $Pb^{2+}(1)$ sites. Along [100], there is only one possibility of finding the $RE^{\cdot}_{K} + V''_{Pb(2)}$ and $RE^{\cdot}_{Pb(2)} + V'_{K}$ defects. Owing to the inversion center located at 0,0,0 (right in the middle of the pseudo-hexagons drawn in Figure 4) three non-equivalent $RE^{\cdot}_{Pb(2)} + K'_{Pb(2)}$ defects can combine. The counting of three-center-type defects proves to be much more cumbersome, not only because of the lack of high-order symmetry elements [note, for example, thirty-six ways of forming $RE^{\cdot}_{Pb(2)} - V''_{Pb(2)} - RE^{\cdot}_{Pb(1)}$], but also because of the many possible combinations of $RE^{\cdot}_{Pb} - RE^{\cdot}_{Pb} - V''_{Pb}$. All in all, checking for the redundancies and with the proviso that the relaxation processes of atomic positions do not entail new symmetry element(s), this brings about more than 100 three-center defects in addition to the 23 two-center ones, all with a distinct formation free energy. Consequently, a distribution of

 © 2006 Wiley-VCH Verlag GmbH & Co. KGaA, Weinheim 

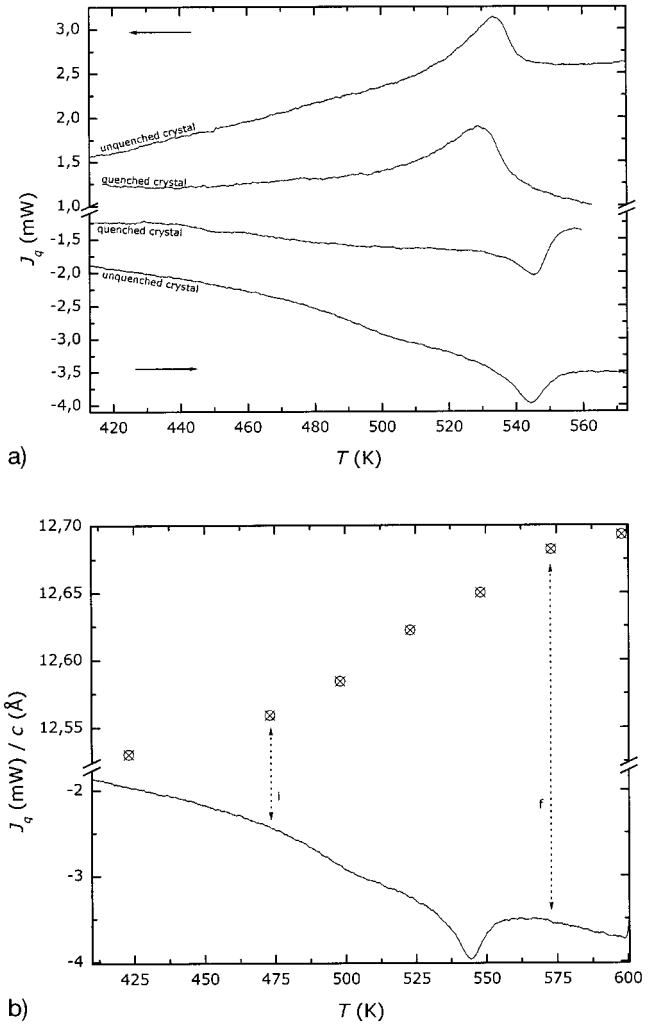


Figure 9. (a) Heat flux vs. temperature curves for raw $KPb_2Cl_5$ single crystals and $KPb_2Cl_5$ single crystals quenched from 633 K; (b) superposition of the unquenched $KPb_2Cl_5$ single crystal $J_q$ vs. $T$ and $c$ vs. $T$ curves. The double arrow labeled "i" indicates the initial peak temperature and that labeled "f" the final peak temperature.

them cannot be discarded a priori. It is even likely that the rare-earth defects' distribution depends on spatial coordinates because the formation free energy of a particular defect is affected by the concentration of its counterparts. These considerations put the recent attempts at characterizing the structure of rare-earth defects into perspective. A $Tb^{\cdot}_{Pb(1)} - V'_{K_4}$ defect, assumed to be the majority, has been supposed to account for the $^{159}Tb^{3+}$ high-frequency EPR spectra obtained in $Tb^{3+}$-doped $KPb_2Cl_5$ single crystals.[16] The labeling of the $K^+$ site is indicated in Figure 6 (a). By means of time-resolved fluorescence line-narrowing spectroscopy performed on $Eu^{3+}$-doped $KPb_2Cl_5$ single crystals, Cascales, Fernández and Balda concluded that three defects form, namely $Eu^{\cdot}_{Pb(2)} - V'_K$ (97%), $Eu^{\cdot}_{Pb(1)} - V'_{K_7}$ (1.9%) and $Eu^{\cdot\cdot}_K - V''_{Pb(?)}$ (1.1%), without unveiling which $K^+$ and $Pb^{2+}$ sites are involved in the latter two defects.[17]

## Thermodynamic and Kinetic Aspects

By making some assumptions, Defay and Prigogine established that the driving force of the transition should vary with time according to $A(t) = k\tau_r\cdot[1 - \exp(-t/\tau_r)]$.[18] Thus, during the phase transition, the value of the affinity $A$ changes from 0 to approximately $k\tau_r$. We suggest to determine $k$ according to $k \approx -\Delta H/\Delta t_t - \Delta V/V_m\cdot R\beta$, in which $\Delta t_t$, the time duration of the phase transition, can be obtained from the $T$ vs. $t$ DSC curve as the interval between the onset time of the baseline deviation and the time of the peak maximum; $\beta$, $\Delta V_m$, and $V_m$ stand for the temperature scanning rate, the molar volume contraction at fixed pressure and temperature, and some mean molar volume of the system in the vicinity of the transition, respectively. While the former is fixed by the experimenter, the latter can be estimated from the XRD data recorded around $T_t$. Our calorimetry and XRD data give $k \approx 11.6\,J\,mol^{-1}\,s^{-1}$. Furthermore, $\tau_r$ can be assigned an upper limit by a quenching experiment: this upper limit is $\tau_c$, the intrinsic cooling time of a crystal and its container quenched from a temperature higher than $T_t$, provided that the quenched sample exhibits the phase transition exactly like the slowly cooled crystals (see Experimental Section). As $\tau_r \leq \tau_c \approx 1.9$ s, we deduce that $A \leq 22\,J\,mol^{-1}$. This value is of the same order of magnitude as the Gibbs free energy change we previously estimated with Smith's formula ($\Delta G \approx 35\,J\,mol^{-1}$).[10] The fact that the affinity remains smaller than both the latent heat ($\Delta H \approx 790\,J\,mol^{-1}$) and the thermal energy at $T_t$ (ca. $4.4\,kJ\,mol^{-1}$), as well as the apparently fast energy relaxation kinetics and vanishingly small affinity threshold for the transition,[10] clearly indicate the close-to-equilibrium character of the transition, and are also consistent with its group-subgroup nature. The positional entropy can be approximated as $R\ln(x_{rt}/x_{ht})$, where $x_{ht}$ and $x_{rt}$ denote the number of atomic-position-independent parameters refined in the high-temperature phase (17) and in the room-temperature one (24), respectively. Hence, $\Delta S_{posn} = 0.345\,R \approx \Delta S_t$. In other words, this transition turns out to be an almost purely cationic order-disorder process, with virtually no phonon mode population redistribution or rotational disorder. Indeed, the extrapolation of the low-temperature part of the $C_p$ vs. $T$ curve falls into the high-temperature one.[10] This behavior of the specific heat baseline before and after the transition, and the fact that $\Delta S_t \approx \Delta S_{posn}$ lend support to the contention that $\Delta S_{vibr} \approx 0\,R$. Furthermore, as we were unable to detect any kind of collective tilt of the $K^+$ and $Pb^{2+}$ polyhedra, we think that $\Delta S_{orient} = 0\,R$. Thus, the increase in $U_{ii}$ values observed in Figure 8 certainly stems from the $K^+/Pb^{2+}(2)$ cations' positional disorder contribution to the Debye–Waller factor.[19] Assuming a $K^+/Pb^{2+}$ lattice interdiffusion coefficient of the order of magnitude of $10^{-11}$–$10^{-12}\,cm^2\,s^{-1}$ around $T_t$,[20] the fact that the same transition entropy is found in samples cooled from 633 K in about 1.9 s and in slowly cooled crystals leads us to presume that this cationic ordering takes place over a characteristic distance shorter than 1000 Å, that is, at the submesoscopic scale. On the other hand, owing to the ap-

 © 2006 Wiley-VCH Verlag GmbH & Co. KGaA, Weinheim 

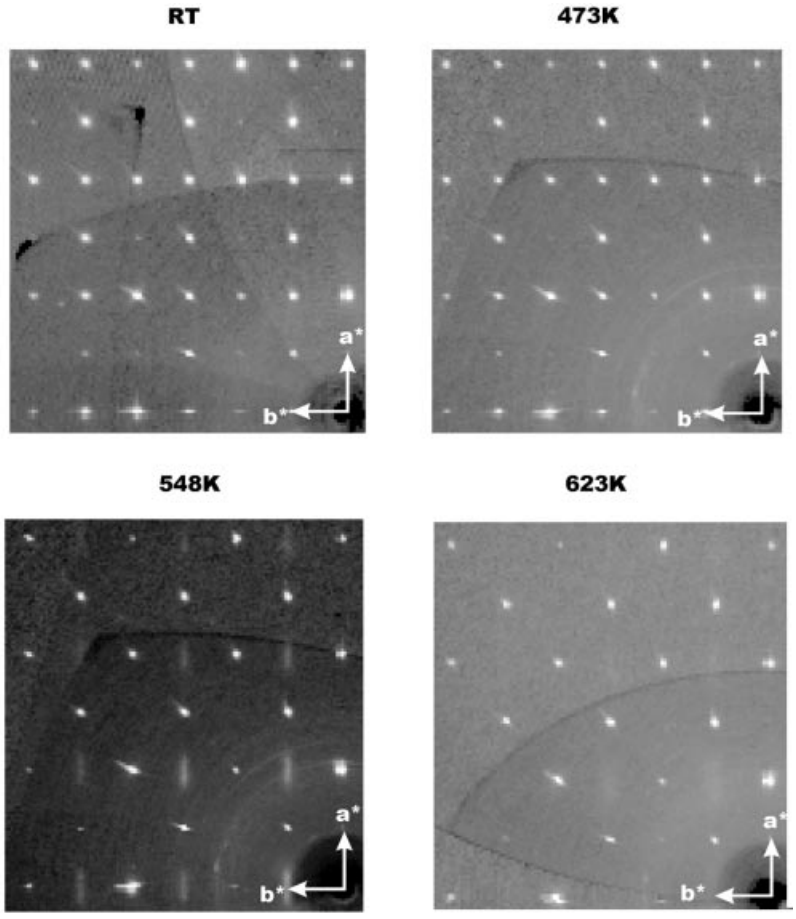


Figure 10. Plots of reciprocal lattice planes assembled from the series of experimental frames taken at various temperatures.

parently fast kinetics, low affinity, and group-subgroup nature of its phase transition, $KPb_2Cl_5$ is expected to belong to one of the two fully ferroelastic *mmmF*2/*m* species of Aizu's theory and display a 2×2 twinned domain microstructure.[21] The absence of splitting of the XRD spots (Figure 10) allows us to discard the possible coexistence of domains with different orientation states in the crystals of this study. This, in turn, suggests that the $K^+/Pb^{2+}$ diffusion upon ordering happens over a length larger than the interatomic distance. Finally, we would like to mention that although the form of the $KPb_2Cl_5$ $C_p$ vs. $T$ curve around the transition and that of $NaClO_4$ in the vicinity of the orthorhombic *Cmcm* to cubic *Fm*3*m* transition temperature are as alike as two peas in a pod,[10,22] the latter situation proves to be fundamentally different because it involves rotational degrees of freedom of the perchlorate anions in the transition mechanism.

## Conclusions

We have presented a consistent set of DSC and single-crystal XRD data that establishes the order-disorder group-subgroup phase transition occurring at 528 K in $KPb_2Cl_5$. This transition is of first order, displays moderately fast kinetics, and can be looked upon as a close-to-equilibrium process. In the high-temperature phase, a $K^+/Pb^{2+}(2)$ disorder takes place in the chains of bicapped trigonal prisms extending infinitely along the [100] direction. The lattice thermal expansion is almost isotropic from room temperature to about 473 K, but doubles its value along the [001] direction in the temperature range of the transition. We have also disentangled the connections between the $Pb^{2+}(1)$ chains embedded into the pseudo-hexagonal network of the $K^+/Pb^{2+}(2)$ chains.

## Experimental Section

**Synthesis and Crystal Growth:** KCl powder (63.4 mmol, Chempur 99.99% used as received) was mixed with $PbCl_2$ powder (126.8 mmol, Chempur 99.999% used as received) in an agate mortar in a ca. 2% wet-nitrogen-filled glovebox, dried in vacuo, and heated in successive stages from 425 to 565 K under electronic-grade HCl gas in a silica tube (mounted to a $10^{-8}$ atm vacuum assembly), in order to promote the solid-state reaction taking place according to $KCl + 2\ PbCl_2 \xrightarrow[425–565\ K]{HCl} KPb_2Cl_5$. Details of the subse-

 © 2006 Wiley-VCH Verlag GmbH & Co. KGaA, Weinheim 

quent crystal growth by the Bridgman-Stockbarger method are given in ref.[10]

**Quenching Procedure:** Fresh $KPb_2Cl_5$ single crystals were taken from various locations of the bulk sample but neither from its beginning nor its end and sealed in a silica ampoule with a thickness of about 1 mm under 0.37 atm of HCl gas. The ampoule was placed in a vertical open furnace and heated at 633 K for 44 h. After this time, the ampoule was thrown into a mixture of ice and water. The intrinsic cooling time can be approximated to $\tau_{SiO_2} + \tau_{KPb_2Cl_5} \approx 1.9$ s, with $\tau_i = \frac{\rho_i C_p L_i^2}{M_i \kappa_i}$, $C_p(KPb_2Cl_5, 633\ K) \approx 40.3\,R$[10] and $\kappa(KPb_2Cl_5, 300\ K) \approx 4.62\ W\,m^{-1}\,K^{-1}$,[23] provided that the surface exchange contributions to heat dissipation can be neglected. The crystals did not seem to undergo mechanical breakdown upon quenching.

**Differential Scanning Calorimetry:** Calorimetric measurements were performed from room temperature to 600 K at a temperature variation rate of $\beta = \pm 10\ °C\,min^{-1} \approx \pm 167\ mK\,s^{-1}$, with a commercial continuous disk-type heat flux differential scanning calorimeter. A piece of fresh $KPb_2Cl_5$ crystal ($m = 34.3 \pm 0.2$ mg), and a quenched specimen ($m = 38.3 \pm 0.2$ mg) were placed without grinding into a stainless-steel crucible in a ca. 2% wet-nitrogen-filled glovebox. The crucibles were then sealed with a stainless-steel top and an Ni ring designed to resist pressures of around 100 atm at 873.15 K. The calorimetry cell was continuously purged with 4N5 $N_2$ gas. Temperature and caloric calibrations are explained in ref.[10] The results are shown in Figure 9 (a).

**Crystal Structure:** The XRD investigation was performed at different temperatures (293, 473, 548, and 623 K), with Mo-$K_\alpha$ radiation, with a Kappa CCD (Bruker Nonius) diffractometer equipped with a Cyberstar gas blower system. Large $\Omega$- and $\Phi$-scans were used to control both the crystalline quality of different samples and determine the unit-cell parameters. A single crystal of suitable size ($100 \times 150 \times 150$ μm) was then selected. The dependency of the cell parameters on the temperature was obtained from large $\Omega$- and $\Phi$-scans performed at different temperatures; the results are reported in Figures 7 (a–c). The evolution of the *c* parameter allowed us to probe the structural transition and fix the most adequate temperature for the data collection process. Suitable data-collection strategies were defined by considering the cell parameters, the spot size, and the obstruction of the diffractometer by the high-temperature conditioning apparatus. For the room-temperature measurement, a scanning angle of 0.8° and a *Dx* (detector–sample distance) of 55 mm were chosen; $\Phi$- and $\Omega$-scans were used. To collect a large number of weak reflections, but avoiding any detector saturation by reflections of strong intensity, two different exposure times (45 s/° and 5 s/°) were used to collect the data. The diffracted intensities were collected up to $\theta = 42°$. One independent monoclinic space was scanned. Plots of reciprocal lattice planes assembled from these series of experimental frames are sufficiently accurate to obtain an overall view of the reciprocal space. The diffraction pattern can be described within a monoclinic cell [cell parameters $a = 8.8492(3)$, $b = 7.9183(5)$, $c = 12.4716(7)$ Å, $\beta = 90.106(3)°$]. The observed conditions limiting the possible reflections, *h0l*: $l = 2n$ and *0k0*: $k = 2n$, are consistent with the $P2_1/c$ space group. The measurements at high temperatures are more tedious. The presence of both the conditioning apparatus and the high-temperature gas flow modifies the environment of the goniometer and generates new shadow zones. To decrease the obstruction near the sample and to avoid collisions or a direct contact of the gas flow with the detector, *Dx* was fixed at 60 mm and only $\Phi$-scans were used. All data collections at high temperatures were undertaken according

Table 1. Details of XRD data and structure refinements for $KPb_2Cl_5$ at selected temperatures.

| | 293 K | 473 K | 548 K | 623 K |
|---|---|---|---|---|
| Empirical formula | $KPb_2Cl_5$ | $KPb_2Cl_5$ | $KPb_2Cl_5$ | $KPb_2Cl_5$ |
| Crystal system | monoclinic | monoclinic | orthorhombic | orthorhombic |
| Space group | $P2_1/c$ (no. 14) | $P2_1/c$ (no. 14) | *Pmcn* (no. 62) | *Pmcn* (no. 62) |
| *Z* | 4 | 4 | 4 | 4 |
| Formula mass [g mol$^{-1}$] | 630.743 | 630.743 | 630.743 | 630.743 |
| *F*(000) | 1072 | 1072 | 1072 | 1072 |
| Radiation | Mo-$K_\alpha$ ($\lambda$ = 0.71073 Å) | Mo-$K_\alpha$ ($\lambda$ = 0.71073 Å) | Mo-$K_\alpha$ ($\lambda$ = 0.71073 Å) | Mo-$K_\alpha$ ($\lambda$ = 0.71073 Å) |
| Crystal size [mm] | 0.10×0.15× 0.15 | 0.10×0.15× 0.15 | 0.10×0.15× 0.15 | 0.10×0.15× 0.15 |
| Diffractometer: Enraf–Nonius | Kappa CCD | Kappa CCD | Kappa CCD | Kappa CCD |
| Monochromator | graphite | graphite | graphite | graphite |
| $\theta$ range [°] | 2–42 | 2–35 | 2–35 | 2–35 |
| Index ranges | $-16 \le h \le 16$ | $-10 \le h \le 10$ | $0 \le h \le 14$ | $0 \le h \le 14$ |
| | $0 \le k \le 14$ | $0 \le k \le 12$ | $0 \le k \le 12$ | $0 \le k \le 12$ |
| | $0 \le l \le 23$ | $0 \le l \le 20$ | $0 \le l \le 20$ | $0 \le l \le 20$ |
| Scan type | $\varphi$ and $\omega$ | φ | φ | φ |
| Independent reflections | 6083 | 2040 | 1383 | 1384 |
| Reflections with $I > 3\sigma(I)$ | 4335 | 1575 | 807 | 819 |
| $R_{int}$ (%) | 4.18 | 3.05 | 2.95 | 3.50 |
| Refinement method | full-matrix least squares on $F^2$ | | | |
| Parameters refined | 75 | 75 | 45 | 45 |
| Weighting scheme | $w = 1/[\sigma^2(F_o^2) + (\alpha P)^2 + \beta P]$, $P = (F_o^2 + 2F_c^2)/3$ | | | |
| Absorption correction | SADABS | SADABS | SADABS | SADABS |
| Extinction coefficient | 0.108(2) | – | 0.052(5) | 0.101(7) |
| Goodness-of-fit on $F^2$ | 1.38 | 1.77 | 4.7 | 3.5 |
| Final *R* factor | | | | |
| $R_1$ [$I > 3\sigma(I)$] | 0.028 | 0.029 | 0.049 | 0.046 |
| $wR_2$ [$I > 3\sigma(I)$] | 0.023 | 0.026 | 0.041 | 0.039 |
| Max. shift/esd | 0.005 | 0.002 | 0.0001 | 0.0002 |
| Largest diff. peaks and holes [e Å$^{-3}$] | +2 [0.50 Å near Pb(1)] | +1.4 (0.70 Å near K) | +3.25 [1 Å near Pb(1)] | +2.33 [0.30 Å near Pb(2)/K] |
| | –2 [0. 55 Å near Pb(2)] | –1.3 [0. 4 Å near Pb(1)] | –3.25 [0. 35 Å near Pb(2)/K] | –3.05 [0. 40 Å near Pb(2)/K] |

 © 2006 Wiley-VCH Verlag GmbH & Co. KGaA, Weinheim 

to the procedure reported in Table 1. The conditions limiting the possible reflections at 473 K are the one observed at room temperature, but at 548 and 623 K new conditions consistent with the *Pmcn* space group appear (*h0l*: $l = 2n$ and *hk0*: $h + k = 2n$; see Figure 10). At 623 K, the cell parameters are $a = 8.851(12)$, $b = 8.015(17)$, $c = 12.683(15)$ Å. It should be noted that *Pmcn* is a supergroup of $P2_1/c$. The existence of diffuse scattering centered on the nodes *hk0*: $h + k = 2n + 1$ in Figure 10 at 548 K should be noted. The EvalCCD software[24] was used to extract reflections from the collected frames and reflections were merged and rescaled as a function of the exposure time. Data were corrected from absorption using the SADABS program[25] developed for scaling and correction of area-detector data. At room temperature a structural model considering the $P2_1/c$ space group was built up with SIR2002[26] using direct methods. Then, the cations and the chloride anions were located. This model was subsequently introduced in the refinement program Jana2000,[27] all the atomic positions were refined, and finally anisotropic atomic displacement parameters were considered for all the atoms. The refinement led to an agreement factor of 2.8%.

It should be noted that the room-temperature data collection and refinement were performed using two different single crystals of the same batch, which gave the same results and that, in particular, none of the crystals investigated were twinned. The structure at 473 K, which exhibits a monoclinic symmetry, was refined using the final result of the room-temperature structure. Except for the ADPs, no significant modifications in the structure were observed (Table 2). The refinements of the structure at higher temperatures were carried out using a model generated in the *Pmcn* space group from the atomic positions determined at room temperature. One should bear in mind that, in the *Pmcn* symmetry, the $Cl^-(1)$ and $Cl^-(4)$ anions as well as the $K^+$ and $Pb^{2+}(2)$ cations become equivalent (Table 2). The behavior of the ADPs as a function of $T$ is displayed in Figure 8 (a) and (b). Further details of the crystal structure investigations may be obtained from the Fachinformationzentrum Karlsruhe, 76344 Eggenstein-Leopoldshafen, Germany [Fax: +49-7247-808-666; E-mail: crysdata@fiz-karlsruhe.de] on quoting the depository numbers CSD-416430 (293 K), -416431 (473 K), -416432 (548 K), and -416433 (623 K).

Table 2. Refined atomic coordinates for $KPb_2Cl_5$ at room temperature ($P2_1/c$ phase) and 623 K (*Pmcn* phase).

| 293 K Atom | Wyckoff position | $x$ | $y$ | $z$ |
|---|---|---|---|---|
| K | 4e | 0.50993(10) | 0.55118(12) | 0.83129(7) |
| Pb(1) | 4e | 0.745007(14) | 0.064158(17) | 0.993373(10) |
| Pb(2) | 4e | 0.006756(16) | 0.506409(19) | 0.825856(11) |
| Cl(1) | 4e | 0.04196(9) | 0.16588(11) | 0.90205(7) |
| Cl(2) | 4e | 0.77048(12) | –0.15544(13) | 0.81152(8) |
| Cl(3) | 4e | 0.76408(10) | 0.31165(12) | 0.72073(7) |
| Cl(4) | 4e | 0.54059(10) | –0.17941(13) | 0.08070(9) |
| Cl(5) | 4e | 0.77812(10) | 0.45939(12) | 0.99858(7) |
| **623 K Atom** | **Wyckoff position** | $x$ | $y$ | $z$ |
| Pb(1) | 4c | 0.25 | 0.05955(6) | –0.00625(3) |
| K/Pb(2) | 8d | 0.50103(7) | –0.48274(8) | –0.17144(6) |
| Cl(1)/Cl(4) | 8d | 0.4616(2) | –0.1721(3) | 0.0892(2) |
| Cl(2) | 4c | 0.75 | –0.1845(4) | –0.2192(3) |
| Cl(3) | 4c | 0.25 | –0.1539(4) | –0.1896(3) |
| Cl(5) | 4c | 0.25 | 0.4560(4) | –0.0004(2) |

Table 3. Selected bond lengths [Å] for $KPb_2Cl_5$ in the room-temperature ($P2_1/c$) and high-temperature (*Pmcn*) phases.

| 293 K[a] | | | | | |
|---|---|---|---|---|---|
| Pb(1)–Cl(1)$^{i}$ | 2.9770(8) | Pb(2)–Cl(1) | 2.8756(9) | K–Cl(2)$^{xi}$ | 3.2826(14) |
| Pb(1)–Cl(1)$^{ii}$ | 2.9263(8) | Pb(2)–Cl(1)$^{vi}$ | 3.1393(9) | K–Cl(2)$^{viii}$ | 3.4625(13) |
| Pb(1)–Cl(2) | 2.8671(10) | Pb(2)–Cl(2)$^{vii}$ | 3.4016(10) | K–Cl(3) | 3.2509(13) |
| Pb(1)–Cl(3)$^{iii}$ | 3.0058(9) | Pb(2)–Cl(2)$^{viii}$ | 2.9114(10) | K–Cl(3)$^{viii}$ | 3.2477(13) |
| Pb(1)–Cl(4)$^{iv}$ | 2.8610(10) | Pb(2)–Cl(3)$^{ix}$ | 2.9492(9) | K–Cl(4)$^{v}$ | 3.1737(14) |
| Pb(1)–Cl(4)$^{v}$ | 2.8398(9) | Pb(2)–Cl(3)$^{viii}$ | 3.2087(9) | K–Cl(4)$^{iii}$ | 3.2978(14) |
| Pb(1)–Cl(5) | 3.1438(9) | Pb(2)–Cl(5)$^{ix}$ | 2.9815(8) | K–Cl(5) | 3.2396(12) |
| | | Pb(2)–Cl(5)$^{x}$ | 2.9113(8) | K–Cl(5)$^{x}$ | 3.3207(12) |
| 623 K[b] | | | | | |
| Pb(1)–Cl(5) | 3.179(3) | | K/Pb(2)–Cl(5)$^{iv}$ | 3.161(2) | |
| Pb(1)–Cl(1) (×2) | 2.916(2) | | K/Pb(2)–Cl(5)$^{i}$ | 3.1246(19) | |
| Pb(1)–Cl(1)$^{i}$ (×2) | 2.930(2) | | K/Pb(2)–Cl(1)$^{v}$ | 2.976(2) | |
| Pb(1)–Cl(2)$^{i}$ | 3.030(3) | | K/Pb(2)–Cl(1)$^{vi}$ | 3.298(3) | |
| Pb(1)–Cl(3) | 2.887(3) | | K/Pb(2)–Cl(2) | 3.324(3) | |
| | | | K/Pb(2)–Cl(2)$^{vii}$ | 3.096(2) | |
| | | | K/Pb(2)–Cl(3) | 3.471(2) | |
| | | | K/Pb(2)–Cl(3)$^{vii}$ | 3.155(2) | |

[a] i: $1 - x, -y, -z$; ii: $1 - x, -y, 2 - z$; iii: $x, 1/2 - y, 1/2 + z$; iv: $-x, -y, 1 - z$; v: $1 - x, -y, 1 - z$; vi: $x, 1/2 - y, 3/2 + z$; vii: $-1 - x, 1 - y, -z$; viii: $1 + x, 1/2 - y, 3/2 + z$; ix: $-1 - x, -y, -z$; x: $1 - x, 1 - y, 2 - z$; xi: $-x,1 - y, -z$. [b] i: $1 - x, -y, -z$; ii: $-1/2 - x, y, z$; iii: $1/2 - x, y, z$; iv: $-x, -1 - y, -z$; v: $1 - x, -1 - y, -z$; vi: $-x, -1/2 + y, -1/2 - z$; vii: $1 - x, -1/2 + y, -1/2 - z$.

 © 2006 Wiley-VCH Verlag GmbH & Co. KGaA, Weinheim 

## Acknowledgments

A. F. is the holder of a PhD thesis DGA fellowship from the French Ministry of Defense. This work was partly supported by the Centre National de la Recherche Scientifique (CNRS) and the Conseil Régional de Basse-Normandie. We would like to acknowledge Miss Hélène Rousselière for her technical help during the high-temperature XRD measurements.

[1] R. Lorenz, W. Ruckstuhl, *Z. Anorg. Chem.* **1907**, *51*, 71–89.
[2] L. I. Isaenko, A. P. Yelisseyev, A. M. Tkachuk, S. E. Ivanova, S. A. Payne, R. H. Page, M. C. Nostrand, *Proc. SPIE – Int. Soc. Opt. Eng.* **2002**, *4900*, 962–972.
[3] J. Schlüter, D. Pohl, S. Britvin, *Neues Jahrb. Mineral., Monatsh.* **2005**, *182*, 95–101.
[4] H. M. Artelt, E. Greinacher, G. Meyer, *J. Prakt. Chem.* **1993**, *335*, 255–261.
[5] S. I. Tkachenko, R. P. Porter, M. A. Korzhinskii, M. D. Van Bergen, K. I. Shmulovich, G. S. Shteinberg, *Geokhimiya* **1999**, *4*, 410–422.
[6] M. Voda, M. Al-Saleh, G. Lobera, R. Balda, J. Fernández, *Opt. Mater.* **2004**, *26*, 359–363.
[7] K. Nitsch, M. Dušek, M. Nikl, K. Polák, M. Rodová, *Prog. Cryst. Growth Charact.* **1995**, *30*, 1–22.
[8] U. N. Roy, Y. Cui, M. Guo, M. Groza, A. Burger, G. J. Wagner, T. J. Carrig, S. A. Payne, *J. Cryst. Growth* **2003**, *258*, 331–336.
[9] L. Isaenko, A. Yelisseyev, A. Tkachuk, S. Ivanova, S. Vatnik, A. Merkulov, S. Payne, R. Page, M. Nostrand, *Mater. Sci. Eng. B* **2001**, *81*, 188–190.
[10] M. Velázquez, A. Ferrier, J.-P. Chaminade, B. Menaert, R. Moncorgé, *J. Cryst. Growth* **2006**, *286*, 324–333.
[11] H. P. Beck, G. Clicqué, H. Nau, *Z. Anorg. Allg. Chem.* **1986**, *536*, 35–44.
[12] A. A. Merkulov, L. I. Isaenko, V. M. Pashkov, V. G. Mazur, A. V. Virovets, D. Ju. Naumov, *J. Struct. Chem.* **2005**, *46*, 103–108.
[13] K. Nitsch, A. Cihlář, Z. Malková, M. Rodová, M. Vaněček, *J. Cryst. Growth* **1993**, *131*, 612–615.
[14] G. Meyer, J. Soose, A. Moritz, V. Vitt, Th. Holljes, *Z. Anorg. Allg. Chem.* **1985**, *521*, 161–172.
[15] R. O. Simmons, R. W. Balluffi, *Phys. Rev.* **1960**, *119*, 600–605.
[16] G. S. Shakurov, B. Z. Malkin, A. R. Zakirov, A. G. Okhrimchuk, L. N. Butvina, N. V. Lichkova, V. N. Zavgorodnev, *Appl. Magn. Reson.* **2004**, *26*, 579–586.
[17] C. Cascales, J. Fernández, R. Balda, *Opt. Express* **2005**, *13*, 2141–2152.
[18] R. Defay, I. Prigogine, in *Thermodynamique Chimique*, 2nd ed., Éditions Desoer, Liège, Éditions Dunod, Paris, **1950**.
[19] W. F. Kuhs, in *International Tables for Crystallography*, vol. D ["Physical properties of crystals", chapter 1.9 ("Atomic displacement parameters")] (Ed.: A. Authier), Kluwer Academic Publishers, Dordrecht, Boston, London, **2003**, pp. 228–242.
[20] G.-M. Schwab, R. Deml, *Z. Phys. Chem. (Muenchen, Ger.)* **1964**, *42*, 280–292.
[21] K. Aizu, *Phys. Rev. B* **1970**, *2*, 754–772.
[22] K. O. Strømme, *Acta Chem. Scand. A* **1974**, *28*, 515–527.
[23] A. M. Tkachuk, S. E. Ivanova, L. I. Isaenko, A. P. Yelisseyev, M.-F. Joubert, Y. Guyot, S. Payne, *Opt. Spectr.* **2003**, *95*, 722–740.
[24] A. Duisenberg, L. Kroon-Batenburg, A. Shreurs, *J. Appl. Crystallogr.* **2003**, *36*, 220.
[25] G. M. Sheldrick, *SADABS, program for scaling and correction of area detector data*, Göttingen, Germany, **1997**.
[26] M. Burla, M. Camalli, B. Carrozzini, G. L. Cascarano, C. Giacovazzo, G. Polidori, R. Spagna, *SIR2002*, Institute of Crystallography, Bari, Italy, **2002**.
[27] V. Petricek, M. Dusek, *Jana 2000, The crystallographic computing system*, Institute of Physics, Praha, Czech Republic, **2000**.

Received: April 16, 2006
Published Online: August 9, 2006

 © 2006 Wiley-VCH Verlag GmbH & Co. KGaA, Weinheim 

DOI: 10.1002/ejic.200600450

# How Do the Different Defect Structures and Element Substitutions Affect the Nonlinear Optical Properties of Lacunary Keggin Polyoxometalates? A DFT Study

**Wei Guan,[a] Guo-Chun Yang,[a] Li-Kai Yan,[a] and Zhong-Min Su*[a]**

**Keywords:** Polyoxometalates / Nonlinear optics / Lacunary species / Tungsten / Density functional theory

Systematic DFT calculations have been carried out on the lacunary α-Keggin polyoxometalate derivatives $[PW_{11}O_{39}]^{7-}$, $[XW_9O_{34}]^{n-}$ (X = $Al^{III}$, $Si^{IV}$, $Ge^{IV}$, $P^V$, $As^V$, and $Sb^V$), $[XW_9M_2O_{39}]^{n-}$, and $[XW_9M_3O_{40}]^{n-}$ (X = $P^V$ and $Si^{IV}$, M = $Mo^{VI}$, $V^V$, $Nb^V$, and $Ta^V$) to investigate the geometric structure and element substitution effects on the molecular nonlinear optical response. Analysis of the computed static second-order polarizability ($\beta_0$) predicts that the molecular nonlinear optical activity of lacunary Keggin polyoxometalate derivatives can be modified by replacing the central heteroatom and the addenda metal atom. Substitution of the central Al atom or the addenda V atom causes significant enhancement in the molecular nonlinearity. Moreover, the $\beta_0$ values are substantially dependent on the defect structures. This class of inorganic complexes possesses remarkably large molecular optical nonlinearity, especially for the partial substitution complex $[SiW_9Nb_2O_{39}]^{10-}$ (**IIIc**), which has a computed $\beta_0$ value of 2071.0 a.u. Thus, lacunary Keggin polyoxometalates could become excellent candidates in the field of second-order NLO.
(© Wiley-VCH Verlag GmbH & Co. KGaA, 69451 Weinheim, Germany, 2006)

## Introduction

Nonlinear optical (NLO) materials based on molecular compounds have continued to be of considerable current interest because they hold promise for potential applications in optical signal processing, switching, and telecommunications. Among inorganic nonlinear materials, borates, phosphates, and niobates (β-$BaB_2O_4$, $LiB_3O_5$, $Li_2B_4O_7$, $CsLiB_6O_{10}$, $KH_2PO_4$, $LiNbO_3$, etc.) have already been widely studied. However, compared with the organic and organometallic compounds that have been extensively examined for their NLO responses recently, NLO studies of inorganic materials are relatively rare even though inorganic compounds are robust and are available as large single crystals. They also possess a large transparency range, suffer very low optical losses, and offer a large variety of structures and a great diversity of electronic properties shaped by the metal-characterized core and therefore may comprise a promising family of NLO materials.

Among the various inorganic compounds, polyoxometalates (POMs) have generated substantial interest in recent years because of their unique structural variety and exciting properties in fields such as catalysis, medicine, materials science, etc.[1] The most representative POM is the well-known α-Keggin heteropolyanion $[XM_{12}O_{40}]^{n-}$ (denoted as α-$XM_{12}$; X = $P^V$, $Si^{IV}$, $Ge^{IV}$, etc.; M = $Mo^{VI}$, $W^{VI}$, or $V^V$). The structure of α-$XM_{12}$ has overall $T_d$ symmetry and consists of a central $XO_4$ tetrahedron that shares its oxygen atoms ($O_a$) with four $M_3O_{13}$ groups. These $M_3O_{13}$ groups, made of three edge-sharing octahedra, are linked together by corners. Lacunary α-Keggin polyanions (species with defect structures) are derived from α-$XM_{12}$ by removing one $MO_6$ octahedron (α-$XM_{11}$, top series in Figure 1) or by removing three $MO_6$ octahedra from different $M_3O_{13}$ groups (A-α-$XM_9$, middle series in Figure 1) or the same $M_3O_{13}$ group (B-α-$XM_9$). In order to synthesize novel POMs with predicted structures, an approach widely used is to treat lacunary POM precursors with transition metal ions or organometallic fragments as lacunary structures possess a reactive nucleophilic polyoxygenated site. Different transition metal ions can partly or wholly fill these vacancies to give rise to compounds with magnetism or catalysts,[2] such as $PW_9Fe_2Ni$, $PW_9Fe_3$, or $PW_{11}Co$. The reactions of organometallic fragments with Keggin-type lacunary polyanions also give numerous novel compounds {e.g., open-type $[SiW_9O_{37}(SnR)_3]^{7-}$ and sandwich-type $[(SnR)_3(SiW_9O_{34})_2]^{7-}$}. Although the study of such lacunary polyanions is receiving considerable attention,[3] they need to be further investigated theoretically.

Murakami et al. have recently shown by the conventional powder second-harmonic generation (SHG) method that nanostructured materials made from lacunary POMs have larger NLO responses than $KH_2PO_4$. They also defined design criteria to obtain a large NLO response.[4] This experi-

[a] Institute of Functional Materials Chemistry, Faculty of Chemistry, Northeast Normal University,
Changchun 130024, P. R. China
Fax: +86-431-568-4009
E-mail: zmsu@nenu.edu.cn
Supporting information for this article is available on the WWW under http://www.eurjic.org or from the author.

 © 2006 Wiley-VCH Verlag GmbH & Co. KGaA, Weinheim 

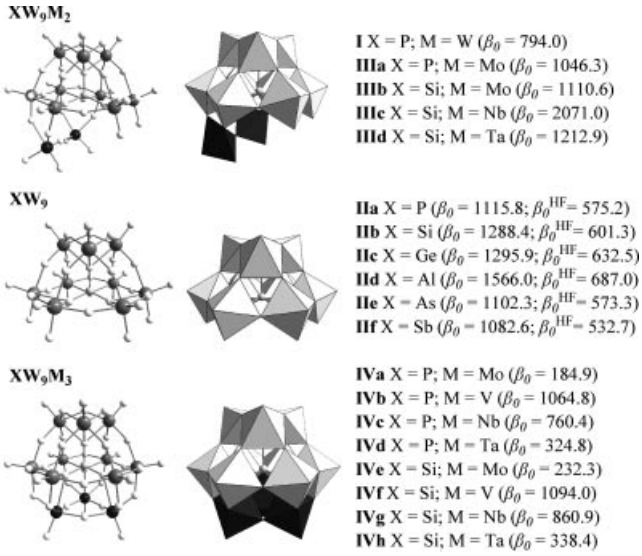


Figure 1. Ball-and-stick and polyhedral representations of the studied complexes. The values in brackets are the respective computed static second-order polarizability (a.u.).

mental result inspired us to further investigate the electronic and NLO properties of lacunary α-Keggin derivatives by a DFT method. In the past decade, DFT has been shown to be able to successfully predict the properties of molecules and materials, including the NLO properties.[5] The modeling of polyoxoanions has also made progress.[6] Recently, we have systematically investigated the bonding character, redox properties, protonation, stability, and NLO properties of $[X_2Mo_5O_{23}]^{6-}$, $[PTi_2W_{10}O_{40}]^{7-}$, $[Mo_6O_{17}R_2]^{2-}$, and $[H_{12}V_{13}O_{40}]^{3-}$ clusters by DFT.[7] Theoretical studies would be helpful in the rationalization of the observed properties and in the design of novel POM-based materials with functional properties by exploiting the unique electronic and structural characteristics of these complexes.

In this paper we present systematic DFT calculations on the static NLO responses of a series of lacunary α-Keggin polyanion derivatives, including $C_s$ systems: $[PW_{11}O_{39}]^{7-}$, $[PW_9Mo_2O_{39}]^{7-}$, $[SiW_9Mo_2O_{39}]^{8-}$, $[SiW_9Nb_2O_{39}]^{10-}$, and $[SiW_9Ta_2O_{39}]^{10-}$; and $C_{3v}$ systems: $[AlW_9O_{34}]^{11-}$, $[SiW_9O_{34}]^{10-}$, $[GeW_9O_{34}]^{10-}$, $[PW_9O_{34}]^{9-}$, $[AsW_9O_{34}]^{9-}$, $[SbW_9O_{34}]^{9-}$, $[PW_9V_3O_{40}]^{6-}$, $[SiW_9V_3O_{40}]^{7-}$, $[PW_9Nb_3O_{40}]^{6-}$, $[SiW_9Nb_3O_{40}]^{7-}$, $[PW_9Ta_3O_{40}]^{6-}$, $[SiW_9Ta_3O_{40}]^{7-}$, $[PW_9Mo_3O_{40}]^{3-}$, and $[SiW_9Mo_3O_{40}]^{4-}$. (Figure 1) The effects of geometric structure and element substitution on the molecular nonlinear response are analyzed and discussed in order to reveal the general rules governing the NLO properties of these polyanions.

## Results and Discussion

### Electronic Structures

The frontier molecular orbitals of all systems have a common character where the occupied orbitals formally delocalize over the p-oxygen orbitals, while the unoccupied d-

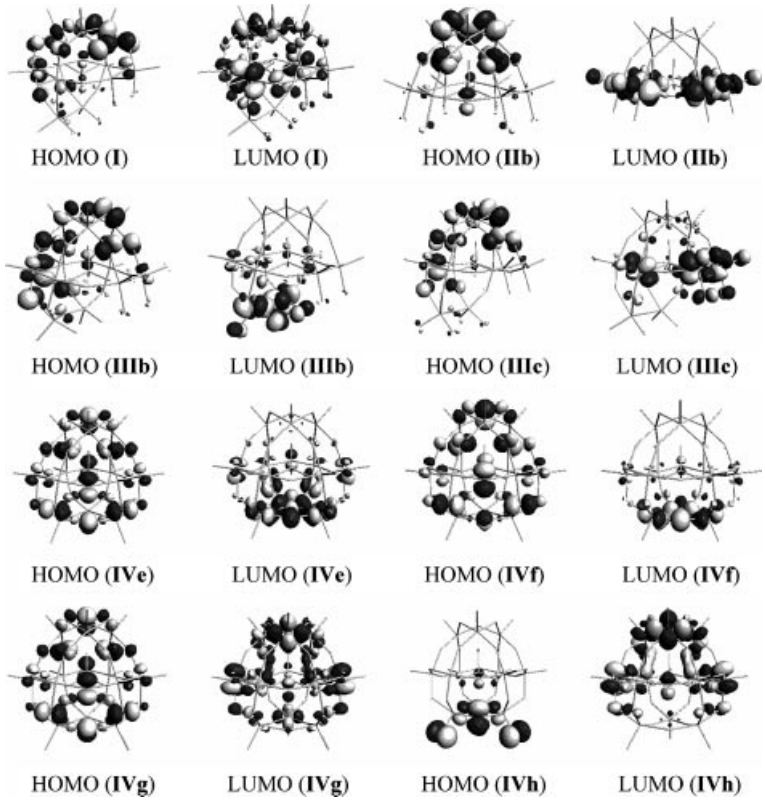


Figure 2. Frontier molecular orbitals of systems **I**, **IIb**, **IIIb**,**c**, and **IVe**–**h**.

 © 2006 Wiley-VCH Verlag GmbH & Co. KGaA, Weinheim 

metal orbitals delocalize over the addenda atoms.[6,7] This kind of charge transfer, namely O→M, must be responsible for the NLO properties of lacunary α-Keggin POM derivatives. The diagrams for the frontier molecular orbitals of eight representative systems (**I**, **IIb**, **IIIb**,**c**, and **IVe**–**h**) are displayed in Figure 2, from which several conclusions can be drawn:

(1) The frontier molecular orbitals of series **II** have similar character (Figure 2, **IIb**) in that the HOMOs formally delocalize over the bridge oxygen atoms that are away from the lacunary sites, which is similar to system **I**. The LUMOs delocalize mostly over the six tungsten atoms that are close to the lacunary sites and partially over the terminal oxygen atoms. In addition, the unoccupied W(d)–O(p) bands have an antibonding interaction in series **II**.

(2) The distribution of HOMOs in series **III** has a similar character to that of series **II**. However, when compared with series **II** the LUMOs in series **III** change significantly as it is the d-orbitals of the Mo atoms that contribute mainly to the LUMO of **IIIa**,**b** (Figure 2). When Mo atoms are substituted by Nb or Ta atoms (**IIIc** and **IIId**), the LUMOs mostly delocalize over the two tungsten atoms that are close to the lacunary sites (Figure 2).

(3) For trisubstituted systems (series **IV**), the HOMOs extensively delocalize over the p-oxygen orbitals, except for the Ta-substituted systems **IVd** and **IVh**, where the HOMOs almost delocalize over the bridge oxygen atom that links two tantalum atoms [O(TaTa)] and the terminal oxygen atom that links to tantalum atoms [O(Ta); Figure 2] The LUMOs of systems **IVa**,**b** and **IVe**,**f** are mainly concentrated on the three substituted addenda atoms (Figure 2), which shows that the d-orbitals of molybdenum and vanadium play an important role in the redox reactions of trisubstituted systems.[6b] However, the delocalization of LUMOs is obviously enhanced by Nb and Ta substitution (Figure 2, **IVg**,**h**).

### Geometric Structure and Element Substitution Effects on $\beta$

In view of the molecular orbital character discussed above, we computed the static second-order polarizabilities ($\beta_0$) of the series of lacunary POM derivatives considered in this investigation by DFT. The static second-order polarizability is also termed the zero-frequency hyperpolarizability and is an estimate of the intrinsic molecular hyperpolarizability in the absence of any resonance effects. Geometric structure and element substitution effects were considered in a set of calculations by choosing mono- and trivacant Keggin derivatives and their mixed addenda species. The computed $\beta_0$ values of the studied complexes are given in Figure 1 (**I**, **IIa**–**c**, **IIIa**, and **IVa**). The results indicate some common trends, which are in agreement with the qualitative predictions of Murakami and co-workers on the NLO response of nanostructured materials made from lacunary POMs.[4] First, the trivacant Keggin complexes (**IIa**, **IIb**, and **IIc**) have larger $\beta_0$ values than the monovacant structure (**I**): all the $\beta_0$ values of **IIa**, **IIb**, and **IIc** are above 1100 a.u. whereas the present calculations predict the $\beta_0$ value of **I** to be just 794.0 a.u. Second, the replacement of the central heteroatom (X) slightly alters the $\beta_0$ values of **IIa**, **IIb**, and **IIc**, which increase as the heavy central atom changes in the order Ge ≥ Si > P; the difference between the $\beta_0$ values of **IIb** and **IIc** is relatively small. Third, partially substituting addenda metal atoms by molybdenum atoms (**IIIa**) causes significant enhancement in the molecular nonlinearity. As can be seen from Figure 1, the $\beta_0$ value of **IIIa** is much larger than that of **IVa**, the difference between the two systems exceeds 800 a.u., and this is confirmed by the frontier molecular orbital character (Figure 2 **IIIb** and **IVe**).

To shed further light on the second-order NLO properties of lacunary Keggin POM derivatives, more complexes (**IId**–**f**, **IIIb**–**d**, and **IVb**–**h**) were systematically calculated to understand the role of the central heteroatom (X) and addenda metal atom (M) in influencing the NLO response. The replacement of X in the trivacant complexes with five elements (Al, Si, P, As and Sb) results in different trends (Figure 3). The substitution by Al results in a larger effect than by Si, which, in turn, has a larger effect than P (**IId** > **IIb** > **IIa**); when X is one of the group 15 elements P, As, and Sb, the computed $\beta_0$ values indicate that the NLO response is **IIa** > **IIe** > **IIf**. As can be seen from two trends above, the magnitude of increase or decrease of $\beta_0$ with respect to the trivacant tungstates depends on both the atomic radius of the central heteroatom (Figure 3A) and its electronegativity (Figure 3B). When X is from the same row of the periodic table (e.g. the third row: Al, Si and P) the $\beta_0$ value is proportional to the atomic radius and is inversely proportional to the electronegativity; however, when X is from the same group (e.g. group 15: P, As, Sb) the opposite trend is observed: the $\beta_0$ value is proportional to the electronegativity and is inversely proportional to the atomic radius. From Figure 1, we also calculated the static second-order polarizabilities for series **II** employing the HF method ($\beta_0^{HF}$). According to the $\beta_0^{HF}$ values, it can be seen that DFT and HF methods give consistent trends for the static second-order polarizabilities. However, the HF method underestimates the second-order polarizabilities of series **II** as there is no correlation consideration in the HF method, while the DFT methods used in this paper overestimate the $\beta$ values. This is in accordance with the literature.[8] Therefore, it can also be concluded that DFT is a feasible method for the present POMs. Moreover, the central heteroatom substitution effects in series **III** and **IV** also obey the trends described above. Substitution by Si results in a larger effect than by P (**IIIb** > **IIIa**, **IVe** > **IVa**, **IVf** > **IVb**, **IVg** > **IVc**, and **IVh** > **IVd**). We believe that the sketch map in Figure 3 will be helpful in designing new NLO materials.

With regard to the role of the addenda metal atom, similar trends (Figure 3) can be seen from the calculated data (Figure 1: **IIIb**–**d** and **IVa**–**h**) obtained for series **III** and **IV**. Unfortunately, it is difficult to obtain a reasonable result for $[SiW_9V_2O_{39}]^{10-}$. The replacement of M with four elements (Mo, V, Nb, and Ta) significantly alters their $\beta_0$ values (Figure 1: **IIIc** > **IIId** > **IIIb**, **IVb** > **IVc** > **IVd** > **IVa**,

 © 2006 Wiley-VCH Verlag GmbH & Co. KGaA, Weinheim 

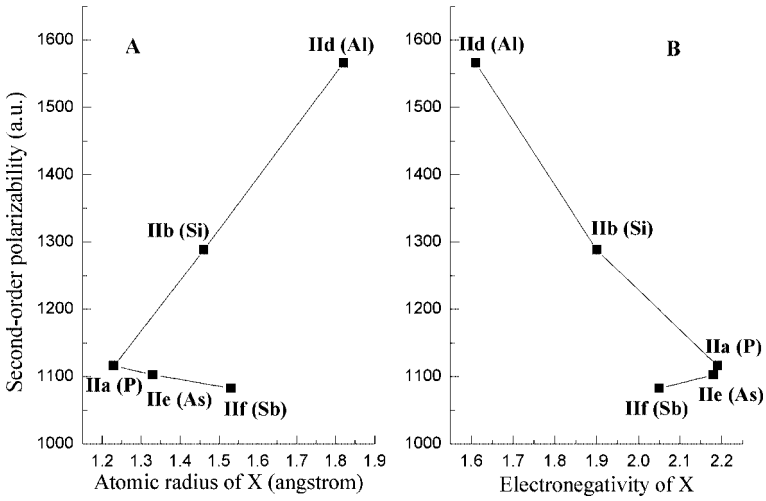


Figure 3. The second-order polarizabilities of trivacant complexes **IIa**–**f** as a function of the atomic radius (A) and electronegativity (B) of the central heteroatom (X).

and **IVf** > **IVg** > **IVh** > **IVe**), which increase as M changes in the order V > Nb > Ta > Mo. Thus, the computed $\beta_0$ values predict that the molecular nonlinear optical activity of lacunary Keggin POM derivatives can be fine-tuned by replacing the central heteroatom or the addenda metal atom. Substitution of the central Al atom or the addenda V atom causes a significant enhancement in the molecular nonlinearity. Furthermore, the defect structure plays a key role in increasing the $\beta_0$ value.

As can be seen from Figure 1, lacunary POMs have larger second-order polarizability coefficients, especially for the partially substituted complexes **IIIc**, whose computed $\beta_0$ value is even larger than that of the $Au_{20}$ cluster with an equivalent molecular size. The present DFT calculations predict the $\beta_0$ value of system **IIIc** to be 2071.0 a.u., whereas the predicted second-order polarizability of $Au_{20}$ is 1655.3 a.u.[9] All these complexes have high transparency in the visible area[4] therefore, in view of the merit of this class of inorganic complexes, they could be an excellent material for use in the second-order NLO field.

## Conclusions

A series of lacunary α-Keggin POM derivatives have been systematically investigated for their molecular nonlinear response, including $[PW_{11}O_{39}]^{7-}$, $[XW_9O_{34}]^{n-}$ (X = $Al^{III}$, $Si^{IV}$, $Ge^{IV}$, $P^{V}$, $As^{V}$, and $Sb^{V}$), $[XW_9M_2O_{39}]^{n-}$, and $[XW_9M_3O_{40}]^{n-}$ (X = $P^{V}$ and $Si^{IV}$; M = $Mo^{VI}$, $V^{V}$, $Nb^{V}$, and $Ta^{V}$). Geometric structure and element substitution effects on the molecular nonlinear response have been analyzed, and the computed $\beta_0$ values reveal the general rules to design a large nonlinearity: (i) the defect structured complex has a larger $\beta$ value than a defect-free complex (series **IV**), especially for trivacant Keggin complexes (series **II**) and partially substituted complexes (series **III**); (ii) the $\beta_0$ value depends on both the atomic radius of the central heteroatom (X) and the addenda metal atom (M) and their electronegativity. When X and M are from the same row of the periodic table (X = Al, Si, and P; M = Nb and Mo) the $\beta_0$ value is proportional to the atomic radius and inversely proportional to the electronegativity, whereas when X and M are from the same group (X = P, As and Sb; M = V, Nb and Ta) the opposite trend is observed. This class of inorganic complexes possesses remarkably large static second-order polarizability, especially for $[SiW_9Nb_2O_{39}]^{10-}$ (**IIIc**), which has a computed $\beta_0$ value of 2071.0 a.u. The frontier molecular orbital character reveals that the main origin of the NLO properties of lacunary α-Keggin POMs derivatives is O→M charge transfer. It is hoped that the results presented in this paper will stimulate experimental research in the field of NLO properties involving lacunary Keggin POM derivatives.

## Computational Details

The DFT calculations were carried out with the ADF2004.01 suite of programs.[10] The zero-order regular approximation (ZORA) was adopted in all the calculations to account for the scalar relativistic effects.[11] The generalized-gradient approximation (GGA) was employed in the geometry optimizations by using the Beck[12] and Perdew[13] (BP86) exchange-correlation (XC) functional. For the calculations, we made use of the standard ADF TZP basis set, which is a triple-ζ plus polarization STO basis set. The cores (O: 1s; Al, Si, P, V: 2p; Ge, As: 3p; Sb: 4p; Nb, Mo: 3d; Ta, W: 4d) were kept frozen. In calculations of the static second-order polarizability, the RESPONSE module[14] implemented in the ADF program was used based on the optimized geometries. The van Leeuwen–Baerends XC potential (LB94) was chosen for calculations of all the response properties.[15] The adiabatic local density approximation (ALDA) was applied for the evaluation of the first and second functional derivatives of the XC potential. Moreover, the value of the numerical integration parameter used to determine the precision of numerical integrals was 6.0. We also calculated the static second-order polarizabilities employing the Hartree–Fock (HF) method based on ab initio quantum chemistry with the GAUSSIAN03 program.[16] The basis set used for Al, Si, P, and O is the standard Gaussian basis set 6-31G(d) in which one set of d-polarization function is included. For 3d, 4d, and 5d transition

 © 2006 Wiley-VCH Verlag GmbH & Co. KGaA, Weinheim 

metals, the LANL2DZ basis set[17] was used, in which the effective core potentials (ECPs) were adopted and mass-velocity, Darwin relativistic effects were incorporated.

**Supporting Information** (see footnote on the first page of this article): Cartesian coordinates of all systems (Tables S1–S19).

## Acknowledgments

The authors gratefully acknowledge financial support from the National Natural Science Foundation of China (projects 20373009 and 20573016) and the Science Foundation for Young Teachers of Northeast Normal University (20060307 and 111494017). We would also like to thank Yuhe Kan for computational support.

[1] a) M. T. Pope, *Heteropoly and Isopoly Oxometalates*, Springer-Verlag, Berlin, **1983**; b) M. T. Pope, A. Müller, *Polyoxometalates: From Platonic Solid to Anti-Retroviral Activity*, Kluwer, Dordrecht, **1994**; c) Special edition on Polyoxometalates: *Chem. Rev.* **1998**, *98*, 1–390 (Ed.: C. L. Hill); d) *Polyoxometalate Chemistry: From Topology via Self-Assembly to Applications* (Eds.: M. T. Pope, A. Müller), Kluwer, Dordrecht, The Netherlands, **2001**.

[2] a) C. L. Hill, C. M. Prosser-McCartha, *Coord. Chem. Rev.* **1995**, *143*, 407–455; b) J. M. Clemente-Juan, E. Coronado, *Coord. Chem. Rev.* **1999**, *193–195*, 361–394; c) N. Mizuno, K. Yamaguchi, K. Kamata, *Coord. Chem. Rev.* **2005**, *249*, 1944–1956.

[3] a) M. Bonchio, O. Bortolini, V. Conte, A. Sartorel, *Eur. J. Inorg. Chem.* **2003**, 699–704; b) K. Kamata, K. Yonehara, Y. Sumida, K. Yamaguchi, S. Hikichi, N. Mizuno, *Science* **2003**, *300*, 964–966; c) D. G. Musaev, K. Morokuma, Y. V. Geletii, C. L. Hill, *Inorg. Chem.* **2004**, *43*, 7702–7708; d) T. M. Anderson, W. A. Neiwert, M. L. Kirk, P. M. B. Piccoli, A. J. Schultz, T. F. Koetzle, D. G. Musaev, K. Morokuma, R. Cao, C. L. Hill, *Science* **2004**, *306*, 2074–2077; e) M. Nyman, A. J. Celestian, J. B. Parise, G. P. Holland, T. M. Alam, *Inorg. Chem.* **2006**, *45*, 1043–1052.

[4] H. Murakami, T. Kozeki, Y. Suzuki, S. Ono, H. Ohtake, N. Sarukura, E. Ishikawa, T. Yamase, *Appl. Phys. Lett.* **2001**, *79*, 3564–3566.

[5] S. J. A. van Gisbergen, J. G. Snijders, E. J. Baerends, *J. Chem. Phys.* **1998**, *109*, 10644–10656.

[6] a) M. M. Rohmer, M. Bénard, J. P. Blaudeau, J. M. Maestre, J. M. Poblet, *Coord. Chem. Rev.* **1998**, *178–180*, 1019–1049 and references cited therein; b) J. M. Poblet, X. López, C. Bo, *Chem. Soc. Rev.* **2003**, *32*, 297–308 and references cited therein; c) A. J. Bridgeman, G. Cavigliasso, *J. Phys. Chem. A* **2003**, *107*, 6613–6621; d) E. M. Zueva, H. Chermette, S. A. Borshch, *Inorg. Chem.* **2004**, *43*, 2834–2844; e) X. Yang, T. Waters, X. B. Wang, R. A. J. O'Hair, A. G. Wedd, J. Li, D. A. Dixon, L. S. Wang, *J. Phys. Chem. A* **2004**, *108*, 10089–10093; f) M. J. Janik, R. J. Davis, M. Neurock, *J. Am. Chem. Soc.* **2005**, *127*, 5238–5245; g) M. J. Watras, A. V. Teplyakov, *J. Phys. Chem. B* **2005**, *109*, 8928–8934; h) X. López, C. Nieto-Draghi, C. Bo, J. B. Avalos, J. M. Poblet, *J. Phys. Chem. A* **2005**, *109*, 1216–1222; i) A. J. Bridgeman, *Chem. Eur. J.* **2006**, *12*, 2094–2102; j) J. Gracia, J. M. Poblet, J. Autschbach, L. P. Kazansky, *Eur. J. Inorg. Chem.* **2006**, 1139–1148; k) J. Gracia, J. M. Poblet, J. A. Fernández, J. Autschbach, L. P. Kazansky, *Eur. J. Inorg. Chem.* **2006**, 1149–1154; l) X. López, J. A. Fernández, J. M. Poblet, *Dalton Trans.* **2006**, 1162–1167; m) M. J. Janik, B. B. Bardin, R. J. Davis, M. Neurock, *J. Phys. Chem. B* **2006**, *110*, 4170–4178; n) D. Laurencin, R. Villanneau, H. Gérard, A. Proust, *J. Phys. Chem. A* **2006**, *110*, 6345–6355.

[7] a) L. K. Yan, Z. M. Su, W. Guan, M. Zhang, G. H. Chen, L. Xu, E. B. Wang, *J. Phys. Chem. B* **2004**, *108*, 17337–17343; b) W. Guan, L. K. Yan, Z. M. Su, S. X. Liu, M. Zhang, X. H. Wang, *Inorg. Chem.* **2005**, *44*, 100–107; c) L. K. Yan, Z. M. Su, K. Tan, M. Zhang, L. Y. Qu, R. S. Wang, *Int. J. Quantum Chem.* **2005**, *105*, 37–42; d) L. K. Yan, G. C. Yang, W. Guan, Z. M. Su, R. S. Wang, *J. Phys. Chem. B* **2005**, *109*, 22332–22336; e) W. Guan, L. K. Yan, Z. M. Su, E. B. Wang, X. H. Wang, *Int. J. Quantum Chem.* **2006**, *106*, 1860–1864.

[8] S. J. A. van Gisbergen, J. G. Snijders, E. J. Baerends, *J. Chem. Phys.* **1998**, *109*, 10657–10668.

[9] K. C. Wu, J. Li, C. S. Lin, *Chem. Phys. Lett.* **2004**, *388*, 353–357.

[10] a) "Chemistry with ADF": G. Te Velde, F. M. Bickelhaupt, E. J. Baerends, C. Fonseca Guerra, S. J. A. van Gisbergen, J. G. Snijders, T. Ziegler, *J. Comput. Chem.* **2001**, *22*, 931–967; b) C. Fonseca Guerra, J. G. Snijders, G. Te Velde, E. J. Baerends, *Theor. Chem. Acc.* **1998**, *99*, 391–403; c) ADF2004.01, SCM, Theoretical Chemistry, Vrije Universiteit, Amsterdam, The Netherlands, http://www.scm.com.

[11] E. van Lenthe, E. J. Baerends, J. G. Snijders, *J. Chem. Phys.* **1993**, *99*, 4597–4610.

[12] A. D. Becke, *Phys. Rev. A* **1988**, *38*, 3098–3100.

[13] J. P. Perdew, *Phys. Rev. B* **1986**, *33*, 8822–8824.

[14] S. J. A. van Gisbergen, J. G. Snijders, E. J. Baerends, *Comput. Phys. Commun.* **1999**, *118*, 119–138.

[15] R. van Leeuwen, E. J. Baerends, *Phys. Rev. A* **1994**, *49*, 2421–2431.

[16] M. J. Frisch, G. W. Trucks, H. B. Schlegel, G. E. Scuseria, M. A. Robb, J. R. Cheeseman, J. A. Montgomery, Jr., T. Vreven, K. N. Kudin, J. C. Burant, J. M. Millam, S. S. Iyengar, J. Tomasi, V. Barone, B. Mennucci, M. Cossi, G. Scalmani, N. Rega, G. A. Petersson, H. Nakatsuji, M. Hada, M. Ehara, K. Toyota, R. Fukuda, J. Hasegawa, M. Ishida, T. Nakajima, Y. Honda, O. Kitao, H. Nakai, M. Klene, X. Li, J. E. Knox, H. P. Hratchian, J. B. Cross, C. Adamo, J. Jaramillo, R. Gomperts, R. E. Stratmann, O. Yazyev, A. J. Austin, R. Cammi, C. Pomelli, J. W. Ochterski, P. Y. Ayala, K. Morokuma, G. A. Voth, P. Salvador, J. J. Dannenberg, V. G. Zakrzewski, S. Dapprich, A. D. Daniels, M. C. Strain, O. Farkas, D. K. Malick, A. D. Rabuck, K. Raghavachari, J. B. Foresman, J. V. Ortiz, Q. Cui, A. G. Baboul, S. Clifford, J. Cioslowski, B. B. Stefanov, G. Liu, A. Liashenko, P. Piskorz, I. Komaromi, R. L. Martin, D. J. Fox, T. Keith, M. A. Al-Laham, C. Y. Peng, A. Nanayakkara, M. Challacombe, P. M. W. Gill, B. Johnson, W. Chen, M. W. Wong, C. Gonzalez, J. A. Pople, *GAUSSIAN03*, Gaussian, Inc., Pittsburgh, PA, **2003**..

[17] P. J. Hay, W. R. Wadt, *J. Chem. Phys.* **1985**, *82*, 299–310.

Received: May 14, 2006
Published Online: August 11, 2006

 © 2006 Wiley-VCH Verlag GmbH & Co. KGaA, Weinheim 

DOI: 10.1002/ejic.200600491

# Assembly and Upconversion Properties of Lanthanide Coordination Polymers Based on Hexanuclear Building Blocks with ($\mu_3$-OH) Bridges

**Danfeng Weng,[a] Xiangjun Zheng,*[a] and Linpei Jin*[a]**

**Keywords:** Hydroxido clusters / Lanthanide coordination polymers / Codoped complexes / Upconversion properties

Three novel hexanuclear core-based hydroxidolanthanide coordination polymers $[Ln_3(BDC)_{3.5}(OH)_2(H_2O)_2]\cdot H_2O$ [Ln = Y (**1**), Yb (**2**) and Er (**3**); BDC = 1,4-benzenedicarboxylate] were prepared by the hydrothermal method. The controlled hydrolysis of lanthanide ions led to an open hexanuclear cluster core. The hexanuclear core containing six ($\mu_3$-OH) bridged $Ln^{III}$ ions from two asymmetric units adopts a chair-like configuration. It behaves as a building block and is linked by the BDC ligands to form a 3D framework. The guest water molecules occupy the 1D channels in the structure. The upconversion spectra of the Y:Er-Yb codoped coordination polymers have been studied. The distinct upconversion emissions come from two-photon or three-photon excitation of Y:Er-Yb codoped coordination polymers and arise from $Er^{III}$ transitions of the type $^4F_{5/2}\rightarrow{}^4I_{15/2}$, $^2H_{11/2}\rightarrow{}^4I_{15/2}$, $^4S_{3/2}\rightarrow{}^4I_{15/2}$ and $^4F_{9/2}\rightarrow{}^4I_{15/2}$.
(© Wiley-VCH Verlag GmbH & Co. KGaA, 69451 Weinheim, Germany, 2006)

## Introduction

Polynuclear hydroxidolanthanide cluster compounds are enjoying increasing popularity due to their optical, electronic and catalytic properties, which may ultimately lead to potential technological applications such as optoelectronic devices, luminescent and biocatalyst materials.[1] Many polynuclear hydroxidolanthanide clusters have been reported in the past two decades. The reported structures show that the basic structural skeletons belong to two motifs, i.e. cubane-like clusters and square pyramids with the $[Ln_4(\mu_3\text{-}OH)_4]^{8+}$ cubane-like building block being regarded as a common structural motif in hydroxidolanthanide clusters.[1b,2] Many tetranuclear hydroxidolanthanide clusters have a cubane-like building block.[1a,b,c;2b;3] Two cubane-like units can be combined to a heptanuclear $[Ln_7(\mu_3\text{-}OH)_8]^{13+}$ cluster sharing one vertex.[4] Four or five vertex-sharing cubane-like cluster units centring around a halide anion template can be assembled to dodeca-[1a,1c] and pentadecanuclear clusters[1a,1c;5] with wheel structures. The pentanuclear square-pyramid unit appears to be another common structural motif in hydroxidolanthanide clusters.[1d,6] The $[Eu_5(\mu_4\text{-}OH)(\mu_3\text{-}OH)_4]^{10+}$ cluster has been reported[7] and the square-pyramidal $Ln_5$ unit can be considered as a building block for hexa-,[1a,1c;8] nona-[6a,9] and tetradecanuclear[1d,6b,10] clusters sharing their apexes or the square bases. To the best of our knowledge, the majority of hexanuclear $[Ln_6(\mu_6\text{-}O)(\mu_3\text{-}OH)_8]^{8+}$ skeletons are octahedral while the $[Ln_6(\mu_3\text{-}OH)_4]^{14+}$ chair-like core as building block has never been reported.

In the past decade, the upconversion of the infrared light into visible light has been extensively studied on various crystalline and amorphous materials for their potential applications in lasers,[11] optical devices, wave-guides, data storage devices, microfabrication,[12] biological labelling,[13] biosensors[14] and so on. The most frequently used upconversion ions are $Er^{III}$ or $Tm^{III}$ combined with $Yb^{III}$ as a sensitiser. Many different RE-doped (RE = rare earths) inorganic materials have been studied such as oxides,[15] silicates and phosphates,[16] oxyfluorides,[17] fluorides[18] and $NaYF_4$.[13b,14a,19] However, very few lanthanide-doped coordination compound materials have been achieved.[20] We report herein three new hexanuclear hydroxidolanthanide cluster coordination polymers $[Ln_3(BDC)_{3.5}(OH)_2(H_2O)_2]\cdot H_2O$ [Ln = Y (**1**), Yb (**2**), Er (**3**)] which are different from the reported motifs and the first examples with upconversion properties of the codoped lanthanide (Y, Er, Yb) coordination polymers.

## Results and Discussion

### Synthesis

The coordination polymers were obtained by hydrothermal synthesis. During the preparation, the pH of the reaction systems was adjusted by aqueous NaOH in the presence of NaAc to control the hydrolysis of the lanthanide ions. Then 1,4-benzenedicarboxylic acid was added to the resultant mixture.

### Structural Description

The single-crystal X-ray diffraction analysis revealed that compounds **1**, **2** and **3** are isomorphous and, consequently,

[a] Department of Chemistry, Beijing Normal University, Beijing 100875, P. R. China
Fax: +86-10-58802075
E-mail: lpjin@bnu.edu.cn

 InterScience © 2006 Wiley-VCH Verlag GmbH & Co. KGaA, Weinheim 

we will only describe the structure of **1** in detail. The asymmetric unit of **1** consists of a neutral trinuclear $[Y_3(BDC)_{3.5}(OH)_2(H_2O)_2]$ unit (Figure 1) and one lattice water molecule. The three $Y^{III}$ ions are all eight-coordinate but surrounded by different numbers of $\mu_3$-OH groups, coordinated $H_2O$ molecules and BDC anions. Around Y1, Y2 and Y3, there are five, five and four BDC ligands, respectively. For BDC, which adopts two coordination modes in the compound, the coordinated carboxyl units are divided into two types: bridging bidentate (I) and chelating/bridging tridentate (II) (Scheme 1). The hydroxy groups adopt a $\mu_3$-mode to bridge three $Y^{III}$ ions, while the water molecule only acts as a terminal ligand. Thus, the three $Y^{III}$ ions are coordinated in markedly different coordination environments (see Table 1). Selected bond lengths of **1** are listed in Table 2.

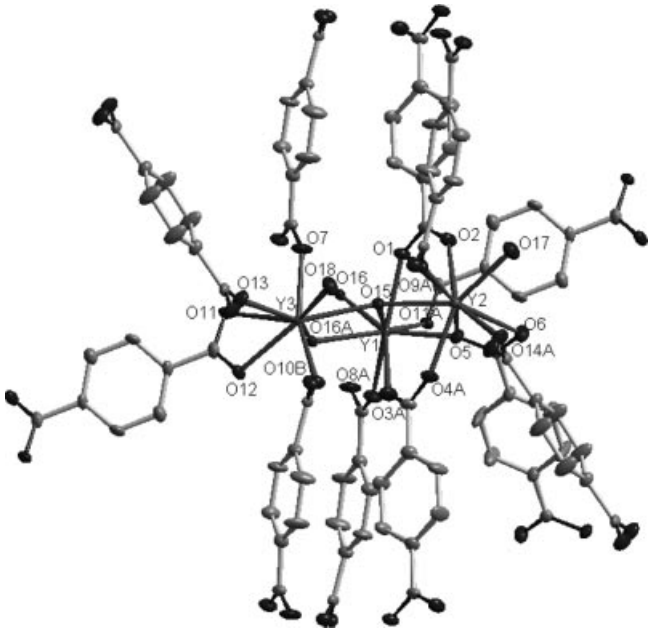


Figure 1. Coordination environment of $Y^{III}$ in complex **1** with ellipsoids drawn at the 30% probability level. All hydrogen atoms and lattice water molecule are omitted for clarity.

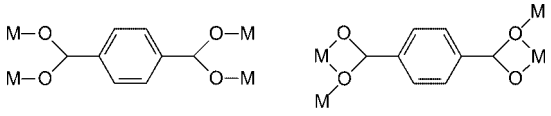


I II

Scheme 1. Coordination modes for the BDC ligands in **1**.

Table 1. The coordination environment of the $Y^{III}$ ions in the asymmetric unit.

| | No. of $\mu_3$-OH | No. of carboxylate oxygen atoms | | No. of $H_2O$ |
|---|---|---|---|---|
| | | I | II | |
| Y1 | 3 | 3 | 2 | 0 |
| Y2 | 1 | 3 | 3 | 1 |
| Y3 | 2 | 3 | 2 | 1 |

Table 2. Selected bond lengths in complex **1** [Å].

| | | |
|---|---|---|
| Y(1)–O(1) 2.362(2) | Y(2)–O(2) 2.336(2) | Y(3)–O(7) 2.226(2) |
| Y(1)–O(3)#1 2.408(2) | Y(2)–O(4)#1 2.335(2) | Y(3)–O(10)#1 2.231(2) |
| Y(1)–O(5) 2.263(2) | Y(2)–O(5) 2.436(2) | Y(3)–O(11) 2.821(2) |
| Y(1)–O(8)#2 2.293(2) | Y(2)–O(6) 2.500(3) | Y(3)–O(12) 2.414(2) |
| Y(1)–O(11)#2 2.431(2) | Y(2)–O(9)#3 2.254(2) | Y(3)–O(13) 2.235(3) |
| Y(1)–O(15) 2.388(2) | Y(2)–O(14)#4 2.300(2) | Y(3)–O(15) 2.479(2) |
| Y(1)–O(16) 2.412(2) | Y(2)–O(15) 2.429(2) | Y(3)–O(16)#2 2.315(2) |
| Y(1)–O(16)#2 2.278(2) | Y(2)–O(17) 2.363(3) | Y(3)–O(18) 2.394(3) |

Symmetry operations: #1: $x + 1, y, z$; #2: $-x + 1, -y + 1, -z + 1$; #3: $-x, -y + 2, -z + 1$; #4: $-x + 1, -y + 2, -z + 1$.

The three $Y^{III}$ ions combine with another three $Y^{III}$ ions from the adjacent asymmetric unit to form a second hexanuclear building block (Figure 2a). Every three adjacent $Y^{III}$ ions are linked by one $\mu_3$-OH group in the centre,

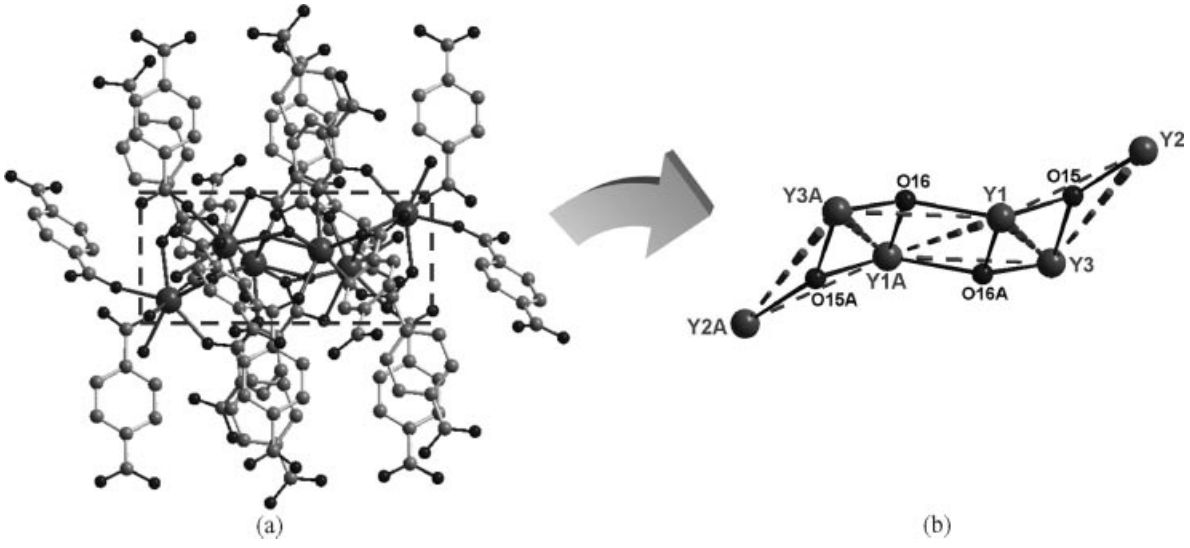


Figure 2. (a) Cell structure of **1**. (b) Chair-like conformation of the hexanuclear core.

 © 2006 Wiley-VCH Verlag GmbH & Co. KGaA, Weinheim 

which is slightly above the basal face and the Y–O($\mu_3$-OH) distances range from 2.278 to 2.479 Å. These distances are comparable with Ln–O($\mu_3$-OH) distances in the reported octahedral hexanuclear compounds with an average of 2.433 Å.[8d,8e] Four $Y_3$($\mu_3$-OH) trigonal pyramids share their adjacent sides to form the hexanuclear cluster with a chair-like conformation (Figure 2b). This chair-like hexanuclear building block is different from the reported structural motifs based on square pyramids and cubane-like cores. The Ln···Ln distances ranging from 3.731 to 4.712 Å are longer than those found in the latter two kinds of clusters (the majority range from 3.5 to 3.8 Å).[1b,3c,4,6,8d,8e,9] This is due to the steric effect of the open construction of the $Ln_6$ entity whereas the reported hexanuclear clusters are all closed clusters.

Among the reported hexanuclear hydroxido clusters, most were almost zero-dimensional.[8a,8b,8d,8e] One 1D example was achieved by linking the hydroxidolanthanide cluster through Pd ions[8c] and a reported pseudo-3D network is based on hydrogen bonds[8f] whereas the hexanuclear cores in the title compounds are linked by the ligand BDC, resulting in 3D coordination polymers. The BDC ligands act as short bridges through one carboxylato end linking the hexanuclear nodes or longer bridges through the two carboxylate groups. The linkages consist of ten BDC ligands along the *a*-axis, four along the [2 0 $\bar{1}$] direction, two along the [0 $\bar{1}$ 1] direction with the remaining two following the [$\bar{1}$ 1 0] direction. The linear rigid BDC ligands take the main role in linking the hexanuclear building blocks into a complicated 3D structure. The lattice water molecules, fixed by hydrogen-bonding interactions to the frameworks, are located in 1D channels in the 3D networks (see Figure 3).

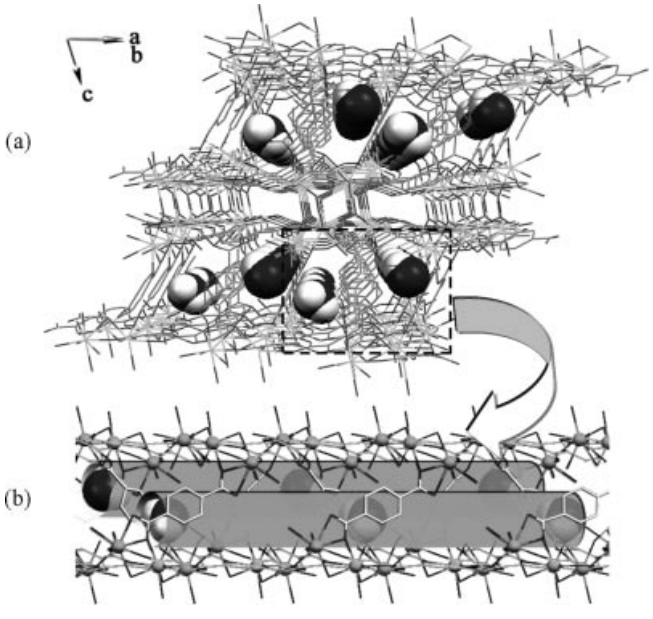


Figure 3. (a) Perspective view of the microporous framework of **1** along the [1 $\bar{1}$ 0] direction, showing 1D channels where guest water molecules reside and the guests are shown as space-filling models. (b) Lateral view of the 1D channels holding the water molecules.

## Upconversion Properties

The upconversion emission spectrum of the Y:Er-Yb codoped coordination polymer under 980 nm laser excitation is shown in Figure 4. The emission spectrum exhibits four bands. The red emission is centred at 654 nm and results from the $^4F_{9/2}(Er^{III})$ to $^4I_{15/2}(Er^{III})$ transition and the green band has centres at 545 and 524 nm and results from the transitions $^4S_{3/2}(Er^{III})/^2H_{11/2}(Er^{III})\rightarrow{}^4I_{15/2}(Er^{III})$. A seldom observed indigo emission centred at 455 nm can also be observed and corresponds to the transition $^4F_{5/2}(Er^{III})\rightarrow{}^4I_{15/2}(Er^{III})$.

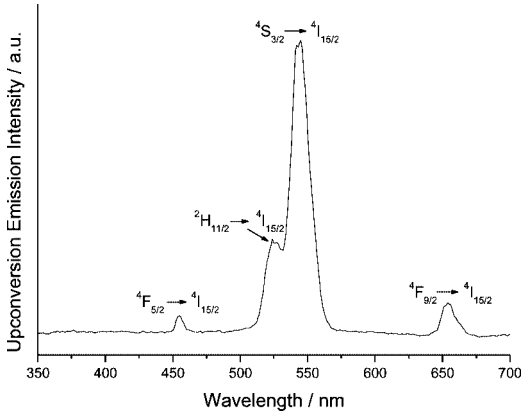


Figure 4. Upconversion emission for the $Er^{III}$ ion in the Y:Yb-Er codoped coordination polymer (laser power used is 640 mW, EM slit = 10.0 nm).

The 545 and 524 nm emissions can be described as a two-photon upconversion excitation mechanism.[15a,18a,18e,18f] First, the $Yb^{III}$ ions are easily excited to their $^2F_{5/2}(Yb^{III})$ level from ground $^2F_{7/2}(Yb^{III})$ level by absorbing a 980 nm photon. The energy is transferred to the $Er^{III}$ ions which become excited from the $^4I_{15/2}(Er^{III})$ level to the $^4I_{11/2}(Er^{III})$ level. A second photon transfer from the excited $Yb^{III}$ ions pumps the $Er^{III}(^4I_{11/2})$ ions to the $^4F_{7/2}(Er^{III})$ level. The $^4F_{7/2}(Er^{III})$ state can decay nonradiatively to the $^4S_{3/2}(Er^{III})$ and $^2H_{11/2}(Er^{III})$ levels.[15a,16c,18a] The green emissions observed result from the $^4S_{3/2}(Er^{III})\rightarrow{}^4I_{15/2}(Er^{III})$ and the $^2H_{11/2}(Er^{III})\rightarrow{}^4I_{15/2}(Er^{III})$ transitions. The decay processes were confirmed by a frequency of 2160 $cm^{-1}$ (1410 $cm^{-1}$ + 750 $cm^{-1}$, see Figure 5) and the peak at 1410 $cm^{-1}$ in the IR spectrum, for which the phonon energy corresponds to the energy gap between the $^4F_{7/2}(Er^{III})$ and $^4S_{3/2}(Er^{III})$ states, and the energy gap between $^4F_{7/2}(Er^{III})$ and $^2H_{11/2}(Er^{III})$ states. The possible channel for the green upconversion luminescence is given below:

$^2F_{5/2}(Yb^{III}) + {}^4I_{15/2}(Er^{III}) \rightarrow {}^2F_{7/2}(Yb^{III}) + {}^4I_{11/2}(Er^{III})$

$^2F_{5/2}(Yb^{III}) + {}^4I_{11/2}(Er^{III}) \rightarrow {}^2F_{7/2}(Yb^{III}) + {}^4F_{7/2}(Er^{III})$

$^4F_{7/2}(Er^{III}) \rightarrow {}^4S_{3/2}(Er^{III})/{}^2H_{11/2}(Er^{III})$ (nonradiative decay)

The 654 nm emission is caused by the transition to the $Er^{III}$ ground state $^4I_{15/2}(Er^{III})$ from the excited $^4F_{9/2}(Er^{III})$ state.[15a,18a,18e,18f] $Er^{III}$ ions in the $^4I_{11/2}(Er^{III})$ state lose their energy in the form of an OH vibration at 3500 $cm^{-1}$ [corresponding to the energy gap between $^4I_{11/2}(Er^{III})$ and $^4I_{13/2}(Er^{III})$], decay to the $^4I_{13/2}(Er^{III})$ state and then jump

 © 2006 Wiley-VCH Verlag GmbH & Co. KGaA, Weinheim 

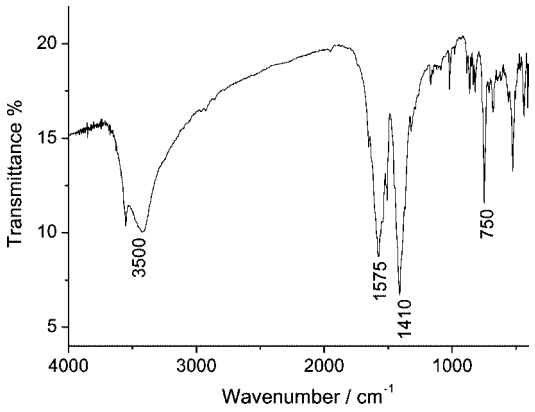


Figure 5. IR spectrum of the Y:Er-Yb codoped coordination polymer.

to the $^4F_{9/2}(Er^{III})$ level by a second pumping photon. This would account for the red emissions from the $^4F_{9/2}(Er^{III})$ level to the ground state. This mechanism can be described as:

$^2F_{5/2}\ (Yb^{III}) + {}^4I_{15/2}(Er^{III}) \rightarrow {}^2F_{7/2}(Yb^{III}) + {}^4I_{11/2}(Er^{III})$

$^4I_{11/2}(Er^{III}) \rightarrow {}^4I_{13/2}(Er^{III})$ (nonradiative decay)

$^2F_{5/2}\ (Yb^{III}) + {}^4I_{13/2}(Er^{III}) \rightarrow {}^2F_{7/2}(Yb^{III}) + {}^4F_{9/2}(Er^{III})$

The 455 nm indigo emission is unusual since upconversion emissions below 490 nm have seldom been observed for $Yb^{III}/Er^{III}$ materials.[15a] A probable three-photon mechanism for the population of the $^4F_{5/2}(Er^{III})$ level can be proposed to explain the indigo emission at 455 nm. There is a possibility that some excited $Er^{III}(^4I_{11/2})$ ions jump back to the lower $^4I_{13/2}(Er^{III})$ level giving the 3500 $cm^{-1}$ IR active decay. The two-photon energy from excited $Yb^{III}(^2F_{5/2})$ pumps the $Er^{III}(^4I_{13/2})$ to the $^2H_{9/2}(Er^{III})$ level via the $^2F_{9/2}(Er^{III})$ bridge and decays to the $^4F_{5/2}(Er^{III})$ level. The $^2H_{9/2}(Er^{III}) \rightarrow {}^4F_{5/2}(Er^{III})$ decay corresponds to 2325 $cm^{-1}$ (1575 $cm^{-1}$ + 750 $cm^{-1}$ in the IR spectrum). Therefore, the possible three-photon mechanism can be expressed as follows:

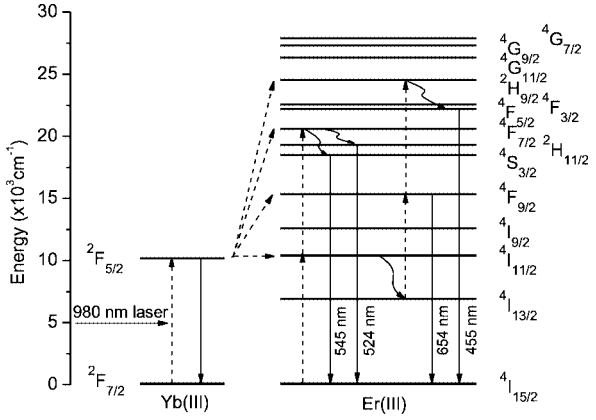


Figure 6. Energy-level diagram for the upconversion mechanism of the Y:Er-Yb codoped coordination polymer under 980 nm excitation.

$^2F_{5/2}\ (Yb^{III}) + {}^4I_{15/2}(Er^{III}) \rightarrow {}^2F_{7/2}(Yb^{III}) + {}^4I_{11/2}(Er^{III})$

$^4I_{11/2}(Er^{III}) \rightarrow {}^4I_{13/2}(Er^{III})$ (nonradiative decay)

$^2F_{5/2}\ (Yb^{III}) + {}^4I_{13/2}(Er^{III}) \rightarrow {}^2F_{7/2}(Yb^{III}) + {}^4F_{9/2}(Er^{III})$

$^2F_{5/2}\ (Yb^{III}) + {}^4F_{9/2}(Er^{III}) \rightarrow {}^2F_{7/2}(Yb^{III}) + {}^2H_{9/2}(Er^{III})$

$^2H_{9/2}(Er^{III}) \rightarrow {}^4F_{5/2}(Er^{III})$ (nonradiative decay)

The energy levels and overall upconversion Scheme of $Er^{III}$ are shown in Figure 6.

## Thermogravimetric Analysis and Powder X-ray Diffraction

We took complex **1** as a representative example for thermogravimetric analysis (see Figure 7). Under atmospheric conditions, thermogravimetric analysis performed on **1** showed the first weight loss of 5.5% in the range of 151–365 °C. This is related to the loss of the two coordinated water molecules and one lattice water molecule (calcd. weight loss 5.8%). The second mass loss began at 480 °C and is associated with the decomposition of the organic and hydroxy groups. The final residue, after the sample was heated to 836 °C, was $Y_2O_3$ (found weight loss 36.2%, calcd. 36.5%).

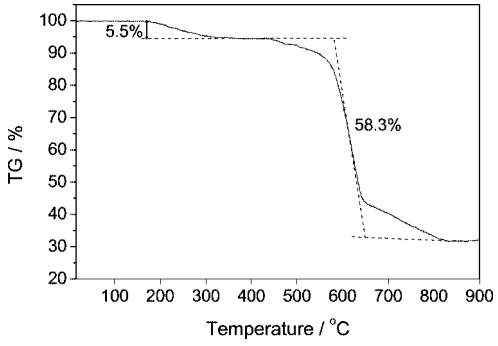


Figure 7. Thermogravimetric trace of **1**.

To confirm the thermogravimetric analysis, complex **1** was characterised by powder X-ray diffraction (PXRD) at 25, 100, 400, 635 and 880 °C (see Figure 8). The PXRD

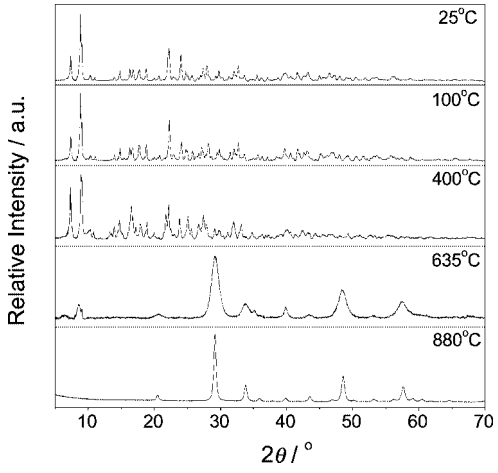


Figure 8. PXRD patterns for **1** taken at 25, 100, 400, 635 and 880 °C.

 © 2006 Wiley-VCH Verlag GmbH & Co. KGaA, Weinheim 

patterns of the sample at 100 and 400 °C, although very similar, are not the same, which indicates the change of the frameworks after the removal of the lattice water and coordinated water molecules. Above 635 °C, the PXRD patterns change completely, suggesting the collapse of the framework. The remaining residue $Y_2O_3$ coincides quite well with the standard $Y_2O_3$ (No. 01-083-0927).

## Conclusions

Three coordination polymers based on hexanuclear building blocks with ($\mu_3$-OH) bridges have been achieved. The hexanuclear building block has an interesting chair-like configuration which is different from the reported motifs based on cubane-like clusters and square pyramids. The structure of the cluster core depends on the extent of the hydrolysis of the Ln ions which is closely related to the pH of the system. Hence, controlled hydrolysis could lead to polymeric materials based on polynuclear clusters exhibiting different configurations. Furthermore, the Y:Er-Yb co-doped coordination polymers have been synthesised successfully. We have demonstrated the feasibility of introducing red, green and indigo light emissions of $Er^{III}$ ions using IR spectroscopy as supporting evidence for the nonradiative decay. The upconversion emissions of the codoped polymers correspond to two-photon and three-photon upconversion excitation mechanisms.

## Experimental Section

**General:** All chemicals were obtained commercially and used without further purification. Elemental analyses of C, H and N were performed with an Elementar Vario EL analyser. The IR spectra were recorded with a Nicolet Avatar 360 FTIR spectrometer using the KBr pellet technique. The thermal stability was investigated using a ZRY-2P thermogravimetric analyser under atmospheric conditions at a heating rate of 10 °C min$^{-1}$, using α-$Al_2O_3$ as a reference. The inductively coupled plasma (ICP) analysis was performed with a JY ULTIMA spectrometer. The powder X-ray diffraction was carried with a PANalytical X'Pert PRO MPD diffractometer using Cu-$K_{\alpha1}$ radiation in the $2\theta$ range of 5°–70°.

**Synthesis of $[Y_3(BDC)_{3.5}(OH)_2(H_2O)_2]\cdot H_2O$(1):** A solution of NaAc·3$H_2O$ (0.020 g, 0.15 mmol), $YCl_3\cdot 6H_2O$ (0.030 g, 0.1 mmol), $H_2O$ (5 mL) and aqueous NaOH (0.3 mL, 0.65 mol L$^{-1}$) was stirred to bring about the hydrolysis of $YCl_3$ and 1,4-benzenedicarboxylic acid (0.017 g, 0.1 mmol) was then added. The pH of the solution was adjusted to 5.1 and the mixture was then sealed in a 25 mL stainless steel reactor with a Teflon liner and heated at 190 °C for 72 h. Colourless block-like crystals of **1** were obtained. Yield: 0.021 g (66.67% based on Y). $C_{28}H_{22}O_{19}Y_3$ (929.19): calcd. C 36.19, H 2.39; found C 36.25, H 2.36. IR (KBr): $\tilde{\nu}$ = 553 (s), 3421 (s), 1651 (m), 1571 (s), 1540 (s), 1510 (m), 1410 (s), 1318 (w), 1169 (w), 1016 (m), 745 (s), 525 (m) cm$^{-1}$.

**Synthesis of $[Yb_3(BDC)_{3.5}(OH)_2(H_2O)_2]\cdot H_2O$(2):** This compound was prepared according to the procedure for **1** but by using $Yb(NO_3)_3\cdot 6H_2O$ instead of $YCl_3\cdot 6H_2O$. Diamond-like crystals of **2** were obtained. Yield: 0.020 g (49.61% based on Yb). $C_{28}H_{22}O_{19}Yb_3$ (1177.54): calcd. C 28.45, H 1.86; found C 28.50, H 2.01. IR (KBr): $\tilde{\nu}$ = 3555 (s), 3435 (s), 1654 (m), 1583 (s), 1539 (s), 1502 (m), 1408 (s), 1320 (w), 1170 (w), 1017 (m), 751 (s), 526 (m) cm$^{-1}$.

**Synthesis of $[Er_3(BDC)_{3.5}(OH)_2(H_2O)_2]\cdot H_2O$(3):** This compound was prepared according to the procedure for **1** but by using $ErCl_3\cdot 6H_2O$ instead of $YCl_3\cdot 6H_2O$. Pink diamond-like crystals of **3** were obtained. Yield: 0.016 g (41.47% based on Er). $C_{28}H_{22}O_{19}Er_3$ (1164.25): calcd. C 28.89, H 1.91; found C 29.08, H 1.89. IR (KBr): $\tilde{\nu}$ = 3550 (s), 3424 (s), 1650 (m), 1578 (s), 1538 (s), 1509 (m), 1408 (s), 1323 (w), 1174 (w), 1019 (m), 749 (s), 520 (m) cm$^{-1}$.

**Synthesis of $[(Y:Er\text{-}Yb)_3(BDC)_{3.5}(OH)_2(H_2O)_2]\cdot H_2O$:** The codoped compounds were prepared according to the procedure for **1** but by using $YCl_3\cdot 6H_2O$, $ErCl_3\cdot 6H_2O$ and $Yb(NO_3)_3\cdot 6H_2O$ (for example, molar ratio: 94.00:2.00:4.00%) instead of 100% $YCl_3\cdot 6H_2O$. Colourless block-like crystals were obtained. Yield: 0.018 g (56.88% based on total Ln). $C_{28}H_{22}O_{19}(Y:Er\text{-}Yb)_3$ (943.83): calcd. C 35.63, H 2.35; found C 35.85, H 2.43. IR (KBr): $\tilde{\nu}$ = 3554 (s), 3423 (s), 1653 (m), 1574 (s), 1535 (s), 1508 (m), 1410 (s), 1319 (w), 1167 (w), 1020 (w), 749 (s), 527 (m) cm$^{-1}$. The ICP analysis showed that the molar ratio of Y/Yb/Er was 94.45:2.17:3.38 in the product.

Table 3. Crystallographic data of **1**, **2** and **3**.

| | **1** | **2** | **3** |
|---|---|---|---|
| Empirical formula | $C_{28}H_{22}O_{19}Y_3$ | $C_{28}H_{22}O_{19}Yb_3$ | $C_{28}H_{24}O_{19}Er_3$ |
| Formula mass | 929.19 | 1177.54 | 1166.25 |
| $T$ [K] | 293(2) | 293(2) | 293(2) |
| Wavelength [Å] | 0.71073 | 0.71073 | 0.71073 |
| Crystal system | triclinic | triclinic | triclinic |
| Space group | $P\bar{1}$ | $P\bar{1}$ | $P\bar{1}$ |
| $a$ [Å] | 11.392(1) | 11.363(3) | 11.408(1) |
| $b$ [Å] | 12.070(1) | 11.989(3) | 12.064(1) |
| $c$ [Å] | 12.996(1) | 12.987(4) | 13.026(1) |
| $\alpha$ [°] | 86.898(1) | 86.741(4) | 86.827(1) |
| $\beta$ [°] | 67.176(1) | 67.084(4) | 67.126(1) |
| $\gamma$ [°] | 72.200(1) | 72.150(4) | 72.137(1) |
| $V$ [Å$^3$] | 1563.9(3) | 1547.1(7) | 1568.0(2) |
| Z | 2 | 2 | 2 |
| $D_c$ [g cm$^{-3}$] | 1.973 | 2.536 | 2.470 |
| $\mu$ [mm$^{-1}$] | 5.608 | 9.082 | 8.043 |
| Reflections collected, unique, $R_{int}$ | 10547, 7180, 0.0187 | 8207, 5447, 0.0336 | 8072, 5504, 0.0207 |
| $R$ indices [$I > 2\sigma(I)$] | $R_1$ = 0.0319, $wR_2$ = 0.0779 | $R_1$ = 0.0350, $wR_2$ = 0.0697 | $R_1$ = 0.0240, $wR_2$ = 0.0609 |
| $R$ indices (all data) | $R_1$ = 0.0457, $wR_2$ = 0.0886 | $R_1$ = 0.0492, $wR_2$ = 0.0749 | $R_1$ = 0.0267, $wR_2$ = 0.0621 |

 © 2006 Wiley-VCH Verlag GmbH & Co. KGaA, Weinheim 

The observed XRD patterns of the Y:Er-Yb codoped coordination polymer and **1** indicate that they are isomorphous.

**X-ray Structure Determination:** Intensity data for **1**, **2** and **3** were collected at 293 K with a Bruker SMART 1000 CCD area detector diffractometer using graphite-monochromated Mo-$K_\alpha$ radiation ($\lambda$ = 0.71073 Å) in $\varphi$ and $\omega$ scan modes with $\theta$ ranges of 1.78–27.88° for **1**, 2.09–25.01° for **2** and 1.70–25.01° for **3**. Semiempirical absorption corrections were applied using the SADABS program.[21] The structures were solved by direct methods[22] and refined by full-matrix least squares on $F^2$ using the SHELXS-97 and SHELXL-97 programs, respectively.[22,23] All non-hydrogen atoms were refined anisotropically. The hydrogen atoms were generated geometrically and treated with a mixture of independent and constrained refinements. Details of the crystallographic data of **1**, **2** and **3** are summarised in Table 3. CCDC-608985 to -608987 contain the supplementary crystallographic data for this paper. These data can be obtained free of charge from the Cambridge Crystallographic Data Centre via www.ccdc.cam.ac.uk/datarequest/cif.

**Luminescence Spectroscopy:** Upconversion spectra were obtained with an LS-50B fluorescence spectrophotometer (Perkin–Elmer Corp., Forster City, CA) with an external 0–800 mW adjustable laser (980 nm, Beijing Hi-Tech Optoelectronic Co., China) as the excitation source, instead of the xenon source in the spectrophotometer and with a fibre-optic accessory.

## Acknowledgments

We acknowledge the support from the National Natural Science Foundation of China (20331010, 20501003). We also thank Prof. Yadong Li from Department of Chemistry, Tsinghua University for help with the upconversion spectroscopic measurements.

[1] a) R. Y. Wang, H. D. Selby, H. Liu, M. D. Carducci, T. Z. Jin, Z. P. Zheng, J. W. Anthis, R. J. Staples, *Inorg. Chem.* **2002**, *41*, 278–286; b) B. Q. Ma, D. S. Zhang, S. Gao, T. Z. Jin, C. H. Yan, G. X. Xu, *Angew. Chem. Int. Ed.* **2000**, *39*, 3644–3646; c) Z. P. Zheng, *Chem. Commun.* **2001**, 2521–2529; d) M. R. Bürgstein, M. T. Gamer, P. W. Roesky, *J. Am. Chem. Soc.* **2004**, *126*, 5213–5218; e) O. Guillou, C. Daiguebonne, in: *Handbook on the Physics and Chemistry of Rare Earths*, Elsevier, Amsterdam, **2004**, vol. 34, p. 359–404.

[2] a) J.-C. G. Bünzli, C. Piguet, *Chem. Rev.* **2002**, *102*, 1897–1928; b) R. Y. Wang, H. Liu, M. D. Carducci, T. Z. Jin, C. Zheng, Z. P. Zheng, *Inorg. Chem.* **2001**, *40*, 2743–2750.

[3] a) J. C. Plakatouras, I. Baxter, M. B. Hursthouse, K. M. A. Malik, J. McAleese, S. R. Drake, *J. Chem. Soc., Chem. Commun.* **1994**, 2455–2456; b) T. Dube′, S. Gambarotta, G. Yap, *Organometallics* **1998**, *17*, 3967–3973; c) B. Q. Ma, D. S. Zhang, S. Gao, T. Z. Jin, C. H. Yan, *New J. Chem.* **2000**, *24*, 251–252; d) S. A. Schuetz, V. W. Day, J. L. Clark, J. A. Belot, *Inorg. Chem. Commun.* **2002**, *5*, 706–710; e) X. K. Fang, T. M. Anderson, C. Benelli, C. L. Hill, *Chem. Eur. J.* **2005**, *11*, 712–718.

[4] X. J. Zheng, L. P. Jin, S. Gao, *Inorg. Chem.* **2004**, *43*, 1600–1602.

[5] R. Y. Wang, Z. P. Zheng, T. Z. Jin, R. J. Staples, *Angew. Chem. Int. Ed.* **1999**, *38*, 1813–1815.

[6] a) G. Xu, Z. M. Wang, Z. He, Z. Lu, C. S. Liao, C. H. Yan, *Inorg. Chem.* **2002**, *41*, 6802–6807; b) R. Y. Wang, D. T. Song, S. N. Wang, *Chem. Commun.* **2002**, 368–369.

[7] R. G. Xiong, J. L. Zuo, Z. Yu, X. Z. You, W. Chen, *Inorg. Chem. Commun.* **1999**, *2*, 490–494.

[8] a) Z. Žák, P. Unfried, G. Giester, *J. Alloys Compd.* **1994**, *205*, 235–242; b) G. Giester, P. Unfried, Z. Žák, *J. Alloys Compd.* **1997**, *257*, 175–181; c) J. P. Liu, E. A. Meyers, S. G. Shore, *Inorg. Chem.* **1998**, *37*, 5410–5411; d) R. Y. Wang, M. D. Carducci, Z. P. Zheng, *Inorg. Chem.* **2000**, *39*, 1836–1837; e) D. S. Zhang, B. Q. Ma, T. Z. Jin, S. Gao, C. H. Yan, T. C. W. Mak, *New J. Chem.* **2000**, *24*, 61–62; f) N. Mahé, O. Guillou, C. Daiguebonne, Y. Gérault, A. Caneschi, C. Sangregorio, J. Y. Chane-Ching, P. E. Car, T. Roisnel, *Inorg. Chem.* **2005**, *44*, 7743–7750.

[9] L. G. Hubert-Pfalzgraf, N. Miele-Pajot, R. Papiernik, J. J. Vaissermann, *J. Chem. Soc., Dalton Trans.* **1999**, 4127–4130.

[10] M. R. Bürgstein, P. W. Roesky, *Angew. Chem. Int. Ed.* **2000**, *39*, 549–550.

[11] a) S. Sanders, R. G. Waarts, D. G. Mehuys, D. F. Welch, *Appl. Phys. Lett.* **1995**, *67*, 1815–1817; b) D. M. Baney, G. Rankin, K. W. Chang, *Appl. Phys. Lett.* **1996**, *69*, 1662–1664.

[12] a) F. Auzel, *Chem. Rev.* **2004**, *104*, 139–173; b) S. Q. Man, Y. B. E. Pun, P. S. Chung, *Appl. Phys. Lett.* **2000**, *77*, 483–485; c) R. Sivaraman, S. J. Clarson, B. K. Lee, A. J. Steckl, B. A. Reinhardt, *Appl. Phys. Lett.* **2000**, *77*, 328–330; d) D. R. Gamelin, H.-U. Güdel, *Acc. Chem. Res.* **2000**, *33*, 235–242.

[13] a) G. S. Yi, H. C. Lu, S. Y. Zhao, Y. Ge, W. J. Yang, D. P. Chen, L. H. Guo, *Nano Lett.* **2004**, *4*, 2191–2196; b) J. H. Zeng, J. Su, Z. H. Li, R. X. Yan, Y. D. Li, *Adv. Mater.* **2005**, *17*, 2119–2123.

[14] a) L. Y. Wang, R. X. Yan, Z. Y. Huo, L. Wang, J. H. Zeng, J. Bao, X. Wang, Q. Peng, Y. D. Li, *Angew. Chem. Int. Ed.* **2005**, *44*, 6054–6057; b) G. Piszczek, I. Gryczynski, B. P. Maliwal, J. R. Lakowicz, *J. Fluoresc.* **2002**, *12*, 15–17.

[15] a) J. Silver, M. I. Martinez-Rubio, T. G. Ireland, G. R. Fern, R. Withnall, *J. Phys. Chem. B* **2001**, *105*, 948–953; b) J. A. Capobianco, F. Vetrone, J. C. Boyer, A. Speghini, M. Bettinelli, *J. Phys. Chem. B* **2002**, *106*, 1181–1187; c) J. A. Capobianco, J. C. Boyer, F. Vertone, A. Speghini, M. Bettinelli, *Chem. Mater.* **2002**, *14*, 2915–2921; d) A. Patra, C. S. Friend, R. Kapoor, P. N. Prasad, *J. Phys. Chem. B* **2002**, *106*, 1909–1912; e) A. Patra, C. S. Friend, R. Kapoor, P. N. Prasad, *Appl. Phys. Lett.* **2003**, *83*, 284–286; f) H. W. Song, B. J. Su, T. Wang, S. Z. Lu, L. M. Yang, B. J. Chen, X. J. Wang, X. G. Kong, *Solid State Commun.* **2004**, *132*, 409–413; g) P. Salas, C. Angeles-Chávez, J. A. Montoya, E. De la Rosa, L. A. Diaz-Torres, H. Desirena, A. Martínez, M. A. Romero-Romo, J. Morales, *Opt. Mater.* **2005**, *27*, 1295–1300; h) C. Strohhöfer, A. Polman, *Opt. Mater.* **2003**, *21*, 705–712; i) G. S. Maciel, A. Biswas, P. N. Prasad, *Opt. Commun.* **2000**, *178*, 65–69.

[16] a) K. Riwotzki, H. Meyssamy, A. Kornowski, M. Haase, *J. Phys. Chem. B* **2000**, *104*, 2824–2828; b) K. Riwotzki, H. Meyssamy, H. Schnablegger, A. Kornowski, M. Haase, *Angew. Chem. Int. Ed.* **2001**, *40*, 573–576; c) F. Song, G. Y. Zhang, M. R. Shang, H. Tan, J. Yang, F. Z. Meng, *Appl. Phys. Lett.* **2001**, *79*, 1748–1750; d) G. A. Hebbink, J. W. Stouwdam, D. N. Reinhoudt, F. C. J. M. van Veggel, *Adv. Mater.* **2002**, *14*, 1147–1150; e) H. K. Jung, J. S. Oh, S. I. Seok, T. H. Lee, *J. Lumin.* **2005**, *114*, 307–313; f) S. Heer, O. Lehmann, M. Haase, H.-U. Güdel, *Angew. Chem. Int. Ed.* **2003**, *42*, 3179–3182.

[17] a) Y. H. Wang, J. Ohwaki, *Appl. Phys. Lett.* **1993**, *63*, 3268–3270; b) F. Lahoz, I. R. Martin, J. M. Calvilla-Quintero, *Appl. Phys. Lett.* **2005**, *86*, 051106; c) X. B. Chen, Z. F. Song, *Solid State Commun.* **2005**, *136*, 313–317.

[18] a) C. T. M. Ribeiro, A. R. Zanatta, L. A. O. Nunes, Y. Messaddeq, M. A. Aegerter, *J. Appl. Phys.* **1998**, *83*, 2256–2260; b) C. M. Bender, J. M. Burlitch, D. Barber, C. Pollock, *Chem. Mater.* **2000**, *12*, 1969–1976; c) J. W. Stouwdam, F. C. J. M. van Veggel, *Nano. Lett.* **2002**, *2*, 733–737; d) X. Wang, Y. D. Li, *Angew. Chem. Int. Ed.* **2003**, *42*, 3497–3500; e) R. X. Yan, Y. D. Li, *Adv. Funct. Mater.* **2005**, *15*, 763–770; f) S. Sivakumar, F. C. J. M. van Veggel, M. Raudsepp, *J. Am. Chem. Soc.* **2005**, *127*, 12464–12465.

[19] a) N. Menyuk, K. Dwight, J. W. Pierce, *Appl. Phys. Lett.* **1972**, *21*, 159–161; b) K. W. Krämer, D. Biner, G. Frei, H. U. Güdel, M. P. Hehlen, S. R. Lüthi, *Chem. Mater.* **2004**, *16*, 1244–1251.

[20] a) L. Luo, W. P. W. Lai, L. K. Wong, W. T. Wong, K. F. Li, K. W. Cheah, *Chem. Phys. Lett.* **2004**, *398*, 372–376; b) K.-L.

 © 2006 Wiley-VCH Verlag GmbH & Co. KGaA, Weinheim 

Wong, W. M. Kwok, W.-T. Wong, D. L. Phillips, K.-W. Cheah, *Angew. Chem. Int. Ed.* **2004**, *43*, 4659–4662.
[21] G. M. Sheldrick, *SADABS, Program for Empirical Absorption Correction of Area Detector Data*, University of Göttingen, Göttingen, Germany, **1997**.
[22] G. M. Sheldrick, *SHELXS 97, Program for Crystal Structure Solution*, University of Göttingen, Göttingen, Germany, **1997**.
[23] G. M. Sheldrick, *SHELXL 97, Program for Crystal Structure Refinement*, University of Göttingen, Göttingen, Germany, **1997**.

Received: May 27, 2006
Published Online: August 10, 2006

 © 2006 Wiley-VCH Verlag GmbH & Co. KGaA, Weinheim 

EurJIC
European Journal of Inorganic Chemistry

Issue 21/2006

Pages 4193–4456

*Papers available ahead of print in Early View at www.interscience.wiley.com*

*Earliest available Table of Contents:*
*Automatically, free of charge by e-mail through*
*www.interscience.wiley.com/alerts*

## COVER PICTURE

**The cover picture shows** the P=C=P backbones of stable, neutral diphosphaallenes along with the publication year of the first example reported for given coordination numbers of the phosphorus atoms. Since the synthesis of hexaphenylcarbodiphosphorane ($Ph_3P{=}C{=}PPh_3$), a $\sigma^4,\sigma^4$-diphosphaallene, in 1961, only two other classes of compounds with P=C=P sequences have been reported in the past decades. Details of the preparation of the phosphavinylidene(oxo)phosphorane Mes*P(O)=C=PMes* (Mes* = 2,4,6-tri-*tert*-butylphenyl), a diphosphaallene featuring $\lambda^5\sigma^3$- and $\lambda^3\sigma^2$-phosphorus atoms, NMR spectroscopic data and the first aspects of its reactivity are described in the article by H. Ranaivonjatovo, J. Escudié et al. on p. 4237 ff.

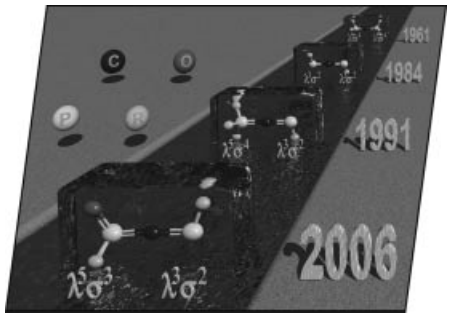


## MICROREVIEW

**Contents**

**4209** **F. A. Cotton,* C. A. Murillo***

Chiral Molecules Containing Metal–Metal Bonds

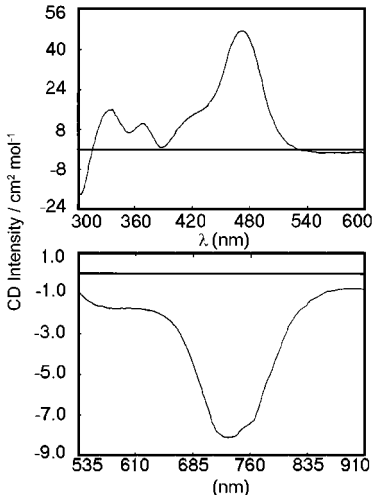


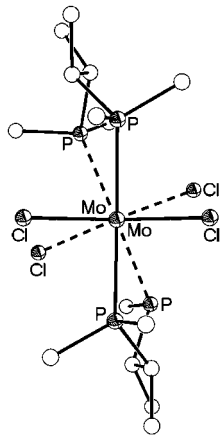


**Keywords:** Metal–metal bonds / Chirality / Chromophores / Orthometalation / Helical molecules

 © 2006 Wiley-VCH Verlag GmbH & Co. KGaA, Weinheim 

# SHORT COMMUNICATIONS


**4219** **M. Ullrich, R. J. F. Berger, C. Lustig, R. Fröhlich, N. W. Mitzel***

"Isomerism" of Coordination Modes and Numbers in Pentanuclear Organozinc Hydroxylamides: An Exercise in Subtle Substituent Size Effects

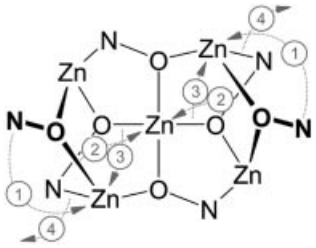

**Keywords:** Zinc / Hydroxylamines / Organometallic / Coordination modes / Crystal structure

**4225** **W. Bi, N. Mercier,* N. Louvain, M. Latroche**

Lead Halide Layers Linked by *trans*-$Cu(Gly)_2$ (Gly = $^{-}O_2C-CH_2-NH_2$) Pillars in Heterometallic Glycinate Based Organic−Inorganic Hybrids

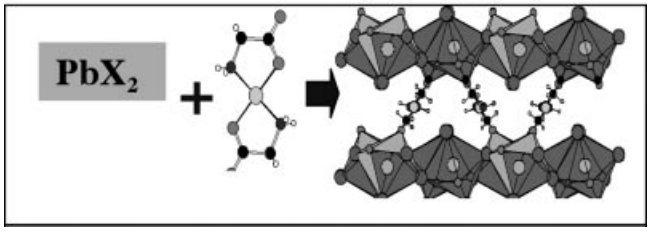


**Keywords:** Amino acids / Lead halide / Layered compounds / Glycinato / Copper

**4229** **M. C. Barral, R. González-Prieto, R. Jiménez-Aparicio,* J. L. Priego, M. R. Torres, F. A. Urbanos**

Molecular Assembly with Axial Cyanato Ligands and Paddlewheel Tetracarboxylatodiruthenium(II,III) Fragments

**Keywords:** Diruthenium compounds / Metal−metal bonds / Molecular assembly / Ruthenium complexes / Cyanato ligands / Silver complexes

**4233** **W. Liao, U. Englert, R. Dronskowski***

A Novel Europium Carbodiimide that Contains Isolated Europium Tetrahedra and Parallel Chains of Edge-Sharing Open Handbag-Like $Eu_6$ Units

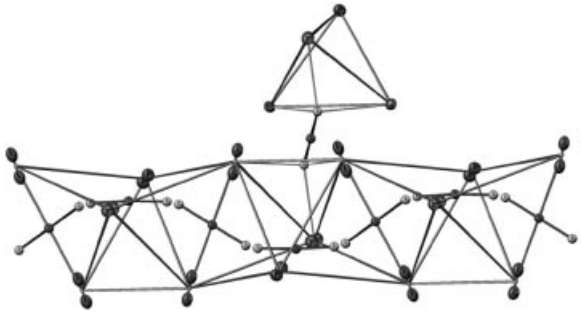

**Keywords:** Europium / Carbodiimide / Lanthanides / Solid-state reactions / Crystal growth


 © 2006 Wiley-VCH Verlag GmbH & Co. KGaA, Weinheim 

# FULL PAPERS


**4237** **R. Septelean, H. Ranaivonjatovo,* G. Nemes, J. Escudié,* I. Silaghi-Dumitrescu, H. Gornitzka, L. Silaghi-Dumitrescu, S. Massou**

Phosphavinylidene(oxo)phosphorane Mes*P(O)=C=PMes*: A Diphosphaallene Featuring $\lambda^5\sigma^3$- and $\lambda^3\sigma^2$-Phosphorus Atoms

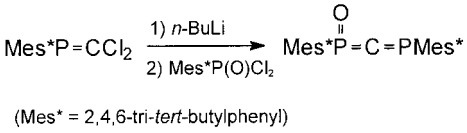


**Keywords:** Heterocumulenes / Phosphorus / Phosphaalkenes / Methylenephosphoranes

**4242** **M. V. Galakhov, M. Gómez,* P. Gómez-Sal, P. Velasco**

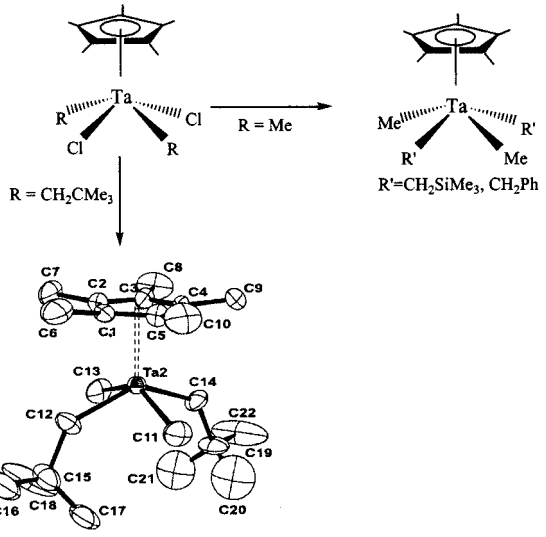


(Alkyl)- and (Alkyl)(alkylidene)(pentamethylcyclopentadienyl)tantalum Complexes

**Keywords:** Tantalum / Alkyl / Alkylidene / Cyclopentadienyl ligands

**4254** **K. Jitsukawa,* T. Mabuchi, H. Einaga, H. Masuda**

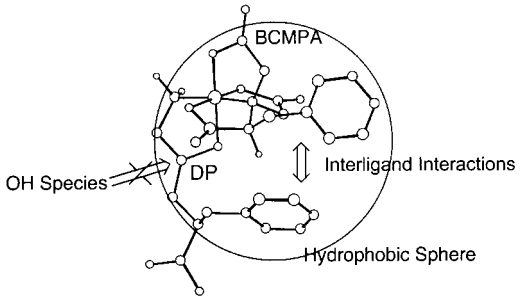


Site-Specific Recognition of Dipeptides Through Non-Covalent Inter-Ligand Interactions for the Hydrolysis of Dipeptide to Amino Acid Ligands Mediated by Ternary Cobalt(III) Complexes

**Keywords:** Ligand design / Hydrolysis / Coordination modes / Cobalt / Host−guest systems

**4264** **H.-P. Jia, W. Li, Z.-F. Ju, J. Zhang***

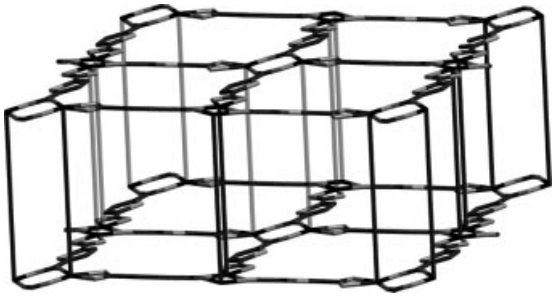

Synthesis, Structure and Magnetism of Metal-Organic Framework Materials with Doubly Pillared Layers

**Keywords:** Metal-organic frameworks / Pillared-layer structure / Iron(II) / Cobalt(II) / Hydrothermal synthesis / Magnetic properties / Carboxylates


 © 2006 Wiley-VCH Verlag GmbH & Co. KGaA, Weinheim 

**4271** **I. A. Portnyagin, M. S. Nechaev, V. N. Khrustalev,* N. N. Zemlyansky, I. V. Borisova, M. Y. Antipin, Y. A. Ustynyuk, V. V. Lunin**

An Unusual Reaction of (β-Dimethylaminoethoxy)triethyltin with Phenyltin Trichloride. The First X-ray Structural Evidence of the Existence of Complexes $R_2SnXY{\cdot}R_2SnXY$ (R = Alkyl, Aryl; X, Y = Hal, OR, X ≠ Y) Both as Unsymmetrical Adducts $[R_2SnX_2{\cdot}R_2SnY_2]$ and Symmetrical Dimers $[R_2SnXY]_2$

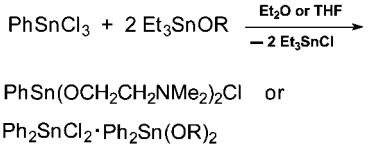


**Keywords:** Complexation / Tin / Dimerization / Stannanes / X-ray diffraction

**4278** **C. C. L. Pereira, S. S. Braga, F. A. A. Paz, M. Pillinger, J. Klinowski, I. S. Gonçalves***

Structural Studies of $[CpMoL_2(CO)_2]^+$ (L = NCMe, $L_2$ = 2,2′-biimidazole) Complexes and Their Inclusion Compounds with Cyclodextrins

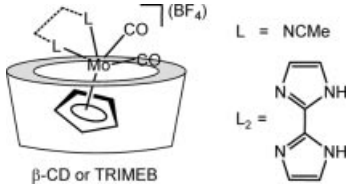


**Keywords:** Cyclodextrins / Inclusion compounds / Half-sandwich complexes / Molybdenum / Cyclopentadienyl metal carbonyls

**4289** **L. Salmon, P. Thuéry, M. Ephritikhine***

Uranium(IV) Complexes of Calix[5]arene

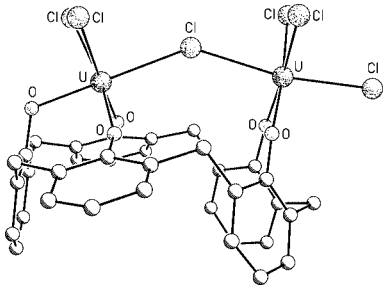


**Keywords:** Uranium / Calix[5]arene / Calixarenes

**4294** **H. Brand, J. F. Liebman, A. Schulz,* P. Mayer, A. Villinger**

Nonlinear, Resonance-Stabilized Pseudohalides: From Alkali Methanides to Ionic Liquids of Methanides

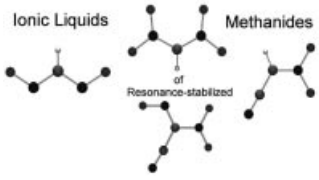


**Keywords:** Ionic liquid / Methanides / Pseudohalides / Resonance / X-ray structure elucidation

**4309** **F. Pelascini, M. Wesolek,* F. Peruch,* P. J. Lutz**

Modified Pyridine-Bis(imine) Iron and Cobalt Complexes: Synthesis, Structure, and Ethylene Polymerization Study

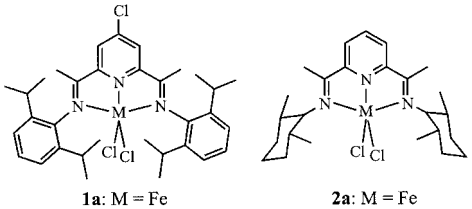


**1a**: M = Fe
**1b**: M = Co

**2a**: M = Fe
**2b**: M = Co

**Keywords:** N ligands / Iron / Cobalt / Ethylene / Polymerization

 © 2006 Wiley-VCH Verlag GmbH & Co. KGaA, Weinheim 

**4317** **X.-M. Liu, X.-Y. Mu, H. Xia, L. Ye, W. Gao, H.-Y. Wang, Y. Mu***

Synthesis, Structures, and Luminescent Properties of $d^{10}$ Group 12 Metal Complexes with Substituted 2,2′-Bipyridine Ligands

**Keywords:** Group 12 metal complexes / 2,2′-Bipyridine / Solid-state structures / Luminescence

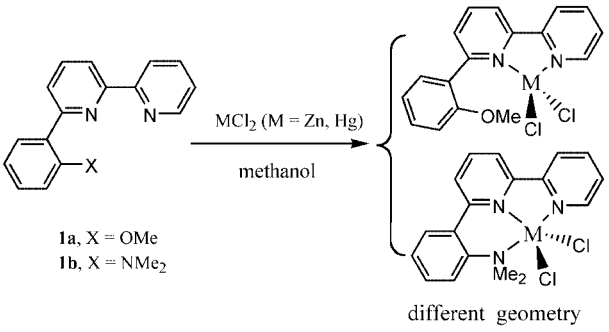


**4324** **L. Sabater, C. Hureau,* G. Blain, R. Guillot, P. Thuéry, E. Rivière, A. Aukauloo***

Chemical and Electrochemical Behaviours of a New Phenolato-Bridged Complex $[(L)Mn^{II}$-$Mn^{II}(L)]^{2+}$. Pathways to Mononuclear Chlorido $[(L)Mn^{II/III/IV}Cl]^{0/1/2+}$ and Dinuclear Mono-μ-Oxido $[(L)Mn^{III}(\mu\text{-}O)Mn^{III/IV}(L)]^{2+/3+}$ Species

**Keywords:** Manganese / N,O Ligands / Chloride ions / Electrochemistry / EPR spectroscopy

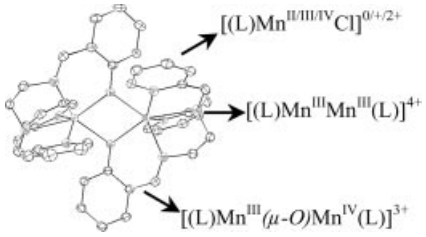


**4338** **F. Agbossou-Niedercorn,* J.-F. Paul***

A Density Functional Study of the Hydrogenation of Ketones Catalysed by Neutral Rhodium-Diphosphane Complexes

**Keywords:** Density functional calculations / Hydrogenation / Ketones / Rhodium / Asymmetric catalysis

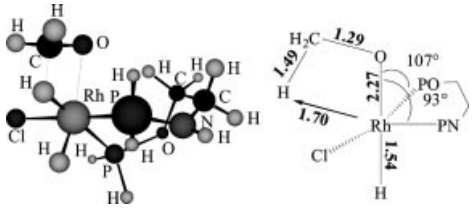


**4349** **B. Li, M. Jing, G. Rong, Y. Xu, Y. Xie***

Morphology Control of CdSe Submicrostructures with High Hierarchy in Solution

**Keywords:** Morphology control / Cadmium selenide / Submicrostructures / Semiconductor

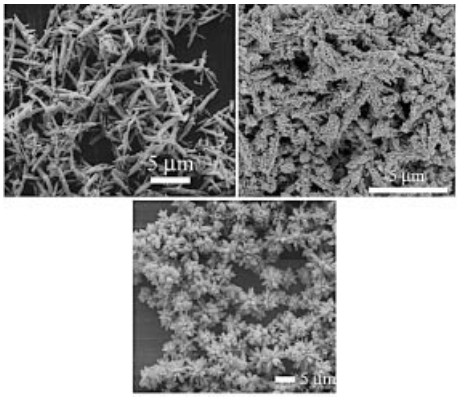


**4355** **H.-B. Fa, L. Zhao, X.-Q. Wang,* J.-H. Yu, Y.-B. Huang, M. Yang, D.-J. Wang**

Chiral Recognition of Mesoporous SBA-15 with an Incorporated Chiral Porphyrin

**Keywords:** Chiral recognition / Porphyrins / Mesoporous materials / SBA-15

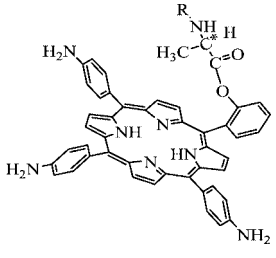

 © 2006 Wiley-VCH Verlag GmbH & Co. KGaA, Weinheim 

## 4362 X. Li,* F. Yu, H. Sun, L. Huang, H. Hou

Reactions of Trimethylphosphane-Supported Cobalt Complexes with Salicylaldimines − Formation and Structures of Cobalt Compounds Containing Salicylaldiminato [*N*:*O*] Ligands

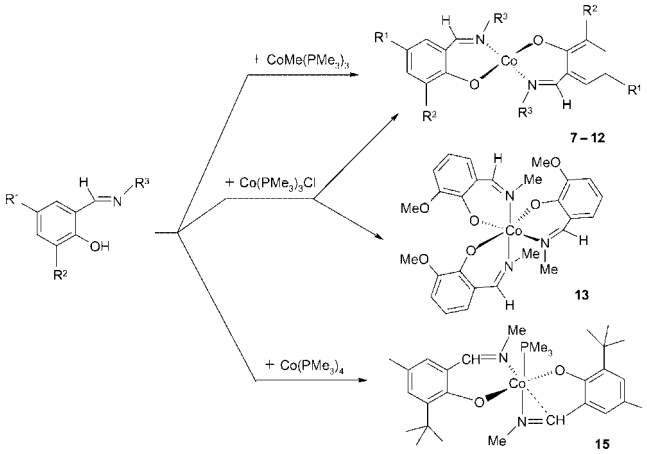


**Keywords:** Cobalt / Salicylaldimines / Trimethylphosphane / Imines

## 4368 Y. Liu, T. Liu, Z. Xiong, J. Hu, G. Wu, P. Chen,* A. T. S. Wee, P. Yang, K. Murata, K. Sakata

Synthesis and Structural Characterization of a New Alkaline Earth Imide: $MgCa(NH)_2$

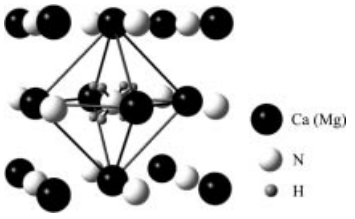


**Keywords:** Solid-state reactions / Amides / Hydrides / EXAFS spectroscopy / Ternary imide

## 4374 D. Benito-Garagorri, K. Mereiter, K. Kirchner*

Selective Phosphoramidite Cleavage as a Route to Novel Chiral and Achiral Pentacoordinated Nickel(II) PNP Pincer Complexes

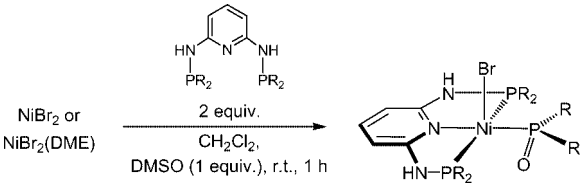


**Keywords:** Nickel complexes / Tridentate ligands / Square-pyramidal complexes / Hydrolysis

## 4380 W. Levason, J. M. Manning, P. Pawelzyk, G. Reid*

Synthesis and Properties of Organometallic $Pt^{II}$ and $Pt^{IV}$ Complexes with Acyclic Selenoether and Telluroether Ligands and Selenoether Macrocycles

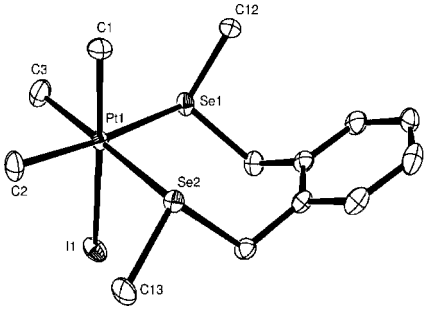


**Keywords:** Selenoether / Telluroether / Platinum / Macrocycles / Organometallic complexes

 © 2006 Wiley-VCH Verlag GmbH & Co. KGaA, Weinheim 

**4391** **C. D. Beard, R. J. Barrie, J. Evans, W. Levason,* G. Reid, M. D. Spicer**

Synthesis and Properties of Complexes of Vanadium(V) Oxide Trichloride with Nitrogen- and Oxygen-Donor Ligands

**Keywords:** Vanadium / Coordination complexes / Multinuclear NMR spectroscopy

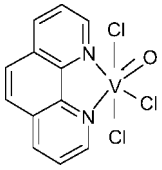


**4399** **C. D. Beard, L. Carr, M. F. Davis, J. Evans, W. Levason, L. D. Norman, G. Reid,* M. Webster**

Studies on Chromium(III) and Vanadium(III) Complexes with Crown Ether and Crown Thioether Coordination − Synthesis, Properties and Structural Systematics

**Keywords:** Chromium / Crown ether / Thioether macrocycle / Vanadium

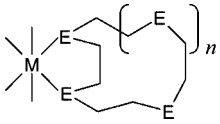


$n = 1, 2, 3$
M = Sc – Cr
E = S or O

**4407** **M. Hölscher, W. Leitner***

DFT-Investigation of the Potential of [H-M-{$(NHCH_2CH_2)_3X$}] Catalysts (M = Mo, Ru, Os; X = N, P) for the Reduction of $N_2$ to $NH_3$ by $H_2$

**Keywords:** DFT calculations / Nitrogen fixation / Nitrogen activation / Nitrogen reduction / Ammonia / Homogeneous catalysis

**4418** **M. F. Erben, C. O. Della Védova,* H. Willner, R. Boese**

Synthesis, Structure and Conformational Properties of Fluoroformylchlorodifluoroacetyl Disulfide, $FC(O)SSC(O)CF_2Cl$: Conformational Transferability in −C(O)SSC(O)− Compounds

**Keywords:** Conformation analysis / Sulfur / Vibrational spectroscopy / X-ray diffraction

**4426** **S. Ghumaan, S. Mukherjee, S. Kar, D. Roy, S. M. Mobin, R. B. Sunoj,* G. K. Lahiri***

An Experimental and Density Functional Theory Approach Towards the Establishment of Preferential Metal- or Ligand-Based Electron-Transfer Processes in Large Quinonoid-Bridged Diruthenium Complexes [{$(aap)_2Ru$}$_2$($\mu$-$BL^{2-}$)]$^{n+}$ (aap = 2-Arylazopyridine)

**Keywords:** Ruthenium / Bridging ligands / Radical ions / Density functional calculations / EPR spectroscopy

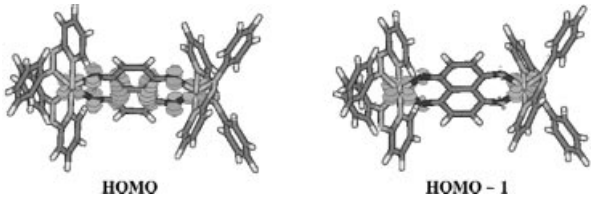


 © 2006 Wiley-VCH Verlag GmbH & Co. KGaA, Weinheim 

**4442** **P. Comba,* R. Krämer, A. Mokhir, K. Naing, E. Schatz**

Synthesis of New Phenanthroline-Based Heteroditopic Ligands − Highly Efficient and Selective Fluorescence Sensors for Copper(II) Ions

**Keywords:** Sensor / Fluorescence / Copper(II) / Selectivity / Ruthenium

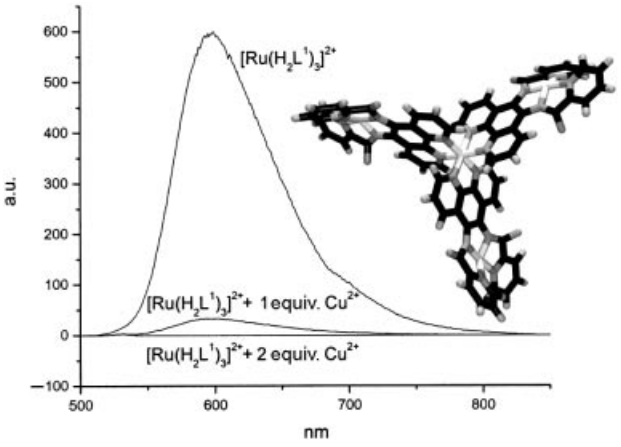


**4449** **M. G. Davidson,* A. L. Johnson, M. D. Jones,* M. D. Lunn, M. F. Mahon**

Titanium(IV) Complexes of Hydrazones and Azines

**Keywords:** Titanium / Coordination modes / Hydrazones / Azines

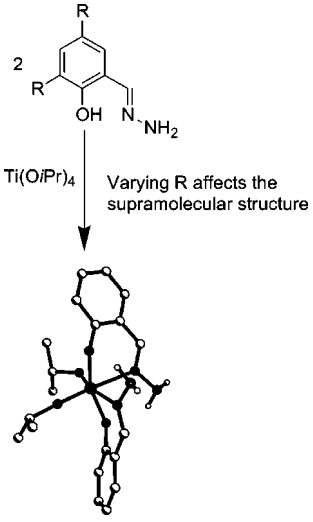

DOI: 10.1002/ejic.200600485

# Chiral Molecules Containing Metal–Metal Bonds

F. Albert Cotton*[a] and Carlos A. Murillo*[a]

**Keywords:** Metal–metal bonds / Chirality / Chromophores / Orthometalation / Helical molecules

Many chiral compounds having metal–metal bonds are now known in which the M–M unit is the chromophore. In this review they are classified as those where it is either (1) an inherently chiral chromophore owing to helical stacking of metal–ligand bonds, or (2) not inherently chiral but surrounded by a collection of ligands bearing chiral substituents. In only a few cases have the actual CD and/or ORD spectra been measured and analyzed. These include $M_2X_4(PP)_2$ molecules (PP = a bridging diphosphane) and $M_2(O_2CR)_4$ molcules where R is chiral. The more recently discovered helical extended metal atom chain (EMAC) molecules are also mentioned.
(© Wiley-VCH Verlag GmbH & Co. KGaA, 69451 Weinheim, Germany, 2006)

## Introduction

The way in which metal–metal (M–M) bonds are influenced by, and exert influence upon, a chiral environment is a topic that has not been comprehensively reviewed. There is now a large enough body of results to justify at least a small (surely at least *micro*) review. In general, metal–metal-bonded compounds are of interest in many areas such as catalysis,[1] medicine[2] and for synthesizing supramolecular arrays.[3]

We preface the main body of the review by reminding the reader that there are two fundamental classes of optically active molecules:[4]

[a] Department of Chemistry and Laboratory for Molecular Structure and Bonding, A&M University, College Station, P. O. Box 30012, Texas 77842-3012, USA
E-mail: cotton@tamu.edu
murillo@tamu.edu

(1) Those with inherently chiral chromophores

(2) Those with achiral chromophores embedded in chiral surroundings

We shall divide this review into two parts based on this difference.

### 1. Inherently Chiral Di- or Polymetal Chromophores

#### *1a. M–M Bond Twist Induced by Chiral Diphosphanes*

The first examples of molecules with the type of structure shown in Figure 1 were discovered by R. A. Walton and co-workers, in 1975 for rhenium compounds[5] and in 1978 for molybdenum compounds.[6] Tungsten analogs were reported in 1980.[7] The compounds with dppe ($Ph_2PCH_2CH_2PPh_2$) are generally regarded as prototypical, but many are known with other $R_2PCH_2CH_2PR_2$ and sim-

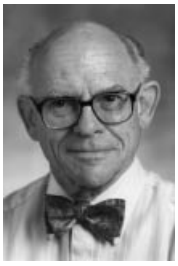

*F. Albert Cotton was born in Philadelphia in 1930. He is the Doherty-Welch Professor of Chemistry and director of the Laboratory for Molecular Structure and Bonding at Texas A&M University. He began his academic career at the Massachusetts Institute of Technology from 1955 to 1971. His successful Ph. D. students number 116. Among his honors are membership in the US National Academy of Sciences and the American Philosophical Society. He received the ACS George C. Pimental Award in Chemical Education in 2006. He is the coauthor of many books and almost 1600 research publications. His main research interest deals with the study of compounds with metal–metal bonds.*

*Carlos A. Murillo received a B. Sc in his native country from the University of Costa Rica in 1973 and a Ph. D. from Texas A&M University (TAMU) in 1976, working with F. A. Cotton. After one year at Princeton University working with M. H. Chisholm he took a position at the University of Costa Rica where he became Professor of Chemistry in 1986. He then moved to TAMU in 1991 where he is a senior lecturer and executive director of the Laboratory for Molecular Structure and Bonding. He is a charter member of the Costa Rican Academy of Sciences, a Fellow of the American Association for the Advancement of Science, a coauthor of Advanced Inorganic Chemistry, a coeditor of Multiple Bonds Between Metal Atoms and coauthor of nearly 250 research publications. His principal research interests are in the synthesis and characterization of compounds with metal-metal bonds.*

 © 2006 Wiley-VCH Verlag GmbH & Co. KGaA, Weinheim 

ilar bridging diphosphanes.[8] The important feature of the $Re_2Cl_4(dppe)_2$ structure shown in Figure 1 is that the conformational requirements of the two six-membered rings that are fused along the metal–metal bond (triple in the rhenium compounds and quadruple for the molybdenum and tungsten ones) induce a partial twist away from an eclipsed conformation. This twist makes the M–M bond an inherently chiral chromophore. For the compounds with quadruple bonds, the δ→δ* transition is a particularly convenient electronic transition for studying the CD/ORD spectra.

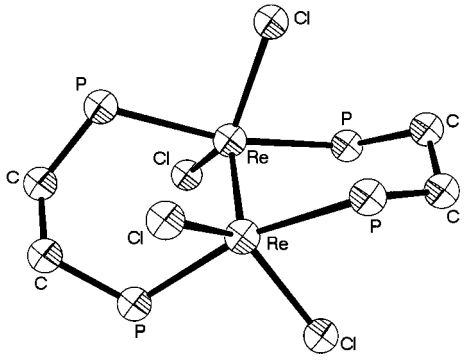


Figure 1. The core of the prototypical $Re_2Cl_4(dppe)_2$ molecule showing the twist away from an eclipsed conformation that produces a chiral chromophore.

No enantiomers of the $M_2X_4(R_2PCH_2CH_2PR_2)_2$ compounds have been resolved, but by introducing chirality into the backbone of the diphosphane, the chirality of the helix around the M–M core can be predetermined. For such work, the prototype compound is Λ-[$Mo_2Cl_4${(*S*,*S*)-dppb}$_2$], shown along with its CD spectrum in Figure 2, where (*S*,*S*)-dppb is (*S*,*S*)-2,3-(diphenylphosphanyl)butane. The structure, with its Λ sense of the twist, is both predicted by conformational analysis and confirmed by X-ray crystallography.[9,10]

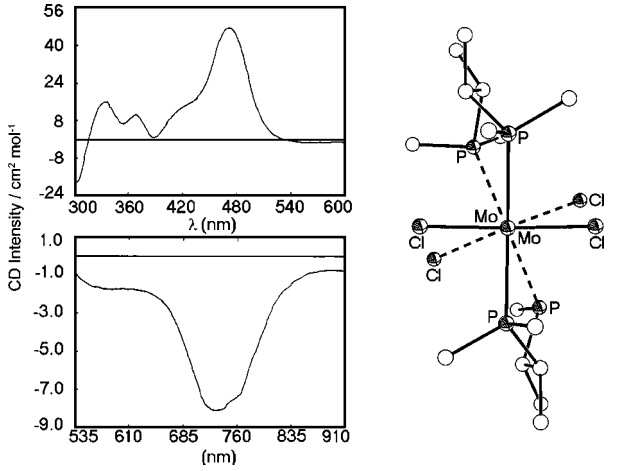


Figure 2. The β-$Mo_2Cl_4${(*S*,*S*)dppb}$_2$ molecule viewed down the Mo–Mo axis (right) and its CD spectrum (left).

The CD spectrum shows two principal features: a negative band at about 13500 $cm^{-1}$ that corresponds to the δ→δ* absorption band in the electronic spectrum and a positive band at about 21300 $cm^{-1}$. These same two principal features are seen in most similar molecules having $Mo_2^{4+}$ units.[11–14]

There is a very straightforward and unequivocal explanation of these CD results. For the δ→δ* transition, we refer to Figure 3, where it can be seen that there is a shift of charge both along and around the metal–metal bond. Therefore, the δ→δ* transition in such a helical molecule is both electric-dipole- and magnetic-dipole-allowed; it must, therefore, be CD allowed. As shown on the left side, when the Λ twist angle is less than 45°, the signs of the CD bands would be reversed for the Λ and Δ isomers. The entire analysis can be conveniently generalized into a sector diagram, as shown in Figure 4. This shows how the CD sign changes, alternating from one octant to the next, as a function of the L–M–M–L angle. Thus, even if it is known from conformational analysis whether to expect the Λ or Δ twist, the extent of the twist must also be known. The first actual test of this octant rule was made with $Mo_2Cl_4${(*R*,*R*)-DIOP}$_2$, where (*R*,*R*)-DIOP is shown in Scheme 1. The twist angle, $\chi$, in the dominant isomer of the dimolybdenum compound is $-45° < \chi < -90°$, and the sign of the CD for the δ→δ* transition is predicted from the sector diagram to be positive. As shown in Figure 5, this is found experimentally. The diamine molecule, $Mo_2Cl_4[(R)\text{-}H_2NCH(CH_3)\text{-}CH_2NH_2]_2$ was also shown to obey the sector diagram.[15]

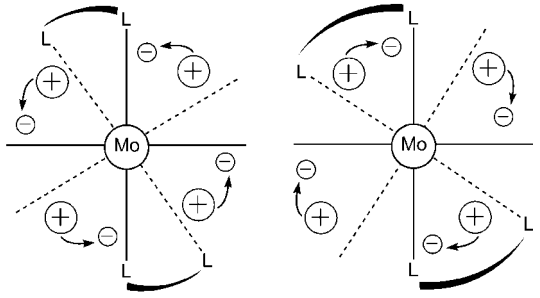


Figure 3. Diagrams of the transient charge distributions for the δ→δ* transition in twisted $Mo_2X_4(LL)_2$ molecules with torsion angle $\theta$ (a) in the range 0 to –45° and (b) in the range –45 to –90°. Note that the two ranges, though in the same direction geometrically, give transient charge distributions of opposite rotational sense.

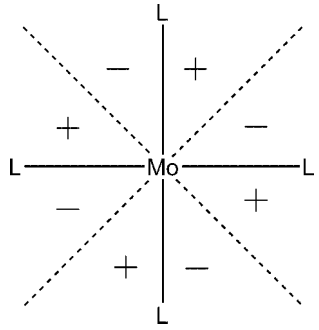


Figure 4. The sign rule for the CD of the δ→δ* transition. The sign of the CD refers to the vector in which the rear set of ligand atoms is found.

 © 2006 Wiley-VCH Verlag GmbH & Co. KGaA, Weinheim 

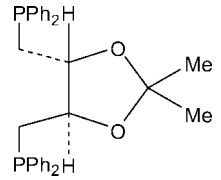


Scheme 1. The (*R*,*R*)-DIOP molecule.

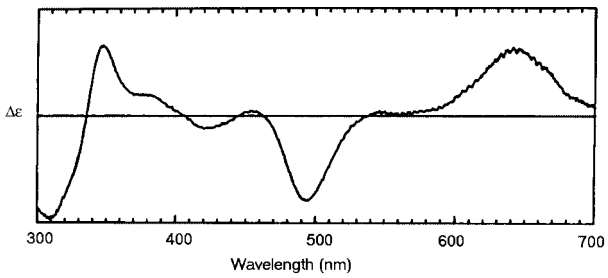


Figure 5. CD spectra of $Mo_2Cl_4\{(R,R)\text{-DIOP}\}_2$ in $CH_2Cl_2$ solution in the range from 300 to 700 nm.

In all of the compounds just discussed, there is a band in the visible spectrum (ca. 22000 $cm^{-1}$) which has the opposite CD sign to that for the δ→δ* transition. This band is due to a $\delta_{xy}\rightarrow\delta_{x^2-y^2}$ transition, and it has been shown that it follows a sector diagram too, but with all of the signs reversed from those shown in Figure 3 for the δ→δ* transition.

### *1b. Molecules with Orthometalated Bridging Phenylphosphanes*

These are compounds with a dimetal unit bridged by two *cisoid* orthometalated phosphanes in a head-to-tail (H,T) arrangement. Two additional equatorial groups such as carboxylates usually complete the paddlewheel arrangement. The compounds *cis*-$Rh_2(C_6H_4PPh_2)_2(OAc)_2\cdot 2CH_3COOH$[16] and $Os_2(C_6H_4PPh_2)_2Cl_4$[17] were the first to be made. The dirhodium compound and its derivatives have been studied in great detail. Because of the H,T arrangement of the two orthometalated bridging ligands, the *cis*-$Rh_2(C_6H_4PPh_2)_2^{2+}$ unit has only $C_2$ symmetry and is therefore chiral. The (*R*) and (*S*) conformations are shown in Scheme 2. The interconversion of (*R*) and (*S*) isomers would require bond breaking and such isomers are not expected to interconvert at ordinary temperatures because of the large energy barriers associated with such processes. As shown in Scheme 3, there is also a secondary source of chirality induced by the twist pattern of each phosphane ligand designated as *P* (for positive torsion angle) and *M* (for negative torsion angle along the axis of the helix) following the nomenclature used for helical molecules.[18] While for the secondary chirality less energy is expected to be required for interconversion than for the primary source of chirality, this value may still be significant. Molecular mechanics calculations have been used to estimate the relative stability of the ($S_M$) and ($S_P$) conformers in *cis*-$Rh_2(C_6H_4PPh_2)_2(CH_3CN)_6^{2+}$,[19] which has a P–Rh–Rh–P torsion angle of –23°. The results indicate that the experimental ($S_M$) conformation is 88.1 kJ $mol^{-1}$ more stable than the ($S_P$) conformation having the same torsion angle, and that the energy barrier between the conformers is estimated to be much greater than $kT$ (153.3 kJ $mol^{-1}$)

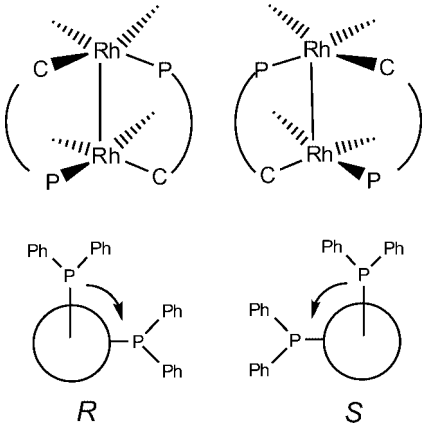


Scheme 2. The (*R*) and (*S*) chirality imposed by the H,T arrangement of the *cisoid* orthometalated groups.

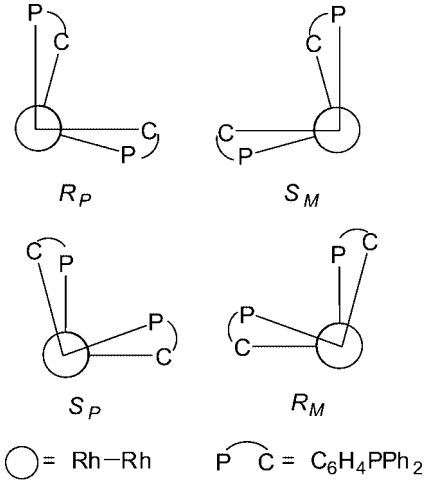


Scheme 3. The second chirality due to the magnitude and sign of the torsion angle along the P–Rh–Rh–P unit.

The stable (*R*) and (*S*) enantiomers have been resolved. The separation procedure makes use of the fact that in (*R*,*S*)-*cis*-$Rh_2(C_6H_4PPh_2)_2(OAc)_2\cdot 2CH_3COOH$, the orthometalated phosphane groups are not labile while the carboxylate groups are. Reaction with ProtosH (*N*-4-methylphenylsulfonyl-L-proline, see Scheme 4) yields (*R*,*S*)-*cis*-$Rh_2(C_6H_4PPh_2)_2(Protos)_2\cdot 2H_2O$ and the diastereoisomers are easily separated by column chromatography using silica gel and elution with a mixture of $CH_2Cl_2/Et_2O$.[20] Many analogs using a great variety of substituted phosphanes have also been synthesized. These compounds have applications in enantioselective C–H insertion of α-diazo ketones and other catalyzed reactions.[20,21]

 © 2006 Wiley-VCH Verlag GmbH & Co. KGaA, Weinheim 

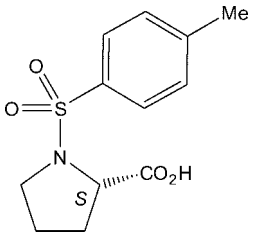


Scheme 4. The chiral ProtosH molecule.

Substitution reactions of the carboxylate groups from the diastereoisomers proceed without racemization, and the group Protos can be easily replaced by other groups such as carboxylates or acetonitrile. The orthometalated dirhodium unit in [(*R*)-*cis*-$Rh_2(C_6H_4PPh_2)_2(CH_3CN)_6](BF_4)_2$ has been useful as a corner piece for the synthesis of enantiopure supramolecular structures. Reaction with the dicarboxylate anions $O_2C(CF_2)_nCO_2$, $n$ = 2 and 3, give molecular loops in which each of the two $Rh_2(C_6H_4PPh_2)_2$ units is also coordinated by two carboxylate groups from each of the two linkers and two axial pyridine molecules, as shown in Figure 6 for $n$ = 2.[22] In this complex, the P–Rh–Rh–P torsion angles [75.7(1) and 74.56(9)°] are smaller than those of C–Rh–Rh–C [–116.9(4) and –119.2(4)°]. Therefore, the overall chirality of this dirhodium compound is ($R_MR_M$). This is uncommon for simple dirhodium compounds, in which the torsion angle of P–Rh–Rh–P is usually larger than that of C–Rh–Rh–C,[23] because of steric repulsions between the bulky phenyl groups in the phosphanes.

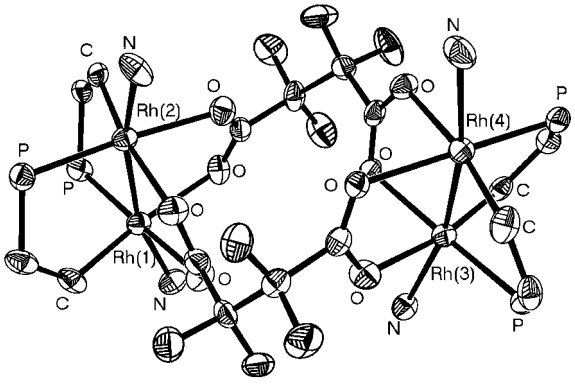


Figure 6. The core of the chiral molecular loop (*RR*)-[*cis*-$Rh_2(C_6H_4PPh_2)_2(py)_2O_2CF_2CF_2CO_2]_2$ for which the overall chirality is ($R_MR_M$).

A series of neutral molecular triangles having the formula [*cis*-$Rh_2(C_6H_4PPh_2)_2]_3$(dicarboxylate)$_3$·$(L_{ax})_6$ where $L_{ax}$ may be one of a variety of donor molecules such as DMF, MeOH or py, $CH_2Cl_2$ have also been made. These compounds, for which a representative core is shown in Figure 7, were first prepared by reaction of racemic [*cis*-$Rh_2(C_6H_4PPh_2)_2(CH_3CN)_6](BF_4)_2$ and tetraethylammonium salts of linear dicarboxylates such as, oxalate, terephthalate and 4,4′-biphenyldicarboxylate.[19] The relative chiralities of the dirhodium units in these triangles were established using a combination of data from X-ray crystallography and $^{31}$P NMR spectroscopy. It should be noted that the combination of the racemic mixture of *cis*-$Rh_2(C_6H_4PPh_2)_2^{2+}$ units with dicarboxylate anions to form triangles can produce four possible stereoisomers: (*RRR*), (*RRS*), (*SSR*), and (*SSS*), and each of these can be either ($R_P$) and ($R_S$), or ($S_P$) and ($S_M$) (see Scheme 3). For the oxalate compound, all the $Rh_2$ units in each triangle have the same chirality, and this compound exists as a mixture of ($R_PR_PR_P$) and ($S_MS_MS_M$) isomers having $D_3$ symmetry. It is notable that no ($R_M$) or ($S_P$) conformers were observed. For the terephthalate analog, the structure shows two dirhodium units with one chirality and the third one with another chirality [(*RRS*) or (*SSR*)] but again there are only ($R_P$) or ($S_M$) conformers.

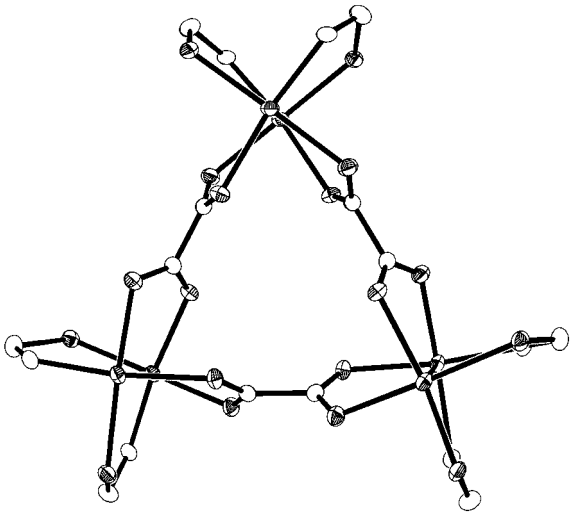

Figure 7. The core of the neutral molecular triangle [*cis*-$Rh_2(C_6H_4PPh_2)_2]_3$(oxalate)$_3$·$(L_{ax})_6$. Only the $Rh_2PCC$ portions of the orthometalated $Rh_2C_6H_4PPh_2$ units are shown. Axially coordinated ligands have also been removed for clarity. Carbon atoms are shown as open ellipsoids.

The $^{31}$P NMR spectra, shown in Figure 8, suggest that the structures observed in the solid state remain unchanged in solution, and that there are no interconversions in solution to other types of oligomers such as squares. For the compounds with oxalate and 4,4′-biphenyldicarboxylate linkers, the doublets are consistent with the high symmetry in the crystal, whereby all the orthometalated phosphane ligands are equivalent. Here, the doublets are due to coupling of the P atoms with the $I$ = 1/2 $^{103}$Rh nucleus. For the terephthalate analog, the three doublets with nearly identical coupling indicate that the (*RRS*) or (*SSR*) chirality of the solid state is again present in solution. The enantiopure analogs [(*RRR*) or (*SSS*)] have also been prepared from reaction of (*R*)- or (*S*)-[*cis*-$Rh_2(C_6H_4PPh_2)_2(CH_3CN)_6](BF_4)_2$ and the dicarboxylate salts.[24] The core structure of (*SSS*)-[*cis*-$Rh_2(C_6H_4PPh_2)_2]_3$(terephthalate)$_3$(py)$_6$ is shown in Figure 9 along with the packing diagram. Catalytic evaluation of these enantiopure triangles show that they are catalytically active and provide good results for the intermolecular cyclopropanation between styrene and ethyl diazoacetate.

 © 2006 Wiley-VCH Verlag GmbH & Co. KGaA, Weinheim 

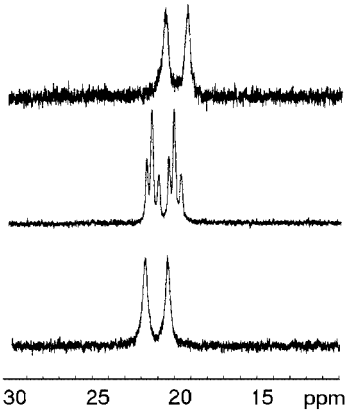


Figure 8. $^{31}P$ NMR in $CD_3Cl$ of the racemic triangular compounds with oxalate, terephthalate and 4,4′-biphenyldicarboxylate linkers shown in the same order from top to bottom.

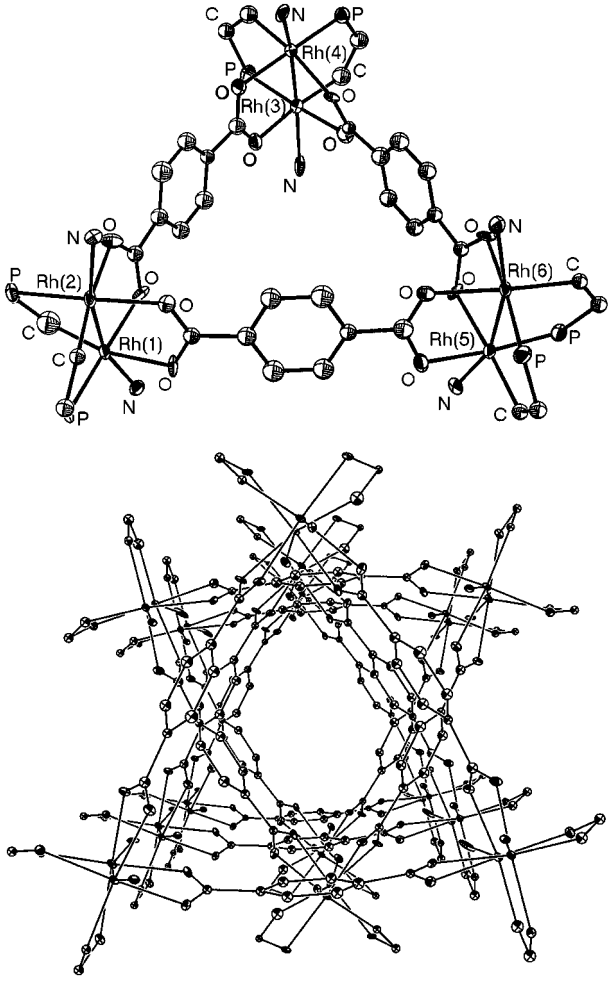


Figure 9. The core structure (top) and packing pattern (bottom) of (*SSS*)-[*cis*-$Rh_2(C_6H_4PPh_2)_2]_3$(terephthalate)$_3(py)_6$. Note that the molecules stack on top of each other, but alternately out of register, leaving a chiral channel. For the oxalate analog, the triangular molecules stack in register.

The same dirhodium corner piece has been used to build a molecule with pure rotational symmetry *T* by reaction of (*R*)-[*cis*-$Rh_2(C_6H_4PPh_2)_2(CH_3CN)_6](BF_4)_2$ and the trianion of benzene-1,3,5-tricarboxylic (trimesic) acid.[25] The compound $\{NEt_4\subset[(R)$-*cis*-$Rh_2(C_6H_4PPh_2)(py)_2]_6(1,3,5$-$C_6H_3(CO_2)_3)_4\}BF_4$, prepared by a designed synthesis and shown in Figure 10, has only eight $C_3$ and three $C_2$ rotations of the group *T*. It encapsulates a $NEt_4^+$ cation within the chiral spheroidal cavity of the cage. In this chiral carceplex there are six *cisoid* (*R*)-$Rh_2(C_6H_4PPh_2)_2^{2+}$ units (B) linked by four trimesate anions (A), each connecting to three different $Rh_2^{4+}$ units to give an $A_4B_6$ type molecule. All oxygen atoms of the trimesate anions are *trans* to either carbon or phosphorus atoms in the orthometalated ligands. The midpoints of the dirhodium units roughly describe an octahedron while the centers of the aryl groups of the anions describe a tetrahedron. Pyridine molecules are found at both axial positions of each dirhodium unit. This carceplex is an all (*R*) isomer.

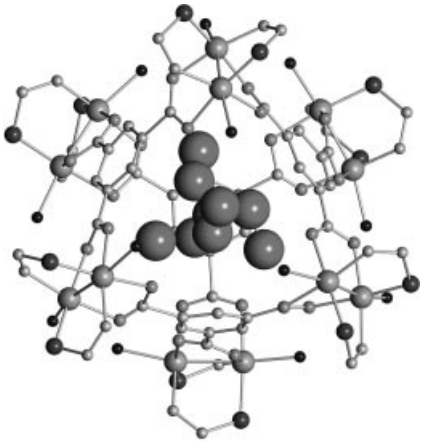

Figure 10. A view of the core structure of the carceplex Λ-$\{NEt_4\subset[(R)$-*cis*-$Rh_2(C_6H_4PPh_2)(py)_2]_6(1,3,5$-$C_6H_3(CO_2)_3)_4\}BF_4$ showing the encapsulated tetraethylammonium cation.

The $^1H$ NMR spectrum offers clear evidence that the tetraethylammonium cation remains encapsulated in solution, and shows two signals at high field (–0.035 and –0.278 ppm) in a ratio of 3:2. The large upfield displacement of these signals relative to those of a non-encapsulated $NEt_4^+$ cation is due to strong shielding by the cage. The $^{31}P$ NMR spectrum of the compound in $CD_2Cl_2$ in the presence of excess pyridine is consistent with the existence of only one highly symmetrical species in solution as it shows only one doublet because of coupling of each P atom to the adjacent $^{103}Rh$ nucleus.

### *1c. Helical Molecules with Three or More Metal Atoms*

The best known compounds are of the type $M_3(dpa)_4X_2$, where dpa = the anion of dipyridylamine, X is a monodentate group, typically a monoanion such as a halide, $PF_6$, acetylide, and others and M = Co, Cr, Rh, Ru, Ni.[26] One remarkable feature of compounds of this type is the tunable metal-to-metal interactions within the trinuclear unit and symmetrical and unsymmetrical arrangements may be obtained depending on the nature of the axial ligands. More importantly for this review is the typical helical arrangement of the four dpa anions about the $M_3$ unit as shown in

 © 2006 Wiley-VCH Verlag GmbH & Co. KGaA, Weinheim 

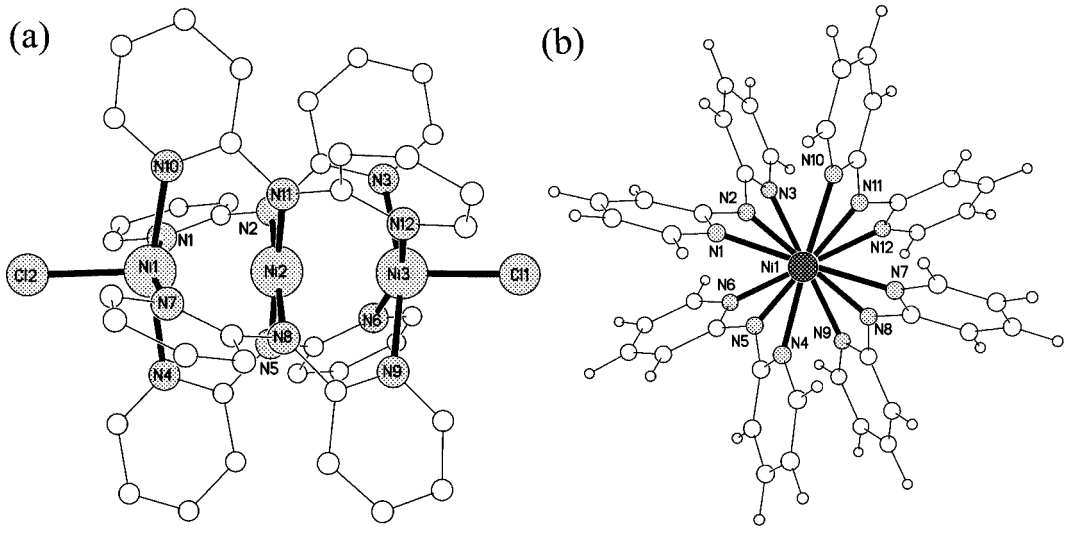


Figure 11. A typical structure of an $M_3(dpa)_4X_2$ as represented by $Ni_3(dpa)_4Cl_2$. The structure is shown (a) perpendicular to the $Ni_3$ axis, and (b) looking down the $Ni_3$ axis to emphasize the helical arrangement of the dpa ligands.

Figure 11 for a typical $M_3$ compound. While the set of four dpa ligands has the capacity to organize an extended metal atom chain (EMAC), it is also forced by internal nonbonded (H···H) contacts to form an overall molecular structure with a helical configuration having right- or left-handed helicity (referred to as Δ or Λ, respectively) as shown in Figure 12.

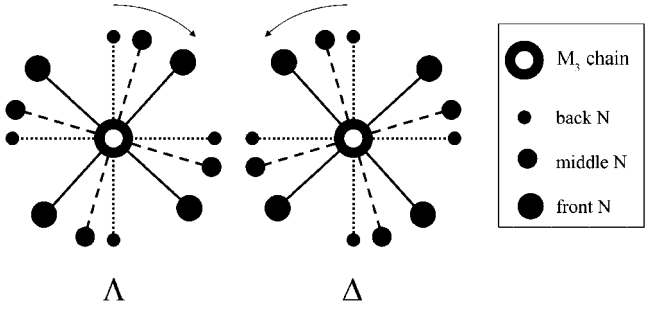


Figure 12. A schematic representation of the Δ and Λ isomers of an EMAC of the type $M_3(dpa)_4X_2$.

Most of the structures of these $M_3(dpa)_4X_2$ compounds are racemic but for $[Co_3(dpa)_4(CH_3CN)_2](PF_6)_2$ single crystals of the Δ and Λ isomers were isolated from solution and manually separated. Their absolute configurations were determined by X-ray crystallography and circular dichroism spectra (Figure 13) were measured on solutions made from crystals of known absolute configuration.[27] Both isomers exhibit significant Cotton effects. The bands were assigned from the electronic spectra with that at 312 nm corresponding to a spin-allowed π–π* transition. The transition at 369 nm was assigned to a charge-transfer band and the lower energy bands at 442 and 544 nm were assigned to metal-centered transitions in the $Co_3^{2+}$ core.[27] In general, the anisotropy or dissymmetry factor given by the $\Delta\varepsilon/\varepsilon$ ratio of circular dichroic to isotropic absorbance is associated with the nature of the transitions.[28] For electric-dipole-allowed and magnetic-dipole-forbidden transitions (CT and ligand π–π* transitions), the $\Delta\varepsilon/\varepsilon$ ratio $\leq 5{\cdot}10^{-3}$ and for magnetic-dipole-allowed and electric-dipole-forbidden transitions (ligand-field transitions, n–π* transitions), $\Delta\varepsilon/\varepsilon$ ratio $\geq 5{\cdot}10^{-3}$. The transition for the Λ isomer at 312 nm has a negative sign ($\Delta\varepsilon/\varepsilon = 8.2{\cdot}10^{-4}$) in the CD spectrum, while the bands at 369 nm ($\Delta\varepsilon/\varepsilon = 1.5{\cdot}10^{-3}$), 442 nm ($\Delta\varepsilon/\varepsilon = 8.25{\cdot}10^{-3}$), and 544 nm ($\Delta\varepsilon/\varepsilon = 5.0{\cdot}10^{-3}$) are positive. The CD spectra for the Δ and Λ isomers are mirror images, as expected for a pair of enantiomers. The CD bands at 312 and 369 nm have small $\Delta\varepsilon/\varepsilon$ values with the former corresponding to a ligand π–π* transition and the latter corresponding to a LMCT transition. Both are electric-dipole-allowed and magnetic-dipole-forbidden transitions. The greater dissymmetry factor $\Delta\varepsilon/\varepsilon$ for the bands at 442 and 544 nm is consistent with these bands being magnetic-dipole-allowed and electric-dipole-forbidden metal-centered transitions. Importantly, the equal intensity but opposite signs of the spectra from the two solutions of isomers having similar concentrations indicates that the two enantiomers do not interconvert in solution.

Spontaneous resolution upon crystallization as just described, is very rare. Normally only racemic crystals are obtainable. However, chromatographic resolution on columns of chiral adsorbants has recently been applied with success to several $M_3(dpa)_4X_2$ compounds.[29] There are two ways to determine the absolute helicity of each enantiomer. The most obvious is to crystallize one (or both) and employ X-ray crystallography. When this cannot be done, vibrational circular dichroism can be used. This has been done in the case of $Ni_3(dpa)_4(OH)_2$.[30] There are preliminary results showing that many other helical EMACs will be treatable by similar methods.

There are also structurally characterized EMACs with longer polypyridylamides having linear $M_5$, $M_7$ and $M_9$ cores. The structures resemble those with $M_3$ cores in that the molecules are helical. An example is that of $Ni_9$-

 © 2006 Wiley-VCH Verlag GmbH & Co. KGaA, Weinheim 

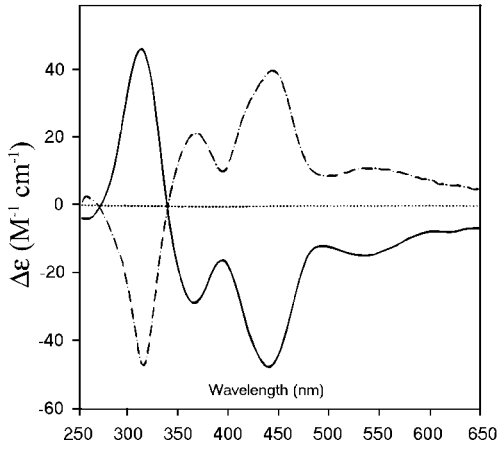


Figure 13. CD spectra of Δ- (solid line) and Λ- (dashed line) $[Co_3(dpa)_4(NCCH_3)_2](PF_6)_2$.

$(peptea)_4Cl_2$ (peptea = the anion of pentapyridyltetraamine),[31] which is shown in Figure 14. Recently examples of complexes with four anions derived from polypyridylnaphthyridine groups (Scheme 5) have been made containing $Co_6^{12+}$ and $Co_6^{11+}$ cores,[32] and $Ni_6^{12+}$ and $Ni_6^{11+}$ cores.[33] A schematic representation of the $Co_6^{n+}$ compounds is given in Figure 15. However, none of these racemic mixtures have been resolved.

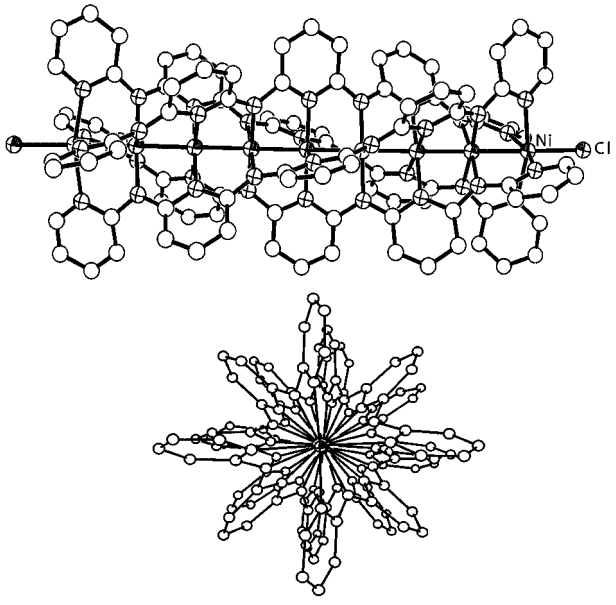


Figure 14. The structure of one of the enantiomers of $Ni_9(peptea)_4Cl_2$ (top). A view along the main axis of this molecule emphasizing the helical arrangement of the polypyridylamido ligands is at the bottom.

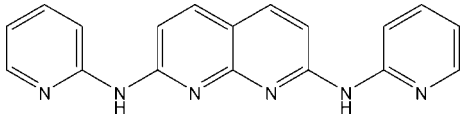

Scheme 5. A schematic drawing of 2,7-bis(α-pyridylamido)-1,8-naphthyridine used in the syntheses of compounds with $M_6^{12+}$ and $M_6^{11+}$ cores, M = Co and Ni.

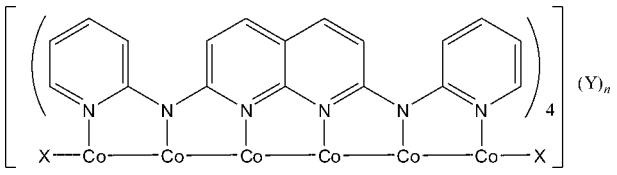


Figure 15. A 2-dimensional representation of the $Co_6^{n+}$ compounds synthesized with the ligand in Scheme 5, X = NCS or triflate anions, and Y = $PF_6$ or triflate anions. The way the EMACs twist is not shown.

## 2. Achiral Dimetal Chromophores in Chiral Environments

It appears that the first structurally characterized quadruply bonded $Mo_2^{4+}$ compound containing chiral ligands was $Mo_2(L\text{-isoleucine})_2(NCS)_4{\cdot}4.5H_2O$, but no spectroscopic data were collected.[34] Later, $Mo_2(\text{L-leucine})_4Cl_2(p\text{-toluenesulfonate})_2{\cdot}2H_2O$ was prepared, structurally characterized, and, because of very favorable alignment of the molecules in the crystal, used for detailed studies of the polarization and vibronic structure of the δ→δ* absorption band.[35] Again, however, no ORD or CD data were collected.

Chiral dicarboxylic acid anions, L-tartrate and D-aspartate, have been used to link $Mo_2(DAniF)_3^+$ units (DAniF = the *N*,*N*′-di-*p*-anisylformamidinate anion).[36] The structure of the tartrate is shown in Figure 16. An enantiomerically pure compound in the form of a loop has two *cis*-$Mo_2(DAniF)_2^{2+}$ units and two chiral dicarboxylates made from hydroquinone and ethyl (*S*)-lactate,[37] **L1**-*para*, shown in Scheme 6. The structure of the loop $[cis\text{-}Mo_2(DAniF)_2]_2(\mathbf{L1}\text{-}para)_2$ is shown in Figure 17. In the crystal, the molecules stack forming channels capable of hosting guest molecules such as $CH_2Cl_2$, as shown in Figure 18.

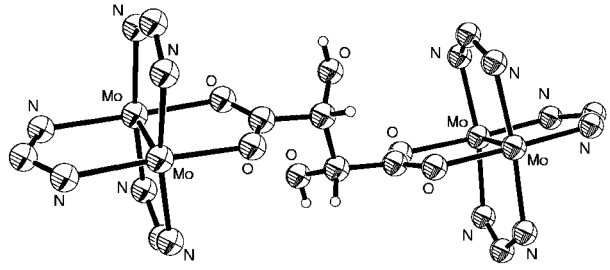


Figure 16. The structure of $[Mo_2(DAniF)_3]_2(L\text{-tartrate})$.

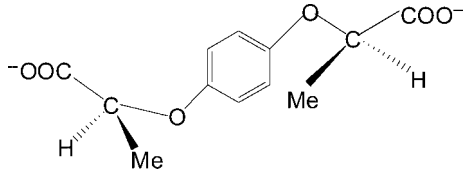


Scheme 6. The ligand **L1**-*para*, $p\text{-}^{-}O_2C(CH_3)(H)(O)\text{–}C_6H_4\text{–}(O)C(CH_3)(H)CO_2^{-}$, made from hydroquinone and ethyl (*S*)-lactate.

Other early work in this area was done by Snatzke,[38] whose goal was to employ the δ→δ* transition in the $Mo_2^{4+}$ chromophore, which is conveniently located at about

 © 2006 Wiley-VCH Verlag GmbH & Co. KGaA, Weinheim 

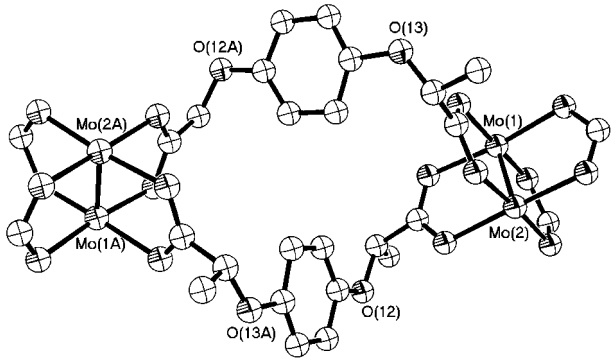


Figure 17. The structure of the molecular loop [*cis*-$Mo_2$(DAniF)$_2$]$_2$-(**L1**-*para*)$_2$.

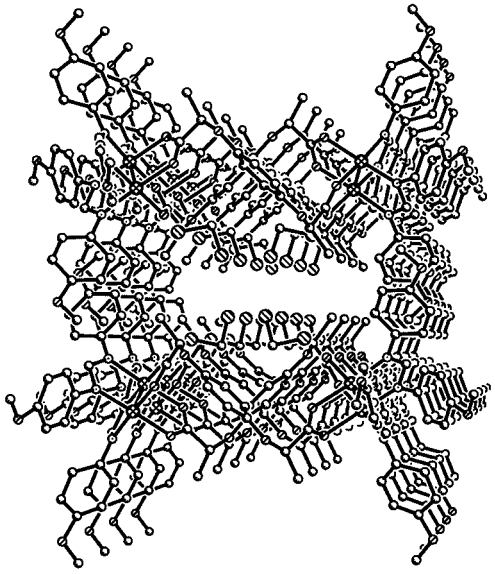

Figure 18. The packing of [*cis*-$Mo_2$(DAniF)$_2$]$_2$(**L1**-*para*)$_2$ showing the chiral intersticies.

20000 $cm^{-1}$, to determine the absolute configurations of functionalized organic molecules. Direct ORD or CD measurements of the organic molecules themselves was challenging because their lowest-energy transition was generally in the ultraviolet. Snatzke's approach was rather empirical; it consisted in simply adding $Mo_2(O_2CCH_3)_4$ to a solution of the organic compound of interest and measuring the CD spectrum in the visible region due to some generally undefined complex between the organic compound and some fragment of the $Mo_2(O_2CCH_3)_4$ molecule that had been introduced. Results varied with absolute and relative concentrations.

It was later proposed[39] that the ability of $Rh_2(O_2CCF_3)_4$ to bind almost every possible organic functionality including simple olefins, at its axial position might lead to a more reliable realization of Snatzke's concept, but there has been no follow up on this. It does not appear that the use of "spectator" dimetal units, either $Mo_2^{4+}$ or $Rh_2^{4+}$ is a very promising technique.

**Dirhodium Compounds**

In 1986 two $Rh_2(O_2CR)_4L_2$ compounds, one with R = CPh(OH)H and L = EtOH and the other with R = CPh(OMe)H and L = THF were structurally characterized and their CD spectra were measured and interpreted.[40] The structure of the (*S*)-mandelate is shown in Figure 19 and it resembles that of the $Mo_2^{4+}$ analog, except for the absence of axial ligands in the latter.[41] The electronic absorption and CD spectra of $Rh_2$[(*S*)-mandelate]$_4$(EtOH)$_2$ are shown in Figure 20. The interpretation, which is much too complex to recapitulate here, was carried out assuming that the central $Rh_2(O_2C–)_4$ core is inherently achiral, having $D_{4h}$ symmetry. A one-electron model of a type previously proposed by others[42] was employed and was found to be consistent with the fact that the CD signs associated with the two prominent absorption bands (at ca. 450 and 600 nm) have the same sign. The fact that both are negative (rather than both positive) was not predictable. However, because both have the same sign, a reversal of the absorption band assignments from those accepted at the time is not ruled out, and indeed MCD measurements reported se-

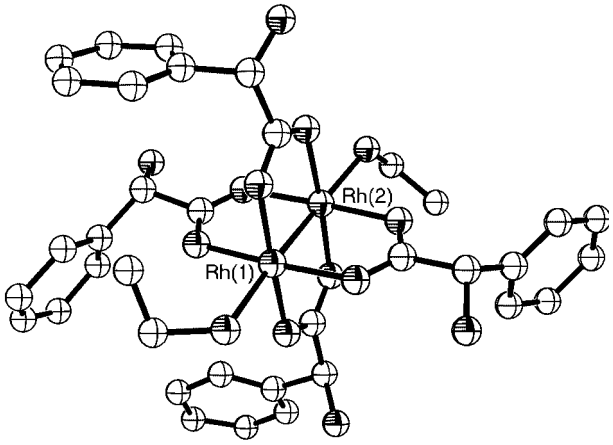


Figure 19. The structure of $Rh_2$[(*S*)-mandelate]$_4$(EtOH)$_2$.

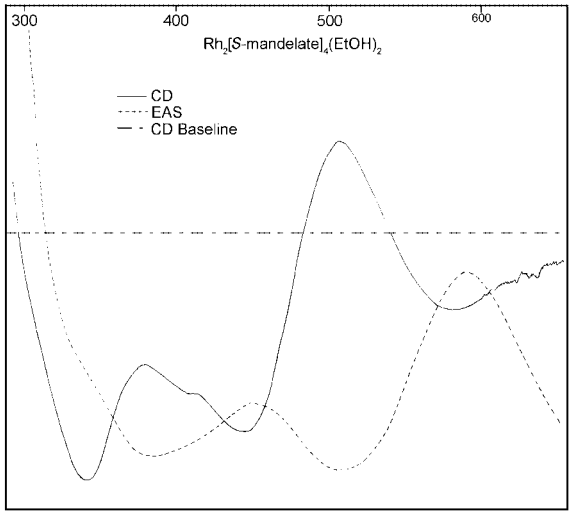


Figure 20. CD and UV-vis spectra of $Rh_2$[(*S*)-mandelate]$_4$(EtOH)$_2$.

 © 2006 Wiley-VCH Verlag GmbH & Co. KGaA, Weinheim 

veral years later[43] showed that such a reversal was required. Thus, while the CD results offer valuable evidence for assigning the electronic spectrum, they are not by themselves definitive.

Chiral dirhodium compounds are some of the most widely studied species with metal–metal bonds due to their applications in catalysis. Because this topic has been reviewed recently we will not elaborate any further here.[44]

## Conclusions

There is considerable diversity of chiral compounds that contain dimetal units. Those cited in this review suggest that there is great scope for further development, along both of the main avenues: (1) compounds in which the ligand arrangement renders the $M_2$ unit itself chiral, and (2) compounds in which the $M_2$ unit is not itself a seat for chirality but is the linchpin for a surrounding set of chiral ligands.

## Acknowledgments

We thank the Robert A. Welch Foundation and Texas A&M University for financial support.

[1] a) M. P. Doyle, T. Ren, *Prog. Inorg. Chem.* **2001**, *49*, 113; b) R. D. Adams, F. A. Cotton (Eds.), *Catalysis by Di- and Polynuclear Metal Cluster Complexes*, Wiley-VCH, New York, **1998**; c) K. Matsumoto, in: *Cisplatin: Chemistry and Biochemistry of a Leading Anticancer Drug* (Ed.: B. Lippert), Wiley-VCH, New York, **1999**, p. 455; d) N. Saeki, N. Nakamura, T. Ishibashi, M. Arime, H. Sekiya, K. Ishihara, K. Matsumoto, *J. Am. Chem. Soc.* **2003**, *125*, 3605; e) M. Pillinger, I. S. Goncalves, P. Ferreira, J. Rocha, M. Schafer, D. Schon, O. Nuyken, F. E. Kühn, *Macromol. Rapid Commun.* **2001**, *22*, 1302; f) E. Whelan, M. Devereux, M. McCann, V. McKee, *Chem. Commun.* **1997**, 427.

[2] a) J. M. Asara, J. S. Hess, E. Lozada, K. R. Dunbar, J. Allion, *J. Am. Chem. Soc.* **2000**, *122*, 8; b) K. V. Catalan, J. S. Hess, M. M. Maloney, D. J. Mindiola, D. L. Ward, K. R. Dunbar, *Inorg. Chem.* **1999**, *38*, 3904; c) L. D. Dale, T. M. Dyson, D. A. Tocher, J. H. Tocher, D. I. Edwards, *Anti-Cancer Drug Des.* **1989**, *4*, 295; d) K. Aoki, H. Yamazaki, *J. Chem. Soc., Chem. Commun.* **1980**, 186; e) R. A. Howard, A. P. Kimball, J. L. Bear, *Cancer Res.* **1979**, *39*, 2568; f) P. Fu, P. M. Bradley, C. Turro, *Inorg. Chem.* **2001**, *40*, 2476; g) K. Aoki, M. A. Salam, *Inorg. Chim. Acta* **2001**, *316*, 50; h) B. Lippert, *Prog. Inorg. Chem.* **1989**, *37*, 1; i) W. Micklitz, G. Müller, B. Huber, J. Riede, F. Rashwan, J. Heinze, B. Lippert, *J. Am. Chem. Soc.* **1988**, *110*, 7084; j) H. T. Chifotides, K. R. Dunbar, *Acc. Chem. Res.* **2005**, *38*, 146.

[3] a) F. A. Cotton, C. Lin, C. A. Murillo, *Acc. Chem. Res.* **2001**, *34*, 759; b) F. A. Cotton, C. Lin, C. A. Murillo, *Proc. Natl. Acad. Sci. USA* **2002**, *99*, 4810; c) M. H. Chisholm, A. M. Mcintosh, *Chem. Rev.* **2005**, *105*, 2949.

[4] A. Moscowitz, *Tetrahedron* **1961**, *13*, 48.

[5] a) J. A. Jaecker, D. P. Murtha, R. A. Walton, *Inorg. Chim. Acta* **1975**, *13*, 21; b) J. R. Ebner, D. R. Tyler, R. A. Walton, *Inorg. Chem.* **1976**, *15*, 833; c) F. A. Cotton, G. G. Stanley, R. A. Walton, *Inorg. Chem.* **1978**, *17*, 2099.

[6] a) S. A. Best, T. J. Smith, R. A. Walton, *Inorg. Chem.* **1978**, *17*, 99; b) H. D. Glicksman, R. A. Walton, *Inorg. Chem.* **1978**, *17*, 3197.

[7] a) F. A. Cotton, T. R. Felthouse, D. G. Lay, *J. Am. Chem. Soc.* **1980**, *102*, 1431; b) F. A. Cotton, T. R. Felthouse, *Inorg. Chem.* **1981**, *20*, 3880.

[8] For full references, see chapters on Mo, W and Re, in: *Multiple Bonds Between Metal Atoms* (Eds.: F. A. Cotton, C. A. Murillo, R. A. Walton), Springer Science and Business Media Inc., New York, **2005**.

[9] P. A. Agaskar, F. A. Cotton, I. F. Fraser, R. D. Peacock, *J. Am. Chem. Soc.* **1984**, *106*, 1851.

[10] P. A. Agaskar, F. A. Cotton, I. F. Fraser, L. Manojlovic-Muir, K. W. Muir, R. D. Peacock, *Inorg. Chem.* **1986**, *25*, 2511.

[11] J.-D. Chen, F. A. Cotton, L. R. Falvello, *J. Am. Chem. Soc.* **1990**, *112*, 1076.

[12] R. D. Peacock, *Polyhedron* **1987**, *6*, 715.

[13] I. F. Fraser, A. McVitie, R. D. Peacock, *Polyhedron* **1986**, *5*, 39.

[14] I. F. Fraser, R. D. Peacock, *J. Chem. Soc., Chem. Commun.* **1985**, 1727.

[15] R. D. Peacock, I. F. Fraser, *Inorg. Chem.* **1985**, *24*, 988.

[16] A. R. Chakravarty, F. A. Cotton, D. A. Tocher, J. H. Tocher, *Organometallics* **1985**, *4*, 8.

[17] F. A. Cotton, R. Poli, *Organometallics* **1987**, *6*, 1743.

[18] R. S. Cahn, C. Ingold, V. Prelog, *Angew. Chem. Int. Ed. Engl.* **1966**, *5*, 385.

[19] F. A. Cotton, C. A. Murillo, X. Wang, R. Yu, *Inorg. Chem.* **2004**, *43*, 8394.

[20] F. Estevan, K. Herbst, P. Lahuerta, M. Barberis, J. Pérez-Prieto, *Organometallics* **2001**, *20*, 950.

[21] a) M. Barberis, J. Pérez-Prieto, K. Herbst, P. Lahuerta, *Organometallics* **2002**, *21*, 1667; b) M. Barberis, P. Lahuerta, J. Pérez-Prieto, M. Sanaú, *Chem. Commun.* **2001**, 439; c) F. Estevan, P. Lahuerta, J. Pérez-Prieto, I. Pereira, S.-E. Stiriba, *Organometallics* **1998**, *17*, 3442; d) F. Estevan, P. Lahuerta, J. Pérez-Prieto, M. Sanaú, S.-E. Stiriba, A. M. Ubeda, *Organometallics* **1997**, *16*, 880.

[22] F. A. Cotton, C. A. Murillo, R. Yu, *Inorg. Chem.* **2005**, *44*, 8211.

[23] a) F. Barceló, F. A. Cotton, P. Lahuerta, M. Sanaú, W. Schwotzer, M. A. Ubeda, *Organometallics* **1987**, *6*, 1105; b) P. Lahuerta, R. Martínez-Mañez, J. Paya, E. Peris, *Inorg. Chim. Acta* **1990**, *173*, 99; c) E. C. Morrison, D. A. Tocher, *J. Organomet. Chem.* **1991**, *408*, 105; d) P. Lahuerta, J. Payá, E. Peris, A. Aguirre, S. García-Granda, F. Gómez-Beltrán, *Inorg. Chim. Acta* **1992**, *192*, 43; e) M. V. Borrachero, F. Estevan, S. García-Granda, P. Lahuerta, J. Latorre, E. Peris, M. Sanaú, *J. Chem. Soc., Chem. Commun.* **1993**, 1864; f) F. Estevan, P. Lahuerta, E. Peris, M. A. Ubeda, S. García-Granda, F. Gómez-Beltrán, E. Pérez-Carreño, G. González, M. Martínez, *Inorg. Chim. Acta* **1994**, *218*, 189; g) F. Estevan, S. García-Granda, P. Lahuerta, J. Latorre, E. Peris, M. Sanaú, *Inorg. Chim. Acta* **1995**, *229*, 365; h) P. Lahuerta, I. Pereira, J. Pérez-Prieto, M. Sanaú, S.-E. Stiriba, D. F. Taber, *J. Organomet. Chem.* **2000**, *612*, 36; i) F. Estevan, P. Krueger, P. Lahuerta, E. Moreno, J. Pérez-Prieto, M. Sanaú, H. Werner, *Eur. J. Inorg. Chem.* **2001**, 105.

[24] F. A. Cotton, C. A. Murillo, R. Yu, *Inorg. Chem.* **2005**, *44*, 8223.

[25] F. A. Cotton, C. A. Murillo, R. Yu, *Dalton Trans.* **2005**, 3161.

[26] J. F. Berry, in: *Multiple Bonds Between Metal Atoms* (Eds.: F. A. Cotton, C. A. Murillo, R. A. Walton), Springer Science and Business Media Inc., New York, **2005**, pp. 669–706. (A review of EMACs with 86 references)

[27] R. Clérac, F. A. Cotton, K. R. Dunbar, T. Lu, C. A. Murillo, X. Wang, *Inorg. Chem.* **2000**, *39*, 3065.

[28] E. L. Eliel, S. H. Wilen, *Stereochemistry of Organic Compounds*, John Wiley & Sons, New York, **1994**.

[29] D. W. Armstrong, F. A. Cotton, unpublished results.

[30] A. G. Petrovic, P. L. Polavarapu, F. A. Cotton, unpublished results.

[31] S.-M. Peng, C.-C. Wang, Y.-L. Yang, Y.-H. Chen, F.-Y. Li, C.-Y. Mou, M.-K. Leung, *J. Magn. Magn. Mater.* **2000**, *209*, 80.

 © 2006 Wiley-VCH Verlag GmbH & Co. KGaA, Weinheim 

[32] C.-H. Chien, J.-C. Chang, C.-Y. Yeh, G.-H. Lee, J.-M. Fang, S.-M. Peng, *Dalton Trans.* **2006**, 2106.
[33] C.-H. Chien, J.-C. Chang, C.-Y. Yeh, G.-H. Lee, J.-M. Fang, Y. Song, S.-M. Peng, *Dalton Trans.* **2006**, 3249.
[34] A. Bino, F. A. Cotton, *Inorg. Chem.* **1979**, *18*, 1381.
[35] A. Bino, F. A. Cotton, P. E. Fanwick, *Inorg. Chem.* **1980**, *19*, 1215.
[36] F. A. Cotton, J. P. Donahue, C. A. Murillo, *Inorg. Chem. Commun.* **2002**, *5*, 59.
[37] J. F. Berry, F. A. Cotton, S. I. Ibragimov, C. A. Murillo, X. Wang, *Dalton Trans.* **2003**, 4297.
[38] a) G. Snatzke, *Angew. Chem. Int. Ed. Engl.* **1979**, *18*, 363; b) G. Snatzke, V. Wagner, H. P. Wolff, *Tetrahedron* **1981**, *37*, 349; c) V. J. Engel, R. Gerger, G. Snatzke, V. Wagner, *Chem.-Ztg.* **1981**, *105*, 85.
[39] F. A. Cotton, L. R. Falvello, M. Gerards, G. Snatzke, *J. Am. Chem. Soc.* **1990**, *112*, 8979.
[40] P. A. Agaskar, F. A. Cotton, L. R. Falvello, S. Han, *J. Am. Chem. Soc.* **1986**, *108*, 1214.
[41] F. A. Cotton, L. R. Falvello, C. A. Murillo, *Inorg. Chem.* **1983**, *22*, 382.
[42] a) S. F. Mason, in: *Optical Activities and Chiral Discrimination* (Ed.: S. F. Mason), D. Riedel, Boston, **1979**, pp. 1–24; b) J. A. Schellman, *Acc. Chem. Res.* **1968**, *1*, 144.
[43] J. W. Trexler Jr, A. F. Schreiner, F. A. Cotton, *Inorg. Chem.* **1988**, *27*, 3265.
[44] D. J. Timmons, M. P. Doyle, in: *Multiple Bonds Between Metal Atoms* (Eds.: F. A. Cotton, C. A. Murillo, R. A. Walton, Eds.), Springer Science and Business Media Inc.: New York, **2005**, pp. 591–632. (A review with 200 references on the catalytic activity of chiral $Rh_2^{4+}$ compounds)

Received: May 24, 2006
Published Online: July 31, 2006

 © 2006 Wiley-VCH Verlag GmbH & Co. KGaA, Weinheim 

DOI: 10.1002/ejic.200600625

# "Isomerism" of Coordination Modes and Numbers in Pentanuclear Organozinc Hydroxylamides: An Exercise in Subtle Substituent Size Effects

**Matthias Ullrich,[a] Raphael J. F. Berger,[a] Christian Lustig,[a] Roland Fröhlich,[b] and Norbert W. Mitzel*[a]**

*Dedicated to Prof. Gerhard Erker on the occasion of his 60th birthday*

**Keywords:** Zinc / Hydroxylamines / Organometallic / Coordination modes / Crystal structure

The first organometallic zinc hydroxylamides $[Zn(RZn)_4(ONMe_2)_6]$ (**1**: R = Me; **2**: R = *i*Pr) and $[Zn(EtZn)_4(ONEt_2)_6]$ (**3**) have been prepared by alkane elimination from dialkylzinc solutions upon treatment with *N*,*N*-dialkylhydroxylamines. The molecular structures of **1** and **2** reveal that a subtle change in the constitution of the aggregates can make a striking difference. By the simple exchange of the $MeZn^+$ groups with *i*PrZn$^+$ groups, the coordination number of the central $Zn^{2+}$ nucleus increases from four (**1**) to six (**2**). The two cluster types are unprecedented in both hydroxylamine and organometallic chemistry. Compounds **1** and **3** adopt a doubly bridged fenestrane-like $Zn_5N_6O_6$ core with two dangling $NR_2$ moieties, whereas *i*PrZn species **2** comprises an octahedroid backbone with all donor atoms attached to the five Zn nuclei with the maintenance of the same heteroatom composition as **1** and **3**. Variable-temperature $^{13}C$ NMR experiments of all-ethyl cluster **3** reveal that the $R_2NO^-$ ligands rapidly exchange between the $RZn^+$ and $Zn^{2+}$ cations. This process is rationalised by a plausible model which also points out that the core structure of **3** could be an intermediate motif in the observed heteroatom connectivity exchange. In line with this, computational investigations reveal that both skeletons are very similar in energy. In sum, the coordination flexibility of the hydroxylamide ligand makes this group of organometallic zinc complexes a highly dynamic family of cluster compounds.
(© Wiley-VCH Verlag GmbH & Co. KGaA, 69451 Weinheim, Germany, 2006)

## Introduction

Compared to organometallics of the trivalent group 13 elements, zinc requires further contact to a donor atom to reach coordination number (CN) four because of its divalent nature. In metal alkoxide/aryloxide chemistry,[1] an increase in aggregate dimensionality is already well established [compare the $Al_2O_2$ ring $\{(Me_2Al)[O(2,6\text{-}iPr_2\text{-}C_6H_3)]\}_2$[2] with the "double cube" $[(MeZn)_3(OMe)_4]_2Zn$[3] (CN = 4, 6)].[4] The highly diverse chemistry of the O–N double-donor array (hydroxylamines or oximes) provides a plethora of aggregation motifs, for example in group 13 complexes,[5–9] and ought to be transferable to zinc for the exploration of similar extensions {compare the six-membered ring dimer $[(Me_2Al)(ON{=}CMe_2)]_2$[5a,5b] with the tetrahedroid oximate $[(MeZn)(ON{=}CMe_2)]_4$[10] (CN = 4)}. The high coordination flexibility of the hydroxylamide ligands that is demonstrated in Al and Ga organometallics (e.g. in the readily fluctuating tetracyclic $Al_3$ cluster $[\{(Me_2Al)[ON(Me)]_2CH_2\}_2(AlMe)]$[6]) can be expected by hypothesis to allow for the construction of highly dynamic Zn-based multinuclear cluster compounds. Zinc, on its own accord, has a very rich alkoxide chemistry.[1,3] However, hydroxylamide derivatives of divalent metals are rather poorly understood and encompass merely inorganic coordination compounds of zinc[11] {e.g. $[(H_2NOH)_2ZnCl_2]$, Crismer's salt[12]}, but organometallic examples are completely unknown.

We report herein the initial evidence to support the above hypothesis. The reaction of *N*,*N*-dialkylhydroxylamines $Me_2NOH$ or $Et_2NOH$ with binary zinc alkyls affords three pentanuclear organozinc cluster compounds: $[Zn(RZn)_4(ONMe_2)_6]$ (**1**: R = Me; **2**: R = *i*Pr) and $[Zn(EtZn)_4(ONEt_2)_6]$ (**3**, vide infra).

## Results and Discussion

With the focus on compounds **1** and **2** (Scheme 1), it is elegantly revealed that the highly flexible coordinating O–N ligands allow Zn atoms to adopt a CN > 4. This

[a] Institut für Anorganische und Analytische Chemie, Westfälische Wilhelms-Universität Münster,
Corrensstrasse 30, 48149 Münster, Germany
Fax: +49-251-8336007
E-mail: mitzel@uni-muenster.de
[b] Organisch-Chemisches Institut, Westfälische Wilhelms-Universität Münster,
Corrensstrasse 40, 48149 Münster, Germany
Supporting information for this article is available on the WWW under http://www.eurjic.org or from the author.

 © 2006 Wiley-VCH Verlag GmbH & Co. KGaA, Weinheim 

stands in contrast to the isoelectronically related organozinc hydrazides (N–N double-donor), where zinc is exclusively tetracoordinate.[13]

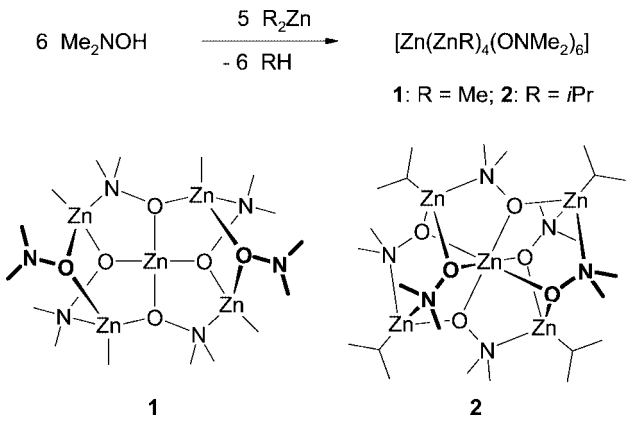


Scheme 1.

Though the formulae of **1** and **2** (apart from the alkyl groups on Zn) are identical, their three-dimensional coordination frameworks differ markedly. The all-methyl cluster $[Zn(MeZn)_4(ONMe_2)_6]$ (**1**) adopts a fenestrane-like motif, as determined by X-ray diffraction analysis (Figure 1).[14] Four O–N moieties coordinate around the central "inorganic" $Zn^{2+}$ ion by their oxygen atoms and are themselves interconnected by $RZn^+$ units via O–Zn–N linkages. The resulting dicationic heterofenestrane $\{[Zn(ONMe_2)_4(ZnMe)_4]^{2+}\}$ is then charge-compensated by two anionic $\mu^2$-O-bridging $Me_2NO^-$ ligands. If the latter are neglected, the core of **1** is reminiscent of a handful of known complexes (e.g. in bioinorganics),[15] but those complexes exhibit solely square-planar coordinated central metal ions and have no M–C bonds. The aggregation motif of **1** (all Zn atoms: CN = 4) is unprecedented in both hydroxylamine and organometallic chemistry.

With a subtle size change of the alkyl group at zinc (from Me to *i*Pr), the core structure of the aggregate completely shifts as revealed by the crystal structure of ether solvate **2**·$OEt_2$ (Figure 2).[14] In this cluster, the ether molecule fills a void but does not contact any of the Zn atoms. The hydroxylamide cluster $[Zn(ONMe_2)_6(Zn\textit{i}Pr)_4]$ (**2**) adopts an octahedral-based structure with all six O–N ligands O-bound to the central $Zn^{2+}$ (CN = 6). Charge compensation of this $[Zn(ONMe_2)_6]^{4-}$ fragment is achieved by four $\textit{i}PrZn^+$ groups, which bind to the six O–N units either in an N,O,O- or in an N,N,O mode. Because all of the O and N atoms are now coordinated to Zn, this contrasts the situation in **1** which has two dangling $NMe_2$ groups – one key feature of the observed coordination "isomerism". Consequently, cluster **2** is one of the limited examples of Zn species that exhibit mixed CNs, whether in organometallic[1,3] or in inorganic chemistry.[16]

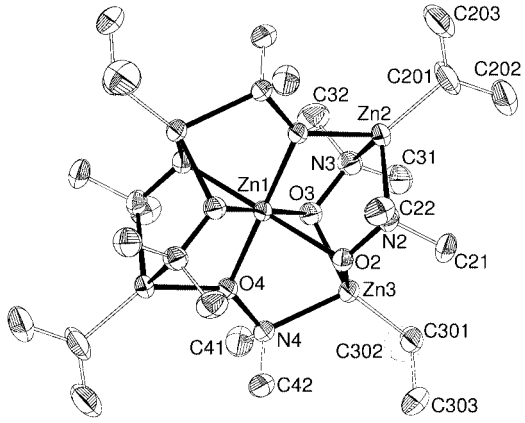


Figure 2. Solid-state structure of **2** in a crystal of the composition **2**·$OEt_2$ (thermal ellipsoids at 50% probability; hydrogen atoms and the $Et_2O$ solvate molecule are omitted; symmetry transformations used to generate equivalent atoms: $-x+1, -y+2, -z$). Selected distances and angles [Å/°]: Zn2–O4′ 1.974(2), Zn1–O2 2.205(2), Zn3–N4 2.135(2), O4–N4 1.433(2), Zn2–C201 1.987(3), N3–C32 1.467(3); O2–Zn1–O3 78.0(1), O2–Zn1–O3′ 102.0(1), O4′–Zn2–N12 85.2(1), O3–Zn3–N4 106.0(1), Zn1–O12–Zn3 102.1(1), Zn2–O3–Zn3 119.3(1), Zn3–O3–N3 108.5(1), Zn2–O3–N3 122.8(1), Zn3–N4–O4 112.2(2), Zn3–N4–C41 109.0(2), O3–N3–C33 106.9(2), C41–N4–C43 110.8(3).

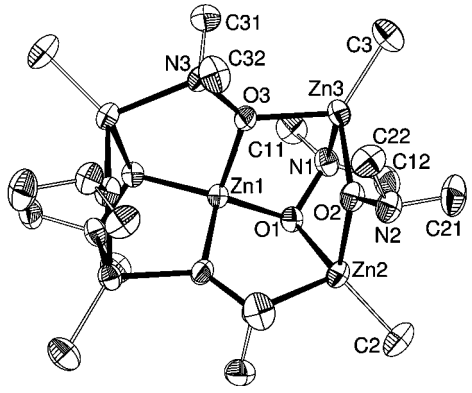


Figure 1. Crystal structure of **1** (thermal ellipsoids at 50% probability; hydrogen atoms are omitted; symmetry transformations used to generate equivalent atoms: $-x+1, y, -z+3/2$). Selected distances and angles [Å/°]: Zn1–O3 1.923(3), Zn2–O1 2.100(2), Zn3–N1 2.175(3), O3–N3 1.435(4), Zn2–C2 1.966(4), N3–C32 1.464(5); O1–Zn2–O2 86.8(1), O1–Zn1–O1′ 132.5(1), O3–Zn3–N1 85.8(1), O2–Zn2–N3′ 103.5(1), Zn1–O1–Zn2 100.0(1), Zn2–O2–Zn3 121.9(1), Zn1–O1–N1 107.9(2), Zn3–O2–N2 123.8(2), Zn3–N1–O1 107.3(2), Zn2–N3′–O3′ 111.6(2), Zn2–N3′–C32′ 110.2(3), O2–N2–C21 107.2(3), C21–N2–C22 109.8(4).

Although the structures of **1** and **2** are not the same, their core compositions are, and thus, the question arises whether a pathway for the interconversion between the two cluster types exists. VT-NMR spectroscopy sheds some light onto this and onto the molecular dynamics of the aggregates. Between 300 and 200 K, the $^1H$ NMR spectra of **1** show some signal broadening but no substantial change to indicate structural variations; the $^{13}C$ NMR spectra give a similar picture. A drawback to these measurements is the limited solubility of **1** especially at low temperatures, which is most probably due to its minimal alkyl periphery.

 © 2006 Wiley-VCH Verlag GmbH & Co. KGaA, Weinheim 

Fortunately, the all-ethyl analogue $[Zn(EtZn)_4(ONEt_2)_6]$ (**3**, Scheme 2) is much more soluble and represents an exquisite VT-NMR substitute for all-methyl cluster **1** because it adopts the same core motif (Figure 3). Furthermore, the fact that **1** and **3** exhibit the same coordination framework underlines that the structural differences between **1** and **2** cannot be accounted for merely by means of the steric congestion of the "organic sphere" about the $Zn_5N_6O_6$ heteroatom core. The number of carbon atoms in that sphere doubles from 16 (compound **1**) to 32 (compound **3**) without any effect on the aggregation motif. Exchange of the $MeZn^+$ groups (compound **1**) by $iPrZn^+$ groups (compound **2**) increases that number only by 8 (from 16 to 24). A simple focus on group sizes – though obvious when only differences between **1** and **2** are examined based on the literature findings of EtZn boryloxides[17] or Stephan's bulky $Me_2Al$ aryloxide[2] (compared to "normal" Al–O organyls with CN $> 4$[1]) – is not a definite reason for the varied CN of the present organozinc hydroxylamides. In fact, if bulkiness of the group had an influence on the CN of the central "inorganic" $Zn^{2+}$ nucleus, the opposite trend in the CN would be expected. The overall packing in the aggregation motif found for **2** is more compact than the one found for **1** and **3**.

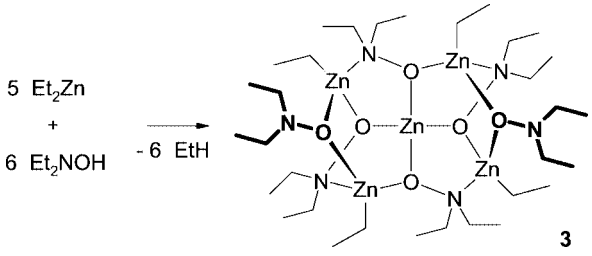


Scheme 2.

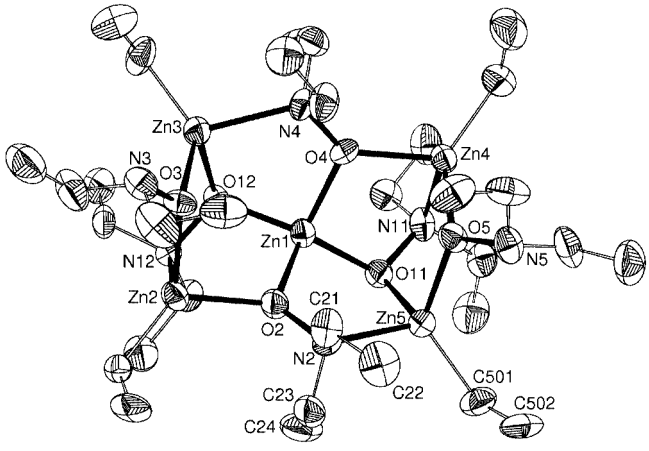


Figure 3. Crystal structure of **3** (thermal ellipsoids at 50% probability; hydrogen atoms and the disorder of the ethyl group at Zn2 are omitted). Selected distances and angles [Å/°]: Zn1–O11 1.944(7), Zn2–O3 2.041(7), Zn4–N11 2.186(9), O2–N2 1.444(11), Zn5–C501 1.972(12), N2–C23 1.461(15); O5–Zn5–O11 88.7(3), O11–Zn1–O12 139.7(3), O2–Zn2–N12 86.2(3), O3–Zn3–N4 107.8(3), Zn1–O11–Zn5 102.3(3), Zn4–O5–Zn5 117.7(3), Zn1–O12–N12 109.7(5), Zn4–O5–N5 121.9(6), Zn4–N11–O11 104.5(5), Zn5–N2–O2 112.9(6), Zn5–N2–C21 112.6(7), O2–N2–C23 106.0(8), C21–N2–C23 110.8(10).

The $^{13}C$ NMR spectrum of **3** at 298 K exhibits broad features for the nitrogen-bound ethyl substituents in the regions between ca. 50 and 60 ppm and between ca. 10 and 15 ppm (Figure 4). At 213 K however, all five resonances are well-resolved and observable. This is in accordance with a $C_2$ molecular symmetry with freely rotating O–N bonds to the dangling $NEt_2$ groups. The ethyl groups at zinc give two sets of sharp resonances at both low and ambient temperatures. Obviously, the $R_2NO^-$ units in compounds **1** and **3** exchange between the five Zn nuclei in a highly fluxional manner.

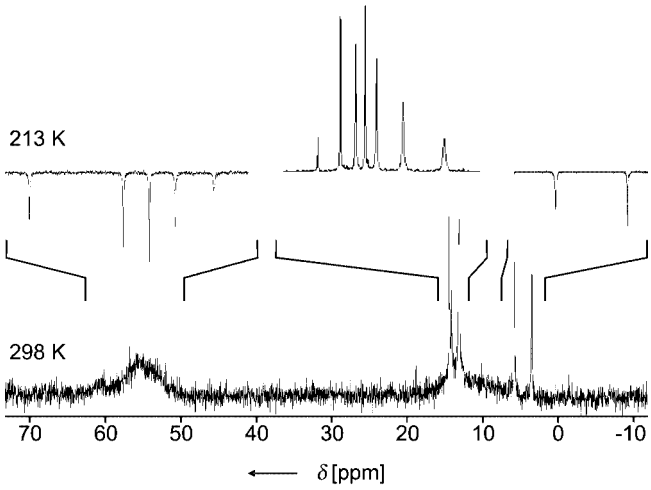


Figure 4. Details of the $^{13}C$ NMR spectra of $[Zn(ZnEt)_4(ONEt_2)_6]$ (**3**) at 298 K (in $[D_6]$benzene) and at 213 K (in $[D_8]$toluene, DEPT 135 mode).

The $^1H$ NMR spectrum of **2** (Figure 5) displays one prominent resonance for the $Me_2NO^-$ units at 300 K, which indicates an exchange on the NMR time scale comparable in magnitude to that found for the $R_2NO^-$ units of **1** and **3**. At temperatures below 270 K, this peak splits into a complex set of signals of rather low resolution. Thus, a drop in the symmetry of the molecule below that of the crystalline state ($C_2$) can be assumed since the latter would require six chemically different *N*–Me groups. From the complexity of the NMR spectrum, the presence of more than one isomeric species in solution is reasonable. The two motifs found in the solid state for **1** and **2** are two likely possibilities.

The observed highly dynamic behaviour is consistent with rapidly isomerising aggregates. A plausible model is illustrated in Scheme 3a with the heteroatom core of **1**. The process by which this core is transformed into itself can be reasoned by the division of the process into four single steps.[18,19] The first two steps involve the bond formation between the peripheral noncoordinated N atom and an $RZn^+$ group [colour code: green (1)]; in addition, there is a change in connectivity of the O atom of the hydroxylamide from a peripheral Zn atom to the central Zn atom [colour code: orange (2)]. The central Zn atom then becomes hexa-

 © 2006 Wiley-VCH Verlag GmbH & Co. KGaA, Weinheim 

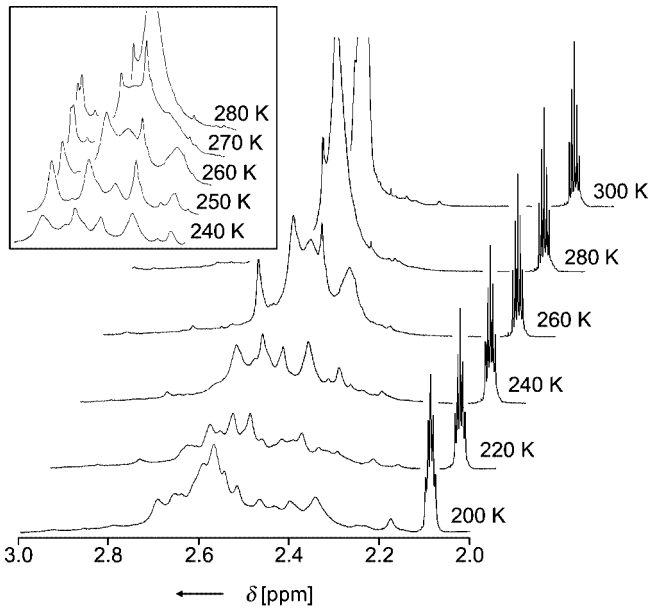


Figure 5. Variable-temperature $^1$H NMR spectra of **2** (in [$D_8$]toluene) in the chemical shift region of the $ONMe_2$ moieties. For clarity, the highlighted temperature range around the coalescence point is provided in steps of 10 K.

coordinate, and this finalises the transformation of the core structure from the type adopted by compound **1** to that of **2** in the crystalline state.

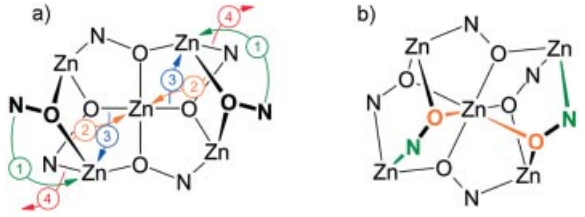


Scheme 3. a) Plausible model for the fluctuation of the O–N ligands. The overall $C_2$ symmetry compels each step to occur twice. b) The isomeric heteroatom cluster core as found for **2** in the solid state – an "intermediate" of the periodical fluctuation.

Two further steps that are reverse in nature to the preceding two allow the ligands to rearrange about the $RZn^+$ and $Zn^{2+}$ atoms to reconstruct the heteroatom connectivity pattern as found in the solid state of **1** {the O atom of one O–N unit moves from the central $Zn^{2+}$ nucleus to a peripheral $RZn^+$ group [colour code: blue (3)], and the N atom of the same O–N unit disconnects from the organozinc residue to become the dangling $NR_2$ group [colour code: red (4)]}.

In order to gain more detailed insight into the energetics of these systems, we calculated the energies of the two cluster types represented by **1** and **2** in the crystalline state for the most simple cases, all-methyl compound **1** and the $MeZn^+$ analogue of **2**, because both are unaffected by substituent conformations. The computations were carried out at the SCF/SV(P) and RI-BP/SV(P) levels of theory and reproduce the core structure parameters of the experimentally determined geometries well. At the SCF/SV(P) level, the aggregation adopted by compound **1** is slightly preferred by 5.4 kcal mol$^{-1}$. At the RI-BP/SV(P) level, the reverse was found; the structure of compound **2** was preferred with an energy difference of 1.2 kcal mol$^{-1}$.[20]

The small differences in the theoretical calculations along with the temperature-dependent NMR studies reveal both aggregation motifs to be very comparable in energy. This explains the sensitivity of the observed aggregation and coordination modes on small substituent effects and the highly dynamic behaviour of the species. Thus, pentanuclear organozinc hydroxylamides **1**–**3** disclose for the first time that a metal can be flexibly coordinated by O–N ligands not only in terms of coordination modes but also numbers. On the basis of the experimental findings and the unique ability of the hydroxylamide ligand to be flexibly coordinating, this group of organometallic zinc complexes forms a highly dynamic family of cluster compounds.

## Experimental Section

**CAUTION:** Pure zinc organyls may spontaneously ignite upon contact to air or moisture!

**Materials and Methods:** All manipulations were carried out under a dry nitrogen atmosphere with standard Schlenk and high-vacuum techniques with double manifolds or in a glove box (MBraun Lab Master 130) operated under an argon atmosphere. All solvents were purified by standard procedures immediately prior to use. $Me_2Zn$ was obtained in its pure form by the fractional distillation of a commercial solution (2.0 M in toluene, Aldrich). $Et_2Zn$ (Crompton GmbH, Bergkamen, Germany) was transferred into glassware in the glove box and used without further purification. $i Pr_2Zn$ was synthesised according to the literature[21] and further purified by fractional condensation (removal of trace $Et_2O$ from synthesis). It was stored in the dark at –78 °C because it decomposes quite quickly upon exposure to light or ambient temperature. $Me_2NOH$ was obtained from its hydrochloride salt (Aldrich) by treatment with excess $NH_3$ at –78 °C and separated from the $NH_4Cl$ residue by distillation.[22] $Et_2NOH$ (Aldrich) was purified by fractional distillation.

**General Synthetic Protocol:** $R_2Zn$ (R = Me, Et or *i*Pr) was condensed into a round-bottomed flask and then diluted with *n*-hexane to generate a ca. 1 M solution. With heavy stirring, a solution of $Me_2NOH$ or $Et_2NOH$ in THF (ca. 1 M) was slowly added at 0 °C. The ice bath was removed, and the reaction mixture was stirred until gas evolution had ceased. All volatiles were evaporated under reduced pressure, and the colourless to light yellow viscous solid was extracted with *n*-hexane/$Et_2O$ and filtered. The resulting solution was carefully concentrated under reduced pressure and stored at –26 °C (**1** and **3**) or –45 °C (**2**) for several days to yield colourless crystals.

**1:** From $Me_2Zn$ (15.8 mmol, 1.51 g) in *n*-hexane (15 mL), and $Me_2NOH$ (19.0 mmol, 1.16 g, 1.30 mL) in THF (20 mL). Colourless cubes. Yield 1.35 g (1.80 mmol, 57%). $^1$H NMR (200.1 MHz, $C_6D_5CD_3$): $\delta$ = –0.68 to –0.15 (m, 12 H, 4×ZnC$H_3$), 2.20–3.00 [m, very br., 36 H, 6×N(C$H_3$)$_2$] ppm. $^{13}$C{$^1$H} NMR (50.3 MHz, $C_6D_5CD_3$): $\delta$ = 3.4, 5.7 [2×(2 C, 2×ZnC$H_3$)], 51–61 [very br., 12 C, 6×N(C$H_3$)$_2$] ppm. $C_{16}H_{48}N_6O_6Zn_5$ (747.47): calcd. C 25.71, H 6.47, N 11.24; found C 25.34, H 6.32, N 11.12.

**2:** From $i Pr_2Zn$ (17.4 mmol, 2.64 g) in *n*-hexane (20 mL), and $Me_2NOH$ (21.0 mmol, 1.28 g, 1.44 mL) in THF (20 mL). Colourless blocks. Yield 2.70 g (2.89 mmol, 83%). $^1$H NMR (200.1 MHz,

 © 2006 Wiley-VCH Verlag GmbH & Co. KGaA, Weinheim 

$CDCl_3$): $\delta$ = 0.53 [sept, $^3J_{H,H}$ = 7.5 Hz, 4 H, 4×ZnC*H*($CH_3$)$_2$], 1.25 [d, $^3J_{H,H}$ = 7.5 Hz, 24 H, 4×ZnCH($CH_3$)$_2$], 2.70 [s, 36 H, 6×N($CH_3$)$_2$] ppm. $^{13}C\{^1H\}$ NMR (50.3 MHz, $CDCl_3$): $\delta$ = 11.6 [4 C, 4×Zn*C*H($CH_3$)$_2$], 24.6 [8 C, 4×ZnCH(*C*H$_3$)$_2$], 52.9 [12 C, 6×N(*C*H$_3$)$_2$] ppm. MS (EI = 70 eV): *m*/*z* (%) = 648 (100) {M + H –(*i*Pr) –[(*i*Pr)ZnONMe$_2$]}$^+$. $C_{24}H_{64}N_6O_6Zn_5$ (859.66): calcd. C 33.53, H 7.50, N 9.78; found C 33.24, H 7.43, N 9.65.

**3:** From $Et_2Zn$ (19.0 mmol, 2.35 g) in *n*-hexane (20 mL), and $Et_2$-NOH (22.9 mmol, 2.04 g, 2.35 mL) in THF (20 mL). Colourless blocks. Yield 3.36 g (3.46 mmol, 91%). $^1H$ NMR (599.8 MHz, 298 K, $C_6D_5CD_3$): $\delta$ = 0.37, 0.37 [2×(q, $^3J_{H,H}$ = 8.1 Hz, 4 H, 2×ZnC*H*$_2$CH$_3$)], ca. 0.85–1.25 [m, very br., 24 H, 4×N$_{coord}$(CH$_2$C*H*$_3$)$_2$], 1.25 [t, $^3J_{H,H}$ = 7.2 Hz, 12 H, 2×N$_{uncoord}$(CH$_2$C*H*$_3$)$_2$], 1.51, 1.53 [2×(t, $^3J_{H,H}$ = 8.1 Hz, 6 H, 2×ZnCH$_2$C*H*$_3$)], ca. 2.70–3.20 [m, very br., 24 H, 6×N(C*H*$_2$-CH$_3$)$_2$] ppm. $^1H$ NMR (599.8 MHz, 213 K, $C_6D_5CD_3$): $\delta$ = 0.40–0.57 (m, 8 H, 4×ZnC*H*$_2$CH$_3$), 0.75, 0.86 (2×{t, br., 2×[3 H, 2×N$_{uncoord}$(CH$_2$C*H*$_3$)$_2$]}), 1.18, 1.21, 1.27, 1.28 (4×{t, br., 2×[3 H, 4×N$_{coord}$(CH$_2$C*H*$_3$)$_2$]}), 1.67, 1.69 [2×(t, br., $^3J_{H,H}$ = 8.3 Hz, 6 H, 2×ZnCH$_2$C*H*$_3$)], 2.27 (q, br., $^3J_{H,H}$ = 6.1 Hz), 2.64 (q, br.), 2.69 (q, br., $^3J_{H,H}$ = 6.3 Hz), 2.81 (q, br., $^3J_{H,H}$ = 6.9 Hz), 2.83 (q, br., $^3J_{H,H}$ = 6.9 Hz), 2.88 (q, br., $^3J_{H,H}$ = 6.4 Hz), 2.97 (q, br., $^3J_{H,H}$ = 6.2 Hz), 3.08 (q, br.), 3.80 (m, br.) {8×(2 H, N$_{coord}$C*H*$_2$CH$_3$); 1×[4×2 H, 2×N$_{uncoord}$(C*H*$_2$CH$_3$)$_2$]} ppm. $^{13}C\{^1H\}$ NMR (50.3 MHz, 298 K, $C_6D_6$): $\delta$ = 3.4, 5.7 [2×(2 C, 2×Zn*C*H$_2$CH$_3$)], ca. 11–17 [very br., 8 C, 4×N$_{coord}$(CH$_2$*C*H$_3$)$_2$], 13.1 [4 C, 2×N$_{uncoord}$(CH$_2$*C*H$_3$)$_2$], 14.1, 14.4 [2×(2 C, 2×ZnCH$_2$*C*H$_3$)], ca. 51–61 {very br., 12 C, 4×[2 C, 2×N$_{coord}$(*C*H$_2$CH$_3$)$_2$]; 1×[4 C, 2×N$_{uncoord}$(*C*H$_2$CH$_3$)$_2$]} ppm. $^{13}C\{^1H\}$ NMR (150.8 MHz, 213 K, $C_6D_5CD_3$): $\delta$ = 2.4, 5.4 [2×(2 C, 2×Zn*C*H$_2$CH$_3$)], 12.3, 13.0 [2×(2 C, 2×ZnCH$_2$*C*H$_3$)], 13.6, 13.8, 13.9, 14.2, 14.7 {4×[2 C, 2×N$_{coord}$(CH$_2$*C*H$_3$)$_2$]; 1×[4 C, 2×N$_{uncoord}$(CH$_2$*C*H$_3$)$_2$]}, 51.8, 53.8, 55.1, 56.4, 61.2 {4×[2 C, 2×N$_{coord}$(*C*H$_2$CH$_3$)$_2$]; 1×[4 C, 2×N$_{uncoord}$(*C*H$_2$CH$_3$)$_2$]} ppm. $C_{32}H_{80}N_6O_6Zn_5$ (971.87): calcd. C 39.55, H 8.30, N 8.65; found C 38.93, H 8.07, N 8.41.

## Acknowledgments

Financial support from the Deutsche Forschungsgemeinschaft is gratefully acknowledged. The authors are indebted to the NRW Graduate School of Chemistry at Münster, GSC-MS (Ph.D. stipend grant for M. U.), and to Dr. K. Bergander and Dr. A. Hepp for conducting the NMR measurements.

[1] D. C. Bradley, R. C. Mehrotra, I. P. Rothwell, A. Singh, *Alkoxo and Aryloxo Derivatives of Metals*, Academic Press, London, San Diego, **2001**.

[2] A. V. Firth, J. C. Stewart, A. J. Hoskin, D. W. Stephan, *J. Organomet. Chem.* **1999**, *591*, 185.

[3] a) J. Lewiński, W. Marciniak, J. Lipkowski, I. Justyniak, *J. Am. Chem. Soc.* **2003**, *125*, 12698; b) M. L. von Ziegler, J. Weiss, *Angew. Chem.* **1970**, *82*, 931; *Angew. Chem. Int. Ed.* **1970**, *9*, 905.

[4] Note that within the metal alkoxides of group 13 (especially those of Al), a strong tendency of the metal/metal complex fragment to be bound by at least one additional donor unit is common and gives the metal a CN >4 (see ref.[1]). This is only suppressed if ligands of elevated steric demand are incorporated (see ref.[2]). Nevertheless, this tendency is mainly due to the Lewis-acidity and/or oxophilicity of the group 13 elements and cannot be accounted for by means of core shell saturation demands, as it is the case with Zn.

[5] a) N. W. Mitzel, C. Lustig, M. Woski, *Z. Naturforsch.* **2003**, *58b*, 363; b) J. R. Jennings, K. Wade, *J. Chem. Soc. A* **1967**, 1333; c) I. Pattison, K. Wade, *J. Chem. Soc. A* **1968**, 2618.

[6] N. W. Mitzel, C. Lustig, *Angew. Chem.* **2001**, *113*, 4521; *Angew. Chem. Int. Ed.* **2001**, *40*, 4390.

[7] a) N. W. Mitzel, C. Lustig, M. Woski, *Dalton Trans.* **2004**, 397; b) H.-D. Hausen, G. Schmöger, W. Schwarz, *J. Organomet. Chem.* **1978**, *153*, 271.

[8] M. Ullrich, N. W. Mitzel, K. Bergander, R. Fröhlich, *Dalton Trans.* **2006**, 714.

[9] N. Voiculescu, *Appl. Organomet. Chem.* **2002**, *16*, 569.

[10] N. A. Bell, H. M. M. Shearer, C. B. Spencer, *Acta Crystallogr., Sect. C* **1984**, *40*, 613.

[11] a) V. A. Kuksa, S. M. S. V. Wardell, P. K. T. Lin, R. A. Howie, *Acta Crystallogr., Sect. E* **2002**, *58*, m68; b) R. Reichenbach-Klinke, M. Zabel, B. König, *Dalton Trans.* **2003**, 141.

[12] J. E. Walker, D. M. Howell, *Inorg. Synth.* **1967**, *9*, 2, and references therein.

[13] S. Jana, R. Fröhlich, N. W. Mitzel, *Chem. Eur. J.* **2006**, *12*, 592.

[14] Crystallographic details: Single-crystals of compounds **1**–**3** were mounted under inert perfluoro-polyether at the tip of a glass fibre and cooled in the cryostream of the diffractometer. The crystallographic data set of **1** was collected at 173(2) K with a Nonius Turbo CAD4 diffractometer; the data sets of **2** and **3** were measured at 198(2) K with a Nonius KappaCCD (both operated with graphite-monochromated Mo-$K_\alpha$ radiation; $\lambda$ = 0.71073 Å). Data collection and reduction was performed with Express[23a] and MolEN[23b] (**1**), or with Collect[23c] and Denzo-SMN[23d] (**2** and **3**). The structures were solved by direct methods and refined against $F^2$ by full-matrix least-squares with SHELXS-97 (**1**)[23e] and SHELXL-97 (**2** and **3**).[23f] In the case of **2**, absorption correction was performed with SORTAV.[23g] CCDC-609256 (**1**), CCDC-609255 (**2**) and CCDC-617869 (**3**) contain the supplementary crystallographic data for this paper. These data can be obtained free of charge from The Cambridge Crystallographic Data Centre via www.ccdc.cam.ac.uk/data_request/cif. **1**: ($C_{16}H_{48}N_6O_6Zn_5$): $M_r$ = 747.47, monoclinic, space group *C*2/c, $a$ = 12.910(1), $b$ = 11.851(2), $c$ = 20.324(2) Å, $\beta$ = 90.02(1)°, $V$ = 3109.2(7) Å$^3$, $Z$ = 4, $\rho_{calcd.}$ = 1.597 g·cm$^{-3}$, $F$(000) = 1536, $\mu$(Mo-$K_\alpha$) = 3.837 mm$^{-1}$. A total of 4837 reflections were measured in the range 4.00° ≤ 2$\theta$ ≤ 53.88°, of which 3101 were unique ($R_{int}$ = 0.041). Final $R$ indices: $R_1$ = 0.034 [$I > 2\sigma(I)$], $wR_2$ = 0.084 (all data); max./min. residual electron density 0.89/–0.37 e·Å$^{-3}$. **2**: ($C_{24}H_{64}N_6O_6Zn_5$·$C_4H_{10}O$): $M_r$ = 933.78, orthorhombic, space group *P*ccn, $a$ = 19.870(1), $b$ = 12.360(1), $c$ = 17.052(1) Å, $V$ = 4187.9(5) Å$^3$, $Z$ = 4, $\rho_{calcd.}$ = 1.481 g·cm$^{-3}$, $F$(000) = 1960, $\mu$(Mo-$K_\alpha$) = 2.867 mm$^{-1}$. A total of 21700 reflections were measured in the range 3.88° ≤ 2$\theta$ ≤ 56.52°, of which 5139 were unique ($R_{int}$ = 0.028). Final $R$ indices: $R_1$ = 0.031 [$I > 2\sigma(I)$], $wR_2$ = 0.074 (all data); max./min. residual electron density 0.64/–0.54 e·Å$^{-3}$. **3**: ($C_{32}H_{80}N_6O_6Zn_5$): $M_r$ = 971.87, monoclinic, space group *C*c, $a$ = 16.480(1), $b$ = 11.595(1), $c$ = 25.073(1) Å, $\beta$ = 108.54(1)°, $V$ = 4542.4(5) Å$^3$, $Z$ = 4, $\rho_{calcd.}$ = 1.421 g·cm$^{-3}$, $F$(000) = 2048, $\mu$(Mo-$K_\alpha$) = 2.644 mm$^{-1}$. A total of 9839 reflections were measured in the range 6.04° ≤ 2$\theta$ ≤ 55.88°, of which 9386 were unique ($R_{int}$ = 0.071). Final $R$ indices: $R_1$ = 0.071 [$I > 2\sigma(I)$], $wR_2$ = 0.199 (all data); max./min. residual electron density 1.83/–1.12 e·Å$^{-3}$.

[15] This research area mainly encompasses pentanuclear $Cu^{2+}$ species; see a) J. J. Bodwin, V. L. Pecoraro, *Inorg. Chem.* **2000**, *39*, 3434; b) J. A. Halfen, J. J. Bodwin, V. L. Pecoraro, *Inorg. Chem.* **1998**, *37*, 5416; c) B. Kurzak, E. Farkas, T. Glowiak, H. Kozlowski, *J. Chem. Soc., Dalton Trans.* **1991**, 163, and references cited therein.

[16] For example, see N. Lalioti, C. P. Raptopoulou, A. Terzis, A. E. Aliev, S. P. Perlepes, I. P. Gerothanassis, E. Manessi-Zoupa, *Chem. Commun.* **1998**, 1513.

[17] Compare the heterocubane [$\mu^3$-(9-BBN-9-O)(ZnEt)]$_4$: S. Luliński, I. Madura, J. Serwatowski, J. Zachara, *Inorg. Chem.* **1999**, *38*, 4937 with [$\mu^2$-($Mes_2$B–O)(ZnEt)]$_2$: R. Anulewicz-Ostrowska, S. Luliński, E. Pindelska, J. Serwatowski, *Inorg. Chem.* **2002**, *41*, 2525.

 © 2006 Wiley-VCH Verlag GmbH & Co. KGaA, Weinheim 

[18] For clarity, the single steps of isomerisation are discussed as if they occurred one after the other. By logic, a nearly simultaneous course of bond formation and disconnection is most likely to exist.
[19] In principle, the whole process of isomerisation of the heteroatom array into itself would consist of six such periods (if the single atoms of a same element were labelled distinguishable). After one period, a molecule equal by connectivity, but of inverted stereochemistry would be furnished. Thus, after three periods, the starting molecule would be reattained in its enantiomeric form. Conversion of this *ent*-molecule back to its original would then call for another three periods.
[20] Supporting Information for computational details is available (see footnote on the first page of this article).
[21] a) I. D. Gridnev, J. M. Serafimov, H. Quiney, J. M. Brown, *Org. Biomol. Chem.* **2003**, *1*, 3811; b) A. Boudier, C. Darcel, F. Flachsmann, L. Micouin, M. Oestreich, P. Knochel, *Chem. Eur. J.* **2000**, *6*, 2748; c) H. Soroos, M. Morgana, *J. Am. Chem. Soc.* **1944**, *66*, 893.
[22] N. W. Mitzel, B. A. Smart, S. Parsons, H. E. Robertson, D. W. H. Rankin, *J. Chem. Soc., Perkin Trans. 2* **1996**, 2727.
[23] a) Nonius B. V., **1994**; b) K. Fair, Enraf Nonius B. V., **1990**; c) Nonius B. V., **1998**; d) Z. Otwinowski, W. Minor, *Methods Enzymol.* **1997**, *276*, 307; e) G. M. Sheldrick, *Acta Crystallogr., Sect Sect. A* **1990**, *46*, 467; f) G. M. Sheldrick, Universität Göttingen, **1997**; g) R. H. Blessing, *Acta Crystallogr., Sect Sect. A* **1995**, *51*, 33; R. H. Blessing, *J. Appl. Crystallogr.* **1997**, *30*, 421.

Received: May 30, 2006
Published Online: September 14, 2006

 © 2006 Wiley-VCH Verlag GmbH & Co. KGaA, Weinheim 

DOI: 10.1002/ejic.200600634

# Lead Halide Layers Linked by *trans*-Cu(Gly)$_2$ (Gly = $^{-}O_2C–CH_2–NH_2$) Pillars in Heterometallic Glycinate Based Organic–Inorganic Hybrids

**Wenhua Bi,[a] Nicolas Mercier,*[a] Nicolas Louvain,[a] and Michel Latroche[b]**

**Keywords:** Amino acids / Lead halides / Layered compounds / Glycinato / Copper

The novel hybrid compounds $Pb_2Cu(O_2C–CH_2–NH_2)_2X_4$ (X = Br, Cl) were prepared and characterized by single-crystal X-ray diffraction. TA analysis and DSC measurements show that the compounds are stable up to 200 °C. As in hybrid perovskites, their layered structures are based on metal(II) halide 2D frameworks, which are here covalently linked by *trans*-Cu(Gly)$_2$ flat SBUs. These rigid pillars are able to accommodate some of the void that exists in between the $PbX_2$ layers. However, the results from hydrogen absorption experiments that were conducted at 77 K indicate that the hybrids are not good candidates for absorption materials.

(© Wiley-VCH Verlag GmbH & Co. KGaA, 69451 Weinheim, Germany, 2006)

## Introduction

During the past decade, organic–inorganic compounds have received considerable attention because of the opportunity that exists to combine useful properties of both components. For example, in hybrid perovskites, whose typical formula is $(R\text{-}NH_3)_2M^{II}X_4$, the organic component allows the solution to be processed as thin films by room temperature techniques such as spin-coating, whereas the inorganic component may possess semiconducting properties.[1] Extensive work has been notably devoted to the study of materials that are based on iodostannate perovskite layers that can be used as semiconducting channels in thin-film field-effect transistors (TFTs)[2] with the potential of relatively high electrical mobility. For instance, a mobility of $0.6\ cm^2\ V^{-1}\ s^{-1}$ is attained in $(C_6H_5C_2H_5NH_3)_2SnI_4$.[2a] Nevertheless, this value remains two orders of magnitude smaller than that evidenced in $CH_3NH_3SnI_3$, which is a 3D perovskite with metallic conductivity.[3] Several strategies have been considered in order to improve the charge carrier mobility of such semiconducting thin film materials. This includes the search of new, possibly nonperovskite, halogenometallate-based salts.[4] Another way is to tune the bandgap that is associated to a given perovskite network. This is made possible because of the incorporation of selected cations that are able to impact the bonding features of the inorganic framework.[5] Hybrids with enhanced structural dimensionality have also been considered.[6,7] In particular, we recently showed that in $[Cu\{O_2C\text{-}(CH_2)_3\text{-}NH_3\}_2]PbBr_4$ the amino carboxylic acid zwitterionic molecules led both to the stabilization of a layered hybrid perovskite and to the formation of a Br–Cu–Cu–Br covalent bond pathway between adjacent perovskite layers.[7] In relation to amino acids, several coordination compounds have been prepared from molecules that adopt their zwitterionic form.[7–9] However, amino acids, which are ubiquitous in biology, are often used in material chemistry (e.g. coordination polymers, open-framework compounds) in their basic form, as they can coordinate to metal ions through both its carboxylate group and its amino group. With a focus on glycine, metal(II) glycinate salts that are based on robust $M^{II}(Gly)_2$ entities are often cluster-type[10] or pseudo 1D compounds;[11] only a few 2D coordination polymers of heterometallic glycinates have been reported.[12]

In this communication, we report the preparation and the X-ray structural characterization of two 3D heterometallic glycinate hybrids $Pb_2Cu(O_2C–CH_2–NH_2)_2X_4$ [X = Br (**1**), Cl (**2**)]. In the structure of both complexes, the adjacent lead halide layers are linked by *trans*-Cu(Gly)$_2$ (Gly = $^{-}O_2C–CH_2–NH_2$) to form 3D frameworks. These layered structures can be conceptually considered as a result of the intercalation of neutral *trans*-Cu(Gly)$_2$ entities in the $PbX_2$ layered network. The rigid pillars do not accommodate much of the void in between the $PbX_2$ layers and the structures are not porous[13] because of the small size of the glycinate ligand.

## Results and Discussion

Reactions of glycine, copper halide, and lead halide (halide = Br, Cl) give rise to two hybrid compounds:

[a] Laboratoire de Chimie, Ingénierie Moléculaire et Matériaux d'Angers, UMR-CNRS 6200, Université d'Angers
2 Bd Lavoisier, 49045 Angers, France
Fax: +33-2-41-73-54-05
E-mail: nicolas.mercier@univ-angers.fr
[b] Laboratoire de Chimie Métallurgique des Terres Rares, CNRS, UPR 209,
2–8 rue Henri Dunant, 94320 Thiais Cedex, France

Supporting information for this article is available on the WWW under http://www.eurjic.org or from the author.

 © 2006 Wiley-VCH Verlag GmbH & Co. KGaA, Weinheim 

$Pb_2Cu(O_2C–CH_2–NH_2)_2X_4$ [X = Br (**1**), Cl (**2**)]. A broad band in the 500–800 nm range with a maximum at about 620 nm, is observed in their UV/Vis absorption spectra, which is correlated to the blue color of the crystals and is assigned to a 3*d*–3*d* electronic transition of cupric ions (ESI). The form of the amino acids ($HO_2C$-R-$NH_2$) in the solution varies according to the pH value of the solution. The amino acids will be in the cationic, zwitterionic, or basic form in acidic, neutral, or basic solutions, respectively. In the field of hybrid perovskites, bifunctional molecules such as $HO_2C$-R-$NH_3^+$ have already been used by us and we demonstrated the role of 1D carboxylic acid supramolecular synthons in the formation of a noncentrosymmetrical hybrid perovskite structure.[14] Recently, we have also shown that $^-O_2C$-$(CH_2)_3$-$NH_3^+$ zwitterionic molecules form a paddle-wheel-type of cluster with copper, which connects the perovskite layers that are stabilized by ammonium counterions.[7] Here, we show that a mixture of glycine, copper, and lead halide, under neutral conditions, affords nice blue crystals of $Pb_2Cu(O_2C–CH_2–NH_2)_2X_4$ (X = Br, Cl) containing $^-O_2C–CH_2–NH_2$ anions. The compound crystallizes in the $P2_1/c$ space group, and the crystal structure can be described as layers of lead(II) halide that are linked together by *trans*-$Cu(Gly)_2$ pillars (Figure 1). Copper ions are at the center of a symmetrical unit that consists of two glycinato ligands, and all non-hydrogen atoms approximately lie in a plane that contains the *c* axis (Figures 1 and 2). Two more weakly bonded bromine atoms complete the [4+2] copper(II) coordination sphere as a result of the Jahn–Teller effect (Figure 1). All bond lengths [**1**: $d_{N–Cu}$ = 1.972(5) Å, $d_{O–Cu}$ = 1.967(4) Å, $d_{Br–Cu}$ = 3.167(4) Å; **2**: $d_{N–Cu}$ = 1.959(4) Å, $d_{O–Cu}$ = 1.976(3) Å, $d_{Cl–Cu}$ = 2.995(4) Å] are in good accordance with those reported in the literature for $Cu(Gly)_2$ entities[10,11] or Cu–Br in [4+2] copper polyhedra.[15]

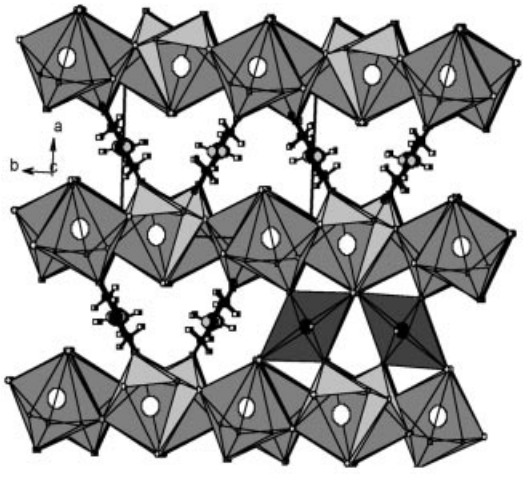


Figure 1. Structure of $Pb_2Cu(O_2C–CH_2–NH_2)_2Br_4$ viewed along the *c* axis that shows layers of lead polyhedra linked by pillars formed by *trans*-$Cu(Gly)_2$ entities. Two copper [4+2] coordination polyhedra, with the weakly bonded bromide atoms taken into account, are shown in deep grey.

Figure 2 shows *trans*-$Cu(Gly)_2$ entities and lead polyhedra that are connected to each other by the carboxylate groups of the organic ligands. The coordination mode of glycinato ligands is $[3.2_{12}\ 2_{23}\ 1_3]$ according to the Harris notation,[16] which means that the whole ligand is bound to three metals and that the donor atoms O1, O2 and N chelate to two $Pb^{2+}$ outer ions, one $Pb^{2+}$ and one inner $Cu^{2+}$ ion, and one inner $Cu^{2+}$ ion, respectively. Each lead atom is surrounded by three oxygen atoms and five bromine atoms to build a distorted polyhedron that can be described as an $O_2Br_4$ trigonal prism capped by two other Br1 and O1 atoms. The last rectangular face that is defined by O1–Br1–Br2–Br2 is open and certainly reveals the stereo effect of the $6s^2$ lone pair of electrons of lead(II) (Figure 2). Pb–O bond lengths are in the range 2.6–2.8 Å [1: O1 2.599(4) Å and 2.720(4) Å, O2 2.820(4) Å; 2: O1 2.585(3) Å and 2.682(3) Å, O2 2.777(7) Å], whereas the distance of the Pb–X bonds are in the range 2.928(1)–3.237(1) Å and 2.796(1) Å–3.120(1) Å for **1** and **2**, respectively. The ability of the soft $Pb^{2+}$ cation to be surrounded by more than six donor atoms together with the weak chelating effect of the bromine atoms allow for the formation of this layered compound which can be conceptually described to result from the intercalation of neutral *trans*-$Cu(Gly)_2$ entities into the $PbX_2$ layered structure. This intercalation would be associated with a concerted electronic effect between both components: copper(II) is stabilized by part of the electronic density that comes from the halide atoms in the lead halide layers, whereas all the lead atoms accept electronic density from the carboxylate moieties of the glycinato ligands (Figure 3).

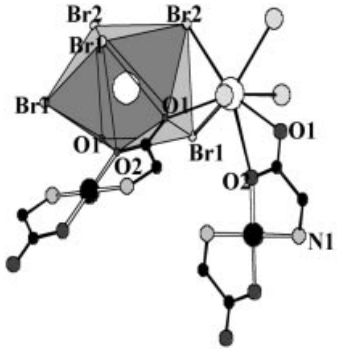


Figure 2. The coordination environment of $Pb^{II}$ and $Cu^{II}$ ions in **1** that shows the *trans*-$Cu(Gly)_2$ entities and the polyhedra of Pb linked together by the carboxylate groups of the organic ligands. The coordination mode of the glycinato ligands is $[2.2_{12}\ 2_{23}\ 1_3]$ according to the Harris notation[16] (All of the hydrogen atoms are omitted for clarity).

The representation of the structure by lead polyhedra and *trans*-$Cu(Gly)_2$ pillars (Figure 1) shows infinite channels that run along the *c* axis. However, the drawing of the [4+2] copper polyhedra in Figure 1, or a space filling representation (see Supporting Information) only show small windows, which reveals that both complexes are not porous structures with infinite channels. Nevertheless, consecutive *trans*-$Cu(Gly)_2$ pillars (or [4+2] copper polyhedra) along the *b* axis are shifted from each other by a distance of *c*/2; there are some discrete lattice voids between the lead halide layers and their spherical volume is defined by a radius of 1.6 Å.

 © 2006 Wiley-VCH Verlag GmbH & Co. KGaA, Weinheim 

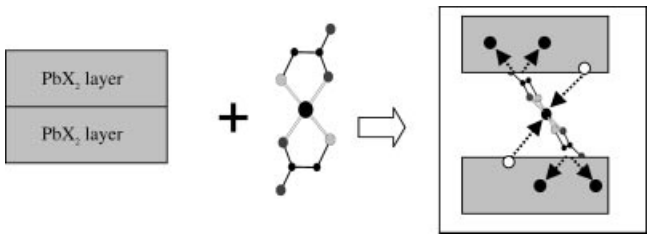


Figure 3. Schematic representation of an hypothetical intercalation of *trans*-Cu(Gly)$_2$ into the $PbX_2$ layered structure, which affords $Pb_2Cu(O_2C–CH_2–NH_2)_2X_4$. Arrows indicate the electron donor effect of the halide and the oxygen atom towards copper(II) and lead(II) ions, respectively.

$H_2$ absorption measurements were then carried out at 77 K under a pressure of up to 25 bars to give a maximum capacity at high pressure of 0.28% weight for the $Pb_2Cu(O_2C–CH_2–NH_2)_2Br_4$ sample (see Supporting Information), which is far from the values that were obtained in MOFs chemistry (1–8% range).[17]

In conclusion, we have described the synthesis and the structural characterization of 3D heterometallic glycinate salts $Pb_2Cu(O_2C–CH_2–NH_2)_2X_4$ (X = Br, Cl). As in hybrid perovskites, their layered structure is based on a metal(II) halide 2D framework, which is here covalently linked by *trans*-Cu(Gly)$_2$ units by the carboxylate groups of glycinato ligands. We now plan to use others such linkers with non-oxidative metals in order to achieve lead(II) or tin(II) iodide based materials that possess semiconducting properties. With regard to the field of coordination polymers, we have shown that the association of the glycinato ligands with both $Cu^{2+}$ and soft $Pb^{2+}$ cations and halide anions leads to an unprecedented 3D architecture. Suitable microporous coordination polymers, especially those that possess small pores or compounds that are based on ligands with incorporated open metal sites,[18] are increasingly sought, and *trans*-$M^{II}(Gly)_2$ could be considered as a building block for the design of such compounds.

## Experimental Section

**Synthesis and Thermal Analysis:** $CuBr_2$ (0.2241 g, 1 mmol, 99%) was dissolved in distilled water (60 mL). The solution was stirred and glycine (0.7539 g, 10 mmol, 99.7%) was then added. After 2 h, $PbBr_2$ (0.7345 g, 2 mmol, 98%) was added to the solution, and the solution was then heated at 60 °C and stirred for another 4 h before it was placed into an aerator. Diamond-like blue crystals were obtained several hours later in a yield of 68.3% (0.646 g, based on $CuBr_2$). The synthesis of **2** was almost the same as **1**, but blue crystals were obtained after one day in a yield of 53.6% (0.411 g, based on $CuCl_2·2H_2O$). For both compounds, X-ray powder diffraction indicated single-phase samples (ESI).

Thermogravimetric analysis measurements and differential scanning calorimetry were performed in the range of 20–900 °C and 20–450 °C, respectively. The first endothermic peak that was observed at about 200 °C was assigned to the melting of the compounds (DSC), and it occurs just before the first weight loss of 10.6% (for **1**) or 13.4% (for **2**) observed in TGA. The second weight loss of 81.3% (for **1**) or 69.8% (for **2**) can be assigned to the departure of $PbX_2$ (theoretical: **1** 77.6%, **2** 72.0%). The first weight loss probably corresponds to the departure of a part of the ligands [$H_2N–CH_2–COOH$: 150 g/mol, observed 99.3 g/mol (for **1**) or 102.9 g/mol (for **2**)], the remaining compound was CuO at higher temperature.

**Crystal Data for 1:** $C_4H_8Br_4CuN_2O_4Pb_2$, $M$ = 945.68, monoclinic, $a$ = 8.556(1) Å, $b$ = 10.971(2) Å, $c$ = 8.376(1) Å, $\beta$ = 108.68(3), $V$ = 744.8(3) Å$^3$, space group $P2_1/c$, $Z$ = 2, calculated density 4.217, crystal dimensions (mm$^3$): 0.12×0.10×0.08, $T$ = 293 K, Bruker Nonius Kappa CCD diffractometer, graphite-monochromated Mo-$K_\alpha$ radiation ($\lambda$ = 0.71073 Å), $\mu$ = 34.69 mm$^{-1}$, $2\theta_{max}$ = 60.04°, 11337 measured reflections of which 2173 were unique ($R_{int}$ = 0.057) and 1744 had $I/\sigma(I) > 2$. The intensities were corrected for Lorentz-polarization effects, as well as for absorption effect (SADABS). The structure was solved by direct methods, and refined by full-matrix least-squares routines against $F^2$ with the use of the SHELXL97 package. Hydrogen atoms were placed in idealized positions in riding mode. The refinements of positions and anisotropic thermal motion parameters of the non-H atoms, converge to $R_{(F)}$ = 0.0274 (1744 reflections, 80 parameters), $wR_{2(F2)}$ = 0.0605 (all data), GOF on $F^2$ = 1.124, $\Delta\rho_{max}$ = 1.224 e Å$^{-3}$.

**Crystal Data for 2:** $C_4H_8Cl_4CuN_2O_4Pb_2$, $M$ = 767.84, monoclinic, $a$ = 8.424(1) Å, $b$ = 10.404(2) Å, $c$ = 8.237(1) Å, $\beta$ = 109.02(3), $V$ = 682.5(3) Å$^3$, space group $P2_1/c$, $Z$ = 2, calculated density 3.736, crystal dimensions (mm$^3$): 0.15×0.10×0.10, $T$ = 293 K, Bruker Nonius Kappa CCD diffractometer, graphite-monochromated Mo-$K_\alpha$ radiation ($\lambda$ = 0.71073 Å), $\mu$ = 26.93 mm$^{-1}$, $2\theta_{max}$ = 60.04°, 8282 measured reflections of which 1987 were unique ($R_{int}$ = 0.039) and 1553 had $I/\sigma(I) > 2$. The intensities were corrected for Lorentz-polarization effects. The structure was solved by direct methods, and refined by full-matrix least-squares routines against $F^2$ with the use of the SHELXL97 package. Hydrogen atoms were placed in idealized positions in riding mode. The refinements of positions and anisotropic thermal motion parameters of the non-H atoms, converge to $R_F$ = 0.0276 (1553 reflections, 79 parameters), $wR_{2(F2)}$ = 0.0445 (all data), GOF on $F^2$ = 1.028, $\Delta\rho_{max}$ = 0.835 e Å$^{-3}$.

CCDC-613293 and -613294 contain the supplementary crystallographic data for this paper. These data can be obtained free of charge from The Cambridge Crystallographic Data Centre via www.ccdc.cam.ac.uk/data_request/cif.

**Hydrogen Storage Measurements:** Hydrogen storage measurements were made with a volumetric device (Sievert's method) equipped with calibrated and thermalized volumes and pressure gauges. In order to remove water and all species that can lie within the pores and channels, the samples were outgassed while heated at 150 °C over a 16 h period under primary vacuum. All weight capacities refer here to outgassed samples. For measurements at 77 K, the sample holder was immersed in liquid nitrogen and the pressure variations due to both gas cooling and hydrogen adsorption were measured with the use of high-purity hydrogen (Alphagaz H22). Under these thermodynamic conditions, the ideal gas law is no longer valid and different equations of state were used depending of the temperature ranges.[19]

**Supporting Information** (see footnote on the first page of this article): UV/Vis absorption and XRPD pattern of crystals **1** and **2**, TGA and DSC graphs of both compounds, absorption analysis and additional figures for structural illustration of **1**.

[1] a) D. B. Mitzi, *Prog. Inorg. Chem.* **1999**, *48*, 1–121; b) D. B. Mitzi, *Chem. Mater.* **2001**, *13*, 3283; c) D. B. Mitzi, *J. Mater. Chem.* **2004**, *14*, 2355.

 © 2006 Wiley-VCH Verlag GmbH & Co. KGaA, Weinheim 

[2] a) C. R. Kagan, D. B. Mitzi, K. Chondroudis, *Science* **1999**, *286*, 945; b) D. B. Mitzi, K. Chondroudis, C. R. Kagan, *IBM J. Res. & Dev.* **2001**, *vol. 45*, n°1; c) D. B. Mitzi, C. D. Dimitrakopoulos, J. Rosner, D. R. Medeiros, Z. Xu, C. Noyan, *Adv. Mater.* **2002**, *14*, 1772.
[3] D. B. Mitzi, C. A. Field, Z. Schlesinger, R. B. Laibowitz, *J. Solid State Chem.* **1995**, *114*, 159.
[4] Z. Xu, D. B. Mitzi, *Inorg. Chem.* **2003**, *42*, 6589.
[5] a) N. Mercier, S. Poiroux, A. Riou, P. Batail, *Inorg. Chem.* **2004**, *43*, 8361; b) Z. Xu, D. B. Mitzi, C. D. Dimitrakopoulos, K. R. Maxcy, *Inorg. Chem.* **2003**, *42*, 2031; c) D. B. Mitzi, C. D. Dimitrakopoulos, L. L. Kosbar, *Chem. Mater.* **2001**, *13*, 3728; d) Z. Xu, D. B. Mitzi, D. R. Medeiros, *Inorg. Chem.* **2003**, *42*, 1400.
[6] a) J. Calabrese, N. L. Jones, R. L. Harlow, N. Herron, D. L. Thorn, Y. Wang, *J. Am. Chem. Soc.* **1991**, *113*, 2328; b) X. H. Zhu, N. Mercier, A. Riou, P. Blanchard, P. Frère, *Chem. Commun.* **2002**, *18*, 2160.
[7] N. Mercier, A. Riou, *Chem. Commun.* **2004**, *7*, 844.
[8] R. Wang, H. Liu, M. D. Carducci, T. Jin, C. Zheng, Z. Zheng, *Inorg. Chem.* **2001**, *40*, 2743.
[9] M. Dan, C. N. Rao, *Chem. Eur. J.* **2005**, *11*, 7102.
[10] a) K. Tomita, I. Nitta, *Bull. Chem. Soc. Jpn.* **1961**, *34*, 286; b) H. C. Freeman, M. R. Snow, I. Nitta, K. Tomita, *Acta Crystallogr.* **1964**, *17*, 1463; c) R. E. Norman, N. J. Rose, R. E. Stenkamp, *Acta Crystallogr., Sect. C* **1990**, *46*, 1; d) L. K. Thomson, Z. Xu, A. E. Goeta, J. A. K. Howard, H. J. Clase, D. O. Miller, *Inorg. Chem.* **1998**, *37*, 3217; e) S. Hu, W. Du, J. Dai, L. Wu, C. Cui, Z. Fu, X. Wu, *J. Chem. Soc., Dalton Trans.* **2001**, 2963.
[11] a) H. O. Davies, R. D. Guillard, M. B. Hursthouse, M. A. Mazid, P. A. Williams, *J. Chem. Soc., Chem. Commun.* **1992**, 226; b) M. A. S. Goher, L. A. Al-Shatti, F. A. Mautner, *Polyhedron* **1997**, *16*, 889.
[12] a) J. J. Zhang, S. Q. Xia, T. L. Sheng, S. M. Hu, G. Leibeling, F. Meyer, X. T. Wu, S. C. Xiang, R. B. Fu, *Chem. Commun.* **2004**, 1186; b) H. an, Y. Guo, Y. Li, E. Wang, J. Lü, L. Xu, C. Hu, *Inorg. Chem. Commun.* **2004**, *7*, 521.
[13] L. J. Barbour, *Chem. Commun.* **2006**, 1163.
[14] N. Mercier, *CrystEngComm* **2005**, *7*, 429.
[15] a) K. Halvorson, R. D. Willet, *Acta Crystallogr., Sect. C* **1988**, *44*, 2071; b) R. D. Willet, *Acta Crystallogr., Sect. C* **1990**, *46*, 565; c) J. K. Garland, K. Emmerson, M. R. Pressprich, *Acta Crystallogr., Sect. C* **1990**, *46*, 1603.
[16] R. A. Coxall, S. G. Harris, D. K. Henderson, S. Parsons, P. A. Tasker, R. E. Winpenny, *J. Chem. Soc., Dalton Trans.* **2000**, 2349.
[17] a) J. L. C. Rowsell, O. M. Yaghi, *Angew. Chem. Int. Ed.* **2005**, *44*, 4670; b) U. Mueller, M. Schubert, F. Teich, H. Puetter, K. Schierle-Arndt, J. Pastre, *J. Mater. Chem.* **2006**, *16*, 626.
[18] S. Kitagawa, S. I. Noro, T. Nakamura, *Chem. Commun.* **2006**, 701.
[19] B. A. Younglove, *J. Phys. Chem.* **1982**, *11*, 4–11.

Received: July 5, 2006
Published Online: September 20, 2006

 © 2006 Wiley-VCH Verlag GmbH & Co. KGaA, Weinheim 

DOI: 10.1002/ejic.200600674

# Molecular Assembly with Axial Cyanato Ligands and Paddlewheel Tetracarboxylatodiruthenium(II,III) Fragments

**M. Carmen Barral,[a] Rodrigo González-Prieto,[a] Reyes Jiménez-Aparicio,*[a] J. Luis Priego[a] M. Rosario Torres[b] and Francisco A. Urbanos[a]**

**Keywords:** Diruthenium compounds / Metal–metal bonds / Molecular assembly / Ruthenium complexes / Cyanato ligands / Silver complexes

Homo and heteropolymetallic chains constructed with $[Ru_2(\mu\text{-}O_2CR)_4]^+$ building blocks and $OCN^-$ and $[Ag(OCN)_2]^-$ connectors are described. In the complexes $[Ru_2\{\mu\text{-}O_2CC(Me)=CHEt\}_4(OCN)]_n$ (**1**) and $\{[Ru_2(\mu\text{-}O_2CMe)_4][Ag(OCN)_2]\}_n$ (**2**) an infrequent $\mu_{1,1}$-*O* coordination mode of the $OCN^-$ ligand is observed. In addition, the formation of a Ag–OCN bond instead of the Ag–NCO coordination mode, which is more usual, is noteworthy in complex **2**.
(© Wiley-VCH Verlag GmbH & Co. KGaA, 69451 Weinheim, Germany, 2006)

## Introduction

The use of $M_2$ paddlewheel species as building blocks to construct polynuclear assemblies has focused great interest in recent years due to the potential applications of these assemblies.[1–3] Especially, the preparation of supramolecular structures based on diruthenium cores has attracted much attention because of the singular electronic and magnetic properties of these structures.[4–7] Thus, numerous polymeric or molecular arrangements with tetracarboxylatodiruthenium(II,III) units that are linked by mononegative anions, neutral molecules or organic radicals have been described.[4,5] However, in spite of the fact that pseudohalide ligands represent an efficient way to generate interactions between metallic centres, these ligands have been little used to connect diruthenium units. Some thiocyanato complexes have been described,[8] but the cyanate group has not been used previously in this chemistry.

The cyanate group is a very versatile ligand that can be bonded in several ways. In Scheme 1 are collected the main coordination modes of this ligand. The N-bonded monodentate mode is the most usual, whereas $\mu_{1,1}$-*O* coordination has been scarcely observed.

On the other hand, the design of heteropolynuclear complexes combining the electronic and stereochemical peculiarities of two different metal ions is a very attractive strategy in obtaining complexes with interesting magnetic, electronic or electric properties.[9]

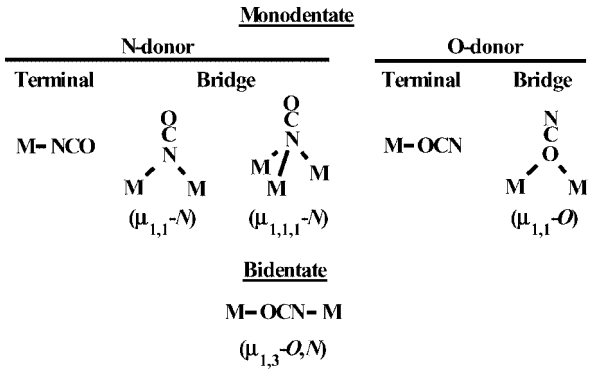


Scheme 1. Main coordination modes of the cyanato ligand.

In this communication we describe the formation of chains constructed by using $[Ru_2(\mu\text{-}O_2CR)_4]^+$ fragments and $OCN^-$ groups. The preparation of one heteropolynuclear species containing diruthenium and silver centres is also described.

## Results and Discussion

Treatment of $[Ru_2\{\mu\text{-}O_2CC(Me)=CHEt\}_4]BF_4$[10] with 5 equiv. sodium cyanate in methanol/water gives brown crystals of $[Ru_2\{\mu\text{-}O_2CC(Me)=CHEt\}_4(OCN)]_n$ (**1**). The X-ray crystal structure of **1** is shown in Figure 1.

This structure has two Ru atoms linked by four *trans*-2-methyl-2-pentenoato bridging ligands; the axial positions are occupied by cyanate groups, giving zigzag chains. These cyanato ligands are coordinated by an infrequent $\mu_{1,1}$-*O* coordination mode. The Ru–Ru and Ru–$O_{axial}$ distances are 2.2793(13) and 2.258(5) Å respectively, typical of those

[a] Departamento de Química Inorgánica, Facultad de Ciencias Químicas, Universidad Complutense de Madrid, Ciudad Universitaria,
28040 Madrid, Spain
Fax: +34-91-3944352
E-mail: qcmm@quim.ucm.es
[b] Centro de Asistencia a la Investigación de Rayos X, Facultad de Ciencias Químicas, Universidad Complutense de Madrid, Ciudad Universitaria,
28040 Madrid, Spain

 © 2006 Wiley-VCH Verlag GmbH & Co. KGaA, Weinheim 

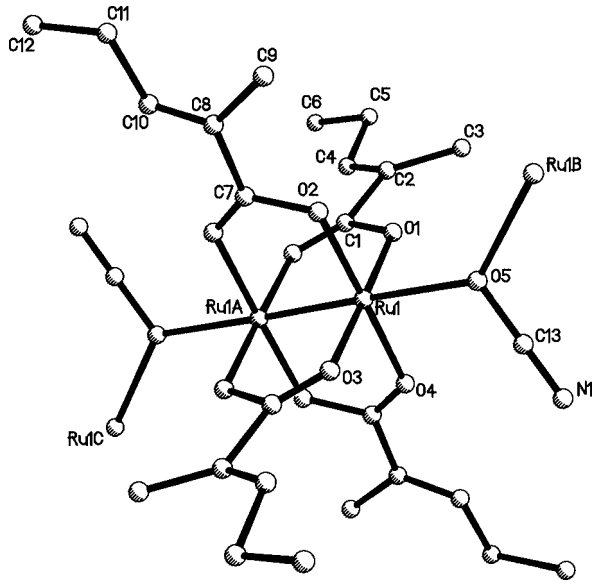


Figure 1. PLUTO view of $[Ru_2\{\mu\text{-}O_2CC(Me)=CHEt\}_4(OCN)]_n$ (**1**). Hydrogen atoms are omitted for clarity.

found in other polymeric complexes with O-donor bridging ligands.[4,5,11] The Ru–O–Ru angle [131.0(6)°] is larger than those found[4,5] in other nonlinear one-dimensional supramolecular structures formed with other bridging ligands. In contrast, the parent chlorido derivative $[Ru_2Cl\{\mu\text{-}O_2CC(Me)=CHEt\}_4]_n$ shows[10] an arrangement of linear chains in the solid state.

A methanol/water solution obtained from the reaction of $[Ru_2Cl(\mu\text{-}O_2CMe)_4]$ with $AgNO_3$ was treated again with 1 equiv. silver nitrate, and 2 equiv. sodium cyanate to give $\{[Ru_2(\mu\text{-}O_2CMe)_4][Ag(OCN)_2]\}_n$ (**2**). The crystal structure of **2** has been determined, and a PLUTO view is shown in Figure 2.

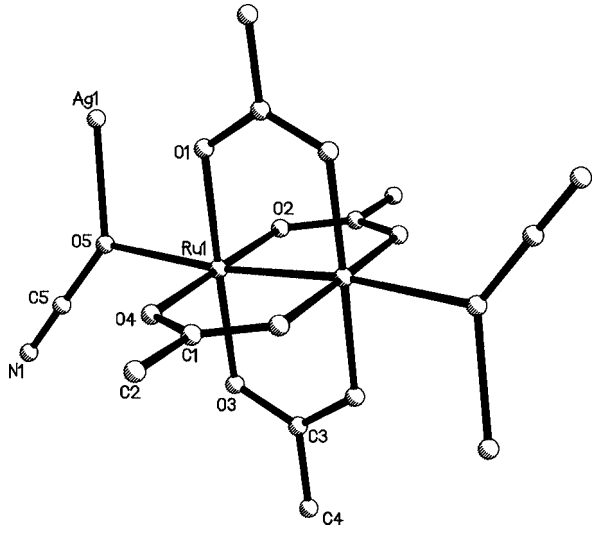


Figure 2. PLUTO view of $\{[Ru_2(\mu\text{-}O_2CMe)_4][Ag(OCN)_2]\}_n$ (**2**). Hydrogen atoms are omitted for clarity.

This compound is formed by zigzag chains that could be considered as $[Ru_2(\mu\text{-}O_2CMe)_4]^+$ units linked by $[Ag(OCN)_2]^-$ groups. The cyanato ligands display the same $\mu_{1,1}$-*O* coordination mode as those in complex **1**, but in this case they bridge the ruthenium and silver atoms (Figure 3).

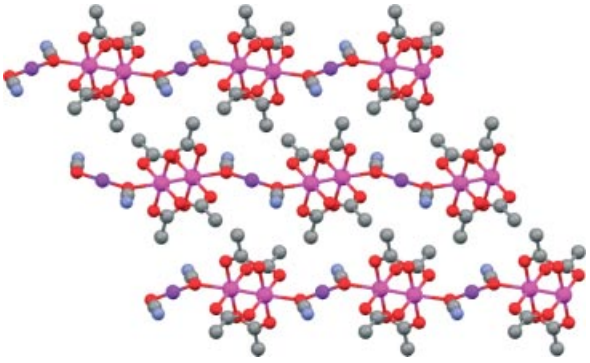

Figure 3. Packing of the zigzag chains of $\{[Ru_2(\mu\text{-}O_2CMe)_4][Ag(OCN)_2]\}_n$ (**2**). Hydrogen atoms are omitted for clarity.

The Ru–Ru bond length is 2.2740(9) Å, and the Ru–$O_{cyanate}$ bond length is 2.271(6) Å. The Ru–O–Ag angle [106.0(2)°] is smaller than the Ru–O–Ru angle in **1**.

An end-to-end (Ru–OCN–Ag) coordination mode for the cyanate group was expected in complex **2**, because the $OCN^-$ ligand is N-bonded in all the structures described[12] for silver complexes. The only exception is the compound $[Ag_2(NCO)_2(dpph)_2]$ [dpph = bis(diphenylphosphanyl)hexane], in which a $\mu_{1,3}$-*N*,*O* coordination mode has been found.[12b] Complex **2** is the first example where the cyanato ligand is coordinated to a silver centre by the oxygen atom, leaving the nitrogen atom uncoordinated. It is also noteworthy that the oxygen atom is shared with the neighbouring ruthenium atom to give $\mu_{1,1}$-*O* coordination. These results contrast with the existence of isocyanato ligands in the complex[13] $(NBu_4)[Ag(NCO)_2]$.

The magnetic measurements of both compounds show magnetic moments at room temperature corresponding to the presence of three unpaired electrons per diruthenium unit. These magnetic moments, 3.69 and 4.15 $\mu_B$ for **1** and **2** respectively, are in accordance with the ground-state configuration $\sigma^2\pi^4\delta^2(\pi^*\delta^*)^3$ proposed by Norman et al.[14] The representation of the magnetic moment vs. temperature shows a decrease in the magnetic moment, mainly at low temperatures (Figure 4).

The molar magnetic susceptibility increases continuously with decreasing temperature. This behaviour has been observed in other zigzag polymeric diruthenium(II,III) compounds and is due to a large zero-field splitting (ZFS) and a weak degree of antiferromagnetic coupling between the dimetallic units.[4–6,11] The magnetic moments for **1** are considerably lower than those for **2** in the whole temperature range. This behaviour indicates the existence of a stronger antiferromagnetic interaction in **1**. In order to estimate the *zJ* values, we have fitted the experimental magnetic data by using the model of Cukiernik et al.,[15] which incorporates

 © 2006 Wiley-VCH Verlag GmbH & Co. KGaA, Weinheim 

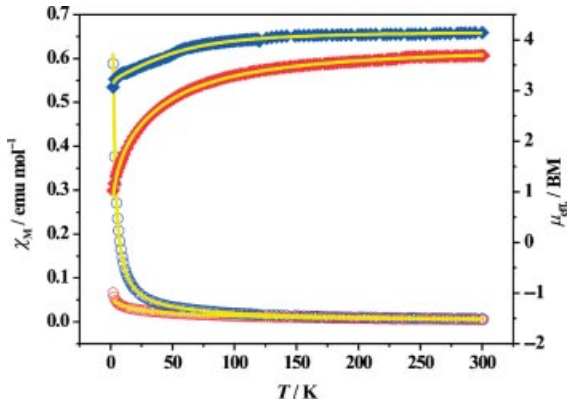


Figure 4. Temperature dependence of the molar magnetic susceptibility (●) and magnetic moment (♦) for **1** (red) and **2** (blue). The solid lines result from least-squares fits with $g = 2.0$, $D = 44.6$ cm$^{-1}$, $zJ = -5.0$ cm$^{-1}$ for **1** and $g = 2.2$, $D = 64.0$ cm$^{-1}$, $zJ = -0.1$ cm$^{-1}$ for **2**.

a strong ZFS as well as a weak intermolecular antiferromagnetism by the molecular field approximation. However, for complex **1** better parameters have been obtained with our model,[16] which introduces into the spin Hamiltonian the ZFS and a strong antiferromagnetic interaction. The fits of the experimental data (Figure 4) confirm the presence of a higher magnetic interaction for **1** (–5.0 cm$^{-1}$) than for **2** (–0.1 cm$^{-1}$). This behaviour could be explained on the basis of two factors: i) the different distances between the diruthenium units in **1** and **2** or ii) the nature of the linker $OCN^-$ or $[Ag(OCN)_2]^-$. However, a strong antiferromagnetic coupling between $Ru_2$(II,III) units with a long linker has been found by Ren et al.[17] Thus, although Ren's complex and **2** are different, we think that the difficulty of the electronic exchange through the diamagnetic $[Ag(OCN)_2]^-$ group is probably the main factor in the low magnetic coupling in complex **2**.

## Conclusions

The present work describes the first diruthenium units linked by $OCN^-$ or $[Ag(OCN)_2]^-$ groups that show an unusual $\mu_{1,1}$-*O* coordination mode. The design strategies reported in this communication lead to chains with a better magnetic interaction through the $OCN^-$ group than the $[Ag(OCN)_2]^-$ fragment. Our further work will explore the preparation of one-dimensional supramolecular structures formed by diruthenium units and anionic metallic cores.

## Experimental Section

**General Remarks:** All reactions were carried out in an inert atmosphere, by using standard Schlenk techniques. The complexes $[Ru_2Cl(\mu\text{-}O_2CMe)_4]$ and $[Ru_2\{\mu\text{-}O_2CC(Me)=CHEt\}_4]BF_4$ were prepared by literature procedures.[10,18] Other chemicals and solvents were obtained from commercial sources and used without further purification.

Elemental analyses were carried out by the Microanalytical Service of the Complutense University of Madrid. IR spectra were recorded with a Midac prospect FT-IR, or a Shimadzu FT-IR Prestige-21 spectrophotometer by using KBr discs. The variable-temperature magnetic susceptibility data were measured with a Quantum Design MPMS*XL* SQUID (Superconducting Quantum Interference Device) susceptometer over a temperature range of 2 to 300 K. All data were corrected for the diamagnetic contribution of both the sample holder and the compound to the susceptibility. The molar diamagnetic corrections for the complexes were calculated on the basis of Pascal's constants. Mass spectra were obtained with a Bruker Esquire-LC with Electrospray Ionization (ESI) by using methanol or dmso as solvent. Nominal molecular masses and isotopic distribution of all peaks were calculated with the MASAS[19] computer program by using a polynomial expansion based on natural abundances of the isotopes.

**Synthesis of $[Ru_2\{\mu\text{-}O_2CC(Me)=CHEt\}_4(OCN)]_n$ (1):** To a methanol solution (15 mL) of $[Ru_2\{\mu\text{-}O_2CC(Me)=CHEt\}_4]BF_4$ (0.22 g, 0.30 mmol) was added an aqueous solution of sodium cyanate (0.10 g, 1.50 mmol, 10 mL). The reaction mixture was stirred for 1 h. A brown precipitate was formed. The solid was filtered out, washed with water (4 × 20 mL) and dried under vacuum to give **1**. Yield: 161 mg (77%). $C_{25}H_{36}NO_9Ru_2$ (696.71): calcd. C 43.10, H 5.21, N 2.01; found C 42.98, H 5.11, N 2.13. Main IR data (KBr disk): 2968 (m), 2935 (m), 2876 (m), 2139 (vs), 2085 (w), 1647 (m), 1435 (v)s, 1415 (vs), 1384 (vs), 1349 (s), 1300 (w), 1258 (w), 1179 (m), 1105 (m), 1067 (w), 1036 (m), 989 (w), 906 (w), 841 (m), 786 w, 752 (m), 684 (s), 651 (w), 623 (w), 530 (s), 479 (w), 431 (w), 421 (w) cm$^{-1}$. $\mu_{eff.}$ (room temp.) = 3.69 $\mu_B$. Mass spectrometric data (ESI$^+$): *m*/*z* = 656 $[Ru_2\{\mu\text{-}O_2CC(Me)=CHEt\}_4]$.

Red-brown crystals of **1** suitable for X-ray diffraction were obtained when a methanol solution of $[Ru_2\{\mu\text{-}O_2CC(Me)=CHEt\}_4]BF_4$ was layered over a water solution of NaOCN.

**Synthesis of $\{[Ru_2(\mu\text{-}O_2CMe)_4][Ag(OCN)_2]\}_n$ (2):** To a suspension of $[Ru_2Cl(\mu\text{-}O_2CMe)_4]$ (0.14 g, 0.30 mmol) in methanol (10 mL) was added a solution of $AgNO_3$ (0.05 g, 0.30 mmol, 5 mL). The reaction mixture was stirred for 10 min to give a solid precipitate of AgCl and a brown solution containing the species $[Ru_2(\mu\text{-}O_2CMe)_4]^+$. The precipitate was removed by filtration, and the solution was treated again with an aqueous solution of $AgNO_3$ (0.05 g, 0.30 mmol, 10 mL) and an aqueous solution of NaOCN (0.04 g, 0.60 mmol, 10 mL). The reaction mixture was stirred for one hour, in the absence of light, and gave a brown precipitate. The solid was filtered out, washed with water (2 × 20 mL) and dried under vacuum to give **2**. Yield: 110 mg (58%). $C_{10}H_{12}AgN_2O_{10}Ru_2$ (630.22): calcd. C 19.06, H 1.92, N 4.44; found C 19.20, H 1.97, N 4.42. Main IR data (KBr disk): 2937 (w), 2155 vs, 2104 (w), 1444 vs, 1398 (m), 1349 (w), 1051 (w), 694 (s), 670 (w), 662 (w), 627 (w), 615 (w) cm$^{-1}$. $\mu_{eff.}$ (room temp.) = 4.15 $\mu_B$. Mass spectrometric data (ESI$^+$): *m*/*z* = 517 $[Ru_2(\mu\text{-}O_2CMe)_4(dmso)]$.

Crystals of **2** were obtained by slow diffusion of the solution containing the species $[Ru_2(\mu\text{-}O_2CMe)_4]^+$ and $Ag^+$ (molar ratio 1:1) over the aqueous solution of NaOCN.

**Crystal Structural Data for 1:** $C_{25}H_{36}NO_9Ru_2$, $M_r$ 696.69, crystal size 0.14 × 0.18 × 0.20 mm, monoclinic, space group *P*2/*c*, $a$ = 9.9698(8), $b$ = 12.0247(9), $c$ = 12.4202(9) Å, $\beta$ = 98.146(2)°, $V$ = 1473.96(19) Å$^3$, $Z$ = 2, $D_c$ = 1.570 g cm$^{-3}$, $F(000)$ = 706, $\mu$ = 1.072 mm$^{-1}$, 3559 independent reflections, $R_I$ [$I > 2\sigma(I)$] = 0.0865, $wR_2$ (all data) = 0.2914.

**Crystal Structural Data for 2:** $C_{10}H_{12}AgN_2O_{10}Ru_2$, $M_r$ 630.23, crystal size 0.04 × 0.04 × 0.32 mm, monoclinic, space group *P*2(1)/*n*, $a$ = 7.3420(6), $b$ = 8.8225(7), $c$ = 13.1580(11) Å, $\beta$ = 92.215(2)°, $V$ = 851.67(12) Å$^3$, $Z$ = 2, $D_c$ = 2.458 g cm$^{-3}$, $F(000)$ = 602, $\mu$ =

 © 2006 Wiley-VCH Verlag GmbH & Co. KGaA, Weinheim 

2.942 $mm^{-1}$, 2051 independent reflections, $R_I$ [$I > 2\sigma(I)$] = 0.0408, $wR_2$ (all data) = 0.1205.

Representative crystals were mounted on a Bruker Smart-CCD diffractometer with graphite monochromated Mo-$K_\alpha$ ($\lambda$ = 0.71073 Å) radiation. Data were collected at 293(2) K over a hemisphere of the reciprocal space by a combination of three exposure sets. The structures were solved by direct methods and refined by full-matrix least-squares on $F^2$ with the SHELXS and SHELXL programs.[20]

CCDC-612317 and CCDC-612318 contain the supplementary crystallographic data for this paper. These data can be obtained free of charge from The Cambridge Crystallographic Data Centre via www.ccdc.cam.ac.uk/data_request/cif.

## Acknowledgments

Financial support by the Ministerio Español de Educación y Ciencia and Comunidad de Madrid (projects no. CTQ2005–00397/BQU and S-0505/MAT/0303) is gratefully acknowledged.

[1] a) J.-W. Ying, D. R. Sobransingh, G.-L. Xu, A. E. Kaifer, T. Ren, *Chem. Commun.* **2005**, 357–359; b) S. K. Hurst, T. Ren, *J. Organomet. Chem.* **2003**, *670*, 188–197; c) T. Ren, G.-L. Xu, *Comments Inorg. Chem.* **2002**, *23*, 355–380.

[2] a) F. A. Cotton, C. Lin, C. A. Murillo, *Proc. Natl. Acad. Sci. USA* **2002**, *99*, 4810–4813; b) F. A. Cotton, C. Lin, C. A. Murillo, *Acc. Chem. Res.* **2001**, *34*, 759–771.

[3] a) M. H. Chisholm, A. M. Macintosh, *Chem. Rev.* **2005**, *105*, 2949–2976; b) B. E. Bursten, M. H. Chisholm, J. S. D′Acchioli, *Inorg. Chem.* **2005**, *44*, 5571–5579; c) M. H. Chisholm, *Acc. Chem. Res.* **2000**, *33*, 53–61.

[4] F. A. Cotton, C. A. Murillo, R. A. Walton (Eds.), *Multiple Bonds between Metal Atoms*, 3rd ed., Springer Science and Business Media Inc., New York, **2005**.

[5] a) M. A. S. Aquino, *Coord. Chem. Rev.* **1998**, *170*, 141–202; b) M. A. S. Aquino, *Coord. Chem. Rev.* **2004**, *248*, 1025–1045.

[6] M. Mikuriya, D. Yoshioka, M. Handa, *Coord. Chem. Rev.* **2006**, *250*, 2194–2211.

[7] For example, see: a) M. C. Barral, T. Gallo, S. Herrero, R. Jiménez-Aparicio, M. R. Torres, F. A. Urbanos, *Inorg. Chem.* **2006**, *45*, 3639–3647; b) B. Liu, P. Yin, X.-Y. Yi, S. Gao, L.-M. Zheng, *Inorg. Chem.* **2006**, *45*, 4205–4213; c) E. V. Dikarev, A. S. Filatov, R. Clérac, M. A. Petrukhina, *Inorg. Chem.* **2006**, *45*, 744–751; d) M. C. Barral, S. Herrero, R. Jiménez-Aparicio, M. R. Torres, F. A. Urbanos, *Angew. Chem. Int. Ed.* **2005**, *44*, 305–307; e) P. Angaridis, F. A. Cotton, C. A. Murillo, D. Villagrán, X. Wang, *J. Am. Chem. Soc.* **2005**, *127*, 5008–5009; f) T. Ren, *Organometallics* **2005**, *24*, 4854–4870; g) W.-Z. Chen, T. Ren, *Organometallics* **2005**, *24*, 2660–2669.

[8] a) M. C. Barral, R. Jiménez-Aparicio, J. L. Priego, E. C. Royer, F. A. Urbanos, U. Amador, *J. Chem. Soc., Dalton Trans.* **1997**, 863–868; b) M. Mukaida, T. Nomura, T. Ishimori, *Bull. Chem. Soc. Jpn.* **1972**, *45*, 2143–2147.

[9] For example, see: a) T. E. Vos, J. S. Miller, *Angew. Chem. Int. Ed.* **2005**, *44*, 2416–2419; b) T. Sugiura, K. Ota, M. Ebihara, T. Kawamura, *C. R. Chim.* **2005**, *8*, 1760–1765; c) O. Kahn, *Acc. Chem. Res.* **2000**, *33*, 647–657.

[10] M. C. Barral, R. Jiménez-Aparicio, D. Pérez-Quintanilla, E. Pinilla, J. L. Priego, E. C. Royer, F. A. Urbanos, *Polyhedron* **1998**, *18*, 371–376.

[11] G. Arribas, M. C. Barral, R. González-Prieto, R. Jiménez-Aparicio, J. L. Priego, M. R. Torres, F. A. Urbanos, *Inorg. Chem.* **2005**, *44*, 5770–5777.

[12] For example, see: a) Effendy, C. Di Nicola, C. Pettinari, A. Pizzabiocca, B. W. Skelton, N. Somers, A. H. White, *Inorg. Chim. Acta* **2006**, *359*, 64–80 and references cited therein; b) Effendy, C. Di Nicola, M. Fianchini, C. Pettinari, B. W. Skelton, N. Somers, A. H. White, *Inorg. Chim. Acta* **2005**, *358*, 763–795; c) G. A. Bowmaker, Effendy, P. C. Junk, A. H. White, *J. Chem. Soc., Dalton Trans.* **1998**, 2131–2138 and references cited therein.

[13] K. Aarflot, K. Ase, *Acta Chem. Scand. Ser. A* **1974**, *28*, 137–144.

[14] J. G. Norman, G. E. Renzoni, D. A. Case, *J. Am. Chem. Soc.* **1979**, *101*, 5256–5267.

[15] F. D. Cukiernik, D. Luneau, J. C. Marchon, P. Maldivi, *Inorg. Chem.* **1998**, *37*, 3698–3704.

[16] R. Jiménez-Aparicio, F. A. Urbanos, J. M. Arrieta, *Inorg. Chem.* **2001**, *40*, 613–619.

[17] Y. Shi, G. T. Yee, G. Wuang, T. Ren, *J. Am. Chem. Soc.* **2004**, *126*, 10552–10553.

[18] R. W. Michell, A. Spencer, G. Wilkinson, *J. Chem. Soc., Dalton Trans.* **1973**, 846–854.

[19] F. A. Urbanos, *MASAS*, version 3.1, University Complutense of Madrid, Madrid, Spain, **2002**.

[20] a) G. M. Sheldrick, *SHELXS-97*, University of Göttingen, Göttingen, Germany, **1997**; b) G. M. Sheldrick, *SHELXL-97*, University of Göttingen, Göttingen, Germany, **1997**.

Received: July 19, 2006
Published Online: September 14, 2006

 © 2006 Wiley-VCH Verlag GmbH & Co. KGaA, Weinheim 

DOI: 10.1002/ejic.200600540

# A Novel Europium Carbodiimide that Contains Isolated Europium Tetrahedra and Parallel Chains of Edge-Sharing Open Handbag-Like $Eu_6$ Units

**Wuping Liao,[a] Ulli Englert,[b] and Richard Dronskowski*[b]**

**Keywords:** Europium / Carbodiimide / Lanthanides / Solid-state reactions / Crystal growth

$Eu_2I_2(NCN)$ is the first compound to contain discrete empty europium tetrahedra and infinite metal chains that are constructed from edge-sharing $Eu_6$ units with an open handbag-like motif. The europium tetrahedra and chains are bridged by coordinating carbodiimide ($NCN^{2-}$) anions in a three-dimensional network.
(© Wiley-VCH Verlag GmbH & Co. KGaA, 69451 Weinheim, Germany, 2006)

## Introduction

Within the past three decades, solid-state (metal) cluster phases have drawn significant attention due to their interesting structural features and physical properties. There are many examples of both empty metal clusters and those filled by interstitial atoms; the differing cluster connectivities result in a large variety of structural motifs.[1] For instance, $Ln_6Z$ *octahedra* (Z = main-group elements such as H, B–O, Si, Ga, and $C_2$ units but also transition metals such as Mn–Cu, Ru–Pd, and Re–Au) serve as characteristic building blocks in the metal-rich rare-earth halides.[2] On the other side, $Ln_4Z$ (Z = N, O) *tetrahedra* are found for a couple of rare-earth halides and sulfides. The different linkages of these $Ln_4Z$ tetrahedra, by corners and/or by edges, lead to a large structural richness that involves oligomeric units, chains, or layers.[3] The polymorph number V of $PrI_2$ was recently reported to contain empty tetrahedral $Pr_4$ units.[4]

Our own research has resulted in novel europium carbodiimide compounds that contain discrete, but also oligomeric, $Eu_4$ tetrahedra and 1D chains that are constructed from the tetrahedra by vertex- and face-sharing $Eu_4$.[5] Nonetheless, there are few reports that outline the coexistence of empty metal clusters and 1D metal chains except for $Ln_{13}Br_{18}B_3$ (Ln = Gd, Tb)[6] which contains both discrete $Ln_{10}B_2$ bioctahedra and 1D metal chains that are constructed from edge-sharing $Ln_6B$ octahedra. In this communication, we present the novel phase $Eu_2I_2(NCN)$, which is another example of a compound that contains discrete metal clusters and chains; the latter are constructed from edge-sharing handbag-like $Eu_6$ units.

[a] Key Laboratory of Rare Earth Chemistry and Physics, Changchun Institute of Applied Chemistry, Chinese Academy of Sciences,
Changchun 130022, P. R. China
[b] Institut für Anorganische Chemie der RWTH Aachen, Landoltweg 1, 52056 Aachen, Germany
E-mail: drons@HAL9000.ac.rwth-aachen.de

## Results and Discussion

The crystal structure of $Eu_2I_2(NCN)$ reveals isolated empty $Eu_4$ tetrahedra and parallel 1D metal chains that are bridged by $NCN^{2-}$ anions in a 3D network in which the iodide anions are located in the interstices (Figure 1, top). To the best of our knowledge, this is the first example of a crystal structure that contains both isolated *empty* metal tetrahedra and infinite metal chains. Another characteristic feature of $Eu_2I_2(NCN)$ is given by the uncommon open handbag-like $Eu_6$ entity (Figure 1, bottom) which *embraces* one $NCN^{2-}$ anion (either located centrally or shifted to the left or right side with partial occupancies) and is capped by another two $NCN^{2-}$ anions. As mentioned above, an octahedral $Ln_6$ entity would be a more typical structure for this type of compound, and the open handbag-like configuration is quite rare and has only been observed in molecular chemistry, namely to describe one of the lowest-energy structures of the water hexamer.[7]

There are four different crystallographic positions found for the Eu units: two fully occupied sites (Eu1 and Eu2) and two other disordered sites (Eu3 and Eu4); all four of the Eu sites differ in their coordination environments with coordination numbers between 6 and 8. While the first two Eu atoms generate the empty $(Eu1)_2(Eu2)_2$ tetrahedron, the other two are responsible for the open handbag-like $(Eu3)_4(Eu4)_2$ entity. The isolated $Eu_4$ tetrahedra are capped over all triangular faces by two kinds of $NCN^{2-}$ anions (Figure 2, top), which is a typical structure. The open handbag-like $Eu_6$ entity, however, is capped by two other $NCN^{2-}$ units as described above (Figure 1, bottom).The $Eu_6$ entities are interconnected to each other by edge-sharing to result in an infinite 1D chain (Figure 1, middle). Note that the encapsulated $NCN^{2-}$ anion excludes the interpretation of the 1D chain as a row of neighboring $Eu_4$ tetrahedra (Figure 2, top) because the filled monomer is nonexistent. The capping $NCN^{2-}$ anions interconnect the $Eu_4$ tetrahedra and the 1D chains into a 3D network that contains quasihexag-

 © 2006 Wiley-VCH Verlag GmbH & Co. KGaA, Weinheim InterScience 

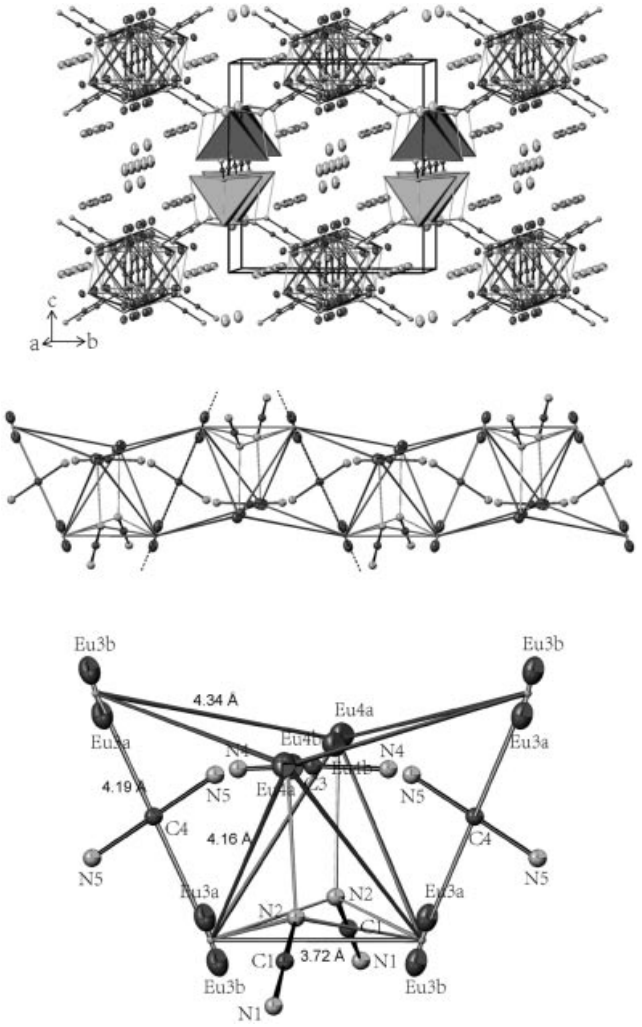


Figure 1. View of the structure of $Eu_2I_2(NCN)$ along the *a* axis which shows isolated $Eu_4$ tetrahedra and 1D metal chains (top), a single 1D metal chain with encapsulated and capping $NCN^{2-}$ anions (middle), and the open handbag-like $Eu_6$ unit coordinated by $NCN^{2-}$ anions (bottom). The I atoms are given as isolated grey spheres, Eu atoms as dark-grey spheres whereas N atoms are shown as small grey and C atoms as small dark-grey spheres.

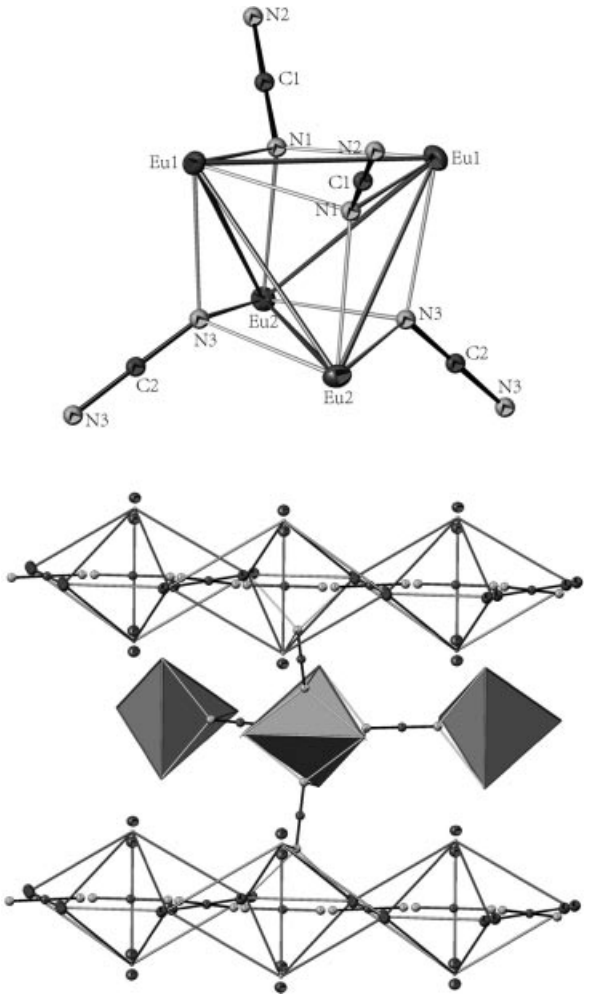


Figure 2. An isolated $Eu_4$ tetrahedron capped by $NCN^{2-}$ anions (top) and its coordination (bottom).

onal and orthorhombic channels for the iodide anions (Figure 1, top). Alternatively, the structure can be viewed as the alternate stacking of one layer of metal chains and two layers of isolated $Eu_4$ tetrahedra along the *c* axis. As a result, one $Eu_4$ tetrahedron is simultaneously interconnected to two metal chains and two other $Eu_4$ tetrahedra (Figure 2, bottom).

The Eu–Eu distances in the isolated $(Eu1)_2(Eu2)_2$ tetrahedron cover a range of 3.97–4.10 Å, which is comparable to 3.98 Å in $LiEu_2(NCN)I_3$ and 3.99–4.12 Å in $LiEu_4(NCN)_3I_3$.[5] The Eu–N bond for isolated $(Eu1)_2$-$(Eu2)_2$ is 2.60–2.62 Å, which is also comparable to 2.62 Å in $LiEu_2(NCN)I_3$ and 2.61–2.66 Å in $LiEu_4(NCN)_3I_3$. In the $(Eu3)_4(Eu4)_2$ entities, the distance between the barycenters of the electron densities of the europium sites cover a range of 3.72–4.45 Å (Figure 1, bottom, the Eu4–Eu4 distance is neglected). The bottom Eu3–Eu3 distance is much shorter (3.72 Å), which might be due to an ionic matrix effect of the nonmetal atoms[8] because there are two N atoms from the $NCN^{2-}$ anions bonded to this edge. The longer distance of the Eu4–Eu4 (4.45 Å) bond and also the Eu3–Eu4 (4.34 Å) bond might be due to the steric effect of the incorporated carbodiimide anion. The Eu–N distances (between the barycenters of Eu and N sites) lie in the range of 2.51–2.72 Å. The wide range goes back, in part, to the distortion of the Eu3 and Eu4 sites. The split positions of the Eu3 and Eu4 sites mirror the two possible sites of the encapsulated carbodiimide anion, either central or shifted to the left or right side of the $Eu_6$ unit. Nonetheless, there is no indication of any Eu valence instability (see Figure 3) and all europium atoms are clearly divalent in nature.

There are four different crystallographic sites for the C atoms which indicate that there are four different $NCN^{2-}$ anions (Table 1). Two of the anions are spatially separated and two are spatially correlated; the latter two correspond to alternatively occupied split positions. All four $NCN^{2-}$ anions have two double C=N bonds with (almost) equiva-

 © 2006 Wiley-VCH Verlag GmbH & Co. KGaA, Weinheim 

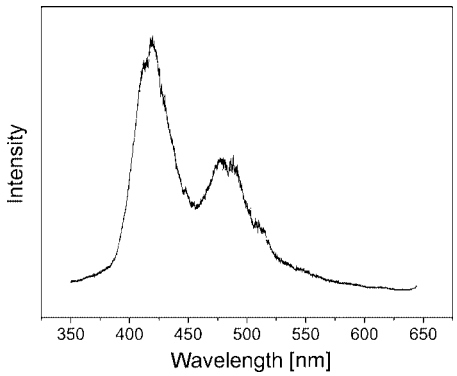


Figure 3. Photoluminescence of $Eu_2I_2(NCN)$ excited at 330 nm which indicates that europium is divalent.

lent distances such that they adopt the classic carbodiimide shape. The shape can be confirmed by analysis of the IR spectra in which characteristic carbodiimide frequencies (around 1958 $cm^{-1}$ for the asymmetric stretch and 665, 656, and 621 $cm^{-1}$ for the deformation vibration) are clearly detected. Different from the alternatively occupied N4–C3–N4 and N5–C4–N5 units, which are located in the interstices of the metal chain, the N2–C1–N1 and N3–C2–N3 units bridge all isolated $Eu_4$ tetrahedra and the metal chains in a 3D network. In particular, the N2–C1–N1 unit bridges the chain (by the N2 atom) and the $Eu_4$ tetrahedron (by the N1 atom), whereas the N3–C2–N3 unit connects two isolated $Eu_4$ tetrahedra. The N4–C3–N4 unit is slightly bent [176(3)°] whereas the other three $NCN^{2-}$ anions are linear (with N–C–N angles of 180°). Note again that an $NCN^{2-}$ unit (with 68% site probability, named N4–C3–N4) is located in the center of the spatially restricted $Eu_6$ entity, but it may also appear (with 32% occupancy, named N5–C4–N5) slightly shifted to the left or right. The very presence of these dislocated $NCN^{2-}$ units indicates the source for the distortion of the Eu3/Eu4 sites.

Table 1. C=N bond lengths [Å] and N=C=N angles [°].

| | | | |
|---|---|---|---|
| C1–N1 | 1.24(2) | N1–C1–N2 | 180(1) |
| C1–N2 | 1.23(2) | N3–C2–N3[i[a]] | 180 |
| C2–N3 | 1.24(2) | N4–C3–N4[ii[a]] | 176(3) |
| C3–N4 | 1.29(2) | N5–C4–N5[iii[a]] | 180 |
| C4–N5 | 1.28(5) | | |

[a] Symmetry codes: (i) $-x, -y, -z + 1$; (ii) $-x + 1/2, -y + 1, z$; (iii) $-x, -y + 1, -z$.

In conclusion, a novel europium carbodiimide iodide serves as the first example of a structure that contains both isolated empty $M_4$ tetrahedra and infinite 1D metal chains. In $Eu_2I_2(NCN)$, the metal chains are constructed from uncommon $Eu_6$ entities that adopt an open handbag-like motif. All metal chains and isolated tetrahedra are bridged by carbodiimide anions in a 3D network with the iodide anions held in the interstices – a structural richness never seen before within europium cluster chemistry.

## Experimental Section

**Synthesis of $Eu_2I_2(NCN)$:** As recently reported, different thermal treatment of identical reactants may lead to the formation of up to three different compounds.[5d] The synthesis of $Eu_2I_2(NCN)$ is another example of a largely temperature-controlled synthesis. Typically, yellow single-crystals of $Eu_2I_2(NCN)$ are synthesized from the reaction of $EuI_2$, NaCN, $NaN_3$, and InI in a 2:1:1:1 ratio at elevated temperatures. $EuI_2$ (99.9%) and InI (99.999%) were used as purchased from Aldrich, and NaCN (95%, Merck) and $NaN_3$ (99%, Alfa) were thoroughly dried in vacuo heated at 160 °C for 3 d. It is important to follow this procedure because even traces of moisture or oxygen will lead to the immediate formation of $Eu_4OI_6$. The mixtures were transported in tantalum ampoules which were sealed with an arc welder and jacketed with quartz; both tasks were performed under an argon atmosphere. The sample was heated to 750 °C at a rate of 6 °C/min. The sample was heated at 750 °C for a week and then slowly cooled to 600 °C at a rate of 2 °C/min. After the sample was annealed at 600 °C for 2 weeks, the mixture was cooled to room temperature at a rate of 2 °C/min. The crystals of the target phase were easily separated from the surplus fluxes because the crystals were of different colors and shapes, and the yield was more than 50%. A single-crystal with a fresh surface was used for X-ray fluorescence (XRF) analysis. It revealed that the Eu and I molar percentiles – Eu/(Eu+I) and I/(Eu+I) – are 51.67% and 48.33%, respectively, which is comparable to the calculated values of 50% and 50%. The elements Na and In were not detected.

Photoluminescence emission spectra excited at 330 nm were recorded at room temperature with a spectrofluorometer (SPEX, DM3000F) equipped with two 0.22 m double monochromators (SPEX, 1680) and a 450 W xenon lamp. Two broad bands were detected with maxima at 417 and 483 nm, which can be assigned to the $4f^6 5d^1 \rightarrow 4f^7$ transition of $Eu^{2+}$. These two independent broad bands indicate two different coordinations of the Eu atoms (either from the isolated $Eu_4$ tetrahedra or from the metal chain). The small splitting of the broad bands may be attributable to the non-identity of chemically similar atoms such as Eu3 and Eu4.

**Crystal data:** $Eu_2I_2(NCN)$, $M$ = 597.75 g/mol, orthorhombic, $a$ = 11.0056(10) Å, $b$ = 10.8921(11) Å, $c$ = 11.5947(11) Å, $V$ = 1389.9(2) $Å^3$, $T$ = 120(2) K, Space group *Pmma* (no. 51), $Z$ = 8, $\mu$(Mo-$K_\alpha$) = 26.655 $mm^{-1}$; diffraction data collected with a Bruker SMART APEX CCD diffractometer with graphite-monochromatized Mo-$K_\alpha$ radiation ($\lambda$ = 0.71073 Å), empirical absorption correction, 38036 reflections measured, 1920 unique ($R_{int}$ = 0.0771) which were all used in the refinements. The final values for $wR_2$ (all data) and $R_1$ [$I > 2\sigma(I)$] were 0.0733 and 0.0312, respectively. Crystal structure solution/refinement was processed by means of SHELX programs.[9] The disordered sites of Eu3, Eu4, and I4 were refined to site occupation factors of 0.757(2) for Eu3a, 1–0.757(2) = 0.243(2) for Eu3b, 0.483(2) for Eu4a, 1–0.483(2) = 0.517(2) for Eu4b, 0.911(3) for I4a, and 1–0.911(3) = 0.089(3) for I4b, respectively. There is no indication whatsoever for a higher symmetry or a superstructure despite the presence of split positions for the Eu3/Eu4 sites. The partially occupied anions N4–C3–N4 and N5–C4–N5 were also refined with a charge constraint (all europium atoms are divalent indicated by the PL spectra), and their site occupation factors arrive at 0.68(3) and 1–0.68(3) = 0.32(3). We believe that the two possible carbodiimide locations induce the aforementioned europium split positions because of the spatial confinement of the $Eu_6$ unit. Further details of the crystal-structure investigation may be obtained from the Fachinformationszentrum Karlsruhe, 76344

 © 2006 Wiley-VCH Verlag GmbH & Co. KGaA, Weinheim 

Eggenstein-Leopoldshafen, Germany, on quoting the depository number CSD-416668.

## Acknowledgments

We thank Tobias Koplin from the Institute of Inorganic Chemistry (RWTH) for the XRF analyses and Deutsche Forschungsgemeinschaft for financial support.

[1] a) A. Simon, *Angew. Chem. Int. Ed. Engl.* **1981**, *20*, 1–22; b) A. Simon, *Angew. Chem. Int. Ed. Engl.* **1988**, *27*, 159–183; c) A. Simon in *Clusters and Colloids – From Theory to Applications* (Ed.: G. Schmid), Verlag Chemie, Weinheim, **1994**, pp. 373–458; d) A. Simon, *J. Alloys Compd.* **1995**, *229*, 158–174; e) S. V. Krivovichev, S. K. Filatov, *Acta Crystallogr., Sect. B: Struct. Sci.* **1999**, *55*, 664–676; f) J. D. Corbett, *Inorg. Chem.* **2000**, *39*, 5178–5191.

[2] For example, see a) G. Meyer, *Chem. Rev.* **1988**, *88*, 93–107; b) M. Lulei, J. D. Martin, L. M. Hoistad, J. D. Corbett, *J. Am. Chem. Soc.* **1997**, *119*, 513–520; c) M. Lulei, *Inorg. Chem.* **1998**, *37*, 777–781; d) H. Mattausch, O. Oeckler, A. Simon, *Inorg. Chim. Acta* **1999**, *289*, 174–190; e) M. Köckerling, J. D. Martin, *Inorg. Chem.* **2001**, *40*, 389–395; f) C. Zheng, O. Oeckler, H. Mattausch, A. Simon, *Z. Anorg. Allg. Chem.* **2001**, *627*, 2151–2162; g) H. Mattausch, C. Zheng, L. Kienle, A. Simon, *Z. Anorg. Allg. Chem.* **2004**, *630*, 2367–2372.

[3] For example, see a) P. E. Caro, *J. Less-Common Met.* **1968**, *16*, 367–377; b) A. Simon, T. Köhler, *J. Less-Common Met.* **1986**, *116*, 279–292; c) T. Schleid, *Eur. J. Solid State Inorg. Chem.* **1996**, *33*, 227–240; d) M. Lulei, J. D. Corbett, *Eur. J. Solid State Inorg. Chem.* **1996**, *33*, 241–250; e) G. M. Ehrlich, M. E. Badding, N. E. Brese, S. S. Trail, F. J. DiSalvo, *J. Alloys Compd.* **1996**, *235*, 133–134; f) F. Lissner, T. Schleid, *Z. Anorg. Allg. Chem.* **2003**, *629*, 1027–1032; g) W. Liao, R. Dronskowski, *Acta Crystallogr., Sect. C: Cryst. Struct. Commun.* **2004**, *60*, i23–i24; h) G. Meyer, N. Gerlitzki, S. Hammerich, *J. Alloys Compd.* **2004**, *380*, 71–78.

[4] a) E. Warkentin, H. Bärnighausen, *Z. Anorg. Allg. Chem.* **1979**, *459*, 187–200; b) N. Gerlitzki, G. Meyer, A. V. Mudring, J. D. Corbett, *J. Alloys Compd.* **2004**, *380*, 211–218.

[5] a) W. Liao, C. Hu, R. K. Kremer, R. Dronskowski, *Inorg. Chem.* **2004**, *43*, 5884–5890; b) W. Liao, R. Dronskowski, *Z. Anorg. Allg. Chem.* **2005**, *631*, 1953–1956; c) W. Liao, B. P. T. Fokwa, R. Dronskowski, *Chem. Commun.* **2005**, 3612–3614; d) W. Liao, R. Dronskowski, *Inorg. Chem.* **2006**, *45*, 3828–3830.

[6] O. Oeckler, L. Kienle, H. Mattausch, A. Simon, *Angew. Chem. Int. Ed.* **2002**, *41*, 4257–4259.

[7] J. Kim, K. S. Kim, *J. Chem. Phys.* **1998**, *109*, 5886–5895.

[8] J. D. Corbett, *J. Chem. Soc., Dalton Trans.* **1996**, 575–587.

[9] G. M. Sheldrick, *SHELXS/SHELXL Computer Programs*, University of Göttingen, Germany.

Received: June 9, 2006
Published Online: September 14, 2006

 © 2006 Wiley-VCH Verlag GmbH & Co. KGaA, Weinheim 

DOI: 10.1002/ejic.200600384

# Phosphavinylidene(oxo)phosphorane Mes*P(O)=C=PMes*: A Diphosphaallene Featuring $\lambda^5\sigma^3$- and $\lambda^3\sigma^2$-Phosphorus Atoms

**Raluca Septelean,[a] Henri Ranaivonjatovo,*[b] Gabriela Nemes,[a] Jean Escudié,*[b] Ioan Silaghi-Dumitrescu,[a] Heinz Gornitzka,[b] Luminita Silaghi-Dumitrescu,[a] and Stéphane Massou[c]**

**Keywords:** Heterocumulenes / Phosphorus / Phosphaalkenes / Methylenephosphoranes

Bis(2,4,6-tri-*tert*-butylphenyl)phosphavinylidene(oxo)phosphorane (**1**) (Mes* = 2,4,6-tri-*tert*-butylphenyl), the first $1\lambda^5\sigma^3,3\lambda^3\sigma^2$-diphosphaallene, has been synthesised by addition of the phosphaalkenyllithium Mes*P=C(Li)Cl to dichlorophosphane oxide Mes*P(O)$Cl_2$. Compound **1** is stable in the solid-state but undergoes a slow intramolecular cyclisation in solution by addition of a C–H bond of an *ortho*-*tert*-butyl group to the $\sigma^3$-P=C double bond. Water adds chemoselectively and regioselectively to the $\lambda^5\sigma^3$-P=C bond, which appears to be more reactive than the $\lambda^3\sigma^2$-P=C bond. This leads to the hydrolysis compound **8** which has been structurally characterised. The new bis(phosphane oxide)-methylene **9** formed from the successive cyclisation of an *ortho*-*tert*-butyl group to the $\lambda^5\sigma^3$-P=C bond and addition of water to the $\lambda^3\sigma^2$-P=C bond has also been structurally characterised.
(© Wiley-VCH Verlag GmbH & Co. KGaA, 69451 Weinheim, Germany, 2006)

## Introduction

The high utility of ketenes, allenes and cumulenes has been well established in organic synthesis.[1] Phosphaallene derivatives, namely compounds with P=C=C or P=C=P skeletons, are phosphorus congeners of allenes and can thus be expected to be useful starting materials for new organophosphorus compounds.

Among the possible neutral heterocumulenes featuring the P=C=P sequence, $1\sigma^4,3\sigma^4$-diphosphaallenes **I**[2] and $1\sigma^2,3\sigma^2$-diphosphaallenes **II**[3,4] have been known for many years. More recently $1\sigma^4,3\sigma^2$-diphosphaallenes **III** have been isolated.[5]

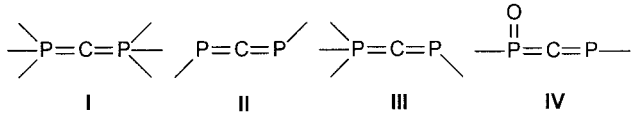


Here we report the synthesis and the first aspects of the chemical behaviour of a hitherto unknown $1\sigma^3,3\sigma^2$-diphosphaallene **IV**. Despite continuing efforts over the past two decades to synthesise low-coordinate multiply bonded phosphorus compounds, such a functionalised molecule has never been described even as an intermediate. Moreover, such a structure is comprised of a methylene(oxo)phosphorane unit of which only two stable –P(O)=C< representatives have been reported to date.[6]

## Results and Discussion

Mes*P(O)=C=PMes*, bis(2,4,6-tri-*tert*-butylphenyl)phosphavinylidene(oxo)phosphorane **1** (Mes* = 2,4,6-tri-*tert*-butylphenyl), was obtained by addition, at –80 °C, of one equiv. of phosphaalkenyllithium **2**[7] to a solution of dichlorophosphane oxide **4**.[8] $^{31}$P NMR spectroscopic analysis of the crude mixture showed the presence of **3**, **4** and **1** in a ratio of 1:1:1. The one-pot preparation of **1** probably involves the preliminary formation of phosphaalkenylphosphane oxide **5** followed by a rapid CCl/CLi exchange with phosphaalkenyllithium **2** leading to the starting dichlorophosphaalkene **3** and intermediate **6**. The latter loses LiCl to afford the title compound **1** (Scheme 1), which could be easily obtained as a yellow powder from the reaction mixture by precipitation with pentane. The structure of **1** was unambiguously determined by sophisticated $^1$H, $^{13}$C and $^{31}$P NMR spectroscopic studies (1D selective $^{31}$P decoupling experiments and 2D HSQC, HMBC) (see supporting information). The $^{31}$P NMR spectrum of **1** displays an AX system at $\delta$ = 261.4 ($\sigma^2$-P) and 117.3 ppm ($\sigma^3$-P) with a coupling constant $^2J_{P,P}$ of 30.5 Hz. A large high-frequency shift of 120 ppm can be observed for the $\lambda^3\sigma^2$-P in comparison with the value reported for the diphosphaallene Mes*P=C=PMes* ($\delta^{31}$P = 140 ppm[4b]). The signal of the

[a] Babes-Bolyai University,
Kogalniceanu 1, 400084 Cluj-Napoca, Romania
[b] Hétérochimie Fondamentale et Appliquée, UMR 5069, Université Paul Sabatier,
118 route de Narbonne, 31062 Toulouse cedex 9, France
[c] Structure Fédérative Toulousaine en Chimie Moléculaire, FR 2599, Université Paul Sabatier,
118 route de Narbonne, 31062 Toulouse cedex 9, France
Supporting information for this article is available on the WWW under http://www.eurjic.org or from the author.

 © 2006 Wiley-VCH Verlag GmbH & Co. KGaA, Weinheim 

$\lambda^5\sigma^3$-phosphorus atom is slightly lower in frequency in relation to those observed for Mes*P(O)=C(R)SiMe$_3$ [$\delta^{31}$P = 153.7 ppm (R = Ph),[6a] 161.1 ppm (R = Me$_3$Si)[6b]]. The sp hybridised carbon atom gives rise to a doublet of doublets at $\delta$ = 229.1 ppm ($^1J_{C,P(O)}$ = 177.4, $^1J_{C,P}$ = 46.8 Hz). The $^1$H NMR spectrum at room temperature shows slow rotation of the Mes* group bonded to the $\lambda^3\sigma^2$-phosphorus atom. Dynamic $^1$H NMR spectroscopy was performed between 213 and 328 K and the coalescence temperatures for the *o*-*t*Bu groups and for the aromatic protons on the Mes* group bonded to the $\lambda^3\sigma^2$-P are 268 and 253 K, respectively, giving a rotation barrier of 12.2 kcal mol$^{-1}$. Similar values have been reported for the rotation barriers of Mes* groups in the phosphaarsaallene Mes*P=C=AsMes* (13.6 kcal mol$^{-1}$)[9] and in the diphosphaallene Mes*P=C=PMes* (14.0 kcal mol$^{-1}$).[10] Hindered rotation can be observed for the Mes* group bonded to the P(O) moiety even at 328 K (two singlets for the *o*-*t*Bu groups and two doublets of doublets for the aromatic protons). A molecular ion peak can be observed in the mass spectrum of **1** with the expected fragments at *m*/*z* = 565 [M – Me]$^+$ and 523 [M – *t*Bu]$^+$.

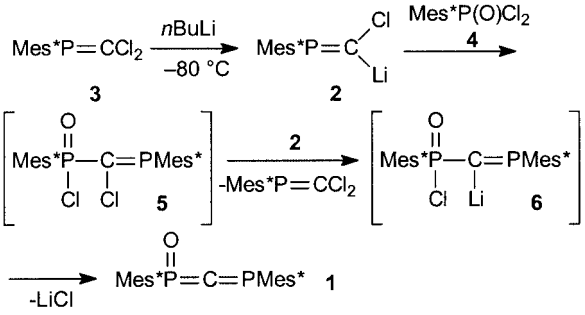


Scheme 1. Synthesis of Mes*P(O)=C=PMes* (**1**).

Compound **1** is stable for months at room temperature in the solid-state but attempts to crystallise it in various solvents at low temperatures did not afford satisfactory single crystals for X-ray diffraction studies. Compound **1** slowly rearranges within one day at room temperature in solution. The rearrangement affords the phosphaalkenylphosphane oxides **7a** and **7b** in near quantitative yield in the form of two geometric isomers in the ratio of 85:15 (Scheme 2). B3LYP/6-31G(d)//ONIOM B3LYP/6-31G(d):PM3 calculations support this easy isomerisation and **7** was found to be lower in energy than **1** by about 54 kcal mol$^{-1}$.

The $^{31}$P NMR spectra of **7a** and **7b** exhibit signals in the typical range for phosphalkenes[11a–11d] [$\delta^{31}$P for P=C in **7a** at $\delta$ = 339.1 ppm (dd, $^2J_{P,P}$ = 70.2 Hz, $^2J_{P,H}$ = 24.4 Hz) and in **7b** at $\delta$ = 353.0 ppm (dd, $^2J_{P,P}$ = 73.3 Hz, $^2J_{P,H}$ = 21.4 Hz, P=C)] and phosphane oxides[11e] [$\delta^{31}$P for P(O) in **7a** at $\delta$ = 49.3 ppm (d, $^2J_{P,P}$ = 70.2 Hz) and in **7b** at $\delta$ = 38.7 ppm (d, $^2J_{P,P}$ = 73.3 Hz)]. Similar chemical shifts at 327 and 10 ppm have been reported for Mes*P=CH–P(O)HMes*.[12] The *E* structure has been tentatively assigned to the major isomer **7a** on the basis of the $^2J_{P,H}$ coupling constant. For example, in the Mes*P=CHR system, the larger

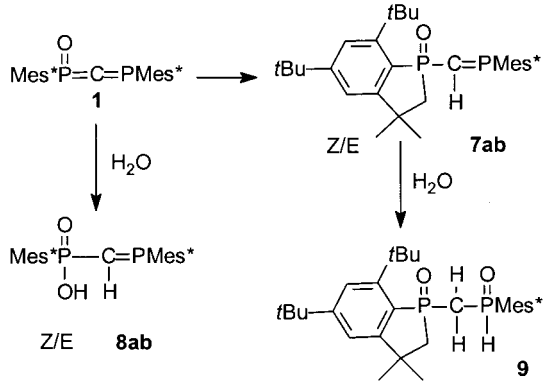


Scheme 2. Rearrangement reaction and hydrolysis of **1**.

coupling constant always corresponds to the *E* isomer [18 Hz (*Z*) and 24.7 Hz (*E*) in Mes*P=C(H)SiMe$_3$].[7a] Moreover ONIOM B3LYP/6-31G(d):PM3 geometry optimisations of **7** place the *Z* isomer higher in energy by 3.63 kcal mol$^{-1}$.

This intramolecular cyclisation results from the addition of a C–H bond of an *ortho*-*tert*-butyl substituent of a supermesityl group to the $\sigma^3$-P=C double bond.[13] This rearrangement shows that the methylene(oxo)phosphorane moiety is much less stable than the phosphane oxide one. In contrast to bis(methylene)phosphoranes RP(=CR′$_2$)$_2$ which isomerise into phosphiranes,[14] the O=P=C unit in **1** does not undergo a similar cyclisation (which would lead to the three-membered ring oxaphosphirane).

The structure of **1** was also established unambiguously from its hydrolysis products. The $\lambda^5\sigma^3$-P=C double bond is much more reactive than the $\lambda^3\sigma^2$-P=C bond since one equiv. of water adds only to this double bond to afford the two geometric isomers **8a** and **8b** (Scheme 2). Again, ONIOM B3LYP/6-31G(d):PM3 optimisations show that **8b** (*E* isomer) is lower in energy by 5.27 kcal mol$^{-1}$.

The $^{31}$P NMR spectra of **8a** and **8b** exhibit characteristic signals of phosphaalkenes [$\delta^{31}$P **8a** = 305.5 ppm (dd, $^2J_{P,P}$ = 47.3 Hz, $^2J_{P,H}$ = 24.4 Hz, P=C), **8b** = 335.4 ppm (dd, $^2J_{P,P}$ = 68.5 Hz, $^2J_{P,H}$ = 24.4 Hz, P=C] and phosphinic acids [$\delta^{31}$P **8a** = 24.6 ppm {d, $^2J_{P,P}$ = 47.3 Hz, P(O)}; **8b** = 34.9 ppm {d, $^2J_{P,P}$ = 68.5 Hz, P(O)}].

This addition is regioselective and gives, as expected, the derivative with the hydrogen atom bonded to the central sp$^2$ carbon atom. However, since the reaction of water with **1** is slow in solution (about one day in pentane at room temperature), the competitive cyclisation products **7a**,**b** are also formed. Compounds **7** and **8** are obtained in the ratio **7a** (25%), **7b** (5%), **8a** (20%) and **8b** (50%). The X-ray structure of the *Z* isomer **8b** has been determined (Figure 1) and displays standard bond lengths and angles.

Addition of water to the *Z*/*E* mixture of **7** afforded, after one week, the new bis(phosphane oxide)methylene **9** in the form of only one diastereoisomer, which was isolated as pale yellow crystals in 85% yield. The $^{31}$P NMR spectrum of **9** displays two doublets at $\delta$ = 52.1 and 4.8 ppm (small coupling constant $^2J_{P,P}$ of 2.7 Hz). In the nondecoupled $^{31}$P NMR spectrum, derivative **9** exhibits a doublet of doublets

 © 2006 Wiley-VCH Verlag GmbH & Co. KGaA, Weinheim 

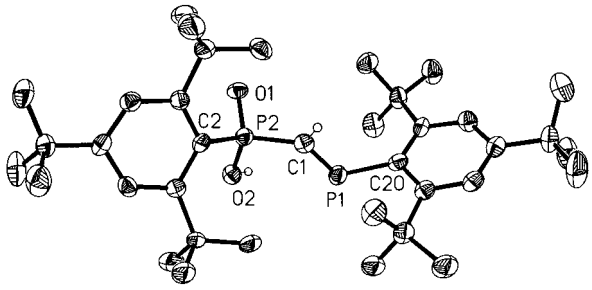


Figure 1. Structure of **8** (*E*) (50% probability level). Selected bond lengths [Å] and angles [°]: P1–C1 1.650(4), P2–C1 1.822(3), P2–C2 1.828(4), P1–C20 1.847(5), P2–O1 1.510(3), P2–O2 1.550(3), P1–C1–P2 122.3(3), O1–P2–C1 108.72(17), O2–P2–C1 107.32(18), O1–P2–C2 108.39(17), O2–P2–C2 105.60(18), C1–P2–C2 116.26(19), C20–P1–C1–P2 168.0.

of triplets for the signal at 4.8 ppm ($^1J_{P,H}$ = 517.4 Hz, $^2J_{P,H}$ = 2.8 Hz, $^2J_{P,P}$ = 2.7 Hz), the very large $^1J_{P,H}$ coupling constant being characteristic of a hydrogen bonded to a $\lambda^5\sigma^4$-phosphorus atom. The $^1$H and $^{13}$C NMR spectra display hindered rotation of the Mes* group. Dynamic $^1$H NMR spectroscopy was performed between 253 and 323 K. The coalescence temperatures for the *o*-*t*Bu groups and for the aromatic protons on the Mes* group bonded to the P(H) atom are 288 K in both cases, corresponding to a rotation barrier of 14.2 kcal mol$^{-1}$ which is 2 kcal mol$^{-1}$ higher than that of the Mes* group bonded to the $\lambda^3\sigma^2$-phosphorus atom in **1**.

The X-ray structure of **9** (Figure 2) displays standard bond lengths and angles.

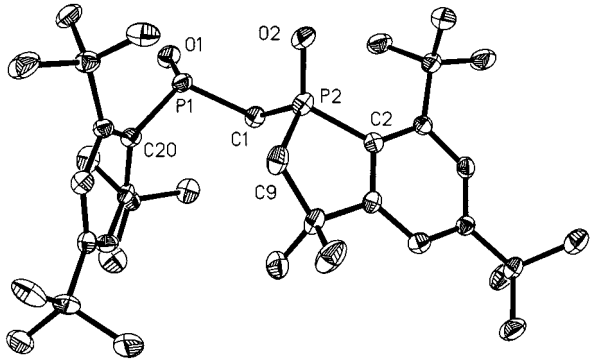


Figure 2. Structure of **9** (50% probability level). Selected bond lengths [Å] and angles [°]: P1–C1 1.827(3), P2–C1 1.822(3), P2–C2 1.819(3), P2–C9 1.794(4), P1–C20 1.818(4), P1–O1 1.482(2), P2–O2 1.481(2), P1–C1–P2 115.14(18), O1–P1–C1 112.78(15), O2–P2–C1 111.13(14), O2–P2–C2 119.96(16), O1–P1–C20 120.11(14).

In conclusion, the first phosphavinylidene(oxo)phosphorane **1**, a derivative with three "cumulated formal double bonds", was obtained as a stable compound in the solid-state in a one-pot procedure. The ability of **1** to form transition metal complexes is now under investigation.

## Experimental Section

**General:** All experiments were carried out in flame-dried glassware under an argon atmosphere using high-vacuum-line techniques. Solvents were dried and freshly distilled from sodium benzophenone ketyl and carefully deoxygenated on a vacuum line by several "freeze-pump-thaw" cycles. NMR spectra were recorded in $CDCl_3$ on the following spectrometers: $^1$H, Bruker Avance 300 (300.13 MHz) and Avance 400 (400.13 MHz); $^{13}$C{$^1$H}, Bruker Avance 300 (75.47 MHz) and Avance 400 (100.62 MHz) (reference TMS); $^{31}$P, Bruker AC200 (81.02 MHz) and Avance 400 (162.04 MHz) (reference $H_3PO_4$). Melting points were determined on a Wild Leitz-Biomed apparatus. Mass spectra were obtained on a Hewlett–Packard 5989A spectrometer by EI at 70 eV.

**Synthesis of Mes*P(O)=C=PMes* (1):** To a solution of Mes*P=CCl$_2$ **3** (3.15 g, 8.67 mmol) in THF (20 mL) cooled to –80 °C was added a solution of *n*-butyllithium (5.7 mL, 1.6 M in hexane, 9.1 mmol). After stirring for 1 h, the solution of Mes*P=C(Cl)Li was transferred by cannula to a solution of Mes*P(O)Cl$_2$ **4** (3.00 g, 8.67 mmol) in THF (30 mL) at –80 °C. The reaction mixture became dark brown and after 15 min stirring and subsequent warming to –20 °C, the solvent was removed under vacuum. Pentane (30 mL) was added to the residue and **3** and **4** dissolved. However **1** and LiCl precipitated due to both being very poorly soluble in pentane. After filtration, **1** was extracted with $CH_2Cl_2$. Removal of the solvent gave a pale yellow powder of **1** (2.01 g, 40%, m.p. 125 °C, dec.).

The carbon and phosphorus atoms are numbered as follows:

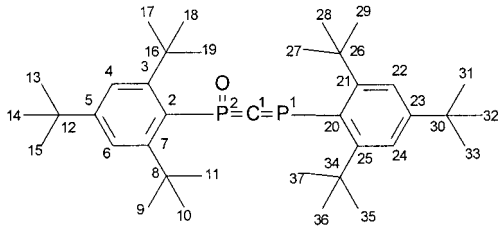

**1**

In order to assign all the signals observed in the $^1$H and $^{13}$C NMR spectra, HSQC, HMBC and selective $^{31}$P decoupling experiments were performed. $^1$H NMR ($CDCl_3$, 400.13 MHz, 213 K): $\delta$ = 1.10 (s, 9 H, H on C27–29), 1.23 (s, 9 H, H on C17–19), 1.34 (s, 9 H, H on C13–15), 1.36 (s, 9 H, H on C31–33), 1.65 (s, 9 H, H on C35–37), 1.79 (s, 9 H, H on C9–11), 7.27 (broad s, 1 H, H on C22), 7.37 (broad d, $^4J_{H,P}$ = 5.2 Hz, 1 H, H on C6), 7.46 (broad s, 1 H, H on C24), 7.48 (broad d, $^4J_{H,P}$ = 6.1 Hz, 1 H, H on C4) ppm. $^{13}$C NMR ($CDCl_3$, 100.62 MHz): $\delta$ = 31.3 (C13–15), 31.5 (C31–33), 32.8 (C17–19), 33.1 (d, $^4J_{C,P1}$ = 6.5 Hz, C27–29), 33.3 (C9–11), 33.9 (C35–37), 35.2 (C30), 35.5 (C12), 37.4 (C26), 38.1 (d, $^3J_{C,P2}$ = 3.1 Hz, C16), 38.5 (C34), 38.7 (d, $^3J_{C,P2}$ = 3.6 Hz, C8), 119.7 (d, $^1J_{C,P2}$ = 127.5 Hz, C2), 121.7 (C22), 122.6 (d, $^3J_{C,P2}$ = 13.8 Hz, C6), 122.7 (C24), 122.9 (d, $^3J_{C,P2}$ = 15.6 Hz, C4), 138.3 (dd, $^1J_{C,P1}$ = 74.6 Hz, $^3J_{C,P2}$ = 28.5 Hz, C20), 150.3 (C23), 152.0 (C21), 153.6 (d, $^2J_{C,P2}$ = 6.7 Hz, C7), 153.9 (C25), 154.2 (d, $^2J_{C,P2}$ = 11.0 Hz, C3), 154.6 (d, $^4J_{C,P2}$ = 2.9 Hz, C5), 227.3 (dd, $^1J_{C,P1}$ = 47.1 Hz, $^1J_{C,P2}$ = 184.7 Hz, C1) ppm.

$^{31}$P NMR ($CDCl_3$, 81.02 MHz, 298 K): $\delta$ = 117.3 (d, $^2J_{P,P}$ = 30.5 Hz, P2), 261.4 (d, $^2J_{P,P}$ = 30.5 Hz, P1) ppm. MS (EI = 70 eV): *m*/*z* (%) = 580 (1) [M]$^+$, 565 (3) [M – Me]$^+$, 523 (20) [M – *t*Bu]$^+$, 467 (5) [M – 2 *t*Bu + 1]$^+$, 335 (30) [M – Mes*]$^+$, 57 (100) [*t*Bu]$^+$. $C_{37}H_{58}OP_2$ (580.81): calcd. C 76.51, H 10.07; found C 76.76, H 9.75. At 253 K, the signals of C21, 22, 24–26, 27–29, 34, and 35–37 ($^{13}$C NMR) and the signals of H on C22, 24, 27–29, 35–37 ($^1$H NMR) are too broad to be observed. At 328 K, the free rotation of Mes* bonded to P1 occurs and the following signals may be

 © 2006 Wiley-VCH Verlag GmbH & Co. KGaA, Weinheim 

observed: 33.8 (C27–29 and C35–37), 37.8 (C26 and C34), 121.9 (C22 and C24) and 153.2 ppm (C21 and C25) in the $^{13}C$ NMR spectrum; 1.39 (s, C27–29 and C35–37) and 7.32 ppm (s, C22 and C24) in the $^{1}H$ NMR spectrum.

**Synthesis of Cyclisation Products 7a and 7b:** A solution of Mes*-P(O)=C=PMes* **1** (1.20 g, 2.01 mmol) in toluene (10 mL) was heated at 80 °C for 1 h. NMR analysis showed the conversion of **1** into **7a** and **7b** in the ratio 85:15. Removal of solvent in vacuo led to a powder of **7a**,**b**. Attempts at fractional crystallisation in various solvents (pentane, $Et_2O$, $CHCl_3$) did not allow the complete separation of the two isomers **7a** and **7b**. Selective $^{31}P$ decoupled $^{1}H$ and $^{13}C$ NMR experiments were performed. At 283 K, signals of some *t*Bu groups were too broad to be observed by $^{1}H$ NMR spectroscopy.

**7a [(*E*) isomer]:** $^{1}H$ NMR ($CDCl_3$, 400.13 MHz, 283 K): $\delta$ = 1.31, 1.48 and 1.56 (3s, 27 H, H from *t*Bu groups), 2.36 [ddd, $^{2}J_{H,H}$ = 15.0 Hz, $^{2}J_{H,P2}$ = 19.3 Hz, $^{4}J_{H,P1}$ = 3.9 Hz, 1 H, H on C9 (carbon atom bonded to P2)], 2.50 (dd, $^{2}J_{H,H}$ = 15.0 Hz, $^{2}J_{H,P2}$ = 7.1 Hz, 1 H, H on C9), 7.16, 7.28, 7.36 and 7.40 (4 broad s, 4 × 1 H, arom H), 7.58 (dd, $^{2}J_{H,P1}$ = 22.3 Hz, $^{2}J_{H,P2}$ = 13.8 Hz, 1 H, H on C1) ppm. $^{13}C$ NMR ($CDCl_3$, 100.62 MHz, 283 K): $\delta$ = 31.2, 31.3 and 32.5 (C13–15, C17–19, C31–33), 34.2 (d, $^{4}J_{C,P1}$ = 7.0 Hz, C27–29, C35–37), 37.5 (C30), 38.3 (C26, C34), 39.0 (d, $^{2}J_{C,P2}$ = 5.8 Hz, C8), 40.0 (d, $J_{C,P2}$ = 2.8 Hz) and 40.8 (d, $J_{C,P2}$ = 3.6 Hz) (C12, C16), 43.7 (dd, $^{1}J_{C,P2}$ = 75.9 Hz, $^{3}J_{C,P1}$ = 6.0 Hz, C9), 118.7 (d, $^{3}J_{C,P2}$ = 13.8 Hz) and 122.8 (d, $^{3}J_{C,P2}$ = 10.0 Hz, C4, C6), 122.2 (C22, C24), 127.1 (d, $^{1}J_{C,P2}$ = 95.6 Hz, C2), 138.8 (dd, $^{1}J_{C,P1}$ = 67.5 Hz, $^{3}J_{C,P2}$ = 17.7 Hz, C20), 150.1 (C23), 153.4 (C21, C25), 154.2 (d, $^{2}J_{C,P2}$ = 7.2 Hz) and 157.0 (d, $^{2}J_{C,P2}$ = 20.2 Hz, C3, C7), 155.7 (d, $^{4}J_{C,P2}$ = 2.5 Hz, C5), 165.3 (dd, $^{1}J_{C,P2}$ = 74.8 Hz, $^{1}J_{C,P1}$ = 63.2 Hz, C1) ppm. $^{31}P$ NMR ($CDCl_3$, 81.02 MHz, 298 K): $\delta$ = 49.3 (d, $^{2}J_{P,P}$ = 70.2 Hz, P2), 339.1 (dd, $^{2}J_{P,P}$ = 70.2 Hz, $^{2}J_{P,H}$ = 24.4 Hz P1) ppm. MS (EI = 70 eV): *m*/*z* (%) = 565 (8) $[M - 15]^+$, 523 (15) $[M - t\text{Bu}]^+$, 335 (100) $[M - \text{Mes*}]^+$, 57 (90) $[t\text{Bu}]^+$.

**7b [(*Z*) isomer]:** $^{1}H$ NMR ($CDCl_3$, 400.13 MHz, 283 K): $\delta$ = 7.82 (dd, $^{2}J_{H,P2}$ = 212.0 Hz, $^{2}J_{H,P1}$ = 17.6 Hz, 1 H, CH=P) ppm (other $^{1}H$ signals and $^{13}C$ signals of the minor isomer could not be assigned unambiguously). $^{31}P$ NMR ($CDCl_3$, 81.02 MHz, 298 K): $\delta$ = 38.7 (d, $^{2}J_{P,P}$ = 73.3 Hz, PO), 353.0 (dd, $^{2}J_{P,P}$ = 73.3 Hz, $^{2}J_{P,H}$ = 21.4 Hz P=C) ppm.

**Hydrolysis of 7a and 7b. Synthesis of 9:** An excess of degassed water was added to the mixture of **7a**,**b** (0.60 g, 1.04 mmol) in $Et_2O$. After stirring for a week at room temperature, NMR analysis showed the formation of **9**. $Et_2O$ was removed under vacuum and recrystallisation from pentane afforded pure **9** as pale yellow crystals (0.48 g, 78%, m.p. 203 °C). HSQC, HMBC, NOESY and selective $^{31}P$ decoupled $^{1}H$ and $^{13}C$ NMR experiments were performed. $^{1}H$ NMR ($CDCl_3$, 400.13 MHz, 253 K): $\delta$ = 0.46 (dd, $^{2}J_{H,P2}$ = 6.2 Hz, $^{2}J_{H,H}$ = 15.3 Hz, 1 H, H on C9, carbon atom bonded to P2), 0.90 and 1.21 (2s, 2 × 3 H, H on C10,11), 1.30 (s, 9 H, H on C13–15), 1.38 (s, 9 H, H on C31–33), 1.52 and 1.65 (2s, 2 × 9 H, H on C27–29 and C35–37), 1.53 (s, 9 H, H on C17–19), 1.54 (dd, $^{2}J_{H,P2}$ = 20.4 Hz, $^{2}J_{H,H}$ = 15.3 Hz, 1 H, H on C9), 2.43 (dddd, $^{2}J_{H,P1}$ = 15.0 Hz, $^{2}J_{H,P2}$ = 7.2 Hz, $^{2}J_{H,H}$ = 15.3 Hz, $^{3}J_{H,H}$ = 7.1 Hz, 1 H, H on C1), 3.30 (dt, $^{2}J_{H,P1}$ and $^{2}J_{H,P2}$ = 16.6 Hz, $^{2}J_{H,H}$ = 15.3 Hz, 1 H, H on C1), 7.07 (dd, $^{4}J_{H,P2}$ = 2.0 Hz, $^{4}J_{H,H}$ = 1.0 Hz, 1 H, H on C4), 7.41 (dd, $^{4}J_{H,P2}$ = 5.2 Hz, $^{4}J_{H,H}$ = 1.0 Hz, 1 H, H on C6), 7.45 (dd, $^{4}J_{H,P1}$ = 2.0 Hz, $^{4}J_{H,H}$ = 1.0 Hz, 1 H, H on C22), 7.54 (dd, $^{4}J_{H,P1}$ = 4.1 Hz, $^{4}J_{H,H}$ = 1.0 Hz, 1 H, H on C24), 8.52 (ddd, $^{1}J_{H,P1}$ = 517.4 Hz, $^{3}J_{H,P2}$ = 2.8 Hz, $^{3}J_{H,H}$ = 7.1 Hz, 1 H, H on P1) ppm. $^{13}C$ NMR ($CDCl_3$, 100.62 MHz, 253 K): $\delta$ = 31.2 (C13–15), 31.4 (C31–33), 31.9 and 33.5 (C10–11), 32.2 (C17–19), 33.6 and 34.3 (C27–29 and C35–37), 35.3 (C30), 35.4 (C12), 37.7 (C16), 38.7 (d, $^{2}J_{C,P2}$ = 6.2 Hz, C8), 39.2 (C26 and C34), 39.6 (d, $^{1}J_{C,P2}$ = 72.1 Hz, C9), 40.6 (dd, $^{1}J_{C,P1}$ = 55.1 Hz, $^{1}J_{C,P2}$ = 50.5 Hz, C1), 118.9 (d, $^{3}J_{C,P2}$ = 14.4 Hz, C4), 123.3 (d, $^{3}J_{C,P2}$ = 10.2 Hz, C6), 123.6 (d, $^{3}J_{C,P1}$ = 11.9 Hz) and 124.1 (d, $^{3}J_{C,P1}$ = 13.4 Hz) (C22 and C24), 125.2 (dd, $^{1}J_{C,P2}$ = 96.5 Hz, $^{3}J_{C,P1}$ = 3.9 Hz, C2), 128.2 (d, $^{1}J_{C,P1}$ = 99.0 Hz, C20), 153.6 (d, $^{4}J_{C,P1}$ = 3.1 Hz, C23), 154.2 (d, $^{2}J_{C,P2}$ = 8.1 Hz, C7), 156.0 (d, $^{2}J_{C,P1}$ = 5.7 Hz, C21), 156.3 (d, $^{2}J_{C,P2}$ = 33.0 Hz, C3), 156.6 (d, $^{4}J_{C,P2}$ = 2.4 Hz, C5), 157.4 (d, $^{2}J_{C,P1}$ = 11.9 Hz, C25) ppm. $^{31}P$ NMR ($CDCl_3$, 81.02 MHz, 298 K): $\delta$ = 4.8 (ddt, $^{2}J_{P,P}$ = 2.7 Hz, $^{1}J_{P,H}$ = 517.4 Hz, $^{2}J_{P,H}$ = 2.8 Hz, P1), 52.1 (d, $^{2}J_{P,P}$ = 2.7 Hz, P2) ppm. MS (EI = 70 eV): *m*/*z* (%) = 599 (2) $[M + 1]^+$, 581 (1) $[M - O - 1]^+$, 541 (100) $[M - t\text{Bu}]^+$, 353 (85) $[M - \text{Mes*}]^+$, 57 (70) $[t\text{Bu}]^+$ $C_{37}H_{60}O_2P_2$ (598.82): calcd.C 74.21, H 10.10; found C 74.56, H 9.85.

**Synthesis of 8a and 8b by Hydrolysis of the P(O)=C Double Bond of 1:** An excess of degassed water was added to a solution of **1** (1.15 g, 1.98 mmol) in pentane (20 mL). After stirring for 2 d at room temperature, NMR analysis showed the formation of a mixture of **7a**,**b** and **8a**,**b**. Attempts at crystallisation from various solvents did not allow complete separation of the two derivatives and only some single crystals of **8**, suitable for an X-ray structure determination, could be obtained by crystallisation from $CHCl_3$ and cyclohexane. $^{31}P$ NMR ($CDCl_3$, 81.02 MHz, 298 K) **8a** (30%), $\delta$ = 24.6 (d, $^{2}J_{P,P}$ = 47.3 Hz, PO), 305.5 ppm (dd, $^{2}J_{P,P}$ = 47.3 Hz, $^{2}J_{P,H}$ = 24.4 Hz, P=C) **8b** (70%), $\delta$ = 34.9 ($^{2}J_{P,P}$ = 68.5 Hz, PO), 335.4 ppm (dd, $^{2}J_{P,P}$ = 68.5 Hz, $^{2}J_{P,H}$ = 24.4 Hz, P=C).

**X-ray Structure Determinations**

**Crystal Data for 8 and 9. Compound 8:** $C_{43}H_{73}Cl_3O_2P_2$, $M$ = 790.30 ($CHCl_3$ and cyclohexane in the lattice), triclinic, $P\bar{1}$, $a$ = 13.998(2), $b$ = 14.106(2), $c$ = 14.348(2) Å, $\alpha$ = 91.531(4), $\beta$ = 119.170(3), $\gamma$ = 108.678(3)°, $V$ = 2285.6(6) Å$^3$, $Z$ = 2, $T$ = 173(2) K. 9004 reflections (5491 independent, $R_{int}$ = 0.0740) were collected. Largest electron density residue: 0.341 e Å$^{-3}$, $R_1$ [for $I > 2\sigma(I)$] = 0.0565 and $wR_2$ = 0.1433 (all data) with $R_1 = \Sigma||F_o| - |F_c||/\Sigma|F_o|$ and $wR_2 = [\Sigma w (F_o^2 - F_c^2)^2/\Sigma w(F_o^2)^2]^{0.5}$. **Compound 9:** $C_{37}H_{60}O_2P_2$, $M$ = 598.79, monoclinic, $P2_1/c$, $a$ = 10.275(1), $b$ = 25.939(2), $c$ = 14.342(1) Å, $\beta$ = 110.884(2)°, $V$ = 3571.4(6) Å$^3$, $Z$ = 4, $T$ = 173(2) K. 15676 reflections (5066 independent, $R_{int}$ = 0.1213) were collected. Largest electron density residue: 0.250 e Å$^{-3}$, $R_1$ [for $I > 2\sigma(I)$] = 0.0558 and $wR_2$ = 0.0943 (all data).

All data for structures reported in this paper were collected at low temperature using an oil-coated shock-cooled crystal on a Bruker-AXS CCD 1000 diffractometer with Mo-$K_\alpha$ radiation ($\lambda$ = 0.71073 Å). The structures were solved by direct methods (SHELXS-97)[15] and all non-hydrogen atoms were refined anisotropically using the least-squares method on $F^2$ (SHELXL-97).[16]

CCDC-605519 (for **8**) and -605520 (for **9**) contain the supplementary crystallographic data for this paper. These data can be obtained free of charge from The Cambridge Crystallographic Data Centre via www.ccdc.cam.ac.uk/data_request/cif.

**Supporting Information:** (for details see the footnote on the first page of this article): variable temperature $^{1}H$ NMR, 2D HSQC and 2D HMBC, $^{13}C\{^{1}H,^{31}P\}$ and $^{13}C\{^{1}H\}$ Jmod spectra of diphosphaallene Mes*P(O)=C=PMes* (**1**), variable-temperature $^{1}H$ NMR spectra of bis(phosphane oxide)methylene **9**.

## Acknowledgments

We thank the CNRS and the Ministry of Foreign Affairs [AI Brancusi no. 08581TK (Fr) and 18015 (Ro)]. R. S. thanks ERASMUS/

 © 2006 Wiley-VCH Verlag GmbH & Co. KGaA, Weinheim 

SOCRATES and CEEX SUPRACOM and G. N. the AUF for a grant.

[1] a) *The Chemistry of Ketenes, Allenes and Related Compounds* (Ed.: S. Patai), **1980**; b) *The Chemistry of Allenes* (Ed.: S. R Landor), **1982**; c) *Allenes in Organic Synthesis* (Eds.: H. F. Schuster, G. M. Coppola), **1984**.

[2] a) F. Ramirez, N. B. Desai, B. Hansen, N. Mc Kelvie, *J. Am. Chem. Soc.* **1961**, *83*, 3539–3540; b) H. J. Bestmann, R. Zimmermann, in: *Methoden der Organische Chemie*, Houben–Weyl, 4th ed., vol. E1, **1982**, pp. 752–758; c) A. W. Johnson, W. C. Kaska, K. A. O. Starzewski, D. A. Dixon, in: *Ylides and Imines of Phosphorus* (Ed.: A. W. Johnson), Wiley-Interscience, New York, **1993**; d) O. I. Kolodiazhnyi, in: *Phosphorus Ylides* (Ed.: O. I. Kolodiazhnyi), Wiley-VCH, Weinheim, **1999**.

[3] For reviews see: a) R. Appel, in: *Multiple Bonds and Low Coordination in Phosphorus Chemistry* (Eds.: M. Regitz, O. J. Scherer), Thieme: Stuttgart, **1990**, p. 157–219; b) J. Escudié, H. Ranaivonjatovo, L. Rigon, *Chem. Rev.* **2000**, *100*, 3639–3696; c) J. Escudié, H. Ranaivonjatovo, M. Bouslikhane, Y. El Harouch, L. Baiget, G. Cretiu-Nemes, *Russ. Chem. Bull.* **2004**, *53*, 1020–1033.

[4] a) R. Appel, P. Fölling, B. Josten, M. Siray, V. Winkhaus, F. Knoch, *Angew. Chem. Int. Ed. Engl.* **1984**, *23*, 618–619; b) H. H. Karsch, F. H. Köhler, H.-U. Reisacher, *Tetrahedron Lett.* **1984**, *25*, 3687–3690; c) M. Yoshifuji, K. Toyota, N. Inamoto, *J. Chem. Soc., Chem. Commun.* **1984**, 689–690; d) M. Gouygou, M. Koenig, J. Escudié, C. Couret, *Heteroat. Chem.* **1991**, *2*, 221–227; e) M. Yoshifuji, S. Sasaki, N. Inamoto, *J. Chem. Soc., Chem. Commun.* **1989**, 1732–1733; f) M. Yoshifuji, T. Niitsu, D. Shiomi, N. Inamoto, *Tetrahedron Lett.* **1989**, *30*, 5433–5436; g) K. Toyota, A. Nakamura, M. Yoshifuji, *Chem. Commun.* **2002**, 3012–3013.

[5] a) U. Krüger, H. Pritzkow, H. Grützmacher, *Chem. Ber.* **1991**, *124*, 329–331; b) H. P. Schrödel, G. Jochem, A. Schmidpeter, H. Nöth, *Angew. Chem. Int. Ed. Engl.* **1995**, *34*, 1853–1856; c) T. Kato, H. Gornitzka, A. Baceiredo, G. Bertrand, *Angew. Chem. Int. Ed.* **2000**, *39*, 3319–3321; d) D. Martin, H. Gornitzka, A. Baceiredo, G. Bertrand, *Eur. J. Inorg. Chem.* **2005**, 2619–2624.

[6] a) R. Appel, C. Casser, *Tetrahedron Lett.* **1984**, *25*, 4109–4112; b) R. Appel, H. Knoch, H. Kunze, *Angew. Chem. Int. Ed. Engl.* **1984**, *23*, 157–158.

[7] a) S. J. Goede, F. Bickelhaupt, *Chem. Ber.* **1991**, *124*, 2677–2684; b) E. Niecke, M. Nieger, O. Schmidt, D. Gudat, W. W. Schoeller, *J. Am. Chem. Soc.* **1999**, *121*, 519–522; c) M. Yoshifuji, S. Ito, *Top. Curr. Chem.* **2003**, *223*, 67–89.

[8] S. Freeman, M. J. P. Harger, *J. Chem. Soc., Perkin Trans. 1* **1987**, 1399–1406.

[9] H. Ranaivonjatovo, H. Ramdane, H. Gornitzka, J. Escudié, J. Satgé, *Organometallics* **1998**, *17*, 1631–1633.

[10] M. Yoshifuji, S. Sasaki, T. Niitsu, N. Inamoto, *Tetrahedron Lett.* **1989**, *30*, 187–188.

[11] For reviews see: a) S. Lochschmidt, A. Schmidpeter, *Phosphorus Sulfur Silicon Relat. Elem.* **1986**, *29*, 73–109; b) R. Appel, F. Knoll, *Adv. Inorg. Chem.* **1989**, *33*, 259–361; c) L. N. Markovski, V. D. Romanenko, *Tetrahedron* **1989**, *45*, 6019–6090; d) L. Weber, *Angew. Chem. Int. Ed. Engl.* **1996**, *35*, 271–288; e) *CRC Handbook of Phosphorus-31 Nuclear Magnetic Resonance Data* (Ed.: J. C. Tebby), CRC Press, Boca Raton, Florida (USA), **1991**.

[12] H. H. Karsch, H.-U. Reisacher, *Phosphorus Sulfur Silicon Relat. Elem.* **1988**, *37*, 241–242.

[13] Such intramolecular cyclisations are well-known in the chemistry of phosphaallenes a) H. H. Karsch, H.-U. Reisacher, *Phosphorus Sulfur Silicon Relat. Elem.* **1988**, *36*, 213–215; b) H. H. Karsch, H.-U. Reisacher, G. Müller, *Angew. Chem. Int. Ed. Engl.* **1986**, *25*, 454–455; c) M. A. David, J. B. Alexander, D. S. Glueck, G. P. A. Yap, L. M. Liable-Sands, A. L. Rheingold, *Organometallics* **1997**, *16*, 378–383; d) M. A. David, S. N. Paisner, D. S. Glueck, *Organometallics* **1995**, *14*, 17–19.

[14] a) R. Appel, Th. Gaitzsch, F. Knoch, G. Lenz, *Chem. Ber.* **1986**, *119*, 1977–1985; b) E. Niecke, D. A. Wildbredt, W. Schoeller, *Angew. Chem. Int. Ed. Engl.* **1981**, *20*, 131–132.

[15] G. M. Sheldrick, *Acta Crystallogr., Sect. A* **1990**, *46*, 467–473.

[16] G. M. Sheldrick, *Program for Crystal Structure Refinement*, University of Göttingen **1997**.

Received: April 27, 2006
Published Online: August 7, 2006

 © 2006 Wiley-VCH Verlag GmbH & Co. KGaA, Weinheim 

DOI: 10.1002/ejic.200600173

# (Alkyl)- and (Alkyl)(alkylidene)(pentamethylcyclopentadienyl)tantalum Complexes

**Mikhail V. Galakhov,[a] Manuel Gómez,*[b] Pilar Gómez-Sal,[b] and Patricia Velasco[b]**

*Dedicated to Prof. Victor Riera on the occasion of his 70th birthday*

**Keywords:** Tantalum / Alkyl / Alkylidene / Cyclopentadienyl ligands

Alkylation of [TaCp*$Cl_4$] (Cp* = $\eta^5$-$C_5Me_5$) with 3 equiv. of $MgCl(CH_2SiMe_3)$ gives the chloridotris(trimethylsilylmethyl) complex [TaCp*$Cl(CH_2SiMe_3)_3$] (**1**). TaCp*$Cl_2Me_2$ reacts with 2 equiv. of LiR (R = $CH_2Ph$, $CH_2SiMe_3$) to give the mixed alkyl derivatives [TaCp*$Me_2R_2$] (R = $CH_2Ph$, **2**; $CH_2SiMe_3$, **3**). The dimethyldineopentyl complex [TaCp*$Me_2(CH_2CMe_3)_2$] (**4**) was obtained by reaction of TaCp*$Cl_2(CH_2CMe_3)_2$ with 2 equiv. of LiMe. The treatment of a toluene solution of TaCp*$Cl_2Me_2$ with 2 equiv. of neophyllithium in a standard vacuum line gave a mixture of three compounds, [{TaCp*$Me_2(CH_2CMe_2Ph)$}$_2$(**μ**-O)] (**5**), [TaCp*$Me_2(CH_2CMe_2$–*o*-$C_6H_4$-κ$^2$*C*,*C*)] (**6**) and [TaCp*$Me(CH_2CMe_2Ph)(CH_2)$] (**7**), which were identified by NMR spectroscopy. However, when the reaction was carried out under rigorously anhydrous conditions, only complexes **6** and **7** were isolated. A chlorido(trimethylsilylmethyl)(trimethylsilylmethylidene) complex [TaCp*$Cl(CH_2SiMe_3)(CHSiMe_3)$] (**8**) was prepared by heating **1** at 60 °C, or by leaving it at room temperature for a long time. A 3:2 (**9**/**10**) mixture of [TaCp*$MeR(CHSiMe_3)$] (R = $CH_2SiMe_3$, **9**; Me, **10**) was obtained by thermal treatment of **3**, which was accompanied by the evolution of $CH_4$ and $SiMe_4$. However, irradiation of a [$D_6$]benzene solution of **3** with a sun lamp gave a mixture of **9** and [TaCp*$(CH_2SiMe_3)R(CH_2)$] (R = Me, **11**; $CH_2SiMe_3$, **12**) in a 2:1:1 (**9**/**11**/**12**) ratio. When a [$D_6$]benzene solution of **4** was heated at 60 °C, a mixture of the (alkyl)(neopentylidene) derivatives [TaCp*$MeR(CHCMe_3)$] (R = Me, **13**; $CH_2CMe_3$, **14**) in a 4:1 (**13**/**14**) ratio was detected by NMR spectroscopy, while irradiation with a sun lamp produced a mixture of alkylidene complexes [TaCp*$(CH_2CMe_3)R(CH_2)$] (R = Me, **15**; $CH_2CMe_3$, **16**) in a 3:1 (**15**/**16**) ratio. On the other hand, the alkylation of TaCp*$Cl_2(CH_2CMe_3)_2$ with 2 equiv. of $LiCH_2SiMe_3$ gave the (alkyl)(alkylidene) complex [TaCp*$(CH_2CMe_3)(CH_2SiMe_3)(CHCMe_3)$] (**17**) with the elimination of $SiMe_4$, whereas the treatment of TaCp*$Cl_2(CH_2SiMe_3)_2$ with the appropriate reagent gave [TaCp*$(CH_2R)(CH_2SiMe_3)(CHR')$] (R = R′ = Ph, **18**; R = $CMe_2Ph$, R′ = $SiMe_3$, **19**) with the elimination of $SiMe_4$ and $CMe_3Ph$, respectively. All compounds were studied by IR and NMR spectroscopy, and the molecular structures of complexes **1**, **4** and **5** were determined by X-ray diffraction methods.

(© Wiley-VCH Verlag GmbH & Co. KGaA, 69451 Weinheim, Germany, 2006)

## Introduction

The study of early-transition-metal compounds in high oxidation states has been a topic of intense research because of their applications in organic synthesis and in catalysis.[1] In particular, metal alkyls and alkylidenes are among the most studied derivatives. Alkyl derivatives have been extensively used as catalysts for the polymerization of olefins,[1,2] while the importance of alkylidenes is demonstrated by a comprehensive study of the olefin metathesis reactions that they are able to catalyse.[3] Further, in combination with stronger Lewis acids they form highly reactive species that are important as catalysts in other processes involving olefins.[3b,3c,4–6] Additionally, μ-alkylidene complexes have been postulated as intermediates in Fischer–Tropsch, olefin metathesis and Ziegler–Natta catalytic processes.[7]

Preliminary reports from our group have focused on the ability of tetrachlorido(cyclopentadienyl)niobium and -tantalum compounds to coordinate with bulky alkyl substituents. Thus, the crowding of the coordination sphere of the metal by the trimethylsilylmethyl group is the basis for the formation of an alkylidene complex by a spontaneous α-hydrogen-elimination process.[8] On the other hand, we reported[9] that the use of the 2-[(dimethylamino)methyl]-phenyl ligand leads to the synthesis of tantalum(V) complexes that can be transformed into new cyclometalated (alkylidene)tantalum derivatives by the activation of carbon–hydrogen bonds in one of the methylamino groups of

[a] Centro de Espectroscopia de RMN, Universidad de Alcalá de Henares,
Campus Universitario, 28871 Alcalá de Henares, Spain
[b] Departamento de Química Inorgánica, Universidad de Alcalá de Henares,
Campus Universitario, 28871 Alcalá de Henares, Spain
Fax: +34-91-885-46-83
E-mail: manuel.gomez@uah.es

Supporting information for this article is available on the WWW under http://www.eurjic.org or from the author.

 © 2006 Wiley-VCH Verlag GmbH & Co. KGaA, Weinheim 

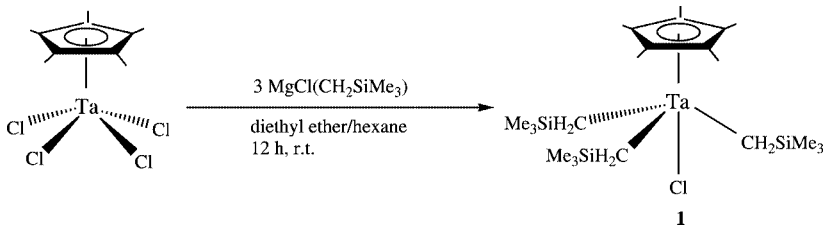


Scheme 1.

the ligand. More recently, the μ-alkylidene complexes $[(TaCp^*Cp')_2(\mu\text{-}CHR)_2]$ ($Cp^*$ = $\eta^5$-$C_5Me_5$, Cp′ = $\eta^5$-$C_5H_4SiMe_3$, R = $C_6H_5$, $SiMe_3$, $CMe_3$) have been prepared by treatment of the (mixed dicyclopentadienyl)tantalum compound $TaCp^*Cp'Cl_2$ with an appropriate amount of the corresponding alkyllithium.[10]

In this article, we report the preparation of new (alkyl)- and (alkyl)(alkylidene)mono(pentamethylcyclopentadienyl)-tantalum(V) complexes. All compounds were studied by spectroscopic methods. In addition, the molecular structures of complexes **1**, **4** and **5** were determined by X-ray diffraction.

## Results and Discussion

$[TaCp^*Cl(CH_2SiMe_3)_3]$ (**1**) was synthesized in good yield by the reaction of $[TaCp^*Cl_4]$ ($Cp^*$ = $\eta^5$-$C_5Me_5$) with 3 equiv. of $MgCl(CH_2SiMe_3)$ (Scheme 1). In contrast, we previously reported[8] the preparation of a dialkyl(alkylidene) derivative $[TaCp^*(CH_2SiMe_3)_2(CHSiMe_3)]$ by the reaction of the tetrachlorido complex with 4 equiv. of an alkylating reagent. Two absorptions bands were observed in the IR spectrum of **1** at $\tilde{\nu}$ = 1026 and 1243 $cm^{-1}$, which can be assigned to $\nu_{C-C}(Cp^*)$[11] and $\delta_{as}(CH_3)(SiMe_3)$,[11c] respectively. The NMR spectra of this complex are in agreement with a $C_{3v}$ local symmetry around the tantalum atom.

The crystal structure of complex **1** (Figure 1) shows a tantalum atom in a distorted trigonal bipyramidal environment with the three alkyl groups occupying the equatorial positions, and the centroid of the pentamethylcyclopentadienyl ring and the chlorine atom at the apical sites. The tantalum atom is displaced towards the Cp* ring by 0.46 Å from the equatorial plane containing the three carbon (alkyl) atoms.[12] The bond lengths for Ta–Cp*(centroid), Ta–C (average), and Ta–Cl are 2.180, 2.160 and 2.481(1) Å, respectively (Table 1). The Ta–C(alkyl) distance is in the range corresponding to normal values for a Ta–C[11d,13,14] single bond, whereas the Ta–Cl distance is shorter than that for a bridging chlorine[15] and longer than that for a terminal chlorine.[11d,14b,16] The angle Cp*–Ta–Cl is 176.84° and confirms the apical position of the chlorine atom. This pentacoordination is unusual, and to the best of our knowledge, no other group 5 metal (alkyl)chlorido(cyclopentadienyl) derivative has this trigonal bipyramidal configuration; all other examples have a four-legged piano-stool arrangement.[11b–d,17,18] In this case, such an arrangement is very unfavourable because of the important steric requirement of the trimethylsilylmethyl substituent.

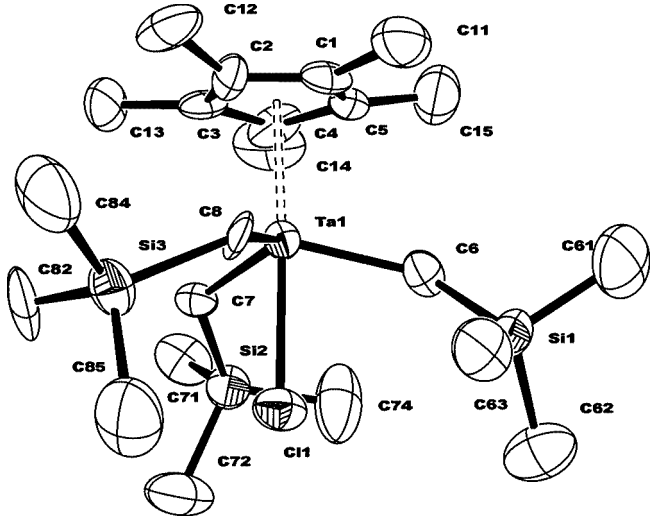


Figure 1. ORTEP drawing of compound **1** with thermal ellipsoids at the 50% probability level.

Table 1. Selected bond lengths [Å] and angles [°] for compound **1**.[a]

| | | | |
|---|---|---|---|
| Ta1–Cl1 | 2.481(5) | Ta1–Cp1 | 2.180 |
| Ta1–C6 | 2.137(16) | Ta1–C7 | 2.188(14) |
| Ta1–C8 | 2.156(16) | Ta1–C1 | 2.430(16) |
| Ta1–C2 | 2.47(2) | Ta1–C3 | 2.52(2) |
| Ta1–C4 | 2.49(2) | Ta1–C5 | 2.480(19) |
| Si1–C6 | 1.911(18) | Si2–C7 | 1.888(15) |
| Si3–C8 | 1.924(15) | | |
| Cp1–Ta1–Cl1 | 176.84 | Cp1–Ta1–C6 | 103.17 |
| Cp1–Ta1–C7 | 100.89 | Cp1–Ta1–C8 | 103.25 |
| C6–Ta1–C8 | 111.7(6) | C6–Ta1–C7 | 114.4(6) |
| C8–Ta1–C7 | 120.3(6) | C6–Ta1–Cl1 | 79.6(5) |
| C7–Ta1–Cl1 | 76.5(4) | C8–Ta1–Cl1 | 76.9(5) |
| Si1–C6–Ta1 | 127.2(9) | Si2–C7–Ta1 | 126.4(9) |
| Si3–C8–Ta1 | 126.9(9) | | |

[a] Cp1 is the centroid of the C1–C5 ring.

The mixed alkyl complexes $[TaCp^*Me_2R_2]$ (R = $CH_2Ph$, **2**; $CH_2SiMe_3$, **3**) were obtained (Scheme 2) at room temperature by treatment of toluene solutions of $TaCp^*Cl_2Me_2$ with stoichiometric amounts of the alkyllithium, LiR, under rigorously anhydrous conditions, while the dimethyldineopentyl complex $[TaCp^*Me_2(CH_2CMe_3)_2]$ (**4**) was synthesized by alkylation, at –78 °C, of the dichloridodineopentyl derivative with 2 equiv. of LiMe in a diethyl ether/hexane mixture.

The mixed alkyl complexes **2**–**4** are extremely air- and moisture-sensitive, are soluble in most organic solvents and were characterised by analytical and spectroscopic methods.

 © 2006 Wiley-VCH Verlag GmbH & Co. KGaA, Weinheim 

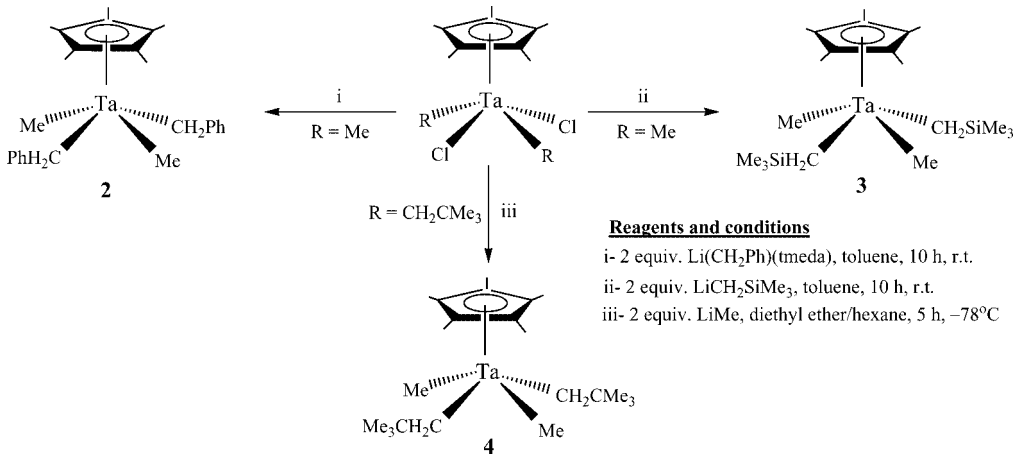


Scheme 2.

Further, the molecular structure of **4** was studied by X-ray diffraction. A view of this molecule is shown in Figure 2, which indicates the atom labelling scheme employed. Selected bond lengths and angles are given in Table 2.

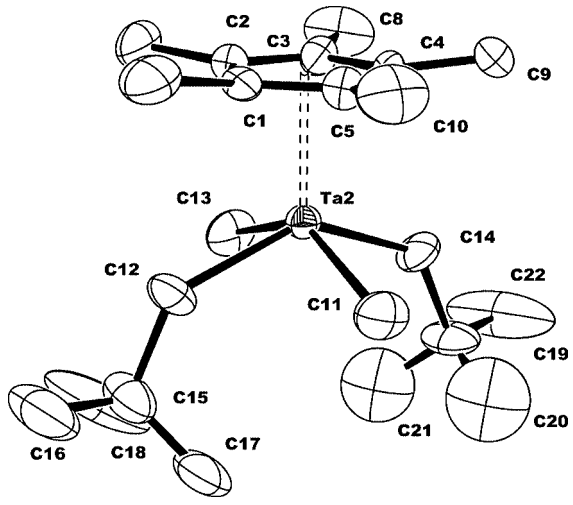


Figure 2. ORTEP drawing of compound **4** with thermal ellipsoids at the 50% probability level.

Table 2. Selected bond lengths [Å] and angles [°] for compound **4**.[a]

| Molecule A | | Molecule B | |
|---|---|---|---|
| Cp1–Ta1 | 2.175 | Cp2–Ta2 | 2.175 |
| C1A–Ta1 | 2.49(2) | C1–Ta2 | 2.48(2) |
| C2A–Ta1 | 2.48(2) | C2–Ta2 | 2.48(2) |
| C3A–Ta1 | 2.50(2) | C3–Ta2 | 2.46(2) |
| C4A–Ta1 | 2.51(2) | C4–Ta2 | 2.48(2) |
| C5A–Ta1 | 2.46(2) | C5–Ta2 | 2.49(3) |
| C11A-Ta1 | 2.20(2) | C11–Ta2 | 2.19(2) |
| C12A-Ta1 | 2.27(2) | C12–Ta2 | 2.26(2) |
| C13A-Ta1 | 2.23(2) | C13–Ta2 | 2.22(2) |
| C14A-Ta1 | 2.245(19) | C14–Ta2 | 2.20(2) |
| C12A-C15A | 1.49(3) | C12–C15 | 1.56(4) |
| C14A-C19A | 1.52(3) | C14–C19 | 1.64(3) |
| Cp1–Ta1–C11A | 109.65 | Cp2–Ta2–C11 | 111.00 |
| Cp1–Ta1–C12A | 111.62 | Cp2–Ta2–C12 | 108.17 |
| Cp1–Ta1–C13A | 109.72 | Cp2–Ta2–C13 | 108.87 |
| Cp1–Ta1–C14A | 108.38 | Cp2–Ta2–C14 | 111.17 |
| C11A–Ta1–C13A | 140.6(8) | C11–Ta2–C13 | 140.1(10) |
| C11A–Ta1–C14A | 83.4(9) | C11–Ta2–C14 | 84.4(11) |
| C13A–Ta1–C14A | 83.7(10) | C14–Ta2–C13 | 81.7(10) |
| C11A–Ta1–C12A | 83.3(9) | C11–Ta2–C12 | 82.1(10) |
| C13A–Ta1–C12A | 83.1(9) | C13–Ta2–C12 | 85.4(10) |
| C14A–Ta1–C12A | 140.0(8) | C14–Ta2–C12 | 140.7(9) |
| C15A-C12A-Ta1 | 133.5(17) | C15–C12–Ta2 | 132(2) |
| C19A-C14A-Ta1 | 128.5(16) | C19–C14–Ta2 | 135(2) |

[a] Cp1 is the centroid of the C1A–C5A ring and Cp2 is the centroid of the C1–C5 ring.

Complex **4** is a monomer, and if Cp* is considered as occupying the apical coordination site, it has distorted square pyramid geometry. Two independent molecules were found in the asymmetric unit, and their geometrical parameters were essentially coincident. The tantalum atom deviates towards the Cp* ring by 0.75 Å from a plane passing through the atoms C11, C12, C13 and C14, and the two methyl groups and the two neopentyl groups are mutually *trans* in order to separate the sterically demanding groups. This arrangement is usual in five-coordinate cyclopentadienyl complexes.[11b,11c,11d,17,18] All the bond lengths and angles are in the normal ranges.

The $^1$H NMR spectrum of **4** in [D$_2$]dichloromethane at 298 K shows two sets of signals in a ratio of 14:1. For the major compound, a quintuplet ($\delta$ = 0.59 ppm) and a septuplet ($\delta$ = 0.20 ppm, $^4J_{H,H}$ = 1.29 Hz) were observed for the Ta–(C$H_3$)$_2$ and the Ta–(C$H_2$CMe$_3$)$_2$ moieties, respectively. On the other hand, the minor component, detected in a NOESY1D spectra (Figure 3), shows an AB spin system ($^2J_{H,H}$ = 12.8 Hz) for the Ta–(C$H_2$CMe$_3$)$_2$ diastereotopic protons.

In contrast to **4**, the Ta–(C$H_2$SiMe$_3$)$_2$ resonance appears as a broad signal ($\Delta\nu_{1/2}$ = 37 Hz) at $\delta$ = –0.25 ppm in the $^1$H NMR spectrum of **3** at 298 K, while the signal corresponding to Ta–(C$H_3$)$_2$ was observed as a quintuplet ($^4J_{H,H}$ = 1.31 Hz) at $\delta$ = 0.44 ppm.

Further, the variable low temperature spectra of **3** indicate the occurrence of a typical spin exchange process between two very differently populated positions. The minor position (10%) was detected by EXSY1D at 213 K and showed an AB spin system ($^2J_{H,H}$ = 11.6 Hz) at $\delta_{av}$ = –0.01 for the Ta–(C$H_2$SiMe$_3$)$_2$ resonance.

 © 2006 Wiley-VCH Verlag GmbH & Co. KGaA, Weinheim 

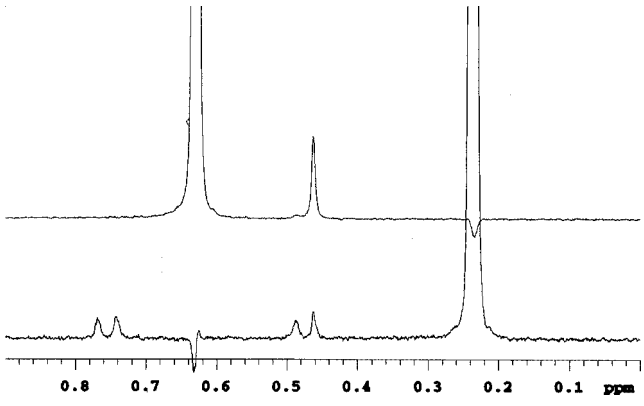


Figure 3. The PFG WFG noesy 1d (mix = 500 ms) proton spectra (spectrum phase = 180°) of complex **4** at 298 K [bottom: Ta–($CH_2CMe_3$)$_2$; top: Ta–($CH_3$)$_2$ resonances].

This spectral behaviour is in agreement with a *trans* arrangement of the methyl and the alkyl groups ($C_{2v}$ local symmetry) in the major component and a *cis* arrangement of the groups in the minor ($C_s$ symmetry) isomers, which undergo the mutual spin-exchange process known as Berry pseudorotation.[14c,14d,16b,18] We hypothesise that in solution both isomers of the **2**–**4** mixed alkyl complexes exhibit pseudo-square-pyramidal geometry in the ground state and a distorted trigonal bipyramidal environment, similar to that of **1**, in the transition state. Moreover, the isomerization process in complex **3** is faster than that in **4**, this is probably caused by the size of the alkyl group. The $^{13}C$ NMR spectra of complexes **2**–**4** show all the expected resonances (see Experimental Section).

The addition of 2 equiv. of $LiCH_2CMe_2Ph$ to a toluene solution of $TaCp^*Cl_2Me_2$ by using a standard vacuum line (Scheme 3) gives a mixture of the dimethyl(neophyl)(μ-oxido) complex [{$TaCp^*Me_2(CH_2CMe_2Ph)$}$_2$(μ-O)] (**5**), the dimethyltantalabenzocyclopentene complex [$TaCp^*Me_2$-($CH_2CMe_2$-*o*-$C_6H_4$-κ$^2$*C*,*C*)] (**6**) and the (methyl)(methylidene)(neophyl) complex [$TaCp^*Me(CH_2CMe_2Ph)(CH_2)$] (**7**), which were observed by NMR spectroscopy. Complexes **5**–**7** can be isolated as pure samples by successive recrystallisations from hexane (see Experimental Section). However, when the same reaction is carried out under rigorously anhydrous conditions (glove box) complex **5** is not formed. We suggest, as a plausible pathway for this alkylation reaction, the initial formation of a mixed alkyl complex "[$TaCp^*Me_2(CH_2CMe_2Ph)_2$]", that, when followed by orthometalation[10,19] of the phenyl ring and by α-hydrogen activation[7e,20] of a methyl group with the elimination of $CMe_3Ph$, produces complexes **6** and **7**, respectively, while the hydrolysis of this mixed alkyl complex produces the μ-oxido complex **5**.

In the IR spectrum of complex **5** the absorption band observed at 740 cm$^{-1}$ could be assigned to $\nu_{Ta-O-Ta}$,[15,21] while all the NMR spectroscopic data (see Experimental Section) are in agreement with a structural formulation that shows a *trans* arrangement of the methyl groups.

The molecular structure of complex **5** (Figure 4) shows two $TaCp^*Me_2(CH_2CMe_2Ph)$ fragments bonded through a bridging oxygen atom, which acts as an inversion centre. The angle Ta1–O1–Ta2 is 180,° and the bond length Ta–O is 1.9227(6) Å (Table 3). This distance is very short and in agreement with the existence of a π-bonding interaction between the oxygen and tantalum atoms.[14c] Each tantalum atom exhibits the normal four-legged piano-stool geometry[11,17,18] in which the pentamethylcyclopentadienyl ring occupies the apical position and the metal centre is displaced towards the Cp* ring by 0.78 Å from a plane formed by the atoms C21, C6, C8 and O1. The bridging oxygen atom is located in a *trans* position with respect to the bulky ligand. This fact, together with the inversion centre, eliminates steric problems. The distance Ta–C21 [2.294(12) Å] is significantly longer than the bonds between the metal and the methyl groups[18] [Ta–C6 2.208(11) Å and Ta–C8 2.194(12) Å], which is probably a result of the *trans* influence.

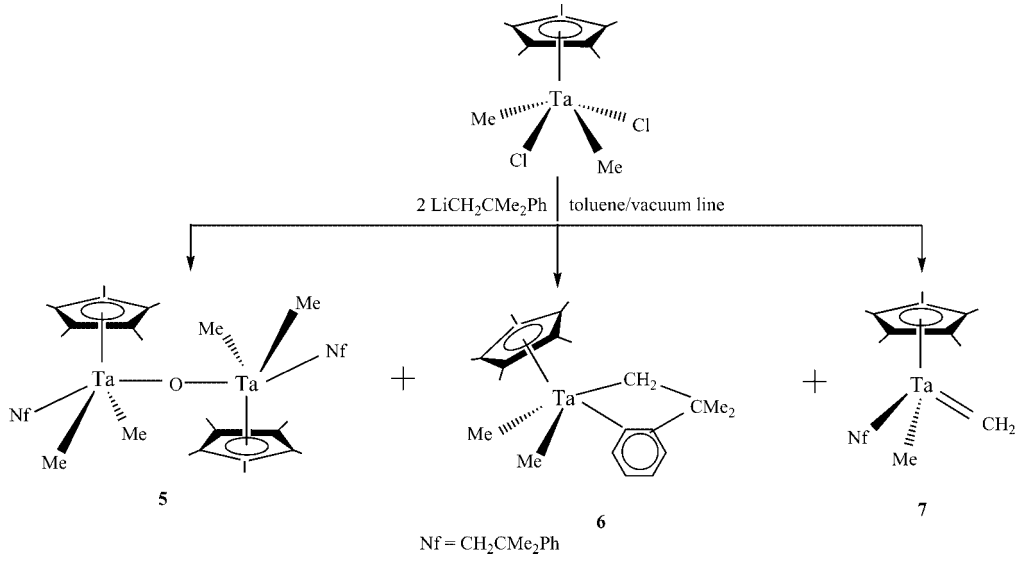


Scheme 3.

 © 2006 Wiley-VCH Verlag GmbH & Co. KGaA, Weinheim 

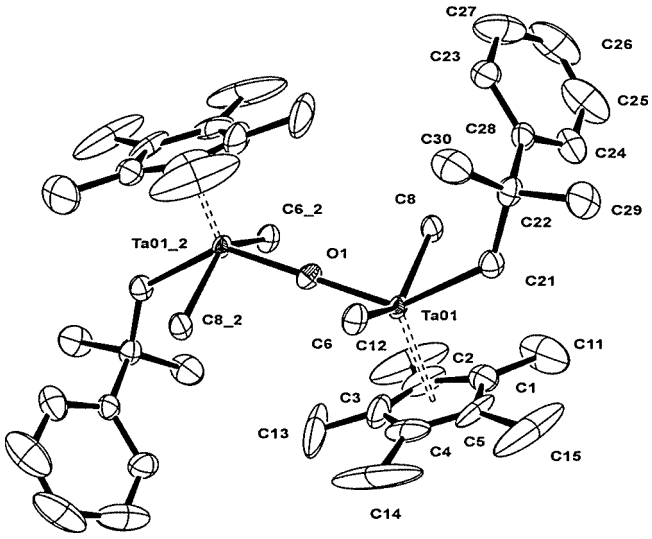


Figure 4. ORTEP drawing of compound **5** with thermal ellipsoids at the 50% probability level.

Table 3. Selected bond lengths [Å] and angles [°] for compound **5**.[a]

| | | | |
|---|---|---|---|
| Ta1–O1 | 1.9227(6) | O1–Ta1#1 | 1.9227(6) |
| Ta1–Cp1 | 2.158 | Ta1–C6 | 2.208(11) |
| Ta1–C8 | 2.194(10) | Ta1–C21 | 2.294(12) |
| Ta1–C1 | 2.502(12) | Ta1–C2 | 2.416(14) |
| Ta1–C3 | 2.366(16) | Ta1–C4 | 2.431(13) |
| Ta1–C5 | 2.533(11) | C21–C22 | 1.538(17) |
| C22–C23 | 1.529(15) | | |
| Ta1#1–O1–Ta1 | 180.00(16) | Cp1–Ta1–O1 | 120.73 |
| Cp1–Ta1–C6 | 109.88 | Cp1–Ta1–C8 | 109.22 |
| Cp1–Ta1–C21 | 103.36 | O1–Ta1–C6 | 84.2(3) |
| C8–Ta1–C6 | 139.2(5) | O1–Ta1–C21 | 135.9(3) |
| O1–Ta1–C8 | 85.9(3) | C8–Ta1–C21 | 79.1(4) |
| C6–Ta1–C21 | 80.9(4) | C23–C22–C21 | 112.9(9) |
| C22–C21–Ta1 | 134.4(8) | | |

[a] Cp1 is the centroid of the C1–C5 ring. Symmetry transformations used to generate equivalent atoms: #1 $-x+1$, $-y+2$, $-z$.

The NMR spectrum of **6**, which is a monomer species [$D = (11.7 \pm 0.2) \times 10^{-11}$ m$^2$s$^{-1}$][22] in [D$_2$]dichloromethane [$D = (29.2 \pm 0.5) \times 10^{-11}$ m$^2$s$^{-1}$] at 298 K, exhibits an ABCD spin system at $\delta$ = 8.1, 7.3, 7.2 and 7.12 ppm corresponding to the $C_6H_4$ moiety, and four singlets for the $\eta^5$-$C_5Me_5$ ($\delta$ = 1.94 ppm, 15 H), Ta–CH$_2$C*Me*$_2$Ph ($\delta$ = 1.15 ppm, 6 H), Ta–C*H*$_2$CMe$_2$Ph ($\delta$ = 0.88 ppm, 2 H, $\Delta\nu_{1/2}$ = 8.7 Hz) and Ta–*Me*$_2$ ($\delta$ = 0.27 ppm, 6 H) proton resonances, which justifies the assignment of $C_s$ symmetry to this complex. Unfortunately, the variable temperature spectra did not show any significant changes ($\Delta\nu_{1/2max}$ = 12.7 Hz) to enable the study of any possible fluxional behaviour. NOE data at 203 K indicate short distances between the pentamethylcyclopentadienyl ring and the –CMe$_2$–, Ta–Me$_2$ and Ta–CH$_2$– moieties, and between Ta–Me$_2$ and the phenyl (H2 proton) ring, suggesting an axial position for the phenyl group in the distorted trigonal bipyramidal structure of **6**, as shown in Scheme 3.

The $^1$H NMR spectrum of complex **7** in [D$_2$]dichloromethane at 298 K shows a singlet for the Cp* ring ($\delta$ = 1.95 ppm), three multiplets for the $C_6H_5$ group ($\delta$ = 7.4, 7.3, 7.13 ppm), two diastereotopic –C*Me*$_2$– ($\delta$ = 1.46, 1.40 ppm) groups and an ABC$_3$ spin system at $\delta$ = 1.26, 0.04 (AB) and –0.52 (d, $^2J_{H,H}$ = 14.8 Hz, $^4J_{H,H}$ = 1.1 Hz) ppm for the Ta–C*H*$_2$CMe$_2$Ph and Ta–*Me* moieties, respectively. Although **7** contains an asymmetric tantalum(V) central atom, the Ta=CH$_2$ resonance is observed as one singlet ($^1$H NMR, $\delta$ = 5.27 ppm; $^{13}$C NMR, $\delta$ = 205.9 ppm, $^1J_{C,H}$ = 126.1 Hz), which is not like an AB spin system. In the variable temperature $^1$H NMR study, the maximum broad line ($\Delta\nu_{1/2}$ = 110 Hz) of the methylidene resonance was observed at 173 K, although the multiplicity could not be resolved. We believe that this experimental result could be due to the fast rotation ($\Delta G^{\neq 173\ K} < 32$ kJ mol$^{-1}$) about the Ta–C vector that accompanies the heterolytic rupture of the double bond, which is in accordance with the reactivity of these complexes. This is known to occur in other methylidene complexes,[18c,23] organic imines[24] and organometallic complexes.[14c,18d]

(Alkyl)(alkylidene)tantalum compounds were obtained by the thermal or photochemical treatment of mixed alkyl derivatives. So, when a toluene or [D$_6$]benzene solution of **1** was heated at 60 °C for 48 h, the (alkyl)(alkylidene)chlorido complex [TaCp*Cl(CH$_2$SiMe$_3$)(CHSiMe$_3$)] (**8**) was formed with the elimination of SiMe$_4$ (Scheme 4). However, complex **1** in [D$_2$]dichloromethane slowly transforms into complex **8** at room temperature.

The $^1$H NMR spectrum of **8** ($D = 13.0 \times 10^{-10}$ m$^2$s$^{-1}$)[22] shows signals at $\delta$ = 5.54 (1 H) and 0.065 ppm (9 H) for Ta=C*H*Si*Me*$_3$ ($^{29}$Si NMR, $\delta$ = –8.2 ppm), an AB spin system at $\delta$ = 0.053 and 0.23 ppm ($^2J_{H,H}$ = 12.65 Hz, 2 H) and one singlet at $\delta$ = 0.12 ppm (9 H) for the Ta–C*H*$_2$Si*Me*$_3$ moiety, and also a resonance for the Cp* ring at $\delta$ = 2.15 ppm. Further, free SiMe$_4$ ($D = 24.5 \times 10^{-10}$ m$^2$s$^{-1}$) that was eliminated from **1** during the reaction was also observed in the solution. The assignment of the trimethylsilyl resonances and the determination of the $^{29}$Si NMR chemical shifts were based on CIGAR data (Figure 5).

When a [D$_6$]benzene solution of **3** was heated at 60 °C for 20 h, a mixture of the dialkyl(alkylidene) compounds [TaCp*MeR(CHSiMe$_3$)] (R = CH$_2$SiMe$_3$, **9**; Me, **10**) was generated in a 3:2 ratio; this mixture was identified by NMR spectroscopy. The reaction occurred with the elimination of CH$_4$ and SiMe$_4$ (Scheme 5). On the other hand, the irradiation of a [D$_6$]benzene solution of **3** with a sun lamp gave a mixture of **9** and [TaCp*(CH$_2$SiMe$_3$)R(CH$_2$)] (R = Me, **11**; CH$_2$SiMe$_3$, **12**) in a 2:1:1 ratio. Both processes, thermal and photochemical, take place by C–Hα activation of the CH$_2$SiMe$_3$ or Me groups. Complex **9** is the major product that results from the preferential elimination of CH$_4$.

In addition, [D$_6$]benzene solutions of the mixed tetraalkyl complex **4** slowly decomposed at room temperature when exposed to a sun lamp, yielding a mixture of the alkylidenes **13**–**16**. When solutions of **4** were heated at 60 °C, the decomposition was faster, and a mixture of (alkyl)(neo-

 © 2006 Wiley-VCH Verlag GmbH & Co. KGaA, Weinheim 

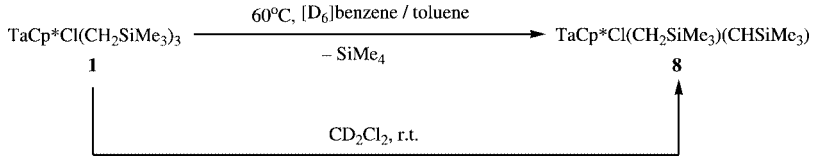


Scheme 4.

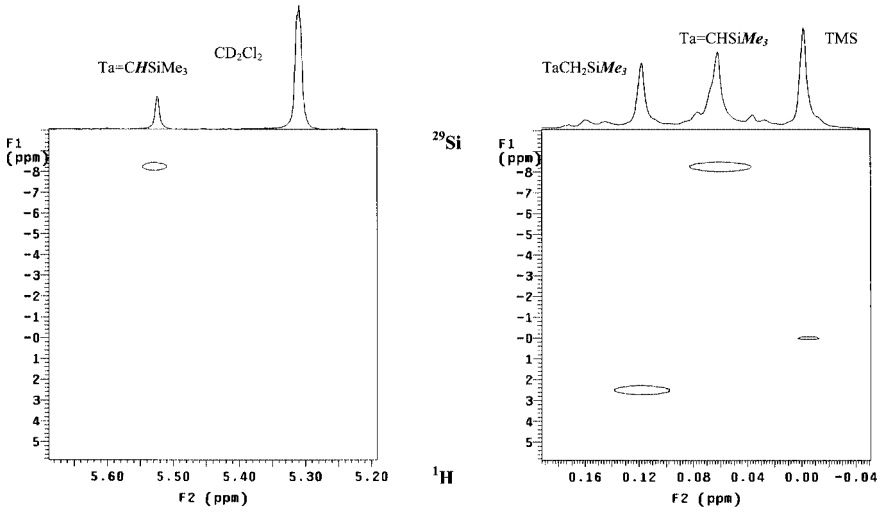


Figure 5. PFG Accord HMBC (CIGAR) $^{1}H$-{$^{29}Si$} spectra of **8** acquired over a period of 20 minutes in a Mercury VX spectrometer with PFG-Z VT 5 mm ATB NMR probe. All parameters were optimized for the $^{1}H$–$^{29}Si$ geminal spin coupling.

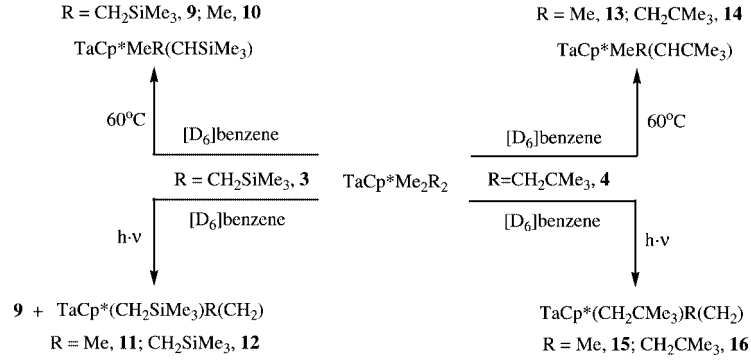


Scheme 5.

pentylidene) derivatives [TaCp*MeR(CHCMe$_3$)] (R = Me, **13**; $CH_2CMe_3$, **14**) in a 4:1 ratio was produced and identified by NMR spectroscopy. Further, a mixture of the (alkyl)(methylidene) complexes [TaCp*($CH_2CMe_3$)R($CH_2$)] (R = Me, **15**; $CH_2CMe_3$, **16**) in a 3:1 ratio was obtained from the irradiation of a [$D_6$]benzene solution of **4** with a sun lamp. These results indicate that a C–Hα bond is activated by thermal (–$CH_2CMe_3$) and photochemical (–$CH_3$) processes, but in both cases the elimination of neopentane is preferential.

A spontaneous α-hydrogen-abstraction process takes place in unstable mixed tetraalkyl intermediates formed by the reaction of complexes [TaCp*$Cl_2$($CH_2R$)$_2$] (R = $CMe_3$, $SiMe_3$) with an alkylating reagent. So, the reaction of [TaCp*$Cl_2$($CH_2CMe_3$)$_2$] with 2 equiv. of $LiCH_2SiMe_3$ gave the (alkyl)(alkylidene) complex [TaCp*($CH_2CMe_3$)($CH_2SiMe_3$)(CHCMe$_3$)] (**17**) with the selective elimination of $SiMe_4$ (Scheme 6). The use of neophyllithium or benzylmagnesium chloride leads to an unidentified mixture of alkylidene derivatives. However, new (alkyl)(alkylidene) derivatives [TaCp*($CH_2R$)($CH_2SiMe_3$)(CHR′)] (R = R′ = Ph, **18**; R = $CMe_2Ph$, R′ = $SiMe_3$, **19**) were prepared by treatment of [TaCp*$Cl_2$($CH_2SiMe_3$)$_2$] with 2 equiv. of the appropriate alkylating reagent; these reactions occur with the elimination of $SiMe_4$ and $CMe_3Ph$, respectively.

For some reported coordinatively unsaturated alkylidene complexes,[8,25] the stretching frequency corresponding to the C–H bond in the IR spectrum was assigned to absorp-

 © 2006 Wiley-VCH Verlag GmbH & Co. KGaA, Weinheim 

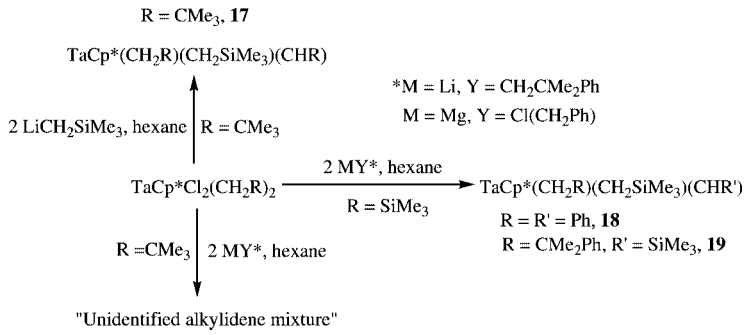


Scheme 6.

tion bands localized in the 2700–2350 $cm^{-1}$ region, which are at a lower wavenumber than those for normal C–H stretches probably as a result of the observed increase in the length of the C–H bond. In the case of (alkyl)(alkylidene) compounds **7** and **17**–**19**, the absorption band localized at $\tilde{\nu}_{average}$ = 2553 $cm^{-1}$ can be assigned to $\nu_{C-H}$.

In accordance with all the NMR spectroscopic data (see Experimental Section) the alkylidene complexes **7**–**19** are monomeric species with the expected three-legged piano-stool geometry.[8,26,27] A large degree of deshielding is observed for the alkylidene carbon resonances ($\delta > 200$ ppm). The direct proton–carbon coupling constants for the Ta=*CH*R signals for complexes **7**, **11**, **12**, **15** and **16** are smaller than the $^1J_{C,H}$ values resulting from coupling involving an $sp^3$ carbon (Ta–*CH*$_2$R groups) and are comparable to other $d^0$ terminal (alkylidene)niobium and -tantalum complexes.[26,27] For the rest of the complexes, we found similar values for the isostructural alkylmethylidene moiety.

## Conclusions

New trialkylchlorido and dialkyldimethyl(pentamethylcyclopentadienyl)tantalum complexes [TaCp*$Cl_xMe_yR_z$] ($x$ = 1, $y$ = 0, $z$ = 3, R = $CH_2SiMe_3$, **1**; $x$ = 0, $y$ = $z$ = 2, R = $CH_2Ph$, **2**; $CH_2SiMe_3$, **3**; $CH_2CMe_3$, **4**) have been prepared by the direct reaction of tetrachlorido or dialkyldichlorido derivatives [TaCp*$Cl_{4-x}R_x$] ($x$ = 0; $x$ = 2, R = Me, $CH_2CMe_3$) with the appropriate alkylating reagent. However, when lithium neophyl is used as the reagent under standard conditions, a different sequence of reactions takes place, which leads to a mixture from which [{TaCp*$Me_2(CH_2CMe_2Ph)$}$_2$(μ-O)] (**5**), [TaCp*$Me_2$-($CH_2CMe_2$–o-$C_6H_4$-κ$^2$*C*,*C*)] (**6**) and [TaCp*Me-($CH_2CMe_2Ph$)($CH_2$)] (**7**) were isolated and identified by NMR spectroscopy. Thermal treatment of toluene or [$D_6$]-benzene solutions of **1** leads to an intramolecular C–Hα bond activation in an alkyl group, giving the (alkyl)(alkylidene)chlorido complex [TaCp*Cl($CH_2SiMe_3$)($CHSiMe_3$)] (**8**) with the evolution of $SiMe_4$. A mixture of dialkyl(alkylidene) derivatives [TaCp*MeR($CHSiMe_3$)] (R = $CH_2SiMe_3$, **9**; Me, **10**) was produced when **3** was heated at 60 °C in [$D_6$]benzene; the mixture was identified by NMR measurements. Further, the direct irradiation of a [$D_6$]benzene solution of **3** gave a mixture of **9** and [TaCp*($CH_2SiMe_3$)-R($CH_2$)] (R = Me, **11**; $CH_2SiMe_3$, **12**). On the other hand, [$D_6$]benzene solutions of **4** slowly decompose at room temperature, giving a mixture of alkylidenes [TaCp*MeR($CHCMe_3$)] (R = Me, **13**; $CH_2CMe_3$, **14**) and [TaCp*($CH_2CMe_3$)R($CH_2$)] (R = Me, **15**; $CH_2CMe_3$, **16**), but the decomposition is faster when activated thermally or photochemically, leading to a mixture of **13**–**14** and **15**–**16**, respectively. Finally, a spontaneous α-hydrogen-abstraction process occurs during the alkylation reaction of TaCp*$Cl_2(CH_2CMe_3)_2$ with $LiCH_2SiMe_3$, which gives [TaCp*($CH_2CMe_3$)($CH_2SiMe_3$)($CHCMe_3$)] (**17**) with selective elimination of $SiMe_4$. However, new (alkyl)(alkylidene) complexes [TaCp*($CH_2$R)($CH_2SiMe_3$)(CHR′)] (R = R′ = Ph, **18**; R = $CMe_2Ph$, R′ = $SiMe_3$, **19**) were obtained by treatment of TaCp*$Cl_2(CH_2SiMe_3)_2$ with 2 equiv. of the appropriate alkylating reagent; these reactions occurred with the elimination of $SiMe_4$ and $CMe_3Ph$, respectively.

## Experimental Section

All operations were carried out under a dry argon atmosphere, by using standard Schlenk tube and cannula techniques, or in a conventional argon-filled glove-box. Solvents were refluxed over an appropriate drying agent, distilled and degassed prior to use: [$D_6$]-benzene and hexane (Na/K alloy), and toluene (Na). Starting materials Ta(η$^5$-$C_5Me_5$)$Cl_4$,[28] Ta(η$^5$-$C_5Me_5$)$Cl_2Me_2$,[13] Ta(η$^5$-$C_5Me_5$)-$Cl_2(CH_2CMe_3)_2$[26a,29] and the alkylating reagents LiR (R = $CH_2SiMe_3$, $CH_2CMe_2Ph$)[30] and Li($CH_2C_6H_5$)(tmeda)[31] were prepared as previously described. Reagent grade LiMe (1.5 M in diethyl ether, Aldrich) and MgCl($CH_2SiMe_3$) (1 M in diethyl ether, Aldrich) were purchased from commercial sources and were used without further purification.

Samples for infrared spectroscopy were prepared as KBr pellets or as Nujol mulls between CsI plates, and the spectra were recorded with a Perkin–Elmer Spectrum 2000 spectrophotometer (4000–400 $cm^{-1}$). The NMR spectra were recorded with Unity 300, Mercury VX 300 and Unity $^{Plus}$ 500 (Varian NMR Systems) spectrometers; chemical shifts were referenced to the $^{13}$C- and residual $^1$H resonances of the deuterated solvents. Microanalyses (C, H) were performed with a LECO CHNS 932 microanalyser.

**[TaCp*Cl($CH_2SiMe_3$)$_3$] (1):** A solution of MgCl($CH_2SiMe_3$) [6.90 mL, 1 M, 6.60 mmol] in diethyl ether was added, at room temperature, to a suspension of TaCp*$Cl_4$ (1.00 g, 2.20 mmol) in hexane (25 mL), and the mixture was stirred for 12 h. The resulting

 © 2006 Wiley-VCH Verlag GmbH & Co. KGaA, Weinheim 

suspension was filtered through Celite and then concentrated to ca. 10 mL, the solution was cooled to –20 °C to give **1** as a yellow microcrystalline solid. Yield 0.90 g (68%). IR (KBr): $\tilde{\nu}$ = 2917 (vs), 1494 (m), 1441 (m), 1380 (s), 1243 (vs), 1105 (s), 1026 (s), 845 (vs), 749 (s), 678 (s), 470 (m), 407 (m) $cm^{-1}$. $^1H$ NMR (300 MHz, [$D_6$]-benzene, 25 °C): $\delta$ = 1.78 (s, 15 H, $C_5Me_5$), 0.65 (s, 6 H, $CH_2SiMe_3$), 0.35 (s, 27 H, $CH_2SiMe_3$) ppm. $^{13}C\{^1H\}$ NMR (75 MHz, [$D_6$]benzene, 25 °C): $\delta$ = 121.5 ($C_5Me_5$), 88.0 ($CH_2SiMe_3$), 12.8 ($C_5Me_5$), 4.2 ($CH_2SiMe_3$) ppm. $C_{22}H_{48}ClSi_3Ta$ (613.28): calcd. C 43.08, H 7.89; found C 43.31, H 7.78.

**[TaCp*Me$_2$(CH$_2$C$_6$H$_5$)$_2$] (2):** This reaction was carried out in a dry box by using darkened glassware designed for photosensitive materials. A solution of Li($CH_2$Ph)(tmeda) (0.31 g, 1.44 mmol) in toluene (20 mL) was added to a solution of TaCp*$Cl_2Me_2$ (0.30 g, 0.72 mmol) in toluene (30 mL) at room temperature, and the mixture was stirred for 10 h. The suspension was concentrated to dryness and the residue extracted with hexane (3 × 20 mL). The solution was filtered, concentrated to ca. 10 mL, and cooled to give **2** as a red microcrystalline solid. Yield 0.29 g (80%). IR (KBr): $\tilde{\nu}$ = 2916 (s), 1591 (m), 1484 (vs), 1450 (m), 1379 (s), 1203 (s), 1150 (m), 1062 (s), 1025 (s), 807 (m), 750 (vs), 698 (vs), 601 (m), 529 (m), 443 (w) $cm^{-1}$. $^1H$ NMR (300 MHz, [$D_6$]benzene, 25 °C): $\delta$ = 7.21 (m, 2 H), 7.11 (m, 2 H), 6.85 (m, 1 H, $H_5C_6CH_2$–Ta), 1.67 (br., 4 H, Ta–$CH_2$Ph), 1.60 (s, 15 H, $C_5Me_5$), 0.86 (br., 6 H, Ta–$Me_2$) ppm. $^{13}C\{^1H\}$ NMR (75 MHz, [$D_6$]benzene, 25 °C): $\delta$ = not detected ($C_i$), 127.9 ($C_m$), 127.3 ($C_o$), 123.2 ($C_p$, $C_6H_5CH_2$–Ta), 119.5 ($C_5Me_5$), 94.8 (Ta–$CH_2C_6H_5$), 81.3 (Ta–$Me_2$), 11.4 ($C_5Me_5$) ppm. $C_{26}H_{35}Ta$ (528.51): calcd. C 59.08, H 6.67; found C 58.98, H 6.70.

**[TaCp*Me$_2$(CH$_2$SiMe$_3$)$_2$] (3):** A stirred suspension of TaCp*$Cl_2Me_2$ (0.50 g, 1.20 mmol) in toluene (30 mL) was treated with a solution of $LiCH_2SiMe_3$ (0.23 g, 2.40 mmol) in toluene (20 mL). The reaction mixture was stirred for 10 h at room temperature, and the resulting suspension was decanted and filtered. The solution was concentrated to dryness and the residue extracted with hexane (3 × 15 mL). The solution was filtered, concentrated to ca. 10 mL, and cooled to –40 °C to give **3** as a yellow microcrystalline solid. Yield 0.35 g (74%). IR (KBr): $\tilde{\nu}$ = 2947 (vs), 1490 (m), 1432 (s), 1380 (m), 1295 (w), 1241 (s), 1160 (m), 1026 (m), 947 (s), 856 (vs), 823 (vs), 744 (m), 718 (s), 676 (m), 612 (m), 521 (w), 442 (m) $cm^{-1}$. $^1H$ NMR (500 MHz, [$D_2$]dichloromethane, 25 °C): $\delta$ = 2.00 (s, 15 H, $C_5Me_5$), 0.40 (quint, $^4J_{H,H}$ = 1.1 Hz, 6 H, Ta–$Me_2$), 0.06 (s, 18 H, Ta–$CH_2SiMe_3$), –0.30 (m, 4 H, Ta–$CH_2SiMe_3$) ppm. $^{13}C\{^1H\}$ NMR (75 MHz, [$D_6$]benzene, 25 °C): $\delta$ = 118.9 ($C_5Me_5$), 83.6 (Ta–$CH_2SiMe_3$), 71.7 (Ta–$Me_2$), 11.7 ($C_5Me_5$), 3.8 ($CH_2SiMe_3$) ppm. $^{13}C\{^1H\}$ NMR (125 MHz, [$D_2$]dichloromethane, 25 °C): $\delta$ = 118.9 ($C_5Me_5$), 83.2 (Ta–$CH_2SiMe_3$), 70.7 (Ta–$Me_2$), 11.1 ($C_5Me_5$), 3.5 ($CH_2SiMe_3$) ppm. $C_{20}H_{43}Si_2Ta$ (520.68): calcd. C 46.12, H 8.32; found C 45.90, H 8.02.

**[TaCp*Me$_2$(CH$_2$CMe$_3$)$_2$] (4):** A solution of LiMe in diethyl ether (1.30 mL, 1.5 M, 1.95 mmol) was added to a solution of TaCp*$Cl_2(CH_2CMe_3)_2$ (0.40 g, 0.75 mmol) in hexane (40 mL) at –78 °C, and the mixture was stirred for 5 h. The suspension was then warmed to room temperature and LiCl filtered off. The solution was concentrated to ca. 10 mL and cooled to –40 °C to give a yellow microcrystalline solid identified as **4**. Yield 0.30 g (81%). IR (KBr): $\tilde{\nu}$ = 2940 (vs), 1431 (m), 1379 (s), 1205 (s), 1157 (m), 1023 (m), 804 (w), 746 (m), 601 (m), 522 (m), 455 (m) $cm^{-1}$. $^1H$ NMR (300 MHz, [$D_6$]benzene, 25 °C): $\delta$ = 1.66 (s, 15 H, $C_5Me_5$), 1.40 (s, 18 H, Ta–$CH_2CMe_3$), 0.92 (6 H, Ta–$Me_2$), 0.34 (4 H, Ta–$CH_2CMe_3$) ppm. $^1H$ NMR (500 MHz, [$D_2$]dichloromethane, 25 °C): $\delta$ = 1.96 (s, 15 H, $C_5Me_5$), 1.07 (s, 18 H, Ta–$CH_2CMe_3$), 0.59 (quint, $^4J_{H,H}$ = 1.3 Hz, 6 H, Ta–$Me_2$), 0.20 (sept, $^4J_{H,H}$ = 1.3 Hz, 4 H, Ta–$CH_2CMe_3$) ppm. $^{13}C\{^1H\}$ NMR (75 MHz, [$D_6$]-benzene, 25 °C): $\delta$ = 118.6 ($C_5Me_5$), 111.2 (Ta–$CH_2CMe_3$), 76.6 (Ta–$Me_2$), not detected (Ta–$CH_2CMe_3$), 36.3 (Ta–$CH_2CMe_3$), 11.7 ($C_5Me_5$) ppm. $C_{22}H_{43}Ta$ (488.53): calcd. C 54.09, H 8.87; found C 53.95, H 8.72.

**[{TaCp*Me$_2$(CH$_2$CMe$_2$Ph)}$_2$(μ-O)] (5):** Complex **5** was isolated together with complexes **6** and **7** by using a standard vacuum line and Schlenk techniques. A mixture of TaCp*$Cl_2Me_2$ (0.50 g, 1.20 mmol) and $LiCH_2CMe_2Ph$ (0.34 g, 2.40 mmol) was stirred in toluene (30 mL) at room temperature for 15 h. LiCl was filtered off, and the resulting solution was concentrated to dryness. The brown residue was extracted with hexane (3 × 10 mL), concentrated to ca. 10 mL, and then cooled to –40 °C to give **5**. The filtrate was cooled to –78 °C to give **6** as a yellow microcrystalline solid, and the final solution was concentrated to dryness to give **7** as a brown oil. IR (KBr): $\tilde{\nu}$ = 2912 (s), 1599 (w), 1491 (m), 1436 (s), 1378 (s), 1203 (w), 1157 (m), 1027 (m), 740 (vs), 709 (s), 650 (m), 555 (w), 466 (m) $cm^{-1}$. $^1H$ NMR (300 MHz, [$D_6$]benzene, 25 °C): $\delta$ = 7.62 (m, 4 H), 7.33 (m, 4 H), 7.12 (m, 2 H, $H_5C_6Me_2C$–$CH_2$–Ta), 1.79 (s, 12 H, Ta–$CH_2CMe_2Ph$), 1.68 (s, 30 H, $C_5Me_5$), 1.04 (s, 4 H, Ta–$CH_2CMe_2Ph$), 0.68 (s, 12 H, Ta–$Me_2$) ppm. $^{13}C\{^1H\}$ NMR (75 MHz, [$D_6$]benzene, 25 °C): $\delta$ = 157.3 ($C_i$), 127.9, 126.3, 124.8 ($H_5C_6Me_2C$–$CH_2$), 117.8 ($C_5Me_5$), 88.3 (Ta–$CH_2CMe_2Ph$), 61.4 (Ta–$Me_2$), 43.7 (Ta–$CH_2CMe_2Ph$), 35.2 (Ta–$CH_2CMe_2Ph$), 11.4 ($C_5Me_5$) ppm.

**[TaCp*Me$_2$(CH$_2$CMe$_2$-*o*-C$_6$H$_4$-κ$^2$*C*,*C*)] (6) and [TaCp*Me(CH$_2$CMe$_2$Ph)(CH$_2$)] (7):** Under rigorously anhydrous conditions (glove box), a solution of TaCp*$Cl_2Me_2$ (0.50 g, 1.20 mmol) in toluene (30 mL) was treated with a solution of $LiCH_2CMe_2Ph$ (0.34 g, 2.40 mmol) in toluene (10 mL), and the mixture was stirred at room temperature for 15 h. The resulting suspension was concentrated to dryness, and the residue extracted with hexane (2 × 15 mL). The solution was filtered, concentrated to ca. 10 mL and cooled to –78 °C over a period of several minutes to give a pale brown microcrystalline solid identified as **6**. Compound **6** was then filtered off, and the solution was concentrated to dryness to give **7** as a sticky brown solid.

Data for **6**: Yield 0.18 g (32%). IR (KBr): $\tilde{\nu}$ = 2909 (vs), 1654 (w), 1574 (w), 1492 (m), 1438 (s), 1377 (s), 1238 (m), 1102 (m), 1024 (m), 762 (s), 731 (vs), 560 (m), 460 (m), 411 (m) $cm^{-1}$. $^1H$ NMR (500 MHz, [$D_2$]dichloromethane, –40 °C): $\delta$ = 8.05 (m, 1 H, $H_4C_6$–*o*-$CMe_2$–$CH_2$–Ta), 7.27 (m, 1 H, $H_4C_6$–*o*-$CMe_2$–$CH_2$–Ta), 7.20 (m, 1 H, $H_4C_6$–*o*-$CMe_2$–$CH_2$–Ta), 7.10 (m, 1 H, $H_4C_6$–*o*-$CMe_2$–$CH_2$–Ta), 1.89 (s, 15 H, $C_5Me_5$), 1.07 (s, 6 H, $H_4C_6$–*o*-$CMe_2$–$CH_2$–Ta), 0.77 (s, 2 H, $H_4C_6$–*o*-$CMe_2$–$CH_2$–Ta), 0.18 (s, 6 H, Ta–$Me_2$) ppm. $^{13}C$ NMR[32] (125 MHz, [$D_2$]dichloromethane, 25 °C): $\delta$ = 219.1 ($C_i$–Ta), 137.1, 124.0, 123.8, 123.2, 160.3 ppm ($H_4C_6$–*o*-$CMe_2$–$CH_2$–Ta), 115.9 ($C_5Me_5$), 112.4 ($H_4C_6$–*o*-$CMe_2$–$CH_2$–Ta), 67.4 (Ta–$Me_2$), 49.5 ($H_4C_6$–*o*-$CMe_2$–$CH_2$–Ta), 34.0 ($H_4C_6$–*o*-$CMe_2$–$CH_2$–Ta), 10.2 ($C_5Me_5$) ppm. $C_{22}H_{33}Ta$ (478.45): calcd. C 55.23, H 6.95; found C 55.10, H 6.75.

Data for **7**: Yield 0.32 g (56%). $^1H$ NMR (500 MHz, [$D_2$]dichloromethane, 25 °C): $\delta$ = 7.41, 7.28, 7.13 ($H_5C_6Me_2C$–$CH_2$–Ta), 5.27 (s, 2 H, Ta=$CH_2$), 1.95 (s, 15 H, $C_5Me_5$), 1.46 (s, 3 H), 1.40 (s, 3 H, $H_5C_6Me_2C$–$CH_2$–Ta), 1.26 (d), 0.04 (q, AB, $^2J_{H,H}$ = 14.8 Hz, 2 H, $H_5C_6Me_2C$–$CH_2$–Ta), –0.52 (d, $^4J_{H,H}$ = 1.1 Hz, 3 H, Ta–*Me*) ppm. $^{13}C\{^1H\}$ NMR (75 MHz, [$D_6$]benzene, 25 °C): $\delta$ = 205.9 (t, $^1J_{C,H}$ = 126.1 Hz, Ta=$CH_2$), 153.5–125.4 ($H_5C_6Me_2C$–$CH_2$–Ta), 113.6 ($C_5Me_5$), 94.8 (t, $^1J_{C,H}$ = 105.6 Hz, $H_5C_6Me_2C$–$CH_2$–Ta), 44 (Ta–*Me*), 40 ($H_5C_6Me_2C$–$CH_2$–Ta), 31.4, 32 ($H_5C_6Me_2C$–$CH_2$–Ta), 11.3 ($C_5Me_5$) ppm.

 © 2006 Wiley-VCH Verlag GmbH & Co. KGaA, Weinheim 

**[TaCp*Cl($CH_2SiMe_3$)($CHSiMe_3$)] (8):** A solution of **1** (0.15 g, 0.24 mmol) in toluene (20 mL) was placed in an ampoule under rigorously anhydrous conditions and then sealed. The solution was heated to 60 °C for 2 days. After the ampoule was opened, the solution was concentrated to dryness, and the brown oil residue was identified as **8**. Yield 0.10 g (80%). IR (KBr): $\tilde{\nu}$ = 2913 (s), 2578 (w), 1584 (m), 1488 (m), 1432 (m), 1378 (m), 1244 (vs), 1097 (m), 1026 (s), 941 (s), 841 (vs), 750 (s), 682 (s), 483 (m), 437 (w) $cm^{-1}$. $^1H$ NMR (500 MHz, [D$_2$]dichloromethane, 25 °C): $\delta$ = 5.54 (s, 1 H, Ta=C*H*SiMe$_3$), 2.15 (s, 15 H, C$_5$*Me*$_5$), 0.23 (AB, $^2J_{H,H}$ = 12.7 Hz, 1 H, Ta–CH*H*SiMe$_3$), 0.12 (s, 9 H, Ta–CH$_2$Si*Me*$_3$), 0.07 (s, 9 H, Ta=CHSi*Me*$_3$), 0.053 (AB, $^2J_{H,H}$ = 12.7 Hz, 1 H, Ta–CH*H*SiMe$_3$) ppm. $^{13}C\{^1H\}$ NMR (125 MHz, [D$_6$]benzene, 25 °C): $\delta$ = 231.5 (d, $^1J_{C,H}$ = 89.0 Hz, Ta=*C*HSiMe$_3$), 116.5 (*C*$_5$Me$_5$), 50.6 (Ta–*C*H$_2$SiMe$_3$), 11.9 (C$_5$*Me*$_5$), 3.4 (Ta–CH$_2$Si*Me*$_3$), 2.5 (Ta=CHSi*Me*$_3$) ppm. $C_{18}H_{36}ClSi_2Ta$ (524.879): calcd. C 41.15, H 6.91; found C 41.18, H 6.81.

**[TaCp*MeR(CHSiMe$_3$)] (R = CH$_2$SiMe$_3$, 9; Me, 10):** A solution of **3** (0.07 g, 0.13 mmol) in [D$_6$]benzene (0.70 mL) was placed into an NMR tube with a valve, and this tube was heated to 60 °C. The reaction was monitored by NMR spectroscopy, and after 20 h the formation of a mixture of the (alkyl)(alkylidene) derivatives **9** and **10** in a 3:2 ratio was confirmed.

Data for **9**: $^1H$ NMR (300 MHz, [D$_6$]benzene, 25 °C): $\delta$ = 4.80 (s, 1 H, Ta=C*H*SiMe$_3$), 1.82 (s, 15 H, C$_5$*Me*$_5$), 0.32 (s, 9 H, Ta–CH$_2$Si*Me*$_3$), 0.28 (s, 9 H, Ta=CHSi*Me*$_3$), 0.06 (s, 3 H, Ta–*Me*), –0.06 (AB, $^2J_{H,H}$ = 12.4 Hz, 1 H, Ta–CH*H*SiMe$_3$), –0.93 (AB, $^2J_{H,H}$ = 12.4 Hz, 1 H, Ta–CH*H*SiMe$_3$) ppm. $^{13}C\{^1H\}$ NMR (75 MHz, [D$_6$]benzene, 25 °C): $\delta$ = 223.3 (d, $^1J_{C,H}$ = 76.9 Hz, Ta=*C*HSiMe$_3$), 114.8 (*C*$_5$Me$_5$), 59.9 (t, $^1J_{C,H}$ = 105.3 Hz, Ta–*C*H$_2$SiMe$_3$), 42.2 (Ta–*Me*), 11.8 (C$_5$*Me*$_5$), 3.7 (Ta–CH$_2$Si*Me*$_3$), 2.8 (Ta=CHSi*Me*$_3$) ppm.

Data for **10**: $^1H$ NMR (300 MHz, [D$_6$]benzene, 25 °C): $\delta$ = 5.81 (s, 1 H, Ta=C*H*SiMe$_3$), 1.79 (s, 15 H, C$_5$*Me*$_5$), 0.37 (s, 9 H, Ta=CHSi*Me*$_3$), 0.13 (s, 6 H, Ta–*Me*$_2$) ppm. $^{13}C\{^1H\}$ NMR (75 MHz, [D$_6$]benzene, 25 °C): $\delta$ = 222.8 (d, $^1J_{C,H}$ = 75.7 Hz, Ta=*C*HSiMe$_3$), 114.7 (*C*$_5$Me$_5$), 47.9 (Ta–*Me*$_2$), 11.6 (C$_5$*Me*$_5$), 3.9 (Ta=CHSi*Me*$_3$) ppm.

**[TaCp*(CH$_2$SiMe$_3$)R(CH$_2$)] (R = Me, 11; CH$_2$SiMe$_3$, 12):** In a standard experiment, a solution of **3** (0.07 g, 0.13 mmol) in [D$_6$]benzene (0.60 mL) was transferred to a valved NMR tube and then irradiated with a sun lamp for 2 h. A mixture of the (alkyl)(alkylidene) compounds **9**, **11** and **12**, in a ratio 2:1:1, together with the elimination products $CH_4$ and $SiMe_4$, was identified in the NMR spectrum of the resulting solution.

Data for **11**: $^1H$ NMR (300 MHz, [D$_6$]benzene, 25 °C): $\delta$ = 6.06 (s, 2 H, Ta=C*H*$_2$), 1.77 (s, 15 H, C$_5$*Me*$_5$), 0.34 (s, 9 H, Ta–CH$_2$Si*Me*$_3$), 0.11 (s, 3 H, Ta–*Me*), –0.14 (AB, $^2J_{H,H}$ = 12.5 Hz, 1 H, Ta–CH*H*SiMe$_3$), –0.69 (AB, $^2J_{H,H}$ = 12.5 Hz, 1 H, Ta–CH*H*SiMe$_3$) ppm. $^{13}C\{^1H\}$ NMR (75 MHz, [D$_6$]benzene, 25 °C): $\delta$ = 207.0 (t, $^1J_{C,H}$ = 125.8 Hz, Ta=*C*H$_2$), 113.3 (*C*$_5$Me$_5$), 60 (Ta–*C*H$_2$SiMe$_3$), 43.1 (Ta–*Me*), 11.3 (C$_5$*Me*$_5$), 2.5 (Ta–CH$_2$Si*Me*$_3$) ppm.

Data for **12**: $^1H$ NMR (300 MHz, [D$_6$]benzene, 25 °C): $\delta$ = 5.89 (s, 2 H, Ta=C*H*$_2$), 1.79 (s, 15 H, C$_5$*Me*$_5$), 0.31 (s, 18 H, Ta–CH$_2$Si*Me*$_3$), 0.06 (AB, $^2J_{H,H}$ = 11.9 Hz, 1 H, Ta–CH*H*SiMe$_3$), –1.05 (AB, $^2J_{H,H}$ = 11.9 Hz, 1 H, Ta–CH*H*SiMe$_3$) ppm. $^{13}C\{^1H\}$ NMR (75 MHz, [D$_6$]benzene, 25 °C): $\delta$ = 205.5 (t, $^1J_{C,H}$ = 126.6 Hz, Ta=*C*H$_2$), 113.2 (*C*$_5$Me$_5$), 56.8 (Ta–*C*H$_2$SiMe$_3$), 11.5 (C$_5$*Me*$_5$), 2.6 (Ta–CH$_2$Si*Me*$_3$) ppm.

**[TaCp*MeR(CHCMe$_3$)] (R = Me, 13; CH$_2$CMe$_3$, 14):** A solution of **4** (0.04 g, 0.08 mmol) in [D$_6$]benzene (0.60 mL) was placed into a sealed NMR tube and then heated to 60 °C for 4 h. The reaction was monitored by NMR, and a mixture of (alkyl)(alkylidene) compounds **13** and **14**, in a 4:1 ratio, together with the organic elimination products $CMe_4$ ($\delta$ = 0.9 ppm) and $CH_4$ ($\delta$ = 0.15 ppm), was identified by NMR spectroscopy.

Data for **13**: $^1H$ NMR (300 MHz, [D$_6$]benzene, 25 °C): $\delta$ = 3.38 (s, 1 H, Ta=C*H*CMe$_3$), 1.84 (s, 15 H, C$_5$*Me*$_5$), 1.30 (s, 9 H, Ta=CHC*Me*$_3$), 0.07 (s, 6 H, Ta–*Me*$_2$) ppm. $^{13}C\{^1H\}$ NMR (75 MHz, [D$_6$]benzene, 25 °C): $\delta$ = 224.2 (d, $^1J_{C,H}$ = 80.3 Hz, Ta=*C*HCMe$_3$), 114.3 (*C*$_5$Me$_5$), 40.9 (Ta–*Me*$_2$), 34.9 (Ta=CH*C*Me$_3$), 33.9 (Ta=CHC*Me*$_3$), 11.3 (C$_5$*Me*$_5$) ppm.

Data for **14**: $^1H$ NMR (300 MHz, [D$_6$]benzene, 25 °C): $\delta$ = 3.26 (s, 1 H, Ta=C*H*CMe$_3$), 1.83 (s, 15 H, C$_5$*Me*$_5$), 1.34 (s, 9 H, Ta=CHC*Me*$_3$), 1.34 (s, 9 H, Ta–CH$_2$C*Me*$_3$), 1.08 (AB, $^2J_{H,H}$ = 14.2 Hz, 1 H, Ta–CH*H*CMe$_3$), –0.07 (s, 3 H, Ta–*Me*), –0.71 (AB, $^2J_{H,H}$ = 14.2 Hz, 1 H, Ta–CH*H*CMe$_3$) ppm. $^{13}C\{^1H\}$ NMR (75 MHz, [D$_6$]benzene, 25 °C): $\delta$ = 226.1 (d, $^1J_{C,H}$ = 78.1 Hz, Ta=*C*HCMe$_3$), 113.9 (*C*$_5$Me$_5$), 94.2 (t, $^1J_{C,H}$ = 102.1 Hz, Ta–*C*H$_2$CMe$_3$), 47.1, 37 (Ta–*Me*), 35.2, 34.0 (Ta=CHC*Me*$_3$, Ta–CH$_2$C*Me*$_3$), 33.7 (Ta=CH*C*Me$_3$, Ta–CH$_2$*C*Me$_3$), 11.6 (C$_5$*Me*$_5$) ppm.

**[TaCp*(CH$_2$CMe$_3$)R(CH$_2$)] (R = Me, 15; CH$_2$CMe$_3$, 16):** In a typical experiment, a yellow solution of **4** (0.04 g, 0.08 mmol) in [D$_6$]-benzene (0.60 mL) was transferred to a valved NMR tube and then irradiated with a sun lamp for 3 h. The (alkyl)(alkylidene) complexes **15** and **16**, in a ratio of 3:1, and the organic elimination products $CMe_4$ and $CH_4$ were identified in the NMR spectrum.

Data for **15**: $^1H$ NMR (300 MHz, [D$_6$]benzene, 25 °C): $\delta$ = 5.92 (s, 2 H, Ta=C*H*$_2$), 1.75 (s, 15 H, C$_5$*Me*$_5$), 1.28 (s, 9 H, Ta–CH$_2$C*Me*$_3$), 1.06 (AB, $^2J_{H,H}$ = 14.4 Hz, 1 H, Ta–CH*H*CMe$_3$), 0.032 (s, 3 H, Ta–*Me*), –0.30 (AB, $^2J_{H,H}$ = 14.4 Hz, 1 H, Ta–CH*H*CMe$_3$) ppm. $^{13}C\{^1H\}$ NMR (75 MHz, [D$_6$]benzene, 25 °C): $\delta$ = 205.5 (t, Ta=*C*H$_2$, $^1J_{C,H}$ = 125.3 Hz), 113.2 (*C*$_5$Me$_5$), 96 (t, Ta–*C*H$_2$CMe$_3$, $^1J_{C,H}$ = 117.2 Hz), 42.9 (Ta–*Me*), 34.8 (Ta–CH$_2$C*Me*$_3$), 32.8 (Ta–CH$_2$*C*Me$_3$), 11.2 (C$_5$*Me*$_5$).

Data for **16**: $^1H$ NMR (300 MHz, [D$_6$]benzene, 25 °C): $\delta$ = 5.80 (s, 2 H, Ta=C*H*$_2$), 1.77 (s, 15 H, C$_5$*Me*$_5$), 1.34 (s, 18 H, Ta–CH$_2$C*Me*$_3$), 1.20 (AB, $^2J_{H,H}$ = 13.0 Hz, 1 H, Ta–CH*H*CMe$_3$), –0.40 (AB, $^2J_{H,H}$ = 13.0 Hz, 1 H, Ta–CH*H*CMe$_3$) ppm. $^{13}C\{^1H\}$ NMR (75 MHz, [D$_6$]benzene, 25 °C): $\delta$ = 209.4 (t, $^1J_{C,H}$ = 126.1 Hz, Ta=*C*H$_2$), 112.8 (C$_5$*Me*$_5$), 92.4 (t, $^1J_{C,H}$ = 110.9 Hz, Ta–*C*H$_2$CMe$_3$), 35 (Ta–CH$_2$C*Me*$_3$), 34 (Ta–CH$_2$*C*Me$_3$), 11.6 (C$_5$*Me*$_5$) ppm.

**[TaCp*(CH$_2$CMe$_3$)(CH$_2$SiMe$_3$)(CHCMe$_3$)] (17):** TaCp*Cl$_2$-(CH$_2$CMe$_3$)$_2$ (0.70 g, 1.30 mmol) and LiCH$_2$SiMe$_3$ (0.25 g, 2.60 mmol) were stirred in hexane (45 mL) at room temperature for 10 h. The resulting suspension was filtered and concentrated to ca. 5 mL and cooled overnight to –40 °C to give **17** as an orange microcrystalline solid. Yield 0.44 (61%). IR (CsI): $\tilde{\nu}$ = 2940 (vs), 2430 (m), 1459 (s), 1434 (m), 1353 (s), 1243 (vs), 1024 (m), 950 (s), 853 (vs), 827 (s), 744 (m), 720 (m), 684 (m), 573 (w), 508 (m), 417 (m) $cm^{-1}$. $^1H$ NMR (500 MHz, [D$_6$]benzene, 25 °C): $\delta$ = 3.10 (s, 1 H, Ta=C*H*CMe$_3$), 1.84 (s, 15 H, C$_5$*Me*$_5$), 1.38 (s, 9 H) and 1.35 (s, 9 H) (Ta=CHC*Me*$_3$ and Ta–CH$_2$C*Me*$_3$), 1.03 (AB, $^2J_{H,H}$ = 13.8 Hz, 1 H, Ta–CH*H*CMe$_3$), 0.32 (s, 9 H, Ta–CH$_2$Si*Me*$_3$), 0.11 (AB, $^2J_{H,H}$ = 12.0 Hz, 1 H, Ta–CH*H*SiMe$_3$), –0.38 (AB, $^2J_{H,H}$ = 13.8 Hz, 1 H, Ta–CH*H*CMe$_3$), –1.44 (AB, $^2J_{H,H}$ = 12.0 Hz, 1 H, Ta–CH*H*SiMe$_3$) ppm. $^{13}C\{^1H\}$ NMR (125 MHz, [D$_6$]benzene, 25 °C): $\delta$ = 226.4 (d, $^1J_{C,H}$ = 77.4 Hz, Ta=*C*HSiMe$_3$), 114 (*C*$_5$Me$_5$), 88.7 (Ta–*C*H$_2$CMe$_3$), 53.7 (Ta–*C*H$_2$SiMe$_3$), 47.6, 35.4, 34.2 (Ta–CH$_2$C*Me*$_3$, Ta=CHC*Me*$_3$), 34.1 (Ta–CH$_2$*C*Me$_3$, Ta=CH*C*Me$_3$), 12.0 (C$_5$*Me*$_5$), 3.2 (Ta–CH$_2$Si*Me*$_3$) ppm. $C_{24}H_{47}SiTa$ (544.663): calcd. C 52.92, H 8.69; found C 52.67, H 8.97.

 © 2006 Wiley-VCH Verlag GmbH & Co. KGaA, Weinheim 

**[TaCp*(CH$_2$Ph)(CH$_2$SiMe$_3$)(CHPh)] (18):** This reaction was carried out in a glove box in darkened glassware designed for photosensitive materials. A 1 M solution of MgCl(CH$_2$Ph) in diethyl ether (1.50 mL, 1.45 mmol) was added to a solution of TaCp*Cl$_2$-(CH$_2$SiMe$_3$)$_2$ (0.40 g, 1.71 mmol) in hexane (30 mL), and the mixture was stirred for 14 h. The resulting suspension was decanted and filtered through Celite. The red solution was concentrated to ca. 5 mL and cooled to –40 °C overnight to give **18** as a red microcrystalline solid. Yield 0.27 g (65%). IR (CsI): $\tilde{\nu}$ = 2914 (vs), 2494 (w), 1856 (w), 1592 (m), 1485 (vs), 1449 (s), 1378 (m), 1242 (s), 1199 (m), 1054 (m), 1027 (s), 950 (m), 850 (vs), 750 (vs), 695 (s), 536 (m), 438 (w) cm$^{-1}$. $^1$H NMR (300 MHz, [D$_6$]benzene, 25 °C): $\delta$ = 7.29–6.86 (several phenyl, $H_5C_6CH_2$–Ta, $H_5C_6CH$=Ta), 5.45 (s, 1 H, Ta=C*H*Ph), 1.79 (s, 15 H, C$_5$*Me*$_5$), 1.68 (AB, $^2J_{H,H}$ = 12.3 Hz, 1 H, Ta–CH*H*Ph), 1.61 (AB, $^2J_{H,H}$ = 12.3 Hz, 1 H, Ta–CH*H*Ph), 0.88 (AB, $^2J_{H,H}$ = 12.1 Hz, 2 H, Ta–CH*H*Ph , Ta–CH*H*SiMe$_3$), 0.09 (s, 9 H, Ta–CH$_2$Si*Me*$_3$), –1.29 (AB, $^2J_{H,H}$ = 12.1 Hz, 2 H, Ta–CH*H*Ph, Ta–CH*H*SiMe$_3$) ppm. $^{13}$C{$^1$H} NMR (75 MHz, [D$_6$]benzene, 25 °C): $\delta$ = 216.7 (d, $^1J_{C,H}$ = 82.6 Hz, Ta=*C*HPh), 151.1–122.9 (several phenyl, $H_5C_6CH_2$–Ta, $H_5C_6CH$=Ta), 114.5 (*C*$_5$Me$_5$), 69.1 (t, $^1J_{C,H}$ = 119.4 Hz, Ta–*C*H$_2$Ph), 64.1 (t, $^1J_{C,H}$ = 104.2 Hz, Ta–*C*H$_2$SiMe$_3$), 11.3 (C$_5$*Me*$_5$), 2.7 (Ta–CH$_2$Si*Me*$_3$) ppm. $C_{28}H_{39}SiTa$ (584.65): calcd. C 57.52, H 6.72; found C 57.48, H 6.75.

**[TaCp*(CH$_2$CMe$_2$Ph)(CH$_2$SiMe$_3$)(CHSiMe$_3$)] (19):** TaCp*Cl$_2$-(CH$_2$SiMe$_3$)$_2$ (0.30 g, 0.53 mmol) and Li(CH$_2$CMe$_2$Ph) (0.16 g, 1.20 mmol) were stirred in toluene (40 mL) at room temperature for 15 h. The volatiles were removed under reduced pressure, and the residual solid was extracted with hexane (2 × 15 mL). The solution was filtered and concentrated to dryness to give **19** as a pale brown oil. Yield 0.26 g (81%). IR (CsI): $\tilde{\nu}$ = 2910 (vs), 2564 (w), 1599 (w), 1492 (m), 1442 (s), 1379 (s), 1242 (vs), 1169 (m), 1028 (m), 945 (vs), 847 (vs), 762 (s), 702 (s), 626 (w), 552 (m), 434 (m) cm$^{-1}$. $^1$H NMR (300 MHz, [D$_6$]benzene, 25 °C): $\delta$ = 7.44 (m, 2 H, $H_5C_6Me_2CCH_2$–Ta), 7.26 (m, 2 H, $H_5C_6Me_2CCH_2$–Ta), 7.09 (m, 1 H, $H_5C_6Me_2CCH_2$–Ta), 4.17(s, 1 H, Ta=C*H*SiMe$_3$), 1.79 (s, 15 H, C$_5$*Me*$_5$), 1.70 (s, 3 H), 1.57 (s, 3 H, Ta–CH$_2$C*Me*$_2$Ph), 1.01 (AB, $^2J_{H,H}$ = 14.4 Hz, 1 H), not detected (AB, $^2J_{H,H}$ = 14.4 Hz, 1 H), 0.40 (AB, $^2J_{H,H}$ = 11.7 Hz, 2 H, Ta–CH*H*CMe$_2$Ph, Ta–CH*H*SiMe$_3$), 0.28 (s, 9 H), 0.14 (s, 9 H, Ta–CH$_2$Si*Me*$_3$, Ta=CHSi-*Me*$_3$), –2.05 (AB, $^2J_{H,H}$ = 11.7 Hz, 2 H, Ta–CH*H*CMe$_2$Ph, Ta–CH*H*SiMe$_3$) ppm. $^{13}$C{$^1$H} NMR (75 MHz, [D$_6$]benzene, 25 °C): $\delta$ = 226.8 (d, $^1J_{C,H}$ = 76.6 Hz, Ta=*C*HSiMe$_3$), 153.6 (C$_i$), 128.5 (C$_o$), 126.4 (C$_m$), 125.5 (C$_p$, $H_5C_6Me_2CCH_2$–Ta), 114.4 (*C*$_5$Me$_5$), 86.7 (t, $^1J_{C,H}$ = 109.5 Hz, Ta–*C*H$_2$CMe$_2$Ph), 64.0 (t, $^1J_{C,H}$ = 103.4 Hz Ta–*C*H$_2$SiMe$_3$), 40.1 (Ta–CH$_2$*C*Me$_2$Ph), 36.9, 31.9 (Ta–CH$_2$C*Me*$_2$Ph), 11.9 (C$_5$*Me*$_5$), 3.6, 2.8 (Ta–CH$_2$Si*Me*$_3$, TaCHSi-*Me*$_3$).

**Crystal Structure Determination for Compounds 1, 4 and 5:** Crystallographic and experimental details of the crystal structure determinations are given in Table 4. Suitably sized crystals were sealed under argon in a Lindemann capillary tube and mounted on an Enraf Nonius CAD 4 automatic four circle diffractometer with graphite monochromated Mo-$K_\alpha$ radiation ($\lambda$ = 0.71073 Å). Intensities were collected at room temperature and corrected for Lorenz and polarization effects in the usual manner. No extinction corrections were made. Empirical absorption corrections (DIFABS)[33] were made to the data for **1** and **4**, and the data for **5** were corrected with $\psi$

Table 4. Crystal data and structure refinement details for **1**, **4** and **5**.[a]

| | **1** | **4** | **5** |
|---|---|---|---|
| Chemical formula | $C_{22}H_{48}ClSi_3Ta$ | $C_{22}H_{43}Ta$ | $C_{44}H_{68}OTa_2$ |
| Formula weight | 613.27 | 488.529 | 974.8 |
| $T$ [K] | 293(2) | 293(2) | 293(2) |
| $\lambda$ (Mo-$K_\alpha$) [Å] | 0.71073 | 0.71073 | 0.71073 |
| Crystal system, space group | Monoclinic, $P2_1/n$ | Monoclinic, $P2_1/c$ | Triclinic, $P\bar{1}$ |
| $a$ [Å]; $\alpha$ [°] | 15.401(1); 90.00 | 9.230(1); 90.00 | 8.639(2); 101.7(2) |
| $b$ [Å]; $\beta$ [°] | 10.945(1); 91.09(2) | 31.913(1); 99.06(5) | 10.278(2); 98.77(2) |
| $c$ [Å]; $\gamma$ [°] | 17.721(1); 90.00 | 16.087(1); 90.00 | 12.159(4); 100.71(2) |
| $V$ [Å]$^3$ | 2986.6(4) | 4679.4(6) | 1018.3(5) |
| Z | 4 | 8 | 1 |
| $\rho_{calcd}$ [g cm$^{-3}$] | 1.364 | 1.3804 | 1.590 |
| $\mu$ [mm$^{-1}$] | 3.896 | 4.698 | 5.399 |
| $F$(000) | 1248 | 1984 | 486 |
| Crystal size [mm$^3$] | 0.27 × 0.30 × 0.33 | 0.35 × 0.30 × 0.20 | 0.35 × 0.35 × 0.10 |
| $\theta$ range [°] | 1.32 to 22.97 | 1.28 to 22.93 | 2.08 to 25.11 |
| Index ranges | –16 ≤$h$≤ 16 | –9 ≤$h$≤ 0 | –10 ≤$h$≤ 0 |
| | –12 ≤$k$≤ 0 | –34 ≤$k$≤ 0 | –12 ≤$k$≤ 12 |
| | 0 ≤$l$≤ 19 | –16 ≤$l$≤ 16 | –14 ≤$l$≤ 14 |
| Number of data collected | 4366 | 6144 | 3873 |
| Number of unique data | 4134 [$R$(int) = 0.0661] | 5711 [$R$(int) = 0.1381] | 3612 [$R$(int) = 0.0172] |
| Number of observed reflections [$I$>2σ($I$)] | 1669 | 2531 | 3368 |
| Absorption correction | Empirical (DIFABS) | Empirical (DIFABS) | $\psi$-scan |
| Max. and min. transmission | 0.702, 0.243 | 0.638, 0.166 | 0.5815, 0.0942 |
| Number of refined parameters | 244 | 390 | 214 |
| Goodness-of-fit on $F^2$ | 0.926 | 0.951 | 1.105 |
| Final $R$ indices [$I$>2σ($I$)] | $R_1$ = 0.0628 | $R_1$ = 0.0677 | $R_1$ = 0.0710 |
| | $wR_2$ = 0.1079 | $wR_2$ = 0.1421 | $wR_2$ = 0.1764 |
| $R$ indices (all data) | $R_1$ = 0.2540 | $R_1$ = 0.2431 | $R_1$ = 0.0744 |
| | $wR_2$ = 0.1469 | $wR_2$ = 0.1870 | $wR_2$ = 0.1802 |
| Largest diff. peak and hole [e Å$^{-3}$] | 0.857 and –1.422 | 0.917 and –1.605 | 5.664 and –5.187 (near Ta) |

[a] $R_1 = \Sigma||F_o|-|F_c||/[\Sigma|F_o|]$; $wR_2 = \{[\Sigma w(F_o^2-F_c)^2]/[\Sigma w(F_o^2)^2]\}^{1/2}$.

 © 2006 Wiley-VCH Verlag GmbH & Co. KGaA, Weinheim 

scan methods. Structures were initially solved by direct methods, completed by the subsequent difference Fourier techniques and refined by full-matrix least-squares on $F^2$ (SHELXL-97).[34] Anisotropic thermal parameters were included in the last cycles of refinement for the non-hydrogen atoms, except for five carbon atoms in compound **5** that remained isotropic. The hydrogen atoms were included from geometrical calculations and refined by using a riding model. All the calculations were performed with the WINGX system.[35]

CCDC-299683(**1**), 299684(**4**) and 299685(**5**) contain the supplementary crystallographic data for this paper. These data can be obtained free of charge from The Cambridge Crystallographic Data Centre via www.ccdc.cam.ac.uk/data_request/cif.

**Supporting Information** (see footnote on the first page of this article): $^1$H NMR spectra of complexes **9-16**.

## Acknowledgments

We thank the MCYT (Project BQU 2002–03754) and Universidad de Alcalá (Project GC 2005/94) for their financial support for this research.

[1] J. S. Moore, *Comprehensive Organometallic Chemistry II*, Pergamon, New York, **1995**, vol. 12, ch. 12.2.

[2] a) G. W. Coates, R. M. Waymouth, *Comprehensive Organometallic Chemistry II*, Pergamon, New York, **1995**, vol. 12, ch. 12.1; b) M. Bochmann, *J. Chem. Soc., Dalton Trans.* **1996**, 255–270; c) W. Kaminsky, M. Arndt, *Adv. Polym. Sci.* **1997**, *127*, 144.

[3] a) J. Feldman, R. R. Schrock, *Prog. Inorg. Chem.* **1991**, *39*, 1–74; b) H. H. Brintzinger, D. Fischer, R. Mülhaupt, B. Rieger, R. M. Waymouth, *Angew. Chem. Int. Ed. Engl.* **1995**, *34*, 1143–1170; c) K. S. Cook, W. E. Piers, S. J. Retting, *Organometallics* **1999**, *18*, 1575–1577; d) R. R. Schrock, *Chem. Rev.* **2002**, *102*, 145–179.

[4] a) B. Temme, G. Erker, R. Fröhlich, M. Grehl, *Angew. Chem. Int. Ed. Engl.* **1994**, *33*, 1480–1482; b) X. Yang, C. L. Stren, T. J. Marks, *J. Am. Chem. Soc.* **1994**, *116*, 10015–10031; c) K. Soga, H. Deng, T. Yano, T. Shiono, *Macromolecules* **1994**, *27*, 7938–7940.

[5] a) B. Temme, J. Karl, G. Erker, *Chem. Eur. J.* **1996**, *2*, 919; b) L. Jia, X. Yang, C. L. Stren, T. J. Marks, *Organometallics* **1997**, *16*, 842–857; c) P. A. Deck, C. L. Beswick, T. J. Marks, *J. Am. Chem. Soc.* **1998**, *120*, 1772–1784.

[6] a) Y. Sun, R. E. v. H. Spence, W. E. Piers, M. Parvez, G. P. A. Yap, *J. Am. Chem. Soc.* **1997**, *119*, 5132–5143; b) R. E. v. H. Spence, W. E. Piers, Y. Sun, M. Parvez, L. R. MacGillivray, M. J. Zaworotko, *Organometallics* **1998**, *17*, 2459–2469; c) D. J. Parks, W. E. Piers, G. P. A. Yap, *Organometallics* **1998**, *17*, 5492–5503; d) Y. Sun, W. E. Piers, G. P. A. Yap, *Organometallics* **1999**, *16*, 2509–2513.

[7] a) M. A. Gallop, W. R. Roper, *Adv. Organomet. Chem.* **1986**, *25*, 121–194; b) M. Brookhart, W. B. Studabaker, *Chem. Rev.* **1987**, 411–432; c) R. M. Bullock, R. T. Hembre, J. R. Norton, *J. Am. Chem. Soc.* **1988**, *110*, 7868–7870; d) B. Denise, D. Navarre, H. Rudler, J. C. Daran, *J. Organomet. Chem.* **1989**, *375*, 273–289; e) T. R. Balderraín, E. Gutiérrez, A. Monge, M. C. Nicasio, M. Paneque, M. L. Poveda, E. Carmona, *Organometallics* **1993**, *12*, 4431–4442.

[8] I. de Castro, J. de la Mata, M. Gómez, P. Gómez-Sal, P. Royo, J. M. Selas, *Polyhedron* **1992**, *11*, 1023–1027.

[9] I. de Castro, M. V. Galakhov, M. Gómez, P. Gómez-Sal, P. Royo, *Organometallics* **1996**, *15*, 1362–1368.

[10] A. Castro, M. V. Galakhov, M. Gómez, P. Gómez-Sal, A. Martín, *Eur. J. Inorg. Chem.* **2002**, 1336–1342.

[11] a) R. B. King, M. B. Bisnette, *J. Organomet. Chem.* **1967**, *8*, 287–297; b) M. V. Galakhov, M. Gómez, G. Jiménez, P. Royo, M. A. Pellinghelli, A. Tiripicchio, *Organometallics* **1995**, *14*, 1901–1910; c) A. Castro, M. V. Galakhov, M. Gómez, P. Gómez-Sal, A. Martín, F. Sánchez, *J. Organomet. Chem.* **2000**, *595*, 36–53; d) M. V. Galakhov, M. Gómez, P. Gómez-Sal, P. Velasco, *Organometallics* **2005**, *24*, 848–856.

[12] a) M. Nardelli, *Comput. Chem.* **1983**, *7*, 95–98; b) M. Nardelli, *J. Appl. Crystallogr.* **1995**, *28*, 659.

[13] M. Gómez, G. Jiménez, P. Royo, J. M. Selas, P. R. Raithby, *J. Organomet. Chem.* **1992**, *439*, 147–154.

[14] a) H. Yasuda, K. Tatsumi, T. Okamoto, K. Mashima, K. Lee, A. Nakamura, Y. Kai, N. Kanehisa, N. Kasai, *J. Am. Chem. Soc.* **1985**, *107*, 2410–2422; b) F. Takusagawa, T. F. Koetzle, P. R. Sharp, R. R. Schrock, *Acta Crystallogr., Sect. C* **1988**, *44*, 439; c) I. de Castro, M. V. Galakhov, M. Gómez, P. Gómez-Sal, A. Martín, P. Royo, *J. Organomet. Chem.* **1996**, *514*, 51–58; d) M. V. Galakhov, M. Gómez, P. Gómez-Sal, P. Velasco, *Organometallics* **2005**, *24*, 3552–3560.

[15] J. de la Mata, R. Fandos, M. Gómez, P. Gómez-Sal, S. Martínez-Carrera, P. Royo, *Organometallics* **1990**, *9*, 2846–2850.

[16] a) M. Gómez, G. Jiménez, P. Royo, M. A. Pellinghelli, A. Tiripicchio, *J. Organomet. Chem.* **1992**, *439*, 309–318; b) A. Castro, M. V. Galakhov, M. Gómez, P. Gómez-Sal, A. Martín, F. Sánchez, P. Velasco, *Eur. J. Inorg. Chem.* **2000**, 2047–2054.

[17] M. Gómez, P. Gómez-Sal, G. Jiménez, A. Martín, P. Royo, J. Sánchez-Nieves, *Organometallics* **1996**, *15*, 3579–3587.

[18] a) L. R. Chamberlain, A. P. Rothwell, I. P. Rothwell, *J. Am. Chem. Soc.* **1984**, *106*, 1847–1948; b) L. R. Chamberlain, I. P. Rothwell, J. C. Huffman, *J. Am. Chem. Soc.* **1986**, *108*, 1502–1509; c) L. R. Chamberlain, I. P. Rothwell, K. Folting, J. C. Huffman, *J. Chem. Soc., Dalton Trans.* **1987**, 155–162; d) M. V. Galakhov, M. Gómez, G. Jiménez, P. Royo, M. A. Pellinghelli, A. Tiripicchio, *Organometallics* **1995**, *14*, 2843–2854; e) K. G. Parker, B. Noll, C. G. Pierpònt, M. R. DuBois, *Inorg. Chem.* **1996**, *35*, 3228–3234; f) S. Cai, D. M. Hoffman, D. A. Wierda, *Organometallics* **1996**, *15*, 1023–1032; g) A. Galindo, M. Gómez, P. Gómez-Sal, A. Martín, D. del Rio, F. Sánchez, *Organometallics* **2002**, *21*, 293–304.

[19] a) I. P. Rothwell, *Polyhedron* **1985**, *4*, 177–200; b) Y.-D. Wu, Z.-H. Peng, K. W. K. Chan, X. Liu, A. A. Tuinman, Z. Xue, *Organometallics* **1999**, *18*, 2081–2090.

[20] a) Y.-D. Wu, K. W. K. Chan, Z. Xue, *J. Am. Chem. Soc.* **1995**, *17*, 9259–9264; b) L. Li, M. Hung, Z. Xue, *J. Am. Chem. Soc.* **1995**, *17*, 12746–12750; c) L. Li, Z. Xue, G. P. A. Yap, A. L. Rheingold, *Organometallics* **1995**, *14*, 4992–4993; d) J. B. Diminnie, H. D. Hall, Z. Xue, *Chem. Commun.* **1996**, 2383–2384; e) R. Andrés, P. Gómez-Sal, E. de Jesús, A. Martín, M. Mena, C. Yélamos, *Angew. Chem. Int. Ed. Engl.* **1997**, *36*, 115–117; f) L. Liu, L. Li, J. B. Diminnie, G. P. A. Yap, A. L. Rheingold, Z. Xue, *Organometallics* **1998**, *17*, 4597–4606; g) M. D. Fryzuk, P. B. Duval, S. S. S. H. Mao, M. J. Zaworotko, L. R. MacGillivray, *J. Am. Chem. Soc.* **1999**, *121*, 2478–2487; h) C. G. Ortiz, K. A. Abboud, J. M. Boncella, *Organometallics* **1999**, *18*, 4253–4260.

[21] a) K. Nakamoto, *Infrared and Raman Spectra of Inorganic and Coordination Compounds*, Wiley, New York, **1978**; b) G. J.-J. Chen, J. W. McDonald, D. C. Bravard, W. E. Newton, *Inorg. Chem.* **1985**, *24*, 2327–2333; c) P. Jernakoff, C. de Meric de Bellefon, G. L. Geoffroy, A. L. Rheingold, S. J. Geib, *Organometallics* **1987**, *6*, 1362–1364; d) J. de la Mata, M. Gómez, P. Gómez-Sal, P. Royo, *Inorg. Chem.* **1993**, *32*, 5454–5457; e) A. Castro, M. Gómez, P. Gómez-Sal, A. Manzanero, P. Royo, *J. Organomet. Chem.* **1996**, *518*, 37–46; f) A. Antiñolo, F. Carrillo-Hermosilla, F. Fernández-Baeza, M. Lanfranchi, A. Lara-Sánchez, A. Otero, E. Palomares, M. A. Pellinghelli, A. M. Rodríguez, *Organometallics* **1998**, *17*, 3015–3019; g) S. W. Schweiger, D. L. Tillison, M. G. Thorn, P. E. Fanwick, I. P. Rothwell, *J. Chem. Soc., Dalton Trans.* **2001**, 2401–2408.

[22] Diffusion coefficients were measured at 25 °C by using "Dbppste" pulse sequence.

 © 2006 Wiley-VCH Verlag GmbH & Co. KGaA, Weinheim 

[23] a) R. R. Schrock, P. R. Sharp, *J. Am. Chem. Soc.* **1978**, *100*, 2389–2399; b) H. C. L. Abbenhuis, N. Feiken, D. M. Grove, J. T. B. H. Jastrzebski, H. Kooijman, P. van der Sluis, W. J. J. Smeets, A. L. Spek, G. van Koten, *J. Am. Chem. Soc.* **1992**, *114*, 9773–9781; c) M. D. Fryzuk, S. S. H. Mao, M. J. Zaworotko, L. P. MacGillivray, *J. Am. Chem. Soc.* **1993**, *115*, 5336–5337.

[24] V. I. Bakmutov, E. I. Fedin, *Bull. Magn. Reson.* **1984**, *6*, 142.

[25] a) M. Brookhart, M. L. H. Green, L.-L. Wong, *Prog. Inorg. Chem.* **1988**, *36*, 1–124; b) T. R. Cundari, M. S. Gordon, *J. Am. Chem. Soc.* **1992**, *114*, 539–548; c) R. B. King, *Encyclopedia of Inorganic Chemistry*, John Wiley & Sons, Chichester, UK, **1994**, vol. 5; d) J. M. Boncella, M. L. Cajigal, K. A. Abboud, *Organometallics* **1996**, *15*, 1905–1912.

[26] a) L. W. Messerle, P. Jennische, R. R. Schrock, G. Stucky, *J. Am. Chem. Soc.* **1980**, *102*, 6744–6752; b) A. J. Schultz, R. K. Brown, J. M. Williams, R. R. Schrock, *J. Am. Chem. Soc.* **1981**, *103*, 169–176; c) F. W. Hartner, J. Schwartz, S. M. Clift, *J. Am. Chem. Soc.* **1983**, *105*, 640–641; d) M. Brookhart, M. L. H. Green, *J. Organomet. Chem.* **1983**, *250*, 395–408; e) S. M. Clift, J. Schwartz, *J. Am. Chem. Soc.* **1984**, *106*, 8300–8301; f) A. van Asselt, B. J. Burger, V. C. Gibson, J. E. Bercaw, *J. Am. Chem. Soc.* **1986**, *108*, 5347–5349; g) W. A. Nugent, J. M. Mayer, *Metal-Ligand Multiple Bonds*, Wiley-Interscience, New York, **1988**; h) K. C. Wallace, D. M. Davis, R. R. Schrock, *Inorg. Chem.* **1990**, *29*, 1104–1106; i) D. H. Berry, T. S. Koloski, P. J. Carroll, *Organometallics* **1990**, *9*, 2952–2962; j) J. S. Freundlich, R. R. Schrock, C. C. Cummins, W. M. Davis, *J. Am. Chem. Soc.* **1994**, *116*, 6476–6477.

[27] a) H. C. L. Abbenhuis, M. H. P. Rietveld, H. F. Haarman, M. P. Hogerheide, A. L. Spek, G. van Koten, *Organometallics* **1994**, *13*, 3259–3268; b) M. H. P. Rietveld, W. Teunissen, H. Hagen, L. van der Water, D. M. Grove, P. A. van der Schaaf, A. Mühlebach, H. Kooijman, W. J. J. Smeets, N. Veldman, A. L. Spek, G. van Koten, *Organometallics* **1997**, *16*, 1674–1684; c) D. Y. Dawson, J. Arnold, *Organometallics* **1997**, *16*, 1111–1113; d) M. H. P. Rietveld, E. G. Klumpers, J. T. B. Jastrzebski, D. M. Grove, N. Veldman, A. L. Spek, G. van Koten, *Organometallics* **1997**, *16*, 4260–4267; e) M. C. W. Chan, J. M. Cole, V. C. Gibson, J. A. K. Howard, C. Lehmann, A. D. Poole, U. Siemeling, *J. Chem. Soc., Dalton Trans.* **1998**, 103–111; f) K. Mashima, M. Kaidzu, Y. Tanaka, Y. Nakayama, A. Nakamura, J. G. Hamilton, J. J. Rooney, *Organometallics* **1998**, *17*, 4183–4195; g) R. Baumann, R. Stumpf, W. M. Davis, L.-C. Liang, R. R. Schrock, *J. Am. Chem. Soc.* **1999**, *121*, 7822–7826; h) S. Courtenay, D. W. Stephan, *Organometallics* **2001**, *20*, 1442–1450; i) K. Mashima, H. Yonekura, T. Yamagata, K. Tani, *Organometallics* **2003**, *22*, 3766–3772; j) P. J. Chirik, D. L. Zubis, L. J. Ackerman, L. M. Henling, M. W. Day, J. E. Bercaw, *Organometallics* **2003**, *22*, 172–187.

[28] a) W. A. Herrmann, W. Kalcher, H. Biersack, J. Bernal, M. Creswick, *Chem. Ber.* **1981**, *114*, 3558–3571; b) R. D. Sanner, S. T. Carter, W. J. Bruton, *J. Organomet. Chem.* **1982**, *240*, 157–162.

[29] S. J. McLain, R. R. Schrock, P. R. Sharp, M. R. Churchill, W. Youngs, *J. Am. Chem. Soc.* **1979**, *101*, 263–265.

[30] C. Tessiers-Youngs, O. T. Beachley Jr, *Inorg. Synth.* **1986**, *24*, 95–97.

[31] W.-P. Leung, C. L. Raston, B. W. Skelton, A. H. White, *J. Chem. Soc., Dalton Trans.* **1984**, 1801–1807.

[32] From gHMQC and gHMBC spectra.

[33] N. Walker, D. Stuart, *Acta Crystallogr. Sect. A* **1983**, *39*, 158–166.

[34] G. M. Sheldrick, SHELXL-97, *Program for Crystal Structure Analysis*, University of Göttingen, Göttingen, Germany, **1983**.

[35] WinGX System; L. J. Farrugia, *J. Appl. Crystallogr.* **1999**, *32*, 837.

Received: February 27, 2006
Published Online: September 14, 2006

 © 2006 Wiley-VCH Verlag GmbH & Co. KGaA, Weinheim 

DOI: 10.1002/ejic.200600400

# Site-Specific Recognition of Dipeptides Through Non-Covalent Inter-Ligand Interactions for the Hydrolysis of Dipeptide to Amino Acid Ligands Mediated by Ternary Cobalt(III) Complexes

**Koichiro Jitsukawa,*[a] Tomohiro Mabuchi,[a] Hisahiko Einaga,[a] and Hideki Masuda[a]**

**Keywords:** Ligand design / Hydrolysis / Coordination modes / Cobalt / Host–guest systems

Molecular recognition of dipeptide (DP) compounds is performed with a ternary cobalt(III) complex containing the tripodal tetradentate ligand bis-*N*,*N*-carboxymethyl-L-phenylalanine ($H_3$bcmpa). The coordination structure of the complex [Co(bcmpa)(dp)]$^-$ (**1**–**14**) was spectroscopically assigned by UV/Vis, CD, and $^1$H NMR spectroscopic methods. Site-specific recognition of the dipeptide on the ternary complex is achieved by various weak, non-covalent, inter-ligand interactions, such as hydrogen bonding, steric repulsion, and electrostatic interaction, etc. Some dipeptides having C-terminal aromatic side-chains also demonstrate inter-ligand CH–π interactions between the aromatic ring and the α-hydrogen of bcmpa. Coordination of the N-terminal nitrogen atom of the dipeptide to cobalt at the *trans*(N)-position to the tertiary nitrogen of bcmpa in the octahedral geometry provides an aminopeptidase model. Under slightly alkaline conditions, the dipeptide ligand of some of these complexes is cleaved to give the ternary complex, [Co(bcmpa)(aa)]$^-$ (aa = amino acidato). The rate for the hydrolysis of dipeptide decreases upon increasing the steric bulkiness of the C-terminal side-chain. In the cases of the ternary complexes [Co(bcmpa)(gly-phe)]$^-$ (**6** and **11**), which have C-terminal L- or D-phenylalanine, the hydrolysis of gly-phe to gly was completely prevented. On the other hand, the ternary cobalt(III) complexes [Co(bcmga)(gly-phe)]$^-$ (**18** and **19**), where $H_3$bcmga (bis-*N*,*N*-carboxymethyl-L-glutamic acid) is the more hydrophilic tripodal ligand, give a small amount of the corresponding cleavage product [Co(bcmga)(gly)]$^-$. The hydrophobic sphere generated around the metal complex in **6** and **11** regulates approach of $OH^-$ ion to the amide carbonyl group. Multi-site interactions mediated on the ternary complexes are available for the design of an artificial hydrolysis enzyme. This is the first report describing the substrate-specific cleavage of peptides using a simple enzyme model complex.

(© Wiley-VCH Verlag GmbH & Co. KGaA, 69451 Weinheim, Germany, 2006)

## Introduction

Various models for the enzyme reaction have been investigated in the course of studying biomimetic catalysis.[1,2] Hydrolysis of the peptide bond is usually carried out in strongly acidic or alkaline conditions as the reaction in neutral aqueous media is very slow. Although hydrolysis of a gly-val compound under non-catalytic conditions requires more than 200 years,[3] the presence of an enzyme accelerates the process remarkably.[4] Kimura has reported the sequential hydrolysis of peptides in the presence of a [Co(trine)(OH)($H_2O$)]$^{2+}$ complex, in which various oligopeptides were cleaved to give amino acids.[5] At around the same time, Bentley et al. also reported cleavage of peptide ligands mediated by the [Co(trine)(OH)($H_2O$)]$^{2+}$ complex.[6] Using this cobalt(III) complex, moreover, Boreham, et al. have reported a mechanistic investigation of the intermediate of the amide cleavage reaction.[7] In these previous studies using cobalt(III) complexes, the selectivity of the cleavage reaction was not discussed. Using cobalt(III) complexes combined with peptide-hapten, Iverson and Lerner reported the sequence-specific hydrolysis of the gly-phe bond.[8] Unlike these previous reports, exopeptidase activity was demonstrated by the regioselective cleavage of lysozyme using [Co($NH_3$)$_4$X($H_2O$)] (X = OH or $H_2O$) complexes as artificial metallopeptidases.[9] Recently, Chae et al. have reported that a cobalt(III) cyclen complex containing a diamide moiety shows an *endo*-selective cleavage activity for peptides.[10] However, there have been few reports demonstrating selectivity for the cleavage of peptides mediated by cobalt(III) complexes. Since Kostic et al. first reported that platinum(II) or palladium(II) ions show catalytic activity for the hydrolysis of peptides,[11] there have been some examples reported of the selective cleavage of peptide compounds. These systems are considered to be an artificial enzyme because the peptide itself becomes a ligand due to coordination of the sulfur or nitrogen atom, for example with peptides including cysteine (cys), methionine (met), or histidine (his).[12] Although a detailed mechanism for the

[a] Department of Applied Chemistry, Nagoya Institute of Technology
Gokiso-cho Showa-ku, Nagoya 466-8555, Japan
Fax: +81-52-735-5240
E-mail: jitsukawa.koichiro@nitech.ac.jp

 © 2006 Wiley-VCH Verlag GmbH & Co. KGaA, Weinheim 

hydrolysis reaction is not yet clear, the carbonyl group of the amide bond to a neighboring cys, met, or his residue was found to be selectively hydrolyzed under mild conditions when platinum(II) complexes containing two substitutionally labile sites were used.[13]

With a view to investigating metalloenzymes, transition metal complexes provide an attractive tool for constructing an artificial enzyme model of peptidase through various weak, non-covalent interactions.[14–18] A combination of non-covalent interactions observed at or near the active site of the enzyme causes high efficiency and specificity for an enzymatic reaction, which is essential for biological reactions involving substrate recognition.[19] For example, various non-covalent interactions, such as hydrogen bonding, hydrophobic interactions, steric repulsions, and electrostatic interactions, have been clearly demonstrated at the active site of the enzyme–substrate complex formed from aminopeptidase and bestatin.[20] Moreover, an interesting approach to delineate the non-covalent bonds between chromium(III) complexes containing a nitrilotriacetate framework and a protein surface has been described that uses NMR and CD spectroscopy.[21] We have hitherto been interested in the construction of molecular recognition models for enzyme–substrate complexes,[22–25] in which the cobalt(III) complex $[Co(bcmpa)(aa)]^-$, which contains the tripodal tetradentate ligand bis-*N*,*N*-carboxymethyl-L-phenylalanine ($H_3$bcmpa), is considered as an enzyme model, with a didentate amino acid (AA) as substrate. Various amino acids were found to coordinate to $Co^{III}$-bcmpa in a *trans*(N) configuration rather than a *cis*(N) one.[22,24] It is very interesting that such a simple metal complex demonstrates the coordination-selective recognition of amino acids through various non-covalent interactions between bcmpa and the amino acid moiety.[17] In addition, this $Co^{III}$-bcmpa complex self-assembled on a Au electrode also becomes a new promoter electrode that recognizes the electron-transfer site in enzymes.[26]

In this study, we report the synthesis of ternary cobalt(III) complexes $[Co(bcmpa)(dp)]^-$ with a dipeptide (DP) ligand and characterize the inter-ligand interactions for the site-selective recognition of dipeptides on the complexes spectroscopically in solution. We also investigate the cleavage reaction of the dipeptide ligand in slightly alkaline solution. Selective hydrolysis of the dipeptide ligand mediated by the ternary cobalt(III) complexes is caused by the various non-covalent inter-ligand interactions, which allow this complex to be considered as an aminopeptidase model.

### Abbreviations

gly-gly: glycylglycine; gly-ala: glycylalanine; ala-gly: alanylglycine; gly-leu: glycylleucine; leu-gly: leucylglycine; gly-phe: glycylphenylalanine; phe-gly: phenylalanylglycine; gly-val: glycylvaline; gly-phg: glycylphenylglycine; gly-β-ala: glycyl-β-alanine; gly-Mala: glycyldimethylglycine.

## Results and Discussion

### Coordination Structure of the Ternary Cobalt(III) Complexes with Dipeptide Ligands

The complexation of $K_2[Co(bcmpa)(CO_3)]$ with various dipeptide compounds in neutral aqueous solution in the presence of active charcoal gave two negatively charged complexes after QAE Sephadex exchange column separation with aqueous KCl solution. One of the separated bands was found to contain the orange-colored complex K[Co(bcmpa)(dp)] (**1**–**14**), whereas the other contained the pink-colored complex K[Co(bcmpa)(aa)]; the ratio of the former to the latter was about 10:1. The UV/Vis spectra of the main band containing cobalt(III) complexes with a dipeptide ligand are very similar to those of the previously reported complexes *trans*(N)-$[Co(bcmpa)(gly)]^-$ and *trans*(N)-$[Co(bcmpa)(leu)]^-$.[22] The first absorption band at $19.6–19.8 \times 10^3$ $cm^{-1}$ ($\log\varepsilon$ = 2.15–2.18) with a shoulder at about $16 \times 10^3$ $cm^{-1}$ ($\log\varepsilon$ = about 1.3) of complexes **1**–**14** indicates that two nitrogen atoms occupy the *trans* position in an octahedral geometry.[24,27,28] Their second absorption bands are found at about $26.2–26.4 \times 10^3$ $cm^{-1}$ ($\log\varepsilon$ = 2.17–2.19). On the basis of the spectral analogy to *trans*(N)-$[Co(N)_2(O)_4]^-$, which is supported by the X-ray single crystal analysis of *trans*(N)-$[Co(bcmpa)(gly)]^-$, *trans*(N)-$[Co(bcmpa)(leu)]^-$, and *trans*(N)-$[Co(bcmle)(phe)]^-$,[22,23] we consider that the *trans* position to the bcmpa nitrogen in the $[Co(bcmpa)(dp)]^-$ complex is occupied by the N-terminal amine nitrogen and the *cis* position by the amide carbonyl oxygen atom.[17,22] The compounds included in the pink-colored minor band were identified as *trans*(N)-$[Co(bcmpa)(aa)]^-$ complexes on the basis of the spectral analogy of their previously reported analogs.[22,24] When the complexation with $K_2[Co(bcmpa)(CO_3)]$ and dipeptide was carried out at higher pH, the yield of the pink-colored band increased and that of the orange-colored one decreased. These findings indicate that complex formation between the dipeptide and $[Co(bcmpa)(CO_3)]^{2-}$ is accompanied by hydrolysis of the amide bond. Moreover, the –1 charge of the reaction product, as determined by the column separation behavior, reveals that the amide carbonyl group of the dipeptide coordinates to the metal center without deprotonation. The hydrogen atom attached to the amide nitrogen of *trans*(N)-$[Co(bcmpa)(dp)]^-$ is not removed in neutral or weakly alkaline media under complex formation conditions.

The character of the ternary cobalt(III) complexes consisting of the optically active bcmpa and dipeptide was also investigated by recording their CD spectra.[27,29] The three positive CD peaks of the *trans*(N)-$[Co(bcmpa)(gly\text{-}gly)]^-$ complex **1** observed at 16.2, 19.6, and $26.0 \times 10^3$ $cm^{-1}$ are very similar to those of *trans*(N)-$[Co(bcmpa)(gly)]^-$.[24] Two dipeptide complexes, namely $[Co(bcmpa)(leu\text{-}gly)]^-$ (**5**) and $[Co(bcmpa)(phe\text{-}gly)]^-$ (**7**), show positive CD peaks at 16.7, 18.7, and $26.4 \times 10^3$ $cm^{-1}$ and a negative one at $20.9 \times 10^3$ $cm^{-1}$, respectively, very similar to complexes of $[Co(bcmpa)(leu)]^-$ with coordinated didentate optically active amino acids.[22,24] Moreover, the intensity of the posi-

 © 2006 Wiley-VCH Verlag GmbH & Co. KGaA, Weinheim 

tive CD peaks of **5** and **7** is relatively strong in comparison with those of [Co(bcmpa)(gly-ala)]$^-$ (**2**), [Co(bcmpa)(gly-leu)]$^-$ (**4**), and [Co(bcmpa)(gly-phe)]$^-$ (**6**). Enhancement of the CD intensity indicates the coordination of the asymmetric amino acid moiety of the dipeptide to the cobalt(III) ion. As shown in Figure 1, the differential CD spectrum between [Co(bcmpa)(gly-D-ala)]$^-$ (**10**) and [Co(bcmpa)(gly-gly)]$^-$ (**1**) has a perfectly antipodal form, as does that between **2** and **1**.[29] Similar differential CD spectra were observed in the complexes coordinated by gly-L-phe (**6**) and gly-D-phe (**11**). The characteristic CD spectra of complexes **1**–**14** reveal that the N-terminal nitrogen atom of the dipeptide coordinates to the cobalt ion in a *trans*(N) manner.

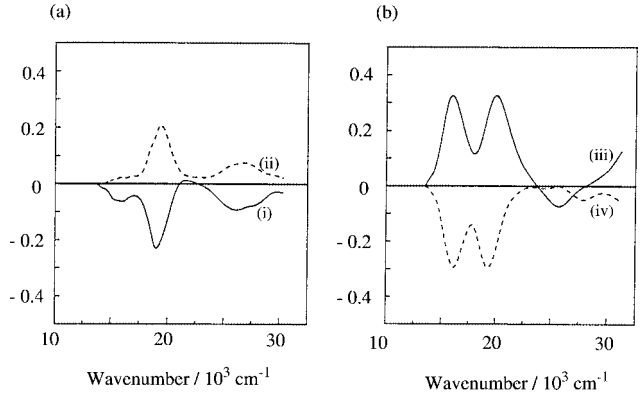


Figure 1. Differential CD spectra of the cobalt(III) complexes with dipeptide ligands. (a) Effect of C-terminal alanine: (i) [Co(bcmpa)(gly-ala)]$^-$ (**2**) – [Co(bcmpa)(gly-gly)]$^-$ (**1**); (ii) [Co(bcmpa)(gly-D-ala)]$^-$ (**10**) – [Co(bcmpa)(gly-gly)]$^-$ (**1**). (b) Effect of C-terminal phenylalanine: (iii) [Co(bcmpa)(gly-phe)]$^-$ (**6**) – [Co(bcmpa)(gly-gly)]$^-$ (**1**); (iv) [Co(bcmpa)(gly-D-phe)]$^-$ (**11**) – [Co(bcmpa)(gly-gly)]$^-$ (**1**).

The coordination structure of the diamagnetic cobalt(III) complex in solution was investigated by $^1$H NMR spectroscopy. The characteristic $^1$H NMR spectra of dipeptide complexes **1**–**14** are summarized in Table 1, where they are compared with those of [Co(bcmpa)(aa)]$^-$ previously identified.[24] In [Co(bcmpa)(gly-gly)]$^-$ (**1**), three pairs of AB patterns are observed in the methylene region. One of these ($\delta$ = 3.98 and 4.63 ppm, $J$ = 18.0 Hz) was assigned to the R-ring hydrogens of bcmpa.[30] The G-ring hydrogens of bcmpa at $\delta$ = 3.20 and 4.13 ppm show a slightly smaller coupling constant of 16.8 Hz.[31] The others at $\delta$ = 4.24 and 4.25 ppm ($J$ = 17.3 Hz) were identified as the N-terminal methylene hydrogens of the coordinating glycine moiety. The ABX pattern demonstrated by two benzyl hydrogens at $\delta$ = 3.51 ($J$ = 15.1 and 10.6 Hz) and 3.64 ppm ($J$ = 15.1 and 4.8 Hz) and the adjacent α-hydrogen at $\delta$ = 4.90 ppm ($J$ = 10.6 and 4.8 Hz) is derived from the Gs-ring of bcmpa.[30] The singlet observed at $\delta$ = 3.82 ppm was identified as the C-terminal methylene hydrogens of the glycine moiety. The aromatic hydrogens of the bcmpa side-chain appear at $\delta$ = 7.4–7.6 ppm. As shown in Table 1, the chemical-shift values of the α-hydrogens of the N-terminal amino acid residue appear slightly downfield in comparison with those of the C-terminal one except for complexes **9** and **12**, which contain a C-terminal phenylglycine moiety. The above complex formation shifts of the N-terminal amino acid moiety indicate N-terminal coordination of the dipeptide to cobalt with formation of an N–O chelate. Taking account of the UV/Vis, CD, and $^1$H NMR spectral investigations, the coordination structure of the dipeptide complex was determined to be that shown in Figure 2 (a), although other structures (b–f) are also possible.

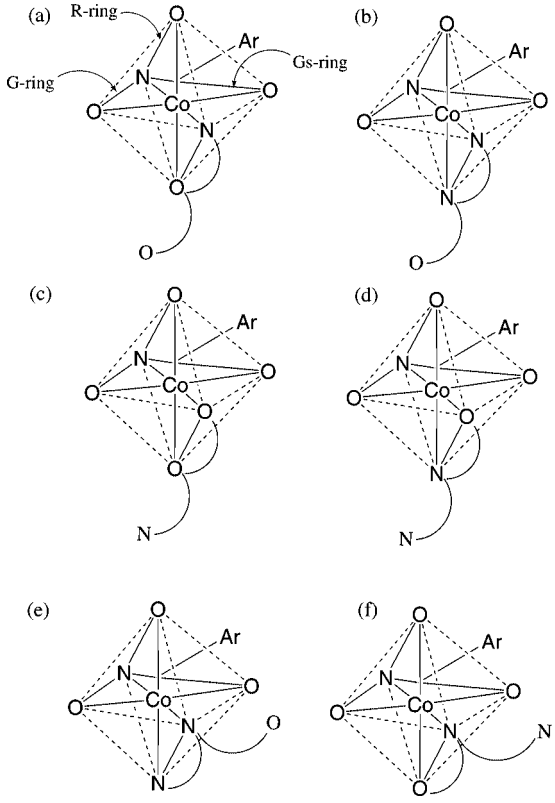


Figure 2. Six possible coordination modes of a dipeptide to a cobalt(III) complex with a tripodal $NO_3$-type ligand: (a) *trans*(N)-NO (coordination of N-terminal amine nitrogen *trans* to the tertiary amine of the tripodal $NO_3$-type ligand and the amide carbonyl oxygen); (b) *trans*(N)-NN (coordination of N-terminal amine nitrogen *trans* to the tertiary amine of the tripodal $NO_3$-type ligand and the amide nitrogen); (c) *trans*(O)-OO (coordination of C-terminal carboxylic oxygen *trans* to the tertiary amine of the tripodal $NO_3$-type ligand and the amide carbonyl oxygen); (d) *trans*(O)-ON (coordination of C-terminal carboxylic oxygen *trans* to the tertiary amine of the tripodal $NO_3$-type ligand and the amide nitrogen); (e) *cis*(N)-NN (coordination of the N-terminal amine nitrogen *cis* to the tertiary amine of the tripodal $NO_3$-type ligand and the amide nitrogen); (f) *cis*(O)-ON (coordination of C-terminal carboxylic oxygen *cis* to the tertiary amine of the tripodal $NO_3$-type ligand and the amide nitrogen).

## Inter-Ligand Interactions Observed for the [Co(bcmpa)(dp)] Complexes

In the $^1$H NMR spectra of the dipeptide complexes, the α-hydrogens of the Gs ring of complexes **1**–**5**, **7**, **8**, **10**, **13**, and **14**, appear at about $\delta$ = 4.8–4.9 ppm, whereas those of complexes **6** and **9** appear at about $\delta$ = 3.8–4.7 ppm. The downfield shift observed in the former complexes indicates

 © 2006 Wiley-VCH Verlag GmbH & Co. KGaA, Weinheim 

Table 1. $^1$H NMR spectroscopic data of [Co(bcmpa)(dp)]$^-$ (**1**–**14**) and [Co(bcmga)(dp)]$^{2-}$ (**15**–**19**) complexes.[a]

| | gly-gly<br>**1** | gly-ala<br>**2** | ala-gly<br>**3** | gly-leu<br>**4** | leu-gly<br>**5** | gly-phe<br>**6** | phe-gly<br>**7** |
|---|---|---|---|---|---|---|---|
| R-ring H | 3.98 (d)<br>4.63 (d)<br>*J* = 18.0 | 3.98 (d)<br>4.64 (d)<br>*J* = 18.0 | 3.98 (d)<br>4.64 (d)<br>*J* = 18.0 | 4.01 (d)<br>4.62 (d)<br>*J* = 18.1 | 3.99 (d)<br>4.62 (d)<br>*J* = 18.0 | 3.96 (d)<br>4.52 (d)<br>*J* = 18.2 | 3.94 (d)<br>4.48 (d)<br>*J* = 17.1 |
| G-ring H | 3.20 (d)<br>4.13 (d)<br>*J* = 16.8 | 3.22 (d)<br>4.15 (d)<br>*J* = 16.5 | 3.22 (d)<br>4.11 (d)<br>*J* = 16.5 | 3.40 (d)<br>4.29 (d)<br>*J* = 16.5 | 3.20 (d)<br>4.11 (d)<br>*J* = 16.5 | 3.39 (d)<br>4.20 (d)<br>*J* = 16.3 | 3.37 (d)<br>4.19 (d)<br>*J* = 16.7 |
| Gs-ring H | 4.90 (dd)<br>*J* = 10.6, 4.8 | 4.93 (dd)<br>*J* = 10.2, 5.2 | 4.87 (dd)<br>*J* = 10.4, 4.8 | 4.87 (dd)<br>*J* = 9.4, 5.4 | 4.87 (dd)<br>*J* = 10.8, 4.8 | 4.32 (dd)<br>*J* = 8.5, 6.4 | 4.80 (m)[b] |
| benzyl H of bcmpa<br>(β-position of bcmga) | 3.51 (dd)<br>*J* = 15.1, 10.6<br>3.64 (dd)<br>*J* = 15.1, 4.8 | 3.53 (dd)<br>*J* = 15.0, 10.2<br>3.64 (dd)<br>*J* = 15.0, 5.2 | 3.53 (dd)<br>*J* = 15.1, 10.4<br>3.66 (dd)<br>*J* = 15.1, 4.8 | 3.56 (dd)<br>*J* = 15.0, 9.4<br>3.63 (dd)<br>*J* = 15.0, 5.4 | 3.52 (dd)<br>*J* = 15.1, 10.8<br>3.61 (dd)<br>*J* = 15.1, 4.8 | 3.51 (m) | 3.52 (m)[b]<br>3.59 (dd)<br>*J* = 14.9, 3.4 |
| N-terminal α-H of dp | 4.24 (d)<br>4.25 (d)<br>*J* = 17.3 | 4.19 (s) | 4.49 (q)<br>*J* = 7.1 | 4.22 (s) | 4.46 (dd)<br>*J* = 8.2, 3.0 | 4.02 (d)<br>4.14 (d)<br>*J* = 17.3 | 4.73 (m) |
| C-terminal α-H of dp | 3.82 (s) | 4.10 (m)[b] | 3.77 (d)<br>3.82 (d)<br>*J* = 16.8 | 4.25 (m)[b] | 3.82 (s) | 4.49 (m)[b] | 3.80 (d)<br>3.91 (d)<br>*J* = 16.8 |

| | gly-val<br>**8** | gly-phg<br>**9** | gly-D-ala<br>**10** | gly-D-phe<br>**11** | gly-D-phg<br>**12** | gly-β-ala<br>**13** |
|---|---|---|---|---|---|---|
| R-ring H | 4.00 (d)<br>4.62 (d)<br>*J* = 18.0 | 3.85 (d)<br>4.84 (d)<br>*J* = 18.2 | 3.98 (d)<br>4.64 (d)<br>*J* = 18.1 | 3.90 (d)<br>4.55 (d)<br>*J* = 18.0 | 3.84 (d)<br>4.54 (d)<br>*J* = 18.2 | 4.02 (d)<br>4.65 (d)<br>*J* = 18.0 |
| G-ring H | 3.40 (d)<br>4.34 (d)<br>*J* = 16.5 | 3.01 (d)<br>4.01 (d)<br>*J* = 16.5 | 3.14 (d)<br>4.05 (d)<br>*J* = 15.8 | 2.96 (d)<br>3.46 (d)<br>*J* = 16.3 | 2.72 (s) | 3.33 (d)<br>4.29 (d)<br>*J* = 16.8 |
| Gs-ring H | 4.86 (dd)<br>*J* = 9.5, 5.5 | 3.85 (dd)<br>*J* = 10.5, 5.3 | 4.88 (dd)<br>*J* = 10.1, 4.6 | 4.75 (dd)<br>*J* = 10.7, 4.6 | 4.57 (dd)<br>*J* = 10.7, 4.8 | 5.00 (dd)<br>*J* = 10.7, 5.2 |
| benzyl H of bcmpa<br>(β-position of bcmga) | 3.55 (dd)<br>*J* = 15.1, 9.5<br>3.63 (dd)<br>*J* = 15.1, 5.5 | 3.23 (dd)<br>*J* = 15.5, 5.3<br>3.36 (dd)<br>*J* = 15.5, 10.5 | 3.51 (dd)<br>*J* = 15.1, 10.1<br>3.64 (dd)<br>*J* = 15.1, 4.6 | 3.47 (dd)<br>*J* = 15.2, 10.7<br>3.60 (dd)<br>*J* = 15.2, 4.6 | 3.45 (dd)<br>*J* = 15.1, 10.7<br>3.61 (dd)<br>*J* = 15.1, 4.8 | 3.55 (dd)<br>*J* = 15.0, 10.7<br>3.66 (dd)<br>*J* = 15.0, 5.2 |
| N-terminal α-H of dp | 4.24 (d)<br>4.25 (d)<br>*J* = 17.2 | 4.30 (d)<br>4.31 (d)<br>*J* = 17.5 | 4.19 (d)<br>4.22 (d)<br>*J* = 17.3 | 4.46 (d)<br>4.48 (d)<br>*J* = 17.1 | 4.19 (d)<br>4.34 (d)<br>*J* = 17.3 | 4.15 (d)<br>4.16 (d)<br>*J* = 17.1 |
| C-terminal α-H of dp | 4.12 (d)<br>*J* = 5.2 | 5.13 (s) | 4.06 (m)[b] | 4.49 (m)[b] | 5.07 (s) | 2.33 (t)<br>*J* = 6.8 |

| | gly-Mala<br>**14** | gly-gly<br>**15**[c] | gly-ala<br>**16**[c] | gly-leu<br>**17**[c] | gly-phe<br>**18**[c] | gly-D-phe<br>**19**[c] |
|---|---|---|---|---|---|---|
| R-ring H | 3.97 (d)<br>4.64 (d)<br>*J* = 18.0 | 4.08 (d)<br>4.39 (d)<br>*J* = 18.3 | 4.08 (d)<br>4.40 (d)<br>*J* = 18.0 | 4.09 (d)<br>4.39 (d)<br>*J* = 18.2 | 4.03 (d)<br>4.29 (d)<br>*J* = 18.3 | 4.04 (d)<br>4.34 (d)<br>*J* = 18.3 |
| G-ring H | 3.21 (d)<br>4.05 (d)<br>*J* = 16.5 | 4.40 (d)<br>4.76 (d)<br>*J* = 16.8 | 4.39 (d)<br>4.69 (d)<br>*J* = 16.7 | 4.44 (d)<br>4.80 (d)<br>*J* = 16.7 | 4.36 (d)<br>4.72 (d)<br>*J* = 16.5 | 4.33 (d)<br>4.47 (d)<br>*J* = 16.2 |
| Gs-ring H | 4.93 (dd)<br>*J* = 10.7, 4.8 | 4.54 (d)<br>*J* = 6.4 | 4.56 (t)<br>*J* = 6.7 | 4.62 (t)<br>*J* = 6.7 | 4.22 (m)[b] | 4.50 (m)[b] |
| benzyl H of bcmpa<br>(β-position of bcmga) | 3.61 (dd)<br>*J* = 15.0, 10.7<br>3.69 (dd)<br>*J* = 15.0, 4.8 | 2.46 (m)[d] | 2.46 (m)[d] | 2.47 (m)[d] | 2.39 (m)[d] | 2.46 (m)[d] |
| N-terminal α-H of dp | 4.13 (d)<br>4.14 (d)<br>*J* = 17.4 | 4.27 (s) | 4.22 (s) | 4.26 (s) | 4.04 (d)<br>4.19 (d)<br>*J* = 17.1 | 4.04 (d)<br>4.19 (d)<br>*J* = 17.1 |
| C-terminal α-H of dp | – | 3.83 (s) | 4.13 (q)<br>*J* = 7.3 | 4.26 (m)[b] | 4.54 (dd)<br>*J* = 10.7, 4.0 | 4.50 (m) [b] |

[a] Chemical shifts ($\delta$) given in ppm relative to DSS in $D_2O$; coupling constants ($J$) given in Hz. [b] An accurate value could not be obtained because of overlap with other peaks. [c] [Co(bcmga)(dp)]$^-$. [d] β-H of the bcmga ligand.

 © 2006 Wiley-VCH Verlag GmbH & Co. KGaA, Weinheim 

a hydrogen-bonding interaction between the α-hydrogen of bcmpa and the coordinating carbonyl oxygen of the dipeptide. This interaction, which is mediated by the cobalt(III) complex with a bcmpa ligand, has also been observed in the crystal structure of amino acid complexes, in which the atomic distances between the α-carbon of bcmpa and the carboxyl oxygen of amino acid in *trans*(N)-[Co(bcmpa)-(leu)]$^-$ are 2.83 and 2.84 Å.[22] These data are within the range for a hydrogen bond.[32] In complex **6**, however, the corresponding signal appears at $\delta$ = 4.32 ppm, which signifies an upfield shift relative to that for **1** ($\delta$ = 4.90 ppm) with no aromatic side-chain. Some α-hydrogens of the Gs-ring in the [Co(bcmpa)(dp)]$^-$ complexes with a C-terminal aromatic amino acid are detected in the high-field region despite the downfield shift caused by the hydrogen bond described above. This is due to the ring current effect of the benzene ring. The larger upfield shift in complex **9** indicates that the benzene ring of the C-terminal phenylglycine residue approaches the α-position more closely in solution. In addition, the G-ring methylene hydrogens in **11** and **12**, which have a C-terminal aromatic D-amino acid residue, appear at $\delta$ = 2.7–3.4 ppm. The highest values of all [Co(bcmpa)(dp)]$^-$ complexes employed here indicate that the aromatic ring of the D-amino acid at the C-terminus of the dipeptide in **11** and **12** approaches the α-position of the bcmpa Gs-ring, which is interpreted in terms of an attractive inter-ligand CH–π interaction.[33] We consider that the CH–π interaction between the aromatic side-chain and the chelate ring methylene group assembles the aromatic rings around the outer coordination sphere of the ternary complex.[33,34]

To confirm the inter-ligand interactions, solvent effects on the $^1$H NMR spectra of some complexes were examined. The α-hydrogen of **6** appears at $\delta$ = 4.40 ppm in less polar solvent (75% [$D_8$]dioxane and 25% $D_2O$) and at $\delta$ = 4.32 ppm in more polar solution ($D_2O$). Notably, all the other hydrogens of **6** appear in the up-field region under less polar conditions. In the cases of **1** and **4**, which have no C-terminal aromatic ring, all hydrogens appear in the upper field region under less polar conditions than those provided by $D_2O$. Hydrophobic interaction such as the CH–π interaction that is present in the aqueous phase does not form under less polar conditions.[33,34] The results are listed in Table 2.

Solvent effects were also investigated by CD spectroscopy. In complexes **1**, **13**, and **14**, whose only asymmetric ligand is bcmpa, no CD spectral variations were observed between polar (water) and less polar (water/dioxane = 1:3) solvents. In the case of **4**, which contains bcmpa and an asymmetric C-terminal bulky aliphatic group, the CD intensity at about $16 \times 10^3$ cm$^{-1}$ in water increases and that at $20 \times 10^3$ cm$^{-1}$ decreases upon addition of dioxane, as shown in Figure 3 (a). Such a spectral change is caused by a conformational change of the asymmetric ligand bound to the cobalt(III) center. On the other hand, in the case of **6**, which contains bcmpa and an asymmetric C-terminal aromatic group, the CD intensities at about 16 and $20 \times 10^3$ cm$^{-1}$ gradually decrease upon addition of dioxane to the aqueous solution, as shown in Figure 3 (b). These findings are interpreted in terms of a hydrophobic inter-ligand interaction between the C-terminal aromatic side-chain of the dipeptide and the benzene ring of bcmpa in the ternary complexes.

We have previously reported that three inter-ligand interactions, such as hydrogen bonds, steric repulsion, and electrostatic interactions, regulate the coordination structure of the ternary cobalt(III) complexes [Co(bcmpa)(aa)]$^-$.[22,24] Two kinds of hydrogen bond in the ternary complexes employed here act between N-terminal amino hydrogens of the dipeptide and carboxyl oxygen atoms of bcmpa and between the α-hydrogen of bcmpa and the amide carbonyl group of the dipeptide. The hydrogen bond plays an important role in the recognition of the dipeptide N-terminus because it supplies a large fraction of energy required for stabilization of the transition state of an enzyme reaction.[35] Steric repulsion of the hydrogen atoms between the methylene groups on the G- or Gs-chelate rings of bcmpa and the N-terminal amino group is expected to promote the formation of the *trans*(N) geometry. An electrostatic interaction is expected to inhibit the formation of the *cis*(N) one because it acts repulsively between the negative charge of the two carboxylate moieties. From the above discussion, which is summarized in Figure 4(a), a ternary cobalt(III) complex coordinated by the N-terminal nitrogen of the dipeptide and bcmpa with a *trans*(N) geometry is formed preferentially. This is an interesting model for mimicking aminopeptidase, even though it is a low-molecular compound. In the case of complexation of a dipeptide having a C-terminal aromatic side-chain, the inter-ligand CH–π interaction assembles the benzene rings of the dipeptide and bcmpa to form a hydrophobic sphere, as shown in Figure 4(b). Although we were not able to obtain a crystal of [Co(bcmpa)(dp)]$^-$, the coordination structures in Figure 4 are proposed based on the above spectral considerations.

Table 2. Solvent effect on the proton chemical shift value in typical [Co(bcmpa)(dp)]$^-$ complexes.[a]

| | gly-gly (**1**) | | | | gly-leu (**4**) | | | | gly-phe (**6**) | | | |
|---|---|---|---|---|---|---|---|---|---|---|---|---|
| Ratio water/dioxane | 100:0 | 75:25 | 50:50 | 25:75 | 100:0 | 75:25 | 50:50 | 25:75 | 100:0 | 75:25 | 50:50 | 25:75 |
| R-ring H | 3.98, 4.63 | 3.92, 4.59 | 3.84, 4.45 | 3.78, 4.45 | 4.01, 4.62 | 3.93, 4.54 | 3.86, 4.46 | 3.80, 4.41 | 3.96, 4.52 | 3.90, 4.44 | 3.83, 4.39 | 3.76, 4.36 |
| G-ring H | 3.20, 4.13 | 3.18, 4.10 | 3.13, 4.06 | 3.11, 4.05 | 3.40, 4.29 | 3.37, 4.28 | 3.36, 4.28 | 3.36, 4.30 | 3.39, 4.20 | 3.36, 4.18 | 3.35, 4.17 | 3.30, 4.17 |
| Gs-ring H | 4.90 | 4.86 | 4.82 | 4.79 | 4.87 | 4.81 | 4.76 | 4.73 | 4.32 | 4.31 | 4.33 | 4.40 |

[a] Chemical shifts ($\delta$) given in ppm relative to DSS in $D_2O$.

 © 2006 Wiley-VCH Verlag GmbH & Co. KGaA, Weinheim 

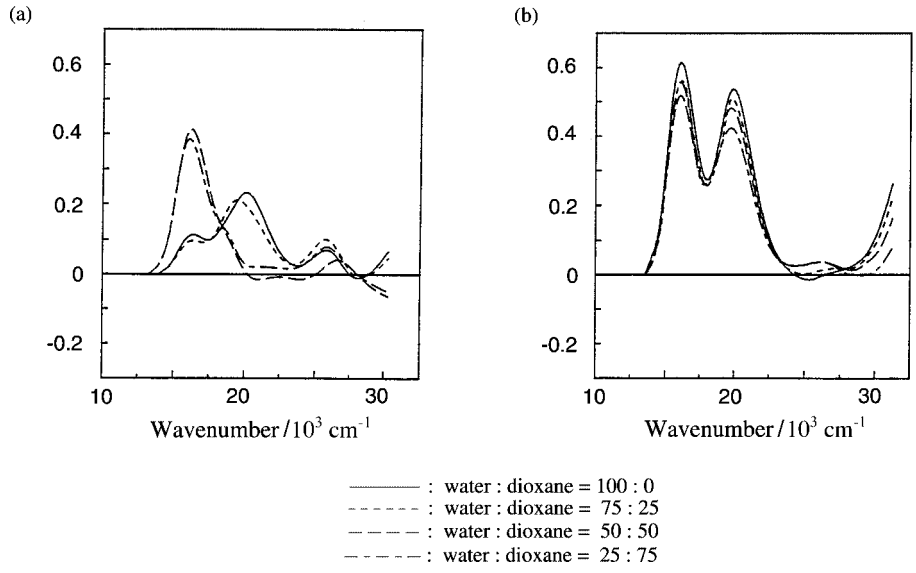


Figure 3. Solvent effects on the inter-ligand interaction between the cobalt(III) ternary complexes and the dipeptide ligand observed by CD spectroscopy: (a) $[Co(bcmpa)(gly\text{-}leu)]^-$ (**4**); (b) $[Co(bcmpa)(gly\text{-}phe)]^-$ (**6**).

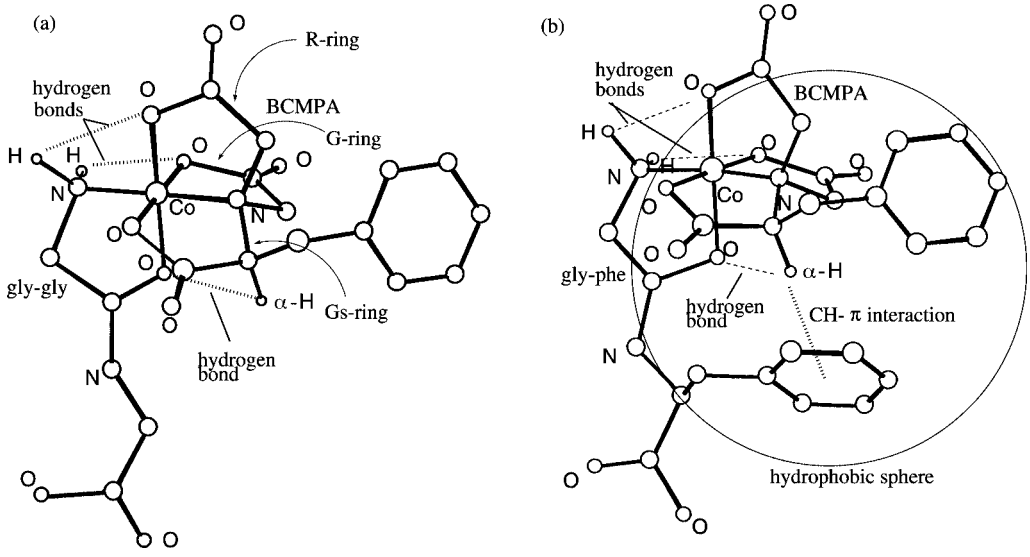


Figure 4. Schematic drawing of the inter-ligand interactions in the ternary complex: (a) $[Co(bcmpa)(gly\text{-}gly)]^-$ (**1**); (b) $[Co(bcmpa)(gly\text{-}phe)]^-$ (**6**), showing the hydrophobic sphere.

### Hydrolysis of Dipeptide Ligands Mediated by the Ternary Cobalt(III) Complexes

*cis*-Diaquacobalt(III) complexes are known to hydrolyze carbonyl esters, amides, nitriles, and phosphate esters by the coordination of these substrates to the metal center.[36] Buckingham et al. have shown that the hydrolysis of amino acid esters and peptides is accelerated 106 times in the presence of a cobalt(III) complex of a linear tetraamine ligand in neutral media.[17,37] These reactions are promoted by the nucleophilic attack of hydroxide at the amide carbonyl group activated by coordination to the metal center. Under these reaction conditions, however, selectivity for the cleavage reaction was not reported.[38] Since the tetraamine ligand has no functional groups for recognition of the peptide, it could not show any selectivity. Exceptionally, a β-$[Co(trien)(OH)(H_2O)]^{2+}$ complex has been reported to show selective hydrolysis of peptides[5] even though no inter-ligand interactions were observed in this complex. Here, we have designed ternary cobalt(III) complexes containing a bcmpa ligand, which is expected to regulate the selective hydrolysis of dipeptides due to its having a recognition site for the aromatic group. From the viewpoint of the selective cleavage of peptide bonds, a ternary cobalt(III) complex having inter-ligand interaction sites becomes a molecular recognition model for aminopeptidases. In order to determine the active species for the hydrolysis of the amide bond, we carried out the reaction with $[Co(bcmpa)(leu\text{-}gly)]^-$ (**5**) under different pH conditions at 40 °C. The yield of the

 © 2006 Wiley-VCH Verlag GmbH & Co. KGaA, Weinheim 

$[Co(bcmpa)(leu)]^-$ complex generated upon hydrolysis of the leu-gly moiety of **5** was higher at higher pH, as shown in Figure 5. This finding indicates that the reaction is promoted by $OH^-$ ion. Since the amount of unidentified cobalt(III) complexes increased in the higher pH region, all reactions were carried out at pH 9.

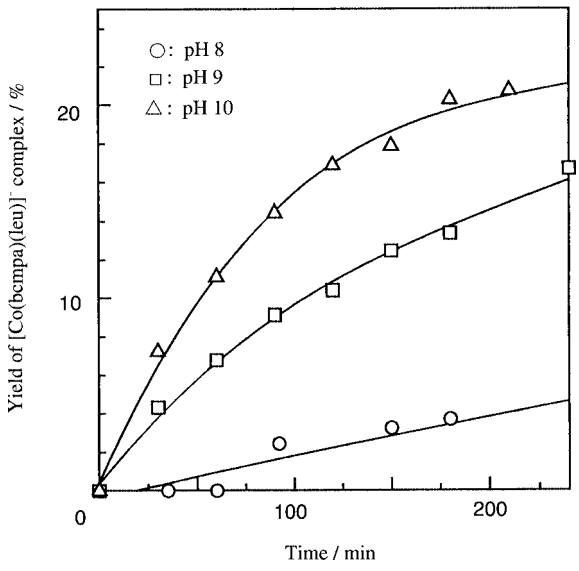


Figure 5. Rate of formation of $[Co(bcmpa)(leu)]^-$ during the hydrolysis of $[Co(bcmpa)(leu\text{-}gly)]^-$ (**5**) and its dependence on pH.

The yields of the cleavage product, $[Co(bcmpa)(aa)]^-$, at the initial stage of the reaction are listed in Table 3. The most striking observation in these reactions is the complete inhibition of hydrolysis of complexes **6** and **11**. The $[Co(bcmpa)(gly)]^-$ complex was not detected even after reaction of **6** and **11** at pH 9.0 and 40 °C for 3 h. This finding is in contrast to a previous report that Co-trien-dp complexes can be used for cleavage reactions of peptides including C-terminal aromatic amino acid residues.[17] The hydrolysis of complexes **1** and **2**, which have a C-terminal glycine or alanine residue, proceeded easily, as shown in Figure 6. On the other hand, the yield of $[Co(bcmpa)(gly)]^-$ from the reaction of **4** and **8**, which have C-terminal bulky dipeptides such as gly-val and gly-leu, was poor. The hydrolysis rate for complex **1** was fivefold higher than those for **4** and **8**. Upon increasing the steric bulkiness of the side chain of the dipeptide at the C-terminus, the yield of the hydrolysis product decreased according to the order glycine (C-0), alanine (C-1), valine (C-3), and leucine (C-4). The reaction of the dipeptide complexes having C-terminal aromatic side-chain (**9** and **12**) did not give the corresponding amino acid complexes, and neither did the complex with C-terminal phenylalanine. In contrast to the above findings, the reaction of **5**, which has an N-terminal bulky substituent, gave $[Co(bcmpa)(leu)]^-$ in moderate yield. In the case of complex **14**, which has an α,α-disubstituted amino acid at the C-terminus, the yield of the $[Co(bcmpa)(gly)]^-$ complex was only 1.7% after 3 h; this was also interpreted in terms of a steric effect.

Table 3. Reactivity for the cleavage reaction of various dipeptides at the ternary cobalt(III) complexes.[a]

| Cobalt(III) complexes | | Yield of gly complex[b] (%) |
|---|---|---|
| bcmpa | gly-gly (**1**) | 24.9 |
| | gly-ala (**2**) | 16.0 |
| | gly-leu (**4**) | 3.9 |
| | leu-gly (**5**) | 13.4[c] |
| | gly-phe (**6**) | 0.0 |
| | gly-val (**8**) | 5.1 |
| | gly-phg (**9**) | 3.7 |
| | gly-D-ala (**10**) | 17.3 |
| | gly-D-phe (**11**) | 0.0 |
| | gly-D-phg (**12**) | 2.0 |
| | gly-Mala (**14**) | 1.7 |
| bcmga | gly-gly (**15**) | 26.3 |
| | gly-ala (**16**) | 8.9 |
| | gly-leu (**17**) | 2.2 |
| | gly-phe (**18**) | 2.9 |
| | gly-D-phe (**19**) | 4.6 |

[a] The reaction was performed on a $1.25 \times 10^{-5}$ mol scale in an aqueous solution of boric buffer (pH 9) at 40 °C for 3 h. [b] Yield of $[Co(bcmpa)(gly)]^-$ or $[Co(bcmga)(gly)]^{2-}$ determined by HPLC analysis based on the starting complexes $[Co(bcmpa)(dp)]^-$ or $[Co(bcmga)(dp)]^{2-}$. [c] $[Co(bcmpa)(leu)]^-$.

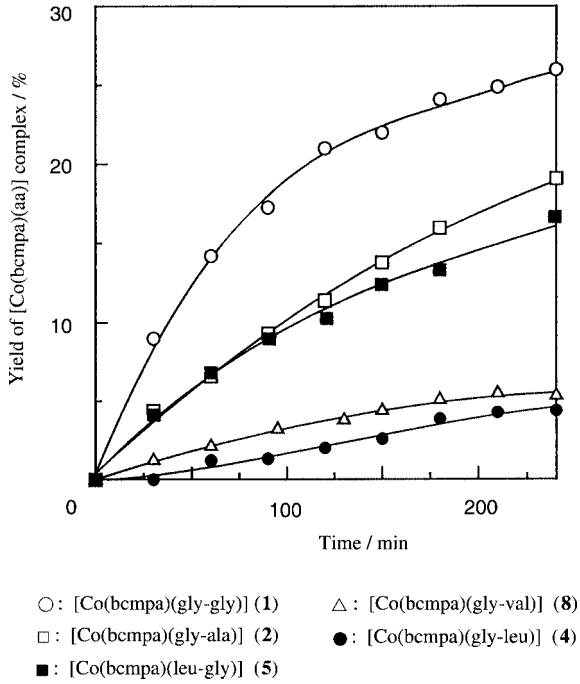


Figure 6. Cleavage reactions of various Co-bcmpa-dp complexes.

Two plausible mechanisms for the hydrolysis of amide compounds mediated by the mononuclear cobalt(III) complex have been proposed.[17,39] One involves external attack of $OH^-$ species on the amide carbonyl group, which is activated by coordination to the metal center,[40] and the other involves internal attack of the $OH^-$ species, which is activated by coordination to the metal center where the amide carbonyl group is coordinated.[41] In the cases of metalloen-

 © 2006 Wiley-VCH Verlag GmbH & Co. KGaA, Weinheim 

zymes containing a mononuclear active site, the internal attack mechanism has been proposed on the basis of the X-ray crystal structural analysis of carboxypeptidase A.[20] However, the ternary cobalt(III) complexes employed here have no coordination site available for the $OH^-$ species, as illustrated in Figure 4, therefore hydrolysis of the dipeptide must occur externally. With bcmpa as ligand hydrolysis of **6** and **11** did not give the corresponding amino acid, in contrast to the reaction with bcmga as ligand. As bcmga has a carboxylate moiety instead of the phenyl moiety of bcmpa, this makes for a more hydrophilic coordination sphere. In the hydrolysis reactivity of dipeptide complexes containing a C-terminal aliphatic side-chain, no difference was found between the bcmpa and bcmga ligands (Table 3). In Figure 7, however, the reactivity of complexes **6**, **11**, **18**, and **19**, which have C-terminal aromatic side-chains is clearly not equal; the dipeptide complexes with bcmga give small amounts of the corresponding cleavage products whereas those with bcmpa give no cleavage products. In the case of the bcmpa system, the hydrophobic interaction around the outer coordination sphere [Figure 4 (b)], which is generated by the assembly of the benzene ring of bcmpa and the C-terminal side-chain of the dipeptide, inhibits the approach of $OH^-$ to the amide carbonyl group. In the case of bcmga, however, such a hydrophobic sphere is not formed around the complex. Although the overall charges of the complexes Co-bcmpa (–1) and Co-bcmga (–2) are different, the effect of the charge on acceleration of the cleavage reaction is not yet clear. The more negatively charged $[Co(bcmga)(dp)]^{2-}$ complex and the carboxylate moiety attached to bcmga seems to attract hydrophilic $OH^-$ species externally. It is interesting that such a simple complex is able to perform the sequence-specific cleavage of peptides by a combination of inter-ligand interactions. We have also reported the selective cleavage of various peptides using simple enzyme model complexes in which the bulkiness of the aliphatic side-chain in the ternary cobalt(III) complex with a terpy ligand controls the specificity of the oxidative degradation of peptides.[42]

In summary, some ternary cobalt(III) complexes ($[Co(bcmpa)(dp)]^-$) containing an asymmetric tripodal ligand and dipeptides have been prepared. Their coordination geometry has been determined by UV/Vis, CD, and $^1H$ NMR spectroscopic methods. Site-specific recognition of dipeptides occurs by various kinds of weak non-covalent inter-ligand interactions. Such interactions are also observed in the ternary complexes with an amino acid ligand, $[Co(bcmpa)(aa)]^-$, some of whose structures have been determined by X-ray crystallography. Under slightly alkaline conditions, the dipeptide ligand of the ternary complexes is cleaved to give $[Co(bcmpa)(aa)]^-$. Selectivity for hydrolysis of the dipeptide ligand is regulated by the above interactions. This is the first report describing selectivity for the cleavage of various peptides using simple enzyme model complexes. The hydrophobic interaction between bcmpa and the C-terminal side-chain of the dipeptide regulates the approach of $OH^-$ to the amide carbonyl group coordinated to the cobalt center. In particular, the CH–π interaction caused by assembly of the benzene ring of bcmpa and the C-terminal aromatic amino acid moiety inhibits the approach of $OH^-$ and prevents hydrolysis of the dipeptide. The present ternary (Co-bcmpa-dp) system provides a method for the selective cleavage of peptide compounds due to multi-site interactions that is superior to the previous ternary (Co-trien-dp) system without the recognition site. We conclude that the multi-site interactions mediated by the metal complexes could be used to design an artificial hydrolysis enzyme.

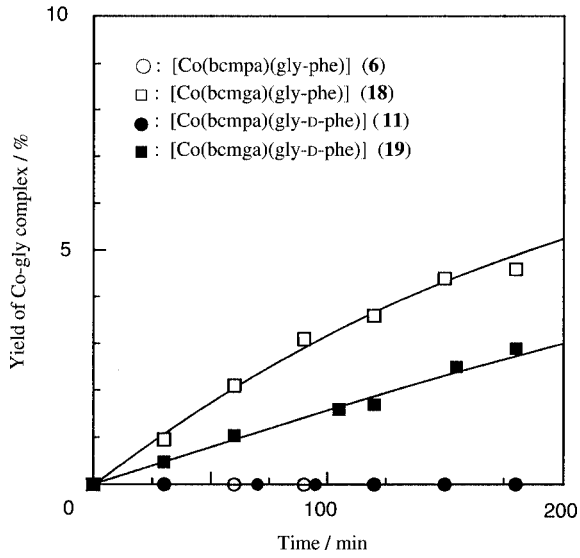


Figure 7. Cleavage reaction of cobalt(III) complexes having a C-terminal aromatic side-chain.

## Experimental Section

**Material:** The $NO_3$-type tripodal tetradentate ligand $H_3$bcmpa, was prepared from L-phenylalanine by a literature procedure.[22,24] $H_3$bcmga [bis-*N*,*N*-carboxymethyl-L-glutamic acid], which is a coordination analogue of bcmpa, was prepared in a similar manner from L-glutamic acid. QAE Sephadex A-25 ($Cl^-$ type) was supplied by Pharmacia. All amino acid derivatives (L- and D-isomers) and gly-gly (grade AA) were obtained from Peptide Institute Inc. and used without further purification. Other dipeptide compounds, namely gly-ala, ala-gly, gly-leu, leu-gly, gly-phe, phe-gly, gly-val, gly-phg, gly-D-ala, gly-D-phe, gly-D-phg, gly-β-ala, and gly-Mala, were synthesized by a DCC coupling method from the corresponding protected amino acid derivatives.

**Measurements:** The UV/Vis spectra were recorded with a JASCO UVDEC-660 spectrophotometer. The circular dichroism (CD) spectra were recorded with a JASCO J-500C spectropolarimeter. All measurements for the ternary cobalt(III) complexes were carried out in water and/or water–dioxane solution at room temperature. $^1H$ NMR spectra were recorded with a JEOL JNM-FX-400 spectrometer in $D_2O$ and/or $D_2O$/[$D_8$]dioxane solvent, with DSS as an internal standard. The HPLC analytical system was constituted by a JASCO Gulliver Series with a finepak SIL $NH_2$-5 column. The analytical conditions of HPLC were as follows: the mobile

 © 2006 Wiley-VCH Verlag GmbH & Co. KGaA, Weinheim 

phase (flow rate: 1 mL min$^{-1}$) was a 2:8 mixture of methanol and $NaHPO_4$ buffer (0.05 M) and the product complexes were monitored with a UV/Vis detector (wavelength: 510 nm).

**Preparation of Ternary Cobalt(III) Complexes with a Dipeptide Ligand:** K[Co(bcmpa)(gly-gly)] was prepared in a manner analogous to K[Co(bcmpa)(aa)].[22,24] An equimolar amount of gly-gly and 0.05 g of active charcoal were added to 10 mL of an aqueous solution of $K_2$[Co(bcmpa)($CO_3$)] (0.2 M). The resulting mixture was stirred for 24 h at 40 °C with addition of dilute HCl to maintain the pH at 6–7. After filtration of active charcoal and desalting with methanol, the resulting mixture was poured onto a QAE Sephadex A-25 column ($Cl^-$ form, 2.5 × 35 cm). The cobalt(III) complexes adsorbed on the anion exchange column were washed with distilled water to remove neutral and cationic complexes, and then two negatively charged bands were separated with KCl solution (0.1 M). The orange-colored first eluting band was the main fraction, which gave 0.49 g of product complex (49% yield) after usual isolation, and the pink-colored second one was the minor product (0.05 g, 5% yield). On the basis of the spectroscopic analysis, the former was identified as the dipeptide complex K[Co(bcmpa)(gly-gly)] (**1**) and the latter as the amino acid complex K[Co(bcmpa)(gly)]. Other negatively charged bands were also eluted in this separation, but they were unable to be identified because of lack of product.

**K[Co(bcmpa)(gly-gly)] (1):** $^1$H NMR ($D_2O$): $\delta$ = 3.20 (d, $J$ = 16.8 Hz, 1 H, G-ring-H),[30] 3.51 (dd, $J$ = 15.1 and 10.6 Hz, 1 H, benzyl-H of bcmpa), 3.64 (dd, $J$ = 15.1 and 4.8 Hz, 1 H, benzyl-H of bcmpa), 3.82 (s, 2 H, C-terminal glycine α-H), 3.98 (d, $J$ = 18.0 Hz, 1 H, R-ring-H), 4.13 (d, $J$ = 16.8 Hz, 1 H, G-ring-H), 4.24 (d, $J$ = 17.3 Hz, 1 H, N-terminal glycine α-H), 4.25 (d, $J$ = 17.3 Hz, 1 H, N-terminal glycine α-H), 4.63 (d, $J$ = 18.0 Hz, 1 H, R-ring-H), 4.90 (dd, 10.6 and 4.8 Hz, 1 H, Gs-ring-H), 7.4–7.6 (m, 5 H, aromatic-H).

The other K[Co(bcmpa)(dp)] complexes **2**–**14** were prepared by the same procedure using the appropriate dipeptide instead of gly-gly. The $K_2$[Co(bcmga)(dp)] complexes **15**–**18** were prepared from $K_3$[Co(bcmga)($CO_3$)]. Their $^1$H NMR spectroscopic data are listed in Table 1.

**Hydrolysis of Dipeptide Ligands:** Hydrolysis of dipeptide ligand mediated by the cobalt complexes was carried out as follows. K[Co(bcmpa)(dp)] or $K_2$[Co(bcmga)(dp)] (about 0.07 g, $1.25 \times 10^{-5}$ mol) was dissolved in 50 mL of an aqueous solution of 0.1 M $H_3BO_3/Na_2HBO_3$ buffer, which was maintained at pH 9.0 and 40 °C. The ionic strength during the reaction was 1.0 M of KCl. An aliquot of the reaction mixture passed through a 0.45-μm filter was analyzed by HPLC at 30 min intervals. After 3 h, the reaction solution was treated with the same isolation method as described above. Mono-negative charged complexes generated by the reaction after QAE Sephadex column separation with 0.1 M KCl solution were characterized by $^1$H NMR, UV/Vis, and CD spectroscopy.


[1] D. R. Garmer, N. Gresh, *J. Am. Chem. Soc.* **1994**, *116*, 3556–3567.
[2] J. Chin, *Acc. Chem. Res.* **1991**, *24*, 145–152.
[3] R. M. Smith, D. E. Hasen, *J. Am. Chem. Soc.* **1998**, *120*, 8910–8913.
[4] R. Wolfenden, M. J. Snider, *Acc. Chem. Res.* **2001**, *34*, 938–945.
[5] E. Kimura, *Inorg. Chem.* **1974**, *13*, 951–954.
[6] K. W. Bentley, E. H. Creaser, *Inorg. Chem.* **1974**, *13*, 1115–1121.
[7] C. J. Boreham, D. A. Buckingham, F. R. Keene, *J. Am. Chem. Soc.* **1979**, *101*, 1409–1421.
[8] B. L. Iverson, R. A. Lerner, *Science* **1989**, *243*, 1184–1188.
[9] C. V. Kumar, A. Buranaprapuk, A. Cho, A. Chaudhari, *Chem. Commun.* **2000**, 597–598.
[10] P. S. Chae, M.-S. Kim, C.-S. Jeung, S. D. Lee, H. Park, S. Lee, J. Suh, *J. Am. Chem. Soc.* **2005**, *127*, 2396–2397.
[11] a) I. E. Burgeson, N. M. Kostic, *Inorg. Chem.* **1991**, *30*, 4299–4305; b) L. Zhu, N. M. Kostic, *Inorg. Chem.* **1992**, *31*, 3994–4001.
[12] N. M. Milovic, J. D. Badjic, N. M. Kostic, *J. Am. Chem. Soc.* **2004**, *126*, 696–697.
[13] a) N. M. Milovic, N. M. Kostic, *Inorg. Chem.* **2002**, *41*, 7053–7063; b) N. M. Milovic, N. M. Kostic, *J. Am. Chem. Soc.* **2002**, *124*, 4759–4769; c) N. M. Milovic, N. M. Kostic, *J. Am. Chem. Soc.* **2003**, *125*, 781–788.
[14] A. Schepartz, R. Breslow, *J. Am. Chem. Soc.* **1987**, *109*, 1814–1826.
[15] J. T. Groves, L. A. Baron, *J. Am. Chem. Soc.* **1989**, *111*, 5442–5448.
[16] L. Zhu, N. M. Kostic, *J. Am. Chem. Soc.* **1993**, *115*, 4566–4570.
[17] P. A. Sutton, D. A. Buckingham, *Acc. Chem. Res.* **1987**, *20*, 357–364, and references cited therein.
[18] O. Yamauchi, A. Odani, S. Hirota, *Bull. Chem. Soc. Jpn.* **2001**, *74*, 1525–1545.
[19] B. Albert, D. Bray, J. Lewis, M. Raff, K. Robert, J. D. Watson, *Molecular Biology of the Cell*, 3rd ed., Garland Publishing, New York, **1994**, p. 89.
[20] D. W. Christianson, W. N. Lipscomb, *Acc. Chem. Res.* **1989**, *22*, 62–69.
[21] a) J. R. Bocarsly, M. Y. Chiang, L. Bryant, J. K. Barton, *Inorg. Chem.* **1990**, *29*, 4898–4907; b) J. R. Bocarsly, J. K. Barton, *Inorg. Chem.* **1992**, *31*, 2827–2834.
[22] K. Jitsukawa, T. Morioka, H. Masuda, H. Ogoshi, H. Einaga, *Inorg. Chim. Acta* **1994**, *216*, 249–251.
[23] H. Kumita, K. Jitsukawa, H. Masuda, H. Einaga, *Inorg. Chim. Acta* **1998**, *283*, 160–166.
[24] H. Kumita, T. Morioka, T. Ozawa, K. Jitsukawa, H. Einaga, H. Masuda, *Bull. Chem. Soc. Jpn.* **2001**, *74*, 1035–1042.
[25] H. Kumita, T. Kato, K. Jitsukawa, H. Einaga, H. Masuda, *Inorg. Chem.* **2001**, *40*, 3936–3942.
[26] I. Takahashi, T. Inomata, Y. Funahashi, T. Ozawa, K. Jitsukawa, H. Masuda, *Chem. Commun.* **2005**, 471–473.
[27] N. Koine, N. Sakata, J. Hidaka, Y. Shimura, *Inorg. Chem.* **1973**, *12*, 859–866.
[28] J. E. Fergusson, *Stereochemistry and Bonding in Inorganic Chemistry*, Prentice-Hall, New York, **1974**.
[29] N. Koine, N. Sakata, J. Hidaka, Y. Shimura, *Bull. Chem. Soc. Jpn.* **1970**, *43*, 1737–1743.
[30] G-ring = guard chelate ring, Gs-ring = substituted guard chelate ring, R-ring = relax chelate ring. See Figure 4.
[31] a) G. L. Blackmer, J. L. Sudmeier, *Inorg. Chem.* **1971**, *10*, 2019–2026; b) K. E. Rohly, B. E. Douglas, C. Maricondi, *Inorg. Chem.* **1986**, *25*, 4119–4125; c) J. B. Mandel, C. Maricondi, B. E. Douglas, *Inorg. Chem.* **1988**, *27*, 2990–2996.
[32] a) G. R. Desiraju, *Acc. Chem. Res.* **1991**, *24*, 290–296; b) T. Steiner, W. Saenger, *J. Am. Chem. Soc.* **1993**, *115*, 4540–4547.
[33] a) K. Jitsukawa, K. Iwai, H. Masuda, H. Ogoshi, H. Einaga, *J. Chem. Soc., Dalton Trans.* **1997**, 3691–3698; b) M. Mizutani, S. Tomosue, H. Kinoshita, K. Jitsukawa, H. Masuda, H. Einaga, *Bull. Chem. Soc. Jpn.* **1999**, *72*, 981–988.
[34] a) M. Nishio, M. Hirota, Y. Umezawa, *The CH/π Interaction. Evidence, Nature and Consequences*, Wiley-VCH, New York, **1998**; b) M. Nishio, *Tetrahedron* **2005**, *61*, 6923–6950.
[35] S. Shan, D. Herschlag, *J. Am. Chem. Soc.* **1996**, *118*, 5515–5518.
[36] J. A. Connolly, J. H. Kim, M. Banaszczyk, M. Drrouin, J. Chin, *Inorg. Chem.* **1995**, *34*, 1094–1099.
[37] H. Kroll, *J. Am. Chem. Soc.* **1952**, *74*, 2036–2039.
[38] B. K. Takasaki, J. H. Kim, E. Rubin, J. Chin, *J. Am. Chem. Soc.* **1993**, *115*, 1157–1159.
[39] J. Chin, *Acc. Chem. Res.* **1991**, *24*, 145–152.


 © 2006 Wiley-VCH Verlag GmbH & Co. KGaA, Weinheim 

[40] R. Breslow, A. Scheparts, *J. Am. Chem. Soc.* **1987**, *109*, 1814–1826.
[41] J. T. Groves, L. A. Baron, *J. Am. Chem. Soc.* **1989**, *111*, 5442–5448.
[42] K. Jitsukawa, H. Takahashi, R. Hyuga, H. Arii, H. Masuda, *Eur. J. Inorg. Chem.* **2004**, 4140–4145.

Received: May 3, 2006
Published Online: August 24, 2006

 © 2006 Wiley-VCH Verlag GmbH & Co. KGaA, Weinheim 

DOI: 10.1002/ejic.200600445

# Synthesis, Structure and Magnetism of Metal-Organic Framework Materials with Doubly Pillared Layers

Hong-Peng Jia,[a] Wei Li,[a] Zhan-Feng Ju,[a] and Jie Zhang*[a]

**Keywords:** Metal-organic frameworks / Pillared-layer structure / Iron(II) / Cobalt(II) / Hydrothermal synthesis / Magnetic properties / Carboxylates

Two novel coordination polymers with a 3D pillared-layer framework, $[M^{II}(Tdc)(4,4'\text{-Bpy})]_n$ [M = Fe (**1**), Co (**2**); Tdc = thiophene-2,5-dicarboxylate; 4,4′-Bpy = 4,4′-bipyridine), have been hydrothermally synthesised and structurally characterised. A simultaneous reduction of iron(III) to iron(II) occurs under hydrothermal conditions in the self-assembly process of complex **1**. The complexes are isostructural and, in each complex, the metal ions are linked by double $\mu_2$-carboxylate bridges in a *syn-syn* mode, giving rise to dinuclear units that are connected to each other by chelating carboxylate groups from the Tdc ligands in an approximately perpendicular orientation to form 2D rectangle-grid layers. The adjacent layers are held together through 4,4′-Bpy molecules in a double-pillar support fashion to give a 3D network with three intersecting perpendicular channels. Variable-temperature magnetic susceptibility measurements revealed weak antiferromagnetic coupling interactions in both complexes and a field-induced magnetic transition can be observed in **2**.

(© Wiley-VCH Verlag GmbH & Co. KGaA, 69451 Weinheim, Germany, 2006)

## Introduction

There has been continuous interest in the design and synthesis of metal-organic coordination polymers and supramolecular architectures due to their potential applications in the fields of magnetism, porous materials, catalysis and nonlinear optical activities or molecular recognition.[1–6] In the rational development of new strategies for the crystal engineering of coordination networks and supramolecular architectures, the pillared-layer assemblies have been shown to be precursors in an efficient route for the construction of porous frameworks with controllable channel sizes and chemical functionalities.[7–9] In particular, the pillared-layer networks based on coordination bonds are more attractive than those based on the hydrogen-bonded assemblies owing to their high structural and thermal stabilities.[10–13] Although the advantages of the pillared-layer assemblies are generally due to their suitability for manipulation of the pore structures by means of simple modifications to the pillar module, the search for new layer-building units is also quite necessary for systematic fine-tuning of structural and functional features. In this paper, we report two novel coordination polymers with a 3D porous pillared-layer framework, namely $[Fe^{II}(Tdc)(4,4'\text{-Bpy})]_n$ (**1**) and $[Co^{II}(Tdc)(4,4'\text{-Bpy})]_n$ (**2**). Thiophene-2,5-dicarboxylate (Tdc) ligands link the metal ions by bridging and chelating carboxylate groups to form a rare type of 2D rectangle-grid layer containing the dimetallic carboxylate subunits in a mutually perpendicular orientation. Each 4,4′-Bpy ligand as a rigid spacer is coordinated to the axial positions of the metal ions, connecting the $[M^{II}(Tdc)]_n$ layers into a 3D coordination framework with twofold interpenetration. An interesting aspect of the structure is that the 4,4′-Bpy ligands bind to the layers in a double-pillar support fashion (Scheme 1), which results in a molecular architecture with a higher thermal stability. In addition, the Tdc ligand displays both chelating and $\mu_2$-bridging carboxylate coordination modes in the assemblies (Scheme 2) and this is the first

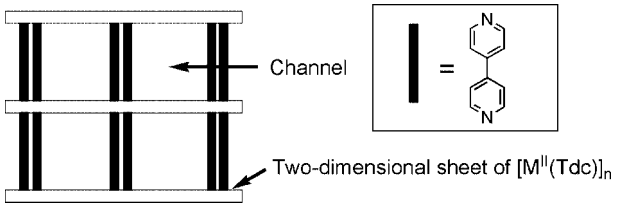


Scheme 1. Schematic representation of the doubly pillared-layer structures of $[M^{II}(Tdc)(4,4'\text{-Bpy})]_n$ (M = Fe, Co).

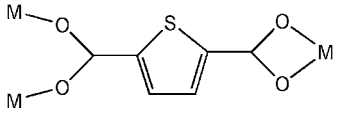


Scheme 2. Coordination mode of Tdc in complexes **1** and **2**.

[a] State Key Laboratory of Structural Chemistry, Fujian Institute of Research on the Structure of Matter, Chinese Academy of Sciences,
Fuzhou, Fujian 350002, China
Fax: +86-591-8371-0051
E-mail: zhangjie@fjirsm.ac.cn

Supporting information for this article is available on the WWW under http://www.eurjic.org or from the author.

 © 2006 Wiley-VCH Verlag GmbH & Co. KGaA, Weinheim 

observation of such behaviour for the Tdc ligand.[14] Variable-temperature magnetic susceptibility measurements revealed weak antiferromagnetic coupling interactions in both complexes and a field-induced magnetic transition can be observed in **2**.

## Results and Discussion

### Synthesis and Structural Description

Single-crystal X-ray diffraction analyses revealed that complexes **1** and **2** are isostructural and crystallise in the orthorhombic space group *Pccn*. As a representative example, the crystal structure of complex **1** is described here in detail. It is interesting to note that a simultaneous reduction of iron (III) to iron (II) occurs in the self-assembly process of complex **1** under hydrothermal conditions. There have been some reports that several metal ions can be reduced in the presence of 4,4′-Bpy under hydrothermal conditions. Although the mechanisms of redox reactions are still unknown, hydrothermal conditions are essential for achieving the reduced product.[15] The fundamental building unit of **1** is composed of a six-coordinate $Fe^{II}$ centre, a Tdc ligand and a 4,4′-Bpy ligand. Each $Fe^{II}$ centre exhibits a distorted octahedral geometry with two pyridyl nitrogen atoms (N1, N2D) from different 4,4′-Bpy ligands at the axial positions and four oxygen atoms in the equatorial plane of which two (O3A, O4B) are from two $\mu_2$-bridging bidentate carboxylate groups from two different Tdc ligands and the other two (O1, O2) are from a chelating carboxylate group of a Tdc ligand, as shown in Figure 1. The Fe–O bond lengths are in the range of 1.999(3)–2.387(3) Å and the Fe–N bond lengths are 2.195(3) and 2.168(3) Å, respectively. The O1–Fe–O2 bite angle of 58.07(10)° is much smaller than the O3A–Fe–O4B bond angle of 117.90(12)°.

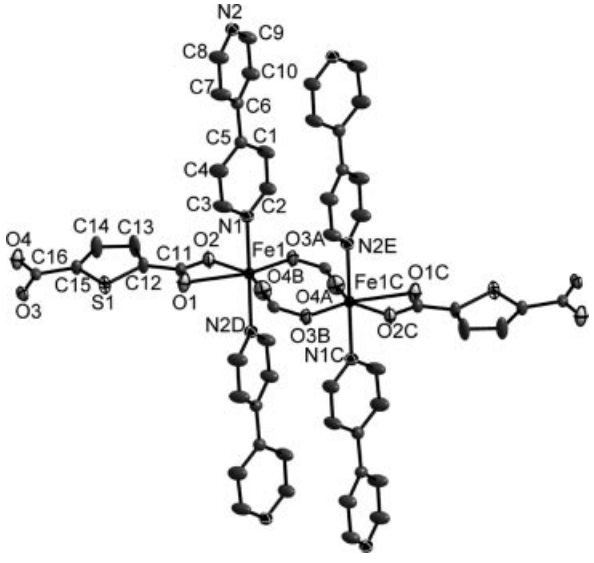


Figure 1. Coordination environment of the $Fe^{II}$ ion with atom labelling in **1**. Hydrogen atoms are omitted for clarity.

Two equivalent $Fe^{II}$ ions related by a twofold axis with a separation of 4.149 Å are bridged by two carboxylate groups from two different Tdc ligands in a *syn-syn* mode to form a dinuclear subunit. These dinuclear units are aligned approximately perpendicular to each other in the *ac* plane and linked further by additional Tdc ligands in a chelating mode to give rise to a neutral 2D sheet with a rectangular window of 8.8 × 11.0 Å (Figure 2). It is worthy of note that the orthogonal arrangement of dimetallic subunits within a 2D layer is still rare in metal carboxylate complexes in which dinuclear units are generally parallel to each other.[16] Each Tdc ligand coordinates to three $Fe^{II}$ ions through the two terminal carboxylate groups in chelating and bridging modes, respectively, illustrating an unreported coordination mode for the Tdc molecule. An interesting aspect of the structure is that the 2D porous sheets are connected by 4,4′-Bpy ligands through the axial positions of both $Fe^{II}$ centres in subunits to form a 3D doubly pillared-layer structure with three intersecting perpendicular channels (Figure 3). The whole structure can also be described as a 3D frame-

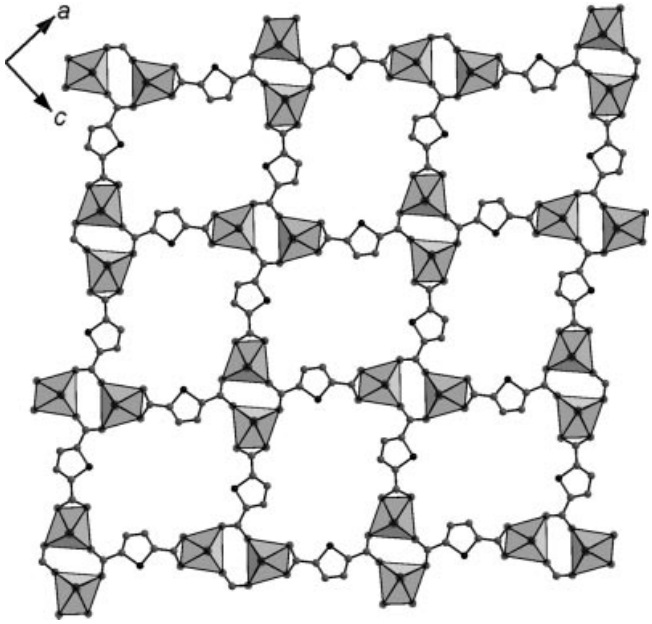


Figure 2. Perspective view of the $[Fe(Tdc)]_n$ sheet subunit with rectangular windows of about 8.8 Å × 11.0 Å. Hydrogen atoms are omitted for clarity.

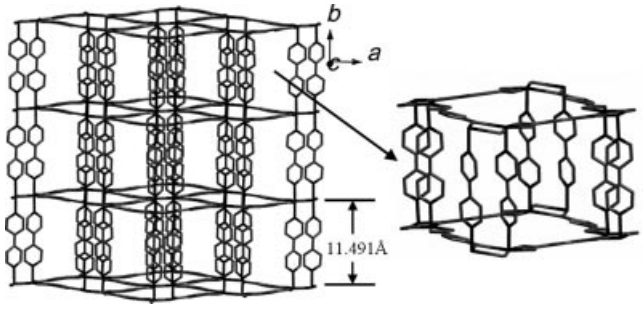


Figure 3. (a) Perspective view of the pillared-layer 3D network of **1**; (b) cuboid-like unit in **1**.

 © 2006 Wiley-VCH Verlag GmbH & Co. KGaA, Weinheim 

work composed of cuboid-like cavities with dimensions of 12.16 × 12.16 × 11.49 Å (based on the centre of the dinuclear subunit). The large cavities in the structure lead to a tendency to form an interpenetrating network. As shown in Figure 4, a twofold interpenetrating topological structure can be observed. The volume of the effective void is about 9.9% of the unit-cell volume in the self-inclusion structure.

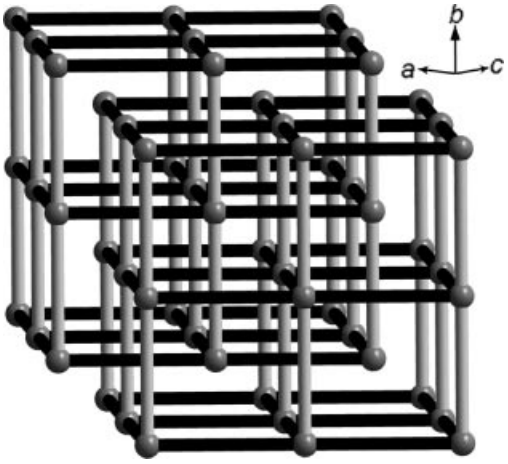


Figure 4. Structure topology of **1** displaying twofold interpenetration (darker and grey rods representing the Tdc and 4,4′-Bpy ligands, respectively).

### Thermogravimetric Analysis

The thermal stabilities of the two complexes were determined by thermogravimetric analysis (TGA) in air with a heating rate of 20 °C min$^{-1}$. Complexes **1** and **2** exhibit high thermal stabilities (Figure S2, Supporting Information). A sharp weight loss occurs in the temperature range 360–470 °C for **1** (74.8%) and 380–480 °C for **2** (72.7%), corresponding to the removal of ligands and decomposition of the framework. The final residues of complexes **1** and **2** were found to be amorphous and could not be identified.

### Magnetic Properties

The temperature dependences of the magnetic susceptibilities of **1** and **2** under an applied field of 5000 Oe are shown in Figure 5 in the form of an $\chi_m T$ vs. $T$ plot, where $\chi_m$ is the molar magnetic susceptibility per formula unit. At room temperature, the $\chi_m T$ value of **1** is 3.35 emu mol$^{-1}$ K per Fe$^{II}$ ion, corresponding to an average $g$ value of 2.11. This is in agreement with the typical value for a high-spin Fe$^{II}$ ion with some orbital contributions.[17] As the temperature is lowered, the $\chi_m T$ value remains almost constant in the range 300–50 K and then rapidly decreases to 1.44 emu mol$^{-1}$ K at 2 K. The magnetic susceptibility above 2.5 K follows the Curie–Weiss equation $\chi_m = C/(T - \theta)$ with $C$ = 3.37 emu mol$^{-1}$ K and $\theta$ = –2.01 K. Such behaviour is consistent with a weak antiferromagnetic coupling interaction between the magnetic centres.

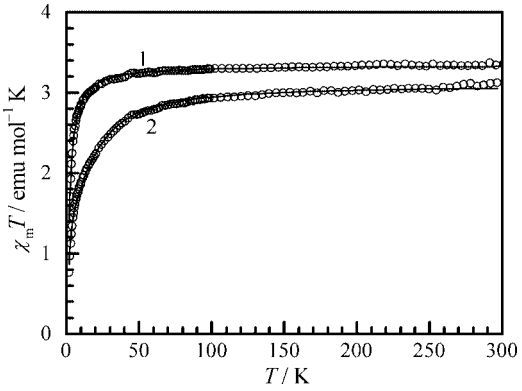


Figure 5. Temperature dependence of $\chi_m T$ for complexes **1** and **2**, the solid lines represent the best fits obtained from the models described in the text.

In the structure of **1**, the carboxylate-bridged dinuclear units are connected by 4,4′-Bpy and Tdc units to form the 3D framework. The Fe–Fe distance of 4.149 Å over the $\mu_2$-carboxylate bridge is much shorter than those over the 4,4′-Bpy (11.49 Å) and the Tdc (10.38 Å) bridges and, consequently, the exchange coupling through the double $\mu_2$-carboxylate bridge in the dinuclear subunits should be dominant. In order to obtain reliable simulation results, the magnetic behaviour of **1** was analysed using an analytical expression[18] based on the Hamiltonian taking into account the anisotropy $g$ and the zero-field-splitting term in Equation (1).

$$H = g_{\perp}\beta H_{\perp}[{}^1/_2(S_1^+ + S_1^- + S_2^+ + S_2^-)] + g_{\parallel}\beta H_{\parallel}(S_{z1} + S_{z2}) - 2J[S_{z1}S_{z2} + {}^1/_2(S_1^+S_2^-) + {}^1/_2(S_1^-S_2^+)] + D(S_{z1}^2 + S_{z2}^2) \quad (1)$$

In addition, a molecular field approximation[19] was applied to Equation (1) to account for the interdimer exchange interaction ($zJ'$) in the 3D system [Equation (2)].

$$\chi_m = \chi_{di}/(1 - 2zJ'\chi_{di}/Ng^2\beta^2) \quad (2)$$

Calculations were performed with the MAGPACK package.[20] The best fit was obtained with the following sets of parameters: $J$ = –0.242 cm$^{-1}$, $g_{\parallel}$ = 2.015, $g_{\perp}$ = 2.289, $D$ = 0.09 cm$^{-1}$, $zJ'$ = 0 and an agreement factor $R$ {defined as $R = \Sigma[(\chi_m T)_{calcd} - (\chi_m T)_{obs}]^2/\Sigma(\chi_m T)_{obs}^2$} of 4.18 × 10$^{-5}$. The value obtained for $D$ is smaller and the ratio of $|J|/D$ is equal to 2.69. When $J$ is much larger or smaller than $D$, exchange coupling or ZFS will be dominant and the smaller term can be treated as a perturbation. Thus, the decreases in $\chi_m T$ at lower temperatures are mainly due to antiferromagnetic coupling for complex **1**.

For **2**, the $\chi_m T$ value at room temperature is equal to 3.15 emu mol$^{-1}$ K, which is much higher than the spin-only value of 1.875 emu mol$^{-1}$ K expected for an isolated high spin Co$^{II}$ ion with $S = {}^3/_2$ and $g$ = 2.00 owing to the orbital contribution of the Co$^{II}$ ion.[21] Upon cooling, the $\chi_m T$ value slightly decreases until around 50 K, then rapidly decreases to 0.76 emu mol$^{-1}$ K at 2 K. Above 32 K, the

 © 2006 Wiley-VCH Verlag GmbH & Co. KGaA, Weinheim 

magnetic data follow the Curie–Weiss law with $C = 3.20\ \text{emu mol}^{-1}\,\text{K}$ and $\theta = -8.8$ K. The negative Weiss constant suggests an antiferromagnetic interaction between the $Co^{II}$ ions. The presence of a small maximum in $\chi_m$ at 2.5 K is indicative of long-range antiferromagnetic ordering (Figure 6a). Complex **2** has the same structure as **1** and in order to fit the magnetic data of **2** quantitatively, we used the MAGPACK package[20] with a similar Hamiltonian model and taking into account the anisotropy $g$, the zero-field splitting parameter $D$ ($S_1 = S_2 = {}^3/_2$) and the molecular field approximation[19] for the interdimer exchange interaction ($zJ'$). The results of the best fit of the experimental data in the whole temperature range are shown in Figure 5 with $J = -0.37\ \text{cm}^{-1}$, $g_{\parallel} = 2.42$, $g_{\perp} = 2.85$, $D = 21.00\ \text{cm}^{-1}$, $zJ' = -0.001\ \text{cm}^{-1}$ and $R = 1.25 \times 10^{-4}$. The $D$ value is larger than the $|J|$ value and so the decreases in $\chi_m T$ at lower temperatures are mainly due to the zero-field splitting of complex **2**. Until now, only a few $Co^{II}$ complexes bridged by carboxylate groups in a *syn-syn* mode have been rigorously studied from a magnetic point of view due to inherent difficulties resulting from strong spin-orbit coupling and magnetic anisotropy orbital degeneracy. Antiferromagnetic interactions are generally observed in these complexes.[22] The complex magnetic behaviour of $Co^{II}$ ions did not allow us to accurately simulate the magnitude of the magnetic interaction taking into account all factors, thus the value of $D$ obtained for **2** is larger than that for **1**.

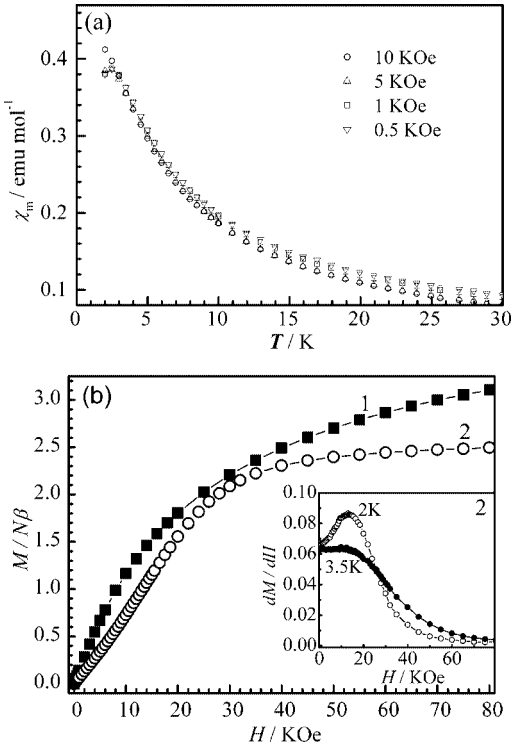


Figure 6. (a) Temperature-dependent molar magnetic susceptibilities of **2** measured at different external fields; (b) field-dependent magnetisations of **1** and **2** at 2 K. The inset shows the d$M$/d$H$ derivative curves of **2** at 2 K and 3.5 K.

In fact, the Fe1–O1 (2.387 Å) and Co1–O1 (2.333 Å) bonds are much longer than the others in the equatorial planes in the structures of **1** and **2**. Ignoring these bonds, we can think of the $Fe^{II}$ and $Co^{II}$ centres as being in distorted trigonal-bipyramidal rather than distorted octahedral environments. The idealised trigonal-bipyramidal geometry belongs to the $D_{3h}$ point group and the orbital momentum is quenched except for the E′ and E″ terms. However, when the structure is distorted and the symmetry deviates from pure $D_{3h}$, the quenching of the ground $^4A_2'$ term may not be sufficient and an admixture of the upper $^4E''$ term may bring the orbital momentum into the ground term, resulting in an obviously high $\mu_{eff}$ value and a deviation of $g$ from 2.0.[23] In **2**, the $\mu_{eff}$ value (5.02 $\mu_B$) is much higher than the spin-only value (3.87 $\mu_B$) but lies in the range of 4.26–5.03 $\mu_B$ for trigonal-bipyramidal cobalt(II) complexes.[24]

In comparison with **1**, the magnetic behaviour of **2** is more complex in the low-temperature range. The small maximum of $\chi_m$ at around 2.5 K only appears at low field. When the external field is increased, this maximum vanishes above 10 kOe (Figure 6a). Furthermore, the field-dependent magnetisation of **1** exhibits a smooth increase at 2 K, reaching 3.1 $N\beta$ at 80 kOe which is less than the expected saturation value of 4 $N\beta$ for a magnetically isolated $Fe^{II}$ centre with $g = 2.0$, while the magnetisation of **2** shows a sigmoid-like curve and gives a saturation value of 2.5 $N\beta$ at 80 kOe (Figure 6b). For the $Co^{II}$ ion, an $S = {}^1/_2$ ground state is usually observed at low temperatures due to the overall effect of the crystal field and spin-orbit coupling. The saturation magnetisation value of **2** is within the range expected for a free cobalt ion with an effective $S = {}^1/_2$ and large anisotropic $g$ values ranging from 4.1 to 5.0.[25]

The disappearance of the $\chi_m$ maximum at higher fields and the sigmoid-like magnetisation curve of **2** suggest the occurrence of a field-induced magnetic transition. The transition field, determined by the d$M$/d$H$ derivative curve is ca. 12 kOe at 2 K (inset in Figure 6b). The AC isothermal magnetisation measurements at 2 K with the DC field from 0 to 50 kOe display a peak value of the in-phase component of the susceptibility ($\chi'$) at 11 kOe, consistent with the transition observed in the d$M$/d$H$ curve. It is worthy of note that a nonzero out-of-phase component of the AC susceptibility ($\chi''$) appears at 17 kOe with a further increase in the applied field, indicating the occurrence of the second magnetic transition. Additional measurements at 3.5 and 5 K show the temperature dependence of the second magnetic transition, the $H$ value increases slightly as the temperature increases (Figure 7).

The magnetic behaviour of **2** is analogous to some observations in the complexes with field-induced spin-flop phase transitions (SF), which is characteristic for antiferromagnetic (AF) systems with weak anisotropy.[26] Although this transition does not generally appear in a system with large anisotropy such as the Ising mode, similar transition behaviour has been discussed for several $Co^{II}$ complexes.[27] In **2**, the spin-flop field ($H_{SF}$) appears at 11 kOe, corresponding to a transition from an antiferromagnetic to a spin-flop state. The AF-SF transition is a first-order transition and there is a discontinuity in the magnetisation on crossing the

 © 2006 Wiley-VCH Verlag GmbH & Co. KGaA, Weinheim 

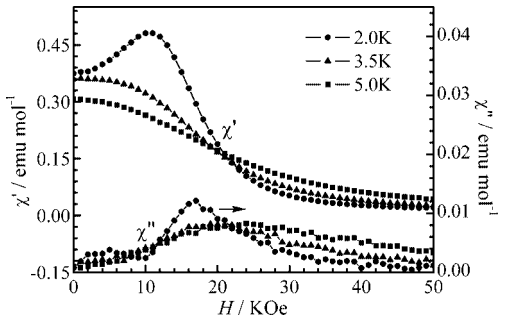


Figure 7. Field-dependent AC magnetic susceptibilities of **2** measured at different temperatures.

AF-SF phase boundary. Thus, an inflexion can be observed in the $M(H)$ curve and a peak also appears in the $\chi'(H)$ plot.[26] Another critical field ($H_C$) is not evident in $\chi'(H)$ although an obvious peak around 17 kOe can be observed in the $\chi''(H)$ curve, which can be identified as the second-order transition field ($H_C$) from a spin-flop to a ferromagnetic-like state.[28,29] The lack of a sharp conversion in $\chi'(H)$ suggests that this second phase-transition process is rather gradual.[29] To further substantiate the spin-flop transition in **2**, additional temperature-dependent AC magnetic susceptibility measurements at different DC fields were carried out (Figure 8). The zero-field AC magnetic susceptibility measurements exhibit a maximum value of $\chi'$ at 2.5 K and a negligible $\chi''$ value, in agreement with the existence of antiferromagnetic ordering. The data measured at 12 kOe clearly show the disappearance of the $\chi'$ maximum, indicating that an antiferromagnetic coupling has been overcome. At an applied field of 17 kOe, $\chi'$ exhibits a new broad peak around 6.9 K, accompanied by a maximum peak of $\chi''$ at somewhat lower temperatures. This feature is quite consistent with a ferromagnetic-like state. It is also notable that the similar small peaks around 6.9 K already appear in $\chi'(T)$ and $\chi''(T)$ plots at 12 kOe, which is in accordance with the continuity and gradualness of this second-order phase transition. With the above results, the anisotropy field $H_A \approx 0.71$ kOe and the exchange field $H_E \approx 1.21$ kOe were estimated based on the mean-field relation $H_{SF} = (2H_EH_A - H_A^2)^{1/2}$ and $H_C = 2H_E - H_A$.[30] The anisotropy constant $a = H_A/H_E$ is 0.59. Although no related parameter can be found in $Co^{II}$ complexes for comparison, a lower anisotropy field in **2** suggests that its magnetisation process can possibly proceed through the spin-flop-like transition.[31]

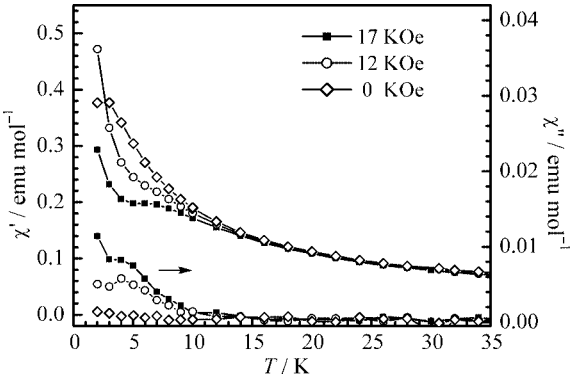


Figure 8. Temperature dependence of the AC magnetic susceptibilities of **2** measured in a field amplitude of 3 Oe (711 Hz) and a DC bias field of 0, 12 and 17 kOe.

## Conclusions

In summary, two novel 3D porous frameworks were hydrothermally synthesised and structurally characterised. Metal ions are connected by chelating and bridging carboxylate groups of Tdc groups to form 2D rectangle-grid layers containing dinuclear subunits in an approximately perpendicular orientation. The interconnection of the 2D layers by the secondary metal linker (4,4′-Bpy) leads to the doubly pillared-layered 3D architecture with twofold interpenetration. Variable-temperature magnetic susceptibility measurements reveal weak antiferromagnetic coupling interactions in both complexes and a field-induced magnetic transition can be observed in **2**.

## Experimental Section

**General:** All the syntheses were performed in Parr Teflon-lined stainless steel autoclaves under autogenous pressure. All chemicals were analytical reagent grade and were used as received. IR spectra were recorded with a Spectrum One FT-IR spectrophotometer in KBr pellets in the range 4000–400 $cm^{-1}$. Elemental analyses were determined with an Elementar Vario EL III elemental analyser. The thermal analysis was performed under air with a Netzsch STA449C thermal analyser at a heating rate of 20 °C $min^{-1}$. Magnetic susceptibilities were measured using a Quantum Design PPMS-9T system. Diamagnetic corrections were estimated from Pascal's constants. The pore-volume analysis was performed with the PLATON software package.

**Synthesis of $[Fe^{II}(tdc)(bpy)]_n$ (1):** This compound was synthesised by the hydrothermal method. A mixture of $FeCl_3·6H_2O$ (65 mg, 0.24 mmol), $H_2Tdc$ (70 mg, 0.41 mmol), NaOH (33 mg, 0.83 mmol) and 4,4′-Bpy (74 mg, 0.47 mmol) in $H_2O$ (5 mL) was homogenised at room temperature for 20 min. The resultant mixture was transferred and sealed in a Teflon-lined steel autoclave (23 mL) at 120 °C for 3 d and was then cooled to room temperature at a rate of 1.7 K $h^{-1}$. The dark-red crystals were isolated in 35.9% yield based on Fe. $C_{16}H_{10}FeN_2O_4S$ (382.17): calcd. C 50.28, H 2.64, N 7.33; found C 49.82, H 2.98, N 7.36. IR (KBr): $\tilde{\nu}$ = 3434 (m), 1604 (s), 1570 (s), 1524 (m), 1490 (w), 1414 (s), 1384 (vs), 1221 (w), 1072 (w), 1046 (w), 1033 (w), 1008 (w), 818 (m), 769 (m), 731 (w), 684 (w), 631 (m), 475 (m) $cm^{-1}$.

**Synthesis of $[Co^{II}(tdc)(bpy)]_n$ (2):** This compound was obtained using a procedure similar to that of **1**, except that $CoCl_2·6H_2O$ was used instead of $FeCl_3·6H_2O$. The pink crystals were isolated in 27.6% yield based on Co. $C_{16}H_{10}CoN_2O_4S$ (385.25): calcd. C 49.88, H 2.62, N 7.27; found C 49.56, H 3.04, N 7.54. IR (KBr): $\tilde{\nu}$ = 3435 (m), 1607 (s),1564 (s),1524 (m),1491 (w),1416 (s),1385 (vs),1221 (w), 1075 (w), 1045 (w), 1029 (w), 1011 (w), 821 (m), 767 (m), 732 (w), 682 (w), 634 (m), 477 (m) $cm^{-1}$.

**X-ray Crystallographic Study:** The intensity data of **1** were collected with a Rigaku CCD diffractometer with graphite-monochromated Mo-$K_\alpha$ radiation ($\lambda$ = 0.71073 Å) at room temperature. An empiri-

 © 2006 Wiley-VCH Verlag GmbH & Co. KGaA, Weinheim 

Table 1. Crystallographic data for complexes **1** and **2**.

| | **1** | **2** |
|---|---|---|
| Empirical formula | $C_{16}H_{10}FeN_2O_4S$ | $C_{16}H_{10}CoN_2O_4S$ |
| Formula mass | 382.17 | 385.25 |
| Crystal system | orthorhombic | orthorhombic |
| Space group | *Pccn* | *Pccn* |
| *a* [Å] | 18.2626(13) | 17.9459(5) |
| *b* [Å] | 11.4913(9) | 11.4012(3) |
| *c* [Å] | 16.0515(10) | 16.2390(5) |
| *V* [Å$^3$] | 3368.6(4) | 3322.58(16) |
| *Z* | 8 | 8 |
| $D_{calcd.}$ [g cm$^{-3}$] | 1.507 | 1.540 |
| *F*(000) | 1640 | 1560 |
| Crystal size [mm] | 0.30 × 0.10 × 0.03 | 0.45 × 0.18 × 0.10 |
| Range for data collection [°] | 3.10–27.48 | 2.12–25.66 |
| Reflections collected | 24699 | 16819 |
| Independent reflections | 3858 | 3140 |
| Number of parameters | 217 | 217 |
| Refinement method | full-matrix least squares on $F^2$ | full-matrix least squares on $F^2$ |
| Goodness-of-fit on $F^2$ | 1.029 | 1.001 |
| $R_1$ [$I > 2\sigma(I)$] | 0.0713 | 0.0656 |
| $wR_2$ (all data) | 0.1410 | 0.1295 |

cal absorption correction for **1** was performed using the CrystalClear program.[32] The crystal structure determination of **2** was performed with a Siemens SMART CCD diffractometer with graphite-monochromated Mo-$K_\alpha$ radiation ($\lambda$ = 0.71073 Å) at room temperature. An empirical absorption correction for **2** was applied using the SADABS program.[33] The structure was solved by direct methods and refined by full-matrix least-squares fitting on $F^2$ using the SHELXS-97[34] and SHELXL-97[35] programs. All non-hydrogen atoms were refined with anisotropic thermal parameters. Hydrogen atoms were located by geometric calculations. Crystallographic data and structural refinements for **1** and **2** are summarised in Table 1. Selected bond lengths and angles for **1** and **2** are listed in Table 2. CCDC-298904 (**1**) and -298903 (**2**) contain the supplementary crystallographic data for this paper. These data can be obtained free of charge from The Cambridge Crystallographic Data Centre via www.ccdc.cam.ac.uk/data_request/cif.

Table 2. Selected bond lengths [Å] and angles [°] for **1** and **2**.

| Complex **1** | | | |
|---|---|---|---|
| Fe1–O1 | 2.387(3) | Fe1–O4B$^{i}$ | 1.999(3) |
| Fe1–O2 | 2.116(3) | Fe1–N2D$^{iii}$ | 2.195(3) |
| Fe1–N1 | 2.198(3) | Fe1–O3A$^{ii}$ | 2.090(3) |
| O1–Fe1–O2 | 58.07(10) | O1–Fe1–N1 | 92.09(12) |
| O2–Fe1–N2D$^{iii}$ | 91.30(13) | O2–Fe1–N1 | 90.25(13) |
| O3A$^{ii}$–Fe1–O2 | 91.29(11) | O3A$^{ii}$–Fe1–N2D$^{iii}$ | 91.27(12) |
| O3A$^{ii}$–Fe1–N1 | 90.37(12) | O3A$^{ii}$–Fe1–O2 | 91.29(11) |
| O4B$^{i}$–Fe1–N1 | 87.64(14) | O4B$^{i}$–Fe1–O3A$^{ii}$ | 117.90(12) |
| O4B$^{i}$–Fe1–O1 | 92.82(12) | O4B$^{i}$–Fe1–O1 | 92.82(12) |
| O4B$^{i}$–Fe1–N2D$^{iii}$ | 90.19(14) | N2D$^{iii}$–Fe1–N1 | 177.71(13) |
| N2D$^{iii}$–Fe1–O1 | 87.31(12) | | |
| Complex **2** | | | |
| Co1–O1 | 2.333(4) | Co1–O4B$^{i}$ | 1.999(3) |
| Co1–O2 | 2.110(4) | Co1–N2D$^{iii}$ | 2.141(4) |
| Co1–N1 | 2.154(4) | Co1–O3A$^{ii}$ | 2.050(3) |
| O1–Co1–O2 | 59.03(13) | O1–Co1–N1 | 92.75(16) |
| O1–Co1–N2D$^{iii}$ | 85.75(16) | O2–Co1–N1 | 88.73(16) |
| O3A$^{ii}$–Co1–O1 | 152.45(14) | O3A$^{ii}$–Co1–N2D$^{iii}$ | 91.88(16) |
| O3A$^{ii}$–Co1–N1 | 90.21(16) | O3A$^{ii}$–Co1–O2 | 93.69(14) |
| O4B$^{i}$–Co1–N1 | 85.99(17) | O4B$^{i}$–Co1–O3A$^{ii}$ | 113.67(15) |
| O4B$^{i}$–Co1–O2 | 152.11(15) | O4B$^{i}$–Co1–O1 | 93.87(14) |
| O4B$^{i}$–Co1–N2D$^{iii}$ | 92.44(17) | N2D$^{iii}$–Co1–N1 | 177.76(17) |
| N2D$^{iii}$–Co1–O2 | 91.93(17) | | |

(i) 1.5 – *x*, *y*, –0.5 + *z*; (ii) –0.5 + *x*, 1 – *y*, 0.5 – *z*; (iii) *x*, –1 + *y*, *z*

**Supporting Information** (see footnote on the first page of this article): Additional two plots including IR spectrum and TGA curve (Figures S1 and S2).

## Acknowledgments

The authors acknowledge the financial support of the Natural Science Foundation of China (No. 50372069/20201010), the Natural Science Foundation of Fujian Province of China (No. E0220003) and the Ministry of Education/Personnel of China.

[1] O. M. Yaghi, H. Li, C. Davis, D. Richardardson, T. L. Groy, *Acc. Chem. Res.* **1998**, *31*, 474–484.
[2] D. L. Long, R. J. Hill, A. J. Blake, N. R. Champness, P. Hubberstey, C. Wilson, M. Schröder, *Chem. Eur. J.* **2005**, *11*, 1384–1391.
[3] L. Pan, D. H. Olson, L. R. Ciemnolonski, R. Heddy, J. Li, *Angew. Chem. Int. Ed.* **2006**, *45*, 616–619.
[4] E. Coronado, J. R. Galán-Mascarós, C. J. Gómez-Garcia, V. Laukhin, *Nature* **2000**, *408*, 447–449.
[5] P. G. Lacroix, I. Malfant, S. Benard, P. Yu, E. Riviere, K. Nakatani, *Chem. Mater.* **2001**, *13*, 441–449.
[6] S. Karasawa, Y. Sano, T. Akita, N. Koga, T. Itoh, H. Iwamura, P. Rabu, M. Drilion, *J. Am. Chem. Soc.* **1998**, *120*, 10080–10087.
[7] B.-B. Ding, Y.-Q. Weng, Z.-W. Mao, C.-K. Lam, X.-M. Chen, B.-H. Ye, *Inorg. Chem.* **2005**, *44*, 8836–8845.
[8] T. K. Maji, K. Uemura, H. Chang, R. Matsuda, S. Kitagawa, *Angew. Chem. Int. Ed.* **2004**, *43*, 3269–3272.
[9] B.-Q. Ma, P. Coppens, *Chem. Commun.* **2003**, 412–413.
[10] M. Kondo, T. Okubo, A. Asami, S.-i. Noro, T. Yoshitomi, S. Kitagawa, T. Ishii, H. Matsuzaka, K. Seki, *Angew. Chem. Int. Ed.* **1999**, *38*, 140–143.
[11] X.-L. Wang, C. Qin, E.-B. Wang, Y.-G. Li, C.-W. Hu, L. Xu, *Chem. Commun.* **2004**, 378–379.
[12] H. Chun, D. N. Dybtsev, H. Kim, K. Kim, *Chem. Eur. J.* **2005**, *11*, 3521–3529.
[13] T. K. Maji, M. Ohba, S. Kitagawa, *Inorg. Chem.* **2005**, *44*, 9225–9231.
[14] B.-L. Chen, K.-F. Mok, S.-C. Ng, M. G. B. Drew, *New J. Chem.* **1999**, *23*, 877–883. A further search in the CCDC data-

 © 2006 Wiley-VCH Verlag GmbH & Co. KGaA, Weinheim 

base (version 1.8) does not show this kind of coordination mode.
[15] O. M. Yaghi, H. Li, *J. Am. Chem. Soc.* **1995**, *117*, 10401–10402.
[16] a) C.-B. Ma, C.-N. Chen, Q.-T. Liu, F. Chen, D.-Z. Liao, L.-C. Li, L.-C. Sun, *Eur. J. Inorg. Chem.* **2003**, 2872–2879 (containing orthogonal dimer); b) R.-Q. Zou, X.-H. Bu, R.-H. Zhang, *Inorg. Chem.* **2004**, *43*, 5382–5386; c) D.-P. Cheng, M. A. Khan, R. P. Houser, *Inorg. Chem.* **2001**, *40*, 6858–6859; d) J. Tao, M.-L. Tong, X.-M. Chen, *J. Chem. Soc., Dalton Trans.* **2000**, 3669–3674.
[17] a) F. E. Mabbs, D. J. Machin, *Magnetism and Transition Metals Complexes*, Chapman and Hall Ltd., London, **1973**; b) R. L. Carlin, *Magnetochemistry*, Springer-Verlag, Berlin, Heidelberg, **1986**.
[18] P. Garge, R. Chikate, S. Padhye, J.-M. Savariault, P. de Loth, J.-P. Tuchagues, *Inorg. Chem.* **1990**, *29*, 3315–3320.
[19] B. E. Myers, L. Berger, S. A. Friedberg, *J. Appl. Phys.* **1968**, *40*, 1149–1151.
[20] a) J. J. Borrás-Almenar, J. M. Clemente-Juan, E. Coronado, B. S. Tsukerblat, *Inorg. Chem.* **1999**, *38*, 6081–6088; b) J. J. Borrás-Almenar, J. M. Clemente-Juan, E. Coronado, B. S. Tsukerblat, *J. Comput. Chem.* **2001**, *22*, 985–991.
[21] M. J. Hossain, M. Yamasaki, M. Mikuriya, A. Kuribayashi, H. Sakiyama, *Inorg. Chem.* **2002**, *41*, 4058–4062.
[22] a) S. Konar, E. Zangrando, M. G. B. Drew, J. Ribas, N. R. Chaudhuri, *Dalton Trans.* **2004**, 260–266; b) D. Ghoshal, G. Mostafa, T. K. Maji, E. Zangrando, T.-H. Lu, J. Ribas, N. R. Chaudhuri, *New J. Chem.* **2004**, *28*, 1204–1213.
[23] a) Md. J. Hossain, H. Sakiyama, *Inorg. Chim. Acta* **2002**, *338*, 255–259; b) S.-Q. Bai, E.-Q. Gao, Z. He, C.-J. Fang, C.-H. Yan, *New J. Chem.* **2005**, *29*, 935–941.
[24] A. K. Patra, M. Ray, R. Mukherjee, *J. Chem. Soc., Dalton Trans.* **1999**, 2461–2466.
[25] a) W. K. Robinson, S. A. Friedberg, *Phys. Rev.* **1960**, *117*, 402–408; b) M. Drillon, E. Coronado, M. Belaiche, R. L. Carlin, *J. Appl. Phys.* **1988**, *63*, 3551–3553.
[26] R. L. Carlin, A. J. Van Duyneveldt, *Acc. Chem. Res.* **1980**, *13*, 231–236.
[27] a) P. Rabu, P. Janvier, B. Bujoli, *J. Mater. Chem.* **1999**, *9*, 1323–1326; b) X.-Y. Wang, H.-Y, Wei, Z.-M. Wang, Z.-D. Chen, S. Gao, *Inorg. Chem.* **2005**, *44*, 572–583.
[28] J. L. Manson, Q.-Z. Huang, J. W. Lynn, H.-J. Koo, M.-H. Whangbo, R. Bateman, T. Otsuka, N. Wada, D. N. Argyriou, J. S. Miller, *J. Am. Chem. Soc.* **2001**, *123*, 162–172.
[29] Y. S. You, J. H. Yoon, H. C. Kim, C. S. Hong, *Chem. Commun.* **2005**, 4116–4118.
[30] J. L. Manson, C. R. Kmety, F. Palacio, A. J. Epstein, J. S. Miller, *Chem. Mater.* **2001**, *13*, 1068–1073.
[31] P. Przychodzeń, K. Lewiński, M. Balanda, R. Pelka, M. Rams, T. Wasiutyński, C. Guyard-Duhayon, B. Sieklucka, *Inorg. Chem.* **2004**, *43*, 2967–2974.
[32] Molecular Structure Corporation & Rigaku, *CrystalClear*, version 1.36, MSC, 9009 New Trails Drive, The Woodland, TX 77381-5209, USA, and Rigaku Corporation, 3-9-12 Akishima, Tokyo, Japan, **2000**.
[33] G. M. Sheldrick, *SADABS, Program for Empirical Absorption Correction of Area Dectector Data*, University of Göttingen, Göttingen, Germany, **1996**.
[34] G. M. Sheldrick, *SHELXS-97, Program for the Solution of Crystal Structure*, University of Göttingen, Germany, **1990**.
[35] G. M. Sheldrick, *SHELXL-97, Program for the Refinement of Crystal Structure*, University of Göttingen, Germany, **1997**.

Received: May 12, 2006
Published Online: September 18, 2006

 © 2006 Wiley-VCH Verlag GmbH & Co. KGaA, Weinheim 

DOI: 10.1002/ejic.200600527

# An Unusual Reaction of (β-Dimethylaminoethoxy)triethyltin with Phenyltin Trichloride. The First X-ray Structural Evidence of the Existence of Complexes $R_2SnXY{\cdot}R_2SnXY$ (R = Alkyl, Aryl; X, Y = Hal, OR, X ≠ Y) Both as Unsymmetrical Adducts $[R_2SnX_2{\cdot}R_2SnY_2]$ and Symmetrical Dimers $[R_2SnXY]_2$

**Ivan A. Portnyagin,[a,b] Mikhail S. Nechaev,[b] Victor N. Khrustalev,*[c] Nikolay N. Zemlyansky,[a] Irina V. Borisova,[a] Mikhail Yu. Antipin,[c] Yuri A. Ustynyuk,[b] and Valery V. Lunin[b]**

**Keywords:** Complexation / Tin / Dimerization / Stannanes / X-ray diffraction

The substituent exchange reaction of $PhSnCl_3$ with $[Et_3Sn(OCH_2CH_2NMe_2)]$ gives rise unexpectedly to the unsymmetrical adduct $[Ph_2SnCl_2{\cdot}Ph_2Sn(OCH_2CH_2NMe_2)_2]$ (**2**). It has been unambiguously proved for the first time that compounds of the $RSnX_3$ type are able to undergo the hydrocarbon substituent redistribution reaction. The analogous tin complexes $[Et_2SnCl_2{\cdot}Et_2Sn(OMe)_2]$ (**5**) and $[Bu_2Sn(OAc)_2{\cdot}Bu_2Sn(OMe)_2]$ (**6**), which have ligands other than β-dimethylaminoethoxy and could be considered as "organotin analogs of Grignard reagents" have symmetrical dimeric structures, i.e., can be formulated as $[Bu_2Sn(OMe)(OAc)]_2$ and $[Et_2Sn(OMe)Cl]_2$, respectively. Both types of structures, viz., unsymmetrical adduct (**2**) and symmetrical dimer (**5**, **6**), have been characterized by X-ray diffraction analysis.
(© Wiley-VCH Verlag GmbH & Co. KGaA, 69451 Weinheim, Germany, 2006)

## Introduction

Redistribution reactions are a convenient and widely used method for the synthesis of organometallic compounds.[1] It has been shown previously that penta- and hexacoordinate organotin compounds such as $[Me_nSnAr_{4-n}]$ and $[Bu_2SnArCl]$, which contain electron-donating groups in the aryl ligands, are more active towards redistribution, and related (transmetallation), reactions than tetracoordinate tin(IV) derivatives.[2] Therefore, the redistribution reactions of hypercoordinate organotin compounds $[R_nSnX_{4-n}]$ containing electron-donating groups in the functional substituents X but not in the hydrocarbon substituents R, have been of significant interest. As a continuation of our investigations into the chemistry of (β-dimethylaminoethoxy)germanium and -tin derivatives,[3] we report here on the surprising results of the interaction between (β-dimethylaminoethoxy)triethyltin and -phenyltin trichloride.

Very recently, we have found that the reaction of $PhGeCl_3$ with $[Et_3Ge(OCH_2CH_2NMe_2)]$ affords $[PhGe(OCH_2CH_2NMe_2)_2Cl]$ in high yield.[3f] However, the analogous reaction in the case of tin unexpectedly results in the unsymmetrical adduct $[Ph_2SnCl_2{\cdot}Ph_2Sn(OCH_2CH_2NMe_2)_2]$ as the main reaction product.

## Results and Discussion

The reaction was carried out by the gradual addition of $[Et_3Sn(OCH_2CH_2NMe_2)]$ to a $PhSnCl_3$ solution in diethyl ether or tetrahydrofuran. In our opinion, it proceeds in three stages. In the first stage, diphenyldichloro- and dichlorodialkoxystannanes are formed. The formation of these products apparently proceeds by the initial formation of a $[PhSn(OCH_2CH_2NMe_2)Cl_2]$ intermediate, which can further disproportionate by two paths: either by the exchange of Ph and $OCH_2CH_2NMe_2$ substituents (path a) or by the exchange of Cl and $OCH_2CH_2NMe_2$ substituents (path b). Path a gives rise immediately to $[Ph_2SnCl_2]$ and $[Cl_2Sn(OCH_2CH_2NMe_2)_2]$, whereas path b first gives rise to $[PhSn(OCH_2CH_2NMe_2)_2Cl]$ (**1**) and $PhSnCl_3$, and a subsequent interchange of the Ph and Cl substituents affords $[Ph_2SnCl_2]$ and $[Cl_2Sn(OCH_2CH_2NMe_2)_2]$ (Scheme 1).

[a] A. V. Topchiev Institute of Petrochemical Synthesis, Russian Academy of Sciences,
29, Leninsky Prospect, 119991 Moscow, Russian Federation
[b] Department of Chemistry, M. V. Lomonosov Moscow State University,
Leninskie Gory, 119899 Moscow, Russian Federation
[c] A. N. Nesmeyanov Institute of Organoelement Compounds, Russian Academy of Sciences,
28 Vavilova str., 119991, Moscow, Russian Federation
Fax: +7-495-135-5085
E-mail: vkh@xray.ineos.ac.ru
Supporting information for this article is available on the WWW under http://www.eurjic.org or from the author.

 © 2006 Wiley-VCH Verlag GmbH & Co. KGaA, Weinheim 

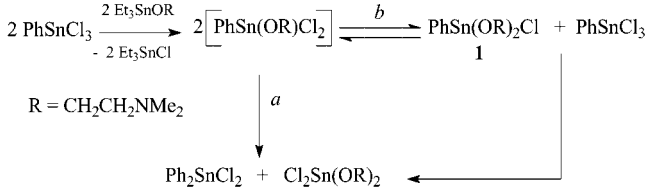


Scheme 1.The first stage of the reaction of $[PhSnCl_3]$ with $[Et_3Sn(OCH_2CH_2NMe_2)]$.

Scheme 1 was confirmed by an NMR spectroscopic study of the products of the reaction between the monochloroorganostannane **1**, which was prepared by an independent method involving reverse order of the reagent mixing (see below), and trichlorophenylstannane. In accordance with the multinuclear NMR spectroscopy data, the reaction mixture contains $[Ph_2SnCl_2]$ and $[Cl_2Sn(OCH_2CH_2NMe_2)_2]$. The latter was identified by comparison of its NMR spectral characteristics with those of the compound prepared by treatment of $HgCl_2$ with $[Sn(OCH_2CH_2NMe_2)_2]$.

A single-crystal X-ray diffraction analysis of **1** (Figure 1, Table 1) provided proof for the proposed structure and revealed that the tin atom is hexacoordinate with one carbon, one chlorine, two oxygen, and two nitrogen atoms, with an overall slightly distorted octahedral *cis-cis-trans* configuration, respectively.

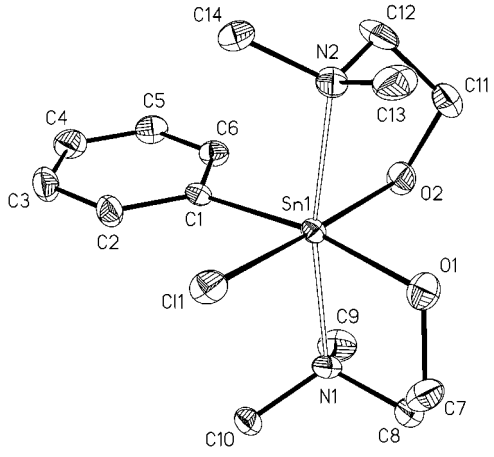


Figure 1.View of compound **1**. The hydrogen atoms have been omitted for clarity. Displacement ellipsoids are scaled to the 50% probability level. The coordination bonds are shown by open lines.

It is important to note that, in contrast to $[PhGe(OCH_2CH_2NMe_2)_2Cl]$, which tends to ionize in hydrogen-bond-donor solvents such as $CHCl_3$ to form the ionic pentacoordinate form $[PhGe(OCH_2CH_2NMe_2)_2][Cl]$ rather than the neutral hexacoordinate form,[3f] compound **1** exists only in the neutral hexacoordinate form.

The second stage is obviously the alkoxylation reaction of $[Ph_2SnCl_2]$, which yields $[Ph_2Sn(OCH_2CH_2NMe_2)_2]$, and the third stage is the complexation reaction between $[Ph_2SnCl_2]$ and $[Ph_2Sn(OCH_2CH_2NMe_2)_2]$, which yields the final poorly soluble complex **2**.

Table 1. Selected bond lengths [Å] and angles [°] for **1**.

| | | | |
|---|---|---|---|
| Sn(1)–O(1) | 2.024(3) | Sn(1)–N(2) | 2.306(3) |
| Sn(1)–O(2) | 2.032(3) | Sn(1)–N(1) | 2.340(3) |
| Sn(1)–C(1) | 2.163(4) | Sn(1)–Cl(1) | 2.5242(11) |
| O(1)–Sn(1)–O(2) | 89.90(14) | C(1)–Sn(1)–N(1) | 93.56(13) |
| O(1)–Sn(1)–C(1) | 170.46(15) | N(2)–Sn(1)–N(1) | 168.42(11) |
| O(2)–Sn(1)–C(1) | 95.82(14) | O(1)–Sn(1)–Cl(1) | 83.51(10) |
| O(1)–Sn(1)–N(2) | 93.60(12) | O(2)–Sn(1)–Cl(1) | 168.11(10) |
| O(2)–Sn(1)–N(2) | 81.38(13) | C(1)–Sn(1)–Cl(1) | 92.10(11) |
| C(1)–Sn(1)–N(2) | 94.80(13) | N(2)–Sn(1)–Cl(1) | 89.15(9) |
| O(1)–Sn(1)–N(1) | 78.80(12) | N(1)–Sn(1)–Cl(1) | 98.55(8) |
| O(2)–Sn(1)–N(1) | 89.82(12) | | |

Proof of the structure of **2** came from a single-crystal X-ray diffraction analysis (Figure 2, Table 2), which revealed that **2** is the adduct $[Ph_2SnCl_2{\cdot}Ph_2Sn(OCH_2CH_2NMe_2)_2]$ formed by the bridging oxygen atoms of the β-dimethylaminoethoxy ligands, with an unsymmetrical arrangement of the substituents at the tin atoms. It is located on a crystallographic $C_2$ axis that passes through the tin atoms. The tin atoms are hexacoordinate, with the phenyl groups in the *trans* configuration. The C–Sn–C angle at Sn1 [132.6(3)°] deviates substantially from the value of 180° (the phenyl rings are shifted towards the longer Sn←N coordination bonds), whereas that at Sn2 is essentially linear [177.3(3)°]. The basal plane of Sn1 is defined by an $N_2O_2$ donor set defined by two chelating β-dimethylaminoethoxy ligands with very long Sn←N bond lengths [2.766(4) Å]. Two chlorine and two oxygen atoms in the *cis* configuration make up the basal plane of Sn2. The bond angles in the equatorial planes vary from 70.8(1)° to 147.8(2)° for Sn1 and from 66.2(2)° to 105.44(7)° for Sn2. Thus, the geometry of Sn1 is best described as skew-trapezoidal bipyramidal, while that of Sn2 is best described as distorted octahedral.

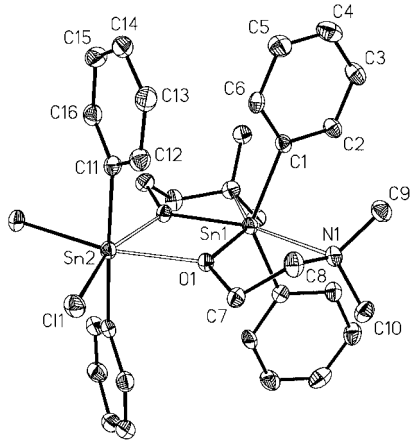


Figure 2.View of complex **2**. The hydrogen atoms have been omitted for clarity. Thermal ellipsoids are scaled to the 40% probability level. The coordination bonds are shown by open lines.

The covalent Sn–O [2.091(3) Å] and coordination Sn←O [2.242(3) Å] bond lengths in the four-membered $Sn_2O_2$ ring are significantly different and close to the corresponding

 © 2006 Wiley-VCH Verlag GmbH & Co. KGaA, Weinheim 

Table 2. Selected bond lengths [Å] and angles [°] for **2**.[a]

| | | | |
|---|---|---|---|
| Sn(1)–O(1) | 2.091(3) | Sn(2)–C(11) | 2.150(5) |
| Sn(1)–C(1) | 2.112(5) | Sn(2)–O(1) | 2.242(3) |
| Sn(1)–N(1) | 2.766(4) | Sn(2)–Cl(1) | 2.5178(14) |
| O(1)–Sn(1)–O(1)$^i$ | 71.66(18) | C(11)–Sn(2)–O(1)$^i$ | 89.13(16) |
| O(1)–Sn(1)–C(1) | 113.44(17) | C(11)–Sn(2)–O(1) | 88.62(17) |
| O(1)–Sn(1)–C(1)$^i$ | 104.69(17) | O(1)–Sn(2)–O(1)$^i$ | 66.15(17) |
| C(1)–Sn(1)–C(1)$^i$ | 132.6(3) | C(11)–Sn(2)–Cl(1)$^i$ | 91.36(15) |
| O(1)–Sn(1)–N(1) | 70.77(14) | O(1)–Sn(2)–Cl(1)$^i$ | 160.36(9) |
| O(1)–Sn(1)–N(1)$^i$ | 141.13(13) | C(11)–Sn(2)–Cl(1) | 90.27(14) |
| C(1)–Sn(1)–N(1) | 81.65(16) | O(1)–Sn(2)–Cl(1) | 94.21(9) |
| C(1)–Sn(1)–N(1)$^i$ | 85.56(17) | Cl(1)–Sn(2)–Cl(1)$^i$ | 105.44(7) |
| N(1)–Sn(1)–N(1)$^i$ | 147.8(2) | Sn(1)–O(1)–Sn(2) | 111.10(14) |
| C(11)–Sn(2)–C(11)$^i$ | 177.3(3) | | |

[a] Symmetry transformations used to generate equivalent atoms: i: $-x$, $y$, $-z + 1/2$.

bond lengths in previously investigated mononuclear hexacoordinate diphenyltin complexes.[4] The Sn–C and Sn–Cl bond lengths are also similar to those found in other related dichloro- and diphenyltin compounds.[4,5]

It is of interest that the result of the reaction of $[PhSnCl_3]$ with $[Et_3Sn(OCH_2CH_2NMe_2)]$ depends to a great extent on the order of reagent mixing. Upon the reverse order of mixing, i.e., when $[PhSnCl_3]$ is added to $[Et_3Sn(OCH_2CH_2NMe_2)]$ solution, di(alkoxy)chlorophenylstannane (**1**) is produced in high yield instead of **2**. Moreover, the use of an excess of $[Et_3Sn(OCH_2CH_2NMe_2)]$ does not allow the complete substitution of all three chlorine atoms in $[PhSnCl_3]$ with β-dimethylaminoethoxy groups. For the sake of comparison, we also carried out the same reaction for the alkyltin derivatives $[MeSnCl_3]$ and $[EtSnI_3]$. However, despite the utilization of similar reactions, in the case of the alkyltin derivatives, the reactions stopped after the first step, affording $[MeSn(OCH_2CH_2NMe_2)_2Cl]$ (**3**) and $[EtSn(OCH_2CH_2NMe_2)_2I]$ (**4**), respectively, in high yields. As for **1**, compounds **3** and **4** exist only in the neutral hexacoordinate form.

It is very important to point out that unique phenyl group migration from $[PhSnCl_3]$ takes place in the reaction described here. Phenyl group migration has previously been observed only for the ionic complexes $[PhSnHal_4]^-$ or $[PhSnHal_5]^{2-}$, in which such migration is promoted by fluoride ion or tributylphosphane.[6,7] Moreover, in these reports the final reaction products were not isolated from the reaction mixture and their structures were not determined unambiguously. In our case, however, only stannanes take part in the reaction and the structures of all key products have been determined by elemental analysis, multinuclear NMR spectroscopy, and X-ray diffraction. Thus, we have unambiguously proved for the first time that compounds of the type $RSnX_3$ are able to undergo a redistribution reaction of the hydrocarbon substituent. A more detailed verification of the supposed reaction scheme will be the subject of further investigations.

Complex **2** is the first compound of the type $R_2SnX_2 \cdot R_2SnY_2$ whose structure has been determined by X-ray diffraction. Previously, Kocheshkov and co-workers have reported the existence of unsymmetrical adducts in solution by studying the interaction of $[R_2Sn(OMe)_2]$ with $[R_2SnCl_2]$ or $[R_2Sn(OAc)_2]$ (R = alkyl) by calorimetric, dielcometric, dielectrometric, and cryoscopic methods.[8] However, as was shown later by Davies and co-workers, the structure of these complexes in solution is additionally complicated by the occurrence of the equilibria presented in Scheme 2. These authors suggested that complexes of the type $R_2SnXY \cdot R_2SnXY$ could be considered to be "organotin analogs of Grignard reagents".[9] However, no unambiguous evidence of the structure of the complexes $R_2SnXY \cdot R_2SnXY$ was available until now. It should be noted that in the paper cited above, the authors gave preference to the symmetrical structure of type **II** for these complexes.

Taking into account the possible application of these reactions to the solution of different synthetic and applied problems,[10] we have decided to fill this gap. To this end, we carried out the reactions of diethyltin dichloride with dimethoxydiethyltin and dibutyltin diacetate with dimethoxydibutyltin. The products obtained were studied by X-ray diffraction analysis. It turned out that they consist of symmetrical dimers $[Et_2Sn(Cl)(OMe)]_2$ (**5**) and $[Bu_2Sn(OAc)(OMe)]_2$ (**6**) (Figures 3 and 4 and Tables 3 and 4), respectively, with Sn atoms linked by bridging methoxy groups in the crystal. The coordination geometry around the metal atoms is a strongly distorted trigonal bipyramid with the two C atoms and the covalently bonded O atom of the bridging methoxy group in the equatorial plane. The coordinated O atom of the bridging methoxy group and Cl or OAc substituents for **5** and **6**, respectively, occupy the axial positions. The distortion from the ideal trigonal-bipyramidal geometry is especially apparent in the C–Sn–C and O–Sn←O angles. The tin atoms in these compounds can also be regarded as [4+1]-coordinate, i.e. they represent model compounds along the transformation path tetrahedron ↔ trigonal bipyramid.

Note that the disposition of the substituents implies the presence of an intrinsic inversion center in both **5** and **6**. However, in the crystal, the crystallographically imposed inversion center is retained only in the case of **5**. In the crystal structure of **6**, two out of the four butyl groups adopt different conformations and are slightly disordered (Figure 4); the inversion center is lost because of this.

Similar to **2**, the covalent Sn–O and coordination Sn←O bond lengths in the four-membered $Sn_2O_2$ rings of **5** and **6** are substantially different [2.054(2) and 2.246(2) Å for **5** and 2.054(2) and 2.277(2) and 2.058(2) and 2.271(2) Å for **6**, respectively]. However, in contrast to **2**, these bonds occupy mutually opposite rather than neighboring positions in the $Sn_2O_2$ rings.

According to the DFT calculations (see Supporting Information), there are no complexes of type **I** on the potential energy surfaces corresponding to the interactions of $[Et_2SnCl_2]$ with $[Et_2Sn(OMe)_2]$ and $[Bu_2Sn(OAc)_2]$ with $[Bu_2Sn(OMe)_2]$. The rearrangement of X and OMe substituents to yield monomeric $[R_2Sn(OMe)X]$ is exothermic ($\Delta H^0 = -1.5$ kcal mol$^{-1}$ for R = Et, X = Cl and

 © 2006 Wiley-VCH Verlag GmbH & Co. KGaA, Weinheim 

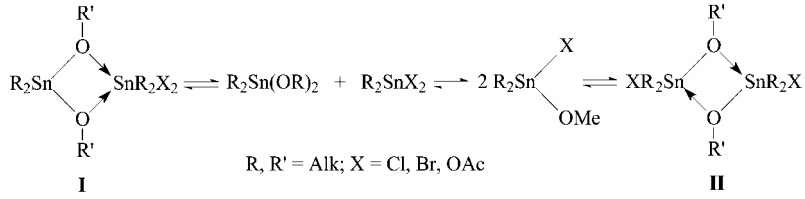


Scheme 2.The equilibria of "organotin analogs of Grignard reagents" in solution.[9]

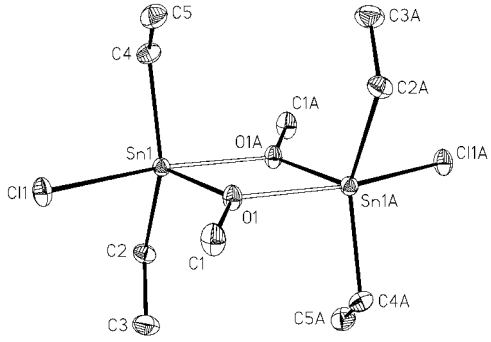


Figure 3.View of complex **5**. The hydrogen atoms have been omitted for clarity. Displacement ellipsoids are scaled to the 50% probability level. The coordination bonds are shown by open lines.

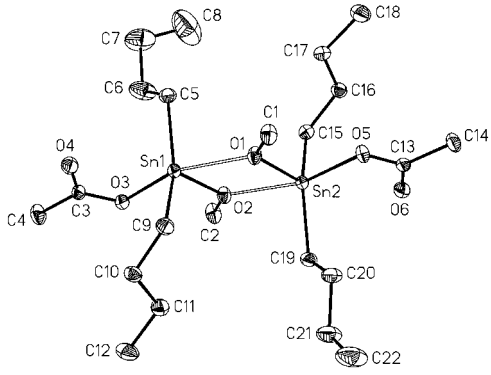


Figure 4.View of complex **6**. The hydrogen atoms have been omitted for clarity. Displacement ellipsoids are scaled to the 50% probability level. The coordination bonds are shown by open lines.

Table 3. Selected bond lengths [Å] and angles [°] for **5**.[a]

| | | | |
|---|---|---|---|
| Sn(1)–O(1) | 2.0539(19) | Sn(1)–O(1)$^{ii}$ | 2.2464(19) |
| Sn(1)–C(4) | 2.125(3) | Sn(1)–Cl(1) | 2.5101(8) |
| Sn(1)–C(2) | 2.126(3) | | |
| O(1)–Sn(1)–C(4) | 106.93(9) | O(1)–Sn(1)–Cl(1) | 91.85(6) |
| O(1)–Sn(1)–C(2) | 108.53(10) | C(4)–Sn(1)–Cl(1) | 93.26(8) |
| C(4)–Sn(1)–C(2) | 143.82(11) | C(2)–Sn(1)–Cl(1) | 92.56(8) |
| O(1)–Sn(1)–O(1)$^{ii}$ | 69.94(9) | Cl(1)–Sn(1)–O(1)$^{ii}$ | 161.79(5) |
| C(4)–Sn(1)–O(1)$^{ii}$ | 91.89(10) | Sn(1)–O(1)–Sn(1)$^{ii}$ | 110.06(9) |
| C(2)–Sn(1)–O(1)$^{ii}$ | 93.56(9) | | |

[a] Symmetry transformations used to generate equivalent atoms: ii: $-x, -y + 1, -z$.

–3.0 kcal mol$^{-1}$ for R = Bu, X = OAc). Their further dimerization leads to complexes of type **II** ($\Delta H^0$ = –16.2 and –14.2 kcal mol$^{-1}$, respectively).

Table 4. Selected bond lengths [Å] and angles [°] for **6**.

| | | | |
|---|---|---|---|
| Sn(1)–O(2) | 2.0538(18) | Sn(2)–O(1) | 2.0577(18) |
| Sn(1)–C(5) | 2.121(3) | Sn(2)–C(19) | 2.129(3) |
| Sn(1)–C(9) | 2.137(3) | Sn(2)–C(15) | 2.133(3) |
| Sn(1)–O(3) | 2.160(2) | Sn(2)–O(5) | 2.1558(19) |
| Sn(1)–O(1) | 2.2769(19) | Sn(2)–O(2) | 2.2714(19) |
| O(2)–Sn(1)–C(5) | 102.24(10) | O(1)–Sn(2)–C(15) | 108.79(10) |
| O(2)–Sn(1)–C(9) | 109.69(10) | C(19)–Sn(2)–C(15) | 143.19(11) |
| C(5)–Sn(1)–C(9) | 144.82(11) | O(1)–Sn(2)–O(5) | 84.57(7) |
| O(2)–Sn(1)–O(3) | 84.87(8) | C(19)–Sn(2)–O(5) | 99.91(9) |
| C(5)–Sn(1)–O(3) | 100.27(9) | C(15)–Sn(2)–O(5) | 98.12(10) |
| C(9)–Sn(1)–O(3) | 96.97(10) | O(1)–Sn(2)–O(2) | 69.74(7) |
| O(2)–Sn(1)–O(1) | 69.70(7) | C(19)–Sn(2)–O(2) | 88.72(10) |
| C(5)–Sn(1)–O(1) | 89.50(9) | C(15)–Sn(2)–O(2) | 88.74(10) |
| C(9)–Sn(1)–O(1) | 88.04(10) | O(5)–Sn(2)–O(2) | 154.24(7) |
| O(3)–Sn(1)–O(1) | 154.22(7) | Sn(2)–O(1)–Sn(1) | 110.09(8) |
| O(1)–Sn(2)–C(19) | 104.65(10) | Sn(1)–O(2)–Sn(2) | 110.44(8) |

## Conclusions

The isolation of complexes **2**, **5**, and **6** provides evidence for the existence of complexes $R_2SnXY{\cdot}R_2SnXY$ (R = Alk, Ar; X, Y = Hal, OR, X ≠ Y) both as unsymmetrical adducts $[R_2SnX_2{\cdot}R_2SnY_2]$ and symmetrical dimers $[R_2SnXY]_2$. Moreover, it has been unambiguously proved for the first time that compounds of the type $[RSnX_3]$ are able to undergo a hydrocarbon substituent redistribution reaction. The similarity of the redistribution reactions of hypercoordinate organotin compounds containing electron-donating groups both in the hydrocarbon R and in the functional X substituents indicates that the chemical properties of these compounds are determined primarily by the coordination mode of the tin atom rather than by the types of ligands. We believe that our findings open-up alluring prospects for the investigation of different transmetallation processes.

## Experimental Section

**General Procedures:** All manipulations were carried out under purified argon using standard Schlenk and high-vacuum-line techniques. The commercially available solvents were purified by conventional methods and distilled immediately prior to use. $[PhSnCl_3]$,[11] $[MeSnCl_3]$,[11] $[EtSnI_3]$,[11] $[Et_3Sn(OCH_2CH_2NMe_2)]$,[3a] $[Et_2Sn(Cl)(OMe)]_2$ (**5**),[8] and $[Bu_2Sn(OAc)(OMe)]_2$ (**6**)[8] were synthesized as described earlier. NMR spectra were recorded with a Bruker AM-360 NMR spectrometer at 360.134 MHz ($^1$H) and 90.555 MHz ($^{13}$C) for samples in $CDCl_3$ or $CD_2Cl_2$. Chemical shifts are relative to $SiMe_4$ for H, C or indirectly refer-

 © 2006 Wiley-VCH Verlag GmbH & Co. KGaA, Weinheim 

enced to TMS via the solvent signals. The accuracy of the coupling constants is ±0.1 Hz, and the accuracy of chemical shift measurements is ±0.01 ppm for $^1H$ and ±0.05 ppm for $^{13}C$. Melting points were measured in sealed capillaries with a SANYO Gallenkamp PLC melting point apparatus without any additional corrections. Elemental analyses were performed on a Carlo Erba EA1108 CHNS-O elemental analyzer.

**$[PhSn(OCH_2CH_2NMe_2)_2Cl]$ (1):** A solution of $[PhSnCl_3]$ (3.78 g, 12.50 mmol) in thf (20 mL) was added to an intensely stirred solution of $[Et_3Sn(OCH_2CH_2NMe_2)]$ (11.85 g, 40.35 mmol) in 70 mL of thf. The solution was stirred for 2 h. The solvent was then removed under vacuum to about one sixth of the initial volume and 70 mL of hexane was added. A white crystalline precipitate was obtained, filtered, and washed three times with hexane (in 30 mL portions) and dried in vacuo. The yield was 3.05 g (60%). M.p. 129–131 °C. $C_{14}H_{25}ClN_2O_2Sn$ (407.50): calcd. C 41.26, H 6.18, N 6.87; found C 40.98, H 6.55, N 6.40. $^1H$ NMR ([D$_8$]thf): $\delta$ = 2.29 (br. s, 12 H, $Me_2N$), 2.62–2.68, 2.76–2.86 (two br. m, 4 H, $NCH_2$), 3.81–3.86, 3.93–3.99 (two br. m, 4 H, $OCH_2$), 7.10–7.40 (m, 3 H, Ph), 8.12–8.40 (br. s, $^3J_{Sn,H}$ = 99.0 Hz, 2 H, Ph) ppm. $^{13}C$ NMR ([D$_8$]thf): $\delta$ = 46.12 (br., $Me_2N$), 58.59 ($NCH_2$), 63.47 ($OCH_2$), 128.60 ($^3J_{Sn,C}$ = 112/108 Hz, $C_m$), 129.52 ($^4J_{Sn,C}$ = 21.6 Hz, $C_p$), 138.04 (br., $^2J_{Sn,C}$ = 61.7 Hz, $C_o$), 148.99 ($C_i$) ppm.

**$[Ph_2SnCl_2{\cdot}Ph_2Sn(OCH_2CH_2NMe_2)_2]$ (2):** A solution of $[Et_3Sn(OCH_2CH_2NMe_2)]$ (7.82 g, 26.63 mmol) in thf (30 mL) was added slowly to a stirred solution of $[PhSnCl_3]$ (4.08 g, 13.50 mmol) in $Et_2O$ (50 mL) or thf (50 mL) at room temperature. A large amount of white precipitate appeared immediately. After stirring the mixture for 2 h and storing it overnight the white precipitate was filtered, washed with benzene, and dried in vacuo. The yield of white solid was 1.33 g (49.7% scaled to the amount of $[PhSnCl_3]$). M.p. 168.7–169 °C. $C_{32}H_{40}Cl_2N_2O_2Sn_2$ (792.94): calcd. C 48.47, H 5.08, N 3.53; found C 48.30, H 5.30, N 3.55. $^1H$ NMR ($CD_2Cl_2$): $\delta$ = 2.36 (br. s, 12 H, $NMe_2$), 2.73–2.78 (br. m, 4 H, $NCH_2$), 3.91–3.96 (br. m, 4 H, $OCH_2$), 7.87–7.91, 7.10–7.50 (two m, 20 H, Ph) ppm. $^{13}C$ NMR ($CD_2Cl_2$): $\delta$ = 45.45 (br., $NMe_2$), 45.60, 45.92 ($NMe_2$), 60.43, 61.06 ($NCH_2$), 62.48 (br., $OCH_2$), 128.87, 129.10 ($C_m$), 129.03, 129.40 ($C_p$), 130.11, 130.51 ($C_o$), 136.03, 136.20 ($C_i$) ppm.

**Reaction of $[PhSn(OCH_2CH_2NMe_2)_2Cl]$ (1) With $[PhSnCl_3]$ (NMR Experiment):** A solution of **1** (0.52 g, 1.3 mmol) and $[PhSnCl_3]$ (0.39 g, 1.3 mmol) in thf (10 mL) was mixed in a vacuum of $10^{-3}$ Torr. The mixture was stored for 1 h at about 20 °C, then thf was removed by evacuation and $CD_2Cl_2$ (1 mL) was introduced. The solution was transferred to a 5-mm NMR tube and sealed. According to the $^1H$ and $^{13}C$ NMR spectra, the solution contained $[Cl_2Sn(OCH_2CH_2NMe_2)_2]$ and $[Ph_2SnCl_2]$ as the main products. $Ph_2SnCl_2$: $^1H$ NMR ($CD_2Cl_2$): $\delta$ = 7.60–7.67 (m, 3 H, Ph), 7.81–7.84 (m, $^3J_{Sn,H}$ = 81.2 Hz, 2 H, Ph) ppm. $^{13}C$ NMR ($CD_2Cl_2$): $\delta$ = 130.32 ($^3J$ = 85.1 Hz, $C_m$), 132.48 ($^4J$ = 18.4 Hz, $C_p$), 135.57 ($^2J$ = 63.6 Hz, $C_o$), 137.50 ($C_i$) ppm.

**$[Cl_2Sn(OCH_2CH_2NMe_2)_2]$:** A solution of $[Sn(OCH_2CH_2NMe_2)_2]$ (1.76 g, 5.96 mmol) in thf (15 mL) was quickly added to an intensely stirred solution of $HgCl_2$ (1.62 g, 5.96 mmol) in thf (20 mL). A large amount of heavy dark-grey precipitate appeared immediately. The mixture was stirred for 30 min and stored overnight. After filtration, the solvent was removed under vacuum to about one sixth of the initial volume. After addition of hexane (50 mL) a white crystalline precipitate was obtained. This was filtered under argon, washed with hexane, and dried in vacuo. The yield was 2.12 g (97%). M.p. 205 °C (with decomp.). $C_8H_{20}Cl_2N_2O_2Sn$

Table 5. Crystallographic data for **1**, **2**, **5**, and **6**.

| | **1** | **2** | **5** | **6** |
|---|---|---|---|---|
| Empirical formula | $C_{14}H_{25}ClN_2O_2Sn$ | $C_{32}H_{40}Cl_2N_2O_2Sn_2$ | $C_{10}H_{26}Cl_2O_2Sn_2$ | $C_{22}H_{48}O_6Sn_2$ |
| *FW* | 407.50 | 792.94 | 486.59 | 645.98 |
| *T* [K] | 120 | 120 | 100 | 100 |
| Crystal size [mm] | 0.2 × 0.2 × 0.1 | 0.2 × 0.2 × 0.2 | 0.3 × 0.2 × 0.2 | 0.3 × 0.2 × 0.2 |
| Crystal system | monoclinic | monoclinic | orthorhombic | monoclinic |
| Space group | $P2_1/c$ | $C2/c$ | $Pbca$ | $P2_1$ |
| *a* [Å] | 11.496(2) | 18.208(3) | 8.5007(16) | 8.2721(4) |
| *b* [Å] | 8.7351(17) | 10.1149(11) | 13.843(3) | 20.433(2) |
| *c* [Å] | 16.660(3) | 19.274(3) | 14.118(3) | 8.3571(5) |
| $\alpha$ [°] | 90 | 90 | 90 | 90 |
| $\beta$ [°] | 90.947(6) | 116.799(5) | 90 | 100.660(5) |
| $\gamma$ [°] | 90 | 90 | 90 | 90 |
| *V* [Å$^3$] | 1672.7(5) | 3168.4(8) | 1661.4(6) | 1388.17(17) |
| *Z* | 4 | 4 | 4 | 2 |
| $D_c$ [g cm$^{-3}$] | 1.618 | 1.662 | 1.945 | 1.545 |
| *F*(000) | 824 | 1584 | 944 | 656 |
| $\mu$ [mm$^{-1}$] | 1.690 | 1.777 | 3.316 | 1.829 |
| $2\theta_{max}$ [°] | 56 | 54 | 56 | 56 |
| Index range | $-15 \le h \le 15$<br>$-11 \le k \le 11$<br>$-19 \le l \le 22$ | $-23 \le h \le 23$<br>$-12 \le k \le 12$<br>$-24 \le l \le 24$ | $-11 \le h \le 11$<br>$-18 \le k \le 18$<br>$-18 \le l \le 18$ | $-10 \le h \le 10$<br>$-27 \le k \le 26$<br>$-11 \le l \le 11$ |
| No. of reflections collected | 13779 | 14829 | 15113 | 13583 |
| No. of unique reflections | 3972 | 3453 | 1984 | 6565 |
| No. of reflections with $I > 2\sigma(I)$ | 3010 | 2434 | 1927 | 6515 |
| Data/restraints/parameters | 3972/6/181 | 3453/0/182 | 1984/0/73 | 6565/10/272 |
| *R*1; *wR*2 [$I > 2\sigma(I)$] | 0.0401; 0.0986 | 0.0496; 0.1121 | 0.0248; 0.0548 | 0.0210; 0.0537 |
| *R*1; *wR*2 (all data) | 0.0570; 0.1100 | 0.0712; 0.1206 | 0.0260; 0.0555 | 0.0213; 0.0538 |
| GOF on $F^2$ | 1.009 | 1.038 | 1.018 | 1.022 |
| $T_{min}$; $T_{max}$ | 0.676; 0.878 | 0.660; 0.730 | 0.390; 0.500 | 0.590; 0.690 |

 © 2006 Wiley-VCH Verlag GmbH & Co. KGaA, Weinheim 

(365.87): calcd. C 26.26, H 5.51, N 7.66; found C 26.05, H 5.41, N 7.40. $^1$H NMR ($CD_2Cl_2$): $\delta$ = 2.73, 2.74 (two s, 12 H, Me); 2.83–2.86 (m, 4 H, $CH_2N$), 3.80–3.85 (m, 4 H, $CH_2O$) ppm. $^{13}$C NMR ($CD_2Cl_2$): $\delta$ = 46.78, 46.87 (two s, $Me_2N$), 58.03 ($^3J_{Sn,C}$ = 24.5 Hz, $CH_2N$), 63.02 ($^2J_{Sn,C}$ = 57.5 Hz, $CH_2O$) ppm.

**[MeSn(OCH$_2$CH$_2$NMe$_2$)$_2$Cl] (3):** A solution of [Et$_3$Sn(OCH$_2$CH$_2$NMe$_2$)] (6.65 g, 23.33 mmol) in $Et_2O$ (20 mL) was added dropwise to a stirred solution of [$MeSnCl_3$] (2.80 g, 11.66 mmol) in $Et_2O$ (30 mL). After two hours of stirring an abundant white precipitate had formed. This was filtered, washed with hexane, and dried in vacuo. The yield was 2.49 g (61.8%). M.p. 139–140 °C. $C_9H_{23}ClN_2O_2Sn$ (345.45): calcd. C 31.29, H 6.71, N 8.11; found C 31.05, H 6.80, N 7.97. $^1$H NMR ($CD_2Cl_2$): $\delta$ = 0.71 (br. s, $^2J_{Sn,H}$ = 99.0/103.6 Hz, 3 H, MeSn), 2.57 (br. s, 12 H, $Me_2N$), 2.70 (br., 4 H, $CH_2N$), 3. 78 (br. m, 4 H, $CH_2O$) ppm. $^{13}$C NMR ($CD_2Cl_2$): $\delta$ = 10.80 (MeSn), 46.27 ($Me_2N$), 58.74 (br., $CH_2N$), 63.61 (br., $CH_2O$) ppm.

**[EtSn(OCH$_2$CH$_2$NMe$_2$)$_2$I] (4):** A solution of [Et$_3$Sn(OCH$_2$CH$_2$NMe$_2$)] (4.47 g, 15.21 mmol) in thf (25 mL) was added dropwise to a stirred solution of $EtSnI_3$ (4.04 g, 7.64 mmol) in $Et_2O$ (30 mL). The mixture was stirred for 2 h and stored overnight. The solvent was removed in vacuo to about one sixth of the initial volume, then 50 mL of hexane was added to give a white crystalline precipitate. This was filtered under argon, washed with hexane, and dried in vacuo. The yield was 1.90 g (56%). M.p. 108–109 °C. $C_{10}H_{25}IN_2O_2Sn$ (450.93): calcd. C 26.64, H 5.59, N 6.21; found C 26.35, H 5.78, N 6.15. $^1$H NMR ($CD_2Cl_2$): $\delta$ = 1.20 (m, 3 H, C*H$_3$*CH$_2$Sn), 1.73 (m, 2 H, CH$_3$C*H$_2$*Sn), 2.63 (br. s, 12 H, $Me_2N$), 2.72 (br., 4 H, $CH_2N$), 3.80 (br. m, 4 H, $CH_2O$) ppm. $^{13}$C NMR ($CD_2Cl_2$): $\delta$ = 10.49 (br., CH$_3$*C*H$_2$Sn), 13.39 ($^2J_{Sn,C}$ = 64.4 Hz, *C*H$_3$CH$_2$Sn), 46.82 (br., $Me_2N$), 58.66 ($CH_2N$), 63.32 ($CH_2O$) ppm.

**X-ray Crystal Structure Determination:** Data were collected on a Bruker three-circle diffractometer equipped with a SMART 1000 CCD detector and corrected for absorption using the SADABS program.[12] Data reduction was performed with the SMART[13] and SAINTPlus[14] programs (see Table 5 for details). The structures were solved by direct methods and refined by full-matrix least-squares on $F^2$ with anisotropic thermal parameters for non-hydrogen atoms. The value of the Flack parameter for complex **6**, 0.363(18), indicates that the absolute structure in this case cannot be determined unambiguously due to the specific centrosymmetric arrangement of the heavy tin atoms as well as most of the substituents (see above). All calculations were carried out using the SHELXTL program (PC Version 5.10).[15]

CCDC-607745 through -607748 contain the supplementary crystallographic data for this paper. These data can be obtained free of charge from The Cambridge Crystallographic Data Centre via www.ccdc.cam.ac.uk/data_request/cif.

**Supporting Information** (see also the footnote on the first page of this article): Details of the quantum-chemical calculations.

## Acknowledgments

This work was supported financially by the Russian Foundation for Basic Research (projects nos. 04-03-32662 and 04-03-32549) and the Russian Academy of Sciences within the frame of the subprogram "Theoretical and experimental study of chemical bonding and mechanisms of chemical reactions and processes". We thank Dr. M. G. Kuznetsova for performing the multinuclear NMR measurements.

[1] Ch. Elschenbroich, A. Salzer, *Organometallics: A Concise Introduction*, Wiley-VCH, Weinheim, New York, Basel, Cambridge, **1992**.
[2] a) R. A. Varga, C. Silvestru, C. Deleanu, *Appl. Organomet. Chem.* **2005**, *19*, 153–160; b) S. H. L. Thoonen, H. van Hoek, E. de Wolf, M. Lutz, A. L. Spek, B.-J. Deelman, G. van Koten, *J. Organomet. Chem.* **2006**, *691*, 1544–1553.
[3] a) N. N. Zemlyansky, I. V. Borisova, M. G. Kuznetsova, V. N. Khrustalev, Yu. A. Ustynyuk, M. S. Nechaev, V. V. Lunin, J. Barrau, G. Rima, *Organometallics* **2003**, *22*, 1675–1681; b) N. N. Zemlyansky, I. V. Borisova, V. N. Khrustalev, M. Yu. Antipin, Yu. A. Ustynyuk, M. S. Nechaev, V. V. Lunin, *Organometallics* **2003**, *22*, 5441–5446; c) V. N. Khrustalev, M. Yu. Antipin, N. N. Zemlyansky, I. V. Borisova, Yu. A. Ustynyuk, V. V. Lunin, J. Barrau, G. Rima, *J. Organomet. Chem.* **2004**, *689*, 478–483; d) V. N. Khrustalev, I. A. Portnyagin, N. N. Zemlyansky, I. V. Borisova, Yu. A. Ustynyuk, M. Yu. Antipin, *J. Organomet. Chem.* **2005**, *690*, 1056–1062; e) V. N. Khrustalev, I. A. Portnyagin, N. N. Zemlyansky, I. V. Borisova, M. S. Nechaev, Yu. A. Ustynyuk, M. Yu. Antipin, V. V. Lunin, *J. Organomet. Chem.* **2005**, *690*, 1172–1177; f) V. N. Khrustalev, I. A. Portnyagin, I. V. Borisova, N. N. Zemlyansky, Yu. A. Ustynyuk, M. Yu. Antipin, M. S. Nechaev, *Organometallics* **2006**, *25*, 2501–2504.
[4] a) F. Caruso, D. Leonesi, F. Marchetti, E. Rivarola, M. Rossi, V. Tomov, C. Pettinari, *J. Organomet. Chem.* **1996**, *519*, 29–44; b) J. E. J. Graudo, N. L. Speziali, A. Abras, M. Horner, C. A. L. Filgueiras, *Polyhedron* **1999**, *18*, 2483–2489; c) E. R. T. Tiekink, *Main Group Met. Chem.* **2000**, *23*, 551–552; d) D. Cunningham, E. M. Landers, P. McArdle, N. N. Chonchubhair, *J. Organomet. Chem.* **2000**, *612*, 53–60; e) R. Garcia-Zarracino, J. Ramos-Quinones, H. Hopfl, *J. Organomet. Chem.* **2002**, *664*, 188–200; f) M. M. Amini, A. Azadmeher, M. Yousefi, S. Foladi, S. W. Ng, *Acta Crystallogr. Sect. E* **2002**, *58*, m58–m60; g) D. Dakternieks, A. Duthie, D. R. Smyth, C. P. D. Stapleton, E. R. T. Tiekink, *Organometallics* **2003**, *22*, 4599–4603; h) M. H. Chisholm, E. E. Delbridge, J. C. Gallucci, *New J. Chem.* **2004**, *28*, 145–152.
[5] a) E. G. Martinez, A. S. Gonzalez, J. S. Casas, J. Sordo, U. Casellato, R. Graziani, U. Russo, *J. Organomet. Chem.* **1993**, *463*, 91–96; b) F. Caruso, M. Giomini, A. M. Giuliani, E. Rivarola, *J. Organomet. Chem.* **1994**, *466*, 69–75; c) M. J. Cox, S. Rainone, G. Siasios, E. R. T. Tiekink, L. K. Webster, *Main Group Met. Chem.* **1995**, *18*, 93–99; d) J. S. Casas, E. E. Castellano, F. J. G. Barros, A. Sanchez, A. S. Gonzalez, J. Sordo, J. Zukerman-Schpector, *J. Organomet. Chem.* **1996**, *519*, 209–216; e) P. A. Boo, M. D. Couce, E. Freijanes, J. S. Casas, A. Castineiras, A. S. Gonzalez, J. Sordo, U. Russo, *J. Organomet. Chem.* **1996**, *506*, 253–258; f) S.-G. Reoh, S.-H. Ang, S.-B. Teo, H.-K. Fun, K.-L. Khew, C.-W. Ong, *J. Chem. Soc., Dalton Trans.* **1997**, 465–468; g) P. A. Boo, J. S. Casas, E. E. Castellano, M. D. Couce, E. Freijanes, A. Furlani, U. Russo, V. Scarcia, J. Sordo, M. Varela, *Appl. Organomet. Chem.* **2001**, *15*, 75–81.
[6] R. Colton, D. Dakternieks, *Inorg. Chim. Acta* **1988**, *143*, 151–159.
[7] D. Dakternieks, H. Zhu, *Organometallics* **1992**, *11*, 3820–3825.
[8] a) I. P. Gol'dstein, N. N. Zemlyansky, O. P. Shamagina, E. N. Gur'yanova, E. M. Panov, N. A. Slovokhotova, K. A. Kocheshkov, *Dokl. Akad. Nauk SSSR* **1965**, *163*, 880–883; b) N. N. Zemlyansky, I. P. Gol'dstein, E. N. Gur′yanova, O. P. Syutkina, E. M. Panov, N. A. Slovokhotova, K. A. Kocheshkov, *Izv. Akad. Nauk SSSR* **1967**, 728–735.
[9] A. C. Chapman, A. G. Davies, P. G. Harrison, W. McFarlane, *J. Chem. Soc. C* **1970**, 821–824.

 © 2006 Wiley-VCH Verlag GmbH & Co. KGaA, Weinheim 

[10] a) T. N. Mitchell, *J. Organomet. Chem.* **1975**, *92*, 311–319; b) A. Boaretto, D. Marton, G. Tagliavini, *J. Organomet. Chem.* **1985**, *288*, 283–287; c) N. Sharma, S. S. Pathania, Archana, S. S. Bhatt, S. C. Chaudhry, *Indian J. Chem., Sect. A* **2004**, *43*, 1672–1675.
[11] K. A. Kocheshkov, N. N. Zemlyansky, N. I. Sheverdina, E. M. Panov, in *Methods of Organoelement Chemistry. Germanium, Tin, Lead* (Eds.: A. N. Nesmeyanov, R. F. Kocheshkov), Nauka, Moscow, **1968**.
[12] G. M. Sheldrick, *SADABS*, v. 2.01, Bruker AXS, Madison, Wisconsin, USA, **1998**.
[13] Bruker AXS, *SMART*, v. 5.059, Bruker AXS, Madison, Wisconsin, USA, **1998**.
[14] Bruker AXS, *SAINTPlus*, v. 6.01, Bruker AXS, Madison, Wisconsin, USA, **1998**.
[15] G. M. Sheldrick, *SHELXTL*, v. 5.10, Bruker AXS, Madison, Wisconsin, USA, **1998**.

Received: June 6, 2006
Published Online: September 13, 2006

 © 2006 Wiley-VCH Verlag GmbH & Co. KGaA, Weinheim 

DOI: 10.1002/ejic.200600551

# Structural Studies of $[CpMoL_2(CO)_2]^+$ (L = NCMe, $L_2$ = 2,2′-biimidazole) Complexes and Their Inclusion Compounds with Cyclodextrins

**Cláudia C. L. Pereira,[a] Susana S. Braga,[a] Filipe A. Almeida Paz,[a] Martyn Pillinger,[a] Jacek Klinowski,[b] and Isabel S. Gonçalves*[a]**

**Keywords:** Cyclodextrins / Inclusion compounds / Half-sandwich complexes / Molybdenum / Cyclopentadienyl metal carbonyls

Protonation of $[CpMo(\eta^3\text{-}C_3H_5)(CO)_2]$ followed by addition of acetonitrile or 2,2′-biimidazole ($H_2$biim) gave the complexes $[CpMo(NCMe)_2(CO)_2](BF_4)$ (**1**) and $[CpMo(H_2biim)(CO)_2](BF_4)$ (**2**) in good yields. The structures of **1** and **2** were determined by single-crystal X-ray diffraction in the orthorhombic *Pbca* and triclinic $P\bar{1}$ space groups, respectively. Both complexes have similar metal ion coordination environments, which can be envisaged as slightly distorted pseudo-square pyramids, a coordination geometry commonly compared with a four-legged piano stool. The two complexes were immobilised in native and permethylated β-cyclodextrins (β CD and TRIMEB) by methods tailored according to the stabilities and solubilities of the individual components and this gave four adducts with a 1:1 host/guest stoichiometry. The formation of true inclusion compounds was supported by powder X-ray diffraction (XRD), thermogravimetric analysis (TGA), $^{13}C\{^1H\}$ CP/MAS NMR and FTIR spectroscopy. In the case of the TRIMEB adduct containing complex **1**, the crystal packing arrangement is markedly similar to that previously reported for the corresponding 1:1 TRIMEB adducts of the neutral guests $[CpMoX(CO)_3]$ (X = Cl, $CH_2CONH_2$), featuring columns in which the macrocycles are arranged along the *b* axis in a tilted fashion.

(© Wiley-VCH Verlag GmbH & Co. KGaA, 69451 Weinheim, Germany, 2006)

## Introduction

Half-sandwich metal carbonyl compounds bearing cyclopentadienyl (Cp = $\eta^5\text{-}C_5H_5$) and $\eta^6$-arene groups have been, and continue to be, investigated for applications in various fields such as catalysis,[1] nonlinear optics[2] and medicine.[3] The bioorganometallic chemistry of these compounds is of particular interest, especially in relation to their use as pharmaceuticals. For example, technetium and rhenium tricarbonyl complexes with derivatised cyclopentadienyl ligands have been investigated for radiopharmaceutical applications in the diagnosis ($^{99m}$Tc) and treatment ($^{188}$Re and $^{186}$Re) of cancer.[4] In these compounds it is the radioactive metal centre that provides the activity, although the ligands attached to the metal centre will ultimately determine the selectivity and efficiency of these compounds towards target diseased cells. Considering the known antitumour action of metallocenes such as $Cp_2TiCl_2$ and $Cp_2MoCl_2$,[5] it is also possible that half-sandwich metal carbonyl compounds containing nonradioactive elements may exhibit anticancer properties. These studies are, however, in their infancy. Researchers have also examined metal carbonyls for applications that directly involve the CO ligands. One of these is their potential use as biological tracer agents.[6] The carbonylmetalloimmunoassay procedure is based on the IR stretching vibrations of organometallic carbonyl groups and has a sensitivity comparable with that of radioactive tracers.[6a] A second example is the use of metal carbonyls as carbon monoxide-releasing molecules.[7]

As indicated above, the primary way to control the properties of half-sandwich metal carbonyl compounds is to modify the steric, electronic and other properties of the first sphere ligands, for example the substituents on the Cp ring. A second approach involves introduction of a second-sphere ligand noncovalently attached to the first-sphere ligands. One of the most promising applications of this idea is the formation of inclusion compounds with cyclodextrins (CDs).[8] CDs and their derivatives are known to bind half-sandwich complexes such as $[CpFeX(CO)_2]$ (X = Cl, Me, CN),[9] $[CpFe(NH_3)(CO)_2](PF_6)$,[10] $[CpMn(CO)_3]$,[11] $[(\eta^6\text{-}C_6H_6)Cr(CO)_3]$,[12] $[CpMoX(CO)_3]$ (X = Cl, $CH_2CONH_2$),[9e,13] $[Cp'Mo(\eta^3\text{-}C_3H_5)(CO)_2]$,[14] $[Cp'Mo(\eta^3\text{-}C_6H_7)(CO)_2]$ and $[Cp'Mo(\eta^4\text{-}C_6H_8)(CO)_2](BF_4)$ (Cp′ = Cp, Ind).[15] Some of these encapsulated metallo-organic complexes exhibit markedly different physical and chemical characteristics in comparison with the bulk material. CD inclusion compounds are interesting for pharmaceutical use because of the enhanced solubility, stability and bioavailability of the drug molecules, as well as the reduced toxic

[a] Department of Chemistry, CICECO, University of Aveiro, 3810-193 Aveiro, Portugal
Fax: +351-234-370084
E-mail: igoncalves@dq.ua.pt
[b] Department of Chemistry, University of Cambridge, Lensfield Road, CB2 1EW Cambridge, United Kingdom

 © 2006 Wiley-VCH Verlag GmbH & Co. KGaA, Weinheim 

side-effects.[16] As part of an ongoing study aimed at improving the properties of potential organometallic pharmaceuticals by encapsulation in CDs, we now report on the encapsulation of the complexes $[CpMo(NCMe)_2(CO)_2](BF_4)$ and $[CpMo(H_2biim)(CO)_2](BF_4)$ ($H_2biim$ = 2,2′-biimidazole) in β-CD and 2,3,6-tris-*O*-methyl-β-CD (TRIMEB). The molecular structures of the "free" dicarbonyl complexes have been determined by single-crystal X-ray diffraction and the inclusion compounds were characterised in the solid state by various techniques.

## Results and Discussion

### Preparation and Crystal Structures of the Molybdenum(II) Dicarbonyl Complexes

Treatment of $[CpMo(\eta^3\text{-}C_3H_5)(CO)_2]$ with $HBF_4{\cdot}Et_2O$ in dichloromethane affords the labile complex $[CpMo(\eta^2\text{-}C_3H_6)(CO)_2(FBF_3)]$,[17] which readily reacts with acetonitrile to give $[CpMo(NCMe)_2(CO)_2](BF_4)$ (**1**) and with 2,2′-biimidazole to give $[CpMo(H_2biim)(CO)_2](BF_4)$ (**2**) (Scheme 1). As expected, complexes **1** and **2** exhibit two ṽ(CO) stretching vibrations in their FTIR spectra, which can be attributed to the *cis*-$(CO)_2$ fragment. The bands for **2** (1976 and 1878 $cm^{-1}$) appear at lower frequencies than those for **1** (1988 and 1893 $cm^{-1}$) because $H_2biim$ is a better electron donor (and acceptor) than acetonitrile and this results in higher Mo→CO back-donation and a weaker C≡O bond.

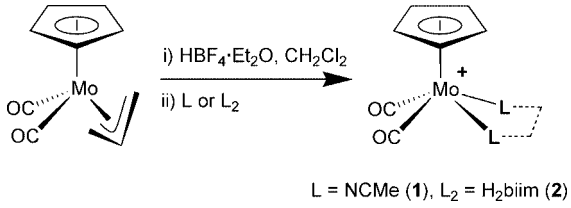


Scheme 1.

The crystal structures of compounds **1** and **2** were elucidated from single-crystal X-ray diffraction studies at low temperature (see Exp. Sect.) and show a number of striking similarities with respect to the geometries of the 18-electron half-sandwich molybdenum(II) cationic complexes and the crystal packing of each material.

Complex **1** crystallises in the orthorhombic *Pbca* space group with the asymmetric unit comprised of four individual residues (two metal complex cations plus two highly disordered tetrafluoroborate anions) and corresponding to the empirical formula $[CpMo(NCMe)_2(CO)_2](BF_4)$. Even though a great number of molybdenum complexes with $\eta^5$-cyclopentadienyl and carbonyl[18] or acetonitrile[19–26] ligands have been reported, only one structure containing the latter two ligands is known.[27] To the best of our knowledge, compound **1** represents the first complex containing all three of these ligands.

As often occurs for transition metal organometallic complexes, the structure of **1** contains two crystallographically independent $[CpMo(NCMe)_2(CO)_2]^+$ cations showing the same structural arrangement and rather similar coordination environments (Figure 1, Table 1). These coordination geometries can be envisaged as slightly distorted pseudo-square pyramids with the basal plane formed by two *cis*-coordinated carbonyl groups and two acetonitrile ligands and the apical position occupied by an $\eta^5$-coordinated cyclopentadienyl which, for clarity, is hereafter regarded as unidentate, with the coordination site being the centroid of the aromatic ring, $C_g$ (Figure 1). This coordination geometry is commonly compared with a four-legged piano-stool[21] in which the metal centre emerges above the basal plane (ca. 0.92 and 0.93 Å for the two crystallographically independent complexes) leading to bond angles which deviate significantly from the ideal 90°. The Mo–C (carbonyl) and Mo–N bond lengths for the two complexes [1.967(4)–1.988(4) and 2.160(3)–2.179(3) Å, respectively] are in good agreement with those typically found in similar Mo/Cp complexes as revealed by a search of the Cambridge Structural Database (CSD) (Version 5.26, updated in August 2005).[28] Thus, while the typical Mo–C (carbonyl) bond lengths were found in the 1.64–2.37 Å range (from 1415 entries with a median of 1.97 Å), the Mo–N (acetonitrile) bond lengths are instead in the 2.12–2.20 Å range (from 16 entries with a median of 2.14 Å). Individual $Mo–C_{aromatic}$ bond lengths (Table 1) are also consistent with the values found in related compounds [2.12–2.74 Å for 2468 entries with a median of 2.34 Å]. However, as commonly encountered for complexes with the four-legged piano-stool resemblance,[29] the observed $Mo–C_{aromatic}$ bond lengths also indicate a slight "slip" from the expected $\eta^5$-coordination mode towards an $\eta^3$-type with the torsion angles between the planes defined by the Cp rings and the N···N···C···C bases of the pyramids being ca. 3.0 and 5.4° [for Mo(1) and Mo(2), respectively]. Indeed, the Mo–C(4,5) and Mo–C(13,14) bond lengths are statistically longer than the remaining distances within each Cp aromatic ring (Table 1). This structural feature is depicted in Figure 1 for one $[CpMo(NCMe)_2(CO)_2]^+$ complex cation. C(4) and C(5) are the closest atoms to the slightly bulkier acetonitrile ligands and the increase in the $Mo–C_{aromatic}$ bond length [$\Delta_{average}$(Mo–C) of ca. 0.09 Å with the largest being ca. 0.12 Å] presumably arises as the result of a tendency to reduce the steric pressure imposed upon the complex. The same occurs for the second complex cation but for atoms C(13) and C(14) instead [not represented – $\Delta_{average}$(Mo–C) and the largest bond length difference are identical to the values for the other complex].

Even though the coordination environments of the two crystallographically independent $[CpMo(NCMe)_2(CO)_2]^+$ cations show several similarities, a few geometric aspects of the square-pyramids are fundamentally different. As summarised in Table 1, the (N,C)–Mo–(N,C) bond angle ranges for the basal planes of the molybdenum square-pyramids are slightly distinct for the two complexes [76.60(10)–79.69(12)° and 74.57(15)–81.47(14)°], these differences arising from the way in which each crystallographically independent complex close-packs in the solid-state. Indeed, one

 © 2006 Wiley-VCH Verlag GmbH & Co. KGaA, Weinheim 

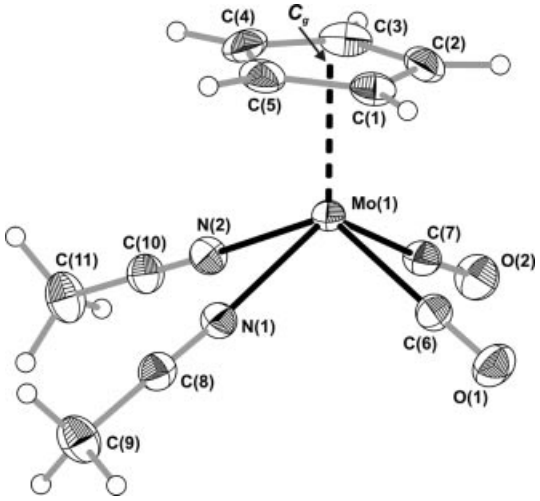


Figure 1. Schematic representation of one crystallographically independent $[CpMo(NCMe)_2(CO)_2]^+$ complex cation present in compound **1**, emphasising the slightly distorted square-pyramidal coordination environment for the $Mo^{2+}$ metal centre and showing the labelling scheme for all non-hydrogen atoms. Displacement ellipsoids are shown at the 30% probability level and hydrogen atoms are represented as small spheres. All Mo–C bonds to the coordinated $\eta^5$-Cp have been omitted for clarity and replaced by a black-filled dashed bond line to the centroid, $C_g$. For selected bond lengths and angles see Table 1.

Table 1. Selected bond lengths [Å] and angles [°] for the molybdenum coordination environments of the two crystallographically independent $[CpMo(NCMe)_2(CO)_2]^+$ complex cations present in **1**.

| | | | |
|---|---|---|---|
| Complex **1** | | | |
| Mo(1)–N(1) | 2.164(3) | N(2)–Mo(1)–N(1) | 76.60(10) |
| Mo(1)–N(2) | 2.160(3) | C(6)–Mo(1)–N(1) | 80.13(12) |
| Mo(1)–C(6) | 1.988(4) | C(6)–Mo(1)–N(2) | 128.58(12) |
| Mo(1)–C(7) | 1.969(4) | C(7)–Mo(1)–N(1) | 125.88(12) |
| Mo(1)–C(1) | 2.299(3) | C(7)–Mo(1)–N(2) | 79.69(12) |
| Mo(1)–C(2) | 2.252(3) | C(7)–Mo(1)–C(6) | 78.05(14) |
| Mo(1)–C(3) | 2.272(3) | $C_g$–Mo(1)–C(6) | 116.33(2) |
| Mo(1)–C(4) | 2.352(3) | $C_g$–Mo(1)–C(7) | 117.99(2) |
| Mo(1)–C(5) | 2.369(3) | $C_g$–Mo(1)–N(1) | 116.11(2) |
| Mo(1)–$C_g$[a] | 1.977(1) | $C_g$–Mo(1)–N(2) | 115.07(2) |
| Complex **2** | | | |
| Mo(2)–N(3) | 2.179(3) | N(4)–Mo(2)–N(3) | 76.96(11) |
| Mo(2)–N(4) | 2.173(3) | C(17)–Mo(2)–N(3) | 80.77(13) |
| Mo(2)–C(17) | 1.967(4) | C(17)–Mo(2)–N(4) | 125.91(12) |
| Mo(2)–C(18) | 1.973(4) | C(17)–Mo(2)–C(18) | 74.57(15) |
| Mo(2)–C(12) | 2.286(4) | C(18)–Mo(2)–N(3) | 127.73(12) |
| Mo(2)–C(13) | 2.366(4) | C(18)–Mo(2)–N(4) | 81.47(14) |
| Mo(2)–C(14) | 2.367(4) | $C_g$–Mo(2)–C(17) | 116.88(2) |
| Mo(2)–C(15) | 2.284(4) | $C_g$–Mo(2)–C(18) | 116.12(2) |
| Mo(2)–C(16) | 2.248(3) | $C_g$–Mo(2)–N(3) | 116.11(2) |
| Mo(2)–$C_g$ | 1.980(1) | $C_g$–Mo(2)–N(4) | 117.20(2) |

[a] $C_g$ corresponds to the centroid of the coordinated $\eta^5$-Cp aromatic rings [C(1)–C(5) and C(12)–C(16)].

complex packs along the [100] direction of the unit cell in a typical interlocked head-to-head fashion, stabilised by π-π interactions between neighbouring $\eta^5$-Cp aromatic rings (distance of ca. 3.5 Å, Figure 2, a). Along this cationic chain the Mo(1)···Mo(1) distances alternate between 5.529(1) and 7.372(1) Å for head-to-head and tail-to-tail packing, respectively. However, the other crystallographically independent complex is instead distributed along the same direction in a head-to-tail fashion [see part c in Figure 2, Mo(2)···Mo(2) distance of 6.441(1) Å] which, in the absence of stabilising interactions between the aromatic ring and the carbonyl and/or acetonitrile moieties, leads to a slightly higher steric pressure on the basal plane, thus resulting in the increase of the (N,C)–Mo–(N,C) bond angles mentioned above.

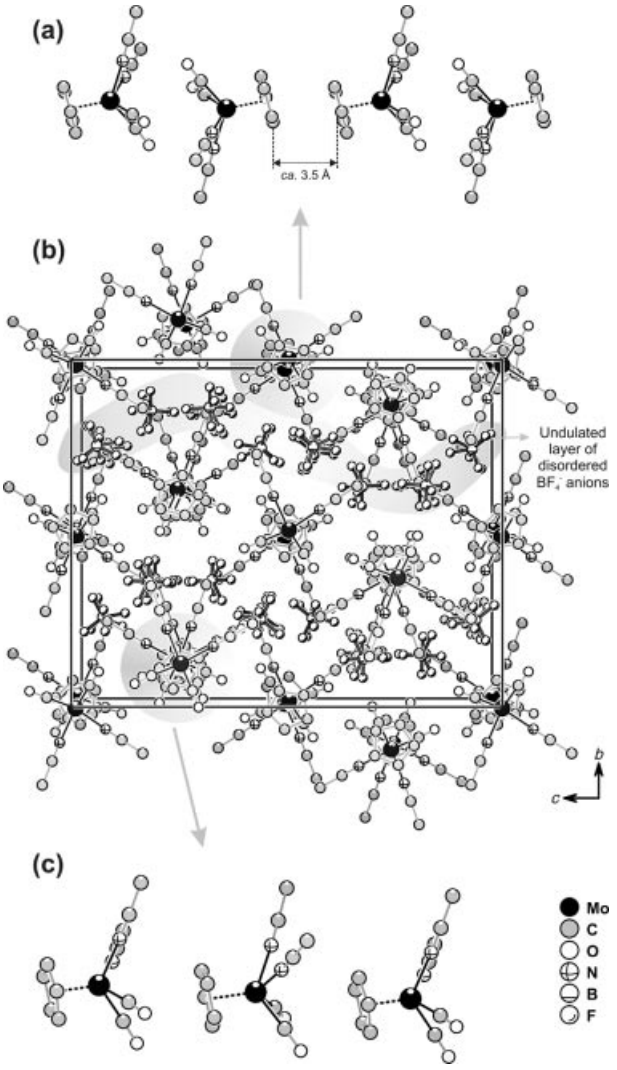


Figure 2. (a) Head-to-head-faced $[CpMo(NCMe)_2(CO)_2]^+$ complex cations in **1** distributed along the [100] direction, showing the π-π interactions between neighbouring $\eta^5$-Cp aromatic rings; (b) Crystal packing of **1** viewed in perspective along the [100] direction of the unit cell, emphasising the alternation in the [010] direction of undulated layers of $[CpMo(NCMe)_2(CO)_2]^+$ complex cations and $BF_4^-$ anions; (c) Head-to-tail-faced $[CpMo(NCMe)_2(CO)_2]^+$ complex cations distributed along the [100] direction. Hydrogen atoms and Mo–C bonds to the coordinated $\eta^5$-Cp have been omitted for clarity.

The crystal packing of **1** is best described as the alternation along the [010] direction of the unit cell of undulated layers formed by the two crystallographically independent $[CpMo(NCMe)_2(CO)_2]^+$ cations with layers of disordered $BF_4^-$ anions (Figure 2). Interactions between these moieties

 © 2006 Wiley-VCH Verlag GmbH & Co. KGaA, Weinheim 

are assured by a large number of weak C–H···F interactions (not shown).

The basic building unit of the complex [CpMo($H_2$biim)(CO)$_2$]($BF_4$) (**2**) is the 18-electron half-sandwich [CpMo($H_2$biim)(CO)$_2$]$^+$ cation, the molecular structure of which was first reported a few years ago by Romão and coworkers for [CpMo($H_2$biim)(CO)$_2$]$ReO_4$ (**2R**).[30] Notably, that report still constitutes, to date, the only crystallographic study of a molybdenum complex with the chelating $H_2$biim ligand. Here we describe the second compound containing this complex cation, in which the tetraoxorhenium(VII) [$ReO_4^-$] moiety has been substituted by tetrafluoroborate anions and the crystal structure determined with increased precision and at low temperature (see Exp. Sect. for crystallographic details for the present study; **2R** was determined at ambient temperature with a very large $R_1$ reliability factor of 9.07%).

For compounds **2** and **2R**, the cation [CpMo($H_2$biim)(CO)$_2$]$^+$ contains the molybdenum centre bound to a chelating $H_2$biim residue, two *cis*-coordinated carbonyl groups and an $\eta^5$-Cp moiety. The coordination geometry is, once again, best described as distorted square-pyramidal and very much resembles a four-legged piano-stool in which the base is formed by the chelating $H_2$biim and the carbonyl residues (Figure 3). The Mo–N and Mo–C (carbonyl) bond lengths are in agreement with those reported for **2R** and related compounds (Table 2). A search in the CSD for typical Mo–N distances of chelating ethanediimines shows values spanning from ca. 2.04 to 2.39 Å with a median of 2.24 Å (from 20 entries in the database). The bite angle of $H_2$biim to the Mo centres is comparable for the two complexes, being ca. 72.8° for **2R** and 72.6° for **2**.

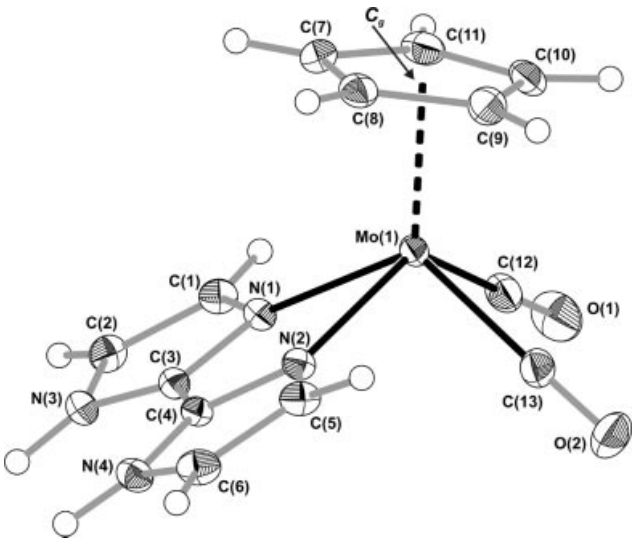


Figure 3. Schematic representation of the [CpMo($H_2$biim)(CO)$_2$]$^+$ complex cation present in the crystal structure of **2**, emphasising the distorted square-pyramidal coordination environment for the $Mo^{2+}$ metal centre and showing the labelling scheme for all non-hydrogen atoms. Displacement ellipsoids are drawn at the 30% probability level and hydrogen atoms are represented as small spheres. All Mo–C bonds to the coordinated $\eta^5$-Cp have been omitted for clarity and replaced by a black-filled dashed bond line to the centroid, $C_g$. For selected bond lengths and angles see Table 2.

Table 2. Selected bond lengths [Å] and angles [°] for the molybdenum coordination environment of the [CpMo($H_2$biim)(CO)$_2$]$^+$ complex cation present in **2**.

| | | | |
|---|---|---|---|
| Mo(1)–N(1) | 2.189(2) | N(2)–Mo(1)–N(1) | 72.55(8) |
| Mo(1)–N(2) | 2.182(2) | C(12)–Mo(1)–N(1) | 80.81(10) |
| Mo(1)–C(12) | 1.981(3) | C(12)–Mo(1)–N(2) | 130.11(9) |
| Mo(1)–C(13) | 1.955(3) | C(13)–Mo(1)–N(1) | 119.59(9) |
| Mo(1)–C(7) | 2.381(3) | C(13)–Mo(1)–N(2) | 80.89(9) |
| Mo(1)–C(8) | 2.396(3) | C(13)–Mo(1)–C(12) | 76.76(12) |
| Mo(1)–C(9) | 2.313(3) | $C_g$–Mo(1)–C(12) | 115.86(2) |
| Mo(1)–C(10) | 2.265(3) | $C_g$–Mo(1)–C(13) | 120.45(2) |
| Mo(1)–C(11) | 2.296(3) | $C_g$–Mo(1)–N(1) | 119.86(2) |
| Mo(1)–$C_g$[a] | 1.996(1) | $C_g$–Mo(1)–N(2) | 113.95(2) |

[a] $C_g$ corresponds to the centroid of the coordinated $\eta^5$-Cp aromatic ring [C(7)–C(11)].

By employing a much smaller anion ($BF_4^-$) to balance the charge of the Mo complex, the crystal packing driving forces mediated by hydrogen bonding interactions (see below) lead to a significant distortion of the geometry of the N···N···C···C base of the pyramid with observed *trans* angles of 130.11(9)° and 119.59(9)°. The corresponding values for **2R** are 124.9(10)° and 126.3(9)°. However, if we consider an average plane for the atoms forming this base, the displacement of the Mo centre towards the $\eta^5$-Cp moiety is ca. 0.96 Å, a value statistically identical to that observed for **2R** [0.94(1) Å]. The latter coordinated moiety is, once again, located at the apex of the distorted square-pyramid and also exhibits a deviation from the ideal $\eta^5$-coordination mode so as to release the steric repulsion with the $H_2$biim molecule. Indeed, compared with the acetonitrile molecules in compound **1**, the $H_2$biim molecule is bulkier and imposes statistically longer Mo–C(7,8) bonds [Table 2; $\Delta_{average}$(Mo–C) of ca. 0.07 Å with the largest being ca. 0.13 Å].

Individual [CpMo($H_2$biim)(CO)$_2$]$^+$ cations close-pack in **2** along the [100] direction in a head-to-tail fashion (Figure 4, a) leading to a chain in which the minimum Mo···Mo separation is 6.531(2) Å. The crystal structure of **2** is formed by the alternation, in the [001] direction of the unit cell, of double layers of [CpMo($H_2$biim)(CO)$_2$]$^+$ complex ions with $BF_4^-$ anions. Interactions between these moieties are assured by strong N–H···F hydrogen bonds (see part b of Figure 4 and Table 3) and, as also reported for compound **1**, by a series of weak C–H···F interactions (not shown).

Table 3. Hydrogen bonding geometry (distances in Å and angles in °) for [CpMo($H_2$biim)(CO)$_2$]($BF_4$) (**2**).[a]

| D–H···A | *d*(D···A) | <(DHA) |
|---|---|---|
| N(3)–H(3)···F(4)$^i$ | 2.868(3) | 144(3) |
| N(4)–H(4)···F(4)$^i$ | 3.116(3) | 139(2) |

[a] Symmetry transformation used to generate equivalent atoms: (i) $x-1, y, z$.

 © 2006 Wiley-VCH Verlag GmbH & Co. KGaA, Weinheim 

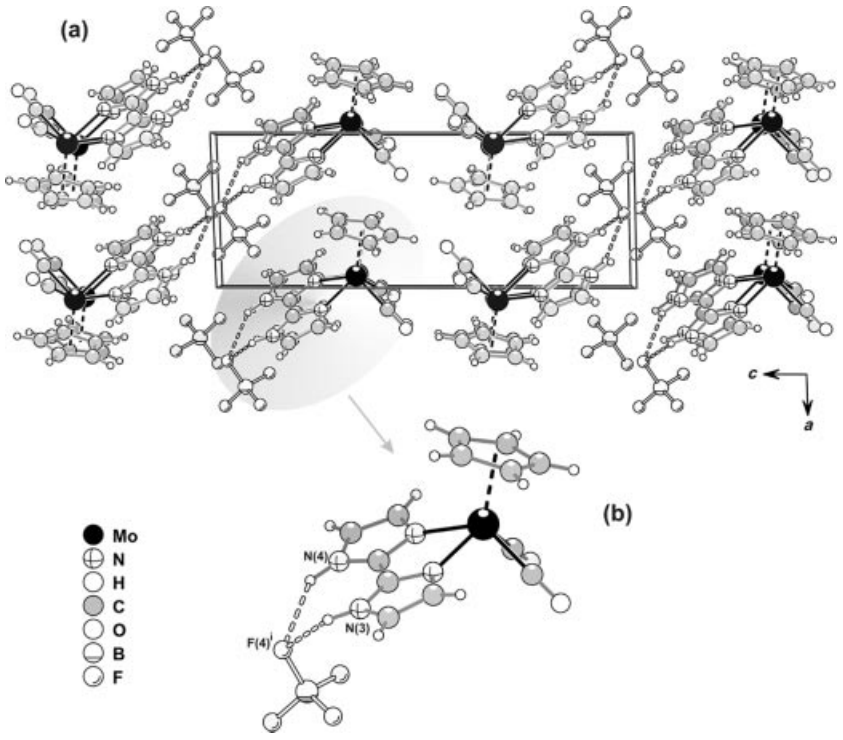


Figure 4. (a) Crystal packing of **2** viewed in perspective along the [010] direction of the unit cell; (b) Strong N–H···F hydrogen bonding interactions linking individual $[CpMo(H_2biim)(CO)_2]^+$ complex cations to neighbouring $BF_4^-$ anions. For further details on the geometry of these interactions see Table 3. As in the previous schematic drawings, Mo–C bonds to the coordinated $\eta^5$-Cp moieties have been replaced by black-filled dashed bond lines to the centroid. Symmetry transformation used to generate equivalent atoms: (i) $x - 1, y, z$.

**Cyclodextrin Inclusion Compounds**

The relative solubilities of β-CD, TRIMEB and the complexes $[CpMo(NCMe)_2(CO)_2](BF_4)$ (**1**) and $[CpMo(H_2biim)(CO)_2](BF_4)$ (**2**) determined the method used for the preparation of the respective inclusion compounds. An initial CD/organometallic molar ratio of 1:1 was always used. For the preparation of β-CD·$[CpMo(NCMe)_2(CO)_2](BF_4)$ (**3**), an acetonitrile solution of **1** was added to an aqueous solution of β-CD, whereas for the preparation of β-CD·$[CpMo(H_2biim)(CO)_2](BF_4)$ (**5**) both components were dissolved in water. Compounds **3** and **5** were obtained as light brown and light brick coloured solids, respectively, after removal of the solvents by freeze-drying. The TRIMEB inclusion compounds TRIMEB·$[CpMo(NCMe)_2(CO)_2](BF_4)$ (**4**) and TRIMEB·$[CpMo(H_2biim)(CO)_2](BF_4)$ (**6**) were obtained by dissolving the components in either dichloromethane (**4**) or a mixture of dichloromethane and ethanol (**6**), followed by evaporation of the solvent(s) under reduced pressure.

X-ray diffraction studies enable the identification of true inclusion complexes of cyclodextrins, mainly based on the empirical evidence that the powder XRD patterns of these complexes should be clearly distinct from those obtained by the superimposition of the diffractograms of the individual components.[9e,31] Figure 5 shows the patterns for complexes **1** and **2**, plain β-CD hydrate, TRIMEB and the adducts **4** and **5**. The diffractograms of the adducts are clearly different from the sum of the individual patterns for complex **1** and TRIMEB, or complex **2** and β-CD. The TRIMEB adduct **4** is quite crystalline and the diffractogram shares similarities with the patterns exhibited by the corresponding 1:1 TRIMEB adducts of $[CpMoX(CO)_3]$ (X = Cl, $CH_2CONH_2$).[9e,13] A hypothetical structural model of the inclusion compound TRIMEB·$[CpMoCl(CO)_3]$ was obtained by global optimisation using simulated annealing.[9e] The compound crystallises in the space group $P2_12_12_1$ and the crystal packing features columns in which the macrocycles are arranged along the *b* axis in a tilted position. The TRIMEB inclusion compound **6** was found to be much less crystalline than **4**, exhibiting very broad and weak features at about 9.1, 11.5, 18.5 and 23.2° for $2\theta$ in the powder XRD pattern (not shown). The β-CD adducts **3** and **5** had moderate crystallinity, with diffraction patterns very similar to that exhibited by the compound β-CD·$[CpMo(CH_2CONH_2)(CO)_3]$.[13]

Thermogravimetric analysis of compounds **3**–**6** was also useful for the recognition of inclusion complex formation. Figure 6 shows the TGA curves for $[CpMo(NCMe)_2(CO)_2](BF_4)$ (**1**), compounds **3** and **4**, and 1:1 physical mixtures of the pure hosts and complex **1**. Complex **1** features a weight loss of about 38% from 100 to 210 °C, which is in good agreement with the expected loss of 36% calculated for the removal of 2 NCMe and 2 CO ligands. A further gradual weight loss of 21% takes place up to 500 °C, leaving a residual mass of 38.2%. The first of these decomposition steps can be clearly seen in the TG profiles for the physical mixtures and is followed by the onset of cyclodextrin decomposition at about 270 °C for β-CD hydrate and

 © 2006 Wiley-VCH Verlag GmbH & Co. KGaA, Weinheim 

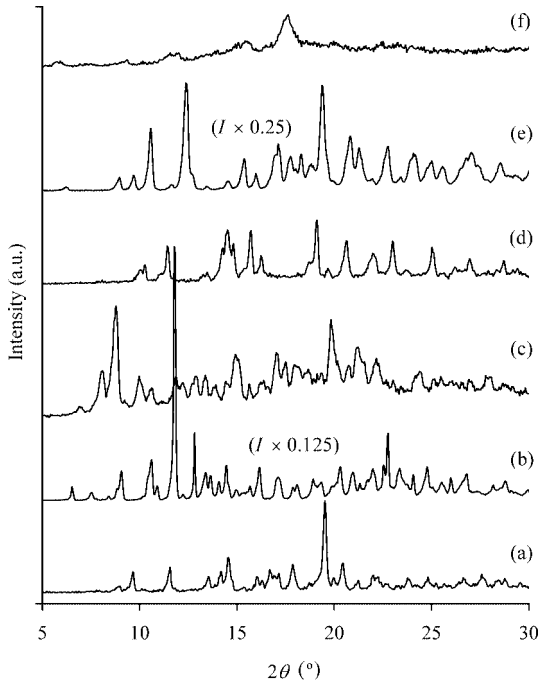


Figure 5. Powder XRD patterns of (a) $[CpMo(NCMe)_2(CO)_2](BF_4)$ (**1**), (b) TRIMEB, (c) the inclusion compound TRIMEB·$[CpMo(NCMe)_2(CO)_2](BF_4)$ (**4**), (d) $[CpMo(H_2biim)(CO)_2](BF_4)$ (**2**), (e) β-CD hydrate and (f) the inclusion compound β-CD·$[CpMo(H_2biim)(CO)_2](BF_4)$ (**5**).

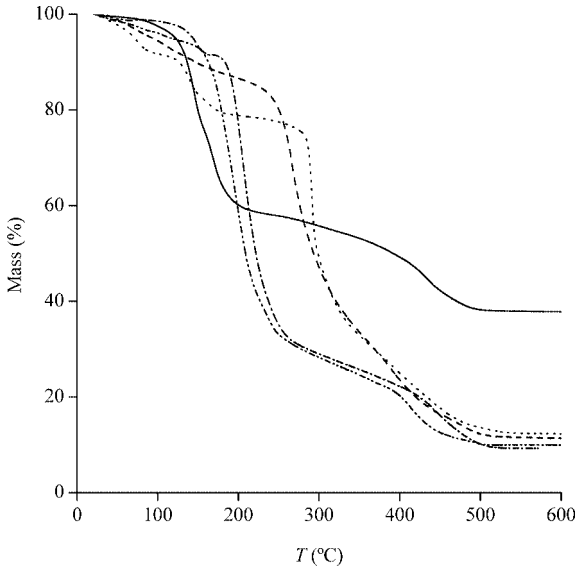


Figure 6. TGA curves of complex **1** (——), a 1:1 physical mixture of **1** and β-CD (·····), a 1:1 physical mixture of **1** and TRIMEB (–·–·) and the inclusion compounds **3** (– – –) and **4** (–··–··).

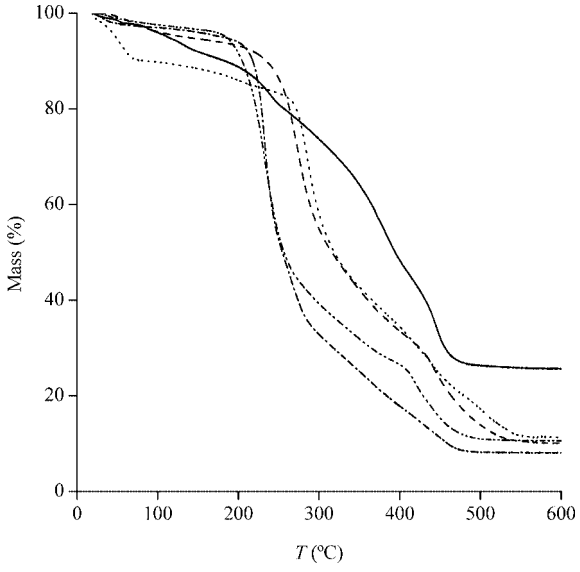


Figure 7. TGA curves of complex **2** (——), a 1:1 physical mixture of **2** and β-CD (·····), a 1:1 physical mixture of **2** and TRIMEB (–·–·) and the inclusion compounds **5** (– – –) and **6** (–··–··).

175 °C for TRIMEB. The TGA profile for the β-CD physical mixture exhibits an additional well-defined step from room temperature to 90 °C corresponding to the removal of water molecules located in the β-CD cavities and also in the interstices between the macrocycles. The TGA profiles for compounds **3** and **4** are very different from those for the physical mixtures. Neither individual steps for dehydration (in the case of the β-CD adduct) nor loss of the ligands from the organometallic complex were observed. Instead, both compounds exhibit a continuous and smooth weight loss from room temperature up to the points where the host macrocycles begin to decompose (230 °C for **3**, 155 °C for TRIMEB). This behaviour, coupled with the early degradation of the hosts (compared with the pure compounds β-CD hydrate and TRIMEB) is characteristic of true inclusion compounds comprising CDs and organometallic molecules. Comparable results were obtained for $[CpMo(H_2biim)(CO)_2](BF_4)$ (**2**) and its inclusion compounds (Figure 7), although the decomposition of the organometallic complex in the physical mixtures is not so obvious since the pure compound **2** decomposes in a series of overlapping steps which extend from room temperature to 475 °C.

The $^{13}C\{^1H\}$ CP/MAS NMR spectra of compounds **1**–**6** are shown in Figure 8 and Figure 9. Although the crystal structure of **1** contains two crystallographically independent $[CpMo(NCMe)_2(CO)_2]^+$ cations, with slightly different geometric features and distinct close-packing configurations, compound **1** gives rise to single peaks at 96.6, 145.1 and 252.6 ppm, assigned to the Cp, CN and CO groups, respectively. On the other hand, three partially revolved lines were observed between $\delta$ = 3 and 5 ppm for the methyl groups of the acetonitrile ligands. In the spectra of the inclusion compounds **3** and **4**, the guest species can be identified by a Cp resonance at about 96 ppm and a Me signal at about 3 ppm, which are essentially unshifted when compared with the resonances for nonincluded **1**. The β-CD carbon atoms in **3** give rise to four single peaks centred around 102.6, 80.6, 72.2 and 60.0 ppm, assigned to C1, C4, C2,3,5 and C6, respectively. This is in sharp contrast to plain β-CD hydrate, which exhibits a complex $^{13}C\{^1H\}$ CP/MAS NMR spectrum containing multiple sharp resonances for each type of carbon atom (not shown).[13] The multiple reso-

 © 2006 Wiley-VCH Verlag GmbH & Co. KGaA, Weinheim 

nances arise due to different torsion angles about the α(1→4) linkages[32] and the torsion angles describing the orientation of the hydroxy groups.[33] The appearance of single peaks in the $^{13}C\{^1H\}$ CP/MAS NMR spectrum of **3**, together with a lower dispersion in the chemical shift for each signal (i.e. the chemical shift range that comprises all of the resonances from the same carbon atom in distinct glycosidic units) are typically attributed to the β-CD macrocycle becoming symmetric, that is, the encapsulation of the guest molecule induces the ring to adopt a less distorted conformation, with each glucose unit in a more similar environment.[9e,13,34] The low crystallinity of compound **3** may also contribute to a broadening of the peaks.

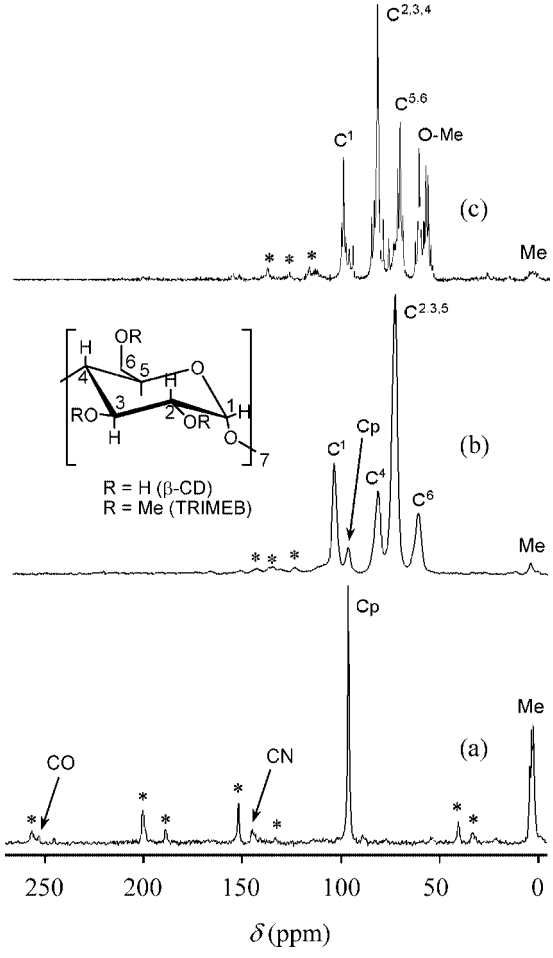


Figure 8. Solid-state $^{13}C\{^1H\}$ CP/MAS NMR spectra of (a) complex **1**, (b) the β-CD inclusion compound **3** and (c) the TRIMEB inclusion compound **4**. Spinning sidebands are denoted by asterisks.

Like plain β-CD hydrate, the $^{13}C\{^1H\}$ CP/MAS NMR spectrum of TRIMEB also contains multiple resonances for each type of carbon atom (not shown).[13] This is because the host assumes a severely collapsed conformation in the solid-state, which minimises the hydrophobic cavity in the absence of a hydrophobic guest.[35] Several resolved lines may also be observed for the inclusion compound **4** and this is consistent with the presence of an ordered crystal-packing arrangement of CD molecules. Indeed, the presence of at least ten sharp lines for the methyl carbon atoms shows that these groups exist in several different well-defined environments. The overall similarity of the spectrum with those previously reported for the adducts TRIMEB·[CpMoX(CO)$_3$] (X = Cl, $CH_2CONH_2$)[9e,13] is in line with the powder XRD results and confirms that the conformations of the host macrocycles and the crystal packing arrangements in the three compounds are similar. On the other hand, a comparison of these spectra with that for plain TRIMEB reveals considerable differences in the number, relative intensities and positions of peaks due to the host, which indicates that the conformation of the macrocycles in the inclusion compounds is different from that in plain TRIMEB.

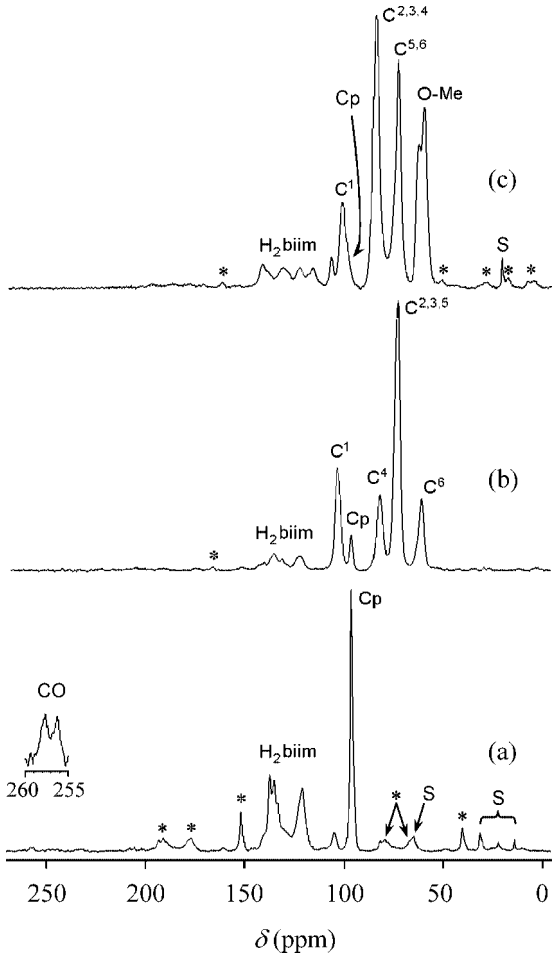


Figure 9. Solid-state $^{13}C\{^1H\}$ CP/MAS NMR spectra of (a) complex **2**, (b) the β-CD inclusion compound **5** and (c) the TRIMEB inclusion compound **6**. Spinning sidebands are denoted by asterisks and peaks due to the presence of residual solvents (diethyl ether, *n*-hexane or ethanol) are indicated by S.

Figure 9 shows the $^{13}C\{^1H\}$ CP/MAS NMR spectra of [CpMo($H_2$biim)(CO)$_2$](BF$_4$) (**2**) and the inclusion compounds β-CD·[CpMo($H_2$biim)(CO)$_2$](BF$_4$) (**5**) and TRIMEB·[CpMo($H_2$biim)(CO)$_2$](BF$_4$) (**6**). The resonances for the carbon atoms of the biimidazole ligand in **2** appear in the range 120–137 ppm and the Cp resonance can be found at $\delta$ = 96.1 ppm. The spectrum for compound **5** is

 © 2006 Wiley-VCH Verlag GmbH & Co. KGaA, Weinheim 

very similar to that of compound **3** with respect to the β-CD carbon resonances. Additional peaks for the guest molecule can be observed at $\delta$ = 95.6 ppm (Cp) and 122–139 ppm ($H_2$biim). For the TRIMEB adduct **6**, the $H_2$biim resonances appear in the range of 115–140 ppm, while the Cp resonance is obscured by a broad peak for the C1 carbon atoms of the host. In fact, in contrast to the spectrum of **4**, the resonances for the host carbon atoms in **6** appear mainly as single broad peaks, which are presumably related to the low crystallinity of the compound as revealed by the powder XRD studies.

For all the inclusion compounds studied, it was not possible to clearly identify the resonances (masked in the background) for the CO groups of the guest molecules, even when contact times of 2 ms were used. The presence of these groups was confirmed by IR spectroscopy. Thus, in addition to the intense and typical bands of the cyclodextrin hosts, the spectra contained two bands in the CO stretching region (1880–2000 $cm^{-1}$). These were mostly shifted by less than 10 $cm^{-1}$ compared with the corresponding bands for the nonincluded complexes **1** and **2**. Only in two cases (1971 $cm^{-1}$ for **3** vs. 1988 $cm^{-1}$ for **1**; 1891 $cm^{-1}$ for **5** vs. 1878 $cm^{-1}$ for **2**) were larger shifts observed. These shifts probably arise because the guest molecules in compounds **3**–**6** are isolated from one another by inclusion in the CD cavities.

### Concluding Remarks

β-CD and TRIMEB inclusion compounds containing the complexes $[CpMo(NCMe)_2(CO)_2](BF_4)$ and $[CpMo(H_2biim)(CO)_2](BF_4)$ have been prepared and characterised. Referring to previous work, we may conclude that neutral, cationic or anionic $\eta^5$-cyclopentadienyl metal carbonyl complexes of the type $[CpML_m(CO)_n]^{z-/z+}$ (M = Mo, Mn or Fe), with three-legged or four-legged piano stool geometries, are readily encapsulated by cyclodextrins. The available experimental and theoretical evidence suggests that the interaction geometries generally involve insertion of the Cp ligand into the host cavities, with the CO and L ligands (L = NCMe, $H_2$biim, Cl, $CH_2CONH_2$ etc) protruding outwards (on the wider secondary side of the host molecules). Indeed, the crystal-packing arrangements in the β-CD and TRIMEB inclusion compounds containing the $[CpMo(NCMe)_2(CO)_2]^+$ complex cation are evidently very similar to the arrangements found in the corresponding inclusion compounds containing the neutral tricarbonyl complex $[CpMoCl(CO)_3]$. We are currently studying how the behaviour of the organometallic complexes as, for example, CO-releasing molecules, catalyst precursors or anti-tumour agents is affected by cyclodextrin encapsulation.

## Experimental Section

**General Remarks:** All air-sensitive operations were carried out using standard Schlenk techniques under an oxygen- and water-free nitrogen atmosphere. Solvents were dried by standard procedures (diethyl ether and ethanol over Na, $CH_2Cl_2$ and NCMe over $CaH_2$), distilled under nitrogen and kept over 3 Å (NCMe) or 4-Å molecular sieves. Microanalyses for C, H and N were performed at the Instituto de Tecnologia Química e Biológica (Oeiras, Portugal) by C. Almeida and Mo was determined by ICP-OES at the Central Laboratory for Analysis (University of Aveiro) by E. Soares. TGA studies were carried out using a Shimadzu TGA-50 system at a heating rate of 5 °C $min^{-1}$ under air. Powder X-ray diffraction data were collected at ambient temperature on a X′Pert MPD Philips diffractometer (Cu-$K_\alpha$ X-radiation, $\lambda$ = 1.54060 Å) equipped with a curved graphite-monochromator and a flat-plate sample holder in a typical Bragg–Brentano *para*-focusing optics configuration (40 kV, 50 mA). Infrared spectra were recorded on a Unican Mattson Mod 7000 FTIR spectrometer. $^{13}C$ NMR spectra in solution were recorded on a Bruker Avance 500 spectrometer. $^{13}C\{^1H\}$ CP/MAS NMR spectra were recorded at 125.72 MHz on a (11.7 T) Bruker Avance 500 spectrometer, with an optimised $\pi/2$ pulse for $^1H$ of 4.5 μs, 2 ms contact time, a spinning rate of 7 kHz and 12 s recycle delays. Chemical shifts are quoted in parts per million relative to tetramethylsilane.

β-Cyclodextrin (Kleptose®) was kindly donated by laboratoires La Roquette (France) and heptakis-2,3,6-tris-*O*-methyl-β-CD was obtained from Fluka. 2,2′-Biimidazole was prepared from glyoxal and concentrated ammonia following the published method.[36] $[CpMo(\eta^3\text{-}C_3H_5)(CO)_2]$ was prepared as described in the literature[16b,16c] and characterised by elemental analysis and FTIR spectroscopy.

**$[CpMo(NCMe)_2(CO)_2](BF_4)$ (1):** A solution of $[CpMo(\eta^3\text{-}C_3H_5)(CO)_2]$ (0.35 g, 1.35 mmol) in $CH_2Cl_2$ was treated with 1 equiv. of $HBF_4{\cdot}Et_2O$. After 10 min, acetonitrile was added in excess and the reaction mixture was stirred for 2 h. The solution was then concentrated to about 5 mL and diethyl ether added to precipitate a red solid. The solid was filtered, washed with diethyl ether and *n*-hexane. Crystals suitable for X-ray analysis were obtained after slow diffusion at 4 °C of diethyl ether into a saturated solution of the crude product in acetonitrile. Yield: 0.48 g, 92%. $C_{11}H_{11}BF_4MoN_2O_2$ (385.96): calcd. C 34.23, N 7.26, H 2.87; found C 33.97, N 7.16, H 2.99. FTIR (KBr): $\tilde{\nu}$ = 3098 m, 3067 m, 3056 m (all $\nu_{CH}$ of Cp), 2972 m, 2965 m, 2915 m, 2902 m (all $\nu_{CH}$ of Me), 2325 w ($\nu_{N\equiv C}$), 2289 w ($\nu_{N\equiv C}$), 1988 vs. ($\nu_{CO}$), 1893 vs. ($\nu_{CO}$), 1621 m, 1434 m, 1422 m, 1366 w, 1352 w, 1305 w, 1300 w, 1083 vs. ($\nu_{BF}$), 1073 s, 1036 s, 928 w, 904 vw, 886 vw, 869 vw, 847 m, 824 w, 772 vw, 713 vw, 588 m, 542 m, 533 m, 522 m, 513 m, 488 m, 458 m, 433 m, 385 m $cm^{-1}$. $^1H$ NMR (300 MHz, [D$_6$]acetone, 25 °C): $\delta$ = 5.80 (s, 5 H, Cp), 2.19 (s, 6 H, Me) ppm. $^{13}C\{^1H\}$ NMR (125.72 MHz, $CDCl_3$, 25 °C): $\delta$ = 249.7 (CO), 142.6 (CN), 96.1 (Cp), 4.8 (Me) ppm. $^{13}C\{^1H\}$ CP/MAS NMR: $\delta$ = 252.6 (CO), 145.1 (CN), 96.6 (Cp), 4.7 (Me) ppm

**$[CpMo(H_2biim)(CO)_2](BF_4)$ (2):** A solution of $[CpMo(\eta^3\text{-}C_3H_5)(CO)_2]$ (0.31 g, 1.19 mmol) in $CH_2Cl_2$ was treated with 1 equiv. of $HBF_4{\cdot}Et_2O$. After 10 min, dimethoxymethane was added in excess and the reaction mixture was stirred for 15 min. 2,2′-biimidazole (0.17 g, 1.30 mmol) was then added and the reaction mixture stirred for 4 h at room temperature. The resultant orange solution was filtered and, after concentrating to about 5 mL, diethyl ether was added to precipitate an orange microcrystalline solid. The solid was filtered and washed several times with diethyl ether and *n*-hexane. Crystals suitable for X-ray analysis were obtained after slow diffusion at 4 °C of diethyl ether into a saturated solution of the crude product in ethanol. Yield: 0.47 g, 90%. $C_{13}H_{11}BF_4MoN_4O_2$ (438.01): calcd. C 35.65, N 12.79, H 2.53; found C 35.52, N 12.51, H 2.38. FTIR (KBr): $\tilde{\nu}$ = 3360 s, br. ($\nu_{NH}$),

 © 2006 Wiley-VCH Verlag GmbH & Co. KGaA, Weinheim 

3265 sh ($\nu_{NH}$), 3156 m, 3140 s, 3122 s ($\nu_{NH}$, $\nu_{CH}$ of Cp and/or $H_2$biim), 2929 m, 2776 m, 1976 vs. ($\nu_{CO}$), 1878 vs. ($\nu_{CO}$), 1707 w, 1638 m, 1534 m, 1512 m, 1429 m, 1420 m, 1359 w, 1321 m, 1284 w, 1253 w, 1123 s, 1100 s, 1068 vs. ($\nu_{BF}$), 1004 m, 978 m, 919 w, 846 m, 822 m, 787 m, 761 s, 695 w, 679 m, 620 m, 612 w, 595 w, 538 m, 520 m, 484 m, 471 w, 435 m, 369 vw, 341 vw, 332 vw, 301 w cm$^{-1}$. $^1$H NMR (300 MHz, [D$_6$]acetone, 25 °C): $\delta$ = 11.6 (NH, $H_2$biim), 7.75 (d, 2 H, $H_2$biim), 7.67 (d, 2 H, $H_2$biim), 5.85 (s, 5 H, Cp) ppm. $^{13}$C{$^1$H} NMR (125.72 MHz, $CDCl_3$, 25 °C): $\delta$ = 253.0 (CO), 136.7, 133.9, 120.7 (all $H_2$biim), 95.2 (Cp) ppm. $^{13}$C{$^1$H} CP/MAS NMR: $\delta$ = 257.6, 256.1 (CO), 137.3, 135.0, 133.3, 120.8 (all $H_2$biim), 104.8, 96.1 (Cp) ppm.

**β-CD·[CpMo(NCMe)$_2$(CO)$_2$](BF$_4$) (3):** A solution of [CpMo(NCMe)$_2$(CO)$_2$](BF$_4$) (**1**) (52.0 mg, 0.134 mmol) in acetonitrile (4.0 mL) was added to a solution of β-CD (152.5 mg, 0.134 mmol) in water (6.0 mL) at 40 °C. The resultant solution was stirred for 1 h and then frozen by immersion of the container in liquid nitrogen. The solvents were removed by freeze-drying to obtain a light-brown solid. FTIR (KBr): $\tilde{\nu}$ = 3375 s, br. ($\nu_{OH}$), 2939 m, 1971 s ($\nu_{CO}$), 1890 s ($\nu_{CO}$), 1640 m, 1536 m, 1509 w, 1422 m, 1367 m, 1334 m, 1300 m, 1244 m, 1157 s, 1101 sh, 1079 vs, 1027 vs, 1003 sh, 946 m, 938 m, 892 w, 860 w, 829 w, 821 w, 762 m, 706 m, 698 m, 670 w, 608 m, 577 m, 527 m, 484 m, 432 m, 356 w, 327 w, 302 w cm$^{-1}$. $^{13}$C{$^1$H} CP/MAS NMR: $\delta$ = 102.6 (β-CD, C1), 95.6 (guest Cp), 80.6 (β-CD, C4), 72.2 (β-CD, C2,3,5), 60.0 (β-CD, C6), 2.8 (guest Me) ppm.

**TRIMEB·[CpMo(NCMe)$_2$(CO)$_2$](BF$_4$) (4):** A solution of TRIMEB (0.558 g, 0.39 mmol) in $CH_2Cl_2$/water (20:1) was added to a solution of [CpMo(NCMe)$_2$(CO)$_2$](BF$_4$) (**1**) (103 mg, 0.26 mmol) in dichloromethane (10 mL) and the mixture was stirred for 48 h at 60 °C. After cooling to ambient temperature, the solution was evaporated to dryness under reduced pressure to obtain a dark-brown microcrystalline solid. FTIR (KBr): $\tilde{\nu}$ = 3463 s, 3106 m ($\nu_{CH}$ of Cp), 2989 s, 2935 s, 2842 s, 2322 vw ($\nu_{N\equiv C}$), 2290 vw ($\nu_{N\equiv C}$), 2074 w, 1988 s ($\nu_{CO}$), 1944 w, 1899 s ($\nu_{CO}$), 1840 w, 1631 m, 1458 m, 1384 m, 1370 m, 1325 m, 1307 m, 1263 m, 1196 s, 1163 s, 1145 s, 1107 vs, 1084 vs, 1072 vs, 1037 vs, 970 s, 951 m, 905 m, 856 m, 823 w, 805 w, 753 m, 734 m, 704 m, 671 vw, 553 m, 534 m, 522 m, 458 w, 434 w, 385 w, 348 w, 328 w, 313 w cm$^{-1}$. $^{13}$C{$^1$H} CP/MAS NMR: $\delta$ = 100.5, 99.6, 99.2, 98.3 (TRIMEB, C1), 96.8, 96.5 (TRIMEB, C1; guest Cp), 94.7 (TRIMEB, C1), 85.4, 84.0, 82.4, 81.9, 81.3, 79.2 (TRIMEB, C2,3,4), 76.4, 74.2, 72.2, 71.0, 69.6 (TRIMEB, C5,6), 63.0, 61.8, 61.2, 60.0, 58.9, 58.1, 57.0, 56.5, 55.4 (TRIMEB, O–Me), 3.8 (guest Me) ppm.

**β-CD·[CpMo(H$_2$biim)(CO)$_2$](BF$_4$) (5):** A solution of β-CD (311 mg, 0.27 mmol) and [CpMo(H$_2$Biim)(CO)$_2$](BF$_4$) (**2**) (120 mg, 0.27 mmol) in water (8 mL) was stirred for 50 min at 50 °C and then frozen with liquid nitrogen. The frozen water was removed by liophilisation to obtain a brick-coloured solid. FTIR (KBr): $\tilde{\nu}$ = 3377 s, br. ($\nu_{OH}$), 2928 m, 1973 s ($\nu_{CO}$), 1891 s ($\nu_{CO}$), 1640 m, 1534 m, 1507 w, 1422 m, 1368 m, 1334 m, 1300 w, 1245 w, 1157 s, 1099 sh, 1079 vs, 1050 sh, 1028 vs, 1005 sh, 944 m, 937 m, 861 w, 828 w, 820 w, 762 m, 706 m, 698 m, 668 m, 607 m, 577 m, 527 m, 483 m, 480 m, 433 m, 356 w, 335 w, 327 w, 302 w cm$^{-1}$. $^{13}$C{$^1$H} CP/MAS NMR: $\delta$ = 139.2, 134.5, 130.2, 122.1 (all guest $H_2$biim), 102.5 (β-CD, C1), 95.6 (guest Cp), 80.7 (β-CD, C4), 71.9 (β-CD, C2,3,5), 59.8 (β-CD, C6) ppm.

**TRIMEB·[CpMo(H$_2$biim)(CO)$_2$]BF$_4$ (6):** A solution of [CpMo(H$_2$biim)(CO)$_2$]BF$_4$ (**2**) (60.0 mg, 0.137 mmol) in a mixture of dichloromethane (12 mL) and ethanol (4 mL) was treated portionwise with TRIMEB (196 mg, 0.137 mmol), allowing each fraction to dissolve before adding the next. The mixture was stirred for 1 h and then evaporated to dryness under reduced pressure to obtain a solid product. FTIR (KBr): $\tilde{\nu}$ = 3142 m ($\nu_{NH}$, $\nu_{CH}$ of Cp and/or $H_2$biim), 2984 s, 2929 s, 2834 s, 2079 w, 1973 m ($\nu_{CO}$), 1885 m ($\nu_{CO}$), 1714 w, 1640 m, 1535 m, 1460 s, 1402 sh, 1369 m, 1322 m, 1304 m, 1259 sh, 1195 s, 1161 vs, 1141 vs, 1110 vs, 1095 vs, 1088 vs, 1072 vs, 1038 vs, 954 s, 937 s, 905 sh, 856 m, 821 w, 756 s, 706 m, 694 m, 666 w, 622 w, 599 sh, 551 m, 517 m, 468 w, 439 w, 377 vw, 346 w, 305 w cm$^{-1}$. $^{13}$C{$^1$H} CP/MAS NMR: $\delta$ = 140.3, 129.7, 121.1, 115.0 (all guest $H_2$biim), 105.0, 99.5 (TRIMEB, C1; guest Cp), 82.2 (TRIMEB, C2,3,4), 71.1 (TRIMEB, C5,6), 60.6, 57.8 (TRIMEB, O–Me) ppm.

**Single-Crystal X-ray Diffraction:** Suitable single-crystals of [CpMo(NCMe)$_2$(CO)$_2$](BF$_4$) (**1**) and [CpMo(H$_2$Biim)(CO)$_2$](BF$_4$) (**2**) were mounted on glass fibres using perfluoropolyether oil.[37] Data were collected at 180(2) K on a Nonius Kappa charge-coupled device area-detector diffractometer (Mo-$K_\alpha$ graphite-monochromated radiation, $\lambda$ = 0.7107 Å) equipped with an Oxford Cryosystems cryostream and controlled by the Collect software package.[38] Images were processed using the Denzo and Scalepack software packages[39] and data were corrected for absorption by the empirical method employed in Sortav.[40] Structures were solved by direct methods using SHELXS-97[41] and refined by full-matrix least-squares on $F^2$ using SHELXL-97.[42] All non-hydrogen atoms were directly located from difference Fourier maps and refined with anisotropic displacement parameters. Selected bond lengths and angles for the $Mo^{2+}$ coordination environments are given in Table 1 and Table 2 for compounds **1** and **2**, respectively. Table 3 summarises the hydrogen bonding geometries reported for compound **2**.

For the two crystal structures, hydrogen atoms bound to carbon were located in their idealised positions using appropriate HFIX instructions in SHELXL (43 for the aromatic and 137 for the terminal methyl groups of the coordinated NCMe moieties) and included in subsequent refinement cycles in the riding-motion approximation with isotropic thermal displacement parameters ($U_{iso}$) fixed at 1.2 (for the aromatic hydrogen atoms) or 1.5 (for the methyl moieties) times $U_{eq}$ of the carbon atom to which they were attached. For compound **1**, the two crystallographically independent $BF_4^-$ anions were found to be severely affected by structural disorder, which was directly reflected in the large thermal displacement parameters calculated for each fluorine atom. This disorder was modelled by considering, on the one hand, two distinct crystallographic positions for each $BF_4^-$ anion with fixed occupancy rates of $^1/_3$ and $^2/_3$ and, on the other, a geometry heavily restrained for each moiety with the B–F and F···F intramolecular distances restrained to variable common factors which ultimately refined to ca. 1.34 and 2.18 Å, respectively. This refinement strategy led to a more reasonable structural model for **1**, even though the checkCIF routines available with the PLATON software package still indicated a rather large discrepancy between the $U_{eq}$ values of the boron and fluorine atoms. The last difference Fourier map synthesis showed, for **1**, the highest peak (0.535 e Å$^{-3}$) and deepest hole (–0.790 e Å$^{-3}$) located at 1.37 Å from H(20C) and 0.79 Å from Mo(1), respectively, while, for **2**, the highest peak (0.616 e Å$^{-3}$) and deepest hole (–0.798 e Å$^{-3}$) were found at 1.65 Å from H(3) and 0.79 Å from Mo(1), respectively.

CCDC-604073 and -604074 (for **1** and **2**) contain the supplementary crystallographic data for this paper. These data can be obtained free of charge from The Cambridge Crystallographic Data Centre via www.ccdc.cam.ac.uk/data_request/cif.

**Crystallographic Data for 1:** $C_{22}H_{22}B_2F_8Mo_2N_4O_4$, $M$ = 771.94, orthorhombic *Pbca*, $a$ = 12.871(3), $b$ = 19.222(4), $c$ = 23.849(5) Å, $V$ = 5900(2) Å$^3$, $Z$ = 8, $D_{calcd.}$ = 1.738 g cm$^{-3}$, $\mu$(Mo-$K_\alpha$) =

 © 2006 Wiley-VCH Verlag GmbH & Co. KGaA, Weinheim 

0.936 $mm^{-1}$, $F(000)$ = 3040, crystal size = 0.28 × 0.16 × 0.10 mm, brown blocks, $\theta$ range = 3.60 to 26.37, index ranges $-16 \le h \le 16$, $-17 \le k \le 24$, $-28 \le l \le 29$, reflections collected = 32704, independent reflections = 6001 ($R_{int}$ = 0.0545), $R_1$, $wR_2$ [$I > 2\sigma(I)$] = 0.0345, 0.0739, $R_1$, $wR_2$ (all data) = 0.0513, 0.0803, weighting scheme $m$, $n$ = 0.0330, 6.4200.

**Crystallographic Data for 2:** $C_{13}H_{11}BF_4MoN_4O_2$, $M$ = 438.01, triclinic $P\bar{1}$, $a$ = 6.5308(13), $b$ = 7.2832(15), $c$ = 16.962(3) Å, $\alpha$ = 92.91(3), $\beta$ = 90.91(3), $\gamma$ = 107.00(3)°, $V$ = 770.2(3) $Å^3$, $Z$ = 2, $D_{calcd.}$ = 1.889 $g\,cm^{-3}$, $\mu$(Mo-$K_\alpha$) = 0.912 $mm^{-1}$, $F(000)$ = 432, crystal size = 0.10 × 0.07 × 0.02 mm, red blocks, $\theta$ range = 3.51 to 30.03, index ranges $-9 \le h \le 9$, $-10 \le k \le 9$, $-23 \le l \le 23$, reflections collected = 10020, independent reflections = 4484 ($R_{int}$ = 0.0406), $R_1$, $wR_2$ [$I > 2\sigma(I)$] = 0.0340, 0.0652, $R_1$, $wR_2$ (all data) = 0.0481, 0.0701, weighting scheme $m$, $n$ = 0, 0.8582.

## Acknowledgments

The authors are grateful to FCT, OE and FEDER for funding (Project POCI//QUI/56109/2004). CCLP is grateful to the FCT for a postdoctoral grant. We wish to thank Professor João Rocha for access to research facilities and Paula Esculcas for assistance in the solid-state NMR experiments. We are also grateful to Celeste Azevedo for carrying out the TGA experiments and to Rosário Soares for collection of the powder diffraction data.

[1] a) F. E. Kühn, A. M. Santos, W. A. Herrmann, *Dalton Trans.* **2005**, 2483–2491; b) A. A. Valente, J. D. Seixas, I. S. Gonçalves, M. Abrantes, M. Pillinger, C. C. Romão, *Catal. Lett.* **2005**, *101*, 127–130; c) J. Zhao, A. M. Santos, E. Herdtweck, F. E. Kühn, *J. Mol. Catal. A* **2004**, *222*, 265–271; d) B. F. M. Kimmich, P. J. Fagan, E. Hauptman, W. J. Marshall, R. M. Bullock, *Organometallics* **2005**, *24*, 6220–6229; e) Y. Kotani, M. Kamigaito, M. Sawamoto, *Macromolecules* **2000**, *33*, 3543–3549; f) O. Buisine, C. Aubert, M. Malacria, *Chem. Eur. J.* **2001**, *7*, 3517–3525; g) J. H. Hardesty, J. B. Koerner, T. A. Albright, G.-Y. Lee, *J. Am. Chem. Soc.* **1999**, *121*, 6055–6067.

[2] a) T. M. Gilbert, F. J. Hadley, C. B. Bauer, R. D. Rogers, *Organometallics* **1994**, *13*, 2024–2034; b) A. R. Dias, M. H. Garcia, M. P. Robalo, A. P. S. Tekheira, L. A. Bulygina, V. I. Sokolov, *Russ. J. Org. Chem.* **2001**, *37*, 620–623; c) M. H. Garcia, S. Royer, M. P. Robalo, A. R. Dias, J.-P. Tranchier, R. Chavignon, D. Prim, A. Auffrant, F. Rose-Munch, E. Rose, J. Vaissermann, A. Persoons, I. Asselberghs, *Eur. J. Inorg. Chem.* **2003**, 3895–3904.

[3] a) J. B. Waern, M. M. Harding, *J. Organomet. Chem.* **2004**, *689*, 4655–4668; b) R. H. Fish, G. Jaouen, *Organometallics* **2003**, *22*, 2166–2177; c) D. L. Mohler, E. K. Barnhardt, A. L. Hurley, *J. Org. Chem.* **2002**, *67*, 4982–4984.

[4] a) J. Bernard, K. Ortner, B. Spingler, H.-J. Pietzsch, R. Alberto, *Inorg. Chem.* **2003**, *42*, 1014–1022; b) M. Saidi, S. Seifert, M. Kretzschmar, R. Bergmann, H.-J. Pietzsch, *J. Organomet. Chem.* **2004**, *689*, 4739–4744.

[5] S. S. Braga, M. P. M. Marques, J. B. Sousa, M. Pillinger, J. J. C. Teixeira-Dias, I. S. Gonçalves, *J. Organomet. Chem.* **2005**, *690*, 2905–2912, and references therein.

[6] a) G. Jaouen, A. Vessières, I. S. Butler, *Acc. Chem. Res.* **1993**, *26*, 361–369; b) D. R. van Staveren, T. Weyhermüller, N. Metzler-Nolte, *Organometallics* **2000**, *19*, 3730–3735; c) J.-M. Heldt, N. Fischer-Durand, M. Salmain, A. Vessières, G. Jaouen, *J. Organomet. Chem.* **2004**, *689*, 4775–4782.

[7] a) T. R. Johnson, B. E. Mann, J. E. Clark, R. Foresti, C. J. Green, R. Motterlini, *Angew. Chem. Int. Ed.* **2003**, *42*, 3722–3729; b) I. J. S. Fairlamb, A.-K. Duhme-Klair, J. M. Lynam, B. E. Moulton, C. T. O'Brien, P. Sawle, J. Hammad, R. Motterlini, *Bioorg. Med. Chem. Lett.* **2006**, *16*, 995–998.

[8] a) F. Hapiot, S. Tilloy, E. Monflier, *Chem. Rev.* **2006**, *106*, 767–781; b) W. Sliwa, T. Girek, *Heterocycles* **2003**, *60*, 2147–2183; c) E. Fenyvesi, L. Szente, N. R. Russel, M. McNamara, in: *Comprehensive Supramolecular Chemistry*, (Eds.: J. Szejtli, T. Osa), Pergamon, Oxford, **1996**, vol. 3, pp. 305–366.

[9] a) M. Shimada, A. Harada, S. Takahashi, *J. Chem. Soc., Chem. Commun.* **1991**, 263–264; b) P. P. Patel, M. E. Welker, *J. Organomet. Chem.* **1997**, *547*, 103–112; c) C. Díaz, A. Arancibia, *J. Inclusion Phenom. Macro. Chem.* **1998**, *30*, 127–141; d) S. S. Braga, I. S. Gonçalves, P. Ribeiro-Claro, A. D. Lopes, M. Pillinger, J. J. C. Teixeira-Dias, J. Rocha, C. C. Romão, *Supramol. Chem.* **2002**, *14*, 359–366; e) S. S. Braga, F. A. Almeida Paz, M. Pillinger, J. D. Seixas, C. C. Romão, I. S. Gonçalves, *Eur. J. Inorg. Chem.* **2006**, 1662–1669.

[10] D. R. Alston, A. M. Z. Slawin, J. F. Stoddart, D. J. Williams, *Angew. Chem. Int. Ed. Engl.* **1985**, *24*, 786–787.

[11] L. Song, Q. Meng, X. You, *J. Organomet. Chem.* **1995**, *498*, C1–C5.

[12] A. Harada, K. Saeki, S. Takahashi, *Organometallics* **1989**, *8*, 730–733.

[13] S. S. Braga, S. Gago, J. D. Seixas, A. A. Valente, M. Pillinger, T. M. Santos, I. S. Gonçalves, C. C. Romão, *Inorg. Chim. Acta*, in press.

[14] S. S. Braga, I. S. Gonçalves, A. D. Lopes, M. Pillinger, J. Rocha, C. C. Romão, J. J. C. Teixeira-Dias, *J. Chem. Soc., Dalton Trans.* **2000**, 2964–2968.

[15] S. Lima, I. S. Gonçalves, P. Ribeiro-Claro, M. Pillinger, A. D. Lopes, P. Ferreira, J. J. C. Teixeira-Dias, J. Rocha, C. C. Romão, *Organometallics* **2001**, *20*, 2191–2197.

[16] a) T. Loftsson, M. E. Brewster, *J. Pharm. Sci.* **1996**, *85*, 1017–1025; b) R. A. Rajewski, V. J. Stella, *J. Pharm. Sci.* **1996**, *85*, 1142–1169.

[17] a) J. Markham, K. Menard, A. Cutler, *Inorg. Chem.* **1985**, *24*, 1581–1587; b) J. R. Ascenso, C. G. de Azevedo, I. S. Gonçalves, E. Herdtweck, D. S. Moreno, C. C. Romão, J. Zühlke, *Organometallics* **1994**, *13*, 429–431; c) J. R. Ascenso, C. G. de Azevedo, I. S. Gonçalves, E. Herdtweck, D. S. Moreno, M. Pessanha, C. C. Romão, *Organometallics* **1995**, *14*, 3901–3919.

[18] a) N. Begum, S. E. Kabir, G. M. G. Hossain, A. Rahman, E. Rosenberg, *Organometallics* **2005**, *24*, 266–271; b) C. M. Alvarez, M. A. Alvarez, M. E. Garcia, A. Ramos, M. A. Ruiz, M. Lanfranchi, A. Tiripicchio, *Organometallics* **2005**, *24*, 7–9; c) C. M. Alvarez, M. A. Alvarez, D. Garcia-Vivo, M. E. Garcia, M. A. Ruiz, D. Saez, L. R. Falvello, T. Soler, P. Herson, *Dalton Trans.* **2004**, 4168–4179; d) M. E. Garcia, V. Riera, M. A. Ruiz, D. Saez, J. Vaissermann, J. C. Jeffery, *J. Am. Chem. Soc.* **2002**, *124*, 14304–14305; e) I. P. Lorenz, S. von Beckerath, H. Noth, *Eur. J. Inorg. Chem.* **1998**, 645–650; f) M. Akita, K. Noda, Y. Takahashi, Y. Morooka, *Organometallics* **1995**, *14*, 5209–5220.

[19] A. J. Bridgeman, M. J. Mays, A. D. Woods, *Organometallics* **2001**, *20*, 2076–2087.

[20] P. Schollhammer, F. Y. Petillon, J. Talarmin, K. W. Muir, *Inorg. Chim. Acta* **1999**, *284*, 107–111.

[21] J. C. Fettinger, H.-B. Kraatz, R. Poli, E. A. Quadrelli, R. C. Torralba, *Organometallics* **1998**, *17*, 5767–5775.

[22] C. G. de Azevedo, M. J. Calhorda, M. Carrondo, A. R. Dias, M. T. Duarte, A. M. Galvão, C. A. Gamelas, I. S. Gonçalves, F. M. da Piedade, C. C. Romão, *J. Organomet. Chem.* **1997**, *544*, 257–276.

[23] A. Fries, M. Green, M. F. Mahon, T. D. McGrath, C. B. M. Nation, A. P. Walker, C. M. Woolhouse, *J. Chem. Soc., Dalton Trans.* **1996**, 4517–4532.

[24] C. Butters, N. Carr, R. J. Deeth, M. Green, S. M. Green, M. F. Mahon, *J. Chem. Soc., Dalton Trans.* **1996**, 2299–2308.

[25] J. C. Fettinger, D. W. Keogh, R. Poli, *J. Am. Chem. Soc.* **1996**, *118*, 3617–3625.

[26] G. R. Willey, T. J. Woodman, M. G. B. Drew, *J. Organomet. Chem.* **1996**, *510*, 213–217.

[27] H. Wadepohl, U. Arnold, H. Pritzkow, M. J. Calhorda, L. F. Veiros, *J. Organomet. Chem.* **1999**, *587*, 233–243.

 © 2006 Wiley-VCH Verlag GmbH & Co. KGaA, Weinheim 

[28] a) F. H. Allen, *Acta Crystallogr. Sect. B Struct. Sci.* **2002**, *58*, 380–388; b) F. H. Allen, W. D. S. Motherwell, *Acta Crystallogr. Sect. B Struct. Sci.* **2002**, *58*, 407–422.
[29] R. Poli, *J. Coord. Chem.* **1993**, *29*, 121–173.
[30] M. G. B. Drew, V. Felix, I. S. Gonçalves, F. E. Kühn, A. D. Lopes, C. C. Romão, *Polyhedron* **1998**, *17*, 1091–1102.
[31] W. Saenger, *Angew. Chem. Int. Ed. Engl.* **1980**, *19*, 344–362.
[32] a) M. J. Gidley, S. M. Bociek, *J. Am. Chem. Soc.* **1988**, *110*, 3820–3829; b) S. J. Heyes, N. J. Clayden, C. M. Dobson, *Carbohydr. Res.* **1992**, *233*, 1–14.
[33] R. P. Veregin, C. A. Fyfe, R. H. Marchessault, M. G. Tayler, *Carbohydr. Res.* **1987**, *160*, 41–56.
[34] L. Cunha-Silva, J. J. C. Teixeira-Dias, *New J. Chem.* **2005**, *29*, 1335–1341.
[35] G. R. Brown, M. R. Caira, L. R. Nassimbeni, B. van Oudtshoorn, *J. Inclusion Phenom. Macro. Chem.* **1996**, *26*, 281–294.
[36] a) M. J. Calhorda, A. R. Dias, *J. Organomet. Chem.* **1980**, *197*, 291–302; b) E. E. Bernarducci, P. K. Bharadwaj, R. A. Lalancette, K. Krogh-Jespersen, J. A. Potenza, H. J. Schugar, *Inorg. Chem.* **1983**, *22*, 3911–3920.
[37] T. Kottke, D. Stalke, *J. Appl. Crystallogr.* **1993**, *26*, 615–619.
[38] R. Hooft, *Collect: Data Collection Software*, Delft, The Netherlands, Nonius B. V., **1998**.
[39] Z. Otwinowski, W. Minor, in: *Methods in Enzymology*, Vol. 276 (Eds.: C. W. Carter Jr, R. M. Sweet), Academic Press, New York, **1997**, p. 307.
[40] a) R. H. Blessing, *Acta Crystallogr. Sect. A* **1995**, *51*, 33–38; b) R. H. Blessing, *J. Appl. Crystallogr.* **1997**, *30*, 421.
[41] G. M. Sheldrick, *SHELXS-97, Program for Crystal Structure Solution*, University of Göttingen, Germany, **1997**.
[42] G. M. Sheldrick, *SHELXL-97, Program for Crystal Structure Refinement*, University of Göttingen, Germany, **1997**.

Received: June 14, 2006
Published Online: September 18, 2006

 © 2006 Wiley-VCH Verlag GmbH & Co. KGaA, Weinheim 

DOI: 10.1002/ejic.200600576

# Uranium(IV) Complexes of Calix[5]arene

Lionel Salmon,[a] Pierre Thuéry,[a] and Michel Ephritikhine*[a]

**Keywords:** Uranium / Calix[5]arene / Calixarenes

The μ-oxo uranium(V) compound $[Hpy]_2[\{U(calix[5]arene–5H)\}_2(\mu_2\text{-}O)]\cdot 4py$ (**1**·4py) was the sole product isolated from the reaction of $UCl_4$ and calix[5]arene unless the last traces of water were eliminated by thoroughly drying the macrocyclic molecule; under such strictly anhydrous conditions, the binuclear $U^{IV}$ complex $[Hpy]_3[U_2(calix[5]arene–5H)Cl_6]\cdot 4py$ (**2**·4py) was obtained. Treatment of $U(OTf)_3$ or $U(OTf)_4$ (OTf = $OSO_2CF_3$) with calix[5]arene gave the dimeric $U^{IV}$ complex $[U(calix[5]arene–4H)(py)]_2\cdot 4py$ (**3**·4py); compound **3** was also formed when no precautions were taken to avoid the presence of traces of water, together with compound **1**. The crystal structures of the complexes were determined.
(© Wiley-VCH Verlag GmbH & Co. KGaA, 69451 Weinheim, Germany, 2006)

## Introduction

We have recently reported on the synthesis and X-ray crystal structures of uranium(IV) complexes with calixarene ligands resulting from reactions of $UCl_4$ with calix[*n*]arenes (*n* = 4, 6 and 8),[1] and of $UX_4$ [X = Cl, MeCOCHCOMe (acac) and $OSO_2CF_3$ (OTf)] or $U(OTf)_3$ with the *O*-dimethylated *p*-*tert*-butylcalix[4]arene ($Me_2$-*t*Bucalix[4]arene).[2] As also outlined in the case of the preparation of the chloride-bridged trimeric complex $[\{U(Me_2\text{-}t\text{Bucalix[4]arene–2H})(\mu\text{-}Cl)_2\}_3]$,[3] the successful isolation of these compounds was critically dependent on the reaction conditions; in particular, the elimination of adventitious traces of water was of major importance to avoid the oxidation of the $U^{IV}$ ion. These difficulties explain why the first attempts to prepare uranium(IV) calixarene compounds by treatment of $UCl_4$ with *p*-*tert*-butylcalix[*n*]arenes (*n* = 4, 5, 6) resulted in the formation of a trinuclear, $\mu_3$-oxo-centred $[U^{VI}_2U^V]$ complex for *n* = 4, dinuclear, $\mu_2$-oxo-centred $U^V$ or $U^{VI}$ complexes for *n* = 5 and a mononuclear $U^{VI}$ homoleptic alkoxide complex for *n* = 6.[4] We encountered the same problems when we studied the reactions of $UX_4$ with calix[5]arene. These reactions seemed to be of special interest to us because metal complexes of calix[5]arene derivatives are rather scarce. A search of the Cambridge Structural Database (CSD, Version 5.27)[5] indicates that only six metal complexes of simple R-calix[5]arene (R = H, *tert*-butyl) have been crystallographically characterised.[4,6–9] Concerning the 5f-element compounds, apart from the binuclear $U^V$ and $U^{VI}$ derivatives cited above,[4] the mononuclear uranyl complex $[HNEt_3]_2[UO_2(p\text{-}tert\text{-butylcalix[5]arene–4H})]$ has also been described.[8] Here we present the synthesis and X-ray crystal structures of the $U^{IV}$ and $U^V$ compounds, which were obtained from reactions of $UX_4$ (X = Cl, OTf) with calix[5]arene.

[a] Service de Chimie Moléculaire, DSM, DRECAM, CNRS URA 331, CEA Saclay,
Bâtiment 125, 91191 Gif-sur-Yvette, France
E-mail: salmon@drecam.cea.fr
pierre.thuery@cea.fr
ephri@drecam.cea.fr

## Results and Discussion

Reaction of $UCl_4$ with 1 molar equiv. of commercial calix[5]arene in pyridine at 20 °C afforded dark orange crystals of the μ-oxo uranium(V) compound $[Hpy]_2[\{U(calix[5]arene–5H)\}_2(\mu_2\text{-}O)]\cdot 4py$ (**1**·4py) in 63% yield. The synthesis of **1** is reminiscent of that of $[Hpy]_2[\{U(p\text{-}tert\text{-butylcalix[5]arene–5H)}\}_2(\mu_2\text{-}O)]$ from $UCl_4$ and *p*-*tert*-butylcalix[5]arene.[4] The crystal structures of both compounds are quite similar and do not merit further discussion; a view of **1** is shown in Figure 1, and selected bond lengths and angles are listed in Table 1.

As the $U^{IV} \rightarrow U^V$ oxidation during the formation of **1** likely resulted from the presence of water in the reaction mixture, it was suspected that commercial calix[5]arene was not anhydrous, and it was heated under vacuum at 130 °C for 1 d, but this had no effect on the course of the reaction. However, the TGA-DTA analysis of this macrocycle revealed a gradual endothermic process between 120 and 210 °C, with a weight loss of 0.9%, which would correspond to the release of half an included water molecule per calix[5]arene. Final drying of the latter was achieved by leaving a pyridine solution on molecular sieves (4 Å) for 5 d; the colourless solution turned pale blue and the $^1H$ NMR signal of the hydroxy protons shifted from $\delta$ = 10.57 to 13.75. Addition of 2 molar equiv. of $UCl_4$ into the anhydrous solution of calix[5]arene gave a green solution, which slowly deposited light green crystals of the uranium(IV) compound $[Hpy]_3[U_2(calix[5]arene–5H)Cl_6]\cdot 4py$ (**2**·4py) in 24% yield.

 © 2006 Wiley-VCH Verlag GmbH & Co. KGaA, Weinheim InterScience 

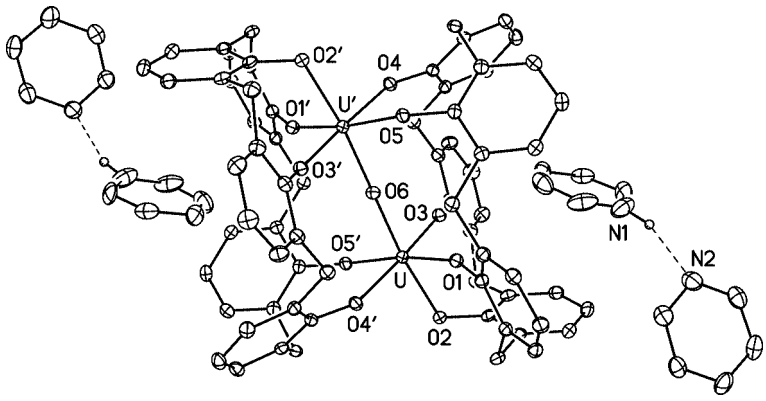


Figure 1. View of complex **1**·4py with displacement ellipsoids drawn at the 30% probability level; two solvent pyridine molecules and hydrogen atoms not involved in hydrogen bonds have been omitted; hydrogen bonds are shown as dashed lines; symmetry code: *–x*, 1 – *y*, *–z*.

Table 1. Selected bond lengths [Å] and angles [°] in compounds **1**–**3**.

| | | | | |
|---|---|---|---|---|
| **1**·4py | U–O1 | 2.157(2) | U–O1–C2 | 156.9(2) |
| | U–O2 | 2.171(2) | U–O2–C9 | 118.52(19) |
| | U–O3 | 2.149(2) | U–O3–C16 | 157.0(2) |
| | U–O4′ | 2.126(2) | U′–O4–C23 | 154.8(2) |
| | U–O5′ | 2.172(2) | U′–O5–C30 | 147.6(2) |
| | U–O6 | 2.08482(12) | | |
| | symmetry code: *–x*, 1 – *y*, *–z* | | | |
| **2**·4py | U1–O1 | 2.140(7) | U1–O1–C2 | 158.4(7) |
| | U1–O2 | 2.144(8) | U1–O2–C9 | 119.3(7) |
| | U1–O3 | 2.177(7) | U1–O3–C16 | 155.5(7) |
| | U1–Cl1 | 2.793(3) | | |
| | U1–Cl2 | 2.693(3) | | |
| | U1–Cl3 | 2.693(3) | | |
| | U2–O4 | 2.110(8) | U2–O4–C23 | 158.7(7) |
| | U2–O5 | 2.107(7) | U2–O5–C30 | 152.3(7) |
| | U2–Cl1 | 2.812(3) | | |
| | U2–Cl4 | 2.679(3) | U1···U2 | 5.2862(8) |
| | U2–Cl5 | 2.650(4) | | |
| | U2–Cl6 | 2.670(3) | | |
| **3**·4py | U–O1 | 2.169(2) | U–O1–C2 | 177.4(2) |
| | U–O2 | 2.671(2) | U–O2–C9 | 97.56(19) |
| | U–O3 | 2.149(2) | U′–O2–C9 | 156.8(2) |
| | U–O4 | 2.239(2) | U–O3–C16 | 172.5(2) |
| | U–O5 | 2.674(2) | U–O4–C23 | 132.9(2) |
| | U–O2′ | 2.222(2) | U–O5–C30 | 107.63(19) |
| | U–N1 | 2.573(3) | U–O2–U′ | 105.46(8) |
| | symmetry code: 2 – *x*, 1 – *y*, 2 – *z* | | | |

The trianionic complex, shown in Figure 2, represents a unique example of two metal atoms bound to a single calix[5]arene ligand. The structure shows a pseudosymmetry plane, which contains the U1, U2, O2, Cl1 and Cl5 atoms, with an rms deviation of 0.027 Å. Both uranium atoms are in six-coordinate environments with *fac*-$O_3Cl_3$ and *cis*-$O_2Cl_4$ octahedral geometry for U1 and U2, respectively. The five donor atoms of the calixarene define a mean $O_5$ plane with an rms deviation of 0.155 Å and the uranium atoms are located 1.125(4) (U1) and 1.626(6) Å (U2) from this mean plane. The macrocycle is in the distorted cone conformation, with dihedral angles between the four aromatic rings and the $O_5$ mean plane of 25.2(2), 87.4(3), 23.3(3), 73.1(3) and 82.9(3)°. These values, with two smaller angles corresponding to aromatic rings almost parallel to the $O_5$ plane, are analogous to those encountered in compound **1**. The mean values of the U–Cl (terminal) and U–$O_{phenoxy}$ bond lengths of 2.677(16) and 2.14(3) Å, respectively, are comparable to those measured in the other uranium(IV) complexes with calix[*n*]arenes (*n* = 4, 6, 8) previously reported.[1,2] The uranium atoms are further bonded to the bridging chlorine atom Cl1, with a U1–Cl1–U2 angle of 141.13(10)°, and they are at a distance of 5.2862(8) Å from one another. The charge of the trianionic complex is balanced by those of three pyridinium ions hydrogen bonded to three pyridine molecules [N1···N2 2.659(17) Å, N3···N4 2.665(10) Å, N5···N6 2.683(17) Å]. The pyridine molecule (or pyridinium ion) containing N3 is further encapsulated in the calixarene cavity, in which it is held by a π–π stacking interaction with the aromatic ring bearing O4 [centroid···centroid distance 3.69 Å, dihedral angle 13°, centroid offset 0.72 Å].

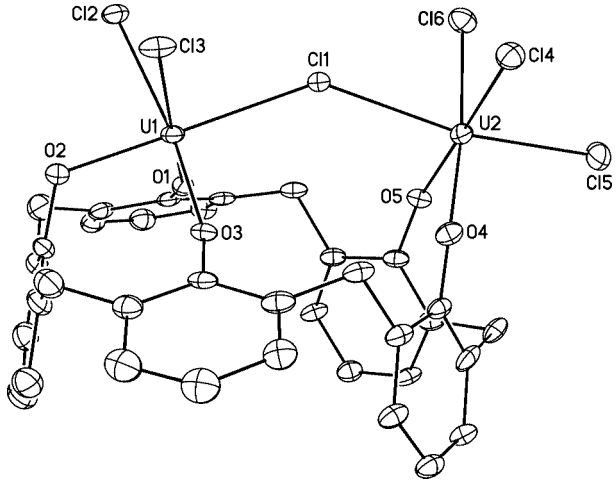


Figure 2. View of the trianion in complex **2**·4py with displacement ellipsoids drawn at the 15% probability level; hydrogen atoms have been omitted.

No reaction was observed between $U(acac)_4$ (acac = MeCOCHCOMe) and calix[5]arene in refluxing THF or pyridine while treatment of $U(acac)_4$ with the sodium salt of the macrocycle led to the sluggish formation of intractable

 © 2006 Wiley-VCH Verlag GmbH & Co. KGaA, Weinheim 

products. The lesser reactivity of $U(acac)_4$ with respect to $UCl_4$ was previously noted with the other calix[*n*]arenes (*n* = 4, 6, 8).[1]

Treatment of $U(OTf)_3$ with commercial calix[5]arene gave a mixture of red crystals of **1**·4py and green crystals of the dimeric complex $[U(calix[5]arene–4H)(py)]_2$·4py (**3**·4py). The latter was obtained from the reactions of $U(OTf)_3$ or $U(OTf)_4$ with the thoroughly dried macrocycle but was contaminated with a brown powder of an unidentified compound. Complex **3** could not be isolated in analytical purity because of its insolubility in organic solvents, a problem which was also encountered with most of the uranium(IV) compounds of calix[*n*]arenes (*n* = 4, 6, 8).[1] The formation of **3** from $U(OTf)_3$ implies oxidation of the uranium(III) centre, as in the case of the synthesis of a bis-calixarene $U^{IV}$ complex by treatment of $U(OTf)_3$ with *O*-dimethylated *p-tert*-butylcalix[4]arene.[2] Such oxidation reactions of trivalent uranium complexes by alcohols and phenols were assumed to proceed either by initial proton transfer followed by a valence disproportionation step,[10] or by the direct oxidation of uranium(III) with concomitant evolution of dihydrogen.[11] All the triflate ligands of $U(OTf)_3$ or $U(OTf)_4$ have been substituted by the phenoxide groups of the macrocycle, contrary to the chloride ligands of $UCl_4$, a difference which has already been noted with the reactions of $UX_4$ (X = Cl, OTf) and other calixarenes,[1,2] and which reflects the lesser coordinating ability of the triflate ligand.

A view of the centrosymmetric complex **3** is shown in Figure 3. The uranium atom is bound to five oxygen atoms from one calixarene, one oxygen atom from the second (O2′) and the nitrogen atom of the pyridine molecule. The resulting seven-coordinate uranium environment is pentagonal bipyramidal with the N1 and O2′ atoms in apical positions. The uranium atom is located 0.0354(11) Å from the $O_5$ mean plane defined by the five oxygen atoms of the ligand (rms deviation 0.313 Å) and is thus close to the centre of the $O_5$ coordination site, like the uranyl ion in the mononuclear complex $[HNEt_3]_2[UO_2$(*p-tert*-butylcalix[5]arene–4H)]. In this respect, complex **3** contrasts with complex **1** and the $U^V$ and $U^{VI}$ complexes with the same stoichiometry previously reported,[4] in which the two metal centres are bound to only two or three phenoxide groups from each calixarene and are located outside the lower rim array. Among the U–O bond lengths, those corresponding to the bridging atom O2 are dissymmetric and larger than the other ones, as well as that associated to atom O5, which is the protonated group (Table 1). The average value for the other bond lengths, 2.19(5) Å, is larger by 0.06 Å than the average value of the $U–O_{phenoxy}$ distances measured in uranium(IV) complexes of calixarenes.[1] Such an increase in the U–O bond length has already been observed in the $[U(Me_2calix)(H_2calix)]$ complex ($Me_2calix$ = *O*-dimethylated *p-tert*-butylcalix[4]arene) and has been attributed to the steric effects generated by the sandwich arrangement.[2] The hydroxy group is involved in a hydrogen bond with the pyridine molecule [O5···N2 2.626(4) Å, O5–H5···N2 157°]. While the uncomplexed calix[5]arene[12] and *p-tert*-butylcalix[5]arene[13] adopt shallow cone conformations, as well as the uranyl complex of *p-tert*-butylcalix[5]arene,[8] the dissymmetric coordination to two metal ions and the presence of an intermolecular hydrogen bond in **3** result in some distortion of the cone geometry; the two phenolic rings associated with metal bridging and hydrogen bonding are more tilted with respect to the $O_5$ mean plane [dihedral angles 12.5(2), 80.93(8), 15.9(2), 53.26(7) and 72.85(8)° for the rings bearing O1–O5, respectively]. This conformation differs from that encountered in the similar dimeric europium complex $[Eu($*p-tert*-butylcalix[5]arene–3H)$(dmso)_2]_2$, which has been described as a distorted 1,2-partial cone conformation.[7]

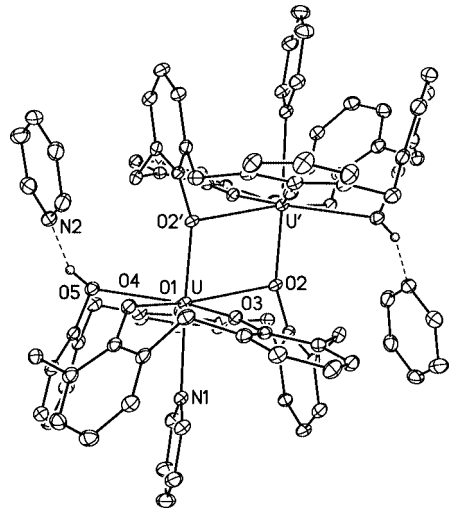


Figure 3. View of complex **3**·4py with displacement ellipsoids drawn at the 30% probability level; two solvent pyridine molecules and hydrogen atoms not involved in hydrogen bonds have been omitted; hydrogen bonds are shown as dashed lines; symmetry code: $2 - x$, $1 - y$, $2 - z$.

## Conclusions

Reactions of $UCl_4$ and $U(OTf)_4$ with calix[5]arene emphasise the extreme sensitivity of uranium(IV) calixarene complexes towards adventitious traces of water and oxygen and their easy oxidation into uranium(V) derivatives. The crystal structure of **2**·4py reveals a novel coordination mode of the calix[5]arene ligand, which was found to be able to accommodate two metal atoms as large as uranium.

## Experimental Section

**General:** All experiments were carried out under argon (<5 ppm oxygen or water) using standard Schlenk-vessel and vacuum-line techniques or in a glovebox. Solvents were dried by standard methods and distilled immediately before use. The $^1H$ NMR spectra were recorded with a Bruker DPX 200 instrument and referenced internally using the residual solvent $^1H$ resonances relative to tetramethylsilane ($\delta$ = 0 ppm). Elemental analyses were performed by Analytische Laboratorien at Lindlar (Germany). Calix[5]arene was purchased from Acros Organics; the TGA-DTA analysis was performed in dry air flow using a SETARAM TGDTA92 analyser; the temperature was increased from ambient to 300 °C applying

 © 2006 Wiley-VCH Verlag GmbH & Co. KGaA, Weinheim 

heating rates of 10 °C min$^{-1}$. $UCl_4$,[14] $U(OTf)_3$ and $U(OTf)_4$[15] were prepared by published methods.

**Crystals of $[Hpy]_2[\{U(calix[5]arene–5H)\}_2(\mu_2\text{-}O)]\cdot 4py$ (1·4py):** A flask was charged with $UCl_4$ (7.2 mg, 0.0188 mmol) and commercial calix[5]arene (10 mg, 0.0188 mmol) in pyridine (0.5 mL). The solution immediately turned orange and dark orange crystals of **1**·4py were deposited after 1 d at room temperature (11 mg, 63%).

**Synthesis of $[Hpy]_3[U_2(calix[5]arene–5H)Cl_6]\cdot 4py$ (2·4py):** Commercial calix[5]arene (50 mg, 0.094 mmol) was dried in pyridine (10 mL) with molecular sieves (4 Å) for 5 d and $UCl_4$ (71 mg, 0.188 mmol) was then added to the solution. After 5 d at 20 °C, the light green crystals of **2**·4py were filtered off and dried under vacuum (38 mg, 24%). $^1$H NMR (200 MHz, [D$_5$]pyridine, 23 °C): $\delta$ = –0.71 and 0.57 (2×2 H, –CH$_2$–), 1.16 (1 H, –CH$_2$–), 1.27 (2 H, –CH$_2$–), 4.46 (1 H, –CH$_2$–), 4.96 (2 H, –CH$_2$–), 7.43 (1 H, aromatic H), 8.51, 9.70, 11.95, 12.97, 13.22, 15.48 and 16.08 (7×2 H, aromatic H) ppm. The elemental analyses were in agreement with the formula $[Hpy]_3[U_2(calix[5]arene–5H)Cl_6]\cdot 3py$. $C_{65}H_{58}Cl_6N_6O_5U_2$ (1691): calcd. C 45.8, H 3.5, N 4.4; found C 46.1, H 3.4, N 4.3.

**Reaction of $U(OTf)_3$ with Calix[5]arene:** An NMR tube was charged with $U(OTf)_3$ (12.9 mg, 0.019 mmol) and commercial calix[5]arene (10 mg, 0.019 mmol) in pyridine (0.5 mL). After 12 h at 20 °C, dark orange crystals of **1**·4py and light green crystals of $[U(calix[5]arene–4H)(py)]_2\cdot 4py$ (**3**·4py) were deposited.

**Reaction of $U(OTf)_4$ with Calix[5]arene:** Commercial calix[5]arene (50 mg, 0.094 mmol) was dried in pyridine (10 mL) with molecular sieves (4 Å) for 5 d and $U(OTf)_4$ (78.7 mg, 0.094 mmol) was then added to the solution. After 5 d at 20 °C, green crystals of **3**·4py contaminated with a brown powder were deposited (35 mg, about 40%). Compound **3**·4py was identified by X-ray diffraction analysis but could not be characterised by $^1$H NMR because of its insolubility.

**X-ray Crystallography:** The data were collected at 100(2) K on a Nonius Kappa-CCD area detector diffractometer using graphite-monochromated Mo-$K_\alpha$ radiation ($\lambda$ = 0.71073 Å). The crystals were introduced into glass capillaries with a protecting "Paratone-N" oil (Hampton Research) coating. The unit cell parameters were determined from ten frames, then refined on all data. The data ($\varphi$- and $\omega$-scans)[16] were processed with HKL2000.[17] The structures were solved by direct methods or Patterson map interpretation with SHELXS-97 and subsequent Fourier-difference synthesis and refined by full-matrix least-squares on $F^2$ with SHELXL-97.[18] Absorption effects were corrected empirically with the program DELABS in PLATON[19] or with SCALEPACK.[17] All non-hydrogen atoms were refined with anisotropic displacement parameters. The hydrogen atoms bound to N1 in **1**·4py and O5 in **3**·4py were found on Fourier-difference maps, but those bound to N atoms in **2**·4py were not found or introduced. All the other hydrogen atoms were introduced at calculated positions. All were treated as riding atoms with an isotropic displacement parameter equal to 1.2 times that of the parent atom. In **2**·4py, one pyridine molecule (containing N7) was affected with a 0.5 occupancy parameter so as to retain acceptable displacement parameters and four solvent pyridine molecules or pyridinium ions, being badly resolved, were refined as idealised hexagons; restraints on displacement parameters had to be applied for the atoms of some pyridine molecules or pyridinium ions. Crystal data and structure refinement details are given in Table 2. The molecular plots were drawn with SHELXTL.[20]

Table 2. Crystal data and structure refinement details.

| | **1**·4py | **2**·4py | **3**·4py |
|---|---|---|---|
| Empirical formula | $C_{100}H_{82}N_6O_{11}U_2$ | $C_{70}H_{63}Cl_6N_7O_5U_2$ | $C_{100}H_{82}N_6O_{10}U_2$ |
| $M$ [g mol$^{-1}$] | 2019.78 | 1771.03 | 2003.78 |
| Crystal system | monoclinic | orthorhombic | monoclinic |
| Space group | $P2_1/n$ | $Pbcn$ | $P2_1/c$ |
| $a$ [Å] | 15.3242(3) | 28.255(2) | 13.6891(4) |
| $b$ [Å] | 15.6437(4) | 22.0276(13) | 16.1392(4) |
| $c$ [Å] | 16.9848(4) | 22.5201(10) | 18.7131(7) |
| $\beta$ [°] | 106.932(2) | 90 | 106.4533(12) |
| $V$ [Å$^3$] | 3895.21(16) | 14016.3(14) | 3965.0(2) |
| $Z$ | 2 | 8 | 2 |
| $\rho_{calcd.}$ [g cm$^{-3}$] | 1.722 | 1.679 | 1.678 |
| $\mu$ (Mo-$K_\alpha$) [mm$^{-1}$] | 4.224 | 4.898 | 4.148 |
| $F$(000) | 1992 | 6864 | 1976 |
| Data collected | 25458 | 212113 | 128725 |
| Unique data | 7300 | 13221 | 7524 |
| Observed data[a] | 6339 | 7607 | 6624 |
| $R_{int}$ | 0.045 | 0.062 | 0.044 |
| Parameters | 538 | 791 | 532 |
| $R_1$ | 0.025 | 0.069 | 0.026 |
| $wR_2$ | 0.055 | 0.199 | 0.071 |
| $S$ | 1.017 | 0.999 | 1.039 |
| $\Delta\rho_{min}$ [e Å$^{-3}$] | –0.62 | –1.32 | –1.40 |
| $\Delta\rho_{max}$ [e Å$^{-3}$] | 0.89 | 2.11 | 1.09 |

[a] $I > 2\sigma(I)$.

CCDC-610617 and -610619 contain the supplementary crystallographic data for this paper. These data can be obtained free of charge from The Cambridge Crystallographic Data Centre via www.ccdc.cam.ac.uk/data_request/cif.

## Acknowledgments

We thank Jean-François Meunier (Laboratoire de Chimie de Coordination, CNRS UPR 8241, Toulouse) for the TGA-DTA analysis.

[1] a) L. Salmon, P. Thuéry, M. Ephritikhine, *Chem. Commun.* **2006**, 856–858; b) L. Salmon, P. Thuéry, M. Ephritikhine, *Dalton Trans.* **2006**, 3629–3637.
[2] L. Salmon, P. Thuéry, Z. Asfari, M. Ephritikhine, *Dalton Trans.* **2006**, 3006–3014.
[3] J. Old, A. A. Danopoulos, S. Winston, *New J. Chem.* **2003**, *27*, 672–674.
[4] P. C. Leverd, M. Nierlich, *Eur. J. Inorg. Chem.* **2000**, 1733–1738.
[5] F. H. Allen, *Acta Crystallogr., Sect. B: Struct. Sci.* **2002**, *58*, 380–388.
[6] A. J. Petrella, N. K. Roberts, D. C. Craig, C. L. Raston, R. N. Lamb, *Chem. Commun.* **2003**, 1728–1729.
[7] L. J. Charbonnière, C. Balsiger, K. J. Schenk, J. C. G. Bünzli, *J. Chem. Soc., Dalton Trans.* **1998**, 505–510.
[8] P. Thuéry, M. Nierlich, *J. Inclusion Phenom. Macrocyclic Chem.* **1997**, *27*, 13–20.
[9] J. W. Steed, C. P. Johnson, R. K. Juneja, J. L. Atwood, R. S. Burkhalter, *Supramol. Chem.* **1996**, *6*, 235–238.
[10] S. D. Stults, R. A. Andersen, A. Zalkin, *Organometallics* **1990**, *9*, 1623–1629.
[11] a) L. Karmazin, M. Mazzanti, J. Pécaut, *Inorg. Chem.* **2003**, *42*, 5900–5908; b) D. L. Clark, A. P. Sattelberger, W. G. Van der Sluys, J. G. Watkin, *J. Alloys Compd.* **1992**, *180*, 303–315.
[12] M. Coruzzi, G. D. Andreetti, V. Bocchi, A. Pochini, R. Ungaro, *J. Chem. Soc., Perkin Trans. 2* **1982**, 1133–1138.
[13] J. F. Gallagher, G. Ferguson, V. Böhmer, D. Kraft, *Acta Crystallogr., Sect. C: Cryst. Struct. Commun.* **1994**, *50*, 73–77.

 © 2006 Wiley-VCH Verlag GmbH & Co. KGaA, Weinheim 

[14] J. A. Hermann, J. F. Suttle, *Inorg. Synth.* **1957**, *5*, 143–145.
[15] J. C. Berthet, M. Lance, M. Nierlich, M. Ephritikhine, *Eur. J. Inorg. Chem.* **1999**, 2005–2007.
[16] R. Hooft, *COLLECT*, Nonius BV, Delft, The Netherlands, **1998**.
[17] Z. Otwinowski, W. Minor, *Methods Enzymol.* **1997**, *276*, 307–326.
[18] G. M. Sheldrick, *SHELXS-97* and *SHELXL-97*, University of Göttingen, Germany, **1997**.
[19] A. L. Spek, *PLATON*, University of Utrecht, The Netherlands, **2000**.
[20] G. M. Sheldrick, *SHELXTL*, Version 5.1, Bruker AXS Inc., Madison, WI, USA, **1999**.

Received: June 20, 2006
Published Online: August 24, 2006

 © 2006 Wiley-VCH Verlag GmbH & Co. KGaA, Weinheim 

DOI: 10.1002/ejic.200600668

# Nonlinear, Resonance-Stabilized Pseudohalides: From Alkali Methanides to Ionic Liquids of Methanides

**Harald Brand,[a] Joel F. Liebman,[b] Axel Schulz,*[a] Peter Mayer,[a] and Alexander Villinger[a]**

*Dedicated to Professor Dr. Karl Otto Christe on the occasion of his 70th birthday*

**Keywords:** Ionic liquid / Methanides / Pseudohalides / Resonance / X-ray structure elucidation

New 1-ethyl-3-methylimidazolium (EMI) salts [EMI][X] (X = $[HC(NO_2)(CN)]^-$, $[C(NO_2)(NO)(CN)]^-$, $[HC(NO)_2]^-$ and $[HC(NO_2)_2]^-$) and 1-*n*-butyl-3-methylimidazolium (BMI) salts [BMI][Y] (Y = $[C(CN)_3]^-$ and $[C(NO_2)(NO)(CN)]^-$) were prepared and characterized. Different synthetic routes to these new resonance-stabilized methanide-based ionic liquids starting either from the explosive silver salts (except from $Ag[C(CN)_3]$) or the easily accessible potassium salts have been described. The melting points of all new salts are lower than 100 °C, in fact, most of them are ionic liquids at room temperature. These strongly colored ionic liquids (besides $[BMI][C(CN)_3]$ which is colorless) are neither heat nor shock sensitive, are thermally stable up to over 52 °C ($[EMI][C(NO_2)(NO)(CN)]$) and 270 °C ($[BMI][C(CN)_3]$) and can be prepared in large quantities. The structure and bonding of resonance-stabilized methanides ($[CR^1R^2R^3]^-$ with $R^{1,2,3}$ = H, $NO_2$, NO, and CN) is discussed on the basis of experimental and theoretical data. X-ray data of $Cs^+[HC(NO_2)(CN)]^-$, $K^+[HC(NO_2)_2]^-$, $[EMI]^+[C(NO_2)(NO)(CN)]^-$, and $[Me_4N]^+[C(NO_2)(NO)(CN)]^-$ reveal almost planar anions with strong cation···anion interactions in the alkali methanides resulting in three-dimensional network structures in the solid state. Only weak interionic interactions are found for the ammonium salts. As shown by different theoretical approaches (charge transfer, resonance energies and NLMO delocalization) resonance effects occur in all three classes of methanides ($NO_2$-, NO-, and CN-substituted), however, the magnitude of such effect strongly differs depending on the degree of substitution.

(© Wiley-VCH Verlag GmbH & Co. KGaA, 69451 Weinheim, Germany, 2006)

## Introduction

The term *pseudohalogen* was first introduced by Lothar Birckenbach[1a] in 1925 and further developed and justified in a series of papers in the following years.[1b–1d] The anions $CN^-$, $CNO^-$, $N_3^-$, $OCN^-$, and $SCN^-$ can be coined *classical linear pseudohalides*. A small species can be classified as a classical pseudohalogen when it fulfills the following criteria with respect to a halogen-like chemical behavior:[2,3] A pseudohalogen (X) forms (i) a strongly bound (linear) univalent radical ($X^{\cdot}$), (ii) a singly charged anion ($X^-$), (iii) a pseudohalogen hydrogen acid of the type HX, (iv) salts of the type $M(X)_n$ with silver, lead and mercuric salts of low solubility, (v) a neutral dipseudohalogen compound (X–X) which disproportionates in water and can be added to double bonds, and (vi) interpseudohalogen species (X–Y). However, not all criteria are always met. While many linear pseudohalogens (e.g. CN, OCN, CNO, $N_3$, SCN) are known, often the corresponding pseudohalide acids, dipseudohalogens, and interpseudohalogens are thermodynamically highly unstable (e.g. $HN_3$, OCN–NCO, NC–SCN) with respect to $N_2$/CO elimination or polymerization or indeed, remain unknown (e.g. $N_3$–$N_3$).

Starting from the binary non-metal hydrides $CH_4$, $NH_3$, $H_2O$ etc. a simple approach can be utilized to derive the hydrogen acids of the classical linear pseudohalides by combining or substituting isolobal (e.g. HC≡/≡N in HCN, HN=/=N=N in $HN_3$, HO–/–CN in HOCN), isosteric (e.g. $N_2$/CO in $HN_3$/HNCO) or isovalence electronic fragments (e.g. CO/CS in HOCN/HSCN).[2]

Nonlinear resonance-stabilized pseudohalides can be derived with the help of the Grimm hydride displacement law, a pseudoelement concept established as early as 1925.[4] This law describes the formation of a new pseudoelement $\cdot AH_n$ when *n* H (*n* = 1–4) atoms are formally added to the element A. The new complexes $\cdot AH_n$ (e.g. ·OH, $\cdot NH_2$ and $\cdot CH_3$) behave like pseudoatoms (in this case like halogens)

[a] Department Chemie und Biochemie, Ludwig-Maximilians-Universität München,
Butenandtstraße 5–13 (Haus F), 81377 München, Germany
E-mail: Axel.Schulz@cup.uni-muenchen.de
[b] Department of Chemistry and Biochemistry, University of Maryland, Baltimore County,
Baltimore, MD 21250, USA

Supporting information for this article is available on the WWW under http://www.eurjic.org or from the author.

 © 2006 Wiley-VCH Verlag GmbH & Co. KGaA, Weinheim 

similar to elements of the group *n* positions to the right in the Periodic Table (e.g. they form singly charged anions: $OH^-$, $NH_2^-$, and $CH_3^-$, or neutral dimers: HO–OH, $H_2N$–$NH_2$ and $H_3C$–$CH_3$). However, chemically there is a significant difference in the basicity between these pseudohalides and the halides as the latter represent only very weak bases while these pseudohalides are strong bases. Only the successive substitution of the hydrogen atoms in $\cdot CH_3$ ($CH_3^-$) and $\cdot NH_2$ ($NH_2^-$) by electron-withdrawing groups such as CN, NO, and $NO_2$, leads to the class of resonance-stabilized, nonlinear pseudohalogens (pseudohalides). Important is also the capability of the electron-withdrawing groups to delocalize the single p-AO-type lone pair (AO = atomic orbital) of the C and N atom in $CH_3$ ($CH_3^-$) and $\cdot NH_2$ ($NH_2^-$), respectively, to decrease the basicity into the range of the halides. A compilation of all resonance-stabilized methanides, $[CR^1R^2R^3]^-$ ($R^{1,2,3}$ = H, $NO_2$, NO, and CN), is displayed in Table S0 (see Supporting Information).

Generally, the synthesis of methanides starts from the free hydrogen acid which often is only generated in situ. Neutralization leads then to the according methanide salt. For instance malonodinitrile (Scheme 1, a)[5] is used to synthesize dicyanomethanides and tricyanomethanides (Scheme 1, b).[6] Nitrosation of malonodinitrile followed by a basic work up yields the nitrosodicyanomethanide, $[C(CN)_2(NO)]^-$, (Scheme 1, c).[7] Oxidation of the nitrosodicyanomethanides with ammonium cerium(IV) nitrate results in the formation of nitrodicyanomethanide, $[C(CN)_2(NO_2)]^-$, (Scheme 1, d),[7c,8] rather than the formation of the dimeric hexasubstituted ethane by radical coupling reactions. In the section "Results and Discussion" the following abbreviations are used: Nt = nitro, N = nitroso, C = cyano, M = methanide, combined with the multiplying prefixes D = di and T = tri; example: NtDCM = nitrodicyanomethanide (see Table S0 in the Supporting Information).

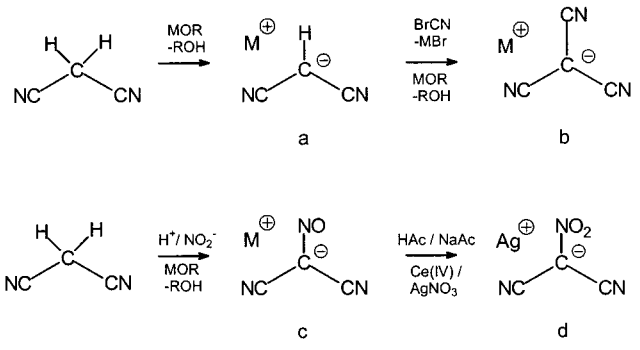


Scheme 1. Synthesis of dicyano, tricyano-, nitrosodicyano- and nitrodicyanomethanides.

Dinitromethanide (DNtM) can be prepared by nitration of barbituric acid followed by an alkaline work up procedure.[9] Access to trinitromethanides (TNtM) is possible by nitration of acetic anhydride followed by neutralization in the presence of sodium sulfite (Scheme 2).[10]

Recently, we have described the synthesis of the trisubstituted nitro(nitroso)cyanomethanides (NtNCM) and the disubstituted dinitrosomethanides (methylnitrosolates, DNM).[11,12] Nitro(nitroso)cyanomethanides can be generated by nitrosation of nitroacetonitrile followed by a basic work up, while treating formamidinium nitrate with hydroxylammonium nitrate and MO*t*Bu (M = alkali metal) in the presence of oxygen yields the deep blue alkali dinitrosomethanides.

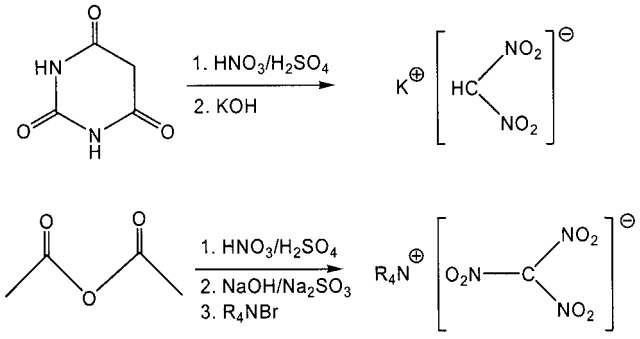


Scheme 2. Synthesis of dinitro- and trinitromethanides.

Herein, we want to report on the synthesis, structure and properties of new ionic liquids based on some resonance-stabilized methanides and alkali methanides as well as on the resonance-stabilization and bonding of these methanides $[CR^1R^2R^3]^-$ ($R^{1,2,3}$ = H, $NO_2$, NO, CN; as well as all permutations of $R^{1,2,3}$).

## Results and Discussion

### Synthesis of Methanide-Based Ionic Liquids

Ionic liquids of resonance-stabilized methanides can easily be prepared from the alkali salts utilizing the properties of a pseudohalogen.[2] The first synthetic step includes the formation of the nearly insoluble silver salts in water (AgX, X = methanide, Scheme 3). Because the silver salts dissolve in 2 N $NH_3$(aq.), adding ethyl(methyl)imidazolium bromide ($EMI^+Br^-$)[13] results in the formation of a water soluble ethyl(methyl)imidazolium methanide ($EMI^+X^-$) which can be separated from the AgBr precipitate by filtration. A specific drying procedure involving stepwise addition and removal of dried methanol, THF and dichloromethane followed by removing traces of water or solvent molecules in high vacuum (HV) is necessary to obtain pure ionic liquids of the type $EMI^+X^-$.

A different approach has been used in case of NtNCM-based ionic liquids because the silver salt, AgNtNCM, is reasonably soluble in water. For this reason KNtNCM was treated with $AgNO_3$ in a 1:1 mixture of methanol and ethanol yielding dissolved AgNtNCM and $KNO_3$ as a white precipitate. Then this AgNtNCM solution is treated by a solution of ethyl(methyl)imidazolium ($EMI^+Br^-$) or *n*-butyl(methyl)imidazolium bromide ($BMI^+Br^-$) in THF resulting in the formation of the ionic liquids $EMI^+NtNCM^-$ and $BMI^+NtNCM^-$, respectively, and a AgBr precipitate which can be separated by filtration. Again, a specific drying procedure is needed to isolate pure NtNCM-based ionic liquids (see Scheme 3).

 © 2006 Wiley-VCH Verlag GmbH & Co. KGaA, Weinheim 

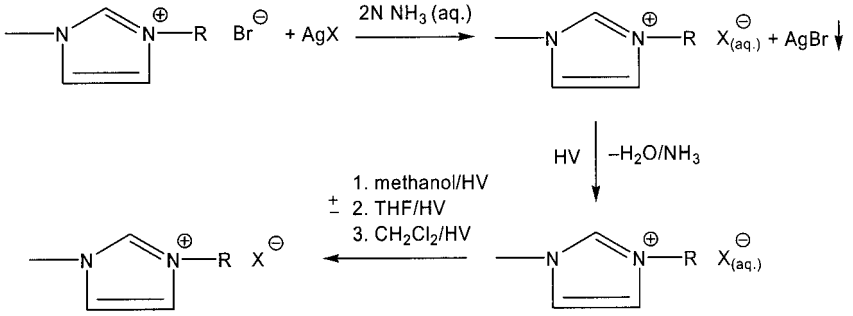


Scheme 3. Synthetic procedure for the isolation of pure, dry ionic liquids of resonance-stabilized methanides (R = Et, *n*Bu; X = methanide; HV = high vacuum, ± = addition and removal of solvent for several times).

An alternative route to ionic liquids of methanides avoiding the explosive silver salts (except from AgTCM) involves the use of imidazolium tetrafluoroborate salts (e.g. $EMI^+BF_4^-$). Because $KBF_4$ precipitates in a methanol/water solution, the reaction of potassium methanides with imidazolium tetrafluoroborate salts yields imidazolium methanides (e.g. $EMI^+X^-$) dissolved in methanol/water.

## Properties of Methanide-Based Ionic Liquids

In contrast to most of the high energy-density alkali and silver (NO- and $NO_2$-substituted) methanides,[11,12] the ionic liquids of methanides with a bulky organic cation are neither heat nor shock sensitive, and hence can be prepared and stored on a large scale. Nevertheless, this type of methanide-based ionic liquids can also be considered as "energetic ionic liquids" because the thermodynamically unstable methanide anion is only kinetically stabilized by the bulky organic cation such as $EMI^+$ or $BMI^+$.[14] Methanide-based ionic liquids are very hygroscopic and immediately absorb water when exposed to air. In the series of the alkali methanides it is mostly the lithium and sodium salts that are hygroscopic and to a much lesser extent are the heavy alkali salts (K, Cs).[11,12]

The decomposition temperature of methanide-based ionic liquids ranges, dependent on the counterion, between $T_{dec}$ = 52 °C [$EMI^+NNtCM^-$] and 270 °C [$BMI^+TCM^-$] (Table 1).[15] As expected, ionic liquids of methanides substituted solely by NO or by $NO_2$ are less stable compared to the pure cyanomethanide-based species. Furthermore, a slow decomposition of the NO- and $NO_2$-substituted methanides (both ionic liquids and alkali salts) is also observed when exposed to air.

Different decomposition reactions can be expected e.g. the oxidation or hydrolysis according to

$$HC(NO)_2^- + 1/2\ O_2 \rightarrow HC(NO)(NO_2)^- \rightarrow NO_2^- + HCNO$$

$$HC(NO)_2^- + H_2O \rightarrow HC(NO)NOH + OH^-$$

$$2\ HC(NO)NOH \rightarrow 2\ HCNO + H_2O + N_2O.$$

The formation of $N_2O$ was experimentally observed when traces of water were present. The decomposition of the free methylnitrosolic acid goes via a dimer. Dimerization of NO species is known for many NO compounds such as HNO and both alkyl and most aryl NO compounds.[16] Hence, NO- and $NO_2$-substituted methanide salts and ionic liquids should be stored under nitrogen at temperatures below –5 °C.

So far we have not been able to crystallize any of the discussed ionic liquids without solvent. Solidification resulted only in glass formation, a well-precedented phenomenon for ionic liquids.[17] However, storing saturated (e.g. ethanolic) solutions of ionic liquids at very low temperature often results in the formation of crystals suitable for single-crystal X-ray investigations (see section X-ray elucidation). The experimentally determined melting points varying between –48 °C ($BMI^+TCM^-$) and 48 °C ($EMI^+DNtM^-$) (Table 1), with the BMI salts always possessing the lower melting point. It can be assumed that both the number and the strength of interionic interactions (Coulomb and hydro-

Table 1. Properties of methanide-based ionic liquids [$RMI^+X^-$] (RMI = R organic group, M = methyl, I = imidazolium; X = resonance-stabilized methanide).

| Methanide | R | FW [g mol$^{-1}$] | $T_m/T_g$ [°C][a] | $T_{dec}$ [°C][a] | $\lambda_{max}$ [nm][b] | Color |
|---|---|---|---|---|---|---|
| TCM[13c] | ethyl | 201.2 | –11[13c] | 240[13c] | 211 | colorless[13c] |
| TCM | *n*-butyl | 229.3 | –48 | 270 | 211 | colorless |
| NtNCM | ethyl | 225.2 | 35 | 52 | 489 | red |
| NtNCM | *n*-butyl | 253.3 | –4 | 65 | 489 | red |
| NtCM | ethyl | 196.2 | 5 | 210 | 364 | brown |
| DNM | ethyl | 184.2 | –6 | 180 | 679 | blue-violet |
| DNtM | ethyl | 216.2 | 48 | 186 | 403 | yellow-orange |

[a] $T_m$ = melting point, $T_g$ = phase-transition temperature, $T_{dec}$ = decomposition onset temperature. [b] UV/Vis from water solution.

 © 2006 Wiley-VCH Verlag GmbH & Co. KGaA, Weinheim 

gen bonding) as well as the size of the ions is responsible for the fairly wide range of observed melting points (see section X-ray elucidation).

On the basis of the characteristic group frequencies [NO (1200–1600 $cm^{-1}$), $NO_2$ (1230–1580 $cm^{-1}$), and CN (2100–2290 $cm^{-1}$)] methanides of the type $[CR^1R^2R^3]^-$ ($R^{1,2,3}$ = H, $NO_2$, NO, CN) are easily identified by Raman and IR spectroscopy.[2,7,11,12] Interestingly, the wavenumber of the characteristic frequency increases with the degree of substitution (Table 3 and Table 4).

As expected, the $^{13}C$ NMR resonance of the methanide C atom strongly depends on the substitution pattern (Table 2). The resonance signal of the methanide C atom attached to a CN group is always observed at smaller $\delta^{13}C$ values compared to the resonance signal of methanide C atoms attached to $NO_2$ and NO groups displaying a stronger deshielded $^{13}C$ nucleus in the latter cases (TCM: $\delta^{13}C$ = 5.1 ppm, NtCM: $\delta^{13}C$ = 80.5 ppm, NtNCM: $\delta^{13}C$ = 149.6 ppm). This is in accord with the larger charge transfer and a smaller negative partial charge localized at the methanide C atom when attached to NO or $NO_2$ groups (see section on bonding). $^{14}N$ NMR spectroscopic data can also be utilized to distinguish between CN, NO and $NO_2$ (NO: broad resonances $\delta^{14}N$ = 250–330, $NO_2$: $\delta^{14}N$ = –25 to –10, CN: $\delta^{14}N$ = –130 to –100 ppm; Table 2).

Nitrosomethanides are deeply colored ionic liquids (NtNCM: dark red, DNM: dark blue), while nitromethanides display a yellow/brown color (DNtM/NtCM) and pure cyanomethanides are colorless (UV/Vis data, Table 2 and Table S4). The UV/Vis spectra of alkali methanide salts, $[CR^1R^2R^3]^-$ exhibit one very strong characteristic $\pi\rightarrow\pi^*$ transition in the non-visible range below 300 nm. However, the color arises from weak $n\rightarrow\pi^*$ HOMO–LUMO electronic transition in the anion, where the HOMO describes a lone pair which lies in the anion plane. A closer inspection of the orbital coefficients composing the HOMO in $[CR^1R^2(NO)]^-$ ($R^1$, $R^2$ = H, $NO_2$, CN) show the largest coefficients for the nitroso group; hence it can be concluded that the nitroso group is mainly responsible for the color in the NO-substituted methanides.[11] We recall that monomeric, neutral nitroso compounds are usually intensely colored while their nitro counterparts and nitriles are generally colorless. It can be assumed that in the mixed-substituted methanides the color is "dominated" by NO > $NO_2$ > CN. Moreover, the color of most alkali methanide salts darkens with increasing heaviness of the alkali-metal counterion which can be attributed to strong cation···anion interactions

Table 3. Calculated group frequencies in methanides (B3LYP/aug-cc-pvTZ).[a]

| R = | CN | NO | $NO_2$ |
|---|---|---|---|
| $H_2CR^-$ | 2138 (690) | 1357 (282)[b]<br>1212 (112)[b] | 1313 (op, 300)<br>1012 (ip, 45)[b] |
| $HCR_2^-$ | 2234 (ip, 87)<br>2185 (op, 955) | 1421 (ip, 0)<br>1315 (op, 827)[b] | 1493 (ip, 499)<br>1436 (op, 74)[b]<br>1343 (ip, 84)<br>1232 (op, 643)[b] |
| $CR_3^-$ | 2292 (ip, 0)<br>2238 (op, 487) | 1529 (ip, 19)<br>1461 (op, 224)<br>1616 (op, 509) | 1578 (as, 377)[c]<br>1507 (ip, 526)[d]<br>1424 (op, 24)[d]<br>1408 (s, 143)[c] |
| $C(CN)(NO)(NO_2)^-$ | 2291 (95) | 1421 (114) | 1503 (as, 326)<br>1193 (s, 3) |

[a] In parenthesis IR intensity in km/mol; ip = in-phase mode, op = out-of-phase mode. [b] Combination with $\delta$CH in-plane. [c] NO stretch of the non-planar arranged $NO_2$ group. [d] NO stretch of the planar arranged $NO_2$ groups.

Table 2. Spectroscopic data of methanide-based ionic liquids $[RMI^+X^-]$ (RMI = R organic group, M = methyl, I = imidazolium; X = resonance-stabilized methanide).

| Methanide | R | Raman[a] | $\delta^{13}C$[c] | $\delta^{14}N$[c] | $\delta^{1}H$[c] |
|---|---|---|---|---|---|
| TCM[b] | ethyl | $\nu_{CN}$ 2230, 2178 | *C*–CN, 5.1<br>C–*C*N, 121.0 | C–C*N*, –122 | – |
| TCM[b] | *n*-butyl | $\nu_{CN}$ 2210, 2166 | *C*–CN, 5.1<br>C–*C*N, 121.0 | C–C*N*, –122 | – |
| NtCM | ethyl | $\nu_{CH}$ 3114,<br>$\nu_{CN}$ 2192,<br>$\nu_{NO}$ 1454, 1340 | *C*–CN, 80.5<br>C–*C*N, 120.6 | C–*N*$O_2$, –14<br>C–C*N*, –117 | *H*–C–$NO_2$, 5.58 |
| NtNCM | ethyl | $\nu_{CN}$ 2211,<br>$\nu_{NO}$ 1495, 1458,<br>1346 | *C*–CN, 149.6<br>C–*C*N, 119.5 | C–*N*O, 265<br>C–*N*$O_2$, –15<br>C–C*N*, –107 | – |
| NtNCM | *n*-butyl | $\nu_{CN}$ 2209,<br>$\nu_{NO}$ 1490, 1458,<br>1340 | *C*–CN, 149.6<br>C–*C*N, 119.5 | C–*N*O, 265<br>C–*N*$O_2$, –15<br>C–C*N*, –107 | – |
| DNM | ethyl | $\nu_{CH}$ 2995 sh,<br>$\nu_{NO}$ 1402 | *C*–NO, 190.0 | C–*N*O, 332 | *H*–C–NO, 8.68 |
| DNtM | ethyl | $\nu_{CH}$ 3142,<br>$\nu_{NO}$ 1447, 1334 | *C*–$NO_2$, 121.7 | C–*N*$O_2$, –21 | *H*–C–$NO_2$, 8.17 |

[a] Only characteristic frequencies of the methanides are listed. [b] Cf. DCM: $\delta^1H$ = 3.38 (*H*–C); $\delta^{13}C$ = 130.6 (C–*C*N), –1.9 (*C*–CN); $\delta^{14}N$ = –135 (C*N*). [c] Only characteristic NMR shifts of the methanides are listed.[35]

 © 2006 Wiley-VCH Verlag GmbH & Co. KGaA, Weinheim 

resulting in small (but visually significant) changes of the HOMO–LUMO gap.[11]

### Structure of Resonance-Stabilized Methanides

Carbanions of the type $[H_2CR^1]^-$, $[HCR^1R^2]^-$, and $[CR^1R^2R^3]^-$ ($R^{1,2,3}$ = CN, NO, $NO_2$ and all possible permutations of $R^{1,2,3}$) can be considered to be resonance-stabilized, nonlinear pseudohalides. All experimentally known resonance-stabilized methanides are reported to be planar or nearly planar (Table S0). To get further inside into the structure and bonding of these anions DFT calculations at the B3LYP/aug-cc-pvTZ level of theory have been carried out (Table 3 and Figures 1 and 2).

While the parent ion, the methanide anion $H_3C^-$, adopts a pyramidal structure [$\Delta E_{planar–pyramidal}$ = 2.35 kcal/mol; $d$(CH) = 1.099 Å, <(HCH) = 109.7°; cf. $d$(CH) = 1.093 Å, <(HCH) = 109.6°],[18] substitution of one H atom by any of the R groups results in planar anions (Figure 1 and Figure 2) other than $H_2C–CN^-$ for which the non-planar $C_S$-symmetric structure is favored by only 0.03 kcal/mol indicating a very flat potential energy surface [cf. 0.15 kcal/mol,

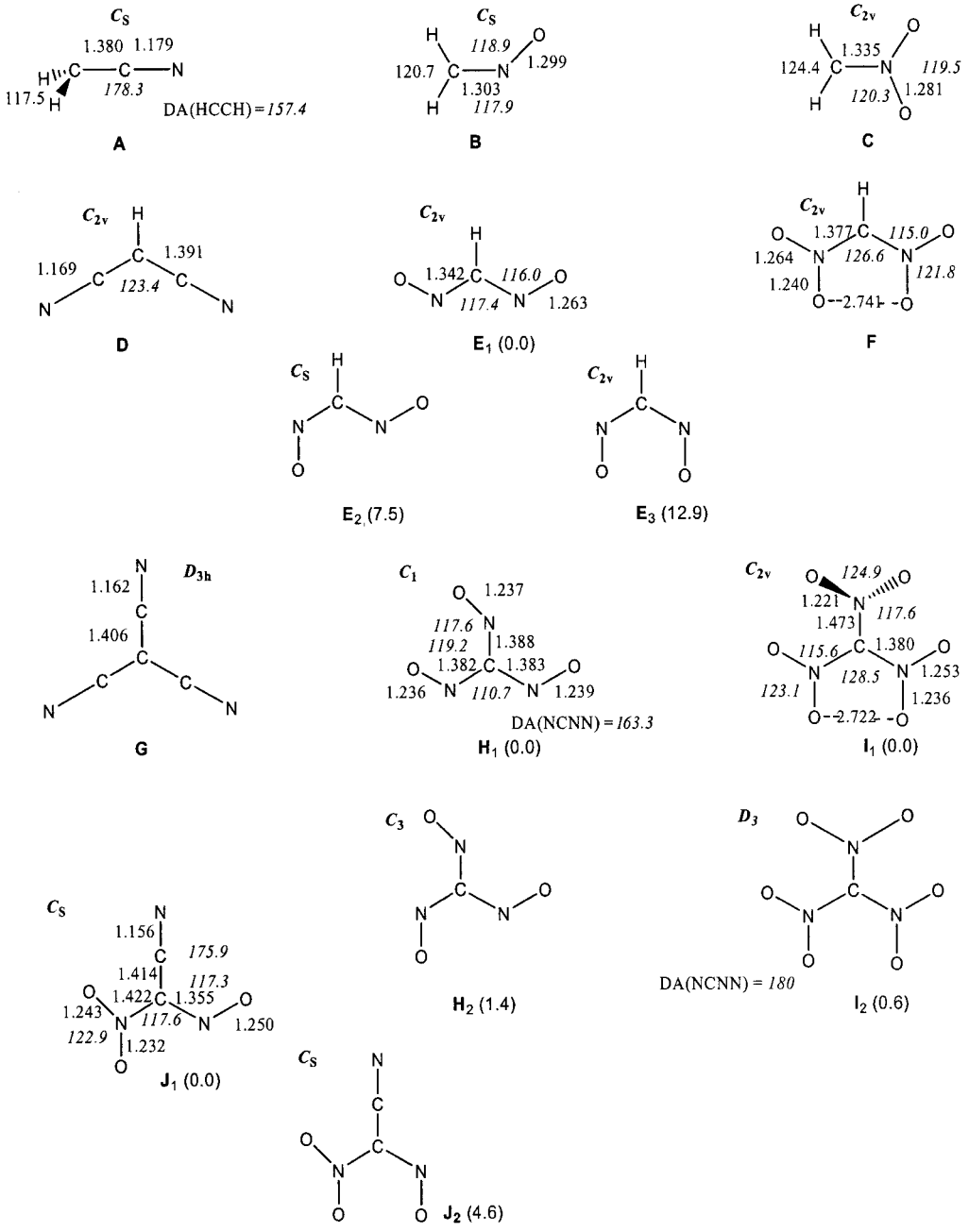


Figure 1. $[CR^1R^2R^3]^-$ ($R^{1,2,3}$ = H, CN, NO, $NO_2$): Molecular models of found isomers A–$J_2$ and selected optimized structural parameters for the global minima [B3LYP/aug-cc-pvTZ, angles in ° (*italics*), bond lengths in Å, DA = dihedral angle, in parenthesis relative energies of isomers in kcal/mol].

 © 2006 Wiley-VCH Verlag GmbH & Co. KGaA, Weinheim 

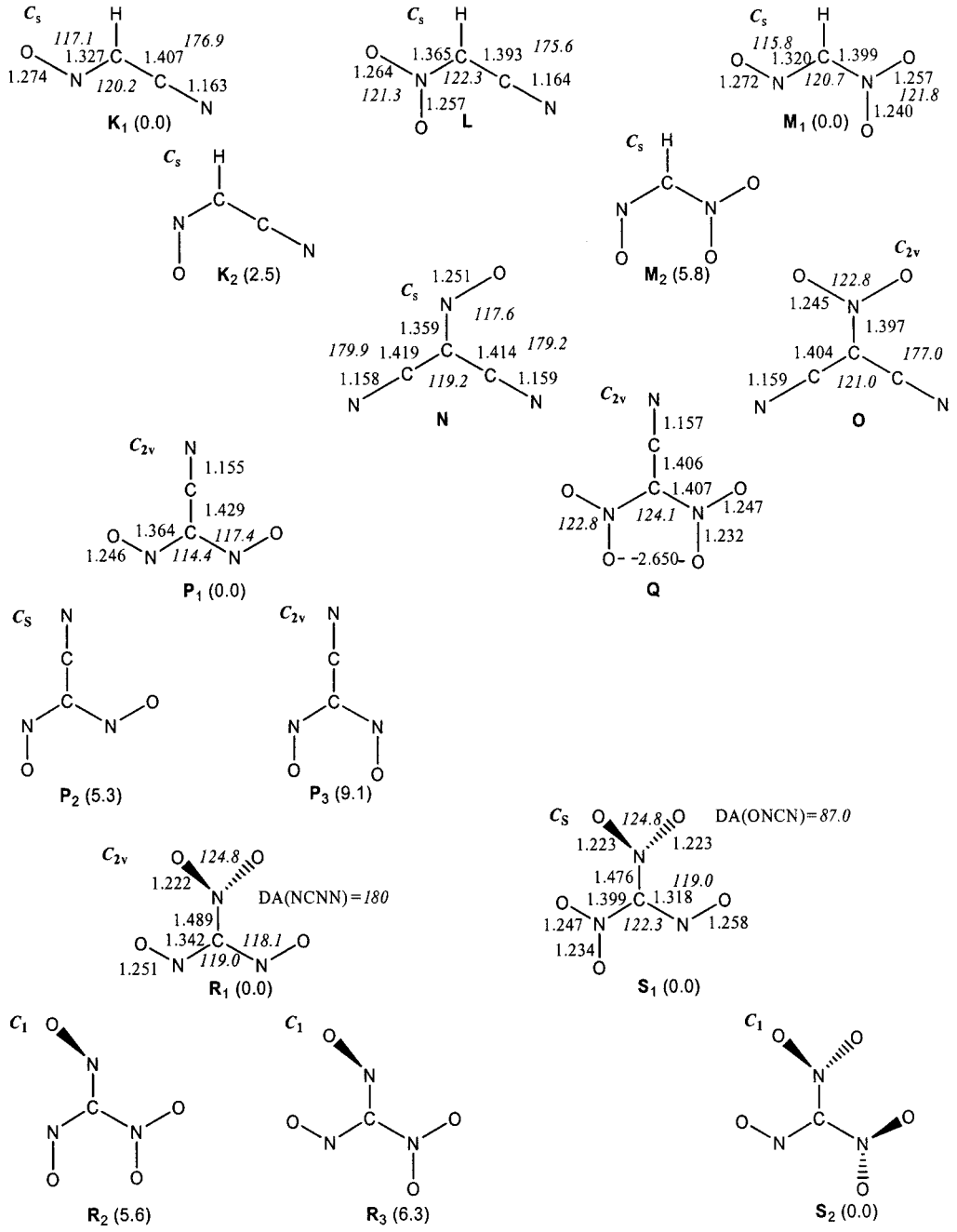


Figure 2. $[CR^1R^2R^3]^-$ ($R^{1,2,3}$ = H, CN, NO, $NO_2$): Molecular models of found isomers K–$S_2$ and selected optimized structural parameters for the global minima [B3LYP/aug-cc-pvTZ, angles in ° (*italics*), bond lengths in Å, DA = dihedral angle, in parenthesis relative energies of isomers in kcal/mol].

out-of-plane deformation angle $\alpha$ = 33.6° at MP2/6-31+G(d)].[19] Inclusion of zero-point vibrational energy at 0 K displays a different picture with the planar structure now being 0.25 kcal/mol [$\Delta(E^{tot}+zpe)$] favored over the non-planar structure. Thermal correction to 298 K slightly increases this value to 0.58 kcal/mol ($\Delta_{298}H$) while explicit consideration of the entropy again favors the non-planar structure with 0.42 kcal/mol ($\Delta_{298}G$). Experimentally, the $H_2C–CN^-$ carbanion was found non-planar with the hydrogen atoms slightly bent out of the molecular plane (out-of-plane deformation angle 30 ± 5°) and a very small inversion barrier of 0.28 ± 0.14 kcal/mol.[20]

The molecular models together with selected calculated data and relative energies are given in Figure 1 and Figure 2. Further substitution of the second H atom again results in planar anions, the same holds for the third substitution in case of R = CN, leading to the $D_{3h}$-symmetric TCM, the most prominent methanide. In case of R = NO and $NO_2$ the third substitution leads either to a propeller type ($D_3$ symmetry) structure with only a small distortion from plan-

 © 2006 Wiley-VCH Verlag GmbH & Co. KGaA, Weinheim 

arity or one $NO_2$ group is twisted by 90°, nevertheless leaving the central carbon in an almost trigonal-planar environment.[21]

It is interesting to note that both the DNM and DNtM anions are planar ($C_{2v}$-symmetric) in the experiment (Figure 3) and theory (Figures 1 and 2), whereas the dinitramide, $[N(NO_2)_2]^-$ (isoelectronic with DNtM) adopts an non-planar ideal $C_2$-symmetric propeller-like structure (but only in the gas phase). Steric repulsion between the lone pairs on the nitrogen and oxygen atoms account for the typically non-planar geometry of the ion $[N(NO_2)_2]^-$, while cation···anion interactions are responsible for a different magnitude of distortions from $C_2$ symmetry (between 3–33°, X-ray data).[22] Consider the analog planar methanide $[HC(NO_2)_2]^-$: N is formally substituted by HC, which means instead of a lone pair a H–C bond is introduced. The electrostatic repulsion is decreased (by formation of two intramolecular C···H···O hydrogen bonds) resulting in a planar structure which allows a maximum of resonance stabilization.

Our calculated structural data display, that obviously only two NO or $NO_2$ groups fit into a planar structure in a methanide as long as $R^3$ is either H or CN. However, when a third NO or $NO_2$ group is introduced in the methanides (TNM, TNtM, DNtNM, NtDNM), the larger electrostatic repulsion forces the anion into a non-planar geometry. Here, the balance between resonance stabilization and steric repulsion results in the torsion of one $NO_2$ or NO group out of the anion plane. Moreover, a $D_3$ propeller-shaped isomer is found being 0.6 kcal/mol less stable (TNtM). In agreement with theory, experimentally for TNtM both isomers are found in single crystal X-ray investigations with dihedral angles between the $NO_2$ planes varying from 60–100°.[10,23]

Moreover, fairly small O···O distances (ranging between 2.60–2.75 Å) are found for all DNtM anions $[R–C(NO_2)_2^-$, Figures 1 and 2]. AIM analyses[24] of DNtM anions show in addition to the expected bond path network, a (3,–1)[25] unusual bond critical point (CP) along $O(NO_2^a)\cdots O(NO_2^b)$ lines (Figure 4). The origin of this bond CP has been described recently by Pinkerton et al. as a bonding closed-shell-type interaction between the negatively charged oxygen atoms belonging to different nitro groups.[26]

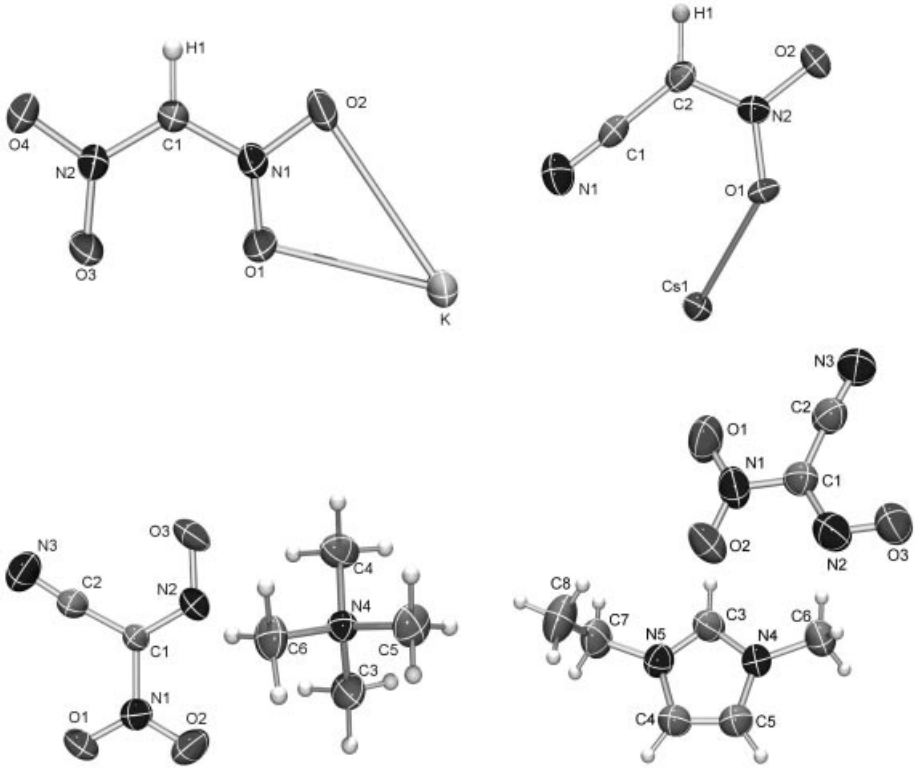


Figure 3. ORTEP Plots of the asymmetric unit in KDNtM, CsNtCM, $[Me_4N]$NtNCM, and [EMI]NtNCM thermal ellipsoid represents 50% probability, selected bond lengths [Å] and angles [°]. Top, left: **KDNtM** K–O1 2.809(2), K–O2 2.893(2), C1–N1 1.359(3), C1–N2 1.362(3), N1–O1 1.243(3), N1–O2 1.265(3); N1–C1–N2 123.5(2), O1–N1–O2 120.1(2). Top, right: **CsNtCM** Cs–O1 3.072(3), C1–N1 1.146(6), C2–N2 1.328(5), C1–C2 1.403(3), N2–O1 1.281(4), N2–O2 1.278(4); N1–C1–C2 178.4(4), N2–C2–C1 119.4(4), O1–N2–O2 119.0(3). Bottom, left: **$[Me_4N]$NtNCM** O1–N1 1.233(2), O2–N1 1.221(3), O3–N2 1.280(2), C1–N1 1.420(3), N2–C1 1.307(3), N3–C2 1.137(4), C1–C2 1.407(4); N3–C2–C1 175.2(3), O3–N2–C1 115.8(2), O2–N1–O1 123.4(2). Bottom, right: **[EMI]NtNCM** O1–N1 1.232(4), O2–N1 1.238(4), O3–N2 1.262(4), C1–N1 1.408(4), N2–C1 1.332(5), N3–C2 1.142(4), C1–C2 1.415(5); N3–C2–C1 174.7(4), O3–N2–C1 116.5(3), O2–N1–O1 122.8(3).

 © 2006 Wiley-VCH Verlag GmbH & Co. KGaA, Weinheim 

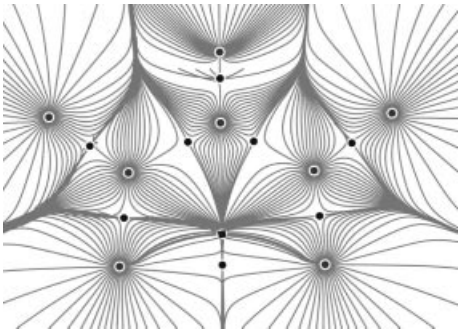

Figure 4. The gradient lines of the electron density in DNtM and the projection of the molecular graph onto the anion plane. The bond CP's are shown as circles and the ring CP's are shown as rectangles.

Balance between resonance and electrostatic repulsion seems to be the important structure factor not only to answer the question of a planar vs. non-planar structure but also to explain the energy differences between different isomers (see Figure 1 and Figure 2, e.g. TNM isomers $\mathbf{I}_1$ and $\mathbf{I}_2$ or NtNCM isomers $\mathbf{J}_1$, and $\mathbf{J}_2$) besides the aforementioned intramolecular hydrogen bonds (see Figures 1 and 2, e.g. DNM isomers $\mathbf{E}_1$, $\mathbf{E}_2$ and $\mathbf{E}_3$, or $\mathbf{R}_1$, $\mathbf{R}_2$ and $\mathbf{R}_3$). Isomeric anions are only found for the NO- and $NO_2$-substituted methanides. In NO-substituted methanides those isomers are energetically favored which adopt an *anti*/*anti* configuration with respect to a second NO or $NO_2$ group. The relative energy difference between different isomers is given in Figures 1 and 2.

All multiply substituted cyanomethanides (DCM, TCM, NCM, NDCM, DNCM, NtCM, NtDCM and DNtCM) adopt a planar structure at the theoretical level applied, nicely in agreement with experimental data.[7c,11,27–29]

A CN group attached to a methanide C atom forms always a linear or nearly linear [<(CCN) = 175°] CCN moiety. Upon further CN substitution the C–CN bond lengths increases (CM: 1.380, DCM: 1.391, TCM: 1.406 Å) while the CN bond lengths decreases (CM 1.179, DCM: 1.169, TCM: 1.162 Å). Similar trends for the C–NO bonds are found along the series NM, DNM and TNM (1.303, 1.342 and 1.380–1.388 Å) as well as for the nitromethanides (1.335, 1.377 and 1.380–1.470 Å), while the NO bonds decrease. The $C–N_{nitroso}$ bond length is significantly smaller than the $C–N_{nitro}$ bond length which again is smaller than the C–CN bond length indicating a stronger π interaction along the $C–N_{nitroso}–O$ moiety [Figure 1, e.g. $d([H_2C–R^1]^–)$: $R^1$ = NO 1.303, $NO_2$ 1.335 and CN 1.380 Å] which nicely agrees with experimental observations.[7c,11,12,29]

### X-ray Elucidation – Interaction between Alkali/Ammonium Cations and Resonance-Stabilized Methanides

In accord with the theoretically derived structural data of resonance-stabilized methanides, the experimental data of KDNtM, CsNtCM, $[Me_4N]$NtNCM and [EMI]NtNCM reveal nearly planar anions, with bond lengths and angles as discussed above. The asymmetric units along with selected bond lengths and angles are displayed in Figure 3. In the following discussion we would like to focus on the interaction between cations and anions.

As shown on numerous occasions, the solid-state structure of alkali methanides consists of an infinite three-dimensional network with coordination numbers between 8 (e.g. KDNtM) and 13 (e.g. CsDNM;[12] see Figures S1–S3 in the Supporting Information, displaying the coordination environment of KDNtM, CsNtCM and $[Me_4N]$NtNCM). Moreover, a great diversity of bonding modi is found. Usually the CN groups coordinate one or two neighboring cation centers, NO one to three cations through the oxygen and/or the nitrogen atoms whereas a $NO_2$ group exclusively coordinates through the oxygen atoms up to three cation centers in both mono and bidentate fashion. These strong cation···anion interactions lead to an interesting three-dimensional network arrangement of the ions (Figure 5, a–b) in the solid with chains of $M^+$ and $[CR^1R^2R^3]^–$ stacked one upon the other. If such interactions are suppressed by using almost non-coordinating cations such as $EMI^+$ or $Me_4N^+$ the anions still show this type of parallel anion arrangement in the solid state (Figure 5, c–d).

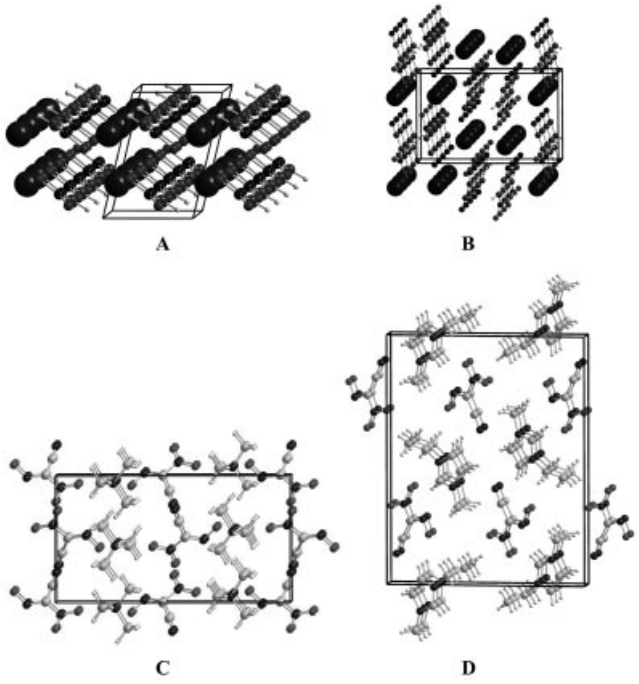


Figure 5. Packing diagram of **A** KDNtM: view along *c* axis, **B** CsNtCM: view along *a* axis, **C** $[Me_4N]$NtNCM: view along *c* axis, and **D** [EMI]NtNCM view along *a* axis.

So far we were not able to crystallize any of our ionic liquids from the melt, however, we succeeded in crystallizing $EMI^+NtNCM^–$ from a saturated ethanolic solution at –30 °C. The unit cell contains one crystallographically independent $EMI^+NtNCM^–$ species (Figure 3). Both the EMI

 © 2006 Wiley-VCH Verlag GmbH & Co. KGaA, Weinheim 

cations and the NtNCM anions form two-dimensional layers which are nearly parallel to each other but two $EMI^+$ layers are always separated by one $NtNCM^-$ layer and vice versa (Figure 5, D). Only very small van der Waals interaction can be assumed between the anion and cation layers, as well as within the anion and cation layers, because fairly long interaction distances are observed [shortest $d(EMI^+\cdots EMI^+)$ = 3.1–3.5, $d(NtNCM^-\cdots NtNCM^-)$ = 3.3, and $d(EMI^+\cdots NtNCM^-)$ = 2.3–2.8 Å] (Figure 6). The interionic distances with 2.3–2.8 Å are significantly shorter than in $EMI^+TCM^-$ (3.05–3.2 Å)[13c] and can be partly attributed to the interionic Coulomb attractive forces; however, for $Me_4N^+NtNCM^-$ there are significantly more interionic interactions (of the type: C–H···O–N–O, C–H···O–N, C–H···N–O, C–H···N–C) in the range between 2.2 and 3.0 Å compared to $EMI^+NtNCM^-$ (cf. Figure 6 and Figure S1/Table S2 in Supporting Information). Hence, it can be assumed that the total interionic interaction decreases along $EMI^+TCM^- < EMI^+NtNCM^- < Me_4N^+NtNCM^-$. In accord with this, the lowest melting point is found for $EMI^+TCM^-$ ($T_m$ = –11 °C),[13c] followed by $EMI^+NtNCM^-$ ($T_m$ = 35 °C, $T_{dec,onset}$ = 52 °C) and $Me_4N^+NtNCM^-$ ($T_m > T_{dec,onset}$ = 70 °C).

### Bonding and Resonance Stabilization in Resonance-Stabilized Methanides

Structural parameters such as the fairly short C–NO, C–$NO_2$ and C–CN bond lengths together with the planarity, indicate the presence of over the whole anion delocalized π bonds. MO and NBO[30] calculations displayed the existence of an ($n$π-electron,$m$-center) bond unit in all methanides (Scheme 4, with $n = 2+4x+2y+2z$ and $m = 1+3x+2y+2z$; $x$ = number of $NO_2$ groups, $y$ = number of NO groups and $z$ number of CN groups in the anion plane).

To gain a quantitative view of the delocalization of the p-type lone pair (LP) localized at the central C atom, the partial charges, occupancies of the p-type LP {*occ*[LP(C)-$p_z$]} and the charge transfer upon substitution have

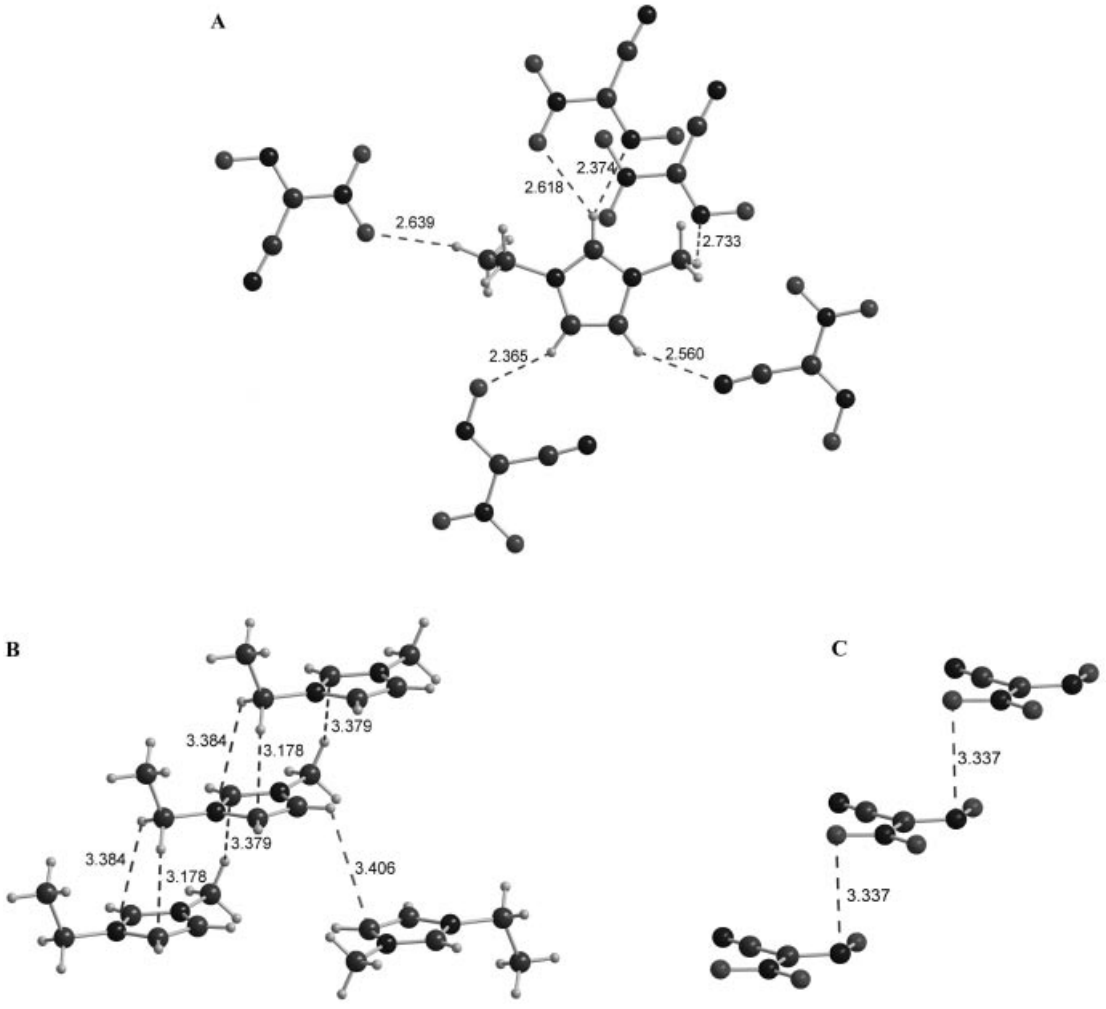


Figure 6. Interionic contacts (in Å) between **A**: EMI cations and NtNCM anions, **B**: EMI cations, and **C**: NtNCM anions in $EMI^+NtNCM^-$. Short contacts are shown by dashed (- - -) lines.

 © 2006 Wiley-VCH Verlag GmbH & Co. KGaA, Weinheim 

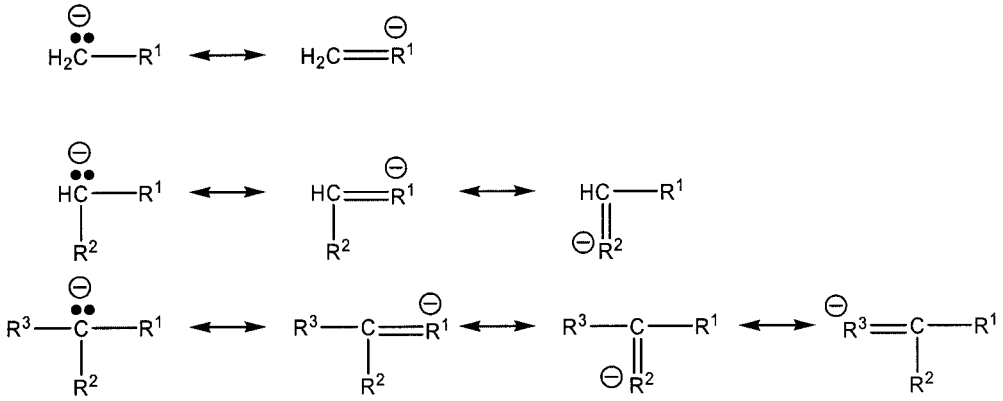

Scheme 4. Resonance stabilization of the lone pair at the central C atom by delocalization into $R^1$, $R^2$, and $R^3$ ($R^1$, $R^2$, $R^3$ = CN, NO, $NO_2$).

Table 4. NPA charges ($q$), occupancies (occ) and charge transfers ($q_{CT}$) in $e$.[a]

| | $q$(C)[$e$] | occ[LP(C)$p_z$] | $q_{CT}(\pi)$ | $q_{CT}(\sigma)$ | $q_{CT}(\pi+\sigma)$ | % C[b] |
|---|---|---|---|---|---|---|
| $CH_3^-$ | –1.45 | 2.00 | 0.00 | +0.45 | +0.45 | 99.7 |
| $C_{2v}$–$CH_2CN^-$ | –0.98 | 1.64 | –0.36 | –0.12 | –0.48 | 81.9 |
| $CH_2NO_2^-$ | –0.47 | 1.37 | –0.63 | –0.34 | –0.97 | 54.9 |
| $CH_2NO^-$ | –0.40 | 1.25 | –0.75 | –0.31 | –1.06 | 55.4 |
| $CH(CN)_2^-$ | –0.73 | 1.51 | –0.49 | –0.22 | –0.71 | 75.1 |
| $CH(NO_2)_2^-$ | –0.10 | 1.28 | –0.72 | –0.63 | –1.35 | 52.5 |
| $CH(NO)_2^-$ | –0.03 | 1.10 | –0.90 | –0.52 | –1.42 | 50.3 |
| $C(CN)_3^-$ | –0.59 | 1.46 | –0.54 | –0.33 | –0.87 | 72.6 |
| $C(NO_2)_3^-$ | 0.15 | 1.33 | –0.67 | –0.93 | –1.60 | 66.7 |
| $C(NO)_3^-$ | 0.14 | 1.15 | –0.85 | –0.74 | –1.59 | – |
| $C(CN)(NO)(NO_2)^-$ | –0.03 | 1.25 | –0.75 | –0.67 | –1.43 | 61.9 |

[a] The data of the mixed species are given in the supporting information. [b] Percent of localization of the methanide lone pair on the carbon atom according to the calculated NLMO (natural localized molecular orbital).

been carefully investigated. The overall charge transfer [$q_{CT}(\pi+\sigma)$] was divided into a π [$q_{CT}(\pi)$] and σ contribution [$q_{CT}(\sigma)$, Table 4]. As displayed in Table 4, the delocalization of the p-type lone pair, $q_{CT}(\pi)$, increases along the series CN < $NO_2$ < NO for all substitution patterns whereas the σ contribution increases along CN < NO < $NO_2$. Introduction of the second group R (R = NO, $NO_2$, CN) results once again in an increase of both the π and σ contribution, although the magnitude strongly decreases especially for the π contribution [e.g. $CH_2NO^-$: –0.75 and –0.15 $e$ for the second NO group in $CH(NO)_2^-$ resulting in an overall $q_{CT}(\pi)$ = –0.90 $e$]. Upon introducing a third group R, the π contribution increases very slightly for TCM but slightly decreases for TNM and TNtM. However, in all cases the σ contribution increases significantly. The dramatic decrease of the partial charge on the C atom (cf. –1.45 in $CH_3^-$ vs. +0.15 $e$ in TNtM) in the methanides is mainly attributed to the delocalization of the p-LP (π contribution) and the increase of the polarization in the σ bonds upon substitution. The σ contribution increases relatively to the π contribution the larger the degree of substitution. The best delocalization of the p-type LP is found in DNM with $q_{CT}(\pi)$ = –0.90 $e$. Molecular orbital, classical VB resonance structures and electron-charge arguments suggest that most of the negative charge in the NO- and $NO_2$-substituted methanides is located on the oxygen atom, which is also the more electronegative element.

To estimate the resonance stabilization energy we have computed the reaction energies of a series of isodesmic reactions[31] according to Equations (1), (2), and (3) (Table 5). The computed resonance stabilization energies reveal a similar picture like the charge transfer/delocalization consideration for the first substitution, displaying the largest resonance energy in $[HC–NO]^-$ followed by the $NO_2$- and CN-substituted methanides (–69.2, –62.6, and –44.8 kcal/mol). The order changes with the second substitution (NO: –44.16 > CN: –42.3 > $NO_2$: –36.7 kcal/mol) and third substitution (CN: –35.7 > $NO_2$: –13.2 > NO: –7.41 kcal/mol), with the cyano group now delivering the largest resonance energy. While the second and the third incremental resonance energies in the CN methanides decrease only very little, a dramatic decrease is observed for the NO and $NO_2$ methanides. However, although the resonance energy for the second substitution strongly decreases for NO and $NO_2$, the overall $\Delta_{res}E$ [Equation (1) + Equation (2)] values are still larger than for DCM (DNM > DNtM > DCM). Only with the third substitution, the cyano compound displays also the largest overall $\Delta_{res}E$ [Equation (1) + Equation (2) + Equation (3)] with –122.8 compared to –120.7 for TNM and –112.5 kcal/mol for TNtM, in accord

 © 2006 Wiley-VCH Verlag GmbH & Co. KGaA, Weinheim 

Table 5. Resonance energies according to Equations 1–3.[a,b]

| $\Delta_{res}E$ | $R^1 = R^2 = R^3 = CN$ | $R^1 = R^2 = R^3 = NO$ | $R^1 = R^2 = R^3 = NO_2$ |
|---|---|---|---|
| $\Delta_{res}E$ [Equation (1)] | –44.83[c] | –69.18 | –62.56 |
| $\Delta_{res}E$ [Equation (2)] | –42.33[c] | –44.16 | –36.75 |
| $\Delta_{res}E$ [Equation (3)] | –35.68 | –7.41 | –13.20 |
| $\Delta_{res}E$ [Equation (1) + Equation (2)] | –87.14 | –113.43 | –99.31 |
| $\Delta_{res}E$ [Equation (1) + Equation (2) + Equation (3)] | –122.82 | –120.75 | –112.51 |
| $\Delta_{res}E$ | $R^1 = CN$, $R^2 = NO$, $R^3 = NO_2$ | $R^1 = CN$, $R^2 = NO_2$, $R^3 = NO$ | $R^1 = NO$, $R^2 = NO_2$, $R^3 = CN$ |
| $\Delta_{res}E$ [Equation (3)] | –27.42 | –31.06 | –21.76 |

[a] Values according to Equation (1) and (2) for the mixed species are given in the supporting information. [b] All resonance energies refer to the best isomer of the H–C bound acid; see Equation (1)–(3). Note: For $R^{1,2,3}$ = H, NO the *aci* form represents always the global minimum while for $R^{1,2,3}$ = H, CN and $NO_2$ the H–C bound acid is the global minimum (values for the *aci* form are given in the supporting information). [c] For planar $C_{2v}$-symmetric $H_2C–CN^-$: $\Delta_{res}E$ [Equation (1)] = –44.80 and $\Delta_{res}E$ [Equation (2)] = –42.36 kcal/mol.

with experimental observations. TCM salts are known and thermally stable while TNtM salts are labile (highly explosive) species, and TNM are not known yet but can be expected to be very labile.

$$[H_3C]^- + H_3C–R^1 \rightarrow [H_2CR^1]^- + H_3C–H \quad (1)$$

$$[H_2CR^1]^- + H_2CR^1R^2 \rightarrow [HCR^1R^2]^- + H_3C–R^1 \quad (2)$$

$$[HCR^1R^2]^- + HCR^1R^2R^3 \rightarrow [CR^1R^2R^3]^- + H_2CR^1R^2 \quad (3)$$

Also the NBO approach[30] can be used to study delocalization effects quantitatively, especially the NLMO (natural localized molecular orbitals) are suitable to display delocalization of a localized natural bond orbital. Here, the contributions of the antibonds represent the delocalization of the bonding orbital, $\varphi_{AB}$, from an idealized, strictly localized Lewis structure, over antibonding orbitals due to non-covalent, hyperconjungative interactions. Thus, the localized MOs offer a direct description of delocalization. Again, the inspection of the delocalization effects in the NLMO describing the methanide lone pair displays similar trends as discussed for the charge transfer, nicely corresponding to the resonance energies (Table 5). While the localization of the p-type lone pair on the methanide C atom steadily decreases for the cyanomethanides (81.9 CM > 75.1 DCM > 72.6% TCM), only a small decrease is found for the second substitution along the $NO_2$- and NO-substituted methanides and an increase is found for the third substitution (e.g. 54.9 NtM > 52.5 DNtM < 66.7% TNtM).

## Conclusions

Different synthetic routes to six new resonance-stabilized methanide-based ionic liquids ($EMI^+NtCM^-$, $EMI^+NtNCM^-$, $BMI^+NtNCM^-$, $EMI^+DNM^-$, $EMI^+DNtM^-$, $BMI^+TCM^-$) starting either from the explosive silver salts (except from AgTCM) or the easily accessible potassium salts have been described. Four of them represent room temperature ionic liquids ($BMI^+TCM^-$, $EMI^+DNM^-$, $BMI^+NtNCM^-$, $EMI^+NtCM^-$) while $EMI^+NtNCM^-$ and $EMI^+DNtM^-$ melt at 35 and 48 °C, respectively. These strongly colored ionic liquids (blue $EMI^+DNM^-$, red $EMI^+NtNCM^-$ and $BMI^+NtNCM^-$, yellow $EMI^+DNtM^-$, brown $EMI^+NtCM^-$, but colorless $BMI^+TCM^-$) are neither heat nor shock sensitive, are thermally stable up to over 52–270 °C and can be prepared in large quantities.

The structure and bonding is discussed on the basis of experimental and theoretical data. X-ray data of $Cs^+NtCM^-$, $K^+DNtM^-$, $EMI^+NtNCM^-$, and $Me_4N^+NtNCM^-$ reveal almost planar anions piled up parallel to each. In case of the alkali metal methanides strong cation···anion interactions result in three-dimensional network type structures in the solid state, while $Me_4N^+NtNCM^-$ and $EMI^+NtNCM^-$ display no such 3D-network which can also be assumed for the other $EMI^+$ or $BMI^+$ salts, not have been structurally characterized. X-ray crystallography of the $EMI^+NtNCM^-$ salt reveals only weak cation/anion, cation/cation and anion/anion contacts.

Structural parameters of the methanides such as the fairly short C–NO, C–$NO_2$ and C–CN bond lengths together with the planarity, indicate the presence of over the whole anion delocalized π bonds. These methanide anions are stabilized relative to the corresponding acids due to resonance stabilization. Charge transfer from the methanide central C atom to the substituent leads to a decrease in the C–$R^{1,2,3}$ bond lengths with the introduction of double bond character and an increase in the bond lengths within the substituent groups ($R^{1,2,3}$). The charge transfer can be divided into a strong π and σ contribution. The π contribution displays the delocalization of the p-type lone pair at the methanide carbon leading to at ambient temperature stable methanide anions.

In summary, as shown by different theoretical approaches (charge transfer, resonance energies and NLMO delocalization) resonance effects occur in all three classes of methanides, however, the magnitude of such effects strongly differs depending on the degree of substitution: (i) For mono-substitution the largest resonance is found for the $NO_2$ and NO species (similarly strong) while a significantly smaller resonance is found for the CN species, $[H_2C–CN]^-$. Hence, geometry optimizations find planar $[H_2C–NO_2]^-$ and $[H_2C–NO]^-$ anions while $[H_2C–CN]^-$ is predicted to be

 © 2006 Wiley-VCH Verlag GmbH & Co. KGaA, Weinheim 

non-planar at the level of theory applied, in agreement with experiment. (ii) For double-substitution the picture changes. Introduction of a second CN group results in a better resonance and the magnitude of the effect of the second CN group only slightly decreases in contrast to the magnitude of the resonance effect of the second $NO_2$ or NO group which dramatically decreases. Combining the resonance effect of the first and the second group, the overall resonance effect is still larger for the $NO_2$ and NO anions (DNtM and DNM) compared to $[HC(CN)_2]^-$ (DCM). In agreement with these strong resonance effects all doubly substituted methanides adopt a planar geometry. (iii) In accord with experimental observations, for the triple-substitution only in case of the CN species a significant resonance effect is found and also for the overall effect (sum over all three resonance steps) the cyano species, $[C(CN)_3]^-$, represents the best stabilized methanide compared to $[C(NO)_3]^-$ (TNM) and $[C(NO_2)_3]^-$ (TNtM). In agreement between theory and experiment TCM salts are stable compounds with a planar TCM anion, while in the highly explosive known TNtM salts non-planar TNtM anions are observed. TNM salts are not known yet, but it can be assumed that according to theory (B3LYP/aug-cc-pvTZ) the TNM anion adopts a non-planar geometry similar to the TNtM salts.

## Experimental Section

**Caution:** Although alkali and silver nitro- and nitrosomethanides are kinetically stable compounds, they are nonetheless energetic materials and appropriate safety precautions (e.g. protection shield when dried substances are used, preparation of small quantities $< 2$ g, keep these salts wet when stored) should be taken, especially when these compounds are prepared on a larger scale.

**General Remarks:** The $^{14}N$ and $^{13}C/^{1}H$ NMR spectra were recorded with a Jeol Eclipse 400 instrument, and chemical shifts were referenced to TMS ($^{13}C/^{1}H$) and $CH_3NO_2$ ($^{14}N$). Raman spectra were recorded with a Perkin–Elmer Spectrum 2000R NIR FT-Raman instrument equipped with a Nd:YAG laser (1064 nm). Elemental analysis was performed with a VARIO-EL Analyser (ELEMENTAR). Melting points are uncorrected (Büchi B540). DSC experiments: Samples (ca. 0.25 mg) were analyzed in closed Al containers with a hole (1 μm) on the top for gas release and a 0.003 × 3/16-inch disk was used to optimize good thermal contact between the sample and container with a nitrogen flow of 20 mL/min. The reference sample was an Al container with air. Experiments were carried out from 30–420 °C. The sample and the reference pan were heated in a differential scanning calorimeter (Perkin–Elmer Pyris 6 DSC, calibrated by standard pure indium and zinc) at different heating rates of 2, 5 and 10 °C/min. For the removal of moisture, the sample was dried in vacuo for 7 d at room temp. and prepared in a dry-box.

**Materials:** Nitroacetonitrile,[32] KTCM,[33] $EMI^+TCM^-$,[13c] KDNM,[12] KNtNCM,[11] KDNtM[9] and $EMI^+BF_4^-$[34] were prepared according to the procedure given in the literature. The following silver salts, AgX [X = $C(CN)_3$, $CH(NO_2)CN$ and $CH(NO)_2$] were synthesized by metathetic reaction of $AgNO_3$ with the corresponding alkali salts (KTCM, CsNtCM and KDNM) in water under exclusion of light. All manipulations for the isolation of the EMI/BMI salts[35] were carried out under an inert atmosphere of nitrogen gas in a dry-box with the rigid exclusion of air and moisture ($H_2O$, $O_2 < 1$ ppm). Solvents (for drying and cleaning procudure) were dried, freshly distilled, and stored under nitrogen.

**Computational Details:** Our goal was to compare the structures and energetics of different substituted methane derivatives and methanide anions. Structural and vibrational data of all considered species were calculated by using the hybrid density functional theory (B3LYP) with the program package Gaussian 98.[36] Three different types of basis sets were used: (i) a 6-31G(d,p) and (ii) an aug-cc-pvDZ and (iii) an aug-cc-pvTZ basis. All stationary points were characterized by a frequency analysis (Table 3) at the B3LYP level. Selected computed geometrical parameters are displayed in Figures 1 and 2. Further details can be obtained in the Supporting Information. If not otherwise stated, all discussed computational data refer to the B3LYP/aug-cc-pvTZ level of theory. Comparison of these data sets shows differences in bond lengths no larger than 0.01–0.02 Å. The bond angles in all these molecules are rather constant and relatively independent of the basis sets.[37] NBO analyses[30] were carried out to investigate the bonding of the methanides at the SCF level utilizing the optimized aug-cc-pvTZ geometry. Details of the NBO analyses are summarized in Table 4. It should be emphasized that the computation was carried out for a single, isolated (gas-phase) anion. There may well be significant differences among gas-phase, solution, and solid-state data.

**X-ray Analysis:** X-ray quality crystals of KDNtM, CsNtCM, $[Me_4N]$NtNCM and [EMI]NtNCM were obtained by recrystallization from ethanol. Data for compound KDNtM were collected with a Nonius Mach3, data for CsNtCM and $[Me_4N]$NtNCM on a KappaCCD, and data for [EMI]NtNCM on a Oxford Excalibur III using Mo-$K_\alpha$ radiation. Crystallographic data are summarized in Table S1 (Supporting Information). The asymmetric unit along with selected bond lengths and angles are displayed in Figure 3. All structures were solved by direct methods (structure solution program: for KDNtM and [EMI]NtNCM SHELXS-97[38] and SIR97[39] for CsNtCM and $[Me_4N]$NtNCM) and refined by full-matrix least-squares methods with SHELXL-97. Hydrogen atoms were included at geometrically idealized positions and were not refined; the non-hydrogen atoms were refined anisotropically.

CCDC-606717 (for CsNtCM), -606718 (for [EMI]NtNCM), -606719 (for KDNtM), and -261892 (for $[Me_4N]$NtNCM) contain the supplementary crystallographic data for this paper. These data can be obtained free of charge from The Cambridge Crystallographic Data Centre via www.ccdc.cam.ac.uk/data_request/cif.

**Synthesis of Cesium Nitrocyanomethanide (CsNtCM, $Cs[CH(NO_2)CN]$):** At 0 °C a solution of nitroacetonitrile (1.87 g, 21.7 mmol) in diethyl ether (70 mL) was slowly dropped to a stirred solution of cesium hydroxide monohydrate (3.60 g, 21.4 mmol) in 2-propanol (30 mL). The resulting suspension was stirred at 0 °C for 30 min and the brown precipitate (CsNTCM) was recrystallized from methanol. Yield 3.92 g (84%). $^1H$ NMR ([D$_6$]DMSO, 400 MHz, 25 °C): $\delta$ = 5.58 (*H*–C) ppm. $^{13}C\{^1H\}$ NMR ([D$_6$]DMSO, 101 MHz, 25 °C): $\delta$ = 120.6 (C–*C*N), 80.5 (*C*–CN) ppm. $^{14}N$ NMR ([D$_6$]DMSO, 28.9 MHz, 25 °C): $\delta$ = –14 (C–*N*O$_2$), –117 (C–C*N*) ppm. Raman (200 mW, 25 °C): $\tilde{\nu}$[cm$^{-1}$] = 3117 (1), 2187 (10), 1452 (7), 1341 (1), 1239 (0.5), 1084 (2), 1025 (0.5), 980 (4), 745 (0.5), 716 (1), 552 (3), 513 (0.5), 442 (0.5), 204 (2), 189 (3), 126 (1). $C_2HN_2CsO_2$ (217.95): calcd. C 11.02, H 0.46, N 12.85; found C 10.70, H 0.51, N 12.34.

**Synthesis of Tetramethylammonium Nitro(nitroso)cyanomethanide ($[Me_4N]$NtNCM, $[Me_4N][C(NO_2)(NO)(CN)]$):** At 0 °C a solution

 © 2006 Wiley-VCH Verlag GmbH & Co. KGaA, Weinheim 

of $H_2SO_4$ (1.10 g, 11.2 mmol, 100%) in 3 mL water was slowly dropped to a stirred solution of nitroacetonitrile (1.80 g, 20.9 mmol) and sodium nitrite (1.50 g, 21.7 mmol) in water (30 mL). The resulting solution was stirred at 0 °C for 30 min and the cyanomethylnitrolic acid was extracted with diethyl ether (4 × 25 mL). The ether solution was dried with anhydrous calcium chloride and filtered. At 0 °C a solution of tetramethylammonium hydroxide pentahydrate (2.60 g, 14.3 mmol) in 10 mL 2-propanol was slowly dropped to the stirred, dried ether solution of cyanomethylnitrolic acid. After recrystallization of the red precipitate from methanol 2.48 g (63%) red crystals of $[Me_4N]$NtNCM were obtained. M.p. decomposition, $T_{dec.,onset}$ = 70 °C. $^{13}C\{^1H\}$ NMR ([D$_6$]DMSO, 101 MHz, 25 °C): $\delta$ = 119.5 (C–*C*N), 149.6 (*C*–CN) ppm. $^{14}N$ NMR ([D$_6$]DMSO, 28.9 MHz, 25 °C): $\delta$ = –107 (C–C*N*), –15 (C–*N*O$_2$), 265 (C–*N*O) ppm. Raman (200 mW, 25 °C): $\tilde{\nu}$[cm$^{-1}$] = 3035 (1), 2957 (1), 2922 (0.5), 2214 (2), 1506 (0.5), 1496 (0.5), 1474 (0.5), 1460 (0.5), 1394 (3), 1340 (10), 1229 (4), 1175 (2), 949 (1), 839 (2), 754 (1), 535 (0.5), 456 (0.5), 244 (2), 170 (2). $C_6H_{12}N_4O_3$ (188.19): calcd. C 38.30, H 6.43, N 29.77; found C 38.34, H 6.32, N 29.94.

**Synthesis of Potassium Dicyanomethanide (KDCM, K[CH(CN)$_2$]):** At 20 °C a solution of malonodinitrile (1.76 g, 26.6 mmol) in 30 mL 2-propanol was slowly dropped to a stirred solution of KO*t*Bu (2.70 g, 24.1 mmol) in 30 mL 2-propanol. After adding 200 mL dichloromethane, a white precipitate (KDCM) is obtained which was washed twice with 100 mL dichloromethane and dried in vacuo. Yield 2.19 g (87%). $^1H$ NMR ([D$_6$]DMSO, 400 MHz, 25 °C): $\delta$ = 3.38 (*H*–C) ppm. $^{13}C\{^1H\}$ NMR ([D$_6$]DMSO, 101 MHz, 25 °C): $\delta$ = 130.6 (s, C–*C*N), –1.9 (*C*–CN). $^{14}N$ NMR ([D$_6$]DMSO, 28.9 MHz, 25 °C): $\delta$ = –135 (C*N*) ppm. Raman (200 mW, 25 °C): $\tilde{\nu}$[cm$^{-1}$] = 3068 (3), 2175 (10), 2122 (1), 1552 (0.5), 1343 (1), 1144 (8), 635 (1), 420 (0.5), 197 (3). $C_3HKN_2$ (104.15): calcd. C 34.60, H 0.97, N 26.90; found C 34.21, H 1.25, N 26.58.

**Synthesis of *n*-Butyl(methyl)imidazolium Tricyanomethanide (BMI$^+$TCM$^-$):** A slight excess of AgTCM (0.59 g, 2.98 mmol) was added to a water solution of ammonia (30 mL, 2 N). This reaction mixture was treated with a solution of BMI$^+$Br$^-$ (0.62 g, 2.83 mmol) in 20 mL distilled water. The resulting suspension was stirred (1 h) in the dark at room temp. and filtered to remove AgBr. The solvent was evaporated in vacuo. The drying and cleaning procedure included successive adding, filtering and removing of 25 mL dried methanol, THF and dichloromethane. Remaining volatiles were evaporated in high-vacuum over a period of 7 d. Yield 0.59 g (91%) colorless liquid (transparent melt). M.p. –48 °C, $T_{dec.,onset}$ = 270 °C. $^{13}C\{^1H\}$ NMR ([D$_6$]DMSO, 101 MHz, 25 °C): $\delta$ = 121.0 (C–*C*N), 5.1 (*C*–CN) ppm. $^{14}N$ NMR ([D$_6$]DMSO, 28.9 MHz, 25 °C): $\delta$ = –122 (C–C*N*) ppm.[35] Raman (200 mW, 25 °C): $\tilde{\nu}$[cm$^{-1}$] = 3167 (0.5, br.), 3110 (0.5), 2962 (3), 2942 (2), 2914 (1), 2875 (1), 2864 (0.5, sh), 2210 (10), 2166 (5), 1418 (2), 1388 (1), 1340 (1), 1112 (0.5), 1024 (2), 600 (0.5), 325 (0.5), 175 (1). $C_{12}H_{15}N_5$ (229.29): calcd. C 62.86, H 6.59, N 30.54; found C 62.70, H 6.25, N 30.73.

**Synthesis of Ethyl(methyl)imidazolium Nitro(cyano)methanide (EMI$^+$NtCM$^-$):** A slight excess of AgNtCM (0.42 g, 2.18 mmol) was added to a water solution of ammonia (25 mL, 2 N). This reaction mixture was treated with a solution of EMI$^+$Br$^-$ (0.40 g, 2.10 mmol) in 10 mL distilled water. The resulting suspension was stirred (1 h) in the dark at room temp. and filtered to remove AgBr. The solvent was evaporated in vacuo. The drying and cleaning procedure included successive adding, filtering and removing of 25 mL dried methanol, THF and dichloromethane. Remaining volatiles were evaporated in high-vacuum over a period of 7 d. Yield 0.32 g (78%) brown liquid (transparent melt). M.p. 5 °C, $T_{dec.,onset}$ = 210 °C. $^1H$ NMR ([D$_6$]DMSO, 400 MHz, 25 °C): $\delta$ = 5.58 (*H*–C) ppm. $^{13}C\{^1H\}$ NMR ([D$_6$]DMSO, 101 MHz, 25 °C): $\delta$ = 120.6 (C–*C*N), 80.5 (*C*–CN). $^{14}N$ NMR ([D$_6$]DMSO, 28.9 MHz, 25 °C): $\delta$ = –13.9 (C–*N*O$_2$), –117 (C–C*N*) ppm.[35] Raman (200 mW, 25 °C): $\tilde{\nu}$[cm$^{-1}$] = 3160 (0.5), 3121 (0.5), 3114 (1), 3070 (0.5, br.), 2960 (1, br.), 2955 (1, br.), 2192 (10), 1454 (7), 1422 (0.5), 1340 (1), 1085 (2), 1021 (0.5), 976 (5), 717 (1), 601 (0.5), 550 (3), 200 (3). $C_8H_{12}N_4O_2$ (196.21): calcd. C 48.97, H 6.16, N 28.55; found C 48.26, H 6.17, N 27.97.

**Synthesis of Ethyl(methyl)imidazolium Dinitrosomethanide (EMI$^+$DNM$^-$):** AgDNM (0.67 g, 3.72 mmol) was added to a water solution of ammonia (35 mL, 2 N). This reaction mixture was treated with a solution of EMI$^+$Br$^-$ (0.71 g, 3.72 mmol) in 20 mL distilled water. The resulting suspension was stirred (1 h) in the dark at room temp. and filtered to remove AgBr. The solvent was evaporated in vacuo. The drying and cleaning procedure included successive adding, filtering and removing of 25 mL dried methanol, THF and dichloromethane. Remaining volatiles were evaporated in high-vacuum over a period of 7 d. Yield 0.61 g (89%) dark blue-violet liquid (transparent melt). M.p. –6 °C, $T_{dec.,onset}$ = 180 °C. $^1H$ NMR ([D$_6$]DMSO, 400 MHz, 25 °C): $\delta$ = 8.68 (*H*–C). $^{13}C\{^1H\}$ NMR ([D$_6$]DMSO, 101 MHz, 25 °C): $\delta$ = 190.0 (*C*–NO). $^{14}N$ NMR ([D$_6$]DMSO, 28.9 MHz, 25 °C): $\delta$ = 332 (C–*N*O).[35] Raman (200 mW, 25 °C): $\tilde{\nu}$[cm$^{-1}$] = 3161 (0.5), 3119 (0.5), 3068 (0.5, br.), 2994 (0.5, sh), 2961 (1, br.), 2952 (1, br.), 1402 (3), 1420 (0.5), 1391 (1), 1340 (1), 1305 (10), 1180 (0.5), 1122 (0.5), 861 (0.5), 601 (0.5), 576 (9), 145 (2). $C_7H_{12}N_4O_2$ (184.20): calcd. C 45.65, H 6.57, N 30.42; found C 44.96, H 6.44, N 29.78.

**Synthesis of *n*-Butyl(methyl)imidazolium Nitro(nitroso)cyanomethanide (BMI$^+$NtNCM$^-$):** KNtNCM (0.47 g, 3.10 mmol) was dissolved in a mixture of 15 mL dried methanol and 15 mL dried ethanol. After adding a solution of $AgNO_3$ (0.53 g, 3.10 mmol) dissolved in 15 mL dried methanol and 15 mL dried ethanol, $KNO_3$ precipitated. After filtration the solvents were evaporated yielding 0.59 g AgNtNCM. A solution of AgNtNCM (0.59 g, 2.65 mmol) in a mixture of 30 mL dried methanol and 30 mL dried ethanol was added to a solution of BMI$^+$Br$^-$ (0.58 g, 2.65 mmol) in 20 mL dried THF. After filtration of AgBr, all solvents were evaporated. The drying and cleaning procedure included successive adding, filtering and removing of 25 mL dried methanol, THF and dichloromethane. Remaining volatiles were evaporated in high-vacuum over a period of 7 d. Yield 0.53 g (68%) red liquid (transparent melt). M.p. –4 °C, $T_{dec.,onset}$ = 65 °C. $^{13}C\{^1H\}$ NMR ([D$_6$]DMSO, 101 MHz, 25 °C): $\delta$ = 119.5 (s, C–*C*N), 149.6 (*C*–CN). $^{14}N$ NMR ([D$_6$]DMSO, 28.9 MHz, 25 °C): $\delta$ = –107 (C–C*N*), –15 (C–*N*O$_2$), 265 (C–*N*O) ppm.[35] Raman (200 mW, 25 °C): $\tilde{\nu}$[cm$^{-1}$] = 3170 (1, br.), 3120 (0.5, br.) 2990 (1), 2964 (0.5, br.), 2880 (0.5, br.), 2209 (6), 1490 (4), 1474 (0.5, br.), 1458 (1), 1418 (3), 1381 (9), 1340 (10), 1346 (10), 1249 (2), 1231 (4), 1178 (2), 1022 (1), 960 (1), 839 (3, br.), 772 (1), 601 (1), 535 (2), 481 (0.5), 251 (4), 176 (2). $C_{10}H_{15}N_5O_3$ (253.26): calcd. C 47.43, H 5.97, N 27.65; found C 48.24, H 6.32, N 26.89.

**Synthesis of Ethyl(methyl)imidazolium Nitro(nitroso)cyanomethanide (EMI$^+$NtNCM$^-$):** KNtNCM (0.75 g, 4.90 mmol) was dissolved in 30 mL methanol and 2 mL water. After adding a solution of EMI$^+$BF$_4^-$ (0.97 g, 4.90 mmol) dissolved in 10 mL methanol, $KBF_4$ precipitated. After filtration the solvents were evaporated. The drying and cleaning procedure included successive adding, filtering and removing of 25 mL dried methanol, THF and dichloromethane. Remaining volatiles were evaporated in high-vacuum over a period of 7 d. Yield 0.95 g (86%) red glass. M.p. 35 °C, $T_{dec.,onset}$ = 52 °C. $^{13}C\{^1H\}$ NMR ([D$_6$]DMSO, 101 MHz, 25 °C): $\delta$ = 119.5

 © 2006 Wiley-VCH Verlag GmbH & Co. KGaA, Weinheim 

(C–*C*N), 149.6 (*C*–CN) ppm. $^{14}$N NMR ([D$_6$]DMSO, 28.9 MHz, 25 °C): $\delta$ = –107 (C–C*N*), –15 (C–*N*O$_2$), 265 (C–*N*O) ppm.[35] Raman (200 mW, 25 °C): $\tilde{\nu}$[cm$^{-1}$] = 3158 (1), 3112 (0.5, br.) 2987 (1), 2964 (0.5, br.), 2878 (0.5), 2211 (5), 1495 (3), 1476 (0.5), 1458 (1), 1417 (3), 1380 (9), 1346 (10), 1248 (2), 1232 (5), 1177 (2), 1021 (1), 959 (1), 838 (3, br.), 772 (1), 600 (1), 536 (2), 480 (0.5), 250 (4), 172 (2). $C_8H_{11}N_5O_3$ (225.21): calcd. C 42.67, H 4.92, N 31.10; found C 43.12, H 4.89, N 30.69.

**Synthesis of Ethyl(methyl)imidazolium Dicyanomethanide (EMI$^+$DCM$^-$):** Adding a solution of KDCM (0.90 g, 8.64 mmol) in 20 mL methanol and 1 mL water, to a solution of EMI$^+$BF$_4^-$ (1.71 g, 8.64 mmol) in 10 mL methanol results in a white precipitate of $KBF_4$. After filtration of $KBF_4$, all solvents were evaporated. The drying and cleaning procedure included successive adding, filtering and removing of 25 mL dried methanol, dried THF and dried dichloromethane. Remaining volatiles were evaporated in high-vacuum over a period of 1 h. Yield 1.27 g (83%) yellow-brown liquid (slowly decomposes at room temperature resulting in a black tar). Raman (200 mW, 25 °C, decomposition in Raman): $\tilde{\nu}$[cm$^{-1}$] = 3121 (1, br.), 2959 (3, br.), 2185 (10, br.), 2157 (8, br.), 2146 (5, br.), 1482 (3), 1420 (3), 1389 (2), 1337 (1), 1236 (0.5), 1091 (0.5), 1023 (1), 704 (0.5), 599 (1), 473 (0.5). $C_9H_{12}N_4$ (176.22): calcd. C 61.34, H 6.86, N 31.79; found C 60.53, H 6.31, N 30.86.

**Synthesis of Ethyl(methyl)imidazolium Dinitromethanide (EMI$^-$DNtM$^+$):** KDNtM (0.73 g, 5.10 mmol) was dissolved in a boiling mixture of 20 mL methanol and 5 mL distilled water. After adding a solution of 1.01 g (5.10 mmol) EMI$^+$BF$_4^-$ in 10 mL methanol, $KBF_4$ precipitated. After filtration of $KBF_4$, all solvents were evaporated. The drying and cleaning procedure included successive adding, filtering and removing of 25 mL dried methanol, THF and dichloromethane. Remaining volatiles were evaporated in high-vacuum over a period of 7 d. Yield 0.79 g (72%) yellow glass. M.p. 48 °C, $T_{dec.,onset}$ = 186 °C. $^1$H NMR ([D$_6$]DMSO, 400 MHz, 25 °C): $\delta$ = 8.17 (*H*–C). $^{13}$C{$^1$H} NMR ([D$_6$]DMSO, 101 MHz, 25 °C): $\delta$ = 121.7 (*C*–NO$_2$) ppm. $^{14}$N NMR ([D$_6$]DMSO, 28.9 MHz, 25 °C): $\delta$ = –21 (C–*N*O$_2$) ppm.[35] Raman (200 mW, 25 °C): $\tilde{\nu}$[cm$^{-1}$] = 3142 (1, br.), 3115 (1, br.), 2963 (10, br.), 2955 (9, br.), 2899 (5, sh), 1668 (1), 1570 (3), 1447 (10, br.), 1375 (5), 1334 (9, br.), 1092 (4), 1023 (5), 999 (4), 960 (3), 794 (3), 780 (3), 750 (2), 702 (2), 431 (3, br.), 255 (4), 162 (5). $C_7H_{12}N_4O_4$ (216.20): calcd. C 38.89, H 5.59, N 25.91; found C 39.27, H 6.08, N 25.39.

**Supporting Information** (see also the footnote on the first page of this article): References, crystallographic data for KDNtM, CsNtCM, [EMI]NtNCM, and [Me$_4$N]NtNCM, and extensive computational data.

## Acknowledgments

This work was supported by the LMU München (financial support for H. B.). A. S. thanks Prof. T. M. Klapötke (LMU München) for his generous support.

[1] a) L. Birckenbach, K. Kellermann, *Ber. Dtsch. Chem. Ges.* **1925**, *58*, 786–794; b) L. Birckenbach, K. Kellermann, *Ber. Dtsch. Chem. Ges.* **1925**, *58*, 2377; c) L. Birckenbach, K. Huttner, W. Stein, *Ber. Dtsch. Chem. Ges.* **1929**, *62*, 2065–2075;L. Birckenbach, K. Huttner, W. Stein, *Ber. Dtsch. Chem. Ges.* **1929**, *62*, 2261–2277; d) L. Birckenbach, M. Linhard, *Ber. Dtsch. Chem. Ges.* **1930**, *63*, 2528–2544; L. Birckenbach, M. Linhard, *Ber. Dtsch. Chem. Ges.* **1930**, *63*, 2544–2558; L. Birckenbach, M. Linhard, *Ber. Dtsch. Chem. Ges.* **1930**, *63*, 2588.

[2] A. M. Golub, H. Köhler, *Chemie der Pseudohalogenide*, VEB Deutscher Verlag der Wissenschaften, Berlin, **1979**.

[3] a) A. Schulz, LMU München, **2001**; b) A. M. Golub, H. Köhler, V. V. Stopenko, *Chemistry of Pseudohalides*, Elsevier, Amsterdam, **1986**.

[4] H. Grimm, *Z. Elektrochem.* **1925**, *31*, 474–480.

[5] a) W. Hiller, S. Frey, J. Straehle, G. Boche, W. Zarges, K. Harms, M. Marsch, R. Wollert, K. Dehnicke, *Chem. Ber.* **1992**, *125*, 87–92; b) M. Armand, Y. Choquette, M. Gauthier, Ch. Michot, *EP 850 921 A1* **1998**.

[6] A. Hantzsch, G. Oswald, *Ber. Dtsch. Chem. Ges.* **1899**, *32*, 641–649.

[7] a) H. Köhler, G. Lux, *Inorg. Nucl. Chem. Lett.* **1968**, *4*, 133–136; b) H. Köhler, V. F. Bolelij, V. V. Skopenko, *Z. Anorg. Allg. Chem.* **1980**, *468*, 179–184; c) N. Arulsamy, D. S. Bohle, B. G. Doletski, *Inorg. Chem.* **1999**, *38*, 2709–2715.

[8] a) H. Köhler, B. Eichler, A. Kolbe, *Z. Chem.* **1970**, *10*, 154; b) H. Matschiner, H. Köhler, R. Matuschke, *Z. Anorg. Allg. Chem.* **1971**, *380*, 267–274.

[9] A. Langlet, N. V. Latypov, U. Wellmar, U. Bemm, P. Goede, J. Bergman, I. Romero, *J. Org. Chem.* **2002**, *67*, 7833–7838.

[10] A. A. Gakh, J. C. Bryan, M. N. Burnett, P. V. Bonnesen, *J. Mol. Struct.* **2000**, *520*, 221–228.

[11] H. Brand, P. Mayer, A. Schulz, J. J. Weigand, *Angew. Chem.* **2005**, *117*, 3998–4001; *Angew. Chem. Int. Ed.* **2005**, *44*, 3929–3932.

[12] H. Brand, P. Mayer, K. Polborn, A. Schulz, J. J. Weigand, *J. Am. Chem. Soc.* **2005**, *127*, 1360–1361.

[13] a) P. Wasserscheid, T. Welton (Eds.), *Ionic liquids in synthesis*, Wiley-VCH, Weinheim, **2003**; b) P. Wasserscheid, W. Keim, *Angew. Chem.* **2000**, *112*, 3926–3945; c) Y. Yoshida, K. Muroi, A. Otsuka, G. Saito, M. Takahashi, T. Yoko, *Inorg. Chem.* **2004**, *43*, 1458–1462, and references therein.

[14] a) H. Xue, J. M. Shreeve, *Adv. Mater.* **2005**, *17*, 2142–2146 and references cited therein; b) H. Xue, Y. Gao, B. Twamley, J. M. Shreeve, *Chem. Mater.* **2005**, *17*, 191–198; c) Y. Gao, S. W. Arritt, B. Twamley, J. M. Shreeve, *Inorg. Chem.* **2005**, *44*, 1704–1712; d) H. Xue, S. W. Arritt, B. Twamley, J. M. Shreeve, *Inorg. Chem.* **2004**, *43*, 7972–7977.

[15] EMI$^+$DCM$^-$ is not stable at room temp. with respect to slow polymerization yielding finally a black tar.

[16] B. G. Gowenlock, G. B. Richter-Addo, *Chem. Soc. Rev.* **2005**, *34*, 797–809 and references cited therein.

[17] a) W. Xu, L. M. Wang, R. A. Nieman, C. A. Angell, *J. Phys. Chem. B* **2003**, *107*, 11749–11756; b) W. Xu, E. I. Cooper, C. A. Angell, *J. Phys. Chem. B* **2003**, *107*, 6170–6178; c) A. R. Choudhury, N. Winterton, A. Steiner, A. I. Cooper, K. A. Johnson, *J. Am. Chem. Soc.* **2005**; *127*, 16792–16793.

[18] a) HF/TZ+2p+d level; T. J. Lee, H. F. Schaefer III, *J. Chem. Phys.* **1985**, *83*, 1784–1794; b) U. Salzner, P. v. R. Schleyer, *Chem. Phys. Lett.* **1992**, *199*, 267–274.

[19] K. B. Wiberg, H. Castejon, *J. Org. Chem.* **1995**, *60*, 6327–6334.

[20] S. Moran, H. B. Ellis, D. J. DeFrees, A. D. McLean, G. B. Ellison, *J. Am. Chem. Soc.* **1987**, *109*, 5996–6003.

[21] J. Cioslowski, S. T. Mixon, E. D. Fleischmann, *J. Am. Chem. Soc.* **1991**, *113*, 4751–4755.

[22] A. A. Pinkerton, J. P. Ritchie, *J. Mol. Struct.* **2003**, *657*, 57–74, and references therein.

[23] a) C. B. Jeffrey, M. N. Burnett, A. A. Gakh, *Acta Crystallogr. Sect. C* **1998**, *54*, 1229–1233; b) L. Liang, *Org. Synth.* **1941**, *21*, 105–107; c) K. D. Scherfise, F. Weller, K. Dehnicke, *Z. Naturforsch., Teil B* **1985**, *40*, 906–912; d) H. L. Ammon, C. S. Choi, R. S. Damvarapu, J. Alster, *Acta Crystallogr. Sect. C* **1990**, *46*, 295–298; e) Z. Berkovitch-Yellin, L. Leiserowitz, *Acta Crystallogr. Sect. B* **1984**, *40*, 159–165.

[24] R. F. W. Bader, *Atoms in Molecules: A Quantum Theory*; The International Series of Monographs of Chemistry, Oxford University Press, **1990**.

[25] For nomenclature definitions of critical points see ref.[24].

 © 2006 Wiley-VCH Verlag GmbH & Co. KGaA, Weinheim 

[26] E. A. Zhurova, V. G. Tsirelson, A. I. Stash, A. Pinkerton, *J. Am. Chem. Soc.* **2002**, *124*, 4574–4575, and references therein.
[27] a) P. Anderson, B. Klewe, *Nature* **1963**, *200*, 464; b) J. Konnert, D. Britton, *Inorg. Chem.* **1966**, *5*, 1193–1196.
[28] a) N. Kuhn, M. Steimann, K. Sweidan, *Z. Naturforsch., Teil B* **2005**, *60*, 123–124; b) J. Ruiz, V. Rodriguez, G. Lopez, J. Casabo, E. Molins, C. Miravittles, *Organometallics* **1999**, *18*, 1177; c) K. Berhalter, U. Thewalt, *J. Organomet. Chem.* **1987**, *332*, 123.
[29] Y. M. Chow, D. Britton, *Acta Crystallogr. Acta Crystallogr., Sect. B* **1974**, *30*, 1117–1118.
[30] a) E. D. Glendening, A. E. Reed, J. E. Carpenter, F. Weinhold, F. *NBO Version 3.1*; b) J. E. Carpenter, F. Weinhold, *J. Mol. Struct. (Theochem)* **1988**, *169*, 41; c) J. P. Foster, F. Weinhold, *J. Am. Chem. Soc.* **1980**, *102*, 7211; d) A. E. Reed, F. Weinhold, *J. Chem. Phys.* **1983**, *78*, 4066; e) A. E. Reed, R. B. Weinstock, F. Weinhold, *J. Chem. Phys.* **1985**, *83*, 735; f) A. E. Reed, P. v. R. Schleyer, *J. Am. Chem. Soc.* **1987**, *109*, 7362; g) A. E. Reed, P. v. R. Schleyer, *Inorg. Chem.* **1988**, *27*, 3969; h) F. Weinhold, J. E. Carpenter, *The Structure of Small Molecules and Ions*, Plenum Press, **1988**, 227.
[31] a) W. J. Hehre, L. Radom, P. v. R. Schleyer, J. Pople, Ab initio *Molecular Orbital Theory*, Wiley, New York, **1986**; b) T. M. Klapötke, A. Schulz, *Quantenmechanische Methoden in der Hauptgruppenchemie*, Spektrum, Heidelberg, Berlin, Oxford, **1996**.
[32] G. H. Reidlinger, H. Junek, *Synthesis* **1991**, *10*, 835–838.
[33] S. Trofimenko, E. L. Little Jr, H. F. Mower, *J. Org. Chem.* **1962**, *27*, 433–438.
[34] P. A. Z. Suarez, J. E. L. Dullius, S. R. Einloft, F. de Souza, J. Dupont, *Polyhedron* **1996**, *15*, 1217–1219.
[35] NMR spectroscopic data of the $EMI^+$ and $BMI^+$ ions are given in the supporting data file.
[36] M. J. Frisch, G. W. Trucks, H. B. Schlegel, G. E. Scuseria, M. A. Robb, J. R. Cheeseman, V. G. Zakrzewski, J. A. Montgomery Jr, R. E. Stratmann, J. C. Burant, S. Dapprich, J. M. Millam, A. D. Daniels, K. N. Kudin, M. C. Strain, O. Farkas, J. Tomasi, V. Barone, M. Cossi, R. Cammi, B. Mennucci, C. Pomelli, C. Adamo, S. Clifford, J. Ochterski, G. A. Petersson, P. Y. Ayala, Q. Cui, K. Morokuma, D. K. Malick, A. D. Rabuck, K. Raghavachari, J. B. Foresman, J. Cioslowski, J. V. Ortiz, B. B. Stefanov, G. Liu, A. Liashenko, P. Piskorz, I. Komaromi, R. Gomperts, R. L. Martin, D. J. Fox, T. Keith, M. A. Al-Laham, C. Y. Peng, A. Nanayakkara, C. Gonzalez, M. Challacombe, P. M. W. Gill, B. Johnson, W. Chen, M. W. Wong, J. L. Andres, M. Head-Gordon, E. S. Replogle, J. A. Pople, Gaussian 98, Revision A7 and A11, Gaussian Inc.: Pittsburgh PA, **1998**.
[37] For more discussion about the basis set dependence of molecular geometries, see T. M. Klapötke, A. Schulz, Ab initio *Methods in Main Group Chemistry* with an invited Chapter of R. D. Harcourt about VB Theory, John Wiley & Sons, New York, **1998**.
[38] G. M. Sheldrick, *SHELXL-97*, *Program for Solution of Crystal Structures*; University of Göttingen: Göttingen, Germany, **1997**.
[39] A. Altomare, M. C. Burla, M. Camalli, G. L. Cascarano, C. Giacorazzo, *J. Appl. Crystallogr.* **1999**, *32*, 115–119.

Received: July 17, 2006
Published Online: August 31, 2006

 © 2006 Wiley-VCH Verlag GmbH & Co. KGaA, Weinheim 

DOI: 10.1002/ejic.200600239

# Modified Pyridine-Bis(imine) Iron and Cobalt Complexes: Synthesis, Structure, and Ethylene Polymerization Study

**Frédéric Pelascini,[a,b] Marcel Wesolek,*[b] Frédéric Peruch,*[a] and Pierre J. Lutz[a]**

**Keywords:** N ligands / Iron / Cobalt / Ethylene / Polymerization

In this paper, we describe the synthesis of two new pyridine-bis(imine)s {4-chloro-2,6-bis[1-(2,6-diisopropylphenylimino)-ethyl]pyridine and 2,6-bis[1-(2,6-dimethylcyclohexylimino)-ethyl]pyridine} and their complexation with iron and cobalt dichloride. The solid-state structure of the iron complexes was solved and found to be very close to catalysts already described by Brookhart and Gibson. Their ability to polymerize ethylene was investigated after activation with MAO. It was thus shown that the substitution of the pyridine ring of the ligand is unfavorable: their catalytic activity is rather low. The replacement of the aromatic rings on the imine functions by dimethylcyclohexyl rings resulted in a complete loss of activity of the iron complex for oligomerization and polymerization of ethylene. With the cobalt analog, polymerization of ethylene could be achieved under the same conditions.

(© Wiley-VCH Verlag GmbH & Co. KGaA, 69451 Weinheim, Germany, 2006)

## Introduction

In 1998, Brookhart and Gibson simultaneously described the synthesis of very active pyridine-bis(imine) iron- or cobalt-based catalysts for the oligomerization or the polymerization of ethylene.[1–3] When the substituents on the ligand were bulky enough, they were found to be extremely efficient for the synthesis of linear polyethylenes. Many modifications of these ligands have already been described, but it was almost always the $R^1$–$R^5$ (Figure 1) groups that were modified; some reviews are listed with the most recent of these references.[4–17] So far, less work has been done on other types of modifications (imine functions replaced by amine functions, aryl rings replaced by amines or pyrrolyl rings, pyridine ring replaced by thiophene or furan ring, and so forth).[18–23] In this paper, we report new kinds of modifications. We focus more specifically on the electronic factors through the synthesis of two new types of pyridine-bis(imine) ligands. With ligand **1**, the presence of the chlorine group in the *para* position of the pyridine ring in the well-known 2,6-bis[1-(2,6-diisopropylphenylimino)ethyl]-pyridine ligand ($R^1 = R^5$ = isopropyl) led us to study the effect of the electronic-withdrawing chlorine group. For ligand **2**, the replacement of the aryl groups by aliphatic rings of another well-known ligand, 2,6-bis-[1-(2,6-dimethylphenylimino)ethyl]pyridine ($R^1 = R^5$ = methyl), was performed. The iron and cobalt complexes, once synthesized, were activated with methylaluminoxane (MAO) and tested for the polymerization of ethylene.

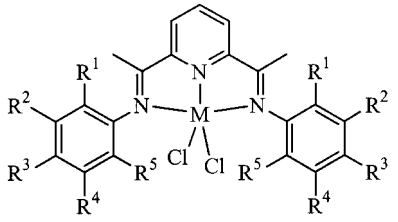


Figure 1. Pyridine-bis(imine) iron or cobalt complexes.

## Results and Discussion

### Synthesis and Characterization of Ligands

4-Chloro-2,6-bis[1-(2,6-diisopropylphenylimino)ethyl]pyridine (**1**) was synthesized according to already published procedures for the synthesis of pyridine-bis(imine).[1,2] The reaction is a condensation between 2,6-diacetyl-4-chloropyridine (synthesis described by Constable[24]) and 2,6-diisopropylaniline (Scheme 1, i). The yellow product was isolated and characterized by elemental analysis, and $^1H$ and $^{13}C$ NMR spectroscopy.

Concerning the synthesis of 2,6-bis[1-(2,6-dimethylcyclohexylimino)ethyl]pyridine (**2**), the same procedure was followed but the substituted aniline was replaced by the corresponding cyclohexylamine to yield aliphatic-substituted imines (Scheme 1, ii). Besides, substituted cycloalkanes exhibit several stereoisomers. In the case of 2,6-dimethylcyclohexylamine, three different stereoisomers can be identified: the

[a] Institut Charles Sadron (UPR CNRS 22),
6 rue Boussingault, B. P. 40016, 67083 Strasbourg Cedex, France
[b] Laboratoire de Chimie des Métaux de Transition et de Catalyse (LC3-UMR CNRS 7177), Institut Le Bel,
4 rue Blaise Pascal, 67070 Strasbourg Cedex, France
E-mail: peruch@enscpb.fr
wesolek@chimie.u-strasbg.fr

 © 2006 Wiley-VCH Verlag GmbH & Co. KGaA, Weinheim 

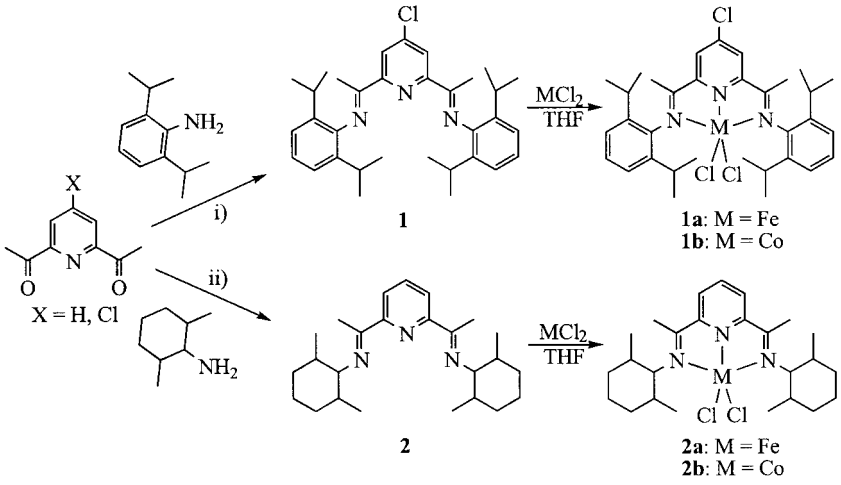


Scheme 1. Synthesis of ligands **1**, **2all-*cis***, **2all-*trans*** and complexes **1a**, **1b**, **2a**, **2b**.

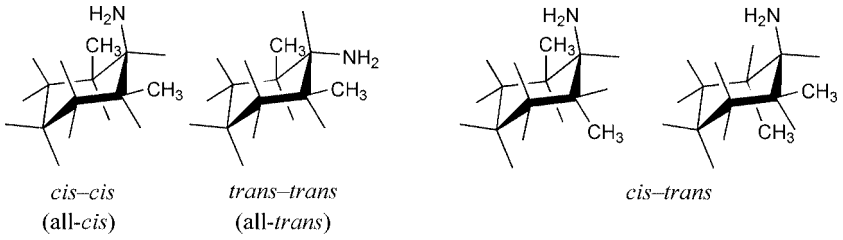


Figure 2. Most stable conformers for each stereoisomer of 2,6-dimethylcyclohexylamine.

*cis–cis* (all-*cis*), the *trans–trans* (all-*trans*), and the *cis–trans* one (Figure 2). It was decided to use only the pure all-*trans* and all-*cis* amines. After double condensation with diacetyl pyridine, these two products will give few conformers compared to the *cis–trans* one. Indeed, in the case of the *cis–trans* amine, the final pyridine-bis(imine) would probably be a mixture of isomers. Moreover, thanks to a thorough conformational analysis, it was shown that each stereoisomer had several conformers of different stabilization energy. For the all-*cis* and all-*trans* amines the most stable conformer is the one where the two methyl groups are in the equatorial position, thus minimizing steric repulsion. For the all-*cis* amine the amino group takes the axial position and for the all-*trans* amine the same group is in an equatorial position. Thus, normally only one conformer will be obtained for each selected amine. Condensation was carried out under ethanol reflux, with a slight excess of amine and some drops of acetic acid.

Both ligands based on the amine, hereafter named **2all-*cis*** and **2all-*trans***, were characterized by elemental analysis, and $^{1}H$ and $^{13}C$ NMR spectroscopy. In order to better allot the resonance peaks, a COSY spectrum was recorded. It was thus established that the molecule is in a blocked configuration at ambient temperature. Indeed, in the case of unsubstituted cyclohexane, it is known that there is a difference of 0.5 ppm between the chemical shifts of the axial and equatorial protons only at low temperature, when the exchange of cycle is slow compared to the timescale of the NMR spectroscopy. In our case, at ambient temperature, the conformational exchange is slow; we observe a difference of 0.3 ppm between the axial and equatorial protons, the equatorial protons being the most strongly shielded.

The attribution of the multiplet between 1.0 and 1.9 ppm was possible thanks to a 2D experiment ($^{1}H$–$^{13}C$). Three broad multiplets that integrate respectively for 10, 2, and 4 protons can be distinguished. One of the main differences between the two NMR spectra is the peak corresponding to the proton of the cycle carried by the carbon linked to the nitrogen atom of the imine function, whose chemical shift changes from 2.9 ppm for the **2all-*trans*** system to 3.7 ppm for the **2all-*cis*** system. Moreover, the coupling constant for the triplet goes from 9.3 Hz to 2.2 Hz. This difference may be easily explained with the Karplus and Conroy

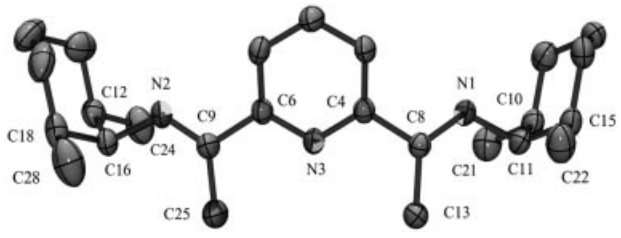


Figure 3. An ORTEP view of the crystal structure of **2all-*cis***. Selected bond lengths [Å] and angles [°]: C(6)–C(9) 1.500(2), C(9)–N(2) 1.270(2), N(2)–C(16) 1.465(2), C(18)–C(28) 1.530(3), C(12)–C(24) 1.523(3), C(9)–N(2)–C(16) 121.85(15), N(2)–C(9)–C(25) 126.92(16), C(16)–C(18)–C(28) 111.60(16), C(18)–C(16)–C(12) 110.92(14).

 © 2006 Wiley-VCH Verlag GmbH & Co. KGaA, Weinheim 

equation. Indeed, $^3J_{180°}$ coupling constants are always strictly higher than $^3J_{60°}$ ones.

The X-ray structure of the ligand **2all-*cis*** has been determined to complete the characterization and is represented in Figure 3. Only one conformer is observed, as expected.

## Synthesis and Characterization of Complexes

### *Synthesis and Structure of Iron and Cobalt Complexes with 4-Chloro-2,6-bis[1-(2,6-diisopropylphenylimino)ethyl]-pyridine (1a and 1b)*

The complexes were obtained from a stoichiometric reaction between the ligand and a suspension of anhydrous $FeCl_2$ or $CoCl_2$ in THF at room temperature. In order to recover the complexes, the solution was concentrated and hexane was added to the reaction medium. The iron complex was isolated with a yield of 83% as a blue-green powder. The cobalt complex was isolated with a yield of 81% as a green powder. The isolated complexes were paramagnetic (according to $^1$H NMR indicating chemical shifts from –40 to 170 ppm) and were characterized by elemental analysis, infrared and X-ray analysis (iron complex only). The elemental analysis results were in agreement with the formula $LMCl_2$.

Recrystallization of the iron complex redissolved in diethyl ether yields crystals suitable for X-ray analysis. In the solid state (Figure 4), the geometry of the metal center can be considered as distorted square-pyramidal. One of the chlorine atoms occupies the apical position, with an almost right angle with the iron and nitrogen of the pyridine [N(1)(2)(3)–Fe–Cl(2) ranging from 89.3° to 102.5°], whereas the second occupies one of the bases of the formed square. The apical bond seems to be the weaker, as the length of the Fe–Cl bond goes from 2.305 Å for the apical position to 2.247 Å for the longitudinal one. This is normally expected for that geometry. The iron atom is slightly above the base of the pyramid [N(3)–Fe–N(1) = 139.2°]. Predictably, the phenyl groups linked to the imine functions are almost perpendicular to the plane formed by the nitrogen atoms, although there is a slight deformation of the molecule, one of the phenyl groups having a dihedral angle of 94.7° and the other 85.1°.

We can examine the effect of the chlorine atom in the *para* position of the pyridine ring by comparing the lengths of the various bonds with X-ray data of the equivalent nonchlorinated iron complex.[2] The molecule is asymmetric in the solid state, one of the Fe–$N_{imine}$ bonds measuring 2.244 Å and the other 2.212 Å. This is probably due to the presence of a molecule of $Et_2O$ in the lattice, but the average value is 2.228(9) Å, very close to the average value 2.224(9) Å for the unsubstituted complex where the lengths of these same bonds are almost identical (in this case half a water molecule is present in the lattice). The decrease in length of the Fe–$N_{py}$ bond for the chlorinated ligand (2.080 instead of 2.091 Å) can be explained by the fact that the chlorine on the pyridine group enhances the π back donation of the iron to the pyridine group. Another expected

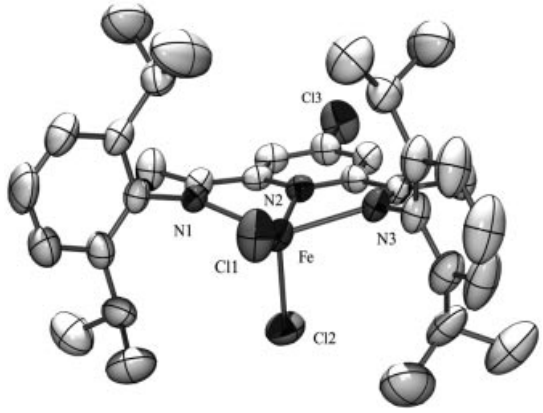


Figure 4. An ORTEP view of the crystal structure of **1a**. Selected bond lengths [Å] and angles [°] for the subunit Fe1: Fe1–N(1) 2.213(4), Fe1–N(2) 2.080(3), Fe1–N(3) 2.243(4), Fe1–Cl(1) 2.247(1), Fe1–Cl(2) 2.305(2), Cl(1)–Fe1–N(1) 100.8(1), Cl(1)–Fe1–N(2) 151.1(1), Cl(1)–Fe1–N(3) 97.2(1), Cl(2)–Fe1–N(1) 100.0(1), Cl(2)–Fe1–N(2) 89.3(1), Cl(2)–Fe1–N(3) 102.5(1), Cl(1)–Fe1–Cl(2) 119.55(7), N(1)–Fe1–N(2) 73.7(1), N(1)–Fe1–N(3) 139.2(1), N(2)–Fe1–N(3) 72.9(1).

difference is the reduction of the length of the Fe–Cl(1) bond *trans* to the pyridine group (2.247 instead of 2.263 Å), while the angle N(2)–Fe–Cl(1) where the chlorine and the nitrogen are *trans* to the basal plane varies from 147.9 to 151.1° (for the chlorinated ligand). The apical iron chlorine bond varies from 2.305 (for the chlorinated ligand) to 2.317 Å, in agreement with the expected electronic effect of the chlorine on the *para* position on the pyridine, that is a decrease of the electronic density on the iron atom. Nevertheless, the solid-state structures of the chlorinated and the nonchlorinated complexes are very close. Besides, as we will see in the structure of {2,6-bis[1-(2,6-dimethylcyclohexylimino)ethyl]pyridine}iron dichloride (**2a**), the crystal packing causes little difference in the structure.

### *Synthesis and Structure of Iron and Cobalt Complexes with 2,6-Bis[1-(2,6-dimethylcyclohexylimino)ethyl]pyridine (2a and 2b)*

With the ligand **2all-*cis***, no iron or cobalt complexes could be isolated. Indeed, during the reaction between iron chloride and the ligand in THF at ambient temperature, the solution became slightly pink, but no precipitation was observed, even after 24 h. The addition of hexane or diethyl ether did not lead to the precipitation of the complex. Evaporation of solvents to dryness yielded a pink powder. IR results prompted us to think that no complexation occurred, as free $FeCl_2$ and free ligand were detected. Similar observations were made when the reaction was run at 50 °C. Thus, the stoichiometric reaction between the ligand **2all-*cis*** and the metal chloride did not lead to the formation of the expected complex of formula $LMCl_2$. We first made the assumption that a steric factor could be the cause of this nonreactivity, but an X-ray of the free ligand shown in Figure 3 does not confirm this hypothesis.

On the contrary, the addition of 1 equiv. of the ligand **2all-*trans*** to 1 equiv. of metal chloride in THF at room

 © 2006 Wiley-VCH Verlag GmbH & Co. KGaA, Weinheim 

temperature led to the formation of the desired complex in good yield (75% for $LFeCl_2$ and 65% for $LCoCl_2$). Crystals suitable for X-ray analysis were obtained by slow crystallization in THF. The X-ray crystal structure contains two independent sets of iron complexes, Fe1 and Fe2, with slightly different angles and distances (Figure 5, Table 1).

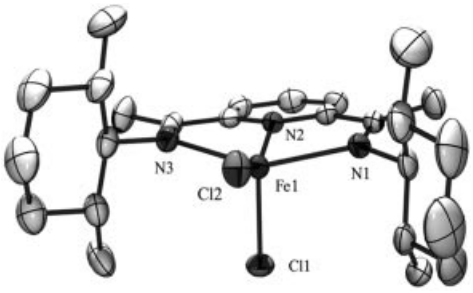


Figure 5. An ORTEP view of the crystal structure of **2a all-*trans***. Only one of the two distinct units is represented. The differences in lengths and angles are shown in Table 1.

Table 1. Selected bond lengths [Å] and angles [°] of the two subunits Fe1 and Fe2 for the complex **2a all-*trans***.

| Bond lengths [Å] | | | |
|---|---|---|---|
| Fe1–N(1) | 2.286(4) | Fe2–N(6) | 2.318(4) |
| Fe1–N(2) | 2.087(4) | Fe2–N(5) | 2.091(4) |
| Fe1–N(3) | 2.295(4) | Fe2–N(4) | 2.308(4) |
| Fe1–Cl(1) | 2.349(1) | Fe2–Cl(3) | 2.329(2) |
| Fe1–Cl(2) | 2.279(1) | Fe2–Cl(4) | 2.286(1) |
| Bond angles [°] | | | |
| Cl(1)–Fe1–N(1) | 97.9(1) | Cl(3)–Fe2–N(6) | 95.9(1) |
| Cl(1)–Fe1–N(2) | 91.8(1) | Cl(3)–Fe2–N(5) | 95.1(1) |
| Cl(1)–Fe1–N(3) | 95.1(1) | Cl(3)–Fe2–N(4) | 102.0(1) |
| Cl(2)–Fe1–N(1) | 103.2(1) | Cl(4)–Fe2–N(6) | 102.2(1) |
| Cl(2)–Fe1–N(2) | 153.4(1) | Cl(4)–Fe2–N(5) | 155.4(1) |
| Cl(2)–Fe1–N(3) | 101.0(1) | Cl(4)–Fe2–N(6) | 102.2(1) |
| Cl(1)–Fe1–Cl(2) | 114.7(1) | Cl(3)–Fe2–Cl(4) | 109.4(1) |
| N(1)–Fe1–N(2) | 73.7(2) | N(5)–Fe2–N(6) | 72.8(2) |
| N(1)–Fe1–N(3) | 144.5(1) | N(4)–Fe2–N(6) | 142.7(2) |
| N(2)–Fe1–N(3) | 73.0(2) | N(4)–Fe2–N(5) | 73.2(2) |

As in the complexes with an aryl group on the imine functions, the geometry of the metal center can be considered as distorted square-pyramidal, with one of the chlorine atoms occupying the apical position, with an almost 90-degree angle with the iron and the nitrogen atoms: N(1)(2)(3)–Fe1–Cl(1) ranging from 91.8° to 97.9° and N(4)(5)(6)–Fe2–Cl(3) ranging from 95.1° to 102.0°. The average apical Fe–Cl bond (2.35 Å) is longer than the average equatorial one (2.28 Å), as expected from this type of geometry. It is noticeable that these lengths are higher than for complexes bearing fully aromatic ligands. This seems to indicate that the electronic density on the iron becomes higher. The iron atom is slightly above the base of the pyramid: N(3)–Fe–N(1) 144.5°, which is close to the value found for the aromatic trimethyl analog described by Gibson et al.,[4] where the value is 145.5°. For comparison, in complex **1a** the angle is 139.2°.

The distances between the iron and both imines are almost identical (average 2.29 Å for Fe1 and 2.31 Å for Fe2). These bonds are a bit longer than for the complex with the 2,4,6-trimethyl aryl substituent[4] (average 2.27 Å), revealing the electronic effect generated by the replacement of an aryl by a cyclohexyl group. Besides, the Fe–$N_{py}$ bond length with an average of 2.09 Å in complex **2a** is shorter than for the aryl analog, where the value is 2.11 Å. The angle N–Fe–Cl where the nitrogen and the chlorine atom are *trans* to the basal plane is somewhat greater, with an average value of 154.4° in complex **2a** compared to 131.3° in the aryl one.[4]

Although the cyclohexyl groups are not planar and adopt a chair conformation with the two methyl substituents and the imine in the equatorial position, they are almost perpendicular to the plane of the square base, like aryl groups (dihedral angles: 117.1° and 111.8°). The average distance between the iron atom and the methyl substituents is about 4.3 Å, as already observed for the equivalent aromatic systems.

### Ethylene Polymerization with Complexes 1a, 1b, 2a, and 2b Activated with MAO

All the complexes were activated with methylaluminoxane and tested for the polymerization of ethylene. The results are summarized in Table 2 together with the experimental conditions.

With complexes **1a** and **1b**, polyethylene was produced with the same activity for the two metals, whereas, iron complexes generally present a higher catalytic activity than their cobalt analogs. This result might be due to faster deactivation processes of **1a** versus **1b**. The activities were compared with those observed for the nonchlorinated pyridine complexes (di*i*PrFe and di*i*PrCo). As indicated in Table 2, the presence of the chlorine atom in the *para* position of the pyridine decreases the catalytic activity, from 2220 to

Table 2. Ethylene polymerization with iron and cobalt complexes/MAO.

| Catalyst[a] | Yield [g] | Activity [g·mmol$^{-1}$·h$^{-1}$·bar$^{-1}$] | Productivity ($g_{PE}/g_{Cat.}$) | $M_n$[b] [g·mol$^{-1}$] | $M_w$[b] [g·mol$^{-1}$] | MMD[c] | $T_m$[d] [°C] | $\chi$[d] |
|---|---|---|---|---|---|---|---|---|
| **1a** | 1.9 | 810 | 295 | 800 | 35000 | 44 | 97; 136 | 0.82 |
| di*i*Pr-Fe | 5.5 | 2220 | 904 | 2200 | 48000 | 22 | 119; 136 | 0.82 |
| **1b** | 1.9 | 810 | 294 | 6400 | 29000 | 4 | 135 | 0.82 |
| di*i*Pr-Co | 3.4 | 1410 | 556 | 7000 | 30000 | 4 | 137 | 0.84 |

[a] Catalyst: 10 μmol; [Al]/[Met] = 400; $P_{Et.}$ = 1 bar; $T$ = 35 °C; $t$ = 15 min; toluene (40 mL). [b] Average molar masses measured by High Temperature Size Exclusion Chromatography in 1,2,4-trichlorobenzene at 150 °C with RI and viscosimetry detection. [c] Molar mass distribution. [d] Melting temperature and crystallinity rate measured by DSC.

 © 2006 Wiley-VCH Verlag GmbH & Co. KGaA, Weinheim 

810 g·mmol$^{-1}$·h$^{-1}$·bar$^{-1}$ for the iron complexes and from 1410 to 810 g·mmol$^{-1}$·h$^{-1}$·bar$^{-1}$ for the cobalt one. It was thought that slightly decreasing the electronic density on the metal would render the interaction with the incoming ethylene more favorable and then would enhance the catalytic activity.

Actually, this is not what happens because lowering the electronic density on the metal simultaneously disfavors the π back donation of the metal to the incoming ethylene. Bennett did not observe significant falls of activity with a cobalt complex substituted by a trifluoromethyl group in the *para* position of the pyridine ring, but experimental conditions were not comparable.[25] As the decrease in the catalytic activity cannot be explained by the small differences in the structures of the chlorinated and the nonchlorinated complex, the possible interaction of the chlorine atom present on the pyridine with MAO, used in a large excess, was studied. To do this we have observed by $^1$H NMR the chemical shifts of chlorobenzene (to mimic the ligand, this one would coordinate first with the nitrogen groups) in deuterated toluene after addition of a quantity of MAO similar to that used in the polymerization experiment. No significant chemical shifts have been observed, which means that there is probably no interaction between the chlorine atom and the TMA present in the MAO, or the MAO itself. Eventually, the loss of activity observed for the chlorinated complexes could be attributed to the lack of stability of the complex. Indeed, as can be seen on the $^1$H NMR spectrum of the complex (Figure 6), a great amount of decomposition product appeared within 20 min; this quantity increases with time. The decomposition process has not been studied in detail.

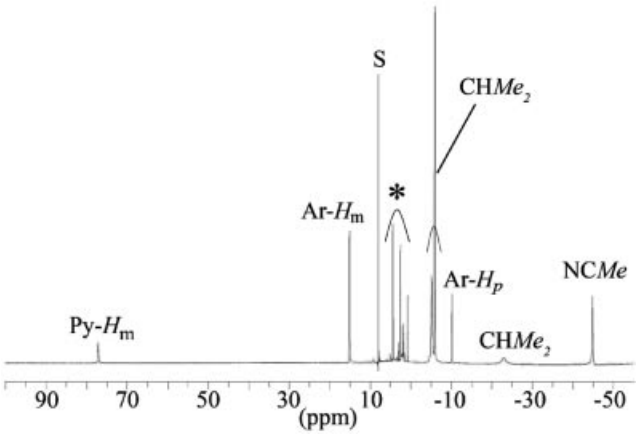


Figure 6. $^1$H NMR spectrum of complex **1a**. The peaks of the decomposition product are marked with * (300 MHz, 293 K, $CDCl_3$).

With the iron complex **2a** no polymers or oligomers have been detected. However, with the cobalt complex **2b** polymers are obtained (no oligomers could be detected by GC). Bianchini obtained oligomers with dissymmetric pyridine-bis(imine) ligands [the imine substituents being an aryl group and a (cyclo)alkyl group].[21] The proton NMR spectra of the iron complex (Figure 7, a) reveals that almost all the peaks are in the region from –8 to 11 ppm; only the peaks attributed to the protons on the pyridine are strongly shifted. Although the spectrum was obtained with a large window, from –55 to 250 ppm, some of the protons of the complex cannot be observed, probably because they are too large. Indeed the integration gives 35 protons instead of the 39 expected. An NMR study at low temperature, down to –90 °C, does not reveal new peaks. On the contrary, the broad peak at –11 ppm broadens even further at –70 °C and is invisible at –90 °C.

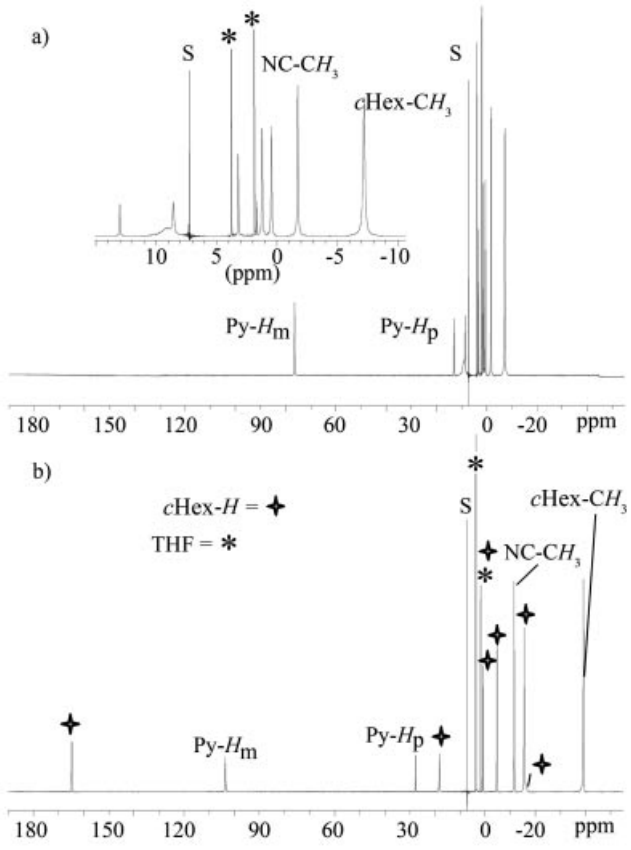


Figure 7. (a) $^1$H NMR spectrum of the iron complex **2a** containing THF marked with *; all the other nonmarked peaks are due to the protons on the cyclohexyl group. (b) $^1$H NMR spectrum of the cobalt complex **2b** containing THF marked with * (300 MHz, 293 K, $CDCl_3$).

All the spectra were recorded with pure crystals that contained THF of crystallization; this is the reason two relatively intense peaks of free THF can always be seen in the spectra. In the case of the cobalt complex the proton NMR shows us more important paramagnetic shift: the peaks are in the range –40 to 166 ppm (Figure 7, b). The integration of the peaks corresponds to what is expected.

These observations and the fact that there is a marked difference in the reactivity between the iron and the cobalt complexes bearing the same ligands prompted us to think that the ligand is in some way hemilabile in the case of iron.

The complete loss of activity can then be explained by the assumption that the addition of MAO can hinder the return of the imine group to the iron. On the contrary, for

 © 2006 Wiley-VCH Verlag GmbH & Co. KGaA, Weinheim 

the cobalt complex **2b**, the spectrum of which is shown in Figure 7 (b), polymerization of ethylene is observed in the presence of MAO. Under 4 bar of ethylene and after 3 h, 150 mg of polyethylene was isolated. We will not go into more detail, as the subject is currently under investigation.

The polymers obtained with **1a** and **1b** were analyzed by $^1$H NMR, DSC, and HT SEC. $^1$H NMR spectra of polyethylenes ($C_2D_2Cl_4$, 130 °C) present a main peak at 1.3 ppm due to $CH_2$ groups, and a small one at 0.9 ppm due to $CH_3$ groups coming from chain ends or branching. Nevertheless, the intensity of the peak at 0.9 ppm is too small to allow reliable integration.

The results of SEC measurements are presented in Table 2. The chlorine atom seems to have no influence on the molar masses or the molar mass distributions when cobalt is employed. For the iron complexes, broad (even bimodal) molar mass distributions were obtained. It is now well established that this is due to transfer to aluminum (TMA present in MAO). It was nevertheless a bit surprising to get such broad distributions, as to avoid this transfer, the MAO we employed had most of its TMA removed by evaporation (5 mol-% residual TMA instead of 30 mol-% in commercial MAO). For cobalt complexes, molar mass distributions were much lower, because these catalytic systems are less sensitive towards transfer to aluminum.

The results of DSC measurements are also presented in Table 2. Like for SEC measurements, no huge differences were observed for the chlorinated and nonchlorinated ligands. The chlorine atom seems to have almost no influence on the melting temperatures and on the crystallinity rate. For all polyethylenes, the crystallinity rate (>0.8) is consistent with highly linear polymers. Polyethylenes obtained with the iron complexes exhibit two melting temperatures corresponding probably to two populations of polymers of different molar masses observed by HT SEC. With the cobalt complexes, only one melting temperature, very close to the one measured for highly linear polyethylene, was observed.

## Conclusion

In summary, two new pyridine-bis(imine)s were synthesized, by substituting the pyridine ring, or by replacing the aryl groups linked to the imine functions by an aliphatic ring. These ligands were complexed with iron and cobalt dichloride and two of these four new complexes were characterized by X-ray analysis. All the complexes were tested in the presence of MAO for the polymerization of ethylene. The introduction of a chlorine atom onto the pyridine ring was unfavorable; indeed the catalytic activity decreases compared to the unsubstituted ligand. For the other ligand two different results were observed. In the case of the iron complex, the loss of aromaticity led to a complete loss of catalytic activity towards ethylene polymerization and oligomerization. On the other hand, for the cobalt system, polyethylene could be obtained.

## Experimental Section

### General Considerations

Anhydrous $FeCl_2$ and $CoCl_2$, diacetylpyridine, chelidamic acid, thionyl chloride, Meldrum's acid, and 2,6-diisopropylaniline (all purchased from Aldrich) were used as received. 2,6-Dimethylcyclohexylamine was kindly provided by BASF AG. Methylaluminoxane (MAO) was purchased from Aldrich as a 10 wt.-% solution in toluene. Toluene and most of the trimethylaluminum (TMA) were removed under vacuum to yield a white powder, still containing 5 mol-% of TMA. Tetrahydrofuran, hexane, and toluene were distilled from sodium benzophenone ketyl. All complex syntheses were performed in a Jacomex glovebox or under thoroughly purified argon using a standard Schlenk technique. 2,6-Diacetyl-4-chloropyridine was prepared according to an already published procedure.[24]

### Characterization

$^1$H and $^{13}$C NMR spectra were recorded with a Bruker Avance-300 apparatus (300 MHz) at room temperature. IR spectra were recorded with a Perkin–Elmer 1600 FTIR spectrometer. Molar masses were measured by Size Exclusion Chromatography using an Alliance GPCV 2000 Permeation Chromatograph equipped with a differential refractive index detector and a viscosimeter in 1,2,4-trichlorobenzene (150 °C) using two Styragel HT 6E and one HT 2 columns. DSC measurements were performed with a Perkin–Elmer DSC4 or DSC7, with a heating rate of 10 °C·min$^{-1}$.

### Synthesis of Ligands

**4-Chloro-2,6-bis[1-(2,6-diisopropylphenylimino)ethyl]pyridine (1):** 2,6-Diacetyl-4-chloropyridine (0.5 g, 2.5 mmol), 2,6-diisopropylaniline (0.98 g, 5.5 mmol), and a small amount of *p*-toluenesulfonic acid were poured into a three-necked round-bottomed flask containing toluene (50 mL). The solution was refluxed for 24 h with a Dean–Stark trap. After lowering the temperature, the toluene was removed under vacuum to yield a brownish oil. The addition of hexane (20 mL) led to a yellow solution and a brown solid. After filtration and drying, a yellow solid was recovered (0.94 g, yield 72%). $^1$H NMR (300 MHz, $CDCl_3$, 293 K): $\delta$ = 8.48 (s, 2 H, py-$H_m$), 7.22–7.09 (m, 6 H, Ar-*H*), 2.74 (sept, $^3J_{H,H}$ = 6.9 Hz, 4 H, C*H*Me$_2$), 2.25 (s, 6 H, N=C-*Me*), 1.17 (d, $^3J_{H,H}$ = 6.9 Hz, 12 H, CH*Me*Me), 1.16 (d, $^3J_{H,H}$ = 6.9 Hz, 12 H, CHMe*Me*) ppm. $^{13}$C NMR (75 MHz, $CDCl_3$, 293 K): $\delta$ = 166.0 (N=*C*), 156.5 (Py-$C_o$), 146.0 (Ar-$C_{ip}$), 145.4 (Py-*C*-Cl), 135.7 (Ar-$C_o$), 123.8 (Ar-$C_p$), 123.0 (Py-$C_m$), 122.2 (Ar-$C_m$), 28.3 (N=C-*Me*), 23.3 (CH*Me*Me), 22.9 (CHMe*Me*), 17.2 (*C*HMe$_2$) ppm. IR: $\tilde{\nu}$ = 1640, 1557, 1317, 1260, 1228, 1189, 1104, 1016, 935, 885, 828, 762, 722, 692, 535, 438 cm$^{-1}$. $C_{33}H_{42}ClN_3$ (516.16): calcd. C 76.79, N 8.14, H 8.20; found C 73.23, N 7.21, H 8.35.

**2,6-Bis[1-(2,6-dimethylcyclohexylimino)ethyl]pyridine (2all-*cis*):** 2,6-Diacetylpyridine (2 g, 12.3 mmol), 2,6-dimethylcyclohexylamine all-*cis* (3.2 g, 25 mmol), and a few drops of acetic acid were poured into a three-necked round-bottomed flask containing ethanol (50 mL). The solution was refluxed for 18 h. After lowering the temperature, a white precipitate appeared. After filtration, washing with pentane and drying, a white solid was recovered (3.7 g, yield 82%). $^1$H NMR (300 MHz, $CDCl_3$, 293 K): $\delta$ = 8.18 (d, $^3J_{H,H}$ = 7.6 Hz, 2 H, py-$H_m$), 7.68 (t, $^3J_{H,H}$ = 7.6 Hz, 1 H, py-$H_p$), 3.71 (t, $^3J_{H,H}$ = 2.2 Hz, 2 H, C$H_{c\text{Hex}}$-N=), 2.38 (s, 6 H, N=C-C$H_3$), 1.88–1.32 (br. m, 16 H, *c*Hex-C$H_2$-), 0.70 (d, $^3J_{H,H}$ = 6.6 Hz, 12 H, *c*Hex-C$H_3$) ppm. $^{13}$C NMR (75 MHz, $CDCl_3$, 293 K): $\delta$ = 164.0 (-*C*=N), 156.5 (py-$C_o$), 135.9 (py-$C_p$), 120.8 (py-$C_m$), 65.2 (C$H_{c\text{Hex}}$-N=), 38.6 (*c*Hex-$C_o$), 28.9 (*c*Hex-$C_m$), 27.1 (*c*Hex-$C_p$), 19.3 (*c*Hex-*C*H$_3$),

 © 2006 Wiley-VCH Verlag GmbH & Co. KGaA, Weinheim 

13.3 ($CH_3$-C=N) ppm. IR: ṽ = 1703, 1638, 1567, 1303, 1237, 1156, 1116, 1086, 995, 980, 950, 857, 838, 818, 626, 558, 530, 491, 440, 338, 277 $cm^{-1}$. $C_{25}H_{39}N_3$ (381.60): calcd. C 78.69, N 11.01, H 10.30; found C 78.70, N 11.11, H 10.34.

**2,6-Bis[1-(2,6-dimethylcyclohexylimino)ethyl]pyridine (2all-*trans*):** 2,6-Diacetylpyridine (2 g, 12.3 mmol), 2,6-dimethylcyclohexylamine all-*trans* (3.2 g, 25 mmol), and a few drops of acetic acid were poured into a three-necked round-bottomed flask containing ethanol (50 mL). The solution was refluxed for 18 h. After lowering the temperature, a white precipitate appeared. After filtration, washing with pentane and drying, a white solid was recovered (3.6 g, yield 76%). $^1$H NMR (300 MHz, $CDCl_3$, 293 K): $\delta$ = 8.09 (d, $^3J_{H,H}$ = 7.7 Hz, 2 H, py-$H_m$), 7.69 (t, $^3J_{H,H}$ = 7.7 Hz, 1 H, py-$H_p$), 2.92 (t, $^3J_{H,H}$ = 9.3 Hz, 2 H, $CH_{c\mathrm{Hex}}$-N=), 2.39 (s, 6 H, N=C Me), 1.82–1.10 (br. m, 16 H, cyclohexyl -$CH_2$-), 0.74 (d, $^3J_{H,H}$ = 6.6 Hz, 12 H, *c*Hex-$CH_3$) ppm. $^{13}$C NMR (75 MHz, $CDCl_3$, 293 K): $\delta$ = 164.8 (-C=N), 156.8 (py-$C_o$), 136.5 (py-$C_p$), 121.0 (py-$C_m$), 72.8 ($CH_{hex}$-N=), 37.9 (*c*Hex-$C_o$), 33.9 (*c*Hex-$C_m$), 25.8 (*c*Hex-$C_p$), 19.5 (*c*Hex-$CH_3$), 14.7 ($CH_3$-C=N) ppm. IR: ṽ = 1643, 1567, 1305, 1237, 1172, 1153, 1116, 1088, 993, 948, 858, 839, 817, 779, 624, 555, 440, 340, 274, 228 $cm^{-1}$. $C_{25}H_{39}N_3$ (381.60): calcd. C 78.69, N 11.01, H 10.30; found C 78.45, N 11.41, H 10.38.

### Synthesis of the Complexes

**{4-Chloro-2,6-bis[1-(2,6-diisopropylphenylimino)ethyl]pyridine}iron Dichloride (1a):** $FeCl_2$ (36 mg, 0.28 mmol) and 4-chloro-2,6-bis[1-(2,6-diisopropylphenylimino)ethyl]pyridine (150 mg, 0.29 mmol) were dissolved in THF (25 mL). The reaction was let run for 16 h. After precipitation with hexane, filtration, and drying, a blue powder was recovered (150 mg, yield 83%). $^1$H NMR (300 MHz, $CDCl_3$, 293 K, $\delta_{solvent}$ = 7.26): $\delta$ = 76.46 (s, 2 H, $H_m$, Py), 14.40 (s, 4 H, $H_m$ Ar), –5.86 (br. s, 12 H, CH*Me*Me), –6.62 (s, 12 H, CHMe*Me*), –10.87 (s, 2 H, $H_p$ Ar), –23.70 (br. s, 4 H, C*H*Me), –45.57 (s, 6 H, NC*Me*) ppm. $C_{33}H_{42}Cl_3FeN_3$ (642.91): calcd. C 61.65, N 6.54, H 6.58; found C 61.88, N 6.01, H 7.35. IR: ṽ = 1689, 1574, 1500, 1320, 1282, 1237, 1115, 1015, 806, 722, 525, 365, 313 $cm^{-1}$.

**{4-Chloro-2,6-bis[1-(2,6-diisopropylphenylimino)ethyl]pyridine}-cobalt Dichloride (1b):** $CoCl_2$ (38 mg, 0.29 mmol) and 4-chloro-2,6-bis[1-(2,6-diisopropylphenylimino)ethyl]pyridine (150 mg, 0.29 mmol) were dissolved in THF (25 mL). The reaction was let run for 16 h. After precipitation with hexane, filtration, and drying, a green powder was recovered (150 mg, yield 81%). $C_{33}H_{42}Cl_3CoN_3$ (646.00): calcd. C 61.36, N 6.50, H 6.55; found C 59.52, N 5.42, H 6.70. IR: ṽ = 1582, 1325, 1264, 1204, 1103, 1057, 1028, 938, 858, 854, 838, 798, 768, 722, 590, 487, 440, 347, 309, 280, 213 $cm^{-1}$.

**{2,6-Bis[1-(2,6-dimethylcyclohexylimino)ethyl]pyridine}iron Dichloride (2a):** $FeCl_2$ (132 mg, 1.04 mmol) and 2,6-bis[1-(2,6-dimethylcyclohexylimino)ethyl]pyridine all-*trans* (400 mg, 1.04 mmol) were dissolved in THF (25 mL). The reaction was let run for 16 h. After precipitation with hexane, filtration, and drying, a blue powder was recovered (400 mg, yield 75%). $^1$H NMR (300 MHz, $CD_2Cl_2$, 298 K, $\delta_{solvent}$ = 5.32): $\delta$ = 78.34 (s, 2 H, py-$H_m$), 10.14 (v br. s, 2 H, $C_{c\mathrm{Hex}}$-*H*), 8.84 (s, 2 H, $C_{c\mathrm{Hex}}$-*H*), 8.58 (s, 1 H, py-$H_p$), 3.46 (s, 2 H, $C_{c\mathrm{Hex}}$-*H*), 1.73 (s, 4 H, $C_{c\mathrm{Hex}}$-*H*), 1.02 (s, 4 H, $C_{c\mathrm{Hex}}$-*H*), –1.29 (s, 6 H, N=C-C$H_3$), –6.99 (br. s, 12 H, $C_{c\mathrm{Hex}}$-C$H_3$) ppm. $C_{25}H_{39}Cl_2FeN_3$ (508.35): calcd. C 59.07, N 8.27, H 7.73; found C 58.52, N 8.40, H 7.71. IR: ṽ = 1582, 1268, 1198, 1020, 948, 842, 816, 718, 639, 568, 314, 285 $cm^{-1}$.

**{2,6-Bis[1-(2,6-dimethylcyclohexylimino)ethyl]pyridine}cobalt Dichloride (2b):** $CoCl_2$ (136 mg, 1.04 mmol) and 2,6-bis[1-(2,6-dimethylcyclohexylimino)ethyl] all-*trans* (400 mg, 1.04 mmol) were dissolved in THF (25 mL). The reaction was let run for 16 h. After precipitation with hexane, filtration, and drying, a green powder

Table 3. Crystal data and structure refinement.

| | **1a** | **2a all-*trans*** | **2all-*cis*** |
|---|---|---|---|
| Empirical formula | $C_{37}H_{52}Cl_3FeN_3O$<br>$C_{33}H_{42}Cl_3FeN_3{\cdot}C_4H_{10}O$ | $C_{112}H_{182}Cl_8Fe_4N_{12}O_4$<br>$C_{100}H_{156}Cl_8Fe_4N_{12}{\cdot}3C_4H_8O{\cdot}H_2O$ | $C_{25}H_{39}N_3$ |
| Formula mass | 717.05 | 2267.8(1) | 381.59 |
| Temperature [K] | 173 | 173 | 173 |
| *Z* | 4 | 4 | 8 |
| Crystal system | monoclinic | monoclinic | orthorhombic |
| Space group | *P*21/*c* | *C*2/*c* | *Pbcn* |
| *a* [Å] | 10.3742(2) | 43.5402(5) | 23.0750(6) |
| *b* [Å] | 20.2225(5) | 12.5601(2) | 14.6860(6) |
| *c* [Å] | 18.6578(4) | 26.2792(3) | 13.7930(9) |
| $\beta$ [°] | 97.982(5) | 117.157(5) | 90.00 |
| *V* [Å$^3$] | 3876.3(1) | 12787.0(6) | 4674.2(4) |
| Color | blue | violet | colorless |
| Crystal size [mm] | 0.20×0.06×0.02 | 0.16×0.12×0.06 | 0.20×0.20×0.15 |
| $D_{calcd.}$ [g·cm$^{-3}$] | 1.23 | 1.17 | 1.085 |
| *F*(000) | 1520 | 4800 | 1680 |
| Absorption coefficient [mm$^{-1}$] | 0.627 | 0.661 | 0.063 |
| Index ranges | $-14 \le h \le 14$<br>$-26 \le k \le 28$<br>$-26 \le l \le 26$ | $0 \le h \le 61$<br>$0 \le k \le 17$<br>$-36 \le l \le 32$ | $-29 \le h \le 29$<br>$-19 \le k \le 19$<br>$-17 \le l \le 17$ |
| $\theta$ range [°] | 2.5–30.55 | 2.5–30.01 | 1.77–27.48 |
| Reflections collected | 12118 | 19449 | 5354 |
| Reflections observed [$I > 3\sigma(I)$] | 3120 | 10571 | 2862 |
| Number of parameters | 406 | 632 | 253 |
| *R* | 0.046 | 0.076 | 0.0555 |
| *Rw* | 0.061 | 0.094 | 0.1278 |
| Goodness-of-fit on $F^2$ | 1.028 | 1.119 | 0.954 |
| Largest difference peak, hole [e·Å$^{-3}$] | 0.350, –0.122 | 0.868, –0.873 | 0.183, –0.186 |

 © 2006 Wiley-VCH Verlag GmbH & Co. KGaA, Weinheim 

was recovered (350 mg, yield 65%). $^1$H NMR (300 MHz, $CDCl_3$, 293 K, $\delta_H$ = 7.26): $\delta$ = 164.79 (s, 2 H, $C_{cHex}$-*H*), 103.50 (s, 2 H, py-$H_m$), 27.73 (s, 1 H, py-$H_p$), 18.21 (s, 2 H, $C_{cHex}$-*H*), 3.70 (s, 2 H, $C_{cHex}$-*H*), 0.79 (s, 2 H, $C_{cHex}$-*H*), –4.72 (s, 4 H, $C_{cHex}$-*H*), –11.59 (s, 6 H, N=C-C$H_3$), –15.58 (s, 4 H, $C_{cHex}$-*H*), –16.02 [s (v br. sh), 2 H, $C_{cHex}$-*H*], –39.19 (s, 12 H, $C_{cHex}$-C$H_3$) ppm. $C_{25}H_{39}Cl_2CoN_3$ (511.44): calcd. C 58.71, N 8.20, H 7.69; found C 58.41, N 8.49, H 7.69. IR: $\tilde{\nu}$ = 1620, 1582, 1266, 1248, 1198, 1115, 1023, 948, 864, 823, 816, 746, 716, 638, 568, 317, 287 cm$^{-1}$.

**Polymerization Procedure:** Polymerizations were conducted in a 250-mL glass Büchi reactor equipped with a magnetic stirrer and a temperature controller. Ethylene pressure was maintained constant in the reactor during the reaction. A typical procedure was: catalyst (10 μmol) in solution in toluene (30 mL) was added to the reactor under nitrogen. The reactor was heated to the reaction temperature and charged with ethylene. A solution of the desired amount of MAO dissolved in toluene (10 mL) was then added to the system. The reactor was charged with the desired differential pressure of ethylene. The reaction was let run for a period of 15 min, after which acidified ethanol (20 mL) was added to the miniclave to stop the polymerization. The content of the reactor was then precipitated in ethanol. The precipitated polymer was washed with ethanol and dried overnight in a vacuum oven at 60 °C.

**X-ray Crystallography:** Crystals of **1a**, **2a**, and **2all-*cis*** coated with vaseline were mounted onto the goniometer and placed on a Nonius Kappa CCD diffractometer with graphite-monochromated Mo-$K_\alpha$ radiation ($\lambda$ = 0.71073 Å). The structures were solved using the Nonius OpenMoleN package and refined against $F^2$ using the SHELXL-97 software[25] with anisotropical thermal parameters for all non-hydrogen atoms (except for one THF and the $H_2O$ in **2a**) and hydrogen atoms were introduced as fixed contribution (SHELXL-97[26]) (except for one THF and the $H_2O$ in **2a**) (see Table 3).

CCDC-255729 (for $C_{33}H_{42}Cl_3FeN_3{\cdot}C_4H_{10}O$, **1a**), -255730 (for $C_{100}H_{156}Cl_8Fe_4N_{12}{\cdot}3OC_4H_8{\cdot}H_2O$, **2a**), and -613556 (for $C_{25}H_{39}N_3$, **2all-*cis***) contain the supplementary crystallographic data for this paper. These data can be obtained free of charge from The Cambridge Crystallographic Data Centre via www.ccdc.cam.ac.uk/data_request/cif.

## Acknowledgments

The authors want to thank the CNRS for financial support, Prof. Richard Blackborow, BASF, and Dr. Rath for providing the 2,6-dimethylcyclohexylamines, Suzanne Zehnacker for DSC measurements, Emmanuel Ibarboure and Prof. Henri Cramail (LCPO, Bordeaux, France) for HT SEC measurements, Jean-Daniel Sauer for the low-temperature NMR measurements, Nathalie Kyritsakas-Gruber for X-ray refinements of the complexes, Dr. André De Cian for all the X-ray measurements and the X-ray refinement of the free ligand, and Dr. Marie-Thérèse Youinou for her helpful advice.

[1] G. J. P. Britovsek, V. C. Gibson, B. S. Kimberley, P. J. Maddox, S. J. McTavish, G. A. Solan, A. J. P. White, D. J. Williams, *Chem. Commun.* **1998**, 849–850.
[2] B. L. Small, M. Brookhart, A. M. A. Bennett, *J. Am. Chem. Soc.* **1998**, *120*, 4049–4050.
[3] B. L. Small, M. Brookhart, *J. Am. Chem. Soc.* **1998**, *120*, 7143–7144.
[4] a) G. J. P. Britovsek, M. Bruce, V. C. Gibson, B. S. Kimberley, P. J. Maddox, S. Mastroianni, S. J. McTavish, C. Redshaw, G. A. Solan, S. Strömberg, A. J. P. White, D. J. Williams, *J. Am. Chem. Soc.* **1999**, *121*, 8728–8740; b) V. C. Gibson, S. K. Spitzmesser, *Chem. Rev.* **2003**, *103*, 283–315.
[5] J. Qiu, Y. Li, Y. Hu, *Polym. Int.* **2000**, *49*, 5–7.
[6] G. J. P. Britovsek, S. Mastroianni, G. A. Solan, S. P. D. Baugh, C. Redshaw, V. C. Gibson, A. J. P. White, D. J. Williams, M. R. J. Elsegood, *Chem. Eur. J.* **2000**, *6*, 2221–2231.
[7] Z. Ma, H. Wang, J. Qiu, D. Xu, Y. Hu, *Macromol. Rapid Commun.* **2001**, *22*, 1280–1283.
[8] R. Chen, C. Qian, J. Sun, *Chin. J. Chem.* **2001**, *19*, 866–869.
[9] A. S. Abu-Surrah, K. Lappalainen, U. Piironen, P. Lehmus, T. Repo, M. Leskelä, *J. Organomet. Chem.* **2002**, *648*, 55–61.
[10] Z. Ma, W.-H. Sun, Z.-L. Li, C.-X. Shao, Y.-L. Hu, *Chin. J. Polym. Sci.* **2002**, *20*, 205–211.
[11] Z. Ma, W.-H. Sun, N. Zhu, Z. Li, C. Shao, Y. Hu, *Polym. Int.* **2002**, *51*, 349–352.
[12] R. Schmidt, U. Hammon, S. Gottfried, M. B. Welch, H. G. Alt, *J. Appl. Polym. Sci.* **2003**, *88*, 476–482.
[13] Y. Chen, R. Chen, C. Qian, X. Dong, J. Sun, *Organometallics* **2003**, *22*, 4312–4321.
[14] Y. Chen, C. Qian, J. Sun, *Organometallics* **2003**, *22*, 1231–1236.
[15] H. Wang, W. D. Yan, T. Jiang, B. B. Liu, W. Q. Xu, J. J. Ma, Y. L. Hu, *Chin. Chem. Lett.* **2003**, *14*, 257–258.
[16] M. E. Bluhm, C. Folli, M. Döring, *J. Mol. Catal. A* **2004**, *212*, 13–18.
[17] a) F. Pelascini, F. Peruch, P. J. Lutz, M. Wesolek, J. Kress, *Eur. Polym. J.* **2005**, *41*, 1288–1295; b) V. C. Gibson, S. K. Spitzmesser, *Chem. Rev.* **2003**, *103*, 283–315; c) S. D. Ittel, L. K. Johnson, M. Brookhart, *Chem. Rev.* **2000**, *100*, 1169–1203; d) R. Mulhaupt, *Macromol. Chem. Phys.* **2003**, *204*, 289–327.
[18] G. J. P. Britovsek, V. C. Gibson, S. Mastroianni, D. C. H. Oakes, C. Redshaw, G. A. Solan, A. J. P. White, D. J. Williams, *Eur. J. Inorg. Chem.* **2001**, 431–437.
[19] G. J. P. Britovsek, V. C. Gibson, B. S. Kimberley, S. Mastroianni, C. Redshaw, G. A. Solan, A. J. P. White, D. J. Williams, *J. Chem. Soc., Dalton Trans.* **2001**, 1639–1644.
[20] C. Amort, M. Malaun, A. Krajete, H. Kopacka, K. Wurst, M. Christ, D. Lilge, M. O. Kristen, B. Bildstein, *Appl. Organomet. Chem.* **2002**, *16*, 506–516.
[21] C. Bianchini, G. Mantovani, A. Meli, F. Migliacci, F. Zanobini, F. Laschi, A. Sommazzi, *Eur. J. Inorg. Chem.* **2003**, 1620–1631.
[22] G. J. P. Britovsek, V. C. Gibson, O. Hoarau, S. K. Spitzmesser, A. J. P. White, D. J. Williams, *Inorg. Chem.* **2003**, *42*, 3454–3465.
[23] V. C. Gibson, S. K. Spitzmesser, A. J. P. White, D. J. Williams, *Dalton Trans.* **2003**, 2718–2727.
[24] R. Ali Fallahpour, E. C. Constable, *J. Chem. Soc., Perkin Trans. 1* **1997**, 2263–2264.
[25] A. M. A. Bennett, World Patent, WO9827124, **1998**.
[26] G. M. Sheldrick, *SHELXL-97*, Program for the Refinement of Crystal Structures, University of Göttingen, Germany, **1997**.

Received: March 16, 2006
Published Online: August 24, 2006

 © 2006 Wiley-VCH Verlag GmbH & Co. KGaA, Weinheim 

DOI: 10.1002/ejic.200600262

# Synthesis, Structures, and Luminescent Properties of $d^{10}$ Group 12 Metal Complexes with Substituted 2,2′-Bipyridine Ligands

**Xiao-ming Liu,[a] Xiao-yue Mu,[a] Hong Xia,[a,b] Ling Ye,[a] Wei Gao,[a] Hao-yu Wang,[a] and Ying Mu*[a]**

**Keywords:** Group 12 metal complexes / 2,2′-Bipyridine / Solid-state structures / Luminescence

Four $d^{10}$ group 12 metal complexes, 6-(2-methoxyphenyl)-2,2′-bipyridinezinc dichloride (**2a**), -mercury dichloride (**2b**), 6-[2-(dimethylamino)phenyl]-2,2′-bipyridinezinc dichloride (**2c**), and -mercury dichloride (**2d**), were synthesized and the structures determined by single-crystal X-ray crystallography. Complexes **2a** and **2b** are four-coordinate and adopt a distorted tetrahedral geometry, while complexes **2c** and **2d** are five-coordinate with a distorted trigonal bipyramidal geometry for the metal center. Luminescent properties of complexes **2a**–**2d** in both solution and the solid state were studied.

(© Wiley-VCH Verlag GmbH & Co. KGaA, 69451 Weinheim, Germany, 2006)

## Introduction

Luminescent coordination complexes have attracted increasing attention because of their potential application in areas of optoelectronic devices and chemical sensors.[1] One of the most important considerations in organic light-emitting diodes (OLEDs) is the design and synthesis of molecules capable of tuning luminescent properties through the modification of ligands.[2,3] The organic compounds with aromatic nitrogen heterocycles, which can be receptors for metal ions, have been studied extensively because they are capable of performing useful light- and/or redox-induced tasks. For example, a large number of complexes based on 8-hydroxyquinoline, 7-azaindole, pyridyl-phenol, and phenyl-pyridine have been investigated during the last decades.[3–5] Particularly, luminescent complexes of $Re^{I}$,[6] $Ru^{II}$,[7] and $Os^{II}$[8] containing bipyridine type ligands have attracted much attention because of their high luminescent efficiency. However, the lower synthetic yields and higher costs of these complexes are disadvantages for their use as optoelectronic materials. The lower-cost $d^{10}$ metal complexes with the nitrogen-containing ligands are of interest because of their photoluminescent and/or electroluminescent properties.[9–11] To develop new complexes of this type with improved luminescent performance, we have synthesized four new complexes of zinc(II) and mercury(II) with modified bipyridine ligands that are synthesized by introducing an aromatic group with a donor at its α position to the 3-position of 2,2′-bipyridine. The ligands were selected considering that larger conjugating systems can be formed in their complexes and better luminescent properties might be expected. We herein report on the preparation, structural characterization, and photoluminescence of these zinc(II) and mercury(II) complexes.

[a] Key Laboratory for Supramolecular Structure and Materials of Ministry of Education, School of Chemistry, Jilin University, 2699 Qianjin Street, Changchun 130012, People's Republic of China
Fax: +86-431-5193421
E-mail: ymu@mail.jlu.edu.cn
[b] State Key Laboratory of Integrated Optoelectronics, College of Electronic Science and Technology, Jilin University, Changchun 130012, People's Republic of China

## Results and Discussion

### Synthesis of Compounds

Ligand **1a** was prepared according to a known procedure (Scheme 1)[12] and ligand **1b** was synthesized by the reaction of dry 2,2′-bipyridine with the aryllithium reagent, obtained from the treatment of 2-bromo-*N*,*N*-dimethylaniline with *n*BuLi, in moderate yield after oxidative rearomatization. Ligand **1a** is a known compound while **1b** is a new compound. The new ligand **1b** was characterized by $^1$H NMR spectroscopy along with elemental analysis. The $^1$H NMR spectrum of **1b** exhibits resonance at $\delta$ = 2.77 ppm for the $CH_3$ proton. Compound **1b** is soluble in most organic solvents. Treatment of $ZnCl_2$ and $HgCl_2$ with equivalent free ligands in methanol at ambient temperature afforded the corresponding $d^{10}$ metal complexes **2a**–**2d** in good yields (>80%) as light yellow or white crystalline solids (Scheme 1). Complexes **2a**–**2d** were all characterized by elemental analyses, $^1$H NMR spectroscopy, and IR spectroscopy, and satisfactory analytic results were obtained on all compounds. All complexes are moderately soluble in DMSO, slightly soluble in dichloromethane, methanol, DMF, and THF, and insoluble in saturated hydrocarbon solvents.

 © 2006 Wiley-VCH Verlag GmbH & Co. KGaA, Weinheim 

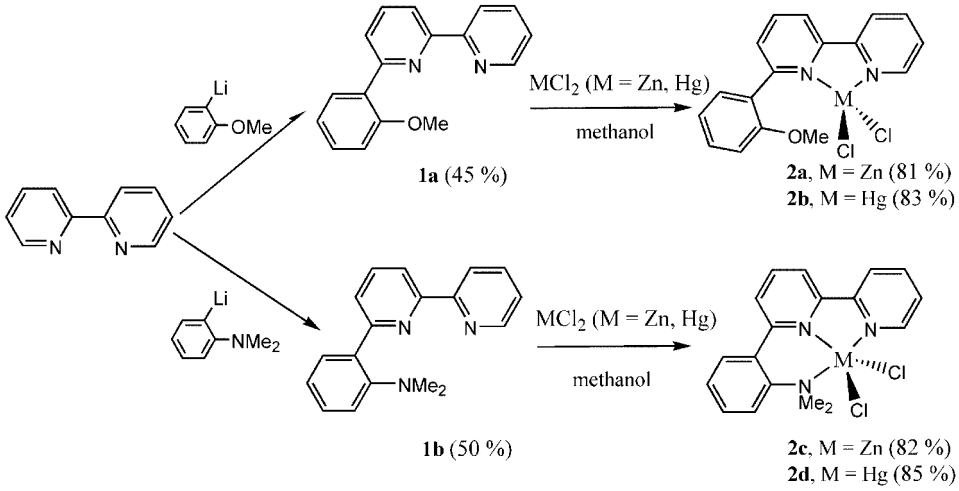


Scheme 1. Synthetic procedure of ligands **1a** and **1b**, and of complexes **2a**–**2d**.

### Crystal Structure

The molecular structures of complexes **2a**, **2b**, **2c**, and **2d** were determined by X-ray crystallographic analysis. Crystals of all four complexes suitable for X-ray crystal structure

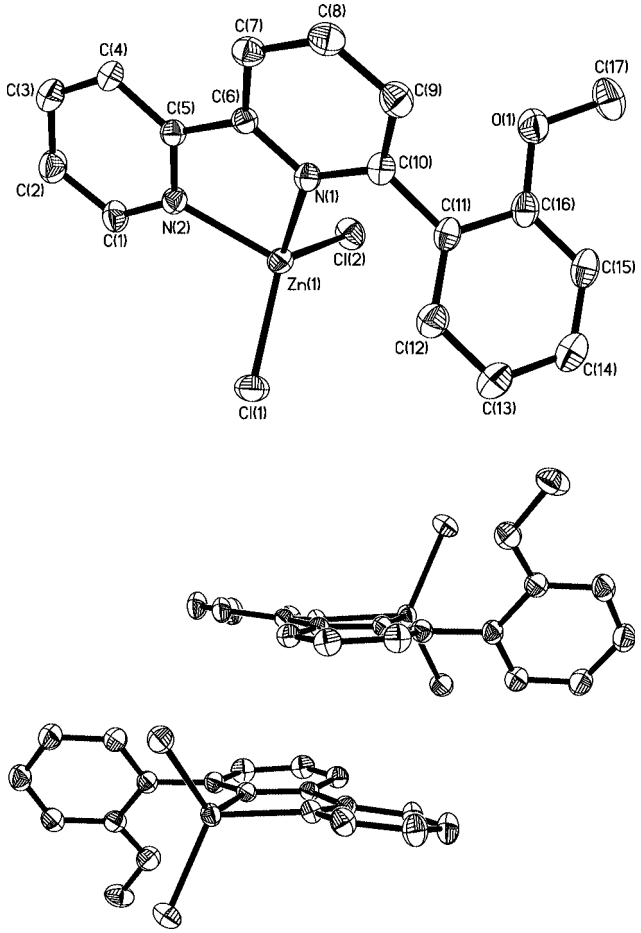


Figure 1. Top: molecular structure of complex **2a**; bottom: crystal packing diagram between two adjacent molecules of **2a** showing the lack of a π–π stacking interaction in the solid state. (Thermal ellipsoids are drawn at the 30% probability level.)

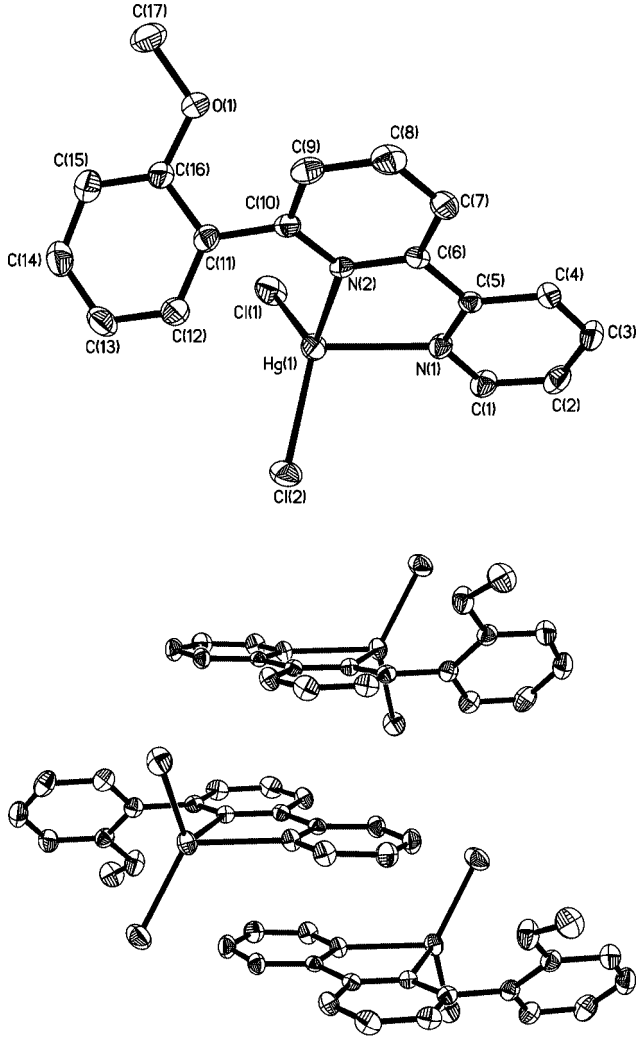


Figure 2. Top: molecular structure of complex **2b**; bottom: the π–π stacking column structure of complex **2b**. (Thermal ellipsoids are drawn at the 30% probability level.)

 © 2006 Wiley-VCH Verlag GmbH & Co. KGaA, Weinheim 

determination were grown from dichloromethane or $CH_3CN$ at room temperature. The ORTEP drawings of the molecular structures of **2a** and **2b** are shown in Figure 1 and Figure 2, respectively. Selected bond lengths and angles for the two complexes are given in Table 1. The X-ray analysis reveals that both complexes adopt a distorted tetrahedral geometry with the metal center chelated by the ligand **1a** through the pyridine nitrogen atoms, and the oxygen atom does not coordinate to the metal center in either complex because of the weak donating ability of the –OMe group. The Zn–N bond lengths in **2a** are 2.071 Å (average), which is close to the values previously reported for similar tetrahedral zinc complexes.[13] In complex **2b**, the two Hg–N bond lengths are slightly different [2.363(3) Å for Hg(1)–N(1) and 2.356(3) Å for Hg(1)–N(2)]. The values are consistent with bond lengths found in other four-coordinate $Hg^{II}$ complexes.[13c,14] The average $M^{II}$–N(pyridyl) bond distances (2.071 Å for Zn–N < 2.359 Å for Hg–N) are consistent with ionic radii. The N–Zn–N bite angle in **2a** [80.27(10)°] is smaller than those found in other pyridyl-containing four-coordinate $Zn^{II}$ complexes,[13a] but larger than the one [70.04(10)°] in its mercury analog **2b**. The dihedral angles between the two pyridyl rings are 10.1° for **2a** and 2.2° for **2b**, and the dihedral angles between the aromatic ring and the adjacent pyridyl ring are 61.0° for **2a** and 50.7° for **2b**. The data of the dihedral angles in two complexes indicate that the conjugated extent of **2b** is larger than that of **2a**. In addition, there is π–π stacking between the pyridyl rings of two neighboring molecules for complex **2a** in the solid state, forming an antiparallel dimeric structure (Figure 1 bottom). The distance between two pyridyl planes is 3.51 Å.[15] In contrast, a π–π stacking column structure was observed in **2b** (Figure 2 bottom). In the column each molecule of **2b** forms antiparallel π–π stacking with two adjacent molecules. The distances between the stacked aromatic planes are 3.46 Å and 3.50 Å, respectively. A similar π–π stacking column structure was also observed in $Hg^{II}$ complexes.[13c]

Table 1. Selected bond lengths (Å) and bond angles (°) for complexes **2a**–**2d**.

| | | | |
|---|---|---|---|
| Complex **2a** | | | |
| Zn(1)–N(1) | 2.079(2) | N(1)–Zn(1)–Cl(1) | 123.53(8) |
| Zn(1)–N(2) | 2.062(2) | N(2)–Zn(1)–Cl(2) | 115.07(8) |
| Zn(1)–Cl(1) | 2.2042(10) | N(1)–Zn(1)–Cl(2) | 108.76(7) |
| Zn(1)–Cl(2) | 2.2104(10) | Cl(1)–Zn(1)–Cl(2) | 117.18(4) |
| N(2)–C(1) | 1.333(4) | C(1)–N(2)–Zn(1) | 125.8(2) |
| N(1)–C(10) | 1.342(4) | C(5)–N(2)–Zn(1) | 113.69(19) |
| N(2)–Zn(1)–N(1) | 80.27(10) | C(10)–N(1)–Zn(1) | 127.7(2) |
| N(2)–Zn(1)–Cl(1) | 106.30(8) | C(6)–N(1)–Zn(1) | 113.09(19) |
| Complex **2b** | | | |
| Hg(1)–N(1) | 2.363(3) | N(1)–Hg(1)–Cl(1) | 118.49(9) |
| Hg(1)–N(2) | 2.356(3) | N(2)–Hg(1)–Cl(2) | 116.07(8) |
| Hg(1)–Cl(1) | 2.3791(14) | N(1)–Hg(1)–Cl(2) | 100.44(9) |
| Hg(1)–Cl(2) | 2.4140(12) | Cl(1)–Hg(1)–Cl(2) | 122.98(4) |
| N(1)–C(1) | 1.344(5) | C(6)–N(2)–Hg(1) | 116.8(2) |
| N(2)–C(10) | 1.344(5) | C(10)–N(2)–Hg(1) | 123.1(2) |
| N(2)–Hg(1)–N(1) | 70.74(10) | C(5)–N(1)–Hg(1) | 116.9(2) |
| N(2)–Hg(1)–Cl(1) | 115.30(8) | C(1)–N(1)–Hg(1) | 123.6(3) |
| Complex **2c** | | | |
| Zn(1)–N(1) | 2.1413(16) | N(2)–Zn(1)–N(3) | 84.17(6) |
| Zn(1)–N(2) | 2.1425(16) | N(2)–Zn(1)–Cl(2) | 118.54(5) |
| Zn(1)–N(3) | 2.3076(16) | N(2)–Zn(1)–Cl(1) | 122.65(5) |
| Zn(1)–Cl(2) | 2.2454(8) | Cl(2)–Zn(1)–N(3) | 97.37(5) |
| Zn(1)–Cl(1) | 2.3066(7) | Cl(1)–Zn(1)–N(3) | 91.39(4) |
| N(1)–Zn(1)–N(2) | 76.34(6) | Cl(2)–Zn(1)–N(3) | 97.37(5) |
| Cl(2)–Zn(1)–Cl(1) | 118.74(3) | Cl(1)–Zn(1)–N(3) | 91.39(4) |
| N(1)–Zn(1)–N(3) | 157.87(6) | C(1)–N(1)–Zn(1) | 125.53(14) |
| Complex **2d** | | | |
| Hg–N(1) | 2.381(10) | N(2)–Hg–N(3) | 76.9(3) |
| Hg–N(2) | 2.440(9) | N(1)–Hg–Cl(2) | 112.4(2) |
| Hg–N(3) | 2.584(10) | Cl(2)–Hg–N(2) | 113.2(2) |
| Hg–Cl(1) | 2.440(3) | N(1)–Hg–Cl(1) | 91.4(2) |
| Hg–Cl(2) | 2.406(3) | N(2)–Hg–Cl(1) | 121.9(2) |
| N(1)–Hg–N(2) | 68.8(3) | Cl(2)–Hg–N(3) | 99.1(2) |
| Cl(1)–Hg–Cl(2) | 124.77(13) | Cl(1)–Hg–N(3) | 89.9(2) |
| N(1)–Hg–N(3) | 140.1(3) | C(1)–N(1)–Hg | 121.3(9) |

The molecular structures of complexes **2c** and **2d** are given in Figure 3 and Figure 4, respectively. Important bond lengths and angles are listed in Table 1. The crystal structure analysis reveals that complexes **2c** and **2d** are five-coordinate and adopt distorted trigonal bipyramidal geometry for the metal center. The ligand **1b** binds to the metal center in tridentate form by three nitrogen atoms, and there-

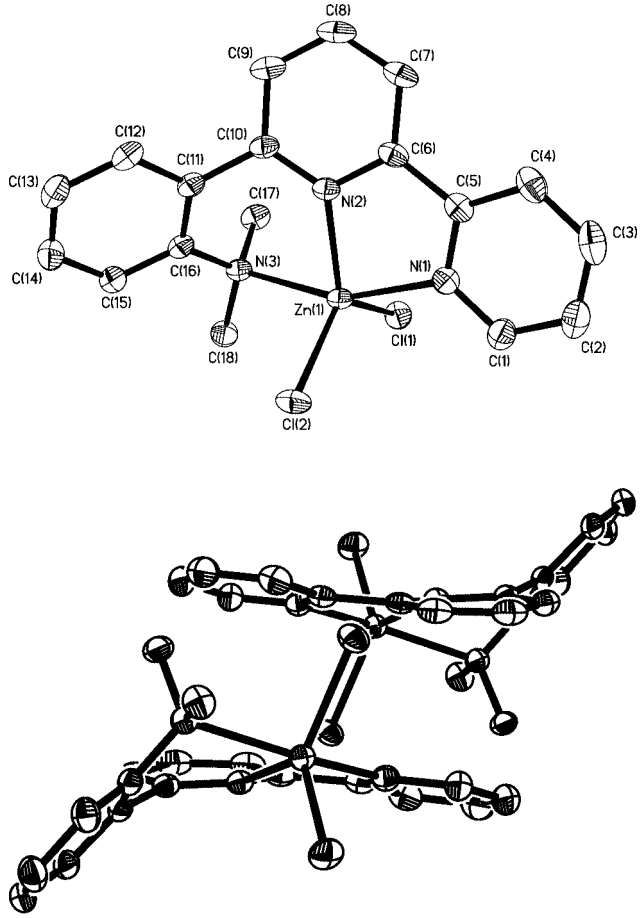


Figure 3. Top: molecular structure of complex **2c**; bottom: the π–π stacking dimer structure of complex **2c**. (Thermal ellipsoids are drawn at the 30% probability level.)

 © 2006 Wiley-VCH Verlag GmbH & Co. KGaA, Weinheim 

fore a five-membered metallacycle and a six-membered metallacycle are constructed. The N(1)–Zn(1)–N(2), N(2)–Zn(1)–N(3), and Cl(1)–Zn(1)–Cl(2) angles are 76.34(6), 84.17(6), and 118.74(3)° in **2c**, respectively. The Zn–N bond lengths, ranging from 2.1413(16) Å [Zn(1)–N(1)] to 2.3076(16) Å [Zn(1)–N(3)], are within the range of 2.098–2.321 Å observed for similar complexes,[16] while they are longer than those (2.079 and 2.062 Å) in the four-coordinate complex **2a**. The dihedral angles between the two pyridyl rings, and between the pyridyl ring and the adjacent aromatic ring are 18.0° and 47.7° for **2c** and 19.1° and 56.3° for **2d**, respectively. In solid state, molecules of **2c** are paired up through intermolecular π–π stacking of the ligand, resulting in the formation of a dimeric structure (Figure 3, bottom). The distance between the planes of the π–π stacked ligand is 3.53 Å. Similar to complex **2b**, a π–π stacking column structure was also observed in the mercury complex **2d** (Figure 4, bottom). The distances between the stacked aromatic planes are 3.42 and 3.65 Å, respectively. The intermolecular π–π interactions suggest that complexes **2a**–**2d** can possess charge transport property, which is essential for electroluminescent material.[17]

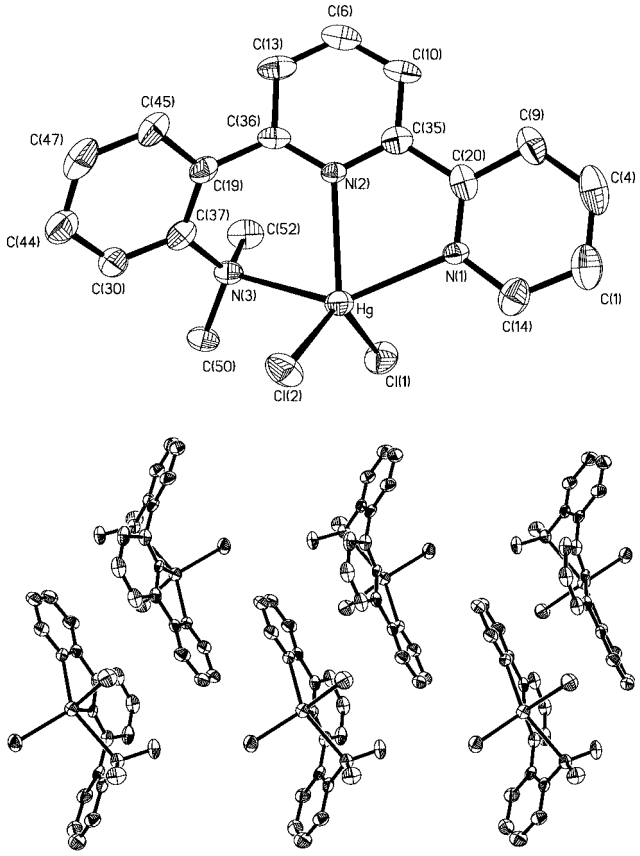


Figure 4. Top: molecular structure of complex **2d**; bottom: the π–π stacking column structure of complex **2d**. (Thermal ellipsoids are drawn at the 30% probability level.)

## Luminescence Properties

Table 2 summarizes the UV/Vis and fluorescent properties of compounds **1a**, **1b** and **2a**–**2d** determined in both solution and the solid state. In solution, the free ligands **1a** and **1b** have emission bands at $\lambda_{max}$ = 431 and 396 nm, respectively. In comparison with the free ligand **1a**, complexes **2a** and **2b** in solution give a broad emission band (bandwidth at half-height = 80–95 nm) with $\lambda_{max}$ = 447 nm and 452 nm, respectively, as shown in Figure 5. The emission maxima of the two complexes are slightly red-shifted compared to that of the free ligand. In contrast to complexes **2a** and **2b**, the emission maxima of **2c** and **2d** in solution are almost the same as that of the free ligand **1b** (see Figure 6). The luminescence of these complexes should be attributed to the transition from π* to π of their ligands. In solution, complex **2a** shows a strongly solvent-dependent emission band and its emission maximum shifts toward a shorter wavelength with the increase in polarity of the solvent. As shown in Figure 7, the emission maximum of **2a** is 461 nm in dichloromethane, while it becomes 358 nm in the polar solvent DMF. This is a rare case, as a red-shift of the emission maximum would be expected for most compounds when solvent polarity increases. The observed blue-shift phenomenon might be attributed to the presence of a highly polarized ground state.[18] The quantum yields of all compounds have been determined in solution. It was found that the quantum yields of the $Zn^{II}$ complexes **2a** and **2c** are slightly higher than those of their free ligands, while the quantum yields of the $Hg^{II}$ complexes **2b** and **2d** are lower than those of their free ligands. These results can be easily understood considering the following factors: the ligand becomes more rigid after coordination with a metal atom, which can reduce the loss of energy by vibrational motions and therefore increase the emission efficiency. On the other hand, the $Hg^{II}$ cation and the chloride anions can quench the fluorescence and result in luminescence decay. The quantum yields of complexes **2a** and **2b** are similar to those of four-coordinate zinc(II) complexes.[13b] The efficiency of **1a** and its corresponding complexes is about 20 times higher than that of **1b** and its corresponding complexes, probably because, in comparison with the –OMe group, the bulkier $–NMe_2$ group reduces the conjugated length and increases vibrational motion in **1b**, **2c**, and **2d**. The emission spectra of compounds **1a**, **1b**, **2a**, **2b**, and **2c** in the solid state are

Table 2. Photoluminescent data for ligands **1a** and **1b** and complexes **2a**–**2d**.

| | Abs. λ (nm) | Ex λ (nm) | Em λ (nm) | Quantum yields[a] | Conditions |
|---|---|---|---|---|---|
| **1a** | 273, 313 | 374 | 431 | 0.108 | $CHCl_3$, 298 K |
| | | | 458, 536 | | solid, 298 K |
| **1b** | 275, 310 | 340 | 394 | 0.005 | $CHCl_3$, 298 K |
| | | | 444 | | solid, 298 K |
| **2a** | 340, 356 | 374 | 447 | 0.113 | $CHCl_3$, 298 K |
| | | | 397 | | solid, 298 K |
| **2b** | 339, 353 | 374 | 452 | 0.083 | $CHCl_3$, 298 K |
| | | | 410 | | solid, 298 K |
| **2c** | 309, 343 | 340 | 395 | 0.006 | $CHCl_3$, 298 K |
| | | | 564 | | solid, 298 K |
| **2d** | 305, 340 | 340 | 394 | 0.003 | $CHCl_3$, 298 K |

[a] Determined using quinine sulfate in sulfuric acid (0.1 M) as a standard in DMF at ambient temperature.

 © 2006 Wiley-VCH Verlag GmbH & Co. KGaA, Weinheim 

shown in Figure 8. Except for **2d**, all compounds in solid state emit bright fluorescence when irradiated by exciting light. The emission maxima of **1a**, **2a**, and **2b** are 536, 397, and 410 nm, respectively. The emission maxima of **2a** and **2b** in the solid state are blue-shifted compared to emission maximum of their ligand **1a**, while the emission maximum of complex **2c** ($\lambda_{max}$ = 564 nm) in the solid state is red-shifted compared to that ($\lambda_{max}$ = 444 nm) of its corresponding ligand **1b**. These properties are probably a result of their π-stacking structures in the solid state.

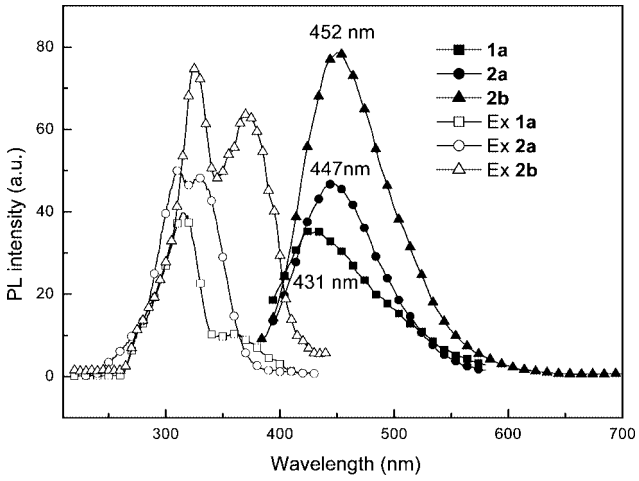


Figure 5. Excitation and emission spectra of compounds **1a**, **2a**, and **2b** in chloroform (ca. $1 \times 10^{-5}$ M).

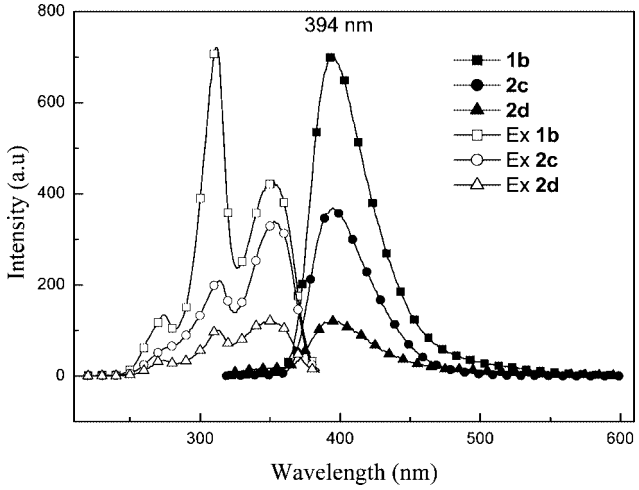


Figure 6. Excitation and emission spectra of compounds **1b**, **2c**, and **2d** in chloroform (ca. $1 \times 10^{-5}$ M).

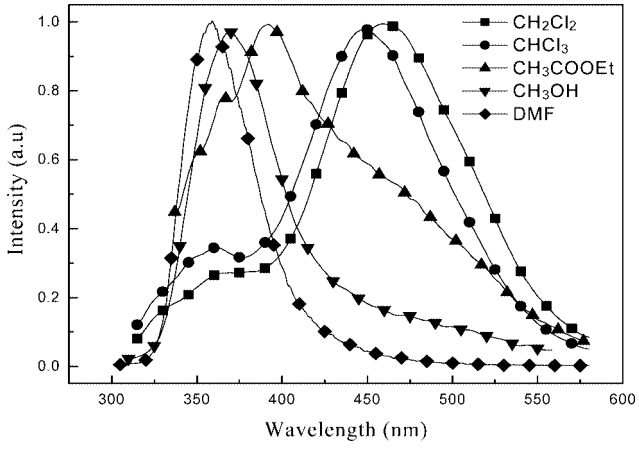


Figure 7. Emission spectra of complex **2a** in various solvents (ca. $1 \times 10^{-5}$ M).

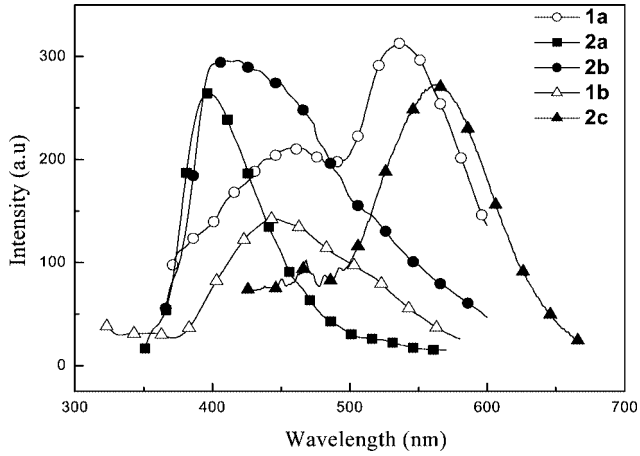


Figure 8. Emission spectra of compounds **1a**, **1b**, **2a**, **2b**, and **2c** in the solid state.

## Conclusions

We have described the syntheses and X-ray structures of a number of d[10] group 12 metal complexes supported by two substituted 2,2′-bipyridine ligands. Crystal structure analysis reveals crystal structures of these complexes are different from each other. It was found that antiparallel dimeric structures are formed for complexes **2a** and **2c** while one-dimensional supramolecular structures are constructed for complexes **2b** and **2d** by π–π stacking in the solid state. These complexes produce fluorescence in both solution and the solid state, and the emission color in the solid state is dramatically affected by their packing structures.

## Experimental Section

All reactions were performed using standard Schlenk techniques in high-purity nitrogen or glovebox techniques. Toluene and diethyl ether were dried by refluxing over sodium and benzophenone and distilled under nitrogen prior to use. $CDCl_3$ was dried with $CaH_2$ for 48 h and vacuum-transferred to an air-free flask. $ZnCl_2$, $HgCl_2$, and *n*BuLi were purchased from Aldrich and used as received. NMR spectra were measured using a Varian Mercury-300 NMR spectrometer. The elemental analysis was performed with a Perkin–Elmer 2400 analyzer. UV/Vis absorption spectra were recorded with a UV-3100 spectrophotometer. Fluorescence measurements were carried out on an RF-5301PC.

**6-[2-(Dimethylamino)phenyl]-2,2′-bipyridine (1b):** A solution of *n*BuLi (30.32 mL, 48.5 mmol) in hexanes was added to a solution of 2-bromo-*N*,*N*-dimethylaniline (9.7 g, 48.5 mmol) in $Et_2O$ (30 mL) under nitrogen at –78 °C. The mixture was allowed to warm to room temperature and stirred overnight. The resulting

 © 2006 Wiley-VCH Verlag GmbH & Co. KGaA, Weinheim 

mixture was added dropwise to an ice-cooled solution of 2,2′-bipyridine (7.57 g, 48.5 mmol) in degassed $Et_2O$ (30 mL), and a wine-red solution was obtained immediately. The resultant mixture was refluxed for 24 h and cooled in an ice bath, then deionized water (25 mL) was added to hydrolyze the products. The yellow organic phase was separated and stirred with $MnO_2$ for 24 h, then filtered and dried with $MgSO_4$. The solid was obtained upon concentration of the solution, and chromatography on silica gel with dichloromethane as eluent afforded a light yellow solid. Yield: 6.7 g (50%). $C_{18}H_{17}N_3$ (275.35): calcd. C 78.52, H 6.22, N 15.26; found C 78.32, H 6.41, N 15.10. $^1$H NMR (300 MHz, $CDCl_3$, 293 K): $\delta$ = 2.77 (s, 6 H, C$H_3$), 7.17 (d, 1 H), 7.32–7.40 (m, 2 H), 7.76–7.84 (m, 4 H), 7.99 (d, 1 H, $J$ = 7.8 Hz), 8.30 (d, 1 H, $J$ = 7.8 Hz), 8.49 (d, 1 H, $J$ = 5.4 Hz), 8.71 (d, 1 H, $J$ = 4.8 Hz) ppm.

**6-(2-Methoxyphenyl)-2,2′-bipyridinezinc Dichloride (2a):** A methanol solution (10 mL) of **1a** (0.2 g, 0.76 mmol) was added to a methanol solution (10 mL) of $ZnCl_2$ (0.11 g, 0.77 mmol). The reaction mixture was stirred for 4 h at room temperature. After filtering, the light yellow precipitate was collected and washed with cold methanol. Pure product was obtained in 81% yield (0.25 g) by recrystallization from $CH_3CN/CH_2Cl_2$. $C_{17}H_{14}Cl_2N_2OZn$ (398.60): calcd. C 51.22, H 3.54, N 7.03; found C 51.40, H 3.67, N 7.15. $^1$H NMR (300 MHz, [$D_6$]DMSO, 293 K): $\delta$ = 3.34 (s, 3 H, C$H_3$), 7.13 (t, 1 H), 7.21 (d, 1 H), 7.41–7.52 (m, 2 H), 7.91–7.99 (m, 4 H), 8.30 (d, 1 H), 8.48 (d, 1 H), 8.72 (d, 1 H) ppm. IR (KBr): $\tilde{\nu}$ = 3072 w, 3007 w, 2959 w, 2850 w, 1600 s, 1569 m, 1484 s, 1459 s, 1441 s, 1401 w, 1299 m, 1260 s, 1248 m, 1179 w, 1162 m, 1119 m, 1055 w, 1023 s, 829 w, 784 s, 755 s, 643 w, 561 w.

**6-(2-Methoxyphenyl)-2,2′-bipyridinemercury Dichloride (2b):** A methanol solution (10 mL) of **1a** (0.2 g, 0.76 mmol) was added to a methanol solution (10 mL) of $HgCl_2$ (0.21 g, 0.77 mmol). The reaction mixture was stirred for 4 h at room temperature. After filtering, the light yellow precipitate was collected and washed with cold methanol. Pure product was obtained in 83% yield (0.34 g) by recrystallization from $CH_3CN$. $C_{17}H_{14}Cl_2HgN_2O$ (533.80): calcd. C 38.25, H 2.64, N 5.25; found C 38.44, H 2.86, N 5.03. $^1$H NMR (300 MHz, [$D_6$]DMSO, 293 K): $\delta$ = 3.35 (s, 3 H, C$H_3$), 7.20 (t, 1 H), 7.23 (d, 1 H), 7.44–7.51 (m, 2 H), 7.91–7.98 (m, 4 H), 8.31 (d, 1 H), 8.47 (d, 1 H), 8.73 (d, 1 H) ppm. IR (KBr): $\tilde{\nu}$ = 3075 w, 3023 w, 2980 w, 2933 w, 2828 w, 1588 s, 1571 m, 1485 s, 1440 s, 1386 m, 1283 m, 1262 s, 1238 s, 1179 m, 1159 m, 1109 m, 1055 w, 1017 s, 1000 s, 946 w, 894 w, 859 w, 824 w, 779 s, 754 s, 734 m, 633 m, 577 w, 616 w.

**6-[2-(Dimethylamino)phenyl]-2,2′-bipyridinezinc Dichloride (2c):** A methanol solution (10 mL) of **1b** (0.2 g, 0.73 mmol) was added to a methanol solution (15 mL) of $ZnCl_2$ (0.11g, 0.74 mmol). The reaction mixture was stirred for 4 h at room temperature. After filtering, the light yellow precipitate was collected and washed with cold methanol. Pure product was obtained in 82% yield (0.25 g) by recrystallization from $CH_3CN/CH_2Cl_2$. $C_{18}H_{17}Cl_2N_3Zn$ (411.64): calcd. C 52.52, H 4.16, N 10.21; found C 52.71, H 4.26, N 10.03. $^1$H NMR (300 MHz, [$D_6$]DMSO, 293 K): $\delta$ = 2.59 (s, 6 H, C$H_3$), 7.13–7.20 (m, 2 H), 7.39 (t, 1 H), 7.52 (s, 1 H), 7.61 (d, 1 H), 7.95–8.13 (m, 3 H), 8.36 (s, 1 H), 8.50 (d, 1 H), 8.71 (d, 1 H) ppm. IR (KBr): $\tilde{\nu}$ = 3061 w, 3015 w, 2984 w, 2928 w, 2873 w, 2833 w, 2362 m, 1601 s, 1568 s, 1446 s, 1401 m, 1298 m, 1262 m, 1246 m, 1156 m, 1130 w, 1104 w, 1053 w, 1021 m, 926 m, 833 m, 783 s, 742 m, 700 w, 655 w, 634 m, 549 w.

**6-[2-(Dimethylamino)phenyl]-2,2′-bipyridinemercury Dichloride (2d):** A methanol solution (10 mL) of **1b** (0.2 g, 0.73 mmol) was added to a methanol solution (15 mL) of $HgCl_2$ (0.21 g, 0.74 mmol). The reaction mixture was stirred for 4 h at room temperature. After filtering, the light yellow precipitate was collected and washed with cold methanol. Pure product was obtained in 85% yield (0.34 g) by

Table 3. Crystal data and structural refinements details for **2a**, **2b**, **2c**, and **2d**.

| | **2a** | **2b** | **2c** | **2d** |
|---|---|---|---|---|
| Empirical formula | $C_{17}H_{14}Cl_2N_2OZn$ | $C_{17}H_{14}Cl_2HgN_2O$ | $C_{18}H_{17}Cl_2N_3Zn$ | $C_{18}H_{17}Cl_2HgN_3$ |
| Formula mass | 398.57 | 533.79 | 411.62 | 546.84 |
| Temp. [K] | 293(2) | 293(2) | 293(2) | 293(2) |
| Wavelength [Å] | 0.71073 | 0.71073 | 0.71073 | 0.71073 |
| Crystal system | monoclinic | monoclinic | monoclinic | triclinic |
| Space group | $P2(1)/n$ | $P2(1)/c$ | $P2(1)/n$ | $P\bar{1}$ |
| $a$ [Å] | 8.2680(17) | 7.5130(15) | 10.236(2) | 8.3858(17) |
| $b$ [Å] | 13.037(3) | 16.718(3) | 13.145(3) | 8.6676(17) |
| $c$ [Å] | 15.433(3) | 13.403(3) | 12.916(3) | 13.173(3) |
| $\alpha$ [°] | 90 | 90 | 90 | 82.56(3) |
| $\beta$ [°] | 95.03(3) | 97.02(3) | 90.08(3) | 89.46(3) |
| $\gamma$ [°] | 90 | 90 | 90 | 73.93(3) |
| $V$ [Å$^3$] | 1657.1(6) | 1670.8(6) | 1737.9(6) | 912.0(3) |
| $Z$ | 4 | 4 | 2 | 2 |
| $D_{calcd.}$ [Mg m$^{-3}$] | 0.799 | 1.061 | 0.787 | 1.991 |
| $F$(000) | 404 | 504 | 420 | 520 |
| Crystal size (mm) | 0.23 × 0.17 × 0.16 | 0.34 × 0.15 × 0.12 | 0.20 × 0.17 × 0.11 | 0.28 × 0.19 × 0.13 |
| $\theta$ range for data collection [°] | 3.08–27.47 | 2.99–27.45 | 3.10–27.46 | 3.00–27.48 |
| Limiting indices | $-10 \le h \le 10$ | $-8 \le h \le 9$ | $-13 \le h \le 11$ | $-9 \le h \le 10$ |
| | $-16 \le k \le 16$ | $-21 \le k \le 21$ | $-17 \le k \le 17$ | $-10 \le k \le 11$ |
| | $-20 \le l \le 17$ | $-17 \le l \le 17$ | $-16 \le l \le 16$ | $-17 \le l \le 17$ |
| Data/restraints/parameters | 3774/0/208 | 3746/0/264 | 3973/0/285 | 3979/0/217 |
| Goodness-of-fit on $F^2$ | 1.079 | 1.004 | 1.055 | 1.102 |
| Final $R$ indices [$I > 2\sigma(I)$] | $R_1$[a] = 0.0414 | $R_1$[a] = 0.0260 | $R_1$[a] = 0.0280 | $R_1$[a] = 0.0663 |
| | $wR_2$[b] = 0.1193 | $wR_2$[b] = 0.0580 | $wR_2$[b] = 0.0670 | $wR_2$[b] = 0.1439 |
| $R$ indices (all data) | $R_1$[a] = 0.0487 | $R_1$[a] = 0.0342 | $R_1$[a] = 0.0371 | $R_1$[a] = 0.0823 |
| | $wR_2$[b] = 0.1222 | $wR_2$[b] = 0.0614 | $wR_2$[b] = 0.0707 | $wR_2$[b] = 0.1517 |
| Largest diff. peak/hole [e Å$^{-3}$] | 0.665, –0.261 | 0.917, –1.172 | 0.315, –0.231 | 2.854, –1.997 |

[a] $R_1 = \Sigma||F_o| - |F_c||/\Sigma|F_o|$. [b] $wR_2 = [\Sigma[w(F_o^2 - F_c^2)^2]/\Sigma[w(F_o^2)^2]]^{1/2}$.

 © 2006 Wiley-VCH Verlag GmbH & Co. KGaA, Weinheim 

recrystallization from $CH_3CN/CH_2Cl_2$. $C_{18}H_{17}Cl_2HgN_3$ (546.84): calcd. C 39.53, H 3.13, N 7.68; found C 39.32, H 3.26, N 7.89. $^1H$ NMR (300 MHz, [D$_6$]DMSO, 293 K): $\delta$ = 2.58 (s, 6 H, C$H_3$), 7.15–7.21 (m, 2 H), 7.41 (s, 1 H), 7.58 (m, 2 H), 7.98–8.09 (m, 3 H), 8.41 (s, 1 H), 8.53 (d, 1 H), 8.72 (d, 1 H) ppm. IR (KBr): $\tilde{\nu}$ = 3064 w, 3013 w, 2964 w, 2869 w, 2835 w, 2795 w, 2364 w, 1594 s, 1568 s, 1443 s, 1288 m, 1259 w, 1233 w, 1185 m, 1159 m, 1126 w, 1110 w, 1049 w, 1008 m, 931 m, 891 w, 826 m, 777 s, 696 w, 630 m, 561 w, 543 w.

**X-ray Structure Determinations of 2a, 2b, 2c, and 2d:** Single crystals of **2a**, **2b**, **2c**, and **2d** suitable for X-ray structural analysis were obtained from dichloromethane or $CH_3CN$. Diffraction data were collected at 293 K on a Rigaku R-AXIS RAPID IP diffractometer equipped with graphite-monochromated Mo-$K_\alpha$ radiation ($\lambda$ = 0.71073 Å) for **2a**, **2b**, **2c**, and **2d**. Details of the crystal data, data collections, and structure refinements are summarized in Table 3. The structures were solved by direct methods[19] and refined by full-matrix least-squares on $F^2$. All non-hydrogen atoms were refined anisotropically and the hydrogen atoms were included in idealized position. All calculations were performed using the SHELXTL[20] crystallographic software packages. For **2d**, the final difference maps revealed residual electron density near the mercury atoms (2.85 and 2.81 e Å$^{-3}$) but no regions of electron density that could be attributed to additional atomic sites.

CCDC-602363 (for **2a**), -602364 (for **2b**), -602365 (for **2c**), and -602366 (for **2d**) contain the supplementary crystallographic data for this paper. These data can be obtained free of charge from The Cambridge Crystallographic Data Centre via www.ccdc.cam.ac.uk/data_request/cif.

## Acknowledgments

This work was supported by the National Natural Science Foundation of China (No. 20374023) and Ministry of Science and Technology of China (No. 2002CB6134003).

[1] a) C. W. Tang, S. A. Vanslyke, *Appl. Phys. Lett.* **1987**, *51*, 913–915; b) S. N. Wang, *Coord. Chem. Rev.* **2001**, *215*, 79–98; c) C. H. Chen, J. Shi, *Coord. Chem. Rev.* **1998**, *171*, 161–174; d) F. Li, M. Zhang, G. Cheng, J. Feng, Y. Zhao, Y. G. Ma, S. Y. Liu, J. C. Shen, *Appl. Phys. Lett.* **2004**, *84*, 148–150; e) Q. S. Zhang, Q. G. Zhou, Y. X. Cheng, L. X. Wang, D. G. Ma, X. B. Jing, F. S. Wang, *Adv. Mater.* **2004**, *16*, 432–436; f) G. B. Cunningham, Y. T. Li, S. X. Liu, K. S. Schanze, *J. Phys. Chem. B* **2003**, *107*, 12569–12572.

[2] a) T. H. Kwon, H. S. Cho, M. K. Kim, J. W. Kim, J. J. Kim, K. H. Lee, S. J. Park, I. S. Shin, H. Kim, D. M. Shin, Y. K. Chung, J. I. Hong, *Organometallics* **2005**, *24*, 1578–1585; b) F. M. Hwang, H. Y. Chen, P. S. Chen, C. S. Liu, Y. Chi, C. F. Shu, F. L. Wu, P. T. Chou, S. M. Peng, G. H. Lee, *Inorg. Chem.* **2005**, *44*, 1344–1353; c) J. Li, P. I. Djurovuch, B. D. Alleyne, M. Yousufuddin, N. N. Ho, J. C. Thomas, J. C. Peters, R. Bau, M. E. Thompson, *Inorg. Chem.* **2005**, *44*, 1713–1727; d) X. M. Liu, W. Gao, Y. Mu, G. H. Li, L. Ye, H. Xia, Y. Ren, S. H. Feng, *Organometallics* **2005**, *24*, 1614–1619.

[3] a) V. A. Montes, G. Li, R. Pohl, J. Shinar, P. Anzenbacher Jr, *Adv. Mater.* **2004**, *16*, 2001–2003; b) R. Pohl, V. A. Montes, J. Shinar, P. Anzenbacher Jr, *J. Org. Chem.* **2004**, *69*, 1723–1725; c) R. Pohl, P. Anzenbacher Jr, *Org. Lett.* **2003**, *5*, 2769–2772.

[4] a) Q. G. Wu, J. A. Lavigne, Y. Tao, M. D'Iorio, S. N. Wang, *Inorg. Chem.* **2000**, *39*, 5248–5254; b) Q. G. Wu, A. Hook, S. N. Wang, *Angew. Chem. Int. Ed.* **2000**, *39*, 3933–3935; c) D. T. Song, S. N. Wang, *Eur. J. Inorg. Chem.* **2003**, 3774–3782; d) Q. G. Wu, J. A. Lavigne, Y. Tao, M. D'Iorio, S. N. Wang, *Chem. Mater.* **2001**, *13*, 17–77.

[5] a) Y. Liu, J. H. Guo, H. D. Zhang, Y. Wang, *Angew. Chem. Int. Ed.* **2002**, *41*, 182–184; b) Y. Q. Li, Y. Liu, W. M. Bu, J. H. Guo, Y. Wang, *Chem. Commun.* **2000**, 1551–1552.

[6] a) W. K. Chan, P. K. Ng, X. Gong, S. J. Hou, *Appl. Phys. Lett.* **1999**, *753*, 3920–3922; b) K. Z. Wang, L. Huang, L. H. Gao, L. P. Jin, C. H. Huang, *Inorg. Chem.* **2002**, *41*, 3353–3358; c) S. Ranjan, S. Y. Lin, K. C. Hwang, Y. Chi, W. L. Ching, C. S. Liu, Y. T. Tao, C. H. Chien, S. M. Peng, G. H. Lee, *Inorg. Chem.* **2003**, *42*, 1248–1255; d) F. Li, M. Zhang, G. Cheng, J. Feng, Y. Zhao, Y. G. Ma, S. Y. Liu, J. C. Shen, *Appl. Phys. Lett.* **2004**, *84*, 148–150.

[7] a) Y. L. Tung, S. W. Lee, Y. Chi, L. S. Chen, C. F. Shu, F. I. Wu, A. J. Carty, P. T. Chou, S. M. Peng, G. H. Lee, *Adv. Mater.* **2005**, *17*, 1059–1063; b) H. Xia, C. Zhang, X. Liu, S. Qiu, P. Lu, F. Shen, J. Zhang, Y. Ma, *J. Phys. Chem. B* **2004**, *108*, 3185–3190; c) H. Xia, C. Zhang, S. Qiu, P. Lu, J. Zhang, Y. Ma, *Appl. Phys. Lett.* **2004**, *84*, 290–292.

[8] a) B. Carlson, G. D. Phelan, W. Kaminsky, L. Dalton, X. Z. Jiang, S. Liu, A. K.-Y. Jen, *J. Am. Chem. Soc.* **2002**, *124*, 14162–14172; b) Y. L. Chen, S. W. Lee, Y. Chi, K. C. Hwang, S. B. Kumar, Y. H. Hu, Y. M. Cheng, P. T. Chou, S. M. Peng, G. H. Lee, S. J. Yeh, C. T. Chen, *Inorg. Chem.* **2005**, *44*, 4287–4294; c) Y. L. Tung, P. C. Wu, C. S. Liu, Y. Chi, J. K. Yu, Y. H. Hu, P. T. Chou, S. M. Peng, G. H. Lee, Y. Tao, J. C. Arthur, C. F. Shu, F. I. Wu, *Organometallics* **2004**, *23*, 3745–3748..

[9] a) Y. G. Ma, C. M. Che, H. Y. Chao, X. M. Zhou, W. H. Chan, J. C. Shen, *Adv. Mater.* **1999**, *11*, 852–857; b) X. M. Zhang, M. L. Tong, M. L. Gong, H. K. Lee, L. Luo, K. F. Li, Y. X. Tong, X. M. Chen, *Chem. Eur. J.* **2002**, *8*, 3187–3194; c) G. Yu, S. W. Yin, Y. Q. Liu, Z. G. Shuai, D. B. Zhu, *J. Am. Chem. Soc.* **2003**, *125*, 14816–14824.

[10] a) W. K. Lo, W. K. Wong, W. Y. Wong, J. P. Guo, *Eur. J. Inorg. Chem.* **2005**, 3950–3954; b) M. R. Haneline, M. Tsunoda, F. P. Gäbbai, *J. Am. Chem. Soc.* **2002**, *124*, 3737–3742; c) R. Q. Fan, D. S. Zhu, Y. Mu, G. H. Li, Y. L. Yang, Q. Su, *Eur. J. Inorg. Chem.* **2004**, 4891–4897.

[11] a) V. W. W. Yam, K. K. W. Lo, W. K. M. Fung, C. R. Wang, *Coord. Chem. Rev.* **1998**, *171*, 17–41; b) H. H. Patterson, S. M. Kanan, M. A. Omary, *Coord. Chem. Rev.* **2000**, *208*, 227–241.

[12] a) M. Schmittel, C. Michel, A. Wiegrefe, V. Kalsani, *Synthesis* **2001**, 1561–1567; b) C. C. Kwok, H. M. Y. Ngai, S. C. Chan, I. H. T. Sham, C. M. Che, N. Y. Zhu, *Inorg. Chem.* **2005**, *44*, 4442–4444.

[13] a) Q. G. Wu, J. A. Lavigne, Y. Tao, M. D'Iorio, S. N. Wang, *Inorg. Chem.* **2000**, *39*, 5248–5254; b) K. Y. Ho, W. Y. Yu, K. K. Cheung, C. M. Che, *J. Chem. Soc., Dalton Trans.* **1999**, 1581–1586; c) Q. D. Liu, R. Y. Wang, S. N. Wang, *Dalton Trans.* **2004**, 2073–2079.

[14] a) S. M. Berry, D. C. Bebout, R. J. Butcher, *Inorg. Chem.* **2005**, *44*, 27–39; b) S. L. Zheng, J. P. Zhang, X. M. Chen, Z. L. Huang, Z. Y. Lin, W. T. Wong, *Chem. Eur. J.* **2003**, *9*, 3888–3896.

[15] C. Janiak, *J. Chem. Soc., Dalton Trans.* **2000**, 3885–3896.

[16] a) R. Q. Fan, D. S. Zhu, H. Ding, Y. Mu, Q. Su, H. Xia, *Synth. Met.* **2005**, *149*, 135–141; b) S. G. Liu, J. L. Zuo, Y. Wang, Y. Z. Li, X. Z. You, *J. Phys. Chem. Solids* **2005**, *66*, 735–740; c) S. Das, C. H. Hung, S. Goswami, *Inorg. Chem.* **2003**, *42*, 5153–5157.

[17] Y. Q. Li, Y. Liu, W. M. Bu, D. Lu, Y. Wu, Y. Wang, *Chem. Mater.* **2000**, *12*, 2672–2675.

[18] E. M. Kosower, *J. Am. Chem. Soc.* **1958**, *80*, 3253–3260.

[19] *SHELXTL*, PC Siemens Analytical X-ray Instruments, Madison, WI, **1993**.

[20] G. M. Sheldrick, *SHELXTL Structure Determination Programs*, Version 5.0, PC Siemens Analytical Systems, Madison, WI, **1994**.

Received: March 25, 2006
Published Online: August 24, 2006

 © 2006 Wiley-VCH Verlag GmbH & Co. KGaA, Weinheim 

DOI: 10.1002/ejic.200600274

# Chemical and Electrochemical Behaviours of a New Phenolato-Bridged Complex $[(L)Mn^{II}Mn^{II}(L)]^{2+}$. Pathways to Mononuclear Chlorido $[(L)Mn^{II/III/IV}Cl]^{0/1/2+}$ and Dinuclear Mono-μ-Oxido $[(L)Mn^{III}(\mu\text{-}O)Mn^{III/IV}(L)]^{2+/3+}$ Species

**Laurent Sabater,[a] Christelle Hureau,*[a,b] Guillaume Blain,[a] Régis Guillot,[a] Pierre Thuéry,[c] Eric Rivière,[a] and Ally Aukauloo*[a]**

**Keywords:** Manganese / N,O Ligands / Chloride ions / Electrochemistry / EPR spectroscopy

The X-ray structure of a new dinuclear phenolato-bridged $Mn_2^{II}$ complex abbreviated as $[(L)MnMn(L)]^{2+}$ (**1**), where LH is the $[N_4O]$ phenol containing ligand *N*,*N*-bis(2-pyridylmethyl)-*N*′-salicylidene-ethane-1,2-diamine ligand, is reported. A *J* value of –3.3 $cm^{-1}$ ($H = -J\hat{S}_1\cdot\hat{S}_2$) was determined from the magnetic measurements and the 9.4 GHz EPR spectra of both powder and frozen acetonitrile solution samples were analyzed with temperature. The cyclic voltammetry of **1** displays a reversible anodic wave at $E^{1/2}$ = 0.46 V vs. SCE associated with the two-electron oxidation of **1** yielding the dinuclear $Mn_2^{III}$ complex $[(L)MnMn(L)]^{4+}$ (**2**). The easy air oxidation of **1** gives the mono-μ-oxido $Mn_2^{III}$ complex $[(L)Mn(\mu\text{-}O)Mn(L)]^{2+}$ (**3**). A rational route to the formation of the mixed-valence $Mn_2^{III,IV}$ complex $[(L)Mn(\mu\text{-}O)Mn(L)]^{3+}$ (**4**) starting from **1** by bulk electrolysis at $E^{p}$ = 0.75 V vs. SCE in the presence of one equiv. of base per manganese ion is also briefly reported. Addition of chloride ions to **1** led to the cleavage of the phenolato bridges to give the mononuclear $Mn^{II}$ complex [(L)MnCl] (**5**). Cyclic voltammetry of **5** displays two reversible anodic waves at $E^{1/2}$ = 0.21 and $E^{1/2}$ = 1.15 V vs. SCE, assigned to the two successive one-electron abstractions giving the $Mn^{III}$ and $Mn^{IV}$ species $[(L)MnCl]^{+}$ (**6**) and $[(L)MnCl]^{2+}$ (**7**), respectively. The electronic signatures from UV/Visible and EPR spectroscopy of the electrochemically prepared samples of **6** and **7** confirmed the respective oxidation states. For instance, **7** displays a broad and intense absorption band characteristic of a phenolato to $Mn^{IV}$ charge-transfer transition at 690 nm (2000 $M^{-1}cm^{-1}$) and its 9.4 GHz EPR spectrum shows a strong transition at $g$ = 5.2 consistent with a rhombically distorted $S$ = 3/2 system with a zero-field splitting dominating the Zeeman effect.

(© Wiley-VCH Verlag GmbH & Co. KGaA, 69451 Weinheim, Germany, 2006)

## Introduction

Manganese ions are involved in the structure and activity of numerous metalloenzymes.[1,2] Their nuclearities may vary from 1 to 4 metal ions and they often carry out multielectron redox reactions. A mononuclear Mn core is encountered in superoxide dismutase[3–5] and in oxalate oxidase[6,7] and oxalate decarboxylase,[6,8] while dinuclear centres are the most common[9] and are found in catalase,[3,9,10] arginase,[11,12] and ribonucleotide reductase.[13] A tetranuclear Mn core is the heart of the oxygen-evolving complex of photosystem II.[14,15] The fact that these manganese containing enzymes perform crucial reactions in different processes for the maintenance of terrestrial life has encouraged the chemists to pay particular attention to their functioning mode together with their intimate structures and spectroscopic characterizations. Furthermore, bioinorganic chemists have set the challenge to devise synthetic low molecular weight models[16–18] to either reproduce the coordination spheres of these Mn containing active sites or even more challenging, to mimic the activity of the target enzyme (see for examples ref.[19–23]).

Results on both bases have until now been encouraging but a great effort is still needed to reach our objectives. Research along this field is being pursued in our laboratory. Recently, we have reported on the metalation of the ligand LH, where LH is the $[N_4O]$ phenol-containing ligand *N*,*N*-bis(2-pyridylmethyl)-*N*′-salicylidene-ethane-1,2-diamine, with $Mn^{II}$ salt giving the $[(LH)MnCl_2]$ complex where the phenol was still in a protonated state.[24] We have shown through various spectroscopic characterizations that upon the first one-electron oxidation process a concerted chemical reaction took place with the concomitant expulsion of one chloride ion from the manganese coordination sphere together with the deprotonation of the phenol and the coor-

[a] Institut de Chimie Moléculaire et des Matériaux d'Orsay, UMR 8182, Université Paris-Sud,
91405 Orsay Cedex, France
E-Mail: christelle.hureau@cea.fr; aukauloo@icmo.u-psud.fr
[b] Current address: Département de Biologie Joliot-Curie, Service de Bioénergétique, URA 2096, CEA Saclay,
91191 Gif-sur-Yvette Cedex, France
[c] CEA Saclay, DRECAM/SCM,
Bâtiment 125, 91191 Gif-sur-Yvette, France

Supporting information for this article is available on the WWW under http://www.eurjic.org or from the author.

 © 2006 Wiley-VCH Verlag GmbH & Co. KGaA, Weinheim 

dination of the phenolate group. The reversibility of this process was also evidenced. We believe that such an electrochemical process is essential to delineate the highly intricate manganese chemistry. Herein we report on the synthesis of the dinuclear phenolato-bridged $Mn_2^{II}$ species $[(L)Mn\text{-}Mn(L)]^{2+}$ (**1**), which has been characterized by X-ray diffraction studies, EPR spectroscopy, and cyclic voltammetry. We show that complex **1** can withstand a two-electron oxidation leading to complex $[(L)MnMn(L)]^{4+}$ (**2**) keeping the phenolate groups as bridging ligands. However, upon air oxidation of **1**, the mono-μ-oxido-bridged $Mn_2^{III}$ complex $[(L)Mn(\mu\text{-}O)Mn(L)]^{2+}$ (**3**) is obtained while the corresponding mixed-valence $Mn_2^{III,IV}$ complex $[(L)Mn(\mu\text{-}O)\text{-}Mn(L)]^{3+}$ (**4**) is electrochemically generated. A more detailed study on the reaction of complex **1** with the biologically ubiquitous chloride ions is described. After addition of chloride ions the mononuclear $Mn^{II}$ species [(L)MnCl] (**5**) is formed. The electrochemical behaviour of **5** exhibits two one-electron reversible-oxidation processes, changing the initial $Mn^{II}$ to $Mn^{III}$ and $Mn^{IV}$ oxidation states, respectively. Spectroscopic characterizations of the $Mn^{III}$ $[(L)\text{-}MnCl]^{+}$ (**6**) and $Mn^{IV}$ $[(L)MnCl]^{2+}$ (**7**) complexes in the $[N_4OCl]$ environment are reported.

## Results

### Characterization of Complex $[(L)MnMn(L)]^{2+}$ (1)

The reaction of ligand LH with $Mn(ClO_4)_2{\cdot}6H_2O$ in ethanol, and in the presence of one equiv. of 2,6-dimethylpyridine gives the complex $\mathbf{1}(ClO_4)_2{\cdot}2H_2O$. In order to attenuate the extremely fast air oxidation of **1** into the mono-μ-oxido-bridged $Mn_2^{III}$ complex $[(L)Mn(\mu\text{-}O)Mn(L)]^{2+}$ (**3**) (see Exp. Sect. for details), the preparation and handling of complex **1**, except for the magnetic measurements, were performed under an argon flux. Nevertheless, unavoidable contamination of solution and solid samples of complex **1** by complex **3** were observed by cyclic voltammetry and by UV/Visible spectroscopy.

### X-ray Crystal Structure of $\mathbf{1}(ClO_4)_2{\cdot}2CH_3CN$

The X-ray structure of complex **1** is shown in Figure 1, and principal bond lengths and angles are listed in Table 1. The structure consists of a discrete cation $[(L)Mn\text{-}Mn(L)]^{2+}$ (**1**), two perchlorate anions, and two acetonitrile solvent molecules. The two $Mn^{II}$ centres are bridged by the phenolato groups of the two $L^-$ ligands. Therefore, a $[N_4O_2]$ donor set forms the distorted octahedral coordination environment of each Mn ion. Bond lengths and angles listed in Table 1 show the distortion from octahedral geometry due to constraints imposed by the ligand.

The Mn···Mn distance of 3.383 Å is slightly longer than those reported for phenolato-bridged $Mn_2^{II}$ complexes of closely related $mL^-$, $Li^-/La^-$ ligands (see Scheme 1),[25–27] but shorter than those obtained for phenolato-bridged $Mn_2^{II}$ complexes obtained with the $[N_3O_2Cl]$ metal environment.[28] As a matter of fact, the $Mn_2O_2$ diamond core structure of **1** differs from those of complexes $[(mL)Mn\text{-}Mn(mL)]^{2+}$ and $[(Li/La)MnMn(Li)]^{2+}$.[29] Values of the average Mn–O–Mn angle and of the dihedral angle are slightly greater than those observed in $[(mL)Mn\text{-}Mn(mL)]^{2+}$ and $[(Li/La)MnMn(Li)]^{2+}$ systems: 103.7° vs. 100.0° and 101.4°, and 17.9° vs. 11.3° and 11.5°, respectively.[26,27] This can be tentatively attributed to the conjugation of the bridging phenolato group to an imine function in the present case.

The wrapping of the Mn ion by the ligand $L^-$ is identical to that observed in the structures of related Mn[24,30] and Fe[31] complexes, with the two pyridine functions in a *trans* position to one another.

### Magnetic Susceptibility Measurements

The molar magnetic susceptibility $\chi_M$ of a powder sample of $\mathbf{1}(ClO_4)_2{\cdot}2H_2O$ was measured between 300 and 2 K. At 300 K the $\chi_M T$ value is equal to 6.8 $cm^3\,mol^{-1}\,K$ and decreases slowly down to 5.0 $cm^3\,mol^{-1}\,K$ at 50 K. Below 50 K the $\chi_M T$ value decreases more rapidly and is equal to 0.3 $cm^3\,mol^{-1}\,K$ at 2 K (Figure S1, open circles). This behaviour is indicative of a weak antiferromagnetic interaction between two high-spin $Mn^{II}$ ions ($S = 5/2$). The best simulation performed on the $\chi_M$ vs. $T$ curve is obtained with a fixed $g$ value of 1.95[32] and $J = -3.2\ cm^{-1}$ ($H = -J\hat{S}_1{\cdot}\hat{S}_2$) (Figure S1, solid line).[33] The best simulation performed on the $\chi_M T$ vs. $T$ curve is obtained with $g = 1.95$[32] and $J = -3.4\ cm^{-1}$ (Figure S1, solid line).[34] The two sets of parameters are in agreement and lead to a $J$ value that is close to $-3.3(0.1)\ cm^{-1}$. This value is consistent with reported $J$ values for systems where the two $Mn^{II}$ ions are bridged by two phenolato groups,[35–38] and is slightly higher than the one published for the closely related $[(mL)MnMn(mL)]^{2+}$ complex.[27]

### EPR Spectroscopy

The 9.4 GHz (X band) EPR spectra recorded at 5 and 30 K, and the 10 K 34 GHz (Q-band) EPR spectrum of a powder sample of $\mathbf{1}(ClO_4)_2{\cdot}2H_2O$ are shown in Figure 2(a,b). The evolution of the 9.4 GHz EPR signatures as a function of temperature was monitored between 5 and 50 K and is given in the Supporting Information (Figure S2). All spectra exhibit features extending from 0–800 mT at 9.4 GHz and from 400–1500 mT at 34 GHz, the intensities of which depend on the temperature. This behaviour is strongly indicative of dinuclear $Mn_2^{II}$ species.[35,38–42] The observed features originate from the superimposition of signatures from the five $S = 1$ to $S = 5$ paramagnetic spin states.[43] The 9.4 and 34 GHz EPR spectra that were

 © 2006 Wiley-VCH Verlag GmbH & Co. KGaA, Weinheim 

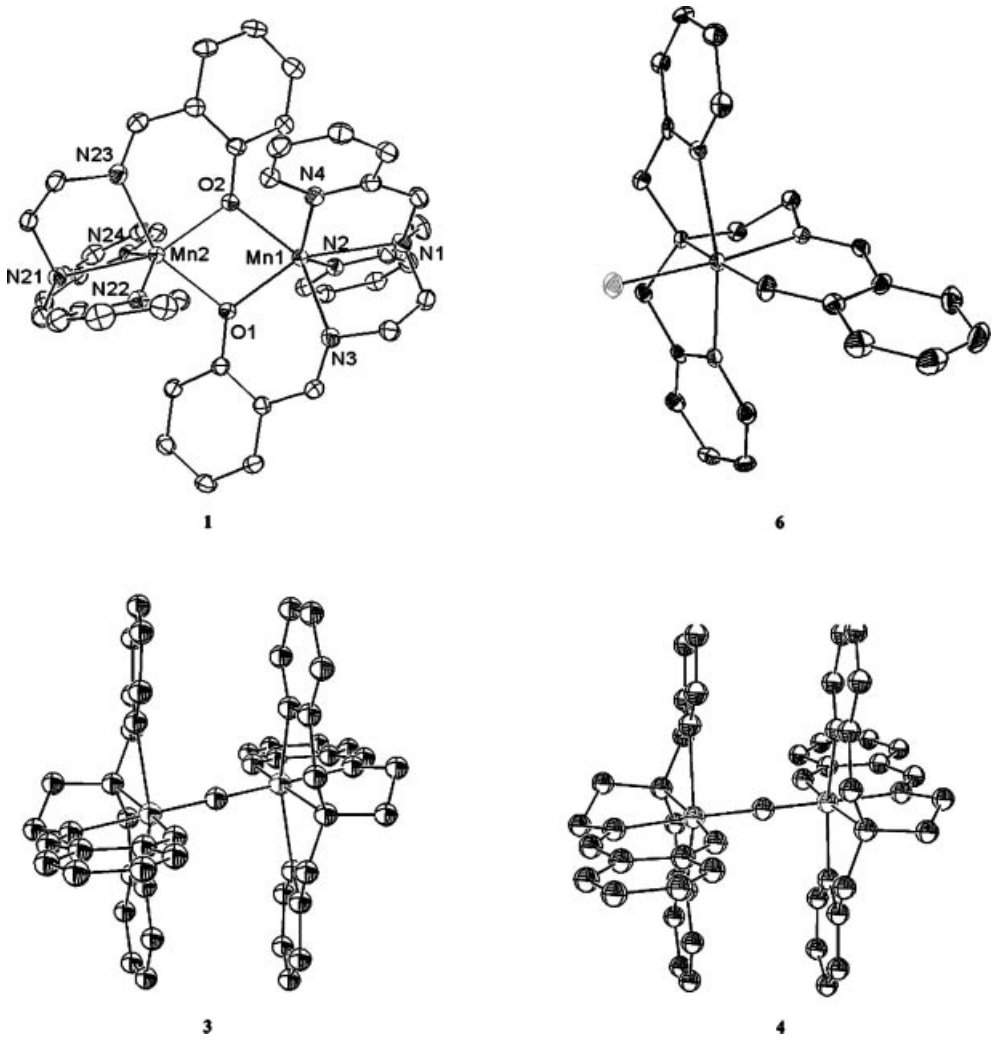


Figure 1. Molecular view of the dication **1**. Displacement ellipsoids are drawn at the 50% probability level. Molecular views of cations **3**, **4**, and **6** from ref.[24,30].

Table 1. Selected bond lengths [Å] and angles [°] for **1**.

| | | | |
|---|---|---|---|
| Mn1–O1 | 2.166(2) | Mn2–O1 | 2.137(2) |
| Mn1–O2 | 2.154(2) | Mn2–O2 | 2.144(2) |
| Mn1–N1 | 2.406(2) | Mn2–N21 | 2.373(3) |
| Mn1–N2 | 2.222(3) | Mn2–N22 | 2.274(3) |
| Mn1–N3 | 2.204(3) | Mn2–N23 | 2.196(3) |
| Mn1–N4 | 2.290(3) | Mn2–N24 | 2.241(3) |
| O1–Mn1–O2 | 73.10(8) | O1–Mn2–O2 | 73.89(10) |
| Mn1–O1–Mn2 | 103.68(10) | Mn1–O2–Mn2 | 103.84(10) |
| O1–Mn1–N1 | 151.69(10) | O2–Mn2–N21 | 156.94(10) |
| O2–Mn1–N1 | 133.31(10) | O1–Mn2–N21 | 128.61(10) |
| O1–Mn1–N2 | 94.95(10) | O2–Mn2–N22 | 118.41(10) |
| O2–Mn1–N2 | 99.90(12) | O1–Mn2–N22 | 84.26(10) |
| O1–Mn1–N3 | 80.95(10) | O2–Mn2–N23 | 82.13(10) |
| O2–Mn1–N3 | 147.47(10) | O1–Mn2–N23 | 149.03(10) |
| O1–Mn1–N4 | 126.60(10) | O2–Mn2–N24 | 100.16(10) |
| O2–Mn1–N4 | 84.48(10) | O1–Mn2–N24 | 101.97(10) |
| N1–Mn1–N2 | 72.90(10) | N21–Mn2–N22 | 73.83(10) |
| N1–Mn1–N3 | 76.81(10) | N21–Mn2–N23 | 78.15(10) |
| N1–Mn1–N4 | 73.47(10) | N21–Mn2–N24 | 72.43(10) |
| N2–Mn1–N3 | 101.58(12) | N22–Mn2–N23 | 90.39(12) |
| N2–Mn1–N4 | 137.04(10) | N22–Mn2–N24 | 140.96(10) |
| N3–Mn1–N4 | 95.94(12) | N23–Mn2–N24 | 101.29(12) |

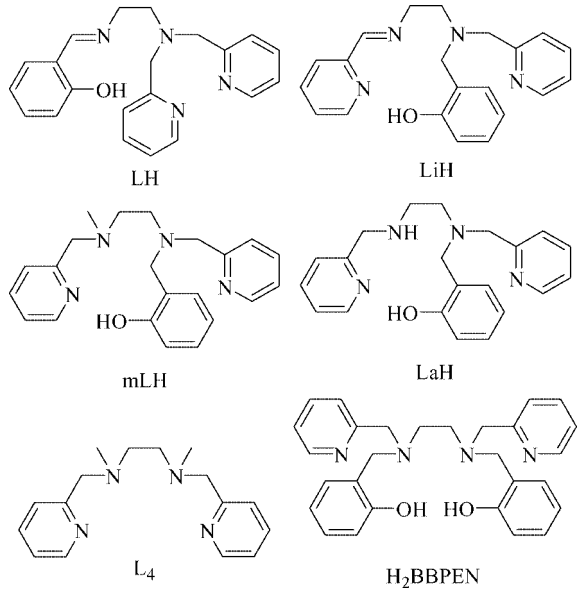


Scheme 1. The LH ligand used in this work and related ligands for comparison.

 © 2006 Wiley-VCH Verlag GmbH & Co. KGaA, Weinheim 

obtained are slightly different from those previously reported for the $[(mL)MnMn(mL)]^{2+}$ complex.[27] More precisely, the 34 GHz EPR spectrum of the $[(mL)MnMn(mL)]^{2+}$ complex shows several lines below 600 mT, which are attributed to inter-S-spin transitions from the competitive effect between the Zeeman and the Heisenberg interactions ($J = -1.8\ cm^{-1}$).[27] Here, the 34 GHz EPR spectrum of **1** shows only one transition below 600 mT, in agreement with the higher $J$ value of $-3.3\ cm^{-1}$.

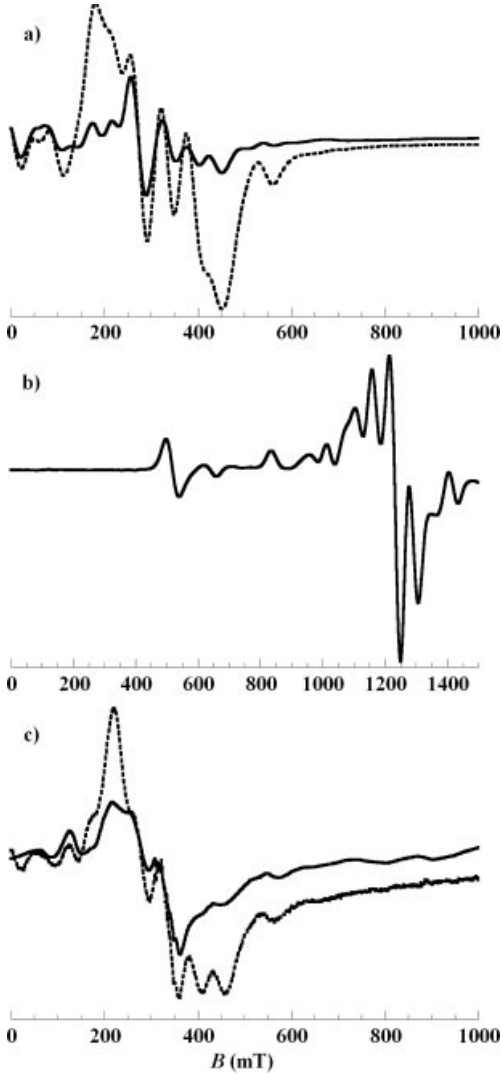


Figure 2. (a) 9.4 GHz EPR spectra recorded on a powder sample of $\mathbf{1}(ClO_4)_2{\cdot}2H_2O$ at 5 K (solid line) and 30 K (dotted line). (b) 34 GHz EPR spectra recorded on a powder sample of $\mathbf{1}(ClO_4)_2{\cdot}2H_2O$ at 10 K. (c) 9.4 GHz EPR spectra recorded on a millimolar solution sample of **1** in acetonitrile containing 0.1 M tetrabutylammonium perchlorate at 5 K (solid line) and 30 K (dotted line). Note that the product of the absorption by the temperature $T$ is plotted as a function of the magnetic field. 9.4 GHz EPR recording conditions: 9.38 GHz microwave frequency, 2.0 mW microwave power, 0.5 mT modulation amplitude, 100 kHz modulation frequency. 34 GHz EPR recording conditions: 34.18 GHz microwave frequency, 2.3 mW microwave power, 1.0 mT modulation amplitude, 100 kHz modulation frequency.

The 9.4 GHz EPR spectra recorded at 5 and 30 K of a frozen acetonitrile solution sample of **1** in the presence of 0.1 M tetrabutylammonium perchlorate are shown in Figure 2 (c). Evolution of the 9.4 GHz EPR signatures as a function of temperature is given in the Supporting Information (Figure S3). The EPR signatures as well as the modifications in the relative intensities of the observed EPR features as a function of temperature conform to that of a dinuclear $Mn_2^{II}$ species. The evolution of the EPR features is similar to the one observed in the powder sample of complex **1**. More precisely, in both powder and solution samples, the features near 200 and 400 mT increase with the temperature. Therefore, we can rationally propose that the dinuclear phenolato-bridged $Mn_2^{II}$ core structure is maintained upon dissolution in acetonitrile. However, no characteristic $^{55}Mn$ hyperfine pattern is observed. This can be attributed either to the superimposition in the same magnetic field range of several lines originating from different transitions that exhibit slightly distinct Mn hyperfine structures, or to a structural heterogeneity that would induce a distribution in the EPR parameters.

### UV/Visible Spectroscopy

The UV/Visible spectrum of complex **1** is shown in Figure 3 (a, dashed line) and the UV/Visible data are reported in Table 2. As expected for $Mn^{II}$ species no transition is observed in the visible region. An intense band is detected at 348 nm, which can be tentatively attributed to the phenolato to $Mn^{II}$ charge-transfer transition by comparison with data obtained from the related $[(L')Mn]^-$ complex, where $L'H_3$ is a triphenol containing ligand with a $[N_2O_3]$ donor set.[25,44] The band detected at 300 nm and indicated by an asterisk in Figure 3 (a) is assigned to the contaminant species **3** (see Table 2).

### Cyclic Voltammetry

The cyclic voltammogram of complex **1** is shown in Figure 4 (a) and its redox data are reported in Table 3. Anodic and cathodic processes assigned to the soil species **3** are indicated by a star in Figure 4 (a). The cyclic voltammetry trace of **1** exhibits a reversible anodic process at $E^{1/2} = 0.46$ V vs. SCE ($\Delta E^P = 133$ mV),[45] and an irreversible anodic peak at $E^P = 1.44$ V vs. SCE. The square wave voltammetry shows that two and one electrons are involved in the first and the second anodic process, respectively. These data indicate that the first anodic process is associated with the formation of the dinuclear phenolato-bridged $Mn_2^{III}$ complex $[(L)MnMn(L)]^{4+}$ (**2**), while the second anodic process is associated with the formation of a $Mn^{IV}$ containing species. Irreversibility of the second anodic process is probably due to the generation of a $Mn^{IV}$ ion, which would spontaneously engender the opening of the dinuclear structure. For comparison purposes redox data of complex **1** together with other related dinuclear phenolato-bridged $Mn_2^{II}$ complexes are given in Table 3. The potential value of the first

 © 2006 Wiley-VCH Verlag GmbH & Co. KGaA, Weinheim 

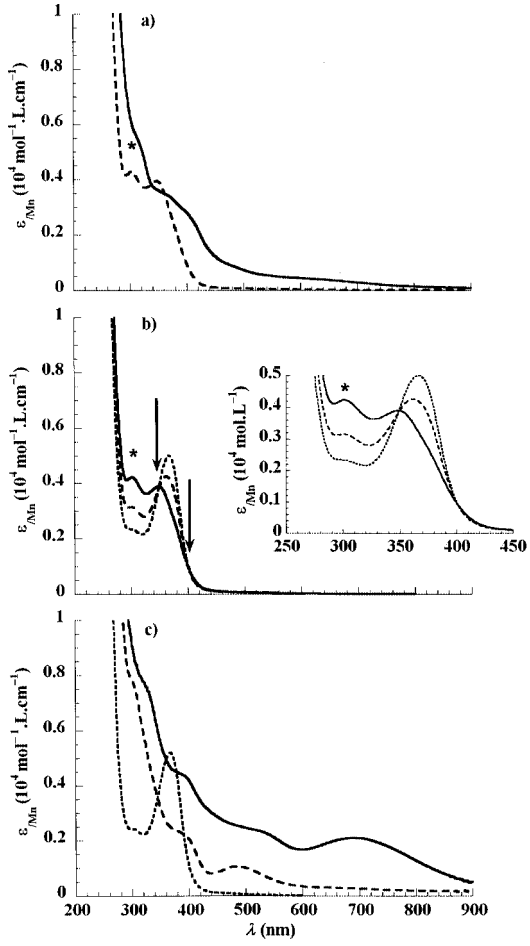


Figure 3. (a) UV/Visible spectrum of complex **1** in acetonitrile containing 0.1 M tetrabutylammonium perchlorate (dashed line) and of complex **2**, generated by exhaustive electrolysis of **1** at $E$ = 0.8 V vs. SCE (solid line); (b) UV/Visible spectrum of 1 mM solution of **1** in acetonitrile containing 0.1 M tetrabutylammonium perchlorate, upon addition of chloride ions. No chloride ion added (solid line), 0.5 equiv. of chloride ion per Mn (dashed line) and 1.0 equiv. of chloride ion per Mn ion (dotted line); (c) UV/Visible spectrum of complex **5**,[60] (dotted line); of complex **6**, generated by exhaustive electrolysis of complex **5** at $E$ = 0.85 V vs. SCE (dashed line), and of complex **7**, generated by exhaustive electrolysis of complex **5** at $E$ = 1.45 V vs. SCE (solid line). (l = 1 mm, $T$ = 20 °C). Note that unless specified the total conversions of **1** were assumed to draw the absorption spectrum. The asterisks * in (a) and (b) indicate the presence of the contaminant species **3**.

anodic process of **1** is lower than those of related phenolato-bridged dinuclear $Mn_2^{II}$ complexes, and the peak-to-peak separation $\Delta E^P$ is distinctly smaller. The possible origins of these differences will be discussed below.

An irreversible cathodic peak is detected at $E^P$ = –1.91 V vs. SCE, while in the related $[(Li/La)MnMn(Li)]^{2+}$ complex[29] reduction of the imine function of the $Li^-$ ligand (see Scheme 1) was observed at $E^P$ = –1.38 V vs. SCE.[26] The conjugation of the imine function to a phenolato group in the $L^-$ is anticipated to render the reduction more difficult, and therefore explain the lower potential value detected here.

### Electrochemical Oxidation of Species 1 into Complex [(L)MnMn(L)]$^{4+}$ (2)

The square wave and the cyclic voltammetry experiments recorded on complex **1** indicate that oxidation of **1** will lead to the dinuclear phenolato-bridged $Mn_2^{III}$ species $[(L)MnMn(L)]^{4+}$ (**2**). Exhaustive electrolysis was performed at $E$ = 0.8 V vs. SCE. The cyclic voltammetry trace recorded after consumption of one electron per Mn ion displays one reversible cathodic process at $E^{1/2}$ = 0.46 V vs. SCE and one irreversible anodic peak $E^P$ = 1.44 V vs. SCE (Figure S4). These data are consistent with the formation of complex **2** in solution. An insignificant amount of the dinuclear mono-μ-oxido-bridged complexes was generated during the electrolysis.

The UV/Visible spectrum recorded after completion of the electrolysis is shown in Figure 3 (a, solid line), and the UV/Visible data reported in Table 2, together with those of related phenolato $Mn^{III}$ complexes. Upon comparison, it is possible to attribute the broad transition detected near 600 nm to $Mn^{III}$ d–d transitions and the shoulder observed at 480 nm to the superimposition of $Mn^{III}$ d–d transitions and phenolato to $Mn^{III}$ charge-transfer transitions. Both the position and the intensity of the two absorption bands detected near 405 nm agree with values reported in the literature for bridging phenolato to $Mn^{III}$ charge-transfer transitions.[44,46–49] The shift of the phenolato to $Mn^{II}$ electronic transition detected in **1** at 348 nm to a lower energy upon oxidation of the Mn ion is reminiscent of what was observed for the successive oxidations of the dinuclear $Mn_2^{II}$ complex $[Mn_2(2\text{-}OHsalpn)_2]^{2-}$.[25,50] The UV/Visible signature of complex **2** is very close to that of complex **3**, except for the strong absorption band at 300 nm only detected in **3**.

9.4 GHz EPR spectra were recorded on the electrolyzed solution using the perpendicular and the parallel detection modes (data not shown). No signal was detected.

### Electrochemical Conversion of Species 1 into Complex [(L)Mn(μ-O)Mn(L)]$^{3+}$ (4)

The electrochemical conversion of mono- and dinuclear $Mn^{II}$ complexes into mixed-valence oxido-bridged $Mn_2^{III,IV}$ systems has been recently described.[27,51,52] An exhaustive electrolysis of the $Mn^{II}$ species is performed in acetonitrile, where the presence of residual water together with an external base leads to the formation of the oxido-bridged species. This method was applied here to obtain the mixed-valence complex $[(L)Mn(\mu\text{-}O)Mn(L)]^{3+}$ (**4**).

The cyclic voltammetry trace of species **1** upon addition of one equiv. of base per Mn ion is shown in Figure 4 (b). When scanning towards anodic potentials, the first oxidation process of species **1** is still partially detected, but at a slightly lower potential value. Furthermore, two new reversible processes are seen at $E^{1/2}$ = 0.55 and $E^{1/2}$ = 1.0 V vs. SCE, which correspond to the two sequential one-electron oxidations of the dinuclear $Mn_2^{III}$ complex $[(L)Mn(\mu\text{-}O)Mn(L)]^{2+}$ (**3**). Both the detection of the oxidation

 © 2006 Wiley-VCH Verlag GmbH & Co. KGaA, Weinheim 

Table 2. Electronic absorption data of complexes **1** to **7** and of the related complexes $[(L_4)MnCl_2]^+$, $[(L_4)MnCl_2]^{2+}$, $[(BBPEN)Mn]^+$, and $[(BBPEN)Mn]^{2+}$.[25]

| Species | $\lambda$, $\varepsilon_{/Mn}$ (nm, $10^3$ M$^{-1}$cm$^{-1}$) | | | | Ref. |
|---|---|---|---|---|---|
| $Mn^{II}$ | | | | | |
| **1** | 348, 3.9 | | | | this work |
| **5** | 367, 5.0 | | | | this work |
| $Mn^{III}$ | | | | | |
| **2** | 370, 3.4 | 405, 2.7 | 480, 0.88 | 600, 0.47 | this work |
| **6** | 298, 7.5 | 392, 2.1 | 479, 0.98 | 494, 1.01 | this work |
| $[(L_4)MnCl_2]^+$ | 291, 7.1 | 394, 1.1 | 500, 0.30 | 536, 0.36 | [52] |
| $[(BBPEN)Mn]^+$ | 258, 29 | 369, 4.2 | 506, 2.1 | | [54] |
| **3** | 300, 10.5 | 400, 2.4 | 500, 0.5 | | [30] |
| $Mn^{IV}$ | | | | | |
| **7** | 325, 7.2 | 390, 4.2 | 523, 2.2 | 690, 2.0 | this work |
| $[(L_4)MnCl_2]^{2+}$ | 314, 8.5 | 409, 2.2 | | | [52] |
| $[(BBPEN)Mn]^{2+}$ | | | 506, 2.7 | 790, 3.7 | [54] |
| **4** | 344, 6.2 | 408, 3.5 | 570, 1.5 | | [30] |

peak of **1** at a lower potential value and of the cyclic voltammetry signature of a new species are symptomatic of an EC (Electrochemical Chemical) mechanism. Oxidation of species **1** leading to the corresponding dinuclear $Mn_2^{III}$ species **2** is followed by the formation of complex **3** at the electrode, because of the presence of residual water and of base in the medium.[53] This EC mechanism is illustrated in Scheme 2.

The cyclic voltammogram, the UV/Visible spectrum, and the 100 K 9.4 GHz EPR spectrum recorded after bulk electrolysis at 0.75 V vs. SCE (Figure 4(c), Figures S5, and S6, respectively, in the Supporting Information) are identical to those reported for the mixed-valence complex **4** obtained by the one-electron oxidation of the chemically prepared species **3**.[30] Both the number of consumed electrons during the electrolysis (3 $e^-$ per complex **1**) and the extinction coefficient values are consistent with the total conversion of species **1** into **4**. This is confirmed by quantification of the EPR trace recorded after the electrolysis of **1** (Figure S6), which shows the formation of **4** with a 95% (±5%) yield (see Exp. Sect. for details).

### Transformation of Complex 1 upon Addition of Chloride Ions

Evolution of the cyclic voltammetry trace of complex **1** upon addition of 0.5 and 1.0 equiv. of chloride ion per Mn ion is shown in Figure 4 (d dashed and solid lines, respectively). The anodic process corresponding to the oxidation of free chloride ions is not observed. Concomitantly with the loss of the anodic processes related to complex **1**, two new reversible anodic processes were detected at $E^{1/2}$ = 0.21 ($\Delta E^P$ = 95 mV) and $E^{1/2}$ = 1.15 V vs. SCE ($\Delta E^P$ = 94 mV). By comparing the potential values with those of related complexes with $[N_4Cl_2]$[52] and $[N_4O_2]$[54] Mn environments (see Table 3) we propose that the coordination sphere of the Mn ion is $[N_4OCl]$ provided by the $L^-$ ligand and one exogenous chloride anion, leading to the neutral $Mn^{II}$ species [(L)MnCl] (**5**). In this hypothesis, the two anodic processes are attributed to the successive one-electron oxidation of species **5** into the mononuclear $Mn^{III}$ $[(L)MnCl]^+$ (**6**) complex and then into the mononuclear $Mn^{IV}$ $[(L)MnCl]^{2+}$ (**7**) complex.

The spectral changes of the UV/Visible spectrum of complex **1** upon addition of 0.5 and 1.0 equiv. of chloride ion per Mn ion are shown in Figure 3 (b, dashed and dotted lines, respectively). The phenolato to $Mn^{II}$ charge transfer transition detected at 348 nm for complex **1** is shifted to lower energies ($\lambda_{max}$ = 367 nm) in species **5**. This spectral modification can be related to the change in the coordination mode of the phenolato arm from bridging to monodendate.

By contrast to the modifications observed by cyclic voltammetry and UV/Visible spectroscopy at room temperature, the EPR signature of complex **1** recorded at 100 K is virtually unmodified upon the addition of one equiv. of chloride ion per Mn ion (Figure 5, a,b). It totally vanishes upon the addition of five equiv. of chloride ions per Mn ion (Figure 5, d). The new spectral features consist of an intense transition at 330 mT ($g$ = 2) and three other transitions of lower intensity at 50 mT, 130 mT, and 225 mT. This signature is consistent with a mononuclear $Mn^{II}$ species, where the Zeeman effect dominates the zero-field splitting interaction.[55–59] The EPR study gives a first insight into the presence of an equilibrium between species **1**, **5**, and the chloride ions, which should be modified by the temperature. The detection of this equilibrium at room temperature was monitored by cyclic voltammetry. Upon addition of two and five equiv. of chloride ions per Mn ion, the cyclic voltammetry trace shows that the potential of the anodic peak is slightly shifted to lower values, whereas the position of the associated cathodic peak observed on the reverse scan remains virtually identical (Figure S7). This behaviour is reminiscent of a CE (Chemical-Electrochemical) mechanism, which is illustrated in Scheme 3. As a working hypothesis, we propose that the chemical reaction, which precedes the electrochemical oxidation of species **5** into **6**, is an equilibrium between species **1** and **5**.

 © 2006 Wiley-VCH Verlag GmbH & Co. KGaA, Weinheim 

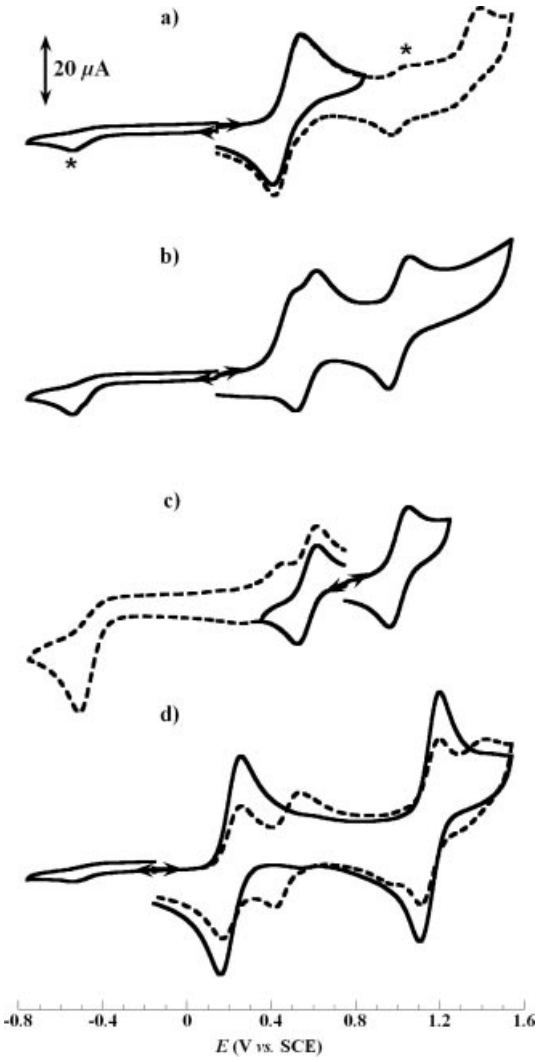


Figure 4. (a) Cyclic voltammograms of 1 mM solution of **1** in acetonitrile containing 0.1 M tetrabutylammonium perchlorate. (b) Cyclic voltammograms of 1 mM solution of **1** in acetonitrile in presence of one equiv. of 2,6-dimethylpyridine per Mn ion. (c) Cyclic voltammograms of 1 mM solution of **1** in acetonitrile in the presence of one equiv. of 2,6-dimethylpyridine per Mn ion, and after bulk electrolysis at $E$ = 0.7 V vs. SCE. ($T$ = 20 °C, scan rate = 100 mV). (d) Cyclic voltammograms of 1 mM solution of **1** in acetonitrile in the presence of 0.5 equiv. of chloride ion per Mn ion (dashed line), and in the presence of 1.0 equiv. of chloride ion per Mn ion (solid line). The stars in (a) indicate the presence of the contaminant species **3**.

It is worth noting that upon the addition of chloride ions, the intensity of anodic and cathodic processes corresponding to the contaminant species **3** fades significantly, as well as the UV band detected at 300 nm and assigned to species **3**. The dissipation of species **3** upon addition of chloride ions will be considered below.

### Electrochemical Oxidations of Complex 5 into Species $[(L)MnCl]^+$ (6) and $[(L)MnCl]^{2+}$ (7)

The cyclic voltammetry signature of complex **5**,[60] which is shown in Figure 4(d), suggests that complex **5** can be oxidized twice electrochemically to generate the corresponding $Mn^{III}$ $[(L)MnCl]^+$ (**6**) and $Mn^{IV}$ $[(L)MnCl]^{2+}$ (**7**) species. Two successive bulk electrolysis of species **5** were performed at $E$ = 0.85 (20 °C) and $E$ = 1.45 V vs. SCE (–30 °C), respectively, and were monitored by UV/Visible and EPR spectroscopy.

The cyclic voltammetry trace recorded after the first consumption of one electron per Mn ion displays one reversible anodic process at $E^{1/2}$ = 1.15 V vs. SCE and one reversible cathodic process at $E^{1/2}$ = 0.21 V vs. SCE (Figure S8, dashed line). These data are consistent with the one-electron oxidation of species **5** leading to the mononuclear $Mn^{III}$ complex **6**.

The UV/Visible spectrum recorded after the first bulk electrolysis is shown in Figure 3 (c, dashed line). Three new transitions are detected in the region from 390 to 495 nm. The UV/Visible data of complex **6** are reported in Table 2, together with other related phenolato and chlorido $Mn^{III}$ complexes. Upon comparison, it is possible to attribute the 390 nm absorption band to the superimposition of chlorido and phenolato to $Mn^{III}$ charge-transfer transitions, and the two transitions detected at 479 and 494 nm to both $Mn^{III}$ d–d transitions and phenolato to $Mn^{III}$ charge-transfer transitions.

No EPR signal was detected using the conventional perpendicular detection mode. However, the 5 K 9.4 GHz EPR spectrum of the electrolyzed solution, recorded in the parallel detection mode displays six ill-resolved hyperfine lines centred at 79 mT ($g$ = 8.5) and spaced by 5.4 mT (Figure 6, a). As previously described in the literature, 9.4 GHz parallel mode EPR spectra are expected for an $S$ = 2 quasi-axial system with a strong zero-field splitting.[61,62] More specifically, the spectroscopic signatures detected here are characteristic of a high-spin $Mn^{III}$ species, where the Jahn–Teller distortion is an elongation.[52,63–69]

The cyclic voltammetry trace recorded after the second one-electron electrolysis of **5** displays two reversible cathodic processes at $E^{1/2}$ = 1.15 and $E^{1/2}$ = 0.21 V vs. SCE (Figure S8, solid line), underlying that the one-electron oxidation of species **6** into the mononuclear $Mn^{IV}$ complex **7** was successful. However, a slightly weaker intensity is observed for the two electrochemical processes, indicating a partial evolution of the $Mn^{IV}$ species, even at –30 °C. It is worth noting that the possibility of a ligand-centred oxidation of species **6** leading to the mononuclear $Mn^{III}$-phenoxyl complex was given some thought. However, it was considered to be an unlikely hypothesis[70] on the basis of the reported oxidation of the $Mn^{III}$ centre at a potential that was 1 V lower than the phenolate ligand in the $Mn^{III}$ species with a phenolate-containing ligand.[71]

The electronic absorption spectrum recorded after the second bulk electrolysis is shown in Figure 3 (c, solid line). Three new intense absorption bands appear at 390, 523, and 690 nm, respectively. The UV/Visible data of complex **7** are reported in Table 3,[72] and compared with related phenolato and chlorido $Mn^{IV}$ complexes. The intense absorption band observed near 400 nm can be attributed to phenolato and chlorido to $Mn^{IV}$ charge-transfer transi-

 © 2006 Wiley-VCH Verlag GmbH & Co. KGaA, Weinheim 

Table 3. $E^{1/2}$ and $E^{p}$ (when the anodic process is irreversible) potential values (V vs. SCE) of complexes **1** and the related complexes $[(mL)MnMn(mL)]^{2+}$ and $[(Li/La)MnMn(Li)]^{2+}$, of complex **5** and the related complexes $[(L_4)MnCl_2]$ and $[(BBPEN)Mn]^{+}$, and of complex **3**.[25] ($T$ = 20 °C).

| Species | $E$ (V vs. SCE), [$\Delta E^{p}$ (mV)] | | Ref. |
|---|---|---|---|
| | $Mn_2^{II}/Mn_2^{III}$ | $Mn_2^{III}/Mn_2^{III,IV}$ | |
| **1** | 0.46 (133) | 1.42 (irr.)[a] | this work |
| $[(mL)MnMn(mL)]^{2+}$ | 0.89, 1.02[b] | | [27] |
| $[(Li/La)MnMn(Li)]^{2+}$ | 0.58 (260) | | [26] |
| | $Mn^{II}/Mn^{III}$ | $Mn^{III}/Mn^{IV}$ | |
| **5** | 0.21 (96) | 1.15 (93) | this work |
| $[(L_4)MnCl_2]$ | 0.74 (70) | 1.46 (irr.)[a] | [52] |
| $[(BBPEN)Mn]^{+}$ | –0.06 (90) | 0.80 (90) | [54] |
| | $Mn_2^{III}/Mn_2^{III,IV}$ | $Mn_2^{III,IV}/Mn_2^{IV}$ | |
| **3** | 0.55 (92) | 1.0 (91) | this work[30] |

[a] irr. = irreversible. [b] The two potential values correspond to the sequential one-electron oxidation of the $Mn_2^{II}$ complex leading to the $Mn_2^{III}$ complex.

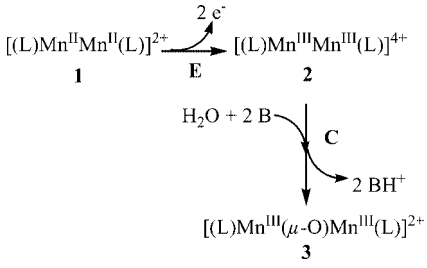


Scheme 2. Proposed Electrochemical Chemical (EC) mechanism to explain the evolution of the cyclic voltammetry trace of **1** upon addition of base.

tions,[71,73] while the shoulder detected at 530 nm may be assigned to $Mn^{IV}$ d–d transitions.[74] However, both the intensity and the position of the broad absorption band observed near 690 nm are reminiscent of absorption features reported for phenolato-containing $Mn^{IV}$ complexes,[27,30,54,71,75–79] and is therefore attributed to a phenolato to $Mn^{IV}$ charge-transfer transition. Therefore, the UV/Vis signature of species **7** also strongly supports the formation of a $Mn^{IV}$ complex instead of a $Mn^{III}$-phenoxyl one. Indeed, in the latter case, the two observed bands at 400 and 690 nm are expected with stronger and much weaker intensities, respectively.[71]

The 5 K 9.4 GHz EPR spectrum of the electrolyzed solution recorded using the perpendicular detection mode is shown in Figure 6 (b). The EPR spectrum exhibits a multiline signal centred at $g$ = 2 due to the presence of traces of uncoordinated $Mn^{II}$ ions. Quantification of this signal (see Exp. Sect.) indicates that uncoordinated $Mn^{II}$ ions account for approximately 5% of the total Mn-based species. Three other broad transitions are detected at 130 mT ($g$ = 5.2), 220 mT ($g$ = 3.0), and 580 mT ($g$ = 1.2), showing no evidence of $^{55}Mn$ hyperfine coupling (Figure 6, b). This EPR signature is indicative of an $S$ = 3/2 $Mn^{IV}$ ion, where the zero-field splitting interaction dominates the Zeeman effect.[54,79–86] For an axial $Mn^{IV}$ system (E/D = 0) the low-field transition is expected at $g_{eff}$ = 4. The diver-

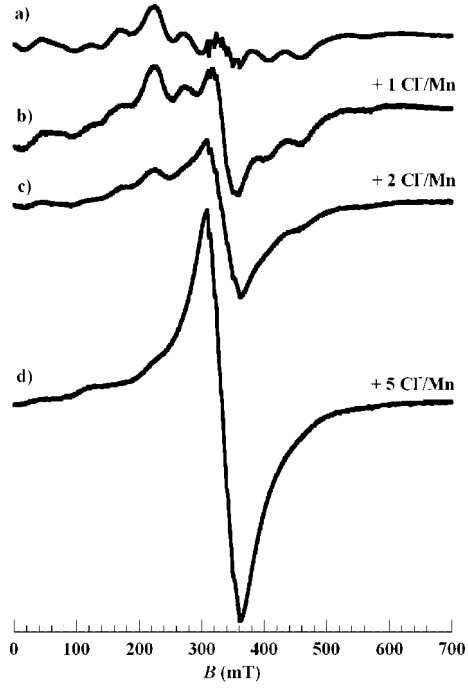


Figure 5. Evolution of the 100 K, 9.4 GHz EPR spectrum of 1 mM solution of **1** in acetonitrile containing 0.1 M tetrabutylammonium perchlorate, upon addition of chloride ions. Recording conditions: 9.38 GHz microwave frequency, 2.0 mW microwave power, 0.5 mT modulation amplitude, 100 kHz modulation frequency.

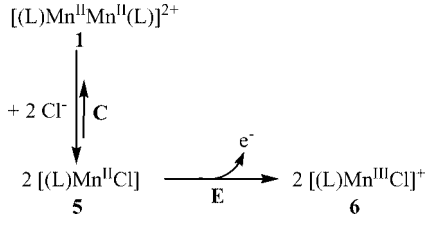


Scheme 3. Proposed Chemical Electrochemical (CE) mechanism to explain the evolution of the cyclic voltammetry trace of **1** upon addition of chloride ions.

 © 2006 Wiley-VCH Verlag GmbH & Co. KGaA, Weinheim 

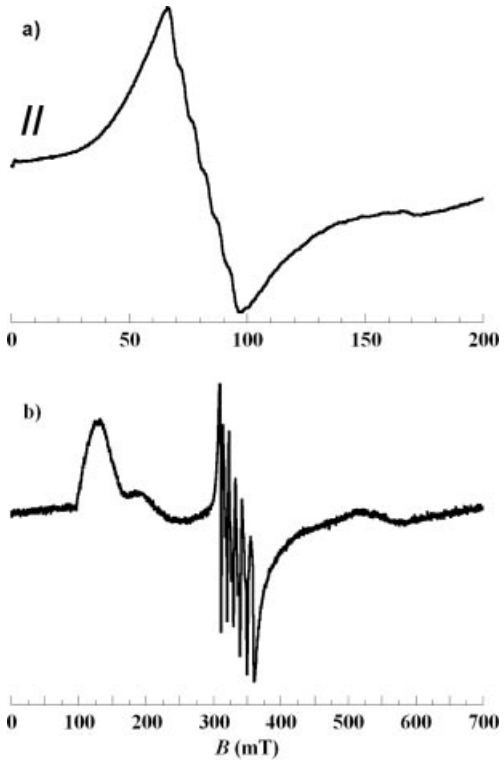


Figure 6. 5 K 9.4 GHz EPR spectra recorded on a 2 mM solution sample of **5**,[60] in acetonitrile containing 0.1 M tetrabutylammonium perchlorate, after bulk electrolysis at $E$ = 0.85 V vs. SCE (a), and after bulk electrolysis at $E$ = 1.45 V vs. SCE (b). Recording conditions: (a) parallel detection mode, 9.42 GHz microwave frequency, 0.8 mW microwave power, 0.5 mT modulation amplitude, 100 kHz modulation frequency, 10 scans. (b) 9.38 GHz microwave frequency, 0.12 mW microwave power, 0.5 mT modulation amplitude, 100 kHz modulation frequency.

gence from this value is characteristic of the rhombicity of the system. In the present case, according to the diagram showing the evolution of the $g_{eff}$ values for the Kramer doublets as a function of E/D,[87] the $g_{eff}$ = 5.2 and $g_{eff}$ = 3.0 values lead to an E/D ratio of 0.20(±0.04).

## Discussion

In the first part of this discussion, we will demonstrate the unique physicochemical properties of the dinuclear phenolato-bridged $Mn_2^{II}$ complex (**1**). As it is not our intention here to make an exhaustive comparison among all dinuclear phenolato-bridged $Mn_2^{II}$ complexes,[26,28] we will limit the comparative study to the recently published [(mL)Mn-Mn(mL)]$^{2+}$ system where the Mn ions have almost the same first coordination spheres as in **1**.[27]

Two main structural differences are observed between complex **1** and complex [(mL)MnMn(mL)]$^{2+}$. In the present case, the two pyridine rings are in a *trans* position, and the nitrogen atoms holding the bridging phenolato groups belong to the plane of the $Mn_2O_2$ core.

These structural peculiarities may support the distinct behaviour found for **1** in solution. More precisely, the enhanced reversibility of the anodic process detected for **1** is assigned to both an easier and nondestructive structural rearrangement from the dinuclear $Mn_2^{II}$ to the dinuclear $Mn_2^{III}$ systems. In the case of complex [(mL)Mn-Mn(mL)]$^{2+}$, it has been proposed that the two successive one-electron oxidations of the dinuclear $Mn_2^{II}$ complex led to the formation of the mononuclear $Mn^{III}$ species.[27] Here, we have shown that the dinuclear structure of complex **1** is maintained upon oxidation. Therefore, we can postulate that the Jahn–Teller distortion axis of the $Mn_2^{III}$ species is along the Py–Mn–Py axis, a direction that is not involved in the bridging motif. Furthermore, oxidation of **1** into **2** is detected at lower potential values than those of the related dinuclear $Mn_2^{II}$ phenolato-bridged complexes (see Table 3). The main difference in the [$N_4O$] donor set of the ligand $L^-$ compared to the one of ligand $mL^-$ (see Scheme 1) is the conjugation of the phenolate group to an imine function. This is in good agreement with the fact that the imine-phenolate fragment stabilizes the high oxidation states of the metal centres.

A two-electron oxidation process was detected for **1** whereas two successive one-electron oxidations were reported for the [(mL)MnMn(mL)]$^{2+}$ complex. The detection of a two-electron oxidation process is in line with what was observed and analyzed by Romero et al.[42] for the $Mn_2^{II}$ complex [$Mn_2(\mu\text{-}Cl)_2(bpea)_2Cl_2$] where bpea is a tetradentate ligand with a [$N_4$] donor set.[25] It was interpreted as arising from the independency of the two Mn ions because of a strong insulating effect of the bridging chloride ions. Indeed the two metal centres in the [$Mn_2(\mu\text{-}Cl)_2(bpea)_2Cl_2$] complex must be electronically uncoupled in order not to bring about any stabilization of the mixed-valence state. In the present case, we favour the hypothesis of an inversion of the potentials of the first- and second-electron transfers during the oxidation of **1**, i.e. the oxidation of the mixed-valence $Mn_2^{II,III}$ complex occurs at a lower potential value than that of complex **1**. Hapiot et al. have illustrated the inversion potential phenomenon in polyconjugated systems. Oxidation of the polyconjugated system leads to the dication, which is stabilized by interaction with the solvent, whereas the radical cation, which is delocalized over the molecular framework and thus less stabilized by interactions with the solvent, is not isolated.[88] We thus propose that in our case the easier oxidation of the mixed-valence $Mn_2^{II,III}$ state than that of the $Mn_2^{II}$ state arises from the better stabilization by the solvent of the $Mn_2^{III}$ state than that of the mixed-valence $Mn_2^{II,III}$ system.

Another clear cut difference is the cyclic voltammetry response upon addition of base to a solution of **1** or a solution of the [(mL)MnMn(mL)]$^{2+}$. In the former case, the dinuclear oxido-bridged species **3** is formed on the time scale of the cyclic voltammetry, whereas the intermediate mononuclear $Mn^{III}$ [(mL)Mn(OH)]$^+$ species was proposed in the latter case.[27] This result clearly indicates that the formation of species **3** is faster than that formed in the corresponding $Mn^{III}$ complex [(mL)Mn($\mu$-O)Mn(mL)]$^{2+}$.

In the second part of the discussion we will examine the various chemical and electrochemical reactions involved be-

 © 2006 Wiley-VCH Verlag GmbH & Co. KGaA, Weinheim 

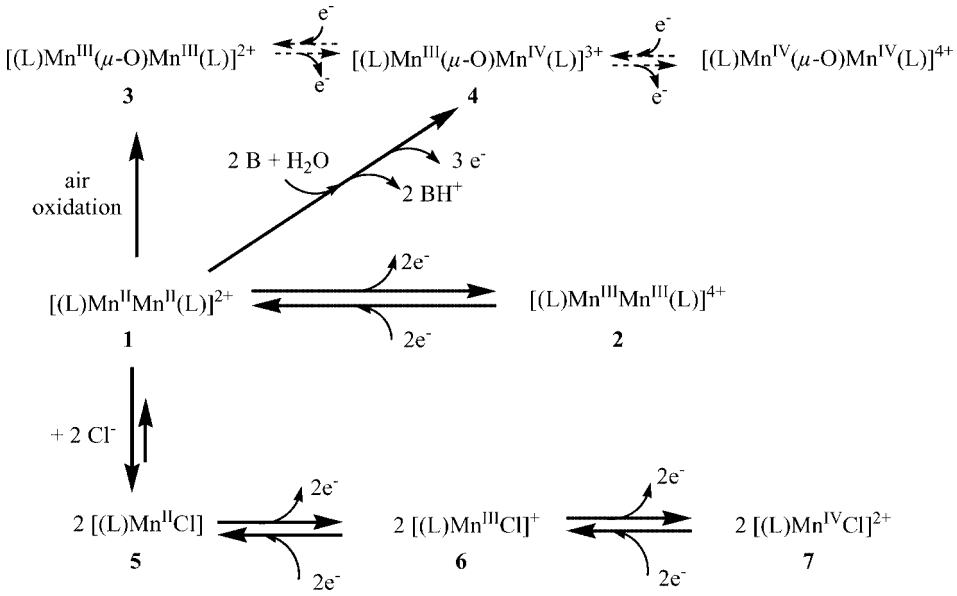


Scheme 4. Scheme of the various chemical or electrochemical reactions involved between species **1** to **7**. Solid arrows correspond to the reactions evidenced in the present work. Dashed arrows correspond to electrochemical processes described in a previous paper.[30]

tween the various Mn species obtained with the ligand $L^-$, which are depicted in Scheme 4. The X-ray structures of complexes **1**, **3**, **4**, and **6** are available in the present study and in the literature.[24,30]

The presence of the contaminant complex **3** in solution and powder samples of complex **1** has been evidenced by various techniques and comes from the air oxidation of **1**. Since all the experiments are not run in a glove box this impurity is hardly avoidable. The mechanism of this air oxidation is still unknown. The fast air oxidation of **1** may be related to the fast electrochemical oxidation of **1** into **3** in the presence of base as evidenced by the cyclic voltammetry study. We have also shown that the phenolato-bridged dinuclear $Mn_2^{III}$ complex **2** is accessible after a two-electron oxidation of **1** and that it does not evolve directly to the formation of the mono-μ-oxido complex **3** under an argon flux. Such an intermediate will certainly provide hints for the mechanistic pathway of the formation of the mono-μ-oxido species.

We have also checked that the mixed-valence mono-μ-oxido complex **4** can be generated by the exhaustive electrolysis of complex **1** in the presence of residual water and one equiv. of base per Mn ion, following a recently described procedure.[27]

The addition of chloride ions to complex **1** leads to the formation of the mononuclear chlorido $Mn^{II}$ species **5**. One more intriguing result is that upon addition of chloride ions to a solution sample of **1** containing species **3** as an impurity (indicated by an asterisk in parts a,b of Figure 3 and part a of Figure 4) leads to the fading of the absorption transition and of the redox waves characteristic of the mono-μ-oxido species. Furthermore, no other signal except that of species **3** was detected. For now, we can only speculate that species **5** is able to reduce species **3**, leading to the breaking of the oxido bridge by a mechanism that has still to be determined.

More importantly, we have shown that complex **5** can be oxidized twice electrochemically into the corresponding $Mn^{III}$ (**6**) and $Mn^{IV}$ (**7**) complexes. To the best of our knowledge no other (X-ray characterized) mononuclear complexes with a $[N_4OCl]$ coordination sphere are reported in the literature. The spectroscopic data for a $Mn^{IV}$ ion in an unusual coordination sphere with four nitrogen atoms, one oxygen, and a chloride ion are reported.[70] Hence, complex **5** is an interesting example of manganese mononuclear systems where three distinct oxidation states are observed and characterized.

## Conclusion

We have shown in this paper the chemical and electrochemical reactivities of a dinuclear phenolato-bridged $Mn_2^{II}$ complex. We have shown that the dinuclear $Mn_2^{II}$ compound could be oxidized in the +III states without alteration of the dinuclear structure of the starting compound. However, addition of chloride ions led to the formation of mononuclear species, which were oxidized and characterized in the +III and the rare +IV oxidation states. Future work will consist of the elucidation of the mechanistic pathways involving the formation of the mono-μ-oxido $Mn_2^{III}$ dinuclear complex.

## Experimental Section

**General Remarks:** Reagents and solvents were purchased commercially and used as received except for the electrochemical experiments for which acetonitrile was distilled under argon over granular $CaCl_2$. Argon U was used in the various experiments.

**Caution:** Perchlorate salts of metal complexes with organic ligands are potentially explosive. Only small quantities of these compounds should be prepared and handled behind suitable protective shields.

 © 2006 Wiley-VCH Verlag GmbH & Co. KGaA, Weinheim 

### Synthesis

***N*,*N*-Bis(2-pyridylmethyl)-*N'*-salicylidene-ethane-1,2-diamine:** Salicyladehyde (210 μL, 2 mmol) was added to a solution of *N*,*N*-bis(2-pyridylmethyl)ethane-1,2-diamine[89] (484 mg, 2 mmol) in methanol (20 mL). The solution was stirred at room temp for 3 h, evaporated, and dried under vacuum to give a pale brown oil (98% yield). $^1$H NMR (250 MHz, $CDCl_3$): $\delta$ = 8.48 (d, 2 H, $J$ = 5 Hz, *H*–$C_6H_3N$), 8.24 (s, 1 H, Ar–C*H*=N), 7.60–6.80 (m, 10 H, *H*–Ar), 3.88 [s, 4 H, N–(C*H*$_2$–Py)$_2$], 3.70 (t, 2 H, $J$ = 6 Hz, CH=N–C*H*$_2$–$CH_2$), 3.46 (s, 1 H, O*H*), 2.90 (t, 2 H, $J$ = 6 Hz, $CH_2$–*N*–C*H*$_2$–$CH_2$) ppm; $^1$H NMR details are given in the Supporting Information. IR: $\tilde{\nu}$ = 3360 (broad), 2944 (strong), 2832 (s), 1634 (medium), 1596 (weak), 1450 (m), 1280 (w), 1028 (s), 762 (w), 660 (br) cm$^{-1}$. ESI-MS: $m/z$ (%) = 347.2 (100) $[M + H]^+$.

**[(L)MnMn(L)](ClO$_4$)$_2$·2(H$_2$O):** Ligand LH (173 mg, 0.5 mmol) and 2,6-dimethylpyridine (58 μL, 0.5 mmol) were mixed in air-free absolute ethanol (10 mL) and placed under an argon atmosphere. $Mn(ClO_4)_2$·$6H_2O$ (181 mg, 0.5 mmol) was dissolved in air-free absolute ethanol (10 mL) and placed under an argon atmosphere. This was then added to the previous mixture. A white precipitate appeared rapidly. It was then filtered under an argon atmosphere, and washed with air-free ether (15 mL). A white powder (105 mg, yield = 42%) was then obtained and kept in a glove box until use. Crystallization of complex **1** was performed in the glove box by slow diffusion of diethyl ether in an acetonitrile solution of **1**, and crystals of **1**$(ClO_4)_2$·$2CH_3CN$ suitable for X-ray crystallography study were obtained. It is worth noting that solution and powder samples of **1** are highly sensitive to air oxidation. When not handled under inert atmosphere, complex **1** spontaneously converts into a dark purple species. An X-ray diffraction study revealed that this species is the previously studied mono-μ-oxido dinuclear $Mn_2^{III}$ complex $[(L)Mn(\mu\text{-}O)Mn(L)]^{2+}$ (**3**).[30] **1**$(ClO_4)_2$·$2H_2O$ (powder) ($C_{42}H_{46}Cl_2Mn_2N_8O_{12}$): calcd. C 48.7, H 4.5, Mn 10.6, N 10.8; found C 49.1, H 4.4, Mn 10.3, N 10.6. Note that in the case of the elemental analysis the contamination by species **3** is unapparent. IR: $\tilde{\nu}$ = 3421 (s, strong), 2918 (w, weak), 1634 (s), 1602 (s), 1570 (w), 1552 (w), 1541 (w), 1471 (m, medium), 1442 (m), 1400 (w), 1342 (w), 1295 (m), 1144 (m), 1115 (m), 1089 (s), 1048 (w), 1016 (w), 907 (w), 766 (m), 637 (m), 625 (w), 594 (w) cm$^{-1}$. ESI-MS: A major peak was detected at $m/z$ = 400 corresponding to $[(L)Mn]^+$.

**Infrared Spectroscopy:** Spectra were recorded on KBr pellets in the range 4000–400 cm$^{-1}$ with a Perkin–Elmer Spectrum 1000 spectrophotometer.

**Electrospray Ionization Mass Spectrometry:** Mass spectra were recorded with a Finnigan Mat95 in a BE configuration at low resolution on a micromolar acetonitrile solution.

**Elemental Analysis:** Analysis was performed by the Service de Microanalyse of the CNRS (Gif-Sur-Yvette, France) for carbon, nitrogen, and hydrogen and by the Service Central d'Analyse (Vernaison, France) for manganese.

**X-ray Crystallography:** Crystal data for $[(L)MnMn(L)](ClO_4)_2$·$2CH_3CN$ [**1**$(ClO_4)_2$·$2CH_3CN$] and the parameters of data collection are summarized in Table 4. Crystal data for **1**$(ClO_4)_2$·$2CH_3CN$ were collected with a Nonius Kappa-CCD area detector diffractometer using graphite-monochromated Mo-$K_\alpha$ radiation. The lattice parameters were determined from ten images recorded with 2 $\varphi$-scans and later refined on all data. The data were recorded at 100°K with an Enraf–Nonius FR558NH nitrogen cryostat. A 180° $\varphi$-range was scanned with two steps with a crystal to detector distance fixed at 40 mm. Data was corrected for Lorentz polarization. The structures were solved by the direct methods with SHELXS-97 and refined by full-matrix least-squares on $F$[2] with anisotropic thermal parameters for all non-H atoms with SHELXL-97. H atoms were found in a difference Fourier map and were introduced at calculated positions as riding atoms, with C–H bond lengths of 0.93 (aromatic CH), 0.98 (aliphatic CH), 0.97 ($CH_2$), and 0.96 Å ($CH_3$), and with $U_{iso}$(H) values of 1.2 $U_{eq}$(C) for CH and $CH_2$ hydrogen atoms, and 1.5 $U_{eq}$(C) for $CH_3$ hydrogen atoms.

Table 4. Details of structure determination, refinement, and experimental parameters for **1**$(ClO_4)_2$·$2CH_3CN$.

| | **1**$(ClO_4)_2$·$2CH_3CN$ |
|---|---|
| Empirical formula | $C_{46}H_{48}Cl_2Mn_2N_{10}O_{10}$ |
| Formula mass [g mol$^{-1}$] | 1081.72 |
| Temperature [K] | 100 (2) |
| Wavelength [Å] | 0.71069 |
| Crystal system | monoclinic |
| Space group | $P21/n$ |
| $a$ [Å] | 8.914(5) |
| $b$ [Å] | 21.075(5) |
| $c$ [Å] | 25.254(5) |
| $\alpha$ [°] | 90.000 |
| $\beta$ [°] | 92.724(5) |
| $\gamma$ [°] | 90.000 |
| Volume [Å$^3$] | 4739(3) |
| $Z$ | 4 |
| $d_{calcd.}$ [g cm$^{-3}$] | 1.516 |
| Absorption coefficient [mm$^{-1}$] | 0.715 |
| Crystal size [mm] | 0.30 × 0.22 × 0.03 |
| Theta range for data collection [°] | 2.09 to 30.64 |
| Index ranges | $0 \le h \le 12$ |
| | $0 \le k \le 29$ |
| | $-35 \le l \le 36$ |
| Reflections collected | 112633 |
| Independent reflections | 13422 |
| | [$R$(int) = 0.056] |
| Data [$I > 2\sigma(I)$] | 10114 |
| Parameters | 655 |
| Goodness-of-fit on $F^2$ | 1.049 |
| Final $R$ indices [$I > 2\sigma(I)$] | $R_1$ = 0.0371 |
| | $wR_2$ = 0.0963 |
| $R$ indices (all data) | $R_1$ = 0.0594 |
| | $wR_2$ = 0.1028 |
| Largest diff. peak/hole [e Å$^{-3}$] | 0.489/–0.497 |

CCDC-279908 contains the supplementary crystallographic data for this paper. These data can be obtained free of charge from The Cambridge Crystallographic Data Centre via www.ccdc.cam.ac.uk/data_request/cif.

**Magnetic Susceptibility Measurements:** Magnetic susceptibility data were recorded with an MPMS5 magnetometer (Quantum Design Inc.). The calibration was made at 298 K using a palladium reference sample furnished by Quantum Design Inc. The data were collected over a temperature range of 2–300 K. Above 100 K, a 1 T magnetic field was applied, while below 100 K, the amplitude was 0.1 T. Data were further corrected for diamagnetism. The $\chi_M$ vs. $T$ and $\chi_M T$ vs. $T$ curves were fitted by the van Vleck formula assuming the same $g$ factor for each $S$-spin state. The total spin $S$ runs from $|S_1 - S_2|$ to $(S_1 + S_2)$ by unit steps. The exchange Hamiltonian used was $H = -J\hat{S}_1 \cdot \hat{S}_2$, where $J$ stands for the exchange coupling constant and $\hat{S}_1$, $\hat{S}_2$ for the spin operators associated with the electronic spin of the $Mn^{II}$ sites ($S_1 = S_2 = 5/2$).

**EPR Spectroscopy:** 9.4 and 34 GHz EPR spectra were recorded with a Bruker ELEXSYS 500 spectrometer. For low temperature studies, an Oxford Instrument continuous-flow liquid helium cryostat and a temperature-control system were used. Solutions spectra

 © 2006 Wiley-VCH Verlag GmbH & Co. KGaA, Weinheim 

were recorded in acetonitrile containing 0.1 M tetrabutylammonium perchlorate. Quantification of uncoordinated $Mn^{II}$ was performed by comparison of the intensities of the $g = 2$ signal with those obtained using solutions of known concentrations of $Mn(ClO_4)_2 \cdot 6H_2O$ under the same recording conditions. Quantification of complex **4** in situ generated by bulk electrolysis of complex **1** in the presence of base was performed by a comparison of the intensities of the signal with those obtained using solutions of known concentrations of **4** (electrochemically prepared from the one-electron oxidation of **3**, and first isolated as a powder) under the same recording conditions.

**UV/Visible Spectroscopy:** UV/Visible spectra were recorded with a Varian Cary 300 Bio spectrophotometer at 20 °C with 0.1-cm quartz cuvettes.

**Cyclic Voltammetry and Bulk Electrolysis:** All electrochemical experiments were run under an Ar atmosphere. Cyclic voltammetry and coulometry measurements were recorded with an EGG PAR potentiostat (M273 model). For the cyclic voltammetry, the counter electrode was a Pt wire and the working electrode a glassy carbon disk carefully polished before each voltammogram with diamond paste (1 μm), sonicated in an ethanol bath and then washed carefully with ethanol. The reference electrode was a $Ag/AgClO_4$ electrode (0.53 V vs. NHE electrode), isolated from the rest of the solution by a fritted bridge. For bulk electrolysis, the counter electrode was a piece of Pt, separated from the rest of the solution with a fritted bridge. The working electrode was a grid of Pt. The solvent used was distilled acetonitrile and tetrabutylammonium perchlorate was added to obtain a 0.1 M supporting electrolyte (20 °C) or a 0.2 M supporting electrolyte (–30 °C). Low temperature regulation was ensured by a Julabo circulation cryostat.

**Supporting Information** (see also the footnote on the first page of this article): Figure S1: Magnetic susceptibility measurements recorded on complex $\mathbf{1}(ClO_4)_2 \cdot 2H_2O$. Figure S2: EPR spectra of complex $\mathbf{1}(ClO_4)_2 \cdot 2H_2O$ as a function of temperature. Figure S3: EPR spectra of the acetonitrile solution of complex $\mathbf{1}(ClO_4)_2 \cdot 2H_2O$ as a function of temperature. Figure S4: Cyclic voltammograms of the acetonitrile solution of **1** before and after bulk electrolysis at $E = 0.8$ V vs. SCE. Figure S5: UV/Visible spectrum of **4**, electrochemically prepared. Figure S6: 9.4 GHz EPR spectrum of **4**, electrochemically prepared. Figure S7: Evolution of the cyclic voltammograms of the acetonitrile solution of **1** upon addition of chloride ions. Figure S8: Cyclic voltammograms of a 2 mM acetonitrile solution of **5**, after bulk electrolysis at $E = 0.85$ and $E = 1.45$ V vs. SCE. Details of the $^1H$ NMR spectrum of ligand LH.

## Acknowledgments

We are grateful to Félix Perez for mass spectrometry measurements and Dr. Pierre Dorlet for the acquisition of the 34 GHz EPR spectrum. We thank Drs. Elodie Anxolabéhère-Mallart and Geneviève Blondin for stimulating discussions. The Conseil Régional de l'Ile de France is acknowledged for its contribution to the acquisition of the Bruker ELEXSYS X band EPR spectrometer. C. H. acknowledges Dr. Sun Un and Dr. William Rutherford, CEA Saclay, for allowing her to complete the work reported in this paper.

[1] E. J. Larson, V. L. Pecoraro in *Introduction to Manganese Enzymes* (Ed.: V. L. Pecoraro), VCH Publishers, Inc., New York, **1992**, pp. 1–28.
[2] J. D. Crowley, D. A. Traynor, D. C. Weatherburn in *Enzymes and Proteins Containing Manganese: an Overview* (Eds.: A. Sigel, H. Sigel), Marcel Dekker, Basel, Switzerland, **2000**, pp. 209–278.
[3] D. W. Yoder, J. Hwang, J. E. Penner-Hahn in *Metal Ions in Biological Processes* (Eds.: A. Sigel, H. Sigel), Marcel Dekker, New York, **2000**, vol. 37, pp. 527–557.
[4] J. W. Whittaker in *Manganese and Its Role in Biological Processes*, Marcel Dekker, New York, **2000**, vol. 37, pp. 587–611.
[5] A.-F. Miller, *Curr. Opin. Chem. Biology* **2004**, *8*, 162–168.
[6] D. Svedruzic, S. Jonsson, C. G. Toyota, L. A. Reinhardt, S. Ricagno, Y. Lindqvist, N. G. J. Richards, *Arch. Biochem. Biophys.* **2005**, *433*, 176–192.
[7] O. Opaleye, R.-S. Rose, M. M. Whittaker, E.-J. Woo, J. W. Whittaker, R. W. Pickersgill, *J. Biol. Chem.* **2006**, *281*, 6428–6433.
[8] V. J. Just, C. E. M. Stevenson, L. Bowater, A. Tanner, D. M. Lawson, S. Bornemann, *J. Biol. Chem.* **2004**, *279*, 19867–19874.
[9] G. C. Dismukes, *Chem. Rev.* **1996**, *96*, 2909–2926.
[10] N. A. Law, M. T. Caudle, V. L. Pecoraro in *Manganese Redox Enzymes and Model Systems: Properties, Structures, and Reactivity* (Ed.: G. B. Sykes), **1998**, vol. 46, pp. 305–440.
[11] Z. F. Kanyo, L. R. Scolnick, D. E. Ash, D. W. Christianson, *Nature* **1996**, *383*, 554–557.
[12] D. W. Christianson, *Acc. Chem. Res.* **2005**, *38*, 191–201.
[13] W. Oehlmann, U. Griepenburg, G. Auling, *Biotechnol. Lett.* **1998**, *20*, 483–488.
[14] K. N. Ferreira, T. M. Iverson, K. Maghlaoui, J. Barber, S. Iwata, *Science* **2004**, *303*, 1831–1838.
[15] A. W. Rutherford, A. Boussac, *Science* **2004**, *303*, 1782–1784.
[16] S. Mukhopadhyay, S. K. Mandal, S. Bhaduri, W. H. Armstrong, *Chem. Rev.* **2004**, *104*, 3981–4026.
[17] A. J. Wu, J. E. Penner-Hahn, V. L. Pecoraro, *Chem. Rev.* **2004**, *104*, 903–938.
[18] T. G. Carrell, A. M. Tyryshkin, G. C. Dismukes, *J. Biol. Inorg. Chem.* **2002**, *7*, 2–22.
[19] S. Durot, F. Lambert, J.-P. Renault, C. Policar, *Eur. J. Inorg. Chem.* **2005**, *14*, 2789–2793.
[20] S. Durot, C. Policar, F. Cisnetti, F. Lambert, J.-P. Renault, G. Pelosi, G. Blain, H. Korri-Youssoufi, J.-P. Mahy, *Eur. J. Inorg. Chem.* **2005**, *17*, 3513–3523.
[21] M. U. Triller, W.-Y. Hsieh, V. L. Pecoraro, A. Rompel, B. Krebs, *Inorg. Chem.* **2002**, *41*, 5544–5554.
[22] A. Gelasco, V. L. Pecoraro, *J. Am. Chem. Soc.* **1993**, *115*, 7928–7929.
[23] A. K. Poulsen, A. Rompel, C. J. McKenzie, *Angew. Chem. Int. Ed. Engl.* **2005**, *44*, 6916–6920.
[24] L. Sabater, C. Hureau, R. Guillot, A. Aukauloo, *Inorg. Chem.* **2006**, *45*, 2373–2375.
[25] LH: *N*,*N*-bis(2-pyridylmethyl)-*N*′-salicylidenethane-1,2-diamine; mLH: *N*,*N*′-bis(2-pyridylmethyl)-*N*-(2-hydroxybenzyl)-*N*′-methylethane-1,2-diamine; LaH: *N*-(2-hydroxybenzyl)-*N*,*N*′-bis(2-pyridylmethyl)ethane-1,2-diamine; LiH: *N*-(2-hydroxybenzyl)-*N*-(2-pyridylmethyl)-*N*′-(2-pyridyliminato)ethane-1,2-diamine; 2-OHsalpn: 1,3-bis(salicylideneimino)-2-propanol; $L'H_3$: *N*,*N*-bis(2-hydroxybenzyl)-*N*′-2-hydroxybenzylidene-1,2-diaminoethane; $H_2$BBPEN: *N*,*N*′-bis(2-hydroxybenzyl)-*N*,*N*′-bis(2-methylpyridyl)ethane-1,2-diamine; BPEA: *N*,*N*-bis(2-pyridylmethyl)ethylamine).
[26] C. Hureau, E. Anxolabéhère-Mallart, M. Nierlich, F. Gonnet, E. Rivière, G. Blondin, *Eur. J. Inorg. Chem.* **2002**, 2710–2719.
[27] C. Hureau, L. Sabater, E. Anxolabéhère-Mallart, M. Nierlich, M.-F. Charlot, F. Gonnet, E. Rivière, G. Blondin, *Chem. Eur. J.* **2004**, *10*, 1998–2010.
[28] N. Reddig, D. Pursche, M. Kloskowski, C. Slinn, S. M. Baldeau, A. Rompel, *Eur. J. Inorg. Chem.* **2004**, 879–887.
[29] This notation indicates that there is a mixture in a 1:1 ratio of two complexes in the sample, i.e. $[(Li)MnMn(Li)]^{2+}$ and $[(La)MnMn(Li)]^{2+}$.
[30] O. Horner, E. Anxolabéhère-Mallart, M.-F. Charlot, L. Tchertanov, J. Guilhem, T. A. Mattioli, A. Boussac, J.-J. Girerd, *Inorg. Chem.* **1999**, *38*, 1222–1232.

 © 2006 Wiley-VCH Verlag GmbH & Co. KGaA, Weinheim 

[31] G. Rogez, A. Marvilliers, P. Sarr, S. Parsons, S. T. Teat, L. Ricard, T. Mallah, *Chem. Commun.* **2002**, 1460–1461.
[32] The *g* value of complex **1** was fixed to 1.95 by analogy to those values of complexes $[(mL)MnMn(mL)]^{2+}$ and $[(Li/La)\text{-}MnMn(Li)]^{2+}$.
[33] Presence of 23% of complex **3** described by $g = 2.0$ and $J = -316\ cm^{-1}$, and of 2.3% of a mononuclear $Mn^{II}$ impurity of half the molar weight of **1** was taken into account.
[34] Presence of 25% of complex **3** described by $g = 2.0$ and $J = -316\ cm^{-1}$, and of 1.5% of a mononuclear $Mn^{II}$ impurity of half the molar weight of **1** was taken into account.
[35] D. P. Kessissoglou, W. M. Butler, V. L. Pecoraro, *Inorg. Chem.* **1987**, *26*, 495–503.
[36] D. Coucouvanis, K. Greiwe, A. Salifoglou, P. Challen, A. Simopoulos, A. Kostikas, *Inorg. Chem.* **1988**, *27*, 593–594.
[37] E. Gallo, E. Solari, N. Re, C. Floriani, A. Chiesi-Villa, C. Rizzoli, *J. Am. Chem. Soc.* **1997**, *119*, 5144–5154.
[38] T. C. Higgs, K. Spartalian, C. J. O'Connor, B. F. Matzanke, C. J. Carrano, *Inorg. Chem.* **1998**, *37*, 2263–2272.
[39] H. Adams, N. A. Bailey, N. Debaeker, D. E. Fenton, W. Kanda, J.-M. Latour, H. Okawa, H. Sakiyama, *Angew. Chem. Int. Ed. Engl.* **1995**, *34*, 2535–2537.
[40] B. Albela, M. Corbella, J. Ribas, I. Castro, J. Sletten, H. Stoeckli-Evans, *Inorg. Chem.* **1998**, *37*, 788–798.
[41] T. Howard, J. Telser, V. J. DeRose, *Inorg. Chem.* **2000**, *39*, 3379–3385.
[42] I. Romero, M.-N. Collomb, A. Deronzier, A. Llobet, E. Perret, J. Pécaut, L. Le Pape, J.-M. Latour, *Eur. J. Inorg. Chem.* **2001**, 69–72.
[43] E. J. Laskowski, D. N. Hendrickson, *Inorg. Chem.* **1978**, *17*, 457–470.
[44] H. Schmitt, R. Lomoth, A. Magnuson, J. Park, J. Fryxelius, M. Kritikos, J. Martensson, L. Hammarström, L. Sun, B. Akermark, *Chem. Eur. J.* **2002**, *8*, 3757–3767.
[45] $E^{1/2}$ is defined as $1/2\cdot(E^{Pa} + E^{Pc})$ and $\Delta E^{P} = |E^{Pa} - E^{Pc}|$ where $E^{Pa}$ ($E^{Pc}$) is defined as the potential of the maximum of current intensity when scanning toward anodic (cathodic) potentials.
[46] J. B. Vincent, K. Folting, J. C. Huffman, G. Christou, *Inorg. Chem.* **1986**, *25*, 996–999.
[47] M. Suzuki, M. Mikuriya, S. Murata, A. Uehara, H. Oshio, S. Kida, K. Saito, *Bull. Chem. Soc. Jpn.* **1987**, *60*, 4305–4312.
[48] H. Diril, H.-R. Chang, M. J. Nigles, X. Zhang, J. A. Potenza, H. J. Schugar, S. S. Isied, D. N. Hendrickson, *J. Am. Chem. Soc.* **1989**, *111*, 5102–5114.
[49] R. Lomoth, P. Huang, J. Zheng, L. Sun, L. Hammarström, B. Akermark, S. Styring, *Eur. J. Inorg. Chem.* **2002**, 2965–2974.
[50] A. Gelasco, M. L. Kirk, J. W. Kampf, V. L. Pecoraro, *Inorg. Chem.* **1997**, *36*, 1829–1837.
[51] C. Hureau, S. Blanchard, M. Nierlich, G. Blain, E. Rivière, J.-J. Girerd, E. Anxolabéhère-Mallart, G. Blondin, *Inorg. Chem.* **2004**, *43*, 4415–4426.
[52] C. Hureau, G. Blondin, M.-F. Charlot, C. Philouze, M. Nierlich, M. Césario, E. Anxolabéhère-Mallart, *Inorg. Chem.* **2005**, *44*, 3669–3683.
[53] The intensity of the cathodic process detected at $E^{P} = -0.52$ V vs. SCE is unchanged upon the addition of the base, confirming that the complex **3** is formed at the electrode and not directly in solution.
[54] A. Neves, S. M. D. Erthal, I. Vencato, A. S. Ceccato, Y. P. Mascarenhas, O. R. Nascimento, M. Hörner, A. A. Batista, *Inorg. Chem.* **1992**, *31*, 4749–4755.
[55] A. Abragam, B. Bleaney, *Electron Paramagnetic Resonance of Transition Ions*, Dover Publications, Inc., New York, **1970**.
[56] F. E. Mabbs, D. Collison, *Electron Paramagnetic Resonance of d Transition Metal Compounds*, Elsevier Science Publishers B. V., Amsterdam, The Netherlands, **1992**, vol. 16.
[57] C. J. H. Jacobsen, E. Pedersen, J. Villadsen, H. Weihe, *Inorg. Chem.* **1993**, *32*, 1216–1221.
[58] D. De Vos, B. M. Weckhuysen, T. Bein, *J. Am. Chem. Soc.* **1996**, *118*, 9615–9622.
[59] L. S. Erre, G. Micera, E. Garribba, A. C. Bényei, *New J. Chem.* **2000**, *24*, 725–728.
[60] It is not rigorously correct to note complex **5** as a mixture of complex **1** and chloride ions in a 1:2 ratio based on the presence of an equilibrium between these three species. However, we will do it for clarity.
[61] M. P. Hendrich, P. G. Debrunner, *Biophys. J.* **1989**, *56*, 489–506.
[62] J. Krzystek, J. Telser, *J. Magn. Reson.* **2003**, *162*, 454–465.
[63] H. J. Gerritsen, E. S. Sabisky, *Phys. Rev.* **1963**, *132*, 1507–1512.
[64] S. L. Dexheimer, J. W. Gohdes, C.-W. Chan, K. S. Hagen, W. H. Armstrong, M. P. Klein, *J. Am. Chem. Soc.* **1989**, *111*, 8923–8925.
[65] K. A. Campbell, E. Yikilmaz, C. V. Grant, W. Gregor, A.-F. Miller, R. D. Britt, *J. Am. Chem. Soc.* **1999**, *121*, 4714–4715.
[66] S. R. Morrissey, T. E. Horton, C. V. Grant, C. G. Hoogstraten, R. D. Britt, V. J. DeRose, *J. Am. Chem. Soc.* **1999**, *121*, 9215–9218.
[67] K. A. Campbell, D. A. Force, P. J. Nixon, F. Dole, B. A. Diner, R. D. Britt, *J. Am. Chem. Soc.* **2000**, *122*, 3754–3761.
[68] K. A. Campbell, M. R. Lashley, J. K. Wyatt, M. H. Nantz, R. D. Britt, *J. Am. Chem. Soc.* **2001**, *123*, 5710–5719.
[69] M. Maneiro, M. R. Bermejo, M. Fondo, A. M. González, J. Sanmartin, J.-C. Garcia-Monteagudo, R. G. Pritchard, A. M. Tyryshkin, *Polyhedron* **2001**, *20*, 711–719.
[70] As pointed out by one of the referees, the one-electron oxidation of species **6** may also lead to the formation of the $Mn^{III}$-phenoxyl species. For the reason given in the text and from the data previously reported in the literature concerning related complexes (see ref. [54,71,75–78]), we strongly favor the formation of a $Mn^{IV}$-phenolate as the predominant species. Therefore, for the sake of clarity, we describe species **7** as the $Mn^{IV}$-phenolate species. However, we acknowledge that we have no conclusive argument to definitively rule out the presence in solution of the $Mn^{III}$-phenoxyl as a minor species. More generally, the correct description of the one-electron oxidation product of the $Mn^{III}$-phenolate species is still an open debate. As suggested by the referee, XAS studies would help to disentangle this issue and should be the subject of future reports.
[71] B. Adam, E. Bill, E. Bothe, B. Goerdt, G. Haselhorst, K. Hildenbrand, A. Sokolowski, S. Steenken, T. Weyhermüller, K. Wieghardt, *Chem. Eur. J.* **1997**, *3*, 308–319.
[72] Note that the molar extinction coefficient values have been estimated assuming the formation of 95% of the $Mn^{IV}$ species.
[73] C. Hureau, Thèse de l'Université Paris-Sud, Orsay, **2003**.
[74] D. R. Gamelin, M. L. Kirk, T. L. Stemmler, S. Pal, W. H. Armstrong, J. E. Penner-Hahn, E. I. Solomon, *J. Am. Chem. Soc.* **1994**, *116*, 2392–2399.
[75] U. Auerbach, T. Weyhermüller, K. Wieghardt, B. Nuber, E. Bill, C. Butzlaff, A. X. Trautwein, *Inorg. Chem.* **1993**, *32*, 508–519.
[76] M. J. Baldwin, T. L. Stemmler, P. J. Riggs-Gelasco, M. L. Kirk, J. E. Penner-Hahn, V. L. Pecoraro, *J. Am. Chem. Soc.* **1994**, *116*, 11349–11356.
[77] C. Hureau, E. Anxolabéhère-Mallart, G. Blondin, E. Rivière, M. Nierlich, *Eur. J. Inorg. Chem.* **2005**, *23*, 4808–4817.
[78] N. A. Law, T. E. Machonkin, J. P. McGornam, E. J. Larson, J. W. Kampf, V. L. Pecoraro, *J. Chem. Soc., Chem. Commun.* **1995**, *19*, 2015–2016.
[79] C. Hureau, L. Sabater, F. Gonnet, G. Blain, J. Sainton, E. Anxolabéhère-Mallart, *Inorg. Chim. Acta* **2006**, *359*, 339–345.
[80] D. T. Richens, D. T. Sawyer, *J. Am. Chem. Soc.* **1979**, *101*, 3681–3683.
[81] D. P. Kessissoglou, X. Li, W. M. Butler, V. L. Pecoraro, *Inorg. Chem.* **1987**, *26*, 2487–2492.
[82] S. K. Chandra, P. Basu, D. Ray, S. Pal, A. Chakravorty, *Inorg. Chem.* **1990**, *29*, 2423–2428.
[83] S. M. Saadeh, M. S. Lah, V. L. Pecoraro, *Inorg. Chem.* **1991**, *30*, 8–15.

 © 2006 Wiley-VCH Verlag GmbH & Co. KGaA, Weinheim 

[84] O. Schlager, K. Wieghardt, B. Nuber, *Inorg. Chem.* **1995**, *34*, 6456–6462.
[85] T. M. Rajendiran, J. W. Kampf, V. L. Pecoraro, *Inorg. Chim. Acta* **2002**, *339*, 497–502.
[86] T. K. Paine, T. Weyhermüller, E. Bothe, K. Wieghardt, P. Chaudhuri, *Dalton Trans.* **2003**, *15*, 3136–3144.
[87] B. H. Huynh, T. A. Kent in *Advances in Mössbauer Spectroscopy* (Eds.: B. V. Thosar, P. K. Iyengar, J. K. Srivastava, S. C. Bhargava), Elsevier, New York, **1983**, p. 490.
[88] P. Hapiot, L. D. Kispert, V. V. Konovalov, J.-M. Savéant, *J. Am. Chem. Soc.* **2001**, *123*, 6669–6677.
[89] O. Horner, M.-F. Charlot, A. Boussac, E. Anxolabéhère-Mallart, L. Tchertanov, J. Guilhem, J.-J. Girerd, *Eur. J. Inorg. Chem.* **1998**, 721–727.

Received: March 28, 2006
Published Online: September 13, 2006

 © 2006 Wiley-VCH Verlag GmbH & Co. KGaA, Weinheim 

DOI: 10.1002/ejic.200600299

# A Density Functional Study of the Hydrogenation of Ketones Catalysed by Neutral Rhodium-Diphosphane Complexes

**Francine Agbossou-Niedercorn*[a] and Jean-François Paul*[b]**

**Keywords:** Density functional calculations / Hydrogenation / Ketones / Rhodium / Asymmetric catalysis

The potential energy profile of $Rh^I$-catalysed hydrogenation of ketones has been computed for the simple model system [Rh{$H_3POCH_2CH_2N(H)PH_3$}(Cl)] using DFT calculations. The general sequence of the catalytic cycle involves coordination of the carbonyl derivative to the neutral $Rh^I$ complex followed by oxidative addition of molecular hydrogen providing rhodium dihydride intermediates. The latter are converted into alkoxy hydrides by a migratory insertion reaction. Reductive elimination of the alcohol and substitution of the latter by the incoming substrate completes the catalytic cycle. Intermediates and transition states of all catalytic steps have been located. Two isomeric derivatives bearing the model substrate have been found for the [Rh{$H_3POCH_2CH_2N(H)PH_3$}(Cl)($H_2CO$)] complex. Eight diastereomeric pathways have been followed for the *cis* addition of molecular hydrogen to [Rh{$H_3POCH_2CH_2N(H)PH_3$}(Cl)($H_2CO$)] leading to eight distinct isomeric dihydride intermediates. Four dihydride complexes can be considered as the more accessible compounds. The site preference for migratory insertion and transition states discriminates the main path of the catalytic reaction. Migratory insertion to form the alkoxy hydride constitute the turn over limiting step of the process. The potential energy profile has been found to be smooth without excessive activation barriers.
(© Wiley-VCH Verlag GmbH & Co. KGaA, 69451 Weinheim, Germany, 2006)

## Introduction

The enantioselective hydrogenation of prochiral ketones, which is one of the most exiting and powerful methods of synthesising chiral alcohols, has been receiving increased attention and has led to notable successes.[1] When ruthenium-based catalysts have been applied in the enantioselective hydrogenation of prochiral ketones,[2] rhodium complexes have proven to lead to very efficient processes along with potential industrial applications.[2–4] Likewise, asymmetric transfer hydrogenation of ketones has been well investigated over the last few decades[5], prompted by the very important contribution of Noyori's group.[6]

The most actively explored asymmetric hydrogenation mechanism has been the enantioselective hydrogenation of C=C bonds catalysed by cationic $Rh^I$-diphosphane complexes. Chemical,[7–14] kinetic[9] and theoretical[15,16] studies have been carried out. As a result, the rhodium-catalysed hydrogenation of dehydroamino acids leading to enantiomerically pure α-amino acids is considered to be a thoroughly understood reaction based on work carried out in the research groups of Halpern[7] and Brown[8] who revealed the underlying steps of the process. It has been demonstrated that the minor diastereomer resulting from the coordination of the enamide to the cationic Rh-diphosphane precursor reacts more rapidly with molecular hydrogen providing the observed prevailing hydrogenated product.[9–13] However, the reason for this increased reactivity is still not clearly understood. In addition, a complete understanding of the stereoselection has not yet been achieved. Finally, as highlighted recently by Rossen,[17] this classical mechanism of Rh-catalysed hydrogenation might not definitely be valid for all bisphosphane and metal combinations.

Much effort has been devoted to characterising transient intermediates in the C=C hydrogenation reactions. Among them, the cationic Rh-diphosphane-enamide complex[7,10,14] and the alkyl monohydride species[8,12] have been characterised by various spectroscopic and X-ray-based methods. Also, the presumed dihydride intermediate has been investigated by PHIP (*para*-hydrogen induced polarisation) NMR spectroscopy, which is a powerful tool for studying hydrogenation reactions.[18] Thus, while utilising *para*-hydrogen and appropriate complexes, elusive species could be detected. In this way, Selke and Bargon[19] observed a rhodium dihydride complex while using a sugar-based bisphosphinite ligand (Scheme 1). More recently, Bargon and Brown[20] reported the observation of an agostic complex which is encountered on the path of hydride transfer to the coordinated substrate (Scheme 1).

[a] Unité Catalyse et Chimie du Solide UMR CNRS 8181, ENSCL-CHIMIE, Bat C7,
B. P. 90108, 59652 Villeneuve d'Ascq Cedex, France
Fax: +33-3-20436585
E-mail: francine.agbossou@ensc-lille.fr
[b] Université des Sciences et Technologies de Lille, C3
Fax: +33-3-20436165,
E-mail: Jean-Francois.paul@univ-lille1.fr

 © 2006 Wiley-VCH Verlag GmbH & Co. KGaA, Weinheim 

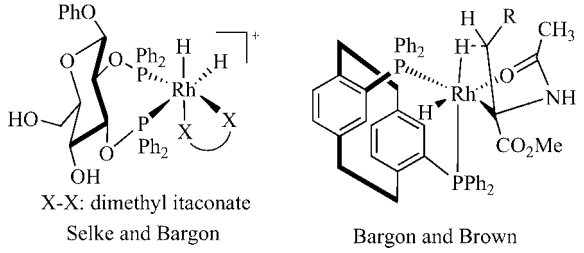


Scheme 1. Characterised dihydride-Rh complexes.

A second mechanism of hydrogenation that has been studied to some extent is related to the transfer hydrogenation of C=O bonds catalysed by $Rh^{I}$[21,22] and $Ru^{II}$ complexes.[23] However, much less is known about the mechanism of the molecular hydrogen-based hydrogenation of ketones catalysed by rhodium species. Although the catalytic results are quite satisfactory in terms of efficiency, little is known experimentally about intermediates and reaction steps and the reaction mechanism has not been elucidated so far. Nevertheless, mechanistic hypotheses have been made in order to take into account the several experimental observations. Primarily, Schrock and Osborn[24] proposed a mechanism for the hydrogenation of ketones catalysed by cationic rhodium complexes bearing basic monophosphanes. One step of the catalytic cycle is an oxidative addition of molecular hydrogen providing a rhodium-dihydride complex. The reported catalytic system is promoted by small quantities of water (ca. 1% of $H_2O$). A study carried out either in the presence of $D_2$ or $D_2O$ gave rise to a mechanism involving an active participation of water that would account for the determined incorporation of deuterium from $D_2O$. Actually, the key points are (1) the participation of a rhodium dihydride intermediate and (2) the promotion of the second hydrogen atom transfer by the small quantity of water as depicted in Scheme 2.

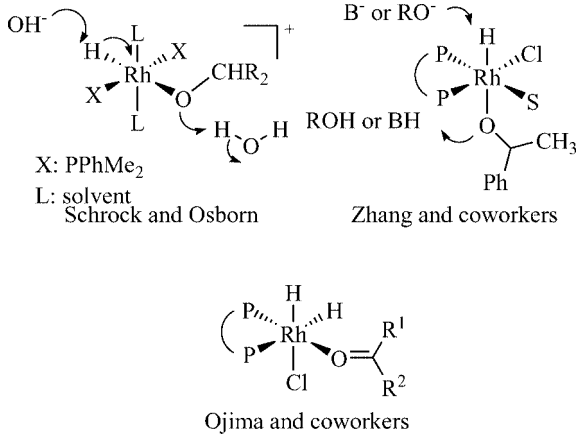


Scheme 2. Examples of reported rhodium-hydride intermediates.

More recently, Zhang[25] proposed a mechanism to take into account the beneficial effect provided by the use of amines which promoted both the activity and selectivity ($\Delta ee$ up to 38%) of the hydrogenation of simple ketones. In the catalytic cycle, an oxidative addition of molecular hydrogen on the rhodium precursor is considered prior to substrate coordination followed by hydride transfer to the coordinated substrate (Scheme 2). Yet, the reaction is carried out in methanol and the possibility of cationic rhodium catalytic intermediates has not been envisioned, the proposed mechanism being based only on noncharged intermediates.

Ojima described the efficient enantioselective hydrogenation of α-keto esters catalysed by neutral Rh–BPPM complexes [BPPM: (2*S*,4*S*)-*N*-*tert*-butoxycarbonyl-4-(diphenylphosphanyl)-2-[(diphenylphosphanyl)methyl]pyrrolidine][26] and proposed a mechanism based on results obtained while varying the solvent.[27] Dry aprotic solvents bestowed the best results both in terms of activity and enantioselectivity. These authors propose that both hydrides (Scheme 2) resulting from the oxidative addition of hydrogen onto the Rh–substrate adduct are successively transferred to the substrate. Meaningfully, it has been suggested that a retention of chloride on rhodium might be the clue for the increased efficiency of the catalyst.

In previous studies, we have shown that the enantioselective hydrogenation of functionalised ketones can be carried out very efficiently in the presence of neutral rhodium precursors bearing aminophosphane phosphinite ligands (AMPP).[28] The potential of such ligands has further been assayed in the highly enantioselective hydrogenation of fluorinated ketones including simple ketones.[29] We have also reported on the use of a combination of molecular mechanics-based methods and extended Hückel calculations in order to have access to the most stable catalytic intermediates and to their reactivity.[30]

Modern efforts have emphasised the potential of computational methods for organometallic catalysis investigations.[31] We became interested in using such methods to examine the catalytic cycle of the hydrogenation of ketones assisted by rhodium-aminophosphanephosphinite catalysts. To address the catalytic cycle, several computational approaches are possible. One deals with the general mechanism and the associated energetic profile while considering neutral catalytic intermediates and a second deals with the quest of the enantiodetermining step of the cycle. Both types of information require different levels of computation and consequently different ranges of calculation times. The aim of this study was to obtain an insight into the most probable energy profile of the catalytic cycle of ketone hydrogenation involving neutral rhodium diphosphane catalysts. Such an approach has not been undertaken to the best of our knowledge. Here, we report on the results of DFT computations of the catalytic reaction potential energy surface for a simple achiral aminophosphane phosphinite-based model system. In this paper, we describe the model system used, the computational method applied, and the overall reaction pathways explored.

 © 2006 Wiley-VCH Verlag GmbH & Co. KGaA, Weinheim 

## Background and Calculation Methods

Despite our many attempts, we were unable to characterise, by NMR, catalytic intermediates under our classical ketone hydrogenation conditions (room temperature, 1 atm $H_2$, toluene). Indeed, only the starting rhodium dimeric complexes of the type $[Rh\{AMPP\}Cl]_2$ could be observed by $^{31}P$ NMR spectroscopy. However, the hydrogenation experiments carried out under various catalytic conditions did provide evidence for the participation of neutral intermediates bearing the chiral diphosphane along with a nonchiral ancillary ligand. For example, when the hydrogenation of benzylbenzoylformamide was run in ethanol in the presence of a cationic precatalyst, a slow reaction ($t_{1/2}$ = 4 h) with a very low *ee* was achieved (5.5% *ee*) (Table 1, entry 1).[32]

Table 1. Enantioselective hydrogenation of benzylbenzoylformamide.[a]

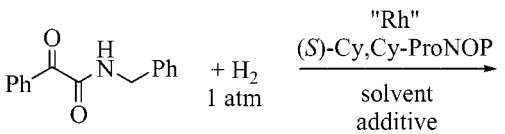


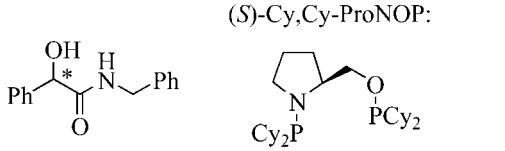


Cy: cyclohexyl

| Entry | "Rh" | Solvent | Additive | $t_{1/2}$ [min][b] | *ee* (%) (conf.) |
|---|---|---|---|---|---|
| 1 | $[Rh(COD)_2]BF_4$ | EtOH | – | 240 | 5.5 (*R*) |
| 2 | $[Rh(COD)Cl]_2$ | EtOH | – | 28 | 64.8 (*S*) |
| 3 | $[Rh(COD)Cl]_2$ | toluene | – | 20 | 74 (*S*) |
| 4 | $[Rh(COD)I]_2$[c] | toluene | – | 25 | 67 (*S*) |
| 5 | $[Rh(COD)_2]BF_4$ | toluene | – | n.d.[d] | 3 (*S*) |
| 6 | $[Rh(COD)_2]BF_4$ | toluene | LiBr | 18 | 69 (*S*) |
| 7 | $[Rh(COD)_2]BF_4$ | toluene | LiI | 40 | 62.2 (*S*) |

[a] Substrate/Rh = 200:1. [b] Time of half conversion of the substrate. [c] F. Agbossou-Niedercorn, unpublished results. [d] n.d.: not determined, substrate/Rh = 45:1, total conversion after 3 d.

Interestingly, if the hydrogenation occurs in ethanol in the presence of a neutral precursor, an enhanced efficiency is attained as the chiral alcohol is produced in ca. 65% *ee* and with a higher rate ($t_{1/2}$ = 28 min) (Table 1, entry 2). The behaviour of diphosphane-rhodium complexes in various solvents deserves some comment. For instance, the reaction of neutral rhodium complexes with an amidophosphane phosphinite results in the formation of a mixture of cationic and neutral compounds in methanol, as shown by Pregosin.[33] Also, an earlier study of Bakos[34] outlined the behaviour of complexes of type "$Rh(P_2)$(diolefin)Cl" in various solvents (dichloromethane, benzene, methanol). Equilibrium between a cationic and a neutral complex could account for the $^{31}P$ NMR features of the corresponding solution. Therefore, the efficiency improvement observed while comparing the two above-mentioned hydrogenations can be reasonably related to the active participation of neutral catalytic species. As further evidence, a reaction carried out in toluene with a neutral precatalyst provides the alcohol with 74 and 67% *ee* and with higher rates for Cl and I, respectively (Table 1, entries 3 and 4). This compares well with hydrogenations carried out while using a cationic precatalyst in toluene in the presence of either LiI or LiBr (Table 1, compare entries 7 and 4). This is consistent with retention of the halide on the catalytic intermediates throughout the entire process. The weak dielectric constant of aromatic solvents is in favour of retention of the halide on the rhodium during catalysis.[35] Finally, note that the reaction performed with a cationic precursor in toluene proceeds with a low rate and an extremely low enantioselectivity (Table 1, entry 5).

Additional earlier results prove the benefit obtained when the hydrogenations of ketopantolactone are performed in the presence of neutral rhodium-halide complexes in toluene, essentially on the enantioselectivity (compare all entries of Table 2).[36] As a matter of fact, 98% *ee* was reached for Rh-iodide-based catalysts.

Table 2. Effect of the ancillary ligand on asymmetric hydrogenation of ketopantolactone.

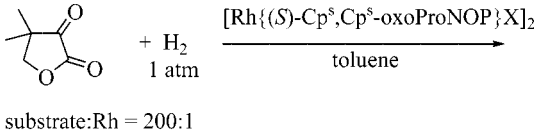


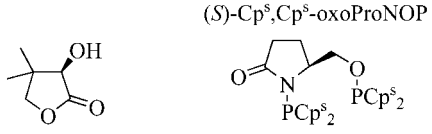


Cp$^s$: cyclopentyl

| Entry | Precatalyst | $t_{1/2}$ [min] | *ee* (%) (conf.) |
|---|---|---|---|
| 8 | $[Rh(COD)_2]BF_4$ | 240 | 5.5 (*R*) |
| 9[a] | $[Rh(COD)Cl]_2$ | 28 | 64.8 (*S*) |
| 10 | $[Rh(COD)Cl]_2$ | 20 | 74 (*S*) |

[a] F. Agbossou-Niedercorn, unpublished results.

The reality of neutral Rh-dihydride-chloride complexes has been shown through the use of PHIP NMR techniques. Indeed, Eisenberg found a way to detect new mononuclear neutral dihydride-rhodium-phosphane-olefin complexes that appear to be intermediates in the catalytic hydrogenation of olefins (Scheme 3).[37]

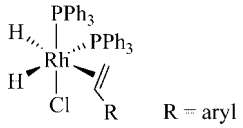


Scheme 3. Schematic representation of the neutral Rh-dihydride-chloride complex.

 © 2006 Wiley-VCH Verlag GmbH & Co. KGaA, Weinheim 

On the basis of these data, a plausible catalytic cycle depicted in Scheme 4 has been proposed for the hydrogenation of ketones catalysed by neutral rhodium complexes in aprotic solvents. Hereafter, we will focus on the computation of the various elementary steps of this catalytic cycle.

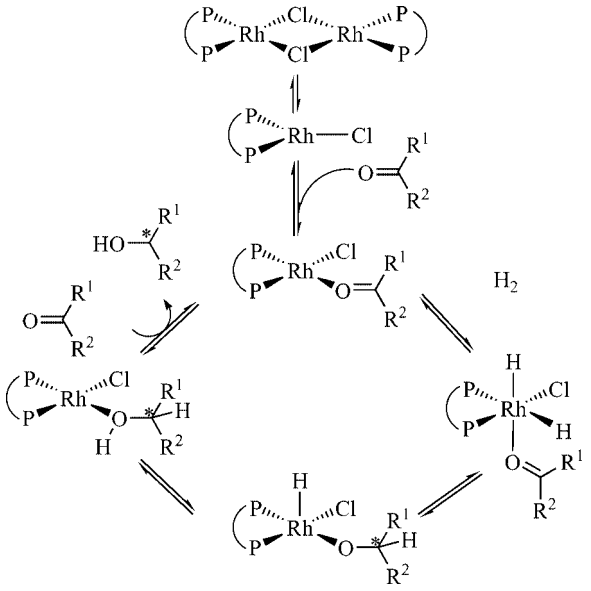

Scheme 4. Proposed reaction mechanism.

### Computational Methods

The calculations were based on the density functional theory (DFT) using Becke's three-parameter hybrid functional (B3) and the Lee, Yang and Parr (LYP) correlation functional for the correlation energies (B3LYP). This method[38] exhibits accuracy comparable to that of sophisticated post-Hartree–Fock methods in transition-metal studies. They were performed using the Gaussian 98 program package (version A9).[39] For the rhodium atom, we used the relativist effective core potential of Hay and Wadt (with 4s and 4p in the valence) and the corresponding double-ζ basis set.[40] For the carbon, oxygen, nitrogen and hydrogen atoms of the ligand a 6–3lG* basis set was used. For the hydrogen atoms on the rhodium and those of the reactant (formaldehyde) and product (methanol) a *p*-orbital of Gaussian type ζ = 1.1 was added. For the chlorine and the phosphorus atoms, a 6-311G* basis set was used. All the used basis sets were implemented in the Gaussian 98 program.

Geometries of reactants and products were fully optimised without any symmetry or internal coordinate constrains. All transition states were characterised by determining the number of imaginary frequencies and a further characterisation of the transition state was achieved by calculation of the intrinsic reaction coordinate (IRC) leading to the corresponding reactants and products.

### Models Used for the Calculation of the Complexes

**The Ligand:** The skeleton of the AMPP ligand {(*S*)-Cp$^s$,Cp$^s$-oxoProNOP} is replaced by an ethanolamine-bridged diphosphane [$H_2POCH_2CH_2N(H)PH_2$] (Scheme 5). Thus, the electronic effects of the oxygen and nitrogen atoms are maintained. In addition, the $CH_2CH_2$ spacer provides the constraint on the carbon backbone of the ligand which mimics the skeleton of the pyrrolidine ring present in the most efficient ligands studied. Hydrogen atoms replace the phosphorus substituents in order to reduce computational time.

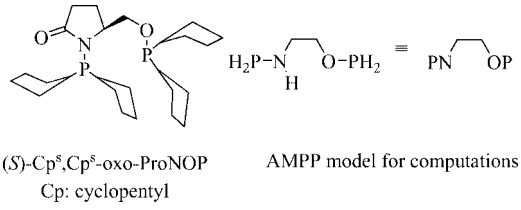

(*S*)-Cp$^s$,Cp$^s$-oxo-ProNOP
Cp: cyclopentyl

AMPP model for computations

Scheme 5. AMPP and the model compound.

**Ketopantolactone:** Calculations were performed by using a model hydrogenation reaction of formaldehyde and when necessary with larger carbonyl compounds.

## Computational Results

### Coordination of the Substrate: Structures of Catalyst–Substrate Adducts

The $d^8$ complex [Rh(Cl){PO∩NP}] is a model for the product expected from the cleavage of the dimeric precursor [Rh{PO∩NP}Cl]$_2$ which leads to the formation of the active species. It is well known that $ML_3$ complexes can be stable in a T-shaped trigonal structure. Nevertheless, the contribution of solvent coordination through a C=C bond providing a square-planar complex has been computed by means of optimisation of Rh(Cl){PO∩NP}($C_6H_6$). The calculations show that the coordination energy of a benzene in the $\eta^2$ mode is almost thermoneutral (around 2 kcal/mol depending upon the geometry). Consequently, and taking into consideration the results related next, the eventual intermediate square-planar complex bearing a solvent molecule was not considered further in the catalytic cycle.

As T-shaped trigonal complexes present a $C_1$ symmetry, two isomeric compounds have to be considered that present the chloride either *trans* to $P_N$ (**1a**) or *trans* to $P_O$ (**1b**) (Figure 1). The energy difference between both optimised complexes is very small (0.2 kcal/mol). The activation energy on going from one isomer to the other is only 4.5 kcal/mol. Furthermore, both experimentally and theoretically, the length of the Rh–$P_O$ and Rh–$P_N$ bonds present only a small difference (0.02–0.03 Å experimentally, 0.03 Å by calculation).[41] Because of these small differences, it can be foreseen that the coordination of the carbonyl substrate *trans* of both moieties, i.e., $P_O$ and $P_N$, will be alike. The relative

 © 2006 Wiley-VCH Verlag GmbH & Co. KGaA, Weinheim 

stabilities are consistent with a larger *trans* influence of the $P_O$ group, an effect which can be observed in the Rh–Cl bond lengths: 2.348 Å when *trans* to $P_N$ and 2.363 Å when *trans* to $P_O$.

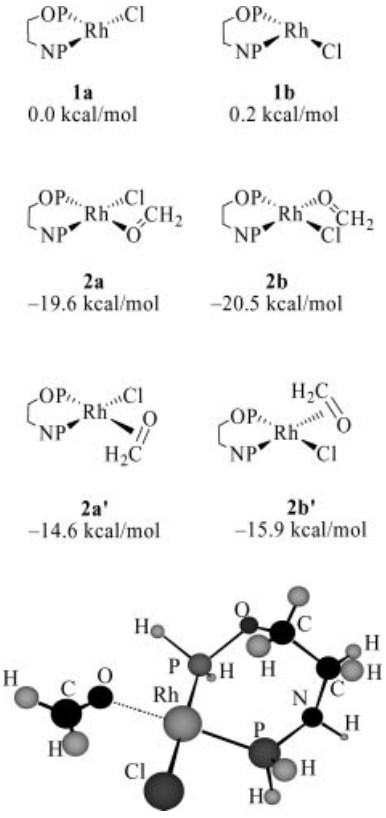


Figure 1. Schematic representation of the intermediates **1** and **2**. Values indicating the relative energies compared to **1a** + $CH_2O$ (top). Geometry of the most stable complex (bottom).

Carbonyl substrates can adopt two fundamental coordination modes on a transition metal complex: end-on coordination ($\eta^1$) by a lone pair of the oxygen atom or side-on coordination ($\eta^2$) through the CO π system.[42] Both modes have been taken into consideration (Figure 1). The $\eta^1$ coordination mode (structures **2a**–**b**) of the substrate provides more stable complexes than the $\eta^2$ one (structures **2a′**–**b′**). As anticipated, the *trans* to $P_N$ $\eta^1$-coordinated formaldehyde complex **2b** is only slightly more stable than **2a** by 0.9 kcal/mol.

The energy differences between the two coordination modes are due to two main effects of the same importance: the deformation energy of the organic molecule and the orbital interaction. The deformation energy of the organic molecule is more important in the $\eta^2$ coordination mode, destabilising the latter. For energetic reasons, the main orbital interaction is between the metal orbital and the $CH_2O$ nonbonding orbital located on the oxygen atom, which is also in favour of the $\eta^1$ coordination. Furthermore, as a test, we considered also acetone coordination on complex **1**. Starting with the molecule coordinated in a $\eta^2$ coordination mode invariably ends with a displacement towards the $\eta^1$ mode. These calculations confirm that the most stable coordination mode on these complexes is $\eta^1$. It should be mentioned that coordination energies of the acetone on the T-shape trigonal complexes are similar to those of the model system (18.2 kcal/mol on complex **1a** and 19.4 kcal/mol on **1b** as compared to 19.5 and 20.6 kcal/mol for the formaldehyde coordination).

### Addition of Molecular Hydrogen

The next elementary step of the proposed mechanism is the hydrogen addition, leading to the formation of a dihydride intermediate. As both complexes **2a** and **2b** bearing the $\eta^1$-coordinated substrate are of equivalent stability, the oxidative addition of molecular hydrogen has to be considered on the two complexes. Furthermore, the oxidative addition of molecular hydrogen to a square-planar complex may occur on either side of the plane, with the molecular hydrogen parallel to either the Rh–$P_O$ or Rh–$P_N$ bond, which leads to eight different dihydrides with *cis* configuration.[15,43] Thus, the addition of molecular hydrogen along eight diastereomeric pathways must be considered in the modelling. These pathways are designated A, B, C, D, E, F, G and H (Figure 2). The search for stable rhodium-dihydrogen intermediates and the transition states for the addition of molecular hydrogen were performed along these pathways. The energy profiles of the approach of molecular hydrogen along the pathways located above and below the square plane are very similar. In fact, the energy difference between the two corresponding transition states (TS) is less than 1.5 kcal/mol. In the TS, the main interaction occurs between the HOMO of the complex ($dz^2$), which is symmetric with respect to the plane, and the LUMO of the molecular hydrogen (σ*) and is therefore independent from the approaching face. Molecular hydrogen complexes of rhodium are not computed as stable intermediates in the process of oxidative addition of molecular hydrogen to the square planar rhodium complex. As a matter of fact, IRC calculations do not end on such complexes but rather on the dissociated species or on the rhodium-dihydride compounds. Interestingly, the activation energies which lead to the displacement of either the chloride or the carbonyl from the square plane are quite different as this motion generates large electronic barriers due to extensive nuclear reorganisation. Indeed, the out-of-plane displacement of the chloride is ca. 5 kcal/mol more energy demanding than the out-of-plane displacement of the carbonyl moiety. Thus, energeti-

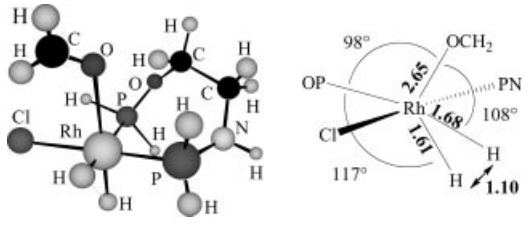


Figure 2. Representation of the transition state between **2a** and **DIHYD-D**.

 © 2006 Wiley-VCH Verlag GmbH & Co. KGaA, Weinheim 

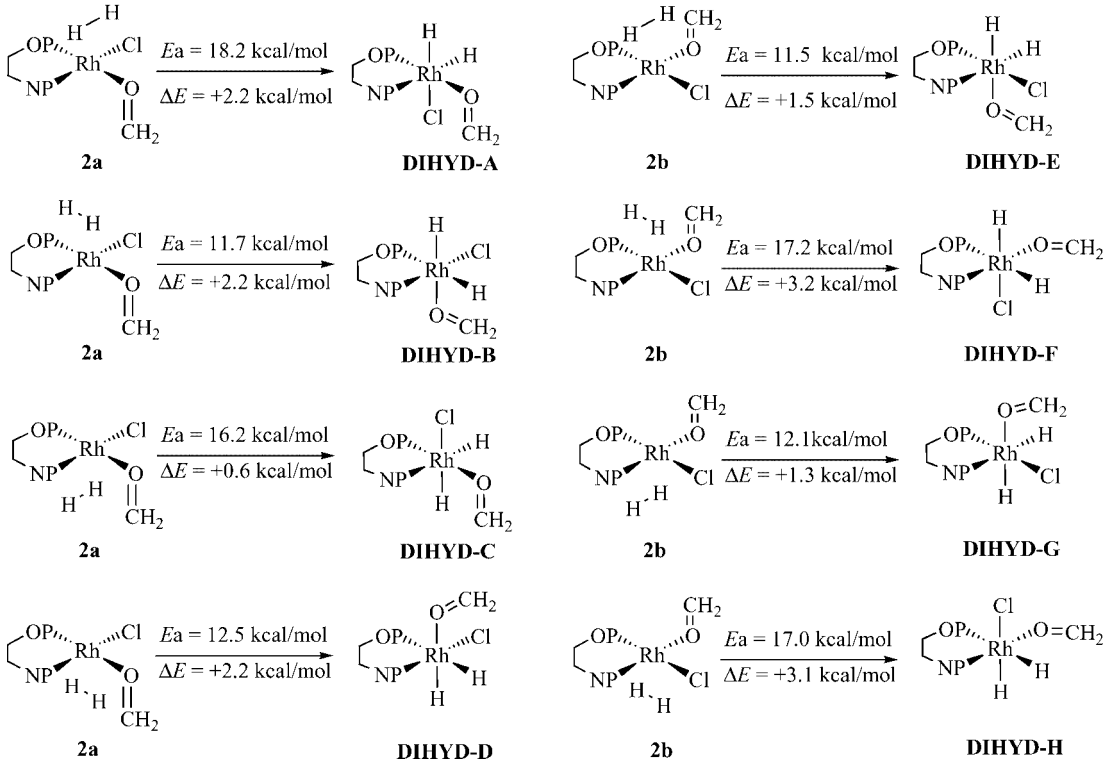


Scheme 6. Reaction and activation energy of the dihydride formation starting from complexes **2a** and **2b**.

cally lower transition states arise from the electronic preference for the chloride to remain in the rhodium-diphosphane plane (Scheme 6).

The transition states in going from **2a** to **DIHYD-B** and **DIHYD-D** and from **2b** to **DIHYD-E** and **DIHYD-G** are favoured. This result supports the final formation of only four isomers under the normal conditions of hydrogenation (room temperature and 1 atm of $H_2$). The geometries of these four transition states are similar: the H–H bond is almost broken while the Rh–O distance is increased to ca. 2.6 Å. The displaced group ($OCH_2$) is almost located in its position in the final products. In the case of the formation of **DIHYD-D**, the geometry of the transition state exhibit a H–H distance of 1.10 Å with the O–Rh length of 2.65 Å ($\Delta d$ = 0.36 Å) (Figure 2). In conclusion, only four dihydride complexes, which result from a *cis* addition of molecular hydrogen, are kinetically accessible minima on the reaction potential surface and are thus viable intermediates. Formation of dihydrides from **2** and molecular hydrogen is ap-

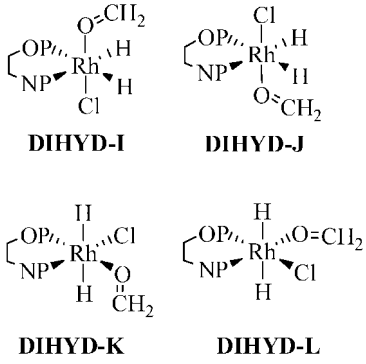


Scheme 7. Schematic representation of the dihydride that cannot be formed in one step, by hydrogen addition on complex **2**.

Table 3. Relative energies of the various intermediates (in kcal/mol).

| Initial complex | | Substrate coordination | | Molecular hydrogen addition | | Alkoxide formation | | Reductive elimination | |
|---|---|---|---|---|---|---|---|---|---|
| **1a** | 0.0 | **2a** | +0.7 | DIHYD-A | +1.6 | | | | |
| | | | | DIHYD-B | +1.8 | **4b** | +0.3 | **5b** | +5.2 |
| | | | | DIHYD-C | 0.0 | | | | |
| | | | | DIHYD-D | +1.5 | **4d** | +0.8 | | |
| **1b** | +0.2 | **2b** | 0.0 | DIHYD-E | +0.3 | **4e** | 0.0 | **5e** | 0.0 |
| | | | | DIHYD-F | +2.0 | | | | |
| | | | | DIHYD-G | +0.1 | **4g** | +2.5 | | |
| | | | | DIHYD-H | +1.9 | | | | |
| **1a** | | **2a′** | +5.7 | DIHYD-I | +19.2 | | | | |
| **1b** | | **2b′** | +4.6 | DIHYD-J | +20.4 | | | | |
| | | | | DIHYD-K | +19.5 | | | | |
| | | | | DIHYD-L | +18.0 | | | | |

 © 2006 Wiley-VCH Verlag GmbH & Co. KGaA, Weinheim 

proximately thermoneutral; reaction enthalpies range from 0.6 to 3.2 kcal/mol.

The complexes possessing either *trans* hydrides or the chlorine and carbonyl in apical positions gave structures much less stable by 18.0 to 20.4 kcal/mol. The transition states to those improbable species have not been studied and these intermediates have not been further considered in the calculations (Scheme 7), as their formation activation energies will be larger than 20 kcal/mol. The relative energies of all intermediates are given in Table 3.

### Transfer of the First Hydride: Conversion of the Dihydrides into Alkoxy Hydrides via Migratory Insertion

A variety of alkoxy hydrides can be obtained by migratory insertion of the C=O bond into the Rh–H bond of a dihydride. As mentioned above, we did not consider structures presenting a *trans* arrangement of the dihydrides nor the structures presenting the *cis* arrangement of the dihydrides in the plane defined by the Rh and the two P atoms; not because they could not give insertion products but because of the improbable participation of such species in the hydrogenation process. The alkoxy formation starting from dihydride without the Cl atom in the RhPP plane has also not been considered as they are much more slowly formed. In conclusion, only the four dihydride complexes **DIHYD-B**, **DIHYD-D**, **DIHYD-E** and **DIHYD-G** have been taken into consideration for this step (Scheme 8). They present *cis* coplanar orientations of the coordinated C=O and one Rh–H being systematically located in the plane containing the diphosphane ligand. The activation energies are reported in Scheme 8 and the relative energies of the obtained intermediates in Table 3. The transition state corresponds to the intramolecular hydride transfer of a H atom into the C–Rh bond that could be created in the case of a $\eta^2$ coordination mode. However, it is not the H atom, which moves toward the C atom, but the opposite. After the H addition, the complexes have an empty coordination site that can be located either in a *trans* position to the H atom or in a *trans* position to one of the phosphorus atoms. The latter geometries are not stable and evolve without activation energies to the one possessing the emty coordination site *trans* to the H atom. The geometry of one transition state is represented in Figure 3.

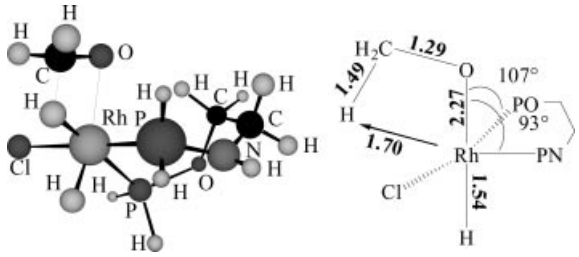


Figure 3. Transition-state geometry for the conversion of **DIHYD-D** into **4d**.

An IRC calculation was carried out for one of the transition-state structures. The final points are, on one side, the 18-electron starting complex with the C=O in a $\eta^2$ coordination mode, and on the other side, a complex with the alkoxy species. This calculation suggests that the substrate changes from a $\eta^1$ coordination to a $\eta^2$ coordination just prior to hydride insertion. The activation energy of this isomerisation is only 4.8 kcal/mol, the resulting dihydride being less stable than the starting one by 3.6 kcal/mol. This step will become improbable with larger carbonyl substrates. For this reason, we have not decomposed the C–H bond formation into two steps in the energetic diagram. This almost elementary step is slightly exothermic ($\Delta E$: –1.4 to –4.7 kcal/mol). The stable intermediates have square-planar pyramidal structures with the alkoxy fragment located in the square plane. The resulting stable structures all have a *cis* arrangement of the remaining H and alkoxy moieties. The site in the *trans* position to the H ligand is empty.

### Conversion of the Alkoxy Hydride into the Hydroxy Complex: Reductive Elimination

The next step is the reductive elimination starting from the four intermediates (**4b**, **4d**, **4e**, **4g**) (Scheme 9). The reductive elimination of the alkoxy hydride provides a square-

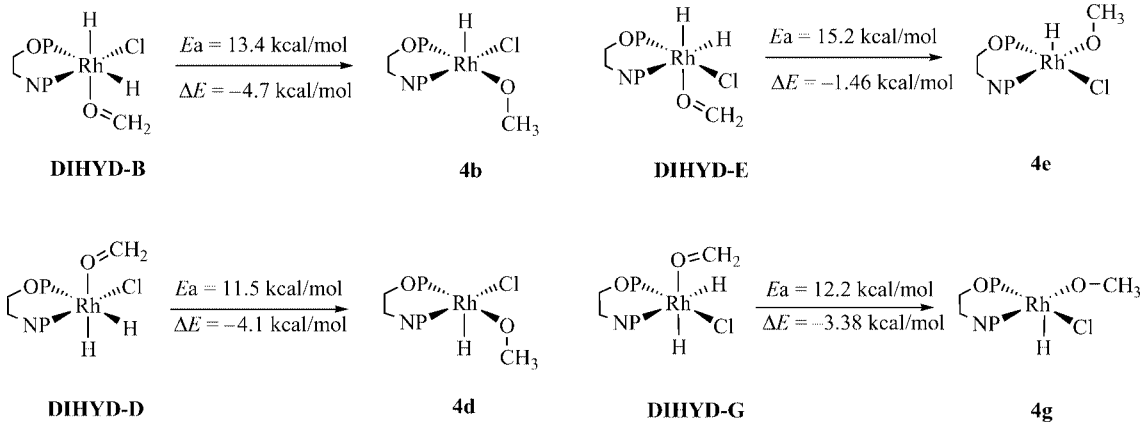


Scheme 8. Reaction and activation energies for the alkoxy formation.

 © 2006 Wiley-VCH Verlag GmbH & Co. KGaA, Weinheim 

planar structure in which the hydroxy species is coordinated to the rhodium.

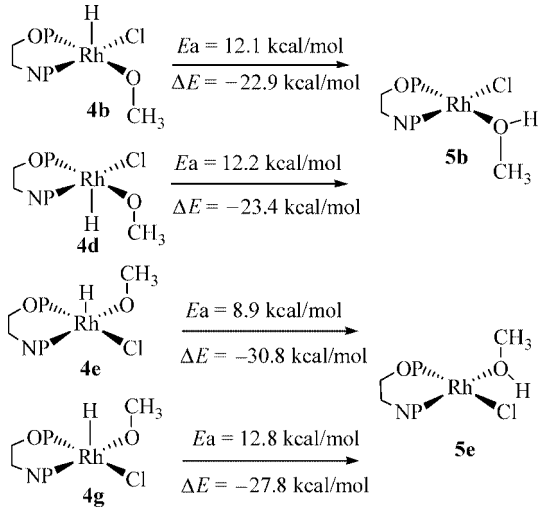


Scheme 9. Reaction and activation energies for the formation of the alcohol.

This structure is closely related to the starting complexes bearing the coordinated substrate C=O. Two structures are obtained with the hydroxy located either *trans* to the $P_O$ moiety or *trans* to the $P_N$ end. The energies are slightly in favour of a *trans* to $P_N$ location as in the case of the complexes resulting from the first step, i.e., coordination of the substrate.

The calculation indicates that the process of reductive elimination resulting in the reduction of $Rh^{III}$ to $Rh^{I}$ is highly exothermic (from –22.9 to –30.0 kcal/mol) (Scheme 9). The reaction coordinate is constituted almost exclusively by the H–Rh–O angle, which decreases from 90° to 15°. The transition state is reached for a value of that angle close to 50° (Figure 4). The activation energy is smaller than 13 kcal/mol for the four reactions path we have studied.

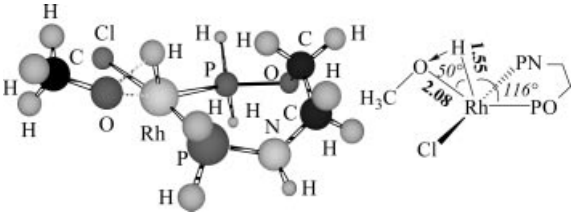

Figure 4. Representation of the transition state between **4b** and **5b**.

Because of the similar energies of the C=O-coordinated structures and the hydroxy coordinated one, it is not unreasonable to consider that the reaction could be inhibited by an excess of hydroxy compounds which might occur in high conversions of the hydrogenation reaction or when the concentration in the produced hydroxy compound becomes higher than that of the ketonic substrate. However, as the partial order of the reaction has not been performed, it is rather difficult to know if such an inhibition effect is observed experimentally.

**Alcohol-Carbonyl Substrate Substitution**

In the catalytic cycle, the last step is a substitution of the hydroxy compound by the carbonyl substrate. This step is almost athermic: slightly exothermic from **5b** and slightly endothermic from **5e** (Scheme 10) and can take place in one step (concerted mechanism). In the transition state, the two Rh–O distances are almost the same [2.60 Å for Rh–O(hydroxy) and 2.54 Å for Rh–O (carbonyl)] (Figure 5). The activation energy of that step is small (5.6 kcal/mol, Scheme 10). An alternative mechanism would be the associative one. However, the reaction involving the carbonyl coordination prior to hydroxy rhodium bond cleavage is an overall endothermic process and the energy loss is similar to the activation energy of the direct exchange reaction, indicating that the substitution should occur in one step.

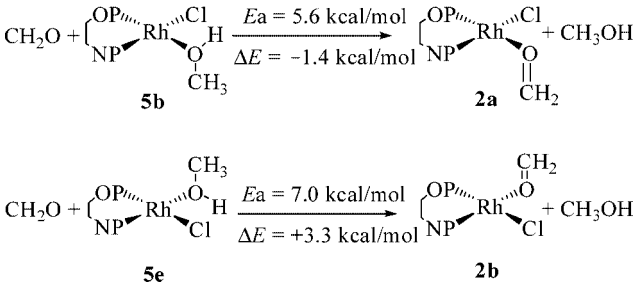


Scheme 10. Reaction and activation energies for the ligand exchange.

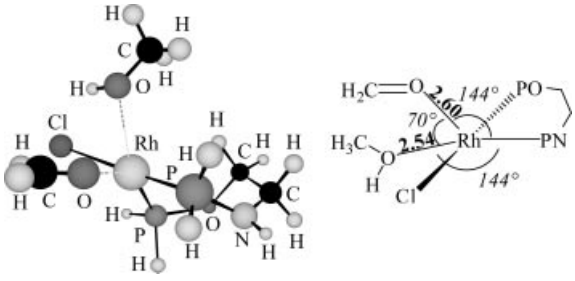

Figure 5. Transition-state geometry for the $CH_3OH/CH_2O$ exchange reaction.

**Catalytic Cycle**

Figure 6 and Figure 7 present the calculated energy profile for the entire catalytic cycle starting from the two complexes presenting the carbonyl substrate in a *trans* position to **2a** or **2b**. All activation energies are reported on the Figures. The energy difference between the final state (**2** + methanol) and the initial state (**2** + formaldehyde + $H_2$) of the cycle is the energy of hydrogenation of formaldehyde. The overall energy profile is smooth. This reaction is highly exothermic. The migratory insertion step [from **2** to the **DIHYD-D** complexes has the most important activation barrier (12.5 kcal/mol)] and might be considered as the rate-limiting step. For the two types of complexes, for steric in-

 © 2006 Wiley-VCH Verlag GmbH & Co. KGaA, Weinheim 

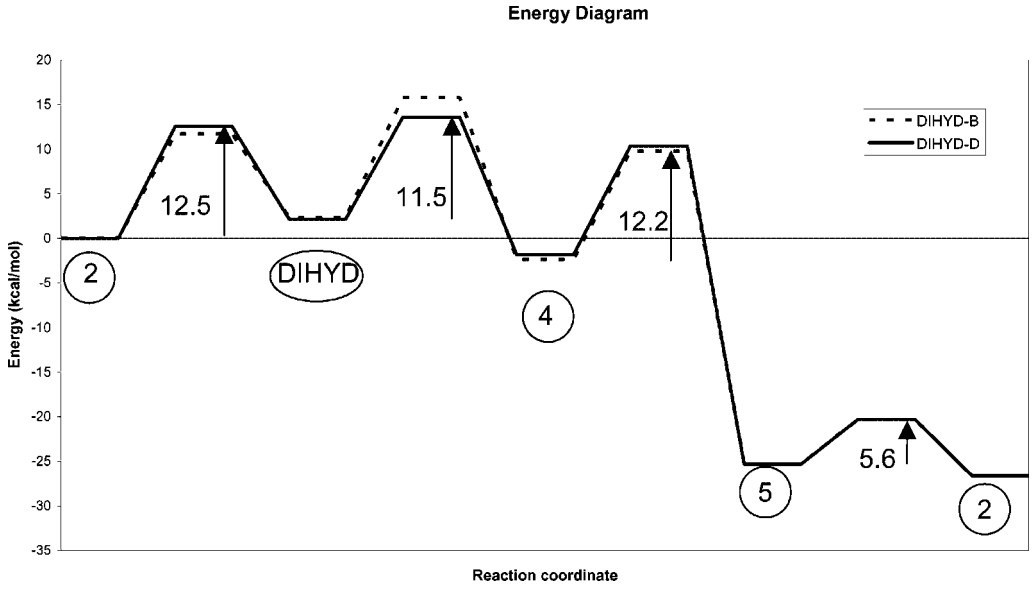


Figure 6. Calculated reaction profile (kcal/mol) of the entire catalytic cycle for the hydrogenation of C=O starting from **2a** (the two last stationary points are common for the two reaction paths).

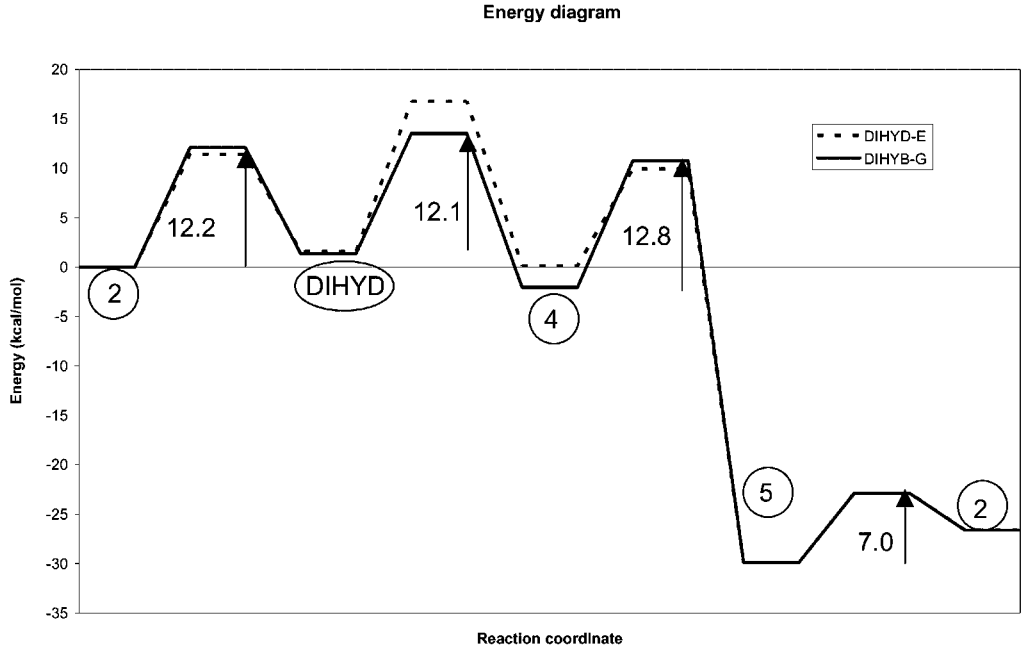


Figure 7. Calculated reaction profile (kcal/mol) of the entire catalytic cycle for the hydrogenation of C=O starting from **2b** (the two last stationary points are common for the two reaction paths).

teraction reasons the C–H formation is favoured when the substrate is located on the same side of the RhPP plane as the C2 chain. These interactions will play an important role for prochiral substrates.

## Conclusions

In this paper, we have presented the possible pathways of the mechanism of hydrogenation of C=O bonds catalysed by neutral rhodium complexes employing the B3LYP density functional method. This theoretical study is the first one carried out on neutral rhodium-based C=O bond hydrogenation. Our purpose was to calculate the most probable pathway for the catalytic reaction. Thus, new insight into our understanding of the reaction is provided here. We performed geometry optimisation for all isomers of intermediates and transition states. Eight diastereomeric pathways have been followed for the *cis* addition of molecular hydrogen to [Rh{$H_2POCH_2CH_2N(H)PH_2$}(CI)($H_2CO$)] leading to eight distinct isomeric dihydride intermediates. The postulated intermediates are minima on the potential surface. Four resulting dihydride complexes have been con-

 © 2006 Wiley-VCH Verlag GmbH & Co. KGaA, Weinheim 

sidered as the more accessible intermediates. In addition, we showed that even if one isomer can be considered as the most stable within a series, several isomeric structures are able to be involved in every step of the cycle and have to be examined in future studies. For formaldehyde hydrogenation, the rate-determining step is difficult to determine on the basis of the energy diagram. However, the calculation of one similar energy path for methanal and propanone indicate that the migratory path of hydride to the carbonyl moiety is the rate-determining step.[44] The overall energy profile of the catalytic cycle is smooth and corresponds to an exothermic process. On the basis of experimental data and on calculations, the hydrogenation of ketones with the participation of only neutral catalytic intermediates bearing a chloride atom during the entire process and without chelation of the substrate is thus likely to proceed. This is strongly supported by the efficiency of such catalysts in the highly efficient hydrogenation of even simple ketones under neutral conditions.[29]

## Acknowledgments

The authors thank Prof. André Mortreux for fruitful discussions and Dr. Corinne Pasquier for preliminary experimental results. We also thank the Centre National de la Recherche Scientifique and the Ministère de la Recherche et de la Technologie for financial support. Finally, we thank CRI (Centre des Ressources Informatiques) of the Université des Sciences et Technologies de Lille (partially founded by FEDER) for their computational support.

[1] a) R. Noyori, *Asymmetric Catalysis in Organic Synthesis*, Wiley, New York, **1994**, ch. 2, pp. 16–94; b) H. Takaya, T. Ohta, R. Noyori, *Catalytic Asymmetric Synthesis* (Ed.: I. Ojima), VCH Publishers, New York, **1993**, chapter 3, pp. 1–39; c) T. Ohkuma, M. Kitamura, R. Noyori, *Catalytic Asymmetric Synthesis*, 2nd ed. (Ed.: I. Ojima), VCH Publishers, New York, **2000**, chapter 1, pp. 1–110.

[2] R. Noyori, T. Ohkuma, *Angew. Chem.* **2001**, *113*, 40–73; *Angew. Chem. Int. Ed.* **2001**, *40*, 40–73.

[3] a) R. Schmid, *Chimia* **1996**, *50*, 110–113; b) R. Schmid, E. A. Broger, *Abstract of Chiral Europe 94*, Nice, September **1994**.

[4] a) H.-U. Blaser, F. Spindler, M. Studer, *Appl. Catal., A* **2001**, *221*, 119–143; b) S. C. Stinson, *Chem. Eng. News* **1999**, *77*, 101–120; c) H. U. Blaser, B. Pugin, F. Spindler, *Applied Homogeneous Catalysis with Organometallic Compounds* (Eds.: B. Cornils, W. A. Herrmann), 2nd ed., Wiley, New York, **2002**, vol. 3, 1131–1149.

[5] M. J. Palmer, M. Wills, *Tetrahedron: Asymmetry* **1999**, *10*, 2045–2061 and references cited therein.

[6] a) R. Noyori, S. Hashiguchi, *Acc. Chem. Res.* **1997**, *30*, 97–102; b) S. Hashiguchi, A. Kujii, T. Takehara, T. Ikariya, R. Noyori, *J. Am. Chem. Soc.* **1995**, *117*, 7562–7563; c) T. Ohkuma, H. Ooka, T. Ikariya, R. Noyori, *J. Am. Chem. Soc.* **1995**, *117*, 10417–10418.

[7] A. S. C. Chan, J. J. Pluth, J. Halpern, *J. Am. Chem. Soc.* **1980**, *102*, 5952–5954.

[8] J. M. Brown, R. A. Chaloner, *J. Chem. Soc., Chem. Commun.* **1980**, 344–346.

[9] C. Landis, J. Halpern, *J. Am. Chem. Soc.* **1987**, *109*, 1746–1754.

[10] J. M. Brown, *Hydrogenation of Functionalized Carbon-Carbon Double Bonds* (Eds.: E. N. Jacobsen, A. Pfaltz, H. Yamamoto), Springer, Berlin, **1999**, vol. l, pp. 119–182.

[11] J. Halpern, D. P. Riley, A. S. C. Chan, J. J. Pluth, *J. Am. Chem. Soc.* **1977**, *99*, 8055–8057.

[12] A. S. C. Chan, J. Halpern, *J. Am. Chem. Soc.* **1980**, *102*, 838–840.

[13] a) A. S. C. Chan, J. Pluth, J. Halpern, *Inorg. Chim. Acta* **1979**, *37*, 477–479; b) J. Halpern, *Science* **1982**, *217*, 401–407.

[14] I. Gridnev, N. Hagashi, K. Asakura, T. Imamoto, *J. Am. Chem. Soc.* **2000**, *122*, 7183–7194 and references cited therein.

[15] a) C. R. Landis, P. Hilfenhaus, S. Feldgus, *J. Am. Chem. Soc.* **1999**, *121*, 8741–8754; b) S. Feldgus, C. R. Landis, *Organometallics* **2001**, *20*, 2374–2386; c) S. Feldgus, C. R. Landis, *J. Am. Chem. Soc.* **2000**, *122*, 12714–12727; d) C. R. Landis, S. Feldgus, *Angew. Chem.* **2000**, *112*, 2985–2988; *Angew. Chem. Int. Ed.* **2000**, *39*, 2863–2866; e) A. Kless, A. Börner, D. Heller, R. Selke, *Organometallics* **1997**, *16*, 2096–2100.

[16] J. S. Giovannetti, C. M. Kelly, C. R. Landis, *J. Am. Chem. Soc.* **1993**, *115*, 4040–4057.

[17] K. Rossen, *Angew. Chem.* **2001**, *113*, 4747–4749; *Angew. Chem. Int. Ed.* **2001**, *40*, 4611–4613.

[18] a) R. Eisenberg, *Acc. Chem. Res.* **1991**, *24*, 110–116; b) J. Bargon, *Applied Homogeneous Catalysis with Organometallic Compounds* (Eds.: B. Cornils, W. A. Herrmann), VCH, Weinheim, **1996**, vol. 2, pp. 672–683.

[19] A. Harthun, R. Kadyrov, R. Selke, J. Bargon, *Angew. Chem.* **1997**, *109*, 1155–1156; *Angew. Chem. Int. Ed. Engl.* **1997**, *36*, 1103–1105.

[20] R. Giernoth, H. Heinrich, N. J. Adams, R. J. Deeth, J. Bargon, J. M. Brown, *J. Am. Chem. Soc.* **2000**, *122*, 12381–12382 and references cited therein.

[21] a) V. Guiral, F. Delbecq, P. Sautet, *Organometallics* **2001**, *20*, 2207–2214; b) M. Bernard, V. Guiral, F. Delbecq, F. Fache, P. Sautet, M. Lemaire, *J. Am. Chem. Soc.* **1998**, *120*, 1441–1446; c) V. Guiral, F. Delbecq, P. Sautet, *Organometallics* **2000**, *19*, 1589–1598.

[22] G. Zassinovitch, G. Mestroni, S. Gladiali, *Chem. Rev.* **1992**, *92*, 1051–1069.

[23] a) D. A. Alonso, P. Brandt, S. J. M. Nordin, P. G. Andersson, *J. Am. Chem. Soc.* **1999**, *121*, 9580–9588; b) M. Yamakawa, H. Ito, R. Noyori, *J. Am. Chem. Soc.* **2000**, *122*, 1466–1478.

[24] R. R. Schrock, J. A. Osborn, *J. Chem. Soc. C* **1970**, 567–568.

[25] Q. Jiang, Y. Jiang, D. Xiao, P. Cao, X. Zhang, *Angew. Chem.* **1998**, *110*, 1203–1207; *Angew. Chem. Int. Ed.* **1998**, *37*, 1100–1103.

[26] I. Ojima, T. Kogure, K. Achiwa, *J. Chem. Soc., Chem. Commun.* **1977**, 428–430.

[27] I. Ojima, T. Kogure, *J. Organomet. Chem.* **1980**, *195*, 239–248.

[28] a) F. Agbossou, J.-F. Carpentier, C. Hatat, N. Kokel, A. Mortreux, P. Betz, R. Goddard, C. Krüger, *Organometallics* **1995**, *14*, 2480–2489; b) F. Agbossou, J.-F. Carpentier, F. Hapiot, I. Suisse, A. Mortreux, *Coord. Chem. Rev.* **1998**, *178–180*, 1615–1645; c) C. Pasquier, S. Naili, A. Mortreux, F. Agbossou, L. Pélinski, J. Brocard, J. Eilers, I. Reiners, V. Peper, J. Martens, *Organometallics* **2000**, *19*, 5723–5732.

[29] a) Y. Kuroki, D. Asada, K. Iseki, *Tetrahedron Lett.* **2000**, *41*, 9853–9858; b) Y. Kuroki, Y. Sakamaki, K. Iseki, *Org. Lett.* **2001**, *3*, 457–459.

[30] a) G. Surpateanu, F. Agbossou, J.-F. Carpentier, A. Mortreux, *Tetrahedron: Asymmetry* **1998**, *9*, 2259–2270; b) F. Agbossou, J.-F. Carpentier, A. Mortreux, G. Surpateanu, A. J. Welch, *New J. Chem.* **1996**, *20*, 1047–1060.

[31] A complete chemical Review issue has been devoted to computational transition chemistry: *Chem. Rev.* **2000**, *100*, 351–801. For recent examples of computation on catalytic reactions, see ref.[21,23].

[32] C. Hatat, A. Karim, N. Kokel, A. Mortreux, F. Petit, *New J. Chem.* **1990**, *14*, 141–152.

[33] N. Keiken, P. Pregosin, G. Trabesinger, *Organometallics* **1998**, *17*, 4510–5518.

[34] J. Bakos, I. Toth, B. Heil, G. Szalontai, L. Parkanyi, V. Fulop, *J. Organomet. Chem.* **1989**, *370*, 263–276.

[35] Dielectric constants taken from the Handbook of Chemistry and Physics, benzene $\varepsilon = 2.284$, methanol $\varepsilon = 33.62$.

 © 2006 Wiley-VCH Verlag GmbH & Co. KGaA, Weinheim 

[36] a) A. Roucoux, M. Devocelle, J.-F. Carpentier, F. Agbossou, A. Mortreux, *Synlett* **1995**, 358–360; b) A. Roucoux, L. Thieffry, J.-F. Carpentier, M. Devocelle, C. Méliet, F. Agbossou, A. Mortreux, A. J. Welch, *Organometallics* **1996**, *15*, 2440–2449.
[37] S. B. Duckett, C. L. Newell, R. Eisenberg, *J. Am. Chem. Soc.* **1994**, *116*, 10548–10556.
[38] a) A. D. Becke, *J. Chem. Phys.* **1993**, *98*, 5648–5652; b) C. Lee, W. Yang, R. G. Parr, *Phys. Rev. B* **1988**, *37*, 785–789.
[39] A. D. Daniels, K. N. Kudin, M. C. Strain, O. Farkas, J. Tomasi, V. Barone, M. Cossi, R. Cammi, B. Mennucci, C. Pomelli, C. Adamo, S. Clifford, J. Ochterski, G. A. Petersson, P. Y. Ayala, Q. Cui, K. Morokuma, D. K. Malick, A. D. Rabuck, K. Raghavachari, J. B. Foresman, J. Cioslowski, J. V. Ortiz, A. G. Baboul, B. B. Stefanov, G. Liu, A. Liashenko, P. Piskorz, I. Komaromi, R. Gomperts, R. L. Martin, D. J. Fox, T. Keith, M. A. Al-Laham, C. Y. Peng, A. Nanayakkara, M. Challacombe, P. M. W. Gill, B. Johnson, W. Chen, M. W. Wong, J. L. Andres, C. Gonzalez, M. Head-Gordon, E. S. Replogle, J. A. Pople, Gaussian, Inc., Pittsburgh, PA, **1998**.
[40] P. J. Hay, W. R. Wadt, *J. Chem. Phys.* **1985**, *82*, 299–310.
[41] The length difference between Rh–PO and Rh–PN bonds was obtained from structures described in ref.[28] where references towards other complexes are also given.
[42] References for isolated aldehyde and ketone complexes: N. Quiros-Méndez, J. W. Seyler, A. M. Arif, J. A. Gladysz, *J. Am. Chem. Soc.* **1993**, *115*, 2323–2334. Theoretical studies: a) F. Delbecq, P. Sautet, *J. Am. Chem. Soc.* **1992**, *114*, 2446–2455; b) J. Joubert, F. Delbecq, *J. Organomet. Chem.* **2006**, *691*, 1030–1038.
[43] a) J. M. Brown, P. L. Evans, *Tetrahedron* **1988**, *44*, 4905–4916; b) P. L. Bogdan, J. J. Irwin, B. Bosnich, *Organometallics* **1989**, *8*, 1450–1453.
[44] For the calculation with acetone, the rate-determining step is clearly the hydride migration ($\Delta E$a = 11 kcal/mol).

Received: April 4, 2006
Published Online: September 5, 2006

 © 2006 Wiley-VCH Verlag GmbH & Co. KGaA, Weinheim 

DOI: 10.1002/ejic.200600412

# Morphology Control of CdSe Submicrostructures with High Hierarchy in Solution

**Benxia Li,[a] Meng Jing,[a] Guoxin Rong,[a] Yang Xu,[a] and Yi Xie*[a]**

**Keywords:** Morphology control / Cadmium selenide / Submicrostructures / Semiconductor

A series of CdSe submicrostructures, including rods, fringy structures, and fasciculate tubes with high hierarchy, have been selectively prepared by a facile one-step solution-based strategy without using any organic surfactants, simply by changing the feeding quantity of aqueous ammonia (25 % $NH_3$). The growth mechanism based on kinetic control is discussed for the selective formation of the CdSe submicrostructures with special morphologies. In the present reaction system, ammonia plays a dual role: providing an alkaline medium for the formation of $Se^{2-}$ and acting as a coordinating agent for cadmium cations in either the solution or the solid phase. The feeding quantity of aqueous ammonia greatly influences the rate of formation of the $Se^{2-}$ anion, and thus determines the final morphology of CdSe crystals. Compared with previous methods of preparing CdSe structures, this concise and novel one-step route has special advantages, suggesting a new path for convenient synthesis of CdSe materials with novel morphology.
(© Wiley-VCH Verlag GmbH & Co. KGaA, 69451 Weinheim, Germany, 2006)

## Introduction

Recently, the synthesis of higher ordered functional materials with specific orientation, complex form, and hierarchy has been an area of active research.[1] More and more studies are focused on synthesizing one-dimensional (1D) nanostructures and their hierarchical assemblies, which are expected to play an important role in fabricating the next generation of microelectronic devices because they can function as both building units and interconnections.[2] The architectural control of functional materials with well-defined shapes between nanoscale and microscale is a key for the success of "bottom-up" approaches toward future microdevice fabrication.[3] In addition, the fabrication of semiconducting metal chalcogenides with micro- or nanosize has attracted intense interest because of the unusual optical and electrical properties of these compounds and their potential applications in microdevices.[4] CdSe is one of the most studied subjects because of its extensive applications in solar cells, luminescent materials, lasing materials, and biomedical imaging.[5] In the past several years, most of the studies on the synthesis of CdSe materials were focused on various 1D nanostructures[6] and tetrapod-branched nanocrystals.[7] Peng et al. have reported the shape control and size distributions of colloidal CdSe nanocrystals and proposed morphological evolution from 0D to 1D nanocrystals.[8] These studies were mostly focused on the synthesis of CdSe nanocrystals with diameters below 100 nm. Little attention was paid to the fabrication of submicro- or micrometer-sized CdSe materials with novel morphology. Recently, Zhang's group has demonstrated that the shapes of CdSe crystals with diameters of 150–1000 nm could be manipulated sequentially from rods to particles to tetrapod structures by a vapor-solid (VS) process at high temperatures.[9] Yet, the controllable synthesis of CdSe materials including 1D, quasi-1D, and 3D microstructures with high hierarchy through a direct low-temperature, solution-based route without the use of any organic additives or the aid of other techniques has been rarely reported.

Because of its easily controlled reaction conditions and facile manipulation, the solution-based route might provide an attractive option for large-scale production of micro- or nanomaterials with special morphology. In as-reported solution-based approaches for controlled synthesis of CdSe nanostructures, a curious feature of the systems has been the ubiquitous use of some organic additives as complexing agents or capping ligands.[10] For the purpose of property studies and future applications, it is desirable to develop convenient strategies to obtain new nanomaterials with desired shapes. Moreover, to meet the needs of designed synthesis of micro- or nanostructures with novel morphology, it is vital to systematically find experimental conditions under which the desired materials with controlled morphology are synthesized in large quantities. In this work, a series of CdSe submicrostructures, including rods, fringy structures, and fasciculate tubes, have been selectively prepared by a facile one-step solution-based strategy without using any

[a] Department of Nanomaterials and Nanochemistry, Hefei National Laboratory for Physical Sciences at Microscale, University of Science and Technology of China,
Hefei, Anhui 230026, P. R. China
Fax: +86-551-360-3987
E-mail: yxie@ustc.edu.cn
Supporting information for this article is available on the WWW under http://www.eurjic.org or from the author.

 © 2006 Wiley-VCH Verlag GmbH & Co. KGaA, Weinheim 

organic surfactants, by simply changing the feeding quantity of aqueous ammonia (25% $NH_3$). Concerning the use of ammonia in the synthetic architecture, a dual role can be identified: providing an alkaline medium for the formation of $Se^{2-}$ anions and acting as a coordinating agent for cadmium cations in either solution or solid phase. This synthetic method provides a simple, environmentally friendly, and reproducible route for the controllable synthesis of CdSe materials.

## Results and Discussion

### Morphologies of the Products

The morphologies of the products obtained in the reaction systems containing different volume ratios of aqueous ammonia (25% $NH_3$) and distilled water were examined by a field-emission scanning electron microscope (FESEM). The FESEM images are shown in Figure 1. As shown in Figure 1 (a), the product obtained by feeding 20 mL aqueous ammonia (25% $NH_3$) was mainly composed of submicrorods with diameters around 500 nm and lengths ranging from 5 μm to 10 μm. When the volume of aqueous ammonia fed into the system was increased to 30 mL, fringy structures with high hierarchy assembled by nanorods was formed with about 85% morphological yield (Figure 1, b). A magnified SEM image in Figure 1 (c) clearly shows that the fringy assembly is formed by many smaller nanorods with diameters of 150 nm growing on a trunk. When aqueous ammonia (25%) was used as the only solvent, the obtained product was a large scale of 3D radial assemblies with an average diameter of about 5 μm, as depicted by the panoramic image (Figure 1, d). Interestingly, these 3D radial assemblies, different from those formed by aggregated nanorods that were reported previously,[11] are formed by fasciculate submicrotubes with diameters of 0.5–1 μm, and the open ends of some submicrotubes can be observed in Figure 1 (d). Parts e and f of Figure 1 show the magnified FESEM images of the assemblies with two representative shapes in the sample. The 3D assembly in Figure 1 (e) is composed of several thick tubes with diameters around 900 nm and wall thickness about 160 nm, which clearly manifests the tubular structure. The other assembly in Figure 1 (f) consists of more tubes with smaller diameters of 500 nm, in which these submicrotubes have cracked ends (arrowheads A) and rough interior walls (arrowhead B).

### Phase and Composition of the Products

The structure and bulk phase of the products were determined by XRD analysis. Figure 2 shows the XRD patterns of as-obtained samples of submicron rods, fringy structures, and fasciculate tubes. All diffraction peaks in these XRD patterns can be well indexed to those of the pure phase of wurtzite CdSe (space group $P6_3mc$, JCPDS card No.2–330). No peaks due to impurities were detected, indicating the high purity of the product. The intense and sharp diffraction peaks suggest that the obtained products are well crystallized. In addition, it is notable that the intensity of {100} and {101} diffraction peaks is degressive and that of the

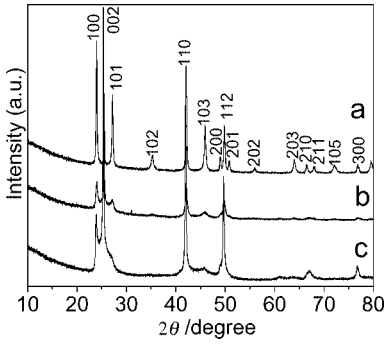


Figure 2. XRD patterns of three as-prepared CdSe samples: (a) submicrorods, (b) fringy structures, and (c) fasciculate submicrotubes.

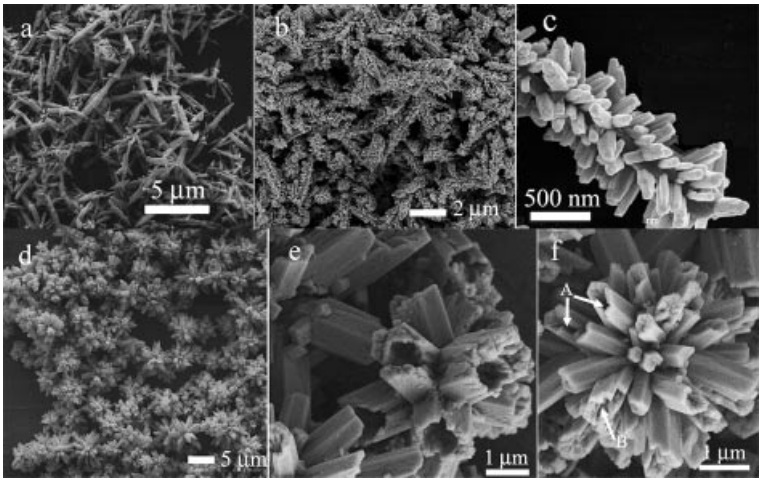


Figure 1. Typical FESEM images of three as-prepared CdSe samples with special morphologies by feeding different amounts of aqueous ammonia (25% $NH_3$): (a) submicrorods, 20 mL aqueous ammonia; (b–c) fringy structures, 30 mL aqueous ammonia; (d–f) fasciculate submicrotubes, 40 mL aqueous ammonia.

 © 2006 Wiley-VCH Verlag GmbH & Co. KGaA, Weinheim 

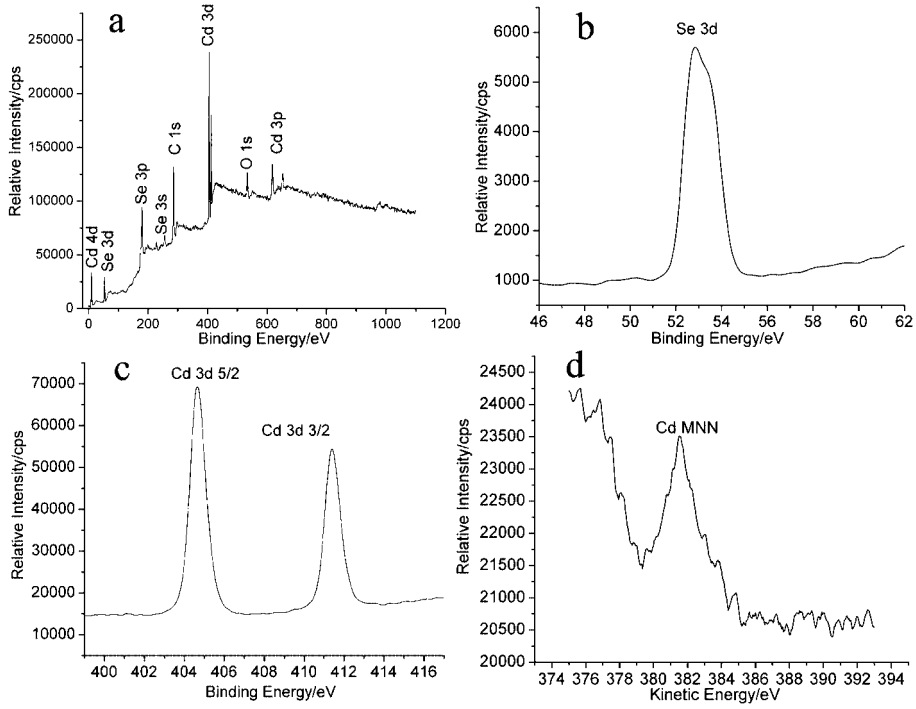


Figure 3. XPS spectra of the as-prepared CdSe fasciculate submicrotubes: (a) survey spectrum, (b) Se 3d, (c) Cd 3d, and (d) Cd MNN. The XPS spectra of other CdSe samples are similar.

{002} diffraction peak strengthens gradually from pattern a to pattern c, which results from the different arrangement of the rods in these CdSe submicrostructures. Thus, the XRD pattern can be indicative of the anisotropic shapes of the three CdSe samples.

In order to obtain the information about the electronic structure of the external ions and the relative composition of the product, three as-prepared CdSe samples with special morphologies were characterized by the XPS technique. Figure 3 shows the XPS spectra of CdSe fasciculate submicrotubes, in which the binding energies were corrected for specimen charging by referencing C 1s to 284.60 eV. The binding energies of Se 3d and Cd 3d were found to be 52.9 and 405.7 eV, respectively. The signals at 10.4 and 381.6 eV can be attributed to the binding energy of Cd 4d and the kinetic energy of Cd MNN. The Auger parameter, defined as the sum of the binding energy of the Cd 3d 5/2 level and the kinetic energy of Cd MNN, is approximately 786 eV, which is consistent with that of the CdSe material.[12]

### Formation Process and Possible Mechanism of CdSe Submicrostructures

To better clarify the nucleation and anisotropic growth of these CdSe submicrocrystals, the morphology and microstructure of their intermediates were further studied by using transmission electron microscopy (TEM) and high-resolution transmission electron microscopy (HRTEM). As shown in Figure 4 (a), the 1-h reaction starting with 20 mL aqueous ammonia engendered very short CdSe rods with different diameters. After 5 h, well-shaped CdSe rods (Figure 4, b) had been formed. The electron diffraction (ED) (Figure 4, b1) and HRTEM image (Figure 4, b2) of a single CdSe rod in Figure 4 (b) indicate that the nanorod has a single-crystalline structure and grows along the <0001> direction. When 30 mL aqueous ammonia was fed into the system, the 1-h reaction gave primary CdSe fringy structures with fewer branches (Figure 4, c). After 5 h, the CdSe fringy structures (Figure 4, d) were almost achieved and resembled their corresponding final products. Figure 4d1 and Figure 4d2 show the ED pattern and HRTEM image taken from a branch (marked with a white rectangle) of the CdSe fringy structure in Figure 4 (d). The ED pattern can be indexed as the [100] zone axis of a wurtzite CdSe crystal, and the lattice spacings of 0.705 nm and 0.372 nm in the HRTEM image correspond to the (0001) and (01$\bar{1}$0) planes of hexagonal CdSe, respectively, indicating that the branches of the CdSe fringy structures grow along the <0001> direction. The ED pattern and HRTEM image of the trunk in the CdSe fringy structure are similar to those from the branch, indicating that the trunk of the CdSe fringy structures also grow along the <0001> direction. In addition, time-dependent experiments for the synthesis of the fasciculate submicrotubes were typically carried out to investigate the formation of the special tubular shapes. TEM images of the intermediate products are shown in Figure 4 (e–f). The 1-h reaction resulted in CdSe aggregations that consisted of many small whiskers (Figure 4, e). After 5 h, the whiskers grew into nanorods with diameters of 200 nm, and the aggregations became 3D radial architectures assembled by nanorods (Figure 4, f). The ED pattern (Figure 4, f1) and HRTEM image (Figure 4, f2), taken form the nanorod marked with a white rectangle in Figure 4 (f), indicate that the nanorods in CdSe are fasciculate crystal-

 © 2006 Wiley-VCH Verlag GmbH & Co. KGaA, Weinheim 

line nanorods that grow along the <0001> direction. The sample obtained after 12 h consists of larger 3D architectures assembled by nanorods, as revealed by its SEM images in Figure 5 (a–b). The magnified image of a typical architecture (Figure 5, b) indicates that the nanorods have very rough and cracked ends.

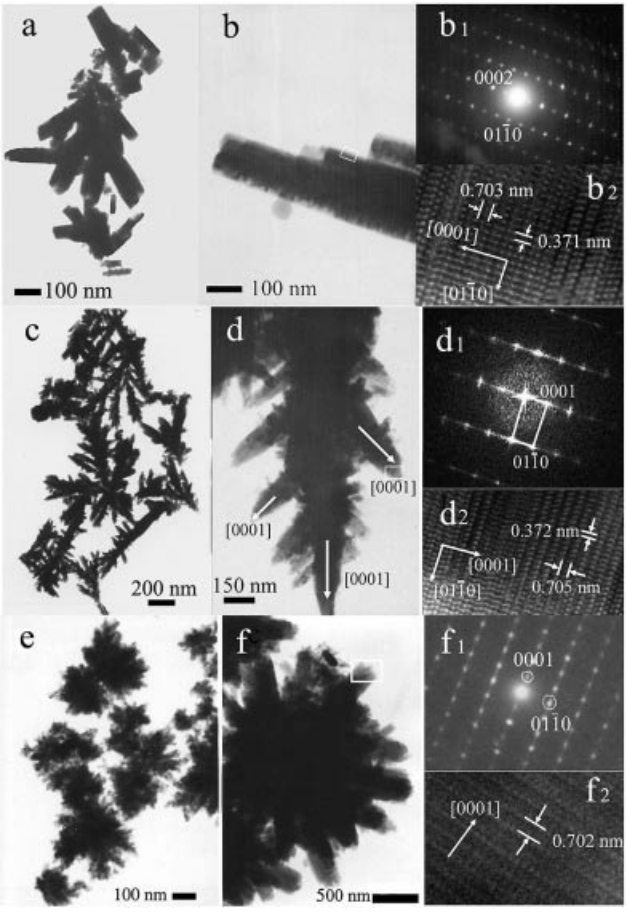


Figure 4. TEM images of the intermediate products of three CdSe submicrostructures: (a) rods obtained after 1 h; (b) rods obtained after 5 h, (b1,2) ED pattern and HRTEM image taken from the rod in Figure b; (c) fringy structure obtained after 1 h; (d) fringy structure obtained after 5 h; (d1,2) ED pattern and HRTEM image taken from the branch of the fringy structure in Figure d; (e) aggregations obtained after 1 h; (f) fasciculate rods obtained after 5 h, (f1,2) ED pattern and HRTEM image taken from the rod marked with a white rectangle in Figure f.

On the basis of the above experimental results, it can be seen that the most important factor that influences the morphology of CdSe crystals in the present approach is the concentration of ammonia in the reaction system. On one hand, our experimental results have indicated that the feeding quantity of aqueous ammonia (25%) in the reaction system also determined the composition of the final product (Figure S1–S2). Moreover, the presence of residual Se in the intermediate products (Figure S3) clarifies the formation process of the CdSe phase in the reaction, which can be illustrated by the series of reactions in Figure 6 (a): First,

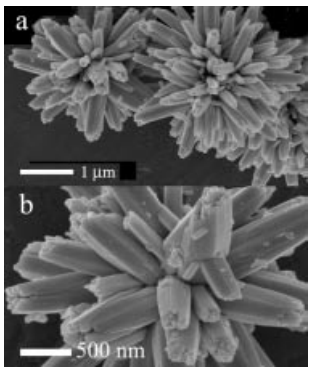


Figure 5. SEM images of CdSe fasciculate rods obtained after 12 h with using aqueous ammonia (25%) as the only solvent (40 mL).

$SeO_3^{2-}$, formed by the dissolution of $SeO_2$ in the solution, is reduced by $NaBH_4$ to Se. Then, under alkaline conditions, Se dismutates into $Se^{2-}$ and $SeO_3^{2-}$,[13] and the latter reacts again as the Se source. Finally, $Se^{2-}$ anions combine with $Cd^{2+}$ cations to form the CdSe phase. The formation of $Se^{2-}$ anions needs proper alkaline conditions, provided by ammonia in our reaction system. On the other hand, it is well known that shape control of the crystals can be achieved by manipulating the growth kinetics.[14] In the present case, the contributing growth-driving force for CdSe crystals is primarily the $Se^{2-}$ concentration, which is determined by the alkalinity of the reaction solution. In our reaction system, the alkalinity was manipulated by changing the feeding quantity of aqueous ammonia. The mechanism of formation of the CdSe submicrostructures with different morphologies is schematically described in Figure 6 (b). When the added volume of aqueous ammonia (25%) was as small as 20 mL, the alkalescence of the reaction solution was relatively weak, and the rate of formation of $Se^{2-}$ anions was low, leading to a lower concentration in solution, which favored the anisotropic nucleation and growth of CdSe crystals. CdSe building units are inclined to grow along the <0001> axis because of the intrinsic structure of CdSe {0001} planes, where $Cd^{2+}$ cations are rich on the positive facet (0001) and $Se^{2-}$ anions are rich on the negative facet (000$\bar{1}$). Thus, one-dimensional nucleation and growth of CdSe nanorods along the <0001> axis took place, and the final CdSe submicrorods were obtained by feeding 20 mL aqueous ammonia (25%) into the present reaction system. With an increased volume of the aqueous ammonia (30 mL), both the alkalinity and the concentration of $Se^{2-}$ anions in the reaction solution increased, giving more CdSe building units. Besides the one-dimensional growth, more nucleation sites around initial CdSe nanorods provided the growth along the <0001> direction of the new CdSe nanorods on the trunks. As a result, the fringy CdSe structures were obtained. When aqueous ammonia (25%) was used as the only solvent (40 mL), both the alkalinity and the concentration of $Se^{2-}$ anions in the reaction solution increased further. The high monomer concentration led to a fast initial nucleation of CdSe, and many newly formed CdSe colloids aggregated together. Then, the concentration

 © 2006 Wiley-VCH Verlag GmbH & Co. KGaA, Weinheim 

of the monomer became lower as the reaction proceeded. The nuclei around the initial CdSe aggregations would grow along the <0001> direction to form 1D nanorods as long as the chemical environment constantly provides reactants. 3D-fasciculate submicrorods were obtained after 12 h. As for the CdSe fasciculate submicrotubes obtained in 40 mL aqueous ammonia (25%) after 24 h, it was deemed that they were formed by a coordination-assisted dissolution and recrystallization process.[15] Because $Cd^{2+}$ cations are rich on the (0001) facet of the CdSe crystal, ammonia molecules tend to be adsorbed on the (0001) plane and coordinate with $Cd^{2+}$ cations [$CdSe + 4\,NH_3 \rightarrow Cd(NH_3)_4^{2+} + Se^{2-}$], leading to the dissolution of solid CdSe. The selective adsorption of ammonia molecules on the tips [plane (0001)] of the CdSe rods would result in selective "etching" on the rods from the tips toward the interior along the <0001> axis. As observed from Figure 5 (b), the tips of these fasciculate rods are very rough and porous, which may be the "etching" effect of ammonia molecules. The transformation from the fasciculate nanorods to the fasciculate submicrotubes was achieved by partial dissolution of CdSe rods from the tips toward the interior along the long axis (<0001> axis). In addition, the diameters of the final tubes are larger than those of the rodlike precursors, indicating that recrystallization accompanied the "etching" process. Thus, final fasciculate submicrotubes were obtained through such a coordination-assisted dissolution and recrystallization process. However, in the rods and the fringy assemblies, obtained with 20 mL and 30 mL aqueous ammonia (25%), respectively, the CdSe crystals cannot adsorb enough ammonia molecules on their surfaces because of the low concentration of $NH_3$, and no tubular structures are formed in either system. Therefore, by adjusting the feeding quantity of aqueous ammonia, the morphology of the CdSe submicrostructures can be varied sequentially from 1D rods to 3D-fasciculate tubes.

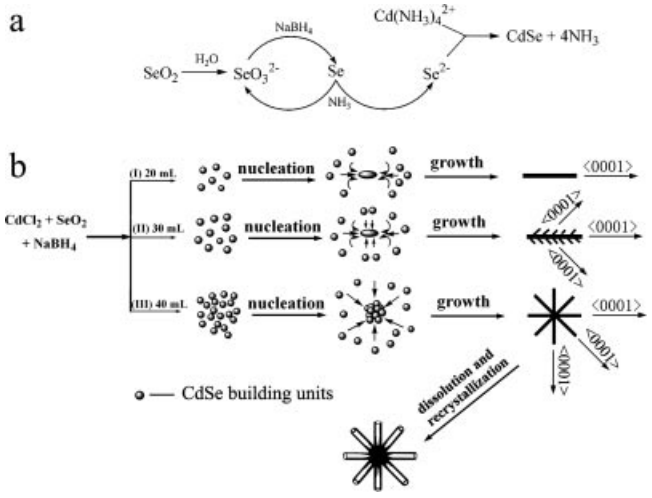


Figure 6. Schematic illustrations: (a) the formation process of CdSe phase in present reaction system; (b) the formation mechanism of CdSe submicrorods, fringy structures, and fasciculate tubes.

## Conclusions

In summary, various morphologies of CdSe, including rods, fringy structures, and fasciculate tubes in submicroscale have been synthesized by a facile one-step, solution-based strategy without using any organic surfactants. The morphology of the CdSe submicrocrystals can be varied sequentially from rods to fringy structures and then to fasciculate tubes by manipulating the volume ratio of aqueous ammonia (25% $NH_3$) and distilled water. In the present reaction system, ammonia acts as a coordinating reagent as well as providing a suitable alkaline environment for the transformation from Se to $Se^{2-}$. The feeding quantity of aqueous ammonia greatly influenced the rate of formation of the $Se^{2-}$ anion and thus its concentration in the reaction solution, which determined the final morphology of CdSe crystals. The rational mechanism based on kinetic control was discussed for the selective formation of these CdSe submicrocrystals with different morphologies. Compared with previous methods of preparing CdSe crystals, this concise one-step route has special advantages, which suggests a new path for the convenient synthesis of CdSe crystals with novel morphology.

## Experimental Section

**Materials and Preparation:** All chemicals were of analytical grade and were used as received without further purification. In a typical procedure, $CdCl_2{\cdot}2.5H_2O$ (ca. 4 mmol), $SeO_2$ (ca. 4 mmol), and $NaBH_4$ (ca. 10 mmol) were dissolved in the solvent (40 mL) containing different volume ratios of aqueous ammonia (25% $NH_3$) and distilled water. The mixed solution was then transferred to a Teflon-lined autoclave with a total capacity of 50 mL. The autoclave was sealed and maintained at 180 °C for 24 h, and then cooled naturally to room temperature. The precipitates were carefully collected and washed with distilled water and absolute ethanol for several times, and then dried in vacuo at 60 °C for 4 h.

**Characterization:** XRD patterns of the products were obtained with a Japan Rigaku DMax-γA rotation anode X-ray diffractometer equipped with graphite-monochromatized Cu-$K_\alpha$ radiation ($\lambda$ = 1.54178 Å). SEM images were taken with a field-emission scanning electron microscope (JEOL JSM-6700F, 15 kV). TEM photographs were taken with a Hitachi Model H-800 transmission electron microscope at an accelerating voltage of 200 kV. The HRTEM images and the corresponding SAED patterns were taken with a JEOL 2010 high-resolution TEM operating at 200 kV. The X-ray photoelectron spectra (XPS) were collected with an ESCALab MKII X-ray photoelectron spectrometer with non-monochromatized Mg-$K_\alpha$ X-ray as the excitation source.

**Supporting Information** (see also the footnote on the first page of this article): XRD patterns of the products obtained under different reaction conditions (Figure S1–S3), room-temperature photoluminescence (PL) emission spectra (Figure S4), and room-temperature Raman spectra (Figure S5).

## Acknowledgments

This work was financially supported by the National Natural Science Foundation of China (No. 20321101). The authors thank Prof. Huagui Zheng for helpful discussions.

 © 2006 Wiley-VCH Verlag GmbH & Co. KGaA, Weinheim 

[1] a) H. T. Shi, L. M. Qi, J. M. Ma, N. Z. Wu, *Adv. Funct. Mater.* **2005**, *15*, 442–450; b) D. Wang, C. M. Lieber, *Nat. Mater.* **2003**, *2*, 355–356; c) G. F. Zou, K. Xiong, C. L. Jiang, H. Li, T. W. Li, J. Du, Y. T. Qian, *J. Phys. Chem. B* **2005**, *109*, 18356–18360.
[2] a) T. K. Sau, C. J. Murphy, *J. Am. Chem. Soc.* **2004**, *126*, 8648–8649; b) Z. R. Tian, J. Liu, J. A. Voigt, H. Xu, M. J. Mcdermott, *Nano Lett.* **2003**, *3*, 89–92; c) K. A. Dick, K. Deppert, M. W. Larsson, T. Martensson, W. Seifert, L. R. Wallenberg, L. Samuelson, *Nat. Mater.* **2004**, *3*, 380–384.
[3] X. Duan, Y. Huang, Y. Cui, J. Wang, C. M. Lieber, *Nature* **2001**, *409*, 66–69.
[4] a) T. C. Harman, P. J. Taylor, M. P. Walsh, B. E. LaForge, *Science* **2002**, *297*, 2229–2232; b) X. T. Zhang, Z. Liu, Q. Li, Y. Leung, K. Ip, S. K. Hark, *Adv. Mater.* **2005**, *17*, 1405–1410; c) I. Robel, B. A. Bunker, P. V. Kamat, *Adv. Mater.* **2005**, *17*, 2458–2463; d) S. C. Erwin, L. J. Zu, M. I. Haftel, A. L. Efros, T. A. Kennedy, D. J. Norris, *Nature* **2005**, *436*, 91–94.
[5] a) D. J. Milliron, A. P. Alivisatos, C. Pitois, C. Edder, J. M. J. Frechet, *Adv. Mater.* **2003**, *15*, 58–61; b) C. Ma, Y. Ding, D. F. Moore, X. Wang, Z. L. Wang, *J. Am. Chem. Soc.* **2004**, *126*, 708–709.
[6] a) W. Nie, L. J. An, B. Z. Jiang, X. L. Ji, *Chem. Lett.* **2004**, *33*, 836–837; b) C. Ma, Z. L. Wang, *Adv. Mater.* **2005**, *17*, 2635–2639.
[7] a) L. Manna, D. J. Milliron, A. Meisel, E. C. Scher, A. P. Alivisatos, *Nat. Mater.* **2003**, *2*, 382–385; b) J. W. Grebinski, K. L. Hull, J. Zhang, T. H. Kosel, M. Kuno, *Chem. Mater.* **2004**, *16*, 5260–5272; c) W. Nie, J. B. He, N. N. Zhao, X. L. Ji, *Nanotechnology* **2006**, *17*, 1146–1149.
[8] a) X. Peng, *Adv. Mater.* **2003**, *15*, 459–463; b) L. Qu, X. Peng, *J. Am. Chem. Soc.* **2002**, *124*, 2049–2055; c) Z. A. Peng, X. Peng, *J. Am. Chem. Soc.* **2001**, *123*, 1389–1395.
[9] Z. Y. Wang, Q. F. Lu, X. S. Fang, X. K. Tian, L. D. Zhang, *Adv. Funct. Mater.* **2006**, *16*, 661–667.
[10] a) Z. A. Peng, X. G. Peng, *J. Am. Chem. Soc.* **2001**, *123*, 1389–1395; b) C. R. Bullen, P. Mulvaney, *Nano Lett.* **2004**, *4*, 2303–2307; c) Q. Pang, L. J. Zhao, Y. Cai, D. P. Nguyen, N. Regnault, N. Wang, S. H. Yang, W. K. Ge, R. Ferreira, G. Bastard, J. N. Wang, *Chem. Mater.* **2005**, *17*, 5263–5267.
[11] a) Z. Q. Li, Y. Ding, Y. J. Xiong, Q. Yang, Y. Xie, *Chem. Eur. J.* **2004**, *10*, 5823–5828; b) C. Z. Wu, Y. Xie, D. Wang, J. Yang, T. W. Li, *J. Phys. Chem. B* **2003**, *107*, 13583–13587.
[12] C. D. Wagner in *Practical Surface Analysis Vol. 1: Auger and X-ray Photoelectron Spectroscopy* (Eds.: D. Briggs, M. P. Seah), John Wiley & Sons, Chichester, **1996**, 2nd ed., p. 595.
[13] a) W. X. Zhang, C. Wang, L. Zhang, X. M. Zhang, X. M. Liu, K. B. Tang, Y. T. Qian, *J. Solid State Chem.* **2000**, *151*, 241–244; b) W. X. Zhang, L. Zhang, Y. W. Cheng, Z. H. Hui, X. M. Zhang, Y. Xie, Y. T. Qian, *Mater. Res. Bull.* **2000**, *35*, 2009–2015.
[14] X. Peng, L. Manna, W. Yang, J. Wickham, E. Scher, A. Kadavanich, A. P. Alivisatos, *Nature* **2000**, *404*, 59–61.
[15] C. J. Jia, L. D. Sun, Z. G. Yan, L. P. You, F. Luo, X. D. Han, Y. C. Pang, Z. Zhang, C. H. Yan, *Angew. Chem. Int. Ed.* **2005**, *44*, 4328–4333.

Received: May 5, 2006
Published Online: September 13, 2006

 © 2006 Wiley-VCH Verlag GmbH & Co. KGaA, Weinheim 

DOI: 10.1002/ejic.200600438

# Chiral Recognition of Mesoporous SBA-15 with an Incorporated Chiral Porphyrin

**Huan-Bao Fa,[a,d] Lang Zhao,[b] Xing-Qiao Wang,*[a] Ji-Hong Yu,[b] Yi-Bing Huang,[c] Min Yang,[a] and De-Jun Wang[a]**

**Keywords:** Chiral recognition / Porphyrins / Mesoporous materials / SBA-15

The incorporation of a chiral porphyrin into the mesoporous molecular sieves SBA-15 by reactions of the surface OH group with an amino group of the porphyrin and its chiral recognition were studied. The resultant material was analyzed by a combination of techniques and it was confirmed that the channels of SBA-15 have been filled with chiral porphyrins, leaving the mesopores unaffected. The investigation of chiral recognition of the porphyrin and the composite SBA-15 shows that the incorporated SBA-15 has a clear CD spectral signal of the chiral porphyrin and exhibits different chiral recognition abilities for small amino acids. The D-alanine is more tightly bound to the mesoporous composite SBA-15 than its optical antipode.

(© Wiley-VCH Verlag GmbH & Co. KGaA, 69451 Weinheim, Germany, 2006)

## Introduction

Chiral recognition is an attractive subject in the area of host-guest chemistry, since it is a fundamental process for a range of chemical and biological phenomena.[1–3] Several types of host molecules for chiral recognition studies have been reported[4–10] because of their biological and chemical importance. Among them, porphyrins are relatively accessible molecules and have been used in recognition studies for the past two decades.[11–16] However, the use of porphyrins for chiral recognition has been restricted due to their poor stability in solution. A useful means to improve the stability of porphyrins is by encapsulating them into microporous materials such as zeolites, since molecular encapsulating is an emerging technology with potential applications in separation, chemical sensing, and catalysis.[17] However, for natural faujasite and synthetic zeolites X and Y the supercage diameter and the aperture to the cages are only 0.7–1.3 nm, which is too small for big complexes such as porphyrin substrates and products to diffuse in and out.[18] The discovery of the mesoporous material SBA-15[19,20] by Zhao and coworkers in 1998 provided the materials needed to achieve porphyrin incorporation since the SBA-15 has a regular hexagonal array of uniform channels with diameters 4.6–30 nm, high internal surface area of about 700–1000 $m^2 g^{-1}$, and high thermal and hydrothermal stabilities.

Incorporation of metal complexes into mesoporous SBA-15 for catalytic purposes has been extensively investigated.[21–26] However, studies on the incorporation of chiral metal complexes into SBA-15 and their chiral recognitions are limited[27] and there are no reports on incorporation of chiral porphyrins and their chiral recognitions. It is, therefore, important to study this system and to focus on chiral recognition of the host for small chiral molecules. It has been proposed that the enantioselectivity of the host for amino acids could be effectively enhanced by constructing a specific chiral environment derived from protected amino acids on the host porphyrin. In this research, we designed and synthesized a porphyrin that contains an amino acid on the porphyrin plane (Figure 1) and incorporated the porphyrin molecule with chiral recognition into the channels of SBA-15 to give it chiral recognition functions. Methods reported to date for organic complex fixation include: (a) impregnation,[28,29] (b) attachment to amine ligands provided by the modification of a mesoporous material surface with an organosilane,[29–31] (c) encapsulation during hydrothermal synthesis,[32] (d) ion exchange between the organic complex cation and the template surfactant species in the non-calcined mesoporous material,[32] and (e) covalent bonding of the amine-functionalized porphyrin to sites created in mesoporous material by doping with Nb.[33] It is well known that the interior surface of SBA-15 is covered with OH groups, so reduction of the nitro group on the porphyrin circumference led to the formation of aminogen with amino groups linking to OH groups of the SBA-15 through hydrogen bonding. In this paper, we report the results of our studies on the incorporation of a chiral porphy-

[a] College of Chemistry, Jilin University,
2519 Jiefang Road, Changchun 130021, China
[b] Key Laboratory of Inorganic Synthesis & Preparative Chemistry, Jilin University,
Changchun 130023, China
[c] Key Laboratory of Molecular Enzymology and Engineering,
Changchun 130021, China
[d] College of Chemistry and Chemical Engineering, Chongqing University,
Chongqing 400044, China

 © 2006 Wiley-VCH Verlag GmbH & Co. KGaA, Weinheim 

rin into SBA-15, and chiral recognition of the mesoporous composite SBA-15/porphyrin using a combination of techniques such as X-ray diffraction (XRD), transmission electron microscopy (TEM), UV/Vis spectroscopy, nitrogen adsorption, and circular dichroism (CD) spectroscopy. At the same time, the enantioselectivity of the chiral porphyrin for an amino acid ester in solution was studied for comparison with the SBA-15/porphyrin.

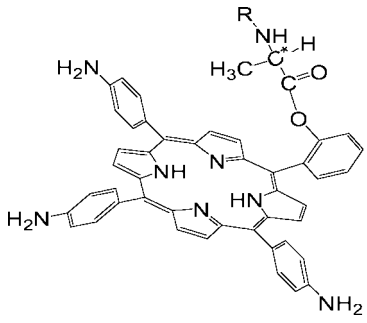


Figure 1. Chemical structure of the chiral porphyrin (R = Boc).

## Results and Discussion

### General Features of the Synthesized Material

The X-ray powder diffraction (XRD) patterns of SBA-15 before (Figure 2, b) and after (Figure 2, a) the incorporation of the chiral porphyrin are given in Figure 2. The XRD patterns of pure SBA-15 and SBA-15/porphyrin show strong (100) peaks, suggesting that framework stability of the mesoporous material is well maintained when the chiral porphyrin is incorporated into the channels of SBA-15. It is to be noted that the relative intensities of (110) and (200) scattering reflections were dramatically decreased for the composite consisting of both the porphyrin and SBA-15 when compared to the same bands for pure SBA-15. The change is interpreted as indicating that the porphyrins are dispersed in the mesoporous channels. TEM measurements were used to analyze the structure of the SBA-15. From the TEM image (Figure 3), it is seen that large ordering domains with highly ordered hexagonal (Figure 3, b) and

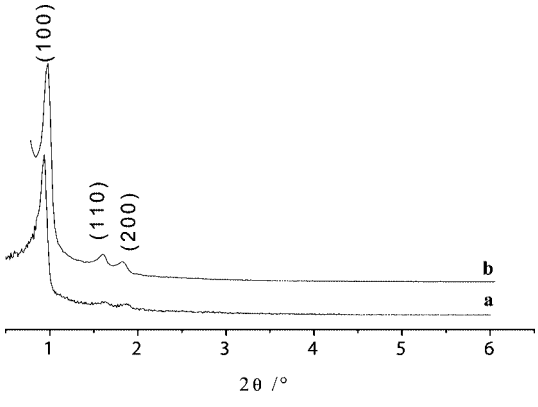


Figure 2. XRD patterns of SBA-15 samples with (a) and without (b) the incorporated chiral porphyrin.

strutlike arrays (Figure 3, a) exist. The SBA-15 after incorporation of chiral porphyrin is shown in Figure 4. When comparing this to Figure 3, it is clear that the hexagonal structure of SBA-15 is preserved after the chiral porphyrin incorporation. However, the TEM images of Figure 4 (part b [110], and part a [100]) show that the hexagonal channels of SBA-15/porphyrin become shaggier. The observed difference can probably be attributed to incorporation of the chiral porphyrin into the channels of SBA-15.

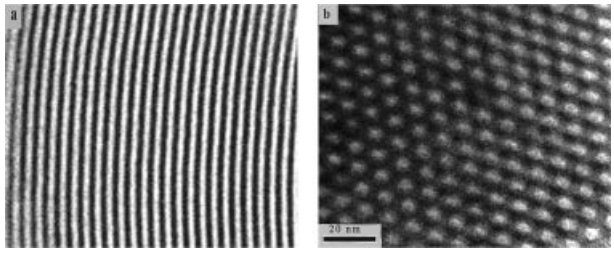


Figure 3. TEM images of SBA-15 along the (a) [100] and (b) [110] directions.

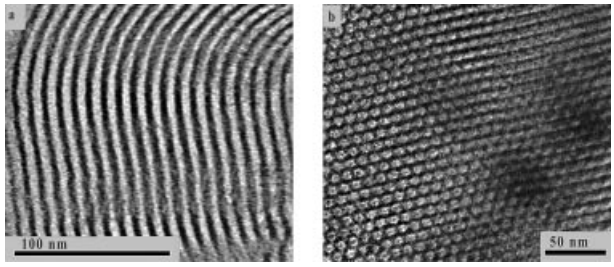


Figure 4. TEM images of SBA-15 with incorporated chiral porphyrin along the (a) [100] and (b) [110] directions.

UV/Vis diffuse reflectance spectrum of the chiral porphyrin, SBA-15/porphyrin, and pure SBA-15 are given in Figure 5. The pure SBA-15 has no characteristic absorption bands over the entire spectral region (Figure 5, a). The chiral porphyrin itself has the Soret bands (438 nm) and four Q-bands (526, 573, 662, 729 nm) (Figure 5, c). The SBA-15/porphyrin has absorption bands at 425 (Soret band), 518, 560, and 698 nm (Figure 5, b). Compared with the pure complex, the Soret band of the chiral porphyrin in SBA-15 is shifted toward shorter wavelengths. This can be attributed to interactions of the porphyrin with the interior surface hydroxyl groups of SBA-15. It has been shown that oxide supports have strong perturbations on the absorption maxima and molar absorption coefficients.[34] A comparison of the characteristic absorption bands of the chiral porphyrin incorporated SBA-15 with that of the chiral porphyrin confirms the incorporation of the chiral porphyrin into the SBA-15 channels. When the chiral porphyrin was incorporated, interactions of the ligands of the porphyrin with their local chemical environment changed the symmetry of the porphyrin. Because of these interactions, the polarity of the surroundings of the porphyrin is increased, as evidenced by the shifts of the absorption bands toward higher energy (shorter wavelength) in the UV/Vis spectra given above.

 © 2006 Wiley-VCH Verlag GmbH & Co. KGaA, Weinheim 

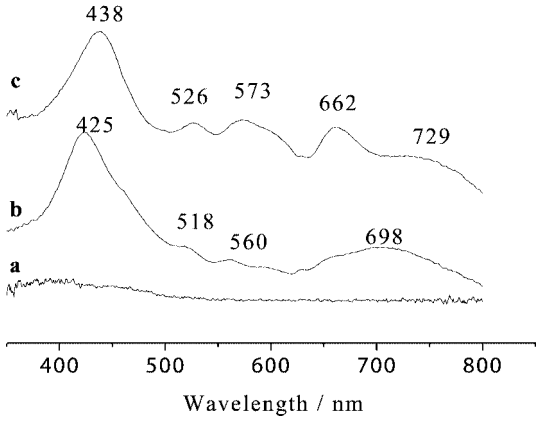


Figure 5. UV/Vis absorption spectra of SBA-15 before (a) and after (b) the incorporation of chiral porphyrin, and also the chiral porphyrin on its own (c).

In order to understand better the texture of the mesoporous composite SBA-15/porphyrin, the nitrogen isothermal adsorption technique was employed. Nitrogen adsorption/desorption isotherms for SBA-15 and SBA-15/porphyrin are shown in Figure 6. When porphyrins were incorporated into SBA-15, the sharpness of the inflection was significantly reduced at the $P/P_0$ range from 0.45 to 0.9, and the inflections were shifted slightly toward lower $P/P_0$ ranges. The inflection point of the relative pressure is related to a diameter in the mesopore range, and the sharpness of these steps indicates the uniformity of the mesopore size distribution.[35,36] Compared to pure SBA-15, the mesoporous composite SBA-15/porphyrin showed a reduction of sharpness, indicating less uniformity of the mesopore size distribution. Table 1 summarizes the results of $N_2$ adsorption analyses. After incorporation of chiral porphyrin into SBA-15, the $S_{BET}$, $V_t$, and $D_{BJH}$ values for SBA-15/porphyrin were 427 $m^2 g^{-1}$, 0.66 $cm^3 g^{-1}$, and 9.0 nm, respectively, and 540 $m^2 g^{-1}$, 0.88 $cm^3 g^{-1}$, and 9.8 nm for pure SBA-15, respectively. Therefore, all parameters of SBA-15/porphyrin decreased compared with pure SBA-15. This is fully consistent with the results of the XRD, UV/Vis, and TEM studies and confirms that the porphyrin was successfully incorporated into the interior surface of the channels of SBA-15. There is a slight decrease of the average pore size ($D_{BJH}$) from 9.8 to 9.0 nm (Figure 6, B), which indicates that some of the nanometer-shaggier void space of the host silica is open, although a portion of the channels may be blocked by the porphyrin molecules. The space is important for guest molecules to diffuse into the host silica, and to contact chiral porphyrin molecules for reactions to proceed.

Table 1. Physical and surface properties of selected samples.

| Sample | $S_{BET}$[a] [$m^2 g^{-1}$] | $V_t$ [$cm^3 g^{-1}$] | $D_{BJH}$ [nm] |
|---|---|---|---|
| SBA-15 | 540 | 0.88 | 9.8 |
| SBA-15/porphyrin | 427 | 0.66 | 9.0 |

[a] $S_{BET}$, BET specific surface area; $V_t$, total pore volume; $D_{BJH}$, pore diameter calculated using the BJH method.

The CD spectra of the chiral porphyrin in solution and the SBA-15/porphyrin in the solid phase are given in Figure 7. The SBA-15 incorporating chiral porphyrin gives CD signals while the pure SBA-15 does not have CD signals. This also confirms the results that the porphyrin has been

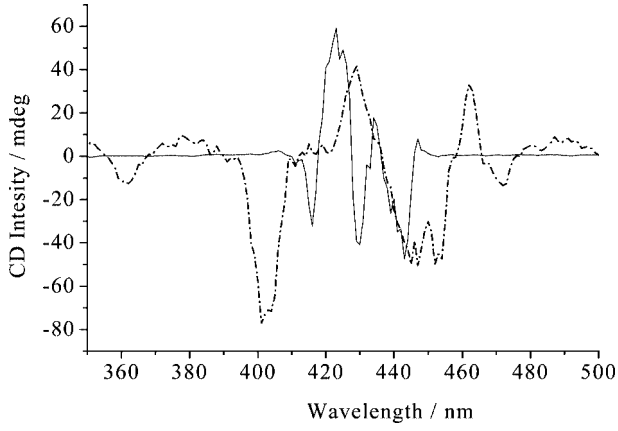


Figure 7. Circular dichroism spectra of the chiral porphyrin (solid line) ($1 \times 10^{-6}$ M) in chloroform and the SBA-15/porphyrin (dash dot line) (solid state) at 298 K.

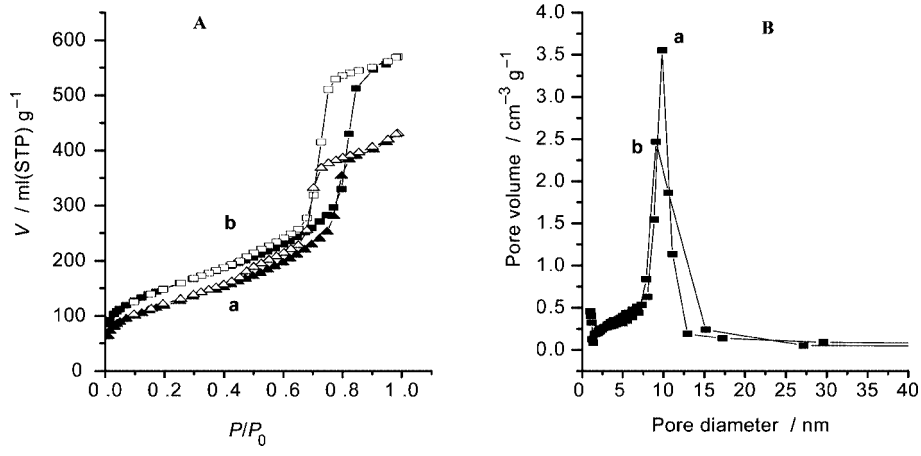


Figure 6. A: Nitrogen adsorption isotherms of pure SBA-15 (a) and SBA-15/porphyrin (b). B: Pore size distribution of the samples calculated from the adsorption branch of the isotherms using the BJH algorithm.

 © 2006 Wiley-VCH Verlag GmbH & Co. KGaA, Weinheim 

successfully incorporated into the channels of SBA-15. The great change in peak shape of the chiral porphyrin upon incorporation also demonstrates that incorporation has indeed occurred. Difference in peak shape is likely attributable to the influence of the channel of mesoporous material by interactions of porphyrins with OH groups of the SBA-15.

### Chiral Recognition

To investigate comparatively the chiral recognition of the chiral porphyrin and mesoporous composite SBA-15/porphyrin for chiral amino acids, visible spectroscopy and circular dichroism spectra were employed to study the enantioselectivity of L and D amino acids.

Figure 8 shows circular dichroism spectra of porphyrin 1 before and after linking L-BocAla. The porphyrin 1 has no spectral signal, but porphyrin 3 has a strong CD spectral signal with a split Cotton effect around its Soret band when chiral amino acid is linked with porphyrin 1 by covalent bonding. The interaction between the excited states of chromophores in unsymmetrical environments gives circular dichroism curves with split Cotton effects.[37] There is strong exciton-coupled action between the porphyrin ring and the acylamide group. Porphyrin 3 exhibits complex curves around its Soret band (Figure 8, b). According to the Tinoco law,[38] the coupling between the electric and magnetic transition moments of the acylamide group and the electric transition moments of porphyrin chromophores leads to the observed Cotton effects.[13,39]

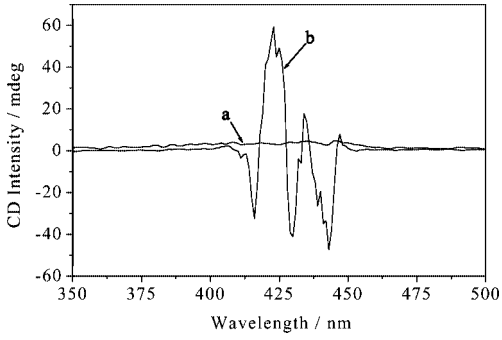


Figure 8. Circular dichroism spectra of porphyrin 1 (a) and chiral porphyrin 3 (b) ($1 \times 10^{-6}$ M).

Absorption spectra of chiral porphyrins binding with amino acid esters of varying concentrations are shown in Figure 9 and Figure 10, which suggest a stepwise binding of the chiral porphyrin with D- and L-alanine methyl ester ($AlaOCH_3$), respectively. The absorption spectral change in the Soret region shows an increase in intensity of the absorption band at 465 nm with a decrease of the absorption at 425 nm, displaying an isosbestic point at 440 nm, which indicates 1:1 complexation between the host and guest molecules. The association constant $K$ is given by Equation (1).

$$\frac{1}{A_0 - A} = \frac{1}{K \cdot a} \cdot \frac{1}{C_L} + \frac{1}{a} \quad (1)$$

where $A_0$ is the absorbance of the porphyrin 3 solution at 425 nm, $A$ is the absorbance in the presence of a guest at concentration $C_L$, and $a$ is a constant. The quantity $1/(A_0 - A)$ has a linear relation to $1/C_L$; the association constant, $K$, can be obtained from the ratio of the intercept to the slope. The results of the association constant of D- and L-$AlaOCH_3$, are $K_D$ = 9526 and $K_L$ = 3834, respectively, which are much larger than that of ZnTPP.[40,41] This is because the electronic effect is more significant than the steric repulsion between the side chain of the amino acid ester and the branch group of the porphyrin. The association constant of D-$AlaOCH_3$ is larger than that of its optical antipode. The structure of the D-enantiomer of the guest molecules can be better aligned with the chiral porphyrin. The steric repulsion between the larger groups in the porphyrin and the L-enantiomer is unfavorable for "close binding" of the host and guest. Accordingly, the association of the porphyrin with the L-guest becomes weaker and the association constant smaller than that with the D-guest.

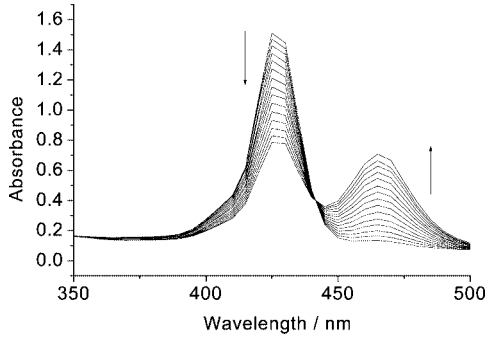


Figure 9. UV/Vis titration of the chiral porphyrin with L-$AlaOCH_3$ in chloroform at 298 K: [3] = $2 \times 10^{-6}$ M; [L-$AlaOCH_3$] = 0, 0.1, 0.2, 0.3, 0.4, 0.5, 0.6, 0.7, 0.8, 0.9, 1.0, 1.1, 1.2, 1.3, and $1.4 \times 10^{-4}$ M.

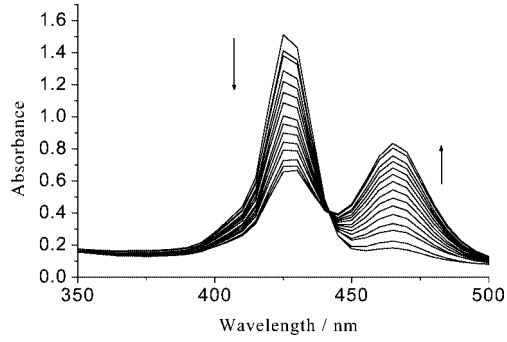


Figure 10. UV/Vis titration of chiral porphyrin with D-$AlaOCH_3$ in chloroform at 298 K: [3] = $1 \times 10^{-6}$ M; [D-$AlaOCH_3$] = 0, 0.1, 0.2, 0.3, 0.4, 0.5, 0.6, 0.7, 0.8, 0.9, 1.0, 1.1, 1.2, 1.3, and $1.4 \times 10^{-4}$ M.

The chiral porphyrin has a higher enantioselectivity in organic solutions, however, the tedious preparation, high cost, and weak stability of the porphyrin, and also the weak solubility of some amino acids in organic solutions obstruct the application of porphyrins in chiral recognition for amino acids. A good approach to circumvent this problem

 © 2006 Wiley-VCH Verlag GmbH & Co. KGaA, Weinheim 

is to incorporate porphyrins into SBA-15, facilitating the host-guest separation. To investigate the enantioselectivity of the mesoporous material SBA-15/porphyrin for chiral amino acids, a $10^{-3}$ M solution of L-alanine and D-alanine in distilled water was prepared. This solution (10 mL) of L-alanine and D-alanine was mixed with SBA-15 (5.6 mg) after incorporation of chiral porphyrin 3. While the mixture was stirred in a round-bottomed flask at room temperature, the solution was monitored by the CD technique. The changes in the CD spectra with time are shown in Figure 11 and Figure 12. Figure 11 gives the CD spectra of L-alanine with a positive response. As time passes, the response intensity of the solution of L-alanine decreases. The intensity at 30 min is half the intensity at 0 min. This indicates that L-alanine is absorbed into the channel and onto the surface of the mesoporous material.

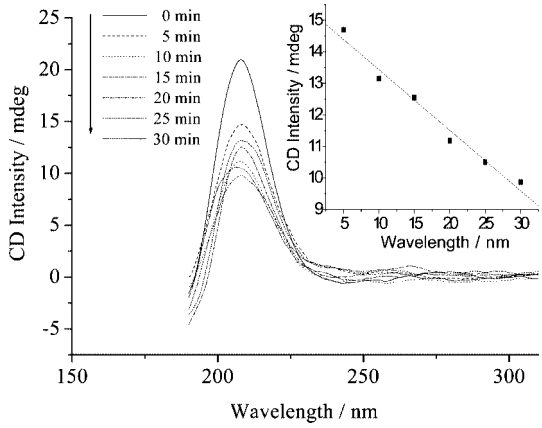


Figure 11. CD spectra of L-alanine at different times after being stirred with SBA-15/porphyrin. Inset shows the CD decrease (ΔCD) vs. time (min).

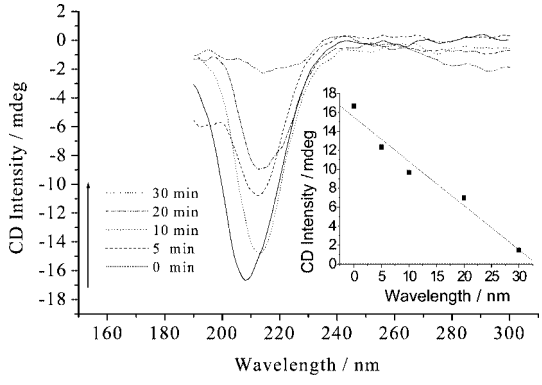


Figure 12. CD spectra of D-alanine solution at different times after being stirred with SBA-15/porphyrin. Inset shows the CD decrease (ΔCD) vs. time (min).

Comparing this with Figure 12, the CD spectra of D-alanine exhibit a negative response and a mirror image of L-alanine. The signal intensity of D-alanine also decreases with time. However, the difference is obvious compared with L-alanine in that the intensity at 30 min is very weak, nearly one ninth of that at 0 min (Figure 12). Also for the same 30 min, the changes of concentration of alanines in their liquid phase are evidently different (inset of Figure 11 and Figure 12). The linear regression parameter for L-alanine is 0.19, and –0.47 for D-alanine. All these results indicated that D-alanine couples more strongly with the mesoporous material, which is consistent with the results of the porphyrin with the amino acid ester. When the porphyrin was not incorporated into the SBA-15, the changes in the CD spectra of the alanines were the same. The observed difference is attributed to incorporation of the chiral porphyrin. The branch groups of the chiral porphyrin provide a chiral cavity for the guest molecules (small amino acids).

## Conclusions

A combination of techniques such as XRD, TEM, UV/Vis, nitrogen adsorption, and CD spectroscopy was employed to confirm that we have successfully incorporated chiral porphyrins into the interior surface of the channels of mesoporous molecular sieves SBA-15. The SBA-15 has a clear CD spectra signal after the incorporation and shows different chiral recognition abilities for small amino acids such as L- and D-alanine. The above experiments demonstrate that the D-alanine is more tightly bound to the host than its optical antipode, which is consistent with the results of porphyrins in organic solutions. The investigation provides an available model for the application of chiral recognition.

## Experimental Section

**Materials and Physical Measurements:** All reagents and solvents were of commercial reagent grade and used without further purification. Boc-alanine(BocAla) was purchased from Aldrich. The SBA-15 was synthesized according to ref.[19]

The powder diffraction of the solid materials was examined by using a Rigaku D/MAX X-ray powder diffractometer with a Cu-$K_\alpha$ X-ray source ($\lambda$ = 0.154 18 nm). Transmission electron microscopic (TEM) images were performed with a JEOL JEM2011 electron microscope operating at 200 kV. UV/Vis spectra of solutions were collected with a Perkin–Elmer Lambda 2 spectrometer. Diffuse reflectance UV/Vis spectra of solids were recorded with a Perkin–Elmer Lambda 9 spectrometer. Circular dichroism (CD) spectra were performed with a JASCO-715 spectropolarimeter equipped with a thermostat cell compartment. Nitrogen adsorption measurements at 77 K were performed with a NOVA 2000e volumetric adsorption analyzer, samples were outgassed for 6 h in the degas port of the adsorption apparatus.

**Synthesis of the Chiral Porphyrin:** The synthesis procedure for the chiral porphyrin is illustrated in Scheme 1.The synthesis was based on the following procedures: The unsymmetrically phenyl-substituted porphyrin **1** was synthesized according to an adaptation of the general Rothemund method for synthesis of *meso*-tetraphenylporphyrins.[42] *o*-Hydroxybenzaldehyde (4.9 g, 1 equiv.) and *p*-nitrobenzaldehyde (6.1 g, 3 equiv.) were added to refluxing propionic acid (300 mL). Once the aldehydes had completely dissolved, freshly distilled pyrrole (6 mL, 4 equiv.) was added within 20 min and refluxed for 1 h. The reaction mixture was then cooled and allowed to stand overnight. After diluting with distilled water (500 mL) and adjusting the pH to 6–7 with aqueous sodium hy-

 © 2006 Wiley-VCH Verlag GmbH & Co. KGaA, Weinheim 

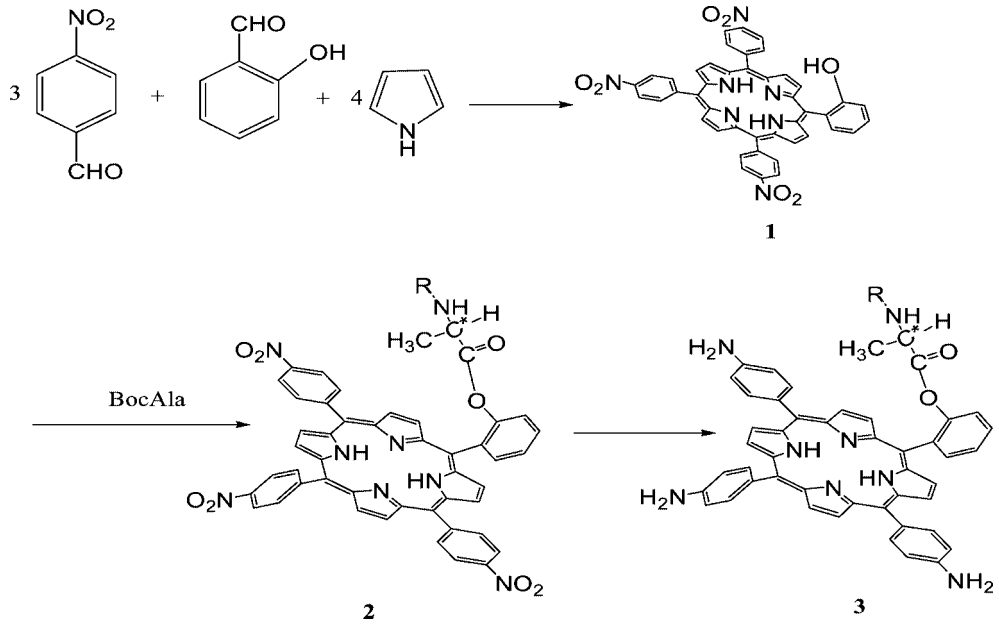


Scheme 1. Synthesis of the tailed chiral amino acid porphyrin chloroform at 298 K.

droxide (6 mol $L^{-1}$), filtration and hot water washing was performed five times. The obtained powder mixture, which was black-purple in color, was then dried in a vacuum oven at 80 °C overnight. The dried powder was extracted with chloroform until the extracts became colorless. After distilling off the solvents under a reduced pressure with a rotary evaporator, a black-purple crude product was obtained. The crude product was separated using silica gel column chromatography eluted first with dichloromethane followed by elution with a chloroform solution. The second elution was collected and the solvents evaporated to dryness, and the product was chromatographed a second time by column chromatography and then TLC. Porphyrin **1** was obtained at the end and dried in a vacuum oven at 80 °C overnight.

$C_{44}H_{27}N_7O_7$ (765.20): calcd. C 69.02, H 3.55, N 12.80; found C 68.85, H 3.50, N 12.63. Visible spectrum ($CHCl_3$): $\lambda$ = 650, 590, 550, 515, 425 nm. IR (KBr): $\tilde{\nu}$ = 3442 (–OH), 3317 (pyrrole N–H) 2921 (C–H), 2850, (–$CH_2$–), 1515, 1346 (–$NO_2$) $cm^{-1}$. MALDI-TOF-MS: *m*/*z* = 765.5 $[M + 1]^+$.

BocAla (30 mg) was dissolved in thionyl chloride (50 mL). This solution was stirred at reflux for 12 h. Thionyl chloride was then removed by distillation under reduced pressure. The crude product was redissolved in benzene (60 mL) and triethylamine (5 mL). A solution of porphyrin 1 (50 mg) in benzene (10 mL) was added. The reaction was stirred for 10 h at reflux. The mixture separated into benzene and water. The organic layer was evaporated under reduced pressure. Flash column chromatography (silica gel, dichloromethane/ethanol, 3:1) afforded 14.1 mg (23%) of pure porphyrin 2.

$C_{52}H_{40}N_8O_{10}$ (936.29): calcd. C 66.66, H 4.30, N 11.96; found C 66.57, H 4.23, N 12.01. Visible spectrum ($CHCl_3$): $\lambda$ = 650, 590, 550, 515, 425 nm. IR (KBr): $\tilde{\nu}$ = 3375 (CON–H), 3317 (pyrrole N–H), 2923 (–$CH_3$), 2852 (–$CH_2$–), 1699 (C=O) $cm^{-1}$. MALDI-TOF-MS: *m*/*z* = 937.2 $[M + 1]^+$.

Porphyrin **2** (24 mg) was dissolved in concentrated hydrochloric acid (36%, 20 mL) at room temperature, in a beaker, followed by addition of excess $SnCl_2{\cdot}2H_2O$ (100 mg). The resulting green mixture was quickly heated to 65–70 °C for 25 min, then cautiously neutralized with concentrated aqueous ammonia. Chloroform (20 mL) was added to the hot suspension and the mixture was stirred for 1 h. The chloroform layer was separated, the aqueous layer extracted several times with chloroform, and all chloroform extracts were combined and filtered. The chloroform solution was reduced in volume (10 mL) on a rotary evaporator, washed first with dilute aqueous ammonia then twice with water, dried with anhydrous sodium sulfate, and evaporated under reduced pressure. Flash column chromatography (silica gel, chloroform, the second elution) afforded 21.7 mg (89%) of pure porphyrin 3.

$C_{52}H_{46}N_8O_4$ (846.36): calcd. C 73.74, H 5.47, N 13.23; found C 73.58, H 5.39, N 13.34. Visible spectrum ($CHCl_3$): $\lambda$ = 650, 590, 550, 515, 425 nm. IR (KBr): $\tilde{\nu}$ = 3429 (N–H), 3359 (CON–H), 3216 (pyrrole N–H), 2921 (–$CH_3$), 2850 (–$CH_2$–), 1700 (C=O) $cm^{-1}$. MALDI-TOF-MS: *m*/*z* = 847.4 $[M + 1]^+$.

**Incorporation of Chiral Porphyrin into SBA-15:** SBA-15 (100 mg) was mixed with porphyrin **3** (10 mg) in a round-bottomed flask (20 mL), and then chloroform (10 mL) was added and stirred for 48 h at room temperature. The solid was filtered and washed with chloroform until no absorption of porphyrin in the UV/Vis spectrum was seen from the solution. The solid was dried at room temperature. The original white powders of SBA-15 turned jade-green after adding the chiral porphyrin, which indicated inclusion of the porphyrins into the SBA-15 frameworks.

For quantitative determination of the porphyrin incorporated into the SBA-15, a mesoporous composite SBA-15/porphyrin sample (14 mg) was dissolved in aqueous sodium hydroxide solution (8 M) to destroy the framework. Thus the porphyrin in the mesoporous composite was released. The porphyrin was extracted with chloroform (10 mL), and the solution was diluted to 1/5 its concentration with chloroform. The OD value of the porphyrin at 425 nm is 0.3141. A reference solution was made with chiral porphyrin (0.5 mg) dissolved in chloroform (100 mL) and its OD value at 425 nm was measured to be 0.5022. By comparing this with the reference, the amount of porphyrin encapsulated in SBA-15 was determined to be 11.2 mg $g^{-1}$ using Beer's law. Because there is no C element in pure SBA-15, the C elemental analysis of the mesopo-

 © 2006 Wiley-VCH Verlag GmbH & Co. KGaA, Weinheim 

rous composite was employed to obtain 0.83%. The amount of porphyrin was estimated to be 11.4 mg g$^{-1}$, which agrees with that obtained by Beer's law.

## Acknowledgments

We gratefully acknowledge the support of this research by the National Science Foundation of China (20071014, 20473033).

[1] V. Schurig, F. Betschinger, *Chem. Rev.* **1992**, *92*, 873–888.
[2] W. H. Pirkle, T. Pochapsky, *Chem. Rev.* **1989**, *89*, 347–362.
[3] J. A. Gladysz, B. T. Boone, *Angew. Chem. Int. Ed. Engl.* **1997**, *36*, 550–583.
[4] M. Almaraz, C. Raposo, M. Martin, M. C. Calallero, J. R. Moran, *J. Am. Chem. Soc.* **1998**, *120*, 3516–3517.
[5] M. Rekarsky, Y. Inoue, *J. Am. Chem. Soc.* **2000**, *122*, 4418–4435.
[6] Z. Tao, T. S. M. Wan, K. Kwang, C. Che, *Anal. Chem.* **2000**, *72*, 5383–5393.
[7] K. Yannakopoulou, D. Mentzafos, I. M. Marridis, K. Dandika, *Angew. Chem. Int. Ed. Engl.* **1996**, *35*, 2480–2482.
[8] C. D. Stevenson, D. K. Cashion, *J. Org. Chem.* **2000**, *65*, 7588–7594.
[9] W. A. Tao, D. Zhang, E. Nikolaev, R. G. Cooks, *J. Am. Chem. Soc.* **2000**, *122*, 10598–10609.
[10] B. Chankvetadze, C. Yamamoto, Y. Okamoto, *Chem. Lett.* **2000**, *10*, 1176–1177.
[11] T. Mizutani, T. Ema, T. Tomita, Y. Kuroda, H. Ogoshi, *J. Am. Chem. Soc.* **1994**, *116*, 4240–4250.
[12] Y. Kuroda, Y. Kato, T. Higashioji, J. Hasegawa, S. Kawanawi, M. Takahashi, N. Shiraishi, K. Tanabe, H. Ogoshi, *J. Am. Chem. Soc.* **1995**, *117*, 10950–10958.
[13] H. Ogoshi, T. Mizutani, *Acc. Chem. Res.* **1998**, *31*, 81–89.
[14] R. J. Abraham, P. Leighton, J. K. M. Sanders, *J. Am. Chem. Soc.* **1985**, *107*, 3472–3478.
[15] R. P. Bonar-Law, L. G. Mackay, C. J. Walter, V. Marvaud, J. K. M. Sanders, *Pure Appl. Chem.* **1994**, *66*, 803–810.
[16] J. P. Collman, Z. Wang, C. Linde, L. Fu, L. Dang, J. I. Brauman, *Chem. Commun.* **1999**, 1783–1784.
[17] a) L. Andersson, *J. Chromatogr. B* **2000**, *745*, 3–13; b) K. Mosbach, *Anal. Chim. Acta* **2001**, *435*, 3–8; c) K. Haupt, K. Mosbach, *Chem. Rev.* **2000**, *100*, 2495–2504; d) B. Sellergen, *J. Chromatogr. A* **2001**, *906*, 227–252; e) D. Kriz, O. Ramstrom, K. Mosbach, *Anal. Chem.* **1994**, *66*, 2636–2639; f) B. Sellergen, *Angew. Chem. Int. Ed.* **2000**, *39*, 1031–1037; g) H. Shi, W.-B. Tsai, M. D. Garrison, S. Ferrari, B. D. Ratner, *Nature* **1999**, *398*, 593–597; h) S. Dai, *Chem. Eur. J.* **2001**, *7*, 763–768; i) M. A. Markowitz, P. R. Kust, G. Deng, P. E. Schoen, J. S. Dordick, D. S. Clark, B. P. Gaber, *Langmuir* **2000**, *16*, 1759–1765.
[18] H. Norman, *J. Coord. Chem.* **1988**, *19*, 25–38.
[19] D. Zhao, J. Feng, Q. Huo, N. Melosh, G. H. Fredrickson, B. F. Chmelka, G. D. Stucky, *Science* **1998**, *279*, 548–552.
[20] D. Zhao, Q. Huo, J. Feng, B. F. Chmelka, G. D. Stucky, *J. Am. Chem. Soc.* **1998**, *120*, 6024–6036.
[21] D. E. D. Vos, M. Dams, B. F. Sels, P. A. Jacobs, *Chem. Rev.* **2002**, *102*, 3615–3640.
[22] P. M. Rao, A. Wolfson, S. Kababya, S. Vega, M. V. Landau, *J. Catal.* **2005**, *232*, 210–225.
[23] Y. Cao, J. Hu, P. Yang, W. Dai, K. Fan, *Chem. Commun.* **2003**, 908–909.
[24] Ch. Nozaki, C. G. Lugmair, A. T. Bell, T. D. Tilley, *J. Am. Chem. Soc.* **2002**, *124*, 13194–13203.
[25] M. S. Zhu, S. H. Zhou, M. Hibino, I. Honma, *J. Mater. Chem.* **2003**, *13*, 1115–1118.
[26] M. Alvaro, A. Corma, D. Das, V. Fornés, H. García, *Chem. Commun.* **2004**, 956–957.
[27] D. Coutinho, A. O. Acevedo, G. R. Dieckmann, K. Balkus Jr, *J. Micropor Mesopor Mat.* **2002**, *54*, 249–255.
[28] H. M. Sung-Suh, Z. Luan, L. Kevan, *J. Phys. Chem. B* **1997**, *101*, 10455–10463.
[29] V. Schünemann, A. X. Trautwein, I. M. C. M. Rietjens, M. G. Boersma, C. Veeger, D. Mandon, R. Weiss, K. Bahl, C. Colapietro, M. Piech, R. N. Austin, *Inorg. Chem.* **1999**, *38*, 4901–4905.
[30] C.-J. Liu, S.-G. Li, W.-Q. Pang, C.-M. Che, *Chem. Commun.* **1997**, 65–66.
[31] C.-J. Liu, W.-Y. Yu, S.-G. Li, C.-M. Che, *J. Org. Chem.* **1998**, *63*, 7364–7369.
[32] B. T. Holland, C. Walkup, A. Stein, *J. Phys. Chem. B* **1998**, *102*, 4301–4309.
[33] L. Zhang, T. Sun, J. Y. Ying, *Chem. Commun.* **1999**, 1103–1104.
[34] a) P. A. Leermkers, H. T. Thomas, L. D. Weis, F. C. James, *J. Am. Chem. Soc.* **1966**, *88*, 5075–5083; b) G. Scheibe, F. Feichtmayr, *J. Phys. Chem.* **1962**, *66*, 2449–2455.
[35] B. L. Newalkar, J. Olanrewaju, S. Komarneni, *Chem. Mater.* **2001**, *13*, 552–557.
[36] Z. Luan, E. M. Maes, M. A. W. Van der Heide, D. Zhao, R. S. Czernuszewicz, L. Keven, *Chem. Mater.* **1999**, *11*, 3680–3686.
[37] a) N. Haraha, K. Nakanishi, *Circular Dichroic Spectroscopy-Exciton Coupling, in: Organic Stereochemistry*; University Science Books: Mill Valley, CA, **1983**; b) K. Nakanishi and N. Berova, in: *Circular Dichroism-Principles and Applications* (Eds.: K. Nakanishi, N. Berova, R. W. Woody), VCH Publishers, New York, **1994**, p. 361.
[38] I. Tinoco, *Adv. Chem. Phys.* **1962**, *4*, 113–117.
[39] T. Mizutani, T. Ema, T. Yoshida, Y. Kuroda, H. Ogoshi, *Inorg. Chem.* **1993**, *32*, 2072–2077.
[40] K. Anzai, T. Hosokawa, K. Hatano, *Chem. Pharm. Bull.* **1986**, *34*, 1865–1870.
[41] Y. Li, W. J. Ruan, C. Z. Wang, Z. A. Zhu, R. Chen, F. M. Miao, X. Wen, *Acta Scientiarum Naturalium Universtatis Nankaiensis* **1999**, *32*, 123–129.
[42] L. R. Milgrom, *J. Chem. Soc., Perkin Trans. 1* **1984**, 1483–1487.

Received: May 11, 2006
Published Online: September 7, 2006

 © 2006 Wiley-VCH Verlag GmbH & Co. KGaA, Weinheim 

DOI: 10.1002/ejic.200600489

# Reactions of Trimethylphosphane-Supported Cobalt Complexes with Salicylaldimines – Formation and Structures of Cobalt Compounds Containing Salicylaldiminato [*N*:*O*] Ligands

**Xiaoyan Li,*[a] Fengli Yu,[a] Hongjian Sun,[a] Liye Huang,[a] and Haoqing Hou[b]**

**Keywords:** Cobalt / Salicylaldimines / Trimethylphosphane / Imines

The reactions of low-valent cobalt complexes $CoMe(PMe_3)_4$, $CoCl(PMe_3)_3$ and $Co(PMe_3)_4$ with salicylaldimines are described to give tetrahedral complexes **7**–**12**, an octahedral complex **13** and a π-coordinated imine complex **15**. The crystal structures of **13** and **15** are reported. The formation and likely mechanisms are discussed.
(© Wiley-VCH Verlag GmbH & Co. KGaA, 69451 Weinheim, Germany, 2006)

## Introduction

At present, there is increasing interest in N-containing chelate ligands forming metallacyclic compounds.[1–6] Large numbers of complexes of transition metals with Schiff bases, which are used as agents in organic synthesis, catalysts and anticancer or antitoxin drugs, have been synthesized and studied in many laboratories.[7–12] Recent progress has been made in the study of Schiff base–Co(II) complexes as dioxygen carriers. These reports have considerable significance in chemical and biochemical processes.[13–15]

Chelate-assisted oxidative addition is a reaction of potential utility for the selective activation of organic functional groups.[16–18] 2-Phosphanylacyl ligands or 2-phosphanylphenol groups containing weakly acidic protons react with metal halides to afford metal hydrides with the oxidative addition of an O–H or C–H bond at the metal centre.[19] According to Equation (1), acylcobalt(III) hydrides are obtained by the reaction of halogenotris(trimethylphosphane)-cobalt(I) complexes with 2-diphenylphosphanylbenzaldehyde.[20] There is increasing interest in this process, since it is generally accepted that acyl hydride intermediates are involved in certain metal-catalyzed carbonylation[21] and decarbonylation processes.[22]

Recently, we have introduced the salicylaldimine ligands, which are isoelectronic to 2-diphenylphosphanylbenzaldehyde. We now report the reactions of electron-rich, low-valent cobalt complexes $CoMe(PMe_3)_4$, $CoCl(PMe_3)_3$ and $Co(PMe_3)_4$ with salicylaldimines, which have afforded tetrahedral bis(chelate) cobalt(II) imine complexes (**7**–**12**), an octahedral tris(chelate) cobalt(III) imine complex **13** as well as a π-coordinate imine complex **15**, which includes trimethylphosphane as a supporting ligand. The neighbouring N-donor of the salicylaldimine ligand plays an active part in the formation of these complexes . The molecular structures of **13** and **15** were determined by X-ray diffraction. Possible formation routes are proposed.

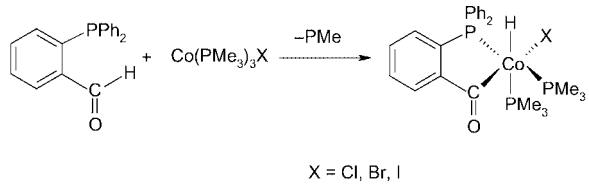


X = Cl, Br, I (1)

## Results and Discussion

### 1. Reactions of $CoMe(PMe_3)_4$ with Salicylaldimines

The reaction between $CoMe(PMe_3)_4$ and salicylaldimines **1**–**4** liberated methane and utilized both the phenolato and N-donor functions to form the paramagnetic cobalt(II) complexes **7**–**10**, which include two salicylaldiminato[*N*:*O*] chelating ligands. The reaction occurs by a disproportionation route, with the concomitant production of tetrakis(trimethylphosphane)cobalt(0) (Scheme 1, route a). Analogous reactions, e.g., leading to a five-membered metallacycle (route b), did not occur, and the corresponding iminoacyl(hydrido)cobalt(III) species was not detected among the products.

In the infrared spectra of complexes **7**–**10**, the characteristic ν(C=N) bands are found between 1600 and 1634 $cm^{-1}$. Complex **10** has pseudo-tetrahedral geometry; the crystal structure of this complex was reported in our previous work.[23]

[a] School of Chemistry and Chemical Engineering, Shandong University,
Shanda Nanlu 27, 250100 Jinan, PR China
Fax: +86-531-88564464
E-mail: xli63@sdu.edu.cn
[b] College of Chemistry and Chemical Engineering, Jiangxi Normal University,
Beijing Xilu 437, 330027 Nanchang, PR China

 InterScience © 2006 Wiley-VCH Verlag GmbH & Co. KGaA, Weinheim 

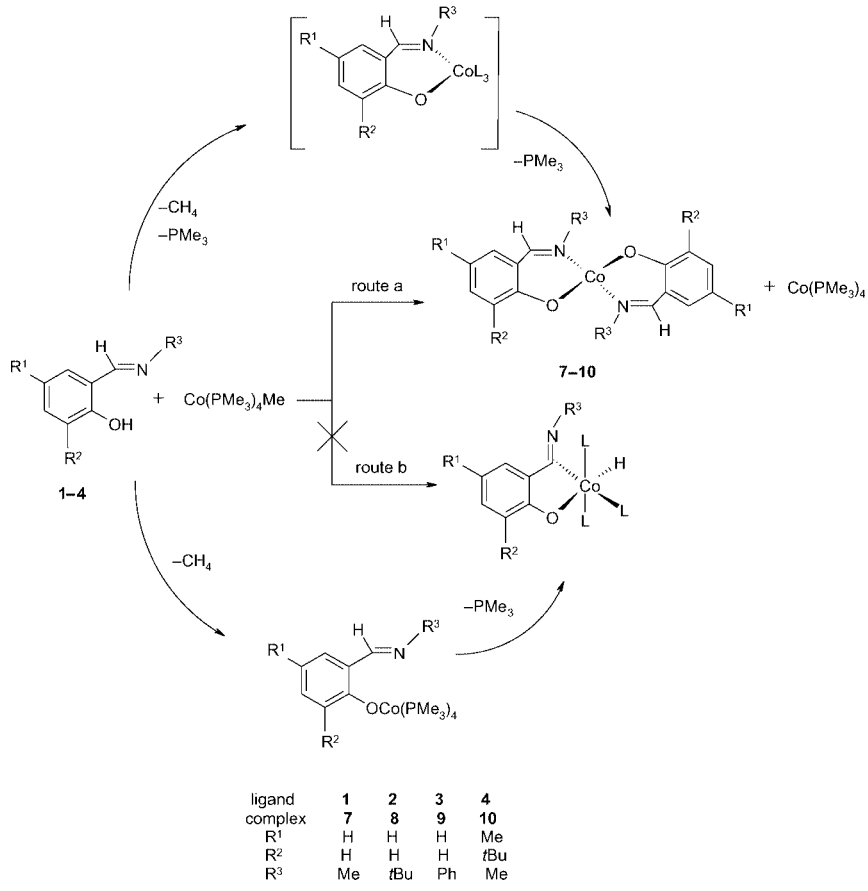


| ligand | 1 | 2 | 3 | 4 |
|---|---|---|---|---|
| complex | 7 | 8 | 9 | 10 |
| $R^1$ | H | H | H | Me |
| $R^2$ | H | H | H | *t*Bu |
| $R^3$ | Me | *t*Bu | Ph | Me |

Scheme 1.

An oxidative addition of salicylaldimine iminoacyl C–H bonds did not occur upon reaction with methyltetrakis(trimethylphosphane)cobalt(I) (Scheme 1, route b). It appears that the preferred coordination of the N-donor prevents the attack of cobalt at the C–H bond. This assumption would also explain the scarcity of iminoacyl metal complexes arising from C–H activation.[24,25]

## 2. Reactions of $CoCl(PMe_3)_3$ with Salicylaldimines

Chloridotris(trimethylphosphane)cobalt(I) reacts with salicylaldimines **3**–**5** to afford the cobalt(II) complexes **9**–**11**, which include two salicylaldiminato[*N:O*] ligands, together with tetrakis(trimethylphosphane)cobalt(0) (Scheme 2). A cobalt hydride is suggested as a plausible intermediate. This unstable species undergoes a reductive elimination reaction liberating hydrogen chloride and giving rise to a reactive cobalt(I) complex, which disproportionates to afford complexes **9**–**11** and tetrakis(trimethylphosphane)cobalt(0).

3-methoxy-*N*-methylsalicylaldimine [ligand **6**, Equation (2)] reacts with chloridotris(trimethylphosphane)cobalt(I) to afford not only the cobalt(II) complex **12** containing salicylaldiminato[*N:O*] ligands but also the cobalt(III) complex **13** containing three salicylaldiminato[*N:O*] ligands [Equation (2)]. To the best of our knowledge, complex **13** is the first cobalt(III) complex with three Schiff base anions.

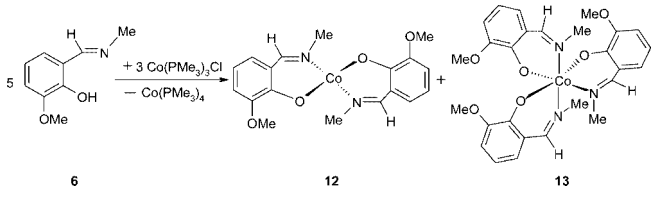


(2)

The $^1$H NMR spectrum of complex **13** shows a resonance at $\delta$ = 7.72 ppm clearly representing the protons of the imino groups. Protons of the benzene rings lie in the range 6.39–6.80 ppm. The $CH_3O$ protons are found at $\delta$ = 3.75 ppm, and the $CH_3N$ protons of are located at $\delta$ = 3.55 ppm. In the $^{13}$C NMR spectrum, resonances at 164.9–166.5 ppm are assigned to the imino carbon atoms. The $CH_3O$ and $CH_3N$ carbon atoms are situated at $\delta$ = 48.0 and 56.0 ppm, respectively. As only the NMR resonances of a single aldimine ligand are observed, the spectra suggest that **13** undergoes a rapid ligand exchange process in $CDCl_3$ solution. It is insoluble in pentane and diethyl ether. Crys-

 © 2006 Wiley-VCH Verlag GmbH & Co. KGaA, Weinheim 

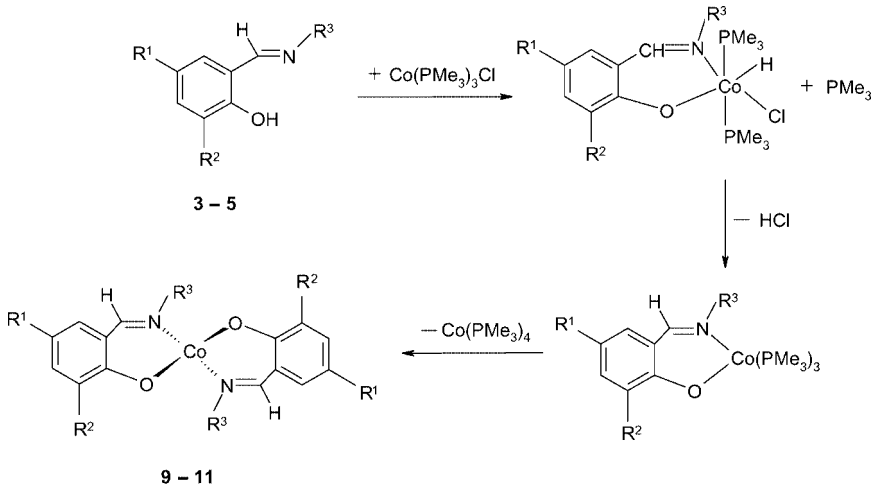


Scheme 2.

tals of **13** were obtained from THF and were analysed by X-ray diffraction. The structure of **13** is shown in Figure 1.

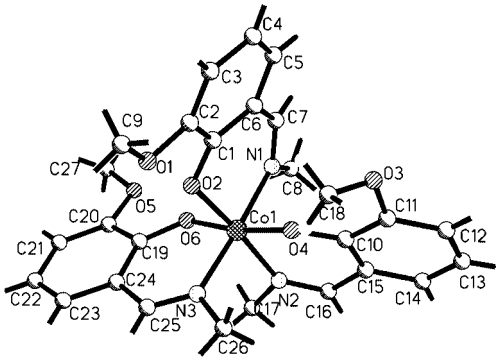

Figure 1. Molecular structure of **13**; selected distances [Å] and angles [°]: Co1–O4 1.883(3), Co1–O6 1.892(3), Co1–O2 1.900(3), Co1–N3 1.935(4), Co1–N2 1.947(3), Co1–N1 1.948(4), N1–C7 1.277(6), N1–C8 1.457(6), N2–C16 1.260(6), N2–C17 1.469(6), N3–C25 1.290(7); O4–Co1–O6 172.33(15), O6–Co1–N3 93.80(16), O4–Co1–N2 92.50(14), O2–Co1–N2 174.11(15), O2–Co1–N1 91.93(15), N3–Co1–N1 176.79(15).

The cobalt atom occupies the central position in an octahedral geometry. Three equivalent salicylaldimine ligands have Co–O and Co–N bond lengths of Co1–O2 1.900(3), Co1–O4 1.883(3), Co1–O6 1.892(3), Co1–N1 1.948(4), Co1–N2 1.947(3), Co1–N3 1.935(4) Å, respectively. Average Co–O and Co–N bond lengths are 1.892 and 1.943 Å, respectively. Complex **13** is a chiral molecule with a meridional configuration. There are two pairs of enantiomers in every crystal cell.

The formation of the cobalt(II) complex **12** is similar to that of complexes **9**–**11** in Scheme 2. A proposed mechanism for the generation of cobalt(III) complex **13** via a cobalt hydride intermediate is illustrated in Scheme 3. The hydridocobalt(III) intermediate, initially formed by oxidative addition of an imino C–H group, reacts with two molecules of Schiff base to afford the cobalt(III) complex **13** with concomitant elimination of hydrogen and hydrogen chloride.

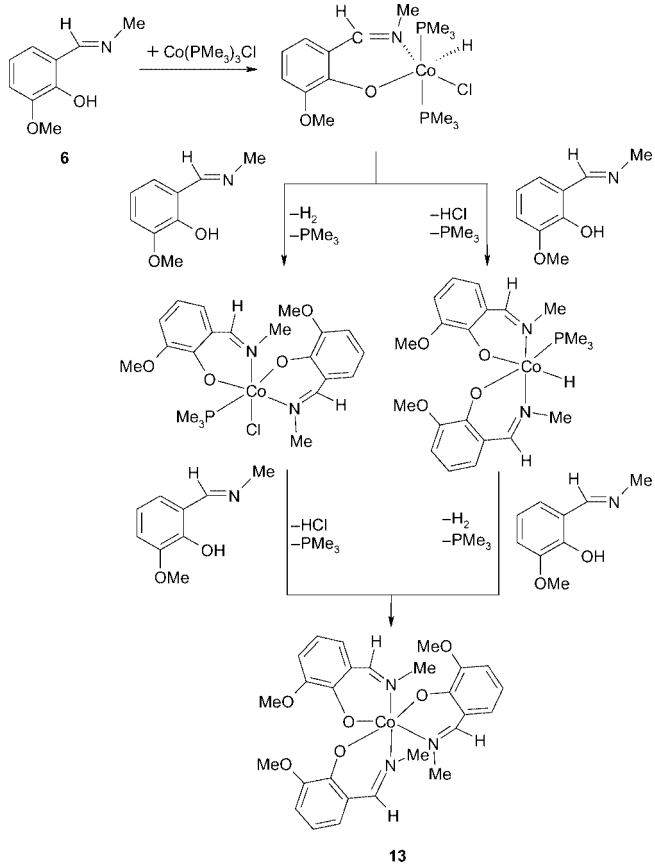


Scheme 3.

 © 2006 Wiley-VCH Verlag GmbH & Co. KGaA, Weinheim 

The formation of complexes **12** and **13** is a competitive process. The stability of the intermediate hydride complex is advantageous for the formation of complex **13**. In Scheme 2, the steric hindrance of groups $R^1$, $R^2$ and $R^3$ and the electronegativities of the substituents have an effect on the stability of the hydride intermediate and therefore on the relative proportions of complexes **12** and **13**. The details of this dependence are not clear and should be further studied with a greater selection of ligands.

### 3. Reactions of $Co(PMe_3)_4$ with Salicylaldimines

Reaction of tetrakis(trimethylphosphane)cobalt(0) with 3-*tert*-butyl-*N*,5-dimethylsalicylaldimine (ligand **4**) should afford a cobalt(II) hydride complex **14** if oxidative addition of the phenolic hydoxy group at the cobalt centre prevails (Scheme 4, route a). However, in the experiment two products were obtained, i.e., the cobalt(II) complex **10** and the π-imine cobalt(II) complex **15**.

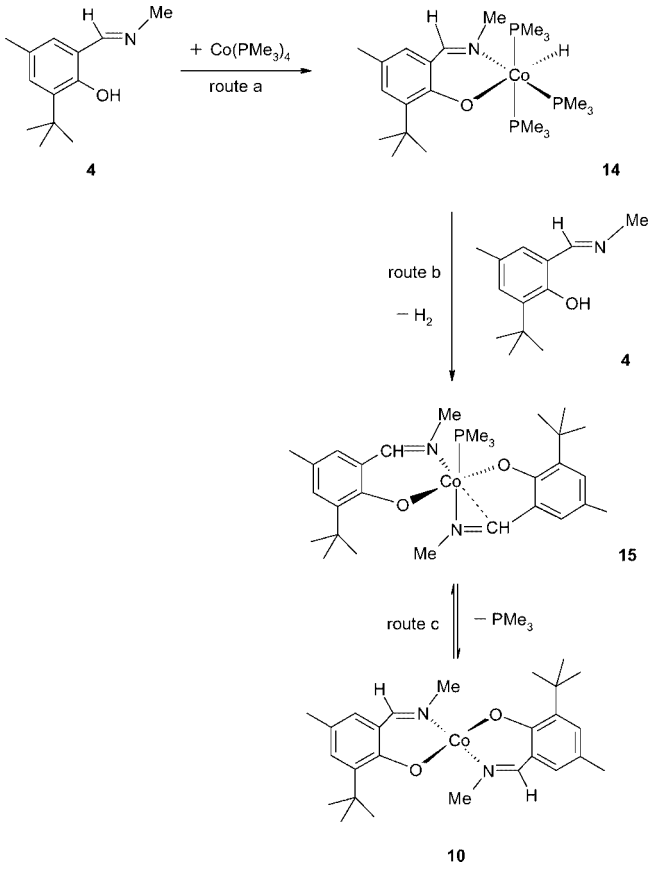


Scheme 4.

The proposed mechanism through an intermediate cobalt(II) hydride complex **14** is illustrated in Scheme 4. The Co–H bond of the reactive hydrido cobalt(II) complex **14** reacts with a phenolic OH group of a further salicylaldimine. Meanwhile, the C=N donor of salicylaldimine π-coordinates to the cobalt atom affording **15** with the elimination of $H_2$ (Scheme 4, route **b**). Dissociation of trimethylphosphane from **15** affords the cobalt(II) complex **10** (Scheme 4, route **c**). We propose that the presence of a trimethylphosphane ligand in complex **15** results from π-imine coordination at the cobalt centre, which competes with the usual N-coordination. In the presence of trimethylphosphane, the interconversion of complexes **15** and **10** is a reversible process.

Yellow crystals of **15** were obtained from pentane at 0 °C. A view of the molecular structure of crystal **15** is given in Figure 2. The cobalt atom occupies the central position of a square plane in a pseudo-square-pyramidal configuration with P1 in the apical position. Two salicylaldimine ligands lie in the square plane with out-of-plane distortion of the π-coordinated C=N bond. The distance between Co1 and C25 [1.929(5) Å] is shorter than that between Co1 and N2 [1.980(4) Å]. Few reports on π-imine compounds of cobalt(II) have appeared.[26]

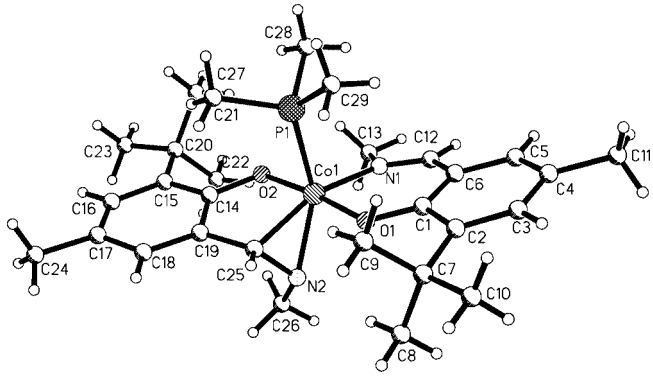


Figure 2. Molecular structure of **15**; selected distances [Å] and angles [°]: Co1–O1 1.918(3), Co1–O2 1.923(3), Co1–C25 1.929(5), Co1–N2 1.980(4), Co1–N1 1.992(4), Co1–P1 2.1954(13); O1–Co1–O2 174.93(13), O1–Co1–C25 89.84(16), O2–Co1–C25 85.28(16), O1–Co1–N2 84.78(15), O2–Co1–N2 90.70(14), C25–Co1–N2 43.15(17), O1–Co1–N1 91.73(14), C25–Co1–N1 156.72(18), N2–Co1–N1 113.91(16), O1–Co1–P1 94.88(10), O2–Co1–P1 87.76(10), C25–Co1–P1 105.46(15), N2–Co1–P1 148.55(13), N1–Co1–P1 97.54(12).

## Conclusions

Methyltetrakis(trimethylphosphane)cobalt(I) and chloridotris(trimethylphosphane)cobalt(I) react with salicylaldimines to form cobalt(II) complexes **7**–**12** which bond to both the phenolato and N-donor functions of two salicylaldiminato[*N*:*O*] ligands. The reaction involves the liberation of methane or hydrochloric acid and subsequent disproportionation to give complexes **7**–**12** and tetrakis(trimethylphosphane)cobalt(0). Steric hindrance and the electronegativities of substituents in the ligands influence the ratio of products in the reaction between chloridotris(trimethylphosphane)cobalt(I) and salicylaldimines. 3-methoxy-*N*-methylsalicylaldimine reacts with chloridotris(trimethylphosphane)cobalt(I) to afford not only cobalt(II) complex **12**, which includes two salicylaldiminato[*N*:*O*] li-

 © 2006 Wiley-VCH Verlag GmbH & Co. KGaA, Weinheim 

gands, but also the cobalt(III) complex **13**, which includes three salicylaldiminato[*N:O*] ligands. Tetrakis(trimethylphosphane)cobalt(0) reacts with salicylaldimine to afford the π-imine cobalt(II) complex **15** and the cobalt(II) complex **10** through a possible cobalt hydride intermediate. However, a chelate-assisted oxidative addition of the OC–H bond, that has been shown to proceed with 2-donor substituted benzaldehydes in complexes of low-valent cobalt,[27] could not be observed for the NC–H group of salicylaldimines under otherwise similar conditions. Such a reaction is probably suppressed by the greater stability of the N-coordination in comparison to an O-coordination in the six-membered cobaltacycle.

## Experimental Section

**General Procedures and Materials:** Standard vacuum techniques were used in manipulations of volatile and air-sensitive materials. Microanalyses: Elemental analysis (C, H and N) was carried out at Shandong University by using a Vario ELIII elemental analyzer. Melting points/decomposition temperatures were determined by using sealed capillaries, uncorrected values are reported. Literature methods were used in the preparation of methyltetrakis(trimethylphosphane)cobalt(I), tetrakis(trimethylphosphane)cobalt(0)[28] and chloridotris(trimethylphosphane)cobalt(I).[29] Salicylaldimines were obtained by the condensation of salicylaldehyde or substituted salicylaldehydes with amines. Other chemicals were used as purchased. All solvents were dehydrated and degassed before use. IR samples were prepared as Nujol mulls and placed between KBr discs; samples were analyzed with a Bruker spectrophotometer of type VECTOR 22. $^1$H NMR spectra were recorded with a Bruker AV 400 MHz spectrometer. X-ray crystallography was performed with a Bruker Smart 1000 diffractometer.

**Bis(*N*-methylsalicylaldiminato)cobalt(II) (7):** Methyltetrakis(trimethylphosphane)cobalt(I) (1.82 g, 4.81 mmol) was dissolved in pentane (50 mL). *N*-Methylsalicylaldimine (0.65 g, 4.81 mmol) in pentane (10 mL) was then added to this solution. The resulting solution was stirred at ambient temperature for 17 h. During this period the solution turned orange, indicating that a reaction had occurred. The mixture was then filtered. The filtrate afforded red crystals of complex **7** (0.57 g, 36.5%). M.p. 165.2–170.5 °C. $C_{16}H_{14}CoN_2O_2$ (325.23): calcd. C 5.91, H 4.34, N 8.61; found C 5.82, H 4.24, N 8.64. IR (Nujol): 1634 s ν(C=N) cm$^{-1}$.

**Bis(*N*-*tert*-butylsalicylaldiminato)cobalt(II) (8):** Methyltetrakis(trimethylphosphane)cobalt(I) (1.0 g, 2.65 mmol) was dissolved in pentane (50 mL). *N*-*tert*-Butylsalicylaldimine (0.47 g, 2.66 mmol) dissolved in pentane (10 mL) was then added to this solution. After being stirred for 18 h at 20 °C, the red-brown mixture was filtered. The filtrate that was stored at –20 °C afforded red microcrystals of complex **8** (0.17 g, 41%). M.p. 208.7–212.5 °C. $C_{22}H_{28}CoN_2O_2$ (411.40): calcd. C 64.23, H 6.86, N 6.81; found C 64.20, H 6.81, N 6.78. IR (Nujol): 1600 (s) ν(C=N) cm$^{-1}$.

**Bis(*N*-phenylsalicylaldiminato)cobalt(II) (9): Method a:** Methyltetrakis(trimethylphosphane)cobalt(I) (0.68 g, 1.80 mmol) was dissolved in pentane (50 mL). *N*-Phenylsalicylaldimine (0.35 g, 1.80 mmol) dissolved in pentane (10 mL) was then added to this solution. The resulting solution was stirred at ambient temperature for 18 h. During this period the reaction solution turned coffee brown. After filtration, the precipitate was recrystallized from diethyl ether at 4 °C to afford red-brown crystals of complex **9** (0.25 g, 31%). **Method b:** *N*-Phenylsalicylaldimine (1.17 g, 5.94 mmol) in diethyl ether (10 mL) was combined with chloridotris(trimethylphosphane)cobalt(I) (1.92 g, 5.95 mmol) in diethyl ether (50 mL) at room temperature. The mixture was stirred for 18 h, during which time a brown-yellow solution formed. The solution was filtered. The filtrate at –27 °C gave red crystals of complex **9** (0.23 g, 17.2%). M.p. 152–155.4 °C. $C_{26}H_{20}CoN_2O_2$ (451.38): calcd. C 69.1, H 4.47, N 6.21; found C 69.08, H 4.52, N 6.31. IR (Nujol): 1604 ν(C=N), 1582 ν(C=C) cm$^{-1}$.

**Bis(3-*tert*-butyl-*N*,5-dimethylsalicylaldiminato)cobalt(II) (10): Method a:** See ref.[23] **Method b:** A solution of 3-*tert*-butyl-*N*,5-dimethylsalicylaldimine (0.67 g, 3.27 mmol) in diethyl ether (10 mL) was added to a stirred solution of chloridotris(trimethylphosphane)cobalt(I) (1.05 g, 3.26 mmol) in diethyl ether (50 mL) at –80 °C. After being warmed up, the mixture was stirred for 18 h at 20 °C. The turbid yellow-brown solution was filtered. The solid residue was then extracted with diethyl ether. The filtrate and ether extracts were combined and kept at 0 °C to afford red crystals **10** (0.16 g, 21%). **Method c:** 3-*tert*-Butyl-*N*,5-dimethylsalicylaldimine (0.90 g, 4.39 mmol) in pentane (10 mL) was combined with tetrakis(trimethylphosphane)cobalt(0) (0.80 g, 2.20 mmol) in pentane (50 mL) at –80 °C. After being warmed up, the mixture was kept stirring for 18 h at 20 °C, during which time a brown-yellow solution formed. The solution was filtered, and the filtrate afforded red crystals of complex **10** (0.20 g, 39%) and yellow crystals of complex **15** (0.27 g, 45%) at 4 °C, respectively, which were separated manually. Crystals of **10**: dec.>159 °C. $C_{26}H_{36}CoN_2O_2$ (467.5): calcd. C 56.6, H 9.44, N 3.15; found C 56.5, H 9.49, N 3.24. IR (Nujol): 1615 ν(C=N), 1538 ν(C=C) cm$^{-1}$.

**Bis(3-methoxy-*N*-phenylsalicylaldiminato)cobalt(II) (11):** 3-methoxy-*N*-phenylsalicylaldimine (1.30 g, 5.73 mmol) in diethyl ether (10 mL) was combined with chloridotris(trimethylphosphane)cobalt(I) (0.62 g, 1.92 mmol) in diethyl ether (50 mL) at room temperature. The mixture was stirred for 18 h, during which time a brown-yellow solution formed. The solution was filtered, and the solid residue was recrystallized from THF at –27 °C affording red crystals of complex **11** (0.13 g, 27%). M.p. ≈ 250 °C (dec.). $C_{28}H_{24}CoN_2O_4$ (511.43): calcd. C 65.76, H 4.73, N 5.48; found C 65.59, H 4.78, N 5.36. IR (Nujol): 1604 ν(C=N), 1582 ν(C=C) cm$^{-1}$.

**Bis(3-methoxy-*N*-methylsalicylaldiminato)cobalt(II) (12) and Tris(3-methoxy-*N*-methylsalicylaldiminato)cobalt(III) (13):** A solution of 3-methoxy-*N*-methylsalicylaldimine (1.25 g, 7.58 mmol) in diethyl ether (10 mL) was added to a stirred solution of chloridotris(trimethylphosphane)cobalt(I) (0.80 g, 2.48 mmol) in diethyl ether (50 mL) at room temperature. After stirring for 18 h, a brown-yellow turbid solution was obtained. The suspension was filtered, and the filtrate was stored at –27 °C to give red crystals of complex **12** (0.06 g, 19%). The solid residue was recrystallized from THF at –27 °C to afford dark green crystals of **13** (0.10 g, 20%). Crystals of **12**: m.p. >250 °C. $C_{18}H_{20}CoN_2O_4$ (387.29): calcd. C 55.82, H 5.20, N 7.23; found C 55.66, H 5.27, N 7.20. IR (Nujol): $\tilde{\nu}$ = 1616 ν(C=N); 1599, 1543 ν(C=C) cm$^{-1}$. Crystals of **13**: m.p. dec.>140 °C. $C_{29}H_{34}CoN_3O_{6.5}$ (587.52): calcd. C 59.32, H 5.83, N 7.15; found C 59.34, H 5.79, N 7.22. IR (Nujol): $\tilde{\nu}$ = 1633 ν(C=N); 1597, 1546 ν(C=C) cm$^{-1}$. $^1$H NMR (300 MHz, $CDCl_3$, 298 K): $\delta$ = 3.55 (s, 3 H, $NCH_3$), 3.75 (s, 3 H, $OCH_3$), 6.39, 6.64, 6.80 (3 H, CH), 7.72 (s, 1 H, N=CH) ppm. $^{13}$C NMR (100 MHz, $CDCl_3$, 298 K): $\delta$ = 47.715, 48.381 (s, $NCH_3$), 56.354, 56.678 (s, $OCH_3$), 112.7, 115.4, 116.4, 116.9, 123.3, 124.9, 125.4, 125.5 (s, CH), 153.3, 153.8, 155.5 (s, C–O), 164.9, 166.5 (s, C=N) ppm.

 © 2006 Wiley-VCH Verlag GmbH & Co. KGaA, Weinheim 

**[η²(*N*,*C*)-(3-*tert*-Butyl-*N*,5-dimethylsalicylaldiminato)](3-*tert*-butyl-*N*,5-dimethylsalicylaldiminato)(trimethylphosphane)cobalt(II) (15):** 3-*tert*-Butyl-*N*,5-dimethylsalicylaldimine (0.90 g, 4.39 mmol) in pentane (10 mL) was combined with tetrakis(trimethylphosphane) cobalt(0) (0.80 g, 2.20 mmol) in pentane (50 mL) at –80 °C. After being warmed up, the mixture was stirred for 18 h, during which time a turbid brown-yellow solution formed. The suspension was filtered, and the filtrate was stored at 4 °C to give red crystals of complex **8** (0.20 g, 38.8%) and yellow crystals of complex **15** (0.27 g, 45.0%), respectively, which were separated manually. Crystals of **15**: m.p. 225.7–228.5 °C (dec.). $C_{29}H_{45}CoN_2O_2P$ (543.57): calcd. C 64.08, H 8.34, N 5.15; found C 64.02, H 8.30, N 5.21. IR (Nujol): 1624 (C=N), 1540 (C=C) $cm^{-1}$.

**X-ray Diffraction:** Crystals of complexes **13** and **15** suitable for X-ray diffraction analysis were grown from THF and pentane at 6 °C. The molecular structures are shown in Figure 1 and Figure 2, respectively, and related crystallographic data are included in Table 1. The structures were solved by direct methods and refined with full-matrix least-squares on all $F^2$ (SHELXL-97) with non-hydrogen atoms anisotropically.

Table 1. Crystallographic data of complexes **13** and **15**.

| | **13** | **15** |
|---|---|---|
| Formula | $C_{29}H_{34}CoN_3O_{6.5}$ | $C_{29}H_{45}CoN_2O_2P$ |
| $M_r$ [g/mol] | 587.52 | 543.57 |
| Colour | dark green | yellow |
| Crystal system | orthorhombic | monoclinic |
| Space group | *Pna*2(1) | *P*2(1)/*c* |
| *a* [Å] | 13.7090(16) | 8.6517(10) |
| *b* [Å] | 11.2224(13) | 48.670(6) |
| *c* [Å] | 19.773(2) | 7.7008(9) |
| *β* [°] | 90 | 107.281(2) |
| *V* [Å³] | 3042.0(6) | 3096.3(6) |
| *Z* | 4 | 4 |
| $\rho_{calcd.}$ [g cm$^{-3}$] | 1.283 | 1.168 |
| $\mu$ [mm$^{-1}$] | 0.609 | 0.631 |
| Scan range [°] | $2.06 \le \theta \le 26.21$ | $0.84 \le \theta \le 25.00$ |
| | $-17 \le h \le 15$ | $-8 \le h \le 10$ |
| | $-11 \le k \le 13$ | $-57 \le k \le 57$ |
| | $-24 \le l \le 23$ | $-9 \le l \le 8$ |
| Reflections collected | 16088 | 15559 |
| $R_{int}$ | 0.0369 | 0.0421 |
| Independent reflections | 6025 | 5456 |
| Data/restraints/parameters | 6025/6/385 | 5456/54/335 |
| Goodness-of-fit on $F_2$ | 1.090 | 1.178 |
| Final *R* indices [$I > 2\sigma(I)$] | $R_1 = 0.0512$ | $R_1 = 0.0668$ |
| | $wR_2 = 0.1359$ | $wR_2 = 0.1291$ |
| *R* indices (all data) | $R_1 = 0.0765$ | $R_1 = 0.0874$ |
| | $wR_2 = 0.1544$ | $wR_2 = 0.1373$ |

CCDC-607934 and CCDC-607935 for **13** and **15** contain the supplementary crystallographic data for this paper. These data can be obtained free of charge from The Cambridge Crystallographic Data Centre via www.ccdc.cam.ac.uk/data_request/cif.

## Acknowledgments

We gratefully acknowledge support by NSFC No. 20572062, 20372042, the Excellent Young Teachers Program of MOE and the 973 Program No. 2004CCA04700.

[1] A. Togni, L. M. Venanzi, *Angew. Chem. Int. Ed. Engl.* **1994**, *33*, 497.
[2] C. M. Thomas, B. Therrien, A. Neels, H. Stoeckli-Evans, G. Suess-Fink, *J. Organomet. Chem.* **2002**, *658*, 251.
[3] Y. J. Park, B.-I. Kwon, J.-A. Ahn, H. Lee, C.-H. Jun, *J. Am. Chem. Soc.* **2004**, *126*, 13892.
[4] C.-H. Jun, D.-Y. Lee, Y.-H. Kim, H. Lee, *Organometallics* **2001**, *20*, 2928.
[5] H.-F. Klein, S. Camadanli, R. Beck, D. Leukel, U. Floerke, *Angew. Chem. Int. Ed.* **2005**, *44*, 975.
[6] H.-F. Klein, R. Beck, U. Floerke, H.-J. Haupt, *Eur. J. Inorg. Chem.* **2003**, 240.
[7] V. G. Gnanasoundari, K. Natarajan, *Transition Met. Chem.* **2004**, *29*, 511.
[8] H.-F. Klein, A. Bickelhaupt, *Inorg. Chim. Acta* **1996**, *248*, 111.
[9] E. Eyhan, A. Karakas, H. Unver, *Chem. Phys.* **2005**, *309*, 251.
[10] B. Clarke, N. Clarke, D. Cunningham, T. Higgins, P. McArdle, M. N. Cholchuin, M. O'Gara, *J. Organomet. Chem.* **1998**, *559*, 55.
[11] T. Nagata, *Angew. Chem. Int. Ed. Engl.* **1995**, *34*, 2145–2147.
[12] T. Yamada, T. Nagata, D. S. Kiyoaki, K. Yorozu, T. Ikeno, Y. Ohtsuka, D. Miyazaki, *Chem. Eur. J.* **2003**, *9*, 4485–4509.
[13] W. Zeng, J. Zh. Li, Zh. H. Mao, Zh. Hong, Sh. Y. Qin, *Adv. Synth. Catal.* **2004**, *346*, 1385.
[14] X. X. Lu, Sh. Y. Qin, Zh. Y. Zhou, V. W.-W. Yam, *Inorg. Chim. Acta* **2003**, *346*, 49.
[15] H. K. Kervinen, M. Korpi, T. R. Leskelä, *J. Mol. Catal. (A)* **2003**, *203*, 9–19.
[16] J. K. Stille, K. S. Y. Lau, *Acc. Chem. Res.* **1977**, *10*, 434.
[17] J. W. J. Suggs, *J. Am. Chem. Soc.* **1979**, *101*, 489.
[18] T. B. Rauchfuss, *J. Am. Chem. Soc.* **1979**, *101*, 1045.
[19] E. F. Landvatter, T. B. Rauchfuss, *Organometallics* **1982**, *1*, 506–513.
[20] H.-F. Klein, U. Lemke, M. Lemke, A. Brand, *Organometallics* **1998**, *17*, 4196–4201.
[21] G. W. Parshall, S. D. Ittel, *Homogeneous Catalysis*, 2nd ed., Wiley, New York, **1992**, p. 109.
[22] D. H. Doughty, L. H. Pignolet, *J. Am. Chem. Soc.* **1978**, *100*, 7083.
[23] X. Li, L. Huang, S. Dong, M. Li, H. Sun, *Acta Crystallogr., Sect. E: Struct. Rep. Online* **2005**, *61*, m465.
[24] H.-F. Klein, R. Beck, U. Flörke, H.-J. Haupt, *Eur. J. Inorg. Chem.* **2002**, 3305.
[25] J. Ko, W. C. Joo, Y. K. Kong, *Bull. Kor. Chem. Soc.* **1986**, *7*, 338–341.
[26] F. L. Yu, X. Y. Xiao, H. J. Sun, *Z. Anorg. Allg. Chem.* **2006**, *632*, 501–504.
[27] H.-F. Klein, S. Haller, H. Sun, X. Li, T. Jung, C. Röhr, U. Flörke, H.-J. Haupt, *Z. Naturforsch. Teil B* **1998**, *53*, 587–598.
[28] H.-F. Klein, H. H. Karsch, *Chem. Ber.* **1975**, *108*, 944–955.
[29] H.-F. Klein, H. H. Karsch, *Inorg. Chem.* **1975**, *14*, 473–477.

Received: May 26, 2006
Published Online: September 8, 2006

 © 2006 Wiley-VCH Verlag GmbH & Co. KGaA, Weinheim 

DOI: 10.1002/ejic.200600492

# Synthesis and Structural Characterization of a New Alkaline Earth Imide: $MgCa(NH)_2$

**Yongfeng Liu,[a] Tao Liu,[a] Zhitao Xiong,[a] Jianjiang Hu,[a] Guotao Wu,[a] Ping Chen,*[a,b] Andrew T. S. Wee,[a] Ping Yang,[c] Kenji Murata,[d] and Ko Sakata[d]**

**Keywords:** Solid-state reactions / Amides / Hydrides / EXAFS spectroscopy / Ternary imide

The ternary imide of $MgCa(NH)_2$ has been successfully synthesized for the first time by the mechanochemical reaction of $Mg(NH_2)_2$ and $CaH_2$ at a molar ratio of 1:1. It was found that ca. four H atoms were desorbed per $Mg(NH_2)_2$-$CaH_2$ after 72 h of ball milling leaving a solid residue with the chemical composition of $MgCa(NH)_2$. The solid residue exhibits an imide N–H stretching vibration at 3151 $cm^{-1}$ and a cubic CaNH-like structure. In addition, X-ray Absorption Fine Structure examination at the Ca *K*-edge indicates that six N atoms occupy the first coordination shell of the Ca center in an anticipated octahedral geometry, and Ca(Mg) atoms occupy the second coordination shell. The distances of Ca–N and Ca–Ca(Mg) in the newly formed $MgCa(NH)_2$ structure calculated by ESDs are 2.46 and 3.47 Å, respectively.
(© Wiley-VCH Verlag GmbH & Co. KGaA, 69451 Weinheim, Germany, 2006)

## Introduction

Significant progress in metal nitride research has been made in the past few decades.[1–6] Binary nitrides of the Group 1 and 2 elements, such as $Li_3N$, $Be_3N_2$, $Mg_3N_2$, and $Sr_3N_2$ have been extensively studied[2–3] and used as solar control coatings for windows,[6] reagents for solid-state metathesis reaction,[7–9] and hydrogen storage materials.[10–12] More recently, ternary and multinary nitrides have also been synthesized and investigated due to the unusual crystal and coordination chemistry.[3–6] Unlike nitrides, however, less work has been performed on metal imides. Some basic structural and electronic properties of binary imides such as $Li_2NH$, $Na_2NH$, CaNH, and BaNH are still unknown or controversial.[13–16] As for ternary imides, limited research was done on $Li_2Mg(NH)_2$ and $Li_2Ca(NH)_2$ only in the past two years, motivated by their remarkable hydrogen storage performances.[17–18] Theoretically, the chemical nature of the –NH group enables it to bond with elements from Groups 1–13. A variety of novel ternary or multinary metal imides with unique physical and chemical properties are expected if suitable synthetic routes can be established. Our recent studies showed that a solid-state reaction between metal amides and hydrides could result in the formation of ternary imides. For example, $Li_2Mg(NH)_2$ was synthesized successfully by reacting $LiNH_2$ with $MgH_2$ (molar ratio 2:1) at around 250 °C.[17] The chemical driving force of the above-mentioned solid-state reaction lies in the strong interaction between $H^{\delta+}$ in amide and $H^{\delta-}$ in hydride. However, the thermal instability of the starting amides may lead to self-decomposition at elevated temperatures, which will inevitably result in synthesis failure especially for reactions with slow kinetics. As thermal decomposition of the starting amides is a highly endothermic process, the synthesis of ternary imides may be favored at lower temperature if the overall interaction is mildly endothermic or exothermic. The mechanochemical route, which can perturb surface-bonded species by pressure and enable uniform occurrence of solid-state reaction with poor kinetics at relatively low temperatures,[19–20] could be advantageously used in such synthesis. In this paper, a novel ternary alkaline earth imide, $MgCa(NH)_2$, has been synthesized for the first time by a mechanochemical reaction. FTIR, XRD, and XAFS characterizations were performed to determine the structure of this newly developed imide.

## Results and Discussion

A gaseous product gradually evolved from the mixture of $Mg(NH_2)_2$ and $CaH_2$ (1:1) during the mechanical ball milling treatment, and was identified to be pure hydrogen by a mass spectrometer (Hiden, HPR20). The corresponding amount of hydrogen released from the starting chemicals was calculated by measuring the pressure of hydrogen and the volume of the ball mill vessel. As shown in Figure 1, the amount of hydrogen desorbed increases with ball

[a] Department of Physics, National University of Singapore, 10 Kent Ridge Crescent, Singapore 117542, Singapore
Fax: +65-6777-6126
E-mail: phychenp@nus.edu.sg
[b] Department of Chemistry, National University of Singapore, 10 Kent Ridge Crescent, Singapore 117543, Singapore
[c] Singapore Synchrotron Light Source, National University of Singapore, 5 Research Link, Singapore 117603, Singapore
[d] The Institute of Applied Energy, Shimbashi SY Bldg, 1-14-2 Nishi-shimbashi, Minato-ku, Tokyo 105-0003, Japan

 © 2006 Wiley-VCH Verlag GmbH & Co. KGaA, Weinheim 

milling time. After 12 h ball milling, 11 psi of hydrogen, which is equivalent to ca. 0.5 H atoms per mixture of $Mg(NH_2)_2$–$CaH_2$, was desorbed. After 72 h ball milling, ca. 3.8 H atoms were found to be detached from the mixture. Taking into consideration the purities of the starting chemicals, the number of H atoms released is close to four, being equivalent to the hydrogen storage capacity of ca. 4.0 wt.-%, which is higher than that of most of the traditional metal hydrides, such as $LaNi_5H_6$ (1.4 wt.-%), $FeTiH_{1.9}$ (1.8 wt.-%), and $Mg_2NiH_4$ (3.6 wt.-%). Moreover, EDS analysis reveals that the Mg/Ca atomic ratio in the solid product is 1.03:1, no other metal contamination, such as Fe, was introduced from the stainless steel ball mill jar and balls during the mechanochemical reaction of ball milling.

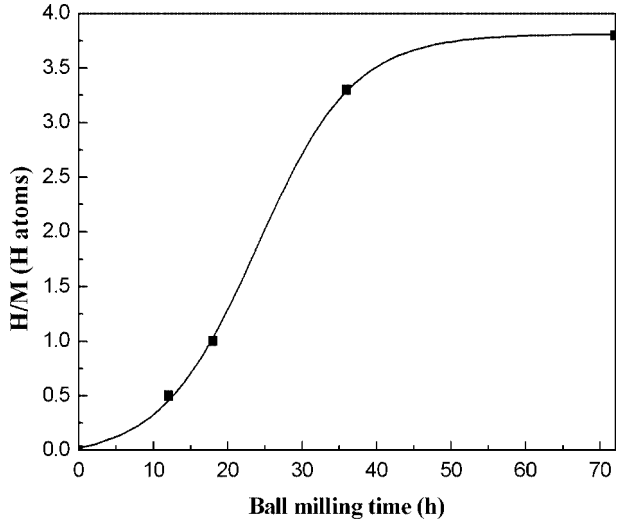


Figure 1. Dependence of the amounts of hydrogen desorption on the ball milling time.

It is well known that $CaH_2$ hardly decomposes to hydrogen at temperatures lower than 600 °C.[21] $Mg(NH_2)_2$, on the other hand, decomposes to $NH_3$ and MgNH at temperatures above 200 °C following the reaction (1).[22–23]

$$Mg(NH_2)_2 \rightarrow MgNH + NH_3 \rightarrow \frac{1}{3}Mg_3N_2 + \frac{4}{3}NH_3 \quad (1)$$

Therefore, hydrogen desorption during the mechanical ball milling should come from the chemical reaction between $Mg(NH_2)_2$ and $CaH_2$ in the present study. Since ca. four H atoms detached from the mixture and no other element was consumed during ball milling, the overall chemical process can be expressed by the following reaction (2).

$$Mg(NH_2)_2 + CaH_2 \rightarrow [MgCa(NH)_2] + 2H_2 \quad (2)$$

The chemical composition of the solid residue indicates that it may be a new ternary imide of Ca and Mg.

It is known that hydrogen atoms in $Mg(NH_2)_2$ are positively charged, while in $CaH_2$ they are negatively charged. The abnormally high enthalpy of the following reaction (3).

$$H^+ + H^- \rightarrow H_2 \ (\Delta H = -17.37 \text{ eV}) \quad (3)$$

is probably the driving force leading reaction (2) to take place under the mechanical ball milling condition.[17] Similar reactions were also observed in other systems such as $LiNH_2$–LiH, $Mg(NH_2)_2$–2LiH, and $LiNH_2$–$CaH_2$ etc. However, it is worth mentioning that it took 72 h for the completion of the reaction under the severe ball milling condition. So the kinetics of the reaction should be very slow. Such slow kinetics will inevitably bring problems to the conventional high temperature synthesis if the starting chemical [like $Mg(NH_2)_2$] or product (the newly developed imide) easily decomposes at elevated temperatures. Therefore, the mechanochemical method developed in the paper could be one of the viable routes for the synthesis of those thermally unstable ternary or multinary imides.

Figure 2 shows the FTIR spectra of the starting chemicals and the solid residues collected at different ball milling times. It can be seen that the N–H symmetric and asymmetric stretching vibrations of $Mg(NH_2)_2$ appear at 3272 and 3326 $cm^{-1}$, respectively. Ca–H vibration in $CaH_2$ is out of the wavenumber range of 3600–2500 $cm^{-1}$. After 12 h ball milling, in addition to the two absorption peaks of $Mg(NH_2)_2$, a broad absorbance at 3151 $cm^{-1}$ was observed, which is located in the N–H vibration range of imide.[13–16] After 72 h ball milling, the characteristic N–H vibrations of $Mg(NH_2)_2$ were almost undetectable. The broad imide-like N–H vibration at 3151 $cm^{-1}$ was enhanced. This result reveals that $Mg(NH_2)_2$ was gradually consumed and an imide-like compound was gradually formed during the ball milling treatment. More importantly, the N–H stretching vibration of the newly developed product of $MgCa(NH)_2$ differs considerably from that of MgNH and CaNH as shown in Figure 2, indicating it is possibly a new ternary imide of Ca and Mg rather than a mixture of MgNH and CaNH.

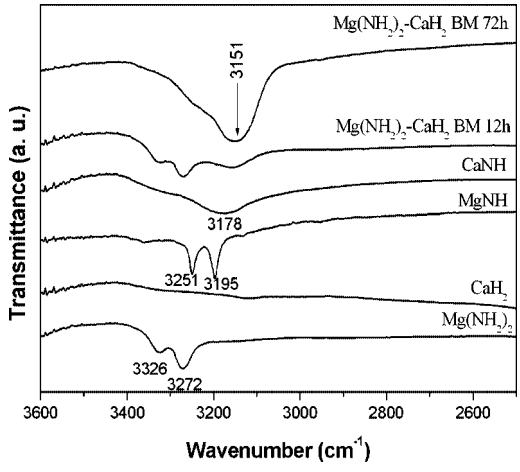


Figure 2. FTIR spectra of the starting chemicals and the Mg–Ca–N–H solid residues after ball milling.

 © 2006 Wiley-VCH Verlag GmbH & Co. KGaA, Weinheim 

Consumption of $CaH_2$ with ball milling was also manifested by the XRD measurements. As shown in Figure 3, the XRD pattern of the post-12 h milled solid residue is mainly composed of the diffraction peaks of orthorhombic $CaH_2$ (refer to the PDF-2 of the JCPDS-ICDD). As $Mg(NH_2)_2$ is easily deformed into an amorphous phase under the energetic ball milling condition,[22] no distinct diffraction peak can be seen. After 72 h ball milling, a new and single phase structure with main diffraction peaks at 30.5, 35.2, and 50.7° was formed (see Figure 3). Matched with the PDF-2 database of the JCPDS-ICDD, the above newly developed solid product possesses a cubic CaNH-like structure. However, compared with CaNH, the diffraction peaks of this product shift to higher angles, revealing a reduction in the unit cell volume. The diffraction pattern is also different from that of MgNH. No other structure assignable to Mg–N or Ca–N can be detected. Combined with the FTIR analyses, it is deducible that this newly developed solid product should be a ternary imide of Ca and Mg, i.e., $MgCa(NH)_2$. Further supportive evidences were obtained from the Temperature-Programmed-Decomposition (TPD) measurements on the $MgCa(NH)_2$, and the mixture of CaNH and MgNH, respectively. Distinct thermal decomposition features were detected. As shown in Figure 4, the solid product decomposes at a peak temperature of 590 °C but the decomposition of the mixture of MgNH and CaNH (1:1) presents two peaks at 650 and 720 °C, respectively.

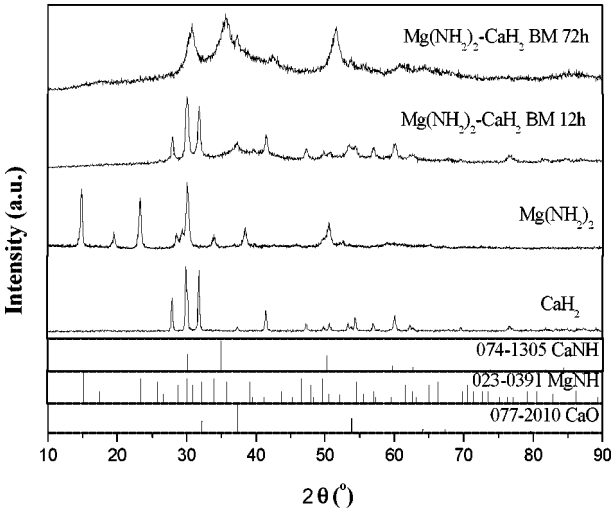


Figure 3. XRD patterns of the starting materials and the Mg–Ca–N–H samples after ball milling.

As can be seen in Figure 3, however, the newly developed imide exhibits rather broad diffraction peaks revealing poor crystallinity in the sample, which is the consequence of the long mechanical ball milling treatment. Because of the poor crystallinity, local structural information could not be convincingly derived from XRD data. The thermal instability of the imide [$MgCa(NH)_2$ decomposes to $NH_3$ at temperatures above 350 °C] defeated our attempt on sample annealing. In order to obtain more structural information on the

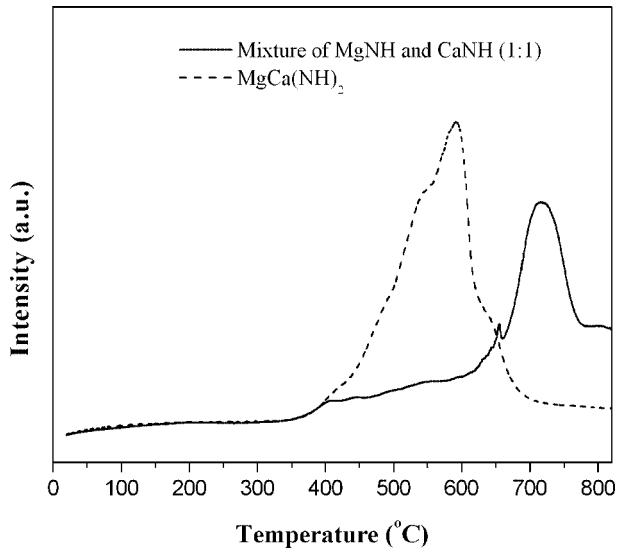


Figure 4. TPD behavior of $MgCa(NH)_2$ and the mixture of MgNH and CaNH.

novel ternary imide, XAFS measurements were conducted. Data of Ca *K*-edge of CaO, CaNH, $Ca(NH_2)_2$, and $MgCa(NH)_2$ were collected and analyzed.

Figure 5 shows the XANES spectra of CaO, CaNH, $Ca(NH_2)_2$, and $MgCa(NH)_2$ samples at Ca *K*-edge, respectively. Obviously all samples exhibit similar spectral features, revealing that they possess the octahedral geometry local structure.[24] Four features can be identified and labeled as A, B, C, and D in Figure 5. Peak A at 4.039 keV can be assigned to the characteristic electron transition from 1*s* to 3*d*.[25] This quadruple transition is usually very weak. However, it is enhanced by the deviation from local centrosymmetry with respect to the central atom (Ca). Compared with CaO, peak A is more obvious in $MgCa(NH)_2$, indicating that the Ca–N octahedrons are somehow distorted. As Mg is more likely to partially replace Ca positions in the second neighboring shell of Ca, the mismatch of atomic radii may result in the distortion of the Ca–N octahedrons. The peak B at 4.042–4.044 keV and peak C at 4.050 keV are ascribed to the dipolar $1s \rightarrow 4p$ transition.[26] Peak B is usually sharp for perfect octahedral sites as shown in CaO.[27] The asymmetry of peak C could be due to the nonequivalent $p_x$, $p_y$, and $p_z$ orbitals of Ca bonded to neighboring nitrogen atoms. Peak C for $MgCa(NH)_2$ shows a shift towards higher energy from 4.049 to 4.050 keV, an indication of a reduced distance between Ca and N compared with that of CaNH. Peak D at 4.058–4.062 keV is related to a middle range ordering as previously demonstrated.[27] Comparatively the ternary $MgCa(NH)_2$ has less middle range ordering, which may be due to its poor crystallinity.

EXAFS looks only at the radial structures of coordination shells around the absorbing atoms. N or O atoms sit in the first coordination shell surrounding the Ca center, and Ca or Mg atoms occupy the second coordination shell. Figure 6 (a) shows Fourier transformed spectra of the various Ca-containing samples. The first peak is assigned to the distance between Ca and the atoms in the first coordination

 © 2006 Wiley-VCH Verlag GmbH & Co. KGaA, Weinheim 

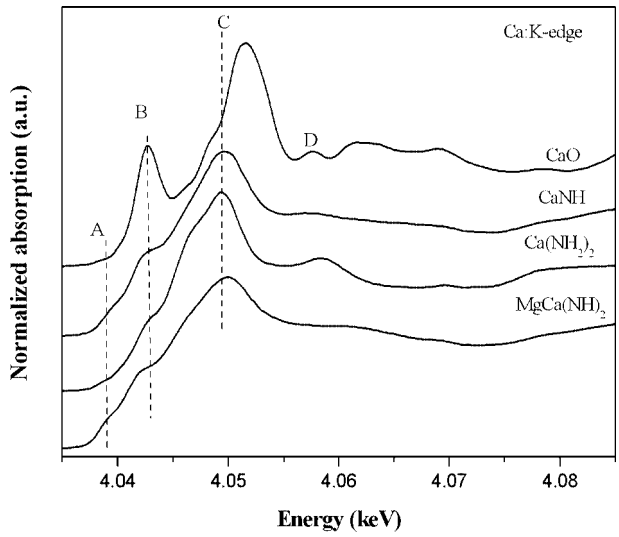


Figure 5. XANES transmission spectra at Ca *K*-edge of the CaO, CaNH, $Ca(NH_2)_2$, and $MgCa(NH)_2$ samples.

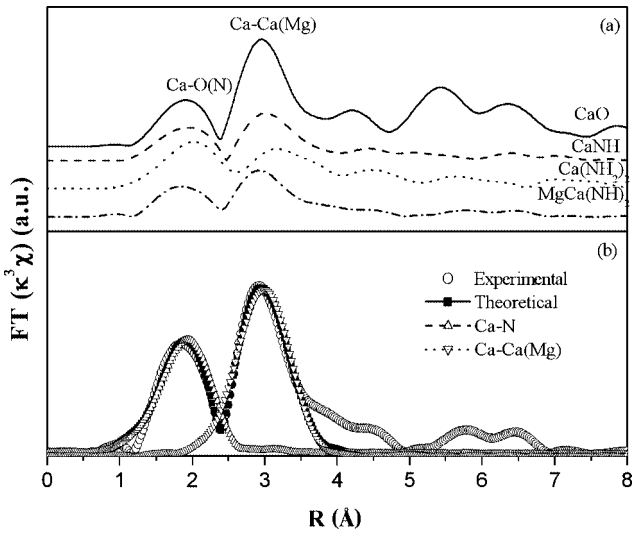


Figure 6. Fourier transformations of the EXAFS spectra of the various Ca-containing samples. (a) Experimental data; (b) fitting results.

shell, i.e., Ca–N or Ca–O; the second peak is attributed to the distance between Ca and the atoms in the second coordination shell, i.e., Ca–Ca and/or Ca–Mg. It should be noted that EXFAS cannot distinguish the positions of Ca and Mg in the second coordination shell of the Ca center. Ca and Mg are more likely to evenly occupy the octahedral center of N in the lattice to minimize energy. Two to three peaks can be identified arising from higher order shells. Figure 6 (b) shows the experimental data and fitting result of $MgCa(NH)_2$, which shows good agreement in the range of 1 to 4 Å. Similar fitting was also performed on CaNH and $Ca(NH_2)_2$, and the results are summarized in Table 1. It is noted that the coordination number (N) of Ca in the first coordination shell is close to 6 for all samples, indicating that octahedral geometry is retained in the first coordination shell, in good agreement with the XRD results. However, the coordination numbers of the second coordination shell are obviously lower than the actual values due to the disorder effects at high coordination shells. Meanwhile, it should be noted that the value of $Ca(NH_2)_2$ (4.4) is lower than that of $MgCa(NH)_2$ (8), which can be attributed to the vacancies of Ca in the second coordination shell due to the lower ratio of the metal atom and N atom (1:2) in the $Ca(NH_2)_2$ structure compared to that in the $MgCa(NH)_2$ structure (1:1).[13] The Ca–N and Ca–Ca distances of CaNH are calculated to be 2.49 and 3.53 Å, respectively, which match well with the values (Ca–N: 2.50 Å, Ca–Ca: 3.54 Å) obtained from the known crystallographic data. On the other hand, the Ca–N and Ca–Ca(Mg) distances of $MgCa(NH)_2$ are calculated to be 2.46 and 3.47 Å, respectively, which are the shortest among the three Ca–N-based structures in the present study. This contraction of atomic distances is in good agreement with the reduction of lattice parameters detected by XRD, which is probably due to the smaller ionic radius of Mg (0.72 Å) compared to Ca (1.0 Å).

Table 1. Structural parameters of CaNH, $Ca(NH_2)_2$, and $MgCa(NH)_2$ obtained from XAFS.[a,b]

| Sample | Shell | Coordination | R [Å] | *N* | $\sigma^2$ [Å$^2$] | Residual [%] |
|---|---|---|---|---|---|---|
| CaNH | 1 | Ca–N | 2.49 | 6.0 | 0.0173 | 9.2 |
| | 2 | Ca–Ca | 3.53 | 6.4 | 0.0132 | |
| $Ca(NH_2)_2$ | 1 | Ca–N | 2.51 | 6.7 | 0.0130 | 16.0 |
| | 2 | Ca–Ca | 3.67 | 4.4 | 0.0078 | |
| $MgCa(NH)_2$ | 1 | Ca–N | 2.46 | 5.9 | 0.0118 | 10.6 |
| | 2 | Ca–Ca(Mg) | 3.47 | 8.0 | 0.0174 | |

[a] Error bars for *R* are 0.01 Å, for *N* and $\sigma^2$, 10%. [b] Data fitting does not include the effects of the H atoms and the oxide contamination.

According to the above discussions, it can be seen that the newly formed ternary imide of $MgCa(NH)_2$ possesses a CaNH-like cubic structure. The half substitution of Ca by Mg does not substantially change the lattice configuration of CaNH, but the lattice has shrunk considerably compared with CaNH, because of the smaller ionic radius of Mg. Figure 7 illustrates a structural model of $MgCa(NH)_2$, in which Ca(Mg) occupies the 4a site (0,0,0) and N occupies the 4b site (1/2,1/2,1/2) of space group Fm-3m, and the N atoms sit in the octahedral holes made of Ca(Mg). However, it is difficult to determine the position of H in the ternary imide by means of XRD and XAFS. There are a number of investigations on the position of H in binary imides, such as CaNH and BaNH.[16,28] As Jacobs et al. pointed out the NH group in CaNH is dynamically disordered at room temperature, and the maximum possibility for the location of hydrogen is the eightfold split position along <111> directions in Ca-octahedra.[16,28] In other words, there are eight possible positions for the H atoms in the structure of CaNH, and every H atom points to the relevant face of the octahedron of Ca. According to the XRD and XAFS analyses, the crystal structure of the newly formed

 © 2006 Wiley-VCH Verlag GmbH & Co. KGaA, Weinheim 

$MgCa(NH)_2$ resembles that of CaNH. Therefore, it is suggested that the situation of the H atoms in $MgCa(NH)_2$ is similar to that in CaNH as shown in Figure 7.

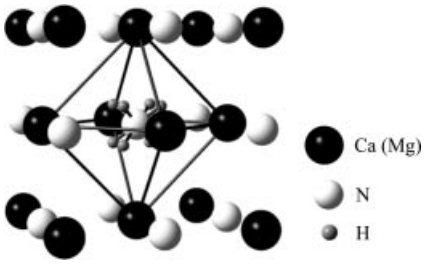


Figure 7. Structural model of $MgCa(NH)_2$.

## Conclusions

In this paper, a novel ternary alkaline earth imide has been synthesized by the mechanochemical reaction of $Mg(NH_2)_2$ and $CaH_2$ with a molar ratio of 1:1. The newly formed ternary imide of $MgCa(NH)_2$ has a CaNH-like cubic structure. Mg atoms partially substitute Ca atoms in the lattice resulting in a distorted local centro-symmetry and poor near and middle range ordering. The Ca–N and Ca–Ca(Mg) distances of $MgCa(NH)_2$ were calculated by ESDs to be 2.46 and 3.47 Å, respectively.

## Experimental Section

All samples were handled in a glovebox (MBRAUN) filled with purified argon ($H_2O$: <1 ppm, $O_2$: <1 ppm). The starting chemicals for the mechanochemical reaction were $Mg(NH_2)_2$ and $CaH_2$. $Mg(NH_2)_2$ was synthesized by reacting pre-milled metallic Mg (99%, Riedel-De Haen) with $NH_3$ (99.98%, BOC GASES) at 300 °C, and its purity was estimated by XRD analyses and measured by thermogravimetric methods, i.e., by measuring the weight loss of a $Mg(NH_2)_2$ sample during the thermal decomposition. Only the diffraction patterns of $Mg(NH_2)_2$ can be detected by XRD examination; and the weight loss was 39.7% as the self-made $Mg(NH_2)_2$ was heated from 25 to 720 °C. The theoretical weight loss was 40.5% when $Mg(NH_2)_2$ was decomposed to $Mg_3N_2$ and $NH_3$. Thus, the purity of the self-made $Mg(NH_2)_2$ is about 98%. $CaH_2$ powder with 95% purity was purchased from Sigma–Aldrich. The mechanochemical reactions were performed on a Retsch PM400 planetary ball mill. In a typical procedure, the starting chemicals of $Mg(NH_2)_2$ (1.4 g) and $CaH_2$ (1.05 g) (molar ratio 1:1) were mixed and then milled at 200 rpm. The ball milling treatment was stopped at different intervals (12–72 h) to measure the pressure changes within the ball mill vessel. After 72 h of mechanochemical reaction, the sample was collected and weighed. Although some of the product adhered to the milling balls and the inner surface of the ball mill vessel, ca. 2.2 g of gray powder was ultimately obtained. The Mg/Ca atomic ratio in the solid product was examined by EDS with a Philips XL30 Scanning Electron Microscope (SEM).

The thermal decomposition of the solid product and the mixture of MgNH and CaNH was carried out with the home-made Temperature-Programmed-Decomposition (TPD) system with an online mass spectrometer (MS) and gas chromatograph (GC) attached. Argon was used as the carrier gas. About 100 mg of sample was loaded and tested each time. The temperature was raised gradually from 20 to 820 °C at 2 °C/min.

N–H vibrations of all samples were detected with a Perkin Elmer FTIR-3000 unit in DRIFT mode. The phase identification was carried out by X-ray diffraction (XRD). A Bruker D8-advance X-ray diffractometer with Cu-$K_\alpha$ radiation at 40 kV and 40 mA equipped with an in-situ cell was used. X-ray absorption fine structure (XAFS) experiments at the Ca *K*-edge (4.038 keV) were performed in transmission mode at room temperature at the XDD beamline in the Singapore Synchrotron Light Source (SSLS).[29] CaO, CaNH, and $Ca(NH_2)_2$ were used as reference samples measured under the same experimental conditions. CaO with 99.9% purity was purchased from Sigma–Aldrich; $Ca(NH_2)_2$ was synthesized by reacting metallic Ca (98.5%, Merck) with $NH_3$ at room temperature.[30] CaNH was obtained by the thermal decomposition of $Ca(NH_2)_2$.[13,31] Each sample was pressed into a pellet by mixing with LiF powder (99%, Fluka) in a weight ratio of 1:10 under a pressure of 2.5 tons; the pellets were subsequently coated with solid wax under an inert atmosphere to protect against air contamination during XAFS measurements. The thickness of the samples was adjusted to achieve a jump of about 1 in absorption coefficient at the absorption edge. Ca *K*-edge XAFS spectra were analyzed following the standard methods using the WINXAS code.[32] The extracted $\chi(k)$ in the range 2.2–9.2 $Å^{-1}$ was weighted by $k^3$ and Fourier transformed into *R* space using the Bessel window function. Data fitting was performed in *R* space without considering the effects of H atoms by filtering out the first and second coordination shells. The other possible error may be generated from the impurities of the reference sample. For all systems, we used the amplitude reduction factor of $S_0^2 = 0.73$, a theoretical value extracted from the fit of CaNH by fixing the known crystallographic data.

## Acknowledgments

We would like to acknowledge the financial support from the Agency for Science, Technology and Research (A*STAR Singapore) and the New Energy and Industrial Technology Development Organization (NEDO, Japan) under the International Joint Research Project "Development for Safe Utilization and Infrastructure of Hydrogen". We also would like to thank Prof. H. O. Moser, SSLS, for discussion and suggestions.

[1] P. Eckerlin, A. Rabenau, *Z. Anorg. Allg. Chem.* **1960**, *304*, 218–219.
[2] O. Reckeweg, F. J. DiSalvo, *Z. Anorg. Allg. Chem.* **2001**, *627*, 371–377.
[3] D. H. Gregory, *Coord. Chem. Rev.* **2001**, *215*, 301–345.
[4] R. Niewa, F. J. DiSalvo, *Chem. Mater.* **1998**, *10*, 2733–2752.
[5] D. H. Gregory, *J. Chem. Soc. Dalton Trans.* **1999**, *3*, 259–270.
[6] P. F. Henry, M. T. Weller, *Angew. Chem. Int. Ed.* **1998**, *37*, 2855–2857.
[7] O. Reckeweg, C. Lind, A. Simon, F. J. DiSalvo, *Z. Naturforsch. Teil B* **2003**, *58*, 159–162.
[8] L. Rao, R. B. Kaner, *Inorg. Chem.* **1994**, *33*, 3210–3211.
[9] E. G. Gillan, R. B. Kaner, *Chem. Mater.* **1996**, *8*, 333–343.
[10] P. Chen, Z. T. Xiong, J. Z. Luo, J. Y. Lin, K. L. Tan, *Nature* **2002**, *420*, 302–304.
[11] Z. T. Xiong, P. Chen, G. T. Wu, J. Y. Lin, K. L. Tan, *J. Mater. Chem.* **2003**, *13*, 1676–1680.
[12] Y. Kojima, Y. Kawai, *Chem. Commun.* **2004**, 2210–2211.
[13] R. Juza, H. Schumacher, *Z. Anorg. Allg. Chem.* **1963**, *24*, 278–286.

 © 2006 Wiley-VCH Verlag GmbH & Co. KGaA, Weinheim 

[14] V. G. Linde, R. Juza, *Z. Anorg. Allg. Chem.* **1974**, *409*, 199–214.
[15] R. Ebmann, H. Jacobs, J. Tomkinson, *J. Alloys Compd.* **1993**, *191*, 131–134.
[16] T. Sichla, H. Jacobs, *Z. Anorg. Allg. Chem.* **1996**, *622*, 2079–2082.
[17] Z. T. Xiong, G. T. Wu, J. J. Hu, P. Chen, *Adv. Mater.* **2004**, *16*, 1522–1525.
[18] W. F. Luo, *J. Alloys Compd.* **2004**, *381*, 284–287.
[19] E. Gutman, *Mechanochemistry of Materials*, Cambridge International Science Publishing, Cambridge, UK, **1997**.
[20] C. Suryanarayana, *Prog. Mater. Sci.* **2001**, *46*, 1–184.
[21] G. G. Libowitz, *The Solid State Chemistry of Binary Metal Hydrides*, W. A. Benjamin, Inc., New York, **1965**.
[22] J. J. Hu, G. T. Wu, Y. F. Liu, Z. T. Xiong, P. Chen, K. Murata, K. Sakata, G. Wolf, *J. Phys. Chem. B* **2006**, *110*, 14688–14692.
[23] Z. T. Xiong, J. J. Hu, G. T. Wu, P. Chen, *J. Alloys Compd.* **2005**, *395*, 209–212.
[24] H. Modrow, S. Bucher, J. J. Rehr, A. L. Ankudinov, *Phys. Rev. B* **2005**, *67*, 035123.
[25] F. de Groot, *Chem. Rev.* **2001**, *101*, 1779–1808.
[26] J. L. Fulton, S. M. Heald, Y. S. Badyal, J. M. Simonson, *J. Phys. Chem. A* **2003**, *107*, 4688–4696.
[27] L. X. Chen, T. Liu, M. C. Thurnauer, R. Csencsits, T. Rahj, *J. Phys. Chem. B* **2002**, *106*, 8539–8546.
[28] B. Wegner, R. Essmann, H. Jacobs, *J. Less-Common Met.* **1990**, *167*, 81–90.
[29] H. O. Moser, B. D. F. Casse, E. P. Chew, M. Cholewa, C. Z. Diao, S. X. D. Ding, J. R. Kong, Z. W. Li, M. Hua, M. L. Ng, B. T. Saw, S. bin Mahmood, S. V. Vidyaraj, O. Wilhelmi, J. Wong, P. Yang, X. J. Yu, X. Y. Gao, A. T. S. Wee, W. S. Sim, D. Lu, R. B. Faltermeier, *Nucl. Instrum. Methods Phys. Res. Sect. B* **2005**, *238*, 83–86.
[30] H. Moissan, *Ann. Chim. Phys.* **1899**, *18*, 289–326.
[31] S. Hino, T. Ichikawa, H. Y. Leng, H. Fujii, *J. Alloys Compd.* **2005**, *398*, 62–66.
[32] T. Ressler, *J. Physique IV* **1997**, *7*, 269–270.

Received: May 27, 2006
Published Online: September 13, 2006

 © 2006 Wiley-VCH Verlag GmbH & Co. KGaA, Weinheim 

DOI: 10.1002/ejic.200600498

# Selective Phosphoramidite Cleavage as a Route to Novel Chiral and Achiral Pentacoordinated Nickel(II) PNP Pincer Complexes

David Benito-Garagorri,[a] Kurt Mereiter,[b] and Karl Kirchner*[a]

**Keywords:** Nickel complexes / Tridentate ligands / Square-pyramidal complexes / Hydrolysis

Treatment of $NiBr_2$(DME) (DME = 1,2-dimethoxyethane) or anhydrous $NiBr_2$ with 2 equiv. of PNP pincer ligands featuring phosphoramidites in $CH_2Cl_2$ yields the novel neutral pentacoordinate complexes [Ni(PNP){$\kappa^1$(P)-$R_2P$=O}Br]. Over the course of this reaction the P–N bonds of the phosphoramidite units of one PNP ligand are selectively cleaved due to hydrolysis affording an anionic $\kappa^1$-(P)-coordinated phosphinite ligand $[R_2P{=}O]^-$, while a second PNP ligand remains intact and is coordinated in a $\kappa^3$-(P,N,P) fashion. The X-ray structure of one [Ni(PNP){$\kappa^1$(P)-$PR_2$=O}Br] complex has been determined.

(© Wiley-VCH Verlag GmbH & Co. KGaA, 69451 Weinheim, Germany, 2006)

## Introduction

Tridentate PNP ligands in which the central pyridine-based ring donor contains $–CH_2PR_2$ substituents in the two *ortho* positions are widely utilized ligands in transition metal chemistry (e.g., Fe, Ru, Rh, Ir, Pd, Pt).[1–10] We have recently designed an alternative and versatile modular approach for the high-yield synthesis of a new generation of tridentate PNP pincer-type ligands based on 2,6-diaminopyridine and $R_2PCl$. The latter may contain both bulky and/or electron-rich dialkylphosphanes as well as various P–O bond containing achiral and chiral phosphite units derived from diols or amino alcohols (Scheme 1).[11] With this synthetic route it is possible to modify both electronic, steric, and stereochemical parameters of the PNP ligands in a simple and straightforward manner avoiding tedious multistep syntheses and expensive starting materials.

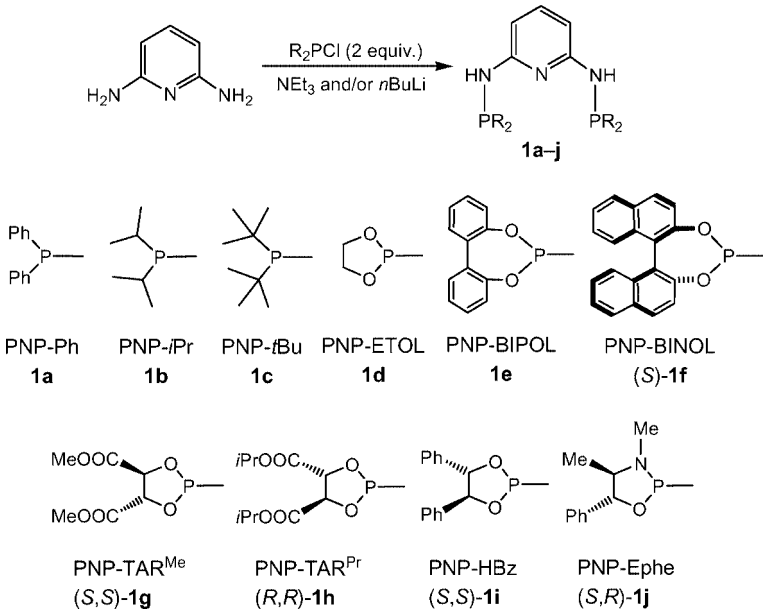


Scheme 1.

[a] Institute of Applied Synthetic Chemistry, Vienna University of Technology,
Getreidemarkt 9, 1060 Vienna, Austria
Fax: +43-1-58801-16399
E-mail: kkirch@mail.zserv.tuwien.ac.at
[b] Institute of Chemical Technologies and Analytics, Vienna University of Technology,
Getreidemarkt 9, 1060 Vienna, Austria

 © 2006 Wiley-VCH Verlag GmbH & Co. KGaA, Weinheim 

Several of these new PNP ligands have recently been successfully applied to the synthesis of square-planar $Ni^{II}$, $Pd^{II}$, and $Pt^{II}$ PNP complexes as shown in Scheme 2.[11] While in the case of palladium and platinum there were no limitations as to the nature of the PNP ligands, surprisingly with nickel the synthesis of square-planar PNP complexes was limited to the alkyl- and aryl-substituted phosphane ligands **1a**–**c**, which lack P–O bonds. In the particular case of phosphite ligands hydrolysis of the P–N bond(s) took place presumably because of the presence of small amounts of water in the solvents leading to the formation of decomposition products. It has to be noted that indeed in some instances $P^{III}$–N bonds turned out to be sensitive towards acid- or base-catalyzed hydrolysis during complexation reactions.[12] In this paper we utilize one such decomposition pathway as a selective high-yield synthetic route to obtain novel pentacoordinated Ni PNP complexes featuring chiral and achiral PNP ligands together with $\kappa^1$-(P)-coordinated phosphinite ligands $R_2P{=}O^-$.

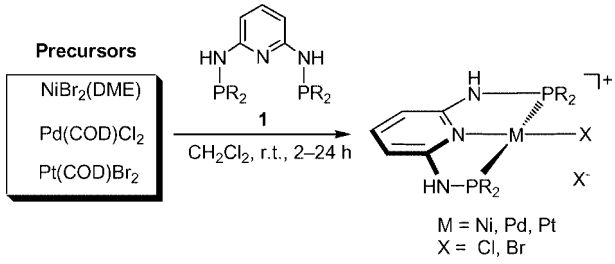


Scheme 2.

## Results and Discussion

Treatment of $NiBr_2$(DME) (DME = 1,2-dimethoxyethane)[13] with 1 equiv. of the PNP ligands **1e**, (*S*,*S*)-**1g**, (*R*,*R*)-**1h**, (*S*,*S*)-**1i**, and (*S*,*R*)-**1j** (see Scheme 1) in $CH_2Cl_2$ at room temperature for 16 h afforded the novel neutral pentacoordinate complexes [Ni(PNP){$\kappa^1$(P)-$PR_2{=}O$}Br] (**2e**,**g**–**j**) (Scheme 3). The isolated yields were typically less than 50%. There was no evidence for the formation of other products such as square-planar complexes of the type [Ni(PNP)Br]Br. The isolated yields of **2e**,**g**–**j** could be significantly improved up to 89% when $NiBr_2$(DME) was treated with ≥1.5 equiv. of PNP ligand in $CH_2Cl_2$ as the solvent for 16 h. The same reaction took place if anhydrous $NiBr_2$ was treated with 2 equiv. of the respective PNP ligands in $CH_2Cl_2$ in the presence of 1 equiv. of DMSO (or DMF). The addition of these solvents resulted in immediate dissolution of the otherwise insoluble nickel precursor accompanied by a color change of the solution from colorless to bright orange indicating the formation of **2e**,**g**–**j**. It has to be emphasized that DMSO does not participate in the reaction as an oxygen-transfer agent but merely increases the solubility of the stated materials. Under these conditions the reaction time could be reduced to 1 h.

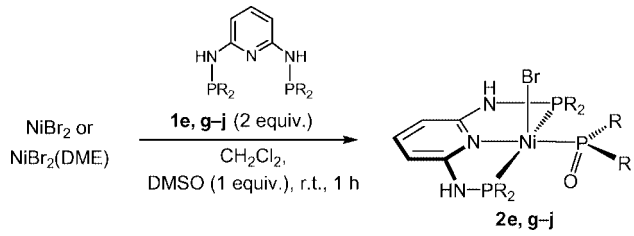


Scheme 3.

All complexes have been characterized by a combination of elemental analysis and $^1H$, $^{13}C\{^1H\}$, and $^{31}P\{^1H\}$ NMR spectroscopy. Most diagnostic is the $^{31}P\{^1H\}$ NMR spectrum exhibiting an $A_2X$ pattern with a doublet in the range of δ = 116–147 ppm, assignable to the intact PNP ligand, and a triplet in the range of δ = 74–87 ppm, assignable to the $\kappa^1$-(P)-coordinated phosphinite ligand $R_2P{=}O^-$. The $J_{PP}$ coupling constant ranges from 90 to 115 Hz.

In order to unequivocally establish the ligand arrangement around the metal center, the structure of **2i** (in the form of **2i**·MeOH) has been determined by X-ray crystallography. A structural view is depicted in Figure 1 with selected bond lengths and angles given in the caption. The nickel atom exhibits a square-pyramidal coordination with the Br atom in the apical position. The diphenylphosphinite ligand is clearly coordinated through the lone-pair at the P atom rather than through the oxygen lone-pairs. The PNP ligand is coordinated in the typical meridional $\kappa^3$-(P,N,P) fashion. Nickel pentacoordination is rare in organometallic chemistry and only about 9% of all complexes adopt this coordination number of which about half belong to the trigonal-bipyramidal and the rest to the square-pyramidal type (Cambridge Structural Data base, CSD, version 5.27, release 2006).[14] Only one compound was found in this database with a square-pyramidal Ni(PNP)(P)Br coordination, however, with the Br atom in the basal and the N atom in the apical position.[15] Another example with a coordination related to **2i**·MeOH is dibromo{bis[2-(diphenylphosphanyl)ethyl]amine}nickel(II)[16] having a Ni(PNP)$Br_2$ square pyramid with a basal Ni–Br bond of 2.33 Å and an apical Ni–Br bond of 2.70 Å, whereas in **2i**·MeOH the latter measures 2.54 Å on average for the two independent complexes.

Over the course of this reaction, the P–N bonds of one PNP ligand were selectively cleaved to afford a complex with one anionic phosphinite ligand $PR_2{=}O^-$ and one intact $\kappa^3$-(P,N,P)-coordinated PNP ligand. Only a few examples of mononuclear complexes with a single $PR_2{=}O^-$ ligand are reported in the literature including [RuCp{=C($CH_2$Ph)-NHPh}($PPh_2$NHPh){$\kappa^1$(P)-$PPh_2{=}O$}],[17] [Pt($PPh_3$)(Ph)-(NC-9-anthracenyl){$\kappa^1$(P)-$PPh_2{=}O$}],[18] and $HNEt_3$-[$W(CO)_5${$\kappa^1$(P)-$PPh_2{=}O$}].[19] However, in many cases phosphinite ligands are found in conjunction with the corresponding phosphinous acids $PR_2OH$ to form $R_2P$–O–H···O=$PR_2$ moieties with very strong and almost symmetric hydrogen bonds of O···O distances as low as 2.40 Å.[20–22]

 © 2006 Wiley-VCH Verlag GmbH & Co. KGaA, Weinheim 

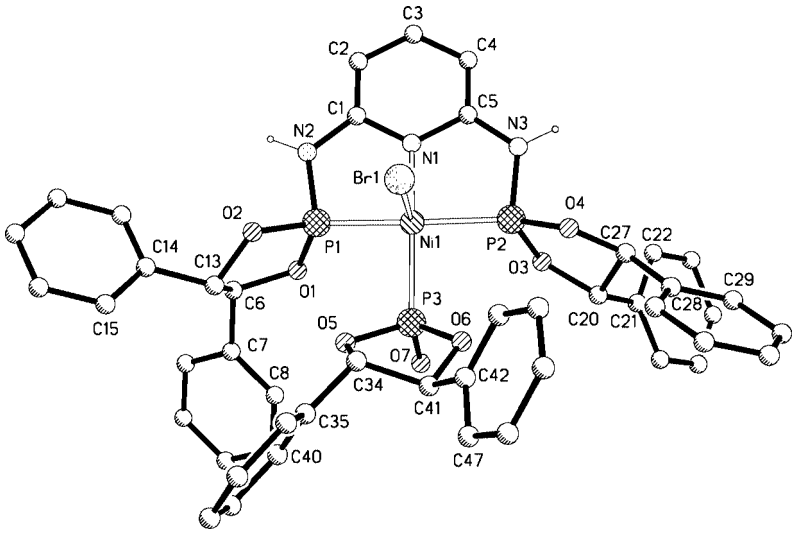


Figure 1. Structural view of [Ni(PNP-HBz){κ$^1$(P)-HBz-P=O}Br] (**2i**·$CH_3OH$) (second independent Ni complex, *C*-bonded H atoms and $CH_3OH$ omitted for clarity). Selected bond lengths [Å] and bond angles [°]: Ni(1)–N(1) 1.913(8), Ni(1)–P(1) 2.144(3), Ni(1)–P(2) 2.114(3), Ni(1)–P(3) 2.132(6), Ni(1)–Br(1) 2.535(4); P(1)–Ni(1)–P(2) 157.6(3), N(1)–Ni(1)–P(3) 163.6(4), Br(1)–Ni(1)–N(1) 97.1(4), Br(1)–Ni(1)–P(1) 98.7(2), Br(1)–Ni(1)–P(2) 101.8(2), Br(1)–Ni(1)–P(3) 99.2(2).

A proposed and plausible mechanism for the formation of **2e**,**g**–**j** supported by $^1$H and $^{31}$P{$^1$H} NMR spectroscopic studies is depicted in Scheme 4. NMR monitoring of the reaction of $NiBr_2$(DME) with varying amounts of PNP-BIPOL (**1e**) ranging from 0.8 to 4 equiv. in $CD_2Cl_2$ revealed in all cases the formation of an intermediate species that exhibits a characteristic $A_2X$ pattern in the $^{31}$P{$^1$H} NMR spectrum with a doublet centered at $\delta$ = 145.7 ppm and a triplet centered at $\delta$ = 122.4 ppm ($J_{PP}$ = 109.8 Hz). This pattern is consistent with a square-pyramidal five-coordinate species **D** where, in contrast to the final product **2e**, the phosphinite ligand is coordinated in the apical position and the Br atom in a basal position. This intermediate isomerizes at room temperature within 16 h to afford quantitatively the final product **2e** exhibiting a doublet centered at $\delta$ = 145.8 ppm and a triplet centered at $\delta$ = 95.4 ppm ($J_{PP}$ = 104.2 Hz). Surprisingly, in all cases there was no evidence for the formation of any additional phosphorus-containing species as a result of PNP decomposition. In fact, if $NiBr_2$(DME) was treated with 0.8 equiv. of **1e**, complex **2e** was cleanly formed after 16 h but the conversion was not quantitative and substantial amounts of the unreacted poorly soluble nickel precursor remained in the NMR tube. If $NiBr_2$(DME) was treated with 1.5 equiv. of **1e**, complete consumption of both $NiBr_2$(DME) and **1e** took place, while with an excess of **1e** (>1.5 equiv.) $NiBr_2$(DME) was completely converted to afford **2e** but unreacted PNP ligand was still present. In the course of all these experiments a white precipitate was formed, which was removed by filtration. Upon dissolution in $CD_3CN$ this compound was unequivocally identified as the 2,6-diaminopyridinium salt **G** giving rise to signals at $\delta$ = 7.46 (t, $J$ = 7.5 Hz, 1 H, H$^5$) and 5.92 (d, $J$ = 7.5 Hz, 2 H, H$^{3,4}$) ppm and broad signals at $\delta$ = 13.4 (1 H, pyN-H) and 7.2 (4 H, $NH_2$) ppm, which is in agreement with an authentic sample[23] of the 2,6-diaminopyridinium cation [cf. the three p$K_a$ values of 2,6-diaminopyridine are 2.16 and 2.90 ($NH_2$ protonation), and 7.22 (protonation of the pyridine nitrogen atom)].[24]

In line with the observed stoichiometry (2 equiv. of nickel salt requires 3 equiv. of PNP ligand for quantitative conversion), despite the absence of other detectable intermediates, the reaction may be initiated by the formation of the cationic square-planar [Ni(PNP)Br]$^+$ complex **A**. Nucleophilic attack of water at one of the two electrophilic phosphorus atoms of the coordinated PNP ligand leads to P–N bond cleavage affording **B**. This compound reacts readily with another PNP ligand to afford **D**. Thereby the monophosphanylated 2,6-diaminopyridine ligand **C** is released, which in turn reacts with $NiBr_2$(DME) to give complex **E** adopting either a square-planar or tetrahedral geometry. The latter reacts again with water to give **F**. The 2,6-diaminopyridine ligand is readily replaced by the tridentate PNP ligand to yield **D** with concomitant release of 2,6-diaminopyridine in the form of its pyridinium cation **G**.

Additional evidence for intermediate **B** comes from the fact that a similar square-planar palladium chloride complex, viz. [Pd{κ$^2$(P,N)-$NH_2$-PN-BIPOL}{κ$^1$(P)-BIPOL-P=O}Cl] (**4**), was obtained during an attempt to obtain crystals of [Pd(PNP-BIPOL)Cl]Cl (**3**) (Scheme 5). Small amounts of pale-yellow crystals of **4** were repeatedly formed by slow solvent evaporation of a DMF solution of **3** at room temperature over a period of 10 d. The molecular structure of this compound (in the form of **4**·DMF) is shown in Figure 2 with selected bond lengths and angles reported in the caption. The Pd center adopts a distorted square-planar geometry defined by two phosphorus atoms, the central nitrogen atom of the PNP ligand, and a chlorine atom. The $PdNP_2Cl$ coordination deviates significantly from planarity most likely because of a short intramolecular contact between C(28)H and Cl (Figure 1). Moreover, there is a stabilizing short intramolecular hydrogen bond N(3)–H···Cl with N···Cl = 3.15 Å. It has to be mentioned

 © 2006 Wiley-VCH Verlag GmbH & Co. KGaA, Weinheim 

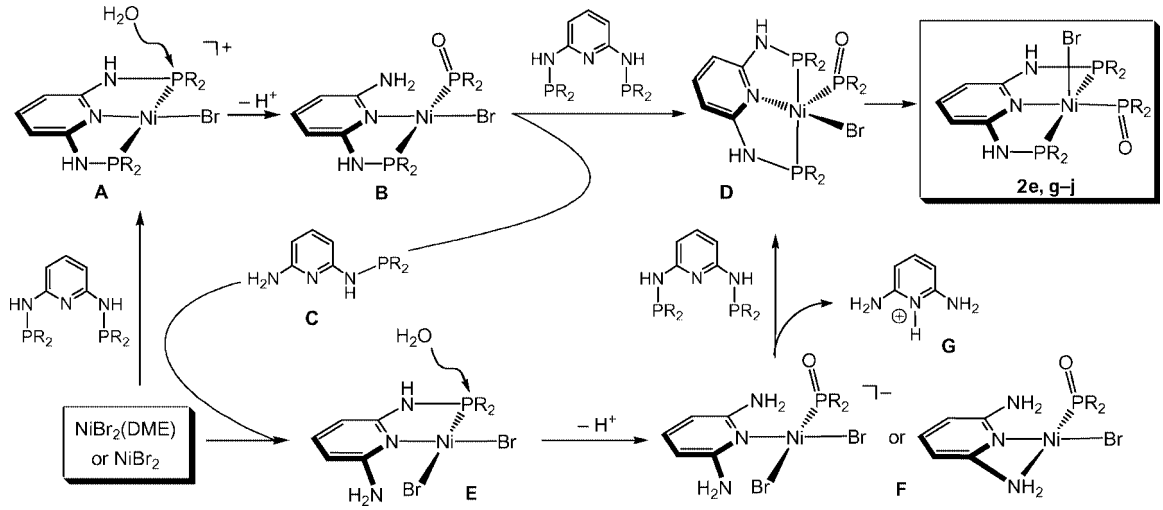


Scheme 4.

that structurally related "one-armed" pincer-type platinum complexes have been reported recently.[25]

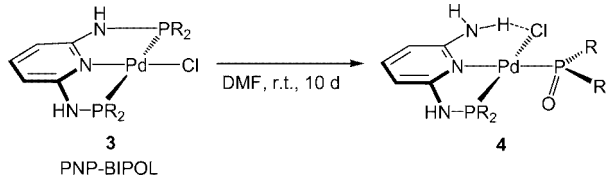


Scheme 5.

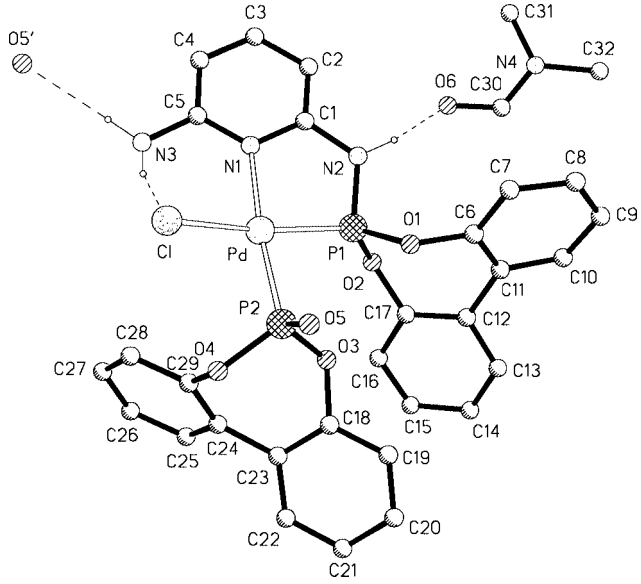

Figure 2. Structural view of [Pd{κ²(P,N)-NH₂-PN-BIPOL}{κ¹(P)-BIPOL-P=O}Cl]·DMF (**4**·DMF) (*C*-bonded H atoms omitted for clarity). Selected bond lengths [Å] and bond angles [°]: Pd–N(1) 2.171(2), Pd–P(1) 2.1787(5), Pd–P(2) 2.2276(6), Pd–Cl 2.3505(5); P(1)–Pd–P(2) 91.78(2), Cl–Pd–P(2) 86.76(2), N(1)–Pd–P(2) 173.51(5), Cl–Pd–P(1) 165.39(2).

Finally, it has to be noted that phosphoramidite PNP ligands are very stable in $CH_2Cl_2$ and comparatively stable also in neat DMSO. In the case of PNP-BIPOL (**1e**) about 50% decomposition is observed at room temperature after 16 h leading to the formation of several intractable materials giving rise to signals in the range of $\delta$ = 6–20 ppm in the $^{31}P\{^1H\}$ NMR spectrum [cf. BIPOL-P(OH)=O, a possible decomposition product, gives rise to a signal at $\delta$ = 5.71 ppm].[26]

## Experimental Section

**General:** All manipulations were performed under argon by using Schlenk techniques. The solvents were purified according to standard procedures. The starting materials (4*S*,5*S*)-2-chloro-4,5-diphenyl-1,3,2-dioxaphospholane,[27] (4*S*,5*R*)-2-chloro-3,4-dimethyl-5-phenyl-1,3,2-oxazaphospholidine,[28] PNP-BIPOL (**1e**), PNP-TAR$^{Me}$ (**1g**), PNP-TAR$^{Pr}$ (**1h**), and [Pd(PNP-BIPOL)Cl]Cl (**3**) were prepared according to literature procedures.[11] The deuterated solvents were purchased from Aldrich and dried with molecular sieves (4 Å). $^1H$, $^{13}C\{^1H\}$, and $^{31}P\{^1H\}$ NMR spectra were recorded with a Bruker AVANCE-250 spectrometer and were referenced to $SiMe_4$ and $H_3PO_4$ (85%), respectively. $^1H$ and $^{13}C\{^1H\}$ NMR signal assignments were confirmed by $^1H$-COSY, 135-DEPT, and HMQC($^1H$-$^{13}C$) experiments.

***N*,*N*′-Bis[(4*S*,5*S*)-4,5-diphenyl-1,3,2-dioxaphospholan-2-yl]-2,6-diaminopyridine (PNP-HBz) (1i):** (4*S*,5*S*)-2-Chloro-4,5-diphenyl-1,3,2-dioxaphospholane (500 mg, 1.8 mmol) was dissolved in toluene (5 mL) and added to a mixture of 2,6-diaminopyridine (98 mg, 0.9 mmol) and triethylamine (0.25 mL, 1.8 mmol) dissolved in toluene (15 mL). The reaction mixture was stirred at 80 °C for 16 h and insoluble materials were removed by filtration. After removal of the solvent under reduced pressure, **1i** was obtained in an analytically pure form as a white solid. Yield: 363 mg (68%). $C_{33}H_{29}N_3O_4P_2$ (593.56): calcd. C 66.78, H 4.92, N 7.08; found C 66.81, H 4.89, N 7.15. $^1H$ NMR ($CDCl_3$, 20 °C): $\delta$ = 7.38–7.11 (m, 21 H, Ph and py[4]), 6.43 (d, $J$ = 8.0 Hz, 2 H, py[3,5]), 6.05 (d, $J$ = 8.2 Hz, 2 H, N*H*), 5.24–5.15 (m, 2 H, C*H*), 5.00–4.81 (m, 2 H, C*H*) ppm. $^{13}C\{^1H\}$ NMR ($CDCl_3$, 20 °C): $\delta$ = 157.6 (py[2,6]), 140.2 (py[4]), 136.5 (Ph[1]), 129.0 (Ph[2,6]), 128.5 (Ph[4]), 126.7 (Ph[3,5]), 100.7 (py[3,5]), 87.2 (*C*H) ppm. $^{31}P\{^1H\}$ NMR ($CDCl_3$, 20 °C): $\delta$ = 130.0 ppm.

***N*,*N*′-Bis[(4*S*,5*R*)-3,4-dimethyl-5-phenyl-1,3,2-oxazaphospholidin-2-yl]-2,6-diaminopyridine (PNP-Ephe) (1j):** This ligand was prepared analogously to **1i** with (4*S*,5*R*)-2-chloro-3,4-dimethyl-5-phenyl-1,3,2-oxazaphospholidine (500 mg, 2.2 mmol), 2,6-diami-

 © 2006 Wiley-VCH Verlag GmbH & Co. KGaA, Weinheim 

nopyridine (118 mg, 1.1 mmol), and triethylamine (0.30 mL, 2.2 mmol). Yield: 283 mg (52%). $C_{25}H_{31}N_5O_2P_2$ (495.50): calcd. C 60.60, H 6.31, N 14.13; found C 60.54, H 6.42, N 14.25. $^1$H NMR ($CDCl_3$, 20 °C): $\delta$ = 7.37–7.15 (m, 13 H, Ph, py$^{3,5}$ and py$^4$), 5.86 (d, $J$ = 7.8 Hz, 2 H, N*H*), 4.71–4.60 (m, 2 H, C*H*Ph), 3.77–3.60 (m, 2 H, C*H*$CH_3$), 2.84–2.63 (m, 6 H, NC*H*$_3$), 0.84–0.63 (m, 6 H, CHC*H*$_3$) ppm. $^{13}$C{$^1$H} NMR ($CDCl_3$, 20 °C): $\delta$ = 157.0 (py$^{2,6}$), 140.1 (py$^4$), 139.6 (Ph$^1$), 128.5 (Ph$^{2,6}$), 126.8 (Ph$^4$), 125.8 (Ph$^{3,5}$), 99.7 (py$^{3,5}$), 81.7 (*C*HPh), 60.2 (*C*HCH$_3$), 29.1 (NCH$_3$), 14.6 (CH*C*H$_3$) ppm. $^{31}$P{$^1$H} NMR ($CDCl_3$, 20 °C): $\delta$ = 119.0 ppm.

**[Ni(PNP-BIPOL){κ$^1$(P)-BIPOL-P=O}Br] (2e):** $NiBr_2$ (150 mg, 0.46 mmol) was suspended in a solution of **1e** (500 mg, 0.93 mmol) in $CH_2Cl_2$ (5 mL). Upon addition of DMSO (33 μL, 0.46 mmol), the solution turned deep orange. The mixture was stirred at room temperature for 1 h and the volume of the solution was reduced under vacuum. The orange product was precipitated with $Et_2O$ and dried under vacuum. Yield: 371 mg (89%). $C_{41}H_{29}BrN_3NiO_7P_3$ (907.23): calcd. C 54.28, H 3.22, N 4.63; found C 54.24, H 3.16, N 3.35. $^1$H NMR ([D$_6$]DMSO, 20 °C): $\delta$ = 7.33–7.09 (m, 20 H, Ph), 6.93–6.88 (m, 4 H, Ph), 6.70 (t, $J$ = 7.3 Hz, 1 H, py$^4$), 6.36 (d, $J$ = 7.3 Hz, 2 H, py$^{3,5}$), 5.80 (d, $J$ = 8.0 Hz, 2 H, N*H*) ppm. $^{13}$C{$^1$H} NMR ([D$_6$]DMSO, 20 °C): $\delta$ = 155.1 (Ph), 154.3 (py$^{2,6}$), 142.2 (py$^4$), 132.3–124.4 (Ph), 100.8 (py$^{3,5}$) ppm. $^{31}$P{$^1$H} NMR ([D$_6$]-DMSO, 20 °C): $\delta$ = 147.7 (d, $J$ = 98.6 Hz, BIPOL-*P*N*P*), 86.6 (t, $J$ = 98.6 Hz, BIPOL-*P*O) ppm.

**[Ni(PNP-TAR$^{Me}$){κ$^1$(P)-TAR$^{Me}$-P=O}Br] (2g):** This complex was prepared analogously to **2e** with $NiBr_2$ (205 mg, 0.94 mmol), **1g** (980 mg, 1.87 mmol), and DMSO (68 μL, 0.94 mmol) as the starting materials. Yield: 672 mg (81%). $C_{35}H_{53}BrN_3NiO_{19}P_3$ (1051.35): calcd. C 39.99, H 5.08, N 4.00; found C 40.09, H 5.00, N 4.10. $^1$H NMR ([D$_6$]DMSO, 20 °C): $\delta$ = 7.44 (t, $J$ = 8.0 Hz, 1 H, py$^4$), 6.40 (d, $J$ = 8.0 Hz, 2 H, py$^{3,5}$), 5.83 (d, $J$ = 8.3 Hz, 2 H, N*H*), 5.03–4.89 (m, 4 H, C*H*), 4.80–4.61 (m, 2 H, C*H*), 1.23–1.14 (m, 18 H, C*H*$_3$) ppm. $^{13}$C{$^1$H} NMR ([D$_6$]DMSO, 20 °C): $\delta$ = 170.2 (*C*O), 166.3 (*C*O), 159.6 (py$^{2,6}$), 142.1 (py$^4$), 100.8 (py$^{3,5}$), 95.1 (*C*H), 76.7 (*C*H), 45.9 (*C*H$_3$), 45.3 (*C*H$_3$) ppm. $^{31}$P{$^1$H} NMR ([D$_6$]DMSO, 20 °C): $\delta$ = 146.2 (d, $J$ = 104.2 Hz, TAR$^{Me}$-*P*N*P*), 85.3 (t, $J$ = 104.2 Hz, TAR$^{Me}$-*P*=O) ppm.

**[Ni(PNP-TAR$^{Pr}$){κ$^1$(P)-TAR$^{Pr}$-PO}Br] (2h):** This complex was prepared analogously to **2e** with $NiBr_2$ (290 mg, 1.33 mmol), **1h** (1.6 g, 2.7 mmol), and DMSO (96 μL, 1.33 mmol) as the starting materials. Yield: 979 mg (70%). $C_{23}H_{29}BrN_3NiO_{19}P_3$ (883.03): calcd. C 31.28, H 3.31, N 4.76; found C 31.21, H 3.40, N 4.66. $^1$H NMR ([D$_6$]DMSO, 20 °C): $\delta$ = 7.42 (t, $J$ = 7.8 Hz, 1 H, py$^4$), 6.41 (d, $J$ = 7.8 Hz, 2 H, py$^{3,5}$), 5.81 (d, $J$ = 8.2 Hz, 2 H, NH), 5.06–4.40 [m, 12 H, C*H* and C*H*(CH$_3$)$_2$], 1.23–1.12 (m, 36 H, [CH(C*H*$_3$)$_2$] ppm. $^{13}$C{$^1$H} NMR ([D$_6$]DMSO, 20 °C): $\delta$ = 170.2 (*C*O), 168.3 (*C*O), 159.8 (py$^{2,6}$), 145.1 (py$^4$), 100.8 (py$^{3,5}$), 95.2 (*C*H), 80.0 (*C*H), 69.1 [*C*H(CH$_3$)$_2$], 68.8 [*C*H(CH$_3$)$_2$], 21.9 [CH(*C*H$_3$)$_2$], 21.7 [CH(*C*H$_3$)$_2$] ppm. $^{31}$P{$^1$H} NMR ([D$_6$]DMSO, 20 °C): $\delta$ = 146.1 (d, $J$ = 100.8 Hz, TAR$^{Pr}$-*P*N*P*), 85.5 (t, $J$ = 100.8 Hz, TAR$^{Pr}$-*P*=O) ppm.

**[Ni(PNP-HBz){κ$^1$(P)-HBz-P=O}Br] (2i):** This complex was prepared analogously to **2e** with $NiBr_2$ (54 mg, 0.24 mmol), **1i** (300 mg, 0.49 mmol), and DMSO (18 μL, 0.24 mmol) as the starting materials. Yield: 132 mg (55%). $C_{47}H_{41}BrN_3NiO_7P_3$ (991.39): calcd. C 56.94, H 4.17, N 4.24; found C 57.04, H 4.19, N 4.31. $^1$H NMR ([D$_6$]DMSO, 20 °C): $\delta$ = 7.29–7.00 (m, 33 H, Ph, py$^4$ and py$^{3,5}$), 5.70 (d, $J$ = 8.0 Hz, 2 H, N*H*), 5.24–4.90 (m, 6 H, C*H*) ppm. $^{13}$C{$^1$H} NMR ([D$_6$]DMSO, 20 °C): $\delta$ = 152.6 (py$^{2,6}$), 144.3 (Ph), 142.5 (py$^4$), 130.1–127.3 (Ph), 98.8 (py$^{3,5}$), 95.1 (*C*H), 87.0 (*C*H) ppm. $^{31}$P{$^1$H} NMR ([D$_6$]DMSO, 20 °C): $\delta$ = 143.4 (d, $J$ = 107.2 Hz, *P*N*P*-HBz), 87.8 (t, $J$ = 107.2 Hz, HBz-*P*=O) ppm.

**[Ni(PNP-Ephe){κ$^1$(P)-Ephe-P=O}Br] (2j):** This complex was prepared analogously to **2e** with $NiBr_2$ (175 mg, 0.40 mmol), **1j** (400 mg, 0.80 mmol), and DMSO (29 μL, 0.40 mmol) as the starting materials. Yield: 213 mg (63%). $C_{35}H_{44}BrN_6NiO_4P_3$ (844.31): calcd. C 49.79, H 5.25, N 9.95; found C 49.69, H 5.09, N 10.05. $^1$H NMR ([D$_6$]DMSO, 20 °C): $\delta$ = 7.40–7.02 (m, 18 H, Ph, py$^4$ and py$^{3,5}$), 5.60 (s, 2 H, N*H*), 4.90–4.74 (m, 3 H, C*H*Ph), 3.64–3.47 (m, 3 H, C*H*CH$_3$), 3.22–3.11 (m, 9 H, NC*H*$_3$), 0.94–0.72 (m, 9 H, CHC*H*$_3$) ppm. $^{13}$C{$^1$H} NMR ([D$_6$]DMSO, 20 °C): $\delta$ = 155.7 (py$^{2,6}$), 143.9 (py$^4$), 141.3 (Ph), 128.6–126.1 (Ph), 99.7 (py$^{3,5}$), 84.5 (*C*HPh), 81.6 (*C*HPh), 65.2 (*C*HCH$_3$), 59.2 (*C*HCH$_3$), 30.9 (NCH$_3$), 28.8 (NCH$_3$), 15.5 (CH*C*H$_3$), 9.5 (CH*C*H$_3$) ppm. $^{31}$P{$^1$H} NMR ([D$_6$]DMSO, 20 °C): $\delta$ = 116.8 (d, $J$ = 114.1 Hz, *P*N*P*-Ephe), 74.5 (t, $J$ = 114.1 Hz, Ephe-*P*=O) ppm.

**X-ray Structure Determination:** Crystals of **2i** were obtained as **2i**·$CH_3OH$ from diethyl ether diffusion into a saturated $CH_3OH$ solution of **2i**. Crystals of **4** were obtained as **4**·DMF by slow concentration of a DMF solution. X-ray data were collected with a Bruker Smart APEX CCD area detector diffractometer using graphite-monochromated Mo-$K_\alpha$ radiation ($\lambda$ = 0.71073 Å) and 0.3° $\omega$-scan frames. Corrections for absorption, $\lambda$/2 effects, and crystal decay were applied.[29] The structures were solved by direct methods using the program SHELXS97.[30] Structure refinement on $F^2$ was carried out with the program SHELXL97.[27] Non-hydrogen atoms were refined anisotropically (for **2i**·MeOH isotropically for C, N, and O atoms). Hydrogen atoms were inserted in idealized positions and were refined riding with the atoms to which they are bonded, except for *N*-bound hydrogen atoms, which were refined in $x$,$y$,$z$ if permitted by data quality. Salient crystallographic data are: **2i**·$CH_3OH$: $C_{48}H_{45}BrN_3NiO_8P_3$, $M_r$ = 1023.40 g mol$^{-1}$, orthorhombic, space group $P2_12_12_1$, $a$ = 15.043(12), $b$ = 19.159(12), $c$ = 33.21(3) Å, $V$ = 9572(12) Å$^3$, $Z$ = 8, $\mu$ = 1.396 mm$^{-1}$, $T$ = 173 K. 11282 independent reflections, reflections were collected up to $\theta_{max}$ = 23.1°; final $R$ indices: $R_1$ = 0.131 [5725 reflections with $I > 2\sigma(I)$], $wR_1$ = 0.365 (all data). All available crystals were thin and bent blades (<0.03 mm), giving broad reflection profiles and poor intensities. Therefore, anisotropic displacement parameters were used only for Ni, Br, and P, and the phenyl rings were refined as idealized rigid groups. Despite the relatively large $R$ values, the structure is sound and hydrogen bonding as well as absolute structure [Flack absolute structure parameter = 0.00(3)] could safely be clarified. The asymmetric unit of the structure contains two independent Ni complexes and methanol molecules mutually linked through hydrogen bonds with N–H and O–H as donors and the Br and phosphinite O atoms as acceptors. Only one of the two independent Ni complexes is shown in Figure 1. **4**·DMF: $C_{32}H_{29}ClN_4O_6P_2Pd$, $M_r$ = 769.38 g mol$^{-1}$, monoclinic, space group $P2_1/c$, $a$ = 9.4778(4), $b$ = 13.7127(6), $c$ = 24.2252(10) Å, $\beta$ = 94.642(1)°, $V$ = 3138.1(2) Å$^3$, $Z$ = 4, $\mu$ = 0.831 mm$^{-1}$, $T$ = 173 K. 9147 independent reflections, reflections were collected up to $\theta_{max}$ = 30.0°; final $R$ indices: $R_1$ = 0.0330 [7211 reflections with $I > 2\sigma(I)$], $wR_1$ = 0.0768 (all data). A view of the molecular structure with all hydrogen bonds is shown in Figure 2. CCDC-608245 (**2i**·$CH_3OH$) and -608246 (**4**·DMF) contain the supplementary crystallographic data for this paper. These data can be obtained free of charge from The Cambridge Crystallographic Data Centre via www.ccdc.cam.ac.uk/data_request/cif.

## Acknowledgments

Financial support by the "Fonds zur Förderung der wissenschaftlichen Forschung" is gratefully acknowledged (Project No.

 © 2006 Wiley-VCH Verlag GmbH & Co. KGaA, Weinheim 

P16600-N11). D. B.-G. thanks the Basque Government (Eusko Jaurlaritza/Gobierno Vasco) for a doctoral fellowship.

[1] W. V. Dahlhoff, S. M. Nelson, *J. Chem. Soc. A* **1971**, 2184.
[2] a) G. Vasapollo, P. Giannoccaro, C. F. Nobile, A. Sacco, *Inorg. Chim. Acta* **1981**, *48*, 125; b) B. D. Steffey, A. Miedaner, M. L. Maciejewski-Farmer, P. R. Bernatis, A. M. Herring, V. S. Allured, V. Carperos, D. L. DuBois, *Organometallics* **1994**, *13*, 4844; c) C. Hahn, J. Sieler, R. Taube, *Chem. Ber./Recueil* **1997**, *130*, 939; d) C. Hahn, A. Vitagliano, F. Giordano, R. Taube, *Organometallics* **1998**, *17*, 2060; e) C. Hahn, M. Spiegler, E. Herdtweck, R. Taube, *Eur. J. Inorg. Chem.* **1999**, 435.
[3] Q. Jiang, D. Van Plew, S. Murtuza, X. Zhang, *Tetrahedron Lett.* **1996**, *37*, 797.
[4] a) M. V. Andreocci, G. Mattogno, R. Zanoni, P. Giannoccaro, G. Vasapollo, *Inorg. Chim. Acta* **1982**, *63*, 225; b) A. Sacco, G. Vasapollo, C. Nobile, A. Piergiovanni, M. A. Pellinghelli, M. Lanfranchi, *J. Organomet. Chem.* **1988**, *356*, 397; c) R. A. T. M. Abbenhuis, I. del Rio, M. M. Bergshoef, J. Boersma, N. Veldman, A. L. Spek, G. van Koten, *Inorg. Chem.* **1998**, *37*, 1749.
[5] a) N. Rahmouni, J. A. Osborn, A. De Cian, J. Fisher, A. Ezzamarty, *Organometallics* **1998**, *17*, 2470; b) R. Sablong, C. Newton, P. Dierkes, J. A. Osborn, *Tetrahedron Lett.* **1996**, *37*, 4933; c) R. Sablong, J. A. Osborn, *Tetrahedron Lett.* **1996**, *37*, 4937; d) L. Barloy, S. Y. Ku, J. A. Osborn, A. De Cian, J. Fischer, *Polyhedron* **1997**, *16*, 291.
[6] a) J. Zhang, G. Leitus, Y. Ben-David, D. Milstein, *J. Am. Chem. Soc.* **2005**, *127*, 10840; b) J. Zhang, M. Gandelman, L. J. W. Shimon, H. Rozenberg, D. Milstein, *Organometallics* **2004**, *23*, 4026; c) D. Hermann, M. Gandelman, H. Rozenberg, L. J. W. Shimon, D. Milstein, *Organometallics* **2002**, *21*, 812.
[7] D. H. Gibson, C. Pariya, M. S. Mashuta, *Organometallics* **2004**, *23*, 2510.
[8] H. Katayama, C. Wada, K. Taniguchi, F. Ozawa, *Organometallics* **2002**, *21*, 3285.
[9] G. Jia, H. M. Lee, I. D. Williams, C. P. Lau, Y. Chen, *Organometallics* **1997**, *16*, 3941.
[10] G. Müller, M. Klinga, M. Leskelä, B. Rieger, *Z. Anorg. Allg. Chem.* **2002**, *628*, 2839.
[11] D. Benito-Garagorri, E. Becker, J. Wiedermann, W. Lackner, M. Pollak, K. Mereiter, J. Kisala, K. Kirchner, *Organometallics* **2006**, *25*, 1900.
[12] a) Z. Fei, N. Biricik, D. Zhao, R. Scopelliti, P. Dyson, *Inorg. Chem.* **2004**, *43*, 2228; b) S. Priya, M. S. Balakrishna, J. T. Mague, S. M. Mobin, *Inorg. Chem.* **2003**, *42*, 1272; c) A. D. Burrows, M. F. Mahon, M. T. Palmer, M. Varrone, *Inorg. Chem.* **2002**, *41*, 1695; d) M. S. Balakrishna, S. S. Krishnamurthy, *Ind. J. Chem.* **1991**, *30A*, 536; e) M. G. Newton, R. B. King, M. Chang, J. Gimeno, *J. Am. Chem. Soc.* **1978**, *100*, 1632; f) J. Geicke, I. P. Lorenz, P. Murschel, K. Polborn, *Z. Naturforsch., Teil B* **1997**, *52*, 593.
[13] A. L. Casalnuovo, T. V. RajanBabu, T. A. Ayers, T. H. Warren, *J. Am. Chem. Soc.* **1994**, *116*, 9869.
[14] F. H. Allen, *Acta Crystallogr., Sect. B* **2002**, *58*, 380.
[15] A. Hessler, J. Fischer, S. Kucken, O. Stelzer, *Chem. Ber.* **1994**, *127*, 481.
[16] P. L. Orioli, C. A. Ghilardi, *J. Chem. Soc. A* **1970**, 1511.
[17] S. Pavlik, K. Mereiter, M. Puchberger, K. Kirchner, *Organometallics* **2005**, *24*, 3561.
[18] W. Beck, M. Keubler, E. Leidl, U. Nagel, M. Schaal, S. Cenini, P. del Buttero, E. Licandro, S. Maiorana, A. C. Villa, *J. Chem. Soc., Chem. Commun.* **1981**, 446.
[19] C. Zeiher, W. Hiller, I.-P. Lorenz, *Chem. Ber.* **1985**, *118*, 3127.
[20] R. Torres-Lubian, M. J. Rosales-Hoz, A. M. Arif, R. D. Ernst, M. A. Paz-Sandoval, *J. Organomet. Chem.* **1999**, *585*, 68.
[21] P. W. N. M. van Leeuwen, C. F. Roobeek, J. H. G. Frijns, A. G. Orpen, *Organometallics* **1990**, *9*, 1211.
[22] B. Walther, H. Hartung, M. Maschmeier, U. Baumeister, B. Messbauer, *Z. Anorg. Allg. Chem.* **1988**, *566*, 121.
[23] S.-H. Liu, J.-D. Chen, L.-S. Liou, J.-C. Wang, *Inorg. Chem.* **2001**, *40*, 6499.
[24] A. Moghimi, R. Alizadeh, A. Shokrollahi, H. Aghabozorg, M. Shamsipur, A. Shockravi, *Inorg. Chem.* **2003**, *42*, 1616.
[25] S. M. Aucott, A. M. Z. Slawin, J. D. Woollins, *J. Chem. Soc., Dalton Trans.* **2000**, 2559.
[26] W. Kuchen, H. F. Mahler, *Phosphorous Sulfur* **1980**, *8*, 139.
[27] H. Park, T. V. RajanBabu, *J. Am. Chem. Soc.* **2002**, *124*, 734.
[28] N. Oka, T. Wada, K. Saigo, *J. Am. Chem. Soc.* **2003**, *125*, 8307.
[29] *SMART*, version 5.625; *SAINT*, version 6.36; *SADABS*, version 2.10; *SHELXTL*, version 6.1: Bruker AXS Inc., Madison, WI, **2003**.
[30] G. M. Sheldrick, *SHELX97, Program System for Crystal Structure Determination*, University of Göttingen, Göttingen, Germany, **1997**.

Received: May 29, 2006
Published Online: September 18, 2006

 © 2006 Wiley-VCH Verlag GmbH & Co. KGaA, Weinheim 

DOI: 10.1002/ejic.200600509

# Synthesis and Properties of Organometallic $Pt^{II}$ and $Pt^{IV}$ Complexes with Acyclic Selenoether and Telluroether Ligands and Selenoether Macrocycles

**William Levason,[a] Joanna M. Manning,[a] Paul Pawelzyk,[a] and Gillian Reid*[a]**

**Keywords:** Selenoether / Telluroether / Platinum / Macrocycles / Organometallic complexes

The first series of planar dimethyl(selenoether)$Pt^{II}$ complexes, $[PtMe_2L]$ [L = $MeSe(CH_2)_nSeMe$ ($n$ = 2 or 3), $o$-$C_6H_4(CH_2SeMe)_2$, [8]ane$Se_2$ (1,5-diselenacyclooctane), or [16]ane$Se_4$ (1,5,9,13-tetraselenacyclohexadecane)], have been obtained by treatment of $[PtMe_2(SMe_2)_2]$ with L in $Et_2O$ solution and characterised by VT $^1H$, $^{13}C\{^1H\}$, $^{77}Se\{^1H\}$ and $^{195}Pt\{^1H\}$ NMR spectroscopy, electrospray MS and microanalysis. The corresponding dimethyl(telluroether)$Pt^{II}$ complexes do not form under similar reaction conditions. The distorted octahedral $[PtMe_3I(L)]$ [L = $o$-$C_6H_4(CH_2SeMe)_2$, [8]ane$Se_2$, [16]ane$Se_4$ or $MeC(CH_2SeMe)_3$] form as stable complexes in good yield from reaction of $PtMe_3I$ with L in refluxing $CHCl_3$ and have been characterised similarly. These all show bidentate selenoether coordination, with fast pyramidal inversion occurring at room temperature. The distorted octahedral coordination environment at $Pt^{IV}$ is also confirmed from a crystal structure of $[PtMe_3I\{o\text{-}C_6H_4(CH_2SeMe)_2\}]$. Rare examples of (telluroether)$Pt^{IV}$ complexes, $[PtMe_3I\{o\text{-}C_6H_4(CH_2TeMe)_2\}]$ and the dinuclear $[Me_3Pt(\mu^2\text{-}I)_2(\mu^2\text{-}MeTeCH_2TeMe)PtMe_3]$, have also been prepared and characterised similarly (and also by $^{125}Te\{^1H\}$ NMR spectroscopy). The [8]ane$Se_2$ and [16]ane$Se_4$ species are the first examples of alkyl $Pt^{II}$ or $Pt^{IV}$ complexes with (macro)cyclic selenoether coordination. Halide abstraction ($TlPF_6$) from $[PtMe_3I(\kappa^2\text{-}[16]aneSe_4)]$ affords $[PtMe_3(\kappa^3\text{-}[16]aneSe_4)]PF_6$; a rare example of a cationic $Pt^{IV}$ selenoether. The (diselenoether)$Pt^{II}$ complexes undergo oxidative addition of MeI to yield the corresponding $Pt^{IV}$ species $[PtMe_3I(diselenoether)]$.
(© Wiley-VCH Verlag GmbH & Co. KGaA, 69451 Weinheim, Germany, 2006)

## Introduction

The chemistry of the neutral ligands derived from the heavier group 16 elements, i.e. selenoethers and telluroethers, is of interest because these are less electronegative than their thioether or ether counterparts, and hence are better σ-donor ligands to transition-metal ions in medium oxidation states compared to their O- and S-donor counterparts.[1,2] The vast majority of transition-metal species involving the selenoether or telluroether ligands are based upon transition-metal halide systems, although we have also shown that homoleptic hexaselenoether or hexatelluroether coordination can be achieved under certain conditions.[3] In contrast, examples of organometallic complexes (involving ligands other than carbonyls) with selenoether and telluroether coordination are rare.[4–7] Abel and Orrell and co-workers have reported some such species based upon $PtMe_3X$ (X = Cl, Br or I) as part of their extensive investigation of the solution dynamics in complexes with dichalcogenoether ligands, in order to understand the fluxional processes occurring and to establish the invertomer populations.[8] However, the reaction chemistry of alkyl(chalcogenoether)transition-metal species has not been investigated. The only examples of dimethyl(chalcogenoether)-$Pt^{II}$ complexes are those involving the $E(CH_2CH{=}CH_2)_2$ ligands (E = S, Se), in which both the chalcogen atom and the alkene functions are coordinated to Pt at low temperature.[9] The preparation of $[PtMeBr\{MeSe(CH_2)_2SeMe\}]$ has also been described.[10]

Here we describe the syntheses and spectroscopic characterisation of a series of methylplatinum(II) and methylplatinum(IV) complexes involving a selected range of acyclic di- and triseleno- and telluroether ligands and macrocyclic selenoethers incorporating between two and four chalcogen atoms and containing a range of linkages between the chalcogen atoms. The $^1H$, $^{13}C\{^1H\}$, $^{77}Se\{^1H\}$, $^{125}Te\{^1H\}$ and $^{195}Pt\{^1H\}$ NMR shifts and coupling constants are discussed and the crystal structure of $[PtMe_3I\{o\text{-}C_6H_4(CH_2SeMe)_2\}]$ described, together with some reaction chemistry.

## Results and Discussion

### Platinum(II) Complexes

Initial attempts to prepare the dimethyl(selenoether)$Pt^{II}$ complexes by treatment of $[PtMe_2(cod)]$ (cod = 1,5-cyclooctadiene) with the ligand in refluxing $CHCl_3$ failed. The $^1H$ NMR spectra of the products show that displacement of the cod is not achieved cleanly, presumably owing to the

[a] School of Chemistry, University of Southampton, Southampton SO17 1BJ, UK

 © 2006 Wiley-VCH Verlag GmbH & Co. KGaA, Weinheim 

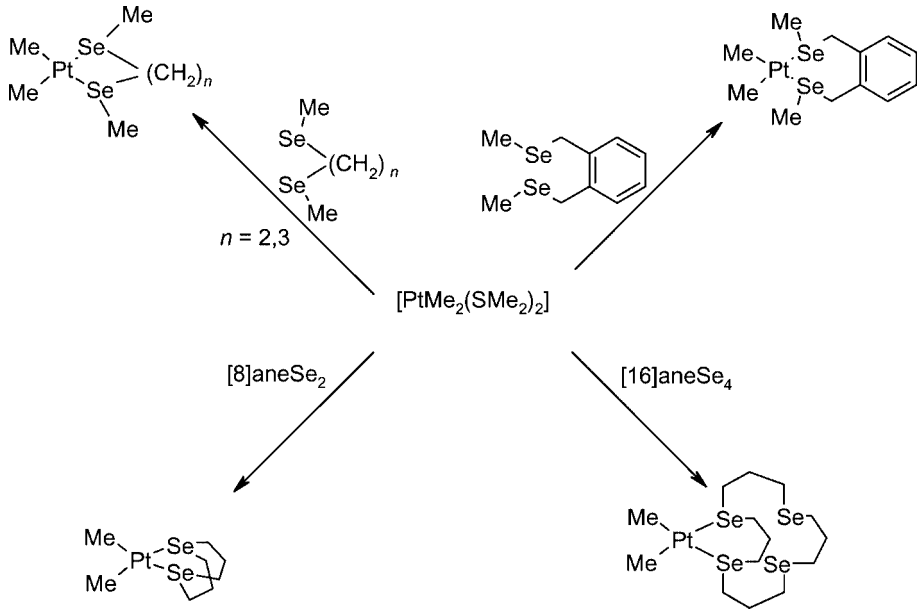


Scheme 1. Synthesis of dimethyl$Pt^{II}$ complexes (note that only one of the possible stereoisomers is shown in each case).

strong σ-donor properties of the Me ligands which occupy the coordination sites *trans* to the cod. However, the (selenoether)$Pt^{II}$ species $[PtMe_2(L\text{-}L)]$ (L-L = $MeSe(CH_2)_nSeMe$, $n$ = 2 or 3, *o*-$C_6H_4(CH_2SeMe)_2$, [8]$aneSe_2$ or [16]$aneSe_4$) were successfully prepared (Scheme 1) by initially treating $[PtCl_2(Me_2S)_2]$ with two mol. equivs. of MeLi in cold $Et_2O$ solution (–78 °C), followed by hydrolysis with water to give $[PtMe_2(SMe_2)_2]$ in situ. Addition of one mol. equiv. of the selenoether to this two-phase mixture and stirring at room temperature gave the products either as solutions in the $Et_2O$ or as yellow solids at the interface. Treatment of [16]$aneSe_4$ with two mol. equivs. of the (dimethyl)$Pt^{II}$ source under these conditions also yielded the 1:1 species $[PtMe_2([16]aneSe_4)]$, hence the product appears to be independent of the ratio used (although this may be a result of the poor solubility of the 1:1 complex which precipitates from the solution and may prevent further complexation to a second $PtMe_2$ unit). The compounds were characterised thoroughly by spectroscopic methods (IR, electrospray MS and variable temperature multinuclear NMR spectroscopy – see Table 1) and microanalysis. On the basis of the *m*/*z* values and the isotopic distributions observed, the electrospray MS show the highest mass peaks corresponding to $[PtMe(L\text{-}L)]^+$ in each case. Attempts to isolate a pure complex from reaction of $[PtMe_2(Me_2S)_2]$ with the $MeSeCH_2SeMe$ under similar conditions were not successful.

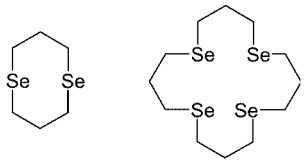


[8]$aneSe_2$ [16]$aneSe_4$

The $^1H$ NMR spectra of $[PtMe_2\{MeSe(CH_2)_nSeMe\}]$ ($n$ = 2 or 3) are consistent with fast pyramidal inversion occurring in chloroform solution at room temperature. Cooling to 223 K reveals sharp resonances associated with both the *meso* and DL forms of the complexes being present in unequal amounts, resulting in two sets of PtMe, SeMe and $SeCH_2$ resonances. Similar behaviour is seen by both $^{13}C\{^1H\}$ and $^{77}Se\{^1H\}$ NMR spectroscopy (Table 1). When recorded at 223 K, the $^{77}Se$ NMR spectra show two distinct Se resonances to high frequency of the uncoordinated selenoether, with $^{195}Pt$ couplings of ca. 420–460 Hz. The relative intensities of the $^{77}Se\{^1H\}$ resonances for $[PtMe_2\{MeSe(CH_2)_2SeMe\}]$ are ca. 1:2, i.e. rather disparate quantities of the *meso* and DL forms, whereas a ratio of ca. 1:1 occurs for $[PtMe_2\{MeSe(CH_2)_3SeMe\}]$. The $^{195}Pt$ NMR spectra (223 K) show resonances for both stereoisomers at approximately –4400 ppm. These resonances are significantly to low frequency of the corresponding $[PtCl_2\{MeSe(CH_2)_nSeMe\}]$, reflecting the better σ-donating properties of the Me ligands.

In separate work we have established that incorporation of the *o*-xylyl linkage in a range of ligand types (diphosphane, distibane, ditelluroether) leads to an increased tendency towards *cis*-chelation compared to aliphatic $C_4$-linked analogues. Therefore, despite the seven-membered ring chelate, these turn out to be very effective ligands for a range of transition-metal ions. We have also reported recently the first series of (alkyl)$Pt^{II}$ and (alkyl)$Pt^{IV}$ complexes involving stibane ligands of this type.[11,12] Furthermore, complexes involving *o*-xylyl-linked wide-angle diphosphanes provide very efficient catalysts for a range of processes such as hydroformylation and hydrocyanation.[13] A number of macrocyclic thioether and selenoethers containing *o*-xylyl linkages have also been reported.[2] We were

 © 2006 Wiley-VCH Verlag GmbH & Co. KGaA, Weinheim 

Table 1. Selected NMR spectroscopic data.

| Compound | $T$ [K][a] | $\delta(^{77}Se$ or $^{125}Te)$ | $^1J_{PtSe/Te}$/Hz | $\delta(^{195}Pt)$ |
|---|---|---|---|---|
| Platinum(II) complexes | | | | |
| $[PtMe_2\{MeSe(CH_2)_2SeMe\}]$ | 243 | 247.9 (major) | 457 | –4383 (major) |
| | | 250.1 (minor) | 438 | –4395 (minor) |
| $[PtMe_2\{MeSe(CH_2)_3SeMe\}]$ | 243 | 114.0 (major) | 427 | –4247 (major) |
| | | 102.1 (minor) | 429 | –4309 (minor) |
| $[PtMe_2\{o\text{-}C_6H_4(CH_2SeMe)_2\}]$ | 193 | 169.1 | 526 | –4308 |
| | | 160.6 | 492 | –4316 |
| | | 155.9 | 438 | |
| $[PtMe_2([8]aneSe_2)]$ | 298 | 140.8 | 323 | –4318 |
| $[PtMe_2([16]aneSe_4)]$ | [b] | [b] | [b] | [b] |
| Platinum(IV) complexes | | | | |
| $[PtMe_3I\{o\text{-}C_6H_4(CH_2SeMe)_2\}]$ | 213 | 114.0 | 289 | –3382 |
| | | 98.7 | 280 | –3468 |
| | | 97.8 | 312 | minor form not obsd. |
| | | 95.5 (minor) | 286 | |
| $[PtMe_3I\{o\text{-}C_6H_4(CH_2TeMe)_2\}]$ | 243 | 189.5 | 602 | –3968 |
| | | 159.9 | 618 | –4022 |
| | | 114.5 | 638 | –4119 |
| | | 110.8 | 537 | |
| $[(PtMe_3I)_2(MeTeCH_2TeMe)]$ | 243 | 173.2 (major) | 713 | –3430 (major) |
| | | 171.1 (minor) | 605 | –3451 (minor) |
| $[PtMe_3I\{MeC(CH_2SeMe)_3\}]$ | 243 | 53.0[c] | 252 | –3446 |
| | | 51.6[c] | 160 | –3543 |
| | | 49.3[c] | 258 | –3550 |
| | | 38.5[c] | 252 | |
| | | 37.4[c] | 162 | |
| | | 37.3[c] | 256 | |
| | | 35.1[d] | – | |
| | | 33.0[d] | – | |
| | | 29.0[d] | – | |
| | | 27.3[d] | – | |
| $[PtMe_3I([8]aneSe_2)]$ | 298 | 65.3 | 244 | –3589 |
| $[PtMe_3I([16]aneSe_4)]$ | 243 | 116.6 (2 Se, coord.) | 266 | –3616 |
| | | 119.5 (2 Se, uncoord.) | – | |
| $[PtMe_3([16]aneSe_4)]PF_6$ | 243 | 70 (3 Se, coord.) | 249 | –3648 |
| | | 138 (1 Se, uncoord.) | – | |

[a] The temperature quoted is that required to clearly resolve the invertomers (see text). [b] Spectra not obtained due to very poor solubility. [c] Coordinated Se. [d] Uncoordinated Se.

therefore interested to investigate the chemistry of *o*-xylyl-linked ligands in this work. Using the wide-angle diselenoether ligand $o\text{-}C_6H_4(CH_2SeMe)_2$ in the procedure described above gives the seven-membered chelate complex $[PtMe_2\{o\text{-}C_6H_4(CH_2SeMe)_2\}]$ in good yield. For square planar $[PtMe_2(L–L)]$ (L–L = bidentate chalcogenoether) two NMR distinguishable forms arise from the chirality at the coordinated chalcogen atom (*meso* and DL). The incorporation of the xylyl linker (which lies out of the square plane) may give rise to further invertomers depending upon the orientation of the SeMe groups with respect to the xylyl backbone. In our recent work on xylyl distibane complexes[11,12] several different conformations of the backbone were identified crystallographically, which serve to illustrate the effect of the backbone. The VT NMR spectroscopic data confirm *cis*-chelation in $[PtMe_2\{o\text{-}C_6H_4(CH_2SeMe)_2\}]$, with two invertomers clearly identifiable, one of which, the DL form, results in two $\delta(^{77}Se)$ resonances of equal intensity (each with $^{195}Pt$ satellites) and one $\delta(^{195}Pt)$ resonance. The other major form is attributed to a *meso*-1 form [one $\delta(^{77}Se)$ and one $\delta(^{195}Pt)$].

The $Pt^{II}$ complexes of the cyclic selenoethers were less soluble, although $[PtMe_2([8]aneSe_2)]$ dissolved in DMF, enabling $^1H$, $^{13}C\{^1H\}$, $^{77}Se\{^1H\}$ and $^{195}Pt\{^1H\}$ NMR spectra to be obtained. The $[PtMe_2([16]aneSe_4)]$ was much less soluble and hence only the $^1H$ NMR spectroscopic data were obtained for this compound, although the formulation was supported by microanalysis and positive ion electrospray MS measurements. The $^1H$ NMR spectra of these cyclic selenoether complexes show resonances associated with coordinated selenoether as well as a singlet around 0.5 ppm due to the Pt–Me groups. The Pt–H couplings (≈ 80 Hz) are in agreement with the expected values. For $[PtMe_2([8]aneSe_2)]$, the $\delta(^{13}C)$ for the Me groups is a singlet at $\delta$ = –7.6 ppm with $^{195}Pt$ satellites (794 Hz). The $^{77}Se$ NMR spectrum is a singlet at 140.8 ppm, thus there is only a very small shift from "free" $[8]aneSe_2$ ($\delta$ = 138 ppm) upon coordination, although the appearance of clear coupling to $^{195}Pt$ ($^1J_{PtSe}$ = 323 Hz) unambiguously confirms the assignment. This compares to $\delta(^{77}Se)$ of 194 ppm ($^1J_{PtSe}$ = 680 Hz) for the corresponding dichloro species $[PtCl_2([8]aneSe_2)]$,[14] consistent with replacement of the chloro ligands with

 © 2006 Wiley-VCH Verlag GmbH & Co. KGaA, Weinheim 

strong σ-donor Me groups which have a much greater *trans* influence and hence substantially reduce the Pt–Se coupling constants. The $^{195}$Pt NMR shift for [$PtMe_2$([8]ane$Se_2$)], –4325 ppm, also compares with a value of –3825 ppm for [$PtCl_2$([8]ane$Se_2$)], reflecting the incorporation of the much stronger σ-donating Me ligands in the former. We note that the cyclic structure of the [8]ane$Se_2$ ligand eliminates the possibility of stereoisomers, hence only one form of the complex is evident. All of the dimethyl(selenoether)$Pt^{II}$ complexes are rather unstable – the solids deteriorate with significant darkening of the powders over a period of days to weeks even when stored under $N_2$. Solutions in chlorocarbons are even less stable, and substantial sample degradation was clearly evident from the NMR spectra recorded after standing in solution for a few hours. Data quoted were therefore recorded from freshly prepared samples.

Attempts to prepare analogous dimethyl(ditelluroether)-$Pt^{II}$ complexes by reaction of [$PtCl_2(SMe_2)_2$] with MeLi in situ, followed by hydrolysis and addition of either $MeTe(CH_2)_3TeMe$ or *o*-$C_6H_4(CH_2TeMe)_2$ gave dark brown, poorly soluble materials which were not the desired species. We also investigated reaction of isolated [$PtMe_2(SMe_2)_2$] with ditelluroether in anhydrous $Et_2O$ both at room temperature and low temperature. These reactions yielded orange/brown materials whose NMR spectra show clear evidence for TeMe units, but no PtMe groups. The electrospray mass spectra from these reaction show common features consistent with diplatinum compounds involving TeMe ligands, strongly indicating significant Te–C bond fission occurs in these reactions.

### Platinum(IV) Complexes

Freshly prepared solutions of the $Pt^{II}$ complexes [$PtMe_2${*o*-$C_6H_4(CH_2SeMe)_2$}] and [$PtMe_2${$MeSe(CH_2)_3$-SeMe}] in $CH_2Cl_2$ were stirred overnight with excess MeI, giving light yellow solids after work-up. The $^1$H and $^{77}$Se{$^1$H} NMR spectra of solutions of these products show that oxidative addition of MeI occurs cleanly, with complete conversion of the $Pt^{II}$ complexes to [$PtMe_3$I{*o*-$C_6H_4(CH_2SeMe)_2$}] and [$PtMe_3$I{$MeSe(CH_2)_3SeMe$}] respectively.

Six-coordinate trimethyl $Pt^{IV}$ complexes with both selenoether and telluroether ligands, [$PtMe_3$I(L-L)] [L-L = *o*-$C_6H_4(CH_2EMe)_2$; E = Se or Te], were obtained in good yield as soluble yellow/orange powdered solids through reaction of $PtMe_3$I with one mol. equiv. of L-L in refluxing $CHCl_3$ (Scheme 2). Surprisingly, these $Pt^{IV}$ compounds are much more stable both as solids and in solution than the $Pt^{II}$ species described above. The formulations follow from variable temperature $^1$H, $^{13}$C{$^1$H}, $^{77}$Se{$^1$H}, $^{125}$Te{$^1$H} and $^{195}$Pt NMR spectroscopic studies, electrospray MS and microanalyses. For bidentate chalcogenoethers coordinated to $PtMe_3$I three NMR distinguishable diastereoisomers are possible (*meso*-1, *meso*-2 and a pair of NMR indistinguishable DL enantiomers – Scheme 3) depending upon the orientations of the Me substituents relative to both the iodo and methyl ligands on Pt. The fact that the planar aromatic unit in the *o*-$C_6H_4(CH_2EMe)_2$ complexes lies out of the $ME_2$ plane leads to further possible stereoisomers for these particular complexes. From the NMR studies we observe that the telluroether complex is undergoing relatively slow pyramidal inversion at 298 K compared to the selenoether analogue. Cooling the solution of [$PtMe_3$I{*o*-$C_6H_4(CH_2SeMe)_2$}] leads to the observation of two significant $\delta$($^{195}$Pt) NMR resonances, while four $\delta$($^{77}$Se) NMR resonances with $^{195}$Pt satellites are evident, albeit one of these is weak, indicating that one isomer (probably a rather sterically crowded *meso*-2 form) has a very low percentage population. Thus, the DL form gives rise to two $\delta$($^{77}$Se) resonances and the *meso* form gives one resonance. Figure 1 shows the low temperature $^{125}$Te{$^1$H} NMR spectrum of [$PtMe_3$I{*o*-$C_6H_4(CH_2TeMe)_2$}], which clearly shows the presence of three invertomers all in significant amounts.

The crystal structure of [$PtMe_3$I{*o*-$C_6H_4(CH_2SeMe)_2$}] (Figure 2) confirms a distorted octahedral coordination sphere at $Pt^{IV}$ derived from three facial Me groups, an iodo ligand and a chelating diselenoether, *d*(Pt–C) = 2.080(3)–2.114(4) Å, *d*(Pt–Se) = 2.5530(4), 2.5629(4) Å, *d*(Pt1–I) = 2.7663(3) Å. The seven-membered chelate ring gives rise to a Se1–Pt1–Se2 angle of 98.317(12)°, and somewhat longer Pt–Se bonds than in [$PtMe_3$I(MeSeCH=CHSeMe)] [2.525(4), 2.532(4) Å],[9] reflecting the considerable steric demands of the wide-angle diselenoether. The selenoether adopts a DL configuration in which the SeMe substituents lie on opposite sides of the $PtSe_2$ plane, and the aromatic ring is oriented towards the Me ligand opposite the sterically large iodo ligand.

Using the ditelluromethane ligand, $MeTeCH_2TeMe$, with two mol. equivs. of $PtMe_3$I gives the dinuclear [($PtMe_3I)_2$-($MeTeCH_2TeMe$)] in good yield. The spectroscopic data are in full accord with a diiodo-bridged species in which the telluroether also bridges between the Pt atoms, i.e. [$Me_3Pt(\mu^2$-I)$_2(\mu^2$-$MeTeCH_2TeMe)PtMe_3$], which leads to two NMR distinguishable invertomers.

In order to investigate the effect of ligand architecture further, reactions were also conducted using the cyclic selenoethers [8]ane$Se_2$ and [16]ane$Se_4$, as well as the tripodal $MeC(CH_2SeMe)_3$. The distorted octahedral (trimethyl)$Pt^{IV}$ complexes, [$PtMe_3$I([8]ane$Se_2$)] and [$PtMe_3$I([16]ane$Se_4$)] were obtained in good yield by treatment of [$PtMe_3$I] with one molar equivalent of the cyclic selenoether in refluxing $CHCl_3$. The products were characterised by IR and multinuclear NMR spectroscopy, electrospray MS and microanalyses and represent the first examples of alkyl $Pt^{IV}$ complexes with (macro)cyclic selenoether coordination. The electrospray MS show clusters of peaks with the correct *m*/*z* and isotope patterns for [$PtMe_3$(L)]$^+$ (L = [8]ane$Se_2$ or [16]-ane$Se_4$). For the [8]ane$Se_2$ complex an additional cluster of peaks corresponding to [PtMe([8]ane$Se_2$)]$^+$ is also clearly evident, presumably a result of facile reductive elimination of ethane from the parent complex in the MS experiment. The NMR spectroscopic data for these species are also summarised in Table 1. The presence of three mutually *fac*

 © 2006 Wiley-VCH Verlag GmbH & Co. KGaA, Weinheim 

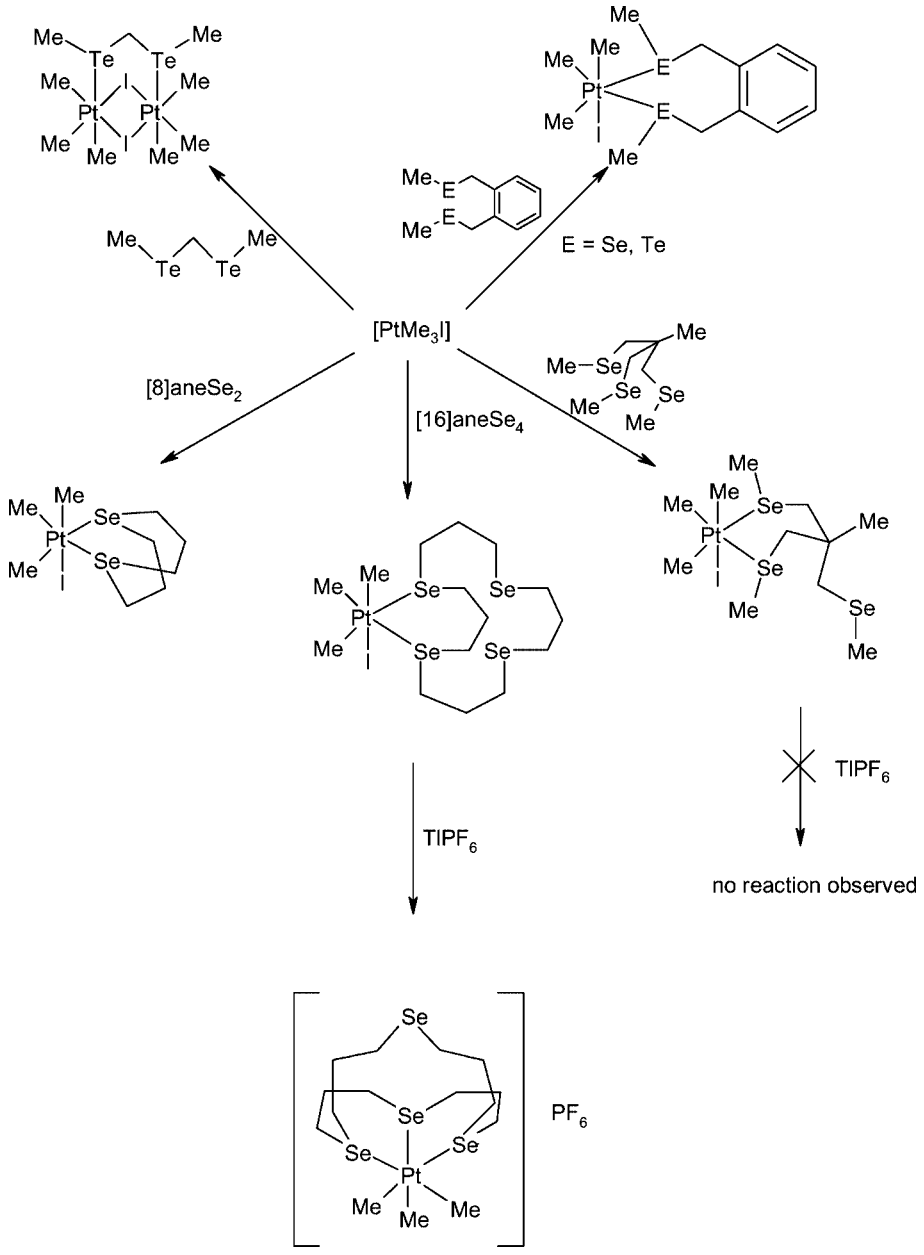


Scheme 2. Synthesis of (trimethyl)$Pt^{IV}$ complexes (note that only one of the possible stereoisomers is shown in each case).

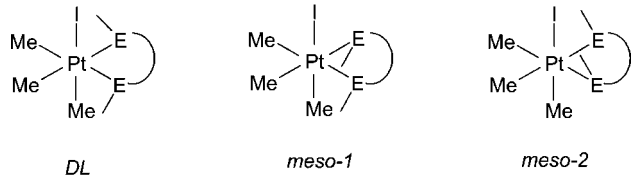


Scheme 3. Diasteroisomers for [$PtMe_3I$(L–L)] (L–L = bidentate dichalcogenoether). Note that the planar phenylene unit present in the xylyl derivatives leads to further stereoisomers depending upon its orientation with respect to the rest of the molecule.

Me groups was confirmed by the $^1H$ and the $^{13}C\{^1H\}$ NMR spectra which show two Me singlets in a 1:2 ratio at low frequency, each with $^{195}Pt$ satellite couplings as expected. The Me group *trans* to I is to low frequency of Me *trans* to Se, as observed for the small number of known examples of (trimethyl)$Pt^{IV}$ complexes with acyclic diselenoethers, and the Pt–H and Pt–C couplings are in also in accord.[7] For [$PtMe_3I$([8]ane$Se_2$)] we find that the coupling constants are consistently smaller than for the planar [$PtMe_2$([8]ane$Se_2$)] described above, as expected based upon the different coordination environments. The absence of axial symmetry in the $Pt^{IV}$ compounds leads to inequivalencies in the macrocyclic $CH_2$ environments, giving rise to four distinct $\delta(CH_2)$ resonances in the $^{13}C\{^1H\}$ NMR spectrum for the [8]ane$Se_2$ complex. For [$PtMe_3I$([16]ane$Se_4$)] seven $\delta(CH_2)$ resonances are clearly evident, consistent with bidentate coordination of the tetraselenoether ligand, giving a six-coordinate $Pt^{IV}$ species with a vertical plane of symmetry. The $^{77}Se$ NMR shifts for the $Pt^{IV}$ species are

 © 2006 Wiley-VCH Verlag GmbH & Co. KGaA, Weinheim 

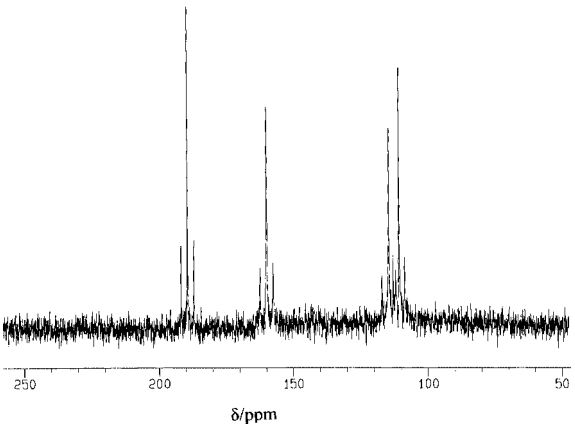


Figure 1. $^{125}Te\{^1H\}$ ($CH_2Cl_2/CDCl_3$, 243 K) spectrum of $[PtMe_3I\{o\text{-}C_6H_4(CH_2TeMe)_2\}]$ showing the presence of all three invertomers.

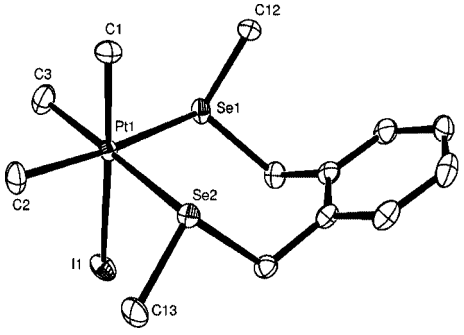


Figure 2. View of the crystal structure of $[PtMe_3I\{o\text{-}C_6H_4(CH_2SeMe)_2\}]$ with numbering scheme adopted. Ellipsoids are drawn at the 50% probability level and H atoms are omitted for clarity.

substantially to low frequency of the "free" ligand values, and surprisingly even the resonance arising from the two uncoordinated Se atoms of the $[16]aneSe_4$ ring is also some 40 ppm to low frequency of $[16]aneSe_4$ itself. This suggests that the presence of the (trimethyl)$Pt^{IV}$ fragment bound to the other two Se atoms significantly influences the electronic environment at the remote, "free" Se atoms – this may suggest that the uncoordinated Se atoms lie near to the iodo ligand.

As with all of the compounds in this study, $^{195}Pt$ NMR spectroscopy in principle provides an excellent and convenient direct probe of the electronic environment at platinum. Each of the $Pt^{IV}$ compounds shows a single resonance at ca. –3600 ppm, to high frequency of that for the planar $[PtMe_2([8]aneSe_2)]$ above. The macrocycle ring size has very little influence on the $^{195}Pt$ chemical shift. These compare with values of –3458 and –3530 ppm for the *meso*-1 and DL forms of $[PtMe_3I\{MeSe(CH_2)_3SeMe\}]$.[7]

Treatment of $[PtMe_3I(\kappa^2\text{-}[16]aneSe_4)]$ with one mol. equiv. of $TlPF_6$ in $CHCl_3$ results in clean abstraction of the iodo ligand, giving $[PtMe_3([16]aneSe_4)]PF_6$, as a white solid. This is the first cationic (alkyl)$Pt^{IV}$ complex with selenoether coordination. Electrospray MS shows intense peaks for the parent $[PtMe_3([16]aneSe_4)]^+$ cation, with lower intensity peaks corresponding to $[PtMe([16]aneSe_4)]^+$, i.e. loss of two Me groups (Figure 3). The generation of a $Pt^{IV}$ cation involving a *fac*-octahedral $Me_3Se_3$ donor set is confirmed by NMR spectroscopy. Although the cation still has $C_s$ local symmetry at $Pt^{IV}$, thus giving rise to two $\delta(^1H)$ and $\delta(^{13}C)$ resonances, this time both the chemical shift values and the Pt–H and Pt–C couplings are similar as the Me ligands are all *trans* to Se. The $^{13}C\{^1H\}$ and $^{77}Se\{^1H\}$ NMR spectra for this cation–anion system show only very broad resonances at room temperature. Upon cooling the sample to 223 K, the spectra sharpen. The dynamic process probably involves "ring-whizzing", resulting in rapid interchange between the "free" and coordinated Se atoms. Abel and coworkers proposed a similar mechanism for the thioether complex $[PtMe_3(\kappa^3\text{-}[12]aneS_4)]^+$ ([12]aneS$_4$ = 1,4,7,10-tetrathiacyclododecane).[15] The occurrence of a $\kappa^3$-bonding mode for $[16]aneSe_4$ is very unusual, the only other known examples are in the carbonyl complexes *fac*-$[M(CO)_3(\kappa^3\text{-}[16]aneSe_4)]^+$ (M = Mn or Re) and *fac*-$[M'(CO)_3(\kappa^3\text{-}[16]aneSe_4)]$ (M′ = Mo or W).[16] At 223 K the $^{77}Se\{^1H\}$ NMR spectrum for $[PtMe_3([16]aneSe_4)]PF_6$ reveals two Se environments at 70 (coordinated Se) and 138 ppm ("free" Se), once again these are both to low frequency of $[16]aneSe_4$ itself ($\delta$ =158 ppm). Replacement of the iodo ligand with a third Se atom leads to a small change in the $^{195}Pt$ NMR spectrum, which is now a singlet at $\delta$ = –3648 ppm. The only other examples of $Pt^{IV}$ complexes involving $[16]aneSe_4$ are the *trans*-$[PtX_2([16]aneSe_4)](PF_6)_2$ (X = Cl or Br) which we have described previously, obtained by halogen oxidation of the planar $[Pt([16]aneSe_4)](PF_6)_2$.[17] Spectroscopic studies of the yellow material obtained following treatment of the dicationic $Pt^{II}$ species, $[Pt([16]aneSe_4)](PF_6)_2$ with excess MeI in either refluxing $CH_2Cl_2$ or acetone solution showed no evidence for oxidative addition of the MeI, contrasting with the halogen oxidation described above.

The successful preparation of the cationic $[PtMe_3([16]aneSe_4)]^+$ with an unusual $Me_3Se_3$ donor set prompted us to investigate the chemistry of the tripodal $MeC(CH_2SeMe)_3$ with $[Me_3PtI]$. The preparation of $[PtMe_3I\{MeC(CH_2SeMe)_3\}]$ was achieved in good yield and the product was characterised by electrospray MS, microanalysis, IR and VT multinuclear NMR spectroscopy. The data are consistent with bidentate coordination of the tripod selenoether at the distorted octahedral $Pt^{IV}$ centre. For $[PtMe_3I\{\kappa^2\text{-}MeC(CH_2SeMe)_3\}]$ at room temperature both the $^1H$ and $^{77}Se\{^1H\}$ NMR spectra were broad and ill-defined. Upon cooling the sample to 223 K, the $^1H$ NMR resonances are sharp and several Pt–Me resonances are clearly evident, consistent with the presence of several invertomers (*meso*-1, *meso*-2 and DL forms, with further isomers arising depending upon the orientation of the uncoordinated arm either towards the iodo ligand or towards a Me group), and the presence of both coordinated and "free" SeMe groups. The mixture of invertomers, together with the low symmetry of the molecule make it very difficult to assign the spectra in detail. The structurally simpler (but spectroscopically still rather complicated)

 © 2006 Wiley-VCH Verlag GmbH & Co. KGaA, Weinheim 

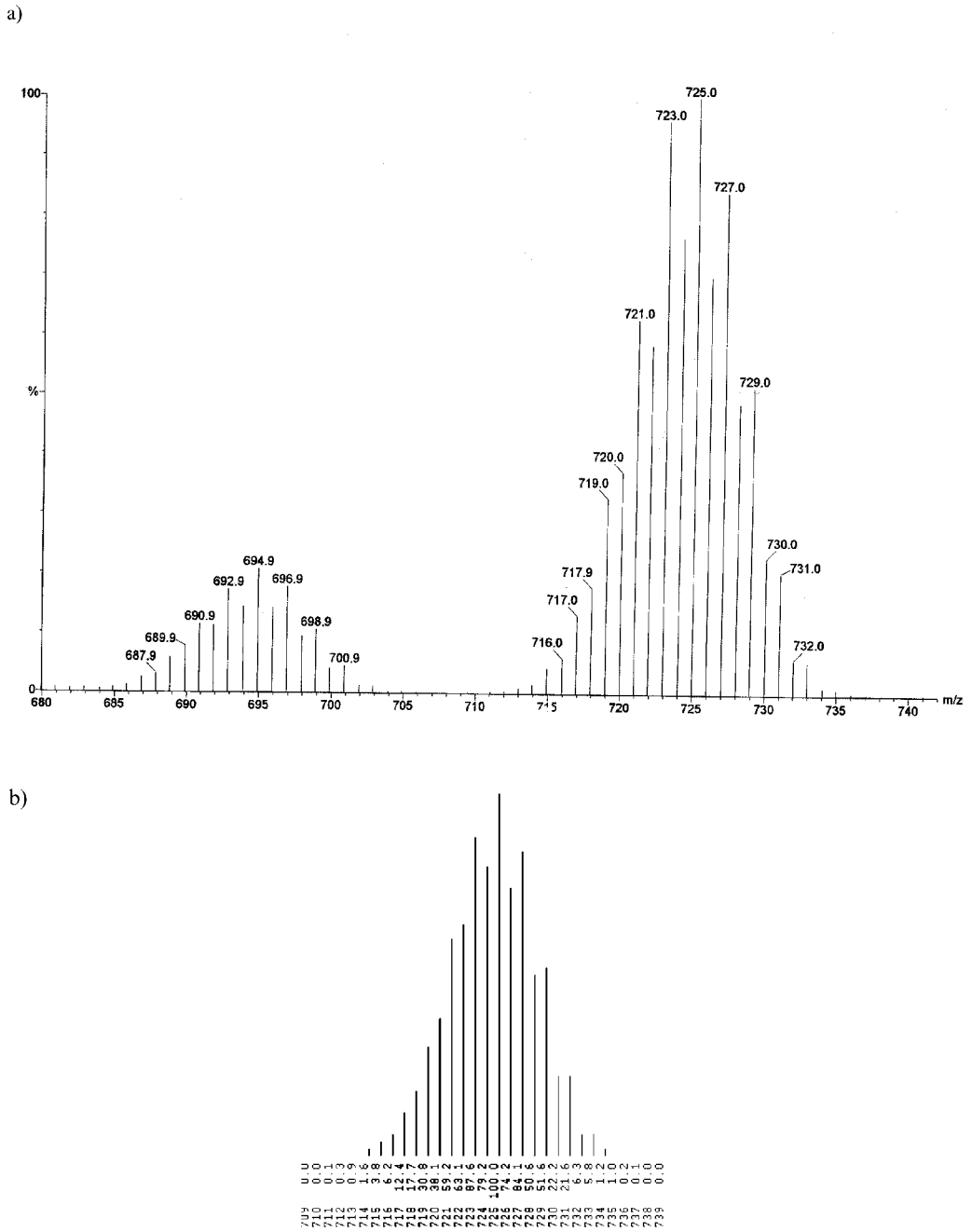


Figure 3. a) Positive ion electrospray MS (MeCN) of $[PtMe_3([16]aneSe_4)]PF_6$ (the cluster of peaks centred at $m/z$ = 725 corresponds to $[PtMe_3([16]aneSe_4)]^+$, while that centred at $m/z$ = 695 corresponds to $[PtMe([16]aneSe_4)]^+$). b). Simulated isotope pattern for $[PtMe_3([16]aneSe_4)]^+$.

$[PtMe_3X\{MeE(CH_2)_nEMe\}]$ ($n$ = 2 or 3) systems have been studied in detail by Abel and co-workers by VT NMR spectroscopy and band-shape analysis.[6–8] However, the identity of the complex as $[PtMe_3I\{\kappa^2\text{-}MeC(CH_2SeMe)_3\}]$ is not in doubt.

At 223 K the $^{13}C\{^1H\}$ NMR spectrum of $[PtMe_3I\{\kappa^2\text{-}MeC(CH_2SeMe)_3\}]$ is extremely complicated owing to the presence of varying amounts of the possible invertomers, the low symmetry of the complexes and the fact that the C atoms of the Pt–Me units occur in the same region of the spectrum as the SeMe groups of the uncoordinated arm of the tripod, resulting in overlapping resonances which are not readily assigned.

The observation of three $^{195}Pt\{^1H\}$ NMR resonances at ca. –3500 ppm at 223 K is consistent with the presence of three significant, NMR distinguishable invertomers. The $^{77}Se\{^1H\}$ NMR spectrum at 223 K is also very complex, revealing three coordinated Se environments in the range 49–53 ppm, each with $^{195}Pt$ satellites, three further coordinated Se environments in the range 37–39 ppm with satellites, and four resonances in the range 27–35 ppm which show no $^{195}Pt$ coupling and hence are attributed to the Se

 © 2006 Wiley-VCH Verlag GmbH & Co. KGaA, Weinheim 

atoms of the uncoordinated arm of the tripod selenoether [$\delta(^{77}Se)$ for $MeC(CH_2SeMe)_3$: +24]. These data strongly suggest that the orientation of the uncoordinated arm of the tripod (either towards the iodide or towards the Me group *trans* to I) are also distinguishable by NMR spectroscopy.

Attempts to promote tridentate selenoether coordination to give $[PtMe_3\{MeC(CH_2SeMe)_3\}]^+$ through treatment of the bidentate complex with $TlPF_6$ either in refluxing MeCN or $CHCl_3$ were not successful. The NMR spectra of the resulting solutions show that $[PtMe_3I\{MeC(CH_2SeMe)_3\}]$ is still the only significant species after the reaction. This suggests that the tripodal $Se_3$-donor ligand is not well-suited to facial coordination on the small trimethylPt$^{IV}$ fragment. The different reactivities of the Pt$^{IV}$ complexes containing the tripodal $Se_3$-donor ligand compared to that containing the macrocyclic selenoether may be due to the different constraints of the two ligands and the different ring-strain effects.

It has been shown that $[PtMe_3I(L–L)]$ (L–L = diphosphane or distibane)[18,12] undergo clean reductive elimination of ethane upon thermolysis. We have therefore probed the thermolysis of the $[PtMe_3I\{o\text{-}C_6H_4(CH_2EMe)_2\}]$ complexes prepared in this work. The telluroether complex $[PtMe_3I\{o\text{-}C_6H_4(CH_2TeMe)_2\}]$ does not melt on heating, but undergoes decomposition at ≈ 130 °C giving a black solid. The corresponding Pt$^{IV}$ selenoether complex melts at ca. 150 °C and then darkens slowly as the temperature is increased, indicating the onset of decomposition. A solid sample of this complex was heated at ca. 160 °C for 1 h and the residue investigated by $^1H$ NMR spectroscopy, which revealed loss of the PtMe and SeMe resonances. Thus, it is clear that these species do not undergo clean reductive elimination under these conditions. This may be a consequence of the well-known susceptibility of group 16 ligands to undergo dealkylation.[1]

## Conclusions

We have developed routes for the synthesis of the first series of dimethyl(selenoether)Pt$^{II}$ complexes, as well as a range of trimethyl(selenoether)Pt$^{IV}$ complexes (including the first macrocyclic examples) and rare examples involving ditelluroethers. The Pt$^{IV}$ species are less reactive than the Pt$^{II}$ complexes, possibly due to the very strong ligand field imparted by the Me ligands in the Pt$^{IV}$ species, together with the fact that these compounds are coordinatively saturated, hence providing limited possibility for metal-assisted E–C bond fission (cf. the Pt$^{II}$ species). The donor type, ligand architecture and denticity clearly play major roles in determining the invertomer populations in these compounds. Using the macrocyclic [16]aneSe$_4$ we have been able to obtain the first cationic trialkyl(selenoether)Pt$^{IV}$, $[PtMe_3(\kappa^3\text{-}[16]aneSe_4)]^+$, whereas surprisingly this was not possible under similar conditions using the tripodal $MeC(CH_2SeMe)_3$. This may also be a consequence of the ligand architecture which for the tripodal $Se_3$ ligand results in low stability on the small Pt$^{IV}$ centre. The new dimethyl(selenoether)Pt$^{II}$ complexes, $[PtMe_2(L\text{-}L)]$, undergo clean and complete oxidative addition of MeI to afford the corresponding Pt$^{IV}$ species $[PtMe_3I(L\text{-}L)]$.

## Experimental Section

Infrared spectra were recorded as Nujol mulls between CsI plates with a Perkin–Elmer 983G spectrometer over the range 4000–200 cm$^{-1}$. Mass spectra were run by positive ion electrospray (MeCN solution) with a VG Biotech platform. $^1H$ NMR spectra were recorded with a Bruker AV300 spectrometer or Bruker DPX400 spectrometer. $^{13}C\{^1H\}$, $^{77}Se\{^1H\}$, $^{125}Te\{^1H\}$ and $^{195}Pt\{^1H\}$ NMR spectra were recorded with a Bruker DPX400 spectrometer operating at 100.6, 76.3, 126.3 or 85.7 MHz, respectively, and are referenced to TMS, external neat $Me_2Se$, external neat $Me_2Te$ and external 1 mol·dm$^{-3}$ $Na_2[PtCl_6]$ in water, respectively. Microanalyses were undertaken by the University of Strathclyde microanalytical service. Solvents were dried prior to use, and all preparations were undertaken using standard Schlenk techniques under $N_2$. The precursors $[PtCl_2(Me_2S)_2]$[19] and $[PtMe_3I]$[20] were prepared by literature methods and the selenoethers and telluroethers were prepared as described previously.[21–24]

### Preparations

#### Pt$^{II}$ Compounds

**$[PtMe_2([8]aneSe_2)]$:** A 1.6 M solution of MeLi (0.2 mL, 0.32 mmol) in $Et_2O$ was slowly added to an ice-cold suspension of $[PtCl_2(SMe_2)_2]$ (0.050 g, 0.128 mmol) in 20 cm$^3$ dry $Et_2O$. After 5 min a further 0.1 mL MeLi (1.6 M in $Et_2O$, 0.16 mmol) were added and the solution was warmed to room temperature. After ca. 10 min the yellow colour disappeared and a white precipitate formed. At this stage 10 mL of $H_2O$ and 1 equiv. of [8]aneSe$_2$ (0.031 g, 0.128 mol) were added. The mixture was stirred for 2.5 h giving a beige precipitate which was filtered off and washed with $Et_2O$. The solid was then dissolved in $CH_2Cl_2$ (10 mL), filtered and the solvent was removed in vacuo. Yield 0.075 g, 64%. $C_8H_{18}PtSe_2$ (467.2): calcd. C 20.6, H 3.9; found C 21.3, H 4.2. Electrospray MS (MeCN): found 494, 453; calcd. for $[^{195}PtMe([8]ane^{80}Se_2)(MeCN)]^+$ *m*/*z* = 495, $[^{195}PtMe([8]ane^{80}Se_2)]^+$ 454. $^1H$ NMR (300 MHz, $CDCl_3$, 298 K): $\delta$ = 0.5 (s, $^2J_{PtH}$ = 82 Hz, 6 H, PtMe), 2.2 (m, 4 H, $CH_2CH_2CH_2$), 2.8 (m, 8 H, $SeCH_2$) ppm. $^{13}C\{^1H\}$ NMR (DMF/$[D_6]Me_2CO$, 298 K): $\delta$ = –7.6 ($^1J_{PtC}$ = 794 Hz, 2 C, PtMe), 24.0 (4 C, $SeCH_2$), 27.3 (2 C, $CH_2CH_2CH_2$) ppm. $^{77}Se\{^1H\}$ NMR (DMF/$[D_6]Me_2CO$, 298 K): $\delta$ = 140.8 ($^1J_{PtSe}$ = 323 Hz) ppm. $^{195}Pt$ NMR ($CH_2Cl_2$/$CDCl_3$, 298 K): $\delta$ = –4318 ppm.

**$[PtMe_2([16]aneSe_4)]$:** Method as above using [16]aneSe$_4$. Yellow solid. Yield 61%. $C_{14}H_{30}PtSe_4$ (709.3): calcd. C 23.7, H 4.3; found C 23.1, H 4.2. Electrospray MS (MeCN): found *m*/*z* = 695; calcd. for $[^{195}PtMe([16]ane^{80}Se_4)]^+$ *m*/*z* = 700. $^1H$ NMR (300 MHz, $[D_6]$-DMSO, 298 K): $\delta$ = 0.48 (s, $^2J_{PtH}$ = 81 Hz, 6 H, PtMe), 1.92 (m, 8 H, $CH_2CH_2CH_2$) 2.61 (t, 16 H, $SeCH_2$) ppm.

**$[PtMe_2\{MeSe(CH_2)_2SeMe\}]$:** Method as above using $MeSe(CH_2)_2SeMe$. Yellow solid. Yield 41%. $C_6H_{16}PtSe_2$ (441.2): calcd. C 16.3, H 3.7; found C 15.9, H 3.3. Electrospray MS (MeCN): found *m*/*z* = 468, 453, 426, 411; calcd. for $[^{195}PtMe\{Me^{80}Se(CH_2)_2{}^{80}SeMe\}(MeCN)]^+$ *m*/*z* = 469, $[^{195}Pt\{Me^{80}Se(CH_2)_2{}^{80}SeMe\}(MeCN)]^+$ 454, $[^{195}PtMe\{Me^{80}Se(CH_2)_2{}^{80}SeMe\}]^+$ 428, $[^{195}Pt\{Me^{80}Se(CH_2)_2{}^{80}SeMe\}]^+$ 413. $^1H$ NMR (400 MHz, $CDCl_3$, 273 K): $\delta$ = 0.72 (s, $^2J_{PtH}$ = 84 Hz, PtMe), 0.77 (s, $^2J_{PtH}$ = 85 Hz, PtMe), 2.16 (s, $^3J_{PtH}$ = 22 Hz, SeMe), 2.36 (s, $^3J_{PtH}$ = 21 Hz,

 © 2006 Wiley-VCH Verlag GmbH & Co. KGaA, Weinheim 

SeMe), 2.55–3.25 (m, 4 H, $SeCH_2$) ppm. $^{13}C\{^1H\}$ NMR ($CDCl_3$, 223 K): $\delta$ = –12.8 ($^1J_{PtC}$ = 760 Hz, PtMe), –12.6 ($J$ = 735 Hz, PtMe), 9.9, 11.1 (SeMe), 29.2, 29.5 ($SeCH_2$) ppm. $^{77}Se\{^1H\}$ NMR ($CDCl_3$, 223 K): $\delta$ = 247.9 (major form, $^1J_{PtSe}$ = 457 Hz), 250.1 (minor form, $J$ = 438 Hz) ppm. $^{195}Pt$ NMR ($CDCl_3$, 223 K): $\delta$ = –4383 (major), –4395 (minor) ppm.

**[$PtMe_2\{MeSe(CH_2)_3SeMe\}$]:** Method as above using $MeSe(CH_2)_3SeMe$. Beige solid. Yield 64%. $C_7H_{18}PtSe_2$ (455.2): calcd. C 18.5, H 4.0; found C 18.6, H 4.2. Electrospray MS (MeCN): found $m/z$ = 482, 466, 425; calcd. for $[^{195}PtMe\{Me^{80}Se(CH_2)_3{}^{80}SeMe\}(MeCN)]^+$ $m/z$ = 483, $[^{195}Pt\{Me^{80}Se(CH_2)_3{}^{80}SeMe\}(MeCN)]^+$ 468, $[^{195}PtMe\{Me^{80}Se(CH_2)_3{}^{80}SeMe\}]^+$ 427. $^1H$ NMR (400 MHz, $CDCl_3$, 248 K): $\delta$ = 0.51 (s, $^2J_{PtH}$ = 84 Hz, PtMe), 0.55 (s, $J$ = 84 Hz, PtMe), 2.20 (br., 2 H, $CH_2CH_2CH_2$), 2.31, 2.33 (s, 6 H, SeMe), 2.83, 2.99 (m, 4 H, $SeCH_2$) ppm. $^{13}C\{^1H\}$ NMR ($CDCl_3$, 223 K): $\delta$ = –8.9 ($^1J_{PtC}$ = 749 Hz, PtMe), –8.7 ($J$ = 748 Hz, PtMe), 10.5, 10.9 (SeMe), 26.0, 26.7, 27.6 ($CH_2$) ppm. $^{77}Se\{^1H\}$ NMR ($CDCl_3$, 223 K): $\delta$ = 114.0 ($^1J_{PtSe}$ = 427 Hz), 102.1 ($J$ = 429 Hz) ppm. $^{195}Pt$ NMR ($CDCl_3$, 223 K): $\delta$ = –4247 (major), –4309 (minor) ppm.

**[$PtMe_2\{o\text{-}C_6H_4(CH_2SeMe)_2\}$]:** Method as above using $o$-$C_6H_4(CH_2SeMe)_2$. Yellow solid. Yield 56%. $C_{12}H_{20}PtSe_2$ (517.3): calcd. C 27.9, H 3.9; found C 28.6, H 3.7. Electrospray MS (MeCN): found $m/z$ = 506; calcd. for $[^{195}PtMe\{o\text{-}C_6H_4(CH_2{}^{80}SeMe)_2\}]^+$ $m/z$ = 504. $^1H$ NMR (400 MHz, $CDCl_3$, 298 K): $\delta$ = 0.34 (s, $^2J_{PtH}$ = 83 Hz, 6 H, PtMe), 2.3 (s, 6 H, SeMe), 4.3 (br., 4 H, $SeCH_2$), 7.0–7.2 (br. m, 4 H, $o$-$C_6H_4$) ppm; (213 K): $\delta$ = 0.23 (s, $^2J_{PtH} \approx$ 80 Hz, PtMe), 0.25 (s, $J \approx$ 80 Hz, PtMe), 1.89, 2.21, 2.44 (s, SeMe), 3.8–5.0 (m, $SeCH_2$), 6.9–7.3 (m, 4 H, $o$-$C_6H_4$) ppm. $^{13}C\{^1H\}$ NMR ($CDCl_3$, 298 K): $\delta$ = –8.6 ($^1J_{PtC}$ = 779 Hz, PtMe), 11.0 (SeMe), 29.8 ($SeCH_2$), 126.0–134.5 ($o$-$C_6H_4$) ppm; (193 K): $\delta$ = –8.8 ($^1J_{PtC}$ = 760 Hz, PtMe), –8.3 (PtMe, $J$ = 751 Hz), –7.4 ($J$ = 763 Hz, PtMe), 10.3, 11.1, 13.2 (SeMe), 27.8, 28.6, 31.3 ($SeCH_2$), 127.4–134.6 ($o$-$C_6H_4$) ppm. $^{77}Se\{^1H\}$ NMR ($CDCl_3$, 298 K): $\delta$ = 171.6 ($^1J_{PtSe}$ = 520 Hz) ppm; (193 K): $\delta$ = 169.1 ($J$ = 526 Hz), 160.6 ($J$ = 492 Hz), 155.9 ($J$ = 438 Hz) ppm. $^{195}Pt$ NMR ($CDCl_3$, 298 K): $\delta$ = –4275; (193 K): $\delta$ = –4308, –4316 ppm.

**Platinum(IV) Compounds**

**[$PtMe_3I([8]aneSe_2)$]:** [$PtMe_3I$] (0.10 g, 0.27 mmol) was dissolved in $CHCl_3$ (10 mL). [8]$aneSe_2$ (0.068 g, 0.28 mmol) in $CHCl_3$ (10 mL) was added slowly. The pale yellow solution was refluxed for 7 h, then stirred at room temperature overnight. The solution was concentrated in vacuo to approximately 5 mL. Diethyl ether (10 mL) was added, producing a cream-coloured solid, which was collected by filtration, washed with diethyl ether and dried in vacuo. Yield 0.075 g, 45%. $C_9H_{21}IPtSe_2$ (609.2): calcd. C 17.7, H 3.4; found C 17.8, H 3.3. Electrospray MS (MeCN): found 494, 483, 453; calcd. for $[^{195}PtMe([8]ane^{80}Se_2)(MeCN)]^+$ 495, $[^{195}PtMe_3([8]ane^{80}Se_2)]^+$ 484, $[^{195}PtMe([8]ane^{80}Se_2)]^+$ 454. $^1H$ NMR (300 MHz, $CDCl_3$, 298 K): $\delta$ = 1.0 (s, $^2J_{PtH}$ = 71.8 Hz, 3 H, PtMe *trans* I), 1.6 (s, $J$ = 65.2 Hz, 6 H, PtMe *trans* Se), 2.1–3.4 (m, 12 H, $CH_2$) ppm. $^{13}C\{^1H\}$ NMR ($CDCl_3$): $\delta$ = 3.5 ($^1J_{PtC}$ = 612 Hz, 1 C, PtMe *trans* I), 3.9 ($J$ = 674 Hz, 2 C, PtMe *trans* Se), 20.8 (2 C), 21.4 (2 C, $SeCH_2$), 22.5 (1 C), 26.8 (1 C, $CH_2CH_2$) ppm. $^{77}Se\{^1H\}$ NMR ($CDCl_3$, 298 K): $\delta$ = 65 ($^1J_{PtSe}$ = 244 Hz) ppm. $^{195}Pt$ NMR ($CDCl_3$): $\delta$ = –3589 ppm.

**[$PtMe_3I([16]aneSe_4)$]:** Method as above, but using [16]$aneSe_4$. Cream solid. Yield 59%. $C_{15}H_{33}IPtSe_4.CHCl_3$ (970.6): calcd. C 19.8, H 3.5; found C 19.4, H 3.8. Electrospray MS (MeCN): found 724; calcd. for $[^{195}PtMe_3([16]ane^{80}Se_4)]^+$ 728. $^1H$ NMR (300 MHz, $CDCl_3$, 298 K): $\delta$ = 1.15 (s, $^2J_{PtH}$ = 71.6 Hz, 3 H, PtMe *trans* I), 1.55 (s, 6 H, PtMe *trans* Se, $J$ = 66.5 Hz), 2.5–3.1 (m, 24 H, $CH_2$) ppm. $^{13}C\{^1H\}$ NMR ($CDCl_3$, 243 K): $\delta$ = 3.7 ($^1J_{PtC}$ = 619 Hz, 2 C, PtMe *trans* Se), 4.35 (1 C, PtMe *trans* I, 654 Hz), 22.1 (1 C), 22.7 (2 C, $SeCH_2$), 23.0 (2 C), 25.7 (2 C), 26.3 (2 C), 29.3 (2 C), 29.9 (1 C, $CH_2$) ppm. $^{77}Se\{^1H\}$ NMR ($CDCl_3$, 243 K): $\delta$ = 116.6 ($^1J_{PtSe}$ = 266 Hz, 1 Se), 119.5 (1 Se) ppm. $^{195}Pt$ NMR ($CDCl_3$, 243 K): $\delta$ = –3616 ppm.

**[$PtMe_3([16]aneSe_4)]PF_6$:** $TlPF_6$ (0.063 g, 0.18 mmol) was added to a solution of [$PtMe_3I$] (0.06 g, 0.163 mmol) and [16]$aneSe_4$ (0.079 g, 0.163 mmol) in $CHCl_3$ (8 mL). The reaction mixture was refluxed under $N_2$ for 2.5 h to give a fine yellow precipitate (TlI) and an almost colourless solution which was separated via cannula. After concentrating the solution in vacuo to ca. 2 mL, $Et_2O$ was added to give a white solid which was collected by filtration, washed with $Et_2O$ and dried in vacuo. Yield 0.049 g, 35%. $C_{15}H_{33}F_6PPtSe_4$ (869.3): calcd. C 20.7, H 3.8, found C 21.3, H 3.7. Electrospray MS (MeCN): found 725, 695; calcd. for $[^{195}PtMe_3([16]ane^{80}Se_4)]^+$ 728, $[^{195}PtMe([16]ane^{80}Se_4)]^+$ 698. $^1H$ NMR (300 MHz, $CDCl_3$, 298 K): $\delta$ = 1.06 (s, $^2J_{PtH}$ = 61 Hz, 3 H, PtMe), 1.13 (s, $J$ = 66 Hz, 6 H, PtMe), 1.8–3.3 (br. m, 24 H, $CH_2$) ppm. $^{13}C\{^1H\}$ NMR ($CH_2Cl_2$/$CDCl_3$, 298 K): very broad (223 K): $\delta$ = 2.4 ($^1J_{PtC}$ = 612 Hz, 1 C, PtMe), 3.0 ($J$ = 647 Hz, 2 C, PtMe), 22.3–29.1 ($CH_2$) ppm. $^{77}Se\{^1H\}$ NMR ($CDCl_3$, 298 K): no spectrum; (223 K): $\delta$ = 138 (1 Se), 70 ($^1J_{PtSe}$ = 249 Hz, 3 Se) ppm. $^{195}Pt$ NMR ($CH_2Cl_2$/$CDCl_3$, 298 K): $\delta$ = –3648 ppm. IR (Nujol): $\tilde{\nu}$ = 840 [$\nu(PF_6^-)$], 557 [$\delta(PF_6^-)$] $cm^{-1}$.

**[$PtMe_3I\{MeC(CH_2SeMe)_3\}$]:** Method as for [$PtMe_3I([16]aneSe_4)$] above, but using $MeC(CH_2SeMe)_3$. Yellow solid. Yield 63%. $C_{11}H_{27}IPtSe_3$ (718.2): calcd. C 18.4, H 3.8, found C 18.7, H 3.5. Electrospray MS (MeCN): found $m/z$ = 591, 561; calcd. for $[^{195}PtMe_3\{MeC(CH_2{}^{80}SeMe)_3\}]^+$ $m/z$ = 594; $[^{195}PtMe\{MeC(CH_2{}^{80}SeMe)_3\}]^+$ 564. $^1H$ NMR (400 MHz, $CDCl_3$, 298 K): very broad (223 K): $\delta$ = 0.9–1.6 (overlapping resonances, PtMe, CMe), 2.0–3.7 (overlapping resonances, SeMe and $SeCH_2$) ppm. $^{13}C\{^1H\}$ NMR ($CDCl_3$, 223 K): $\delta$ = 0.35–1.06 (s, PtMe *trans* I), 5.9–6.8 (s, PtMe *trans* Se), 7.8–12.4 (SeMe), 25.2–25.5 (MeC), 31.5–42.5 ($SeCH_2$) ppm. $^{77}Se\{^1H\}$ NMR ($CDCl_3$, 298 K): no spectrum; (223 K): $\delta$ = 53.0 ($^1J_{PtSe}$ = 252 Hz), 51.6 ($J$ = 160 Hz), 49.3 ($J$ = 258 Hz), 38.5 ($J$ = 252 Hz), 37.4 ($J$ = 162 Hz), 37.3 ($J$ = 256 Hz), 35.1, 33.0, 29.0, 27.3 (uncoordinated Se) ppm. $^{195}Pt$ NMR ($CDCl_3$, 223 K): $\delta$ = –3446, –3543, –3550 ppm.

**[$PtMe_3I\{o\text{-}C_6H_4(CH_2SeMe)_2\}$]:** Method as above, but using $o$-$C_6H_4(CH_2SeMe)_2$. Cream solid. Yield 75%. $C_{13}H_{23}IPtSe_2{\cdot}1/2Et_2O$ (696.3): calcd. C 25.9, H 4.0, found C 26.3, H 3.8. Electrospray MS (MeCN): found 533; calcd. for $[^{195}PtMe_3\{o\text{-}C_6H_4(CH_2{}^{80}SeMe)_2\}]^+$ 534. $^1H$ NMR (400 MHz, $CDCl_3$, 298 K): broad (223 K): $\delta$ = 0.90 (s, $^2J_{PtH}$ = 79 Hz, PtMe), 1.12 (s, $J$ = 70 Hz, PtMe), 1.20 (s, $J$ = 70 Hz, PtMe), 1.22 (s, $J$ = 70 Hz, PtMe), 1.36 (s, $J$ = 68 Hz, PtMe), 2.3 (sh), 2.55, 2.6 (sh, 6 H, SeMe), 3.9–5.2 (m, 4 H, $CH_2$), 7.05–7.45 (m, 4 H, $o$-$C_6H_4$) ppm. $^{13}C\{^1H\}$ NMR ($CDCl_3$, 298 K): broad (213 K): $\delta$ = 1.8 ($^1J_{PtC}$ = 628 Hz, PtMe), 2.6 ($J$ = 622 Hz, PtMe), 5.2 ($J$ = 616 Hz, PtMe), 5.85 ($J$ = 624 Hz, PtMe), 6.2 ($J$ = 660 Hz, PtMe), 13.7, 14.5, 14.69, 14.72 (SeMe), 27.7, 28.6, 34.3 (sh), 34.6 ($SeCH_2$), 126.8–139.9 ($o$-$C_6H_4$) ppm. $^{77}Se\{^1H\}$ NMR ($CDCl_3$, 298 K): not observed; (213 K): $\delta$ = 114.0 ($^1J_{PtSe}$ = 289 Hz) ppm; 98.7 ($J$ = 280 Hz), 97.8 ($J$ = 312 Hz), 95.5 ($J$ = 286 Hz) (minor isomer) ppm. $^{195}Pt$ NMR ($CDCl_3$, 298 K): not observed; (213 K): $\delta$ = –3382, –3468 (the minor isomer is not observed) ppm.

**[$PtMe_3I\{o\text{-}C_6H_4(CH_2TeMe)_2\}$]:** Method as above, but using $o$-$C_6H_4(CH_2TeMe)_2$. Orange solid. Yield 60%. $C_{13}H_{23}IPtTe_2{\cdot}1/2Et_2O$ (793.6): calcd. C 22.7, H 3.6, found C 23.1, H 3.5. Electrospray MS (MeCN): found 629; calcd. for $[^{195}PtMe_3\{o\text{-}C_6H_4(CH_2{}^{130}TeMe)_2\}]^+$

 © 2006 Wiley-VCH Verlag GmbH & Co. KGaA, Weinheim 

634. $^1$H NMR (400 MHz, $CDCl_3$, 298 K): broad (248 K): $\delta$ = 0.85–1.6 (s, PtMe), 2.1–3.1 (s, TeMe), 3.9–5.0 (m, 4 H, $CH_2$), 6.9–8.1 (m, 4 H, *o*-$C_6H_4$) ppm. $^{13}C\{^1H\}$ NMR ($CDCl_3$, 298 K): broad (243 K): $\delta$ = –12.45, –12.4, –6.7, –5.7 (TeMe), 1.8 ($^1J_{PtC}$ = 638 Hz, PtMe), 2.9 ($J$ = 635 Hz, PtMe), 3.9 ($J$ = 687 Hz, PtMe), 4.3 ($J$ = 607 Hz, PtMe), 7.3 ($J$ = 592 Hz, PtMe), 10.4, 12.4, 16.7, 16.9 ($TeCH_2$), 126.5–135.3 (*o*-$C_6H_4$) ppm. $^{125}Te\{^1H\}$ NMR ($CDCl_3$, 243 K): $\delta$ = 189.5 ($^1J_{PtTe}$ = 602 Hz) ppm; 159.9 ($J$ = 618 Hz), 114.5 ($J$ = 638 Hz), 110.8 ($J$ = 537 Hz) ppm. $^{195}$Pt NMR ($CDCl_3$, 298 K): not observed; (223 K): $\delta$ = –3968, –4022, –4119 ppm.

**[($PtMe_3I)_2$(MeTe$CH_2$TeMe)]:** Method as above, but using 0.5 mol. equivs. of MeTe$CH_2$TeMe. Orange solid. Yield 68%. $^1$H NMR (400 MHz, $CDCl_3$, 298 K): broad (248 K): $\delta$ = 1.06 (s, $^2J_{PtH}$ = 76 Hz, PtMe), 1.14 (s, $J$ = 72 Hz, PtMe), 1.16 (s, $J$ = 74 Hz, PtMe), 1.22 (s, $J$ = 76 Hz, PtMe), 2.06 (s, $J$ = 68 Hz, PtMe), 2.07 (s, $J$ = 68 Hz, PtMe), 2.01, 2.18 (s, TeMe), 4.46, 4.55 (m, $TeCH_2$) ppm. $^{13}C\{^1H\}$ NMR ($CDCl_3$, 298 K): broad (243 K): $\delta$ = –18.7 (major form, $TeCH_2$) –16.1 (minor form, $TeCH_2$), –8.5 (major form, TeMe), –7.95 (minor form, TeMe), 6.55 ($^1J_{PtC}$ = 670 Hz, PtMe), 7.0 ($J$ = 678 Hz, PtMe), 7.7 ($J$ = 600 Hz, PtMe), 7.8 ($J$ = 660 Hz, PtMe), 9.1 ($J$ = 607 Hz, PtMe) ppm. $^{125}Te\{^1H\}$ NMR ($CDCl_3$, 243 K): $\delta$ = 173.2 ($^1J_{PtTe}$ = 713 Hz) ppm. 171.1 ($J$ = 605 Hz) ppm. $^{195}$Pt NMR ($CDCl_3$, 223 K): $\delta$ = –3430 (major), –3451 (minor) ppm.

**X-ray Crystallography:** Selected bond lengths and angles for this species are presented in Table 2. Details of the crystallographic data collection and refinement parameters are given in Table 3. Yellow/orange single crystals of [$PtMe_3I${*o*-$C_6H_4(CH_2SeMe)_2$}] were obtained by diffusion of hexane into a solution of the complex in $CH_2Cl_2$. Data collection used a Nonius Kappa CCD diffractometer ($T$ = 120 K) and with graphite-monochromated Mo-$K_\alpha$ X-radiation ($\lambda$ = 0.71073 Å). Structure solution and refinement were routine.[25,26]

CCDC-609594 contains the supplementary crystallographic data for this paper. These data can be obtained free of charge from The Cambridge Crystallographic Data Centre via www.ccdc.cam.ac.uk/data_request/cif.

Table 2. Selected bond lengths [Å] and angles [°] for [$PtMe_3I${*o*-$C_6H_4(CH_2SeMe)_2$}].

| | |
|---|---|
| C1–Pt1 | 2.085(4) |
| C2–Pt1 | 2.080(3) |
| C3–Pt1 | 2.114(4) |
| Se1–Pt1 | 2.5530(4) |
| Se2–Pt1 | 2.5629(4) |
| I1–Pt1 | 2.7663(3) |
| C2–Pt1–C1 | 84.28(15) |
| C2–Pt1–C3 | 87.39(15) |
| C1–Pt1–C3 | 88.25(16) |
| C2–Pt1–Se1 | 172.68(11) |
| C1–Pt1–Se1 | 95.03(11) |
| C3–Pt1–Se1 | 85.30(10) |
| C2–Pt1–Se2 | 88.97(11) |
| C1–Pt1–Se2 | 89.06(11) |
| C3–Pt1–Se2 | 175.67(11) |
| Se1–Pt1–Se2 | 98.317(12) |
| C2–Pt1–I1 | 94.58(11) |
| C1–Pt1–I1 | 177.53(11) |
| C3–Pt1–I1 | 89.51(12) |
| Se1–Pt1–I1 | 85.815(11) |
| Se2–Pt1–I1 | 93.116(10) |

Table 3. Crystallographic parameters.[a]

| Complex | [$PtMe_3I${*o*-$C_6H_4(CH_2SeMe)_2$}] |
|---|---|
| Empirical formula | $C_{13}H_{23}IPtSe_2$ |
| $M$ | 659.22 |
| Crystal system | monoclinic |
| Space group | C2/*c* |
| *a* [Å] | 13.3002(7) |
| *b* [Å] | 11.6116(7) |
| *c* [Å] | 22.5391(12) |
| $\alpha$ [°] | 90 |
| $\beta$ [°] | 102.788(2) |
| $\gamma$ [°] | 90 |
| $V$ [Å] $^3$ | 3394.5(3) |
| $Z$ | 8 |
| $\mu$(Mo-$K_\alpha$) [$mm^{-1}$] | 14.356 |
| $R_{int}$ | 0.0224 |
| Total no. reflections | 10840 |
| Unique reflections | 3861 |
| No. of parameters | 159 |
| $R_1$ [$I_o > 2\sigma(I_o)$] | 0.0196 |
| $R_1$ [all data] | 0.0215 |
| $wR_2$ [$I_o > 2\sigma(I_o)$] | 0.0443 |
| $wR_2$ [all data] | 0.0451 |

[a] $R_1 = \Sigma||F_o|-|F_c||_i/\Sigma|F_o|$; $wR_2 = [\Sigma w(F_o^2-F_c^2)^2/\Sigma wF_{oi}^4]^{1/2}$.

## Acknowledgments

We thank the EPSRC for support (J. M. M.) and Johnson Matthey plc for generous loans of platinum salts. We also thank Dr N. Tsoureas for the crystallographic data analysis.

[1] a) E. G. Hope, W. Levason, *Coord. Chem. Rev.* **1993**, *122*, 109–170; b) W. Levason, S. D. Orchard, G. Reid, *Coord. Chem. Rev.* **2002**, *225*, 159–199; c) A. K. Singh, S. Sharma, *Coord. Chem. Rev.* **2000**, *209*, 49–98.
[2] W. Levason, G. Reid, in *Comprehensive Coordination Chemistry II* (Eds.: J. A. McCleverty, T. J. Meyer), Elsevier, **2003**, vol. 1, 391–398 and 399–410.
[3] a) W. Levason, S. D. Orchard, G. Reid, *Chem. Commun.* **1999**, 1071–1072; b) S. D. Orchard, W. Levason, G. Reid, *Inorg. Chem.* **2000**, *39*, 3853–3859.
[4] W. Levason, S. D. Orchard, G. Reid, J. M. Street, *J. Chem. Soc., Dalton Trans.* **2000**, 2537–2543.
[5] E. W. Abel, D. G. Evans, J. R. Koe, M. B. Hursthouse, M. Mazid, *J. Chem. Soc., Dalton Trans.* **1992**, 663–667.
[6] a) E. W. Abel, K. G. Orrell, S. P. Scanlon, D. Stephenson, T. Kemmitt, W. Levason, *J. Chem. Soc., Dalton Trans.* **1991**, 591–595; b) H. B. Singh, A. V. Regina, J. P. Jasinski, E. S. Paight, R. J. Butcher, *J. Organomet. Chem.* **1994**, *466*, 283–289.
[7] a) E. W. Abel, A. R. Khan, K. Kite, K. G. Orrell, V. Sik, *J. Chem. Soc., Dalton Trans.* **1980**, 1169–1174; b) E. W. Abel, K. G. Orrell, A. W. G. Platt, *J. Chem. Soc., Dalton Trans.* **1983**, 2345–2351.
[8] a) K. G. Orrell, *Coord. Chem. Rev.* **1989**, *96*, 1–48; b) E. W. Abel, K. G. Orrell, *Prog. Inorg. Chem.* **1984**, *32*, 1–118.
[9] E. W. Abel, D. G. Evans, J. R. Koe, M. B. Hursthouse, M. Mazid, *J. Chem. Soc., Dalton Trans.* **1992**, 663–667.
[10] E. W. Abel, S. K. Bhargava, K. Kite, K. G. Orrell, V. Sik, B. L. Williams, *Polyhedron* **1982**, *1*, 289–298.
[11] a) W. Levason, M. L. Matthews, G. Reid, M. Webster, *Dalton Trans.* **2004**, 51–58; b) W. Levason, M. L. Matthews, G. Reid, M. Webster, *Dalton Trans.* **2004**, 554–561.
[12] M. D. Brown, W. Levason, G. Reid, M. Webster, *Dalton Trans.* **2006**, 1667–1674.
[13] P. W. N. M. van Leeuwen, P. C. J. Kamer, J. N. H. Reek, P. Dierkes, *Chem. Rev.* **2000**, *100*, 2741–2770.

 © 2006 Wiley-VCH Verlag GmbH & Co. KGaA, Weinheim 

[14] N. R. Champness, W. Levason, J. J. Quirk, G. Reid, C. S. Frampton, *Polyhedron* **1995**, *14*, 2753–2758.
[15] E. W. Abel, P. D. Beer, I. Moss, K. G. Orrell, V. Sik, P. A. Bates, M. B. Hursthouse, *J. Organomet. Chem.* **1988**, *341*, 559–567.
[16] M. K. Davies, M. C. Durrant, W. Levason, G. Reid, R. L. Richards, *J. Chem. Soc., Dalton Trans.* **1999**, 1077–1083.
[17] W. Levason, J. J. Quirk, G. Reid, C. S. Frampton, *Inorg. Chem.* **1994**, *33*, 6120–6122.
[18] P. P. Brown, R. J. Puddephatt, C. E. E. Upton, *J. Chem. Soc., Dalton Trans.* **1974**, 2457–2465.
[19] G. S. Hill, M. J. Irwin, C. J. Levy, L. M. Rendina, R. J. Puddephatt, *Inorg. Synth.* **1998**, *32*, 149–153.
[20] J. C. Baldwin, W. C. Kaska, *Inorg. Chem.* **1975**, *14*, 2020.
[21] R. J. Batchelor, F. W. B. Einstein, I. D. Gay, J.-H. Gu, B. D. Johnston, B. M. Pinto, *J. Am. Chem. Soc.* **1989**, *111*, 6582–6591.
[22] T. Kemmitt, E. G. Hope, W. Levason, *Organometallics* **1988**, *7*, 78–83.
[23] D. J. Gulliver, E. G. Hope, W. Levason, S. G. Murray, D. M. Potter, G. L. Marshall, *J. Chem. Soc., Perkin Trans. 2* **1984**, 429–434.
[24] W. Levason, B. Patel, G. Reid, A. J. Ward, *J. Organomet. Chem.* **2001**, *619*, 218–225.
[25] G. M. Sheldrick, SHELXS-97, program for crystal structure solution, University of Göttingen, Germany, **1997**.
[26] G. M. Sheldrick, SHELXL-97, program for crystal structure refinement, University of Göttingen, Germany, **1997**.

Received: May 31, 2006
Published Online: September 5, 2006

 © 2006 Wiley-VCH Verlag GmbH & Co. KGaA, Weinheim 

DOI: 10.1002/ejic.200600513

# Synthesis and Properties of Complexes of Vanadium(V) Oxide Trichloride with Nitrogen- and Oxygen-Donor Ligands

**Charlotte D. Beard,[a] Rosalind J. Barrie,[b] John Evans,[a] William Levason,*[a] Gillian Reid,[a] and Mark D. Spicer[b]**

**Keywords:** Vanadium / Coordination complexes / Multinuclear NMR spectroscopy

Intensely coloured, extremely moisture sensitive complexes $[VOCl_3(L)]$ (L = pyridine, quinoline, $Ph_3PO$, $Ph_3AsO$, pyridine *N*-oxide), $[VOCl_3(L)_2]$ (L = pyridine, $Me_3PO$, pyridine *N*-oxide), $[VOCl_3(L–L)]$ [L–L = 2,2′-bipyridyl, 1,10-phenanthroline, $Ph_2P(O)CH_2P(O)Ph_2$, $MeOCH_2CH_2OMe$, 15-crown-5 or $Me_2NCH_2CH_2NMe_2$] and $[Cl_3OV(\mu\text{-}L–L)VOCl_3]$ [L–L =18-crown-6 or $Ph_2P(O)CH_2P(O)Ph_2$] have been prepared from $VOCl_3$ and the appropriate ligands in dichloromethane solution. These constitute the first extended series of complexes of vanadium(V) with neutral donor ligands. They have been fully characterised by analysis, IR, UV/Visible and multinuclear ($^1H$, $^{31}P$, $^{51}V$) NMR spectroscopy, and their solution behaviour probed as a function of temperature using $^{51}V$ NMR spectroscopy. Reducing ligands including phosphanes, arsanes, thio- and selenoethers immediately reduce $VOCl_3$ to give $V^{IV}$ or $V^{III}$ species. Oxygen atom transfer reactions of some of the complexes with $Ph_3P$, $Ph_3As$, $Me_2Se$ and $Bu_2S$, leading to the corresponding ligand oxides are also described.

(© Wiley-VCH Verlag GmbH & Co. KGaA, 69451 Weinheim, Germany, 2006)

## Introduction

The chemistry of vanadium(V) is dominated by oxido species including $V_2O_5$, iso- and hetero-polyvanadates and alkoxides.[1] The only binary halide is $VF_5$; early claims for the existence of $VCl_5$ having been shown to be erroneous,[2] and there are three oxide trihalides $VOX_3$ (X = F, Cl or Br).[1] Adducts of $VOCl_3$ with a variety of neutral ligands have been explored by in situ $^{51}V$ NMR studies,[3–5] but structurally characterised examples are limited to the nitriles, $[VOCl_3(PhCN)_2]$ (octahedral, but with Cl/O disorder) and $[VOCl_3(RCN)]$ (R = Me, Ph, $PhCH_2$),[6–8] the surprisingly robust carbene $[VOCl_3\{(mes)N^aCH_2CH_2N(mes)\text{-}C^a(N^a–C^a)\}]$,[9] and $[VOCl_3(adamantan\text{-}2,2'\text{-}homoadamantan\text{-}3\text{-}one)]$,[10] all of which approximate to square pyramids with the V=O apical. In the six-coordinate $[VOCl_3\{(2\text{-}nitrophenyl)pyridine\text{-}2\text{-}carboxamide\}]$ the chlorines are *mer* and the V=O *trans* to the amide oxygen.[11] The isolation of other complexes has been reported from time to time,[12–17] but the data are very limited and frequently inconsistent. The problems arise both from the extreme moisture sensitivity of $VOCl_3$ and many of its complexes, and from the ease with which the vanadium is reduced to $V^{IV}$ or $V^{III}$. In passing, we note that $VOBr_3$ is reported to be reduced by all *neutral* ligands examined.[18,19] We are currently exploring the use of molecular high-valent vanadium complexes as single source CVD precursors, and to provide comparator compounds for that work we have investigated complexes of $VOCl_3$ with a range of neutral group 15 and 16 donor ligands. We have also explored the solution chemistry using $^{51}V$ NMR spectroscopy and investigated some oxygen atom transfer reactions of the resulting complexes. The chemistry of high-valent vanadium species is also of relevance to vanadium in biological systems such as the vanadate-dependent haloperoxidases most of which occur in marine organisms.[20]

[a] School of Chemistry, University of Southampton, Southampton SO17 1BJ, UK
[b] Department of Pure and Applied Chemistry, University of Strathclyde, Glasgow G1 1XL, UK

## Results and Discussion

$VOCl_3$ is extremely easily hydrolysed, and all reactions were carried out in rigorously dried glassware using freshly dried ligands and solvents. Many of the complexes are also photochemically unstable and typically were stored in foil-wrapped containers in a dry-box. Even with these precautions, many of the solid samples deteriorate over a few days, hence all measurements were made on freshly prepared samples. Decomposition in solution is faster and, despite many attempts, X-ray quality crystals of the complexes have not proved to be obtainable. The two commonest products of hydrolysis are the dark red $[VOCl_4]^-$ and yellow $[VO_2Cl_2]^-$ anions,[21,22] which are readily detected by $^{51}V$ NMR spectroscopy [$^{51}V$:[23] 99.76%, I = 7/2, $\Xi$ = 26.29 MHz, $Q = -5.2\cdot10^{-30}$ m$^2$, $D_c$ (receptivity relative to $^{13}C$) = 2150], (Table 1). The $^{51}V$ chemical shift of the former is slightly solvent-dependent and lies in the range $\delta$ = +45 to +50 ppm, which is to high frequency of the resonances of

 © 2006 Wiley-VCH Verlag GmbH & Co. KGaA, Weinheim 

Table 1. Selected spectroscopic data.

| Complex | υ(V=O)[a] [cm$^{-1}$] | υ(VCl) [cm$^{-1}$] | $\delta$($^{51}$V)[b] | $E_{max}$[c] [cm$^{-1}$] |
|---|---|---|---|---|
| [$VOCl_3$(2,2′-bipy)] | 978 | 381, 358, 348 | –103 (370) | 17200 (sh),19120 (sh), 21370, 32260 |
| [$VOCl_3$(1,10-phen)] | 973 | 386, 347, 319 | –108 (560) | 18000 (sh), 22220, 32895 |
| [$VOCl_3$(py)] | 1020 | 419, 383, 344 | –36 (800)[d] | 16024 (sh), 20900, 33000 |
| [$VOCl_3(py)_2$] | 978 | 393, 372, 347 | –58 (300)[d] | 20240 (vb), 27940 |
| [$VOCl_3$(quinoline)] | 1022 | 409, 375, 330 | –39 (2500) | 16600 (sh), 19250, 20800, 3200 |
| [$VOCl_3(Ph_3PO)$] | 1020 | 403, 372, 336 | –83 (700) | 15900 (sh), 19400, 21900 (sh), 32000 |
| [$VOCl_3(Me_3PO)_2$] | 952 | 381, 367 (br) | –92 (740) | 17240 (sh), 19840 (sh), 21930, 28100 |
| [$VOCl_3(Ph_3AsO)$] | 1016 | 393, 365, 347 | –141 (400) | 15500 (sh), 19840, 21750, 29760 |
| [$VOCl_3${$Ph_2P(O)CH_2P(O)Ph_2$}] | 970 | 395, 337, 320 | –81 (2500) | 17600 (sh), 22320, 29070 |
| "[{$VOCl_3$}$_2$[$Ph_2P(O)CH_2P(O)Ph_2$]]"[e] | 1023 | 390, 371, 360 | see text | 18800 (sh), 20800, 25000 |
| [{$VOCl_3$}$_2$(18-crown-6)] | 993 | 408 (sh), 359 (vbr) | –6 (2000) | ca. 16000 (sh), 21000 (vbr) |
| [$VOCl_3$(15-crown-5)] | 983 | 395, 351 (br) | –21 (350) | 16000 (sh), 20620 |
| [$VOCl_3(MeOCH_2CH_2OMe)$] | 983 | 359, 348 (br) | –32 (150) | 16050 (sh), 20830, 24750, 33800 |
| [$VOCl_3$(pyNO)] | 1006 | 393, 371, 330 | see text | 16000 (sh), 19700, 22000, 31700 |
| [$VOCl_3(pyNO)_2$] | 976 | 373, 348, 325 | –67 (800) | 18000 (br), 27200 |
| [$VOCl_3(Me_2NCH_2CH_2NMe_2)$] | 993 | 360 (sh), 343, 290 (sh) | [f] | 16000 (sh), 21000, 30100 |
| [$Ph_4As$][$VOCl_4$] | 1025 | 394, 373 | +48 (300) | 19840, 25000, 30490 |
| [$Ph_4As$][$VO_2Cl_2$] | 967, 957 | 431 | –362 (160) | 24630, 33000 |

[a] Nujol mull. [b] $^{51}$V Chemical shift in $CH_2Cl_2$ solution at 298 K relative to neat $VOCl_3$, $w_{1/2}$ (Hz) in parenthesis. [c] Diffuse reflectance UV/Vis spectra. [d] See text. [e] Not obtained analytically pure, see text. [f] Insufficiently soluble.

the neutral complexes prepared in this study. The $[VO_2Cl_2]^-$ anion is relatively resistant to further hydrolysis and the $^{51}$V chemical shift ($\delta \approx -362$ ppm) is less solvent-dependent. It seems probable that resonances at ca. $\delta = -360$ to $-370$ ppm originally ascribed to oligomeric $\{VOCl_3L\}_n$ adducts in in situ studies,[4] are in fact due to hydrolysis to $[VO_2Cl_2]^-$. Reduction of $VOCl_3$ to blue-green $[VOCl_2L_n]$ species is also common in the presence of reducing ligands, but the $VO^{2+}$ species are easily identified by the presence of a strong, broad feature at ca. 12000–15000 cm$^{-1}$ in their UV/Visible spectra.[24]

**N-Donor Ligands** (Scheme 1): The reaction of $VOCl_3$ with 2,2′-bipyridyl or 1,10-phenanthroline (L–L), in anhydrous $CH_2Cl_2$ or toluene produced [$VOCl_3$(L–L)] in good yield, as diamagnetic, very dark red-brown powders. These two complexes are amongst the more stable simple adducts of $VOCl_3$, although even these solids decompose in a few weeks at room temperature, hydrolyse rapidly in air, and decompose quite rapidly in solution. The solids show strong υ(VO) bands at 978 and 973 cm$^{-1}$, respectively, and three strong features in the region 300–400 cm$^{-1}$ assigned as υ(VCl) (Table 1). In $VOCl_3$ complexes υ(VO) ranges from ca. 950–1040 cm$^{-1}$ and, comparing data only on structurally characterised compounds, the value falls from the four-coordinate $VOCl_3$ (1035 cm$^{-1}$), to five-coordinate [$VOCl_3$(RCN)], $[VOCl_4]^-$, [$VOCl_3${(mes)N$^a$$CH_2CH_2$N(mes)-C$^a$($N^a$–$C^\alpha$)}] (1025–1016 cm$^{-1}$), to six-coordinate [$VOCl_3(RCN)_2$] (below ca. 1000 cm$^{-1}$).[6–9,25,26] This is

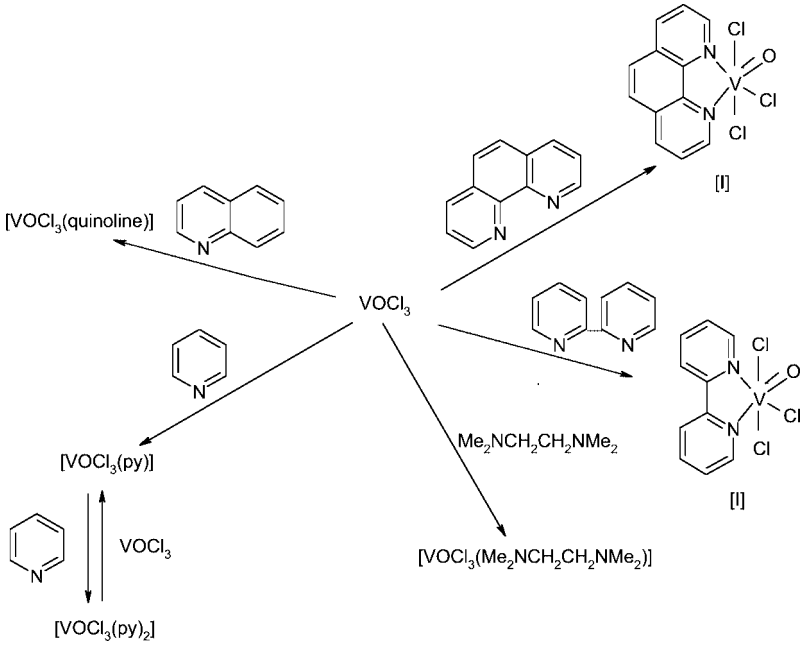


Scheme 1.

 © 2006 Wiley-VCH Verlag GmbH & Co. KGaA, Weinheim 

clearly consistent with the two diimine complexes containing six-coordinate vanadium. In solution the $^1H$ NMR spectra show significant high-frequency shifts of the ring protons and the complex pattern (see Exp. Sect.) shows that the isomer present is the unsymmetrical I (see Scheme 1), rather than the isomer with both N atoms *trans* to Cl which would have given a maximum of four resonances of equal intensity for each complex. The $^{51}V$ NMR resonances are relatively sharp lines some 100 ppm to low frequency from $VOCl_3$ (Table 1). The UV/Visible spectra in anhydrous $CH_2Cl_2$ solution consist of strong broad features at ca. 21000 $cm^{-1}$ which are assigned as $\pi(Cl)\rightarrow V$ charge transfer, with several strong overlapping features at higher energy. The diffuse reflectance spectra are similar although the bands are broader and the first bands have weak shoulders to lower energy. Several attempts to produce crystals of the deep red 2,2′-bipy complex reproducibly formed a few very small orange crystals identified as the oxido-bridged dimeric hydrolysis product. The structure (Figure 1) consists of two six-coordinate V atoms linked through a bridging oxido group. The V–O2 distances favour an oxido rather than hydroxo bridge [compare the V–O(H) distance in $[VOCl_3(OH)]^-$ 2.033(4) Å[22]] leading to $V^V$ and on each V the two Cl atoms are in *trans* position. There are two molecules in the asymmetric unit which are very similar.[27] Several X-ray data sets were obtained from crystals grown both in Strathclyde and Southampton, and all showed the same rather poor crystal quality. The origin of this is probably related to the similarity of the triclinic cell to a monoclinic C-lattice cell and the occurrence of twinning, which was particularly marked for one data set.

Quinoline and $VOCl_3$ react in dry $CH_2Cl_2$ to form dark red $[VOCl_3(quinoline)]$ which has the $\upsilon(VO)$ at 1022 $cm^{-1}$ and $\upsilon(VCl)$ at 409, 375 and 330 $cm^{-1}$, the higher frequency of $\upsilon(VO)$ is in agreement with five-coordination at the vanadium centre based on the trends described above [if significant V=O···V interactions occur such that a six-coordinate oligomer description is appropriate $\upsilon(VO)$ would be much lower]. At ambient temperature the $^{51}V$ NMR spectrum is a broad ($w_{1/2}$ = 2500 Hz) line at $\delta$ = –39 ppm, which sharpens on cooling the solution, but with little change in the chemical shift. In contrast, the $VOCl_3$–pyridine system is more complicated and initial attempts to isolate reproducible materials from the reaction of $VOCl_3$ with pyridine in either a 1:1 or 1:2 molar ratio in anhydrous $CH_2Cl_2$ were unsuccessful. Using a 2:1 $VOCl_3$/py ratio led to red-brown $[VOCl_3(py)]$, whilst a 1:4 ratio gave $[VOCl_3(py)_2]$, but with stoichiometric ratios of the reagents only mixtures are produced. In this respect the pyridine systems seem to resemble the nitrile complexes.[6–8] The IR spectra show $\upsilon(VO)$ at 1020 and 978 $cm^{-1}$ for the 1:1 and 1:2 complexes, respectively (Table 1), consistent with assignment as five- and six-coordinate vanadium. The $\upsilon(VCl)$ modes in $[VOCl_3(py)_2]$ have a very similar pattern to those in $[VOCl_3(L–L)]$ (L–L = 2,2′-bipy or 1,10-phenanthroline) and strongly suggest the same isomer is present with *mer* chlorines and one pyridine ligand *trans* to Cl and the second *trans* to O. The diffuse reflectance spectra are similar, although the lowest energy feature in the 1:1 complex is at slightly lower energy than that of the 1:2 complex. It seems that the charge-transfer spectra are not suited to distinguishing reliably five- and six-coordination in these systems. The solution spectroscopic data obtained from either $[VOCl_3(py)]$ or $[VOCl_3(py)_2]$ are similar, consistent with equilibrium mixtures in solution. In particular, the $^{51}V$ NMR spectra show only single resonances for solutions of either complex, which vary with concentration and temperature. However, at –90 °C $CH_2Cl_2$ solutions of $[VOCl_3(py)_2]$ containing excess pyridine show a relatively sharp resonance at $\delta$ = –58 ppm, which broadens and drifts to higher frequency on warming. This is probably due to the 1:2 complex. Similarly, at –90 °C a $CH_2Cl_2$ solution of $[VOCl_3(py)]$ containing excess $VOCl_3$ shows two resonances at $\delta$ = –6 and –38 ppm, which broaden and then coalesce (–40 °C) on warming. These are tentatively attributed to $VOCl_3$ and $[VOCl_3(py)]$ respectively, although the lines are still broad, indicating that the low temperature limit has not been reached. However, further cooling results in precipitation of the complex. The reaction of $VOCl_3$ with amines was violent and generated considerable heat and decomposition. We were unable to obtain pure complexes with $Et_3N$ or $Et_2NH$, but adding a $CH_2Cl_2$ solution of $VOCl_3$ to a solution of $Me_2NCH_2CH_2NMe_2$ in $CH_2Cl_2$ frozen in liquid nitrogen, and slowly allowing the mixture to thaw, gave dark brown $[VOCl_3(Me_2NCH_2CH_2NMe_2)]$. The complex is very poorly soluble in chlorocarbons, preventing useful solution-phase spectroscopic data being obtained, but the IR and UV/Visible data (Table 1) are consistent with six-coordinate $V^V$.

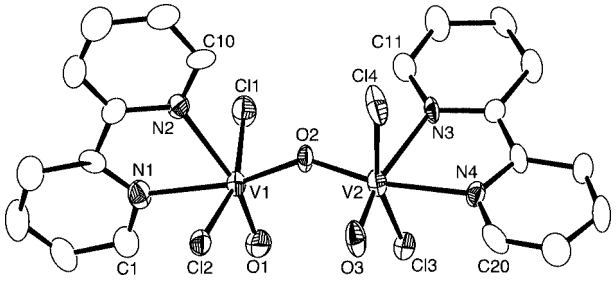


Figure 1. Structure of one of the two vanadium-containing molecules in the asymmetric unit of $[V_2Cl_4O_3(2,2'\text{-bipy})_2]\cdot 1.75CH_2Cl_2$. Displacement ellipsoids are drawn at the 50% probability level and H atoms omitted for clarity. Selected bond lengths [Å] and angles [°]: V1–Cl1 2.308(4); V1–Cl2 2.330(3); V1–O1 1.578(8); V1–N1 2.164(10); V1–N2 2.258(10); V1–O2 1.783(7); V2–Cl3 2.309(4); V2–Cl4 2.290(4); V2–O3 1.595(8); V2–N3 2.228(9); V2–N4 2.167(9); V2–O2 1.785(8); Cl1–V1–Cl2 163.6(2); N1–V1–N2 72.1(4); N1–V1–O2 163.0(4); N2–V1–O1 164.3(4); V1–O2–V2 145.8(5); Cl3–V2–Cl4 163.2(2); N3–V2–N4 72.7(4); N4–V2–O2 164.1(3); N3–V2–O3 164.8(4). The second molecule involving V3 and V4 has very similar bond lengths and angles.

Comparison of the data above shows that adducts of $VOCl_3$ with nitrogen heterocycles form readily under anhydrous conditions. For the rigid chelates, 2,2′-bipyridyl and 1,10-phenanthroline, the complexes are six-coordinate, whilst for the bulky monodentate quinoline, five-coordina-

 © 2006 Wiley-VCH Verlag GmbH & Co. KGaA, Weinheim 

tion is preferred. The formation of both 1:1 and 1:2 complexes with the smaller pyridine suggests that electronically the stability of the five- and six-coordinate complexes are similar. Paul et al.[16] reported dark brown $[VOCl_3(L)_3]$ (L = py, 1-, 2-, or 3-picoline, or quinoline), described as hygroscopic and insoluble in common solvents. We have been unable to reproduce these results, and the coordination of seven monodentate ligands to the small $V^V$ centre seems highly unlikely. The only examples of "seven-coordinate" $V^V$ are with small-angle chelates such as $[VO(NO_3)_3]$ or $[VO(S_2CNR_2)_3]$, or in "side-on" peroxido complexes.[1] The complexes described above are easily soluble in organic solvents, although some insoluble decomposition or hydrolysis products we have obtained include dark brown or sometimes green solids, which often show evidence of protonation of the heterocycle in the IR spectra.

**O-Donor Ligands** (Scheme 2): Reaction of excess $VOCl_3$ with 15-crown-5 and 18-crown-6 in $CH_2Cl_2$ under rigorously anhydrous conditions gave dark red-brown solutions from which removal of the solvent and excess $VOCl_3$ in vacuo, left very moisture sensitive, red-brown powders. The products were identified as $[VOCl_3(15\text{-crown-5})]$ and $[(VOCl_3)_2(18\text{-crown-6})]$ by analysis. Repeated attempts to obtain a pure complex with 12-crown-4 were unsuccessful. The presence of $V^V$ was confirmed by their diamagnetism, and by broad features in the UV/Visible spectra of both the solids and $CH_2Cl_2$ solution at ca. 21000 $cm^{-1}$ assigned as $(\pi)Cl\rightarrow V^V$ charge transfer, the absence of features to lower energy ruling out lower oxidation states of vanadium.[24] The IR spectra show broad, intense features in the regions between ca. 1100 and ca. 800 $cm^{-1}$ attributable to $(COC)_{asym}$ and $(COC)_{sym}$ vibrations, respectively, of the crowns. ν(VO) is assigned as the broad medium intensity features at 983 $cm^{-1}$ (15-crown-5) or 993 $cm^{-1}$ (18-crown-6) and ν(VCl) as overlapping bands at ca. 360–430 $cm^{-1}$. The compounds are extremely moisture sensitive and labile in solution. In rigorously dry $CD_2Cl_2$ the $^1H$ NMR spectra show singlet methylene resonances over the range +25 to –95 °C, indicating reversible ligand dissociation or "ring whizzing". The $^{51}V$ NMR spectrum of $[VOCl_3(15\text{-crown-5})]$ shows a single line at $\delta$ = –21 ppm and that of $[(VOCl_3)_2$-(18-crown-6)] a broad feature at $\delta$ = –6 ppm, both of which drift upfield on cooling the solutions, the effects reversing on warming to ambient temperatures. This is consistent with reversible dissociation on the vanadium NMR timescale, and from mixtures with added $VOCl_3$ we were unable to observe separate resonances for the complex and $VOCl_3$ even at –90 °C. The data are consistent with six-coordinate vanadium centres, with the $VOCl_3$ coordinated to two crown ether oxygen atoms. The behaviour of these complexes is reminiscent of the $[TiCl_4(crown)]$ systems,[28] although in these the exchange processes were slowed sufficiently at low temperatures for the different methylene environments to be observed in the $^1H$ NMR spectra, consistent with the stronger Lewis acidity of $TiCl_4$ compared with $VOCl_3$. Hydrolysis of the $V^V$ complexes with traces of water in chlorocarbon solvents produce $[VO_2Cl_2]^-$ $\delta(^{51}V)$ = –363 ppm, and the $^{51}V$ resonance of a $CH_2Cl_2$ solution of $[Ph_4As][VO_2Cl_2]$ is unshifted on adding 18-crown-6 showing no interaction with the crown in solution.

The acyclic ether, 1,2-bis(methoxy)ethane (dme) gave a dark red complex $[VOCl_3(dme)]$, which was also very labile in solution and deliquescent in the solid state. The very similar IR and $^{51}V$ NMR spectra of this complex (Table 1) to those of the two crown ethers is strong evidence for the $\kappa^2$-coordination of the crown proposed above.

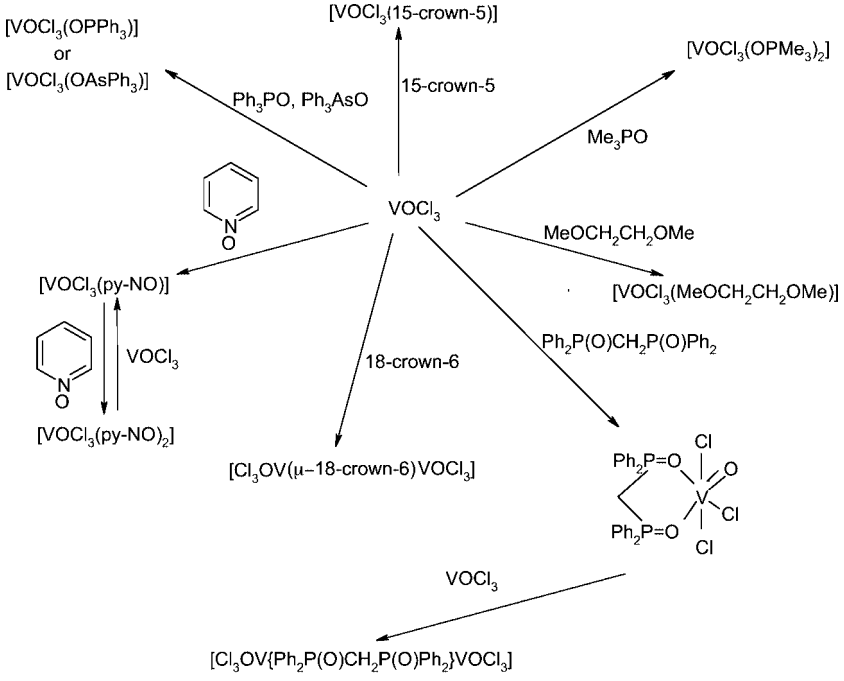


Scheme 2.

 © 2006 Wiley-VCH Verlag GmbH & Co. KGaA, Weinheim 

The reaction of $VOCl_3$ with $Ph_3PO$ and $Me_3PO$ gave $[VOCl_3(Ph_3PO)]$ and $[VOCl_3(Me_3PO)_2]$ irrespective of the V/L ratio used. The former is a dark brown solid which exhibits υ(PO) at 1050 $cm^{-1}$ and υ(VO) at 1020 $cm^{-1}$, whilst the latter is dark red-brown and has υ(PO) at 1085 $cm^{-1}$ and υ(VO) at 952 $cm^{-1}$, the differences in υ(VO) suggesting these are five- and six-coordinate species, respectively. The dry solids are relatively resistant to hydrolysis and may be handled briefly in air, although in solution hydrolysis to chlorido-oxidovanadates occurs readily ($^{51}V$ NMR evidence). In solution the complexes exhibit large high-frequency coordination shifts in the $^{31}P\{^1H\}$ NMR spectra, consistent with coordination to a high-valent metal centre, and have $\delta(^{51}V)$ at –83 and –92 ppm, respectively. The observation of single $^1H$ and $^{31}P$ NMR resonances for $[VOCl_3(Me_3PO)_2]$ even at low temperatures, suggests a single isomer with equivalent phosphane oxides is present, and the single υ(PO) vibration tentatively suggests the $R_3PO$ groups are mutually *trans*. The corresponding reaction of $VOCl_3$ with $Ph_3AsO$ in $CH_2Cl_2$ produced an extremely moisture-sensitive dark red solid $[VOCl_3(Ph_3AsO)]$, which from its spectroscopic signature [υ(VO) at 1016 $cm^{-1}$, υ(AsO) at 803 $cm^{-1}$, $\delta(^{51}V)$ = –141 ppm] appears to be analogous to the $OPPh_3$ complex.

The diphosphane dioxide $Ph_2P(O)CH_2P(O)Ph_2$, reacts with 1 equiv. of $VOCl_3$ to form dark brown $[VOCl_3\{Ph_2P(O)CH_2P(O)Ph_2\}]$. In the solid state the complex exhibits bands at 1164 and 1080 $cm^{-1}$ assigned as υ(PO) and 970 υ(VO), suggesting a six-coordinate vanadium centre. In $CH_2Cl_2$ solution the complex is labile and exhibits a $^{31}P$ NMR resonance only on cooling, and at –70 °C the spectrum reveals doublets of equal intensity at $\delta$ = 48.2 and 34.5 ppm ($^2J$ = 12 Hz) ["free" $Ph_2P(O)CH_2P(O)Ph_2$ has $\delta(^{31}P)$ = 25 ppm]. The $^{51}V$ ($\delta$ = –81 ppm) resonance is broad ($w_{1/2}$ ca. 2500 Hz) at room temperature, and sharpens on cooling, although the chemical shift varies only slightly with temperature. The large difference in υ(PO) in the IR spectrum and the inequivalence of the phosphorus centres in solution strongly suggest the structure of this complex has the phosphinoyl groups *trans* to VO and VCl, respectively, and hence has *mer*-Cl atoms. Evaporation of a $CH_2Cl_2$ solution of $[VOCl_3\{Ph_2P(O)CH_2P(O)Ph_2\}]$ with excess $VOCl_3$ and pumping to dryness in vacuo, gave a second complex which was not obtained analytically pure, but which appears to be $[(VOCl_3)_2\{\mu\text{-}Ph_2P(O)CH_2P(O)Ph_2\}]$ with υ(PO) at 1094 $cm^{-1}$ and υ(VO) at 1023 $cm^{-1}$, and which from NMR studies was undergoing ligand exchange in solution even down to very low temperatures. The data show that like the pyridine systems above, the balance between five- and six-coordination in the phosphane oxide systems is subtle. In the case of the $Ph_2P(O)CH_2P(O)Ph_2/VOCl_3$ system the relative mismatch of the small vanadium centre and the large chelate bite in the six-membered ring is probably responsible for the dynamic behaviour in solution. Attempts to isolate a complex of $VOCl_3$ with the diphosphane dioxide $o\text{-}C_6H_4\{P(O)Ph_2\}_2$, which is both more rigid and sterically larger, were unsuccessful.

Pyridine *N*-oxide afforded two complexes, red $[VOCl_3(pyNO)]$ and darker red-black $[VOCl_3(pyNO)_2]$, depending upon the experimental conditions. The υ(VO) at 976 $cm^{-1}$ in the latter is within the range of other six-coordinate complexes, whilst for the former the υ(VO) at 1006 $cm^{-1}$ is at the lowest frequency observed for an (assumed) five-coordinate vanadium centre. The complexes also show strong υ(NO) at 1195 and 1200 $cm^{-1}$, lowered from the value of 1228 $cm^{-1}$ in pyridine *N*-oxide.[29] The $^{51}V$ NMR spectrum of $[VOCl_3(pyNO)_2]$ in anhydrous $CH_2Cl_2$ solution at ambient temperatures is a very broad resonance at $\delta$ = –67 ppm ($w_{1/2}$ = 800 Hz) which on cooling the solution sharpens and shows a small low-field shift. In the presence of added pyNO the limiting chemical shift is $\delta$ = –72 ppm ($w_{1/2}$ = 1000 Hz) at –70 °C, which probably corresponds to the 1:2 complex. In contrast, a $CH_2Cl_2$ solution of $[VOCl_3(pyNO)]$ only shows a $^{51}V$ NMR resonance below ca. –30 °C as a very broad feature at ca. $\delta$ = –25 ppm, which does not sharpen appreciably on cooling the solution, although as expected, addition of excess pyNO replicates the behaviour observed from $[VOCl_3(pyNO)_2]$. Overall, the data suggest that neutral O-donor ligand complexes of $VOCl_3$ are less stable, particularly in solution, than the N-donor adducts, and with the exception of the phosphane oxides, the lability precludes using solution NMR spectroscopic data to identify the isomer present in the six-coordinate complexes. Again examples of both five- and six-coordination are found, the coordination number presumably largely driven by steric factors.

**S-, Se-, P- and As-Donor Ligands:** The reaction of $VOCl_3$ with $R_2S$ (R = Me, Et or Bu) in chlorocarbons or hydrocarbons even at low temperatures gave dark solutions, which became blue-green in seconds. The UV/Visible spectrum of the latter ($E_{max}$ = 13500 $cm^{-1}$) showing reduction to a vanadyl $VO^{2+}$ species, as reported by Baker et al.[15] Similar reduction occurred with $Ph_2S$ and $PhSCH_2CH_2SPh$. The reaction of $Me_2Se$, $MeSeCH_2CH_2SeMe$, $Ph_3P$, $Ph_2PCH_2CH_2PPh_2$, or $o\text{-}C_6H_4(AsMe_2)_2$ with $VOCl_3$ even at –78 °C caused instant reduction to $V^{IV}$ or $V^{III}$ (identified by in situ UV/Visible spectroscopy).

**Oxygen Atom Transfer Reactions:** The results above clearly show that the $V^V$ complexes are extremely reactive and unstable towards reduction. Hence we have investigated their possible utility as O-atom transfer reagents towards $R_3E$ (E = P or As) and $R_2E'$ (E′ = S or Se). Many high valent metal oxido complexes have been shown to behave as O-atom transfer reagents to organic molecules.[30] The addition of 1 equiv. of $Ph_3P$ to $CH_2Cl_2$ solutions of $[VOCl_3(2,2'\text{-bipy})]$, $[VOCl_3(py)_2]$ or $[VOCl_3(quinoline)]$ resulted in instant loss of the dark red $V^V$ complexes, leaving pale pink solutions, and in situ $^{31}P$ NMR studies showed clean conversion to $Ph_3PO$ ($\delta$ = +28 ppm). The corresponding reactions with $Me_3As$ and $Ph_3As$ with $[VOCl_3(quinoline)]$ also resulted in rapid discharge of the colour, and after hydrolysis with aqueous ammonia, a mixture of the corresponding $R_3AsO$ and quinoline were isolated from the organic extracts, and identified by comparison of their IR and $^1H$ NMR spectra with literature data.[31] The reaction

 © 2006 Wiley-VCH Verlag GmbH & Co. KGaA, Weinheim 

of [$VOCl_3$(quinoline)] with $Me_2Se$ was also rapid, and in this case the product was identified as $Me_2SeO$ by its $^{77}Se$ NMR [$\delta$($CH_2Cl_2$ solution) = +825 ppm; ref.[32] +812 ppm (in $H_2O$)] which, given the solvent-dependence of selenium chemical shifts, is good agreement. In contrast, the reactions of [$VOCl_3$(quinoline)] with thioethers, including $nBu_2S$ and $Ph_2S$, were slow, taking several hours to discharge the deep red colour (contrast the rapid reduction of $VOCl_3$ by these ligands described above). In these cases, after hydrolysis with aqueous ammonia and extraction with $CH_2Cl_2$, evaporation of the organic solvents left the corresponding[33] colourless liquid sulfoxides, $R_2SO$.

## Conclusions

A range of five- and six-coordinate oxido $V^V$ complexes incorporating neutral N- and O-donor ligands has been isolated and characterised spectroscopically and analytically. This represents the first detailed characterisation of an extended series of adducts of $VOCl_3$. The compounds are highly reactive and undergo moderately rapid degradation both in solution and in the solid state even in the dark. They are immediately decomposed by water or alcohols and reduced by ligands containing the heavier groups 15 or 16 donors, and for selected examples we have shown that this decomposition involves oxygen atom transfer to the group 15/16 atom. $^{51}V$ NMR studies show resonances to low frequency of $VOCl_3$ for all of the complexes reported here. Variable temperature studies have shown that most of the complexes are labile in chlorocarbon solvents. Although for some of the monodentate ligands both 1:1 and 1:2 ligand/metal complexes have been isolated as solids, in solution these are in fast equilibrium.

## Experimental Section

All reactions were conducted under anhydrous conditions under dry dinitrogen using standard vacuum line, Schlenk and glove-box techniques. $VOCl_3$ (Aldrich) was used as received. Solvents were dried by distillation from $CaH_2$ ($CH_2Cl_2$), Na/benzophenone ketyl (hexane and diethyl ether). 2,2′-Bipyridyl, 1,10-phenanthroline, $Ph_3PO$, $Ph_3AsO$ and pyridine *N*-oxide were dried by heating in vacuo, $Me_3PO$ was freshly sublimed in vacuo. 18-crown-6, 15-crown-5 and 12-crown-4 were dried by refluxing with excess $SOCl_2$, followed by vacuum drying at 60 °C. 1,2-bis(methoxy)ethane was dried by distillation from Na pellets. Quinoline, pyridine and $Me_2NCH_2CH_2NMe_2$ were refluxed over BaO and freshly distilled. [$Ph_4As$][$VOCl_4$] and [$Ph_4As$][$VO_2Cl_2$] were made by literature methods.[20,21] $^{51}V$ NMR spectra were recorded in 10-mm o.d. tubes from dry $CH_2Cl_2$ solutions containing 5% $CD_2Cl_2$ as lock, with a Bruker DPX400 operating at 105.2 MHz, and referenced to external neat $VOCl_3$ ($\delta$ = 0 ppm). Other physical measurements were made as described.[9,28] Analytical data were obtained from the microanalytical laboratory of Strathclyde University.

**[$VOCl_3$(2,2′-bipy)]:** A solution of $VOCl_3$ (0.23 g, 1.3 mmol) in dry $CH_2Cl_2$ (5 mL) was added to a solution of 2,2′-bipyridyl (0.2 g, 1.3 mmol) in dry $CH_2Cl_2$ (10 mL). The dark red solution was concentrated to ca. 5 mL in vacuo, dry hexane (5 mL) added and the red-black solid isolated by filtration, and dried in vacuo. Yield 0.30 g, 70%. $C_{10}H_8Cl_3N_2OV$ (329.5): calcd. C 36.5, H 2.5, N 8.5; found C 37.1, H 2.1, N 8.2. $^1H$ NMR (300 MHz, $CDCl_3$, 298 K): $\delta$ = 7.6 (m, 2 H), 8.5 (m, 4 H), 9.35 (s, H), 9.70 (s, H) ppm. IR (Nujol): $\tilde{\nu}$ = 1314 (m), 1261 (m), 1157 (w), 1104 (w), 1026 (m), 978 (s), 802 (m), 763 (s), 658 (m), 381 (s), 358 (s), 348 (s) $cm^{-1}$. UV/Vis: $E_{max}$ [$cm^{-1}$] ($\varepsilon_{mol}$, $cm^{-1}$ $dm^3$ $mol^{-1}$) = 19250 (sh), 21550 (1325), 22730 (1300), 26310 (sh), ca. 33000 (ca. 20000).

**[$VOCl_3$(1,10-phen)]:** Prepared similarly from $VOCl_3$ (0.29 g, 1.6 mmol) and 1,10-phenanthroline (0.29 g, 1.6 mmol). A dark red-brown solid was isolated. Yield 0.32 g, 55%. $C_{12}H_8Cl_3N_2OV$ (353.2): calcd. C 40.7, H 2.3, N 7.9; found C 39.8, H 2.0, N 7.5. $^1H$ NMR (300 MHz, $CDCl_3$, 298 K): $\delta$ = 8.0 (m, 4 H), 8.65 (s, 2 H), 9.75 (s, H), 9.95 (s, H) ppm. IR (Nujol): $\tilde{\nu}$ = 1308 (w), 1258 (w), 1171 (m), 1140 (s), 1023 (w), 973 (s), 839 (s), 776 (m), 431 (m), 386 (s), 347 (s), 319 (sh) $cm^{-1}$. UV/Vis ($CH_2Cl_2$): $E_{max}$ [$cm^{-1}$] ($\varepsilon_{mol}$, $cm^{-1}$ $dm^3$ $mol^{-1}$) = 18200 (sh), 21505 (1680), 22730 (1730), ca. 33000 (ca. 15000).

**[$VOCl_3(py)_2$]:** A solution of pyridine (0.4 g, 5.0 mmol) in $CH_2Cl_2$ (5 mL) was added to $VOCl_3$ (0.21 g, 1.2 mmol) in $CH_2Cl_2$ (5 mL) producing an immediate precipitate. The mixture was stirred briefly, concentrated in vacuo to small volume and hexane (5 mL) added. The red solid was filtered off, rinsed with hexane, and dried in vacuo. Yield 0.23 g, 51%. $C_{10}H_{10}Cl_3N_2OV$ (331.5): Calcd. C 36.2, H 3.0, N 8.5; found C 36.3, H 3.9, N 8.3. $^1H$ NMR (300 MHz, $CDCl_3$, 298 K): $\delta$ = 7.3–7.5 (m) ppm. IR (Nujol): $\tilde{\nu}$ = 1604 (m), 1375 (m), 1325 (w), 1263 (w), 1161 (w), 1054 (m), 978 (s), 800 (s), 750 (s), 671 (s), 426 (s), 393 (m), 372 (m), 347 (m) $cm^{-1}$. UV/Vis ($CH_2Cl_2$): $E_{max}$ [$cm^{-1}$] = 19800 (sh), 21740, 28730.

**[$VOCl_3$(py)]:** A solution of pyridine (0.2 g, 2.5 mmol) in $CH_2Cl_2$ (5 mL) was added to $VOCl_3$ (0.84 g, 4.8 mmol) in $CH_2Cl_2$ (25 mL) producing an immediate precipitate. The solution was stirred for 30 min and then pumped to dryness in vacuo at room temperature. The dark brown powder produced was rinsed with hexane (5 mL), the solid filtered off and dried in vacuo. Yield 0.40 g, 64%. $C_5H_5Cl_3NOV$ (252.4): calcd. C 23.8, H 2.0, N 5.6; found C 23.1, H 2.1, N 5.4. $^1H$ NMR (300 MHz, $CDCl_3$, 298 K): $\delta$ = 7.5 (s, 2 H), 8.0 (s, H), 8.9 (s, 2 H) ppm. IR (Nujol): $\tilde{\nu}$ = 1604 (w), 1361 (m), 1250 (w), 1236 (w), 1158 (m), 1071 (m), 1020 (s), 964 (w), 869 (m), 757 (s), 734 (s), 687 (s), 642 (m), 419 (s), 385 (s), 344 (s) $cm^{-1}$. UV/Vis ($CH_2Cl_2$): $E_{max}$ [$cm^{-1}$] = 21500, 29110.

**[$VOCl_3$(quinoline)]:** A solution of quinoline (0.26 g, 2.0 mmol) in $CH_2Cl_2$ (10 mL) was added to $VOCl_3$ (0.52 g, 3.0 mmol) in $CH_2Cl_2$ (25 mL) producing an immediate red-black precipitate. The solution was stirred for 30 min and then pumped to dryness in vacuo at room temperature. The dark brown powder produced was stirred with hexane (5 mL) for 15 min, the solid filtered off and dried in vacuo. Yield 0.45 g, 74%. $C_9H_7Cl_3NOV$ (302.5): calcd. C 35.7, H 2.3, N 4.6; found C 35.5, H 2.4, N 4.5. $^1H$ NMR (300 MHz, $CDCl_3$, 298 K): $\delta$ = 7.7 (s, H), 7.9 (s, H), 8.1 (s, 2 H), 8.4 (s, H), 8.7 (s, H), 9.4 (s, H) ppm. IR (Nujol): $\tilde{\nu}$ = 1610 (w), 1354 (m), 1298 (w), 1261 (m), 1091 (m),1022 (s), 798 (s), 771 (m), 710 (s), 634 (w), 596 (m), 496 (s), 458 (m), 409 (sh), 375 (s), 330 (sh) $cm^{-1}$. UV/Vis ($CH_2Cl_2$): $E_{max}$ [$cm^{-1}$] = 21600, 27700.

**[$VOCl_3(Me_2NCH_2CH_2NMe_2)$]:** A solution of $Me_2NCH_2CH_2NMe_2$ (0.12 g, 1.0 mmol) in $CH_2Cl_2$ (20 mL) was frozen in liquid nitrogen and a solution of $VOCl_3$ (0.17 g, 1.0 mmol) in $CH_2Cl_2$ (10 mL) syringed in. The mixture was allowed to thaw and then warm slowly to room temperature to produce a dark brown solution. The solution was stirred for 30 min and then concentrated to ca. 10 mL in vacuo. The dark red-brown solid was filtered off and dried in vacuo. Yield 0.25 g, 86%. $C_6H_{16}Cl_3N_2O_3V$ (281.5): calcd. C 24.9, H 5.6, N 9.7; found C 24.3, H 6.0, N 9.5. IR (Nujol): $\tilde{\nu}$ = 1590

 © 2006 Wiley-VCH Verlag GmbH & Co. KGaA, Weinheim 

(w), 1260 (m), 1161 (w), 1080 (sh), 993 (s), 946 (m), 914 (w), 803 (s), 733 (s), 525 (w), 360 (sh), 343 (s), 290 (sh) $cm^{-1}$. UV/Vis ($CH_2Cl_2$): $E_{max}$ [$cm^{-1}$] = 20830, 32100.

**[$VOCl_3$(15-crown-5)]:** $VOCl_3$ (0.14 g, 0.8 mmol) in dry $CH_2Cl_2$ (5 mL) was added to 15-crown-5 (0.17 g, 0.77 mmol) in dry $CH_2Cl_2$ (10 mL) and the solution pumped to dryness under vacuum. The solid was washed with pentane (10 mL), filtered off and dried in vacuo. Yield 0.2 g, 64%. $C_{10}H_{20}Cl_3O_6V$ (393.5): calcd. C 30.5, H 5.2; found C 29.4, H 5.7. IR (Nujol): $\tilde{\nu}$ = 1304 (w), 1261 (m), 1098 (vs), 1022 (s), 983 (m), 940 (m), 802 (s), 610 (w), 428 (m), 395 (m), 351 (m) $cm^{-1}$. UV/Vis ($CH_2Cl_2$): $E_{max}$ [$cm^{-1}$] = 22420. $^1H$ NMR (300 MHz, $CDCl_3$, 298 K): $\delta$ = 3.6 (br. s) ppm. $^{51}V$ NMR ($CH_2Cl_2$, 223 K): $\delta$ = –54 ($w_{1/2}$ = 1000 Hz) ppm.

**[{$VOCl_3$}$_2$(18-crown-6)]:** Excess $VOCl_3$ (0.42 g, 2.4 mmol) in dry $CH_2Cl_2$ (5 mL) was added to 18-crown-6 (0.2 g, 0.76 mmol) in dry $CH_2Cl_2$ (10 mL) and worked up as described for [$VOCl_3$(15-crown-5)]. Red-brown solid. Yield 0.2 g, 30%. $C_{12}H_{24}Cl_6O_8V_2$ (610.9): calcd. C 23.6, H 4.0; found C 24.3, H 4.6. IR (Nujol): $\tilde{\nu}$ = 1300 (w), 1260 (m), 1146 (w), 1098 (vs), 1027 (s), 993 (m), 927 (m), 803 (s), 563 (m), 408 (sh), 359 (s,br), 306 (m) $cm^{-1}$. UV/Vis ($CH_2Cl_2$): $E_{max}$ [$cm^{-1}$] = 22320. $^1H$ NMR (300 MHz, $CDCl_3$, 298 K): $\delta$ = 3.66 (s) ppm. $^{51}V$ NMR ($CH_2Cl_2$, 203 K): $\delta$ = –47 ($w_{1/2}$ = 2000 Hz) ppm.

**[$VOCl_3$($Ph_3PO$)]:** A solution of triphenylphosphane oxide (0.56 g, 2.0 mmol) in $CH_2Cl_2$ (5 mL) was added to $VOCl_3$ (0.35 g, 2.0 mmol) in $CH_2Cl_2$ (5 mL), the dark solution stirred briefly and then concentrated in vacuo. The solution was treated with hexane (5 mL) and refrigerated to give a red-brown solid, which was filtered off and dried in vacuo. Yield 0.53 g, 58%. $C_{18}H_{15}Cl_3PO_2V$ (451.6): calcd. C 47.9, H 3.3; found C 48.5, H 3.3. $^1H$ NMR (300 MHz, $CDCl_3$, 298 K): $\delta$ = 7.4–7.8 (m, Ph) ppm. $^{51}V$ ($CH_2Cl_2$, 200 K): $\delta$ = –102 ($w_{1/2}$ = 850 Hz) ppm. $^{31}P\{^1H\}$ ($CH_2Cl_2$, 295 K): $\delta$ = 56 ppm. IR (Nujol): $\tilde{\nu}$ = 1312 (w), 1260 (m), 1182 (m), 1119 (s), 1050 (s, PO), 1020 (s), 992 (m), 749 (s), 688 (s), 535 (vs), 432 (m), 403 (m), 372 (m), 336 (m), 311 (m) $cm^{-1}$. UV/Vis ($CH_2Cl_2$) $E_{max}$ [$cm^{-1}$] ($\varepsilon_{mol}$, $cm^{-1}\,dm^3\,mol^{-1}$) = 17000 (110), 23250 (500), 31000 (15000).

**[$VOCl_3$($Me_3PO$)$_2$]:** A solution of trimethylphosphane oxide (0.09 g, 1.0 mmol) in $CH_2Cl_2$ (5 mL) was added to $VOCl_3$ (0.09 g, 0.5 mmol) in $CH_2Cl_2$ (5 mL), the dark brown solution which was stirred briefly, filtered, and the solvents evaporated to dryness in vacuo. Yield 0.16 g, 88%. $C_6H_{18}Cl_3O_3P_2V$ (357.5): calcd. C 20.1, H 5.0; found C 20.6, H 5.3. $^1H$ NMR (300 MHz, $CDCl_3$, 298 K): $\delta$ = 2.0 (br., $CH_3$) ppm. $^{31}P\{^1H\}$ ($CH_2Cl_2$, 295 K): $\delta$ = 74 ppm, essentially unchanged on cooling to 210 K. IR (Nujol): $\tilde{\nu}$ = 1297 (s), 1260 (m), 1085 (vs, PO), 1016 (s), 952 (s), 863 (m), 801 (m), 757 (w), 608 (w), 468 (sh), 431 (m), 381 (sh), 367 (br., m) $cm^{-1}$. UV/Vis ($CH_2Cl_2$): $E_{max}$ [$cm^{-1}$] = 17240 sh, 18380, 23580, 33000.

**[$VOCl_3$[$Ph_2P(O)CH_2P(O)Ph_2$]]:** A solution of the diphosphane dioxide (0.27 g, 0.65 mmol) in $CH_2Cl_2$ (10 mL) was added to $VOCl_3$ (0.11 g, 0.65 mmol) in $CH_2Cl_2$ (5 mL), and the dark solution stirred briefly. Hexane (5 mL) was added and the dark-brown precipitate filtered off and dried in vacuo. Yield 0.175 g, 46%. $C_{25}H_{22}Cl_3O_3P_2V$ (589.7): calcd. C 50.9, H 3.8; found C 50.9, H 3.5. $^1H$ NMR (300 MHz, $CDCl_3$, 298 K): $\delta$ = 7.4–7.9 (m, Ph), 3.95 (br. s, $CH_2$) ppm; no change at 210 K. $^{51}V$ ($CH_2Cl_2$, 200 K) $\delta$ = –85 ($w_{1/2}$ = 1100 Hz) ppm. $^{31}P\{^1H\}$ ($CH_2Cl_2$, 223 K): $\delta$ = 48 (br., P), 35 (br., P) ppm; (200 K): $\delta$ = 48.2 (d, $^2J_{P-P}$ = 12 Hz, P), 34.5 (d, $^2J_{P-P}$ = 12 Hz, P) ppm. IR (Nujol): $\tilde{\nu}$ = 1260 (m), 1164 (s, PO), 1125 (s), 1099 (m), 1080 (m, PO), 1055 (m), 1025 (m), 970 (w), 777 (s), 687 (s), 517 (s), 395 (m), 337 (s), 320 (sh) $cm^{-1}$. UV/Vis ($CH_2Cl_2$): $E_{max}$ [$cm^{-1}$] ($\varepsilon_{mol}$, $cm^{-1}\,dm^3\,mol^{-1}$) = 17980 (1300), 22730 (3750), 30490 (2200).

**[$VOCl_3$($Ph_3AsO$)]:** Triphenylarsane oxide (0.32 g, 1.0 mmol) was melted in vacuo after 20 min the melt was cooled to room temperature, dissolved in dry $CH_2Cl_2$ (10 mL) and added to $VOCl_3$ (0.35 g, 2.0 mmol) in $CH_2Cl_2$ (5 mL). (Unless rigorously anhydrous conditions are used this reaction gives the product as a black oil which appears spectroscopically identical to the solid complex.) The dark solution stirred briefly and then concentrated in vacuo. The solution was treated with hexane (5 mL) to give a red-black solid, which was filtered off and dried in vacuo. Yield 0.40 g, 80%. $C_{18}H_{15}AsCl_3O_2V{\cdot}CH_2Cl_2$ (580.5): calcd. C 39.3, H 3.0; found C 39.6, H 2.7. $^1H$ NMR (300 MHz, $CDCl_3$, 298 K): $\delta$ = 7.4–7.8 (m, Ph), 5.4 (s, $CH_2Cl_2$) ppm. $^{51}V$ ($CH_2Cl_2$, 298 K): $\delta$ = –142 ($w_{1/2}$ = 400 Hz) ppm. IR (Nujol): $\tilde{\nu}$ = 1363 (m), 1260 (m), 1087 (s), 1016 (s), 801 (m, AsO), 735 (s), 684 (m), 530 (w), 461 (m), 393 (m), 365 (m), 347 (sh) $cm^{-1}$. UV/Vis ($CH_2Cl_2$): $E_{max}$ [$cm^{-1}$] ($\varepsilon_{mol}$, $cm^{-1}\,dm^3\,mol^{-1}$) = 16000 (sh) (ca. 200), 21550 (3100), 30490 (2295).

**[$VOCl_3$($MeOCH_2CH_2OMe$)]:** A solution of dme (0.18 g, 2.0 mmol) in $CH_2Cl_2$ (10 mL) was added to $VOCl_3$ (0.19 g, 1.0 mmol) in $CH_2Cl_2$ (25 mL) producing a very dark solution. The solution was stirred for 30 min, and then pumped to dryness in vacuo at room temperature. The dark red-black powder produced was stirred with hexane (5 mL) for 15 min, the solid filtered off and dried in vacuo. Yield 0.35 g, 66%. $C_4H_{10}Cl_3O_3V$ (263.4): calcd. C 18.3, H 3.8; found C 18.7, H 4.2. $^1H$ NMR (300 MHz, $CDCl_3$, 298 K): $\delta$ = 3.8 (br) ppm; (220 K): $\delta$ = 4.01 (s, 2 H, $CH_2$), 4.05 (s, 3 H, $CH_3$) ppm. IR (Nujol): $\tilde{\nu}$ = 1346 (m), 1278 (w), 1260 (m), 1240 (m), 1190 (m), 1107 (s), 1076 (s), 1026 (s), 999 (s), 983 (s), 864 (m), 820 (m), 770 (m), 421 (m), 359 (s), 348 (vbr), 282 (w) $cm^{-1}$. UV/Vis ($CH_2Cl_2$): $E_{max}$ [$cm^{-1}$] = 19840, 26050 (sh), 32000.

**[$VOCl_3$(pyNO)]:** A solution of pyridine *N*-oxide (0.55 g, 5.8 mmol) in toluene (50 mL) was treated dropwise with $VOCl_3$ (1.0 g, 5.8 mmol). A dark red precipitate was formed immediately and the mixture stirred for 2 h. The supernatant was removed by cannula and the solid residue washed with hexane (15 mL). Filtration yielded a red solid which was dried in vacuo. Yield 0.96 g, 62%. $C_5H_5Cl_3NO_2V$ (268.4): calcd. C 22.4, H 1.9, N 5.2; found C 22.1, H 1.7, N 5.7. $^1H$ NMR (400 MHz, $CDCl_3$, 298 K): $\delta$ = 8.85 (s, 2 H), 9.20 (s, 1 H), 9.65 (s, 2 H). IR (Nujol): $\tilde{\nu}$ = 1605 (w), 1258 (m), 1197 (s), 1172 (m), 1092 (m), 1006 (s), 979 (m), 836 (m), 768 (s), 727 (m), 690 (m), 393 (m), 371 (s), 330 (s) $cm^{-1}$. UV/Vis ($CH_2Cl_2$): $E_{max}$ [$cm^{-1}$] = 16000 (sh), 19700, 22000, 31700.

**[$VOCl_3$(pyNO)$_2$]:** A solution of pyridine *N*-oxide (0.55 g, 5.8 mmol) in $CH_2Cl_2$ (30 mL) was treated with $VOCl_3$ (0.5 g, 2.8 mmol). A very dark red-black solution resulted. After stirring for 1 h. the mixture was taken to dryness in vacuo at room temperature. The resulting dark red solid was suspended in hexane (10 mL) and stirred for 15 min, the solid filtered off and dried in vacuo. Yield 0.86 g, 82%. $C_{10}H_{10}Cl_3N_2O_3V$ (363.5): calcd. C 33.0, H 2.8, N 7.7; found C 32.7, H 2.6, N 7.1 $^1H$ NMR (400 MHz, $CDCl_3$, 298 K): $\delta$ = 8.82 (s, 2 H), 9.15 (s, 1 H), 9.60 (s, 2 H). IR (Nujol): $\tilde{\nu}$ = 1605 (w), 1258 (m), 1200 (s), 1175 (m), 1092 (s), 996 (s), 976 (m), 830 (m), 768 (s), 727 (m), 695 (m), 373 (m), 348 (s), 325 (s) $cm^{-1}$. UV/Vis ($CH_2Cl_2$): $E_{max}$ [$cm^{-1}$] = 18000 (br), 27200.

**Oxidation Reactions:** General method: $Ph_3P$ (0.026 g, 0.1 mmol) was dissolved in $CH_2Cl_2$ (5 mL) and a solution of the vanadium complex (0.1 mmol) in $CH_2Cl_2$ (5 mL) added. After 5 min the mixture was pumped to dryness in vacuo, and the residue shaken up with aqueous ammonia (5 mL of 4 mol·$dm^{-3}$) and $CH_2Cl_2$ (5 mL). The organic phase was separated and used for $^{31}P$ NMR studies. The reactions with $Me_3As$, $Ph_3As$, $Me_2Se$, $nBu_2S$ and $Ph_2S$ were

 © 2006 Wiley-VCH Verlag GmbH & Co. KGaA, Weinheim 

conducted similarly, the products being identified by $^{1}H$, $^{77}Se$ NMR and IR spectroscopy as appropriate.

**X-ray Data:** CCDC-608276 contains the supplementary crystallographic data for this paper. These data can be obtained free of charge from The Cambridge Crystallographic Data Centre via www.ccdc.cam.ac.uk/data_request/cif.

## Acknowledgments

We thank EPSRC for support and Dr M. Webster for assistance with the X-ray crystallographic studies.

[1] F. A. Cotton, G. Wilkinson, M. Bochmann, C. A. Murillo, *Advanced Inorganic Chemistry*, 6th ed., Wiley, New York, **1998**.
[2] I. M. Griffiths, D. Nichols, *J. Chem. Soc. C* **1970**, 713–714.
[3] W. Priebsch, D. Rehder, *Inorg. Chem.* **1985**, *24*, 3058–3062.
[4] C. Weidemann, D. Rehder, *Inorg. Chim. Acta* **1986**, *120*, 15–20.
[5] D. Rehder, *Z. Naturforsch., Teil B* **1977**, *32*, 771–775.
[6] J.-C. Daran, A. Gourdon, Y. Jeannin, *Acta Crystallogr., Sect. B* **1980**, *36*, 309–312.
[7] A. Gourdon, Y. Jeannin, *Acta Crystallogr., Sect. B* **1980**, *36*, 304–309.
[8] J. C. Daran, Y. Jeannin, G. Constant, R. Morancho, *Acta Crystallogr., Sect. B* **1975**, *31*, 1833–1837.
[9] C. D. Abernethy, G. M. Codd, M. D. Spicer, M. K. Taylor, *J. Am. Chem. Soc.* **2003**, *125*, 1128–1129.
[10] T. Wistuba, C. Limburg, H. Pritzkow, *Z. Anorg. Allg. Chem.* **2002**, *628*, 2340–2344.
[11] T. A. Kabanos, A. D. Keramidas, A. Papaioannou, A. Terzis, *Inorg. Chem.* **1994**, *33*, 845–846.
[12] H.-L. Krauss, G. Gnatz, *Chem. Ber.* **1962**, *95*, 1023–1032.
[13] K. Behzadi, A. Thompson, *J. Less-Common Met.* **1987**, *132*, 49–55.
[14] H. Funk, W. Weiss, M. Zeising, *Z. Anorg. Allg. Chem.* **1958**, *296*, 36–45.
[15] K. L. Baker, D. A. Edwards, G. W. A. Fowles, R. G. Williams, *J. Inorg. Nucl. Chem.* **1967**, *29*, 1881–1885.
[16] R. C. Paul, N. C. Sharma, Y. P. Sahi, S. L. Chadha, K. Ashok, *Ind. J. Chem.* **1975**, *13*, 1191–1193.
[17] A. Hills, D. L. Hughes, G. J. Leigh, F. Pietro-Alcon, *J. Chem. Soc., Dalton Trans.* **1993**, 3609–3617.
[18] D. Nichols, K. R. Seddon, *J. Chem. Soc., Dalton Trans.* **1973**, 2747–2750.
[19] D. Nichols, K. R. Seddon, *J. Chem. Soc., Dalton Trans.* **1973**, 2751–2754.
[20] a) D. C. Crans, J. J. Smee, in: *Comprehensive Coordination Chemistry II* (Eds.: J. A. McCleverty, T. J. Meyer), **2004**, *4*, 175–239; b) R. Weaver, K. Kustin, *Adv. Inorg. Chem.* **1990**, *35*, 81–115.
[21] G. Beindorf, J. Strahle, W. Liebelt, K. Dehnicke, *Z. Naturforsch., Teil B* **1980**, *35*, 522–525.
[22] a) E. Ahlborn, E. Diemann, A. Muller, *Z. Anorg. Allg. Chem.* **1972**, *394*, 1–7; b) D. Fenske, A.-F. Shihada, H. Schwab, K. Dehnicke, *Z. Anorg. Allg. Chem.* **1980**, *471*, 140–146; c) A. Noll, S. Rabe, U. Mueller, *Z. Naturforsch. Teil B* **1999**, *54*, 591–596.
[23] J. Mason, *Multinuclear NMR*, Plenum, New York, **1987**.
[24] A. B. P. Lever, *Inorganic Electronic Spectroscopy*, 2nd ed., Elsevier, New York, **1985**, chapter 6.
[25] J.-P. Brunette, R. Heimburger, M. F. J. Leroy, *C R. Seances Acad. Sci., Ser C* **1971**, *272*, 2147–2150.
[26] J. E. Drake, J. E. Vekris, J. S. Wood, *J. Chem. Soc. A* **1969**, 345–349.
[27] Small orange crystals were grown from a $CH_2Cl_2$ solution of $[VOCl_3(2,2'\text{-bipy})]$ layered with hexane. Crystal data for $[V_2Cl_4O_3(2,2'\text{-bipy})_2]\cdot 1.75CH_2Cl_2$: $M$ = 752.76; triclinic, space group $P\bar{1}$ (no. 2), $Z$ = 4, $a$ = 13.522(4), $b$ = 13.833(3), $c$ = 16.784(5) Å, $\alpha$ = 105.216(12), $\beta$ = 103.871(12), $\gamma$ = 90.483(16)°, $U$ = 2932.4(14) Å$^3$; $T$ = 120 K, 10279 unique data gave $R_1$ = 0.105, $wR_2$ = 0.223 [$I > 2\sigma(I)$] based upon 678 independent parameters with $S$ = 1.03.
[28] W. Levason, M. C. Popham, G. Reid, M. Webster, *Dalton Trans.* **2003**, 291–294.
[29] R. G. Garvey, J. H. Nelson, R. O. Ragsdale, *Coord. Chem. Rev.* **1968**, *3*, 375–407.
[30] a) R. H. Holm, *Chem. Rev.* **1987**, *87*, 1401–1449; b) Y. Zhang, R. H. Holm, *Inorg. Chem.* **1990**, *29*, 911–917; c) H. Schmidt, M. Bashirpoor, D. Rehder, *J. Chem. Soc., Dalton Trans.* **1996**, 3865–3870.
[31] W. Levason, B. Patel, M. C. Popham, G. Reid, M. Webster, *Polyhedron* **2001**, *20*, 2711–2720.
[32] W. McFarlane, R. J. Wood, *J. Chem. Soc. A* **1972**, 1397–1402.
[33] W. F. Currier, J. H. Weber, *Inorg. Chem.* **1967**, *6*, 1539–1543.

Received: June 1, 2006
Published Online: September 8, 2006

 © 2006 Wiley-VCH Verlag GmbH & Co. KGaA, Weinheim 

DOI: 10.1002/ejic.200600573

# Studies on Chromium(III) and Vanadium(III) Complexes with Crown Ether and Crown Thioether Coordination – Synthesis, Properties and Structural Systematics

**Charlotte D. Beard,[a] Loretta Carr,[a] Martin F. Davis,[a] John Evans,[a] William Levason,[a] Louise D. Norman,[a] Gillian Reid,*[a] and Michael Webster[a]**

**Keywords:** Chromium / Crown ether / Thioether macrocycle / Vanadium

A series of six-coordinate chloro $Cr^{III}$ and $V^{III}$ complexes involving crown ether, crown thioether and mixed ether/thioether crowns, $[MCl_3(crown)]$ (M = Cr or V; crown = 12-crown-4, 15-crown-5,18-crown-6, [12]aneS$_4$, [15]aneS$_5$, [9]aneS$_2$O, [15]aneS$_2$O$_3$, [18]aneS$_3$O$_3$) has been prepared by the reaction of $[MCl_3(thf)_3]$ with rigorously dried crown in anhydrous $CH_2Cl_2$. In the presence of small amounts of water the monoaquo species $[MCl_3(H_2O)$(15-crown-5)] and $[MCl_3(H_2O)$(18-crown-6)] are obtained. The products have been characterised by IR and UV/Visible spectroscopy, microanalyses and for $[CrCl_3(H_2O)$(18-crown-6)], $[VCl_3(H_2O)$(15-crown-5)] and $[CrCl_3$([15]aneS$_5$)], by X-ray crystallography. The unexpected affinity of specifically the 15-crown-5 and 18-crown-6 complexes to pick up $H_2O$ is rationalised in terms of the strain within the two adjacent five-membered chelate rings in the anhydrous ($\kappa^3$-coordinated) species, and a wider survey of the structures reported for six-coordinate $M^{III}$ crown complexes (M = Sc – Cr) with RECH$_2$CH$_2$ER (E = O or S) reveals that while the S–M–S angles in five-membered chelate rings are typically around 82°, those involving O–M–O are very substantially more acute at around 75°. Thus, the $[MCl_3(\kappa^3$-crown ether)] complexes are much less stable and can alleviate some of this significant ring strain by switching to $\kappa^2$-crown coordination with the $H_2O$ ligand completing the six coordination. In contrast, the crown thioether complexes have much less tendency to do this and hence appear to be more stable. Furthermore, using the structurally related (dimethylene linkages) mixed thia/oxa crowns to probe the M–O vs. M–S binding competitively, strongly indicates that the $Cr^{III}$ and $V^{III}$ preferentially coordinate to the thioether rather than the ether donor atoms, contrary to normal expectation based upon HSAB theory.
(© Wiley-VCH Verlag GmbH & Co. KGaA, 69451 Weinheim, Germany, 2006)

## Introduction

The coordination chemistry of crown ether ligands is dominated by the group 1 and 2 metals and the lanthanides.[1–3] Two main types of metal–crown ether complex are known – primary coordination, where the crown bonds directly to the metal by some or all of the ether oxygen atoms, and secondary coordination, where the crown is not directly bonded to the metal, but interacts through H bonding with the metal complex. Relatively few studies of transition metal crown ether complexes have been reported. For the early 3d metals, scandium(III) forms primary coordination complexes under anhydrous conditions, including $[ScCl_2$(15-crown-5)][SbCl$_6$], [ScCl(15-crown-5)(MeCN)]-[SbCl$_6$]$_2$, $[ScCl_2$(18-crown-6)][SbCl$_6$] and $[Sc(12\text{-crown-}4)_2]^{3+}$, whilst in the presence of water secondary coordination occurs as in $[ScCl_3(H_2O)_3]\cdot$crown (crown = 15-crown-5, 18-crown-6).[4–6] Titanium(IV) halides produce the very moisture sensitive $[TiX_4(\kappa^2$-crown)] (crown = 12-crown-4, 15-crown-5, 18-crown-6; X = Cl or Br) and $[TiCl_3$(15-crown-5)(MeCN)][SbCl$_6$]; two hydrolysis products $[Ti_2Cl_6(\mu$-O)(18-crown-6)$_2$] and $[Ti_4(\mu$-O)$_4$Cl$_8$(15-crown-5)$_4$] have also been structurally characterised.[7–9]

Titanium(III), vanadium(III) and chromium(III) are represented by some scattered structurally characterised complexes, viz. $[MCl_3(H_2O)$(18-crown-6)] (M = Ti or V),[10,11] [VCl$_2$(15-crown-5)][VOCl$_4$],[12] $[CrCl_3(H_2O)$(15-crown-5)],[13] and $[CrCl_3(H_2O)_3]\cdot$(15-crown-5),[14] but the systematic chemistry with these trivalent metals has not been investigated. We have also been probing the chemistry of early transition-metal centres with softer thioether ligands and macrocycles in order to explore the effects of combining these soft ligands with hard metals. In this context we have described previously the preparations and properties of a series of neutral $Cr^{III}$ and $V^{III}$ halide complexes of the form $[MX_3(L)]$ (X = Cl or Br; L = [9]aneS$_3$, [10]aneS$_3$ [1,4,7-trithiacyclodecane] or [18]aneS$_6$ [1,4,7,10,13,16-hexathiacyclooctadecane]) and the cationic $[CrX_2([n]$aneS$_4$)]PF$_6$ ($n$ = 14 or 16) ([14]aneS$_4$ = 1,4,8,11-tetrathiacyclotetradecane, [16]aneS$_4$ = 1,5,9,13-tetrathiacyclohexadecane).[15] The crystal structure of $[CrCl_3(\kappa^3$-[18]aneS$_6$)] has also been described by Grant and co-workers.[16] Chromium(III) complexes with thioether-containing ligands, e.g.

[a] School of Chemistry, University of Southampton, Southampton SO17 1BJ, UK
E-mail: g.reid@soton.ac.uk

 © 2006 Wiley-VCH Verlag GmbH & Co. KGaA, Weinheim 

$[CrCl_3\{RS(CH_2)_2NH(CH_2)_2SR\}]$ (R = Me, Et, *n*Bu, *n*-decyl) have also been shown to be important catalyst precursors which, when combined with methylaluminoxane, promote the selective trimerisation of ethene to produce 1-hexene.[17] The nature of the ligand plays an important role in determining the product distribution in these processes.

Here we report the results of our systematic studies on the synthesis, characterisation and structures of complexes of the three crown ethers 12-crown-4, 15-crown-5 and 18-crown-6, the thiamacrocycles [12]ane$S_4$ (1,4,7,10-tetrathiacyclododecane) and [15]ane$S_5$ (1,4,7,10,13-pentathiacyclopentadecane) and the mixed thia-oxa macrocycles [9]ane$S_2O$ (1-oxa-4,7-dithiacyclononane), [15]ane$S_2O_3$ (1,4,7-trioxa-10,13-dithiacyclopentadecane) and [18]ane$S_3O_3$ (1,4,7-trioxa-10,13,16-trithiacyclooctadecane) with $Cr^{III}$ and $V^{III}$ chlorides. The macrocyclic ligands were specifically chosen to provide a direct comparison between ether and thioether coordination and the mixed S/O systems to probe the ligation to S or O competitively. The crystal structures of three complexes are reported and an analysis of the structural parameters of these species, together with the structurally characterised examples in the literature reveal some quite marked trends in the angles subtended at the metal. These are discussed in terms of donor atom type, ring size and complex stability.

## Results and Discussion

The reaction of $[MCl_3(thf)_3]$ with rigorously dry (either by prolonged heating in vacuo or by pre-treatment with $SOCl_2$ in refluxing $CH_2Cl_2$) 15-crown-5 in $CH_2Cl_2$ under anhydrous conditions yields pink-purple (Cr) and pink (V) powders $[MCl_3(\kappa^3\text{-15-crown-5})]$, whilst in the presence of small amounts of water the products are $[MCl_3(H_2O)(\kappa^2\text{-15-crown-5})]$. The structure of $[CrCl_3(H_2O)$(15-crown-5)] has been reported[13] and consists of a pseudo-octahedral chromium centre bonded to three facial chlorines, a water molecule and $\kappa^2$ to the crown. The anhydrous and aqua complexes are readily distinguishable by their IR spectra (the presence or absence of water bands), have distinguishable spectra in the fingerprint region and also differ in the far IR ν(M–Cl) vibrations (Experimental Section). The anhydrous $[MCl_3(\kappa^3\text{-15-crown-5})]$ readily convert to $[MCl_3(H_2O)(\kappa^2\text{-15-crown-5})]$ upon stirring in $CH_2Cl_2$ solution with small amounts of added water under $N_2$ (larger amounts of water completely displace the crown – see below). Crystals of $[VCl_3(H_2O)(\kappa^2\text{-15-crown-5})]$ were obtained from $CH_2Cl_2$/hexane. The structure shows (Figure 1, Table 1) the V coordinated to three facial Cl atoms 2.309(2)–2.335(2) Å, one $H_2O$ ligand [2.064(5) Å] and two adjacent ether O atoms from the crown [2.070(4) and 2.122(4) Å]. The O–V–O angle within the chelate ring is 76.23(18)°. The O5···O6···O4a angle is a plausible 102.3°. The structure of $[VCl_3(H_2O)(\kappa^2\text{-18-crown-6})]$ reported by Atwood and co-workers shows similar geometric parameters.[8] Although the H atoms bonded to the water O6 were not convincingly identified, there are only two suitable O···O distances for O–H···O H-bonding interactions. Thus O6···O5 [2.784(6) Å] is an intramolecular H-bond and O6···O4a [2.676(6) Å, a: *y*, *x*, –*z*] an intermolecular interaction to crown O atoms.

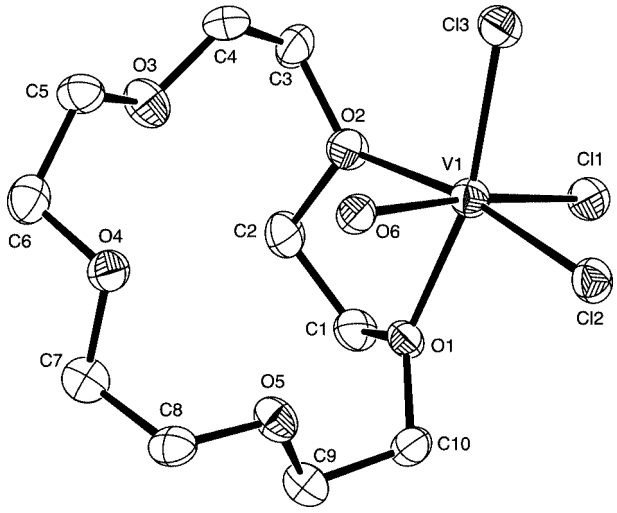


Figure 1. View of the structure of $[VCl_3(H_2O)$(15-crown-5)] with numbering scheme adopted. H atoms have been omitted for clarity and the ellipsoids are drawn at the 50% probability level.

Table 1. Selected bond lengths [Å] and angles [°] for $[VCl_3(H_2O)$(15-crown-5)]·3/4$CH_2Cl_2$.

| | | | |
|---|---|---|---|
| V1–O1 | 2.070(4) | V1–Cl1 | 2.319(2) |
| V1–O2 | 2.122(4) | V1–Cl2 | 2.335(2) |
| V1–O6 | 2.064(5) | V1–Cl3 | 2.309(2) |
| | | | |
| O6–V1–O1 | 82.72(19) | O6–V1–O2 | 88.12(18) |
| O1–V1–O2 | 76.23(18) | O6–V1–Cl3 | 89.08(14) |
| O1–V1–Cl3 | 166.19(14) | O2–V1–Cl3 | 92.46(14) |
| O6–V1–Cl1 | 172.78(14) | O1–V1–Cl1 | 90.07(15) |
| O2–V1–Cl1 | 89.73(14) | Cl3–V1–Cl1 | 97.90(8) |
| O6–V1–Cl2 | 89.08(13) | O1–V1–Cl2 | 94.00(13) |
| O2–V1–Cl2 | 170.10(14) | Cl3–V1–Cl2 | 96.98(8) |
| Cl1–V1–Cl2 | 91.89(8) | | |

Stirring a $CH_2Cl_2$ solution of this complex overnight with a further added water leads to deposition of blue crystals. These were shown (unit cell determination) to be the $V^{IV}$ species $[VOCl_2(H_2O)_2]$·(15-crown-5) whose structure has been determined previously and shows secondary bonding interactions between the $H_2O$ ligands on the vanadyl centre and the crown ether.[18]

The corresponding reactions of $[MCl_3(thf)_3]$ with 12-crown-4 gave $[MCl_3(\kappa^3\text{-12-crown-4})]$. Similarly, reaction of $[MCl_3(thf)_3]$ with 18-crown-6 affords $[MCl_3(\kappa^3\text{-18-crown-6})]$ and $[MCl_3(H_2O)(\kappa^2\text{-18-crown-6})]$ (the latter with M = Cr was characterised by an X-ray study – below), while using a 2:1 ratio of M/crown gives the binuclear $[(MCl_3)_2$(18-crown-6)]. The anhydrous $[MCl_3(\kappa^3\text{-18-crown-6})]$ are particularly moisture sensitive, much more so than $[MCl_3(\kappa^3$-12-crown-4)], which may indicate that the water is first associated with the "free" O atoms of the crown and then transferred to the metal, which will be less easy in the smaller ring. The structure of $[CrCl_3(H_2O)$(18-crown-6)] shows two

 © 2006 Wiley-VCH Verlag GmbH & Co. KGaA, Weinheim 

independent molecules in the asymmetric unit, one of which is shown in Figure 2, Table 2. The $Cr^{III}$ is in a distorted octahedral environment, coordinated to three facial Cl atoms, two adjacent ether O atoms from the crown and a water molecule. For the Cr1 molecule (see Figure 2) each of the O13 H atoms is involved in an intramolecular H bond to a crown O atom [O13···O4 2.813(4), O13···O6 2.842(4) Å]. A similar situation applies to the Cr2 containing-molecule and O14. The Cr–O distances within the crown are ca. 2.05 Å, while the Cr–$OH_2$ distances are slightly shorter in each case. The O–Cr–O angles within the chelate rings are notable at only 79.22(11) and 76.93(12)°. The structural features in this species parallel those in $[CrCl_3(H_2O)(\kappa^2\text{-15-crown-5})]$ reported by Dehnicke and co-workers,[13] which shows intramolecular H-bonding interactions between the coordinated $H_2O$ ligand and two of the uncoordinated O atoms of the crown.

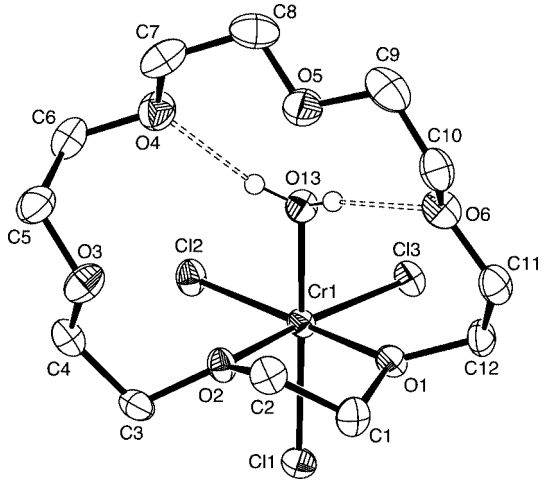


Figure 2. View of the structure of one of the two independent $[CrCl_3(H_2O)(18\text{-crown-6})]$ molecules with numbering scheme adopted. H atoms on C have been omitted for clarity and the ellipsoids are drawn at the 50% probability level. The other molecule is very similar.

As before, the anhydrous and the aqua complexes can be distinguished by their IR spectra, and the IR spectra of the dinuclear complexes are quite distinct in the fingerprint region. All of the $M^{III}$ complexes contain pseudo-octahedral metal centres, as shown by their diffuse reflectance spectra (Table 3) (some solution spectra were obtained but a combination of poor solubility and extreme moisture sensitivity of the dilute solutions meant they were poorly reproducible and are not quoted).

The $d^3$ chromium complexes typically showed two d–d bands assigned (in $O_h$ symmetry) as $^4A_{2g}\rightarrow{}^4T_{2g}$ and $^4A_{2g}\rightarrow{}^4T_{1g}(F)$, respectively, and a third band was usually evident of the edge of intense features in the UV, which may be the $^4A_{2g}\rightarrow{}^4T_{1g}(P)$ transition (Table 3).[19] Although the actual metal-centre symmetry is lower than $O_h$, no clearly resolved splitting of the bands was observed, although the lowest energy feature was often asymmetric. The band maxima show small shifts consistent with the ligand field strengths $Cl < O_{crown} < H_2O$. For the $d^2$ vanadium complexes the two transitions observed are assigned to $^3T_{1g}\rightarrow{}^3T_{2g}$, and $^3T_{1g}\rightarrow{}^3T_{1g}(P)$, respectively, based on $O_h$ symmetry and trends are discussed below.

Table 2. Selected bond lengths [Å] and angles [°] for $[CrCl_3(H_2O)(18\text{-crown-6})]$.

| | | | |
|---|---|---|---|
| Cr1–O1 | 2.060(3) | Cr1–Cl1 | 2.3047(13) |
| Cr1–O2 | 2.047(3) | Cr1–Cl2 | 2.2704(12) |
| Cr1–O13 | 2.034(3) | Cr1–Cl3 | 2.2780(12) |
| Cr2–O7 | 2.072(3) | Cr2–Cl4 | 2.3017(13) |
| Cr2–O8 | 2.069(3) | Cr2–Cl5 | 2.2892(12) |
| Cr2–O14 | 2.016(3) | Cr2–Cl6 | 2.2717(12) |
| O13–Cr1–O2 | 86.41(12) | O13–Cr1–O1 | 86.05(12) |
| O2–Cr1–O1 | 79.22(11) | O13–Cr1–Cl2 | 89.84(9) |
| O2–Cr1–Cl2 | 94.26(8) | O1–Cr1–Cl2 | 172.49(9) |
| O13–Cr1–Cl3 | 90.94(9) | O2–Cr1–Cl3 | 169.63(8) |
| O1–Cr1–Cl3 | 90.60(8) | Cl2–Cr1–Cl3 | 95.75(4) |
| O13–Cr1–Cl1 | 173.43(9) | O2–Cr1–Cl1 | 87.82(9) |
| O1–Cr1–Cl1 | 89.78(9) | Cl2–Cr1–Cl1 | 93.73(5) |
| Cl3–Cr1–Cl1 | 94.18(5) | O14–Cr2–O8 | 85.70(12) |
| O14–Cr2–O7 | 86.76(12) | O8–Cr2–O7 | 76.93(12) |
| O14–Cr2–Cl6 | 88.74(9) | O8–Cr2–Cl6 | 171.29(10) |
| O7–Cr2–Cl6 | 96.08(9) | O14–Cr2–Cl5 | 90.23(9) |
| O8–Cr2–Cl5 | 91.43(9) | O7–Cr2–Cl5 | 168.16(9) |
| Cl6–Cr2–Cl5 | 95.29(4) | O14–Cr2–Cl4 | 174.83(9) |
| O8–Cr2–Cl4 | 91.73(9) | O7–Cr2–Cl4 | 88.29(9) |
| Cl6–Cr2–Cl4 | 93.27(5) | Cl5–Cr2–Cl4 | 94.33(5) |

Grant and co-workers have described the reaction of $CrCl_3\cdot6H_2O$ with the thioether macrocycles [12]aneS$_4$ and [15]aneS$_5$ in refluxing MeCN; however, unsurprisingly, in the presence of water the substitutions are not clean and no pure products were isolated.[16] We have obtained the thioether macrocyclic complexes $[CrCl_3(\kappa^3\text{-[12]aneS}_4)]$ and $[CrCl_3(\kappa^3\text{-[15]aneS}_5)]$ readily and in good yield from $[CrCl_3(thf)_3]$ and the thiamacrocycle in anhydrous $CH_2Cl_2$ solution and isolated them as purple/blue solids. Despite the softer nature of the ligand donor atoms, once isolated these compounds show a much reduced tendency to pick up $H_2O$ in the metal coordination sphere cf. the crown ethers above (IR evidence). $[VCl_3(\kappa^3\text{-[12]aneS}_4)]$ was obtained similarly.

A crystal structure of $[CrCl_3([15]aneS_5)]$ confirms (Figure 3, Table 4) the distorted octahedral coordination at Cr through three facial Cl atoms and three facial and mutually adjacent S atoms of the macrocycle, $d$(Cr–Cl) = 2.2849(8)–2.3028(9) Å; $d$(Cr–S) = 2.4161(10)–2.4942(8) Å, the bond lengths and angles compare well with those in the crystallographically characterised neutral $[CrCl_3([18]aneS_6)]$[16] and the cationic *cis*-$[CrX_2([14]aneS_4)]PF_6$.[15] The UV/Visible spectra show clearly that the thioether donors present a stronger ligand field than the O–donor ligands, giving the overall order $Cl^- < O_{crown} < H_2O < S_{thiacrown}$ (Table 3).

The mixed thia-oxa macrocyclic complexes $[MCl_3(\kappa^3\text{-[9]aneS}_2O)]$, $[MCl_3(\kappa^3\text{-[15]aneS}_2O_3)]$ and $[MCl_3(\kappa^3\text{-[18]aneS}_3O_3)]$ were obtained from similar reactions as purple/blue (Cr) or pink (V) coloured solids. These compounds have a much lower tendency to pick up $H_2O$ compared to the crown ether complexes.

The diffuse reflectance UV/Visible spectra for the thia and thia-oxa macrocyclic complexes are also consistent

 © 2006 Wiley-VCH Verlag GmbH & Co. KGaA, Weinheim 

Table 3. UV/Visible data [$cm^{-1}$].[a]

| Complex[b] | $^4A_{2g}\rightarrow{}^4T_{2g}$ | $^4A_{2g}\rightarrow{}^4T_{1g}$(F) | $^4A_{2g}\rightarrow{}^4T_{1g}$(P) |
|---|---|---|---|
| $[CrCl_3(thf)_3]$ | 13666 (sh), 14450 | 19680 | 27320 |
| $[CrCl_3$(12-crown-4)] | 13510 | 19050 | – |
| $[CrCl_3$(15-crown-5)] | 13195 | 19230 | 27930 |
| $[CrCl_3(H_2O)$(15-crown-5)] | 13660 | 19650 | 29250 (sh) |
| $[CrCl_3$(18-crown-6)] | 13200 (sh), 13500 | 19380 | 28900 (sh) |
| $[CrCl_3(H_2O)$(18-crown-6)] | 13570 | 19685 | 29270 (sh) |
| $[(CrCl_3)_2$(18-crown-6)] | 13400, 13960 (sh) | 19450 | – |
| $[CrCl_3$([12]ane$S_4$)] | 14050 | 19840 | 29900 (sh) |
| $[CrCl_3$([15]ane$S_5$)] | 14290 | 19380 | 30490 (sh) |
| $[CrCl_3$([9]ane$S_2O$)] | 14880 | 19970 | – |
| $[CrCl_3$([15]ane$S_2O_3$)] | 14450 | 20000 | 30860 (sh) |
| $[CrCl_3$([18]ane$S_3O_3$)] | 14350 | 19660 | 30300 |
| Complex[b] | $^3T_{1g}\rightarrow{}^3T_{2g}$ | $^3T_{1g}\rightarrow{}^3T_{1g}$(P) | |
| $[VCl_3(thf)_3]$ | 12820 | 20490 | |
| $[VCl_3$(12-crown-4)] | 11870 | 18900 | |
| $[VCl_3$(15-crown-5)] | 11500 (sh), 12830 | 19380 | |
| $[VCl_3(H_2O)$(15-crown-5)] | 11300 (sh), 12690 | 19190 | |
| $[VCl_3$(18-crown-6)] | 12900 | 18950 | |
| $[VCl_3(H_2O)$(18-crown-6)] | 11900 (sh), 13400 | 19800 | |
| $[(VCl_3)_2$(18-crown-6)] | 12320 | 19230 | |
| $[VCl_3$([12]ane$S_4$)] | 12690 | 18250 | |
| $[VCl_3$([9]ane$S_2O$)] | 13440 | 18880 | |
| $[VCl_3$([15]ane$S_2O_3$)] | 12940, 13400 (sh) | 19850 | |
| $[VCl_3$([18]ane$S_3O_3$)] | 12800 | 19690 | |

[a] Spectra recorded by diffuse reflectance; frequencies quoted have errors estimated as +/– 100 $cm^{-1}$. [b] For $Cr^{III}$ $\nu_1$ gives 10Dq directly; for both $Cr^{III}$ and $V^{III}$ semi-quantitative fitting of the spectra (in $O_h$ symmetry) to the appropriate Tanabe–Sugano diagram gave consistent trends, i.e. the average 10 Dq increases with incorporation of S-donor atoms and is accompanied by a small decrease in the B parameter.[19]

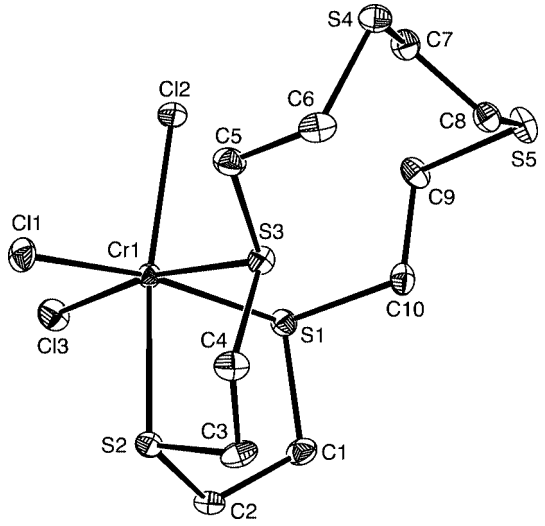


Figure 3. View of the structure of $[CrCl_3$([15]ane$S_5$)] with numbering scheme adopted. H atoms are omitted for clarity and the ellipsoids are drawn at the 50% probability level.

Table 4. Selected bond lengths [Å] and angles [°] for $[CrCl_3$([15]ane$S_5$)].

| | | | |
|---|---|---|---|
| Cr1–Cl1 | 2.2849(8) | Cr1–S1 | 2.4942(8) |
| Cr1–Cl2 | 2.2885(9) | Cr1–S2 | 2.4166(9) |
| Cr1–Cl3 | 2.3028(9) | Cr1–S3 | 2.4261(10) |
| Cl1–Cr1–Cl2 | 96.13(3) | Cl1–Cr1–Cl3 | 94.45(3) |
| Cl2–Cr1–Cl3 | 99.08(3) | Cl1–Cr1–S2 | 87.74(3) |
| Cl2–Cr1–S2 | 171.22(3) | Cl3–Cr1–S2 | 88.43(3) |
| Cl1–Cr1–S3 | 90.21(3) | Cl2–Cr1–S3 | 88.46(3) |
| Cl3–Cr1–S3 | 170.64(3) | S2–Cr1–S3 | 83.64(3) |
| Cl1–Cr1–S1 | 172.12(3) | Cl2–Cr1–S1 | 91.71(3) |
| Cl3–Cr1–S1 | 83.62(3) | S2–Cr1–S1 | 84.58(3) |
| S3–Cr1–S1 | 90.68(2) | | |

with distorted octahedral geometries. For the $[MCl_3$([9]ane$S_2O$)] complexes, $S_2O$ coordination of the macrocycle is imposed, giving the metal an $S_2OCl_3$ donor set overall, and as expected, the UV/Visible spectra of $[MCl_3$([9]ane$S_2O$)] (Table 3) much more closely resemble those of the thioether crown analogues ($S_3Cl_3$ donor set) rather than the crown ether analogues ($O_3Cl_3$ donor set). Importantly, comparison of the energies of the d-d transitions in the $Cr^{III}$ thia-oxa species clearly shows that even the [15]ane$S_2O_3$ and [18]ane$S_3O_3$ systems involve S-coordination (although this technique does not readily discriminate between $S_3$ vs. $S_2O$ vs. $SO_2$ coordination). Unfortunately, despite repeated efforts to obtain single crystals of one or more of the complexes with these ligands to provide definitive proof of the metal donor set, we have not been successful.

## Analysis of Structural Data

Evidence from this work shows that the $\kappa^3$-coordinated crown ether complexes may be obtained only under stringently anhydrous conditions, with traces of water leading to partial hydrolysis and isolation of the mono-aqua complexes, with the crown now only $\kappa^2$-coordinated. On the other hand, the thiamacrocycles readily yield $S_3$-coordinated species, which appear to be considerably less susceptible to hydrolysis. At first sight this seems surprising because on the basis of Pearson's HSAB theory, one would antici-

 © 2006 Wiley-VCH Verlag GmbH & Co. KGaA, Weinheim 

pate that the crown ether ligands (O-donor) would result in more stable complexes than the softer thioether macrocycles. In order to explain these results we have therefore examined the structural parameters in these species, together with the crystallographically determined parameters in all other reported six-coordinate (octahedral) complexes of early transition metals (Sc, Ti, V and Cr) with ether and thioether ligands of the form $RE(CH_2)_2ER$ and $RE(CH_2)_2E(CH_2)_2ER$ (E = O or S; R = alkyl) and S- or O-donor macrocycles involving dimethylene linkages. The results obtained using the Cambridge Crystallographic Database[20,21] are presented in Figure 4, which shows histograms depicting the E–M–E angles within the five-membered chelate rings for E = O (a) and for E = S (b). The average O–M–O angles in these species are 74.8°, with values ranging from 68.6–79.0°, while the average S–M–S chelate angles are 82.2°, with values ranging from 75.7–86.8°. The data obtained from the three crystal structures presented above are consistent with the data in Figure 4. This surprisingly large difference is consistent with the crown ether complexes being more strained, and may well explain why the $\kappa^3$-crown complexes are so readily hydrolysed – incorporating two adjacent very acute five-membered chelates leads to a very strained species which will readily scavenge another donor ligand such as $H_2O$ and convert to $\kappa^2$-crown to relieve the strain within the coordination sphere. In contrast, the S–M–S chelate angles of ca. 82° are closer to the idealised 90° angle in a regular octahedron. In support of this we note that the O–Cr–O angles in *mer*-$[CrCl_3(thf)_3]$ are 86.0(1) and 86.5(1)° – the monodentate thf ligands remove chelate constraints as a consideration, and hence presumably reflect the preferred relative positioning of the ligands.[22]

The magnitude of the chelate angle subtended at the metal M is a consequence of both the M–E distances and the E–C distances. The M–S distances are ca. 0.4 Å longer than *d*(M–O) in these species. The reason for the large difference in E–M–E angles presumably originates from the difference between *d*(O–C) (typically ca. 1.47 Å) vs. *d*(S–C) (typically ca. 1.83 Å) – thus an O–C–C–O linkage is too short to accommodate idealised octahedral angles at a coordinated early transition metal without introducing significant angle strain at the O and the C atoms.

We previously reported the preparation and properties of the $Ti^{IV}$ complex $[TiCl_4(\kappa^2\text{-}[15]aneS_2O_3)]$, the $^1H$ NMR spectrum of which unexpectedly showed that coordination to Ti is through the two thioether S atoms, not the ether O atoms.[9] This result, together with the results of the present studies, suggest that the substantially different ring-strain effects introduced upon chelation of $–OCH_2CH_2O–$ cf. $–SCH_2CH_2S–$ linkages plays a dominant role in determining the donor set at Ti and offsets the fact that the thioethers are softer donor ligands than the ethers.

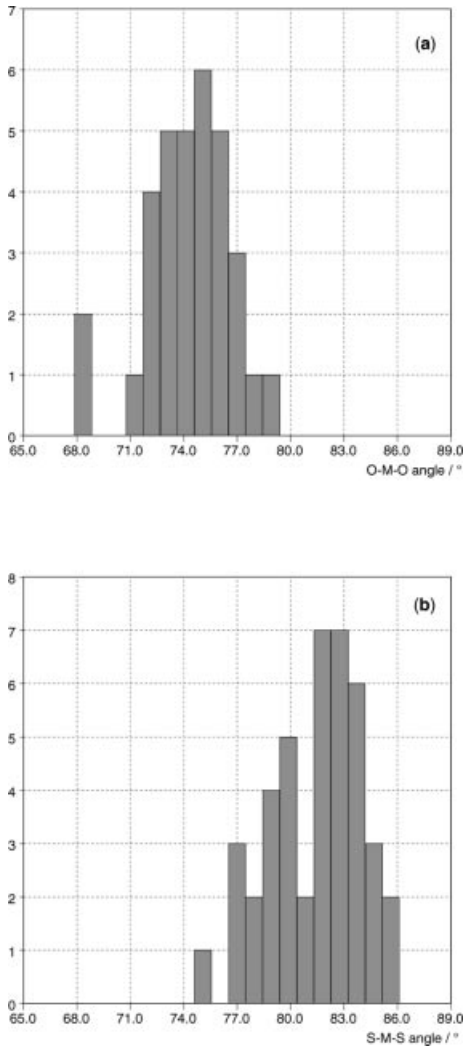


Figure 4. Histograms showing the crystallographically determined E–M–E angles within saturated five-membered chelate rings on an octahedral metal centre (M = Sc, Ti, V, Cr). (**a**) E = O, mean O–M–O angle 74.8(2.4)°. The lowest angles are for $[Sc(CH_2SiMe_3)_3$-(12-crown-4)] which contains two adjacent five-membered chelate rings.[28] (b) E = S, mean S–M–S angle 82.2(2.6)°. The lowest angles are for those complexes involving the macrocycle [9]ane$S_3$ containing three adjacent five-membered chelate rings.

## Conclusions

We describe here a series of neutral chloro $Cr^{III}$ and $V^{III}$ complexes with crown ether, crown thioether and mixed thia-oxa crown ligands. The $\kappa^3$-crown ether complexes show a marked tendency to dissociate one O atom and pick up a $H_2O$ ligand – an observation also noted for other early transition-metal crown ether complexes both by ourselves and by other workers. Furthermore, competitive binding studies using mixed S/O crowns with various ring sizes, but still maintaining the dimethylene linking groups strongly suggest that *S*-coordination is preferred.

This work has shown that despite the prediction that the hard, oxophilic early transition metals are likely to coordinate more favourably with ether-based ligands than the softer thioethers, ring strain within the resulting five-membered chelates plays a critical role and destabilises the crown ether complexes cf. the crown thioether analogues in these systems. This result suggests that the linkage between the O atoms of crown ether ligands may be of fundamental

 © 2006 Wiley-VCH Verlag GmbH & Co. KGaA, Weinheim 

importance in determining complex stability and that judicious choice of crown design (ring size and substitution pattern) may influence significantly the stability of transition metal–crown ether complexes and allow a much wider range of transition metal complexes with this important family of ligands to be prepared. Work is underway in our laboratories currently to investigate this more fully. Finally, we note that these considerations are not relevant to the *endo*-coordinated crowns in the seven-coordinate species such as $[ScCl_2(\kappa^5\text{-15-crown-5})]^+$, $[ScCl(\kappa^5\text{-15-crown-5})(MeCN)]^{2+}$ [4–6] and $[VCl_2(\kappa^5\text{-15-crown-5})]^+$,[12] since in these species the crown occupies five positions in a pentagonal plane, with idealised O–M–O angles of 72° which can be easily accommodated by the five-membered chelate rings.

## Experimental Section

**Physical Measurements:** Infrared spectra were recorded as Nujol mulls between CsI discs with a Perkin–Elmer 983G spectrometer over the range 4000–180 $cm^{-1}$. UV/Visible spectra were obtained in diffuse reflectance mode from samples diluted with $BaSO_4$ using a Perkin–Elmer Lambda19 spectrometer or as solutions in $CH_2Cl_2$ using quartz cells. Microanalyses were performed by the University of Strathclyde micro-analytical service. In some cases the compounds retained some $CH_2Cl_2$ which was evident from the microanalyses, IR and by $^1H$ NMR spectroscopy; partial $CH_2Cl_2$ is also evident in some of the crystal structures. $[CrCl_3(thf)_3]$ was made by the literature route.[23] $[VCl_3(thf)_3]$ and the macrocycles 12-crown-4, 15-crown-5, 18-crown-6, [12]ane$S_4$ and [15]ane$S_5$ were obtained from Aldrich. The mixed thia-oxa crowns, [9]ane$S_2O$, [15]ane$S_2O_3$ and [18]ane$S_3O_3$ were prepared by the literature methods.[24] The anhydrous crown ethers were obtained either by prolonged heating in vacuo or by refluxing the crown with thionyl chloride in $CH_2Cl_2$. The aqua complexes either used the crowns treated as above and subsequent addition of small amounts of water, or using crowns which were "dried" by pumping in vacuo at room temperature for a few hours (under these conditions $^1H$ NMR and IR spectra provide evidence for retention of some water). The anhydrous crowns were stored in Schlenk flasks and manipulated in a dry box. All complexes were manipulated in a dry box (<5 ppm water).

### Chromium(III) Complexes

**$[CrCl_3(12\text{-crown-4})]$:** $[CrCl_3(thf)_3]$ (0.4 g, 1.1 mmol) in dry $CH_2Cl_2$ (5 mL) was combined with dry 12-crown-4 (0.2 g, 1.1 mmol) in dry $CH_2Cl_2$ (5 mL). A precipitate was formed; this was then filtered off and dried in vacuo. The product was a pink solid. Yield 0.10 g, 24%. $C_8H_{16}Cl_3CrO_4\cdot 1/2CH_2Cl_2$ (377.0): calcd. C 27.1, H 4.5; found C 27.5, H 4.9. IR (Nujol): $\tilde{\nu}$ = 1299 (s), 1261 (m), 1228 (m), 1145 (s), 1063 (s), 1026 (vs), 934 (m), 908 (s), 838 (s), 363 (sh), 356 (s), 340 (sh) $cm^{-1}$.

**$[CrCl_3(15\text{-crown-5})]$:** $[CrCl_3(thf)_3]$ (0.13 g, 0.34 mmol) in dry $CH_2Cl_2$ (5 mL) was added to anhydrous 15-crown-5 (0.07 g, 0.34 mmol) in dry $CH_2Cl_2$ (5 mL) and the solution was stirred for 30 min. A solid was produced and then filtered off and dried in vacuo. Pink solid. Yield 0.06 g, 38%. $C_{10}H_{20}Cl_3CrO_5\cdot CH_2Cl_2$ (463.5): calcd. C 28.5, H 4.8; found C 27.5, H 5.8. IR (Nujol): $\tilde{\nu}$ = 1304 (m), 1263 (m), 1231 (m), 1147 (s), 1126 (s), 1111 (s), 1081 (s), 1064 (vs), 1021 (vs), 934 (s), 928 (sh), 906 (sh), 841 (s), 798 (s), 728 (s), 380 (sh), 362 (s), 349 (s) $cm^{-1}$.

**$[CrCl_3(H_2O)(15\text{-crown-5})]$:** $[CrCl_3(thf)_3]$ (0.10 g, 0.27 mmol) in dry $CH_2Cl_2$ (5 mL) was added to 15-crown-5 (0.17 g, 0.28 mmol) in dry $CH_2Cl_2$ (5 mL) and the solution was stirred for 1 h. The precipitate was filtered off and dried in vacuo. The product was a pink solid. Yield 0.05 g, 37%. $C_{10}H_{22}Cl_3CrO_6$ (396.6): calcd. C 30.3, H 5.6; found C 29.5, H 6.1. IR (Nujol): $\tilde{\nu}$ = 3300 (br), 1630 (m), 1303 (m), 1249 (m), 1140 (s), 1120 (s), 1110 (s), 1073 (vs), 1035 (vs), 1006 (m), 933 (s), 919 (m), 854 (s), 828 (w), 786 (w), 365 (sh), 343 (m), 321 (m) $cm^{-1}$.

**$[CrCl_3(18\text{-crown-6})]$:** $[CrCl_3(thf)_3]$ (0.3 g, 0.8 mmol) in dry $CH_2Cl_2$ (5 mL) was combined with dry 18-crown-6 (0.2 g, 1.0 mmol) in dry $CH_2Cl_2$ (5 mL). The solution was stirred for 5 min the solid produced was then filtered off and dried in vacuo. The product produced was a pink solid. Yield 0.05 g, 10%. $C_{12}H_{24}Cl_3CrO_6\cdot 1/2CH_2Cl_2$ (465.1): calcd. C 32.3, H 5.4; found C 32.5, H 6.0. IR (Nujol): $\tilde{\nu}$ = 1306 (m), 1260 (w), 1120 (s), 1166 (s), 1022 (s), 937 (m), 922 (m), 822 (m), 797 (m), 377 (m), 352 (s) $cm^{-1}$.

**$[CrCl_3(H_2O)(18\text{-crown-6})]$:** $[CrCl_3(thf)_3]$ (0.14 g, 0.37 mmol) in dry $CH_2Cl_2$ (10 mL) was combined with 18-crown-6 (0.1 g, 0.4 mmol) in dry $CH_2Cl_2$ (10 mL). The solution was stirred for 1 h. Addition of dry *n*-hexane (5 mL) produced a precipitate, which was then filtered off and dried in vacuo. The product produced was a pink solid. Yield 0.03 g, 19%. $C_{12}H_{26}Cl_3CrO_7$ (440.7): calcd. C 32.7, H 6.0; found C 31.9, H 7.0. IR (Nujol): $\tilde{\nu}$ = 3300 (br), 1617 (m), 1299 (w), 1261 (m), 1148 (m), 1093 (vs), 1046 (sh), 1019 (s), 951 (w), 865 (s), 810 (m), 356 (m), 323 (m) $cm^{-1}$.

**$[(CrCl_3)_2(18\text{-crown-6})]$:** $[CrCl_3(thf)_3]$ (0.19 g, 0.50 mmol) was dissolved in anhydrous $CH_2Cl_2$ (20 mL) and a solution of dry 18-crown-6 (0.06 g, 0.23 mmol) in anhydrous $CH_2Cl_2$ (10 mL) added and the mixture stirred for 30 min. The solution was concentrated in vacuo to 10 mL, and dry hexane (10 mL) added dropwise to the vigorously stirred solution. After stirring for 10 min the purple solid which had separated was filtered off and dried in vacuo. Yield 0.09 g, 67%. $C_{12}H_{24}Cl_6Cr_2O_6$ (581.0): calcd. C 24.8, H 4.2; found C 25.7, H 5.9. IR (Nujol): $\tilde{\nu}$ = 1346 (w), 1306 (w), 1258 (m), 1210 (w), 1147 (sh), 1092 (s), 1064 (s), 1018 (s), 936 (m), 921 (sh), 852 (m), 821 (m), 707 (m), 587 (w), 367 (sh), 350 (s) $cm^{-1}$.

**$[CrCl_3([12]aneS_4)]$:** [12]ane$S_4$ (0.03 g, 0.13 mmol) was dissolved in $CH_2Cl_2$ (5 mL) and combined with a solution of $[CrCl_3(thf)_3]$ (0.05 g, 0.13 mmol) in $CH_2Cl_2$ (5 mL). The solution turned blue immediately and a small amount of blue precipitate formed. The solution was concentrated further to ca. 3 mL in vacuo. The resulting blue solid was then filtered off and dried in vacuo. Yield 0.04 g, 76%. $C_8H_{16}Cl_3CrS_4$ (398.8): calcd. C 24.1, H 4.0; found C 24.4, H 4.6. IR (Nujol): $\tilde{\nu}$ = 1300 (w), 1262 (m), 1093 (m), 1017 (m), 951 (w), 923 (w), 861 (m), 802 (m), 744 (m), 366 (m), 329 (w) $cm^{-1}$.

**$[CrCl_3([15]aneS_5)]$:** Prepared similarly to $[CrCl_3([12]aneS_4)]$ using [15]ane$S_5$. Purple solid. Yield 88%. $C_{10}H_{20}Cl_3CrS_5$ (459.0): calcd. C 26.2, H 4.4; found 25.6, H 4.9. IR (Nujol): $\tilde{\nu}$ = 1260 (s), 1096 (s), 1021 (s), 800 (m), 340 (m), 315 (sh) $cm^{-1}$.

**$[CrCl_3([9]aneS_2O)]$:** Prepared similarly to $[CrCl_3([12]aneS_4)]$ using [9]ane$S_2O$. Purple solid. Yield 58%. $C_6H_{12}Cl_3CrOS_2\cdot 1/4thf$ (340.67): calcd. C 24.7, H 4.1; found 25.0, H 4.0. IR (Nujol): $\tilde{\nu}$ = 1297 (w), 1200 (w), 1188 (w), 1056 (m), 1012 (m), 989 (s), 934 (m), 912 (s), 836 (m), 772 (w), 686 (w), 487 (w), 358 (s), 343 (sh) $cm^{-1}$.

**$[CrCl_3([15]aneS_2O_3)]$:** Prepared similarly to $[CrCl_3([12]aneS_4)]$ using [15]ane$S_2O_3$. Purple solid. Yield 40%. $C_{10}H_{20}Cl_3CrO_3S_2$ (410.8): calcd. C 29.2, H 4.9; found C 28.9, H 5.3. IR (Nujol): $\tilde{\nu}$ = 1304 (m), 1260 (m), 1095 (s), 1021 (s), 917 (w), 868 (w), 802 (m), 366 (m), 345 (w) $cm^{-1}$.

**$[CrCl_3([18]aneS_3O_3)]$:** $[CrCl_3(thf)_3]$ (0.18, 0.52 mmol) was dissolved in anhydrous $CH_2Cl_2$ (15 mL) and added to a solution of

 © 2006 Wiley-VCH Verlag GmbH & Co. KGaA, Weinheim 

[18]ane$S_3O_3$ (0.16 g, 0.52 mmol) in anhydrous $CH_2Cl_2$ (15 mL), when an intensely blue solution formed immediately which rapidly deposited a blue solid. The mixture was stirred for 30 min, dry hexane (10 mL) was added dropwise and the mixture stirred for a further 1 h. The deep blue solid was filtered off and dried in vacuo. Yield 0.16 g, 82%. $C_{12}H_{24}Cl_3CrO_3S_3 \cdot 1/2CH_2Cl_2$ (513.3): calcd. C 29.2, H 4.9; found C 28.9, H 5.3. IR (Nujol): $\tilde{\nu}$ = 1348 (w), 1295 (m), 1260 (m), 1130 (sh), 1101 (s), 1070 (sh), 1023 (s), 914 (w), 849 (w), 801 (s), 470 (w), 355 (sh), 345 (s) $cm^{-1}$.

**Vanadium(III) Complexes**

**[$VCl_3$(12-crown-4)]:** [$VCl_3(thf)_3$] (0.38 g, 1.0 mmol) and dry 12-crown-4 (0.18 g, 1.0 mmol) were combined in dry $CH_2Cl_2$ (10 mL). The pink powder that precipitated was filtered off after 2 h and dried in vacuo. Yield 0.28 g, 33%. $C_8H_{16}Cl_3O_4V$ (333.5): calcd. C 28.8, H 4.8; found C 28.8, H 5.6. IR (Nujol): $\tilde{\nu}$ = 1298 (s), 1261 (w), 1231 (m), 1145 (s), 1066 (s), 1027 (s), 937 (m), 909 (s), 837 (s), 483 (m), 364 (m), 339 (s) $cm^{-1}$.

**[$VCl_3$(15-crown-5)]:** Prepared similarly to [$VCl_3$(12-crown-4)] using anhydrous 15-crown-5. Pink powder. Yield 0.15 g, 25%. $C_{10}H_{20}Cl_3O_5V \cdot CH_2Cl_2$ (462.5): calcd. C 28.5, H 5.2; found C 27.5, H 5.3. IR (Nujol): $\tilde{\nu}$ = 1304 (m), 1262 (w), 1228 (w), 1149 (m), 1113 (m), 1080 (sh), 1068 (vs), 1027 (s), 933 (m), 918 (m), 846 (m), 793 (m), 367 (m), 342 (s), 324 (s) $cm^{-1}$.

**[$VCl_3(H_2O)$(15-crown-5)]:** [$VCl_3(thf)_3$] (0.17 g, 0.48 mmol) in dry $CH_2Cl_2$ (5 mL) was added to 15-crown-5 (0.11 g, 0.48 mmol) in dry $CH_2Cl_2$ (5 mL) and the solution was stirred for 1 h. The pink precipitate was filtered off and dried under vacuo. Yield 0.15 g, 38%. $C_{10}H_{22}Cl_3O_6V \cdot CH_2Cl_2$ (480.5): calcd. C 27.5, H 5.0; found C 27.5, H 6.1. IR (Nujol): $\tilde{\nu}$ = 3300 (br), 1630 (m), 1303 (m), 1260 (m), 1140 (s), 1120 (s), 1110 (s), 1073 (vs), 1035 (vs), 1006 (m), 933 (s), 919 (m), 854 (s), 828 (w), 786 (w), 362 (sh), 331 (m), 321 (m) $cm^{-1}$.

**[$VCl_3$(18-crown-6)]:** [$VCl_3(thf)_3$] (0.37 g, 1.0 mmol) was dissolved in anhydrous $CH_2Cl_2$ (20 mL) and added to a solution of 18-crown-6 (0.26 g, 1.0 mmol) in anhydrous $CH_2Cl_2$ (10 mL), and the purple-pink solution stirred for 1 h. The pink solid which separated on concentration of the solution to ca. 15 mL in vacuo, was filtered off and dried. Yield 0.21 g, 50%. $C_{12}H_{24}Cl_3O_6V \cdot CH_2Cl_2$ (506.5): calcd. C 30.8, H 5.2; found C 31.2, H 6.5. IR (Nujol): $\tilde{\nu}$ = 1350 (w), 1297 (m), 1261 (m), 1240 (w), 1100 (sh), 1057 (s), 1033 (s), 928 (s), 833 (s), 799 (s), 485 (w), 432 (w), 359 (sh), 340 (s) $cm^{-1}$.

**[$VCl_3(H_2O)$(18-crown-6)]:** The filtrate from the [$VCl_3$(18-crown-6)] preparation above was treated with 0.1 mL $H_2O$ and stirred for 1 h, concentrated in vacuo to ca. 10 mL to give a pink solid which was filtered off and dried in vacuo. Yield 35%. $C_{12}H_{26}Cl_3O_7V$ (439.6): calcd. C 32.8, H 6.0; found C 32.4, H 6.3. IR (Nujol): $\tilde{\nu}$ = 3400 (br), 1630 (m), 1290 (m), 1256 (m), 1150 (sh), 1093 (br.,s), 1000 (s), 952 (s), 920 (m), 837 (m), 808 (m), 389 (w), 333 (s), 310 (sh) $cm^{-1}$.

**[($VCl_3$)$_2$(18-crown-6)]:** Prepared similarly to [$VCl_3$(18-crown-6)] from anhydrous 18-crown-6 and two mol. equiv. [$VCl_3(thf)_3$]. Pink solid. Yield 45%. $C_{12}H_{24}Cl_6O_6V_2$ (578.9): calcd. C 24.9, H 4.2; found C 24.4, H 4.4. IR (Nujol): $\tilde{\nu}$ = 1298 (m), 1275 (m), 1097 (sh), 1056 (s), 1031 (s), 930 (m), 833 (m), 794 (w), 365 (sh), 341 (s) $cm^{-1}$.

**[$VCl_3$([12]ane$S_4$)]:** Prepared similarly to [$VCl_3$(18-crown-6)], using [12]ane$S_4$. Pink solid. Yield 30%. $C_8H_{16}Cl_3S_4V$ (397.8): calcd. C 24.2, H 4.1; found C 25.1, H 5.3. IR (Nujol): $\tilde{\nu}$ = 1345 (w), 1260 (s), 1090 (s), 1041 (m), 1015 (s), 925 (w), 841 (m), 801 (s), 677 (w), 361 (w), 346 (m) $cm^{-1}$.

**[$VCl_3$([9]ane$S_2O$)]:** Prepared similarly to [$VCl_3$(18-crown-6)] using [9]ane$S_2O$. Pink solid. Yield 52%. $C_6H_{12}Cl_3OS_2V$ (321.6): calcd. C 22.4, H 3.8; found C 22.4, H 3.7. IR (Nujol): $\tilde{\nu}$ = 1300 (w), 1260 (m), 1182 (w), 1096 (s), 1072 (sh), 1051 (m), 1013 (s), 998 (w), 976 (w), 935 (m), 910 (m), 797 (s), 483 (w), 356 (sh), 339 (m) $cm^{-1}$.

**[$VCl_3$([15]ane$S_2O_3$)]:** [$VCl_3(thf)_3$] (0.21 g, 0.55 mmol) was dissolved in anhydrous $CH_2Cl_2$ (15 mL) and added to a solution of [15]ane$S_2O_3$ (0.14 g, 0.55 mmol) in anhydrous $CH_2Cl_2$ (10 mL), and the purple-pink solution stirred for 1 h. The pink solid which separated on standing was filtered off and dried in vacuo. Yield 0.12 g, 54%. $C_{10}H_{20}Cl_3O_3S_2V \cdot 2CH_2Cl_2$ (579.5): calcd. C 24.8, H 4.2; found C 24.6, H 4.9. IR (Nujol): $\tilde{\nu}$ = 1290 (m), 1260 (m), 1208 (w), 1190 (m), 1126 (s), 1116 (s), 1064 (s), 1015 (sh), 917 (m), 905 (m), 811 (s), 796 (sh), 485 (w), 416 (w), 360 (s), 322 (s) $cm^{-1}$.

**[$VCl_3$([18]ane$S_3O_3$)]:** [$VCl_3(thf)_3$] (0.11 g, 0.29 mmol) was dissolved in anhydrous $CH_2Cl_2$ (15 mL) and added to a solution of

Table 5. Crystallographic parameters.[a]

| Complex | [$CrCl_3(H_2O)$(18-crown-6)] | [$CrCl_3$([15]ane$S_5$)] | [$VCl_3(H_2O)$(15-crown-5)]·3/4$CH_2Cl_2$ |
|---|---|---|---|
| Formula | $C_{12}H_{26}Cl_3CrO_7$ | $C_{10}H_{20}Cl_3CrS_5$ | $C_{10}H_{22}Cl_3O_6V \cdot 0.75(CH_2Cl_2)$ |
| $M_r$ | 440.68 | 458.91 | 459.26 |
| Crystal system | monoclinic | orthorhombic | trigonal |
| Space group | $P2_1/c$ (no. 14) | $Pna2_1$ (no. 33) | $P3_22_1$ (no. 154) |
| $a$ [Å] | 15.663(3) | 12.942(3) | 12.153(2) |
| $b$ [Å] | 13.0981(16) | 8.4682(15) | 12.153(2) |
| $c$ [Å] | 19.216(4) | 16.040(3) | 22.773(3) |
| $\alpha$ [°] | 90 | 90 | 90 |
| $\beta$ [°] | 109.352(8) | 90 | 90 |
| $\gamma$ [°] | 90 | 90 | 120 |
| $U$ [Å$^3$] | 3719.5(11) | 1757.8(6) | 2912.9(9) |
| $Z$ | 8 | 4 | 6 |
| $\mu$(Mo-$K_\alpha$) [$mm^{-1}$] | 1.074 | 1.684 | 1.150 |
| $R_{int}$ | 0.1258 | 0.0393 | 0.1990 |
| Total no. reflections | 43927 | 13098 | 27190 |
| Unique reflections | 8505 | 3972 | 4408 |
| No. of parameters | 428 | 172 | 209 |
| $R_1$ [$I_o > 2\sigma(I_o)$] | 0.0580 | 0.0292 | 0.0681 |
| $R_1$ (all data) | 0.1402 | 0.0380 | 0.1787 |
| $wR_2$ [$I_o > 2\sigma(I_o)$] | 0.1062 | 0.0537 | 0.1180 |
| $wR_2$ (all data) | 0.1314 | 0.0567 | 0.1490 |

[a] $R_1 = \Sigma||F_o|-|F_c||/\Sigma|F_o|$; $wR_2 = [\Sigma_w(F_o^2-F_c^2)^2/\Sigma\ wF_o^4]^{1/2}$.

 © 2006 Wiley-VCH Verlag GmbH & Co. KGaA, Weinheim 

[18]aneS$_3$O$_3$ (0.09 g, 0.29 mmol) in anhydrous $CH_2Cl_2$ (10 mL), and the pale purple-pink solution stirred for 1 h. The solution was concentrated in vacuo to 10 mL, and dry hexane (10 mL) was added dropwise to the vigorously stirred solution. After stirring for 10 min the pale pink solid which had separated was filtered off and dried in vacuo. Yield 0.07 g, 52%. $C_{12}H_{24}Cl_3O_3S_3V$ (469.8): calcd. C 30.7, H 5.2; found C 31.2, H 5.6. IR (Nujol): $\tilde{\nu}$ = 1346 (w), 1300 (m), 1258 (s), 1210 (w), 1100 (s), 1072 (s), 1033 (s), 919 (m), 848 (w), 805 (s), 477 (m), 355 (sh), 343 (s) cm$^{-1}$.

**X-ray Crystallography:** Details of the crystallographic data collection and refinement parameters are given in Table 5. Crystals of [$CrCl_3(H_2O)$(18-crown-6)], [$CrCl_3$([15]aneS$_5$)] and [$VCl_3(H_2O)$(15-crown-5)]·3/4$CH_2Cl_2$ were obtained by layering $CH_2Cl_2$ solutions of the complexes with hexane. Data collection used a Nonius Kappa CCD diffractometer ($T$ = 120 K) and with graphite-monochromated Mo-$K_\alpha$ radiation ($\lambda$ = 0.71073 Å). Structure solution and refinement were routine.[25,26] H atoms bonded to C were introduced in calculated positions (C–H 0.99 Å). H atoms on the water molecules (O13 and O14) were located in [$CrCl_3(H_2O)$(18-crown-6)] from later electron-density maps and introduced into the model and refined using DFIX commands on the four O–H distances [target 0.84(2) Å]. Refinement converged leaving satisfactory H–O–H and H–O–Cr angles. Water H atoms were not identified on O6 in the V compound. The $U_{iso}$ for H atoms was either a common refined parameter or 1.2$U_{eq}$ of the bonded C atom (in [$CrCl_3$([15]aneS$_5$)] only). The absolute structures of the crystals used for [$VCl_3(H_2O)$(15-crown-5)] and [$CrCl_3$([15]aneS$_5$)] were established from the Flack parameter.[27] Selected bond lengths and angles are given in Table 1, 2 and 4.

CCDC-607029 (for Cr/O), -607030 (for V), and -607031 (for Cr/S) contain supplementary crystallographic data for this paper. These data can be obtained free of charge from the Cambridge Crystallographic Data Centre via www.ccdc.cam.ac.uk/data_request/cif.

## Acknowledgments

We thank the EPSRC for support and access to the EPSRC's Chemical Database Service at Daresbury.

[1] R. D. Rogers, C. B. Bauer, in: *Comprehensive Supramolecular Chemistry* (Eds.: J. L. Atwood, J. E. D. Davies, D. D. MacNicol, F. Vögtle), Elsevier, Amsterdam, **1996**, *1*, 315–355.
[2] T. P. Hanusa, in: *Comprehensive Coordination Chemistry II* (Eds.: J. A. McCleverty, T. J. Meyer), Elsevier, Amsterdam, **2004**, *3*, 1–92.
[3] S. A. Cotton, in: *Comprehensive Coordination Chemistry II* (Eds.: J. A. McCleverty, T. J. Meyer), Elsevier, Amsterdam, **2004**, *3*, 93–188.
[4] G. R. Willey, M. T. Lakin, N. W. Alcock, *J. Chem. Soc., Dalton Trans.* **1993**, 3407–3411.
[5] G. R. Willey, P. R. Meehan, M. D. Rudd, M. G. B. Drew, *J. Chem. Soc., Dalton Trans.* **1995**, 811–817.
[6] M. D. Brown, W. Levason, D. C. Murray, M. C. Popham, G. Reid, M. Webster, *Dalton Trans.* **2003**, 857–865.
[7] M. Plate, G. Frenzen, K. Dehnicke, *Z. Naturforsch., Teil B* **1993**, *48*, 149–155.
[8] S. G. Bott, H. Prinz, A. Alvanipour, J. L. Atwood, *J. Coord. Chem.* **1987**, *16*, 303–309.
[9] W. Levason, M. C. Popham, G. Reid, M. Webster, *Dalton Trans.* **2003**, 291–294.
[10] S. G. Bott, U. Kynast, J. L. Atwood, *J. Inclusion Phenom.* **1986**, *4*, 241–246.
[11] U. Kynast, S. G. Bott, J. L. Atwood, *J. Coord. Chem.* **1988**, *17*, 53–61.
[12] G. Frenzen, W. Massa, T. Ernst, K. Dehnicke, *Z. Naturforsch., Teil B* **1990**, *45*, 1393–1397.
[13] T. Ernst, K. Dehnicke, H. Goesmann, D. Fenske, *Z. Naturforsch., Teil B* **1990**, *45*, 967–970.
[14] P. C. Junk, J. L. Atwood, *J. Organomet. Chem.* **1998**, *565*, 179–186.
[15] N. R. Champness, S. R. Jacob, G. Reid, C. S. Frampton, *Inorg. Chem.* **1995**, *34*, 396–398; M. C. Durrant, S. Davies, D. L. Hughes, C. Le Floc′h, R. L. Richards, J. R. Sanders, N. R. Champness, S. J. A. Pope, G. Reid, *Inorg. Chim. Acta* **1996**, *251*, 13–14; N. R. Champness, S. J. A. Pope, G. Reid, *J. Chem. Soc., Dalton Trans.* **1997**, 1639–1644; W. Levason, G. Reid, S. M. Smith, *Polyhedron* **1997**, *16*, 4253–4256; S. C. Davies, M. C. Durrant, D. L. Hughes, C. LeFloc'h, S. J. A. Pope, G. Reid, R. L. Richards, J. R. Sanders, *J. Chem. Soc., Dalton Trans.* **1998**, 2191–2198.
[16] G. J. Grant, K. E. Rogers, W. N. Setzer, D. G. VanDerveer, *Inorg. Chim. Acta* **1995**, *234*, 35–45.
[17] D. S. McGuinness, P. Wasserscheid, D. H. Morgan, J. T. Dixon, *Organometallics* **2005**, *24*, 552–556; D. S. McGuinness, P. Wasserscheid, W. Keim, D. H. Morgan, J. T. Dixon, A. Bollman, H. Maumela, F. Hess, U. Englert, *J. Am. Chem. Soc.* **2003**, *125*, 5272–5273.
[18] N. Azuma, T. Ozawa, K. Ishizu, *Polyhedron* **1994**, *13*, 1715–1723.
[19] A. B. P. Lever, *Inorganic Electronic Spectroscopy*, 2nd ed., Elsevier, Amsterdam, **1984**.
[20] D. A. Fletcher, R. F. McMeeking, D. Parkin, *J. Chem. Inf. Comput. Sci.* **1996**, *36*, 746–749.
[21] I. J. Bruno, J. C. Cole, P. R. Edgington, M. Kessler, C. F. Macrae, P. McCabe, J. Pearson, R. Taylor, *Acta Crystallogr., Sect. B* **2002**, *58*, 389–397.
[22] F. A. Cotton, S. A. Duraj, G. L. Powell, W. J. Roth, *Inorg. Chim. Acta* **1986**, *113*, 81–85.
[23] W. Herzig, H. H. Zeiss, *J. Org. Chem.* **1958**, *23*, 1404.
[24] J. S. Bradshaw, J. Y. Hui, B. L. Haymore, J. J. Christensen, R. M. Izatt, *J. Heterocycl. Chem.* **1973**, *10*, 1–4; J. S. Bradshaw, J. Y. Hui, Y. Chan, B. L. Haymore, R. M. Izatt, J. J. Christensen, *J. Heterocycl. Chem.* **1974**, *11*, 45–49.
[25] G. M. Sheldrick, SHELXS-97, Program for crystal structure solution, University of Göttingen, Germany, **1997**.
[26] G. M. Sheldrick, SHELXL-97, Program for crystal structure refinement, University of Göttingen, Germany, **1997**.
[27] H. D. Flack, *Acta Crystallogr., Sect. A* **1983**, *39*, 876–881.
[28] B. R. Elvidge, S. Arndt, P. M. Zeimentz, T. P. Spaniol, J. Okuda, *Inorg. Chem.* **2005**, *44*, 6777–6788.

Received: May 15, 2006
Published Online: September 7, 2006

 © 2006 Wiley-VCH Verlag GmbH & Co. KGaA, Weinheim 

DOI: 10.1002/ejic.200600548

# DFT Investigation of the Potential of [H-M{$(NHCH_2CH_2)_3X$}] Catalysts (M = Mo, Ru, Os; X = N, P) for the Reduction of $N_2$ to $NH_3$ by $H_2$

**Markus Hölscher[a] and Walter Leitner*[a]**

**Keywords:** DFT calculations / Nitrogen fixation / Nitrogen activation / Nitrogen reduction / Ammonia / Homogeneous catalysis

DFT calculations of model complexes [H-M{$(NHCH_2CH_2)_3$-X}] (M = Mo, Ru, Os; X = N, P) were carried out to investigate the catalytic potential of these complexes towards the reduction of $N_2$ to $NH_3$ using only $H_2$ as the reducing agent. Closed catalytic cycles were calculated for all three metal hydrides. The calculations showed that [H-Mo{$(NHCH_2CH_2)_3$-N}], **1**-Mo, is not an appropriate catalyst due to very high activation barriers for several steps of the reaction ($\Delta H^{\ddagger}_{max}$ = 69.1 kcal/mol). Much lower activation barriers were found for the Ru and Os catalysts [H-Ru{$(NHCH_2CH_2)_3N$}], **1**-Ru, and [H-Os{$(NHCH_2CH_2)_3P$}], **1**-Os(P). With $\Delta H^{\ddagger}_{max}/\Delta G^{\ddagger}_{max}$ = 29.3/35.7 kcal/mol, **1**-Os(P) shows potential for future theoretical work. QM/MM calculations were used to investigate some properties of the Ru system empolying the hexaisopropylterphenyl ligand (HIPT). The results indicate that an HIPT substituent at the ligand core has a benefical influence on some reaction steps by lowering the activation barriers, while for other steps the activation energies increase.
(© Wiley-VCH Verlag GmbH & Co. KGaA, 69451 Weinheim, Germany, 2006)

## Introduction

The reduction of dinitrogen ($N_2$) to ammonia ($NH_3$) has been of significant importance to chemical research for many years.[1] The conversion of the very inert $N_2$ molecule to $NH_3$ is currently put into practice by both natural and manmade processes, which have some important differences, such as the following: For the in vivo reaction of $N_2$ with the FeMoco-Cofactor of nitrogenase, protons and reducing agents are required. This process can be considered as a homogeneously catalyzed reaction. Conversely, the industrial reduction of $N_2$ to $NH_3$ (Haber–Bosch process) is a hetereogeneously catalyzed reaction in which $N_2$ is directly reduced by $H_2$. Any kind of synthetic, well-defined transition metal complex that catalyzes either of these reactions ($H^+$/reducing agent, or $H_2$ reduction) is of general interest, allowing for a greater understanding of the natural and technical processes, as they can provide important information about the individual reaction steps on the molecular level. Furthermore, routes to new processes might be identified in this way.

Especially important in this context is the seminal work published very recently by Schrock et al., who showed [$N_2$–Mo{$(N(HIPT)CH_2CH_2)_3N$}] (HIPT = hexaisopropylterphenyl) **I** to be an active catalyst for the reduction of $N_2$ to $NH_3$.[2] In the presence of **I**, protons, and a reducing agent, $N_2$ can be reduced in a stepwise protonation/reduction cycle to yield $NH_3$.

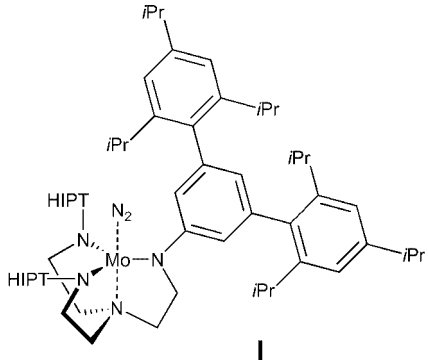


**I**

These experimental results were recently rationalized by Tuczek and Studt using DFT calculations.[3] The reaction mechanism as postulated by Schrock et al. was supported by these calculations, and the energetic requirements for the reaction were related to the energetics of the reducing agent ATP which led to an experimentally, and theoretically, well-rounded picture of this synthetic $N_2$ reduction. Independently, Reiher et al. investigated, by means of DFT calculations, the geometries and electronic structures of complexes that participate in this type of nitrogen activation/transformation reaction and considered how the structures vary as a function of the ligand structure. The authors were able to prove the assumptions that were postulated by the Schrock

[a] Institut für Technische und Makromolekulare Chemie, Rheinisch-Westfälische Technische Hochschule Aachen, Worringer Weg 1, 52074 Aachen, Germany
E-mail: leitner@itmc.rwth-aachen.de
Fax: +49-241-8022177
Supporting information for this article is available on the WWW under http://www.eurjic.org or from the author.

 © 2006 Wiley-VCH Verlag GmbH & Co. KGaA, Weinheim 

group with regards to some of the individual reaction steps.[4,5] Also, the work by Reiher et al. made it clear that the ligand structures (that is the HIPT substituent or other substituents at the trisamidoamine core of the ligand) can lead to significantly different energy profiles over multiple reaction steps. Furthermore, it was shown that the charge of the complex is crucial in enabling the catalyst to release $NH_3$ at the end of the reaction cycle, and for coordination to a new $N_2$ molecule. Cao et al. also reported DFT calculations using model complexes derived from **I**.[6] On the whole there is agreement between experimental and theoretical results that the reaction at the molybdenum center can take place because firstly, the HIPT substituent at the amido nitrogen centers of the ligand core efficiently shields the metal center and thus prevents the formation of nitrogen-bridged, unreactive complex dimers, and secondly, it leaves enough space to allow $N_2$ and $H^+$ to approach the metal center thus enabling the reaction to take place. For the release of $NH_3$ at the end of the catalytic cycle Reiher et al. suggested that a neutral or anionic pathway would be the most probable way for re-establishment of the original catalyst. Furthermore, experiments made it clear that the substituent at the trisamidoamine ligand core exerts a significant electronic influence, as Schrock et al. showed that changing the HIPT substituent to the HTBT substituent (HTBT = hexa-*tert*-butylterphenyl) results in a significant lowering of the catalytic activity, while the activities of catalysts with *para*-BrHIPT substituents are similar to the those catalysis carrying the HIPT substituent.[2e] Electronically, molybdenum seems to be a mandatory component of the catalyst as it was shown experimentally that the corresponding tungsten compound [$N_2$-W{(N(HIPT)$CH_2CH_2)_3$N}] **II** does not catalyze $NH_3$ formation under identical reaction conditions.[7]

Stimulated by these fascinating experimental and theoretical results, we became interested in finding out if complexes of the general formula [H-M{$(NHCH_2CH_2)_3$X}] (M = Mo, Ru, Os; X = N, P) could be suitable general catalysts for the reduction of $N_2$ to $NH_3$ using *only* $H_2$. If this is the case, the gap that presently exists in catalytic $N_2$ reduction chemistry could be closed, and one could arrive at the homogeneously catalyzed reduction of $N_2$ to $NH_3$ using a $N_2$/$H_2$ reactant gas mixture and well-defined transition metal complexes as catalysts, without the presence of any other reagents. As Schrock et al. have already reported the synthesis of, and analytical data for, [H-Mo{(N(HIPT)-$CH_2CH_2)_3$N}][2d] we considered model complexes [H-Mo{$(NHCH_2CH_2)_3$N}] (**1**-Mo), [H-Ru{$(NHCH_2$-$CH_2)_3$N}] (**1**-Ru) and [H-Os{$(NHCH_2CH_2)_3$P}] (**1**-Os(P)) to be potentially useful catalyst candidates for DFT investigations aimed at exploring the $N_2$ reduction reaction. Our aim was to check if closed catalytic cycles can be found in all cases, and if they exist, which energy profiles one would have to expect. To the best of our knowledge calculations of this kind have not yet been carried out.[8] We found for all three complexes, **1**-Mo, **1**-Ru and **1**-Os(P) that catalytic cycles do exist, but differ from one another, in some parts significantly so. With regards to a potential experimental application of catalysts of this kind, we postulate in accordance with our calculations and the experimental work by Schrock et al.[9] that **1**-Mo will not be a suitable catalyst for the generation of $NH_3$ using $N_2$/$H_2$. Whether or not complexes **1**-Ru and **1**-Os(P) will be suitable cannot be answered conclusively at this point; however, there is a higher probability that these compounds will be of potential use. Furthermore, they should be interesting starting points for theoretical and experimental investigations of modified ligands (vide infra). Our main aim in this first theoretical catalyst screening is to answer the following question: can an experimental search for potential catalysts be considered profitable in view of the high activation barriers that must be expected for this reaction?

DFT calculations using the B3LYP hybrid function were carried out successfully by Tuczek and Studer,[3] and by Reiher and co-workers,[4,5] using models of molybdenum complexes relevant to the $N_2$ reduction reaction, as reported by Schrock et al. Yates and co-workers compared the results of B3LYP and CCSD(T) calculations for nitrogen activation at model trigonal coordinated molybdenum complexes, and found both calculation methods yielded energies being well in accord with each other.[10] Thus, calculations using the B3LYP hybrid function can be considered a reasonable compromise between justifiable computer time for the calculations of model complexes, and the degree of accuracy with which the structures and energies are obtained from these calculations. Moreover, calculations of this kind are considered to predict reactivity trends correctly. A multitude of theoretical investigations of transition metal hydrides,[11] among them ruthenium[12] and osmium hydrides[13] also show the B3LYP hybrid function to be appropriate for obtaining plausible structures and energy trends. For this reason we used the B3LYP hybrid function in this work.[14] In a few selected cases we used QM/MM calculations to estimate the influence of the HIPT substituent on the calculated properties (see Computational Details). In the following discussion of energies and energy differences we refer to the reaction enthalpy, $H$,[15] as well as the Gibb's free energy, $G$ (as well as to the activation enthalpies $H^{\ddagger}$ and Gibb's free activation energies $G^{\ddagger}$).

## Results and Discussion

The catalytic cycle that was obtained using **1**-Mo is shown in Scheme 1 and an energy profile is depicted in Figure 1. Figures showing the structures and selected structural parameters are included in the supporting information. Complex **1**-Mo is more stable, by –14.2 kcal/mol, in the triplet state than in the singlet state, which is in accord with the experimentally observed paramagnetism of **1**-Mo.[2d,16] However, all other compounds of the Mo cycle are either significantly more stable in the singlet state, or they could not be located in the triplet state. To start the reaction cycle, $N_2$ or $H_2$ could be added to **1**-Mo, resulting in the formation of **2**-Mo and **3**-Mo, respectively. With regard to a closed catalytic cycle, only the addition of $N_2$ would be successful. A low lying transition state for the conversion of

 © 2006 Wiley-VCH Verlag GmbH & Co. KGaA, Weinheim 

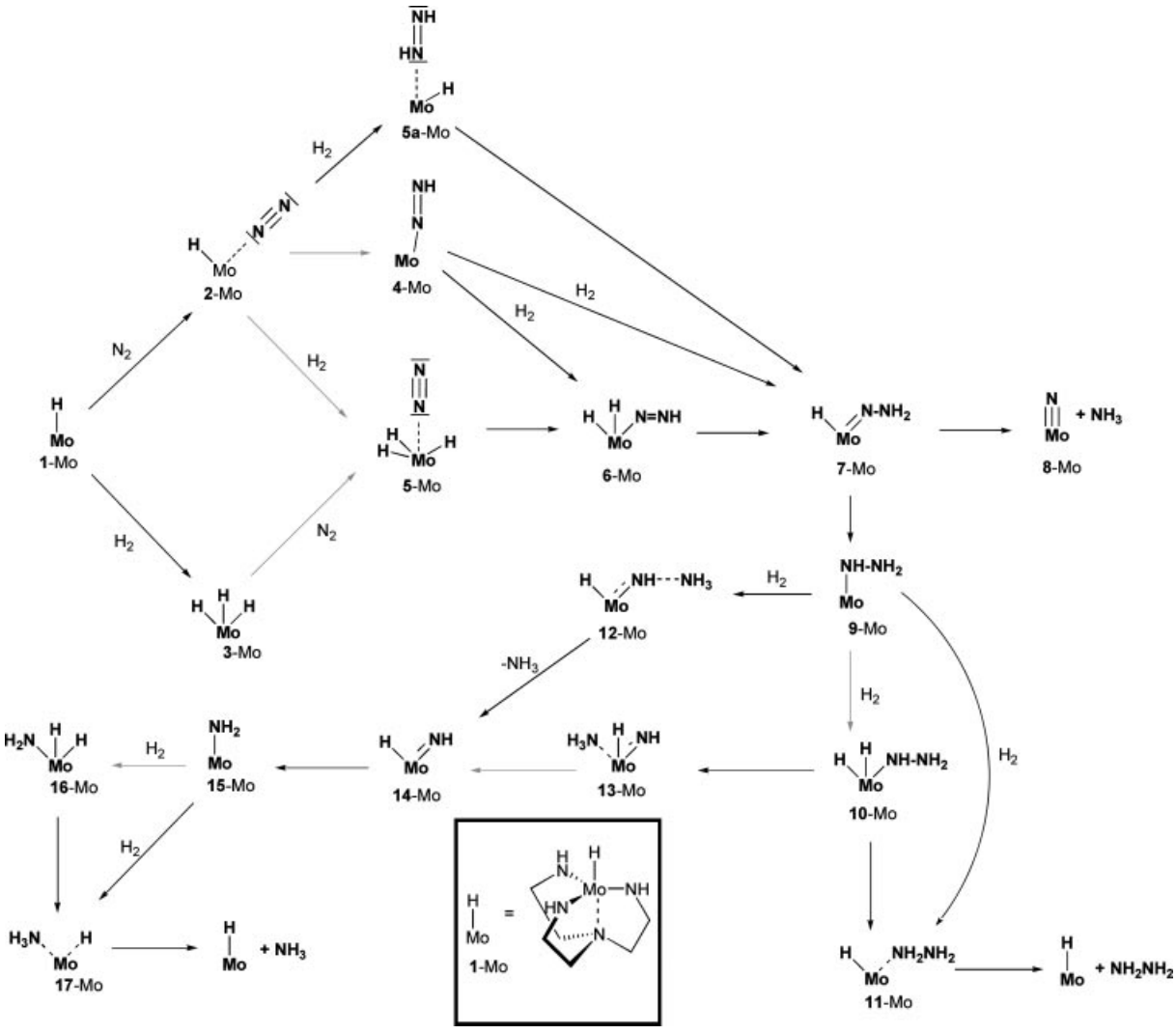


Scheme 1. Catalytic cycle as calculated for **1**-Mo. Arrows in grey denote reactions for which a transition state could not be located.

**1**-Mo to **3**-Mo was located, but the addition of $N_2$ to **3**-Mo to give **5**-Mo is not feasible as a transition state leading to **5**-Mo could not be located. There is a transition state for the conversion of **1**-Mo to **2**-Mo ($\Delta H^{\ddagger}$ = 17.8 kcal/mol), but not for the oxidative addition of $H_2$ to **2**-Mo leading to **5**-Mo. As a result **5**-Mo cannot be formed in this way. Also the transfer of the metal bound hydride in **2**-Mo to a coordinated $N_2$ molecule does not seem to be possible. The corresponding product **4**-Mo, which has been characterized crystallographically,[2f] is a stable local minimum, however no transition state for the conversion of **2**-Mo to give **4**-Mo exists. However in an interesting, though energetically very unfavorable, σ-bond metathesis process $H_2$ can be added to **2**-Mo thus generating **5a**-Mo.

During this reaction the metal bound hydride is transferred to one of the nitrogen atoms of the $N_2$ molecule that is coordinated to the metal, while one of the hydrogen atoms of the $H_2$ molecule is transferred to the other nitrogen atom, and the second hydrogen atom is transferred to the metal center. However, the activation enthalpy $\Delta H^{\ddagger}$ for this step is extremely high (69.1 kcal/mol). A local minimum in which the incoming $H_2$ molecule initially coordinates in a non-classical manner to the metal center of **2**-Mo without being cleaved, was searched for, but not located. Complex **7**-Mo can be obtained from **5a**-Mo by hydrogen migration from the internal N atom of the Mo–NH=NH unit to the external N atom. Energetically speaking this reaction is slightly more unfavorable than the reaction of **4**-Mo with $H_2$ that also generates **7**-Mo, in both cases transition states were located. The activation enthalpies for both reactions are very high (52.3 and 43.4 kcal/mol, respectively). However, the reaction of $H_2$ and **4**-Mo to produce **6**-Mo is not possible. Complexes **6**-Mo and **5**-Mo can only be formed from **7**-Mo. With **7**-Mo as the staring material, two reactions can take place, either the metal bound hydrogen is transferred to the $NH_2$ unit generating one molecule of ammonia and the extremely stable molybdenum nitride complex **8**-Mo, or the H atom is transferred to the internal N atom of the $N{=}NH_2$ unit generating **9**-Mo. The latter reaction is kinetically preferred with respect to the formation of **8**-Mo due to its lower activation enthalpy ($\Delta H^{\ddagger}$ = 21.7 kcal/mol); the formation of **8**-Mo and $NH_3$ requires

 © 2006 Wiley-VCH Verlag GmbH & Co. KGaA, Weinheim 

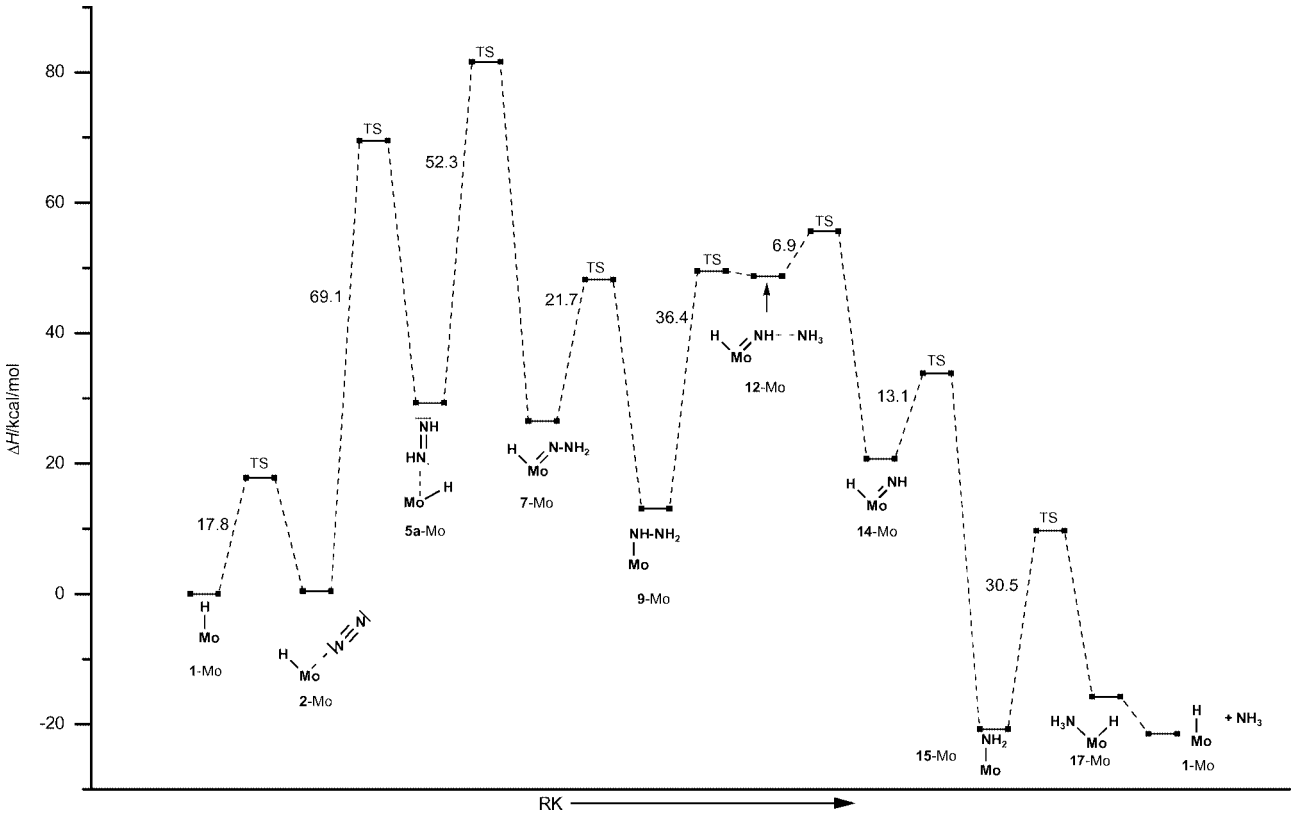


Figure 1. Energy profile ($\Delta H$/kcal/mol) as calculated for the only completely closed cycle obtained with **1**-Mo. Relative activation energies ($\Delta H^{\ddagger}$/kcal/mol) are noted at the corresponding barriers.

an activation enthalpy higher by ca. 20 kcal/mol ($\Delta H^{\ddagger}$ = 39.7 kcal/mol). However, thermodynamically speaking the formation of **8**-Mo and $NH_3$ is clearly preferred. The reintroduction of **8**-Mo into the catalytic cycle by the addition of $H_2$ is impossible.

Complex **9**-Mo can also react in two ways. The addition/cleavage of $H_2$ generates **11**-Mo, which can be considered as the adduct of **1**-Mo and hydrazine. Hydrazine can leave the complex while the catalytic cycle is endothermically closed ($\Delta H$ = 57.8 kcal/mol). The oxidative addition of $H_2$ to **9**-Mo does not seem to be possible, as the reaction product **10**-Mo exists on the hyper surface, but this is not case for the corresponding transition state that leads to **10**-Mo. However, the transfer of one metal bound hydride of **10**-Mo to the NH–$NH_2$ unit to form **11**-Mo is possible, and the corresponding activation enthalpy is comparatively low ($\Delta H^{\ddagger}$ = 16.2 kcal/mol).

Alternatively, **9**-Mo can react with one $H_2$ molecule to produce **12**-Mo. By cleavage of $H_2$ one molecule of $NH_3$ is generated, which participates in attractive interactions with a neighboring N atom. The $NH_3$ molecule can be cleaved off easily ($\Delta H^{\ddagger}$ = 6.9 kcal/mol) thus forming **14**-Mo. The rearrangement of **14**-Mo to give **15**-Mo requires only a comparatively small amount of energy ($\Delta H^{\ddagger}$ = 13.1 kcal/mol), and the product **15**-Mo is significantly more stable than **14**-Mo ($\Delta H$ = –37.8 kcal/mol).

Complex **15**-Mo cannot participate in an oxidative addition reaction with $H_2$ to produce **16**-Mo, as the corresponding transition state does not exist. Instead, the $H_2$ molecule is cleaved directly upon reaction with **15**-Mo generating **17**-Mo, which is an adduct of $NH_3$ and **1**-Mo. The activation enthalpy for this reaction that generate **17**-Mo amounts to 30.5 kcal/mol. In the last step $NH_3$ is cleaved off from the complex, and **1**-Mo is regenerated.[17]

Due to the high activation enthalpies, which amount to very high values at the beginning of the reaction cycles (i.e. **2**-Mo → **5a**-Mo, **5a**-Mo → **7**-Mo), it cannot be expected that **1**-Mo would be a useful catalyst for the reduction of $N_2$ to $NH_3$ using only $H_2$, this is in accordance with experimental results.[9] As an alternative to molybdenum, we considered ruthenium to be interesting, as a variety of molecular ruthenium hydrides have been synthesized[18] and have been employed as catalysts by us[19] and others.[20] Furthermore, novel heterogeneous ruthenium catalysts[21] have been developed recently, and Haber–Bosch ruthenium-containing catalysts are also known. Additionally, by keeping the formal oxidation state of the metal center the same, by exchanging molybdenum with ruthenium (and also osmium, vide infra) one obtains a catalyst system possessing an additional two electrons. This should enable direct information to be generated as to whether or not, for the given ligand core, an electron-rich metal center is most useful for promoting the $N_2$ reduction reaction. Interestingly, a closed catalytic cycle for the $N_2$ reduction reaction could also be calculated using **1**-Ru as the catalyst. However, this cycle is different from the molybdenum cycle in some ways.

 © 2006 Wiley-VCH Verlag GmbH & Co. KGaA, Weinheim 

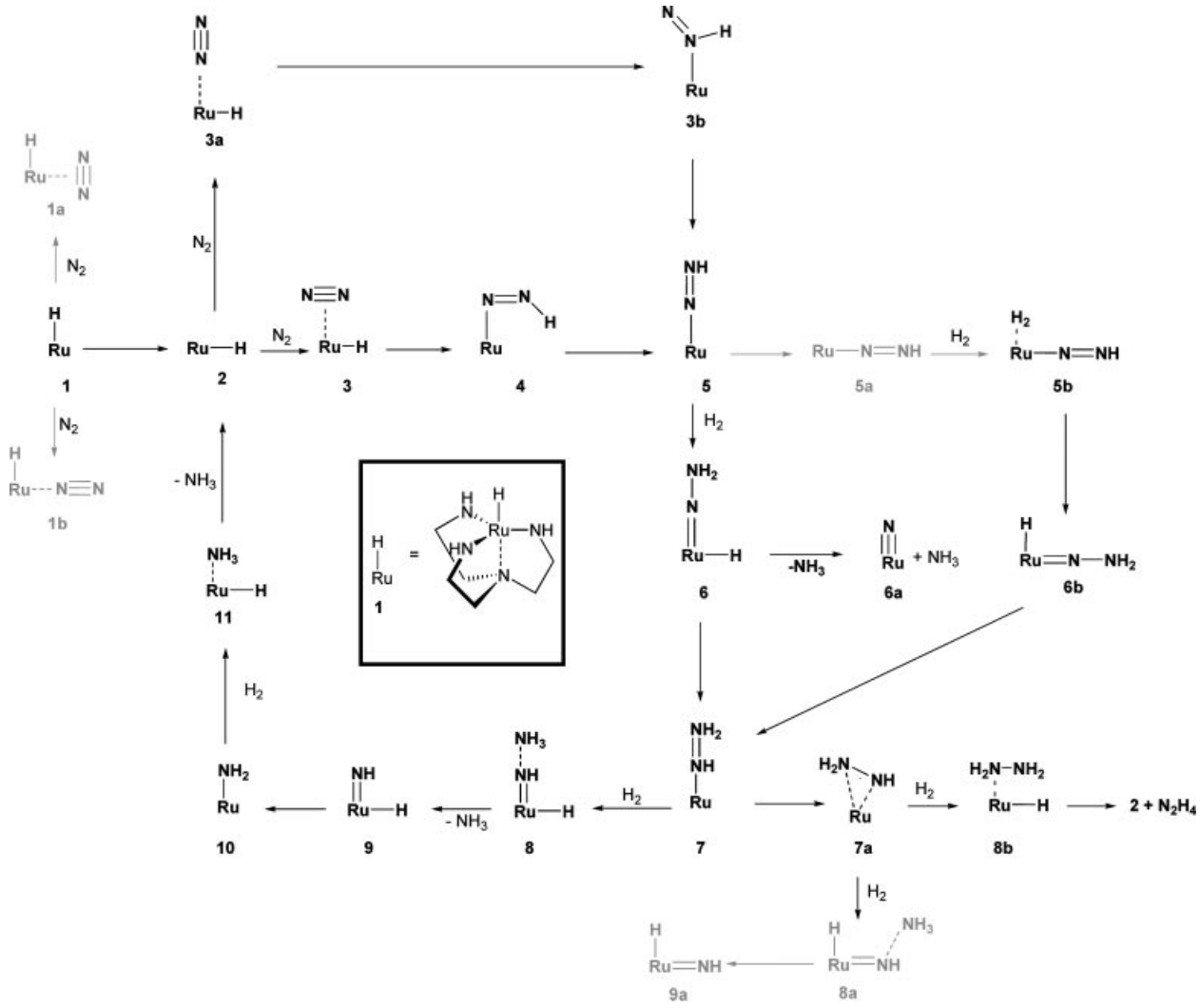


Scheme 2. Catalytic cycle as calculated for **1**-Ru. Compounds and arrows in grey denote structures and reactions which were not located, respectively.

The catalytic cycle obtained with **1**-Ru is shown in Scheme 2 and Figure 2 contains the corresponding energy profile (the supporting information contains graphical representations of the calculated structures). The cycle for the Ru catalyst was calculated with all compounds being in the singlet spin state (this was also the case for the cycle incorporating Os compounds, vide infra). Both the side-on and end-on addition of $N_2$ to **1**-Ru forming **1a**-Ru and **1b**-Ru, respectively, are not possible ($H_2$ could not be coordinated side-on, or end-on, to **1**-Ru either).

However, in contrast to **1**-Mo, the hydride in **1**-Ru can flip from the axial to the equatorial position generating **2**-Ru. This flipping requires a significant amount of energy ($\Delta H^{\ddagger}/\Delta G^{\ddagger}$ = 43.5/43.2 kcal/mol) and product **2**-Ru is significantly richer in energy ($\Delta H$ = 42.9) than the reactant. Dinitrogen can coordinate to **2**-Ru at the axial position in either end-on (**3a**-Ru) or side-on (**3**-Ru) fashion, with end-on-addition clearly being exergonic relative to **2**-Ru ($\Delta H/\Delta G$ = –24.1/–13.3 kcal/mol), while side-on addition yields only a small energy gain ($\Delta H$ = –5.0 kcal/mol), which is compensated for by the unfavorable entropic contribution ($\Delta G$ = 4.7 kcal/mol). Transfer of the Ru bound hydride in **3**-Ru to the coordinated $N_2$ molecule leads to **4**-Ru, and the activation enthalpy for this reaction amounts to $\Delta H^{\ddagger}$ = 19.4 kcal/mol ($\Delta G^{\ddagger}$ = 20.9 kcal/mol). This is clearly different to the molybdenum system in which hydride transfer is not possible in this way. Complex **4**-Ru can rearrange to give the slightly more stable complex **5**-Ru, which is also obtainable via **3a**-Ru. The transfer of the hydride of **3a**-Ru to form **3b**-Ru is possible, however, energetically it is much more unfavorable than the reaction sequence already described, namely the transformation of **3**-Ru to **5**-Ru via **4**-Ru. Indeed, the activation barrier for the formation of **3b**-Ru from **3a**-Ru is higher by ca. 20 kcal/mol ($\Delta H^{\ddagger}/\Delta G^{\ddagger}$ = 42.0/41.9 kcal/mol), and the barrier for the reaction of **3b**-Ru to give **5**-Ru is very high with $\Delta H^{\ddagger}$ and $\Delta G^{\ddagger}$ values of 47.2 and 46.8 kcal/mol, respectively. The sequence **3**-Ru → **4**-Ru → **5**-Ru requires much less energy.

It can be envisaged that the reaction continues from **5**-Ru via the equatorial conformer **5a**-Ru. For the subsequent steps (reaction of **5b**-Ru to **6b**-Ru and **7**-Ru) the corresponding minima and transition states were located, and

 © 2006 Wiley-VCH Verlag GmbH & Co. KGaA, Weinheim 

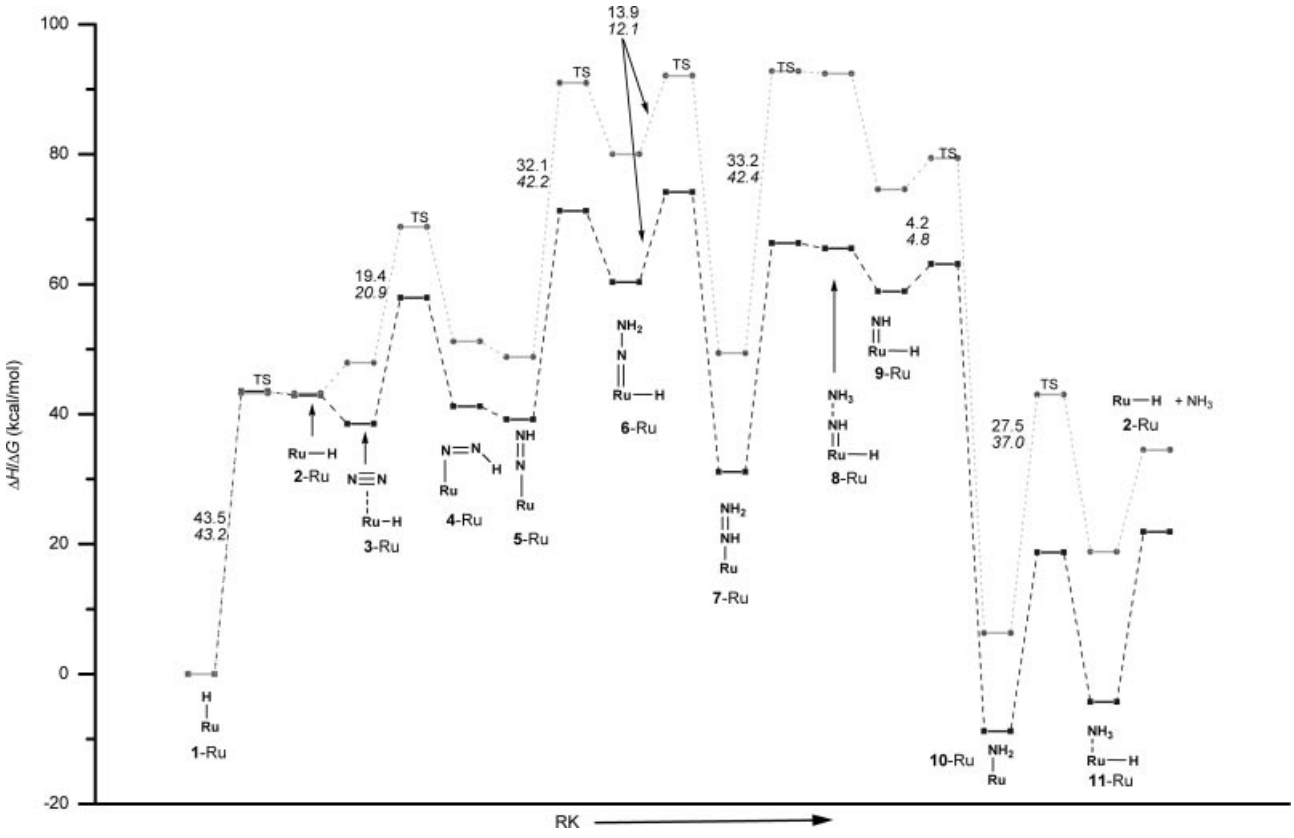


Figure 2. Energy profile ($\Delta H$ [squares; broken lines] and $\Delta G$ [circles; dotted lines], all in kcal/mol) as calculated for the main cycle obtained for **1**-Ru. Relative activation energies ($\Delta H^{\ddagger}/\Delta G^{\ddagger}$ plain/italics) are noted at the corresponding barriers.

the energies of these were low. For example, the activation energies for the conversion of **5b**-Ru to **6b**-Ru are $\Delta H^{\ddagger}/\Delta G^{\ddagger}$ = 9.5/10.5 kcal/mol. Complex **6b**-Ru can then be transformed to **7**-Ru, a process that also has a low activation barrier ($\Delta H^{\ddagger}/\Delta G^{\ddagger}$ = 9.4/9.5 kcal/mol). However, it was not possible to locate compound **5a**-Ru, making the reaction sequence **5**-Ru → **5a**-Ru → **5b**-Ru → **6b**-Ru → **7**-Ru questionable.

Conversely, if an $H_2$ molecule approaches **5**-Ru, the H–H bond is cleaved and **6**-Ru is formed. One hydrogen atom is transferred to the terminal NH group, and the other hydrogen atom migrates to the metal. Transfer of the Ru bound hydride of **6**-Ru to the terminal $NH_2$ group of the $NNH_2$ unit generates the first $NH_3$ molecule of this cycle. In an analogous manner to the molybdenum system, the corresponding ruthenium nitride complex **6a**-Ru is formed. In a similar way to the molybdenum system, this reaction step has a large activation energy ($\Delta H^{\ddagger}/\Delta G^{\ddagger}$ = 43.6/43.3 kcal/mol), however, the reaction products are strongly endothermic ($\Delta H/\Delta G$ = 51.7/58.2 kcal/mol) relative to the sum of the energies for **1**-Ru, $N_2$ and $H_2$, and this is in clear contrast to the molybdenum system. According to these results ruthenium nitride, **6a**-Ru, is significantly less stable than the analogous molybdenum nitride complex, **8**-Mo.

Alternatively, the hydride in **6**-Ru can be transferred from the metal center to the internal N atom of the $NNH_2$ unit generating complex **7**-Ru ($\Delta H/\Delta G$ = 31.1/49.4 kcal/mol) that is significantly lower in energy. The Gibb's free energy required for the formation of **7**-Ru from **6**-Ru is relatively small ($\Delta G^{\ddagger}$ = 12.1 kcal/mol), and clearly differs from the Gibb's free energies for the steps described so far. The even less energy consuming complex **7**-Ru is obtained following the alternative route (which is not completely closed) **5b**-Ru to **6b**-Ru, and then from **6b**-Ru complex **7**-Ru can be obtained, with a Gibb's free energy of only 9.5 kcal/mol.

By rotating the $NHNH_2$ unit that is bound to the metal center in **7**-Ru to a side-on coordination mode, complex **7a**-Ru is formed in which both N atoms of the $NHNH_2$ unit have bonding interactions with the ruthenium center, as can be deduced from the N–Ru distances of 2.081 ($NH_2$–Ru) and 2.186 Å (NH–Ru). With **7a**-Ru as a starting material one can arrive at **8b**-Ru (the adduct of **2**-Ru and hydrazine), and the imidoruthenium complex **8a**-Ru can also be formed, from which the second ammonia molecule of the cycle is generated, which shows bonding interactions with the imido unit.[22] However, the resultant product **9a**-Ru could not be located, and as a result the cycle cannot be continued in this way. Due to the formation of hydrazine and **2**-Ru the catalytic cycle ends endothermically as expected.

If $H_2$ is added to **7**-Ru the H–H bond is cleaved, and the axial imidoruthenium complex **8**-Ru is formed. The newly formed $NH_3$ molecule that is incorporated in this complex has bonding interactions with the imido group. The acti-

 © 2006 Wiley-VCH Verlag GmbH & Co. KGaA, Weinheim 

vation barrier for this reaction ($\Delta H^{\ddagger}/\Delta G^{\ddagger}$ = 33.2/42.4 kcal/mol) is significantly higher than the barrier for the conversion of **7a**-Ru to **8a**-Ru ($\Delta H^{\ddagger}/\Delta G^{\ddagger}$ = 28.2/28.6 kcal/mol).

Alternatively, the $NH_3$ molecule can be cleaved from **8**-Ru and the resultant imido complex **9**-Ru can then react to give the amido complex **10**-Ru, which requires only a small amount of activation energy ($\Delta H^{\ddagger}/\Delta G^{\ddagger}$ = 4.2/4.8 kcal/mol). The reaction of **10**-Ru with $H_2$ cleaves the H–H bond and generates complex **11**-Ru that can be considered as an adduct of **2**-Ru and $NH_3$. This reaction requires an activation energy of $\Delta H^{\ddagger}/\Delta G^{\ddagger}$ = 27.5/36.7 kcal/mol. Cleaving $NH_3$ off **11**-Ru generates a second ammonia molecule, and regenerates the catalyst **2**-Ru.[16]

In summary, a closed catalytic cycle could be calculated using **1**-Ru with local minima and transition states that enable a plausible reaction scheme to be suggested. It is interesting to note that the highest activation barriers of this cycle are much lower than those for the molybdenum system. However, some activation enthalpies and Gibb's free energies (i.e. reactions **5**-Ru → **6**-Ru and **7**-Ru → **8**-Ru) have values of ca. 30 and 40 kcal/mol, respectively and thus are probably too high to enable the reaction to occur in practice. Also we note that the usage of the real HIPT ligand seems to influence the reaction trend. Some steps of the cycle (**1**-Ru → **2**-Ru; **3**-Ru → **4**-Ru; **10**-Ru → **11**-Ru, **5b**-Ru → **6b**-Ru) were re-optimized, using the HIPT ligand, by applying QM/MM-methods (see Computational Details). Interestingly, the presence of the real ligand reduces the activation barrier, in comparison to the model ligand, by ca. 10 kcal/mol for the reaction **1**-Ru → **2**-Ru ($\Delta H^{\ddagger}/\Delta G^{\ddagger}$ = 30.8/31.4 kcal/mol). Conversely, the activation barriers for the reactions **3**-Ru → **4**-Ru and **5b**-Ru → **6b**-Ru are slightly higher relative to the model ligand. An even clearer increase in the activation barrier was found for the **10**-Ru → **11**-Ru reaction. For this reaction the activation enthalpy $\Delta H^{\ddagger}$ is raised by 3.3 kcal/mol, and the Gibb's free activation energy, $\Delta G^{\ddagger}$, rises by 4.1 kcal/mol relative to the model ligand system. These results indicate that fine tuning of the ligand may be crucial in future experimental work.

In the third part of this evaluation of the potential of transition metal complexes with TREN- and TREN-type ligands, we investigated the behavior of **1**-Os(P). In this complex the ligand core is not tris(2-aminoethyl)amine, but tris(2-aminoethyl)phosphane. Phosphanes of this kind can be obtained synthetically and have been structurally characterized.[23] Similar phosphanes were used for the syntheses of zirconium complexes.[24] In test calculations of a few steps of the cycles involving **1**-Os and **1**-Os(P) it turned out that the usage of the triamidophosphane ligand seems to be slightly more favorable, with regards to activation barriers, than the other ligands discussed thus far. Accordingly, we

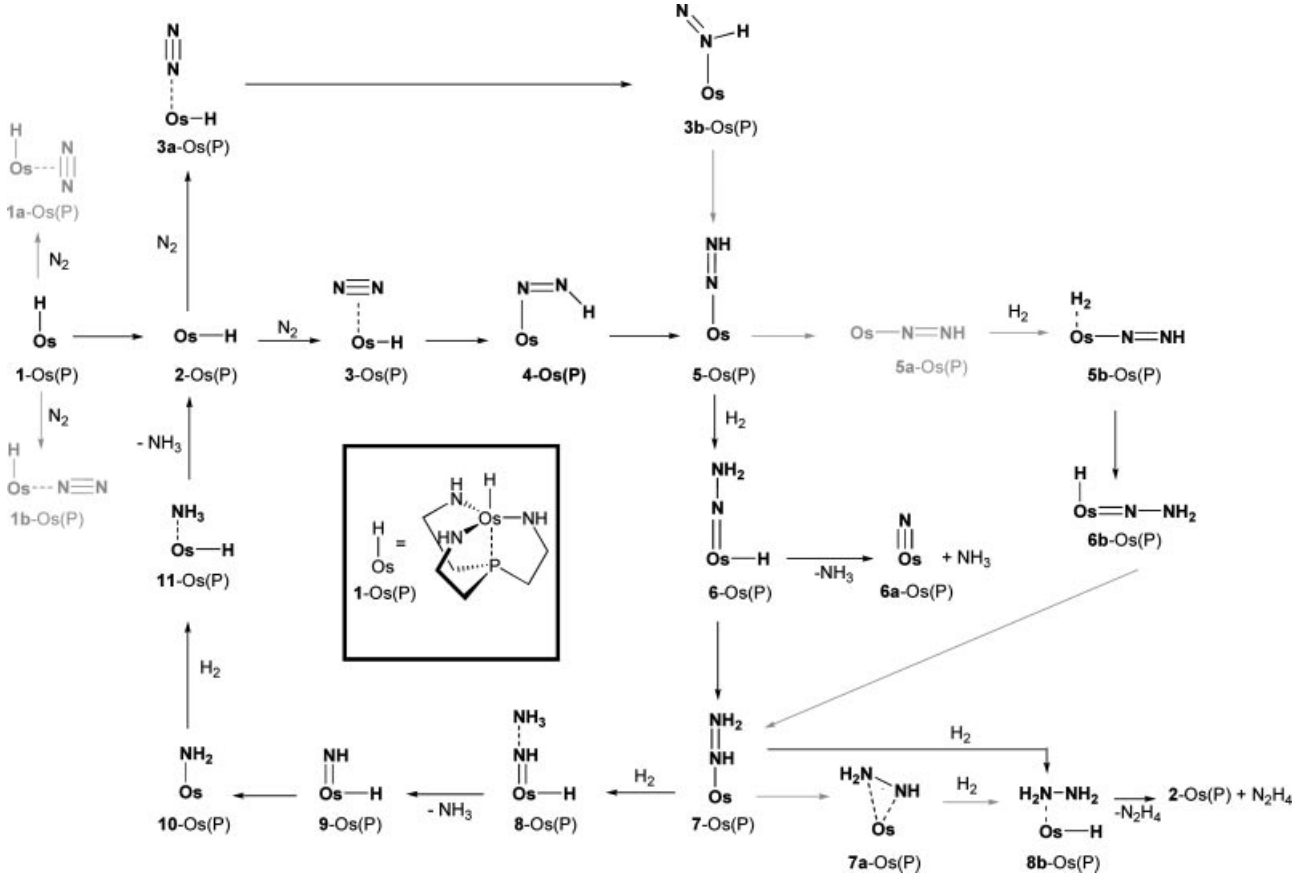


Scheme 3. Catalytic cycle as calculated for **1**-Os(P). Compounds and arrows in grey denote structures and reactions which were not located, respectively.

 © 2006 Wiley-VCH Verlag GmbH & Co. KGaA, Weinheim 

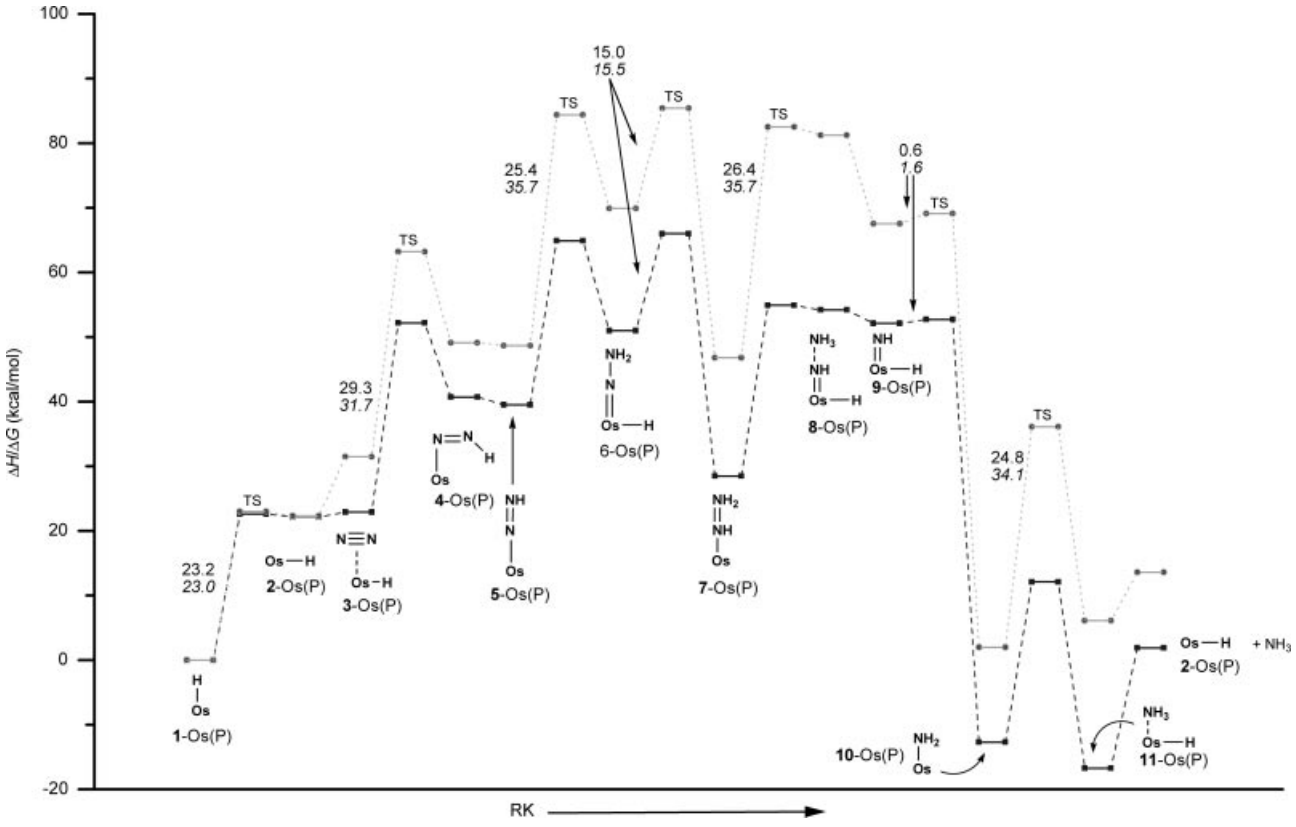


Figure 3. Energy profile ($\Delta H$ [squares; broken lines] and$\Delta G$ [circles; dotted lines], all kcal/mol) as calculated for the main cycle obtained for **1**-Os(P). Relative activation barriers ($\Delta H^{\ddagger}/\Delta G^{\ddagger}$ plain/italics) are noted at the corresponding barriers.

used this ligand for the calculation of the following cycle. All of our investigations hint that the cycle proposed for **1**-Ru would be applicable to **1**-Os(P) with a few small differences.[25] Accordingly the cycle is discussed only briefly. Scheme 3 and Figure 3 show the corresponding catalytic cycle and the energy profile for **1**-Os(P), respectively.

With regards to the main cycle it is striking that some activation barriers and Gibb's free activation energies are lower – in some cases significantly lower – compared to the ruthenium system. For example the Gibb's free activation energy, $\Delta G^{\ddagger}$, for the flipping of the hydride from the axial position in **1**-Ru to the equatorial position in **2**-Ru amounts to 43.2 kcal/mol, while for the conversion of **1**-Os(P) to **2**-Os(P) it is only 23.0 kcal/mol. Also for the conversion of **5**-Os(P) to **6**-Os(P) the Gibb's free activation barrier ($\Delta G^{\ddagger}$ = 35.7 kcal/mol) is lower by 6.5 kcal/mol than the barrier for the conversion of **5**-Ru to **6**-Ru ($\Delta G^{\ddagger}$ = 42.2 kcal/mol). Less pronounced is the reduction in the Gibb's free activation barrier in the osmium system for the conversion of **10**-Os(P) to **11**-Os(P) when compared to the analogous reaction within the ruthenium system. The barrier is $\Delta G^{\ddagger}$ = 34.1 kcal/mol for the conversion of **10**-Os(P) to **11**-Os(P), while for the conversion of **10**-Ru to **11**-Ru 36.7 kcal/mol of energy are required. In an analogous manner to the Ru system, complexes **1a**-Os(P), **1b**-Os(P) and **5a**-Os(P) could not be located. Additionally, relative to the Ru system there is a drastic increase in the activation energy for the conversion of **3**-Os(P) to **4**-Os(P) ($\Delta H^{\ddagger}/\Delta G^{\ddagger}$ = 29.3/31.7 kcal/mol with respect to $\Delta H^{\ddagger}/\Delta G^{\ddagger}$ = 19.4/20.9 kcal/mol for the Ru system).

In summary, for **1**-Os(P) a closed catalytic cycle can be calculated for the $N_2$ reduction reaction. In this cycle the highest Gibb's free activation barriers, $\Delta G^{\ddagger}$, using the model ligand, only amounts to 35.7 kcal/mol [**5**-Os(P) → **6**-Os(P) and **7**-Os(P) → **8**-Os(P)],[26] while the activation enthalpy $\Delta H^{\ddagger}$ has a maximum value of 29.3 kcal/mol [**3**-Os(P) → **4**-Os(P)]. Compared to the molybdenum system ($\Delta H^{\ddagger}_{max}$ = 69.1 kcal/mol) the activation energies are generally much lower for this system. These results are encouraging as it can be expected that, as in the case of the ruthenium system, the osmium system with the use of HIPT or other real ligands might prove useful by actively reducing the activation barriers further.

## Summary

We have showed that all three metal hydrides investigated in the calculations reported herein yield closed catalytic cycles for the reduction of $N_2$ to $NH_3$ by $H_2$. The extremely high activation barriers of the molybdenum system, in accordance with experimental work by Schrock et al., hint at the fact that **1**-Mo is not a suitable catalyst for such a $N_2$ reduction reaction. The activation barriers are much lower

 © 2006 Wiley-VCH Verlag GmbH & Co. KGaA, Weinheim 

in catalytic cycles incorporating **1**-Ru and **1**-Os(P), however the Gibb's free activation barriers, $\Delta G^{\ddagger}$, have values that are significantly higher than 30 kcal/mol for some reaction steps. As a result, predictions as to the experimental behavior of catalysts of this type cannot be made accurately at this point, and further clarification is need, especially with regards to the influence of real substituents at the ligand core, and the effects of solvent. According to QM/MM calculations for some of the reaction steps for the Ru system, the presence of the HIPT ligand seems to be beneficial with regards to lowering the activation barriers. However, for other steps it seems to generate slightly higher activation barriers. In general it is important to note that by varying the metal center (Mo, Ru, Os), as well as varying the type of ligand, it has been shown clearly that it may be possible to create catalyst systems that lead to reactions with comparatively low activation barriers. We believe that these results are promising, and proved a starting point for further theoretical work.

## Computational Details

The geometry optimizations reported herein were carried out using the Gaussian 03 and the Turbomole 5.7 suite of programs.[27] Table 1 lists relative energies for all compounds. Tables S1 (Mo), S2 (Ru) and S3 (Os) in the supporting information list energies, enthalpies and free enthalpies in atomic units obtained from the different computational studies. Cartesian coordinates for all calculated compounds are contained in the supporting information. Ball-and-Stick representations of the calculated structures are shown in Figures S4 (Mo), S5 (Ru) and S6 (Os) in the supporting information.

**Mo:** The structures were first optimized using Gaussian 03 (B3LYP[28] hybrid function) with the 6-31G(d) basis set[29] for elements C, N and H. For Mo, a quasirelativistic small-core ECP[30] was used with a (441/2111/31) valence basis set. This basis set shall be called basis set BII.[31] The relaxed structures were inputted into frequency calculations to successfully characterize the nature of the stationary points ($i$ = 0 for local minima, and 1 for saddle points of order 1; frequency calculations were carried out throughout this

Table 1. Relative enthalpies $\Delta H$ [kcal/mol] and Gibb's free enthalpies $\Delta G$ [kcal/mol] and the number of imaginary frequences $i$ [$cm^{-1}$] for the compounds calculated in this work.[a]

| Compd.[b] | $\Delta H$ | $i$ | Compd.[c] | $\Delta H$ | $\Delta G$ | $i$ | Compd.[c] | $\Delta H$ | $\Delta G$ | $i$ |
|---|---|---|---|---|---|---|---|---|---|---|
| **1**-Mo($^{3\Sigma}$) | 0.0 | 0 | **1**-Ru | 0.0 | 0.0 | 0 | **1**-Os(P) | 0.0 | 0.0 | 0 |
| **1**-Mo($^{1\Sigma}$) | 14.8 | 0 | **2**-Ru | 42.9 | 43.0 | 0 | **2**-Os(P) | 22.6 | 22.3 | 0 |
| **2**-Mo | 0.4 | 0 | **3**-Ru | 38.5 | 47.9 | 0 | **3**-Os(P) | 22.9 | 31.5 | 0 |
| **3**-Mo | 1.7 | 0 | **3a**-Ru | 19.4 | 29.9 | 0 | **3a**-Os(P) | 7.6 | 17.7 | 0 |
| **4**-Mo | 2.9 | 0 | **3b**-Ru | 51.0 | 60.6 | 0 | **3b**-Os(P) | 50.2 | 60.0 | 0 |
| **5**-Mo | 36.7 | 0 | **4**-Ru | 41.2 | 51.2 | 0 | **4**-Os(P) | 40.7 | 49.1 | 0 |
| **5a**-Mo | 29.3 | 0 | **5**-Ru | 39.2 | 48.8 | 0 | **5**-Os(P) | 39.5 | 48.7 | 0 |
| **6**-Mo | 47.3 | 0 | **5b**-Ru | 67.4 | 86.0 | 0 | **5b**-Os(P) | 56.8 | 75.4 | 0 |
| **7**-Mo | 26.5 | 0 | **6**-Ru | 60.3 | 80.0 | 0 | **6**-Os(P) | 51.0 | 69.9 | 0 |
| **8**-Mo | –17.5 | 0 | **6a**-Ru | 51.7 | 58.2 | 0 | **6a**-Os(P) | 49.1 | 56.2 | 0 |
| **9**-Mo | 13.1 | 0 | **6b**-Ru | 64.8 | 83.8 | 0 | **6b**-Os(P) | 55.3 | 74.4 | 0 |
| **10**-Mo | 35.9 | 0 | **7**-Ru | 31.1 | 49.4 | 0 | **7**-Os(P) | 28.5 | 46.8 | 0 |
| **11**-Mo | 21.8 | 0 | **7a**-Ru | 45.9 | 65.6 | 0 | **7a**-Os(P) | 36.8 | 56.6 | 0 |
| **12**-Mo | 48.7 | 0 | **8**-Ru | 65.5 | 92.4 | 0 | **8**-Os(P) | 54.2 | 81.2 | 0 |
| **13**-Mo | 23.1 | 0 | **8b**-Ru | 36.7 | 63.3 | 0 | **9**-Os(P) | 52.1 | 67.5 | 0 |
| **14**-Mo | 20.7 | 0 | **9**-Ru | 58.9 | 74.6 | 0 | **10**-Os(P) | –12.7 | 2.0 | 0 |
| **15**-Mo | –20.8 | 0 | **10**-Ru | –8.8 | 6.3 | 0 | **11**-Os(P) | –16.7 | 6.1 | 0 |
| **16**-Mo | 8.3 | 0 | **11**-Ru | –4.3 | 18.8 | 0 | TS(**1**,**2**-Os(P)) | 23.2 | 23.0 | 1(–128.3) |
| **17**-Mo | –15.8 | 0 | TS(**1**,**2**-Ru) | 43.5 | 43.2 | 1(–267.2) | TS(**3**,**4**-Os(P)) | 52.2 | 63.2 | 1(–754.8) |
| TS(**1**,**2**-Mo) | 17.8 | 1(–115.6) | TS(**3**,**4**-Ru) | 57.9 | 68.8 | 1(–929.5) | TS(**3a**,**3b**-Os(P)) | 58.2 | 68.3 | 1(–810.0) |
| TS(**1**,**3**-Mo) | 18.9 | 1(–255.0) | TS(**3a**,**3b**-Ru) | 61.4 | 71.8 | 1(–808.3) | TS(**5**,**6**-Os(P)) | 64.9 | 84.4 | 1(–1300.9) |
| TS(**2**,**5a**-Mo) | 69.5 | 1(–501.6) | TS(**3b**,**5**-Ru) | 98.2 | 107.4 | 1(–2185.0) | TS(**6**,**7**-Os(P)) | 66.0 | 85.4 | 1(–902.4) |
| TS(**5**,**6**-Mo) | 53.1 | 1(–802.3) | TS(**5**,**6**-Ru) | 71.3 | 91.0 | 1(–1488.3) | TS(**6**,**6a**-Os(P)) | 103.2 | 122.8 | 1(–1509.6) |
| TS(**4**,**7**-Mo) | 46.3 | 1(–1449.3) | TS(**5b**,**6b**-Ru) | 76.9 | 96.5 | 1(–1190.4) | TS(**7**,**8**-Os(P)) | 54.9 | 82.5 | 1(–1089.5) |
| TS(**5a**,**7**-Mo) | 81.6 | 1(–2059.0) | TS(**6**,**6a**-Ru) | 103.9 | 123.3 | 1(–1453.5) | TS(**7**,**8b**-Os(P)) | 55.0 | 82.2 | 1(–512.5) |
| TS(**6**,**7**-Mo) | 72.9 | 1(–1572.7) | TS(**6**,**7**-Ru) | 74.2 | 92.1 | 1(–951.8) | TS(**9**,**10**-Os,P)) | 52.7 | 69.1 | 1(–630.1) |
| TS(**7**,**8**-Mo) | 66.2 | 1(–1524.2) | TS(**7**,**7a**-Ru) | 59.3 | 78.0 | 1(–336.0) | TS(**10**,**11**-Os(P)) | 12.1 | 36.1 | 1(–393.0) |
| TS(**7**,**9**-Mo) | 48.2 | 1(–1054.9) | TS(**7**,**8**-Ru) | 64.3 | 91.8 | 1(–1109.8) | | | | |
| TS(**9**,**11**-Mo) | 42.3 | 1(–1127.6) | TS(**7a**,**8a**-Ru)[d] | 65.3 | 93.2 | 1(–979.1) | | | | |
| TS(**10**,**11**-Mo) | 52.1 | 1(–1075.0) | TS(**7a**,**8b**-Ru) | 61.4 | 88.8 | 1(–541.6) | | | | |
| TS(**9**,**12**-Mo) | 49.5 | 1(–1124.4) | TS(**9**,**10**-Ru) | 63.1 | 79.4 | 1(–763.3) | | | | |
| TS(**10**,**13**-Mo) | 58.1 | 1(–1326.4) | TS(**10**,**11**-Ru) | 18.7 | 43.0 | 1(–412.6) | | | | |
| TS(**12**,**14**-Mo) | 55.6 | 1(–499.4) | | | | | | | | |
| TS(**14**,**15**-Mo) | 33.8 | 1(–1327.4) | | | | | | | | |
| TS(**15**,**17**-Mo) | 9.7 | 1(–1047.3) | | | | | | | | |
| TS(**16**,**17**-Mo) | 18.8 | 1(–1083.8) | | | | | | | | |

[a] Structures and energies for compounds located in the triplet state (Mo system only) are included in the supporting information. [b] Calculated on B3LYP/BII. [c] Calculated on B3LYP/BIII. [d] The transition state TS(**7a**,**8a**-Ru) was unequivocally established. However, no energy value for **8a**-Ru is reported here, as no true minimum could be located for this compound. Frequency calculations showed four imaginary frequencies related to skeletal vibrations and $NH_3$ rotations.[22]

 © 2006 Wiley-VCH Verlag GmbH & Co. KGaA, Weinheim 

work with $T$ = 298.15 K and $p$ = 1 atm). Furthermore, optimized transition state geometries were inputted into IRC calculations to check if the transition states correspond to the correct reactants and products. The zero-point vibrational energies (*ZPE*) were used without scaling. To gain an insight into the relative energy differences for the different spin states, the optimized structures were then geometry optimized for the triplet state (B3LYP/BII), and for the cases were local minima or transition state structures could be found, their energies, relative to the energy of the singlet state, are reported in Table S1 in the supporting information. To obtain more accurate structures and energies, the B3LYP/BII geometries were inputted into geometry optimization calculations at the B3LYP level of theory employing the TZVP basis set designed by Ahlrichs[32] et al. for elements C, H and N. For Mo, the Stuttgart/Köln relativistic effective core potential was used in combination with a (311111/22111/411) valence basis.[33] This basis set is denoted as basis set BIII. For the calculations of the Mo system the Turbomole 5.7 program was used. In the Discussion section of the text the enthalpies $H$ obtained from the B3LYP/BII calculations are quoted. Comparison of these values with the B3LYP/BIII-derived energies showed that the deviations between these values were small, and consequently do not to require extra discussion (see Table S1, supporting information).

**Ru and Os:** Geometry optimizations were carried out using Gaussian03 (B3LYP) with the TZVP basis set for elements C, H, N, P.[32] For Ru and for Os the Stuttgart/Köln relativistic effective core potential was used in combination with a (311111/22111/411) valence basis.[33] This is denoted as basis set BIII. The stationary points obtained from these calculations were characterized as local minima or transition states according to frequency calculations ($i$ = 0 for local minima, and 1 for saddle points of order 1), and in some cases IRC calculations were carried out. Zero point energies were used without scaling. Relative enthalpies, $H$, and Gibbs free energies, $G$, are listed in Table 1 and are quoted in the Discussion section of the text. Tables S2 and S3 in the supporting information show energies, enthalpies, and free enthalpies in atomic units.

**QM/MM Calculations:** For some ruthenium compounds the HIPT ligand, as developed by Schrock et al., was used. For these large molecules QM/MM calculations were employed using the ONIOM method:[34] The ruthenium center, all atoms of the reacting substrates, the TREN part of the ligand, and the phenyl rings attached to the amido nitrogen centers were treated at the DFT level (BLYP[35] function) using the 6-31G(d) basis set for elements C, H, N. For Ru, a quasirelativistic small-core ECP[29,30] was used with a (441/2111/31) valence basis set. The DFT part of the calculations was run using the density fitting approximation[36] employing the density fitting set developed by Godbout et al.[37] and Sosa et al.[38] The atoms of the phenyl rings bearing the isopropyl groups, as well as the isopropyl groups themselves, were treated at the molecular mechanics level using the UFF force field.[39] The boundary atoms were treated as H atoms at the highest calculation level. Figure 4 gives a graphical example of the two layers. The optimized local minima and transition states were successfully characterized by frequency calculations ($i$ = 0 and $i$ = 1 for minima and saddle points of order 1, respectively).

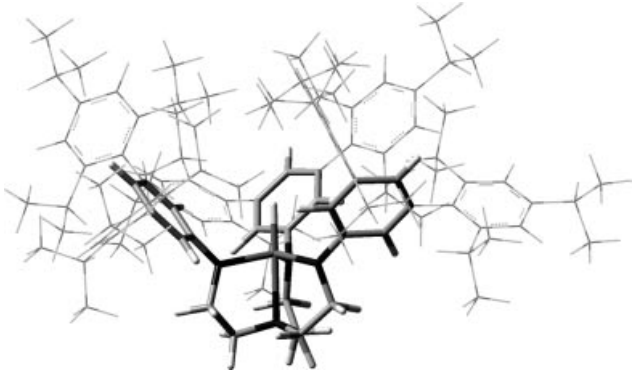

Figure 4. Assignment of atoms to layers in QM/MM calculations with **1**-Ru(HIPT) as an example. The atoms in the high layer are shown with a stick representation, whereas the atoms in the low layer appear as a wireframe representation.

**Supporting Information:** Energies and figures for most of the compounds calculated in this work, as well as the Cartesian coordinates employed.

## Acknowledgments

The generous allocation of computer time by the Calculation and Communication Centre of the RWTH Aachen is gratefully acknowledged.

[1] R. Schlögl, *Angew. Chem.* **2003**, *115*, 2050 and literature cited therein.
[2] a) D. V. Yandulov, R. R. Schrock, *J. Am. Chem. Soc.* **2002**, *124*, 6252; b) D. V. Yandulov, R. R. Schrock, *Science* **2003**, *301*, 76; c) R. R. Schrock, *Chem. Commun.* **2003**, 2389; d) D. V. Yandulov, R. R. Schrock, A. L. Rheingold, C. Ceccarelli, W. M. Davis, *Inorg. Chem.* **2003**, *42*, 796; e) V. Ritleng, D. V. Yandulov, W. W. Weare, R. R. Schrock, A. S. Hock, W. M. Davis, *J. Am. Chem. Soc.* **2004**, *126*, 6150; f) D. V. Yandulov, R. R. Schrock, *Inorg. Chem.* **2005**, *44*, 1103; g) R. R. Schrock, *Acc. Chem. Res.* **2005**, *38*, 955.
[3] F. Studt, F. Tuczek, *Angew. Chem.* **2005**, *117*, 5783.
[4] B. Le Guennic, B. Kirchner, M. Reiher, *Chem. Eur. J.* **2005**, *11*, 7448. In this investigation the authors compared a variety of complexes for which the electronic properties were calculated with the B3LYP and BP86 functions. It was found that the structures were in good agreement with each other.
[5] M. Reiher, B. Le Guennic, B. Kirchner, *Inorg. Chem.* **2005**, *44*, 9640.
[6] Z. Cao, Z. Zhou, H. Wan, Q. Zhang, *Int. J. Quantum Chem.* **2005**, *103*, 344.
[7] D. V. Yandulov, R. R. Schrock, *Can. J. Chem.* **2005**, *83*, 341.
[8] Ab initio and DFT calculations investigating the characteristics of Mo–P triple bonds were carried out on numerous complexes with different nitrogen ligands. The triamidoamine ligand is included in this study: T. Wagener, G. Frenking, *Inorg. Chem.* **1998**, *37*, 1805.
[9] Schrock et al. tried to use **I** as a catalyst for $NH_3$ production from $H_2$ and $N_2$, employing temperatures of up to 100 °C and pressures of up to 100 atm. However, the conditions used did not result in the formation of $NH_3$ (personal communication, R. R. Schrock).
[10] D. C. Graham, G. J. O. Beran, M. Head-Gordon, G. Christian, R. Stranger, B. F. Yates, *J. Phys. Chem. A* **2005**, *109*, 6762.
[11] F. Maseras, A. Lledós, E. Clot, O. Eisenstein, *Chem. Rev.* **2000**, *100*, 601.
[12] R. Gelabert, M. Moreno, J. M. Lluch, A. Lledós, *J. Am. Chem. Soc.* **1997**, *119*, 9840.
[13] I. Bytheway, G. B. Bacskay, N. S. Hush, *J. Phys. Chem.* **1996**, *100*, 6023.
[14] Reiher et al.[4] noted that in calculations with the B3LYP hybrid function, different substituents at the amido nitrogen centers of **1**-Mo yield pyramidal (H-substituted) and trigonal planar (C-substituted) N centers, which would lead to errors when the energy profiles between compounds with different

 © 2006 Wiley-VCH Verlag GmbH & Co. KGaA, Weinheim 

substituents are compared in detail, and these errors must be considered.

[15] For the Mo system only enthalpies $H$ and $H^{\ddagger}$ are included in the energy profile, as these values clearly show the activation barriers to be very high. Gibb's free energies are expected to be, and were shown by us, to be significantly higher for a few steps (as can be seen in the energy profiles of the Ru and the Os systems), but as no new relevant information can be deduced from the $\Delta G$ curve, it is not included in the energy profile. In the case of the Ru and Os catalysts some of the $H^{\ddagger}$ values are fairly low, which calls for the inclusion of $G$ and $G^{\ddagger}$ in these systems to obtain an impression of how large the differences between the enthalpies $H/H^{\ddagger}$ and Gibb's free energies $G^{\ddagger}/G^{\ddagger}$ really are.

[16] The calculated structures of compounds **4**-Mo and **8**-Mo are in good agreement with the structures carrying the HIPT substituent that have been determined crystallographically by Schrock et al..

[17] Attempts to locate transition states for the cleavage of $NH_3$ from **17**-Mo, as well as $N_2H_4$ from **11**-Mo, were not successful. Instead only local minima were found, in which the N centers of the $NH_3$ and $N_2H_4$ molecules are bridged by the protons at the amido N centers of the complex. For this reason we have not attempted to locate these transition states in the ruthenium and osmium systems. If the real HIPT ligand was employed this would not occur, as in the real system C atoms are attached to the amido N centers.

[18] A. F. Borowski, B. Donnadieu, J.-C. Daran, S. Sabo-Etienne, B. Chaudret, *Chem. Commun.* **2000**, 543.

[19] D. Giunta, M. Hölscher, C. W. Lehmann, R. Mynott, C. Wirtz, W. Leitner, *Adv. Synth. Catal.* **2003**, *345*, 1139.

[20] a) M. Grellier, L. Vendier, B. Chaudret, A. Albinati, S. Rizzato, S. Mason, S. Sabo-Etienne, *J. Am. Chem. Soc.* **2005**, in print; b) A. F. Borowski, S. Sabo-Etienne, B. Donnadie, B. Chaudret, *Organometallics* **2003**, *22*, 1630.

[21] H. Bielawa, O. Hinrichsen, A. Birkner, M. Muhler, *Angew. Chem.* **2001**, *113*, 1093.

[22] For complex **8a**-Ru no real minimum could be located, as the corresponding frequency calculation showed the existence of four imaginary vibrations, which can be attributed to $NH_3$ rotations and skeletal vibrations. This is the reason why Table 1 does not contain an entry for **8a**-Ru.

[23] a) A. Heßler, S. Kucken, O. Stelzer, J. Blotevogel-Baltronat, W. S. Sheldrick, *J. Organomet. Chem.* **1995**, *501*, 293; b) F. Bitterer, S. Kucken, O. Stelzer, *Chem. Ber.* **1995**, *128*, 275; c) F. Kasparek, Z. Travnicek, M. Posolda, Z. Sindelar, J. Marek, *J. Coord. Chem.* **1998**, *44*, 61.

[24] R. R. Schrock, S. W. Seidel, Y. Schrodi, W. M. Davis, *Organometallics* **1999**, *18*, 428.

[25] a) Complex **8a**-Os(P), as well as the transition states TS(**7**,**7a**-Os(P)) and TS(**7a**,**10**-Os(P)), could not be located.

[26] For reactions like the conversion of **5**-Os(P) to **6**-Os(P), in which the H–H bond of a $H_2$ molecule is broken, it can be seen that this process is energetically more favorable than in the Ru system (and also the Mo system). However, we agree with the opinion of one referee that these barriers are high. Therefore this issue needs to be addressed in further analyses of the electronic structure of the catalysts, with the aim of developing modified catalyst structures.

[27] a) Gaussian 03, Revision B.03, M. J. Frisch, G. W. Trucks, H. B. Schlegel, G. E. Scuseria, M. A. Robb, J. R. Cheeseman, J. A. Montgomery Jr, T. Vreven, K. N. Kudin, J. C. Burant, J. M. Millam, S. S. Iyengar, J. Tomasi, V. Barone, B. Mennucci, M. Cossi, G. Scalmani, N. Rega, G. A. Petersson, H. Nakatsuji, M. Hada, M. Ehara, K. Toyota, R. Fukuda, J. Hasegawa, M. Ishida, T. Nakajima, Y. Honda, O. Kitao, H. Nakai, M. Klene, X. Li, J. E. Knox, H. P. Hratchian, J. B. Cross, C. Adamo, J. Jaramillo, R. Gomperts, R. E. Stratmann, O. Yazyev, A. J. Austin, R. Cammi, C. Pomelli, J. W. Ochterski, P. Y. Ayala, K. Morokuma, G. A. Voth, P. Salvador, J. J. Dannenberg, V. G. Zakrzewski, S. Dapprich, A. D. Daniels, M. C. Strain, O. Farkas, D. K. Malick, A. D. Rabuck, K. Raghavachari, J. B. Foresman, J. V. Ortiz, Q. Cui, A. G. Baboul, S. Clifford, J. Cioslowski, B. B. Stefanov, G. Liu, A. Liashenko, P. Piskorz, I. Komaromi, R. L. Martin, D. J. Fox, T. Keith, M. A. Al-Laham, C. Y. Peng, A. Nanayakkara, M. Challacombe, P. M. W. Gill, B. Johnson, W. Chen, M. W. Wong, C. Gonzalez, and J. A. Pople, Gaussian, Inc., Pittsburgh PA, **2003**; b) Turbomole 5.7, R. Ahlrichs, M. Bär, H.-P. Baron, R. Bauernschmitt, S. Böcker, P. Deglmann, M. Ehrig, K. Eichkorn, S. Elliott, F. Furche, F. Haase, M. Häser, H. Horn, C. Hättig, C. Huber, U. Huniar, M. Kattannek, A. Köhn, C. Kölmel, M. Kollwitz, K. May, C. Ochsenfeld, H. Öhm, H. Patzelt, O. Rubner, A. Schäfer, U. Schneider, M. Sierka, O. Treutler, B. Unterreiner, M. von Arnim, F. Weigend, P. Weis, H. Weiss, The Quantum Chemistry Group, University of Karlsruhe, 1988–2005.

[28] a) A. D. Becke, *J. Chem. Phys.* **1993**, *98*, 5648; b) C. Lee, W. Yang, R. G. Parr, *Phys. Rev.* **1988**, *37*, 785; c) S. H. Vosko, L. Wilk, M. Nusair, *Can. J. Phys.* **1980**, *58*, 1200; d) P. J. Stephens, F. J. Delvin, C. F. Chabalowski, M. J. Frisch, *J. Phys. Chem.* **1994**, *98*, 11623.

[29] a) R. Ditchfield, W. J. Hehre, J. A. Pople, *J. Chem. Phys.* **1971**, *54*, 724; b) W. J. Hehre, R. Ditchfield, J. A. Pople, *J. Chem. Phys.* **1972**, *56*, 2257; c) P. C. Hariharan, J. A. Pople, *Mol. Phys.* **1974**, *27*, 209; d) M. S. Gordon, *Chem. Phys. Lett.* **1980**, *76*, 163; e) P. C. Hariharan, J. A. Pople, *Theor. Chim. Acta* **1973**, *28*, 213.

[30] P. J. Hay, W. R. Wadt, *J. Chem. Phys.* **1985**, *82*, 299.

[31] G. Frenking, I. Antes, M. Böhne, S. Dapprich, A. W. Ehlers, V. Jonas, A. Neuhaus, M. Otto, R. Stegmann, A. Veldkamp, S. F. Vyboishchikov, *Reviews in Computational Chemistry* (Eds.: K. B. Lipkowitz, D. B. Boyd), Wiley-VCH, New York, **1996**, vol. 8, p. 63–144.

[32] A. Schäfer, C. Huber, R. Ahlrichs, *J. Chem. Phys.* **1994**, *100*, 5829.

[33] D. Andrae, U. Haeussermann, M. Dolg, H. Stoll, H. Preuss, *Theor. Chim. Acta* **1990**, *77*, 123.

[34] a) K. Morukuma, F. Maseras, *J. Comput. Chem.* **1995**, *16*, 1170; b) S. Humbel, S. Sieber, K. Morokuma, *J. Chem. Phys.* **1996**, *105*, 1959; c) T. Matsubara, S. Sieber, K. Morokuma, *Int. J. Quantum Chem.* **1996**, *60*, 1101; d) M. Svensson, S. Humbel, R. D. J. Foese, T. Matsubara, S. Sieber, K. Morokuma, *J. Phys. Chem.* **1996**, *100*, 19357; e) M. Svensson, S. Humbel, K. Morokuma, *J. Chem. Phys.* **1996**, *105*, 3654; f) S. Dapprich, I. Komaromia, K. S. Byun, K. Morokuma, M. J. Frisch, *J. Mol. Struct. (Theochem)* **1999**, *462*, 1.

[35] a) A. D. Becke, *Phys. Rev. A* **1988**, *38*, 3098; b) C. Lee, W. Yang, R. G. Parr, *Phys. Rev. B* **1988**, *37*, 785; c) B. Miehlich, A. Savin, H. Stoll, H. Preuss, *Chem. Phys. Lett.* **1989**, *157*, 200.

[36] a) B. I. Dunlap, *J. Chem. Phys.* **1983**, *78*, 3140; b) B. I. Dunlap, *J. Mol. Struct. (Theochem)* **2000**, *529*, 37.

[37] N. Godbout, D. R. Salahub, J. Andzelm, E. Wimmer, *Can. J. Chem.* **1992**, *70*, 560.

[38] C. Sosa, J. Andzelm, B. C. Elkin, E. Wimmer, K. D. Dobbs, D. A. Dixon, *J. Phys. Chem.* **1992**, *96*, 6630.

[39] A. K. Rappe, C. J. Casewit, K. S. Colwell, W. A. Goddard III, W. M. Skiff, *J. Am. Chem. Soc.* **1992**, *114*, 10024.

Received: June 14, 2006
Published Online: September 13, 2006

 © 2006 Wiley-VCH Verlag GmbH & Co. KGaA, Weinheim 

DOI: 10.1002/ejic.200600604

# Synthesis, Structure and Conformational Properties of Fluoroformylchlorodifluoroacetyl Disulfide, $FC(O)SSC(O)CF_2Cl$: Conformational Transferability in –C(O)SSC(O)– Compounds

**Mauricio F. Erben,[a] Carlos O. Della Védova,*[a,b] Helge Willner,[c] and Roland Boese[d]**

**Keywords:** Conformation analysis / Sulfur / Vibrational spectroscopy / X-ray diffraction

Pure fluoroformylchlorodifluoroacetyl disulfide, FC(O)SSC(O)$CF_2Cl$, has been prepared by the reaction of FC(O)SCl and $CF_2ClC(O)SH$ in quantitative yield. The conformational properties of the novel molecule have been studied by vibrational spectroscopy (IR – gas phase, Raman – liquid phase) and quantum chemical calculations (B3LYP and MP2 methods). The gaseous compound exhibits a conformational equilibrium at room temperature where the most stable form adopts a $C_1$ symmetry and a *syn*-periplanar (*sp*) orientation of both carbonyl groups with respect to the disulfide bond. A second form, observed in the IR spectrum of the vapor, corresponds to a conformer in which the carbonyl bond of the FC(O) moiety adopts an *anti*-periplanar (*ap*) position with respect to the S–S single bond, and *gauche* with respect to the ClC–C=O moiety in the chlorodifluoroacetyl group. The experimental free energy difference value $\Delta G^0 = G^0_{(ap-sp)} - G^0_{(sp-sp)}$ = 1.4(3) kcal/mol (IR) is reproduced well by the B3YLP/6-311+G(3df) (1.1 kcal/mol) and the MP2/6-31G* (1.8 kcal/mol) methods. In addition, the structure of a single-crystal, grown in situ, was determined by X-ray diffraction analysis at low temperature. The crystalline solid [monoclinic, $P2_1/n$, $a$ = 5.579(3) Å, $b$ = 16.615(7), $c$ = 8.455(4) Å, $\beta$ = 106.876(8)°] consists exclusively of molecules with the (*sp*–*sp*) conformation and the usual *gauche* orientation around the disulfide bond [$\phi$(CS–SC) = 84.2°]. Conformational transferability is thus demonstrated once again for species that contain the –C(O)SSC(O)– group as part of a systematic program designed to analyze the behavior of this class of molecules.

(© Wiley-VCH Verlag GmbH & Co. KGaA, 69451 Weinheim, Germany, 2006)

## Introduction

One of the most fundamental concepts in chemistry is that of a functional group; the idea that a linked group of atoms can exhibit a set of characteristic geometric and chemical properties. This concept is especially useful to understand the chemistry of biological macromolecules which consist of polymeric combinations of a small number of building blocks. From this empirical cornerstone of chemistry – atoms and functional groups possess characteristic and additive properties that in many cases exhibit a remarkable transferability between different molecules – a series of methodologies have been developed, especially in relation to the study of protein folding.[1–5] The transferability principle can be used to deduce the properties of large molecules from smaller, readily accessible molecules whose geometric parameters are experimentally known. Knowledge of the structural properties and conformational preference of simple molecules containing distinct functional groups is therefore of prime interest.

Geometric structures of symmetrically substituted noncyclic disulfides, XSSX, in the gas phase are characterized by a *gauche* conformation around the S–S bond, with dihedral angles $\phi$(XS–SX) close to 90° (e.g. 90.76(6)° in HSSH,[6] 87.7(4)° in FSSF,[7] 85.2(2) in ClSSCl,[8] 85.3(37) in $CH_3SSCH_3$,[9] and 104.4(40)° in $CF_3SSCF_3$).[10] In this conformation, the *p*-shaped lone pairs of the sulfur atoms are perpendicular to each other and their mutual repulsion is minimized. Furthermore, such a structure is favored by the anomeric effect by electron donation from the sulfur lone pairs into the empty $\sigma^*$ orbitals of the opposing S–X bonds.[11,12] Disulfides with very bulky substituents, such as *t*BuSS*t*Bu, have dihedral angles which are considerably larger than 90° [$\phi$(CS–SC) = 128.2(27)].[13] On the other hand, the dihedral angle for FC(O)SSC(O)F has been reported to be 82.2(19).[14] Structural data for nonsymmetrically substituted disulfides of the type XSSY are more sparse in both experimental and theoretical terms. FC(O)-

[a] CEQUINOR (CONICET-UNLP), Departamento de Química, Facultad de Ciencias Exactas, Universidad Nacional de La Plata,
47 esq. 115 (B1900AJL), C. C. 962, La Plata, Buenos Aires, República Argentina
E-mail: carlosdv@quimica.unlp.edu.ar
[b] Laboratorio de Servicios a la Industria y al Sistema Científico (UNLP-CIC-CONICET) Camino Centenario,
Gonnet, Buenos Aires, República Argentina
[c] FB C, Anorganische Chemie, Bergische Universität Wuppertal, Gaußstrasse 20, 47097 Wuppertal, Germany
[d] Institut für Anorganische Chemie, Universität Duisburg–Essen, Universitätsstr. 5–7, 45117 Essen, Germany

Supporting information for this article is available on the WWW under http://www.eurjic.org or from the author.

 © 2006 Wiley-VCH Verlag GmbH & Co. KGaA, Weinheim 

$SSCF_3$[15] and $FC(O)SSCH_3$[16] have been studied in the gas phase and display φ(CS–SC) dihedral angles of 95.0(27)° and 83.5(15)°, respectively.

Additionally, the presence of a carbonyl group attached to the S–S bond, as in $FC(O)SSC(O)F$,[17] $FC(O)SSCH_3$,[15] and $FC(O)SSCF_3$,[16] may promote a conformational equilibrium, but this depends on the relative orientation of the C=O and S–S bonds. The *syn*-periplanar (*sp*) orientation, with φ(SS–C=O) = 0°, is the prevailing form for these species.

In order to gain additional experimental and theoretical information about the structural and conformational behavior of acyl-substituted disulfides, we became interested in molecules containing the –C(O)SSC(O)– fragment with two carbonyl groups bonded to the disulfide bond. Thus, fluoroformyltrifluoroacetyl disulfide, $FC(O)SSC(O)CF_3$, has been recently synthesized and its structural properties studied in both the gas and condensed phases.[18] In the present study, we have extended the analysis to the related $FC(O)SSC(O)CF_2Cl$ molecule, a novel compound for which the geometric structure and conformational properties have been determined by experimental and theoretical methods.

## Results

### Synthesis, Characterization, and Physical Properties

The synthesis of $FC(O)SSC(O)CF_2Cl$ was adapted from that recently reported for $FC(O)SSC(O)CF_3$,[18] by the reaction of chlorodifluorothioacetic acid, $CF_2ClC(O)SH$, with fluorocarbonylsulfenyl chloride, FC(O)SCl, according to Equation (1).

$$CF_2ClC(O)SH + FC(O)SCl \rightarrow FC(O)SSC(O)CF_2Cl + HCl \quad (1)$$

The new compound is a colorless liquid with the characteristic overpowering sulfenylcarbonyl odor. In the liquid or gaseous state, the compound is stable for days at room temperature. The vapor pressure, measured in a small section of the vacuum line (total volume ca. 15 mL) with a capacitance manometer over the temperature range 247–291 K, follows the equation $\log p = 5.857 - 2383/T$ (*p*/bar, *T*/K), and gives an extrapolated normal boiling point of 407 K (134 °C).

In the $^{19}F$ NMR spectrum of the liquid, two singlets with an intensity ratio of 1:2 were observed. The more intense signal is located at $\delta$ = –62.6 ppm, whereas the second signal appears at $\delta$ = 42.3 ppm. The related trifluoromethyl species shows corresponding signals at $\delta$ = –74.9 ppm [$CF_3C(O)$– group] and 41.4 ppm [FC(O)– group].[18]

Additional evidence for the identity of $FC(O)SSC(O)CF_2Cl$ comes from the IR spectrum of the vapor and the Raman spectrum of the liquid (Figure 1 and Table SI1 in the Supporting Information). Two intense bands in the carbonyl stretching region at 1847 and 1771 $cm^{-1}$ are characteristic of the FC=O and $CF_2ClC=O$ groups, respectively. The strongest band in the IR spectrum of the vapor centered at 1060 $cm^{-1}$, is assigned to the $F–C_{sp^2}$ stretching mode. In addition, the characteristic disulfide stretching mode is observed in the Raman spectrum of the liquid as a signal of medium intensity at 535 $cm^{-1}$.

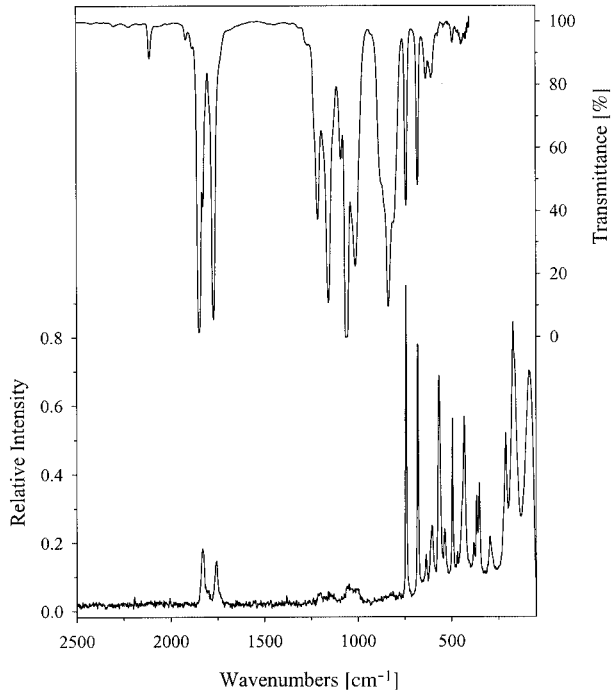


Figure 1. Gas IR at 5.0 mbar (glass cell, 200 mm optical path length, Si windows, 0.5 mm thick) and liquid Raman spectra for $FC(O)SSC(O)CF_2Cl$.

### Quantum Chemical Calculations

In a first step, the potential function for the internal rotation around the S–S bond was derived by structure optimizations at fixed φ(CS–SC) dihedral angles, whereas near-*sp* mutual orientations were supposed for both C=O double bonds and the S–S bond. The potential function obtained with the B3LYP/6-31G* method is shown in Figure 2. Minima occur at dihedral angles around ±75°, whereas a rather flat maximum in the region of a *trans* C–S–S–C skeleton is observed, with imaginary frequencies, at φ(CS–SC) = 180°.

Besides the two enantiomeric forms that are related by rotation around the disulfide bond, several conformations are feasible, in principle, for $FC(O)SSC(O)CF_2Cl$, but they depend on the orientation of the C=O bonds of the FC(O) and the $CF_2ClC(O)$ groups. Each of them can be *syn*-periplanar (*sp*) or *anti*-periplanar (*ap*) relative to the S–S bond. This leads to four possible conformers: (*sp–sp*), (*ap–sp*), (*sp–ap*), and (*ap–ap*) [the first orientation refers to the FC(O) group and the second to the $CF_2ClC(O)$ group, see Scheme 1].

The potential functions for the internal rotation around both S–C bonds were calculated (B3LYP/6-31G*) by full geometry optimization at fixed φ(SS–C=O) torsional angles (Figure 3). As expected, both curves possess minima for *sp* [φ(SS–C=O) = 0°] and *ap* [φ(SS–C=O) = 180°] orientations.

 © 2006 Wiley-VCH Verlag GmbH & Co. KGaA, Weinheim 

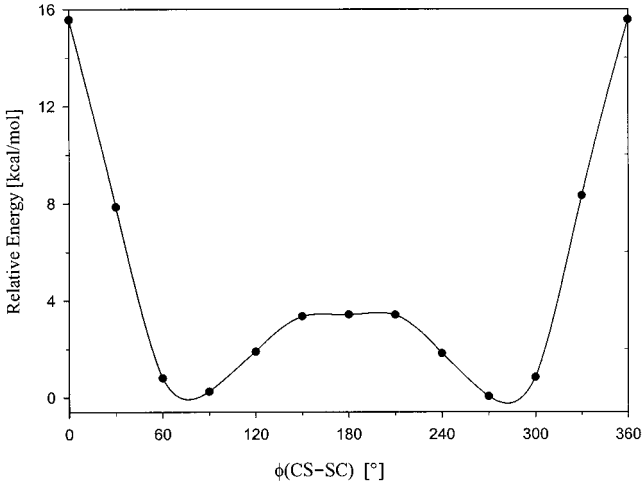


Figure 2. Calculated potential function (B3LYP/6-31G*) for the internal rotation around the S–S bond in FC(O)SSC(O)$CF_2Cl$.

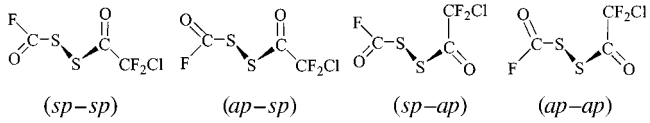


Scheme 1. Representation of the conformers of FC(O)SSC(O)-$CF_2Cl$.

The calculated maxima for near-perpendicular orientations [ϕ(SS–C=O) ≈ 90°] have similar energy values in both cases, which are characterized as torsional transition states (TS, $N_{imag}$ = 1). The geometries of the four minima were fully optimized, including frequency calculations, with the B3LYP method and with the use of the 6-31G* and 6-311+G(3df) basis sets and the MP2/6-31G* approximation. Calculated relative energies (corrected for zero-point energy) and vibrational frequencies of the C=O stretches with their IR intensities are collected in Table 1. All three computational methods predict that the four different conformers correspond to stable structures and agree with respect to the conformational preference. In the lowest-energy conformer, both carbonyl bonds adopt an *sp* orientation with respect to the S–S bond, whereas the second most stable conformer possesses an *ap* orientation of the FC(O) group with respect to the S–S single bond. Moreover, structures with *ap* orientation of the $CF_2ClC(O)$ group with respect to the S–S bond are considerably higher in energy ($\Delta G^0 \approx$ 4.0 kcal/mol or even more) and are not expected to be detectable in our experiments.

Table 1. Calculated relative energies (corrected by zero-point energy) and vibrational frequencies of the C=O stretching modes [$cm^{-1}$] with IR intensities [km/mol] in parentheses for FC(O)-SSC(O)$CF_2Cl$.

| Conformer[a] | Method of calculation | $\Delta E^0$ | ν(FC=O) | ν(O=C$CF_2Cl$) |
|---|---|---|---|---|
| (*sp–sp*) | B3LYP/6-31G* | 0.00[b] | 1922 (231) | 1851 (192) |
| | B3LYP/6-311+G(3df) | 0.00[c] | 1892 (249) | 1827 (214) |
| | MP2/6-31G* | 0.00[d] | 1894 (177) | 1784 (127) |
| (*ap–sp*) | B3LYP/6-31G* | 0.89 | 1903 (379) | 1847 (190) |
| | B3LYP/6-311+G(3df) | 1.14 | 1866 (453) | 1826 (204) |
| | MP2/6-31G* | 1.76 | 1881 (301) | 1780 (127) |
| (*sp–ap*) | B3LYP/6-31G* | 4.48 | 1923 (245) | 1827 (250) |
| | B3LYP/6-311+G(3df) | 3.74 | 1893 (267) | 1804 (288) |
| | MP2/6-31G* | 6.05 | 1897 (183) | 1759 (163) |
| (*ap–ap*)[e] | B3LYP/6-31G* | 5.29 | 1901 (327) | 1826 (295) |
| | MP2/6-31G* | 7.93 | 1872 (250) | 1759 (195) |

[a] First orientation (*sp* or *ap*) refers to FC(O) group, second orientation (*sp* or *ap*) to $CF_2ClC(O)$ group. [b] $E^0$ = –1820.807875 hartree. [c] $E^0$ = –1817.714699 hartree. [d] $E^0$ = –1821.140101 hartree. [e] The (*ap–ap*) was not calculated at the B3LYP/6-311+G(3df) approximation.

In regard to the chlorodifluoromethyl group, the predominant conformer possesses a *gauche* structure with ClC–C=O values close to 80°; the C–F bond deviates from the eclipsed orientation [ϕ(FC–C=O) = 42°]. From the potential energy curve obtained by the rotation of the $CF_2Cl$ group around the C–C single bond (Figure 4) both *cis*

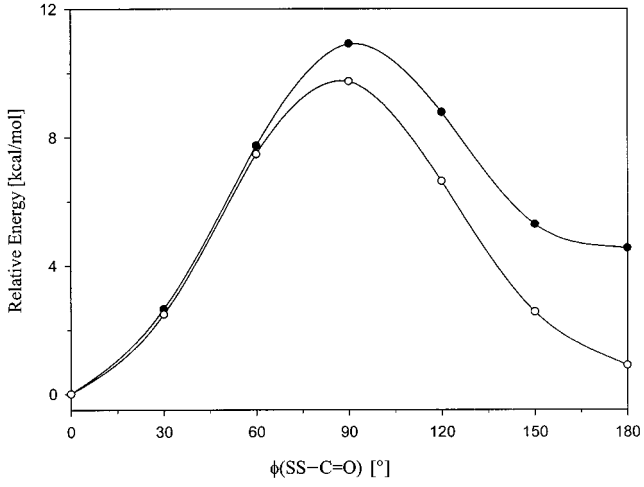


Figure 3. Potential energy curves for FC(O)SSC(O)$CF_2Cl$ as a function of the ϕ(SS–C=O) dihedral angles calculated with the B3LYP/6-31G* approximation. [○: ϕ(SS–C1=O1), ●: ϕ(SS–C2=O2), for atom numbering see Figure 5].

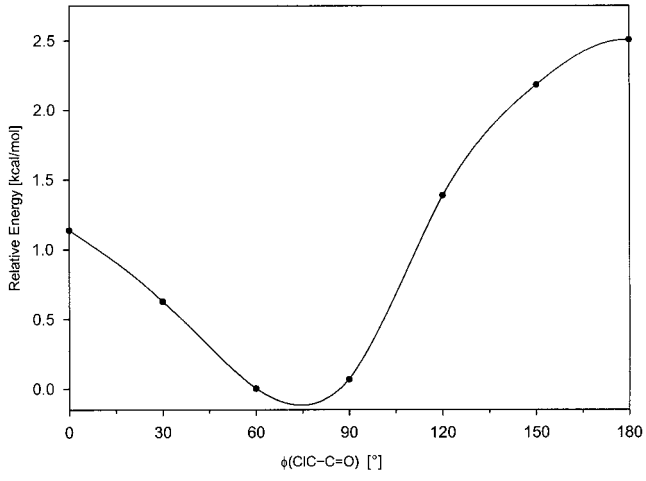


Figure 4. Potential energy curves for FC(O)SSC(O)$CF_2Cl$ as a function of the ϕ(ClC–C=O) dihedral angle calculated with the B3LYP/6-31G* approximation.

 © 2006 Wiley-VCH Verlag GmbH & Co. KGaA, Weinheim 

[$\phi$(ClC–C=O) = 0°] and *trans* [$\phi$(ClC–C=O) = 180°] forms correspond to torsional transition states ($N_{imag}$ = 1). The calculated barrier heights (corrected for zero-point energies) are 1.1 and 2.5 kcal/mol, respectively.

### Vibrational Spectra

The IR spectrum of the vapor and the Raman spectrum of liquid $FC(O)SSC(O)CF_2Cl$ are shown in Figure 1. Both spectra are similar to those of $FC(O)SSC(O)CF_3$.[18] A tentative assignment of the observed bands was performed by comparison with the calculated spectrum and the approximate description of modes is based on the calculated displacement vectors for the fundamental modes of vibration, as well as on comparisons with the spectra of related molecules, especially FC(O)SSC(O)F[17] and $CF_2ClC(O)Cl$.[19] Experimental and calculated [B3LYP/6-311+G(3df)] frequencies for the (*sp–sp*) and (*ap–sp*) conformers, together with the tentative assignments, are given in the Supporting Information (Table SI1).

The ab initio calculations indicate that the (*sp–sp*) conformer is more stable than the (*ap–sp*) conformer. The vibrational spectra are consistent with this prediction, but the presence of a second conformer in the vapor phase becomes apparent. It is known that the $\nu$(C=O) normal mode of carbonyl compounds is very sensitive to conformational properties.[20,21] As observed in Figure 5, two intense bands occur in the IR spectrum of $FC(O)SSC(O)CF_2Cl$ vapor at 1847 and 1771 $cm^{-1}$, whereas a third band of low intensity appears at 1827 $cm^{-1}$. The first two bands are assigned to the C=O stretching modes of the FC=O and $CF_2ClC$=O groups in the most abundant (*sp–sp*) conformer. Comparison with the calculated frequencies then allows the assignment of the third band to the FC=O group in the (*ap–sp*) form. Thus, the calculated wavenumber difference [B3LYP/6-311+G(3df)] for the C=O stretching mode of the FC(O) group [$\nu$(FC=O), Table 1] between the (*sp–sp*) and the (*ap–sp*) forms is +26 $cm^{-1}$, a value that is in good agreement with the experimentally observed value of +20 $cm^{-1}$. No significant difference is expected in the wavenumbers of the $CF_2ClC$=O stretching mode between the (*sp–sp*) and (*ap–sp*) forms; the calculated difference is about 2 $cm^{-1}$. Accordingly, the stretching mode of the (*ap–sp*) conformer is assigned to the band at 1771 $cm^{-1}$, which is masked by the band of the corresponding stretching mode of the (*sp–sp*) form. The conformational composition was derived from the integrated intensities of the C=O vibrations for the (*sp–sp*) and (*ap–sp*) forms, with the intensities calculated by the B3LYP/6-311+G(3df) method taken into account (Table 1). This analysis leads to a composition of 92(5)% of the more stable (*sp–sp*) form at ambient temperature (the estimated error limit includes uncertainties in the measured areas and in the calculated intensities).

A conformational equilibrium was also evident in the F–C(O) stretching region [$\nu(C_{sp^2}–F)$, Table SI1 given in the Supporting Information] through the presence of two bands in the IR spectrum of the vapor. The more intense band is located at 1060 $cm^{-1}$, which can be assigned to this mode in the main (*sp–sp*) conformer; the second band, at 1089 $cm^{-1}$, can be assigned to the same mode of the less stable (*ap–sp*) form. Quantum chemical calculations correctly reproduce this frequency shift of 19 $cm^{-1}$. According to the calculations, the other fundamental modes of the (*sp–sp*) and (*ap–sp*) conformers either differ by less than 2 $cm^{-1}$ or have too low an intensity to be observed in our experiments.

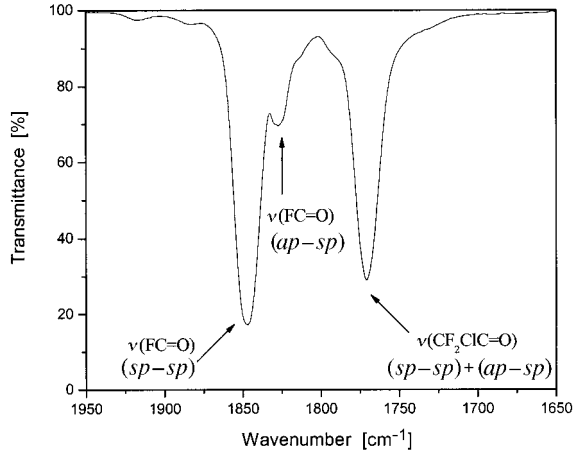


Figure 5. C=O vibrational stretching region in the IR spectrum of gaseous $FC(O)SSC(O)CF_2Cl$ at 5.0 mbar (glass cell, 200 mm optical path length, Si windows, 0.5 mm thick).

### Crystal Structure

Because simple covalent disulfides are liquids or gases at ambient temperatures and because they are frequently labile species, very little is known about their structures in the solid state. Only with the development of special crystallization techniques has it become possible to extend detailed structural studies to the crystalline state. By using the in situ crystallization technique developed at Essen,[22] an appropriate single-crystal of $FC(O)SSC(O)CF_2Cl$ was grown at 193 K. The compound crystallizes in the monoclinic system ($P2_1/n$ spatial group) with the following unit cell dimensions: $a$ = 5.579(3) Å, $b$ = 16.615(7) Å, $c$ = 8.455(4) Å, and $\alpha = \gamma = 90°$ and $\beta$ = 106.876(8)°, $Z$ = 4 (for the full crystallographic data and treatment information, see Table SI2 in the Supporting Information). Only the (*sp–sp*) conformer is observed in the crystal, with a *gauche* orientation around the S–S bond. The structure of the molecule is shown in Figure 6, and Table 2 includes the main geometric parameters derived from the structure refinement, as well as those obtained from quantum chemical calculations. The overall crystal packing, as viewed along the *ab* plane, is shown in Figure 7.

Intermolecular interactions that are dominated by F···F contacts are common for fluorinated molecules where there is no other choice for the stabilization of the packing. According to quantum chemical calculations, F···F contacts in aromatic systems can contribute up to 14 kcal/mol of local stabilization energy.[23] In the present case, the chlorodifluo-

 © 2006 Wiley-VCH Verlag GmbH & Co. KGaA, Weinheim 

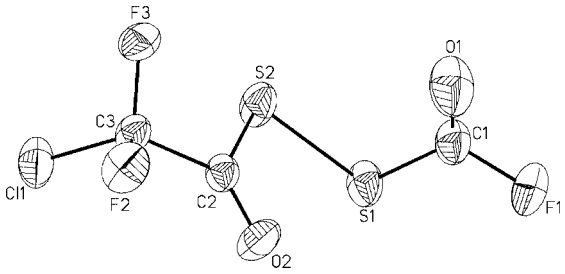


Figure 6. Molecular model with atom numbering scheme for the single-crystal structure of $FC(O)SSC(O)CF_2Cl$.

Table 2. Experimental and calculated geometric parameters for the *gauche* (*sp–sp*) conformer of $FC(O)SSC(O)CF_2Cl$.[a]

| Parameter | X-ray[b] | B3LYP | | MP2/6-31G* |
|---|---|---|---|---|
| | | 6-31G* | 6-311+G(3df) | |
| S1–S2 | 2.029 (1) | 2.074 | 2.050 | 2.049 |
| S1–C1 | 1.759 (4) | 1.790 | 1.785 | 1.774 |
| S2–C3 | 1.796 (3) | 1.824 | 1.813 | 1.794 |
| C1–C2 | 1.556 (4) | 1.553 | 1.557 | 1.539 |
| C1=O1 | 1.179 (4) | 1.196 | 1.187 | 1.211 |
| C3=O2 | 1.165 (4) | 1.182 | 1.176 | 1.194 |
| $(C2–F)_{mean}$ | 1.335 (4) | 1.340 | 1.339 | 1.354 |
| C3–F4 | 1.342 (4) | 1.342 | 1.347 | 1.358 |
| C–Cl | 1.739 (3) | 1.785 | 1.773 | 1.753 |
| S2–S1–C1 | 99.7 (1) | 99.8 | 101.4 | 98.2 |
| S1–S2–C3 | 99.1 (1) | 101.4 | 100.4 | 99.4 |
| S1–C1=O1 | 126.7 (2) | 125.7 | 126.2 | 126.0 |
| S2–C3=O2 | 131.1 (3) | 129.7 | 130.5 | 129.7 |
| S1–C1–C2 | 111.8 (2) | 112.1 | 112.2 | 112.9 |
| F–C2–F | 107.1 (2) | 108.5 | 108.0 | 108.5 |
| S2–C3–F4 | 106.7 (2) | 106.6 | 106.3 | 106.6 |
| $(F–C–C)_{mean}$ | 109.5 (3) | 109.6 | 110.0 | 108.7 |
| Cl–C–C | 110.7 (2) | 110.0 | 109.6 | 110.3 |
| $(Cl–C–F)_{mean}$ | 110.0 (3) | 109.6 | 109.6 | 109.9 |
| ϕ(SS–C=O1) | 0.8 (4) | 2.9 | 0.9 | 2.0 |
| ϕ(SS–C=O2) | 4.8 (3) | 2.0 | 2.7 | 2.9 |
| ϕ(CS–SC) | 84.2 (2) | 77.4 | 83.5 | 71.1 |
| ϕ(ClC–C=O) | 102.3 (4) | 68.8 | 78.9 | 77.2 |

[a] See Figure 6 for atom numbering. [b] Uncertainties are σ values.

romethyl groups interact through C–F···F–C contact which measure 2.817 Å. This value is within the range found in comparable structural studies, in which C–F···F–C contacts of 2.777 and 2.868 Å are identified as packing motifs.[24,25] The sum of the van der Waals radii would suggest 2.7 Å as a contact distance, but this does not obviously hold for carbon-bonded fluorine.

The investigation of short nonbonded intramolecular 1,4 S···O contacts have attracted much attention because S···O distances in the range 2.77–3.16 Å have been observed in crystals.[26] These values are much shorter than the sum of the sulfur and oxygen van der Waals radii (3.3 Å).[27] The presence of such short S···O contacts in these compounds, each of which crystallizes in a different packing environment, indicates that the conformational feature results from a nonbonded intramolecular interaction. Computational results suggest that electronic conjugation gives rise to the observed S···O close contact.[28] In molecules which contain the –C(O)SSC(O)– moiety, there are two 1,4 S···O distances, defined by one sulfur atom of the disulfide bond and the

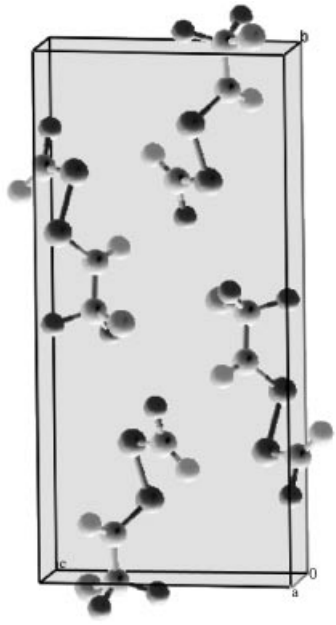

Figure 7. Stereoscopic illustration of the crystal packing of $FC(O)SSC(O)CF_2Cl$ at 193 K.

oxygen atom in the carbonyl group bonded to the other sulfur atom. Following Figure 6, these 1,4 S···O distances for $FC(O)SSC(O)CF_2Cl$ are labeled as S1···O2 and S2···O1, with values of 3.016 Å and 3.078 Å, respectively. The ϕ(SS–C=O) dihedral angles around the corresponding C–S bonds are 4.8 and 0.8°, respectively. Following Burling et al.,[28] these nearly planar conformations favor electronic delocalization of the nonbonded π electrons of the sulfur atom, which results in an increased attractive interaction between the sulfur and oxygen atoms.

## Discussion

According to the vibrational spectra, the title molecule exists in the gas phase as a mixture of two conformers that differ in the relative orientation of the FC(O) group and the S–S single bond, with the *sp* conformer prevailing over the *ap* form. At room temperature, the more stable conformer accounts for 92(5)% of the vapor species. The standard Gibbs free-energy difference [$\Delta G^0 = G^0_{(ap–sp)} - G^0_{(sp–sp)}$] derived from the IR spectrum of the vapor (1.4 kcal/mol) is reproduced satisfactorily at the B3LYP/6-311+G(3df), B3LYP/6-31G*, and MP2/6-31G* levels of calculation. On the other hand, only the *sp* conformation is observed for the mutual orientation of the $CF_2ClC=O$ double bond and the S–S single bond, with a calculated mean value of $\Delta G^0 = G^0_{(sp–ap)} - G^0_{(sp–sp)}$ of 4.7 kcal/mol. This behavior parallels that recently reported for $FC(O)SSC(O)CF_3$, with $\Delta G^0 = G^0_{(ap–sp)} - G^0_{(sp–sp)} = 1.14(15)$ kcal/mol from the IR spectrum of the matrix isolated vapor and *sp* orientation of the S–S single bond with respect to the C=O double bond in the $–C(O)CF_3$ moiety.[18]

The chlorodifluoroacetyl group adopts a *gauche* orientation in the crystal, with a corresponding dihedral angle

 © 2006 Wiley-VCH Verlag GmbH & Co. KGaA, Weinheim 

φ(ClC–C=O) of 102.3(4)° [φ(F3C3–C=O) = 136.4(3)°]. As already commented in this paper, quantum chemical calculations predict a different behavior for a molecule with the (*sp–sp*) conformation, with φ(ClC–C=O) and φ(F3C3–C=O) dihedral angles of 78.9 and 160.7°, respectively. The predominant conformer found experimentally for chlorodifluoroacetyl chloride [$CF_2ClC(O)Cl$] in the gas phase possesses a *gauche* orientation of the chlorine atoms [φ(ClC–C=O) = 104.6(10)°],[29] whereas a second stable conformer where the C–Cl bond eclipses the C=O bond is higher in energy by $\Delta G^0$ = 1.1(3) kcal/mol.[29] From a study of the Raman spectrum of the liquid at different temperatures, a $\Delta H^0$ value of 1.03(11) kcal/mol was determined, whereas for the sample dissolved in liquid xenon, this value decreases to 0.71(17) kcal/mol.[19] For the free molecule of the title compound, this last conformation corresponds to a rotational transition state; the calculated barrier is only 1.1 kcal/mol. Thus, the barrier to rotation appears to be quite low for the chlorodifluoroacetyl moiety, and the discrepancy between the X-ray structure and the calculated geometrical properties probably reflects the distortions induced by the crystal packing.

Transferability is then evident in the conformational properties of $FC(O)SSC(O)CF_2Cl$. Extensive studies of carbonylsulfenyl compounds with the general formula XC(O)SY have established the preference for a *syn*-periplanar conformation around the C–S bond.[20,30–33] In the case of disulfides (so that Y corresponds to an –SR group), the preferred mutual orientation of the C=O and S–S bonds is also *sp*.[12,14–16] It has also been established experimentally that the *ap* conformation appears as a second stable form that makes appreciable contributions to the vapor at room temperature when X is a fluorine atom,[14,17,34,35] whereas only the *sp* conformation is adopted by species containing the $CF_3C(O)S$ moiety.[36–38]

Breitzer et al.[39] have reported the analysis of the crystal structures of several disulfides. A plot of the S–S bond length versus the disulfide torsion angles reveals the greatest density of data points in the bond length region 2.00–2.06 Å and torsion angles between 75 and 90°. A similar pattern has also been observed for the structures of gaseous disulfides. In accordance with this trend, the disulfide bond length and torsion angle in crystalline $FC(O)SSC(O)CF_2Cl$ are 2.029(1) Å and 84.2(2)°, respectively.

The two computational methods we have used predict dihedral angles for the molecular skeleton with values similar to those obtained from the X-ray analysis. The methods are less successful in the reproduction of the lengths of some of the bonds around sulfur. Thus, even with large basis sets [6-311+G(3df)], the B3LYP method predicts the S–X bonds to be too long (by up to 0.026 Å for the S1–C1 bond). While these bonds are better described by the MP2 method with the modest 6-31G* basis set, this method fails to reproduce the C=O double bond lengths well, which are also made out to be too long (0.032 Å for the C1 = O1 bond). In practice, however, the contraction of polar bonds is to be expected upon crystallization and compensation for this phenomenon allows both methodologies to satisfactorily reproduce the molecular dimensions of the crystalline solid.

## Experimental Section and Instrumentation

**General Procedure:** Volatile materials were manipulated in a glass vacuum line equipped with two capacitance pressure gauges (221 AHS-1000 and 221 AHS-10, MKS Baratron, Burlington, MA), three U-traps and valves with PTFE stems (Young, London, UK). The vacuum line was connected to an IR cell (optical path length 200 mm, Si windows 0.5 mm thick) contained in the sample compartment of an FTIR instrument (Impact 400D, Nicolet, Madison, WI). This allowed us to monitor the purification processes and to follow the course of the reactions. The pure compound was stored in flame-sealed glass ampules under liquid nitrogen in a long-term Dewar vessel. The ampules were opened with an ampule key on the vacuum line, an appropriate amount of the compound was taken out for the experiments, and then the ampules were flame-sealed again.[40]

$CF_2ClC(O)SH$ was synthesized by the reaction of either $CF_2ClC(O)Cl$ or $[CF_2ClC(O)]_2O$ (98% Aldrich) with $H_2S$ (98% Linde, Germany) in a metal reactor.[41] This method was adapted from the literature procedure for the synthesis of $CF_3C(O)SH$.[42] $CF_2ClC(O)Cl$ was synthesized by the reaction of chlorodifluoroacetic acid (98% Merck) with $PCl_5$ according to the usual method. FC(O)SCl was obtained by the reaction of commercial ClC(O)SCl (Aldrich 95%) with $SbF_5$ following the reported method.[43,44]

Conventional vacuum techniques were used to condense equimolar quantities (typically 2.5 mmol) of $CF_2ClC(O)SH$ and FC(O)SCl into a 6 mm o.d. glass ampule. The vessel was flame-sealed and placed in a –40 °C ethanol bath. At this temperature, the reaction proceeded rapidly, as judged by the disappearance of the yellow color [due to FC(O)SCl] of the reaction mixture. The mixture was then warmed to –10 °C and preserved at that temperature for about 1 h. Subsequently the products were separated by "trap-to-trap" condensation through traps held at –30 °C, –60 °C and –196 °C. Pure $FC(O)SSC(O)CF_2Cl$ was retained as a colorless liquid in the –60 °C trap. The yield was nearly quantitative and, apart from the HCl generated in the reaction, only minor quantities of OCS and $SiF_4$ were observed as byproducts in the U-trap at –196 °C.

**X-ray Diffraction at Low Temperature:** An appropriate crystal of $FC(O)SSC(O)CF_2Cl$ ca. 0.3 mm in diameter was obtained on the diffractometer at a temperature of 193(2) K with a miniature zone melting procedure with the use of focused infrared laser radiation.[22] The diffraction intensities were measured at low temperatures with a Nicolet R3m/V four-circle diffractometer. Intensities were collected with graphite–monochromatized Mo-$K_\alpha$ radiation with the ω-scan technique. The crystallographic data, conditions and some features of the structure are listed in Table SI2 (Supporting Information). The structure was solved by Patterson syntheses and refined by full-matrix least-squares methods on *F* with the SHELXTL-Plus program.[45] Absorption correction details are given in Table SI2 (Supporting Information). All atoms were assigned anisotropic thermal parameters. Further details of the crystal structure investigation may be obtained from the Fachinformationszentrum Karlsruhe, 76344 Eggenstein-Leopoldshafen, Germany (Fax: +49-7247-808-666, E-mail: crysdata@fiz-karlsruhe.de) on quoting the depository number CSD-416694.

**Vibrational Spectroscopy:** Gas-phase infrared spectra were recorded with a resolution of 1 $cm^{-1}$ in the range 4000–400 $cm^{-1}$ with a Bruker IFS 66v FTIR instrument and Raman spectra of liquid

 © 2006 Wiley-VCH Verlag GmbH & Co. KGaA, Weinheim 

$FC(O)SSC(O)CF_2Cl$ with a Bruker RFS 100/S FT-Raman spectrometer. The liquid sample was contained in a 4 mm glass capillary and the spectrum excited with 500 mW of 1064 nm radiation from a Nd:YAG laser (ADLAS, DPY 301, Lübeck, Germany).

**NMR Spectroscopy:** For the $^{19}F$ NMR measurements, neat samples were held in flame-sealed, thin-walled 3 mm o.d. tubes placed inside 5 mm NMR tubes. The spectra were recorded with a Bruker Avance DRX-300 spectrometer operating at 282.41 MHz. The spectrum was measured with the sample at room temperature with a mixture of $CD_3CN$ and $CFCl_3$ as an external lock and reference, respectively.

**Theoretical Calculations:** All quantum chemical calculations were performed with the GAUSSIAN03 program package[46] under the Linda parallel execution environment with two coupled PC's. MP2 and B3LYP methods with standard basis sets up to 6-311+G(3df) and gradient techniques were used for the geometry optimizations and calculation of the vibrational properties. Transition states were optimized by the Synchronous Transit-guided Quasi-Newton (STQN) method, and torsional barrier heights were calculated from the relative energies of the TS and the stable structure with the zero-point energies of the species taken into account. All the computed TS structures show only one imaginary frequency, which corresponds to the torsion involved in the conformational transition.

**Supporting Information** (see footnote on the first page of this article): Observed and calculated vibrational data for (*sp–sp*) and (*ap–sp*) conformers; X-ray crystallographic data and structural refinement details.

## Acknowledgments

Financial support by the Volkswagen-Stiftung and the Deutsche Forschungsgemeinschaft is gratefully acknowledged. The Argentinean authors thank the ANPCYT-DAAD for the German-Argentinean cooperation Awards (PROALAR) and the DAAD Regional Program of Chemistry for Argentina. They also thank the Consejo Nacional de Investigaciones Científicas y Técnicas (CONICET), the Comisión de Investigaciones Científicas de la Provincia de Buenos Aires (CIC), República Argentina. They are indebted to the Facultad de Ciencias Exactas, Universidad Nacional de La Plata, República Argentina for financial support. M.F.E. and C.O.D.V. would like to express their gratitude to Holger Pernice, Plácido García, Mike Finze, Stefan Balters, and Stefan von Ahsen for friendship and valuable help in the laboratory work during their stay in Duisburg. C.O.D.V. especially acknowledges the DAAD, which generously sponsors the DAAD Regional Program of Chemistry for the Republica Argentina to support Latin-American students to study for their PhD in La Plata.

[1] M. L. Chodkiewicz, *J. Chem. Phys.* **2005**, *122*, 224107–224114.
[2] Y. A. Arnautova, A. Jagielska, H. A. Scheraga, *J. Phys. Chem. B* **2006**, *110*, 5025–5044.
[3] C. F. Matta, R. F. W. Bader, *Proteins Struct. Funct. Genet.* **2003**, *52*, 360–399.
[4] C. F. Matta, R. F. W. Bader, *Proteins Struct. Funct. Genet.* **2002**, *48*, 519–538.
[5] C. F. Matta, R. F. W. Bader, *Proteins Struct. Funct. Genet.* **2000**, *40*, 310–329.
[6] C. J. Marsden, B. J. Smith, *J. Phys. Chem.* **1988**, *92*, 347–353.
[7] C. J. Marsden, H. Oberhammer, O. Losking, H. Willner, *J. Mol. Struct.* **1989**, *193*, 233–245.
[8] C. J. Marsden, R. D. Brown, P. D. Godfrey, *J. Chem. Soc., Chem. Commun.* **1979**, 399–401.
[9] A. Yokozeki, S. H. Bauer, *J. Phys. Chem.* **1976**, *80*, 618–625.
[10] C. J. Marsden, B. Beagley, *J. Chem. Soc., Faraday Trans.* **1981**, *2*, 2213–2221.
[11] D. R. Alleres, D. L. Cooper, T. P. Cunningham, J. Gerratt, P. B. Karadakov, M. Raimondi, *J. Chem. Soc., Faraday Trans.* **1995**, *91*, 3357–3362.
[12] M. F. Erben, C. O. Della Védova, *Helv. Chim. Acta* **2003**, *86*, 2379–2395.
[13] H. Oberhammer, unpublished results.
[14] H.-G. Mack, C. O. Della Védova, H. Oberhammer, *J. Phys. Chem.* **1992**, *96*, 9215–9217.
[15] A. Hermann, S. E. Ulic, C. O. Della Védova, H. G. Mack, H. Oberhammer, *J. Fluorine Chem.* **2001**, *112*, 297–305.
[16] A. C. Fantoni, C. O. Della Védova, *J. Mol. Spectrosc.* **1992**, *154*, 240–245.
[17] S. E. Ulic, C. O. Della Védova, P. J. Aymonino, *J. Raman Spectrosc.* **1989**, *20*, 655–662.
[18] M. F. Erben, C. O. Della Védova, H. Willner, F. Trautner, H. Oberhammer, R. Boese, *Inorg. Chem.* **2005**, *44*, 7070–7077.
[19] J. R. Durig, J. F. Davis, G. A. Guirgis, *J. Mol. Struct.* **1994**, *328*, 19–35.
[20] M. F. Erben, C. O. Della Védova, R. M. Romano, R. Boese, H. Oberhammer, H. Willner, O. Sala, *Inorg. Chem.* **2002**, *41*, 1064–1071.
[21] N. L. Campbell, C. J. Gillis, D. Klapstein, W. M. Nau, W. J. Balfour, S. G. Fougère, *Spectrochim. Acta Sect. A* **1995**, *51*, 787–798.
[22] R. Boese, M. Nussbaumer, "In Situ Crystallisation Techniques" in *Organic Crystal Chemistry* (Ed.: D. W. Jones), Oxford University Press: Oxford, UK, **1994**, pp. 20–37.
[23] C. F. Matta, N. Castillo, R. J. Boyd, *J. Phys. Chem. A* **2005**, *109*, 3669–3681.
[24] A. R. Choudhury, U. K. Urs, T. N. GuruRow, K. Nagarajan, *J. Mol. Struct.* **2002**, *605*, 71–77.
[25] D. Chopra, K. Nagarajan, T. N. GuruRow, *Cryst. Growth Des.* **2005**, *5*, 1035–1039.
[26] F. T. Burling, B. M. Goldstein, *Acta Crystallogr., Sect. B* **1993**, *49*, 738–744.
[27] A. Bondi, *J. Phys. Chem.* **1964**, *68*, 441–451.
[28] F. T. Burling, B. M. Goldstein, *J. Am. Chem. Soc.* **1992**, *114*, 2313–2320.
[29] K. I. Gobbato, C. Leibold, S. Centeno, C. O. Della Védova, H.-G. Mack, H. Oberhammer, *J. Mol. Struct.* **1996**, *380*, 55–61.
[30] Q. Shen, R. Krisak, K. Hagen, *J. Mol. Struct.* **1995**, *346*, 13–19.
[31] C. O. Della Védova, R. M. Romano, H. Oberhammer, *J. Org. Chem.* **2004**, *69*, 5395–5398.
[32] R. M. Romano, C. O. Della Védova, A. J. Downs, H. Oberhammer, S. Parson, *J. Am. Chem. Soc.* **2001**, *123*, 12623–12631.
[33] M. F. Erben, C. O. Della Védova, *Inorg. Chem.* **2002**, *41*, 3740–3748.
[34] C. O. Della Védova, *Spectrochim. Acta Sect. A* **1991**, *47*, 1619–1626.
[35] H.-G. Mack, H. Oberhammer, C. O. Della Védova, *J. Phys. Chem.* **1991**, *95*, 4238–4241.
[36] K. I. Gobbato, C. O. Della Védova, H. G. Mack, H. Oberhammer, *Inorg. Chem.* **1996**, *35*, 6152–6157.
[37] S. E. Ulic, C. O. Della Védova, A. Hermann, H. G. Mack, H. Oberhammer, *Inorg. Chem.* **2002**, *41*, 5699–5705.
[38] S. E. Ulic, K. I. Gobbato, C. O. Della Védova, *J. Mol. Struct.* **1997**, *407*, 171–175.
[39] J. G. Breitzer, A. I. Smirnov, L. F. Szczepura, S. R. Wilson, T. B. Rauchfuss, *Inorg. Chem.* **2001**, *40*, 1421–1429.
[40] W. Gombler, H. Willner, *J. Phys. E* **1987**, *20*, 1286–1288.
[41] M. F. Erben, C. O. Della Védova, H. Willner, R. Boese, unpublished results.
[42] R. Minkwitz, J. Sawatzki, *Z. Anorg. Allg. Chem.* **1988**, *566*, 151–159.
[43] A. Haas, H. Reinke, *Angew. Chem.* **1967**, *79*, 687–688.
[44] A. Haas, H. Reinke, *Chem. Ber.* **1969**, *102*, 2718–2727.

 © 2006 Wiley-VCH Verlag GmbH & Co. KGaA, Weinheim 

[45] *SHELTX-Plus Version SGI IRIS Indigo*, a Complex Software Package for Solving, Refining and Displaying Crystal Structures; Siemens: Germany, **1991**.
[46] M. J. Frisch, G. W. Trucks, H. B. Schlegel, G. E. Scuseria, M. A. Robb, J. R. Cheeseman, J. A. Montgomery Jr, T. Vreven, K. N. Kudin, J. C. Burant, J. M. Millam, S. S. Iyengar, J. Tomasi, V. Barone, B. Mennucci, M. Cossi, G. Scalmani, N. Rega, G. A. Petersson, H. Nakatsuji, M. Hada, M. Ehara, K. Toyota, R. Fukuda, J. Hasegawa, M. Ishida, T. Nakajima, Y. Honda, O. Kitao, H. Nakai, M. Klene, X. Li, J. E. Knox, H. P. Hratchian, J. B. Cross, C. Adamo, J. Jaramillo, R. Gomperts, R. E. Stratmann, O. Yazyev, A. J. Austin, R. Cammi, C. Pomelli, J. W. Ochterski, P. Y. Ayala, K. Morokuma, G. A. Voth, P. Salvador, J. J. Dannenberg, V. G. Zakrzewski, S. Dapprich, A. D. Daniels, M. C. Strain, O. Farkas, D. K. Malick, A. D. Rabuck, K. Raghavachari, J. B. Foresman, J. V. Ortiz, Q. Cui, A. G. Baboul, S. Clifford, J. Cioslowski, B. B. Stefanov, G. Liu, A. Liashenko, P. Piskorz, I. Komaromi, R. L. Martin, D. J. Fox, T. Keith, M. A. Al-Laham, C. Y. Peng, A. Nanayakkara, M. Challacombe, P. M. W. Gill, B. Johnson, W. Chen, M. W. Wong, C. Gonzalez, J. A. Pople, *Gaussian 03*, revision B.04, Gaussian, Inc., Pittsburgh PA, **2003**.

Received: June 1, 2006
Published Online: September 7, 2006

 © 2006 Wiley-VCH Verlag GmbH & Co. KGaA, Weinheim 

DOI: 10.1002/ejic.200600638

# An Experimental and Density Functional Theory Approach Towards the Establishment of Preferential Metal- or Ligand-Based Electron-Transfer Processes in Large Quinonoid-Bridged Diruthenium Complexes $[\{(aap)_2Ru\}_2(\mu\text{-}BL^{2-})]^{n+}$ (aap = 2-Arylazopyridine)

**Sandeep Ghumaan,[a] Sriparna Mukherjee,[a] Sanjib Kar,[a] Dipankar Roy,[a] Shaikh M. Mobin,[a] Raghavan B. Sunoj,*[a] and Goutam Kumar Lahiri*[a]**

**Keywords:** Ruthenium / Bridging ligands / Radical ions / Density functional calculations / EPR spectroscopy

A group of ten quinonoid-bridged diruthenium(II) complexes $[(aap)_2Ru^{II}(\mu\text{-}BL_1^{2-})Ru^{II}(aap)_2](ClO_4)_2$, [**1a**–**1c**]$(ClO_4)_2$ and $[(pap)_2Ru^{II}(\mu\text{-}BL_n^{2-})Ru^{II}(pap)_2](ClO_4)_2$ [**2**–**8**]$(ClO_4)_2$ [aap = 2-arylazopyridine, $NC_5H_4$–N=N–$C_6H_4$(R) {R = H (pap) [**1a**]$(ClO_4)_2$, *m*-Me [**1b**]$(ClO_4)_2$, *m*-Cl [**1c**]$(ClO_4)_2$}; $BL^{2-}$ = 5,8-dioxido-1,4-napthoquinone ($BL_1^{2-}$), 2,3-dichloro-5,8-dioxido-1,4-napthoquinone ($BL_2^{2-}$), 6,11-dioxido-5,12-naphthacenedione ($BL_3^{2-}$), 1,4-dioxido-9,10-anthraquinone ($BL_4^{2-}$), 2,3-dimethyl-1,4-dioxido-9,10-anthraquinone ($BL_5^{2-}$), 6,7-dichloro-1,4-dioxido-9,10-anthraquinone ($BL_6^{2-}$), 1,4-diimino-9,10-anthraquinone ($BL_7^{2-}$), 1,5-dioxido-9,10-anthraquinone ($BL_8^{2-}$)] have been synthesized. The crystal structures of [**1a**]$(ClO_4)_2{\cdot}H_2O$ and [**3**]$(ClO_4)_2$ suggest the preferential crystallization of the *meso* isomer in both cases. The two similar C–O distances in coordinated $BL_1^{2-}$ [C2–O1/C4–O2 1.278(5)/1.291(4) Å] and $BL_3^{2-}$ [C2–O1/C4–O2 1.282(7)/1.280(7) Å] in [**1a**]$(ClO_4)_2$ and [**3**]$(ClO_4)_2$, respectively, and the corresponding intraring distances suggest a delocalized keto-enol state of the coordinated $BL^{2-}$. $[\mathbf{1}\text{–}\mathbf{8}]^{2+}$ exhibit two successive one-electron oxidation processes and multiple reductions in both $CH_3CN$ and $CH_2Cl_2$. The first oxidation potential varies substantially depending on a variety of factors associated with $BL^{2-}$ and follows the order: $[\mathbf{8}]^{2+} >> [\mathbf{2}]^{2+} > [\mathbf{6}]^{2+} > [\mathbf{1a}]^{2+} \geq [\mathbf{4}]^{2+} > [\mathbf{3}]^{2+} > [\mathbf{5}]^{2+} >> [\mathbf{7}]^{2+}$. The separation in potentials between the successive oxidation processes translates to comproportionation constant ($K_c$) values in the ranges $2.5\times10^4$–$2.6\times10^5$ and $1.7\times10^3$–$1.3\times10^6$ in $CH_3CN$ and $CH_2Cl_2$, respectively. The intermediate paramagnetic species $[\mathbf{1}\text{–}\mathbf{8}]^{3+}$ systematically exhibit closely spaced rhombic or axial-type EPR spectra at 77 K corresponding to *g* values close to the free-electron value of 2.0023, thereby suggesting a radical complex formulation of $\{Ru^{II}(\mu\text{-}BL^{\cdot-})Ru^{II}\}$ instead of the usually expected alternative mixed-valence formulation of $\{Ru^{II}(\mu\text{-}BL^{2-})Ru^{III}\}$. Consequently, $[\mathbf{1}\text{–}\mathbf{7}]^{3+}$ display intense near-infrared transitions in the range 1200–1500 nm with a band width at half height ($\Delta\nu_{1/2}$) of 1900–3800 $cm^{-1}$ which is lower than the calculated value of 3800–4600 $cm^{-1}$ obtained using the Hush formula for a localized class II mixed-valence system. Electrogenerated EPR-inactive second-step oxidized species $[\mathbf{1}\text{–}\mathbf{8}]^{4+}$ have been described as spin-coupled radical-bridged mixed-valence ruthenium(II)(III) species, $\{Ru^{II}(\mu\text{-}BL^{\cdot-})Ru^{III}\}$. $[\mathbf{1}\text{–}\mathbf{8}]^{2+}$ exhibit multiple ligand-based reductions involving coordinated $BL^{2-}$ as well as aap. The above preferential metal- or ligand-based accessible electron-transfer processes in the complexes have been further substantiated by DFT calculations on the geometry-optimized structure of $[\mathbf{1a}]^{2+}$.

(© Wiley-VCH Verlag GmbH & Co. KGaA, 69451 Weinheim, Germany, 2006)

## Introduction

The design of newer classes of ligand-bridged polyruthenium systems in combination with selective ancillary ligands $[\{(AL)Ru\}_n(\mu\text{-}BL)]^{n+}$ (AL = ancillary ligand and BL = bridging ligand) has drawn special attention in recent years,[1] particularly from the perspective of tuning intermetallic electronic coupling processes in their mixed-valence states, which, in turn, finds partial applications in fabricating molecular electronic devices[2] as well as the theoretical understanding of electron-transfer processes.[3] A large number of polyruthenium derivatives have been studied and a wide variation of coupling aspects, including moderately coupled localized class II, strongly coupled delocalized class III, and hybrid or borderline class II–III situations[4,5] have emerged that primarily depend on the electronic states of the specific set of bridging and ancillary ligands. Although different kinds of molecular frameworks have been utilized as bridging ligands for assembling metal fragments in place, only a limited number of diruthenium complexes with the following redox-active polynucleating quinonoid bridging (BL) units along with selective ancillary ligands (AL) are known so far: 1,10-phenanthroline-5,6-dione (AL =

[a] Department of Chemistry, Indian Institute of Technology, Powai, Mumbai 400076, India
Fax: +91-22-2572-3480
E-mail: lahiri@chem.iitb.ac.in

Supporting information for this article is available on the WWW under http://www.eurjic.org or from the author.

 © 2006 Wiley-VCH Verlag GmbH & Co. KGaA, Weinheim 

acac$^-$[6]/bpy[7]), 1,10-phenanthroline-5,6-diimine (acac$^-$),[6] 2,5-dioxido-1,4-benzoquininediimines (bpy/acac$^-$),[8] 2,5-dioxido-1,4-benzoquinones (bpy),[9] 5,8-dioxido-1,4-naphthoquinone (bpy),[10] 1,4-dioxidoanthraquinone (bpy),[11] 1,5-dioxidoanthraquinone (bpy),[11] 1,2,4,5-tetraimino-3,6-diketocyclohexane (bpy),[12] 3,3′,4,4′-tetraoxybiphenyl (bpy),[13] 3,3′,4,4′-tetraiminobiphenyl (acac$^-$[14]/bpy[15]), and *p*-benzoquinonediimine(NH$_3$)[16] (bpy = 2,2′-bipyridine, acac$^-$ = acetylacetonate). The remarkable mixing of ruthenium and quinonoid frontier orbitals[17] is expected to facilitate the bridging-ligand-mediated intermetallic coupling processes in such systems; however, it also creates additional challenges in assigning the precise valence state combinations of the metal ion and the bridging ligand in the native state as well as towards the accessible electron-transfer processes. The extent of mixing of ruthenium- and quinonoid-based orbitals and their subsequent participation in the electron-transfer processes are also influenced by the involvement of the ancillary ligands (AL)[8,14,15] in the resultant molecular orbitals, and this is essentially the reason for the present program of developing larger quinonoid-bridged diruthenium complexes encompassing strongly π-accepting 2-arylazopyridine (aap) as ancillary ligands.

The present article thus describes the synthesis of a group of ten diruthenium complexes [(aap)$_2$Ru$^{II}$(μ-BL$_n^{2-}$)-Ru$^{II}$(aap)$_2$](ClO$_4$)$_2$ [**1a**–**1c**](ClO$_4$)$_2$ and [**2**–**8**](ClO$_4$)$_2$ {BL$^{2-}$ = 5,8-dioxido-1,4-napthoquinone (BL$_1^{2-}$), 2,3-dichloro-5,8-dioxido-1,4-napthoquinone (BL$_2^{2-}$), 6,11-dioxido-5,12-naphthacenedione (BL$_3^{2-}$), 1,4-dioxido-9,10-anthraquinone(BL$_4^{2-}$), 2,3-dimethyl-1,4-dioxido-9,10-anthraquinone (BL$_5^{2-}$), 6,7-dichloro-1,4-dioxido-9,10-anthraquinone (BL$_6^{2-}$), 1,4-diimino-9,10-anthraquinone (BL$_7^{2-}$), and 1,5-dioxido-9,10-anthraquinone (BL$_8^{2-}$); aap = 2-arylazopyridine} and the crystal structures of two selected derivatives, namely [**1a**](ClO$_4$)$_2$ and [**3**](ClO$_4$)$_2$. The primary involvement of metal-, bridging-ligand-, or ancillary-ligand-based orbitals or a mixed situation in the accessible electron-transfer processes of the complexes has been scrutinized by UV/Vis/NIR spectroelectrochemistry and EPR investigations in combination with DFT/TDDFT calculations on the selected complex [**1a**]$^{2+}$. The specific effect of aap as an ancillary ligand in [**1**–**8**]$^{n+}$ with special reference to complexes with bpy[10,11] and BL$_1^{2-}$, BL$_4^{2-}$, and BL$_8^{2-}$ as bridging ligands are also highlighted.

## Results and Discussion

### Synthesis and Characterization

The present study deals with the eight quinonoid-based bridging ligands abbreviated as H$_2$BL$_{1-8}$. The bridging ligands differ in terms of their ring size (naphthaquinone- or anthraquinone-based frameworks), the substituents on the rings, and the positions of the donor centers in the rings. H$_2$BL$_7$ is the amine (NH$_2$) version of the hydroxy-containing H$_2$BL$_4$ (Scheme 1).

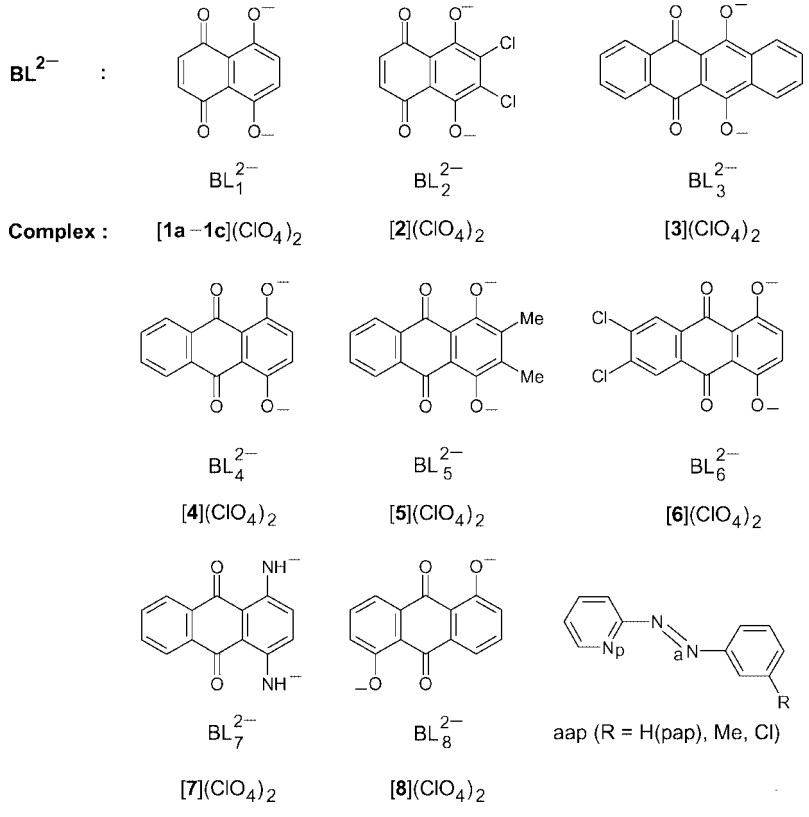


Scheme 1.

 © 2006 Wiley-VCH Verlag GmbH & Co. KGaA, Weinheim 

The complexes $[(pap)_2Ru^{II}(\mu\text{-}BL^{2-})Ru^{II}(pap)_2](ClO_4)_2$ {[**1a**]$(ClO_4)_2$ and [**2**–**8**]$(ClO_4)_2$; Scheme 1} were synthesized by following a general procedure involving treatment of the respective quinones ($H_2BL$) with an ethanolic solution of the metal precursor *ctc*-$[Ru^{II}(pap)_2(H_2O)_2](ClO_4)_2$ [pap = 2-phenylazopyridine; *ctc* = *cis*-*trans*-*cis* with respect to the aqua, pyridine ($N_p$), and azo ($N_a$) nitrogen atoms of pap, respectively} in the presence of sodium acetate as base under dinitrogen, followed by chromatographic purification on a neutral alumina column. The complexes [**1b**]$(ClO_4)_2$ and [**1c**]$(ClO_4)_2$ have 2-(*m*-tolylazo)pyridine and 2-(*m*-chlorophenylazo)pyridine, respectively, as ancillary ligands in combination with $BL_1^{2-}$ (Scheme 1).

The *tc*-configuration [*tc* = *trans* and *cis* with respect to the pyridine ($N_p$) and azo ($N_a$) nitrogens, respectively] as well as the $Ru^{II}$ state of the precursor metal fragment $\{Ru^{II}(pap)_2\}$ remain unaltered in complexes [**1**–**8**]$(ClO_4)_2$ (see below).

Although the reactions ideally lead to a mixture of *meso* ($\Delta\Lambda$) and *rac* ($\Delta\Delta/\Lambda\Lambda$) isomers,[18] the appearance of only one band, even on the preparatory TLC plate, in each case suggests either the presence of one particular diastereoisomeric form or an intimate mixture of *meso* and *rac* isomers in solution. The crystal structures of [**1a**]$(ClO_4)_2$ and [**3**]$(ClO_4)_2$ suggest the preferential crystallization of the *meso* isomer in both cases (see below).

The complexes are fairly soluble in polar ($CH_3CN$, DMF) as well as nonpolar ($CH_2Cl_2$) solvents. The diamagnetic (low-spin $Ru^{II}$, $t_{2g}^6$) complexes [**1**–**8**]$(ClO_4)_2$ are 1:2 conductors in $CH_3CN$ and their microanalytical data (C,H,N) are in good agreement with the calculated values (see Exp. Sect.). The formation of the complexes was further confirmed by their electrospray mass spectroscopic data in $CH_3CN$ (see Table 1 and Figure 1). The $^1H$ NMR spectra in $CDCl_3$ or $(CD_3)_2SO$ show partially overlapping signals corresponding to half of the molecule due to internal symmetry (see Figure 2 and Exp. Sect.). The closeness of the chemical shifts of the signals of several protons makes them appear as overlapping clusters. The ν(C=O) stretching frequency of the free $H_2BL$ ligands (1616–1636 $cm^{-1}$) is absent in the IR spectra of the complexes, where a sharp peak appears in the range 1520–1582 $cm^{-1}$, thus indicating a delocalized keto-enol state of the coordinated bridging ligand $BL^{2-}$.[19] The delocalized keto-enol state of $BL^{2-}$ is also clearly evidenced in the crystal structures of [**1a**]$(ClO_4)_2$ and [**3**]$(ClO_4)_2$ (see below). The $ClO_4^-$ vibrations for all the complexes and the NH stretching fre-

Table 1. Mass spectroscopic data (*m*/*z*) in acetonitrile for [**1**–**8**]$(ClO_4)_2$.

| Compound | Observed | Assignment | Calculated |
|---|---|---|---|
| [**1a**]$(ClO_4)_2$ | 1224.18 | $[\{\mathbf{1a}\}ClO_4]^+$ | 1223.08 |
| [**1b**]$(ClO_4)_2$ | 1279.14 | $[\{\mathbf{1b}\}ClO_4]^+$ | 1279.14 |
| [**1c**]$(ClO_4)_2$ | 1359.78 | $[\{\mathbf{1c}\}ClO_4]^+$ | 1358.93 |
| [**2**]$(ClO_4)_2$ | 1290.51 | $[\{\mathbf{2}\}ClO_4]^+$ | 1291.01 |
| [**3**]$(ClO_4)_2$ | 1322.97 | $[\{\mathbf{3}\}ClO_4]^+$ | 1323.12 |
| [**4**]$(ClO_4)_2$ | 1273.27 | $[\{\mathbf{4}\}ClO_4]^+$ | 1273.10 |
| [**5**]$(ClO_4)_2$ | 1301.41 | $[\{\mathbf{5}\}ClO_4]^+$ | 1301.13 |
| [**6**]$(ClO_4)_2$ | 1340.86 | $[\{\mathbf{6}\}ClO_4]^+$ | 1341.02 |
| [**7**]$(ClO_4)_2$ | 1270.95 | $[\{\mathbf{7}\}ClO_4]^+$ | 1271.13 |
| [**8**]$(ClO_4)_2$ | 1274.02 | $[\{\mathbf{8}\}ClO_4]^+$ | 1273.10 |

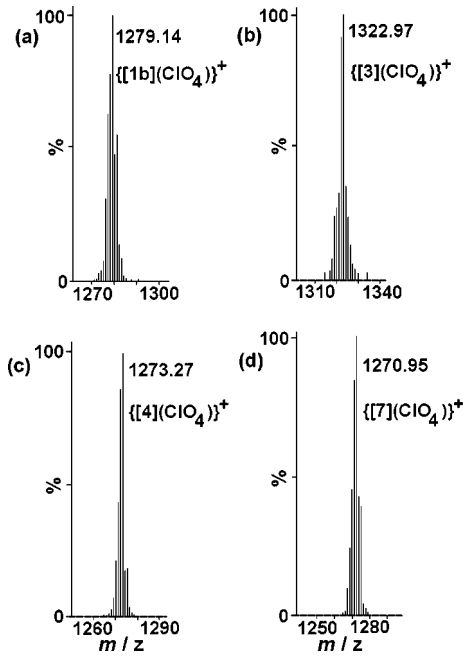


Figure 1. Mass spectra of [**1b**]$(ClO_4)_2$ (a), [**3**]$(ClO_4)_2$ (b), [**4**]$(ClO_4)_2$ (c), and [**7**]$(ClO_4)_2$ (d) in $CH_3CN$.

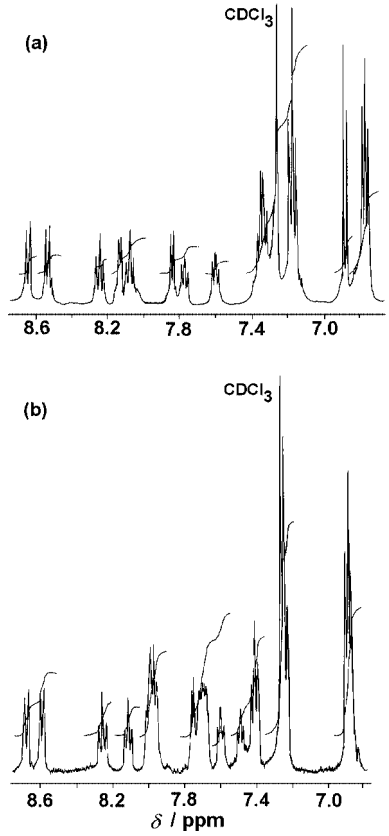


Figure 2. $^1H$ NMR spectra of [**1a**]$(ClO_4)_2$ (a) and [**3**]$(ClO_4)_2$ (b) in $CDCl_3$.

 © 2006 Wiley-VCH Verlag GmbH & Co. KGaA, Weinheim 

quency of the coordinated $BL_7^{2-}$ in [**7**]$(ClO_4)_2$ appear in the expected positions of 1100/625 and 3260 $cm^{-1}$, respectively (see Exp. Sect.).

### Crystal Structures of [1a]$(ClO_4)_2 \cdot H_2O$ and [3]$(ClO_4)_2$

The crystal structures of [**1a**]$(ClO_4)_2 \cdot H_2O$ and [**3**]$(ClO_4)_2$ are shown in Figures 3 and 4, respectively. Selected crystallographic parameters are given in the Exp. Sect. and bond lengths and angles are listed in Table 2. Both structures contain a crystallographic inversion center. Each Ru ion is bonded symmetrically to the dianionic bridging ligand $BL^{2-}$ through the two oxygen donor centers at each end. The Ru centers are nearly coplanar with the bridging ligand; the angles between the planes consisting of the chelate ring containing the Ru ion to the bridging ligand and the planar bridging ligand are 1.57(0.71)° and 3.17(0.81)° for [**1a**]$(ClO_4)_2$ and [**3**]$(ClO_4)_2$, respectively. The $RuO_2N_4$ chromophore is in a distorted octahedral arrangement, as can be seen from the angles around the metal ion (Table 2). The two similar C–O distances in coordinated $BL_1^{2-}$ [C2–O1/C4–O2 1.278(5)/1.291(4) Å] and $BL_3^{2-}$ [C2–O1/C4–O2 1.282(7)/1.280(7) Å] and the corresponding intra-ring distances (Table 2) in [**1a**]$(ClO_4)_2$ and [**3**]$(ClO_4)_2$, respectively, signify the delocalized keto-enol state of the coordinated $BL^{2-}$.[19–21] The calculated (B3LYP/SDD, 6-31G* level of theory) bond lengths/angles and atomic charges of the dianionic form of free $BL_1^{2-}$ (Figure 5 and Table 3; coordinates for the optimized $BL_1^{2-}$ are given in Table S1 in the Supporting Information) also suggest its delocalized state. The $Ru^{II}$–O($BL^{2-}$) distances [Ru1–O1/Ru1–O2 2.025(3)/2.038(3) and 2.009(4)/2.016(4) Å in [**1a**]$(ClO_4)_2$ and [**3**]$(ClO_4)_2$, respectively] agree well with known $Ru^{II}$–O (acetylacetonate, keto-enol delocalized form) distances.[21] The Ru–Ru separations in [**1a**]$(ClO_4)_2$ and [**3**]$(ClO_4)_2$ are 8.327 and 8.338 Å, respectively.

The {Ru(pap)$_2$} fragment is in a *tc*-configuration (*tc* = *trans* and *cis* with respect to the pyridine and azo nitrogens

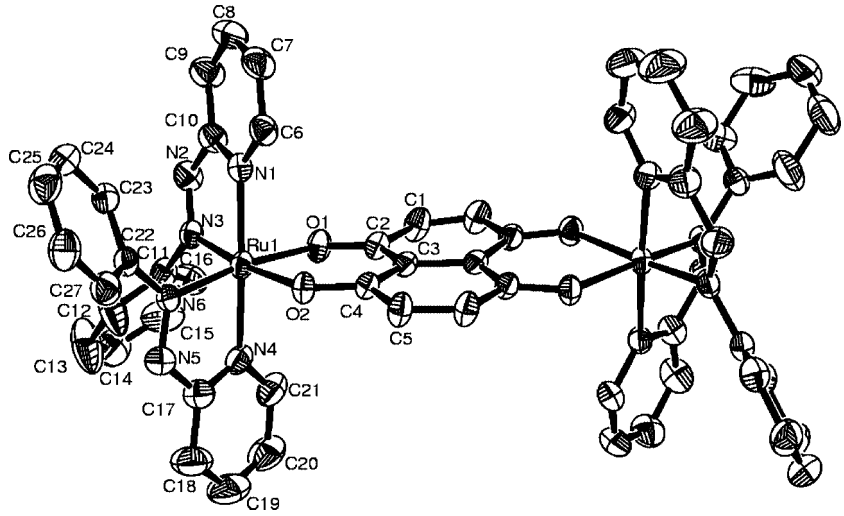


Figure 3. Crystal structure of the cation of [**1a**]$(ClO_4)_2$. Ellipsoids are drawn at 30% probability.

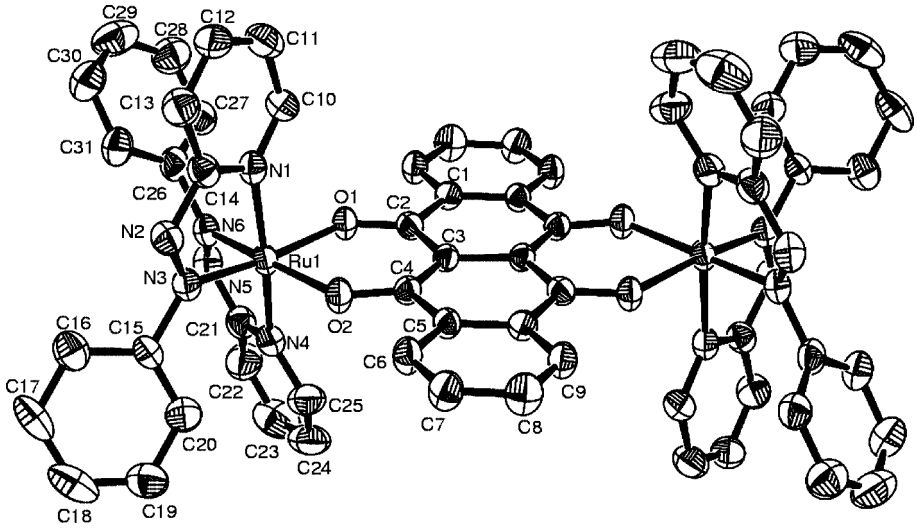


Figure 4. Crystal structure of the cation of [**3**]$(ClO_4)_2$. Ellipsoids are drawn at 30% probability.

 © 2006 Wiley-VCH Verlag GmbH & Co. KGaA, Weinheim 

Table 2. Experimental and calculated bond lengths [Å] and angles [°] for [**1a**]$(ClO_4)_2$ and [**3**]$(ClO_4)_2$.

| | [**1a**]$(ClO_4)_2$ Exp.[a] | Comp.[b] | [**3**]$(ClO_4)_2$ Exp. | | [**1a**]$(ClO_4)_2$ Exp.[a] | Comp.[b] | [**3**]$(ClO_4)_2$ Exp. |
|---|---|---|---|---|---|---|---|
| Ru(1)–N(1) | 2.041(4) | 2.071 | 2.030(6) | N(3)–Ru(1)–N(6) | 98.53(14) | 101.8 | 98.1(2) |
| Ru(1)–N(3) | 1.957(3) | 2.035 | 2.006(6) | N(3)–Ru(1)–O(1) | 87.92(14) | 86.3 | 169.1(2) |
| Ru(1)–N(4) | 2.034(4) | 2.071 | 2.058(6) | N(6)–Ru(1)–O(1) | 170.97(12) | 169.5 | 87.20(19) |
| Ru(1)–N(6) | 2.018(3) | 2.035 | 1.959(5) | N(3)–Ru(1)–N(4) | 98.85(15) | 102.7 | 106.5(2) |
| Ru(1)–O(1) | 2.025(3) | 2.059 | 2.009(4) | N(6)–Ru(1)–N(4) | 76.86(15) | 76.8 | 76.6(3) |
| Ru(1)–O(2) | 2.038(3) | 2.059 | 2.016(4) | O(1)–Ru(1)–N(4) | 95.97(15) | 94.9 | 83.9(2) |
| N(2)–N(3) | 1.284(5) | 1.286 | 1.298(7) | N(3)–Ru(1)–O(2) | 172.99(13) | 169.5 | 89.13(19) |
| N(5)–N(6) | 1.288(5) | 1.286 | 1.281(8) | N(6)–Ru(1)–O(2) | 86.54(12) | 86.3 | 171.8(2) |
| C(2)–O(1) | 1.278(5) | 1.289 | 1.282(7) | O(1)–Ru(1)–O(2) | 87.61(12) | 86.6 | 86.27(17) |
| C(4)–O(2) | 1.291(4) | 1.289 | 1.280(7) | N(4)–Ru(1)–O(2) | 86.99(13) | 85.7 | 97.8(2) |
| C(1)–C(2) | 1.443(6) | 1.450 | 1.457(9) | N(3)–Ru(1)–N(1) | 77.21(14) | 76.8 | 76.4(2) |
| C(2)–C(3) | 1.426(5) | 1.433 | 1.424(8) | N(6)–Ru(1)–N(1) | 103.17(14) | 102.7 | 94.8(2) |
| C(3)–C(4) | 1.408(5) | 1.433 | 1.412(8) | O(1)–Ru(1)–N(1) | 84.36(13) | 85.7 | 93.7(2) |
| C(4)–C(5) | 1.438(6) | 1.450 | 1.466(8) | N(4)–Ru(1)–N(1) | 176.05(14) | 179.2 | 171.2(2) |
| C(5)–C(6) | – | – | 1.410(8) | O(2)–Ru(1)–N(1) | 96.97(13) | 94.9 | 90.5(2) |
| C(6)–C(7) | – | – | 1.369(10) | O(1)–C(2)–C(3) | 126.6(4) | 126.9 | 126.3(6) |
| C(7)–C(8) | – | – | 1.359(10) | C(3)–C(2)–C(1) | 118.6(4) | 118.6 | 120.1(6) |
| C(8)–C(9) | – | – | 1.413(9) | C(4)–C(3)–C(2) | 121.6(3) | 120.8 | 120.6(5) |
| C(1)–C(1)#1 | 1.326(9) | 1.351 | – | O(2)–C(4)–C(3) | 126.8(3) | 129.9 | 126.0(5) |
| C(3)–C(3)#1 | 1.469(7) | 1.464 | 1.452(11) | C(3)–C(4)–C(5) | 118.8(3) | 118.6 | 119.9(5) |
| C(5)–C(5)#1 | 1.327(8) | 1.351 | – | | | | |
| C(1)–C(5)#1 | – | – | 1.383(8) | | | | |
| C(5)–C(1)#1 | – | – | 1.383(8) | | | | |

[a] From X-ray crystal data. [b] Calculated at the B3LYP level of theory (see Exp. Sect.).

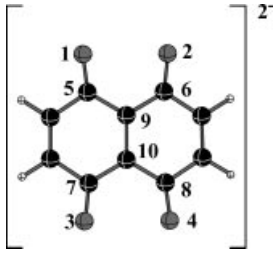


Figure 5. The B3LYP,6-31G*-optimized geometry for the singlet ground state of $[BL_1]^{2-}$.

Table 3. Selected geometrical parameters and atomic charges for the free $BL_1^{2-}$ ligand optimized at the B3LYP/6-31G* level of theory.

| Bond lengths [Å] | | Bond and dihedral angles [°] | |
|---|---|---|---|
| O1–C5 | 1.262 | O1–C5–C9 | 127.5 |
| O2–C6 | 1.262 | O2–C6–C9 | 127.5 |
| O3–C7 | 1.262 | O3–C7–C10 | 127.5 |
| O4–C8 | 1.262 | O4–C8–C10 | 127.5 |
| C5–C9 | 1.459 | O1–C5–C6–O2 | 0.00 |
| C9–C6 | 1.459 | O3–C7–C8–O4 | 0.00 |
| C9–C10 | 1.474 | O1–C5–C8–O4 | 180.0 |
| C7–C10 | 1.459 | O2–C6–C7–O3 | 180.0 |
| C10–C8 | 1.459 | | |
| Atomic charges | | | |
| O1 | –0.64 | C5 | 0.34 |
| O2 | –0.64 | C6 | 0.34 |
| O3 | –0.64 | C7 | 0.34 |
| O4 | –0.64 | C8 | 0.34 |

of pap, respectively), as is the case in the precursor complex.[22] The shortness of the Ru–N(azo) bonds [Ru1–N3 1.957(3) and 2.006(6), Ru1–N6 2.018(3) and1.959(5) Å for [**1a**]$(ClO_4)_2$ and [**3**]$(ClO_4)_2$, respectively] compared to the Ru–N(pyridine) bonds [Ru1–N1 2.041(4) and 2.030(6), Ru1–N4 2.034(4) and2.058(6) Å in [**1a**]$(ClO_4)_2$ and [**3**]$(ClO_4)_2$, respectively] reflects the π-back-bonding interaction $Ru^{II}(d\pi)\rightarrow pap(\pi*)$, where the pap(π*) level is predominantly azo in character.[23] A consequence of this is that the azo(N=N) distances of the coordinated pap ligand [N2–N3 1.284(5) and 1.297(7), N5–N6 1.288(5) and 1.281(8) Å in [**1a**]$(ClO_4)_2$ and [**3**]$(ClO_4)_2$, respectively] are significantly longer than that calculated (B3LYP,6-31G* level of theory) for the free pap ligand (1.259 Å, see Figure 6 and Table 4; coordinates for the optimized pap ligand are given in Table S2 in the Supporting Information), as is also the case in other reported complexes of arylazopyridine ligands.[24]

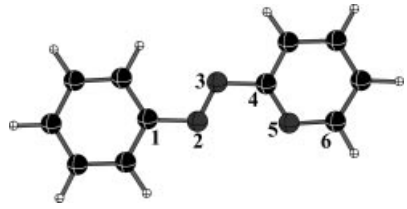


Figure 6. The B3LYP,6-31G*-optimized geometry for the singlet ground state of pap.

The optimized geometry of $[\mathbf{1a}]^{2+}$ is shown in Figure 7 and a selected list of optimized geometrical details of $[\mathbf{1a}]^{2+}$ is provided in Table 2 (coordinates and a full list of bond lengths and angles for the optimized $[\mathbf{1a}]^{2+}$ are provided in Tables S3 and S4, respectively, in the Supporting Information). In general, the computed structural details of $[\mathbf{1a}]^{2+}$ are in good agreement with the experimental param-

 © 2006 Wiley-VCH Verlag GmbH & Co. KGaA, Weinheim 

Table 4. Selected geometrical parameters and atomic charges of the free 2-(phenylazo)pyridine (pap) ligand obtained at the B3LYP/6-31G* level of theory.

| Bond lengths [Å] | | Bond and dihedral angles [°] | |
|---|---|---|---|
| C1–N2 | 1.419 | C1–N2–N3 | 114.45 |
| N2–N3 | 1.259 | N2–N3–C4 | 114.86 |
| N3–C4 | 1.425 | N3–C4–N5 | 121.76 |
| C4–N5 | 1.340 | C4–N5–C6 | 117.21 |
| N5–C6 | 1.333 | C1–N2–N3–C4 | 179.27 |
| | | N2–N3–C4–N5 | 8.38 |
| | | N3–C4–N5–C6 | 179.55 |
| Atomic charges | | | |
| C1 | 0.26 | C4 | 0.46 |
| N2 | –0.26 | N5 | –0.43 |
| N3 | –0.31 | C6 | 0.04 |

eters (Table 2). The calculated bond lengths of the coordinated $BL_1^{2-}$ ligand in $[\mathbf{1a}]^{2+}$ also suggest its delocalized keto-enol nature.

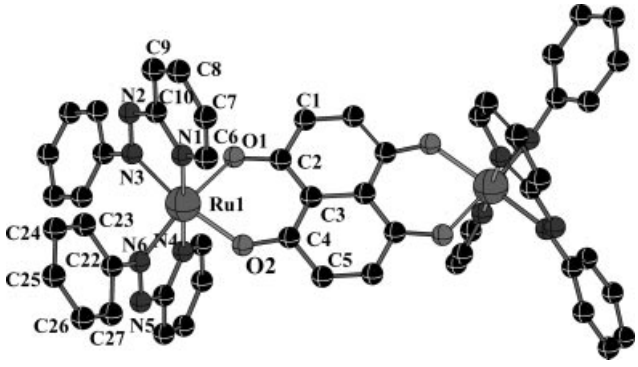


Figure 7. The B3LYP/SDD,6-31G*-optimized geometry for the singlet ground state of $[\mathbf{1a}]^{2+}$.

It should be noted that to the best of our knowledge $[\mathbf{1a}](ClO_4)_2$ and $[\mathbf{3}](ClO_4)_2$ are the first structurally characterized diruthenium complexes bridged by $BL^{2-}$, although the crystal structures of $[\{Co(tripod)\}_2(\mu\text{-}BL_1^{2-})]^{2+}$/$[\{Co(tripod)\}_2(\mu\text{-}BL_4^{2-})]^{2+}$ [tripod = $MeC(CH_2PPh_2)_3$],[25] $[\{Ph_4Sb\}_2(\mu\text{-}BL_1^{2-})]$,[26] $[Cu_2(dien)_2(\mu\text{-}BL_1^{2-})](BPh_4)_2$ (dien = diethylenetriamine),[27] $[\{Fe(salen)\}_2(\mu\text{-}BL_4^{2-})]$ [salen = *N*,*N*′-bis(salicylaldehyde)ethylenediimine],[28] and $[\{Rh(CO)(PPh_3)\}_2(\mu\text{-}BL_7^{2-})]$[29] have been reported.

## Electrochemistry, EPR Spectroscopy, Spectrolectrochemistry, and Density Functional Calculations

Complexes $[\mathbf{1}–\mathbf{8}](ClO_4)_2$ exhibit two successive one-electron oxidation processes and multiple reductions in both $CH_3CN$ and $CH_2Cl_2$ (Figure 8 and Table 5). The first oxidation potential of $BL_1^{2-}$-bridged $[\mathbf{1a}]^{2+}$–$[\mathbf{1c}]^{2+}$ varies slightly based on the electronic effect of the R group attached to the framework of the ancillary ligand (Scheme 1).[30]

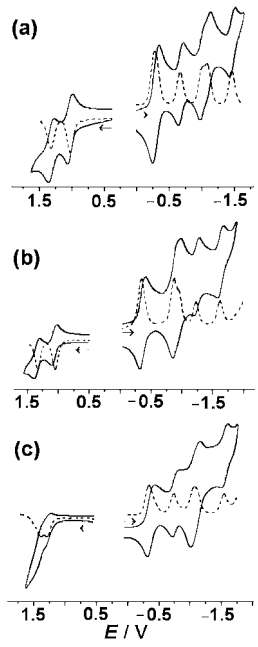


Figure 8. Cyclic voltammograms (—) and differential pulse voltammograms (----) of $10^{-3}$ M solutions of $[\mathbf{1a}](ClO_4)_2$ (a), $[\mathbf{4}](ClO_4)_2$ (b), and $[\mathbf{8}](ClO_4)_2$ (c) in $CH_3CN$/0.1 M $Et_4NClO_4$ at 298 K (scan rate: 50 mV $s^{-1}$).

The potentials of the complexes with pap in combination with different $BL^{2-}$ ligands ($[\mathbf{1a}]^{2+}$ and $[\mathbf{2}]^{2+}$–$[\mathbf{8}]^{2+}$) vary substantially due to a variety of parameters associated with $BL_n^{2-}$, such as (i) the electronic nature of the substituents in $BL_n^{2-}$, (ii) the number of fused rings involved, (iii) the relative position of the oxygen donor centers in the anthracene ring ($BL_4^{2-}$ and $BL_8^{2-}$), and (iv) the difference in donor centers in $BL_4^{2-}$ (oxido) and $BL_7^{2-}$ (iminium). The first oxidation potential follows the order $[\mathbf{8}]^{2+} >> [\mathbf{2}]^{2+} > [\mathbf{6}]^{2+} > [\mathbf{1a}]^{2+} \geq [\mathbf{4}]^{2+} > [\mathbf{3}]^{2+} > [\mathbf{5}]^{2+} >> [\mathbf{7}]^{2+}$ in both $CH_3CN$ and $CH_2Cl_2$ (Table 5). The separation in potentials between the successive oxidation processes ($\Delta E$) translates to the comproportionation constant $K_c$ [derived from $RT\ln K_c = nF(\Delta E)$[31]], which has values in the range of $2.3\times10^2$–$1.2\times10^5$ in $CH_3CN$ (Table 5). The variation of the electronic nature of the substituents in the framework of the ancillary ligands (H, Me, Cl) with the same $BL_1^{2-}$ bridging unit in $[\mathbf{1a}]^{2+}$–$[\mathbf{1c}]^{2+}$ has a small effect on the coupling processes. However, it is significantly large as in pap complexes $[\mathbf{1a}]^{2+}$ and $[\mathbf{2}]^{2+}$–$[\mathbf{8}]^{2+}$ with different $BL_n^{2-}$ ligands. Complex $[\mathbf{8}]^{2+}$ shows the smallest electrochemical coupling ($K_c$) due to its larger Ru–Ru separation, which is a result of the spreading of donor centers (O,O,O,O) over all three available rings in the anthracene backbone unlike all other complexes ($[\mathbf{1}]^{2+}$–$[\mathbf{7}]^{2+}$), where only two consecutive fused rings are involved. The $\Delta E$ value, however, increases in $CH_2Cl_2$ in each case, leading to relatively higher $K_c$ values of $1.7\times10^3$–$1.3\times10^6$ (Table 5). The $K_c$ values of the complexes are suggestive of an electrochemically moderately coupled, localized, class II mixed-valence situation.[32] The only other related diruthenium derivatives of large quinones (Scheme 1) with AL = bpy, namely $[\{(bpy)_2Ru\}_2(\mu\text{-}$

 © 2006 Wiley-VCH Verlag GmbH & Co. KGaA, Weinheim 

Table 5. Electrochemical data in acetonitrile (AN) and dichloromethane (DCM).

| | Solv. | Oxidation couple $E°_{298}$ [V] ($\Delta E_p$ [mV]) | $\Delta E$ [mV], $K_c$ | Reduction couple $E°_{298}$ [V] ($\Delta E_p$ [mV]) |
|---|---|---|---|---|
| $[\mathbf{1a}]^{2+}$ | AN | 1.06 (69), 1.36 (70) | 300, $1.2\times10^5$ | –0.30 (97),[a] –0.68 (72), –1.00 (62), –1.12 (64), –1.47 (75) |
| | DCM | 1.13 (58), 1.46 (76) | 330, $3.9\times10^5$ | –0.33 (160),[a] –0.86 (118), –1.10 (96), –1.24 (92), –1.55 (126) |
| $[\mathbf{1b}]^{2+}$ | AN | 1.05 (61), 1.34 (60) | 290, $8.2\times10^4$ | –0.40 (65),[a] –0.85 (100),[a] –0.94 (80), –1.18 (90), –1.53 (93) |
| | DCM | 1.11 (57), 1.43 (58) | 320, $2.6\times10^5$ | –0.22 (81), –0.61 (109), –0.78 (40), –1.18 (100), –1.68 (50) |
| $[\mathbf{1c}]^{2+}$ | AN | 1.09 (71), 1.40 (71) | 310, $1.8\times10^5$ | –0.26 (100),[a] –0.67 (53), –0.89 (120),[a] –1.48 (68) |
| | DCM | 1.16 (90), 1.48 (50) | 320, $2.6\times10^5$ | –0.27 (110), 0.56 (30), –0.75 (40), –0.90 (50), –1.04 (80), –1.42 (80) |
| $[\mathbf{2}]^{2+}$ | AN | 1.14 (76), 1.41 (80) | 270, $3.8\times10^4$ | –0.36 (90),[a] –0.71 (66), –1.07 (60), –1.20 (62), –1.50 (61) |
| | DCM | 1.20 (86), 1.52 (68) | 320, $2.6\times10^5$ | –0.29 (89),[a] –0.82 (40), –1.19 (60), –1.48 (40) |
| $[\mathbf{3}]^{2+}$ | AN | 0.99 (79), 1.25 (80) | 260, $2.5\times10^4$ | –0.40 (59),[a] –0.94 (66),[a] –1.43 (60), –1.76 (73) |
| | DCM | 1.10 (72), 1.38 (60) | 280, $5.5\times10^4$ | –0.31 (130),[a] –0.99 (62),[a] –1.42 (42), –1.76 (93) |
| $[\mathbf{4}]^{2+}$ | AN | 1.04 (79), 1.33 (79) | 290, $8.2\times10^4$ | –0.38 (95),[a] –0.88 (120),[a] –0.97 (68), –1.24 (79), –1.63 (78) |
| | DCM | 1.13 (168), 1.47 (162) | 340, $5.7\times10^5$ | –0.33 (110),[a] –0.96 (55), –1.14 (150), –1.49 (170), –1.85 (150) |
| $[\mathbf{5}]^{2+}$ | AN | 0.98 (59), 1.28 (69) | 300, $1.2\times10^5$ | –0.40 (81), –0.93 (120),[a] –1.37 (67), –1.76 (63) |
| | DCM | 1.05 (121), 1.41 (142) | 360, $1.3\times10^6$ | –0.35 (130),[a] –0.98 (120), –1.15 (140), –1.51 (180), –1.84 (170) |
| $[\mathbf{6}]^{2+}$ | AN | 1.08 (74), 1.36 (86) | 280, $5.6\times10^4$ | –0.37 (120),[a] –0.90 (126),[a] –1.57 (74), –1.95 (60) |
| | DCM | 1.17 (131), 1.52 (110) | 350, $8.5\times10^5$ | –0.30 (144),[a] –1.00 (140),[a] –1.37 (160), –1.70 (180) |
| $[\mathbf{7}]^{2+}$ | AN | 0.54 (95), 0.84 (76) | 300, $1.2\times10^5$ | –0.47 (96),[a] –0.80 (46), –1.04 (72),[a] –1.64 (80), –1.90 (67) |
| | DCM | 0.60 (115), 0.93 (105) | 330, $4.0\times10^5$ | –0.42 (180),[a] –0.95 (140), –1.13 (120), –1.68 (160) |
| $[\mathbf{8}]^{2+}$ | AN | 1.26 (34), 1.40 (74) | 140, $2.3\times10^2$ | –0.36 (80),[a] –0.75 (65), –1.05 (43),[a] –1.56 (57) |
| | DCM | 1.36 (77), 1.55 (54) | 190, $1.7\times10^3$ | –0.31 (151),[a] –0.88 (100), –1.16 (170), –1.41 (110), –1.58 (60) |

[a] Two-electron transfer process.

$BL_1^{2-})]^{2+}$,[10] $[\{(bpy)_2Ru\}_2(\mu\text{-}BL_4^{2-})]^{2+}$,[11] and $[\{(bpy)_2Ru\}_2(\mu\text{-}BL_8^{2-})]^{2+}$,[11] exhibit $K_c$ values of $1.8\times10^5$, $3.7\times10^4$ and $3.4\times10^2$, respectively, in $CH_3CN$, similar to those of the corresponding pap complexes $[\mathbf{1}]^{2+}$, $[\mathbf{4}]^{2+}$, and $[\mathbf{8}]^{2+}$ (Table 5) in spite of the much stronger π-acceptor characteristics of pap relative to bpy.[33]

Both the metal ion and the bridging ligand in $[\mathbf{1}]^{2+}$–$[\mathbf{8}]^{2+}$ (Scheme 2) are able to undergo successive two-step one-electron oxidations with formation of paramagnetic intermediate species. Therefore, the preferential involvement of metal- or ligand-based frontier orbitals in the first oxidation process was ascertained from the EPR characteris-

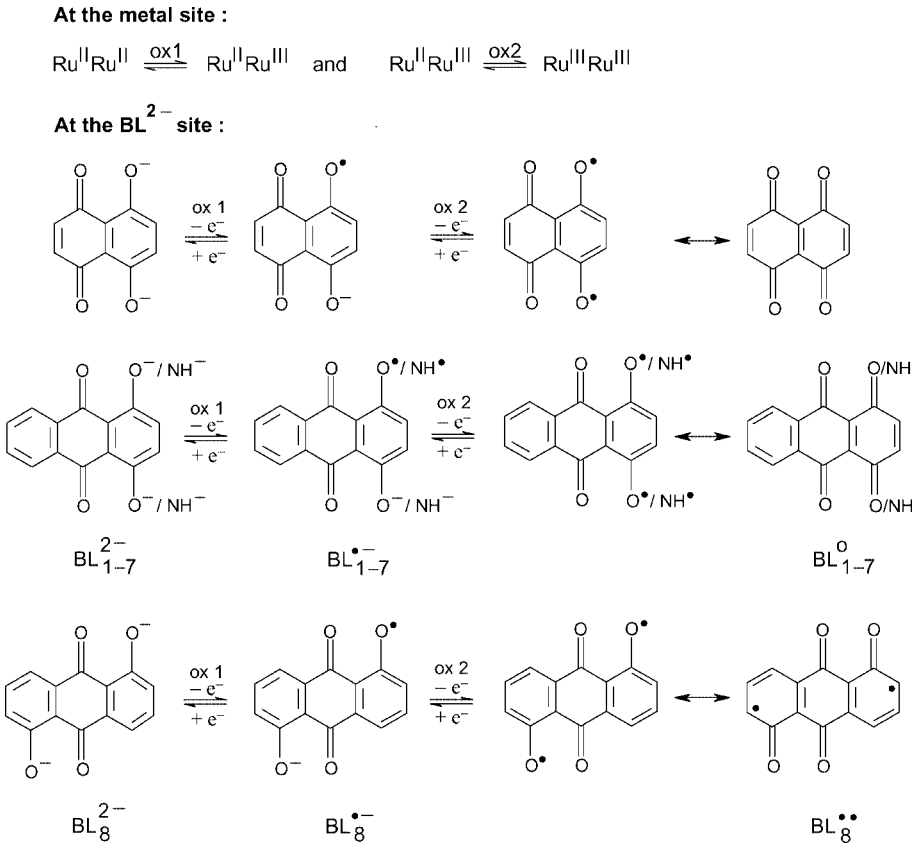


Scheme 2.

 © 2006 Wiley-VCH Verlag GmbH & Co. KGaA, Weinheim 

tics of the electrogenerated one-electron oxidized species in each case. The intermediate paramagnetic species $[\mathbf{1}–\mathbf{8}]^{3+}$ systematically exhibit closely spaced rhombic or axial-type EPR spectra at 77 K (Figure 9 and Table 6). However, analysis of the EPR spectra, especially the small $g$ anisotropy ($\Delta g = g_1 - g_3 = 0.0078–0.0642$) and the average $g$ $\{<g> = [(g_1^2 + g_2^2 + g_3^2)/3]^{1/2} \approx 2.00\}$,[34] which is close to the free electron value of 2.0023, clearly suggest a radical complex[35] with the formulation $Ru^{II}(\mu\text{-}BL^{\cdot-})Ru^{II}$ for $[\mathbf{1}–\mathbf{8}]^{3+}$ instead of the mixed-valence alternative $Ru^{II}(\mu\text{-}BL^{2-})Ru^{III}$. However, the observed small splitting of the EPR spectra implies a minority contribution of a paramagnetic $Ru^{III}$ ion in the singly occupied molecular orbital (SOMO) as well, which leads to the alternative mixed-valence formulation $Ru^{II}(\mu\text{-}BL^{2-})Ru^{III}$.[36] The appreciable effect of the electronic structure of $BL^{2-}$ on the first oxidation potential of $[\mathbf{1}–\mathbf{8}]^{2+}$ (Table 5) indeed justifies its preferential involvement. The above assignments are in good agreement with the computed HOMO energies of $[\mathbf{1a}]^{2+}$ at the B3LYP level (Figure 10 and Table 7). The contribution of 68% $\pi(BL_1^{2-})$ along with 22% $d\pi(Ru)$ in the HOMO level essentially justifies the preferential primary involvement of $BL_1^{2-}$ instead of $Ru^{II}$ in the first oxidized state, as clearly evidenced in the EPR spectra of $[\mathbf{1}–\mathbf{8}]^{3+}$. The intermediate one-electron oxidized species for the analogous bpy complexes $[\{(bpy)_2Ru\}_2(\mu\text{-}BL_1^{2-})]^{3+}$,[10] $[\{(bpy)_2Ru\}_2(\mu\text{-}BL_4^{2-})]^{3+}$,[11] and $[\{(bpy)_2Ru\}_2(\mu\text{-}BL_8^{2-})]^{3+}$[11] were, however, ascribed to a mixed-valence $Ru^{II}Ru^{III}$ situation based on the EPR spectrum of the isolated polycrystalline $[\{(bpy)_2Ru\}_2(\mu\text{-}BL_1^{2-})]^{3+}$ at 77 K ($g_1 = 2.33$, $g_2 = 2.01$, and $g_3 = 1.88$; $\Delta g = 0.45$ and $<g> = 2.08$) and the near-IR transition at 2083 nm in $CH_3CN$ ($\varepsilon = 9120\ M^{-1}cm^{-1}$, $\Delta\nu_{1/2} = 3000\ cm^{-1}$). The preferential involvement of the bridging ligand in the first oxidation process has been described recently in the smaller quinonoid-based diruthenium(II)-bpy complex $[\{(bpy)_2Ru^{II}\}_2(\mu\text{-}H_2L^{2-})]^{2+}$ ($H_2L^{2-}$ = 2,5-dioxido-1,4-benzoquinonediimine).[7] However, the $K_c$ value for the successive oxidation processes in $[\{(bpy)_2Ru^{II}\}_2(\mu\text{-}H_2L^{2-})]^{2+}$ is much higher ($6.5\times10^8$ in $CH_3CN$) than that in the present cases (ca. $10^2$–$10^5$), as normally expected for ligand-based processes.[14,36]

Electrochemically generated further one-electron oxidized species $[\mathbf{1}–\mathbf{8}]^{4+}$ are found to be EPR inactive even when frozen in a glass (77 K). The diamagnetic nature of the doubly oxidized species $[\mathbf{1}–\mathbf{8}]^{4+}$ suggests their probable alternative formulation as $\{Ru^{II}(\mu\text{-}BL^{\circ})Ru^{II}\}$, with involvement of the bridging ligand in the second step oxidation process, or $\{Ru^{II}(\mu\text{-}BL^{\cdot-})Ru^{III}\}$, with involvement of the metal ion in the second step oxidation process and subsequent antiferromagnetic spin pairing of the unpaired electrons associated with $BL^{\cdot-}$ and $Ru^{III}$. The computed orbital compositions in $[\mathbf{1a}]^{2+}$ at the B3LYP level suggest that the HOMO–1 and HOMO–2 are primarily dominated by Ru (61% and 70%, respectively), with only a minor contribution (ca. 10%) from $BL_1^{2-}$ (Figure 10 and Table 7), which rules out the alternative possibility of a bridging-ligand-based second oxidation process. It should be noted that the stabilization of alternative spin-coupled singlet states by the involvement of a mixed-valence $Ru^{II}Ru^{III}$ configuration and an azo anion radical-based bridging ligand in $[(acac)_2Ru^{II}(\mu\text{-}L^{\cdot-})Ru^{III}(acac)_2]$ $\{L^{\cdot-} = NC_5H_4(N{=}N^{\cdot-})H_4C_5N\}$[18a] or partially coupled semiquinone form of 1,10-phenanthroline-5,6-dione ($L_1^{\cdot-}$) bridged $[(acac)_2Ru^{II}(\mu\text{-}L_1^{\cdot-})Ru^{III}(acac)_2]$ (acac = acetylacetonate) has been reported recently.[6] The consideration of a ruthenium-based second-step oxidation process ($Ru^{II}\rightarrow Ru^{III}$) instead of further oxidation of $BL^{\cdot-}$ can easily be understood, particularly in the case of $[\mathbf{8}]^{4+}$, as the alternative option leads to the formation of an unstable diradical-bridged triplet species $Ru^{II}(\mu\text{-}BL_8^{\cdot\cdot})Ru^{II}$ (Scheme 2). It is interesting to note that the occupied frontier orbitals (HOMO to HOMO–2) exhibit a fairly good mixing with the π orbitals of pap in $[\mathbf{1a}]^{2+}$ (Figure 10 and Table 7).

The formulations of analogous two-electron-oxidized bpy complexes $[\{(bpy)_2Ru\}_2(\mu\text{-}BL_1)]^{4+}$[10] and $[\{(bpy)_2Ru\}_2(\mu\text{-}BL_4)]^{4+}/[\{(bpy)_2Ru\}_2(\mu\text{-}BL_8)]^{4+}$ [11] were, on the other hand, proposed as $\{Ru^{II}(\mu\text{-}BL_1^{\circ})Ru^{II}\}$ and $\{Ru^{III}(\mu\text{-}BL_{4/8}^{2-})Ru^{III}\}$, respectively.

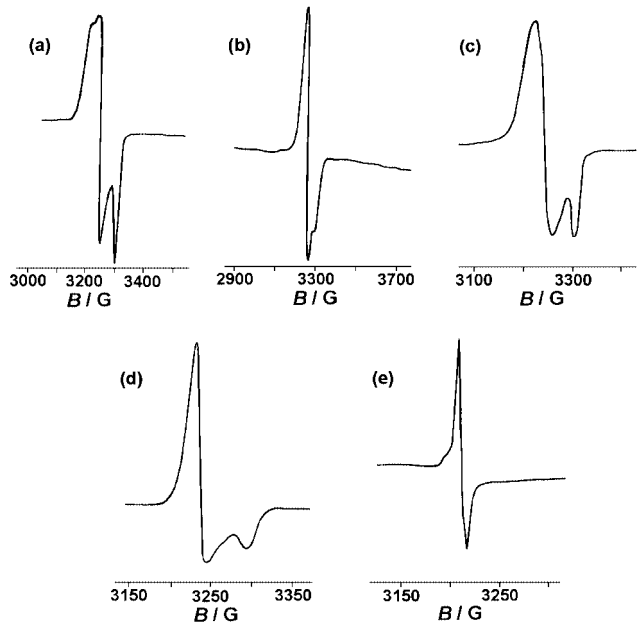


Figure 9. EPR spectra of $[\mathbf{1a}]^{3+}$ (a), $[\mathbf{3}]^{3+}$ (b), $[\mathbf{4}]^{3+}$ (c), $[\mathbf{7}]^{3+}$ (d), and $[\mathbf{8}]^{3+}$ (e) in $CH_3CN/Et_4NClO_4$ at 77 K.

Table 6. EPR data of electrogenerated $[\mathbf{1}–\mathbf{8}]^{3+}$ in acetonitrile at 77 K.

| Compd. | $g_1$ | $g_2$ | $g_3$ | $\Delta g$[a] | $<g>$[b] |
|---|---|---|---|---|---|
| $[\mathbf{1a}]^{3+}$ | 2.0242 | 2.0023 | 1.9659 | 0.0583 | 1.9976 |
| $[\mathbf{1b}]^{3+}$ | 2.0273 | 2.0023 | 1.9630 | 0.0642 | 1.9977 |
| $[\mathbf{1c}]^{3+}$ | 2.0273 | 2.0023 | 1.9660 | 0.0613 | 1.9987 |
| $[\mathbf{2}]^{3+}$ | 2.0254 | 1.9992 | 1.9629 | 0.0625 | 1.9960 |
| $[\mathbf{3}]^{3+}$ | 2.0085 | 2.0023 | 1.9737 | 0.0348 | 1.9949 |
| $[\mathbf{4}]^{3+}$ | 2.0147 | 2.0023 | 1.9648 | 0.0499 | 1.9940 |
| $[\mathbf{5}]^{3+}$ | 2.0146 | 2.0047 | 1.9661 | 0.0485 | 1.9952 |
| $[\mathbf{6}]^{3+}$ | 2.0211 | 2.0035 | 1.9628 | 0.0583 | 2.0064 |
| $[\mathbf{7}]^{3+}$ | 2.0057 | 2.0026 | 1.9661 | 0.0396 | 1.9915 |
| $[\mathbf{8}]^{3+}$ | 2.0054 | 2.0023 | 1.9976 | 0.0078 | 2.0018 |

[a] $\Delta g = g_1 - g_3$. [b] $<g> = [(g_1^2 + g_2^2 + g_3^2)/3]^{1/2}$.

 © 2006 Wiley-VCH Verlag GmbH & Co. KGaA, Weinheim 

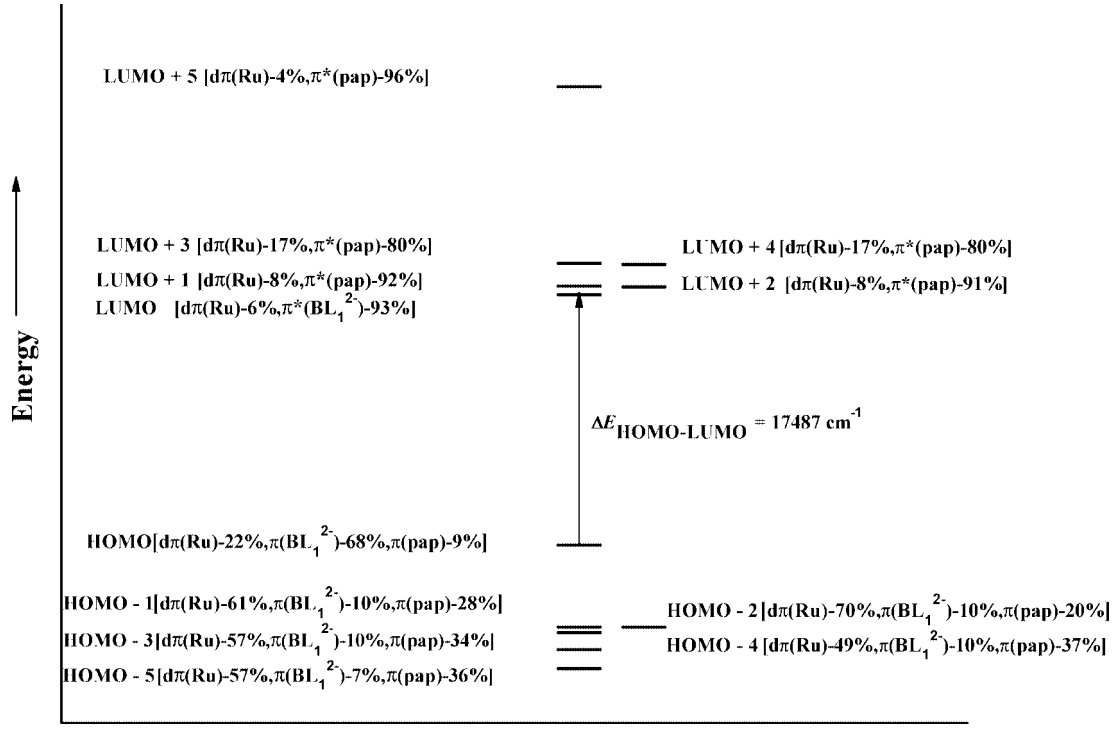


Figure 10. Orbital energy diagram for $[\mathbf{1a}]^{2+}$ computed at the B3LYP/SDD,6-31G* level of theory.

Table 7. Orbital energies and percent contributions of frontier molecular orbitals of $[\mathbf{1a}]^{2+}$ computed at the B3LYP level of theory by employing the SDD basis set for Ru and 6-31G* for all other atoms.

| | Ru center | Bridging ligand ($BL_1^{2-}$) | Ancillary ligand (pap) |
|---|---|---|---|
| LUMO+5 (–0.197)[a] | 3.6 | – | 96.0 |
| LUMO+4 (–0.254) | 17.0 | 2.3 | 80.0 |
| LUMO+3 (–0.254) | 17.0 | 1.7 | 80.0 |
| LUMO+2 (–0.263) | 8.2 | 1.2 | 90.8 |
| LUMO+1 (–0.263) | 8.0 | 0.6 | 92.0 |
| LUMO (–0.265) | 6.2 | 92.9 | – |
| HOMO (–0.346) | 2.4 | 68.5 | 9.2 |
| HOMO–1 (–0.373) | 61.4 | 10.3 | 28.4 |
| HOMO–2 (–0.373) | 70.0 | 9.7 | 20.0 |
| HOMO–3 (–0.374) | 56.6 | 9.8 | 33.6 |
| HOMO–4 (–0.380) | 48.8 | 10.1 | 37.2 |
| HOMO–5 (–0.387) | 56.8 | 7.0 | 36.0 |

[a] Values in parentheses are orbital energies in atomic units.

Both the ancillary (aap)[37] and bridging ligand ($BL^{2-}$)[10,11] are known to successively accept two electrons each in their LUMOs (Scheme 3), therefore ideally a total of ten one-electron reduction processes (eight from four aap ligands and two from $BL^{2-}$) are expected for $[\mathbf{1}–\mathbf{8}]^{2+}$. The complexes indeed display multiple reductions in $CH_3CN$ or $CH_2Cl_2$ (Figure 8 and Table 5) within the accessible potential limit of –2.0 V. However, instead of ten successive one-electron reduction processes, simultaneous two-electron processes are also detected along with the clear one-electron responses, as confirmed by comparing the current heights of their respective DPVs (differential pulse voltammograms) with that of the coulometrically established one-electron oxidation processes. Since the ruthenium ion in $[\mathbf{1}–\mathbf{8}]^{2+}$ is in the +2 state, aap and $BL^{2-}$ ligands are naturally involved in the reduction processes. Consequently, the reduction potentials vary systematically depending on the electronic structures of both aap and $BL^{2-}$ (Table 5). The two-electron nature of the first reduction process for most of the complexes does not permit the radical intermediate to be electrogenerated (Scheme 3). However, the first one-electron reduced species for $[\mathbf{5}]^{+}$ in $CH_3CN$ displays a free radical EPR signal at 77 K with $g = 1.998$ (Figure 11) without any hyperfine splitting, which might suggest that the unpaired electron resides on the oxygen center of $BL_5^{\cdot 3-}$ instead of the nitrogen center of the azo group of pap.[35,38] The B3LYP/6-31G* Kohn–Sham orbitals show that the LUMO is primarily dominated by the π* orbital of $BL_1^{2-}$ (93%) whereas LUMO+1/LUMO+2 consist of π* orbitals of pap (>90%; Figure 10 and Table 7). The closeness in energy between the $BL_1^{2-}$-based LUMO and the pap-based higher vacant orbitals (LUMO+1/LUMO+2) justifies the observed simultaneous two-electron first step reduction process (Figure 8).

The spectral features of the complexes both in the native state $[\mathbf{1}–\mathbf{8}]^{2+}$ and also in the oxidized $[\mathbf{1}–\mathbf{8}]^{3+}/[\mathbf{1}–\mathbf{8}]^{4+}$ states follow a general trend in $CH_3CN$ (Figure 12 and Table 8). The spectral features of $[\mathbf{1a}–\mathbf{1c}]^{n+}$ ($n$ = 2, 3, 4) in $CH_2Cl_2$ also show a similar general trend and no significant solvent effect on the spectral aspects is observed. Multiple ligand-based π–π*/n–π* transitions appear in the UV region. In addition, intense metal-to-ligand charge transfer (MLCT) transitions are observed near 550 nm, which are associated with a moderately intense shoulder(s) at the lower energy part near 650 nm. The Gaussian analysis of the visible region part of the spectra of $[\mathbf{1a}]^{2+}$ in $CH_3CN$ and $CH_2Cl_2$

 © 2006 Wiley-VCH Verlag GmbH & Co. KGaA, Weinheim 

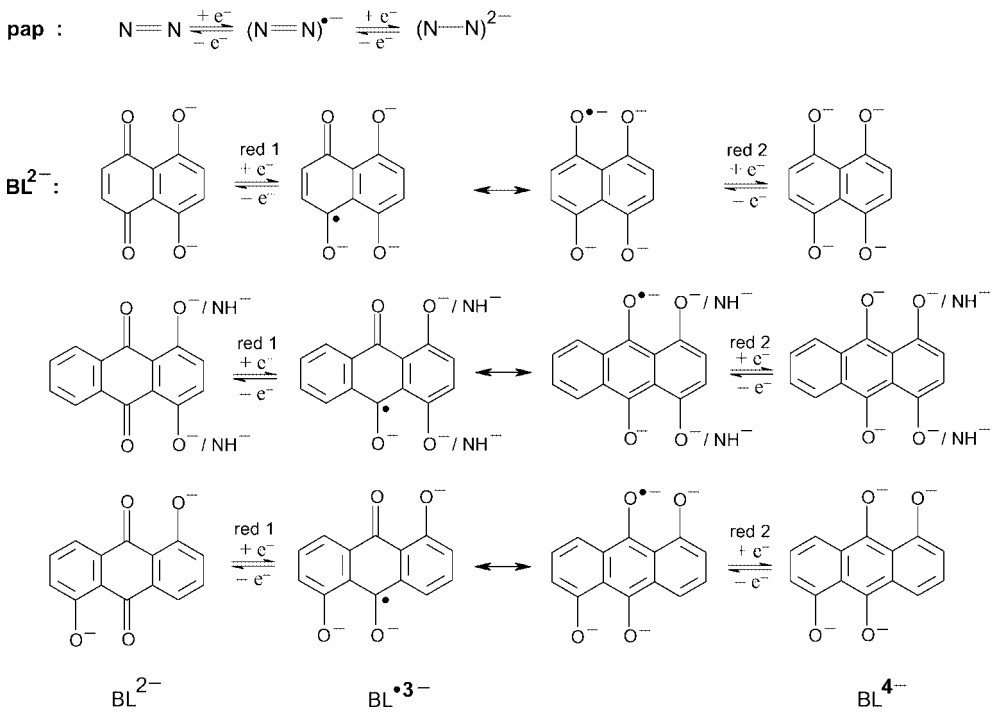


Scheme 3.

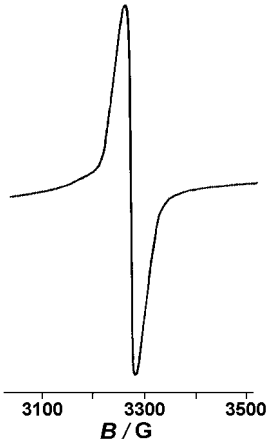


Figure 11. EPR spectrum of $[5]^+$ in $CH_3CN/Et_4NClO_4$ at 77 K.

shows a total of four bands at $\lambda$ ($\varepsilon$) = 742 nm (4396 $M^{-1}cm^{-1}$), 639 (5580), 565 (11821), and 517 (22069) (see part a in Figure 12, inset) and 748 (4800), 656 (5739), 570 (11120), and 522 (23527) (Figure 12, part b, inset), respectively. A selected list of vertical excitation energies computed with the TD-DFT/B3LYP formalism for the B3LYP/SDD,6-31G* geometry of $[\mathbf{1a}]^{2+}$ in its singlet ground state are summarized in Table 9 (complete lists are given in Table S5 in the Supporting Information).[39] Here, a comparison between observed and computed transitions is performed by examining transitions of comparable intensities guided by their respective oscillator strengths and absorptivity values.[40] The nature of the excited states is assigned based on the percent Kohn–Sham orbital contributions of the orbitals involved in the electronic transitions. Based on the oscillator strengths, the comparable predicted transitions appear at $\lambda$ = 743.91 (HOMO→LUMO+1), 696.64 (HOMO→LUMO/HOMO→LUMO+4), 539.14 (HOMO–2→LUMO/HOMO–1→LUMO+2) and 514.30 nm (HOMO–5→LUMO+1/HOMO–4→LUMO+2) (Table 9, Figure 13, and Figure S1 in the Supporting Information).

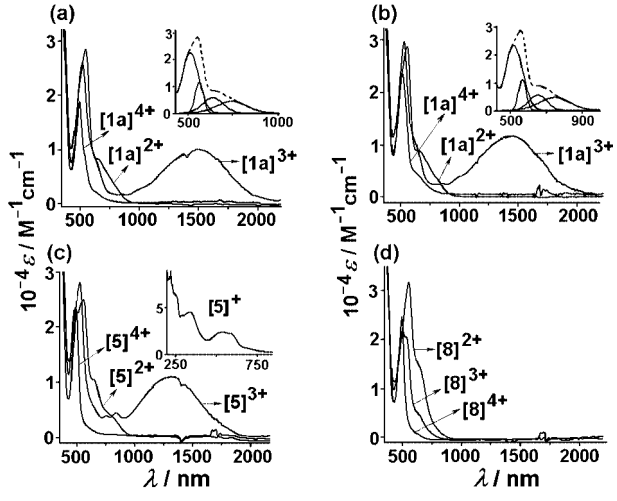


Figure 12. Electronic spectra of (a) $[\mathbf{1a}]^{n+}$ ($n$ = 2–4) in $CH_3CN/Et_4NClO_4$. The inset shows the Gaussian analysis of the visible region of the spectrum for $n$ = 2. (b) $[\mathbf{1a}]^{n+}$ ($n$ = 2–4) in $CH_2Cl_2/Et_4NClO_4$. The inset shows the Gaussian analysis of the visible region of the spectrum for $n$ = 2. (c) $[\mathbf{5}]^{n+}$ ($n$ = 2–4) in $CH_3CN/Et_4NClO_4$. The inset shows the spectrum of $[\mathbf{5}]^+$. (d) $[\mathbf{8}]^{n+}$ ($n$ = 2, 3, 4) in $CH_3CN/Et_4NClO_4$.

The charge-transfer bands of $[\mathbf{1}–\mathbf{8}]^{3+}$ are blue shifted upon oxidation, with a reduction in intensity, and a new low-energy, intense transition appears in the range 1200–

 © 2006 Wiley-VCH Verlag GmbH & Co. KGaA, Weinheim 

Table 8. Spectroelectrochemical data for $[\mathbf{1a}]^{n+}$–$[\mathbf{1c}]^{n+}$ in dichloromethane (DCM) and $[\mathbf{1}]^{n+}$–$[\mathbf{8}]^{n+}$ in acetonitrile (AN) ($n$ = 2–4).

| | Solvent | $\lambda_{max}$ [nm] ($\varepsilon$ [$M^{-1}cm^{-1}$]) |
|---|---|---|
| $[\mathbf{1a}]^{2+}$ | AN | 669 (8260, sh), 554 (28300), 503 (22100, sh), 332 (35900), 286 (31200, sh) |
| | DCM | 666 (8910, sh), 561 (28800), 505 (22400, sh), 344 (38400), 288 (31900, sh) |
| $[\mathbf{1a}]^{3+}$ | AN | 1500 (9960, 3007,[a] 3924[b]), 623 (9120, sh), 526 (25870), 502 (23400, sh), 363 (37100), 313 (33300, sh), 283 (37000) |
| | DCM | 1439 (11600, 3246,[a] 4006[b]), 645 (9590, sh), 534 (29700), 496 (21900, sh), 367 (39500), 313 (33600, sh), 287 (36300) |
| $[\mathbf{1a}]^{4+}$ | AN | 550 (8540, sh), 502 (18800), 471 (12300, sh), 363 (34800), 310 (30300, sh), 282 (34500) |
| | DCM | 641 (4510, sh), 519 (23500), 485 (16100, sh), 367 (43900), 308 (39700, sh), 287 (41600) |
| $[\mathbf{1b}]^{2+}$ | AN | 668 (10300, sh), 551 (32600), 507 (27100, sh), 346 (52300), 280 (35300) |
| | DCM | 661 (7620, sh), 556 (22400), 504 (17900, sh), 356 (30900), 284 (24000) |
| $[\mathbf{1b}]^{3+}$ | AN | 1482 (8400, 3156,[a] 3948[b]), 613 (9500, sh), 520 (22000), 470 (14200, sh), 370 (35900), 355 (34100, sh), 283 (33700) |
| | DCM | 1484 (8930, 3104,[a] 3945[b]), 638 (8630, sh), 535 (22000), 497 (16500, sh), 374 (31300), 314 (24100, sh), 284 (27100) |
| $[\mathbf{1b}]^{4+}$ | AN | 548 (9460, sh), 501 (21400), 471 (15100, sh), 370 (43300), 311 (33700, sh), 280 (40800) |
| | DCM | 624 (9500, sh), 517 (23800), 490 (19800, sh), 371 (42400), 310 (45700, sh), 285 (44600) |
| $[\mathbf{1c}]^{2+}$ | AN | 666 (10400 sh), 541 (31800), 505 (27400, sh), 323 (46800), 284 (41000, sh) |
| | DCM | 689 (8930, sh), 549 (26200), 514 (23800, sh), 336 (40100), 284 (32800, sh) |
| $[\mathbf{1c}]^{3+}$ | AN | 1416 (8880, 3130,[a] 4039[b]), 629 (8670, sh), 520 (27200), 470 (17300, sh), 351 (46400), 308 (43600, sh), 284 (45200) |
| | DCM | 1405 (11000, 3387,[a] 4054[b]), 641 (10200, sh), 537 (28900), 495 (20800, sh), 356 (40700), 284 (37400) |
| $[\mathbf{1c}]^{4+}$ | AN | 545 (11100, sh), 504 (28400), 470 (18500, sh), 346 (52300), 310 (49300, sh), 280 (54400) |
| | DCM | 636 (5050, sh), 522 (23800), 493 (18900, sh), 349 (46600), 284 (44800) |
| $[\mathbf{2}]^{2+}$ | AN | 655 (9280, sh), 553 (32400), 496 (22600, sh), 329 (38600), 285 (32500, sh) |
| $[\mathbf{2}]^{3+}$ | | 1530 (10100, 3063,[a] 3885[b]), 642 (8490, sh), 527 (26000), 481 (17800, sh), 362 (35400), 309 (33600, sh), 284 (35900) |
| $[\mathbf{2}]^{4+}$ | | 524 (9680, sh), 501 (22200), 362 (41300), 472 (14800, s), 306 (35400, sh), 280 (44900) |
| $[\mathbf{3}]^{2+}$ | AN | 802 (4250, sh), 618 (12500, sh), 569 (25100), 531 (20800, sh), 480 (19600), 370 (39000, sh), 335 (42300), 275 (70700) |
| $[\mathbf{3}]^{3+}$ | | 1286 (9200, 3810,[a] 4238[b]), 623 (6510, sh), 534 (23600), 499 (21200, sh), 365 (38200), 275 (66800) |
| $[\mathbf{3}]^{4+}$ | | 556 (5630, sh), 501 (20800), 476 (15000, sh), 362 (44600), 309 (35900, sh), 280 (44400) |
| $[\mathbf{4}]^{2+}$ | AN | 807 (2920, sh), 666 (8620, sh), 558 (23000), 488 (20300, sh), 335 (36200), 283 (34800) |
| $[\mathbf{4}]^{3+}$ | | 1381 (5720, 3522,[a] 4090[b]), 612 (4450, sh), 530 (15100), 501 (13200, sh), 360 (20200), 310 (19400, sh), 283 (21800) |
| $[\mathbf{4}]^{4+}$ | | 542 (3280, sh), 501 (12200), 475 (8620, sh), 361 (24300), 307 (19300, sh), 280 (22700) |
| $[\mathbf{5}]^{+}$ | AN | 706 (6160, sh), 597 (22200), 530 (23800), 341 (45100), 293 (41900, sh), 246 (65500, sh) |
| $[\mathbf{5}]^{2+}$ | | 792 (4270, sh), 657 (10500, sh), 561 (25100), 488 (23500, sh), 336 (42900), 268 (59400) |
| $[\mathbf{5}]^{3+}$ | | 1320 (10900, 3608,[a] 4183[b]), 648 (5710, sh), 534 (28100), 503 (25100, sh), 362 (38800), 283 (42200, sh), 265 (59400) |
| $[\mathbf{5}]^{4+}$ | | 519 (14900, sh), 500 (22900), 472 (15900, sh), 358 (46100), 306 (35000, sh), 278 (43800) |
| $[\mathbf{6}]^{2+}$ | AN | 662 (8210, sh), 550 (22500), 493 (19300, sh), 329 (34000), 274 (44000) |
| $[\mathbf{6}]^{3+}$ | | 1416 (8220, 3677 ,[a] 4039[b]), 622 (6930, sh), 528 (21100), 506 (20100, sh), 363 (30500), 282 (39600) |
| $[\mathbf{6}]^{4+}$ | | 530 (5750, sh), 501 (17500), 473 (12400, sh), 361 (87100), 306 (27100, sh), 279 (35500) |
| $[\mathbf{7}]^{2+}$ | AN | 943 (4310, sh), 664 (6260, sh), 550 (20500), 491 (21500), 349 (38800), 304 (40700), 237 (60400, sh) |
| $[\mathbf{7}]^{3+}$ | | 1274 (7170, 1913,[a] 4258[b]), 911 (8870, sh), 539 (21100, sh), 504 (24800), 373 (36700), 317 (31900, sh), 228 (54400, sh) |
| $[\mathbf{7}]^{4+}$ | | 892 (21100), 499 (26100), 370 (39000), 282 (34300, sh), 234 (48500, sh) |
| $[\mathbf{8}]^{2+}$ | AN | 653 (14400, sh), 561 (31700), 487 (18800, sh), 360 (40500, sh), 319 (44700), 250 (61600, sh), 225 (85900) |
| $[\mathbf{8}]^{3+}$ | | 638 (4960, sh), 546 (20300, sh), 508 (21500), 472 (16000, sh), 356 (44800), 308 (45000), 284 (42700, sh) |
| $[\mathbf{8}]^{4+}$ | | 501 (24800), 475 (17600, sh), 363 (44800), 307 (36600, sh), 280 (45400) |

[a] Experimental band width at half height ($\Delta\nu_{1/2}$). [b] Calculated band width at half height ($\Delta\nu_{1/2}$).

Table 9. Selected list of higher intensity vertical excitations computed at the TD-DFT/B3LYP//B3LYP/6-31G* level[a] for $[\mathbf{1a}]^{2+}$.

| Excitation energy[a] ($10^3$ $cm^{-1}$)[b] | Oscillator strength | $\varepsilon$[c] | $\psi_o \rightarrow \psi_v$[d] | Type of transition[e] |
|---|---|---|---|---|
| 13.442 (743.91) | 0.0648 | 4548.96 | HOMO→LUMO+1 (0.67)[f] | dπ(Ru), π($BL_1^{2-}$)→dπ(Ru), π*(pap) |
| 14.354 (696.64) | 0.0229 | 1607.58 | HOMO→LUMO (0.41) | dπ(Ru), π($BL_1^{2-}$)→dπ(Ru), π*($BL_1^{2-}$) |
| | | | HOMO→LUMO+4 (0.46) | dπ(Ru), π($BL_1^{2-}$)→dπ(Ru), π*(pap) |
| 18.548 (539.14) | 0.0990 | 6949.8 | HOMO-2→LUMO (0.57) | dπ(Ru), π($BL_1^{2-}$)→dπ(Ru), π*($BL_1^{2-}$) |
| | | | HOMO-1→LUMO+2 (0.32) | dπ(Ru), π($BL_1^{2-}$)→dπ(Ru), π*(pap) |
| 19.444 (514.30) | 0.0455 | 3194.1 | HOMO-5→LUMO+1 (0.17) | dπ(Ru)→dπ(Ru), π*(pap) |
| | | | HOMO-4→LUMO+2 (0.34) | dπ(Ru)→dπ(Ru), π*(pap) |

[a] Singlet excitation energies. [b] Wavelength values in nm given in parentheses. [c] $M^{-1}cm^{-1}$. [d] Occupied and virtual orbitals. [e] $BL_1^{2-}$ stands for the bridging ligand and pap represents the 2-(phenylazo)pyridine ligand. [f] Transition coefficients.

1500 nm ($\varepsilon$ = 5000–11000 $M^{-1}cm^{-1}$) with a band width at half height ($\Delta\nu_{1/2}$) of 1900–3800 $cm^{-1}$ (Figure 12 and Table 8). The experimentally obtained $\Delta\nu_{1/2}$ values are smaller than would be expected (3900–4300 $cm^{-1}$) from the Hush formula [$\Delta\nu_{1/2} = (2310\ E_{op})^{1/2}$][41] for a localized class-II mixed-valence system. This disagreement between experimental and calculated $\Delta\nu_{1/2}$ values and the high intensity of the NIR band supports the notion of a ligand-based oxidation to $Ru^{II}(\mu\text{-}BL^{\cdot-})Ru^{II}$ instead of metal-based oxidation to $Ru^{II}(\mu\text{-}BL^{2-})Ru^{III}$, as previously implied by the free-radi-

 © 2006 Wiley-VCH Verlag GmbH & Co. KGaA, Weinheim 

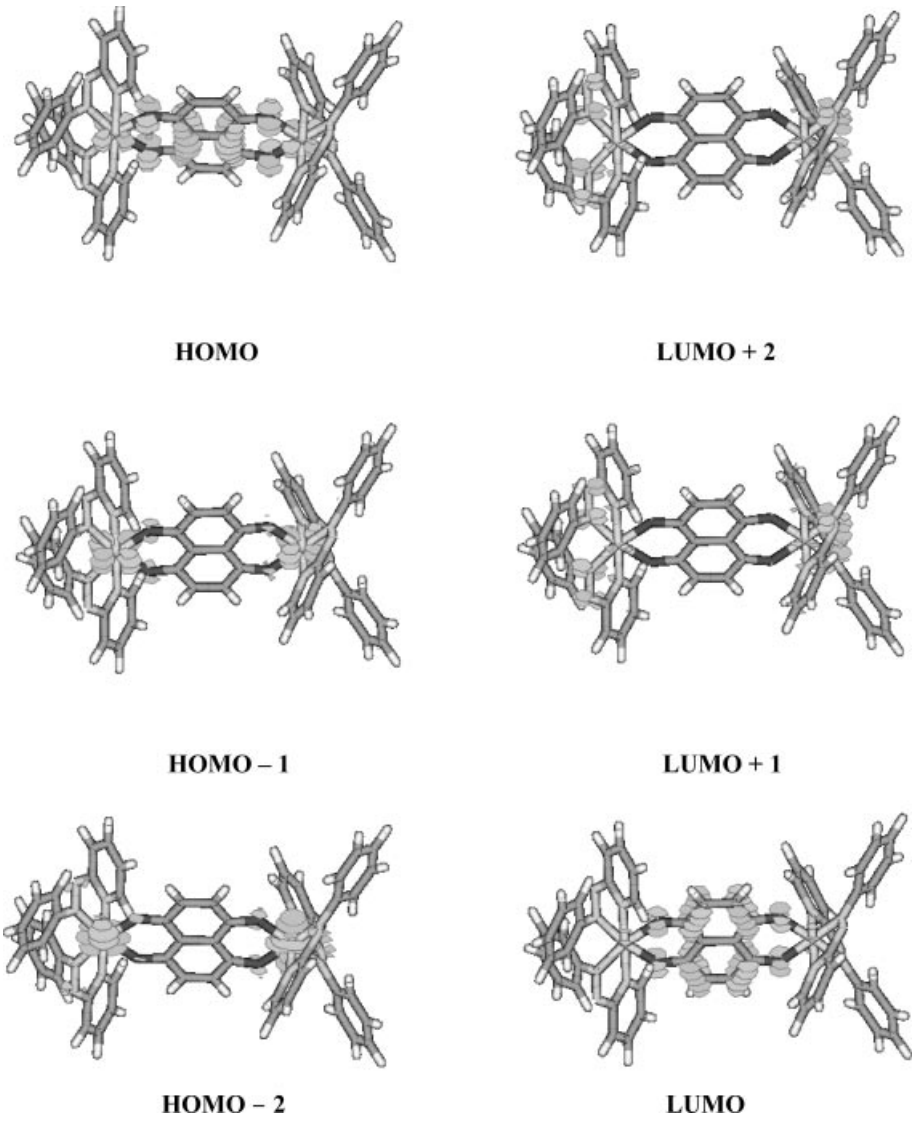


Figure 13. Kohn–Sham orbital contours of the frontier MOs of [**1a**]$^{2+}$ involved in the intense long-wavelength transitions.

cal EPR signal of [**1**–**8**]$^{3+}$ (Table 6). The low-energy NIR band is thus assigned as an intraligand transition involving the reduced component of the bridging ligand to the oxidized SOMO of its counterpart. Although the spectral features of [**8**]$^{2+/3+/4+}$ in the UV/Vis region are akin to those in other complexes, the expected NIR band for the intermediate [**8**]$^{3+}$ has not been detected (Figure 12, d, Table 8). On further oxidation to the spin-coupled diamagnetic $Ru^{II}$(μ-$BL^{\cdot-}$)$Ru^{III}$ state in [**1**–**8**]$^{4+}$, the near-IR band disappears and the charge-transfer (MLCT/LMCT) bands are blue shifted. Unlike other complexes, the low-energy shoulder in [**7**]$^{4+}$ appears as an intense band at 892 nm (Table 8). The reduction of [**5**]$^{2+}$ to the radical species [**5**]$^{\cdot+}$ results in a red shift of the MLCT band from 561 to 597 nm with comparable intensity [Figure 12, c (inset), Table 8].

In summary, experimental results in combination with DFT calculations have established that the large quinonoid ($BL^{2-}$)-bridged diruthenium complexes [$(aap)_2Ru^{II}$(μ-$BL^{2-}$)$Ru^{II}(aap)_2$]$^{2+}$ [**1**–**8**]$^{2+}$ containing strongly π-accepting ancillary ligands (AL = arylazopyridine) undergo preferential first-step oxidation at the bridging ligand to give the paramagnetic radical-bridged diruthenium(II) species [$(aap)_2Ru^{II}$(μ-$BL^{\cdot-}$)$Ru^{II}(aap)_2$]$^{3+}$ [**1**–**8**]$^{3+}$. However, second-step oxidation selectively takes place at the metal center to give antiferromagnetically coupled singlet species, namely the mixed-valence $Ru^{II}Ru^{III}$ species [$(aap)_2Ru^{II}$(μ-$BL^{\cdot-}$)-$Ru^{III}(aap)_2$]$^{4+}$ [**1**–**8**]$^{4+}$, which are bridged by a radical bridging ligand (Scheme 4). Successive reductions, however, take place at the ligand centers. The first-step reduction process takes place either as a single electron transfer to the bridging ligand ($BL^{\cdot3-}$) or, in most cases, as a simultaneous two-electron transfer process involving the bridging ligand (μ-$BL^{4-}$) or a mixed situation of bridging ($BL^{\cdot3-}$) and ancillary ($aap^{\cdot-}$) ligands (Scheme 4).

 © 2006 Wiley-VCH Verlag GmbH & Co. KGaA, Weinheim 

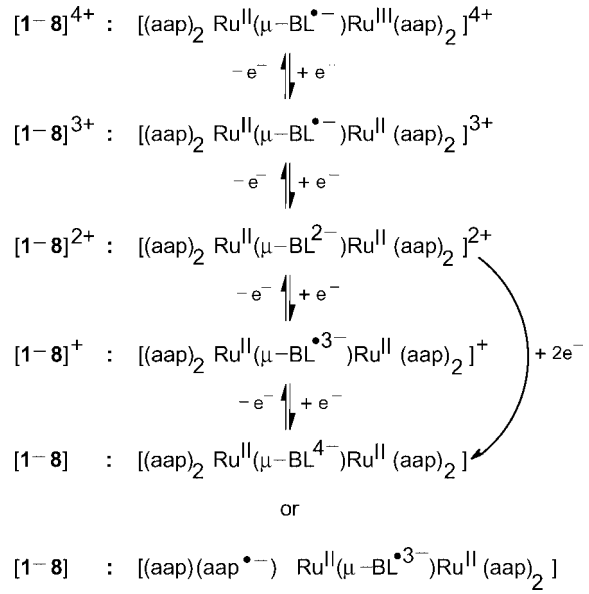


Scheme 4.

## Experimental Section

**Materials and Instrumentation:** The precursor compounds *ctc*-$[Ru(aap)_2(H_2O)_2](ClO_4)_2{\cdot}H_2O$ and aap ligands were prepared according to the reported procedures.[42] The dinucleating ligand precursors 5,8-dihydroxy-1,4-napthoquinone ($H_2BL_1$), 2,3-dichloro-5,8-dihydroxy-1,4-napthoquinone ($H_2BL_2$), 6,11-dihydroxy-5,12-naphthacenedione ($H_2BL_3$), 1,4-dihydroxy-9,10-anthraquinone ($H_2BL_4$), 1,4-dihydroxy-2,3-dimethyl-9,10-anthraquinone ($H_2BL_5$), 6,7-dichloro-1,4-dihydroxy-9,10-anthraquinone ($H_2BL_6$), 1,4-diamino-9,10-anthraquinone ($H_4BL_7$), and 1,5-dihydroxy-9,10-anthraquinone ($H_2BL_8$) were purchased from Aldrich (USA). HPLC-grade solvents were used for spectroscopic and electrochemical studies. UV/Vis/NIR spectra in $CH_3CN$ or $CH_2Cl_2$/0.1 M $Et_4NClO_4$ at 298 K were recorded with a Perkin–Elmer 950 lambda spectrophotometer. FT-IR spectra were recorded with a Nicolet spectrophotometer with samples prepared as KBr pellets. Solution electrical conductivity was checked using a Systronic 305 conductivity bridge. $^1$H NMR spectra were obtained with a 300 or 400 MHz Varian FT spectrometer. The EPR measurements were made with a Varian model 109C E-line X-band spectrometer fitted with a quartz dewar for measurements at 77 K. Cyclic voltammetric, differential pulse voltammetric, and coulometric measurements were carried out using a PAR model 273A electrochemistry system. Platinum wire working and auxiliary electrodes and an aqueous saturated calomel reference electrode (SCE) were used in a three-electrode configuration. The supporting electrolyte was 0.1 M $[NEt_4]ClO_4$ and the solute concentration was about $10^{-3}$ M. The half-wave potential $E^\circ_{298}$ was set equal to $0.5(E_{pa} + E_{pc})$, where $E_{pa}$ and $E_{pc}$ are the anodic and cathodic cyclic voltammetric peak potentials, respectively. A platinum wire-gauze working electrode was used in the coulometric experiments. The elemental analyses were carried out with a Perkin–Elmer 240C elemental analyzer. Electrospray mass spectra were recorded with a Micromass Q-ToF mass spectrometer.

***CAUTION!*** *Perchlorate salts of metal complexes with organic ligands are potentially explosive. Heating of dried samples must be avoided and handling of small amounts has to proceed with great caution using protection.*

Complexes [**1**–**8**]$(ClO_4)_2$ were prepared by following a general procedure. The details are given for [**1a**]$(ClO_4)_2$.

**[(pap)$_2$Ru$^{II}$(μ-BL$_1^{2-}$)Ru$^{II}$(pap)$_2$](ClO$_4$)$_2$ [1](ClO$_4$)$_2$:** The bridging ligand $H_2BL_1$ (0.013 g, 0.068 mmol) was added to the starting complex *ctc*-$[Ru(aap)_2(OH_2)_2](ClO_4)_2{\cdot}H_2O$ (0.1 g, 0.138 mmol) in absolute ethanol (20 mL) and the resulting mixture was heated to reflux under a dinitrogen atmosphere for 12 h. The initial purple solution gradually changed to violet. The solvent of the reaction mixture was then evaporated to dryness under reduced pressure. The resulting mixture was purified on a neutral alumina column. Initially, a blue compound corresponding to $[Ru(pap)_2Cl_2]$ was eluted with $CH_2Cl_2/CH_3CN$ (15:1 v/v), followed by a violet compound with $CH_2Cl_2/CH_3CN$ (5:1 v/v) corresponding to [**1a**]$(ClO_4)_2$. Evaporation of the solvent under reduced pressure yielded pure complex [**1a**]$(ClO_4)_2$. Yield: 0.046 g (50%). $C_{54}H_{40}Cl_2N_{12}O_{12}Ru_2$: calcd. C 49.02, H 3.05, N 12.71; found C 48.45, H 3.20, N 11.78. $\Lambda_M$ ($\Omega^{-1}$ cm$^2$ M$^{-1}$) in acetonitrile at 25 °C: 219. IR (KBr disk): $\tilde{\nu}$ = 1089, 622 cm$^{-1}$. $^1$H NMR (400 MHz, $CDCl_3$, 298 K): $\delta$ = 8.64 (d, $J$ = 8.4 Hz, 1 H), 8.53 (d, $J$ = 8.0 Hz, 1 H), 8.24 (t, $J$ = 8.0, 7.9 Hz, 1 H), 8.13 (d, $J$ = 5.2 Hz, 1 H), 8.08 (t, $J$ = 7.2, 7.6 Hz, 1 H), 7.84 (d, $J$ = 5.6 Hz, 1 H), 7.78 (t, $J$ = 7.2, 7.6 Hz, 1 H), 7.6 (t, $J$ = 7.2, 7.9 Hz, 1 H), 7.35 (m, 3 H), 7.18 (t, $J$ = 7.6, 7.2 Hz, 3 H), 6.88 (d, $J$ = 7.2 Hz, 2 H), 6.77 (t, $J$ = 8.7, 6.4 Hz, 4 H) ppm.

**[1b](ClO$_4$)$_2$:** Yield: 0.041 g (45%). $C_{58}H_{48}Cl_2N_{12}O_{12}Ru_2$: calcd. C 50.50, H 3.51, N 12.19; found C 50.63, H 3.07, N 11.99. $\Lambda_M$ ($\Omega^{-1}$ cm$^2$ M$^{-1}$) in acetonitrile at 25 °C: 214. IR (KBr disk): $\tilde{\nu}$ = 1088, 623 cm$^{-1}$. $^1$H NMR (400 MHz, $CDCl_3$, 298 K): $\delta$ = 8.65 (d, $J$ = 8.0 Hz, 1 H), 8.55 (d, $J$ = 8.0 Hz, 1 H), 8.25 (q, $J$ = 7.9, 7.6, 7.6 Hz, 1 H), 8.09 (t, $J$ = 6.4, 7.6 Hz, 2 H), 7.82 (d, $J$ = 5.2 Hz, 1 H), 7.76 (t, $J$ = 6.0, 6.8 Hz, 1 H), 7.61 (t, $J$ = 6.4, 6.0 Hz, 1 H), 7.15 (m, 2 H), 7.04 (m, 2 H), 6.87 (d, $J$ = 5.2 Hz, 2 H), 6.57 (s, 2 H), 6.48 (m, 2 H), 2.17 (s, 3 H), 2.15 (s, 3 H) ppm.

**[1c](ClO$_4$)$_2$:** Yield: 0.039 g (42%). $C_{54}H_{36}Cl_6N_{12}O_{12}Ru_2$: calcd. C 44.45, H 2.49, N 11.53; found C 44.19, H 2.83, N 11.22. $\Lambda_M$ ($\Omega^{-1}$ cm$^2$ M$^{-1}$) in acetonitrile at 25 °C: 236. IR (KBr disk): $\tilde{\nu}$ = 1090, 621 cm$^{-1}$. $^1$H NMR (400 MHz, $CDCl_3$, 298 K): $\delta$ = 8.69 (d, $J$ = 7.6 Hz, 1 H), 8.27 (t, $J$ = 7.6, 6.8 Hz, 1 H), 7.92 (d, $J$ = 5.2 Hz, 1 H), 7.69 (t, $J$ = 6.0, 6.0 Hz, 1 H), 7.34 (m, 1 H), 7.16 (t, $J$ = 8.0 Hz, 1 H), 6.89 (s, 1 H), 6.72 (d, $J$ = 8.4 Hz, 1 H), 6.65 (s, 1 H) ppm.

**[2](ClO$_4$)$_2$:** Yield: 0.030 g (31%). $C_{54}H_{38}Cl_4N_{12}O_{12}Ru_2$: calcd. C 46.62, H 2.76, N 12.09; found C 46.45, H 2.89, N 11.83. $\Lambda_M$ ($\Omega^{-1}$ cm$^2$ M$^{-1}$) in acetonitrile at 25 °C: 212. IR (KBr disk): $\tilde{\nu}$ = 1085, 623 cm$^{-1}$. $^1$H NMR [400 MHz, $(CD_3)_2SO$, 298 K]: $\delta$ = 8.96 (t, $J$ = 7.2, 5.6 Hz, 2 H), 8.34 (m, 2 H), 7.97 (m, 1 H), 7.75 (t, $J$ = 6.0, 6.8 Hz, 1 H), 7.61 (m, 1 H), 7.44 (t, $J$ = 4.8, 4.0 Hz, 2 H), 7.30 (t, $J$ = 7.9, 6.0 Hz, 5 H), 6.94 (d, $J$ = 15.9 Hz, 1 H), 6.85 (t, $J$ = 9.5, 8.3 Hz, 2 H), 6.79 (t, $J$ = 7.5, 7.9 Hz, 2 H) ppm.

**[3](ClO$_4$)$_2$:** Yield: 0.048 g (48%). $C_{62}H_{44}Cl_2N_{12}O_{12}Ru_2$: calcd. C 52.32, H 3.12, N 11.82; found C 52.36, H 3.22, N 11.50. $\Lambda_M$ ($\Omega^{-1}$ cm$^2$ M$^{-1}$) in acetonitrile at 25 °C: 205. IR (KBr disk): $\tilde{\nu}$ = 1091, 623 cm$^{-1}$. $^1$H NMR (400 MHz, $CDCl_3$, 298 K): $\delta$ = 8.68 (d, $J$ = 8.0 Hz, 1 H), 8.59 (d, $J$ = 7.6 Hz, 1 H), 8.25 (t, $J$ = 6.8, 7.6 Hz, 1 H), 8.11 (t, $J$ = 7.6 Hz, 1 H), 7.97 (m, 3 H), 7.75 (d, $J$ = 4.8 Hz, 1 H), 7.69 (m, 4 H), 7.59 (t, $J$ = 6.4, 6.0 Hz, 1 H), 7.49 (t, $J$ = 5.6 Hz, 1 H), 7.41 (t, $J$ = 7.6 Hz, 1 H), 7.24 (m, 2 H), 6.89 (t, $J$ = 7.6, 5.2 Hz, 5 H) ppm.

**[4](ClO$_4$)$_2$:** Yield: 0.035 g (35%). $C_{58}H_{42}Cl_2N_{12}O_{12}Ru_2$: calcd. C 50.73, H 3.09, N 12.25; found C 50.64, H 3.29, N 12.01. $\Lambda_M$ ($\Omega^{-1}$ cm$^2$ M$^{-1}$) in acetonitrile at 25 °C: 223. IR (KBr disk): $\tilde{\nu}$ = 1088, 622 cm$^{-1}$. $^1$H NMR (400 MHz, $CDCl_3$, 298 K): $\delta$ = 8.68 (t, $J$ = 8.6 Hz, 1 H), 8.61 (d, $J$ = 8.1 Hz, 1 H), 8.55 (d, $J$ = 7.8 Hz, 1 H),

 © 2006 Wiley-VCH Verlag GmbH & Co. KGaA, Weinheim 

8.26 (m, 2 H), 8.11 (m, 2 H), 7.93 (m, 2 H), 7.86 (d, $J$ = 4.8 Hz, 1 H), 7.69 (m, 2 H), 7.38 (m, 3 H), 7.20 (m, 3 H), 6.96 (d, $J$ = 6.3 Hz, 1 H), 6.86 (t, $J$ = 6.0, 8.9 Hz, 1 H), 6.78 (t, $J$ = 8.9, 6.0 Hz, 1 H) ppm.

**[5](ClO$_4$)$_2$:** Yield: 0.030 g (31%). $C_{60}H_{46}Cl_2N_{12}O_{12}Ru_2$: calcd. C 51.43, H 3.31, N 12.00; found C 50.94, H 3.38, N 11.92. $\Lambda_M$ ($\Omega^{-1}$ cm$^2$ M$^{-1}$) in acetonitrile at 25 °C: 240. IR (KBr disk): $\tilde{\nu}$ = 1089, 623 cm$^{-1}$. $^1$H NMR (400 MHz, $CDCl_3$, 298 K): $\delta$ = 8.67 (t, $J$ = 8.1, 4.8 Hz, 1 H), 8.61 (d, $J$ = 10.7 Hz, 1 H), 8.54 (d, $J$ = 8.1 Hz, 1 H), 8.30 (t, $J$ = 8.1, 7.8 Hz, 1 H), 8.19 (m, 1 H), 8.02 (t, $J$ = 7.5, 8.1 Hz, 1 H), 7.93 (m, 1 H), 7.85 (d, $J$ = 5.1 Hz, 1 H), 7.66 (m, 2 H), 7.39 (d, $J$ = 7.5 Hz, 2 H), 7.19 (m, 4 H), 6.86 (t, $J$ = 3.3, 5.1 Hz, 2 H), 6.76 (t, $J$ = 6.0, 4.2 Hz, 2 H), 1.64 (s, 3 H) ppm.

**[6](ClO$_4$)$_2$:** Yield: 0.036 g (38%). $C_{58}H_{40}Cl_4N_{12}O_{12}Ru_2$: calcd. C 48.33, H 2.80, N 11.67; found C 48.65, H 2.93, N 11.43. $\Lambda_M$ ($\Omega^{-1}$ cm$^2$ M$^{-1}$) in acetonitrile at 25 °C: 243. IR (KBr disk): $\tilde{\nu}$ = 1088, 622 cm$^{-1}$. $^1$H NMR (400 MHz, $CDCl_3$, 298 K): $\delta$ = 8.66 (m, 1 H), 8.56 (t, $J$ = 7.6, 6.4 Hz, 1 H), 8.25 (d, $J$ = 11.1 Hz, 1 H), 8.19 (t, $J$ = 8.4, 5.6 Hz, 1 H), 8.12 (t, $J$ = 7.6, 7.9 Hz, 1 H), 8.02 (d, $J$ = 5.6 Hz, 1 H), 7.92 (s, 1 H), 7.72 (m, 1 H), 7.61 (t, $J$ = 5.6, 7.2 Hz, 1 H), 7.54 (m, 1 H), 7.20 (m, 3 H), 6.95 (d, $J$ = 6.4 Hz, 1 H), 6.84 (t, $J$ = 7.2, 7.9 Hz, 3 H), 6.78 (t, $J$ = 6.4, 6.8 Hz, 3 H) ppm.

**[7](ClO$_4$)$_2$:** Yield: 0.030 g (34%). $C_{58}H_{44}Cl_2N_{14}O_{10}Ru_2$: calcd. C 50.80, H 3.24, N 14.31; found C 50.43, H 3.36, N 14.86. $\Lambda_M$ ($\Omega^{-1}$ cm$^2$ M$^{-1}$) in acetonitrile at 25 °C: 239. IR (KBr disk): $\tilde{\nu}$ = 3260, 1087, 625 cm$^{-1}$. $^1$H NMR (400 MHz, $CDCl_3$, 298 K): $\delta$ = 9.55 (s, NH), 8.65 (d, $J$ = 6.0 Hz, 1 H), 8.53 (d, $J$ = 6.0 Hz, 1 H), 8.08 (m, 3 H), 7.33 (d, $J$ = 8.9 Hz, 2 H), 7.20 (m, 8 H), 6.98 (d, $J$ = 7.5 Hz, 3 H), 6.84 (d, $J$ = 7.2 Hz, 3 H) ppm.

**[8](ClO$_4$)$_2$:** Yield: 0.035 g (37%). $C_{58}H_{42}Cl_2N_{12}O_{12}Ru_2$: calcd. C 50.73, H 3.09, N 12.25; found C 50.62, H 3.38, N 12.33. $\Lambda_M$ ($\Omega^{-1}$ cm$^2$ M$^{-1}$) in acetonitrile at 25 °C: 202. IR (KBr disk): $\tilde{\nu}$ = 1088, 622 cm$^{-1}$. $^1$H NMR [400 MHz, $(CD_3)_2SO$, 298 K]: $\delta$ = 8.94 (m, 2 H), 8.32 (m, 2 H), 7.94 (m, 2 H), 7.46 (m, 4 H), 7.30 (m, 5 H), 7.21 (d, $J$ = 8.0 Hz, 1 H), 7.06 (m, 1 H), 6.93 (d, $J$ = 7.6 Hz, 2 H), 6.84 (d, $J$ = 5.6 Hz, 2 H) ppm.

**X-ray Crystallography:** Single crystals of [**1a**](ClO$_4$)$_2$·H$_2$O and [**3**](ClO$_4$)$_2$ were grown by slow evaporation of a 1:1 dichloromethane/hexane solution. Data were collected with an OXFORD XCALIBUR-S CCD diffractometer (see Table 10 for further details). The structures were solved and refined by full-matrix least-squares techniques on $F^2$ with SHELX-97.[43] The absorption corrections were done by multi-scan (SHELXTL program package) and all the data were corrected for Lorentz polarization effects. Hydrogen atoms were included in the refinement process with a riding model. CCDC-606432 {[**1a**](ClO$_4$)$_2$·H$_2$O} and -606433 {[**3**](ClO$_4$)$_2$} contain the supplementary crystallographic data for this paper. These data can be obtained free of charge from The Cambridge Crystallographic Data Centre via www.ccdc.cam.ac.uk/data_request/cif.

**Computational Details:** Full geometry optimization of [**1a**]$^{2+}$ was carried out using the density functional theory method at the (R)B3LYP level.[44a,44b] All elements except ruthenium were assigned the 6-31G* basis set. The SDD basis set with effective core potential was employed for the ruthenium atoms.[44c,44d] Calculations were performed with Gaussian98 and Gaussian03.[44e,44f] Vertical electronic excitations based on B3LYP optimized geometries were computed using the time-dependent density functional theory (TD-DFT) formalism[44g] with the B3LYP functional using the above combination of basis sets. Molecular orbital compositions were analyzed using the AOMIX program.[44h–44j]

Table 10. Crystallographic data for [**1a**](ClO$_4$)$_2$·H$_2$O and [**3**](ClO$_4$)$_2$.

| | [**1a**](ClO$_4$)$_2$·H$_2$O | [**3**](ClO$_4$)$_2$ |
|---|---|---|
| Formula | $C_{27}H_{20}ClN_6O_7Ru$ | $C_{31}H_{22}ClN_6O_6Ru$ |
| $M_r$ | 677.01 | 711.07 |
| Crystal size [mm] | 0.33×0.26×0.21 | 0.15×0.10×0.10 |
| Crystal system | monoclinic | orthorhombic |
| Space group | *C*2/*c* | *Pbca* |
| *Z* | 8 | 8 |
| *a* [Å] | 35.069(5) | 14.5179(18) |
| *b* [Å] | 9.5143(13) | 19.265(2) |
| *c* [Å] | 19.5817(18) | 22.516(3) |
| *α* [°] | 90 | 90 |
| *β* [°] | 122.597(12) | 90 |
| *γ* [°] | 90 | 90 |
| *V* [Å$^3$] | 5504.4(11) | 6297.5(14) |
| $\rho_{calcd.}$ [g cm$^{-3}$] | 1.634 | 1.500 |
| *T* [K] | 293(2) | 293(2) |
| *μ* [mm$^{-1}$] | 0.725 | 0.635 |
| *F*(000) | 2728 | 2872 |
| *hkl* range | $-41 \le h \le 41$ | $-17 \le h \le 17$ |
| | $-11 \le k \le 11$ | $-22 \le k \le 22$ |
| | $-22 \le l \le 23$ | $-26 \le l \le 26$ |
| *θ* range [°] | 2.98–25.00 | 3.00–25.00 |
| Reflections collected | 23331 | 24895 |
| Unique reflections [$R_{int}$] | 4779 [0.0224] | 5533 [0.0572] |
| Data/restraints/parameters | 4779/14/388 | 5533/0/406 |
| *R*1 [$I > 2\sigma(I)$] | 0.0475 | 0.0621 |
| *wR*2 [all data] | 0.1424 | 0.1909 |
| Goodness-of-fit | 1.076 | 0.910 |
| Residual electron density [e Å$^{-3}$] | 0.872, –0.714 | 1.328, –0.429 |

**Supporting Information** (for details see the footnote on the first page of this article): Kohn−Sham orbitals of [**1a**]$^{2+}$ (Figure S1); optimized coordinates for $BL_1^{2-}$ (Table S1), pap (Table S2) and [**1a**]$^{2+}$ (Table S3); calculated bond lengths and angles of [**1a**]$^{2+}$ (Table S4) and TD-DFT data for [**1a**]$^{2+}$ (Table S5).

## Acknowledgments

Financial support received from the Department of Science and Technology, and Council of Scientific and Industrial Research, New Delhi (India) is gratefully acknowledged. X-ray structural studies for [**1a**](ClO$_4$)$_2$ and [**3**](ClO$_4$)$_2$ were carried out at the National Single Crystal Diffractometer Facility, Indian Institute of Technology, Bombay. Special acknowledgment is made to the Sophisticated Analytical Instrument Facility (SAIF) and the Computer Center, Indian Institute of Technology Bombay, respectively, for providing the EPR and computational facilities.

[1] a) W. Kaim, A. Klein, M. Glöckle, *Acc. Chem. Res.* **2000**, *33*, 755; b) M. D. Ward, *Chem. Soc. Rev.* **1995**, *24*, 121; c) J. A. McCleverty, M. D. Ward, *Acc. Chem. Res.* **1998**, *31*, 842; d) R. J. Crutchley, in *Comprehensive Coordination Chemistry II* (Eds.: J. A. McCleverty, T. J. Meyer), **2004**, vol. 2, pp. 235; e) J. T. Hupp, in *Comprehensive Coordination Chemistry II* (Eds.: J. A. McCleverty, T. J. Meyer), **2004**, vol. 2, pp. 709; f) B. K. Breedlove, T. Yamaguchi, T. Ito, C. H. Londergan, C. P. Kubiak, in *Comprehensive Coordination Chemistry* II (Eds.: J. A. McCleverty, T. J. Meyer), **2004**, vol. 2, pp. 717; g) G. Giuffrida, S. Campagna, *Coord. Chem. Rev.* **1994**, *135–136*, 517; h) B. S. Brunschwig, C. Creutz, N. Sutin, *Chem. Soc. Rev.* **2002**, *31*, 168.

 © 2006 Wiley-VCH Verlag GmbH & Co. KGaA, Weinheim 

[2] a) V. Balzani, M. Venturi, A. Credi, in *Molecular Devices and Machines*: *A Journey into the Nanoworld*, Wiley-VCH, Weinheim, Germany, **2003**; b) B. L. Feringa, in *Molecular Switches*, Wiley-VCH, Weinheim, Germany, **2001**; c) F. Paul, C. Lapinte, *Coord. Chem. Rev.* **1998**, *178–180*, 431; d) M. D. Ward, *Chem. Ind.* **1997**, 640; e) M. D. Ward, *Chem. Ind.* **1996**, 568; f) O. Kahn, J.-P. Launay, *Chemtronics* **1988**, *3*, 140; g) S. Fraysse, C. Coudret, J.-P. Launay, *J. Am. Chem. Soc.* **2003**, *125*, 5880; h) S. Fraysse, C. Coudret, J.-P. Launay, *Eur. J. Inorg. Chem.* **2000**, *7*, 1581; i) M. D. Ward, *J. Chem. Educ.* **2001**, *78*, 321.

[3] a) B. S. Brunschwig, N. Sutin, *Coord. Chem. Rev.* **1999**, *187*, 233; b) A. Bencini, I. Ciofini, C. A. Daul, A. Ferretti, *J. Am. Chem. Soc.* **1999**, *121*, 11418.

[4] a) D. E. Richardson, H. Taube, *Coord. Chem. Rev.* **1984**, *60*, 107; b) C. E. B. Evans, M. L. Naklicki, A. R. Rezvani, C. A. White, V. V. V. Kondratiev, R. J. Crutchley, *J. Am. Chem. Soc.* **1998**, *120*, 13096; c) F. Barriere, N. Camire, W. E. Geiger, U. T. Mueller-Westerhoff, R. Sanders, *J. Am. Chem. Soc.* **2002**, *124*, 7262; d) G. M. Brown, N. Sutin, *J. Am. Chem. Soc.* **1979**, *101*, 883.

[5] a) M. Al-Noaimi, G. P. A. Yap, R. J. Crutchley, *Inorg. Chem.* **2004**, *43*, 1770; b) K. D. Demadis, C. M. Hartshorn, T. J. Meyer, *Chem. Rev.* **2001**, *101*, 2655.

[6] S. Ghumaan, B. Sarkar, S. Patra, J. van Slageren, J. Fiedler, W. Kaim, G. K. Lahiri, *Inorg. Chem.* **2005**, *44*, 3210.

[7] A. Shukla, A. Das, *Polyhedron* **2000**, *19*, 2605.

[8] S. Kar, B. Sarkar, S. Ghumaan, D. Janardanan, J. van Slageren, J. Fiedler, V. G. Puranik, R. B. Sunoj, W. Kaim, G. K. Lahiri, *Chem. Eur. J.* **2005**, *11*, 4901.

[9] M. D. Ward, *Inorg. Chem.* **1996**, *35*, 1712.

[10] a) A. Dei, D. Gatteschi, L. Pardi, *Inorg. Chem.* **1990**, *29*, 1442; b) S. Bruni, F. Cariati, A. Dei, D. Gatteschi, *Inorg. Chim. Acta* **1991**, *186*, 157.

[11] G. G. Sadler, N. R. Gordon, *Inorg. Chim. Acta* **1991**, *180*, 271.

[12] H. Masui, A. L. Freda, M. C. Zerner, A. B. P. Lever, *Inorg. Chem.* **2000**, *39*, 141.

[13] L. F. Joulie, E. Schatz, M. D. Ward, F. Weber, L. J. Yellowlees, *J. Chem. Soc., Dalton Trans.* **1994**, 799.

[14] S. Patra, B. Sarkar, S. Ghumaan, J. Fiedler, S. Zalis, W. Kaim, G. K. Lahiri, *Dalton Trans.* **2004**, *5*, 750.

[15] P. R. Auburn, A. B. P. Lever, *Inorg. Chem.* **1990**, *29*, 2551.

[16] S. Joss, H. Reust, A. Ludi, *J. Am. Chem. Soc.* **1981**, *103*, 981.

[17] a) S. Patra, B. Sarkar, S. M. Mobin, W. Kaim, G. K. Lahiri, *Inorg. Chem.* **2003**, *42*, 6469; b) P. Ghosh, A. Begum, D. Herebian, E. Bothe, K. Hildenbrand, T. Weyhermüller, K. Wieghardt, *Angew. Chem.* **2003**, *115*, 581; *Angew. Chem. Int. Ed.* **2003**, *42*, 563; c) K. S. Min, T. Weyhermüller, K. Wieghardt, *Dalton Trans.* **2003**, 1126; d) C. Remenyi, M. Kaupp, *J. Am. Chem. Soc.* **2005**, *127*, 11399; e) H. Chun, E. Bill, E. Bothe, T. Weyhermüller, K. Wieghardt, *Inorg. Chem.* **2002**, *41*, 5091; f) W. Kaim, M. Wanner, A. Knödler, S. Zalis, *Inorg. Chim. Acta* **2002**, *337*, 163; g) C. G. Pierpont, *Coord. Chem. Rev.* **2001**, *219–221*, 415; h) P. Chaudhuri, C. N. Verani, E. Bill, E. Bothe, T. Weyhermüller, K. Wieghardt, *J. Am. Chem. Soc.* **2001**, *123*, 2213; i) C. G. Pierpont, A. S. Attia, *Collect. Czech. Chem. Commun.* **2001**, *66*, 33; j) J. Rall, M. Wanner, M. Albrecht, F. M. Hornung, W. Kaim, *Chem. Eur. J.* **1999**, *5*, 2802; k) C. N. Verani, S. Gallert, E. Bill, T. Weyhermüller, K. Wieghardt, P. Chaudhuri, *Chem. Commun.* **1999**, 1747; l) M. Ebadi, A. B. P. Lever, *Inorg. Chem.* **1999**, *38*, 467; m) J. Rall, E. Waldhör, B. Schwederski, M. Schwach, S. Kohlmann, W. Kaim, in *Bioinorganic Chemistry: Transition Metals in Biology and their Coodination Chemistry* (Ed.: A. X. Trautwein), VCH, Weinheim, **1997**, pp. 476; n) R. A. Metcalfe, A. B. P. Lever, *Inorg. Chem.* **1997**, *36*, 4762; o) G. Speier, A. Whalen, J. Csihony, C. G. Pierpont, *Inorg. Chem.* **1995**, *34*, 1355; p) C. G. Pierpont, C. W. Lange, *Prog. Inorg. Chem.* **1994**, *41*, 331; q) J. Rall, W. Kaim, *J. Chem. Soc., Faraday Trans.* **1994**, *90*, 2905; r) H. Masui, A. B. P. Lever, E. S. Dodsworth, *Inorg. Chem.* **1993**, *32*, 258; s) B. Schwederski, W. Kaim, *Inorg. Chim. Acta* **1992**, *195*, 123; t) N. Bag, G. K. Lahiri, P. Basu, A. Chakravorty, *J. Chem. Soc., Dalton Trans.* **1992**, 113; u) H. Masui, A. B. P. Lever, P. Auburn, *Inorg. Chem.* **1991**, *30*, 2402; v) S. Ernst, P. Hänel, J. Jordanov, W. Kaim, V. Kasack, E. Roth, *J. Am. Chem. Soc.* **1989**, *111*, 1733; w) S. Ernst, V. Kasack, C. Bessenbacher, W. Kaim, *Z. Naturforsch., Teil B* **1987**, *42*, 425; x) M. Haga, E. S. Dodsworth, A. B. P. Lever, *Inorg. Chem.* **1986**, *25*, 447; y) R. B. Salmonsen, A. Abelleira, M. J. Clarke, *Inorg. Chem.* **1984**, *23*, 387; z) A. Dei, D. Gatteschi, C. Sangregorio, L. Sorace, *Acc. Chem. Res.* **2004**, *37*, 827.

[18] a) B. Sarkar, S. Patra, J. Fiedler, R. B. Sunoj, D. Janardanan, S. M. Mobin, M. Niemeyer, G. K. Lahiri, W. Kaim, *Angew. Chem. Int. Ed.* **2005**, *44*, 5655; b) J. A. Zampese, F. R. Keene, P. J. Steel, *Dalton Trans.* **2004**, 4124.

[19] S. Patra, B. Mondal, B. Sarkar, M. Niemeyer, G. K. Lahiri, *Inorg. Chem.* **2003**, *42*, 1322.

[20] G. K. J. Chao, R. L. Sime, R. J. Sime, *Acta Crystallogr., Sect. B* **1973**, *29*, 2845.

[21] S. Kar, N. Chanda, S. M. Mobin, F. A. Urbanos, M. Niemeyer, V. G. Puranik, R. Jimenez-Aparicio, G. K. Lahiri, *Inorg. Chem.* **2005**, *44*, 1571.

[22] A. Seal, S. Ray, *Acta Crystallogr., Sect. C* **1984**, *40*, 929.

[23] B. K. Santra, G. A. Thakur, P. Ghosh, A. Pramanik, G. K. Lahiri, *Inorg. Chem.* **1996**, *28*, 3050.

[24] a) A. Mostad, C. Romming, *Acta Chem. Scand.* **1971**, *25*, 3561; b) C. H. Chang, R. F. Porter, S. H. Bauer, *J. Am. Chem. Soc.* **1970**, *92*, 5313; c) S. P. Sengupta, T. Roy, *Cryst. Struct. Commun.* **1980**, *9*, 965; d) N. Bag, A. Pramanik, G. K. Lahiri, A. Chakravorty, *Inorg. Chem.* **1992**, *31*, 40; e) R. A. Krause, K. Krause, *Inorg. Chem.* **1982**, *21*, 1714; f) A. K. Deb, P. C. Paul, S. Goswami, *J. Chem. Soc., Dalton Trans.* **1988**, 2051; g) A. Saha, C. Das, S. Goswami, S.-M. Peng, *Indian J. Chem. Sect. A* **2001**, *40*, 198.

[25] K. Heinze, S. Mann, G. Huttner, L. Zsolnai, *Chem. Ber.* **1996**, *129*, 115.

[26] S. Arnold, V. Mansel, G. Klar, *Z. Naturforsch., Teil B* **1990**, *45*, 369.

[27] C. G. Pierpont, L. C. Francesconi, D. N. Hendrickson, *Inorg. Chem.* **1978**, *17*, 3470.

[28] M. J. Maroney, R. O. Day, T. Psyris, L. M. Fleury, J. P. Whitehead, *Inorg. Chem.* **1989**, *28*, 173.

[29] A. Elduque, F. Aguilera, F. J. Lahoz, J. A. Lopez, L. A. Oro, M. T. Pinillos, *Inorg. Chim. Acta* **1998**, *274*, 15.

[30] a) A. Bharath, B. K. Santra, P. Munshi, G. K. Lahiri, *J. Chem. Soc., Dalton Trans.* **1998**, 2643; b) B. K. Santra, G. K. Lahiri, *J. Chem. Soc., Dalton Trans.* **1998**, 139; c) B. K. Santra, G. K. Lahiri, *J. Chem. Soc., Dalton Trans.* **1997**, 129.

[31] C. Creutz, *Prog. Inorg. Chem.* **1983**, *30*, 1.

[32] S. Patra, T. A. Miller, B. Sarkar, M. Niemeyer, M. D. Ward, G. K. Lahiri, *Inorg. Chem.* **2003**, *42*, 4707.

[33] B. Mondal, M. G. Walawalkar, G. K. Lahiri, *J. Chem. Soc., Dalton Trans.* **2000**, 4209.

[34] N. Chanda, B. Sarkar, J. Fiedler, W. Kaim, G. K. Lahiri, *Dalton Trans.* **2003**, 3550.

[35] S. Patra, B. Sarkar, S. Maji, J. Fiedler, F. A. Urbanos, R. Jimenez-Aparicio, W. Kaim, G. K. Lahiri, *Chem. Eur. J.* **2006**, *12*, 489.

[36] S. Chakraborty, R. H. Laye, R. L. Paul, R. G. Gonnade, V. G. Puranik, M. D. Ward, G. K. Lahiri, *J. Chem. Soc., Dalton Trans.* **2002**, 1172.

[37] B. Mondal, H. Paul, V. G. Puranik, G. K. Lahiri, *J. Chem. Soc., Dalton Trans.* **2001**, 481.

[38] a) S. Patra, B. Sarkar, S. Ghumaan, J. Fiedler, W. Kaim, G. K. Lahiri, *Dalton Trans.* **2004**, 754; b) N. Chanda, R. H. Laye, S. Chakraborty, R. L. Paul, J. C. Jeffery, M. D. Ward, G. K. Lahiri, *J. Chem. Soc., Dalton Trans.* **2002**, 3496; c) S. Patra, B. Sarkar, S. Ghumaan, J. Fiedler, W. Kaim, G. K. Lahiri, *Inorg. Chem.* **2004**, *43*, 6108.

 © 2006 Wiley-VCH Verlag GmbH & Co. KGaA, Weinheim 

[39] a) J. M. Villegas, S. R. Stoyanov, W. Huang, L. J. Lockyear, J. H. Reibenspies, D. P. Rillema, *Inorg. Chem.* **2004**, *43*, 6383; b) S. R. Stoyanov, J. M. Villegas, D. P. Rillema, *Inorg. Chem.* **2002**, *41*, 2941; c) S. R. Stoyanov, J. M. Villegas, D. P. Rillema, *Inorg. Chem. Commun.* **2004**, *7*, 838.
[40] Conversion of calculated oscillator strength to molar absorptivity was done based on the following references: a) R. S. Drago, in *Physical Methods for Chemists*, 2nd ed., Saunders College Publishing, Ft. Worth, Texas, **1992**; b) J. E. Monat, J. H. Rodriguez, J. K. McCusker, *J. Phys. Chem. A* **2002**, *106*, 7399.
[41] N. S. Hush, *Prog. Inorg. Chem.* **1967**, *8*, 391.
[42] S. Goswami, A. R. Chakravarty, A. Chakravorty, *Inorg. Chem.* **1983**, *22*, 602.
[43] G. M. Sheldrick, *SHELXS-97*, Program for Crystal Structure Solution and Refinement, University of Göttingen, Germany, **1997**.
[44] a) A. D. Becke, *Phys. Rev. A* **1988**, *38*, 3098; b) C. Lee, W. Yang, R. G. Parr, *Phys. Rev. B* **1988**, *37*, 785; c) D. Andrae, U. Haeussermann, M. Dolg, H. Stoll, H. Preuss, *Theor. Chim. Acta* **1990**, *77*, 123; d) P. Fuentealba, H. Preuss, H. Stoll, L. V. Szentpaly, *Chem. Phys. Lett.* **1989**, *89*, 418; e) M. J. Frisch, et al. *Gaussian03*, revision C.02; Gaussian, Inc.: Wallingford CT, **2004**; f) Frisch et al. *Gaussian 98*, revision A.11. 4; Gaussian, Inc.: Pittsburgh, PA, **1998**; g) M. Casida, in *Recent Advances in Density Functional Methods* (Ed.: D. P. Chong), World Scientific Press, Singapore, **1995**, vol. I, pp. 155; h) G. Schaftenaar, J. H. Noordik, *J. Comput.-Aided Mol. Design* **2000**, *14*, 123; i) S. I. Gorelsky, *AOMIX* program, http://www.sg-chem.net/; j) S. I. Gorelsky, A. B. P. Lever, *J. Organomet. Chem.* **2001**, *635*, 187.

Received: May 3, 2006
Published Online: August 24, 2006

 © 2006 Wiley-VCH Verlag GmbH & Co. KGaA, Weinheim 

DOI: 10.1002/ejic.200600469

# Synthesis of New Phenanthroline-Based Heteroditopic Ligands – Highly Efficient and Selective Fluorescence Sensors for Copper(II) Ions

**Peter Comba,*[a] Roland Krämer,[a] Andriy Mokhir,[a] Kyaw Naing,[a] and Erik Schatz[a]**

**Keywords:** Sensor / Fluorescence / Copper(II) / Selectivity / Ruthenium

The heteroditopic phenanthroline derivatives 5,6-bis(2-pyridylcarboxamido)-1,10-phenanthroline ($H_2L^1$) and 5,6-bis[(4-methoxy-2-pyridyl)carboxamido]-1,10-phenanthroline ($H_2L^2$) have been prepared and characterized, together with their luminescent ruthenium(II) complexes $[Ru(bpy)_2(H_2L^{1,2})](PF_6)_2$ and $[Ru(H_2L^1)_3](PF_6)_2$ and the corresponding iron(II) complex $[Fe(H_2L^1)_3](PF_6)_2$. In these complexes, the metal ion is coordinated by the bidentate phen site of $H_2L$. The luminescence of the ruthenium complexes ($\lambda_{ex}$ = 450 nm, $\lambda_{em}$ ca. 620 nm) is completely quenched by $Cu^{2+}$ ions in the micromolar concentration range and, to a lesser extent, by other metal ions. At pH 5, the response of the luminescent sensors is highly $Cu^{2+}$-selective. Heterodinuclear complexes $[Ru(bpy)_2(LM)](PF_6)_2$, $[Ru(LM)_3](PF_6)_2$, and $[Fe(LM)_3](PF_6)_2$ have been isolated for M = $Cu^{2+}$, $Ni^{2+}$, $Co^{2+}$, and $Pd^{2+}$. It is suggested that M is coordinated to the tetradentate N4 site of L by two deprotonated amide N atoms and two pyridyl groups. This coordination type is confirmed by the EPR spectrum of the compound $[Ru^{II}(bpy)_2(L^1Cu^{II})](PF_6)_2$.

(© Wiley-VCH Verlag GmbH & Co. KGaA, 69451 Weinheim, Germany, 2006)

## Introduction

For many good reasons di- and oligonuclear transition-metal complexes are attracting much interest. Cooperativity in general and, more specifically, electron and energy transfer as well as magnetic interactions have been recognized as important and rather general features in biological systems,[1,2] and there is an increasing range of applications in areas such as catalysis,[3,4] analytical chemistry (metal-ion- and anion-selective sensors),[5,6] and information technology (switches).[7] Most of these applications imply that the two metal centers in a dinuclear complex have different functions and, therefore, different properties. Synthetically, the required ligand asymmetry is often a demanding task.[8] An attractive approach is to couple a photoactive coordination site covalently to a ligand, which selectively coordinates another metal ion or has a second coordination center that selectively binds anions or activates substrates. Tris(bipyridine)ruthenium(II)-derived systems have been used frequently in this area,[9,10] and metal-ion- and anion-selective sensors,[10–16] photocatalysts,[12–14] and photoactive pharmaceuticals[15,16] have been reported.

Generally, the synthesis of this type of system relies on a suitable ditopic ligand with a multidentate or macrocyclic donor set, coupled to 1,10-phenanthroline (phen) or 2,2′-bipyridine (bpy). We report here on the synthesis of the two heteroditopic ligands $H_2L^1$ and $H_2L^2$ (Scheme 1) based on 5,6-diamino-1,10-phenanthroline and the synthesis of the corresponding ruthenium(II) complexes ($[Ru(bpy)_2(H_2L^{1,2})]^{2+}$ and $[Ru(H_2L^1)_3]^{2+}$) and their hetero-oligonuclear transition-metal complexes ($[Ru(bpy)_2\{(L^{1,2})M\}]^{2+}$ and $[Ru\{(L^1)M\}_3]^{2+}$, M = divalent transition-metal ion, e.g. $Cu^{2+}$). Of specific interest are the strong and selective coordination of first-row transition-metal ions to the coordina-

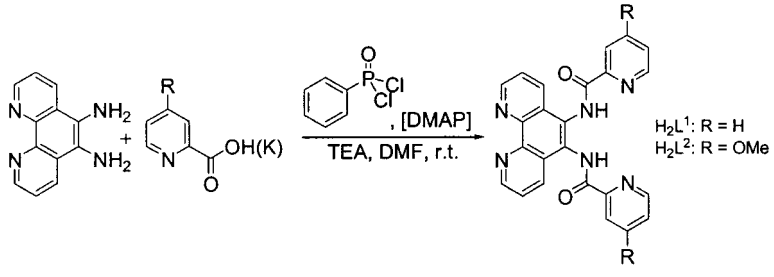


Scheme 1.

[a] Universität Heidelberg, Anorganisch-Chemisches Institut, Im Neuenheimer Feld 270, 69120 Heidelberg, Germany
Fax: +49-6221-54-66-17
E-mail: peter.comba@aci.uni-heidelberg.de


© 2006 Wiley-VCH Verlag GmbH & Co. KGaA, Weinheim

tion site offered by $L^1$ and $L^2$ and the quenching of the fluorescence of the tris(bipyridine-type)ruthenium(II) site by this selective coordination event.

## Results and Discussion

### Syntheses and Characterization

The heteroditopic ligands $H_2L^1$ and $H_2L^2$ are prepared in respectable yields from 5,6-diamino-1,10-phenanthroline[17–19] (obtained in high yield by the reduction of 1,10-phenanthroline-5,6-dione dioxime with sodium dithionite[20] or formamidinesulfinic acid[21]) and picolinic acid or its methoxy derivative, respectively (Scheme 1). Because of solubility problems, air sensitivity, and poor reactivity of the amine groups, the acylation is performed under inert conditions in DMF, with DMAP[22] as the acylation catalyst, phenylphosphonic acid dichloride[23–26] as the activation reagent for the carboxylic group, and TEA as base. The $Ru^{2+}$ complexes $[Ru(bpy)_2(H_2L^{1,2})]^{2+}$ and $[Ru(H_2L^1)_3]^{2+}$ are obtained by the usual methods and in high yields.[10] Low-spin $Fe^{2+}$ complexes have also been obtained but are not discussed here in detail. The red mononuclear $Ru^{2+}$ complexes have the characteristic MLCT transitions at around 450 nm, they show resonances in the $^1H$ NMR spectra for the amide protons at around 10.5 ppm and have the expected vibrations for amide bonds in the infrared spectra at approximately 1680 and 1570 $cm^{-1}$, as well as the amide N–H transitions at approximately 3300 $cm^{-1}$. Upon coordination of metal ions to the $L^1$ ($L^2$) sites, the N–H vibration disappears, the amide transitions shift to a lower energy (ca. 30–50 $cm^{-1}$), and the MLCT transitions are shifted to a higher energy.

The EPR spectra of the mono- and tris-$Cu^{II}$ complexes are similar to each other and typical for tetragonal $Cu^{II}$ sites, with $g$ and $A$ values ($g_\parallel = 2.213$, $A_\parallel = 180 \times 10^{-4}$ $cm^{-1}$) that are typical for tetrahedrally distorted coordination sites.[9] The similarity of the EPR spectra indicates that there is no $Cu^{II}\cdots Cu^{II}$ magnetic exchange interaction and only a very weak, i.e. negligible, dipolar coupling interaction (Figure 1b). A model of the structure (Figure 1a), obtained by force field calculations,[27,28] visualizes the $Cu^{II}$ planes that are distorted because of the α-H atoms of the pyridine donors and indicates a distance of ca. 13 Å between the $Cu^{II}$ centers.

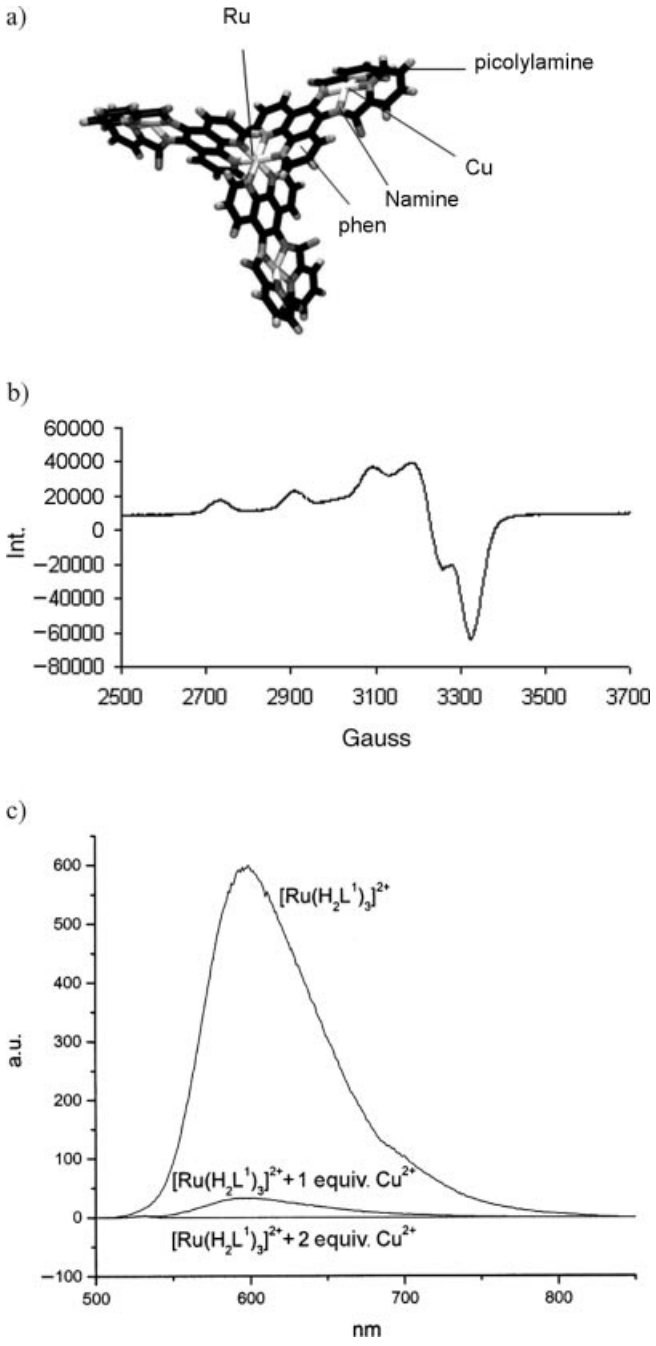


Figure 1. (a) Structural model of $[Ru\{(L^1)Cu\}_3]^{2+}$; (b) X-band EPR spectrum of $[Ru\{\mu\text{-}(L^1)Cu\}_3](PF_6)_2$ (ca. $10^{-3}$ M, DMF-$H_2O$-glass (2:1), 110 K); and (c) relative fluorescence intensities ($\lambda_{ex}$ = 450 nm, $\lambda_{em}$ = 620 nm) in aqueous solution at pH 7 (lutidine buffer) of $[Ru(H_2L^1)_3](PF_6)_2$ alone (10 μM), and after addition of 1 or 2 equiv. $CuSO_4$.

### Fluorescence Measurements

The luminescence spectra of $[Ru(bpy)_2(H_2L^1)]^{2+}$, $[Ru(bpy)_2(H_2L^2)]^{2+}$, and $[Ru(H_2L^1)_3]^{2+}$ are as expected for $Ru^{2+}$ polypyridine chromophores (transition at ca. 620 nm,[13] see Figure 1c); also shown in Figure 1c is the efficient fluorescence quenching of $[Ru(H_2L^1)_3]^{2+}$ with $Cu^{2+}$ ($[Ru^{2+}]/[Cu^{2+}]$ = 1:0, 1:1, 1:2). Similar effects are observed with $[Ru(bpy)_2(H_2L^1)]^{2+}$ and $[Ru(bpy)_2(H_2L^2)]^{2+}$, i.e. these complexes are, as expected, good on/off sensors for metal ions, specifically for $Cu^{2+}$ and $Ni^{2+}$, which have electronic transitions at similar energies and are known to strongly bind to amide donors already at physiological pH.[10,29]

To fully characterize the $L^1$- and $L^2$-based $Cu^{2+}$ sensors, the luminescence intensities (aqueous solutions, $[Ru^{2+}] = 10^{-5}$ M) were studied as a function of pH, buffer base, anion, and $M^{n+}$ concentration (M = $Cu^{2+}$, $Ni^{2+}$, $Co^{2+}$, $Fe^{2+/3+}$, $Zn^{2+}$, $Al^{3+}$, $Nd^{3+}$, $Mn^{2+}$, $Pb^{2+}$, alkali, and alkaline earth

 © 2006 Wiley-VCH Verlag GmbH & Co. KGaA, Weinheim 

metal ions; see Table 1 for an overview of the most relevant results.). Buffer bases such as acetate, citrate, carbonate, phosphate, and lutidine as well as EDTA do not quench the fluorescence. Aminoalkylsufonates (e.g., MOPS, MES) lead to an approximately 50% reduction of the luminescence intensity, i.e., these are not suited as buffer bases in our systems. Usual inorganic anions or carboxylates do not affect the fluorescence intensity (see Table 1 and above). In addition, $Al^{3+}$, $Nd^{3+}$, $Mn^{2+}$, $Pb^{2+}$, and group 1 and 2 cations do not alter the luminescence spectra. Interestingly, protonation of the pyridine donors and deprotonation of an amide site lead to drastic changes in the luminescence properties (Figure 2). This is in contrast to other $Ru(bpy)_2$-amide sensors,[10] which have pH-independent luminescence intensities over a pH range of 2–12. This indicates that the published and present systems probably differ with respect to the mechanism of quenching of the excited state [electron (PET) vs. energy transfer (EET)].[12]

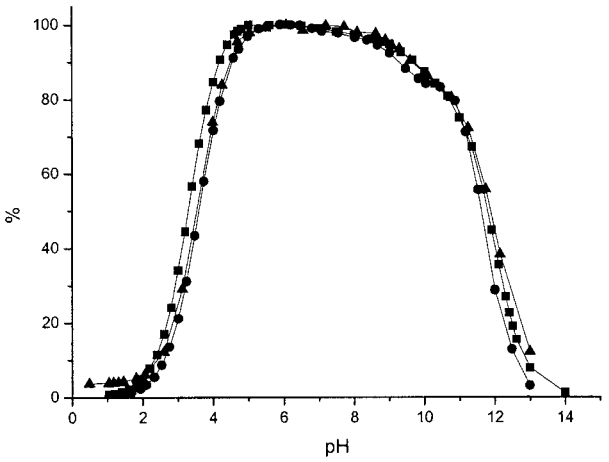


Figure 2. pH-dependence of the relative fluorescence intensity of 10 μM aqueous solutions of the complexes ($\lambda_{ex}$ = 450 nm, $\lambda_{em}$ = 620 nm) $[Ru(bpy)_2(H_2L^1)]^{2+}$ (■), $[Ru(H_2L^1)_3]^{2+}$ (▲), and $[Ru(bpy)_2(H_2L^2)]^{2+}$ (●).

Table 1. Reduction of the fluorescence intensity (in %) of $[Ru(bpy)_2(H_2L^1)]^{2+}$ as a function of added metal ions and pH.

| Added metal ion | pH | % Reduction of fluorescence intensity of $[Ru(bpy)_2(H_2L^1)]^{2+}$ |
|---|---|---|
| 1 equiv. $Cu^{2+}$ | 5 | 99 |
| 2 equiv. $Cu^{2+}$ | 5 | 99 |
| 10 equiv. $Co^{2+}$ | 5 | 2 |
| 10 equiv. $Fe^{2+}$ | 5 | 1 |
| 1 equiv. $Ni^{2+}$ | 5 | 0 |
| 10 equiv. $Ni^{2+}$ | 5 | 5 |
| 10 equiv. $Zn^{2+}$ | 5 | 1 |
| 10 equiv. $Fe^{2+}$ + 1 equiv. $Cu^{2+}$ | 5 | 98 |
| 100 equiv. $Ni^{2+}$ + 1 equiv. $Cu^{2+}$ | 5 | 99 |
| 10 equiv. $Zn^{2+}$ + 1 equiv. $Cu^{2+}$ | 5 | 99 |
| 1 equiv. $Cu^{2+}$ | 7 | 98 |
| 1 equiv. $Co^{2+}$ | 7 | 70 |
| 10 equiv. $Co^{2+}$ | 7 | 90 |
| 10 equiv. $Fe^{2+}$ | 7 | 80 |
| 10 equiv. $Mn^{2+}$ | 7 | 3 |
| 1 equiv. $Ni^{2+}$ | 7 | 80 |
| 10 equiv. $Ni^{2+}$ | 7 | 85 |
| 1 equiv. $Zn^{2+}$ | 7 | 40 |
| 10 equiv. $Pb^{2+}$ | 7 | 0 |
| 10 equiv. $Cu^{2+}$ | 7 | 0 |
| 10 equiv. $Mg^{2+}$ | 7 | 0 |
| 1 equiv. $Cu^{2+}$ + 10 equiv. $Co^{2+}$ | 7 | 99 |
| 1 equiv. $Cu^{2+}$ + 10 equiv. $Fe^{2+}$ | 7 | 99 |
| 1 equiv. $Cu^{2+}$ + 10 equiv. $Pb^{2+}$ | 7 | 99 |

From the plot in Figure 2, it follows that for $[Ru(bpy)_2(H_2L^1)]^{2+}$ the luminescence intensity is virtually constant over the pH range 4.5–8.5. For $[Ru(bpy)_2(H_2L^2)]^{2+}$ and $[Ru(H_2L^{1,2})_3]^{2+}$ the pH ranges of approximately constant luminescence are similar (pH 4.7–9.0). At a lower pH, the fluorescence intensity drops sharply to nearly zero at pH < 2. The sigmoidal curves suggest p$K_a$ values of ≈3, which is in the expected range for substituted pyridine groups [p$K_a$(20–25 °C) = 2.1–2.4].[30] The decrease in the luminescence intensity at high pH (luminescence intensity approximately zero at pH > 14, p$K_a$ ≈ 11.5) suggests a deprotonation of an amide donor, and this also occurs in the expected range [p$K_a$(25 °C) ≈ 12].[33]

Figure 3 shows the pH-dependent luminescence of $[Ru(bpy)_2(H_2L^1)]^{2+}$ together with that of the $[Ru(bpy)_2(H_2L^1)]^{2+}/Cu^{2+}$ system (1 equiv. $Cu^{2+}$). Also shown in Figure 3 is the $Cu^{2+}$-concentration dependence of the fluorescence intensity at pH 4.9 (acetate buffer). At pH 5, no other metal ion leads to any fluorescence quenching, i.e. at pH 5 the $[Ru(bpy)_2(H_2L^1)]^{2+}$ on/off fluorescence sensor is selective for $Cu^{2+}$.

All three systems, $[Ru(bpy)_2(H_2L^1)]^{2+}$, $[Ru(bpy)_2(H_2L^2)]^{2+}$, and $[Ru(H_2L^1)_3]^{2+}$, show very similar behavior with respect to the metal-ion-induced fluorescence quenching, specifically in terms of the metal-ion- and pH-dependencies and the competition with other ligands (Table 1): (i) at pH 5 (acetate buffer), $Cu^{2+}$ is the only metal ion that leads to significant quenching; the addition of an excess of any other metal ion does not have any influence on the fluorescence intensity observed with $Cu^{2+}$ alone; (ii) at pH 7 (lutidine buffer), the reduction of the fluorescence intensity with one equivalent of $Cu^{2+}$ is ≈100%, those due to $Ni^{2+}$, $Fe^{2+/3+}$, $Co^{2+}$, and $Zn^{2+}$ are significantly smaller (40–85%), all other metal ions studied do not lead to any quenching; the kinetics of complex formation with $Ni^{2+}$ is very slow, full equilibration (pH 7; 1 or 10 equiv. $Ni^{2+}$) needs at least 1 h (complexation of all other metal ions is fast, i.e., equilibration within minutes); (iii) at pH 7, acetate does not lead to any significant reduction of the quenching efficiency of $Cu^{2+}$, with citrate there is some competition, and with EDTA fluorescence quenching is only observed after complexation with EDTA is complete [from semiquantitative experiments and the known stability constants $\log K^{ML}$(Cu–acetate) = 1.75,[31] $\log K^{ML}$(Cu–citrate) = 4.5,[32] $\log K^{ML}$(Cu–EDTA) = 19.2,[33] an approximate value of $\log K^{ML}([Ru(bpy)_2\{(H_2L^1)Cu\}]^{2+}) = 12 \pm 2$ may be deduced].

 © 2006 Wiley-VCH Verlag GmbH & Co. KGaA, Weinheim 

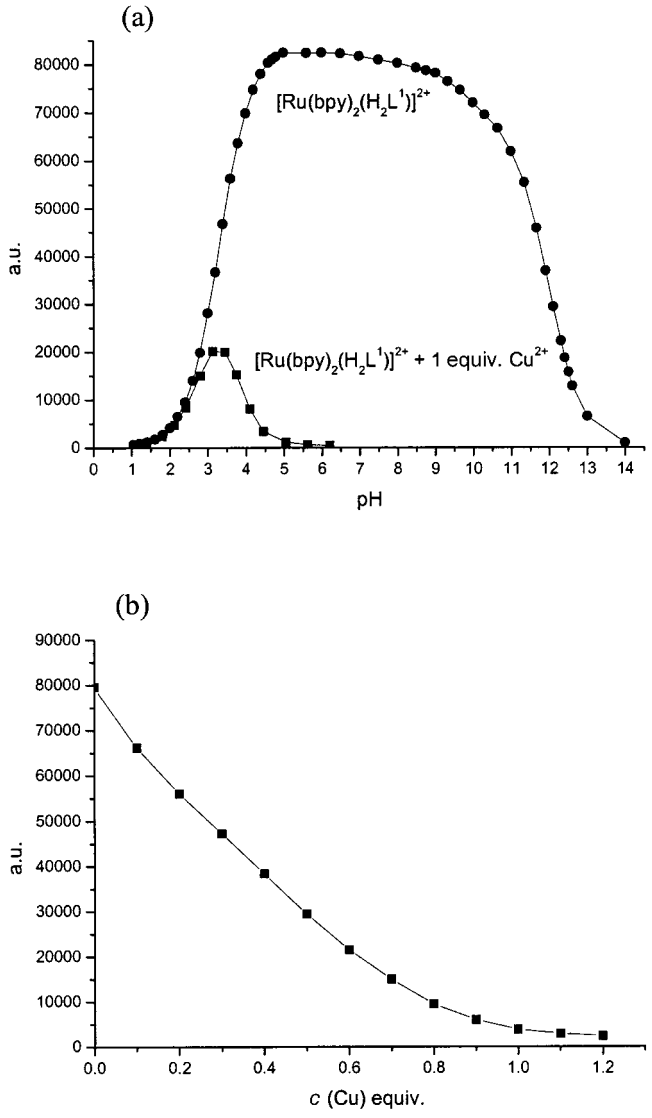


Figure 3. (a) pH-dependence of the luminescence of $[Ru(bpy)_2(H_2L^1)]^{2+}$ (10 μM aqueous solution) with or without 1 equiv. of $Cu^{2+}$, $\lambda_{ex}$ = 450 nm, $\lambda_{em}$ = 620 nm. (b) Fluorimetric titration of $[Ru(bpy)_2(H_2L^1)]^{2+}$ ($10^{-5}$ M) with $Cu^{2+}$ in acetate buffer (100 equiv.) at pH 4.9.

## Conclusions

The synthesis of a rigid ditopic ligand with a 1,10-phenanthroline and a bis(pyridinamide) coordination site, based on a general strategy, which may be used to prepare a variety of 1,10-phenanthroline-derived ditopic ligands with a range of donor sets, has led to $Ru^{2+}$-polypyridine-based fluorescence on/off sensors that are highly selective for $Cu^{2+}$ in aqueous solution at low pH. The rational design of the structure and donor set of the host, which, upon coordination of a metal ion, leads to fluorescence quenching,[34–36] should make possible the development of systems that show a range of specific selectivities in various pH regions.

## Experimental Section

**Materials and Measurements:** Commercially available chemicals were used without further purification; solvents were dried by standard methods; solvents and chemicals for spectroscopy were of the highest possible grade and used as purchased. 1,10-Phenanthroline-5,6-dione dioxime was obtained by oxidation of 1,10-phenanthroline to 1,10-phenanthroline-5,6-dione[37] and subsequent reaction with hydroxylamine.[18] (4-Chloro-2-pyridyl)carboxylic acid methyl ester and (4-methoxy-2-pyridyl)carboxylic acid methyl ester were obtained as described from picolinic acid.[38]

UV/Vis/NIR spectra ($CH_3CN$, ambient temperature) were recorded with a Cary 1E or a JASCO V-570 spectrophotometer. IR spectra (KBr pellets) were obtained with a Perkin–Elmer 16C FTIR instrument. $^1H$ NMR spectra were recorded at room temperature with a Bruker ARX 200 or a Bruker Avance 500 spectrometer; the chemical shifts are relative to the solvent that is used as the internal standard. Electrochemical data were obtained by cyclic voltammetry [100 mV/sec., complex solutions ($2\times10^{-3}$ M), ambient temperature, tetrabutylammonium hexafluorophosphate (0.1 M) in $CH_3CN$], measured with a BAS100B electrochemical analyzer (data analysis with Digisim), by using a glassy carbon working electrode, a Pt-wire auxiliary, and a $Ag/AgNO_3$ reference electrode (0.01 M $AgNO_3$); ferrocene was used as an external standard. EPR spectra were recorded with a Bruker ELEXSYS E500 spectrometer [frozen solutions (approx. $10^{-3}$ M) in $DMF/H_2O$ = 2:1] at 110 K. Mass spectra were recorded with a Finnigan 8400 or a JEOL JMS700 sector field instrument (EI or FAB) with a nitrobenzyl alcohol matrix (Nibeol, NBA) for the FAB spectra; electrospray mass spectra were recorded with a Finnigan TSQ 700 triple-quadrupole or a Q-Tof Ultima API mass spectrometer (Micromass/Waters, ESI) with analyte solutions in acetonitrile or methanol in the concentration range $10^{-6}$–$10^{-5}$ M. For HR-EI, HR-FAB, and HR-ESI spectra deviations from the theoretical mass are generally smaller than 5 mD, the internal standards used are reported with the experimental data. Emission spectra were recorded with a Varian Cary Eclipse fluorescence spectrophotometer at an excitation wavelength of 450 nm (intensities not calibrated). Fluorimetric titrations were performed in aqueous solutions (equilibrated in air, $\mu$ = 0.1; NaCl; the concentrations of the ruthenium complexes were $10^{-5}$ M). Metal ions were added as the chloride, perchlorate, or sulfate salts, and there was no dependence on the type of anion within this group. Standard HCl and NaOH solutions were used for adjusting the pH. Buffers at pH 4.7–5 and 7 were made by using the acetate/acetic acid and the lutidine/lutidinium couples, respectively.

**Syntheses**

**5,6-Diamino-1,10-phenanthroline**[17–19]

**Method A:** A suspension of phenanthroline-5,6-dione dioxime (2.88 g, 12 mmol) in ethanol (80 mL) was heated under $N_2$ (70 °C). A solution of sodium dithionite (85%, 9 g, 45 mmol) in aqueous ammonia (3%, 80 mL) was quickly added. An additional amount of sodium dithionite (85%, 3 g, 15 mmol) in aqueous ammonia (3%, 40 mL) solution was added when the yellow product started to precipitate as yellow flakes after dissolution of the dioxime. The reaction was then kept for 45 min at 85 °C. After being cooled to ambient temperature, the product was filtered under $N_2$, washed 3 times with diluted ammonia and then with THF, and dried overnight under high vacuum. Yield: 2.17 g (10.3 mmol, 86%), deep yellow solid.

**Method B:** Ethanol (150 mL, 50%) and a concentrated ammonia solution (10 mL) were added to a mixture of phenanthroline-5,6-dione dioxime (2.4 g, 10 mmol) and thiourea *S*,*S*-dioxide (5 g, 46.3 mmol) under nitrogen whilst stirring. The mixture was placed in a preheated (80 °C) oil bath and left to react for 45 min. The 5,6-diamino-1,10-phenanthroline started to precipitate after ≈15 min. After being cooled to room temperature, the product was isolated

 © 2006 Wiley-VCH Verlag GmbH & Co. KGaA, Weinheim 

as described above. Yield: 1.79 g (8.1 mmol, 81%). $C_{12}H_{10}N_4 \cdot \frac{1}{6}H_2O$ (213.23): calcd. C 67.59, H 4.88, N 26.27; found C 67.81, H 4.62, N 26.03. MS (EI+): $m/z$ = 210 [$M^+$].

**Potassium Salts of Substituted Picolinic Acids:** KOH (0.95 equiv.) in a minimum amount of EtOH was added to a stirred solution of the methyl ester of the corresponding substituted picolinic acid derivative in dry ethanol (2 mL/mmol). After 6 h, $Et_2O$ (1/5 volume) was added. The product was filtered, washed with EtOH/$Et_2O$, and dried under high vacuum.

**Potassium (4-Cloro-2-pyridyl)carboxylate:** Yield: 84%. M.p. > 350 °C. $C_6H_3ClKNO_2$ (195.64): calcd. C 36.83, H 1.55, N 7.16; found C 36.98, H 1.82, N 7.22. MS (ESI-): $m/z$ = 156 [M – $H^-$]. $^1$H NMR (200 MHz, $D_2O$): $\delta$ = 7.63 (dd, $^3J$ = 5.3 Hz, $^4J$ = 1.9 Hz, 1 H), 7.99 (d, $^4J$ = 1.90 Hz, 1 H), 8.55 (d, $^3J$ 5.3 Hz, 1 H) ppm.

**Potassium (4-Methoxy-2-pyridyl)carboxylate:** (4-Methoxy-2-pyridyl)carboxylic acid methyl ester (0.84 g, 5 mmol) and KOH (0.27 g) were added together to give (4-methoxy-2-pyridyl)carboxylic acid potassium salt (0.76 g). Yield: 80%. M.p. > 350 °C. $C_7H_6KNO_3 \cdot \frac{1}{4}H_2O$ (195.73): calcd. C 42.95, H 3.35, N 7.16; found C 43.06, H 3.21, N 7.17. MS (ESI-): $m/z$ = 152 [M – $H^-$]. $^1$H NMR (200 MHz, $D_2O$): $\delta$ = 3.92 (s, 3 H, OC$H_3$), 7.07 (dd, $^3J$ = 5.8 Hz, $^4J$ = 2.5 Hz, 1 H), 7.46 (d, $^4J$ = 2.5 Hz, 1 H), 8.38 (d, $^3J$ = 5.76 Hz, 1 H) ppm.

**5,6-Bis(2-pyridylcarboxamido)-1,10-phenanthroline, $H_2L^1$:** Picolinic acid (1.11 g, 9 mmol) and DMAP (0.12 g, 1 mmol, 33 mol-%) in absolute DMF (25 mL) were added to a stirred suspension/solution of 5,6-diamino-1,10-phenanthroline (0.63 g, 3 mmol) in a 100-mL Schlenk flask under nitrogen at ambient temperature. TEA (1.4 mL, 10 mmol) was then added by syringe, followed by the addition of phenylphosphonic acid dichloride (0.9 mL, 6.4 mmol) and more TEA (2.8 mL, 20 mmol) over a period of 5 h. After an additional 4 h, the reaction was quenched by the addition of water (1 mL). The product was isolated by precipitation (addition of $H_2O$, 5 volumes), filtration, washing with $H_2O$, and drying under high vacuum. Yield: 0.68 g (1.62 mmol, 54%). M.p. 294–298 °C. $C_{24}H_{16}N_6O_2 \cdot 1\frac{2}{3}\ H_2O$ (450.45): calcd. C 63.99, H 4.33, N 18.66, found C 64.01, H 4.10, N 18.39. MS (ESI+): $m/z$ = 421 [M + $H^+$]. $^1$H NMR (500 MHz, [$D_7$]DMF): $\delta$ = 7.70 (ddd, $^3J$ = 7.6 Hz, $^3J$ = 4.7 Hz, $^4J$ = 1.2 Hz, 2 H, py-*H*), 7.85 (dd, $^3J$ = 8.3 Hz, $^3J$ = 4.2 Hz, 2 H, phen-*H*), 8.11 (td, $^3J$ = 7.7 Hz, $^4J$ = 1.5 Hz, 2 H, py-*H*), 8.25 (ddd,$^3J$ = 7.7 Hz, $^4J$ = 1.2 Hz, $^5J$ = 0.6 Hz, 2 H, py-*H*), 8.62 (dd, $^3J$ = 8.3 Hz, $^4J$ = 1.6 Hz, 2 H, phen-*H*), 8.75 (ddd, $^3J$ = 4.7 Hz, $^4J$ = 1.5 Hz, $^5J$ = 0.6 Hz, 2 H, py-*H*), 9.21 (dd, $^3J$ = 4.2 Hz, $^4J$ = 1.6 Hz, 2 H, phen-*H*), 11.10 (s, 2 H, N*H*) ppm. IR (KBr): 3298 (m), 3236 (m) (N–H); 3076 (w), 3050 (m) (C–H); 1676 (s), 1570 (m) (C=$O_{amide}$); 1616 (m) (C=N); 1590 (m), 1496 (m) (C=C) $cm^{-1}$.

**5,6-Bis[(4-methoxy-2-pyridyl)carboxamido]-1,10-phenanthroline, $H_2L^2$:** Obtained as described above by using 5,6-diamino-1,10-phenanthroline (0.21 g,1 mmol). Yield: 0.25 g, (0.52 mmol, 52%). M.p. 246–249 °C. $C_{26}H_{20}N_6O_4 \cdot 2H_2O$ (516.51): calcd. C 60.46, H 4.68, N 16.27, found C 60.57, H 4.76, N 15.96. MS (ESI+): $m/z$ = 481 [M + $H^+$]. $^1$H NMR (500 MHz, [$D_7$]DMF): $\delta$ = 4.00 (s, 6 H, OC$H_3$), 7.26 (dd, $^3J$ = 5.7 Hz, $^4J$ = 2.6 Hz, 2 H, py-*H*), 7.73 (d, $^4J$ = 2.6 Hz, 2 H, py-*H*), 7.85 (dd, $^3J$ = 8.4 Hz, $^3J$ = 4.2 Hz, 2 H, phen-*H*), 8.57 (d, $^3J$ = 5.7 Hz, 2 H, py-*H*), 8.59 (dd, $^3J$ = 8.4 Hz, $^4J$ = 1.5 Hz, 2 H, phen-*H*), 9.20 (dd, $^3J$ = 4.2 Hz, $^4J$ = 1.5 Hz, 2 H, phen-*H*), 11.02 (s, 2 H, N*H*) ppm. IR (KBr): 3298 (s) (N–H); 3090 (w), 3066 (w), 3010 (w), 2934 (w) (C–H); 1684 (s), 1566 (m) (C=$O_{amide}$); 1602 (s), 1496 (s) (C=N, C=C) $cm^{-1}$.

**5,6-Bis[(4-chloro-2-pyridyl)carboxamido]-1,10-phenanthroline:** Obtained as described above by using 5,6-diamino-1,10-phenanthroline (0.21 g, 1 mmol) and (4-chloro-2-pyridyl)carboxylic acid potassium salt (0.59 g, 3 mmol). Yield: 0.37 g crude product. HR-ESI-MS: calcd. for [M + $H^+$] ($C_{24}H_{15}Cl_2N_6O_2$) 489.0634; found 489.0610 (–2.4 mD, standard: $H_3PO_4$).

**Tris[5,6-bis(2-pyridylcarboxamido)-1,10-phenanthroline]ruthenium Hexafluorophosphate, $[Ru(H_2L^1)_3](PF_6)_2$:** A mixture of $RuCl_3 \cdot 3H_2O$ (0.026 g, 0.1 mmol) and 5,6-bis(2-pyridylcarboxamido)-1,10-phenanthroline (0.15 g, 0.35 mmol) was heated (160 °C) in ethylene glycol (5 mL) for 30 min. After being cooled to room temperature, the mixture was diluted with water (1/6 volume), and the excess ligand was removed by filtration. The complex was precipitated by the addition of $NH_4PF_6$, filtered off, washed with small amounts of $H_2O$ and $Et_2O$, and dried under high vacuum. Yield: 0.11 g (0.06 mmol, 66%) black-violet powder. $C_{72}H_{48}F_{12}N_{18}O_6P_2Ru \cdot 6H_2O$ (1760.25): calcd. C 49.12, H 3.44, N 14.32; found C 49.29, H 3.54, N 13.87. HR-FAB-MS: calcd. for [M – $PF_6^-$] ($C_{72}H_{48}F_6N_{18}O_6PRu$) 1507.2689; found 1507.2656 (–3.3 mD, standard: PEG1500). $^1$H NMR (500 MHz, $CD_3CN$): $\delta$ = 7.61 (dd,$^3J$ = 7.5 Hz, $^3J$ = 4.5, 6 H, py-*H*), 7.72 [m(br), 6 H, phen-*H*], 8.01 (t, $^3J$ = 7.5 Hz, 6 H, py-*H*), 8.19 [s(sh), 6 H, phen-*H*], 8.20 (d, $^3J$ = 7.5 Hz, 6 H, py-*H*), 8.65 (d, $^3J$ = 4.5 Hz, 6 H, py-*H*), 8.69 (d, $^3J$ = 7.8 Hz, 6 H, phen-*H*), 10.71 (s, 6 H, N*H*) ppm. IR (KBr): 3280 (s) (N–H); 3076 (m), 3054 (m) (C–H); 1680 (s), 1570 (m) (C=$O_{amide}$); 1620 (m) (C=N); 1590 (m), 1496 (s) (C=C); 844 (s) ($PF_6^-$) $cm^{-1}$. UV/Vis ($CH_3CN$): $\lambda_{max}$ = 451 nm ($\varepsilon$ = $2.2 \times 10^4$ L $mol^{-1}$ $cm^{-1}$).

**Bis(2,2′-bipyridine)[5,6-bis(2-pyridylcarboxamido)-1,10-phenanthroline]ruthenium Hexa-fluorophosphate, $[Ru(bpy)_2(H_2L^1)](PF_6)_2$:** $Ru(bpy)_2Cl_2 \cdot 2H_2O$ (0.15 g, 0.3 mmol) and 5,6-bis(2-pyridylcarboxamido)-1,10-phenanthroline (0.15 g, 0.35 mmol) were refluxed in 50% aqueous ethanol (20 mL) under nitrogen for 4 h. After being evaporated to near dryness, the residue was treated with water (10 mL), and the excess ligand was removed by filtration. The complex was precipitated with $NH_4PF_6$, filtered off, washed with $H_2O$ and $Et_2O$, and dried under vacuum. Yield: 0.27 g (0.233 mmol, 78%) orange-red powder. $C_{44}H_{32}F_{12}N_{10}O_2P_2Ru \cdot 2H_2O$ (1159.80): calcd. C 45.56, H 3.13, N 12.08; found C 45.40, H 3.13, N 11.90. HR-FAB-MS: calcd. for [M – $PF_6^-$] ($C_{44}H_{32}F_6N_{10}O_2PRu$) 979.1395; found 979.1415 (+2.0 mD, standard: PEG1000). $^1$H NMR (500 MHz, $CD_3CN$): δ = 7.29 (ddd, $^3J$ = 7.3 Hz, $^3J$ = 5.4 Hz, $^4J$ = 1.0 Hz, 2 H, bpy-*H*), 7.46 (ddd, $^3J$ = 7.3 Hz, $^3J$ = 5.4 Hz, $^4J$ = 1.0 Hz, 2 H, bpy-*H*), 7.61 (ddd, $^3J$ = 7.5 Hz, $^3J$ = 4.8 Hz, $^4J$ = 1.0 Hz, 2 H, py-*H*), 7.63 (d, $^3J$ = 5.4 Hz, 2 H, bpy-*H*), 7.75 (dd, $^3J$ = 8.4 Hz, $^3J$ = 5.2 Hz, 2 H, phen-*H*), 7.85 (d, $^3J$ = 5.4 Hz, 2 H, bpy-*H*), 8.00 (ddd, $^3J$ = 8.2 Hz, $^3J$ = 7.3 Hz, $^4J$ = 1.0 Hz, 2 H, bpy-*H*), 8.02 (ddd, $^3J$ = 8.2 Hz, $^3J$ = 7.3 Hz, $^4J$ = 1.0 Hz, 2 H, bpy-*H*), 8.10 (ddd, $^3J$ = 8.0 Hz, $^3J$ = 7.5 Hz, $^4J$ = 0.9 Hz, 2 H, py-*H*), 8.12 (dd, $^3J$ = 5.2 Hz, $^4J$ = 0.8 Hz, 2 H, phen-*H*), 8.19 (d, $^3J$ = 8.0 Hz, 2 H, py-*H*), 8.51 (d, $^3J$ = 8.2 Hz, 2 H, bpy-*H*), 8.54 (d, $^3J$ = 8.2 Hz, 2 H, bpy-*H*), 8.65 (d, $^3J$ = 4.8 Hz, 2 H, py-*H*), 8.66 (d, $^3J$ = 8.4 Hz, 2 H, phen-*H*), 10.67 (s, 2 H, NH) ppm. IR (KBr): 3322 (s) (N–H); 3076 (m) (C–H); 1684 (m), 1570 (w) (C=$O_{amide}$); 1622 (m) (C=N); 1604 (m), 1496 (m) (C=C); 842 (s) ($PF_6^-$) $cm^{-1}$. UV/Vis ($CH_3CN$): $\lambda_{max}$ = 450 nm ($\varepsilon \approx 1.3 \times 10^4$ L $mol^{-1}$ $cm^{-1}$).

**Bis(2,2′-bipyridine){5,6-bis[(4-methoxy-2-pyridyl)carboxamido]-1,10-phenanthroline}ruthenium Hexafluorophosphate, $[Ru(bpy)_2(H_2L^2)](PF_6)_2$:** Obtained as described above by using $Ru(bpy)_2Cl_2 \cdot 2H_2O$ (0.09 g, 0.173 mmol) and 5,6-bis[(4-methoxy-2-pyridyl)-carboxamido]-1,10-phenanthroline (0.1 g, 0.2 mmol). Yield: 0.19 g (0.152 mmol, 88%) orange-red powder. $C_{46}H_{36}F_{12}N_{10}O_4P_2Ru \cdot 3.5H_2O$ (1246.87): calcd. C 44.31, H 3.48, N 11.23; found C 44.02, H 3.15, N 11.06. HR-FAB-MS: calcd. for [M – $PF_6^-$]

 © 2006 Wiley-VCH Verlag GmbH & Co. KGaA, Weinheim 

($C_{46}H_{36}F_6N_{10}O_4PRu$) 1039.1608; found 1039.1649 (+4.1 mD, standard: PEG1000); calcd. for [M – 2 $PF_6^-$] ($C_{46}H_{36}N_{10}O_4PRu$) 894.1966; found 894.1955 (–1.1 mD). $^1$H NMR (500 MHz, $CD_3CN$): $\delta$ = 3.92 (s, 6 H, $OCH_3$), 7.12 (dd, $^3J$ = 5.2 Hz, $^4J$ = 2.8 Hz, 2 H, py-*H*), 7.29 [m(br), 2 H, bpy-*H*], 7.46 [m(br), 2 H, bpy-*H*], 7.63 (d, $^3J$ = 4.2 Hz, 2 H, bpy-*H*), 7.70 (d, $^4J$ = 2.8 Hz, 2 H, py-*H*), 7.74 (dd, $^3J$ = 8.2 Hz, $^3J$ = 4.8 Hz, 2 H, phen-*H*), 7.85 (d, $^3J$ = 4.2 Hz, 2 H, bpy-*H*), 8.02 [m(br), 2 H, bpy-*H*], 8.10 [m(br), 2 H, bpy-*H*], 8.11 (d, $^3J$ = 4.8 Hz, 2 H, phen-*H*), 8.46 (d, $^3J$ = 5.2 Hz, 2 H, py-*H*), 8.51 (d, $^3J$ = 7.9 Hz, 2 H, bpy-*H*), 8.54 (d, $^3J$ = 7.9 Hz, 2 H, bpy-*H*), 8.63 (d, $^3J$ = 8.2 Hz, 2 H, phen-*H*), 10.67 (s 2 H, N*H*) ppm. IR (KBr): 3318 (s) (N–H); 3074 (m), 2932 (w) (C–H); 1684 (m), 1566 (m) (C=$O_{amide}$); 1614 (m) (C=N); 1600 (s), 1308 (s) (C=C); 840 (s) ($PF_6^-$) $cm^{-1}$. UV/Vis ($CH_3CN$): $\lambda_{max}$ = 447 nm ($\varepsilon \approx 1.9 \times 10^4$ $L\,mol^{-1}\,cm^{-1}$).

**[Ru(bpy)$_2$(μ-L$^1$M)](PF$_6$)$_2$, M = Cu$^{2+}$, Ni$^{2+}$, Pd$^{2+}$:** [Ru(bpy)$_2$-($H_2L^1$)]($PF_6$)$_2$·2$H_2O$ (0.034 g, 0.03 mmol) and the corresponding metal salt (0.03 mmol) were refluxed in MeOH (15 mL) for 20 min. After being cooled to room temperature, the dinuclear complexes were precipitated by addition of $Et_2O$, isolated by centrifugation or filtration, and dried under high vacuum.

**[Ru(bpy)$_2$(μ-L$^1$Cu)](PF$_6$)$_2$:** Cu$(AcO)_2$·$H_2O$ (0.006 g). Yield: 0.022 g (0.017 mmol, 57%) dark brown solid. $C_{44}H_{30}CuF_{12}N_{10}O_2P_2Ru$·6$H_2O$ (1293.39): calcd. C 40.86, H 3.27, N 10.83; found C 40.63, H 3.03, N 10.60. IR (KBr): 3074 (m) (C–H); 1654 (m) (C=$O_{amide}$); 1624 (m) (C=N); 1600 (m), 1488 (m) (C=C); 838 ($PF_6^-$) $cm^{-1}$.

**[Ru(bpy)$_2$(μ-L$^1$Ni)](PF$_6$)$_2$:** Ni$(AcO)_2$·4$H_2O$ (0.0075 g). Yield: 0.027 g (0.023 mmol, 75%) bright red solid.

**[Ru(bpy)$_2$(μ-L$^1$Pd)](PF$_6$)$_2$:** Pd(benzonitrile)$_2Cl_2$ (0.0115 g) in $CH_3CN$ (2 mL), followed by 0.05 mL TEA. Yield: 0.031 g (0.024 mmol, 80%) orange-red solid. $C_{44}H_{30}F_{12}N_{10}O_2P_2PdRu$·2MeOH (1292.26): calcd. C 42.75, H 2.96, N 10.84; found C 42.59, H 3.16, N 11.12. IR (KBr): 3062 (m) (C–H); 1684 (w) (C=$O_{amide}$); 1626 (m) (C=N); 1600 (m), 1494 (w) (C=C); 842 (s) ($PF_6^-$) $cm^{-1}$.

**[Ru(bpy)$_2$(μ-L$^2$M)](PF$_6$)$_2$, M = Cu$^{2+}$, Ni$^{2+}$, Pd$^{2+}$:** Obtained as described above, but with [Ru(bpy)$_2$($H_2L^2$)]($PF_6$)$_2$·3.5$H_2O$ (0.038 g, 0.03 mmol).

**[Ru(bpy)$_2$(μ-L$^2$Cu)](PF$_6$)$_2$:** Cu$(AcO)_2$·$H_2O$ (0.006 g). Yield: 0.027 g (0.02 mmol, 68%) red-brown solid. $C_{46}H_{34}CuF_{12}N_{10}O_2P_2Ru$·3$H_2O$·1.5MeOH (1319.42): calcd. C 42.34, H 3.44, N 10.39; found C 42.40, H 3.64, N 10.61. IR (KBr): 3072 (w), 2926 (w) (C–H); 1656 (m) (C=$O_{amide}$); 1634 (s) (C=N); 1604 (s), 1310 (m) (C=C); 842 (s) ($PF_6^-$) $cm^{-1}$.

**[Ru(bpy)$_2$(μ-L$^2$Ni)](PF$_6$)$_2$:** Ni$(AcO)_2$·4$H_2O$ (0.0075 g). Yield: 0.029 g (0.022 mmol, 74%) red solid. $C_{46}H_{34}NiF_{12}N_{10}O_2P_2Ru$·3$H_2O$ (1268.02): calcd. C 42.68, H 3.11, N 10.82; found C 42.69, H 3.16, N 10.77. IR (KBr): 3074 (m), 2934 (w) (C–H); 1640 (m) (C=$O_{amide}$); 1612 (s) (C=N); 1584 (w), 1310 (m) (C=C); 838 (s) ($PF_6^-$) $cm^{-1}$.

**[Ru(bpy)$_2$(μ-L$^2$Pd)](PF$_6$)$_2$:** Pd(benzonitrile)$_2Cl_2$ (0.0115 g) in $CH_3CN$ (2 mL), followed by 0.05 mL TEA. Yield: 0.03 g (0.022 mmol, 74%) orange-red solid. $C_{46}H_{34}PdF_{12}N_{10}O_2P_2Ru$·4$H_2O$ (1333.77): calcd. C 40.62, H 3.11, N 10.30; found C 40.45, H 3.13, N 10.22. IR (KBr): 3066 (m), 2926 (w) (C–H); 1654 (sh) (C=$O_{amide}$); 1626 (s) (C=N); 1604 (s), 1308 (m) (C=C); 842 (s) ($PF_6^-$) $cm^{-1}$.

**[Ru(μ-L$^1$M)$_3$](PF$_6$)$_2$, M = Cu$^{2+}$, Ni$^{2+}$, Pd$^{2+}$:** The synthesis was carried out as described above, but with [Ru($H_2L^1$)$_3$]($PF_6$)$_2$·6$H_2O$ (0.035 g, 0.02 mmol), along with double the amount of the corresponding metal salts and double the volume of solvent.

**[Ru(μ-L$^1$Cu)$_3$](PF$_6$)$_2$:** Cu$(AcO)_2$·$H_2O$ (0.012 g). Yield after recrystallization from DMF/MeOH: 0.029 g (0.014 mmol, 69%) dark brown solid. $C_{72}H_{42}Cu_3F_{12}N_{18}O_6P_2Ru$·2DMF·5$H_2O$·MeOH (2105.06): calcd. C 45.07, H 3.35, N 13.31; found C 45.21, H 3.46, N 13.15. HR-ESI-MS: calcd. for [M – 2 $PF_6^-$] ($C_{72}H_{42}Cu_3$-$N_{18}O_6Ru$) 1545.0466; found 1545.0432 (–3.4 mD, standard: $H_3PO_4$). IR (KBr): 3066 (w) (C–H); 1650 (sh) (C=$O_{amide}$); 1620 (s) (C=N); 1596 (s) (C=C); 842 (s) ($PF_6^-$) $cm^{-1}$. UV/Vis ($CH_3CN$): $\lambda_{max}$ = 419 nm ($\varepsilon \approx 1.0 \times 10^4$ $L\,mol^{-1}\,cm^{-1}$), $\lambda_{max}$ = 473 nm ($\varepsilon \approx 0.9 \times 10^4$ $L\,mol^{-1}\,cm^{-1}$).

**[Ru(μ-L$^1$Ni)$_3$](PF$_6$)$_2$:** Ni$(AcO)_2$·4$H_2O$ (0.015 g). Yield: 0.031 g (0.017 mmol, 85%) red solid. HR-ESI-MS: calcd. for [M – 2 $PF_6^-$] ($C_{72}H_{42}N_{18}Ni_3O_6Ru$) 1530.0639; found 1530.0640 (+0.1 mD, standard: $H_3PO_4$).

**[Ru(μ-L$^1$Pd)$_3$](PF$_6$)$_2$:** Pd(benzonitrile)$_2Cl_2$ (0.023 g) in $CH_3CN$ (4 mL), followed by TEA (0.1 mL). Yield: 0.037 g (0.022 mmol, 74%) red solid. ESI-MS: calcd. for [M – 2 $PF_6^-$] ($C_{72}H_{42}N_{18}O_6P$-$d_3Ru$) 1673.97; found 1674.

**Tris[5,6-bis(2-pyridylcarboxamido)-1,10-phenanthroline]iron Hexafluorophosphate, [Ru(H$_2$L$^1$)$_3$](PF$_6$)$_2$:** A mixture of $FeSO_4$·7$H_2O$ (0.028 g, 0.1 mmol), 5,6-bis(2-pyridylcarboxamido)-1,10-phenanthroline (0.15 g, 0.35 mmol), hydroxylammonium chloride (0.01 g), and sulfuric acid (50 μL) was stirred in $H_2O$ (10 mL) for 6 h at ambient temperature. After filtration (excess ligand), the complex was precipitated from the dark red solution by addition of $NH_4PF_6$, collected on a filter, washed with small amounts $H_2O$ and $Et_2O$, and dried under high vacuum. Yield: 0.15 g (0.09 mmol, 90%) bordeaux red powder. $C_{72}H_{48}F_{12}FeN_{18}O_6P_2$·4$H_2O$ (1679.00): calcd. C 51.50, H 3.36, N 15.02; found C 51.67, H 3.55, N 15.13. HR-ESI-MS: calcd. for [M – 2$PF_6^-$] ($C_{72}H_{48}FeN_{18}O_6$) 1316.3354; found 1316.3366 (+1.2 mD, standard: $H_3PO_4$). $^1$H NMR (500 MHz, $CD_3CN$): $\delta$ = 7.62 (dd, $^3J$ = 7.5 Hz, $^3J$ = 4.2 Hz, 6 H, py-*H*), 7.69 [m(br), 6 H, phen-*H*], 7.82 (d, $^3J$ = 3.4 Hz, 6 H, phen-*H*), 8.01 (t, $^3J$ = 7.5 Hz, 6 H, py-*H*), 8.21 (d, $^3J$ = 7.5 Hz, 6 H, py-*H*), 8.65 (d, $^3J$ = 4.2 Hz, 6 H, py-*H*), 10.74 (s, 6 H, N*H*) ppm. IR (KBr): 3274 (m) (N–H); 3074 (w), 3054 (w) (C–H); 1570 (m), 1680 (s) (C=$O_{amide}$); 1622 (m) (C=N); 1588 (m), 1500 (s) (C=C); 844 (s) ($PF_6^-$) $cm^{-1}$. UV/Vis ($CH_3CN$): $\lambda_{max}$ = 515 nm ($\varepsilon \approx 0.8 \times 10^4$ $L\,mol^{-1}\,cm^{-1}$).

**[Fe(μ-L$^1$M)$_3$](PF$_6$)$_2$, M = Cu$^{2+}$, Ni$^{2+}$, Pd$^{2+}$:** [Fe($LpicH_2$)$_3$]($PF_6$)$_2$·4$H_2O$ (0.034 g, 0.02 mmol) and the corresponding metal salt (0.06 mmol) were refluxed in MeOH (15 mL) for 20 min. After cooling, the tetranuclear complexes were precipitated by addition of $Et_2O$, isolated by centrifugation or filtration, and dried under high vacuum.

**[Fe(μ-L$^1$Cu)$_3$](PF$_6$)$_2$:** Cu$(AcO)_2$·$H_2O$ (0.012 g). Yield: 0.03 g (0.0157 mmol, 79%) dark red-brown solid. $C_{72}H_{42}Cu_3F_{12}FeN_{18}$-$O_6P_2$·6$H_2O$ (1899.62): calcd. C 45.52, H 2.87, N 13.27; found C 45.56, H 3.04, N 13.17. HR-ESI-MS: calcd. for [M – 2$PF_6^-$] ($C_{72}H_{42}Cu_3FeN_{18}O_6$) 1499.0772; found 1499.0804 (+3.2 mD, standard: $H_3PO_4$). IR (KBr): 3068 (m) (C–H); 1654 (m) (C=$O_{amide}$); 1622 (s) (C=N); 1596 (s) (C=C); 844 (s) ($PF_6^-$) $cm^{-1}$. UV/Vis ($CH_3CN$): $\lambda_{max}$ = 387 nm ($\varepsilon \approx 1.0 \times 10^4$ $L\,mol^{-1}\,cm^{-1}$), $\lambda_{max}$ = 524 nm ($\varepsilon \approx 0.9 \times 10^4$ $L\,mol^{-1}\,cm^{-1}$).

**[Fe(μ-L$^1$Ni)$_3$](PF$_6$)$_2$:** Ni$(AcO)_2$·4$H_2O$ (0.015 g). Yield: 0.025 g (0.0132 mmol, 66%) red solid. $C_{72}H_{42}F_{12}FeN_{18}Ni_3O_6P_2$·2$H_2O$·3MeOH (1906.09): calcd. C 47.18, H 3.06, N 13.21; found C 47.22, H 2.92, N 12.96. ESI-MS: calcd. for [M – 2 $PF_6^-$] ($C_{72}H_{42}FeN_{18}Ni_3O_6$) 1484; found 1483.9. IR (KBr): 3078 (w) (C–H); 1660 (sh) (C=$O_{amide}$); 1636 (s) (C=N); 1604 (w), 1586 (m) (C=C); 842 (s) ($PF_6^-$) $cm^{-1}$. UV/Vis ($CH_3CN$): $\lambda_{max}$ = 451 nm ($\varepsilon \approx$

 © 2006 Wiley-VCH Verlag GmbH & Co. KGaA, Weinheim 

$1.3 \times 10^4$ L mol$^{-1}$ cm$^{-1}$), $\lambda_{max}$ = 485 nm ($\varepsilon \approx 1.3 \times 10^4$ L mol$^{-1}$ cm$^{-1}$), $\lambda_{max}$ = 527 nm ($\varepsilon \approx 1.3 \times 10^4$ L mol$^{-1}$ cm$^{-1}$).

**[Fe(μ-L$^1$Pd)$_3$](PF$_6$)$_2$:** Pd(benzonitrile)$_2$Cl$_2$ (0.023 g) in $CH_3CN$ (4 mL), followed by TEA (0.1 mL). Yield: 0.032 g (0.0164 mmol, 82%) red solid. $C_{72}H_{42}F_{12}FeN_{18}O_6P_2Pd_3 \cdot 9H_2O$ (2082.29): calcd. C 41.53, H 2.90, N 12.11; found C 41.28, H 2.76, N 11.97. ESI-MS: calcd. for [M – 2 $PF_6^-$] ($C_{72}H_{42}FeN_{18}O_6$ $Pd_3$) 1628; found 1628. IR (KBr): 3064 (m) (C–H); 1650 (sh) (C=O$_{amide}$); 1626 (s) (C=N); 1598 (s) (C=C); 844 (m) ($PF_6^-$) cm$^{-1}$.

## Acknowledgments

Generous financial support by the Deutsche Forschungsgemeinschaft (DFG) and a generous gift of palladium and ruthenium salts by Degussa AG are gratefully acknowledged.

[1] S. J. Lippard, J. M. Berg, *Principles of Bioinorganic Chemistry*, University Science Books, **1994**.
[2] R. J. P. Williams, *Bringing Chemistry to Life*, Oxford University Press, **2000**.
[3] P. Braunstein, X. Morise, *Organometallics* **1998**, *17*, 540.
[4] P. Comba, A. Mayboroda, H. Pritzkow, *Eur. J. Inorg. Chem.* **2003**, 3042.
[5] P. D. Beer, *Acc. Chem. Res.* **1998**, *31*, 71.
[6] P. D. Beer, M. W. Wong, *Macrocyclic Chemistry – Current Trends and Future Perspectives* (Ed.: E. K. Gloe), Springer, **2005**.
[7] V. Balzani, A. Credi, M. Venturi, *ChemPhysChem* **2003**, *3*, 49.
[8] C. Fraser, L. Johnston, A. L. Rheingold, B. S. Haggerty, G. K. Williams, J. Whelan, B. Bosnich, *Inorg. Chem.* **1992**, *31*, 1835.
[9] E. Kimura, S. Wada, M. Shionoga, T. Takahashi, Y. Iitaca, *J. Chem. Soc., Chem. Commun.* **1990**, 397.
[10] F. Bolletta, I. Costa, L. Fabbrizzi, M. Licchelli, M. Montalti, P. Pallavicini, L. Prodi, N. Zaccheroni, *J. Chem. Soc., Dalton Trans.* **1999**, 1381.
[11] C. Lodeiro, F. Pina, A. J. Parola, A. Bencini, A. Bianchi, C. Bazzicalupi, S. Ciattini, C. Giorgi, A. Masotti, B. Valtancoli, J. S. de Melo, *Inorg. Chem.* **2001**, *40*, 6813.
[12] V. Balzani, F. Scandola, *Supramolecular Photochemistry*, Horwood, **1991**.
[13] A. Juris, V. Balzani, F. Barigelletti, S. Campagna, P. Belser, A. von Zelewsky, *Coord. Chem. Rev.* **1988**, *84*, 85.
[14] M. K. Nazeeruddin, M. Graetzel in *Conversion and Storage of Solar Energy Using Dye-Sensitized Nanocrystalline $TiO_2$ Cells* (Eds.: M. K. Nazeeruddin, M. Graetzel), Oxford, **2004**.
[15] V. Nikolenko, R. Yuste, L. Zayat, L. M. Baraldo, R. Etchenique, *Chem. Commun.* **2005**, *13*, 1752.
[16] A. Bouskila, E. Amouyal, C. Verchere-Beaur, I. Sasaki, A. Gaudemer, *J. Photochem. Photobiol. B* **2004**, *76*, 69.
[17] J. Bolger, A. Gourdon, E. Ishow, J.-P. Launay, *Inorg. Chem.* **1996**, *35*, 2937.
[18] S. Bodige, F. M. MacDonnell, *Tetrahedron Lett.* **1997**, *38*, 8159.
[19] H. Camren, M.-Y. Chang, L. Zeng, M. E. McGuire, *Synth. Commun.* **1996**, *26*, 1247.
[20] O. Luis-Andre, G. Gelbard, *Bull. Soc. Chim. Fr.* **1986**, 565.
[21] E. de Barry Barnet, *J. Chem. Soc.* **1910**, 63.
[22] R. Murugan, E. F. V. Scriven, *Aldrichim. Acta* **2003**, *36*, 21.
[23] A. Michaelis, F. Rothe, *Ber. Dtsch. Chem. Ges.* **1892**, *25*, 1747.
[24] K. Sasse in *Organische Phosphorverbindungen, Teil 1* (Ed.: K. Sasse), **1963**.
[25] L. Anschütz, H. Wirth, *Ber. Dtsch. Chem. Ges.* **1956**, 688.
[26] M. F. Hershman, L. F. Audrieth, *J. Org. Chem.* **1958**, *23*, 1889.
[27] P. Comba, T. W. Hambley, N. Okon, G. Lauer, *MOMEC97, A Molecular Modeling Package for Inorganic Compounds*, ed. CVS, **1997**.
[28] J. E. Bol, C. Buning, P. Comba, J. Reedijk, M. Ströhle, *J. Comput. Chem.* **1998**, *19*, 512.
[29] H. A. O. Hill, K. A. Raspin, *J. Chem. Soc., Sect. A* **1968**, 3036.
[30] A. Weiss, S. Fallab, H. Erlenmeyer, *Helv. Chim. Acta* **1955**, *38*, 263.
[31] P. W. Lindner, R. G. Torrington, U. A. Seemann, *Talanta* **1983**, *30*, 295.
[32] H. Azab, A. M. El-Nady, A. Hassan, R. S. A. Akzal, *Monatsh. Chem.* **1993**, *124*, 637.
[33] E. Baumann, *J. Inorg. Nucl. Chem.* **1974**, *36*, 1827.
[34] P. Comba, *Coord. Chem. Rev.* **1999**, *185*, 81.
[35] P. Comba, T. W. Hambley, *Molecular Modeling of Inorganic Compounds*, 2nd ed., with a tutorial based on MOMEClite, Wiley-VCH, **2001**.
[36] P. Comba, B. Martin in *Modeling of Macrocyclic Ligand Complexes* (Ed.: K. Gloe), **2005**.
[37] W. Paw, R. Eisenberg, *Inorg. Chem.* **1997**, *36*, 2287.
[38] R. J. Sundberg, S. Jiang, *Org. Prep. Proc. Int.* **1997**, *29*, 117.

Received: May 19, 2006
Published Online: September 12, 2006

 © 2006 Wiley-VCH Verlag GmbH & Co. KGaA, Weinheim 

DOI: 10.1002/ejic.200600501

# Titanium(IV) Complexes of Hydrazones and Azines

**Matthew G. Davidson,*[a] Andrew L. Johnson,[a] Matthew D. Jones,*[a] Matthew D. Lunn,[b] and Mary F. Mahon[c]**

**Keywords:** Titanium / Coordination modes / Hydrazones / Azines

The coordination modes of various azines (C=N–N=C) and hydrazones (C=N–$NR_2$) with titanium(IV) are investigated. Five ligands were studied, two hydrazones **1H–2H** and three azines **$3H_2$–$5H_2$**, and it was found that hydrazones form monomers and azines form dimers in the solid state. The hydrogen-bonded arrays observed for the hydrazones were significantly different for the two ligands, with one forming a ribbon like structure and the other a chain. For the azines the supramolecular structures are also discussed. A pronounced twist is observed in the azine ligand upon complexation to the metal centre, which is rationalised in terms of the favourable interactions observed in the solid-state.
(© Wiley-VCH Verlag GmbH & Co. KGaA, 69451 Weinheim, Germany, 2006)

## Introduction

There is continuing interest in the synthesis of new titanium(IV) complexes for use in catalysis and supramolecular chemistry.[1–7] As a consequence it is pertinent to design new ligands that may impart different steric effects at the metal centre. Thus, we have investigated the coordination of $Ti^{IV}$ with a variety of hydrazone (C=N–$NR_2$) and azine (C=N–N=C) ligands. To the best of our knowledge, there are only two reported titanium–azine crystal structures and no titanium–hydrazone complexes, where R = H, have been structurally characterised.[8,9] Azine complexes of transition metals, for example ruthenium, iron, copper and zinc are known to form dimers in the solid state, with either a *cis* or *trans* configuration, Figure 1.[10–14]

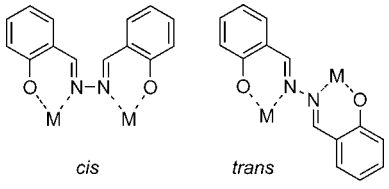


Figure 1. Two possible isomers for azine complexes.

In contrast, hydrazone complexes of transition metals (e.g. vanadium and copper) tend to form monomeric structures.[15–17] Hydrazones (where R = H) can form supramolecular arrays in the solid state due to the presence of the protic $NH_2$ group available for hydrogen bonding, a feature which is being exploited in the crystal engineering field.[18–23] The ligands chosen for this study are shown in Figure 2, with the expectation of conveying different steric demands on the titanium(IV) centre and facilitating the formation of different arrays in the solid state.

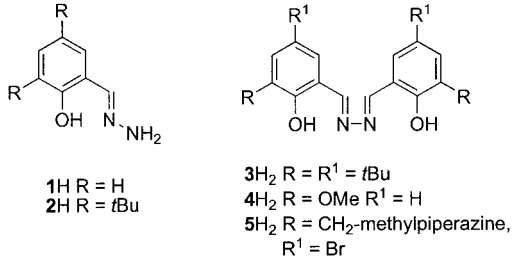


Figure 2. Hydrazones **1**H and **2**H, azines $\mathbf{3}H_2$, $\mathbf{4}H_2$ and $\mathbf{5}H_2$.

## Results and Discussion

Two equivalents of each hydrazone **1**H and **2**H react readily with $Ti(OiPr)_4$ to form the desired complexes $Ti(\mathbf{1})_2(OiPr)_2$ and $Ti(\mathbf{2})_2(OiPr)_2$. Each of the ligands is deprotonated at the phenolic moiety and chelates to the metal centre through the resulting phenoxide and the imine nitrogen of the hydrazone group. The amine group does not coordinate to the metal centre. The coordination sphere of the titanium is completed by two terminal isopropoxide ligands, Figure 3.

Each titanium centre has a distorted octahedral geometry with the two aryl oxide ligands adopting a *trans* configuration and the imine donors assuming a *cis* configuration, see Table 1 for selected bond lengths and angles. The bond lengths and angles are in agreement with literature pre-

[a] Department of Chemistry, University of Bath, Claverton Down, Bath BA2 7AY, UK
Fax: +44-1225-386231
E-mail: m.g.davidson@bath.ac.uk; mj205@bath.ac.uk
[b] Johnson Matthey Catalysts, P. O. Box 1, Belasis Avenue, Billingham, Cleveland TS23 1LB, UK
[c] Bath Chemical Crystallography Unit, Department of Chemistry, University of Bath, Claverton Down, Bath BA2 7AY, UK
Fax: +44-1225-386231

 © 2006 Wiley-VCH Verlag GmbH & Co. KGaA, Weinheim 

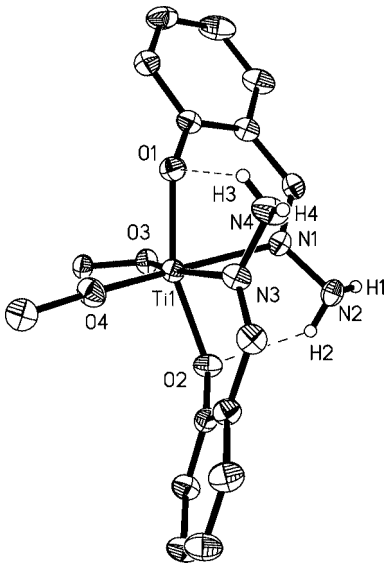


Figure 3. Crystal structure of complex Ti(**1**)$_2$(O*i*Pr)$_2$. Ellipsoids are shown at the 50% probability level, the hydrogen atoms not involved in hydrogen bonding and the isopropoxide methyl groups have been omitted for clarity. The same labelling scheme was used for complex Ti(**2**)$_2$(O*i*Pr)$_2$. The dashed lines represent the *intramolecular* hydrogen bonding, between H(2)–O(2) and H(3)–O(1). The hydrogen atoms were located in the penultimate difference Fourier map and refined freely.

cedent.[24–30] The $^1$H and $^{13}$C NMR spectra of the complexes suggest that the gross solid-state structures are maintained in solution with well-defined resonances for the isopropoxide region.

Table 1. Selected bond lengths [Å] and angles [°] for complexes Ti(**1**)$_2$(O*i*Pr)$_2$ and Ti(**2**)$_2$(O*i*Pr)$_2$.

| | Ti(**1**)$_2$(O*i*Pr)$_2$ | Ti(**2**)$_2$(O*i*Pr)$_2$ |
|---|---|---|
| Ti(1)–O(1) | 1.950(1) | 1.912(2) |
| Ti(1)–O(2) | 1.940(1) | 1.913(2) |
| Ti(1)–O(3) | 1.846(1) | 1.778(2) |
| Ti(1)–O(4) | 1.761(1) | 1.852(2) |
| Ti(1)–N(1) | 2.268(1) | 2.282(2) |
| Ti(1)–N(3) | 2.264(1) | 2.271(2) |
| O(1)–Ti(1)–O(2) | 158.89(5) | 160.80(7) |
| O(3)–Ti(1)–O(4) | 102.79(5) | 101.75(8) |
| O(1)–Ti(1)–O(4) | 97.78(5) | 94.33(7) |
| N(1)–Ti(1)–N(3) | 79.90(5) | 81.86(7) |

Both *intra*- and *intermolecular* hydrogen bonds are observed. The intramolecular hydrogen bonds are shown in Figure 3, where one hydrogen atom of each $NH_2$ group interacts with a phenoxide oxygen centre, see Table 2 for the hydrogen bonding parameters, which are similar for both complexes. The main structural distinction between Ti(**1**)$_2$(O*i*Pr)$_2$ and Ti(**2**)$_2$(O*i*Pr)$_2$ arises due to their patterns of intermolecular hydrogen bonding. For Ti(**1**)$_2$(O*i*Pr)$_2$ both H(1) and H(4) are invoked in hydrogen bonding (Figure 4) forming a ribbon-like structure in the solid state. H(1) bonds to an isopropoxide oxygen {O(3)} of a neighbouring molecule and H(4) binds to a hydrazone $NH_2$ group {N(2)} of a third molecule. For Ti(**2**)$_2$(O*i*Pr)$_2$ only *one* intermolecular hydrogen bond is seen in the solid state, between H(1) and an isopropoxide O(4), and this forms a chain-like structure. The absence of a hydrogen bond from H(4) to N(2) of an adjacent molecule is presumably related to the increase in steric bulk of the ligand.

One equivalent of each azine was treated with two equivalents of Ti(O*i*Pr)$_4$ to form complexes Ti$_2$(**3**)(O*i*Pr)$_6$, Ti$_2$(**4**)(O*i*Pr)$_6$ and Ti$_2$(**5**)(O*i*Pr)$_6$. The structure of Ti$_2$(**4**)(O*i*Pr)$_6$ is shown in Figure 5. In all cases the azine bridges between two titanium centres in a *cis* fashion. The coordination sphere around each titanium atom being completed by coordination of two terminal and two bridging isopropoxide moieties. The titanium centre is pseudooctahedral with the bond lengths and angles in the expected range, Table 3.[24–30] The core of each complex consists of three rings, one Ti$_2$O$_2$ ring made up of the two titanium centres and the two bridging alkoxides, and two five-membered rings made up of the two titanium centres, a bridging alkoxide and the azine N–N bond. The $^1$H and $^{13}$C NMR spectra suggests that the solid-state structure is maintained in solution, with distinct resonances observed for the isopropoxide moieties; for example for the azine complexes three distinct O*i*Pr methine resonances are observed in both the $^1$H and $^{13}$C NMR spectra.

The ligand shows a distortion away from planarity, which manifests itself by analysis of the torsion angle {C(8)–N(1)–N(1A)–C(8A)} of 55.7(4)° for complex Ti$_2$(**4**)(O*i*Pr)$_6$. The ligand distortion suggests that there is little conjugation between the two salicylaldimine units of the azine and that the N–N bond has little π-bonding character. For complex Ti$_2$(**3**)(O*i*Pr)$_6$ this torsion angle is very similar at 53.2(5)° to Ti$_2$(**4**)(O*i*Pr)$_6$. However, there is a significant increase in this torsion angle for complex Ti$_2$(**5**)(O*i*Pr)$_6$ at 66.6(4)°. A possible explanation is that the ligand distorts to form favourable Br···N interactions with a neighbouring molecule, Figure 6. The interaction results in an ordering of the piperazine amine nitrogen atom such that its lone pair is directed towards the bromine atom of a neighbouring molecule, with

Table 2. Summary of the hydrogen bonding parameters for complexes Ti(**1**)$_2$(O*i*Pr)$_2$ and Ti(**2**)$_2$(O*i*Pr)$_2$, the hydrogen atoms were freely refined in all cases. [1]: $-x+1, -y+1, -z+1$; [2]: $x, y, z$; [3]: $-x, -y+1, -z+1$; [4]: $-x+1, y+1/2, -z+1/2$.

| | Ti(**1**)$_2$(O*i*Pr)$_2$ | | | | Ti(**2**)$_2$(O*i*Pr)$_2$ | | | | |
|---|---|---|---|---|---|---|---|---|---|
| D–H···A | *d*(D–H) | *d*(H···A) | *d*(D···A) | <(DHA) | D–H···A | *d*(D–H) | *d*(H···A) | *d*(D···A) | <(DHA) |
| N(2)–H(1)···O(3)[1] | 0.88(2) | 2.19(3) | 3.055(2) | 175(2) | N(2)–H(1)···O(4)[4] | 0.87(3) | 2.18(3) | 3.013(3) | 159(3) |
| N(2)–H(2)···O(2)[2] | 0.90(2) | 2.17(2) | 2.845(2) | 131(2) | N(2)–H(2)···O(2)[2] | 0.85(3) | 2.23(3) | 2.875(3) | 133(3) |
| N(4)–H(3)···O(1)[2] | 0.86(2) | 2.27(2) | 2.821(2) | 122(2) | N(4)–H(3)···O(1)[2] | 0.80(3) | 2.29(3) | 2.876(3) | 130(3) |
| N(4)–H(4)···N(2)[3] | 0.86(2) | 2.42(2) | 3.252(2) | 162(2) | | | | | |

 © 2006 Wiley-VCH Verlag GmbH & Co. KGaA, Weinheim 

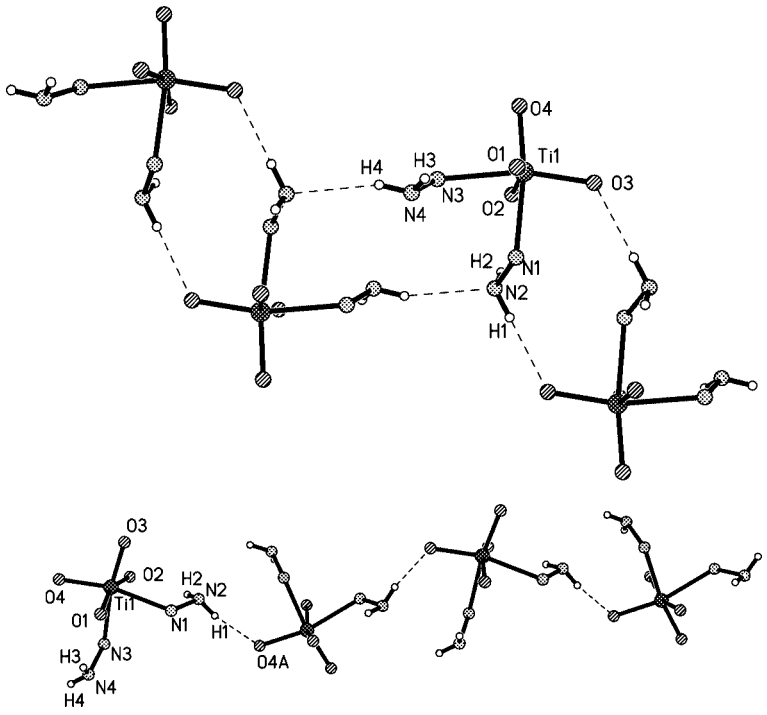


Figure 4. Hydrogen-bonded supramolecular arrays formed in the case of Ti(**1**)$_2$(O*i*Pr)$_2$ (top) containing $R_2^2(10)$ and $R_2^2(12)$ ring motifs[31,32] and Ti(**2**)$_2$(O*i*Pr)$_2$ (bottom). The dashed lines represent the intermolecular hydrogen bonds.

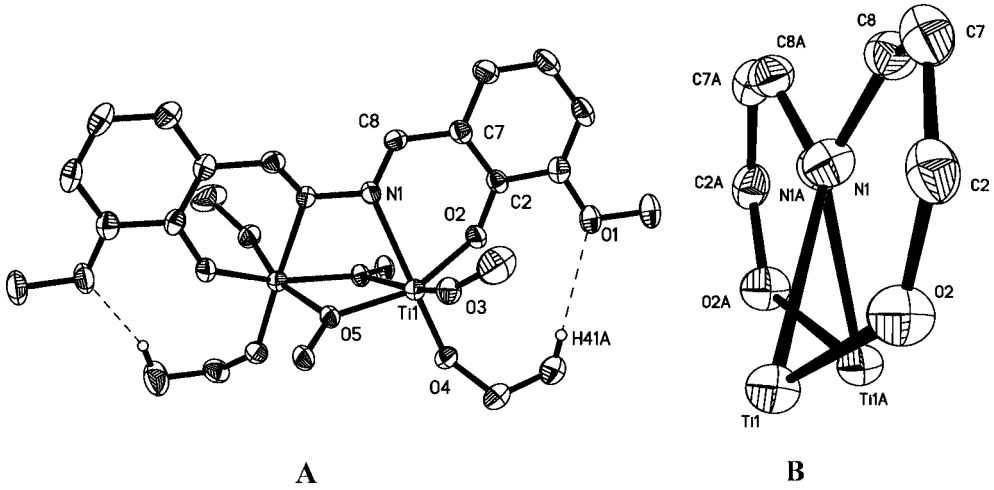


Figure 5. **A** The crystal structure of complex Ti$_2$(**4**)(O*i*Pr)$_6$. The ellipsoids are shown at the 50% probability level and the hydrogen atoms not involved in the weak intramolecular interaction have been removed for clarity. In the case of Ti$_2$(**4**)(O*i*Pr)$_6$ a weak interaction is observed between H(41A) and O(1), D–H 0.86(4) Å, H···A 2.67(4) Å, D···A 3.474(4) Å, <(DHA) 155(4)°, and is shown as a dashed line, H(41A) was identifiable in the penultimate difference Fourier map and refined freely. **B** View down the N(1)–N(1A) bond highlighting the {C(8)–N(1)–N(1A)–C(8A)} torsion angle.

Table 3. Selected bond lengths [Å] and angles [°] for complexes Ti$_2$(**3**)(O*i*Pr)$_6$, Ti$_2$(**4**)(O*i*Pr)$_6$ and Ti$_2$(**5**)(O*i*Pr)$_6$.

| Ti$_2$(**3**)(O*i*Pr)$_6$ | | Ti$_2$(**4**)(O*i*Pr)$_6$ | | Ti$_2$(**5**)(O*i*Pr)$_6$ | |
|---|---|---|---|---|---|
| Ti(1)–O(1) | 1.921(3) | Ti(1)–O(2) | 1.930(2) | Ti(1)–O(1) | 1.934(2) |
| Ti(1)–O(4) | 1.786(3) | Ti(1)–O(3) | 1.797(2) | Ti(1)–O(2) | 1.796(2) |
| Ti(1)–O(5) | 1.799(3) | Ti(1)–O(4) | 1.798(2) | Ti(1)–O(3) | 2.003(2) |
| Ti(1)–O(6) | 2.007(3) | Ti(1)–O(5) | 1.990(2) | Ti(1)–O(4) | 1.795(2) |
| Ti(1)–O(7) | 2.060(3) | Ti(1)–N(1) | 2.320(2) | Ti(1)–N(1) | 2.315(2) |
| Ti(1)–N(1) | 2.317(3) | N(1)–Ti(1)–O(4) | 165.34(7) | N(1)–Ti(1)–O(4) | 169.52(7) |
| N(1)–Ti(1)–O(5) | 166.86(1) | O(2)–Ti(1)–O(5) | 157.79(7) | O(2)–Ti(1)–O(3) | 92.95(7) |
| O(6)–Ti(1)–O(7) | 73.04(9) | O(2)–Ti(1)–O(3) | 93.53(8) | O(4)–Ti(1)–O(3) | 99.15(7) |

 © 2006 Wiley-VCH Verlag GmbH & Co. KGaA, Weinheim 

a Br–N interaction of 3.034 Å, which falls within the typical range,[33–35] to render the formation of a supramolecular ladder.

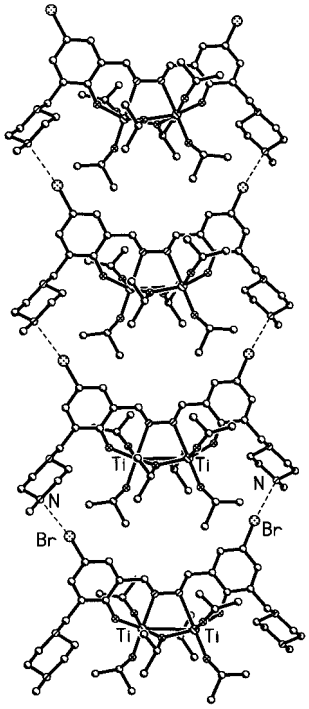


Figure 6. Bromine–nitrogen interactions in complex $Ti_2$(**5**)(O*i*Pr)$_6$.

## Conclusions

In conclusion X-ray structures of five novel titanium(IV) azine and hydrazone complexes are reported. The hydrazone complexes form monomers which have interesting supramolecular structures, with Ti(**1**)$_2$(O*i*Pr)$_2$ forming a ribbon-like array and Ti(**2**)$_2$(O*i*Pr)$_2$ forming a chain-like structure. By increasing the steric bulk the hydrogen bonding motifs are significantly altered. The azine complexes form dimers in the solid state. At the molecular level the substituents on the salicylaldimine aryl oxide groups had little effect on the structures. However, on the supramolecular level introduction of Lewis basic groups in the *ortho* position allowed formation of a weak intramolecular C–H···O interaction and intermolecular N–Br interactions, which induced the formation of a supramolecular ladder.

## Experimental Section

For the preparation and characterisation of complexes, all reactions and manipulations were performed under argon using standard Schlenk or glove-box techniques and all solvents were freshly distilled from suitable drying agents and degassed prior to use. Ligand **1**H was purchased from Aldrich, **2**H and **3**H$_2$–**5**H$_2$ were synthesised using literature procedures[36] and recrystallised from petroleum ether prior to use. Ti(O*i*Pr)$_4$ was purchased from Aldrich and purified by vacuum distillation prior to use. $^1$H/$^{13}$C NMR spectra were recorded with a Bruker Avance 300 MHz spectrometer and referenced to residual solvent peaks. Coupling constants are given in Hertz. Elemental analysis was performed by Mr. A. K. Carver at the Department of Chemistry, University of Bath. Due to the propensity of the complexes to hydrolyse reliable elemental analysis could not be obtained in some cases. Crystallographic data were collected on a Nonius KappaCCD area detector diffractometer using Mo-$K_\alpha$ radiation ($\lambda$ = 0.71073 Å) at a temperature of 150(2) K, and all structures were solved by direct methods and refined on all $F^2$ data using the SHELXL-97 suite of programs.[37] Hydrogen atoms not involved in hydrogen bonding were included in idealised positions and refined using the riding model. Absorption corrections were applied on merit. See Table 4 for full crystallographic parameters.

CCDC-607937 to -607941 contain the supplementary crystallographic data for this paper. These data can be obtained free of charge from The Cambridge Crystallographic Data Centre via www.ccdc.cam.ac.uk/data_request/cif.

**Ti(1)$_2$(O*i*Pr)$_2$:** A solution of salicylaldehyde hydrazone (0.82 g, 6 mmol), was prepared in dry toluene (10 mL) under an inert atmosphere. To this Ti(O*i*Pr)$_4$ (0.9 mL, 3 mmol) was added to give a bright yellow solution. This solution was vigorously stirred for 1 h. The solvent was removed in vacuo to give a pale yellow solid product. This product was suspended in hexane and toluene added until dissolution occurred on warming. Standing at room temperature yielded a crop of yellow blocks. Yield 1.12 g (85%). M.p. 140–143 °C. $^1$H NMR ($CDCl_3$): $\delta$ = 1.04 [d, $J$ = 6 Hz, 12 H, CH(C$H_3$)$_2$], 4.63 [sept, $J$ = 6 Hz, 2 H,C$H$(CH$_3$)$_2$], 5.57 (s, 4 H, NH$_2$), 6.69 (dd, $J$ = 5 and 1 Hz, 2 H, Ar-H), 6.78 (d, $J$ = 8 Hz, 2 H, Ar-H), 7.00 (d, $J$ = 8 Hz, 2 H, Ar-H), 7.18 (m, 2 H, Ar-H), 7.62 (s, 2 H, imine CH) ppm. $^{13}$C{$^1$H} ($CDCl_3$): $\delta$ = 25.6 [CH(*C*H$_3$)$_2$], 79.2 [*C*H(CH$_3$)$_2$], 118.5, 118.9, 122.0, 131.3, 132.3 (Ar), 146.9 (NCH), 162.4 (Ar-O) ppm. $C_{20}H_{28}N_4O_4Ti$ (436.3): calcd. C 55.1, H 6.47, N 12.84; found C 54.8, H 6.40, N 12.70.

**Ti(2)$_2$(O*i*Pr)$_2$:** An analogous procedure to that for Ti(**1**)$_2$(O*i*Pr)$_2$ was followed. Yield 0.39 g (59%), m.p. 220–224 °C (dec.) $^1$H NMR ($CDCl_3$): $\delta$ = 0.90 [two overlaying doublets, $J$ = 6 Hz, 12 H, CH(C$H_3$)$_2$], 1.22 [s, 18 H, C(CH$_3$)$_3$], 1.46 [s, 18 H, C(CH$_3$)$_3$], 4.55 [sept, $J$ = 6 Hz, 2 H, C$H$(CH$_3$)$_2$], 5.48 (s, 4 H, NH$_2$), 6.87 (s, 2 H, Ar-H), 7.29 (s, 2 H, Ar-H), 7.70 (s, 2 H, NCH) ppm. $^{13}$C{$^1$H} NMR ($CDCl_3$): $\delta$ = 26.0 [CH(*C*H$_3$)$_2$], 30.2 [C(*C*H$_3$)$_3$], 31.9 [C(*C*H$_3$)$_3$], 34.5 [*C*(CH$_3$)$_3$], 35.6 [*C*(CH$_3$)$_3$], 78.6 [*C*H(CH$_3$)$_2$], 121.2, 125.9, 127.1, 137.6, 139.6 (Ar), 148.7 (NCH), 159.7 (Ar-O) ppm. $C_{36}H_{60}N_4O_4Ti$ (660.8): calcd. C 65.4, H 9.15, N 8.48; found C 66.2, H 9.35, N 7.90.

**Ti$_2$(3)(O*i*Pr)$_6$:** A solution of 2,4-di(*tert*-butyl)salicylaldehyde azine (0.36 g, 1 mmol), was prepared in dry toluene (10 mL) under an inert atmosphere. To this Ti(O*i*Pr)$_4$ (0.6 mL, 2 mmol) was added to give a yellow solution. This solution was vigorously stirred for 1 h. Reduction in volume of the toluene and standing at room temperature yielded a crop of yellow blocks. Yield 0.46 g (57%), m.p. 243–246 °C. $^1$H NMR ($CDCl_3$): $\delta$ = 0.77 [br., 12 H, CH(C$H_3$)$_2$], 1.02 [d, $J$ = 6 Hz, 6 H, CH(C$H_3$)$_2$], 1.20 [d, $J$ = 6 Hz, 6 H, CH(C$H_3$)$_2$], 1.21–1.29 [m, 30 H, 2× CH(C$H_3$)$_2$ and 2× C(CH$_3$)$_3$)], 1.46 [s, 18 H, C(CH$_3$)$_3$], 4.37 [sept, $J$ = 6 Hz, 2 H, C$H$(CH$_3$)$_2$], 4.77 [sept, $J$ = 6 Hz, 2 H, C$H$(CH$_3$)$_2$], 4.88 [sept, $J$ = 6 Hz, 2 H, C$H$(CH$_3$)$_2$], 7.12 (s, 2 H, Ar-H), 7.37 (s, 2 H, Ar-H), 7.89 (s, 2 H, NCH) ppm. $^{13}$C{$^1$H} NMR ($CDCl_3$): $\delta$ = 22.0 [CH(*C*H$_3$)$_2$], 22.1 [CH(*C*H$_3$)$_2$], 23.7 [CH(*C*H$_3$)$_2$], 23.7 [CH(*C*H$_3$)$_2$], 23.8 [CH(*C*H$_3$)$_2$], 23.9 [CH(*C*H$_3$)$_2$], 27.9 [C(*C*H$_3$)$_3$], 29.5 [C(*C*H$_3$)$_3$], 32.1 [*C*(CH$_3$)$_3$], 33.3 [*C*(CH$_3$)$_3$], 72.3 [*C*H(CH$_3$)$_2$], 75.1 [*C*H(CH$_3$)$_2$], 75.9 [*C*H(CH$_3$)$_2$], 117.8, 126.2, 127.0, 135.8, 136.4 (Ar), 149.6 (NCH), 159.8 (Ar-O) ppm. $C_{48}H_{84}N_2O_8Ti_2$ (912.9): calcd. C 63.2, H 9.27, N 3.07; found C 63.0, H 9.14, N 3.39.

 © 2006 Wiley-VCH Verlag GmbH & Co. KGaA, Weinheim 

Table 4. Crystal data of the complexes Ti(**1**)$_2$(O*i*Pr)$_2$, Ti(**2**)$_2$(O*i*Pr)$_2$, Ti$_2$(**3**)(O*i*Pr)$_6$, Ti$_2$(**4**)(O*i*Pr)$_6$ and Ti$_2$(**5**)(O*i*Pr)$_6$.

| Complex | Ti(**1**)$_2$(O*i*Pr)$_2$ | Ti(**2**)$_2$(O*i*Pr)$_2$ | Ti$_2$(**3**)(O*i*Pr)$_6$ | Ti$_2$(**4**)(O*i*Pr)$_6$ | Ti$_2$(**5**)(O*i*Pr)$_6$ |
|---|---|---|---|---|---|
| Empirical formula | $C_{20}H_{28}N_4O_4Ti$ | $C_{39}H_{67}N_4O_4Ti$ | $C_{55}H_{92}N_2O_8Ti_2$ | $C_{34}H_{56}N_2O_{10}Ti_2$ | $C_{44}H_{74}Br_2N_6O_8Ti_2$ |
| Formula mass | 436.36 | 703.87 | 1005.11 | 748.61 | 1070.71 |
| Crystal system | triclinic | monoclinic | triclinic | monoclinic | monoclinic |
| Space group | $P\bar{1}$ | $P2_1/c$ | $P\bar{1}$ | $C2/c$ | $C2/c$ |
| $a$ [Å] | 9.644(2) | 17.118(3) | 13.433(3) | 11.172(1) | 30.193(4) |
| $b$ [Å] | 10.188(3) | 13.160(2) | 14.276(3) | 15.376(2) | 9.862(1) |
| $c$ [Å] | 11.142(3) | 18.425(3) | 17.623(4) | 22.973(4) | 17.667(3) |
| $\alpha$ [°] | 97.437(1) | 90 | 77.595(1) | 90 | 90 |
| $\beta$ [°] | 92.913(1) | 98.237(1) | 72.174(1) | 95.451(1) | 95.214(1) |
| $\gamma$ [°] | 94.571(1) | 90 | 64.645(1) | 90 | 90 |
| $V$ [Å$^3$] | 1080.0(5) | 4107.8(1) | 2893.6(1) | 3928.5(9) | 5238.8(1) |
| $Z$ | 2 | 4 | 2 | 4 | 4 |
| $D_{calcd.}$ [g cm$^{-3}$] | 1.342 | 1.138 | 1.154 | 1.266 | 1.358 |
| Reflections collected | 12218 | 52194 | 37102 | 18362 | 33197 |
| $\theta$ range [°] | 3.28–27.50 | 3.61–27.49 | 3.65–25.68 | 3.56–26.37 | 3.82–27.51 |
| Independent reflections [$R_{int}$] | 4922 [0.0350] | 9332 [0.0793] | 10966 [0.1136] | 3934 [0.1257] | 5985 [0.044] |
| Goodness-of-fit | 1.002 | 1.045 | 1.025 | 1.029 | 1.057 |
| $R_1$,$wR_2$ [$I > 2\sigma(I)$][a] | 0.0374, 0.0975 | 0.0566, 0.1449 | 0.0683, 0.1630 | 0.0494, 0.1138 | 0.0340, 0.0810 |
| $R_1$, $wR_2$ [all data][a] | 0.0486, 0.1043 | 0.0890, 0.1648 | 0.1245, 0.1935 | 0.0787, 0.1289 | 0.0407, 0.0865 |

[a] $R_1 = \Sigma||F_o|-|F_c||/\Sigma|F_o|$, $wR_2 = [\Sigma(F_o^2-F_c^2)^2/\Sigma w(F_o^2)^2]^{1/2}$.

**Ti$_2$(4)(O*i*Pr)$_6$:** An analogous procedure to that for Ti$_2$(**3**)(O*i*Pr)$_6$ was followed. Yield 0.86 g (57%), m.p. 147–148 °C. $^1$H NMR ($CDCl_3$): $\delta$ = 0.80 [2 overlaying doublets, $J$ = 6 Hz, 12 H, CH(C$H_3$)$_2$], 1.12 [2 overlaying doublets $J$ = 6 Hz, 12 H, CH(C$H_3$)$_2$], 1.23 [d, $J$ = 6 Hz, 6 H, CH(C$H_3$)$_2$], 1.32 [d, $J$ = 6 Hz, 6 H, CH(C$H_3$)$_2$], 3.84 (s, 6 H, OCH$_3$), 4.39 [sept, $J$ = 6 Hz, 2 H, C$H$(CH$_3$)$_2$], 4.71 [sept, $J$ = 6 Hz, 2 H, C$H$(CH$_3$)$_2$], 4.95 [sept, $J$ = 6 Hz, 2 H, C$H$(CH$_3$)$_2$], 6.59 (m, 2 H, Ar-H), 6.85 (s, 2 H, Ar-H), 6.92 (s, 2 H, Ar-H), 7.87 (s, 2 H, NCH) ppm. $^{13}$C{$^1$H}($CDCl_3$): $\delta$ = 25.2 [CH(*C*H$_3$)$_2$], 26.1 [CH(*C*H$_3$)$_2$], 27.0 [CH(*C*H$_3$)$_2$], 27.2 [CH(*C*H$_3$)$_2$], 27.5 [CH(*C*H$_3$)$_2$], 27.5 [CH(*C*H$_3$)$_2$], 59.4 (OCH$_3$), 76.3 [*C*H(CH$_3$)$_2$], 79.6 [*C*H(CH$_3$)$_2$], 80.7 [*C*H(CH$_3$)$_2$], 118.1, 120.6, 122.2, 126.1, 151.5 (Ar), 152.8 (NCH), 158.8 (Ar-O). $C_{34}H_{56}N_2O_{10}Ti_2$ (748.6): calcd. C 54.6, H 7.54, N 3.74; found C 54.5, H 7.49, N 3.69.

**Ti$_2$(5)(O*i*Pr)$_6$:** An analogous procedure to that for Ti$_2$(**3**)(O*i*Pr)$_6$ was followed. Yield 0.89 g (83%), m.p. 175–179 °C. $^1$H NMR ($CDCl_3$): $\delta$ = 0.80 [2 overlaying doublets, $J$ = 6 Hz, 12 H, CH(C$H_3$)$_2$], 0.99 [d, $J$ = 6 Hz, 6 H, CH(C$H_3$)$_2$], 1.12 [d, $J$ = 6 Hz, 6 H, CH(C$H_3$)$_2$], 1.24 [2 overlaying doublets, $J$ = 6 Hz, 12 H, CH(C$H_3$)$_2$], 2.24 [s, 6 H, NCH$_3$], 2.41 [br. m, 16 H, piperazine CH$_2$], 3.47–3.68 [m, 4 H, NCH$_2$Ph], 4.34 [sept, $J$ = 6 Hz, 2 H, C$H$(CH$_3$)$_2$], 4.64 [sept, $J$ = 6 Hz, 2 H, C$H$(CH$_3$)$_2$], 4.89 [sept, $J$ = 6 Hz, 2 H, C$H$(CH$_3$)$_2$], 7.20 [s, 2 H, Ar-H], 7.53 (s, 2 H, Ar-H), 7.74 (s, 2 H, NCH) ppm. $^{13}$C{$^1$H} ($CDCl_3$): $\delta$ = 22.8 [CH(*C*H$_3$)$_2$], 23.1 [CH(*C*H$_3$)$_2$], 24.6 [CH(*C*H$_3$)$_2$], 24.8 [CH(*C*H$_3$)$_2$], 24.9 [CH(*C*H$_3$)$_2$], 24.9 [CH(*C*H$_3$)$_2$], 45.2 [NCH$_3$], 52.3, 54.3 (piperazine CH$_2$), 55.0 (N*C*H$_2$Ar), 73.8 [*C*H(CH$_3$)$_2$], 77.0 [*C*H(CH$_3$)$_2$], 78.0 [*C*H(CH$_3$)$_2$], 106.9, 119.9, 129.5, 131.3, 135.7 (Ar), 149.0 (NCH), 161.5 (Ar-O) ppm. $C_{44}H_{74}N_6O_8Ti_2Br_2$ (1070.6): calcd. C 49.4, H 6.97, N 7.85; found C 48.1, H 6.61, N 7.52.

## Acknowledgments

We would like to thank the EPSRC and Johnson-Matthey for funding this work.

[1] D. A. Pennington, W. Clegg, S. J. Coles, R. W. Harrington, M. B. Hursthouse, D. L. Hughes, M. E. Light, M. Schormann, M. Bochmann, S. J. Lancaster, *Dalton Trans.* **2005**, 561.
[2] M. Bochmann, *J. Organomet. Chem.* **2004**, *689*, 3982.
[3] A. Parssinen, T. Luhtanen, M. Klinga, T. Pakkanen, M. Leskela, T. Repo, *Eur. J. Inorg. Chem.* **2005**, 2100.
[4] L. S. Natrajan, C. Wilson, J. Okuda, P. L. Arnold, *Eur. J. Inorg. Chem.* **2004**, 3724.
[5] J. M. Tanski, P. T. Wolczanski, *Inorg. Chem.* **2001**, *40*, 2026.
[6] T. P. Vaid, E. B. Lobkovsky, P. T. Wolczanski, *J. Am. Chem. Soc.* **1997**, *119*, 8742.
[7] T. P. Vaid, J. M. Tanski, J. M. Pette, E. B. Lobkovsky, P. T. Wolczanski, *Inorg. Chem.* **1999**, *38*, 3394.
[8] H. Hefele, H. Jancke, S. Sawusch, U. Schilde, E. Uhlemann, *Struct. Chem.* **1997**, *8*, 211.
[9] M. Albrecht, S. Kamptmann, R. Frohlich, *Polyhedron* **2003**, *22*, 643.
[10] M. Trivedi, M. Chandra, D. S. Pandey, M. C. Puerta, P. Valerga, *J. Organomet. Chem.* **2004**, *689*, 879.
[11] S. K. Singh, M. Chandra, D. S. Pandey, *J. Organomet. Chem.* **2004**, *689*, 2073.
[12] S. Pal, *Inorg. Chem.* **2001**, *40*, 4807.
[13] J. Saroja, V. Manivannan, P. Chakraborty, S. Pal, *Inorg. Chem.* **1995**, *34*, 3099.
[14] H. Mo, C. J. Fang, C. Y. Duan, Y. T. Li, Q. J. Meng, *Dalton Trans.* **2003**, 1229.
[15] D. L. Hughes, G. J. Leigh, J. R. Sanders, *J. Chem. Soc., Dalton Trans.* **1990**, 3235.
[16] M. A. Halcrow, C. A. Kilner, J. Wolowska, E. J. L. McInnes, A. J. Bridgeman, *New J. Chem.* **2004**, *28*, 228.
[17] E. Amadei, M. Carcelli, S. Ianelli, P. Cozzini, P. Pelagatti, C. Pelizzi, *J. Chem. Soc., Dalton Trans.* **1998**, 1025.
[18] N. S. Oxtoby, A. J. Blake, N. R. Champness, C. Wilson, *Chem. Eur. J.* **2005**, *11*, 4643.
[19] D. Braga, S. L. Giaffreda, M. Polito, F. Grepioni, *Eur. J. Inorg. Chem.* **2005**, 2737.
[20] A. M. Beatty, *Coord. Chem. Rev.* **2003**, *246*, 131.
[21] P. J. Hagrman, D. Hagrman, J. Zubieta, *Angew. Chem. Int. Ed.* **1999**, *38*, 2639.
[22] G. R. Desiraju, *Acc. Chem. Res.* **2002**, *35*, 565.
[23] A. D. Burrows, D. M. P. Mingos, A. J. P. White, D. J. Williams, *Chem. Commun.* **1996**, 97.
[24] D. A. Pennington, S. J. Coles, M. B. Hursthouse, M. Bochmann, S. J. Lancaster, *Chem. Commun.* **2005**, 3150.
[25] R. D. Kohn, P. Kampe, G. Kociok-Kohn, *Eur. J. Inorg. Chem.* **2005**, 3217.
[26] R. K. J. Bott, M. Hammond, P. N. Horton, S. J. Lancaster, M. Bochmann, P. Scott, *Dalton Trans.* **2005**, 3611.

 © 2006 Wiley-VCH Verlag GmbH & Co. KGaA, Weinheim 

[27] S. Groysman, E. Sergeeva, I. Goldberg, M. Kol, *Inorg. Chem.* **2005**, *44*, 8188.
[28] S. Groysman, E. Y. Tshuva, I. Goldberg, M. Kol, Z. Goldschmidt, M. Shuster, *Organometallics* **2004**, *23*, 5291.
[29] A. J. Chmura, M. G. Davidson, M. D. Jones, M. D. Lunn, M. F. Mahon, *Dalton Trans.* **2006**, 887.
[30] M. G. Davidson, M. D. Jones, M. D. Lunn, M. F. Mahon, *Inorg. Chem.* **2006**, *45*, 2282.
[31] M. C. Etter, J. C. Macdonald, J. Bernstein, *Acta Crystallogr., Sect. B: Struct. Sci.* **1990**, *46*, 256.
[32] M. C. Etter, *Acc. Chem. Res.* **1990**, *23*, 120.
[33] D. S. Reddy, D. C. Craig, A. D. Rae, G. R. Desiraju, *J. Chem. Soc., Chem. Commun.* **1993**, 1737.
[34] S. C. Blackstock, J. P. Lorand, J. K. Kochi, *J. Org. Chem.* **1987**, *52*, 1451.
[35] S. C. Blackstock, J. K. Kochi, *J. Am. Chem. Soc.* **1987**, *109*, 2484.
[36] B. Khera, A. K. Sharma, N. K. Kaushik, *Bull. Chem. Soc. Jpn.* **1985**, *58*, 793.
[37] G. M. Sheldrick, SHELXL-97, University of Göttingen, Germany, **1997**.

Received: May 30, 2006
Published Online: August 29, 2006

 © 2006 Wiley-VCH Verlag GmbH & Co. KGaA, Weinheim 

EurJIC
European Journal of Inorganic Chemistry

Issue 22/2006

Pages 4457–4704

*Papers available ahead of print in Early View at www.interscience.wiley.com*

*Earliest available Table of Contents:*
*Automatically, free of charge by e-mail through*
*www.interscience.wiley.com/alerts*

## COVER PICTURE

**The cover picture shows** some various examples of terminal imido–titanium complexes of the general formula $Ti(=NR)Cl_2(NHMe_2)_2$ that are accessible through the reported one-pot reaction of $Ti(NMe_2)_4$ with a primary amine $RNH_2$ in the presence of excess chlorotrimethylsilane. This procedure appears to be general to the generation of a wide range of imido groups: alkyl-, silyl-, and arylimido groups, as well as functional organoimido, chiral imido, and diimido ligands. $Ti(=NR)Cl_2(NHMe_2)_2$ complexes are of particular interest as organometallic synthons and for further applications in the field of homogeneous catalysis and materials science. The background photo of the famous palm tree vault of the Jacobins church (Toulouse, France, founded in the 13th–14th centuries) symbolizes the diversity of the compounds – arranged in arc around the palm tree vault – that can be prepared by using our promising synthetic strategy, and provides a solid foundation – the pillar – for attractive applications. Details are discussed in the article by C. Lorber et al. on p. 4503 ff. The authors acknowledge Christian Bergounhou (LCC Toulouse) for the Palm Tree photograph.

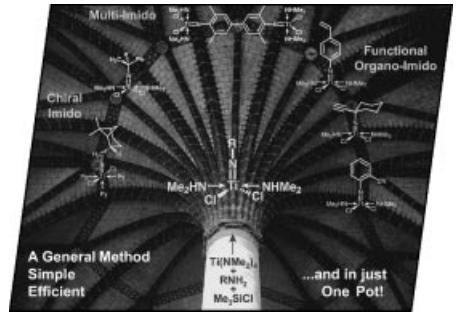


## MICROREVIEW

Contents

**4473** **M. Bassetti***

Kinetic Evaluation of Ligand Hemilability in Transition Metal Complexes

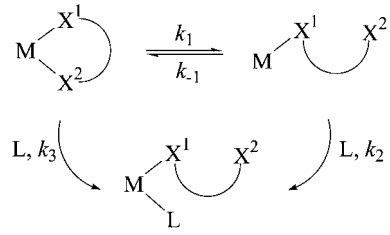

**Keywords:** Ligand hemilability / Oxidative addition / Platinum metals / Kinetics / Reaction mechanisms

 © 2006 Wiley-VCH Verlag GmbH & Co. KGaA, Weinheim 

# SHORT COMMUNICATIONS


**4483** **G. Yong, S. Qiao, Y. Xie, Z. Wang***

Cadmium(II) and Zinc(II) Coordination Polymers with 1D Ladder and 2D Basket Weave Layer Structures Constructed from a New T-Shaped Ligand

**Keywords:** Pyridinones / Polymers / T-shaped ligands / Luminescence / Coordination modes

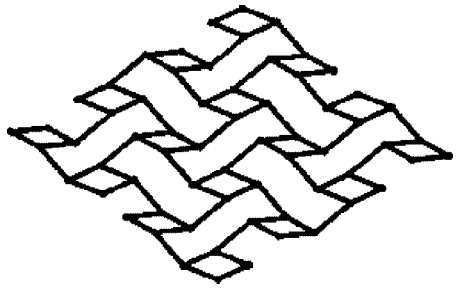

**4489** **D. D. Díaz, S. Sen Gupta, J. Kuzelka, M. Cymborowski, M. Sabat, M. G. Finn***

Bis(formamidine−urea) Complexes of $Ni^{II}$ and $Cu^{II}$: Synthesis, Characterization, and Reactivity

**Keywords:** Formamidine ligand / Urea ligand / Nickel / Copper / Catalysis

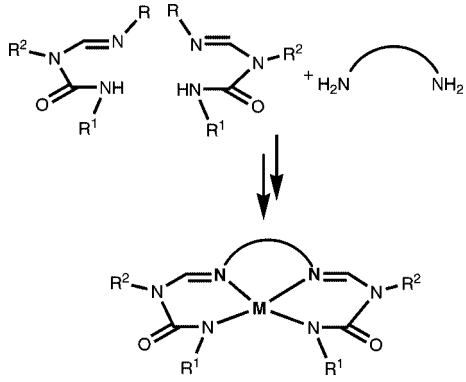

**4494** **H. Sugimoto,* M. Tarumizu, H. Miyake, H. Tsukube**

Bis(dithiolene) Molybdenum Complex that Promotes Combined Coupled Electron−Proton Transfer and Oxygen Atom Transfer Reactions: A Water-Active Model of the Arsenite Oxidase Molybdenum Center

**Keywords:** Bioinorganic chemistry / Electrochemistry / Molybdenum / Reaction mechanism / S ligands

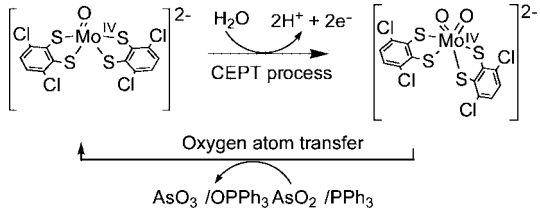


**4498** **M. Schulz-Dobrick, M. Jansen***

Supramolecular Intercluster Compounds Consisting of Gold Clusters and Keggin Anions

**Keywords:** Supramolecular chemistry / Cluster compounds / Polyoxometalates / Nanomaterials / Gold clusters

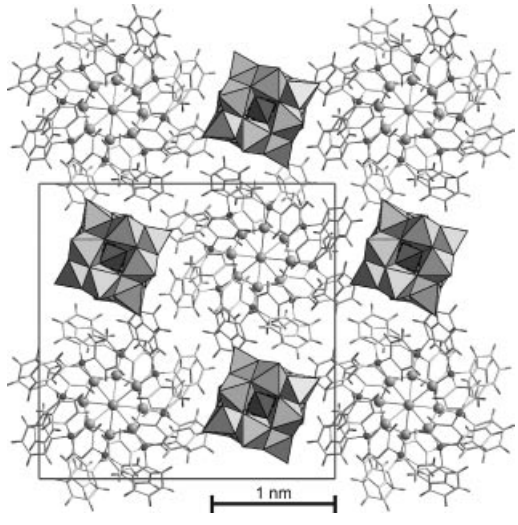



 © 2006 Wiley-VCH Verlag GmbH & Co. KGaA, Weinheim 

# FULL PAPERS


**4503** **C. Lorber,* R. Choukroun, L. Vendier**

A General and Facile One-Step Synthesis of Imido−Titanium(IV) Complexes: Application to the Synthesis of Compounds Containing Functionalized or Chiral Imido Ligands and Bimetallic Diimido Architectures

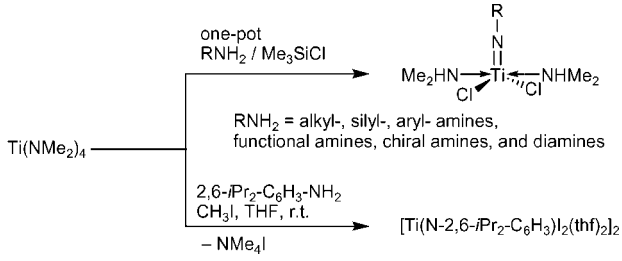


**Keywords:** Imido / N ligands / Multiple bonds / Titanium / Synthesis design

**4519** **E. V. Mutseneck, Z. A. Starikova, K. A. Lyssenko, P. V. Petrovskii, P. Zanello, M. Corsini, A. R. Kudinov***

Slipped μ-Indenyl Triple-Decker Complexes Containing $(C_4Me_4)Co$ and $(C_5R_5)Ru$ Fragments

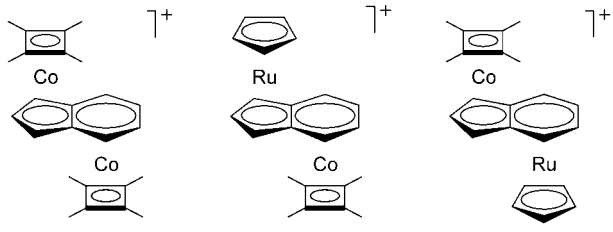


**Keywords:** Cobalt / Ruthenium / Sandwich compounds / Triple-decker complexes / Electrochemistry

**4528** **F. Šimko,* A. Rakhmatullin, M. Boča, V. Daněk, C. Bessada**

A High-Temperature Multinuclear NMR Study of $Na_3AlF_6$/FeO and $Na_3AlF_6$/$Fe_2O_3$ Melts

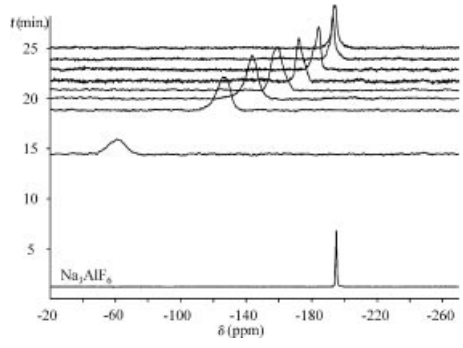


**Keywords:** Electrolysis / NMR spectroscopy / Cryolitic melts / Aluminium / Iron

**4533** **P. Di Bernardo,* P. Zanonato, A. Bismondo, H. Jiang, A. Y. Garnov, J. Jiang, L. Rao***

Complexation of Uranium(VI) with Thiodiacetic Acid in Solution at 10−85 °C

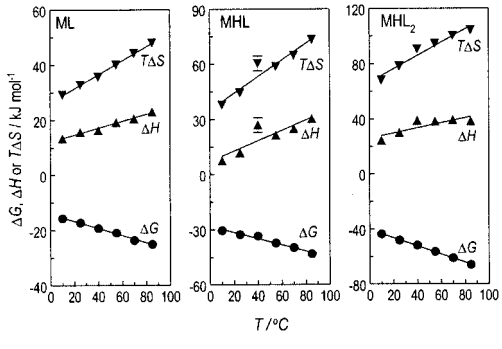


**Keywords:** Uranium / Thermodynamics / Carboxylate ligands / EXAFS spectroscopy / Temperature effect


 © 2006 Wiley-VCH Verlag GmbH & Co. KGaA, Weinheim 

**4541** **H. Jin, Y. F. Qi, E. B. Wang,* Y. G. Li, C. Qin, X. L. Wang, S. Chang**

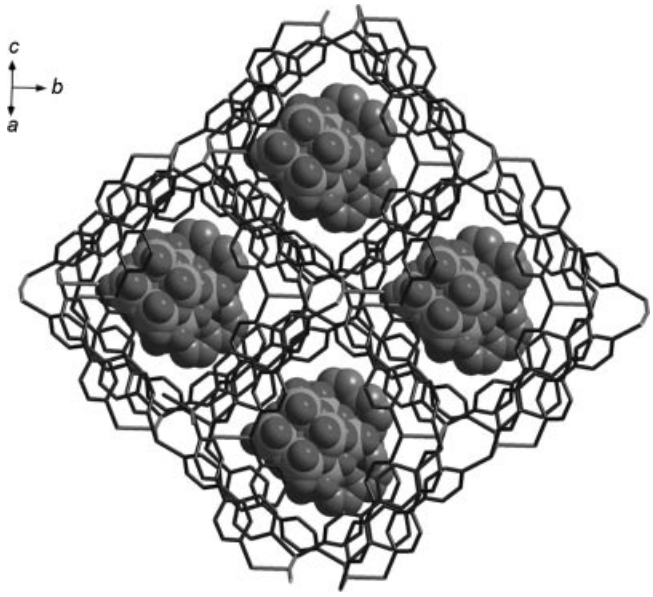


A Novel Copper(I) Halide Framework Templated by Organic−Inorganic Hybrid Polyoxometalate Chains Formed In Situ: A New Route for the Design and Synthesis of Porous Frameworks

**Keywords:** Coordination polymers / Organic−inorganic hybrid composites / Polyoxometalates / Template synthesis

**4546** **P. Gruene, C. Trage, D. Schröder,* H. Schwarz**

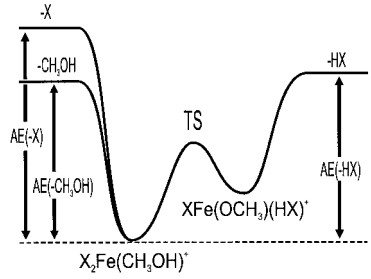


Solvent and Ligand Effects on the Structures of Iron Halide Cations in the Gas Phase

**Keywords:** Hydrogen transfer / Iron halides / Ligand effects / Mass spectrometry / Solvent effects

**4553** **T. J. Boyle,* L. J. Tribby, S. D. Bunge**

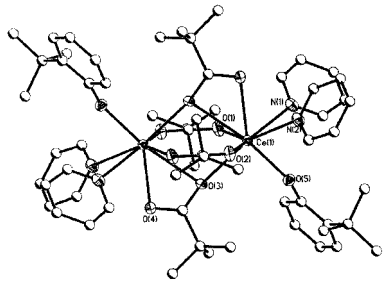

$$Ce(OAr)_3 + HORc \xrightarrow{py} [Ce(OAr)(\mu\text{-}ORc)(\mu_c\text{-}ORc)(py)]_2$$

[shown OR = oBP, ORc = OBc: **10**]

Synthesis and Structural Characterization of a Series of Carboxylic Acid Modified Cerium(III) Alkoxides

**Keywords:** Metal alkoxides / Cerium alkoxides / Carboxylate ligands / Chelates

 © 2006 Wiley-VCH Verlag GmbH & Co. KGaA, Weinheim 

**4564** **I. Senkovska, S. Kaskel***

Solvent-Induced Pore-Size Adjustment in the Metal-Organic Framework $[Mg_3(ndc)_3(dmf)_4]$ (ndc = naphthalene dicarboxylate)

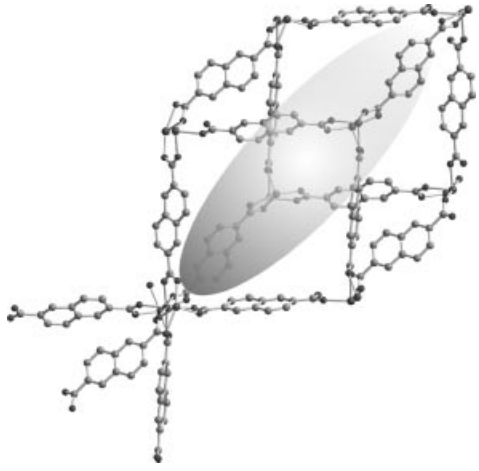

**Keywords:** Metal-organic frameworks / Magnesium / Carboxylate ligands / Adsorption

**4570** **R. Pietschnig,* A. Orthaber**

The Relative Stabilities of 1,3-Diphospha-2-sila-allene and Some of Its Isomers

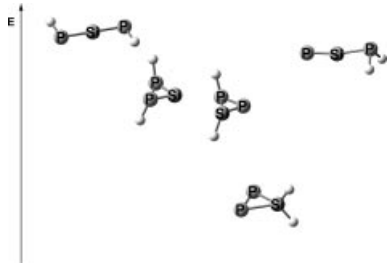

**Keywords:** Multiple bonds / Silicon / Phosphorus / Allenes / Ab initio calculations

**4577** **M. Sato,* Y. Kubota, A. Tanemura, G. Maruyama, T. Fujihara, J. Nakayama, T. Takayanagi, K. Takahashi, K. Unoura**

Synthesis and Some Properties of Bis(ruthenocenyl)thiophene Derivatives − Possible Spin-Coupling in the Two-Electron Oxidized Species of Dinuclear Ruthenocenes Bridged by Thiophene Derivatives

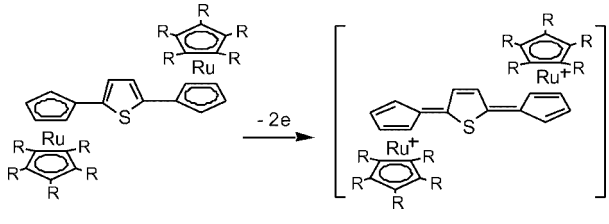


**Keywords:** Metallocenes / Redox chemistry / Cations / Sulfur heterocycles / Oxidation / Metal−metal interactions

 © 2006 Wiley-VCH Verlag GmbH & Co. KGaA, Weinheim 

**4589** **V. Cappello, J. Baumgartner, A. Dransfeld, K. Hassler***

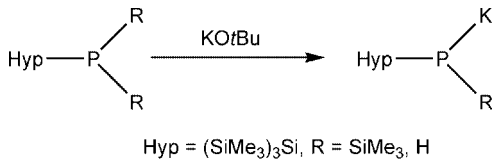


Monophosphanes and Diphosphanes with the Hypersilyl Substituent

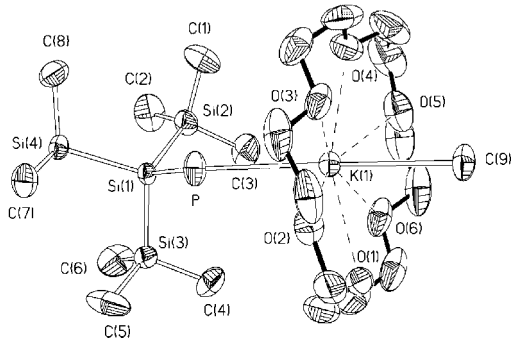


**Keywords:** Hypersilylphosphanes / Potassium phosphanides / Ab initio calculations / *P*-Silylhalophosphanes / Silicon

**4600** **S. Gosiewska, S. Herreras Martinez, M. Lutz, A. L. Spek, G. van Koten, R. J. M. Klein Gebbink***

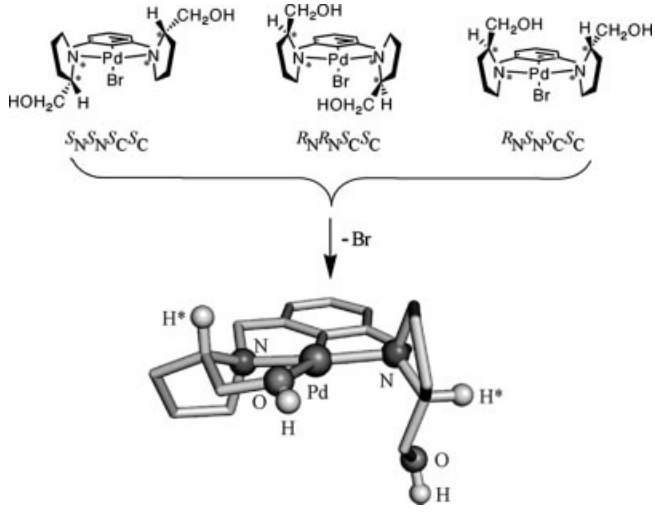


Diastereopure Cationic NCN-Pincer Palladium Complexes with Square Planar $\eta^4$-*N,C,N,O* Coordination

**Keywords:** Palladium / NCN-pincer / Amino acids / Ligand design / Hydrogen bonds

**4608** **D. Carriazo, C. Martín, V. Rives***

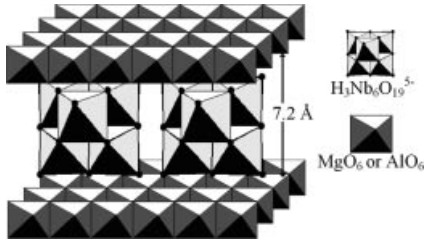


Thermal Evolution of a MgAl Hydrotalcite-Like Material Intercalated with Hexaniobate

**Keywords:** Layered double hydroxides / Polyoxometalates / Nb-Mg-Al mesoporous oxides / Intercalations

**4616** **D. Taher, A. I. Wallbank, E. A. Turner, H. L. Cuthbert, J. F. Corrigan***

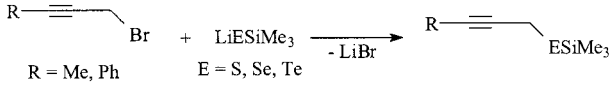


Alk-2-ynyl Trimethylsilyl Chalcogenoethers by Nucleophilic Substitution of Propargyl Bromides

**Keywords:** Chalcogens / Silicon / Propargyl complexes

 © 2006 Wiley-VCH Verlag GmbH & Co. KGaA, Weinheim 

**4621** **K. Strohfeldt, H. Müller-Bunz, C. Pampillón, N. J. Sweeney, M. Tacke***

Glycol Methyl Ether and Glycol Amine Substituted Titanocenes as Antitumor Agents

**Keywords:** Anticancer drugs / *cis*-Platin / Titanocene / Super hydride / Lithiation / Titanium

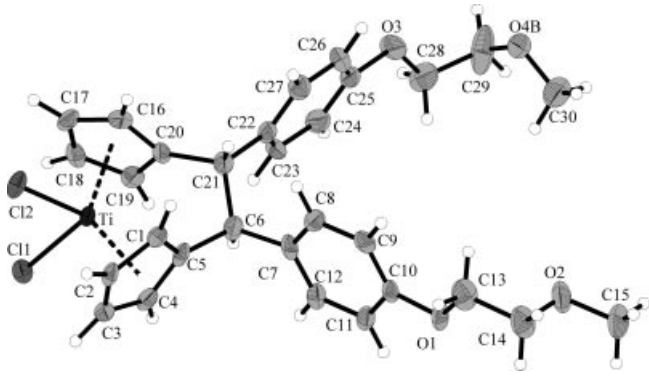


**4629** **M. Carbó, N. Marín, R. Navarro, T. Soler, E. P. Urriolabeitia***

Synthesis and Structure of Pd and Pt Complexes with Doubly Stabilized Phosphorus Ylides

**Keywords:** Ylides / Metallacycles / Palladium / Platinum / Coordination modes

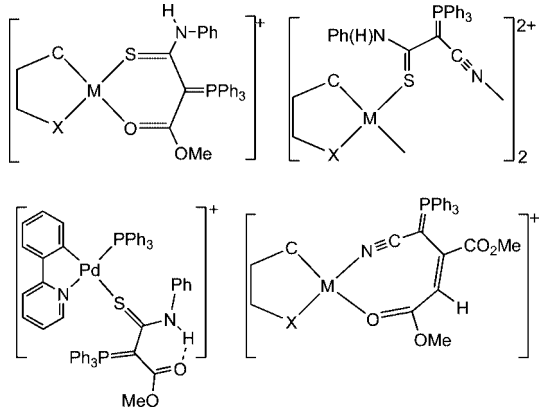


**4642** **M.-T. Chen, C.-A. Huang, C.-T. Chen***

Synthesis, Characterization, and Catalytic Applications of Palladacyclic Complexes Bearing C,N,S-Donor Ligands

**Keywords:** Palladacyclic complexes / Pendant thioether / Suzuki reaction / Heck reaction / Palladium

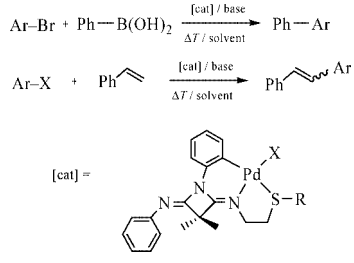


**4649** **P. Pallavicini,* G. Dacarro,* C. Mangano, S. Patroni, A. Taglietti, R. Zanoni**

pH-Driven $Cu^{2+}$ Translocation in Ferrocene-Containing Ligands

**Keywords:** Molecular devices / Macrocyclic ligands / Copper / Ferrocene / N ligands

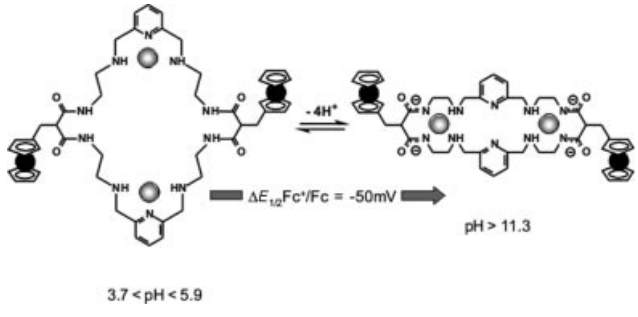


 © 2006 Wiley-VCH Verlag GmbH & Co. KGaA, Weinheim 

**4658** **L. Yang, Y. Shen,* A. Xie, J. Liang, S. Li, Q. Zhang**

Size- and Shape-Controlled Synthesis and Assembly of a Silver Nanocomplex in UV-Irradiated TSA Solution

**Keywords:** Nanostructures / Silver / Photochemistry / Self-assembly

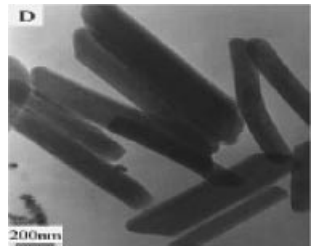


**4665** **A. Baunemann, M. Winter, K. Csapek, C. Gemel, R. A. Fischer***

Mixed Amido/Imido/Guanidinato Complexes of Tantalum: Effects of Ligand Substitution on Thermal Properties

**Keywords:** X-ray diffraction / Chelates / N ligands / Tantalum / Nitrides

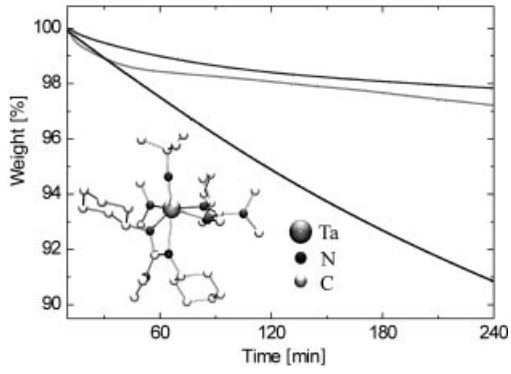


**4673** **A. Karmakar, R. J. Sarma, J. B. Baruah***

Mechanochemical Control of Synthesis and Structures of Aqua-Bridged Binuclear Nickel(II) Benzoate Complexes

**Keywords:** Nickel / Aqua-bridged complexes / Solvation / Hydrogen bonds

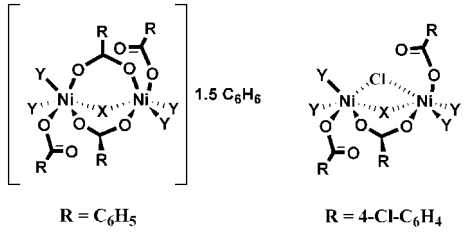


**4679** **J. Hou, X.-J. Peng,* J.-F. Liu, Y.-L. Gao, X. Zhao, S. Gao, K.-L. Han**

A Binuclear Isocyanide Azadithiolatoiron Complex Relevant to the Active Site of Fe-Only Hydrogenases: Synthesis, Structure and Electrochemical Properties

**Keywords:** Bioinorganic chemistry / Density functional calculations / Hydrogenases / Iron / Isocyanide ligands

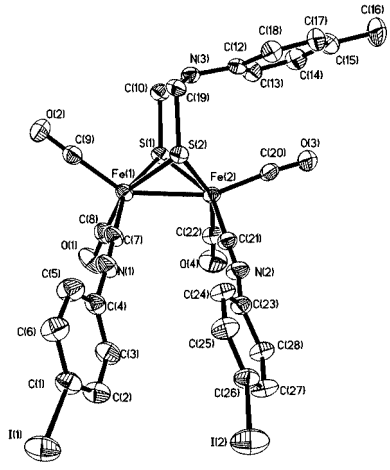

 © 2006 Wiley-VCH Verlag GmbH & Co. KGaA, Weinheim 

**4687** **T. Dhanalakshmi, E. Suresh, H. Stoeckli-Evans, M. Palaniandavar***

New Copper(II) Complexes as Efficient Catalysts for Olefin Aziridination: The Effect of Ligand Steric Hindrance on Reactivity

**Keywords:** Aziridination / Copper / N ligands / Tridentate ligands / Steric hindrance

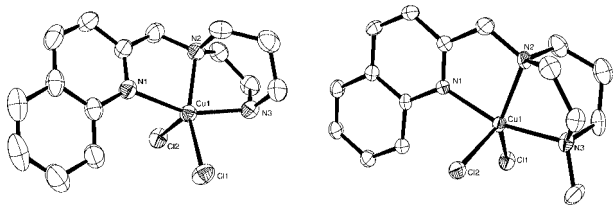


# CORRECTION

**4697** **S. Lachaize, S. Sabo-Etienne***

σ-Silane Ruthenium Complexes: The Crucial Role of Secondary Interactions

**Keywords:** σ-Complexes / Ruthenium / Silanes / Hydrides / Coordination modes / Intramolecular interactions / Oxidative addition / Hypervalent compounds

**RSS Feed**

Journal content prior to print publication can be found online on our Early View page at wwweurjic.org. Stay updated on the latest journal content by registering for our free e-mail alerts at http://interscience.wiley.com/alerts.

Keep up with the latest research with our RSS feed, which provides the titles, authors, and the Digital Object Identifiers (DOIs) of Early View articles, including links to the full texts. RSS is an XML-based format for sharing and distributing web content. To receive the RSS feed, just click on the orange feed icon at www.eurjic.org, or visit http://interscience.wiley.com/rss for more information.

DOI: 10.1002/ejic.200600212

# Kinetic Evaluation of Ligand Hemilability in Transition Metal Complexes

**Mauro Bassetti*[a]**

**Keywords:** Ligand hemilability / Oxidative addition / Platinum metals / Kinetics / Reaction mechanisms

Hemilability is the property of hybrid ligands to undergo a reversible metal chelate opening process by rupture of the weakest coordinative bond, yielding a coordinatively unsaturated complex. While experimental evidences of the process rely on the observation of fluxional behavior in the metal complex or on the spectroscopic detection of the species with different chelating bites, various effects are speculatively attributed to hemilability. In this review, this property is discussed in the context of its effects on the rate and mechanisms of bimolecular reactions. Examples of kinetics performed on ligand substitution, oxidative addition, alkyne tautomerization, and dehydrobromination reactions illustrate that the ligand hemilability process can be detected through simple kinetic analyses and can be quantitatively evaluated with respect to alternative reaction pathways. Since this concept affects various fields of chemistry, e.g. catalysis, supramolecular chemistry, molecular sensing, and materials, the kinetic approach may assist the rational design of ligands with the expected properties.

(© Wiley-VCH Verlag GmbH & Co. KGaA, 69451 Weinheim, Germany, 2006)

## 1. Introduction

Bidentate or polydentate ligands characterized by the presence of different donor atoms (X) bind to metal centers forming complexes with one or more metallacyclic rings. Because of the different strengths of the metal–heteroatom bonds, the metal complex may undergo a ring-opening process by the preferential rupture of the weakest coordinative bond. When the ligand free arm is easily recoordinated, the process becomes reversible (Scheme 1).[1,2]

Scheme 1. Hemilability of a bifunctional ligand $X^1$–$X^2$.

[a] CNR, Istituto di Metodologie Chimiche, Sezione Meccanismi di Reazione, and Dipartimento di Chimica, Università La Sapienza,
00185 Roma, Italy
Fax: +39-06-490-421
E-mail: mauro.bassetti@uniroma1.it

This feature, defined as hemilability, arises from the mixed bonding characteristics of hybrid ligands. It should be emphasized that while the term hybrid identifies the bifunctional structure of the ligand, the term hemilabile refers to the property of undergoing selective metal-donor bond breaking in the corresponding metal complex.[3]

Hemilability has been discussed in excellent reviews written in the last few years, which have focussed on definition and properties, and have described either the different classes of ligands according to the donor atoms involved in the chelate[1] or specific ligand systems with hemilabile character.[2] The use of potentially hemilabile ligands in catalysis has also been reviewed.[4]

The expression "hemilabile ligands" was first formulated by Jeffrey and Rauchfuss,[5] following from the early examples of transition metal complexes with bifunctional ligands.[6] These investigations were motivated by the expectation that bifunctional, for instance phosphane-amine or phosphane-ether, ligands would bind strongly enough to form chelate complexes but would readily dissociate the hard (N or O) ligand component in order to create a vacant site for substrate binding. Since then, the transition metal

*Mauro Bassetti was born in Milano in 1953. He studied Chemistry at Università "La Sapienza" in Roma, where he obtained the Laurea cum laude in 1978 with a thesis on the mercuration of olefins, under the supervision of Barbara Floris and the late Gabriello Illuminati. He was a National Institute of Health postdoctoral fellow at Auburn University and Virginia Commonwealth University in the years 1979–1982, working with Lidia Vallarino on the synthesis of lanthanide chelate complexes. After joining the Centro CNR di Studio sui Meccanismi di Reazione in 1984, he was a visiting scientist at the University of Sheffield during the 1990s in the group of Peter Maitlis, and at the University of Virginia in 1998. He has been a WG coordinator of projects related to ruthenium chemistry for catalysis, in the program COST Chemistry, Actions D12 and D24. His current research interests include organometallic reaction mechanisms, macrocyclic chemistry, olefin metathesis, and catalytic properties of ruthenium complexes.*

 © 2006 Wiley-VCH Verlag GmbH & Co. KGaA, Weinheim 

coordination chemistry of hemilabile ligands has expanded impressively and, while the initial motivation still remains the essential leitmotiv, hemilability is now considered a useful approach to induce molecular activation and create new systems for homogeneous catalysis and functional materials. Ligand design, synthesis of transition metal complexes with enhanced reactivities, biomimetic modelling, enantioselective catalysis, supramolecular coordination chemistry, and sensing of small molecules are some of the topics which have been affected by this concept.[1,2]

As a striking example of the impact that may arise from the strategic use of hemilability in catalysis, it is worth mentioning the case of the Hoveyda–Grubbs catalysts, which have significantly expanded the application profile of olefin metathesis in organic chemistry,[7] a subject now at the forefront of the chemical scenario.[8]

The key feature of these ruthenium complexes is the presence of the bidentate *o*-isopropyloxybenzylidene ligand, which binds to ruthenium through both the carbene functionality and the ethereal oxygen atom. When in action, the molecule allows the coordination of the olefinic substrate by substitution of the bound oxygen moiety (Scheme 2). On the other hand, the ethereal group stabilizes the complex when dormant in solution, thus reducing the decomposition pathways that occur more easily in the corresponding benzylidene phosphane complexes. In addition, this stabilizing effect allows for the recovery of the complex at the end of the reaction by column chromatography.

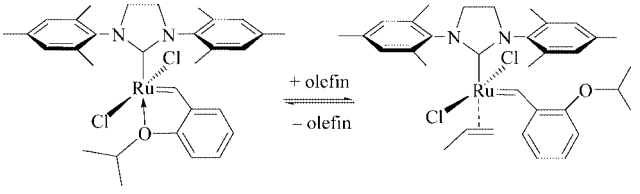


Scheme 2. Activation of a Hoveyda–Grubbs metathesis catalyst by substitution of the oxygen-bound chelate by an olefin.

The combination of a strong, substitutionally inert, and a weak, substitutionally labile, donor atom within the ligand molecular frame is the rationale for obtaining hemilability, which results from the relative metal–donor bond strengths in the complex. In fact, the strong bond ensures stability to the system when monocoordinated, while the weak bond allows for ring opening and closing of the metallacycle. Although it can be generically stated that the net effect arises from a combination of steric and electronic properties, it is nowadays difficult to predict a hemilabile character because of the variety of factors coming into play, for instance relative donicity toward a specific metal ion, interplay of soft and hard donor properties, ring size of the chelate, influence of ancillary ligands, ring substituents, solution effects, etc. The net outcome is that the game of hemilability is ruled by subtle and elusive energy differences, still difficult to control. It is with regard to this that an understanding of this property at a kinetic level may assist a rational design of ligands and complexes with the expected functions.

## 2. Properties of Hemilabile Complexes

The most significant feature exhibited by transition metal complexes of bifunctional ligands with hemilabile character is a fluxional behavior arising from the dissociation and rebinding of the weakly bonding moiety by intramolecular ligand exchange processes (Scheme 1).[9] The exchange involves a transient species which is either coordinatively unsaturated if formed from a dissociative pathway or saturated by solvent or by a counterion molecule. The intimate mechanistic features of fluxional processes of hemilabile systems have been documented in detail and are understood in depth, with a corresponding development of appropriate spectroscopic techniques and evaluative criteria.[1] A second important feature that may arise from hemilability in the complex is the facility to undergo ligand displacement reactions with external molecules, in which a monodentate ligand, a small molecule, or an organic substrate coordinates to the metal ion via the door opened by the substitutionally labile group. Reversible decoordination followed by chelate formation corresponds to hemilability (Scheme 3).[10]

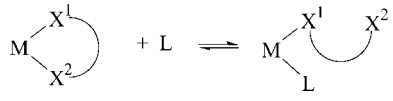


Scheme 3. Substitution reaction in the complex with a hemilabile ligand.

This property moves hemilability from a strictly intramolecular process toward a bimolecular phenomenon, with the obvious implications for molecular sensing, supramolecular design, and enhanced catalytic activity. However, in addition to the isolation of the corresponding substituted complexes and the qualitative observation of intriguing effects in stoichiometric or catalytic reactions, attributed to hemilability, the reaction mechanisms of transition metal complexes with bifunctional ligands in bimolecular reactions have not been studied extensively from the point of view of hemilability. In this regard, since the ring opening represents an easy access to a structural isomer of the chelate complex with altered reactivity, kinetic studies can provide an additional criterion for the identification of hemilability and a quantitative evaluation of its role along the reaction coordinate. In fact, it is within the exclusive realm of chemical kinetics that many reactive species are detected and evaluated, specifically when these are elusive toward any spectroscopic detection.

## 3. Kinetic Studies

Although the mechanisms of metal-chelate ring-opening processes of polydentate ligands have been studied extensively from a kinetic viewpoint,[11] the first article dealing

 © 2006 Wiley-VCH Verlag GmbH & Co. KGaA, Weinheim 

with the reaction of a metal complex of a bifunctional ligand was described by Knebel and Angelici in 1974.[12] The purpose of the work was to study the effect of the chelate ring structure on the rates of ring opening for reactions in which the product contained a bidentate ligand in the monocoordinated mode. This effect was obtained using a series of bifunctional ligands $Ph_2P(CH_2)_2NR_2$ (R = Me, Et, H) and $Ph_2P(CH_2)_3NMe_2$ (P-N) in the reaction of the complexes $[M(CO)_4(\kappa^2\text{-}P,N)]$ (**1**) with carbon monoxide, by taking advantage of the different binding abilities of a relatively inert phosphorus-donor and a labile nitrogen-donor atom. In fact, the substitution reactions of analogous bidentate N–N, S–S, CS–CS, As–As ligands in Cr, Mo, and W complexes had always proceeded with complete displacement of the bidentate ligand, affording no experimental evidence for the ring-opened monodentate species.

The reactions of complexes **1** with CO to give $[Mo(CO)_5(\kappa^1\text{-}P,N)]$ (**2**) were found to be first order in the metal complex and in CO, and second order overall. Such a relatively simple kinetic behavior is in agreement with at least two mechanisms, implying either direct attack of CO on the starting complex or reversible dissociation of the N-donor group followed by CO attack on the five-coordinate intermediate $[Mo(CO)_4(\kappa^1\text{-}P,N)]$ (**3**), this latter case being outlined in Scheme 4.

With the assumption that $k_{-2}$ is negligible, application of the steady-state approximation to the open intermediate yields the rate expression (1) (L = CO), which implies a first-order dependence on the CO concentration in the reasonable case that $k_{-1} >> k_2[CO]$. This is in agreement with the observed linear dependence of the $k_{obs}$ values on the concentration of carbon monoxide.

$$k_{obs} = \frac{k_1 k_2[L]}{k_{-1} + k_2[L]} \quad (1)$$

Since the second-order behavior does not give direct evidence for the existence of an intermediate along the reaction pathway, discrimination between the two mechanisms was possible from the observation that the reactivity, expressed by $k_{obs}$, became independent of [CO], hence zero order, upon performing the reaction in the presence of trifluoroacetic acid. This is because of the fast protonation of the nitrogen atom of the intermediate, which prevents any possibility of ring closing, resulting in the starting complex, and allows rapid trapping of the five-coordinate species by CO to give the product $[Mo(CO)_5(\kappa^1\text{-}P,NH^+)]$ (**4**) (Scheme 5).

Under these conditions, the rate is only limited by the value of $k_1$. Therefore, the kinetics in the presence of acid allowed the rate constant of the ring-opening process to be obtained, i.e. the Mo–N bond breaking, being $k_{obs} = k_1$. The operation of a purely dissociative mechanism yielding the "open arm" five-coordinate intermediate $[Mo(CO)_4(\kappa^1\text{-}P,NH^+)]$ was supported from the evidence of zero-order dependence on [CO] for the substitution reactions of corresponding monodentate N-ligand complexes under analogous conditions, with a lack of rate enhancements in the presence of acid. The $k_1$ values were found to increase by an order of magnitude with the bulkiness of the N substituents (H = Me > Et) in the five-membered chelate complexes $[Mo(CO)_5(\kappa^2\text{-}P,N)\text{-}Ph_2P(CH_2)_2NR_2]$, while a 50-fold rate increase was observed in the corresponding six-membered chelate (R = Me) as the result of the larger release of ring strain in the transition state.

Having established from kinetic data the hemilabile character of the P–N complexes, the $k_{obs}$/[CO] values in the absence of acid yield $k_1k_2/k_{-1}$, from which the ratio $k_2/k_{-1}$ can be derived. This value represents the competition for the intermediate species between ring closure and reaction with CO. The data indicated that ring closure ($k_{-1}$) is approximately one thousand times faster than the uptake of CO ($k_2$) and that the five-coordinate intermediate is insensitive to the nature of the N donor group or to the size of the incipient ring. Thermodynamic parameters in addition to kinetic data were determined for the reactions of complexes $[M(CO)_4(\kappa^2\text{-}P,N)]$ with carbon monoxide, P–N being a series of *o*-phosphanepyridyl ligands.[13]

These articles represented the most informative kinetic studies on the reaction of a bifunctional system proceeding by substitution of the weakly bound donor moiety with an external ligand, and showing in quantitative terms the competition of the monodentate intermediate between ring closure ($k_{-1}$) and the bimolecular reaction ($k_2$). In these cases, (i) the only reactive pathway is provided by chelate-ring opening, and (ii) the incoming ligand does not participate in further reactions. The backward reaction can be suppressed by trapping the ligand free arm into a group that is

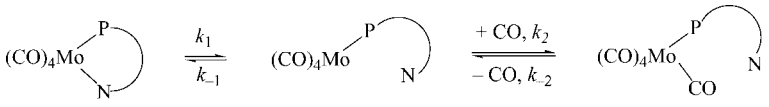


Scheme 4. Mechanism of the substitution reaction of complexes $[M(CO)_4(\kappa^2\text{-}P,N)]$ with carbon monoxide.

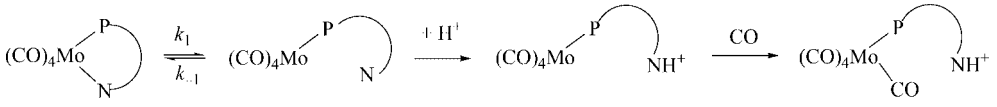


Scheme 5. Mechanism of the substitution reaction of complexes $[M(CO)_4(\kappa^2\text{-}P,N)]$ with carbon monoxide in the presence of acid.

 © 2006 Wiley-VCH Verlag GmbH & Co. KGaA, Weinheim 

unsuitable for rebinding, such as by protonation. Kinetics of the acid-promoted chelate-ring opening have often been reported for a variety of transition metal complexes with hybrid ligands.[14]

The case of competitive reactivity of the chelate molecule and of the open monodentate species has emerged during our studies on the reaction of the rhodium(I) carbonyl complex [Rh(κ$^3$-L)(CO)]$PF_6$ (**5**) with methyl iodide, in which L is the tridentate $NS_2$ ligand 2,6-bis(benzylthiomethyl)pyridine binding to rhodium in a square-planar geometry through a *trans*-dithioether coordination. The complex, as well others from the same family containing the $NS_2$ ligand set, exhibits a fluxional behavior at room temperature arising from configurational inversion at the stereogenic sulfur centers and occurring by the debinding and rebinding of the sulfur donor groups.[15] The reaction of **5** with methyl iodide proceeds by consecutive oxidative addition–carbonyl insertion reactions, which is typical of many monodentate and bidentate rhodium(I) carbonyl complexes, and results in the isolation of the final $Rh^{III}$ acyl complex [Rh(κ$^3$-L)(COMe)I]$PF_6$ (**6**) (Scheme 6).[16]

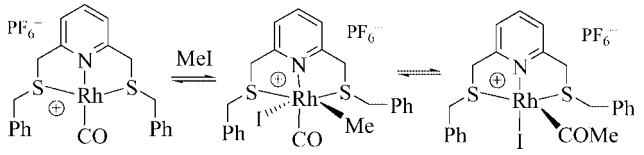


Scheme 6. Consecutive oxidative addition–migratory insertion steps in the reaction of complex **5** with methyl iodide.

Rate studies on the oxidative addition step, giving the intermediate $Rh^{III}$ methyl species [Rh(L)(CO)(Me)I]$PF_6$ (first stage in Scheme 6), have been carried out in solvents of different polarity. The data indicated the presence of two parallel routes, one involving the four-coordinate complex **5**, and one involving a rearranged form of this complex. This evidence emerged from a relatively simple kinetic behavior expressed from the plots of $k_{obs}$ vs. the concentration of MeI in acetonitrile, acetone, and dichloromethane (Figure 1), which showed a linear dependence on MeI and a nonzero intercept on the *y* axis. While the linear dependence identifies a reaction route characterized by the presence of both the rhodium complex and the electrophile in the rate-determining step, overall second-order, the nonzero intercept indicates an alternative pathway that is first order in the rhodium complex but zero order in MeI, in which the electrophile comes into play after the rate-limiting step.

The concept arising from the observed kinetic behavior, represented graphically in Scheme 7, corresponds to the case of a generic substrate S that can react as such (second-order route) or in the form of a more reactive species S* (first-order route) to give the same final product P.[17] The transient molecule S* is either captured by the reagent R with rate $k_2$ or transformed back into the original complex with rate $k_{-1}$. Since both of these steps are faster than its formation, this rearranged form of the starting material is subject only to kinetic but not to spectroscopic detection.

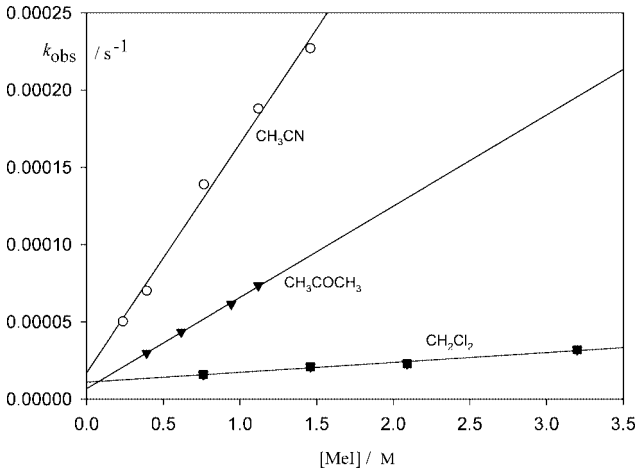


Figure 1. Plot of $k_{obs}$ values for the oxidative addition of methyl iodide to complex [Rh(κ$^3$-L)(CO)]$PF_6$ (**5**) [L = 2,6-bis(benzylthiomethyl)pyridine] in acetonitrile, acetone, and dichloromethane, at 31 °C.

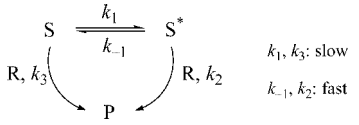


Scheme 7. Schematic representation of parallel first- and second-order routes in the reaction of substrate S with reagent R to give product P.

The kinetic analysis of Scheme 7 yields Equation (2) from the application of the steady-state approximation to the intermediate S*.

$$k_{obs} = k_1 + k_3[R] \quad (2)$$

At this stage, the next step takes us from facts to interpretation. Although various speculations can be done as to the origin of a highly reactive species arising from the tridentate complex, logic and indirect evidences suggest that hemilability of the $NS_2$ ligand plays a role in the pathway which is zero order in MeI. In fact, the fluxional character of this system indicates the presence of an equilibration process specifically involving the methylene groups of the ligand. The dissociation of one ligand arm by rupture of the sulfur–rhodium bond would provide a 14 electron and coordinatively unsaturated complex, expected to be highly reactive toward the electrophilic methyl iodide. The mechanistic version of Scheme 7 in terms of the structural features of complex **5** is represented in Scheme 8.

The intercept on the *y* axis represents the rate of formation of the κ$^2$-*N*,*S* complex ($k_1$), which is slower than the reaction with MeI ($k_2$) or the rebinding of the thioether group ($k_{-1}$). Analysis of the first-order rate constants, $k_1$, reveals a small dependence on the nature of the solvent, which is typical for a limiting-ligand dissociative step from a platinum group metal.[18] This is in sharp contrast with the values of the second-order rate constants, $k_3$, which vary by a factor of 20 between the polar solvent acetonitrile and the less polar dichloromethane, implying separation of charge in the attack of rhodium to the methyl group during

 © 2006 Wiley-VCH Verlag GmbH & Co. KGaA, Weinheim 

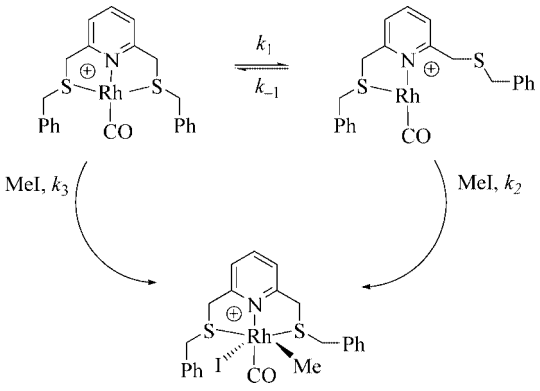


Scheme 8. First ($k_1$: slow; $k_2$: fast) and second-order ($k_3$) routes for the reaction of complex **5** with methyl iodide.

the slowest step, clearly associated with methyl iodide bond rupture.[19] Values of $k_1$ and $k_3$, along with the ratios $k_1/([\text{MeI}]\times k_3)$, which represent the relative weight of the two pathways at different concentrations of methyl iodide, are reported in Table 1.

Table 1. Values of rate constants for the reaction of complex $[Rh(\kappa^3\text{-}NS_2)(CO)]PF_6$ (**5**) with MeI in different solvents (31 °C).

| Solvent | $\varepsilon$[a] | $k_1$ / $s^{-1}$ | $k_3$ / $M^{-1}s^{-1}$ | $k_1/k_3\times$[MeI][b] | $k_1/k_3\times$[MeI][c] |
|---|---|---|---|---|---|
| $CH_2Cl_2$ | 9.1 | $1.1\times10^{-5}$ | $6.4\times10^{-6}$ | 3.4 | 1.7 |
| $Me_2CO$ | 20.7 | $6.7\times10^{-6}$ | $5.9\times10^{-5}$ | 0.23 | 0.11 |
| MeCN | 37.5 | $1.7\times10^{-5}$ | $1.4\times10^{-4}$ | 0.24 | 0.12 |

[a] Dielectric constant. [b] $c$ = 0.5 M. [c] $c$ = 1.0 M.

In addition to the fluxional character of complex **5**, a convincing indirect evidence that supports the interpretation based on hemilability is that the reactions of rhodium(I) complexes with MeI, as well as those of platinum group metal complexes in general, display kinetic plots characterized by linear dependence on the electrophilic concentrations and zero intercepts on the $y$ axis, indicating the availability of only one reactive route.[20] Moreover, significant solvent effects are observed in these reactions, which proceed by means of an SN2 pathway, in contrast to the lack of any correlation with the solvent donor ability in the clockwise route ($k_1$) of Scheme 8. A kinetic pattern showing a nonzero intercept was found once in the case of the rhodium(I) complex [Rh(cupf)(CO)($PPh_3$)], containing the bidentate anionic ligand *N*-nitrosophenyloxyamine PhN(NO)-$O^-$ (cupf).[21] In this case, the presence of mixed first- and second-order pathways was interpreted as the result of an intramolecular rearrangement of the complex induced by the attack of solvent and involving a change of the coordinative mode of the bifunctional ligand, thus generating a reactive species in equilibrium with the starting material. Linear plots with a positive intercept on the $y$ axis and described by an equation formally identical to 2 are found for equilibrium processes in which substrate and product remain spectroscopically observable at the end of the reaction. Such a case can be found in the oxidative addition of methyl iodide to the iodocarbonyl complex [Rh(CO)-$(L_{Me})_2$I] containing the N-heterocyclic carbene 3,5-dimethylimidazoline-2-ylidene ($L_{Me}$) ligand.[22] It is usually easy to differentiate between parallel and reversible processes from the final spectra.

An interesting kinetic pattern was observed for the reaction of complex **5** in methanol, in which the $k_{obs}$ values as a function of [MeI] exhibit a saturation behavior, i.e. tend toward a limiting value with increasing concentration of the electrophile.[15] This situation corresponds to the formation of a reactive species in equilibrium with the substrate, often induced by solvent, with comparable values of the forward reaction with the reagent and of the step leading back to the starting material.[23] The kinetic analysis on treatment of the intermediate under steady-state conditions yields the same Equation (1) (L = MeI) which was derived from the case of the P–N complexes **1**, the saturation effect here arising from the similarity of $k_{-1}$ and $k_2$. Although the separate values cannot be determined, the analysis yields the ratio $k_{-1}/k_2$ and the rate constant $k_1$. In the present case, these correspond to 1.8, and to the same rate of methyl iodide attack and ring closure at [MeI] = 1.8 M, and to $1.7\times10^{-4}$ $s^{-1}$, respectively. Therefore, it appears that in methanol the preferred route is the one involving a methanol solvated bidentate $\kappa^2$-*N*,*S* complex, along the clockwise pathway of Scheme 8, with no evidence for the second-order route. For the sake of comparison with the reaction of the bidentate P–N complexes **1** with carbon monoxide, the ratio of ring closure to CO attack ($k_{-1}/k_2$) from the five-coordinate intermediate [Mo(CO)$_4$($\kappa^1$-*P*,N)] is about one thousand at the conditions employed ([CO] = $5\times10^{-3}$ M, 69.6 °C in 1,2-dichlorobutane), while extrapolation at a concentration of carbon monoxide of about 1 M yields a similar ratio to the one observed for the reaction of **5** in methanol.

We have performed rate studies on the second step of the reaction of complex **5** with MeI (Scheme 6), which is the migratory insertion process giving the isolable product $[Rh(\kappa^3\text{-}L)(COMe)I]PF_6$ (**6**). The reaction is characterized by no rate dependence on the MeI concentration as expected for an intramolecular process, and we had no experimental evidence for any role of hemilability. However, in light of more information now available about the reactivity of rhodium(I) complexes with tridentate ligands, it appears that the presence of harder donor atoms or of less flexible ligand structures inhibit the migratory-insertion step. In fact, the oxidative addition of MeI stops at the methyl carbonyl rhodium(I) species for [N–N–N] complexes of 2,6-bis(oxazoline)pyridine,[24] bis(imino)carbazolide,[20q] or of [C–N–C] 2,6-bis(alkylimidazol-2-ylidene)pyridine ligands,[20r] while it proceeds to spontaneous migratory CO insertion for rhodium(III) complexes of hybrid [P–N–O] or [N–O–N] ligands.[25–26] The contribution of the association/dissociation process of a dangling ligand arm in carbonylation reactions was proposed for rhodium(I) complexes of mixed phosphane-phosphite or phosphane-ether bidentate ligands.[2a,c,20e,27]

 © 2006 Wiley-VCH Verlag GmbH & Co. KGaA, Weinheim 

Analogous cases of parallel first- and second-order kinetics were found in the study of the reactions of ruthenium complexes coordinated by the hybrid allylphosphane ligand, $Ph_2PCH_2CH=CH_2$, which acts in a bidentate fashion through the coordination of both the phosphorus atom and the allylic double bond to the metal center. Mixed alkenyl-phosphane or alkynyl-phosphane ligands have attracted a large interest because of the potential hemilabile character in the corresponding transition metal complexes.[28] The Cp* ruthenium complex $[Ru(\eta^5\text{-}C_5Me_5)\{\kappa^1\text{-}P\text{-}Ph_2PCH_2CH=CH_2\}\{\kappa^3\text{-}P,C,C\text{-}Ph_2PCH_2CH=CH_2\}][PF_6]$ (**7**), containing two molecules of allylphosphane in different, monodentate and bidentate, coordinative modes, reacts with nucleophiles (L = NaNCS, CO, PhC≡CH) yielding corresponding neutral or cationic complexes in which both molecules are monodentate. In addition, complex **7** reversibly binds acetonitrile (Scheme 9).[29]

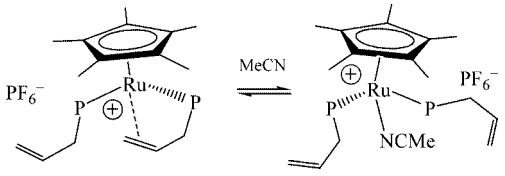


Scheme 9. Reversible coordination of acetonitrile to complex **7**.

These reactions occur readily by substitution of the coordinated alkenyl group, which forms a weaker bond to the metal than the phosphorus donor. The specific hemilabile character of allylphosphane was suggested by a fluxional behavior exhibited by complex **7** at room temperature, and confirmed by variable temperature NMR spectroscopic studies. Substitution reactions and dynamic properties have been interpreted as the result of a dissociative mechanism involving binding and rebinding of the allylic moiety, typical of hemilability. In analogy, the cationic indenyl complexes $[Ru(\eta^5\text{-}C_9H_7)(PPh_3)\{\kappa^3\text{-}P,C,C\text{-}Ph_2PCHRCH=CH_2\}]PF_6$ (**8**, R = H; **9**, R = Me) containing allylphosphane derivatives undergo substitution reactions of the allylic double bond by nitriles (MeCN, BzCN) or by sodium azide yielding the corresponding monodentate cationic or neutral complexes.[30] In contrast with the behavior of the Cp* complex **7**, dynamic processes were not observed in the $^1H$ or $^{31}P$ NMR spectra of complexes **8** or **9**, performed between –90 and 50 °C. Because of their rich chemistry, rate studies were performed on the reactions of these indenyl complexes.

In particular, complex $[Ru(\eta^5\text{-}C_9H_7)\{\kappa^3\text{-}(P,C,C)\text{-}PPh_2(CH_2CH=CH_2)\}(PPh_3)][PF_6]$ (**8**) reacts with terminal alkynes RC≡CH (R = Ph, *p*-$MeC_6H_4$, $SiMe_3$) yielding bicyclic cyclobutadienylidene compounds.[31] This reaction stems from the action of the allylphosphane ligand, which first decoordinates the allylic double bond allowing the incoming alkyne to π-coordinate to ruthenium and then undergoes an unprecedented [2+2] cycloaddition with the tautomerized vinylidene moiety (Scheme 10). The reaction is highly diastereoselective yielding only one isomer of the bicyclic derivative, which contains three stereogenic centers.

In the case of aryl alkynes, the intermediate vinylidene species, observable by $^{31}P$ NMR spectroscopy, were also independently prepared from the corresponding alkynyl derivatives and shown to proceed under thermal activation to the same bicyclic products. In addition to the novelty of such a [2+2] cycloaddition occurring smoothly just above room temperature, the process appears peculiar among those of complexes with hybrid ligands since it involves both a transformation of the alkyne at the metal center and its further reaction with the dissociated arm of the bifunctional molecule.

Although the first step of this process, i.e. the formation of the vinylidene intermediates, is associated with a change of the binding mode of the allylphosphane ligand from $\kappa^3$-*P,C,C* to monodentate $\kappa^1$-*P* coordination, a case of hemilability cannot be identified due to the lack of fluxional behaviour. Kinetic experiments were performed by $^{31}P$ NMR spectroscopy for the formation of the vinylidene species from complex **8** and the aryl alkynes *p*-$XC_6H_4C{\equiv}CH$ (X = H, Cl) in chloroform-*d* solution.[32] The reactions were found to be first order in **8** and the values of $k_{obs}$ were obtained at different concentrations of the alkynes. Figure 2 shows the corresponding plots. Analogous to the results obtained for the rhodium complex **5**, the graph reveals finite intercepts on the *y* axis and points to the mechanistic hypothesis of Scheme 7, which when adapted to the structural features of complex **8** yields Scheme 11. In this case the positive values of the intercepts on the *y* axis represent the rate of dissociation of the allylic double bond from ruthenium ($k_1$). These were found to be $k_1 = 9(\pm2.5)\times10^{-5}\ s^{-1}$ for phenylacetylene and $7(\pm1.5)\times10^{-5}\ s^{-1}$ for *p*-chlorophenylacetylene, corresponding to the rate of formation of the vinylidene species $[Ru(\eta^5\text{-}C_9H_7)(=C=CHC_6H_4\text{-}p\text{-}X)\{\kappa^1\text{-}(P)\text{-}PPh_2(CH_2CH=CH_2)\}(PPh_3)]^+$, existing in equilibrium with the chelate complex. It is worth mentioning that a chelate complex analogous to **8** coordinated by the homoallylphosphane ligand $PPh_2(CH_2CH_2CH=CH_2)$ is inert to-

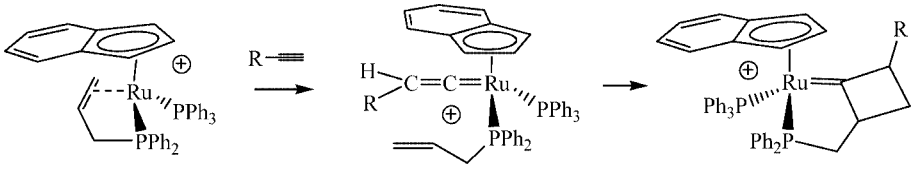


Scheme 10. Reaction of complex **8** with terminal alkynes.

 © 2006 Wiley-VCH Verlag GmbH & Co. KGaA, Weinheim 

ward reactions with either nitrile or alkynes.[28] This information indicates that enlarging the chelate by one additional methylene group in the carbon chain imparts greater stability to the ring and to the ruthenium–olefin bond, which does not undergo either spontaneous or induced ring opening.

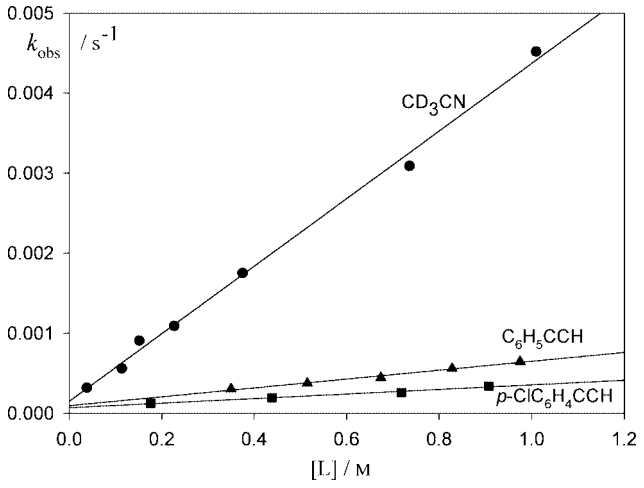


Figure 2. Plot of $k_{obs}$ values for the substitution reaction of complex $[Ru(\eta^5\text{-}C_9H_7)\{\kappa^3\text{-}(P,C,C)\text{-}PPh_2(CH_2CH{=}CH_2)\}(PPh_3)][PF_6]$ (**8**) with $CD_3CN$ (●), compared with the $k_{obs}$ values for the reactions with PhC≡CH (▲) and $p$-$ClC_6H_4C{\equiv}CH$ (■), in [$D_1$]chloroform at 38.1 °C.

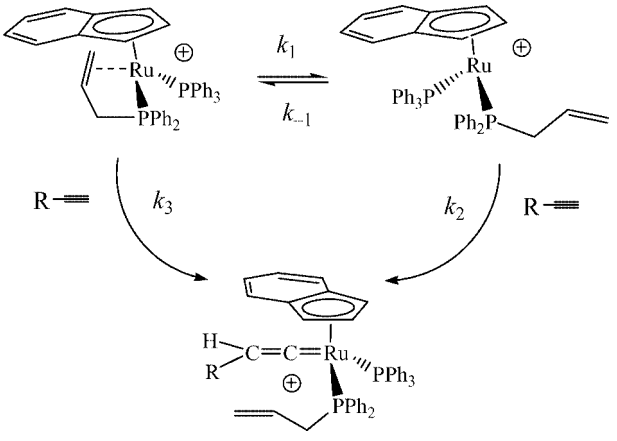


Scheme 11. Direct SN2 attack of the alkyne at complex **8** ($k_3$, slow) or at the transient $[Ru(\eta^5\text{-}C_9H_7)\{\kappa^1\text{-}(P)\text{-}PPh_2(CH_2CH{=}CH_2)\}(PPh_3)][PF_6]$ ($k_2$, fast).

With regard to the mechanistic analysis presented for the reaction of complex **5**, there is an additional feature of relevance in the concept of kinetic detection of hemilability. In fact, the rate data in the case of the $NS_2$ rhodium complex $[Rh(\kappa^3\text{-}L)(CO)]PF_6$ were obtained for the reaction with the same MeI in different solvents, while here different alkynes have been made to react with the indenyl ruthenium complex. The zero-order dependence on the alkyne implicit in the finite $y$ intercept and the observation of Scheme 11 points out that $k_1$ values must be independent not only of the concentration of the alkyne but also of its nature, since the alkyne is supposed to interact with the ruthenium complex after the rate-determining dissociation of the allylic double bond. In agreement with this consideration, the values of the intercept on the $y$ axis obtained from phenylacetylene and $p$-chlorophenylacetylene are the same within experimental error of the measurements. In line with the basic principle of chemical kinetics for which information is attainable only up to the rate-limiting step along the reaction coordinate, the rate of dissociation of the weakest bond of the hybrid ligand is not affected by the evolution of the resulting intermediate. In contrast, the values of the second-order rate constants obtained from the slopes of the linear plots, which are $k_2 = 5.5(\pm0.4)\times10^{-4}$ for phenylacetylene and $2.8(\pm0.3)\times10^{-4}$ $M^{-1}s^{-1}$ for $p$-chlorophenylacetylene, depend on the nature of the alkyne interacting with the metal complex in the slowest step of this pathway. In particular, the smaller value for the $p$-chloro derivative indicates that an electron-withdrawing ring substituent reduces the electron density on the triple bond and its reactivity toward the ruthenium center.

The concept that the rate of formation of a monodentate intermediate arising from ring opening must be independent of the concentration and nature of the reagent found a further example in the reactions of complex **8** with nitriles (L), proceeding quantitatively to the formation of the substituted complexes $[Ru(\eta^5\text{-}C_9H_7)(PPh_3)\{\kappa^1(P)\text{-}Ph_2PCH_2CH{=}CH_2\}(L)]PF_6$ (L = MeCN, BzCN),[30] differently from that of the equilibrium observed for the bisallyl Cp* complex **7** (Scheme 9). The kinetics for the reaction with [$D_3$]acetonitrile exhibited mixed first- and second-order routes, with the second-order rate constant $k_2 = 4.2(\pm0.1)\times10^{-3}$ $M^{-1}s^{-1}$, in agreement with a larger nucleophilic character of a nitrile with respect to an arylalkyne. In contrast, the first-order rate constant $k_1 = 1.5(\pm0.6)\times10^{-4}$ $s^{-1}$ was within experimental error of the values obtained from the reactions with $p$-$XC_6H_4C{\equiv}CH$ (X = H, Cl). Therefore, because of the nature of $k_1$ its value is independent of the reaction in which the coordinatively unsaturated intermediate becomes involved, i.e. of its final destiny. This concept is represented graphically in Scheme 12.

As previously pointed out, consistent circumstantial evidence should assist the proposal of a reaction mechanism, especially when highly reactive or spectroscopically undetectable species are involved. The possibility of an intermediate arising from the dissociation of $PPh_3$ instead of the allylic double bond was excluded by the observation that the rate of the reaction of complex **8** with phenylacetylene was not depressed in the presence of a large excess of the monodentate phosphane. In addition, the attribution of the first-order pathway to a rate-limiting $\eta^5$-$\eta^3$ shift of the indenyl ring can be excluded from the fact that substitution reactions of indenyl complexes exhibit second-order behavior.[33] The substitution reaction in the indenyl complex is first-order overall when the rate-determining dissociation of another ligand generates a 16-electron coordinatively unsaturated species and the free ligand, the indenyl group remains $\eta^5$-bound.[34] What occurs in the case of complex **8** is exactly the intramolecular version of this phenomenon,

 © 2006 Wiley-VCH Verlag GmbH & Co. KGaA, Weinheim 

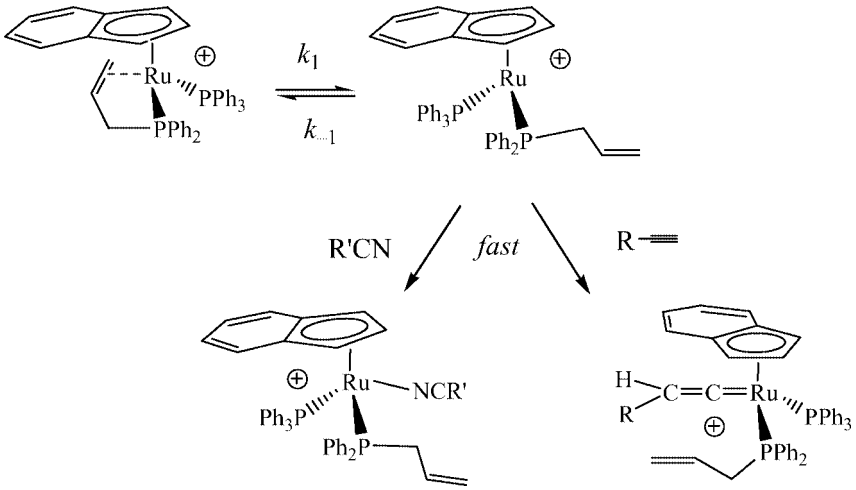


Scheme 12. The reactivity of complex [Ru($\eta^5$-$C_9H_7$){$\kappa^3$-(*P*,*C*,*C*)-$PPh_2(CH_2CH{=}CH_2)$}($PPh_3$)][$PF_6$] is dominated by the rate of dissociation of the allylic double bond ($k_1$).

with the allylphosphane ligand remaining bound to the ruthenium through the phosphorus atom. Cases of parallel first- and second-order kinetics involving monodentate ligands and exhibiting the same kinetic pattern observed here were also reported.[35]

A simple analysis of the plots in Figure 1 and Figure 2 allows the contribution of the arm-off mechanism to the overall reactivity to be estimated. This is done graphically from the ratio of $k_1$ over the interpolated $k_{obs}$ value on the *y* axis at a given concentration of the reagent. For instance, the rhodium complex **5** reacts with MeI via the $\kappa^2$-*N*,*S* intermediate for about 10% in acetone or in acetonitrile, and for about 60% in dichloromethane, at [MeI] ≈ 1 M. The contribution of hemilability increases to about 19% in the more polar solvents and to 78% in dichloromethane at [MeI] ≈ 0.5 M. The reaction of the indenyl ruthenium complex **9** proceeds via the monodentate intermediate for about 25% in the case of phenylacetylene and 33% in the case of the *p*-chloroderivative, at an alkyne concentration of 0.5 M. At the same concentration of phenylacetylene, only 5% of the reaction with [$D_3$]acetonitrile occurs via the open arm intermediate of the allylphosphane complex. The effect of hemilability is minimized under those conditions of solvent or reagent that favor the SN2 attack to the chelate complex, while it tends to become dominant at concentrations of the reagent approaching zero.

The substitution reactions of the homoditopic S–S ligands of [Pt(Ph)$_2${$\kappa^2$-(*S*,*S*)-$Ph_2S(CH_2)_nSPh_2$}] (*n* = 2,3) by a diphosphane were found to proceed according to Equation (2), indicating the formation of a monodentate $\kappa^1$-*S* transient species.[36] Parallel first- and second-order kinetics were also observed for the acid-promoted ring opening and displacement by chloride of the bidentate chelate ligand from dichloro[pyridine-2-(α-methoxymethanolato)]-gold(III).[14d]

The effect of hemilabile ligands on the rates of 1,2-dehydrobromination reactions mediated by lithium diisopropylamide (LDA) were studied in detail by Collum and coworkers. The process itself served as the reference reaction for addressing key issues in organolithium chemistry, in particular aggregation and solvation effects.[37] The reaction in the presence of hemilabile O–N ligands instead of BuOMe can be accelerated by up to four orders of magnitude because of the intervention of monomer and dimer based pathways. Kinetic and spectroscopic experiments carried out using either BuOMe, bidentate ethers such as dimethoxyethane, or different hybrid aminoethers have shown that ground state structures are dimeric complexes bearing a monodentate ligand, while transition state structures are chelated monomeric species (Scheme 13).

The subject has been investigated with various approaches, including thermodynamic, kinetic, and computa-

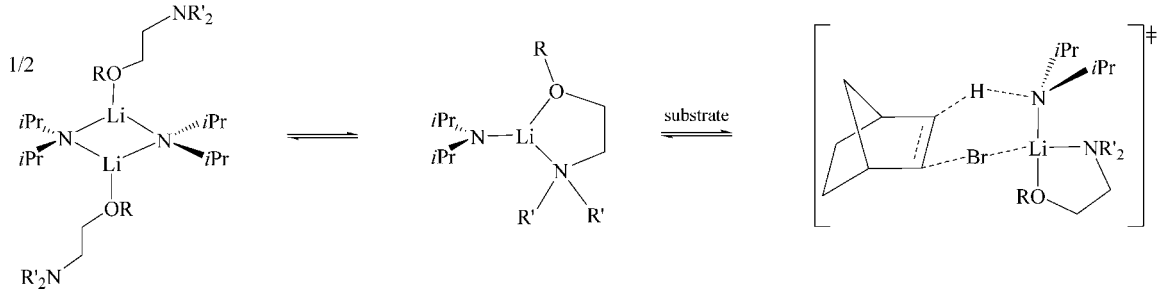


Scheme 13. Equilibrium between dimeric monodentate and monomeric bidentate complexes, and the transition state structure in the 1,2-dehydrobromination of (±)-2-*exo*-bromonorbornane, mediated by lithium diisopropylamide complexes.

 © 2006 Wiley-VCH Verlag GmbH & Co. KGaA, Weinheim 

tional work, which has allowed the authors to show and prove some fundamental mechanistic concepts. In particular, effects on relative reaction rates were dissected into the rate retarding influence due to ground state stabilization and the rate accelerating influence due to transition state stabilization. The rate acceleration imparted by dimethoxyethane and related aminoethers is due to selective stabilization of the transition state structure arising from a chelate effect of the hybrid ligands, and not to an increased solvation ability with respect to a monodentate ligand. This case, when compared with the examples described previously, shows an opposite situation among the effects, which hybrid hemilabile ligands may exert on the reactivity of a metal center. In fact, while complexes **1**, **5**, and **8** are chelated in the ground state and change into monocoordinated complexes by the arm-off mechanism to become reactive toward a substrate, the lithium diisopropylamide complexes are dimeric monodentate species in solution but use bidentation at the transition state to access lower energy pathways for the reaction. The transition state stabilization and hence the reaction rates can be tuned by changing the structure of the hybrid ligand in the following ways: (i) altering the length of the hydrocarbon chain and so the chelate ring size, (ii) varying the alkyl substituents on both the oxygen and nitrogen donors, (iii) introducing ramification on the carbon chain. A recent work addressing the last issue has concluded that rate accelerations based on the *gem*-dimethyl effect are nonexistent for lithium ion chelation.[38] The *gem*-dimethyl effect applies when destabililizing effects due to unfavorable steric interactions of alkyl substituents in an open carbon chain are alleviated by ring closure and can give pronounced substituent-dependent rate accelerations.[39]

Although many hybrid ligands have been used successfully in catalysis,[2,4] the establishment of contributions from the reversible association/dissociation of one labile function during the catalytic cycle remains a key question, which appears more difficult to address than it is for stoichiometric reactions.[40] Because of the interchange of various metal species, the alternation of dangling or chelate ligand modes may occur frequently during the cycle and affect the relative stability/reactivity in each step. To devise kinetic experiments that are as informative for catalysis as they are for stoichiometric reactions represents an important challenge, however, it is fundamental for understanding the role of hemilability in cyclic multistep processes.

## 4. Concluding Remarks

This review describes the information attainable from kinetic studies about the hemilability of hybrid ligands coordinated to transition metal complexes. In particular, it shows that the kinetic method allows for the detection of the reversible association/dissociation process of the hemilabile ligand function, even in the absence of fluxional behavior, as well as a quantitative evaluation of its weight along the coordinate of a bimolecular reaction. Cases in which the only available reaction pathway involves a transient species arising from dissociation of the ligand arm, cases in which such species reacts in parallel with the chelate complex, and opposite cases in which only the chelate is reactive are described. The kinetic approach may serve as a basis for the rational design of hemilabile systems and for the development of targeted applications.

## Acknowledgments

The author expresses his gratitude to the collaborators and coauthors involved in the studies on hemilability, and in particular to the group of Josè Gimeno in Oviedo, where the chemistry of the indenyl allylphosphane complexes was developed.

[1] C. S. Slone, D. A. Weinberger, C. A. Mirkin, *Progr. Inorg. Chem. Vol. 48* (Ed.: K. D. Karlin), Wiley, New York, **1999**, pp. 233–350.
[2] a) P. Braunstein, F. Naud, *Angew. Chem. Int. Ed.* **2001**, *40*, 680–699; b) P. Espinet, K. Soulantica, *Coord. Chem. Rev.* **1999**, *193–195*, 499–556; c) A. Bader, E. Lindner, *Coord. Chem. Rev.* **1991**, *108*, 27–110.
[3] In principle, while a metal complex of a hybrid ligand may not display hemilability, a chelate complex of a homofunctional polydentate ligand can exhibit reversible decoordination of one ligand arm, e.g., G. Kiss, I. T. Horváth, *Organometallics* **1991**, *10*, 3798–3799.
[4] a) J. J. Schneider, *Nachr. Chem.* **2000**, *48*, 614–616; J. J. Schneider, *Nachr. Chem.* **2000**, *48*, 618–620; b) K. N. Gavrilov, A. I. Polosukhin, *Russ. Chem. Rev.* **2000**, *69*, 661–682; c) G. Delapierre, G. Buono, *Actualite Chimique* **2003**, *2*, 3–11.
[5] J. C. Jeffrey, T. B. Rauchfuss, *Inorg. Chem.* **1979**, *18*, 2658–2666.
[6] a) J. F. Sieckhaus, T. Layloff, *Inorg. Chem.* **1967**, *6*, 2185–2190; b) M. Bacci, S. Midollini, *Inorg. Chim. Acta* **1971**, *5*, 220–222; c) D. H. Payne, Z. A. Payne, R. Rohmer, H. Frye, *Inorg. Chem.* **1973**, *12*, 2540–2543; d) T. B. Rauchfuss, D. M. Roundhill, *J. Am. Chem. Soc.* **1974**, *96*, 3098–3105; e) S. O. Grim, L. C. Satek, C. A. Tolman, J. P. Jesson, *Inorg. Chem.* **1975**, *14*, 656–660; f) P. Braunstein, D. Matt, F. Mathey, D. Thavard, *J. Chem. Res. Synop.* **1978**, 232–233.
[7] J. S. Kingsbury, J. P. A. Harrity, P. J. Bonitatebus, A. H. Hoveyda, *J. Am. Chem. Soc.* **1999**, *121*, 791–799; S. B. Garber, J. S. Kingsbury, B. L. Gray, A. H. Hoveyda, *J. Am. Chem. Soc.* **2000**, *122*, 868–8179.
[8] R. H. Grubbs, *Tetrahedron* **2004**, *60*, 7117–7140.
[9] In the study of the exchange processes associated with hemilability, various expressions have been introduced to represent the reversible decoordination of one ligand arm: interchange, tick-tock, wind-screen wiper, opening and closing, arm-off mechanism (see ref.[1]).
[10] The formation of a stable monochelate product indicates that selective decoordination of one ligand arm has occurred, but does not imply that the bis-chelate complex was involved in the reversible motion which identifies hemilability.
[11] For example: T. R. Webb, T. Y. Dong, *Inorg. Chem.* **1982**, *21*, 114–116; S. Siddiqui, R. E. Shepherd, *Inorg. Chem.* **1983**, *22*, 3726–3733; G. R. Dobson, S. S. Basson, C. B. Dobson, *Inorg. Chim. Acta* **1985**, *105*, L17–L19; D. A. Buckingham, C. R. Clark, *Inorg. Chem.* **1994**, *33*, 6171–6179.
[12] W. J. Knebel, R. J. Angelici, *Inorg. Chem.* **1974**, *13*, 627–631.
[13] W. J. Knebel, R. J. Angelici, *Inorg. Chem.* **1974**, *13*, 632–637.
[14] For example: a) A. Peloso, *J. Chem. Soc. Dalton Trans.* **1979**, 2033–2036; b) E. Kita, M. Laczna, *Transition Met. Chem.* **2001**, *26*, 510–516; c) J. Favier, M. Gómez, J. Granell, M. Martínez, X. Solans, M. Font-Bardía, *Dalton Trans.* **2005**, 123–132;

 © 2006 Wiley-VCH Verlag GmbH & Co. KGaA, Weinheim 

d) G. Marangoni, B. Pitteri, G. Annibale, M. Bortoluzzi, *Eur. J. Inorg. Chem.* **2006**, 765–771.

[15] M. Bassetti, A. Capone, M. Salamone, *Organometallics* **2004**, *23*, 247–252.

[16] M. Bassetti, A. Capone, L. Mastrofrancesco, M. Salamone, *Organometallics* **2003**, *22*, 2535–2538.

[17] J. D. Atwood, *Inorganic and Organometallic Reaction Mechanisms*, Brooks/Cole Publishing Company, Monterey, CA, **1985**, p. 14.

[18] M. R. Plutino, L. Monsù Scolaro, R. Romeo, A. Grassi, *Inorg. Chem.* **2000**, *39*, 2712–2720, and references therein.

[19] a) A. J. Hart-Davis, W. A. G. Graham, *Inorg. Chem.* **1970**, *9*, 2658–2663; b) T. R. Griffin, D. B. Cook, A. Haynes, J. M. Pearson, D. Monti, G. E. Morris, *J. Am. Chem. Soc.* **1996**, *118*, 3029–3030; c) G. Aullon, S. Alvarez, *Inorg. Chem.* **1996**, *35*, 3137–3144; d) D. Lamprecht, G. J. Lamprecht, *J. Comput. Chem.* **2000**, *21*, 692–703.

[20] a) P. B. Chock, J. Halpern, *J. Am. Chem. Soc.* **1966**, *88*, 3511–3514; b) R. Ugo, A. Pasini, A. Fusi, S. Cenini, *J. Am. Chem. Soc.* **1972**, *94*, 7364–7370; c) D. J. A. de Waal, T. I. A. Gerber, W. J. Louw, *Inorg. Chem.* **1982**, *21*, 1259–1260; d) J. P. Collman, J. I. Brauman, A. M. Madonik, *Organometallics* **1986**, *5*, 310–322; e) R. W. Wegman, A. G. Abatjoglou, A. M. Harrison, *J. Chem. Soc. Chem. Commun.* **1987**, 1891–1892; f) G. J. Vanzyl, G. J. Lamprecht, J. G. Leipoldt, T. W. Swaddle, *Inorg. Chim. Acta* **1988**, *143*, 223–227; g) A. Fulford, C. E. Hickey, P. M. Maitlis, *J. Organomet. Chem.* **1990**, *398*, 311–323; h) M. Bassetti, D. Monti, A. Haynes, J. M. Pearson, I. A. Stanbridge, P. M. Maitlis, *Gazz. Chim. Ital.* **1992**, *122*, 391–393; i) M. R. Wilson, H. Liu, A. Prock, W. P. Giering, *Organometallics* **1993**, *12*, 2044–2050; j) C. Dueker-Benfer, R. van Eldik, A. J. Canty, *Organometallics* **1994**, *13*, 2412–2414; k) L. Gonsalvi, H. Adams, G. J. Sunley, E. Ditzel, A. Haynes, *J. Am. Chem. Soc.* **1999**, *121*, 11233–11234; l) J. K. Jawad, F. N. K. Al-Obaidy, J. A. Hammud, F. Al-Azab, *J. Organomet. Chem.* **2000**, *599*, 166–169; m) A. Roodt, G. J. J. Steyn, *South Afr. J. Chem.* **2001**, *54*, 1–22; n) L. Gonsalvi, H. Adams, G. J. Sunley, E. Ditzel, A. Haynes, *J. Am. Chem. Soc.* **2002**, *124*, 13597–13612; o) V. Chauby, J.-C. Daran, C. Serra-Le Berre, F. Malbosc, P. Kalck, O. Delgado Gonzales, C. E. Haslam, A. Haynes, *Inorg. Chem.* **2002**, *41*, 3280–3290; p) L. Gonsalvi, J. A. Gaunt, H. Adams, A. Castro, G. J. Sunley, A. Haynes, *Organometallics* **2003**, *22*, 1047–1054; q) J. A. Gaunt, V. C. Gibson, A. Haynes, S. K. Spitzmesser, A. J. P. White, D. J. Williams, *Organometallics* **2004**, *23*, 1015–1023; r) J. M. Wilson, G. J. Sunley, H. Adams, A. Haynes, *J. Organomet. Chem.* **2005**, *690*, 6089–6095.

[21] S. S. Basson, J. G. Leipoldt, A. Roodt, J. A. Venter, *Inorg. Chim. Acta* **1987**, *128*, 31–37.

[22] H. C. Martin, N. H. James, J. Aitken, J. A. Gaunt, H. Adams, A. Haynes, *Organometallics* **2003**, *22*, 4451–4458.

[23] a) R. J. Mawby, F. Basolo, R. G. Pearson, *J. Am. Chem. Soc.* **1964**, *86*, 3994–3999; b) J. P. Collman, L. S. Hegedus, J. R. Norton, R. G. Finke, *Principles and Applications of Organotransition Metal Chemistry*; University Science Book, Mill Valley, CA, **1987**, p. 357.

[24] D. Cuervo, J. Díez, M. Pilar Gamasa, S. García-Granda, J. Gimeno, *Inorg. Chem.* **2002**, *41*, 4999–5001.

[25] P. Pelagatti, A. Bacchi, C. Bobbio, M. Carcelli, M. Costa, C. Pelizzi, C. Vivorio, *Organometallics* **2000**, *19*, 5440–5446.

[26] D. A. Cooper, S. J. Rettig, A. Storr, *Can. J. Chem.* **1986**, *64*, 566–574.

[27] P. Das, M. Sharma, N. Kumari, D. Konwar, D. K. Dutta, *Appl. Organomet. Chem.* **2002**, *16*, 302–306.

[28] J. Díez, M. P. Gamasa, J. Gimeno, E. Lastra, A. Villar, *Eur. J. Inorg. Chem.* **2006**, 78–87, and references therein.

[29] L. P. Barthel-Rosa, K. Maitra, J. H. Nelson, *Inorg. Chem.* **1998**, *37*, 633–639.

[30] P. Alvarez, E. Lastra, J. Gimeno, P. Braña, J. A. Sordo, J. Gomez, L. R. Falvello, M. Bassetti, *Organometallics* **2004**, *23*, 2956–2966.

[31] P. Alvarez, E. Lastra, J. Gimeno, M. Bassetti, L. R. Falvello, *J. Am. Chem. Soc.* **2003**, *125*, 2386–2387.

[32] M. Bassetti, P. Alvarez, E. Lastra, J. Gimeno, *Organometallics* **2004**, *23*, 5127–5134.

[33] a) M. E. Rerek, F. Basolo, *J. Am. Chem. Soc.* **1984**, *106*, 5908–5912; b) J. S. Merola, R. T. Kacmarcik, D. Van Engen, *J. Am. Chem. Soc.* **1986**, *108*, 329–331; c) A. K. Kakkar, N. J. Taylor, T. B. Marder, J. K. Shen, N. Hallinan, F. Basolo, *Inorg. Chim. Acta* **1992**, *198–200*, 219–231; d) T. Foo, R. G. Bergman, *Organometallics* **1992**, *11*, 1811–1819; e) C. Bonifaci, G. Carta, A. Ceccon, A. Gambaro, S. Santi, *Organometallics* **1996**, *15*, 1630–1636; f) M. Bassetti, P. Casellato, M. P. Gamasa, J. Gimeno, C. González-Bernardo, B. Martín-Vaca, *Organometallics* **1997**, *16*, 5470–5477; g) M. Bassetti, S. Marini, J. Díaz, M. P. Gamasa, J. Gimeno, Y. Rodriguez-Álvarez, *Organometallics* **2002**, *21*, 4815–4822.

[34] a) D. J. Jones, R. J. Mawby, *Inorg. Chim. Acta* **1972**, *6*, 157–160; b) K. A. Pevear, M. M. Banaszak Holl, G. B. Carpenter, A. L. Rieger, P. H. Rieger, D. A. Sweigart, *Organometallics* **1995**, *14*, 512–523; c) M. P. Gamasa, J. Gimeno, C. Gonzalez-Bernardo, B. Martín-Vaca, D. Monti, M. Bassetti, *Organometallics* **1996**, *15*, 302–308.

[35] a) A. J. Hart-Davis, C. White, R. J. Mawby, *Inorg. Chim. Acta* **1970**, *4*, 441–446; b) N. N. Turaki, J. M. Huggins, L. Lebioda, *Inorg. Chem.* **1988**, *27*, 424–427.

[36] R. Romeo, L. Monsù Scolaro, M. R. Plutino, A. Romeo, F. Nicolò, A. Del Zotto, *Eur. J. Inorg. Chem.* **2002**, 629–638.

[37] J. F. Remenar, D. B. Collum, *J. Am. Chem. Soc.* **1997**, *119*, 5573–5582.

[38] A. Ramírez, E. Lobkovsky, D. B. Collum, *J. Am. Chem. Soc.* **2003**, *125*, 15376–15387.

[39] R. F. Brown, N. M. Van Gulick, *J. Org. Chem.* **1956**, *21*, 1046–1049; C. Galli, G. Giovannelli, G. Illuminati, L. Mandolini, *J. Org. Chem.* **1978**, *44*, 1258–1261; C. Wang, G. A. Russell, *J. Org. Chem.* **1999**, *64*, 2066–2069; J. B. Sperry, D. L. Wright, *J. Am. Chem. Soc.* **2005**, *127*, 8034–8035.

[40] J. Andrieu, J.-M. Camus, P. Richard, R. Poli, L. Gonsalvi, F. Vizza, M. Peruzzini, *Eur. J. Inorg. Chem.* **2006**, 51–61, and references cited therein.

Received: March 9, 2006
Published Online: August 11, 2006

 © 2006 Wiley-VCH Verlag GmbH & Co. KGaA, Weinheim 

DOI: 10.1002/ejic.200600713

# Cadmium(II) and Zinc(II) Coordination Polymers with 1D Ladder and 2D Basket Weave Layer Structures Constructed from a New T-Shaped Ligand

**Guoping Yong,[a] Shu Qiao,[a] Yu Xie,[a] and Zhiyong Wang*[a]**

**Keywords:** Pyridinones / Polymers / T-shaped ligands / Luminescence / Coordination modes

A novel imidazo[1,2-*a*]pyridin-2-one ligand, 3,3-bis(carboxymethyl)imidazo[1,2-*a*]pyridin-2-one ($H_2L$), was conveniently synthesized and acts as a three-connecting T-shaped building block. Hydrothermal treatment of the $H_2L$ ligand with $Cd(ClO_4)_2 \cdot 6H_2O$ or $Zn(ClO_4)_2 \cdot 6H_2O$ gives two new coordination polymers, $[CdL(H_2O)_2]_n$ (**1**) or $[ZnL(H_2O)]_n$ (**2**). Compound **1** consists of a rare 1D ladder-like chain and **2** is the first example of a polymer with a 2D basket weave network. Solid-state photoluminescent analyses of **1** and **2** show that they display strong fluorescent emissions.
(© Wiley-VCH Verlag GmbH & Co. KGaA, 69451 Weinheim, Germany, 2006)

## Introduction

In the past decades, coordination polymers have been subjected to a vast number of studies owing to their potential applications in catalysis, molecular adsorption, magnetism, nonlinear optics, luminescence, and molecular sensing,[1,2] as well as their intriguing structural motifs.[3] Recently, increasing investigations have been focused on the construction of coordination polymers with the use of heterocyclic carboxylic acids such as pyridine-,[4] pyrazole-,[5] and imidazolecarboxylic acids[6] as building blocks. These building blocks contain multioxygen and nitrogen atoms and can coordinate with metal ions in different ways, which results in the formation of various metal–organic frameworks with specific topologies and useful properties. It is well-known that organic ligands play crucial roles in the design and construction of desirable frameworks because changes in the flexibility, length, and symmetry of the organic ligands can result in a remarkable class of coordination polymers bearing diverse architectures and functions.[7] Our previous work had shown that the N-containing polycarboxylate ligands could be used to construct novel coordination polymers.[8] Herein, we turn our attention to a novel N-containing polycarboxylate ligand, 3,3-bis(carboxymethyl)imidazo[1,2-*a*]pyridin-2-one ($H_2L$). This ligand consists of a rigid imidazo[1,2-*a*]pyridin-2-one ring and flexible diacetic acid moieties; it is possible that the combination of these specialties may lead to the formation of interesting topologies.

A number of infinite ladder-like coordination polymers have been reported;[9] however, most of them were constructed with two-connecting ligands such as 4,4′-bipy. In principle, it is difficult to obtain a T-shaped geometry around the metal center, which is essential for the ladder structure, by using two-connecting ligands.[10] One strategy that can be used to overcome this difficulty is to use three-connecting T-shaped ligands as building units.[11] Hitherto, only a few ladder-like compounds containing T-shaped ligands have been reported.[10–12] Comparatively, less effort has been made in the construction of 2D layers by using three-connecting T-shaped ligands.[11b,13] According to the definition of Wells,[14] five types of 2D architectures (brick wall, herringbone, bilayer, basket weave, and long and short brick) can be expected for a T-shaped geometry, but only the first three types have already been realized so far.[3c]

During our research on the $H_2L$ ligand, we have obtained two new coordination polymers, $[CdL(H_2O)_2]_n$ (**1**) and $[ZnL(H_2O)]_n$ (**2**). The ladder-like chain built from the T-shaped ligand as found in **1** is rare. To the best of our knowledge, compound **2** is the first example of a coordination polymer whose 2D basket weave network is constructed from the combination of metal centers with a T-shaped geometry and ligands with T-shaped structure simultaneously. Herein, we report the syntheses, X-ray single-crystal analyses, and photoluminescent properties of **1** and **2**.

## Results and Discussion

### Synthesis of 3,3-Bis(carboxymethyl)imidazo[1,2-*a*]pyridin-2-one ($H_2L$)

Imidazo[1,2-*a*]pyridine derivatives have been attracting considerable interest because of their significant pharmaceutical importance.[15] They are also versatile intermediates

[a] Hefei National Laboratory for Physical Science at Microscale and Department of Chemistry, University of Science and Technology of China,
Hefei 230026, P. R. China
E-mail: zwang3@ustc.edu.cn
Supporting information for this article is available on the WWW under http://www.eurjic.org or from the author.

 © 2006 Wiley-VCH Verlag GmbH & Co. KGaA, Weinheim 

for synthetic transformations.[16] However, less effort has been made in the synthesis of imidazo[1,2-*a*]pyridin-2-one derivatives. We exploit a novel and facile synthetic method for these imidazo[1,2-*a*]pyridin-2-one derivatives (Scheme 1). 3,3-Bis(carboxymethyl)imidazo[1,2-*a*]pyridin-2-one ($H_2L$) was obtained as a free acid from the reaction of potassium chloroacetate and 2-aminopyridine in aqueous alkaline solution heated at 86 °C, followed by acidification of the mixture with aqueous HCl and concentration under boiling conditions. After cooling of the mixture to remove the precipitated KCl (ice bath), the desired acid was precipitated and removed by filtration. The negative ion electrospray mass spectrum ($H_2O$) of $H_2L$ shows the characteristic molecular ion peak around $m/z$ = 248.97, which provides strong evidence for the formula $C_{11}H_{10}N_2O_5$. The molecular structure is also supported by microanalysis, IR, and NMR spectroscopic results.

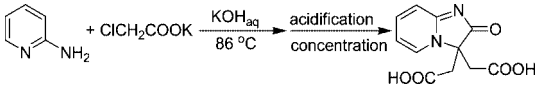


Scheme 1. Synthesis of 3,3-bis(carboxymethyl)imidazo[1,2-*a*]pyridin-2-one.

### Syntheses of Compounds 1 and 2

Compounds **1** and **2** were readily obtained in good yields (Scheme 2) by treating the corresponding metal perchlorate salts and $H_2L$ in a mixture of DMF and $H_2O$ at 120 °C for two days. Their formulations are supported by IR, microanalysis and thermogravimetric analysis (TGA) results. The phase purities were revealed by powder diffraction patterns of the bulk samples, which are consistent with the theoretical patterns generated from their single-crystal X-ray diffraction data (see Supporting Information).

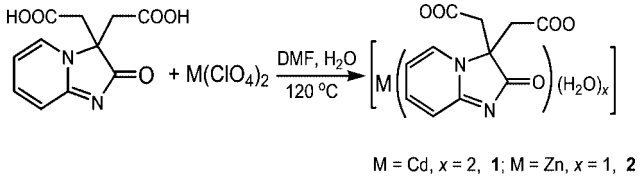


Scheme 2. Syntheses of compounds **1** and **2**.

### Description of Crystal Structure

#### *[CdL(H$_2$O)$_2$]$_n$ (1)*

Compound **1** has a 1D infinite ladder structure that is assembled through metal–nitrogen and metal–oxygen coordination bonds. The coordination geometry of each $Cd^{II}$ ion is a distorted octahedron, in which the $Cd^{II}$ ion is coordinated to two water oxygen atoms, three carboxylate oxygen atoms, and one nitrogen atom from three $L^{2-}$ ligands (Figure 1). The five Cd–O bond lengths range from 2.234(2) to 2.508(2) Å, and the Cd–N bond length is 2.264(2) Å (Table 1).

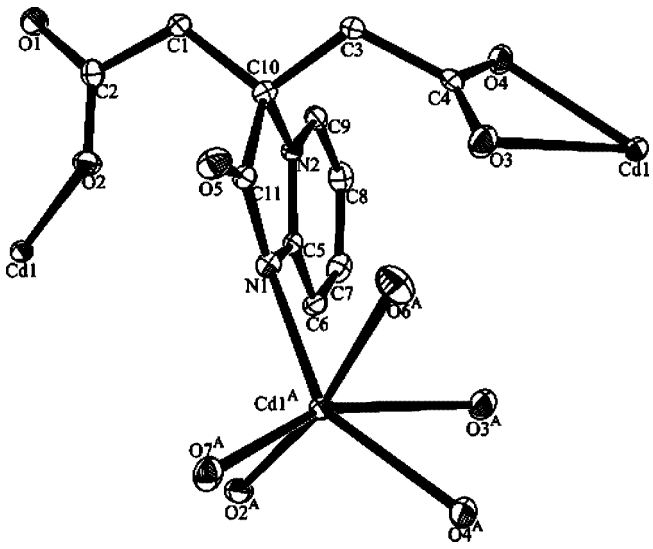


Figure 1. ORTEP drawing at the 50% probability level showing the $Cd^{II}$ coordination environment and T-shaped ligand in **1**. Hydrogen atoms are omitted for clarity. Symmetry code: A: –*x*, –*y*, –*z*.

Table 1. Selected bond lengths [Å] and angles [°] for compounds **1** and **2**.

| **1**[a] | | **2**[b] | |
|---|---|---|---|
| Cd1–O2 | 2.234(2) | Zn1–O2#2 | 1.980(2) |
| Cd1–O3 | 2.508(2) | Zn1–O3#3 | 2.075(2) |
| Cd1–O4 | 2.296(2) | Zn1–O6 | 2.034(2) |
| Cd1–O6 | 2.423(2) | Zn1–N1 | 2.010(2) |
| Cd1–O7 | 2.253(2) | | |
| Cd1–N1#3 | 2.264(2) | | |
| O2–Cd1–O3 | 96.59(7) | O2#2–Zn1–O3#3 | 125.43(8) |
| O2–Cd1–O4 | 104.72(6) | O2#2–Zn1–O6 | 99.54(10) |
| O2–Cd1–O6 | 169.89(7) | O2#2–Zn1–N1 | 114.13(8) |
| O2–Cd1–O7 | 89.80(7) | O3#3–Zn1–O6 | 94.20(9) |
| O2–Cd1–N1#3 | 89.11(7) | O3#3–Zn1–N1 | 116.62(9) |
| O3–Cd1–O4 | 54.83(6) | O6–Zn1–N1 | 95.72(10) |
| O3–Cd1–O6 | 89.50(7) | | |
| O3–Cd1–O7 | 152.41(6) | | |
| O3–Cd1–N1#3 | 93.37(7) | | |
| O4–Cd1–O6 | 85.39(7) | | |
| O4–Cd1–O7 | 97.59(6) | | |
| O4–Cd1–N1#3 | 146.02(7) | | |
| O6–Cd1–O7 | 88.49(8) | | |
| O6–Cd1–N1#3 | 82.45(7) | | |
| O7–Cd1–N1#3 | 113.61(7) | | |

[a] Symmetry transformations used to generate equivalent atoms: #3: –*x*, –*y*, –*z*. [b] Symmetry transformations used to generate equivalent atoms: #2: –*x* + 1/2, *y* + 1/2, –*z* + 1/2; #3: –*x*, –*y*, –*z*.

As a rail and rung simultaneously, each $L^{2-}$ ligand bridges three Cd atoms through its two carboxylate groups and one nitrogen atom to form a ladder extending along the *a* axis, as shown in Figure 2. As a result, the $L^{2-}$ ligand can be described as a three-connecting T-shaped building block. The Cd atom can be taken as a three-connecting node with a T-shaped geometry if two coordinated water molecules are disregarded. The T-shaped configurations of both the $Cd^{II}$ center and the $L^{2-}$ ligand have thus accommodated the formation of a 1D ladder. Interestingly, the two flexible acetate groups bridge two Cd atoms in the monodentate

 © 2006 Wiley-VCH Verlag GmbH & Co. KGaA, Weinheim 

and chelating fashion, respectively, to form the side rail of the ladder, while one nitrogen atom is linked to the third Cd atom. As a result, the rigid imidazo[1,2-*a*]pyridin-2-one ring acts as the rung. Because of the distorted T-joints and the unequal separations between the Cd1 and C10 atoms across the adjacent carboxylate groups, the 1D ladder is composed of two kinds of alternating rhombic rings with step lengths of 4.78 and 5.16 Å, respectively. The structure of **1** is a rare ladder motif consisting of two kinds of step lengths.[17]

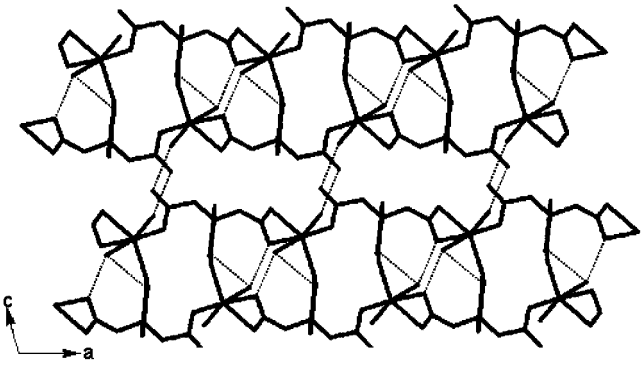


Figure 2. View along the *b* axis of the 2D hydrogen bonding network (dotted lines) of **1**.

As shown in Figure 2, the ladders extending along the *a* axis are organized by the O7···O1 [2.700(2) Å] hydrogen bonds that exist between two adjacent chains to form a layer that lies in the *a*,*c* plane. There are also intra-chained hydrogen bonding interactions [O6···O5 2.856(3) and O6···O3 2.807(3) Å] between coordinating water molecules, carbonyl oxygen atoms, and carboxylate oxygen atoms (Table 2). It is interesting to note that the stack of undulating 2D hydrogen bonding layers through the O···O hydrogen bonding interactions [O7···O5 2.739(3) Å] gives rise to a 3D supramolecular network with rhombic channels occupied by the pendent pyridine rings of the $L^{2-}$ ligands (see Supporting Information).

Table 2. Hydrogen bond geometries for compounds **1** and **2**.

| | D–H···A | *d*(D···A) [Å] | <(D–H···A) [°] |
|---|---|---|---|
| **1**[a] | O6–H01···O3$^{i}$ | 2.807(3) | 153(4) |
| | O6–H02···O5$^{i}$ | 2.856(3) | 149(4) |
| | O7–H03···O5$^{ii}$ | 2.739(3) | 173(4) |
| **2**[b] | O6–H02···O1$^{i}$ | 2.615(3) | 178(4) |
| | O6–H01···O5$^{ii}$ | 2.688(3) | 168(4) |

[a] Symmetry codes for **1**: $^{i}$: $-x$, $-y$, $-z$; $^{ii}$: $-x$, $y+1/2$, $-z+1/2$. [b] Symmetry codes for **2**: $^{i}$: $x-1/2$, $-y-1/2$, $z-1/2$; $^{ii}$: $-x+1/2$, $y+1/2$, $-z+1/2$.

### *[ZnL(H$_2$O)]$_n$ (2)*

Compound **2** possesses a 2D basket weave network based on the three-connecting T-shaped ligand. As shown in Figure 3, each $Zn^{II}$ ion adopts a distorted tetrahedral coordination environment by coordinating one water molecule, two carboxylate oxygen atoms, and one nitrogen atom from three $L^{2-}$ ligands with the Zn–O bond lengths ranging from 1.980(2) to 2.075(2) Å, and the Zn–N bond length of 2.010(2) Å (Table 1).

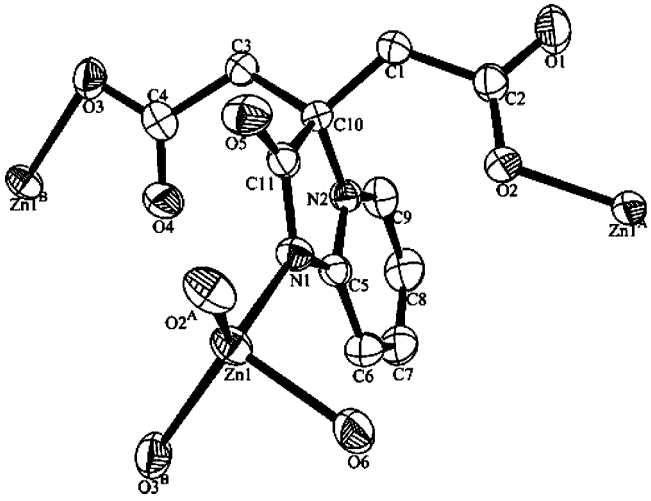


Figure 3. ORTEP drawing at the 50% probability level showing the $Zn^{II}$ coordination environment and T-shaped ligand in **2**. Hydrogen atoms are omitted for clarity. Symmetry code: A: $-x+1/2$, $y+1/2$, $-z+1/2$; B: $-x$, $-y$, $-z$.

The $L^{2-}$ ligand also acts as a three-connecting T-shaped building block, bridging three Zn atoms through its two monodentate carboxylate groups and one nitrogen atom. The Zn atom can also be taken as a three-connecting node with a T-shaped geometry if one coordinated water molecule is disregarded (the aqua ligand does not bridge). Interestingly, four arms (two acetate groups and two imidazo[1,2-*a*]pyridin-2-one rings) from two different $L^{2-}$ ligands bridge two Zn atoms to form a four-membered metallacycle with four three-connecting nodes (two C10 atoms and two Zn1 atoms). Such metallacycles are further extended to form not a ladder as observed in **1**, but a 2D basket weave network lying in the *a*,*b* plane, as shown in Figure 4. In principle, the transformation from the 1D ladder of **1** to the 2D basket weave network of **2** only requires the alternate breaking of opposite side rails of one ladder and then the connection to the neighboring parallel ladders (see Supporting Information). Thus, the present case is the first coordination network having a 2D basket weave architecture that is constructed from the combination of metal ions with T-shaped geometries and ligands with T-shape structures simultaneously. There are intralayered hydrogen bonding interactions [O6···O5 2.688(3) Å] between coordinating water molecules and carbonyl oxygen atoms. It is very interesting to notice that the 2D basket weave network of **2** exhibits beautiful sinusoidal 2D layers extending along the *a*,*c* plane, which further assemble into a 3D supramolecular network through the interlayered hydrogen bonding interactions [O6···O1 2.615(3) Å] (see Supporting Information).

It is worthy to note that the structural differences between **1** and **2** with the same $L^{2-}$ ligands and the same synthetic conditions may mainly be attributed to the radii of the metal atoms with the Cd atom having a larger atomic radius than the Zn atom, which results in different coordi-

 © 2006 Wiley-VCH Verlag GmbH & Co. KGaA, Weinheim 

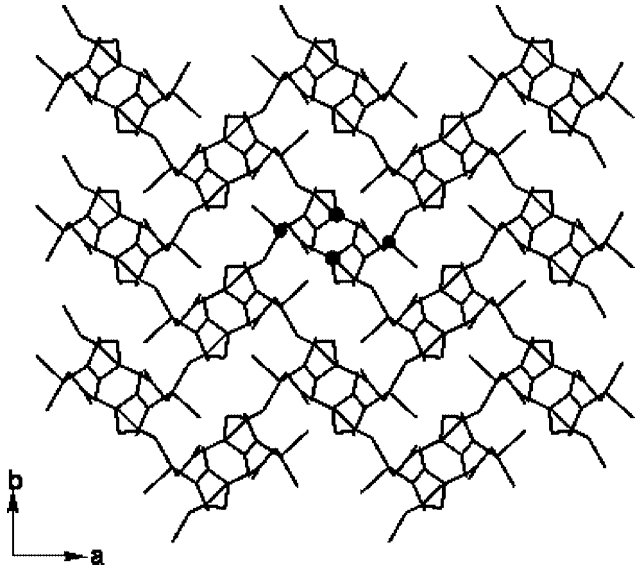


Figure 4. View of the 2D basket weave network lying in the *a*,*b* plane of **2**. Pyridine rings are omitted for clarity, and the black spheres represent three-connecting nodes.

nation environments ($Cd^{II}$ with octahedron geometry and $Zn^{II}$ with tetrahedron geometry).[18]

### Thermogravimetric Analyses

TG analysis of **1** reveals that its first weight loss appears at ca. 152 °C due to the loss of two coordinating water molecules (calcd. 9.1%; found 9.2%). The second weight loss occurs between 252 °C and 550 °C and is characteristic of the decomposition of the organic moiety. Coordination polymer **2** shows the first weight loss at ca.168 °C with the loss of one coordinating water molecule (calcd. 5.4%; found 5.1%), and the second weight loss occurs between 355 °C and 472 °C and is characteristic of the decomposition of the organic moiety (see Supporting Information).

### Photoluminescent Properties

The emission spectra of **1** and **2** in the solid state at room temperature are depicted in Figure 5. Compounds **1** and **2** display similar shoulder peaks, and their maximum emission peaks occur at 400 nm upon excitation at 210 nm and 250 nm, respectively. The emissions of **1** and **2** can probably be assigned to intraligand fluorescent emission,[19] since the free $H_2L$ ligand reveals the same maximum emission band (400 nm) upon excitation at 313 nm (see Supporting Information). These results imply that the coordination of the $L^{2-}$ ligand with the $Cd^{II}$ and $Zn^{II}$ ions, although yielding different topological structures, has no influence on the emission mechanism of the metal coordination polymer.[20] Compared to that of the free $H_2L$ ligand, **1** and **2** show significantly stronger photoluminescence, probably due to the coordination of the $H_2L$ ligand to the metal ions, which increases the ligand conformational rigidity;[21] the nonradiative decay of the intraligand excited state is thereby reduced. The metallacycles of **1** and **2** built by T-shaped $L^{2-}$ ligands probably cause significant enhancement to the rigidity of the ligand. The difference in the emission intensities of **1** and **2** is probably due to the differences in the metal ions and the coordination environment around them.[22] These observations suggest that compounds **1** and **2** may be excellent candidates for potential photoactive materials,[23] since these condensed materials are thermally stable and insoluble in water and common organic solvents.

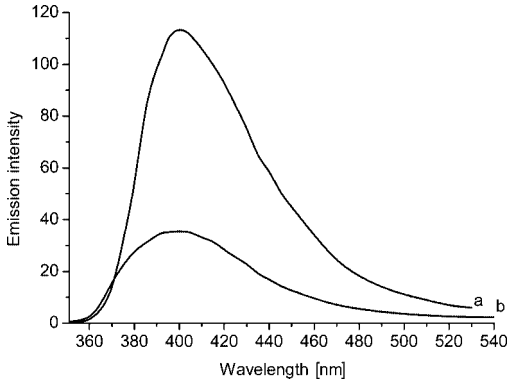


Figure 5. Solid-state emission spectra of a) **1** and b) **2** at room temperature.

## Conclusions

A novel imidazo[1,2-*a*]pyridin-2-one derivative ($H_2L$) was conveniently synthesized and characterized. By a combination of the different coordination environments of the metal ions and the T-shaped coordination mode of the $L^{2-}$ ligand, we have successfully synthesized two new coordination polymers, of which **1** has a rarely reported ladder motif and **2** is the first example having a 2D basket weave network. Toward the synthesis and design of 1D ladder chains or 2D basket weave networks, we think that T-shaped ligands are very suitable and promising for the syntheses of compounds with novel structures such as ladders, brickwalls, herringbones, bilayers, basket weaves, and long and short bricks.

## Experimental Section

**General Methods:** All reagents are commercially available and used as purchased without further purification. Elemental analysis was carried out with an Elementar Vario EL III microanalyser. The FTIR spectra were recorded with a Bruker Vector 22 spectrophotometer in the 4000–400 $cm^{-1}$ region. Mass spectra were obtained by negative ion electrospray ($H_2O$ solution) with a LCQ Advantage Max mass spectrometer. $^1H$- and $^{13}C$ NMR spectra were recorded with a Bruker AV300 and AV400 spectrometer, respectively. The emission spectra for the solid samples were recorded at room temperature with a Hitachi 850 fluorescence spectrophotometer. Thermogravimetric analyses were performed under air with a heating rate of 10 °C $min^{-1}$ with a Shimadzu TGA-50H TG analyzer. Powder X-ray diffraction (PXRD) patterns were obtained with a MXPAHF rotation anode X-ray diffractometer. ***Caution:*** Cd-

 © 2006 Wiley-VCH Verlag GmbH & Co. KGaA, Weinheim 

$(ClO_4)_2 \cdot 6H_2O$ and $Zn(ClO_4)_2 \cdot 6H_2O$ are potentially explosive and should be used with care!!

**Synthesis of 3,3-Bis(carboxymethyl)imidazo[1,2-*a*]pyridin-2-one ($H_2L$):** A solution of KOH (33.6 g, 0.6 mol) in water (75 mL) was added dropwise to an ice-bath cooled solution of chloroacetic acid (28.4 g, 0.3 mol) in water (75 mL). To the resulting alkaline solution, 2-aminopyridine (9.4 g, 0.1 mol) was slowly added, and the mixture was heated under reflux at 86 °C for 30 h. HCl (6 N, 53 mL) was added to neutralize the solution, which was concentrated under boiling conditions and then cooled (ice-bath) to remove KCl. After the mother liquor (pH = 2–3) was allowed to stand in the refrigerator for three days, the desired acid ($H_2L$) was separated out and collected by filtration. The solid was recrystallized from hot ethanol/water (1:1), and the colorless product was then collected by filtration and air-dried. Yield: 5.75 g (23%, based on 2-aminopyridine). $C_{11}H_{10}N_2O_5$ (250.21): calcd. C 52.80, H 4.03, N 11.20; found C 52.48, H 4.05, N 10.93. MS (ES–, $H_2O$): *m*/*z* = 250 $[M]^+$. $^1H$ NMR (300 MHz, $D_2O$, 25 °C): $\delta$ = 8.77 (d, $^3J_{H,H}$ = 6.8 Hz, 1 H, 5-H), 8.48 (dd, $^3J_{H,H}$ = 6.8, 8.4 Hz, 1 H, 6-H), 7.67 (m, 2 H, 7-H, 8-H), 3.44 (s, 4 H, $CH_2$) ppm. $^{13}C$ NMR (100 MHz, $D_2O$, 25 °C): $\delta$ = 175.5 (C-2), 172.0 (*C*OOH), 153.2 (C-9), 147.9 (C-5), 136.2 (C-7), 120.4 (C-8), 111.6 (C-6), 69.8 (C-3), 42.5 (*C*$H_2$) ppm. IR (KBr pellet): $\tilde{\nu}$ = 3434 (m), 3077(m), 2972(m), 2876(w), 2792(w), 2683(w), 1771(s), 1708(m), 1649(s), 1580(m), 1519(s), 1414(m), 1185(s), 807(m), 598(m), 440(m) $cm^{-1}$.

**Synthesis of $[CdL(H_2O)_2]_n$ (1):** A mixture of $Cd(ClO_4)_2 \cdot 6H_2O$ (0.15 mmol) and $H_2L$ (0.15 mmol) was placed in a heavy-walled Pyrex tube containing DMF (0.3 mL) and $H_2O$ (0.3 mL). The tube was frozen in liquid $N_2$, sealed under vacuum, and then heated at 120 °C for two days. The colorless crystals were collected and washed with ethanol. Yield: 0.042 g [70%, based on $Cd(ClO_4)_2 \cdot 6H_2O$]. $C_{11}H_{12}CdN_2O_7$ (396.63): calcd. C 33.28, H 3.02, N 7.06; found C 33.54, H 2.69, N 7.07. IR (KBr pellet): $\tilde{\nu}$ = 3333 (s), 3053(w), 2967(w), 1709(s), 1653(s), 1593(s), 1559(s), 1496(s), 1440(m), 1391(s), 1348(m), 1297(w), 1227(m), 1162(w), 1140(m), 1089(w), 1026(w), 934(w), 920(m), 839(m), 771(s), 701(m), 606(m), 508(m) $cm^{-1}$.

**Synthesis of $[ZnL(H_2O)]_n$ (2):** A mixture of $Zn(ClO_4)_2 \cdot 6H_2O$ (0.15 mmol) and $H_2L$ (0.15 mmol) was placed in a heavy-walled Pyrex tube containing DMF (0.3 mL) and $H_2O$ (0.3 mL). The tube was frozen in liquid $N_2$, sealed under vacuum, and then heated at 120 °C for two days. The colorless crystals were collected and washed with ethanol. Yield 0.027 g [54%, based on $Zn(ClO_4)_2 \cdot 6H_2O$]. $C_{11}H_{10}N_2O_6Zn$ (331.58): calcd. C 39.81, H 3.01, N 8.44; found C 39.71, H 2.77, N 8.42. IR (KBr pellet): $\tilde{\nu}$ = 3322 (s), 3051(w), 2971(w), 1710(s), 1630(s), 1567(w), 1497(s), 1408(s), 1346(s), 1293(m), 1238(m), 1167(m), 1143(m), 1085(w), 1024(w), 943(w), 916(m), 866(w), 769(s), 703(m), 625(m), 524(m) $cm^{-1}$.

**X-ray Crystallographic Study:** Diffraction intensities for **1** and **2** were collected at 293 K with a Bruker P4 diffractometer by employing graphite-monochromated Mo-$K_\alpha$ radiation ($\lambda$ = 0.71073 Å). Empirical absorption correction was applied with the use of the SADABS program.[24] The structures were solved by direct methods and refined by full-matrix least-squares on $F^2$ by using the SHELXS-97 and SHELXL-97 programs, respectively.[25] All non-hydrogen atoms were refined anisotropically. The C–H hydrogen atoms were placed in geometrically calculated positions; the O–H hydrogen atoms were located from Fourier difference maps and kept fixed in that position. The selected bond lengths and bond angles for **1** and **2** are listed in Table 1, and the crystallographic data are summarized in Table 3.

Table 3. Crystal data and structure refinement parameters for compounds **1** and **2**.

| | **1** | **2** |
|---|---|---|
| Chemical formula | $C_{11}H_{12}CdN_2O_7$ | $C_{11}H_{10}N_2O_6Zn$ |
| Crystal system | monoclinic | monoclinic |
| Space group | $P2_1/c$ | $P2_1/n$ |
| Formula weight | 396.63 | 331.58 |
| *a* [Å] | 9.124(2) | 11.669(2) |
| *b* [Å] | 14.398(3) | 8.101(2) |
| *c* [Å] | 9.844(2) | 12.733(3) |
| $\alpha$ [°] | 90.00 | 90.00 |
| $\beta$ [°] | 99.66(3) | 94.82(3) |
| $\gamma$ [°] | 90.00 | 90.00 |
| *V* [Å$^3$] | 1274.7(4) | 1199.4(4) |
| *Z* | 4 | 4 |
| *F*(000) | 784 | 672 |
| $D_c$ [g cm$^{-3}$] | 2.067 | 1.836 |
| *T* [K] | 293(2) | 293(2) |
| $\theta$ range [°] | 2.26–28.46 | 2.27–28.29 |
| $\mu$ [mm$^{-1}$] | 1.751 | 2.077 |
| GOF | 1.065 | 0.887 |
| Reflections collected | 6857 | 6797 |
| Independent reflections ($R_{int}$) | 3001 (0.0188) | 2832 (0.0305) |
| Observed reflections | 2740 | 2102 |
| $R_1$, $wR_2$ [$I > 2\sigma(I)$] | 0.0251, 0.0588 | 0.0382, 0.0715 |
| $R_1$, $wR_2$ [all data] | 0.0283, 0.0599 | 0.0538, 0.0763 |

CCDC-260674 and -260675 for **1** and **2**, respectively, contain the supplementary crystallographic data for this paper. These data can be obtained free of charge from the Cambridge Crystallographic Data Centre via www.ccdc.cam.ac.uk/data_request/cif.

**Supporting Information** (see footnote on the first page of this article): Luminescent curve of $H_2L$. Additional figures, PXRD patterns and TGA curves of **1** and **2**.

## Acknowledgments

This work was supported by the National Natural Science Foundation of China (No. 20472078) and the Foundation of Education Department of Anhui Province (2002kj330ZD).

[1] a) M. Eddaoudi, D. B. Moler, H. Li, B. Chen, T. M. Reineke, M. O'Keeffe, O. M. Yaghi, *Acc. Chem. Res.* **2001**, *34*, 319–330; b) O. R. Evans, W. B. Lin, *Acc. Chem. Res.* **2002**, *35*, 511–522; c) S. Kitagawa, R. Kitaura, S.-i. Noro, *Angew. Chem. Int. Ed.* **2004**, *43*, 2334–2375; d) D. Maspoch, D. Ruiz-Molina, J. Veciana, *J. Mater. Chem.* **2004**, *14*, 2713–2723.

[2] a) N. G. Pschirer, D. M. Ciurtin, M. D. Smith, U. H. F. Bunz, H. C. zur Loye, *Angew. Chem. Int. Ed.* **2002**, *41*, 583–585; b) G. S. Papaefstathiou, Z. Zhong, L. Geng, L. R. MacGillivray, *J. Am. Chem. Soc.* **2004**, *126*, 9158–9159; c) J. S. Seo, D. Whang, H. Lee, S. I. Jun, J. Oh, Y. J. Jeon, K. Kim, *Nature* **2000**, *404*, 982–986; d) Z. Ni, A. Yassar, T. Antoun, O. M. Yaghi, *J. Am. Chem. Soc.* **2005**, *127*, 12752–12753; e) S. N. Wang, H. Xing, Y. Z. Li, J. F. Bai, Y. Pan, M. Scheer, X. Z. You, *Eur. J. Inorg. Chem.* **2006**, 3041–3053.

[3] a) S. R. Batten, R. Robson, *Angew. Chem. Int. Ed.* **1998**, *37*, 1460–1494; b) A. J. Blake, N. R. Champness, P. Hubberstey, W. S. Li, M. A. Withersby, M. Schröder, *Coord. Chem. Rev.* **1999**, *183*, 117–138; c) B. Moulton, M. J. Zaworotko, *Chem. Rev.* **2001**, *101*, 1629–1658.

[4] a) P. Ayyappan, O. R. Evans, W. B. Lin, *Inorg. Chem.* **2001**, *40*, 4627–4632; b) M. L. Tong, S. Hu, J. Wang, S. Kitagawa, S. W. Ng, *Cryst. Growth Des.* **2005**, *5*, 837–839; c) Y. Xu, L. Han, Z. Z. Lin, C. P. Liu, D. Q. Yuan, Y. F. Zhou, M. C. Hong, *Eur.*

 © 2006 Wiley-VCH Verlag GmbH & Co. KGaA, Weinheim 

*J. Inorg. Chem.* **2004**, 4457–4462; d) B. Zhao, P. Cheng, Y. Dai, C. Cheng, D. Z. Liao, S. P. Yan, Z. H. Jiang, G. L. Wang, *Angew. Chem. Int. Ed.* **2003**, *42*, 934–936.
[5] L. Pan, N. Ching, X. Y. Huang, J. Li, *Chem. Eur. J.* **2001**, *7*, 4431–4437.
[6] a) Y. L. Liu, V. Kravtsov, R. D. Walsh, P. Poddar, H. Srikanth, M. Eddaoudi, *Chem. Commun.* **2004**, 2806–2807; b) M. T. Caudle, J. W. Kampf, M. L. Kirk, P. G. Rasmussen, V. L. Pecoraro, *J. Am. Chem. Soc.* **1997**, *119*, 9297–9298; c) E. Shimizu, M. Kondo, Y. Fuwa, R. P. Sarker, M. Miyazawa, M. Ueno, T. Naito, K. Maeda, F. Uchida, *Inorg. Chem. Commun.* **2004**, *7*, 1191–1194; d) P. Angaridis, J. W. Kampf, V. L. Pecoraro, *Inorg. Chem.* **2005**, *44*, 3626–3635; e) P. Mahata, S. Natarajan, *Eur. J. Inorg. Chem.* **2005**, 2156–2163; f) J. Y. Lu, Z. H. Ge, *Inorg. Chim. Acta* **2005**, *358*, 828–833; g) Z. F. Fei, D. B. Zhao, T. J. Geldbach, R. Scopelliti, P. J. Dyson, S. Antonijevic, G. Bodenhausen, *Angew. Chem. Int. Ed.* **2005**, *44*, 5720–5725; h) W. G. Lu, L. Jiang, X. L. Feng, T. B. Lu, *Cryst. Growth Des.* **2006**, *6*, 564–571.
[7] a) X. H. Bu, W. Chen, S. L. Lu, R. H. Zhang, D. Z. Liao, W. M. Bu, M. Shionoya, F. Brisse, J. Ribas, *Angew. Chem. Int. Ed.* **2001**, *40*, 3201–3203; b) D. N. Dybtsev, H. Chun, K. Kim, *Angew. Chem. Int. Ed.* **2004**, *43*, 5033–5036.
[8] a) G. P. Yong, S. Qiao, Z. Y. Wang, Y. Cui, *Inorg. Chim. Acta* **2005**, *358*, 3905–3913; b) G. P. Yong, Z. Y. Wang, Y. Cui, *Eur. J. Inorg. Chem.* **2004**, 4317–4323.
[9] a) K. Biradha, M. Fujita, *Chem. Commun.* **2002**, 1866–1867; b) A. J. Barton, A. R. J. Genge, W. Levason, G. Reid, *J. Chem. Soc., Dalton Trans.* **2000**, 2163–2166; c) M. Fujita, Y. J. Kwon, O. Sasaki, K. Yamaguchi, K. Ogura, *J. Am. Chem. Soc.* **1995**, *117*, 7287–7288; d) L. Carlucci, G. Ciani, D. Proserpio, *Coord. Chem. Rev.* **2003**, *246*, 247–289; e) M. Fujita, O. Sasaki, K. Y. Watanabe, K. Ogura, K. Yamaguchi, *New J. Chem.* **1998**, *22*, 189–191.
[10] P. Gamez, P. de Hoog, M. Lutz, A. L. Spek, J. Reedijk, *Inorg. Chim. Acta* **2003**, *351*, 319–325.
[11] a) P. Gamez, P. de Hoog, O. Roubeau, M. Lutz, W. L. Driessen, A. L. Spek, J. Reedijk, *Chem. Commun.* **2002**, 1488–1489; b) M. S. Wang, G. C. Guo, M. L. Fu, L. Xu, L. Z. Cai, J. S. Huang, *Dalton Trans.* **2005**, 2899–2907.
[12] a) P. Ayyappan, O. R. Evans, B. M. Foxman, K. A. Wheeler, T. H. Warren, W. B. Lin, *Inorg. Chem.* **2001**, *40*, 5954–5961; b) B. W. Sun, Z. M. Wang, S. Gao, *Inorg. Chem. Commun.* **2001**, *4*, 79–81.
[13] M. S. Wang, G. C. Guo, L. Z. Cai, W. T. Chen, B. Liu, A. Q. Wu, J. S. Huang, *Dalton Trans.* **2004**, 2230–2236.
[14] A. F. Wells, *Three-dimensional Nets and Polyhedra*, Wiley, New York, **1977**.
[15] a) M. Anderson, J. F. Beattie, G. A. Breault, J. Breed, K. F. Byth, J. D. Culshaw, R. P. A. Ellston, S. Green, C. A. Minshull, R. A. Norman, R. A. Pauptit, J. Stanway, A. P. Thomas, P. J. Jewsbury, *Bioorg. Med. Chem. Lett.* **2003**, *13*, 3021–3026; b) A. Gueiffier, S. Mavel, M. Lhassani, A. Elhakmaoui, R. Snoeck, G. Andrei, O. Chavignon, I. C. Teulade, M. Witvrouw, J. Balzarini, E. De Clercq, J. P. Chapat, *J. Med. Chem.* **1998**, *41*, 5108–5112; c) G. Trapani, A. Latrofa, M. Franco, A. Carrieri, S. Cellamare, M. Serra, E. Sanna, G. Biggio, G. Liso, *Eur. J. Pharm. Sci.* **2003**, *18*, 231–240; d) L. Almirante, L. Polo, A. Mugnaini, E. Provinciali, P. Rugarli, A. Biancotti, A. Gamba, W. Murmann, *J. Med. Chem.* **1965**, *8*, 305–312; e) S. Z. Langer, S. Arbilla, J. Benavides, B. Scatton, *Adv. Biochem. Psychopharmacol.* **1990**, *46*, 61–72.
[16] a) M. E. Baumann, H. Bosshard, W. Breitenstein, G. Rihs, T. Winkler, *Helv. Chim. Acta* **1984**, *67*, 1897–1905; b) J. C. Teulade, G. Grassy, R. Escale, J.-P. Chapat, *J. Org. Chem.* **1981**, *46*, 1026–1030.
[17] Y. Zou, W. L. Liu, S. Gao, J. L. Xie, Q. J. Meng, *Chem. Commun.* **2003**, 2946–2947.
[18] a) O. R. Evans, W. B. Lin, *Chem. Mater.* **2001**, *13*, 3009–3017; b) A. Q. Wu, Y. Li, F. K. Zheng, G. C. Guo, J. S. Huang, *Cryst. Growth Des.* **2006**, *6*, 444–450.
[19] a) S. T. Wang, Y. Hou, E. B. Wang, Y. G. Li, L. Xu, J. Peng, S. X. Liu, C. W. Hu, *New J. Chem.* **2003**, *27*, 1144–1147; b) X. D. Chen, M. Du, T. C. W. Mak, *Chem. Commun.* **2005**, 4417–4419.
[20] a) M. P. Clares, J. Aguilar, R. Aucejo, C. Lodeiro, M. T. Albelda, F. Pina, J. C. Lima, A. J. Parola, J. Pina, S. de Melo, C. Soriano, E. García-España, *Inorg. Chem.* **2004**, *43*, 6114–6122; b) F. Bolletta, I. Costa, L. Fabbrizzi, M. Licchelli, M. Montalti, P. Pallavicini, L. Prodi, N. Zaccheroni, *J. Chem. Soc., Dalton Trans.* **1999**, 1381–1385; c) S. A. Zabin, C. R. Jejurkar, *J. Polym. Mater.* **1997**, *14*, 239–243.
[21] a) S. L. Zheng, J. H. Yang, X. L. Yu, X. M. Chen, W. T. Wong, *Inorg. Chem.* **2004**, *43*, 830–838; b) L. Y. Zhang, J. P. Zhang, Y. Y. Lin, X. M. Chen, *Cryst. Growth Des.* **2006**, *6*, 1684–1689.
[22] a) L. Y. Zhang, G. F. Liu, S. L. Zheng, B. H. Ye, X. M. Zhang, X. M. Chen, *Eur. J. Inorg. Chem.* **2003**, 2965–2971; b) Q. R. Fang, G. S. Zhu, M. Xue, J. Y. Sun, F. X. Sun, S. L. Qiu, *Inorg. Chem.* **2006**, *45*, 3582–3587.
[23] J. C. Dai, X. T. Wu, Z. Y. Fu, S. M. Hu, W. X. Du, C. P. Cui, L. M. Wu, H. H. Zhang, R. Q. Sun, *Chem. Commun.* **2002**, 12–13.
[24] Bruker, *SMART, SAINT and SADABS*, Bruker AXS Inc., Madison, Wisconsin, USA, **2002**.
[25] G. M. Sheldrick, *SHELXTL-97*, *Program for the Refinement of Crystal Structures*, University of Göttingen, Germany, **1997**.

Received: August 1, 2006
Published Online: October 5, 2006

 © 2006 Wiley-VCH Verlag GmbH & Co. KGaA, Weinheim 

DOI: 10.1002/ejic.200600686

# Bis(formamidine–urea) Complexes of $Ni^{II}$ and $Cu^{II}$: Synthesis, Characterization, and Reactivity

**David D. Díaz,[a][‡] Sayam Sen Gupta,[a] Jane Kuzelka,[a] Marcin Cymborowski,[c] Michal Sabat,[b] and M. G. Finn*[a]**

**Keywords:** Formamidine ligand / Urea ligand / Nickel / Copper / Catalysis

A novel chelating chiral bis(formamidine–urea) ligand was synthesized and used to prepare the corresponding $Ni^{II}$ and $Cu^{II}$ complexes. Spectroscopic and X-ray crystallographic analysis of the former revealed that the urea moiety of the acyclic tetradentate ligand is deprotonated and binds to the square-planar $Ni^{2+}$ ion through amide nitrogen atoms. This complex showed quasi-reversible redox behavior in cyclic voltammetry, with $E_{1/2}$ = 640 mV vs. $Cp_2Fe^+/Cp_2Fe$ corresponding to the $Ni^{III}/Ni^{II}$ couple. The Cu complex was shown by EPR spectroscopy to also adopt a square-planar geometry [$g_{\|}$ = 2.25 ($A_{\|}$ = 184 G), $g_{\perp}$ = 2.06 at 6 K], and reduction was found to be irreversible, perhaps due to the rigid nature of the tetradentate ligand. The nickel complex was found to be a modestly active catalyst for epoxidation of electron-rich alkenes under Mukaiyama's conditions, likely involving a radical mechanism.
(© Wiley-VCH Verlag GmbH & Co. KGaA, 69451 Weinheim, Germany, 2006)

## Introduction

The coordination chemistry of urea and substituted ureas with nickel(II) is a topic of significant interest primarily because these compounds serve as structural and functional models of the metalloenzyme urease.[1–4] This enzyme activates the otherwise inert urea molecule toward hydrolysis by coordination of the substrate to one or both $Ni^{II}$ ions located at the active site, ultimatedly affording carbon dioxide and ammonia.[5–7] Considerable research has been dedicated to investigating the interaction of nickel(II) with urea[1–3,8–10] and urea derivatives.[11–13] X-ray crystallographic analysis of these compounds indicates that the geometry around the metal ion is typically octahedral and coordination of urea to $Ni^{2+}$ occurs predominately through the oxygen atom, although cases in which urea nitrogen atoms are involved in binding have been identified.[13,14] It is possible to stabilize higher oxidation states of nickel by coordination of deprotonated amides, as demonstrated by tetra(amido) macrocyclic ligands.[15,16] Because high-valent nickel complexes are believed to be the active catalytic species in epoxidation reactions,[17] complexes in which urea binds nickel(II) through a deprotonated amide nitrogen atom may function as robust oxidation catalyst precursors.

We recently reported a practical synthesis of the formamidine–ureas **1** by condensation of substituted urea derivatives with isocyanides in the presence of acid chloride (Scheme 1).[18] The imine fragment of these compounds undergoes exchange with primary nitrogen nucleophiles to afford the derivatives **2**, at rates determined primarily by the electron-donating ability of the formamidine–urea substituents.[19–21] Using this synthetic methodology, we report the preparation and characterization of the chiral bis(formamidine–urea) ligand **4** and its mononuclear nickel(II) (**5**) and copper(II) (**6**) complexes (Scheme 2). To the best of our knowledge, this is the first example of a chiral multidentate urea-based acyclic ligand that binds metal ions through the *endo* nitrogen of the deprotonated urea in a square-planar

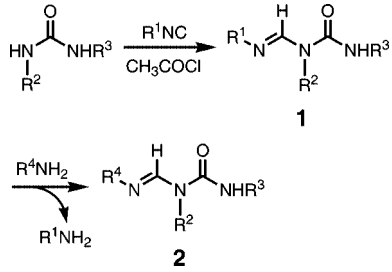


Scheme 1. Synthesis of formamidine–ureas **1** and subsequent imine exchange with primary amines to afford formamidine–urea derivatives **2**.

[a] Department of Chemistry and The Skaggs Institute for Chemical Biology, The Scripps Research Institute,
10550 North Torrey Pines Road, La Jolla, California 92037, USA
Fax: +1-858-784-8850
E-mail: mgfinn@scripps.edu
[b] Department of Chemistry, University of Virginia,
McCormick Rd., Charlottesville, VA 22901, USA
[c] Department of Molecular Physiology and Biological Physics, University of Virginia,
McCormick Rd., Charlottesville, VA 22901, USA
[‡] Present address: Departamento de Química Orgánica, Universidad Autónoma de Madrid,
28049 Madrid, Spain
Supporting information for this article is available on the WWW under http://www.eurjic.org or from the author.

 © 2006 Wiley-VCH Verlag GmbH & Co. KGaA, Weinheim 

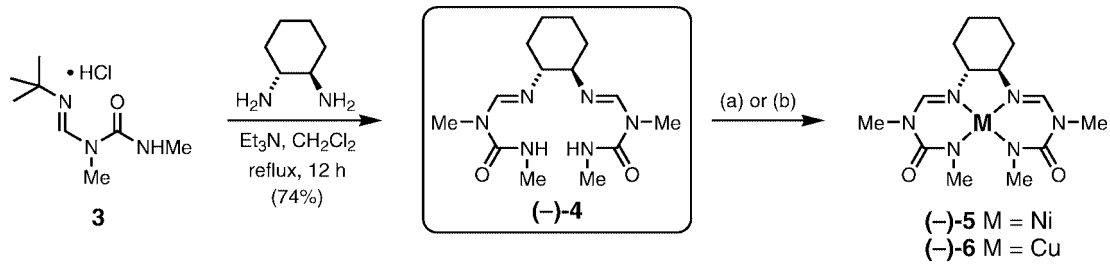


Scheme 2. Synthesis of compounds [Ni($N_4$L)] (**5**) and [Cu($N_4$L)] (**6**). (a) 3 equiv. $Ni(OAc)_2{\cdot}4H_2O$, $CH_3CN$, 45 °C, 91%. (b) 1 equiv. $Cu(OAc)_2{\cdot}H_2O$, $CH_3OH$, 50 °C, 76%.

geometry. The ability of **5** to catalyze olefin epoxidation is also described.

## Results and Discussion

### Synthesis of Ligand $H_2N_4L$ (4) and Coordination Compounds [Ni($N_4$L)] (5) and [Cu($N_4$L)] (6)

The displacement of *tert*-butylamine from 2 equiv. of 1-(*tert*-butyliminomethyl)-1,3-dimethylurea hydrochloride (**3**) and (1*R*,2*R*)-(–)-1,2-diaminocyclohexane afforded the bis(formamidine–urea) ligand **4** in 74% yield (Scheme 2). Although ligand **4** was very easily made, the practical synthesis of bis(formamidine–ureas) cannot yet be said to be modular, because changes in the components gave widely different yields and sometimes severe difficulties in purification (data not shown). Addition of excess nickel(II) acetate to a gently heated solution of **4** in MeCN gave the red-brown complex **5**. Deprotonation of both amide nitrogen atoms of **4** (substantiated by electrospray ionization mass spectrometry with good agreement of the isotopically resolved mass peaks with the theoretical distribution, elemental analysis, and single-crystal X-ray crystallography) was achieved without addition of external base. The analogous reaction of **4** and copper(II) acetate afforded the purple complex **6**, in which ligand **4** was again found to be in its doubly-deprotonated form. Attempts to obtain pure complexes of other transition metals were not successful.

### Structural Characterization of [Ni($N_4$L)] (5)

Single X-ray quality crystals of compound **5** were obtained by slow vapor diffusion of $Et_2O$ into a saturated solution of **5** in $CH_3CN$. X-ray structure analysis revealed the geometry of the metal center to be approximately square planar, as shown in Figure 1. Ligation of the nickel ion by tetradentate **4** is accomplished by the two imine and two deprotonated urea nitrogen atoms. Due to the greater basicity of the oxygen lone pair, it is typical for the urea oxygen atom rather than the nitrogen atom to bind transition metals. Both coordination modes should be accessible with ligand **4**, and we suggest that binding through the nitrogen atom is not geometrically enforced. The preference for N-donor coordination may be linked to the low spin nature of $Ni^{II}$ in **5**. The average $Ni–N_{urea}$ bond length is approximately 1.89 Å, which compares favorably with Ni–N bond lengths in complexes bearing anionic N-based ligands.[8,14,22,23] Deprotonation of the nitrogen atom results in delocalization through the urea moiety as evidenced by the short N(1)–C(1) and N(6)–C(6) distances of ca. 1.34 Å. These bond lengths are in good agreement with those of a related nickel(II) complex bearing both deprotonated NH (N–C ca. 1.31 Å) and neutral $NH_2$ urea groups (N–C ca. 1.43 Å).[8] The geometry at the deprotonated urea nitrogen atom is approximately trigonal planar with bond angles ranging from 111–121°. The Ni atom rests centrally in the binding pocket (the $N_{urea}–Ni–N_{imine}$ bond angles are both approximately 89.5°) and the ligand is twisted to relieve potential steric interactions between the two terminal urea *N*-methyl groups, presumably in a manner dictated by the chiral 1,2-diaminocyclohexane backbone.

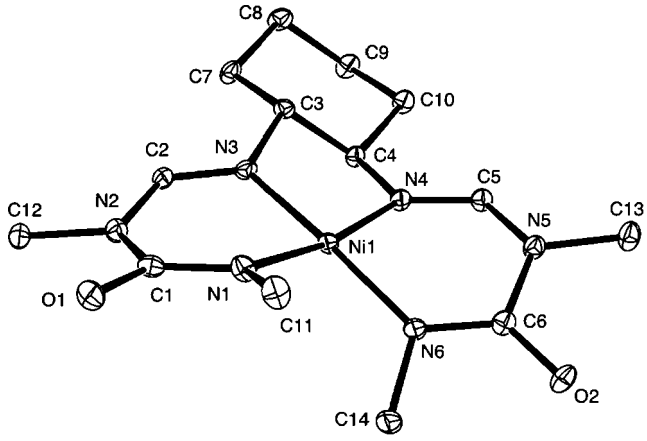


Figure 1. ORTEP diagram of [Ni($N_4$L)] (**5**) showing 50% probability ellipsoids for all non-hydrogen atoms.

### EPR Spectroscopy of [Cu($N_4$L)] (6)

Compound **6** was obtained as a crystalline solid from MeOH/$Et_2O$. The crystals suffered from the same crystallographic difficulties as **5** (pseudomerohedral twinning) and satisfactory refinement of the molecule was not possible. Examination of **6** by EPR spectroscopy, however, provided insight into the metal ion coordination geometry. A frozen glass of **6** (2:1 EtOH/MeOH) gave a four-line EPR spectrum at 6 K typical of square-planar copper(II) compounds, as shown in Figure 2.[24] ESI-MS and elemental

 © 2006 Wiley-VCH Verlag GmbH & Co. KGaA, Weinheim 

analysis of **6** indicate loss of two protons from the ligand, and we speculate that the detailed structure of this compound is very similar to its nickel(II) analogue **5**.

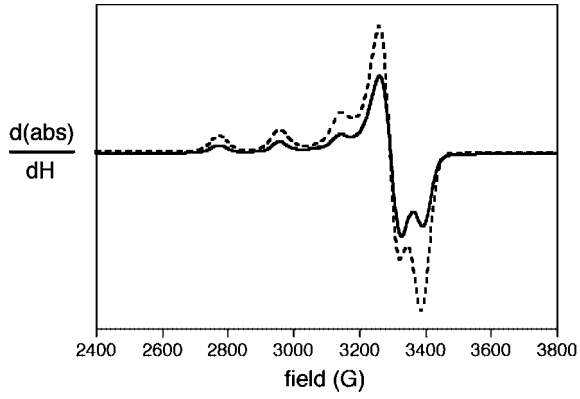


Figure 2. Solid line: X-band EPR spectrum of [Cu($N_4$L)] (**6**) as a frozen solution (5 mM in 2:1 EtOH/MeOH) at 6 K. Dotted line: simulated spectrum giving the values $g_{\|}$ = 2.248 ($A_{\|}$ = 185 G), $g_{\perp}$ = 2.08, linewidth parameter = 55 G.

### Electrochemical Studies

Cyclic voltammograms (CVs) of **5** in $CH_2Cl_2$ were recorded to investigate the ease of oxidation of the $Ni^{II}$ center. The CV of compound **5** reveals a quasi-reversible one-electron redox wave with an $E_{1/2}$ value of 650 mV ($\Delta E_p$ = 80 mV) vs. $Cp_2Fe^+/Cp_2Fe$, corresponding to the $Ni^{III}/Ni^{II}$ couple (see Supporting Information). The $E_{1/2}$ value of **5** is 1.2 V more positive than that of a related square-planar nickel(II) tetra(amide) macrocycle,[15] but comparable to square-planar $[Ni(cyclam)]^{2+}$ ($E_{1/2}$ = 560 mV vs. $Cp_2Fe^+/Cp_2Fe$) and its derivatives.[16,25,26] The deprotonated urea ligand of **5**, therefore, does not favor the formation of a high valent $Ni^{III}$ species. The CV of complex **6** shows an irreversible reduction wave (data not shown). The enforced square-planar geometry of the bis(formamidine–urea) ligand does not permit the corresponding copper(I) species to form. This finding is not surprising, given the preference of $Cu^{I}$ for nonplanar coordination geometries.

### Epoxidation Studies

Nickel(II) complexes of macrocyclic tetraamines such as cyclam,[17] salen-type ligands,[27] and *N*,*N*′-disubstituted oxamides[28] are catalysts for epoxidation reactions using iodosylbenzene or dioxygen (in presence of aldehydes) as oxidants. The similarity in $E_{1/2}$ values between **5** and $[Ni(cyclam)]^{2+}$ complexes prompted us to explore the catalytic activity of **5**, and *trans*-stilbene was chosen as the model substrate for a variety of oxidation conditions. The results of our initial experiments are outlined in Scheme 3. In the presence of 2-methylpropanal, dioxygen and **5** at 50 °C (Mukaiyama's conditions[29]), *trans*-stilbene oxide was produced in 73% yield. The use of aqueous sodium hypochloride with 4-Å molecular sieves afforded the epoxide in 66% yield, but twice as much catalyst was needed, presumably due to partial hydrolysis of **5** in the presence of water (see below). No epoxidation was observed when PhIO was used as terminal oxidant in $CH_2Cl_2$ in the presence of 10 mol-% of **5**, and low yields of epoxide were obtained with *t*BuOOH (10 mol-% **5**, 3 equiv. *t*BuOOH in isooctane, 2 equiv. pyridine, $CH_2Cl_2$). Activated alkenes such as *trans*-anethole were unreactive under Mukaiyama conditions (Table 1), and $Ni(OAc)_2{\cdot}5H_2O$ as catalyst did not promote the epoxidation of substrates for which **5** was effective, demonstrating that complexation of $Ni^{II}$ to **4** is necessary for catalysis.

- **5** (10 mol-%), $O_2$ (1 atm), 2 $Me_2CHCHO$, 50 °C, 1,2-dichloroethane, 15 h, 73%
- **5** (20 mol-%), 4 NaOCl (aq.), 4-Å mol. sieves, r.t., $CH_3CN$, 15 h, 66%
- **5** (10 mol-%), 1 PhIO, r.t., $CH_2Cl_2$, 15 h, no reaction

Scheme 3. Epoxidation of *trans*-stilbene using [Ni($N_4$L)] (**5**) as catalyst under different conditions.

Table 1. Epoxidation of olefins using [Ni($N_4$L)] (**5**) as catalyst under Mukaiyama's conditions (1 equiv. alkene, 0.1 equiv. **5**, 1 atm $O_2$, 2 equiv. isobutyraldehyde, $CH_2Cl_2$, 50 °C, 12–20 h). Yields are of products purified by column chromatography on alumina and giving satisfactory spectroscopic characterization. Isomer ratios were determined by $^1$H NMR spectroscopy.

| Entry | Olefin | Product | Yield [%] |
|---|---|---|---|
| 1 | *trans*-stilbene | *trans*-epoxide | 73 |
| 2 | *cis*-stilbene | *cis*- + *trans*-epoxides | 4, 61 |
| 3 | styrene | epoxide | 58 |
| 4 | α-Me-styrene | epoxide | 51 |
| 5 | *trans*-β-Me-styrene | *trans*-epoxide + benzaldehyde | 62, 4 |
| 6 | *p*-OMe-*trans*-β-Me-styrene | *trans*-epoxide + aldehyde | 65, 5 |
| 7 | 1,2-dihydronaphthalene | epoxide | 26 |
| 8 | cyclohexene | epoxide | 53 |
| 9 | 1-Me-cyclohexene | epoxide | 47 |
| 10 | cyclooctene | epoxide | 51 |
| 11 | 1-octene | epoxide | 49 |
| 12 | 2-hexen-1-ol | epoxide | 31 |
| 13 | 1-bromo-4-pentene | epoxide | 44 |
| 14 | geranyl benzoate | 6,7-epoxide + diepoxide | 41, 29 |

Table 1 summarizes the ability of **5** to epoxidize a variety of unfunctionalized alkenes under Mukaiyama's conditions using 10 mol-% catalyst (the use of less catalyst gives very poor yields of oxidized products after 24 h). Epoxides were obtained in moderate yields from *trans* di- and tri-substituted alkenes (Entries 1, 5, 6, 12, 14). Geranyl benzoate, bearing electronically dissimilar double bonds, afforded a mixture of regioisomers (Entry 14). Both *cis* and *trans* epoxides (1:15, Entry 2) were isolated from *cis*-stilbene, whereas *trans*-stilbene gave the *trans*-epoxide exclusively (Entry 1). In two cases, approximately 5% of benzaldehyde was also formed (Entries 5, 6). Di- and tri-substituted cyclic olefins were found to be modestly reactive (Entries 7, 8, 9, 10). Acid-sensitive epoxides could be isolated in moderate yields (Entries 3, 4, 5, 8), and a variety of functional groups

 © 2006 Wiley-VCH Verlag GmbH & Co. KGaA, Weinheim 

were tolerated (Entries 6, 12, 13, 14). However, electron-deficient olefins such as 2-cyclohexen-1-one or methyl methacrylate were unreactive to **5**. No enantiomeric excess was detected in products isolated from reactions catalyzed by enantiopure **5**.

The above observations are all consistent with the dominance of a radical oxidation mechanism. Furthermore, epoxidation does not occur in the presence of the one-electron acceptor 2,6-di-*tert*-butyl-4-methylphenol. Aside from requiring somewhat higher concentrations, the catalytic properties of **5** are similar to those of nickel(II) compounds supported by tetradentate sulfonamide,[26] and di-*N*,*N*′-substituted oxamide ligands,[27] and differ from the cyclam- and salen-based systems, which are not catalytically active under Mukaiyama's conditions. Compound **5**, in the presence of aldehyde and dioxygen, probably generates an acylperoxy radical, as proposed by Valentine and co-workers,[30] which has been shown to be a competent oxidant for olefin epoxidation. Although the $E_{1/2}$ values of **5** and $[Ni(cyclam)]^{2+}$ complexes are comparable, epoxidation of alkenes by **5** and PhIO was not observed. This is probably due to the inability of **5** to generate the kind of high-valent oxo–nickel species that is the active oxidant in such processes.[17]

## Conclusions

Complexes of a bis(formamidine–urea) ligand have been made here for the first time in the form of the mononuclear species [Ni($N_4$L)] (**5**) and [Cu($N_4$L)] (**6**). X-ray crystallography and EPR studies indicate that these coordination compounds adopt a square-planar geometry. In contrast to most nickel(II) urea complexes, the urea component of this multidentate urea-based acyclic ligand binds the metal center through a deprotonated amide nitrogen bond. Examination of **5** by CV indicates that access to the +3 oxidation state is possible, as indicated by quasi-reversible redox waves, although the redox potentials are more comparable to nickel complexes of tetra(amine) ligands than tetra(amido) derivatives. Compound **5** was found to be a moderately active epoxidation catalyst for electron-rich olefins operating by a radical mechanism, as evidenced by product distributions and the quenching of the process upon addition of a radical scavenger. We are currently preparing variations in the general structure, with the goal, among others, of producing a more active and enantioselective $Ni^{II}$ catalyst.

## Experimental Section

**General Remarks:** All solvents and reagents were ACS reagent grade or better and were used as received or purified in an appropriate manner. Compound **3** was synthesized according to the published procedure.[18]

**A) Physical Measurements:** Optical spectra were collected with a Hewlett–Packard 8453 diode-array spectrophotometer. NMR spectra were obtained with a 200 MHz Varian Mercury instrument. Elemental analyses were performed by Microanalytical Labs (Indianapolis, IN), and high-resolution MS by the mass spectrometry facility at The Scripps Research Institute. ESI-MS were recorded with an Agilent 1100 LC/MS spectrometer eluting with $CH_3OH$/$H_2O$ (90:10). IR spectra were obtained with a MIDAC FTIR instrument using samples dispersed on a horizontal attenuated total reflectance (HATR) accessory (Pike Instruments). Melting points were measured in a Thomas Hoover capillary melting point apparatus and are uncorrected. TLC analysis was facilitated by the use of phosphomolybdic acid or anisaldehyde/EtOH stains, in addition to UV light with fluorescent-indicating plates (silica gel on aluminum, Sigma). Analytical HPLC was performed with Hewlett–Packard series 1100 instrument, using a commercial chiral column (Chiralcel OD; *i*PrOH/hexane, 0.5 mL min$^{-1}$).

**B) Electrochemistry:** Cyclic voltammograms were recorded with a Bioanalytical Systems Epsilon potentiostat. The cell contained a glassy carbon working electrode, a Pt wire pseudoreference electrode, and a platinum wire auxiliary electrode, with 0.5 M $Bu_4N(PF_6)$ in $CH_2Cl_2$ as the supporting electrolyte. All measurements were externally referenced to ferrocene.

**C) EPR Study:** Frozen solution EPR spectra of **6** were recorded at 6 K with a Bruker Model E500 of the ELEXSYS series spectrometer operating at 9.47 GHz (University of California, San Diego). The spectrum was simulated using the Bruker SimFonia program as a powder spectrum for $S = 1/2$, $I = 3/2$ (assuming 100% natural abundance $^{63}Cu^{2+}$), with the resulting parameters listed in the caption to Figure 2. The simulated spectrum closely matches the observed one with the use of only an axial g tensor, with no need to include a rhombic distortion.

**D) X-ray Crystallographic Study:** X-ray quality crystals were obtained by slow vapor diffusion of $Et_2O$ into a saturated of **5** in $CH_3CN$. Data collection was carried out at 103 K with a Rigaku R-AXIS RAPID single-crystal diffractometer equipped with the R-AXIS3S area detector.[31] Intensities were corrected for absorption with the transmission factors ranging 0.854–0.900. Successful structure solution by direct methods and full-matrix refinement[32] were accomplished in the monoclinic space group $P2_1$ with two independent molecules of the complex in the unit cell. The final $R$ and $R_w$ values were 0.035 and 0.084, respectively, for 10404 reflections with $I > 2\sigma(I)$. All H atoms were found in difference Fourier maps and refined with isotropic thermal displacement parameters. The final difference Fourier map was essentially featureless with the highest peak of 0.45 e/Å$^3$.

CCDC-615365 contains the supplementary crystallographic data for this paper. These data can be obtained free of charge from The Cambridge Crystallographic Data Centre via www.ccdc.cam.ac.uk/data_request/cif.

**E) Typical Procedure for Epoxidation Studies:** 2-Methylpropanal (21 μL, 0.22 mmol) and **5** (10 μL of 1.0 M $CH_2Cl_2$, 0.01 mmol) were added to a solution of *trans*-stilbene (20 mg, 0.11 mmol) in 1,2-dichloroethane (1.1 mL) at room temperature. The reaction mixture was warmed to 50 °C and vigorously stirred for 15 h under $O_2$ (1 atm). The solvent was evaporated under reduced pressure and the residue was purified by column chromatography ($SiO_2$, 2% EtOAc/*n*-hexane) to give *trans*-stilbene oxide as a white solid (15.7 mg, 73%).

**Characterization Data**

***N*,*N*′-Dimethyl-*N*-[(*E*)-({1*R*,2*R*)-2-[((*E*)-{methyl[(methylamino)-carbonyl]amino}methylidene)amino]cyclohexyl}imino)methyl]urea ($H_2N_4L$, 4):** $Et_3N$ (0.75 mL, 5.31 mmol) was added to a solution of 1-(*tert*-butyliminomethyl)-1,3-dimethylurea hydrochloride (**3**) (1.0 g, 4.8 mmol) in dry $CH_2Cl_2$ (20 mL) and the resulting solution

 © 2006 Wiley-VCH Verlag GmbH & Co. KGaA, Weinheim 

was stirred for 5 min at room temperature under nitrogen. A solution of (1*R*,2*R*)-(–)-1,2-diaminocyclohexane (188 mg, 1.61 mmol) in dry $CH_2Cl_2$ (5 mL) was added and the mixture was refluxed for 12 h. The solvent was then removed by rotary evaporation and the residue was triturated with THF. The precipitate was separated by filtration and the filtrate was concentrated under reduced pressure. The residue was purified by flash chromatography on silica gel ($MeOH/CH_2Cl_2$, 9:1; $R_f$ = 0.5) to afford **4** as a hygroscopic white solid (370 mg, 74%). $^1H$ NMR ($CDCl_3$): $\delta$ = 1.23–1.39 (m, 6 H), 1.80 (m, 4 H), 2.78 (s, 6 H), 3.12 (s, 6 H), 7.65 (s, 2 H), 9.2 (br. s, 2 H) ppm. $^{13}C$ NMR ($CDCl_3$): $\delta$ = 24.9, 26.9, 34.1, 34.3, 70.2, 152.0, 157.0 ppm. IR (thin film): $\tilde{\nu}$ = 3347, 3055, 2937, 2857, 1659, 1545, 1307, 1079 $cm^{-1}$. ESI-MS: +*m*/*z* (rel. int.) = 333 $[M + Na]^+$ (45), 312 (20), 311 $[M + 1H]^+$ (100). HRMS (+*m*/*z*): calcd for $C_{14}H_{27}N_6O_2$, 311.219; found 311.2190. M.p. 136 °C.

**$[Ni(N_4L)]$ (5):** Solid $Ni(OAc)_2{\cdot}4H_2O$ (119 mg, 0.48 mmol) was added to a stirred solution of **4** (50 mg, 0.16 mmol) in $CH_3CN$ (2 mL). The resulting red mixture was heated to 45 °C for 1 min, after which time TLC analysis showed complete consumption of **4**. Excess $Ni(OAc)_2{\cdot}4H_2O$ was removed by filtration and the solvent was evaporated under reduced pressure to afford **5** as a red oil (53 mg, 91%). For epoxidation studies, **5** was recrystallized from $CH_3CN/Et_2O$ to afford a red-brown crystalline solid. $^1H$ NMR (200 MHz, $CD_3OD$): $\delta$ = 1.17–1.23 (m, 4 H), 1.74–1.75 (m, 2 H), 1.94 (s, 2 H), 2.09–2.11 (s, 2 H), 2.41 (s, 6 H), 3.11 (s, 6 H), 7.30 (s, 2 H) ppm. $^{13}C$ NMR (50 MHz, $CD_3OD$): $\delta$ = 25.5, 29.3, 36.7, 38.1, 68.4, 153.5, 158.2 ppm. IR ( thin film): $\tilde{\nu}$ = 3297, 2886, 1687, 1590, 1470, 1289, 983, 858, 757 $cm^{-1}$. ESI-MS: +*m*/*z* (rel. int.) = 366 (100) $[M]^+$, 367 (19) $[M + 1H]^+$, 368 (39) $[M + 2H]^+$, 369 (9), 370 (5), 372 (1). For recrystallized material: $C_{14}H_{24}N_6NiO_2$: calcd. C 45.81, H 6.59, N 22.89; found C 45.86, H 6.64, N 22.91. UV/Vis (MeCN): $\lambda_{max}$ ($\varepsilon$, $M^{-1}cm^{-1}$) = 439 nm (23.3).

**$[Cu(N_4L)]$ (6):** Solid $Cu(OAc)_2{\cdot}H_2O$ (31.9 mg, 0.16 mmol) was added to a solution of **4** (50 mg, 0.16 mmol) in MeOH (5 mL) in a single portion. The purple mixture was heated to 50 °C for 5 min, after which time TLC analysis showed complete reaction of **4**. Evaporation of the solvent under reduced pressure afforded a residue that was successively washed with cold $CH_3CN$ (2 × 1 mL) and $Et_2O$ (2 × 1 mL). The resulting solid was dried under high vacuum for 48 h to afford **6** as hygroscopic blue-purple solid (45 mg, 76% yield). Single crystals were grown by slow vapor diffusion of $Et_2O$ into a saturated solution of **6** in MeOH. IR (thin film): $\tilde{\nu}$ = 3238, 2860, 1661, 1598, 1481, 1293, 906, 862, 767 $cm^{-1}$. ESI-MS: +*m*/*z* (rel. int.) = 371 (100) $[M]^+$, 372 (18) $[M + 1H]^+$, 373 (47) $[M + 2H]^+$, 374 (7). $C_{14}H_{24}CuN_6O_2$: calcd. C 45.21, H 6.50, N 22.60; found C 45.22, H 6.49, N 22.62. UV/Vis (MeCN): $\lambda_{max}$ ($\varepsilon$, $M^{-1}cm^{-1}$) = 573 nm (119).

**Supporting Information** (see also the footnote on the first page of this article): Two pages with hydrolysis kinetics and cyclic voltammetry data.

## Acknowledgments

We thank the Skaggs Institute for Chemical Biology for support of this work. D. D. thanks the Spanish MECD for a postdoctoral fellowship. We are grateful to Professor Karsten Meyer at the University of California San Diego for allowing us access to his EPR spectrometer, Mr. Patrick Feng for collecting the spectrum of **6**, and Prof. David Goodin of TSRI for its simulation. We also acknowledge Dr. A. D. Lozano at McMaster University for useful suggestions and the Mass Spectrometry Laboratories of TSRI and UAM (SIdI).

[1] A. M. Barrios, S. J. Lippard, *J. Am. Chem. Soc.* **2000**, *122*, 9172–9177.
[2] M. Konrad, F. Meyer, A. Jacobi, P. Kircher, P. Rutsch, L. Zsolnai, *Inorg. Chem.* **1999**, *38*, 4559–4566.
[3] K. Yamaguchi, S. Koshino, F. Akagi, M. Suzuki, A. Uehara, S. Suzuki, *J. Am. Chem. Soc.* **1997**, *119*, 5752–5753.
[4] M. A. Halcrow, G. Christou, *Chem. Rev.* **1994**, *94*, 2421–2481.
[5] P. A. Karplus, M. A. Pearson, R. P. Hausinger, *Acc. Chem. Res.* **1997**, *30*, 330–337.
[6] E. Jabri, M. B. Carr, R. P. Hausinger, P. A. Karplus, *Science* **1995**, *268*, 998–1004.
[7] E. Mack, D. S. Villars, *J. Am. Chem. Soc.* **1923**, *45*, 505–510.
[8] F. Meyer, M. Konrad, E. Kaifer, *Eur. J. Inorg. Chem.* **1999**, 1851–1854.
[9] S. Mukherjee, T. Weyhermuller, E. Bothe, K. Wieghardt, P. Chaudhuri, *Eur. J. Inorg. Chem.* **2003**, 863–875.
[10] H. E. Wages, K. L. Taft, S. J. Lippard, *Inorg. Chem.* **1993**, *32*, 4985–4987.
[11] A. M. Barrios, S. J. Lippard, *Inorg. Chem.* **2001**, *40*, 1250–1255.
[12] F. Kyriakidou, A. Panagiotopoulos, S. P. Perlepes, E. Manessi-Zoupa, C. P. Raptopoulou, A. Terzis, *Polyhedron* **1996**, *15*, 1031–1034.
[13] a) P. Maslak, J. J. Sczepanski, M. Parvez, *J. Am. Chem. Soc.* **1991**, *113*, 1062–1063; b) C. E. MacBeth, P. L. Larsen, T. N. Sorrell, D. Powell, A. S. Borovik, *Inorg. Chim. Acta* **2002**, *341*, 77–84; c) F. Meyer, *Chem. Commun.* **1998**, 1555–1556; d) S. Buchler, F. Meyer, E. Kaifer, H. Pritzkow, *Inorg. Chim. Acta* **2002**, *337*, 371–386.
[14] For examples of *N*-bonded isomers of other metals, see: a) D. P. Fairlie, W. G. Jackson, *Inorg. Chim. Acta* **1988**, *150*, 81–100; b) D. P. Fairlie, W. G. Jackson, G. M. McLaughlin, *Inorg. Chem.* **1989**, *28*, 1983–1989; c) T. C. Woon, W. A. Wickramasinghe, D. P. Fairlie, *Inorg. Chem.* **1993**, *32*, 2190–2194; d) D. P. Fairlie, T. C. Woon, W. A. Wickramasinghe, A. C. Willis, *Inorg. Chem.* **1994**, *33*, 6425–6428.
[15] T. J. Collins, T. R. Nichols, E. S. Uffelman, *J. Am. Chem. Soc.* **1991**, *113*, 4708–4709.
[16] R. I. Haines, A. McAuley, *Coord. Chem. Rev.* **1981**, *39*, 77–119.
[17] J. F. Kinneary, T. R. Wagler, C. J. Burrows, *Tetrahedron Lett.* **1988**, *29*, 877–880.
[18] a) A. S. Ripka, D. D. Díaz, K. B. Sharpless, M. G. Finn, *Org. Lett.* **2003**, *5*, 1531–1533; b) D. D. Díaz, A. S. Ripka, M. G. Finn, *Org. Synth.* **2005**, *82*, 59–63.
[19] D. D. Díaz, M. G. Finn, *Chem. Eur. J.* **2004**, *10*, 303–309.
[20] D. D. Díaz, M. G. Finn, *Org. Lett.* **2004**, *6*, 43–46.
[21] D. D. Díaz, W. G. Lewis, M. G. Finn, *Chem. Lett.* **2005**, *34*, 78–79.
[22] H. Nie, C. L. Stern, B. M. Hoffman, A. G. M. Barrett, *Chem. Commun.* **1999**, 703–704.
[23] X. H. Bu, X. C. Cao, Z. H. Zhang, Z. A. Zhu, Y. T. Chen, *Polyhedron* **1996**, *15*, 1203–1205.
[24] T. Sawada, K. Fukumaru, H. Sakurai, *Chem. Pharm. Bull.* **1996**, *44*, 1009–1016.
[25] F. V. Lovecchio, E. S. Gore, D. H. Busch, *J. Am. Chem. Soc.* **1974**, *96*, 3109–3118.
[26] E. K. Barefield, F. V. Lovecchio, N. E. Tokel, E. Ochiai, D. H. Busch, *Inorg. Chem.* **1972**, *11*, 283–288.
[27] R. Irie, Y. Ito, T. Katsuki, *Tetrahedron Lett.* **1991**, *32*, 6891–6894.
[28] I. Fernandez, J. R. Pedro, A. L. Rosello, R. Ruiz, X. Ottenwaelder, Y. Journaux, *Tetrahedron Lett.* **1998**, *39*, 2869–2872.
[29] T. Mukaiyama, *Aldrichimica Acta* **1996**, *29*, 59–76.
[30] W. Nam, H. J. Kim, S. H. Kim, R. Y. N. Ho, J. S. Valentine, *Inorg. Chem.* **1996**, *35*, 1045–1049.
[31] Z. Otwinowski, W. Minor, *Methods Enzymol.* **1997**, *276*, 307–326.
[32] G. M. Sheldrick, SHELXTL-97, Version 5.10, Bruker AXS, Madison, WI 53719, **1997**.

Received: July 22, 2006
Published Online: October 5, 2006

 © 2006 Wiley-VCH Verlag GmbH & Co. KGaA, Weinheim 

DOI: 10.1002/ejic.200600785

# Bis(dithiolene) Molybdenum Complex that Promotes Combined Coupled Electron–Proton Transfer and Oxygen Atom Transfer Reactions: A Water-Active Model of the Arsenite Oxidase Molybdenum Center

**Hideki Sugimoto,*[a] Makoto Tarumizu,[a] Hiroyuki Miyake,[a] and Hiroshi Tsukube[a]**

**Keywords:** Bioinorganic chemistry / Electrochemistry / Molybdenum / Reaction mechanism / S ligands

Combined CEPT (coupled electron–proton transfer)/OAT (oxygen atom transfer) reactions were accomplished in $(Bu_4N)_2[Mo^{IV}O(bdtCl_2)_2]$ (**1**) and $(Bu_4N)_2[Mo^{VI}O_2(bdtCl_2)_2]$ (**2**) complexes in aqueous media. The reaction mechanism of the CEPT reaction was analyzed electrochemically and the conversion of **1** to **2** was revealed to proceed by a two-proton two-electron oxidative process. The structural and reaction profiles provide a new model for the arsenite oxidase catalytic center.

(© Wiley-VCH Verlag GmbH & Co. KGaA, 69451 Weinheim, Germany, 2006)

One of the most challenging themes in the field of bioinorganic chemistry is to develop active site models that work in aqueous media. The molybdenum-containing oxotransferases typically utilize water as the ultimate source or sink of oxygen in the overall catalytic reaction, and the reaction is combined with coupled electron–proton transfer (CEPT) and oxygen atom transfer (OAT) reactions.[1] Thus, a model of the catalytic centers is an intriguing target. Interestingly, in all members of the DMSO reductase family, the molybdenum center consists of reduced ($Mo^{IV}$) and oxidized ($Mo^{VI}$) states, and is essentially coordinated by two dithiolene ligands.[1]

A large number of OAT reactions from the enzymatic substrates, $R_3NO$, $R'_2SO$, or $SeO_4^{2-}$, to the $Mo^{IV}$ complexes that have two dithiolene ligands have been used to model some reductases.[2] Furthermore, OAT reactions from $Mo^{VI}$ complexes having two dithiolene ligands to substrates have also been extensively explored.[3] However, the CEPT process has yet to be accomplished with Mo complexes having dithiolene ligands. Even in the large number of mononuclear $Mo^{VI}$ complexes reported,[4] only two complexes have been reported to promote CEPT processes. $[LMo^{IV}O(py)(SC_6H_5)]$ and $[LMo^{IV}(p\text{-}O\text{-}C_6H_4\text{-}OC_2H_5)_2]\text{-}NO_3$ [L = hydrotris(3,5-dimethyl-1-pyrazolyl-borato)] were successfully converted to $[LMo^{VI}O_2(SC_6H_5)]$ and $[LMo^{VI}O(p\text{-}O\text{-}C_6H_4\text{-}OC_2H_5)_2]NO_3$, respectively, in water-containing solvents by two-step CEPT processes, and the resulting $Mo^{VI}$ complexes exhibited OAT reactions.[5]

We report herein the first example of chemistry that combines CEPT/OAT reactions in molybdenum complexes having dithiolene ligands. The $(Bu_4N)_2[Mo^{IV}O(bdtCl_2)_2]$ complex (**1**) ($bdtCl_2$ = 3,6-dichloro-1,2-benzenedithiolate) is readily converted to $(Bu_4N)_2[Mo^{VI}O_2(bdtCl_2)_2]$ (**2**) in aqueous media ($CH_3CN/H_2O$, 5:7) by a CEPT process, and **2** further transfers the oxygen atom to arsenite. The structures and conversion process of **1**/**2** are very similar to those of the molybdenum center in arsenite oxidase (A.O.) (Scheme 1).[6] The reaction mechanism of the CEPT reactivity of **1** and a difference in the reactivity of **1**, **3** of bdt, and **5** of mnt are discussed (Figure 1: bdt = 1,2-benzenedithiolate and mnt = maleonitrile-1,2-ethylenedithiolate).

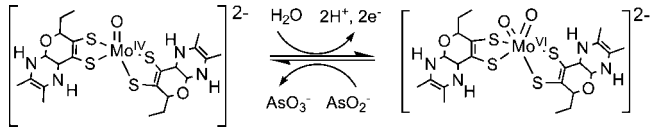


Scheme 1. Catalytic cycle mediated by the active site in arsenite oxidase.

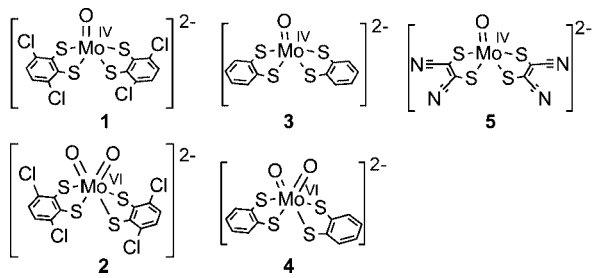


Figure 1. Structures of $[Mo^{IV}O(dithiolene)_2]^{2-}$ and $[Mo^{VI}O_2(dithiolene)_2]^{2-}$ complexes.

[a] Department of Chemistry, Graduate School of Science, Osaka City University,
Sumiyoshi-ku 3-3-138, Osaka 558-8585, Japan
Fax: +81-6-6605-2522
E-mail: sugimoto@sci.osaka-cu.ac.jp

Supporting information for this article is available on the WWW under http://www.eurjic.org or from the author.


© 2006 Wiley-VCH Verlag GmbH & Co. KGaA, Weinheim

We have newly synthesized **1** because the solubility of previously reported $(Et_4N)_2[MoO(bdtCl_2)_2]$[3e] in aqueous media is very low. Five coordinate complex **1** exhibited one reversible $Mo^{V/IV}$ redox couple at 0.04 V (versus SCE) in $CH_3CN/H_2O$ (5:7) solution (pH = 9.0).[7] As the pH of the solution was increased from 9.0 to 12.5, the intensity of the current for the anodic process ($E_{pa}$) increased, whereas that of the cathodic process ($E_{pc}$) decreased (Figure 2, inset). This observation indicates that **1** is irreversibly oxidized at high pH. The electrolysis of the solution at pH = 12.0 and $E$ = 0.2 V was monitored by electronic spectral changes (Figure 2). As the electrolysis proceeded, the band centered at 540 nm increased in intensity and the color of the solution changed from yellow to red. The final spectrum was consistent with the electronic spectrum of **2**. A coulometric measurement during the electrolysis confirmed this reaction to be a two-electron oxidative process.

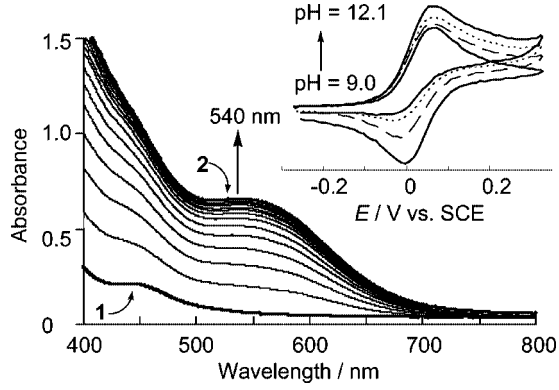


Figure 2. Electronic spectral changes during electrolysis of **1** ($3.5\cdot10^{-4}$ M) at 0.2 V (versus SCE) in $CH_3CN/H_2O$ (5:7) pH = 12.0. Spectra were recorded every six minutes. (inset) pH-dependent cyclic voltammograms (pH = 9.0, 11.3, 11.8, and 12.1, scan rate = 100 mV $s^{-1}$) of **1** ($5.4\cdot10^{-4}$ M) in $CH_3CN/H_2O$ (5:7).

Similarly, chemical oxidation of **1** with 2 equiv. of $K_3[Fe(CN)_6]$ in the presence of 2 equiv. of *t*BuOK in $CH_3CN/H_2O$ (5:7) yielded $(Bu_4N)_2[MoO_2(bdtCl_2)_2]$ (**2**). Isolated **2** exhibited $\nu(Mo{=}O)_{asym}$ at 836 $cm^{-1}$ (IR: solid) and an ESI-MS peak cluster attributed to $\{[Mo^{VI}O_2(bdtCl_2)_2]^{2-} + Bu_4N^+\}^-$ (in $CH_3CN$). When 98% $H_2{}^{18}O$ was used instead of $H_2O$, $(Bu_4N)_2[Mo^{VI}O^{18}O(bdtCl_2)_2]$ (**2a**) was stoichiometrically formed and isolated in 95% yield, which exhibited $\nu(Mo{=}O)_{asym}$ at 801 $cm^{-1}$ (IR: solid) and gave an ESI-MS peak cluster attributed to $\{[Mo^{VI}O^{18}O(bdtCl_2)_2]^{2-} + Bu_4N^+\}^-$ (in $CH_3CN$, Figures 3 and S1).

In nonaqueous $CH_3CN$, **2** was obtained from **1** in the presence of $Bu_4NOH$ by the CEPT process.[8] The reversible $Mo^{V/IV}$ couple at –0.07 V[3e] became an irreversible wave upon addition of $Bu_4NOH$ to the $CH_3CN$ solution of **1**, increasing and decreasing the current intensities of $E_{pa}$ and $E_{pc}$, respectively. A plot of the $\Delta I_{pa}$ value against [$Bu_4NOH$]/[**1**] indicated that 2 equiv. of $Bu_4NOH$ was consumed in the conversion of **1** to **2** (Figure S2). The coulometric and UV/Vis measurements (Figure S3) during the electrolysis at 0.2 V also supported that the conversion of **1** to **2** was a two-electron oxidative process.

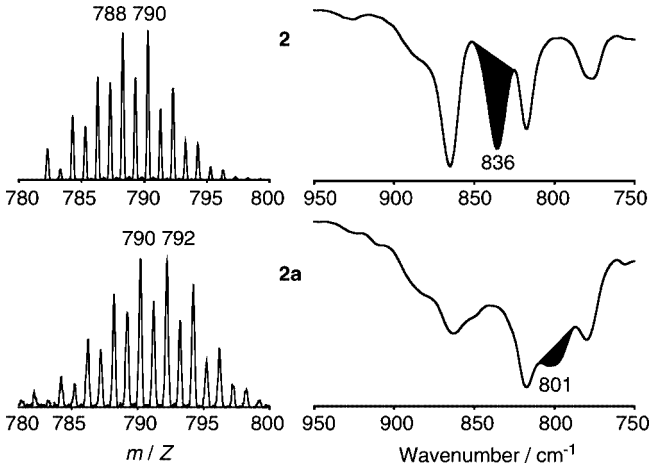


Figure 3. IR (solid) and ESI-MS (in $CH_3CN$) spectra of **2** (upper) with those of **2a** (lower).

The above results obtained in aqueous and $CH_3CN$ solutions of **1** clearly indicate that the conversion of **1** to **2** occurs by a two-proton two-electron oxidative process. Because the irreversible structural change of **1** to **2** obeys the electrochemical *EC* mechanism, $OH^-$ binding with $[Mo^{V}O(bdtCl_2)_2]^-$ is involved in the rate-determining step (Scheme 2).[9] Stoichiometries of the conversions from **1** to **2** in $CH_3CN/H_2O$ (5:7) and $CH_3CN$ solutions are described in Equations (1) and (2). The reaction mechanism from **1** to **2** is quite different from that of the pyrazolylborate system.[5] The $MoO_2$ core having two $bdtCl_2$ ligands is formed in the $Mo^{VI}$ state and a $Mo^{V}$ species was not detected during the CEPT process. However, both $[LMo^{VI}O_2(SC_6H_5)]$ and $[LMo^{VI}O(p\text{-}O\text{-}C_6H_4\text{-}OC_2H_5)_2]NO_3$ are formed by two-step CEPT processes, in which the $MoO_2$ and MoO cores, respectively, are formed in the $Mo^{V}$ states; the intermediates $[LMo^{V}O_2(SC_6H_5)]^-$ and $[LMo^{V}O(p\text{-}O\text{-}C_6H_4\text{-}OC_2H_5)_2]$ have been characterized.[5,10] Furthermore, the coordination number of the molybdenum center changes from five to six when **1** is converted to **2** in our system, whereas the molybdenum centers maintain their six coordination structures in both the $Mo^{IV}$ and $Mo^{VI}$ complexes in the pyrazolylborate system. The electrochemical behavior of **1** is similar to that of the molybdenum center of arsenite oxidase; in both systems, five coordinate $Mo^{IV}O$ is converted to six coordinate $Mo^{VI}O_2$ by a two-proton two-electron process.[6]

$$[Mo^{IV}O(bdtCl_2)_2]^{2-}\ (\mathbf{1}) + H_2O \rightarrow [Mo^{VI}O_2(bdtCl_2)_2]^{2-}\ (\mathbf{2}) + 2H^+ + 2e^-\ (CH_3CN\text{-}H_2O) \quad (1)$$

$$[Mo^{IV}O(bdtCl_2)_2]^{2-}\ (\mathbf{1}) + 2OH^- \rightarrow [Mo^{VI}O_2(bdtCl_2)_2]^{2-}\ (\mathbf{2}) + H_2O + 2e^-\ (CH_3CN) \quad (2)$$

$[Mo^{IV}O(bdt)_2]^{2-}$ (**3**) and $[Mo^{IV}O(mnt)_2]^{2-}$ (**5**) exhibited markedly different reactivities in the CEPT process from that of **1** under the same conditions ([Mo] = 0.5 mM). Complex **3** was converted to $[Mo^{VI}O_2(bdt)_2]^{2-}$ (**4**) in $CH_3CN$ by a CEPT process in the presence of 2 equiv. of $Bu_4NOH$; however, **3** did not afford **4** by the CEPT process in

 © 2006 Wiley-VCH Verlag GmbH & Co. KGaA, Weinheim 

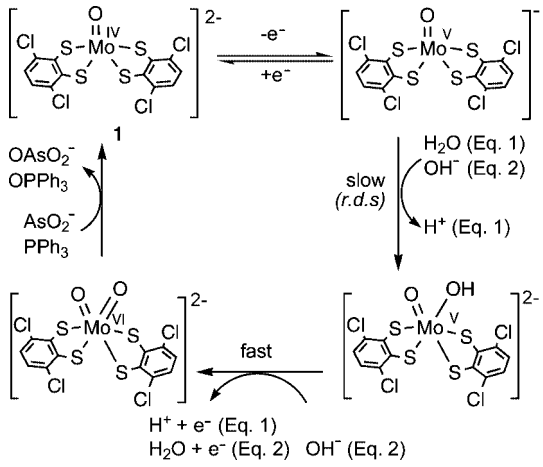


Scheme 2. Proposed mechanism for the conversion of **1** to **2** by the CEPT process in $CH_3CN/H_2O$ (5:7) [Equation (1)] and $CH_3CN$ [Equation (2)] solutions, and further oxygen atom transfer.

$CH_3CN/H_2O$ (5:7). An aspect of the reversible $Mo^{V}/^{IV}$ wave at –0.20 V in $CH_3CN/H_2O$ (5:7) was intact up to pH = 14, and the electrolysis of the solution at 0.1 V resulted in the formation of $[Mo^{V}O(bdt)_2]^-$. On the other hand, **5** decomposed to $Mo_2O_7^{2-}$ by oxidative electrolysis at 0.55 V (versus SCE) both in $CH_3CN/H_2O$ (5:7) and $CH_3CN$ solutions.[11] The drastic difference in the reactivities observed among **1**, **3**, and **5** may be based on the electron donating properties of the dithiolene ligands employed, which controls the stability of each $Mo^{V}O$ center. The values of the $Mo^{V}/^{IV}$ couples (0.04 for **1**, –0.20 V for **3**,[2a] and 0.45 V for **5**[3a] in solutions of $CH_3CN/H_2O$) indicate that the electron donating properties of the dithiolene ligands increases in the order bdt > $bdtCl_2$ > mnt. The comparison of the CEPT reactivity of **1** with those of **3** and **5** suggests that $bdtCl_2$ offers a $Mo^{V}O$ center with suitable acidity to bind $OH^-$ to afford a $Mo^{V}O(OH)$ complex which undergoes successive CEPT processes without decomplexation (Scheme 2).[12] The bdt ligand probably provides a weaker acidic $Mo^{V}O$ center. Thus, the $Mo^{V}O$ complex is stable, less reactive, and does not readily bind to $OH^-$ in aqueous media, in where the activities of both the $Mo^{V}O$ center and the $OH^-$ anion are decreased by the buffer action of $H_2O$. Therefore, $Mo^{V}O$ can bind the $OH^-$ anion of $Bu_4NOH$ in the $CH_3CN$ solution, in where the activities of both the $Mo^{V}O$ center and the $OH^-$ anion are increased by solvent effects. Conversely the mnt ligand provides a $Mo^{V}O$ center with high acidity. Because the $Mo^{V}O$ center is too unstable, it can be concluded that $Mo^{V}O(OH)$ decomposes by oxidative hydrolysis before the complex undergoes the CEPT process, although the decomplexation process is unclear at this stage.

It was found that **2** stoichiometrically oxidized $AsO_2^-$ and $PPh_3$ to $AsO_3^-$ and $OPPh_3$, respectively, and was converted to **1** in the $CH_3CN/H_2O$ solution (Scheme 2).[13]

The present study has achieved, for the first time, a combination of CEPT/OAT reactions in aqueous media for molybdenum complexes having dithiolene ligands (Scheme 2). The $Mo^{IV}O$ complex of $bdtCl_2$, **1**, was converted into the $Mo^{VI}O_2$ complex, **2**, by a one-step CEPT process and the reaction mechanism was analyzed electrochemically. The similarity of the reaction profile of our system with that of the molybdenum center of the arsenite oxidase system suggests that this model can be very helpful in understanding the reaction mechanism occurring at the molybdenum center of the arsenite oxidase as well as to develop active site models that work in water.

## Experimental Section

**General:** All reagents and solvents were used as received unless otherwise noted. $CH_3CN$ was dried with $CaH_2$ and then $P_2O_5$ and distilled under an atmosphere of nitrogen prior to use. A dry 10% $Bu_4NOH/CH_3OH$ solution was purchased from Tokyo Chemical Industry (TCI) and stored in the presence of molecular sieve. Each reaction was carried out under an atmosphere of argon in either a Schlenk tube or a Miwa DB0–1KP glove box.

**Preparations:** All complexes were synthesized under an atmosphere of nitrogen. Complexes **3** and **5** were prepared as described in the literature.[2a,3a]

$(Bu_4N)_2[Mo^{IV}O(bdtCl_2)_2]$ (**1**) was prepared in the same manner as $(Et_4N)_2[Mo^{IV}O(bdtCl_2)_2]$[3e] with the use of $(Bu_4N)_2[Mo^{VI}O_2(bdtCl_2)_2]$ (**2**) instead of $(Et_4N)_2[Mo^{VI}O_2(bdtCl_2)_2]$.[3e] $C_{44}H_{76}Cl_4MoN_2OS_4$ (1015.12): calcd. C 52.06, H 7.55, N 2.76; found C 51.99, H 7.53, N 2.76.

$(Bu_4N)_2[Mo^{VI}O_2(bdtCl_2)_2]$ (**2**): *Method A:* **1** (13.9 mg, 0.014 mmol), $K_3[Fe(CN)_6]$ (9.2 mg, 0.028 mmol), and *t*BuOK (3.1 mg, 0.028 mmol) were dissolved in $CH_3CN/H_2O$ (5:7, 300–420 μL). The red solution was concentrated to about 300 μL. Red microcrystalline powder precipitated out of the solution, which was collected by filtration. Yield: 13.7 mg (95%). $C_{44}H_{76}Cl_4MoN_2O_2S_4$ (1031.11): calcd. C 51.25, H 7.43, N 2.72; found C 50.90, H 7.41, N 2.61. *Method B:* **2** was prepared in the same manner as $(Et_4N)_2[Mo^{VI}O_2(bdtCl_2)_2]$[3e] with the use of $Bu_4NOH$ instead of $Et_4NOH$.

$(Bu_4N)_2[Mo^{VI}O^{18}O(bdtCl_2)_2]$ (**2a**) was prepared by method A as per **2** with the use of 98% $H_2{}^{18}O$ instead of $H_2O$. Yield: 13.7 mg (95%). $C_{44}H_{76}Cl_4MoN_2O^{18}OS_4$ (1033.11): calcd. C 51.15, H 7.41, N 2.71; found C 51.29, H 7.58, N 2.74.

**Physical Measurement:** FTIR spectra were recorded with a Perkin–Elmer Spectrum One. UV/Vis spectra were recorded with a Unisoku USP-801 spectrometer with an optical fiber attachment. Molar absorption coefficients were corrected by measuring $[Ru(2,2'\text{-bipyridyl})_3](PF_6)_2$ as an authentic sample. GC- and ESI-MS spectra were recorded with a Shimazu GC–MS-QP5050A and a JEOL JMS-700S, respectively. Cyclic voltammograms were recorded under an atmosphere of nitrogen with the use of a Hokuto Denko HZ-3000 potentiostat. A three-electrode configuration consisting of a glassy-carbon working electrode, a SCE reference electrode, and a platinum counter electrode was used.

**Supporting Information** (see footnote on the first page of this article): The isotope distribution pattern of the calculated mass spectrum as $\{[MoO^{18}O(bdtCl_2)_2]^{2-} + Bu_4N^+\}^-$ (Figure S1), cyclic voltammograms of **1** in $CH_3CN$ in the presence of 0–2 equiv. $Bu_4NOH$ and a plot of $\Delta I_{pa}$ versus $[Bu_4NOH]/[\mathbf{1}]$ (Figure S2), and electronic spectral changes during electrolysis of **1** in the presence of 2 equiv. $Bu_4NOH$ at 0.2 V (versus SCE) in $CH_3CN$ (Figure S3).

 © 2006 Wiley-VCH Verlag GmbH & Co. KGaA, Weinheim 

## Acknowledgments

The authors are grateful to Professor Koji Tanaka of the Institute for Molecular Science for valuable comments. This work was partly supported by a grant for Scientific Research (No. 18750052 to H. S.).

[1] a) R. Hille, *Chem. Rev.* **1996**, *96*, 2757–2816; b) S. J. N. Burgmayer, *Prog. Inorg. Chem.* **2004**, *52*, 491–537; c) J. Kuper, A. Liamas, H. J. Hecht, R. Mendel, G. Schwarz, *Nature* **2004**, *430*, 803–806.

[2] a) S. Boyde, S. R. Ellis, C. D. Garner, W. Clegg, *J. Chem. Soc., Chem. Commun.* **1986**, 1541–1543; b) D. Coucouvanis, A. Hadjikyriacou, A. Toupadakis, S.-M. Koo, O. Ileperuma, M. Draganjac, A. Salifoglou, *Inorg. Chem.* **1991**, *30*, 754; c) H. Oku, N. Ueyama, A. Nakamura, *Inorg. Chem.* **1995**, *34*, 3667; d) H. Oku, N. Ueyama, A. Nakamura, *Inorg. Chem.* **1997**, *36*, 1505–1516; e) E. S. Davies, R. L. Beddoes, D. Collison, A. Dinsmore, A. Docrat, J. A. Joue, C. R. Wilson, C. D. Garner, *J. Chem. Soc., Dalton Trans.* **1997**, 3985–3995; f) B. S. Shim, R. H. Holm, *J. Am. Chem. Soc.* **2001**, *123*, 1920–1930; g) H. Sugimoto, M. Harihara, M. Shiro, K. Sugimoto, K. Tanaka, H. Tsukube, *Inorg. Chem.* **2005**, *44*, 6386–6392; h) H. Sugimoto, T. Sakurai, H. Miyake, K. Tanaka, H. Tsukube, *Inorg. Chem.* **2005**, *44*, 6927–6929; i) K. Baba, T. Okamura, C. Suzuki, H. Yamamoto, T. Yamamoto, M. Ohama, N. Ueyama, *Inorg. Chem.* **2006**, *45*, 894–901; j) J.-J. Wang, C. Tessier, R. H. Holm, *Inorg. Chem.* **2006**, *45*, 2979–2988; k) H. Sugimoto, R. Tajima, T. Sakurai, H. Ohi, H. Miyake, S. Itoh, H. Tsukube, *Angew. Chem. Int. Ed.* **2006**, *45*, 3520–3522.

[3] a) S. K. Das, P. K. Chaudhury, D. Biswas, S. Sarkar, *J. Am. Chem. Soc.* **1994**, *116*, 9061–9070; b) N. Ueyama, H. Oku, M. Kondo, T. Okamura, N. Yoshinaga, A. Nakamura, *Inorg. Chem.* **1996**, *35*, 643–650; c) C. Lorber, M. R. Plutino, L. I. Elding, E. Nordlander, *J. Chem. Soc., Dalton Trans.* **1997**, 3997–4003; d) G. C. Tucci, J. P. Donahue, R. H. Holm, *Inorg. Chem.* **1998**, *37*, 1602–1608; e) H. Sugimoto, M. Tarumizu, K. Tanaka, H. Miyake, H. Tsukube, *Dalton Trans.* **2005**, 3558–3565.

[4] a) J. H. Enemark, C. G. Young, *Adv. Inorg. Chem.* **1993**, *41*, 1–88; b) J. H. Enemark, J. J. A. Cooney, J.-J. Wang, R. H. Holm, *Chem. Rev.* **2004**, *104*, 1175–1200; c) J. McMaster, J. M. Tunney, C. D. Garner, *Prog. Inorg. Chem.* **2004**, *52*, 539–583.

[5] a) Z. Xiao, C. G. Young, J. H. Enemark, A. G. Wedd, *J. Am. Chem. Soc.* **1992**, *114*, 9194–9195; b) Z. Xiao, M. A. Bruck, J. H. Enemark, C. G. Young, A. G. Wedd, *Inorg. Chem.* **1996**, *35*, 7508–7515; c) V. N. Nemykin, S. R. Davie, S. Mondal, N. Rubie, M. L. Kirk, A. Somogyi, P. Basu, *J. Am. Chem. Soc.* **2002**, *124*, 756–757.

[6] a) P. J. Ellis, T. Conrads, R. Hille, P. Kuhn, *Structure* **2001**, *9*, 125–132; b) T. Conrads, C. Hemann, G. N. George, I. J. Pickering, R. C. Prince, R. Hille, *J. Am. Chem. Soc.* **2002**, *124*, 11276–11277; c) K. R. Hoke, N. Cobb, F. A. Armstrong, R. Hille, *Biochemistry* **2004**, *43*, 1667–1674.

[7] Because **1** still does not dissolve in $H_2O$, mixed solvent, $CH_3CN/H_2O$ (5:7), was used instead. This ratio offered a maximized % volume of $H_2O$.

[8] A dry 10% $Bu_4NOH/CH_3OH$ solution was used.

[9] The $Mo^{IV}$ center of **1** does not bind $H_2O$ or $OH^-$ because the $E_{pa}$ value of the $Mo^{IV/V}$ couple and the electronic spectrum did not change at high concentrations of $OH^-$. $[Mo^{V}O(bdtCl_2)_2]^-$ that was characterized structurally and spectroscopically[3e] was stable only in aqueous media at pH < 9 and in $CH_3CN$.

[10] Recently, it was reported that $[Mo^{VI}(bdt)_3]$ was converted to $[Mo^{VI}OH(bdt)_3]^{2-}$ in the presence of $H_2O$, and the two $[Mo^{VI}(OH)(bdt)_3]^-$ oxidized one $PPh_3$ to give one $OPPh_3$, one $H_2O$, and two $[Mo^{V}(bdt)_3]^-$. In that case, the six coordination structure of $[Mo(bdt)_3]^{n-}$ may require a $Mo^{VI}$ center of strong acidity to bind $OH^-$, whereas in the case of $[MoO(bdtCl_2)_2]^{n-}$, the $Mo^{V}$ center can bind $OH^-$ because of the five coordinate structure. A. Cervilla, F. Perez-Pla, E. Llopis, M. Piles, *Inorg. Chem.* **2005**, *44*, 4106–4108.

[11] $Mo_2O_7^{2-}$ was identified by ESI-MS of the solution. Sarkar et al. reported that the oxidation of $[MoO(mnt)_2]^{2-}$ resulted in the formation of $MoO_4^{2-}$.[3a] In solution, $Mo_2O_7^{2-}$ and $MoO_4^{2-}$ are in an acid–base equilibrium.

[12] The $\nu(Mo^{IV,V}=O)$ stretching values (IR: solid) 910 and 941 $cm^{-1}$ for the $bdtCl_2$ complexes, 905 and 935 $cm^{-1}$ for the bdt complexes, and 928 $cm^{-1}$ [$\nu(Mo^{IV}=O)$] for the mnt complex support that the order of acidity of the molybdenum centers is bdt < $bdtCl_2$ < mnt. The $Mo^{V}$ complex of mnt is too unstable to be isolated and characterized.[3a]

[13] The stoichiometric oxidations of $PPh_3$ and $AsO_2^-$ by **2** were confirmed by $^1H$ NMR, UV/Vis, and ESI-MS spectroscopy. However, the reaction mechanism of the oxidation of $AsO_2^-$ by **2** could not be analyzed because the reaction was too fast to follow. The oxidation of $PPh_3$ by **2** was kinetically analyzed in ref.[3e]

Received: August 25, 2006
Published Online: October 12, 2006

 © 2006 Wiley-VCH Verlag GmbH & Co. KGaA, Weinheim 

DOI: 10.1002/ejic.200600790

# Supramolecular Intercluster Compounds Consisting of Gold Clusters and Keggin Anions

Martin Schulz-Dobrick[a] and Martin Jansen*[a]

**Keywords:** Supramolecular chemistry / Cluster compounds / Polyoxometalates / Nanomaterials / Gold clusters

Supramolecular intercluster compounds, that is, assemblies of different, well-defined inorganic building blocks with diameters of >1 nm, consisting of $[Au_9(PPh_3)_8]^{3+}$ clusters and Keggin anions $[PW_{12}O_{40}]^{3-}$ were synthesized as single-crystals by a diffusion method. Depending on the solvent combination, two modifications with different core geometries of the gold cluster and different overall packing type can be obtained as a single-phase in macroscopic amounts. This approach leads toward the study of nanostructured matter with high translational symmetry and the principles of nanoscopic self-assembly.

(© Wiley-VCH Verlag GmbH & Co. KGaA, 69451 Weinheim, Germany, 2006)

## Introduction

Supramolecular chemistry aims to organize molecular building blocks by means of noncovalent interactions into complex arrangements.[1] Efforts to synthesize suitable building blocks, to develop methods for their assembly, and understand the underlying fundamental principles are currently driven over all magnitudes – ranging from molecules to nano-, *meso*-, and macroscopic compounds.[1,2] In particular, nanoscopic self-assembly is envisioned to be the alternative to lithographic techniques for future electronic or optic devices. By the assembly of different building blocks into superlattices, materials can be obtained that exhibit new properties that are due to cooperative effects. One step in this direction are binary nanoparticle superlattices.[3] Recently, progress has been made in the experimental realization of such compounds, which gives insight into the driving forces of nanoparticle crystallization.[4] Depending on the types of interaction (van der Waals, hard sphere, or ionic interaction) and the relative size of the ligand stabilized nanoparticles, a whole variety of packing types were observed.

Although the principles of self-assembly and the interparticle interactions vary over the different magnitudes, one rule holds for all: the quality of the arrangements depends on the uniformity of the building blocks. This prerequisite is commonly fulfilled very well for a molecular assembly but not for the assembly of nanoparticles (except protein crystallization), which exhibit an intrinsic size distribution. The resulting violations of translational symmetry on the atomic scale would undermine at least some of the enthusiastic expectations connected to the properties of nanostructured matter. Anyhow, such defects would thwart structure determinations with atomic resolution, which is an important prerequisite for a detailed understanding of structure-directing forces and the resulting physical properties. Our approach for overcoming these limitations is based on the generation of supramolecular intercluster compounds (SICC), that is, assemblies of different, well defined, inorganic building blocks with diameters of 1 nm or larger.

The variety of inorganic clusters that have been studied in manifold, and clusters of several nanometers in size have been uniformly synthesized and crystallized.[5,6] Only a few examples of compounds consisting of different inorganic clusters have been reported and all are constructed of different polyoxometalates as anionic building blocks.[7,8]

SICCs can be seen as a bridge between the molecular self-assembly and the self-assembly of nanoparticles. While the latter is dominated by nondirectional interactions of spherical particles leading to more or less densely-packed structures that can mostly be derived from simple ionic or intermetallic compounds, the arrangements in the former are strongly dependent on the shape of the molecules and directional interactions, which can lead to structures with either low symmetry or density. For SICCs, a tendency for structures with a dense packing of the clusters can be expected. However, because of deviations from a perfect spherical shape, local directional, or steric interactions, a wide range of arrangements might be realized. Because of the size of the building blocks, voids filled with solvent molecules are likely to occur in such arrangements. Unlike binary nanoparticle superlattices, it is possible to grow SICCs as single-crystals with high translational order, such that details of the supramolecular arrangements can be elucidated by X-ray diffraction.

[a] Max Planck Institute for Solid State Research,
Heisenbergstraße 1, 70569 Stuttgart, Germany
Fax: +49-711-689-1502
E-mail: M.Jansen@fkf.mpg.de

Supporting information for this article is available on the WWW under http://www.eurjic.org or from the author.

 © 2006 Wiley-VCH Verlag GmbH & Co. KGaA, Weinheim 

## Results and Discussion

In this communication, we report the crystallization and structural characterization of the first supramolecular intercluster compounds consisting of different types of building units, the gold cluster $[Au_9(PPh_3)_8]^{3+}$ and the Keggin anion $\alpha$-$[PW_{12}O_{40}]^{3-}$. It is noteworthy that the $[Au_9(PPh_3)_8]^{3+}$ cluster although being one of the first gold clusters to be discovered,[9,10] accessible in gram-scale quantities, and widely investigated, has never been characterized by single-crystal X-ray diffraction because of heavy disorder. Structural characterization of $Au_9^{3+}$ clusters was successful only by the employment of *para*-substituted ligands.[10–12] In the solid state, two skeletal isomers of $[Au_9(PR_3)]^{3+}$ clusters were found; in solution the clusters undergo fast rearrangements.

The mixing of solutions of $[Au_9(PPh_3)_8](NO_3)_3$ and $(NBu_4)_3[PW_{12}O_{40}]$ in acetonitrile leads to a microcrystalline, orange precipitate of the 1:1 compound $[Au_9(PPh_3)_8][PW_{12}O_{40}]$ (**1**). For growing single-crystals for X-ray diffraction, an interdiffusion method was employed. The building blocks were separately dissolved in solvents of different density and layered carefully on top of each other. Depending on the types of solvents and the concentration, two types of crystals were obtained, orange needles of compound **1** and greenish-black plates or prisms of a second compound **2**. Both compounds contain $[Au_9(PPh_3)_8]^{3+}$ and $\alpha$-$[PW_{12}O_{40}]^{3-}$ in a 1:1 ratio, but exhibit different $Au_9$ skeletal isomers and packing types. Although in some solvent combinations simultaneous growth of both compounds was observed, **1** and **2** can be obtained selectively in DMF-acetonitrile and DMF-acetone, respectively.

Compound **1** crystallizes in the tetragonal space group *P*4/*n* with two formula units in the unit cell.[13] The skeletal geometry of the $[Au_9(PPh_3)_8]^{3+}$ cluster, which is located on a four-fold axis, resembles the shape of a centered crown with eight Au atoms surrounding the central Au1 atom (Figure 1a). The radial Au–Au bond lengths are 266.2(1) pm and 266.9(1) pm and the peripheral bond lengths are 277.7(1) pm and 280.6(1) pm. This centered crown geometry was first observed in the related $[Au_9\{P(p\text{-}C_6H_4OMe)_3\}_8](BF_4)_3$.[12] The central P atom of the Keggin anion $\alpha$-$[PW_{12}O_{40}]^{3-}$ resides on a position exhibiting $\bar{4}$ symmetry (Wyckhoff position 2a) and the whole anion is found to be ordered (Figure 1b). The W–O and P–O bond lengths of this well-known anion are in agreement with those previously found in other crystal structure determinations.[14] Figure 2 shows the overall packing of **1**, which can be derived from the CsCl structure type. Both the gold cluster and the Keggin anion are coordinated by each other in the form of distorted cubes. The distortion originates mainly from the nonspherical shape of the $Au_9$ cluster. Furthermore, the eight peripheral Au atoms can be divided into an upper and lower part of the crown. Four Au atoms, respectively, are bonded to $PPh_3$ ligands pointing directly towards the corners (4 × Au2) and the edges (4 × Au3) of the coordination cube (Figure 3). The distances between the central Au1 and the central P1 of the Keggin anions are 1339 pm and 1444 pm. This separation leads to the slight distortion of the $Au_9$ skeleton from the $D_{4d}$ symmetry with the Au2–Au2 distances [344.8(1) pm] being shorter than the Au3–Au3 distances [350.2(1) pm]. The gold clusters exhibit close contacts not only to the eight Keggin anions (H···O distances 230–250 pm) but also to six neighboring gold clusters (H···H distances <270 pm), which is expected for the CsCl packing type. The Au1–Au1 distances are 1367 pm and 1723 pm and can be regarded as an approximation for the short and long van der Waals diameters of the gold cluster. The van der Waals diameters of $[PW_{12}O_{40}]^{3-}$, which is not perfectly spherical as well, can be estimated to range from 1050 pm to 1350 pm. As both building blocks are oriented with their short diameters parallel to the *c* axis, a relatively dense packing is achieved. The estimated radii ratios of 0.75–0.80 are close to the theoretical value of 0.73, which is calculated for touching spheres with cubic coordination. Although the estimation of the radii ratios for such building blocks with a rather irregular surface seems to be a rough approximation, it can be concluded that the CsCl structure-type is at least a very dense and therefore effective packing for this intercluster compound. A search for voids in the crystal structure (PLATON,[15] probe radius 1.2 Å) led to a value of 11.5% of the accessible volume. The largest voids (202 Å$^3$) can be found in between two adjacent Keggin anions that lie along [001].

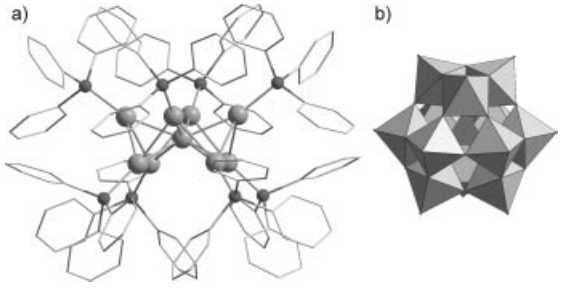


Figure 1. a) Structure of the crown isomer of the $[Au_9(PPh_3)_8]^{3+}$ cluster. Hydrogen atoms are omitted for clarity. b) Structure of the Keggin anion $\alpha$-$[PW_{12}O_{40}]^{3-}$ in polyhedral representation.

Compound **2** crystallizes in the space group *C*2/*c* with four formula units in the unit cell.[13] Different from **1**, the $[Au_9(PPh_3)_8]^{3+}$ cluster is not in the crown skeletal geometry but in a "butterfly-shaped" geometry (Figure 4a), which was first observed in the compound $[Au_9\{P(p\text{-}C_6H_4Me)_3\}_8](PF_6)_3$.[12] The cluster resides on a crystallographic site of $C_2$ symmetry (4e). While the ligand shell exhibits only this $C_2$ symmetry, the symmetry of the Au skeleton is close to $D_{2h}$. The radial Au···Au bond lengths range from 266.1(1) pm to 273.8(1) pm and the corresponding peripheral bond lengths vary from 278.8(1) pm to 292.6(1) pm. Thus, the average Au···Au bond lengths and their variations are considerably larger than those of the crown isomer. The Keggin anion was found to be disordered over two orientations with the resulting superposition exhibiting inversion symmetry (Wyckhoff position 4d). This kind of disorder has been encountered several times before for Keggin anions and can be realized by 90° rotations

 © 2006 Wiley-VCH Verlag GmbH & Co. KGaA, Weinheim 

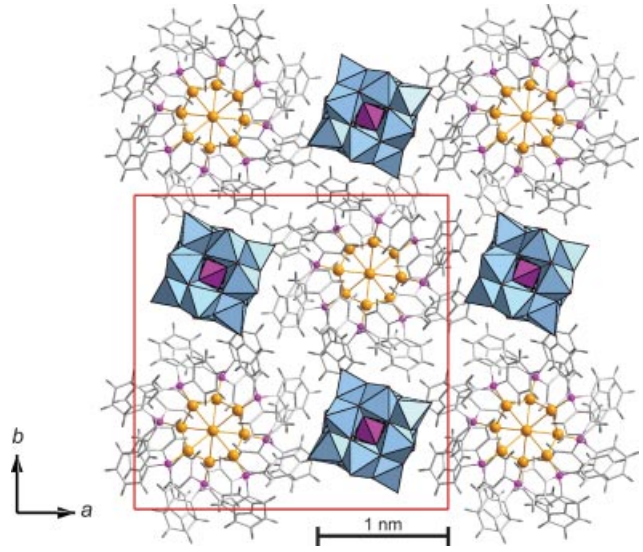


Figure 2. View of the crystal structure along [001]. The Keggin anions are located at $z = 0$ and the gold clusters at $z = 0.42$ and $z = 0.58$, respectively.

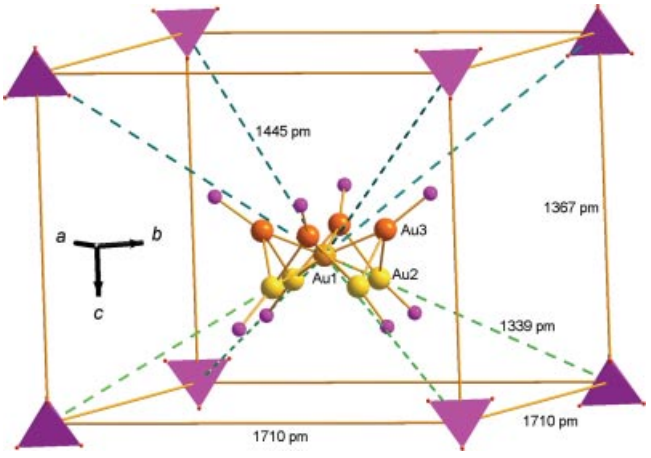


Figure 3. Coordination of the gold cluster by eight anions. The ligands of the peripheral Au atoms are pointing directly towards (Au2, yellow spheres) or in between (Au3, orange spheres) the anions.

along one of the $\bar{4}$ axes of the central tetrahedron.[16] In Figure 4b, it can be seen that the outer silhouette of the two orientations is almost equal, so that this crystallographic disorder is likely to occur. The packing scheme of **2** can be derived from the NaCl structure-type (Figure 5). The Keggin anions are coordinated by six $[Au_9(PPh_3)_8]^{3+}$ clusters (shortest O···H contacts <250 pm) in the form of a distorted octahedra with center-to-center distances of 1300, 1304, and 1391 pm. Vice versa, the gold clusters are coordinated by six Keggin anions octahedrally as well. The gold clusters are oriented in such a way that the eight $PPh_3$ ligands, which surround the Au skeleton in almost a cubic fashion, point towards the eight faces of the coordination octahedron.

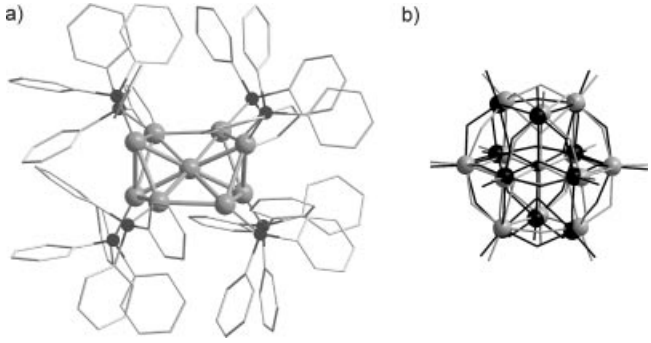


Figure 4. a) Structure of the "butterfly-shaped" isomer of the $[Au_9(PPh_3)_8]^{3+}$ cluster. Hydrogen atoms are omitted for clarity. b) Superposition of the two orientations of the α-$[PW_{12}O_{40}]^{3-}$ anion in **2**.

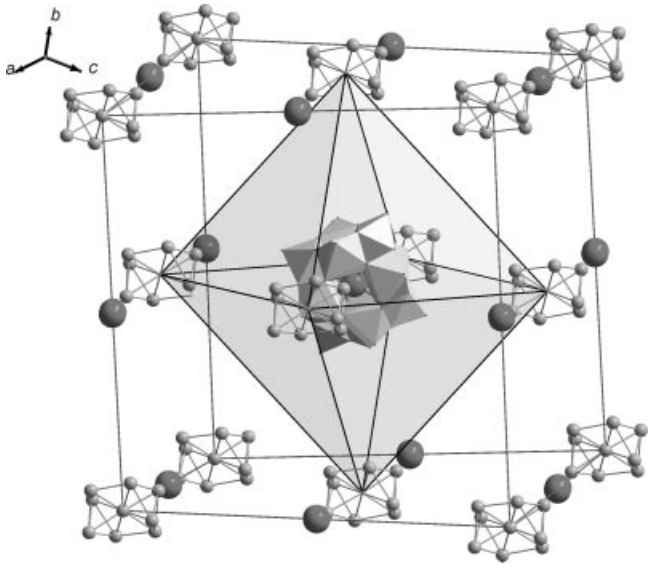


Figure 5. Similarity of the packing of **2** to the NaCl structure type: the gold clusters are packed face-centered cubic and the Keggin anions (dark grey spheres) occupy the octahedral voids.

The effective van der Waals diameter of the "butterfly-shaped" $[Au_9(PPh_3)_8]^{3+}$ isomer can be estimated to be about 1650 pm to 1750 pm. The silhouette of this isomer is more spherical than that of the crown isomer. In case of a regular closed packing of touching hard spheres with this diameter, the octahedral voids could occupy spheres with a diameter not greater than about 700 pm. The diameter of the Keggin anion (1050 pm to 1350 pm) is significantly larger than that, which has several consequences. First, not all of the twelve neighboring gold clusters are in close contact to the central gold cluster. The center-to-center distances in the distorted cuboctahedron vary from 1680 pm to 2108 pm. Furthermore, the misfit of the Keggin anions leads to substantial voids. The solvent accessible volume was calculated to be 19.6%. There appear to be four crystallographically equivalent solvent pockets per unit cell (average coordinates 0, 0.185, 0.25), but single solvent molecules could not be located during crystal structure refinement because of disorder. The crystals lose solvent molecules rapidly upon re-

 © 2006 Wiley-VCH Verlag GmbH & Co. KGaA, Weinheim 

moval from the mother liquid. From geometric considerations about six molecules (DMF or acetone) per formula unit would fit into the voids.

## Conclusions

In conclusion, we have synthesized two representatives of SICCs in macroscopic amounts and determined their crystal structures. We think that this may become a versatile and efficient approach to new, well-defined, nanostructured materials. Currently, we are modifying the building-blocks in order to study the underlying principles of such supramolecular structures and their formation.

## Experimental Section

$Au_9(PPh_3)_8(NO_3)_3$ ("$Au_9$") and $Au_8(PPh_3)_8(NO_3)_2$ ("$Au_8$") were prepared by the reduction of $AuPPh_3NO_3$ with $NaBH_4$, and its subsequent reaction with excess triphenylphosphane according to the procedure given in ref.[17] α-$[n Bu_4N]_3PW_{12}O_{40}$ ("$PW_{12}$") was prepared by precipitation of an aqueous solution of commercially available tungstophosphoric acid with $nBu_4NBr$ and subsequent recrystallization from acetone.[18] **1**: Upon mixing acetonitrilic solutions of $Au_9$ and $PW_{12}$, an orange, microcrystalline powder of **1** precipitates immediately. Larger crystals can be obtained by an interdiffusion method, which was optimized in glass tubes with a diameter of 8 mm at 20 °C. Single-crystals of **1** were obtained by the careful layering of $Au_9$ in DMF (0.3 mL, 1 μmol/mL) followed by DMF/acetonitrile (1:1, 1.0 mL), and $PW_{12}$ in acetonitrile (0.3 mL, 1.5 μmol/mL). After several days, orange needles that tend to dendritic intergrowth form. If the diffusion is carried out with $Au_8$ as starting material, the $Au_8$ cluster rearranges back to the $Au_9$ cluster and **1** crystallizes as the only compound, which was checked by X-ray diffractometry. Interestingly, the obtained crystals are larger and less intergrown than those obtained with $Au_9$ as the starting material. Single-crystals suitable for X-ray diffraction were washed with acetonitrile, dried in air, and mounted on glass capillaries. Larger scale synthesis of **1** was carried out in glass tubes with a diameter of 2 cm. $[(nBu_4N)]_3PW_{12}O_{40}$ (133 mg, 36.9 μmol) in DMF (8 mL) was carefully layered with DMF/acetonitrile (1:1, 4 mL), followed by $Au_9(PPh_3)_8(NO_3)_3$ (100 mg, 24.6 μmol) in acetonitrile (8 mL). After 5 to 7 d, the orange needles were collected on a fine glass frit, washed with acetonitrile, and dried under vacuum. Yield: 142 mg (85%). ATR-IR (neat sample), $Au_9(PPh_3)_8^{3+}$: $\tilde{\nu}$ = 1586(w), 1571(w), 1479(m), 1436(m), 1384(w), 1331(w), 1310(w), 1185(w), 1161(w), 1097(m), 1028(w), 987(sh), 738(m), 707(m), 686(m); $PW_{12}O_{40}^{3-}$: $\tilde{\nu}$ = 1079(s), 977(s), 893(m), 808(s). The PXRD pattern corresponds to the calculated pattern from the single-crystal X-ray structure determination (see Supporting Information). Room-temperature unit cell parameters of $a$ = 2433.2 pm and $b$ = 1386.5 pm were determined by the Le Bail method.

The preparation of **2** as a single phase is more difficult, as the formation of **2** and **1** is dependent on the concentrations in the crystallization zone. In 8 mm tubes $Au_9$ in DMF (0.3 mL, 2.5 μmol/mL) followed by DMF/acetone (1:1, 0.8 mL) and $PW_{12}$ in acetone (0.3 mL, 3.0 μmol/mL) are carefully layered. After several days, greenish-black crystals appear, and the solution is still slightly yellow. The crystals lose solvent rapidly upon removal from the mother liquid and, as a consequence, turn opaque and diffract poorly. Thus, single-crystals for X-ray diffraction were directly transferred into inert oil, picked with a loop and cooled with liquid nitrogen. Up-scaling of the crystallization in larger tubes was not successful, as substantial amounts of **1** formed simultaneously. Instead, larger amounts of **2** were prepared by simply filling 12 to 16 of the small tubes at once. Yield: ca. 3.3 mg per tube (ca. 60%). ATR-IR (neat sample), $Au_9(PPh_3)_8^{3+}$: $\tilde{\nu}$ = 1584(w), 1569(w), 1478(m), 1434(m), 1383(w), 1308(w), 1182(w), 1161(w), 1096(m), 1027(w), 986(sh), 740(m), 706(m), 687(m); $PW_{12}O_{40}^{3-}$: $\tilde{\nu}$ = 1077(s), 974(s), 892(s), 806(s). The solvent loss is at least partially reversible. If the dried crystals are put into solvent, they turn transparent again. For powder X-ray diffraction the crystals were washed with DMF/acetone and acetone, dried in air, ground, and filled into a 0.7 mm capillary with additional solvent. The PXRD pattern corresponds to the calculated pattern from the single-crystal X-ray structure determination (see Supporting Information).

**Supporting Information** (see footnote on the first page of this article): Experimental and calculated PXRD patterns of **1** and **2**.

## Acknowledgments

The authors want to thank Dipl.-Chem. Hanne Nuss and Dr. Jürgen Nuss for single-crystal X-ray measurements, Alexandra Müller and Sven Drescher for preparative assistance, and the Fonds der Chemischen Industrie for financial support.

[1] a) J. M. Lehn, *Supramolecular Chemistry: Concepts and Perspectives*, VCH, Weinheim, **1995**; b) J. L. Atwood, J. E. D. Davies, D. D. MacNicol, F. Vögtle, J. M. Lehn, *Comprehensive Supramolecular Chemistry*, Pergamon, Oxford, **1996**.

[2] a) G. M. Whitesides, B. Grzybowski, *Science* **2002**, *295*, 2418–2421; b) G. M. Whitesides, M. Boncheva, *Proc. Natl. Acad. Sci.* **2002**, *99*, 4769–4774.

[3] a) C. J. Kiely, J. Fink, M. Brust, D. Bethell, D. J. Schiffrin, *Nature* **1998**, *396*, 444–446; b) C. J. Kiely, J. Fink, M. Brust, D. Bethell, D. J. Schiffrin, *Nature* **1998**, *396*, 444–446; c) A. L. Rogach, *Angew. Chem.* **2004**, *116*, 150–151; *Angew. Chem. Int. Ed.* **2004**, *43*, 148–149.

[4] a) E. V. Shevchenko, D. V. Talapin, N. A. Kotov, S. O'Brien, C. B. Murray, *Nature* **2006**, *439*, 55–59; b) E. V. Shevchenko, D. V. Talapin, C. B. Murray, S. O'Brien, *J. Am. Chem. Soc.* **2006**, *128*, 3620–3637; c) A. M. Kalsin, M. Fialkowski, M. Paszewski, S. K. Smoukov, K. J. M. Bishop, B. A. Grzybowski, *Science* **2006**, *312*, 420–424.

[5] a) D. Fenske, N. Y. Zhu, T. Langetepe, *Angew. Chem.* **1998**, *110*, 2783–2788; *Angew. Chem. Int. Ed.* **1998**, *37*, 2640–2644; b) X. J. Wang, T. Langetepe, C. Persau, B. S. Kang, G. M. Sheldrick, D. Fenske, *Angew. Chem.* **2002**, *114*, 3972–3977; *Angew. Chem. Int. Ed.* **2002**, *41*, 3818–3822; c) D. Fenske, C. Persau, S. Dehnen, C. E. Anson, *Angew. Chem.* **2004**, *116*, 309–313; *Angew. Chem. Int. Ed.* **2004**, *43*, 305–309; d) D. Fenske, C. E. Anson, A. Eichhofer, O. Fuhr, A. Ingendoh, C. Persau, C. Richert, *Angew. Chem.* **2005**, *117*, 5376–5381; *Angew. Chem. Int. Ed.* **2005**, *44*, 5242–5246.

[6] a) A. Müller, E. Krickemeyer, J. Meyer, H. Bögge, F. Peters, W. Plass, E. Diemann, S. Dillinger, F. Nonnenbruch, M. Randerath, C. Menke, *Angew. Chem.* **1995**, *107*, 2293–2295; *Angew. Chem. Int. Ed. Engl.* **1995**, *34*, 2122–2124; b) A. Müller, E. Krickemeyer, H. Bögge, M. Schmidtmann, C. Beugholt, P. Kögerler, C. Z. Lu, *Angew. Chem.* **1998**, *110*, 1278–1281; *Angew. Chem. Int. Ed.* **1998**, *37*, 1220–1223; c) A. Müller, E. Krickemeyer, H. Bögge, M. Schmidtmann, F. Peters, *Angew. Chem.* **1998**, *110*, 3567–3571; *Angew. Chem. Int. Ed.* **1998**, *37*, 3360–3363.

[7] a) J. H. Son, H. Choi, Y. U. Kwon, *J. Am. Chem. Soc.* **2000**, *122*, 7432–7433; b) J. H. Son, Y. U. Kwon, O. H. Han, *Inorg. Chem.* **2003**, *42*, 4153–4159; c) J. H. Son, Y. U. Kwon, *Inorg. Chem.* **2004**, *43*, 1929–1932; d) J. H. Son, Y. U. Kwon, *Inorg.*

 © 2006 Wiley-VCH Verlag GmbH & Co. KGaA, Weinheim 

*Chim. Acta* **2005**, *358*, 310–314; e) P. Mialane, A. Dolbecq, L. Lisnard, A. Mallard, J. Marrot, F. Secheresse, *Angew. Chem.* **2002**, *114*, 2504–2507; *Angew. Chem. Int. Ed.* **2002**, *41*, 2398–2401.

[8] a) S. Uchida, M. Hashimoto, N. Mizuno, *Angew. Chem.* **2002**, *114*, 2938–2941; *Angew. Chem. Int. Ed.* **2002**, *41*, 2814–2817; b) S. Uchida, N. Mizuno, *J. Am. Chem. Soc.* **2004**, *126*, 1602–1603; c) S. Uchida, R. Kawamoto, T. Akatsuka, S. Hikichi, N. Mizuno, *Chem. Mater.* **2005**, *17*, 1367–1375.

[9] F. Cariati, L. Naldini, *J. Chem. Soc., Dalton Trans.* **1972**, 2286–2287.

[10] a) P. L. Bellon, F. Cariati, M. Manassero, L. Naldini, M. Sansoni, *J. Chem. Soc., D* **1971**, 1423–1424; b) J. M. M. Smits, P. T. Beurskens, J. J. Bour, F. A. Vollenbroek, *J. Crystallogr. Spectrosc. Res.* **1983**, *13*, 365–372.

[11] C. E. Briant, K. P. Hall, D. M. P. Mingos, *J. Chem. Soc., Chem. Commun.* **1984**, 290–291.

[12] K. P. Hall, B. R. C. Theobald, D. I. Gilmour, D. Michael, P. Mingos, A. J. Welch, *J. Chem. Soc., Chem. Commun.* **1982**, 528–530.

[13] Crystal data and structure refinement for **1**: $C_{144}H_{120}Au_9P_9W_{12}O_{40}$, needle ($0.3 \times 0.1 \times 0.03$ mm$^3$), tetragonal, space group *P*4/*n*, $a$ = 2417.8(2), $c$ = 1367.1(2) pm, $V$ = 7991.8(14)·10$^6$ pm$^3$, $\rho_{calcd.}$ = 2.804 g cm$^{-3}$, $Z$ = 2, $\mu$(Mo-$K_\alpha$) = 16.98 mm$^{-1}$, $F$(000) = 6076, $\lambda$ = 71.073 pm, Bruker-AXS-Smart-APEX-diffractometer, graphite monochromator, $T$ = 100 K, $\omega$-Scan, 72914 measured reflections, 6282 symmetry independent reflections ($2\theta_{max}$ = 48.00°), 483 refined parameters; semiempirical absorption correction (SADABS[19]); structure solution and refinement with SHELXTL:[20] $R_1$ = 0.0545, $wR_2$ = 0.1376 [4967 $F_o > 2\sigma(F_o)$], $R_1$ = 0.0746, $wR_2$ = 0.1523 (all data). Non-hydrogen atoms were refined with anisotropic displacement parameters. Hydrogen atoms were calculated with the use of HFIX. No residual electron density for solvent molecules was detected. **2**: $C_{144}H_{120}Au_9P_9W_{12}O_{40}$, rhombic ($0.15 \times 0.12 \times 0.10$ mm$^3$), monoclinic, space group *C*2/*c*, $a$ = 2932.1(2), $b$ = 2107.8(2), $c$ = 3243.8(2) pm, $V$ = 18246(2)·10$^6$ pm$^3$, $\rho_{calcd.}$ = 2.457 g cm$^{-3}$, $Z$ = 4, $\mu$(Mo-$K_\alpha$) = 14.87 mm$^{-1}$, $F$(000)= 12152, $\lambda$ = 71.073 pm, Bruker-AXS-Smart-APEX-diffractometer, graphite monochromator, $T$ = 100 K, $\omega$-Scan, 76985 measured reflections, 19919 symmetry independent reflections ($2\theta_{max}$ = 54.12°), 646 refined parameters; semiempirical absorption correction (SADABS[19]); structure solution and refinement with SHELXTL:[20] $R_1$ = 0.0499, $wR_2$ = 0.1193 [16370 $F_o > 2\sigma(F_o)$], $R_1$ = 0.0616, $wR_2$ = 0.1238 (all data). The $[PW_{12}O_{40}]^{3-}$ anion is disorderd over an inversion center, with the positions of the W and outer O atoms being very close to each other (see Figure 4b). Thus, chemically equivalent W–O bonds were restraint to common values. All C and O atoms were refined with isotropic displacement parameters and hydrogen atoms were calculated with the use of HFIX. Diffuse solvent molecules could not be found properly in the difference fourier map. Their contribution was eliminated by the SQUEEZE subprogram.[21] CCDC-615444 and -615445 contain the supplementary crystallographic data for this paper. These data can be obtained free of charge from The Cambridge Crystallographic Data Centre via www.ccdc.cam.ac.uk/data_request/cif.

[14] G. M. Brown, M. R. Noespirlet, W. R. Busing, H. A. Levy, *Acta Crystallogr., Sect. B* **1977**, *33*, 1038–1046.

[15] A. L. Spek, Utrecht University, **2005**.

[16] H. T. Evans, M. T. Pope, *Inorg. Chem.* **1984**, *23*, 501–504.

[17] J. W. A. van der Velden, J. J. Bour, W. P. Bosman, J. H. Noordik, *Inorg. Chem.* **1983**, *22*, 1913–1918.

[18] J. Fuchs, A. Thiele, R. Palm, *Angew. Chem.* **1982**, *94*, 804–805; *Angew. Chem. Int. Ed. Engl.* **1982**, *21*, 789–790.

[19] G. M. Sheldrick, 2.10 ed., Bruker AXS, Madison, WI, USA, **2003**.

[20] G. M. Sheldrick, Version 6.10 ed., Bruker AXS, Madison, WI, USA, **2000**.

[21] P. van der Sluis, A. L. Spek, *Acta Crystallogr., Sect. A* **1990**, *46*, 194–201.

Received: August 25, 2006
Published Online: October 2, 2006

 © 2006 Wiley-VCH Verlag GmbH & Co. KGaA, Weinheim 

DOI: 10.1002/ejic.200600475

# A General and Facile One-Step Synthesis of Imido–Titanium(IV) Complexes: Application to the Synthesis of Compounds Containing Functionalized or Chiral Imido Ligands and Bimetallic Diimido Architectures

**Christian Lorber,*[a] Robert Choukroun,[a] and Laure Vendier[a]**

**Keywords:** Imido / N ligands / Multiple bonds / Titanium / Synthesis design

One-pot reactions of $Ti(NMe_2)_4$ with a wide range of primary alkyl, aryl, and silylamines $RNH_2$ in the presence of excess chlorotrimethylsilane produced the corresponding imido–titanium(IV) complexes $[Ti(=NR)Cl_2(NHMe_2)_2]$ (**1a–j**), in which R = *t*Bu, 1-adamantane, $Ph_3C$, $Ph_3Si$, Ph, 2,6-*i*$Pr_2$–$C_6H_3$, 2,6-$Cl_2$–$C_6H_3$, 2,6-$Br_2$–4-Me–$C_6H_2$, $C_6F_5$, and 3,5-$(F_3C)_2$–$C_6H_3$. This general synthesis, which starts from commercially available reagents, represents a simple and direct route to imido complexes. Reaction of complexes **1** with pyridine afforded the six-coordinate tris-pyridine adducts $[Ti(=NR)Cl_2(Py)_3]$ (**2**). Another advantage of this method is its tolerance to other functional groups; complexes that contain halides, ether, dialkylamino, cyano, ethynyl, olefin, and nitro substituents on the imido moiety have been prepared. The use of enantiomerically pure primary amines affords the first group of titanium complexes that contain chiral imido groups, and the use of diamines produces diimido complexes. Alternatively, $CH_3I$ has been used as an alkylating agent to generate titanium–imido complexes of the type $[Ti(NR)I_2(THF)_2]_2$. All compounds were fully characterized by spectroscopic methods (IR, $^1H$ NMR, $^{13}C$ NMR) and elemental analysis. Some of the compounds were also analyzed by single-crystal X-ray diffraction studies.

(© Wiley-VCH Verlag GmbH & Co. KGaA, 69451 Weinheim, Germany, 2006)

## Introduction

The last two decades have witnessed a strong interest in the coordination chemistry of transition-metal complexes that contain imido ligands $[NR]^{2-}$ (R = alkyl or aryl).[1] The dianionic π-donor terminal imido functional group is involved in many facets of chemistry that can be subdivided into two types: (1) reactions in which the imido group acts as a spectator ligand, the $[NR]^{2-}$ moiety is isolobal with $[C_5H_5]^-$[2] (e.g. in alkene metathesis[3] or olefin polymerization[1c,4–6]), (2) reactions in which the M = NR linkage itself is involved in stoichiometric or catalytic transformations such as metathesis reactions (with imines,[7] nitro- and nitrosoarenes,[8] or oxo–imido exchange[9]), C–H activation,[10] reactions with unsaturated C–C[11] or C–X bonds,[12] alkyne hydroaminations,[13,14] carboamination reactions,[15] and ring-opening reactions of strained heterocycles.[10d,16] Moreover, some imido derivatives have also found applications in material chemistry (OMCVD,[17] polyoxometalate[18]) and have been implicated in the ammoxidation of propene.[19]

As part of an ongoing study of vanadium complexes supported by various ligands,[20] we recently described the synthesis and molecular structure of the new terminal aryl–imido, and rare Cp-free, vanadium(IV)complex $[V(=N–2,6\text{-}iPr_2–C_6H_3)Cl_2(NHMe_2)_2]$.[5] We have further demonstrated that various aryl–imido groups could be very conveniently introduced by a one-pot synthesis from $V(NMe_2)_4$, the corresponding aniline, and chlorotrimethylsilane.[21] We have also studied the coordination chemistry of these new complexes with N- or P-donor neutral ligands,[21,22] and the results suggest that imido compounds of this type could lead to a large variety of vanadium coordination compounds. Furthermore, some of these imido–vanadium species have been shown to possess catalytic activities in olefin polymerization[5] and in alkyne hydroamination.[13a] Terminal imido–titanium complexes $[Ti(=N–t\text{Bu})Cl_2L_n]$ [$L_n$ = $(NHMe_2)_2$, $Py_2$, $Py_3$, TMEDA] have proven to be very useful synthons for the preparation of many other imido derivatives through chloride and/or ligand base exchange metathesis; aryl– and silyl–imido derivatives are available by transimination reactions with the appropriate aryl and silylamine.[6a,13d,17c,23–26] Some of these imido–titanium complexes present potential activity in olefin polymerization,[6] alkyne hydroamination,[13] and have been used for the synthesis of TiN thin films,[17a–17c] which further justifies the quest for the cheapest and the most direct route for the preparation of such useful precursors.

[a] Laboratoire de Chimie de Coordination, CNRS UPR 8241, lié par convention à l'Université Paul Sabatier,
205 route de Narbonne, 31077 Toulouse Cedex 04, France
Fax: +33-5-61-55-30-03
E-mail: lorber@lcc-toulouse.fr

Supporting information for this article is available on the WWW under http://www.eurjic.org or from the author.

 © 2006 Wiley-VCH Verlag GmbH & Co. KGaA, Weinheim 

Two routes are commonly employed for the preparation of the now widely used synthon $[Ti(=N–R)Cl_2L_n]$ [$L_n$ = $(NHMe_2)_2$, $Py_3$]. In the first method, $[Ti(=N–tBu)Cl_2Py_3]$ is prepared from $TiCl_4$, $tBuNH_2$, and pyridine.[23] Nevertheless, other analogues (i.e. aryl–imido) cannot be obtained this way, and their synthesis requires a second step that consists of an imido/amine exchange reaction (transimination) of $[Ti(=N–tBu)Cl_2Py_3]$ with the appropriate arylamine.[23] Moreover, the presence of pyridine renders these compounds somewhat insoluble, and pyridine ligands may be unwanted for certain applications. During the course of our studies, imido–titanium complexes $[Ti(=N–R)Cl_2(NHMe_2)_2]$ have been prepared by Mountford et al. with a procedure based on the reaction of $Ti(NMe_2)_2Cl_2$ with a primary alkyl- or arylamine.[26] Although this route appears more general than the one with $TiCl_4$, the precursor $Ti(NMe_2)_2Cl_2$ is not commercially available and needs to be prepared from $TiCl_4$ and $Ti(NMe_2)_4$.[27]

In this paper, and as an extension of our imido–vanadium method[21] to titanium, we report on a very convenient, one-pot synthesis of a series of alkyl–, aryl–, and silyl–imido derivatives of titanium(IV) complexes of the general formula $[Ti(=NR)Cl_2(NHMe_2)_2]$ (**1**), where R is an alkyl-, an aryl-, or a silyl group. Part of this work [synthesis of $Ti(=NPh)Cl_2(NHMe_2)_2$] has been previously communicated.[13a] Our method presents the advantage to afford the imido derivative in one single step with the use of a very simple one-pot synthesis from commercially available $Ti(NMe_2)_4$, the corresponding primary amine $RNH_2$, and an excess of chlorotrimethylsilane. Another important goal of this study was to explore the selectivity and the functional group tolerance of the reaction. Amines that contain additional functionality on their skeletons (e.g. ether, dialkylamino, cyano, ethynyl, olefin, or nitro substituents) were successfully used to generate original imido derivatives. In consequence, our procedure appears to be applicable to a wide range of primary amines including enantiomerically pure amines (to afford chiral imido functions) and diamines (to afford diimido complexes). Related complexes with pyridine ligands prepared by the substitution of the $NHMe_2$ ligands in $[Ti(=NR)Cl_2(NHMe_2)_2]$ by pyridine (Py) donors is also described. Finally, an alternative preparation for the related iodo analogue complex $[Ti(NAr)I_2(thf)_2]_2$ is also described; this method is based on the use of $CH_3I$ instead of $Me_3SiCl$ (Scheme 3).

## Results and Discussion

This work constitutes a systematic investigation of the synthetic and structural chemistry of imido–titanium(IV) complexes of the general formula $[Ti(=NR)Cl_2(NHMe_2)_2]$ that are prepared directly from a one-pot reaction of $Ti(NMe_2)_4$, $RNH_2$, and $Me_3SiCl$, as well as some related compounds. The synthesis and proposed structures of the imido complexes of titanium(IV) are summarized in Schemes 1–3. The structures of eleven complexes are set out in Figures 2–7, and Figures 9, 10, 12, and 14, selected metric data are collected in Tables 1 and 2.

### 1. General Synthesis of the Imido Complexes $[Ti(=NR)Cl_2(NHMe_2)_2]$ and $[Ti(=NR)Cl_2Py_3]$

In our previous study,[21] we described the synthesis of paramagnetic aryl–imido–vanadium complexes $[V(=NAr)Cl_2(NHMe_2)_2]$ from the reaction of an aniline with $V(NMe_2)_4$ in toluene followed by the addition of an excess of chlorotrimethylsilane. Inspired by this result, we attempted to use a similar one-pot synthesis for the production of related titanium–imido analogue complexes, and the scope of this method was first illustrated with a range of primary amines listed in Scheme 2.

| | | | |
|---|---|---|---|
| $[Ti(=N–tBu)Cl_2(NHMe_2)_2]$ | **1a** | $[Ti(=N–3\text{-}O_2N–6\text{-}Me–C_6H_3)Cl_2(NHMe_2)_2]$ | **1q** |
| $[Ti(=N–1\text{-}adamantane)Cl_2(NHMe_2)_2]$ | **1b** | $[Ti\{=N(C_6H_{10}C=CH)\}Cl_2(NHMe_2)_2]$ | **1r** |
| $[Ti(=N–CPh_3)Cl_2(NHMe_2)_2]$ | **1c** | $[Ti\{=N–[(S)\text{-}(–)\text{-}CHMePh]\}Cl_2(NHMe_2)_2]$ | **1s*** |
| $[Ti(=N–SiPh_3)Cl_2(NHMe_2)_2]$ | **1d** | $[Ti\{=N–[(–)\text{-}cis\text{-}myrtanyl]\}Cl_2(NHMe_2)_2]$ | **1t*** |
| $[Ti(=N–Ph)Cl_2(NHMe_2)_2]$ | **1e** | $[Ti(=N–SiPh_3)Cl_2(Py)_3]$ | **2d** |
| $[Ti(=N–2,6\text{-}iPr_2–C_6H_3)Cl_2(NHMe_2)_2]$ | **1f** | $[Ti(=N–4\text{-}NC–C_6H_4)Cl_2(Py)_3]$ | **2l** |
| $[Ti(=N–2,6\text{-}Cl_2–C_6H_3)Cl_2(NHMe_2)_2]$ | **1g** | $[Ti[=N(C_6H_{10}C=CH)]Cl_2(Py)_3]$ | **2r** |
| $[Ti(=N–2,6\text{-}Br_2–4\text{-}Me–C_6H_2)Cl_2(NHMe_2)_2]$ | **1h** | $[Ti\{=N–[(S)\text{-}(–)\text{-}CHMePh]\}Cl_2(Py)_3]$ | **2s*** |
| $[Ti(=N–C_6F_5)Cl_2(NHMe_2)_2]$ | **1i** | $[Ti\{=N–[(–)\text{-}cis\text{-}myrtanyl]\}Cl_2(Py)_3]$ | **2t*** |
| $[Ti(=N–3,5\text{-}(F_3C)_2–C_6H_3)Cl_2(NHMe_2)_2]$ | **1j** | $[Ti(N–2\text{-}EtO–C_6H_4)Cl_2(NHMe_2)_1]_2]$ | **3** |
| $[Ti(=N–4\text{-}Et_2N–C_6H_4)Cl_2(NHMe_2)_2]$ | **1k** | $[Ti[N–CH_2(CHO(CH_2)_3)]Cl_2(NHMe_2)_1]_2$ | **4** |
| $[Ti(=N–4\text{-}NC–C_6H_4)Cl_2(NHMe_2)_2]$ | **1l** | $[Ti[N–CH_2(CHO(CH_2)_3)]Cl_2(Py)_1]_2$ | **5** |
| $[Ti(=N–2\text{-}NC–C_6H_4)Cl_2(NHMe_2)_2]$ | **1m** | $[Ti\{=N–[(S)\text{-}(–)\text{-}CHMePh]\}Cl_2(NHMe_2)_1]_2$ | **6*** |
| $[Ti(=N–4\text{-}H_2C=CH–C_6H_4)Cl_2(NHMe_2)_2]$ | **1n** | $[(Me_2HN)_2Cl_2Ti(=N–Me_2C_6H_2–C_6H_2Me_2–N=)TiCl_2(NHMe_2)_2]$ | **7** |
| $[Ti(=N–2\text{-}MeC=CH_2–C_6H_4)Cl_2(NHMe_2)_2]$ | **1o** | $[(Py)_3Cl_2Ti(=N–Me_2C_6H_2–C_6H_2Me_2–N=)TiCl_2(Py)_3]$ | **8** |
| $[Ti(=N–3\text{-}HC=C–C_6H_4)Cl_2(NHMe_2)_2]$ | **1p** | $[Ti(N–2,6\text{-}iPr_2–C_6H_3)I_2(thf)_2]_2$ | **9** |

Scheme 1. Designation of imido–titanium complexes described in this study.

 © 2006 Wiley-VCH Verlag GmbH & Co. KGaA, Weinheim 

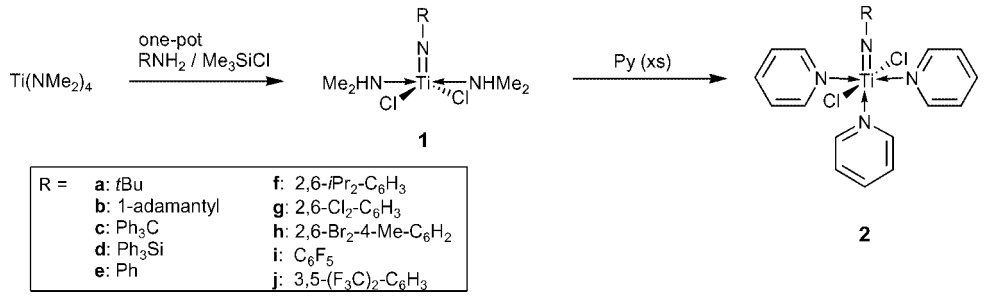


| R = | | |
|---|---|---|
| | **a**: *t*Bu | **f**: 2,6-*i*Pr$_2$-C$_6$H$_3$ |
| | **b**: 1-adamantyl | **g**: 2,6-Cl$_2$-C$_6$H$_3$ |
| | **c**: Ph$_3$C | **h**: 2,6-Br$_2$-4-Me-C$_6$H$_2$ |
| | **d**: Ph$_3$Si | **i**: C$_6$F$_5$ |
| | **e**: Ph | **j**: 3,5-(F$_3$C)$_2$-C$_6$H$_3$ |

Scheme 2. General synthesis of imido–titanium(IV) complexes **1** and **2**.

When a toluene solution of $Ti(NMe_2)_4$ is reacted with one equiv. of $RNH_2$ [with R = *t*Bu, 1-adamantyl, $Ph_3C$, $Ph_3Si$, Ph, 2,6-*i*Pr$_2$–C$_6$H$_3$, 2,6-Cl$_2$–C$_6$H$_3$, 2,6-Br$_2$–4-Me–C$_6$H$_2$, C$_6$F$_5$, and 3,5-(F$_3$C)$_2$–C$_6$H$_3$] and an excess of chlorotrimethylsilane[28] (typically about 8 equiv.) at room temp. overnight, yellow–orange compounds $[Ti(=NR)Cl_2(NHMe_2)_2]$ [R = *t*Bu (**1a**), 1-adamantyl (**1b**), $Ph_3C$ (**1c**), $Ph_3Si$ (**1d**), Ph (**1e**), 2,6-*i*Pr$_2$–C$_6$H$_3$ (**1f**), 2,6-Cl$_2$–C$_6$H$_3$ (**1g**), 2,6-Br$_2$–4-Me–C$_6$H$_2$ (**1h**), C$_6$F$_5$ (**1i**), and 3,5-(F$_3$C)$_2$–C$_6$H$_3$ (**1j**)] are formed exclusively (Scheme 2). These complexes often separated by crystallization (while the reaction proceeds or upon the addition of pentane) as large, generally yellow–orange (for alkyl–imido) or red (for aryl–imido) needles or crystals with good yields (73–96%).

The detailed experimental protocols and full characterization are given in the Experimental Section. Compounds **1a**–**j** have been characterized by infrared spectroscopy (with strong $\nu_{NH}$ absorptions around 3250 cm$^{-1}$), multinuclear NMR spectroscopy, elemental analysis, and by X-ray structure determination for some (vide infra). The products are consistent with the proposed structure of a monomeric five-coordinate compound with 2 dimethylamine ligands that occupy the axes of the bipyramid. This one-pot synthesis cleanly affords a wide range of alkyl–, silyl–, and aryl–imido complexes $Ti(=NR)Cl_2(NHMe_2)_2$. It is important to note that titanium silyl–imido complexes remain comparatively rarer than their alkyl- or aryl analogues.[10b,12d,25,29]

When dissolved in pyridine, bis-dimethylamine adducts **1** are instantly and generally quantitatively converted into tris-pyridine complexes $[Ti(=NR)Cl_2(Py)_3]$ (**2**). In a few cases, it has been reported that the substitution of $NHMe_2$ ligands by pyridine is difficult or produces mixed $NHMe_2$–pyridine adducts.[21,26] Within this study, we have only experienced difficulties (vide infra) in the synthesis of one compound (namely **5** from **4**). We will not insist on this substitution reaction that has already been described by us on vanadium analogues,[21] and by Mountford on titanium complexes,[26] but these tris-pyridine complexes are generally obtained as large crystals with good X-ray quality that facilitates their structural characterization, vide infra (although they are sometimes poorly soluble in common organic solvents). In consequence, in this article we will refer to this substitution reaction only when a related tris-pyridine–imido compound was structurally characterized.

Single crystals of **2d** were grown from a $CH_2Cl_2$/pyridine solution of **2d** layered with pentane at room temp. and were analyzed by X-ray crystallography. A thermal ellipsoid plot is presented in Figure 1 along with selected bond lengths and angles in Table 1.

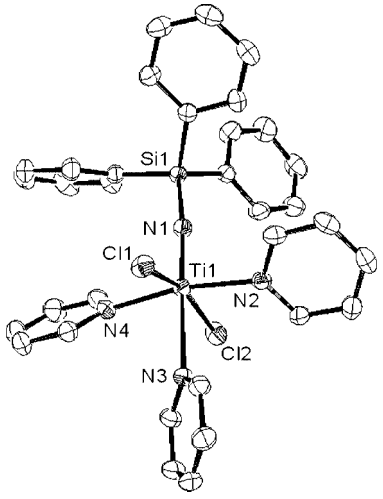


Figure 1. Molecular structure of **2d** with selected bond lengths [Å] and angles [°], which shows 50% probability ellipsoids and partial atom-labeling schemes. Hydrogen atoms are omitted for clarity.

Compound **2d** adopts a pseudooctahedral geometry around the metal center with mutually *trans* chloride and pyridine ligands. The third pyridine ligand is disposed *trans* to the imido group. Bond lengths and angles are unexceptional and were found to be very similar to those observed in titanium[23,25] and vanadium[21] analogues; the titanium–nitrogen bond lengths of the imido fragment is 1.7110(13) Å, with an almost linear Ti–N$_{imido}$–Si angle [171.12(9)°], and an average Ti–Cl ca. 2.39 Å. The *trans* Ti–N(Py) of 2.4742(14) Å is significantly longer than the average *cis* Ti–N(Py) bond lengths [2.224(2) Å], which reflects the *trans*-labilizing ability of the imido ligand.

### 2. Tolerance to Functional Groups on the Imido Moiety in $[Ti(=NR)Cl_2(NHMe_2)_2]$ and $[Ti(=NR)Cl_2Py_3]$ Complexes

Functionalized organoimido complexes of titanium, that is complexes that contain additional functional groups on the imido moiety, are extremely rare.[23,30] Since we have easy

 © 2006 Wiley-VCH Verlag GmbH & Co. KGaA, Weinheim 

Table 1. Comparison of the average interatomic distances [Å] and angles [°] in $Ti(=NR)Cl_2(NHMe_2)_2$ and $Ti(=NR)Cl_2(Py)_3$ complexes.

| | **1k** | **1o** | **1p** | **1s*** | **2d** | **2l** | **2r** |
|---|---|---|---|---|---|---|---|
| $Ti–N_{imido}$ | 1.6955(18) | 1.7028(11) | 1.700(2) | 1.682(4) | 1.7110(13) | 1.726(2) | 1.6988(12) |
| $N_{imido}–C_{ipso}$/Si | 1.390(2) | 1.3889(16) | 1.384(4) | 1.455(6) | 1.7098(14)[a] | 1.357(3) | 1.4448(18) |
| Ti–Cl | 2.3567(9) | 2.3393(4) | 2.3261(9) | 2.3602(15) | 2.3752(5) | 2.3756(4) | 2.4353(5) |
| | 2.3553(11) | 2.3509(4) | 2.3301(9) | 2.3393(17) | 2.4037(5) | | 2.3999(5) |
| $Ti–N_{NHMe_2}$ | 2.2185(18) | 2.2005(11) | 2.207(3) | 2.196(5) | – | – | – |
| | 2.2186(17) | 2.2119(11) | 2.210(2) | 2.214(5) | | | |
| $Ti–N_{Py}$(*trans*) | – | – | – | – | 2.4742(14) | 2.425(2) | 2.4000(12) |
| $Ti–N_{Py}$(*cis*) | – | – | – | – | 2.2140(14) | 2.2201(13) | 2.2433(12) |
| | | | | | 2.2339(14) | | 2.2314(13) |
| $H_{NHMe_2}\cdots Cl$ | 2.516 | 2.391 | 2.708 | 2.563 | – | – | – |
| | 2.530 | | | | | | |
| $Ti–N_{imido}–C_{ipso}$/Si | 178.21(15) | 178.86(10) | 169.4(2) | 168.8(4) | 171.12(9) [b] | 180.0 | 174.31(10) |
| Cl–Ti–Cl | 132.86(3) | 131.357(16) | 134.01(4) | 140.12(6) | 162.03(2) | 164.59(3) | 163.780(18) |
| $N_{NHMe_2}–Ti–N_{NHMe_2}$ | 167.27(6) | 169.29(4) | 168.35(10) | 160.43(16) | – | – | – |
| $N_{N_{imido}}–Ti–N_{NHMe_2}$ | 96.39(8) | 95.36(5) | 93.64(11) | 100.88(18) | – | – | – |
| | 96.33(8) | 95.31(5) | 97.85(11) | 98.65(19) | | | |
| $N_{Py}$(*cis*)–Ti–$N_{Py}$(*cis*) | – | – | – | – | 169.87(5) | 169.32(7) | 168.24(4) |
| $N_{imido}–Ti–Cl$ | 113.97(7) | 115.08(4) | 115.41(10) | 112.79(15) | 91.44(4) | 97.705(15) | 98.77(4) |
| | 113.17(6) | 113.54(4) | 110.45(10) | 107.04(15) | 99.15(5) | | 97.37(4) |
| $N_{imido}–Ti–N_{Py}$(*trans*) | – | – | – | – | 178.09(6) | 169.32(7) | 179.23(5) |
| N–H···Cl | 153.63 | 164.94 | 153.17 | 147.90 | – | – | – |
| | 151.20 | | | | | | |
| functional group | $N_{Et}–C_{Ar}$ | C=C 1.338(2) | C≡C 1.183(5) | – | – | N≡C 1.144(4) | C≡C 1.187(2) |
| | 1.386(3) | | | | | | |
| | | | C–C≡C | | | N≡C–C | C–C≡C |
| | | | 175.5(4) | | | 180.0 | 178.93(18) |

[a] $N_{imido}$–Si bond length. [b] Ti–$N_{imido}$–Si angle.

access to various Ti–imido complexes from readily available amines, it was of interest to probe the tolerance of our synthetic procedure towards the presence of functional groups on the alkyl/arylamine backbone, and also to learn the stability of the resulting functionalized imido compounds. The added functionality of the organoimido compounds may serve as an anchor to graft the complexes to a support, and their reactivity could be studied as well. We have already shown in the previous section that halides and $CF_3$-substituted anilines can be employed, and we have screened several other anilines and amines that contain ether, dialkylamine, cyano, alkyne, olefin, or nitro groups under the same conditions used above [$Ti(NMe_2)_4$, $RNH_2$, $Me_3SiCl$, toluene, room temp.]. These amines are depicted in Figure 2.

The general one-pot procedure proceeded as anticipated with anilines substituted with *p*-$NEt_2$, *p*-CN, *o*-CN, *p*-$HC=CH_2$, *o*-$MeC=CH_2$, *m*-C≡CH, and *m*-$NO_2$ groups with the formation of the expected corresponding bis-dimethylamine adducts $[Ti(=NAr)Cl_2(NHMe_2)_2]$ (**1k**–**q**) [with Ar = *p*-$Et_2N–C_6H_4$ (**1k**), *p*-$NC–C_6H_4$ (**1l**), *o*-$NC–C_6H_4$ (**1m**), *p*-$H_2C=CH–C_6H_4$ (**1n**), *o*-$MeC=CH_2–C_6H_4$ (**1o**), *m*-$HC≡C–C_6H_4$ (**1p**), and *m*-$O_2N$–*o*-$Me–C_6H_3$ (**1q**)]. Not surprisingly, some of these compounds have been easily converted into their tris-pyridine adducts $[Ti(=NAr)Cl_2(Py)_3]$ (**2**) by the addition of an excess of pyridine to the corresponding dimethylamine precursor. Only [Ti(=N–*p*-$NC–C_6H_4$)$Cl_2(Py)_3$] (**2l**) will be described later on as its molecular structure has been established (vide infra). These functional organoimido species have been characterized by means of spectroscopic methods (NMR, IR), and combustion analysis. The solution $^1H$- and $^{13}C$ NMR spectroscopic data present features similar to those of their nonfunctional analogues – a single set of resonances for the coordinated $NHMe_2$ ligands (in **1**) or two different pyridine ligands in the ratio 2:1 (in **2**), and resonances attributable to the or-

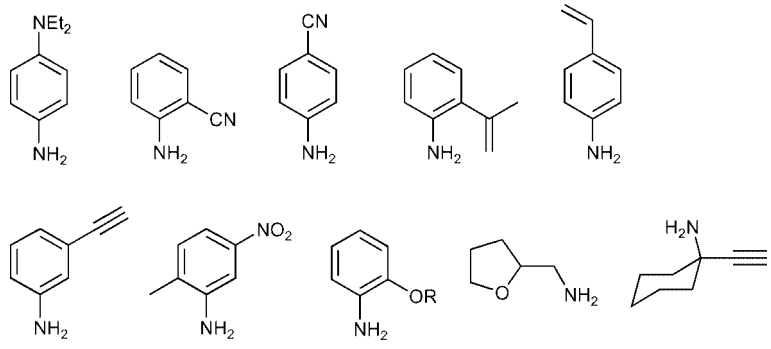


Figure 2. Functional amines used in this study.

 © 2006 Wiley-VCH Verlag GmbH & Co. KGaA, Weinheim 

ganoimido group. These data are consistent with the functional group that does not interact with the metal center. Indeed, according to the IR data, some of these functional groups are clearly observed in their normal regions ($\nu_{C\equiv N}$ 2243, 2242, and 2221 $cm^{-1}$, respectively, for **1l**, **1m**, and **2l**; $\nu_{C=C}$ 1624 and 1629 $cm^{-1}$, respectively, for **1n** and **2o**; $\nu_{C\equiv C}$ 2208 $cm^{-1}$ for **1p**; $\nu_{NO_2}$ 1517 $cm^{-1}$ for **1q**).

When reacted with $Ti(NMe_2)_4$ in the presence of chlorotrimethylsilane, 1-ethynylcyclohexylamine gave the imido complex $Ti[=N(C_6H_{10}C\equiv CH)]Cl_2(NHMe_2)_2$ (**1r**). Again, spectroscopic ($^1H$- and $^{13}C$ NMR) data suggest that the carbon–carbon triple bond does not coordinate to the titanium center. The corresponding pyridine analogue $[Ti[=N(C_6H_{10}C\equiv CH)]Cl_2(Py)_3]$ (**2r**), formed upon the addition of excess pyridine to **1r**, has been characterized by X-ray structure determination (vide infra) that clearly shows the free C≡C–H fragment.

Single-crystals suitable for X-ray diffraction studies were obtained for these functionalized organoimido compounds from room temp. toluene (**1k**, **1o**), cold toluene/pentane (**1p**), or pyridine-toluene/pentane (**2l**, **2r**) solutions. Thermal ellipsoid plots are presented in Figures 3, 4, 5, 6, 7; selected metric parameters are given in Table 1.

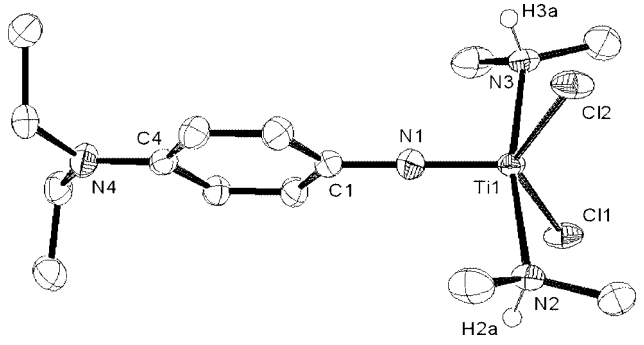


Figure 3. Molecular structure of **1k** with selected bond lengths [Å] and angles [°], which shows 50% probability ellipsoids and partial atom-labeling schemes. Hydrogen atoms are omitted for clarity.

In the solid state, the molecular structure of the three $NHMe_2$ adducts (**1k**, **1o**, **1p**) is best described as distorted trigonal bipyramid with axial dimethylamine ligands [$\tau$ = 0.58 (**1k**), 0.63 (**1o**), and 0.57 (**1p**)],[31] with $N_{imido}$–Ti–Cl angles in the range 110–115°, and $N_{imido}$–Ti–$N_{NHMe_2}$ angles in the range 93–98°. The distances and angles associated with the titanium center and the ligands are comparable to those found in other $[M(=NR)Cl_2(NHMe_2)_2]$ complexes (M = Ti,[26] V[21]). Adducts **1k**, **1o**, and **1p** exhibit a short Ti–$N_{imido}$ distance of 1.6955(18) Å for **1k**, 1.7028(11) Å for **1o**, and 1.700(2) Å for **1p**. The imido linkage is almost linear [Ti–$N_{imido}$–$C_{ipso}$ angle = 178.21(15), 178.86(10), and 169.4(2)°, respectively, in **1k**, **1o**, and **1p**], and is consistent with the donation of the lone pair on nitrogen to an acceptor orbital on titanium (the imido Ti–N bond can be considered as a triple bond). The crystal structure determinations also unambiguously show noninteracting functional -$NEt_2$ (**1k**), -C(Me)=$CH_2$ (**1o**), and –C≡CH (**1p**) groups, with normal metric parameters that are listed in Table 1. Both of the chlorine atoms occupy equatorial sites

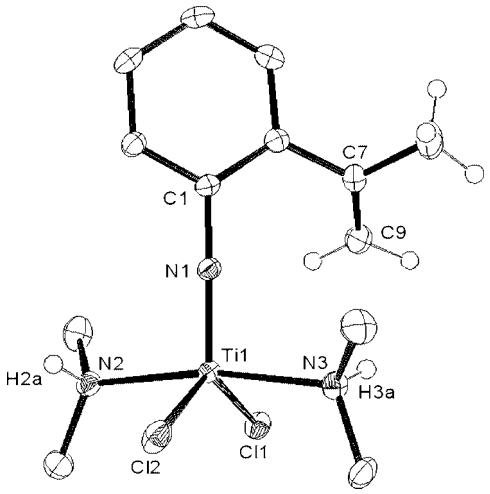


Figure 4. Molecular structure of **1o** with selected bond lengths [Å] and angles [°], which shows 50% probability ellipsoids and partial atom-labeling schemes. Hydrogen atoms are omitted for clarity.

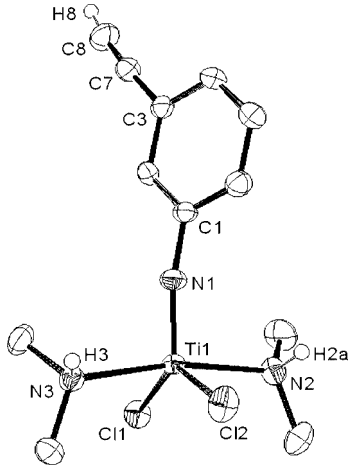


Figure 5. Molecular structure of **1p** with selected bond lengths [Å] and angles [°], which shows 50% probability ellipsoids and partial atom-labeling schemes. Hydrogen atoms are omitted for clarity.

in the trigonal bipyridine with a Cl1–Ti–Cl2 angle of 132.86(3)°, 131.357(16)°, and 134.01(4) Å for **1k**, **1o**, and **1p**, respectively, and mean Ti–Cl bond lengths of 2.36 Å, 2.34 Å, and 2.33 Å for **1k**, **1o**, and **1p**, respectively. The two *trans* dimethylamino ligands form the axis of the bipyramid, and have mean Ti–$N_{NHMe_2}$ bonds of ca. 2.21 Å for the three compounds. The supramolecular structure is dominated by $Me_2N$–H···Cl hydrogen bonding (NH···Cl bond lengths are in the range 2.391 to 2.708 Å; associated N–H···Cl angles are 164.94 to 147.64°); features that they share with Mountford's related compounds.[26]

An ORTEP drawing of the molecular structure of **2l** and **2r** is shown in Figures 6 and 7, respectively. Crystals of **2r** contain one residual molecule of pyridine (not shown in Figure 6). In **2l**, the Ti–$N_{imido}$ and C≡N vectors lie on a crystallographic two-fold rotation axis. The pendant functional cyano (**2l**) and ethynyl (**2r**) group on the imido moieties do not bind to the titanium center. Compounds **2l** and **2r** adopt a pseudooctahedral geometry around the titanium

 © 2006 Wiley-VCH Verlag GmbH & Co. KGaA, Weinheim 

center similar to the one described above for **2d** (with mutually *trans* chloride and pyridine ligands, the third pyridine ligand is disposed *trans* to the imido group). Bond lengths and angles are normal, and found to be very similar to those observed in titanium[23] and vanadium[21] analogues, as well as in previously described **2d** (Table 1). The titanium–nitrogen bond length of the imido fragments are 1.726(2) Å (**2l**) and 1.6988(12) Å (**2r**) with an angle Ti–$N_{imido}$–$C_{ipso}$ of 180.0° (**2l**) and 174.31(10)° (**2r**), and Ti–Cl bond length of 2.3756(4) Å (**2l**) and 2.4353(5) and 2.3999(5) Å (**2r**).

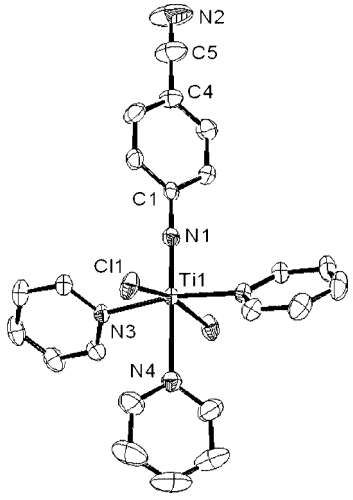


Figure 6. Molecular structure of **2l** with selected bond lengths [Å] and angles [°], which shows 50% probability ellipsoids and partial atom-labeling schemes. Hydrogen atoms are omitted for clarity.

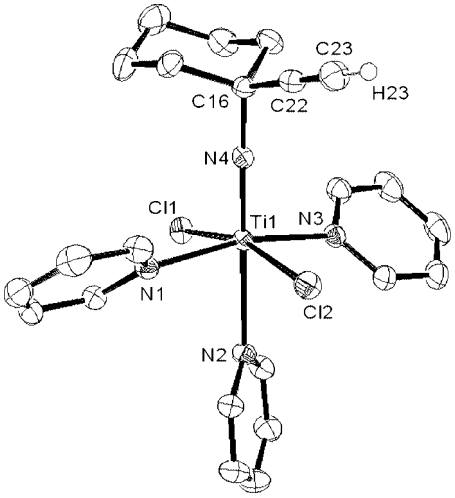


Figure 7. Molecular structure of **2r** with selected bond lengths [Å] and angles [°], which shows 50% probability ellipsoids and partial atom-labeling schemes. Hydrogen atoms and residual solvent (one molecule of pyridine) of crystallization are omitted for clarity.

Unlike the previous functional anilines, however, amines that contain an additional ether-function {i.e. 2-EtO–$C_6H_4NH_2$ and tetrahydrofurfurylamine [$H_2NCH_2$-$(CHO(CH_2)_3)$]} did not generate the bis-dimethylamine adduct, but rather reacted to afford the mono-dimethylamine adduct of the general formula [Ti($NR^o$)$Cl_2$($NHMe_2$)] [with $R^o$ = 2-EtO–$C_6H_4$ (**3**), and $CH_2(CHO(CH_2)_3)$ (**4**)] (Figure 8), as judged by spectroscopic ($NHMe_2$/$NR^o$, 1:1) and analytical data. The $^1$H- and $^{13}$C NMR spectra of **3** reveal diastereotopic methyl groups for the $NHMe_2$ ligand. Because of their poor solubility in common organic solvents, these compounds are probably imido-bridged dimers with the oxygen atom coordinated to the metal center.

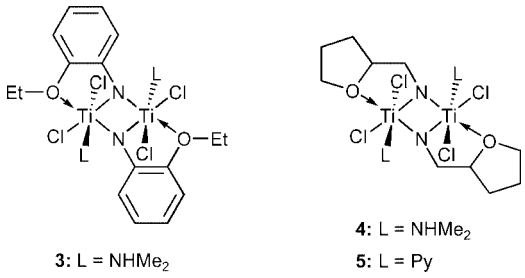


Figure 8. Proposed structure for complexes **3**–**5**.

Indeed, molecular structure determination (Figure 9) has unambiguously established that **3** is the centrosymmetric dimer [Ti[$\mu_2$-[N]-$\eta^1$[O]-N–2-EtO–$C_6H_4$]$Cl_2$($NHMe_2$)]$_2$, with two aryl–imido ligands that bridge two ($Me_2HN$)$Cl_2$Ti moieties. The O atom of the ether function is coordinated *cis* to the N atom of its own ligand set, *trans* to the N atom of the other imido group, and the chlorine atoms are mutually *cis* to one another. The coordination geometry of titanium is distorted octahedral. The $Ti_2N_2$ core is planar (torsion angle 0°) and is characterized by a short Ti···Ti distance common in imido dimers[32] [Ti1···Ti1′ = 2.889(3) Å] with two Ti–$N_{imido}$ bond lengths of 1.830(6) Å and 2.027(6) Å. The ($Me_2HN$)$Cl_2$Ti moiety is normal with the expected Ti–$N_{amine}$ and Ti–Cl bond lengths and angles [Ti–$N_{amine}$ 2.226(6) Å, Ti–Cl avg. 2.346 Å].

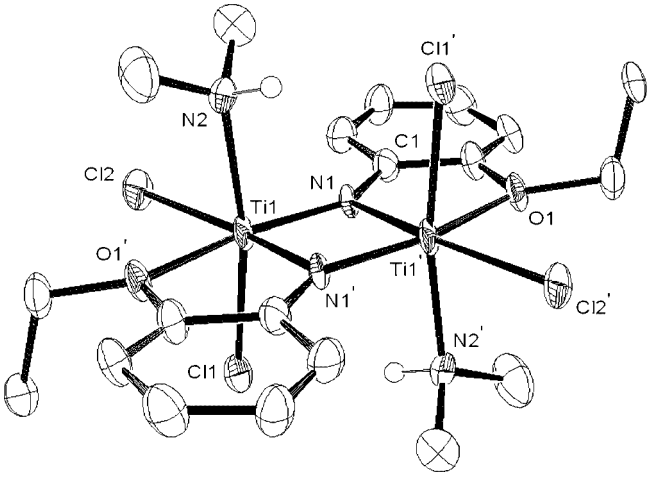


Figure 9. Molecular structure of **3** with selected bond lengths [Å] and angles [°], which shows 50% probability ellipsoids and partial atom-labeling schemes. Hydrogen atoms are omitted for clarity.

Addition of pyridine to **4** affords the pyridine complex [Ti($\mu$2-[N]-$\eta^1$[O]–$NR^o$)$Cl_2$(Py)]$_2$ (**5**) [$R^o$ = $CH_2(CHO(CH_2)_3)$] and its molecular structure has also been assessed on the basis of X-ray structure determination. The ORTEP

 © 2006 Wiley-VCH Verlag GmbH & Co. KGaA, Weinheim 

drawing is shown in Figure 10, and selected bond lengths and angles are given in Table 2. Like **3**, compound **5** is dimeric in the solid state, and the overall geometry, distances, and angles are broadly comparable to those of **3**. Complex **5** is an imido-bridged dimer with two edge-sharing octahedral metal coordination spheres. Each distorted octahedron is completed by two mutually *cis* chlorine atoms [Ti–Cl avg. 2.367(2) Å, Cl–Ti–Cl 90.69(4)°], one pyridine ligand [Ti–$N_{Py}$ 2.254(3) Å] and the O atom of the furan link [Ti–O 2.177(3) Å]. The $Ti_2N_2$ core is planar (torsion angle 0°) and is characterized by a short Ti···Ti distance [2.8502(13) Å]. The disymmetric imido bridges are characterized by two Ti–$N_{imido}$ bond lengths of 1.821(3) Å and 2.013(3) Å, that are longer by ca. 0.1/0.3 Å than those generally observed in terminal imido complexes. The angle formed by the bridging nitrogen atoms with the two metal centers [Ti–$N_{imido}$–Ti′ = 95.92(14)°] deviates significantly from that expected for an $sp^2$ nitrogen atom. The (Py)$Cl_2$Ti moiety is normal with the expected Ti–$N_{Py}$ and Ti–Cl bond lengths and angles [Ti–$N_{Py}$ 2.254(3) Å, Ti–Cl avg. 2.367(2) Å].

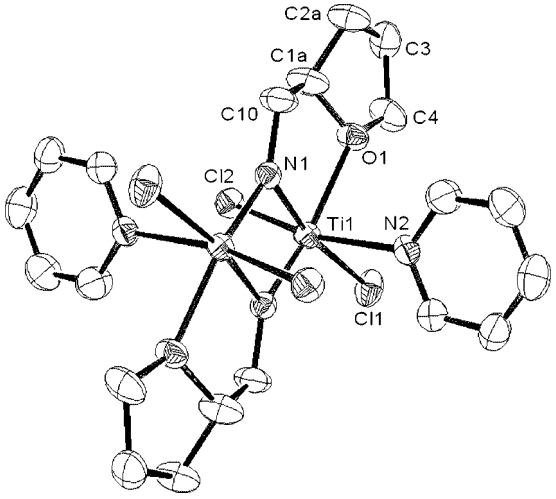


Figure 10. Molecular structure of **5** with selected bond lengths [Å] and angles [°], which shows 50% probability ellipsoids and partial atom-labeling schemes. Hydrogen atoms are omitted for clarity.

### 3. Application to the Synthesis of Diimido Complexes and Chiral Imido Complexes

In relation to the possible use of chiral imido complexes in catalysis for stereoselective olefin polymerization[33] and their involvement in alkyne/alkene hydroamination,[34] we have initiated the synthesis of chiral imido groups on titanium complexes from enantiomerically pure chiral amines.

Table 2. Comparison of the average interatomic distances [Å] and angles [°] in dimers **3**, **5**, **6***, and **8**.

| | **3** | **5** | **6*** | **8** |
|---|---|---|---|---|
| Ti–$N_{imido}$ | Ti1–N1 1.830(6)<br>Ti1–N1′ 2.027(6) | Ti1–N1 2.013(3)<br>Ti1–N1′ 1.821(3) | Ti1–N1 1.821(4)<br>Ti2–N1 1.965(4)<br>Ti1–N2 1.840(4)<br>Ti2–N2 1.971(4) | Ti1–N1 1.719(4)<br>Ti2–N5 1.710(4) |
| $N_{imido}$–$C_{ipso}$ | N1–C1 1.395(10) | N1–C10 1.452(5) | N1–C1 1.494(6)<br>N2–C9 1.487(6) | N1–C16 1.374(6)<br>N5–C27 1.378(6) |
| Ti–Cl | Ti1–Cl1 2.360(2)<br>Ti1–Cl2 2.333(2) | Ti1–Cl1 2.3592(12)<br>Ti1–Cl2 2.3755(11) | Ti1–Cl1 2.2542(17)<br>Ti1–Cl2 2.2482(16)<br>Ti2–Cl3 2.3500(16)<br>Ti2–Cl4 2.3588(16) | Ti1–Cl1 2.4075(16)<br>Ti1–Cl2 2.4059(18)<br>Ti2–Cl3 2.4185(17)<br>Ti2–Cl4 2.3893(16) |
| Ti–$N_{NHMe_2}$ or Ti–$N_{Py}$ | 2.226(6) | Ti1–N1 2.254(3) | Ti2–N3 2.215(4)<br>Ti2–N4 2.233(4) | Ti1–N2 2.249(5)<br>Ti1–N3 2.386(4)<br>Ti1–N4 2.235(5)<br>Ti2–N6 2.223(4)<br>Ti2–N7 2.406(4)<br>Ti2–N8 2.236(5) |
| Ti–O | Ti1–O1′ 2.240(5) | Ti1–O1 2.177(3) | – | – |
| $H_{NHMe_2}$···Cl | – | – | 2.638 | – |
| Ti···Ti | 2.889(3) | 2.8502(13) | 2.8239(14) | 13.33 |
| Ti–$N_{imido}$–$C_{ipso}$ | Ti1–N1–C1 143.9(5)<br>Ti1′–N1–C1 119.2(5) | Ti1–N1–C10 118.1(3)<br>Ti1′–N1–C10 145.6(3) | C1–N1–Ti1 130.2(3)<br>C1–N1–Ti2 133.0(3)<br>C9–N2–Ti1 132.4(3)<br>C9–N2–Ti2 132.0(3) | Ti1–N1–C16 174.6(4)<br>Ti2–N5–C27 178.1(4) |
| Cl–Ti–Cl | 90.34(9) | 90.69(4) | Cl1–Ti1–Cl2 114.10(7)<br>Cl3–Ti2–Cl4 95.91(6) | Cl1–Ti1–Cl2 163.93(7)<br>Cl3–Ti2–Cl4 166.35(6) |
| $N_{imido}$–Ti–Cl | N1–Ti–Cl1 98.3(2)<br>N1–Ti–Cl2 109.7(2) | N1–Ti–Cl1 169.36(11)<br>N1–Ti–Cl2 94.52(9) | | N1–Ti1–Cl1 98.51(15)<br>N1–Ti1–Cl2 97.32(15)<br>N5–Ti1–Cl3 95.76(16)<br>N5–Ti2–Cl4 97.89(16) |
| misc. | N1–Ti1–O1′ 157.7(2)<br>N1–Ti1′–O1 74.8(2)<br>Ti1–N1–Ti1′ 96.9(3)<br>N1–Ti1–N1′ 83.1(3) | N1–Ti1–O1 76.25(12)<br>N1′–Ti1–O1 159.71(12)<br>Ti1–N1–Ti1′ 95.92(14)<br>N1–Ti1–N1′ 84.08(14) | N–H···Cl 147.64<br>N3–Ti2–N4 163.95(16)<br>Ti1–N1–Ti2 96.41(19)<br>Ti1–N2–Ti2 95.57(19)<br>N1–Ti1–N2 87.56(18)<br>N1–Ti2–N2 80.10(17) | N1–Ti1–N3 177.00(19)<br>N5–Ti2–N7 178.20(18)<br>N2–Ti1–N4 166.03(17)<br>N6–Ti2–N8 165.37(16) |

 © 2006 Wiley-VCH Verlag GmbH & Co. KGaA, Weinheim 

Following our one-pot procedure, the chiral amine (*S*)-(–)-α-methylbenzylamine was treated with $Ti(NMe_2)_4$ in the presence of excess $Me_3SiCl$, and the resulting yellow complex $[Ti\{=N\text{-}[(S)\text{-}(-)\text{-}CHMePh]\}Cl_2(NHMe_2)_2]$ (**1s***) was obtained in good yields (74%) (Figure 11). By the treatment with pyridine, **1s*** was transformed into the tris-pyridine adduct $[Ti\{=N\text{-}[(S)\text{-}(-)\text{-}CHMePh]\}Cl_2(Py)_3]$ (**2s***). These complexes represent the first examples of a chiral imido group on titanium complexes.[35]

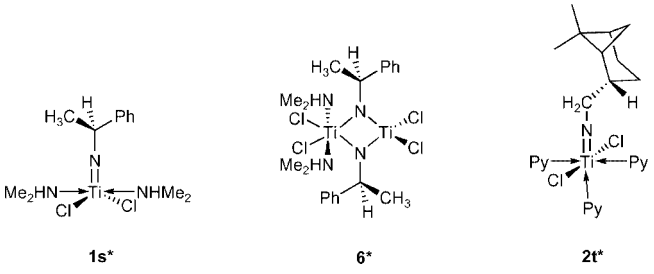


Figure 11. Chiral imido–titanium(IV) complexes.

Single-crystals of **1s*** (yellow blocks) were obtained from a toluene/pentane solution at room temp., and the crystal structure was determined. Complex **1s*** crystallized in the monoclinic space group $P2_1$.[36] A thermal ellipsoid plot is presented in Figure 12 along with selected bond lengths and angles in Table 1. In the solid state, the molecular structure of **1s*** resembles that of other five-coordinate $M(=NR)\text{-}Cl_2(NHMe_2)_2$ complexes described in this article and by others (M = Ti,[26] V[21]), and the metric parameters are comparable [avg. $N_{imido}$–Ti–Cl 109.9°, avg. $N_{imido}$–Ti–$N_{NHMe_2}$ 99.8, Ti–$N_{imido}$ distance of 1.682(4) Å, Ti–$N_{imido}$–C1 angle = 168.8(4)°, Cl–Ti–Cl angle of 140.12(6)°, mean Ti–Cl bond lengths of 2.350 Å, Ti–$N_{amine}$ bond lengths of avg. 2.205 Å]. In this case, the geometry around the metal center is closer to square planar ($\tau$ = 0.34).

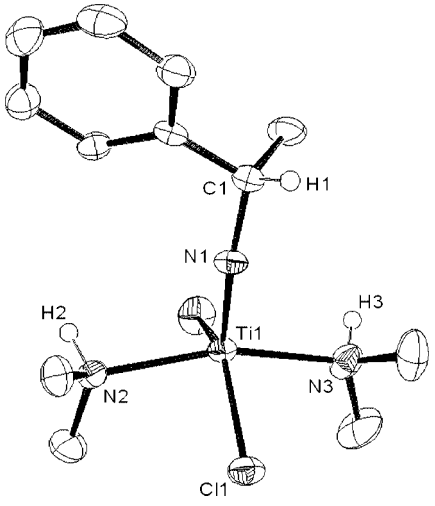


Figure 12. Molecular structure of **1s*** with selected bond lengths [Å] and angles [°], which shows 50% probability ellipsoids and partial atom-labeling schemes. Hydrogen atoms are omitted for clarity.

Note that when less than 1 equiv. of chiral benzylic amine is used, we have observed by $^1H$ NMR spectroscopy the concomitant formation of another imido species **6*** as a minor side product. The lower solubility of **6*** allowed us to selectively obtain a few crystals and to determine its solid-state structure. **6s*** crystallized in the tetragonal space group $P4_2$. The molecular structure is presented in Figure 13 and selected distances and angles are summarized in Table 2. Compound **6*** is an imido-bridged dimer formulated as $[Cl_2Ti\{\mu\text{-}N\text{-}[(S)\text{-}(-)\text{-}CHMePh]\}_2TiCl_2(NHMe_2)_2]$ that consists of one four- and one six-coordinate titanium center.[37] Molecules of **6*** possess approximately tetrahedral (Ti1) and octahedral (Ti2) metals linked by bridging aryl–imido ligands. The Ti–Cl [average Ti1–Cl 2.25 Å, average Ti2–Cl 2.35 Å] and Ti–$N_{imido}$ [Ti1–N1 1.821(4) Å, Ti1–N2 1.840(4) Å, Ti2–N1 1.965(4) Å, Ti2–N2 1.971(4) Å] distances for Ti2 are longer than those for Ti1 by ca. 0.1 Å (Ti–Cl) and ca. 0.13 Å (Ti–$N_{imido}$), which is consistent with the higher coordination number of Ti2. The torsion angle Ti1–N1–Ti2–N2 of the $Ti_2N_2$ core is 4.5(2)°.

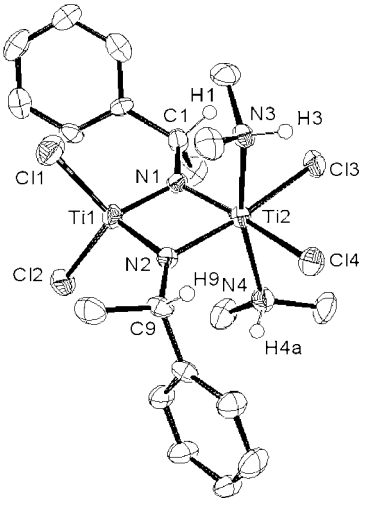


Figure 13. Molecular structure of **6*** with selected bond lengths [Å] and angles [°], which shows 50% probability ellipsoids and partial atom-labeling schemes. Hydrogen atoms are omitted for clarity.

Similarly, we have attempted the synthesis of the related imido complex $[Ti\{=N\text{-}[(-)\text{-}cis\text{-myrtanyl}]\}Cl_2(NHMe_2)_2]$ (**1t***) that has a *cis*-myrtanyl function (Figure 11). However, we have not been able to isolate **1t*** in a pure form – the resulting orange material probably contains a mixture of imido compounds with a lower number of dimethylamine coligands as judged by its poor solubility and by the low *N*-content determined by combustion analysis (unfortunately the $^1H$ NMR spectrum was extremely broad and a full assignment of the signals was not possible). Nevertheless, a subsequent addition of pyridine afforded the desired pyridine complex $[Ti\{=N\text{-}[(-)\text{-}cis\text{-myrtanyl}]\}Cl_2(Py)_3]$ (**2t***) as the unique product.[38]

Interestingly, as an extension, our procedure may be used to generate multimetallic architectures held together by imido functions.[39] For instance, diimido complexes have been obtained directly from diamines. The reaction of

 © 2006 Wiley-VCH Verlag GmbH & Co. KGaA, Weinheim 

3,3′,5,5′-tetramethyl[1,1′-biphenyl]-4,4′-diamine ($H_2N$–*BP*–$NH_2$) with 2 equiv. of $Ti(NMe_2)_4$ in the presence of an excess of $Me_3SiCl$ afforded the binuclear derivative $[(Me_2HN)_2Cl_2Ti(=N–BP–N=)TiCl_2(NHMe_2)_2]$ (**7**, Figure 14). Replacement of the dimethylamine ligands was prompted by the addition of pyridine to **7** and afforded the pyridine analogue $[(Py)_3Cl_2Ti(=N–BP–N=)TiCl_2(Py)_3]$ (**8**). An X-ray structure determination of a crystal of **8** (Figure 15 and Table 2) reveals a binuclear titanium complex with a bridging spacer composed of the diimido unit. The two titanium centers have an octahedral geometry with structure, bond lengths, and angles similar to the monometallic species. The titanium–nitrogen bond length of the imido fragments are 1.719(4) Å and 1.710(4) Å, the imido fragment were found to be almost linear [Ti–$N_{imido}$–$C_{ipso}$ 174.6(4)° and 178.1(4)°], and Ti–Cl bond lengths are in the range 2.39–2.42 Å. The dihedral angle between the planes of the two benzene rings of the biphenyl unit is 14.0(2)°.

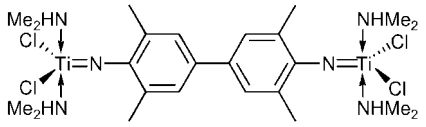


**7**

Figure 14. Diimido-titanium(IV) complex **7**.

### 4. Alternative Synthesis of Imido–Titanium Species

The reaction of $Ti(NMe_2)_4$ with 2,6-*i*$Pr_2$–$C_6H_3NH_2$ in THF with an excess of $CH_3I$ in place of chlorotrimethylsilane can be used to generate an aryl–imido complex. This reaction proceeds at room temperature (Scheme 3), with alkylation of the four dimethylamido groups.[40] After filtration of the insoluble $Me_4NI$ salt, the imido complex formulated as $[Ti(NAr)I_2(thf)_2]$ (**9**) (Ar = 2,6-*i*$Pr_2$–$C_6H_3$), as judged by $^1H$ NMR spectroscopy and combustion analysis, is obtained in 79% yield. This compound is most probably a dimer with bridging iodides as in the structurally established phenylimido analogue $[Ti(=NPh)Cl(\mu\text{-}Cl)(thf)_2]_2$.[4c] This new synthesis could be important as an alternative method for the preparation of imido complexes when N-donor coligands ($NHMe_2$) are not wanted. The scope of this synthesis will be developed elsewhere.

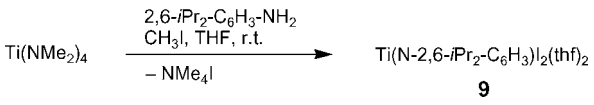


Scheme 3. Alternative synthesis of imido–titanium(IV) compounds.

## Conclusions

We have reported a direct and efficient method to generate titanium(IV) complexes of the type $Ti(=NR)Cl_2(NHMe_2)_2$ from commercially available $Ti(NMe_2)_4$ and a wide range of primary amines under simple and mild conditions. We have also demonstrated the functional group tolerance of this reaction, and it has been applied to the synthesis of titanium complexes that have an additional functionality on the imido moiety. The reactivity of these functionalized imido groups can now be ascertained and the added functionality may also serve as an anchor to graft this species onto a support. Also of great interest, we have been able to prepare complexes with diimido ligands, as well as the first Ti compounds that contain chiral imido supporting ligands. As an alternative method, we have reported some preliminary results on the synthesis of imido–titanium complexes of the type $[Ti(NAr)I_2(thf)_2]_2$ that use $CH_3I$ as a reagent.

## Experimental Section

**General Methods and Instrumentation:** All manipulations were carried out with a standard Schlenk line or dry box techniques under an atmosphere of argon. Solvents were refluxed and dried with the appropriate drying agents under an atmosphere of argon, and collected by distillation. NMR spectra were recorded with a Bruker AM200, AM250, ARX250, DPX300, or Avance500 spectrometers, referenced internally to residual protio-solvent ($^1H$) resonances, and are reported relative to tetramethylsilane ($\delta$ = 0 ppm). $^{19}F$ NMR spectra were recorded with a Bruker AM200 spectrometer (reference $CF_3CO_2H$). $^{29}Si$ NMR spectra were recorded with a Bruker Avance500 spectrometer. Infrared spectra were prepared under an argon atmosphere in a glove box and were recorded with

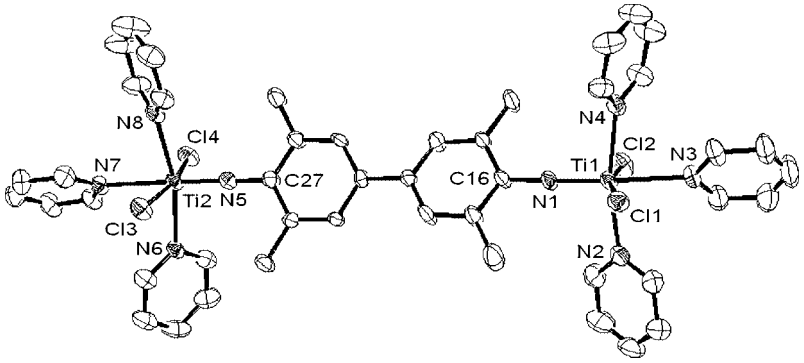


Figure 15. Molecular structure of **8** with selected bond lengths [Å] and angles [°], which shows 50% probability ellipsoids and partial atom-labeling schemes. Hydrogen atoms are omitted for clarity.

 © 2006 Wiley-VCH Verlag GmbH & Co. KGaA, Weinheim 

a Perkin–Elmer Spectrum GX FT-IR spectrometer. Elemental analyses were performed at the Laboratoire de Chimie de Coordination (Toulouse, France) (C, H, N) or by the Service Central de Microanalyses du CNRS at Vernaison (France) (C, H, N, Cl).

The $Ti(NMe_2)_4$ used in this study was prepared by a modification of a literature procedure,[41] or purchased from commercial sources (Aldrich, Acros). Liquid anilines and amines were dried with KOH or $CaH_2$, refluxed, distilled, and stored over 4 Å molecular sieves under an argon atmosphere before use. Trimethylchlorosilane was distilled and stored over 4 Å molecular sieves under an argon atmosphere before use. The optical purity of the enantiomerically pure chiral amines used in this study [(*S*)-(–)-α-methylbenzylamine and (–)-*cis*-myrtanylamine] was 98% (Aldrich).

**Crystal Structure Determination:** Crystals of **1k** (dark-green blocks), **1o** (orange plates), **1p** (orange plates), **1s*** (yellow blocks), **2d** (yellow blocks), **2l** (orange plates), **2r** (orange parallelepipeds), **3** (dark-red blocks), **5** (orange blocks), **6*** (green plates), and **8** (orange blocks) were obtained. Crystal data collection and processing parameters are given in Table 3 and Table 4. The selected crystals, sensitive to air and moisture, were mounted on a glass fiber with perfluoropolyether oil and cooled rapidly to 180 K in a stream of cold $N_2$. Data were collected at low temperature (T = 180 K) with a Stoe Imaging Plate Diffraction System (IPDS) equipped with an Oxford Cryosystems Cryostream Cooler Device or an Oxford Diffraction Kappa CCD Excalibur diffractometer equipped with an Oxford Instrument cryojet, with graphite-monochromated Mo-$K_\alpha$ radiation ($\lambda$ = 0.71073 Å). Final unit cell parameters were obtained by means of a least-squares refinement of a set of 8000 well-measured reflections, and crystal decay was monitored during data collection by the measurement of 200 reflections by image; no significant fluctuation of intensities has been observed. Structures have been solved by means of Direct Methods with the program SIR92,[42] and subsequent difference Fourier maps. Models were refined by least-squares procedures on a $F^2$ with SHELXL-97[43] integrated in the package WINGX version 1.64;[44] empirical absorption corrections were applied on the data.[45] All hydrogen atoms have been located on differences Fourier maps, and introduced into the refinement as fixed contributors with a riding model with an isotropic thermal parameter fixed at 20% higher than those of the $Csp^2$ atoms and 50% for the $Csp^3$ atoms to which they were connected. The methyl groups were refined with the torsion angle as a free variable. Some exceptions for a few specific hydrogen atoms were made, which have been isotropically refined (like nitrogen bound hydrogens). For the seven structures all non-hydrogen atoms were anisotropically refined, and in the last cycles of the refinement weighting schemes were used, where weights are calculated from the following formula: $w = 1/[\sigma^2(F_o^2) + (aP)^2 + bP]$ where $P = (F_o^2 + 2F_c^2)/3$. The poor quality of the structure determination of **3** is due to the small size of the crystal, and was not sufficient to give precise bond lengths and angles. For **8** it was not possible to resolve diffuse electron-density residuals (enclosed solvent molecules). Treatment with the SQUEEZE facility from PLATON,[46] with a localized void of about 1730 $Å^3$ and 75 recovered electrons, resulted in a smooth refinement. Since a few low-order reflections are missing from the data set, the electron count will be underestimated. Thus, the values given for $D_{calc}$, $F(000)$ and the molecular weight are only valid for the ordered part of the structure. For **1s***, the Flack parameter[47] was refined to a value of 0.11(7). Although, the standard deviation on this parameter is rather high, inversion of the configuration gave a value of 0.89, and so the absolute configuration could be determined and it agrees with the synthetic pathway [in addition, the Flack parameter for complex **6***, which is derived from **1s***, was refined to a satisfying value of 0.04(3)]. The deviation of the Flack parameter from 0 is probably due to the weak anomalous diffusion of Ti and Cl atoms. CCDC-608174 to -608184 contain the supplementary crystallographic data for this paper. These data can be obtained free of charge from The Cambridge Crystallographic Data Centre via www.ccdc.cam.ac.uk/data_request/cif.

Table 3. Crystallographic data, data collection and refinement parameters for compounds **1k**, **1p**, **1o**, **1s***, **2d**, and **2l**.

| | **1k** | **1o** | **1p** | **1s***[a] | **2d** | **2l** |
|---|---|---|---|---|---|---|
| Chemical formula | $C_{14}H_{28}Cl_2N_4Ti$ | $C_{13}H_{23}Cl_2N_3Ti$ | $C_{12}H_{19}Cl_2N_3Ti$ | $C_{12}H_{23}Cl_2N_3Ti$ | $C_{33}H_{30}Cl_2N_4SiTi$ | $C_{22}H_{19}Cl_2N_5Ti$ |
| Formula weight | 371.20 | 340.14 | 324.10 | 328.10 | 629.50 | 472.22 |
| Crystal system | triclinic | monoclinic | monoclinic | monoclinic | monoclinic | monoclinic |
| Space group | $P\bar{1}$ | $P2_1/c$ | $P2_1/a$ | $P2_1$ | $P2_1/c$ | $C2/c$ |
| *a* [Å] | 9.182(5) | 13.9252(7) | 8.9189(7) | 9.0267(9) | 10.8267(5) | 8.2536(6) |
| *b* [Å] | 9.694(5) | 10.2394(5) | 20.246(2) | 10.5665(18) | 11.2667(5) | 23.3710(11) |
| *c* [Å] | 12.436(5) | 12.1777(6) | 9.1104(8) | 9.0580(12) | 26.8863(14) | 12.5545(6) |
| *α* [°] | 107.181(5) | 90.0 | 90.0 | 90.0 | 90.0 | 90.0 |
| *β* [°] | 109.035(5) | 89.897(4) | 98.747(10) | 103.210(10) | 107.819(4) | 105.544(5) |
| *γ* [°] | 94.289(5) | 90.0 | 90.0 | 90.0 | 90.0 | 90.0 |
| *V*( [Å]$^3$) | 981.6(8) | 1736.36(15) | 1626.0(2) | 841.1(2) | 3122.3(3) | 2333.1(2) |
| Z | 2 | 4 | 4 | 2 | 4 | 4 |
| $D_{calc}$ (g cm$^{-3}$) | 1.256 | 1.301 | 1.324 | 1.296 | 1.339 | 1.344 |
| $\mu$ (Mo-$K_\alpha$) [mm$^{-1}$] | 0.708 | 0.792 | 0.842 | 0.815 | 0.513 | 0.614 |
| *F*(000) | 392 | 712 | 672 | 344 | 1304 | 968 |
| $\theta$ range [°] | 3.51–32.06 | 3.54–32.15 | 2.48–25.68 | 2.87–32.04 | 2.96–32.26 | 3.49–25.68 |
| Measured reflections | 10407 | 17009 | 12282 | 8603 | 26117 | 7813 |
| Unique reflections/Rint | 6192/0.0223 | 5707/0.0277 | 3070/0.0549 | 3962/0.0746 | 10210/0.0209 | 2215/0.0242 |
| Parameters/restraints | 196/0 | 183/3 | 166/1 | 169/1 | 370/0 | 140/0 |
| Final *R* indices [$I>\sigma 2(I)$] | $R_1$ = 0.0424 | $R_1$ = 0.0338 | $R_1$ = 0.0509 | $R_1$ = 0.0552 | $R_1$ = 0.0452 | $R_1$ = 00.0304 |
| | $wR_2$ = 0.1131 | $wR_2$ = 0.0819 | $wR_2$ = 0.1082 | $wR_2$ = 0.1067 | $wR_2$ = 0.1080 | $wR_2$ = 0.0703 |
| Final *R* indices all data | $R_1$ = 0.0516 | $R_1$ = 0.0497 | $R_1$ = 0.0583 | $R_1$ = 0.1065 | $R_1$ = 0.0578 | $R_1$ = 0.0346 |
| | $wR_2$ = 0.1170 | $wR_2$ = 0.0873 | $wR_2$ = 0.1106 | $wR_2$ = 0.1383 | $wR_2$ = 0.01157 | $wR_2$ = 0.0731 |
| Goodness of fit | 1.077 | 1.067 | 1.167 | 0.841 | 1.070 | 1.051 |
| $\Delta\rho$max and $\Delta\rho$min | 0.905 and –0.514 | 0.531 and –0.311 | 0.349 and –0.305 | 0.360 and –0.407 | 0.462 and –0.529 | 0.264 and –0.210 |

[a] Absolute structure parameter: 0.11(7).

 © 2006 Wiley-VCH Verlag GmbH & Co. KGaA, Weinheim 

Table 4. Crystallographic data, data collection and refinement parameters for compounds **2r**, **3**, **5**, **6***, and **8**.

| | **2r** | **3** | **5** | **6***[a] | **8** |
|---|---|---|---|---|---|
| Chemical formula | $C_{23}H_{26}Cl_2N_4Ti$, $C_5H_5N$ | $C_{20}H_{32}Cl_4N_4O_2Ti_2$ | $C_{20}H_{28}Cl_4N_4O_2Ti_2$ | $C_{20}H_{32}Cl_4N_4Ti_2$ | $C_{46}H_{46}Cl_4N_8Ti_2$ |
| Formula weight | 556.38 | 598.04 | 594.06 | 566.10 | 948.51 |
| Crystal system | monoclinic | monoclinic | monoclinic | tetragonal | monoclinic |
| Space group | $P\bar{1}$ | $P2_1/n$ | $P2_1/n$ | $P4_2$ | $P2_1/n$ |
| $a$ [Å] | 9.1233(9) | 9.868(2) | 10.1969(15) | 13.043(2) | 15.7668(12) |
| $b$ [Å] | 10.3422(11) | 7.9255(16) | 11.9115(13) | 13.043(2) | 17.2900(12) |
| $c$ [Å] | 15.5338(13) | 16.575(3) | 11.0227(15) | 15.073(3) | 21.7813(19) |
| $\alpha$ [°] | 76.531(8) | 90.0 | 90.0 | 90.0 | 90.0 |
| $\beta$ [°] | 80.338(8) | 90.77(3) | 112.931(15) | 90.0 | 96.202(7) |
| $\gamma$ [°] | 87.611(9) | 90.0 | 90.0 | 90.0 | 90.0 |
| $V$( [Å]$^3$) | 1405.2(2) | 1296.2(4) | 1233.0(3) | 2564.2(8) | 5903.0(8) |
| Z | 2 | 2 | 2 | 4 | 4 |
| $D_{calc}$ (g cm$^{-3}$) | 1.315 | 1.532 | 1.600 | 1.466 | 1.067 |
| $\mu$ (Mo-$K_\alpha$) [mm$^{-1}$] | 0.520 | 1.053 | 1.107 | 1.055 | 0.484 |
| $F$(000) | 580 | 616 | 608 | 1168 | 1960 |
| $\theta$ range [°] | 2.73–32.05 | 3.30–23.25 | 2.64–25.68 | 3.12–24.69 | 3.02–26.37 |
| Measured reflections | 14916 | 7332 | 9348 | 17232 | 41980 |
| Unique reflections/Rint | 8919/0.0312 | 1854/0.1297 | 2332/0.1180 | 4373/0.1019 | 12047/0.1418 |
| Parameters/restraints | 325/0 | 148/0 | 145/0 | 277/1 | 545/0 |
| Final $R$ indices [I>σ2(I)] | $R_1$ = 0.0372 $wR_2$ = 0.0923 | $R_1$ = 0.0996 $wR_2$ = 0.2462 | $R_1$ = 0.0432 $wR_2$ = 0.0951 | $R_1$ = 0.0431 $wR_2$ = 0.0549 | $R_1$ = 0.0950 $wR_2$ = 0.2361 |
| Final $R$ indices all data | $R_1$ = 0.0544 $wR_2$ = 0.1045 | $R_1$ = 0.1203 $wR_2$ = 0.2684 | $R_1$ = 0.0853 $wR_2$ = 0.1051 | $R_1$ = 0.0765 $wR_2$ = 0.0622 | $R_1$ = 0.1510 $wR_2$ = 0.2649 |
| Goodness of fit | 0.958 | 1.058 | 0.851 | 0.784 | 0.993 |
| $\Delta\rho$max and $\Delta\rho$min | 0.488 and –0.586 | 1.322 and –1.089 | 0.308 and –0.321 | 0.274 and –0.254 | 0.634 and –0.792 |

[a] Absolute structure parameter 0.04(3).

**[Ti(=NR)Cl$_2$(NHMe$_2$)$_2$] (1a–t). General Synthetic Procedure:** To a toluene solution (5 mL) of Ti(NMe$_2$)$_4$ (250 mg, 1.115 mmol), amine RNH$_2$ (1 equiv. 1.115 mmol) was added at room temperature. To this solution Me$_3$SiCl (1.00 g) was slowly added at room temperature. The resulting solution was stirred overnight at room temp. (or at 60 °C for **1a**, for the other compounds we did not notice significant changes in yields when the reaction was performed at 60 °C). Depending on the amine RNH$_2$ used, the product separates from the solution as a crystalline compound (without or upon the addition of pentane), or the volatiles were removed under reduced pressure. The yellow–orange microcrystalline solid was then washed with pentane (2×10 mL), and dried under vacuum to afford the analytically and spectroscopically pure material. Pure **1** was obtained by recrystallization from toluene/pentane. Yields are calculated on the basis of 250-mg scale reaction of Ti(NMe$_2$)$_4$. Some of these compounds have been prepared with up to 2 g of Ti(NMe$_2$)$_4$ with similar yields.

**[Ti(=N–*t*Bu)Cl$_2$(NHMe$_2$)$_2$] (1a):** Yield 260 mg (93%) (yellow). $^1$H NMR (250 MHz, CD$_2$Cl$_2$): $\delta$ = 3.46 (br. m, 2 H, N*H*), 2.71 (d, $^3J$ = 6.2 Hz, 12 H, NH*Me$_2$*), 1.05 (s, 9 H, *t*Bu) ppm. $^{13}$C{$^1$H} NMR (62.90 MHz, CD$_2$Cl$_2$): $\delta$ = 73.6 (*C*Me$_3$), 41.1 (NH*Me$_2$*), 31.5 (C*Me$_3$*) ppm. IR (KBr): $\tilde{\nu}$ = 3234 (s, NH), 2973 (s), 1517 (m), 1363 (w), 1244 (m), 1184 (m), 1090 (m), 1015 (s), 975 (s), 901 (m), 810 (w), 557 (m), 498 (w) cm$^{-1}$. C$_8$H$_{23}$Cl$_2$N$_3$Ti (280.06): calcd. C 34.31, H 8.28, N 15.00; found C 34.33, H 8.35, N 14.86.

**[Ti(=N–1-Adamantane)Cl$_2$(NHMe$_2$)$_2$] (1b):** Yield 320 mg (80%) (yellow). $^1$H NMR (300 MHz, CD$_2$Cl$_2$): $\delta$ = 3.48 (br. m, 2 H, N*H*), 2.71 (d, $^3J$ = 6.0 Hz, 12 H, NH*Me$_2$*), 1.89 (br. s, 3 H, C*H*$_{ada}$), 1.66 (br. s, 6 H, C*H*$_{2ada}$), 1.48 (br. s, 6 H, C*H*$_{2ada}$) ppm. $^{13}$C{$^1$H} NMR (75.47 MHz, CD$_2$Cl$_2$): $\delta$ = 75.4 (*C*$_q$), 45.4 (*C*$_q$), 41.2 (NH*Me$_2$*), 36.5 (*C*$_{ada}$), 30.1 (*C*$_{ada}$) ppm. IR (KBr): $\tilde{\nu}$ = 3233 (w, NH), 2921 (vs), 1465 (m), 1365 (m), 1237 (s), 1097 (m), 1016 (m), 894 (s), 499 (w) cm$^{-1}$. C$_{14}$H$_{29}$Cl$_2$N$_3$Ti (358.17): calcd. C 46.95, H 8.16, N 11.73; found C 47.05, H 8.19, N 11.60.

**[Ti(=N–CPh$_3$)Cl$_2$(NHMe$_2$)$_2$] (1c):** Yield 475 mg (91%) (yellow). $^1$H NMR (250 MHz, CD$_2$Cl$_2$): $\delta$ = 7.21–7.38 (m, 15 H, C$_6$*H*$_5$), 3.27 (br. sept, 2 H, N*H*), 2.44 (d, $^3J$ = 6.1 Hz, 12 H, NH*Me$_2$*) ppm. $^{13}$C{$^1$H} NMR (62.90 MHz, CD$_2$Cl$_2$): $\delta$ = 147.7, 129.0, 128.0, 126.9 (*C*$_6$H$_5$, one signal not observed), 40.7 (NH*Me$_2$*) ppm. IR (KBr): $\tilde{\nu}$ = 3233 (m, NH), 2929 (m), 2780 (m), 1596 (m), 1467 (m), 1443 (m), 1209 (m), 1020 (m), 991 (w), 893 (m), 755 (m), 699 (s), 636 (m), 420 (m) cm$^{-1}$. C$_{23}$H$_{29}$Cl$_2$N$_3$Ti (466.27): calcd. C 59.25, H 6.27, N 9.01; found: C 59.07, H 6.24, N 8.87.

**[Ti(=N–SiPh$_3$)Cl$_2$(NHMe$_2$)$_2$] (1d):** Yield 490 mg (91%) (yellow). $^1$H NMR (250 MHz, CD$_2$Cl$_2$): $\delta$ = 7.72 (m, 6 H, C$_6$*H*$_5$), 7.38 (m, 9 H, C$_6$*H*$_5$), 3.39 (br. sept, 2 H, N*H*), 2.55 (d, $^3J$ = 6.2 Hz, 12 H, NH*Me$_2$*) ppm. $^{13}$C{$^1$H} NMR (125.81 MHz, CD$_2$Cl$_2$): $\delta$ = 136.9, 135.5, 130.6, 129.7 (*C*$_6$H$_5$), 41.2 (NH*Me$_2$*) ppm. $^{29}$Si NMR (99.40 MHz, CD$_2$Cl$_2$): $\delta$ = –43 ppm. IR (KBr): $\tilde{\nu}$ = 3242 (s, NH), 1465 (m), 1427 (m), 1111 (vs), 893 (w), 703 (s), 507 (s) cm$^{-1}$. C$_{22}$H$_{29}$Cl$_2$N$_3$SiTi (482.34): calcd. C 54.78, H 6.06, N 8.71; found C 54.66, H 6.07, N 8.66.

**[Ti(=N–Ph)Cl$_2$(NHMe$_2$)$_2$] (1e):** Yield 273 mg (81%) (red–orange). $^1$H NMR (250 MHz, CD$_2$Cl$_2$): $\delta$ = 7.07 (t, 2 H, C$_6$*H*$_5$), 6.82 (m, 3 H, C$_6$*H*$_5$), 3.56 (br. sept, 2 H, N*H*), 2.76 (d, $^3J$ = 6.2 Hz, 12 H, NH*Me$_2$*) ppm. C$_{10}$H$_{19}$Cl$_2$N$_3$Ti (300.05): calcd. C 40.03, H 6.38, N 14.00; found C 39.86, H 6.41, N 13.92.

**[Ti(=N–2,6-*i*Pr$_2$–C$_6$H$_3$)Cl$_2$(NHMe$_2$)$_2$] (1f):** Yield 410 mg (96%) (orange). $^1$H NMR (300 MHz, C$_6$D$_6$): $\delta$ = 6.99 (d, $^3J$ = 7.5 Hz, 2 H, C$_6$*H*$_3$), 6.85 (t, $^3J$ = 7.6 Hz, 1 H, C$_6$*H*$_3$), 4.67 (sept, $^3J$ = 6.7 Hz, 2 H, C*H*Me$_2$), 2.91 (br. m, 2 H, N*H*), 2.27 (d, $^3J$ = 6.3 Hz, 12 H, NH*Me$_2$*), 1.44 (d, $^3J$ = 6.9 Hz, 12 H, CH*Me$_2$*) ppm. $^{13}$C{$^1$H} NMR (75.47 MHz, C$_6$D$_6$): $\delta$ = 157.8, 144.7, 123.8, 122.7 (*C*$_6$H$_3$), 40.8 (NH*Me$_2$*), 28.0 (*C*HMe$_2$), 24.6 (CH*Me$_2$*) ppm. IR (KBr): $\tilde{\nu}$ = 3255 (w, NH), 2961 (m), 1465 (s), 1334 (s), 1288 (s), 1021 (m), 896 (m), 753 (s), 668 (vs) cm$^{-1}$. C$_{16}$H$_{31}$Cl$_2$N$_3$Ti (384.21): calcd. C 50.02, H 8.13, N 10.94; found C 49.93, H 8.20, N 10.81.

 © 2006 Wiley-VCH Verlag GmbH & Co. KGaA, Weinheim 

**[Ti(=N–2,6-$Cl_2$–$C_6H_3$)$Cl_2$($NHMe_2$)$_2$] (1g):** Yield 300 mg (73%) (orange). $^1$H NMR (250 MHz, $C_6D_6$): $\delta$ = 6.90 (d, $^3J$ = 8.0 Hz, 2 H, $C_6H_3$), 6.13 (t, $^3J$ = 7.9 Hz, 1 H, $C_6H_3$), 2.97 (br. m, 2 H, N*H*), 2.28 (d, $^3J$ = 6.2 Hz, 12 H, NH$Me_2$) ppm. $^{13}$C{$^1$H} NMR (62.90 MHz, $C_6D_6$): $\delta$ = 158.0, 130.6, 122.2 ($C_6H_3$, one signal not observed, probably obscured under $C_6D_6$), 41.2 (NH$Me_2$) ppm. IR (KBr): $\tilde{\nu}$ = 3251 (s, NH), 2977 (m), 2931 (m), 2783 (m), 1610 (w), 1468 (m), 1434 (vs), 1397 (m), 1332 (s), 1258 (w), 1192 (w), 1071 (w), 1011 (s), 983 (m), 894 (s), 788 (s), 759 (m), 718 (m), 568 (m), 458 (w), 425 (w) cm$^{-1}$. $C_{10}H_{17}Cl_4N_3Ti$ (368.94): calcd. C 32.55, H 4.64, N 11.39; found C 32.53, H 4.60, N 11.25.

**[Ti(=N–2,6-$Br_2$–4-Me–$C_6H_2$)$Cl_2$($NHMe_2$)$_2$] (1h):** Yield 451 mg (96%) (orange). $^1$H NMR (250 MHz, $C_6D_6$): $\delta$ = 6.97 (d, 2 H, $C_6H_2$), 3.17 (br. m, 2 H, N*H*), 2.36 (d, $^3J$ = 6.1 Hz, 12 H, NH$Me_2$), 1.69 (s, 3 H, $Me_{Ar}$) ppm. $^{13}$C{$^1$H} NMR (62.90 MHz, $C_6D_6$): $\delta$ = 152.7, 133.7, 132.4, 120.5 ($C_6H_2$), 41.4 (NH$Me_2$), 20.2 ($Me_{Ar}$) ppm. IR (KBr): $\tilde{\nu}$ = 3248 (s, NH), 3008 (w), 2975 (w), 2937 (w), 2781 (w), 1465 (m), 1442 (s), 1332 (s), 1255 (w), 1011 (s), 896 (s), 850 (m), 741 (s), 713 (m), 581 (m), 568 (m), 459 (w), 423 (w) cm$^{-1}$. $C_{11}H_{19}Br_2Cl_2N_3Ti$ (471.87): calcd. C 28.00, H 4.06, N 8.91; found C 28.05, H 4.08, N 8.89.

**[Ti(=N–$C_6F_5$)$Cl_2$($NHMe_2$)$_2$] (1i):** Yield 405 mg (93%) (orange). $^1$H NMR (250 MHz, $C_6D_6$): $\delta$ = 2.70 (br. m, 2 H, N*H*), 2.21 (d, $^3J$ = 6.1 Hz, 12 H, NH$Me_2$) ppm. $^{19}$F NMR ($C_6D_6$, 188.3 MHz): $\delta$ = –78.8 (d, 2F, *o*-$C_6F_5$), –89.5 (t, 2F, *m*-$C_6F_5$), –90.3 (t, 1F, *p*-$C_6F_5$) ppm. $C_{10}H_{14}Cl_2F_5N_3Ti$ (390.00): calcd. C 30.80, H 3.62, N 10.77; found C 30.75, H 3.57, N 10.70.

**[Ti[=N–3,5-($F_3C$)$_2$–$C_6H_3$]$Cl_2$($NHMe_2$)$_2$] (1j):** Yield 380 mg (87%) (red–orange). $^1$H NMR (250 MHz, $C_6D_6$): $\delta$ = 7.36 (br. s, 3 H, $C_6H_3$), 2.36 (br. m, 2 H, N*H*), 2.11 (d, $^3J$ = 6.0 Hz, 12 H, NH$Me_2$) ppm. $^{13}$C{$^1$H} NMR (62.90 MHz, $C_6D_6$): $\delta$ = 159.1, 132.7, 124.3, 123.7 ($C_6H_3$), 115.4 ($CF_3$), 41.0 (NH$Me_2$) ppm. $^{19}$F NMR (188.3 MHz, $C_6D_6$): $\delta$ = 13.31 ppm. IR (KBr): $\tilde{\nu}$ = 3229 (m, NH), 3008 (w), 2982 (w), 1598 (w), 1466 (m), 1460 (m), 1387 (s), 1278 (vs), 1177 (s), 1132 (vs), 1040 (s), 1022 (m), 894 (m), 876 (m), 682 (m), 426 (w) cm$^{-1}$. $C_{12}H_{17}Cl_2F_6N_3Ti$ (436.05): calcd. C 33.05, H 3.93, N 9.64; found C 33.03, H 3.94, N 9.51.

**[Ti(=N–4-$Et_2$N–$C_6H_4$)$Cl_2$($NHMe_2$)$_2$] (1k):** Yield 345 mg (93%) (green). $^1$H NMR (250 MHz, $C_6D_6$): $\delta$ = 7.11 (d, $^3J$ = 8.9 Hz, 2 H, $C_6H_4$), 6.40 (d, $^3J$ = 9.0 Hz, 2 H, $C_6H_4$), 2.94 [q, $^3J$ = 7.0 Hz, 4 H, N($CH_2CH_3$)$_2$], 2.80 (br. m, 2 H, N*H*), 2.36 (d, $^3J$ = 6.1 Hz, 12 H, NH$Me_2$), 0.86 [t, $^3J$ = 7.0 Hz, 6 H, N($CH_2CH_3$)$_2$] ppm. $^{13}$C{$^1$H} NMR (250 MHz, $C_6D_6$): $\delta$ = 156.2, 144.2, 125.9, 112.7 ($C_6H_4$), 45.2 [N($CH_2CH_3$)$_2$], 41.2 (NH$Me_2$), 13.4 [N($CH_2CH_3$)$_2$] ppm. IR (KBr): $\tilde{\nu}$ = 3249 (s, NH), 2973 (s), 1597 (m), 1499 (vs), 1465 (m), 1320 (m), 1265 (vs), 1005 (m), 896 (m), 815 (s), 458 (w) cm$^{-1}$. $C_{14}H_{28}Cl_2N_4Ti$ (371.17): calcd. C 45.30, H 7.60, N 15.09; found C 45.12, H 7.74, N 14.99.

**[Ti(=N–4-NC–$C_6H_4$)$Cl_2$($NHMe_2$)$_2$] (1l):** Yield 280 mg (77%) (orange). $^1$H NMR (250 MHz, $CD_2Cl_2$): $\delta$ = 7.39 (d, $^3J$ = 8.6 Hz, 2 H, $C_6H_4$), 6.85 (d, $^3J$ = 8.5 Hz, 2 H, $C_6H_4$), 3.54 (br. m, 2 H, N*H*), 2.75 (d, $^3J$ = 6.3 Hz, 12 H, NH$Me_2$) ppm. The low solubility of **1l** precluded its $^{13}$C{$^1$H} NMR analysis. IR (KBr): $\tilde{\nu}$ = 3214 (m, NH), 2978 (w), 2923 (w), 2243 (s, CN), 1586 (s), 1487 (s), 1441 (s), 1168 (m), 1021 (m), 961 (w), 897 (m), 836 (m), 773 (w), 551 (w) cm$^{-1}$. $C_{11}H_{18}Cl_2N_4Ti$ (325.06): calcd. C 40.64, H 5.58, N 17.24; found C 40.54, H 5.52, N 17.12.

**[Ti(=N–2-NC–$C_6H_4$)$Cl_2$($NHMe_2$)$_2$] (1m):** Yield 350 mg (96%) (orange). $^1$H NMR (250 MHz, $CD_2Cl_2$): $\delta$ = 7.31 (app. t, app. $^3J$ = 8.6 Hz, 2 H, $C_6H_4$), 6.85 (app. t, app. $^3J$ = 7.3 Hz, 2 H, $C_6H_4$), 3.82 (br. m, 2 H, N*H*), 2.78 (d, $^3J$ = 5.6 Hz, 12 H, NH$Me_2$) ppm. $^{13}$C{$^1$H} NMR (62.90 MHz, $CD_2Cl_2$): $\delta$ = 160.5, 133.3, 131.9, 129.2, 128.3, 123.8, 122.0, 41.3 (NH$Me_2$) ppm. IR (KBr): $\tilde{\nu}$ = 3228 (m, NH), 2971 (w), 2934 (w), 2242 (s, CN), 1570 (s), 1462 (s), 1446 (s), 1350 (s), 1262 (m), 1018 (m), 995 (m), 973 (w), 898 (m), 765 (s) cm$^{-1}$. $C_{11}H_{18}Cl_2N_4Ti$ (325.06): calcd. C 40.64, H 5.58, N 17.24; found C 40.37, H 5.44, N 17.06.

**[Ti(=N–4-$H_2$C=CH–$C_6H_4$)$Cl_2$($NHMe_2$)$_2$] (1n):** Yield 240 mg (74%) (red). $^1$H NMR (250 MHz, $C_6D_6$): $\delta$ = 7.15 (d, $^3J$ = 8.3 Hz, 2 H, $C_6H_4$), 6.96 (d, $^3J$ = 8.3 Hz, 2 H, $C_6H_4$), 5.57 (dd, $J$ = 17.6 and 11.8 Hz, 1 H, =C*H*), 5.53 (d, $^3J$ = 18.5 Hz, 1 H, =C*H*), 5.02 (d, $^3J$ = 12.0 Hz, 1 H, =C*H*), 2.62 (m, 2 H, N*H*), 2.25 (d, $^3J$ = 6.1 Hz, 12 H, NH$Me_2$) ppm. $^{13}$C{$^1$H} NMR (62.90 MHz, $C_6D_6$): $\delta$ = 161.5 ($C_6H_4$), 137.2 (=*C*H), 132.6, 127.0, 124.5 ($C_6H_4$), 112.7 (=*C*H$_2$), 41.0 (NH$Me_2$) ppm. IR (KBr): $\tilde{\nu}$ = 3266 (m, NH), 3237 (m, NH), 2973 (m), 2935 (m), 1624 (w, C=C), 1588 (w), 1491 (s), 1466 (s), 1400 (w), 1326 (s), 1264 (m), 1114 (m), 1018 (s), 893 (s), 842 (s), 609 (w) cm$^{-1}$. $C_{12}H_{21}Cl_2N_3Ti$ (326.09): calcd. C 44.20, H 6.49, N 12.89; found C 44.10, H 6.50, N 12.54.

**[Ti(=N–2-MeC=$CH_2$–$C_6H_4$)$Cl_2$($NHMe_2$)$_2$] (1o):** Yield 250 mg (73%) (red). $^1$H NMR (250 MHz, $C_6D_6$): $\delta$ = 7.31 (dd, $^3J$ = 9.0 Hz, 1 H, $C_6H_4$), 7.07 (dd, $^3J$ = 7.6 Hz, 1 H, $C_6H_4$), 7.00 (td, $^3J$ = 9.6 Hz, 1 H, $C_6H_4$), 6.74 (t, $^3J$ = 7.4 Hz, 1 H, $C_6H_4$), 5.26 (app d, app. $J$ = 12.9 Hz, 2 H, C$H_2$), 2.77 (br. m, 2 H, N*H*), 2.52 (s, 3 H, C$H_3$), 2.26 (d, $^3J$ = 6.3 Hz, 12 H, NH$Me_2$) ppm. $^{13}$C{$^1$H} NMR (62.90 MHz, $C_6D_6$): $\delta$ = 158.8, 147.2, 136.0 ($C_6H_4$, 1 peak obscured under $C_6D_6$), 123.2 (*C*=CH$_2$), 115.2 (C=*C*H$_2$), 41.0 (NH$Me_2$), 25.0 (*C*H$_3$) ppm. IR (KBr): $\tilde{\nu}$ = 3226 (m, NH), 2973 (w), 2934 (w), 1629 (w, C=C), 1517 (w), 1466 (s), 1430 (s), 1322 (s), 1115 (w), 1094 (w), 1020 (m), 997 (w), 973 (w), 982 (w), 894 (m), 750 (m), 573 (w), 472 (w) cm$^{-1}$. $C_{13}H_{23}Cl_2N_3Ti$ (340.11): calcd. C 45.91, H 6.82, N 12.35; found C 45.83, H 6.98, N 11.91.

**[Ti(=N–3-HC≡C–$C_6H_4$)$Cl_2$($NHMe_2$)$_2$] (1p):** Yield 260 mg (72%) (red). $^1$H NMR (500 MHz, $CD_2Cl_2$): $\delta$ = 7.07 (t, $^3J$ = 8.0 Hz, 1 H, $C_6H_4$), 6.99 (s, 1 H, $C_6H_4$), 6.98 (d, $^3J$ = 8.5 Hz, 1 H, $C_6H_4$), 6.85 (d, $^3J$ = 8.6 Hz, 1 H, $C_6H_4$), 3.60 (br. m, 2 H, N*H*), 3.11 (s, 1 H, ≡C*H*), 2.78 (d, $^3J$ = 6.1 Hz, 12 H, NH$Me_2$) ppm. $^{13}$C{$^1$H} NMR (125.81 MHz, $CD_2Cl_2$): $\delta$ = 159.6, 128.4, 126.7, 126.0, 123.8, 121.9 ($C_6H_4$), 83.3 (*C*≡CH), 76.7 (≡*C*H), 40.8 (NH$Me_2$) ppm. IR (KBr): $\tilde{\nu}$ = 3270 (m, NH), 3255 (m, NH), 2977 (m), 2208 (w, C≡C), 1577 (w), 1467 (s), 1407 (m), 1329 (s), 1261 (m), 1099 (m), 1025 (s), 993 (s), 794 (s), 676 (m) cm$^{-1}$. $C_{12}H_{19}Cl_2N_3Ti$ (324.07): calcd. C 44.47, H 5.91, N 12.97; found C 45.94, H 6.53, N 11.91. We were unable to obtain satisfactory elemental analysis for this compound even on a recrystallized sample (from cold toluene/pentane solutions). A $^1$H NMR spectrum is provided in the supporting information.

**[Ti(=N–3-$O_2$N–6-Me–$C_6H_3$)$Cl_2$($NHMe_2$)$_2$] (1q):** Yield 270 mg (67%) (brown). $^1$H NMR (250 MHz, $CD_2Cl_2$): $\delta$ = 7.70 (s, 1 H, *o*-$C_6H_3$), 7.54 (d, $^3J$ = 8.3 Hz, 1 H, *p*-$C_6H_3$), 7.12 (d, $^3J$ = 8.3 Hz, 1 H, *m*-$C_6H_3$), 3.57 (br. m, 2 H, N*H*), 2.78 (d, $^3J$ = 5.6 Hz, 12 H, NH$Me_2$), 2.56 (s, 3 H, $C_6H_3Me$) ppm. $^{13}$C{$^1$H} NMR (125.81 MHz, $CD_2Cl_2$): $\delta$ = 130.0 ($C_6H_3$), 40.9 (NH$Me_2$), 35.4 ($C_6H_3Me$) ppm (because of poor solubility, not all $C_6H_3$ resonances are observed). IR (KBr): $\tilde{\nu}$ = 3281 (s, NH), 2976 (w), 2934 (w), 2776 (w), 1517 (vs, $NO_2$), 1468 (s), 1400 (m), 1353 (vs), 1313 (m), 1250 (w), 1099 (w), 1020 (m), 1002 (m), 894 (s), 844 (m), 740 (m), 640 (w), 420 (w) cm$^{-1}$. $C_{12}H_{20}Cl_2N_4O_2Ti$ (359.07): calcd. C 36.79, H 5.61, N 15.60; found C 36.58, H 5.48, N 15.38.

**[Ti{=N($C_6H_{10}$C≡CH)}$Cl_2$($NHMe_2$)$_2$] (1r):** Yield 220 mg (60%) (yellow). $^1$H NMR (500 MHz, $C_6D_6$): $\delta$ = 2.78 (m, 2 H, N*H*), 2.36 (d, $^3J$ = 6.0 Hz, 12 H, NH$Me_2$), 2.10 (s, 1 H, ≡C*H*), 1.91 (br. m, 2 H, C$H_2$), 1.62 (br. m, 2 H, C$H_2$), 1.54 (br. m, 4 H, C$H_2$), 1.41 (br. m, 1 H, C$H_a$H$_b$), 1.07 (br. m, 1 H, CH$_a$H$_b$) ppm. $^{13}$C{$^1$H}

 © 2006 Wiley-VCH Verlag GmbH & Co. KGaA, Weinheim 

NMR (125.81 MHz, $C_6D_6$): $\delta$ = 88.0 (*C*≡CH), 73.0 (*C*N), 71.0 (C≡*C*H), 41.7 (*C*H$_2$), 41.5 (NH*Me$_2$*), 26.1 (*C*H$_2$), 23.7 (*C*H$_2$) ppm. IR (KBr): $\tilde{\nu}$ = 3278 (s, ≡CH), 3263, 3248 (m, NH), 2935 (s), 1466 (m), 1342 (m), 1266 (s), 1198 (s), 1005 (s), 895 (s), 668 (m), 655 (m), 600 (w), 537 (w), 487 (w), 419 (w) cm$^{-1}$. $C_{12}H_{25}Cl_2N_3Ti$ (330.12): calcd. C 43.66, H 7.63, N 12.73; found C 43.50, H 7.72, N 12.34.

**[Ti{=N–[(*S*)-(–)-CHMePh]}Cl$_2$(NHMe$_2$)$_2$] (1s*):** Yield 270 mg (74%) (yellow). $^1$H NMR (250 MHz, $CD_2Cl_2$): $\delta$ = 7.45 (d, $^3J$ = 8.4 Hz, 2 H, *o*-C$_6$*H*$_5$), 7.31 (app t, app. *J* = 7.8 Hz, 2 H, *m*-C$_6$*H*$_5$), 7.20 (t, $^3J$ = 7.3 Hz, 1 H, *p*-C$_6$*H*$_5$), 4.41 (q, $^3J$ = 6.5 Hz, 1 H, C*H*Me), 3.38 (br. m, 2 H, N*H*), 2.61 (d, $^3J$ = 6.3 Hz, 12 H, NH*Me$_2$*), 1.31 (d, $^3J$ = 6.7 Hz, 3 H, CH*Me*) ppm. $^{13}$C{$^1$H} NMR (62.90 MHz, $CD_2Cl_2$): $\delta$ = 146.0, 128.5, 126.6, 126.1 (*C*$_6$H$_5$), 77.4 (*C*HMe), 40.8 (NH*Me$_a$*Me$_b$), 40.7 (NHMe$_a$*Me$_b$*), 25.7 (CH*Me*) ppm. IR (KBr): $\tilde{\nu}$ = 3203 (s, NH), 3013 (w), 2979 (w), 2790 (w), 1465 (m), 1452 (m), 1261 (w), 1112 (w), 1070 (w), 1051 (w), 1015 (m), 933 (m), 893 (s), 766 (m), 706 (m), 659 (m), 581 (m), 458 (m) cm$^{-1}$. $C_{12}H_{23}Cl_2N_3Ti$ (328.10): calcd. C 43.93, H 7.07, N 12.81; found C 43.74, H 7.12, N 12.66.

**[Ti(=N–SiPh$_3$)Cl$_2$(Py)$_3$] (2d):** Complex **1d** (180 mg) was dissolved in dichloromethane (2 mL) and pyridine (1 mL) was added. The resulting solution stood overnight and was then layered with toluene (ca. 1 mL) and pentane (20 mL) to afford **2d** as a crystalline sample. The crystals were collected and washed with pentane (3 × 5 mL) and dried under vacuum. Yield 220 mg (93%) (yellow). $^1$H NMR (500 MHz, $CD_2Cl_2$): $\delta$ = 9.01 (d, $^3J$ = 5.5 Hz, 4 H, *cis*-Py), 8.61 (br. s, 2 H, *trans*-Py), 7.81 (t, $^3J$ = 7.5 Hz, 2 H, *cis*-Py), 7.64 (d, $^3J$ = 8.3 Hz, 6 H, C$_6$*H*$_5$), 7.38 (s, 1 H, *trans*-Py), 7.35 (d, $^3J$ = 7.5 Hz, 3 H, C$_6$*H*$_5$), 7.30–7.25 (m, 12 H, *cis*-Py, *trans*-Py, C$_6$*H*$_5$) ppm. $^{13}$C{$^1$H} NMR (75.81 MHz, $CD_2Cl_2$): $\delta$ = 151.6 (Py), 150.3 (Py), 139.2 (Py), 136.4 (*C*$_6$H$_5$), 135.5 (*C*$_6$H$_5$), 129.5 (*C*$_6$H$_5$), 127.8 (*C*$_6$H$_5$), 127.8 (Py), 124.4 (Py), 123.8 (Py) ppm. $^{29}$Si NMR (99.40 MHz, $CD_2Cl_2$): $\delta$ = –43 ppm. IR (KBr): $\tilde{\nu}$ = 3050 (w), 1603 (m), 1595 (m), 1485 (m), 1442 (m), 1425 (m), 1217 (m), 1109 (vs), 1068 (m), 755 (w), 693 (s), 511 (s) cm$^{-1}$. $C_{33}H_{30}Cl_2N_3SiTi$ (629.48): calcd. C 62.97, H 4.80, N 8.90; found C 62.90, H 4.70, N 8.81.

**[Ti(=N–4-NC–C$_6$H$_4$)Cl$_2$(Py)$_3$] (2l):** This compound was obtained from **1l** (100 mg) with a procedure similar to the one described for **2d**. Yield 145 mg (99%) (orange). $^1$H NMR (500 MHz, $CD_2Cl_2$): $\delta$ = 9.07 (br. d, 4 H, *cis*-Py), 8.65 (br. s, *trans*-Py), 7.93 (br. t, 2 H, *cis*-Py), 7.73 (br. s, *trans*-Py), 7.46 (br. t, 4 H, *cis*-Py), 7.37 (d, $^3J$ = 8.3 Hz, 2 H, C$_6$*H*$_4$), 7.32 (br. s, *trans*-Py), 6.84 (d, $^3J$ = 8.5 Hz, 2 H, C$_6$*H*$_4$) ppm (integration of the *trans*-Py signals is not given because of the poor solubility and partial decomposition of **2l** in $CD_2Cl_2$, which makes the integration of the *trans*-Py obscured by free pyridine signals). $^1$H NMR (250 MHz, [D$_5$]Pyridine): $\delta$ = 7.40 (d, 2 H, C$_6$*H*$_4$), 7.14 (d, 2 H, C$_6$*H*$_4$) ppm. The low solubility and partial decomposition of **2l** in $CD_2Cl_2$ precluded its $^{13}$C NMR analysis. IR (KBr): $\tilde{\nu}$ = 2221 (s, CN), 1603 (s), 1587 (s), 1484 (s), 1442 (s), 1347 (s), 1212 (m), 1160 (m), 1043 (m), 966 (m), 841 (s), 759 (m), 700 (s), 680 (m), 638 (m), 549 (m). $C_{22}H_{19}Cl_2N_5Ti$ (472.19): calcd. C 55.96, H 4.06, N 14.83; found C 55.64, H 3.96, N 14.63.

**[Ti[=N(C$_6$H$_{10}$C≡CH)]Cl$_2$(Py)$_3$] (2r):** This compound was obtained from **1r** (100 mg) with a procedure similar to the one described for **2d**. Yield 100 mg (69%) (ochre). $^1$H NMR (500 MHz, $CD_2Cl_2$): $\delta$ = 9.20 (d, $^3J$ = 5.0 Hz, 4 H, *cis*-Py), 8.65 (br. s, 2 H, *trans*-Py), 7.85 (t, $^3J$ = 7.6 Hz, 2 H, *cis*-Py), 7.66 (br. s, 1 H, *trans*-Py), 7.40 (t, $^3J$ = 6.6 Hz, 4 H, *cis*-Py), 7.18 (br. s, 2 H, *trans*-Py), 2.36 (s, 1 H, ≡C*H*), 1.64–1.48 (m, 6 H, C*H*$_2$), 1.33–1.22 (br. m, 3 H, C*H*$_2$, C*H$_a$*H$_b$), 1.13 (m, 1 H, CH$_a$*H$_b$*) ppm. $^{13}$C{$^1$H} NMR (125.81 MHz, $CD_2Cl_2$): $\delta$ = 152.6 (*cis*-Py), 152.0 (*trans*-Py), 138.7 (*cis*-Py), 136.7 (*trans*-Py), 123.9 (*cis*-Py), 123.5 (*trans*-Py), 87.1 (*C*≡CH), 71.1 (*C*N), 69.9 (C≡*C*H), 39.5 (*C*H$_2$), 25.3 (*C*H$_2$), 22.6 (*C*H$_2$) ppm. $C_{23}H_{26}Cl_2N_4Ti$ (477.25): calcd. C 57.88, H 5.49, N 11.74; found C 57.86, H 5.44, N 11.78.

**[Ti{=N–[(*S*)-(–)-CHMePh]}Cl$_2$(Py)$_3$] (2s*):** This compound was obtained from **1s*** (250 mg) with a procedure similar to the one described for **2d**. Yield 160 mg (44%) (orange needles). $^1$H NMR (250 MHz, $CD_2Cl_2$): $\delta$ = 9.04 (d, $^3J$ = 4.9 Hz, 4 H, Py), 8.64 (s, 2 H, Py), 7.85 (t, $^3J$ = 7.5 Hz, 2 H, Py), 7.69 (s, 1 H, Py), 7.38 (app. t, app. *J* = 7.0 Hz, 6 H, Py, C$_6$*H*$_5$), 7.13–7.24 (m, 4 H, Py, C$_6$*H*$_5$), 4.49 (q, $^3J$ = 6.7 Hz, 1 H, C*H*Me), 1.26 (d, $^3J$ = 6.7 Hz, 3 H, CH*Me*) ppm. $^{13}$C{$^1$H} NMR (62.90 MHz, $CD_2Cl_2$): $\delta$ = 146.0, 128.5, 126.6, 126.1 (*C*$_6$H$_5$), 77.4 (*C*HMe), 40.8 (NH*Me$_a$*Me$_b$), 40.7 (NHMe$_a$*Me$_b$*), 25.7 (CH*Me*) ppm. $C_{23}H_{24}Cl_2N_4Ti$ (475.24): calcd. C 58.13, H 5.09, N 11.79; found C 57.96, H 4.97, N 11.56.

**[Ti{=N–[(–)-*cis*-myrtanyl]}Cl$_2$(Py)$_3$] (2t*):** This compound was prepared from unisolated **1t*** [prepared from Ti(NMe$_2$)$_4$ and (–)-*cis*-myrtanylamine/Me$_3$SiCl as described above for **1a**] with a procedure similar to the one described for **2d**. Yield 250 mg [44% based on starting Ti(NMe$_2$)$_4$] (orange). $^1$H NMR (250 MHz, $C_6D_6$): $\delta$ = 9.45 (br. s, 3 H, Py), 8.81 (br. s, 3 H, Py), 6.85 (br. t, 3 H, Py), 6.58 (br. d, 6 H, Py), 4.00 (s, 1 H, C*H*), 3.58 (dd, $^3J$ = 7.5 Hz, 2 H, C*H*$_2$N), 2.52 (m, 1 H, C*H*), 2.28 (br. s, 2 H, C*H*$_2$), 1.95 (br. m, 1 H, C*H*), 1.83–1.74 (br. s, 3 H, C*H*, C*H*$_2$), 1.35 (m, 1 H, C*H*), 1.11 (s, 3 H, C*H*$_3$), 0.87 (s, 3 H, C*H*$_3$) ppm. $^{13}$C{$^1$H} NMR (125.81 MHz, $C_6D_6$): $\delta$ = 152.2, 151.5, 138.3, 136.8, 124.1, 76.4, 55.1, 44.9, 42.2, 39.1, 34.1, 28.6, 27.1, 23.9, 20.1 ppm. $C_{25}H_{32}Cl_2N_4Ti$ (507.32): calcd. C 59.19, H 6.36, N 11.04; found C 59.04, H 6.35, N 10.91.

**[Ti(N–2-EtO–C$_6$H$_4$)Cl$_2$(NHMe$_2$)$_1$]$_2$ (3):** This compound was obtained from a procedure similar to the one described for **1a**–**t**. Pure **3** was obtained after recrystallization from a THF/toluene solution layered with pentane. Yield 235 mg (70%) (dark red). $^1$H NMR (250 MHz, $CD_2Cl_2$): $\delta$ = 7.58 (dd, $^3J$ = 7.8 Hz, 2 H, C$_6$*H*$_4$), 7.05 (m, 4 H, C$_6$*H*$_4$), 6.91 (dd, $^3J$ = 8.1 Hz, 2 H, C$_6$*H*$_4$), 5.37 (m, 2 H, N*H*), 5.02 (qd, $^3J$ = 7.1 Hz, 4 H, OC*H*$_2$CH$_3$), 2.48 (d, $^3J$ = 5.8 Hz, 6 H, NH*Me$_a$*Me$_b$), 2.35 (d, $^3J$ = 6.1 Hz, 6 H, NHMe$_a$*Me$_b$*), 1.62 (t, $^3J$ = 7.0 Hz, 6 H, OCH$_2$C*H*$_3$) ppm. $^{13}$C{$^1$H} NMR (125.81 MHz, $CD_2Cl_2$): $\delta$ = 144.2, 142.3, 128.2, 126.7, 124.7, 111.4 (*C*$_6$H$_4$), 71.7 (O*C*H$_2$CH$_3$), 42.5 (NH*Me$_a$*Me$_b$), 40.0 (NHMe$_a$*Me$_b$*), 13.40 (OCH$_2$*C*H$_3$) ppm. IR (KBr): $\tilde{\nu}$ = 3149 (w, NH), 2978 (m), 1473 (s), 1254 (s, CO), 1191 (m), 1112 (m), 1041 (m), 1002 (m), 922 (m), 896 (m), 751 (m), 652 (w), 419 (w) cm$^{-1}$. $C_{20}H_{32}Cl_4N_4O_2Ti_2$ (598.04): calcd. C 40.17, H 5.39, N 9.37; found C 40.20, H 5.41, N 9.39.

**[Ti[N–CH$_2$(CH(OCH$_2$)$_3$)]Cl$_2$(NHMe$_2$)$_1$]$_2$ (4):** This compound was obtained from a procedure similar to the one described for **1a**–**t**. Yield 260 mg (89%) (orange). The very poor solubility of **4** in $CD_2Cl_2$ and in [D$_8$]THF precluded its $^1$H and $^{13}$C NMR analysis. In [D$_5$]Py the HNMe$_2$ ligands are displaced by [D$_5$]Py ligands. $^1$H NMR (250 MHz, [D$_5$]Py): $\delta$ = 4.13 (br., 2 H), 3.90–3.25 (br., app t), 1.96 (br., 4 H), 1.75–1.56 (br., 4 H) ppm. IR (KBr): $\tilde{\nu}$ = 3215 (w, NH), 2983 (m), 2917 (s), 2773 (s), 1459 (m), 1257 (w, CO), 1126 (s), 1043 (s), 1029 (s), 981 (m), 893 (m), 821 (m), 699 (m), 463 (m) cm$^{-1}$. $C_{14}H_{32}Cl_4N_4O_2Ti_2$ (525.98): calcd. C 31.97, H 6.13, N 10.65; found C 32.07, H 6.09, N 10.66.

**[Ti[N–CH$_2$(CHO(CH$_2$)$_3$)]Cl$_2$(Py)$_1$]$_2$ (5):** This compound was only obtained as a few red crystals by the crystallization of **4** in pyridine/toluene solutions. Attempted large scale synthesis (even in hot pyridine) gave only insoluble materials (precluding NMR analysis), and with an elemental analysis close to that of **4** which proves that

 © 2006 Wiley-VCH Verlag GmbH & Co. KGaA, Weinheim 

the substitution of $NHMe_2$ in **4** by Py is difficult (vide infra). In consequence, **5** was only characterized by X-ray analysis.

**[Ti{=N–[(*S*)-(–)-CHMePh]}$Cl_2(NHMe_2)_1]_2$ (6*):** This compound was observed in the synthesis of **1s*** when only 0.8 equiv. of the chiral amine was treated with $Ti(NMe_2)_4$ (1 equiv.) and $Me_3SiCl$ (10 equiv.). $^1H$ NMR (250 MHz, $CD_2Cl_2$): $\delta$ = 7.70 (d, $^3J$ = 8.3 Hz, 4 H, $C_6H_5$), 7.40 (m, 6 H, $C_6H_5$), 5.62 (q, $^3J$ = 6.8 Hz, 2 H, C*H*Me), 3.00 (br. m, 4 H, N*H*), 2.59 (d, $^3J$ = 6.1 Hz, 6 H, NH$Me_2$), 2.45 (d, $^3J$ = 5.9 Hz, 6 H, NH$Me_2$), 1.80 (d, $^3J$ = 6.8 Hz, 6 H, CH*Me*) ppm.

**[$(Me_2HN)_2Cl_2Ti$(=N–$Me_2C_6H_2$–$C_6H_2Me_2$–N=)$TiCl_2(NHMe_2)_2$] (7):** This compound was obtained from a procedure similar to the one described for **1a**–**t**. Yield 280 mg (77%) (yellow). $^1H$ NMR (250 MHz, $CD_2Cl_2$): $\delta$ = 6.98 (s, 4 H, $C_6H_2$), 3.59 (m, $^3J$ = 6.1 Hz, 4 H, N*H*), 2.75 (d, $^3J$ = 6.2 Hz, 24 H, NH$Me_2$), 2.56 (s, 12 H, $C_6H_2Me_2$) ppm. $^{13}C\{^1H\}$ NMR (125.81 MHz, $CD_2Cl_2$): $\delta$ = 159.4, 134.2, 133.9, 124.9 ($C_6H_2$), 41.0 (NH$Me_2$), 19.0 ($C_6H_2Me_2$) ppm. IR (KBr): $\tilde{\nu}$ = 3251 (s, NH), 2972 (m), 2936 (m), 1465 (m), 1459 (m), 1311 (s), 1117 (w), 1093 (w), 1020 (m), 1006 (m), 894 (m), 859 (m), 803 (w), 758 (w), 735 (w), 462 (w), 415 (w) $cm^{-1}$. $C_{24}H_{44}Cl_4N_6Ti_2$ (654.19): calcd. C 44.06, H 6.78, N 12.85; found C 43.93, H 6.84 N 12.62.

**[$(Py)_3Cl_2Ti$(=N–$Me_2C_6H_2$–$C_6H_2Me_2$–N=)$TiCl_2(Py)_3$] (8):** This compound was obtained from **7** (100 mg) with a procedure similar to the one described for **2d**. Yield 137 mg (94%) (orange). $^1H$ NMR (250 MHz, [$D_5$]Py): $\delta$ = 7.31 (s, 4 H, $C_6H_2$), 2.79 (s, 12 H, Me) ppm. The very poor solubility in $CD_2Cl_2$ precluded its $^{13}C$ NMR analysis. IR (KBr): $\tilde{\nu}$ = 1604 (s), 1444 (vs), 1299 (s), 1217, 1069, 1012 (m), 681 (w), 754 (m), 695 (vs), 637, 429 (m) $cm^{-1}$. $C_{46}H_{46}Cl_4N_8Ti_2$ (948.46): calcd. C 58.25, H 4.89, N 11.81; found C 57.99, H 4.71, N 11.55.

**[$Ti(N$–2,6-$iPr_2$–$C_6H_3)I_2(thf)_2]_2$ (9):** A THF solution (5 mL) of $Ti(NMe_2)_4$ (250 mg, 1.115 mmol) was treated with 2,6-$iPr_2$–$C_6H_3NH_2$ (1 equiv., 1.115 mmol) at room temperature. To this solution, MeI (1.58 g) was slowly and carefully added. The resulting solution was stirred at room temp. for 1 d. Toluene (5 mL) were added and the white precipitate of $Me_4NI$ was filtered and washed with toluene(2 × 3 mL). The volatiles were removed under vacuum, and the resulting sticky solid was washed with pentane (2 × 10 mL) and dried under vacuum to afford the product. Yield 550 mg (79%) (orange). $^1H$ NMR (250 MHz, $C_6D_6$): $\delta$ = 6.96 (d, $^3J$ = 7.7 Hz, 2 H, $C_6H_3$), 6.82 (t, $^3J$ = 7.6 Hz, 1 H, $C_6H_3$), 4.89 (sept, $^3J$ = 6.8 Hz, 2 H, C*H*$Me_2$), 4.32 (br. t, 8 H, O$CH_2$), 1.45 (d, $^3J$ = 6.8 Hz, 12 H, CH$Me_2$), 1.24 (br. t, 8 H, $CH_2$) ppm. $^{13}C\{^1H\}$ NMR (62.90 MHz, $C_6D_6$): $\delta$ = 160.0, 144.3, 125.0, 122.8 ($C_6H_3$), 77.1 (O$CH_2$), 28.6 (*C*H$Me_2$), 25.2 ($CH_2$), 24.8 (CH$Me_2$) ppm. IR (KBr): $\tilde{\nu}$ = 2954 (vs), 1459 (s), 1326 (s), 1279 (s), 1175 (w), 1037 (w), 1011 (s), 921 (m), 853 (vs), 751 (s), 686 (w), 544 (w) $cm^{-1}$. $C_{20}H_{33}I_2NO_2Ti$ (621.16): calcd. C 38.67, H 5.35, N 2.25; found C 35.99, H 4.96, N 2.05 (the elemental analysis always gave low C and N content).

**Supporting Information** (see footnote on the first page of this article): $^1H$ NMR spectra of complexes **1p** and **9**.

## Acknowledgments

We are grateful to the CNRS for financial support.

[1] a) D. E. Wigley, *Progress in Inorganic Chemistry*. (Ed.: K. D. Karlin), Interscience: **1994**, vol. 42, 239–482; b) W. A. Nugent, J. M. Mayer, *Metal-Ligand Multiple Bonds*. Wiley-Interscience, New York, **1998**; c) P. D. Bolton, P. Mountford, *Adv. Synth. Catal.* **2005**, *347*, 355–366; d) P. Mountford, *Chem. Commun.* **1997**, 2127–2134; e) L. H. Gade, P. Mountford, *Coord. Chem. Rev.* **2001**, *216–217*, 65–97; f) A. P. Duncan, R. G. Bergman, *Chem. Rec.* **2002**, *2*, 431–445.

[2] D. N. Williams, J. P. Mitchell, A. D. Poole, U. Siemeling, W. Clegg, D. C. R. Hockless, P. A. O'Neil, V. C. Gibson, *J. Chem. Soc., Dalton Trans.* **1992**, 739–751.

[3] R. R. Schrock, *Acc. Chem. Res.* **1990**, *23*, 158–165.

[4] a) M. C. W. Chan, K. C. Chen, C. I. Dalby, V. C. Gibson, A. Kohlmann, I. R. Little, W. Reed, *Chem. Commun.* **1998**, 1673–1674; b) S. Scheuer, J. Fischer, J. Kress, *Organometallics* **1995**, *14*, 2627–2629; c) D. A. Pennington, M. Bochmann, S. J. Lancaster, P. N. Horton, M. B. Hursthouse, *Polyhedron* **2005**, *24*, 151–156.

[5] C. Lorber, B. Donnadieu, R. Choukroun, *J. Chem. Soc., Dalton Trans.* **2000**, 4497–4498.

[6] a) A. J. Nielson, M. W. Glenny, C. E. F. Rickard, *J. Chem. Soc., Dalton Trans.* **2001**, 232–239; b) N. A. H. Male, M. E. G. Skinner, S. Y. Bylikin, P. J. Wilson, P. Mountford, M. Schröder, *Inorg. Chem.* **2000**, *39*, 5483–5491; c) N. Adams, P. D. Bolton, S. R. Dubberley, A. J. Sealey, A. R. Cowley, P. Mountford, P. J. Wilson, M. Schröder, D. Cowell, C. M. Grant, N. Friederichs, B. Wang, M. Kranenburg, H. J. Arts, *Chem. Commun.* **2004**, *10*, 434–435.

[7] a) K. E. Meyer, P. J. Walsh, R. G. Bergman, *J. Am. Chem. Soc.* **1995**, *117*, 974–982; b) K. E. Meyer, P. J. Walsh, R. G. Bergman, *J. Am. Chem. Soc.* **1994**, *116*, 2669–2670; c) G. K. Cantrell, T. Y. Meyer, *Chem. Commun.* **1997**, *2*, 1551–1552; d) G. K. Cantrell, T. Y. Meyer, *Organometallics* **1997**, *16*, 5381–5883; e) J. M. McInnes, P. Mountford, *Chem. Commun.* **1998**, 1669–1670.

[8] S. A. Blum, R. G. Bergman, *Organometallics* **2004**, *23*, 4003–4005.

[9] W. A. Nugent, *Inorg. Chem.* **1983**, *22*, 955–969.

[10] a) S. Y. Lee, R. G. Bergman, *J. Am. Chem. Soc.* **1995**, *117*, 5877–5878; b) J. L. Bennett, P. T. Wolczanski, *J. Am. Chem. Soc.* **1997**, *119*, 10696–10709; c) A. J. Blake, P. E. Collier, P. Mountford, L. H. Gade, M. Schubart, M. McPartlin, I. J. Scowen, *Chem. Commun.* **1997**, *2*, 1555–1556; d) P. J. Walsh, F. J. Hollander, R. G. Bergman, *J. Am. Chem. Soc.* **1993**, *12*, 3705–3723; e) H. M. Hoyt, F. E. Michael, R. G. Bergman, *J. Am. Chem. Soc.* **2004**, *126*, 1018–1019.

[11] a) D. J. M. Trösch, P. E. Collier, A. Bashall, L. H. Gade, M. McPartlin, P. Mountford, S. Radojevic, *Organometallics* **2001**, *20*, 3308–3313; b) P. J. Walsh, A. M. Baranger, R. G. Bergman, *J. Am. Chem. Soc.* **1992**, *114*, 1708–1719; c) S. Y. Lee, R. G. Bergman, *Tetrahedron* **1995**, *51*, 4255–4276; d) J. L. Polse, R. A. Andersen, R. G. Bergman, *J. Am. Chem. Soc.* **1998**, *120*, 13405–13414; e) B. D. Ward, A. Maisse-François, L. H. Gade, P. Mountford, *Chem. Commun.* **2004**, *10*, 704–705; f) K. S. Lokare, J. T. Ciszewski, A. L. Odom, *Organometallics* **2004**, *23*, 5386–5388; g) F. E. Michael, A. P. Duncan, Z. K. Sweeney, R. G. Bergman, *J. Am. Chem. Soc.* **2005**, *127*, 1752–1764.

[12] a) S. M. Pugh, P. Mountford, D. J. M. Trösch, L. H. Gade, D. J. Wilson, F. G. N. Cloke, P. B. Hitchcock, J. F. Nixon, A. Bashall, M. McPartlin, *Organometallics* **2000**, *19*, 3205–3210; b) I. Meisel, G. Hertl, K. Weiss, *J. Mol. Catal.* **1986**, *36*, 159–162; c) S.-H. Hsu, J.-C. Chang, C.-L. Lai, C.-H. Hu, H. M. Lee, G.-H. Lee, S.-M. Peng, J.-H. Huang, *Inorg. Chem.* **2004**, *43*, 6786–6792; d) T. E. Hanna, I. Keresztes, E. Lobkovsky, W. H. Bernskoetter, P. J. Chirik, *Organometallics* **2004**, *23*, 3448–3458.

[13] For some examples of hydroamination with imido–titanium catalysts, see a) C. Lorber, R. Choukroun, L. Vendier, *Organometallics* **2004**, *23*, 1845–1850; b) L. Ackermann, R. G. Bergman, R. N. Loy, *J. Am. Chem. Soc.* **2003**, *125*, 11956–11963; c) T.-G. Ong, G. P. A. Yap, D. S. Richeson, *Organometallics* **2002**, *21*, 2839–2841; d) H. Wang, H.-S. Chan, Z. Xie, *Organometallics* **2005**, *24*, 3772–3779.

 © 2006 Wiley-VCH Verlag GmbH & Co. KGaA, Weinheim 

[14] For selected examples of hydroamination with Group 4 precatalysts, see a) Y. H. Li, Y. H. Shi, A. L. Odom, *J. Am. Chem. Soc.* **2004**, *126*, 1794–1803; b) L. Ackermann, *Organometallics* **2003**, *22*, 4367–4368; c) B. Ramanathan, J. A. Keith, D. Armstrong, A. L. Odom, *Org. Lett.* **2004**, *6*, 2957–2960; d) F. Pohlki, I. Bytschov, H. Siebeneicher, A. Heutling, W. A. König, S. Doye, *Eur. J. Org. Chem.* **2004**, 1967–1972; e) J. A. Bexrud, J. D. Beard, D. C. Leitch, L. L. Schafer, *Org. Lett.* **2005**, *7*, 1959–1962; f) A. Tillack, V. Khedkar, H. J. Jiao, M. Beller, *Eur. J. Org. Chem.* **2005**, 5001–5012; g) D. V. Gribkov, K. C. Hultzsch, *Angew. Chem. Int. Ed.* **2004**, *44*, 5542–5546.

[15] a) R. T. Ruck, R. G. Bergman, R. L. Zuckerman, S. W. Krska, *Angew. Chem. Int. Ed.* **2004**, *43*, 5372–5374; b) R. T. Ruck, R. G. Bergman, *Angew. Chem. Int. Ed.* **2004**, *43*, 5375–5377; c) F. Basuli, H. Aneetha, J. C. Huffman, D. J. Mindiola, *J. Am. Chem. Soc.* **2005**, *127*, 17992–17993.

[16] S. A. Blum, V. A. Rivera, R. T. Ruck, F. E. Michael, R. G. Bergman, *Organometallics* **2005**, *24*, 1647–1659.

[17] a) C. J. Carmalt, A. Newport, I. P. Parkin, P. Mountford, A. J. Sealey, S. R. Dubberley, *J. Mater. Chem.* **2003**, *13*, 84–87; b) C. J. Carmalt, A. C. Newport, I. P. Parkin, A. J. P. White, D. J. Williams, *J. Chem. Soc., Dalton Trans.* **2002**, 4055–4059; c) C. H. Winter, P. H. Sheridan, T. S. Lewkebandara, M. J. Heeg, J. W. Proscia, *J. Am. Chem. Soc.* **1992**, *114*, 1095–1097; d) O. J. Bchir, K. M. Green, M. S. Hlad, T. J. Anderson, B. C. Brooks, C. B. Wilder, D. H. Powell, L. McElwee-White, *J. Organomet. Chem.* **2003**, *684*, 338–350; e) O. J. Bchir, K. M. Green, H. M. Ajmera, E. A. Zapp, T. J. Anderson, B. C. Brooks, L. L. Reitfort, D. H. Powell, K. A. Abboud, L. McElwee-White, *J. Am. Chem. Soc.* **2005**, *127*, 7825–7833.

[18] a) Z. Peng, *Angew. Chem. Int. Ed.* **2004**, *43*, 930–935; b) A. R. Moore, H. Kwen, A. M. Beatty, E. A. Maatta, *Chem. Commun.* **2000**, 1793–1794; c) J. B. Strong, G. P. A. Yap, R. Ostrander, L. M. Liable-Sands, A. L. Rheingold, R. Thouvenot, P. Gouzerh, E. A. Maatta, *J. Am. Chem. Soc.* **2000**, *122*, 639–649.

[19] T. E. Hanna, *Coord. Chem. Rev.* **2004**, *248*, 429–440.

[20] a) F. Wolff, C. Lorber, R. Choukroun, B. Donnadieu, *Eur. J. Inorg. Chem.* **2004**, 2861–2867; b) F. Wolff, R. Choukroun, C. Lorber, B. Donnadieu, *Eur. J. Inorg. Chem.* **2003**, 628–632; c) F. Wolff, C. Lorber, R. Choukroun, B. Donnadieu, *Inorg. Chem.* **2003**, *42*, 7839–7845; d) C. Lorber, B. Donnadieu, R. Choukroun, *Organometallics* **2000**, *19*, 1963–1966; e) R. Choukroun, C. Lorber, B. Donnadieu, *Organometallics* **2004**, *23*, 1434–1437; f) R. Choukroun, C. Lorber, L. Vendier, B. Donnadieu, *Organometallics* **2004**, *23*, 5488–5492; g) R. Choukroun, C. Lorber, B. Donnadieu, *Organometallics* **2002**, *21*, 1124–1126; h) R. Choukroun, B. Donnadieu, C. Lorber, P. M. Pellny, W. Baumann, U. Rosenthal, *Chem. Eur. J.* **2000**, *6*, 4505–4509; i) C. Lorber, F. Wolff, R. Choukroun, L. Vendier, *Eur. J. Inorg. Chem.* **2005**, 2850–2859.

[21] C. Lorber, R. Choukroun, B. Donnadieu, *Inorg. Chem.* **2002**, *41*, 4217–4226.

[22] C. Lorber, R. Choukroun, B. Donnadieu, *Inorg. Chem.* **2003**, *42*, 673–675.

[23] A. J. Blake, P. E. Collier, S. C. Dunn, W.-S. Li, P. Mountford, O. V. Shishkin, *J. Chem. Soc., Dalton Trans.* **1997**, 1549–1558.

[24] a) A. J. Nielson, *Inorg. Chim. Acta* **1988**, *154*, 177–182; b) T. S. Lewkebandara, P. H. Sheridan, M. J. Heeg, A. L. Rheingold, C. H. Winter, *Inorg. Chem.* **1994**, *33*, 5879–5889.

[25] Y. Li, S. Banerjee, A. L. Odom, *Organometallics* **2005**, *24*, 3272–3278.

[26] N. Adams, H. R. Bigmore, T. L. Blundell, C. L. Boyd, S. R. Dubberley, A. J. Sealey, A. R. Cowley, M. E. G. Skinner, P. Mountford, *Inorg. Chem.* **2005**, *44*, 2882–2894.

[27] E. Benzing, W. Kornicker, *Chem. Ber.* **1961**, *94*, 2263–2267.

[28] For some typical examples of the use of $Me_3SiCl$ as a chlorinating agent for the cleavage of Ti–$N_{amido}$ bond in Group 4 complexes, see a) D. J. Arney, M. A. Bruck, S. R. Huber, D. E. Wigley, *Inorg. Chem.* **1992**, *31*, 3749–3755; b) G. M. Diamond, R. F. Jordan, J. L. Petersen, *Organometallics* **1996**, *15*, 4030–4037; c) R. Baumann, W. M. Davis, R. R. Schrock, *J. Am. Chem. Soc.* **1997**, *119*, 3830–3831.

[29] a) C. C. Cummins, C. P. Schaller, G. D. Van Duyne, P. T. Wolczanski, A. W. C. Chan, R. Hoffmann, *J. Am. Chem. Soc.* **1991**, *113*, 2985–2994; b) J. L. Bennett, P. T. Wolczanski, *J. Am. Chem. Soc.* **1994**, *116*, 2179–2180; c) H. Bürger, U. Wannagat, *Monatsh. Chem.* **1963**, *94*, 761–764; d) N. W. Alcock, M. Pierce-Butler, G. R. Willey, *J. Chem. Soc., Dalton Trans.* **1976**, 707–713; e) R. Wollert, S. Wocadlo, K. Dehnicke, H. Goesmann, D. Fenske, *Z. Naturforsch., Teil B* **1992**, *47*, 1386; f) R. Schlichenmaier, J. Strähle, *Z. Anorg. Allg. Chem.* **1993**, *619*, 1526–1529; g) L. M. Slaughter, P. T. Wolczanski, T. R. Klinckman, T. R. Cundari, *J. Am. Chem. Soc.* **2000**, *122*, 7953–7975; h) M. A. Putzer, B. Neumüller, K. Dehnicke, *Z. Anorg. Allg. Chem.* **1998**, *624*, 57–64; i) J. D. Gardner, D. A. Robson, L. H. Rees, P. Mountford, *Inorg. Chem.* **2001**, *40*, 820–824; j) J. R. Hagadorn, J. Arnold, *Organometallics* **1998**, *17*, 1355–1368.

[30] J. E. Hill, P. E. Fanwick, I. P. Rothwell, *Inorg. Chem.* **1991**, *30*, 1143–1144.

[31] $\tau$ is the angular parameter commonly used to describe the geometry around the metal center in pentacoordinate complexes and defined as $\tau = (\alpha–\beta)/60$ ($\alpha$ and $\beta$ are the two largest L–M–L bond angles, with $\alpha \geq \beta$). A. W. Addison, T. N. Rao, J. Reedijk, J. V. van Rijn, *J. Chem. Soc., Dalton Trans.* **1984**, 1349–1356.

[32] a) D. L. Thorn, W. A. Nugent, *J. Am. Chem. Soc.* **1981**, *103*, 357–363; b) W. A. Nugent, B. L. Haymore, *Coord. Chem. Rev.* **1980**, *31*, 123–175; c) S. Gambarotta, C. Floriani, A. Chiesi-Villa, C. Guastini, *J. Chem. Soc., Chem. Commun.* **1982**, 1015–1017.

[33] For a review on the stereochemistry of polymerization, and an example of polymerization with the use of an enantiomerically pure catalyst, see a) G. W. Coates, *Chem. Rev.* **2000**, *100*, 1223–1252; b) A. E. Cherian, E. B. Lobkovsky, G. W. Coates, *Chem. Commun.* **2003**, 2566–2567.

[34] For some examples of the use of enantiomerically pure amines as substrates for Ti-catalyzed hydroamination of alkynes, see ref.[13a] and ref.[14c].

[35] For an example of a chiral molybdenum diimido complex, see E. A. Kretzschmar, J. Kipke, J. Sundermeyer, *Chem. Commun.* **1999**, 2381–2388.

[36] Complex **1s*** has also been obtained as yellow needles that crystallized in the orthorhombic space group $P2_12_12_1$ [*a*: 6.5483(2), *b*: 7.7647(3), *c*: 33.3440(9)]. Bond lengths and angles are similar, but the overall structure differs by the position of the N–H bonds: *syn* in the $P\,2_1$ structure versus *anti* in the $P\,2_12_12_1$ structure, and by the NH···Cl network.

[37] Overall, complex **6s*** only differs from **1s*** by the loss of one $NHMe_2$ ligand/Ti center. To explain its formation, we suspect the concomitant formation [when $Ti(NMe_2)_4/R^*NH_2$ ratio > 1] of a small amount of $[TiCl_3(NMe_2)(HNMe_2)]_2$ that would trap some of the $HNMe_2$ ligand needed to form **1s*** and thus **6s*** is formed. These studies, that are related to the mechanism of the general reaction $Ti(NMe_2)_4/RNH_2/Me_3SiCl$, are under current investigations and will be reported in due course.

[38] The chiral imido–vanadium analogue complex has been prepared similarly and its structure has been established by X-ray structure determination. C. Lorber, Unpublished result.

[39] Selected examples of Group 5/6 diimido complexes: a) E. A. Maatta, D. D. Devore, *Angew. Chem. Int. Ed. Engl.* **1988**, *27*, 569–571; b) D. E. Wheeler, J.-F. Wu, E. A. Maatta, *Polyhedron* **1998**, *17*, 969–976; c) A. Antinolo, I. Dorado, M. Fajardo, A. Garces, I. Lopez-Solera, C. Lopez-Mardomingo, M. M. Kubicki, A. Otero, S. Prashar, *Eur. J. Inorg. Chem.* **2004**, 1299–1310; d) S. Prashar, M. Fajardo, A. Garces, I. Dorado, A. Antinolo, A. Otero, I. Lopez-Solera, C. Lopez-Mardomingo, *J. Organomet. Chem.* **2004**, *689*, 1304–1314.

[40] For an example of cleavage of Ti–$NMe_2$ with $CH_3I$, see A. R. Johnson, P. W. Wanandi, C. C. Cummins, D. M. Davis, *Organometallics* **1994**, *13*, 2907–2909.


 © 2006 Wiley-VCH Verlag GmbH & Co. KGaA, Weinheim 

[41] D. C. Bradley, I. M. Thomas, *J. Chem. Soc.* **1960**, 3857–3861.
[42] A. Altomare, G. Cascarano, G. Giacovazzo, A. Guagliardi, M. C. Burla, G. Polidori, M. Camalli, *J. Appl. Crystallogr.* **1994**, *27*, 435.
[43] G. M. Sheldrick, *SHELX97 [Includes SHELXS97, SHELXL97, CIFTAB] - Programs for Crystal Structure Analysis (Release 97–2). Institut für Anorganische Chemie der Universität, Tammanstrasse 4, D-3400 Göttingen, Germany*, 1998.
[44] L. J. Farrugia, *J. Appl. Crystallogr.* **1999**, *32*, 837–838.
[45] N. Walker, D. Stuart, *Acta Crystallogr., Sect. A* **1983**, *39*, 158–166.
[46] A. L. Spek, *Acta Crystallogr., Sect. A* **1990**, *46*, C34.
[47] G. Bernardinelli, H. D. Flack, *Acta Crystallogr., Sect. A* **1985**, *41*, 500–511.

Received: May 22, 2006
Published Online: August 7, 2006

 © 2006 Wiley-VCH Verlag GmbH & Co. KGaA, Weinheim 

DOI: 10.1002/ejic.200600264

# Slipped μ-Indenyl Triple-Decker Complexes Containing $(C_4Me_4)Co$ and $(C_5R_5)Ru$ Fragments[‡]

**Elena V. Mutseneck,[a] Zoya A. Starikova,[a] Konstantin A. Lyssenko,[a] Pavel V. Petrovskii,[a] Piero Zanello,[b] Maddalena Corsini,[b] and Alexander R. Kudinov*[a]**

**Keywords:** Cobalt / Ruthenium / Sandwich compounds / Triple-decker complexes / Electrochemistry

Slipped triple-decker complexes with a bridging indenyl ligand, namely $[Cb^*Co(\mu{:}\eta^5{:}\eta^6\text{-}C_9H_7)CoCb^*]^+$ (**2**, $Cb^* = C_4Me_4$) and $[Cb^*Co(\mu{:}\eta^5{:}\eta^6\text{-}C_9H_7)Ru(C_5R_5)]^+$ (R = H, **5a**; Me, **5b**), have been synthesised by electrophilic stacking of $[Cb^*Co(\eta^5\text{-}C_9H_7)]$ (**1**) with $[Cb^*Co(MeCN)_3]^+$ or $[(C_5R_5)Ru(MeCN)_3]^+$ (R = H, Me), respectively. A similar reaction of $[(C_5R_5)Ru(\eta^5\text{-}C_9H_7)]$ (R = H, **3a**; Me, **3b**) with $[Cb^*Co(MeCN)_3]^+$ affords the cations $[(C_5R_5)Ru(\mu{:}\eta^5{:}\eta^6\text{-}C_9H_7)CoCb^*]^+$ (R = H, **4a**; Me, **4b**), which are isomeric with **5a**,**b**. Stacking of $[Ru(\eta^5\text{-}C_9H_7)_2]$ (**7**) with $[Cb^*Co(MeCN)_3]^+$ or $[Cb^*CoI]_x/TlBF_4$ gives the triple-decker complex $[(\eta^5\text{-}C_9H_7)Ru(\mu{:}\eta^5{:}\eta^6\text{-}C_9H_7)CoCb^*]^+$ (**8**). Further reaction of **8** with $[Cp^*RuCl]_4/TlBF_4$ unexpectedly affords the slipped tetradecker ruthenium complex $[Cp^*Ru(\mu{:}\eta^5{:}\eta^6\text{-}C_9H_7)Ru(\mu{:}\eta^5{:}\eta^6\text{-}C_9H_7)RuCp^*]^{2+}$ (**11**). The structures of **[4b]**$[Co(\eta\text{-}7,8\text{-}C_2B_9H_{11})_2]$ and $[Cp^*Ru(\eta^6\text{-}C_9H_7)]$ (**6**) have been determined by X-ray diffraction, and the electrochemical behaviour of the complexes prepared has been studied.
(© Wiley-VCH Verlag GmbH & Co. KGaA, 69451 Weinheim, Germany, 2006)

## Introduction

The presence of two fused π-systems in pentalene, indenyl and naphthalene makes them able to form slipped triple-decker complexes with an *anti* coordination of the metal atoms.[2] The first example of such compounds, $[(\eta^3\text{-allyl})Ni(\mu{:}\eta^5{:}\eta^5\text{-}C_8H_6)Ni(\eta^3\text{-allyl})]$, was described by Miyake and Kanai in 1971.[3] Manriquez et al. have synthesised a series of fused metallocenes with the formula $[Cp^*M(\mu{:}\eta^5{:}\eta^5\text{-}C_8H_6)M'Cp^*]$ (M, M′ = Fe, Co, Ni, Ru) along with other related compounds.[4] Their most interesting feature is a strong electronic interaction between the metal centres, as established by electrochemical and spectroscopic studies. A few μ-naphthalene triple-decker complexes are known: $[(\eta^6\text{-}C_6H_6)Cr(\mu{:}\eta^6{:}\eta^6\text{-}C_{10}H_8)Cr(\eta^6\text{-}C_6H_6)]$,[5] $[(C_5R_5)M(\mu{:}\eta^6{:}\eta^6\text{-}C_{10}H_8)M(C_5R_5)]$ (M = V, Fe[6]), and $[(cod)Ru(\mu{:}\eta^6{:}\eta^6\text{-}C_{10}H_8)Ru(cod)]$.[7] μ-Indenyl derivatives are the least studied, and the first examples, the ruthenium complexes $[(C_5R_5)Ru(\mu{:}\eta^5{:}\eta^6\text{-}C_9H_7)Ru(C_5R_5)]^+$,[8] were prepared by electrophilic stacking of $[(C_5R_5)Ru(\eta^5\text{-}C_9H_7)]$ with $[(C_5R_5)Ru]^+$ fragments.[9]

Recently we have developed convenient methods for the preparation of (tetramethylcyclobutadiene)cobalt complexes.[10–13] The acetonitrile complex $[Cb^*Co(MeCN)_3]^+$ ($Cb^* = C_4Me_4$) has been shown to be the most useful synthon of the Cb*Co fragment. In particular, its reaction with the indenide anion gives the $\eta^5$-indenyl derivative $[Cb^*Co(\eta^5\text{-}C_9H_7)]$ (**1**).[12] Herein we describe the synthesis and electrochemical behaviour of dicobalt and cobalt-ruthenium triple-decker complexes with a bridging indenyl ligand.[14]

## Results and Discussion

### Synthesis

Electrophilic stacking of **1** with $[Cb^*Co(MeCN)_3]^+$ in nitromethane affords the slipped dicobalt triple-decker complex $[Cb^*Co(\mu{:}\eta^5{:}\eta^6\text{-}C_9H_7)CoCb^*]^+$ (**2**) in 54% yield (Scheme 1). Similar reactions of the $(\eta^5$-indenyl)ruthenium derivatives $[(C_5R_5)Ru(\eta^5\text{-}C_9H_7)]$ (R = H, **3a**; Me, **3b**) give the cobalt-ruthenium complexes $[CpRu(\mu{:}\eta^5{:}\eta^6\text{-}C_9H_7)CoCb^*]^+$ (**4a**, 23%) and $[Cp^*Ru(\mu{:}\eta^5{:}\eta^6\text{-}C_9H_7)CoCb^*]^+$ (**4b**, 54%; Scheme 2). Both reactions are reversible, with nucleophilic degradation of the products by acetonitrile being the back reaction. The low yield of **4a** suggests it degrades easier than **4b**, which is apparently connected with the poorer donor ability of the CpRu fragment. Nevertheless, we were able to increase the yield up to 78% by using a fivefold excess of **3a** and removing acetonitrile from the reaction mixture.

[‡] (Tetramethylcyclobutadiene)cobalt Complexes, 6. For part 5 see ref.[1]

[a] A. N. Nesmeyanov Institute of Organoelement Compounds, Russian Academy of Science,
28 ul. Vavilova, 119991 Moscow, GSP-1, Russian Federation
Fax: +7-495-135-5085
E-Mail: arkudinov@ineos.ac.ru
[b] Dipartimento di Chimica, Università di Siena,
Via Aldo Moro, 53100 Siena, Italy

Supporting information for this article is available on the WWW under http://www.eurjic.org or from the author.

 © 2006 Wiley-VCH Verlag GmbH & Co. KGaA, Weinheim 

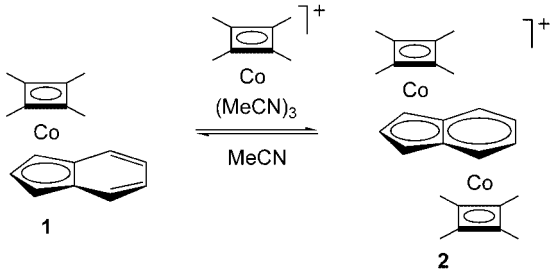


Scheme 1. Synthesis of the $Co_2$ complex **2**.

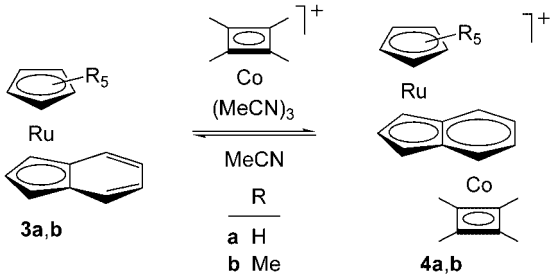


Scheme 2. Synthesis of the CoRu complexes **4a**,**b**.

The cobalt atom in complexes **4a**,**b** is coordinated at the six-membered ring of the indenyl ligand. The isomeric cations $[Cb^*Co(\mu{:}\eta^5{:}\eta^6\text{-}C_9H_7)Ru(C_5R_5)]^+$ (R = H, **5a**; Me, **5b**) with the cobalt atom at the five-membered ring were prepared by stacking of **1** with $[(C_5R_5)Ru(MeCN)_3]^+$ (R = H, Me; Scheme 3). Alternatively, complex **5b** was obtained by treatment of the $\eta^6$-indenyl derivative $[Cp^*Ru(\eta^6\text{-}C_9H_7)]$ (**6**) with $[Cb^*Co(MeCN)_3]^+$ (Scheme 4).

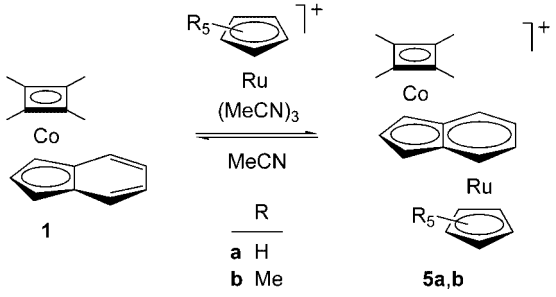


Scheme 3. Synthesis of the CoRu complexes **5a**,**b**.

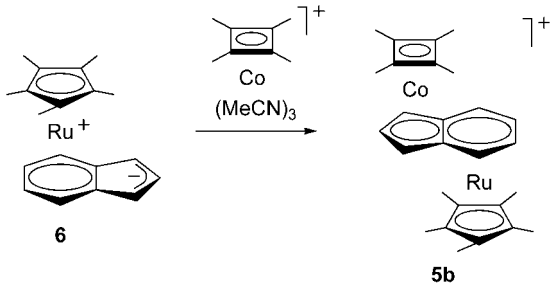


Scheme 4. Synthesis of **5b** from the $\eta^6$-indenyl complex **6**.

It has been shown previously that stacking of bis(indenyl)ruthenium $[Ru(\eta^5\text{-}C_9H_7)_2]$ (**7**) with $[(C_5R_5)Ru(MeCN)_3]^+$ affords either triple- or tetra-decker complexes such as $[(C_5R_5)Ru(\mu{:}\eta^5{:}\eta^6\text{-}C_9H_7)Ru(\eta^5\text{-}C_9H_7)]^+$ and $[(C_5R_5)Ru(\mu{:}\eta^5{:}\eta^6\text{-}C_9H_7)Ru(\mu{:}\eta^5{:}\eta^6\text{-}C_9H_7)Ru(C_5R_5)]^{2+}$ as a result of addition of one or two fragments, respectively.[8a] However, a similar reaction of **7** with $[Cb^*Co(MeCN)_3]^+$ gives only the slipped triple-decker complex $[(\eta^5\text{-}C_9H_7)Ru(\mu{:}\eta^5{:}\eta^6\text{-}C_9H_7)CoCb^*]^+$ (**8**, 15–20%), irrespective of the reagent ratio (Scheme 5). The yield was greatly increased (up to 65%) by using a new method for the generation of the $[Cb^*Co]^+$ fragment. This utilizes halide abstraction from the iodide complex $[Cb^*CoI]_x$ by treatment with $TlBF_4$ in thf. The advantage of this method is the absence of strongly coordinating acetonitrile. In particular, it has proved to be very effective for the preparation of arene complexes $[Cb^*Co(arene)]^+$ containing acceptor ligands (dichlorobenzene, acetophenone and anthracene).[15]

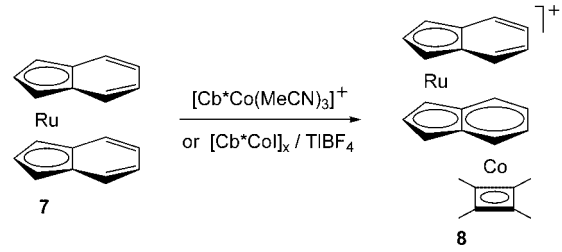


Scheme 5. Synthesis of the CoRu complex **8**.

However, the reaction of **7** with two equivalents of $[Cb^*CoI]_x/TlBF_4$ does not give the expected tetra-decker complex $[Cb^*Co(\mu{:}\eta^5{:}\eta^6\text{-}C_9H_7)Ru(\mu{:}\eta^5{:}\eta^6\text{-}C_9H_7)CoCb^*]^{2+}$. We propose that the insolubility of the primary product **8**·$BF_4$ in thf precludes its further stacking reaction.[16] However, the salt $[\mathbf{8}][Co(\eta\text{-}7,8\text{-}C_2B_9H_{11})_2]$, which is well soluble in thf, also proved to be unreactive towards $[Cb^*CoI]_x/Tl[Co(\eta\text{-}7,8\text{-}C_2B_9H_{11})_2]$.

The reaction of the triple-decker cation **8** with the $[Cp^*Ru]^+$ fragment, generated as a labile solvate from $[Cp^*RuCl]_4/TlBF_4$ in $MeNO_2$ (Scheme 6), proved to be very intriguing. A 1:1 molar ratio resulted in a mixture of the slipped triple-decker complexes **8** (25%) and $[Cp^*Ru(\mu{:}\eta^5{:}\eta^6\text{-}C_9H_7)Ru(\eta^5\text{-}C_9H_7)]^+$ (**10**, 15%) along with the slipped tetra-decker complex $[Cp^*Ru(\mu{:}\eta^5{:}\eta^6\text{-}C_9H_7)Ru(\mu{:}\eta^5{:}\eta^6\text{-}C_9H_7)RuCp^*]^{2+}$ (**11**, 60%), whereas with a 1:2 ratio only complex **11** (59%) was isolated. The unstable cobalt-ruthenium tetra-decker cation $[Cb^*Co(\mu{:}\eta^5{:}\eta^6\text{-}C_9H_7)Ru(\mu{:}\eta^5{:}\eta^6\text{-}C_9H_7)RuCp^*]^{2+}$ (**9**) is believed to be an intermediate. Its further degradation leads to the diruthenium cation **10** by elimination of the $[Cb^*Co]^+$ fragment. Subsequent reaction of **10** with a second equivalent of $[Cp^*Ru]^+$ gives the stable $Ru_3$ tetra-decker cation **11**.

 © 2006 Wiley-VCH Verlag GmbH & Co. KGaA, Weinheim 

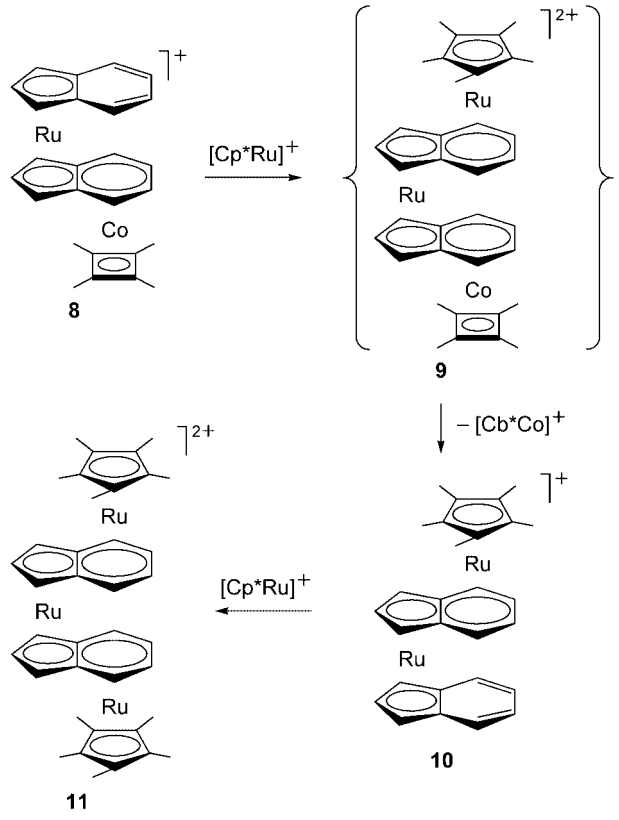


Scheme 6. Formation of the $Ru_3$ complex **11**.

### Nucleophilic Degradation

Nucleophilic degradation of triple-decker complexes by solvent molecules is the back reaction to electrophilic stacking.[17] As shown above, this process complicates the preparation of μ-indenyl triple-decker complexes, stimulating us to study degradation of the permethylated cations **2**, **4b** and **5b** by acetone and acetonitrile.

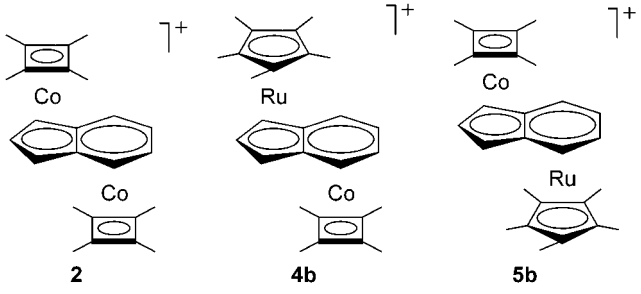


In accordance with the $^1H$ NMR spectroscopic data, all the cations slowly decompose in [$D_6$]acetone with the formation of a mononuclear $\eta^5$-indenyl complex (**1** or **3b**) and a solvate cationic complex ([Cb*Co($Me_2CO$)$_3$]$^+$ or [Cp*Ru($Me_2CO$)$_3$]$^+$). After one day, the 30% conversion of **4b** was observed. Further standing for one week did not cause any further changes. The behaviour of complexes **2** and **5b** is slightly different: the initially formed mononuclear cobalt compound **1** decomposes within several days, apparently owing to its oxidation by cationic solvate complexes. The absence of secondary processes for **4b** is in agreement with the higher oxidation potential of **3b** (+0.50 V, vide supra) compared with **1** (+0.33 V).[12]

The nucleophilic degradation rate increases in the order **5b** < **2** < **4b**. Cations **2** and **4b** differ by the fragment coordinated at the five-membered ring of the indenyl ligand. The Cp*Ru fragment accepts electron density of this ring to a greater extent than Cb*Co (due to the more covalent bonding of the ruthenium atom), which results in a higher positive charge at the $\eta^6$-coordinated cobalt atom and, as a consequence, to easier degradation of **4b**. Comparing **2** and **5b**, the [Cp*Ru]$^+$ fragment is more strongly bonded with the six-membered ring than [Cb*Co]$^+$, which explains the lower reactivity of **5b**.

Dissolution of complexes **2**, **4b** and **5b** in acetonitrile results in immediate decomposition. In the case of **4b**, a yellow solution was formed. $^1H$ NMR spectroscopy detected the starting compounds, **3b** and [Cb*Co(MeCN)$_3$]$^+$ resulting from nucleophilic degradation. The decomposition of **2** and **5b** leads to green solutions that show only very broad signals indicative of paramagnetic species. This behaviour contradicts with the preparation of triple-decker cations from acetonitrile complexes. However, we have shown that **5b** decomposes only slowly in the presence of two equivalents of MeCN in $CD_2Cl_2$, thus resolving the contradiction. As in the case of degradation by acetone, the more complex behaviour of derivatives **2** and **5b** with the cobalt atom coordinated at the five-membered ring may be explained by the easier oxidation of **1** compared with **3b**.

### X-ray Diffraction Study

The structures of complexes **6** and [**4b**][Co(η-7,8-$C_2B_9H_{11}$)$_2$][18] were investigated by X-ray diffraction (Figures 1 and 2, respectively). Selected bond lengths are given in Tables 1 and 2, respectively.

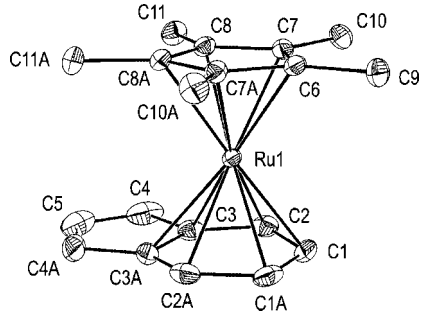


Figure 1. Structure of complex **6**. Ellipsoids are shown at the 50% level.

The structure of **6** is the first example of a mononuclear complex with an $\eta^6$-coordinated indenyl ligand. The structure has a symmetry plane. The ruthenium atom is not quite symmetrically coordinated with the six-membered ring, the distances from the Ru atom to the bridgehead C3 and C3A atoms (2.367 Å) being noticeably longer than other Ru–C distances (2.202 and 2.228 Å). This elongation (0.139–0.165 Å) is much greater than that for the isomeric $\eta^5$-indenyl complex **3b** (0.02–0.06 Å).[19] The six-membered ring

 © 2006 Wiley-VCH Verlag GmbH & Co. KGaA, Weinheim 

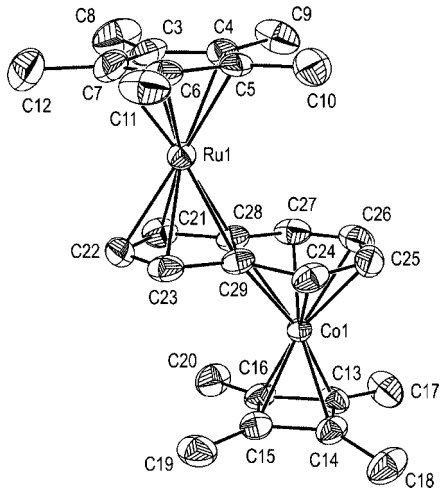


Figure 2. Structure of cation **4b**. Ellipsoids are shown at the 50% level.

Table 1. Selected bond lengths [Å] for complex **6**.

| | | | |
|---|---|---|---|
| Ru1–C1 | 2.202(1) | C1–C1A | 1.422(3) |
| Ru1–C2 | 2.228(1) | C1–C2 | 1.415(2) |
| Ru1–C3 | 2.367(1) | C2–C3 | 1.427(2) |
| Ru1–C6 | 2.165(2) | C3–C3A | 1.473(2) |
| Ru1–C7 | 2.169(1) | C3–C4 | 1.411(2) |
| Ru1–C8 | 2.169(1) | C4–C5 | 1.400(3) |

Table 2. Selected bond lengths [Å] for complex **4b**.

| | | | |
|---|---|---|---|
| Ru1–C4 | 2.125(4) | Co1–C13 | 2.006(4) |
| Ru1–C5 | 2.146(4) | Co1–C14 | 2.011(4) |
| Ru1–C7 | 2.147(5) | Co1–C16 | 2.014(5) |
| Ru1–C3 | 2.149(5) | Co1–C15 | 2.014(5) |
| Ru1–C6 | 2.153(4) | Co1–C24 | 2.098(4) |
| Ru1–C21 | 2.176(4) | Co1–C25 | 2.099(5) |
| Ru1–C22 | 2.176(5) | Co1–C26 | 2.099(5) |
| Ru1–C23 | 2.186(4) | Co1–C27 | 2.102(5) |
| Ru1–C28 | 2.217(4) | Co1–C28 | 2.185(4) |
| Ru1–C29 | 2.218(4) | Co1–C29 | 2.202(4) |
| C3–C7 | 1.394(7) | C13–C14 | 1.447(6) |
| C3–C4 | 1.406(7) | C13–C16 | 1.480(7) |
| C4–C5 | 1.455(6) | C14–C15 | 1.443(6) |
| C5–C6 | 1.427(6) | C15–C16 | 1.469(7) |
| C6–C7 | 1.412(7) | C24–C25 | 1.409(7) |
| C21–C22 | 1.417(7) | C24–C29 | 1.444(7) |
| C21–C28 | 1.454(7) | C25–C26 | 1.386(8) |
| C22–C23 | 1.408(7) | C26–C27 | 1.374(8) |
| C23–C29 | 1.414(6) | C27–C28 | 1.421(6) |
| C28–C29 | 1.477(6) | | |

is folded along the line C2–C2a (by 6.4°). For comparison, the distances from the metal atom to the non-bonded carbon atoms of the $\eta^4$-coordinated arene ligand in the ruthenium compound $[(\eta^6\text{-}C_6Me_6)Ru(\eta^4\text{-}C_6Me_6)]$ (av. 3.028 Å) are 0.838–0.950 Å longer than the other Ru–C distances (av. 2.148 Å); the folding angle is 43°.[20] The much shorter elongation for **6**, along with the requirement of an 18-electron configuration, confirms the $\eta^6$-bonding mode of the indenyl ligand.

Compound **6** can be represented by three limiting structures (Scheme 7). The elongation of the Ru–C3(3A) distances and folding of the six-membered ring can be explained by a considerable contribution of the neutral structures with an $\eta^5$-coordinated indenyl ligand. Following the same reasoning, in the case of the related $\eta^6$-fluorenyl-iron[21] and -manganese[22] complexes the six-membered ring is also folded, with considerable elongation of the distance from the metal atom to one of the bridgehead carbon atoms.

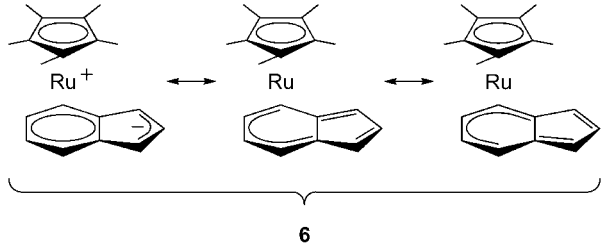


Scheme 7. Limiting structures of **6**.

Cation **4b** has a slipped triple-decker structure with a central $\eta^5$:$\eta^6$-indenyl ligand. This ligand is essentially planar, with maximum deviations of the C(24) and C(27) atoms by 0.060 and 0.046 Å, respectively, towards the cobalt atom. The ligand planes are essentially coplanar, the dihedral angles Cp*/$C_9H_7$ and Cb*/$C_9H_7$ being 3.4° and 0.6°, respectively.

A more detailed consideration of the structure revealed a folding of the five- and six-membered rings along the axes C(21)–C(23) (2.5°) and C(24)–C(27) (7.4°). Likewise, the metal atoms are not quite symmetrically coordinated with the rings. For instance, the distances from the Ru atom to the bridgehead C(28) and C(29) atoms (2.217 and 2.218 Å, respectively) are longer than the other Ru–C distances (2.176, 2.176 and 2.186 Å). However, this elongation (0.03–0.04 Å) is rather small and comparable with that for the mononuclear complex **3b** (0.02–0.06 Å),[19] thus confirming the $\eta^5$-bonding mode of the indenyl ligand.[23] The Ru···($\eta^5$-$C_9H_7$) distance (1.835 Å) in cation **4b** is slightly shorter than that in **3b** (1.840 Å),[19] which suggests stronger bonding in the case of **4b**. The Ru···Cp* distance (1.772 Å) in **4b** is also shorter than that in **3b** (1.792 Å).[19]

The bonding of the cobalt atom with the six-membered ring is even more asymmetrical. The Co–C(28) and Co–C(29) distances (2.185 and 2.202 Å, respectively) are longer than the other Co–C distances (2.098, 2.099, 2.099 and 2.102 Å) by 0.09–0.10 Å. This elongation is practically the same as that for the M($\eta^6$-$C_9H_7$) fragment in $[CpRu(\mu{:}\eta^5{:}\eta^6\text{-}C_9H_7)RuCp^*]^+$ (**12a**; 0.08–0.10 Å)[8a] and $[(cod)Rh(\mu{:}\eta^5{:}\eta^6\text{-}C_9H_7)Cr(CO)_3]$ (0.09–0.12 Å),[24] slightly longer than that in the naphthalene complex $[Cb^*Co(C_{10}H_8)]^+$ (0.04–0.06 Å)[15] but smaller than in **6** (0.14–0.17 Å), the $\eta^6$-coordination mode in which is clear.

The triple-decker cation **4b** could be considered as an arene complex in which the sandwich compound **3b** acts as a six-electron ligand towards the $[Cb^*Co]^+$ fragment. The Co···Cb* distance in **4b** (1.726 Å) is significantly longer than that for cations $[Cb^*Co(C_6H_6)]^+$ (1.702 Å) and $[Cb^*Co(C_{10}H_8)]^+$ (1.707 Å),[15] thus suggesting the greater acceptor ability of **3b** compared with benzene and naphthalene.

 © 2006 Wiley-VCH Verlag GmbH & Co. KGaA, Weinheim 

The C–C bonds within the five-membered ring of the indenyl ligand in **4b** are generally longer than those in **3b**. The bond between the bridgehead carbon atoms is the most elongated (1.477 Å in **4b** and 1.446 Å in **3b**), in accordance with a greater loosening of the π bond upon bifacial coordination. A similar elongation has been observed for the triple-decker complex **12a** (av. 1.481 Å).[8a]

### Electrochemistry

In this section we describe the redox properties of the μ-indenyl triple-decker complexes **2**, **4b** and **5a**,**b** and their diruthenium analogues **12a**–**c**. Let us start with the homometallic $Ru_2$ derivatives. In order to understand their electron-transfer ability, Figure 3 compares the cyclic voltammetric response of the building unit **3b** (Figure 3, a) with that of the dinuclear monocation **12b** (Figure 3, b).

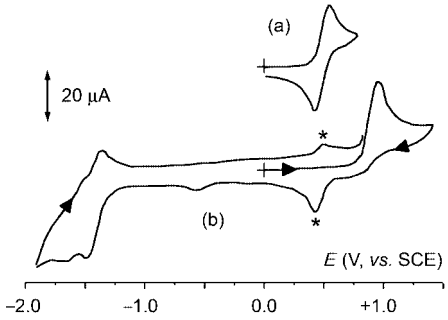


Figure 3. Cyclic voltammetric responses recorded at a platinum electrode for $CH_2Cl_2$ solutions of: a) **3b** ($0.9\times10^{-3}$ M) and b) **12b** ($1.0\times10^{-3}$ M). $[NBu_4]PF_6$ (0.2 M) as supporting electrolyte. Scan rate: 0.5 $V\,s^{-1}$.

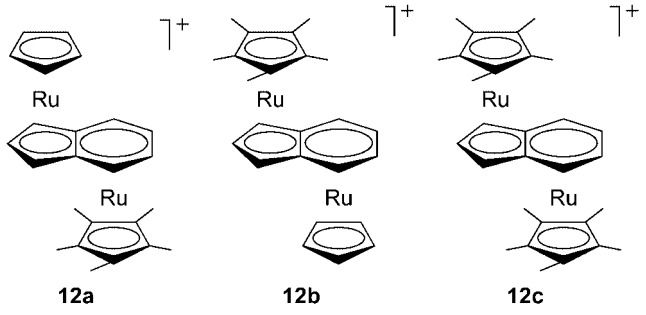


Complex **3b** undergoes a coulometrically measured one-electron oxidation that exhibits features of chemical reversibility on the cyclic voltammetric timescale. In fact, analysis of the responses with progressively increasing scan rates from 0.2 to 1.0 $V\,s^{-1}$ shows that: (i) the current ratio $i_{pc}/i_{pa}$ is constantly equal to 1; (ii) the current function $i_{pa}\cdot v^{-1/2}$ decreases by about 10% with a tenfold increase of the scan rate; and (iii) the peak-to-peak separation increases progressively from 98 to 130 mV. These parameters are diagnostic of a chemically reversible, but electrochemically quasi-reversible, one-electron process.[25] In reality, cyclic voltammetric tests carried out on the exhaustively oxidised solution ($E_w$ = +0.7 V) show partial decomposition of the electrogenerated monocation. A similar behaviour is exhibited by the parent compound **3a** except for the fact that the corresponding monocation is unstable even on the cyclic voltammetric timescale (the $i_{pc}/i_{pa}$ ratio reaches unity only at 5.0 $V\,s^{-1}$).

The voltammetric pattern exhibited by the triple-decker cation **12b** is more complex. It essentially undergoes an irreversible oxidation and a reduction displaying features of partial chemical reversibility. The rather positive and negative potential values of the two processes prevent a reliable determination of the number of electrons involved by controlled potential coulometry. Nevertheless, the cyclic voltammetric comparison with the one-electron oxidation of *N*,*N*-dimethyl-1-[1′,2-bis(diphenylphosphanyl)ferrocenyl]-ethylamine ($E^{\circ\prime}$ = +0.55 V) (an appropriate calibrant due to its similar molecular weight of 625.5)[25] supports the two-electron nature of the anodic step.[26] Since the cathodic process possesses a peak height similar to the anodic one, we assume that the reduction also involves a two-electron process. As a matter of fact, the minor reduction following the main cathodic step can be assigned to the by-product arising from the primary reduction as it tends to disappear with an increase of the scan rate.

We finally underline that the starred peak system that appears in the back-scans after traversing the anodic peak occurs at potential values coincident with those of **3b**, thus suggesting that the electron transfers trigger decomposition of the triple-decker derivative **12b** and regeneration of the precursor **3b**. A qualitatively similar redox picture holds for complexes **12a** and **12c**. The pertinent electrode potentials are compiled in Table 3.

Table 3. Formal electrode potentials [V vs. SCE] and peak-to-peak separations [mV] for the redox processes of the $Ru_2$ complexes and their mononuclear precursors in $CH_2Cl_2$ solution.

| Complex | $E^{\circ\prime}_{Ox}$ | $\Delta E_p$[a] | $E^{\circ\prime}_{Red}$ | $\Delta E_p$[a] |
|---|---|---|---|---|
| **3a** | +0.73[b,c] | 127 | – | – |
| **3b** | +0.50[b,d] | 96 | – | – |
| **12a** | +0.92[a,e,f] | – | –1.74[c,e] | 120 |
| **12b** | +0.92[a,e,f] | – | –1.43[c,e] | 66 |
| **12c** | +0.89[a,e,f] | – | –1.73[c,e] | 110 |
| $FeCp_2$ | +0.39[b] | 72 | | |

[a] Measured at 0.2 $V\,s^{-1}$. [b] One-electron process. [c] Complicated by chemical reactions. [d] See refs.[19,29] [e] Two-electron process. [f] Peak-potential value for irreversible processes.

In principle, the occurrence of single two-electron processes in binuclear derivatives would imply the lack of any electronic communication between metal centres.[27] We must, however, consider that the two ruthenium centres in cations **12a**–**c** are in different ligand surroundings: one is coordinated to the five-membered ring while the other is coordinated to the six-membered ring, which results in different charges at the metal centres. Therefore, two simultaneous one-electron processes at the two metal centres can be excluded. Most likely, the two-electron reduction occurs at the atom coordinated to the six-membered ring as it has a more positive charge whereas the two-electron oxidation is centred on the ruthenium atom coordinated to the five-

 © 2006 Wiley-VCH Verlag GmbH & Co. KGaA, Weinheim 

membered ring. Such an assumption is supported by a comparison between the redox behaviour of ruthenocene and the benzene complex $[CpRu(C_6H_6)]^+$, which can be considered as the fused parts of the parent triple-decker cation $[CpRu(\mu{:}\eta^5{:}\eta^6\text{-}C_9H_7)RuCp]^+$ ($[\mathbf{A}]^+$). The arene complex is reduced at –2.02 V but not oxidized up to +2.5 V,[28] whereas ruthenocene is oxidized at +0.8 V,[19] but, to the best of our knowledge, is not reduced up to –2 V.

As shown in Scheme 8, the two-electron reduction would result in anion $[\mathbf{A}]^-$, in which one ruthenium atom is $\eta^4$-coordinated to the six-membered ring of the indenyl ligand. Both metal atoms have 18 valence electrons (VE), in accordance with the strong preference of ruthenium for an 18 VE configuration. The two-electron oxidation would give cation $[\mathbf{A}]^{3+}$ with one 16 VE metal centre, which could be stabilized by coordination with a solvent molecule or a counterion (a similar process for mononuclear indenyl complexes is known[29]). Apparently, $[\mathbf{A}]^{3+}$ decomposes to give cation $[\mathbf{3a}]^+$, thereby explaining its appearance in the backscans.

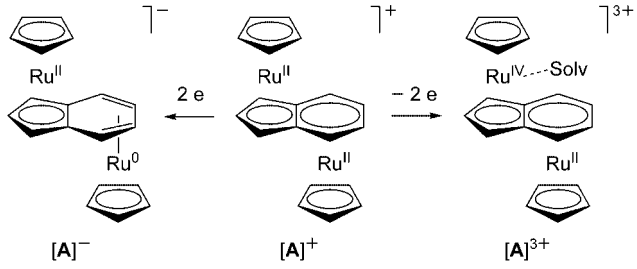


Scheme 8. Reduction and oxidation of $[CpRu(\mu{:}\eta^5{:}\eta^6\text{-}C_9H_7)RuCp]^+$.

Let us now move on to the CoRu complexes **4b** and **5a**,**b**. The pertinent electrode potentials are compiled in Table 4. Cation **4b** obviously represents the simplest comparative connection with the preceding diruthenium derivatives. In fact, as illustrated in Figure 4, it affords a redox profile substantially similar to that of **12b**. The usual comparison with an equimolar amount of *N*,*N*-dimethyl-1-[1′,2-bis(diphenylphosphanyl)ferrocenyl]ethylamine supports the two-electron nature of the anodic process (and hence of the cathodic one). Also in this case, the chemical complication accompanying the oxidation process generates the monomeric building block **3b** (starred peak system).

Table 4. Formal electrode potentials [V vs. SCE] and peak-to-peak separations [mV] for the redox processes of the $Co_2$ complex **2** and CoRu complexes **4** and **5** in $CH_2Cl_2$ solution.

| Complex | $E_{pOx(I)}$ | $E_{pOx(II)}$ | $E^{\circ\prime}_{Red}$ | $\Delta E_p$[a] |
|---|---|---|---|---|
| **2** | +0.72[b] | ≈ +1.6[b,c,d] | –1.74[e] | 74 |
| **4b** | ≈ +0.93[b,e] | ≈ +0.93[b,e] | –1.67[c] | 102 |
| **5a** | +1.04[b,e] | [d] | –1.40[b,c] | – |
| **5b** | +0.70[b,e] | ≈ +1.5[b,e] | –1.81[b,c] | – |

[a] Measured at 0.2 V s$^{-1}$. [b] Peak-potential value for irreversible processes. [c] Two-electron process. [d] Substantially overlapped by the solvent discharge. [e] One-electron process.

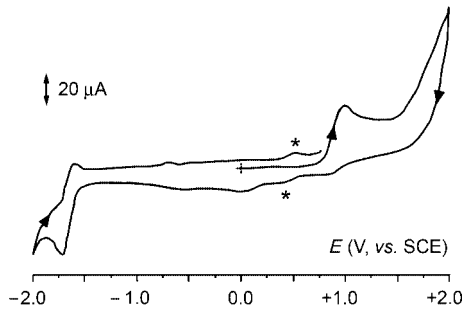


Figure 4. Cyclic voltammetric response recorded at a platinum electrode for a $CH_2Cl_2$ solution of **4b** ($0.8\times10^{-3}$ M). $[NBu_4]PF_6$ (0.2 M) as supporting electrolyte. Scan rate: 0.5 V s$^{-1}$.

In reality, Osteryoung square-wave voltammetry shows a slight inflection of the oxidation process, probably due to a very slight difference between the oxidation potentials of the $Ru^{II/III}$ and the $Ru^{III/IV}$ processes. A difference of about 0.08 V can be estimated from Figure S2 in the Supporting Information, even though the relative peak heights do not seem to support the one-electron nature of both processes. It cannot, however, be ruled out that this apparent discrepancy might be due to the mathematical treatment.

A different redox pattern is exhibited by complexes **5a**,**b**, which have the cobalt atom coordinated to the five-membered ring. As illustrated in Figure 5 for **5b**, they undergo two separate oxidations (the second of which is partially overlapped by the solvent discharge) and one reduction, which are irreversible in character. The peak height of the reduction is about twice that of each oxidation step. Comparison with the response of *N*,*N*-dimethyl-1-[1′,2-bis(diphenylphosphanyl)ferrocenyl]ethylamine supports the one-electron nature of the first anodic step.

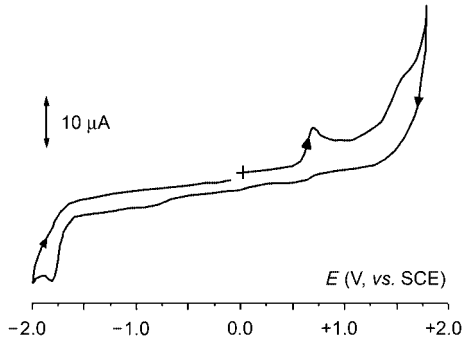


Figure 5. Cyclic voltammetric response recorded at a gold electrode for a $CH_2Cl_2$ solution of **5b** ($1.0\times10^{-3}$ M). $[NBu_4]PF_6$ (0.2 M) as supporting electrolyte. Scan rate: 0.2 V s$^{-1}$.

As a final consideration, we will briefly mention the redox behaviour of the $Co_2$ complex **2**. In $CH_2Cl_2$ solution, it exhibits a cyclic voltammetric profile which is qualitatively reminiscent of that exhibited by complexes **4b** and **5**, even though, as indicated in Table 4, some differences hold in the number of electrons involved either in the cathodic or the most anodic processes.

In view of the preceding discussion on the nucleophilic degradation of the present complexes in MeCN solution, it is interesting to compare the anodic response recorded in

 © 2006 Wiley-VCH Verlag GmbH & Co. KGaA, Weinheim 

$CH_2Cl_2$ solution with that recorded in MeCN solution, at low temperature (250 K). As illustrated in Figure 6, in MeCN solution the irreversible oxidation of the complex apparently occurs at notably lower potential values ($E_p$ = –0.09 V) and is followed by a main oxidation process with features of chemical reversibility ($E°'$ = +0.22 V). It should be noted that an increase of the temperature makes the two oxidation processes disappear (the first oxidation disappearing more quickly than the second one).

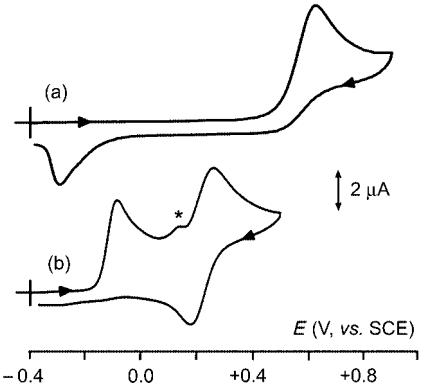


Figure 6. Cyclic voltammetric responses exhibited by **2** at a platinum electrode, under the following experimental conditions: a) $CH_2Cl_2$ solution ($0.7\times10^{-3}$ M), b) MeCN solution ($0.8\times10^{-3}$ M). $[NBu_4]PF_6$ (0.2 M) as supporting electrolyte. $T$ = 250 K. Scan rate: 0.2 V $s^{-1}$.

We would like to assign the second reversible oxidation present in MeCN solution to the decomposition product **1** even though the couple **1**/[**1**]$^+$ exhibits a rather congruent potential value ($E°'$ = +0.33 V) in $CH_2Cl_2$ solution.[12] The starred peak at +0.13 V could be attributed to the second decomposition product $[Cb*Co(MeCN)_3]^+$.[30] The assignment of the first irreversible oxidation is, in reality, rather less straightforward. In fact, even though it is conceivable that the low temperature might attenuate the lability of complex **2**, thus allowing us to detect the oxidation of the residual original product, the difference of about 0.7 V in redox potentials on passing from $CH_2Cl_2$ to MeCN solution makes such a proposal questionable. It is more likely that the first irreversible oxidation is due to the transient product $[Cb*Co(\mu{:}\eta^5{:}\eta^4\text{-}C_9H_7)Co(MeCN)Cb*]^+$, which arises from partial solvolysis of **2**.

## Conclusions

Electrophilic stacking reactions of indenyl sandwich complexes with the acetonitrile derivatives $[Cb*Co(MeCN)_3]^+$ and $[(C_5R_5)Ru(MeCN)_3]^+$ have proved to be effective for the preparation of slipped triple-decker cations. However, the acetonitrile eliminated can induce nucleophilic degradation of the product, thereby reducing the yield. The new method using $[Cb*CoI]_x/TlBF_4$ lacks this limitation and allows to obtain the target compounds in high yield.

## Experimental Section

**General:** All reactions were carried out under argon in anhydrous solvents that were purified and dried using standard procedures. The isolation of products was conducted in air unless otherwise stated. Starting materials were prepared as described in the literature: **1**,[12] **3a**,**b**, **6**,[8a] **7**,[31] $[Cb*Co(CO)_2I]$,[11,12] $[Cb*Co(MeCN)_3]PF_6$,[11,12] $[Cp*RuCl]_4$,[32] $[(C_5R_5)Ru(MeCN)_3]PF_6$[33,34] and $Tl[Co(\eta\text{-}7,8\text{-}C_2B_9H_{11})_2]$.[35] Irradiation was conducted in a Schlenk tube using a high-pressure mercury vapour lamp with phosphor-coated bulb (400 W). Both the tube and the lamp were placed in a vessel of appropriate volume covered inside with aluminium foil; cooling was accomplished with running water. The $^1H$ and $^{11}B$ NMR spectra were recorded with a Bruker AMX 400 spectrometer operating at 400.13 and 128.38 MHz, respectively. Materials and apparatus for electrochemistry have been described elsewhere.[36]

**Preparation of the Benzene Complex $[Cb*Co(C_6H_6)]I$:** A mixture of $[Cb*Co(CO)_2I]$ (3.5 g, 10 mmol), anhydrous aluminium chloride (13.3 g, 100 mmol) and benzene (70 mL) was vigorously stirred under reflux for 8 h. After cooling, the reaction mixture was carefully hydrolysed with cold water (ca. 100 mL). The aqueous phase was separated, filtered and stirred with $Me_3NO{\cdot}2H_2O$ (ca. 0.2 g, 1.2 mmol) and $NaI{\cdot}2H_2O$ (ca. 0.4 g, 2 mmol) for 4 h. The resulting brown precipitate of $[Cb*Co(CO)_2I]$ was filtered off. The filtrate was stirred with $NaI{\cdot}2H_2O$ (2.8 g, 15 mmol) and extracted with $CH_2Cl_2$ (4 × 50 mL). The organic phase was separated, dried under $MgSO_4$ and eluted through a short layer of silica gel (ca. 5 cm) with $CH_2Cl_2$. The filtrate was evaporated in vacuo to about 50 mL and diethyl ether (ca. 100 mL) was added. The yellow solid was filtered off and dried in vacuo. Yield: 2.3 g (63%). $^1H$ NMR ([$D_6$]-acetone): $\delta$ = 6.72 (s, 6 H, $C_6H_6$), 1.70 (s, 12 H, Cb*) ppm. $C_{14}H_{18}CoI$ (372.13): calcd. C 45.18, H 4.87; found C 45.01, H 4.93.

**Preparation of Slipped Triple-Decker Complexes Starting from $[Cb*Co(MeCN)_3]PF_6$ and $[(C_5R_5)Ru(MeCN)_3]PF_6$. $[Cb*Co(\mu,\eta^5{:}\eta^6\text{-}C_9H_7)CoCb*]PF_6$ (2·$PF_6$):** A mixture of $[Cb*Co(MeCN)_3]PF_6$ (57 mg, 0.13 mmol) and **1** (45 mg, 0.16 mmol) in $MeNO_2$ (3 mL) was stirred overnight. The solvent was then removed in vacuo and the residue was dissolved in $CH_2Cl_2$ (ca. 1 mL). Addition of diethyl ether (ca. 10 mL) gave a dark pink precipitate which was twice re-precipitated from $CH_2Cl_2$ by addition of diethyl ether. Yield: 42 mg (54%). $^1H$ NMR ($CDCl_3$): $\delta$ = 6.86 (m, 2 H, 4,7-H), 5.98 (m, 2 H, 5,6-H), 5.32 (t, $^3J$ = 2.4 Hz, 1 H, 2-H), 5.29 (d, $^3J$ = 2.4 Hz, 2 H, 1,3-H), 1.27 (s, 12 H, Cb*, $\eta^6$), 1.23 (s, 12 H, Cb*, $\eta^5$) ppm.[37] $C_{25}H_{31}Co_2F_6P$ (594.34): calcd. C 50.52, H 5.26; found C 50.29, H 5.18.

The following compounds were prepared in a similar way.

**$[Cp*Ru(\mu,\eta^5{:}\eta^6\text{-}C_9H_7)CoCb*]PF_6$ (4b·$PF_6$):** Yellow-orange solid. Yield: 73 mg (79%) from **3b** (56 mg, 0.16 mmol) and $[Cb*Co(MeCN)_3]PF_6$ (61 mg, 0.14 mmol) in $MeNO_2$ (3 mL). $^1H$ NMR ($CD_2Cl_2$): $\delta$ = 6.72 (m, 2 H, 4,7-H), 5.80 (m, 2 H, 5,6-H), 5.00 (d, $^3J$ = 2.4 Hz, 2 H, 1,3-H), 4.86 (t, $^3J$ = 2.4 Hz, 1 H, 2-H), 1.67 (s, 15 H, Cp*), 1.30 (s, 12 H, Cb*) ppm.[37] $C_{27}H_{34}CoF_6PRu$ (663.52): calcd. C 48.87, H 5.16; found C 48.77, H 5.17.

**$[Cb*Co(\mu,\eta^5{:}\eta^6\text{-}C_9H_7)RuCp]PF_6$ (5a·$PF_6$):** All manipulations were carried out under argon. Red solid. Yield: 38 mg (54%) from **1** (37 mg, 0.13 mmol) and $[CpRu(MeCN)_3]PF_6$ (52 mg, 0.12 mmol) in thf (10 mL). $^1H$ NMR ($CD_2Cl_2$): $\delta$ = 6.93 (m, 2 H, 4,7-H), 5.67 (m, 2 H, 5,6-H), 5.20 (br., 2 H, 1,3-H), 5.13 (br., 1 H, 2-H), 4.89 (s, 5 H, Cp), 1.29 (s, 12 H, Cb*) ppm.[37] $C_{22}H_{24}CoF_6PRu{\cdot}0.5CH_2Cl_2$ (635.86): calcd. C 42.50, H 3.96; found C 42.60, H 3.91.

**$[Cb*Co(\mu,\eta^5{:}\eta^6\text{-}C_9H_7)RuCp*]PF_6$ (5b·$PF_6$):** Dark red solid. Yield: 89 mg (79%) from **1** (53 mg, 0.19 mmol) and $[Cp*Ru(MeCN)_3]PF_6$

 © 2006 Wiley-VCH Verlag GmbH & Co. KGaA, Weinheim 

(86 mg, 0.17 mmol) in $CH_2Cl_2$ (10 mL). Alternatively, this complex was prepared by treatment of **6** (77 mg, 0.22 mmol) with [Cb*Co(MeCN)$_3$]$PF_6$ (83 mg, 0.19 mmol) in thf (10 mL); yield 76 mg (60%). $^1$H NMR ($CD_2Cl_2$): $\delta$ = 6.27 (m, 2 H, 4,7-H), 5.37 (m, 3 H, 2,5,6-H), 5.04 (d, $^3J$ = 2.4 Hz, 2 H, 1,3-H), 1.65 (s, 15 H, Cp*), 1.27 (s, 12 H, Cb*) ppm.[37] $C_{27}H_{34}CoF_6PRu$ (663.52): calcd. C 48.87, H 5.16; found C 48.93, H 5.19.

**[CpRu(μ,η$^5$:η$^6$-$C_9H_7$)CoCb*]$PF_6$ (4a·$PF_6$):** All manipulations were carried out under argon. A mixture of [Cb*Co(MeCN)$_3$]$PF_6$ (52 mg, 0.12 mmol) and **3a** (194 mg, 0.6 mmol) in $MeNO_2$ (3 mL) was stirred for 1 h. The solvent was then removed in vacuo, a new portion of $MeNO_2$ (3 mL) was added and stirring was continued for 1 h. This solvent removal-addition cycle followed by stirring for 1 h was repeated twice more. The volume was then reduced in vacuo to about 0.5 mL. Addition of diethyl ether (10 mL) gave a yellow-orange precipitate, which was twice re-precipitated from $MeNO_2$ by addition of diethyl ether. Yield: 55 mg (78%). $^1$H NMR ($CDCl_3$): $\delta$ = 7.04 (m, 2 H, 4,7-H), 5.81 (m, 2 H, 5,6-H), 5.47 (d, $^3J$ = 2.7 Hz, 2 H, 1,3-H), 5.02 (t, $^3J$ = 2.6 Hz, 1 H, 2-H), 4.45 (s, 5 H, Cp), 4.29 (s, 2 H, $MeNO_2$), 1.35 (s, 12 H, Cb*) ppm.[37] $C_{22}H_{24}CoF_6PRu·0.75MeNO_2$ (639.17): calcd. C 42.75, H 4.14; found C 42.86, H 4.26.

**Preparation of Slipped Triple-Decker Complexes Starting from [Cb*CoI]$_x$. [(η$^5$-$C_9H_7$)Ru(μ,η$^5$:η$^6$-$C_9H_7$)CoCb*]$BF_4$ (8·$BF_4$):** All manipulations were carried out under argon. The iodide complex [Cb*CoI]$_x$ was prepared from [Cb*Co($C_6H_6$)]I and used without further purification. A solution of [Cb*Co($C_6H_6$)]I (100 mg, 0.27 mmol) in acetonitrile (3 mL) was irradiated for 4 h, resulting in a colour change from yellow to red. The solvent was removed in vacuo to give [Cb*Co(MeCN)$_3$]I as a dark-red microcrystalline solid. This was heated in vacuo (ca. 0.01 Torr) at 50–60 °C for 15 min to afford crude [Cb*CoI]$_x$ as a dark-green solid. The latter was dissolved in thf (5 mL) to give a clear, dark-green solution. Complex **7** (106 mg, 0.32 mmol) and $TlBF_4$ (79 mg, 0.27 mmol) were then added and the mixture was stirred overnight. The yellow-orange precipitate was filtered off, washed with diethyl ether and dissolved in $CH_2Cl_2$ (ca. 5 mL). The orange-red solution obtained was filtered and concentrated in vacuo to about 0.5 mL. Addition of diethyl ether (ca. 10 mL) gave an orange solid, which was re-precipitated from $CH_2Cl_2$ by addition of diethyl ether. Yield: 103 mg (65%). $^1$H NMR ($CDCl_3$): $\delta$ = 6.87 (m, 4 H, 4–7-H, η$^5$-$C_9H_7$), 6.49 (m, 2 H, 4,7-H, μ-$C_9H_7$), 5.81 (m, 2 H, 5,6-H, μ-$C_9H_7$), 5.29 (s, 1 H, $CH_2Cl_2$), 5.12 (m, 4 H, 1,3-H, $C_9H_7$), 4.98 (t, $^3J$ = 2.6 Hz, 1 H, 2-H, μ-$C_9H_7$), 4.75 (t, $^3J$ = 2.4 Hz, 1 H, 2-H, η$^5$-$C_9H_7$), 1.35 (s, 12 H, Cb*) ppm.[37] $C_{26}H_{26}BCoF_4Ru·0.5CH_2Cl_2$ (627.77): calcd. C 50.70, H 4.34; found C 50.87, H 4.41. In a similar way, complex 8·$PF_6$ (69%) was prepared using $TlPF_6$ instead of $TlBF_4$.

**[Cp*Ru(μ,η$^5$:η$^6$-$C_9H_7$)CoCb*][Co(η-7,8-$C_2B_9H_{11}$)$_2$] ([4b][Co(η-7,8-$C_2B_9H_{11}$)$_2$]):** The title compound was prepared similar to 8·$BF_4$ from [Cb*Co($C_6H_6$)]I (100 mg, 0.27 mmol), **3b** (112 mg, 0.32 mmol) and Tl[Co(η-7,8-$C_2B_9H_{11}$)$_2$] (143 mg, 0.27 mmol). Yield: 164 mg (72%) of a dark-red solid. $^1$H NMR ($CD_2Cl_2$): $\delta$ = 6.72 (m, 2 H, 4,7-H), 5.77 (m, 2 H, 5,6-H), 5.00 (d, $^3J$ = 2.6 Hz, 2 H, 1,3-H), 4.88 (t, $^3J$ = 2.6 Hz, 1 H, 2-H), 3.95 (br., 4 H, CH), 1.67 (s, 15 H, Cp*), 1.31 (s, 12 H, Cb*) ppm.[37] $^{11}$B NMR: $\delta$ = 5.8 (d, $J_{B,H}$ = 144 Hz, 1 B), 1.4 (d, $J_{B,H}$ = 141 Hz, 1 B), –5.5 (d, $J_{B,H}$ = 107 Hz, 2 B), –6.8 (d, $J_{B,H}$ = 125 Hz, 2 B), –17.3 (d, $J_{B,H}$ = 154 Hz, 2 B), –22.7 (d, $J_{B,H}$ = 168 Hz, 1 B) ppm.

**Formation of the Slipped Tetra-Decker Complex [Cp*Ru(μ,η$^5$:η$^6$-$C_9H_7$)Ru(μ,η$^5$:η$^6$-$C_9H_7$)RuCp*][$PF_6$]$_2$ ([11][$PF_6$]$_2$):** A mixture of 8·$PF_6$ (39 mg, 0.06 mmol), [Cp*RuCl]$_4$ (33 mg, 0.03 mmol) and $TlPF_6$ (42 mg, 0.12 mmol) in $MeNO_2$ (3 mL) was stirred overnight. The solvent was then removed in vacuo. The residue was extracted with $CH_2Cl_2$/petroleum ether (10:1) and filtered. The filtrate was concentrated in vacuo to about 0.5 mL. Addition of petroleum ether (10 mL) gave an orange-red precipitate, which was twice re-precipitated from $CH_2Cl_2$ by addition of petroleum ether. Yield: 28 mg (43%). $^1$H NMR ($CDCl_3$): $\delta$ = 6.38 (m, 4 H, 4,7-H), 5.45 (m, 4 H, 5,6-H), 5.20 (br., 6 H, 1–3-H), 1.66 (s, 30 H, Cp*) ppm. According to $^1$H NMR spectroscopy, a similar reaction with a 4:1 molar ratio of 8·$PF_6$ and [Cp*RuCl]$_4$ resulted in a mixture of complexes **8** (25%), **10** (15%) and **11** (60%).

**X-ray Crystallography:** Crystals of [**4b**][Co(η-7,8-$C_2B_9H_{11}$)$_2$] suitable for X-ray diffraction were grown by slow interdiffusion of a two-phase system containing diethyl ether and a $CH_2Cl_2$ solution of the complex. Crystals of **6** were obtained by cooling a hexane solution to –15 °C. X-ray diffraction experiments were carried out with a Bruker SMART 1000 CCD at 120 K. The adsorption correction was applied semi-empirically using equivalent reflections. Crystallographic data and structure refinement parameters are given in Table 5. All calculations were performed on an IBM PC/AT using the SHELXTL software.[38]

Table 5. Crystallographic data and structure refinement parameters for [**4b**][Co(η-7,8-$C_2B_9H_{11}$)$_2$] and **6**.

| Compound | [**4b**][Co(η-7,8-$C_2B_9H_{11}$)$_2$] | **6** |
|---|---|---|
| Empirical formula | $C_{31}H_{56}B_{18}Co_2Ru$ | $C_{19}H_{21}Ru$ |
| Molecular weight | 842.27 | 350.43 |
| Crystal colour, habit | orange, prism | yellow, prism |
| Crystal system | monoclinic | orthorhombic |
| Space group | $P2_1/c$ | $Pnma$ |
| $a$ [Å] | 12.406(2) | 11.4039(6) |
| $b$ [Å] | 13.040(2) | 12.4270(7) |
| $c$ [Å] | 24.781(4) | 10.6831(6) |
| $\beta$ [°] | 90.619(4) | 90 |
| $V$ [Å$^3$] | 4008.6(12) | 1513.97(14) |
| $Z$ ($Z$) | 4(1) | 4(0.5) |
| $D_{calcd.}$ [g cm$^{-3}$] | 1.214 | 1.537 |
| $2\theta$ max [°] | 52 | 60 |
| Abs. coeff., $\mu$(Mo-$K_\alpha$) [cm$^{-3}$] | 12.14 | 10.23 |
| $T_{max}/T_{min}$ | 0.7121/0.7932 | 0.7489/0.8216 |
| Collected reflections | 34252 | 39865 |
| Independent reflections ($R_{int}$) | 7669 (0.0417) | 2252 (0.0462) |
| Observed reflections [$I > 2\sigma(I)$] | 6127 | 2129 |
| Parameters | 469 | 114 |
| $R_1$ (on $F$ for obsd. reflections)[a] | 0.0525 | 0.0218 |
| $wR_2$ (on $F^2$ for all reflections)[b] | 0.1167 | 0.0553 |
| $F$(000) | 1720 | 716 |
| GOF | 1.001 | 1.023 |
| Largest diff. peak and hole [e Å$^{-3}$] | 1.221/–0.742 | 0.569/–0.662 |

[a] $R_1 = \Sigma||F_o| - |F_c||/\Sigma(F_o)$ for observed reflections. [b] $wR_2 = \{\Sigma[w(F_o^2 - F_c^2)^2]/\Sigma[w(F_o^2)^2]\}^{0.5}$ for all reflections.

CCDC-602655 (for [**4b**][Co(η-7,8-$C_2B_9H_{11}$)$_2$]) and -602656 (for **6**) contain the supplementary crystallographic data for this paper. These data can be obtained free of charge from The Cambridge Crystallographic Data Centre via www.ccdc.cam.ac.uk/data_request/cif.

**Supporting Information** (see also the footnote on the first page of this article): Cyclic voltammetric responses of **12b** after the addition of an equimolar amount of *N*,*N*-dimethyl-1-[1′,2-bis(diphenylphosphanyl)ferrocenyl]ethylamine and the OSWV response of **4b**.

 © 2006 Wiley-VCH Verlag GmbH & Co. KGaA, Weinheim 

## Acknowledgments

P.Z. gratefully acknowledges the financial support of the University of Siena (PAR, 2005). Z.A.S. thanks the Russian Foundation for Basic Research (grant no. 03-03-32214).

[1] E. V. Mutseneck, D. S. Perekalin, J. Holub, Z. A. Starikova, P. V. Petrovskii, P. Zanello, M. Corsini, B. Štíbr, A. R. Kudinov, *Organometallics* **2006**, *25*, 2419–2426.

[2] For recent reviews see: a) A. Ceccon, S. Santi, L. Orian, A. Bisselo, *Coord. Chem. Rev.* **2004**, *248*, 683–724; b) S. Barlow, D. O'Hare, *Chem. Rev.* **1997**, *97*, 637–669; c) O. T. Summerscales, F. G. N. Cloke, *Coord. Chem. Rev.* **2006**, *250*, 1122–1140.

[3] A. Miyake, A. Kanai, *Angew. Chem. Int. Ed. Engl.* **1971**, *10*, 801–802.

[4] a) J. M. Manriquez, M. D. Ward, W. M. Reiff, J. C. Calabrese, N. L. Jones, P. J. Carroll, E. E. Bunel, J. S. Miller, *J. Am. Chem. Soc.* **1995**, *117*, 6182–6193; b) E. E. Bunel, L. Valle, N. L. Jones, P. J. Carroll, C. Barra, M. Gonzalez, N. Munoz, G. Visconti, A. Aizman, J. M. Manriquez, *J. Am. Chem. Soc.* **1988**, *110*, 6596–6598; c) B. Oelckers, I. Chávez, J. M. Manriquez, E. Román, *Organometallics* **1993**, *12*, 3396–3397.

[5] B. F. Bush, V. M. Lynch, J. J. Lagowski, *Organometallics* **1987**, *6*, 1267–1275.

[6] K. Jonas, *Pure Appl. Chem.* **1990**, *62*, 1169–1174.

[7] M. A. Bennett, H. Neumann, M. Thomas, X. Q. Wang, P. Pertici, P. Salvadori, G. Vitulli, *Organometallics* **1991**, *10*, 3237–3245.

[8] a) A. R. Kudinov, P. V. Petrovskii, Yu. T. Struchkov, A. I. Yanovskii, M. I. Rybinskaya, *J. Organomet. Chem.* **1991**, *421*, 91–115; b) A. R. Kudinov, M. I. Rybinskaya, *Metalloorg. Khim.* **1988**, *1*, 1429–1430 [*Organomet. Chem. USSR* **1988**, *1*, 781–782 (Engl. Transl.)].

[9] In the related CrRh complexes [(diene)Rh(μ:η$^5$:η$^6$-$C_9H_7$)$Cr(CO)_3$] the metal atoms adopt either a *syn* or *anti* disposition: a) C. Bonifaci, A. Ceccon, A. Gambaro, F. Manoli, L. Mantovani, P. Ganis, S. Santi, A. Venzo, *J. Organomet. Chem.* **1998**, *557*, 97–109; b) C. Bonifaci, A. Ceccon, A. Gambaro, P. Ganis, S. Santi, G. Valle, A. Venzo, *J. Organomet. Chem.* **1995**, *492*, 35–39.

[10] A. R. Kudinov, E. V. Mutseneck, D. A. Loginov, *Coord. Chem. Rev.* **2004**, *248*, 571–585.

[11] M. V. Butovskii, U. Englert, A. A. Fil'chikov, G. E. Herberich, U. Koelle, A. R. Kudinov, *Eur. J. Inorg. Chem.* **2002**, 2656–2663.

[12] E. V. Mutseneck, D. A. Loginov, D. S. Perekalin, Z. A. Starikova, D. G. Golovanov, P. V. Petrovskii, P. Zanello, M. Corsini, F. Laschi, A. R. Kudinov, *Organometallics* **2004**, *23*, 5944–5957.

[13] E. V. Mutseneck, D. S. Perekalin, J. Holub, K. A. Lyssenko, P. V. Petrovskii, B. Štíbr, A. R. Kudinov, *Eur. J. Inorg. Chem.* **2006**, 1737–1742.

[14] For a preliminary communication see: E. V. Mutseneck, P. V. Petrovskii, A. R. Kudinov, *Izv. Akad. Nauk Ser. Khim.* **2004**, 2003–2004 [*Russ. Chem. Bull.* **2004**, *53*, 2090–2091 (Engl. Transl.)].

[15] Manuscript in preparation.

[16] Other polar solvents such as $CH_2Cl_2$ and $MeNO_2$ rapidly decompose $[Cb^*CoI]_x$.

[17] G. E. Herberich, U. Englert, F. Marken, P. Hofmann, *Organometallics* **1993**, *12*, 4039–4045.

[18] Crystals of salts **4b**·$BF_4$ and **4b**·$PF_6$ proved to be unsuitable for X-ray diffraction study.

[19] P. G. Gassman, C. H. Winter, *J. Am. Chem. Soc.* **1988**, *110*, 6130–6135.

[20] G. Huttner, S. Lange, *Acta Crystallogr., Sect. B* **1972**, *28*, 2049–2060.

[21] J. W. Johnson, P. M. Treichel, *J. Am. Chem. Soc.* **1977**, *99*, 1427–1436.

[22] P. M. Treichel, K. P. Fivizzani, K. J. Haller, *Organometallics* **1982**, *1*, 931–934.

[23] S. A. Westcott, A. K. Kakkar, G. Stringer, N. J. Taylor, T. B. Marder, *J. Organomet. Chem.* **1990**, *394*, 777–794.

[24] A. Ceccon, A. Gambaro, S. Santi, G. Valle, A. Venzo, *J. Chem. Soc., Chem. Commun.* **1989**, 51–53.

[25] P. Zanello, *Inorganic Electrochemistry. Theory, Practice and Application*, Royal Society of Chemistry, Cambridge, **2003**.

[26] See Supporting Information for details.

[27] D. Astruc, *Electron Transfer and Radical Processes in Transition-Metal Chemistry*, Wiley-VCH, New York, **1995**.

[28] O. V. Gusev, M. A. Ievlev, M. G. Peterleitner, S. M. Peregudova, L. I. Denisovich, P. V. Petrovskii, N. A. Ustynyuk, *J. Organomet. Chem.* **1997**, *534*, 57–66.

[29] S. V. Kukharenko, V. V. Strelets, A. R. Kudinov, A. Z. Kreidlin, M. G. Peterleitner, L. I. Denisovich, M. I. Rybinskaya, *J. Organomet. Chem.* **1996**, *519*, 1–5.

[30] Under the same experimental conditions $E°' = +0.14$ V for $[Cb^*Co(MeCN)_3]^+$, generated in situ from the naphthalene complex $[Cb^*Co(C_{10}H_8)]^+$.

[31] N. S. Crossley, J. C. Green, A. Nagy, G. Stringer, *J. Chem. Soc., Dalton Trans.* **1989**, 2139–2147.

[32] P. J. Fagan, M. D. Ward, J. C. Calabrese, *J. Am. Chem. Soc.* **1989**, *111*, 1698–1719.

[33] T. P. Gill, K. R. Mann, *Organometallics* **1982**, *1*, 485–488.

[34] J. L. Schrenk, A. M. McNair, F. B. McCormick, K. R. Mann, *Inorg. Chem.* **1986**, *25*, 3501–3504.

[35] M. F. Hawthorne, D. C. Young, T. D. Andrews, D. V. Howe, R. L. Pilling, A. D. Pitts, M. Reintjes, L. F. Warren, Jr., P. A. Wegner, *J. Am. Chem. Soc.* **1968**, *90*, 879–896.

[36] F. Fabrizi de Biani, M. Corsini, P. Zanello, H. Yao, M. E. Bluhm, R. N. Grimes, *J. Am. Chem. Soc.* **2004**, *126*, 11360–11369.

[37] The H(4,7) and H(5,6) protons appear as multiplets characteristic of the A and B components of an AA′BB′ spin system.

[38] G. M. Sheldrick, *SHELXTL-97*, v. 5.10, Bruker AXS Inc., Madison, WI 53719, USA.

Received: March 27, 2006
Published Online: October 12, 2006

 © 2006 Wiley-VCH Verlag GmbH & Co. KGaA, Weinheim 

DOI: 10.1002/ejic.200600538

# A High-Temperature Multinuclear NMR Study of $Na_3AlF_6$–FeO and $Na_3AlF_6$–$Fe_2O_3$ Melts

**František Šimko,*[a] Aydar Rakhmatullin,[b] Miroslav Boča,[a] Vladimír Daněk,[a] and Catherine Bessada[b]**

**Keywords:** Electrolysis / NMR spectroscopy / Cryolitic melts / Aluminium / Iron

In the Hall–Héroult process for the industrial production of aluminum, iron oxide impurities are known to lower the current efficiency as well as the metal quality. Iron can be present in the di- or trivalent form. The nature of dissolved $Fe^{III}$ and $Fe^{II}$ species and the reactions taking place in cryolitic melts have been investigated by high-temperature NMR spectroscopy. The evolution of $^{27}Al$, $^{23}Na$, and $^{19}F$ NMR chemical shifts are reported in the $Na_3AlF_6$–FeO and $Na_3AlF_6$–$Fe_2O_3$ systems for different iron oxide contents. They express the formation of oxofluoroaluminate species. For the $Na_3AlF_6$–FeO system, the $^{19}F$ signal appears only after 14 minutes at 1020 °C. The line position is shifted with heating time. This evolution is associated with a narrowing of the $^{27}Al$ signal due to a decrease in the content of paramagnetic compounds in the sample. This effect is probably caused by the evaporation of an $Fe^{II}$ compound, as already mentioned in the literature. For the $Na_3AlF_6$–$Fe_2O_3$ system we have never observed the $^{19}F$ NMR spectra over the full heating time (ca. 30 min). This could be due to the influence of paramagnetic $Fe^{III}$ nuclei, probably in $FeF_6^{3-}$ species present in the melt.

(© Wiley-VCH Verlag GmbH & Co. KGaA, 69451 Weinheim, Germany, 2006)

## Introduction

Aluminum is produced industrially by the Hall–Héroult electrolytic process. The impurities present during the process represent a critical problem because they negatively influence the current efficiency and may lower the metal quality.[1,2] Iron is one of the predominant impurities in the industrial production and can be present in the di- or trivalent state, especially as oxides (FeO, $Fe_2O_3$). Iron is introduced with the raw materials and/or by corrosion of the different cell parts. The nature of the dissolved species and different reactions taking place upon dissolution of $Fe_2O_3$ and FeO into cryolite (the major component of the electrolyte) is a crucial question. Because of the experimental difficulties due to the corrosive properties of fluoride melts at high temperature, only a few data have been reported, mainly deduced from solubility measurements.[3–9] From cryoscopy measurements, Diep[5] has suggested that $Fe_2O_3$ dissolves in cryolite to form nonvolatile sodium hexafluoroferrite ($Na_3FeF_6$), while for $Fe^{II}O$ the formation of $Na_xFeF_{(2+x)}$ complexes has been assumed by Jentofsen.[8,9] In both systems, the formation of oxofluoroaluminate complexes ($Al_2OF_6^{2-}$ and $Al_2O_2F_4^{2-}$) has also been proposed depending on the iron oxide concentration in the melt. Up to now, no direct detection of the ionic species formed in both kinds of melts has been attempted. Therefore, we propose in this paper to present their in situ NMR description. This spectroscopy is sensitive to the local environment around a selected nucleus, therefore it allows both qualitative and quantitative information about the different species existing in the bath to be determined.[10,11] The presence of $Fe^{II}$ in the melts can cause some paramagnetic effects on the NMR signal of the different nuclei, mainly broadening and shift and shape distortion of the line. These effects can be large enough to dramatically decrease the signal intensity and make any observation impossible. We will try to take advantage of this interaction and its effects on the spectra that we can associate with the detection of $Fe^{II}$ formation in the melt, and its implication on the ionic species.

We report in this paper $^{27}Al$, $^{23}Na$, and $^{19}F$ NMR measurements at high temperature in the $Na_3AlF_6$–FeO and $Na_3AlF_6$–$Fe_2O_3$ binary systems. The combination of the structural information given by the NMR signal of the different nuclei enables us to give the first experimental evidence of the formation of new species due to dissolution of iron oxide in these high-temperature melts.

## Results and Discussion

### $^{27}Al$ NMR Spectra

The HT $^{27}Al$ NMR spectra of molten $Na_3AlF_6$ with different amounts of FeO are shown in Figure 1.

[a] Institute of Inorganic Chemistry, Slovak Academy of Sciences, Dúbravská cesta 9, 84536 Bratislava, Slovakia
E-mail: uachsim@savba.sk
Fax: +421-2-5941-0444
[b] Centre de Recherches sur les Matériaux à Haute Température CNRS,
1D av. de la Recherche Scientifique, 45071 Orléans, France

 © 2006 Wiley-VCH Verlag GmbH & Co. KGaA, Weinheim 

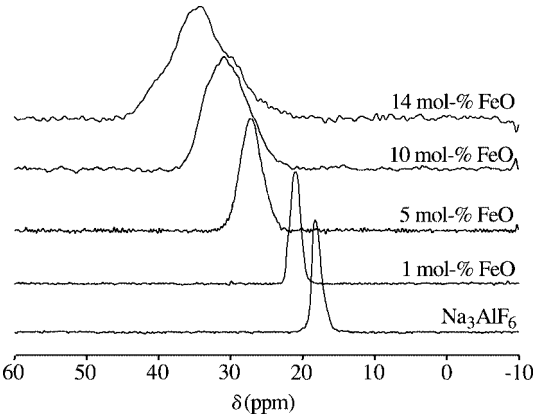


Figure 1. HT $^{27}$Al NMR spectra of $Na_3AlF_6$–FeO melts at 1020 °C.

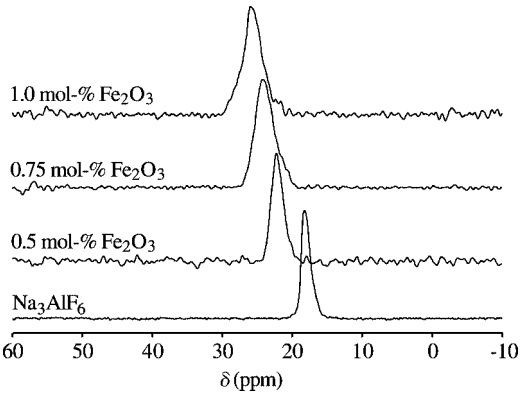


Figure 2. HT $^{27}$Al NMR spectra of $Na_3AlF_6$–$Fe_2O_3$ melts at 1020 °C.

Because of the dynamics existing in the melt, and the rapid exchange between the different possible species involving the nucleus under observation, all the HT NMR spectra consist of a single Lorentzian-shaped line. In pure cryolite, a sharp line at $\delta$ = 18.3 ppm is observed, in good agreement with the value reported by Lacassagne et al.[11] Upon addition of FeO the signal is shifted towards higher chemical shifts and broadens progressively with increased FeO content. For 1 mol-% added FeO, the line position is moved slightly to $\delta$ = 21 ppm, and the linewidth is unchanged. For 14 mol-% FeO, however, the peak is centered at $\delta$ = 34 ppm with an important modification of the lineshape ($\Delta_{1/2}$ = 900 Hz; Table 1). We observe the same kind of evolution for very low $Fe_2O_3$ additions (Figure 2), with a shift of 7 ppm for 1 mol-% added $Fe_2O_3$.

Table 1. Composition, $^{27}$Al and $^{23}$Na NMR chemical shifts, and linewidths in $Na_3AlF_6$–FeO and $Na_3AlF_6$–$Fe_2O_3$ melts at 1020 °C.

| $x$(FeO) [mol-%] | $\delta$($^{27}$Al) [ppm] | $\Delta_{1/2}$ [Hz] | $\delta$($^{23}$Na) [ppm] | $\Delta_{1/2}$ [Hz] |
|---|---|---|---|---|
| 0.0 | 18.8 | 149 | –6.5 | 130 |
| 1 | 21.0 | 179 | –6.4 | 179 |
| 5 | 27.3 | 398 | – | – |
| 10 | 30.9 | 765 | – | – |
| 14 | 34.3 | 903 | – | – |
| $x$($Fe_2O_3$) [mol-%] | $\delta$($^{27}$Al) [ppm] | $\Delta_{1/2}$ [Hz] | $\delta$($^{23}$Na) [ppm] | $\Delta_{1/2}$ [Hz] |
| 0.0 | 18.8 | 149 | –6.5 | 130 |
| 0.5 | 22.2 | 256 | –5.5 | 199 |
| 0. 75 | 24.2 | 326 | –5.0 | 262 |
| 1 | 26.0 | 361 | –4.8 | 296 |

These shifts can be caused by a) a modification in the local environment of the aluminum nucleus and the formation of new aluminum species with higher chemical shifts and b) the existence of unpaired electrons in the system that affect the local magnetic field around the observed nucleus and cause a shift and broadening of the line.

Let us discuss the first point. In the liquid phase, the observed peak position is the average of the chemical shifts of individual species present in the melt weighted by their respective populations [Equation (1)] and $\sum_i X^{Al}(A_i) = 1$.

$$\delta^{Al}{}_{mes} = \sum_i X^{Al}(A_i)\cdot\delta^{Al}(A_i) \quad (1)$$

where $X^{Al}(A_i)$ is the atomic fraction of Al atoms in the $A_i$ species and $\delta^{Al}(A_i)$ its chemical shift.

The $^{27}$Al chemical shift range for aluminum in oxide and fluoride materials is known to correlate strongly with the nature and number of the nearest neighbors around the aluminum atom and thus to its coordination. For $\{AlO_4\}$ tetrahedral sites in oxides the $\delta$ values fall in the range $\delta$ = 55 to 90 ppm and in the range $\delta$ = –20 to +20 ppm for the $\{AlO_6\}$ octahedral sites. $\{AlO_5\}$ groups have been characterized in different aluminosilicate structures with $\delta$ values of about 30 to 40 ppm. In fluorides, significantly different chemical shift ranges have also been reported for $AlF_4^-$, $AlF_5^{2-}$, and $AlF_6^{3-}$ units. They are clearly shifted towards lower chemical shifts: $\delta$ = 4 to –15 ppm for $AlF_6^{3-}$, $\delta$ = 40 to 35 ppm for $AlF_4^-$, and around $\delta$ = 20 ppm for $AlF_5^{2-}$ (Table 2).[10]

Table 2. $^{27}$Al chemical shift ranges for Al–O and Al–F coordination.[11]

| Al coordination | $\delta$($^{27}$Al) [ppm] |
|---|---|
| $AlO_4$ | 90–55 |
| $AlO_5$ | 40–30 |
| $AlO_6$ | 20 to –20 |
| $AlF_4$ | 35–40 |
| $AlF_5$ | 20 |
| $AlF_6$ | 4 to –15 |

These chemical-shift ranges will help us to better understand the chemical-shift evolution measured in the melts. An increase of the $^{27}$Al chemical shift can thus be related to a decrease of the average coordination number of the aluminum atoms and the formation of species with a lower coordination number.

It is also expected that the addition of oxides ($Al_2O_3$, FeO, $Fe_2O_3$) to molten cryolite will result in the formation of oxygen-containing entities, the most probable being the oxofluoroaluminate species $Al_2OF_6^{2-}$ and $Al_2O_2F_4^{2-}$ depending on the oxide content. From an NMR point of view, the local configuration around the aluminum atom in each of these two anions corresponds to tetrahedral environments $\{AlOF_3\}$ and $\{AlO_2F_2\}$. Lacassagne et al.[11] have determined the $^{27}$Al chemical shifts of these species as $\delta^{Al}{}_{Al_2OF_6^{2-}} = 50.0 \pm 0.5$ ppm and $\delta^{Al}{}_{Al_2O_2F_4^{2-}} =$

 © 2006 Wiley-VCH Verlag GmbH & Co. KGaA, Weinheim 

58.5 ± 0.5 ppm, which lie between the chemical-shift ranges of $\{AlO_4\}$ and $\{AlF_4\}$ tetrahedral units. The formation of such oxofluoroaluminate species in the melt by dissolution of iron oxides should thus contribute to an increase of the measured $^{27}Al$ chemical shifts in molten cryolite, where aluminum atoms are essentially involved in pure fluoride environments.

Because of the line-shape distortion observed for high FeO amounts it is difficult to interpret the position of the line unambiguously. This distortion can be assigned to a paramagnetic effect that causes a line broadening and should certainly contribute to the shift of the line observed.

Iron in the +2 and +3 oxidation states may exist in a low-spin or a high-spin state, depending on the ligand-field strength. In both systems, $F^-$ and $O^{2-}$ ligands create a rather soft ligand field.[12] Thus, the high-spin state will be preferred [$(t_{2g})^4(e_g)^2$ for $Fe^{II}$ and $(t_{2g})^3(e_g)^2$ for $Fe^{III}$]. This is also supported by the increasing Boltzman distribution of the higher states with temperature increase. The important line broadening indicates that the distribution of local magnetic fields is spread over the sample. The broadening of the resonance signal reflects the extent of interaction between the unpaired electrons and the nucleus.[13]

We can calculate the $^{27}Al$ chemical shifts in the $Na_3AlF_6$–10 mol-% FeO system, by taking into account only the aluminum species involved in the suggested reaction (A).

$$2\,Na_3AlF_6(l) + 2\,FeO(s) \leftrightharpoons 2\,Na_2FeF_4(g) + Na_2Al_2O_2F_4(l) \quad (A)$$

At this FeO concentration, the $Al_2O_2F_4^{2-}$ anion is supposed to be formed in the melt in addition to the fluoroaluminate species $AlF_6^{3-}$, $AlF_5^{2-}$, and $AlF_4^-$ due to a dissociation reaction of unreacted molten cryolite.[1,14–18] Thus, starting from 90 mol of $Na_3AlF_6$ and 10 mol of FeO, we assume the formation of 5 mol of $Al_2O_2F_4^{2-}$ by reaction with 10 mol of $Na_3AlF_6$. After the reaction our system would contain 5 mol of $Al_2O_2F_4^{2-}$ and 80 mol of unreacted $Na_3AlF_6$.

From the mass-balance equation expressed for aluminum, we can calculate the anionic molar fractions of the different species in the melt. $x_i = \frac{N_i}{N_T}$, where $N_i$ is the number of mols of the species $i$ and $N_T$ the total number of mols. The atomic fractions can then be easily deduced and substituted in Equation (2) to give Equation (1).

$$\delta^{27}_{Al}(\text{calcd.})\,[\text{ppm}] = 0.0588\cdot\delta^{27}_{Al}(Al_2O_2F_4^{2-}) + 0.9412\cdot\delta^{27}_{Al}\left(\sum_{x=4}^{6} AlF_x^{(x-3)-}\right) \quad (2)$$

In this calculation, the contribution of unpaired electrons is not taken into account. $\delta^{27}_{Al}\left(\sum_{x=4}^{6} AlF_x^{(x-3)-}\right) = 18.8$ ppm is the chemical shift measured in molten cryolite, and $\delta^{27}_{Al}(Al_2O_2F_4^{2-}) = 58.5$ ppm is the $^{27}Al$ chemical shift value reported by Lacassagne et al.[11] for the $Al_2O_2F_4^{2-}$ species. This gives Equation (3).

$$\delta^{27}_{Al}(\text{calcd.})\,[\text{ppm}] = 0.0588\times 58.5 + 0.9412\times 18.8 = 21.1 \quad (3)$$

This calculated value is different from the experimental chemical shift measured in the melt of $\delta$ = 30.9 ppm. This difference can be associated with the presence of the unpaired electrons of iron in the oxidation state +2, as mentioned above.

In the ($Na_3AlF_6$–$Fe_2O_3$) system the formation of two oxofluoroaluminate anions should be considered even at such a low iron oxide content according to reaction B.[18,19]

$$4\,Na_3AlF_6 + Fe_2O_3 \leftrightharpoons 2\,Na_3FeF_6 + Na_2Al_2O_2F_4 + Na_2Al_2OF_6 + 2NaF \quad (B)$$

Addition of 1 mol of $Fe_2O_3$ to cryolite results in the formation of 1 mol of $Al_2OF_6^{2-}$ and 1 mol of $Al_2O_2F_4^{2-}$ by reaction with 4 mols of $Na_3AlF_6$. After the reaction, the system contains 1 mol of $Al_2OF_6^{2-}$, 1 mol of $Al_2O_2F_4^{2-}$, and 95 mols of unreacted $Na_3AlF_6$ and other species that do not contain Al atoms and thus that will not contribute to the $^{27}Al$ chemical shift. Normalization gives Equations (4) and (5).

$$\delta^{27}_{Al}(\text{calcd.})\,[\text{ppm}] = 0.0103\cdot\delta^{27}_{Al}(Al_2O_2F_4^{2-}) + 0.9794\cdot\delta^{27}_{Al}\left(\sum_{x=4}^{6} AlF_x^{(x-3)-}\right) \quad (4)$$

$$\delta^{27}_{Al}(\text{calcd.})\,[\text{ppm}] = 0.0103\times 50 + 0.0103\times 58 + 0.9794\times 18.3 = 19.0 \quad (5)$$

The difference between the calculated and the experimental chemical shift of $\delta$ = 26.0 ppm can again be attributed to the presence of unpaired electrons of iron in the oxidation state +3.

### $^{23}Na$ NMR Spectra

No significant modifications of the $^{23}Na$ chemical shift were observed in both systems. In the $Na_3AlF_6$–FeO system, when the amount of FeO is increased, the line is enlarged and distorted. This indicates the proximity of a paramagnetic element to the $^{23}Na$ surroundings but no direct bonding in a defined ionic species.

### $^{19}F$ NMR Spectra

No $^{19}F$ NMR signal was detected on melting. This can be explained by the existence of a strong paramagnetic effect that can disturb the signal and make it disappear. For $Na_3AlF_6$-10 mol-% FeO a small $^{19}F$ signal was observed but only after 14 minutes of heating. This means that some reaction has started that changes the local environment around the fluorine atoms.

In order to follow the kinetics of the dissolution of iron oxides in both systems, NMR spectra were recorded successively for the $^{27}Al$ and $^{19}F$ nuclei during 30 minutes at 1020 °C.

The evolution of the $^{19}F$ NMR spectra of the $Na_3AlF_6$-10 mol-% FeO mixture at 1020 °C is shown in Figure 3 as a function of time. When the heating duration is increased the position and the shape of the signal are modified. The signal position moves towards the position measured in

 © 2006 Wiley-VCH Verlag GmbH & Co. KGaA, Weinheim 

pure cryolite and at the same time the line becomes narrower (Table 3). This evolution can be explained by a continuous evolution of the nucleus shielding due to a decrease of the concentration of paramagnetic compounds in the investigated sample.

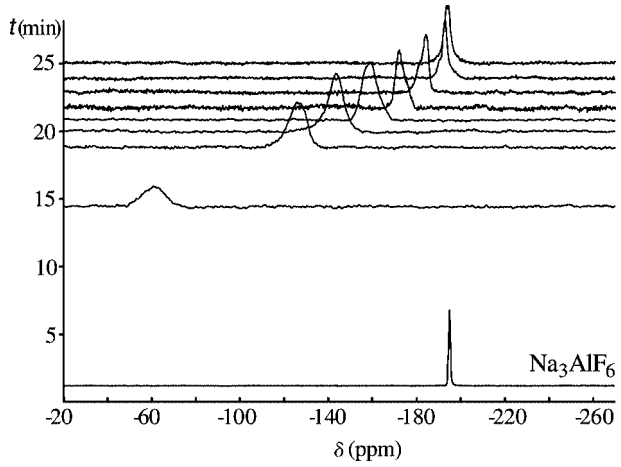


Figure 3. HT $^{19}F$ NMR spectra of $Na_3AlF_6$–10 mol-% FeO at 1020 °C vs. heating time.

Table 3. Time dependence of $^{27}Al$ and $^{19}F$ signal position ($\delta$) and linewidth ($\Delta_{1/2}$) in the $Na_3AlF_6$–10 mol-% FeO and $Na_3AlF_6$–1 mol-% $Fe_2O_3$ systems at 1020 °C.

| $Na_3AlF_6$–FeO | | | | | | $Na_3AlF_6$–$Fe_2O_3$ | | |
|---|---|---|---|---|---|---|---|---|
| $t$ [min] | $\delta(^{27}Al)$ [ppm] | $\Delta_{1/2}$ [Hz] | $t$ [min] | $\delta(^{19}F)$ [ppm] | $\Delta_{1/2}$ [Hz] | $t$ [min] | $\delta(^{27}Al)$ [ppm] | $\Delta_{1/2}$ [Hz] |
| 4 | 30.9 | 762 | 6 | – | – | 3 | 24.6 | 336 |
| 7 | 31.2 | 1052 | 11 | – | – | 11 | 24.6 | 313 |
| 12 | 31.5 | 717 | 14 | –61.5 | 9618 | 16 | 25.1 | 323 |
| 16 | 27.6 | 394 | 19 | –126.2 | 2100 | 24 | 25.5 | 379 |
| 20 | 22.8 | 302 | 20 | –145.2 | 1859 | 28 | 26.0 | 366 |
| 25 | 22.6 | 488 | 21 | –160.5 | 1835 | | | |
| 30 | 23.2 | 441 | 22 | –172.0 | 1494 | | | |
| 31 | 23.2 | 475 | 23 | –184.4 | 1183 | | | |
| | | | 24 | –193.1 | 971 | | | |
| | | | 25 | –194.8 | 829 | | | |

The decreasing concentration of paramagnetic iron in the sample is probably caused by the volatilization of $Fe^{II}$ compounds from the melt. The solidified sample was investigated by X-ray diffraction and no crystalline phase containing iron was detected. This confirms the formation of volatile compounds of the type $Na_xFeF_{2+x}$ ($x$ = 1, 2),[19,20] as already proposed in the literature.[8,9]

The same kind of measurements were made for the second system with $Fe_2O_3$ oxide ($Na_3AlF_6$ + 1 mol-% $Fe_2O_3$). In this case we were not able to observe any $^{19}F$ signal even after more than 30 minutes in the melt. The non-observation of the $^{19}F$ signal suggests the presence of stable, nonvolatile fluoride species in the melt involving the paramagnetic nuclei, probably in the form of $FeF_6^{3-}$ ions.[5,19] The paramagnetic effect seems to be strong enough to strongly affect the signal detection.

In the case of $^{27}Al$ in $Na_3AlF_6$ + 10 mol-% FeO, we observed a particular behavior of the spectrum with time whilst heating, with a shift of the line position and a progressive broadening of the line up to 14 minutes of heating (Figure 4). This evolution is then inversed and we observed a decrease of the chemical shift and a narrowing of the peak. This modification appears approximately at the same time as the $^{19}F$ signal is observed (Figure 3). These observations support the suggestion of a continuous decrease of the concentration of paramagnetic iron in the sample with FeO caused by evaporation of $Fe^{II}$ compounds from the system.

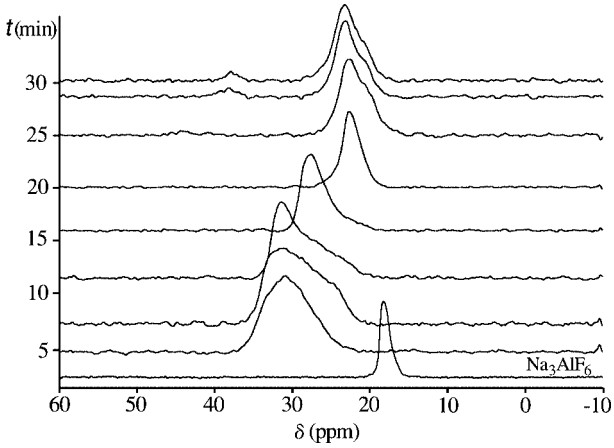


Figure 4. HT $^{27}Al$ NMR spectra of $Na_3AlF_6$–10 mol-% FeO at 1020 °C vs. heating time.

As mentioned above, the calculated value of the $^{27}Al$ chemical shift ($Na_3AlF_6$ + 10 mol-% FeO), assuming reaction B and no influence of the unpaired electrons, is $\delta$ = 20.6 ppm. This calculated value is in good agreement with the experimental value of $\delta$ = 23.0 ppm for the sample after 30 minutes of heating.

In the case of $Fe_2O_3$ (after five minutes of heating), the $^{27}Al$ chemical shift remains constant during further heating (Figure 5). This observation confirms the presence of stable, nonvolatile fluoride species in the melt involving the $Fe^{III}$ paramagnetic iron nuclei.

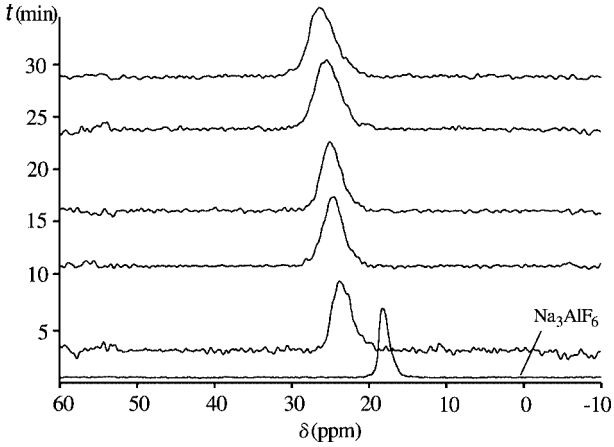


Figure 5. HT $^{27}Al$ NMR spectra of $Na_3AlF_6$–1 mol-% $Fe_2O_3$ at 1020 °C vs. heating time.

 © 2006 Wiley-VCH Verlag GmbH & Co. KGaA, Weinheim 

## Conclusions

High-temperature NMR experiments have been performed in molten cryolite with addition of different amounts of FeO or $Fe_2O_3$. The selective observation of the $^{27}Al$, $^{23}Na$, and $^{19}F$ signals in the melts at 1020 °C and their evolution with increasing iron oxide content has allowed us to confirm the formation of oxofluoroaluminate species. The non-observation of the $^{19}F$ signal caused by the paramagnetic influence of the $Fe^{II}$ ion in the melt is associated with the formation of "fluorinated iron" species. Even though this paramagnetic effect causes a strong broadening and distortion of the signals, we can still take advantage of this interaction and follow the formation and/or loss of the $Fe^{II}$ species. In the $Na_3AlF_6$–FeO melts, the $^{19}F$ signal was finally detected after 14 minutes heating, which would coincide with the evaporation of $Fe^{II}$ species. However, it was not observed at all in the $Na_3AlF_6$–$Fe_2O_3$ system due to the presence of stable, nonvolatile species involving the paramagnetic iron nuclei.

## Experimental Section

Samples were prepared by mixing $Na_3AlF_6$ (natural, from Ivigtut) and FeO or $Fe_2O_3$ (reagent grade, Aldrich). The compositions ranged from 0 to 14 mol-% of FeO and from 0 to 1 mol-% of $Fe_2O_3$ (see Table 1).

All NMR experiments were carried out using a Bruker DSX 400 (9.4 T) NMR spectrometer operating at frequencies of 104.2 MHz for $^{27}Al$, 105.8 MHz for $^{23}Na$, and 376.3 MHz for $^{19}F$. $^{27}Al$, $^{23}Na$, and $^{19}F$ chemical shifts are referenced to 1 M aqueous solutions of $Al(NO_3)_3$, NaCl, and $CFCl_3$ at room temperature, respectively. High temperature (HT) NMR experiments were performed using the previously described laser-heated system developed at the CRMHT (Orléans, France).[13] Every sample was placed in a high purity boron nitride (Carborundum) crucible tightly closed by a screwed BN cap and placed inside the RF coil, in the center of the cryomagnet. The crucible was then heated with a $CO_2$ laser beam ($\lambda$ = 10.6 μm, 120 W). The HT NMR spectra were obtained using single-pulse excitation with 20-, 30-, and 18-μs pulses for $^{27}Al$, $^{23}Na$, and $^{19}F$ measurements, respectively. Recycle delays of between 500 ms and 2 s (for $^{19}F$) were used, and 64 scans were measured to obtain a reliable signal-to-noise ratio. The powder mixtures were heated and melted up to 1020 °C. $^{27}Al$, $^{23}Na$, and $^{19}F$ NMR spectra were recorded for every composition after 4 min for temperature stabilization. In order to follow the kinetics of the iron oxide dissolution, $^{27}Al$, $^{23}Na$, and $^{19}F$ NMR spectra were recorded repeatedly up to 30 min at 1020 °C.

The NMR parameters (chemical shifts, line widths, quadrupolar coupling constants) were fitted to the experimental spectra with the Winfit program.[21]

## Acknowledgments

We would like to acknowledge the financial support of the EEC (contract HPMC-CT-2000-00169) in the framework of the Marie Curie training site "high resolution solid/high temperature liquid nuclear magnetic resonance in materials sciences" (Orleans, France), and Slovak Grant Agencies (VEGA-2/4107/23, APVT-51-008104)

[1] K. Grjotheim, C. Krohn, M. Malinovský, K. Matiašovský, J. Thonstad, *Aluminium Electrolysis. Fundamentals of the Hall–Héroult Process*, 2nd ed., Aluminium Verlag GmbH, Düsseldorf, **1982**.
[2] Å. Sterten, P. A. Solli, E. Skybakmoen, *J. Appl. Electrochem.* **1998**, *28*, 781–789.
[3] J. H. Choi, G. W. Suh, Y. H. Paik, *J. Korean Inst. Met. Mater.* **1991**, *29*, 1283–1285.
[4] K. Horinouchi, N. Tachikawa, K. Yamada, "DSA in Aluminium Reduction Cells." Proc. 1st Int. Symp. Molten Salt Chem. Technology, Kyoto, Japan, **1983**, pp. 66–72.
[5] Q. B. Diep, Dr. Ing. Thesis, Norwegian University of Science and Technology, Trondheim, **1998**.
[6] H. G. Johansen, Dr. Ing. Thesis, Norwegian University of Science and Technology, Trondheim, **1975**.
[7] H. G. Johansen, A. Sterten, J. Thonstad, *Acta Chem. Scand.* **1989**, *43*, 417–420.
[8] T. E. Jentofsen, E. W. Dewing, G. M. Haarberg, J. Thonstad, *Proc. Electrochem. Soc.* **1999**, *99*, 473–484.
[9] T. E. Jentofsen, Dr. Ing. Thesis, Norwegian University of Science and Technology, Trondheim, **2000**.
[10] C. Bessada, V. Lacassagne, D. Massiot, P. Florian, J.-P. Coutures, E. Robert, B. Gilbert, *Z. Naturforsch., Teil A* **1999**, *54*, 162–166.
[11] V. Lacassagne, C. Bessada, P. Florian, S. Bouvet, B. Ollivier, J.-P. Coutures, D. Massiot, *J. Phys. Chem. B* **2002**, *106*, 1862–1868.
[12] D. F. Shiver, P. W. Atkins, C. H. Langford, *Inorganic Chemistry*, Oxford University Press, Oxford, 2nd edition, **1994**.
[13] V. Lacassagne, C. Bessada, B. Ollivier, D. Massiot, P. Florian, J.-P. Coutures, *C. R. Acad. Sci. Paris, Ser. IIb.* **1997**, *325*, 91–98.
[14] B. Gilbert, G. Mamantov, G. M. Begun, *J. Chem. Phys.* **1975**, *62*, 950.
[15] F. N. Xiang, H. Kvande, *Acta Chem. Scand.* **1986**, *A40*, 622.
[16] B. Gilbert, T. Materne, *Appl. Spectrosc.* **1990**, *44*, 299.
[17] H. Zhou, Dr. Ing. Thesis, Norwegian University of Science and Technology, Trondheim, **1991**.
[18] F. Šimko, V. Daněk, *Chem. Pap.* **2001**, *55*, 269–272.
[19] F. Šimko, Dr. Ing. Thesis, The Institute of Inorganic Chemistry SAS, Bratislava, **2003**.
[20] G. Scholz, R. Stösser, *J. Fluorine Chem.* **1997**, *86*, 31–142.
[21] D. Massiot, F. Fayon, M. Capron, I. King, S. Le Calvé, B. Alonso, J.-O. Durand, B. Bujoli, Z. Gan, G. Hoatson, *Magn. Reson. Chem.* **2002**, *40*, 70–76.

Received: June 9, 2006
Published Online: September 22, 2006

 © 2006 Wiley-VCH Verlag GmbH & Co. KGaA, Weinheim 

DOI: 10.1002/ejic.200600554

# Complexation of Uranium(VI) with Thiodiacetic Acid in Solution at 10–85 °C

**Plinio Di Bernardo,*[a] PierLuigi Zanonato,[a] Arturo Bismondo,[b] Huijian Jiang,[c] Alexander Yu. Garnov,[c] Jun Jiang,[c] and Linfeng Rao*[c]**

**Keywords:** Uranium / Thermodynamics / Carboxylate ligands / EXAFS spectroscopy / Temperature effect

The protonation of thiodiacetate and its complexation with uranium(VI) in 1.05 mol kg$^{-1}$ $NaClO_4$ are studied at variable temperatures (10–85 °C). Three $U^{VI}$ complexes ($UO_2L$, $UO_2HL^+$, and $UO_2HL_2^-$, where L is thiodiacetate) are identified in this temperature range. The formation constants and the enthalpies of complexation are determined by potentiometry and calorimetry. The complexation of uranium(VI) with thiodiacetate becomes more endothermic at higher temperatures. However, the complexes become stronger due to increasingly more positive entropies of complexation at higher temperatures, which exceeds the increase in the unfavorable enthalpy of complexation. The values of the heat capacity of complexation ($\Delta C_p°$) are 122 ± 16, 302 ± 26, and 242 ± 23 J K$^{-1}$ mol$^{-1}$ for $UO_2L$, $UO_2HL^+$, and $UO_2HL_2^-$, respectively. The effect of temperature on the thermodynamics of the complexation is discussed in terms of the electrostatic model and the change in the solvent structure.

(© Wiley-VCH Verlag GmbH & Co. KGaA, 69451 Weinheim, Germany, 2006)

## Introduction

There has been significant interest in studies of the complexation of actinides with organic materials in solution at elevated temperatures due to the demand for scientific information to aid the safe management of nuclear wastes. The temperature of nuclear wastes in the storage tanks and the vicinity of the waste repository is known or estimated to be significantly above ambient temperature. For example, the temperature in the storage tanks is up to 90 °C and the temperature in the nuclear waste repository could be close to 100 °C thousands of years after the closure of the repository. Failure of the engineering barriers of the waste form could result in the contact of nuclear wastes with groundwater and possible migration of actinides into the environment. Prediction of the chemical behavior of actinides in waste processing and in the repository requires thermodynamic data on the complexation of actinides at elevated temperatures. At present, the majority of the thermodynamic data on actinide complexation are obtained at or near 25 °C.[1] The lack of data at elevated temperatures therefore makes it difficult to predict the behavior of actinides in waste processing and disposal, where elevated temperatures are expected.

While providing data to support the safe management of nuclear wastes, studies of the complexation of actinides at elevated temperatures could improve the fundamental understanding of the coordination chemistry of actinides as well. For example, the change in temperature perturbs the structure of solvent in the bulk and in the vicinity of the ions, alters its dielectric property, and thus affects the energetics of the complexation.[2,3] Therefore, the trends in thermodynamic parameters over a wide range of temperature could provide insight into the nature of the actinide complex and the solvent effect.

The liquid nuclear wastes in storage tanks are complex in composition and extremely diverse in acidity/basicity, ranging from strongly acidic to highly basic solutions. Many ligands could affect the behavior of actinides in liquid nuclear wastes by forming complexes. We have studied a series of mono- and dicarboxylic acids at elevated temperatures, including acetic,[4–7] malonic,[8] and oxydiacetic[9] acids. Some of the ligands exist in the nuclear wastes as degradation products of more complex organic compounds whose complexation with actinides has a direct impact on the behavior of actinides in waste storage and processing. Other ligands may not exist in nuclear wastes, but they are members of a series of structurally related ligands to allow a systematic study to help reveal the structure–function relationship. In this work, the complexation of $U^{VI}$ with thiodiacetate was studied at 10 to 85 °C. This system has been previously studied at 25 °C,[10,11] but not at elevated temperatures. Furthermore, due to the unavailability of tech-

[a] Dipartimento di Scienze Chimiche, Università di Padova, via Marzolo 1, 35131 Padova, Italy
Fax: +39-049-827-5161,
E-mail: plinio.dibernardo@unipd.it
[b] Istituto di Chimica Inorganica e delle Superfici del C.N.R. of Padova,
Corso Stati Uniti 4, 35127, Padova, Italy
[c] Chemical Sciences Division, Lawrence Berkeley National Laboratory,
Berkeley, CA 94720, U.S.A.
Fax: +1-510-486-5596,
E-mail: lrao@lbl.gov

Supporting information for this article is available on the WWW under http://www.eurjic.org or from the author.

 © 2006 Wiley-VCH Verlag GmbH & Co. KGaA, Weinheim 

niques to characterize the coordination modes, no structural information on the $U^{VI}$-thiodiacetate complexes in solution was obtained in the earlier studies. Therefore, the primary objectives in this work are: (1) to extend the thermodynamic database for the complexation of $U^{VI}$ with thiodiacetate to elevated temperatures; (2) to gain insight into the energetics of the complexation and the effect of temperature; and (3) to establish the coordination modes in the complexes. Thermodynamic parameters, including formation constants, enthalpy, and entropy, were determined by potentiometry and calorimetry. EXAFS was used, in conjunction with the thermodynamic data, to establish the coordination modes in the complexes.

## Results and Discussion

### Protonation of Thiodiacetate at 10–85 °C

The protonation constants of thiodiacetate at different temperatures were calculated from the data obtained by potentiometry. These constants were then used in the calculation of the enthalpies of protonation from the data obtained by calorimetry at the same temperature. The results are summarized in Table 1. The values obtained at 25 °C are in good agreement with the values at 20 and 25 °C in the literature.[10,12]

As is typical of many carboxylic acids,[13] the enthalpies of protonation of thiodiacetate are small (a few kilojoules per mol) and become more endothermic when the temperature is increased (Table 1). On the other hand, the entropy of protonation increases from 76 $J K^{-1} mol^{-1}$ (10 °C) to 100 $J K^{-1} mol^{-1}$ (85 °C) for HL, and from 130 $J K^{-1} mol^{-1}$ (10 °C) to 172 $J K^{-1} mol^{-1}$ (85 °C) for $H_2L$, thus favoring the protonation at higher temperatures. The increase in the entropy term ($T\Delta S$) is slightly larger than the increase in the enthalpy, which results in a net increase in the protonation constants when the temperature is increased.

Comparison between the thermodynamic functions concerning the protonation reactions of $TDA^{2-}$ and $ODA^{2-}$ may give additional information about these species in solution. Figure 1 shows the entropy and enthalpy of the first protonation of $TDA^{2-}$ and $ODA^{2-}$ ($H + L^{2-} \leftrightharpoons HL^-$) at different temperatures. The entropies of protonation of $TDA^{2-}$ and $ODA^{2-}$ are almost identical in the entire temperature region, whereas the enthalpies of protonation of $TDA^{2-}$ and $ODA^{2-}$ are parallel to each other, with a constant difference of 1.5 $kJ mol^{-1}$, at any given temperature. The fact that the $T\Delta S$ terms for $TDA^{2-}$ and $ODA^{2-}$ are identical at any temperature implies that the same degree of

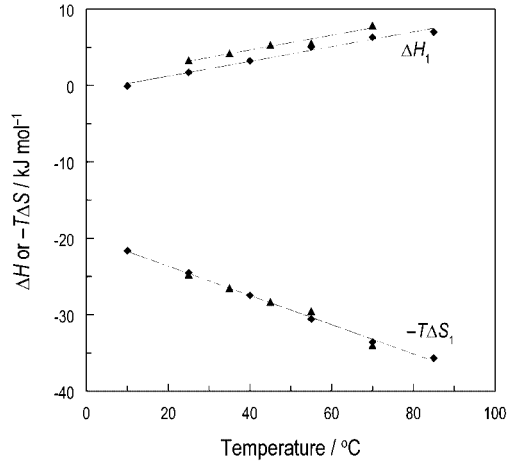


Figure 1. The thermodynamic parameters for the first protonation reaction of thiodiacetate (♦) and oxydiacetate (▲).[9] $I$ = 1.05 $mol kg^{-1}$ $NaClO_4$.

Table 1. Protonation of thiodiacetate ($I$ = 1.05 $mol kg^{-1}$ $NaClO_4$); the error limits represent 3σ.

| | $T$ [°C] | $\log\beta_{H,M}$ | $\log\beta_{H,m}$ | $-\Delta G$ [$kJ mol^{-1}$] | $\Delta H$ [$kJ mol^{-1}$] | $\Delta S$ [$J K^{-1} mol^{-1}$] | Ref. |
|---|---|---|---|---|---|---|---|
| $H^+ + L^{2-} \leftrightharpoons HL^-$ | 10 | 4.02 ± 0.02 | 4.00 ± 0.02 | 21.68 ± 0.11 | –(0.05 ± 0.03) | 76.4 ± 0.4 | |
| | 20 | 4.04 ± 0.02 | | | | | [10] |
| | 25 | 4.01 ± 0.02 | 3.99 ± 0.02 | 22.77 ± 0.11 | 1.73 ± 0.06 | 82.2 ± 0.4 | |
| | | 3.99 ± 0.01 | | | 1.82 ± 0.11 | | [12] |
| | 40 | 4.06 ± 0.03 | 4.04 ± 0.03 | 24.22 ± 0.18 | 3.24 ± 0.09 | 87.7 ± 0.6 | |
| | 55 | 4.08 ± 0.01 | 4.06 ± 0.01 | 25.50 ± 0.06 | 5.05 ± 0.15 | 93.1 ± 0.5 | |
| | 70 | 4.17 ± 0.01 | 4.15 ± 0.01 | 27.26 ± 0.07 | 6.3 ± 0.4 | 97.8 ± 1.2 | |
| | 85 | 4.20 ± 0.01 | 4.18 ± 0.01 | 28.66 ± 0.07 | 7.0 ± 0.3 | 99.6 ± 0.9 | |
| $2 H^+ + L^{2-} \leftrightharpoons H_2L$ | 10 | 7.21 ± 0.02 | 7.17 ± 0.02 | 38.87 ± 0.11 | –(2.16 ± 0.03) | 129.6 ± 0.4 | |
| | 20 | 7.18 ± 0.02 | | | | | [10] |
| | 25 | 7.21 ± 0.02 | 7.17 ± 0.02 | 40.92 ± 0.11 | 1.13 ± 0.10 | 141.0 ± 0.5 | |
| | | 7.13 ± 0.01 | | | 1.36 ± 0.15 | | [12] |
| | 40 | 7.25 ± 0.02 | 7.21 ± 0.02 | 43.22 ± 0.12 | 3.84 ± 0.07 | 150.3 ± 0.4 | |
| | 55 | 7.28 ± 0.01 | 7.24 ± 0.01 | 45.48 ± 0.06 | 6.96 ± 0.27 | 159.8 ± 0.8 | |
| | 70 | 7.39 ± 0.01 | 7.35 ± 0.01 | 48.28 ± 0.07 | 9.3 ± 0.7 | 167.8 ± 2.0 | |
| | 85 | 7.40 ± 0.01 | 7.36 ± 0.01 | 50.46 ± 0.07 | 11.0 ± 0.3 | 171.6 ± 0.9 | |
| $H^+ + OH^- \leftrightharpoons H_2O$ | 10 | 14.46 ± 0.01 | | | –58.75 | | |
| | 25 | 13.78 ± 0.01 | | | –56.27 | | |
| | 40 | 13.20 ± 0.01 | | | –52.99 | | |
| | 55 | 12.88 ± 0.06 | | | –50.8 | | |
| | 70 | 12.54 ± 0.01 | | | –48.6 | | |
| | 85 | 12.10 ± 0.10 | | | –45.3 | | |

 © 2006 Wiley-VCH Verlag GmbH & Co. KGaA, Weinheim 

disorder is generated when these two doubly charged anions are protonated. The fact that the enthalpy of protonation of $ODA^{2-}$ is higher than that of $TDA^{2-}$ at all temperatures probably results from the lower basicity of $ODA^{2-}$ than $TDA^{2-}$, which is due to a higher inductive effect exerted by the ether oxygen in $ODA^{2-}$ than the sulfur in $TDA^{2-}$. Since this inductive effect is likely to be independent of temperature, the difference in the enthalpies of protonation for $TDA^{2-}$ and $ODA^{2-}$ remains constant (approx. 1.5 kJ mol$^{-1}$) at any temperature and parallel trends in the enthalpy are observed.

## Complexation of Uranium(VI) with Thiodiacetate

### *Stability Constants at 10–85 °C*

Two representative potentiometric titrations at 10 and 85 °C are shown in Figure 2. The best model to fit the potentiometric data in the entire temperature range includes the formation of three $U^{VI}$/TDA complexes (ML, MHL, and $MHL_2$):

$UO_2^{2+} + L^{2-} \leftrightharpoons UO_2L(aq)$

$UO_2^{2+} + H^+ + L^{2-} \leftrightharpoons UO_2HL^+$

$UO_2^{2+} + H^+ + 2L^{2-} \leftrightharpoons UO_2HL_2^-$

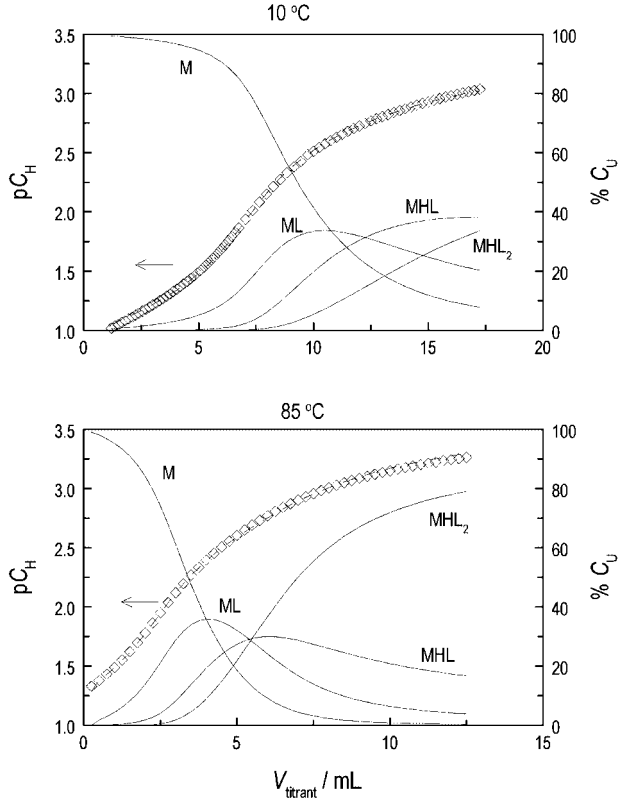


Figure 2. Potentiometric titrations of $U^{VI}$/thiodiacetate complexation. $I$ = 1.05 mol kg$^{-1}$ $NaClO_4$. Top: $T$ = 10 °C; $V^0$ = 32.0 cm$^3$, $C_H^0$ = 110.0 mM, $C_U^0$ = 19.22 mM; titrant $C_H/C_{TDA}$ = 0.485:0.481 M. Bottom: $T$ = 85 °C; $V^0$ = 29.0 cm$^3$, $C_H^0$ = 51.35 mM, $C_U^0$ = 21.19 mM; titrant $C_H/C_{TDA}$ = 0.556:0.556 M. Symbols: ◊: experimental data (p$C_H$); dashed curve: fit (p$C_H$); solid lines: percentage of $U^{VI}$ species (right $y$ axis).

The formation constants and Gibbs free energy of complexation at different temperatures were calculated and are given in Table 2. The model developed for the entire temperature range (from 10 to 85 °C) from this study is identical to the model for 25 °C from a previous study,[11] and the values at 25 °C from both studies agree well (Table 2). The data from this work indicate that the complexation between uranium(VI) and thiodiacetate is enhanced at elevated temperatures. The ML, MHL, and $MHL_2$ complexes at 85 °C are 6, 5, and 40 times as strong as those at 10 °C, respectively. The enhancement of complexation at elevated temperatures is consistent with the predictions by a simple electrostatic model that was developed to interpret the effect of temperature on the formation of lanthanide and actinide carboxylate complexes.[6–9,14]

### *Enthalpy and Entropy of Complexation at 10–85 °C*

A representative set of four calorimetric titrations at 25 °C is shown in part a of Figure 3. Similar titrations with solutions of different concentrations ($C_U$ and $C_H$) were performed at 10, 40, 55, 70, and 85 °C (see Table S3 in the Supporting Information). Using the formation constants of the complexes calculated from potentiometry, in conjunction with the constants and enthalpies of protonation (Table 1), the enthalpies of complexation for ML, MHL, and $MHL_2$ were calculated from the calorimetric titration data (see Table 2).

Using the thermodynamic values for protonation and complexation in Tables 1 and 2, simulated calorimetric titration curves for 10, 40, and 85 °C were calculated (Figure 3, b). The excellent agreement between the curves and experimental points confirms the mutual consistency of the calorimetric and potentiometric data on the complexation as well as the reliability of the data on protonation.

The data in Table 2 show that, as the temperature is increased, both the enthalpy and entropy of complexation increase, making opposite contributions to the temperature effect on the Gibbs free energy (and thus on the overall stability of the complexes). The overall stability constants increase because the increase in the entropy term ($T\Delta S$) exceeds the increase in the enthalpy. These trends are similar to previous observations for the $U^{VI}$/acetate,[7] $U^{VI}$/malonate,[8] and $U^{VI}$/oxydiacetate[9] systems, and are expected for typical hard acid–hard base interactions.[3] The increase of entropy with temperature could be the consequence of a more disordered bulk water structure due to the perturbation by more thermal motion at higher temperatures. In the process of complexation, the solvating water molecules are released to a more disordered bulk solvent. As a result, the gain in the complexation entropy is larger at higher temperatures. Meanwhile, the released water molecules would form fewer and/or weaker hydrogen bonds with the bulk water due to the thermal motion, thus resulting in less favorable enthalpy of complexation at higher temperatures. Detailed discussions on this point are given elsewhere.[6–9,14]

Figure 4 shows that the molar enthalpies of complexation for the three complexes increase monotonously as the temperature is increased. From these data, the heat capacity

 © 2006 Wiley-VCH Verlag GmbH & Co. KGaA, Weinheim 

Table 2. Complexation of $U^{VI}$ with thiodiacetate ($I$ = 1.05 mol kg$^{-1}$ $NaClO_4$); the error limits represent 3σ.

| | $T$ [°C] | $\log\beta_M$ | $\log\beta_m$ | $-\Delta G$ [kJ mol$^{-1}$] | $\Delta H$ [kJ mol$^{-1}$] | $\Delta S$ [J K$^{-1}$ mol$^{-1}$] | Ref. |
|---|---|---|---|---|---|---|---|
| $UO_2^{2+} + L^{2-} \leftrightharpoons UO_2L(aq)$ | 10 | 2.91 ± 0.03 | 2.89 ± 0.03 | 15.67 ± 0.16 | 13.4 ± 0.4 | 102.6 ± 1.5 | |
| | 20 | 3.16 ± 0.03 | | | | | [10] |
| | 25 | 3.04 ± 0.03 | 3.02 ± 0.03 | 17.24 ± 0.17 | 15.7 ± 0.7 | 110.5 ± 2.4 | |
| | | 2.97 ± 0.02 | | | 14.8 ± 0.2 | | [11] |
| | 40 | 3.23 ± 0.03 | 3.21 ± 0.03 | 19.24 ± 0.18 | 16.3 ± 0.9 | 113.5 ± 2.9 | |
| | 55 | 3.35 ± 0.05 | 3.33 ± 0.05 | 20.9 ± 0.3 | 19.2 ± 1.2 | 122.3 ± 3.8 | |
| | 70 | 3.62 ± 0.03 | 3.60 ± 0.03 | 23.65 ± 0.20 | 20.5 ± 1.8 | 129 ± 5 | |
| | 85 | 3.68 ± 0.05 | 3.66 ± 0.05 | 25.1 ± 0.3 | 23.0 ± 1.8 | 134 ± 5 | |
| $UO_2^{2+} + H^+ + L^{2-} \leftrightharpoons UO_2HL^+$ | 10 | 5.66 ± 0.04 | 5.62 ± 0.04 | 30.46 ± 0.22 | 7.5 ± 0.6 | 134.1 ± 2.2 | |
| | 25 | 5.76 ± 0.06 | 5.72 ± 0.06 | 32.6 ± 0.3 | 11.9 ± 1.2 | 150 ± 4 | |
| | | 5.43 ± 0.10 | | | 17.8 ± 0.4 | | [11] |
| | 40 | 5.63 ± 0.07 | 5.59 ± 0.07 | 33.5 ± 0.4 | 27 ± 4 | 193 ± 13 | |
| | 55 | 5.98 ± 0.07 | 5.94 ± 0.07 | 37.3 ± 0.4 | 21.4 ± 2.1 | 179 ± 6 | |
| | 70 | 6.10 ± 0.08 | 6.06 ± 0.08 | 39.8 ± 0.5 | 25 ± 3 | 189 ± 9 | |
| | 85 | 6.34 ± 0.08 | 6.30 ± 0.08 | 43.2 ± 0.6 | 30.3 ± 2.7 | 205 ± 8 | |
| $UO_2^{2+} + H^+ + 2L^{2-} \leftrightharpoons UO_2HL_2^-$ | 10 | 8.10 ± 0.08 | 8.04 ± 0.08 | 43.6 ± 0.4 | 24.3 ± 0.6 | 239.7 ± 2.6 | |
| | 20 | 8.42 ± 0.06 | | | | | [10] |
| | 25 | 8.48 ± 0.07 | 8.42 ± 0.07 | 48.1 ± 0.4 | 30.0 ± 1.2 | 262 ± 4 | |
| | | 8.39 ± 0.11 | | | 25.7 ± 0.2 | | [11] |
| | 40 | 8.70 ± 0.07 | 8.64 ± 0.07 | 51.8 ± 0.4 | 38.6 ± 3.6 | 289 ± 12 | |
| | 55 | 9.03 ± 0.07 | 8.97 ± 0.07 | 56.4 ± 0.4 | 38.0 ± 1.5 | 288 ± 5 | |
| | 70 | 9.36 ± 0.07 | 9.30 ± 0.07 | 61.1 ± 0.5 | 39.0 ± 2.5 | 292 ± 7 | |
| | 85 | 9.69 ± 0.08 | 9.63 ± 0.08 | 66.0 ± 0.6 | 38.2 ± 2.4 | 291 ± 7 | |

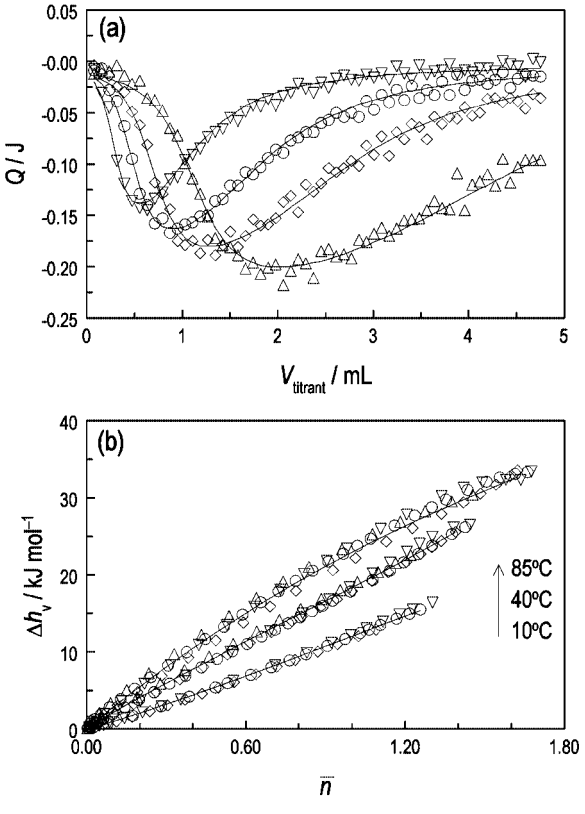


Figure 3. Calorimetric titrations of the uranium(VI) thiodiacetate system. $I$ = 1.05 mol kg$^{-1}$ $NaClO_4$. (a) $Q$ vs. $V_{titrant}$ at 25 °C, four titrations with different $C_M$ and $C_H$; (b) $\Delta h_v$ vs. $\bar{n}$ at 10, 40, and 85 °C; three or four titrations with different $C_M$ and $C_H$ were conducted at each temperature. The number of points in the figure has been reduced for clarity. Detailed conditions for ◊, ○, △, and ▽ are given in Table S3 of the Supporting Information.

of complexation, $\Delta C_p°$, was calculated to be 122 ± 16, 302 ± 26, and 242 ± 23 J K$^{-1}$ mol$^{-1}$ for $UO_2L$, $UO_2HL^+$, and $UO_2HL_2^-$, respectively.

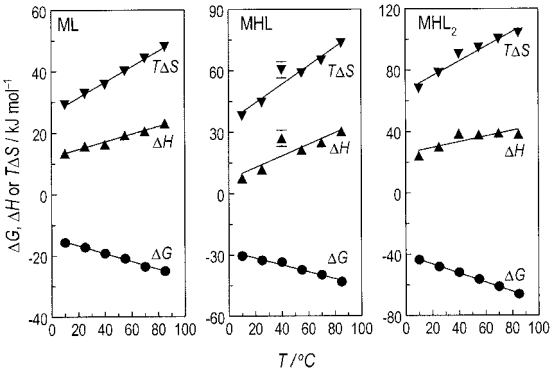


Figure 4. Overall thermodynamic parameters for the complexation of $U^{VI}$ with thiodiacetate. $I$ = 1.05 mol kg$^{-1}$ $NaClO_4$.

### *Coordination Modes*

The results of EXAFS experiments with three $U^{VI}$ solutions are shown in Figure 5 and Table 3. Solution I contains 100% free $UO_2^{2+}$. Speciation calculations with the stability constants in Table 2 indicate that the major species in solution II are $UO_2HL^+$ (51%) and free $UO_2^{2+}$ (30%), while the major species in solution III is $UO_2HL_2^-$ (86%). The FT magnitudes for solutions I and II are quite similar and are fitted with two U–O scattering paths at 1.77–1.78 Å and five U–O scattering paths at 2.40–2.41 Å. The two oxygens at 1.77–1.78 Å are the axial oxygens in the $UO_2^{2+}$ moiety and the five oxygens at 2.40–2.41 Å are from the water and/or the thiodiacetate ligands in the equatorial plane of

 © 2006 Wiley-VCH Verlag GmbH & Co. KGaA, Weinheim 

Table 3. Fitting parameters for uranium $L_{III}$-edge EXAFS.

| Samples | Shell | $R$[a] [Å] | $N$[a] | $\sigma$[b] [Å] | $\Delta E_0$ [eV] |
|---|---|---|---|---|---|
| Solution I[c] | $U–O_{ax}$ | 0.77 | 1.8 | 0.0385 | –13.69 |
| (0.02 M $U^{VI}$/0.1 M $HClO_4$) | $U–O_{eq}$ | 2.41 | 5.5 | 0.0871 | –13.69 |
| Solution II | $U–O_{ax}$ | 0.78 | 2.0 | 0.0531 | –13.77 |
| (0.02 M $U^{VI}$/0.5 M TDA, pH 2.0) | $U–O_{eq}$ | 2.40 | 5.4 | 0.1040 | –13.77 |
| Solution III | $U–O_{ax}$ | 0.79 | 2.0 | 0.0526 | –16.58 |
| (0.02 M $U^{VI}$/0.5 M TDA, pH 3.5) | $U–O_{eq1}$ | 2.34 | 1.7 | 0.0368 | –16.58 |
| | $U–O_{eq2}$ | 2.49 | 2.7 | 0.0573 | –16.58 |

[a] The 95% confidence limits for the bond lengths ($R$) and coordination numbers ($N$) for each shell are: $U–O_{ax}$ = 0.01 Å and ±15%; $U–O_{eq}$ = 0.02 Å and ±25%, respectively. [b] $\sigma$ is the EXAFS Debye–Waller term which accounts for the effects of thermal and static disorder through damping of the EXAFS oscillations by the factor $\exp(-2k^2\sigma^2)$. [c] Data from ref.[8]

$UO_2^{2+}$. The FT magnitude for solution III shows, besides the prominent peak for the two axial oxygens, two distinct shells in the range of 1.7–2.3 Å (phase shift not corrected) and is fitted with two U–O scattering paths at 2.34 Å and three U–O scattering paths at 2.49 Å. In the following discussion, these structural data are used in conjunction with the thermodynamic parameters of complexation to shed light on the coordination modes in the $UO_2L$, $UO_2HL^+$, and $UO_2HL_2^-$ complexes.

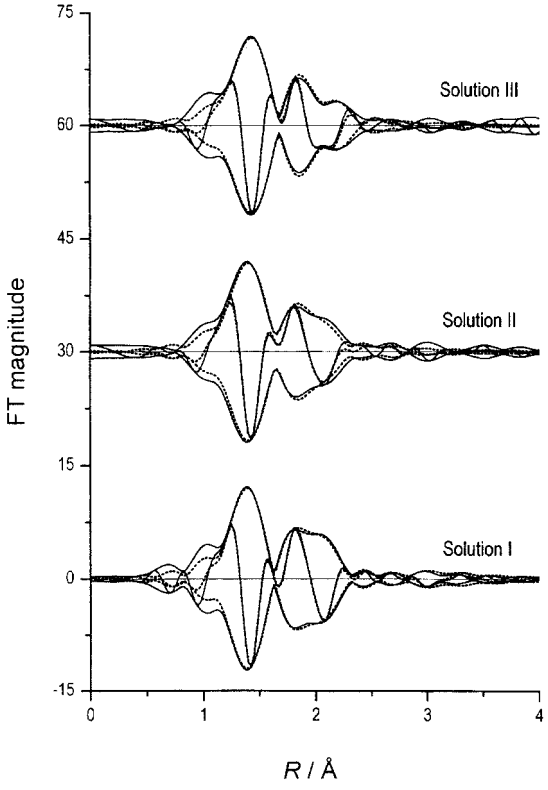


Figure 5. Fourier (FT) transform magnitude $\chi(k)\times k^3$ of the uranium $L_{III}$-edge EXAFS. Solid lines: experimental, dotted lines: fitted. Fitting results are given in Table 3.

### *$UO_2HL_2^-$*

Because this species is dominant (86%) in solution III, it is possible to propose a structure for this species based on the EXAFS data. In this complex, one TDA is fully deprotonated ($L^{2-}$) and the other TDA ligand is partially protonated ($HL^-$). As discussed in a previous study for the complexation of $U^{VI}$ with oxydiacetate (ODA),[9] the partially protonated ligand ($HL^-$) is likely to prefer a "terminal" didentate coordination mode in the complex, leaving the protonated carboxylate group free from metal binding. A proposed structure of the $UO_2HL_2^-$ complex is shown in Figure 6 (a), where one TDA ($L^{2-}$) is coordinated with $U^{VI}$ in a "global" didentate mode while the other TDA ($HL^-$) is in a "terminal" didentate mode similar to that in the uranium(VI) acetate complex described in the literature.[7] The U–O distance in the "global" didentate mode is shorter (2.34 Å) than that in the "terminal" didentate mode (2.49 Å). The oxygen from the water molecule is at a similar distance to the two oxygens of the "terminal" didentate carboxylate group and is not resolved by EXAFS.

### *$UO_2HL^+$*

Solution II contains 51% $UO_2HL^+$ and 30% free $UO_2^{2+}$ (30%). Therefore, the EXAFS data reflect the average coordination of $U^{VI}$ in these two major species. Because the partially protonated TDA ligand ($HL^-$) is likely to take a "terminal" didentate coordination mode in the complex, the structure of the $UO_2HL^+$ complex is proposed as shown in Figure 6 (b). The two oxygens from the terminal carboxylate group and the three oxygens from water molecules are all around 2.40 Å, resulting in a similar coordination shell of five oxygens as in the free $UO_2(H_2O)_5^{2+}$ (Solution I).

### *$UO_2L$*

This complex is not a major species in either solution I or solution II. Therefore, the EXFAS data do not provide information on the coordination mode of TDA in this complex. However, based on the structures of $UO_2HL_2^-$ (Figure 6, a) and $UO_2HL^+$ (Figure 6, b) proposed from the EXFAS data, it is reasonable to assume that the sulfur atom in $UO_2L$ does not participate in bonding with $U^{VI}$. Moreover, since the entropy of complexation primarily reflects the effect of dehydration and chelate formation, comparison of the entropy of complexation between TDA and structurally related dicarboxylates (e.g., ODA) could help reveal the coordination mode(s). A previous study has shown that, at 25 °C, one carboxylate group contributes approximately 50 $J\,K^{-1}\,mol^{-1}$ to the overall entropy of complexation.[9] For example, the value of $\Delta S_{298}$ for the didentate $U^{VI}$–phenylene-1,2-dioxydiacetate complex is 103 $J\,K^{-1}\,mol^{-1}$, while the values of $\Delta S_{298}$ for the tridentate $U^{VI}$–oxydiacetate and

 © 2006 Wiley-VCH Verlag GmbH & Co. KGaA, Weinheim 

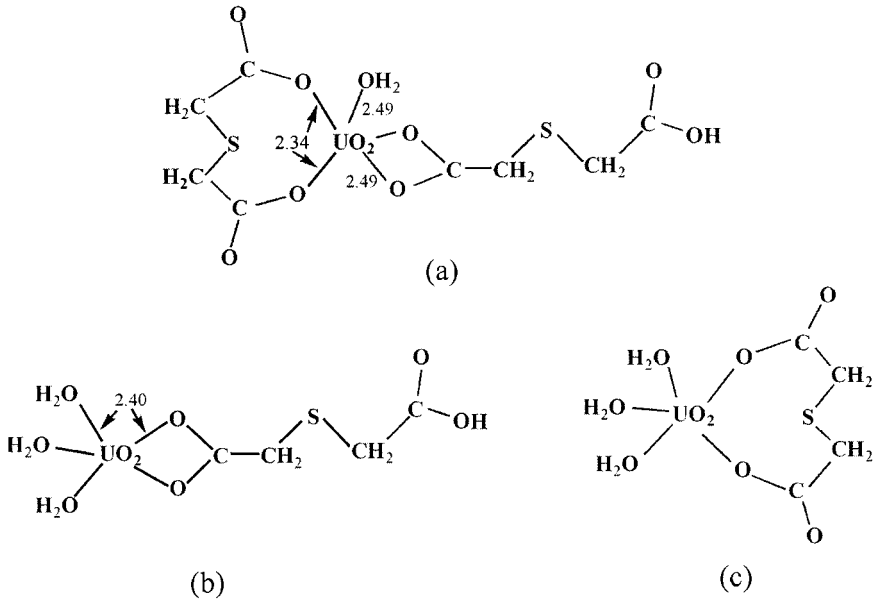


Figure 6. Proposed structures of uranium(VI) thiodiacetate complexes in solution: (a) $UO_2HL_2^-$, (b) $UO_2HL^+$, (c) $UO_2L$(aq), where $L^{2-}$ stands for the thiodiacetate anion.

$U^{VI}$–iminodiacetate complexes are 152 and 161 $J\,K^{-1}\,mol^{-1}$, respectively. The oxydiacetate and iminodiacetate ligands in these complexes are tridentate because the ether oxygen or the nitrogen atoms participate in the complexation.[9] The value of $\Delta S_{298}$ for the $U^{VI}$-TDA complex ($UO_2L$) is 110 $J\,K^{-1}\,mol^{-1}$ from this work (Table 2), similar to that for the didentate $U^{VI}$–phenylene-1,2-dioxydiacetate complex but much smaller than those for the tridentate $U^{VI}$-ODA and $U^{VI}$-IDA complexes. Thus, the thermodynamic data are consistent with a didentate mode in the 1:1 $U^{VI}$-TDA complex. Both carboxylate groups of TDA coordinate with $U^{VI}$ while the sulfur atom does not participate in the complexation. A proposed structure for $UO_2L$ is shown in Figure 6 (c).

## Conclusions

In the temperature range from 10 to 85 °C, three uranium(VI) thiodiacetate complexes ($UO_2L$, $UO_2HL^+$, and $UO_2HL_2^-$) have been identified by potentiometry and calorimetry. Both the enthalpy and entropy of complexation increase as the temperature is increased, although they make opposite contributions to the overall stability of the complexes. The complexes become stronger at higher temperatures due to a larger contribution from the entropy, which exceeds the unfavorable effect of enthalpy. The thermodynamic parameters, in conjunction with the structural information from EXAFS, suggest that TDA coordinates with $U^{VI}$ through the carboxylate group(s) and that the sulfur atom does not participate in the complexation. In $UO_2L$, the fully deprotonated TDA is in a "global" didentate mode through both carboxylate groups. However, in $UO_2HL^+$ and $UO_2HL_2^-$, the partially protonated TDA is probably in a "terminal" didentate mode, with the protonated carboxylate group free from metal bonding.

## Experimental Section

**Chemicals:** All chemicals were reagent grade or higher. Distilled and deionized water was used in preparations of all the solutions. The stock solution of uranium(VI) perchlorate was prepared by dissolving uranium trioxide ($UO_3$) in perchloric acid. The concentration of uranium(VI) in the stock solution was determined by absorption spectrophotometry and fluorimetry.[15] Gran's potentiometric method[16] was used to determine the concentration of perchloric acid in the stock solution. Volumetric standard sodium hydroxide solutions were purchased from Brinkmann Instruments, Inc. or Sigma–Aldrich, Inc. and verified to be carbonate-free prior to use. Solutions of sodium thiodiacetate were prepared by adding calculated amounts of sodium hydroxide to solutions of thiodiacetic acid. The ionic strength of all the solutions used in potentiometry and calorimetry was adjusted to 1.0 M at 25 °C by adding appropriate amounts of sodium perchlorate as the background electrolyte.

**Potentiometry:** The protonation constants of thiodiacetate (TDA) and the stability constants of the uranium(VI) TDA complexes were determined by potentiometric titrations in a temperature range from 10 to 85 °C. A specially designed titration vessel was used to avoid the problem of water condensation during the titrations at temperatures above the ambient. Details of the titration setup have been provided elsewhere.[6]

Electromotive force (EMF, in millivolts) was measured with a Metrohm pH meter (Model 713) equipped with a Ross combination pH electrode (Orion Model 8102). Because potassium perchlorate is much less soluble than sodium perchlorate, precipitation of the former could result in the clogging of the electrode frit glass septum. As a result, the original electrode filling solution (3.0 M potassium chloride) was replaced with 1.0 M sodium chloride. The electrode potential (mV) in acidic solutions can be expressed as Equation (1).

$$E = E^0 + RT/F \ln[H^+] + \gamma_H[H^+] \quad (1)$$

$R$ is the gas constant, $F$ is the Faraday constant, and $T$ is the temperature in Kelvin. The last term in Equation (1), $\gamma_H[H^+]$, is the

 © 2006 Wiley-VCH Verlag GmbH & Co. KGaA, Weinheim 

electrode junction potential for the hydrogen ion. Prior to each protonation or complexation titration, an acid/base titration with standard perchloric acid and sodium hydroxide solutions was performed to obtain the parameters $E^0$ and $\gamma_H$. These parameters allowed the calculation of hydrogen ion concentrations from the electrode potential in the subsequent titration. Corrections for the electrode junction potential for the hydroxide ion are not necessary in this work because all the experiments were conducted in acidic solutions, where the junction potential for the hydroxide ion is negligible.

Detailed conditions for the potentiometric titrations are provided in Tables S1 and Table S2 in the Supporting Information. Multiple titrations were conducted at each temperature with solutions of different concentrations ($C_{TDA}$, $C_H$, and $C_U$). 50–70 Data points were collected in each titration. The protonation constants of TDA, $K_{H,M}$, and the formation constants of $U^{VI}$-TDA complexes, $\beta_{j,M}$, on the molarity scale were calculated with the program Hyperquad.[17] To allow the comparison at different temperatures, the constants in molarity were converted into the constants in molality according to Equation (2).[18]

$$\log_{10}K_m = \log_{10}K_M + \Sigma_r v_r \log_{10}\vartheta \quad (2)$$

$K_m$ and $K_M$ are the equilibrium constants of a reaction in molality and molarity, respectively, $\vartheta$ is the ratio of the values of molality to molarity for the specific ionic medium. For the 1.0 M $NaClO_4$ used in this study, $\vartheta$ equals 1.05 L of solution per kilogram of water. $\Sigma_r v_r$ is the sum of stoichiometric coefficients of the reaction ($v_r$ is positive for products and negative for reactants.)

**Calorimetry:** Calorimetry was used to determine the enthalpy of thiodiacetate protonation and complexation with $U^{VI}$. The calorimetric titrations were conducted with both an isoperibol calorimeter (Model ISC-4285, Calorimetry Sciences Corp.) at the Lawrence Berkeley National Laboratory (for $T$ from 25 to 85 °C) and an isothermal microcalorimeter (Thermometric 2277 Thermal Activity Monitor, nanoWatt model) at the University of Padova (for $T$ = 10 °C). The performance of the isoperibol calorimeter was tested by measuring the enthalpy of protonation of 2-bis(2-hydroxyethyl)amino-2-(hydroxymethyl)propane-1,3-diol at different temperatures. The results are –29.1 ± 0.3 kJ mol$^{-1}$ at 45 °C and –29.3 ± 0.3 kJ mol$^{-1}$ at 70 °C, in good agreement with those in the literature (–28.4 ± 0.3 kJ mol$^{-1}$ at 45 °C and –29.3 ± 0.2 kJ mol$^{-1}$ at 70 °C).[19]

Detailed conditions for the calorimetric titrations are provided in Table S3 in the Supporting Information. Multiple titrations were performed at each temperature to obtain the enthalpy of protonation of TDA and the enthalpy of complexation between $U^{VI}$ and TDA, using different concentrations of the titrant or $UO_2(ClO_4)_2$ and $HClO_4$ in the cell. For each titration run, $n$ experimental values of the total heat produced in the reaction vessel ($Q_{ex,j}$, $j$ = 1 to $n$, usually $n$ = 50–70), were calculated as a function of the volume of the added titrant. These values, corrected for the heat of dilution of the titrant ($Q_{dil,j}$, determined in separate runs), gave the net reaction heat: $Q_{r,j} = Q_{exp,j} - Q_{dil,j}$. A quantity, $\Delta h_v$, was then calculated for the stepwise addition by Equation (3).

$$\Delta h_v = \sum_{j=1}^{j=n} (Q_{r,j} - Q_{p,j})/n \quad (3)$$

For the protonation titrations, $Q_{p,j}$ is the heat of water formation and $n$ is the number of mols of TDA in the cell. For the complexation titrations, $Q_{p,j}$ is the sum of the heat calculated for the water formation and ligand protonation while $n$ is the number of mols of $U^{VI}$ in the cell. The enthalpies of reaction were calculated, with a home modified version of the computer program Letagrop,[20] to use $\Delta h_v$ as the error-carrying variable while assigning equal weight to all the titrations with different amounts of uranium(VI) (for the U/TDA systems) or TDA (for the H/TDA systems).

**EXAFS Spectroscopy:** Three uranium(VI) solutions were prepared for EXAFS experiments. Solution I contained 0.02 M $UO_2(ClO_4)_2$ in 0.1 M $HClO_4$ with no thiodiacetic acid. Solutions II and III contained 0.02 M $UO_2(ClO_4)_2$ and 0.5 M thiodiacetic acid at pH 2.0 and 3.5, respectively. Approximately 2 mL of each solution was sealed in a polyethylene tube (5 mm i.d.) and mounted on an aluminum sample positioner with Scotch tape for the experiments.

Uranium $L_{III}$-edge EXAFS spectra were collected at the Stanford Synchrotron Radiation Laboratory (SSRL) on beamline 4-1 under normal ring operating conditions (3.0 GeV, 50–100 mA). Energy scans of the polychromatic X-ray beam were obtained using a Si(220) double-crystal monochromator. The vertical slit width was 0.5 mm, which reduced the effects of beam instabilities and monochromator glitches while providing ample photon flux. The higher order harmonic content of the beam was reduced by detuning the crystals in the monochromator so that the incident flux was reduced to 50% of its maximum at the scan ending energy. The EXAFS data were collected in both the transmission mode using argon-filled ionization chambers and the fluorescence mode using a four-element Ge detector, up to $k_{max} \approx 15$ Å$^{-1}$. Usually three or four scans were performed for each sample. Energy calibration was based on assigning the first inflection point of the absorption edge for uranium dioxide to 17166 eV. The EXAFS spectra were fitted with the R-space X-ray Absorption Package (RSXAP),[21] using parameterized phase and amplitude functions generated by the program FEFF7.[22] Single scattering interactions of U–$O_{ax}$ (axial oxygen) and U–$O_{eq}$ (equatorial oxygen) were included.

**Supporting Information** (see footnote on the first page of this article): Tables S1 and S2: Experimental conditions of potentiometry for proton/thiodiacetate and uranium(VI)/thiodiacetate systems, respectively. Table S3. Experimental conditions of calorimetry for thiodiacetate protonation and uranium(VI)/thiodiacetate complexation.

## Acknowledgments

This work was supported by the Director, Office of Science, Office of Basic Energy Sciences, Division of Chemical Sciences, under U.S. Department of Energy Contract No. DE-AC02-05CH11231 at Lawrence Berkeley National Laboratory and by the Ministero dell'Università e della Ricerca Scientifica e Tecnologica (MURST, Roma) within the program COFIN02. The EXAFS experiments were conducted at SSRL, which is operated by the Department of Energy, Division of Chemical Sciences.

[1] E. Martell, R. M. Smith, *Critical Stability Constants*, vol. 3, Plenum Press, New York, **1977**; first suppl., **1982**; second suppl., **1989**.

[2] T. M. Seward, *Metal Complex Formation in Aqueous Solutions at Elevated Temperatures and Pressures*, in *Chemistry and Geochemistry of Solutions at High Temperatures and Pressures*, Physics and Chemistry of the Earth, volumes 13 and 14 (Eds.: D. T. Rickard, F. E. Wickman), Pergamon Press, New York, **1981**, 113–128.

[3] E. N. Rizkalla, G. R. Choppin, *Lanthanides and Actinides Hydration and Hydrolysis*, in *Handbook on the Physics and Chem-*

 © 2006 Wiley-VCH Verlag GmbH & Co. KGaA, Weinheim 

*istry of Rare Earths*, vol. 18, *Lanthanides/Actinides: Chemistry* (Eds.: K. A. Gschneider Jr, L. Eyring, G. R. Choppin, G. H. Lander), Elsevier Science B. V., New York, **1994**.
[4] D. A. Wruck, P. Zhao, C. E. A. Palmer, R. J. Silva, *J. Solution Chem.* **1997**, *26*, 267–275.
[5] S. A. Wood, D. J. Wesolowski, D. A. Palmer, *Chem. Geol.* **2000**, *167*, 231–253.
[6] P. Zanonato, P. Di Bernardo, A. Bismondo, L. Rao, G. R. Choppin, *J. Solution Chem.* **2001**, *30*, 1–18.
[7] J. Jiang, L. Rao, P. Di Bernardo, P. Zanonato, A. Bismondo, *J. Chem. Soc., Dalton Trans.* **2002**, 1832–1836.
[8] L. Rao, J. Jiang, P. Zanonato, P. Di Bernardo, A. Bismondo, A. Y. Garnov, *Radiochim. Acta* **2002**, *90*, 581–588.
[9] L. Rao, A. Yu. Garnov, J. Jiang, P. Di Bernardo, P. Zanonato, A. Bismondo, *Inorg. Chem.* **2003**, *42*, 3685–3692.
[10] A. Cassol, P. Di Bernardo, R. Portanova, L. Magon, *Inorg. Chim. Acta* **1973**, *7*, 353–358.
[11] P. Di Bernardo, G. Tomat, A. Bismondo, O. Traverso, L. Magon, *J. Chem. Res. (M)* **1980**, 3144–3171.
[12] I. Dellien, I. Grenthe, G. Hessler, *Acta Chem. Scand.* **1973**, *27*, 2431–2440.
[13] A. E. Martell and R. M. Smith, *Critical Stability Constants*, vol. 6, Plenum Press, New York, **1989**.
[14] L. Rao, Z. C. Zhang, P. Zanonato, P. Di Bernardo, A. Bismondo, S. B. Clark, *Dalton Trans.* **2004**, 2867–2872.
[15] C. W. Sill, H. E. Peterson, *Anal. Chem.* **1947**, *19*, 646–651.
[16] G. Gran, *Analyst* **1952**, *77*, 661–671.
[17] P. Gans, A. Sabatini, A. Vacca, *Talanta* **1996**, *43*, 1739–1753.
[18] W. Hummel, G. Anderegg, I. Puigdomenech, L. Rao, O. Tochiyama; *Chemical Thermodynamics of Compounds and Complexes of U, Np, Pu, Am, Tc, Zr, Ni, and Se with Selected Organic Ligands* (Eds.: F. J. Mompean, M. Illemassène, J. Perrone), Elsevier Science B. V., Amsterdam, **2005**.
[19] R. Smith, P. Zanonato, G. R. Choppin, *J. Chem. Thermodyn.* **1992**, *24*, 99–106.
[20] R. Arnek, *Arkiv Kemi* **1970**, *32*, 81.
[21] B. J. E. Penner-Hahn, *Coord. Chem. Rev.* **1999**, *190–192*, 1101–1123.
[22] http://lise.lbl.gov/RSXAP.

Received: June 15, 2006
Published Online: September 20, 2006

 © 2006 Wiley-VCH Verlag GmbH & Co. KGaA, Weinheim 

DOI: 10.1002/ejic.200600558

# A Novel Copper(I) Halide Framework Templated by Organic–Inorganic Hybrid Polyoxometalate Chains Formed In Situ: A New Route for the Design and Synthesis of Porous Frameworks

**Hua Jin,[a] Yanfei Qi,[a] Enbo Wang,*[a] Yangguang Li,[a] Chao Qin,[a] Xinlong Wang,[a] and Song Chang[a]**

**Keywords:** Coordination polymers / Organic–inorganic hybrid composites / Polyoxometalates / Template synthesis

A 1D organic–inorganic hybrid polyoxometalate chain has been used as a non-coordinating anionic template for the construction of a novel 3D copper halide 4,4′-bipy framework, namely $[Cu_3^{I}Cl(4,4'\text{-bipy})_4][Cu^{II}(1,10\text{-phen})_2Mo_8O_{26}]$. X-ray diffraction experiments revealed that the title compound consists of chloride-bridged trinuclear $Cu^{I}$ units linked by neutral organic 4,4′-bipy groups into a 3D framework with hexagon-like channels in which 1D organic–inorganic hybrid polyoxometalate chains reside. This is the first example of a 1D organic–inorganic hybrid polyoxometalate chain functioning as a novel anionic template for the construction of a 3D framework.
(© Wiley-VCH Verlag GmbH & Co. KGaA, 69451 Weinheim, Germany, 2006)

## Introduction

Porous materials have attracted much attention because of interest in the creation of nanometer-sized spaces and their potential applications in gas storage, separation, ion exchange, or heterogeneous catalysis.[1] A promising approach toward the synthesis of these porous materials is the design of metal-organic frameworks built up from transition-metal ions and bridging organic ligands.[2] In this field, copper halides bridged by organic species have been subjected to a vast number of studies owing to the fact that the architectures of copper halides can be tuned at the molecular level so as to design and control, at least partly, the molecular structures of the final products,[3] especially since the so-called secondary building block (SBU) concept was proposed and extended by Yaghi and co-workers.[4] However, it is still important to synthesize robust 3D frameworks with high porosity.[5]

Anions are capable of directing the formation of some porous entities through either cation–anion interactions or hydrogen-bonding interactions between an organic host and an anionic guest.[6] Compared to simple anionic templates, POMs are bigger, have more diverse topologies, a higher charge, and are more suitable as guest units in the metal-organic host as they lead to larger pores, channels, and cavities. In this field, several interesting host–guest complex with various dimensional structures have been prepared.[7] Zubieta and co-workers, for example, have reported $[Fe(tpypor)_3Fe][Mo_6O_{19}]\cdot xH_2O$[7a] (tpypor = tetrapyridylporphyrin), which possesses a 3D $[Fe(tpypor)_3Fe]^{2+}$ host framework with a $[Mo_6O_{19}]^{2-}$ molecule encapsulated, and Zheng et al. have recently reported the novel decavanadate-anion-templated copper framework $[Cu_3(2\text{-pzc})_4(H_2O)_2(V_{10}O_{28}H_4)]\cdot 6.5H_2O$ (2-pzc = 2-pyrazinecarboxylate).[7b] In 2002, the Keller group first prepared the novel compound $[Cu_3(4,4'\text{-bipy})_5(MeCN)_2]PW_{12}O_{40}\cdot 2C_6H_5CN$[7c] constructed from a 3D Cu-4,4′-bipy coordination polymer with a large pore as host and Keggin-type heteropolyoxoanions as template. More recently, the 2D layer-like compound $Na_3[4,4'\text{-Hbipy}]\{Cu_4(4,4'\text{-bipy})_8(H_2O)_8\}[PW_{11}CuO_{39}(H_2O)][PW_{10}Cu_2O_{38}(H_2O)_2]\cdot 38H_2O$[7d] with Keggin-type POMs as guests has been characterized by the Dolbecq group. As part of our continuing efforts in the construction of functional porous coordination polymers,[8] we have exploited the Lindquist-type POM $[Mo_6O_{19}]^{2-}$ to synthesize several novel polyoxometalate-templated, supramolecular networks based on lanthanide dimers.[9] To the best of our knowledge, no metal-organic frameworks using an organic–inorganic hybrid polyoxometalate chain as template has been reported thus far.

In the hope that the combination of copper halides with POMs not only shows value-added properties and possible synergistic effects but also allows the creation of new networks with unique physical properties, we report here the unprecedented compound $[Cu_3^{I}Cl(4,4'\text{-bipy})_4][Cu^{II}(1,10\text{-phen})_2Mo_8O_{26}]$ (**1**), which exhibits a novel 3D copper halide 4,4′-bipy framework templated by a 1D organic–inorganic hybrid polyoxometalate chain. Additionally, we have also

[a] Department of Chemistry, Institute of Polyoxometalate Chemistry, Northeast Normal University,
Changchun, Jilin 130024, P. R. China
Fax: +86-431-509-8787
E-mail: wangenbo@public.cc.jl.cn
Supporting information for this article is available on the WWW under http://www.eurjic.org or from the author.

 © 2006 Wiley-VCH Verlag GmbH & Co. KGaA, Weinheim 

prepared another compound by changing the reaction conditions, namely $(H_3O)[Cu^{I}(4,4'\text{-bipy})]_3[Mo_8O_{26}]$, which exhibits a new 2D supramolecular network consisting of β-$[Mo_8O_{26}]^{4-}$ clusters and copper-organonitrogen coordination polymer chains via weak long-range Cu–O interactions.

## Results and Discussion

### Syntheses

The successful isolation of compounds **1** and **2** depends on the use of hydrothermal techniques. Hydrothermal synthesis has recently been proved to be a particularly useful technique for the preparation of organic–inorganic hybrid materials.[10] The exploitation of hydrothermal conditions requires a paradigm shift from the thermodynamic to the kinetic such that equilibrium phases are replaced by structurally more complex metastable phases.[11] In the hydrothermal environment, the reduced viscosity of the solvent results in enhanced rates of solvent extraction of solids and crystal growth from solution. Furthermore, since different solubility problems can be minimized, a variety of organic and inorganic precursors can be introduced. However, hydrothermal synthesis is still a relatively complex process because many factors can influence the outcome of reaction, such as the type of initial reactants, starting concentrations, pH values, reaction time, and temperature.[12]

Parallel experiments showed that the pH value of the reaction system is crucial for the crystallization of compound **1**: dark-green crystals of compound **1** could only be obtained in the pH range 3.9–4.5. In addition, the nature of the divalent transition metal is crucial for the formation of compound **1**. We tried to replace $CuCl_2{\cdot}2H_2O$ with $NiCl_2{\cdot}6H_2O$, $CoCl_2{\cdot}6H_2O$, $MnCl_2{\cdot}4H_2O$, or $FeCl_2{\cdot}4H_2O$ in the synthesis of compound **1**, but no isostructural compounds were obtained. When $CuCl_2{\cdot}2H_2O$ was replaced with $NiCl_2{\cdot}6H_2O$ or $CoCl_2{\cdot}6H_2O$ $[\{Ni(1,10\text{-phen})_2\}_2(\xi\text{-}Mo_8O_{26})]{\cdot}H_2O$[13] or $\{Co(1,10\text{-phen})_3\}_2[Mo_6O_{19}][Mo_8O_{26}]{\cdot}2H_2O$[14] could be synthesized. However, when $CuCl_2{\cdot}2H_2O$ was replaced with $MnCl_2{\cdot}4H_2O$ or $FeCl_3{\cdot}6H_2O$ no crystalline phase was formed. $[Cu(1,10\text{-phen})]_2[\{Cu(1,10\text{-phen})\}_2\text{-}Mo_8O_{26}]{\cdot}2H_2O$[15] could be synthesized without 4,4′-bipy, and compound **2** could be synthesized without 1,10-phen.

### Structure Description

The single X-ray structural analysis revealed that the structure of **1** is constructed from a coordination complex $\{[Cu_3^{I}Cl(4,4'\text{-bipy})_4]\}_n^{2n+}$ scaffolding and encapsulating organic–inorganic hybrid $\{Cu^{II}(1,10\text{-phen})_2Mo_8O_{26}\}_n^{2n-}$ polyoxometalate chains.

The metal-organic framework is composed of hexagon-grid layers pillared by 4,4′-bipy ligands in which there are two distinct copper centers: one resides in the corner of the hexagon lattice in each layer and is additionally coordinated to three nitrogen atoms of 4,4′-bipy and one chlorine atom, while the second copper center is coordinated to two pyridyl nitrogen donors and one chlorine atom, thus two Cu(3) and one Cu(2) are connected into a trinuclear copper cluster through the chlorine atom. The hexagon-grid layer lies parallel to the *ab* plane (Figure 1). Each layer consists of hexagonal lattices, in which the Cu atoms are located at the corners, while the 4,4′-bipy ligands and Cl atoms are located at the edges. As shown in Figure 2, there is no interpenetration between the layers, thus this type of arrangement leads to hexagonal channels of about $5.3\times11.1\times11.1$ Å$^3$, in which organic–inorganic hybrid $\{Cu^{II}(1,10\text{-phen})_2Mo_8O_{26}\}_n^{2n-}$ polyoxometalate chains are located. The octamolybdate $[Mo_8O_{26}]^{4-}$ cluster, which is built up from eight distorted $\{MoO_6\}$ edge-shared octahedra, is a typical β-octamolybdate. The valence sum calculations[16] show that all molybdenum atoms are in the +6 oxidation state; the average value is +5.952. The oxygen atoms can be divided into four categories: 1.694(2)–1.706(3) Å for Mo–O(t), 1.908(2)–2.305(2) Å for Mo–O(μ2), 1.943(8)–2.331(2) Å for Mo–O(μ3), and 2.184(2)–2.462(2) Å for Mo–O(μ5); the mean values are 1.700(1), 1.999(7), 2.146(9), and 2.314(4) Å, respectively. All these bond lengths are within the normal ranges and in close agreement with those described in the literature.[17] It is noteworthy that the polyoxoanion acts as a ligand covalently bonded to two $[Cu^{II}(1,10\text{-phen})_2]^{2+}$ units to form a 1D chain (see Figure 3) through terminal oxygen atoms, with Cu–O distances of 2.663(7) Å.[18] In the $[Cu^{II}(1,10\text{-phen})_2]^{2+}$ unit, Cu is coordinated by four N atoms of two 1,10-phen ligands and one terminal oxygen atom of the β-octamolybdate anion to form a distorted octahedron with Cu–N distances in the range 1.974(3)–2.014(4) Å. Thus, the three crystallographically unique copper atoms have three different coordination geometries: Cu(1) exhibits a octahedral geometry in the

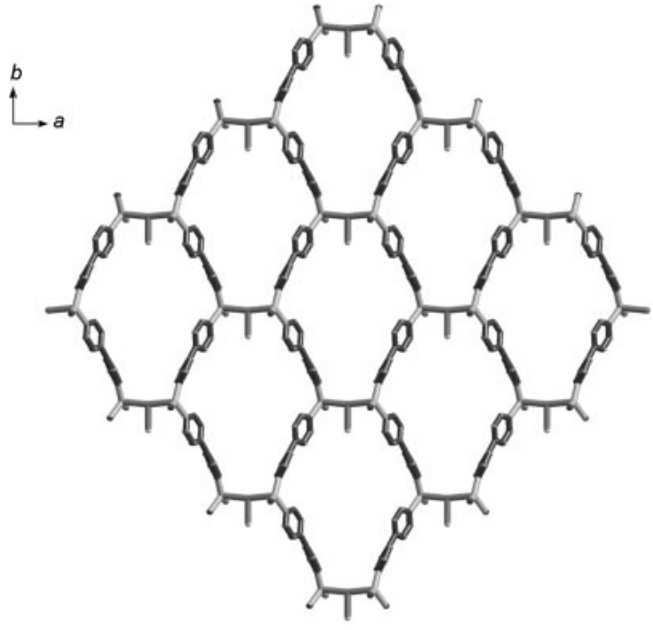


Figure 1. View of the hexagon-grid layer in **1**; all the hydrogen atoms have been omitted for clarity.

 © 2006 Wiley-VCH Verlag GmbH & Co. KGaA, Weinheim 

form of $\{CuN_4O_2\}$, Cu(2) displays a distorted $\{CuN_3Cl\}$ tetrahedral geometry, while Cu(3) shows trigonal $\{CuN_2Cl\}$ geometry. Valence sum calculations on the Cu sites give values of 1.848, 1.127, and 1.239 for Cu(1), Cu(2), and Cu(3), respectively. Having studied the literature, we noticed that the exploitation of discrete POMs as guests in the construction of 3D frameworks has been reported;[7a,7c] however, there are no examples of organic–inorganic POM chain-templated frameworks to date (see Figure 4a).

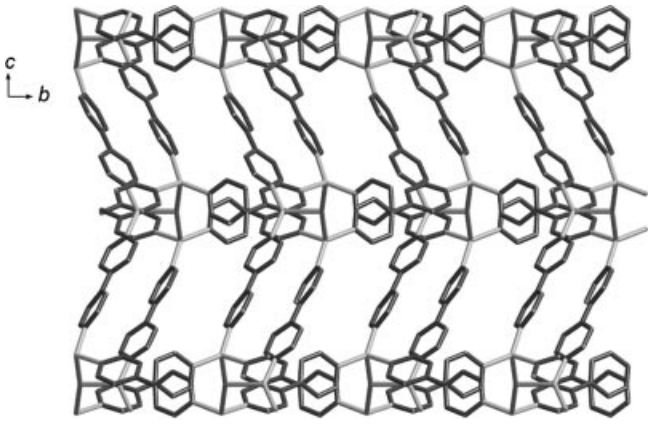


Figure 2. View of the $\{[Cu_3^{I}Cl(4,4'\text{-bipy})_4]\}_n^{2n+}$ coordination complex scaffolding composed of hexagon-grid layers pillared by 4,4′-bipy ligands in **1**; all the hydrogen atoms have been omitted for clarity.

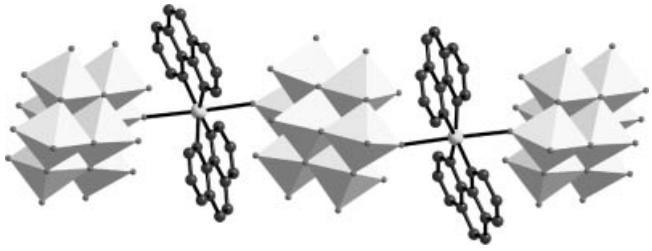

Figure 3. Polyhedral representation of the organic–inorganic hybrid polyoxometalate chain in **1**; all the hydrogen atoms have been omitted for clarity.

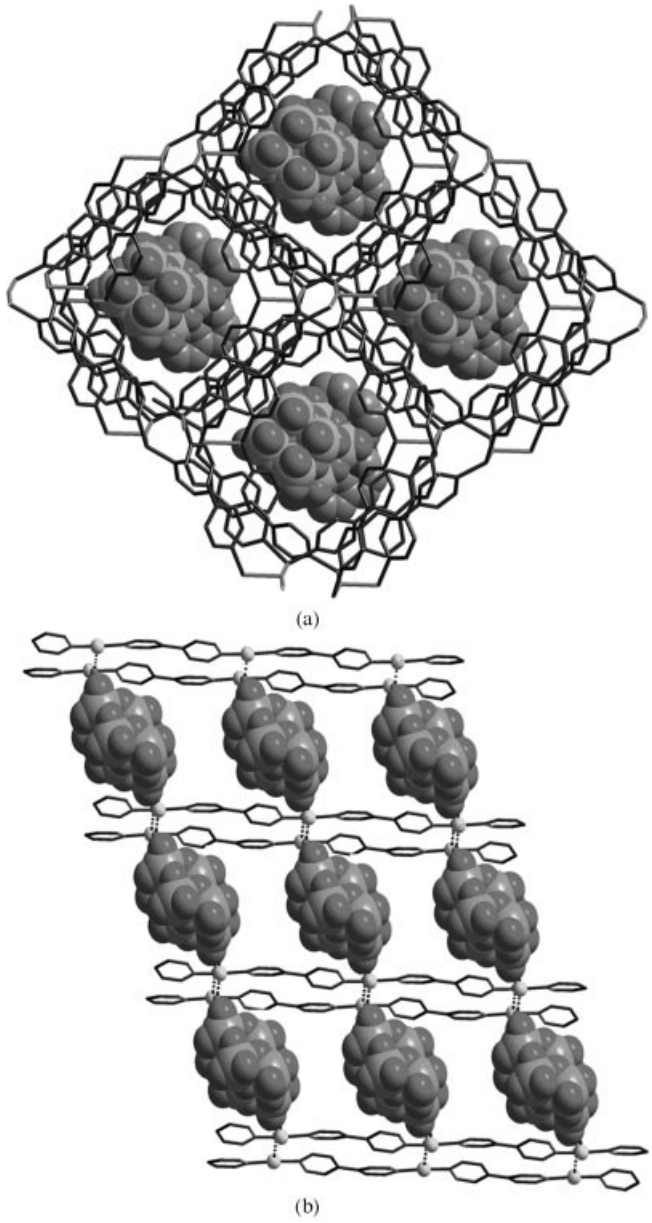


Figure 4. (a) Projection of the 3D framework of **1**; all the hydrogen atoms have been omitted for clarity. (b) View of the 2D supramolecular structure of **2**; all the hydrogen atoms and the water molecules have been omitted for clarity.

The single X-ray structural analysis revealed that the structure of **2** is composed of β-$[Mo_8O_{26}]^{4-}$, $\{Cu(4,4'\text{-bipy})\}_n^{n+}$ chains, and lattice water molecules. The structure of $[Mo_8O_{26}]^{4-}$ is a typical β-$[Mo_8O_{26}]^{4-}$ anion, similar to that of compound **1**. The Mo–O bonds can be divided into four groups, i.e. Mo–$O_t$, Mo–O(μ2), Mo–O(μ3), and Mo–O(μ5) bonds, with bond lengths in the ranges 1.685(2)–1.702(6), 1.746(9)–2.259(8), 2.149(8)–2.394(2), and 2.149(8)–2.450(8) Å, respectively; the mean values are 1.696(9), 1.944(7), 2.104(3), and 2.334(6) Å. All the mean values of the Mo–O distances are shorter than those of compound **1**. These results may be due to the influence of the outer coordination environment in compound **1**.

As shown in Figure 4b, the β-$[Mo_8O_{26}]^{4-}$ clusters link the $\{Cu(4,4'\text{-bipy})\}_n^{n+}$ chains into a 2D supramolecular structure with a weak, long-range Cu–O interaction of 2.501(66)–2.563(27) Å.

## EPR Spectroscopy

The EPR spectrum of **1** at room temperature shows a $Cu^{2+}$ signal with $g_{[par]} = 2.2281$ and $g_{\perp} = 2.0506$ (Figure 5), in good accordance with the valence sum calculation.

 © 2006 Wiley-VCH Verlag GmbH & Co. KGaA, Weinheim 

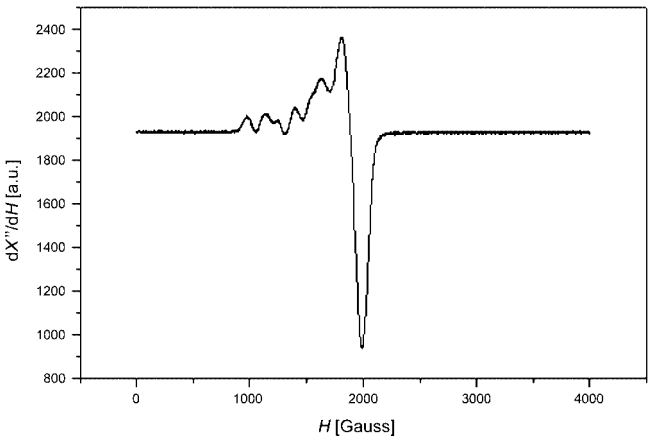


Figure 5. The EPR spectrum of **1**.

### Electrochemistry

The POM-modified carbon paste electrode (CPE) was fabricated as follows: 1.0 g of graphite powder and 40 mg of POM **1** or **2** were mixed and ground together with an agate mortar and pestle to achieve an even, dry mixture. Nujol (0.66 mL) was then added to the mixture and stirred with a glass rod. The homogenized mixture was used to pack 3-mm inner diameter glass tubes, and the surface was wiped with weighing paper. Electrical contact was established with a copper rod through the back of the electrode. Platinum gauze was used as counter electrode and an SCE was used as reference electrode.

Figure S1 shows the voltammetric behavior of the working electrodes made from **1** and **2** in 30 mL of aqueous 1 M $H_2SO_4$ solution at a scan rate of 100 mV s$^{-1}$. It can be seen that one reversible redox peak appears in the potential range –800 to +1000 mV. In compounds **1** and **2**, the mean peak potential $E_{1/2} = (E_{pa} + E_{pc})/2$ is 11.6 and –58.5 mV, respectively. The redox peaks might be ascribed to the $Mo^{VI}/Mo^{V}$ couple.[19]

### FT-IR Spectroscopy

In the IR spectrum of compound **1** (Figure S2), the characteristic bands at 943, 915, 842, 730, 704, and 655 cm$^{-1}$ can be attributed to the Mo=O and Mo–O–Mo vibrations. On comparing the IR spectrum of compound **1** with that of β-$[Mo_8O_{26}]^{4-}$,[20] it can be seen that the shape of the peaks in the range 600–1000 cm$^{-1}$ is nearly identical to that of β-$[Mo_8O_{26}]^{4-}$ except for slight shifts of some peaks due to the effect of coordination, which indicates that the polyoxoanion in compound **1** still retains the basic β-$[Mo_8O_{26}]^{4-}$ structure. This is in agreement with the result of the single-crystal X-ray diffraction analysis. In addition, bands in the 1601–1408 cm$^{-1}$ region can be assigned to characteristic peaks of the ligands 4,4′-bipy and 1,10-phen.

## Conclusions

In summary, compound **1** provides an unprecedented 3D host–guest structure with an organic–inorganic hybrid polyoxometalate chain-like template and confirms the utility of hydrothermal methods for the synthesis of new compounds with novel structures. Furthermore, compound **1** demonstrates that both the vast class of polyoxoanion clusters and organic–inorganic polyoxometalate chains may act as templates in the design of higher organic–inorganic hybrid porous materials. Given the variations in the organic–inorganic polyoxometalate chains and metal-organic frameworks, the scope for the further synthesis of POM-based porous materials appears to be very promising.

## Experimental Section

**Materials:** All chemicals purchased were of reagent grade and were used without further purification.

**Physical Methods:** Elemental analyses (C, H, and N) were performed on a Perkin–Elmer 2400 CHN elemental analyzer. Mo and Cu were determined with a Leaman inductively coupled plasma (ICP) spectrometer. The FTIR spectra were recorded in the range 400–4000 cm$^{-1}$ on an Alpha Centaurt FT/IR spectrophotometer as pressed KBr pellets. TG analyses were performed on a Perkin–Elmer TGA7 instrument in flowing $N_2$ at a heating rate of 10 °C min$^{-1}$. The EPR spectrum was recorded with a Bruker ER 200D spectrometer at room temperature. All electrochemical measurements were carried out on a CHI 660 electrochemical workstation at room temperature (25–30 °C).

**Synthesis of Compound 1:** A mixture of $(NH_4)_6Mo_7O_{24}\cdot 6H_2O$ (0.1 mmol), $CuCl_2\cdot 2H_2O$ (0.3 mmol), 4,4′-bipy (0.3 mmol), 1,10-phen (0.2 mmol), and $H_2O$ (10 mL) was stirred for half an hour in air. The pH was then adjusted to 4.0 with 4 M HCl, and the mixture transferred to a Teflon-lined, 23-mL autoclave and kept at 165 °C for 4 d. After slowly cooling to room temperature, dark-green crystals were filtered off, washed with distilled water, and dried in a desiccator at room temperature. Yield: 0.153 g (54.8% based on Mo). $C_{64}H_{44}ClCu_4Mo_8N_{12}O_{26}$ (2454.2): calcd. C 31.24, H 1.96, Cu 10.34, Mo 31.22, N 6.84; found C 31.54, H 2.13, Cu 10.67, Mo 30.86, N 7.07.

**Synthesis of Compound 2:** A mixture of $(NH_4)_6Mo_7O_{24}\cdot 6H_2O$ (0.1 mmol), $CuCl_2\cdot 2H_2O$ (0.3 mmol), 4,4′-bipy (0.3 mmol), and $H_2O$ (10 mL) was stirred for half an hour in air. The pH was then adjusted to 4.8 with 4 M HCl and the mixture transferred to a Teflon-lined, 23-mL autoclave and kept at 165 °C for 4 d. After slowly cooling to room temperature, orange crystals were filtered off, washed with distilled water, and dried in a desiccator at room temperature. Yield: 0.079 g (37.5% based on Mo). $C_{30}H_{27}Cu_3Mo_8N_6O_{27}$ (1861.7): calcd. C 19.35, H 1.46, Cu 10.24, Mo 41.23, N 4.52; found C 19.49, H 1.53, Cu 10.09, Mo 41.08, N 4.68.

**X-ray Crystallography:** Crystallographic data for **1** and **2** were collected at 298 K with a Rigaku R-axis Rapid IP diffractometer using graphite-monochromated Mo-$K_\alpha$ radiation ($\lambda$ = 0.710373 Å) and the IP technique. The structure was solved by direct methods and refined by full-matrix least-squares on $F^2$ using the SHELXTL-97 crystallographic software package.[21] Anisotropic thermal parameters were used to refine all non-hydrogen atoms. Carbon-bound hydrogen atoms were placed in geometrically calculated positions; oxygen-bound hydrogen atoms were located in the difference Fourier maps. Further details of the X-ray structural analysis are given in Table 1. Selected bond lengths and angles for compounds **1** and **2** are listed in Tables S1 and S2 in the Supporting Information. CCDC-600762 (**1**) and -600763 (**2**) contain the supplementary crystallographic data for this paper. These data can be obtained free

 © 2006 Wiley-VCH Verlag GmbH & Co. KGaA, Weinheim 

of charge from The Cambridge Crystallographic Data Centre via www.ccdc.cam.ac.uk/data_request/cif.

Table 1. Crystal data and structure refinement for **1** and **2**.

| | **1** | **2** |
|---|---|---|
| Chemical formula | $C_{64}H_{44}ClCu_4Mo_8N_{12}O_{26}$ | $C_{30}H_{27}Cu_3Mo_8N_6O_{27}$ |
| Formula weight | 2454.24 | 1861.74 |
| Crystal system | monoclinic | triclinic |
| Space group | *C*2/c | $P\bar{1}$ |
| *a* [Å] | 19.748(4) | 10.837(2) |
| *b* [Å] | 17.494(4) | 11.274(2) |
| *c* [Å] | 22.160(4) | 11.321(2) |
| *α* [°] | 90 | 68.49(3) |
| *β* [°] | 109.83(3) | 83.08(3) |
| *γ* [°] | 90 | 64.04(3) |
| *V* [Å$^3$] | 7202(2) | 1155.7(4) |
| *Z* | 4 | 1 |
| *D* [mg m$^{-3}$] | 2.264 | 2.701 |
| *T* [K] | 293(2) | 293(2) |
| Reflns. collected | 34103 | 9534 |
| Reflns. unique | 8222 | 4270 |
| *R*(int) | 0.0283 | 0.0322 |
| Goodness of fit on $F^2$ | 0.895 | 0.747 |
| $R_1$[a] | 0.0286 | 0.0256 |
| $wR_2$[b] | 0.1038 | 0.0622 |

[a] $R1 = \sum||F_o| - |F_c||/\sum|F_o|$. [b] $wR_2 = \sum[w(F_o^2 - F_c^2)^2]/\sum[w(F_o^2)^2]^{1/2}$.

**Supporting Information** (see footnote on the first page of this article): Cyclic voltammograms, IR spectra, and selected bond lengths and angles for compounds **1** and **2**.

## Acknowledgments

This work was supported by the National Science Foundation of China (grant no. 20371011).

[1] a) K. Biradha, Y. Hongo, M. Fujita, *Angew. Chem. Int. Ed.* **2000**, *39*, 3843–3845; b) B. Moulton, M. J. Zaworotko, *Chem. Rev.* **2001**, *101*, 1629–1658; c) M. Eddaoudi, D. B. Moler, H. L. Li, B. L. Chen, T. M. Reineke, M. O'Keeffe, O. M. Yaghi, *Acc. Chem. Res.* **2001**, *34*, 319–330; d) U. Kortz, S. S. Hamzeh, N. A. Nasser, *Chem. Eur. J.* **2003**, *9*, 2945–2952; e) C. N. R. Rao, S. Natarajan, R. Vaidhyanathan, *Angew. Chem. Int. Ed.* **2004**, *43*, 1466–1496; f) Y. Q. Sun, J. Zhang, Y. M. Chen, G. Y. Yang, *Angew. Chem. Int. Ed.* **2005**, *44*, 5814–5817; g) Z. E. Lin, J. Zhang, J. T. Zhao, S. T. Zheng, C. Y. Pan, G. M. Wang, G. Y. Yang, *Angew. Chem. Int. Ed.* **2005**, *44*, 6881–6884.

[2] a) S. S. Y. Chui, S. M. F. Lo, J. P. H. Charmant, A. G. Orpen, I. D. Williams, *Science* **1999**, *283*, 1148–1150; b) S. Kitagawa, R. Kiaura, S. I. Noro, *Angew. Chem. Int. Ed.* **2004**, *43*, 2334–2375; c) Y. Q. Tian, C. X. Cai, X. M. Ren, C. Y. Duan, Y. Xu, S. Gao, X. Z. You, *Chem. Eur. J.* **2003**, *9*, 5673–5685; d) Z. Shi, L. R. Zhang, S. Gao, G. Y. Yang, J. Hua, L. Gao, S. H. Feng, *Inorg. Chem.* **2000**, *39*, 1990–1993; e) J. P. Zhang, Y. Y. Lin, W. X. Zhang, X. M. Chen, *J. Am. Chem. Soc.* **2005**, *127*, 14162–14163.

[3] a) J. Lu, G. Crisci, T. Niu, A. J. Jacobson, *Inorg. Chem.* **1997**, *36*, 5140–5141; b) J. Y. Lu, B. R. Cabrera, R. J. Wang, J. Li, *Inorg. Chem.* **1998**, *37*, 4480–4481; c) R. P. Hammond, M. Cavaluzzi, R. C. Haushalter, J. Zubieta, *Inorg. Chem.* **1999**, *38*, 1288–1292; d) R. D. Willett, *Inorg. Chem.* **2001**, *40*, 966–971; e) S. T. Wang, Y. G. Li, E. B. Wang, G. Y. Luan, C. W. Hu, N. H. Hu, H. Q. Jia, *J. Solid State Chem.* **2002**, *167*, 402–406.

[4] a) H. Li, M. Eddaoudi, M. O'Keeffe, O. M. Yaghi, *Nature* **1999**, *402*, 276–279; b) B. Chen, M. Eddaoudi, S. T. Hyde, M. O'Keeffe, O. M. Yaghi, *Science* **2001**, *291*, 1021–1023; c) M. Eddaoudi, J. Kim, N. Rosi, D. Vodak, D. V. Wachter, M. O'Keeffe, O. M. Yaghi, *Science* **2002**, *295*, 469–472; d) N. L. Rosi, J. Eckert, M. Eddaoudi, D. T. Vodak, J. Kim, M. O'Keeffe, O. M. Yaghi, *Science* **2003**, *300*, 1127–1129.

[5] a) X. H. Bu, M. L. Tong, H. C. Chang, S. Kitagawa, S. R. Batten, *Angew. Chem. Int. Ed.* **2004**, *43*, 192–195; b) B. Zhao, P. Cheng, X. Y. Chen, C. Cheng, W. Shi, D. Z. Liao, S. P. Yan, Z. H. Jiang, *J. Am. Chem. Soc.* **2004**, *126*, 3012–3013.

[6] a) R. Vilar, D. M. P. Mingos, A. J. P. White, D. J. Williams, *Angew. Chem. Int. Ed.* **1998**, *37*, 1258–1261 and references cited therein; b) G. Bianchi, E. Garcia-España, K. Bowman-James, *Supramolecular Chemistry of Anions*, Wiley-VCH, Weinheim, **1997**.

[7] a) D. Hagrman, P. J. Hagrman, J. Zubieta, *Angew. Chem. Int. Ed.* **1999**, *38*, 3165–3168; b) L. M. Zheng, Y. S. Wang, X. Q. Wang, J. D. Korp, A. J. Jacobson, *Inorg. Chem.* **2001**, *40*, 1380–1385; c) C. Inman, J. M. Knaust, S. W. Keller, *Chem. Commun.* **2002**, 156–157; d) L. Lisnard, A. Dolbecq, P. Mialane, J. Marrot, E. Codjovi, F. Sécheresse, *Dalton Trans.* **2005**, 3913–3920.

[8] a) H. Y. An, E. B. Wang, D. R. Xiao, Y. G. Li, Z. M. Su, L. Xu, *Angew. Chem. Int. Ed.* **2006**, *45*, 904–908; b) Y. Lu, Y. G. Li, E. B. Wang, J. Lü, L. Xu, R. Clérac, *Eur. J. Inorg. Chem.* **2005**, 1239–1244.

[9] a) X. L. Wang, Y. Q. Guo, Y. G. Li, E. B. Wang, C. W. Hu, N. H. Hu, *Inorg. Chem.* **2003**, *42*, 4135–4140; b) X. L. Wang, Y. Q. Guo, E. B. Wang, L. Y. Duan, X. X. Xu, C. W. Hu, *J. Mol. Struct.* **2004**, *691*, 171–180.

[10] a) M. Yuan, Y. G. Li, E. B. Wang, C. G. Tian, L. Wang, C. W. Hu, N. H. Hu, H. Q. Jia, *Inorg. Chem.* **2003**, *42*, 3670–3676; b) D. Q. Chu, J. Q. Xu, L. M. Duan, T. G. Wang, A. Q. Tang, L. Ye, *Eur. J. Inorg. Chem.* **2001**, 1135–1137.

[11] a) J. Gopalakrishnan, *Chem. Mater.* **1995**, *7*, 1265–1275; b) D. Hagrman, C. Sangregorio, C. J. O'Connor, J. Zubieta, *J. Chem. Soc., Dalton Trans.* **1998**, 3707–3709.

[12] P. J. Hagrman, D. Hagrman, J. Zubieta, *Angew. Chem. Int. Ed.* **1999**, *38*, 2638–2684.

[13] J. Q. Xu, R. Z. Wang, G. Y. Yang, Y. H. Xing, D. M. Li, W. M. Bu, S. Q. Liu, L. Ye, Y. G. Fan, G. D. Yang, Y. Xing, Y. H. Lin, H. Q. Jia, *Chem. Commun.* **1999**, 983–984.

[14] B. K. Koo, U. Lee, *Inorg. Chim. Acta* **2006**, *359*, 2067–2071.

[15] R. Z. Wang, J. Q. Xu, G. Y. Yang, W. M. Bu, Y. H. Xing, D. M. Li, S. Q. Liu, L. Ye, Y. G. Fan, *Polyhedron* **1999**, *18*, 2971–2975.

[16] D. Brown, D. Altermatt, *Acta Crystallogr., Sect. B* **1985**, *41*, 244–247.

[17] a) A. Kitamura, T. Ozeki, A. Yagasaki, *Inorg. Chem.* **1997**, *36*, 4275–4279; b) D. Hagrman, C. Zubita, D. J. Rose, J. Zubieta, R. C. Haushalter, *Angew. Chem. Int. Ed. Engl.* **1997**, *36*, 873–876; c) C. D. Wu, C. Z. Lu, H. H. Zhuang, J. S. Huang, *Inorg. Chem.* **2002**, *41*, 5636–5637; d) J. Lü, E. H. Shen, Y. G. Li, D. R. Xiao, E. B. Wang, L. Xu, *Cryst. Growth Des.* **2005**, *5*, 65–67; e) D. G. Allis, E. Burkholder, J. Zubieta, *Polyhedron* **2004**, *23*, 1145–1152; f) D. Hagrman, H. D. Hagrman, J. Zubieta, *Inorg. Chim. Acta* **2000**, *300–302*, 212–224.

[18] a) E. Burkholder, J. Zubieta, *Chem. Commun.* **2001**, 2056–2057; b) L. Lisnard, A. Dolbecq, P. Mialane, J. Marrot, F. Sécheresse, *Inorg. Chim. Acta* **2004**, *357*, 845–852.

[19] C. Qin, X. L. Wang, Y. F. Qi, E. B. Wang, C. W. Hu, L. Xu, *J. Solid State Chem.* **2004**, *177*, 3263–3269.

[20] W. G. Klemperer, W. Shum, *J. Am. Chem. Soc.* **1976**, *98*, 8291–8293.

[21] a) G. M. Sheldrick, *SHELXL-97, Program for Crystal Structure Refinement*; University of Göttingen, Germany, **1997**; b) G. M. Sheldrick, *SHELXS-97, Program for Crystal structure Solution*; University of Göttingen, Germany, **1997**.

Received: June 16, 2006
Published Online: September 25, 2006

 © 2006 Wiley-VCH Verlag GmbH & Co. KGaA, Weinheim 

DOI: 10.1002/ejic.200600587

# Solvent and Ligand Effects on the Structures of Iron Halide Cations in the Gas Phase

Philipp Gruene,[a,b] Claudia Trage,[c] Detlef Schröder,*[a,d] and Helmut Schwarz[a]

**Keywords:** Hydrogen transfer / Iron halides / Ligand effects / Mass spectrometry / Solvent effects

The effects of the oxidation state, the ligand, and the solvent on structures and energetics of cationic iron complexes are investigated by means of electrospray-ionization mass spectrometry. Insights into the potential-energy surfaces of $FeX^+$, $FeX_2^+$, and $XFe(OCH_3)^+$ ions (X = F, Cl, Br, I) with a variable number of coordinated methanol molecules are obtained by means of collision experiments and complementary thermochemical considerations. It is shown that upon change of the halide ligand, the weakly solvated ions respond differentially to the increasing need for stabilization of the partial charge on the metal center. For example, whereas $F_2Fe(CH_3OH)_n^+$ ions tend to lose mainly HF for $n$ = 1–3, the loss of HBr is not observed at all for $Br_2Fe(CH_3OH)_n^+$. Instead, the iron-bromide cations undergo reductive loss of atomic bromine. $Cl_2Fe(CH_3OH)_n^+$ bears an intermediate position in that both reduction as well as elimination of HCl can occur.
(© Wiley-VCH Verlag GmbH & Co. KGaA, 69451 Weinheim, Germany, 2006)

## Introduction

One important factor for the success of mass spectrometry as a tool for investigating the elementary steps of various catalytic reactions is its ability to design and to probe model systems of variable complexity. Many experiments focus exclusively on the intrinsic properties of reactive centers by studying isolated, ligand-free atomic metal ions or their clusters, and the knowledge that has been accumulated for these systems is rather astonishing.[1] More complex systems have also been addressed, even including consideration of extrinsic factors such as ligands and counterions.[2–5] While investigations of gaseous metal clusters can largely assist in bridging the gap between gas-phase reactions and heterogeneous catalysis, understanding the often crucial role of the solvent is necessary in order to translate gas-phase chemistry data to processes taking place in solution. Different approaches have been pursued in order to include solvent molecules in mass spectrometry.[6–9] The unique features of electrospray ionization (ESI)[10,11] mass spectrometry allow the straightforward generation of a large number of solvated ions.[3,4,12–15] Here, we report a systematic study of the cationic complexes formed upon ESI of methanolic solutions of $FeX_2$ (X = F, Cl, Br, I) and $FeX_3$ (X = F, Cl, Br). Iron was investigated because of its growing importance in the field of catalysis[16] and biochemistry.[17] Halides were chosen because of their sufficient solubility in organic solvents,[18] which is reflected in their frequent use as catalysts and, additionally, they permit the investigation of periodic trends regarding the role of ligands. Methanol was used for its excellent performance as an ESI solvent and furthermore because it allows for various types of solvation mechanisms, like mere association, solvolysis, hydrogen bonding, etc. and, moreover, also has a potential for bond activation processes.[15]

[a] Institut für Chemie der Technischen Universität Berlin, Strasse des 17. Juni 135, 10623 Berlin
[b] Fritz-Haber-Institut der Max-Planck-Gesellschaft, Faradayweg 4–6, 14195 Berlin
[c] BASF AG, GKA/S – E 210, 67056 Ludwigshafen
[d] Institute of Organic Chemistry and Biochemistry, Czech Academy of Sciences, Flemingovo nám. 2, 16610 Prague 6, Czech Republic
E-mail: Detlef.Schroeder@uochb.cas.cz

## Results and Discussion

**$FeX_2$ (X = F, Cl, Br, I):** In general, two different types of mononuclear ions are formed upon ESI of methanolic $FeX_2$ solutions: $XFe(CH_3OH)_n^+$ with $n \leq 5$ and $Fe(OCH_3)(CH_3OH)_n^+$ with $n \leq 3$. In addition, iron clusters of the formal composition $(Fe_mX_{2m-1})(CH_3OH)_n^+$ are formed, in which $m$ can reach numbers of up to six and $n$ up to eight. Reduced clusters of the type $(Fe_mX_{2m-2})(CH_3OH)_n^+$ are only observed for the heavy halogens, i.e. bromine and iodine. Here, we focus on the mononuclear $XFe(CH_3OH)_n^+$ ions. At very low cone voltage (≈0 V), which corresponds to rather mild ionization conditions, multiply solvated complexes $XFe(CH_3OH)_n^+$ with $n$ = 3–5 are formed. With rising cone voltage (30–50 V), the ions lose their weakly bound solvent molecules, and $XFe(CH_3OH)_n^+$ ions with $n$ = 0–3 dominate the spectra. Under these conditions, also $Fe(OCH_3)(CH_3OH)_n^+$ ions with $n$ = 0–3 are observed in substantial quantities. At very high cone voltages, the complexes undergo consecutive fragmentation and are finally reduced to bare atomic iron(I) $Fe^+$.

 © 2006 Wiley-VCH Verlag GmbH & Co. KGaA, Weinheim 

Qualitative insight into the potential-energy surfaces of the solvated iron(II)halide cations and estimations of the binding energies to the solvent molecules are achieved by means of collision-induced dissociation (CID) experiments (Table 1). The exclusive exit channel for $XFe(CH_3OH)_n^+$ cations with $n$ = 3–5 corresponds to the loss of an intact methanol solvent molecule. For $n$ = 4 and 5, the methanol ligands are that weakly bound that they are already lost at thermal energies; accordingly, the determination of *AEs* is not reasonable anymore, because it would result in negative values. The findings for $n$ = 1–3 reveal two trends. First, the binding energies between the metal core and the solvent molecule appear to decrease with increasing solvation. Obviously, the partial charge on the metal center is effectively stabilized by the first methanol molecules, so that additional solvation accompanied by increased steric hindrance becomes less and less significant. Secondly, the binding energies decrease from fluorine to bromine, which can be attributed to the fact that the more electronegative fluorine induces a much higher charge on the metal center than bromine. For $n$ = 0–2 in the case of X = Cl, Br and $n$ = 0, 1 in the case of X = F, the reductive loss of a halogen atom is available as an additional fragmentation channel. Given the qualitative nature of the *AE* measurements, we note in passing that the experimental values for the unsolvated species are in rather good agreement with values reported in the literature ($FeF^+$: 4.5; $FeCl^+$: 3.5; $FeBr^+$: 2.7; $FeI^+$: 2.6 eV).[19–23] Further, the binding energies for the cleavage of the Fe–X-bonds also increase with solvation, the origin of which has been discussed previously.[15]

If solvated with only one or two methanol molecules, the $FFe(CH_3OH)_n^+$ ions exhibit elimination of HF as yet another fragmentation channel. Consequently, the mere description of the complex as a $FeF^+$ core to which the solvent molecules are coordinated seems insufficient, because direct loss of HF from such a structure is considered less likely compared to the loss of the coordinated methanol ligand. Instead, a rearrangement according to Reaction (1) must take place prior to fragmentation.

$$FFe(CH_3OH)_n^+ \rightleftharpoons (HF)Fe(OCH_3)(CH_3OH)_{(n-1)}^+ \quad (1)$$

The breakdown graph (Figure 1) for the CID fragments of mass-selected $FFe(CH_3OH)^+$ provides some further insight into the potential-energy surface of this system. The loss of HF bears the lowest appearance energy of about 0.5 eV and shows a characteristic increase in intensity, reaching a maximum at about $E_{CM}$ = 2 eV, and then declines at higher collision energies, whereas the loss of methanol increases until about $E_{CM}$ = 5 eV. This kind of behavior points to the operation of a kinetic hindrance, i.e. the presence of the two isomers $FFe(CH_3OH)^+$ and (HF)-$Fe(OCH_3)^+$ separated by a barrier that is of comparable height as the appearance energy for the elimination of HF. On the basis of thermochemical considerations, $FFe(CH_3OH)^+$ is indicated to be more stable than (HF)-$Fe(OCH_3)^+$ (see Appendix). However, the loss of HF represents the energetically lowest-lying exit channel. At low collision energies, the system will accordingly rearrange and dissociate to the $Fe(OCH_3)^+$ fragment. Once direct loss of methanol is energetically accessible at about 1.6 eV, this route of fragmentation is preferred, since the density of states for the direct bond cleavage resulting in two molecules is orders of magnitude higher than the density of states for the tight transition state connecting the two tautomers. For a detailed discussion, including DFT calculations, of the related $Cl_2Fe(CH_3OH)^+$/$ClFe(HCl)(OCH_3)^+$ system, see ref.[15]

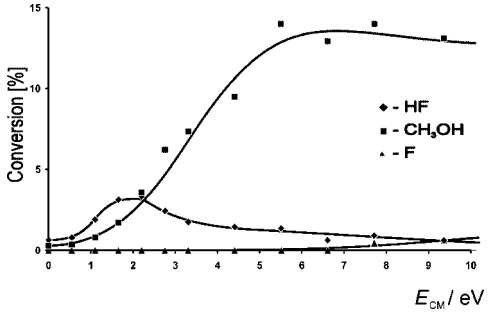


Figure 1. Breakdown graph of the CID fragments of mass-selected $FFe(CH_3OH)^+$ as a function of collision energy in the center of mass frame.

**$FeX_3$ (X = F, Cl, Br):** Three different iron(III) species are formed upon ESI of methanolic $FeX_3$ solutions: $X_2Fe(CH_3OH)_n^+$, $XFe(OCH_3)(CH_3OH)_n^+$, and $Fe(OCH_3)_2(CH_3OH)_n^+$, with $n$ up to five. In addition, some reduced ions are observed, namely, the iron(II)cations $XFe(CH_3OH)_n^+$ and $Fe(OCH_3)(CH_3OH)_n^+$ as well as the formal iron(I) clusters $Fe(CH_3OH)_n^+$. The spectra also show the presence of small amounts of binuclear clusters of the formal compositions $Fe_2X_m(CH_3OH)_n^+$ ($m$ = 3–5, $n$ = 0–4). At low cone voltages, ESI produces by and large the same type of solvated $FeX_2^+$ cations from all three solutions of $FeF_3$, $FeCl_3$, and $FeBr_3$ in methanol, respectively. How-

Table 1. Phenomenological appearance energies [eV] for the losses of $CH_3OH$ as well as X upon CID of mass-selected $XFe(CH_3OH)_n^+$ ions (X = F, Cl, Br, I).

| $XFe(CH_3OH)_n^+$ | *AE* [eV] (-$CH_3OH$) | | | | *AE* [eV] (-X) | | | |
|---|---|---|---|---|---|---|---|---|
| $n$ vs. X | F | Cl | Br | I | F | Cl | Br | I |
| 0 | | | | | 5.2±0.9 | 3.7±0.4 | 3.2±0.6 | 2.3±0.6 |
| 1 | 1.6±0.2 | 1.6±0.2 | 1.1±0.2 | 1.1±0.2 | 7±1 | 5.4±0.5 | 5.3±0.4 | 4.7±0.6 |
| 2 | 0.9±0.2 | 0.8±0.2 | 0.5±0.2 | 0.6±0.2 | | 6.5±0.9 | 6.6±0.8 | 6.5±0.5 |
| 3 | 0.4±0.2 | 0.1±0.1 | 0.2±0.2 | 0.1±0.1 | | | | |

 © 2006 Wiley-VCH Verlag GmbH & Co. KGaA, Weinheim 

ever, the similarities vanish once solvation decreases. Hence, the need for stabilization of the partial charge on the metal center is even larger than in the case of the iron(II) compounds. Generally, the ions react in two different ways. The first route corresponds to the elimination of HX resulting in new iron(III) complexes; this pathway is mainly observed for X = F. Alternatively, reductive loss of a halogen atom takes place, which dominates in the case of $FeBr_2^+$ ions. Obviously, there exist substantial differences in the respective potential-energy surfaces regarding the rearrangement/dissociation energy requirements between the two tautomers $X_2Fe(CH_3OH)_n^+$ and $XFe(OCH_3)(HX)(CH_3OH)_{(n-1)}^+$.

All appearance energies for the elimination of methanol from the solvated iron(III) halide cations are larger than those of the corresponding iron(II) species (Table 2 vs. Table 1). This finding can be attributed to the increased partial charge of the metal center, which hence leads to a larger ion-dipole interaction between the metal center and the methanol molecules and thus increased binding energies of the ligands.

Loss of HF from the complexes $F_2Fe(CH_3OH)_n^+$ ($n$ = 1–3) is observed with rather low *AE*s of 0.5 eV, hence suggesting that hydrogen migrations to form the tautomeric ions $FFe(OCH_3)(HF)(CH_3OH)_{(n-1)}^+$ are facile. Evaporations of hydrogen chloride are observed for $Cl_2Fe(CH_3OH)_n^+$ ($n$ = 1, 2). Here, the importance of the oxidation state of the metal becomes evident, for HCl elimination has not been detected for any solvated iron(II) chloride cation. Just like in the case of HF elimination, the *AE*s for the loss of HCl from $Cl_2Fe(CH_3OH)_n^+$ ($n$ = 1, 2) do not change much with the degree of solvation, which can be attributed to the operation of two opposing effects. On the one hand, the partial charge on the metal center is lowered with increasing solvation as discussed above, and accordingly the binding energy to HX, which is based mainly on ion-dipole interaction, decreases. On the other hand, the hydrogen migration, which is crucial for formation of HX, may be favored upon increasing solvation, because the ligands are brought to closer vicinity. The cations $F_2Fe(CH_3OH)_n^+$ ($n$ = 0, 1) and $X_2Fe(CH_3OH)_n^+$ (X = Cl, Br; $n$ = 0–2) exhibit loss of a halogen atom as an additional fragmentation channel, which formally corresponds to a reduction of the oxidation state of the metal. In fact, for all iron(III)-bromide cations the reduction of the metal via elimination of a halogen atom completely suppresses the formation of HX via hydrogen rearrangement. The appearance energies for the dissociation of the $XFe^+$–X-bond of the naked species seem to be somewhat lower compared with existing literature values [$D_o(ClFe^+–Cl$ = 2.19; 2.53)].[21,24,25] Interestingly, the trend of binding energy of the metal-halide bond responds differently to a changing degree of solvation. Whereas with coordination of the first methanol molecule the *AE* for the loss of fluorine increases by as much as 1.4 eV, it changes only by 0.8 and 0.1 eV for the ejection of chlorine and bromine atoms, respectively (Table 2).

Figure 2 shows the breakdown graphs for the CID fragments of mass-selected $X_2Fe(CH_3OH)^+$ ions (X = F, Cl,

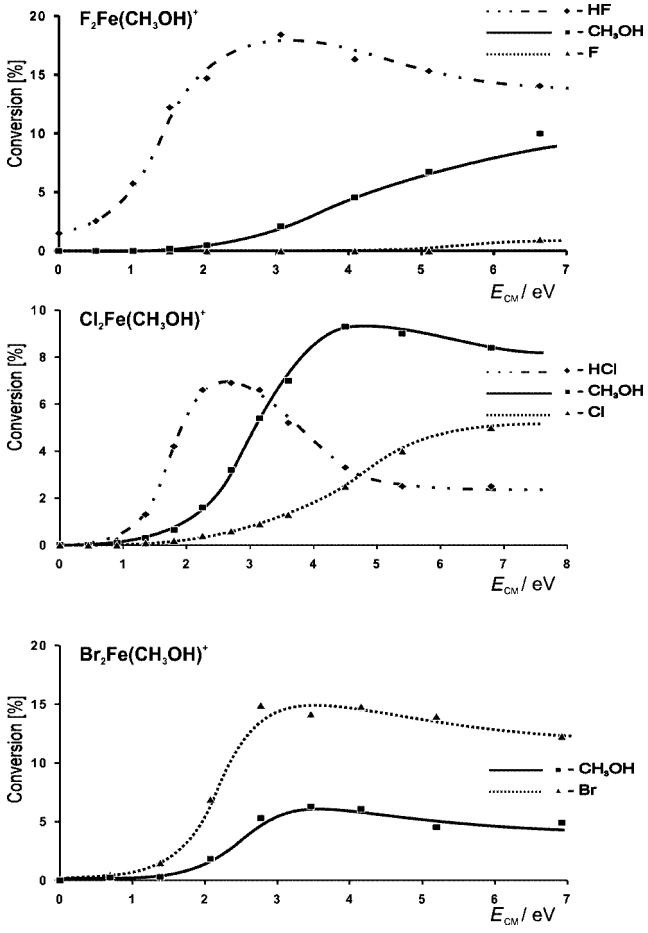


Figure 2. Breakdown graphs of the CID fragments of mass-selected $X_2Fe(CH_3OH)^+$ cations as a function of collision energy in the center of mass frame.

Table 2. Phenomenological appearance energies [eV] for the losses of $CH_3OH$, X, and HX upon CID of mass-selected $X_2Fe(CH_3OH)_n^+$ ions.

| $XFe(CH_3OH)_n^+$ | *AE* [eV] (-$CH_3OH$) | | | *AE* [eV] (-X) | | *AE* [eV] (-HX) | | |
|---|---|---|---|---|---|---|---|---|
| *n* vs. X | F | Cl | Br | F | Cl | Br | F | Cl |
| 0 | | | | 1.8±0.3 | 1.6±0.3 | 1.4±0.3 | | |
| 1 | 2.2±0.3 | 1.9±0.2 | 1.6±0.3 | 3.2±0.2 | 2.4±0.5 | 1.5±0.4 | 0.5±0.2 | 1.2±0.1 |
| 2 | 1.5±0.2 | 1.3±0.1 | 0.8±0.2 | | 3.0±0.5 | 2.5±0.5 | 0.5±0.2 | 1.0±0.1 |
| 3 | 0.5±0.2 | 0.4±0.2 | 0.2±0.1 | | | | 0.5±0.2 | |
| 4 | <0.5 | 0.3±0.2 | <0.2 | | | | | |
| 5 | <0.5 | <0.3 | <0.2 | | | | | |

 © 2006 Wiley-VCH Verlag GmbH & Co. KGaA, Weinheim 

Br), and the influence of the halide becomes quite evident upon comparison. For X = F, elimination of HF corresponds to the dominant fragmentation channel with the lowest *AE* and the largest intensity, while evaporation of the solvent exhibits a higher *AE* as well as a lower intensity. Reductive loss of the fluorine atom is negligible over the whole energy regime studied. In the case of X = Cl, the energy behavior reveals a kinetic hindrance of HCl elimination, which still exhibits the lowest *AE* and thus is the most intense fragmentation channel at low collision energies, but becomes less pronounced than evaporation of the solvent at collision energies above 3.3 eV and even less intense than the reductive elimination of atomic chlorine at collision energies above 5 eV. For X = Br, reductive cleavage of the Fe–X-bond even dominates over the loss of the solvent both in terms of appearance energy and intensity.

The assumption that the $X_2Fe(CH_3OH)^+$ isomer is more stable than $XFe(OCH_3)(HX)^+$ implies qualitative potential-energy surfaces for the competing losses of $CH_3OH$, X, and HX as depicted in Figure 3.

On the very left, the energies of the $XFe(CH_3OH)^+$ cation and the halogen radical as well as the naked $FeX_2^+$ cation and the free methanol molecule are shown. The binding energy of the radical to the iron(II) species $\Delta E_1$ and the binding energy of the solvent molecule to the iron(III) halide cation $\Delta E_2$ are assumed to correspond to the *AEs* for the reductive loss of the halogen and the elimination of methanol, respectively. As discussed above for X = F and Cl, the barrier separating the tautomers ($\Delta E_3$) has to be smaller or of comparable height than that of the exit channel for the loss of HX ($\Delta E_5$). Finally, the stability difference of the isomers **A** and **B** ($\Delta E_4$) can be derived by estimations based on Equation (2) and Equation (3), where the key parameters are the changes of Fe-X and H-X binding energies (for details, see Appendix).

$$\Delta_f H(X_2Fe(CH_3OH)^+) = \Delta_f H(FeX_2^+) + \Delta_f H(CH_3OH) - BDE(X_2Fe^+ - (CH_3OH)) \quad (2)$$

$$\Delta_f H(XFe(OCH_3)(HX)^+) = \Delta_f H(XFe(OCH_3)^+) + \Delta_f H(HX) - BDE((OCH_3)XFe^+ - (HX)) \quad (3)$$

Using an approach analogous to that described above for the iron(II) species (also see Appendix), some semi-quantitative estimates can be made for the energy differences $\Delta E_1$–$\Delta E_5$, and the results are summarized in Table 3.

Table 3. Energy differences $\Delta E_1$ to $\Delta E_5$ [eV] (as defined in Figure 3) for the competing losses of methanol, HX, and X from cationic $X_2Fe(CH_3OH)^+$ complexes (X = F, Cl, Br).[a]

| | F | $Cl_{exp}$ | $Cl_{theo}$ | Br |
|---|---|---|---|---|
| $\Delta E_1$ | 3.2 | 2.4 | | 1.5 |
| $\Delta E_2$ | 2.2 | 1.9 | 1.93 | 1.6 |
| $\Delta E_3$ | <0.5 | <1.2 | 1.35 | >0.83 |
| $\Delta E_4$ | <0.5 | <1.2 | 0.83 | >0.83 |
| $\Delta E_5$ | 0.5 | 1.2 | 1.40 | –[b] |

[a] In the estimation of the values for X = F and $Cl_{exp}$, thermodynamic control is assumed. The values of $Cl_{theo}$ are taken from theoretical data given in ref.[15]. [b] Loss of HBr is not observed experimentally.

From the CID experiments alone it cannot be deduced, whether the *AE* of HX elimination is determined by the energy demand of the exit channel (Case **a** in Figure 3), hence the fragmentation is thermodynamically controlled, or if the height of the barrier is crucial (Case **b** in Figure 3) such that the fragmentation is subject to kinetic control.[26] For the system $Cl_2Fe(CH_3OH)^+$, computational results have demonstrated that the fragmentation is subject to thermodynamic control.[15]

Iron(III) alkoxide ions $XFe(OCH_3)(CH_3OH)_n^+$ are formally accessible from $X_2Fe(CH_3OH)_{n+1}^+$ via loss of HX according to Equation (4).

$$X_2Fe(CH_3OH)_{n+1}^+ \rightleftharpoons XFe(OCH_3)(CH_3OH)_n^+ + HX \quad (4)$$

In this respect, the maximum number of coordinated solvent molecules gives a hint, whether the reaction has already taken place in solution or if it occurs only in the ESI process after evaporation. Multiply solvated ions, already present in solution, should appear at the mildest ionization conditions, whereas ions formed via collisional activation in the mass spectrometer should only be produced under more drastic ESI conditions.

For X = F, $FFe(OCH_3)^+$ cations are observed with one or two solvent molecules attached to it. Keeping in mind that solvated $FeF_2^+$ ions lose HF unless more than three methanol molecules are coordinated, this is exactly the result expected for ion formation in the evaporation process. The same holds true for the $ClFe(OCH_3)^+$ ions. Only iron(III) bromide cations never lose HBr in CID experiments, and yet, $BrFe(OCH_3)^+$ ions with up to four coordi-

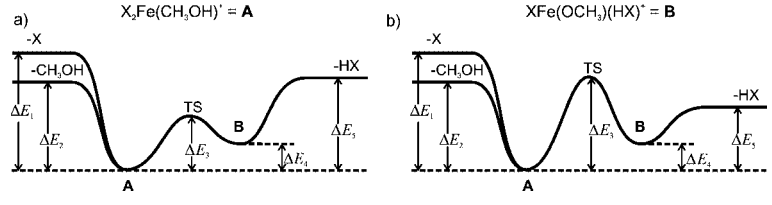


Figure 3. Possible free-energy profiles for the competing losses of methanol, HX, and X (X = F, Cl, Br) from cationic $X_2Fe(CH_3OH)^+$ complexes **A** as well as the isomeric $XFe(OCH_3)(HX)^+$ complexes **B** with the central transition structure lower [case a)] and higher in energy [case b)] than the lowest lying exit channels for ion dissociation. We note in passing that for X = Br the experimental data implies $\Delta E_1 < \Delta E_2$.

 © 2006 Wiley-VCH Verlag GmbH & Co. KGaA, Weinheim 

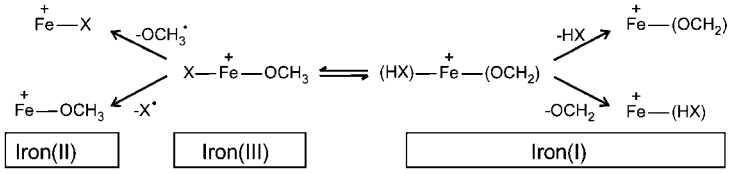


Figure 4. Redox tautomerization in the fragmentations of $XFe(OCH_3)^+$ (X = Cl, Br); loss of $H_2CO$ is only observed for X = Br.

nated methanol molecules are observed in the spectra, thus suggesting that for X = Br, reaction (4) can already occur in solution.

The fragmentation patterns of the two unsolvated ions $ClFe(OCH_3)^+$ and $BrFe(OCH_3)^+$ reveals interesting redox properties of these species. In both cases, loss of hydrogen halide corresponds to the lowest-lying exit channel [*AE*(-HCl) = 0.5 eV; *AE*(-HBr) = 0.7 eV]. This requires a redox tautomerization in which $CH_3O^-$ is oxidized to $H_2CO$ and the electrons are formally transferred intramolecularly to the iron center, leading to an iron(I) complex $(HX)Fe(CH_2O)^+$ (X = Cl, Br) (Figure 4). The ability of methoxo ligands to transfer hydrogen atoms to the metal center via a ß-hydrogen shift has been long known[27,28] and it seems reasonable to assume that hydrogen is transferred to the halide ligand in a similar manner. Such rearrangements, in which an iron(III) species is reduced to iron(I) via a hydrogen transfer, have also been reported for the reaction of bare $Fe^+$ with dimethylperoxide.[29] Nevertheless, a direct tautomerization via a multicentered transition structure is also conceivable.[30]

For $BrFe(OCH_3)^+$, in line with the respective *AE*s, the loss of HBr prevails over the evaporation of $CH_2O$ [*AE*(-$CH_2O$) = 1.5 eV], which indicates a stronger binding of formaldehyde to the metal center than hydrogen bromide. In the case of X = Cl, the difference in bond strength is so distinct that the expulsion of $H_2CO$ is not observed at all upon CID. The *AEs* corresponding to the respective direct homolytic bond cleavages show that breaking of the $ClFe^+$–($OCH_3$) bond is easier [*AE*(-$OCH_3$) = 2.4 eV] than breaking the Cl–$Fe(OCH_3)^+$ bond [*AE*(-Cl) = 3.5 eV]. In contrast, cleavage of the Br–$Fe(OCH_3)^+$ bond [*AE*(-Br) = 2.3 eV] is easier than breaking the $BrFe^+$–($OCH_3$) bond [*AE*(-$OCH_3$) = 2.8 eV]. Once solvent molecules are attached to these complexes, these mechanistically indicative evaporations of formaldehyde are not observed anymore, such that on the basis of the CID experiments, a further distinction of the structures of the parent ions is impossible. When two methanol molecules surround the ion core, i.e. for $XFe(OCH_3)(CH_3OH)_2^+$, the influence of the ligand again becomes most obvious: While the fluoride species loses HF besides methanol, evaporation of the solvent is the only fragmentation channel for $ClFe(OCH_3)(CH_3OH)_2^+$; for X = Br, also reductive cleavage of the iron-halide bond concomitant with the expulsion of atomic bromine from the precursor complex is observed.

## Conclusions

The effects of the formal oxidation state, the nature of the halide, and the number of solvent molecules on the structures and energetics of iron-halide complexes are studied by electrospray mass spectrometry of methanolic $FeX_m$ solutions (X = F, Cl, Br, I; *m* = 2, 3). The most abundant ions formed can be described as consisting of covalently bound $FeX^+$, $FeX_2^+$, and $XFe(OCH_3)^+$ cores, respectively, which are stabilized by various amounts of methanol molecules. For some halide ligands, solvolysis becomes energetically accessible upon collisional excitation once the effects of solvation are less dominant. This effect is particularly pronounced for all species containing fluorine as formation of HF via an intracomplex hydrogen transfer from a methanol molecule provides a strong thermodynamic driving force. The presence of methoxo ligands in turn facilitates the occurrence of C–H bond activation reactions via hydrogen migration leading to iron(I) compounds. In contrast, $Br_2Fe(CH_3OH)_n^+$-ions do not at all undergo intramolecular hydrogen transfer processes, and a pronounced tendency to undergo reductive loss of atomic bromine prevails instead. In comparison of the iron(II)- and iron(III) compounds, in line with general expectations solvation strongly stabilizes the iron(III) state. With decreasing solvation of the iron(III) species, the binding energies of the methanol accordingly enlarge and likewise the probability of the occurrence of redox reactions leading to either iron(II) or even iron(I) compounds increases.

## Experimental Section

The mass spectrometric experiments were carried out with a commercial VG BIO-Q mass spectrometer described elsewhere.[31] In brief, the VG BIO-Q consists of an ESI source combined with a tandem mass spectrometer of QHQ configuration (Q: quadrupole, H: hexapole). In the present experiments, mmolar solutions of anhydrous $FeX_2$ (X = F, Cl, Br, I) and $FeX_3$ (X = F, Cl, Br) in methanol were introduced through a syringe pump (flow rate 5 μL/min) to the fused silica capillary of the ESI source. The source temperature was kept at 80 °C. For each ion of interest, the instrument parameters were optimized for maximal ion abundance. The most crucial parameter is the cone voltage $U_C$ which determines the extent of collisional activation of the ions evolving from solution in the differential pumping system of the ESI source. At low cone voltages, multiply solvated ions are formed, which then lose the weakly bound solvent molecules at increased $U_C$, followed by evaporation of more strongly bound ligands including the cleavage of covalent bonds, electron-transfer processes, and atomic metal cations are obtained at very high cone voltages.

Collision-induced dissociation experiments were performed with Q1-selected ions and xenon was admitted as a collision gas to the hexapole at various collision energies ($E_{lab}$ = 0–40 eV) and a pressure of about $2.5 \cdot 10^{-4}$ mbar, which approximately corresponds to single collision conditions.[31] The product ions formed in the hexa-

 © 2006 Wiley-VCH Verlag GmbH & Co. KGaA, Weinheim 

pole were then analyzed by scanning Q2. The collision energies were converted into the center-of-mass frame, $E_{CM} = [m/(M + m)] \cdot E_{lab}$, in which $M$ and $m$ are the masses of the collision gas and the ionic species, respectively. Variation of the collision energy led to breakdown diagrams that enabled the determination of phenomenological appearance energies (*AEs*)[32] of the various fragmentation channels by linear extrapolation of the signal onsets to the baseline. The corresponding experimental errors were estimated by applying linear extrapolations with gradients deviating from the best possible fits, but which are still in reasonable agreement with the experimental data. It is to be pointed out that the *AEs* given below do not directly correspond to thermochemical thresholds of the respective ion dissociations, but nevertheless provide a frame for the energy demands of the various fragmentations.

**Appendix. Thermochemical Estimates**

In order to evaluate the stability of the two tautomers $FFe(CH_3OH)^+$ and $(HF)Fe(OCH_3)^+$, their heats of formation are estimated using Equation (5) and (6).[33]

$$\Delta_f H(FFe(CH_3OH)^+) = \Delta_f H(FeF^+) + \Delta_f H(CH_3OH) - BDE(FFe^+ - (CH_3OH)) \quad (5)$$

$$\Delta_f H((HF)Fe(OCH_3)^+) = \Delta_f H(Fe(OCH_3)^+) + \Delta_f H(HF) - BDE((OCH_3)Fe^+ - (HF)) \quad (6)$$

The exact values for the binding energies are unknown and have to be estimated using existing data. The binding energy of methanol to $FeF^+$ must be within the window of the binding energies of methanol to bare $Fe^+$ and to the iron(II)-chloride cation. Both these values can be found in the literature[15,34] (Table 4), and the binding energy to $FeF^+$ is estimated to correspond to their average [Equation (7)]. Note the excellent agreement with the *AE* for the loss of methanol from $FeF^+$ in Table 1.

$$BDE(FFe^+ - (CH_3OH)) \approx \tfrac{1}{2}\left[BDE(Fe^+ - (CH_3OH)) + BDE((Cl)_2Fe^+ - (CH_3OH)\right] = (1.6 \pm 0.3)eV \quad (7)$$

Table 4. Literature thermochemistry used.

| | $\Delta_f H$ [eV] | Ref. | | *BDE* [eV] | Ref. |
|---|---|---|---|---|---|
| $FeF^+$ | 8.0 ± 0.2 | [33] | $Fe^+$–$CH_3OH$ | 1.39 ± 0.09 | [34] |
| $FeOCH_3^+$ | 8.76 ± 0.08 | [28] | $FeCl_2^+$–$CH_3OH$ | 1.79 | [15] |
| $CH_3OH$ | –1.94 ± 0.02 | [39] | $Cu^+$–HF | 0.76 | [35] |
| HF | –2.64 ± 0.01 | [39] | $Cu^+$–$H_2O$ | 1.41 | [35] |
| | | | $Cu^+$–$NH_3$ | 1.98 | [35] |
| | | | $Cr^+$–HF | 0.66 | [36] |
| | | | $Cr^+$–$H_2O$ | 1.23 | [36] |
| | | | $Cr^+$–$NH_3$ | 1.67 | [36] |
| | | | $Fe^+$–$H_2O$ | 1.27 ± 0.05 | [38] |
| | | | $Fe^+$–$H_2O$ | 1.72 ± 0.09 | [37] |

The binding energy of HF to $Fe(OCH_3)^+$ is even more difficult to evaluate. A first simplification is to neglect the methoxide ligand, thus estimating the binding energy of HF to bare $Fe^+$. Unfortunately, even this value is unknown, but values for binding energies of HF to $Cu^+$ and $Cr^+$ exist, as well as values for the binding energies of $H_2O$ and $NH_3$ to $Cu^+$, $Cr^+$, and $Fe^+$.[35–38] On the basis of this data, a rough approximation according to Equation (8), (9), and (10) is possible.

$$BDE(Cu^+ - (HF)) = x_1 \cdot BDE(Cu^+ - (H_2O)) = x_2 \cdot BDE(Cu^+ - (NH_3)) \quad (8)$$

$$BDE(Cr^+ - (HF)) = x_2 \cdot BDE(Cr^+ - (H_2O)) = y_2 \cdot BDE(Cr^+ - (NH_3)) \quad (9)$$

$$BDE(Fe^+ - (HF)) \approx x_{1,2} \cdot BDE(Fe^+ - (H_2O)) \approx y_{1,2} \cdot BDE(Fe^+ - (NH_3)) \quad (10)$$

The resulting binding energies range from 0.66 to 0.69 eV. Obviously the binding energy of HF to the iron(II) species $Fe(OCH_3)^+$ is larger than the one estimated to $Fe^+$; however, this should be a somewhat reasonable value. Inserting all data, including the known values for the heats of formation of $FeF^+$,[28] $Fe(OCH_3)^+$,[33] methanol and HF,[39] the following results are obtained:

$\Delta_f H[FFe(CH_3OH)^+] = (4.5 \pm 0.5)$ eV

$\Delta_f H[(HF)Fe(OCH_3)^+] = (5.5 \pm 0.2)$ eV

As some of the approximations made in the estimation of these quantities are quite crude, we do not claim the exactness of the results; nevertheless these considerations can at least provide a guideline for the understanding of the experimentally observed trends among the different halogens. In the particular case discussed here, the energy difference of about 1 eV clearly implies the conclusion that the iron-fluoride complex $FFe(CH_3OH)^+$ is energetically more favorable than the iron-methoxo isomer $(HF)Fe(OCH_3)^+$.

## Acknowledgments

Financial support from the Deutsche Forschungsgemeinschaft and the Fonds der Chemischen Industrie is gratefully acknowledged. P. G. thanks the Studienstiftung des Deutschen Volkes for a scholarship.

[1] D. K. Böhme, H. Schwarz, *Angew. Chem. Int. Ed.* **2005**, *44*, 2336–2354.
[2] D. Schröder, H. Schwarz, *Angew. Chem. Int. Ed. Engl.* **1995**, *34*, 1973–1995.
[3] D. A. Plattner, *Int. J. Mass Spectrom.* **2001**, *207*, 125–144.
[4] P. Chen, *Angew. Chem. Int. Ed.* **2003**, *42*, 2832–2847.
[5] K. A. Zemski, D. R. Justes, A. W. Castleman, Jr., *J. Phys. Chem. B* **2002**, *106*, 6136–6148.
[6] G. Niedner-Schatteburg, V. E. Bondybey, *Chem. Rev.* **2000**, *100*, 4059–4086.
[7] B. S. Fox, O. P. Balaj, I. Balteanu, M. K. Beyer, V. E. Bondybey, *Chem. Eur. J.* **2002**, *8*, 5534–5540.
[8] M. Meot-Ner, *Int. J. Mass Spectrom.* **2003**, *227*, 525–554.
[9] S. J. Ye, R. M. Moision, P. B. Armentrout, *Int. J. Mass Spectrom.* **2005**, *240*, 233–248.
[10] M. Yamashita, J. B. Fenn, *J. Phys. Chem.* **1984**, *88*, 4451–4459.
[11] M. Yamashita, J. B. Fenn, *J. Phys. Chem.* **1984**, *88*, 4671–4675.
[12] J. S. Klassen, Y. Ho, A. T. Blades, P. Kebarle, *Adv. Gas Phase Ion Chem.* **1998**, *3*, 255–318.
[13] M. Y. Combariza, A. M. Fahey, A. Milshteyn, R. W. Vachet, *Int. J. Mass Spectrom.* **2005**, *244*, 109–124.

 © 2006 Wiley-VCH Verlag GmbH & Co. KGaA, Weinheim 

[14] N. G. Tsierkezos, D. Schröder, H. Schwarz, *J. Phys. Chem. A* **2003**, *107*, 9575–9581.
[15] C. Trage, M. Diefenbach, D. Schröder, H. Schwarz, *Chem. Eur. J.* **2006**, *12*, 2454–2464.
[16] C. Bolm, J. Legros, J. Le Paih, L. Zani, *Chem. Rev.* **2004**, *104*, 6217–6254.
[17] W. Kaim, B. Schwederski, *Bioinorganic Chemistry*, 3rd ed., Wiley, New York, **2001**.
[18] $FeF_2$ and $FeF_3$ are poorly soluble in methanol, however, ESI of their saturated solution provides enough ion intensity for analysis.
[19] C. W. Bauschlicher, Jr., *Chem. Phys.* **1996**, *211*, 163–169.
[20] M. N. Glukhovtsev, R. D. Bach, C. J. Nagel, *J. Phys. Chem. A* **1997**, *101*, 316–323.
[21] D. Schröder, S. Bärsch, H. Schwarz, *Int. J. Mass Spectrom.* **1999**, *192*, 125–139.
[22] D. Schröder, J. Hrušák, H. Schwarz, *Helv. Chim. Acta* **1992**, *75*, 2215–2218.
[23] M. Grade, W. Rosinger, *Surf. Sci.* **1985**, *156*, 920–929.
[24] R. D. Bach, D. S. Shobe, H. B. Schlegel, C. J. Nagel, *J. Phys. Chem.* **1996**, *100*, 8770–8776.
[25] D. Schröder, J. Loos, H. Schwarz, R. Thissen, O. Dutuit, *Inorg. Chem.* **2001**, *40*, 3161–3169.
[26] W. A. Brand, T. Baer, *J. Am. Chem. Soc.* **1984**, *106*, 3154–3160.
[27] C. J. Cassady, B. S. Freiser, *J. Am. Chem. Soc.* **1985**, *107*, 1566–1573.
[28] A. Fiedler, D. Schröder, H. Schwarz, B. L. Tjelta, P. B. Armentrout, *J. Am. Chem. Soc.* **1996**, *118*, 5047–5055.
[29] C. A. Schalley, R. Wesendrup, D. Schroeder, K. Schroeter, H. Schwarz, *J. Am. Chem. Soc.* **1995**, *117*, 12235–12242.
[30] M. C. Holthausen, G. Hornung, D. Schröder, S. Sen, W. Koch, H. Schwarz, *Organometallics* **1997**, *16*, 3135–3147.
[31] D. Schröder, T. Weiske, H. Schwarz, *Int. J. Mass Spectrom.* **2002**, *219*, 729–738.
[32] a) D. Schröder, M. Engeser, M. Brönstrup, C. Daniel, J. Spandl, H. Hartl, *Int. J. Mass Spectrom.* **2003**, *228*, 743–757; b) J. Roithová, J. Hrušák, D. Schröder, H. Schwarz, *Inorg. Chim. Acta* **2005**, *358*, 4287–4292.
[33] D. Schröder, H. Schwarz, *Int. J. Mass Spectrom.* **2003**, *227*, 121–134.
[34] R. Wesendrup, C. A. Schalley, D. Schröder, H. Schwarz, *Organometallics* **1996**, *15*, 1435–1440.
[35] A. M. El-Nahas, K. Hirao, *J. Phys. Chem. A* **2000**, *104*, 138–144.
[36] M. Trachtman, C. W. Bock, *J. Mol. Struct. (THEOCHEM)* **2004**, *672*, 75–96.
[37] D. Walter, P. B. Armentrout, *J. Am. Chem. Soc.* **1998**, *120*, 3176–3187.
[38] N. F. Dalleska, K. Honma, L. S. Sunderlin, P. B. Armentrout, *J. Am. Chem. Soc.* **1994**, *116*, 3519–3528.
[39] From: http://webbook.nist.gov/chemistry/.

Received: June 21, 2006
Published Online: September 28, 2006

 © 2006 Wiley-VCH Verlag GmbH & Co. KGaA, Weinheim 

DOI: 10.1002/ejic.200600616

# Synthesis and Structural Characterization of a Series of Carboxylic Acid Modified Cerium(III) Alkoxides

**Timothy J. Boyle,*[a] Louis J. Tribby,[a] and Scott D. Bunge[a]**

**Keywords:** Metal alkoxides / Cerium alkoxides / Carboxylate ligands / Chelates

A series of cerium alkoxides were synthesized from the reaction of $Ce\{N[Si(CH_3)_3]_2\}_3$ and the appropriate alcohol: neopentyl alcohol [$H–OCH_2C(CH_3)_3$ = H-ONep], *tert*-butyl alcohol [$H–OC(CH_3)_3$ = H-O*t*Bu], *o*-(*tert*-butyl)phenol {$H–OC_6H_4[C(CH_3)_3]$-2 = H-*o*BP}, 2,6-dimethylphenol [$H–OC_6H_3(CH_3)_2$-2,6 = H-DMP], 2,6-diisopropylphenol {$H–OC_6H_3[CH(CH_3)_2]_2$-2,6 = H-DIP}, 2,6-di-*tert*-butylphenol {$H–OC_6H_3[C(CH_3)_3]_2$-2,6 = H-DBP}, or 2,6-diphenylphenol [$H–OC_6H_3(C_6H_5)_2$-2,6 = H-DPP] using toluene (tol), tetrahydrofuran (THF) or pyridine (py). The precursors were characterized as $[Ce(\mu\text{-ONep})_2(ONep)]_4$ (**1**), $Ce_4(\mu_3\text{-O}t\text{Bu})_3(\mu\text{-O}t\text{Bu})_4(O t\text{Bu})_5$ (**2**), $Ce_3(\mu_3\text{-O}t\text{Bu})_3(\mu\text{-O}t\text{Bu})_3(O t\text{Bu})_3(\text{H-O}t\text{Bu})_2$ (**2a**), $Ce(o\text{BP})_3(THF)_3$ (**3**), $[Ce(\mu\text{-DMP})(DMP)_2(solv)_2]_2$ [solv = THF (**4**) and py (**4a**)], $Ce(DIP)_3(THF)_3$ (**5**), $Ce(DPP)_3(THF)_2$ (**6**). Once isolated, several of these species were further reacted with a series of sterically varied carboxylic acid modifiers including isobutyric acid [$H–O_2CCH(CH_3)_2$ = H-OPc] and trimethylacetic acid [$H–O_2CC(CH_3)_3$ = H-OBc]. The products were isolated as $[Ce(OR)(\mu\text{-ORc})(\mu_c\text{-ORc})(py)]_2$ [OR = *o*BP, OBc: **7**; DMP, OPc: **8**; DMP, OBc: **9**; DIP, OPc: **10**]. These compounds were identified by single-crystal X-ray diffraction and powder XRD analyses. Several novel structure types are added to the cerium alkoxide family of compounds.

(© Wiley-VCH Verlag GmbH & Co. KGaA, 69451 Weinheim, Germany, 2006)

## Introduction

The role of metal alkoxide [$M(OR)_x$] precursors in ceramic materials synthetic routes such as, chemical solution (or the so-called "sol-gel"), metal organic chemical vapor deposition (MOCVD), or emerging nanoparticle synthetic methods have continued to expand. The growth is mainly due to their commercial availability, low crystallization temperatures, high solubility, high volatility, and other physical properties. In addition, these compounds are easily modified through the manipulation of their ligand set which allows for optimization of the final materials properties without increasing the complexity of the processing conditions. Typically, tailoring hydrolysis and condensation pathways of the $M(OR)_x$ precursors is of interest and accomplished by introducing a variety of ligands, including carboxylic acids (H–ORc). We have previously explored the structures obtained for group 4 alkoxides, modified with a series of H–ORc reagents, including: formic acid ($H–O_2CH$ = H-OFc), acetic acid ($H–O_2CCH_3$ = H-OAc), isobutyric acid [$H–O_2CCH(CH_3)_2$ = H-OPc], trimethylacetic acid [$H–O_2CC(CH_3)_3$ = H-OBc], or *tert*-butylacetic acid [$H–O_2CCH_2C(CH_3)_3$ = H-ONc], in an effort to understand how structure affects the final densification of thin films.[1,2] A number of general constructs were isolated for these systems but the partially hydrolyzed smaller trinuclear species proved to be the most useful for the generation of highly dense $TiO_2$ films and simple dinuclear species for $ZrO_2$ thin films.[1,2]

Recently, we have become interested in thin films of cerium oxide ($CeO_x$) as an anticorrosion material. In addition, $CeO_x$ has demonstrated a wide variety of other applications, such as barrier layers,[3–5] counter electrodes for electrochromic glasses,[6] catalysts,[7–11] electrolytes for solid oxide fuel cells,[12–14] polishing agents for soft and hard optical glasses,[15,16] and numerous other applications. Due to the widespread use of $CeO_x$, it is surprising that only a few structurally characterized cerium alkoxides [$Ce(OR)_3$] have been reported in the literature,[17–29] and no systematic studies were possible from this eclectic mix of potential precursors. Because it is critical to know the structure of the precursor to be able to optimize the properties of the final $CeO_x$ materials, it was necessary to develop a family of well-characterized, systematically structurally diverse $Ce(OR)_3$ precursors. Understanding the structural changes available for these precursors is critical prior to generating tailored-property $CeO_x$ thin films.

Therefore, we undertook the synthesis and characterization of a series of $Ce(OR)_3$ that would fill in several gaps in the alkyl and aryl oxide derivatives to develop a systematic family of structurally characterized $Ce(OR)_3$ complexes which could be used to explore tailored materials. An alcohol amide metathesis reaction pathway was selected to synthesize these compounds [Equation (1)] in toluene (tol),

[a] Sandia National Laboratories, Advanced Materials Laboratory, 1001 University Boulevard SE, Albuquerque, New Mexico, 87105, USA
Fax: +1-505-272-7336
E-mail: tjboyle@Sandia.gov

 © 2006 Wiley-VCH Verlag GmbH & Co. KGaA, Weinheim 

tetrahydrofuran (THF), or pyridine (py). The products were identified as: $[Ce(\mu\text{-}ONep)_2(ONep)]_4$ where ONep = $OCH_2C(CH_3)_3$ (**1**), $Ce_4(\mu_3\text{-}OtBu)_3(\mu\text{-}OtBu)_4(OtBu)_5$ (**2**), $Ce_3(\mu_3\text{-}OtBu)_3(\mu\text{-}OtBu)_3(OtBu)_3(H\text{-}OtBu)_2$ (**2a**), where $OtBu = OC(CH_3)_3$, $Ce(oBP)_3(THF)_3$ {**3**, *o*BP = $OC_6H_4$-[$C(CH_3)_3$]-2}, $[Ce(\mu\text{-}DMP)(DMP)_2(solv)]_2$ [DMP = $OC_6H_3(CH_3)_2$-2,6, solv = THF (**4**); solv = py (**4a**)], $Ce(DIP)_3(THF)_3$ [**5**, DIP = $OC_6H_3[CH(CH_3)_2]_2$-2,6], and $Ce(DPP)_3(THF)_3$ [**6**, DPP = $OC_6H_3(C_6H_5)_2$-2,6]. Compounds **1**–**5** were further reacted with a series of sterically varied H–ORc modifiers and their products identified as: $[Ce(OR)(\mu\text{-}ORc)(\mu_c\text{-}ORc)(py)]_2$ [OR = *o*BP, OBc (**7**); DMP, OPc (**8**); DMP, OBc (**9**); DIP, OPc (**10**), py = pyridine; $\mu$ = bridging; $\mu_c$ = chelating bridge]. The synthesis, characterization, and crystal structures of **1**–**10** are discussed below.

$$Ce(NR_2)_3 + 3\ H\text{–}OR \rightarrow Ce(OR)_3 + 3\ H\text{–}NR_2 \quad (1)$$

## Results and Discussion

As mentioned previously, we are interested in understanding the structural types available from simple OR- and ORc-modified Ce-based compounds prior to generating tailor-made $CeO_x$ thin films. Only a limited number of X-ray crystallographically characterized $Ce(OR)_3$ species have been reported: $[Ce(\mu\text{-}OiPr)(OiPr)_3(H\text{–}OiPr)]_2$ [O*i*Pr = $OCH(CH_3)_2$],[27,28] $Ce_4(\mu_4\text{-}O)(\mu_3\text{-}OiPr)_2(\mu\text{-}OiPr)_4(OiPr)_8$,[24,29] $Ce_3(\mu_3\text{-}OtBu)_2(\mu\text{-}OtBu)_3(OtBu)_5(NO_3)$,[20] $[Ce(\mu\text{-}OR)(OR)_2]_2$ where OR = O*t*Bu[23] or $OCH(tBu)_2$,[26] $Ce[OC(tBu)_3]_3(CNtBu)_2$,[22] $[Ce\{OCH(tBu)_2\}_3(\mu\text{-}DMAE)]_2$ [DMAE = $Me_2N\text{–}C_2H_4\text{–}NMe\text{–}C_2H_4\text{–}O^-$],[21] and $[Ce\{OC(tBu)_3\}_3]_2(OC_6H_4O)$.[23] In contrast, significantly fewer aryl oxide derivatives have been isolated, including $Ce[OC_6H_3(tBu)_2]_3$,[25] $Ce[OC_6H_3(tBu)_2]_3(CNtBu)$,[25] and $Ce[OC_6H_3(C_6H_5)_2]_3$.[17] It is of note that other Ce-containing species are available with fluorinated ligands, siloxide ligands,[19] or the inclusion of other metals.[30,31]

This nonsystematic family of compounds does not lend insight into the possible structure types available for $CeO_x$ precursors and thus necessitated the controlled synthesis of a series of $Ce(OR)_3$. Initial attempts focused on the aryl oxide ligands due to the dearth of structures available, the ease with which steric bulk can be introduced in the *ortho* positions, and our previous success using these ligands to produce high-quality thin films. We were also interested in several sterically demanding alkyl derivatives ONep and O*t*Bu due to our previous success using these ligands for materials synthesis and their lack of availability in the literature as homoleptic precursors.[20]

### Cerium Alkoxides

Several routes to these $Ce(OR)_3$ were considered prior to initiating this investigation. The first attempts were made using a liquid ammonia route wherein $CeCl_3$ was added to $Na^0$ dissolved in $NH_3$(l) at –78 °C followed by addition of H-DIP in toluene. Crystallization of the hexanes-soluble fraction of this reaction mixture yielded $[Ce(\mu\text{-}DIP)(DIP)_2]_2$. Unfortunately, when altering the pendant chain to an alkyl group, Na contamination was observed.[32] This prevented us from using a standard route to the family of $Ce(OR)_3$ that we were interested in isolating. It was therefore necessary to adjusted our synthetic strategy, and we switched to an amide alcohol metathesis route [Equation (1)] based on our previous success with this route.[32] It is critical for the synthesis of these compounds that a very pure $Ce(NR_2)_3$ be used, which was obtained by repeated sublimations and crystallizations.

### Synthesis

For each reaction, the $Ce(NR_2)_3$ was dissolved in toluene yielding a pale yellow solution. Upon addition of the desired alcohol, the reaction mixture was warmed slightly and turned clear with no precipitates observed for any of these samples. Crystals were isolated by drastically reducing the volume of the reaction and cooling the mixture to –25 °C. FTIR data indicates for each sample that the crystals did not possess any amide ligands and that the alcohols had fully reacted. Solution-state NMR could not be obtained due to the paramagnetic nature of the $Ce^{III}$ species isolated, therefore, it was necessary to obtain single-crystal X-ray structures to identify these compounds. The results of these experiments are shown in Figure 1 to Figure 12 for **1**–**10**, respectively.

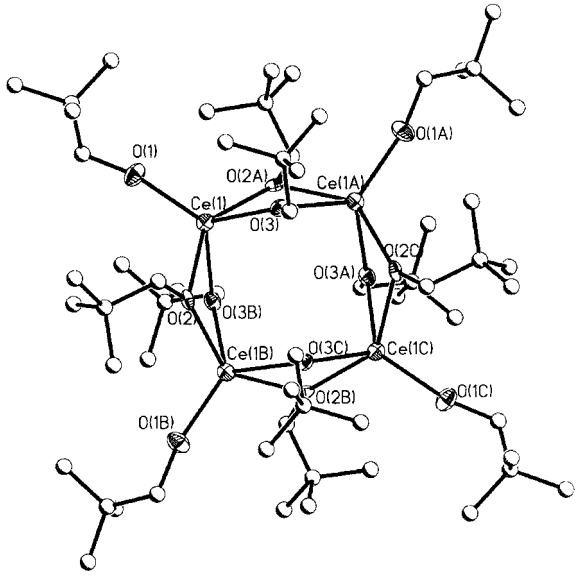


Figure 1. Structure plot of **1**. Thermal ellipsoids of heavy atoms drawn at 30% level. Carbon atoms are drawn as ball and stick for clarity.

### Crystal Structures

For **1**, the least sterically hindering ONep ligand led to the formation of a tetranuclear species, which is identical

 © 2006 Wiley-VCH Verlag GmbH & Co. KGaA, Weinheim 

to what was reported for the all of the lanthanide ONep derivative, see Figure 1.[32–34] The central core consists of four Ce metal centers arranged in a square, interconnected by four bridging μ-ONep ligands and one terminal ONep ligand per metal. Each of the Ce cations is five-coordinated adopting a square-base-pyramidal (SBP) geometry. As reported for the other $[Ln(ONep)_3]_4$ species,[32–34] there is significant H-bonding interaction noted for this compound.

Increasing the steric demands from the ONep to the O*t*Bu ligand, under stoichiometric conditions, led to the isolation of another tetranuclear species **2** (Figure 2). For **2**, the four octahedrally bound ($O_h$) metals are again arranged in a square linked by μ-O*t*Bu ligands; however, in contrast to **1**, three $\mu_3$-O*t*Bu link the metal centers: Ce(1), Ce(2), and Ce(3) through the use two of the $\mu_3$-O*t*Bu while the remaining $\mu_3$-O*t*Bu bridges Ce(1), Ce(2), and Ce(4). To complete the $O_h$ geometry, Ce(1), Ce(2) and Ce(3) bind one terminal O*t*Bu ligand each and Ce(4) coordinates two ligands. This structure is similar to what was observed for $Ce_4(\mu_4\text{-}O)[\mu_3\text{-}OCH(CH_3)_2]_2[\mu\text{-}OCH(CH_3)_2]_4[OCH(CH_3)_2]_8$,[24,29] which uses an oxo ligand to achieve this structure; however, this is the first structural arrangement of this type noted for homoleptic $Ln(OR)_3$. When excess H-O*t*Bu is used, a centrosymmetric trinuclear species **2a** (Figure 3), similar to other lanthanide alkoxides is isolated in the presence of Lewis base solvents. For **2a**, each Ce is bound by two $\mu_3$-O*t*Bu, two μ-O*t*Bu and two terminal O*t*Bu ligands adopting a distorted trigonal bipyramidal (TBP) arrangement. By charge balance, two of these ligands must be protonated, as is commonly noted for metal alkoxides.[35,36] The increased steric bulk of the bound Lewis base H-O*t*Bu does not allow for large clusters to form. The mixed charge $NO_3$ derivative $Ce_3[\mu_3\text{-}OC(CH_3)_3]_2[\mu\text{-}OC(CH_3)_3]_3[OC(CH_3)_3]_5(NO_3)$,[20] and other solvated $Ln(OR)_3$ are known to adopt this structure as well.[37] It is interesting to note that the primary alcohol H-ONep is often considered to be less sterically hindering than the tertiary H-O*t*Bu, but in this system, the ONep-ligated species yields Ce metal centers with a lower coordination number. One explanation for this phenomenon may be the significantly greater cone angle swept out by the ONep ligand as compared to that of the O*t*Bu ligand.

Because only slight changes in the structure were noted for the pure alkoxides isolated above, in comparison to the literature species, further probing of the influence of sterics on the structure of these compounds led to an investigation of aryl oxide derivatives. For this system, it was necessary to use Lewis base solvents to maintain solubility. Using an asymmetrically substituted aryl oxide (*o*BP) wherein the steric bulk of one of the *ortho* sites is increased to a *tert*-butyl group, the first mono-substituted alkyl phenoxide lanthanide alkoxide complex was isolated as **3** (Figure 4). It is of note that several lanthanide alkali metal double alkoxides with 4-methylphenoxides[38,39] have been isolated previously.[39,40] The *tert*-butyl groups of the *o*BP ligands all point away from the metal center allowing the coordination of three THF solvent molecules forming a *fac* $O_h$ metal center.

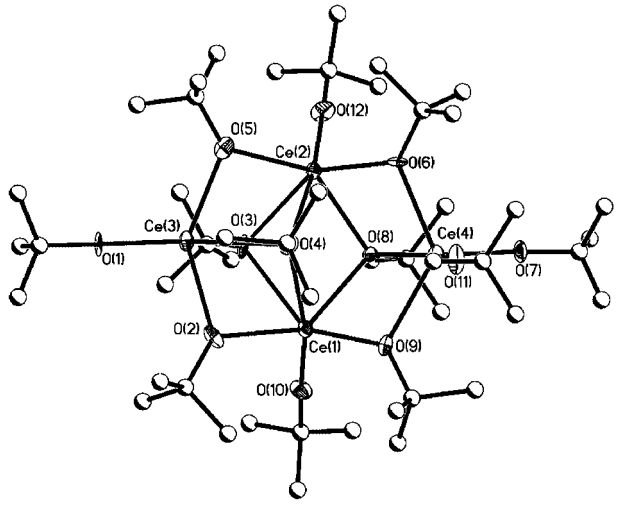


Figure 2. Structure plot of **2**. Thermal ellipsoids of heavy atoms drawn at 30% level. Carbon atoms are drawn as ball and stick for clarity.

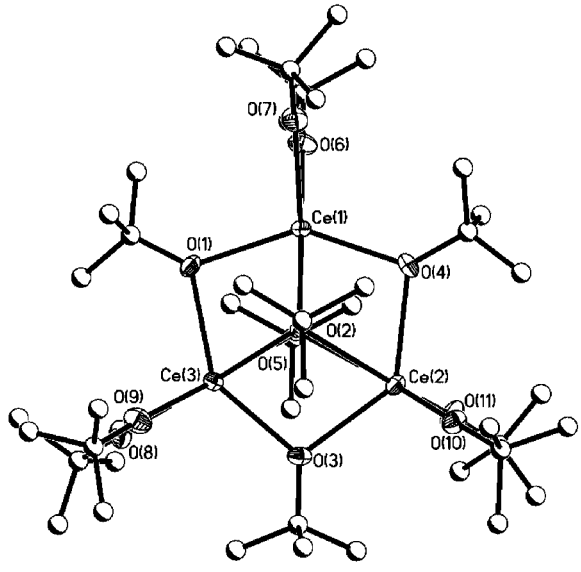


Figure 3. Structure plot of **2a**. Thermal ellipsoids of heavy atoms drawn at 30% level. Carbon atoms are drawn as ball and stick for clarity.

Systematically increasing the steric bulk by placing a methyl group in each *ortho* position, surprisingly led to the isolation of the dinuclear species **4**, shown in Figure 5. Each of the Ce metal centers adopts a distorted $O_h$ geometry by binding two μ-DMP, two terminal DMP, and two THF solvent molecules in the axial position. It was thought that the delicate balance between steric bulk and coordination strength of the solvent allowed a monomer to form as noted for **3** vs. the dinuclear for **4**. Therefore, a stronger Lewis base was used in the synthesis to see if **4** could be converted to a mononuclear species. Surprisingly, switching to py, lead to the isolation of **4a** which adopts an identical dinuclear structure as observed for **4** but the THF ligands are replaced by py ligands (Figure 6). This is the first py adduct of $Ce(OR)_3$ reported to date. Compounds **4** and **4a** are

 © 2006 Wiley-VCH Verlag GmbH & Co. KGaA, Weinheim 

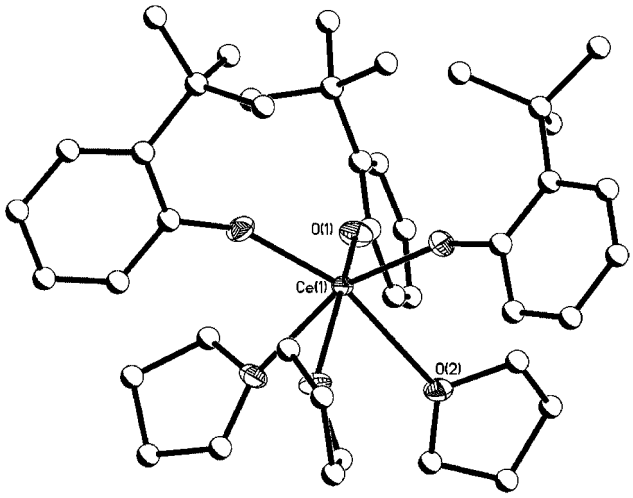


Figure 4. Structure plot of 3. Thermal ellipsoids of heavy atoms drawn at 30% level. Carbon atoms are drawn as ball and stick for clarity.

analogous to $[Y(\mu\text{-DMP})(DMP)_2(THF)]_2$ structure previously reported.[41]

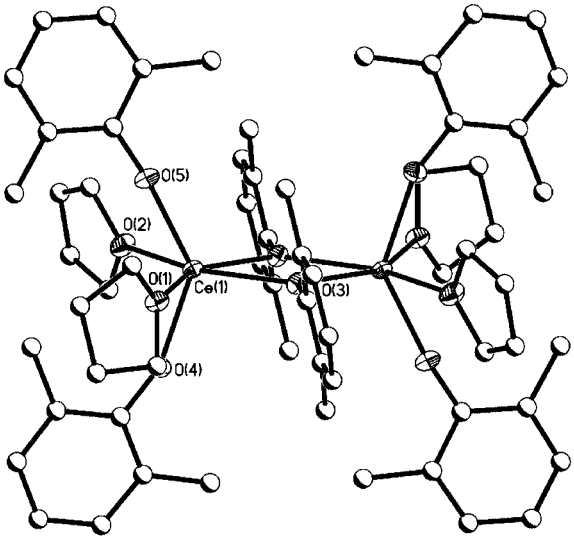


Figure 5. Structure plot of **3a**. Thermal ellipsoids of heavy atoms drawn at 30% level. Carbon atoms are drawn as ball and stick for clarity.

For compound **5** shown in Figure 7, the further increase in steric bulk of the *ortho* positions to isopropyl groups coupled with the use of Lewis base solvents, led to the formation of a monomer. The Ce metal center is $O_h$ bound by three DIP and three THF ligands in a *fac* arrangement, as noted for the *o*BP ligated species and numerous literature reports of solvated lanthanide monomers.[40] In comparison, the larger La cation only used two solvent molecules to complete its coordination sphere for the same ligand set;[42] however, smaller cations have also been found to yield trisolvated species such as $Sm(DIP)_3(THF)_3$.[43] Therefore, the number of solvent molecules coordinated can not be directly related to the size of the cations employed. A similar mononuclear structural arrangement was observed for the DPP (**6**, Figure 8) ligated compound; however, for **6** only two THF molecules are present. The previously reported DPP derivative was also a monomer but had π interactions from the *ortho* phenyl groups,[17–29] therefore, the addition of coordinated solvent noted for **6** is not unexpected. For the $Ln(DPP)_3(THF)_2$ Ln = La,[42,44] Nd,[42,44] Yb[45,46] complexes, the large *trans* effect of the OAr and the THF ligands was also observed for **6**.

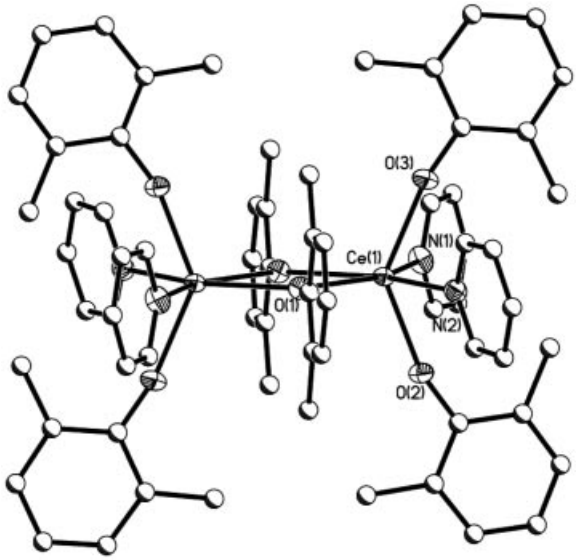


Figure 6. Structure plot of **4**. Thermal ellipsoids of heavy atoms drawn at 30% level. Carbon atoms are drawn as ball and stick for clarity.

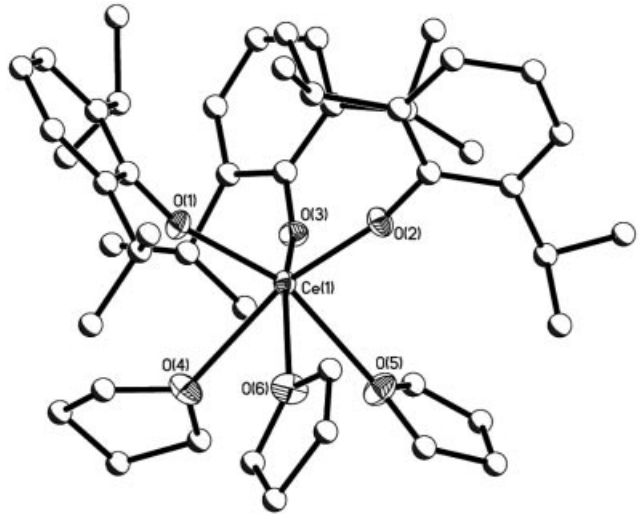


Figure 7. Structure plot of **5**. Thermal ellipsoids of heavy atoms drawn at 30% level. Carbon atoms are drawn as ball and stick for clarity.

The bond lengths and angles of this family of $Ce^{III}$ alkoxides, **1**–**6**, are consistent with those of previously reported $Ce(OR)_3$.[17–29,32–34,47,48] For **1**, as the second largest cation

 © 2006 Wiley-VCH Verlag GmbH & Co. KGaA, Weinheim 

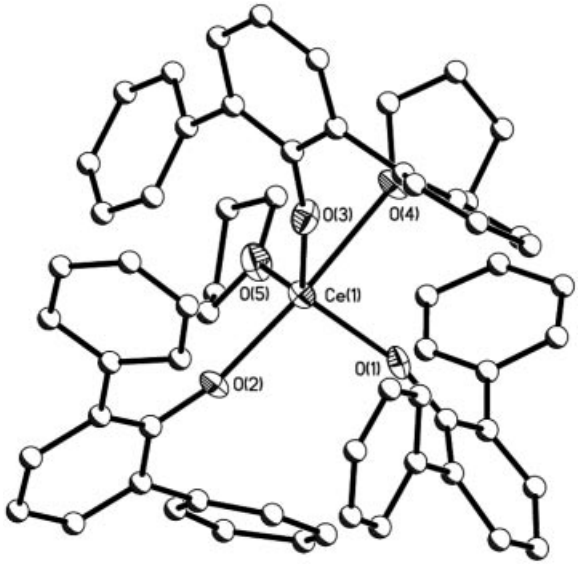


Figure 8. Structure plot of **6**. Thermal ellipsoids of heavy atoms drawn at 30% level. Carbon atoms are drawn as ball and stick for clarity.

in the ONep family of $[Ln(\mu\text{-}ONep)_2(ONep)]_4$ it falls on the long end of the Ln···Ln separations which systematically decrease from 3.86 to 3.28 Å. Terminal Ln–O distances of 2.14 Å for Ce fall within the range 2.16 Å (La, average value) to 1.89 Å (Sc) with an overall average distance of 2.06 Å. Ce is the second largest cation so obviously the Ce–O distance falls at the longer end of the observed bond lengths.

The O*t*Bu derivative **2** was found to adopt a novel structure type and no acceptable models were available for structural comparisons; however, the Ce(III/IV) oxo isopropoxide[24,29] was the closest in terms of connectivity and composition. The average terminal Ce–OR distances of 2.12, Ce(μ-OR) of 2.31, and Ce($\mu_3$-OR) of 2.47 Å were *not* found to be in agreement with **2** [2.24 (terminal), 2.44 (μ) Å]. This is most likely a reflection of the varied oxidation state and oxo species for the Ce(III/IV) oxo isopropoxide[24,29] complex vs. the $Ce^{III}$ alkoxide for **2**. There is also a trinuclear Ce(III/IV) O*t*Bu derivative structurally consistent with **2a**; however, the average Ce–OR, Ce(μ-OR), and Ce($\mu_3$-OR) distances of 2.08, 2.37, and 2.52 Å, respectively, are *not* in agreement with **2a** [2.23 (terminal) and 2.45 (μ) Å]. These differences are not surprising due to the mixed valent Ce(III/IV) species. Because the lanthanides systematically vary in cation size due to the lanthanide contraction, it is valid to use the isostructural La derivatives for metrical comparisons. In general, the bond lengths and angles of **2a** were found to be in agreement with $La_3(O\mathit{t}Bu)_9(H\text{-}O\mathit{t}Bu)_2$.[49] For example, the average $\mu_3$-OR–Ln distances are 2.55 Å for **2a** and 2.57 Å for La.

The dinuclear species **4** and **4a** have average Ce–OR and Ce(μ-OR) distances of 2.25 and 2.45 Å, respectively; **5** has an average Ce–OR distance of 2.22 Å. The dinuclear $O\mathit{t}Bu/OC\mathit{t}Bu_3$,[23] O*i*Pr,[27,28] $OC(CH_3)_2(\mathit{i}Pr)$,[48] and $OC(H)(\mathit{t}Bu)_2$[26] have average distances of 2.14 Å for Ce–OR and 2.36 Å for Ce(μ-OR). The monomeric species that are solvated[17,25,48] also have a similar average Ce–OR distance of 2.17 Å. The mononuclear solvated **6** was found to be in agreement with the metrical data reported for the unsolvated but π-bound DPP;[17–29] the average Ce–OR distances were 2.21 Å for **5** and 2.24 Å for **6**.

### Carboxylic Acid Modified Cerium Alkoxides

It was of interest to add more protective groups to the metal center to reduce the sensitivity to hydrolysis as well as introduce new constructs for $Ce(OR)_3$. This was undertaken using H-ORc. Previous studies[1,50,51] have shown that substantial changes in the rate of hydrolysis and condensation can be wrought through the introduction of H-ORc modifiers both through esterification oxolation pathways and the steric hindrance introduced by the bidentate nature of the ORc ligand. It is of note that the μ- and $\mu_c$-ORc ligands (also referred to as bidentate and tridentate, respectively) have been observed in a variety of lanthanide carboxylate systems wherein over 1500 structures have been identified revealing a variety of binding modes available for Ln–ORc species.[40] A further search of the literature reveals many Ce–ORc compounds have been structurally characterized but the majority of these are the homoleptic species.[52–62] with no structurally characterized carboxylate-modified alkoxide compounds available.

### Synthesis

Therefore, we investigated the modification of the $Ce(OR)_3$ isolated above with a series of sterically varied carboxylic acids. In general, the compounds were dissolved in py and then added to a stirring solution of the carboxylic acid dissolved in py. No precipitates were observed. Because the $Ce^{III}$ metal center is paramagnetic, solution identification of these compounds by NMR methods was not possible. Further, the volatility of the bound solvent prevents clean identification of the bulk powder by thermal elemental analyses. Therefore, while we have isolated numerous powders from these reactions, only those that were structurally characterized will be discussed below.

After numerous attempts, only the OAr–ORc modified species were structurally characterized. This phenomenon was mainly attributed to the ability of the steric bulk of the aryl oxide to prevent larger less soluble precursors to form. This is clearly illustrated by the larger oligomers observed for both the ONep and O*t*Bu ligated species **1**–**2** in comparison to the OAr derivatives **3**–**5**.

### X-ray Crystal Structure

Figure 9 shows the structure plot of **7**, the OBc-modified species of **3** that was isolated as the substituted dinuclear species. The OBc ligands have replaced two of the *o*BP ligands and bridge between the metal centers in two coordination modes: bridging (μ-ORc) and bridging chelating ($\mu_c$-

 © 2006 Wiley-VCH Verlag GmbH & Co. KGaA, Weinheim 

ORc) modes. By binding two py and the original *o*BP ligands, this forms eight-coordinate Ce metal centers forming a dodecahedron[63] arrangement. Independent of an increase in steric bulk of the pendant ORc chain, an identical core was observed for each of the various modified species [DMP/OPc **8** (Figure 10); DMP/OBc **9** (Figure 11), and DIP/OPc **10** (Figure 12)]. Interestingly, no esterification or redox behavior was noted for any of these reactions which is in stark contrast to the early transition metal ORc-modified compounds, wherein, esterification products were isolated for all but the most sterically hindering ligands.[1,2,64,65]

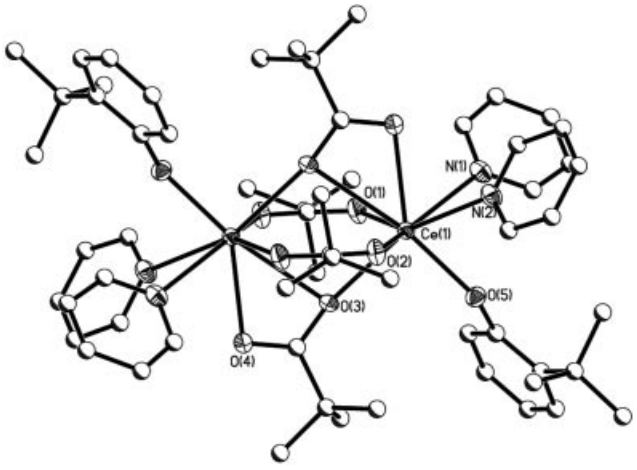


Figure 9. Structure plot of **7**. Thermal ellipsoids of heavy atoms drawn at 30% level. Carbon atoms are drawn as ball and stick for clarity.

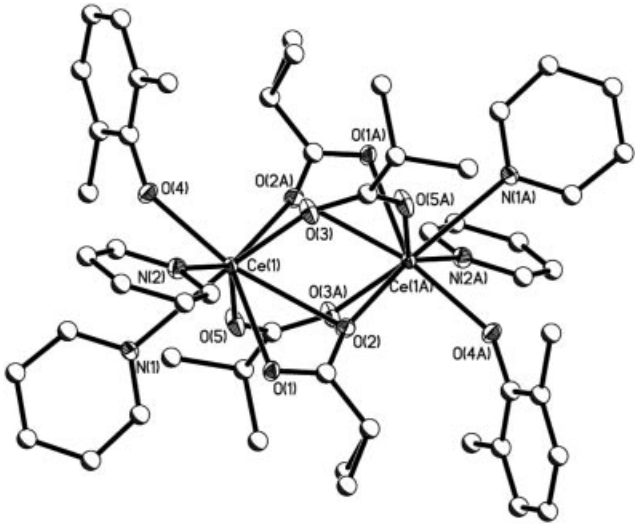


Figure 10. Structure plot of **8**. Thermal ellipsoids of heavy atoms drawn at 30% level. Carbon atoms are drawn as ball and stick for clarity.

The bond lengths and angles of the alkoxides[17–29,32–34,47,48] and the carboxylates moieties[52–62] are consistent with literature reports. The terminal distances of the aryl oxides are on the order of 2.24 to 2.27 Å and as noted above are within the expected range.[17–29,32,33,47,48] The bite angle of the $\mu_c$-ORc in the literature[52–62] have

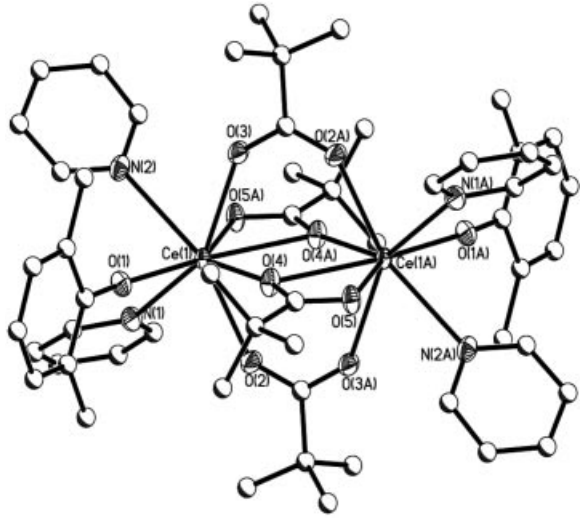


Figure 11. Structure plot of **9**. Thermal ellipsoids of heavy atoms drawn at 30% level. Carbon atoms are drawn as ball and stick for clarity.

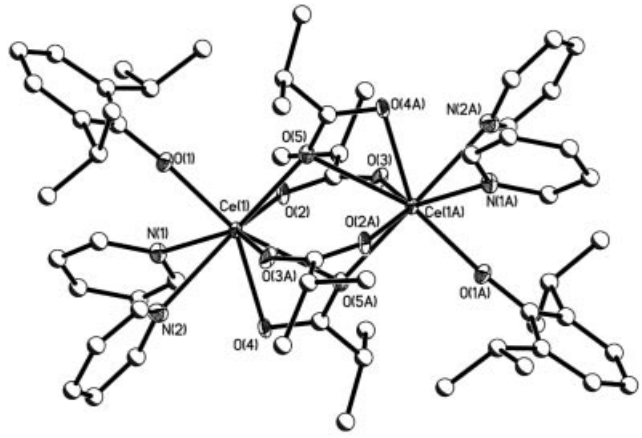


Figure 12. Structure plot of **10**. Thermal ellipsoids of heavy atoms drawn at 30% level. Carbon atoms are drawn as ball and stick for clarity.

values ranging from 116° to 128° with an average value of 120.7°. The angles noted for **7**–**10** (121.3°, 121.3°, 120.9°, 119.6°, respectively) fall within this range. The μ-ORc ligands are limited to a few species with a smaller bite angle range (119° to 126°) with an average value of 123.4°, which is similar to the average values noted for **7**–**10**: 123.8°, 125.2°, 124.9°, 125.6°, respectively.

### Bulk Powder Characterization

In an effort to characterize the bulk powder, several analytical methods were investigated. Typically, solution NMR can be employed to elucidate purity; however, the paramagnetic nature of the $Ce^{III}$ metal centers prevents obtaining any meaningful data by these techniques. Solid-state NMR spectroscopic data also proved inconclusive due to broad and numerous peaks expected for these structures. These phenomena were also attributed to the paramagnetic nature

 © 2006 Wiley-VCH Verlag GmbH & Co. KGaA, Weinheim 

of the $Ce^{III}$ and packing disorders, because the ligands are not free to rotate in the solid state numerous peaks are often observed.

The elemental analyses of the bulk powders of **1**–**10**, in general, agree with the unsolvated compounds. Compound **4a** is a solvated species and the slight variation in the elemental analysis was attributed to either "trapped" and/or bound solvent. These conditions are often reported to cause variations from ideal conditions.[50,51,66,67] FTIR spectra of **1**–**10** revealed the presence of the appropriate stretches expected for the various alkoxide ligands and shifts of the ORc ligands consistent with them bound to a metal center. It is of note that there are some reports that indicate these compounds can undergo a reaction with KBr under high pressure, yielding spectra that may not reflect the actual species but a metathesis products instead.[68] However, these spectra are useful in terms of identifying the resultant products. Further investigations of these materials by TGA/DTA revealed that most samples did not show consistent weight losses or thermal behavior during processing. This is attributed to high reactivity with the ambient atmosphere as an artefact with our current experimental setup. This led to total weight losses that were rarely in agreement with the crystal structure. Due to the complexity of the above data, it is not possible to conclusively deduce the purity of the bulk powder and alternative methods were investigated.

Therefore, microXRD spectra were obtained on the $Ce(OR)_3$ bulk powders sealed in glass capillary tubes and compared to calculated patterns from the obtained single crystal structures. In general, the resulting spectra matched what was expected for the powder XRD patterns. Figure 13 and Figure 14 show the obtained microXRD results for **2a** and **6** and their general agreement with the theoretical spectrum (inset). The variations noted can be contributed to two factors (i) the calculated patterns generated from the crystal structure are based on a truly random powder and the crystals have preferential orientation and (ii) the powders are not solvated as are the crystal structures. Therefore, an exact match was not obtained; however, the powders do appear to agree to a significant degree with the calculated patterns.

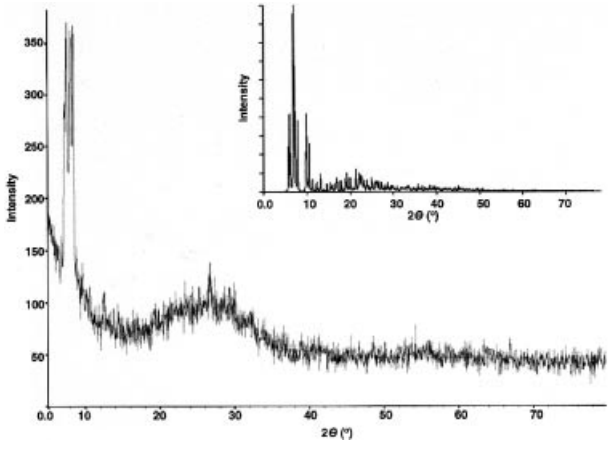


Figure 13. MicroXRD spectrum of **2a**. Inset is the calculated pattern.

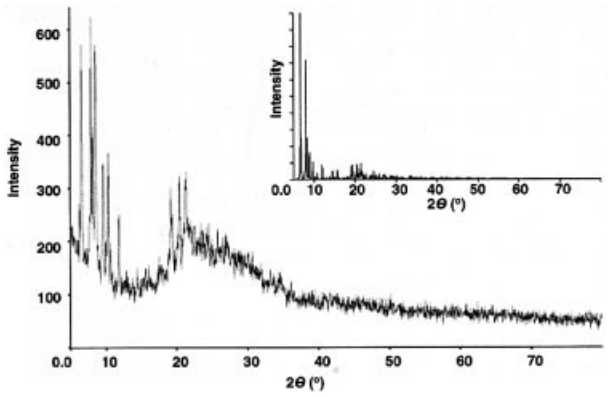


Figure 14. MicroXRD spectrum of **6**. Inset is the calculated pattern.

## Summary and Conclusion

A family of $Ce^{III}$ alkoxides were isolated through an alcohol–amide exchange reaction pathway. In general, as the steric bulk of the pendant alkoxy moiety increased and the presence of a Lewis base, the nuclearity of the molecule decreased. Species ranged from tetra- to mono-nuclear species with several novel solvents as ligands and arrangements noted for this family of compounds. The successful modification of the aryl oxide complexes led to the first alkoxy carboxylate structures isolated for Ce. These compounds were identified as dinuclear species with μ-ORc and $\mu_c$-ORc ligands. The change in steric bulk of the OAr or the ORc ligand had no effect on the final structure. Interestingly, none of the ORc–$Ce(OR)_3$ possessed an oxo species indicating that esterification did not occur. These compounds are being investigated as precursors to $CeO_x$ nanoparticles and thin films wherein the ligand set controls the structure and reactivity, which imparts control to the final properties of these $CeO_x$ materials.

## Experimental Section

All reactions were performed under a dry, inert atmosphere using standard Schlenk line and glovebox techniques. The following chemicals were used as received (Aldrich): $CeBr_3$, $KN[Si(CH_3)_3]_2$ ($KNR_2$), H-ONep, H-O*t*Bu, H-DMP, H-DIP, H-DPP, H-*o*BP, H-OPc, H-OBc, and H-ONc. H-OFc and H-OAc were dried according to literature preparative methods.[69] All solvents were used as received in anhydrous (Sure/Seal™) bottles. $Ce(NR_2)_3$ [where R = $Si(CH_3)_3$] was isolated from the reaction of $CeBr_3$ and 3 equiv. of $KNR_2$.[35,36] FT-IR spectroscopic data were obtained with a Bruker Vector 22 spectrometer using KBr pellets pressed under argon and handled under flowing nitrogen. Elemental analyses were performed with a Perkin–Elmer 2400 CHN-S/O elemental analyzer. Micro powder X-ray diffraction was performed with several samples that were prepared in a glass (Quartz) capillary and mounted vertically on an XYZ stage of a Bruker D8 Discover diffractometer

 © 2006 Wiley-VCH Verlag GmbH & Co. KGaA, Weinheim 

using Cu-$K_\alpha$ radiation ($\lambda$ = 1.5406 Å). The X-ray beam was collimated to 1 mm size and scans are typically taken from 10 to 80 ° $2\theta$ at 0.04 degree steps at 2 s per step. Diffraction scan interpretation was done using MDI, Inc. Jade 7 software.

**General Alkoxide Synthesis:** Due to the similarity of the synthesis of compounds **1**–**6**, a general description will be provided. The appropriate alcohol was dissolved in the solvent of choice and slowly added to a stirring solution of $Ce(NR_2)_3$ dissolved in the same solvent. The resulting solutions were stirred for 12 h and then the volume of the volatile material was drastically reduced by rotary evaporation. After this, the mixture was cooled to –25 °C until crystals formed.

**$[Ce(\mu\text{-}ONep)_2(ONep)]_4$ (1):** Used $Ce(NR_2)_3$ (0.60 g, 0.97 mmol), H-ONep (0.25 g, 2.9 mmol) in toluene (tol). Yield: 87% (0.34 g). FT-IR (KBr): $\tilde{\nu}$ = 2951 (w), 2864 (m), 2803 (m), 2687 (s), 1478 (m), 1460 (m), 1390 (s), 1358 (m), 1254 (s), 1215 (s), 1106 (w), 1059 (m), 1019 (m), 932 (s), 896 (s), 749 (s), 702 (s), 592 (m), 561 (s), 426 (s) $cm^{-1}$. $C_{60}H_{132}Ce_4O_{12}$ (1606.20): calcd C 44.87, H 8.28; found C 44.67, H 8.17.

**$Ce_4(\mu_3\text{-}OtBu)_3(\mu\text{-}OtBu)_4(OtBu)_5$ (2):** Used $Ce(NR_2)_3$ (0.61 g, 0.98 mmol), H-O*t*Bu (0.22 g, 3.0 mmol) in tol. Yield: 89% (0.32 g). FT-IR (KBr, $cm^{-1}$): $\tilde{\nu}$ = 2960 (w), 2865 (w), 2150 (s), 2120 (s), 1936 (s), 1848 (s) 1466 (w), 1356 (w), 1187 (w), 974 (w), 929 (w), 878 (w), 829 (w), 767 (w), 740 (w), 693 (s), 677 (s), 655 (s), 595 (m). $C_{48}H_{108}Ce_4O_{12}$ (1437.87): calcd C 40.09, H 7.57; found C 39.78, H 7.68.

**$Ce_3(\mu_3\text{-}OtBu)_3(\mu\text{-}OtBu)_3(OtBu)_3(H\text{-}OtBu)_2$ (2a):** Used $Ce(NR_2)_3$ (0.61 g, 0.98 mmol), H-O*t*Bu (0.29 g, 3.9 mmol) in tol. Yield: 90% (0.36 g). FT-IR (KBr, $cm^{-1}$): $\tilde{\nu}$ = 2965 (w), 2925 (w), 2865 (w), 1467 (m), 1370 (m), 1356 (w), 1020 (m), 968 (w), 927 (w), 878 (w), 768 (m), 759 (m), 740 (s), 511 (w), 488 (w). $C_{44}H_{101}Ce_3O_{11}$ (1226.65): calcd. C 43.08, H 8.30; found C 42.78, H 8.09.

**$Ce(oBP)_3(THF)_3$ (3):** Used $Ce(NR_2)_3$ (1.3 g, 2.9 mmol), H-*o*BP (0.91 g, 6.1 mmol) in tol. Yield: 92% (1.5 g). FT-IR (KBr, $cm^{-1}$): $\tilde{\nu}$ = 3056 (s), 2952 (m), 1587 (m), 1561 (m), 1478 (w), 1439 (w), 1301 (w), 1260 (w), 1217 (m), 1124 (s), 1088 (s), 1068 (s), 1047 (s), 1035 (s), 1003 (s), 868 (w), 823 (m), 748 (w), 703 (w), 597 (s). $C_{42}H_{63}CeO_6$ (804.09): calcd. C 62.74, H 7.90; found C 62.36, H 7.81.

**$[Ce(\mu\text{-}DMP)(DMP)_2(THF)_2]_2$ (4):** Used $Ce(NR_2)_3$ (0.22 g, 0.35 mmol), H-DMP (0.13 g, 1.10 mmol) in tetrahydrofuran (THF). Yield: 95% (0.22 g). FT-IR (KBr, $cm^{-1}$): $\tilde{\nu}$ = 2971 (s), 1591 (m), 1465 (m), 1425 (m), 1367 (s), 1269 (w), 1233 (w), 1211 (w), 1094 (m), 1068 (s), 1027 (m), 850 (w), 761 (m), 697 (m), 678 (s), 565 (s), 524 (s), 492 (s). $C_{64}H_{86}Ce_2O_{10}$ (1295.63): calcd. C 59.33, H 6.69; found C 59.16, H 7.05.

**$[Ce(\mu\text{-}DMP)(DMP)_2(py)_2]_2$ (4a):** $Ce(NR_2)_3$ (0.97 g, 1.6 mmol), H-DMP (0.58 g, 4.7 mmol) in tol and pyridine (py). Yield: 95% (0.98 g). FT-IR (KBr, $cm^{-1}$): $\tilde{\nu}$ = 3068 (m), 3049 (m), 3012 (m), 2964 (m), 2909 (s), 1596 (w), 1465 (w), 1442 (w), 1424 (w), 1270 (w), 1234 (w), 1210 (w), 1150 (s), 1092 (w), 1067 (m), 1035 (m), 1003 (m), 850 (w), 837 (w), 747 (w), 621 (m), 564 (s), 526 (m). $C_{68}H_{74}Ce_2N_4O_6$ (1323.61): calcd. C 61.70, H 5.64, N 4.23; found C 60.87, H 5.66, N 4.48.

**$Ce(DIP)_3(THF)_3$ (5):** Used $Ce(NR_2)_3$ (0.22 g, 0.36 mmol), H-DIP (0.19 g, 1.1 mmol) in tol and THF. Yield: 96% (0.22 g). FT-IR (KBr, $cm^{-1}$): $\tilde{\nu}$ = 3054 (s), 2958 (w), 2867 (m), 1586 (s), 1380 (s), 1357 (s), 1327 (m), 1264 (w), 1206 (m), 1095 (s), 1042 (m), 1021 (m), 885 (m), 855 (w), 796 (s), 752 (m), 687 (m), 561 (m). $C_{48}H_{75}CeO_6$ (888.25): calcd. C 64.91, H 8.51; for $C_{36}H_{51}CeO_3$ (without 3THF, 671.92): calcd. C 64.35, H 7.65; found C 63.96, H 8.04.

**$Ce(DPP)_3(THF)_2$ (6):** Used $Ce(NR_2)_3$ (0.24 g, 0.39 mmol), H-DPP (g, 1.2 mmol) in THF. Yield: 99% (0.39 g). FT-IR (KBr, $cm^{-1}$): $\tilde{\nu}$ = 3054 (m), 3027 (m), 2975 (m), 2874 (m), 1596 (w), 1581 (m), 1495 (w), 1453 (w), 1405 (w), 1307 (w), 1261 (w), 1176 (m), 1156 (s), 1086 (w), 1069 (w), 1025 (w), 914 (m), 856 (w), 803 (s), 702 (w), 626 (s), 600 (w). $C_{62}H_{55}CeO_5$ (1020.24): calcd. C 72.99, H 5.43; found C 72.64, H 5.79.

**General Modified Alkoxide Synthesis:** Due to the similarity of the synthesis of compounds **7**–**10**, a general description will be provided. To a stirring solution of the appropriate $Ce(OR)_3$ (**1**–**5**), 1 equiv. of the appropriate H-ORc was added. The reaction was stirred for 12 h and then the volatile portion was allowed to slowly evaporate until crystals formed.

**$[Ce(oBP)(\mu\text{-}OBc)(\mu_c\text{-}OBc)(py)_2]_2$ (7):** Used compound **3** (0.26 g, 0.32 mmol), H-OBc (0.066 g, 0.65 mmol) in py. Yield: 92% (0.20 g). FT-IR (KBr, $cm^{-1}$): $\tilde{\nu}$ = 2962 (m), 1524 (w), 1483 (w), 1459 (w), 1418 (w), 1375 (w), 1224 (m), 1032 (s), 897 (s), 802 (s), 601 (s), 540 (s). $C_{60}H_{82}Ce_2N_4O_{10}$ (1299.58): calcd. C 55.45, H 6.36, N 4.31; found C 55.19, H 6.81, N 4.01.

**$[Ce(DMP)(\mu\text{-}OPc)(\mu_c\text{-}OPc)(py)_2]_2$ (8):** Used compound **4** (0.28 g, 0.22 mmol), H-OPc (0.038 g, 0.43 mmol) in py. Yield: 37% (0.10 g). FT-IR (KBr, $cm^{-1}$): $\tilde{\nu}$ = 2968 (w), 2930 (m), 1581 (w), 1477 (w), 1422 (w), 1373 (m), 1359 (m), 1238 (m), 1217 (w), 1092 (w), 1035 (m), 1004 (m), 850 (w), 753 (w), 702 (w), 663 (s), 619 (m), 547 (m), 531 (m), 518 (m). $C_{52}H_{66}Ce_2N_4O_{10}$ (1187.37): calcd. C 52.60, H 5.60, N 4.71; found C 52.39, H 5.52, N 4.19.

**$[Ce(DMP)(\mu\text{-}OBc)(\mu_c\text{-}OBc)(py)_2]_2$ (9):** Used compound **4** (0.44 g, 0.34 mmol), H-OBc (0.069 g, 0.68 mmol) in py. Yield: 53% (0.22 g). FT-IR (KBr, $cm^{-1}$): $\tilde{\nu}$ = 3607 (s), 2961 (w), 2929 (w), 2871 (w), 1541 (w), 1483 (w), 1460 (w), 1420 (w), 1375 (w), 1361 (w), 1285 (m), 1263 (w), 1224 (w), 1090 (m), 1033 (m), 896 (w), 839 (m), 803 (m), 791 (m), 756 (m), 700 (m), 601 (w), 552 (m), 517 (s). $C_{56}H_{74}Ce_2N_4O_{10}$ (1243.48): calcd. C 54.09, H 6.00, N 4.50; found C 54.51, H 6.39, N 4.31.

**$[Ce(DIP)(\mu\text{-}OPc)(\mu_c\text{-}OPc)(py)_2]_2$ (10):** Used compound **5** (0.26 g, 0.29 mmol), H-OPc (0.052 g, 0.58 mmol) in py. Yield: 60% (0.12 g). FT-IR (KBr, $cm^{-1}$): $\tilde{\nu}$ = 3062 (s), 3036 (s), 2968 (w), 2930 (m), 2870 (m), 1581 (w), 1477 (w), 1442 (w), 1422 (w), 1373 (m), 1359 (s), 1283 (w), 1263 (m), 1238 (s), 1217 (s), 1092 (m), 1035 (m), 1004 (s), 850 (m), 753 (m), 702 (m), 619 (s), 547 (s), 531 (s), 518 (s). $C_{60}H_{82}Ce_2N_4O_{10}$ (1299.58): calcd. C 55.45, H 6.36, N 4.31; found C 55.90, H 6.81, N 4.33.

**General X-ray Crystal Structure Information:**[70] Each crystal was mounted onto a thin glass fiber from a pool of Fluorolube™ and immediately placed under a liquid $N_2$ stream, on a Bruker AXS diffractometer. The radiation used was graphite-monochromatized Mo-$K_\alpha$ radiation ($\lambda$ = 0.7107 Å). The lattice parameters were optimized from a least-squares calculation on carefully centered reflections. Lattice parameter determination and data collection were carried out using SMART Version 5.054 software. Data reduction was performed using SAINT Version 6.01 software. The structure refinement was performed using XSHELL 3.0 software. The data were corrected for absorption using the SADABS program within the SAINT software package. General collection parameters for **1**–**3** and **4**–**10** are shown in Table 1 and Table 2, respectively. Additional information concerning the structure of these compounds can be found by accessing the final CIF files through the Cambridge Crystallographic Data Base. In general, each structure was solved by direct methods. This procedure yielded the heavy atoms,

 © 2006 Wiley-VCH Verlag GmbH & Co. KGaA, Weinheim 

Table 1. Data collection parameters for **1**–**3**.

| Compound | **1(·8tol)** | **2** | **2a(·2tol)** | **3(·3THF)** |
|---|---|---|---|---|
| Empirical formula | $C_{116}H_{196}Ce_4O_{12}$ | $C_{48}H_{108}Ce_4O_{12}$ | $C_{58}H_{115}Ce_3O_{11}$ | $C_{54}H_{87}CeO_9$ |
| Formula weight | 2343.32 | 1437.82 | 1408.92 | 1020.36 |
| Temp. [K] | 168(2) | 168(2) | 178(2) | 168(2) |
| Space group | tetragonal | monoclinic | monoclinic | rhombohedral |
| | *P*-42(1)c | *P*21/*c* | *P*2(1) | *R*-3 |
| *a* [Å] | 20.5590(18) | 18.673(12) | 14.1032(17) | 14.663(2) |
| *b* [Å] | 20.5590(18) | 11.382(7) | 18.952(2) | 14.663(2) |
| *c* [Å] | 11.908(2) | 29.308(18) | 14.5646(17) | 14.663(2) |
| *α* [°] | | | | 68.220(3) |
| *β* [°] | | 91.335(15) | 115.902(2) | 68.220(3) |
| *γ* [°] | | | | 68.220(3) |
| *V* [Å$^3$] | 5033.1(11) | 6227(7) | 3501.7(7) | 2617.3(6) |
| *Z* | 2 | 4 | 2 | 2 |
| $D_{calcd}$ [Mg/m$^3$] | 1.060 | 1.534 | 1.336 | 1.295 |
| $\mu$ (Mo-$K_\alpha$) [mm$^{-1}$] | 1.838 | 2.917 | 1.965 | 0.922 |
| $R_1$[a] (%) (all data) | 7.78 (22.60) | 8.55 (16.70) | 7.23 (11.87) | 4.23 (9.60) |
| $wR_2$[b] (%) (all data) | 12.30 (25.05) | 17.00 (19.94) | 11.09 (13.25) | 5.90 (9.83) |

[a] $R_1 = \Sigma||F_o|-|F_c||/\Sigma|F_o| \times 100$. [b] $wR_2 = [\Sigma w(F_o^2-F_c^2)^2/\Sigma(w|F_o|^2)^2]^{1/2} \times 100$.

Table 2. Data collection parameters for **4**–**10**.

| Compound | **4(·2THF)** | **4a(·2tol)** | **5(·tol)** | **6(·2THF)** |
|---|---|---|---|---|
| Empirical formula | $C_{72}H_{100}Ce_2O_{12}$ | $C_{82}H_{90}Ce_2N_4O_6$ | $C_{55}H_{83}CeO_6$ | $C_{70}H_{71}CeO_7$ |
| Formula weight | 1439.78 | 1507.82 | 980.33 | 1164.45 |
| Temp. [K] | 168(2) | 178(2) | 178(2) | 203(2) |
| Space group | monoclinic | monoclinic | monoclinic | monoclinic |
| | *P*21/*c* | *P*21/*n* | *P*21/*n* | *P*2(1) |
| *a* [Å] | 12.748(2) | 14.600(3) | 11.1537(16) | 10.220(2) |
| *b* [Å] | 18.883(3) | 19.504(4) | 35.671(5) | 21.968(5) |
| *c* [Å] | 15.343(3) | 14.690(3) | 13.4253(19) | 13.461(3) |
| *α* [°] | | | | |
| *β* [°] | 112.723(3) | 118.254(2) | 96.293(3) | 101.110(4) |
| *γ* [°] | | | | |
| *V* [Å$^3$] | 3406.6(11) | 3684.7(11) | 5309.2(13) | 2965.4(11) |
| *Z* | 2 | 2 | 4 | 2 |
| $D_{calcd}$ [Mg/m$^3$] | 1.404 | 1.359 | 1.226 | 1.143 |
| $\mu$ (Mo-$K_\alpha$) [mm$^{-1}$] | 1.379 | 1.274 | 0.903 | 0.810 |
| $R_1$[a] (%) (all data) | 3.40 (8.51) | 2.74 (6.75) | 7.49 (14.48) | 4.51 (8.54) |
| $wR_2$[b] (%) (all data) | 4.07 (8.90) | 3.15 (6.97) | 13.89 (17.16) | 5.51 (8.96) |
| Compound | **7(·py)** | **8** | **9** | **10(·2py)** |
| Empirical formula | $C_{65}H_{87}Ce_2N_5O_{10}$ | $C_{52}H_{66}Ce_2N_4O_{10}$ | $C_{56}H_{74}Ce_2N_4O_{10}$ | $C_{70}H_{92}Ce_2N_6O_{10}$ |
| Formula weight | 1391.36 | 1187.33 | 1243.43 | 1457.74 |
| Temp. [K] | 203(2) | 168(2) | 178(2) | 168(2) |
| Space group | monoclinic | monoclinic | triclinic | monoclinic |
| | *P*21/*n* | *C*2/*c* | *P*$\bar{1}$ | *P*21/*c* |
| *a* [Å] | 11.660(3) | 20.9692(13) | 11.8503(16) | 9.883(3) |
| *b* [Å] | 15.714(5) | 13.4977(13) | 11.9179(16) | 20.157(7) |
| *c* [Å] | 19.113(6) | 20.1132(14) | 12.9071(17) | 18.208(6) |
| *α* [°] | | | 86.896(2) | |
| *β* [°] | 99.253(5) | 107.972(2) | 65.609(2) | 103.471(7) |
| *γ* [°] | | | 65.482(2) | |
| *V* [Å$^3$] | 3456.5(17) | 5415.0(7) | 1495.3(3) | 3528(2) |
| *Z* | 2 | 4 | 1 | 2 |
| $D_{calcd}$ [Mg/m$^3$] | 1.337 | 1.456 | 1.381 | 1.372 |
| $\mu$ (Mo-$K_\alpha$) [mm$^{-1}$] | 1.358 | 1.717 | 1.558 | 1.333 |
| $R_1$[a] (%) (all data) | 8.96 (22.76) | 3.82 (10.01) | 4.38 (8.37) | 7.76 (12.19) |
| $wR_2$[b] (%) (all data) | 9.80 (23.07) | 4.34 (10.30) | 5.63 (8.81) | 13.50 (13.95) |

[a] $R_1 = \Sigma \; | \; |F_o|-|F_c| \; | / \Sigma \; |F_o| \times 100$. [b] $wR_2 = [\Sigma \; w \; (F_o^2-F_c^2)^2/\Sigma \; (w \; |F_o|^2)^2]^{1/2} \times 100$.

along with a number of the C, O, and N atoms when present. Subsequent Fourier synthesis yielded the remaining atom positions. The hydrogen atoms were fixed in positions of ideal geometry and refined within the XSHELL software. These idealized hydrogen atoms had their isotropic temperature factors fixed at 1.2 or 1.5 times the equivalent isotropic *U* of the C atoms to which they were bonded. The final refinement of each compound included anisotropic thermal parameters on all non-hydrogen atoms. Final crystal solutions that contain alkoxides are well known to possess ligand positional disorder issues.

 © 2006 Wiley-VCH Verlag GmbH & Co. KGaA, Weinheim 

CCDC-614454 to -614465 contain the supplementary crystallographic data for this paper. These data can be obtained free of charge from The Cambridge Crystallographic Data Centre via www.ccdc.cam.ac.uk/data_request/cif. Any variations from standard structural solution associated with the representative compounds are discussed below. All CIF files were checked for errors using the free on-line Checkcif service provided by the International Union of Crystallography (available on the Web at http://checkcif.iucr.org/).

## Acknowledgments

For support of this research, the authors would like to thank the Office of Basic Energy Sciences of the Department of Energy and the United States Department of Energy. Sandia is a multiprogram laboratory operated by Sandia Corporation, a Lockheed Martin Company, for the United States Department of Energy under contract DE-AC04-94AL85000.

[1] T. J. Boyle, R. P. Tyner, T. M. Alam, B. L. Scott, J. W. Ziller, B. G. J. Potter, *J. Am. Chem. Soc.* **1999**, *121*, 12104.
[2] T. J. Boyle, L. A. Ottley, M. A. Rodriguez, *Polyhedron* **2005**, *24*, 1727.
[3] S. N. Jacobsen, L. D. Madsen, U. Kelmersson, *J. Mater. Res.* **1999**, *14*, 2385.
[4] M. A. Arranz, B. Holzapfel, N. Reger, J. Eickemeyer, L. Schultz, *Physica C* **2002**, *266*, 109.
[5] C. S. Oh, C. I. Kim, K. H. Kwon, *J. Vac. Sci. Technol.* **2001**, *19*, 1068.
[6] R. Reisfeld, M. Zayat, H. Minti, A. Zastrow, *Sol. Energy Mater. Sol. Cells* **1998**, *54*, 109.
[7] G. S. Qi, R. T. Yang, R. Chang, *Appl. Catal., B* **2004**, *51*, 93.
[8] K. Tomishige, M. Asadullah, K. Kunimori, *Catal. Today* **2004**, *89*, 389.
[9] C. H. Wang, S. S. Lin, *Appl Catal., A* **2004**, *268*, 227.
[10] N. Kakuta, H. Ohkita, T. Mizushima, *J. Rare Earths* **2004**, *22*, 1.
[11] X. M. Qi, M. Flytzani-Stephanopoulos, *Ind. Eng. Chem. Res.* **2004**, *43*, 3055.
[12] J. Soler, T. Gonzalez, M. J. Escudero, T. Rodrigo, L. Daza, *J. Power Sources* **2002**, *106*, 189.
[13] C. Hatchwell, N. M. Sammes, I. W. M. Brown, *Solid State Ionics* **1999**, *126*, 201.
[14] A. Atkinson, *Solid State Ionics* **1997**, *95*, 249.
[15] R. Sabia, H. J. Stevens, *Machining Sci. Technol.* **2000**, *4*, 235.
[16] B. K. Tanner, T. P. A. Hase, H. Z. Wu, *Philos. Magn. Lett.* **2001**, *81*, 351.
[17] G. B. Deacon, T. C. Feng, C. M. Forsyth, A. Gitlits, D. C. R. Hockless, S. Qi, B. W. Skelton, A. H. White, *J. Chem. Soc., Dalton Trans.* **2000**, 961–966.
[18] W. J. Evans, T. J. Deming, J. M. Olofson, J. W. Ziller, *Inorg. Chem.* **1989**, *28*, 4027.
[19] P. S. Gradeff, K. Yunlu, T. J. Deming, J. M. Olofson, *Inorg. Chem.* **1990**, *29*, 420.
[20] Y. K. Gun'ko, S. D. Elliott, P. B. Hitchcock, M. F. Lappert, *J. Chem. Soc., Dalton Trans.* **2002**, 1852.
[21] L. G. Hubert-Pfalzgraf, N. El Khokh, J.-C. Daran, *Polyhedron* **1992**, *11*, 59.
[22] A. Sen, A. L. Rheingold, M. B. Allen, *Private Communication with Cambridge Data Base* **1996**.
[23] A. Sen, H. A. Stecher, A. L. Rheingold, *Inorg. Chem.* **1992**, *31*, 473.
[24] C. Sirio, L. G. Hubert-Pfalzgraf, C. Bois, *Polyhedron* **1997**, *16*, 1129.
[25] H. A. Stecher, A. Sen, A. L. Rheingold, *Inorg. Chem.* **1988**, *27*, 1130–1132.
[26] H. A. Stecher, A. Sen, A. L. Rheingold, *Inorg. Chem.* **1989**, *28*, 3280.
[27] P. Tolendao, F. Ribot, C. Sanchez, *Acta Crystallogr., Sect. C* **1990**, *46*, 1419.
[28] B. A. Vaarstrstra, J. C. Huffman, P. S. Gradeeff, L. G. Hubert-Pfalzgraf, J. C. Daran, S. Parraud, K. Yunlu, K. G. Caulton, *Inorg. Chem.* **1990**, *29*, 3126.
[29] K. Yunlu, P. S. Gradeff, N. Edelstein, W. Kot, G. Shalimoff, W. E. Steib, B. A. Vaartstra, K. G. Caulton, *Inorg. Chem.* **1991**, *30*, 2317–2321.
[30] L. G. Hubert-Pfalzgraf, V. Abada, J. Vaissermann, *Polyhedron* **1999**, *8*, 3497.
[31] L. G. Hubert-Pfalzgraf, C. Sirio, C. Bois, *Polyhedron* **1998**, *17*, 821.
[32] T. J. Boyle, S. D. Bunge, P. G. Clem, J. Richardson, J. T. Dawley, L. A. M. Ottley, M. A. Rodriguez, B. A. Tuttle, G. Avilucea, R. G. Tissot, *Inorg. Chem.* **2005**, *44*, 1588.
[33] T. J. Boyle, L. A. M. Ottley, L. J. Tribby, S. D. Bunge, C. J. Gordon, *Chem. Mater.* **2005**, (*in preparation*).
[34] D. M. Barnhart, D. L. Clark, J. C. Gordon, J. C. Huffman, J. G. Watkin, B. D. Zwick, *J. Am. Chem. Soc.* **1993**, *115*, 8461.
[35] D. C. Bradley, R. C. Mehrotra, D. P. Gaur, *Metal Alkoxides*, Academic Press, New York, **1978**.
[36] D. C. Bradley, R. C. Mehrotra, I. P. Rothwell and A. Singh, *Alkoxo and Aryloxo Derivatives of Metals*, Academic Press, New York, **2001**, p. 704.
[37] T. J. Boyle, S. D. Bunge, P. G. Clem, J. Richardson, J. T. Dawley, L. A. M. Ottley, M. A. Rodriguez, B. A. Tuttle, G. R. Avilucea, R. G. Tissot, *Inorg. Chem.* **2005**, *44*, 1588.
[38] W. J. Evans, R. E. Golden, J. W. Ziller, *Inorg. Chem.* **1993**, *32*, 3041.
[39] W. J. Evans, M. A. Ansari, J. W. Ziller, *Polyhedron* **1997**, *16*, 3429.
[40] The database of The Cambridge Crystallographic Data Centre, 12 Union Road, Cambridge CB2 1EZ, United Kingdom, www.ccdc.cam.ac.uk, was searched using ConQuest v 5.27 (Jan. **2006**).
[41] W. J. Evans, J. M. Olofson, J. W. Ziller, *Inorg. Chem.* **1989**, *28*, 4308–4309.
[42] G. B. Deacon, F. Tiecheng, B. W. Skelton, A. H. White, *Aust. J. Chem.* **1995**, *48*, 741.
[43] Z. Xie, K. Chui, Q. Yang, T. C. W. Mak, J. Sun, *Organometallics* **1998**, *17*, 3937.
[44] G. B. Deacon, B. M. Gatehouse, Q. Shen, G. N. Ward, E. R. T. Tiekink, *Polyhedron* **1993**, *12*, 1289.
[45] G. B. Deacon, S. Nickel, P. Mackinnon, E. R. T. Tiekink, *Aust. J. Chem.* **1990**, *43*, 1245.
[46] G. B. Deacon, F. Tiecheng, S. Nickel, M. I. Ogden, A. H. White, *Aust. J. Chem.* **1992**, *45*, 671.
[47] D. M. Barnhart, D. L. Clark, J. C. Gordon, J. C. Huffman, R. L. Vincent-Hollis, J. G. Watkin, B. D. Zwick, *Inorg. Chem.* **1994**, *33*, 3487.
[48] S. Suh, J. Guan, L. A. Miinea, J.-S. M. Lehn, *Chem. Mater.* **2004**, *16*, 1667.
[49] D. C. Bradley, H. Chudzynska, M. B. Hursthouse, M. Motevalli, *Polyhedron* **1991**, *10*, 1049–1059.
[50] T. J. Boyle, N. L. Andrews, T. A. Alam, M. A. Rodriguez, J. M. Santana, B. L. Scott, *Polyhedron* **2002**, *21*, 2333.
[51] T. J. Boyle, T. A. Alam, C. J. Tafoya, B. L. Scott, *Inorg. Chem.* **1998**, *37*, 5588.
[52] W. Brzysk, Z. Rzaczynska, E. Swita, R. Mrozek, T. Glowiak, *J. Coord. Chem.* **1997**, *41*, 1.
[53] U. Baish, D. B. Dell'Amico, F. Calderazzo, L. Labella, *J. Mol. Catal. A* **2003**, *204*, 259.
[54] P. C. Junk, C. J. Kepert, W. M. Lu, B. W. Skelton, A. H. White, *Aust. J. Chem.* **1999**, *52*, 437–457.
[55] Z. Long-Guan, Y. Qing-Sen, X. Xue-Peng, *Jiegou Huaxue (Chin.) Chinese J. Struct. Chem.* **1998**, *17*, 281.
[56] C.-Y. Xian, L.-G. Zhu, Q.-S. Yu, *Wuji Huaxue Xuebao (Chin.)* **1999**, *15*, 813.

 © 2006 Wiley-VCH Verlag GmbH & Co. KGaA, Weinheim 

[57] S.-H. Zhao, C.-Y. Xian, *Wuji Huaxue Xuebao (Chin.)* **2002**, *18*, 639.
[58] A. Panagiotopoulos, T. F. Zafiropopulos, S. P. Perlepes, E. Bakalbassis, I. Masson-Ramade, O. Kahn, A. Terzis, C. P. Raptopoulou, *Inorg. Chem.* **1995**, *34*, 4918.
[59] L.-Z. Cai, W.-T. Chen, M.-S. Wang, G.-G. Guo, J.-S. Huang, *Inorg. Chem. Commun.* **2004**, *7*, 611.
[60] B. Wu, Y.-S. Guo, *Acta Crystallogr., Sect E. Struct. Rep. Onlin Sect. E* **2004**, *60*, m1261.
[61] A.-Y. Fu, S.-Z. Fu, T. Yu, *Acta Crystallogr., Sect E. Struct. Rep. Onlin Sect. E* **2005**, *61*, m223.
[62] L.-L. Wen, B.-G. Zhang, Z.-H. Peng, *Wuji Huaxue Xuebao (Chin.)* **2004**, *20*, 1228.
[63] F. A. Cotton and G. Wilkinson, *Advanced Inorganic Chemistry, Fifth Edition*, John Wiley & Sons, New York, **1988**, p.
[64] T. J. Boyle, L. A. M. Ottley, M. A. Rodriguez, *Polyhedron* **2005**, *24*, 1727.
[65] T. J. Boyle, N. L. Andrews, T. M. Alam, M. A. Rodriguez, J. M. Santana, B. L. Scott, *Polyhedron* **2002**, *21*, 2333.
[66] T. J. Boyle, N. L. Andrews, M. A. Rodriguez, C. Campana, T. Yiu, *Inorg. Chem.* **2003**, *42*, 5357.
[67] T. J. Boyle, D. M. Pedrotty, T. M. Alam, S. C. Vick, M. A. Rodriguez, *Inorg. Chem.* **2000**, *39*, 5133–5146.
[68] G. B. Deacon, R. J. Phillips, *Coord. Chem. Rev.* **1980**, *33*, 227–250.
[69] D. D. Perrin and W. L. F. Armarego, *Purification of Laboratory Chemicals*, Pergamon Press, New York, **1988**, p.
[70] The listed versions of SAINT, SMART, XSHELL, XPOW in SHELXTL, and SADABS software from Bruker Analytical X-ray Systems Inc., 6300 Enterprise Lane, Madison, WI 53719 were used in the analysis.

Received: June 29, 2006
Published Online: September 20, 2006

 © 2006 Wiley-VCH Verlag GmbH & Co. KGaA, Weinheim 

DOI: 10.1002/ejic.200600635

# Solvent-Induced Pore-Size Adjustment in the Metal-Organic Framework $[Mg_3(ndc)_3(dmf)_4]$ (ndc = naphthalenedicarboxylate)

**Irena Senkovska[a] and Stefan Kaskel*[a]**

**Keywords:** Metal-organic frameworks / Magnesium / Carboxylate ligands / Adsorption

Two new compounds containing magnesium and the bidentate ligand 2,6-naphthalenedicarboxylate (ndc), namely $[Mg(dmf)_2(H_2O)_4]$·ndc (**1**) (dmf = *N*,*N*-dimethylformamide) and $[Mg_3(ndc)_3(dmf)_4]$ (TUDMOF-2) (**2**), have been obtained from $Mg(NO_3)_2$·$6H_2O$ and the pure acid using a solvothermal route. According to single-crystal X-ray studies both compounds are monoclinic. Complex **1** crystallizes in the space group $P2_1/c$ [$a$ = 12.317(3), $b$ = 12.582(2), $c$ = 15.353(3) Å, $\beta$ = 110.96(3)°]. The compound consists of an isolated tetraaquabis-*N*,*N*-dimethylformamide cation and the deprotonated ligand with hydrogen bonds linking the cations and anions. The metal-organic framework **2** crystallizes in the space group $C2/c$ [$a$ = 13.451(3), $b$ = 18.043(4), $c$ = 20.937(5) Å, $\beta$ = 99.79(3)°] with trinuclear magnesium clusters connected to six dicarboxylate ligands that link the clusters into a three-dimensional network. In contrast to $[Mg_3(ndc)_3(def)_4]$ (def = *N*,*N*-diethylformamide; **3**), the dmf molecules coordinated to magnesium in TUDMOF-2 (**2**) not only cause a distortion of the network but induce accessibility for the adsorption of nitrogen. TUDMOF-2 has a Langmuir surface area of 520 $m^2 g^{-1}$ and a hydrogen adsorption capacity of 0.78 wt.-% at 77 K and 760 Torr.
(© Wiley-VCH Verlag GmbH & Co. KGaA, 69451 Weinheim, Germany, 2006)

## Introduction

Metal-organic frameworks (MOFs) are a new family of porous crystalline inorganic–organic hybrid materials that are attracting increasing interest due to their rich structural chemistry and potential applications in gas storage, separation processes, and catalysis.[1] The modular concept allows for a rational design of porous solids in which a multinuclear complex (cluster) is used as a connecting node and an organic bi- or trifunctional linker to link the nodes into a three-dimensional network of predefined topology. An often observed structural motif in transition metal MOFs is the paddle-wheel unit acting as a four-connecting node.[2] Such copper-, zinc-, or molybdenum-containing networks may be useful for hydrogen storage applications.[3] The most prominent 6-connector is the $Zn_4O^{6+}$ cluster in MOF-5 and the IRMOF family.[4]

Although transition-metal-containing MOFs have been widely investigated, the coordination chemistry of alkaline earth metals has until now remained a largely underdeveloped area, and reports on magnesium coordination polymers are very rare.[5] Magnesium carboxylates seldom form coordination polymers and extended three-dimensional structures because of the high affinity of $Mg^{2+}$ for oxygen donor atoms of polar solvents. Additionally, the coordination chemistry of magnesium is less flexible than that of zinc, and octahedral complexes are often found.[6] In the case of polyfunctional ligands used for the synthesis of Mg-based MOFs, competitive coordination by water or other solvent ligands may result in low-dimensional network topologies or isolated complexes, and thus porosity cannot be expected. However, the first magnesium-based metal-organic framework with permanent porosity and accessibility for very small molecules ($H_2$, $O_2$) was recently reported by Dinća and Long.[7] $[Mg_3(ndc)_3(def)_4]$ (**3**) (def = *N*,*N*-diethylformamide) was found to adsorb $O_2$ and $H_2$ preferentially, although the pores were too small to allow the access of $N_2$.

Below we describe the structure of two new magnesium carboxylates, namely $[Mg(dmf)_2(H_2O)_2]$·ndc (**1**) and $[Mg_3(ndc)_3(dmf)_4]$ (TUDMOF-2, **2**). TUDMOF-2 (Technical University Dresden Metal Organic Framework no. 2) has the same network topology as $[Mg_3(ndc)_3(def)_4]$ but the smaller solvent molecule induces significant structural changes, resulting in a larger pore diameter and permanent porosity with pores accessible for $N_2$ molecules.

## Results and Discussion

### Synthesis and Structural Characterization of 1 and 2

Solvothermal reaction of $Mg(NO_3)_2$·$6H_2O$ and ndc in dmf at 110 °C results in the formation of yellow crystals of **2**. White crystals of **1** were obtained from the same reaction carried out in aqueous dmf (5 vol-% $H_2O$). In spite of their

[a] Department of Inorganic Chemistry, Technical University Dresden
Mommsenstr. 6, 01069 Dresden, Germany
Fax: +49-351-4633-7287
E-mail: Stefan.Kaskel@chemie.tu-dresden.de

 InterScience © 2006 Wiley-VCH Verlag GmbH & Co. KGaA, Weinheim 

very similar synthetic conditions, complexes **1** and **2** have completely different architectures.

Single-crystal X-ray diffraction was used to determine the structure of compound **1**. Instead of carboxylate ligands coordinating to $Mg^{2+}$, the compound consists of isolated $[Mg(H_2O)_4(dmf)_2]^{2+}$ cations and $ndc^{2-}$ anions (Figure 1). The $Mg^{2+}$ ion has a sixfold coordination and is surrounded by four water molecules and two oxygen atoms of dmf molecules, resulting in a somewhat distorted octahedral geometry. Figure 2 shows a packing diagram of **1**. Hydrogen bonds link the water molecules to the carboxylate O atoms (O···O = 2.68–2.75 Å) to form a three-dimensional hydrogen-bonded network.

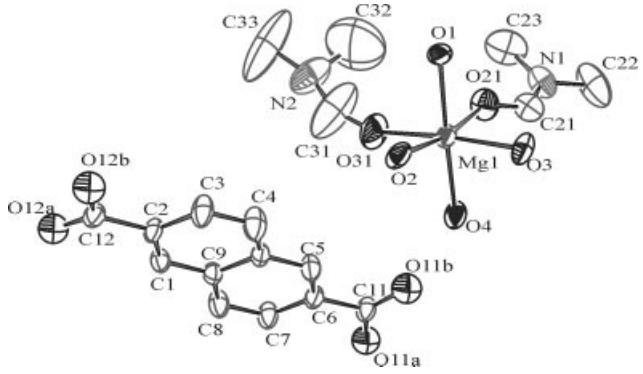


Figure 1. The asymmetric unit and labelling scheme for compound **1**. Displacement ellipsoids are drawn at the 50% probability level. H atoms have been omitted.

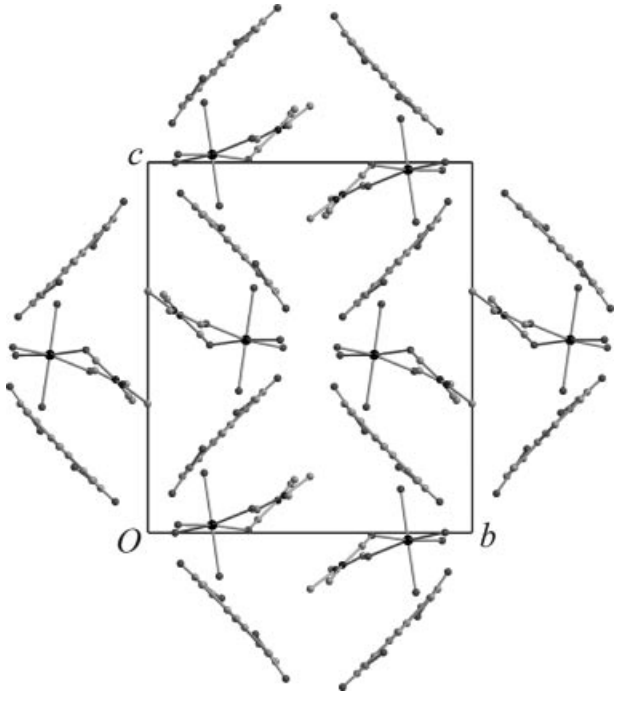


Figure 2. The crystal packing of **1** viewed along the crystallographic *a* axis.

Complex **2** crystallizes in the monoclinic space group *C*2/*c* and is a structural analogue of $[Mg_3(ndc)_3(def)_4]$ (**3**) reported by Dinća and Long.[7] However, the channels in **2** are filled with dmf instead of def, which results in a significantly reduced lattice constant *a* of 13.451 Å compared to that of **3** (*a* = 15.045 Å). All other lattice parameters are very close to those reported for **3** with differences of below 0.1 Å for *b* and *c* and below 2° for the monoclinic angle.

The structure of **2** contains two independent magnesium centers (Figure 3a). Mg1 is positioned on a twofold rotation axis and Mg2 is located at a general position (*8f*). The $ndc^{2-}$ anions are positioned on an inversion center located in the middle of the central C–C bond in the naphthalene system. Two distinct carboxylate coordination modes are observed. The C16 and C26 carboxylate groups form didentate bridges, whereas the C6 carboxylate group chelates to Mg2, with each of the O atoms also bound to Mg1. This tridentate bridging mode is postulated to be an important intermediate in "carboxylate-shift" chemistry[8] and is a key factor for the formation of the trinuclear metal cluster. Consequently, Mg1 is connected to two adjacent Mg2 centers to form a linear $[Mg_3(\mu_3\text{-}O)_2(\mu_2\text{-}O)_4]$ unit with a nonbonding Mg–Mg distance of 3.582(6) Å (Figure 3a). These trinuclear magnesium clusters represent a 6-connecting secondary building unit (Figure 3b).[9] They are linked by naphthalenedicarboxylate bridges to form a three-dimensional network (Figure 3c and Figure 4).

A trinuclear SBU has been reported earlier as a discrete molecular cluster.[10] Furthermore, this structural motif has been found in networks such as $Zn_3(bdc)_3{\cdot}6CH_3OH$ (bdc = benzenedicarboxylate) (MOF-3),[11] $[Cd_3(bdc)_3(L)_2(H_2O)_2]$ (L = 1,4-bis(1,2,4-triazol-1-yl)butane),[12] $[CoT(p\text{-}CO_2)PPCo_{1.5}(C_5H_5N)_3(H_2O)]{\cdot}11C_5H_5N$ (PIZA-1),[13] and $[Co_3(bpdc)_3(bpy)]{\cdot}4dmf{\cdot}H_2O$ (bpdc = biphenyldicarboxylate, bpy = 4,4′-bipyridine) (IRPM-1),[14] each of which contains $M^{II}_3$ clusters linked together to form a rigid framework with accessible internal channels and/or cages and permanent porosity.

In contrast to the compressed central $MgO_6$ octahedron of Mg1 in **3**, the magnesium–oxygen octahedron in the trinuclear cluster of **2** is elongated, with axial Mg1–O61 bond lengths of 2.109(3) Å and equatorial bond lengths of 2.077(3)–2.084(3) Å. The three $Mg^{2+}$ ions in the trinuclear motif form an almost linear chain. The Mg2–Mg1–Mg2$^i$ (symmetry code: *i*: –*x*, *y*, 1/2 – *z*) angle in the $Mg_3$ units of **2** is 174.36(7)° and is thus somewhat smaller than the corresponding angle in **3** [176.14(1)°].

The Mg1–Mg2 distance in **2**, however, is longer than in **3** [3.530(2) Å] because of the longer Mg–O bonds in the former. Thus, the structural changes within the $Mg_3$ cluster are not responsible for the compressed *a* axis, whereas the orientation of the linker in the 6-connecting SBU allows for compression or elongation along the *a* axis, resulting in a high flexibility and breathing of the $Mg_3(ndc)_3$ network.

The reason for the contraction along the *a* axis observed in **2** as compared to **3** is the predefined orientation of solvent molecules upon coordination to Mg2. The ethyl groups of the def molecules in **3** are oriented along the *a* axis and thus occupy more space in this direction. The orientation is similar for dmf in **2**, thus allowing for a compression along the *a* axis. The dmf molecules in **2** can be re-

 © 2006 Wiley-VCH Verlag GmbH & Co. KGaA, Weinheim 

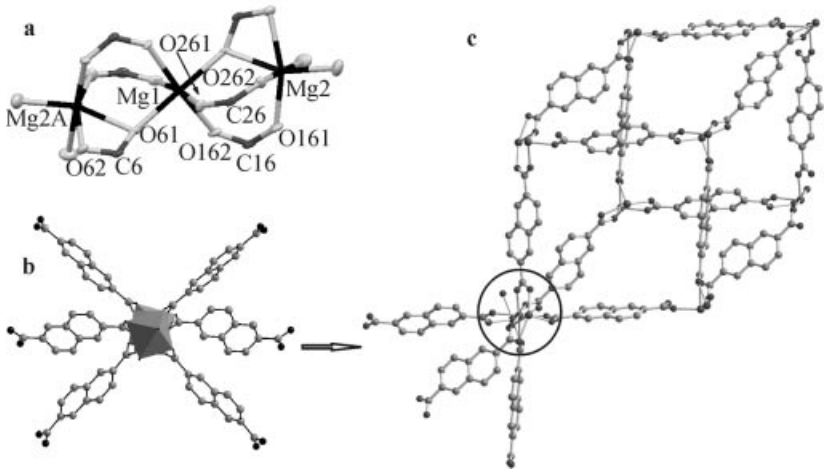


Figure 3. a) Trinuclear Mg-carboxylate cluster; b) representation of the inorganic 6-connecting SBU; c) the three-dimensional network in **2**.

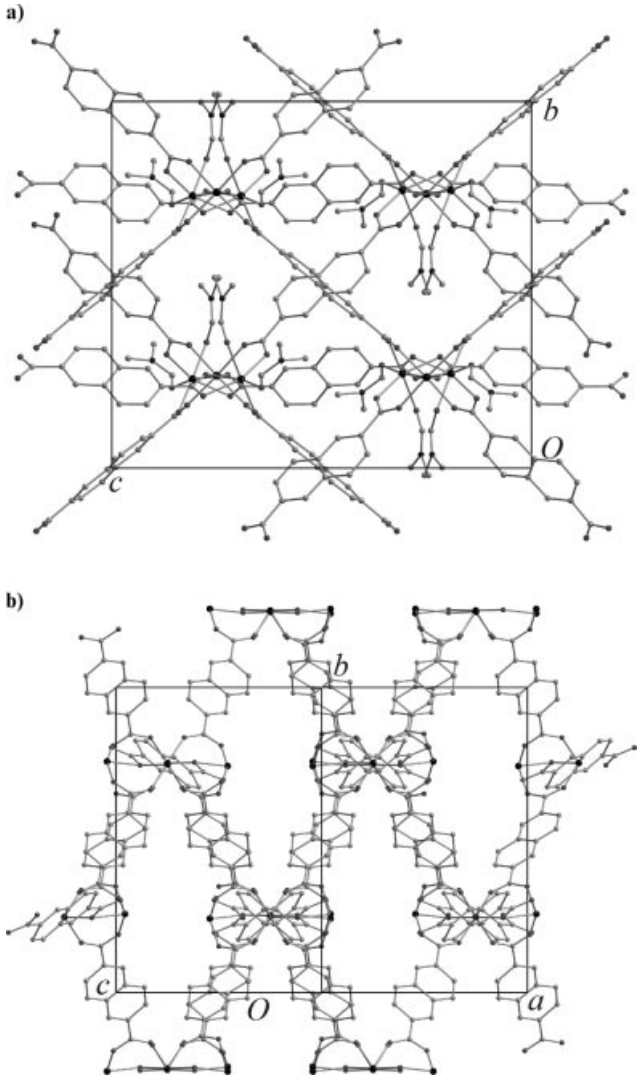


Figure 4. Extended structure of **2** viewed along: a) the crystallographic *a* axis; b) along [101] (dmf molecules have been omitted).

moved from the voids to give a porous network having open magnesium sites. This open framework has channels along the [100] and [101] directions (Figure 4). The minor differences in structure cause significant changes in the gas adsorption properties of **2** and **3**.

### Thermal Stability

Thermogravimetric analysis (TGA) shows the desolvation of compound **1** in one step at a temperature above 90 °C. The weight loss of 41% for **1** from 90 to 170 °C corresponds to the loss of four $H_2O$ and two dmf molecules from the structure (calcd.: 42.13%). The second step in the range from 500 to 540 °C indicates the decomposition of the ligand.

The framework of **2** has a high thermal stability up to 500 °C. For compound **2**, a total weight loss of 29% is observed between 120 and 400 °C, corresponding to four dmf molecules per $Mg_3$ unit. This weight loss is consistent with the elemental analysis and the empirical formula deduced from the single-crystal X-ray analysis. The desolvated framework is hereafter denoted as **2a**. The X-ray powder diffraction pattern of **2** changes after removal of the guest molecules as compared to the product obtained from the solvothermal synthesis. The reflections of **2a** show an apparent shift to the lower angle region, and several of the reflections disappear (Figure 5b), thereby indicating a slight structural deformation of the framework upon desolvation. After treatment of **2a** with dmf, the virgin framework of **2** regenerates (Figure 5a), thus indicating a reversible transformation (Scheme 1).

However, some additional peaks appear too. Treating **2a** with def molecules should afford **3** (Figure 5c) and, due to the larger size of the def molecules, the latter is expected to expand the lattice constant *a* as discussed above. This host flexibility can improve the efficiency of the adsorption by the aid of host structural transformation suited for the guest molecules.[15] The XRD pattern of **2a** shows diffraction peaks similar to those of desolvated **3**. The evacuated framework of **3** is hereafter indicated as **3a**. However, a detailed comparison of the XRD patterns reveals a significant

 © 2006 Wiley-VCH Verlag GmbH & Co. KGaA, Weinheim 

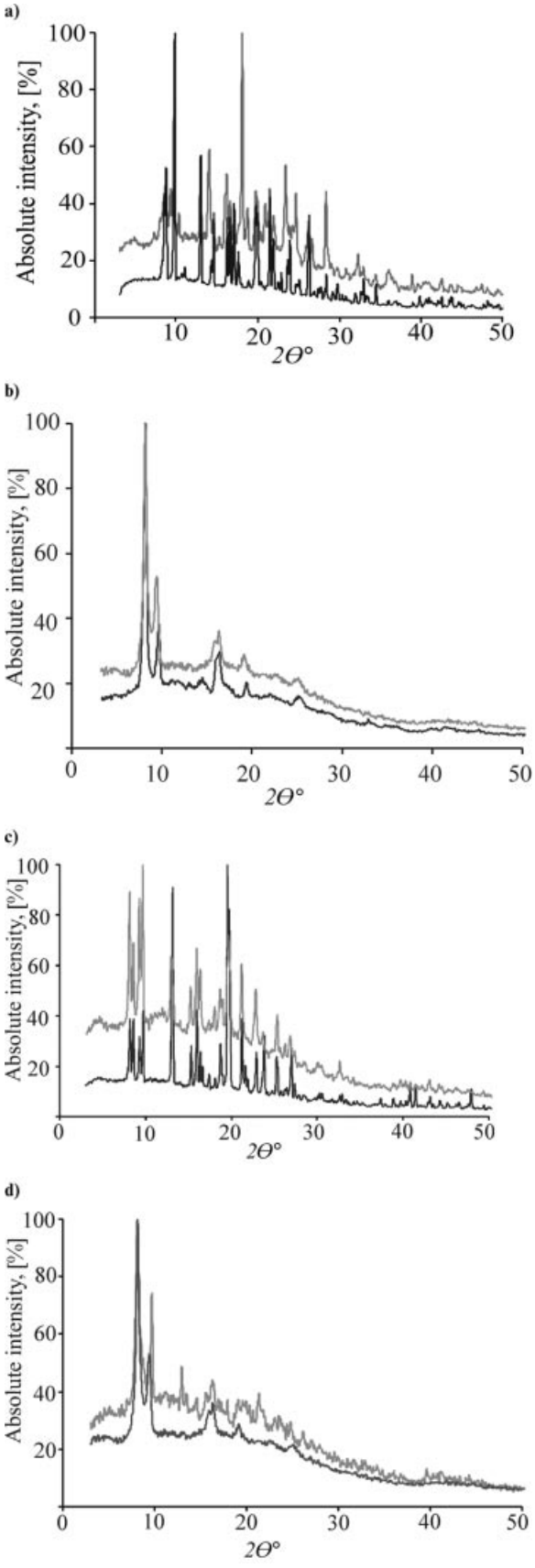


Figure 5. X-ray powder diffraction patterns: a) for **2** as synthesized (black) and **2a** resolvated with dmf (grey); b) for **2a** (black) and **3a** (grey); c) for **3** as synthesized (black) and **2a** resolvated with def (grey); d) for **3a** (black) and **3a** resolvated with dmf (grey).

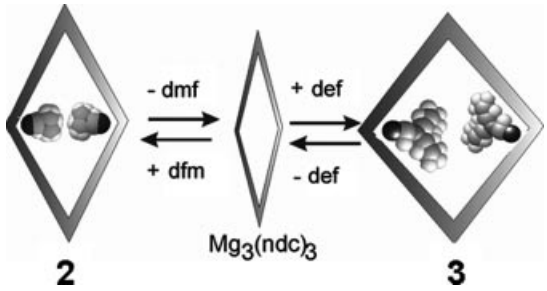


Scheme 1. The reversible structural transformation of **2** and **2a**.

shift for selected peaks (Figure 5b). Treating **2a** with def affords an XRD pattern identical to that of the as-synthesized **3** (Figure 5c). On the other hand, treating **3a** with dmf does not allow us to convert the framework into compound **2** (Figure 5d). Thus, **2** can be converted into **3** via **2a** but not vice versa. The porous materials **2a** and **3a** obtained from the different networks show small structural differences according to the X-ray powder patterns. This resembles a sort of memory effect induced by the different solvents and causes different sorption properties for the two compounds.

## Sorption Properties

Compound **1** is essentially nonporous and has only a low $N_2$ adsorption capacity and a type II adsorption isotherm (Figure 6). Compound **2** shows a type I nitrogen adsorption isotherm at 77 K typical of a microporous material (Figure 6). The sorption isotherm was fitted to a Langmuir equation, resulting in a specific surface area of 520 $m^2 g^{-1}$ for the activated framework.

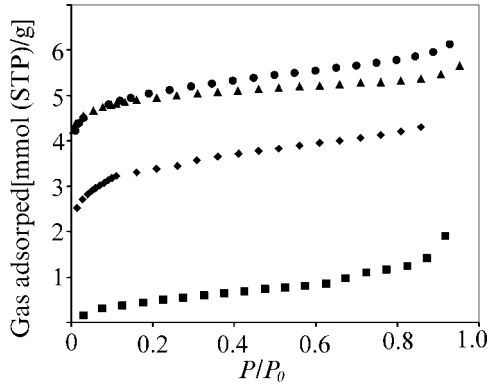


Figure 6. The $N_2$ (triangle), $O_2$ (circle), and $CH_4$ (diamond) adsorption isotherms of $[Mg_3(ndc)_3]$ (**2a**) and the $N_2$ (square) adsorption isotherm of $[Mg(dmf)_2(H_2O)_2]$·ndc (**1**) at 77 K.

Significant differences between $[Mg_3(ndc)_3(dmf)_4]$ (**2**) and $[Mg_3(ndc)_3(def)_4]$ (**3**) are also observed in the gas adsorption properties. The as-synthesized sample of **2** was activated by drying under vacuum at 468 K for 72 h. The mass loss of 28.8% was close to the 29.0% estimated for complete removal of four dmf molecules.

 © 2006 Wiley-VCH Verlag GmbH & Co. KGaA, Weinheim 

Whereas for **3** essentially no $N_2$ adsorption was detected, for TUDMOF-2 (**2**) the adsorbed amount of nitrogen (5.0 mmol $g^{-1}$ at 0.9 $P/P_0$) is surprisingly large. TUDMOF-2 also shows a type I isotherm for the adsorption of $CH_4$ (kinetic diameter of 3.8 Å) (Figure 6). However, only oxygen and hydrogen adsorption was observed for **3**, thus indicating a limited accessibility only for smaller gas molecules due to the small pore size. The limited accessibility of nitrogen in **3** could indicate incomplete removal of def molecules in the activation, which would cause pore blocking for larger molecules such as $N_2$. The latter is reasonable due to the higher boiling point and more effective encapsulation of def as a result of the larger size of def relative to dmf. Thus, even though a compression of the *a* axis is detected for **2**, the more effective removal of dmf is responsible for a larger pore size in the desolvated form and larger specific pore volume. Another reason for the differences in porosity are the structural differences of **3** and **2**, which result in a memory effect and cause structural differences also in the desolvated forms of **3** and **2**. An indication for the latter is the experimentally observed difference in the XRD powder patterns of the activated forms.

The hydrogen adsorption isotherms measured at 77 K are shown in Figure 7. The hydrogen storage capacity is 3.9 mmol $g^{-1}$ (0.78 wt.-%) at 760 Torr and is thus slightly higher than for $[Mg_3(ndc)_3(def)_4]$ but lower than for other MOFs.[3]

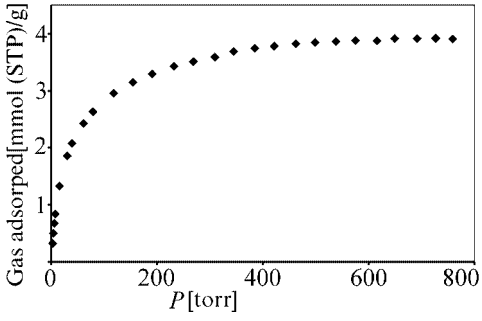


Figure 7. $H_2$ adsorption isotherm of $[Mg_3(ndc)_3]$ (**2a**) at 77 K.

In summary, we have presented two new magnesium carboxylates. Whereas in the presence of water molecules preferred coordination of $H_2O$ and dmf hinders the formation of extended three-dimensional networks, a porous network structure is obtained in the absence of water. The resulting $[Mg_3(ndc)_3(dmf)_4]$ network is microporous, and the pores are accessible for $H_2$, $O_2$, $N_2$, and $CH_4$. Small structural changes induced by coordinating dmf molecules play a key role in adjusting the pore size of the network and are responsible for the size exclusion of nitrogen.

Due to the low weight of magnesium, the design of Mg-MOFs with higher specific surface areas is, in principle, feasible, although identification of suitable structural building units allowing for a high porosity remains a challenge.

## Experimental Section

**General:** All chemicals (Aldrich) were reagent grade and were used as received. Microanalyses (C, H, N) were performed with a Fison's EA1108 CHNS analyzer. IR spectra were recorded as KBr discs using an Excalibur FTS 3000 spectrometer in the range 480–4000 $cm^{-1}$. Powder X-ray diffraction (PXRD) data were collected on a Stoe STADI P powder diffractometer with Cu-$K_{\alpha1}$ radiation. Thermogravimetric analyses were carried out using a Netzsch STA 409 thermal analyzer. Physisorption isotherms were measured at 77 K using a Quantachrome Autosorb1C apparatus. Prior to the measurement, the samples were evacuated at 468 K for 72 h. High purity gases were used (nitrogen: 99.999%, hydrogen: 99.999%, oxygen 99.999%, methane 99.995%). To prevent condensation of $O_2$ and $CH_4$ at 77 K, the oxygen adsorption isotherm was recorded below 156 Torr and the adsorption isotherm of methane was recorded below 9.4 Torr. The specific surface areas and porosity parameters were derived from the $N_2$ adsorption data.

**$[Mg(dmf)_2(H_2O)_4]$·ndc (1):** $Mg(NO_3)_2·6H_2O$ (0.9 g, 3.5 mmol) was mixed with 2,6-naphthalenedicarboxylic acid (0.7 g, 3.24 mmol) in dmf (18 mL) and deionized water (1 mL). The solution was filled in a 40-mL Teflon liner, placed in an autoclave, heated to 373 K for 24 h, and then cooled to room temperature. Colorless crystals of **1** were isolated from the solution at room temperature after several days. Yield: 1.06 g (71%). $C_{18}H_{28}MgN_2O_{10}$ (456.73): calcd. C 47.34, H 6.18, N 6.13; found C 46.87, H 6.28, N 6.33. IR: $\nu_{C=O}$ = 1676 (s), 1659 (vs), 1606 (s), 1560 (s), 1495 (m), 1394 (s), 1358 (s) $cm^{-1}$.

**$[Mg_3(ndc)_3(dmf)_4]$ (2):** A mixture of $Mg(NO_3)_2·6H_2O$ (1.5 g, 5.85 mmol) and 2,6-naphthalenedicarboxylic acid (0.9 g, 4.16 mmol) in dmf (60 mL) was filled in a 250-mL Teflon liner, placed in an autoclave, heated to 383 K for 24 h, and then cooled to room temperature at a rate of 0.05 K $min^{-1}$. The resulting pale-yellow crystals were collected, washed with dmf, and dried under argon to give **2**. Yield: 0.9 g (64.2%). $C_{48}H_{46}Mg_3N_4O_{16}$ (1007.8): calcd. C 57.21, H 4.60, N 5.56; found C 56.77, H 4.36, N 5.81. IR: $\nu_{C=O}$ = 1680 (s), 1655 (s), 1621 (s), 1566 (s), 1497 (m), 1406 (vs), 1359 (m) $cm^{-1}$.

**X-ray Crystallography:** Single-crystal X-ray diffraction data for complexes **1** and **2** were recorded with a STOE IPDS I image plate diffractometer with Mo-$K_\alpha$ radiation. The structures were solved by direct methods with the help of SHELXS-97[16] and refined by full-matrix least-squares techniques using SHELXL-97.[17] Non-hydrogen atoms were refined with anisotropic temperature parameters, and the hydrogen atoms of the ligands and dmf molecules were refined as rigid groups. The hydrogen atoms of the water molecules of **1** were located from the difference Fourier maps. Further details of the structural analysis are summarized in Table 1.

Table 1. Summary of X-ray crystallographic data for compounds **1** and **2**.

| Compound | **1** | **2** |
|---|---|---|
| Formula | $C_{18}H_{28}O_{10}MgN_2$ | $C_{48}H_{46}O_{16}Mg_3N_4$ |
| Molar mass | 456.73 | 1007.82 |
| Space group | $P2_1/c$ | $C2/c$ |
| *a* [Å] | 12.317(3) | 13.451(3) |
| *b* [Å] | 12.582(2) | 18.043(4) |
| *c* [Å] | 15.353(3) | 20.937(5) |
| $\beta$ [°] | 110.96(3) | 99.79(3) |
| $V$ [$Å^3$] | 2221.9(9) | 5007(2) |
| $Z$, $D_{calcd.}$ [g $cm^{-3}$] | 4, 1.365 | 4, 1.334 |
| Reflns. collected/unique | 18500/3448 | 14280/2522 |
| Reflns. obsd. [$I > 2\sigma(I)$] | 1946 | 1973 |
| GOF on $F^2$ | 1.038 | 1.009 |
| $R1$, $wR_2$ (obsd.) | 0.0779, 0.1939 | 0.0558, 0.1489 |
| Max., min. peaks [e $Å^{-3}$] | 1.162 | 0.532 |

 © 2006 Wiley-VCH Verlag GmbH & Co. KGaA, Weinheim 

CCDC-607099 (**1**) and -607100 (**2**) contain the supplementary crystallographic data for this paper. These data can be obtained free of charge from the Cambridge Crystallographic Data Centre via www.ccdc.cam.ac.uk/data_request/cif.

## Acknowledgments

This work was supported by the German Ministry of Science and Education (BMBF: FK 03X0011B).

[1] For recent reviews regarding the development of MOFs see, for example: a) S. Kitagawa, R. Kitaura, S. Noro, *Angew. Chem.* **2004**, *116*, 2388; *Angew. Chem. Int. Ed.* **2004**, *43*, 2334; b) S. Kaskel, in *Handbook of Porous Solids*, Wiley-VCH, Weinheim **2002**, p. 1190; c) J. L. C. Rowsell, O. M. Yaghi, *Microporous Mesoporous Mater.* **2004**, *73*, 3; d) O. M. Yaghi, M. O'Keeffe, N. W. Ockwig, H. K. Chae, M. Eddaoudi, J. Kim, *Nature* **2003**, *423*, 705.

[2] a) S. S.-Y. Chui, S. M.-F. Lo, J. P. H. Charmant, A. G. Orpen, I. D. Williams, *Science* **1999**, *283*, 1148; b) K. Schlichte, T. Kratzke, S. Kaskel, *Microporous Mesoporous Mater.* **2004**, *73*, 81; c) H. Li, M. Eddaoudi, T. L. Groy, O. M. Yaghi, *J. Am. Chem. Soc.* **1998**, *120*, 8571; d) M. Kramer, U. Schwarz, S. Kaskel, *J. Mater. Chem.* **2006**, *16*, 2245.

[3] a) P. Krawiec, M. Kramer, M. Sabo, R. Kunschke, H. Fröde, S. Kaskel, *Adv. Eng. Mater.* **2006**, *8*, 293; b) B. Chen, N. W. Ockwig, A. R. Millward, D. S. Contreras, O. M. Yaghi, *Angew. Chem. Int. Ed.* **2005**, *44*, 4745; c) B. Panella, M. Hirscher, H. Puetter, U. Mueller, *Adv. Funct. Mater.* **2006**, *16*, 520.

[4] a) H. Li, M. Eddaoudi, M. O'Keeffe, O. M. Yaghi, *Nature* **1999**, *402*, 276; b) M. Eddaoudi, J. Kim, N. Rosi, D. Vodak, J. Wachter, M. O'Keeffe, O. M. Yaghi, *Science* **2002**, *295*, 469.

[5] J. L. C. Rowsell, O. M. Yaghi, *Angew. Chem.* **2005**, *117*, 4748; *Angew. Chem. Int. Ed.* **2005**, *44*, 4670.

[6] O. Carugo, K. Djinović, M. Rizzi, *J. Chem. Soc., Dalton Trans.* **1993**, 2127.

[7] M. Dinća, J. R. Long, *J. Am. Chem. Soc.* **2005**, *127*, 9376.

[8] R. L. Rardin, W. B. Tolman, S. J. Lippard, *New J. Chem.* **1991**, *15*, 417.

[9] M. Eddaoudi, D. B. Moler, H. Li, B. Chen, T. M. Reineke, M. O'Keeffe, O. M. Yaghi, *Acc. Chem. Res.* **2001**, *34*, 319.

[10] W. Clegg, I. R. Little, B. P. Straughan, *J. Chem. Soc., Chem. Commun.* **1985**, 73.

[11] H. Li, C. E. Davis, T. L. Groy, D. G. Kelley, O. M. Yaghi, *J. Am. Chem. Soc.* **1998**, *120*, 2186.

[12] X.-L. Wang, C. Qin, E.-B. Wang, Z.-M. Su, *Chem. Eur. J.* **2006**, *12*, 2680.

[13] M. E. Kosal, J.-H. Chou, S. R. Wilson, K. S. Suslick, *Nat. Mater.* **2002**, *1*, 118.

[14] L. Pan, H. Liu, X. Lei, X. Huang, D. H. Olson, N. J. Turro, J. Li, *Angew. Chem.* **2003**, *115*, 560; *Angew. Chem. Int. Ed.* **2003**, *42*, 542.

[15] K. Uemura, R. Matsuda, S. Kitagawa, *J. Solid State Chem.* **2005**, *178*, 2420.

[16] G. M. Sheldrick, *SHELXS-86*: *Program for Crystal Structure Determination*, University of Göttingen, Germany, **1986**.

[17] G. M. Sheldrick, *SHELXL-97*: *Program for Crystal Structure Refinement*, University of Göttingen, Germany, **1993/1997**.

Received: July 5, 2006
Published Online: September 25, 2006

 © 2006 Wiley-VCH Verlag GmbH & Co. KGaA, Weinheim 

DOI: 10.1002/ejic.200600581

# The Relative Stabilities of 1,3-Diphospha-2-silaallene and Some of Its Isomers

Rudolf Pietschnig*[a] and Andreas Orthaber[a]

**Keywords:** Multiple bonds / Silicon / Phosphorus / Allenes / Ab initio calculations

An ab initio investigation of the relative stability of 1,3-diphospha-2-silaallenes (RP=Si=PR) with respect to potential isomers shows that the allene isomer is not the global minimum throughout a series of several substituents (R = H, $SiH_3$, $CH_3$, Ph, F) – the siladiphosphirene isomer is significantly more stable for all these substituents. The stability of the diphosphasilaallene relative to other isomers depends on the nature of the adjacent substituents. Thus, for simple carbon and silyl substituents alternative ring-closed isomers are favored over the diphosphasilaallene, which, depending on the substituent, can show silylene or phosphasilene character. The results obtained at the DFT level are compared with those at other levels of theory for the parent system.

(© Wiley-VCH Verlag GmbH & Co. KGaA, 69451 Weinheim, Germany, 2006)

## Introduction

Numerous investigations dealing with the stabilization and bonding situation of multiply bonded phosphorus and silicon compounds have initiated a fertile research area. Multiple bonds between silicon and phosphorus are synthetically especially challenging due to the high reactivity of such unsaturated systems. Nevertheless, sterically protected Si=P double bonds have been generated and structurally characterized.[1–5] Similarly, phosphaallenes[6–15] as well as silaallenes,[16–19] trisilaallenes,[20–22] and even a 1-phospha-3-silaallene[23] have been synthesized and studied theoretically,[24–30] although the combination of both heteroatoms directly bonded to each other within a single allene system remains unknown so far. Earlier attempts to generate 1,3-diphospha-2-silaallenes by hydrogen chloride abstraction from suitable precursors with sterically hindered bases resulted either in Si–P bond cleavage or addition of the base to the Si–P unit.[31,32] The availability of seemingly suitable precursors of the type $(RPH)_2SiCl_2$ combined with a lack of information concerning the outcome of attempted synthesis of 1,3-diphospha-2-silaallenes prompted us to investigate their stability with respect to possible isomers theoretically. According to our findings, the 1,3-diphospha-2-silaallene structure, despite being a local minimum, is not the global minimum on the potential energy hypersurface. For all substituents considered in our investigation the cyclic siladiphosphirene is by far the most stable isomer. Which isomer is the next most stable one depends significantly on the nature of the adjacent substituent. However, in neither case was the silaallene the second most stable isomer. For systems bearing carbon substituents we find that a cyclic phosphasilene isomer is more stable than the silaallene, while for more electropositive substituents a cyclic diphosphasilylene structure is lower in energy. As our results show, the relative stability of the isomers explored by us strongly depends on the electronic properties of the adjacent substituents.

## Results and Discussion

In order to investigate the energetic separation of 1,3-diphospha-2-silaallene and its isomers, we performed ab initio quantum chemical calculations using the program package Gaussian 03,[33] employing a 6-311G(d) basis set[34–37] at the Hartree–Fock and DFT(B3LYP) level.[38,39] The harmonic vibrational frequencies and their infrared intensities for all of the optimized structures were evaluated by the B3LYP method. Complete reports of the vibrational frequencies and infrared intensities are given in the Supporting Information. These results were used to determine if a structure is a genuine minimum. The final energy values include zero-point correction and thermal correction to 298 K. The reliability of the B3LYP method for the calculation of the structures and the stability of the group of compounds under investigation was tested by the higher correlated MP2 method for the hydrogen-substituted parent systems of all isomers.

For our calculations we considered the diphosphasilaallene structure **1**, the cyclic diphosphasilylene structures with the adjacent substituents adopting a *cis* and a *trans* position (**2** and **3**), the ring-opened diphosphenyl silylene structure **4**, the cyclic phosphasilene **5**, siladiphosphirene **6**, and finally phosphasilyne **7** (Scheme 1). Other isomers such as the vinylidene silylene **8** or phosphanylidenes like **9** were not taken into account since exploratory calculations on the parent system at the B3LYP//6-311G(d) level showed that

[a] Institut für Chemie, Karl-Franzens-Universität, Schuberstraße 1, 8010 Graz, Austria

Supporting information for this article is available on the WWW under http://www.eurjic.org or from the author.

 InterScience © 2006 Wiley-VCH Verlag GmbH & Co. KGaA, Weinheim 

they are roughly 20 kcal mol$^{-1}$ higher in energy than the least stable of the other isomers. To explore the electronic influence of different substituents on the relative energies of these isomers, we investigated the hydrogen-substituted parent systems **1**–**7a**, the silyl derivatives **1**–**7b**, the methyl derivatives **1**–**7c**, the phenyl derivatives **1**–**7d**, and the fluorine-substituted derivatives **1**–**7e**. Since we were mainly interested in exploring the effect of the electronic properties of different substituents on the stability of the 1,3-diphospha-2-silaallene, we focused our attention only on its monomeric isomers. Nevertheless, it is obvious that in the case of insufficient steric protection dimers or oligomers of these isomers will be even lower in energy. Although it appears worthwhile to investigate this aspect, it exceeds the scope of this investigation, which is mainly aimed at the possibility of predicting the electronic influence of the substituents in order to realize the unsaturated isomers discussed herein synthetically.

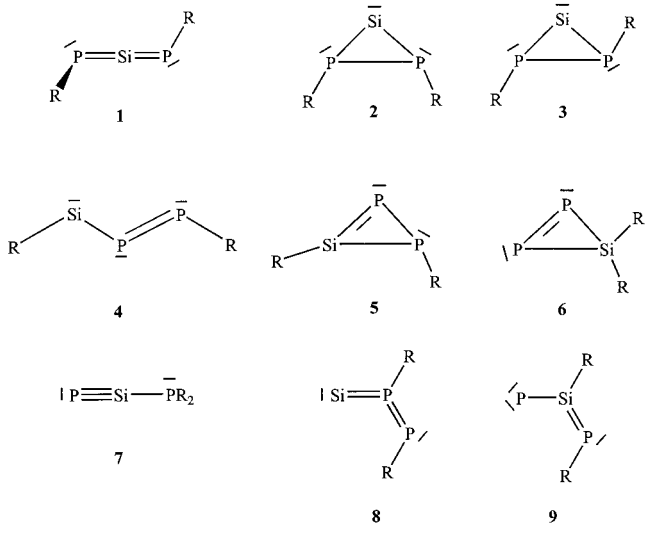


Scheme 1. Idealized structures of isomers of 1,3-disphospha-2-silaallenes (R = H, $SiH_3$, $CH_3$, Ph, F).

The relative energies obtained for the differently substituted isomers **1**–**7** are summarized in Table 1. As is evident from these data, the 1,3-diphospha-2-silaallene is not the global minimum on the energy hypersurface. Nevertheless, the diphosphasilaallene structure is a local minimum for all these substituents.

For all substituents considered in our investigation (R = H, $SiH_3$, $CH_3$, Ph, F) the siladiphosphirene structure **6** is the most stable isomer. The relative stability of this isomer is most pronounced for the fluorine-substituted **6e** and lowest for the silyl-substituted **6b**. The geometric parameters of this isomer show a related trend (Table 2). As expected, the P=P bond in most examples of isomer **6** shows values typical for a double bond and the Si–P distance is typical for the corresponding single bond. Interestingly, these bonds show a counteracting trend for **6e** and **6b**. Thus, the P=P bond in **6b** (2.056 Å) is the shortest observed in this series while the corresponding Si–P bond is the longest (2.250 Å). The opposite is observed for the highly electronegative fluorine substituted **6e**, which shows the longest P=P bond in this series (2.124 Å) along with the shortest Si–P bond (2.160 Å). In fact for the fluorine derivative, both of these values are right in the middle between typical single and double bonds of these elements. Concomitant with this trend of the bond lengths, the angles associated with the substituents also show related effects. For fluorine as substituent the R–Si–R angle (ca. 105°) is the smallest in this series, while for silyl substituents this angle is the largest (ca. 118°).

Table 2. Geometrical parameters for the structural isomer **6**.

| | P–P [Å] | Si–P [Å] | P–P–Si [°] | R–S–P [°] | P–Si–P [°] | R–Si–R [°] |
|---|---|---|---|---|---|---|
| R = H (**6a**) | 2.069 | 2.220 | 62.28 | 119.19 | 55.58 | 113.09 |
| R = $SiH_3$ (**6b**) | 2.056 | 2.250 | 62.91 | 117.27 | 54.25 | 117.99 |
| R = $CH_3$ (**6c**) | 2.079 | 2.220 | 62.14 | 119.70 | 55.71 | 111.82 |
| R = Ph (**6d**) | 2.078 | 2.220 | 62.24 | 119.70 | 55.72 | 113.20 |
| R = F (**6e**) | 2.124 | 2.160 | 60.56 | 122.03 | 58.88 | 104.94 |

These findings can be rationalized based on the considerations that have been developed for phosphirenes. where the phosphirene ring is considered as the combination of a (hetero)carbene and a triple bond.[40,41] Similarly, the diphosphirene could be considered as the combination of a silylene and P≡P. The stronger the interaction of these fragments, the higher should be the P–Si bond order and hence the shorter this bond length. In contrast, the P–P bond order should be reduced by increasing interaction of $P_2$ with the silylene fragment and the P–P bond length should therefore increase. Consequently, the main effect of the substituents in **6** would be to affect the electronic nature of the silylene fragment and hence the extent of its interaction with the $P_2$ fragment. It is well known that fluoro-substituted silylenes possess a singlet ground state that is more favorable to interact with a $P_2$ unit, while the triplet ground state is stabilized by silyl substituents. The strong interaction between these fragments in **6e** should also be increased

Table 1. Relative energies [kcal mol$^{-1}$] for isomers **1**–**7** including ZPE and thermal energy correction for 298.2 K computed at the B3LYP//6-311g(d) level. TS = one imaginary frequency.

| | **1** | **2** | **3** | **4** | **5** | **6** | **7** |
|---|---|---|---|---|---|---|---|
| R = H (**a**) | 24.53 | 16.67 | 16.13 | 36.07 | 24.06 | 0.00 | 25.09 |
| R = $SiH_3$ (**b**) | 14.98 | 9.56 | 7.42 | 33.70 | 18.17 | 0.00 | 19.07 |
| R = $CH_3$ (**c**) | 44.60 | 32.77 | 31.77 | 77.31 (TS) | 27.54 | 0.00 | 36.63 |
| R = Ph (**d**) | 39.08 | 27.26 | 24.97 | 33.48 | 23.95 | 0.00 | 36.60 |
| R = F (**e**) | 92.28 | 83.65 (TS) | 79.43 (TS) | 46.79 | 49.24 | 0.00 | 75.41 |

 © 2006 Wiley-VCH Verlag GmbH & Co. KGaA, Weinheim 

by additional negative hyperconjugation,[42,43] where σ*(Si-F) states act as acceptors towards bonding π(P≡P) states.

Apart from the most stable siladiphosphirene **6**, the nature of the next stable isomer depends significantly on the properties of the adjacent substituent. For the hydrogen- and silyl-substituted species the cyclic diphosphasilylene structure **3** carrying the substituents in a *trans* orientation is the second most stable isomer. Structure **3** is around 8 kcal mol$^{-1}$ more stable than the 1,3-disphospha-2-silaallene structure **1**. For all substituents the *cis* isomer **2a**–**e** is only around 1–4 kcal mol$^{-1}$ less stable than the *trans* isomers **3a**–**e**, thus indicating only a minor repulsive interaction between the substituents. On changing the substituents to methyl or phenyl a somewhat different picture is obtained. In these cases the phosphasilene structure **5**, to which some partial silyl cation character might be attributed, is the second most stable isomer rather than the diphosphasilylene structure **3**. The energy difference between these two isomers is not large (1–4 kcal mol$^{-1}$), however.

The relative stability of isomers **3** and **5** can be rationalized by taking the charge distribution within the PPSi system into account. On the grounds of Mulliken charges calculated for the phosphorus and silicon atoms within isomers **3** and **5** it is obvious that for hydrogen- and silyl-substituted derivatives the charge distribution differs substantially from the carbon- and fluorine-substituted derivatives. Of the isomers under question those with the more negative (less positive) charge at the more electronegative phosphorus atoms represents the energetically more favored structure (Table 3). Consequently for R = $CH_3$, Ph, and F the phosphasilene isomer **5** is more stable, while the cyclic *trans* isomer **3** is favored for R = H and $SiH_3$.

Table 3. Sums of Mulliken charges for the P and Si atoms in isomers **3** and **5**.

| | Phosphasilene **5** | | *trans* Ring **3** | |
|---|---|---|---|---|
| R = H (**a**) | q(Si) | 0.207 | q(Si) | 0.238 |
| | Σq(PP) | –0.271 | Σq(PP) | –0.348 |
| R = $SiH_3$ (**b**) | q(Si) | 0.126 | q(Si) | 0.200 |
| | Σq(PP) | –0.337 | Σq(PP) | –0.350 |
| R = $CH_3$ (**c**) | q(Si) | 0.459 | q(Si) | 0.220 |
| | Σq(PP) | –0.113 | Σq(PP) | 0.042 |
| R = Ph (**d**) | q(Si) | 0.435 | q(Si) | 0.127 |
| | Σq(PP) | –0.099 | Σq(PP) | 0.197 |
| R = F (**e**) | q(Si) | 0.567 | q(Si) | 0.221 |
| | Σq(PP) | 0.191 | Σq(PP) | 0.514 |

For fluorine as substituent the second most stable isomer is the ring-opened structure **4**. The latter is about 2 kcal mol$^{-1}$ more stable than the cyclic phosphasilene **5e** and about 33 kcal mol$^{-1}$ more stable than the *trans* oriented cyclic structure **3e**. Apart from the global minimum **6e**, structures **4e** and **5e** are the only isomers with direct Si–F bonds, therefore their relative stability is likely to be a consequence of the strength of the silicon–fluorine bond. In contrast, structure **4** is about 10–50 kcal mol$^{-1}$ higher in energy than the second most stable isomer for most other substituents (R = H, $CH_3$, $SiH_3$). In fact, structure **4a**–**c** is the least stable isomer for these substituents and even a transition state for R = $CH_3$ which transforms into **5c** and connects the two enantiomeric forms of **5** as we found based on IRC calculations. Interestingly, the phenyl substituent has a somewhat intermediate position and **4d** is only 10 kcal mol$^{-1}$ less stable than **5d**. This indicates that the π-donor properties of fluorine and phenyl stabilize structure **4**.

For structure **4** a delocalized bond situation can be expected. Formally, this could be described as a silylene-substituted diphosphene. However, it is obvious that other resonance forms have to be considered. This isomer is probably best described as a 2π-SiPP allylic system where significant interaction of the substituents with the central unit can be neglected (Scheme 2). However, such a description requires a planar or nearly planar arrangement of the SiPP unit and the adjacent substituents. According to our findings (Table 4), such a situation is realized only in the methyl- and fluoro-substituted derivatives **4c**,**e** and to a lesser extent for phenyl-substituted **4d**. In contrast, the substituents adjacent to the SiPP unit in the hydrogen- and silyl-substituted derivatives **4a**,**b** deviate by almost 90° from the planar geometry. Nevertheless, the geometric parameters in **4b**,**c** show almost equally long Si–P and P–P bond lengths, which differ by 0.08–0.09 Å. The Si–P distances in **4b**,**c** (2.02 and 2.11 Å, respectively) are in a range for P–Si bond lengths that is significantly shorter than a P–Si single bond (2.25 Å).[3,5] In contrast to the σ-acceptor, π-donor substituents fluorine and phenyl, this P–Si bond length increases substantially to 2.31 and 2.35 Å, which is in the range for a single bond. Hydrogen-substituted **4a** shows an intermediate situation, with an Si–P bond length of 2.22 Å. The central Si–P–P angle follows a similar trend (86–90°) and is markedly smaller for fluorine- and phenyl-substituted derivatives **4d**,**e** than for the other substituents (**4a**–**c**: 117–144°).

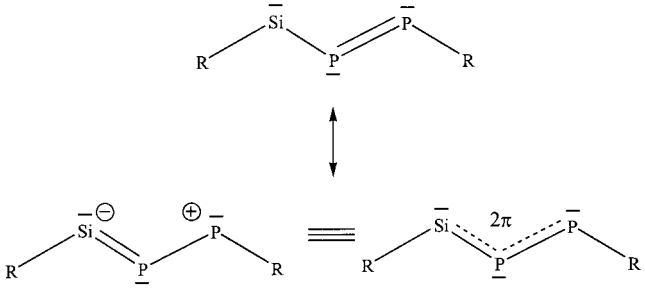


Scheme 2. Mesomeric Lewis structures of **4**.

The trends observed for the structures of isomers **4a**–**e** (Table 4) can be interpreted as a dominant contribution of the silylene-substituted diphosphene resonance structure. Interaction of π-donor substituents such as phenyl and fluorine can stabilize the adjacent silylene center to an extent that makes this isomer more stable than the cyclic isomer **3**, as in the case of fluorine. Given a nearly planar arrangement, such a stabilized silylene center (as in **4d**,**e**) shows only a low tendency to interact with the neighboring diphosphene unit. For less stabilized and therefore more electrophilic silylene centers such as in **4c**, interaction with the adjacent diphosphene unit is much stronger. In nonplanar

 © 2006 Wiley-VCH Verlag GmbH & Co. KGaA, Weinheim 

arrangements such as found for **4a**,**b**, an effective Si–P–π interaction is precluded by the geometric situation, which tends to lead to an isolated (i.e. short) P=P bond along with a rather long Si–P bond.

Table 4. Geometric parameters for the structural isomer **4**.

| | Si–P–P [°] | Si–P [Å] | P–P [Å] | R–Si–P [°] | P–P–R [°] | RSi···PR [°] |
|---|---|---|---|---|---|---|
| R = H (**4a**) | 116.93 | 2.220 | 2.040 | 91.27 | 94.87 | 84.80 |
| R = $SiH_3$ (**4b**) | 143.48 | 2.110 | 2.030 | 91.66 | 97.72 | 88.94 |
| R = $CH_3$ (**4c**) | 129.75 | 2.020 | 2.110 | 144.22 | 96.40 | 0.00 |
| R = Ph (**4d**) | 90.00 | 2.310 | 2.060 | 100.41 | 89.99 | 10.06 |
| R = F (**4e**) | 86.13 | 2.350 | 2.020 | 96.05 | 105.33 | 0.00 |

Isomer **3** can be described as a cyclic diphosphasilylene in which the silylene center can interact with the adjacent phosphorus atoms. The structure of this isomer is almost invariant to the adjacent substituents with respect to the central ring (Table 5). Only for R = F it is not a minimum structure and ring opens to **1**. Generally, the Si–P bond length is about 2.28–2.29 Å, in the typical single bond range for these elements. The P–P bond length varies slightly more and is shortest in fluorine-substituted **3e** (2.12 Å); it is between 2.22 and 2.28 Å for the other substituents. The central P–Si–P angle varies only slightly (55–60°) and is close to experimental values in diphosphasiliranes.[44] Similarly, the P–P–Si angle of the three-membered ring shows values in a narrow range between 60–63°. In contrast to the central ring unit, more significant differences are observed for the angles involving the adjacent substituents, i.e. the R–P–Si and the dihedral angle R–P–P–R. For R–P–Si the angle increases with the π-donor character of R. In contrast, the dihedral angle R–P–P–R decreases in the same direction (Table 5).

Table 5. Geometric parameters for the structural isomer **3**.

| | P–Si–P [°] | Si–P [Å] | P–P–Si [°] | R–P–Si [°] | P–P [Å] | R–P–P–R [°] |
|---|---|---|---|---|---|---|
| R = H (**3a**) | 58.85 | 2.290 | 60.57 | 92.79 | 2.259 | 178.26 |
| R = $SiH_3$ (**3b**) | 59.81 | 2.280 | 60.09 | 87.88 | 2.283 | 170.54 |
| R = $CH_3$ (**3c**) | 58.11 | 2.280 | 60.76 | 110.27 | 2.222 | 155.72 |
| R = Ph (**3d**) | 59.11 | 2.260 | 59.25 | 91.05 | 2.266 | 158.22 |
| R = F (**3e**) | 55.05 | 2.290 | 62.47 | 121.05 | 2.123 | 126.79 |

The structural parameters for the 1,3-disphospha-2-silaallenes **1a**–**e** also show some interesting trends depending on the nature of the adjacent substituents (Table 6). The deviation from linearity of the central P=Si=P unit [P–Si–P angle of 135° (**1e**) and 155° (**1d**)] is strongest for the π-donating substituents fluorine and phenyl. Concomitant with this bending is an increase of the P–Si bond length to 2.12 (**1e**) and 2.09 Å (**1d**). The corresponding hydrogen- and silyl-substituted analogues (**1a**,**b** 169–171°) are closer to linearity and the P–Si bond (2.06 Å) is shorter than for the phenyl- and fluorine-substituted derivatives (**1e**,**d**).

Table 6. Geometric parameters for the structural isomer **1**.

| | P–Si–P [°] | Si–P [Å] | R–P–Si [°] | RP···PR [°] |
|---|---|---|---|---|
| R = H (**1a**) | 168.87 | 2.060 | 89.83 | 88.69 |
| R = $SiH_3$ (**1b**) | 171.36 | 2.060 | 93.50 | 89.14 |
| R = $CH_3$ (**1c**) | 161.98 | 2.080 | 102.89 | 90.58 |
| R = Ph (**1d**) | 155.38 | 2.090 | 102.17 | 94.16 |
| R = F (**1e**) | 135.46 | 2.120 | 104.40 | 99.34 |

Among all isomers of 1,3-disphospha-2-silaallene the cyclic phosphasilene **5** shows the least impact of the electronic properties of the substituents on its structural parameters (Table 7). Thus, in **5a**–**e** the formal double bond between the silicon atom and phosphorus atom without any exocyclic substituent shows values in the range of 2.04–2.06 Å. The formal single bond from silicon to the other phosphorus atom is characteristically longer, with values between 2.17 and 2.23 Å that are in agreement with a description as a short single bond. The P–P distances (2.38–2.41 Å) are rather long, and the angles are in a narrow range for all substituents that we investigated. Thus, the P–Si–P angles in **5a**–**e** vary only from 68° to 69° and similarly the P(R)–P–Si angles are all within the range of 58° to 59°.

Table 7. Geometric parameters for the structural isomer **5**.

| | Si–P [Å] | Si–P(R) [Å] | P–P [Å] | P–Si–P [°] | P(R)–P–Si [°] | R–Si–P–R [°] |
|---|---|---|---|---|---|---|
| R = H (**5a**) | 2.046 | 2.210 | 2.410 | 68.91 | 58.79 | 87.74 |
| R = $SiH_3$ (**5b**) | 2.059 | 2.230 | 2.390 | 67.88 | 59.43 | 85.76 |
| R = $CH_3$ (**5c**) | 2.051 | 2.200 | 2.390 | 68.38 | 58.86 | 84.57 |
| R = Ph (**5d**) | 2.057 | 2.200 | 2.380 | 67.95 | 58.94 | 77.88 |
| R = F (**5e**) | 2.040 | 2.170 | 2.380 | 69.02 | 58.06 | 78.60 |

The cyclic isomers of 1,3-diphospha-2-silaallene (**2**, **3**, **5**, and **6**) are generally not as structurally flexible as the ring-opened isomers **1** and **4**. One might be tempted to interpret this rigidity as an indication of a limited or even negligible interaction between the substituents and the cyclic $P_2Si$ unit. However, the presence and significance of such an interaction is evident from the prominent influence of different substituents on the relative stabilities of these isomers, including the cyclic ones.

Finally, the last isomer investigated by us is the phosphanyl-substituted phosphasilyne **7** (Table 8). Since the substituents in this isomer are not bonded directly to a low-valent main group atom, structural differences based on their conjugative properties are not likely to be pronounced. Accordingly, the formal triple bond shows a constant P–Si distance of roughly 1.97 Å for all substituents. The adjacent Si–P single bond (2.23 Å) is shortest for silyl-substituted **7a** and longest for fluorine-substituted **7e** (2.35 Å). The angles around the tricoordinate phosphorus atom are smallest for the hydrogen-substituted compound and largest for its phenyl-substituted congener, which suggests steric reasons for this observation.

 © 2006 Wiley-VCH Verlag GmbH & Co. KGaA, Weinheim 

Table 8. Geometric parameters for the structural isomer **7**.

| | Si≡P [Å] | Si–$PR_2$ [Å] | P–Si–P [°] | Si–P–R [°] | R–P–R [°] | P–Si–P–R [°] |
|---|---|---|---|---|---|---|
| R = H (**7a**) | 1.966 | 2.260 | 170.38 | 93.95 | 93.72 | 132.97 |
| R = $SiH_3$ (**7b**) | 1.968 | 2.230 | 175.34 | 98.23 | 100.48 | 128.97 |
| R = $CH_3$ (**7c**) | 1.971 | 2.270 | 170.55 | 100.23 | 100.57 | 128.28 |
| R = Ph (**7d**) | 1.971 | 2.270 | 168.48 | 100.33 | 105.20 | 110.32 |
| R = F (**7e**) | 1.976 | 2.350 | 154.16 | 98.81 | 98.56 | 129.99 |

In order to check the reliability of the B3LYP method and the basis set of our choice for the structurally rather flexible compounds investigated here we tested the structure and energy calculations for the hydrogen-substituted parent systems of all isomers by reoptimization using the MP2 method. Table 9 and Scheme 3 summarize the results obtained for isomers **1**–**7a** with the 6-311g(d) and 6-311g(d,p) basis sets using the DFT and MP2 approach to include electron correlation. As is evident from these data, the differences with respect to correlation method and basis set are only marginal and the same trend in the relative energies of isomers **1**–**7a** is observed in all cases, which indicates that the DFT approach is well suited to exploring the energy hypersurface of this type of compounds. A minor issue is observed for isomer **4**, which is the least stable isomer for all methods. Interestingly, structure **4** is identified as a minimum when employing the B3LYP functional while two negative vibrations at low frequency are found at the MP2 level. Bearing in mind that DFT methods are known to sometimes incorrectly predict minima on a very flat energy hypersurface and for spin contaminated states,[45] it might be possible that this isomer could in fact be a transition state in other cases as well. Actually, methyl-substituted **4c** is a TS even at the DFT level and this isomer is generally the least stable one, except for **4d**,**e**. Therefore, for the fluorine-substituted system, where structure **4e** is quite relevant due to its high relative stability, the minimum was confirmed also at the MP2 level.

Table 9. Relative energies [kcal mol$^{-1}$] for isomers **1**–**7a** (R = H) including ZPE and thermal energy correction for 298.2 K at different levels of theory.

| | **1** | **2** | **3** | **4** | **5** | **6** | **7** |
|---|---|---|---|---|---|---|---|
| B3LYP//6-311g(d) | 24.5 | 16.7 | 16.1 | 36.1 | 24.1 | 0.0 | 25.1 |
| B3LYP//6-311g(d,p) | 22.5 | 15.1 | 14.5 | 35.2 | 23.2 | 0.0 | 23.9 |
| MP2//6-311g(d) | 32.3 | 26.1 | 25.9 | 59.2 | 28.0 | 0.0 | 26.2 |
| MP2//6-311g(d,p) | 28.4 | 22.8 | 22.4 | 57.5 | 26.6 | 0.0 | 24.5 |

A limitation of our study that should be relevant for the synthetic realization of such systems is the fact that we focused strictly on the electronic properties of the adjacent substituents and did not consider steric effects and the bulk of the substituents. Nevertheless, it is obvious that sterically very demanding substituents will destabilize structures in which both substituents are connected to the same atom, as

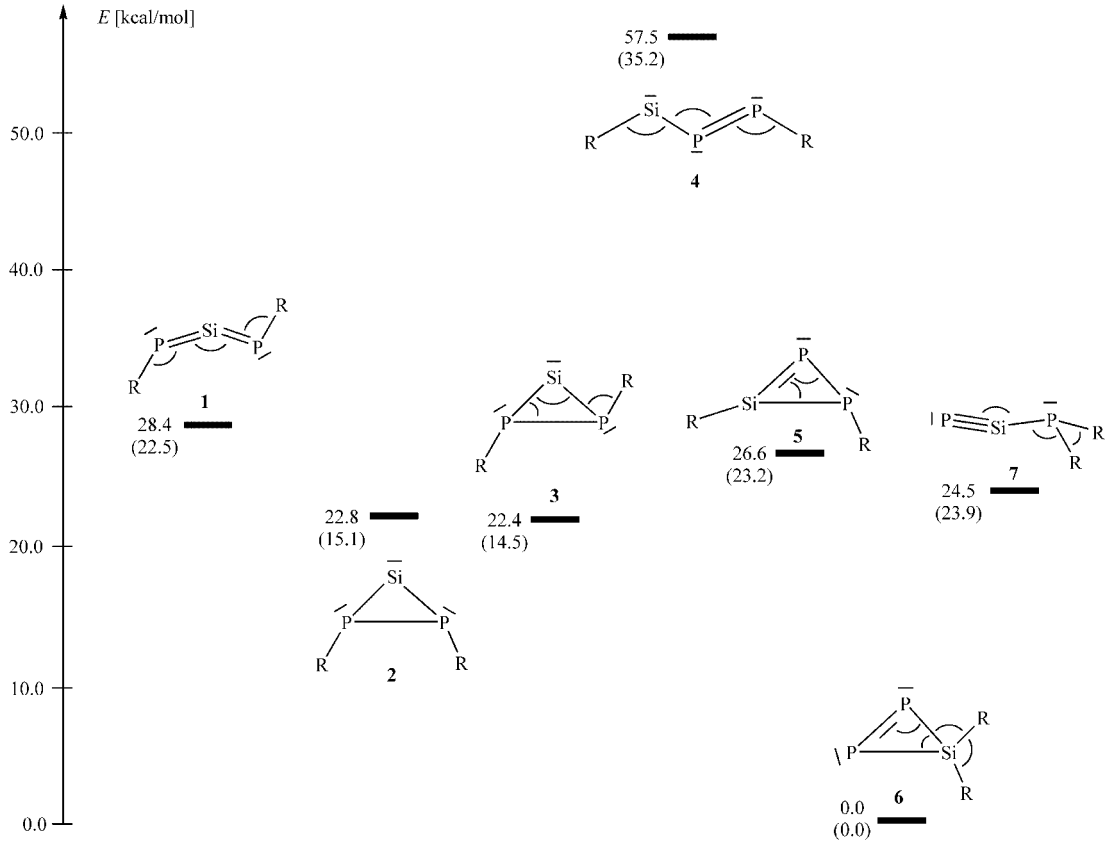


Scheme 3. Overview of relative energies [kcal mol$^{-1}$] for isomers **1**–**7a** (R = H) at the MP2 level (B3LYP in brackets) using a 6-311g(d,p) basis set including ZPE and thermal energy correction for 298.2 K.

 © 2006 Wiley-VCH Verlag GmbH & Co. KGaA, Weinheim 

in **7** or the global minimum **6**, whereas the other isomers should benefit from such an influence.

In summary, our exploration of the relative stabilities of 1,3-diphospha-2-silaallenes and their isomers shows that the goal to prepare a stable 1,3-diphospha-2-silaallene will be a hard one to achieve as the siladiphosphirene isomer is significantly more stable for all substituents considered in this study. The stability of the diphosphasilaallene relative to other isomers depends strongly on the nature of the adjacent substituents. Thus, for simple carbon and silyl substituents alternative ring-closed isomers are favored over the diphosphasilaallene, which, depending on the substituent, can show silylene or phosphasilene character. Given sufficient steric protection, the latter species themselves will surely be challenging synthetic goals to pursue.

## Computational Details

Quantum chemical calculations were carried out using the Gaussian 03 suite of programs.[33] In related work studying the effect of basis sets and electron correlation on several double-bonded silicon species using different basis sets and several correlation methods, it was found that the geometry is not sensitive to the basis set and good results are expected with standard density functional theory methods.[30,46,47]

The optimized geometry was confirmed as a minimum on the potential surface by second-derivative calculations. All the calculated energy data were corrected with the zero-point energy (ZPE) and the thermal energy correction to 298 K ($E = E_0 + E_{vib} + E_{rot} + E_{transl}$).

**Supporting Information** (see also the footnote on the first page of this article): Complete data of harmonic vibrational frequencies, optimized geometries, total energies ($E$, in hartrees), and number of imaginary vibrational frequencies are provided for all isomers.

## Acknowledgments

The authors would like to thank the computational center of the Karl-Franzens Universität for computational resources and the Austrian Science Fund (FWF) for financial support (grant no. P 18591-B03).

[1] C. N. Smit, F. M. Look, F. Bickelhaupt, *Tetrahedron Lett.* **1984**, *25*, 3011.
[2] C. N. Smit, F. Bickelhaupt, *Organometallics* **1987**, *6*, 1156.
[3] E. Niecke, E. Klein, M. Nieger, *Angew. Chem. Int. Ed. Engl.* **1989**, *28*, 751.
[4] M. Driess, S. Rell, H. Pritzkow, *J. Chem. Soc., Chem. Commun.* **1995**, 253.
[5] D. Lange, E. Klein, H. Bender, E. Niecke, M. Nieger, R. Pietschnig, W. W. Schoeller, H. Ranaivonjatovo, *Organometallics* **1998**, *17*, 2425.
[6] R. Appel, P. Fölling, B. Josten, M. Siray, V. Winkhaus, F. Knoch, *Angew. Chem. Int. Ed. Engl.* **1984**, *23*, 619.
[7] H. H. Karsch, H. U. Reisacher, G. Mueller, *Angew. Chem. Int. Ed. Engl.* **1984**, *23*, 618.
[8] R. Appel, V. Winkhaus, F. Knoch, *Chem. Ber.* **1986**, *119*, 2466.
[9] G. Märkl, U. Herold, *Tetrahedron Lett.* **1988**, *29*, 2935.
[10] G. Märkl, S. Reithinger, *Tetrahedron Lett.* **1988**, *29*, 463.
[11] G. Märkl, P. Kreitmeier, *Angew. Chem. Int. Ed. Engl.* **1988**, *27*, 1360.
[12] M. Yoshifuji, K. Toyota, T. Niitsu, N. Inamoto, Y. Okamoto, R. Aburatani, *J. Chem. Soc., Chem. Commun.* **1986**, 1550.
[13] M. Yoshifuji, S. Sasaki, N. Inamoto, *Tetrahedron Lett.* **1989**, *30*, 839.
[14] M. Yoshifuji, S. Sasaki, N. Inamoto, *J. Chem. Soc., Chem. Commun.* **1989**, 1732.
[15] M. Yoshifuji, T. Niitsu, D. Shiomi, N. Inamoto, *Tetrahedron Lett.* **1989**, *30*, 5433.
[16] G. E. Miracle, J. L. Ball, D. R. Powell, R. West, *J. Am. Chem. Soc.* **1993**, *115*, 11598.
[17] M. Trommer, G. E. Miracle, B. E. Eichler, D. R. Powell, R. West, *Organometallics* **1997**, *16*, 5737.
[18] B. Eichler, R. West, in *Advances in Organometallic Chemistry*, vol. 46, **2001**, pp. 1.
[19] B. E. Eichler, G. E. Miracle, D. R. Powell, R. West, *Main Group Met. Chem.* **1999**, *22*, 147.
[20] S. Ishida, T. Iwamoto, C. Kabuto, M. Kira, *Nature* **2003**, *421*, 725.
[21] T. Iwamoto, T. Abe, C. Kabuto, M. Kira, *Chem. Commun.* **2005**, 5190.
[22] T. Iwamoto, H. Masuda, C. Kabuto, M. Kira, *Organometallics* **2005**, *24*, 197.
[23] L. Rigon, H. Ranaivonjatovo, J. Escudie, A. Dubourg, J. P. Declercq, *Chem. Eur. J.* **1999**, *5*, 774.
[24] D. J. Berger, P. P. Gaspar, R. S. Grev, F. Mathey, *Organometallics* **1994**, *13*, 640.
[25] M. S. Gordon, R. D. Koob, *J. Am. Chem. Soc.* **1981**, *103*, 2939.
[26] G. Maier, H. Pacl, H. P. Reisenauer, *Angew. Chem. Int. Ed. Engl.* **1995**, *34*, 1439.
[27] J. C. Barthelat, G. Trinquier, G. Bertrand, *J. Am. Chem. Soc.* **1979**, *101*, 3785.
[28] M. H. Lien, A. C. Hopkinson, *Chem. Phys. Lett.* **1981**, *80*, 114.
[29] M. T. Nguyen, H. Vansweevelt, L. G. Vanquickenborne, *Chem. Ber.* **1992**, *125*, 923.
[30] T. Veszprémi, K. Petrov, C. T. Nguyen, *Organometallics* **2006**, *25*, 1480.
[31] K. Hassler, F. Mitter, B. Reiter, *J. Organomet. Chem.* **1989**, *376*, C1.
[32] E. Niecke, E. Klein, personal communication.
[33] M. J. Frisch, G. W. Trucks, H. B. Schlegel, G. E. Scuseria, M. A. Robb, J. R. Cheeseman, J. Montgomery, J. A., T. Vreven, K. N. Kudin, J. C. Burant, J. M. Millam, S. S. Iyengar, J. Tomasi, V. Barone, B. Mennucci, M. Cossi, G. Scalmani, N. Rega, G. A. Petersson, H. Nakatsuji, M. Hada, M. Ehara, K. Toyota, R. Fukuda, J. Hasegawa, M. Ishida, T. Nakajima, Y. Honda, O. Kitao, H. Nakai, M. Klene, X. Li, J. E. Knox, H. P. Hratchian, J. B. Cross, V. Bakken, C. Adamo, J. Jaramillo, R. Gomperts, R. E. Stratmann, O. Yazyev, A. J. Austin, R. Cammi, C. Pomelli, J. W. Ochterski, P. Y. Ayala, K. Morokuma, G. A. Voth, P. Salvador, J. J. Dannenberg, V. G. Zakrzewski, S. Dapprich, A. D. Daniels, M. C. Strain, O. Farkas, D. K. Malick, A. D. Rabuck, K. Raghavachari, J. B. Foresman, J. V. Ortiz, Q. Cui, A. G. Baboul, S. Clifford, J. Cioslowski, B. B. Stefanov, G. Liu, A. Liashenko, P. Piskorz, I. Komaromi, R. L. Martin, D. J. Fox, T. Keith, M. A. Al-Laham, C. Y. Peng, A. Nanayakkara, M. Challacombe, P. M. W. Gill, B. Johnson, W. Chen, M. W. Wong, C. Gonzalez, J. A. Pople, *Gaussian 03*, Revision C.02 ed., Gaussian, Inc., Wallingford CT, **2004**.
[34] K. Raghavachari, J. A. Pople, E. S. Replogle, M. Head-Gordon, *J. Phys. Chem.* **1990**, *94*, 5579.
[35] M. J. S. Dewar, C. H. Reynolds, *J. Comput. Chem.* **1986**, *7*, 140.
[36] A. D. McLean, G. S. Chandler, *J. Chem. Phys.* **1980**, *72*, 5639.
[37] R. Krishnan, J. S. Binkley, R. Seeger, J. A. Pople, *J. Chem. Phys.* **1980**, *72*, 650.
[38] C. Lee, W. Yang, R. G. Parr, *Phys. Rev. B* **1988**, *37*, 785.
[39] A. D. Becke, *J. Chem. Phys.* **1993**, *98*, 5648.
[40] F. Mathey, *Chem. Rev.* **1990**, *90*, 997.
[41] D. Gonbeau, G. Pfister-Guillouzo, *Nouv. J. Chim.* **1985**, *9*, 71.
[42] A. J. Kos, P. v. R. Schleyer, *Tetrahedron* **1983**, *39*, 1141.

 © 2006 Wiley-VCH Verlag GmbH & Co. KGaA, Weinheim 

[43] A. E. Reed, P. v. R. Schleyer, *J. Am. Chem. Soc.* **1990**, *112*, 1434.
[44] M. Weidenbruch, M. Herrndorf, A. Schäfer, *J. Organomet. Chem.* **1985**, *295*, 7.
[45] C. J. Cramer, *Essentials of Computational Chemistry*, John Wiley & Sons, New York, **2004**.
[46] T. Veszprémi, M. Takahashi, J. Ogasawara, K. Sakamoto, M. Kira, *J. Am. Chem. Soc.* **1998**, *120*, 2408.
[47] T. Veszprémi, M. Takahashi, B. Hajgató, M. Kira, *J. Am. Chem. Soc.* **2001**, *123*, 6629.

Received: June 20, 2006
Published Online: October 5, 2006

 © 2006 Wiley-VCH Verlag GmbH & Co. KGaA, Weinheim 

DOI: 10.1002/ejic.200600370

# Synthesis and Some Properties of Bis(ruthenocenyl)thiophene Derivatives – Possible Spin-Coupling in the Two-Electron Oxidized Species of Dinuclear Ruthenocenes Bridged by Thiophene Derivatives

**Masaru Sato,*[a] Yusuke Kubota,[a] Atsushi Tanemura,[a] Genta Maruyama,[a] Takashi Fujihara,[a] Juzo Nakayama,[a] Toshiyuki Takayanagi,[a] Kenta Takahashi,[a] and Kei Unoura[b]**

**Keywords:** Metallocenes / Redox chemistry / Cations / Sulfur heterocycles / Oxidation / Metal–metal interactions

The binuclear ruthenocene derivatives bridged by thiophene, 3,4-ethylenedioxythiophene, 2,2′-bithiophene, thieno[3,2-*b*]thiophene, or 3,6-dimethylthieno[3,2-*b*]thiophene were prepared by the Suzuki coupling of 2-ruthenocenyl-4,5-tetramethyl-1,3-dioxaborolane with the corresponding diiodo compounds. In addition, thiophene- and bithiophene-bridged binuclear pentamethylruthenocenes were prepared by the reaction of bis(pentamethylruthenocenyl)diyne and -tetrayne with NaSH, respectively. The cyclic voltammograms of these complexes exhibit one-step two-electron redox waves in the lower potential region (0–0.3 V versus $FcH/FcH^+$). The two-electron oxidized species of the thiophene-bridged binuclear ruthenocene derivatives are comparatively stable and adopt the spin-coupled and structurally isomerized fulvene complex-type structure. The solid structure of the oxidized species of bis(pentamethylruthenocenyl)thiophene was determined by X-ray diffraction analysis. The thieno[3,2-*b*]thiophene-bridged analog shows a temperature-dependent $^1H$ NMR spectrum in $CD_3NO_2$. The dicationic species exist as a $Ru^{II}$–$Ru^{IV}$ mixed-valence species in $CD_3CN$.

(© Wiley-VCH Verlag GmbH & Co. KGaA, 69451 Weinheim, Germany, 2006)

## Introduction

Significant interest has been focused on carbon-rich organometallics that contain rigid, π-conjugated chains or aromatics because organometallic assemblies are important for electron-transfer processes,[1] the formation of liquid crystalline materials,[2] and the construction of molecular devices.[3] In particular, numerous investigations have been concentrated on polyynediyl complexes, $[L_nM–(C\equiv C)_m–ML_n]$ ($m$ = 1,2, etc.),[4] because they are attractive candidates for use in the preparation of molecular wires and nanoscale electronic devices; this comes by virtue of their possible charge delocalization along the entire conjugated backbone.[5] Ferrocenyl derivatives also present themselves as fascinating candidates for use in the design of such materials because of a stable one-electron redox system (i.e. stability in both the neutral and oxidized forms).[6] Enormous effort has been expended in the synthesis of dinuclear ferrocene derivatives with π-conjugation.[7] In addition, much attention is currently focused on materials that are based on oligothiophenes and polythiophenes because of their remarkable electronic and optoelectronic properties.[8,9] Therefore, the incorporation of these compounds between two ferrocenyl sites may be expected to promote or inhibit electron delocalization in these types of conjugated systems.[10] Only a few studies have been published with regard to ruthenocene derivatives bridged by π-conjugated chains probably because of the irreversible redox behavior of ruthenocene itself. For example, biruthenocene undergoes one-step two-electron oxidation to afford the dicationic complex that possesses a uniquely coordinated fulvalene as a result of structural isomerization caused by spin-coupling.[11] Bis(ruthenocenyl)oligoenes are oxidized reversibly by the one-step two-electron redox process to afford stable dicationic bis(fulvene)-type complexes.[12] The spin coupling that leads to this structural isomerization is maintained despite the length of the conjugation, at least up to the tetraene derivatives. Bis(ruthenocenyl)ethynes also afford the novel dicationic $\mu_2$-bis(cyclopentadienylidene)ethene diruthenium complexes upon two-electron oxidation.[13] In contrast with the case of the two-electron oxidized species of the oligoene derivatives, the stability of the two-electron oxidized species in the oligoyne derivatives declines with increasing length of the conjugation. In cyclic voltammograms, these dinuclear ruthenocene derivatives show two-electron oxidation waves in the low-potential region, which suggests the formation of a stable, two-electron oxidized

[a] Department of Chemistry, Faculty of Science, Saitama University,
Saitama, Saitama 338-8570, Japan
[b] Department of Chemistry, Faculty of Science, Yamagata University,
Yamagata, Yamagata 990-8560, Japan

 © 2006 Wiley-VCH Verlag GmbH & Co. KGaA, Weinheim 

species. However, the bis(ruthenocenyl) derivatives that are bridged by benzenoid aromatics show only a small or no two-electron oxidation wave in their cyclic voltammograms.[14] The published reports on the ferrocenes and transition-metal complexes bridged by thiophene derivatives[9,10] have stimulated us to investigate complexes that incorporate thiophene derivatives between two ruthenocenyl sites because thiophenes have an enhanced olefinic character and have less aromaticity compared with those of benzenoid compounds. In this report, we describe the synthesis and some properties of bis(ruthenocenyl)thiophene derivatives. Recently, a bis(ruthenocenyl)thiophene derivative has been reported to show an interesting redox behavior.[15]

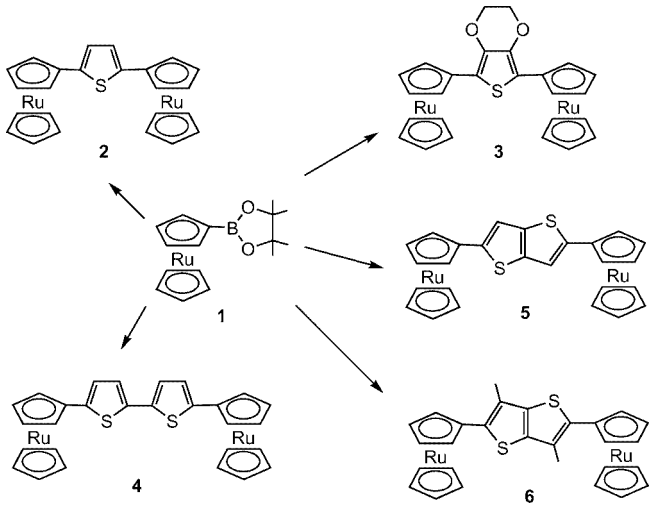


Scheme 1.

## Results and Discussion

### Preparation of Bis(ruthenocenyl)thiophene Derivatives

It has been reported that the Suzuki coupling reaction of 2-ruthenocenyl-4,5-tetramethyl-1,3-dioxaborolane (**1**) with the appropriate halide is a useful method for the preparation of binuclear ruthenocene derivatives bridged by an aromatic compound.[14] Complex **1** was heated with 2,5-diiodothiophene in the presence of (dppf)$PdCl_2$ and 3 M aqueous NaOH in DME in a sealed tube to afford 2,5-bis(ruthenocenyl)thiophene (**2**) in 23% yield. In a similar manner, the reaction of **1** with 3,4-ethylenedioxy-2,5-diiodothiophene, 5,5′-diiodo-2,2′-bithiophene, 2,5-diiodothieno[3,2-*b*]thiophene, or 2,5-diiodo-3,6-dimethylthieno[3,2-*b*]thiophene also proceeded successfully under the similar conditions to afford the corresponding binuclear ruthenocene derivatives **3**, **4**, **5**, or **6** with yields of 33%, 23%, 18%, or 25%, respectively (Scheme 1). Complex **2** was also prepared by the reaction of 1,4-bis(ruthenocenyl)buta-1,3-diyne with NaSH in DMF in an 87% yield. Complexes **2**, **4**, and **5** were scarcely soluble in common organic solvents. Assignment of their structures was carried out on the basis of the corresponding spectroscopic data. For example, the $^1$H NMR spectrum of **4** shows the η-$C_5H_4$-ring protons at $\delta$ = 4.63 and 4.98 ppm as triplets ($J$ = 1.8 Hz), the η-$C_5H_5$-ring protons at $\delta$ = 4.53 ppm as a singlet, and the ring protons of bithiophene at $\delta$ = 6.82 and 6.86 ppm as doublets ($J$ = 3.8 Hz). The $^{13}$C NMR spectrum of **4** supports the structure assigned by the $^1$H NMR spectrum. The structure of **3** was confirmed by single-crystal X-ray diffraction. The crystallographic data are listed in Table 5, and selected bond lengths and angles are listed in Table 1. The ORTEP view of **3** is shown in Figure 1. The two η-$C_5H_4$-ring planes of the ruthenocenyl (abbreviated as Rc hereafter) parts are tilted by 18.89(4)° and 24.83(4)° toward the central thiophene-ring plane probably because of the steric hindrance that is due to the dioxolane ring fused to the thiophene ring. The two η-$C_5H_5$Ru moieties of the Rc parts are positioned on opposite sides of the central thiophene ring. Other bond lengths and angles are the same as those of the ruthenocene and thiophene derivatives.

Table 1. Selected bond lengths and bond angles for **3**.

| Bond lengths [Å] | | | |
|---|---|---|---|
| C(11)–C(12) | 1.380(11) | C(12)–C(15) | 1.400(11) |
| C(15)–C(16) | 1.367(11) | C(12)–O(1) | 1.378(9) |
| O(1)–C(13) | 1.38(2) | C(13)–C(14) | 1.31(2) |
| C(14)–O(2) | 1.432(14) | O(2)–C(15) | 1.366(10) |
| S(1)–C(11) | 1.742(9) | S(1)–C(16) | 1.735(8) |
| C(1)–C(11) | 1.413(12) | C(16)–C(17) | 1.425(12) |
| Ru(1)–C(Cp) | 2.176(av.) | C(Cp)-C(Cp) | 1.42(av.) |
| **Bond angles [°]** | | | |
| C(11)–S(1)–C(16) | 94.4(4) | S(1)–C(11)–C(12) | 107.1(6) |
| C(11)–C(12)–C(15) | 115.7(7) | S(1)–C(16)–C(15) | 108.9(6) |
| C(12)–C(15)–C(16) | 113.8(7) | | |

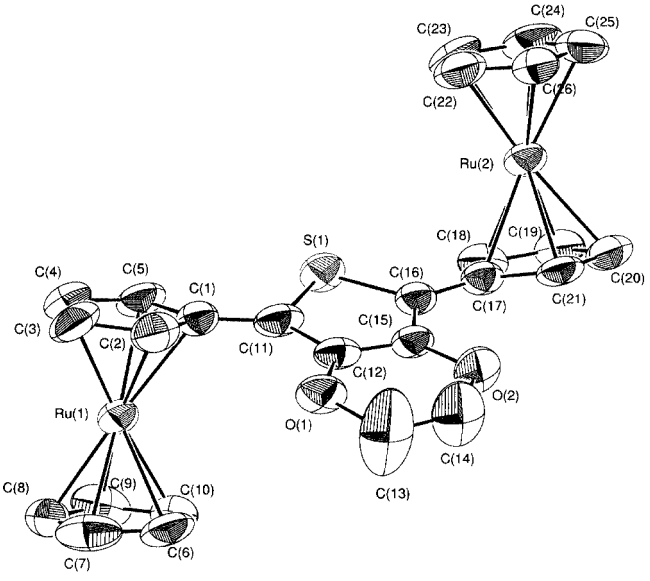


Figure 1. ORTEP view of complex **3**.

 © 2006 Wiley-VCH Verlag GmbH & Co. KGaA, Weinheim 

1,4-Bis(1′′,2′′,3′′,4′′,5′′-pentamethylruthenocenyl)buta-1,3-diyne was allowed to react with NaSH in DMF heated at 100 °C under an argon atmosphere to afford 2,5-bis(1′′,2′′,3′′,4′′,5′′-pentamethylruthenocenyl)thiophene (**7**) in 92% yield. The similar reaction of 1,8-bis-(1′′,2′′,3′′,4′′,5′′-pentamethylruthenocenyl)-1,3,5,7-octatetrayne afforded 5,5′-bis(1′′,2′′,3′′,4′′,5′′-pentamethylruthenocenyl)-2,2′-bithiophene (**8**) in 64% yield (Scheme 2). The structures of these compounds were assigned on the basis of the corresponding $^1$H- and $^{13}$C NMR spectroscopic data. The structure of **7** was also confirmed by X-ray diffraction analysis. The crystallographic data are listed in Table 5, and selected bond lengths and angles are shown in Table 2. The ORTEP view of **7** is shown in Figure 2. The thiophene ring is almost coplanar with the plane of the η-$C_5H_4$-rings of the two 1′,2′,3′,4′,5′-pentamethylruthenocenyl (abbreviated as Rc* hereafter) groups; the twisted angles are 3.60(5)° and 2.36(5)°. The two η-$C_5Me_5$Ru moieties of the Rc* parts adopt the *trans* orientation with respect to the linker ligand. Other bond lengths and angles are the same as the corresponding parameters for the ruthenocene and thiophene derivatives.

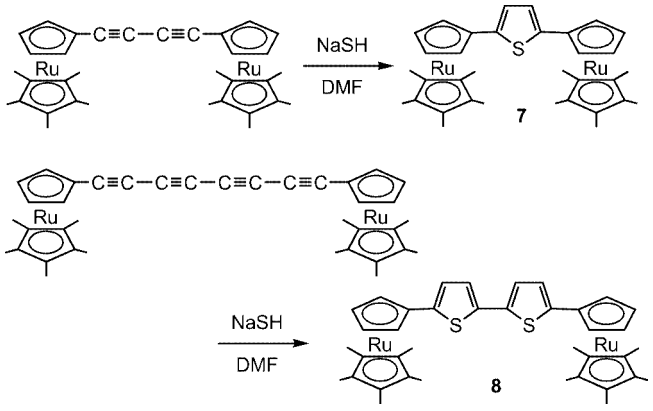


Scheme 2.

Table 2. Selected bond lengths and bond angles for **7**.

| Bond lengths [Å] | | | |
|---|---|---|---|
| Ru(1)–C(Cp) av. | 2.187 | C–C(Cp) av. | 1.42 |
| S(1)–C(1) | 1.736(9) | S(1)–C(4) | 1.748(8) |
| C(1)–C(2) | 1.352 (13) | C(2)–C(3) | 1.390(12) |
| C(3)–C(4) | 1.336 (12) | C(1)–C(20) | 1.445(11) |
| C(4)–C(5) | 1.443(12) | | |
| **Bond angles [°]** | | | |
| S(1)–C(1)–C(2) | 109.0(7) | S(1)–C(4)–C(3) | 109.0(7) |
| S(1)–C(4)–C(5) | 120.3(6) | S(1)–C(1)–C(20) | 121.1(7) |
| C(1)–C(2)–C(3) | 114.1(13) | C(2)–C(3)–C(4) | 115.0(8) |
| C(1)–S(1)–C(4) | 92.5(4) | | |

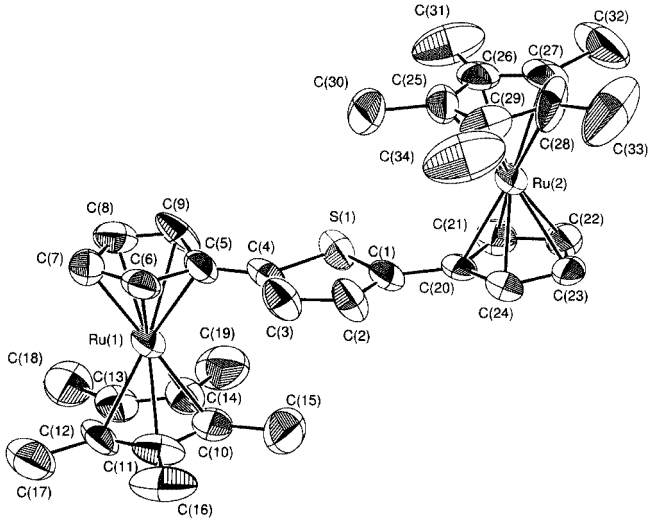


Figure 2. ORTEP view of complex **7**.

## Redox Behavior

The cyclic voltammograms of **2**–**8** were measured in a solution of 0.1 M $n$Bu$_4$NBF$_4$ in $CH_2Cl_2$ with the use of a glassy carbon electrode and a sweep rate of 0.1 V s$^{-1}$ (Figure 3). The electrochemical data are summarized in Table 3. As seen in Figure 3, the cyclic voltammograms are much more complex than those of bis(ruthenocenyl)ethenes that were previously reported to contain a pair of oxidation and reduction waves in a similar region.[12] However, the cyclic voltammograms exhibit a definite oxidation wave near 0.3 V, along with a similar wave near 0.5 V in the Rc series **2**–**6**. The magnitude of the former oxidation wave is almost equal to that of the latter, probably because the electron-rich thiophene bridge promotes the one-step two-electron redox process. This observation differs greatly from the finding that similar dinuclear ruthenocene derivatives bridged by aromatics only show a small or no oxidation wave near 0.3 V.[14] In these complexes, the peak current parameter $I_{pa}$ at about 0.3 V is about 2500 μAV$^{-1/2}$s$^{1/2}$ cm$^{-2}$mM$^{-1}$, with the exception of **4**, and the $n_{app}$ value in the thin-layer coulometry[16] is approximately 2; this suggests that the first oxidation wave near 0.3 V can be assigned to the two-electron oxidation process that corresponds to the Ru$^{II}$–Ru$^{III}$ couple at the two ruthenocenyl sites. The large peak current parameter for the first oxidation peak of **4** appears to be due to an overlap of the first oxidation peak with part of an adjacent, second oxidation peak. Although the redox behavior of the second wave of each complex is relatively complex, the second wave near 0.5 V may be assigned to Ru$^{III}$–Ru$^{IV}$ oxidation. Moreover, if the backwards scan is analyzed at the end of the first wave near 0.3 V, the $I_{pa}$ of this oxidation wave is almost identical to the $I_{pc}$ of the reduction wave near 0.2 V. Surprisingly, in **7** and **8** one oxidation wave and one reduction wave appear near 0.0 V with equal magnitudes, although small additional peaks are also observed. The methyl-substituted ruthenocene ring seems to assist the one-step two-electron redox process. In particular, the oxidation potential of **7** is in the low potential region, which is similar to those of bis(ruthenocenyl)-ethenes (which are comparable to that of ferrocene!).[12] These observations suggest that the redox waves observed at <0.25 V correspond to a one-step two-electron process and that the two-electron oxidized species of complexes **2**–**8** are stable.

 © 2006 Wiley-VCH Verlag GmbH & Co. KGaA, Weinheim 

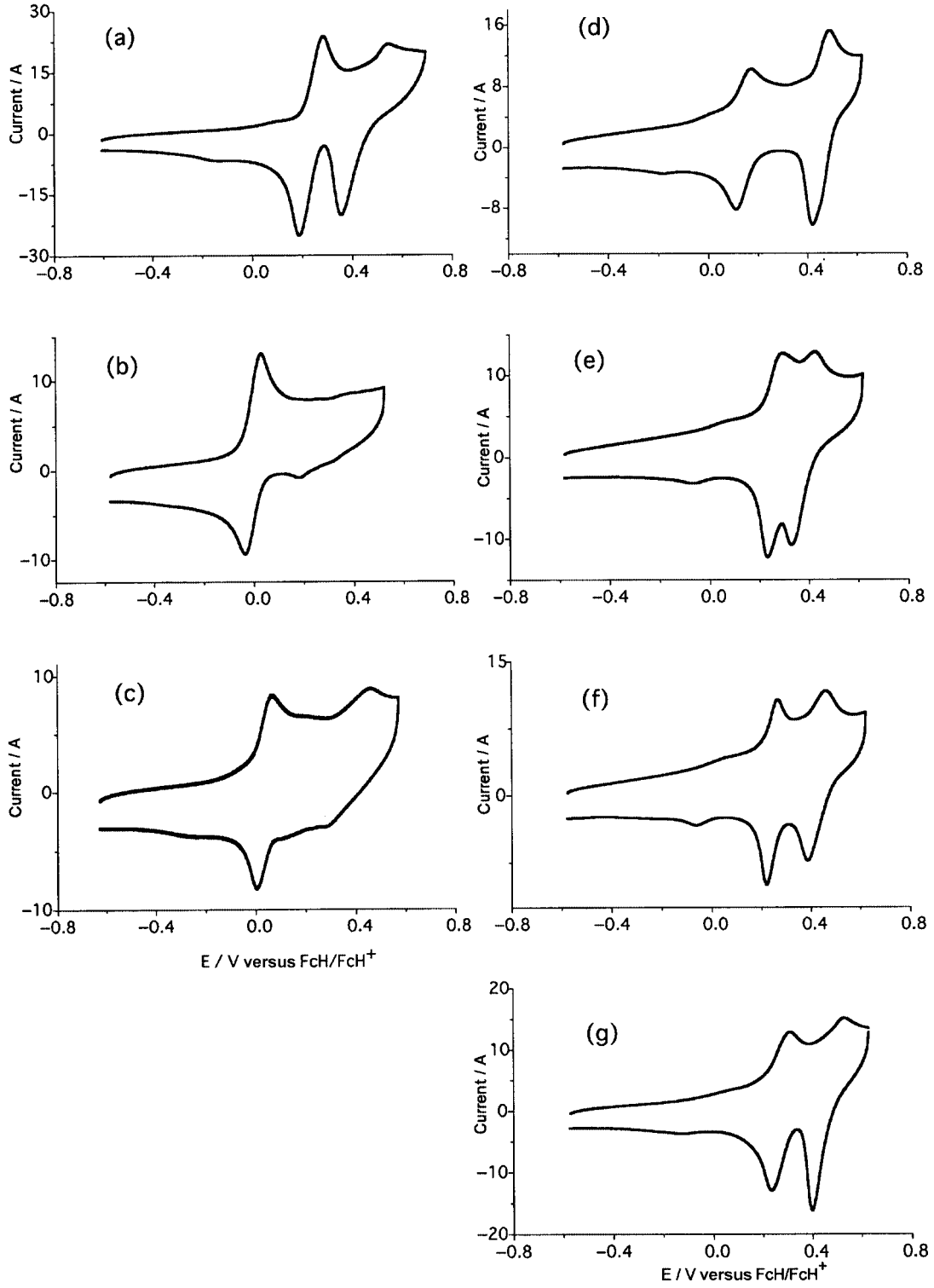


Figure 3. Cyclic voltammograms of **2**–**8**: (a) complex **2**, (b) complex **7**, (c) complex **8**, (d) complex **3**, (e) complex **4**, (f) complex **5**, (g) complex **6**.

It is noteworthy that the oxidation potentials observed for the present complexes show no change or increased only slightly with increases in conjugation of the linker: **2** (+0.281 V) ≈ **5** (+0.265 V) ≈ **4** (+0.276 V), and **7** (+0.028 V) < **8** (+0.069 V). A similar but clearer trend is observed in the Rc*(C≡C)$_n$Rc* series.[13a] However, this tendency is different from that observed for the dinuclear ruthenocene derivatives bridged by oligoenes, the oxidation potentials of which are shifted to a lower potential region with an increase in the number of CH=CH units.[12a] The lower susceptibility of the oxidation potential to the length of conjugation in the present system seems to be related to

 © 2006 Wiley-VCH Verlag GmbH & Co. KGaA, Weinheim 

Table 3. Cyclic voltammetric[a] and coulometric data for the first oxidation process of bis(ruthenocenyl)thiophene derivatives in $CH_2Cl_2$.

| Complex | $E_{pa}$ [V] vs. $FcH/FcH^+$ | $E_{pc}$ [V] vs. $FcH/FcH^+$ | $E_{1/2}$ [V][b] vs. $FcH/FcH^+$ | $\Delta E_p$ [mV][c] | $I_{pa}$ [$U$][d] | $I_{pc}/I_{pa}$ | $n_{app}$[e] |
|---|---|---|---|---|---|---|---|
| **2** | 0.281 | 0.201 | 0.241 | 80 | 2900 | 1.1 | 2.2(1) |
| **3** | 0.174 | 0.111 | 0.143 | 63 | 2500 | 1.2 | 1.9(1) |
| **4** | 0.276 | 0.229 | 0.253 | 47 | 4400 | 1.6 | –[f] |
| **5** | 0.265 | 0.224 | 0.245 | 41 | 3000 | 1.4 | –[g] |
| **6** | 0.307 | 0.230 | 0.269 | 77 | 2400 | 1.5 | 1.8(1) |
| **7** | 0.028 | –0.039 | –0.005 | 67 | 2700 | 1.0 | 2.1(2) |
| **8** | 0.069 | 0.007 | 0.038 | 62 | 2700 | 1.3 | –[g] |

[a] Sweep rate = 0.1 $Vs^{-1}$. [b] $E_{1/2} = (E_{pa} + E_{pc})/2$. [c] $\Delta E = E_{pa} - E_{pc}$. [d] Peak current parameter: $U = \mu A V^{-1/2} s^{1/2} cm^{-2} mM^{-1}$. [e] The number of electrons ($n_{app}$) concerned with the first oxidation of the complexes with standard deviation given in parentheses is determined from the results of thin-layer coulometry. [f] The second oxidation is observed at the potential close to the first oxidation. [g] Solubility is too low to determine $n_{app}$.

the fact that the aromaticity of the thiophene ring works as cross-conjugation for the electronic interaction between two metal sites in the bis(ruthenocenyl)thiophene derivatives.

### Chemical Oxidation

A suspension of thiophene-bridged dinuclear ruthenocene **2** in $CHCl_3$ was oxidized with *p*-BQ/$BF_3$·$OEt_2$ (*p*-BQ = *p*-benzoquinone) at 0 °C to yield **9** as fine brown crystals. The deep red–brown solution of **9** in $CD_3NO_2$ was found to be stable at 0 °C. The $^1H$ NMR spectrum shows one singlet for the η-$C_5H_5$ ring protons at $\delta$ = 5.26 ppm, the four signals for the η-$C_5H_4$ ring protons at $\delta$ = 5.75, 5.90, 6.32, and 6.40 (2 H each) ppm, and one singlet for the thiophene ring protons at $\delta$ = 7.46 ppm, which suggest that the molecule has a mirror plane or a center of symmetry but that the α- and β-protons of the η-$C_5H_4$ ring are nonequivalent because of the lack of symmetry in the η-$C_5H_4$ ring. The η-$C_5H_5$ ring ($\Delta\delta$ = 1.61 ppm) and the thiophene ring protons ($\Delta\delta$ = 0.77 ppm) are shifted to a lower field compared with the corresponding signals of **2**, which indicates the accumulation of positive charges on the Rc moiety and the thiophene ring. This type of spectral pattern accords with the appearance of the fulvene complex-type structure (**9B** in Scheme 3), as seen for the oxidized species of bis(ruthenocenyl)ethene.[12] This hypothesis is supported by the $^{13}C$ NMR spectrum of **9** in which signals for the α- and β-η-$C_5H_4$ ring carbons are observed at $\delta$ = 77.42, 78.72, 90.33, and 90.66 ppm. This signal pattern is also observed for [(η-$C_5H_5$)Ru(μ$_2$-η$^6$:η$^6$-$C_5H_4CHCHC_5H_4$)Ru(η-$C_5H_5$)]-$(BF_4)_2$.[12]

Oxidation of **7** with *p*-BQ/$BF_3OEt_2$ in $CH_2Cl_2$ at 0 °C and subsequent dilution with benzene produced **11** as black powdery crystals that are stable when stored in the freezer. The $^1H$ NMR spectrum of the red–violet solution of **11** in $CD_3NO_2$ at –5 °C exhibits the η-$C_5H_4$ ring proton signals at $\delta$ = 5.53 (m, 4 H) and 5.90 (m, 4 H) ppm and the thiophene ring proton signals at $\delta$ = 7.41 ppm. This signal pattern is different from that observed for **9**, which implies that the α- and β-protons of the η-$C_5H_4$ ring are in a symmetrical environment. The signals for the η-$C_5H_4$ ($\Delta\delta$ = 1.30 and 1.33 ppm) and thiophene ring ($\Delta\delta$ = 0.75 ppm) protons in **12** show a lower-field shift similar to those seen for **9**. Therefore, the spectral pattern indicates the presence of species **11A** shown in Scheme 3, in which the two spins of the molecule are coupled to each other, but they do not lead to structural isomerization. However, the $^{13}C$ NMR spectrum of **11** in $CD_3NO_2$ shows four η-$C_5H_4$ ring carbon signals at $\delta$ = 75.85, 77.10, 93.81, and 93.99 ppm. This signal pattern is similar to that seen for **9**, which indicates the presence of a fulvene complex-type structure (**11B**) for the dicationic species. The appearance of two signals for the η-$C_5H_4$ ring protons in the $^1H$ NMR spectrum of **11** in $CD_3NO_2$ may be due to an accidental superimposition because the signals are observed as a quintet and a sextet rather than two triplets, if they are examined in detail. Furthermore, in $CD_2Cl_2$ or $(CD_3)_2CO$ three signals are observed for the η-$C_5H_4$ ring protons.

The NMR spectra of **9** and **11** in $CD_3CN$ show quite different patterns from those in $CD_3NO_2$, and two sets of the signals for the Rc part and the thiophene ring are observed. For example, the set of signals for the Rc ring protons [$\delta$ = 4.57 (s, 5 H), 5.02 (t, 2 H), and 5.36 (t, 2 H) ppm] is similar to that of the neutral ruthenocenyl group, and the other set of signals [$\delta$ = 5.90 (s, 5 H), 6.01 (t, 2 H), 6.27 (t, 2 H) ppm] resembles that of the ruthenocenium cation. The protons of the thiophene ring appear at $\delta$ = 7.40 and 8.05 ppm as doublets ($J$ = 4.5 Hz). The spectral pattern indicates that **9** reacts with $CD_3CN$, passes through intermediate **9C**, to generate $Ru^{II}$–$Ru^{IV}$ mixed-valence complex **10**. Similarly, the $^1H$ NMR spectrum of **11** in $CD_3CN$ shows the presence of mixed-valence complex **12**. This type of conversion has been reported for the dissolution of the two-electron oxidized species of biruthenocene in $CD_3CN$,[11] but has not been observed for the oxidized species of the dinuclear ruthenocenes bridged by oligoenes and oligoynes in $CD_3CN$.[12,13] This difference may be due to the level of stability of the fulvene complex-type structure. It is considered that the two-electron oxidized species of bis(ruthenocenyl)oligoenes are sufficiently stabilized by the fulvene complex-type structure, whereas the fulvene complex-type structure in **9** or **11** is not very stable in solution because of lower spin coupling. These results also suggest that the replacement of the Rc group with the Rc* group exerts little influence on the structures of the two-electron oxidized species of the thiophene-bridged binuclear derivatives.

 © 2006 Wiley-VCH Verlag GmbH & Co. KGaA, Weinheim 

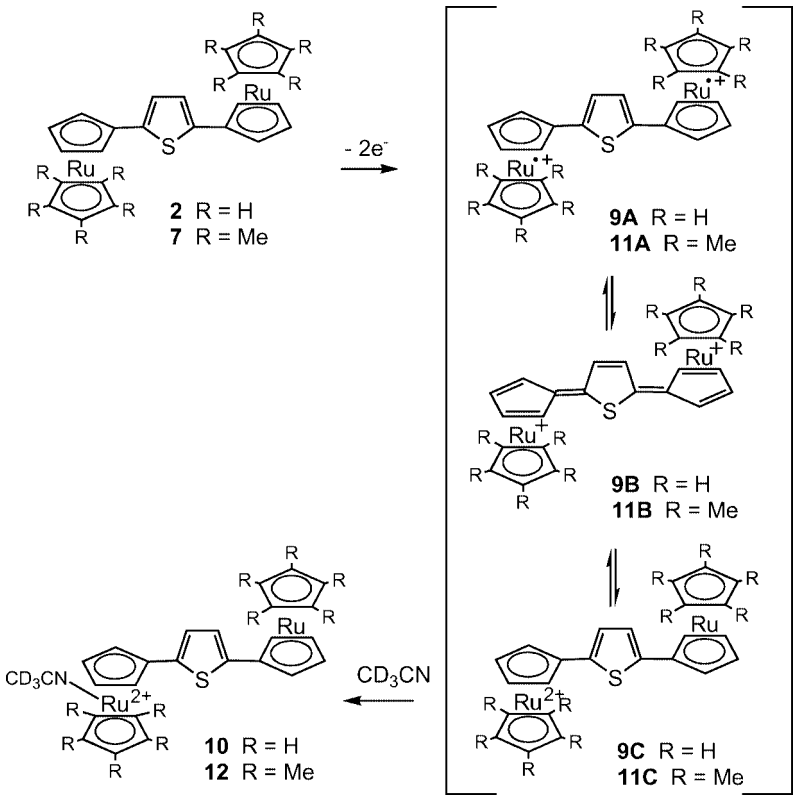


Scheme 3.

The oxidation of **7** with ferricenium tetra[3,5-bis(trifluoromethyl)phenyl]borate in $CH_2Cl_2$ yielded stable oxidized species **13** as dark violet fine needles. The $^1H$ NMR spectrum of **13** in $CD_3NO_2$ exhibits two $C_5H_4$-ring protons at $\delta$ = 5.52 (m, 4 H) and $\delta$ = 5.90 (m, 4 H) ppm and shows no change when **13** is cooled to –30 °C ($CH_3NO_2$, m.p. –29 °C). This spectral pattern is similar to that observed for **11**, which suggests that the counter anion has no influence on the degree of structural isomerization. Complex **13** was recrystallized from $CH_2Cl_2$/diethyl ether in diffusion mode to produce black–violet cubes, which were suitable for X-ray diffraction analysis. The crystallographic data for **13** are listed in Table 5, and selected bond lengths and angles are shown in Table 4. The ORTEP view for the cationic part of **13** is shown in Figure 4. The cationic molecule of **13** is located at an inversion center. Two molecules of diethyl ether are involved in the crystal. As seen in Figure 4, a disorder exists in the central thiophene ring of **13**. It is clear that the Rc* part of **13** adopts a fulvene complex-type structure. The Ru(1)–C(16) bond length is 2.111(5) Å, which is somewhat shorter than the corresponding bond lengths observed in $[Ru(\eta\text{-}C_5H_5)(\eta^6\text{-}C_5H_4CH_2)]^+$ [2.272(4) Å],[17] $[(\eta\text{-}C_5Me_5)Ru(\eta^6{:}\eta^6\text{-}C_5H_4CHCHC_5H_4)Ru(\eta\text{-}C_5Me_5)^{2+}$ [2.410 Å],[12] and $[(\eta\text{-}C_5Me_5)Ru(\eta^6{:}\eta^6\text{-}C_5H_4C{=}CC_5H_4)Ru(\eta\text{-}C_5Me_5)^{2+}$ [2.254(3) Å].[13] The C(15)–C(16) bond length is 1.381(7) Å, which is shorter than the $C(sp^2)$–$C(sp^2)$ bond length (1.465 Å). Similar short bond lengths are found in the fulvene complexes $[Ru(\eta\text{-}C_5Me_5)(\eta^6\text{-}C_5Me_4CH_2)]^+$ [1.401(4) Å][18] and $[Ru(\eta\text{-}C_5H_5)(\eta^6\text{-}C_5H_4CH_2)]^+$ [1.405(5) Å].[17] The C(15)–C(16) bond is folded by 30.5° from the $\eta\text{-}C_5H_4$ ring plane. This tilt angle is smaller than those of $[Ru(\eta\text{-}C_5H_5)(\eta^6\text{-}C_5H_4CH_2)]^+$ (42.6°),[17] $[Ru(\eta\text{-}C_5Me_5)(\eta^6\text{-}C_5Me_4CH_2)]^+$ (40.3°),[19] $[(\eta\text{-}C_5Me_5)Ru(\eta^6{:}\eta^6\text{-}C_5H_4CHCHC_5H_4)Ru(\eta\text{-}C_5Me_5)]^{2+}$ (40.4°)[12] and $[(\eta\text{-}C_5Me_5)Ru(\eta^6{:}\eta^6\text{-}C_5H_4C{=}CC_5H_4)Ru(\eta\text{-}C_5Me_5)]^{2+}$ (41.3°),[13b] but close to that of $[(\eta\text{-}C_5H_5)Ru(\eta^6{:}\eta^6\text{-}C_5Me_4C{=}CC_5Me_4)Ru(\eta\text{-}C_5H_5)]^{2+}$ (32.7°).[13a] In addition, some bond alternation is observed in the $\eta\text{-}C_5H_4$ ring of the Rc* moiety. The C(16)–C(17) and C(17)–C(18) bond lengths are 1.753(13) and 1.306(14) Å, respectively, which indicates that the former is a single bond and the latter is a double bond, although these measurements are not precise because of the presence of disorder in the system. This relationship is reverse to that noted for neutral thiophene deriv-

Table 4. Selected bond lengths and bond angles for **13**.

| Bond lengths [Å] | | | |
|---|---|---|---|
| Ru(1)–C(Cp) av. | 2.182 | C–C(Cp) av. | 1.397 |
| S(1)–C(16) | 1.560(8) | S(1)–C(16′) | 1.539(8) |
| C(16)–C(17) | 1.735(13) | C(17)–C(18) | 1.306(14) |
| C(16′)–C(18) | 1.754(13) | C(15)–C(16) | 1.381(7) |
| C(11)–C(15) | 1.439(9) | C(11)–C(12) | 1.405(16) |
| C(12)–C(13) | 1.346(19) | C(13)–C(14) | 1.357(14) |
| C(14)–C(15) | 1.439(9) | Ru(1)–C(16) | 2.111(5) |
| **Bond angles [°]** | | | |
| S(1)–C(16)–C(17) | 105.6(5) | S(1)–C(16′)-C(18) | 105.7(5) |
| S(1)–C(16)–C(15) | 141.8(7) | S(1)–C(16′)-C(15′) | 143.6(7) |
| C(16)–C(17)–C(18) | 110.5(9) | C(17)–C(18)–C(16′) | 109.9(9) |
| C(15′)–C(16′)–C(18) | 109.3(7) | C(16)–S(1)–C(16′) | 108.2(3) |

 © 2006 Wiley-VCH Verlag GmbH & Co. KGaA, Weinheim 

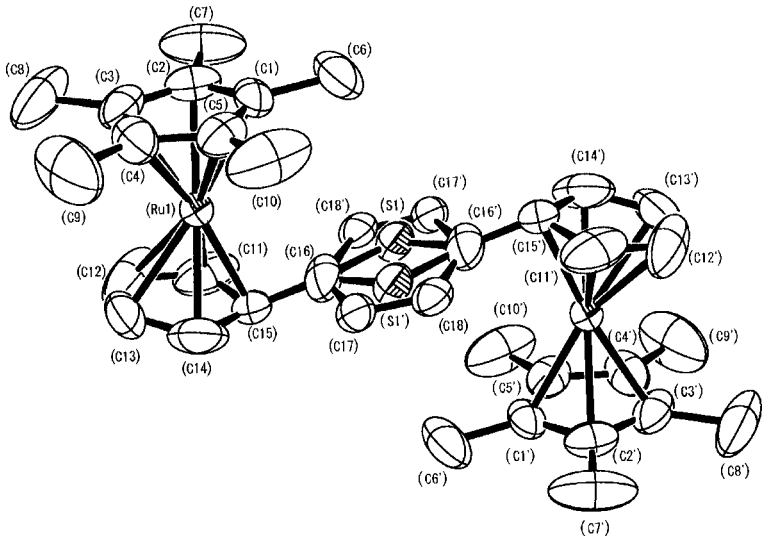


Figure 4. ORTEP view of complex **13**.

ative **7**. Therefore, the bridging ligand in **13** can be formulated as a fully conjugated 2,5-bis(fulvalenylidene)thiophene.

3,4-Ethylenedioxythiophene derivative **3** and bithiophene derivatives **4** and **8** were oxidized under similar conditions to generate the corresponding oxidized species, which gave no clear-cut $^1$H NMR spectrum of a sole product in $CD_3NO_2$. Oxidation of thieno[3,2-*b*]thiophene derivative **5** under similar conditions afforded two-electron oxidized species **14** as a black powder which is relatively stable at room temperature in the solid form. The $^1$H NMR spectrum of **14** in $CD_3NO_2$ at 20 °C shows η-$C_5H_4$ ring protons as triplets at $\delta$ = 5.93 and 6.30 ppm, which suggests that the structure of **14** has a plane or center of symmetry. The signals for the η-$C_5H_4$ ring protons broaden when the temperature is lowered, and the signal at $\delta$ = 5.93 ppm splits at –30 °C and is clearly observed as two signals at –35 °C (the limit of the measurement). This suggests the presence of a certain dynamic process. The structures **14A**–**14C** shown in Scheme 4 can be attributed to the structure of the two-electron oxidized species **14** in $CD_3NO_2$. The structure at low temperature that produces the four signals for the η-$C_5H_4$ ring protons (albeit two signals were still superimposed) seems to be fulvene complex-type structure **14B**. Thus, the structure at room temperature would be symmetrical structure **14A** or **14C**. The low-field shifts of the proton signals of η-$C_5H_5$ ($\Delta\delta$ = 0.74 ppm), η-$C_5H_4$ ($\Delta\delta$ = 1.25–1.30 ppm), and the thieno[3,2-*b*]thiophene rings ($\Delta\delta$ = 0.52 ppm) upon oxidation of **5** are smaller than those seen for **9**. The small shifts observed for the η-$C_5H_5$ and η-$C_5H_4$ ring protons suggest a decrease in the positive charge on the Ru atom of **14**. The lower-field shift of the thieno[3,2-*b*]thiophene ring protons may be explained by a counterbalancing of the increase in the positive charge by the destruction of the aromaticity in the thiophene ring of **14C**. Thus, **14C** seems to be the preferred structure at room temperature, and the dynamic process described above may be attributed to simultaneous charge transfer between **14B** and **14C**. However, a dynamic process due to spin-coupling and spin uncoupling between **14B** and **14A** cannot presently be ruled out. On the other hand, the $^1$H NMR spectrum of **14** in $CD_3CN$ shows two sets of signals for the (η-$C_5H_5$)Ru(η-$C_5H_4$)-moiety and two signals for the thieno[3,2-*b*]thiophene ring as observed for **10** and **12** in $CD_3CN$, which indicates that **15** reacts with $CD_3CN$ via **14C** to generate $Ru^{II}$–$Ru^{IV}$ mixed-valence complex **15**.

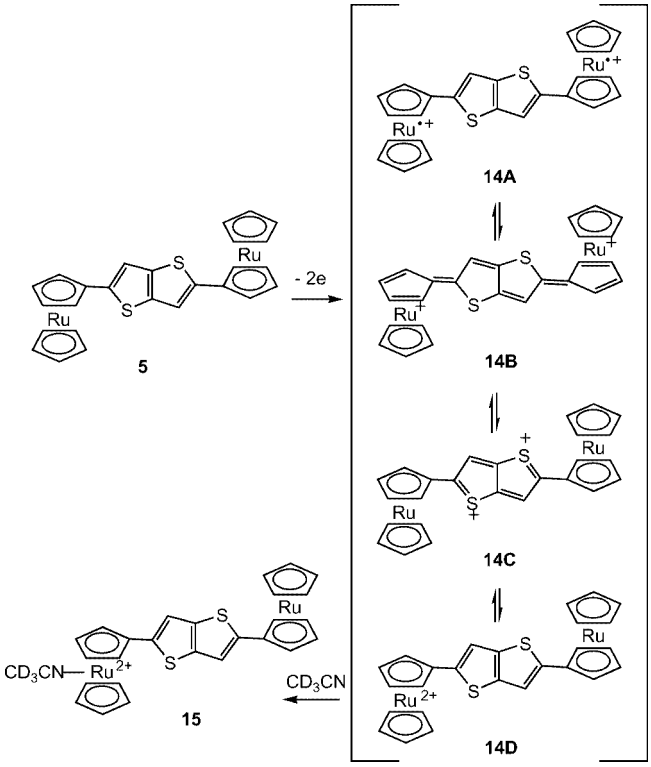


Scheme 4.

 © 2006 Wiley-VCH Verlag GmbH & Co. KGaA, Weinheim 

### Theoretical Considerations

Density function theory (DFT) calculations were performed for the cationic part of two-electron oxidized species **9**, **11**, and **14**. Because the B3LYP/3-21G level calculation for the optimized structures of **9** and **11** did not reproduce the structures determined by the NMR spectra and X-ray diffraction analyses, local spin density approximation (LSDA) was employed for all calculations described in this paper, and in result could revive the actual structure.

The Rc* part of the two-electron oxidized species of thiophene-bridged complex **11** was found to adopt a fulvene complex-type structure, as shown in Figure 5. Thus, the Ru(1)–C(16) distance was found to be 2.50 Å, which is close to that found experimentally for **13** [2.529(5) Å]. The C(15)–C(16) bond length was calculated to be 1.412 Å, which is similar to that of the coordinated ethene bond and approximates the observed length [1.381(7) Å]. The C(15)–C(16) bond was found to be folded by 31.0° from the η-$C_5H_4$ ring plane, which is consistent with the experimental finding that the tilt angle in **13** is 30.5°, although this angle is smaller than those seen for fulvene complexes [Ru(η-$C_5H_5$)(η$^6$-$C_5H_4CH_2$)]$^+$ (42.6°)[17] and [Ru(η-$C_5Me_5$)(η$^6$-$C_5Me_4CH_2$)]$^+$ (40.3°).[18] The calculated C(16)–C(17) bond length (1.431 Å) resembles a single bond and the C(17)–C(18) bond length (1.354 Å) resembles a double bond, which coincides with the trend observed in **13**. The Mulliken charge distribution in two-electron oxidized species **11** was calculated, in which +0.929 of the positive charge was found to be located on one Ru atom and +0.001 of the positive charge was found to be located on the S atom. These results suggest that the structure of **11B** is that of the two-electron oxidized species **11**.

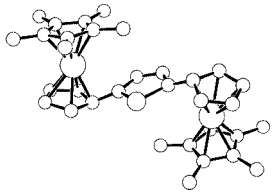

Figure 5. Optimized structure of the dication of **2**.

The optimized structure for the two-electron oxidized species of thieno[3,2-*b*]thiophene-bridged complex **14** was calculated to be also a fulvene complex-type structure (i.e. **14B**). This structure was experimentally detected at low temperature, although it was inconsistent with the structure at room temperature (vide supra). The calculation of the Mulliken charge distribution of **14** assigns a positive charge of about +0.3 on the sulfur atom, which suggests some contribution from **14C**. It was calculated that the conformer that possesses the thiophene ring perpendicular to the η-$C_5H_4$ ring, which explains the $^1$H NMR spectrum at room temperature, has 125 kJ mol$^{-1}$ more energy than the fulvene complex-type structure. In addition, calculations that considered both "broken-symmetry" and higher spin states were carried out. As a result, it was confirmed that the singlet states are electronic ground states in all cases and that the positive charge is equally distributed in the two terminal ruthenocene moieties. However, the lowest triplet states lie only about 40 kJ mol$^{-1}$ higher in energy above the singlet ground states at the DFT levels of theory employed, and the optimized structures of the lowest triplet states have no fulvene complex-type structure. As one possible idea, the triplet state may be the ground state for **14** in solution, but there is no evidence to support this assumption at present. More systematic calculations that include solvent effects will be necessary, but this is beyond the scope of this paper.

## Summary

The binuclear ruthenocene derivatives bridged by thiophene derivatives were newly prepared. The cyclic voltammograms for these complexes exhibited the one-step two-electron redox waves in a lower potential region, contrary to those for derivatives bridged by benzenoid aromatics.[11] This finding is probably related to increases in the electron-rich and olefinic properties of the thiophene derivatives. The stability levels and structures of the two-electron oxidized species were found to be mainly dependent on the types of bridging thiophene derivatives. The two-electron oxidized species of **3**, **4**, and **8** are unstable, whereas those of **2**, **5**, and **7** are stable. The two-electron oxidized species of **2** and **7** adopt the spin-coupled and structurally isomerized fulvene complex-type structures **9B** and **11B**, respectively. The structure of **11B** was determined by X-ray diffraction analysis. If thiophene is regarded as a sulfur-bridged butadiene, the behaviors exhibited upon the oxidation of **2** and **7** is very similar to those seen for bis(ruthenocenyl)butadienes.[12] The two-electron oxidized species **14** derived from **5** was also found to be stable but showed a temperature-dependent $^1$H NMR spectrum in $CD_3NO_2$. This species exists as a fulvene complex-type structure (**14B**) at low temperature, but appears in a different form (**14A** or **14C**) at room temperature. Thus, the behavior of the electronic spins in the two-electron oxidized species of biruthenocenes bridged by thiophene derivatives, that is, the fate of the fulvene complex-type structure, seems to depend largely on the character of the thiophene derivatives, although no product has been detected that corresponds to the appearance of the triplet spins in the two-electron oxidized species of bis(ruthenocenyl)butadiynes.[13]

## Experimental Section

### General

All reactions were carried out under an atmosphere of $N_2$ and/or Ar and workups were performed without precaution to exclude air. NMR spectra were recorded with Bruker AC300P, AM400, or ARX400 spectrometers. Dry solvents were prepared by distillation from the appropriate drying agent prior to use as follows: $CH_2Cl_2$ ($CaH_2$), $ClCH_2CH_2Cl$ ($CaCl_2$), $CH_3CN$ ($CaH_2$), benzene (Na), THF (Na-benzophenone), and DMF ($CaH_2$). 2-Ruthenocenyl-1,3-dioxaborolane (**1**),[14] 1,4-bis(ruthenocenyl)buta-1,3-diyne,[19] 1,4-bis(1′′,2′′,3′′,4′′,5′′-pentamethylruthenocenyl)buta-1,3-diyne,[13]

 © 2006 Wiley-VCH Verlag GmbH & Co. KGaA, Weinheim 

1,8-bis(1′′,2′′,3′′,4′′,5′′-pentamethylruthenocenyl)octa-1,3,5,7-tetrayne,[13] thieno[3,2-*b*]thiophene,[20] 3,6-dimethylthieno[3,2-*b*]-thiophene,[21] 2,5-diiodo-3,4-ethylenedioxythiophene,[22] dichloro-[1,1′-bis(diphenylphosphanyl)ferrocene]palladium, (dppf)$PdCl_2$,[23] and ferricenium tetra{3,5-bis(trifluoromethyl)phenyl}borate[24] were prepared according to the literature procedures. Other reagents were used as received from commercial suppliers.

Cyclic voltammetric and thin-layer coulometric measurements[16] were carried out with an ALS 400A Electrochemical Analyzer at 20 °C. A three-electrode cell containing of a glassy carbon disk working electrode (diameter 0.3 cm), Pt-coil counter electrode and an Ag/AgCl (3 M NaCl) reference electrode were employed. The ferrocene/ferrecenium ($FcH/FcH^+$) redox couple was used as an internal standard of the potential. Tetrabutylammonium tetrafluoroborate ($n$Bu)$_4BF_4$ (Nacalai Tesque Inc.) was purified by recrystallization to be used as a supporting electrode. All solutions were degassed with high-purity argon prior to the electrochemical measurements.

**2,5-Diiodo-thieno[3,2-*b*]thiophene:** To a solution of thieno[3,2-*b*]-thiophene (0.11 g, 0.80 mmol) in dry benzene (10 mL) was slowly added iodine (0.43 g, 1.70 mmol) and HgO (0.17 g, 0.80 mmol) which were grinded together. The mixture was refluxed for 2 h and then cooled to room temp. After filtration, the residue was washed with $CH_2Cl_2$. The filtrate and the washings were combined, washed with a saturated solution of $Na_2S_2O_3$, and then dried with $MgSO_4$. After evaporation of the solvent, the residue was recrystallized from EtOH. Colorless crystals. Yield 0.20 g, 63%. M.p. 188–189 °C. $^1$H NMR (300 MHz, $CDCl_3$): $\delta$ = 7.35 (s, 2 H, =CH) ppm. $^{13}$C NMR (100 MHz, $CDCl_3$): $\delta$ = 75.6 (=C–I), 127.6 (=CH), 144.0 (=C) ppm. $C_6H_2I_2S_2$ (392.01): calcd. C 18.38, H 0.51; found C 18.56, H 0.44.

**2,5-Diiodo-3,6-dimethylthieno[3,2-*b*]thiophene:** This compound was prepared from 3,6-dimethylthieno[3,2-*b*]thiophene (0.21 g, 1.25 mmol) according to the procedure described above. Colorless crystals. Yield 0.30 g, 58%., M.p. >200 °C. $^1$H NMR (300 MHz, $CDCl_3$): $\delta$ = 2.26 (s, 6 H, Me) ppm. $^{13}$C NMR (100 MHz, $CDCl_3$): $\delta$ = 16.9 (Me), 99.7 (=C–I), 134.3 (=CH), 142.2 (=C) ppm. $C_8H_6I_2S_2$ (420.07): calcd. C 22.87, H 1.44; found C 23.13, H 1.35.

**2,5-Bis(ruthenocenyl)thiophene (2):** *Method A*: A mixture of 1,4-bis(ruthenocenyl)buta-1,3-diyne (0.102 g, 0.2 mmol) and NaSH (0.23 g, 4 mmol) in DMF (10 mL) was heated at 100 °C for 24 h under an atmosphere of Ar. After the reaction was cooled, $H_2O$ (40 mL) was added to the solution, and the mixture was stirred for 0.5 h. The resulting crystals were collected by filtration under reduced pressure. The crystals were recrystallized from $CHCl_3$/hexane (2:1) to afford the title complex (97 mg, 87%) as yellow needles. M.p. 199–199.5 °C. $^1$H NMR (400 MHz, $CDCl_3$): $\delta$ = 4.52 (s, 10 H), 4.60 (t, $J$ = 1.9 Hz, 4 H), 4.94 (t, $J$ = 1.9 Hz, 4 H), 6.69 (s, 2 H) ppm. $^{13}$C NMR (100 MHz, $CDCl_3$): $\delta$ = 69.91 (η-$C_5H_4$), 70.44 (η-$C_5H_4$), 71.74 (η-$C_5H_5$), 84.22 (η-$C_5H_4$-*ipso*), 123.11 (=CH), 146.01 (=CS) ppm. $C_{24}H_{20}Ru_2S$ (542.63): calcd. C 53.12, H 3.72; found C 52.97, H 3.65.

*Method B*: 2,5-Diiodothiophene (0.12 g, 0.30 mmol), **1** (0.29 g, 1.6 mmol), (dppf)$PdCl_2$ (20 mg), DME (3 mL), and NaOH (10% aqueous solution, 3 mL) was sealed in an ample tube under an atmosphere of Ar. The ample tube was heated at 100 °C for 12 h. After the reaction was cooled to room temperature, the contents of the ampule were washed out with $CH_2Cl_2$, and the mixture was filtered. The organic layer was washed with water and then dried with $Mg_2SO_4$. After evaporation, the residue was dissolved in benzene, and the solution was then chromatographed on $Al_2O_3$ by elution with hexane/benzene to afford pale yellow crystals (42 mg, 23%). $^1$H NMR (300 MHz, $CDCl_3$): $\delta$ = 4.52 (s, 10 H), 4.60 (t, $J$ = 2 Hz, 4 H), 4.94 (t, $J$ = 2 Hz, 4 H), 6.69 (s, 2 H) ppm. $^{13}$C NMR (100 MHz, $CDCl_3$): $\delta$ = 69.91, 70.44, 71.74, 84.22, 123.11, 146.01 ppm.

**2,5-Bis(ruthenocenyl)-3,4-ethylenedioxythiophene (3):** This compound was prepared from 2,5-diiodo-3,4-ethylenedioxythiophene according to *Method B* described above. Yellow crystals. Yield 38%. M.p. 253–254 °C. $^1$H NMR (400 MHz, $CDCl_3$): $\delta$ = 4.19 (s, 4 H, $CH_2$), 4.53 (s, 10 H, η-$C_5H_5$), 4.59 (t, $J$ = 1.6 Hz, 4 H, η-$C_5H_4$), 5.00 (t, $J$ = 1.6 Hz, 4 H, η-$C_5H_4$) ppm. $^{13}$C NMR (100 MHz, $CDCl_3$): $\delta$ = 64.59 ($CH_2$), 69.95 (η-$C_5H_4$), 70.12 (η-$C_5H_4$), 71.44 (η-$C_5H_5$), 81.81 (*ipso*- η-$C_5H_4$), 111.52 (=C–S), 137.08 (=C–O) ppm. $C_{26}H_{22}O_2Ru_2S$ (660.66): calcd. C 51.99, H 3.69; found C 52.34, H 3.52.

**5,5′-Bis(ruthenocenyl)-2,2′-bithiophene (4):** This compound was prepared from 5,5′-diiodo-2,2′-bithiophene according to the procedure described above. Yellow crystals. Yield 23%. M.p. 253–254 °C. $^1$H NMR (400 MHz, $CDCl_3$): $\delta$ = 4.53 (s, 10 H, η-$C_5H_5$), 4.63 (t, $J$ = 1.8 Hz, 4 H, η-$C_5H_4$), 4.98 (t, $J$ = 1.8 Hz, 4 H, η-$C_5H_4$), 6.82 (d, $J$ = 3.8 Hz, 2 H, =CH), 6.86 (d, $J$ = 3.8 Hz, 2 H, =CH) ppm. $^{13}$C NMR (100 MHz, $CDCl_3$): $\delta$ = 69.86 (η-$C_5H_4$), 70.63 (η-$C_5H_4$), 71.88 (η-$C_5H_5$), 83.57 (*ipso*-η-$C_5H_4$), 122.94 (=CH), 123.79 (=CH), 135.08 (=C–S), 141.24 (=C–S) ppm. $C_{28}H_{22}Ru_2S_2$·1/4$CHCl_3$ (654.60): calcd. C 51.61, H 3.44; found C 51.50, H 3.35.

**2,5-Bis(ruthenocenyl)thieno[3,2-*b*]thiophene (5):** This compound was prepared from 2,5-diiodothieno[3,2-*b*]thiophene according to the procedure described above (reaction time: 2 h). Yellow crystals. Yield 18%. M.p. >250 °C. $^1$H NMR (400 MHz, $CDCl_3$): $\delta$ = 4.53 (s, 10 H, η-$C_5H_5$), 4.64 (t, $J$ = 1.8 Hz, 4 H, η-$C_5H_4$), 5.00 (t, $J$ = 1.8 Hz, 4 H, η-$C_5H_4$), 7.00 (s, 2 H, =CH) ppm. $^{13}$C NMR (100 MHz, $CDCl_3$): $\delta$ = 69.99 (η-$C_5H_4$), 70.62 (η-$C_5H_4$), 71.90 (η-$C_5H_5$), 115.27 (=CH) ppm. No quaternary carbon was observed because of its insolubility. $C_{26}H_{20}Ru_2S_2$ (598.71): calcd. C 52.16, H 3.37; found C 52.16, H 3.36.

**2,5-Bis(ruthenocenyl)-3,6-dimethylthieno[3,2-*b*]thiophene (6):** This compound was prepared from 2,5-diiodo-3,6-dimethylthieno[3,2-*b*]-thiophene according to the procedure described above (reaction time: 5 h). Yellow crystals. Yield 25%. M.p. >250 °C. $^1$H NMR (400 MHz, $CDCl_3$): $\delta$ = 2.28 (s, 6 H, Me), 4.58 (s, 10 H, η-$C_5H_5$), 4.64 (t, $J$ = 1.7 Hz, 4 H, η-$C_5H_4$), 4.93 (t, $J$ = 1.7 Hz, 4 H, η-$C_5H_4$) ppm. $^{13}$C NMR (100 MHz, $CDCl_3$): $\delta$ = 70.43 (η-$C_5H_4$), 71.73 (η-$C_5H_5$), 71.78 (η-$C_5H_4$), 84.66 (*ipso*-η-$C_5H_4$), 126.03 (=C–C), 135.44 (=C–S), 137.50 (=C–S) ppm. $C_{28}H_{24}Ru_2S_2$ (626.76): calcd. C 53.66, H 3.86; found C 53.48, H 3.56.

**2,5-Bis(1′′,2′′,3′′,4′′,5′′-pentamethylruthenocenyl)thiophene (7):** A mixture of 1,4-bis(1′′,2′′,3′′,4′′,5′′-pentamethylruthenocenyl)buta-1,3-diyne (97 mg, 0.15 mmol) and NaSH (84 mg, 1.5 mmol) in DMF (20 mL) was stirred and heated at 100 °C for 24 h under an atmosphere of Ar. After the reaction was cooled, the mixture was diluted with benzene (50 mL). The solution was washed twice with saturated aqueous LiCl and subsequently with $H_2O$ and then dried with $MgSO_4$. After evaporation, the residue was chromatographed on $Al_2O_3$ (deactivated with 5% $H_2O$) and eluted with hexane/benzene (10:1) to afford the title complex (94 mg, 92%) as yellow solid. M.p. 243 °C. $^1$H NMR (400 MHz, $C_6D_6$): $\delta$ = 1.81 (s, 15 H, Me), 4.23 (t, $J$ = 1.7 Hz, 4 H, η-$C_5H_4$), 4.57 (t, $J$ = 1.7 Hz, 4 H, η-$C_5H_4$) 6.66 (s, 2 H, =CH) ppm. $^{13}$C NMR (100 MHz, $C_6D_6$): $\delta$ = 11.58 (Me), 70.86 (η-$C_5H_4$), 73.20 (η-$C_5H_4$), 84.36 (*ipso* -η-$C_5H_4$), 85.39 (η-$C_5Me_5$), 121.48 (=CH), 137.56 (=C–S) ppm. $C_{34}H_{40}Ru_2S$ (682.90): calcd. C 59.80, H 5.90; found C 59.69, H 5.86.

**5,5′-Bis(1′′,2′′,3′′,4′′,5′′-pentamethylruthenocenyl)-2,2′-bithiophene (8):** This compound was prepared from 1,8-bis(1′′,2′′,3′′,4′′,5′′-

 © 2006 Wiley-VCH Verlag GmbH & Co. KGaA, Weinheim 

pentamethylruthenocenyl)octa-1,3,5,7-tetrayne according to the procedure described above (reaction temperature: 110 °C). Red–orange solid. Yield 64%. M.p. 230 °C (dec.). $^1$H NMR (400 MHz, $CDCl_3$): $\delta$ = 1.79 (s, 30 H, Me), 4.29 (t, $J$ = 1.6 Hz, 4 H, η-$C_5H_4$), 4.53 (t, $J$ = 1.6 Hz, 4 H, η-$C_5H_4$), 6.69 (d, $J$ = 3.8 Hz, 2 H, =CH), 6.90 (d, $J$ = 3.8 Hz, 2 H, =CH) ppm. $^{13}$C NMR (100 MHz, $CDCl_3$): $\delta$ = 11.33 (Me), 70.64 (η-$C_5H_4$), 73.24 (η-$C_5H_4$), 82.96 (*ipso*-η-$C_5H_4$), 85.52 (η-$C_5Me_5$), 121.12 (=CH), 122.81 (=CH), 133.63 (=C–S), 140.07 (=C–S) ppm. $C_{38}H_{42}Ru_2S_2$ (765.02): calcd. C 59.66, H 5.53; found C 59.47, H 5.42.

**Chemical Oxidation of Complex 2:** To a solution of **2** (16.3 mg, 0.03 mmol) and *p*-BQ (6.3 mg, 0.06 mmol) in $CHCl_3$ (3 mL) chilled at 0 °C by an ice bath was added $BF_3$·$OEt_2$ (2 drops from a capillary) under an atmosphere of nitrogen. After the resulting dark brown solution had been stirred for 5 min at 0 °C, dry benzene (3 mL) was added to the solution and then kept for 30 min at the same temperature. The mixture was filtered under reduced pressure and washed with pentane to afford a black powder (16 mg) (The product contained hydroquinone). $^1$H NMR (400 MHz, $CD_3NO_2$, 0 °C): $\delta$ = 5.26 (s, 10 H), 5.75 (br. s, 2 H), 5.90 (br. s, 2 H), 6.32 (br. s, 2 H), 6.40 (br. s, 2 H), 7.46 (s, 2 H) ppm. $^1$H NMR (400 MHz, $CD_3CN$, –5 °C): $\delta$ = 4.57 (s, 5 H, η-$C_5H_5$), 5.02 (t, $J$ = 1.8 Hz, 2 H, η-$C_5H_4$), 5.36 (t, $J$ = 1.8 Hz, 2 H, η-$C_5H_4$), 5.88 (s, 5 H, η-$C_5H_5$), 6.01 (t, $J$ = 2.6 Hz, 2 H, η-$C_5H_4$), 6.27 (t, $J$ = 2.6 Hz, 2 H, η-$C_5H_4$), 7.40 (d, $J$ = 4.5 Hz, 1 H, =CH), 8.05 (d, $J$ = 4.5 Hz, 1 H, =CH) ppm. $^{13}$C NMR (100 MHz, $CD_3NO_2$, –5 °C): $\delta$ = 77.42 (η-$C_5H_4$), 78.72 (η-$C_5H_4$), 86.24 (η-$C_5H_5$), 90.33 (η-$C_5H_4$), 90.66 (η-$C_5H_4$), 92.90 (*ipso*-η-$C_5H_4$), 129.96 (=C–S), 137.01 (=CH) ppm.

**Chemical Oxidation of Complex 7:** *Method A*: To a solution of **7** (20.5 mg, 0.03 mmol) and *p*-BQ (6.3 mg, 0.06 mmol) in dry $CH_2Cl_2$ (3 mL) chilled at 0 °C by an ice bath was added $BF_3$·$OEt_2$ (1 drop from a capillary) under an atmosphere of nitrogen. After the resulting red–violet solution had been stirred for 3 min at 0 °C, dry benzene (6 mL) was added to the solution, and the stirring was then stopped. After the solution had been kept for 30 min at 0 °C, dry benzene (9 mL) was added to the solution, and the solution was then kept for 1 h at the same temperature. The mixture was filtered under reduced pressure and washed with pentane to afford black powdery crystals (16 mg) (The product contained hydroquinone). The crystals were comparably stable when stored in the freezer. The solution of the product in $CD_3NO_2$ or $CD_3CN$ immediately after its preparation produced a clear $^1$H NMR spectrum. $^1$H NMR (400 MHz, $CD_3NO_2$, –5 °C): $\delta$ = 1.79 (s, 30 H), 5.53 (t, $J$ = 2.0 Hz, 4 H), 5.90 (m, 4 H), 7.41 (s, 2 H) ppm. $^1$H NMR (400 MHz, $CD_3CN$, 0 °C): $\delta$ = 1.66 (s, 15 H), 1.92 (s, 15 H), 4.78 (t, $J$ = 1.8 Hz, 2 H), 4.94 (br. s, 2 H), 5.57 (t, $J$ = 2.3 Hz, 2 H), 5.69 (m, 2 H), 7.11 (d, $J$ = 4.6 Hz, 1 H), 7.99 (d, $J$ = 4.6 Hz, 1 H) ppm. $^{13}$C NMR (100 MHz, $CD_3NO_2$, –5 °C): $\delta$ = 7.39 (Me), 75.85 (η-$C_5H_4$), 77.10 (η-$C_5H_4$), 93.81 (η-$C_5H_4$), 93.99 (η-$C_5H_4$), 95.34 (*ipso*-η-$C_5H_4$), 98.49 (η-$C_5Me_5$), 132.93 (=C–S), 136.58 (=CH) ppm.

*Method B*: To a solution of **7** (13.7 mg, 0.02 mmol) in dry $CH_2Cl_2$ (3 mL) was added ferricenium tetra{3,5-bis(trifluoromethyl)-phenyl}borate (42 mg, 0.04 mmol) at 0 °C under an atmosphere of nitrogen. After the resulting red–violet solution had been stirred for 15 min at 0 °C, dry benzene (6 mL) was added to the solution and the stirring was then stopped. After the solution had been kept for 30 min at 0 °C, dry benzene (9 mL) was added to the solution, and the solution was then kept for 1.5 h at the same temperature. The resulting fine crystals were collected by filtration under reduced pressure. Dark red–violet fine crystals (37 mg). $^1$H NMR (400 MHz, $CD_2Cl_2$, 0 °C): $\delta$ = 1.70 (s, 30 H, Me), 5.19 (m, 2 H, η-$C_5H_4$), 5.24 (m, 2 H, η-$C_5H_4$), 5.65 (t, $J$ = 2.1 Hz, 4 H, η-$C_5H_4$), 7.02 (s, 2 H, =CH), 7.56 (br. s, 8 H, $C_6H_3$), 7.72 (br. s, 16 H, $C_6H_3$) ppm. $^1$H NMR (400 MHz, [D$_6$]acetone, 0 °C): $\delta$ = 1.83 (s, 30 H, Me), 5.81 (br. s, 2 H, η-$C_5H_4$), 5.89 (br. s, 2 H, η-$C_5H_4$), 6.17 (br. s, 4 H, η-$C_5H_4$), 7.68 (br. s, 8 H, $C_6H_3$), 7.77 (br. s, 16 H, $C_6H_3$), 7.83 (s, 2 H, =CH) ppm. $^1$H NMR (400 MHz, $CD_3NO_2$, 0 °C): $\delta$ = 1.80 (s, 30 H, Me), 5.52 (m, 4 H, η-$C_5H_4$), 5.90 (m, 4 H, η-$C_5H_4$), 7.41 (s, 2 H, =CH), 7.67 (br. s, 8 H, $C_6H_3$), 7.84 (br. s, 16 H, $C_6H_3$) ppm. $^1$H NMR (400 MHz, $CD_3CN$, –10 °C): $\delta$ = 1.65 (s, 15 H, Me), 1.91 (s, 15 H, Me), 4.78 (t, $J$ = 1.8 Hz, 2 H, η-$C_5H_4$), 4.93 (m, 2 H, η-$C_5H_4$), 5.56 (t, $J$ = 2.4 Hz, 4 H, η-$C_5H_4$), 5.67 (m, 2 H, η-$C_5H_4$), 7.10 (d, $J$ = 4.6 Hz, 1 H, =CH), 7.35 (br. s, 8 H, $C_6H_3$), 7.67 (br. s, 16 H, $C_6H_3$), 7.98 (d, $J$ = 4.6 Hz, 1 H, =CH) ppm. $C_{98}H_{64}B_2F_{48}Ru_2S$ (2409.35): calcd. C 48.85, H 2.68; found C 48.42, H 2.61.

**Chemical Oxidation of Complex 5:** To a solution of **5** (8.0 mg, 0.015 mmol) and *p*-BQ (3.2 mg, 0.03 mmol) in $CHCl_3$ (3 mL) chilled at 0 °C by an ice bath was added $BF_3$·$OEt_2$ (2 drops from a capillary) under an atmosphere of nitrogen. After the resulting dark brown solution had been stirred for 1 h at 0 °C, dry $Et_2O$ (6 mL) was added to the solution and the stirring was then stopped. The solution was kept for 1 h at the same temperature. The reaction was filtered under reduced pressure and washed with pentane to afford black crystals (6.5 mg) that were stable when stored in the freezer. The solution of the product in $CD_3NO_2$ (deep blue–violet) or $CD_3CN$ (deep blue) produced a clear $^1$H NMR spectrum. $^1$H NMR (400 MHz, $CD_3NO_2$, 20 °C): $\delta$ = 5.27 (s, 10 H), 5.93 (t, $J$ = 1.9 Hz, 4 H), 6.30 (t, $J$ = 1.9 Hz, 4 H), 7.53 (s, 2 H) ppm. $^{13}$C NMR (100 MHz, $CD_3NO_2$, 20 °C): $\delta$ = 76.50 (η-$C_5H_4$), 84.18 (η-$C_5H_5$), 88.79 (η-$C_5H_4$), 95.77 (*ipso*- η-$C_5H_4$), 125.88 (=CH) ppm. $^1$H NMR (400 MHz, $CD_3NO_2$, –35 °C): $\delta$ = 5.24 (s, 10 H), 5.88 (br. s, 2 H), 5.98 (br. s, 2 H), 6.27 (br. s, 4 H), 7.51 (s, 2 H) ppm. $^1$H NMR (400 MHz, $CD_3CN$, 0 °C): $\delta$ = 4.55 (s, 5 H), 4.93 (br. s, 2 H), 5.29 (br. s, 2 H), 5.90 (s, 5 H), 6.12 (br. s, 5 H), 6.34 (br. s, 2 H), 7.45 (s, 1 H), 8.32 (s, 1 H) ppm.

### Electronic Structure Calculation

DFT calculations were performed with the Gaussian 03 package program.[25] The calculation at the B3LYP hybrid density-functional levels[26,27] with the 3-21G basis set did not reproduce the optimized structure of the two-electron oxidized species in the present series determined by the NMR spectra and X-ray analysis. In order to understand this source, extensive DFT calculations for ruthenocene ($C_{10}H_{10}Ru$ with $D_{5h}$ symmetry) have also been performed with various combinations of exchange and correlation functionals. As a result, we have chosen to use the local spin density approximation (LSDA) with the Vosko–Wilk–Nusair exchange-correlation potential[28] for the calculation of our systems, because the previous theoretical study[29,30] at this level for ruthenocene showed relatively good agreement with the experimental data and give the order of $3e'_2 < 5a'_1 < 4e''_1$ [$(3e'_2)^4(5a'_1)^2(4e''_1)^0$]. Notice that the HOMO of ruthenocene is an $a_{1g}$ orbital and this gives a significant result in the ionization state of ruthenocene and the structure of the dications of binuclear ruthenocene derivatives. Thus, it may be suggested that the extraction of an electron from the $a_{1g}$ orbital of the ruthenocene moiety of **2** and **7** is likely to cause the deformation of the bridging ligand in **10** and **12**, respectively.

A Stuttgart–Dresden–Bonn quasirelativistic ECP28 MWB (SDD) effective core potential[31] have been employed for ruthenium atoms. The standard 6-311G basis sets were used for C and H atoms, whereas the 6-311G(*d*) basis set was used to describe the

 © 2006 Wiley-VCH Verlag GmbH & Co. KGaA, Weinheim 

Table 5. Crystallographic data for **3**, **7**, and **13**.

| | **3** | **7** | **13** |
|---|---|---|---|
| Empirical formula | $C_{26}H_{22}O_2Ru_2S$ | $C_{34}H_{40}Ru_2S$ | $C_{106}H_{84}B_2F_{48}O_2Ru_2S$ |
| Formula mass | 600.664 | 682.898 | 2557.55 |
| Crystal system | Monoclinic | Triclinic | Triclinic |
| Space group | $P21/c$ | $P\bar{1}$ | $P\bar{1}$ |
| $a$ [Å] | 11.8770(10) | 7.8370(8) | 14.0768(7) |
| $b$ [Å] | 14.3180(10) | 13.5590(13) | 14.4758(7) |
| $c$ [Å] | 12.7840(10) | 15.458(2) | 15.5151(8) |
| $\alpha$ [°] | 90 | 105.672(6) | 88.9260(10) |
| $\beta$ [°] | 92.372(7) | 102.038(5) | 76.1620(10) |
| $\gamma$ [°] | 90 | 99.768(10) | 63.8540(10) |
| $V$ [Å$^3$] | 2172.1(3) | 1501.5(3) | 2742.0(2) |
| $Z$ | 4 | 2 | 1 |
| $D_{calcd.}$ [Mg m$^{-3}$] | 1.837 | 1.510 | 1.549 |
| Crystal size [mm] | 0.20 × 0.15 × 0.08 | 0.18 × 0.06 × 0.02 | 0.28 × 0.14 × 0.12 |
| Radiation ($\lambda$ [Å]) | Mo-$K_\alpha$ (0.71073) | Mo-$K_\alpha$ (0.71073) | Mo-$K_\alpha$ (0.71073) |
| Reflection ($hkl$) limits | $-15 \le h \le 15$ | $-9 \le h \le 9$ | $-18 \le h \le 17$ |
| | $0 \le k \le 18$ | $-15 \le k \le 15$ | $-19 \le k \le 15$ |
| | $0 \le l \le 15$ | $0 \le l \le 19$ | $-17 \le l \le 20$ |
| Total reflections measured | 4466 | 5203 | 20164 |
| Unique reflections | 4314 | 5198 | 12980 |
| Linear abs. coeff. [mm$^{-1}$] | 1.508 | 1.10 | 0.424 |
| Reflections used in L.S. | 4314 | 5198 | 12980 |
| R | 0.0688 | 0.0681 | 0.0789 |
| $R$w | 0.1886 | 0.1881 | 0.2131 |
| $S$ | 1.087 | 1.035 | 0.997 |
| Max peak in final Fourier map [e Å$^{-3}$] | 0.792 | 0.861 | 1.092 |
| Min peak in final Fourier map [e Å$^{-3}$] | –1.432 | –0.922 | –0.788 |

hypervalency of the sulfur atom. In order to further examine the effect of polarization, larger basis sets of 6-311G(*d*) have also been employed for C and H and 6-311G(2*d*) for S.

**Structure Determination**

The crystallographic data are listed in Table 5 for **3**, **7**, and **13**. Data collection of crystal data for **3** and **7** was performed at room temperature with a Mac Science DIP3000 image processor. The structures of **3** and **7** were solved with the Dirdif-Patty method in MAXUS (software package for structure determination) and refined finally by full-matrix least-squares procedure with SHELEX. Crystal data for **13** were collected at –196 °C (liquid $N_2$) with a Bruker Apex diffractometer with graphite monochromated Mo-$K_\alpha$ radiation and an 18-kW rotating anode generator. The structure of **13** was solved and refined by SHELEX. Absorption correction for **3** and **7** was carried out by the Sortav method and anisotropic refinement for non-hydrogen atom was carried out. The hydrogen atoms, located from difference Fourier maps or calculation, were isotropically refined.

CCDC-298964 (**3**), -298965 (**7**), and -298966 (**13**) contain the supplementary crystallographic data for this paper. These data can be obtained free of charge from The Cambridge Crystallographic Data Centre via www.ccdc.cam.ac.uk/data_request/cif..


[1] a) M. D. Ward, *Chem. Soc. Rev.* **1995**, *24*, 121–134; b) V. Grosshenny, A. Harriman, R. Ziessel, *Angew. Chem. Int. Ed. Engl.* **1995**, *34*, 1100–1102.

[2] a) M. Altmann, U. F. H. Bunz, *Angew. Chem. Int. Ed. Engl.* **1995**, *34*, 569–571; b) L. Oriol, J. L. Serrano, *Adv. Mater.* **1995**, *7*, 348–369.

[3] J.-M. Lehn, *Suppramolecular Chemistry: Concepts and Perspectives*, VCH Publishers, Weinheim, Germany, **1995**.

[4] M. I. Bruce, P. J. Low, *Adv. Organomet. Chem.* **2004**, *50*, 179–444.

[5] a) F. Paul, C. Lapinte, *Coord. Chem. Rev.* **1998**, *178–180*, 431–509; b) U. H. Bunz, *Angew. Chem. Int. Ed. Engl.* **1996**, *35*, 969–971; c) A. Nakamura, *Bull. Chem. Soc. Jpn.* **1995**, *68*, 1515–1521; d) N. J. Long, *Angew. Chem. Int. Ed. Engl.* **1995**, *34*, 21–38; e) H. Lang, *Angew. Chem. Int. Ed. Engl.* **1994**, *33*, 547–550; f) W. Beck, B. Niemer, M. Wieser, *Angew. Chem. Int. Ed. Engl.* **1993**, *32*, 923–949.

[6] D. Astruc, *Electron Transfer and Radical Process in Transition-Metal Chemistry*, VCH, New York, **1995**.

[7] a) G.-L. Xu, R. J. Crutchley, M. C. DeRosa, Q.-J. Pan, H.-X. Zhang, X. Wang, T. Ren, *J. Am. Chem. Soc.* **2005**, *127*, 13354–13363; b) W. Skibar, H. Kopacka, K. Wurst, C. Salzmann, K.-H. Ongania, F. Fabrizi de Biani, P. Zanello, B. Bildstein, *Organometallics* **2004**, *23*, 1024–1041; c) J. H. K. Yip, J. Wu, K.-Y. Wong, K. P. Ho, C. S.-N. Pun, J. J. Vittal, *Organometallics* **2002**, *21*, 5292–5300; d) N. J. Long, *Metallocens: An Introduction to Sandwich Complexes*, Blackwell Science, Oxford, UK, **1998**; e) A. Hradsky, B. Bildstein, N. Schuler, H. Schottenberger, P. Jaitner, K.-H. Ongania, K. Wurst, J.-P. Laumay, *Organometallics* **1997**, *16*, 392–402; f) N. D. Jones, M. O. Wolf, D. M. Giaquinta, *Organometallics* **1997**,*16*, 1352–1354; g) M. C. B. Colbert, J. Lewis, N. J. Long, P. R. Raithby, A. J. P. White, D. J. Williams, *J. Chem. Soc., Dalton Trans.* **1997**, 99–104; h) A.-C. Ribou, J.-P. Launay, M. L. Sachtleben, H. Li, C. W. Spangler, *Inorg. Chem.* **1996**, *35*, 3735–3740; i) Z. Yuan, G. Stringer, I. R. Jobe, D. Kreller, L. Koch, N. J. Taylor, T. B. Marder, *J. Organomet. Chem.* **1993**, *452*, 115–120.

[8] a) S.-M. Lee, M. Marcaccio, J. A. McCleverty, M. D. Ward, *Chem. Mater.* **1998**, *10*, 3272–3274; b) R. D. McCullough, *Adv. Mater.* **1998**, *10*, 93–116; c) J. Roncali, *Chem. Rev.* **1997**, *97*, 173–205; d) J. M. Tour, *Chem. Rev.* **1996**, *96*, 537–553; e) M. C. B. Colbert, D. Hodgson, J. Lewis, P. R. Raithby, N. J. Long, *Polyhedron* **1995**, *14*, 2759–2766.

[9] a) P. Li, B. Ahrens, H. Feeder, P. R. Raithby, S. T. Teat, M. S. Khan, *Dalton Trans.* **2005**, 874–883; b) M. Landman, H. Görls, S. Lotz, *Eur. J. Inorg. Chem.* **2001**, 233–238; c) R. D. A. Hudson, A. R. Manning, D. F. Nolan, I. Asselberghs, R. V. Boxe-


 © 2006 Wiley-VCH Verlag GmbH & Co. KGaA, Weinheim 

151l, A. Persoons, J. F. Gallagher, *J. Organomet. Chem.* **2001**, *619*, 141; d) S. L. Stang, F. Paul, C. Lapinte, *Organometallics* **2000**, *19*, 1035–1043; e) M. C. B. Colbert, J. Lewis, N. J. Long, P. R. Raithby, M. Younus, A. J. P. White, D. J. Williams, N. N. Payne, L. Yellowlees, D. Beljonne, N. Chawdhury, R. H. Friend, *Organometallics* **1998**, *17*, 3034–3043; f) J. Lewis, N. J. Long, P. R. Raithby, G. P. Shields, W.-Y. Wong, M. Younus, *J. Chem. Soc. Dalton Trans.* **1997**, 4283–4288.

[10] a) B. Jacques, J.-P. Tranchier, F. Rose-Munch, E. Rose, *Organometallics* **2004**, *23*, 184–193; b) W.-Y. Wong, G.-L. Lu, A.-F. Ng, K.-H. Choi, Z. Lin, *J. Chem. Soc. Dalton Trans.* **2001**, 3250–3260; c) Y. Zhu, M. O. Wolf, *J. Am. Chem. Soc.* **2000**, *122*, 10121–10125; d) K. R. Justin Thomas, J. T. Lin, Y. S. Wen, *Organometallics* **2000**, *19*, 1008–1012; e) M. Sato, M. Shiraogawa, *CACS Forum* **1993**, *13*, 30–32.

[11] M. Watanabe, M. Sato, T. Takayama, *Organometallics* **1999**, *18*, 5201–5203.

[12] a) M. Sato, T. Nagata, A. Tanemura, T. Fujihara, S. Kumakura, K. Unoura, *Chem. Eur. J.* **2004**, *10*, 2166–2178; b) M. Sato, Y. Kawata, A. Kudo, A. Iwai, H. Saitoh, S. Ochiai, *J. Chem. Soc. Dalton Trans.* **1998**, 2215–2224; c) M. Sato, A. Kudo, Y. Kawata, H. Saitoh, *Chem. Commun.* **1996**, 25–26.

[13] a) M. Sato, Y. Kubota, Y. Kawata, T. Fujihara, K. Unoura, A. Oyama, *Chem. Eur. J.* **2006**, *12*, 2282–2292; b) M. Sato, M. Watanabe, *Chem. Commun.* **2002**, 1574–1575.

[14] M. Sato, G. Maruyama, A. Tanemura, *J. Organomet. Chem.* **2002**, *655*, 23–30.

[15] D. Obendorf, H. Schottenberger, K. Wurst, N. Schuler, G. Laus, *J. Organomet. Chem.* **2005**, *690*, 811–817.

[16] K. Unoura, A. Iwase, H. Ogino, *J. Electro. Chem. Interfacial Electrochem.* **1990**, *295*, 385–392.

[17] S. Barlow, A. Cowley, J. C. Green, T. J. Brunker, T. Hascall, *Organometallics* **2001**, *20*, 5351–5359.

[18] A. I. Yanovsky, Yu. T. Struchkov, A. Z. Kleindlin, M. I. Rybinskaya, *J. Organomet. Chem.* **1989**, *369*, 125–130.

[19] O. Hofer, K. Schlögl, *J. Organomet. Chem.* **1968**, *13*, 443–456.

[20] L. S. Fuller, B. Iddon, K. A. Smith, *J. Chem. Soc. Perkin Trans. 1* **1977**, 3465–3470.

[21] K. S. Choi, K. Sawada, H. Dong, M. Hoshino, J. Nakayama, *Heterocycles* **1994**, *38*, 143–149.

[22] H. Meng, D. F. Perepichka, M. Bendikov, F. Wudl, G. Z. Pan, W. Yu, W. Dong, B. Brown, *J. Am. Chem. Soc.* **2003**, *125*, 15151–15162.

[23] T. Hayashi, M. Konishi, Y. Kobori, M. Kumada, T. Higuchi, K. Hirotsu, *J. Am. Chem. Soc.* **1984**, *106*, 158–163.

[24] I. Chávez, A. Alverez-Carena, E. Molins, A. Roig, W. Maniu-Kiewicz, A. Arancibia, V. Arencibia, H. Brand, I. M. Manríquez, *J. Organomet. Chem.* **2000**, *601*, 126–132.

[25] M. J. Frisch, G. W. Trucks, H. B. Schlegel, G. E. Scuseria, M. A. Robb, J. R. Cheeseman, J. A. Montgomery Jr, T. Vreven, K. N. Kudin, J. C. Burant, J. M. Millam, S. S. Iyengar, J. Tomasi, V. Barone, B. Mennucci, M. Cossi, G. Scalmani, N. Rega, G. A. Petersson, H. Nakatsuji, M. Hada, M. Ehara, K. Toyota, R. Fukuda, J. Hasegawa, M. Ishida, T. Nakajima, Y. Honda, O. Kitao, H. Nakai, M. Klene, X. Li, J. E. Knox, H. P. Hratchian, J. B. Cross, C. Adamo, J. Jaramillo, R. Gomperts, R. E. Stratmann, O. J. Yazyev, A. Austin, R. Cammi, C. Pomelli, J. W. Ochterski, P. Y. Ayala, K. Morokuma, G. A. Voth, P. Salvador, J. J. Dannenberg, V. G. Zakrzewski, S. Dapprich, A. D. Daniels, M. C. Strain, O. Farkas, D. K. Malick, A. D. Rabuck, K. Raghavachari, J. B. Foresman, J. V. Ortiz, Q. Cui, A. G. Baboul, S. Clifford, J. Cioslowski, B. B. Stefanov, G. Liu, A. Liashenko, P. Piskorz, I. Komaromi, R. L. Martin, D. J. Fox, T. Keith, M. A. Al-Laham, C. Y. Peng, A. Nanayakkara, M. Challacombe, P. M. W. Gill, B. Johnson, W. Chen, M. W. Wong, C. Gonzalez, J. A. Pople, *Gaussian 03*, Revision C.02, Gaussian, Inc., Wallingford, CT, **2004**.

[26] A. D. Becke, *J. Chem. Phys.* **1993**, *98*, 5648–5652.

[27] C. Lee, W. Yang, R. G. Parr, *Phys. Rev. B* **1988**, *37*, 785–789.

[28] S. H. Vosko, L. Wilk, N. Nusair, *Can. J. Phys.* **1980**, *58*, 1200–1211.

[29] C. Daul, H.-U. Güdel, J. Weber, *J. Chem. Phys.* **1993**, *98*, 4023–4029.

[30] F. Gilardoni, J. Weber, A. Hauser, C. Daul, *J. Chem. Phys.* **1998**, *109*, 1425–1434.

[31] A. Bergner, M. Dolg, W. Kuechle, H. Stoll, H. Preuss, *Mol. Phys.* **1993**, *80*, 1431–1441.

Received: April 26, 2006
Published Online: September 18, 2006

 © 2006 Wiley-VCH Verlag GmbH & Co. KGaA, Weinheim 

DOI: 10.1002/ejic.200600444

# Monophosphanes and Diphosphanes with the Hypersilyl Substituent

**Vittorio Cappello,[a] Judith Baumgartner,[a][‡] and Alk Dransfeld,[a][‡‡] and Karl Hassler*[a]**

**Keywords:** Hypersilylphosphanes / Potassium phosphanides / Ab initio calculations / *P*-Silylhalophosphanes / Silicon

The synthesis of $(SiMe_3)_3SiPH_2$ (**1**) (further on denoted as hypersilylphosphane, $HypPH_2$) was achieved by two methods: by the reaction of $(SiMe_3)_3Si(OSO_2CF_3)$ with $PH_3$, and alternatively, by the reaction of $NaPH_2$ with $(SiMe_3)_3SiCl$ (hypersilylchloride). The latter reaction also afforded bis(hypersilyl)phosphane $Hyp_2PH$ (**2**). By the reaction of **1** and known hypersilylbis(trimethylsilyl)phosphane (**3**) with *t*BuOK, the novel hypersilylphosphanides HypPHK (**4**) and $Hyp(SiMe_3)PK$ (**5**) were prepared. Compound **1** also reacted with *n*BuLi to form HypPHLi (**6**) and $HypPLi_2$ (**7**). Furthermore, **3** reacted with hexachloroethane and 1,2-dibromotetrachloroethane to give $HypPCl(SiMe_3)$ (**8**) and $HypPBr(SiMe_3)$ (**9**) as well as $HypPCl_2$ (**10**) and $HypPBr_2$ (**11**). Compounds **4** and **5** reacted smoothly with 1,2-dibromoethane to give diphosphane HypHPPHHyp (**12**) as a mixture of the *meso*- and *rac*-D,L-diastereomers and $Hyp(SiMe_3)PP(SiMe_3)Hyp$ (**13**) as the D,L-modification only. By reducing the known compound *t*BuHypPCl with potassium, the D,L-modification of *t*BuHypPPHyp*t*Bu (**14**) was obtained. All compounds were characterized by $^{29}Si$- and $^{31}P$ NMR spectroscopy and elemental analyses with the exception of the phosphanides which were characterized spectroscopically only. The crystal structures of **3** and **4** and of diphosphanes **10**, **11** and **13** are reported. From temperature-dependent $^{31}P$ NMR experiments, the coalescence temperature for the *meso*↔D,L interconversion of **12** was determined at 110 °C and gave an inversion barrier of roughly 69.4 kJ mol$^{-1}$, which is corroborated by results of ab initio calculations at the B3LYP/6-31G(d) level. Two diastereomeric inversion transition structures for diphosphanes R–PH–PH–R with either a *syn* or an *anti* arrangement of the P–H bond and the phosphorus lone pair of electrons could be located; bulky substituents seem to prefer the *anti* arrangement.

(© Wiley-VCH Verlag GmbH & Co. KGaA, 69451 Weinheim, Germany, 2006)

## Introduction

The bulky tris(trimethylsilyl)silyl group, often denoted as the hypersilyl group [a term coined by Nils Wiberg[1] to distinguish it from the tri(*tert*-butyl)silyl group which he named supersilyl], has been used extensively in the past to stabilize and protect uncommon bonding states of main group elements and transition elements. Despite the bulkiness of the group, a number of geminal dihypersilyl derivatives were also synthesized successfully, essentially with heavier main group elements. We will not give a full account of all the compounds that have been prepared so far, as this can be found in refs.[2–4] and the literature cited therein. K. Klinkhammer even succeeded to synthesize $NaSnHyp_3$, the only known compound with three hypersilyl groups on one central atom.[5]

Despite this widespread use of the hypersilyl group, the number of known hypersilyl compounds of the elements of group V (N, P, As, Sb, and Bi) is surprisingly small. With nitrogen, $HypNH_2$, HypNHLi, $HypNH(SiMe_3)$ and $HypNLi(SiMe_3)$ have been described,[6] and some derivatives such as tris(trimethylsilyl)silylamides of zinc,[7] tin and mercury have also been reported.[8]

The first hypersilyl phosphorus compound, HypP*t*BuCl, was described by Cowley.[9] It is a thermally stable silylhalophosphane that undergoes a silicon–halogen exchange reaction at about 100 °C. Hypersilyldiphenylphosphane was prepared for mass spectroscopic purposes in 1993.[10] Regitz et al. introduced the hypersilyl group into 1*H*-phosphirenes, which undergo isomerization to furnish trimethylsilyl-substituted phosphasiletanes upon irradiation.[11] Klingebiel reported the preparation of stable hypersilylfluorophosphanes that have an amino group as the third substituent on the P atom, for instance $(SiMe_3)_2N$.[12] The synthesis of $HypPMe(NRP{=}NR)$ with R = 2,4,6-$(Me_3C)_3C_6H_2$ was reported in 1991.[13] Recently, C. Marschner reported the synthesis of a bis(hypersilyl)phosphane, $Hyp_2PNR$.[14]

In our group, bis(trimethylsilyl)hypersilylphosphane was prepared some years ago by the reaction of bis(trimethylsilyl)lithiumphosphanide with hypersilylchloride (Scheme 1).[15]

[a] Institute of Inorganic Chemistry, University of Technology, Stremayrgasse 16, 8010 Graz, Austria
E-mail: vittorio.cappello@tugraz.at
judith.baumgartner@tugraz.at
alk.dransfeld@tugraz.at
karl.hassler@tugraz.at
[‡] X-ray structures
[‡‡]Ab initio calculations

 © 2006 Wiley-VCH Verlag GmbH & Co. KGaA, Weinheim 

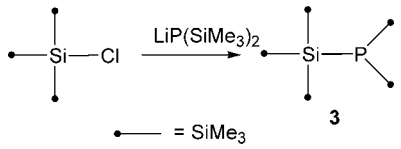


Scheme 1.

Recently, we also reported the synthesis of air-stable tri(hypersilyl)heptaphosphane,[16] which undergoes an interesting reaction with *t*BuOK even at temperatures as low as –60 °C. In the first step of the reaction, a silicon–silicon bond is cleaved with concomitant formation of $tBuOSiMe_3$. The resulting potassium silanide rearranges into a heptaphosphanide anion and bis(trimethylsilyl)silylene that inserts into a P–P bond of the three-membered ring at the base of the $P_7$-cage.[17]

At present, no compounds with the hypersilyl group attached to arsenic, antimony or bismuth are known.

The desire to have at our disposal some hypersilyl–phosphorus synthons which can be used widely, for instance for the preparation of hypersilyldiphosphanes and hypersilyloligophosphanes, motivated us to investigate various possibilities for the preparation of $HypP(SiMe_3)X$ and $HypPX_2$, (X = halogen), HypPHK and $HypP(SiMe_3)K$. Here we report on the successful synthesis of these phosphanes and phosphanides as well as on some reactions they can undergo.

## Results and Discussion

### Syntheses

#### *Synthesis of $HypPH_2$ (1) and $(Hyp)_2PH$ (2)*

Reactions of silyltriflates with $PH_3$ that form Si–P bonds were first described by W. Uhlig.[18] We transferred this methodology to the synthesis of $(SiMe_3)_3Si(OSO_2CF_3)$ (prepared from $(SiMe_3)_3SiPh$[19] and $HOSO_2CF_3$), which reacts cleanly with $PH_3$ in the presence of triethylamine to give $HypPH_2$ in almost quantitative yield. No disubstitution with the hypersilyl group at the phosphorus atom could be observed in this reaction. An alternative route starts from $NaPH_2$, which can be prepared from $PH_3$ and sodium in liquefied ammonia.[20] If the reaction is heated at reflux in toluene, $(SiMe_3)_3SiCl$ and $NaPH_2$ slowly react over a period of a week to give a 1:1 mixture of hypersilyl- and dihypersilylphosphane (Scheme 2).

As minor byproducts of the reaction that are easily identified with $^{31}P$ NMR spectroscopy, HypPHHPHyp and $P_7Hyp_3$ are also formed, probably through the decomposition of $NaPH_2$ at 110 °C:

$$2\ NaPH_2 \rightarrow Na_2PH + PH_3$$

$$3\ NaPH_2 \rightarrow Na_3P + 2\ PH_3$$

As $HypPH_2$ and $(Hyp)_2PH$ can easily be separated and purified by fractional sublimation in vacuo, this procedure simultaneously affords both phosphanes on a preparative scale.

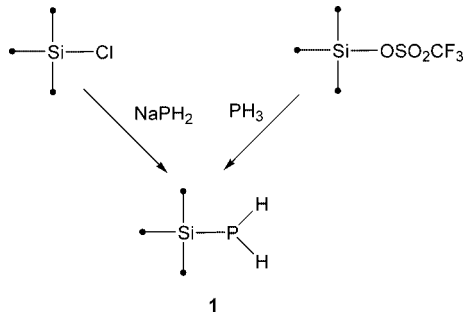


Scheme 2.

#### *Synthesis of HypPHK (4), $HypP(SiMe_3)K$ (5), and HypPHLi (6)*

It is well known from the work of G. Fritz[21] that P–Si bonds can be cleaved by alkyllithium reagents to form silylated Li-phosphanides. However, these phosphanides are not very stable at room temperature. For instance, $(SiMe_3)_2PP(SiMe_3)Li$ decomposes quickly to form a plethora of compounds such as $P(SiMe_3)_3$, $LiP(SiMe_3)_2$ and $Li_3P$.

To obtain some understanding of the thermal stability of hypersilyllithiumphosphanides, we treated $HypPH_2$ with *n*BuLi in THF at –60 °C. As expected, the only initial product that was formed was HypPHLi, which decomposed slowly to form $HypP(SiMe_3)Li$ and $HypPLi_2$ as well as $(SiMe_3)_2PLi$ besides some other unidentified products. The intensity of the signal in the $^{31}P$ NMR spectrum of HypPHLi gradually diminished with time.

We therefore chose to investigate the reaction of $HypPH_2$ with *t*BuOK. Though *t*BuOK is known to cleave P–Si bonds of $P(SiMe_3)_3$[22] to give $(SiMe_3)_2PK$ and $tBuOSiMe_3$, it was our expectation that the hypersilyl group might not be attacked due to its bulkiness and that PH would be transformed into PK.

As could easily be followed by $^{31}P$ NMR spectroscopy, the reaction cleanly gave HypPHK in about 90% yield in THF. A minor byproduct of the reaction was $HypPK_2$, besides some $HypPH_2$ (Scheme 3). Most importantly, HypPHK turned out to be stable for more than a week at room temperature. It can be crystallized from hexane in the presence of 18-crown-6 for further purification.

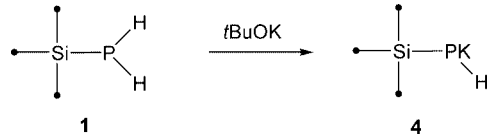


Scheme 3.

Because of the bulkiness of the hypersilyl group, *t*BuOK reacts with $HypP(SiMe_3)_2$ by the cleavage of only one trimethylsilyl group to form $HypPK(SiMe_3)$ in excellent yields (>90%). As a minor byproduct, HypPHK was always present in the reaction mixtures. $HypPK_2$ can also be obtained from $HypP(SiMe_3)_2$ by adjusting the stoichiometry, albeit in moderate yields.

 © 2006 Wiley-VCH Verlag GmbH & Co. KGaA, Weinheim 

### *Synthesis of HypP(SiMe$_3$)H*

Over a period of three weeks, **3** (Scheme 4) reacts slowly with *t*BuOH at room temperature to form HypP(SiMe$_3$)H and Me$_3$SiO*t*Bu as a byproduct. No cleavage of the hypersilyl–phosphorus bond occurs, and no HypPH$_2$ can be detected in the reaction mixture. HypP(SiMe$_3$)H is easily separated from unreacted **3** by vacuum sublimation.

**3** **5**

Scheme 4.

### *Synthesis of HypPX(SiMe$_3$) and HypPX$_2$, X = Cl, Br (8, 9, 10, 11)*

By the reaction of *t*BuP(SiMe$_3$)$_2$ with C$_2$Cl$_6$, Appel[23] et al. were able to prepare *t*BuP(SiMe$_3$)Cl, the first moderately stable P-chloro–P-silylphosphane with $t_{1/2} \approx 13$ min at ambient temperature. We were curious to know if the substitution of the *t*Bu group with hypersilyl would also give stable chlorosilylphosphanes, which it did. The synthesis was achieved by the reaction of HypP(SiMe$_3$)$_2$ with one or two equiv. of C$_2$Cl$_6$ (Scheme 5). All attempts to crystallize the samples failed despite the fact that the compounds were formed in excellent yields.

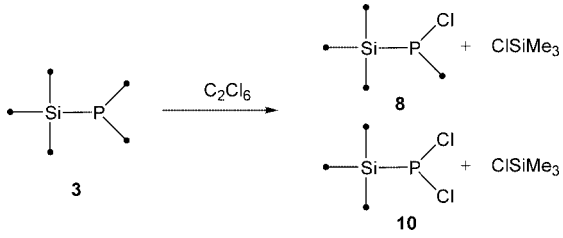


**3** **8** **10**

Scheme 5.

The chlorodisilylphosphane turned out to be astonishingly stable and survived several days heated at 70 °C as a solution in toluene. When heated at reflux in toluene, it decomposed quickly to give a plethora of unidentified products. From the observed shifts in the $^{31}$P NMR spectra it can be concluded that some of these products contain P–P bonds, which supports the evidence that ClSiMe$_3$ is eliminated with concomitant formation of hypersilylphosphanylidene which then undergoes all sorts of insertion reactions. It is of some note that no change in colour occurred upon the thermal elimination of ClSiMe$_3$. The thermal stability of the compound is noticeably decreased in THF, where decomposition occurs at a temperature as low as 40 °C.

HypP(SiMe$_3$)$_2$ reacts cleanly and quantitatively with BrCl$_2$CCCl$_2$Br to form HypPBr(SiMe$_3$) (**9**) and HypPBr$_2$ (**11**), which are both fairly stable at room temperature (Scheme 6). We were unable to obtain crystals of these two silylhalophosphanes that were suitable for X-ray diffraction experiments. When HypPCl(SiMe$_3$) reacts with BrCl$_2$CCCl$_2$Br, a mixture of HypPBr$_2$ and HypPClBr (≈ 90:10) forms, which can be observed by analysis of the $^{31}$P NMR spectrum.

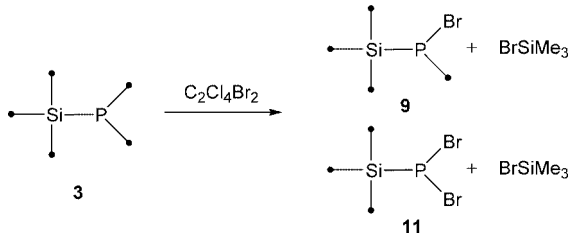


**3** **9** **11**

Scheme 6.

As reported elsewhere, HypP(SiMe$_3$)Cl is an excellent precursor to hypersilylphosphanylidene.[24] When it is added dropwise to a solution of *t*BuOK in THF, the colour changes immediately to brown and then to a deep violet and the triphosphaallyl anion [Hyp$_2$P$_3$]$^-$ forms. By reversing the procedure, bis(hypersilyl)diphosphane is formed when a solution of *t*BuOK is added to a solution of HypP(SiMe$_3$)-Cl by dimerization of hypersilylphosphanylidene which is generated under these reaction conditions (Scheme 7).

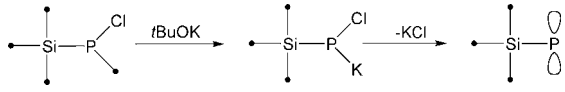


Scheme 7.

The reaction of HypP(SiMe$_3$)K (**5**) with C$_2$Cl$_6$ does not give HypPClK through Si–P bond cleavage, followed by KCl elimination and formation of the phosphanylidene HypP. Instead, chlorophosphane **8** is formed quantitatively (Scheme 8). A diphosphane is also not formed by the reaction of unreacted **5** with **8**.

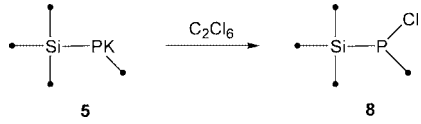


**5** **8**

Scheme 8.

Attempts to prepare a disilylfluorophosphane, HypP(SiMe$_3$)F, by the reaction of **5** with FCl$_2$CCCl$_2$F were unsuccessful.

### *Synthesis of (Hypersilyl)diphosphanes*

HypPHK and HypPK(SiMe$_3$) cleanly react with 1,2-dibromoethane to give the bulky diphosphanes HypPHHPHyp (**12**) and Hyp(SiMe$_3$)PP(SiMe$_3$)Hyp (**13**) Scheme 9. As follows from the $^{31}$P NMR spectra, 1,2-dihypersilyldiphosphane forms as a mixture of *meso*- and *rac*-D,L-diastereomers which differ in their $^{31}$P–$^{31}$P coupling constants (see section NMR spectroscopy). 1,2-Bis(hypersilyl)-1,2-bis(trimethylsilyl)diphosphane shows a single resonance in the $^{31}$P NMR spectrum that originates from the D,L-diastereomers. This interpretation is corroborated by the X-ray structure.

We also investigated the reaction of HypPH$_2$ with *t*Bu$_2$Hg in an attempt to prepare a cyclotetraphosphane

 © 2006 Wiley-VCH Verlag GmbH & Co. KGaA, Weinheim 

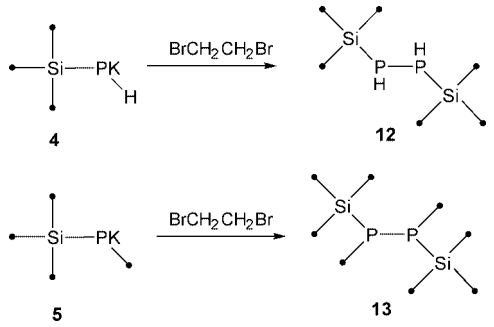


Scheme 9.

which is known to form when $(SiMe_3)PH_2$ is used.[25] Because of the bulkiness of the hypersilyl group, the reaction stops with the formation of bis(hypersilyl)diphosphane even when an excess of $tBu_2Hg$ is used. Here again, a mixture of the *meso*- and *rac*-D,L-diastereomers is formed.

By reducing the known compound *t*Bu(Hyp)PCl[9] with potassium, we were able to prepare the even bulkier diphosphane *t*Bu(Hyp)PP(Hyp)*t*Bu (**14**), which again possesses a single resonance in the $^{31}P$ NMR spectrum (Scheme 10). X-ray diffraction experiments again show that it is the D,L-racemic modification that is formed.

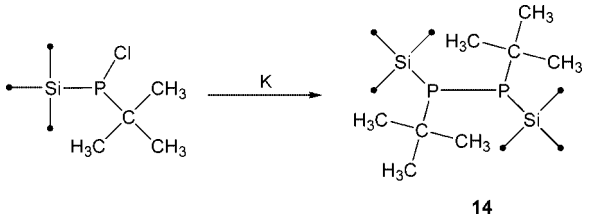


Scheme 10.

We will report on our attempts to prepare tetra(hypersilyl)diphosphane in a forthcoming paper.

## $^{29}Si$ and $^{31}P$ NMR Spectroscopy

### *Shift Data and Coupling Constants*

All compounds were characterized by $^{29}Si$- and $^{31}P$ NMR spectroscopy. The relevant shift data and the coupling constants are summarized in Table 1, which includes data for compounds that were not isolated in their pure form such as HypPClBr.

### *$^{31}P$ NMR Spectrum and Inversion Barrier of Bis(hypersilyl)diphosphane (12)*

Figure 1 presents the experimental proton-coupled $^{31}P$- and $^{1}H$ NMR spectra of **12** which both display two AA′ (or XX′) subspectra of two AA′XX′ spin systems (A = P, X = H) originating from the *meso*- and *rac*-D,L-**12** and the racemic modification. The coupling with the hypersilyl protons is negligibly small, which causes a broadening of the lines only. Because of the size of the hypersilyl group, all diastereomers are expected to adopt the *anti* conformation only at room temperature to minimize the steric repulsion between the two hypersilyl groups (see section X-ray Crystallography).

As Figure 2 shows, with the help of Newman projections, the two phosphorus lone pairs of electrons will be *trans* ($\omega \approx 180°$) to each other for the *meso* form and *gauche* ($\omega \approx 60°$) to each other for the D,L-diastereomer. As is known from numerous studies, the absolute value of the one bond P–P coupling constant $|^1J_{P,P}|$ is large for a *gauche* arrangement of the lone pairs of electrons and comparatively small for the *trans* arrangement.[26] For instance, ab initio calculations at the B3LYP/6-31+G*//B3LYP/IGLO-III level of theory for 180° and 60° electron lone pair dihedral angles of $P_2H_4$ predict $^1J_{P,P}$ values of +2.5 and –187.9 Hz, respectively.[27] For *meso*-1,2-di(*tert*-butyl)diphosphane, –162.7 Hz is reported in the literature and –206.6 Hz is reported for the D,L-diastereomer.[28]

Table 1. Chemical shifts {[ppm], $\delta(^{29}Si)$ against TMS, $\delta(^{31}P)$ against $H_3PO_4$}, and coupling constants [Hz] for hypersilylmonophosphanes and hypersilyldiphosphanes.

| Compound | No. | Solvent | Hypersilyl group | | | | | | $SiMe_3$ group | | | | |
|---|---|---|---|---|---|---|---|---|---|---|---|---|---|
| | | | $\delta(^{31}P)$ | $\delta(^{29}Si^*)$ | $\delta(^{29}Si)$ | $^1J(PSi^*)$ | $^2J(PSi)$ | $^2J(Si^*H)$ | $\delta(^{29}Si)$ | $^1J(PSi)$ | $^1J(P,H)$ | $^2J(P,H)$ | $^1J(P,P)$ |
| $HypP(SiMe_3)_2$ | **3** | toluene | –268.8 | –100.2 | –10.5 | 90.5 | 8.8 | – | +3.6 | 32.4 | – | – | – |
| $HypPH(SiMe_3)$ | | toluene | –257.3 | –101.5 | –10.6 | 65.5 | 10.1 | – | +3.9 | 32.2 | – | – | – |
| $HypPH_2$ | **1** | toluene | –265.4 | –102.4 | –11.8 | 46.7 | 9.0 | 0.6 | – | – | 178.7 | – | – |
| $Hyp_2PH$ | **2** | toluene | –272.0 | –93.9 | –10.0 | 88.7 | 11.4 | 16.4 | – | – | 195.1 | – | – |
| HypPHK | **4** | THF | –352.9 | –91.4 | –14.5 | 98.5 | 11.9 | 1.1 | – | – | 144.3 | – | – |
| HypPHLi | **6** | THF | –358.2 | –94.6 | –14.1 | 85.9 | 10.6 | 1.1 | – | – | 144.3 | – | – |
| $HypPK(SiMe_3)$ | **5** | toluene | –352.7 | –94.6 | –14.1 | 121.9 | 11.2 | – | +0.7 | 9.1 | – | – | – |
| $HypPK_2$ | | toluene | –367.4 | –76.7 | –17.1 | 107.9 | 13.9 | – | – | – | – | – | – |
| $HypPLi_2$ | **7** | THF | –371.4 | – | – | – | – | – | – | – | – | – | – |
| *meso*-$[HypPH]_2$ | **12** | toluene | –202.0 | –93.7 | –9.6 | 29.0[a] | 8.0[a] | – | – | – | 170.6 | 15.9 | –80.9 |
| D,L-$[HypPH]_2$ | **12** | toluene | –212.0 | –94.4 | –9.5 | 26.5[a] | 7.0[a] | – | – | – | 171.9 | 12.0 | –254.1 |
| D,L-$[HypP(SiMe_3)]_2$ | **13** | toluene | –201.2 | –82.3 | –9.4 | 35.9[a] | 10.5[a] | – | +4.5 | 28.7 | – | – | – |
| D,L-$[HypPtBu]_2$ | **14** | toluene | –41.8 | –83.0 | –9.8 | 46.0[a] | 12.3[a] | – | – | – | – | – | – |
| $HypP(SiMe_3)Cl$ | **8** | toluene | +38.1 | –83.5 | –8.6 | 102.3 | 12.2 | – | +9.3 | 51.3 | – | – | – |
| $HypP(SiMe_3)Br$ | **9** | toluene | +7.5 | –84.3 | –8.5 | 103.2 | 12.0 | – | +7.3 | 54.4 | – | – | – |
| $HypPCl_2$ | **10** | toluene | +236.2 | –62.8 | –8.8 | 103.8 | 14.6 | – | – | – | – | – | – |
| $HypPBr_2$ | **11** | toluene | +206.5 | –62.0 | –7.1 | 108.6 | 15.3 | – | – | – | – | – | – |
| HypPBrCl | | toluene | +222.9 | – | – | – | – | – | – | – | – | – | – |

[a] Pseudotriplet, given is the observed line spacing.

 © 2006 Wiley-VCH Verlag GmbH & Co. KGaA, Weinheim 

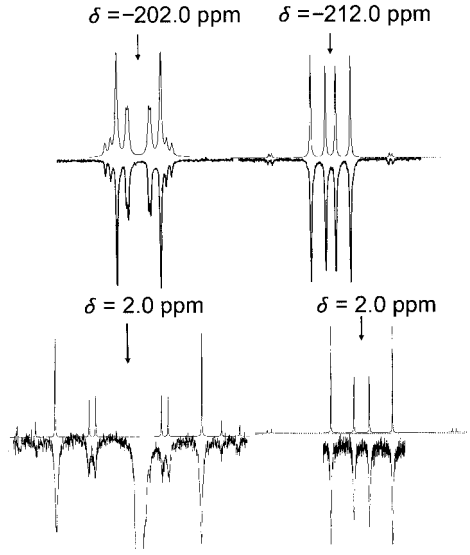


Figure 1. Calculated (positive intensities) and observed $^{31}$P- (top) and $^{1}$H NMR spectra of *meso*- (–202.0, 2.0 ppm, respectively) and D,L-bis(hypersilyl)diphosphane (–212.0, 2.9 ppm).

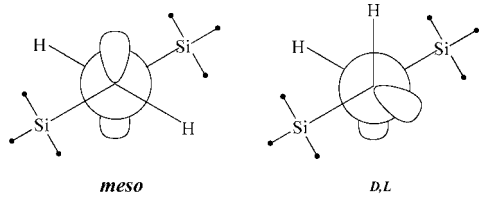


Figure 2. Newman projections for the *anti* conformers [$\omega$(Si–P–P–Si) ≈ 180°] of *meso*- and D,L-HypPHHPHyp.

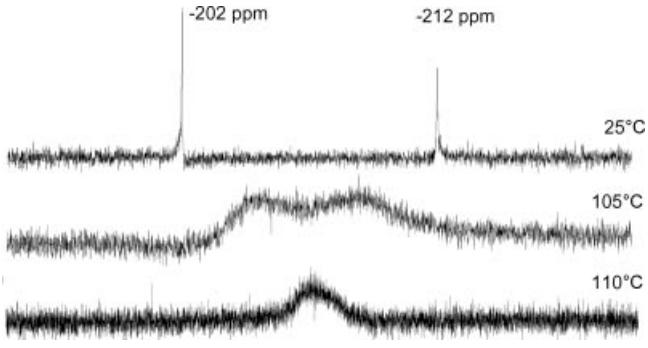


Figure 3. Proton-decoupled $^{31}$P NMR spectrum of a solution of **12** in toluene at three different temperatures. The frequency separation $\delta\nu$ at 25 °C is 1214.2 Hz.

From the simulated spectra, $^{1}J_{P,P}$ values of –80.9 Hz are obtained for the *meso*-diastereomer, and –254.1 Hz for the D,L-diastereomer. The difference is much larger than that of 1,2-di(*tert*-butyl)diphosphane, but it is close to the difference calculated for $P_2H_4$.

Figure 3 presents the proton-decoupled $^{31}$P NMR spectrum of a solution of **12** in toluene at three different temperatures. Coalescence due to rapid interconversion of *meso*↔D,L occurs at $T_c$ = 110 °C. $\Delta G^{\neq}$ can be approximated by $\Delta G^{\neq} = 19.13\ T_c(9.97 + \log T_c/\delta\nu)$[29], the barrier for phosphorus inversion can be estimated to be 69.4 kJ mol$^{-1}$.

### Ab initio Calculation of the Phosphorus Inversion Barrier of 12

Dynamic NMR experiments have been used for the determination of the inversion barriers ($\Delta E_{inv}$) of silylphosphanes as early as 1970. For $C_6H_5P(i\text{Pr})SiMe_3$ and $C_6H_5P(SiMe_2H)_2$ values of 78 and 51 kJ mol$^{-1}$ were reported, respectively.[30,31] These are smaller that those obtained for organophosphanes. The observed lowering of $\Delta E_{inv}$ upon silyl substitution has been related to three effects, which include a destabilization of the pyramidal structure and a stabilization of the transition structure by either π-acceptor or σ-donor properties.[32] Earlier ab initio calculations by one of the authors (A. Dransfeld[33]) predicted that replacement of a hydrogen atom of $PH_3$ with $PH_2$ ($PH_3 \rightarrow H_2PPH_2$) is accompanied by a lowering of $\Delta E_{inv}$ from 147.9 to 114.1 kJ mol$^{-1}$. Thus, disilyldiphosphanes, RHPPHR, are predicted to possess even smaller barriers than those of organophosphanes, which is fully confirmed by the NMR results of **12**.

To gain some deeper understanding of the nature of the inversion barrier of disilyldiphosphanes, ab initio calculations for a small series of representative species, RHPPHR with R = H, Me, $CMe_3$, $SiH_3$, $Si(SiH_3)_3$ and $Si(SiMe_3)_3$, have been performed at the B3LYP/6-31G* level of theory. Optimized transition structures were evaluated on the basis of the analysis of vibration modes at the same level of theory.

An interesting feature of the inversion of these diphosphanes is the occurrence of two alternative, diastereomeric transition structures which we term *anti* and *syn* as they differ by the dihedral angle between the lone pair of electrons at the pyramidal P atom and the P–H bond of the planar (inverting) P atom. Schematic drawings of these structures are presented in Figure 4, and relative energies as well as Mulliken charges of the phosphorus atoms are summarized in Table 2. The reader may note that the *anti* TS of diphosphane $P_iRH–P_pRH$ with the (*R*) configuration at $P_p$ is enantiomeric to the *anti* TS of the corresponding diphosphane with the (*S*) configuration at $P_p$. Therefore, the energy of the *anti* TS and the *syn* TS in Table 2 are independent of the chirality at $P_p$.

For small substituents R = Me and $SiH_3$, the *syn* transition structure is preferred, as seen from Table 2. With increasing bulkiness of the substituent [R = $CMe_3$, $Si(SiH_3)_3$ and $Si(SiMe_3)_3$], the *anti* transition structure with an approximate 180° dihedral angle between the lone pair of electrons at the pyramidal phosphorus and the P–H bond at the inverting P atom becomes lower in energy. Although the preference for the *anti* structure for large R groups is sufficiently explained by steric arguments, the preference for the *syn* geometry in the case of R = methyl is due to conjugation of the lone pair of electrons at the pyramidal P atom with the antibonding $\sigma(P_iH)$ orbital.

 © 2006 Wiley-VCH Verlag GmbH & Co. KGaA, Weinheim 

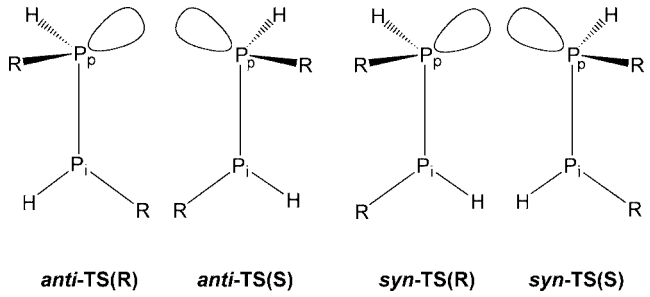


Figure 4. Schematic representation of the *anti* and *syn* transition structures of diphosphanes RHP–PHR. $P_i$ denotes the planar P atom that undergoes inversion, $P_p$ the pyramidal phosphorus atom.

Table 2. Relative energies [kJ mol$^{-1}$] and Mulliken charges $Q$ of the P atoms for the *anti* and *syn* transition states of diphosphanes RHP–PHR and of monophosphanes $H_2P$–R. $P_i$ denotes the inverting P atom.

| R | RHP–PHR | | | | $H_2P$–R | | |
|---|---|---|---|---|---|---|---|
| | $E_{rel}$ | Type of TS | $Q(P_i)$ | $Q(P_p)$ | $E_{rel}$ | Type of TS | $Q$(P) |
| H | 116.4 | *anti* = *syn* | 0.03 | –0.25 | 148.8 | | –0.27 |
| $CH_3$ | 113.3 | *anti* | 0.16 | –0.11 | 149.7 | *eclipsed* | –0.14 |
| $CH_3$ | 112.1 | *syn* | 0.16 | –0.12 | | | |
| $CMe_3$ | 99.3 | *anti* | 0.14 | –0.12 | 147.6 | *eclipsed* | –0.16 |
| $CMe_3$ | 100.9 | *syn* | 0.15 | –0.13 | | | |
| $SiH_3$ | 80.1 | *anti* | –0.07 | –0.32 | 104.8 | *eclipsed* | –0.33 |
| $SiH_3$ | 79.4 | *syn* | –0.06 | –0.33 | | | |
| $SiMe_3$ | 72.2 | *anti* | –0.12 | –0.35 | 96.6 | *eclipsed* | –0.38 |
| $SiMe_3$ | 75.5 | *syn* | –0.10 | –0.37 | | | |
| $Si(SiH_3)_3$ | 76.9 | *anti* | –0.02 | –0.27 | 103.6 | *gauche* | –0.29 |
| $Si(SiH_3)_3$ | 80.6 | *syn* | –0.02 | –0.28 | | | |
| $Si(SiMe_3)_3$ | 74.8 | *anti* | –0.08 | –0.33 | 98.9 | *gauche* | –0.36 |
| $Si(SiMe_3)_3$ | 97.2 | *syn* | –0.08 | | | | |

With a value of 74.8 kJ mol$^{-1}$, the calculated inversion barrier of **12** is in excellent agreement with the experimental value and also fits nicely into trends observed for various R substituents. As reported previously,[33] methyl substituents reduce the inversion barrier more than $PH_3$ does, which is due to electronic effects (σ-acceptor), and *t*Bu decreases the barrier because it destabilizes the steric effects in the pyramidal minimum structure. A distinct lowering of $\Delta E_{inv}$ occurs for a silyl group because of its σ-donor character. Additional steric effects in the minimum structure further reduce $\Delta E_{inv}$ in $H_2P$–$SiMe_3$. Noteworthy, further increase of the bulkiness of R in $H_2PR$ does not lower the barrier more than $H_2P$–$SiMe_3$. In general, donation from the substituent is reflected in the phosphorus charge in the transition state of all of the $H_2P$–$SiX_3$ molecules. The more negatively charged the P atom is in the TS, the lower the $\Delta E_{inv}$. To quantify these trends, results of the calculations for the monophosphanes $H_2PR$ (R = $CX_3$ or $SiX_3$) have been included in Table 2. Here again, transition structures for different R groups are observed which differ in the dihedral angle $\omega$ between a P–H and a C–X or Si–X bond, which we term *syn* ($\omega \approx 0°$) and *gauche* ($\omega \approx 60°$) as shown in Figure 5. For large R groups, the *gauche* TS is adopted.

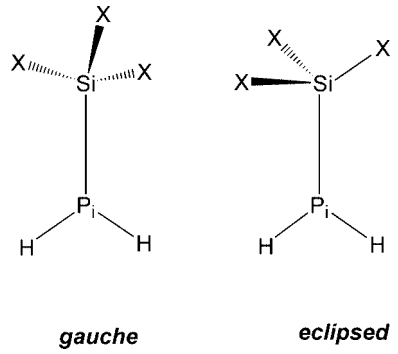


Figure 5. *Gauche* and *eclipsed* transition structures for monophosphanes $H_2PCX_3$ and $H_2PSiX_3$.

Diphosphanes can be considered as phosphanyl substituted monophosphanes. Because of the small electronegativity difference between H and P, $H_2PPHR$ and $H_2PR$ molecules should have similar inversion barriers, and 1,2-disilylated diphosphanes should have smaller inversion barriers, than those of $H_2PPH_2$ and the alkylated derivatives RHPPHR. To some extent, the results summarized in Table 2 confirm these expectations. Silyl substituents do lower $\Delta E_{inv}$, and the $PH_2$ substituent lowers it less than the silyl group $SiH_3$. Both effects ($PH_2$: –32 kJ mol$^{-1}$; $SiH_3$: –44 kJ mol$^{-1}$) are roughly additive, as can be seen for $SiH_3$–PH–PH–$SiH_3$. The calculated barrier is ≈ 80 kJ mol$^{-1}$, the predicted value is ≈ 73 kJ mol$^{-1}$.

## X-ray Crystallography

Compounds **3**, **4**, **12**, **13** and **14** were subjected to single-crystal X-ray analysis; details of the data collection and crystal data have been summarized in the Experimental Section. Selected bond lengths, bond angles and torsion angles are presented in Table 3.

The molecular structure of the 18-crown-6 salt of potassium phosphanide **4** and the arrangement of the molecules in the crystal is presented in Figure 6. Structural reports for potassium phosphanides are available for a small number of compounds only. Examples are K(thf)P($SiMe_3$)$_2$, which displays a ladder-type structure,[22] KHPSi*t*Bu$_3$,[34] polymeric KHPMes* (Mes* = 2,4,6-*t*Bu$_3$C$_6$H$_{12}$)[35] and dimeric [K(thf)$_2$P(2,4,6-Me$_3$C$_6$H$_2$)Si*t*Bu$_2$]$_2$.[36] Because of the large size of the hypersilyl group and the presence of 18-crown-6, each phosphorus atom in **4** is coordinated to one potassium atom only, which is different from the above-mentioned examples where coordination numbers two or three are observed. The potassium phosphorus distance (see Table 3) is 326 pm, which compares well with values between 320–360 pm which are reported in the literature. Each potassium atom, in addition to being coordinated to the P atom and the crown ether, has a contact [$d_{P-C}$ = 335pm] with a methyl group from the hypersilyl group of a

 © 2006 Wiley-VCH Verlag GmbH & Co. KGaA, Weinheim 

Table 3. Selected bond lengths [pm], bond angles [°] and dihedral angles [°] with estimated standard deviations in parentheses for **3**, **4**, **12**, **13** and **14**.

| | **3** | **4** | **12** | **13** | **14** |
|---|---|---|---|---|---|
| P–P | – | – | 220.2(3) | 219.61(18) | 215.90(40) |
| P–K | – | 326.19(13) | – | – | – |
| P–$Si_{(Hyp)}$ | 231.56(8) | 221.36(13) | 226.86(18) | 229.31(20) | 230.10(40) |
| P–$Si_{(Me)}$ | 228.7(11) | – | – | 225.80(20) | – |
| Si–Si | 240.19(9) | 233.19(13) | 234.31(17) | 237.35(20) | 237.80(40) |
| | 241.60(10) | 233.36(15) | 234.63(17) | 237.85(20) | 233.00(40) |
| | 242.61(11) | 234.35(12) | 235.16(16) | 238.95(20) | 239.00(40) |
| P–C | – | – | – | – | 188.9(10) |
| P–P–$Si_{(Hyp)}$ | – | – | 102.49(9) | 109.11(8) | 109.47(15) |
| P–P–$Si_{(Me)}$ | – | – | – | 115.98(8) | – |
| P–Si–Si | 108.04(3) | 107.30(5) | 108.19(7) | 109.29(8) | 104.65(16) |
| | 121.64(3) | 110.17(6) | 101.42(7) | 123.29(8) | 130.40(16) |
| | 103.52(4) | 112.39(5) | 112.26(7) | 106.47(9) | 104.65(16) |
| $Si_{(Me)}$ –P–$Si_{(Hyp)}$ | 108.55(3) | – | – | 109.14(8) | – |
| | 113.77(4) | – | – | – | – |
| C–P–$Si_{(Hyp)}$ | – | – | – | – | 110.20(40) |
| P–P–C | – | – | – | – | 115.55(40) |
| $Si_{(Hyp)}$–P–P–$Si_{(Hyp)}$ | – | – | 180.0 | 139.27(7) | 162.48(14) |
| $Si_{(Me)}$–P–P–$Si_{(Me)}$ | – | – | – | 26.66(11) | – |
| C–P–P–C | – | – | – | – | 52.50(50) |

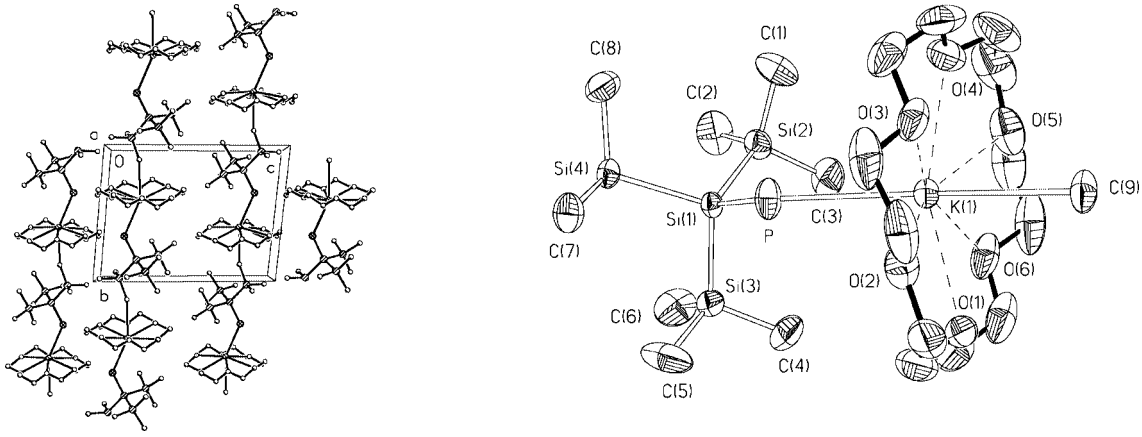


Figure 6. Molecular structure of the 18-crown-6 salt of **4** and arrangement in the crystal.

neighbouring molecule. The structure thus displays a zigzag chain $[PKC(H_3)SiSi]_n$ as shown in Figure 6. Noteworthy, the P–Si–Si angles within the hypersilyl group differ by not more than 5° from each other, which is due to the absence of steric strain. Moreover, the three Si–Si distances in the hypersilyl group are almost equal (233–234 pm), and they are the shortest compared those found for **3**, **12**, **13** and **14**.

The molecular structures of compounds **3**, **12**, **13** and **14** are presented together in Figure 7. The presence of two trimethylsilyl groups in **3** certainly increases the steric strain, which leads to quite long Si–P (231.6 and 228.7 pm) and Si–Si bonds (240.2–242.6 pm). The hypersilyl group is quite severely distorted from local $C_3$ symmetry, with P–Si–Si angles of 108.0°, 121.6° and 103.5°, respectively.

The strain in bis(hypersilyl)diphosphane **12** is considerably smaller than that in **3**, which results in shorter Si–P and Si–Si bonds and smaller variations in the P–Si–Si bond angles (Table 3). The two hydrogen atoms which are attached to the phosphorus atoms are located well inside the molecule and have no noticeable effect on the Si–P–P–Si dihedral angles that the diastereomers possess in the crystal form. Both the *meso*- and the D,L-diastereomers are present, which we corroborated by dissolving a single crystal in toluene and recording a $^{31}P$ NMR spectrum.

Despite the bulkiness of the substituents that diphosphanes **13** and **14** bear, the P–P bond lengths (220 and 216 pm, respectively) are in a range considered as normal. However, P–Si and Si–Si bonds are longer than those found for **4** and **12**. The X-ray structures together with the $^{31}P$ NMR spec-

 © 2006 Wiley-VCH Verlag GmbH & Co. KGaA, Weinheim 

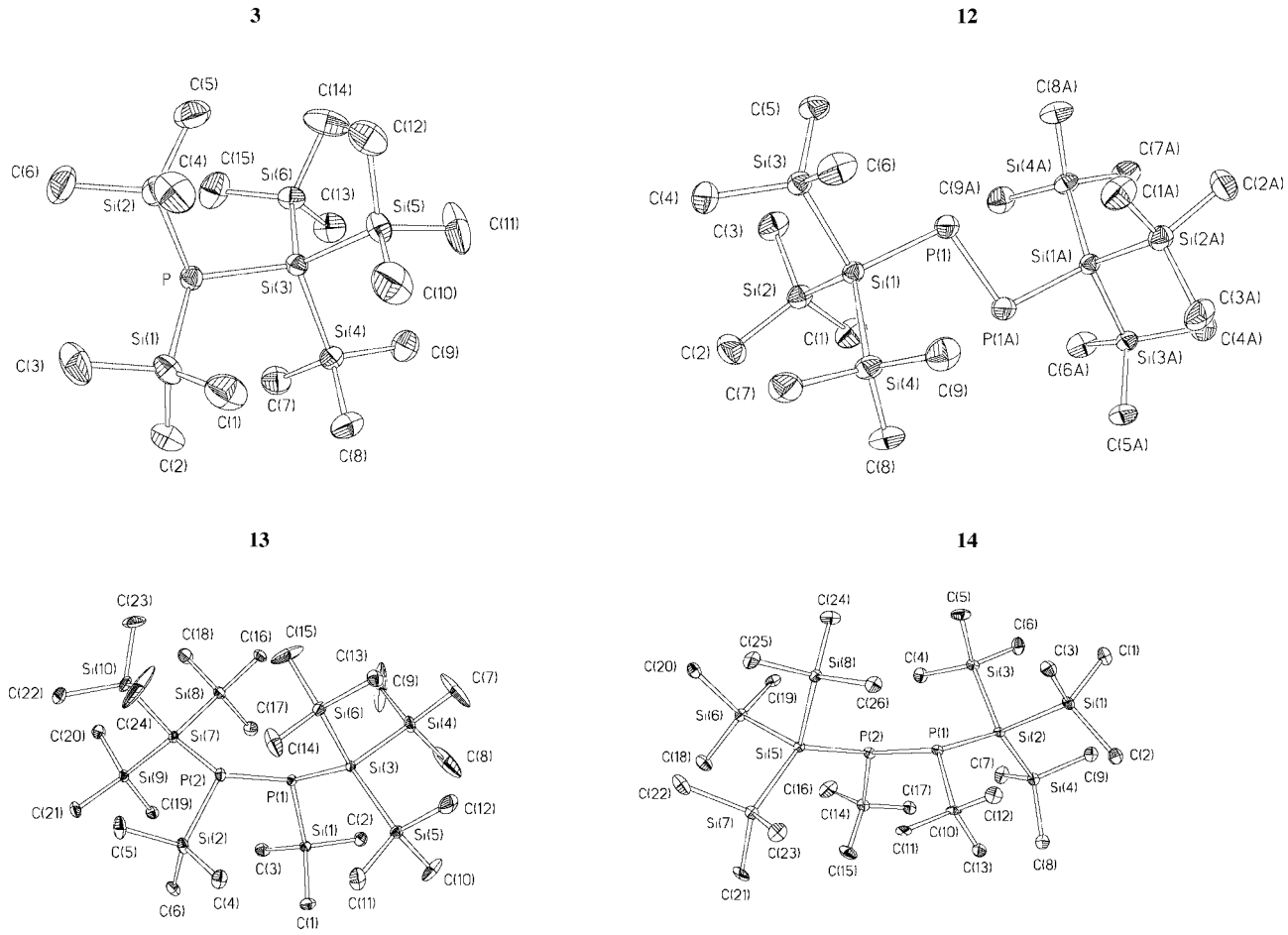


Figure 7. ORTEP plots (30% probabilities) of the molecular structures of **3**, **12**, **13** and **14**.

tra prove that it is the D,L-modifications which are formed exclusively. We were unable to detect even traces of the *meso*-diastereomers. Similar observations were made during the synthesis of $(SiMe_3)PhPPPh(SiMe_3)$, $(SiMe_3)t$BuPP$t$Bu$(SiMe_3)$ and $t$BuPhPPPh$t$Bu. All three diphosphanes display a single resonance in the $^{31}$PNMR spectrum, but it is not clear in all three cases whether it originates from the *meso*- or the D,L-diastereomers.[37]

## Experimental Section

**NMR Spectroscopy:** NMR spectra were recorded with a BRUKER MSL 300 or a VARIAN Unity Inova 300 spectrometer. The $^{29}$Si NMR and $^{31}$P NMR spectra of the samples were measured as solutions in THF or toluene in 10 mm tubes with capillaries of $D_2O$ to serve as an external lock.

**X-ray Structure Analysis:** The crystals were mounted onto the tip of a glass fibre, and the data collection was performed with a BRUKER-AXS SMART APEX CCD diffractometer. Graphite-monochromated Mo-$K_\alpha$ radiation (71.073 pm) was used for the measurements. The data were reduced to $F^2_o$ and corrected for absorption effects with SAINT and SADABS, respectively. The structures were solved by direct methods and refined by full-matrix least-squares method (SHELXL97). All non-hydrogen atoms were refined with anisotropic displacement parameters. All hydrogen atoms were located in calculated positions to correspond to standard bond lengths and angles. Relevant data are presented in Table 4. Because of the formation of thin plates, the quality of the structure data for **13** and **14** is poor. All attempts to obtain better crystals failed.

CCDC-605545 (for **3**), -605546 (for **4**), -605542 (for **12**), -605543 (for **13**) and -605544 (for **14**) contain the supplementary crystallographic data for this paper. These data can be obtained free of charge from The Cambridge Crystallographic Data Centre via www.ccdc.cam.ac.uk/data_request/cif.

**Ab Initio Calculations:** For geometry optimization, the B3LYP/6-31G(d) method has been applied as implemented in the GAUSSIAN package programs.[38] In the population analysis, the Mulliken method was conducted for both phosphorus atoms.[39] Unless otherwise stated, the optimized structures are minima on the potential energy hypersurfaces (only positive harmonic frequencies at the B3LYP/6-31G(d)//B3LYP/6-31G(d) level). The considered transition structures, TS, were characterized by a single vibration mode of inversion character at phosphorus.

**General Remarks for the Syntheses:** All syntheses and manipulations were carried out under an inert atmosphere of either $N_2$ or Ar with the use of standard Schlenk techniques. Solvents were distilled from sodium, potassium, sodium–potassium alloy or $LiAlH_4$ prior to use. Amines such as $NEt_3$ were dried with molecular sieves. Elemental analyses were performed with a HERAEUS Vario Elementar.

**Synthesis of $HypPH_2$ (1) and $Hyp_2PH$ (2) from $NaPH_2$ and $(SiMe_3)_3SiCl$:** HypCl (13.6 g, 48.1 mmol) was dissolved in a mix-

 © 2006 Wiley-VCH Verlag GmbH & Co. KGaA, Weinheim 

Table 4. Crystal data and structure refinement for compounds **3**, **4**, **12**, **13** and **14**.

| | **3** | **4** | **12** | **13** | **14** |
|---|---|---|---|---|---|
| Formula | $C_{15}H_{45}PSi_6$ | $C_{21}H_{52}KO_6PSi_4$ | $C_{18}H_{56}P_2Si_8$ | $C_{24}H_{72}P_2Si_{10}$ | $C_{26}H_{72}P_2Si_8$ |
| Formula weight | 425.02 | 583.06 | 559.19 | 703.66 | 671.495 |
| $T$ [K] | 213(1) | 293(2) | 200(2) | 100(2) | 100(2) |
| Wavelength [Å] | 0.71073 | 0.71069 | 0.71073 | 0.71073 | 0.71073 |
| Crystal system | monoclinic | triclinic | triclinic | triclinic | triclinic |
| Space group | $C2/c$ | $P\bar{1}$ | $P\bar{1}$ | $P\bar{1}$ | $P\bar{1}$ |
| $a$ [Å] | 15.707(3) | 9.7417(19) | 9.5970(19) | 10.191(2) | 9.6834(19) |
| $b$ [Å] | 11.599(2) | 11.839(2) | 13.266(3) | 13.097(3) | 14.090(3) |
| $c$ [Å] | 33.006(7) | 15.711(3) | 15.805(3) | 17.971(4) | 16.090(3) |
| $\alpha$ [°] | 90.0 | 94.59(3) | 81.28(3) | 98.62(3) | 79.58(3) |
| $\beta$ [°] | 100.91(3) | 94.19(3) | 84.79(3) | 97.98(3) | 89.44(3) |
| $\gamma$ [°] | 90.0 | 101.88(3) | 69.44(3) | 103.98(3) | 74.00(3) |
| $V$ [Å$^3$] | 5904(2) | 1759.9(6) | 1860.7(6) | 2262.7(8) | 2073.6(7) |
| $Z$ | 8 | 2 | 2 | 2 | 2 |
| $\rho_{calcd.}$ [g cm$^{-3}$] | 0.956 | 1.100 | 0.998 | 1.033 | 1.075 |
| Absorption coefficient [mm$^{-1}$] | 0.335 | 0.360 | 0.381 | 0.375 | 0.351 |
| $F(000)$ | 1872 | 632 | 612 | 772 | 740 |
| $\theta$ range [°] | $1.26 < \theta < 23.25$ | $1.77 < \theta < 23.26$ | $1.97 < \theta < 24.71$ | $1.17 < \theta < 25.00$ | $1.29 < \theta < 22.00$ |
| $h$, $k$, $l$ Indices range | $-17 < h < 17$ | $-10 < h < 10$ | $-11 < h < 11$ | $-12 < h < 12$ | $-10 < h < 10$ |
| | $-12 < k < 12$ | $-13 < k < 12$ | $-15 < k < 15$ | $-15 < k < 15$ | $-14 < k < 14$ |
| | $-36 < l < 38$ | $-17 < l < 17$ | $-18 < l < 18$ | $-21 < l < 21$ | $-16 < l < 16$ |
| Reflections collected / unique | 17157 / 4228 | 10812 / 5020 | 13046 / 6278 | 15965 / 7821 | 11017 / 5005 |
| Completeness to $\theta$ [°]/[%] | 23.25/99.7 | 23.26/99.3 | 24.71/98.7 | 25.00/98.2 | 22.00/98.4 |
| Absorption correction | SADABS | SADABS | SADABS | SADABS | SADABS |
| Refinement method | Full-matrix least-squares on $F^2$ | Full-matrix least-squares on $F^2$ | Full-matrix least-squares on $F^2$ | Full-matrix least-squares on $F^2$ | Full-matrix least-squares on $F^2$ |
| Data/restraints/parameters | 4228/0/214 | 5020/0/322 | 6278/0/279 | 7821/0/349 | 5005/0/349 |
| Goodness-of-fit on $F^2$ | 1.064 | 1.032 | 1.017 | 1.1312 | 1.143 |
| Final $R$ indices [$I > 2\sigma(I)$] | $R1 = 0.0370$ | $R1 = 0.0492$ | $R1 = 0.0622$ | $R1 = 0.0881$ | $R1 = 0.1235$ |
| | $wR2 = 0.0995$ | $wR2 = 0.1285$ | $wR2 = 0.1208$ | $wR2 = 0.2038$ | $wR2 = 0.3025$ |
| $R$ indices (all data) | $R1 = 0.0422$ | $R1 = 0.0575$ | $R1 = 0.0936$ | $R1 = 0.0939$ | $R1 = 0.1406$ |
| | $wR2 = 0.1024$ | $wR2 = 0.1352$ | $wR2 = 0.1343$ | $wR2 = 0.2078$ | $wR2 = 0.3145$ |
| Largest diff. peak/hole [e Å$^{-3}$] | 0.238/–0.152 | 0.328/–0.160 | 0.440/–0.275 | 1.315/–1.041 | 1.301/–0.678 |

ture of toluene (30 mL) and $Et_2O$ (30 mL). $NaPH_2$ (5.4 g, 96.2 mmol) was then added, and the suspension was heated at reflux for 2 d. $^{29}$Si NMR spectroscopy was used to monitor the consumption of HypCl. Upon completion, the liquid phase which contained **1** and **2** and traces of $Hyp_3P_7$ was separated from the salts (NaCl) by decantation. The solvent was then removed by evaporation in vacuo. From the oily residue, **1** was separated by fractional distillation, b.p. 65–68 °C (0.03 mbar). It solidified at room temperature to a colourless sticky wax. From the residue, **2** (1.4 g, 11%) can be obtained by sublimation in vacuo at a temperature of 120–125 °C. Compound **2** can also be prepared from HypPHK and HypCl in excellent yield (see later on). Yield of **1** 7.4 g (55%). $C_9H_{29}PSi_4$ (280.66): calcd. C 38.51, H 10.41; found C 38.70, H 9.70.

**Synthesis of $HypPH_2$ (1) from $PH_3$, $HOSO_2CF_3$, and $(SiMe_3)_3SiPh$:** $(SiMe_3)_3SiPh$ (10 g, 28.1 mmol) was dissolved in toluene (50 mL). The solution was cooled to –30 °C, and $CF_3SO_3H$ (4.21 g, 28.1 mmol) was added dropwise over a period of one hour. The reaction mixture was warmed up to room temperature and was stirred for another 2 h. Triethylamine (2.84 g, 28.1 mmol) was then added, and a moderate stream of $PH_3$ was passed through the solution. Immediately, a colourless oil of $[CF_3SO_3]^-[NHEt_3]^+$ formed. After completion, the solution of $HypPH_2$ was separated from the oil by decantation. The solvent then was removed by evaporation in vacuo, and **1** was purified by sublimation as described previously. Yield 75%.

**Synthesis of HypPHK (4):** Compound **1** (0.5 g, 1.80 mmol) was dissolved in toluene (10 mL) and cooled to –50 °C. With vigorous stirring, KO*t*Bu (0.22 g, 2.0 mmol) and 18-crown-6 (0.52 g, 2.0 mmol) was added with a spatula. The solution turned yellow/orange slowly. After 2 h, the reaction was complete. Product **4** crystallized from toluene at –80 °C in the form of yellow crystals that were suitable for X-ray analysis. Yield 0.38 g (≈ 60%).

**Synthesis of $Hyp_2PH$ (2) from 4 and HypCl:** Compound **4** (2.0 mmol; prepared from 0.6 g of **1** as described above) was dissolved in toluene (10 mL). The solution was vigorously stirred and a solution of HypCl (0.56 g, 2.0 mmol) in toluene (10 mL) was added slowly at a temperature of –40 °C. After one hour, the mixture was warmed up to room temperature. The liquid phase was separated from the salts by decantation. Sublimation in vacuo (0.03 mbar, 120–125 °C) afforded **2** (2.46 g, 80%) as a colourless waxy solid. M.p. 160 °C. $C_{18}H_{55}PSi_8$ (527.33): calcd. C 41.00, H 10.51; found C 39.79, H 9.94.

**Synthesis of HypPHLi (6):** $HypPH_2$ (1.67 g, 5.95 mmol) was dissolved in THF (20 mL) and cooled with ice to 0 °C. With constant stirring, *n*BuLi (5.95 mmol, hexane solution) was added with a syringe. The solution turned red slowly. Compound **6** (≈ 95%) was afforded, and traces of $(Me_3Si)_2PLi$, $Li_3P_7$ and $HypPLi_2$ (**7**) could be detected in the solution by $^{31}$P NMR spectroscopy.

**Synthesis of HypP(SiMe$_3$)K (5):** $HypP(SiMe_3)_2$ (1.28 g, 3.01 mmol) was dissolved in toluene (60 mL). The solution was cooled to –50 °C and KO*t*Bu (0.34 g, 3.03 mmol) and 18-crown-6 (0.80 g, 3.03 mmol) was added as a solid. The solution turned orange slowly. After two hours the reaction was complete. From analysis of the $^{31}$P NMR spectrum, a yield of ≈ 95% could be deduced. Minor byproducts were $HypPK_2$ and HypPHK.

 © 2006 Wiley-VCH Verlag GmbH & Co. KGaA, Weinheim 

**Synthesis of HypP(SiMe$_3$)H:** HypP(SiMe$_3$)$_2$ (0.33 g, 0.78 mmol) was dissolved in toluene (60 mL). Dry *t*BuOH (0.06 g) was then added, and the reaction mixture was stirred for three weeks at room temperature. Analysis of the $^{31}$P NMR spectrum revealed a 1:1 mixture of HypP(SiMe$_3$)H and the starting material. If the reaction was heated at 100 °C under a vacuum of 0.03 mbar, HypP(SiMe$_3$)H was obtained as a waxy, colourless solid. $C_{12}H_{37}PSi_5$ (352.86): calcd. C 40.85, H 10.57; found C 39.70, H 10.33.

**Synthesis of HypPHHPHyp (12):** HypPH$_2$ (**1**) (12.1 g, 43.1 mmol) was dissolved in toluene (100 mL). With vigorous stirring, (*t*Bu)$_2$Hg (8.0 g, 26.0 mmol) was added at room temperature. The solution was then heated at 60 °C. After 2 h, a small quantity of mercury had formed and the colour of the solution had turned to a yellowish–green. At –80 °C, crystals of HypPHHPHyp precipitated as yellow needles. Yield 10.8 g (90%).

Alternatively, **1** (1.0 g, 4.0 mmol) was dissolved in toluene (15 mL) and solid KO*t*Bu (0.5 g, 4.5 mmol) and solid 18-crown-6 (1.2 g, 4.5 mmol) was added at –50 °C. The solution turned yellow slowly. After 3 h at –50 °C, $BrCH_2CH_2Br$ (0.43 g, 2.25 mmol) was added. The colour changed immediately to a yellowish–green. The solution was decanted from the salts and stored in a freezer at –80 °C where **12** (1.00 g, 90%) crystallized. $C_{18}H_{56}P_2Si_8$ (559.33): calcd. C 38.65, H 10.09; found C 37.60, H 9.41.

**Synthesis of Hyp(SiMe$_3$)PP(SiMe$_3$)Hyp (13):** HypP(SiMe$_3$)$_2$ (**3**) (1.00 g, 2.35 mmol) was dissolved in toluene (30 mL). With vigorous stirring, solid KO*t*Bu (0.30 g, 2.67 mmol) and solid 18-crown-6 (0.70 g, 2.65 mmol) was added at –50 °C. The solution turned yellow immediately. After three hours the reaction mixture was warmed up to room temperature. The solution of Hyp(SiMe$_3$)PK then was again cooled to –50 °C and $BrCH_2CH_2Br$ (0.25 g, 1.33 mmol) was added. The colour of the solution slowly turned green. After one hour, the salts were separated by decantation and the solution was stored in a freezer at –80 °C. Product **13** (0.62 g, 65%) crystallized as yellowish thin plates. $C_{24}H_{72}P_2Si_{10}$ (703.70): calcd. C 40.96, H 10.31; found C 41.40, H 10.26.

**Synthesis of Hyp(tBu)PP(tBu)Hyp (14):** *t*BuPClHyp (1.00 g, 2.70 mmol) was dissolved in toluene (20 mL). With vigorous stirring, K/Na alloy (5:1; 0.20 g, excess) was added with a syringe at room temperature. The solution was then heated at 80 °C for three hours. The liquid phase was the separated from the salts by decantation and stored at –80 °C in a freezer. Product **14** (0.73 g, 80%) was obtained as yellowish thin plates. $C_{26}H_{72}P_2Si_8$ (671.55): calcd. C 46.50, H 10.72; found C 45.48, H 10.11.

**Synthesis of HypPCl(SiMe$_3$) (8):** HypP(SiMe$_3$)$_2$ (**3**) (1.54 g, 3.62 mmol) was dissolved in toluene (20 mL). With vigorous stirring solid $C_2Cl_6$ (0.86 g, 3.63 mmol) was added. at room temperature. The reaction proceeds slowly and is complete after 24 h at room temperature. After removal of all volatile products by evaporation in vacuo, a nearly pure **8** (1.27 g, 92%) is obtained as a viscous yellowish oil. Further purification by sublimation turned out to be impossible as the compound decomposed quickly when warmed. Attempts to obtain crystals were unsuccessful. $C_{12}H_{36}ClPSi_5$ (387.30): calcd. C 37.21, H 9.37; found C 36.59, H 8.86.

**Synthesis of HypPCl$_2$ (10):** HypP(SiMe$_3$)$_2$ (**3**) (0.27 g, 0.64 mmol) was dissolved in toluene (20 mL) and solid $C_2Cl_6$ (0.35 g, 1.45 mmol) was added with a spatula. After 24 h at room temperature and under vigorous stirring, the reaction was complete. Analysis of the $^{31}$P NMR spectrum revealed that besides HypPCl$_2$ (≈ 70%), cyclotriphosphane P$_3$Hyp$_2$Cl (≈ 15%) and bis(hypersilyl)-bicyclotetraphosphane P$_4$Hyp$_2$ (≈ 15%) were also present in the reaction mixture. Attempts to isolate or purify **10** by fractional crystallization were not successful.

**Synthesis of HypP(SiMe$_3$)Br (9):** HypP(SiMe$_3$)$_2$ (**3**) (1.00 g, 2.35 mmol) was dissolved in toluene (30 mL) and solid $BrCl_2CCCl_2Br$ (0.76 g, 2.35 mmol) was added with a spatula. After two hours at room temperature and vigorous stirring, the reaction was complete. All volatile products were then removed by evaporation in vacuo. Pure **9** (1.0 g, ≈ 100%) was obtained as a yellowish waxy solid. Further purification by sublimation was impossible due to decomposition. Attempts to obtain crystals were also unsuccessful. $C_{12}H_{36}BrPSi_5$ (431.75): calcd. C 33.38, H 8.40; found C 32.49, H 8.33.

**Synthesis of HypPBr$_2$ (11):** HypP(SiMe$_3$)$_2$ (**3**) (0.23 g, 0.54 mmol) was dissolved in toluene (10 mL) and solid $BrCl_2CCCl_2Br$ (0.35 g, 1.08 mmol) was added with a spatula. The colour of the solution turned a yellowish brown. After two hours at room temperature, the reaction was complete. All volatile products were removed by evaporation in vacuo to afford **11** (0.22 g, 95%) of as a yellow, viscous oil. Noticeable amounts of byproducts could not be detected in the analysis of the $^{31}$P NMR spectrum. $C_9H_{27}Br_2PSi_4$ (438.47): calcd. C 24.65, H 6.21; found C 22.87, H 5.26.

## Acknowledgments

Financial support by the "Fonds zur Förderung der wissenschaftlichen Forschung", Vienna, is gratefully acknowledged (project P 18176-N11).

[1] Hypersilane and supersilane were proposed as trivial names for tris(trimethylsilyl)silane and tri(*tert*-butyl)silane by N. Wiberg during the Xth International Symposium on Organosilicon Chemistry in Poznan, Poland **1993**.
[2] T. Gross, H. Reinke, H. Oehme, *Can. J. Chem.* **2000**, *78*, 1399–1404.
[3] H. Bock, J. Meuret, R. Baur, K. Ruppert, *J. Organomet. Chem.* **1993**, *446*, 113–122.
[4] F. H. Elsner, T. D. Tilley, *J. Am. Chem. Soc.* **1988**, *110*, 313–314.
[5] K. W. Klinkhammer, *Chem. Eur. J.* **1997**, *3*, 1418–1431.
[6] M. Westerhausen, W. Schwarz, *Z. Anorg. Allg. Chem.* **1993**, *619*, 1053–1063.
[7] M. Westerhausen, M. Wieneke, B. B. Rademacher, W. Schwarz, *Chem. Ber./Recueil* **1997**, *130*, 1499–1505.
[8] M. Westerhausen, J. Greul, H.-D. Hausen, W. Schwarz, *Z. Anorg. Allg. Chem.* **1996**, *622*, 1295–1305.
[9] A. H. Cowley, T. H. Newman, *Organometallics* **1982**, *1*, 1412–1413.
[10] T. W. Kim, W. S. Jahng, C. H. Kim, M. E. Lee, *Rapid Commun. Mass Spectrom.* **1993**, *7*, 898–901.
[11] S. Haber, M. Schmitz, U. Bergsträßer, J. Hoffmann, M. Regitz, *Chem. Eur. J.* **1999**, *5*, 1581–1589.
[12] M. Haase, U. Klingebiel, *Z. Naturforsch. Teil B* **1986**, *41*, 697–701; M. Haase, U. Klingebiel, L. Skoda, *Z. Naturforsch. Teil B* **1984**, *39*, 1500–1504.
[13] J. Hein, C. Gärtner-Winkhaus, M. Nieger, E. Niecke, *Heteroat. Chem.* **1991**, *2*, 409–415.
[14] J. Markov, R. Fischer, H. Wagner, N. Noormofidi, J. Baumgartner, C. Marschner, *Dalton Trans.* **2004**, *14*, 2166–2169.
[15] K. Hassler, *J. Organomet. Chem.* **1988**, *348*, 33–39.
[16] H. Siegl, W. Krumlacher, K. Hassler, *Monatsh. Chem.* **1999**, *130*, 139–145.
[17] J. Baumgartner, V. Cappello, A. Dransfeld, K. Hassler in *Silicon Chemistry, From the Atom to Extended Systems* (Eds.: P Jutzi, U. Schubert), Wiley-VCH, Weinheim **2004**.

 © 2006 Wiley-VCH Verlag GmbH & Co. KGaA, Weinheim 

[18] W. Uhlig, *Z. Anorg. Allg. Chem.* **1990**, *588*, 133–138.
[19] U. Baumeister, K. Schenzel, R. Zink, K. Hassler, *J. Organomet. Chem.* **1997**, *543*, 117–124.
[20] G. Brauer, *Handbuch der präparativen Anorganischen Chemie*, Ferdinand Enke, Stuttgart, **1975**.
[21] G. Fritz, J. Härer, K. H. Schneider, *Z. Anorg. Allg. Chem.* **1982**, *487*, 44–58.
[22] U. Englich, K. Hassler, K. Ruhland-Senge, F. Uhlig, *Inorg. Chem.* **1998**, *37*, 3532–3537.
[23] R. Appel, W. Paulen, *Angew. Chem. Int. Ed. Engl.* **1981**, *20*, 869–870.
[24] V. Cappello, J. Baumgartner, A. Dransfeld, M. Flock, K. Hassler, *Eur. J. Inorg. Chem.* **2006**, 2393–2405.
[25] M. Baudler, G. Hoffmann, M. Hallab, *Z. Anorg. Allg. Chem.* **1980**, *466*, 71–75.
[26] for instance, see A. H. Cowley, W. D. White, *J. Am. Chem. Soc.* **1969**, *91*, 1913–1917; J. P. Albrand, D. Gagnaire, J. B. Robert, *J. Am. Chem. Soc.* **1973**, *95*, 6498–6500; J. P. Albrand, J. B. Robert, *J. Chem. Soc. Chem. Commun.* **1974**, *16*, 644–645; J. P. Albrand, H. Faucher, D. Gagnaire, J. B. Robert, *Chem. Phys. Lett.* **1976**, *38*, 521–523.
[27] Private communication with M. Flock, unpublished results.
[28] M. Baudler, C. Gruner, H. Tschäbunin, J. Hahn, *Chem. Ber.* **1982**, *115*, 1739–1745.
[29] H. Günther, *NMR Spektroskopie*, Georg Thieme, Stuttgart/N. Y., **1983**.
[30] R. D. Baechler, K. Mislow, *J. Am. Chem. Soc.* **1970**, *92*, 4758–4759.
[31] R. D. Baechler, K. Mislow, R. J. Cook, G. H. Senkler, *J. Am. Chem. Soc.* **1972**, *94*, 2859–2861.
[32] A. Rauk, J. D. Andose, W. G. Frick, R. Tang, K. Mislow, *J. Am. Chem. Soc.* **1971**, *93*, 6507–6515; C. C. Levin, *J. Am. Chem. Soc.* **1975**, *97*, 5649–5655.
[33] A. Dransfeld, Thesis, Erlangen, **1998**.
[34] M. Westerhausen, S. Weinrich, B. Schmid, S. Schneiderbauer, M. Suter, H. Nöth, H. Piotrowski, *Z. Anorg. Allg. Chem.* **2003**, *629*, 625–633.
[35] G. W. Raabe, G. P. A. Yap, A. L. Rheingold, *Inorg. Chem.* **1997**, *36*, 1990–1991.
[36] M. Andrianarison, D. Stalke, U. Klingebiel, *Chem. Ber.* **1990**, *123*, 71–73.
[37] H. Schumann, R. Fischer, *J. Organomet. Chem.* **1975**, *88*, C13–C16; M. Baudler, M. Hallab, A. Zarkadas, E. Tolls, *Chem. Ber.* **1973**, *106*, 3962–3969.
[38] M. J. Frisch, G. W. Trucks, H. B. Schlegel, G. E. Scuseria, M. A. Robb, J. R. Cheeseman, J. A. Montgomery Jr., T. Vreven, K. N. Kundin, J. C. Burant, J. M. Millam, S. S. Iyengar, J. Tomasi, V. Barone, B. Mennucci, M. Cossi, G. Scalmani, N. Rega, G. A. Petersson, H. Nakatsuji, M. Hada, M. Ehara, K. Toyota, R. Fukuda, J. Hasegawa, M. Ishida, T. Nakajima, Y. Honda, O. Kitao, H. Nakai, M. Klene, X. Li, J. E. Knox, H. P. Hratchian, J. B. Cross, C. Adamo, J. Jaramillo, R. Gomperts, R. E. Stratmann, O. Yazyev, A. J. Austin, R. Cammi, C. Pomelli, J. W. Ochterski, P. Y. Ayala, K. Morokuma, G. A. Voth, P. Salvador, J. J. Dannenberg, V. G. Zakrzewski, S. Dapprich, A. D. Daniels, M. C. Strain, O. Farkas, D. K. Malick, A. D. Rabuck, K. Raghavachari, J. B. Foresman, J. V. Ortiz, Q. Cui, A. G. Baboul, S. Clifford, J. Cioslowski, B. B. Stefanov, G. Liu, A. Liashenko, P. Piskorz, I. Komaromi, R. L. Martin, D. J. Fox, T. Keith, M. A. Al-Laham, C. Y. Peng, A. Nanayakkara, M. Challacombe, P. M. W. Gill, B. Johnson, W. Chen, M. W. Wong, C. Gonzalez, J. A. Pople, *GAUSSIAN03/Revison C.02*, Gaussian, Inc., Wallingford CT, **2004**.
[39] R. S. Mulliken, *J. Phys. Chem.* **1962**, *36*, 3428–3439.

Received: May 12, 2006
Published Online: October 2, 2006

 © 2006 Wiley-VCH Verlag GmbH & Co. KGaA, Weinheim 

DOI: 10.1002/ejic.200600508

# Diastereopure Cationic NCN-Pincer Palladium Complexes with Square Planar $\eta^4$-*N,C,N,O* Coordination

**Silvia Gosiewska,[a] Sara Herreras Martinez,[a] Martin Lutz,[b] Anthony L. Spek,[b] Gerard van Koten,[a] and Robertus J. M. Klein Gebbink*[a]**

**Keywords:** Palladium / NCN-pincer / Amino acids / Ligand design / Hydrogen bonds

Neutral NCN-pincer palladium bromide complex **2** containing the monoanionic, enantiopure pincer ligand 2,6-bis{[(*S*)-2-hydroxymethyl-1-pyrrolidinyl]methyl}phenyl bromide (**1**) with bis-*ortho*-(*S*)-prolinol substituents was synthesized and isolated as a mixture of three stereoisomers [($S_N$,$S_N$,$S_C$,$S_C$), ($R_N$,$S_N$,$S_C$,$S_C$), and ($R_N$,$R_N$,$S_C$,$S_C$)] in a 1:1:1 ratio. Upon abstraction of the bromide ion from the unresolved mixture of **2**, single diastereoisomers of the cationic complexes [**3**]$BF_4$ and [**3**]$PF_6$, respectively, were formed with a unique $\eta^4$-*N,C,N,O* coordination mode of ligand **1**. X-ray crystal structure determination established the intramolecular $\eta^4$-*N,C,N,O* coordination of **1** to palladium where the typical *mer*-$\eta^3$-*N,C,N* pincer coordination is accompanied by coordination of one of the hydroxy groups of the (*S*)-prolinol moieties. The water molecule that was cocrystallized in the crystal structure of [**3**]$PF_6$ does not coordinate to palladium, but instead is involved in a hydrogen bonding network. The catalytic potential of both cationic complexes, [**3**]$BF_4$ and [**3**]$PF_6$, was tested in an aldol reaction of aldehydes with methyl isocyanoacetate to yield the oxazoline products as racemic mixtures.

(© Wiley-VCH Verlag GmbH & Co. KGaA, 69451 Weinheim, Germany, 2006)

## Introduction

Organometallic pincer complexes containing the terdentate, monoanionic ECE ligand, (ECE = [2,6-$(ECH_2)_2$-$C_6H_3$]$^-$, where E is a neutral two-electron donor such as $NR_2$, $PR_2$, $AsR_2$, OR, or SR; Figure 1), have attracted widespread interest in catalysis and materials science.[1] The M–C σ bond in these complexes is complemented and stabilized by coordination of the E-donors through a double *ortho*-metalation and results in relatively robust organometallic complexes. Coordination of the two donor E-substituents furthermore controls the accessibility and the electronic fine tuning of the metal. Another important feature of the pincer ligand system is the possibility to introduce stereochemical information at various positions of the pincer skeleton, for example, at the benzylic carbons of the pincer backbone,[2,3] on the donor unit E,[4–7] or a combination of both.[8] Especially in the case of NCN-pincer systems, the presence of stereogenic centers in the N-donor substituents offers facile synthetic access to chiral metal complexes.

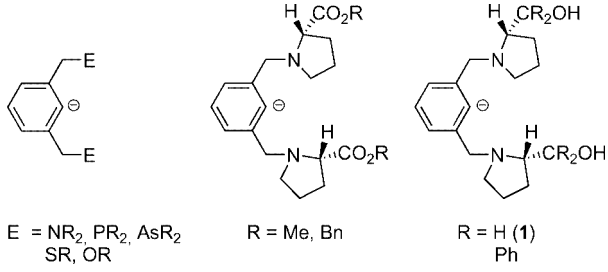


Figure 1. ECE pincer ligands.

Previously, we reported the synthesis and structural analysis of neutral and cationic palladium(II) complexes of monoanionic NCN-pincer ligands in which ester prolinate auxiliaries were used as the N-donor (Figure 1).[9] Depending on both the bulkiness of the prolinate ester substituents and the actual $\eta^3$-*N,C,N* or $\eta^4$-*N,C,N,O* coordination mode of the ligand, the palladium complexes were formed either as mixtures of three diastereoisomers or as single diastereoisomers both in the solid state and solution. These studies led us to develop a new class of enantiopure NCN-pyrrolidine ligands where the ester groupings were replaced by $CR_2OH$ groups (R = H, Ph; Figure 1). Here we present the synthesis of the ligand PhBr$(ProOH)_2$ (**1**), with R = H, and the studies of its coordination toward Pd. In order to probe the stereogenity at Pd in the resulting complexes, we have used these complexes as catalysts in the aldol reaction between benzaldehyde and methyl isocyanoacetate.

[a] Organic Chemistry and Catalysis, Faculty of Science, Utrecht University,
Padualaan 8, 3584 CH Utrecht, The Netherlands
Fax: +31-302523615
E-mail: r.j.m.kleingebbink@chem.uu.nl
[b] Bijvoet Center for Biomolecular Research, Faculty of Science, Crystal and Structural Chemistry, Utrecht University,
Padualaan 8, 3584 CH Utrecht, The Netherlands

 © 2006 Wiley-VCH Verlag GmbH & Co. KGaA, Weinheim 

## Results and Discussion

### Synthesis

The ligand precursor PhBr(ProOH)$_2$ (**1**) was synthesized in a one-step procedure with the use of 2.5 equiv. of (*S*)-prolinol with respect to 1-bromo-2,6-bis(bromomethyl)benzene in a biphasic $CH_2Cl_2/H_2O$ system with 10% of $n$Bu$_4$NCl as a phase-transfer catalyst and $K_2CO_3$ as the base (Scheme 1).

According to this procedure, ligand precursor **1** was obtained in 58% yield after purification by column chromatography. Phase transfer catalytic conditions were used in order to obtain the desired product in higher yield, since under basic conditions ($Et_3N$) in $CH_2Cl_2$ the yield of **1** was only 24%. Arylpalladium complex **2** was synthesized under an inert atmosphere by the oxidative addition reaction of aryl bromide **1** with $[Pd_2(dba)_3]\cdot CHCl_3$ in degassed benzene at 50 °C. The product was isolated in 63% yield after purification by column chromatography (Scheme 1). $^1$H and $^{13}$C{$^1$H} NMR spectra of the isolated product showed a complicated peak pattern, which was interpreted to result from a mixture of three diastereoisomers in a 1:1:1 molar ratio. Reaction of this mixture of diastereoisomers of **2** with either $AgBF_4$ in acetone/water (10:1, v/v) or with aqueous $NH_4PF_6$ in methanol yielded the cationic complexes [**3**]BF$_4$ and [**3**]PF$_6$ in moderate to good yields (76 and 46%, respectively). Analysis of the NMR spectrum showed the formation of these complexes as single diastereoisomers (vide infra).

All compounds were characterized by $^1$H and $^{13}$C{$^1$H} NMR, IR spectroscopy, ESI-MS, and elemental analysis. The structures of complexes [**3**]BF$_4$ and [**3**]PF$_6$ were confirmed by X-ray crystal structure determination.

### Description of Crystal Structures of [3]BF$_4$ and [3]PF$_6$

Single-crystals suitable for X-ray diffraction were obtained by vapor diffusion of $Et_2O$ into a saturated solution of either [**3**]BF$_4$ in acetone or [**3**]PF$_6$ in $CH_2Cl_2$. Regrettably, all attempts to crystallize **2** failed. In the crystal structures, two independent molecules of both [**3**]BF$_4$ and [**3**]PF$_6$ are present which differ only in the conformation of the noncoordinated hydroxymethylene group of the ligand. One of the independent molecules of [**3**]BF$_4$ is shown in Figure 2, and Quaternion overlay plots of both cations of [**3**]BF$_4$ (left) and [**3**]PF$_6$ (right) are shown in Figure 3. Relevant bond lengths and angles are displayed in Table 1 and crystallographic details are listed in the Experimental Section. Both structures crystallize in chiral space groups and their absolute structure could be determined from the Flack parameter.[10] Besides the two cations of **3** and two $PF_6$ anions, one molecule of water also crystallizes in the asymmetric unit of [**3**]PF$_6$.

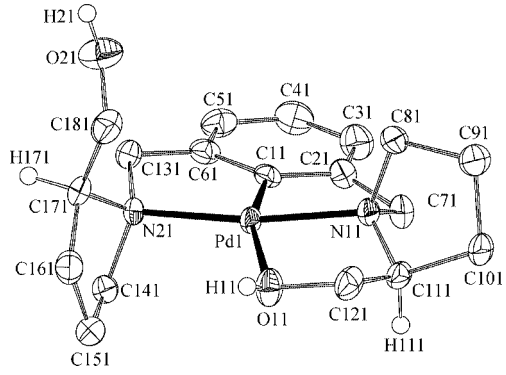


Figure 2. Displacement ellipsoid plot (50% probability) of cation [**3**]BF$_4$; hydrogen atoms of the hydroxy groups and of the stereogenic C-atoms are depicted; the remaining hydrogen atoms and noncoordinated $BF_4$ anions are omitted for clarity. Only one of two independent molecules is shown.

In all four molecules of [**3**]BF$_4$ and [**3**]PF$_6$, the coordinated nitrogen atoms have an ($R_N$) configuration, while the C-stereogenic centers have the expected ($S_C$) configuration. The two independent molecules of [**3**]BF$_4$ and [**3**]PF$_6$ have an essentially identical, four-coordinate $\eta^4$-*N*,*C*,*N*,*O*-ligand coordination around the palladium center that comprises C1, both N atoms, as well as the oxygen atom of one of the hydroxy groups. However, the noncoordinated hydroxy-

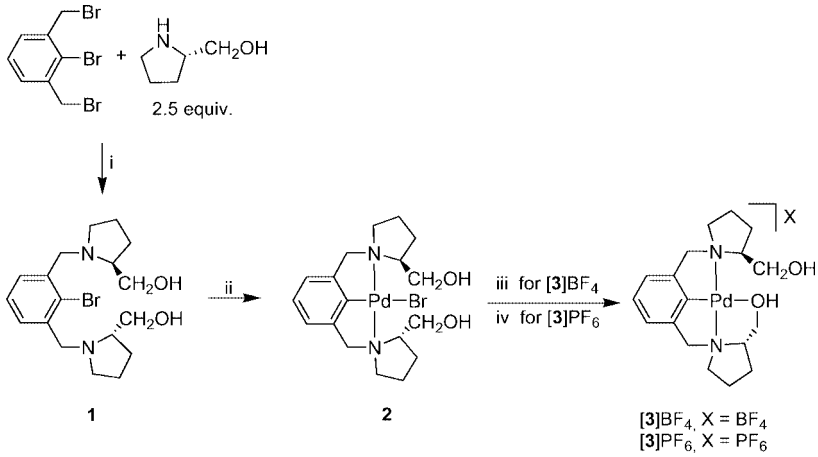


Scheme 1. Synthesis of compounds **1**–**3**. Conditions: (i) $K_2CO_3$, $n$Bu$_4$NCl, $CH_2Cl_2/H_2O$, reflux, 16 h; (ii) $[Pd_2(dba)_3]\cdot CHCl_3$, $C_6H_6$, 50 °C, 3 h; (iii) $AgBF_4$, acetone/$H_2O$, room temp.; (iv) $NH_4PF_6/H_2O$, $CH_3OH$, room temp.

 © 2006 Wiley-VCH Verlag GmbH & Co. KGaA, Weinheim

Figure 3. Quaternion fit[13] of the two independent molecules of cation **3** in the crystal structure of [**3**]$BF_4$ (left) and [**3**]$PF_6$ (right). Molecule 1 is drawn in black; molecule 2 is drawn in grey. The only significant difference is in the conformation of the noncoordinated hydroxymethylene group. Hydrogen atoms, noncoordinated water molecules, and noncoordinated $BF_4$ and $PF_6$ anions are omitted for clarity.

Table 1. Relevant bond lengths [Å] and angles [°] of complexes [**3**]$BF_4$ and [**3**]$PF_6$.

| | [**3**]$BF_4$ | | [**3**]$PF_6$ | |
|---|---|---|---|---|
| | Molecule 1 | Molecule 2 | Molecule 1 | Molecule 2 |
| Pd–C1 | 1.901(3) | 1.894(3) | 1.900(3) | 1.906(3) |
| Pd–N1 | 2.049(3) | 2.049(2) | 2.047(2) | 2.048(2) |
| Pd–N2 | 2.118(3) | 2.124(2) | 2.116(2) | 2.117(2) |
| Pd–O1 | 2.205(3) | 2.247(2) | 2.227(2) | 2.201(2) |
| C1–Pd–O1 | 160.95(11) | 156.45(11) | 163.60(10) | 165.05(10) |
| N1–Pd–N2 | 164.88(11) | 164.95(9) | 163.42(9) | 163.48(10) |
| C1–Pd–N1 | 82.87(12) | 83.14(11) | 82.61(11) | 82.57(11) |
| C1–Pd–N2 | 82.19(12) | 81.98(11) | 80.80(11) | 80.92(11) |
| O1–Pd–N1 | 80.74(10) | 79.32(8) | 81.43(9) | 82.88(9) |
| O1–Pd–N2 | 114.38(10) | 115.62(9) | 115.13(9) | 113.64(9) |
| N2–C17–C18–O2 | 73.9(4) | –68.7(3) | 172.0(2) | 178.0(2) |
| C1–C2–C7–N1 | –23.6(4) | –23.8(3) | –28.0(4) | –30.0(4) |
| C1–C6–C13–N2 | –22.5(4) | –21.1(4) | –20.0(3) | –22.6(4) |

methylene groups in [**3**]$BF_4$ and [**3**]$PF_6$ have different orientations. In the structure of [**3**]$BF_4$, both of these groups point towards the palladium center with Pd···O2 distances of 3.966(3) and 2.862(3) Å, whereas in [**3**]$PF_6$, both groups point away from the palladium center and have Pd···O2 distances of 4.680(2) and 4.639(2) Å. These differences result from the different hydrogen bond network that is present in both complexes. The Pd-coordination environment in these complexes, including bond lengths and angles, is very similar to that observed for structurally related cationic NCN-pincer palladium complexes containing methyl or benzyl prolinate substituents, where one carbonyl group of the ester moieties is coordinated to palladium (Figure 1).[9]

In cationic NCN-pincer complexes which do not contain additional donor atoms in the ligand, the *mer*-$\eta^3$-*N*,*C*,*N* coordination of the pincer ligand is complemented by an $\eta^1$-*O* water molecule.[11,12] Apparently, the intramolecular $\eta^1$-*O*-coordination of the hydroxy group of the ligand in [**3**]$BF_4$ and [**3**]$PF_6$ is preferred over water coordination. A water molecule is actually found in the crystal structure of [**3**]$PF_6$; it is however not coordinated to Pd, but instead is involved in a hydrogen bonding network. As a result of the extra $\eta^1$-*O* coordination of the hydroxy group of the ligand, the complexes [**3**]$BF_4$ and [**3**]$PF_6$ lack any element of symmetry, in contrast to the pincer [Pd(NCN)$(OH_2)$]$BF_4$ complexes which usually have an overall $C_2$ symmetry.[12] Importantly, both complexes [**3**]$BF_4$ and [**3**]$PF_6$ exist as single diastereoisomers with an ($R_N$,$R_N$,$S_C$,$S_C$) configuration.

Because of the presence of cocrystallized, noncoordinated water molecules in [**3**]$PF_6$, the hydrogen bond networks and hence the three dimensional structures are very different in the crystal structures of [**3**]$BF_4$ and [**3**]$PF_6$. The relevant distance and angles of the hydrogen bonds for [**3**]$BF_4$ and [**3**]$PF_6$ are shown in Table 2. In the structure of [**3**]$BF_4$, both coordinated and noncoordinated hydroxy groups donate hydrogen bonds, and thus, this results in four independent donor groups. Three fluoride atoms of the first $BF_4$ anion act as acceptors, whereas only one fluoride of the second $BF_4$ is a hydrogen-bond acceptor. This hydrogen bonding arrangement results in discrete aggregates consisting of four cations and four anions (Figure 4).

Table 2. Selected hydrogen bond lengths [Å] and angles [°] of complexes [**3**]$BF_4$ and [**3**]$PF_6$.[a]

| Complex | Donor–H···Acceptor | D–H | H···A | D···A | D–H···A |
|---|---|---|---|---|---|
| [**3**]$BF_4$ | O11–H11···F1$^{i}$ | 0.71(4) | 2.01(4) | 2.717(4) | 170(4) |
| | O12–H12···F8 | 0.76(4) | 1.95(4) | 2.693(3) | 166(4) |
| | O21–H21···F4$^{ii}$ | 0.97(4) | 1.84(6) | 2.777(4) | 161(5) |
| | O22–H22···F2 | 0.79(4) | 2.15(4) | 2.934(3) | 174(4) |
| [**3**]$PF_6$ | O21–H21O···F7$^{iii}$ | 0.71 | 2.53 | 3.043(4) | 131 |
| | O22–H22O···O3$^{iv}$ | 0.82 | 1.91 | 2.712(3) | 165 |
| | O11–H110···O21$^{v}$ | 0.73 | 1.95 | 2.671(3) | 174 |
| | O12–H120···O22$^{iv}$ | 0.74 | 1.92 | 2.651(3) | 170 |
| | O3–H130···F12 | 0.97 | 1.94 | 2.905(3) | 170 |
| | O3–H230···F6A | 0.88 | 2.09 | 2.796(6) | 136 |

[a] Symmetry operations: *i*: $x-0.5$, $y+0.5$, $z$; *ii*: $1.5-x$, $y+0.5$, $1-z$; *iii*: $1-x$, $y+0.5$, $-z$; *iv*: $1-x$, $y-0.5$, $1-z$; *v*: $1-x$, $y-0.5$, $-z$.

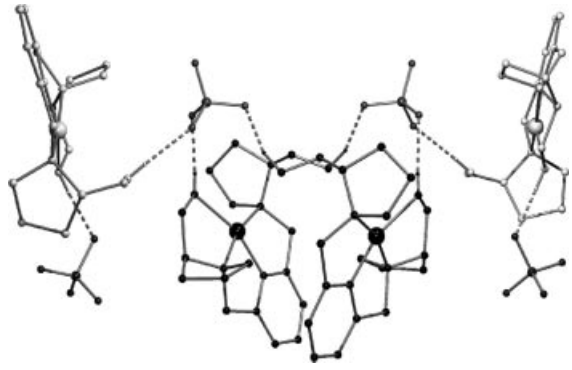

Figure 4. Hydrogen-bonded aggregate of four cations and four anions in [**3**]$BF_4$. Dashed lines indicate hydrogen bonds between the hydroxy groups as donors and the $BF_4$ anions as acceptors. C–H hydrogen atoms are omitted for clarity.

In the crystal structure of [**3**]$PF_6$, both coordinated hydroxy groups of the two independent molecules form intermolecular hydrogen bonds with the noncoordinated hydroxy groups as acceptors, which results in the formation of a hydrogen bonded dimer of two cations of [**3**]$PF_6$. The noncoordinated hydroxy group of the first molecule donates a hydrogen bond with a $PF_6$ fluoride as acceptor, while the noncoordinated hydroxy group of the second molecule forms a hydrogen bond with the water molecule as acceptor. The water molecule forms two hydrogen bonds

 © 2006 Wiley-VCH Verlag GmbH & Co. KGaA, Weinheim 

with $PF_6$ anions as acceptors. By means of these hydrogen bonds, an infinite two-dimensional network is formed in the crystallographic *b*,*c*-plane (Figure 5).

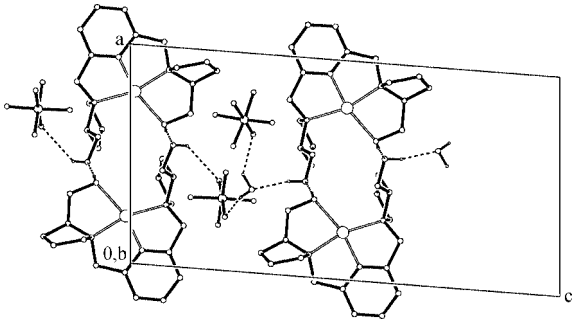


Figure 5. Infinite, two-dimensional hydrogen bond network in [**3**]$PF_6$ in the crystallographic *b*,*c*-plane. View along the *b* axis. Dashed lines indicate hydrogen bonds between the hydroxy groups and water molecules as donors and the $PF_6$ anions as acceptors. Note that the two cations of [**3**] form a hydrogen bonded dimer. C–H hydrogen atoms are omitted for clarity. Only one orientation of the disordered $PF_6$ anion is shown.

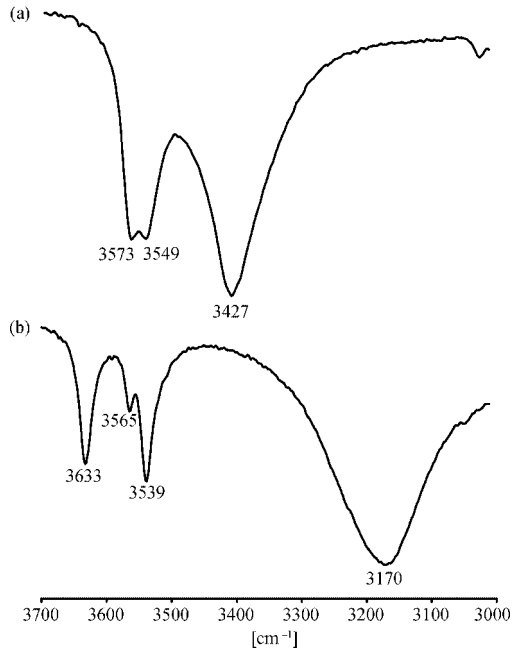


Figure 6. The *ν*(OH) valence vibration region of IR spectra of a) [**3**]$BF_4$ and b) [**3**]$PF_6$.

## IR Spectra

The different bonding nature of the hydroxy groups in **1**–**3** is reflected in their IR spectra in the region of the *ν*(OH) valence vibration. The broader *ν*(OH) band, which in the spectrum of ligand **1** is present at 3410 $cm^{-1}$, is slightly shifted to lower wavenumbers in palladium bromide complex **2** [*ν*(OH) 3383 $cm^{-1}$]. In the spectrum of [**3**]$BF_4$, two sharp vibrations at higher wavenumbers are observed (Figure 6a). The *ν*(OH) at 3427 $cm^{-1}$ is assigned to the vibration of a Pd-coordinated hydroxy group, whereas the second, split band [*ν*(OH) at 3549 and 3573 $cm^{-1}$] is assigned to the two different orientations of the noncoordinated hydroxy group as shown in the X-ray crystal structure.

In the spectrum of [**3**]$PF_6$, one broad vibration at 3170 $cm^{-1}$ and three sharp vibrations at higher wavenumbers appear (Figure 6b). The presence of water in the structure of [**3**]$PF_6$ is represented by the broad vibration at 3170 $cm^{-1}$. The other three *ν*(OH) bands were tentatively assigned to the hydroxy group of the ligands that are coordinated (at 3539 $cm^{-1}$) and noncoordinated (at 3565 and 3633 $cm^{-1}$) to Pd. The dissimilar wavenumbers and shape of the bands of the hydroxy groups that are observed in the IR spectra of [**3**]$PF_6$ compared with the *ν*(OH) in the spectrum of [**3**]$BF_4$ is a consequence of the different hydrogen bonding patterns that are found in the crystal structures of these two compounds. The dominant bands in the spectra of cationic complexes **3** are the typical vibrations belonging to the anions [i.e. $BF_4$ (986 $cm^{-1}$) and $PF_6$ (834 $cm^{-1}$), respectively].

## NMR Studies of Complexes 2–3

The $^1H$ and $^{13}C\{^1H\}$ NMR spectra of neutral complex **2** showed various resonance patterns pointing to the presence of a mixture of species. This observation is in line with those for neutral Pd-halide complexes derived from prolinate ester NCN-pincers.[9] In that case, a mixture of three diastereoisomers [($S_N$,$S_N$,$S_C$,$S_C$), ($R_N$,$S_N$,$S_C$,$S_C$), and ($R_N$,$R_N$,$S_C$,$S_C$)] is present in the temperature range of –80 °C to +95 °C. The $^1H$ and $^{13}C\{^1H\}$ NMR spectra were analyzed for these ester derivatives by applying a number of different one- and two-dimensional NMR techniques [$^1H$-$^1H$ COSY, $^1H$-$^{13}C$ HETCOR, $^1H$ NOESY, EXSY, and DEPT (angle) experiments]. On the basis of the structural similarity with these prolinate ester complexes, the $^1H$ NMR spectroscopic data of **2** were interpreted to result from a 1:1:1 mixture of three diastereoisomers (Figure 7). The ratio of the diastereoisomers of **2** was determined based on the resonances of the aromatic hydrogens ($C_{meta}$ to $C_{ipso}$), which are the only doublet resonances that are well-enough resolved (Figure 8). A full assignment of the $^1H$ and $^{13}C\{^1H\}$ NMR of **2** was not attempted because the aliphatic methylene groups of the pyrrolidine and hydroxymethylene moieties gave very complicated patterns and very similar shifts of the $^{13}C$ atoms.[14] The $^1H$ NMR spectrum of **2** measured in [$D_6$]benzene showed the best-resolved resonances, whereas in [$D_6$]acetone, broader resonances were observed.

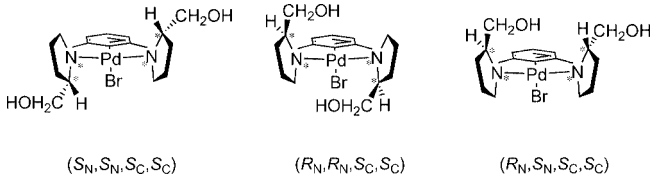


Figure 7. The three diastereoisomers of **2**; hydrogen atoms and the hydroxymethylene groups on the stereogenic carbon atom are depicted; the remaining hydrogen atoms are omitted for clarity.

 © 2006 Wiley-VCH Verlag GmbH & Co. KGaA, Weinheim 

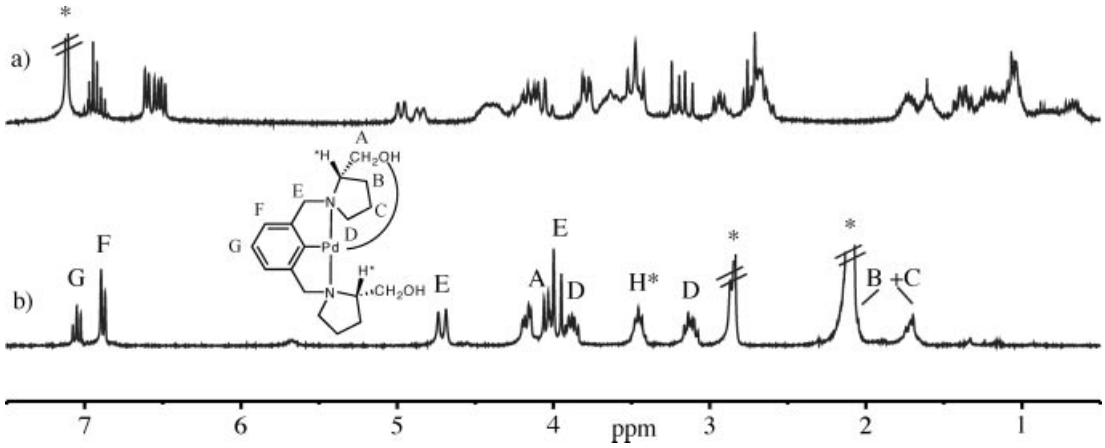


Figure 8. The $^1$H NMR spectra of a) **2** in [D$_6$]benzene and b) [**3**]BF$_4$ in [D$_6$]acetone with the assignment of the hydrogen atoms of the ligand for the cationic complex (asterisk denotes residual solvent peaks).

The formation of three isomers of neutral complex **2** is a consequence of the interconversion between the different diastereoisomers that is caused by dissociation of the Pd–N bond followed by pyramidal inversion at nitrogen, rotation, and recoordination. The $^1$H NMR spectrum of **2** (measured in [D$_6$]acetone) was temperature independent in the range between –80 °C to +50 °C, which indicates the presence of all three diastereoisomers in the 1:1:1 ratio in this temperature range. Apparently, the hydroxymethylene groups are too small to prevent the diastereoisomer interconversion even at lower temperatures, and sterically more hindered substituents seemingly have to be part of the pyrrolidine moieties in order to stabilize a single diastereoisomer of the neutral NCN-Pd-Br complex. Indeed, substitution of the hydrogen atoms of the hydroxymethylene group in **2** for phenyl groups resulted in the formation of a single diastereoisomer with the ($R_N$,$R_N$,$S_C$,$S_C$) configuration.[15]

The $^1$H and $^{13}$C{$^1$H} NMR spectra obtained for the cationic complexes [**3**]BF$_4$ and [**3**]PF$_6$ showed one, almost identical resonance pattern. The presence of only one species in the NMR spectrum ($^1$H NMR spectrum of [**3**]BF$_4$ is depicted in Figure 8; aliphatic hydrogen atoms were assigned with $^1$H-$^1$H COSY) and the information obtained from X-ray crystallography leads to the conclusion that a single stereoisomer with the ($R_N$,$R_N$,$S_C$,$S_C$) configuration is present, regardless of the ratio of stereoisomers in starting material **2**. Only in this ($R_N$,$R_N$,$S_C$,$S_C$) conformer, both hydroxymethylene groups point towards the palladium center and are within suitable distance for coordination to the metal (Figures 2 and 3). In the stereoisomers with the ($R_N$,$S_N$,$S_C$,$S_C$) and ($S_N$,$S_N$,$S_C$,$S_C$) configurations either one or both hydroxymethylene moieties point away from palladium; thus, they lack the dual intramolecular coordination ability and these stereoisomers are apparently less favored. In solution, fast exchange of the hydroxy group that is coordinated to the palladium center is anticipated in [**3**]BF$_4$ and [**3**]PF$_6$, and therefore, a resonance pattern in the $^1$H and $^{13}$C{$^1$H} NMR spectra that is consistent with an overall $C_2$ symmetry was observed for both complexes. No spectral changes were observed in their $^1$H NMR spectra in the range between –80 °C to +50 °C. Coordination of one of the hydroxy group to the metal seems crucial for the ultimate stereochemistry of the resulting cationic palladium complexes.

## Catalysis

In the course of this study, the catalytic potential of cationic complexes [**3**]BF$_4$ and [**3**]PF$_6$ was tested in the aldol condensation between aromatic aldehydes and methyl α-isocyanoacetate (MIC) in the presence of 10 mol-% of *i*Pr$_2$EtN at ambient temperature (Table 3). Both complexes were

Table 3. Aldol reaction of methyl α-isocyanoacetate with aldehydes catalyzed by [**3**]PF$_6$ and [**3**]BF$_4$.[a]

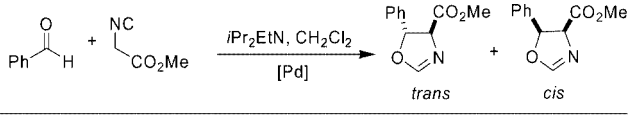


| Entry | Aldehyde | Complex | Conv. [%][b] | *trans*/*cis*[b] | *trans* (*ee*) (4*S*,5*R*)[c] |
|---|---|---|---|---|---|
| 1 | 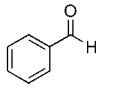 | [**3**]PF$_6$ | 84 | 72/28 | <5 |
| 2 | | [**3**]BF$_4$ | 75 | 69/31 | <5 |
| 3 | 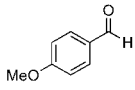 | [**3**]PF$_6$ | 73 | 64/36 | <5 |
| 4 | 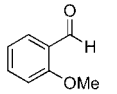 | [**3**]PF$_6$ | 81 | 67/33 | <5 |
| 5 | 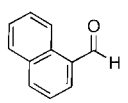 | [**3**]PF$_6$ | 80 | 85/15 | 9 |

[a] Reaction conditions: aldehyde (1.6 mmol), CNCH$_2$CO$_2$Me (1.6 mmol), catalyst (0.016 mmol, 1 mol-%), *i*Pr$_2$EtN (0.16 mmol), CH$_2$Cl$_2$ (5 mL), 20 °C, 24 h. [b] Determined by $^1$H NMR analysis. [c] Determined by chiral HPLC (Daicel CHIRALCEL OD, hexane/*i*PrOH = 95:5) and configuration was determined by $^1$H NMR analysis with the use of Eu(dcm)$_3$ as a chiral shift reagent.[17]

 © 2006 Wiley-VCH Verlag GmbH & Co. KGaA, Weinheim 

tested in the reaction with benzaldehyde (Entries 1 and 2). As [**3**]$PF_6$ gave the product in slightly higher yield, subsequent reactions with substituted aromatic aldehydes were performed with [**3**]$PF_6$ only (Table 3, Entries 2–5) as the catalyst. The highest *trans*/*cis* ratio and enantioselectivity for the *trans*-oxazoline product was obtained with naphthaldehyde as the substrate (Table 3, entry 5). In all cases, the *trans*-oxazoline derivative was obtained as the major product in good yields, albeit without significant enantioselectivity.

The preference for the *trans*-oxazoline product is commonly observed for achiral and chiral pincer complexes.[2b,3a,3c,5c,5k,5j,6a,16] Apparently, the pyrrolidine moieties with the hydroxymethylene groups are too small to generate a deep cavity around the palladium and the intermediate Pd-enolate complex and it is this cavity that would normally favor the formation of either one of the two enantiomers of the *trans*- or *cis*-oxazoline product.

## Experimental Section

**General:** (*S*)-Prolinol,[18] 2,6-bis(bromomethyl)-1-bromobenzene,[19] and [$Pd_2(dba)_3$·$CHCl_3$][20] were prepared according to previously published procedures. $^1H$ and $^{13}C\{^1H\}$ NMR spectra were recorded with a Varian Inova 300 spectrometer. Optical rotations were measured with a Perkin polarimeter 241. Elemental microanalyses were carried out by Microanalytisches Laboratorium Dornis und Kolbe, Mülheim a.d. Ruhr, Germany. The solid state infrared spectra were recorded with a Perkin–Elmer Spectrum One FTIR instrument. Mass spectrometry was carried out in a Voyager, Biosystems, MALDI-TOF. HPLC analyses were performed with a Perkin–Elmer Series 200 machine, equipped with a Diode Array II detector and LC pump with the use of a Daicel Chiracel OD column.

**2,6-Bis{[(*S*)-2-(hydroxymethyl)-1-pyrrolidinyl]methyl}phenyl Bromide (1):** (*S*)-prolinol (2.5 equiv., 30 mmol, 3 g) and bis(bromomethyl)-phenyl bromide (12 mmol, 4.1 g) were dissolved in $CH_2Cl_2$ (45 mL). Subsequently, to the reaction mixture was added $K_2CO_3$ (3 equiv., 36 mmol, 5 g) dissolved in water (45 mL) followed by the addition of $n$$Bu_4NCl$ (10 mol-%, 1.2 mmol, 0.33 g), and the mixture was vigorously stirred at reflux for 16 h. The organic layer was separated and the water layer was extracted with $CH_2Cl_2$ (2 × 30 mL). The solvent was evaporated in vacuo and the crude oil was purified by column chromatography [$SiO_2$, ethyl acetate/hexane = 5:1]. The product was obtained as a pale yellow solid in 58% yield (3 g). $C_{18}H_{27}BrN_2O_2$ (383.32): calcd. C 56.40, H 7.10, N 7.31; found C 56.29, H 6.93, N 7.24. MALDI-TOF: *m*/*z* = 383.33 [M + H]$^+$. $[\alpha]_D^{21}$ = –65.36 (*c* = 1.07, $CHCl_3$). IR: $\tilde{\nu}$ = 3410 (br), 2948 (s), 2872 (s), 2798 (m), 2758 (m), 1459 (m), 1446 (m), 1424 (m), 1403 (m), 1372 (m), 1351 (m), 1313 (w), 1264 (w), 1244 (w), 1194 (w), 1144 (w), 1113 (w), 1078 (m), 1048 (s), 1024 (s), 971 (w), 920 (w), 901 (w), 854 (w), 805 (w), 792 (w), 763 (w), 732 (m) cm$^{-1}$. $^1H$ NMR (300.1 MHz, $CDCl_3$, 25 °C): $\delta$ = 1.70–1.77 (m, 4 H, C*$CH_2$C$H_2$ ring), 1.82–1.99 (m, 4 H, C*C$H_2$ ring), 2.30–2.39 (m, 2 H, NCH*H* ring), 2.77–2.83 (m, 2 H, C**H*), 2.96–3.02 (m, 2 H, NC*H*H ring), 3.41 (dd, AB, $^2J_{H,H}$ = 11.1 Hz, $^3J_{H,H}$ = 2.1 Hz, $^3J_{H,H}$ = 3.6 Hz, 2 H, C$H_2$OH), 3.70 (dd, AB, $^2J_{H,H}$ = 11.1 Hz, $^3J_{H,H}$ = 2.1 Hz, $^3J_{H,H}$ = 3.6 Hz, 2 H, C$H_2$OH), 3.55 (d, AB, $^2J_{H,H}$ = 13.5 Hz, 2 H, $^2J_{H,H}$ = 13.5 Hz, 2 H, ArC$H_2$N), 4.08 (d, AB, $^2J_{H,H}$ = 13.5 Hz, 2 H, ArC$H_2$N), 7.22–7.33 (m, 3 H) ppm. $^{13}C\{^1H\}$ NMR (75.5 MHz, $CDCl_3$, 25 °C): $\delta$ = 23.85 (C*$CH_2$C$H_2$ ring), 27.82 (C*C$H_2$ ring), 54.93 (NC$H_2$ ring), 59.35 (ArC$H_2$N), 62.11 (C$H_2$OH), 65.04 (C*), 126.66 (*C*Br), 127.04 ($C_{para}$ to CBr), 129.93 ($C_{meta}$ to CBr), 139.18 (ArCCH$_2$N) ppm.

**2,6-Bis{[(*S*)-2-(hydroxymethyl)-1-pyrrolidinyl]methyl}phenylpalladium(II) Bromide (2):** Solid [$Pd_2(dba)_3$]·$CHCl_3$ (1.3 mmol, 1.39 g) was added to a solution of **1** (2.6 mmol, 1 g) in degassed benzene (60 mL). The resulting mixture was stirred at 50 °C for 3 h, filtered through Celite, and the solvent was evaporated in vacuo. Purification of the crude product by column chromatography [$SiO_2$, dba was eluted with hexanes/ethyl acetate = 1:1, the product with ethyl acetate/methanol = 5:1] yielded a yellowish solid in 63% yield (0.8 g). $C_{18}H_{27}BrN_2O_2Pd$ (489.74): C 44.14, H 5.56, N 5.72; found C 43.99, H 5.52, N 5.64. MALDI-TOF: *m*/*z* = 490.13 [M + H]$^+$, 410.22 [M – Br]$^+$. $[\alpha]_D^{21}$ = –10 (*c* = 0.6, acetone). IR: $\tilde{\nu}$ = 3383 (br), 2928 (s), 2877 (s), 1573 (w), 1459 (m), 1439 (m), 1429 (m), 1388 (w), 1352 (w), 1263 (w), 1094 (w), 1037 (s), 971 (m), 880 (w), 835 (w), 763 (m), 703 (w) cm$^{-1}$.

**2,6-Bis{[(*S*)-2-(hydroxymethyl)-1-pyrrolidinyl]methyl}phenylpalladium(II) Tetrafluoroborate ([3]$BF_4$):** Solid $AgBF_4$ (0.4 mmol, 80 mg) was added to a solution of **2** (0.4 mmol, 200 mg) in an acetone/water mixture (10:1, 20 mL). The reaction mixture was stirred for 30 min. The resulting suspension was filtered through Celite to yield a colorless filtrate. The solvent was removed in vacuo to leave the title compound as a white solid in 76% yield (153 mg). Crystals suitable for X-ray diffraction were obtained by slow diffusion of $Et_2O$ into an acetone solution of [**3**]$BF_4$. $C_{18}H_{27}BF_4N_2O_2Pd$ (496.74): C 43.53, H 5.48, N 5.64; found C 43.28, H 5.40, N 5.52. MALDI-TOF: *m*/*z* = 410.14 [M – $BF_4$]$^+$. $[\alpha]_D^{21}$ = +83.4 (*c* = 1.05, acetone). IR: $\tilde{\nu}$ = 3573 (m), 3549 (m), 4327 (m), 2973 (m), 2956 (m), 2929 (m), 2886 (m), 1585 (w), 1571 (w), 1461 (m), 1442 (m), 1430 (m), 1363 (w), 1340 (m), 1290 (w), 1270 (w), 1253 (w), 1228 (w), 1216 (w), 1077 (s), 1041 (s), 1010 (s), 986 (s), 955 (m), 899 (m), 861 (w), 842 (w), 823 (w), 761 (m), 701 (w) cm$^{-1}$. $^1H$ NMR (300.1 MHz, [$D_6$]acetone, 25 °C): $\delta$ = 1.64–1.68 (m, 6 H, C*$CH_2$CH*H* ring, C*C$H_2$ ring), 2.04–2.09 (m, 2 H, C*$CH_2$C*H*H ring), 3.08–3.16 (m, 2 H, NCH*H* ring), 3.43–3.46 (m, 2 H, C**H*), 3.88 (quintet, $^3J_{H,H}$ = 5.1 Hz, 2 H, NC*H*H ring), 3.94 (d, AB, $^2J_{H,H}$ = 11.7 Hz, 1 H, CH*H*OH), 4.23 (d, AB, $^2J_{H,H}$ = 11.7 Hz, 1 H, CH*H*OH), 3.98 (d, AB, $^2J_{H,H}$ = 11.4 Hz, 1 H, C*H*HOH), 4.24 (d, AB, $^2J_{H,H}$ = 11.4 Hz, 1 H, C*H*HOH), 3.92 (d, AX, $^2J_{H,H}$ = 14.7 Hz, 4 H, ArC$H_2$N), 4.69 (d, AX, $^2J_{H,H}$ = 14.7 Hz, 4 H, ArC$H_2$N), 5.67 (br. s, 1 H, OH), 6.84 (d, $^3J_{H,H}$ = 7.5 Hz, 2 H), 7.01 (t, $^3J_{H,H}$ = 8.1 Hz, 1 H) ppm. $^{13}C\{^1H\}$ NMR (75.5 MHz, [$D_6$]acetone, 25 °C): $\delta$ = 21.24 (C*$CH_2$C$H_2$), 24.16 (C*C$H_2$ ring), 60.47 (NC$H_2$), 66.32 (ArC$H_2$N), 68.52 (C*), 69.87 (C$H_2$OH), 120.60 ($C_{meta}$ to $C_{ipso}$), 125.11 ($C_{para}$ to $C_{ipso}$), 146.89 (ArCCH$_2$N), 151.00 ($C_{ipso}$) ppm.

**2,6-Bis{[(*S*)-2-(hydroxymethyl)-1-pyrrolidinyl]methyl}phenylpalladium(II) Hexafluorophosphate ([3]$PF_6$):** An excess of $NH_4PF_6$ (1.5 g) in water (15 mL) was added to a solution of **2** (0.43 mmol, 213 mg) in methanol (15 mL), and the reaction mixture was stirred for 16 h at ambient temperature. Subsequently, water (15 mL) was added to the reaction mixture which resulted in the precipitation of the product. After filtration of the reaction mixture, the crude product was redissolved in acetone and precipitated with $Et_2O$ to afford the product as a light yellow solid in 46% yield (110 mg). Crystals suitable for X-ray diffraction were obtained by slow diffusion of $Et_2O$ into a dichloromethane solution of [**3**]$PF_6$. $C_{18}H_{27}F_6N_2O_2PPd$ (554.8): C 38.97, H 4.91, N 5.05; found C 39.10, H 4.98, N 4.94. MALDI-TOF: *m*/*z* = 410.27 [M – $PF_6$]$^+$. $[\alpha]_D^{21}$ = +77.4 (*c* = 0.5, acetone). IR: $\tilde{\nu}$ = 3633 (m), 3565 (w), 3539 (m), 3170 (br), 2987 (m), 2959 (m), 2881 (m), 1624 (w), 1568 (w), 1463 (m), 1446 (m), 1426 (m), 1386 (w), 1360 (w), 1264 (w), 1231 (w),

 © 2006 Wiley-VCH Verlag GmbH & Co. KGaA, Weinheim 

1181 (w), 1097 (w), 1084 (w), 1048 (m), 1034 (m), 1018 (m), 1004 (m), 990 (m), 948 (w), 834 (s), 770 (m), 742 (m), 666 (w) $cm^{-1}$. $^1H$ NMR (300.1 MHz, [D$_6$]acetone, 25 °C): $\delta$ = 1.64–1.68 (m, 6 H, C*CH$_2$CH*H* ring, C*C*H*$_2$ ring), 2.04–2.09 (m, 2 H, C*CH$_2$C*H*H ring), 3.05–3.12 (m, 2 H, NCH*H* ring), 3.28–3.42 (m, 2 H, C**H*), 3.83 (quintet, $^3J_{H,H}$ = 5.1 Hz, 2 H, NC*H*H ring), 3.91 (d, AB, $^2J_{H,H}$ = 11.7 Hz, 1 H, CH*H*OH), 4.20 (d, AB, $^2J_{H,H}$ = 11.7 Hz, 1 H, CH*H*OH), 3.96 (d, AB, $^2J_{H,H}$ = 11.4 Hz, 1 H, C*H*HOH), 4.16 (d, AB, $^2J_{H,H}$ = 11.4 Hz, 1 H, C*H*HOH), 3.92 (d, AX, $^2J_{H,H}$ = 14.7 Hz, 2 H, ArC*H*$_2$N), 4.69 (d, AX, $^2J_{H,H}$ = 14.7 Hz, 2 H, ArC*H*$_2$N), 5.79 (br. s, 1 H, OH), 6.84 (d, $^3J_{H,H}$ = 7.5 Hz, 2 H), 7.01 (t, $^3J_{H,H}$ = 8.1 Hz, 1 H) ppm. $^{13}C\{^1H\}$ NMR (75.5 MHz, [D$_6$]acetone, 25 °C): $\delta$ = 21.22 (C*CH$_2$*C*H$_2$), 24.17 (C**C*H$_2$ ring), 60.48 (N*C*H$_2$), 66.37 (Ar*C*H$_2$N), 68.55 (*C**), 69.95 (*C*H$_2$OH), 120.71 (*C$_{meta}$* to C$_{ipso}$), 125.23 (*C$_{para}$* to C$_{ipso}$), 146.83 (Ar*C*CH$_2$N) 150.92 (*C$_{ipso}$*) ppm.

**General Procedure for Aldol Condensation of Methyl α-Isocyanoacetate with Aldehydes:** To a solution of the palladium complex (0.016 mmol, 1 mol-%) in $CH_2Cl_2$ (5 mL) was sequentially added methyl α-isocyanoacetate (145 μL, 1.6 mmol), aldehyde (1.6 mmol), and diisopropylethylamine (28 μL, 0.16 mmol). The reaction mixture was stirred at ambient temperature for 24 h. Subsequently, the solvent was evaporated in vacuo, and $^1H$ NMR samples and HPLC samples were prepared. The yield and ratio of *cis*- and *trans*-isomers was determined by $^1H$ NMR and the enantiomeric excess by HPLC. The configurations of the *trans*- and *cis*-product were determined after separation of the *trans*/*cis* mixture (column chromatography, $SiO_2$, ethyl acetate/hexane = 1:2) by $^1H$ NMR analysis of the spectrum with the use of Eu(dcm)$_3$ as the chiral shift reagent.[23]

**X-ray Crystal Structure Determinations:** X-ray intensities were measured with a Nonius Kappa CCD diffractometer with a rotating anode (graphite monochromator, $\lambda$ = 0.71073 Å) up to a resolution of $(\sin\theta/\lambda)_{max}$ = 0.65 $Å^{-1}$ at a temperature of 150 K. The structures were solved with automated Patterson methods[21] ([**3**]BF$_4$) or Direct Methods[22] ([**3**]PF$_6$) and refined with SHELXL-97[23] against $F^2$ of all reflections. Geometry calculations and checks for higher symmetry were performed with the PLATON[13] program. CCDC-605998 (for [**3**]BF$_4$) and -605999 (for [**3**]PF$_6$) contain the supplementary crystallographic data for this paper. These data can be obtained free of charge from The Cambridge Crystallographic Data Centre via www.ccdc.cam.ac.uk/data_request/cif.

**X-ray Crystal Structure Determination of [3]BF$_4$:** $C_{18}H_{27}N_2O_2Pd{\cdot}BF_4$, *FW* = 496.63, yellowish hexagonal plate, 0.30 × 0.30 × 0.06 $mm^3$, monoclinic, C2 (no. 5), $a$ = 18.5640(1), $b$ = 10.7289(1), $c$ = 20.6534(2) Å, $\beta$ = 108.8572(3)°, $V$ = 3892.78(6) $Å^3$, $Z$ = 8, $D_x$ = 1.695 g/$cm^3$. Number of reflections measured: 37429. An absorption correction based on multiple measured reflections was applied ($\mu$ = 1.01 $mm^{-1}$, 0.72–0.94 correction range). Unique reflections: 8777 ($R_{int}$ = 0.052). Non-hydrogen atoms were refined with anisotropic displacement parameters. All hydrogen atoms were located in the difference Fourier map. OH hydrogen atoms were refined freely with isotropic displacement parameters; CH hydrogen atoms were refined with a riding model. Number of parameters refined with one restraint: 521. *R*1/*wR*2 [$I > 2\sigma(I)$]: 0.0277/0.0620. *R*1/*wR*2 (all refl.): 0.0301/0.0647. $S$ = 1.033. Flack parameter[10] $x$ = –0.043(16). Residual electron density between –0.57 and 0.58 e/$Å^3$.

**X-ray Crystal Structure Determination of [3]PF$_6$:** $C_{18}H_{27}N_2O_2Pd{\cdot}PF_6{\cdot}0.5H_2O$, *FW* = 563.79, colorless block, 0.30 × 0.24 × 0.12 $mm^3$, monoclinic, $P2_1$ (no. 4), $a$ = 10.9459(10), $b$ = 9.2189(3), $c$ = 21.5229(9) Å, $\beta$ = 94.430(7)°, $V$ = 2165.4(2) $Å^3$, $Z$ = 4, $D_x$ = 1.729 g/$cm^3$. Number of reflections measured: 59398. An absorption correction based on multiple measured reflections was applied ($\mu$ = 1.00 $mm^{-1}$, 0.77–0.89 correction range). Unique reflections; 9936 ($R_{int}$ = 0.025). Non-hydrogen atoms were refined with anisotropic displacement parameters. All hydrogen atoms were located in the difference Fourier map. OH hydrogen atoms were kept fixed on their located positions, CH hydrogen atoms were refined with a riding model. One $PF_6$ anion was orientationally disordered. Number of parameters refined with 415 restraints: 605. *R*1/*wR*2 [$I > 2\sigma(I)$]: 0.0203/0.0449. *R*1/*wR*2 (all refl.): 0.0246/0.0463. $S$ = 1.040. Flack parameter[10] $x$ = –0.031(15). Residual electron density between –0.34 and 0.44 e/$Å^3$.

## Acknowledgments

The work described here was financially supported by the National Research School Combination-Catalysis (NRSC-C) (S.G.) and the Council for Chemical Sciences of the Netherlands Organization for Scientific Research (CW-NWO) (M.L., A.L.S.).

[1] For reviews on pincer complexes, see a) M. Albrecht, G. van Koten, *Angew. Chem. Int. Ed.* **2001**, *40*, 3750–3781; b) M. E. van der Boom, D. Milstein, *Chem. Rev.* **2003**, *103*, 1759–1792; c) J. T. Singleton, *Tetrahedron* **2003**, *59*, 1837–1857; for a general review on palladacycles, see d) J. Dupont, C. S. Consorti, J. Spencer, *Chem. Rev.* **2005**, *105*, 2527–2571.

[2] For the NCN-pincer complexes, see a) J. G. Donkervoort, J. L. Vicario, J. T. B. H. Jastrzebski, W. J. J. Smeets, A. L. Spek, G. van Koten, *J. Organomet. Chem.* **1998**, *551*, 1–7; b) M. Albrecht, B. M. Kocks, A. L. Spek, G. van Koten, *J. Organomet. Chem.* **2001**, *624*, 271–286; c) E. Diez-Barra, J. Guerra, I. Lopez-Solera, S. Merino, J. Rodrigues-Lopez, P. Sanchez-Verdu, J. Tejeda, *Organometallics* **2003**, *22*, 541–547.

[3] For the PCP complexes see a) F. Gorla, A. Togni, L. M. Venanzi, A. Albinati, F. Lianza, *Organometallics* **1994**, *13*, 1607–1616; b) J. M. Longmire, X. Zhang, *Tetrahedron Lett.* **1997**, *38*, 1725–1728; c) J. M. Longmire, X. Zhang, M. Shang, *Organometallics* **1998**, *17*, 4374–4379; d) P. Dani, M. Albrecht, G. P. M. van Klink, G. van Koten, *Organometallics* **2000**, *19*, 4468–4476.

[4] For the NCN-pincer complexes, see a) J. A. M. van Beek, G. van Koten, M. J. Ramp, N. C. Coenjaarts, D. Grove, K. Goubitz, M. C. Zoutberg, C. H. Stam, W. J. J. Smeets, A. L. Spek, *Inorg. Chem.* **1991**, *30*, 3059–3068; b) L. van Kuil, Y. S. J. Veldhuizen, D. Grove, J. W. Zwikker, J. W. Jenneskens, W. Drenth, W. J. J. Smeets, A. L. Spek, G. van Koten, *Recl. Trav. Chim. Pays-Bas* **1994**, *113*, 267–277; c) I. G. Jung, S. U. Son, K. H. Park, K.-C. Chung, J. W. Lee, Y. K. Chung, *Organometallics* **2003**, *22*, 4715–4720.

[5] For the Phebox-pincer complexes, see a) Y. Motoyama, N. Makihara, Y. Mikami, K. Aoki, H. Nishiyama, *Chem. Lett.* **1997**, 951–952; b) S. E. Denmark, R. A. Stavenger, A.-M. Faucher, J. P. Edwards, *J. Org. Chem.* **1997**, *62*, 3375–3389; c) M. A. Stark, C. J. Richards, *Tetrahedron Lett.* **1997**, *38*, 5881–5884; d) Y. Motoyama, Y. Mikami, H. Kawakami, K. Aoki, H. Nishiyama, *Organometallics* **1999**, *18*, 3584–3588; e) Y. Motoyama, H. Narusawa, H. Nishiyama, *Chem. Commun.* **1999**, 131–132; f) M. A. Stark, G. Jones, C. J. Richards, *Organometallics* **2000**, *19*, 1282–1291; g) M. Gerisch, J. R. Krumper, R. G. Bergman, T. D. Tilley, *J. Am. Chem. Soc.* **2001**, *123*, 5818–5819; h) Y. Motoyama, M. Okano, H. Narusawa, N. Makihara, K. Aoki, H. Nishiyama, *Organometallics* **2001**, *20*, 1580–1591; i) Y. Motoyama, Y. Koga, H. Nishiyama, *Tetrahedron* **2001**, *57*, 853–860; j) Y. Motoyama, K. Shimozono, K. Aoki, H. Nishiyama, *Organometallics* **2002**, *21*, 1684–1694; k) Y. Motoyama, H. Kawakami, K. Shimozono, K. Aoki, H. Nishiyama, *Organometallics* **2002**, *21*, 3408–3416; l) Y. Motoyama, Y. Koga, K. Kobayashi, K. Aoki, H. Nishiyama, *Chem. Eur. J.* **2002**, *8*,

 © 2006 Wiley-VCH Verlag GmbH & Co. KGaA, Weinheim 

2968–2975; m) M. Gerisch, J. R. Krumper, R. G. Bergman, T. D. Tilley, *Organometallics* **2003**, *22*, 47–58; n) H. Nishiyama, T. Shiomi, Y. Tsuchiya, I. Matsuda, *J. Am. Chem. Soc.* **2005**, *127*, 6972–6973.

[6] For the PCP complexes, see a) B. S. Wiliams, P. Dani, M. Lutz, A. L. Spek, G. van Koten, *Helv. Chim. Acta* **2001**, *84*, 3519–3530; b) D. Morales-Morales, R. E. Cramer, C. M. Jensen, *J. Organomet. Chem.* **2002**, *654*, 44–50; c) S. Medici, M. Gagliardo, B. S. Williams, P. A. Chase, S. Gladiali, M. Lutz, A. L. Spek, G. P. M. van Klink, G. van Koten, *Helv. Chim. Acta* **2005**, *88*, 694–705.

[7] For the SCS-pincer complexes, see D. R. Evans, M. Huang, W. M. Seganish, J. C. Fettinger, T. L. Williams, *Organometallics* **2002**, *21*, 893–900.

[8] a) K. Takenaka, Y. Uozumi, *Org. Lett.* **2004**, *6*, 1833–1835; b) K. Takenaka, Y. Uozumi, *Adv. Synth. Catal.* **2004**, *346*, 1693–1696; c) K. Takenaka, M. Minakawa, Y. Uozumi, *J. Am. Chem. Soc.* **2005**, *127*, 12273–12281.

[9] S. Gosiewska, M. Huis in't Veld, J. J. M. de Pater, P. C. A. Bruijnincx, M. Lutz, A. L. Spek, R. J. M. Klein Gebbink, G. van Koten, *Tetrahedron: Asymmetry* **2006**, *17*, 674–686.

[10] H. D. Flack, *Acta Crystallogr., Sect. A* **1983**, *39*, 876–881.

[11] a) M. A. Stark, G. Jones, C. J. Richards, *Organometallics* **2000**, *19*, 1282–1291; b) Y. Motoyama, K. Shimozono, K. Aoki, H. Nishiyama, *Organometallics* **2002**, *21*, 1684–1694; c) J. van den Broeke, J. J. H. Heeringa, A. V. Chuchuryukin, H. Kooijman, A. M. Mills, A. L. Spek, J. H. van Lenthe, P. J. A. Ruttink, B.-J. Deelman, G. van Koten, *Organometallics* **2004**, *23*, 1287–1294.

[12] J. Vicente, A. Arcas, *Coord. Chem. Rev.* **2005**, *249*, 1135–1154.

[13] A. L. Spek, *J. Appl. Crystallogr.* **2003**, *36*, 7–13.

[14] The ($S_N$,$S_N$,$S_C$,$S_C$) and ($R_N$,$R_N$,$S_C$,$S_C$) enantiomers both contain a $C_2$ axis and this symmetry element reduces the amount of signals by half. The ($R_N$,$S_N$) isomer does not contain any element of symmetry, and therefore, all hydrogen and carbon atoms are magnetically inequivalent [the stereoisomers with the ($R_N$,$S_N$,$S_C$,$S_C$) and ($S_N$,$R_N$,$S_C$,$S_C$) configurations are superimposable upon 180° rotation around the C–Pd axis and are therefore identical].

[15] S. Gosiewska, S. Herreras Martinez, M. Lutz, A. L. Spek, R. W. A. Havenith, G. P. M. van Klink, G. van Koten, R. J. M. Klein Gebbink, manuscript in preparation.

[16] N. C. Mehendale, R. J. M. Klein Gebbink, G. van Koten, manuscript in preparation.

[17] a) Tris(δ,δ-dicampholylmethanato)europium(III): M. D. McCreary, D. W. Lewis, D. L. Wernick, G. M. Whitesides, *J. Am. Chem. Soc.* **1974**, *96*, 1038–1054; b) Y. Ito, M. Sawamura, T. Hayashi, *J. Am. Chem. Soc.* **1986**, *108*, 6405–6406.

[18] D. Enders, P. Fey, H. Kipphardt, *Organic Syntheses* (Ed.: J. P. Freeman), Wiley, New York, **1993**, vol. 8, p. 26.

[19] C. H. M. Amijs, G. P. M. van Klink, G. van Koten, *Green Chem.* **2003**, *5*, 470–474.

[20] S. Komiya (Ed.), *Synthesis of Organometallic Compounds*, Wiley, Chichester, U. K., **1997**.

[21] P. T. Beurskens, G. Admiraal, G. Beurskens, W. P. Bosman, S. Garcia-Granda, R. O. Gould, J. M. M. Smits, C. Smykalla, *The DIRDIF99 Program System*, Technical Report of the Crystallography Laboratory, University of Nijmegen, The Netherlands, **1999**.

[22] G. M. Sheldrick, *SHELXS-97*, Program for crystal structure solution, University of Göttingen, Germany, **1997**.

[23] G. M. Sheldrick, *SHELXL-97*, Program for crystal structure refinement, University of Göttingen, Germany, **1997**.

Received: May 31, 2006
Published Online: September 28, 2006

 © 2006 Wiley-VCH Verlag GmbH & Co. KGaA, Weinheim 

DOI: 10.1002/ejic.200600580

# Thermal Evolution of a MgAl Hydrotalcite-Like Material Intercalated with Hexaniobate

Daniel Carriazo,[a] Cristina Martín,[a] and Vicente Rives*[a]

**Keywords:** Layered double hydroxides / Polyoxometalates / Nb-Mg-Al mesoporous oxides / Intercalations

A MgAl hydrotalcite-like material intercalated with hexaniobate has been prepared by the anion exchange method from the corresponding nitrate precursor; the sample and the oxides obtained upon its calcination were characterized by element chemical analysis, powder X-ray diffraction, thermal analyses (thermogravimetric and differential), nitrogen adsorption-desorption isotherms at –196 °C, transmission electron microscopy, and FT-IR and UV/Vis spectroscopy. The results show the formation of a microporous hydrotalcite-type solid with a gallery height of 7.2 Å where the $H_3Nb_6O_{19}^{5-}$ anions are oriented with their $C_3$ axes perpendicular to the layers. This material preserves its layered structure upon calcination up to 400 °C; calcination above this temperature causes decomposition of the hexaniobate and the layered structure collapses, giving rise to amorphous mesoporous solids (Nb-Mg-Al-O) with a large specific surface area (157 $m^2 g^{-1}$). At 800 °C crystallization of $Mg_4Nb_2O_9$ takes place. FT-IR studies on the acid-basic properties carried out by pyridine and 2-propanol adsorption, showed that all solids obtained through hydrotalcite calcination present Lewis-type acid and Brönsted-type basic sites.

(© Wiley-VCH Verlag GmbH & Co. KGaA, 69451 Weinheim, Germany, 2006)

## Introduction

Layered Double Hydroxides (LDHs), also known as hydrotalcite-like compounds or anionic clays, are lamellar materials generally described by the empirical formula $M^{2+}_{1-x}M^{3+}_x(OH)_2(A^{m-})_{x/m}\cdot nH_2O$, where $A^{m-}$ is the anion balancing the net positive charge of the brucite-like layers[1–3] developed by a partial $M^{2+}/M^{3+}$ substitution. A large number of compounds with this structure have been synthesized in the last decades varying the nature and the molar ratio of the cations in the layers and the nature of the interlayer anions. These compounds have shown their suitability in different fields, acting as anion scavengers in wastewater, biomolecule reservoirs or as polymer additives to improve its properties.[4–6] Nevertheless, there is no doubt that it is in the field of catalysis where they find the widest number of applications, as catalysts, catalyst precursors or supports.[7] These last applications are mainly due to the fact that calcination of the mentioned materials gives rise to systems constituted by different phases (mixed metal oxides) which usually show higher stability, larger surface development and longer life-time than others prepared by conventional methods.

Polyoxometalates (POMs) are anionic compounds with a cluster structure formed by linked oxygen octahedra coordinating transition metals (V, Mo, W, isopolyoxometalates), although in many cases a heteroatom (P, Si) in a tetrahedrally coordinated unit is included in the structure (heteropolyoxometalates).[8] These compounds have also deserved much attention because of the multiple applications they find in many different fields, such as medicine, materials science and catalysis.[9–11] POMs containing niobium have been scarcely studied and, contrary to those containing V, Mo or W, are synthesized under basic pH conditions.[12] The best-known niobium POM is hexaniobate ($Nb_6O_{19}^{8-}$), which has the Lindqvist structure, and is obtained through alkaline fusion of $Nb_2O_5$. Niobium compounds are extensively used in many heterogeneous catalytic processes where they can act as catalyst supports or as the active phase.[13]

In order to modify the textural properties and to develop acid and electron acceptor centres in the hydrotalcite basic structure and thereby improve its catalytic properties, many authors have reported the intercalation of different oxo- or polyoxometalates between the LDH layers,[14,15] giving rise to very selective catalysts in some oxidation reactions such as dehydrogenation or alkene epoxidation.[16–18] In a previous work Evans et al. reported the intercalation of some hexametalates with the Lindqvist structure [$V_2W_4O_{19}^{4-}$ and $Nb_xW_{6-x}O_{19}^{(x+2)-}$ where $x$ = 2, 3, 4] within the interlayers of hydrotalcite,[19] but a study of the intercalation of hexaniobate is lacking in the literature, and so herein we report the synthesis of a new MgAl LDH intercalated with hexaniobate ($H_3Nb_6O_{19}^{5-}$) prepared by anion exchange, starting from a nitrate LDH (MgAl-$NO_3$) precursor. Its characterization, as well as of the oxides obtained upon its calcination, by element chemical analyses, Powder X-ray Diffraction (PXRD), Thermogravimetric (TG) and Differential

[a] Departamento de Química Inorgánica, Universidad de Salamanca,
37008 Salamanca, Spain

 © 2006 Wiley-VCH Verlag GmbH & Co. KGaA, Weinheim 

Table 1. Elemental chemical analyses of the prepared samples and their corresponding formulae.

| Sample | Mg[a] | Al[a] | N[a] | Nb[a] | K[a] | C[a] | Formula |
|---|---|---|---|---|---|---|---|
| MgAl-$NO_3$ | 18.5 | 10.1 | 5.2 | – | – | – | $[Mg_{0.67}Al_{0.33}(OH)_2](NO_3)_{0.33}\cdot 0.44H_2O$ |
| $K_8Nb_6O_{19}$ | – | – | – | 40.0 | 22.5 | – | $K_8Nb_6O_{19}\cdot 13H_2O$ |
| MgAlNb | 12.9 | 6.7 | – | 25.9 | – | 0.1 | $[Mg_{0.68}Al_{0.32}(OH)_2](H_3Nb_6O_{19})_{0.06}(CO_3)_{0.01}\cdot 0.70H_2O$ |

[a] Weight percentage.

Thermal Analyses (DTA), nitrogen adsorption-desorption at –196 °C, Scanning and Transmission Electron Microscopy (SEM and TEM), and Fourier Transform Infrared (FT-IR) and Vis-UV spectroscopy are also reported. Crystalline potassium hexaniobate, which was synthesized for preparation of MgAl-hexaniobate LDH, has also been characterized and used as a reference. The acid-base properties of the solids obtained by calcination of the MgAl-hexaniobate LDH were tested by FT-IR spectroscopy after pyridine or 2-propanol adsorption.

## Results and Discussion

Element chemical analysis carried out for potassium hexaniobate as well as for both layered samples lead to the following formulae: $K_8Nb_6O_{19}\cdot 13H_2O$, $[Mg_{0.67}Al_{0.33}(OH)_2](NO_3)_{0.33}\cdot 0.44H_2O$ and $[Mg_{0.68}Al_{0.32}(OH)_2](H_3Nb_6O_{19})_{0.06}(CO_3)_{0.01}\cdot 0.70H_2O$, respectively (values have been rounded to two figures after the decimal point) (Table 1). This last formula has been calculated considering $H_3Nb_6O_{19}^{5-}$ as the interlayer anion since this is the predominant species at the pH conditions (12.5) at which the exchange process was performed.[13] The amount of interlayer water (0.70 molecules per LDH mol) has been determined from the TG curve (see below). The slight increase of the Mg/Al molar ratio from 2 (MgAl-$NO_3$) to 2.1 (MgAlNb) after the exchange process is probably due to a partial dissolution of the aluminum cations as aluminate as a consequence of its amphoteric character and the extremely high pH used during the exchange process to stabilize the niobium POM, although this small difference could also be ascribed to the experimental error of the technique.

It should be mentioned that different intercalation attempts, such as direct synthesis from metal nitrate salts or exchange using meixnerite (a MgAl LDH containing hydroxyl as the interlayer anion) as a precursor were tested and none of them produced the hexaniobate intercalation, the unique layered phase detected using these synthesis routes being hydrotalcite, MgAl-$CO_3$. Addition of the LDH-$NO_3$ as a slurry, as recommended by other authors to facilitate anion exchange,[20] was also unsuccessful, probably due to changes in pH leading to $Nb_2O_5$ precipitation.

Although the procedure followed to synthesize potassium hexaniobate is described in the literature to produce the single-protonated form, element chemical analyses and the PXRD pattern in Figure 1, from comparison with the JCPDS file 14-0288, confirm that the niobium polyoxometalate formed in this case was octo-potassium hexaniobate ($K_8Nb_6O_{19}\cdot 13H_2O$). To study its thermal stability the PXRD patterns of the products obtained upon its calcination at different temperatures were recorded and are also shown in this Figure. As can be observed, potassium hexaniobate completely decomposes below 300 °C and two different crystallographic forms of potassium niobate, $KNbO_3$, have been identified, one at 300 °C and the other at 600 °C, matching with the 32-0821 and 32-0822 JCPDS files, respectively.

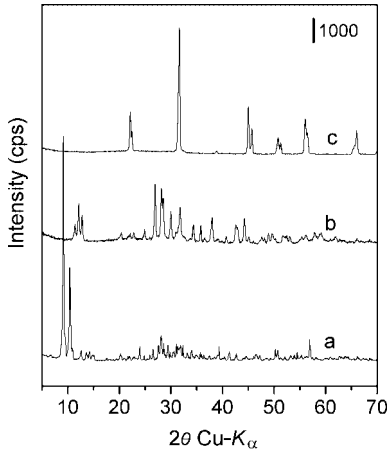


Figure 1. PXRD patterns of $K_8Nb_6O_{19}$ (a) uncalcined, and calcined at (b) 300 °C and (c) 600 °C.

The powder XRD patterns of sample MgAlNb, both original and calcined at increasing temperatures, are shown in Figure 2. The first one is characteristic of materials with the hydrotalcite-like structure in which the intercalation of hexaniobate has led to an increase in the basal spacing from 8.8 Å (corresponding to a phase with intercalated nitrate anions in an upwards configuration) to 12.0 Å, which means a gallery height of 7.2 Å, once the brucite-like layers width (4.8 Å)[21] is subtracted. This value is in agreement with the height of a hexaniobate anion, ($Nb_6O_{19}^{8-}$)[22,23] with its $C_3$ axis perpendicular to the layers (Figure 3). The basal spacing, usually measured from the $d_{003}$ diffraction peak (assuming a$R\bar{3}m$ layers stacking) was calculated in this sample from the positions of the peaks due to other basal planes, (006) and (009), recorded at 6.0 and 4.0 Å, respectively, because the peak due to (003) planes is partially hidden by a broad peak centred at 11 Å. The pattern is similar to that reported by different authors for other POM-LDHs systems.[20,21,24–31] Regarding the broad reflection between 10–12 Å some authors have claimed that it is produced by a poorly crystallized phase of a $M^{2+}/M^{3+}$-POM salt in low quantities,[20,26] while other authors have proposed different alternatives.[27–30] The unexpected low intensity of the peak due to diffraction by the (003) planes (weaker than the other two basal reflections recorded) is due to the presence

 © 2006 Wiley-VCH Verlag GmbH & Co. KGaA, Weinheim 

of species (POMs) with high scattering factors in the interlayers.[29]

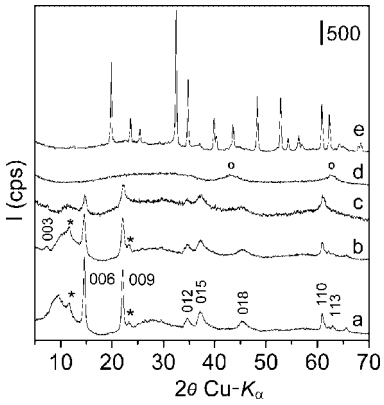


Figure 2. PXRD patterns of samples MgAlNb: (a) uncalcined and calcined at (b) 150 °C, (c) 300 °C, (d) 450 °C and (e) 800 °C. (*) MgAl-$CO_3$; (o) MgO. Miller indexes are labelled for the layered phase.

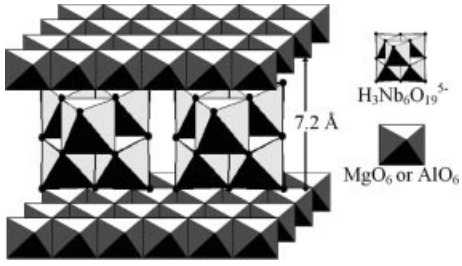


Figure 3. Scheme of MgAl LDH pillared with hexaniobate.

Additionally, and in agreement with the chemical analyses, a small amount of another layered crystalline phase, ascribed to hydrotalcite (MgAl-$CO_3$), is also present, even though extreme care was taken to avoid $CO_2$. This phase could have been formed during the exchange process due to the high affinity that these materials have towards carbonate under the strongly basic conditions (pH = 12.5) at which the reaction was carried out, or it could have been incorporated during post-synthesis treatments while the solid was still wet (during washing or drying processes).

The PXRD pattern recorded for the sample calcined at 150 °C (Figure 2, b) is rather similar to that recorded for the uncalcined one, but a decrease in the intensity of the broad peak centred at 11 Å allows the weak (003) reflection to be distinguished at the position expected (12 Å) taking into account the positions of the peaks due to diffraction by planes (006) and (009). The diffractograms are quite similar for samples calcined below 300 °C, although some differences are observed in the PXRD pattern of the sample calcined at 300 °C, Figure 2 (c); the reflections due to the MgAl-$CO_3$ phase have vanished, and a decrease in the intensities of all the peaks is also observed. The characteristic reflections due to planes (003), (006), (009) and (110) of a hydrotalcite-like material are still observed at 400 °C, which means that the POM ions hosted in the interlayers are thermally more stable than when they are isolated as a potassium salt (decomposition is observed at 300 °C). The PXRD pattern for the sample calcined at 450 °C, Figure 2 (d), is typical of an amorphous material, indicating that the layered structure has collapsed, giving rise to amorphous oxides for which the PXRD diagram shows only weak peaks at 2.1 and 1.5 Å ascribed to the MgO periclase phase (JCPDS file: 4-0829). Similar patterns are observed for samples calcined up to 700 °C, but at 800 °C the PXRD pattern (MgAlNb800, Figure 2, e) shows sharp diffraction maxima characteristic of a crystalline phase ascribed to magnesium niobate, $Mg_4Nb_2O_9$ (JCPDS file: 36-1381). No crystalline phase containing aluminum has been identified at any calcination temperature, suggesting that it must be well dispersed or forming amorphous phases. At these calcination temperatures, the niobium in excess which has not reacted with magnesium (Mg/Nb = 1.8) to form magnesium niobate must be, as well as aluminum, forming an amorphous phase, since no peaks corresponding to crystalline $Nb_2O_5$ were detected by PXRD.

The FT-IR spectra of potassium hexaniobate and of LDH-niobate (MgAlNb sample) are shown in Figure 4. Apart from the bands due to the LDH matrix, the spectra are very similar, suggesting that the hexaniobate structure is maintained after the exchange. Bands at 3462 $cm^{-1}$ (broad) and at 1640 $cm^{-1}$ for the potassium salt are due to the hydroxyl groups stretching mode and the bending mode of water molecules, respectively. The bands due to Nb=O and Nb–O–Nb stretching vibrations are recorded in the 900–400 $cm^{-1}$ range (844, 697, 528, and 415 $cm^{-1}$), in agreement with those previously reported elsewhere for this compound.[32] After intercalation into the LDH structure, bands ascribed to Nb–O stretching modes in hexaniobate units (844, 770, and 542 $cm^{-1}$) are still recorded, together with other bands at 664, 447, and 402 $cm^{-1}$ due to υ(Mg–O) and Mg/Al–OH translational modes of the layers.[33] Another band due to the $\nu_3$ mode of carbonate anions associated to the LDH-carbonate phase identified by XRD is clearly recorded at 1369 $cm^{-1}$.

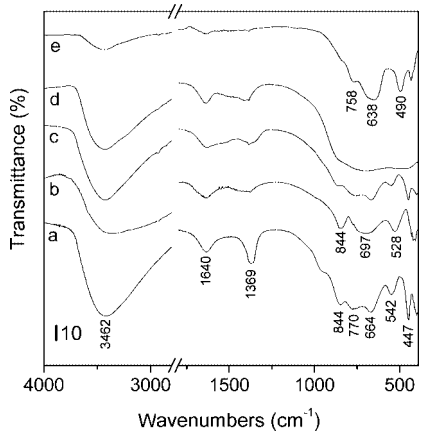


Figure 4. FT-IR spectra of MgAlNb (a) and calcined at (c) 250 °C, (d) 450 °C and (e) 800 °C; (b) FT-IR spectrum of potassium hexaniobate.

The small shift observed for some of the bands ascribed to the hexaniobate unit, when compared with their positions for the potassium salt, is presumably a consequence

 © 2006 Wiley-VCH Verlag GmbH & Co. KGaA, Weinheim 

of the interaction between the anion and the brucite-like layers.

The FT-IR spectra recorded for calcined MgAlNb samples are also included in Figure 4. Similar spectra to that recorded for the uncalcined sample are observed when the calcination is carried out up to 400 °C, and only an appreciable decrease in the intensity of the bands, especially the one due to carbonate, is observed, in agreement with the PXRD results.

Calcination at 450 °C gives rise to decomposition of hexaniobate and collapse of the layered structure, the spectrum showing a broad band in the 900–400 $cm^{-1}$ range, typical of amorphous oxide species. The spectrum is similar for samples calcined up to 700 °C, but when the solid is calcined at 800 °C, new bands at 758, 638, 490 and 432 $cm^{-1}$ characteristic of the $Mg_4Nb_2O_9$ phase, already identified in this solid by PXRD, develop.

The TG and DTA curves recorded for potassium hexaniobate and the MgAlNb sample are shown in Figure 5. Three thermal effects can be distinguished in the DTA curve of the potassium salt (dashed line in panel A); the first two (at 115 and 290 °C) are endothermic effects and correspond to removal of structural water, the second also coincides with potassium hexaniobate decomposition (observed from the PXRD at 300 °C) to potassium niobate. The exothermic effect recorded at 592 °C can be ascribed to transformation of $KNbO_3$ into another crystalline phase, also observed by PXRD. The TG curve (solid line in panel A) reveals that the structural water, which is the only volatile species in the sample, is lost in different steps. The weight losses represent ca. 16% of the total weight which means 13 water molecules per mol potassium hexaniobate.

Two well-resolved weight losses are recorded in the TG curve for sample MgAlNb (Figure 5B), although the DTA curve shows three endothermic effects; the first one, at 126 °C, can be ascribed to removal of surface adsorbed water. The second effect, at 265 °C is due to removal of interlayer water and the third, recorded at 443 °C, is a consequence of dehydroxylation of the brucite-like layers, matching with the hexaniobate decomposition into amorphous Mg-Al-Nb-O and water, as detected by FT-IR and PXRD between 400 and 450 °C.

Carbonate decomposition to $CO_2$ around 300 °C, as concluded by PXRD and FT-IR spectroscopy, can be partially included in the peak recorded at 265 °C, although its contribution to the weight loss is almost undetectable due to the low amount of $CO_3^{2-}$ present in the sample. Moreover, the peak at 126 °C could be partially due to the evaporation of some intercalated water, because water adsorbed on the external surface of the crystallites generally is totally evolved at 110 °C. This overlap does not allow ascribing accurately the weight loss to the different processes detected. Consequently, the amount of intercalated water given in the formula of the MgAlNb sample (0.70 molecules per mol of LDH) has been determined in an approximate way from the weight loss recorded between 110 and 270 °C.

The UV/Vis spectra (not shown) recorded for all samples show only an absorption band in the UV range, corresponding to a $Nb^{5+}\leftarrow O^{2-}$ charge-transfer process. A shift from 260 (potassium hexaniobate) to 245 nm (MgAlNb) is observed upon intercalation of hexaniobate in the LDH structure (Table 2). This small hypsochromic shift is probably due to the POM confinement within the layered host. No appreciable change is observed in the spectra of the calcined samples, where only a sharper absorption peak at 253 nm is recorded in the spectrum of the sample calcined at 800 °C (Table 2).

The nitrogen adsorption-desorption isotherm recorded for the MgAlNb sample, Figure 6, previously degassed at 120 °C for 2 h, is in between types I and II of the IUPAC classification,[34] characteristic of microporous solids. The specific surface area determined by the BET method is 24 $m^2 g^{-1}$ (Table 2), 40% of which corresponds to adsorption on micropores (as calculated from the t-plot)[35] and the external surface area corresponds to 14 $m^2 g^{-1}$. Layered double hydroxides intercalated with small anions are not microporous, as the width of the interlayer (ca. 3 Å) is not large enough to host nitrogen molecules. Interlayer micro-

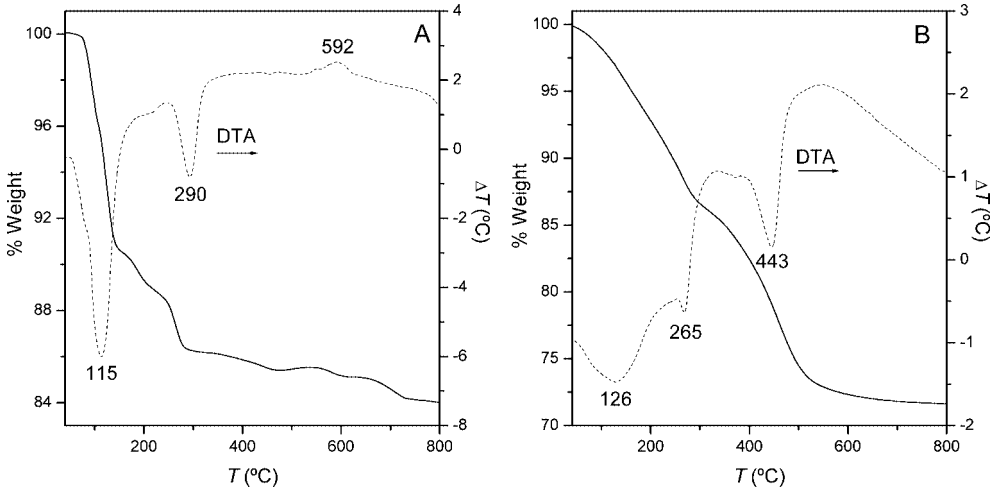


Figure 5. TG (solid lines) and DTA (dotted lines) of (A) potassium hexaniobate and (B) sample MgAlNb, recorded under oxygen.

 © 2006 Wiley-VCH Verlag GmbH & Co. KGaA, Weinheim 

Table 2. Specific surface areas ($S_{BET}$: BET method; $S_m$ microporous equivalent surface area, $S_{ext}$ external surface area and $V_t$ total pore volume) and position of the maximum in the UV/Vis spectra for potassium niobate and several layered samples (* determined from the *t*-plot).

| Sample | $S_{BET}$[a] | $S_m$[a]* | $S_{ext}$[a]* | $V_t$[b] | λ[c] |
|---|---|---|---|---|---|
| MgAl-$NO_3$ | 26 | – | 27 | 0.08 | – |
| MgAlNb | 24 | 10 | 14 | 0.06 | 245 |
| MgAlNb500 | 157 | – | 160 | 0.20 | 239 |
| MgAlNb800 | 45 | 6 | 39 | 0.12 | 253 |
| $K_8Nb_6O_{19}$ | 1 | – | – | – | 260 |

[a] $m^2 g^{-1}$. [b] mL $g^{-1}$ (determined at $p/p = 0.95$). [c] nm.

porosity only develops when the interlayers are swelled after intercalation of large anions with a large formal charge, rendering large spaces between them.

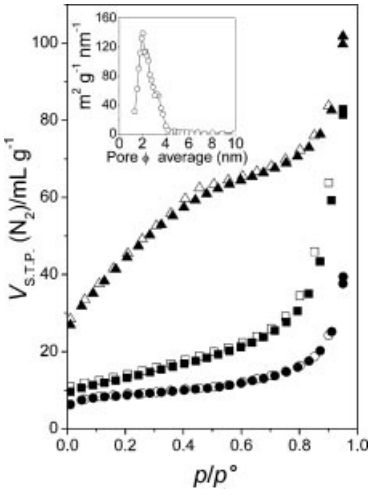


Figure 6. Nitrogen adsorption–desorption isotherms (filled symbols and open symbols, respectively) at –196 °C for the original sample MgAlNb (circles) and calcined at 500 °C (triangles) or 800 °C (squares). The inset shows the pore size distribution for sample MgAlNb500.

The isotherms recorded for the samples calcined between 450 and 600 °C are similar to each other and very different to that recorded for the MgAlNb sample. The isotherm for sample MgAlNb500 (Figure 6) can be classified as type IV, characteristic of mesoporous solids, since it shows a significant increase of the adsorbed amount at an intermediate relative pressure range, produced by a multilayer filling mechanism. The BET surface area for this sample shows an appreciable increase (157 $m^2 g^{-1}$) in comparison to that for the uncalcined one (Table 2). No adsorption on micropores was detected (the zero intercept of the t-plot approached zero) and the corresponding external surface area was calculated as 160 $m^2 g^{-1}$. The pore size distribution plot (Figure 6), shows a very intense and slightly asymmetric curve, which indicates that most of the pores have diameters ranging between 1.8 and 4 nm. A considerable increase in the pore volume (0.20 $cm^3 g^{-1}$) is also observed upon calcination. These textural properties change with calcination above 700 °C. Thus, the MgAlNb800 sample (Figure 6) shows an isotherm similar to that recorded for the pristine layered material. The BET surface area decreases to 45 $m^2 g^{-1}$, probably due to crystallization of magnesium niobate, $Mg_4Nb_2O_9$, (detected by PXRD), although it remains larger than that measured for crystalline potassium hexaniobate and its calcination products (between 1 and 2 $m^2 g^{-1}$), suggesting that other phases corresponding to aluminum-containing amorphous species also exist. For this sample a small fraction of micropores is also found.

Representative scanning and transmission electron micrographs (SEM and TEM) for calcined and uncalcined samples are shown in Figure 7 and Figure 8. At first sight, when potassium hexaniobate crystallizes from solution, enlarged prismatic-shaped crystals are formed. From the SEM micrographs it can be observed that these crystals have a hexagonal section (see parts a and b in Figure 7), and a closer view reveals small, smooth crystalline particles with sizes between 2 and 5 μm (Figure 7, c).

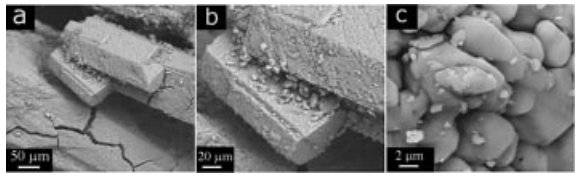


Figure 7. SEM pictures of potassium hexaniobate with different magnification.

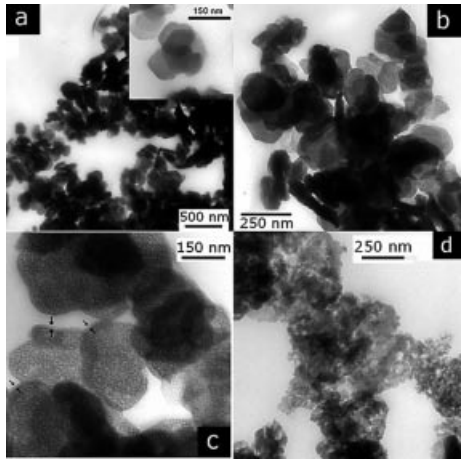


Figure 8. TEM pictures of the original sample MgAlNb (a), inset closer view and calcined at 500 °C (b, c) and 800 °C (d).

The typical hydrotalcite morphology, hexagonal platelet particles, is clearly observed by TEM for the as-synthesized MgAlNb sample (Figure 8, a). The size of the hexagonal crystals is ca. 100 ± 50 nm and their thickness 20 ± 10 nm. Calcination between 450 and 600 °C produces a smoothing of the particle edges (Figure 8, parts b and c), which are now more rounded than those observed for the uncalcined ones. A quite homogeneous pore distribution is simultaneously developed, in agreement with the results obtained by the nitrogen adsorption study. The particles are surrounded by an amorphous wall with a thickness of 10 nm (indicated by arrows in Figure 8, c).

 © 2006 Wiley-VCH Verlag GmbH & Co. KGaA, Weinheim 

For the sample calcined at 800 °C (Figure 8, d) the morphology completely changes; aggregates of very small irregular-shaped particles (between 20 and 50 nm) are observed, indicating that the magnesium hexaniobate ($Mg_4Nb_2O_9$) phase (detected by PXRD and FT-IR), is well mixed or embedded in an amorphous phase (formed by Al-Nb oxides).

The textural and morphological properties observed for sample MgAlNb calcined between 450 and 600 °C have not been previously reported for LDH-POM calcined systems.[30,36,37] In these last cases, as well as for LDHs intercalated with permanent (nonvolatile) anions, a decrease in the surface areas is usually observed upon calcination. On the other hand, calcination of hydrotalcites intercalated with volatile anions ($CO_3^{2-}$, $NO_3^-$, etc.)[36,38] results in the development of porosity and, as a consequence, an enhancement of their surface areas. Different factors influence this process, such as the preparation method, nature of the metal ions in the layers, the sort of anion, etc., and it is ascribed to the evolved gases ($NO_2$, $CO_2$, $O_2$, etc.) produced upon anion decomposition, escaping through the crystal basal faces. However, in previous reports where TEM pictures of calcined hydrotalcites are shown,[36] no particles as well defined as in our case have been observed.

Because of the high basicity of the hexaniobate anion in comparison with other polyoxometalates (heptamolybdate or polyoxotungstates), a delay of the reaction between hexaniobate and the magnesium existing in the layers may be produced, enhancing its thermal stability, so POM decomposition and layer dehydroxylation take place in a narrow temperature range. This may be the reason why an amorphous solid (Mg-Al-Nb-O) with these special textural properties is formed.

### Acid-Base Properties

To gain insight into the surface properties of solid MgAlNb500 we have tested its acid-base properties by the adsorption of pyridine and 2-propanol monitored by FT-IR spectroscopy.

### Pyridine Adsorption

The FT-IR spectrum of the MgAlNb500 sample after pyridine adsorption at room temperature and outgassing at the same temperature is shown in part A of Figure 9; only bands at 1608, 1586, 1575, 1487 and 1443 $cm^{-1}$ are recorded, ascribed to modes 8a, 8b, 19a and 19b, respectively, of pyridine bonded to surface Lewis acid sites. The splitting observed for the band originated by mode 8a (1608, 1586 $cm^{-1}$) clearly shows the presence of two different types of surface Lewis acid sites on the surface of this solid. The positions of the bands are similar to those previously recorded upon adsorption of py on alumina, and so the bands here recorded should be ascribed to pyridine adsorbed on tetrahedrally (1608 $cm^{-1}$) or octahedrally coordinated (1586 $cm^{-1}$) $Al^{3+}$ cations,[39] although the first one could also be ascribed to py bonded to coordinatively unsaturated (cus) $Nb^{5+}$ ions, since its position coincides with that of the band recorded after adsorption of pyridine on $Nb_2O_5$.[40] When the outgassing temperature is increased up to 300 °C, Figure 9 (A), the intensity of the bands are markedly reduced, but they are still observed, indicating that the Lewis-type acid centres are strong.

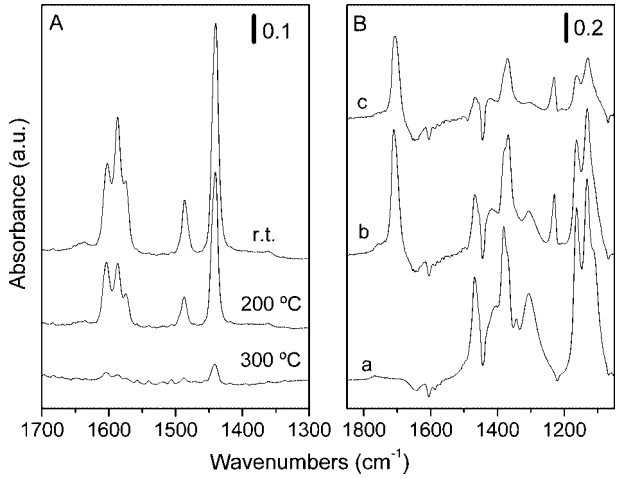


Figure 9. (A) FT-IR spectra of pyridine adsorbed at room temperature on MgAlNb500 and outgassing at the temperatures given (in °C); (B) FT-IR spectra of 2-propanol adsorbed at room temp. on MgAlNb500 (a) and heated at (b) 200 °C and (c) 300 °C.

The FT-IR spectrum of pyridine adsorbed on sample MgAlNb800 (not shown) is similar to that recorded upon adsorption on the sample calcined at 500 °C, where only Lewis acid sites are detected, but they are weaker than for the sample calcined at 500 °C, as they were removed after outgassing merely at 200 °C.

Some authors have reported the existence of Brönsted acid sites in niobium-containing samples when they are exposed to water,[41] but they were not observed in our samples; the FT-IR spectra recorded after adsorption of py on samples previously exposed in situ to water vapour are similar to that recorded for the unwetted samples.

### Isopropanol Adsorption

The FT-IR spectrum of 2-propanol (ISP) adsorbed on sample MgAlNb500 at room temperature is displayed in part B of Figure 9. It shows a broad band at ca. 3255 $cm^{-1}$ (not shown) which corresponds to new surface hydroxyl groups developed on the surface of the solid by a dissociative adsorption mechanism. Sharp bands at 2970, 2936, 2878, and 2728 $cm^{-1}$ correspond to stretching modes of the methyl group and the bands in the low wavenumbers region, at 1468, 1382, 1308, 1164, and 1135 $cm^{-1}$ [ascribed to $\delta(CH_3)$, $\nu(CO)$, and $\nu(CC)$], are characteristic of alcoholate species formed via dissociative adsorption of the ISP molecule. When the solid is heated in situ at increasing temperatures, Figure 9 (B), the intensities of the bands originated by the isopropoxide species decrease; new bands develop above 200 °C at 1709 and 1230 $cm^{-1}$, which correspond to $\nu(C{=}O)$ and $\nu_{as}(C–C–C)$ modes of acetone weakly coordinated through the oxygen atom of the carbonyl group to surface Lewis acid sites. The latter bands disappear upon outgassing at low temperature (100 °C). Adsorption of ISP

 © 2006 Wiley-VCH Verlag GmbH & Co. KGaA, Weinheim 

on sample MgAlNb calcined at 800 °C (not shown) gives rise to similar spectra, although the bands assigned to acetone are less intense.

ISP decomposition to acetone or propene is considered as a test reaction in the study of the acid-base and redox properties of metal oxide heterogeneous catalysts[42,43] since Brönsted acid sites are needed for propene formation via dehydration, while Lewis-type acid and basic, and redox centres are required for acetone formation via oxidative dehydrogenation, but only acid and basic sites if the acetone is produced via simple dehydrogenation. In our case, formation of acetone (detected by FT-IR) has to be produced through this last process, since temperature programmed reduction (TPR) studies carried out on our samples did not show any hydrogen consumption due to $Nb^{5+}$ reduction. The reaction may proceed through the following steps: (1) ISP is first dissociatively adsorbed on Lewis-type acid sites as an isopropoxide species and the proton is adsorbed on basic centres−surface exposed oxide anions−and (2) the abstraction of a second hydrogen atom from the alcohol takes place. On desorption, acetone and $H_2$ are the reaction products.

In summary, Lewis-type acid and Brönsted-type basic centres are present in the calcined samples.

## Conclusions

All the results reported here support the successful intercalation for the first time of hexaniobate between the MgAl brucite-like layers, rendering a new microporous layered material which retains its structure during calcination in air up to 400 °C, i.e., an enhancement in POM thermal stability is achieved upon its intercalation. Calcination at 450 °C produces dehydroxylation of the layered structure and POM decomposition, giving rise to amorphous mesoporous solids, with a large specific surface area (157 $m^2 g^{-1}$); further calcination at 800 °C leads to magnesium niobate crystallization which is embedded in an amorphous Nb-Al-containing phase. All calcined solids show surface Lewis-type acid and Brönsted-type basic sites, which are responsible for acetone formation by simple dehydrogenation of 2-propanol.

In addition to succeeding in preparing a novel, thermally stable MgAl-hexaniobate LDH, an amorphous mesoporous solid, Mg-Al-Nb-O, which seems suitable to be used as a catalyst support or adsorbent, was formed through its calcination between 450–600 °C.

## Experimental Section

All reagents were purchased from Aldrich and used without any further purification.

Potassium hexaniobate ($K_8Nb_6O_{19}·13H_2O$) was synthesized following a preparation method similar to that described elsewhere;[44] $Nb_2O_5$ (13.3 g, 50 mmol) was slowly added to a KOH (26 g, 394 mmol) melt in a nickel crucible; once the addition was completed the mixture was further heated for 30 min and then it was poured into decarbonated water (100 mL). After filtering the solution the volume was reduced to 50 mL and the solution was cooled overnight at 0 °C. The crystals that formed were filtered off and washed with a 1:1 (v/v) ethanol/water mixture and dried under vacuum in a desiccator.

The MgAl-$NO_3$ hydrotalcite−$Mg_2Al(OH)_6(NO_3)·1.33H_2O$−was prepared by coprecipitation from the corresponding metal nitrate salts, following a method previously described:[45] a solution formed by dissolving $Mg(NO_3)_2·6H_2O$ (12.8 g, 50 mmol) and $Al(NO_3)_3·9H_2O$ (9.4 g, 25 mmol) in water (150 mL) was added dropwise under nitrogen to $CO_2$-free water (150 mL). The pH was maintained close to 10 by simultaneous addition of a 2-M NaOH solution, and the mixture was stirred for 24 h at room temperature and then it was treated for five days at 70 °C under hydrothermal conditions in a Teflon-lined steel autoclave at autogenous pressure. The suspension was finally washed with decarbonated water, centrifuged and dried under vacuum.

The MgAl-hexaniobate LDH was prepared by anion exchange, by adding dry $Mg_2Al(OH)_6(NO_3)·1.33H_2O$ (1.0 g, 3.8 mmol) to a solution of $K_8Nb_6O_{19}·13H_2O$ (1.5 g, 1.1 mmol) in $CO_2$-free water (70 mL). The pH finally achieved was 12.5. The mixture was kept under nitrogen and refluxed at 90 °C for 6 h; the resulting solid was centrifuged and washed with boiling water and finally dried under vacuum in a desiccator. The sample obtained in this way is designated as MgAlNb, and the samples obtained upon calcination are labelled as MgAlNbT (where *T* is the calcination temperature in °C).

**Instrumentation:** Element chemical analyses were carried out in Servicio General de Análisis Químico Aplicado (University of Salamanca, Spain); Mg, Al and Nb were determined by atomic absorption in a Mark-2 EEL 240 apparatus, while carbon and nitrogen contents were determined with a CHNS 932 Leco analyzer.

The powder X-ray diffraction (PXRD) patterns were obtained with a Siemens D-500 diffractometer, using Cu-$K_{\alpha 1}$ radiation ($\lambda$ = 1.54050 Å).

Differential thermal analysis (DTA) and thermogravimetric (TG) analysis curves were recorded in DTA-7 and TG-7 instruments, respectively, from Perkin–Elmer. The analyses were carried out in flowing (30 mL $min^{-1}$) oxygen from L'Air Liquide (Spain) at a heating rate of 10 °C $min^{-1}$.

The nitrogen adsorption-desorption isotherms for specific surface area measurements were recorded at –196 °C in a Gemini instrument from Micromeritics. The samples were previously outgassed at 120 °C for 2 h. The pore size distribution plotted for MgAlNb500 was obtained from the Cranston and Inkley method.[46]

The UV/Vis spectra were recorded in the 200–1100 nm range with a Perkin–Elmer Lambda 35 apparatus equipped with a Labsphere RSA-PE-20 accessory by the diffuse reflectance technique; MgO was used as a reference.

Fourier Transform infrared spectra (FT-IR) were collected with a Perkin–Elmer FT-1730 instrument using the KBr pellet technique.

The FT-IR technique was also used to assess the surface acidity/basicity properties using pyridine or 2-propanol as probe molecules. These spectra were recorded with a Perkin–Elmer 16 PC spectrometer using self-supported discs; the sample was degassed in situ in a special cell[47] with $CaF_2$ windows at 400 °C for 2 h at $10^{-4}$ N $m^{-2}$, prior to the adsorption experiments. After degassing, the probe molecule vapour was adsorbed at room temperature and, in the case of pyridine (py), the spectra were recorded after outgassing at increase temperatures (from room temp. to 400 °C), while

 © 2006 Wiley-VCH Verlag GmbH & Co. KGaA, Weinheim 

2-propanol (ISP) was adsorbed at room temp. and, without removing the gas phase, the solid was heated at increasing temperatures (100–400 °C).

Scanning electron micrographs (SEM) were obtained with a model 940 Digital Scanning-Microscope from Zeiss.

Transmission electron micrographs (TEM) were obtained with a Zeiss-902 apparatus equipped with a digital camera, the samples were prepared on a copper grid after evaporating a drop of sample dispersed in water.

## Acknowledgments

The authors acknowledge financial support from MEC (grant MAT2003-06605-C02-01) and ERDF; DC also thanks a grant from Universidad de Salamanca.

[1] V. Rives (Ed.), *Layered Double Hydroxides: Present and Future*, Nova Science Publishers, Inc., New York, **2001**.
[2] E. Wypych, K. G. Satyanarayana (Eds.), *Clay Surfaces: Fundamental and Applications*, Elsevier, Amsterdam, **2004**.
[3] D. G. Evans, R. C. T. Slade, *Struct. Bond.* **2006**, *119*, 1–87.
[4] N. K. Lazaridis, T. A. Pandi, K. A. Matis, *Ind. Eng. Chem. Res.* **2004**, *43*, 2209–2215.
[5] J. H. Choy, S. Y. Kwak, Y. J. Jeong, J. S. Park, *Angew. Chem. Int. Ed.* **2000**, *39*, 4042–4045.
[6] L. Li, R. Z. Ma, Y. Ebina, N. Iyi, T. Sasaki, *Chem. Mater.* **2005**, *17*, 4386–4391.
[7] S. Albertazzi, F. Basile, A. Vaccari in *Clay Surfaces: Fundamental and Applications* (Eds.: E. Wypych, K. G. Satyanarayana), Elsevier, Amsterdam, **2004**, p. 497–546.
[8] M. T. Pope, *Heteropoly and Isopoly Oxometalates*; Springer-Verlag, New York **1983**.
[9] I. V. Kozhevnikov, *Chem. Rev.* **1998**, *98*, 171–198.
[10] N. Mizuno, M. Misono, *Chem. Rev.* **1998**, *98*, 199–217.
[11] J. T. Rhule, C. L. Hill, D. A. Judd, R. F. Schinazi, *Chem. Rev.* **1998**, *98*, 327–357.
[12] M. Nyman, F. Bonhomme, T. M. Alam, M. A. Rodriguez, B. R. Cherry, J. L. Krumhansl, T. M. Nenoff, A. M. Sattler, *Science* **2002**, *297*, 996–998.
[13] I. Nowak, M. Ziolek, *Chem. Rev.* **1999**, *9*, 3603–3624.
[14] T. Kwon, G. A. Tsigdinos, T. J. Pinnavaia, *J. Am. Chem. Soc.* **1988**, *110*, 3653–3654.
[15] V. Rives, M. A. Ulibarri, *Coord. Chem. Rev.* **1999**, *181*, 61–120.
[16] B. F. Sels, D. E. de Vos, P. A. Jacobs, *Angew. Chem. Int. Ed.* **2005**, *44*, 310–313.
[17] T. Tatsumi, K. Yamamoto, H. Tajima, H. Tominaga, *Chem. Lett.* **1992**, *5*, 815–818.
[18] E. Gardner, T. J. Pinnavia, *Appl. Catal. A* **1998**, *167*, 65–74.
[19] J. Evans, M. Pillinger, J. J. Zhang, *J. Chem. Soc., Dalton Trans.* **1996**, 2963–2974.
[20] S. K. Yun, T. J. Pinnavaia, *Inorg. Chem.* **1996**, *35*, 6853–6860.
[21] M. A. Drezdzon, *Inorg. Chem.* **1988**, *27*, 4628–4632.
[22] I. Lindqvist, *Arkiv Kemi* **1953**, *5*, 247–250.
[23] R. Rhomer, J. E. Guerchais, *Bull. Soc. Chim. Fr.* **1961**, 324–334.
[24] M. R. Weir, J. Moore, R. A. Kydd, *Chem. Mater.* **1997**, *9*, 1686–1690.
[25] M. R. Weir, R. A. Kydd, *Inorg. Chem.* **1998**, *37*, 5619–5624.
[26] E. Narita, P. D. Kaviratna, T. J. Pinnavaia, *J. Chem. Soc., Chem. Commun.* **1993**, 60–62.
[27] J. D. Wang, Y. Tian, R. C. Wang, A. Clearfield, *Chem. Mater.* **1992**, *4*, 1276–1282.
[28] R. S. Weber, P. Gallezot, F. Lefebvre, S. L. Suib, *Microporous Mater.* **1993**, *1*, 223–227.
[29] T. Hibino, A. Tsunashima, *Chem. Mater.* **1997**, *9*, 2082–2089.
[30] M. del Arco, D. Carriazo, S. Gutiérrez, C. Martín, V. Rives, *Inorg. Chem.* **2004**, *43*, 375–384.
[31] F. L. Sousa, M. Pillinger, R. A. S. Ferreira, C. M. Granadeiro, A. M. V. Cavaleiro, J. Rocha, L. D. Carlos, T. Trindade, H. I. S. Nogueira, *Eur. J. Inorg. Chem.* **2006**, *4*, 726–734.
[32] F. J. Farrell, V. A. Maroni, T. G. Spiro, *Inorg. Chem.* **1969**, *8*, 2638–2642.
[33] J. T. Kloprogge, L. Hickey, R. L. Frost, *J. Raman Spect.* **2004**, *35*, 967–974.
[34] K. S. W. Sing, D. H. Everett, R. A. W. Haul, L. Moscou, R. Pierotti, J. Rouquerol, T. Sieminiewska, *Pure Appl. Chem.* **1985**, *57*, 603–619.
[35] B. C. Lippens, J. H. de Boer, *J. Catal.* **1965**, *4*, 319–323.
[36] V. Rives in *Layered Double Hydroxides: Present and Future* (Ed.: V. Rives), Nova Sci. Pub. Inc., New York, **2001**, p. 229–250, and references therein.
[37] D. Carriazo, C. Domingo, C. Martín, V. Rives, *Inorg. Chem.* **2006**, *45*, 1243–1251.
[38] W. T. Reichle, S. Y. Kang, D. S. Everhardt, *J. Catal.* **1986**, *101*, 352–369.
[39] C. Morterra, S. Coluccia, E. Garrone, G. Ghiotti, *J. Chem. Soc., Faraday Trans. 1* **1979**, *75*, 289–304.
[40] C. Martín, G. Solana, P. Malet, V. Rives, *Catal. Today* **2003**, *78*, 365–376.
[41] C. L. T. da Silva, V. L. L. Camorim, J. L. Zotin, M. L. R. D. Pereira, A. D. Faro, *Catal. Today* **2000**, *57*, 209–217.
[42] B. Grzybowska-Swierkosz, *Mater. Chem. Phys.* **1987**, *17*, 121–144.
[43] M. Ai, *J. Catal.* **1977**, *49*, 305–312.
[44] M. Filowitz, R. K. C. Ho, W. G. Klemperer, W. Shum, *Inorg. Chem.* **1979**, *18*, 93–103.
[45] M. del Arco, S. Gutiérrez, C. Martín, V. Rives, J. Rocha, *J. Solid State Chem.* **2000**, *151*, 272–280.
[46] R. W. Cranston, F. A. Inkley, *Adv. Catal.* **1957**, *9*, 143–154.
[47] V. Rives, C. Martín, A. Montero, Spanish Patent, 200100688, **2001**.

Received: June 20, 2006
Published Online: September 22, 2006

 © 2006 Wiley-VCH Verlag GmbH & Co. KGaA, Weinheim 

DOI: 10.1002/ejic.200600583

# Alk-2-ynyl Trimethylsilyl Chalcogenoethers by Nucleophilic Substitution of Propargyl Bromides

**Deeb Taher,[a] Andrew I. Wallbank,[a] Elizabeth A. Turner,[a] Heather L. Cuthbert,[a] and John F. Corrigan*[a]**

**Keywords:** Chalcogens / Silicon / Propargyl complexes

Lithium (trimethylsilyl)chalcogenolates have been generated and used to prepare a series of alk-2-ynyl trimethylsilyl chalcogenoethers from the corresponding propargyl bromides in good yield. The thermal decomposition of the telluroethers has also been studied.

(© Wiley-VCH Verlag GmbH & Co. KGaA, 69451 Weinheim, Germany, 2006)

## Introduction

Trimethylsilyl chalcogenoethers of the general formula $RESiMe_3$ (R = alkyl or aryl, E = S, Se, Te) are a powerful class of reagents due to their demonstrated ability to react smoothly with metal salts (M–X) to form metal chalcogenolate cluster and nanocluster complexes $(M–ER)_x$, through the thermodynamically favorable elimination of $XSiMe_3$.[1–9] This includes their use in nanoparticle chemistry, where silylated reagents have been utilized to passivate the surface of metal chalcogenide cores.[10,11]

Despite their wide ranging utility, only a relatively limited number of $RESiMe_3$ reagents of the heavier congeners Se and Te have been reported, and this can likely be attributed to the difficulty of introducing the $Me_3Si$ moiety onto $RE^-$. For the elements Se and Te, this typically involves silylation reactions of salts RE-M[12–29] (M = Li, Na) or REMgX (X = Cl, Br) with $ClSiMe_3$.[30–33]

Segi and co-workers have reported a general route to asymmetric thio- and selenoethers by the in situ generation of $Me_3SiE^-$ nucleophiles from the silylated chalcogenides $E(SiMe_3)_2$ and alkyllithium reagents (Scheme 1).[34] Utilizing this methodology, we set out to combine the reactive lithium (trimethylsilyl)chalcogenolates with a series of propargyl bromides (Scheme 2). The coordination chemistry of both the chalcogen group(s) and the propargyl functionality could provide for a wide variety of structural types when complexed to metal centers.[35] In this paper, we report the preparation and spectral characterization of the series of

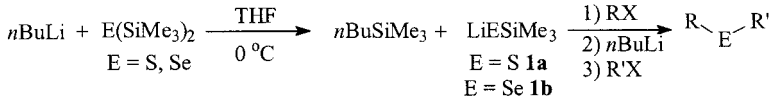


Scheme 1. Route to asymmetric chalcogenoethers as reported by Segi et al.[34]

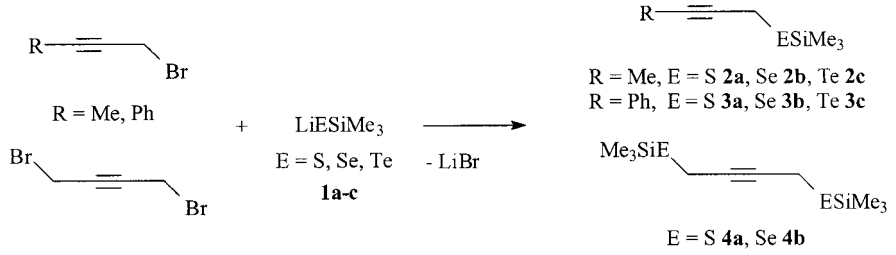


Scheme 2.

Li[$ESiMe_3$] and its utility for the synthesis of propargyl chalcogenoethers. The chalcogenoethers have been characterized by nuclear magnetic resonance spectroscopy and

[a] Department of Chemistry, The University of Western Ontario, London, Ontario, N6A 5B7 Canada

 © 2006 Wiley-VCH Verlag GmbH & Co. KGaA, Weinheim 

mass spectrometry, along with decomposition studies of the highly unstable tellurium congeners.

## Results and Discussion

The reagents $LiESiMe_3$ **1a**–**c**, provide ready access to reactive trimethylsilyl chalcogenolate fragments. Reported by Segi as reactive intermediates as part of a catalytic cycle,[39] the use of *n*BuLi and bis(trimethylsilyl) chalcogenide as the starting materials yields the desired product $[Me_3SiE]Li$ through reductive cleavage of the E–Si bond, without any complications due to formation of $Li_2E$.[40] The NMR chemical shifts of **1a**–**c** are reported in Table 1. In compounds **1a**–**c**, the chalcogen centers produce a downfield trend in the $^1H$ and $^{13}C$ chemical shifts and an upfield trend in the $^{29}Si$ NMR going from S < Se < Te. The $^{77}Se$ and $^{125}Te$ chemical shifts values of **1b** and **1c** are similar to those reported for related alkylsilylchalcogenolates[41] and are also close to the values reported for phosphane-stabilized copper trimethylsilylchalcogenolates.[42,43]

Table 1. NMR spectroscopic data for **1a**–**c** in $C_6D_6$. Chemical shifts are reported in ppm.

| | $-Si(CH_3)_3$ $^1H$ | $^{13}C$ | $^{29}Si$ | $^{77}Se/^{125}Te$ |
|---|---|---|---|---|
| **1a** | 0.58 | 7.32 | 7.22 | – |
| **1b** | 0.70 | 7.87 | 4.10 | –518.1 |
| **1c** | 0.88 | 9.71 | –19.43 | –1294.3[a] |

[a] Recorded in $[H_8]$thf.

Chalcogen-substituted propargyl complexes can be prepared from propargyl bromides and metal chalcogenolates,[44–52] although demonstrated radical routes have recently been documented for the preparation of propargyl selenols from diselenides.[53] The demonstrated clean conversion of $E(SiMe_3)_2$ to $[Me_3SiE]Li$ using *n*-butyllithium has allowed for the successful preparation of a range of chalcogenoethers from alkyl bromides, including 1-bromo-2-propyne (propargyl bromide).[34] Our attempts to isolate pure $HC{\equiv}CCH_2ESiMe_3$ under a variety of reaction conditions with either **1a** or **1b** were unsuccessful. On occasion, the desired product was isolated but in extremely low yield, due to either the acidity of the alkynyl proton or the general instability of any $HC{\equiv}CCH_2ESiMe_3$ formed.[50] Indeed, with all propargyl bromides $RC{\equiv}CCH_2Br$ used as the starting materials in this study, the $Me_3SiE^-$ anion proved to be too reactive under the conditions previously reported (thf, 0 °C) for the generation of selenoethers.[34] As nucleophilic displacements of this type are well known to proceed through the expected $S_N2$ reaction mechanism,[50] lower polarity solvents and low reaction temperatures were used to control the reaction. Propargyl–allenyl isomerization via a 1,3-hydride shift is quite common in chalcogen substituted propargyl complexes and in tellurium systems, the allenyl form is generally favored.[50] No evidence for isomerization was observed in this study. The lithium chalcogenolates **1a**–**c** are all soluble in hydrocarbon solvents, presumably due to the presence of the trimethylsilyl groups and the tightly bound thf molecules. Qualitatively, the reactivity of the lithium chalcogenolates increases on going from S < Se < Te and the reactivity of the propargyl bromides $RC{\equiv}CCH_2Br$ increases on going from R = Ph < Me < $BrCH_2$. Slight excesses of the lithium chalcogenolates were used in the preparation of **3a**,**b** and **4a**,**b** to ensure complete consumption of the starting propargyl bromides. The synthesis of **3a** and **4a** required refluxing temperatures of 65 °C and 35 °C, respectively, while the tellurium analogs **2c** and **3c** were not stable for extended periods of time at any accessible temperature, although dilute solutions maintained at –80 °C could be kept for 2 or 3 d before significant decomposition (as evidenced by the precipitation of tellurium metal) occurred. All of the compounds are highly water-, oxygen- and photosensitive. The sulfur and selenium derivatives are highly malodorous oils while the tellurium derivatives are obtained as yellow solids.

Selected NMR spectroscopic data are provided in Table 2. The $^1H$ chemical shifts of the methylene groups attached to the chalcogen centers show an upfield trend upon substitution by a heavier, less electronegative chalcogen while the trimethylsilyl resonances shift downfield. The chemical shifts of 3.05–3.25 ppm for the methylene group in the sulfur derivatives are upfield of those reported for S-aryl-substituted derivatives.[49,54] The $^{13}C$ chemical shifts of the methylene groups remain virtually constant upon varying R but are highly dependent on the chalcogen. The upfield shifts for the methylene carbons attached to selenium and tellurium are consistent with those observed previously[51,55] but were assigned conclusively by heteronuclear single-bond quantum correlation (HSQC) NMR spectroscopy techniques.

Table 2. Selected NMR spectroscopic data for **2**–**4** in $C_6D_6$. Chemical shifts are reported in ppm.

| | $^1H$ | | $^{13}C$ | | | | $^{77}Se/^{125}Te$ |
|---|---|---|---|---|---|---|---|
| | $CH_2$ | $Si(CH_3)_3$ | R–C≡C– | ≡C–$CH_2$ | $CH_2$ | $Si(CH_3)_3$ | |
| **2a** | 3.10 | 0.25 | 77.97 | 78.42 | 14.44 | 0.79 | – |
| **2b** | 2.97 | 0.32 | 78.41 | 78.53 | 2.53 | 1.49 | 2.1 |
| **2c**[a] | 2.80 | 0.42 | 77.11 | 79.88 | 3.61 | 2.31 | –80.9 |
| **3a** | 3.25 | 0.25 | 88.71 | 83.03 | 14.73 | 0.89 | – |
| **3b** | 3.14 | 0.34 | 89.39 | 83.18 | 2.55 | 1.51 | 12.4 |
| **3c**[b] | 2.89 | 0.42 | 91.27 | 81.67 | 5.00 | 2.21 | –56.7 |
| **4a** | 3.05 | 0.24 | 81.13 | | 14.29 | 0.83 | – |
| **4b** | 2.96 | 0.32 | 81.87 | | 2.68 | 1.87 | 4.0 |

[a] Recorded at –50 °C in $C_7D_8$. [b] Recorded at –80 °C in $C_7D_8$.

### Thermal Decomposition of 2c and 3c

Initial attempts at extending this chemistry to tellurium met with poor results as the reaction solutions rapidly decomposed to tellurium metal and colored tars. Maintaining the entire reaction at low temperatures resulted in beige-yellow solutions, which would decompose even at –25 °C. Although unstable, $RC{\equiv}CCH_2TeSiMe_3$ (**2c**, R = Me; **3c**, R = Ph) can be isolated provided reaction conditions are maintained below –40 °C. (Scheme 3) Although solid samples of **3c** decomposed significantly at –80 °C after 3 d, the

 © 2006 Wiley-VCH Verlag GmbH & Co. KGaA, Weinheim 

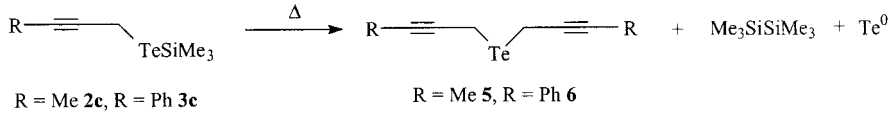


Scheme 3. Decomposition pathway of **2c** and **3c**.

slightly higher stability vs. **2c** allowed for its decomposition pathway to be studied. An aliquot of a reaction mixture of **3c** was isolated and dried (below –40 °C) and then, over a period of 5 d, the reaction flask was maintained at –25 °C and aliquots were taken and isolated at this temperature to monitor the reaction. $^{125}$Te NMR spectra showed clearly that **3c** ($\delta$ = –56.7 ppm) was converting cleanly to a new compound **6** ($\delta$ = +679.7 ppm) and observation of the flask indicated the presence of $Te^0$. Due to the wide range of $^{125}$Te chemical shifts for telluroethers (e.g. $Me_2Te$ $\delta$ = 0 ppm, $tBu_2Te$ $\delta$ = 999 ppm)[56] and ditellurides ($Me_2Te_2$ $\delta$ = 69 ppm, $MeTe_2tBu$ $\delta$ = 617 ppm)[57] a chemical shift value of +679.7 ppm is not diagnostic. The identity of the species as the telluroether $(PhC{\equiv}CCH_2)_2Te$ **6** could be inferred via the $^{125}$Te-$^1$H spectrum which displayed a quintet at +679.7 ppm ($^2J_{Te-H}$ = 29 Hz) in addition to a multiplet at $\delta$ = –56.7 ppm assigned to **3c**. A $^2J_{TeH}$ value of 29 Hz observed for the peak centered at +679.7 ppm is consistent with this structural assignment.[58] Mass spectra of partially decomposed solutions of **2c** and **3c** were obtained and parent ions for the telluroethers **5** and **6**, respectively, were observed. If samples of **5** and **6** are exposed to the air, further deposition of $Te^0$ is observed and GC-MS analysis of the supernatant displays predominantly the corresponding propargyl alcohol $RC{\equiv}CCH_2OH$. Attempts to synthesize an authentic sample of **6** via the reaction of two equivalents of 1-bromo-3-phenyl-2-propyne with $Na_2Te$ or $Li_2Te$[59] were unsuccessful in our hands due to the formation of the coupled product, 1,6-diphenylhexa-1,5-diyne. The ability of $Te^{2-}$ to couple allyl halides has been reported by Clive and co-workers[60] and is thought to proceed via homolytic fission of the telluroether initially formed. In their study, high reaction temperatures were required to force the elimination of the $Te^0$ but they found that the stability of the organic radical thus generated was the primary thermodynamic barrier. In the case of **6**, both radicals would be extremely delocalized and thus the dissociation may proceed easily. Similar, but more complex reaction mixtures were observed for the attempted synthesis of **5** from $M_2Te$.

## Experimental Section

All syntheses were carried out using standard inert atmosphere Schlenk and glovebox techniques. Bis(trimethylsilyl) sulfide,[36] bis(trimethylsilyl) selenide and bis(trimethylsilyl) telluride were synthesized according to the literature procedure reported for bis(trimethylsilyl) sulfide. 1-Bromo-3-phenyl-2-propyne, 1-bromo-2-butyne and 1,4-dibromo-2-butyne were synthesized from the corresponding propargyl alcohols using phosphorus tribromide.[37] *n*BuLi (1.6 M in hexanes) was used as received from Aldrich Chemical Co. Reaction solvents were dried by passing through packed columns of alumina using commercially available (MBraun) solvent drying towers. $C_6D_6$ was dried with Na/K alloy. Celite was dried under vacuum by heating at 100 °C for several days. NMR spectra were obtained with a Varian INOVA 400 MHz spectrometer. $^1$H and $^{13}$C spectra were referenced to internal solvent peaks relative to tetramethylsilane (TMS) at 0 ppm. $^{77}$Se{$^1$H} and $^{125}$Te{$^1$H} spectra were indirectly referenced to external $PhESiMe_3$ (+85.6, E = Se; +11.6, E = Te) relative to $Me_2E$ at 0 ppm.[26,38] $^{29}$Si spectra were obtained indirectly via a $^1$H{$^{29}$Si} heteronuclear multiple bond correlation (HMBC) pulse sequence with a magnetization transfer time of 83 ms (coupling constant of 6 Hz) and were referenced to internal silicone grease at –21.5 ppm relative to TMS at 0 ppm. Chemical Analyses were performed by Chemisar Laboratories Inc. (Guelph Ontario). Due to their sensitivity, elemental analyses were not possible for the Se/Te derivatives **2b–c**, **3c** and **4b–c**. Mass spectra and precise mass determinations were performed with a Finnigan MAT 8200 instrument. Gas Chromatography-Mass Spectrometry measurements were performed on a Varian CP-3800 Gas Chromatograph with a Varian Saturn 2000 GC-MS analyzer.

**Synthesis of $LiESiMe_3$ (1a–c):** In a modification of the published procedure,[34] bis(trimethylsilyl) sulfide (0.20 mL, 0.953 mmol) was diluted in tetrahydrofuran (THF, 20 mL) and cooled to 0 °C. *n*-Butyllithium (1.6 M in hexanes, 0.60 mL, 0.953 mmol) was added dropwise causing a slight yellow color to develop which faded as the addition was completed. The cooling bath was removed after 30 min and the reaction was stirred for a further 30 min. Removal of the solvent in vacuo afforded an oily white solid, **1a**.

The syntheses of **1b** and **1c** were performed by the same method, although the preparation of **1c** required cooling the reaction solution to –40 °C. While **1a** and **1b** were relatively stable under an inert atmosphere at ambient temperatures, **1c** began to decompose within an hour after drying and so was used immediately in further reactions.

**1a·0.84thf:** $^1$H NMR ($C_6D_6$): $\delta$ = 3.90 (thf), 1.50 (thf), 0.58 (–$SiMe_3$) ppm. $^{13}$C{$^1$H} NMR: $\delta$ = 68.81 (thf), 25.45 (thf), 7.32 (–$SiMe_3$) ppm. $^{29}$Si NMR: $\delta$ = 7.2 ppm.

**1b·0.88thf:** $^1$H NMR ($C_6D_6$): $\delta$ = 3.93 (thf), 1.50 (thf), 0.70 (–$SiMe_3$) ppm. $^{13}$C{$^1$H} NMR: $\delta$ = 68.99 (thf), 25.44 (thf), 7.87 (–$SiMe_3$) ppm. $^{29}$Si NMR: $\delta$ = 4.10 ppm. $^{77}$Se NMR: $\delta$ = –518.1 ppm.

**1c·3.4thf:** $^1$H NMR ($C_6D_6$): $\delta$ = 3.76 (thf), 1.48 (thf), 0.88 (–$SiMe_3$) ppm. $^{13}$C{$^1$H} NMR: $\delta$ = 68.69 (thf), 25.53 (thf), 9.71 (–$SiMe_3$) ppm. $^{29}$Si NMR: $\delta$ = –19.43 ppm. $^1$H NMR ([$H_8$]thf): $\delta$ = 0.33 (–$SiMe_3$) ppm. $^{13}$C{$^1$H} NMR: $\delta$ = 9.25 (–$SiMe_3$) ppm. $^{125}$Te{$^1$H} NMR: $\delta$ = –1294.3 ppm.

**Synthesis of 1-Trimethylsilylthio-2-butyne (2a):** A freshly prepared sample of $LiSSiMe_3$ (2.38 mmol) was dissolved in pentane (50 mL). The flask was covered with aluminum foil and cooled to –78 °C. A cold (–78 °C) solution of 1-bromo-2-butyne (0.32 g, 2.38 mmol) in hexane (10 mL) was added dropwise and the solution was stirred at low temperature for 2 h and then the bath was warmed. After stirring at room temperature for 5 h, a ubiquitous white suspension had formed. Reaction completion was confirmed by monitoring via GC-MS and the reaction solution was filtered twice over celite to ensure removal of LiBr. The solvent was removed in vacuo from

 © 2006 Wiley-VCH Verlag GmbH & Co. KGaA, Weinheim 

the colorless filtrate to afford analytically pure **2a** as a colorless oil in 60% yield (0.23 g). $^1$H NMR ($C_6D_6$): $\delta$ = 3.10 (q, $^5J$ = 2.6 Hz, 2 H, –$CH_2$–), 1.47 ( t, $^5J$ = 2.6 Hz, 3 H, –$CH_3$,), 0.25 (s, 9 H, –$SiMe_3$) ppm. $^{13}C\{^1H\}$ NMR: $\delta$ = 78.42 (C≡C), 77.97 (C≡C), 14.44 ($CH_2$), 3.35 ($CH_3$), 0.79 (–$SiMe_3$) ppm. $^{29}$Si NMR: $\delta$ = 16.25 ppm. $C_7H_{14}SSi$ (158.3): calcd. C 53.10, H 8.91; found C 52.86, H 9.11. Exact mass: calculated 158.058549, found 158.058489.

**Synthesis of 1-Trimethylsilylseleno-2-butyne (2b):** A freshly prepared sample of $LiSeSiMe_3$ (2.31 mmol) was dissolved in pentane (50 mL). The flask was covered with aluminum foil and cooled to –78 °C. A cold (–78 °C) solution of 1-bromo-2-butyne (0.31 g, 2.31 mmol) in hexane (10 mL) was added dropwise and the solution was stirred at low temperature for 2 h. The bath was warmed and after stirring at room temperature for 2 h, a ubiquitous white suspension had formed. Reaction completion was confirmed by monitoring via GC-MS and the reaction solution and the reaction solution was filtered twice over celite to ensure removal of LiBr. The solvent was removed in vacuo from the filtrate to afford **2b** as a pale yellow oil in 94% yield (0.45 g).$^1$H NMR ($C_6D_6$): $\delta$ = 2.97 (q, $^5J$ = 2.6 Hz, 2 H, –$CH_2$–), 1.49 (t, $^5J$ = 2.6 Hz, 3 H, –$CH_3$), 0.32 (s, 9 H, –$SiMe_3$) ppm. $^{13}C\{^1H\}$ NMR: $\delta$ = 78.53 (C≡C), 78.41 (C≡C), 3.55 ($CH_3$), 2.53 ($CH_2$), 1.49 (–$SiMe_3$) ppm. $^{29}$Si NMR: $\delta$ = 14.3 ppm. $^{77}Se\{^1H\}$ NMR: $\delta$ = 2.1 ppm. Exact mass: calculated 206.002999, found 206.003044.

**Synthesis of 1-Trimethylsilyltelluro-2-butyne (2c):** A freshly prepared sample of $LiTeSiMe_3$ (2.34 mmol) was dissolved in pentane (50 mL) to give a beige solution due to slight decomposition of the $LiTeSiMe_3$. The flask was covered with aluminum foil and cooled to –78 °C. A cold (–78 °C) solution of 1-bromo-2-butyne (0.31 g, 2.34 mmol) in hexane (10 mL) was added dropwise and the solution was stirred at low temperature for 2 h to ensure reaction completion although a white solid was evident after 10 min. Attempts to confirm reaction completion by GC-MS failed as only a small amount of bis(trimethylsilyl) telluride was observed along with several unidentified organic compounds. The beige-yellow suspension was filtered at –78 °C through a cold bath jacketed filter and the receiver flask was also kept at low temperature. Removal of the solvent in vacuo at or below –40 °C afforded a **2c** as a yellow solid which decomposed significantly over a period of three days even when kept at –80 °C. $^1$H NMR ($C_7D_8$, –50 °C): $\delta$ = 2.80 (q, $^5J$ = 2.7 Hz, 2 H, –$CH_2$–), 1.45 (t, $^5J$ = 2.7 Hz, 3 H, –$CH_3$), 0.42 (s, 9 H, –$SiMe_3$) ppm. $^{13}C\{^1H\}$ NMR: $\delta$ = 79.88 (C≡C), 77.11 (C≡C), 5.19 ($CH_3$), 3.61 ($CH_2$), 2.31 (–$SiMe_3$) ppm. $^{29}$Si NMR: $\delta$ = –2.44 ppm. $^{125}Te\{^1H\}$ NMR: $\delta$ = –80.9 ppm.

**Synthesis of 3-Phenyl-1-trimethylsilylthio-2-propyne (3a):** A freshly prepared sample of $LiSSiMe_3$ (2.38 mmol) was dissolved in hexane (50 mL). The flask was covered with aluminum foil and cooled to 0 °C. A cold (0 °C) solution of 1-bromo-3-phenyl-2-propyne (0.44 g, 2.26 mmol) in hexane (10 mL) was added dropwise and the solution was stirred at low temperature for 1 h and then the bath was warmed. After stirring at room temperature for 1 h, the reaction was heated to reflux for 5 h by which time a ubiquitous white suspension had formed. Reaction completion was confirmed by monitoring via GC-MS and the reaction solution and the reaction solution was filtered twice over celite to ensure removal of LiBr. The solvent was removed in vacuo from the colorless filtrate to afford **3a** as a pale yellow oil in 75% yield (0.37 g). $^1$H NMR ($C_6D_6$): $\delta$ = 7.39 (m, 2 H, $H_{ortho}$), 6.97 (m, 3 H, $H_{meta/para}$), 3.25 (s, 2 H, –$CH_2$–), 0.25 (s, 9 H, –$SiMe_3$) ppm. $^{13}C\{^1H\}$: 131.81 ($C_{ortho}$), 128.55 ($C_{para}$), 128.20 ($C_{meta}$), 123.89 ($C_{ipso}$), 88.71 (C≡C), 83.03 (C≡C), 14.73 ($CH_2$), 0.89 (–$SiMe_3$) ppm. $^{29}$Si NMR: $\delta$ = 17.72 ppm. $C_{12}H_{16}SSi$ (220.4): calcd. C 65.39, H 7.32; found C 65.19, H 7.76. Exact mass: calculated 220.074199, found 220.074223

**Synthesis of 3-Phenyl-1-trimethylsilylseleno-2-propyne (3b):** A freshly prepared sample of $LiSeSiMe_3$ (2.31 mmol) was dissolved in pentane (50 mL). The flask was covered with aluminum foil and cooled to –78 °C. A cold (–78 °C) solution of 1-bromo-3-phenyl-2-propyne (0.43 g, 2.19 mmol) in hexane (20 mL) was added dropwise and the solution was stirred at low temperature for 2 h and then the bath was warmed. After stirring at room temperature for 3 h, a yellow solution with a ubiquitous white solid had formed. Reaction completion was confirmed by monitoring via GC-MS and the reaction solution and the reaction solution was filtered twice over celite to ensure removal of LiBr. The solvent was removed in vacuo from the yellow filtrate to afford **3b** as a yellow oil in 80% yield (0.47 g). $^1$H NMR ($C_6D_6$): $\delta$ = 7.41 (m, 2 H, $H_{ortho}$), 6.96 (m, 3 H, $H_{meta/para}$), 3.14 (s, 2 H, –$CH_2$–), 0.34 (s, 9 H, –$SiMe_3$) ppm. $^{13}C\{^1H\}$ NMR: $\delta$ = 131.78 ($C_{ortho}$), 128.54 ($C_{para}$), 128.11 ($C_{meta}$), 124.06 ($C_{ipso}$), 89.39 (C≡C), 83.18 (C≡C), 2.55 ($CH_2$), 1.51 (–$SiMe_3$) ppm. $^{29}$Si NMR: $\delta$ = 13.84 ppm. $^{77}Se\{^1H\}$ NMR: $\delta$ = 12.4 ppm. $C_{12}H_{16}SeSi$ (267.3): calcd. C 53.92, H 6.03; found C 53.83, H 5.85. Exact mass: calculated 268.018649, found 268.018393

**Synthesis of 3-Phenyl-1-trimethylsilyltelluro-2-propyne (3c):** A freshly prepared sample of $LiTeSiMe_3$ (2.34 mmol) was dissolved in pentane (50 mL) to give a beige solution due to slight decomposition of the $LiTeSiMe_3$. The flask was covered with aluminum foil and cooled to –78 °C. A cold (–78 °C) solution of 1-bromo-3-phenyl-2-butyne (0.46 g, 2.34 mmol) in hexane (20 mL) was added dropwise and the solution was stirred at low temperature for 2 h to ensure reaction completion although a white solid was evident after 10 min. Attempts to confirm reaction completion by GC-MS failed as only a small amount of bis(trimethylsilyl) telluride, along with several unidentified organic compounds, was observed. The beige-yellow suspension was filtered at –78 °C through a cold bath jacketed filter and the receiver flask was also kept at low temperature. Removal of the solvent in vacuo at or below –40 °C afforded a **3c** as a yellow solid. Solutions of **3c** decomposed slowly at –25 °C but were more stable at lower temperatures. $^1$H NMR (–80 °C, $C_7D_8$): $\delta$ = 7.39 (m, 2 H, $H_{ortho}$), 6.87 (m, 3 H, $H_{meta/para}$), 2.89 (s, 2 H, –$CH_2$–), 0.42 (s, 9 H, –$SiMe_3$) ppm. $^{13}C\{^1H\}$ NMR: $\delta$ = 131.49 ($C_{ortho}$), 127.86 ($C_{para}$), 125.01 ($C_{meta}$), 123.88 ($C_{ipso}$), 91.27 (C≡C), 81.67 (C≡C), 5.00 ($CH_2$), 2.21 (–$SiMe_3$) ppm. $^{29}$Si NMR: $\delta$ = –0.68 ppm. $^{125}Te\{^1H\}$ NMR: $\delta$ = –56.7 ppm.

**Synthesis of 1,4-Bis(trimethylsilylthio)-2-butyne (4a):** A freshly prepared sample of $LiSSiMe_3$ (2.38 mmol) was dissolved in pentane (50 mL). The flask was covered with aluminum foil and cooled to 0 °C. A solution of 1,4-dibromo-2-butyne (0.24 g, 1.13 mmol) in hexane (2 mL) was added dropwise and the solution was stirred at low temperature for 1 h. The bath was removed and after stirring at room temperature for 1 h, the reaction was heated to reflux for 3 h by which time a ubiquitous white suspension had formed. Reaction completion was confirmed by monitoring with GC-MS and the reaction solution and the reaction solution was filtered twice over celite to ensure removal of LiBr. The solvent was removed in vacuo from the colorless filtrate to afford **4a** as a light colored oil in 74% yield (0.22 g). $^1$H NMR ($C_6D_6$): $\delta$ = 3.05 (s, 2 H, –$CH_2$–), 0.24 (s, 9 H, –$SiMe_3$) ppm. $^{13}C\{^1H\}$: 81.13 (C≡C), 14.29 ($CH_2$), 0.83 (–$SiMe_3$); $^{29}$Si: 15.85 ppm. $C_{10}H_{22}S_2Si_2$ (262.6): calcd. C 45.74, H 8.44; found C 46.20. H 8.29. Exact mass: calculated 262.070150, found 262.070121.

**Synthesis of 1,4-Bis(trimethylsilylseleno)-2-butyne (4b):** A freshly prepared sample of $LiSeSiMe_3$ (2.31 mmol) was dissolved in pen-

 © 2006 Wiley-VCH Verlag GmbH & Co. KGaA, Weinheim 

tane (50 mL). The flask was covered with aluminum foil and cooled to –78 °C. A cold (–78 °C) solution of 1,4-dibromo-2-butyne (0.23 g, 1.09 mmol) in hexane (20 mL) was added dropwise and the solution was stirred at low temperature for 2 h. The bath was warmed and after stirring at room temperature for 2 h, a pale yellow solution with a ubiquitous white solid had formed. Reaction completion was confirmed by GC-MS and the reaction was filtered to remove the LiBr. The solvent was removed in vacuo from the colorless filtrate to afford **4b** as a pale yellow oil in 80% yield (0.31 g).

N.B. Extreme care to reduce exposure of this compound to ambient light is required as otherwise decomposition to an insoluble white solid occurs. $^1$H NMR ($C_6D_6$): $\delta$ = 2.96 (s, 2 H, –$CH_2$–), 0.32 (s, 9 H, –$SiMe_3$) ppm. $^{13}$C{$^1$H}: 81.87 (C≡C), 2.68 ($CH_2$), 1.87 (–$SiMe_3$) ppm. $^{29}$Si NMR: $\delta$ = 13.69 ppm. $^{77}$Se{$^1$H} NMR: $\delta$ = 4.0 ppm. Exact mass: calculated 357.959049, found 357.958961.

## Acknowledgments

We gratefully acknowledge the Natural Sciences and Engineering Research Council (NSERC) of Canada and the Academic Development Fund (UWO) for funding support. A.I. W. thanks the Government of Ontario for postgraduate scholarships (OGS, OGSST) and D. Hairsine and M.W. Degroot at UWO for the mass spectrometry work. H.L. C. and E.A. T. both thank the NSERC for a postgraduate scholarship.

[1] S. Dehnen, A. Eichhöfer, D. Fenske, *Eur. J. Inorg. Chem.* **2002**, 279.
[2] N. Zhu, D. Fenske, *J. Chem. Soc., Dalton Trans.* **1999**, 1067.
[3] D. Fenske, N. Zhu, *J. Cluster Sci.* **2000**, *11*, 135.
[4] M. W. DeGroot, J. F. Corrigan, *J. Chem. Soc., Dalton Trans.* **2000**, 1235.
[5] J. F. Corrigan, D. Fenske, *Chem. Commun.* **1997**, 1837.
[6] S. Behrens, M. Bettenhausen, A. C. Deveson, A. Eichhöfer, D. Fenske, A. Lohde, U. Woggon, *Angew. Chem. Int. Ed. Engl.* **1996**, *35*, 2215.
[7] M. W. DeGroot, M. W. Cockburn, M. S. Workentin, J. F. Corrigan, *Inorg. Chem.* **2001**, *40*, 4678.
[8] S. Behrens, M. Bettenhausen, A. Eichhöfer, D. Fenske, *Angew. Chem. Int. Ed.* **1997**, *36*, 2797.
[9] M. Bettenhausen, D. Fenske, *Z. Anorg. Allg. Chem.* **1998**, *624*, 1245.
[10] D. Fenske, N. Zhu, T. Langetepe, *Angew. Chem. Int. Ed.* **1998**, *37*, 2639.
[11] M. L. Steigerwald, A. P. Alivasatos, J. M. Gibson, T. D. Harris, R. Kortan, A. J. Muller, A. M. Thayer, T. M. Duncan, D. C. Douglass, L. E. Brus, *J. Am. Chem. Soc.* **1988**, *110*, 3046.
[12] A. I. Wallbank, J. F. Corrigan, *Chem. Commun.* **2001**, 377.
[13] T. P. Lebold, D. L. B. Stringle, M. S. Workentin, J. F. Corrigan, *Chem. Commun.* **2003**, 1398.
[14] J. E. Drake, R. T. Hemmings, *J. Chem. Soc., Dalton Trans.* **1976**, 1730.
[15] R. S. Sukhai, L. Brandsma, *Synthesis* **1979**, 455.
[16] W.-W. du Mont, S. Kubiniok, L. Lange, S. Pohl, W. Saak, I. Wagner, *Chem. Ber.* **1991**, *124*, 1315.
[17] N. Miyoshi, H. Ishii, K. Kondo, S. Murai, N. Sonoda, *Synthesis* **1979**, 300.
[18] M. R. Detty, *Tetrahedron Lett.* **1978**, *13*, 5087.
[19] V. Yu. Vvdensky, L. Brandsma, E. D. Shtefan, B. A. Trofimov, *Tetrahedron* **1997**, *53*, 13079.
[20] V. Yu. Vvdensky, L. Brandsma, E. D. Shtefan, B. A. Trofimov, *Tetrahedron* **1997**, *53*, 16783.
[21] U. Herzog, *J. Prakt. Chem.* **2000**, *342*, 379.
[22] U. Herzog, *Main Group Met. Chem.* **2001**, *24*, 31.
[23] K. Sasaki, Y. Aso, T. Otsubo, F. Ogura, *Tetrahedron Lett.* **1985**, *26*, 453.
[24] J. E. Drake, R. T. Hemmings, *Inorg. Chem.* **1980**, *19*, 1879.
[25] J. F. Corrigan, S. Balter, D. Fenske, *J. Chem. Soc., Dalton Trans.* **1996**, 729.
[26] H. Poleschner, M. Heydenreich, U. Schilde, *Eur. J. Inorg. Chem.* **2000**, 1307.
[27] T. M. Klapotke, B. Krumm, P. Mayer, K. Polborn, O. P. Ruscitti, *Phosphorus Sulfur Silicon Relat. Elem.* **2001**, *171–172*, 373.
[28] M. David, *Synlett* **2001**, 445.
[29] M. Clarembeau, A. Cravador, W. Dumont, L. Hevesi, A. Krief, J. Lucchetti, D. Van Ende, *Tetrahedron* **1985**, *41*, 4793.
[30] C. H. W. Jones, R. D. Sharma, *J. Organomet. Chem.* **1984**, *268*, 113.
[31] J. W. Anderson, G. K. Barker, J. E. Drake, M. Rodger, *J. Chem. Soc., Dalton Trans.* **1973**, 1716.
[32] K. Praefcke, C. Weichsel, *Synthesis* **1980**, 216.
[33] M. Schmidt, E. Kiewert, H. Lux, C. Sametschek, *Phosphorus Sulfur Silicon Relat. Elem.* **1986**, *26*, 163.
[34] a) M. Segi, T. Nakajima, S. Suga, S. Murai, I. Ryu, A. Ogawa, N. Sonoda, *J. Am. Chem. Soc.* **1988**, *110*, 1976; b) M. Segi, M. Kato, T. Nakajima, S. Suga, N. Sonoda, *Chem. Lett.* **1989**, 1009.
[35] P. Mathur, B. Manimaran, R. Trivedi, C. V. V. Satyanarayana, R. K. Chadha, *J. Cluster Sci.* **1998**, *9*, 45.
[36] a) J. So, P. Boudjouk, *Synthesis* **1989**, 306; b) M. W. DeGroot, N. J. Taylor, J. F. Corrigan, *J. Mater. Chem.* **2004**, *14*, 654.
[37] A. Padwa, M. Meske, Z. Ni, *Tetrahedron* **1995**, *51*, 89.
[38] C. H. W. Jones, R. D. Sharma, S. P. Taneja, *Can. J. Chem.* **1986**, *64*, 980.
[39] M. Segi, M. Takahashi, T. Nakajima, S. Suga, *Synth. Commun.* **1989**, *19*, 2431.
[40] K. Steliou, P. Salama, J. Corriveau, *J. Org. Chem.* **1985**, *50*, 4969.
[41] G. A. Kraus, B. Andersh, *Tetrahedron Lett.* **1991**, *32*, 2189.
[42] D. T. T. Tran, J. F. Corrigan, *Organometallics* **2000**, *19*, 5202.
[43] A. I. Wallbank, J. F. Corrigan, *Can. J. Chem.* **2002**, *80*, 1592.
[44] M. J. Dabdoub, J. C. G. Rotta, *Synlett* **1996**, 526.
[45] Y. Zheng, W. Bao, Y. Zhang, *Synth. Commun.* **1997**, *27*, 79.
[46] M. Brudermüller, H. Musso, A. Wagner, *Chem. Ber.* **1988**, *121*, 2239.
[47] B. S. Thyagarajan, K. C. Majumdar, D. K. Bates, *J. Heterocycl. Chem.* **1975**, *12*, 59.
[48] K. Shimada, S. Akimoto, Y. Takikawa, C. Kabuto, *Chem. Lett.* **1994**, 2283.
[49] R. Mantione, A. Alves, P. P. Montijn, G. A. Wildschut, H. J. T. Bos, L. Brandsma, *Recl. Trav. Chim.* **1970**, *89*, 97.
[50] G. Pourcelot, P. Cadiot, *Bull. Soc. Chim. Fr.* **1956**, *9*, 3016.
[51] T. Kanda, Y. Ando, S. Kato, N. Kambe, N. Sonoda, *Synlett* **1995**, 745.
[52] R. Gleiter, S. Rittinger, H. Langer, *Chem. Ber.* **1991**, *124*, 357.
[53] E. H. Riague, J.-C. Guillemin, *Organometallics* **2002**, *21*, 68.
[54] K. B. Simonsen, N. Thorup, J. Becher, *Synthesis* **1997**, 1399.
[55] H. B. Singh, A. V. Regini, J. P. Jasinski, E. S. Paight, R. J. Butcher, *J. Organomet. Chem.* **1994**, *464*, 87.
[56] D. H. O'Brien, N. Dereu, C.-K. Huang, K. J. Irgolic, *Organometallics* **1983**, *2*, 305.
[57] D. H. O'Brien, N. Dereu, R. A. Grigsby, K. J. Irgolic, F. F. Knapp, Jr., *Organometallics* **1982**, *1*, 513.
[58] R. W. Gedridge, Jr., K. T. Higa, R. A. Nissan, *Magn. Reson. Chem.* **1995**, *33*, 441.
[59] M. R. Detty, M. D. Seidler, *J. Org. Chem.* **1982**, *47*, 1354.
[60] D. L. J. Clive, P. C. Anderson, N. Moss, A. Singh, *J. Org. Chem.* **1982**, *47*, 1641.

Received: June 21, 2006
Published Online: September 18, 2006

 © 2006 Wiley-VCH Verlag GmbH & Co. KGaA, Weinheim 

DOI: 10.1002/ejic.200600586

# Glycol Methyl Ether and Glycol Amine Substituted Titanocenes as Antitumor Agents

**Katja Strohfeldt,[a] Helge Müller-Bunz,[a] Clara Pampillón,[a] Nigel J. Sweeney,[a] and Matthias Tacke*[a]**

**Keywords:** Anticancer drugs / *cis*-Platin / Titanocene / Super hydride / Lithiation / Titanium

6-[4-(2-Methoxyethoxy)phenyl]fulvene (**3a**) and 6-{4-[2-(dimethylamino)ethoxy]phenyl}fulvene (**3b**) were prepared as the starting materials for the synthesis of three different classes of titanocenes, which are *ansa*-titanocenes, diarylmethyl-substituted titanocenes and benzyl-substituted titanocenes. Because the synthetic possibilities seem to be limited, only *ansa*-titanocene {1,2-bis(cyclopentadienyl)-1,2-bis[4-(2-methoxyethoxy)phenyl]ethanediyl}titanium dichloride (**4a**) and benzyl-substituted titanocene bis-{[4-(2-methoxyethoxy)benzyl]cyclopentadienyl}titanium(IV) dichloride (**6a**) were obtained and characterised. The change in the substitution pattern of the phenyl moiety from an oxygen atom to a nitrogen atom had such a big influence on the reaction that not one compound of the three titanocene classes could be synthesised, and it was also not possible to obtain diarylmethyl-substituted titanocenes with the use of either of the fulvenes. When benzyl-substituted titanocene **6a** was tested against pig kidney cells (LLC-PK), an antiproliferative effect that results in an $IC_{50}$ value of 43 μM, was observed. This $IC_{50}$ value is in the lower range of the cytotoxicities evaluated for titanocenes up to now. *ansa*-Titanocene **4a** surprisingly showed, when tested on the same cell line, a proliferative effect together with a fast rate of hydrolysis.

(© Wiley-VCH Verlag GmbH & Co. KGaA, 69451 Weinheim, Germany, 2006)

## Introduction

The introduction of *cis*-platin into clinics in 1978 started a broad search for other cytotoxic metal complexes. Despite the resounding success of *cis*-platin and closely related platinum antitumor agents, the movement of other transition-metal anticancer drugs towards the clinic has been exceptionally slow.[1–3] In general, metallocene dichlorides ($Cp_2MCl_2$) with M = Ti, V, Nb and Mo show remarkable antitumor activity,[4,5] and titanocene dichloride, $Cp_2TiCl_2$, has especially become a very promising candidate as an anticancer drug. $Cp_2TiCl_2$ shows medium–high cytotoxicity in vitro and a high efficacy in the animal models. Unfortunately, the efficacy in Phase II clinical trials in patients with metastatic renal-cell carcinoma[6] or metastatic breast cancer[7] was too low to be pursued.

In order to increase the cytotoxicity of $Cp_2TiCl_2$, different highly substituted analogues were synthesised. Within this paper we introduce three different types of substituted titanocenes: *ansa*-titanocenes, diarylmethyl-substituted titanocenes, and benzyl-substituted titanocenes.

*ansa*-Titanocenes, which contain a carbon–carbon bridge, can be synthesised by reacting titanium dichloride with fulvenes.[8–19] By using this method we have synthesised {1,2-bis(cyclopentadienyl)-1,2-bis[4-(dimethylamino)-phenyl]ethanediyl}titanium dichloride (titanocene **X**), which showed an $IC_{50}$ value of $2.7 \times 10^{-4}$ M when tested for cytotoxic effects on the LLC-PK cell line.[16]

The diarylmethyl-substituted titanocene analogues were synthesized and they showed a significant increase in their cytotoxicity. These titanocenes can be obtained by a carbolithiation reaction of 6-arylfulvene with the corresponding aryllithium species followed by transmetallation with titanium tetrachloride.[20] With this new method, bis{bis[4-(dimethylamino)phenyl]methylcyclopentadienyl}titanium(IV) dichloride has been synthesised, which shows an $IC_{50}$ value of $3.8 \times 10^{-5}$ M when tested for cytotoxic effects on the LLC-PK cell line.[20]

A third method that is used for the preparation of benzyl-substituted titanocenes allowed for the synthesis of titanocene **Y**, which is so far our best titanocene in terms of cytotoxicity.[21] Bis-[(4-methoxybenzyl)cyclopentadienyl]-titanium(IV) dichloride (titanocene **Y**), which has an $IC_{50}$ value of $2.1 \times 10^{-5}$ M when tested on the LLC-PK cell line, was synthesised from fulvene and super hydride ($LiBEt_3H$) followed by transmetallation with titanium tetrachloride. The structures of the three mentioned titanocene classes are shown in Figure 1.

The first in vitro and ex vivo tests with titanocenes **X** and **Y** showed that prostate, cervix and renal cell cancer are prime targets for these types of titanocenes. Both titano-

[a] UCD School of Chemistry and Chemical Biology, Conway Institute of Biomolecular and Biomedical Research, Centre for Synthesis and Chemical Biology (CSCB), University College Dublin,
Belfield, Dublin 4, Ireland
E-mail: matthias.tacke@ucd.ie

 © 2006 Wiley-VCH Verlag GmbH & Co. KGaA, Weinheim 

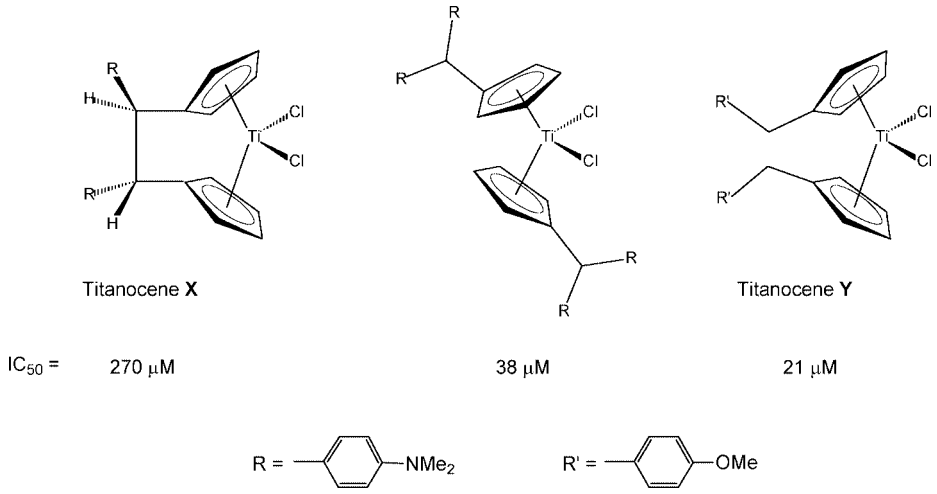


Figure 1. Molecular structures of the titanocenes.

cenes have been studied in a 36 human carcinoma cell panel for their antiproliferative activity.[22] Furthermore, titanocene **X** has been tested on four freshly explanted human tumors.[23] First mechanistic studies showed that both titanocenes induce apoptosis, especially in prostate cancer cells.[24] Furthermore, very successful animal studies with the use of titanocene **Y** on Caki-1 tumor-bearing mice and xenograft Ehrlich's ascites tumor in mice were performed.[25,26]

The main idea behind the research presented in this paper was to convert the methoxy group of titanocene **Y**, our most cytotoxic titanocene, into a glycol methyl ether or glycol amine side chain in order to improve the cytotoxicity and availability in the cell. Within this paper, we present the synthetic possibilities and limits of introducing a glycol methyl ether or a glycol amine group in all three mentioned classes of titanocenes and comparing the antiproliferative effects of the new synthesised titanocenes.

## Results and Discussion

### *Synthesis*

6-Arylfulvenes are the starting materials for all three classes of titanocenes and their main function is to introduce the substitution pattern at the cyclopentadienide rings. These fulvenes can be synthesised according to the published procedure[18] by reacting the corresponding benzaldehyde with cyclopentadiene in the presence of pyrrolidine as a base. Benzaldehydes **2a** and **2b** were not commercially available, and therefore, they were synthesised from 4-hydroxybenzaldehyde (**1**) and the corresponding alkyl chloride.[27] Afterwards, 6-[4-(2-methoxyethoxy)phenyl]fulvene (**3a**) and 4-[2-(dimethylamino)ethoxy]benzaldehyde (**3b**) were obtained in the described condensation reaction as orange solids in yields of 78% and 51%, respectively (Scheme 1).

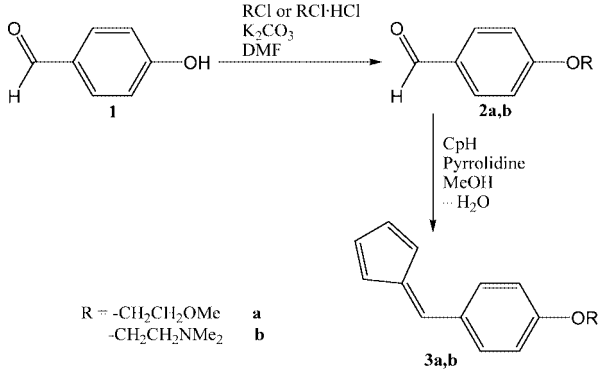


Scheme 1. Synthesis of fulvenes **3a** and **3b**.

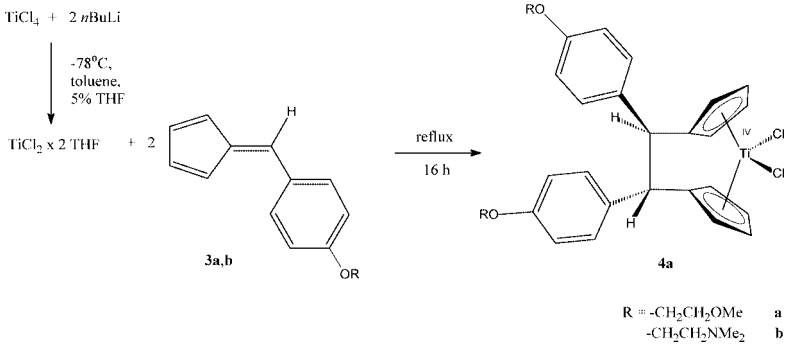


Scheme 2. Synthesis of *ansa*-titanocene **4a**.

 © 2006 Wiley-VCH Verlag GmbH & Co. KGaA, Weinheim 

*ansa*-Titanocenes can be obtained by the reductive dimerisation of the corresponding fulvene with titanium dichloride (Scheme 2), which is synthesised by the reduction of $TiCl_4$ with *n*BuLi as described in refs.[12,13]

With the use of this method, fulvenes **3a** and **3b** were tested for the synthesis of the corresponding *ansa*-titanocenes. *ansa*-Titanocene **4a** was obtained from fulvene **3a** as a black solid in a yield of 22%, and the determined *cis–trans* ratio at the carbon–carbon bridge was 44:56. Surprisingly, with the use of fulvene **3b** and the above-described procedure, no *ansa*-titanocene was formed and merely a black polymer was obtained.

A second synthetic pathway starting with 6-arylfulvenes leads to the corresponding benzyl-substituted titanocenes. This method includes a hydride transfer to the exocyclic double bond of the fulvene with the use of $LiBEt_3H$ (super hydride) and results in the formation of the appropriate substituted lithium cyclopentadienyl intermediate. Two moles of this lithium intermediate undergo a transmetallation reaction with $TiCl_4$ to give the corresponding unbridged substituted titanocenes (Scheme 3).[21]

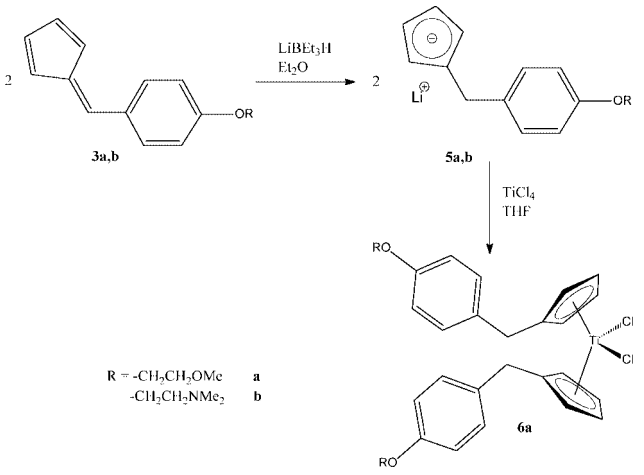


Scheme 3. Synthesis of benzyl-substituted titanocene **6a**.

These benzyl-substituted titanocenes do not have stereocentres; therefore, unlike their *ansa* analogues, stereoisomers of this compound do not exist, which, in terms of in vivo and in vitro cell testing, is advantageous. Our most cytotoxic titanocene, titanocene **Y**, has been synthesised by this reaction.

Again, both fulvenes **3a** and **3b** were tested for their ability to form the corresponding benzyl-substituted titanocenes. With the use of this method, unbridged titanocene **6a** was obtained as a brown solid in a yield of 67% from **3a**. Again, the use of fulvene **3b** did not lead to any success; therefore, the unbridged titanocene substituted with a glycol amine group could not be formed. The reactivity of lithium intermediate **5b** was so high that it immediately decomposed after its formation and substituted lithium cyclopentadienide **5b** could not be isolated and consequently reacted with $TiCl_4$.

A third synthetic route that leads to the formation of achiral diarylmethyl-substituted titanocenes was evaluated again for both fulvenes **3a** and **3b**.[20] The first step was a bromine–lithium exchange reaction and resulted in the formation of lithiated intermediates **9a** and **9b**. Bromine compounds **8a** and **8b** were synthesised beforehand by refluxing 4-hydroxyphenylbromide (**7**) with the appropriate alkyl chloride.[28] Afterwards, lithium intermediates **9a** and **9b** were intended to undergo a carbolithiation reaction that would result in the formation of corresponding substituted lithium cyclopentadienide **5a** and **5b**, which could then be transmetallated with $TiCl_4$ (Scheme 4). However, neither the use of fulvene **3a** nor the use of fulvene **3b** led to the formation of the expected diarylmethyl-substituted titanocene.

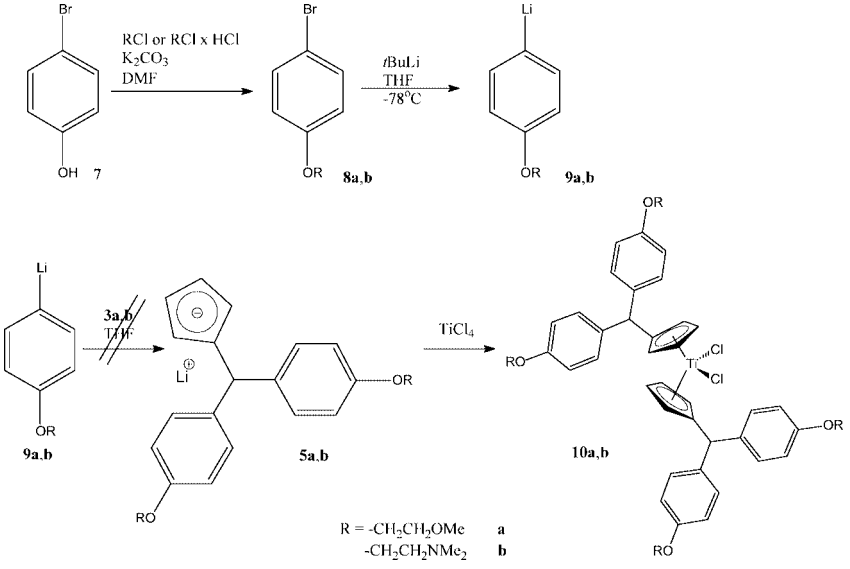


Scheme 4. Synthesis of diarylmethyl-substituted titanocene.

 © 2006 Wiley-VCH Verlag GmbH & Co. KGaA, Weinheim 

Closer investigations of the lithium–bromine exchange reaction showed that the *para*-substituted lithium intermediate was not the only product formed. The formation of a mixture of lithium compounds might be due to the *ortho*-directing property of the glycol methyl ether or glycol amine side chain. To carry out these investigations the bromine compound was treated with *tert*-butyllithium in THF and afterwards reacted with chlorotrimethylsilane.

### Structural Discussion

Suitable single-crystals of titanocene **4a** for X-ray diffraction experiments were obtained by the slow diffusion of pentane into a saturated solution of dichloromethane. The collection and refinement data for **4a** are shown in Table 2.

Because of the presence of stereoisomers, *ansa*-titanocenes seem to be a difficult class of compounds in terms of crystallisation experiments. Therefore, there are very few examples of molecular structures of titanocenes in the crystal form and their crystallisation behaviour strongly depends on the substitution pattern. In the crystal structure of titanocene **4a**, only the *trans* isomer is found, and in accordance with the centrosymmetric space group $P\bar{1}$, the (*R*,*R*)- and (*S*,*S*) isomers are present in equal amounts. The molecule itself has a *pseudo*-$C_2$ symmetry in the solid state. The cyclopentadienyl bond lengths are of the expected values for titanocenes and range from 138 pm to 142 pm, as well as the ring centroid distances to the metal centre (205 and 206 pm). The Ti–Cl bond lengths, both of them being 236 pm, and the Cl–Ti–Cl angle, being 95.0°, are also typical of titanocenes (Table 1). The carbon–carbon *ansa*-bridge has a length of 152 pm and is therefore in the expected range for a carbon–carbon single bond. Despite the *ansa*-bridge, the angle centroid–metal–centroid is 128°, which is nearly the same as that in unbridged titanocene **Y** (131°)[21] and suggests that there is no strain on the ethylene bridge.

One of the glycol methyl ether side chains shows an orientational disorder with O4 and is distributed over two positions. In the final refinement, the position of the two adjacent carbon atoms, C29 and C30, has been treated as unaffected and leads to some unusual bond lengths and angles (Table 1). These unusual bond lengths and angles show that C29 is, in fact, disordered as well and that the two positions are very close to each other (<20 pm). Therefore, the dataset with a resolution of 87 pm does not allow a separate refinement of the two C29 sites.

The unit cell of the determined structure of **4a** shows an absence of any solvent molecules; the assumed free space between the titanocenes is filled by the glycol methyl ether group. This is in contrast to the molecular structure of an analogue of *ansa*-titanocene that is substituted with a pentamethyl phenyl group at the cyclopentadienyl rings. In this analogue, the aromatic substituents form a channel in which the solvent molecules are situated.[18] In terms of biological applications, the absence of solvent molecules in the obtained crystals is advantageous as the compounds are known to be of high purity and the cytotoxic effects that are observed can not be due to the presence of chlorinated solvents.

Table 1. Selected bond lengths and angles for **4a**.

| Bond lengths [Å] | | | |
|---|---|---|---|
| Cl1–Ti | 2.3553(11) | C2–C3 | 1.375(5) |
| Cl2–Ti | 2.3559(11) | C3–C4 | 1.399(5) |
| Ti–C1 | 2.352(3) | C4–C5 | 1.387(5) |
| Ti–C2 | 2.397(3) | C5–C6 | 1.522(5) |
| Ti–C3 | 2.391(3) | C16–C17 | 1.397(5) |
| Ti–C4 | 2.360(3) | C16–C20 | 1.408(5) |
| Ti–C5 | 2.367(3) | C17–C18 | 1.377(6) |
| Ti–Cent1 | 2.054(3) | C18–C19 | 1.399(5) |
| Ti–C16 | 2.359(4) | C19–C20 | 1.394(5) |
| Ti–C17 | 2.401(4) | C20–C21 | 1.508(5) |
| Ti–C18 | 2.394(4) | C6–C21 | 1.521(5) |
| Ti–C19 | 2.341(3) | C29–O4A | 1.564(10) |
| Ti–C20 | 2.383(3) | C29–O4B | 1.467(7) |
| Ti–Cent2 | 2.058(2) | O4A–C30 | 1.252(9) |
| C1–C2 | 1.406(5) | O4B–C30 | 1.374(7) |
| C1–C5 | 1.418(5) | | |
| **Bond angles [°]** | | | |
| Cl1–Ti–Cl2 | 95.04(4) | | |
| Cent1–Ti–Cent2 | 128.15(3) | | |
| C28–C29–O4A | 86.8(5) | | |
| C28–C29–O4B | 119.8(5) | | |
| C29–O4A–C30 | 109.9(7) | | |
| C29–O4B–C30 | 109.1(4) | | |

### Cell Tests

The in vitro cytotoxicity of compounds **4a** and **6a** was determined by MTT-based assays[29] that involves a 48 hour drug exposure period, followed by 24 hours of recovery time. Compounds were tested for their activity on pig kidney cells (LLC-PK) and the results are shown in Figures 2 and 3.

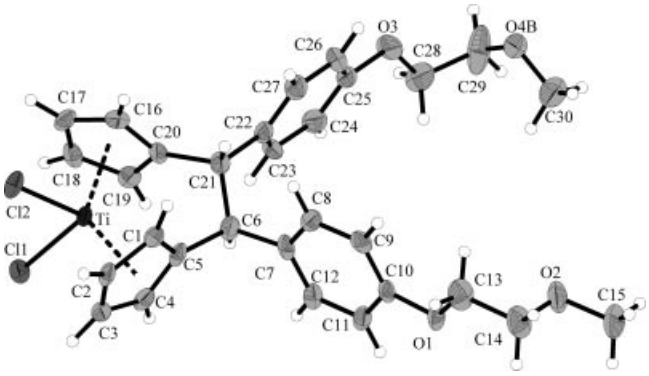


Figure 2. Molecular structure of a crystal of **4a**, thermal ellipsoids are drawn at the 50% probability level and disorder has been neglected.

In our workgroup, *ansa*-titanocenes have been synthesised which show cytotoxic effects with $IC_{50}$ values in the range of 930 to 210 μM when tested on the LLC-PK cell line, depending on the substitution pattern of the phenyl ring. Most of the *ansa*-titanocenes show poor water solubil-

 © 2006 Wiley-VCH Verlag GmbH & Co. KGaA, Weinheim 

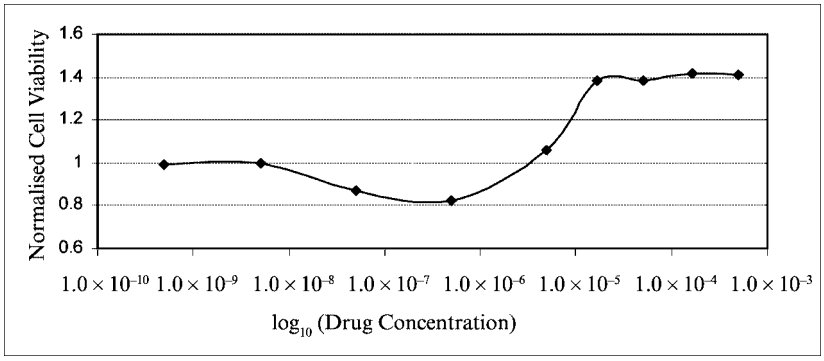


Figure 3. Cytotoxicity curve from typical MTT assays that show the effect of compound **4a** on the viability of pig kidney (LLC-PK) cells.

ity, and therefore, the introduction of the glycol methyl ether group was supposed to improve the water solubility and the availability of the titanocene in the cell.

The water solubility of *ansa*-titanocene **4a** was significantly improved, but unfortunately a few seconds after the titanocene dissolved in the medium, a white solid precipitated despite the fact that the titanocene is completely soluble in 0.7% DMSO. Cell tests with this solution showed very surprising results. *ansa*-Titanocene **4a**, which was dissolved in the medium with 0.7% DMSO, showed nearly no cytotoxic effect under physiological conditions. Quite the opposite result, a proliferative effect, was observed and the cell growth was significantly increased when tested on the LLC-PK cell line. Only at very low concentrations in the range of $10^{-5}$ to $10^{-8}$ M can a small cytotoxic effect be noticed (Figure 3). The proliferative result can be explained by a very fast hydrolysis rate of the *ansa*-titanocene, which results from the substitution pattern of the phenyl rings.

A similar unexpected proliferate effect was observed by G. Jaouen and coworkers when a titanocene derivative of the anticancer drug tamoxifen was tested on the human hormone-dependent breast cancer cell line MCF-7. This compound contains an analogous glycol amine group and further explanations concerning the hydrolysis process can be found within the literature[30] and the studies of P. Sadler.[31]

Cytotoxic studies with the use of analogous benzyl-substituted titanocene **6a** were undertaken in order to determine whether the hydrolysis rate is dependant only on the side chain of the phenyl moiety or whether there is an additional correlation with the structure of the titanocene.

Titanocene **6a** was tested in the typical MTT-based assay with the use of the LLC-PK cell line and it showed an $IC_{50}$ value of 43 μM (Figure 4). However, this value, when compared with that of benzyl-substituted titanocene **Y**, is twice as large. In comparison to *cis*-platin, this represents an approximate thirteen-fold increase. Nevertheless, this value shows an approximate fifty-fold decrease in magnitude when compared with that of titanocene dichloride; its $IC_{50}$ value is $2.0 \times 10^{-3}$ M when tested on the same cell line.[16] Samples prepared for the cell tests showed a significantly slower rate of hydrolysis compared with that of *ansa*-titanocene **4a**. This resulted in the formation of a lesser amount of the white precipitate. Nevertheless, there might still be a rapid rate of hydrolysis, which has a counterproductive impact on the cytotoxic effect.

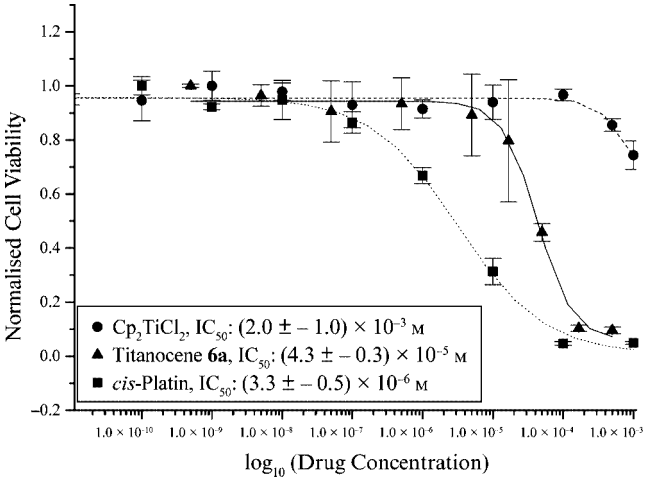


Figure 4. Cytotoxicity curve from typical MTT assays that show the effect of compound **6a** on the viability of pig kidney (LLC-PK) cells.

Furthermore, benzyl-substituted titanocene **6a** does not have stereocentres, and therefore, stereoisomers do not exist, unlike their *ansa* analogue **4a**. In terms of in vivo and in vitro cell testing, this is advantageous. Previously, the presence of unseparated stereoisomers meant that the issue of whether the compounds' cytotoxicities were related to specific isomers was not addressed. This is not of concern for achiral compound **6a**.

## Conclusions and Outlook

6-Arylfulvenes can be very useful starting materials for the synthesis of different types of titanocenes. Fulvenes **3a** and **3b**, which have a glycol methyl ether or a glycol amine side chain at the phenyl moiety, were obtained in good yields as orange solids. Their application towards the synthesis of titanocenes was very limited. Only the glycol methyl ether analogues of *ansa*-titanocene and of benzyl-substituted titanocene were obtained, whereas it was not possible to synthesise any of the three types of titanocenes

 © 2006 Wiley-VCH Verlag GmbH & Co. KGaA, Weinheim 

bearing a glycol amine side chain. Both fulvenes could not be used for the successful synthesis of a diarylmethyl-substituted titanocene. This study shows how limited the various methods are and that not every 6-arylfulvene can be used for the synthesis of the corresponding titanocenes.

When tested for cytotoxicity on the LLC-PK cell line, the $IC_{50}$ value of **6a** was in the lower $10^{-5}$ M range and showed a clear dose dependent antiproliferative effect. This represents an increase in cytotoxicity when compared to that of unsubstituted titanocene dichloride; however, **6a** is two times less cytotoxic than the most cytotoxic of the titanocenes so far, titanocene **Y**, which has a methoxybenzyl functionality. Compound **6a** is also approximately fifteen times less cytotoxic than *cis*-platin when tested on the LLC-PK cell line.

Surprisingly, *ansa*-titanocene **4a** showed a proliferative effect when tested on the same cell line. This might be due to the fast rate of hydrolysis, which was observed during the preparation of the sample for the cell tests. Nevertheless, this was the first time that a proliferative effect with this class of titanocenes was observed. We could show that a glycol methyl ether side chain at the phenyl moiety helps to improve the water solubility, but unfortunately it increases the hydrolysis rate as well. Furthermore, we were able to see that the hydrolysis rate is strongly dependent on the class of titanocenes.

Future work will focus on the exchange of the chlorines in order to decrease the hydrolysis rate. If this can be achieved, both titanocenes might be very interesting compounds for further studies in terms of their availability in the cell.

## Experimental Section

**General Conditions:** Titanium tetrachloride, *n*-butyllithium (2.0 M in cyclohexane), *tert*-butyllithium (1.7 M in pentane), 4-hydroxybenzaldehyde, 4-bromophenol, $K_2CO_3$, NaI, DMF, (2-chloroethyl)-methyl ether, 2-(dimethylamino)ethyl chloride and super hydride ($LiBEt_3H$, 1.0 M solution in THF) were obtained commercially from Aldrich Chemical Co. THF, toluene, pentane and diethyl ether were dried with Na and benzophenone. Solvents were freshly distilled and collected under an atmosphere of argon prior to use. Cyclopentadiene was collected under an atmosphere of nitrogen from freshly cracked dicyclopentadiene and pyrrolidine was distilled under an atmosphere of argon prior to use. Manipulations of air- and moisture-sensitive compounds were done with the use of standard Schlenk techniques, under an argon atmosphere. NMR spectra were measured with either a Varian 300 or a Varian 400 spectrometer. Chemical shifts are referenced to TMS. IR spectra were recorded with a Perkin–Elmer Paragon 1000 FT-IR Spectrometer. UV/Vis spectra were recorded with a Unicam UV2 Spectrometer. Electron spray mass spectrometry of **4a** and **6a** were performed with a quadrupole tandem mass spectrometer (Quattro Micro, Micromass/Water's Corp., USA) with the use of solutions that were made up in 50% dichloromethane and 50% methanol.

Single-crystals of **4a** suitable for X-ray diffraction experiments were grown by the diffusion of pentane into a saturated solution of dichloromethane at room temperature. X-ray diffraction data for the compound was collected with a BRUKER Smart Apex diffractometer. A semi-empirical absorption correction on the raw data was performed with the program SADABS.[32] The crystal structure was then solved by direct methods (SHELXS-NT 97)[33] and refined by full-matrix least-squares methods against $F^2$. Further details about the data collection are listed in Table 2, as well as reliability factors. CCDC-610549 contains the supplementary crystallographic data for this paper. These data can be obtained free of charge from The Cambridge Crystallographic Data Centre via www.ccdc.cam.ac.uk/data_request/cif.

Table 2. Crystal data and structure refinements for **4a**.

| | |
|---|---|
| Empirical formula | $C_{30}H_{32}O_4Cl_2Ti$ |
| Formula weight | 575.36 |
| Temperature [K] | 100(2) |
| Wavelength [Å] | 0.71073 |
| Crystal system | triclinic |
| Space group | $P\bar{1}$(#2) |
| Unit cell dimensions [Å], [°] | $a$ = 7.7841(11), $\alpha$ = 102.085(2)<br>$b$ = 13.0191(18), $\beta$ = 100.794(3)<br>$c$ = 14.358(2), $\gamma$ = 102.998(3) |
| Volume [Å$^3$] | 1343.7(3) |
| $Z$ | 2 |
| Density$_{calcd.}$ [Mg/m$^3$] | 1.422 |
| Absorption coefficient [mm$^{-1}$] | 0.552 |
| $F$(000) | 600 |
| Crystal size [mm$^3$] | 0.20 × 0.10 × 0.02 |
| $\theta$ range for data collection [°] | 1.66 to 24.00 |
| Index ranges | $-8 \le h \le 8$, $-14 \le k \le 14$, $-16 \le l \le 16$ |
| Reflections collected | 14440 |
| Independent reflections | 4207 [$R$(int) = 0.0460] |
| Completeness to $\theta$ = 24.00° [%] | 99.8 |
| Absorption correction | Semi-empirical from equivalents |
| Max. and min. transmission | 0.9890 and 0.8143 |
| Refinement method | Full-matrix least–squares on $F^2$ |
| Data/restraints/parameters | 4207/0/345 |
| Goodness-of-fit on $F^2$ | 1.052 |
| Final $R$ indices [$I > 2\sigma(I)$] | $R1$ = 0.0468, $wR2$ = 0.1177 |
| $R$ indices (all data) | $R1$ = 0.0680, $wR2$ = 0.1312 |
| Largest diff. peak and hole [e/Å$^{-3}$] | 0.717 and –0.328 |

In vitro cell tests were performed on LLC-PK cells obtained from the ATCC (American Tissue Cell Culture Collection) and maintained in Dulbecco's Modified Eagle Medium containing FCS (foetal calf serum) [10% (v/v)], penicillin streptomycin [1% (v/v)] and L-glutamine [1% (v/v)]. Cells were seeded in 96-well plates containing 200-μL-microtitre wells at a density of 5,000 cells/200 μL of medium and were incubated at 37 °C for 24 h to allow for exponential growth. The compounds used for the testing were then dissolved in a medium solution containing DMSO (0.7%) to obtain stock solutions of $5 \times 10^{-4}$ M in concentration. The cells were then treated with varying concentrations of the compounds and incubated for 48 h at 37 °C. The solutions were then removed from the wells and the cells were washed with PBS (phosphate buffer solution) and fresh medium was added to the wells. After a recovery period of 24 h incubation at 37 °C, individual wells were treated with a solution of MTT (200 μL) [3-(4,5-dimethylthiazol-2-yl)-2,5-diphenyltetrazolium bromide] in medium. The solution consisted of MTT (30 mg) in the medium (30 mL). The cells were incubated for 3 h at 37 °C. The medium was then removed and the purple formazan crystals were dissolved in DMSO (200 μL per well). Absorbance was then measured at 540 nm by a Wallac Victor (Multilabel HTS Counter) Plate Reader. Cell viability was expressed as a percentage of the absorbance recorded for control wells. The mean values used for the dose response curves represent

 © 2006 Wiley-VCH Verlag GmbH & Co. KGaA, Weinheim 

the values obtained from four consistent MTT-based assays for each compound tested.

**4-(2-Methoxyethoxy)benzaldehyde (2a):** This compound was synthesised according to the published procedure and obtained as a nearly colourless oil in a yield of 72%.[27] The spectroscopic data were in correspondence to the published data.

**4-[2-(Dimethylamino)ethoxy]benzaldehyde (2b):** 4-Hydroxybenzaldehyde (1.00 g, 8.19 mmol) was heated at 80 °C together with 2-(dimethylamino)ethyl chloride (1.2 equiv., 1.41 g, 9.83 mmol) and $K_2CO_3$ (4 equiv., 4.52 g, 32.76 mmol) in abs. DMF (50 mL) for 3 d under an atmosphere of argon. $H_2O$ (30 mL) was added, and the reaction mixture was extracted with diethyl ether (4 × 20 mL). The combined organic layers were dried with $Na_2SO_4$ and the solvent was removed in vacuo. A red oil was obtained in a yield of 76%. $^1$H NMR ($CDCl_3$, 300 MHz): $\delta$ = 2.33 [s, 3 H, N(C$H_3$)$_2$], 2.75 [t, $^3J$ = 5.7 Hz, 2 H, (CH$_3$)$_2$NC$H_2$CH$_2$], 4.14 [t, $^3J$ = 5.7 Hz, 2 H, (CH$_3$)$_2$NCH$_2$C$H_2$O], 7.02 (d, $J_{A,B}$ = 8.4 Hz, 2 H, OCC*H*CH), 7.81 (d, $J_{A,B}$ = 8.7 Hz, 2 H, C*H*C), 9.86 (s, 1 H, CHO) ppm.

**6-[4-(2-Methoxyethoxy)phenyl]fulvene (3a):** Pyrrolidine (2.58 mL, 2.20 g, 30.94 mmol) was added to a solution of 4-(2-methoxyethoxy)benzaldehyde (5.20 g, 30.94 mmol) and cyclopentadiene (5.11 mL, 77.34 mmol) in methanol (60 mL). After this addition, the solution turned from colourless to deep red and a solid was formed. After 12 h, acetic acid (1.86 g, 1.77 mL, 30.94 mmol) was added. $H_2O$ (30 mL) was added, and the mixture was extracted with $CH_2Cl_2$ (4 × 20 mL). The combined organic layers were dried with $Na_2SO_4$, and the solvent was removed in vacuo to afford a dark red oil. The crude product was purified on a silica column (15–5 cm) with $CH_2Cl_2$ as the solvent. After removal of the solvent under vacuum, the product was obtained as an orange solid in yield of 78% (5.49 g, 24.07 mmol). $^1$H NMR ($CDCl_3$, 300 MHz): $\delta$ = 2.43 (s, 3 H, OC$H_3$), 2.74 (t, $^3J$ = 5.7 Hz, 2 H, CH$_3$OC$H_2$CH$_2$), 4.11 (t, $^3J$ = 5.7 Hz, 2 H, CH$_3$OCH$_2$C$H_2$), 6.30–6.31, 6.47–6.49, 6.64–6.67, 6.71–6.73 (m, 4 H, C$_5H_4$), 6.95 (d, $J_{A,B}$ = 8.7 Hz, 2 H, OCC*H*CHC), 7.15 (s, 1 H, C$_6$H$_4$C*H*C$_5$H$_4$), 7.56 (d, $J_{A,B}$ = 8.7 Hz, 2 H, OCCHC*H*C) ppm. $^{13}$C NMR ($CDCl_3$, 75 MHz): $\delta$ = 45.9 (O*C*H$_3$), 58.2, 66.1 (2 C) (CH$_3$O*C*H$_2$*C*H$_2$O), 114.9 (2 C) (C-2,6 OC$_6$H$_4$), 119.9 (C$_5$H$_4$*C*HC$_6$H$_4$), 127.4, 129.6, 134.9, 138.3 (4 C) (C-2,3,4,5 C$_5$H$_4$), 132.4 (2 C) (C-3,5 OC$_6$H$_4$), 143.3 (C-1 C$_5$H$_4$), 159.9 (C-1 OC$_6$H$_4$) ppm. $C_{15}H_{16}O_2$ (228.12): calcd. C 78.98, H 7.07; found C, 78.68, H, 7.05.

**6-{4-[2-(Dimethylamino)ethoxy]phenyl}fulvene (3b):** Pyrrolidine (4.97 mL, 4.24 g, 59.55 mmol) was added to a solution of 4-[2-(dimethylamino)ethoxy]benzaldehyde (11.50 g, 59.55 mmol) and cyclopentadiene (9.84 g, 148.88 mmol) in methanol (100 mL). After this addition, the solution turned from colourless to deep red. After 12 h, acetic acid (3.58 g, 3.41 mL, 59.55 mmol) was added. $H_2O$ (40 mL) were added, and the mixture was extracted with $CH_2Cl_2$ (4 × 40 mL). The combined organic layers were dried with $Na_2SO_4$, and the solvent was removed by vacuum to afford a dark red oil. The crude product was purified on an aluminium oxide column (15–5 cm) with $CH_2Cl_2$ as the solvent. After removal of the solvent under vacuum, the product was obtained as an orange solid in yield of 51% (7.34 g, 30.44 mmol). $^1$H NMR ($CDCl_3$, 400 MHz): $\delta$ = 2.35 [s, 6 H, N(C$H_3$)$_2$], 2.75 [t, $^3J$ = 5.7 Hz, 2 H, (CH$_3$)$_2$NC$H_2$CH$_2$], 4.11 [t, $^3J$ = 5.7 Hz, 2 H, (CH$_3$)$_2$NCH$_2$C$H_2$O], 6.30–6.35, 6.45–6.50, 6.65–6.67, 6.70–6.75 (m, 4 H, C$_5H_4$), 6.96 (d, $J_{A,B}$ = 8.6 Hz, 2 H, C-2,6 OC$_6H_4$), 7.15 (s, 1 H, C$_5$H$_4$C*H*C$_6$H$_4$), 7.56 (d, $J_{A,B}$ = 8.6 Hz, 2 H, C-3,5 OC$_6H_4$) ppm. $^{13}$C NMR ($CDCl_3$, 100 MHz): $\delta$ = 46.2 (2 C) [N(*C*H$_3$)$_2$], 58.4 [(CH$_3$)$_2$N*C*H$_2$CH$_2$], 66.2 [(CH$_3$)$_2$NCH$_2$*C*H$_2$O], 115.1 (2 C) (C-2,6 OC$_6$H$_4$), 120.1 (C$_6$H$_4$*C*HC$_5$H$_4$), 127.6 (C$_5$H$_4$), 129.8 (C-4 OC$_6$H$_4$), 130.0 (C$_5$H$_4$), 132.7 (2 C) (C-3,5 OC$_6$H$_4$), 135.1, 138.5 (C$_5$H$_4$), 143.5 (C-1 C$_5$H$_4$), 160.1 (C-1 OC$_6$H$_4$) ppm. $C_{16}H_{19}NO$ (241.15): calcd. C 79.63, H 7.94, N 5.80; found C 79.85, H 7.92, N 5.79.

**{1,2-Dicyclopentadienyl-1,2-bis[4-(2-methoxyethoxy)phenyl]ethanediyl}titanium Dichloride, [1,2-{4-(2-MeO-C$_2$H$_4$O)-C$_6$H$_2$}$_2$C$_2$H$_2${η$^5$-C$_5$H$_4$}$_2$]TiCl$_2$ (4a):** $TiCl_4$ (0.46 mL, 0.79 g, 4.18 mmol) was added to dry toluene (50 mL) and dry THF (5 mL). The solution turned immediately from colourless to pale yellow. The solution was stirred and cooled down to –78 °C and then was treated dropwise with *n*BuLi (4.18 mL, 8.36 mmol). The solution turned from yellow to brown during the addition. After this addition, the mixture was warmed up slowly to room temp., and the solution finally turned black. After 20 h of stirring, a solution of 6-[4-(2-methoxyethoxy)phenyl]fulvene (1.91 g, 8.36 mmol) in dry toluene was added to the solution of $TiCl_2$·2THF at room temp. under an atmosphere of argon. The mixture was then stirred under reflux for another 16 h. The solvent was removed under vacuum. The resulting black solid was extracted with $CH_3Cl$ (3 × 20 mL) and filtered through celite and twice through a Whatman No. 1 filter paper. The solvent was removed under vacuum, and the residue was triturated with pentane (40 mL) to give 0.53 g (22% yield) of a black solid. The ratio of *trans* and *cis* isomers was 44% to 56%. $^1$H NMR ($CDCl_3$, 400 MHz): $\delta$ = 3.42–3.48 (m, 2 H, C$H_3$), 3.69–3.79 (m, 4 H, CH$_3$OC$H_2$CH$_2$), 4.01–4.10 (m, 4 H, CH$_3$OCH$_2$C$H_2$O), 4.68, 5.40 (s, 2 H, *cis*- and *trans*-PhC*H*Cp), 6.12–6.33, 6.76–7.17 (m, 16 H, C$_6H_4$, C$_5H_4$) ppm. $^{13}$C NMR ($CDCl_3$, 100 MHz): $\delta$ = 49.0, 51.8 (2 C) (*cis*- and *trans*-Ph*C*HCp), 57.2 (2 C) (O*C*H$_3$), 65.1, 68.8 (4 C) (O*C*H$_2$*C*H$_2$O), 107.1, 111.3, 111.6, 111.9, 114.1, 114.2, 123.4, 125.3, 125.6, 126.8, 127.1, 127.6, 129.6, 130.7, 134.4, 135.6, 153.9, 154.5 (22 C) (*cis*- and *trans*-$C_6H_4$ and $C_5H_4$) ppm. IR (KBr): $\tilde{\nu}$ = 3104 (m), 2924 (m), 1612 (s), 1514 (s), 1453 (s), 1440 (s), 1254 (w), 1180 (s), 1059 (s), 1037 (s), 860 (m), 771 (m) cm$^{-1}$. UV/Vis ($CH_2Cl_2$): $\lambda$ ($\varepsilon$, L mol$^{-1}$ cm$^{-1}$) = 227 (23600), 271 (19666), 378 (1666), 387 (1767), 524 (233) nm. MS (ESI–): *m*/*z* = 610.99 [M + Cl]$^+$. $C_{30}H_{32}Cl_2O_4Ti$ (574.12): calcd. C 62.63, H 5.61; found C 65.65, H 6.14.

**Bis{[4-(2-methoxyethoxy)benzyl]cyclopentadienyl}titanium(IV) Dichloride, [{η$^5$-C$_5$H$_4$-CH$_2$-C$_6$H$_4$–O(CH$_2$)$_2$OCH$_3$}$_2$Ti]Cl$_2$ (6a):** LiBEt$_3$H (12.44 mL) was concentrated by removal of the solvent by heating it to 90 °C under a vacuum of $10^{-2}$ mbar for 2 h. The concentrated reagent was dissolved in diethyl ether (30 mL) and transferred to a solution of 6-[4-(2-methoxyethoxy)phenyl]fulvene (2.25 g, 9.86 mmol) in diethyl ether (10 mL). The solution was stirred for 20 min and then pentane (40 mL) was added, after which point lithium cyclopentadienide intermediate **5a** precipitated from the solution. The precipitate was immediately filtered, and **5a** was then collected on a frit and washed with pentane (25 mL), dried briefly in vacuo and transferred to a Schlenk flask under an atmosphere of argon. White lithium cyclopentadienide intermediate **5a** (1.88 g, 7.96 mmol, 81% yield) was dissolved in THF (20 mL) and was added dropwise to a solution of $TiCl_4$ (0.44 mL, 3.98 mmol) in THF (80 mL) at 0 °C. The resultant dark red solution was heated under reflux for 16 h. The solution was then cooled, and the solvent was removed under reduced pressure. The remaining residue was extracted with $CH_2Cl_2$ (75 mL) and filtered through celite to remove the LiCl. The dark red filtrate was filtered twice more by gravity filtration. The solvent was removed under reduced pressure to yield a brown solid, which was dried in vacuo (1.54 g, 2.67 mmol, 67% yield). $^1$H NMR ($CDCl_3$, 300 MHz): $\delta$ = 3.44 (s, 6 H, OC$H_3$), 3.74 (t, $^3J$ = 4.6 Hz, 4 H, CH$_3$OC$H_2$CH$_2$), 4.02 (s, 4 H, C$_6$H$_4$C$H_2$C$_5$H$_4$), 4.09 (t, $^3J$ = 4.6 Hz, 4 H, CH$_3$OCH$_2$C$H_2$O), 6.29 (s, 8 H, C$_5H_4$), 6.86, 7.11 (d, $J_{A,B}$ = 8.4 Hz, 8 H, C$_6H_4$) ppm. $^{13}$C NMR ($CDCl_3$, 75 MHz): $\delta$ = 36.0 (2 C) (C$_6$H$_4$*C*H$_2$C$_5$H$_4$), 59.2

 © 2006 Wiley-VCH Verlag GmbH & Co. KGaA, Weinheim 

(2 C) ($OCH_3$), 67.3, 71.1 (4 C) ($CH_3OCH_2CH_2OC_6H_4$), 114.7, 130.0 (4 C) (C-2,3,5,6 $C_6H_4$), 116.2, 122.2 (8 C) (C-2,3,4,5 $C_5H_4$), 131.7, 137.7 (4 C) (C-1 $C_5H_4$; C-6 $C_6H_4$), 157.5 (2 C) (C-1, $OC_6H_4$) ppm. IR (KBr): $\tilde{\nu}$ = 3104 (m), 2924 (m), 1612 (s), 1514 (s), 1453 (s), 1440 (s), 1254 (w), 1180 (s), 1059 (s), 1037 (s), 860 (m), 771 (m) $cm^{-1}$. MS (ESI–): 611.05 $[M + Cl]^+$. UV/Vis ($CH_2Cl_2$): $\lambda$ ($\varepsilon$, $L\,mol^{-1}\,cm^{-1}$) = 227 (26600), 262 (24600), 316 (8600), 396 (3500), 524(400) nm. $C_{30}H_{34}Cl_2O_4Ti$ (576.13): calcd. C 62.41, H 5.99, Cl 12.28; found C 62.84, H 6.08, Cl 12.12.

**1-Bromo-4-(2-methoxyethoxy)benzene (8a):** This compound was synthesised according to the known procedure and obtained as an orange oil in a yield of 75%.[28] $^1H$ NMR ($CDCl_3$, 400 MHz): $\delta$ = 3.39 (s, 3 H, $OCH_3$), 3.65–3.70 (m, 2 H, $CH_3OCH_2CH_2$), 4.00–4.05 (m, 2 H, $CH_3CH_2CH_2O$), 6.75 (d, $J_{A,B}$ = 9.1 Hz, 2 H, $OCCHCH$), 7.31 (d, $J_{A,B}$ = 8.9 Hz, 2 H, $OCHCHC$) ppm. $^{13}C$ NMR ($CDCl_3$, 100 MHz): $\delta$ = 59.4 ($OCH_3$), 67.7, 71.1 (2 C) ($OCH_2CH_2OCH_3$), 116.6 (2 C) (C-3,5 $BrC_6H_4$), 117.6 (C-1 $BrC_6H_4$), 132.4 (2 C) (C-2,6 $BrC_6H_4$), 158.1 (C-4 $BrC_6H_4$). $C_9H_{11}BrO_2$ (229.99): calcd. C 46.78, H 4.80; found C 46.80, H 4.81.

**1-Bromo-4-[2-(dimethylamino)ethoxy]benzene (8b):** A mixture of 4-bromophenol (3.75 g, 21.81 mmol), NaI (3.25 g, 21.68 mmol), $K_2CO_3$ (4 equiv. 12.03 g, 87.24 mmol) and 2-(dimethylamino)ethyl chloride (3.74 g, 26.17 mmol) in DMF (100 mL) was stirred at 80 °C for 4 d. $H_2O$ (50 mL) was added, and the reaction mixture was extracted with diethyl ether (5 × 50 mL). The combined organic layers were additionally washed with aq. KOH (3 × 20 mL). Afterwards, the aqueous layers were extracted with diethyl ether (5 × 15 mL). The combined organic layers were dried with $Na_2SO_4$ and concentrated in vacuo to give a dark red oil. The oil was distilled at 96 °C ($4 \times 10^{-1}$ mbar) to afford a light yellow oil in a yield of 52% (2.76 g, 11.34 mmol). $^1H$ NMR ($CDCl_3$, 400 MHz): $\delta$ = 2.31 [s, 6 H, $N(CH_3)_2$], 2.69 [t, $^3J$ = 5.7 Hz, 2 H, $(CH_3)_2NCH_2CH_2$], 3.99 [t, $^3J$ = 5.7 Hz, 2 H, $(CH_3)_2NCH_2CH_2O$], 6.78 (d, $J_{A,B}$ = 9.1 Hz, 2 H, $OCHCH$), 7.34 (d, $J_{A,B}$ = 9.1 Hz, 2 H, $OCHCHC$) ppm. $^{13}C$ NMR ($CDCl_3$, 100 MHz): $\delta$ = 46.1 (2 C) $[N(CH_3)_2]$, 58.4 $[(CH_3)_2NCH_2CH_2]$, 66.4 $[(CH_3)_2NCH_2CH_2O]$, 113.0 (C-1 $BrC_6H_4$), 116.6 (2 C) (C-3,5 $BrC_6H_4$), 132.4 (2 C) (C-2,6 $BrC_6H_4$), 158.2 (C-4 $BrC_6H_4$) ppm. $C_{10}H_{14}BrNO$: calcd. C 49.20, H 5.78, N 5.74; found C 48.90, H 5.68, N 5.65.

## Acknowledgments

The authors want to thank the Science Foundation Ireland (SFI) for funding through grant (04/BRG/C0682). In addition, funding from the Higher Education Authority (HEA) and the Centre for Synthesis and Chemical Biology (CSCB) through the HEA PRTLI cycle 3 as well as COST D39 was provided.

[1] A. Gelasco, S. J. Lippard, *Top. Biol. Inorg. Chem.* **1999**, *1*, 1–43.
[2] E. R. Jamieson, S. J. Lippard, *Chem. Rev.* **1999**, *99*, 2467–2498.
[3] N. Farrell, Y. Qu, J. D. Roberts, *Top. Biol. Inorg. Chem.* **1999**, *1*, 99–115.
[4] a) P. Köpf-Maier, H. Köpf, *Chem. Rev.* **1987**, *87*, 1137–1152; b) P. Köpf-Maier, H. Köpf, *Struct. Bonding (Berlin)* **1988**; *70*, 103–194.
[5] F. Caruso, M. Rossi, *Met. Ions Biol. Sys.* **2004**, *42*, 353–384.
[6] G. Lummen, H. Sperling, H. Luboldt, T. Otto, H. Rubben, *Cancer Chemother. Pharmacol.* **1998**, *42*, 415–417.
[7] N. Kröger, U. R. Kleeberg, K. B. Mross, L. Edler, G. Saß, D. K. Hossfeld, *Onkologie* **2000**, *23*, 60–62.
[8] R. Teuber, G. Linti, M. Tacke, *J. Organomet. Chem.* **1997**, *545–546*, 105.
[9] F. Hartl, L. Cuffe, J. P. Dunne, S. Fox, T. Mahabiersing, M. Tacke, *J. Mol. Struct., Theochem* **2001**, *559*, 331–339.
[10] M. Tacke, J. P. Dunne, S. Fox, G. Linti, R. Teuber, *J. Mol. Struct.* **2001**, *570*, 197–202.
[11] S. Fox, J. P. Dunne, D. Dronskowski, D. Schmitz, M. Tacke, *Eur. J. Inorg. Chem.* **2002**, 3039–3046.
[12] J. J. Eisch, S. Xian, F. A. Owuor, *Organometallics* **1998**, *17*, 5219–5221.
[13] J. J. Eisch, F. A. Owuor, S. Xian, *Organometallics* **1999**, *18*, 1583–1585.
[14] K. M. Kane, P. J. Shapiro, A. Vij, R. Cubbon, A. L. Rheingold, *Organometallics* **1997**, *16*, 4567–4571.
[15] S. Fox, J. P. Dunne, M. Tacke, J. F. Gallagher, *Inorg. Chim. Acta* **2004**, *357*, 225–234.
[16] M. Tacke, L. T. Allen, L. P. Cuffe, W. M. Gallagher, Y. Lou, O. Mendoza, H. Müller-Bunz, F.-J. K. Rehmann, N. Sweeney, *J. Organomet. Chem.* **2004**, *689*, 2242–2249.
[17] F.-J. K. Rehmann, L. P. Cuffe, O. Mendoza, D. K. Rai, N. Sweeney, K. Strohfeldt, W. M. Gallagher, M. Tacke, *Appl. Organomet. Chem.* **2005**, *19*, 293–300.
[18] M. Tacke, L. P. Cuffe, W. M. Gallagher, Y. Lou, O. Mendoza, H. Müller-Bunz, F.-J. K. Rehmann, N. Sweeney, *J. Inorg. Biochem.* **2004**, *98*, 1987–1994.
[19] F.-J. K. Rehmann, A. Rous, O. Mendoza, C. Pampillon, K. Strohfeldt, N. Sweeney, W. M. Gallagher, M. Tacke, *Polyhedron* **2005**, *24*, 1250–1255.
[20] a) C. Pampillón, O. Mendoza, N. Sweeney, K. Strohfeldt, M. Tacke, *Polyhedron* **2006**, *25*, 2101–2108; b) C. Pampillón, N. Sweeney, K. Strohfeldt, M. Tacke, *Inorg. Chim. Acta* **2006**, *359*, 3969–3975.
[21] a) N. Sweeney, O. Mendoza, H. Müller-Bunz, C. Pampillón, F.-J. K. Rehmann, K. Strohfeldt, M. Tacke, *J. Organomet. Chem.* **2005**, *690*, 4537–4544; b) N. J. Sweeney, H. Müller-Bunz, C. Pampillón, K. Strohfeldt, M. Tacke, *J. Inorg. Biochem.* **2006**, 100, 1479–1486.
[22] G. Kelter, N. Sweeney, K. Strohfeldt, H. H. Fiebig, M. Tacke, *Anti-Cancer Drugs* **2005**, *16*, 1091–1098.
[23] O. Oberschmidt, A. R. Hanauske, F.-J. K. Rehmann, K. Strohfeldt, N. Sweeney, M. Tacke, *Anti-Cancer Drugs* **2005**, *16*, 1071–1073.
[24] K. O'Connor, C. Gill, M. Tacke, F.-J. K. Rehmann, K. Strohfeldt, N. Sweeney, J. M. Fitzpatrick, R. W. G. Watson, *Apoptosis* **2006**, *11*, 1205–1214.
[25] I. Fichtner, C. Pampillón, N. J. Sweeney, K. Strohfeldt, M. Tacke, *Anti-Cancer Drugs* **2006**, *17*, 333–339.
[26] M. C. Valadares, A. L. Ramos, F.-J. K. Rehmann, N. J. Sweeney, K. Strohfeldt, M. Tacke, M. L. S. Queiroz, *Eur. J. Pharmacol.* **2006**, *534*, 264–270.
[27] H. Brunner, K.-M. Schellerer, *Inorg. Chim. Acta* **2003**, *350*, 39–48.
[28] M. Seto, Y. Aramaki, T. Okawa, N. Miyamoto, K. Aikawa, N. Kanzaki, S. Niwa, Y. Iizawa, M. Baba, M. Shiraishi, *Chem. Pharm. Bull.* **2004**, *52*, 577–590.
[29] T. Mosmann, *J. Immunol. Methods* **1983**, *65*, 55–63.
[30] S. Top, E. B. Kaloun, A. Vessieres, I. Laios, G. Leclercq, G. Jaouen, *J. Organomet. Chem.* **2002**, *643–644*, 350–356.
[31] M. Guo, S. Hongzhe, H. J. McArdle, L. Gambling, P. J. Sadler, *Biochemistry* **2000**, *39*, 10023–10033.
[32] G. M. Sheldrick, *SADABS*. Version 2.03, University of Göttingen, Germany, **2002**.
[33] G. M. Sheldrick, *SHELXS97* and *SHELXL97*, University of Göttingen, Germany, **1997**.

Received: June 21, 2006
Published Online: September 20, 2006

 © 2006 Wiley-VCH Verlag GmbH & Co. KGaA, Weinheim 

DOI: 10.1002/ejic.200600599

# Synthesis and Structure of Pd and Pt Complexes with Doubly Stabilized Phosphorus Ylides

**Marta Carbó,[a] Nérida Marín,[a] Rafael Navarro,[a] Tatiana Soler,[b] and Esteban P. Urriolabeitia*[a]**

**Keywords:** Ylides / Metallacycles / Palladium / Platinum / Coordination modes

The doubly stabilized P-ylide ligands $Ph_3P{=}C(CO_2Me)$-$C(=S)N(H)Ph$ (**L1**), $Ph_3P{=}C(CN)C(=S)N(H)Ph$ (**L2**), and $Ph_3P{=}C(CN)$–[(*E*)-$C(CO_2Me){=}CH(CO_2Me)$] (**L3**) have been prepared and fully characterized. The X-ray structures of **L1** and **L2** are reported. The reactivity of **L1**, **L2**, and **L3** towards cationic $Pd^{II}$ and $Pt^{II}$ precursors with two vacant coordination sites has been studied. Adducts of general formula $[M(C\hat{}X)$-$(\mathbf{L}n)]ClO_4$, $[M(C\hat{}X)(\mathbf{L}n)_2]ClO_4$, and $[M(\mu\text{-}\mathbf{L}n)(C\hat{}X)]_2(ClO_4)_2$ ($C\hat{}X$ = ancillary ligands) were obtained. The ylides **L*n*** coordinate to the metal center through their heteroatoms (O, N, S), while the C bonding of **L*n*** has not been observed in any of the cases studied.
(© Wiley-VCH Verlag GmbH & Co. KGaA, 69451 Weinheim, Germany, 2006)

## Introduction

We have recently shown that the α-stabilized P-ylides $Ph_3P{=}C(H)R$ [R = CN, C(O)R′; R′ = Me, Ph, OMe, $NMe_2$] behave as versatile ligands towards $Pd^{II}$ and $Pt^{II}$ precursors, and several coordination modes of these ylides have been characterized. Thus, the ylide can coordinate to the metal center through the $C_\alpha$ atom, the carbonyl oxygen, or the N atom of the cyano group. We have even characterized situations in which the same ylide shows a combination of bonding modes.[1] An interesting fact is that, in spite of the presence of several potential donor atoms on the same ylide, they always behave as ambidentate ligands,[1] that is, using only one donor atom each time. Further replacement of the ylidic H atom by other functional groups increases the functionality of the ylides and should expand their bonding capabilities. In this context, we have now focused our attention on doubly stabilized P-ylides. The introduction of an additional stabilizing functional group can be achieved through several simple synthetic procedures: acylation,[2] reactivity towards alkynes or other unsaturated compounds,[3] reactivity of iminophosphoranes with alkynes,[4] retro-Wittig reactions,[5] and other less common processes.[6]

While the chemistry of P-ylide compounds with two stabilizing groups, and their organic applications, has been the subject of intensive research, their coordination chemistry and bonding properties towards transition metals are scarcely represented.[7] Representative examples are the reaction of $Hg^{II}$ halides $HgX_2$ (X = Cl, Br, I) or different $U^{VI}$ salts with $Ph_3P{=}C[C(O)Me][C(O)Ph]$ (ABPPY), which results in the formation of mono- and dinuclear complexes with the *O*(acetyl)-bonded ABPPY ylide.[7a,7d] It is remarkable that the reactivity of the same $HgX_2$ precursors towards $Ph_3P{=}C(H)C(O)Ph$ (BPPY) results in *C*-bonded mono- and polynuclear complexes.[8] On the other hand, the reaction of $[PtCl_2(NCC_6F_5)_2]$ with $Ph_3P{=}C(H)CO_2Me$ gives the imine-ylide complex $[PtCl_2\{NH{=}C(C_6F_5)$-$C(=PPh_3)C(O)Me\}_2]$,[7b] in which the generated doubly stabilized ylide remains bonded to the Pt center through the imine N atom. As can be observed, all complexes with doubly stabilized ylides share a common feature, namely their bonding to the metal through the heteroatoms. Aiming to expand the knowledge on the bonding properties of doubly stabilized P-ylides, we have studied the reactivity of $Ph_3P{=}C(CO_2Me)C(=S)N(H)Ph]$ (**L1**),[3a] $Ph_3P{=}C(CN)C$-$(=S)N(H)Ph$ (**L2**),[3a] and $Ph_3P{=}C(CN)$–[(*E*)-$C(CO_2$-$Me){=}CH(CO_2Me)]$ (**L3**)[3b] towards orthometalated bis-solvato derivatives of $Pd^{II}$ and $Pt^{II}$. We have found different stoichiometries and different bonding modes for each ylide (monodentate, didentate, chelating, bridging), and we have also found that in none of the cases studied does the ylide bond to the metal center through the ylidic $C_\alpha$ atom.

[a] Departamento de Compuestos Organometálicos, Instituto de Ciencia de Materiales de Aragón, Universidad de Zaragoza-C.S.I.C,
Plaza de San Francisco s/n, 50009 Zaragoza, Spain
Fax: +34-976-761187
E-Mail: esteban@unizar.es
[b] Servicio Técnicos de Investigación, Facultad de Ciencias Fase II,
03690 San Vicente de Raspeig, Alicante, Spain

## Results and Discussion

### Synthesis and Reactivity of L1

The ylide $Ph_3P{=}C(CO_2Me)C(=S)N(H)Ph$ (**L1**) was prepared following reported methods[3a] by treatment of

 © 2006 Wiley-VCH Verlag GmbH & Co. KGaA, Weinheim 

$Ph_3P{=}C(H)CO_2Me$[9b] with phenyl isothiocyanate (PhNCS). Since in the original work this compound was poorly characterized, and also for comparative purposes, a complete characterization of **L1** was performed. The IR spectrum of **L1** shows an intense absorption at 1629 $cm^{-1}$, attributed to the C=O stretch, and two very intense absorptions at 1526 and 1107 $cm^{-1}$, assigned to the stretch of the C=N and C=S bonds of the thioamide group, respectively.[10] The N–H stretch was not observed in the IR spectrum. The $^1H$ NMR spectrum of **L1** shows a very broad singlet at $\delta$ = 12.25 ppm due to the NH proton. This strongly deshielded position can be easily explained by taking into account the formation of an intramolecular hydrogen bond between the NH group and the carbonyl oxygen, as depicted in Figure 1. The formation of this hydrogen bond could also account for the lack of observation of the $\nu_{NH}$ band in the IR spectrum, which is shifted to lower energies with respect to its expected position (about 3400 $cm^{-1}$)[10] and is probably hidden under the polyethylene absorptions (2800–3000 $cm^{-1}$). A similar intramolecular H bond has been found in the related N-ylide $H_5C_5NC[C(O)Ph]C(S)N(H)Ph$.[11] The $^{31}P\{^1H\}$ NMR spectrum of **L1** shows the presence of a single signal at $\delta$ = 11.33 ppm, and the $^{13}C\{^1H\}$ NMR spectrum also shows a good agreement with the proposed structure. Key features are the signal due to the P=C carbon at $\delta$ = 71.48 ppm (d, $^1J_{P,C}$ = 143.1 Hz), and that due to the C=S carbon at $\delta$ = 189.01 ppm (d, $J$ = 16.6 Hz).[12] These observations agree with the structures depicted in Figure 1 for **L1**. The X-ray structure of **L1** has also been determined.

A molecular drawing of **L1** is shown in Figure 2, the most relevant parameters concerning data collection and structure solution and refinement are given in the Experimental Section, and selected bond lengths and angles are collected in Table 1. The molecular skeleton of **L1** is very similar to that reported previously for the closely related ylide $H_5C_5NC[C(O)Ph]C(S)N(H)Ph$.[11] Key features are the cisoid arrangement of the P=C and C=S bonds, also observed in other thiocarbonyl stabilized ylides,[13] and the transoid arrangement of the P=C and C=O bonds, as usually observed in ester-stabilized ylides.[2f,14] The atoms P(1), C(19), C(20), O(1), C(22), S(1), and N(1) are nearly coplanar, since the maximum deviation of the best least-squares plane is 0.13 Å (C20). The P=$C_\alpha$ bond length is elongated [P(1)–C(19) 1.751(2) Å] and both $C_\alpha$–C bond lengths are identical [C(19)–C(22) 1.436(3), C(19)–C(20) 1.437(3) Å]. These values are shorter than the standard value for a $C(sp^2)$–$C(sp^2)$ single bond (1.478 Å),[15] but are longer than those found in free[2f,16] or *O*-bonded[9a,17] ylides [range: 1.366–1.394 Å] containing a single functional group. The C(22)–S(1) bond length [1.690(2) Å] is identical to that found in related ylides [1.693(2) Å],[11] and is slightly longer than usual values for C=S double bonds [1.671 Å].[15] All these facts also show an extensive delocalization of the ylidic charge density through the chain of atoms O(1)–C(20)–C(19)–C(22)–S(1), probably due to the simultaneous presence of two delocalizing groups. In good agreement with the NMR spectroscopic data, an intramolecular hydrogen bond between the NH proton and the carbonyl oxygen can be established and characterized with the following param-

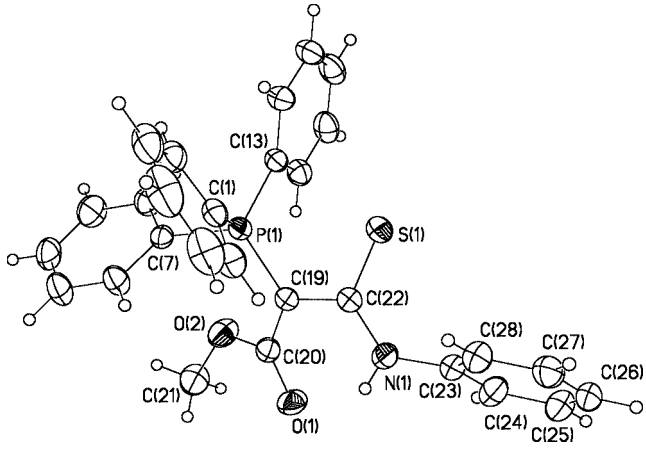


Figure 2. Thermal ellipsoid plot of **L1**. Non-hydrogen atoms are drawn at the 50% probability level.

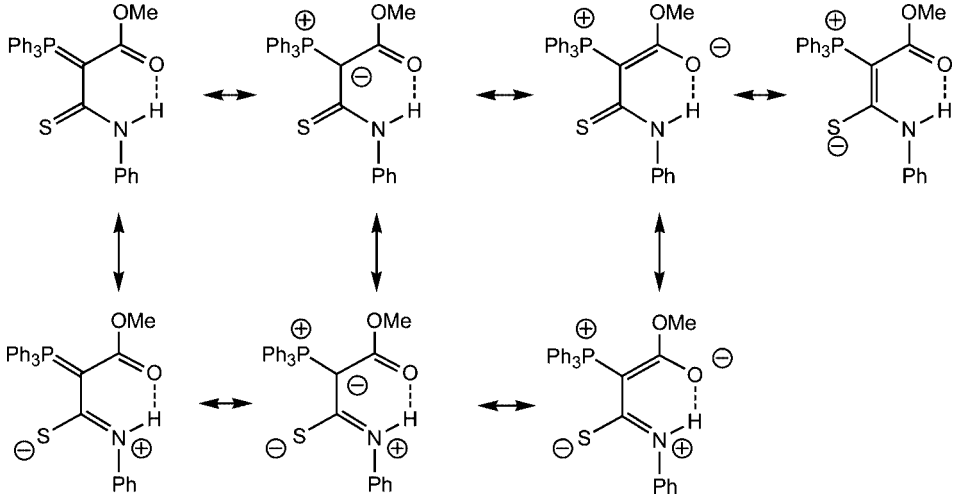


Figure 1. Resonance forms for ligand **L1**.

 © 2006 Wiley-VCH Verlag GmbH & Co. KGaA, Weinheim 

eters: H(1A)···O(1) 1.939(3) and N(1)···O(1) 2.642(3) Å; N(1)–H(1A)···O(1) 138.14(15)°. The intramolecular P(1)–S(1) distance is 3.034 Å, which is shorter than those found in other ylides[13] and is much shorter than the sum of the van der Waals radii (3.60 Å).[18] The P(1)–C(19)–C(22)–S(1) torsion angle is –8.9° and the P(1)–C(19)–C(22) bond angle is 115.19(15)°, a value smaller than expected for an $sp^2$-hybridised carbon.

Table 1. Selected bond lengths [Å] and angles [°] for **L1**.

| | | | |
|---|---|---|---|
| P(1)–C(19) | 1.751(2) | P(1)–C(13) | 1.801(2) |
| P(1)–C(1) | 1.805(2) | P(1)–C(7) | 1.817(2) |
| C(19)–C(22) | 1.436(3) | C(19)–C(20) | 1.437(3) |
| C(20)–O(1) | 1.216(3) | C(20)–O(2) | 1.334(3) |
| O(2)–C(21) | 1.438(3) | C(22)–N(1) | 1.340(3) |
| C(22)–S(1) | 1.690(2) | N(1)–C(23) | 1.420(3) |
| O(1)–C(20)–O(2) | 120.4(2) | O(1)–C(20)–C(19) | 126.2(2) |
| O(2)–C(20)–C(19) | 113.3(2) | C(20)–O(2)–C(21) | 118.6(2) |
| N(1)–C(22)–C(19) | 117.89(19) | N(1)–C(22)–S(1) | 122.22(17) |
| C(19)–C(22)–S(1) | 119.85(17) | C(22)–N(1)–C(23) | 127.9(2) |

The resonance forms shown in Figure 1 suggest that there are at least four potential donor atoms for **L1** (two O atoms, one S, and the $C_\alpha$). We thus explored the reactivity of **L1** towards the bis-solvate complexes $[Pd(C^X)(thf)_2]ClO_4$ (see Scheme 1), prepared as usual by reaction of the corresponding dinuclear chlorido-bridged derivatives with $AgClO_4$ (1:2 molar ratio) in thf. Treatment of freshly prepared solutions of $[M(C^X)(thf)_2]ClO_4$ with **L1** (1:1 molar ratio) in thf at 25 °C resulted in the formation of the cationic derivatives $[Pd(C^X)(\mathbf{L1})]ClO_4$ (**1**–**5**), which show elemental analyses and mass spectra (FAB+) in good agreement with the proposed stoichiometry. The IR spectra of **1**–**5** show several remarkable features: (i) a notable decrease in the position of the $\nu_{CO}$ absorption with respect to free **L1**; (ii) a shift of the $\nu_{CN}$ absorption to high energies with respect to free **L1**, while the $\nu_{CS}$ band is found shifted to lower energies; and (iii) a weak band due to the NH group. All these facts suggest strongly that ligand **L1** is bonded to the Pd atom through the S atom of the thioamide unit and through the carbonyl oxygen of the resonance-stabilized $CO_2Me$ group, and that the ylidic $C_\alpha$ atom is not involved in bonding with the metal atom. This bonding mode also implies that the NH···O hydrogen bond is broken, and hence explains the increase in the NH stretch, since the ylide must rotate around the $C_\alpha$–C(S) bond to adopt the final bonding mode.

The NMR spectra of **1**–**5** give additional structural information. The $^1H$ NMR spectra show that the molecular plane behaves as a symmetry plane, excluding the C coordination of **L1**, and also show a broad signal ($\delta$ = 7.20–7.50 ppm) due to the NH proton. This shift can be explained by the cleavage of the H bond after coordination of **L1**. The $^{13}C\{^1H\}$ NMR spectra of **1**–**5** show a doublet at $\delta$ = 72 ppm ($^1J_{P,C}$ = 104 Hz) due to the ylidic C atom, and the $^{31}P\{^1H\}$ NMR spectra show the presence of a peak at $\delta$ = 19–20 ppm. All these data confirm the absence of an interaction between the $C_\alpha$ atom and the Pd center,[9a] and therefore the S,O bonding mode of **L1**. This should, in principle, give two geometric isomers but, according to the NMR spectroscopic data, only one of them is obtained. A tentative structure, depicted in Scheme 1, can be proposed taking into account the hard/soft nature of the donor atoms bonded directly to the Pd atom and the antisymbiotic effect[19] shown by the Pd center. This reasoning has been successfully applied in the coordination chemistry of α-stabilized ylides.[1a] In agreement with this, it is sensible to suppose that *trans* to the aryl C atom (soft donor) the oxygen atom of **L1** (hard donor) would be more stabilized than the S atom (soft donor).[20]

The S,O-chelating bonding mode can be transformed into an S-monodentate mode by simple addition of L ligands. Thus, complex **4** reacts with $PPh_3$ (1:1 molar ratio) in $CDCl_3$ to give **6** (see Scheme 2). The NMR spectroscopic data of **6** show that the intramolecular H bond has been restored, since the signal attributed to the NH proton ap-

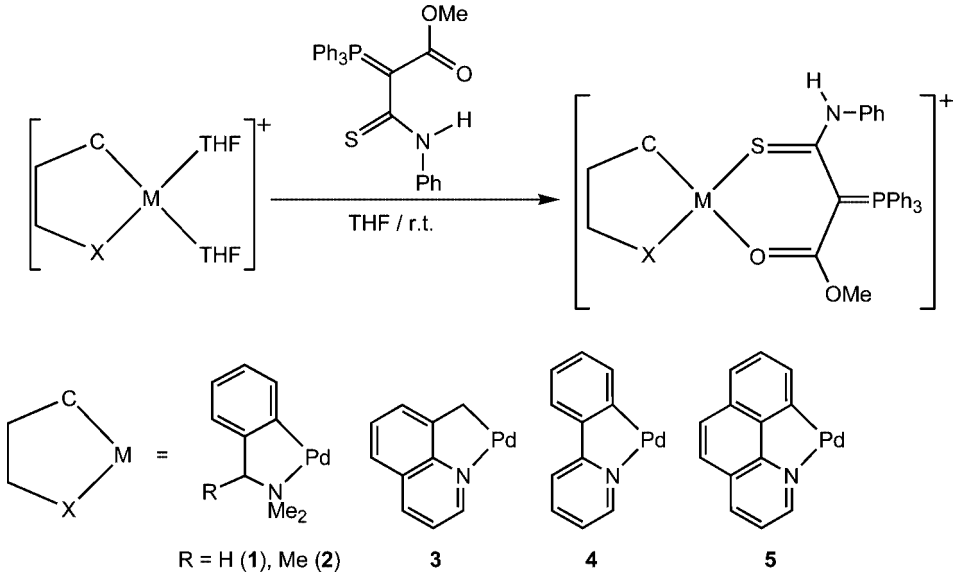


Scheme 1.

 © 2006 Wiley-VCH Verlag GmbH & Co. KGaA, Weinheim 

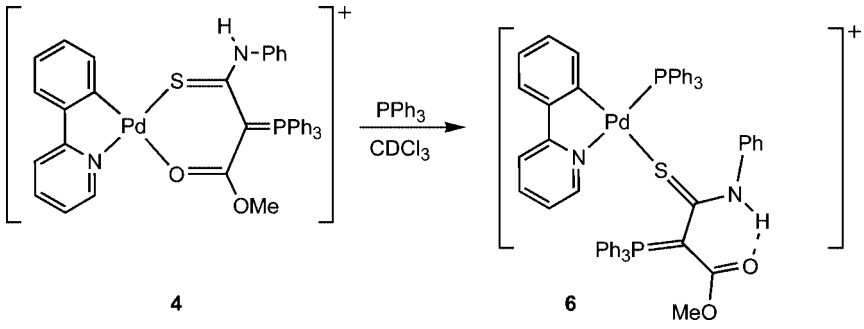


4 6

Scheme 2.

pears at $\delta$ = 11.61 ppm, a position close to that found in free **L1** ($\delta$ = 12.25 ppm). A plausible structure for **6** is shown in Scheme 2, taking into account the known reluctance of $PPh_3$ ligands to coordinate *trans* to metalated $C_{aryl}$ atoms.

### Synthesis and Reactivity of L2

The exchange of the $CO_2Me$ group for the CN group promotes notable differences of reactivity. The ylide $Ph_3P{=}C(CN)C(=S)N(H)Ph$ (**L2**) was prepared following reported methods[3a] by reaction of $Ph_3P{=}C(H)CN$[3d] with PhNCS. The IR spectrum of **L2** shows intense absorptions at 3262 (NH), 2159 (CN), and 1524 and 1108 $cm^{-1}$ (thioamide).[21] The shifts of the CN[22] and thioamide bands suggest an extensive delocalization of the charge density, and this fact agrees with the presence of the resonance forms shown in Figure 3. The $^1H$ NMR spectrum of **L2** shows a singlet at $\delta$ = 8.49 ppm due to the NH proton. This signal is shifted upfield when compared with **L1** meaning, probably, that a similar hydrogen bond is not present in solution. The ylidic $C_\alpha$ atom appears in the $^{13}C\{^1H\}$ NMR spectrum as a doublet at $\delta$ = 49.62 ppm ($^1J_{P,C}$ = 162 Hz), while the CS atom ($\delta$ = 189.68 ppm) appears at higher field than expected (usually about $\delta$ = 205 ppm).[12,21] The X-ray structure of **L2** has also been determined.

The molecular skeleton of **L2** (Figure 4 and Table 2) is very similar to that reported for **L1**, and the geometrical parameters of the P–$C_\alpha$–C(S)–N–C unit are nearly the same as those found in **L1**. For instance, the P–$C_\alpha$ [1.7401(17) Å], $C_\alpha$–$C_\beta$(S) [1.432(2) Å], and $C_\beta$–S [1.6831(17) Å] bond lengths are identical, within experimental error, to the corresponding values found in **L1** [1.751(2), 1.436(3), and 1.690(2) Å, respectively], and similar conclusions can be derived from a comparison of the bond angles. Thus, ligand **L2** also shows an extensive delocalization of the charge density, as can be deduced from the spectroscopic data. The C(1)–N(1) bond length [1.152(2) Å] is slightly longer than those reported for typical C≡N bonds (1.136 Å),[15] but is similar to those found in other cyano-stabilized ylides which contain additional stabilizing groups.[22] This elongation can be related to the presence of an intermolecular hydrogen bond between the N(2)–H(2) dipole of one molecule and the N(1)–C(1) group of another molecule. As a result of this, **L2** forms dimers in the crystal. This H bond is characterized by the following parameters: N(1)···N(2) 3.009(3), N(1)···H(2) 2.251(3) Å; N(1)···H(2)–N(2) 152.23(2)°. The intramolecular P(1)–S(1) distance is 3.090 Å, slightly longer than that found in **L1**, but is shorter

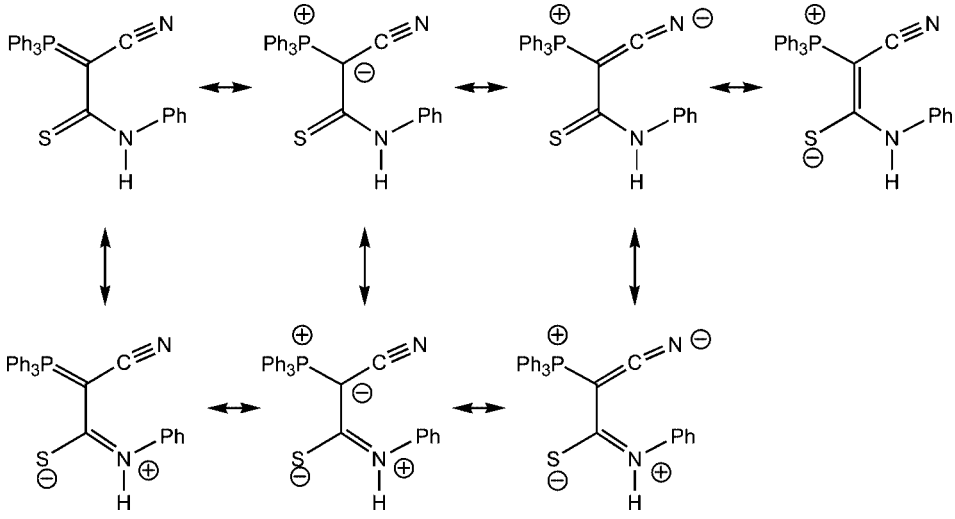


Figure 3. Resonance forms for ligand **L2**.

 © 2006 Wiley-VCH Verlag GmbH & Co. KGaA, Weinheim 

than the sum of the van der Waals radii (3.60 Å),[18] while the torsion angle P(1)–C(2)–C(3)–S(1) is –10.29°.

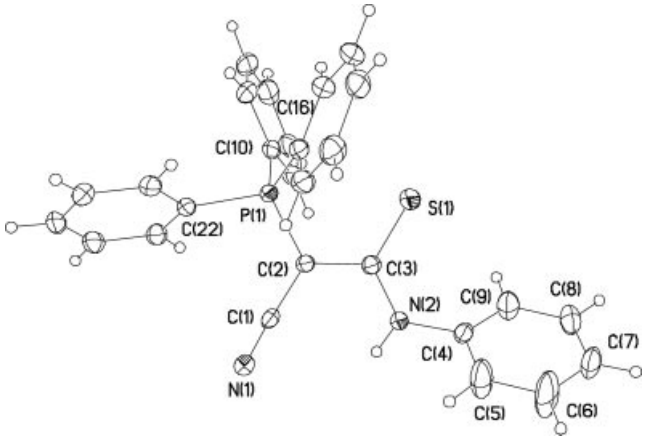


Figure 4. Thermal ellipsoid plot of **L2**. Non-hydrogen atoms are drawn at the 50% probability level.

Table 2. Selected bond lengths [Å] and angles [°] for **L2**.

| | | | |
|---|---|---|---|
| P(1)–C(2) | 1.7401(17) | P(1)–C(10) | 1.7945(18) |
| P(1)–C(16) | 1.8036(17) | P(1)–C(22) | 1.8047(17) |
| C(1)–N(1) | 1.152(2) | C(1)–C(2) | 1.409(2) |
| C(2)–C(3) | 1.432(2) | S(1)–C(3) | 1.6831(17) |
| C(3)–N(2) | 1.356(2) | N(2)–C(4) | 1.421(2) |
| N(1)–C(1)–C(2) | 176.82(18) | C(1)–C(2)–C(3) | 121.22(15) |
| C(1)–C(2)–P(1) | 119.83(12) | C(3)–C(2)–P(1) | 118.16(12) |
| N(2)–C(3)–C(2) | 117.30(15) | N(2)–C(3)–S(1) | 123.35(13) |
| C(2)–C(3)–S(1) | 119.34(13) | C(3)–N(2)–C(4) | 126.39(15) |
| C(3)–N(2)–H(2) | 117.3(14) | C(4)–N(2)–H(2) | 114.1(14) |

The reaction of $[M(C\hat{}X)(thf)_2]ClO_4$ with **L2** (1:1 molar ratio, thf, room temp.) gives complexes of stoichiometry $[M(C\hat{}X)(\mathbf{L2})](ClO_4)$ (**7**–**12**, Scheme 3). Their mass spectra (FAB+) show intense peaks due to a mononuclear stoichiometry, and those of **10** and **12** show additional peaks at 1968 and 1480 amu, respectively, with the correct isotopic distribution for an $[M_2(C\hat{}X)_2(\mathbf{L2})_2(ClO_4)]^+$ stoichiometry, and suggesting that **7**–**12** are dinuclear in nature. The IR spectra of **7**–**12** show the $\nu_{CN}$ stretch in the 2195–2206 $cm^{-1}$ region, and the $\nu_{CS}$ stretch in the 1027–1064 $cm^{-1}$ range. With these data, two structures can be envisaged: a mononuclear one with **L2** as a $C_\alpha$,S-chelate,[23] and a binuclear compound with the ylide acting as an N,S- or $C_\alpha$,S-bridging ligand. In this case, chelation through the N-cyano and S atoms is discarded because of the constraint imposed by the nitrile group. The measurement of $\Lambda_M$ in solution could be a convenient tool to determine the nuclearity of complexes **7**–**12**, through the determination of the slope of the Onsager equation.[24] However, **7**–**12** are extremely insoluble in the usual noncoordinating solvents and they only show a moderate solubility in strongly coordinating solvents such as dmso or acetonitrile. This means that in solution the solvent could be incorporated into the coordination sphere of the metal, with concomitant changes of nuclearity or bonding modes of the ylide. The IR spectrum of **11** in MeCN shows the absorption of the $\nu_{CS}$ stretch at 1102 $cm^{-1}$, virtually at the same position as in free **L2** (1108 $cm^{-1}$), while the $\nu_{CN}$ stretch appears at 2181 $cm^{-1}$ and two new bands at 2293 and 2248 $cm^{-1}$ are also seen. These facts suggest that MeCN is bonded to the Pd atom replacing the S atom, which is no longer bonded, and that the environment of the C(H)–CN group is the same in solution and in the solid state.

The NMR spectra of **7**–**12** provide additional valuable information. Key features of the NMR spectra are: (i) the behavior of the molecular plane as a symmetry plane; (ii) the low-field shift of $\delta$(P) in the $^{31}P\{^1H\}$ NMR spectrum with respect to **L2**; (iii) the similarity of $\delta(C_\alpha)$ and $^1J_{P,C}$ values in **7**–**12** and in free **L2**.[23] According to our previous experience,[23] all these observations exclude the C coordination of the ylide and strongly suggest the N-cyano bonding of **L2** to the Pd atom. In conclusion, we propose a dinuclear structure with an N,S-bridging ylide ligand for complexes **7**–**12**, as depicted in Scheme 3. Finally, and as explained for **L1**, the absence of symmetry in **L2** should also result in two geometric isomers after coordination. For similar reasons to those reported for complexes **1**–**5**, and also

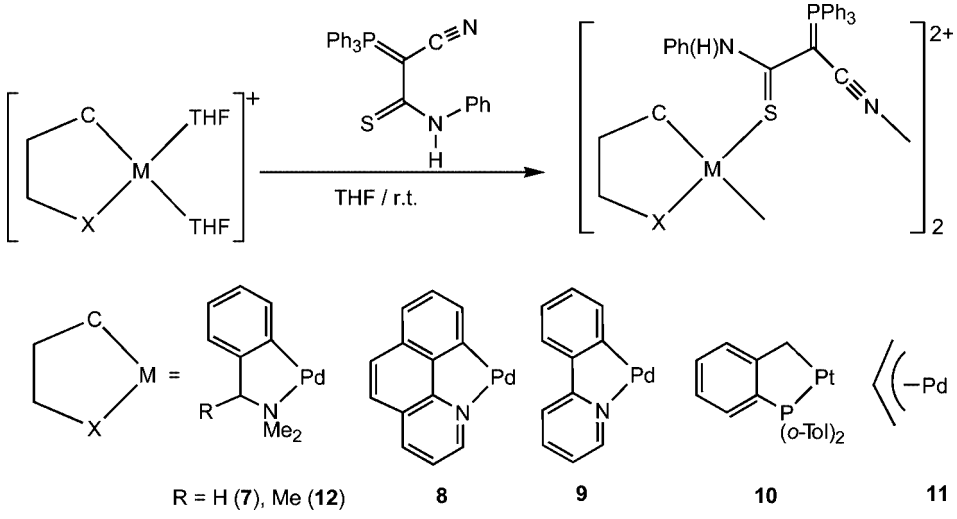


Scheme 3.

 © 2006 Wiley-VCH Verlag GmbH & Co. KGaA, Weinheim 

due to the previously described coordinating behavior of cyano ylides,[23] we propose the bonding of the N atom of the ylide *trans* to the orthometalated C atom.

### Synthesis and Reactivity of L3

The ylide $Ph_3P{=}C(CN)C(CO_2Me){=}C(H)CO_2Me$ (**L3**) was prepared following the procedure reported by Trippett et al.[3b] by reaction of $Ph_3P{=}C(H)CN$[3d] with DMAD (dimethylacetylenedicarboxylate) in refluxing MeOH, as a yellow solid stable to the air and to moisture. The yield for **L3** has been improved with respect to methods reported previously (65% of analytic and spectroscopically pure product vs. 43%). In addition, **L3** has been fully characterized spectroscopically because very few details were given in the original report.[3b] The IR spectrum of **L3** shows absorptions of all expected functional groups, at 2169 ($\nu_{CN}$), 1744, 1689 ($\nu_{COO}$), and 1531 ($\nu_{CC}$) $cm^{-1}$. The NMR parameters of **L3** follow a close relationship with those reported for **L1** and **L2**. For instance, the $^{13}C\{^1H\}$ NMR spectrum shows the signal due to $C_\alpha$ at $\delta$ = 32.27 ppm as a doublet ($^1J_{P,C}$ = 130 Hz) that is strongly downfield shifted with respect to the starting ylide. The $^1H$ NMR spectrum shows the expected signals, although the (*E*)- or (*Z*)-configuration of the C=C double bond is not defined. A 1D-NOESY experiment performed for **L3** shows a small, but detectable, NOE in the signals of the OMe groups when the signal due to the =CH proton ($\delta$ = 4.81 ppm) is irradiated, which clearly agrees with an (*E*) configuration.

The ligand **L3** is multidentate, as is evident from the resonance forms shown in Figure 5. Plausible donor atoms are the $C_\alpha$ atom, the cyano N atom, the carbonyl oxygens, and even the C=C double bond. The reactivity of **L3** towards bis-solvate derivatives of $Pd^{II}$ and $Pt^{II}$ has been studied. The reaction of $[M(C\hat{}X)(thf)_2]ClO_4$ with **L3** (1:1 molar ratio, thf, room temp.) gives solids of stoichiometry $[M(C\hat{}X)(\mathbf{L3})](ClO_4)$ (**13**–**18**), as derived from their elemental analyses (Scheme 4). The mass spectra (FAB+) of **13**–**18** show the presence of peaks due to the stoichiometry $[M(C\hat{}X)(\mathbf{L3})]^+$, with the correct isotopic distribution. We have not observed peaks due to species of higher nuclearity, as observed for **L2**. The use of the ESI-MS as an identification tool of the nuclearity of the species in solution is a well established fact.[25] In the case of complexes **13**–**18**, the analysis of their NCMe solutions only showed, once again, peaks due to the $[M(C\hat{}X)(\mathbf{L3})]^+$ stoichiometry. This fact suggests that these complexes are mononuclear in nature. Additional proof can be derived from molar conductivity measurements[24] and from NMR diffusion experiments.[26]

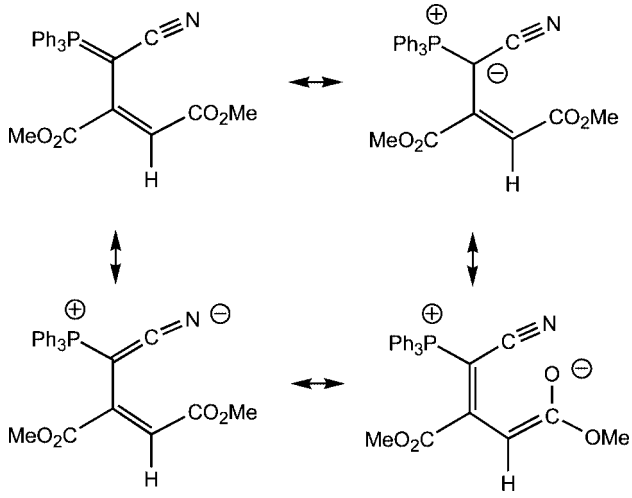


Figure 5. Resonance forms for ligand **L3**.

Since these complexes are adequately soluble in the usual organic solvents, the value of the molar conductivity can be determined. For complex **13**, the values determined for $\Lambda_M$ are 114.0 (acetone, $c = 2\times10^{-4}$ M) and 81.7 $\Omega^{-1}cm^2mol^{-1}$ ($MeNO_2$, $c = 1\times10^{-3}$ M). These values are typical of 1:1 electrolytes[3b] and mean that **13**–**18** could be mononuclear with **L3** acting as a chelating ligand. The IR spectra of **13**–**18** show two relevant features: (i) an increase of the $\nu_{CN}$ stretch; and (ii) a slight decrease of one of the $\nu_{CO}$ stretches,

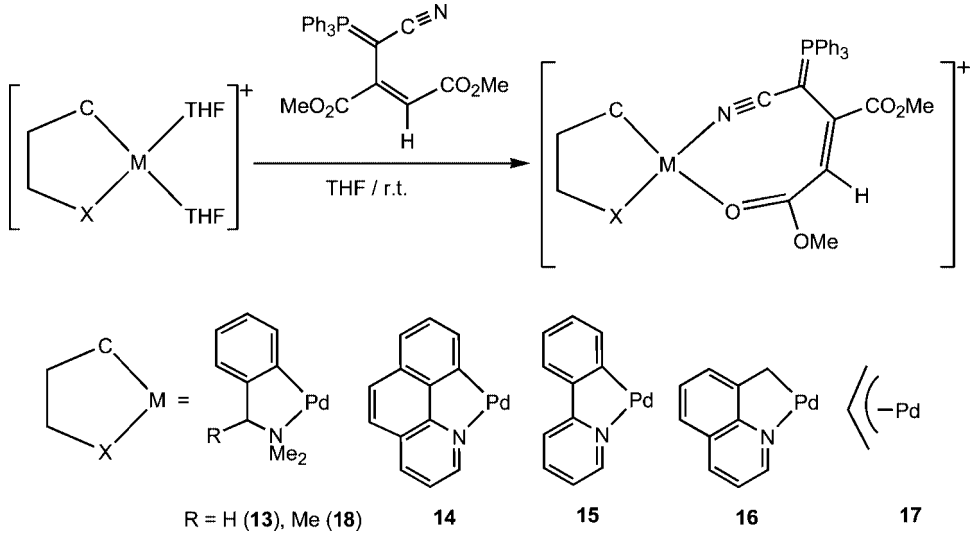


Scheme 4.

 © 2006 Wiley-VCH Verlag GmbH & Co. KGaA, Weinheim 

both with respect to **L3**. As we have seen, the increase of the $\nu_{CN}$ stretch could be due either to the C(ylide) or the N(cyano) bonding to the metal, while the decrease of the $\nu_{CO}$ indicates the coordination of the oxygen of one carbonyl group. Interestingly, the IR spectra of **13**–**18** in solution are virtually the same as in the solid state, thereby suggesting that the bonding mode of the ylide remains the same in solution. The NMR spectra of **13**–**18**, measured in nonbonding solvents ($CDCl_3$) and compared with **L3**, show similar features to those described for **L1** and **L2**. The small variations of $\delta$(P), $\delta(C_\alpha)$, and $^1J_{P,C}$ mean that the P=C moiety in coordinated **L3** is not involved in bonding with the Pd atom. According to the IR and NMR spectroscopic data, the ylide **L3** coordinates to the metal center in **13**–**18** through the N atom of the cyano group and through one oxygen atom of one carbonyl group. The mass spectra and the conductivity measurements suggest, in addition, that the complexes are mononuclear and that **L3** acts as a chelating ligand. The pulsed gradient spin-echo (PGSE) NMR diffusion methods (DOSY) have proved to be a valuable tool for the determination of relative molecular sizes in solution.[26] We have compared the diffusion coefficients of one representative of **13**–**18** with those obtained for other mononuclear complexes with the same ligands. We have shown that complexes **1**–**5** behave as mononuclear in solution. The determination of the value of *D* for **3** [8-mq as ancillary ligand, see Equation (1)] gives a value of $5.93\times10^{-10}$ $m^2s^{-1}$ (2 mM, $CDCl_3$, 300 K, $\delta$ = 1.7 ms, $\Delta$ = 100 ms). This value fits very well with that determined for complex **16** (8-mq as ancillary ligand, *D* = $5.92\times10^{-10}$ $m^2s^{-1}$) under the same experimental conditions (2 mM, $CDCl_3$, 300 K, $\delta$ = 1.8 ms, $\Delta$ = 100 ms). Thus, it is sensible to suppose that **13**–**18** are also mononuclear (Scheme 4), even taking into account the geometric constraint imposed by the cyano group. Two factors could contribute to the stabilization of the chelating mode of **L3**. The first one could be the formation of a highly flexible eight-membered ring, and the second one is the possible bent coordination of the CN group, as has been shown previously.[27]

The behavior of the cyclometalated complex [Pt{*o*-$CH_2C_6H_4P(o\text{-tol})_2$}$(S)_2$]$ClO_4$ (S = solvent) towards **L3** is slightly different. In this case, when the reaction is carried out in a 1:1 molar ratio, a low yield of **19** is obtained together with some decomposition to $Pt^0$. The yield of **19** improves up to 80% when the reaction is performed with a 1:2 (Pt/**L3**) molar ratio (see Scheme 5). Even when a substoichiometrict amount of **L3** is employed, complex **19** is the only species isolated. The characterization of **19** is straightforward. The $^1$H NMR spectrum shows the incorporation of two **L3** ligands per cyclometalated unit since only one peak is observed for the Me of the tolyl groups while the peaks due to the ligand appear duplicated. The $^{31}P\{^1H\}$ NMR spectrum shows the presence of three singlets with relative intensities 1:1:1 at $\delta$ = 19.97 (**L3**), 19.69 (**L3**), and 18.09 ppm.

The reluctance of $C_\alpha$ to bond to the metal center is a recurrent fact throughout the bonding modes of **L1**–**L3**. A plausible explanation for this lack of reactivity could be centered on the fact that the charge density of $C_\alpha$ is delocalized throughout the molecular skeleton, including the two stabilizing groups. This should lead to a decrease of the formal charge of $C_\alpha$, which becomes a poor donor and which cannot compete against the heteroatoms present in the same molecule (N, S, O, ...).

## Conclusions

The ylides **L1**, **L2**, and **L3**, all of which contain two stabilizing groups at the ylidic $C_\alpha$ atom, have been prepared and characterized. The X-ray crystal structures of **L1** and **L2** have been determined; they show extensive delocalization of the ylidic charge density. Ligands **L1**–**L3** coordinate to $Pd^{II}$ and $Pt^{II}$ solvates in a variety of forms. Ligand **L1** bonds as a chelate through the S atom and the resonance-stabilized C=O group; ligand **L2** coordinates as a bridging ligand through the S atom and the cyano N atom; and ligand **L3** can coordinate as a chelate, through the cyano N atom and one oxygen of a C=O group, or as a monodentate ligand through the cyano N atom. In spite of the presumed nucleophilic properties of $C_\alpha$, this atom does not coordinate to the metal center in any of the cases studied due to delocalization of its charge density.

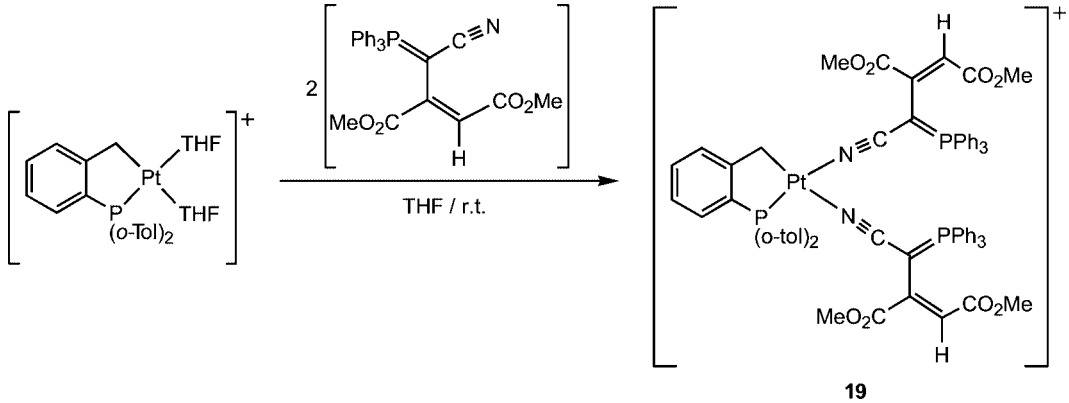


**19**

Scheme 5.

 © 2006 Wiley-VCH Verlag GmbH & Co. KGaA, Weinheim 

## Experimental Section

**CAUTION:** Perchlorate salts of metal complexes with organic ligands are potentially explosive. Only small amounts of these materials should be prepared and they should be handled with great caution. See *J. Chem. Educ.* **1973**, *50*, A335–A337.

**General Methods:** Solvents were dried and distilled under argon using standard procedures before use. Elemental analyses were carried out with a Perkin–Elmer 2400-B microanalyser. IR spectra (4000–400 $cm^{-1}$) were recorded with a Perkin–Elmer Spectrum One IR spectrophotometer from nujol mulls between polyethylene sheets. $^1H$ (300.13, 400.13 MHz), $^{13}C\{^1H\}$ (75.47, 100.61 MHz), and $^{31}P\{^1H\}$ (121.49, 161.97 MHz) NMR spectra were recorded in $CDCl_3$, $CD_2Cl_2$, or [D$_6$]DMSO solutions at 25 °C (other temperatures are specified) with Bruker ARX300 and Avance400 spectrometers ($\delta$ in ppm, J in Hz). The $^1H$ and $^{13}C\{^1H\}$ NMR spectra were referenced using the solvent signal as internal standard whereas $^{31}P\{^1H\}$ NMR spectra were externally referenced to $H_3PO_4$ (85%). The $^1H$ SELNO-1D and SELRO-1D NMR experiments were performed with optimized mixing times (D8, P15) depending on the irradiated signal. ESI/APCI mass spectra were recorded using an Esquire 3000 ion-trap mass spectrometer (Bruker Daltonik GmbH, Bremen, Germany) equipped with a standard ESI/APCI source. Samples were introduced by direct infusion with a syringe pump. Nitrogen served both as the nebulizer gas and the dry gas. Helium served as cooling gas for the ion trap and collision gas for $MS^n$ experiments. Other mass spectra (positive ion FAB) were recorded from $CH_2Cl_2$ solutions on a V. G. Autospec spectrometer. The starting materials $Ph_3P{=}C(H)CO_2Me$,[9b] $Ph_3P{=}C(H)CN$,[3d] [Pd(μ-Cl)($C_6H_4CH_2NMe_2$-$C^2$,$N$)]$_2$,[28] [Pd(μ-Cl){$SC_6H_4C(H)MeNMe_2$-$C^2$,$N$}]$_2$,[28] [Pd(μ-Cl)($NC_{13}H_8$-$C^{10}$,$N$)]$_2$,[29] [Pd(μ-Cl)($CH_2NC_9H_6$-$C^8$,$N$)]$_2$,[30] [Pd(μ-Cl)($C_6H_4$-2-$NC_5H_4$-$C^2$,$N$)],[31] [M(μ-Cl)(*o*-$CH_2C_6H_4$)P(*o*-tol)$_2$]$_2$ (M = Pd,[32] Pt[33]), and [Pd(μ-Br)($\eta^3$-$C_3H_5$)]$_2$,[34] were prepared following reported methods. Other reagents such as DMAD ($MeO_2C$-C≡C-$CO_2Me$) or PhN=C=S were purchased from commercial sources (Aldrich) and used without further purification.

**$Ph_3P{=}C(CO_2Me)C(=S)N(H)Ph$ (L1):** The ylide **L1** was prepared following the method described in the literature by Bestmann and Pfohl[3a] by reaction of $Ph_3P{=}C(H)CO_2Me$ with PhNCS in toluene (66% yield). The characterization of **L1** is reported here since no data were given in the original paper. $C_{28}H_{24}NO_2PS$ (469.54): calcd. C 71.62, H 5.15, N 2.98, S 6.83; found C 71.45, H 5.11, N 2.84, S 6.77. MS (FAB+): *m*/*z* (%) 469 (18) [M$^+$]. IR: $\tilde{\nu}$ = 1107 ($\nu_{CS}$), 1526 ($\nu_{CN}$), 1584 (Ph), 1629 ($\nu_{CO}$) $cm^{-1}$. $^1H$ NMR ($CDCl_3$): $\delta$ = 3.00 (s, 3 H, OMe), 7.03 (tt, $^3J_{H,H}$ = 7.2, $^4J_{H,H}$ = 0.9, 1 H, $H_p$, NPh), 7.24 (t, $^3J_{H,H}$ = 7.2, 2 H, $H_m$, NPh), 7.32–7.51 (m, 9 H, $PPh_3$), 7.69 (dd, 2 H, $H_o$, NPh), 7.73–7.82 (m, 6 H, $H_o$, $PPh_3$), 12.25 (s, 1 H, NH) ppm. $^{13}C\{^1H\}$ NMR ($CDCl_3$): $\delta$ = 49.67 (OMe), 71.47 (d, $^1J_{P,C}$ = 143.1, P=C), 123.71 ($C_{meta}$, NPh), 124.31 ($C_{para}$, NPh), 128.20 ($C_{ortho}$, NPh), 128.36 (d, $^3J_{P,C}$ = 12.7, $C_{meta}$, $PPh_3$), 128.50 (d, $^1J_{P,C}$ = 97, $C_{ipso}$, $PPh_3$), 131.12 (d, $^4J_{P,C}$ = 2.6, $C_{para}$, $PPh_3$), 132.94 (d, $^2J_{P,C}$ = 9.3, $C_{ortho}$, $PPh_3$), 140.38 ($C_{ipso}$, NPh), 168.93 (d, $^2J_{P,C}$ = 16.4, C=O), 189.01 (d, $^2J_{P,C}$ = 16.6, C=S) ppm. $^{31}P\{^1H\}$ NMR ($CDCl_3$): $\delta$ = 11.33 ppm.

**Synthesis of 1:** $AgClO_4$ (0.045 g, 0.217 mmol) was added to a suspension of [Pd(μ-Cl)($C_6H_4CH_2NMe_2$-$C^2$,$N$)]$_2$ (0.060 g, 0.108 mmol) in dry thf (20 mL) under an Ar atmosphere. The resulting suspension was stirred for 20 min at room temperature with exclusion of light, and then filtered through a Celite pad in order to remove the AgCl. The ylide **L1** (0.102 g, 0.217 mmol) was added to this freshly prepared solution of the solvate derivative. The resulting solution was stirred for 30 min and then the solvent evaporated to dryness. Treatment of the residue with $Et_2O$ (25 mL) and vigorous stirring gave **1** as a yellow solid, which was filtered, washed with additional $Et_2O$ (10 mL), and air dried. Yield: 0.060 g (34.1%). Complex **1** was recrystallized from $CH_2Cl_2$/$Et_2O$ to give yellow crystals of **1**·0.5$CH_2Cl_2$, which were used for analytic and spectroscopic purposes. The amount of $CH_2Cl_2$ was determined by integration of the signal in the $^1H$ NMR spectrum. $C_{37}H_{36}ClN_2O_6PPdS$·0.5$CH_2Cl_2$ (852.06): calcd. C 52.86, H 4.38, N 3.29, S 3.76; found C 52.93, H 4.31, N 3.12, S 3.83. MS (FAB+): *m*/*z* (%) 709 (15) [M – $ClO_4$]$^+$. IR: $\tilde{\nu}$ = 1066 ($\nu_{CS}$), 1575 ($\nu_{CN}$), 1596 ($\nu_{CO}$), 3260 ($\nu_{NH}$) $cm^{-1}$. $^1H$ NMR ($CDCl_3$): $\delta$ = 2.81 (s, 6 H, $NMe_2$), 3.08 (s, 3 H, OMe), 4.03 (s, 2 H, $CH_2N$), 6.58–6.61 (m, 2 H, $H_o$, NPh), 6.77–6.82 (m, 2 H, $C_6H_4$), 6.98–7.00 (m, 2 H, $C_6H_4$), 7.21 (m, 3 H, $H_m$, $H_p$, NPh), 7.27 (br. s, 1 H, NH), 7.67–7.96 (m, 15 H, $PPh_3$) ppm. $^{13}C\{^1H\}$ NMR ($CD_2Cl_2$): $\delta$ = 51.16 ($NMe_2$), 52.80 (OMe), 71.53 (d, $^1J_{P,C}$ = 103.6, P=C), 71.81 ($CH_2N$), 122.42 (d, $^1J_{P,C}$ = 91.3, $C_{ipso}$, $PPh_3$), 123.17, 125.33, 126.00, 133.49, 137.83, 142.57 ($C_6H_4$), 126.06 ($C_{meta}$), 128.20 ($C_{para}$), 129.40 ($C_{ortho}$), 148.65 ($C_{ipso}$) (NPh), 130.69 (d, $^2J_{P,C}$ = 12.5, $C_{ortho}$), 133.67 (d, $^3J_{P,C}$ = 9.9, $C_{meta}$), 134.71 ($C_{para}$) ($PPh_3$), 172.49 (d, $^2J_{P,C}$ = 10.2, C=O), 186.70 (d, $^2J_{P,C}$ = 4.1, CS) ppm. $^{31}P\{^1H\}$ NMR ($CDCl_3$): $\delta$ = 19.29 ppm.

**Synthesis of 2:** Complex **2** was obtained following the same synthetic procedure as reported for **1**. [Pd(μ-Cl){(*S*)-$C_6H_4CH(Me)NMe_2$-$C^2$,$N$}]$_2$ (0.060 g, 0.103 mmol) was treated with $AgClO_4$ (0.043 g, 0.207 mmol) and **L1** (0.097 g, 0.207 mmol) in thf to give **2** as an orange solid. Yield: 0.113 g (66.3%). Complex **2** was recrystallized from $CH_2Cl_2$/$Et_2O$ to give orange crystals of **2**·0.5$CH_2Cl_2$, which were used for analytic and spectroscopic purposes. The amount of $CH_2Cl_2$ was determined by integration of the signal in the $^1H$ NMR spectrum. $C_{38}H_{38}ClN_2O_6PPdS$·0.5$CH_2Cl_2$ (866.09): calcd. C 53.39, H 4.54, N 3.23, S 3.70; found C 53.28, H 4.34, N 3.39, S 3.88. MS (FAB+): *m*/*z* (%) 723 (30) [M – $ClO_4$]$^+$. IR: $\tilde{\nu}$ = 1080 ($\nu_{CS}$), 1575 ($\nu_{CN}$), 1600 ($\nu_{CO}$), 3220 ($\nu_{NH}$) $cm^{-1}$. $^1H$ NMR ($CDCl_3$): $\delta$ = 1.63 (d, $^3J_{H,H}$ = 6.3, 3 H, Me), 2.63 (s, 3 H, $NMe_2$), 2.87 (s, 3 H, $NMe_2$), 3.08 (s, 3 H, OMe), 4.03 (q, 1 H, CH), 6.59 (m, 2 H, $H_o$, NPh), 6.83 (m, 2 H, $C_6H_4$), 6.92–7.03 (m, 2 H, $C_6H_4$), 7.22 (m, 3 H, $H_m$, $H_p$, NPh), 7.25 (br. s, 1 H, NH), 7.65–7.96 (m, 15 H, $PPh_3$) ppm. $^{31}P\{^1H\}$ NMR ($CDCl_3$): $\delta$ = 19.25 ppm.

**Synthesis of 3:** Complex **3** was obtained following the same synthetic procedure as reported for **1**. [Pd(μ-Cl)($CH_2NC_9H_6$-$C^8$,$N$)]$_2$ (0.061 g, 0.107 mmol) was treated with $AgClO_4$ (0.044 g, 0.212 mmol) and **L1** (0.101 g, 0.215 mmol) in thf to give **3** as a yellow solid. Yield: 0.122 g (69.5%). $C_{38}H_{32}ClN_2O_6PPdS$ (817.57): calcd. C 55.83, H 3.94, N 3.42, S 3.92; found C 56.26, H 3.74, N 3.14, S 4.10. MS (FAB+): *m*/*z* (%) 717 (27) [M – $ClO_4$]$^+$. IR: $\tilde{\nu}$ = 1065 ($\nu_{CS}$), 1564 ($\nu_{CN}$), 1599 ($\nu_{CO}$), 3216 ($\nu_{NH}$) $cm^{-1}$. $^1H$ NMR ($CD_2Cl_2$): $\delta$ = 3.21 (s, 3 H, OMe), 3.36 (s, 2 H, $CH_2Pd$), 6.57 (br., 2 H, $H_o$, NPh), 7.21 (br. s, 3 H, NH, $NC_9H_6$), 7.51–7.60 [m, 4 H, $H_m$, $H_p$ (NPh), $NC_9H_6$], 7.66–7.80 [m, 10 H, $H_m$, $H_p$ ($PPh_3$) + $NC_9H_6$], 7.90–7.97 (m, 6 H, $H_o$, $PPh_3$), 8.41 (d, $^3J_{H,H}$ = 8.1, 1 H, $NC_9H_6$), 8.66 (br. s, 1 H, $NC_9H_6$) ppm. $^{13}C\{^1H\}$ NMR ($CD_2Cl_2$): $\delta$ = 21.60 ($PdCH_2$), 52.69 (OMe), 70.63 (d, $^1J_{P,C}$ = 106.1, P=C), 125.08 (d, $^1J_{P,C}$ = 93, $C_{ipso}$, $PPh_3$), 121.98, 124.56, 126.87, 128.25, 137.92, 138.88, 147.42, 149.08, 152.21 ($NC_9H_6$), 126.21 ($C_{meta}$), 128.93 ($C_{para}$), 129.42 ($C_{ortho}$), 148.99 ($C_{ipso}$) (NPh), 130.65 (d, $^2J_{P,C}$ = 11.1, $C_{ortho}$), 133.60 (d, $^3J_{P,C}$ = 9.5, $C_{meta}$), 134.59 ($C_{para}$) ($PPh_3$) ppm; the CO and CS signals were not observed. $^{31}P\{^1H\}$ NMR ($CD_2Cl_2$): $\delta$ = 19.69 ppm.

**Synthesis of 4:** Complex **4** was obtained following the same synthetic procedure as reported for **1**. [Pd(μ-Cl)($C_6H_4$-2-$NC_5H_4$-$C^2$,$N$)]$_2$ (0.062 g, 0.105 mmol) was treated with $AgClO_4$ (0.044 g, 0.212 mmol) and **L1** (0.101 g, 0.215 mmol) to give **4** as a yellow

 © 2006 Wiley-VCH Verlag GmbH & Co. KGaA, Weinheim 

solid. Yield: 0.088 g (50.3%). $C_{39}H_{32}ClN_2O_6PPdS$ (829.58): calcd. C 56.47, H 3.89, N 3.38, S 3.86; found C 56.46, H 3.76, N 3.33, S 4.21. MS (FAB+): *m/z* (%) 729 (30) $[M - ClO_4]^+$. IR: $\tilde{\nu}$ = 1080 ($\nu_{CS}$), 1578 ($\nu_{CN}$), 1600 ($\nu_{CO}$), 3259 ($\nu_{NH}$) $cm^{-1}$. $^1H$ NMR ($CD_2Cl_2$): $\delta$ = 3.21 (s, 3 H, OMe), 6.64 (dd, $^3J_{H,H}$ = 5.7, $^4J_{H,H}$ = 1.6, 2 H, $H_o$, NPh), 7.02 (td, $^3J_{H,H}$ = 7.5, $^4J_{H,H}$ = 1.2, 1 H, Phpy), 7.04 (s, 1 H, NH), 7.14 (td, $^3J_{H,H}$ = 6.6, $^4J_{H,H}$ = 1.8, 1 H, Phpy), 7.24–7.27 [m, 4 H, $H_m$+$H_p$ (NPh) + Phpy], 7.32 (td, $^3J_{H,H}$ = 6.6, $^4J_{H,H}$ = 0.9, 1 H, Phpy), 7.55 (d, $^3J_{H,H}$ = 7.5, 1 H, Phpy), 7.68–7.99 (m, 17 H, $PPh_3$ + Phpy), 8.45 (d, $^3J_{H,H}$ = 5.0, 1 H, Phpy) ppm. $^{13}C\{^1H\}$ NMR ($CD_2Cl_2$): $\delta$ = 53.09 (OMe), 71.67 (d, $^1J_{P,C}$ = 102.8, P=C), 119.59, 123.32, 124.74, 125.77, 130.06, 134.20, 137.82, 140.10, 146.47, 147.07, 164.27 (Phpy), 122.18 (d, $^1J_{P,C}$ = 91, $C_{ipso}$, $PPh_3$), 126.16 ($C_{meta}$), 128.44 ($C_{para}$), 129.50 ($C_{ortho}$), 149.73 ($C_{ipso}$) (NPh), 130.77 (d, $^2J_{P,C}$ = 12.4, $C_{ortho}$), 133.68 (d, $^3J_{P,C}$ = 9.7, $C_{meta}$), 134.78 ($C_{para}$) ($PPh_3$), 186.47 (d, $^2J_{P,C}$ = 4.4, C=S) ppm; the CO signal was not observed. $^{31}P\{^1H\}$ NMR ($CD_2Cl_2$): $\delta$ = 19.27 ppm.

**Reaction of 4 with $PPh_3$:** $PPh_3$ was added in small portions to a suspension of **4** in $CD_2Cl_2$ (0.6 mL) in an NMR tube. NMR spectra were measured each time, until complete transformation of **4**. At this point, complete dissolution had occurred. The amount of $PPh_3$ required matched a 1:1 molar ratio (**4**:$PPh_3$), and gave complex **6** as a single isomer in 100% spectroscopic yield. Selected NMR spectroscopic data of **6**: $^1H$ NMR ($CD_2Cl_2$): $\delta$ = 3.00 (s, 3 H, OMe), 6.31 (t, $^3J_{H,H}$ = 6.9, 1 H, Phpy), 6.46–6.59 (m, 6 H, NPh + Phpy), 6.91 (t, $^3J_{H,H}$ = 7.2, 1 H, Phpy), 7.24–7.74 (m, 33 H, $PPh_3$ + Phpy), 7.89 (br. s, 1 H, Phpy), 7.96 (td, $^3J_{H,H}$ = 7.5, $^4J_{H,H}$ = 1.5, 1 H, Phpy), 11.61 (s, 1 H, NH) ppm. $^{31}P\{^1H\}$ NMR ($CD_2Cl_2$): $\delta$ = 17.65 (P=C), 38.09 ppm (Pd–$PPh_3$).

**Synthesis of 5:** Complex **5** was obtained following the same synthetic procedure as reported for **1**. $[Pd(\mu\text{-}Cl)(bhq\text{-}C,N)]_2$ (bhq = $NC_{13}H_8$; 0.066 g, 0.102 mmol) was treated with $AgClO_4$ (0.042 g, 0.205 mmol) and **L1** (0.096 g, 0.205 mmol) to give **5** as a yellow solid. Yield: 0.115 g (65.7%). Complex **5** was recrystallized from $CH_2Cl_2/Et_2O$ to give crystals of **5**·$0.5CH_2Cl_2$ (determined by NMR), which were used for analytic and spectroscopic purposes. $C_{41}H_{32}ClN_2O_6PPdS{\cdot}0.5CH_2Cl_2$ (896.07): calcd. C 55.62, H 3.71, N 3.13, S 3.58; found C 55.36, H 3.88, N 2.87, S 3.74. MS (FAB+): *m/z* (%) 753 (10) $[M - ClO_4]^+$. IR: $\tilde{\nu}$ = 1060 ($\nu_{CS}$), 1586 (br., $\nu_{CN}$ + $\nu_{CO}$), 3225 ($\nu_{NH}$) $cm^{-1}$. $^1H$ NMR ($CD_2Cl_2$): $\delta$ = 3.28 (s, 3 H, OMe), 6.68 (dd, $^3J_{H,H}$ = 5.7, $^4J_{H,H}$ = 1.8, 2 H, $H_o$, NPh), 7.19 (d, $^3J_{H,H}$ = 7.2, 1 H, $NC_{13}H_8$), 7.28 (m, 3 H, $H_m$+$H_p$, NPh), 7.34 (t, $^3J_{H,H}$ = 7.5, 1 H, $NC_{13}H_8$), 7.38 (s, 1 H, NH), 7.63 (m, 2 H, $NC_{13}H_8$), 7.67–7.73 [m, 7 H, $H_m$ ($PPh_3$) + $NC_{13}H_8$], 7.76–7.82 [m, 4 H, $H_p$ ($PPh_3$) + $NC_{13}H_8$], 7.90–7.98 (m, 6 H, $H_o$, $PPh_3$), 8.42 (dd, $^3J_{H,H}$ = 8.1, $^4J_{H,H}$ = 1.2, 1 H, $H_4$, $NC_{13}H_8$), 8.66 (dd, $^3J_{H,H}$ = 5.1, 1 H, $H_2$, $NC_{13}H_8$) ppm. $^{13}C\{^1H\}$ NMR ($CD_2Cl_2$): $\delta$ = 53.12 (OMe), 72.07 (d, $^1J_{P,C}$ = 103.0, P=C), 122.31 (d, $^1J_{P,C}$ = 91.2, $C_{ipso}$, $PPh_3$), 122.40, 122.46, 124.01, 124.06, 127.49, 128.96, 131.22, 134.44, 137.89, 138.31, 141.93, 146.27, 153.71 ($NC_{13}H_8$), 126.09 ($C_{meta}$), 128.30 ($C_{para}$), 129.45 ($C_{ortho}$), 147.33 ($C_{ipso}$) (NPh), 130.71 (d, $^2J_{P,C}$ = 12.5, $C_{ortho}$), 133.74 (d, $^3J_{P,C}$ = 9.4, $C_{meta}$), 134.69 ($C_{para}$) ($PPh_3$), 172.82 (d, $^2J_{P,C}$ = 10.0, C=O), 186.38 (d, $^2J_{P,C}$ = 4.7, C=S) ppm. $^{31}P\{^1H\}$ NMR ($CD_2Cl_2$): $\delta$ = 19.62 ppm.

**$Ph_3P$=C(CN)C(S)N(H)Ph (L2):** PhN=C=S (0.543 mL, 0.614 g, 4.55 mmol) was added to a suspension of $Ph_3P$=C(H)CN (1.370 g, 4.55 mmol) in freshly distilled toluene (50 mL). The resulting mixture was refluxed for 1 h and then stirred for 72 h at 25 °C to give a yellow suspension. This suspension was evaporated to dryness and the residue treated with $Et_2O$ (50 mL) to give **L2** as a white solid. Yield: 1.122 g (56.5%). $C_{27}H_{21}N_2PS$ (436.52): calcd. C 74.29, H 4.85, N 6.41, S 7.34; found C 74.78, H 4.84, N 7.11, S 7.63. MS (FAB+): *m/z* (%) 437 (100) $[M + H]^+$. IR: $\tilde{\nu}$ = 1108 ($\nu_{CS}$), 1524 ($\nu_{C=N}$), 2159 ($\nu_{CN}$), 3262 ($\nu_{NH}$) $cm^{-1}$. $^1H$ NMR ($CDCl_3$): $\delta$ = 7.09 (t, 1 H, $H_{para}$, Ph), 7.28 (t, $^3J_{HmHp}$ = $^3J_{HmHo}$ = 7.5, 2 H, $H_{meta}$, Ph), 7.41–7.52 [m, 8 H, $H_{meta}$($PPh_3$) + $H_{ortho}$(Ph)], 7.56–7.60 (m, 3 H, $H_{para}$, $PPh_3$), 7.71–7.80 (m, 6 H, $H_{ortho}$, $PPh_3$), 8.49 (br. s, 1 H, NH) ppm. $^{13}C\{^1H\}$ NMR ($CD_2Cl_2$): $\delta$ = 49.62 (d, $^1J_{P,C}$ = 162, P=C), 120.99 (d, $^1J_{P,C}$ = 20.7, $C_{ipso}$, $PPh_3$), 124.02 ($C_{meta}$, Ph), 125.16 ($C_{para}$, Ph), 125.29 (CN), 128.47 ($C_{ortho}$, Ph), 128.96 (d, $^3J_{P,C}$ = 13, $C_{meta}$, $PPh_3$), 132.65 (d, $^4J_{P,C}$ = 2.8, $C_{para}$, $PPh_3$), 133.75 (d, $^2J_{P,C}$ = 9.8, $C_{ortho}$, $PPh_3$), 139.47 (d, $^4J_{P,C}$ = 1.5, $C_{ipso}$, Ph), 189.68 (d, $^2J_{P,C}$ = 15.4, C=S) ppm. $^{31}P\{^1H\}$ NMR ($CDCl_3$): $\delta$ = 14.80 (s, C=$PPh_3$) ppm.

**Synthesis of 7:** $AgClO_4$ (0.053 g, 0.257 mmol) was added to a suspension of $[Pd(\mu\text{-}Cl)(C_6H_4CH_2NMe_2\text{-}C^2,N)]_2$ (0.071 g, 0.128 mmol) in 20 mL of freshly distilled thf under argon. The resulting mixture was stirred at room temperature with exclusion of light for 30 min, then filtered through a Celite pad. This freshly prepared solution was treated with a stoichiometric amount of **L2** (0.112 g, 0.257 mmol) giving, after a few seconds, a deep yellow precipitate of **7**. This suspension was stirred at room temperature for an additional 20 min, then the yellow solid was filtered, washed with thf (5 mL) and $Et_2O$ (20 mL), dried by suction, and subsequently identified as **7**. Yield: 0.141 g (70.5%). $C_{36}H_{33}ClN_3O_4PPdS$ (776.57): calcd. C 55.68, H 4.28, N 5.41, S 4.13; found C 55.81, H 4.50, N 5.11, S 4.03. MS (FAB+): *m/z* (%) 676 (100) $[M/2 - ClO_4]^+$. IR: $\tilde{\nu}$ = 1060 ($\nu_{CS}$), 1558 ($\nu_{C=N}$), 2196 ($\nu_{CN}$), 3203 ($\nu_{NH}$) $cm^{-1}$. $^1H$ NMR ([$D_6$]DMSO): $\delta$ = 2.24 (s, 6 H, $NMe_2$), 3.53 (s, 2 H, $CH_2N$), 6.26 (d, $^3J_{H,H}$ = 7.5, 1 H, $C_6H_4$), 6.64 (m, 1 H, $C_6H_4$), 6.76 (d, $^3J_{H,H}$ = 6.6, 1 H, $C_6H_4$), 6.84 (t, $^3J_{H,H}$ = 6.9, 1 H, $C_6H_4$), 7.13–7.19 (m, 3 H, $H_o$+$H_p$, Ph), 7.28 (t, $^3J_{H,H}$ = 7.2, 2 H, $H_m$, Ph), 7.73–7.93 (m, 15 H, $PPh_3$), 10.33 (s, 1 H, NH) ppm. $^{31}P\{^1H\}$ NMR ([$D_6$]DMSO): $\delta$ = 20.22 (s, C=$PPh_3$) ppm.

**Synthesis of 8:** Complex **8** was prepared following a synthetic procedure similar to that reported for **7**. Thus, $[Pd(\mu\text{-}Cl)(bhq\text{-}C,N)]_2$ (bhq = $C_{13}H_8N$, 0.078 g, 0.122 mmol) was treated with $AgClO_4$ (0.050 g, 0.244 mmol) and **L2** (0.110 g, 0.244 mmol), in thf (20 mL), to give **8** as a yellow solid. Yield: 0.110 g (55%). $C_{40}H_{29}ClN_3O_4PPdS$ (820.58): calcd. C 58.55, H 3.56, N 5.12, S 3.91; found C 58.85, H 3.41, N 4.76, S 3.82. MS (FAB+): *m/z* (%) 720 (27) $[M/2 - ClO_4]^+$. IR: $\tilde{\nu}$ = 1056 ($\nu_{CS}$), 1568 ($\nu_{C=N}$), 2195 ($\nu_{CN}$), 3188 ($\nu_{NH}$) $cm^{-1}$. $^1H$ NMR ([$D_6$]DMSO): $\delta$ = 6.66 (d, $^3J_{H,H}$ = 9, 1 H, bhq), 6.79 (t, $^3J_{H,H}$ = 9, 1 H, bhq), 7.00–7.24 (m, 5 H, Ph), 7.57 (d, $^3J_{H,H}$ = 6, 1 H, bhq), 7.65–7.69 (m, 2 H, bhq), 7.76–8.01 (m, 16 H, $PPh_3$ + 1 H bhq), 8.54 (br. d, $^3J_{H,H}$ = 9, 2 H, bhq), 10.58 (br. s, 1 H, NH) ppm. $^{31}P\{^1H\}$ NMR ([$D_6$]DMSO), $\delta$ = 21.08 (s, C=$PPh_3$) ppm.

**Synthesis of 9:** Complex **9** was prepared following a synthetic procedure similar to that reported for **7**. Thus, $[Pd(\mu\text{-}Cl)(NC_5H_5\text{-}2\text{-}C_6H_4\text{-}C,N)]_2$ (0.080 g, 0.134 mmol) was treated with $AgClO_4$ (0.056 g, 0.269 mmol) and **L2** (0.117 g, 0.269 mmol), in thf (20 mL), to give **9** as a yellow solid. Yield: 0.140 g (70%). $C_{38}H_{29}ClN_3O_4PPdS$ (796.56): calcd. C 57.30, H 3.67, N 5.27, S 4.02; found C 57.09, H 3.20, N 5.08, S 3.65. MS (FAB+): *m/z* (%) 696 (100) $[M/2 - ClO_4]^+$. IR: $\tilde{\nu}$ = 1059 ($\nu_{CS}$), 1538 ($\nu_{C=N}$), 2197 ($\nu_{CN}$), 3196 ($\nu_{NH}$) $cm^{-1}$. $^1H$ NMR ([$D_6$]DMSO): $\delta$ = 6.48 (d, $^3J_{H,H}$ = 6, 1 H, Phpy), 6.84 (t, $^3J_{H,H}$ = 6, 1 H, Phpy), 6.88 (t, $^3J_{H,H}$ = 6, 1 H, Phpy), 7.00 (t, $^3J_{H,H}$ = 9, 1 H, Phpy), 7.15 (m, 4 H, $H_o$+$H_m$, Ph), 7.33 (t, $^3J_{H,H}$ = 6, 1 H, $H_p$, Ph), 7.50 (d, $^3J_{H,H}$ = 9, 1 H, Phpy), 8.08–7.56 (m, 17 H, $PPh_3$ + Phpy), 8.19 (s, 1 H, Phpy), 10.53 (s, 1 H, NH) ppm. $^{13}C\{^1H\}$ NMR ([$D_6$]DMSO): $\delta$ = 50.80 (d, $^1J_{P,C}$ = 137.7, P=C), 117.65 (d, $^2J_{P,C}$ = 14.7, CN), 119.03 (NPh, $C_{meta}$), 121.60 (d, $^1J_{P,C}$ = 93.9, $C_{ipso}$, $PPh_3$), 122.75, 124.14, 124.48, 125.65,

 © 2006 Wiley-VCH Verlag GmbH & Co. KGaA, Weinheim 

133.36, 136.46, 140.05, 145.39, 147.35, 149.56, 163.04 (Phpy), 125.37 (NPh, $C_{ortho}$), 128.37 ($C_{para}$, $PPh_3$), 129.23 (NPh, $C_{para}$), 129.69 (d, $^3J_{P,C}$ = 12.7, $C_{meta}$, $PPh_3$), 134.05 (d, $^2J_{P,C}$ = 10.0, $C_{ortho}$, $PPh_3$), 139.23 ($C_{ipso}$, NPh), 183.27 (d, $^2J_{P,C}$ = 14.5, C=S) ppm. $^{31}P\{^1H\}$ NMR ([D$_6$]DMSO): $\delta$ = 20.92 (C=$PPh_3$) ppm.

**Synthesis of 10:** Complex **10** was prepared following a synthetic procedure similar to that reported for **7**. Thus, [Pt(μ-Cl)[*o*-$CH_2C_6H_4P$(*o*-$MeC_6H_4)_2$]]$_2$ (0.103 g, 0.096 mmol) was treated with $AgClO_4$ (0.040 g, 0.193 mmol) and **L2** (0.084 g, 0.193 mmol), in thf (20 mL), to give **10** as a yellow solid. Yield: 0.0461 g (23%). $C_{48}H_{41}ClN_2O_4P_2PtS$ (1034.42): calcd. C 55.73, H 4.00, N 2.71, S 3.10; found C 55.47, H 3.71, N 2.94, S 2.61. MS (FAB+): *m*/*z* (%) 934 (37) [M/2 – $ClO_4$]$^+$. IR: $\tilde{\nu}$ = 1027 ($\nu_{CS}$), 1530 ($\nu_{C=N}$), 2199 ($\nu_{CN}$), 3180 ($\nu_{NH}$) cm$^{-1}$. $^1$H NMR ([D$_6$]DMSO): $\delta$ = 2.11 (s, 6 H, Me), 2.78 (s, 2 H, $PtCH_2$), 7.95–6.87 (m, 32 H, $PPh_3$ + $C_6H_4$), 10.90 (br. s, 1 H, NH) ppm. $^{31}P\{^1H\}$ NMR ([D$_6$]DMSO): $\delta$ = 20.25 (C=$PPh_3$), 32.09 ($^1J_{PtP}$ = 3843, C^P–Pt) ppm.

**Synthesis of 11:** Complex **11** was prepared following a synthetic procedure similar to that reported for **7**. Thus, [Pd(μ-Br)($\eta^3$-$C_3H_5$)]$_2$ (0.0664 g, 0.146 mmol) was treated with $AgClO_4$ (0.061 g, 0.292 mmol) and **L2** (0.127 g, 0.292 mmol), in thf (20 mL), to give **11** as a green-yellow solid. Yield: 0.159 g (79.4%). $C_{30}H_{26}ClN_2O_4PPdS$ (683.44): calcd. C 52.72, H 3.83, N 4.10, S 4.69; found C 51.95, H 4.15, N 3.72, S 4.53. MS (FAB+): *m*/*z* (%) 583 (47) [M/2 – $ClO_4$]$^+$. IR: $\tilde{\nu}$ = 1027 ($\nu_{CS}$), 1530 ($\nu_{C=N}$), 2181 ($\nu_{CN}$), 3240 ($\nu_{NH}$) cm$^{-1}$. $^1$H NMR ([D$_6$]DMSO): $\delta$ = 2.98 (br. s, 2 H, $CH_2$), 4.17 (br. s, 2 H, $CH_2$), 5.37 (m, 1 H, CH), 6.91 (m, 2 H, Ph), 7.12–7.18 (m, 3 H, Ph), 7.39–7.87 (m, 15 H, $PPh_3$), 10.70 (br. s, 1 H, NH) ppm. $^{31}P\{^1H\}$ NMR ([D$_6$]DMSO): $\delta$ = 20.13 (s, C=$PPh_3$) ppm.

**Synthesis of 12:** Complex **12** was prepared following a synthetic procedure similar to that reported for **7**. Thus, [Pd(μ-Cl)-{(*S*)-$C_6H_4CH(Me)NMe_2$-$C^2$,*N*}]$_2$ (0.0731 g, 0.126 mmol) was treated with $AgClO_4$ (0.052 g, 0.252 mmol) and **L2** (0.110 g, 0.252 mmol), in thf (20 mL), to give **12** as a yellow solid. Yield: 0.120 g (60%). $C_{37}H_{35}ClN_3O_4PPdS$ (790.59): calcd. C 56.21, H 4.46, N 5.31, S 4.05; found C 56.28, H 4.15, N 4.86, S 4.81. MS (FAB+): *m*/*z* (%) 690 (40) [M/2 – $ClO_4$]$^+$. IR: $\tilde{\nu}$ = 1064 ($\nu_{CS}$), 1542 ($\nu_{C=N}$), 2206 ($\nu_{CN}$), 3232 ($\nu_{NH}$) cm$^{-1}$. $^1$H NMR ([D$_6$]DMSO): $\delta$ = 1.18 (d, $^3J_{H,H}$ = 6, 3 H, Me), 2.09 (s, 3 H, $NMe_2$), 2.34 (s, 3 H, $NMe_2$), 3.72 (d, $^3J_{H,H}$ = 6, 1 H, CH), 6.30 (d, $^3J_{H,H}$ = 6.9, 1 H, $C_6H_4$), 6.66 (m, 2 H, $C_6H_4$), 6.85 (t, $^3J_{H,H}$ = 7.5, 1 H, $C_6H_4$), 7.13–7.36 (m, 5 H, Ph), 7.73–7.92 (m, 15 H, $PPh_3$), 10.23 (br. s, 1 H, NH) ppm. $^{13}C\{^1H\}$ NMR ([D$_6$]DMSO): $\delta$ = 15.13 (Me), 43.91 ($NMe_2$), 48.63 ($NMe_2$), 51.29 (d, $^1J_{P,C}$ = 134.7, P=C), 71.92 (CH), 118.05 (d, $^2J_{P,C}$ = 15.9, CN), 121.55 (d, $^1J_{P,C}$ = 24.5, $C_{ipso}$, $PPh_3$), 122.50 (s, $C_{para}$, NPh), 124.02, 125.46, 128.98, 135.06, 142.98, 152.54 ($C_6H_4$), 124.95 ($C_{meta}$, NPh), 128.48 ($C_{ortho}$, NPh), 129.68 (d, $^3J_{P,C}$ = 12.7, $C_{meta}$, $PPh_3$), 133.97 (d, $^2J_{P,C}$ = 10.2, $C_{ortho}$, $PPh_3$), 133.98 ($C_{para}$, $PPh_3$) 139.44 ($C_{ipso}$, NPh), 183.71 (d, $^2J_{P,C}$ = 13.7, C–S) ppm. $^{31}P\{^1H\}$ NMR ([D$_6$]DMSO): $\delta$ = 20.40 (s, C=$PPh_3$) ppm.

**$Ph_3P$=C(CN)-[(*E*)-C($CO_2Me$)=CH($CO_2Me$)] (L3):** A suspension of $Ph_3P$=C(H)CN (1.000 g, 3.32 mmol) and DMAD ($MeO_2C$–C≡C–$CO_2Me$) (0.41 mL, 0.472 g, 3.32 mmol) in MeOH (20 mL) was refluxed for 20 min under argon. Once cooled, the reaction mixture was further stirred at room temperature for 18 h to give a yellow suspension. The precipitated solid of **L3** was filtered, washed with MeOH (10 mL) and $Et_2O$ (20 mL), and dried by suction. Yield: 0.951 g (64.6%). IR: $\tilde{\nu}$ = 1531 ($\nu_{CC}$), 1689 ($\nu_{COO}$), 1744 ($\nu_{COO}$), 2169 ($\nu_{CN}$) cm$^{-1}$. $^1$H NMR ($CDCl_3$): $\delta$ = 3.46 (s, 3 H, OMe), 3.54 (br. s, 3 H, OMe), 4.81 (s, 1 H, =CH), 7.51–7.70 (m, 15 H, $PPh_3$) ppm. $^{13}C\{^1H\}$ NMR ($CDCl_3$): $\delta$ = 32.27 (d, $^1J_{P,C}$ = 129.9, P=C), 49.36 (OMe), 51.01 (OMe), 97.74 (d, $^3J_{P,C}$ = 6.6, =CH), 120.26 (d, $^1J_{P,C}$ = 91.8, $C_{ipso}$, $PPh_3$), 120.44 (d, $^2J_{P,C}$ = 15.4, CN), 128.04 (d, $^3J_{P,C}$ = 12.8, $C_{meta}$, $PPh_3$), 132.37 (d, $^4J_{P,C}$ = 2.8, $C_{para}$, $PPh_3$), 132.58 (d, $^2J_{P,C}$ = 10.3, $C_{ortho}$, $PPh_3$), 150.90 (d, $^2J_{P,C}$ = 8.8, =C), 165.15 (COO), 167.35 (COO) ppm. $^{31}P\{^1H\}$ NMR ($CDCl_3$): $\delta$ = 19.95 ppm.

**Synthesis of 13:** $AgClO_4$ (0.0935 g, 0.451 mmol) was added to a suspension of [Pd(μ-Cl)($C_6H_4CH_2NMe_2$-$C^2$,*N*)]$_2$ (0.124 g, 0.225 mmol) in thf (20 mL) under Ar. The resultant mixture was stirred at room temperature for 20 min with exclusion of light, then filtered through a Celite pad. The freshly prepared solution of the bis(solvate) was treated with **L3** (0.200 g, 0.451 mmol) to give a yellow solution, which was stirred for an additional 30 min. The yellow solution was then evaporated to dryness and the yellow residue was treated with $Et_2O$ (30 mL) and stirred continuously to give **13** as a yellow solid. Yield: 0.316 g (89.5%). $C_{35}H_{34}ClN_2O_8PPd$ (783.49): calcd. C 53.65, H 4.37, N 3.57; found C 53.50, H 4.59, N 3.24. MS (FAB+): *m*/*z* (%) 683 (100) [M – $ClO_4$]$^+$. IR: $\tilde{\nu}$ = 1557 ($\nu_{CC}$), 1698 ($\nu_{COO}$), 1732 ($\nu_{COO}$), 2192 ($\nu_{CN}$) cm$^{-1}$. $^1$H NMR ($CDCl_3$, 213 K): $\delta$ = 2.26 (s, 3 H, $NMe_2$), 2.70 (s, 3 H, $NMe_2$), 3.60 (br., 2 H, $CH_2N$), 3.63 (s, 3 H, OMe), 3.76 (br. s, 3 H, OMe), 4.81 (s, 1 H, =CH), 6.38 (d, $^3J_{H,H}$ = 7.2, 1 H, $C_6H_4$), 6.68 (t, $^3J_{H,H}$ = 7.8, 1 H, $C_6H_4$), 6.80 (d, $^3J_{H,H}$ = 7.2, 1 H, $C_6H_4$), 6.91 (t, $^3J_{H,H}$ = 7.2, 1 H, $C_6H_4$), 7.59–7.77 (m, 15 H, $PPh_3$) ppm. $^{13}C\{^1H\}$ NMR ($CDCl_3$): $\delta$ = 33.66 (d, $^1J_{P,C}$ = 127.8, P=C), 51.13 (OMe), 52.88 (OMe), 52.20 ($NMe_2$), 72.93 ($CH_2N$), 102.62 (d, $^3J_{P,C}$ = 5.1, =CH), 120.54 (d, $^1J_{P,C}$ = 92, $C_{ipso}$, $PPh_3$), 121.88, 125.19, 130.17, 134.62, 150.12 ($C_6H_4$, one of the quaternary C atoms was not observed), 125.79 (d, $^2J_{P,C}$ = 15.37, CN), 129.96 (d, $^3J_{P,C}$ = 12.7, $C_{meta}$, $PPh_3$), 133.96 (d, $^2J_{P,C}$ = 10.4, $C_{oho}$, $PPh_3$), 134.44 (s, $C_{para}$, $PPh_3$), 149.86 (d, $^2J_{P,C}$ = 7.4, =C), 165.90 (COO), 168.20 (d, $^3J_{P,C}$ = 11.1, COO) ppm. $^{31}P\{^1H\}$ NMR ($CDCl_3$): $\delta$ = 20.18 (C=$PPh_3$) ppm.

**Synthesis of 14:** Complex **14** was prepared following a synthetic procedure similar to that reported for **13**. Thus, [Pd(μ-Cl)(bhq-*C*,*N*)]$_2$ (bhq = $C_{13}H_8N$, 0.144 g, 0.225 mmol) was treated with $AgClO_4$ (0.0932 g, 0.45 mmol) and **L3** (0.200 g, 0.45 mmol), in thf (20 mL), to give **14** as a yellow solid. Yield: 0.167 g (45%). $C_{39}H_{30}ClN_2O_8PPd$ (827.50): calcd. C 56.61, H 3.65, N 3.38; found C 56.26, H 3.98, N 2.96. MS (ESI, positive ions): *m*/*z* = 726.9 [M – $ClO_4$]$^+$. IR: $\tilde{\nu}$ = 1557 ($\nu_{CC}$), 1698 ($\nu_{COO}$), 1733 ($\nu_{COO}$), 2212 ($\nu_{CN}$) cm$^{-1}$. $^1$H NMR ($CDCl_3$): $\delta$ = 3.51 (s, 3 H, OMe), 3.71 (br. s, 3 H, OMe), 4.85 (s, 1 H, =CH), 6.94 (d, $^3J_{H,H}$ = 6.3, 1 H, bhq), 7.25 (t, $^3J_{H,H}$ = 7.8, 1 H, bhq), 7.47 (m, 1 H, bhq), 7.53 (d, $^3J_{H,H}$ = 8.1, 1 H, bhq), 7.57–7.82 [m, 17 H, $PPh_3$ + 2 H(bhq)], 8.23 (d, $^3J_{H,H}$ = 7.8, 1 H, bhq), 8.74 (br. s, 1 H, bhq) ppm. $^{13}C\{^1H\}$ NMR ($CDCl_3$): $\delta$ = 34.84 (d, $^1J_{P,C}$ = 127.7, P=C), 51.20 (OMe), 53.22 (OMe), 102.81 (d, $^3J_{P,C}$ = 4.6, =CH), 120.37 (d, $^1J_{P,C}$ = 91.8, $C_{ipso}$, $PPh_3$), 121.93, 123.48, 126.69, 128.35, 128.63, 129.54, 131.85, 133.43, 137.69, 140.29, 143.19, 148.97, 153.55 (bhq), 126.49 (d, $^2J_{P,C}$ = 15.37, CN), 130.08 (d, $^3J_{P,C}$ = 13.0, $C_{meta}$, $PPh_3$), 134.05 (d, $^2J_{P,C}$ = 10.4, $C_{ortho}$, $PPh_3$), 134.47 (s, $C_{para}$, $PPh_3$), 149.86 (d, $^2J_{P,C}$ = 7.4, =C), 165.68 (COO), 168.68 (COO) ppm. $^{31}P\{^1H\}$ NMR ($CDCl_3$): $\delta$ = 20.28 (C=$PPh_3$) ppm.

**Synthesis of 15:** Complex **15** was prepared following a synthetic procedure similar to that reported for **13**. Thus, [Pd(μ-Cl)($NC_5H_5$-2-$C_6H_4$-*C*,*N*)]$_2$ (0.074 g, 0.124 mmol) was treated with $AgClO_4$ (0.052 g, 0.25 mmol) and **L3** (0.110 g, 0.25 mmol), in thf (20 mL), to give **15** as a pale-yellow solid. Yield: 0.190 g (95%). $C_{37}H_{30}ClN_2O_8PPd$ (803.48): calcd. C 55.31, H 3.76, N 3.49; found C 55.26, H 3.98, N 3.17. MS (ESI, positive ions): *m*/*z* 702.9 [M – $ClO_4$]$^+$. IR: $\tilde{\nu}$ = 1558 ($\nu_{CC}$), 1698 ($\nu_{COO}$), 1732 ($\nu_{COO}$), 2192 ($\nu_{CN}$)

 © 2006 Wiley-VCH Verlag GmbH & Co. KGaA, Weinheim 

cm$^{-1}$. $^1$H NMR ($CDCl_3$): $\delta$ = 3.49 (s, 3 H, OMe), 3.63 (s, 3 H, OMe), 4.84 (s, 1 H, =CH), 6.63 (d, $^3J_{H,H}$ = 7.8, 1 H, Phpy), 6.87 (t, $^3J_{H,H}$ = 7.2, 1 H, Phpy), 7.05 (t, $^3J_{H,H}$ = 7.2, 1 H, Phpy), 7.13 (t, $^3J_{H,H}$ = 6.6, 1 H, Phpy), 7.29 (d, $^3J_{H,H}$ = 7.5, 1 H, Phpy), 7.56 – 7.78 [m, 17 H, $PPh_3$ + 2 H (Phpy)], 7.85 (m, 1 H, Phpy) ppm. $^{13}C\{^1H\}$ NMR ($CDCl_3$): $\delta$ = 34.79 (d, $^1J_{P,C}$ = 126.8, P=C), 51.18 (OMe), 52.85 (OMe), 102.77 (d, $^3J_{P,C}$ = 4.9, =CH), 118.97, 123.10, 123.71, 125.68, 129.48, 133.63, 140.04, 149.93, 145.12, 149.77, 150.06 (Phpy), 120.33 (d, $^1J_{P,C}$ = 92, $C_{ipso}$, $PPh_3$), 126.25 (d, $^2J_{P,C}$ = 15.8, CN), 130.07 (d, $^3J_{P,C}$ = 13.0, $C_{meta}$, $PPh_3$), 133.92 (d, $^2J_{P,C}$ = 10.3, $C_{ortho}$, $PPh_3$), 134.72 (s, $C_{para}$, $PPh_3$), 149.72 (d, $^2J_{P,C}$ = 7.4, =C), 165.89 (d, $^2J_{P,C}$ = 5.1, COO), 168.38 (d, $^3J_{P,C}$ = 11.6, COO) ppm. $^{31}P\{^1H\}$ NMR ($CDCl_3$): $\delta$ = 20.24 (C=$PPh_3$) ppm.

**Synthesis of 16:** Complex **16** was prepared following a synthetic procedure similar to that reported for **13**. Thus, [Pd(μ-Cl)($NC_9H_6CH_2$-C,N)]$_2$ (0.0718 g, 0.126 mmol) was treated with $AgClO_4$ (0.0524 g, 0.253 mmol) and **L3** (0.112 g, 0.253 mmol), in thf (20 mL), to give **16** as a yellow solid. Yield: 0.189 g (94%). $C_{36}H_{30}ClN_2O_8PPd$ (791.47): calcd. C 54.63, H 3.82, N 3.53; found C 54.37, H 3.92, N 3.18. MS (ESI, positive ions): *m*/*z* = 690.9 [M – $ClO_4$]$^+$. IR: $\tilde{\nu}$ = 1557 ($\nu_{CC}$), 1698 ($\nu_{COO}$), 1731 ($\nu_{COO}$), 2200 ($\nu_{CN}$) cm$^{-1}$. $^1$H NMR ($CDCl_3$): $\delta$ = 3.46 (br. s, 2 H, $CH_2Pd$), 3.49 (s, 3 H, OMe), 3.69 (br. s, 3 H, OMe), 4.81 (s, 1 H, =CH), 7.40 (m, 2 H, 8-mq), 7.66 (m, 17 H, $PPh_3$ + 8-mq), 8.22 (br. s, 2 H, 8-mq) ppm. $^{13}C\{^1H\}$ NMR ($CDCl_3$): $\delta$ = 25.58 ($PdCH_2$), 34.50 (d, $^1J_{P,C}$ = 127.5, P=C), 51.16 (OMe), 52.97 (OMe), 102.41 (d, $^3J_{P,C}$ = 2.9, =CH), 120.41 (d, $^1J_{P,C}$ = 91.9, $C_{ipso}$, $PPh_3$), 121.87, 124.30, 126.60, 128.20, 128.47, 129.31, 138.50, 150.51, 150.27 (8-mq), 130.05 (d, $^3J_{P,C}$ = 12.9, $C_{meta}$, $PPh_3$), 133.97 (d, $^2J_{P,C}$ = 10.3, $C_{ortho}$, $PPh_3$), 134.89 ($C_{para}$, $PPh_3$), 145.99 (d, $^2J_{P,C}$ = 4.8, =C), 166.01 (COO), 168.60 (d, $^3J_{P,C}$ = 10.4, COO) ppm. $^{31}P\{^1H\}$ NMR ($CDCl_3$): $\delta$ = 20.12 (C=$PPh_3$) ppm.

**Synthesis of 17:** Complex **17** was prepared following a synthetic procedure similar to that reported for **13**. Thus, [Pd(μ-Br)($\eta^3$-$C_3H_5$)]$_2$ (0.066 g, 0.145 mmol) was treated with $AgClO_4$ (0.060 g, 0.290 mmol) and **L3** (0.120 g, 0.29 mmol), in thf (20 mL), to give **17** as an orange solid. Yield: 0.154 g (77%). $C_{29}H_{27}ClNO_8PPd$ (690.36): calcd. C 50.45, H 3.94, N 2.03; found C 50.23, H 3.91, N 1.98. MS (FAB+): *m*/*z* (%) 590 (47) [M – $ClO_4$]$^+$. IR: $\tilde{\nu}$ = 1557 ($\nu_{CC}$), 1695 ($\nu_{COO}$), 1732 ($\nu_{COO}$), 2192 ($\nu_{CN}$) cm$^{-1}$. $^1$H NMR ($CDCl_3$): $\delta$ = 2.22 (br., 2 H, $CH_2$, allyl), 2.73 (d, $^3J_{H,H}$ = 10.5, 2 H, $CH_2$, allyl), 3.48 (s, 3 H, OMe), 3.71 (br. s, 3 H, OMe), 4.76 (s, 1 H, =CH), 5.33 (q, 1 H, CH, allyl), 7.50 (m, 15 H, $PPh_3$) ppm. $^{13}C\{^1H\}$ NMR ($CDCl_3$): $\delta$ = 33.99 (d, $^1J_{P,C}$ = 127.2, P=C), 51.14 (OMe), 52.74 (OMe), 62.89 ($CH_2$ allyl), 102.33 (d, $^3J_{P,C}$ = 4.6, =CH), 115.67 (CH allyl), 120.40 (d, $^1J_{P,C}$ = 92, $C_{ipso}$, $PPh_3$), 127.63 (d, $^2J_{P,C}$ = 12.4, CN), 130.20 (d, $^3J_{P,C}$ = 12.9, $C_{meta}$, $PPh_3$), 133.90 (d, $^2J_{P,C}$ = 10.4, $C_{ortho}$, $PPh_3$), 134.35 (d, $^4J_{P,C}$ = 5.5, $C_{para}$, $PPh_3$), 150.00 (d, $^2J_{P,C}$ = 7.6, =C), 165.92 (COO), 168.21 (d, $^3J_{P,C}$ = 11.3, COO) ppm. $^{31}P\{^1H\}$ NMR ($CDCl_3$): $\delta$ = 20.27 (C=$PPh_3$) ppm.

**Synthesis of 18:** Complex **18** was prepared following a synthetic procedure similar to that reported for **13**. Thus, [Pd(μ-Cl){(*S*)-$C_6H_4CH(Me)NMe_2$-$C^2$,*N*}]$_2$ (0.0725 g, 0.125 mmol) was treated with $AgClO_4$ (0.052 g, 0.250 mmol) and **L3** (0.111 g, 0.25 mmol), in thf (20 mL), to give **18** as a yellow solid. Yield: 0.1964 g (98.2%). $C_{36}H_{36}ClN_2O_8PPd$ (797.52): calcd. C 54.22, H 4.55, N 3.51; found C 54.20, H 4.47, N 3.30. MS (ESI, positive ions): *m*/*z* = 696.9 [M – $ClO_4$]$^+$. IR: $\tilde{\nu}$ = 1558 ($\nu_{CC}$), 1698 ($\nu_{COO}$), 1732 ($\nu_{COO}$), 2199 ($\nu_{CN}$) cm$^{-1}$. $^1$H NMR ($CDCl_3$): $\delta$ = 1.45 (d, $^3J_{H,H}$ = 6.0, 3 H, CMe), 2.52 (s, 3 H, $NMe_2$), 2.70 (s, 3 H, $NMe_2$), 3.48 (s, 3 H, OMe), 3.67–3.74 (br. s, 4 H, OMe+CH), 4.81 (s, 1 H, =CH), 6.37 (d, $^3J_{H,H}$ = 7.8, 1 H, $C_6H_4$), 6.67–6.73 (m, 2 H, $C_6H_4$), 6.92 (t, $^3J_{H,H}$ = 7.8, 1 H, $C_6H_4$), 7.24–7.75 (m, 15 H, $PPh_3$) ppm. $^{13}C\{^1H\}$ NMR ($CDCl_3$): $\delta$ = 18.91 (Me), 34.45 (d, $^1J_{P,C}$ = 127.3, P=C), 46.15 ($NMe_2$), 51.16 (OMe), 51.49 ($NMe_2$), 53.16 (OMe), 74.85 (CHN), 102.70 (d, $^4J_{P,C}$ = 4.9, =CH), 119.85 (d, $^1J_{P,C}$ = 91.9, $C_{ipso}$, $PPh_3$), 122.15, 122.92, 125.10, 125.34, 152.21 ($C_6H_4$; $C_2$ was not observed), 125.95 (d, $^2J_{P,C}$ = 16.2, CN), 130.03 (d, $^3J_{P,C}$ = 12.9, $C_{meta}$, $PPh_3$), 133.99 (d, $^2J_{P,C}$ = 10.4, $C_{ortho}$, $PPh_3$), 134.42 (d, $^4J_{P,C}$ = 2.3, $C_{para}$, $PPh_3$), 149.78 (d, $^2J_{P,C}$ = 7.6, =C), 165.82 ($CO_2$), 168.04 (d, $^3J_{P,C}$ = 10.8, $CO_2$) ppm. $^{31}P\{^1H\}$ NMR ($CDCl_3$): $\delta$ = 20.17 (s, C=$PPh_3$) ppm.

**Synthesis of 19:** Complex **19** was prepared following a synthetic procedure similar to that reported for **13**. Thus, [Pt(μ-Cl){*o*-$CH_2C_6H_4P$(*o*-$MeC_6H_4)_2$}]$_2$ (0.103 g, 0.096 mmol) was treated with $AgClO_4$ (0.040 g, 0.192 mmol) and **L3** (0.170 g, 0.384 mmol), in thf (20 mL), to give **19** as a yellow solid. Yield: 0.161 g (80.2%). $C_{71}H_{64}ClN_2O_{12}P_3Pt$ (1460.76): calcd. C 58.38, H 4.42, N 1.92; found C 59.05, H 4.29, N 1.65. MS (FAB+): *m*/*z* (%) 941 (100) [M – ylide – $ClO_4$]$^+$. IR: $\tilde{\nu}$ = 1564 ($\nu_{CC}$), 1699 ($\nu_{COO}$), 1733 ($\nu_{COO}$), 2198 ($\nu_{CN}$) cm$^{-1}$. $^1$H NMR ($CDCl_3$): $\delta$ = 2.26 (s, 6 H, Me), 3.19 (s, 3 H, OMe), 3.48 (s, 2 H, $PtCH_2$), 3.50 (s, 6 H, 2 OMe), 3.69 (s, 3 H, OMe), 4.80 (s, 1 H, =CH), 4.85 (s, 1 H, =CH), 6.85–7.76 (m, 42 H, $PPh_3$ + $C_6H_4$) ppm. $^{13}C\{^1H\}$ NMR ($CDCl_3$): $\delta$ = 12.19 ($PtCH_2$), 23.08 (d, $^3J_{P,C}$ = 7.0, Me), 33.94 (d, $^1J_{P,C}$ = 127.7, P=C), 34.31 (d, $^1J_{P,C}$ = 128.3, P=C), 51.10 (OMe), 51.20 (OMe), 52.21 (OMe), 52.78 (OMe), 102.44 (d, $^4J_{P,C}$ = 6.5, =CH), 103.25 (d, $^4J_{P,C}$ = 5.2, =CH), 120.29 (d, $^1J_{P,C}$ = 92.1, $C_{ipso}$, $PPh_3$), 120.62 (d, $^1J_{P,C}$ = 92.1, $C_{ipso}$, $PPh_3$), 124.04 (d, $^2J_{P,C}$ = 15.9, CN), 125.07 (d, $^2J_{P,C}$ = 16.2, CN), 126.04 (d, $J_{P,C}$ = 10.8, $C_6H_4$), 129.77 (d, $^3J_{P,C}$ = 12.9, $C_{meta}$, $PPh_3$), 130.13 (d, $^3J_{P,C}$ = 12.9, $C_{meta}$, $PPh_3$), 131.30 (d, $J_{P,C}$ = 8.9, $C_6H_4$), 131.71 (d, $J_{P,C}$ = 11.6, $C_6H_4$), 133.33 (d, $J_{P,C}$ = 5.0, $C_6H_4$), 133.34 (d, $J_{P,C}$ = 25.5, $C_6H_4$), 133.88 (d, $^2J_{P,C}$ = 10.4, $C_{ortho}$, $PPh_3$), 134.40 (d, $^4J_{P,C}$ = 2.6, $C_{para}$, $PPh_3$), 134.74 (d, $^4J_{P,C}$ = 1.9, $C_{para}$, $PPh_3$), 141.59 (d, $J_{P,C}$ = 10.7, $C_6H_4$), 149.18 (d, $^2J_{P,C}$ = 30.9, =C), 149.29 (d, $^2J_{P,C}$ = 30.3, =C), 157.26 (d, $^1J_{P,C}$ = 27.0, $C_6H_4$), 165.83 (COO), 165.99 (COO), 167.68 (d, $^3J_{P,C}$ = 13.9, COO), 167.82 (d, $^3J_{P,C}$ = 15.9, COO) ppm. $^{31}P\{^1H\}$ NMR ($CDCl_3$): $\delta$ = 18.09 ($^1J_{Pt,P}$ = 4605, C^P–Pt), 19.69 (C=$PPh_3$), 19.97 (C=$PPh_3$) ppm.

**Crystallography. Data Collection:** X-ray quality crystals were grown by slow vapor diffusion of $Et_2O$ into a $CH_2Cl_2$ solution of the corresponding crude compound. A single crystal of dimensions 0.25×0.18×0.16 mm$^3$ (**L1**) or 0.30×0.24×0.06 mm$^3$ (**L2**) was mounted at the end of a quartz fiber in a random orientation and covered with epoxy. Data collection was performed on a Bruker Smart CCD diffractometer using graphite-monochromated Mo-$K_\alpha$ radiation ($\lambda$ = 0.71073 Å). A hemisphere of data was collected in each case based on three $\omega$-scan runs (starting $\omega$ = –30°) at values $\varphi$ = 0°, 90° and 180° with the detector at 2$\theta$ = 30°. For each of these runs, frames (606, 435, and 230, respectively) were collected at 0.3° intervals and 10 s per frame. The diffraction frames were integrated using the program SAINT[35] and the integrated intensities were corrected for absorption with SADABS.[36]

**Structure Solution and Refinement:** The structures were solved and developed by Patterson and Fourier methods.[37] All non-hydrogen atoms were refined with anisotropic displacement parameters. The hydrogen atoms were placed at idealized positions and treated as riding atoms. Each hydrogen atom was assigned an isotropic displacement parameter equal to 1.2-times the equivalent isotropic displacement parameter of its parent atom. The structures were refined to $F_o^2$, and all reflections were used in the least-squares calculations.[38]

**Crystallographic Data for L1:** $C_{28}H_{24}NO_2PS$, $M$ = 469.51, $T$ = 291(2) K, monoclinic $C2/c$, $a$ = 26.710(3), $b$ = 9.5585(1), $c$ =

 © 2006 Wiley-VCH Verlag GmbH & Co. KGaA, Weinheim 

20.620(2) Å, $\beta$ = 114.396(2)°, $V$ = 4794.4(9) Å$^3$, $Z$ = 8, $D_{calcd.}$ = 1.301 Mg m$^{-3}$, $\mu$ = 0.228 mm$^{-1}$, a total of 15869 reflections were collected, of which 5764 [$R_{int}$ = 0.0366] independent reflections were used in the refinement of 299 parameters and 0 restraints. The final $R$ factors were $R_1$ = 0.0516, $wR_2$ = 0.1129 for $I > 2\sigma(I)$ and $R_1$ = 0.0940, $wR_2$ = 0.1303 for all reflections, Goof = 1.022.

**Crystallographic Data for L2:** $C_{27}H_{21}N_2PS$, $M$ = 436.49, $T$ = 100(1) K, monoclinic $P2_1/c$, $a$ = 11.1040(2), $b$ = 12.2318(2), $c$ = 16.2397(2) Å, $\beta$ = 94.980(1)°, $V$ = 2197.38(6) Å$^3$, $Z$ = 4, $D_{calcd.}$ = 1.319 Mg m$^{-3}$, $\mu$ = 0.238 mm$^{-1}$, a total of 37050 reflections were collected, of which 5033 [$R_{int}$ = 0.0546] independent reflections were used in the refinement of 284 parameters and 0 restraints. The final $R$ factors were $R_1$ = 0.0433, $wR_2$ = 0.1048 for $I > 2\sigma(I)$ and $R_1$ = 0.0548, $wR_2$ = 0.1095 for all reflections, Goof = 1.061.

CCDC-612165 (for **L1**) and -612166 (for **L2**) contain the supplementary crystallographic data for this paper. These data can be obtained free of charge from The Cambridge Crystallographic Data Centre via www.ccdc.cam.ac.uk/data_request/cif.

## Acknowledgments

Funding by the Dirección General de Investigación Científica y Técnica (DGICYT) Spain (projects CTQ2005-01037 and CTQ2005-03141) is gratefully acknowledged. T.S. thanks the MECD (Spain) for a postdoctoral fellowship.

[1] a) R. Navarro, E. P. Urriolabeitia, *J. Chem. Soc., Dalton Trans.* **1999**, 4111 and references cited therein; b) A. W. Johnson, *Ylides and Imines of Phosphorus*, Wiley, Chichester, **1993**; c) O. I. Kolodiazhnyi, *Phosphorus Ylides, Chemistry and Applications in Organic Synthesis*, Wiley-VCH, Weinheim, **1999**.

[2] For some representative examples, see: a) S. T. D. Gough, S. Trippett, *J. Chem. Soc.* **1962**, 2333; S. T. D. Gough, S. Trippett, *J. Chem. Soc.* **1962**, 2337; b) P. A. Chopard, R. J. G. Searle, F. H. Devitt, *J. Org. Chem.* **1965**, *30*, 1015; c) H. H. Wasserman, D. S. Ennis, C. A. Blum, V. M. Rotello, *Tetrahedron Lett.* **1992**, *33*, 6003; d) H. H. Wasserman, A. K. Petersen, *J. Org. Chem.* **1997**, *62*, 8972; e) R. A. Aitken, H. Hérion, C. E. R. Horsburg, N. Karodia, S. Seth, *J. Chem. Soc., Perkin Trans. 1* **1996**, 485; f) R. A. Aitken, N. Karodia, P. Lightfoot, *J. Chem. Soc., Perkin Trans. 2* **2000**, 333; g) M. K. Wong, C. W. Yu, W. H. Yuen, D. Yang, *J. Org. Chem.* **2001**, *66*, 3606.

[3] a) H. Bestmann, S. Pfohl, *Angew. Chem. Int. Ed. Engl.* **1969**, *8*, 762; b) S. Trippett, *J. Chem. Soc.* **1962**, 4733; c) P. J. Butterfield, J. C. Tebby, T. J. King, *J. Chem. Soc., Perkin Trans. 1* **1978**, 1237; d) S. Trippett, D. M. Walker, *J. Chem. Soc.* **1959**, 3874; e) Y. Ohshiro, Y. Mori, T. Minami, T. Agawa, *J. Org. Chem.* **1970**, *35*, 2076; f) Y. Ohshiro, Y. Mori, M. Komatsu, T. Agawa, *J. Org. Chem.* **1971**, *36*, 2029; g) J. B. Hendrickson, C. Hall, R. Rees, J. F. Templeton, *J. Org. Chem.* **1965**, *30*, 3312.

[4] a) W. Lwowski, B. J. Walker, *J. Chem. Soc., Perkin Trans. 1* **1975**, 1309; b) E. M. Briggs, G. W. Brown, W. T. Dawson, J. Jiricny, *J. Chem. Soc., Chem. Commun.* **1975**, 641; c) T. C. W. Mak, J. Trotter, *Acta Crystallogr.* **1965**, *18*, 81; d) J. Barluenga, F. López, F. Palacios, *J. Chem. Soc., Chem. Commun.* **1985**, 1681; e) J. Barluenga, F. López, F. Palacios, *J. Chem. Soc., Chem. Commun.* **1986**, 1574; f) J. Barluenga, F. López, F. Palacios, F. Sánchez-Ferrando, *Tetrahedron Lett.* **1988**, *29*, 381; g) J. Barluenga, F. López, F. Palacios, *J. Chem. Soc., Perkin Trans. 1* **1989**, 2273; h) J. Barluenga, I. Merino, F. Palacios, *Tetrahedron Lett.* **1989**, *30*, 5493; i) J. Barluenga, I. Merino, F. Palacios, *J. Chem. Soc., Perkin Trans. 1* **1991**, 341.

[5] E. Ciganek, *J. Org. Chem.* **1970**, *35*, 1725.

[6] H. Grützmacher, H. Pritzkow, *Chem. Ber.* **1989**, *122*, 1411.

[7] a) P. Laavanya, U. Venkatasubramanian, K. Panchanatheswaran, J. A. Krause Bauer, *Chem. Commun.* **2001**, 1660; b) J. Vicente, M. T. Chicote, M. A. Beswick, M. C. Ramírez-de-Arellano, *Inorg. Chem.* **1996**, *35*, 6592; c) J. Vicente, M. T. Chicote, M. C. Lagunas, P. G. Jones, *Inorg. Chem.* **1995**, *34*, 5441; d) E. C. Spencer, B. Kalyanasundari, M. B. Mariyatra, J. A. Howard, K. Panchanatheswaran, *Inorg. Chim. Acta* **2006**, *359*, 35.

[8] a) M. Kalyanasundari, K. Panchanatheswaran, W. T. Robinson, H. Wen, *J. Organomet. Chem.* **1995**, *491*, 103; b) B. Kalyanasundari, K. Panchanatheswaran, V. Parthasarathi, W. T. Robinson, *Bull. Chem. Soc. Jpn.* **1999**, *72*, 33.

[9] a) L. R. Falvello, S. Fernández, R. Navarro, I. Pascual, E. P. Urriolabeitia, *J. Chem. Soc., Dalton Trans.* **1997**, 763; b) O. Isler, H. Gutmann, M. Montavon, R. Ruegg, G. Ryser, P. Zeller, *Helv. Chim. Acta* **1957**, *40*, 1242.

[10] E. Pretsch, P. Bühlmann, C. Affolter, A. Herrera, R. Martínez, *Determinación Estructural de Compuestos Orgánicos*, Springer-Verlag Ibérica, Barcelona, **2001**.

[11] V. N. Nesterov, V. E. Shklover, Y. T. Struchkov, Y. A. Sharanin, A. M. Shestopalov, A. S. Demerkov, *Acta Crystallogr., Sect. C* **1991**, *47*, 1927.

[12] a) H. J. Bestmann, A. Pohlschmidt, K. Kumar, *Tetrahedron Lett.* **1992**, *33*, 5955; b) L. Kniezo, P. Kristian, J. Imrich, *Tetrahedron* **1988**, *44*, 543.

[13] a) G. Bombieri, E. Forsellini, U. Chiacchio, P. Fiandaca, G. Purrello, E. Foresti, R. Graziani, *J. Chem. Soc., Perkin Trans. 2* **1976**, 1404; b) C. Puke, G. Erker, N. C. Aust, E.-U. Würthwein, R. Fröhlich, *J. Am. Chem. Soc.* **1998**, *120*, 4863; c) L. Van Meervelt, G. S. Schuerman, V. S. Brovarets, N. I. Mishchenko, E. A. Romanenko, B. S. Drach, *Tetrahedron* **1995**, *51*, 1471; d) J. Hasek, K. Huml, H. Schenk, K. Goubitz, R. de Jong, D. Heijdenrijk, *Acta Crystallogr., Sect. C* **1990**, *46*, 843.

[14] A. Lledós, J. J. Carbó, E. P. Urriolabeitia, *Inorg. Chem.* **2001**, *40*, 4913.

[15] F. H. Allen, O. Kennard, D. G. Watson, L. Brammer, A. G. Orpen, R. Taylor, *J. Chem. Soc., Perkin Trans. 2* **1987**, S1–S19.

[16] a) M. Geoffroy, G. Rao, Z. Tancic, G. Bernardinelli, *J. Am. Chem. Soc.* **1990**, *112*, 2826; b) M. Shao, X. Jin, Y. Tang, Q. Huang, Y. Huang, *Tetrahedron Lett.* **1982**, *23*, 5343; c) M. Kalyanasundari, K. Panchanatheswaran, V. Parthasarathi, W. T. Robinson, H. Wen, *Acta Crystallogr., Sect. C* **1994**, *50*, 1738; d) P. D. Boyle, *Acta Crystallogr., Sect. C* **1996**, *52*, 2859.

[17] L. R. Falvello, S. Fernández, R. Navarro, E. P. Urriolabeitia, *Inorg. Chem.* **1996**, *35*, 3064.

[18] A. Bondi, *J. Phys. Chem.* **1964**, *68*, 441.

[19] a) R. G. Pearson, *Inorg. Chem.* **1973**, *12*, 712; b) J. Vicente, A. Arcas, D. Bautista, P. G. Jones, *Organometallics* **1997**, *16*, 2127; c) C. Bartolomé, P. Espinet, L. Vicente, F. Villafañe, J. P. H. Charmant, A. G. Orpen, *Organometallics* **2002**, *21*, 3536; d) J. Vicente, J. A. Abad, E. Martínez-Viviente, P. G. Jones, *Organometallics* **2002**, *21*, 4454; e) J. Vicente, A. Arcas, D. Bautista, M. C. Ramírez de Arellano, *J. Organomet. Chem.* **2002**, *663*, 164; f) J. Vicente, J. A. Abad, A. D. Frankland, M. C. Ramírez de Arellano, *Chem. Eur. J.* **1999**, *5*, 3066.

[20] a) R. G. Pearson, *J. Chem. Educ.* **1968**, *45*, 581; b) G. Schwarzenbach, M. Shellenberg, *Helv. Chim. Acta* **1965**, *48*, 28; c) S. Ahrland, *Coord. Chem. Rev.* **1996**, *154*, 13; d) R. B. Martin, *Inorg. Chim. Acta* **2002**, *339*, 27.

[21] E. Pretsch, J. Seibl, W. Simon, J. Clerc, *Tablas para la determinación estructural por métodos espectroscópicos*, Springer-Verlag Ibérica, Barcelona, **1998**, pp. I220 and C203.

[22] a) L. Pandolfo, G. Facchin, R. Bertani, P. Ganis, G. Valle, *Angew. Chem. Int. Ed. Engl.* **1994**, *33*, 576; b) L. VanMeerrelt, R. N. Vydzhak, V. S. Brovarets, N. I. Mischenko, B. S. Drasch, *Tetrahedron* **1994**, *50*, 1889.

[23] L. R. Falvello, S. Fernández, R. Navarro, E. P. Urriolabeitia, *Inorg. Chem.* **1997**, *36*, 1136.

[24] a) G. Geary, *Coord. Chem. Rev.* **1971**, *7*, 81; b) R. D. Feltham, R. G. Hayter, *J. Chem. Soc.* **1964**, 4587.

 © 2006 Wiley-VCH Verlag GmbH & Co. KGaA, Weinheim 

[25] a) H. Schmitt, R. Lomoth, A. Magnuson, J. Park, J. Fryxelius, M. Kritikos, J. Mårtensson, L. Hammarström, L. Sun, B. Åkermark, *Chem. Eur. J.* **2002**, *8*, 3757; b) B. F. G. Johnson, S. Hermans, T. Khimyak, *Eur. J. Inorg. Chem.* **2003**, 1325; c) W. Henderson, B. K. Nicholson, *Inorg. Chim. Acta* **2004**, *357*, 2231; d) C. Decker, W. Henderson, B. K. Nicholson, *J. Organomet. Chem.* **2004**, *689*, 1691.
[26] a) P. S. Pregosin, P. G. Anil Kumar, I. Fernández, *Chem. Rev.* **2005**, *105*, 2977; b) P. S. Pregosin, E. Martínez-Viviente, P. G. Anil Kumar, *Dalton Trans.* **2003**, 4007.
[27] R. J. Parker, K. D. Lu, S. R. Batten, B. Moubaraki, K. S. Murray, L. Spiccia, J. D. Cashion, D. Rae, A. C. Willis, *J. Chem. Soc., Dalton Trans.* **2002**, 3723.
[28] A. C. Cope, E. C. Friedrich, *J. Am. Chem. Soc.* **1968**, *90*, 909.
[29] a) A. Kasara, *Bull. Chem. Soc. Jpn.* **1968**, *41*, 1272; b) B. N. Cockburn, D. V. Howe, T. Keating, B. F. G. Johnson, J. Lewis, *J. Chem. Soc., Dalton Trans.* **1973**, 404.
[30] a) A. J. Deeming, I. P. Rothwell, M. B. Hursthouse, L. New, *J. Chem. Soc., Dalton Trans.* **1978**, 1490; b) J. Forniés, R. Navarro, V. Sicilia, *Polyhedron* **1988**, *7*, 2659; c) G. E. Hawell, R. V. Lawrence, M. J. Smas, *J. Chem. Soc. C* **1970**, 912.
[31] M. A. Gutiérrez, G. R. Newkome, J. Selbin, *J. Organomet. Chem.* **1980**, *202*, 341.
[32] a) W. A. Herrmann, C. Brossman, K. Öfele, C. Reisinger, T. Priermeier, M. Beller, H. Fischer, *Angew. Chem. Int. Ed. Engl.* **1995**, *34*, 1844; b) L. R. Falvello, J. Forniés, A. Maín, R. Navarro, V. Sicilia, P. Villarroya, *Inorg. Chem.* **1997**, *36*, 6166.
[33] J. Forniés, A. Maín, R. Navarro, V. Sicilia, P. Villarroya, *Organometallics* **1996**, *15*, 1826.
[34] Y. Tatsuno, T. Yoshida, S. Otsuka, *Inorg. Synth.* **1990**, *28*, 342.
[35] SAINT Version 5.0: Bruker Analytical X-ray Systems, Madison, WI.
[36] G. M. Sheldrick, SADABS: Empirical absorption correction program, Göttingen University, **1996**.
[37] G. M. Sheldrick, SHELXS-86, *Acta Crystallogr., Sect. A* **1990**, *46*, 467.
[38] G. M. Sheldrick, SHELXL-97: FORTRAN program for the refinement of crystal structures from diffraction data, Göttingen University, **1997**. Molecular graphics were done using the commercial package SHELXTL-PLUS, Release 5.05/V, Siemens Analytical X-ray Instruments, Inc., Madison, Wisconsin, **1996**.

Received: June 26, 2006
Published Online: September 22, 2006

 © 2006 Wiley-VCH Verlag GmbH & Co. KGaA, Weinheim 

DOI: 10.1002/ejic.200600601

# Synthesis, Characterization, and Catalytic Applications of Palladacyclic Complexes Bearing C,N,S-Donor Ligands

**Ming-Tsz Chen,[a] Chi-An Huang,[a] and Chi-Tien Chen*[a]**

**Keywords:** Palladacyclic complexes / Pendant thioether / Suzuki reaction / Heck reaction / Palladium

The preparations of novel tridentate C,N,S-donor ligand precursors, PhN=C($CMe_2$)(NPh)C=N($CH_2$)$_2$SR [R = $CMe_3$ (**2**); R = Ph (**3**)] are described. Treatment of **2** and **3** with 1 equiv. of $Pd(OAc)_2$ affords the orthometallated palladium(II) complexes [PhN=C($CMe_2$)(N-$\eta^1$-Ph)C=N($CH_2$)$_2$SR]Pd(OAc) [R = $CMe_3$ (**4**); R = Ph (**5**)]. Reaction of **4** and **5** with an excess of LiCl in methanol affords the orthometallated palladium(II) complexes [PhN=C($CMe_2$)(N-$\eta^1$-Ph)C=N($CH_2$)$_2$SR]PdCl [R = $CMe_3$ (**6**); R = Ph (**7**)]. Crystal structures are reported for compounds **3** and **4**. The application of these novel palladacyclic complexes as catalyses for the Suzuki and Heck reactions with aryl halide substrates was examined.
(© Wiley-VCH Verlag GmbH & Co. KGaA, 69451 Weinheim, Germany, 2006)

## Introduction

Due to the powerful application of, and versatile methods for, the formation of carbon-carbon bonds, palladium-catalyzed coupling reactions have been an attractive area of research.[1–19] Among these studies, the search for appropriate ancillary ligands that can serve as catalyst precursors is of current interest. Palladacycles bearing a metallated carbon atom and dative group(s) are the most active catalyst precursors for the promotion of such reactions.[2–8,11–17,19] These complexes are usually formed as dinuclear species with bridged ligands, or as mononuclear species in the presence of ligands with neutral dative groups. In order to improve the stability and efficiency of catalytic palladium complexes, various families of palladium based catalyst precursors have been developed. Recently, some sulfur containing palladacycles that function as excellent catalyst precursors for coupling reactions have been reported. [20–30] Their success in catalyzing cross-coupling reactions encouraged us to study the catalytic performance exhibited by palladacycles with pendant thioether functionalities. Following our previous work on four-membered ring diimino palladacycles,[31] we report here the synthesis and characterization of novel mononuclear palladacycles incorporating unsymmetrical C,N,S-donor ligands. Their catalytic activities toward the Suzuki and Heck reactions were investigated.

[a] Department of Chemistry, National Chung Hsing University, Taichung 402, Taiwan, Republic of China
Fax: +886-4-22862547
E-mail: ctchen@dragon.nchu.edu.tw

## Results and Discussion

### Syntheses and Characterization of Ligand Precursors and Palladacycles

Pre-ligand compound **1** was prepared by the reaction of 2,2-dimethyl-*N*,*N*′-diphenylpropanediimidoyl dichloride with 3.0 equiv. of 2-chloroethylamine hydrochloride in the presence of 4.0 equiv. of $NEt_3$ using a similar procedure to that reported in the literature.[31] The new ligand precursors **2** and **3** were synthesized from **1** via a nucleophilic substitution reaction with the corresponding thiol [R = $C(CH_3)_3$ for **2**; R = Ph for **3**].[20] Compounds **1**, **2**, and **3** were characterized by NMR spectroscopy and elemental analysis, which indicated that they are four-membered ring diimine compounds with the different functionalities. A summary of the synthetic route and the proposed structures is shown in Scheme 1. The X-ray structure of **3** features a four-membered diimine ring bearing a pendant thioether functional group. The molecular structure is shown in Figure 1, and selected bond lengths and angles are listed in Table 1. The C(1)–N(1) [1.253(2) Å] and C(3)–N(3) [1.257(2) Å] bond lengths are consistent with these bonds possessing significant double bond character, and the bond angles around the imino C and N atoms are indicative of $sp^2$ hybridized centers.

Treatment of **2** and **3** with 1 equiv. of $Pd(OAc)_2$ at room temperature yields complexes **4** and **5**, respectively, as pale brown solids. Similar to the results reported previously,[31] an additional tertiary carbon was found in the phenyl ring region of the $^{13}C\{^1H\}$ NMR spectrum that indicates the presence of a metallated carbon atom, which was created during the reactions. Crystals of **4** suitable for structural determination were obtained from a $CH_2Cl_2$/hexane solu-

 © 2006 Wiley-VCH Verlag GmbH & Co. KGaA, Weinheim 

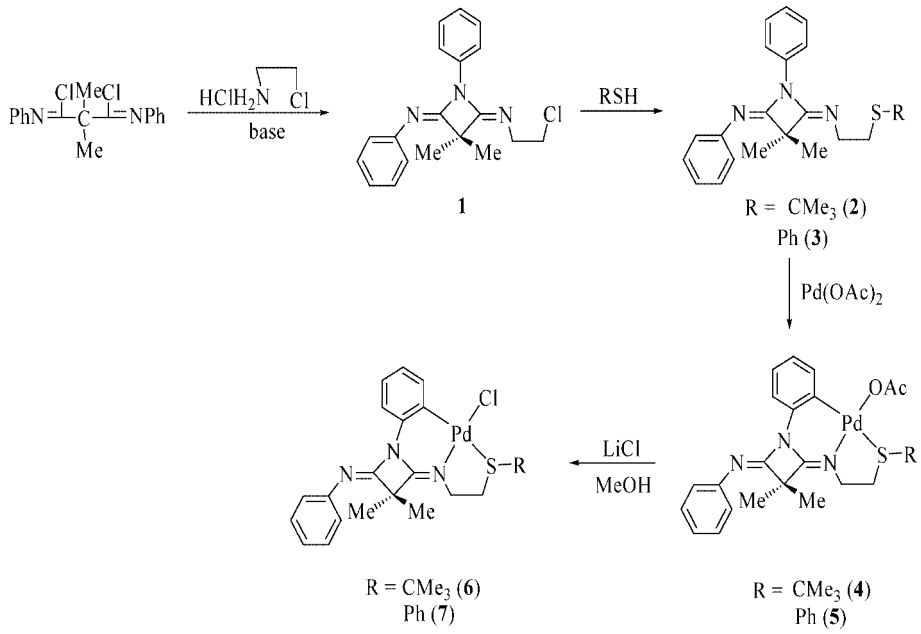


Scheme 1.

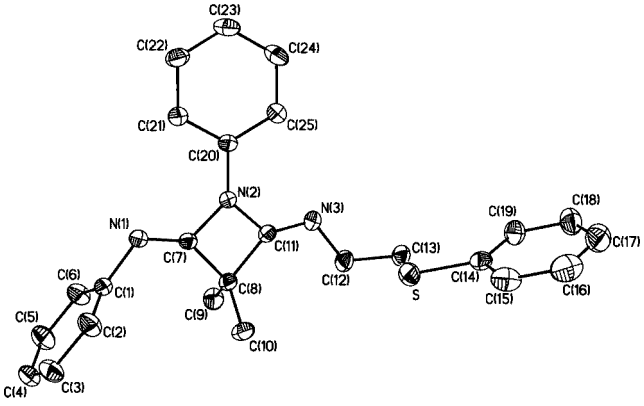

Figure 1. Molecular structure of compound **3**. Hydrogen atoms bound to carbon atoms have been omitted for clarity.

Table 1. Selected bond lengths [Å] and angles [°] for **3**.

| | | | |
|---|---|---|---|
| S–C(14) | 1.751(2) | S–C(13) | 1.789(2) |
| N(1)–C(7) | 1.252(2) | N(1)–C(1) | 1.427(2) |
| N(2)–C(7) | 1.403(2) | N(2)–C(11) | 1.411(2) |
| N(2)–C(20) | 1.413(2) | N(3)–C(11) | 1.251(2) |
| N(3)–C(12) | 1.467(3) | | |
| C(14)–S–C(13) | 104.20(10) | C(7)–N(1)–C(1) | 119.15(15) |
| C(7)–N(2)–C(11) | 93.61(13) | C(7)–N(2)–C(20) | 133.05(15) |
| C(11)–N(2)–C(20) | 133.33(16) | C(11)–N(3)–C(12) | 118.34(17) |
| N(1)–C(7)–N(2) | 128.08(16) | N(1)–C(7)–C(8) | 140.33(17) |
| N(2)–C(7)–C(8) | 91.58(14) | C(7)–C(8)–C(11) | 83.57(13) |
| N(3)–C(11)–N(2) | 127.21(17) | N(3)–C(11)–C(8) | 141.54(17) |
| N(2)–C(11)–C(8) | 91.22(14) | | |

tion. The molecular structure is shown in Figure 2, and selected bond lengths and angles are listed in Table 2. The bond angles [in the range of 84.62(8) to 93.47(12)°] around the palladium metal center indicate that the complex has a slightly distorted square planar geometry, in which the palladium metal center is coordinated to one imine nitrogen atom, one thioether sulfur atom, one carbon atom, and one OAc oxygen atom. The N–Pd–$C_{metallated}$ bite angle [93.47(12)°] involving the imino nitrogen and metallated carbon atoms is similar to those [93.20(104)°, 93.77(8)°, and 94.51(10)°] found in our previous work.[31] The N–Pd–S bite angle [84.62(8)°] involving the imino nitrogen atom and the pendant group is in the range [84.46(10)–85.1(1)°] found for C,N,S-donor complexes with two carbon spacer atoms

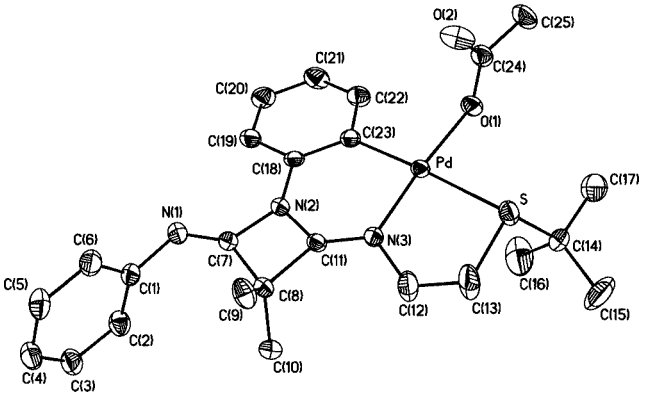

Figure 2. Molecular structure of complex **4**. Hydrogen atoms bound to carbon atoms have been omitted for clarity. Dichloromethane and water molecules are omitted for clarity.

Table 2. Selected bond lengths [Å] and angles [°] for **4**.

| | | | |
|---|---|---|---|
| Pd–N(3) | 2.011(3) | Pd–C(23) | 2.022(4) |
| Pd–O(1) | 2.036(2) | Pd–S | 2.4093(9) |
| N(3)–Pd–C(23) | 93.47(12) | N(3)–Pd–O(1) | 174.95(11) |
| C(23)–Pd–O(1) | 91.47(13) | N(3)–Pd–S | 84.62(8) |
| C(23)–Pd–S | 176.85(11) | O(1)–Pd–S | 90.40(8) |

 © 2006 Wiley-VCH Verlag GmbH & Co. KGaA, Weinheim 

between the nitrogen and sulfur atoms.[32–34] The Pd–S bond length [2.4093(9) Å] is in the range [2.240(1)–2.422(1) Å] found for palladium complexes containing thioether functionalities.[23,25,30,32–37] The Pd–$C_{metallated}$ bond length [2.022(4) Å] is in the range [1.964(3)–2.034(2) Å] found for palladacycles with metallated carbon.[23,31–34,38] The Pd–$N_{C=N}$ bond length [2.011(3) Å] is within the range [1.985(3)–2.098(2) Å] found for palladacycles.[31–34,38] The Pd–$O_{OAc}$ bond length [2.036(2) Å] is comparable to those [2.0027(9)–2.105(2) Å] found in the literature.[31,39–41] The reaction of **4** and **5** with an excess of lithium chloride, in methanol at room temperature, yielded complexes **6** and **7**, respectively, as yellow solids.[42] Compounds **6** and **7** were characterized by NMR spectroscopy and elemental analysis. Basically, **6** and **7** are quite similar to **4** and **5**, but with Cl coordinated to the metal centre instead of an OAc group.

## Catalytic Studies

Due to the success of some sulfur containing palladacycles in catalyzing cross-coupling reactions,[20–30] the palladacycles discussed above are expected to catalyze carbon-carbon coupling reactions. For the purpose of comparing the reactivity of complexes **4**–**7** with other palladacycles, the Suzuki reaction was chosen to demonstrate the catalytic activities of these sulfur containing complexes, as shown in Scheme 2. The potential catalyst precursor candidates **4**–**7** were investigated in the coupling of 4-bromoacetophenone with phenylboronic acid at 50 °C, over a period of 1 h on a 1 mol-% scale. Selected results are listed in Table 3. The optimum conditions for the reaction were found to be $K_3PO_4$/toluene, $Cs_2CO_3$/DMA, and $Cs_2CO_3$/DMF for **4** (entries 1–3); $K_3PO_4$/DMF for **5** (entry 4); $Cs_2CO_3$/THF, $Cs_2CO_3$/toluene, and $Cs_2CO_3$/DMA for **6** (entries 5–7); $Cs_2CO_3$/THF for **7** (entry 8). Higher reactivity was observed, under optimum conditions, for palladacycles containing a pendant *t*BuS moiety. Moreover, compounds containing an acetate group demonstrated slightly higher catalytic activities than those containing a Cl group.

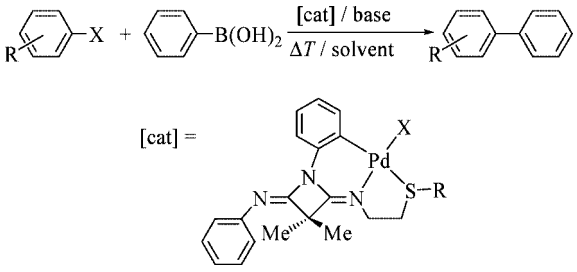


Scheme 2. Application of the palladacycles in the Suzuki reaction.

Although both sets of optimized conditions, $K_3PO_4$/toluene and $Cs_2CO_3$/DMF, for **4** exhibited similar conversion levels with electronically activated aryl bromide (entries 1–2 and 9–12), poor conversion levels were observed for reactions with electronically deactivated compounds using $Cs_2CO_3$/DMF (entries 14–15 and 17–18). Therefore the op-

Table 3. Suzuki coupling reactions catalysed by the new palladium complexes.[a]

| Entry | Catalyst | Aryl halide | Base | Solvent | [Pd] (mol-%) | *T* [°C] | *t* [h] | Conversion (%)[b] | Yield (%)[c] |
|---|---|---|---|---|---|---|---|---|---|
| 1 | **4** | 4-bromoacetophenone | $K_3PO_4$ | toluene | 1 | 50 | 1 | 96 | 90 |
| 2 | **4** | 4-bromoacetophenone | $Cs_2CO_3$ | DMF | 1 | 50 | 1 | 98 | 92 |
| 3 | **4** | 4-bromoacetophenone | $Cs_2CO_3$ | DMA | 1 | 50 | 1 | 94 | 83 |
| 4 | **5** | 4-bromoacetophenone | $K_3PO_4$ | DMF | 1 | 50 | 1 | 92 | 85 |
| 5 | **6** | 4-bromoacetophenone | $Cs_2CO_3$ | THF | 1 | 50 | 1 | 87 | 82 |
| 6 | **6** | 4-bromoacetophenone | $Cs_2CO_3$ | toluene | 1 | 50 | 1 | 90 | 88 |
| 7 | **6** | 4-bromoacetophenone | $Cs_2CO_3$ | DMA | 1 | 50 | 1 | 88 | 85 |
| 8 | **7** | 4-bromoacetophenone | $Cs_2CO_3$ | THF | 1 | 50 | 1 | 87 | 76 |
| 9 | **4** | 4-bromobenzaldehyde | $K_3PO_4$ | toluene | 1 | 50 | 1 | 99 | 92 |
| 10 | **4** | methyl 4-bromobenzoate | $K_3PO_4$ | toluene | 1 | 50 | 1 | 99 | 95 |
| 11 | **4** | 4-bromobenzaldehyde | $Cs_2CO_3$ | DMF | 1 | 50 | 1 | 96 | 90 |
| 12 | **4** | methyl 4-bromobenzoate | $Cs_2CO_3$ | DMF | 1 | 50 | 1 | 99 | 94 |
| 13 | **4** | 4-bromotoluene | $K_3PO_4$ | toluene | 1 | 110 | 0.75 | 99 | 90 |
| 14 | **4** | 4-*tert*-butylbromobenzene | $K_3PO_4$ | toluene | 1 | 70 | 3.5 | 92 | 86 |
| 15 | **4** | 4-bromoanisole | $K_3PO_4$ | toluene | 1 | 70 | 4 | 97 | 90 |
| 16 | **4** | 4-bromotoluene | $Cs_2CO_3$ | DMF | 1 | 135 | 0.75 | 99 | 89 |
| 17 | **4** | 4-*tert*-butyl-bromobenzene | $Cs_2CO_3$ | DMF | 1 | 70 | 3.5 | 83 | 75 |
| 18 | **4** | 4-bromoanisole | $Cs_2CO_3$ | DMF | 1 | 70 | 4 | 83 | 76 |
| 19 | **4** | 4-bromoacetophenone | $K_3PO_4$ | toluene | 0.01 | 80 | 2.5 | 87 | 81 |
| 20 | **4** | 4-bromoacetophenone | $K_3PO_4$ | toluene | 0.002 | 80 | 5 | 99 | 96 |
| 21 | **4** | 4-chloroacetophenone | $K_3PO_4$ | toluene | 1 | 80 | 4 | 9 | – |
| 22 | **4** | 4-chloroacetophenone | $Cs_2CO_3$ | DMF | 1 | 80 | 4 | 85 | 80 |
| 23 | **4** | methyl 4-chlorobenzoate | $Cs_2CO_3$ | DMF | 1 | 80 | 4 | 72 | 70 |
| 24 | **4** | 4-chloroanisole | $Cs_2CO_3$ | DMF | 1 | 80 | 7 | 82 | 75 |
| 25 | **4** | 4-chloroacetophenone | $Cs_2CO_3$ | DMF | 1 | 135 | 4 | 92 | 90 |

[a] Reaction conditions: 1.0 mmol aryl halide, 1.5 mmol phenylboronic acid, 2.0 mmol base, 2 mL solvent. [b] Determined by $^1$H NMR spectroscopy. [c] Isolated yield (average of two experiments).

 © 2006 Wiley-VCH Verlag GmbH & Co. KGaA, Weinheim 

timized conditions, $K_3PO_4$/toluene, were chosen for use in further studies to examine the limitations of the catalytic capability of compound **4**. Due to the high reactivity of **4**, lower catalyst concentrations were required, catalyst/substrate ratios from $10^{-4}$ to $2\times10^{-5}$ were employed, leading to turnover numbers of up to 48000 within a 5 h period (entries 19–20). Similar conditions were applied during the reaction of the electronically activated aryl chloride with 1 mol-% catalyst loading; however, poor conversion levels were observed after 4 h (entry 21). Surprisingly, the percentage conversion increased to 85% after 4 h (entry 22) using $Cs_2CO_3$/DMF. These conditions were employed in a reaction using methyl 4-chlorobenzoate and resulted in percentage conversion levels of up to 72% within 4 h (entry 23). A similar conversion level was observed using electronically deactivated aryl chloride and 4-chloroanisole as substrates; however, the reaction took up to 7 h (entry 24). In order to compare the catalytic activities with the sulfur containing palladacycles,[22] the optimized conditions at 110 °C and 135 °C were employed in the reaction with 4-bromotoluene as the substrate, this gave conversion levels of up to 99% within 0.75 h (entries 13 and 16). A similar conversion level was observed using electronically activated aryl chloride and 4-chloroacetophenone as the substrates; however, the reaction took up to 4 h at 135 °C (entry 25).

In order to determine the influence of the pendant functionality on the catalytic activity,[21] compounds **4**–**7** were investigated as catalysts in the Heck coupling reaction of 4-bromoacetophenone with styrene at 135 °C over a period of 1.5 h on a 1 mol-% scale, as shown in Scheme 3. Selected results are listed in Table 4. The optimum conditions were found to be $Cs_2CO_3$/DMF for **4** (entry 1); KF/DMA for **5** (entry 2); $K_3PO_4$/DMA for **6** (entry 3); KF/DMA for **7** (entry 4). High reactivity was observed for **4** under optimized conditions. A similar conversion level was observed using methyl 4-bromobenzoate as the substrate (entry 5). Similar conditions were applied to the reactions employing the electronically deactivated aryl bromide compounds; however, the reactions took up to 6 h (4-bromotoluene) and 12 h (4-bromoanisole) at 135 °C (entries 6 and 7). Lower catalyst concentrations, catalyst/substrate ratios of $10^{-3}$ to $10^{-5}$, led to percentage conversion levels of 81% after 6 h and 21% after 24 h (entries 8 and 9). Compound **4** also showed catalytic activity for reactions involving both electronically activated and deactivated aryl chlorides; however, higher catalyst loadings were necessary (entries 10 and 11).

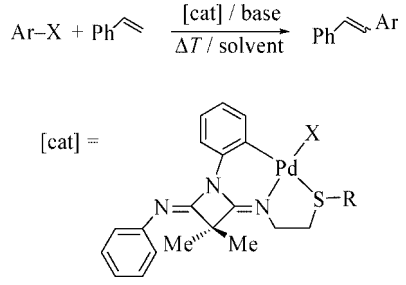


Scheme 3. Application of the palladacycles in the Heck reaction.

## Summary

Mononuclear phosphane-free palladacycles have been prepared using tridentate ligands containing carbon, nitrogen, and sulfur. Under optimized conditions, palladacycle **4** exhibits catalytic activity comparable to existing sulfur containing palladacyclic systems employed in the Suzuki coupling reaction. Complex **4** exhibits higher catalytic activity in some cases than in others. The catalyst productivity for the coupling of an electronically activated aryl bromide with phenylboronic acid was observed with a turnover of up to 48000 during a 5 h period. Complex **4** also demonstrates catalytic activity with less reactive aryl chlorides containing both electron withdrawing and electron donating groups. In the case of the four-membered diimine palladacyclic system, the thioether containing palladacycle exhibits better catalytic activity for the Heck coupling reaction than the nitrogen containing palladacycles reported in our previous work. Studies relating to the fine-tuning of the ligands, and investigations into further catalytic applications for metal complexes are currently underway.

Table 4. Heck coupling reactions catalysed by the new palladium complexes.[a]

| Entry | Catalyst | Aryl halide | Base | Solvent | [Pd] (mol-%) | $T$ [°C] | $t$ [h] | Conversion (%)[b] | Yield (%)[c] |
|---|---|---|---|---|---|---|---|---|---|
| 1 | **4** | 4-bromoacetophenone | $Cs_2CO_3$ | DMF | 1 | 135 | 1.5 | 92 | 86 |
| 2 | **5** | 4-bromoacetophenone | KF | DMA | 1 | 135 | 1.5 | 84 | – |
| 3 | **6** | 4-bromoacetophenone | $K_3PO_4$ | DMA | 1 | 135 | 1.5 | 80 | – |
| 4 | **7** | 4-bromoacetophenone | KF | DMA | 1 | 135 | 1.5 | 89 | – |
| 5 | **4** | methyl 4-bromobenzoate | $Cs_2CO_3$ | DMF | 1 | 135 | 1.5 | 95 | 90 |
| 6 | **4** | 4-bromotoluene | $Cs_2CO_3$ | DMF | 1 | 135 | 6 | 99 | 87 |
| 7 | **4** | 4-bromoanisole | $Cs_2CO_3$ | DMF | 1 | 135 | 12 | 96 | 91 |
| 8 | **4** | 4-bromoacetophenone | $Cs_2CO_3$ | DMF | 0.1 | 135 | 6 | 81 | 75 |
| 9 | **4** | 4-bromoacetophenone | $Cs_2CO_3$ | DMF | 0.001 | 135 | 24 | 21 | – |
| 10 | **4** | 4-chloroacetophenone | $Cs_2CO_3$ | DMF | 3 | 135 | 48 | 57 | – |
| 11 | **4** | 4-chloroanisole | $Cs_2CO_3$ | DMF | 5 | 135 | 48 | 56 | – |

[a] Reaction conditions: 1.0 mmol aryl halide, 1.3 mmol styrene, 1.5 mmol base, 2 mL solvent. [b] Determined by $^1$H NMR spectroscopy. [c] Isolated yield (average of two experiments).

 © 2006 Wiley-VCH Verlag GmbH & Co. KGaA, Weinheim 

## Experimental Section

**General Procedure:** All manipulations were carried out under nitrogen using standard Schlenk-line or drybox techniques. Solvents (THF, toluene, $CH_2Cl_2$ and hexane) were refluxed over an appropriate drying agent and distilled prior to use. Methanol (Merck, 99.9%), DMA (TEDIA, 99%) and DMF (TEDIA, 95%) were used as supplied. Deuterated solvents were dried over molecular sieves.

$^1H$ and $^{13}C\{^1H\}$ NMR spectra were recorded on Varian Gemini-200 (200 MHz), Varian Mercury-400 (400 MHz) and Varian Inova-600 (600 MHz) spectrometers. Spectra were recorded in chloroform-*d* at ambient temperature unless otherwise stated, and referenced internally to the residual solvent peak, and reported as parts per million relative to tetramethylsilane. Elemental analyses were performed with an Elementar Vario ELIV instrument.

Chemicals were used as supplied unless otherwise stated. $NEt_3$ was dried with $CaH_2$ and distilled before use. 2,2-Dimethyl-*N*,*N*′-diphenyl-malonamide and 2,2-dimethyl-*N*,*N*′-diphenylpropanediimidoyl dichloride were prepared by a method reported in the literature.[31]

**PhN=C$^A$(C$^B$Me$_2$)(N$^B$Ph)C$^C$=N(CH$_2$)$_2$Cl(*C$^A$–N$^B$*)(*C$^B$–C$^C$*) (1):** To a flask containing 2,2-dimethyl-*N*,*N*′-diphenylpropanediimidoyl dichloride (2.5 g, 8.0 mmol) and $NEt_3$ (4.5 mL, 32 mmol), 40 mL $CH_2Cl_2$, 2-chloroethylamine hydrochloride (2.8 g, 24 mmol) was added at 0 °C. The reaction mixture was warmed to room temperature and left to react overnight. After 14 h of stirring, the volatiles were removed in vacuo, and the residue was extracted with 30 mL toluene. After removal of solvent, the residue was washed with 5 mL hexane to afford a white solid. Yield, 1.84 g, 70.5%. $^1H$ NMR (600 MHz, $CDCl_3$): $\delta$ = 1.46 [s, 6 H, C(C$H_3$)$_2$], 3.74 [m, 4 H, (C$H_2$)$_2$], 6.94 (d, $^3J$ = 7.2 Hz, 2 H, *o*-Ph), 7.08 (t, $^3J$ = 7.8 Hz, 1 H, *p*-Ph), 7.16 (t, $^3J$ = 7.2 Hz, 1 H, *p*-Ph), 7.30 (t, $^3J$ = 7.8 Hz, 2 H, *m*-Ph), 7.39 (t, $^3J$ = 7.8 Hz, 2 H, *m*-Ph), 8.27 ppm (d, $^3J$ = 7.8 Hz, 2 H, *o*-Ph). $^{13}C\{^1H\}$ NMR (150 MHz, $CDCl_3$): $\delta$ = 21.7 [s, C(*C*H$_3$)$_2$], 45.0 [s, (*C*H$_2$)$_2$], 50.4 [s, (*C*H$_2$)$_2$], 58.0 [s, *tert*-*C*(CH$_3$)$_2$], 119.4, 121.4, 123.4, 124.6, 128.7 (overlap) (*o*, *m*, *p*-$C_6H_5$), 137.1, 146.7, 157.8, 159.6 ppm (two $C_{ipso}$-$C_6H_5$ and two *C*=*N* groups). $C_{19}H_{20}N_3Cl$ (325.84): calcd. C 70.04, H 6.19, N 12.90; found C 69.88, H 6.28, N 12.74.

**PhN=C$^A$(C$^B$Me$_2$)(N$^B$Ph)C$^C$=N(CH$_2$)$_2$S(CMe$_3$)(*C$^A$–N$^B$*)(*C$^B$–C$^C$*) (2):** To a flask containing **1** (0.49 g, 1.5 mmol) and $K_2CO_3$ (0.62 g, 4.5 mmol), 40 mL DMF, 2-methyl-2-propanethiol (0.34 mL, 3.0 mmol) was added. The reaction mixture was heated to 70 °C and left to react overnight. After 16 h of stirring, the resulting suspension was cooled to room temperature. Water (ca. 30 mL) was added into the suspension, which was then put into the fridge, and subsequently afforded a white solid. Yield, 0.49 g, 85.4%. $^1H$ NMR (600 MHz, $CDCl_3$): $\delta$ = 1.35 [s, 9 H, C(C$H_3$)$_3$], 1.45 [s, 6 H, C(C$H_3$)$_2$], 2.80 (t, $^3J$ = 7.2 Hz, 2 H, C$H_2$), 3.57 (t, $^3J$ = 7.8 Hz, 2 H, C$H_2$), 6.93 (d, $^3J$ = 7.2 Hz, 2 H, *o*-Ph), 7.07 (t, $^3J$ = 7.2 Hz, 1 H, *p*-Ph), 7.14 (t, $^3J$ = 7.2 Hz, 1 H, *p*-Ph), 7.28 (t, $^3J$ = 7.8 Hz, 2 H, *m*-Ph), 7.38 (t, $^3J$ = 7.8 Hz, 2 H, *m*-Ph), 8.27 ppm (d, $^3J$ = 7.8 Hz, 2 H, *o*-Ph). $^{13}C\{^1H\}$ NMR (150 MHz, $CDCl_3$): $\delta$ = 21.7 [s, C(*C*H$_3$)$_2$], 30.2 (s, *C*H$_2$), 31.0 [s, C(*C*H$_3$)$_3$], 42.2 [s, *C*(CH$_3$)$_3$], 49.1 (s, *C*H$_2$), 58.0 [s, *C*(CH$_3$)$_2$], 119.4, 121.5, 123.3, 124.4, 128.6 (overlap) (*C*H-$C_6H_5$), 137.2, 146.8, 158.0, 158.4 ppm (two $C_{ipso}$-$C_6H_5$, and two *C*=*N* groups). $C_{23}H_{29}N_3S$ (379.56): calcd. C 72.78, H 7.70, N 11.07; found C 72.35, H 7.30, N 11.01.

**PhN=C$^A$(C$^B$Me$_2$)(N$^B$Ph)C$^C$=N(CH$_2$)$_2$SPh(*C$^A$–N$^B$*)(*C$^B$–C$^C$*) (3):** The procedure for the preparation of **3** was similar to that used for **2**. A white solid was obtained. Yield, 0.46 g, 91.0%. $^1H$ NMR (600 MHz, $CDCl_3$): $\delta$ = 1.34 [s, 6 H, C(C$H_3$)$_2$], 3.19 (t, $^3J$ = 7.2 Hz, 2 H, C$H_2$), 3.63 (t, $^3J$ = 7.2 Hz, 2 H, C$H_2$), 6.91 (d, $^3J$ = 7.2 Hz, 2 H, *o*-Ph), 7.06 (t, $^3J$ = 7.2 Hz, 1 H, *p*-Ph), 7.14 (t, $^3J$ = 7.2 Hz, 1 H, *p*-Ph), 7.16 (t, $^3J$ = 7.2 Hz, 1 H, *p*-Ph), 7.26 (m, overlap, 4 H, Ph), 7.37 (m, overlap, 4 H, Ph), 8.24 ppm (d, $^3J$ = 7.8 Hz, 2 H, *o*-Ph). $^{13}C\{^1H\}$ NMR (150 MHz, $CDCl_3$): $\delta$ = 21.5 [s, C(*C*H$_3$)$_2$], 35.2 (s, *C*H$_2$), 48.3 (s, *C*H$_2$), 58.0 [s, *C*(CH$_3$)$_2$], 119.4, 121.4, 123.3, 124.5, 126.1, 128.6 (overlap), 128.9, 129.3 (*C*H-$C_6H_5$), 136.1, 137.1, 146.7, 157.9, 168.8 ppm (three $C_{ipso}$-$C_6H_5$, and two *C*=*N* groups). $C_{25}H_{25}N_3S$ (399.55): calcd. C 75.15, H 6.31, N 10.52; found C 75.31, H 6.09, N 10.55.

**[PhN=C$^A$(C$^B$Me$_2$)(N$^B$-η$^1$-C$_6$H$_4$)C$^C$=N(CH$_2$)$_2$S(CMe$_3$)(*C$^A$–N$^B$*)-(*C$^B$–C$^C$*)]Pd(OAc) (4):** To a flask containing $Pd(OAc)_2$ (0.11 g, 0.50 mmol) and **2** (0.19 g, 0.50 mmol), 30 mL THF was added at room temperature. After 12 h of stirring, the yellow suspension was filtered and the filtrate was dried in vacuo to afford a pale brown solid. Yield, 0.22 g, 79.2%. $^1H$ NMR (600 MHz, $CDCl_3$): $\delta$ = 1.47 [s, 6 H, C(C$H_3$)$_2$], 1.58 [s, 9 H, C(C$H_3$)$_3$], 2.16 [s, 3 H, O-C(=O)-C$H_3$], 2.71 (t, $^3J$ = 6.0 Hz, 2 H, C$H_2$), 3.76 (t, $^3J$ = 6.0 Hz, 2 H, C$H_2$), 6.94 (d, $^3J$ = 7.2 Hz, 2 H, *o*-Ph), 7.06 (t, $^3J$ = 7.2 Hz, 1 H, C*H*-Ph), 7.13 (t, $^3J$ = 7.2 Hz, 1 H, C*H*-Ph), 7.17 (t, $^3J$ = 7.2 Hz, 1 H, C*H*-Ph), 7.33 (t, $^3J$ = 7.8 Hz, 2 H, *m*-Ph), 7.59 (d, $^3J$ = 8.4 Hz, 1 H, C*H*-Ph), 8.09 ppm (d, $^3J$ = 7.8 Hz, 1 H, C*H*-Ph). $^{13}C\{^1H\}$ NMR (150 MHz, $CDCl_3$): $\delta$ = 21.0 [s, C(*C*H$_3$)$_2$], 24.6 [s, O-C(=O)-*C*H$_3$], 30.0 [s, C(*C*H$_3$)$_3$], 30.7 (s, *C*H$_2$), 48.6 [s, *C*(CH$_3$)$_3$], 52.6 (s, *C*H$_2$), 57.0 [s, *C*(CH$_3$)$_2$], 116.6, 120.8, 124.1, 124.8, 125.5, 129.0, 134.1 (*C*H-$C_6H_5$), 129.6, 129.9, 145.5, 153.2, 158.7 (one η$^1$-Ph, two $C_{ipso}$-$C_6H_5$ and two *C*=*N* groups), 177.6 ppm [s, O-*C*(=O)-CH$_3$]. $C_{25}H_{31}N_3O_2PdS$ (544.02): calcd. C 55.19, H 5.74, N 7.72; found C 54.72, H 5.99, N 7.34.

**[PhN=C$^A$(C$^B$Me$_2$)(N$^B$-η$^1$-C$_6$H$_4$)C$^C$=N(CH$_2$)$_2$SPh(*C$^A$–N$^B$*)(*C$^B$–C$^C$*)]Pd(OAc) (5):** The procedure for the preparation of **5** was similar to that used for **4**; however, compound **3** was used instead of **2**. A pale brown solid was obtained. Yield, 0.18 g, 61.9%. $^1H$ NMR (600 MHz, $CDCl_3$): $\delta$ = 1.44 [s, 6 H, C(C$H_3$)$_2$], 2.08 [s, 3 H, OC(O)C$H_3$], 2.98 (t, $^3J$ = 6.0 Hz, 2 H, C$H_2$), 3.65 (t, $^3J$ = 6.0 Hz, 2 H, C$H_2$), 6.93 (m, 2 H, C*H*-Ph), 7.11 (m, 1 H, C*H*-Ph), 7.13 (m, 1 H, C*H*-Ph), 7.21 (m, 1 H, C*H*-Ph), 7.33 (m, 2 H, C*H*-Ph), 7.43 (m, 3 H, C*H*-Ph), 7.78 (m, 1 H, C*H*-Ph), 8.13 ppm (m, 3 H, C*H*-Ph). $^{13}C\{^1H\}$ NMR (150 MHz, $CDCl_3$): $\delta$ = 21.0 [s, C(*C*H$_3$)$_2$], 24.0 [s, O-C(=O)-*C*H$_3$], 39.2 (s, *C*H$_2$), 52.1 (s, *C*H$_2$), 57.1 [s, *C*(CH$_3$)$_2$], 116.7, 120.8, 124.2, 124.9, 125.8, 129.0, 129.6, 129.7, 133.5, 134.4 (*C*H-$C_6H_5$), 129.76, 129.82, 129.87, 145.5, 153.2, 158.8 (one η$^1$-Ph, three $C_{ipso}$-$C_6H_5$ and two *C*=*N* groups), 177.3 ppm [s, O-*C*(=O)-CH$_3$]. $C_{27}H_{27}O_2N_3PdS$ (564.01): calcd. C 57.50, H 4.83, N 7.45; found C 57.26, H 5.08, N 7.36.

**[PhN=C$^A$(C$^B$Me$_2$)(N$^B$-η$^1$-C$_6$H$_4$)C$^C$=N(CH$_2$)$_2$S(CMe$_3$)(*C$^A$–N$^B$*)-(*C$^B$–C$^C$*)]PdCl (6):** To a flask containing **4** (0.14 g, 0.25 mmol) and LiCl (0.04 g, 1.0 mmol) 30 mL methanol was added at room temperature. After 0.5 h of stirring, the yellow suspension was filtered and the precipitate was washed with 20 mL deionized water followed by 20 mL hexane to afford a yellow solid. Yield, 0.068 g, 52.4%. $^1H$ NMR (600 MHz, $CDCl_3$): $\delta$ = 1.50 [s, 6 H, C(C$H_3$)$_2$], 1.66 [s, 9 H, C(C$H_3$)$_3$], 2.71 (t, $^3J$ = 6.6 Hz, 2 H, C$H_2$), 3.79 (t, $^3J$ = 6.6 Hz, 2 H, C$H_2$), 6.95 (m, 2 H, C*H*-Ph), 7.07 (t, $^3J$ = 6.6 Hz, 1 H, C*H*-Ph), 7.14 (t, $^3J$ = 7.2 Hz, 1 H, C*H*-Ph), 7.16 (t, $^3J$ = 7.2 Hz, 1 H, C*H*-Ph), 7.34 (t, $^3J$ = 7.8 Hz, 1 H, C*H*-Ph), 8.10 (d, $^3J$ = 7.8 Hz, 1 H, C*H*-Ph), 8.41 ppm (d, $^3J$ = 7.8 Hz, 1 H, C*H*-Ph). $^{13}C\{^1H\}$ NMR (150 MHz, $CDCl_3$): $\delta$ = 21.1 [s, C(*C*H$_3$)$_2$], 30.6 [s, C(*C*H$_3$)$_3$], 31.3 (s, *C*H$_2$), 49.9 [s, *C*(CH$_3$)$_3$], 53.1 (s, *C*H$_2$), 57.0 [s, *C*(CH$_3$)$_2$], 116.8, 120.8, 124.2, 125.1, 125.5, 129.0, 138.9 (*C*H-$C_6H_5$), 130.1, 130.2, 145.5, 153.1, 158.7 ppm (one η$^1$-Ph, two $C_{ipso}$-$C_6H_5$, and two *C*=*N* groups). $C_{23}H_{28}ClN_3PdS$ (520.43): calcd. C 53.08, H 5.42, N 8.07; found C 53.29, H 5.36, N 8.40.

 © 2006 Wiley-VCH Verlag GmbH & Co. KGaA, Weinheim 

**[PhN=C$^A$(C$^B$Me$_2$)(N$^B$-η$^1$-C$_6$H$_4$)C$^C$=N(CH$_2$)$_2$SPh(C$^A$–N$^B$)(C$^B$–C$^C$)]PdCl (7):** The procedure for the preparation of **7** was similar to that used for **6**; however, compound **5** was used instead of **4**.A yellow solid was obtained. Yield, 0.274 g, 87.0%. $^1$H NMR (600 MHz, $CD_2Cl_2$): $\delta$ = 1.46 [s, 6 H, C(C$H_3$)$_2$], 2.99 (t, $^3J$ = 6.0 Hz, 2 H, C$H_2$), 3.76 (br., 2 H, C$H_2$), 6.97 (d, $^3J$ = 7.2 Hz, 2 H, *o*-Ph), 7.04 (m, 1 H, C*H*-Ph), 7.14 (t, $^3J$ = 7.2 Hz, 1 H, C*H*-Ph), 7.19 (t, $^3J$ = 7.2 Hz, 1 H, C*H*-Ph), 7.35 (t, $^3J$ = 7.8 Hz, 2 H, *m*-Ph), 7.47 (m, 3 H, C*H*-Ph), 8.11 (m, 2 H, C*H*-Ph), 8.17 (d, $^3J$ = 8.4 Hz, 1 H, C*H*-Ph), 8.40 ppm (m, 1 H, C*H*-Ph). $^{13}$C{$^1$H} NMR (150 MHz, $CD_2Cl_2$): $\delta$ = 21.0 [s, C(*C*H$_3$)$_2$], 39.2 (s, *C*H$_2$), 53.3 (s, *C*H$_2$), 57.4 [s, *C*(CH$_3$)$_2$], 117.1, 120.9, 124.3, 124.7, 125.7, 129.2, 129.8, 130.0, 133.4, 138.9 (*C*H-*C*$_6$H$_5$), 129.6, 130.3, 130.7, 145.8, 153.7, 159.0 ppm (one η$^1$-Ph, three *C$_{ipso}$*-*C*$_6$H$_5$, and two *C*=*N* groups). $C_{25}H_{24}ClN_3PdS$ (540.42): calcd. C 55.56, H 4.48, N 7.78; found C 55.47, H 4.070, N 7.80.

**General Procedure for the Suzuki-Type Coupling Reaction:** Prescribed amounts of catalyst, base (2.0 equiv.), boronic acid (1.5 equiv.), and aryl halide (1.0 equiv.) were placed under nitrogen in a Schlenk tube. Solvent (2 mL) was added by syringe, and the reaction mixture was heated at the prescribed temperature for the prescribed amount of time.

**General Procedure for the Heck Reaction:** Prescribed amount of catalysts, base (1.5 equiv.) and aryl halide (1 equiv.) were placed under nitrogen in a Schlenk tube. Solvent (2 mL) and styrene (1.3 equiv.) were added by syringe, and the reaction mixture was heated at the prescribed temperature for the prescribed amount of time.

**Crystal Structure Data:** Crystals were grown from $CHCl_3$ solution (**3**) or a $CH_2Cl_2$/hexane solution (**4**), and then isolated by filtration. Suitable crystals of **3** or **4** were sealed in thin walled glass capillaries under nitrogen and mounted on a Bruker AXS SMART 1000 diffractometer. Absorption corrections were based on symmetry equivalent reflections and applied using the SADABS program. Space group determinations were based on the Laue symmetries and systematic absences exhibited by the diffraction patterns, and were confirmed by the structure solutions. The structures were solved by direct methods using the SHELXTL package. All non-hydrogen atoms were located from successive difference Fourier maps, and hydrogen atoms were refined using a riding model. Anisotropic thermal parameters were used for all non-hydrogen atoms, and fixed isotropic parameters were used for the hydrogen atoms. The asymmetric unit of **4** contains a severely disordered molecule of dichloromethane, and a molecule of water. Crystallographic data collection and refinement details are given in Table 5.

Table 5. Summary of crystal data for compounds **3** and **4**.

| | **3** | **4** |
|---|---|---|
| Formula | $C_{25}H_{25}N_3S$ | $C_{26}H_{35}Cl_2N_3O_3PdS$ |
| Fw | 399.54 | 646.93 |
| $T$ [K] | 293(2) | 293(2) |
| Crystal system | triclinic | monoclinic |
| Space group | $P\bar{1}$ | $C2/c$ |
| $a$ [Å] | 7.9986(8) | 22.7849(14) |
| $b$ [Å] | 11.6307(11) | 13.2886(8) |
| $c$ [Å] | 12.1069(11) | 20.8977(13) |
| $\alpha$ [°] | 90.187(2) | 90 |
| $\beta$ [°] | 98.050(2) | 112.7370(10) |
| $\gamma$ [°] | 100.699(2) | 90 |
| $V$ [Å$^3$] | 1095.32(18) | 5835.7(6) |
| $Z$ | 2 | 8 |
| $\rho_{calc}$ [Mg/m$^3$] | 1.211 | 1.473 |
| $\mu$(Mo-$K_\alpha$) [mm$^{-1}$] | 0.163 | 0.922 |
| Reflections collected | 6263 | 16054 |
| No. of parameters | 262 | 335 |
| $R1$[a] | 0.0491 | 0.0422 |
| $wR2$[a] | 0.1452 | 0.1332 |
| GoF[b] | 1.065 | 1.14 |

[a] $R1 = [\Sigma(|F_o| - |F_c|)/\Sigma |F_o|]$; $wR2 = [\Sigma w(F_o^2 - F_c^2)^2/\Sigma w(F_o^2)^2]^{1/2}$, $w$ = 0.10. [b] GoF = $[\Sigma w(F_o^2 - F_c^2)^2/(N_{rflns} - N_{params})]^{1/2}$.

CCDC-269677 and -269678 for compounds **3** and **4** contain the supplementary crystallographic data for this paper. These data can be obtained free of charge from The Cambridge Crystallographic Data Centre via www.ccdc.cam.ac.uk/data_request/cif.

## Acknowledgments

We would like to thank the National Science Council of the Republic of China for financial support.

[1] N. Miyaura, A. Suzuki, *Chem. Rev.* **1995**, *95*, 2457–2483.
[2] W. A. Herrmann, V. P. W. Böhm, C.-P. Reisinger, *J. Organomet. Chem.* **1999**, *576*, 23–41.
[3] A. Suzuki, *J. Organomet. Chem.* **1999**, *576*, 147–168.
[4] I. P. Beletskaya, A. V. Cheprakov, *Chem. Rev.* **2000**, *100*, 3009–3066.
[5] J. Dupont, M. Pfeffer, J. Spencer, *Eur. J. Inorg. Chem.* **2001**, 1917–1927.
[6] N. J. Whitcombe, K. K. Hii, S. E. Gibson, *Tetrahedron* **2001**, *57*, 7449–7476.
[7] A. F. Littke, G. C. Fu, *Angew. Chem. Int. Ed.* **2002**, *41*, 4176–4211.
[8] S. Kotha, K. Lahiri, D. Kashinath, *Tetrahedron* **2002**, *58*, 9633–9695.
[9] J. Hassan, M. Sévignon, C. Gozzi, E. Schulz, M. Lemaire, *Chem. Rev.* **2002**, *102*, 1359–1470.
[10] E. Negishi, L. Anastasia, *Chem. Rev.* **2003**, *103*, 1979–2018.
[11] R. B. Bedford, *Chem. Commun.* **2003**, 1787–1796.
[12] I. P. Beletskaya, A. V. Cheprakov, *J. Organomet. Chem.* **2004**, *689*, 4055–4082.
[13] V. Farina, *Adv. Synth. Catal.* **2004**, *346*, 1553–1582.
[14] H.-U. Blaser, A. Indolese, F. Naud, U. Nettekoven, A. Schnyder, *Adv. Synth. Catal.* **2004**, *346*, 1583–1598.
[15] R. B. Bedford, C. S. J. Cazin, D. Holder, *Coord. Chem. Rev.* **2004**, *248*, 2283–2321.
[16] U. Christmann, R. Vilar, *Angew. Chem. Int. Ed.* **2005**, *44*, 366–374.
[17] A. Zapf, M. Beller, *Chem. Commun.* **2005**, 431–440.
[18] A. C. Frisch, M. Beller, *Angew. Chem. Int. Ed.* **2005**, *44*, 674–688.
[19] J. Dupont, C. S. Consorti, J. Spencer, *Chem. Rev.* **2005**, *105*, 2527–2572.
[20] D. E. Bergbreiter, P. L. Osburn, Y.-S. Liu, *J. Am. Chem. Soc.* **1999**, *121*, 9531–9538.
[21] A. S. Gruber, D. Zim, G. Ebeling, A. L. Monteiro, J. Dupont, *Org. Lett.* **2000**, *2*, 1287–1290.
[22] D. Zim, A. S. Gruber, G. Ebeling, J. Dupont, A. L. Monteiro, *Org. Lett.* **2000**, *2*, 2881–2884.
[23] J. Dupont, A. S. Gruber, G. S. Fonseca, A. L. Monteiro, G. Ebeling, *Organometallics* **2001**, *20*, 171–176.
[24] P. B. Silveira, V. R. Lando, J. Dupont, A. L. Monteiro, *Tetrahedron Lett.* **2002**, *43*, 2327–2329.
[25] C. S. Consorti, G. Ebeling, F. R. Flores, F. Rominger, J. Dupont, *Adv. Synth. Catal.* **2004**, *346*, 617–624.
[26] V. V. Thakur, N. S. C. R. Kumar, A. Sudalai, *Tetrahedron Lett.* **2004**, *45*, 2915–2918.
[27] Z. Xiong, N. Wang, M. Dai, A. Li, J. Chen, Z. Yang, *Org. Lett.* **2004**, *6*, 3337–3340.

 © 2006 Wiley-VCH Verlag GmbH & Co. KGaA, Weinheim 

[28] R. B. Bedford, C. S. J. Cazin, M. B. Hursthouse, M. E. Light, V. J. M. Scordia, *Dalton Trans.* **2004**, 3864–3868.
[29] K. Yu, W. Sommer, J. M. Richardson, M. Weck, C. W. Jones, *Adv. Synth. Catal.* **2005**, *347*, 161–171.
[30] J. Spencer, D. P. Sharratt, J. Dupont, A. L. Monteiro, V. I. Reis, M. P. Stracke, F. Rominger, I. M. McDonald, *Organometallics* **2005**, *24*, 5665–5672.
[31] C.-T. Chen, Y.-S. Chan, Y.-R. Tzeng, M.-T. Chen, *Dalton Trans.* **2004**, 2691–2696.
[32] X. Riera, A. Caubet, C. López, V. Moreno, E. Freisinger, M. Willermann, B. Lippert, *J. Organomet. Chem.* **2001**, *629*, 97–108.
[33] A. Fernández, D. Vázquez-García, J. J. Fernández, M. López-Torres, A. Suárez, S. Castro-Juiz, J. M. Ortigueira, J. M. Vila, *New J. Chem.* **2002**, *26*, 105–112.
[34] S. Pérez, C. López, A. Caubet, R. Bosque, X. Solans, M. F. Bardía, A. Roig, E. Molins, *Organometallics* **2004**, *23*, 224–236.
[35] J. Dupont, M. Pfeffer, J. C. Daran, Y. Jeannin, *Organometallics* **1987**, *6*, 899–901.
[36] J. Dupont, N. R. Basso, M. R. Meneghetti, R. A. Konrath, R. Burrow, M. Horner, *Organometallics* **1997**, *16*, 2386–2391.
[37] G. Ebeling, M. R. Meneghetti, F. Rominger, J. Dupont, *Organometallics* **2002**, *21*, 3221–3227.
[38] A. Fernández, D. Vázquez-García, J. J. Fernández, M. López-Torres, A. Suárez, R. Mosteiro, J. M. Vila, *J. Organomet. Chem.* **2002**, *654*, 162–169.
[39] Y. Li, S. Selvaratnam, J. J. Vittal, P.-H. Leung, *Inorg. Chem.* **2003**, *42*, 3229–3236.
[40] P. Štěpnička, I. Císařová, *Organometallics* **2003**, *22*, 1728–1740.
[41] G. A. Grasa, R. Singh, E. D. Stevens, S. P. Nolan, *J. Organomet. Chem.* **2003**, *687*, 269–279.
[42] J. Bravo, C. Cativiela, R. Navarro, E. P. Urriolabeitia, *J. Organomet. Chem.* **2002**, *650*, 157–172.

Received: June 27, 2006
Published Online: September 22, 2006

 © 2006 Wiley-VCH Verlag GmbH & Co. KGaA, Weinheim 

DOI: 10.1002/ejic.200600607

# pH-Driven $Cu^{2+}$ Translocation in Ferrocene-Containing Ligands

**Piersandro Pallavicini,*[a] Giacomo Dacarro,*[a] Carlo Mangano,[a] Stefano Patroni,[a] Angelo Taglietti,[a] and Robertino Zanoni[b]**

**Keywords:** Molecular devices / Macrocyclic ligands / Copper / Ferrocene / N ligands

The ligands **L1**$H_4$, **L2**$H_2$, and **L**3$H_4$ have been synthesized, featuring two, one, and two ferrocene-functionalized diamino-diamido compartments, respectively. The coordination chemistry of the ligands towards $Cu^{2+}$ has been fully characterized by means of potentiometric and spectrophotometric titrations, which allowed us to determine the protonation constants of the ligands, the formation constants of their complexes, and their coordination geometry. **L1**$H_4$ and **L2**$H_2$ feature additional diaminopyridine and bis(aminoquinoline) binding sites, respectively, and are capable of the pH-driven translocation of two and one $Cu^{2+}$ cations, respectively. Electrochemical experiments (CV) coupled with pH-metric titrations demonstrate that while the coordination of $Cu^{2+}$ to the compartments more distant from ferrocene (Fc), i.e. diaminopyridine in **L1**$H_4$ and bis(aminoquinoline) in **L2**$H_2$ leaves the oxidation potential of Fc unchanged, the translocation of the $Cu^{2+}$ cation(s) inside the diamino-diamido compartment(s) is signaled by a peculiar lowering of the Fc oxidation potential.

(© Wiley-VCH Verlag GmbH & Co. KGaA, 69451 Weinheim, Germany, 2006)

## Introduction

The controlled translocation of metal cations is a recent development of coordination chemistry in solution based on the concepts elaborated by supramolecular chemistry,[1] and is at the edge of one of the hot topics of nanotechnology, i.e. molecular machines and controlled motions at the molecular level.[2]

However, few papers have been published so far in this field. As a first example, the chemically promoted redox-driven translocation of one iron cation inside a polytopic ligand was reported by the group of Shanzer in 1995,[3a] and the same author reported the redox-controlled translocation of one copper cation in 2002.[3b]

Using a different approach, we are involved in a long-term research effort concerning the translocation of transition metal cations in aqueous solutions driven by the variation of a classical bulk property, i.e. pH.[4,5] This approach has also been exploited by a few other groups.[6] Recent results obtained by our group include the simultaneous pH-driven translocation of two $Cu^{2+}$ cations inside large macrocyclic ligands containing two dioxo232 and two diaminopyridine binding sites, and functionalized either with a benzyl[7] or a propargyl[8] unit on the central carbon of the malonic amide groups. For the latter examples, the pH-driven double translocation process can be summarized as follows: at slightly acidic or neutral pH values, the two $Cu^{2+}$ cations reside in the diaminopyridine compartments (Scheme 1: $[\mathbf{BZ}H_4Cu_2]^{4+}$ blue, $\lambda_{max}$ = 660 nm, and $[\mathbf{PG}H_4Cu_2]^{4+}$ blue, $\lambda_{max}$ = 660 nm) but when the pH is raised enough, the two dioxo232 compartments lose their amido protons and the $Cu^{2+}$ cations move inside the very effective diamino-diimido binding units to form a neutral complex ($[\mathbf{BZ}Cu_2]$ and $[\mathbf{PG}Cu_2]$ in Scheme 1). The overall molecular shape and $Cu^{2+}$ coordination number and geometry in the neutral complexes depend on the bulkiness of the substituent: the slim propargyl allows folding and apical coordination of one pyridine to each $Cu^{2+}$ cation (square-pyramidal geometry, purple, $\lambda_{max}$ = 575 nm), while the bulky benzyl prevents folding, resulting in square-planar $Cu^{2+}$ cations (pink, $\lambda_{max}$ = 515 nm). Visual and instrumental recognition of the double movement is based on the color change.

In this paper we report a double pH-driven $Cu^{2+}$ translocation inside the ligand **L1**$H_4$, whose backbone is identical to that of **BZ**$H_4$ and **PG**$H_4$ but features two ferrocene (Fc) groups instead of benzyl and propargyl moieties. For sake of comparison the Fc-containing **L2**$H_2$ and **L**3$H_4$ ligands, which are capable of single $Cu^{2+}$ translocation and inclusion of two $Cu^{2+}$ cations with no translocation, respectively, on changing pH, have also been studied. As Fc is reversibly oxidizable and its potential is significantly influenced by nearby charges or dipoles, the study of the Fc redox potential as a function of the absence/presence and position of $Cu^{2+}$ cation(s) in these new systems has two goals: i) obtaining an electrochemical signal, as an alternative to color[4,7,8] or fluorescence changes,[4,5] that can be

[a] Dipartimento di Chimica Generale, Università di Pavia, viale Taramelli 12, 27100 Pavia, Italy
E-mail: psp@unipv.it
[b] Dipartimento di Chimica n. 4, Università La Sapienza, piazzale Aldo Moro 5, 00185 Roma, Italy

 © 2006 Wiley-VCH Verlag GmbH & Co. KGaA, Weinheim 

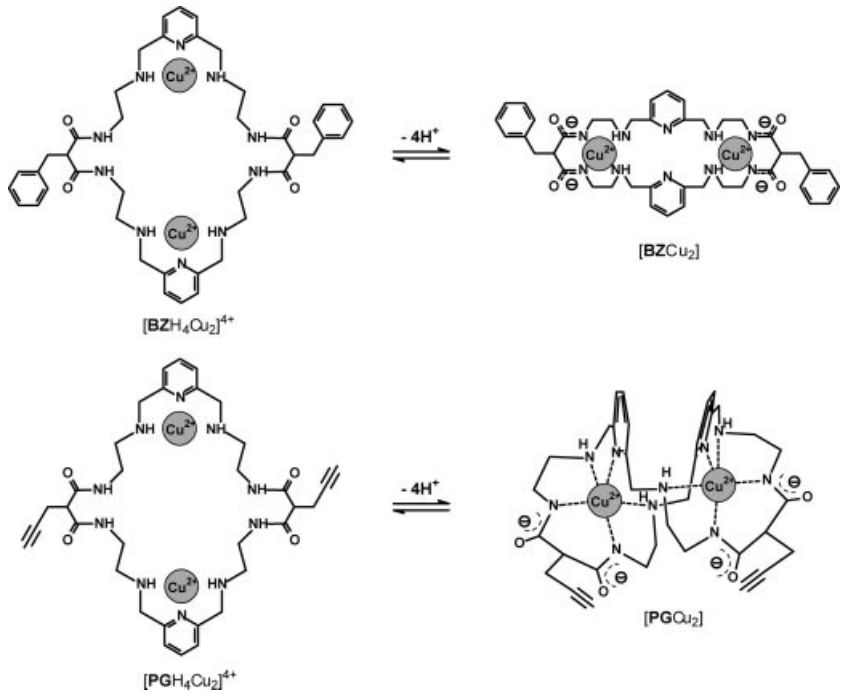


Scheme 1. Pictorial representation of pH-driven double $Cu^{2+}$ translocation (upper equilibrium, ref.[6]) and pH-driven double $Cu^{2+}$ translocation plus folding (lower equilibrium, ref.[7]) in ligands **BZ**$H_4$ and **PG**$H_4$.

used to monitor the position(s) of the cation(s) inside the ligands; and ii) evaluating how a change in the overall charge and in the charge distribution upon $Cu^{2+}$ translocation can electrostatically influence the space region occupied by ferrocenes. These are linked to a long-term research project of ours concerning the grafting of ligands on Si surfaces,[9] which may be achieved by surface reactions of the propargyl groups[10] and is thus accessible for ligands like **PG**$H_4$.

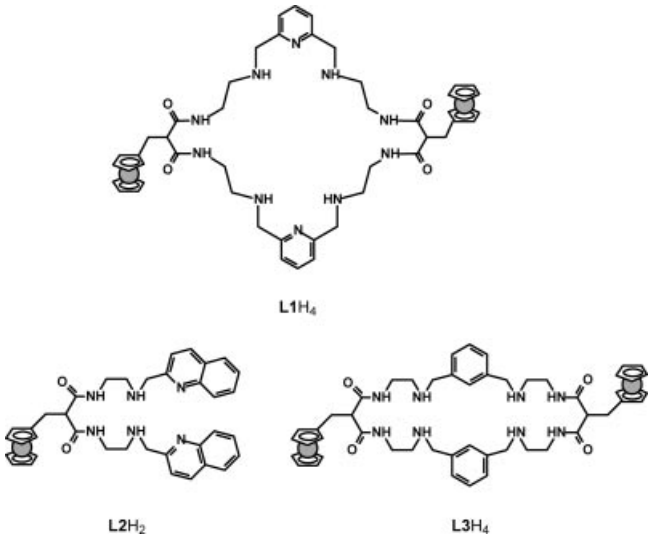


Accordingly, we report here the full characterization in aqueous solution of ligands **L1**$H_4$, **L2**$H_2$, and **L3**$H_4$ and of their copper complexes, by means of the determination of the protonation and complexation constants of the forms present in the pH range 2–12. The pH values between which double and single $Cu^{2+}$ translocation takes place in **L1**$H_4$ and **L2**$H_2$, respectively, are determined. The nature and the coordination geometry of the pertinent copper complexes are investigated by UV/Vis spectroscopy. Finally, electrochemical (CV) investigations on the Fc redox potential have been carried out in aqueous solution as a function of pH, in the presence and in the absence of $Cu^{2+}$, to determine the effect of the metal cations and of their positions on the Fc oxidation potential.

## Results and Discussion

### Copper Complexes in Aqueous Solution and pH-Driven Translocation

The protonation and complexation constants of the ferrocene-containing ligands **L1**$H_4$, **L2**$H_2$, and **L3**$H_4$ were determined by means of potentiometric titrations in a water/dioxane (1:4, v/v) mixture due to the hydrophobic nature of the ferrocene molecule, which does not allow solubilization of the three ligands in pure water. Titrations were carried out automatically by addition of base to solutions containing first ligand only plus excess acid (for the determination of the protonation constants) and then to solutions containing ligand, the pertinent quantity of $Cu(CF_3SO_3)_2$ (2, 1, and 2 equiv. in the case of **L1**$H_4$, **L2**$H_2$, and **L3**$H_4$, respectively), and excess acid. The $\log K$ (protonation and complexation) values were obtained by elaboration of the emf vs. volume of added base data obtained by means of the Hyperquad program suite.[11] Experimental conditions

 © 2006 Wiley-VCH Verlag GmbH & Co. KGaA, Weinheim 

and details are described in the Experimental Section. The calculated logarithmic protonation constants data are collected in Table 1.

Table 1. Logarithmic step protonation constants for ligands. Uncertainties are indicated in parentheses.[a]

| | $\log K_1$ | $\log K_2$ | $\log K_3$ | $\log K_4$ |
|---|---|---|---|---|
| **L1**$H_4$ | 8.78(0.01) | 7.77(0.01) | 6.91(0.01) | 6.15(0.02) |
| **L2**$H_2$ | 7.98(0.01) | 6.78(0.01) | 3.35(0.02) | |
| **L3**$H_4$ | 7.89(0.01) | 7.80(0.01) | 6.87(0.02) | 6.04(0.02) |

[a] Data obtained in dioxane/water (8:2, v/v), 0.05 M $NaNO_3$, $T$ = 25 °C.

Table 3. Formation constants of the $Cu^{2+}$-containing species for the ligand featuring one dioxo232 compartment. Column 1 reports the relative equilibrium for each value relative to a generic diamido ligand $LH_2$. Uncertainties are indicated in parentheses.[a]

| | **L2**$H_2$ |
|---|---|
| $LH_2 + Cu^{2+} \leftrightharpoons [LH_2Cu]^{2+}$ | 10.90(0.01) |
| $[LH_3]^+ + Cu^{2+} \leftrightharpoons [LH_3Cu]^{3+}$ | 14.86(0.01) |
| $LH_2 + Cu^{2+} + H_2O \leftrightharpoons [LH_2Cu(OH)]^+ + H^+$ | 5.04(0.01) |
| $LH_2 + Cu^{2+} \leftrightharpoons [LCu] + 2H^+$ | –2.56(0.02) |

[a] Data obtained in dioxane/water (8:2, v/v), 0.05 M $NaNO_3$, $T$ = 25 °C.

The number and $\log K$ values of the found protonation steps are in agreement with those already described for similar ligands in the same solvent mixture.[4,5] The formation constants of the copper complexes of the three ligands and the relative equilibria are reported, as logarithmic values, in Tables 2 (**L1**$H_4$ and **L3**$H_4$) and 3 (**L2**$H_2$) The distribution diagrams in Figure 1 (parts A–C), in which the percentage of each species (with respect to total ligand) is expressed as a function of pH, can be drawn from the data in all these tables.

From Figure 1 (A) it can be seen that the system containing ligand **L1**$H_4$ and $Cu^{2+}$ in a 1:2 molar ratio allows the efficient translocation of the two $Cu^{2+}$ cations.

The species $[\mathbf{L1}H_4Cu_2]^{4+}$ (see Scheme 2) contains the neutral ligand and two copper cations, each of which is chelated to the tridentate diaminopyridine units. The large formation constant of this species (24.12 log units) reflects the chelating nature of the two donor sets and the coordination of two $Cu^{2+}$ cations, and is in good agreement with the values already found for the analogous species $[\mathbf{BZ}H_4Cu_2]^{4+}$ and $[\mathbf{PG}H_4Cu_2]^{4+}$ (Scheme 1, $\log K$ = 25.31[7] and 25.30,[8] respectively). This species is the prevalent one in a large pH range (i.e. between pH 3 and 7), and accounts for over 95% at 3.7 < pH < 5.9. Its formulation was confirmed by mass spectrometry (ESI) with solutions containing ligand and $Cu(CF_3SO_3)_2$ in a 1:2 stoichiometry and with the pH set at between 4 and 5. Peaks were observed for $[\mathbf{L1}H_4Cu_2 - H]^{3+}$, $[\mathbf{L1}H_4Cu_2 + CF_3SO_3]^{3+}$, and $[\mathbf{L1}H_4Cu_2 + 2CF_3SO_3]^{2+}$ (*m*/*z* 368, 369; 418, 419; and 701, 703 respectively). In the analogous complexes $[\mathbf{BZ}H_4Cu_2]^{4+}$ and $[\mathbf{PG}H_4Cu_2]^{4+}$, each $Cu^{2+}$ cation was found to be five-coordinate (diaminopyridine chelate + two water molecules) with a trigonal-bipyramidal geometry on the basis of the visible absorption spectra. A d–d absorption band centered at 670 nm ($\varepsilon$ = 190 $M^{-1}cm^{-1}$) can also be observed for $[\mathbf{L1}H_4Cu_2]^{4+}$ when spectra are taken at 3.7 < pH < 5.9, despite the absorption band of ferrocene in the visible range ($\lambda_{max}$ = 440 nm, $\varepsilon$ = 186 $M^{-1}cm^{-1}$). Figure 2 shows a spectrum taken for this species at pH 5.1. The solution has a green color due to the combination of blue (band at 670 nm) and yellow-orange (ferrocene band at 440 nm).

On increasing the pH above 6, the two hydroxide species $[\mathbf{L1}H_4Cu_2(OH)]^{3+}$ and $[\mathbf{L1}H_4Cu_2(OH)_2]^{2+}$ are formed by deprotonation of the coordinated water molecules. A p$K_a$ of 7.19 and 8.68 may be calculated for the first and second deprotonation steps. These values are too large to suggest bridging of $OH^-$ between the two $Cu^{2+}$ cations.[12] The d–d absorption band of coordinated copper does not change significantly on passing from $[\mathbf{L1}H_4Cu_2]^{4+}$ to $[\mathbf{L1}H_4Cu_2(OH)]^{3+}$ and $[\mathbf{L1}H_4Cu_2(OH)_2]^{2+}$ (a shift of $\lambda_{max}$ to 675 nm and a lowering of $\varepsilon$ to 160 are observed), similarly to the analogous complexes of **BZ**$H_4$ and **PG**$H_4$.[7,8] When the pH is raised to above 9.8 the solution takes a brown-purple color due to the neutral species $[\mathbf{L1}Cu_2]$, which is the prevalent one at pH > 10.8 (> 95% at pH > 11.3). In this species the two $Cu^{2+}$ cations have translocated inside the diamino-diimido compartments (see Scheme 2). Mass spectra measured at pH > 11.3 display the peak for $[\mathbf{L1}Cu_2 + H]^+$ (*m*/*z* 1101, 1103). The interpretation of the UV/Vis spectrum of this species is complicated by the presence of the ferrocene band. While the band at 670 nm disappears when $[\mathbf{L1}Cu_2]$ is formed (see part A of Figure 1, black triangles, for an $Abs_{670}$ vs. pH plot), the band for this species falls under the Fc absorption, as can be seen in Figure 2 for a spectrum taken at pH 11.5. The effect of the formation of $[\mathbf{L1}Cu_2]$ is to shift the apparent absorption maximum of Fc to longer wavelengths and to increase the intensity of the band. Subtracting the spectrum at pH 5.1 from that at pH 11.5 gives the profile shown in the inset of Figure 2, which gives an indication that the absorption maximum of $[\mathbf{L1}Cu_2]$ is closer to 515 nm (absorption of $[\mathbf{BZ}Cu_2]$[7]) than to 575 nm (absorption of $[\mathbf{PG}Cu_2]$[8]). This

Table 2. Formation constants of the $Cu^{2+}$-containing species for the ligands featuring two dioxo232 compartments. Column 1 reports the relative equilibrium for each value relative to a generic tetra-amido ligand $LH_4$. Uncertainties are indicated in parentheses.[a]

| | **L1**$H_4$ | **L3**$H_4$ |
|---|---|---|
| $LH_4 + 2Cu^{2+} \leftrightharpoons [LH_4Cu_2]^{4+}$ | 24.12(0.01) | 10.63(0.01) |
| $LH_4 + 2Cu^{2+} + H_2O \leftrightharpoons [LH_4Cu_2(OH)]^{3+} + H^+$ | 16.93(0.02) | –1.23(0.02) |
| $LH_4 + 2Cu^{2+} + 2H_2O \leftrightharpoons [LH_4Cu_2(OH)_2]^{2+} + 2H^+$ | 8.25(0.02) | |
| $LH_4 + 2Cu^{2+} \leftrightharpoons [LCu_2] + 4H^+$ | –13.17(0.02) | –14.89(0.03) |

[a] Data obtained in dioxane/water (8:2, v/v), 0.05 M $NaNO_3$, $T$ = 25 °C.

 © 2006 Wiley-VCH Verlag GmbH & Co. KGaA, Weinheim 

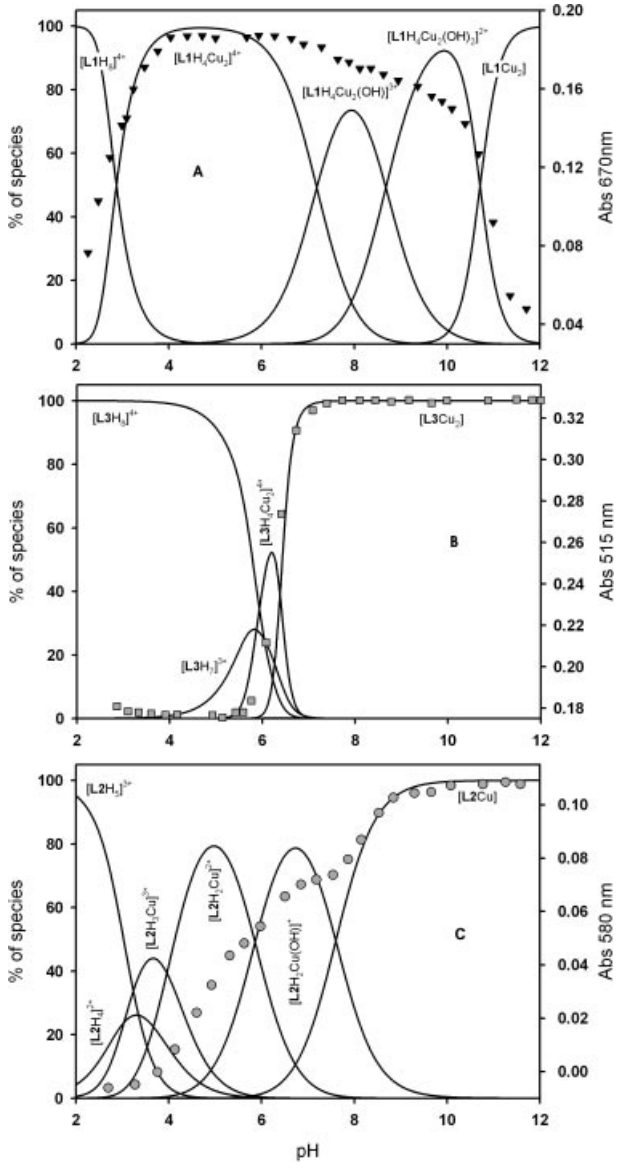


Figure 1. Distribution diagrams for the three systems, expressed as percentage of species (with respect to total ligand) vs. pH. Each diagram has been calculated for a $10^{-3}$ M ligand concentration. The species relative to each curve are reported on the diagram. A: **L1**$H_4$ + $2Cu^{2+}$; black triangles indicate the absorbance at 670 nm (i.e. at $\lambda_{max}$ for $[\mathbf{L1}H_4Cu_2]^{4+}$) vs. pH. B: **L3**$H_4$ + $2Cu^{2+}$; grey squares indicate the absorbance at 515 nm (i.e. at the expected maximum of absorption for the $Cu^{2+}$-centered d–d transition) vs. pH. C: **L2**$H_2$ + $Cu^{2+}$; grey circles indicate the absorbance at 580 nm (i.e. at $\lambda_{max}$ for [**L2**Cu]) vs. pH.

fits well with a structure in which each $Cu^{2+}$ is square planar, as shown in Scheme 2, which is indeed what would be expected if we consider the bulkiness of the ferrocene group, which should prevent the folding of the ligand structure and thus not allow apical coordination of $Cu^{2+}$ by the pyridine moiety.[8]

According to these findings, translocation of the $Cu^{2+}$ cations from the diaminopyridine compartments to the diamino-diimido ones (and vice versa) can occur as shown in Scheme 2, i.e. by changing the pH between two values chosen in the range 3.7–5.9 and >11.3. The movement is reversible and can be performed repeatedly, as confirmed by adding first excess base to a solution at pH 4.0 and then the same quantity of acid 10 times: the recorded spectra for $[\mathbf{L1}H_4Cu_2]^{4+}$ and [**L1**$Cu_2$] are superimposable, apart from a negligible lowering of the intensity due to dilution. Kinetic characterization of the translocation process is beyond the scope of this paper. However, it can be noticed that the process is relatively fast: an instantaneous (i.e. not progressive) color change was observed visually upon addition of acid or base, and even though only a few seconds were needed to add the acid or base and transfer a sample of the bulk solution to a cuvette, the sequence of constant absorption spectra obtained subsequently indicated that the translocation process was already complete. In this connection, the question may be raised whether the cation translocation is an *intra-* or an *inter*molecular process. Careful kinetic measurements would be needed to give a reliable answer to this question, and again these are outside the scope of this paper. However, the hypothesis that the movement is intramolecular can be put forward. First of all it should be stressed that the probability of the translocation process is much higher between two compartments belonging to the same ligand molecule than between two compartments of different ligand molecules (binding of $Cu^{2+}$ to the starting compartment means that the receiving compartment belonging to the same molecule would feel an enormously increased local concentration of $Cu^{2+}$). Moreover, kinetic studies carried out on closely related systems always show the intramolecular nature of the cation translocation processes.[4a,5]

It is interesting to compare these findings with those found for the non-translocating system containing the macrocyclic bis-dioxo232 ligand **L3**$H_4$ and $Cu^{2+}$ in a 1:2 molar ratio. In this case, the structure of the ligand does not allow chelation and formation of stable $Cu^{2+}$ complexes, apart from the square-planar, neutral bis-$Cu^{2+}$ species [**L3**$Cu_2$], which is obtained by the release of the four amido protons. Accordingly, the distribution diagram (Figure 1, B) is dominated by the tetraprotonated, non-metalated species $[\mathbf{L3}H_8]^{4+}$ and by [**L3**$Cu_2$], which is prevalent at pH > 6.2 and accounts for more than 95% at pH 6.8. Indeed, a species in which two $Cu^{2+}$ cations interact with the free ligand, i.e. $[\mathbf{L3}H_4Cu_2]^{4+}$, is observed with a very low formation constant (10.63 log units), and may be representative of the coordination of each $Cu^{2+}$ to a single amine nitrogen. This species forms in low quantities and in a limited pH range (it goes over 5% only between pH 5.6 and 6.5, reaching a maximum of around 50%) and is not competitive with respect to [**L3**$Cu_2$]. As a consequence, no translocation is possible in this system and formation of the neutral, square-planar species [**L3**$Cu_2$] is anticipated, on the pH axis, with respect to what is found for [**L1**$Cu_2$]. In particular, [**L3**$Cu_2$] goes over 95% at pH > 6.8, while [**L1**$Cu_2$] goes over 95% at pH > 11.3, with a dramatic shift of 4.5 pH units. As regards the UV/Vis spectra, at acidic pH values this system displays only the ferrocene absorption ($\lambda_{max}$ = 440 nm, $\varepsilon$ = 210 $M^{-1}cm^{-1}$, orange color) in the visible

 © 2006 Wiley-VCH Verlag GmbH & Co. KGaA, Weinheim 

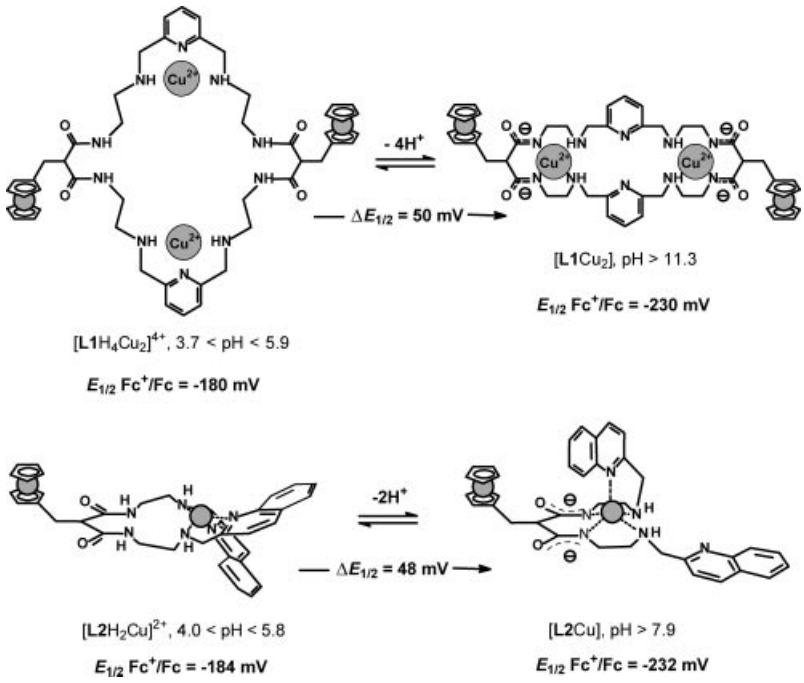


Scheme 2. Pictorial representation of pH-driven double $Cu^{2+}$ translocation and pH-driven single $Cu^{2+}$ translocation plus folding in ligands **L1**$H_4$ and **L2**$H_2$. The change in the Fc oxidation potential, which depends on the position(s) of the $Cu^{2+}$ cation(s), is also evidenced.

range, as can be seen in part B of Figure 2 (spectrum measured at pH 4.0). At the pH values in which the formation of [**L3**$Cu_2$] begins, the Fc band shifts to longer wavelengths, increases in intensity, and gains a shoulder due to the intrinsic absorption of $Cu^{2+}$ inside the diamino-diimido compartments (the solution takes a brown-purple color). Above pH 7 a series of superimposable spectra are obtained. Figure 2 (part B) also shows a spectrum recorded at pH 8.5. The inset B of Figure 2 displays the profile obtained by subtracting the spectrum recorded at pH 4.0 from that recorded at pH 8.5: noticeably, a curve similar to the inset A of Figure 2 is obtained, which can be considered a further indication of the square-planar nature of $Cu^{2+}$ in [**L1**$Cu_2$]. Moreover, plotting the absorbance at 515 nm vs. pH gives a profile (Figure 1 B, grey triangles) that perfectly superimposes the profile of the percentage of [**L3**$Cu_2$] vs. pH.

Finally, the behavior of the system containing **L2**$H_2$ and one equivalent of $Cu^{2+}$ was examined. In this case, the structure of the ligand allows only single $Cu^{2+}$ translocation. Indeed, the ligand resembles two very similar ones that we have already studied, in which a benzyl group[4b] or a propargyl group[8] are present instead of $FcCH_2$ in the same position. In both cases, a single pH-driven $Cu^{2+}$ translocation is possible from the bis(aminoquinoline) compartment to the diamino-diimido one, and vice versa. However, translocation is accompanied by an overall folding of the system as the $Cu^{2+}$ cation coordinated in the diamino-diimido compartment is also apically coordinated by quinoline. We have recently demonstrated that this kind of translocation + folding process always takes place when $Cu^{2+}$ moves in open (i.e. non-cyclic) ligands of this kind, independently of the nature of the substituent on the central carbon of the malonic amide group.[8] Accordingly, we would expect a behavior like that sketched in Scheme 2 for **L2**$H_2$/$Cu^{2+}$, and this is confirmed by the experimental results. Calculation of the potentiometric titrations and formation constants allows us to draw the distribution diagram for this system (Figure 2, C). [**L2**$H_2$Cu]$^{2+}$ is the species in which the $Cu^{2+}$ cation is coordinated by the two bis(aminoquinoline) chelating units (plus one water molecule), as has already been found for the systems based on similar benzyl- and propargyl-containing ligands.[4b,8] It forms at pH values above 3 and is prevalent between 4.0 and 5.8, reaching a maximum of 80% at pH 5.1. In the UV/Vis spectra (Figure 2 C, spectrum taken at pH 5.2), beside the ferrocene absorption (somewhat masked by the strong quinoline absorption band, which has a shoulder in the visible range), a d–d transition is observed at 660 nm ($\varepsilon$ = 90 $M^{-1}cm^{-1}$), typical of trigonal-bipyramidal $Cu^{2+}$ in these kind of complexes.[4b,8] At a pH between 4 and 6 the solution has a green color due to a combination of the ferrocene absorption and the $Cu^{2+}$ d–d transition. Mass spectra (ESI) reveal the expected peaks at *m*/*z* 730, 732 for [**L2**$H_2$Cu-H]$^+$ and at *m*/*z* 880, 882 for [**L2**$H_2$Cu + $CF_3SO_3$]$^+$. On raising the pH the monohydroxide species [**L2**$H_2$Cu(OH)]$^+$ forms, with $Cu^{2+}$ remaining in the bis(aminoquinoline) compartment, thanks to the deprotonation of coordinated water. The absorption spectrum of this species is similar to that of [**L2**$H_2$Cu]$^{2+}$. What is observed is a moderate shift of the absorption maximum towards shorter wavelengths and no perceivable change in the color of the solution. The solution color changes when the pH is raised over 7 and [**L2**Cu] forms in significant amounts. This species is that in which $Cu^{2+}$ has translocated into the diamino-diimido compartment. It becomes prevalent above pH 7.9 and accounts for over 95% at a pH above 9.5. At this pH or higher, the

 © 2006 Wiley-VCH Verlag GmbH & Co. KGaA, Weinheim 

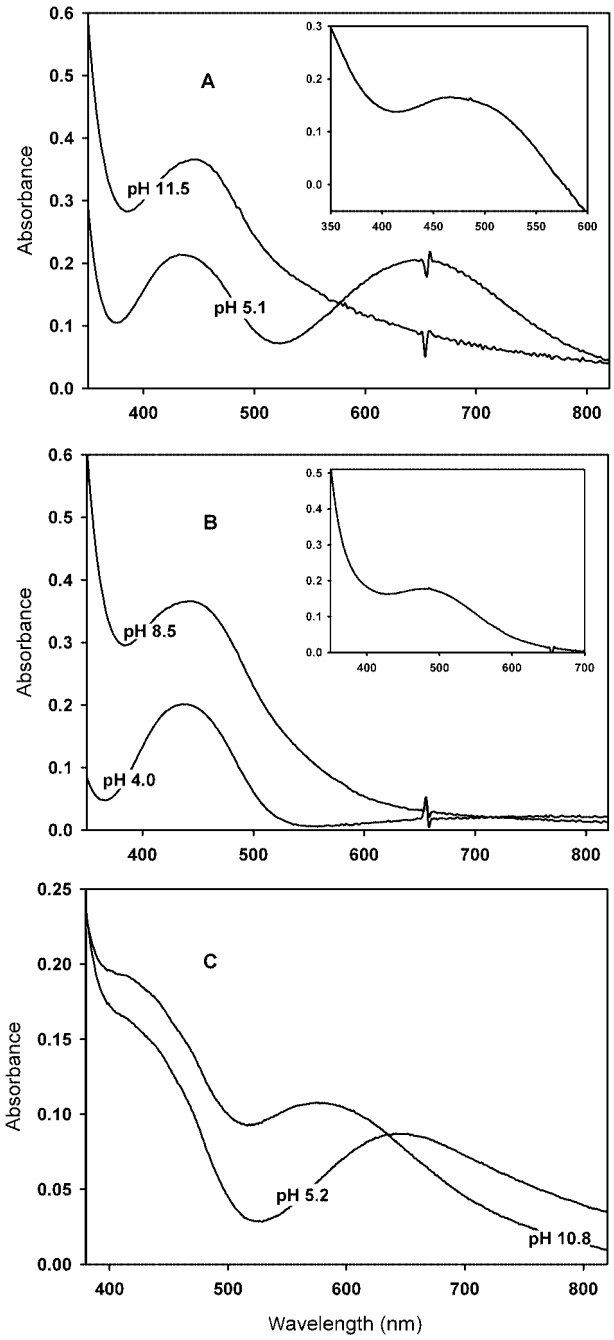


Figure 2. A: absorption spectra for the system $\mathbf{L1}H_4$ + $2Cu^{2+}$ at $1.1\times10^{-3}$ M ligand concentration; the spectrum recorded at pH 5.1 belongs to $[\mathbf{L1}H_4Cu_2]^{4+}$, the spectrum recorded at pH 11.5 belongs to $[\mathbf{L1}Cu_2]$. Subtraction of the spectrum at pH 5.1 from the spectrum at pH 11.5 is shown in the inset. B: Absorption spectra for the system $\mathbf{L3}H_4$ + $2Cu^{2+}$ at $1.0\times10^{-3}$ M ligand concentration; the spectrum recorded at pH 4.0 belongs to $[\mathbf{L3}H_8]^{4+}$ and the very weak and large band (between 600 and 900 nm) is due to free $Cu^{2+}$ (not complexed at this pH value, see also Figure 1, B), i.e. it is the d–d transition of the solvated cation; the spectrum recorded at pH 8.5 belongs to $[\mathbf{L3}Cu_2]$; the subtraction of spectrum at pH 4.0 from spectrum at pH 8.5 is shown in the inset. C: Absorption spectra for the system $\mathbf{L2}H_4$ + $Cu^{2+}$ at $1.0\times10^{-3}$ M ligand concentration; the spectrum recorded at pH 5.2 belongs to $[\mathbf{L2}H_2Cu]^{2+}$, the spectrum recorded at pH 10.8 belongs to [**L2**Cu].

solution display a green/brown color and the UV/Vis spectra show that the $Cu^{2+}$ d–d band has shifted to 580 nm ($\varepsilon$ = 110 $M^{-1}cm^{-1}$). This is the typical value for a pentacoordinate, square-pyramidal $Cu^{2+}$ cation inside a diamino-diimido compartment and apically coordinated by quinoline.[4b,8] (Figure 2 C, spectrum taken at pH 10.8). By means of a coupled pH-metric/spectrophotometric titration it is possible to obtain a plot of the absorbance at 580 nm vs. pH (part C of Figure 1, grey circles), which shows superimposition with the relevant percentage of species vs. pH curves. The observed step profile of $Abs_{580}$ vs. pH is due to the fact that both $[\mathbf{L2}H_2Cu]^{2+}$ and $[\mathbf{L2}H_2Cu(OH)]^{+}$ also have a significant absorbance at 580 nm. The ESI mass spectra show a peak at *m*/*z* 730, 732 for $[\mathbf{L2}Cu + H]^{+}$. Accordingly, single $Cu^{2+}$ translocation plus folding can take place, as illustrated in Scheme 2. The reversibility of the backwards and forwards movements was checked by preparing a solution of $[\mathbf{L2}H_2Cu]^{2+}$ at pH 5.2 and adding first excess strong base and then the same quantity of strong acid for ten cycles, always obtaining superimposable spectra for $[\mathbf{L2}H_2Cu]^{2+}$ and [**L2**Cu], with a negligible effect due to dilution.

## The Effect of the Translocation Process on the Ferrocene Oxidation Potential

A huge number of multicomponent molecular systems that contain Fc and one or more binding units are capable of electrochemically signaling the coordination of metal cations to the binding units or the protonation of the donor atoms of the latter. The proximity of $M^{n+}$ (or, for example, of $NH_2^+$) makes the oxidation potential of Fc increase due to obvious electrostatic repulsion effects between the positive charge and ferricinium.[13]

We first examined the effect of protonation of the amine groups on the Fc oxidation potential in our ligands in the absence of metal cations. Each ligand was dissolved in the same solvent used for complexation studies (dioxane/water, 4:1 v/v) to a $10^{-3}$ M concentration, with 0.1 M $NaNO_3$ as the background electrolyte, and a series of CV experiments were carried out spanning the 2–12 pH interval by means of addition of excess standard $HNO_3$ and microadditions of standard NaOH. Quite interestingly, the oxidation potential of Fc does not change significantly with protonation, even at the lower limit of the examined interval, i.e. pH 2. At the more acidic pH values the found $E_{1/2}$ values are –175, –178, and –170 mV for the species $[\mathbf{L1}H_8]^{4+}$, $[\mathbf{L2}H_5]^{3+}$, and $[\mathbf{L3}H_8]^{4+}$ respectively (potential values referenced to $Ag/Ag^+$ electrode; see Exp. Sect. for details), while at more basic values the measured values are –182, –184, and –180 mV for $\mathbf{L1}H_4$, $\mathbf{L2}H_2$, and $\mathbf{L3}H_4$, respectively (reversible waves are found in all cases, with a peak separation of around 120 mV at a scan rate of 400 mV $s^{-1}$). These values are close to the average for a mono-alkyl-substituted ferrocene, and the absence of significant changes on protonation is indeed not unexpected as it has already been demonstrated that a distance of more than three carbon atoms between ferrocene and the group changing its charge makes any electrostatic effects almost negligible.[14] However it is

 © 2006 Wiley-VCH Verlag GmbH & Co. KGaA, Weinheim 

worth stressing that even in +4 charged systems as $[\mathbf{L1}H_8]^{4+}$ and $[\mathbf{L3}H_8]^{4+}$ the peripheral ferrocene moieties do not experience any significant change (<10 mV) in the potential of their oxidation process.

After obtaining these data we examined the effect on the Fc oxidation potential of the presence/absence of $Cu^{2+}$ cations, and of their translocation, in the three ligands by means of coupled pH-metric titrations and electrochemical measurements. We coupled pH-metric titrations and CV measurements by adding base to acidic solutions containing ligand + $2Cu^{2+}$ (**L1**$H_4$ and **L3**$H_4$) or ligand + $Cu^{2+}$ (**L2**$H_2$). In the case of the double translocating system **L1**$H_4$/$2Cu^{2+}$ at the pH values at which $[\mathbf{L1}H_4Cu_2]^{4+}$, $[\mathbf{L1}H_4Cu_2(OH)]^{3+}$, and $[\mathbf{L1}H_4Cu_2(OH)_2]^{3+}$ exist, the $E_{1/2}$ for $Fc^+$/Fc oxidation remains constant at –180 mV vs. $Ag^+$/Ag (reversible, peak separation = 120 mV at a scan rate of 400 mV $s^{-1}$), i.e. roughly the same value observed both for the free and the protonated ligand. This clearly indicates that when the $Cu^{2+}$ cations are located in the diamino-pyridine compartments they are too far from Fc to exert any significant effect on it. On the other hand, when the pH is raised enough (>9.8) to translocate the two $Cu^{2+}$ cations inside the deprotonated dioxo232 compartments and form [**L1**$Cu_2$], a significant shift in the Fc redox potential is observed, with $E_{1/2}$ decreasing to a final value of –230 mV vs. $Ag^+$/Ag (reversible, peak separation = 120 mV at a scan rate of 400 mV $s^{-1}$), obtained at pH values above 11.2, i.e. where [**L1**$Cu_2$] accounts for more than 95% of the species present in solution. A nice superimposition of the $E_{1/2}$ vs. pH profile is observed with the formation curve of [**L1**$Cu_2$], as shown in Figure 3. It should be noted that the *lowering* of the oxidation potential of ferrocene due to the presence of a nearby metal cation is unusual but not new, as has already been reported in a ligand containing ferrocene and a simple dioxo232 ligand.[15] The overall charge in the complex is zero, but in each $Cu^{2+}$/diamino-diimido compartment a dipole is formed by $Cu^{2+}$ and the two negative charges (delocalized between the oxygen atoms and the conjugated imido nitrogens) that points its negative end towards the region of space in which the ferrocene moiety is located.

The same kind of result is found for the single $Cu^{2+}$ translocating system **L2**$H_2$/$Cu^{2+}$. At the pH values in which $Cu^{2+}$ is in the bis(aminoquinoline) compartment (up to pH 6) the observed $E_{1/2}$ for Fc oxidation is –184 mV (i.e. roughly the same as for the free or protonated ligand), while a negative shift is observed when the pH is raised and [**L2**Cu] begins to form. A final value of –232 mV vs. $Ag^+$/Ag is observed at pH 9.5 or higher ([**L2**Cu] > 95%).

Accordingly, this behavior allows electrochemical signaling of the pH-driven translocation of the $Cu^{2+}$ cations. Moreover, this result gives a clear indication that the two different positions in which the $Cu^{2+}$ cations can be located should have sharply different effects (e.g. as regards electrical capacity) on a surface to which **L1**$H_4$ and **L2**$H_2$ ligands are grafted by reaction of a $HC{\equiv}C–CH_2–$ group bound to the same carbon bearing the $FcCH_2$ substituent. Finally, it should be mentioned that, obviously, the same negative shift effect is observed for the **L3**$H_4$/$2Cu^{2+}$ system. However, as in this case no species exists to any significant degree in which the $Cu^{2+}$ cations are located on the ligand, except [**L3**$Cu_2$], a shift in the ferrocene $E_{1/2}$ is observed on going from the protonated ligand (–180 mV) to the [**L3**$Cu_2$] complex (–224 mV), i.e. it is not due to a translocation process.

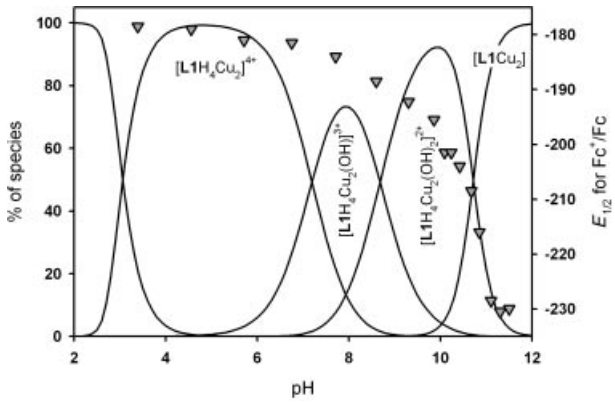


Figure 3. Distribution diagram for the system **L1**$H_4$/$2Cu^{2+}$ at $10^{-3}$ M ligand concentration, with superimposed (grey triangles) $E_{1/2}$ values for the $Fc^+$/Fc couple as a function of pH, showing the negative shift that occurs on changing the position of the copper cations from the diaminopyridine to the diamino-diimido units.

## Conclusions

Two new ligands have been studied in which double and single pH-driven $Cu^{2+}$ translocation has been demonstrated to take place. Due to the bulkiness of the ferrocene group, in the macrocyclic and double translocating system (**L1**$H_4$/$2Cu^{2+}$), translocation to the diamino-diimido compartments produces an authentic square planar $Cu^{2+}$ complex. On the other hand, in the open ligand and single translocating system (**L2**$H_2$/$Cu^{2+}$) translocation to the diamino-diimido compartment results in a five-coordinate $Cu^{2+}$ center, with one quinoline folding to coordinate copper in one of its apical positions. From an electrochemical point of view, positioning of the $Cu^{2+}$ cations in the compartments that are more distant from the Fc unit does not influence its redox potential at all. However, translocation inside the diamino-diimido compartments influences the oxidation of the ferrocene groups, which becomes easier by around 50 mV, thus allowing electrochemical signaling of the pH-driven translocation process. The unusual negative shift of the Fc oxidation potential on complexation of $Cu^{2+}$ in the diamino-diimido compartment reflects the formation of a dipole that has its negative end pointing towards the region of space in which the ferrocene is located. Beside adding an electrochemical tool for signaling cation translocation processes, this work also gives an indication that, if molecules with the same structure as those studied here could be grafted on a conducting surface through the covalent binding of groups located in the same position as ferrocene, the surface could change its properties (e.g. impedance) upon translocation of the $Cu^{2+}$ cation(s).

 © 2006 Wiley-VCH Verlag GmbH & Co. KGaA, Weinheim 

## Experimental Section

**Synthesis:** The syntheses of the three ligands use $N^1$,$N^3$-bis(2-aminoethyl)-2-(ferrocenylmethyl)malonamide (Ferrocene-methyldioxo232) as the starting material, which was prepared according to a literature procedure.[15] 2-Quinolinecarboxaldehyde and 2,6-pyridinedicarboxaldehyde were purchased from Aldrich and used without further purification.

**L1**$H_4$**:** 2,6-Pyridinedicarboxaldehyde (134 mg, 1 mmol) was dissolved in 60 mL of $CH_3CN$. Ferrocene-methyldioxo232 (386 mg, 1 mmol) dissolved in 40 mL of $CH_3CN$ was then added dropwise over a 2 h period under nitrogen and the mixture was kept under magnetic stirring overnight. An orange brown product (the tetraimino macrocycle) was collected by suction filtration, dissolved in methanol, and reduced with excess $NaBH_4$ (600 mg for each mol of C=N, considering 100% yield from the previous step), which was added in small portions, at room temperature, to avoid foaming. After the addition, the mixture was heated at reflux for 2 h, then cooled to room temperature and the solvent evaporated on a rotary evaporator. Water (100 mL) was added to the crude semisolid mixture, and the hydrolyzed suspension was extracted with three 30-mL portions of $CH_2Cl_2$. The organic portions were gathered, dried with $MgSO_4$, filtered, and the solvent removed on a rotary evaporator to give a yellow solid (237.5 mg, 0.243 mmol, 47.1% yield). ESI-MS: *m*/*z* 979 [**L1**$H_4$ + H]$^+$. $^1$H NMR (DMSO): $\delta$ = 7.94 (t, 4 H, CO-N*H*-$CH_2$), 7.68 (t, 2 H, py-H), 7.24 (d, 4 H, py-H), 4.11 (s, 10 H, H of ferrocene), 4.02 (s, 4 H, H of ferrocene), 4.00 (s, 4 H, H of ferrocene), 3.4–3.0 [m, 14 H, amine protons + CO-C*H*(*R*)-CO + CO-NH-C$H_2$], 2.74 (d, 4 H, Fc-C$H_2$-CH), 2.50 (m, C$H_2$-NH-$CH_2$ + DMSO) ppm. $C_{50}H_{62}Fe_2N_{10}O_4{\cdot}CH_2Cl_2$ (1063.7): calcd. C 57.63, H 6.07, N 13.18; found C 57.58, H 6.05, N 13.15.

**L2**$H_2$**:** Quinoline-2-carboxaldehyde (628.7 mg, 4 mmol) was dissolved in 20 mL of ethanol. Ferrocenemethyl-dioxo232 (772 mg, 2 mmol) was dissolved in 30 mL of ethanol and added dropwise at room temperature, with magnetic stirring, under nitrogen. After 18 h the solution (containing the diimine) was treated in situ with excess $NaBH_4$ (600 mg for each mol of C=N). The subsequent workup was identical to that of **L1**$H_4$. A brown oily product was obtained, which was transformed into a yellow solid after repeated washing with diethyl ether (1.21 g, 90% yield). ESI-MS: *m*/*z* 669 [**L2**$H_2$ + H]$^+$. $^1$H NMR (DMSO): $\delta$ = 8.5–7.5 (m, 14 H, quinoline protons and CO-N*H*-$CH_2$), 4.2–3.8 (m, 13 H, H of ferrocene and NH-C$H_2$-quinoline), 3.2 (m, 5 H, CO-CHR-CO and CO-NH-C$H_2$), 2.8 (d, 2 H, Fc-C$H_2$-CH), 2.6 (t, 4 H, C$H_2$-NH-$CH_2$) ppm. $C_{38}H_{40}FeN_6O_2{\cdot}H_2O$ (686.6): calcd. C 66.47, H 6.16, N 12.24; found C 66.44, H 6.18, N 12.21.

**L3**$H_4$**:** The synthesis of this ligand followed the same procedure described for **L1**$H_4$, but with isophthalaldehyde instead of 2,6-pyridinedicarboxaldehyde. The product was obtained as a yellow solid in 60.6% yield. ESI-MS: *m*/*z* 977 [**L3**$H_4$ + H]$^+$. $^1$H NMR (DMSO): $\delta$ = 7.86 (s, 4 H, CO-N*H*-$CH_2$), 7.15–7.25 (m, 8 H, H of the phenyl rings), 4.10 (s, 10 H, H of ferrocene), 4.02 (s, 4 H, H of ferrocene), 3.99 (s, 4 H, H of ferrocene), 3.61 (s, 8 H, NH-C$H_2$-arene), 3.35 (broad, 4 H, amine protons), 3.2–3.0 [m, 10 H, CO-C*H*(*R*)-CO + CO-NH-C$H_2$], 2.74 (d, 4 H, Fc-C$H_2$-CH), 2.50 (m, C$H_2$-NH-$CH_2$ + DMSO) ppm. $C_{52}H_{64}Fe_2N_8O_4{\cdot}0.5CH_2Cl_2$ (1019.3): calcd. C 61.86, H 6.43, N 10.99; found C 61.89, H 6.45, N 11.02.

**Potentiometric Titrations:** Protonation equilibria for ligands **L1**$H_4$, **L2**$H_2$, and **L3**$H_4$ were studied in dioxane/water (8:2, v/v) made up to 0.05 M in $NaNO_3$, thermostatted at 25 °C, with a Radiometer automatic system (Titralab TIM900) under nitrogen. In a typical experiment, a volume of 20 mL of a $10^{-3}$ M ligand solution was treated with 1.0 M standard $HNO_3$ in a quantity corresponding to the mols of ligand multiplied by the number of basic groups (amines + quinolines or pyridines) and augmented by two. Titrations were run by adding 20-μL portions of standard 0.1 M NaOH and collecting 80–100 points for each titration. Complexation equilibria were studied by means of titrations run under the same conditions, except that the starting solutions also contained $Cu(CF_3SO_3)_2$ in a 1:1 (**L2**$H_2$) or 2:1 (**L1**$H_4$ and **L3**$H_4$) molar ratio with respect to the ligand. Prior to each potentiometric titration, a titration according to the Gran method[16] was run to determine the $E°$ of the glass electrode in the chosen conditions. Protonation data (emf vs. volume of added base) were processed with the Hyperquad package[11] to determine protonation constants.

**Spectrophotometric Titrations:** Coupled spectrophotometric–pH-metric titrations were run with a procedure and under conditions similar to that described for potentiometric titrations. However, in this case, standard base was added manually by means of a 10- or 20-μL Rainin Pipet-Lite pipette. After each addition, a portion of the solution was transferred into a quartz cuvette and its absorption spectrum recorded. After recording the spectrum, the solution was transferred back to the bulk solution. The spectra recorded after each addition were associated with a pH value measured in the bulk solution by means of a glass electrode.

**Electrochemistry:** Cyclic voltammetric measurements were carried out in a three electrode cell, using a platinum electrode as the working electrode, a silver/silver ion electrode as the reference [clean silver wire into an electrolyte containing silver ion. The electrode filling solution was dioxane/water (8:2, v/v) made up to $7\times10^{-3}$ M in $AgNO_3$, with 0.1 M $NaNO_3$ as the background electrolyte]. Dioxane/water (8:2, v/v) was used as solvent, made up to 0.1 M in $NaNO_3$. Ligand + metal solutions were at concentrations $\geq 5\times10^{-4}$ M. pH was regulated by means of microadditions of standard acid or base, and checked with a glass electrode dipped in the electrochemical solution before measurements. Scan rates were in the 200–400 mV $s^{-1}$ range.

**Instrumentation:** Mass spectra were recorded with a Finnigan MAT TSQ 700 instrument, and NMR spectra with a Bruker AMX 400. Spectrophotometric measurements were performed with a diode array HP 8452A spectrophotometer or a Varian CARY 1000 SCAN spectrophotometer. The pH-metric titrations were made with a Radiometer TitraLab 90 titration system. Electrochemistry was obtained with a BAS100B/W instrument.

## Acknowledgments

We would like to thank MIUR (COFIN – PRIN 2005 national program) and INSTM (FIRB, project RBNE019H9K "Manipolazioni molecolari per macchine nanometriche") for financial support.

[1] J.-M. Lehn, *Angew. Chem. Int. Ed. Engl.* **1990**, *29*, 1304.
[2] a) V. Balzani, A. Credi, M. Venturi, *Chem. Eur. J.* **2002**, *8*, 5524; b) C. Dietrich-Buchecker, M. C. Jimenez-Molero, V. Sartor, J. P. Sauvage, *Pure Appl. Chem.* **2003**, *75*, 1383; c) J. P. Collin, V. Heitz, J.-P. Sauvage, *Top. Curr. Chem.* **2005**, *262*, 29.
[3] a) L. Zelikovich, J. Libman, A. Shanzer, *Nature* **1995**, *374*, 790; b) D. Kalny, M. Elhabiri, T. Moav, A. Vaskevich, I. Rubinstein, A. Shanzer, A.-M. Albrecht-Gary, *Chem. Commun.* **2002**, 1426.
[4] a) V. Amendola, L. Fabbrizzi, C. Mangano, P. Pallavicini, A. Perotti, A. Taglietti, *J. Chem. Soc., Dalton Trans.* **2000**, 185; b)

 © 2006 Wiley-VCH Verlag GmbH & Co. KGaA, Weinheim 

V. Amendola, C. Brusoni, L. Fabbrizzi, C. Mangano, H. Miller, P. Pallavicini, A. Perotti, A. Taglietti, *J. Chem. Soc., Dalton Trans.* **2001**, 3528; c) V. Amendola, L. Fabbrizzi, C. Mangano, P. Pallavicini, *Acc. Chem. Res.* **2001**, *34*, 488.

[5] V. Amendola, L. Fabbrizzi, C. Mangano, H. Miller, P. Pallavicini, A. Perotti, A. Taglietti, *Angew. Chem. Int. Ed.* **2002**, *41*, 2553.

[6] a) P. Arranz, C. Bazzicalupi, A. Bencini, A. Bianchi, S. Ciattini, P. Fornasari, C. Giorgi, B. Valtancoli, *Inorg. Chem.* **2001**, *40*, 6383; b) s. Tamburini, P. A. Vigato, M. Gatos, L. Bertolo, U. Casellato, *Inorg. Chim. Acta* **2006**, *359*, 183.

[7] L. Fabbrizzi, F. Foti, S. Patroni, P. Pallavicini, A. Taglietti, *Angew. Chem. Int. Ed.* **2004**, *43*, 5073.

[8] A. Aurora, M. Boiocchi, G. Dacarro, F. Foti, C. Mangano, P. Pallavicini, S. Patroni, A. Taglietti, R. Zanoni, *Chem. Eur. J.* **2006**, *12*, 5535.

[9] a) E. A. Dalchiele, A. Aurora, G. Bernardini, F. Cattaruzza, P. Pallavicini, R. Zanoni, F. Decker, *J. Electroanal. Chem.* **2005**, *579*, 133; b) R. Zanoni, F. Cattaruzza, C. Coluzza, E. A. Dalchiele, F. Decker, G. Di Santo, A. Flamini, L. Funari, A. G. Marrani, *Surf. Sci.* **2005**, *575*, 260.

[10] a) E. G. Robins, M. P. Stewart, J. M. Buriak, *Chem. Commun.* **1999**, 2479; b) P. T. Hurley, A. E. Ribbe, J. M. Buriak, *J. Am. Chem. Soc.* **2003**, *125*, 11334.

[11] P. Gans, A. Sabatini, A. Vacca, *Talanta* **1996**, *43*, 1739–1753.

[12] R. Menif, J. Reibenspies, A. E. Martell, *Inorg. Chem.* **1991**, *30*, 3446.

[13] a) P. D. Beer, K. Y. Wild, *Polyhedron* **1996**, *15*, 775; b) P. D. Beer, D. K. Smith, *J. Chem. Soc., Dalton Trans.* **1998**, 417; c) J. M. Lloris, R. Martinez-Mañez, M. E. Padilla-Tosta, T. Pardo, J. Soto, P. D. Beer, J. Cadman, D. K. Smith, *J. Chem. Soc., Dalton Trans.* **1999**, 2359; d) F. Oton, A. Tarraga, M. D. Velasco, P. Molina, *Dalton Trans.* **2005**, 1159.

[14] G. De Santis, L. Fabbrizzi, M. Licchelli, P. Pallavicini, *Inorg. Chim. Acta* **1994**, *225*, 293.

[15] a) G. De Santis, L. Fabbrizzi, M. Licchelli, P. Pallavicini, A. Perotti, *J. Chem. Soc., Dalton Trans.* **1992**, 3283; b) G. De Santis, L. Fabbrizzi, M. Licchelli, P. Pallavicini, A. Perotti, A. Poggi, *Supramolec. Chem.* **1994**, *3*, 115.

[16] G. Gran, *Analyst (London)* **1952**, *77*, 661.

Received: June 27, 2006
Published Online: September 28, 2006

 © 2006 Wiley-VCH Verlag GmbH & Co. KGaA, Weinheim 

DOI: 10.1002/ejic.200600621

# Size- and Shape-Controlled Synthesis and Assembly of a Silver Nanocomplex in UV-Irradiated TSA Solution

**Liangbao Yang,[a] Yuhua Shen,*[a] Anjian Xie,[a] Jianjun Liang,[b] Shikuo Li,[a] and Qingfeng Zhang[a]**

**Keywords:** Nanostructures / Silver / Photochemistry / Self-assembly

In this paper we describe the size-controlled synthesis of a silver nanocomplex based on the reduction of silver nitrate ($AgNO_3$) by UV-irradiated tungstosilicate acid [$H_4(SiW_{12}O_{40})$, TSA] solution. This method allows the synthesis of ellipsoidal particles with an average size that is tunable between 2.4 and 84 nm by varying the molar ratio of silver nitrate to TSA, the pH of the reaction solution, and the reaction temperature. Silver nanorods can be formed from the ellipsoidal nanoparticles by controlling the aging time. The formation mechanism of these nanorods is also discussed. The nanoparticles are characterized by UV/Vis spectroscopy, FTIR spectroscopy, XRD analysis, XPS, electron diffraction (ED), TEM, and with a Zetasizer instrument.

(© Wiley-VCH Verlag GmbH & Co. KGaA, 69451 Weinheim, Germany, 2006)

## Introduction

Metal nanoparticles are being investigated in considerable detail due to their exciting potential applications in catalysis,[1] biological and chemical sensing,[2,3] and optoelectronics.[4] One of the most important current challenges is to develop experimental recipes that would enable nanoparticle shape-control in addition to size and polydispersity. A number of nanoparticle morphologies such as wires,[5] rods,[6] cubes,[7] and nanotriangles/prisms[8] can now be routinely synthesized by different chemical methods.

Silver nanoparticles, in particular, are of great interest because of their ability to efficiently interact with light by virtue of plasmon resonances, which are the collective oscillations of the conduction electrons in the metal. Silver nanoparticles certainly have the potential to be the building blocks of future photonic and plasmonic devices as the field of nanotechnology matures.

A requirement for this progress is the development of a method that can reliably produce large quantities of silver nanoparticles with a controlled size distribution as different applications will require particles with various dimensions and the ability to tailor surface chemistry. The ideal method of synthesis should yield essentially naked particles so that different surface functionalities can be readily introduced for template-assisted or self-assembly based fabrication methods for nanoscale devices.

The use of tungstosilicate acid [$H_4(SiW_{12}O_{40})$, TSA] to synthesize silver nanoparticles is an important synthetic method. TSA ions form a subset of polyoxometalates of the Keggin structure. These polyoxometalates have the general formula $(XM_{12}O_{40})^{(8-n)-}$, where M is W or Mo and X is a heteroatom such as P, Si, or Ge, with $n$ being the valency of X.[9] The TSA ions, accompanying cations, and other components such as water are arranged in a well-defined secondary three-dimensional structure, the stability of which depends on the nature of the counterions, the amount of water, etc.[10] It is well known that Keggin ions undergo stepwise multielectron redox processes without a structural change[11] and can be reduced electrolytically, photochemically, and chemically (with suitable reducing agents). They are a large category of metal oxygen cluster anions with well-defined structures and properties and have diverse applications in the fields of analytical chemistry, biochemistry, and solid state devices, and have been used as antiviral and antitumor reagents. Their redox chemistry is characterized by their ability to accept and release a certain number of electrons, in distinct steps, without decomposition.[12] Recently, Papaconstantinou and co-workers have shown that photochemically reduced polyoxometalates of the Keggin structure phosphotungstic acid $(PW_{12}O_{40})^{3-}$[13] lead to the formation of the corresponding metal nanoparticles. Sastry and co-workers have used $(PW_{12}O_{40})^{3-}$ ions for making phase-pure core–shell nanoparticles.[14] They have also used $(PW_{12}O_{40})^{3-}$ ions as a template for the in-situ growth of metal nanoparticles,[15,16] star-shaped calcium carbonate crystals,[17] and CdS nanoparticles.[18]

[a] School of Chemistry and Chemical Engineering, Anhui University,
Hefei 230039, P. R. China
E-mail: s_yuhua@163.com
Fax: +86-551-510-7342
[b] Chuzhou Vocational Technology College,
Chuzhou 239000, P. R. China

Supporting information for this article is available on the WWW under http://www.eurjic.org or from the author.

 InterScience © 2006 Wiley-VCH Verlag GmbH & Co. KGaA, Weinheim 

$(PW_{12}O_{40})^{3-}$ is stable at a pH of around 1, whereas TSA is stable up to a pH of about 5.[5] It should be noted that these two Keggin ions have a similar photochemical behavior except that the reaction rates with $(PW_{12}O_{40})^{3-}$ appear to be about two to three times faster than those with TSA.[19] This faster reaction rate often leads to difficulty in controlling the morphologies of the particles, therefore TSA is preferable. In this paper, a general synthetic method that produces silver nanoparticles in water is proposed. The method offers the advantages of being easily scalable and able to produce particles that exhibit long-term stability. The sizes of the synthesized particles can be varied from several to eighty nanometers simply by varying the reaction conditions such as the molar ratio of silver nitrate to TSA, the pH value of the reaction solution, or the reaction temperature. At the same time, silver nanorods can be obtained by varying the aging time. The role of the TSA in directing the morphology of the Ag-TSA colloidal particles for the growth of nanoparticles of a range of chemical compositions is an exciting aspect of the work with important future implications in nanoparticle design. Another area where applications of such composites could arise is in the area of catalysis. Combining the Keggin-ion scaffold with catalytically active metal nanoparticles, such as Rh or Pd, could lead to novel catalysts wherein the Keggin ion and metal components catalyze different reactions simultaneously.[16] To the best of our knowledge, this is the first time to study the size-controlled and shape-controlled synthesis of silver nanoparticles by the templates of TSA colloidal particles. The TSA template may be removed by simple dissolution in an alkaline medium leaving behind reasonably intact silver nanoparticle superstructures. Presented below are details of this investigation.

## Results and Discussion

A representative Keggin structure $(SiW_{12}O_{40})^{4-}$ was chosen to study the reaction between $(SiW_{12}O_{40})^{5-}$ and $Ag^+$ ions. The $(SiW_{12}O_{40}]^{5-}$ ion was obtained by photolysis ($\lambda >$ 280 nm) of a deaerated 2-propanol/$(SiW_{12}O_{40})^{4-}$ aqueous solution, in the presence of, for instance, 2-propanol as a sacrificial reagent[20] [Equation (1)].

$$2(SiW_{12}O_{40})^{4-} + (CH_3)_2CHOH \rightarrow 2(SiW_{12}O_{40})^{5-} + (CH_3)_2C{=}O + 2H^+ \quad (1)$$

After UV irradiation, the above solution gradually turned from colorless to grey (Ag) [Equation (2)]. This should be due to two reasons: one is the ability of the reduced $(SiW_{12}O_{40})^{5-}$ to transfer the electrons efficiently to silver ions;[21] the other is the lower potential of the one-equivalent-reduced tungstate couple $(SiW_{12}O_{40})^{4-}$/$(SiW_{12}O_{40})^{5-}$ (0.057 V vs. NHE;) relative to $Ag^+/Ag^0$ (0.799 V vs. NHE).

$$(SiW_{12}O_{40})^{5-} + Ag^+ \rightarrow (SiW_{12}O_{40})^{4-} + Ag \quad (2)$$

Furthermore, TSA ions can be utilized cyclically as oxidizing agent or reducing agent according to Equations (1) and (2).

Figure 1 shows the UV/Vis spectra recorded for a mixture of 1 mM $AgNO_3$ and 1 mM TSA at different stages of treatment. Prior to UV irradiation, it can be seen that there is no absorption in the visible region (0 h, Figure 1A), whereas after UV irradiation absorption bands are observed in the region 460–478 nm with the reaction time ranging from 20 to 300 min. These absorption bands are characteristic of silver nanoparticles and are caused by excitation of surface-plasmon vibrations.[22] Figure 1B shows the changes of wavelength and absorbance with different reaction time. From Figure 1, we can see that the absorption band becomes sharper and the resonance intensity increases, both of which are due to the increase of the number of silver nanoparticles during the whole process. A gradual shift of surface plasmon band (from 460 to 478 nm) is commensurate with the increasing $(SiW_{12}O_{40})^{5-}$ mol fraction. It can be seen that all the peaks are located at positions between those for pure $(SiW_{12}O_{40})^{5-}$ and Ag nanoparticle plasmon bands (730 and 413 nm, respectively, as reported

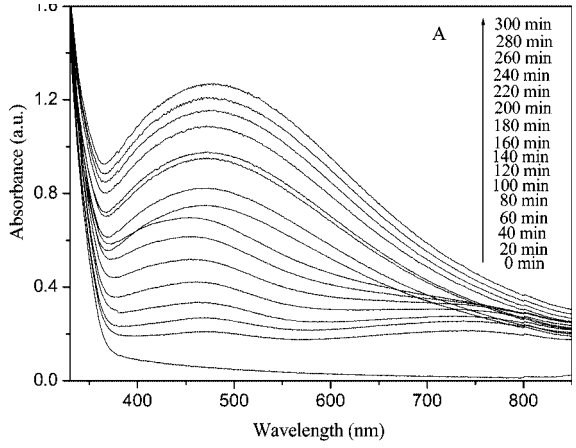


Figure 1. (A) UV/Vis spectra (330–850 nm) recorded for an aqueous mixture of 1 mM $AgNO_3$ and 1 mM TSA at different times of treatment. 0 h: before UV irradiation; 20–300 min: after UV irradiation. (B) Changes of wavelength and absorbance with reaction time. The inset shows one of the spectra of Figure 1A in the region from 210 to 330 nm.

 © 2006 Wiley-VCH Verlag GmbH & Co. KGaA, Weinheim 

earlier).[13,23,24] The presence of only one plasmon resonance, which shifts gradually from nanosilver to $(SiW_{12}O_{40})^{5-}$ ion particle plasmon bands clearly suggests the formation of TSA-silver nanocomposites rather than a segregated structure, as two bands would be observed in the latter case.[14] Thus, the UV-irradiated TSA ions reduce the $Ag^+$ ions, presumably on the surface of the TSA colloidal particles. It is notable that, in all experiments, the tungstosilicate acid structure remains intact in the process, as determined by the stability of the absorbance peak at 263 nm (shown in the inset of Figure 1B), which is characteristic of the oxidized form of TSA.[13]

In order to study the interaction between $AgNO_3$ and TSA during UV irradiation, the dynamic process of Ag-TSA colloid formation was analyzed by monitoring the conductance of a mixture consisting of equal volumes of 1 mM TSA and 1 mM $AgNO_3$ solutions (the conductance value of 1 mM aqueous TSA is 1.060 mS while that of 1 mM $AgNO_3$ is 0.532 mS). Figure 2 shows the conductance of the Ag-TSA reaction mixture measured as a function of the reaction time. After $AgNO_3$ is added to the TSA solution, it can be seen that the conductivity increases slowly. The reason for this is that the silver cations react with TSA anions to form a strong electrostatic complexation in solution. During complexation of silver ions with TSA anions, it is expected that the mobility of ions in solution would decrease, although the concentration of the ions increases swiftly. As UV irradiation progresses, the silver ions are reduced. At the end of the reaction the silver ions have been reduced completely, complexation of the silver cations and TSA anions in solution disappears, and plenty of TSA anions are generated. This means that the solution conductivity increases steadily and saturates after about 5 h of reaction, which is therefore an estimate of the optimum reaction time for the formation of this colloidal Ag nanocomplex.

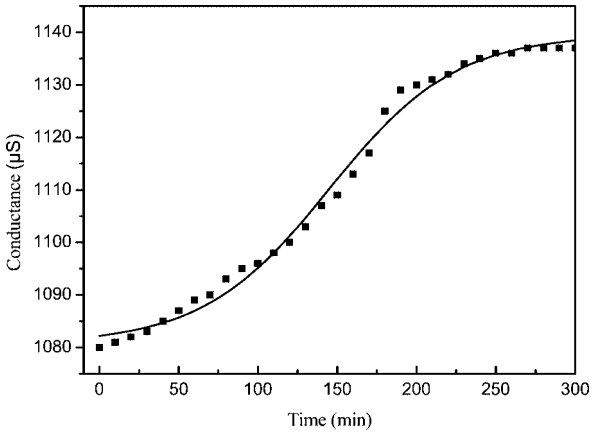


Figure 2. Conductivity measured as a function of time after mixing equal-volume aqueous solutions of 1 mM TSA and 1 mM $AgNO_3$ and irradiating for 5 h.

The XRD pattern recorded from a drop-coated film of the UV-irradiated sample on a glass substrate is shown in Figure 3. The (111), (200), (220), and (311) Bragg reflections of face-centered cubic (fcc) silver are clearly observed. Some of the Bragg reflections corresponding to the TSA structure (indicated by an asterisk) indicate that the formation of silver nanoparticles on the $Ag^+$-TSA colloidal particle template does not disrupt the basic structure of TSA. The XRD pattern recorded from a drop-coated film of the Ag-TSA nanocomplex solution after alkali dissolution of the TSA scaffold is shown as curve b in Figure 3. It is clear that the Bragg reflections of the TSA scaffold have disappeared, leaving behind just the Bragg reflections of the Ag nanoparticle assembly.

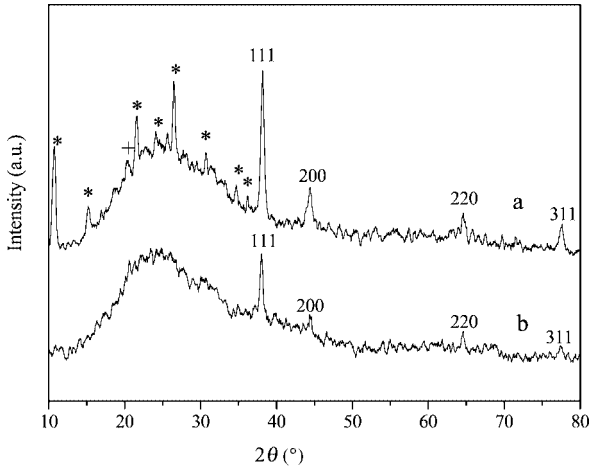


Figure 3. XRD patterns recorded from drop-coated films on glass substrates of silver nanoparticles synthesized by reaction of UV-irradiated TSA solution with aqueous $AgNO_3$ before (curve a) and after base treatment (curve b). The Bragg reflections marked * correspond to TSA.

Figure 4 shows the XPS $W_{4f}$ and $Ag_{3d}$ core-level spectra recorded from drop-coated films of the Ag-TSA solution on a Si (111) substrate. Figure 4A shows the $W_{4f}$ spectrum recorded from the Ag-TSA film. This spectrum can be resolved into spin-orbit pairs (splitting $\approx$ 2.15 eV) with a $4f_{7/2}$ binding energy (BE) of 35.19 eV (curve 1 in Figure 4A). Figure 4B shows the $Ag_{3d}$ core-level spectrum. The $Ag_{3d}$ spectrum resolves into two spin-orbit components. The Ag $3d_{5/2}$ and $3d_{3/2}$ peaks occur at a BE of 367.8 and 373.8 eV, respectively, and correspond to metallic silver.[25] The result demonstrates that only one form of Ag is present in solution, in the form of $Ag^0$. There is no evidence for additional components in the $Ag_{3d}$ spectrum, which indicates the complete reduction of the $Ag^+$ ions in the UV-irradiated TSA solution.

Figure 5A–D show representative TEM images recorded from a drop-coated film of the Ag-TSA solution after aging for 1, 6, 24, and 48 h, respectively. Figure 5A clearly show that there are only densely populated ellipsoidal or irregular structures. The crystalline nature of the silver nanoparticles forming the ellipsoidal or irregular crystal is revealed by the typical electron diffraction pattern shown in the inset of Figure 5A. The four fringe patterns observed, with spacings of 2.360, 2.021, 1.408, and 1.230 Å, are consistent with the fcc polycrystalline silver (111), (200), (220), and (311) spacings of 2.359, 2.044, 1.445, and 1.231 Å. Figure 5D shows

 © 2006 Wiley-VCH Verlag GmbH & Co. KGaA, Weinheim 

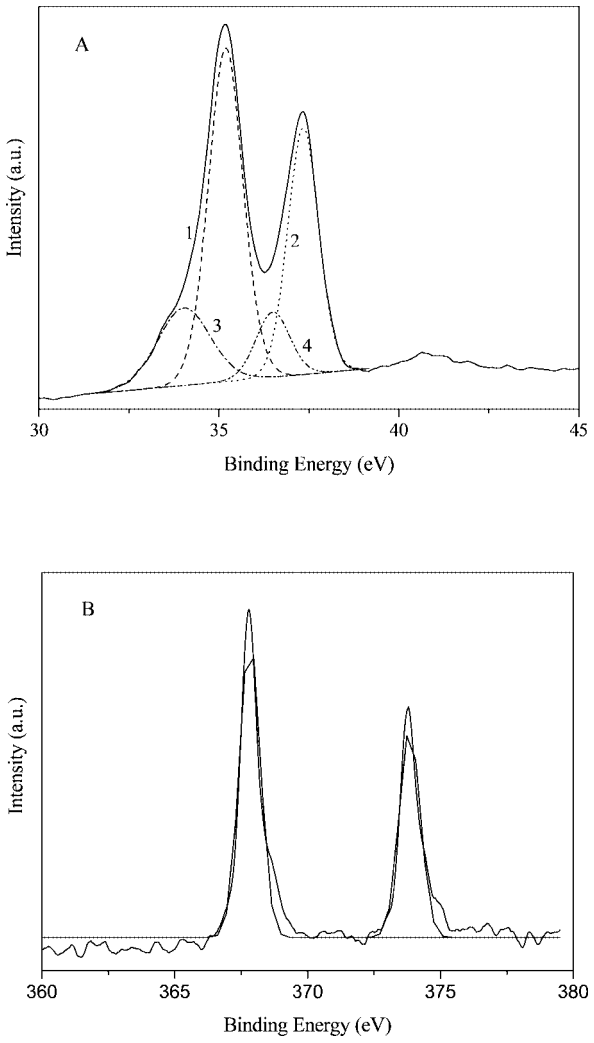


Figure 4. XPS recorded from drop-coated films of the Ag-TSA solution on a Si(111) substrate. (A) W 4f core-level spectrum together with two spin-orbit pairs (1, 2 and 3, 4). (B) Ag 3d core-level spectrum.

a representative TEM image recorded from a drop-coated film of the silver-nanocomplex solution after aging for 48 h. The surface of the rods is smooth and their structure is well-defined, with an average length and diameter of 1250 and 80 nm, respectively (a particle-size-distribution measurement was made from 140 nanorods). The aspect ratio (AR) of the silver nanorods in Figure 5D is estimated to be $13.2 \pm 5.0$. From the TEM image, it can be seen that the nanorods are smooth. In addition to the rod-shaped silver crystals, a lot of irregular crystals are also observed at the bottom left-hand corner of the image (Figure 5D), which implies that the nanorods possibly develop from the original irregular crystals.

The crystallinity of the nanorods was further studied by electron diffraction. As can be seen in the inset of Figure 5D, the ED patterns demonstrate the highly crystalline nature of the particles. From the electron diffraction analysis, the reflection assignments agree well with the results of nanowires reported previously,[26–28] thus demonstrating

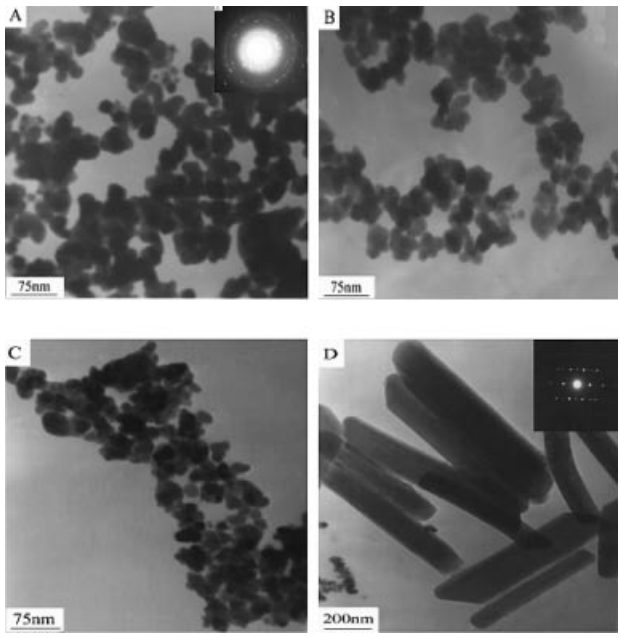


Figure 5. Representative TEM images of Ag nanocrystals obtained at different aging times after reaction (A–D). The insets in A and D are the electron diffraction patterns.

that the rod is formed by a cyclic penta-tetrahedral twin crystal in which five {111} twin boundaries are arranged radially to the [110] direction of the elongation axis. The rod has a pentagonal cross-section and is bound by five {100} side faces and five {111} faces at each end. In accordance with this structure feature, the rod should grow through the decahedral twinned particles with a diameter similar to the transverse length of the rods. The longitudinal and transverse lengths of the rods normally increase in the cases of smaller amounts of seeds. The rod formation possibly occurs in the early aggregation step of the initial particles.

It has been noticed that this kind of reaction takes place within a few seconds.[16] A lot of silver is generated in the first few seconds, so silver "seeds" can be formed, although no silver nanorods are generated at this stage. However, this in itself is not enough to form silver nanorods from silver seeds. Nanorod nucleation is thought to require twinned seed particles, so seed aggregation as a source of twinning may be an important step of nanorod synthesis.[29] On the other hand, the distance between two silver seeds is short, therefore some silver monomers can easily move and adsorb onto the deposited seeds and these aggregated seeds can form nanorods by subsequent recrystallization. So, we think that the growth mode for nanorods in our work is a type of seed-mediated growth mechanism.[29–31]

To understand the formation of large silver nanorod assemblies better, the kinetics of crystallization were monitored as a function of aging time. After aging for 1 h, ellipsoidal or irregular-shaped particles were obtained (Figure 5A). After aging for 6 h the long, irregular crystals begin to take shape and the number of ellipsoidal crystals decreases (Figure 5B). This is the initial stage of silver nano-

 © 2006 Wiley-VCH Verlag GmbH & Co. KGaA, Weinheim 

rod formation from ellipsoidal silver particle seeds. After aging for 24 h (Figure 5C) the Ag nanorods have almost formed, and when the aging time is prolonged to 48 h the silver nanorods grow into a well-organized shape (Figure 5D). The silver cubes are stable when they are separated from solvents. We found that the dry silver cubes do not change at all after being kept in air for several months.

To discount the possibility of UV-irradiated 2-propanol being the reducing agent for silver ions and thus for nanoparticle formation, a control experiment was performed in which 2 mL of 2-propanol was added to 20 mL of a 1 mM aqueous, deaerated solution of $AgNO_3$ and irradiated for 5 h. There was no change in color of the $AgNO_3$ solution after UV irradiation, which indicates that the product of UV-irradiated 2-propanol is not responsible for the reduction of $AgNO_3$. In the UV/Vis spectrum, the characteristic silver absorption band cannot be observed (see UV/Vis spectrum in Figure S1 in the Supporting Information).

Figure 6 shows the dependence of the particle diameter on the different molar ratios of $Ag^+$ ion to TSA. Parts A–D of Figure 6 show four samples of Ag-TSA nanoparticles corresponding to 1:10, 1:4, 1:2, and 2:1 molar ratios, respectively. These samples have mean diameters of 2.4, 22, 38, and 75.3 nm, respectively. As demonstrated in Figure 6, the size of these Ag-TSA nanoparticles can be conveniently controlled simply by varying the molar ratio, which changes from 0.1 to 2. The diameter increases monotonically from about 2.4 to about 75.3 nm. However, the growth rate decreases gradually, and when the molar ratio is above 2 there is only a small increase in the diameter of the silver nanoparticles. We also noticed that the color reflects the nanoparticle size in our experiments. By following the evolution of the color changes, we observed that a black color represents a colloidal size of about 70 nm and that the suspension of 10-nm-diameter Ag-TSA nanoparticles has, in fact, a grayish appearance, although it appears at lower concentrations. These changes may be directly related to the absorption features of the particles in the visible region of the spectra. It is not unusual that the size of the particles increases as a result of decreasing the relative concentrations of the reducing agent. This behavior is similar to that found in many chemical reduction approaches to nanosystems because the nucleation and growth sequences are both affected by the relative concentrations of the reducing agent and the precursor.[32] In our case, we think that the nucleation process is overwhelmingly faster than particle growth at the higher relative concentrations of the reducing agent, which results in smaller sized particles.

Figure 7 shows the dependence of the Ag-TSA nanoparticles' diameter on the pH of the solution. Parts A–D of Figure 8 show four samples of Ag-TSA nanoparticles corresponding to pH 1, 2, 3, and 4, respectively. The mean diameters of these four samples are 82, 22.8, 5.7, and 2.8 nm, respectively. Figure 7 clearly shows that the diameter decreases continuously with an increase in pH from 1 to 4. However, the rate of decrease diminishes gradually, and when the pH is near 4 there is only a small decrease in the diameter of the nanoparticles. The variation of pH does not

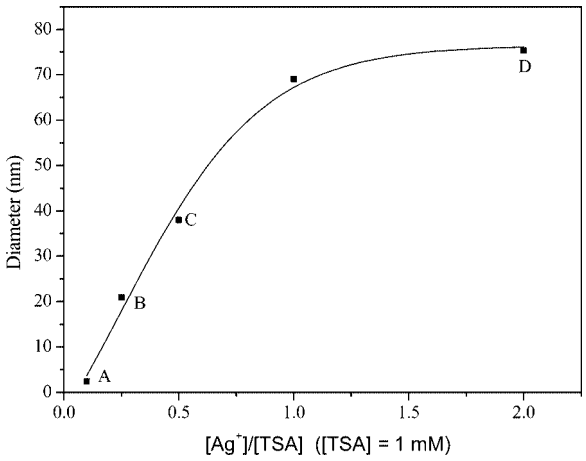


Figure 6. Dependence of the Ag-TSA nanoparticle diameter on the different molar ratio of $Ag^+$ ion to TSA. A–D show four samples of Ag-TSA nanoparticles corresponding to 1:10, 1:4, 1:2, and 2:1 molar ratios ($T$ = 20 °C; [$Ag^+$] = 1 mM; reaction time: 5 h; aging time: 1 h).

alter the rate of metal ions' recovery during the reaction.[33] In other words, varying the pH does not alter the redox power of TSA, so the influence of pH on the particle diameter has nothing to do with this. We suppose that an electrostatic interaction leads to the dependence of the particle diameter on pH. Thus, with a decrease in pH the electrostatic interaction between the silver cations and TSA anions in solution becomes weaker, which allows the size of the particles to increase.

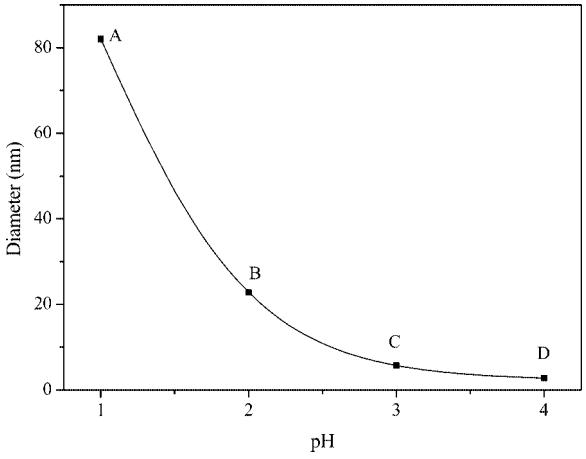


Figure 7. Dependence of the Ag-TSA nanoparticle diameters on pH. A–D show four samples of Ag-TSA nanoparticles with different diameters obtained at pH 1, 2, 3, and 4, respectively ($T$ = 20 °C; [TSA] = 1 mM; [Ag+] = 1 mM; reaction time: 5 h; aging time: 1 h).

The dependence of the diameter of the Ag-TSA nanoparticles on temperature was also studied, as shown in Figure 8. Parts A–D of Figure 8 show four samples of Ag-TSA nanoparticles with different diameters obtained at 20, 40, 60, and 80 °C, respectively. The mean diameters of these four samples are 38, 7.6, 3.4, and 2.7 nm. As demonstrated in Figure 8, the size of these colloids can be conveniently controlled by simply varying the temperature. That is, the

 © 2006 Wiley-VCH Verlag GmbH & Co. KGaA, Weinheim 

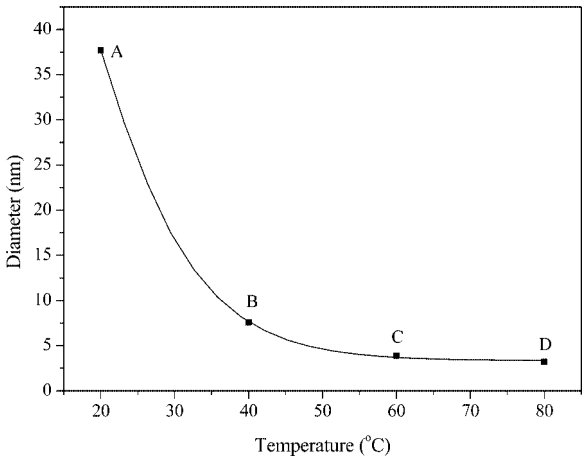


Figure 8. Dependence of the Ag-TSA nanoparticle diameters on reaction temperature. A–D show four samples of Ag-TSA nanoparticles with different diameters obtained at 20, 40, 60,and 80 °C, respectively.

diameter undergoes a continuous decrease with increasing temperature. However, the decrease rate diminishes gradually, and at 80 °C only a small decrease of the diameter of the particles is observed. With increasing temperature the silver ions have higher energies, which are larger than the affinity between TSA ions and silver ions, therefore these silver ions can move anywhere in the solution. That is to say, with an increase of temperature the rate of nucleation of silver nanoparticles accelerates, therefore the nucleation process is faster than the particle growth under these conditions and the size of the particles decreases.

To sum up, since the size of these Ag-TSA nanoparticle colloids can be conveniently controlled by simply varying the molar ratio of silver nitrate to TSA, the pH of the reaction solution, or the reaction temperature, the procedure described here should provide an effective route to ellipsoidal nanoparticles of Ag with controllable size. In principle, this procedure can be extended to several other noble metals that have been prepared as nanoparticles by reduction with TSA.

## Conclusions

In conclusion, a facile method has been proposed to synthesize size-controlled silver nanocomplexes. The size of the nanoparticles can be controlled by varying the reaction conditions, and nanorods of silver can be formed by prolonging the aging time. The rods are found to generate through aggregation to form decahedral seeds followed by elongation along the [110] direction. The possibility of using the TSA framework as a UV-switchable reducing matrix is exciting and may be extended to the creation of other highly organized hybrid inorganic structures with possible applications in nanomaterials.

## Experimental Section

**Materials:** $H_4(SiW_{12}O_{40})$ (TSA), $AgNO_3$, and 2-propanol were all obtained as A.R. grade from Shanghai Reagent Co. All other reagents were used as received.

**Synthesis of the Silver Nanocomplex:** In a typical experiment, 2-propanol (2 mL) and an aqueous deaerated solution of $AgNO_3$ (20 mL, 1 mM) were added to an aqueous deaerated solution of TSA (20 mL) under continuous stirring for 10 min and then allowed to age for 30 min. This mixture was irradiated with UV light (Pyrex filter, >280 nm, 450 W Hanovia medium pressure lamp) for 5 h. The solution changed to gray gradually, thus indicating the formation of silver nanoparticles. The corresponding control experiments under different reaction conditions, such as molar ratio of silver nitrate to TSA, pH of the reaction solution, and reaction temperature are similar to the above experiments.

To discount the possibility of UV-irradiated 2-propanol being the reducing agent for silver ions, and thus for nanoparticle formation, a control experiment was performed in which 2 mL of 2-propanol was added to 20 mL of a 1 mM aqueous deaerated solution of $AgNO_3$ and irradiated for 5 h.

**Sample Characterization:** UV/Vis spectroscopy measurements of the Ag-TSA solution at different stages of treatment were carried out with a TU-1901 model UV/Vis double beam spectrophotometer (Beijing Purkinje General Instrument Co., Ltd, China) operating at a resolution of 2 nm. XPS measurements of the silver nanoparticles synthesized by reduction of $Ag^+$ ions in a UV-irradiated TSA solution were carried out with a VG ESCALAB MKII instrument at a pressure greater than $10^{-6}$ Pa. The general scan and Ag 3d and W 4f core-level spectra were recorded with non-monochromated Mg-$K_\alpha$ radiation (photon energy = 1253.6 eV). The core-level binding energies (BEs) were aligned with respect to the C 1s binding energy (BE) of 285 eV. Samples for TEM analysis were prepared by drop-coating films of the Ag-TSA solution at different stages of reaction on carbon-coated copper TEM grids, allowing the grid to stand for 2 min, and then removing the excess solution with blotting paper. TEM measurements were performed with a JEM model 100SX electron microscope instrument (Japan Electron Co.) at an accelerating voltage of 80 kV. Selected-area electron diffraction measurements of the Ag nanoparticles were also carried out. XRD analysis of drop-coated films of the Ag-TSA solution on glass substrates was carried out with a MAP18AHF instrument (Japan MAC Science Co.). Conductance measurements were carried out to characterize the interaction between $Ag^+$ ions and TSA. The conductance of a mixture consisting of equal volumes of 1 mM TSA and 1 mM silver nitrate solutions was investigated. The conductivity of this solution as a function of reaction time was measured with a DDSJ-308A model conductivity meter (Shanghai Precision & Scientific Instrument Co., Ltd). The size distributions of nanoparticles were measured by PCS on a Zetasizer $3000HS_A$ instrument (Malvern Instruments Limited) at different molar ratios of silver nitrate to TSA, pH of the reaction solution, and reaction temperature.

**Supporting Information** (see footnote on the first page of this article): UV/Vis spectrum of a mixture of 2 mL 2-propanol and 20 mL of a 1 mM aqueous, deaerated solution of $AgNO_3$ after irradiation for 5 h.

## Acknowledgments

This work was supported by the National Science Foundation of China (20471001, 20371001), the Specific Project for Talents of Science and Technology of the Universities of Anhui Province (2005hbz03), the Key Laboratory of Environment-Friendly Polymer Materials of Anhui Province, and the Science Foundation of Anhui Province (2006KJ155B).

 © 2006 Wiley-VCH Verlag GmbH & Co. KGaA, Weinheim 

[1] S. Mandal, D. Roy, R. V. Chaudhari, M. Sastry, *Chem. Mater.* **2004**, *16*, 3714–3724.
[2] T. A. Taton, C. A. Mirkin, R. L. Letsinger, *Science* **2000**, *289*, 1757–1760.
[3] N. Krasteva, I. Besnard, B. Guse, R. E. Bauer, K. Mullen, A. Yasuda, T. Vossmeyer, *Nano Lett.* **2002**, *2*, 551–555.
[4] M. L. Brongersma, J. W. Hartman, H. A. Atwater, *Phys. Rev. B* **2000**, *62*, 356–359.
[5] K. K. Caswell, C. M. Bender, C. J. Murphy, *Nano Lett.* **2003**, *3*, 667–669.
[6] F. Kim, J. H. Song, P. Yang, *J. Am. Chem. Soc.* **2002**, *124*, 14316–14317.
[7] Y. Sun, Y. Xia, *Science* **2002**, *298*, 2176.
[8] a) R. Jin, Y. Cao, C. A. Mirkin, K. L. Kelly, G. C. Schatz, J. G. Zheng, *Science* **2001**, *294*, 1901–1903; b) S. S. Shankar, A. Rai, B. Ankamwar, A. Singh, A. Ahmad, M. Sastry, *Nat. Mater.* **2004**, *3*, 482–488.
[9] J. A. Huheey, *Inorganic Chemistry*, 3rd ed., Harper and Row, New York, **1983**, p. 698.
[10] M. Misono, *Mater. Chem. Phys.* **1987**, *17*, 103–108.
[11] a) M. T. Pope, A. Muller, *Angew. Chem. Int. Ed. Engl.* **1991**, *30*, 34–48; b) V. Kogan, Z. Izenshtat, R. Neumann, *Angew. Chem. Int. Ed.* **1999**, *38*, 3331–3334.
[12] M. T. Pope in *Inorganic Chemistry Concepts*, Springer Verlag, West Berlin, **1983**, vol. 8, p. 101.
[13] A. Troupis, A. Hiskia, E. Papaconstantinou, *Angew. Chem. Int. Ed.* **2002**, *41*, 1911–1914.
[14] S. Mandal, P. R. Selvakannan, R. Pasricha, M. Sastry, *J. Am. Chem. Soc.* **2003**, *125*, 8440–8441.
[15] S. Mandal, D. Rautaray, M. Sastry, *J. Mater. Chem.* **2003**, *13*, 3002–3005.
[16] A. Sanyal, S. Mandal, M. Sastry, *Adv. Funct. Mater.* **2005**, *15*, 273–280.
[17] D. Rautaray, S. R. Sainkar, M. Sastry, *Langmuir* **2003**, *19*, 10095–10099.
[18] S. Mandal, D. Rautaray, A. Sanyal, M. Sastry, *J. Phys. Chem. B* **2004**, *108*, 7126–7131.
[19] A. Hiskia, A. Troupis, A. Hiskia, E. Papaconstantinou, *Environ. Sci. Technol.* **2001**, *35*, 2358–2364.
[20] a) E. Papaconstantinou, *Chem. Soc. Rev.* **1989**, *16*, 1–31; b) A. Hiskia, A. Mylonas, E. Papaconstantinou, *Chem. Soc. Rev.* **2001**, *30*, 62–69; c) A. Mylonas, A. Hiskia, E. Androulaki, D. Dimotikali, E. Papaconstantinou, *Phys. Chem. Chem. Phys.* **1999**, *1*, 437–440.
[21] I. A. Weinstock, *Chem. Rev.* **1998**, *98*, 113–170.
[22] S. Link, Z. I. Wang, M. A. El-Sayed, *J. Phys. Chem. B* **1999**, *103*, 3529–3533.
[23] P. Mukherjee, S. Senapati, D. Mandal, A. Ahmad, M. I. Khan, R. Kumar, M. Sastry, *ChemBioChem* **2002**, *3*, 461–463.
[24] A. Ahmad, P. Mukherjee, S. Senapati, D. Mandal, M. I. Khan, R. Kumar, M. Sastry, *Colloids Surf. B* **2003**, *28*, 313–318.
[25] C. S. Fadley, D. A. Shirley, *J. Res. Natl. Bur. Stand.* **1970**, *74A*, 543.
[26] a) Y. Sun, B. Mayers, T. Herricks, Y. Xia, *Nano Lett.* **2003**, *3*, 955–960; b) H. Hofmeister, S. A. Nepijko, D. N. Ievlev, W. Schulze, G. Ertl, *J. Cryst. Growth* **2002**, *234*, 773–781.
[27] C. J. Johnson, E. Dujardin, S. A. Davis, C. J. Murphy, S. Mann, *J. Mater. Chem.* **2002**, *12*, 1765–1770.
[28] I. Lisiecki, A. Filankembo, H. Sack-Kongehl, K. Weiss, M. P. Pileni, *J. Phys. Rev. B* **2000**, *61*, 4968–4974.
[29] H. Liao, J. H. Hafner, *J. Phys. Chem. B* **2004**, *108*, 19276–19280.
[30] a) Z. Wei, A. J. Mieszawska, F. P. Zamborini, *Langmuir* **2004**, *20*, 4322–4326; b) Z. Wei, F. P. Zamborini, *Langmuir* **2004**, *20*, 11301–11304.
[31] N. Taub, O. Krichevski, G. Markovich, *J. Phys. Chem. B* **2003**, *107*, 11579–11582.
[32] Z. H. Lin, C. R. Chris Wang, *Mater. Chem. Phys.* **2005**, *92*, 591–594.
[33] A. Troupis, A. Hiskia, E. Papaconstantinou, *Environ. Sci. Technol.* **2002**, *36*, 5355–5362.

Received: July 2, 2006
Published Online: September 20, 2006

 © 2006 Wiley-VCH Verlag GmbH & Co. KGaA, Weinheim 

DOI: 10.1002/ejic.200600653

# Mixed Amido/Imido/Guanidinato Complexes of Tantalum: Effects of Ligand Substitution on Thermal Properties

**Arne Baunemann,[a] Manuela Winter,[a] Karoly Csapek,[a] Christian Gemel,[a] and Roland A. Fischer*[a]**

**Keywords:** X-ray diffraction / Chelates / N ligands / Tantalum / Nitrides

Mixed amido/imido/guanidinato tantalum complexes $[Ta(NR^1R^2)\{C(NR^1R^2)(NR^3)_2\}_2(NR^4)]$ [$R^1$,$R^2$ = methyl, ethyl; $R^3$ = cyclohexyl (cy), isopropyl; $R^4$ = *tert*-butyl, *n*-propyl] have been synthesized by the insertion of carbodiimides into tantalum–amide bonds. All compounds have been characterized by means of NMR spectroscopy, mass spectrometry, and CHN analysis. Additionally, single crystal structures of five compounds (**4**: $R^1$ = Me, $R^2$ = Et, $R^3$ = *i*Pr, $R^4$ = *t*Bu; **5**: $R^1$, $R^2$ = Et, $R^3$ = *i*Pr, $R^4$ = *t*Bu; **6**: $R^1$, $R^2$ = Me, $R^3$ = cy, $R^4$ = *t*Bu; **8**: $R^1$, $R^2$ = Et, $R^3$ = cy, $R^4$ = *t*Bu; **9**: $R^1$, $R^2$ = Et, $R^3$ = *i*Pr, $R^4$ = *n*Pr) have been determined and relevant structural issues are discussed. The thermal properties of all complexes have been investigated by TGA/DTA measurements. Thus, complexes originating from diisopropylcarbodiimide (*i*Pr-cdi) are significantly more volatile than complexes derived from dicyclohexylcarbodiimide (cy-cdi). In contrast, variations of $R^1$, $R^2$, and $R^4$ have only a small impact on the thermal behavior of the complexes. Finally, selected compounds have been pyrolyzed at 600 °C, and the decomposition products studied by GC-MS and $^1$H NMR spectroscopy.
(© Wiley-VCH Verlag GmbH & Co. KGaA, 69451 Weinheim, Germany, 2006)

## Introduction

Thin films of tantalum nitride (TaN) play an important role in the ongoing process of device optimization in microelectronics. Conducting TaN films serve as gate electrode materials in metal oxide semiconductor field-effect transistors as well as diffusion barriers for the inhibition of copper or silver diffusion into the silicon substrates.[1] A rough literature survey shows that 492 patents on the production, processing, and use of TaN films were filed in 2005 alone. TaN thin films can be deposited by various methods, including sputtering processes and gas-phase deposition techniques such as MOCVD (metal organic chemical vapor deposition), plasma-enhanced CVD (PECVD), or atomic layer deposition (ALD). These gas-phase-based techniques make use of binary metal halides, although more recently metal-organic tantalum coordination complexes have also been used. Key parameters for precursors in MOCVD or ALD processes include volatility, thermal decomposition behavior, chemical reactivity, accessibility, and safety issues. Several tantalum–ligand systems have been tested for the deposition of TaN films, amongst which mixed amido/imido tantalum complexes are the most prominent.[2] While most compounds in this class are liquid and have a sufficiently high vapor pressure, they tend to be chemically and thermally rather fragile and show problems in terms of long-term stability at vaporization temperatures as well as a high sensitivity towards moisture or reactive gases. Thus, the use of didentate ligands such as hydrazines has been suggested.[3] In this paper we wish to report on an extension of this approach by introducing guanidinates as suitable chelating ligands for mixed amido/imido tantalum complexes. The use of guanidinates has already shown promising results for the deposition of Ti(C)N or $HfO_2$ thin films in CVD processes.[4,5] Moreover, we recently published a communication on the synthesis and characterization of mixed amido/imido/guanidinato complexes **3**–**5** and showed the successful deposition of conductive, almost carbon-free TaN (C content $< 1\%$) thin films using compound **4** as a single source precursor.[6] This is a rather surprising result considering the fact that less complex amido/imido compounds of tantalum with a considerably lower relative carbon content produce films with much higher carbon contents of around 10%.[7] These results encouraged us to carry out a more detailed examination of the tantalum guanidinato/amido/imido complex system and the impact of substituent variations at different ligand sites on the chemical and thermal properties of the resulting complexes. Table 1 gives a summary of all complexes synthesized and characterized in this paper.

[a] Lehrstuhl für Anorganische Chemie II – Organometallics and Materials Chemistry, Ruhr-University Bochum
44870 Bochum, Germany
Fax: +49-234-321-4174
E-mail: roland.fischer@rub.de
Supporting information for this article is available on the WWW under http://www.eurjic.org or from the author.

 © 2006 Wiley-VCH Verlag GmbH & Co. KGaA, Weinheim 

Table 1. Overview of compounds **3**–**10** in this publication.

| Compound | $R^1$ | $R^2$ | $R^3$ | $R^4$ | M.p. [°C] |
|---|---|---|---|---|---|
| **3**[a] | Me | Me | *i*Pr | *t*Bu | 232 |
| **4**[b] | Me | Et | *i*Pr | *t*Bu | 217 |
| **5**[b] | Et | Et | *i*Pr | *t*Bu | 210 |
| **6** | Me | Me | cy | *t*Bu | 210 |
| **7** | Me | Et | cy | *t*Bu | 218 |
| **8** | Et | Et | cy | *t*Bu | 204 |
| **9** | Et | Et | *i*Pr | *n*Pr | 195 |
| **10** | Et | Et | cy | *n*Pr | 205 |

[a] Included for reasons of comparison. [b] Crystal structure has not been published so far.

## Results and Discussion

Two basic pathways are known in the literature for the synthesis of metal guanidinate complexes: (i) salt metathesis reactions in which sodium or lithium guanidinates are treated with the metal halides[4,8] and (ii) the insertion of carbodiimides into metal–amido bonds, which is a more convenient pathway that does not involve the formation of LiX or NaX byproducts.[6,9] In the case of tantalum guanidinates, previous work from Tin et al. includes the synthesis of $[Ta(NMe_2)_4\{C(NMe_2)(NR'')_2\}]$ (R″ = cy, *i*Pr) as well as the preparation of tantalum complexes of the neutral, protonated guanidine ligand.[10] The large variety of compounds published before 2001 have been summarized in a recent review.[11]

The synthesis of the starting compounds $[Ta(NR^1R^2)_3(NR^4)]$ followed published procedures.[12] At first the intermediate compound $[TaCl_3(N\text{-}n\text{Pr})(py)_2]$ (**1**) was formed by reaction of $TaCl_5$ with *n*-propylamine, chlorotrimethylsilane, and pyridine. It should be noted that on scaling up the literature procedure it is possible to keep the amount of solvent almost constant by increasing the amount of pyridine, which significantly increases the solubility of **1** in toluene and thus allows the separation of the product from the precipitated ammonium salts (see Experimental Section). In a second step, this pyridine-stabilized salt was treated with $LiNEt_2$ in order to form $[Ta(NEt_2)_3(N\text{-}n\text{Pr})]$ (**2**). Higher yields of **2** can be obtained when stoichiometric amounts of lithium amide are added to **1** at –60 °C instead of an excess at room temperature. The mixed amido/imido tantalum complexes were then treated with the respective carbodiimides in hexane to give the guanidinato/amido/imido complexes **3**–**10** (Scheme 1).

The synthesis of **3**–**5** has already been described in a previous communication.[6a] It is noteworthy that no insertion products could be isolated when sterically encumbering carbodiimides such as $(t\text{Bu})_2C_2N$ or $(SiMe_3)_2C_2N$ were used, even after refluxing the reaction mixtures for 24 h in the presence of a large excess of the carbodiimides. On the other hand, reaction with the unsubstituted carbodiimide (which exists as its tautomer $H_2NC{\equiv}N$) did not lead to isolable products but instead gave an orange solid which is insoluble in organic solvents. It is likely that transamination reactions lead to the formation of insoluble, oligomeric tantalum amides.

Compounds **3**–**10** can be prepared in high yields (>80%) and are white solids with rather high melting points of 195–230 °C. All compounds are highly soluble in hexane, benzene, or toluene and their elemental analyses are in good agreement with their suggested molecular formulae. The mass spectra of **3**–**10** show differences between the bis(cyclohexyl)carbodiimide (cy-cdi) containing compounds and their (*i*Pr-cdi) based congeners. Thus, the intensities of the $[M^+]$ peaks of **6**, **7**, **8**, and **10** (cy-cdi) are below 1% of the base peak (if visible at all), while they are above 10% for **3**, **4**, **5**, and **9** (*i*Pr-cdi). As will be shown below, this is consistent with the thermal properties of these compounds, since cy-cdi based compounds generally show significant decomposition during evaporation. The most intense peaks for **6**, **7**, **8**, and **10** are observed at *m*/*z* 41, 43 and 55 and are due to the cyclohexyl fragments $C_3H_5^+$, $C_3H_7^+$, and $C_4H_7^+$.

### NMR Analysis

All NMR assignments are based on two-dimensional NMR spectra of the previously published compounds **3**–**5**.[6a] The $^1H$ NMR spectra of **3**–**10** show rather large differences in the exact chemical shifts of the diastereotopic alkyl substituents of the Ta-amido groups, which also show a hindered rotation due to the partial π character of the Ta–N bond. In the case of the dimethyl-substituted amido group (**6**), the two singlets are separated by 0.5 ppm and in the case of the diethyl-substituted amido group (**8**, **9**, and **10**), the four doublets of quartets ($ABX_3$ spin system) are found in a range of 1.5 ppm. Of these four multiplets, three are close to each other while the other is strongly high-field shifted, probably because of the anisotropic magnetic field of the guanidinate π systems. The $^1H$ and $^{13}C$ NMR spectra

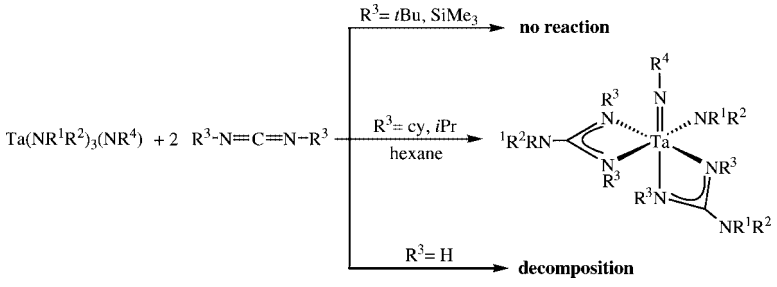


Scheme 1. Synthesis of compounds **3**–**10**.

 © 2006 Wiley-VCH Verlag GmbH & Co. KGaA, Weinheim 

of **7** (MeEtN substitution) could not be fully assigned due to the formation of rotational isomers, which leads to a mixture of several interconvertible isomers and thus highly complex solution spectra. The $^1$H NMR spectra of the cycdi based complexes **6**, **7**, **8**, and **10** show broad signals for the cyclohexyl groups, with only the $C_\alpha$ proton being slightly low-field shifted. The assignment of all $^{13}$C NMR spectra, with the exception of **7**, was straightforward and is therefore not discussed here in detail.

### X-ray Analysis

Single crystals of **4**, **5**, **6**, **8**, and **9** were obtained by recrystallization of the compounds from toluene at –30 °C. Several attempts to obtain crystals of **7** or **10** suitable for single-crystal X-ray analysis failed. Compounds **4** and **5** crystallize in an orthorhombic crystal system while the crystal systems of **6**, **8**, and **9** are of lower symmetry, i.e. monoclinic for **6** and **8** and triclinic for **9**. The molecular structures of **6** and **9** are displayed in Figure 1 as representatives of all solid-state structures.[13] Table 2 contains bond lengths, angles, and dihedral angles for all the above complexes.

The molecular structures of all compounds are very similar to each other and to that of compound **3**, which has already been discussed in an earlier publication.[6a] Thus, only the solid-state structure of **6** will be discussed here in more detail. The tantalum(V) center in **6** is sixfold coordinated by two didentate guanidinato ligands, one amido, and one imido group, resulting in a highly distorted octahedron. The Ta–N(6)–C(18) unit of the imido ligand is almost linear [170.6(4)°] and the Ta–N(6) bond is relatively short (1.79 Å), which indicates an almost sp-hybridized imido ligand. Due to the strong π-donating effect of this imido ligand,[14] the Ta(1)–N(3) bond of the guanidinato ligand opposite to the imido group is lengthened [2.437(5) Å], while the second Ta–N bond in the same guanidinato ligand [Ta(1)–N(4) = 2.123(5) Å] is considerably shorter. Obviously, the π-donating effect of the imido group results in an unsymmetrical charge distribution within the delocalized π system of the guanidinato ligand, which is also well reflected in a rather large difference in the N–C bond lengths [N(3)–C(2) = 1.308(9), N(4)–C(2) = 1.363(9) Å]. Scheme 2 illustrates the mesomeric structures for the metal–guanidinato interactions, with structure **a** describing best the observed bond lengths in the solid-state structure.

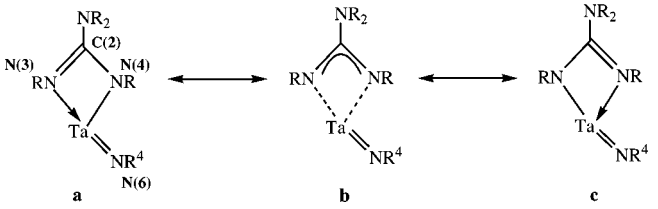


Scheme 2. Mesomeric structures for metal–guanidinato interactions.

The second guanidinato ligand [N(1)–C(1)–N(2)] is more symmetric – the two Ta–N bond lengths are 2.168(6) Å [Ta–N(1)] and 2.279(5) Å [Ta(1)–N(2)]. Again, the longer Ta–N bond is found *trans* to the more basic ligand, i.e. the amido group. The noncoordinated $NR_2$ groups of the guanidinato ligands are almost planar, with angular sums around the nitrogen atoms of 355.1° and 359°, respectively. A rather weak π-donating effect of the $NR_2$ groups to the guanidinato π-systems is suggested by a relatively large tilt angle of the C–N–C planes of 45.3° and 40.6°, respectively, which is obviously an effect of the steric repulsions of the alkyl substituents. However, an even weaker interaction is found in $[Ta(NMe_2)_4\{C(NMe_2)(N\text{-}cy)_2\}]$,[10a] which shows a tilt angle of the two CNC planes of more than 80°. Indeed, the C–N bond length of the exocyclic nitrogen ligand to the guanidinato core is elongated by 0.03 Å compared to **6**.

### Analysis of Thermal Properties

The thermal properties of compounds **6**–**10** were analyzed by classic melting point determinations, standard TG/DTA measurements, isothermal analyses, and sublimation

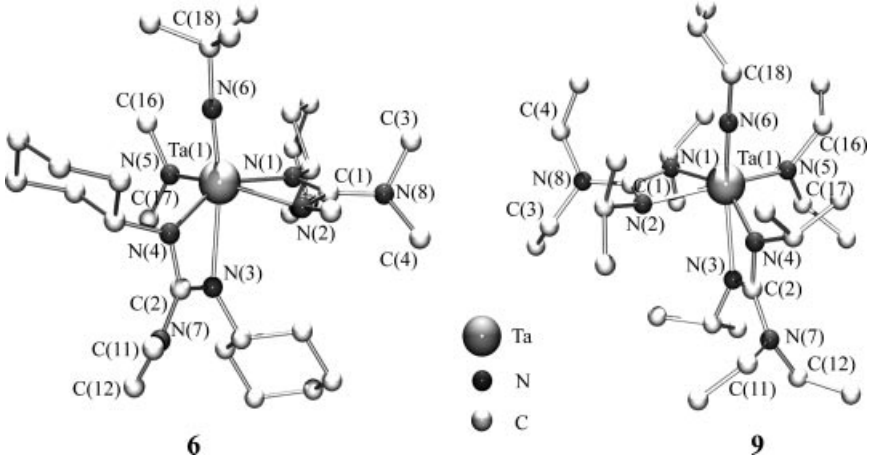


Figure 1. Povray/Ortep drawings of the molecular structures of **6** and **9** in the solid state. All hydrogen atoms have been omitted for clarity.

 © 2006 Wiley-VCH Verlag GmbH & Co. KGaA, Weinheim 

Table 2. Selected bond lengths [Å] and bond and torsion angles [°] for **3**,[a] **4**, **5**, **6**, **8**, and **9**.

| | **3** | **4** | **5**·Et | **6** | **8**·Et | **9**·Et |
|---|---|---|---|---|---|---|
| Ta(1)–N(1) | 2.174(4) | 2.185(7) | 2.198(8) | 2.168(6) | 2.198(4) | 2.192(4) |
| Ta(1)–N(2) (opp. amido) | 2.254(4) | 2.251(7) | 2.275(8) | 2.279(5) | 2.269(4) | 2.250(4) |
| Ta(1)–N(3) (opp. imido) | 2.396(5) | 2.409(7) | 2.408(8) | 2.437(5) | 2.408(4) | 2.433(4) |
| Ta(1)–N(4) | 2.129(4) | 2.127(7) | 2.126(8) | 2.123(5) | 2.136(4) | 2.122(4) |
| Ta(1)–N(5) (Ta-amido) | 2.014(5) | 2.002(8) | 2.023(8) | 2.005(5) | 2.008(4) | 2.013(4) |
| Ta(1)–N(6) (Ta-imido) | 1.785(5) | 1.791(8) | 1.790(10) | 1.786(6) | 1.797(4) | 1.780(4) |
| N(1)–C(1) | 1.345(7) | 1.352(11) | 1.327(13) | 1.389(8) | 1.342(6) | 1.329(6) |
| N(2)–C(1) | 1.309(7) | 1.318(11) | 1.327(14) | 1.318(9) | 1.319(6) | 1.325(6) |
| N(3)–C(2) | 1.320(7) | 1.319(11) | 1.323(13) | 1.308(9) | 1.320(6) | 1.308(6) |
| N(4)–C(2) | 1.361(7) | 1.356(11) | 1.359(13) | 1.363(9) | 1.363(6) | 1.359(6) |
| N(5)–C(16) | 1.456(7) | 1.453(12) | 1.464(13) | 1.451(8) | 1.457(7) | 1.471(6) |
| N(5)–C(17) | 1.463(7) | 1.468(13) | 1.465(12) | 1.453(8) | 1.464(6) | 1.454(7) |
| N(6)–C(18) | 1.444(7) | 1.453(12) | 1.449(14) | 1.457(9) | 1.440(7) | 1.439(7) |
| N(7)–C(2) | 1.390(7) | 1.382(11) | 1.400(13) | 1.388(9) | 1.400(6) | 1.388(6) |
| N(7)–C(11) | 1.442(7) | 1.454(12) | 1.464(14) | 1.465(9) | 1.456(7) | 1.467(6) |
| N(7)–C(12) | 1.440(8) | 1.447(12) | 1.467(16) | 1.443(9) | 1.446(7) | 1.457(6) |
| N(8)–C(1) | 1.393(7) | 1.391(11) | 1.393(13) | 1.397(8) | 1.393(7) | 1.393(6) |
| N(8)–C(3) | 1.444(8) | 1.437(13) | 1.444(14) | 1.455(8) | 1.456(8) | 1.451(7) |
| N(8)–C(4) | 1.450(7) | 1.447(12) | 1.461(14) | 1.459(9) | 1.483(10) | 1.463(7) |
| N(1)–Ta(1)–N(2) | 59.56(18) | 59.4(3) | 58.8(3) | 60.3(2) | 59.14(15) | 59.38(14) |
| N(2)–Ta(1)–N(5) | 155.36(19) | 154.8(3) | 158.7(3) | 153.7(2) | 156.64(17) | 155.50(16) |
| N(3)–Ta(1)–N(4) | 58.92(16) | 58.1(3) | 58.5(3) | 58.0(2) | 58.62(14) | 58.05(14) |
| N(3)–Ta(1)–N(6) | 162.19(19) | 161.1(3) | 160.6(4) | 161.4(2) | 161.69(16) | 156.78(16) |
| N(1)–C(1)–N(2) | 112.0(5) | 111.0(7) | 111.6(9) | 111.3(6) | 111.9(4) | 112.1(4) |
| N(3)–C(2)–N(4) | 113.2(5) | 112.0(8) | 112.5(8) | 113.0(6) | 112.9(4) | 113.2(4) |
| C(1)–N(8)–C(3) | 122.7(5) | 120.6(8) | 120.6(9) | 121.0(6) | 120.3(5) | 120.0(4) |
| C(1)–N(8)–C(4) | 121.9(5) | 121.4(8) | 120.1(8) | 119.0(5) | 118.4(5) | 121.8(4) |
| C(3)–N(8)–C(4) | 115.3(5) | 117.2(8) | 118.5(9) | 115.1(5) | 120.9(5) | 116.9(4) |
| C(2)–N(7)–C(11) | 120.7(5) | 122.9(8) | 121.4(8) | 123.0(6) | 121.1(4) | 120.6(4) |
| C(2)–N(7)–C(12) | 122.8(5) | 120.7(8) | 121.4(8) | 120.9(6) | 121.1(4) | 119.1(4) |
| C(11)–N(7)–C(12) | 116.5(5) | 116.1(8) | 117.2(8) | 115.1(6) | 116.0(4) | 118.2(4) |
| Ta(1)–N(6)–C(18) | 170.6(4) | 175.7(7) | 174.9(8) | 175.7(5) | 172.3(4) | 176.2(4) |
| Ta(1)–N(5)–C(16)–C(17) | 178.5(7) | 179.4(12) | 178.4(14) | 175.7(10) | 180.0(7) | 178.0(5) |
| C(2)–N(7)–C(11)–C(12) | 179.8(9) | 174.6(11) | 179.0(14) | 169.0(10) | 166.2(6) | 163.6(4) |
| C(1)–N(8)–C(3)–C(4) | 176.3(9) | 169.9 (12) | 169.9(14) | 155.5(10) | 172.4(5) | 166.8(5) |
| C(3)–N(8)–C(4) plane vs. N(1)–C(1)–N(2)–plane | 45.5(13) | 50.4(18) | 53.7(14) | 45.3(10) | 58.6(6) | 48.7(8) |
| C(11)–N(7)–C(12) plane vs. N(3)–C(2)–N(4)–plane | 44.2(13) | 45.0(18) | 42.2(14) | 40.6(10) | 46.2(7) | 45.9(6) |

[a] The data of **3** have already been published and are only given here for comparison.

experiments under vacuum conditions. The melting points of all compounds are relatively high (195–232 °C, see Table 1) and cannot be rationalized by the type of ligand substitution ($R^1$–$R^4$). It can be concluded from the DTA spectra that the melting process is accompanied by the initiation of decomposition reactions. The compounds do not melt fully at the documented temperatures but undergo some sort of waxy transition phase over a temperature range of approximately 5 °C (vide infra).

The nature of the carbodiimide substituents (cy vs. *i*Pr) has a big influence on the volatility of the compounds. Thus, **3**, **4**, **5**, and **9** (*i*Pr-cdi) can be sublimed without any residues at 120 °C in vacuo ($10^{-4}$ mbar) whereas **6**, **7**, **8**, and **10** (cy-cdi) do not sublime at all under these conditions. Isothermal studies at 120 °C underline these results. After 240 min at ambient pressure the weight loss of **3**, **4**, **5**, and **9** is approximately 10% in all cases, while compounds **6** and **7**, for example, show a weight loss of only 2.5% (Figure 2). The mass transport of these complexes is highest for **9** (4.9 $\mu g\,min^{-1}$) and significantly lower for **6** and **7** (0.93 and 0.59 $\mu g\,min^{-1}$, respectively). The simplest explanation for this observation is the higher molecular masses of the cy-cdi based compounds. However, by changing $R^1$ and $R^2$ from methyl to ethyl (e.g. **3** to **5**) no significant effect on the volatility is observed. Obviously, the variation of $R^3$ has a significant effect on the interactions between the molecules in the solid state, for example by a different packing of the moieties.

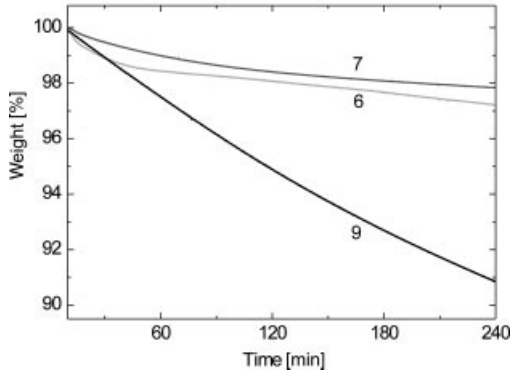


Figure 2. Isothermal analysis of **6**, **7**, and **9**. The spectra were recorded at a temperature of 120 °C, 300 sccm nitrogen flow for 4 h. Heating from 25 °C to 120 °C at a rate of 10 °C $min^{-1}$.

 © 2006 Wiley-VCH Verlag GmbH & Co. KGaA, Weinheim 

The residual masses after TG/DTA measurements from cy-cdi based complexes are higher than the theoretical masses (residual masses for **6**–**8**, **10**: 29–35%, theoretical content of TaN: 22–24%). This indicates the incorporation of significant amounts of carbon during the decomposition. In contrast, the *i*Pr-cdi based complexes **4**, **5**, and **9** show considerably lower residual masses and thus cleaner decomposition processes (residual masses: 10–12%, theoretical content of TaN: 27–28%).

With the exception of **7**, all compounds show one or two endothermic peaks at temperatures below their melting/decomposition points (Figure 3). Due to the fact that no weight loss can be observed in any case, a phase change of the solids is possibly responsible for this behavior. This phase change is not reversible, which means that running a program in which the sample is heated, cooled down, and heated again shows endothermic peaks only in the first period of heating. The position of the peaks is strongly dependent on the nature of the alkyl substituents $R^1$, $R^2$, and $R^3$. Going from methyl to ethyl for the amido substituents $R^1$ and $R^2$ results in a shift of these peaks to higher temperatures (**3**→**4**→**5**: 52 °C→70 °C→110 °C; **6**→**8**: 112 °C→139 °C). The same is true for the variation of $R^3$ from *i*Pr to cy (**3**→**6**: 52 °C→112 °C; **5**→**8**: 110 °C→139 °C; **9**→**10**: 82 °C→140 °C). It can be concluded, that the onset of the temperature for phase changes depends on the mobility of the molecules in the solid state, which supposedly increases with higher chain lengths and/or size of the substituents.

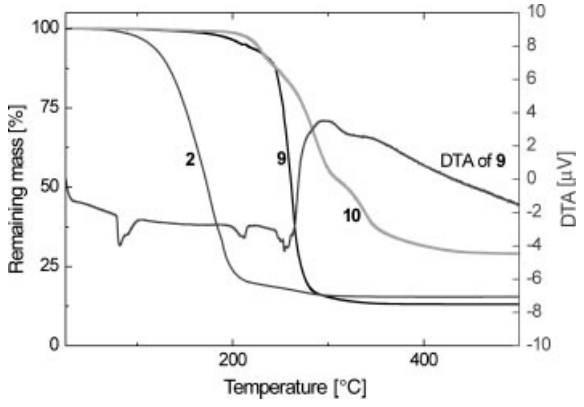


Figure 3. TG/DTA spectrum of **9** and TG curves of **2** and **10**. Heating rate: 5 °C min$^{-1}$.

### Decomposition Experiments of 3–5

The nature of the thermal decomposition of potential MOCVD precursors into the desired materials is crucial. Thus, compounds **3**–**5** were evaporated at 120 °C in vacuo, with a constant flow of argon providing a continuous transport of the precursor through a decomposition tube at 600 °C (Figure 4). The decomposition products were subsequently trapped at –196 °C (liquid nitrogen) in a slightly modified cooling trap. After full evaporation of the precursor (300 mg), deuterated benzene was injected into the cooling trap, and the resulting $C_6D_6$ solutions analyzed by $^1$H NMR spectroscopy and GC-MS measurements. The $^1$H NMR spectra revealed the formation of the corresponding free amines for **3**–**5** ($HNMe_2$, HNMeEt and $HNEt_2$), small amounts of $t$BuNH$_2$ (resulting from the former imido ligand), as well as free carbodiimide. At these very high temperatures (600 °C) carbodiimide could be released from the guanidinato ligand by deinsertion analogous to the behavior of amidinate complexes.[15] It should be noted that although these compounds represent the major part of decomposition products, smaller peaks were also present which could not be unequivocally assigned. GC-MS measurements confirm these $^1$H NMR results and additionally show the presence of small amounts of isopropylamine as well as several unidentified species containing the carbodiimide group. Although the relatively large variety of decomposition products suggests rather complex decomposition mechanisms, preliminary MOCVD experiments of compound **4** as a single-source precursor showed the possibility of carbon-free (atomic concentration < 1%)[6] TaN deposition, which requires clean thermal decomposition processes.

Figure 4. Setup for the decomposition experiments of **3**–**5**.

## Conclusions

We have presented the synthesis and characterization of several new guanidinato/amido/imido complexes of the type $[Ta(NR^1R^2)\{C(NR^1R^2)(NR^3)_2\}_2(NR^4)]$ {$R^1$,$R^2$ = methyl, ethyl; $R^3$ = cyclohexyl (cy), isopropyl; $R^4$ = *tert*-butyl, *n*-propyl}. All complexes are structurally very similar, the bond lengths and angles of the solid-state structures showing only minor variations. TG/DTA measurements and isothermal studies reveal the low volatility of the cy-cdi based complexes. This is rather unexpected considering the fact that the structural and chemical behaviors of compounds **3**–**10** are very similar. Thus, cy-cdi based complexes are, in general, not suitable for MOCVD purposes due to a supposedly weak precursor transport. However, application of the compounds derived from cy-cdi in liquid injection MOCVD is feasible. The choice of substituents of the amido or imido groups does not seem to have a significant impact on the thermal behavior of the resulting complexes. Finally, thermal decomposition experiments of **3**–**5** clearly show that highly complex pyrolysis reactions are taking place, although they lead to a clean decomposition of the selected precursors in all cases.

## Experimental Section

All manipulations of air- and moisture-sensitive compounds were performed on a conventional vacuum/argon line using standard

 © 2006 Wiley-VCH Verlag GmbH & Co. KGaA, Weinheim 

Schlenk techniques. Preparations of samples for further analysis were carried out in argon-filled glove boxes. All solvents were purified by an MBraun solvent purification system (SPS) and stored over activated molecular sieves (4 Å). $C_6D_6$ was degassed and dried with activated molecular sieves. Elemental analysis was performed by the analytical service of our Chemistry Department (CHNSO Vario EL 1998). $^1H$ and $^{13}C$ NMR spectra were recorded on a Bruker Advance DPX-250 spectrometer. EI mass spectra were recorded with a Varian MAT spectrometer. Simultaneous TG/DTA analysis was carried out using a Seiko TG/DTA 6300S11 at ambient pressure (sample weight ≈ 10 mg). GC-MS measurements were carried out on a Shimadzu QP2010 instrument at a column temperature of 290 °C. The tantalum-containing starting compounds, namely [Ta(NMe$_2$)$_3$(N-*t*Bu)], [Ta(NMeEt)$_3$(N-*t*Bu)], [Ta(NEt$_2$)$_3$(N-*t*Bu)], and [Ta(NEt$_2$)$_3$(N-*n*Pr)] were synthesized in batches of 15–40 g following modified literature procedures.[12] Reagents were purchased from the following companies and used without further purification: butyllithium (1.6 N solution in hexane, Merck), diethylamine (>99% purity, Merck), methylethylamine (> 97% purity, Fluka), pyridine (Normapur grade, VWR), chlorotrimethylsilane (98%, Acros), lithium dimethylamide (95%, Aldrich), diisopropylcarbodiimide (99%, careful: very toxic, Acros), and dicyclohexylcarbodiimide (99%, Aldrich). The synthesis and characterization of **3**–**5** was described in a previous publication.[6a] For a brief summary of the crystallographic data see Table 3. CCDC-611058 to -611062 (**4**–**6**, **8**, and **9**, respectively) contain the supplementary crystallographic data for this paper. These data can be obtained free of charge from The Cambridge Crystallographic Data Centre via www.ccdc.cam.ac.uk/data_request/cif.

**[TaCl$_3$(N-*n*Pr)(py)$_2$] (1):** *N*-Propylamine (20.2 mL, 14.52 g, 246 mmol) and chlorotrimethylsilane (15 mL, 118 mmol) were added to a cooled suspension of TaCl$_5$ (20 g, 55.8 mmol) in toluene (150 mL). The color of the suspension changed to slight yellow-greenish. After stirring the reaction mixture at room temperature for 25 min, pyridine was added (25 mL, 24.5 g, 310 mmol). After 24 h, the clear, yellow-green solution was filtered, and the solvents removed in vacuo. The crude product was recrystallized from hot toluene (100 °C, ca. 120 mL). Yield: 22.2 g (44.2 mmol, 79% based on TaCl$_5$). $C_{13}H_{17}Cl_3N_3Ta$ (502.63): calcd. C 31.13, H 3.39, N 8.38; found C 31.14, H 3.67, N 8.67. All other analyses (NMR, MS) were in accordance with the previously published results.

**[Ta(NEt$_2$)$_3$(N-*n*Pr)] (2):** A suspension of lithium diethylamide (62 mmol) was prepared in situ by adding 40 mL of a 1.6 M BuLi solution (hexane) to diethylamine (7.5 mL, 62 mmol) at –60 °C. After stirring the reaction mixture for 24 h at room temperature, the resulting suspension was added to a suspension of **1** (10 g, 20.8 mmol) in hexane at –60 °C. The reaction mixture slowly turned yellow/orange and was filtered after stirring for an additional 24 h. The yellow/orange filtrate was concentrated in order to obtain the dark orange product **2**. Yield: 8.38 g (18.4 mmol, 92% based on **1**). $C_{15}H_{37}N_4Ta$ (454.43): calcd. C 39.65, H 8.20, N 12.33; found C 39.87, H 7.80, N 12.49. All other analyses (NMR, MS) were in accordance with the previously published results.

**[Ta(NMe$_2$){(N-cy)$_2$C(NMe$_2$)}$_2$(N-*t*Bu)] (6):** A solution of dicyclohexylcarbodiimide (1.52 g, 7.83 mmol) in hexane (20 mL) was added to a solution of [Ta(NMe$_2$)$_3$(N-*t*Bu)] (1.55 g, 4.03 mmol) in hexane (40 mL). The temperature of the solution increased to about 45 °C

Table 3. Crystallographic data and structure refinement details for **4**, **5**, **6**, **8**, and **9**.

| | **4** (CVD82) | **5** (CVD72) | **6** (CVD101) | **8** (CVD76) | **9** (CVD99) |
|---|---|---|---|---|---|
| Empirical formula | $C_{27}H_{61}N_8Ta$ | $C_{30}H_{67}N_8Ta$ | $C_{36}H_{71}N_8Ta$ | $C_{42}H_{83}N_8Ta$ | $C_{29}H_{65}N_8Ta$ |
| Formula mass | 678.79 | 720.87 | 796.96 | 881.11 | 706.84 |
| $T$ [K] | 108(2) | 105(2) | 113(2) | 108(2) | 111(2) |
| Crystal system | orthorhombic | orthorhombic | triclinic | monoclinic | monoclinic |
| Space group | *Pbca* | *Pbca* | $P\bar{1}$ | $P2_1/c$ | $P2_1/n$ |
| $a$ [Å] | 10.7124(7) | 11.4691(11) | 10.1139(9) | 14.4945(9) | 11.0993(12) |
| $b$ [Å] | 18.2835(10) | 18.1889(18) | 16.8089(14) | 17.4746(8) | 19–395(4) |
| $c$ [Å] | 34.0026(18) | 34.854(3) | 23.796(2) | 21.6152(14) | 15.960(2) |
| $\alpha$ [°] | 90 | 90 | 80.815(7) | 90 | 90 |
| $\beta$ [°] | 90 | 90 | 88.860(7) | 98.182(5) | 91.702(9) |
| $\gamma$ [°] | 90 | 90 | 78.771(7) | 90 | 90 |
| $V$ [Å$^3$] | 6659.8(7) | 7270.8(12) | 3916.8(6) | 5045.2(5) | 3434.2(9) |
| $Z$ | 8 | 8 | 4 | 4 | 4 |
| Density (calcd.) [g cm$^{-3}$] | 1.354 | 1.317 | 1.351 | 1.160 | 1.367 |
| $\mu$(Mo-$K_\alpha$) [mm$^{-1}$] | 3.328 | 3.053 | 2.841 | 2.211 | 3.230 |
| $T_{max.}/T_{min.}$ | 0.967/0.787 | 0.643/0.589 | 0.833/0.465 | 0.733/0.556 | 0.529/0.298 |
| $F$(000) | 2816 | 3008 | 1664 | 1856 | 1472 |
| Crystal size [mm] | 0.21×0.06×0.01 | 0.16×0.10×0.07 | 0.18×0.08×0.03 | 0.16×0.11×0.07 | 0.25×0.17×0.11 |
| $\theta$ range [°] | 2.99–25.00 | 2.92–25.00 | 2.60–25.00 | 3.01–27.56 | 2.76–25.00 |
| Completeness to $\theta$ [%] | 99.8 | 98.2 | 99.7 | 99.9 | 99.8 |
| Index ranges | $-12 \le h \le 12$ | $-13 \le h \le 13$ | $-12 \le h \le 12$ | $-17 \le h \le 15$ | $-13 \le h \le 13$ |
| | $-21 \le k \le 19$ | $-21 \le k \le 21$ | $-19 \le k \le 19$ | $-22 \le k \le 19$ | $-23 \le k \le 23$ |
| | $-40 \le l \le 40$ | $-39 \le l \le 40$ | $-28 \le l \le 27$ | $-28 \le l \le 28$ | $-18 \le l \le 18$ |
| Reflections collected | 48057 | 48479 | 53636 | 50240 | 42514 |
| Independent reflections | 5852 | 6292 | 13711 | 11646 | 6019 |
| Data/restraints/parameters | 5852/0/325 | 6292/0/369 | 13711/6/811 | 11646/0/460 | 6019/0/358 |
| Goodness-of-fit on $F^2$ | 1.393 | 1.058 | 1.229 | 1.113 | 1.097 |
| $R$ indices [$I>2\sigma(I)$] $R_1$ | 0.0869 | 0.0707 | 0.0662 | 0.0562 | 0.0406 |
| $wR_2$ | 0.1086 | 0.1447 | 0.0960 | 0.1119 | 0.0977 |
| $R$ indices (all data) $R_1$ | 0.1041 | 0.1197 | 0.0861 | 0.0797 | 0.0440 |
| $wR_2$ | 0.1138 | 0.1663 | 0.1016 | 0.1221 | 0.1000 |
| Largest diff. peak/hole [e Å$^{-3}$] | 2.699/–1.589 | 4.998/–1.103 | 1.771/–0.725 | 3.882/–1.493 | 2.954/–1.558 |

 © 2006 Wiley-VCH Verlag GmbH & Co. KGaA, Weinheim 

during addition; no color change was observed. After stirring the mixture for 24 h, the solvent was removed in vacuo. Small, white crystallites suitable for X-ray analysis were obtained by recrystallizing the crude product from toluene. M.p. 210 °C (uncorrected). Yield: 2.73 g (3.43 mmol, 85% based on [Ta(NMe$_2$)$_3$(N-*t*Bu)]). $C_{36}H_{71}N_8Ta$ (796.96): calcd. C 45.27, H 8.71, N 17.60; found C 45.22, H 9.00, N 17.83. $^1$H NMR (25 °C, 250 MHz, $C_6D_6$): $\delta$ = 1.30–2.10 (m, cyclohexyl), 1.58 [s, 9 H, Ta{NC(C*H*$_3$)$_3$}], 2.58, 2.62 [2 × s, 2 × 6 H, Ta{(N-cy)$_2$C[N(C*H*$_3$)$_2$]}], 3.2–3.7 (m, 4 H, cyclohexyl, N–C–*H*) 3.59 [s, 3 H, Ta–N(C*H*$_3$)$_2$], 4.20 [s, 3 H, Ta–N(C*H*$_3$)$_2$] ppm. $^{13}$C NMR (25 °C, 62.5 MHz, $C_6D_6$): $\delta$ = 26.2, 26.5, 26.6 (2×), 26.7 (3×), 27.1 (2×), 27.2, 27.4 (2×) (cyclohexyl, 3,4-position), 35.2 [Ta{NC(*C*H$_3$)$_3$}], 34.3, 34.5, 35.2, 36.3, 36.6, 37.0, 37.1, 37.5 (cyclohexyl, 2-position), 40.3 [Ta{(N-cy)$_2$C[N(*C*H$_3$)$_2$]}], 49.1, 59.3 [Ta{N(*C*H$_3$)$_2$}], 55.1, 56.0, 57.3, 57.5 (cyclohexyl, N-*C*), 63.6 [Ta{N*C*(CH$_3$)$_3$}], 164.8, 169.3 [Ta{(N-cy)$_2$*C*(NMe$_2$)}] ppm. EI-MS (70eV): *m*/*z* (%) = 796 (0.5) [M$^+$], 590 (15) [M$^+$ – cy-cdi], 206 (25) [cy-cdi$^+$], 124 (45) [cy-N=C=N–H$^+$], 83 (80) [cy$^+$], 55 (100) [$C_4H_7^+$], 43 (70) [$C_3H_7^+$], 41 (75) [$C_3H_5^+$].

**[Ta(NEtMe){(N-cy)$_2$C(NEtMe)}$_2$(N-*t*Bu)] (7):** The synthesis of **7** followed the same procedure as for **6** but with [Ta(NEtMe)$_3$(N-*t*Bu)] (1.72 g, 4.03 mmol) and dicyclohexylcarbodiimide (1.52 g, 7.83 mmol). M.p. 218 °C (uncorrected). Yield: 2.77 g (3.30 mmol, 82% based on [Ta(NEtMe)$_3$(N-*t*Bu)]). $C_{39}H_{77}N_8Ta$ (839.03): calcd. C 53.98, H 9.25, N 13.36; found C 53.62, H 9.34, N 13.48. $^1$H NMR (25 °C, 250 MHz, $C_6D_6$): $\delta$ = 0.9–1.1 [3 × q, 3 × 3 H, 2 × Ta{(N-*cy*)$_2$C[N(CH$_2$C*H*$_3$)Me]} and Ta{N(CH$_2$C*H*$_3$)Me}], 1.10–2.10 (m, cyclohexyl), 1.57 [s, 9 H, Ta{NC(C*H*$_3$)$_3$}], 2.62, 2.63, 2.64 [no assignment possible, most probably Ta{(N-*cy*)$_2$C[N(C*H*$_3$)Et]}], 2.9–3.7 [m, cyclohexyl, N–C–*H*, Ta{(N-*cy*)$_2$C[N(C*H*$_2$CH$_3$)Me]} and Ta{N[C*H*$_2$CH$_3$]Me}], 4.25 [s, 3 H, Ta{NEt(C*H*$_3$)}] ppm. $^{13}$C NMR (25 °C, 62.5 MHz, $C_6D_6$): $\delta$ = 14.0 [Ta{(N-cy)$_2$C-[N(CH$_2$*C*H$_3$)Me]}], 15.2 [Ta{[N(CH$_2$*C*H$_3$)Me]}], 35.4 [Ta{N-[C(*C*H$_3$)$_3$]}], 54.5, 54.6 [Ta{N(*C*H$_2$CH$_3$)Me} and Ta{NEt(C*H*$_3$)}], 63.8 [Ta{N*C*(CH$_3$)$_3$}], 166.1 [Ta{(N-cy)$_2$*C*(NMeEt)}] ppm; peaks that cannot be clearly assigned: $\delta$ = 26.0, 26.7, 27.1, 27.3 27.5, 24.4, 35.1, 36.6, 37.0, 56.5, 57.4 ppm. EI-MS (70eV): *m*/*z* (%) = 576 (3) [M$^+$ – guanidinate], 265 (10) [guanidinate$^+$], 206 (10) [cy-cdi$^+$], 163 (37) [cy-cdi$^+$ – $C_3H_7$], 124 (35) [cy-N=C=N–H$^+$], 83 (67) [cy$^+$], 55 (97) [$C_4H_7^+$], 43 (100) [$C_3H_7^+$], 41 (97) [$C_3H_5^+$].

**[Ta(NEt$_2$){(N-cy)$_2$C(NEt$_2$)}$_2$(N-*t*Bu)] (8):** The synthesis of **8** followed the same procedure as for **6** but with [Ta(NEt$_2$)$_3$(N-*t*Bu)] (1.89 g, 4.03 mmol) and dicyclohexylcarbodiimide (1.52 g, 7.83 mmol). M.p. 204 °C (uncorrected). Yield: 3.09 g (3.50 mmol, 87% based on [Ta(NEt$_2$)$_3$(N-*t*Bu)]). $C_{42}H_{83}N_8Ta$ (881.11): calcd. C 57.25, H 9.49, N 12.72; found C 57.41, H 10.18, N 11.96. $^1$H NMR (25 °C, 250 MHz, $C_6D_6$): $\delta$ = 0.9–1.1 [m, 12 H, 4 of 6 CH$_3$ groups of Ta{(N-cy)$_2$C[N(CH$_2$C*H*$_3$)$_2$]} and Ta{N[CH$_2$C*H*$_3$]$_2$}], 1.40, 1.46 [m, 2 of 6 CH$_3$ groups of Ta{(N-cy)$_2$C[N(CH$_2$C*H*$_3$)$_2$]} and Ta{N[CH$_2$C*H*$_3$]$_2$}], 1.20–2.20 (m, cyclohexyl), 1.58 [s, 9 H, Ta{NC(C*H*$_3$)$_3$}], 2.9–3.2 [m, 8 H, Ta{(N-*i*Pr)$_2$C[N(C*H*$_2$CH$_3$)$_2$]}], 3.30–3.70 [m, 4 H, cyclohexyl, N-C-*H*, and 1 H, Ta–N(C*H*$_2$CH$_3$)], 4.44, 4.66, 5.00 [3 × d of q, $^1J$ = 6.5, 6.2, 6.3 Hz, 3 × 1 H, Ta–N(C*H*$_2$CH$_3$)] ppm. $^{13}$C NMR (25 °C, 62.5 MHz, $C_6D_6$): $\delta$ = 13.5, 14.3, 15.7, 15.9 [Ta{(N-cy)$_2$C[N(CH$_2$*C*H$_3$)$_2$]} and TaN(CH$_2$*C*H$_3$)] 26.0, 26.5, 26.6 (2×), 26.7, 26.8 (2×), 26.9, 27.2, 27.3, 27.5, 27.6 (cyclohexyl, 3,4-position), 34.0, 34.5, 34.6, 35.9, 36.4, 37.1, 37.6, 38.7 (cyclohexyl, 2-position), 35.2 [Ta{NC(*C*H$_3$)$_3$}], 41.5, 43.0, 43.1 (br), 44.6 (br) [Ta{(N-cy)$_2$C[N(*C*H$_2$CH$_3$)$_2$]}], 47.5, 58.1 [TaN(*C*H$_2$CH$_3$)], 55.6, 56.2, 57.5, 58.8 (cyclohexyl, N-*C*), 64.1 [Ta{N*C*(CH$_3$)$_3$}], 166.2, 170.2 [Ta{(N-cy)$_2$*C*(NEt$_2$)}] ppm. EI-MS (70eV): *m*/*z* (%) = 810 (3) [M$^+$ – NEt$_2$], 604 (calcd. 605) (3) [M$^+$ – cy-cdi], 206 (27) [cy-cdi$^+$], 163 (48) [cy-cdi$^+$ – $C_3H_7$], 124 (44) [cy-N=C=N–H$^+$], 83 (81) [cy$^+$], 55 (100) [$C_4H_7^+$], 43 (70) [$C_3H_7^+$], 41 (71) [$C_3H_5^+$].

**[Ta(NEt$_2$){(N-*i*Pr)$_2$C(NEt$_2$)}$_2$(N-*n*Pr)] (9):** The synthesis of **9** followed, in general, the same procedure as for **6** but with [Ta(NEt$_2$)$_3$(N-*n*Pr)] (1.83 g, 4.03 mmol) and diisopropylcarbodiimide (1.01 g, 8.06 mmol). The diimide was used without dissolving it in hexane. M.p. 195 °C (uncorrected). Yield: 2.39 g (3.38 mmol, 84% based on [Ta(NEt$_2$)$_3$(N-*n*Pr)]). $C_{29}H_{65}N_8Ta$ (706.84): calcd. C 49.28, H 9.27, N 15.85; found C 49.28, H 9.17, N 16.10. $^1$H NMR (25 °C, 250 MHz, $C_6D_6$): $\delta$ = 0.89 [t, $^1J$ = 6.9 Hz, 3 H, Ta(NCH$_2$CH$_2$C*H*$_3$)], 0.91, 2 × 0.96, 1.06, 1.07, 1.47 [6 × t, $^1J$ = 6.7, 2 × 7.0, 7.4, 6.8, 7.0 Hz, 6 × 3 H, 4 × Ta{(N-*i*Pr)$_2$C[N(CH$_2$C*H*$_3$)$_2$]} and 2 × TaN[CH$_2$C*H*$_3$]$_2$], 1.16, 1.23, 1.35, 1.38, 2 × 1.40, 1.47, 1.58 [8 × d, $^1J$ = 6.4, 6.4, 6.5, 6.0, 2 × 6.0, 6.4, 6.5 Hz, 24 H, Ta{[N[CH(C*H*$_3$)$_2$]]$_2$C(NEt$_2$)}], 1.72 [sextet, $^1J$ = 7.3 Hz, 2 H, Ta(NCH$_2$C*H*$_2$CH$_3$)], 2.80–3.15 {m, 8 H, Ta{(N-*i*Pr)$_2$C[N-(C*H*$_2$CH$_3$)$_2$]}}, 3.41, 4.25, 4.59, 4.73 [4 × d of q, $^1J$ = 6.3, 6.0, 6.0, 5.9 Hz, 4 H, TaN(C*H*$_2$CH$_3$)], 3.76, 3.87, 3.94, 4.10 [4 × septet, $^1J$ = 6.5, 6.4, 6.4, 6.5 Hz, 4 H, Ta{{N[C*H*(CH$_3$)$_2$]}$_2$C(NEt$_2$)}], 4.31, 4.37 [2 × d of t, $^1J$ = 6.8, 6.7 Hz, 2 H, Ta(NC*H*$_2$CH$_2$CH$_3$)] ppm. $^{13}$C NMR (25 °C, 62.5 MHz, $C_6D_6$): $\delta$ = 12.40 [Ta(NCH$_2$CH$_2$*C*H$_3$)], 13.6, 14.0, 14.8, 15.7, 17.0 [Ta{(N-*i*Pr)$_2$C[N(CH$_2$*C*H$_3$)$_2$]} and TaN(CH$_2$*C*H$_3$)] 23.5, 24.5, 25.0, 25.2, 25.9, 26.1, 26.5, 28.0 [Ta{[N{CH(*C*H$_3$)$_2$}]$_2$C(NEt$_2$)}], 28.5 [Ta(NCH$_2$*C*H$_2$CH$_3$)], 41.4, 42.3, 43.7 (br) [Ta{(N-*i*Pr)$_2$C[N(*C*H$_2$CH$_3$)$_2$]}], 46.8, 56.7 [TaN(*C*H$_2$CH$_3$)], 47.2, 47.5, 48.4, 48.8 [Ta{[N{*C*H(CH$_3$)$_2$}]$_2$C-(NEt$_2$)}], 61.9 [Ta(N*C*H$_2$CH$_2$CH$_3$)], 166.5, 170.3 [Ta{N(*i*Pr)$_2$*C*-(NEt$_2$)}] ppm. EI-MS (70eV): *m*/*z* (%) = 706 (12) [M$^+$], 635 (79) [M$^+$ – NEt$_2$], 509 (100) [M$^+$ – guanidinate], 466 (29) [M$^+$ – guanidinate – *i*Pr], 407 (calcd. 409) (10) [M$^+$ – *i*Pr – N-Pr (*i* or *n*)], [M$^+$ – guanidinate], 198 (4) [guanidinate$^+$], 141 (15) [N(*i*Pr)$_2$C(NH)$^+$], 126 (5) [*i*Pr-N=C=N-*i*Pr$^+$], 69 (34) [*i*Pr-N–C$^+$], 58 (10) [HN-Pr$^+$], 43 (10) [*i*Pr].

**[Ta(NEt$_2$){(N-cy)$_2$C(NEt$_2$)}$_2$(N-*n*Pr)] (10):** The synthesis of **10** followed the same procedure as for **6** but with [Ta(NEt$_2$)$_3$(N-*n*Pr)] (1.83 g, 4.03 mmol) and dicyclohexylcarbodiimide (1.52 g, 7.83 mmol). M.p. 205 °C (uncorrected). Yield: 2.27 g (2.62 mmol, 65% based on [Ta(NEt$_2$)$_3$(N-*n*Pr)]). $C_{41}H_{81}N_8Ta$ (866.61): calcd. C 56.80, H 9.41, N 12.92; found C 56.13, H 10.04, N 13.20. $^1$H NMR (25 °C, 250 MHz, $C_6D_6$): $\delta$ = 0.97, 0.98, 2 × 1.02, 1.08, 1.09 [6 × t, coupling constants could not be determined, 18 H, Ta(NCH$_2$CH$_2$C*H*$_3$), 3 × Ta{(N-cy)$_2$C[N(CH$_2$C*H*$_3$)$_2$]} and 2 × Ta{N[CH$_2$C*H*$_3$]$_2$}], 1.49 [t, $^1J$ = 7.1 Hz, 3 H, Ta{(N-cy)$_2$C-[N(CH$_2$C*H*$_3$)$_2$]}], 1.73 [m, Ta (NCH$_2$C*H*$_2$CH$_3$)], 1.2–2.3 (m, cyclohexyl), 2.90–3.20 [m, 8 H, Ta{(N-cy)$_2$C[N(C*H*$_2$CH$_3$)$_2$]}], 3.30–3.80 [m, 5 H, 4 × cyclohexyl (N–C–*H*) and 1 × Ta{N(C*H*$_2$CH$_3$)$_2$}], 4.25–4.50 [m, 3 H, 2 × Ta(NCH$_2$CH$_2$C*H*$_3$) + 1 × Ta[N(C*H*$_2$CH$_3$)$_2$]], 4.62, 4.76 [2 × sextet, $^1J$ = 5.8, 6.0 Hz, 2 H, Ta{N(C*H*$_2$CH$_3$)$_2$}] ppm. $^{13}$C NMR (25 °C, 62.5 MHz, $C_6D_6$): $\delta$ = 12.56 [Ta(NCH$_2$CH$_2$*C*H$_3$)], 13.6, 13.9, 14.90 (br), 15.9, 16.8 [Ta{(N-cy)$_2$C[N(CH$_2$*C*H$_3$)$_2$]} and TaN(CH$_2$*C*H$_3$)], 26.5, 2 × 26.6, 26.7, 26.8, 26.9, 2 × 27.0, 2 × 27.1, 27.5, 27.6, 28.5 [12 × cyclohexyl (3,4-position), 1 × Ta{(NCH$_2$CH$_2$CH$_3$)$_3$}], 33.5, 34.8, 35.7, 35.8, 36.6, 2 × 36.7 (cyclohexyl, 2-position), 39.1, 41.5, 42.5, 44.0 (br) [Ta{(N-cy)$_2$-C[N(*C*H$_2$*C*H$_3$)$_2$]}], 47.5 [1 × TaN(*C*H$_2$CH$_3$)$_2$], 55.7 55.9, 56.2, 56.9, 58.0, 58.3 [1 × TaN(*C*H$_2$CH$_3$)$_2$, 4 × cyclohexyl (N–*C*)], 62.0 [Ta(N*C*H$_2$CH$_2$CH$_3$)], 166.6, 170.3 [Ta{N(cy)$_2$*C*(NEt$_2$)}] ppm. Small amounts of free cy-cdi were detected in the $^{13}$C NMR spectrum of this compound. EI-MS (70eV): *m*/*z* (%) = 795 (calcd. 794) (0.5) [M$^+$ – NEt$_2$], 589 (calcd. 588) (0.5) [M$^+$ – guanidinate], 206 (20) [cy-N=C=N-cy$^+$], 82 (61) [cy$^+$], 56 (100), 55 ($C_4H_7^+$), 43 (60) [$C_3H_7^+$], 41 (67) [$C_3H_5^+$].

 © 2006 Wiley-VCH Verlag GmbH & Co. KGaA, Weinheim 

**Supporting Information** (see footnote on the first page of this article): Ortep/Povray drawings of the molecular structures of **4**, **5**, and **8** in the solid state.

## Acknowledgments

The authors would like to thank the Deutsche Forschungsgemeinschaft, the Fonds der Chemischen Industrie, and H. C. Starck for financial support.

[1] a) C.-L. Cheng, K.-S. Chang-Liao, T.-C. Wang, T.-K. Wang, H. C.-H. Wang, *IEEE Electron Device Lett.* **2006**, *27*, 148–150; b) M. Kadoshima, K. Akiyama, K. Yamamoto, H. Fujiwara, T. Yasuda, T. Nabatame, A. Toriumi, *J. Vac. Sci. Technol. B* **2005**, *23*, 42–47; c) A. E. Kaloyeros, E. Eisenbraun, *Annu. Rev. Mater. Sci.* **2000**, *30*, 363–385; d) D. Adams, G. F. Malgas, N. D. Theodore, R. Gregory, H. C. Kim, E. Misra, T. L. Alford, J. W. Mayer, *J. Vac. Sci. Technol. B* **2004**, *22*, 2345–2352.

[2] a) X. Zhao, N. P. Magtoto, J. A. Kelber, *Thin Solid Films* **2005**, *478*, 188–195; b) O. van der Straten, Y. Zhu, J. Rullan, K. Topol, K. Dunn, A. Kaloyeros, *Mat. Res. Soc. Symp. Proc.* **2004**, *812 D*, 165–170; c) O. van der Straten, Y. Zhu, K. Dunn, E. T. Eisenbraun, A. E. Kaloyeros, *J. Mater. Res.* **2004**, *19*, 447–453; d) J.-S. Park, H.-S. Park, S.-W. Kang, *J. Electrochem. Soc.* **2002**, *149*, C28–C32; e) J. W. Hong, K. I. Choi, Y. K. Lee, S. G. Park, S. W. Lee, J. M. Lee, S. B. Kang, G. H. Choi, S. T. Kim, U.-I. Chung, J. T. Moon, *Proceedings of the 7th IEEE International Interconnect Technology Conference*, San Francisco, CA, USA, June 7–9, **2004**; f) K. I. Choi, B. H. Kim, S. W. Lee, J. M. Lee, W. S. Song, G. H. Choi, U.-I. Chung, J. T. Moon, *Proceedings of the 6th IEEE International Interconnect Technology Conference*, San Francisco, CA, USA, June 2–4, **2003**.

[3] A. Baunemann, Y. Kim, M. Winter, R. A. Fischer, *Dalton Trans.* **2006**, 121–128.

[4] C. J. Carmalt, A. C. Newport, S. A. O'Neill, I. P. Parkin, A. J. P. White, D. J. Williams, *Inorg. Chem.* **2005**, *44*, 615–619.

[5] A. P. Milanov, R. K. Bhakta, A. Baunemann, M. Winter, A. Devi, *Inorg. Chem.*, submitted.

[6] a) A. Baunemann, Y. Kim, M. Winter, R. A. Fischer, *Dalton Trans.* **2005**, 3051–3055; b) A. Baunemann, M. Lemberger, A. J. Bauer, H. Parala, R. A. Fischer, *Chem. Vap. Dep.*, DOI: 10.1002/cvde.200606514.

[7] M. H. Tsai, S. C. Sun, H. T. Chiu, C. E. Tsai, S. H. Chuang, *Appl. Phys. Lett.* **1995**, *67*, 1128–1130.

[8] a) D. Rische, A. Baunemann, M. Winter, R. A. Fischer, *Inorg. Chem.* **2006**, *45*, 269–277; b) A. A. Trifonov, D. M. Lyubov, E. A. Fedorova, G. K. Fukin, H. Schumann, S. Muehle, M. Hummert, M. N. Bochkarev, *Eur. J. Inorg. Chem.* **2006**, 747–756.

[9] a) C. N. Rowley, G. A. Dilabio, S. T. Barry, *Inorg. Chem.* **2005**, *44*, 1983–1991; b) A. P. Kenney, G. P. A. Yap, D. S. Richeson, S. T. Barry, *Inorg. Chem.* **2005**, *44*, 2926–2933; c) M. P. Coles, P. B. Hitchcock, *Eur. J. Inorg. Chem.* **2004**, 2662–2672.

[10] a) M. K. T. Tin, G. P. A. Yap, D. S. Richeson, *Inorg. Chem.* **1999**, *38*, 998–1001; b) N. Thirupathi, G. P. A. Yap, D. S. Richeson, *Chem. Commun.* **1999**, 2483–2484; c) N. Thirupathi, G. P. A. Yap, D. S. Richeson, *Organometallics* **2000**, *19*, 2573–2579; d) M. K. T. Tin, T. Natesan, G. P. A. Yap, D. S. Richeson, *J. Chem. Soc., Dalton Trans.* **1999**, 2947–2951.

[11] P. J. Bailey, S. Pace, *Coord. Chem. Rev.* **2001**, *214*, 91–141.

[12] H.-T. Chiu, S.-H. Chuang, C.-E. Tsai, G.-H. Lee, S.-M. Peng, *Polyhedron* **1998**, *17*, 2187–2190.

[13] Molecular structures of **4**, **5**, and **8** in the solid state are available as Supporting Information.

[14] D. E. Wigley, *Prog. Inorg. Chem.* **1994**, *42*, 239.

[15] A. L. Brazeau, Z. Wang, C. N. Rowley, S. T. Barry, *Inorg. Chem.* **2006**, *45*, 2276.

Received: July 12, 2006
Published Online: September 25, 2006

 © 2006 Wiley-VCH Verlag GmbH & Co. KGaA, Weinheim 

DOI: 10.1002/ejic.200600667

# Mechanochemical Control of Synthesis and Structures of Aqua-Bridged Binuclear Nickel(II) Benzoate Complexes

**Anirban Karmakar,[a] Rupam J. Sarma,[a] and Jubaraj B. Baruah*[a]**

**Keywords:** Nickel / Aqua-bridged complexes / Solvation / Hydrogen bonds

Synthetic and structural aspects of a few binuclear nickel(II) complexes, having two bridging carboxylate groups and aqua groups are reported. Intramolecular O–H···O hydrogen bonding interactions between the bridging aqua group and the monodentate benzoate groups stabilises the bridging structures. Aqua-bridged nickel(II) benzoate complex is stable irrespective of solvent system and also can include solvent molecules such as toluene and benzene. A mixed chloro, aqua and 4-chloro-benzoato-bridged $Ni^{II}$ binuclear complex was synthesised and structurally characterised.
(© Wiley-VCH Verlag GmbH & Co. KGaA, 69451 Weinheim, Germany, 2006)

## Introduction

The crystal structures of the active sites of binuclear nickel(II) metallo-enzymes have shown that the metal centres are bridged by carboxylates as well as water or hydroxide ions.[1] The binuclear metal active site of the urease isolated from *Klebseilla aerogenes*, has aqua-bridged binuclear nickel(II) centres with pseudo-octahedral and square-pyramid geometry around the nickel ions.[2] So the design of binuclear aqua-bridged nickel(II) complexes is important in biological modelling.[3] Study of the structure and properties of binuclear transition-metal complexes containing bridging groups such as aqua groups[3] are expected to increase our understanding of the crucial factors that determine the catalytic activity of metalloenzymes.[4] We recently described the synthesis and catalytic activity of a binuclear nickel(II) benzoate complex that contains an aqua group in the bridging position.[5] We also communicated that the solid state and solution synthetic route results in a variation of the structure of nickel carboxylate complexes.[5] In the biological environment the reactions of substrates takes place in confined media, so, it is necessary to understand how different types of motifs can be developed from the complexes that have close structural resemblance to biological active sites. It is also necessary to understand the stability of such complexes in the presence of various neutral molecules in the lattice. With these objectives in mind we investigated multiple component solid-state synthesis of binuclear nickel(II) carboxylate complexes and the structural aspects of aqua-bridged nickel complexes in the presence of different neutral molecules in the lattice.

[a] Department of Chemistry, Indian Institute of Technology, Guwahati, 781039, India
E-mail: juba@iitg.ernet.in

## Results and Discussion

We have observed that the reaction of nickel(II) chloride hexahydrate, and sodium benzoate in 1:2 stoichiometry (Scheme 1) in the solid-state followed by addition of pyridine gave the nickel(II) benzoate complex, **2a**. The synthetic procedure is important because the analogous reaction in solution results in the formation of a mononuclear species.[6] The complex is soluble in chloroform, benzene or toluene and could subsequently be crystallised from benzene in $P2_1/c$ space group as light blue blocks. The crystal structure of **2a** shows that each of the nickel centres have octahedral geometry involving two bridging benzoate groups (Figure 1), two coordinated pyridine molecules and a monodentate benzoate apart from a bridging aqua group;

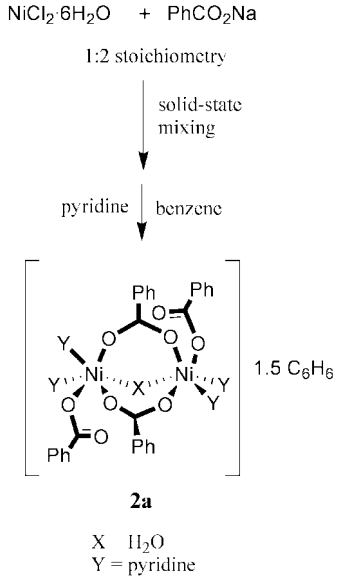


**2a**

X $H_2O$
Y = pyridine

Scheme 1.

 © 2006 Wiley-VCH Verlag GmbH & Co. KGaA, Weinheim 

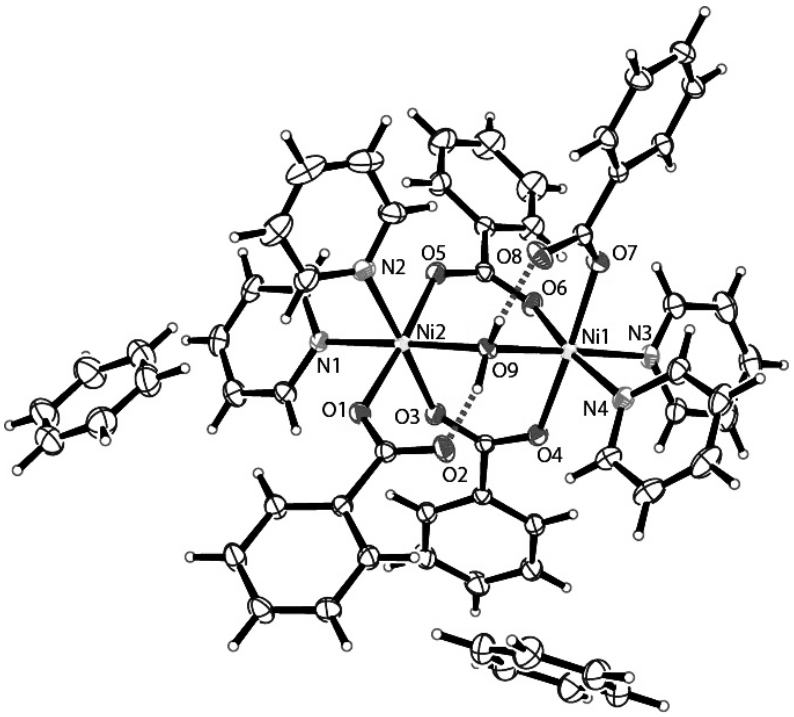


Figure 1. Crystal structure of **2a** with included benzene molecules (thermal ellipsoids drawn to 30% probability).

the Ni(1)···Ni(2) distance in this complex is 3.506(3) Å. The monodentate benzoate groups are intramolecularly hydrogen-bonded to the bridging aqua group through O(9)–H···O(2) [2.565(3) Å, 166(3)°] and O(9)–H···O(8) [2.572(3) Å, 170(3)°] interactions. The Ni(1)–O(9) and Ni(2)–O(9) bond lengths in this complex are 2.093(2) and 2.094(2) Å while the corresponding Ni(1)–O(9)–Ni(2) bond angle is 113.7(8)°.

There is a distorted octahedral geometry around each of the nickel centres. The compound has an absorption maximum at 645 nm due to a $^3A_2$ to $^3T_1$ transition arising from $d^8$-electronic configuration in a weak field. The assembly is stabilised by weak aromatic C–H···π interactions ($d_{C\cdots\pi}$ 3.87 Å) involving the C60–H of the benzene molecule as the donor and the aromatic ring of the benzoate groups of the molecule as the acceptor. In this case, the self-assembly of the binuclear nickel(II) benzoate complex leads to the inclusion of two benzene molecules in the crystal lattice that are stabilised by weak intermolecular C–H···π interactions.

The complex $[Ni_2(H_2O)(O_2CPh)_4(Py)_4]$ when crystallised from toluene results in the formation of a polymorph that contains included benzoic acid and toluene molecules and we have reported this structure in the past.[5] When this complex was dissolved in ethanol and layered over water the complex $[Ni_2(H_2O)(O_2CPh)_4(Py)_4]H_2O$ (**2b**) was crystallised; the crystals were found to have crystallised in the orthorhombic *Pbcn* space group. The structure of this complex is shown in Figure 2. Intra-molecular O(4)–H···O(2) [2.573(17) Å, 166(3)°] hydrogen bonding interactions are also observed between the bridging aqua group and the monodentate benzoate group as shown in Figure 2. It is observed that the Ni(1)–O(4) bond length in **2b** is 2.104(9) Å, which is slightly longer than that in **2a**, while the Ni(1)–O(4)–Ni(1′) bond angle is 115.25(8)°. This complex, **2b**, is a polymorph of **2a** and is characterised by a similar binuclear nickel(II) core except for the presence of a lattice water molecule that is intermolecularly hydrogen-bonded to the monodentate benzoate group through O(6)–H···O(2) [2.910(2) Å, 164(3)°] interactions. Solid-state FT-IR spectroscopy of this complex shows broad signals at 3537 and 3478 $cm^{-1}$ arising from intramolecular and intermolecularly hydrogen bonded O–H stretching vibrations. In methanol, the UV/Visible spectrum of **2b** shows an absorption band at 648 nm that may be assigned to the $^3A_2$ to $^3T_1$ transition.

Addition of pyridine to a mixture of nickel(II) chloride hexahydrate, 1-naphthoic acid and potassium hydroxide in toluene/methanol (1:1 v/v) gave a blue solution, from which the corresponding aqua-bridged binuclear complex, $[Ni_2(H_2O)(O_2CNp)_4(Py)_4]$ (**2c**), was obtained (where Np is naphthyl). The crystal structure of the complex is shown in Figure 3 (a), which shows that the bridging aqua group is hydrogen bonded to the monodentate naphthoate group through O(9)–H···O(8) [2.566(4) Å, 169(5)°] and O(9)–H···O(2) [2.533(4) Å, 162(6)°] interactions. The structure of the complex shows that the two nickel(II) centres are bridged by a water molecule and two naphthoate groups such that the Ni(1)–O(9)–Ni(2) bond angle is 117.78(9)°, with a Ni(1)···Ni(2) distance of 3.593(7) Å.

In a similar manner to the one discussed above, a corresponding binuclear nickel(II) complex of 2-nitrobenzoic acid was also prepared and could be crystallised from toluene as blue-green plates in the *C*2/*c* space group. Crystal structure analysis shows that the corresponding aqua bridge

 © 2006 Wiley-VCH Verlag GmbH & Co. KGaA, Weinheim 

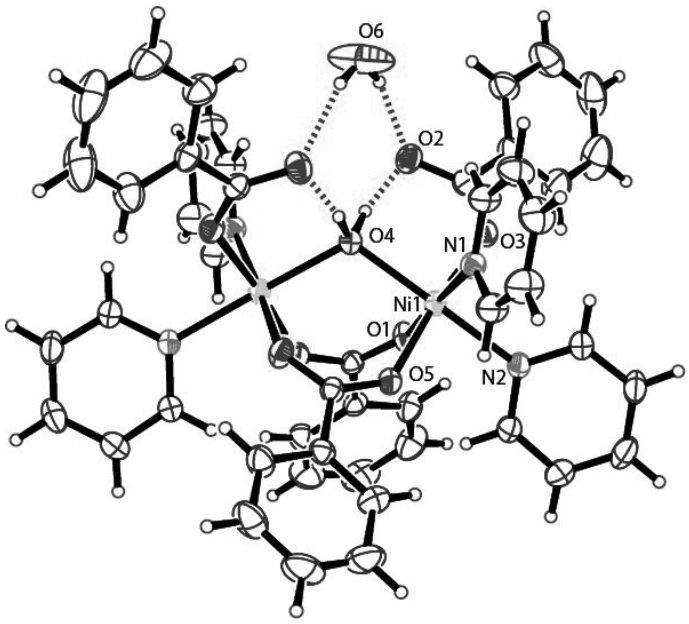


Figure 2. The structure of **2b** containing a hydrogen-bonded water molecule; symmetry for equivalent atoms [ $-x$, $y$, $-z + 1/2$] (thermal ellipsoids drawn to 30% probability).

in the binuclear nickel(II) complex with 2-nitrobenzoic acid **2d** is structurally similar to that of **2c** (Figure 3, b). It is observed that solvent molecules are not included in the crystal lattice of this complex apparently due to the steric crowding caused by the nitro substituent on the aromatic carboxylic acid molecules. As described earlier, each nickel(II) centre in complex **2d** is coordinated to the monodentate benzoate groups and two pyridine molecules, apart from the two bridging benzoate and bridging aqua group, which gives a six-coordinate octahedral geometry. The aqua molecule in this complex is intramolecularly hydrogen bonded to the monodentate benzoate through O(9)–H···O(2) [2.571(16) Å, 167(2)°] interactions; in this case the Ni(1)–O(9) bond length is 2.089(9) Å with the Ni(1)–O(9)–Ni(2) bond angle being 117.05(8)°.

So far in the above reactions we have obtained systematically aqua-bridged complexes, starting from nickel(II) chloride as the inorganic salt. However, in the reaction of 4-chlorobenzoic acid under analogous conditions a chloro-bridged complex $[Ni_2(H_2O)(Cl)(O_2CAr)_3(Py)_4]$ (**2e**) was formed. The crystal structure of this complex revealed the presence of an aqua bridge (Figure 4) and a benzoate bridge unlike complexes **2a**–**2d**, along with a chloride bridging group between the two nickel centres. In this case the presence of three monodentate 4-chlorobenzoate groups led to the binuclear tribridged $[Ni_2(H_2O)(Cl)(O_2CAr)_3(Py)_4]$

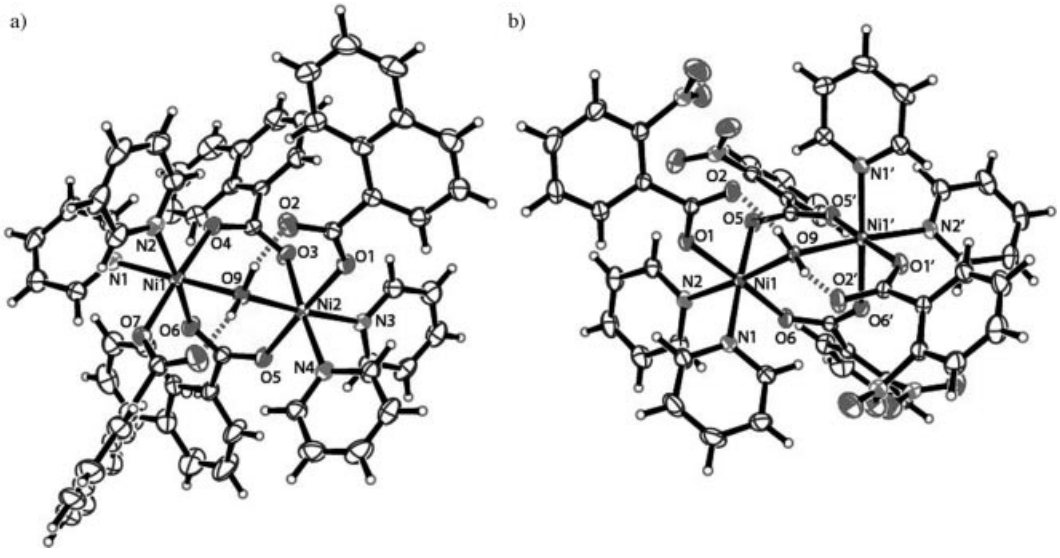


Figure 3. Crystal structures of (a) **2c** and (b) **2d** showing the intramolecular hydrogen bonding interactions between the bridging aqua molecule and the monodentate carboxylate groups (thermal ellipsoids drawn to 30% probability).

 © 2006 Wiley-VCH Verlag GmbH & Co. KGaA, Weinheim 

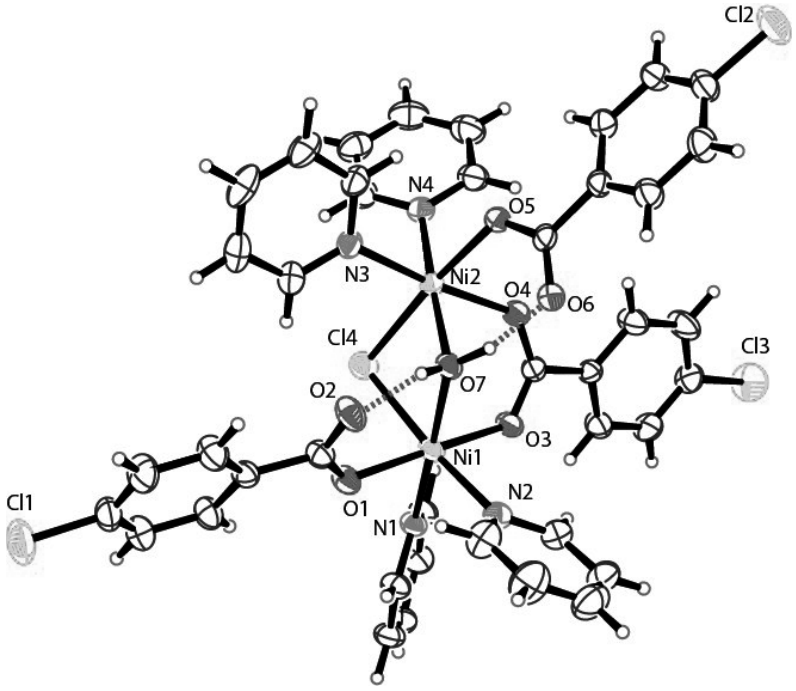


Figure 4. Crystal structure of **2e** (thermal ellipsoids drawn to 30% probability).

complex, (**2e**) as shown in Figure 4. The complex also has distorted octahedral geometry around the nickel centres and has an electronic absorption at 633 nm due to the $^3A_2$ to $^3T_1$ transition.

It is observed that in complex **2e**, the bridging aqua molecule is intramolecularly hydrogen bonded to the carboxylate units of the monodentate 4-chlorobenzoate groups via O(7)–H···O(2) [2.593(3) Å, 165(3)°] and O(7)–H···O(6) [2.561(3) Å, 165(4)°] interactions. The corresponding Ni(1)–O(7) and Ni(2)–O(7) bond lengths are 2.126(2) and 2.121(2) Å respectively while the Ni(1)–O(7)–Ni(2) bond angle is found to be 101.18(9)°. Although the Ni(1)···Ni(2) distance is 3.281(2) Å it is substantially shorter than **2a** or **2c** (Table 1). The reported values for Ni···Ni distance of separation in aqua-bridged complexes ranges from 3.497–3.676 Å.[7] However, the effect of the substituent on the aromatic ring as well as solvation on the Ni–$O_{aqua}$–Ni angle becomes prominent in the complexes **2c** and **2d**, which are close to the reported bond angles.[7] When the Ni–$O_{aqua}$–Ni angles among **2a** and **2b** are compared it is found that **2a** < **2b**. This happens because the hydrogen bonding interaction of the bridging water molecules in each case is different. In the case of complex **2b**, the hydrogen bonding interaction involving the interstitial water molecules draws the carbonyl closer, making the Ni–$O_{aqua}$–Ni bond angle smaller than in **2a**. In the case of complex **2e** the bond angle is the smallest in comparison to **2a**–**2d** because both the chloro and aqua groups bridge it.

Table 1. Bond lengths (in Å) and angles (in °).

| | **2a** | **2b** | **2c** | **2d** | **2e** |
|---|---|---|---|---|---|
| Ni(1)–$O_{aqua}$ | 2.094(2) | 2.139(2) | 2.088(2) | 2.089(9) | 2.126(2) |
| Ni(2)–$O_{aqua}$ | 2.094(2)[a] | 2.143(2) | 2.108(2) | 2.089(9)[a] | 2.121(2) |
| Ni(1)–$O_{aqua}$–Ni(2) | 113.7(8) | 111.87(11) | 117.78(9) | 117.05(8) | 101.18(9) |
| Ni(1)···Ni(2) | 3.506(5) | 3.554(3) | 3.593(7) | 3.563(6) | 3.281(2) |

[a] Symmetry equivalence Ni(1) and Ni(2) in **2a** and **2d**.

## Conclusion

In summary, we have described the synthetic and structural aspects of a few binuclear nickel(II) complexes, having two bridging carboxylate groups and aqua groups. Intramolecular O–H···O hydrogen bonding interactions between the bridging aqua group and the monodentate benzoate groups are observed in these complexes which add to the stability of the bridging structure. From this structural study on aqua-bridged structures we could show the structural implications of solvent molecules in different types of co-crystals. Aqua-bridged nickel(II) benzoate complexes are stable irrespective of solvent system and also can include solvent molecules such as toluene and benzene. A mixed chloro, aqua and 4-chloro-benzoato-bridged $Ni^{II}$ binuclear complex is formed from the reaction of 4-chlorobenzoate with nickel(II) chloride in the presence of pyridine. This suggests that a substituent on the aromatic ring has a role in deciding the mechanochemical process during the solid-state synthesis.

## Experimental Section

The reagents used were procured from commercial sources (Sigma–Aldrich or Fluka) and used as received unless otherwise stated. Solvents such as benzene, toluene, methanol and acetonitrile were distilled and used.

 © 2006 Wiley-VCH Verlag GmbH & Co. KGaA, Weinheim 

Table 2. Crystal data and refinement parameters for **2a**–**e**.

| | **2a** | **2b** | **2c** | **2d** | **2e** |
|---|---|---|---|---|---|
| Formula | $C_{57}H_{51}N_4Ni_2O_9$ | $C_{48}H_{44}N_4Ni_2O_{10}$ | $C_{64}H_{50}N_4Ni_2O_9$ | $C_{48}H_{38}N_8Ni_2O_{17}$ | $C_{41}H_{34}Cl_4N_4Ni_2O_7$ |
| Mol. weight | 1053.40 | 954.29 | 1136.50 | 1116.28 | 953.94 |
| Crystal system | monoclinic | orthorhombic | monoclinic | monoclinic | monoclinic |
| Space group | $P2_1/c$ | $Pbcn$ | $P2_1/c$ | $C2/c$ | $P2_1/c$ |
| Temperature [K] | 296 | 296 | 296 | 296 | 296 |
| Wavelength [Å] | 0.71073 | 0.71073 | 0.71073 | 0.71073 | 0.71073 |
| $a$ [Å] | 10.7917(2) | 14.2706(6) | 10.490(4) | 15.9027(5) | 12.9935(5) |
| $b$ [Å] | 38.3193(7) | 21.2846(8) | 20.917(9) | 13.5204(5) | 14.3654(5) |
| $c$ [Å] | 12.5877(2) | 15.2229(6) | 25.180(11) | 23.6140(10) | 22.6612(8) |
| $\alpha$ [°] | 90 | 90 | 90 | 90 | 90 |
| $\beta$ [°] | 91.3750(1) | 90 | 96.16(3) | 99.906(2) | 97.762(3) |
| $\gamma$ [°] | 90 | 90 | 90 | 90 | 90 |
| $V$ [Å$^3$] | 5203.90(16) | 4623.9(3) | 5493.0(4) | 5001.6(3) | 4191.1(3) |
| $Z$ | 4 | 4 | 4 | 4 | 4 |
| Density [Mg m$^{-3}$] | 1.345 | 1.371 | 1.374 | 1.482 | 1.512 |
| Abs. coeff. [mm$^{-1}$] | 0.784 | 0.876 | 0.748 | 0.834 | 1.207 |
| Abs. correction | none | none | none | none | none |
| $F$(000) | 2196 | 1984 | 2360 | 2296 | 1952 |
| Total no. of reflections | 50748 | 34247 | 39758 | 21611 | 41439 |
| Reflections, $I > 2\sigma(I)$ | 12870 | 5768 | 12863 | 6153 | 10403 |
| Max. $2\theta$ [°] | 28.33 | 28.32 | 28.28 | 28.33 | 28.32 |
| Ranges ($h$, $k$, $l$) | $-11 \le h \le 14$<br>$-51 \le k \le 45$<br>$-16 \le l \le 16$ | $-13 \le h \le 19$<br>$-28 \le k \le 28$<br>$-16 \le l \le 20$ | $-13 \le h \le 13$<br>$-27 \le k \le 27$<br>$-27 \le l \le 33$ | $-16 \le h \le 21$<br>$-17 \le k \le 16$<br>$-31 \le l \le 31$ | $-16 \le h \le 17$<br>$-19 \le k \le 19$<br>$-30 \le l \le 30$ |
| Complete to $2\theta$ (%) | 99.1 | 99.9 | 94.4 | 98.9 | 99.7 |
| Refinement method | full-matrix least squares on $F^2$ | full-matrix least squares on $F^2$ | full-matrix least squares on $F^2$ | full-matrix least squares on $F^2$ | full-matrix least squares on $F^2$ |
| Data/restraints/parameters | 12870/0/657 | 5768/0/298 | 12863/0/720 | 6153/0/343 | 10403/0/531 |
| Goof ($F^2$) | 1.016 | 1.021 | 0.948 | 0.993 | 0.974 |
| $R$ indices [$I > 2\sigma(I)$] | 0.0417 | 0.0332 | 0.0472 | 0.0319 | 0.0451 |
| $R$ indices (all data) | 0.0761 | 0.0556 | 0.1025 | 0.0452 | 0.1146 |

The X-ray data were collected at 296 K with Mo-$K_\alpha$ radiation ($\lambda$ = 0.71073 Å) with a Bruker Nonius SMART CCD diffractometer equipped with a graphite monochromator (Table 2). The SMART software was used for data collection and also for indexing the reflections and determining the unit cell parameters; the collected data were integrated using SAINT software. The structures were solved by direct methods and refined by full-matrix least-squares calculations using the SHELXTL software.[8] All the non-H atoms were refined in the anisotropic approximation against $F^2$ of all reflections. The H-atoms, except those attached to N, O and F were placed at their calculated positions and refined in the isotropic approximation; those attached to heteroatoms (N, O and F) were located in the difference Fourier maps, and refined with isotropic displacement coefficients.

CCDC numbers 614270–614274 contain the supplementary crystallographic data for this paper. These data can be obtained free of charge from The Cambridge Crystallographic Data Centre via www.ccdc.cam.ac.uk/data_request/cif.

**Preparation of 2a:** Nickel(II) chloride hexahydrate (0.238 g, 1 mmol) and sodium benzoate (0.28 g, 2 mmol) were finely ground in a mortar and heated at 100 °C for 15 min. The solid mixture was cooled to room temperature and transferred into a round-bottomed flask and benzene (20 mL) was added and the heterogeneous mixture was stirred at room temp. for 5 min followed by the addition of pyridine (0.158 g, 2 mmol). The blue supernatant liquid was filtered off and was left undisturbed. Blue crystals were collected after 3 d and dried in air. Yield: 0.371 g, 34% (based on Ni). FT-IR (KBr): $\tilde{\nu}$ = 3412 (b), 3065 (w), 3032 (w), 1630 (s), 1602 (m), 1572 (m), 1530 (w), 1481 (w), 1445 (m), 1394 (s), 1215 (m), 1067 (m), 1037 (m), 814 (m), 757 (m), 716 (s), 696 (s), 676 (s) cm$^{-1}$. $\lambda_{max}$(methanol) = 645 nm, $\varepsilon$ = 18.91 M$^{-1}$ cm$^{-1}$, 383 nm, $\varepsilon$ = 65.6 M$^{-1}$ cm$^{-1}$

**Preparation of 2b:** Benzoic acid (0.24 g, 2 mmol), potassium hydroxide (0.116 g, 2 mmol) and nickel(II) chloride hexahydrate (0.238 g, 1 mmol) were finely ground in the mortar and heated at 100 °C for 15 min. The solid mixture was cooled to room temperature and transferred into a round-bottomed flask. Toluene (20 mL) was added to the solid mass and the heterogeneous mixture was stirred at room temperature for 5 min. To this mixture pyridine (0.158 g, 2 mmol) was added. The residue was filtered off and the blue filtrate was left undisturbed. From this solution blue crystals were obtained after 3 d and dried in air. The blue crystals were further dissolved in ethanol and water (1:1) mixture (5 mL) to obtain crystals of **2b**. Yield: 0.553 g, 58% (based on Ni). FT-IR (KBr): $\tilde{\nu}$ = 3537 (w), 3478 (w), 3060 (w), 2065 (w), 1630 (s), 1602 (m), 1572 (s), 1528 (m), 1484 (m), 1447 (s), 1397 (s), 1215 (m), 1152 (w), 1070 (m), 1039 (m), 825 (s), 760 (m), 720 (s), 697 (s), 674 (s) cm$^{-1}$. $\lambda_{max}$(methanol) = 648 nm, $\varepsilon$ = 16.55 M$^{-1}$ cm$^{-1}$; 389 nm, $\varepsilon$ = 36.63 M$^{-1}$ cm$^{-1}$.

The complexes **2c**–**2e** were prepared from the corresponding acid in an analogous manner to that for **2b**. However, for the crystallisations different solvents were used.

**2c:** Crystallised from a toluene and methanol mixture (1:1). Yield: 0.296 g, 26%. IR (KBr): $\tilde{\nu}$ = 3423 (w), 3043 (m), 2071 (w), 1626 (s), 1614 (s), 1588 (w), 1525 (w), 1484 (w), 1445 (m), 1410 (s), 1374 (s), 1256 (w), 1215 (m), 1152 (w), 1070 (w), 1039 (w), 891 (w), 861 (m), 787 (s), 697 (s), 655 (m), 628 (w) cm$^{-1}$. $\lambda_{max}$(methanol) 649 nm, $\varepsilon$ = 19.53 M$^{-1}$ cm$^{-1}$; 388 nm, $\varepsilon$ = 55.45 M$^{-1}$ cm$^{-1}$.

 © 2006 Wiley-VCH Verlag GmbH & Co. KGaA, Weinheim 

**2d:** Crystallised from toluene. Yield: 0.235 g, 21%. IR (KBr): $\tilde{\nu}$ = 3445 (m), 3071 (m), 2071 (w), 1637 (s), 1604 (m), 1555 (w), 1520 (s), 1486 (m), 1448 (s), 1396 (s), 1363 (s), 1303 (w), 1218 (w), 1155 (w), 1071 (w), 858 (w), 824 (m), 781 (m), 736 (s), 701 (s) $cm^{-1}$. $\lambda_{max}$(acetonitrile) = 638 nm, $\varepsilon$ = 12.09 $M^{-1}cm^{-1}$.

**2e:** Crystallised from an ethanol and acetonitrile mixture (2:1). Yield: 0.134 g, 14%. IR (KBr): $\tilde{\nu}$ = 3420 (w), 3065 (w), 1703 (w), 1614 (s), 1566 (w), 1533 (w), 1484 (w), 1445 (m), 1400 (s), 1218 (m), 1166 (m), 1091 (m), 1039 (w), 1012 (w), 850 (w), 820 (m), 772 (m), 697 (m), 631 (w), 532 (s) $cm^{-1}$. $\lambda_{max}$ (methanol) 633 nm, $\varepsilon$ = 24.42 $M^{-1}cm^{-1}$; 389 nm, $\varepsilon$ = 40.92 $M^{-1}cm^{-1}$.

## Acknowledgments

The authors thank the Department of Science and Technology, New-Delhi, India for supporting the X-ray facility.

[1] a) J. T. Groves, L. Ann Baron, *J. Am. Chem. Soc.* **1989**, *111*, 5442–5448; b) H. Shim, F. M. Raushel, *Biochemistry* **2000**, *39*, 7357–7364; c) A. Messerschmidt, A. Huber, T. Poulos, K. Wieghardt (Eds.), *Handbook of Metalloproteins*, Wiley, Chichester, **2001**.

[2] E. Jabri, M. B. Carr, R. A. Hausinger, P. A. Karplus, *Science* **1995**, *268*, 998–1004.

[3] a) R. C. Holz, *Coord. Chem. Rev.* **2002**, *232*, 5–26; b) Y.-H. Liu, H.-L. Tsai, Y.-L. Lu, Y.-S. Wen, J.-C. Wang, K.-L. Lu, *Inorg. Chem.* **2001**, *40*, 6426–6431; c) R. A. Reynolds III, W. R. Dunham, D. Coucouvanis, *Inorg. Chem.* **1998**, *37*, 1232–1241; d) S.-B. Yu, S. J. Lippard, I. Shweky, A. Bino, *Inorg. Chem.* **1992**, *31*, 3502–3504.

[4] a) R. Lachicotte, A. Kitaygorodskiy, K. S. Hagen, *J. Am. Chem. Soc.* **1993**, *115*, 8883–8884; b) D. M. Kurtz, *Chem. Rev.* **1996**, *96*, 585–606; C. He, S. J. Lippard, *J. Am. Chem. Soc.* **1998**, *120*, 105–113; c) A. M. Barrios, S. J. Lippard, *J. Am. Chem. Soc.* **2000**, *122*, 9172–9177; d) D. Lee, P.-L. Hung, B. Spingler, S. J. Lippard, *Inorg. Chem.* **2002**, *41*, 521–531; e) A. Caneschi, F. Ferraro, D. Gatteschi, M. C. Melandri, P. Rey, R. Sessoli, *Angew. Chem. Int. Ed. Engl.* **1989**, *28*, 1365–1367; f) V. Calvo-Perez, S. Ostrovsky, A. Vega, J. Pelikan, E. Spodine, W. Haase, *Inorg. Chem.* **2006**, *45*, 644–649; g) Y.-H. Liu, H.-L. Tsai, Y.-L. Lu, Y.-S. Wen, J.-C. Wang, K.-L. Lu, *Inorg. Chem.* **2001**, *40*, 6426–6431.

[5] A. Karmakar, K. Deka, R. J. Sarma, J. B. Baruah, *Inorg. Chem. Commun.* **2006**, *9*, 836–838.

[6] K. Deka, N. Barooah, R. J. Sarma, J. B. Baruah, *J. Mol. Structure*, in press.

[7] a) B.-H. Ye, I. D. Willams, X.-Y. Li, *J. Inorg. Biochem.* **2002**, *92*, 128–136; b) U. Turpeinen, R. Hamalainen, J. Reedijk, *Polyhedron* **1987**, *6*, 1603–1610; c) M. Ahlgren, U. Turpeinen, *Acta Crystallogr. Sect. B* **1982**, *38*, 276–279; d) D. W. Christianson, C. A. Fierke, *Acc. Chem. Res.* **1996**, *29*, 331–339.

[8] a) G. M. Sheldrick, *SHELXS97*, Program for the solution of crystal structures, Univ. of Göttingen, Germany, **1997**; b) G. M. Sheldrick, *SHELXS97*, Program for the refinement of crystal structures, Univ. of Göttingen, Germany, **1997**.

Received: July 17, 2006
Published Online: October 2, 2006

 © 2006 Wiley-VCH Verlag GmbH & Co. KGaA, Weinheim 

DOI: 10.1002/ejic.200600452

# A Binuclear Isocyanide Azadithiolatoiron Complex Relevant to the Active Site of Fe-Only Hydrogenases: Synthesis, Structure and Electrochemical Properties

**Jun Hou,[a] Xiaojun Peng,*[a] Jifeng Liu,[b] Yunling Gao,[b] Xing Zhao,[a] Shang Gao,[a] and Keli Han[b]**

**Keywords:** Bioinorganic chemistry / Density functional calculations / Hydrogenases / Iron / Isocyanide ligands

An aromatic isocyanide-substituted diiron complex **5** has been synthesized as a mimic for the active site of Fe-only hydrogenases. Its structure has been fully characterized by X-ray crystallography. The 4-iodophenylisocyanide ligands in **5** are in the basal positions and are nearly parallel to each other, with π–π stacking interactions. Four isomeric geometries of complex **5** have been optimized by DFT calculations, and the electrochemical properties of **5** have been investigated by cyclic voltammetry in the absence and presence of *p*-toluenesulfonic acid (HOTs). Analysis of the cyclic voltammetric curve indicates that the reduction event at about –1.43 V is electrocatalytically active to proton reduction. This potential is more positive than that of any functionalized propanedithiolatodiiron complex.
(© Wiley-VCH Verlag GmbH & Co. KGaA, 69451 Weinheim, Germany, 2006)

## Introduction

Proton reduction to hydrogen in proteins, according to the reaction $2H^+ + 2e^- \rightleftarrows H_2$, is catalyzed in a highly efficient manner by Fe-only hydrogenases ([Fe]$H_2$ases), with rates in the range of 6000–9000 per second.[1–3] Because of this significant efficiency, [Fe]$H_2$ases have drawn considerable attention from chemists in the past few years.

As revealed by a combination of X-ray crystallography[4,5] and IR spectroscopy,[6,7] the active site of [Fe]$H_2$ases is comprised of a 2Fe2S subunit linked to a 4Fe4S cluster by a cysteinyl-S bridge. The 4Fe4S unit is probably responsible for electron transfer while the 2Fe2S subsite is utilized as a catalytic center for hydrogen formation and activation. The two iron atoms in the 2Fe2S subunit are bridged by the sulfur atoms of a propanedithiolato (PDT) ligand and bear the biologically unusual ligands CO and $CN^-$. Theoretical studies support the assignment of the bridging ligand as having the structure $–SCH_2NCH_2S–$ (ADT),[8,9] and the nitrogen heteroatom likely plays an important role in $H_2$ production in the natural system.

The unique structure of the active site has inspired bioinorganic chemists to synthesize structural and functional models.[10–15] Numerous biomimetic models of the PDT-[16] or ADT-bridged[17,18] all-carbonyl diiron complexes, as well as of their isocyanide,[19,20] thioether,[21–23] and phosphane/cyano-substituted[24,25] analogues have been prepared. Recently, Pickett and co-workers have reported their assembly by linking of an $[Fe_4S_4]$ cluster to a diiron unit, which offers the prospect of understanding the catalytic mechanisms of [Fe]$H_2$ases.[26] Rauchfuss et al. have developed syntheses of mixed-ligand diferrous dithiolate complexes by the oxidative decarbonylation of diiron dithiolates,[27,28] and Darensbourg and co-workers have described the electrocatalytic production of $H_2$ by PDT-bridged diiron derivatives [(μ-PDT)$Fe_2(CO)_4(PR_3)_2$] in the presence of the weak acid HOAc.[29,30] Rauchfuss et al. have demonstrated that the mixed-ligand substituted diiron system [(μ-PDT)$Fe_2(CO)_4$-$PMe_3(CN)]^-$ is an electrocatalyst for $H_2$ production with the strong acid *p*-toluenesulfonic acid (HOTs).[31,32] However, relatively more negative potentials are required to drive the reduction of protons to $H_2$ with these synthetic systems. Sun and co-workers have reported that the introduction of nitrogen in the ADT bridge shifts the reduction potential to a more positive value.[33] Thus, the synthesis of functionalized azadithiolatodiirons may be an alternative in the search for synthetic catalysts with [Fe]$H_2$ase-like capability. Although ADT-bridged diiron complexes have been extensively studied,[34–39] to the best of our knowledge there is no report on the electrocatalytic reduction of protons catalyzed by functionally substituted azadithiolatodiiron derivatives in the literature to date. With this in mind, we present here a binuclear isocyanide azadithiolatoiron complex **5** in which the isocyanide ligand was chosen because it can be used as a surrogate for the relevant $CN^-$ without complicating the reactivity of the cyanide nitrogen in catalytic reactions.[19,20] We describe the preparation, structural charac-

[a] State Key Laboratory of Fine Chemicals, Dalian University of Technology,
Dalian 116012, P. R. China
Fax: +86-411-8899-3906
E-mail: pengxj@dlut.edu.cn
[b] State Key Laboratory of Molecular Reaction Dynamics, Dalian Institute of Chemical Physics, Chinese Academy of Science,
Dalian 116022, P. R. China
Supporting information for this article is available on the WWW under http://www.eurjic.org or from the author.

 © 2006 Wiley-VCH Verlag GmbH & Co. KGaA, Weinheim 

terization, and DFT calculations of the possible isomers of **5**, as well as the electrochemical properties of **5** in the absence and presence of the moderately strong acid HOTs.

## Results and Discussion

### Synthesis and Spectroscopic Characterization of Complexes 3 and 5

The complex [{(μ-$SCH_2$)$_2$N(4-$CH_3C_6H_4$)}$Fe_2(CO)_6$] (**3**) was prepared by a similar procedure to that reported by Rauchfuss (Scheme 1).[34] The lithium salt of hexacarbonyldisulfidodiiron (**1**),[40] freshly derived from [(μ-S)$_2$$Fe_2$-$(CO)_6$], was treated with *N*,*N*-bis(chloromethyl)-4-methylaniline (**2**) to give complex **3** in moderate yield. The synthesis of [{(μ-$SCH_2$)$_2$N(4-$CH_3C_6H_4$)}$Fe_2(CO)_4$(4-$IC_6H_4NC$)$_2$] (**5**) from complex **3** and 4-iodophenylisocyanide (**4**) turned out to be a challenge. Treatment of **3** with two equivalents of **4** in $CH_2Cl_2$ or $CH_3CN$ solution afforded complex **5** in very low yield, and attempts to afford disubstituted isocyanide derivative **5** in refluxing MeCN solution by Rauchfuss' protocol[19] were unsuccessful because **4** is thermally unstable. However, reaction of complex **3** with **4** in $CH_3CN$/$CH_2Cl_2$ (2:1, v/v) solution in the presence of the decarbonylating agent $Me_3NO{\cdot}2H_2O$ at room temperature gave the desired product **5** in reasonable yield after purification by column chromatography on silica gel. Complexes **3** and **5** are stable to air in the solid state but moderately sensitive in solution.

Complexes **3** and **5** were characterized by IR and $^1$H and $^{13}$C NMR spectroscopy and mass spectrometry. The IR spectrum of complex **3** in $CH_2Cl_2$ shows three major bands in the CO region at 2071, 2030, and 2000 cm$^{-1}$, in agreement with those of other azadithiolatodiiron derivatives.[34–36] The IR spectrum of complex **5** in $CH_2Cl_2$ exhibits NC bands at 2122 and 2094 cm$^{-1}$ and CO bands at 1996, 1980, and 1950 cm$^{-1}$. Compared with the signals of **3**, the stretching frequencies of CO are shifted to lower wavenumbers by about 50 cm$^{-1}$ on average, consistent with the better electron-donating ability of 4-iodophenylisocyanide with respect to the CO ligand. This indicates that the introduction of aromatic isocyanide ligands to the diiron center increases the electron density of the Fe–Fe bond.

### Structures of Complexes 3 and 5

The solid-state structures of **3** and **5** were determined by X-ray diffraction. The structure of **3** is shown in Figure 1 and selected bond lengths and bond angles are listed in Table 1. The 2Fe2S unit has a pseudo-square-pyramidal geometry, similar to those of previously reported azadithiolatodiiron derivatives.[34–36] The 4-methylphenyl ring slants towards the Fe(2)$(CO)_3$ unit, and the axis containing N(1), C(9), C(12), and C(15) atoms is nearly parallel to the apical C(6)O(6) ligand on the Fe(2) atom. It is noteworthy that the C(6)–Fe(2)–Fe(1) angle is about 7° larger than the C(2)–Fe(1)–Fe(2) angle, thus indicating an interaction between the arene group and Fe(2)$(CO)_3$ unit. The Fe–Fe distance of 2.5090(10) Å agrees well with those found in other (μ-ADT)$Fe_2(CO)_6$ structures.

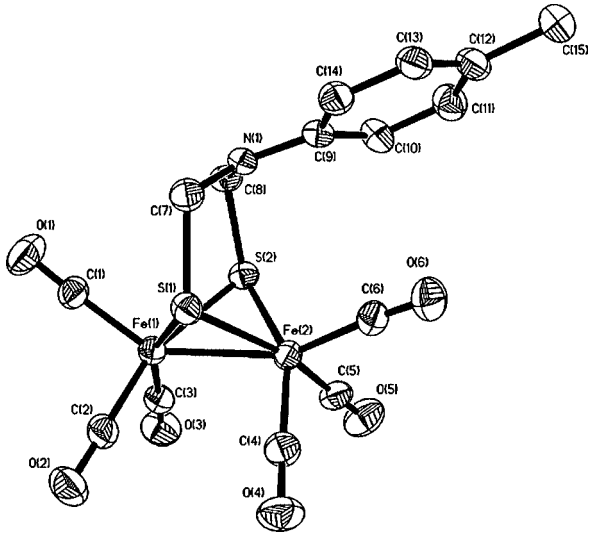


Figure 1. ORTEP view of **3** (ellipsoids at 30% probability level).

The molecular structure of **5** in the solid state is displayed in Figure 2 and selected lengths and angles are listed in Table 2. Like the "parent" **3**, the central 2Fe2S unit of **5** adopts a face-shared bi-octahedral structure. The Fe–Fe bond length of 2.5121(11) Å is somewhat longer than that observed in **3** and is similar to that found in an isocyanide-substituted PDT-bridged diiron complex.[20] This indicates that the metal–metal distance in diiron(I) compounds is

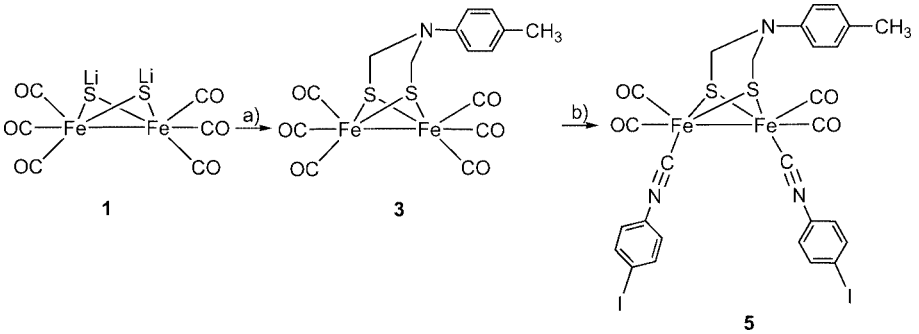


Scheme 1. a) $(ClCH_2)_2N(4\text{-}CH_3C_6H_4)$ (**2**), thf, –78 °C, 2 h; b) 4-iodophenyl isocyanide (**4**), $Me_3NO{\cdot}2H_2O$, $CH_3CN/CH_2Cl_2$ (1:1, v/v), room temp., 48 h.

 © 2006 Wiley-VCH Verlag GmbH & Co. KGaA, Weinheim 

Table 1. Selected bond lengths [Å] and angles [°] for **3**.

| | | | |
|---|---|---|---|
| Fe(1)–Fe(2) | 2.5090(10) | Fe(1)–S(1)–Fe(2) | 67.44(4) |
| Fe(1)–S(1) | 2.2614(14) | Fe(1)–S(2)–Fe(2) | 67.28(4) |
| Fe(1)–S(2) | 2.2626(15) | S(1)–Fe(1)–S(2) | 85.05(5) |
| Fe(2)–S(1) | 2.2585(14) | S(1)–Fe(2)–S(2) | 85.02(5) |
| Fe(2)–S(2) | 2.2666(15) | C(7)–S(1)–Fe(1) | 110.7(2) |
| Fe(1)–C(1) | 1.797(6) | C(8)–S(2)–Fe(1) | 107.59(19) |
| Fe(1)–C(2) | 1.783(6) | C(1)–Fe(1)–C(3) | 99.3(3) |
| Fe(1)–C(3) | 1.797(6) | C(3)–Fe(1)–C(2) | 90.2(3) |
| N(1)–C(7) | 1.420(8) | C(2)–Fe(1)–C(1) | 99.3(3) |
| N(1)–C(8) | 1.411(8) | C(1)–Fe(1)–S(1) | 101.99(19) |
| N(1)–C(9) | 1.413(7) | C(1)–Fe(1)–S(2) | 99.4(2) |
| | | C(9)–N(1)–C(8) | 121.3(5) |
| | | C(9)–N(1)–C(7) | 122.3(5) |
| | | C(7)–N(1)–C(8) | 113.8(5) |

slightly affected by the nature of terminal ligands with a better electron-donating ability. The p-π conjugation between the 4-methylphenyl ring and the bridging N p orbital is somewhat weakened, therefore the bridging N atom is not in the plane defined by the atoms C(12), C(10), and C(19). The sum of the C–N–C angles around N(3) is 354°. The 4-methylphenyl ring in an axial position is approximately parallel to the apical carbonyl ligand C(22)O(3) on the Fe(2) site, as found in **3**. The C(20)–Fe(2)–Fe(1) angle in **5** [156.5(2)°] is enlarged by about 3.6° compared to the corresponding angle [C(6)–Fe(2)–Fe(1)] in **3** [152.83(19)°], thus suggesting the effect of the phenylisocyanide ligands on the diiron unit. The C(7)–N(1)–C(4) angle [177.3(7)°] on the Fe(1) unit is relatively linear, whereas the C(21)–N(2)–C(23) angle [168.1(7)°] on the Fe(2) unit is slightly bent. The bending at the N(2) atom is probably due to a steric influence of the bulky isocyanide ligands. The average Fe–C(N) distance of 1.846(6) Å is slightly larger than that of Fe–C(O) [av. 1.7805(7) Å]. It is interesting to note that the two phenylisocyanide ligands in the basal positions on each iron unit are nearly parallel to each other, thus indicating a crystal stacking interaction between them. Figure 3 displays the packing view along the *b* axis. It shows π–π stacking interactions of the 4-iodophenylisocyanide ligands within the column. Complex **5** is unusual compared to related diiron isocyanide complexes where the two isocyanide ligands are in apical positions in the solid state and are not parallel to each other.[20]

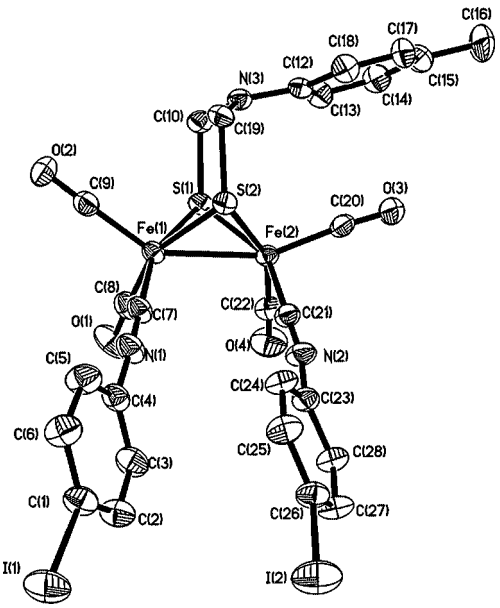


Figure 2. ORTEP view of **5** (ellipsoids at 30% probability level).

Table 2. Selected bond lengths [Å] and angles [°] for **5**.

| | | | |
|---|---|---|---|
| Fe(1)–Fe(2) | 2.5121(11) | Fe(1)–S(1)–Fe(2) | 67.29(5) |
| Fe(1)–S(1) | 2.2642(16) | Fe(1)–S(2)–Fe(2) | 67.25(5) |
| Fe(1)–S(2) | 2.2698(17) | S(1)–Fe(1)–S(2) | 84.93(6) |
| Fe(2)–S(1) | 2.2698(17) | S(1)–Fe(2)–S(2) | 84.87(6) |
| Fe(2)–S(2) | 2.2668(17) | C(10)–S(1)–Fe(1) | 107.6(2) |
| Fe(1)–C(7) | 1.846(6) | C(19)–S(2)–Fe(1) | 109.3(2) |
| Fe(1)–C(8) | 1.758(8) | C(9)–Fe(1)–C(8) | 101.1(3) |
| Fe(1)–C(9) | 1.806(7) | C(8)–Fe(1)–C(7) | 90.1(3) |
| N(1)–C(7) | 1.158(8) | C(7)–Fe(1)–C(9) | 100.1(3) |
| N(1)–C(4) | 1.409(8) | C(9)–Fe(1)–S(1) | 99.8(2) |
| N(2)–C(21) | 1.165(8) | C(9)–Fe(1)–S(2) | 101.5(2) |
| N(2)–C(23) | 1.397(8) | C(12)–N(3)–C(19) | 121.0(5) |
| N(3)–C(12) | 1.396(7) | C(12)–N(3)–C(10) | 121.7(5) |
| N(3)–C(10) | 1.398(8) | C(10)–N(3)–C(19) | 111.5(5) |
| N(3)–C(19) | 1.434(8) | C(7)–Fe(1)–S(1) | 159.8(2) |
| I(1)–C(1) | 2.092(7) | C(7)–Fe(1)–S(2) | 87.6(2) |
| | | N(1)–C(7)–Fe(1) | 178.9(7) |
| | | N(2)–C(21)–Fe(2) | 177.7(6) |
| | | C(4)–N(1)–C(7) | 177.3(7) |
| | | C(23)–N(2)–C(21) | 168.1(7) |

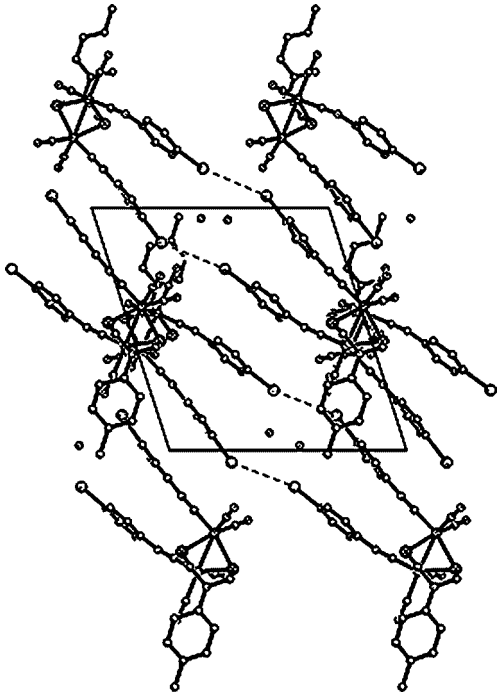

Figure 3. Crystal packing diagram for **5** viewed along the *b* axis. Thermal ellipsoids are drawn at the 50% possibility level.

In contrast to the solid structure, complex **5** exists as isomers, with two different CN stretching frequencies at 2122 and 2094 $cm^{-1}$, respectively, in solution. This phenomenon is analogous to that described for the related isocyanide

 © 2006 Wiley-VCH Verlag GmbH & Co. KGaA, Weinheim 

derivative $[(\mu\text{-}S_2C_3H_6)Fe_2(CO)_4(t\text{Bu}_4\text{NC})_2]$.[20] In general, complexes of this type can share several isomeric geometries in solution on the basis of ligands in apical or axial positions.

### DFT Structure Calculations for 5

To gain insight into the possible isomeric structures based on the different positions of the two isocyanide ligands, the possible geometries of **5** were optimized by using DFT methods. Theoretically, there are four possible isomers for doubly substituted diiron complexes, that is ap/ap, ba/ap, ba/ba, and ap/ba configuration modes. Four optimized structures of the relevant isomers of **5** are shown in Figure 4. Selected geometrical parameters are summarized in the Supporting Information. A comparison of these structures reveals that the Fe–Fe distance is affected by the arrangement of the CO and 4-$IC_6H_4NC$ groups. This effect can be partly attributed to the competition between π-acceptors for the π electrons. The crystallographically characterized isomer **5** is analogous to the computed complex **5.4**. Notably, the bond lengths and angles are in good agreement with the X-ray data and the two phenylisocyanide groups in the basal positions are close to parallel.

From the relative energies of the four isomers shown in Table S1, it can be seen that in the monomer case the stabilization sequence of the four conformations for **5** in the gas phase is **5.2** > **5.3** > **5.4** > **5.1**. When considering the solvent effect, we found that the stabilization sequence changes and isomer **5.4** becomes the most stable one in $CCl_4$ solution at 298 K. The stabilization sequence in $CCl_4$ solution is **5.4** > **5.1** > **5.3** > **5.2**. Theoretical calculations show an important role for the solvent effect on structure selection

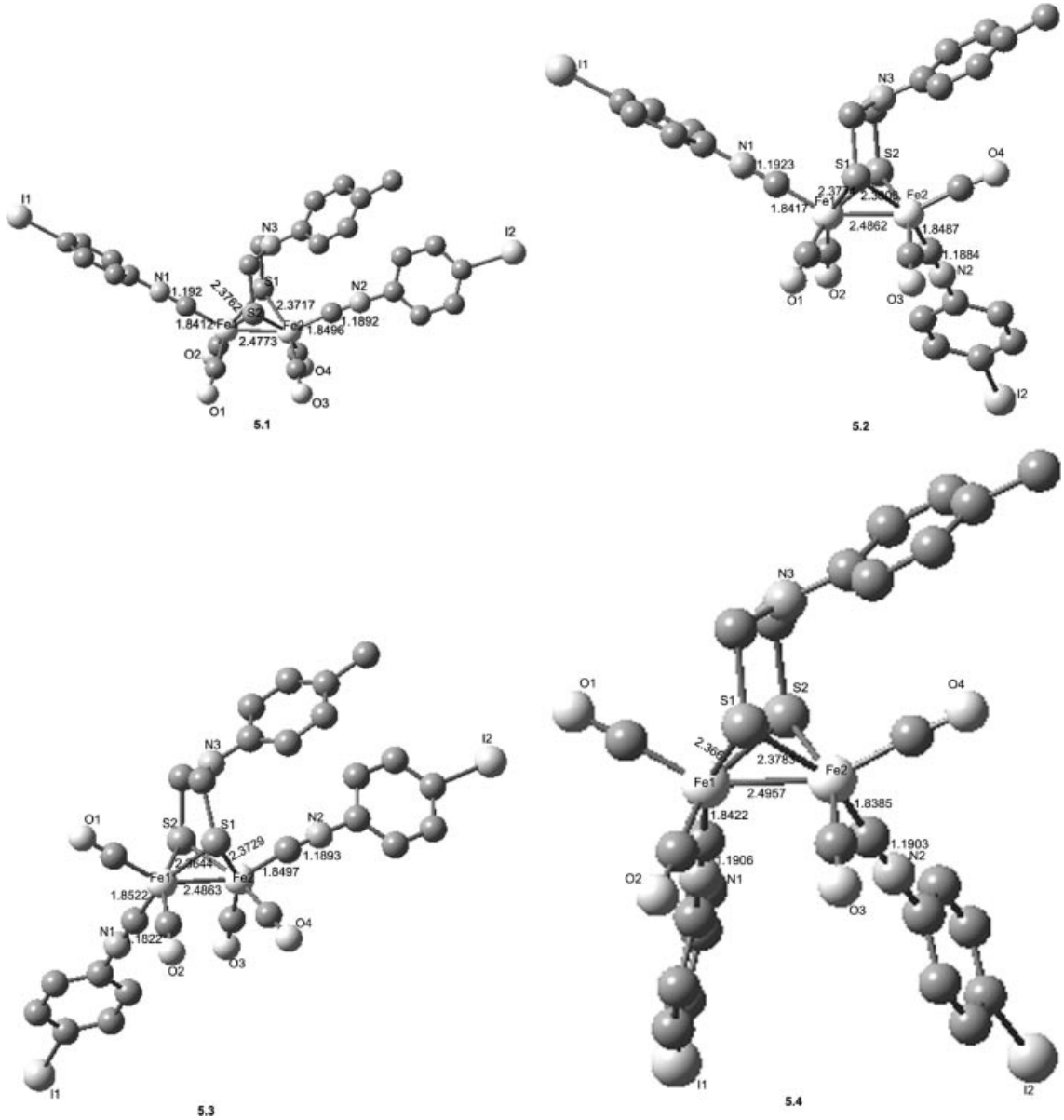


Figure 4. DFT-optimized structures of the four isomers of complex **5**. Selected bond lengths [Å] are given.

 © 2006 Wiley-VCH Verlag GmbH & Co. KGaA, Weinheim 

during the crystallization of complex **5**. The energy difference between isomers is less than 15 kJ mol$^{-1}$, which means that isomers of complex **5** can interchange easily.

### Electrochemistry of Complexes 3 and 5

The ADT-bridged diiron hexacarbonyl compounds [(μ-ADT)$Fe_2(CO)_6$][33,35] and their phosphane-substituted derivatives[36] have been reported to undergo an electrochemically quasi-reversible/irreversible reduction at moderately negative potentials depending on the electron-donating abilities of the ligands on the diiron core. The cyclic voltammograms of complexes **3** and **5** shown in Figure 5 were recorded in $CH_3CN$ solution (with 0.1 M $n$Bu$_4$NPF$_6$ as electrolyte) and proceed, as indicated, in the cathodic direction. Complexes **3** and **5** display a quasi-reversible reduction peak and an irreversible oxidation wave, respectively. By comparison with electrochemical data for PDT-bridged diiron complexes[29,30] and ADT-bridged diiron analogues,[33,35,36] the reduction peaks at –1.55 V for **3** and –1.70 V for **5** vs. $Fc^+$/Fc can be assigned to the one-electron reduction process of $Fe^IFe^I$ to $Fe^IFe^0$. The oxidation peaks at 0.55 V for **3** and at 0.13 V for **5** can be attributed to a net one-electron process, but further work is needed to establish this aspect of the electrochemistry. In comparison to that of the parent complex **3**, the reduction potential of **5** shifts by about 0.15 V to a more negative value, and the oxidation peak shifts by about 0.42 V to a less positive value. These shifts of potential indicate that the introduction of 4-iodophenylisocyanide ligands in **5** makes the reduction of the iron core more difficult and the oxidation easier, which is consistent with the better donor capacity of 4-iodophenylisocyanide relative to CO. A similar trend in the diiron analogue [{(μ-$SCH_2)_2$N(4-$BrC_6H_4$)}$Fe_2(CO)_5$-$PPh_3$] has been reported by Sun and co-workers.[36]

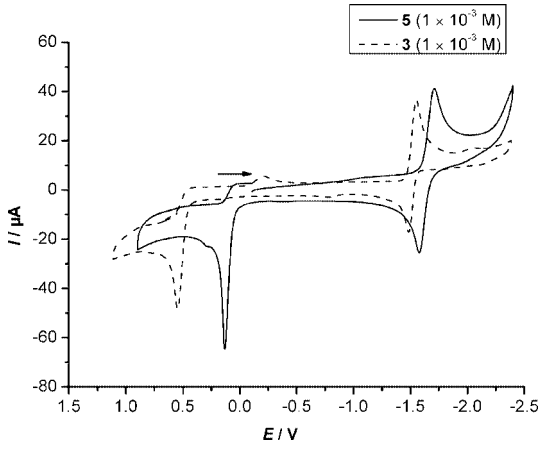


Figure 5. Cyclic voltammograms of **3** and **5** (1 mM) in 0.1 M $n$Bu$_4$NPF$_6$/$CH_3CN$ solution at a potential scan rate of 100 mV s$^{-1}$.

### Electrocatalytic Proton Reduction in $CH_3CN$ Solution

The electrocatalytic proton reduction by **5** was investigated by cyclic voltammetry in the presence of the moderately strong acid HOTs. The cyclic voltammogram recorded in $CH_3CN$ solution at different acid concentrations (0–4 mM) is shown in Figure 6. Upon addition of 1 mM of HOTs, two new reduction peaks were observed at around –1.20 and –1.43 V. As can be seen in Figure 6, the current height of the reduction peak around –1.20 V displays a slight increase with an increase of acid concentration, while the reduction wave at around –1.43 V shows a significant electrocatalytic response. The current intensity of this reduction peak gradually increases and the potential is shifted to a relatively more negative value with increasing acid concentration. The current intensity ($I_{pc}$) of this reduction displays a linear increase with an increase of the concentration of HOTs, as shown in Figure 7. The steeper slope is indicative of the sensitivity of the reduction to acid concentration. These features are typical of a catalytic proton reduction process.[41] At [$H^+$]/[**5**] ≥ 5, the reduction peak at around –1.70 V disappears and the height of the reduction event around –1.43 V also increases and its potential shifts to a more negative value (Figure S1). We conclude that the reduction peak around –1.43 V displays an electrocatalytic response to proton reduction. The reduction peak around –1.20 V may be the reduction process of a protonated product, and further work is needed to define it properly. To further confirm the catalytic activity of **5** around –1.43 V, bulk electrolysis of solutions of 2 mM **5** with 50 mM HOTs was performed at –1.50 V. After passage of 20 C of charge through the cell, a sample of gas was collected and analyzed. Analysis by gas chromatography showed the gas evolved during electrolysis to be $H_2$.

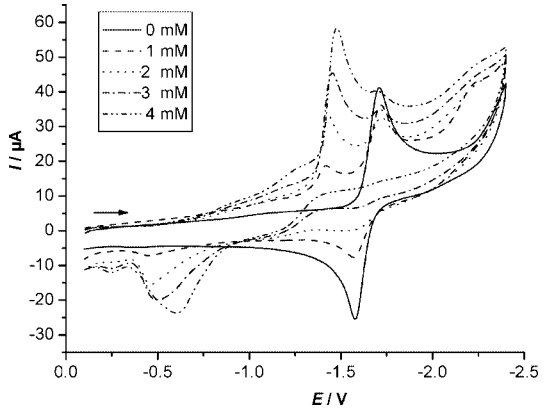


Figure 6. Cyclic voltammograms of **5** (1 mM) with 0–4 mM HOTs in 0.1 M $n$Bu$_4$NPF$_6$/$CH_3CN$ solution at a potential scan rate of 100 mV s$^{-1}$.

Electrocatalytic $H_2$ production by the cyano/phosphane-substituted diiron derivative [(μ-PDT){$Fe(CO)_2PMe_3$}-{$Fe(CO)_2CN$}]$^-$ has been reported by Rauchfuss and coworkers under similar acid conditions (HOTs).[31,32] The potential for the reduction of protons was found to be $E_p^{red}$ = –1.2 V vs. Ag/AgCl (corresponding to –1.69 V vs. $Fc^+$/Fc),[42] which means that the potential of complex **5** is shifted by about 260 mV to a more positive value. Compared with all other functionalized PDT-bridged substituted diiron compounds,[29,30] complex **5** also has a con-

 © 2006 Wiley-VCH Verlag GmbH & Co. KGaA, Weinheim 

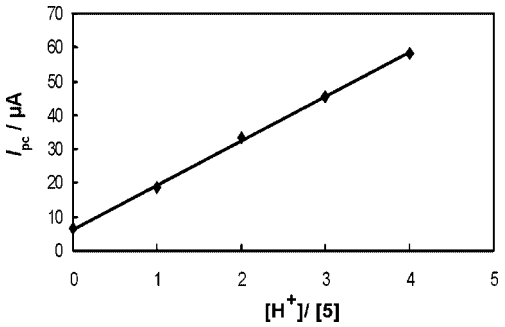


Figure 7. Dependence of current intensity of the reduction events of **5** (1 mM) around –1.43 V on concentration of HOTs.

siderably more positive potential of proton reduction. A reasonable interpretation for this is that the utilization of the basicity of the ADT heteronitrogen atom[43] and the introduction of isocyanide ligands shift the potential to a more positive value and therefore makes the reduction of protons remarkably easier.

Upon addition of acid, an irreversible event is observed at around –0.6 V on the reverse scan. This presumably results from a reduction-derived decomposition product.[29,44]

## Conclusions

The binuclear aromatic isocyanide substitute [{(μ-$SCH_2$)$_2$-N(4-$CH_3C_6H_4$)}$Fe_2(CO)_4$(4-$IC_6H_4NC$)$_2$] (**5**) has been prepared as an active site model of iron-only hydrogenases. Both **5** and its parent complex **3** have been fully characterized by X-ray diffraction. The structure of **5** is highly unusual in that the two phenylisocyanide ligands are in basal positions and are nearly parallel to each other. This suggests that steric or crystal packing forces control the stereochemistry of CO and the aromatic isocyanide ligands. The introduction of the isocyanide ligands in **5** makes the CO stretching frequencies shift to lower values. These lower values of $\nu_{(CO)}$ indicate that the diiron core is more electron-rich, which is also consistent with the shift of the reduction potential of **5** to a more negative value.

The results of DFT calculations show that the binuclear active site of **5** has four possible isomers. One of these was isolated and characterized crystallographically because of the potential for isomeric complexity. It is likely that the π–π stacking interaction between molecules of complex **5** makes the isomer **5.4** stable enough to crystallize from solution.

On the basis of electrochemical analyses of **5**, the reduction peak around –1.43 V is electrocatalytically active in the presence of HOTs. The iodo functionality in **5** could be used for further elaboration by incorporating a redox species. This offers a possibility of linking a ruthenium photosensitizer to the azadithiolatodiiron system **5** in an attempt to produce $H_2$ by action of light.[15] Further experimental efforts in these directions are underway.

## Experimental Section

**Reagents and Instrumentation:** All reactions and operations were carried out under $N_2$ using standard Schlenk techniques. All solvents were dried and distilled prior to use according to standard methods. Tetrahydrofuran was purified by distillation under $N_2$ from sodium/benzophenone. Acetonitrile was distilled once from $CaH_2$ and once from $P_2O_5$ and freshly distilled from $CaH_2$ prior to use. Dichloromethane was distilled from $P_2O_5$ under $N_2$. The following materials were commercially available reagents and used without further purification: paraformaldehyde, 4-methylaniline, and 4-iodoaniline. $LiEt_3BH$ was purchased from Aldrich and used as received. *N*,*N*-Bis(chloromethyl)-4-methylaniline (**2**), [(μ-S)$_2$-$Fe_2(CO)_6$], [(μ-LiS)$_2Fe_2(CO)_6$] (**1**), and 4-iodophenylisocyanide (**4**) were synthesized according to the literature procedures.[34,40,45,46]

Infrared spectra were recorded with a FT-IR spectrophotometer. $^1H$ and $^{13}C$ NMR spectra were recorded on a Varian INOVA 400 NMR spectrometer. Mass spectra were recorded with a HP 100 MSD. HR mass spectra were recorded on a Q-TOF mass spectrometer or a GC-TOF instrument (Micromass).

**Synthesis of [{(μ-$SCH_2$)$_2$N(4-$CH_3C_6H_4$)}$Fe_2(CO)_6$] (3):** $LiEt_3BH$ solution (1 M solution in thf, 2.9 mL, 2.9 mmol) was added to a solution of [(μ-S)$_2Fe_2(CO)_6$] (500 mg, 1.45 mmol) in thf (30 mL) by syringe at –78 °C over 30 min. A solution of *N*,*N*-bis(chloromethyl)-4-methylaniline (**2**) in thf (20 mL) was added to the resulting green solution, causing an immediate change of color to dark red. After stirring for 2 h at –78 °C and for 1 h at room temperature, the solvent was removed in vacuo and the resulting dark-red solid was purified by column chromatography on silica gel using $CH_2Cl_2$/hexane (1:10) as eluent to afford a dark-red solid. Yield: 57% (recrystallized from $CH_2Cl_2$/hexane). $^1H$ NMR (400 MHz, $CDCl_3$): $\delta$ = 7.12 (s, 2 H), 6.66 (s, 2 H), 4.31 (s, 4 H), 2.28 (s, 3 H) ppm. $^{13}C$ NMR (100 MHz, $CDCl_3$): $\delta$ = 209.0, 207.2, 142.8, 130.6, 130.2, 116.3, 53.6, 50.2, 19.5 ppm. IR ($CH_2Cl_2$): $\nu_{(CO)}$ = 2071, 2030, 1999 $cm^{-1}$. MS (API-ES): (*m*/*z*): 478 $[M + H]^+$. HR-MS (ESI) calcd. for $[M + H]^+$: 477.8805; found 477.8793.

**Synthesis of [{(μ-$SCH_2$)$_2$N(4-$CH_3C_6H_4$)}$Fe_2(CO)_4$(4-$IC_6H_4NC$)$_2$] (5). Method A:** A solution of complex **3** (1 g, 2.09 mmol) in $CH_3CN$ (30 mL) was treated with a solution of 4-$IC_6H_4NC$ (0.96 g, 4.19 mmol) in $CH_2Cl_2$ (30 mL) at room temperature, followed by the addition of $Me_3NO{\cdot}H_2O$ (0.465 g, 4.19 mmol) in $CH_3CN$ (20 mL). The solution immediately turned dark purple, and after 5 h the color had changed again to dark red. The mixture was stirred at room temperature for 48 h and TLC showed the reaction was complete. The solvent was removed in vacuo and the dark-red residue was purified by column chromatography on silica gel eluting with hexane/dichloromethane (5:1). Two main bands were observed: the first red band, containing [{(μ-$SCH_2$)$_2$N(4-$CH_3C_6H_4$)}-$Fe_2(CO)_5$(4-$IC_6H_4NC$)] [IR ($CH_2Cl_2$): $\nu_{CN}$ = 2124 $cm^{-1}$, $\nu_{CO}$ = 2040, 2000, 1975 $cm^{-1}$], was collected with around 600 mL of eluent, and the second red band (**5**), with a further 1000 mL of eluent, was collected to give the red product **5**. Yield: 640 mg (34%) (recrystallized from $CH_2Cl_2$/hexane). $^1H$ NMR (400 MHz, [$D_6$]acetone): $\delta$ = 7.77 (d, *J* = 8.4 Hz, 2 H), 7.11 (d, *J* = 8.4 Hz, 2 H), 7.03 (d, *J* = 8.0 Hz, 2 H), 6.77 (d, *J* = 8.0 Hz, 2 H), 4.38 (s, 4 H), 2.14 (s, 3 H) ppm. $^{13}C$ NMR (100 MHz, $CDCl_3$): $\delta$ = 211.5 (CN), 205.5, 202.5 (CO), 147.0, 143.5, 138.6, 130.2, 128.7, 127.5, 115.8, 93.3, 49.8, 20.5 ppm. IR ($CH_2Cl_2$): $\nu_{(CN)}$ = 2122, 2094 $cm^{-1}$; $\nu_{(CO)}$ = 1996, 1980, 1950 $cm^{-1}$. HR-MS (EI) calcd. for $[M^+]$: 878.7605; found 878.7601.

**Methods B:** A 100-mL Schlenk flask was charged with [{(μ-$SCH_2$)$_2$-N(4-$CH_3C_6H_4$)}$Fe_2(CO)_6$] (**3**; 500 mg, 1.04 mmol) and 4-$IC_6H_4NC$

 © 2006 Wiley-VCH Verlag GmbH & Co. KGaA, Weinheim 

(479 mg, 2.09 mmol), 50 mL of $CH_2Cl_2$ was added to this flask, and the solution was stirred 48 h at room temperature. The solvent was removed in vacuo and the residue was purified by column chromatography on silica gel, eluting with hexane/dichloromethane (5:1). The first band, containing a large quantity of the monoisocyanide-substituted product, was collected with about 800 mL of eluent, and the second red band containing **5** with a further 200 mL. Yield of **5**: 92 mg (10%; recrystallized from $CH_2Cl_2$/hexane).

**X-ray Structure Determinations:** The single-crystal X-ray data were collected with a Siemens SMART CCD diffractometer for **3**, while the measurement for **5** was performed on a Siemens P4 four-circle diffractometer. In all cases, the data were collected at 293 K using graphite monochromated Mo-$K_\alpha$ radiation ($\lambda$ = 0.71073 Å) in the $\omega$–2$\theta$ scan mode. Data processing was accomplished with the SAINT processing program.[47] Intensity data were corrected for absorption with empirical methods. The structures of complexes **3** and **5** were solved by direct methods and refined on $F_o^2$ against full-matrix least-squares with the SHELXTL 97 program package.[48] All non-hydrogen atoms were refined anisotropically. Hydrogen atoms were located by geometrical calculation, but their positions and thermal parameters were fixed during the structure refinement. A summary of the crystallographic data and structural determinations for **3** and **5** is provided in Table 3.

Table 3. X-ray crystallographic data for **3** and **5**.

| | **3** | **5** |
|---|---|---|
| Formula | $C_{15}H_{11}Fe_2NO_6S_2$ | $C_{27}H_{23}Fe_2I_2N_3O_6S_2$ |
| $M_r$ [g mol$^{-1}$] | 475.05 | 915.12 |
| $\lambda$ [Å] | 0.71073 | 0.71073 |
| Crystal system | triclinic | monoclinic |
| Space group | $P\bar{1}$ | $P2_1/c$ |
| $a$ [Å] | 7.8394(3) | 13.3600(8) |
| $b$ [Å] | 9.6753(3) | 21.6360(14) |
| $c$ [Å] | 12.4508(3) | 12.4395(8) |
| $\alpha$ [°] | 99.2350(10) | 90.00 |
| $\beta$ [°] | 101.954(2) | 107.7380(10) |
| $\gamma$ [°] | 90.124(2) | 90.00 |
| $V$ [Å$^3$] | 911.31(5) | 3424.8(4) |
| $Z$ | 2 | 4 |
| $T$ [K] | 293 | 293 |
| $\rho_{calcd.}$ [g cm$^{-3}$] | 1.731 | 1.771 |
| $\mu$ [mm$^{-1}$] | 1.850 | 2.812 |
| $F$ [000] | 478 | 1772 |
| Total reflections | 3177 | 7895 |
| Reflections observed | 2789 | 5453 |
| Parameters | 236 | 379 |
| Goodness-of-fit on $F^2$ | 1.091 | 1.035 |
| $R1$[a] [$I > 2\sigma(I)$] | 0.0694 | 0.0697 |
| $wR$[b] [$I > 2\sigma(I)$] | 0.2061 | 0.2265 |
| Max. peak/hole [e Å$^{-3}$] | 1.583/– 0.937 | 2.844/–1.054 |

[a] $R1 = (\Sigma||F_o| - |F_c||)/(\Sigma|F_o|)$. [b] $wR2 = [\Sigma w(F_o^2 - F_c^2)^2/\Sigma w(F_o^2)^2]^{1/2}$.

CCDC-293055 (for **3**) and -289306 (for **5**) contain the supplementary crystallographic data for this paper. These data can be obtained free of charge from The Cambridge Crystallographic Data Center via www.ccdc.cam.ac.uk/data_request/cif.

**Computational Methods:** The density functional theory (DFT) method was used to optimize the isomeric geometries of complex **5**. Calculations were performed with the B3LYP functional[49] included in the Gaussian 03 program package.[50] The D95 basis set[51] was used for all atoms except Fe and I, for which the LANL2DZ basis set[52] was used with the effective core potential (ECP) of LANL2DZ. The effect of solvent on the stability of the isomers was considered by optimizing all the geometries in $CCl_4$ solution using the PCM method[53] included in Gaussian 03.

**Electrochemistry:** Acetonitrile used for electrochemical measurements was distilled once from $CaH_2$ and once from $P_2O_5$ and freshly distilled from $CaH_2$ under $N_2$. Measurements were made with a BAS 100B electrochemical workstation. All cyclic voltammograms were obtained in a conventional three-electrode cell under argon and at ambient temperature. The working electrode was a glassy carbon electrode (diameter 3 mm) that was successively polished with 3-μm and 1-μm alumina pastes and sonicated in ion-free water for 15 min prior to use. The supporting electrolyte was 0.1 M $n$Bu$_4$NPF$_6$ (Fluka, electrochemical grade). The experimental reference electrode was a nonaqueous Ag/Ag$^+$ electrode (0.01 M $AgNO_3$/0.1 M $n$Bu$_4$NPF$_6$ in $CH_3CN$). Ferrocene was used as an internal standard. All potentials reported in this paper are relative to the Fc$^+$/Fc couple. The counter electrode was platinum wire. During the electrocatalytic experiments under argon, increments of acid were added by microsyringe. Bulk electrolysis experiments were performed under argon with a BAS 100 B/W electrochemical analyzer, which was carried out on a glassy carbon rod ($A$ = 3.14 cm$^2$) in a gas-tight H-type electrolysis cell containing about 14 mL of $CH_3CN$ solution. Gas chromatography was performed with a GC 920 instrument equipped with a thermal conductivity detector (TCD) under isothermal conditions with argon as carrier gas.

**Supporting Information** (see also the footnote on the first page of this article): Energetic properties of isomers of complex **5** calculated both in the gas phase and $CCl_4$ solution using PCM method. Geometrical bond lengths and angles calculated for the isomers **5.1**–**5.4**.

## Acknowledgments

We are grateful to the Ministry of Education of China and the National Natural Science Foundation of China (projects 20128005, 20376010, and 20472012). We also thank the Supercomputing Center of CNIC (CAS) for the support of calculations.

[1] M. W. W. Adam, *Biochim. Biophys. Acta* **1990**, *1020*, 115–145.
[2] J. W. Peters, *Curr. Opin. Struct. Biol.* **1999**, *9*, 670–676.
[3] M. Frey, *ChemBioChem* **2002**, *3*, 152–160.
[4] J. W. Peters, W. N. Lanzilotta, B. J. Lemon, L. C. Seefeldt, *Science* **1998**, *282*, 1853–1858.
[5] Y. Nicolet, C. Piras, P. Legrand, C. E. Hatchikian, J. C. Fontecilla-Camps, *Structure* **1999**, *7*, 13–23.
[6] A. L. De Lacey, C. Stadler, C. Cavazza, E. C. Hatchikian, V. M. Fernandez, *J. Am. Chem. Soc.* **2000**, *122*, 11232–11233.
[7] Z. Chen, B. J. Lemon, S. Huang, D. J. Swartz, J. W. Peters, K. A. Bagley, *Biochemistry* **2002**, *41*, 2036–2043.
[8] Y. Nicolet, A. L. de Lacey, X. Vernède, V. M. Fernandez, E. C. Hatchikian, J. C. Fontecilla-Camps, *J. Am. Chem. Soc.* **2001**, *123*, 1596–1601.
[9] H.-J. Fan, M. B. Hall, *J. Am. Chem. Soc.* **2001**, *123*, 3828–3829.
[10] M. Y. Darensbourg, *Nature* **2005**, *433*, 589–591.
[11] M. Y. Darensbourg, E. J. Lyon, J. J. Smee, *Coord. Chem. Rev.* **2000**, *206–207*, 533–561.
[12] M. Y. Darensbourg, E. J. Lyon, X. Zhao, I. P. Georgakaki, *Proc. Natl. Acad. Sci. USA* **2003**, *7*, 3683–3688.
[13] D. J. Evans, C. J. Pickett, *Chem. Soc. Rev.* **2003**, *32*, 268–275.
[14] T. B. Rauchfuss, *Inorg. Chem.* **2004**, *43*, 14–26.
[15] L. Sun, B. Åkermark, S. Ott, *Coord. Chem. Rev.* **2005**, *249*, 1653–1663.
[16] E. J. Lyon, I. P. Georgakaki, J. H. Reibenspies, M. Y. Darensbourg, *Angew. Chem. Int. Ed.* **1999**, *38*, 3178–3180.

 © 2006 Wiley-VCH Verlag GmbH & Co. KGaA, Weinheim 

[17] J. D. Lawrence, H. Li, T. B. Rauchfuss, M. Bénard, M.-M. Rohmer, *Angew. Chem. Int. Ed.* **2001**, *40*, 1768–1771.
[18] H. Li, T. B. Rauchfuss, *J. Am. Chem. Soc.* **2002**, *124*, 726–727.
[19] J. D. Lawrence, T. B. Rauchfuss, S. R. Wilson, *Inorg. Chem.* **2002**, *41*, 6193–6195.
[20] J. L. Nehring, D. M. Heinekey, *Inorg. Chem.* **2003**, *42*, 4288–4292.
[21] M. Razavet, S. C. Davies, D. L. Hughes, C. J. Pickett, *Chem. Commun.* **2001**, 847–848.
[22] S. J. George, Z. Cui, M. Razavet, C. J. Pickett, *Chem. Eur. J.* **2002**, *8*, 4037–4046.
[23] L. Song, Z. Yang, H. Bian, Q. Hu, *Organometallics* **2004**, *23*, 3082–3084.
[24] E. J. Lyon, I. P. Georgakaki, J. H. Reibenspies, M. Y. Darensbourg, *J. Am. Chem. Soc.* **2001**, *123*, 3268–3278.
[25] F. Gloaguen, J. D. Lawrence, M. Schmidt, S. R. Wilson, T. B. Rauchfuss, *J. Am. Chem. Soc.* **2001**, *123*, 12518–12527.
[26] C. Tard, X. Liu, S. K. Ibrahim, M. Bruschi, L. D. Gioia, S. C. Davies, X. Yang, L.-S. Wang, G. Sawers, C. J. Pickett, *Nature* **2005**, *433*, 610–613.
[27] C. A. Boyke, T. B. Rauchfuss, S. R. Wilson, M.-M. Rohmer, M. Bénard, *J. Am. Chem. Soc.* **2004**, *126*, 15151–15160.
[28] C. A. Boyke, J. I. van der Vlugt, T. B. Rauchfuss, S. R. Wilson, G. Zampella, L. De Gioia, *J. Am. Chem. Soc.* **2005**, *127*, 11010–11018.
[29] D. Chong, I. P. Georgakaki, R. Mejia-Rodriguez, J. Sanabria-Chinchilla, M. P. Soriaga, M. Y. Darensbourg, *Dalton Trans.* **2003**, 4158–4163.
[30] R. Mejia-Rodriguez, D. Chong, J. H. Reibenspies, M. P. Soriaga, M. Y. Darensbourg, *J. Am. Chem. Soc.* **2004**, *126*, 12004–12014.
[31] F. Gloaguen, J. D. Lawrence, T. B. Rauchfuss, *J. Am. Chem. Soc.* **2001**, *123*, 9476–9477.
[32] F. Gloaguen, J. D. Lawrence, T. B. Rauchfuss, M. Bénard, M.-M. Rohmer, *Inorg. Chem.* **2002**, *41*, 6573–6582.
[33] S. Ott, M. Kritikos, B. Åkermark, L. Sun, R. Lomoth, *Angew. Chem. Int. Ed.* **2004**, *43*, 1006–1009.
[34] J. D. Lawrence, H. Li, T. B. Rauchfuss, *Chem. Commun.* **2001**, 1482–1483.
[35] T. Liu, M. Wang, Z. Shi, H. Cui, W. Dong, J. Chen, B. Åkermark, L. Sun, *Chem. Eur. J.* **2004**, *10*, 4474–4479.
[36] S. Ott, M. Borgström, M. Kritikos, R. Lomoth, J. Bergquist, B. Åkermark, L. Hammarström, L. Sun, *Inorg. Chem.* **2004**, *43*, 4683–4692.
[37] F. Wang, M. Wang, X. Liu, K. Jin, W. Dong, G. Li, B. Åkermark, L. Sun, *Chem. Commun.* **2005**, 3221–3223.
[38] W. Dong, M. Wang, X. Liu, K. Jin, G. Li, F. Wang, L. Sun, *Chem. Commun.* **2006**, 305–307.
[39] L. Schwartz, G. Eilers, L. Eriksson, A. Gogoll, R. Lomoth, S. Ott, *Chem. Commun.* **2006**, 520–522.
[40] D. Seyferth, R. S. Henderson, L. C. Song, *Organometallics* **1982**, *1*, 125–133.
[41] I. Bhugun, D. Lexa, J.-M. Savéant, *J. Am. Chem. Soc.* **1996**, *118*, 3982–3983.
[42] The different reference systems were compared by using [(μ-PDT)$Fe_2(CO)_6$] as a calibrating agent, which is reduced at –1.16 V vs. Ag/AgCl (see ref. 25). With our system, and under the same conditions, the complex is reduced at –1.65 V, which gives a $\Delta E$ value of 0.49 V.
[43] H.-J. Fan, M. B. Hall, *J. Am. Chem. Soc.* **2001**, *123*, 3828–3829.
[44] S. J. Borg, T. Behrsing, S. P. Best, M. Razavet, X. Liu, C. J. Pickett, *J. Am. Chem. Soc.* **2004**, *126*, 16988–16999.
[45] D. Seyferth, R. S. Henderson, *J. Organomet. Chem.* **1981**, *218*, C34–C36.
[46] R. Obreht, R. Herrmann, I. Ugi, *Synthesis* **1985**, 400–402.
[47] SMART and SAINT, Siemens Analytical X-ray Instruments Inc., Madison, WI, USA, **1996**.
[48] SHELXTL, Version 5.1, Siemens Industrial Automation, Inc., **1997**.
[49] A. D. Becke, *J. Chem. Phys.* **1993**, *98*, 5648–5652.
[50] M. J. Frisch, G. W. Trucks, H. B. Schlegel, G. E. Scuseria, M. A. Robb, J. R. Cheeseman, J. A. Montgomery Jr, T. Vreven, K. N. Kudin, J. C. Burant, J. M. Millam, S. S. Iyengar, J. Tomasi, V. Barone, B. Mennucci, M. Cossi, G. Scalmani, N. Rega, G. A. Petersson, H. Nakatsuji, M. Hada, M. Ehara, K. Toyota, R. Fukuda, J. Hasegawa, M. Ishida, T. Nakajima, Y. Honda, O. Kitao, H. Nakai, M. Klene, X. Li, J. E. Knox, H. P. Hratchian, J. B. Cross, C. Adamo, J. Jaramillo, R. Gomperts, R. E. Stratmann, O. Yazyev, A. J. Austin, R. Cammi, C. Pomelli, J. W. Ochterski, P. Y. Ayala, K. Morokuma, G. A. Voth, P. Salvador, J. J. Dannenberg, V. G. Zakrzewski, S. Dapprich, A. D. Daniels, M. C. Strain, O. Farkas, D. K. Malick, A. D. Rabuck, K. Raghavachari, J. B. Foresman, J. V. Ortiz, Q. Cui, A. G. Baboul, S. Clifford, J. Cioslowski, B. B. Stefanov, G. Liu, A. Liashenko, P. Piskorz, I. Komaromi, R. L. Martin, D. J. Fox, T. Keith, M. A. Al-Laham, C. Y. Peng, A. Nanayakkara, M. Challacombe, P. M. W. Gill, B. Johnson, W. Chen, M. W. Wong, C. Gonzalez, and J. A. Pople, *Gaussian 03*, Revision C.02, Gaussian, Inc., Wallingford CT, **2004**.
[51] T. H. Dunning Jr, P. J. Hay, in *Modern Theoretical Chemistry* (Ed.: H. F. Schaefer III), vol. 3, Plenum, New York, **1976**, 1–28.
[52] P. J. Hay, W. R. Wadt, *J. Chem. Phys.* **1985**, *82*, 270–283; W. R. Wadt, P. J. Hay, *J. Chem. Phys.* **1985**, *82*, 284–298; P. J. Hay, W. R. Wadt, *J. Chem. Phys.* **1985**, *82*, 299–310.
[53] M. T. Cancès, B. Mennucci, J. Tomasi, *J. Chem. Phys.* **1997**, *107*, 3032–3041.

Received: May 15, 2006
Published Online: September 18, 2006

 © 2006 Wiley-VCH Verlag GmbH & Co. KGaA, Weinheim 

DOI: 10.1002/ejic.200600490

# New Copper(II) Complexes as Efficient Catalysts for Olefin Aziridination: The Effect of Ligand Steric Hindrance on Reactivity

**Thirumanasekaran Dhanalakshmi,[a] Eringathodi Suresh,[b] Helen Stoeckli-Evans,[c] and Mallayan Palaniandavar*[a]**

**Keywords:** Aziridination / Copper / N ligands / Tridentate ligands / Steric hindrance

Three new copper(II) complexes derived from the tridentate $N_3$ ligands 4-methyl-1-(pyrid-2-ylmethyl)-1,4-diazacycloheptane (L1), 1-(quinol-2-ylmethyl)-1,4-diazacycloheptane (L2), and 4-methyl-1-(quinol-2-ylmethyl)-1,4-diazacycloheptane (L3) have been prepared and examined as copper catalysts for olefin aziridination. In the X-ray crystal structures of the complexes $[Cu(L2)Cl_2]$ (**2**) and $[Cu(L3)Cl_2]$ (**3**) copper(II) adopts a trigonal-bipyramidal distorted square-based pyramidal geometry (TBDSBP) as seen from the values of the trigonality index $\tau$ (0.08 for **2** and 0.48 for **3**). The enhanced trigonal distortion in **3** is due to the presence of an N-Me group, the lone pair orbital of which is not oriented exactly along the $d_{x^2-y^2}$ orbital of copper(II). While $[Cu(L1)(H_2O)](ClO_4)_2$ (**1**) assumes a tetragonal geometry in solution, complexes **2** and **3** adopt a distorted tetragonal geometry, as revealed by UV/Vis and EPR spectral studies. The complexes undergo quasi-reversible $Cu^{II}/Cu^{I}$ redox behavior in methanol solution. The ability of the complexes to mediate nitrene transfer from PhINTs to olefins to form *N*-tosylaziridines has been studied. The complexes are found to be efficient catalysts (in 5 mol-% amounts) for the aziridination of the reactive olefin styrene, with yields varying from 80 to 90% (with respect to PhINTs). They exhibit significant catalytic nitrene transfer reactivity (yields of 30 to 60%) also towards the less reactive olefins cyclohexene and cyclooctene. A remarkable observation is the significantly accelerated rate of aziridination by **3**, which is ascribed to the steric crowding around copper(II) imposed by the bulky quinolyl and N-Me groups of the tridentate ligand L3.

(© Wiley-VCH Verlag GmbH & Co. KGaA, 69451 Weinheim, Germany, 2006)

## Introduction

Similar to epoxides, aziridine rings enjoy special attention in organic synthesis, particularly as intermediates[1,2] in the synthesis of amines and amino alcohols. Furthermore, naturally occurring azinomycin and mitomycin, which contain aziridines in their core, exhibit cytotoxic properties.[3] The development of new catalysts for the preparation of aziridines has therefore been an active area of investigation. Of the two different catalytic processes that lead to the formation of aziridines,[4–6] that involving addition of an "NR" nitrene unit to a C=C double bond (alkene; Scheme 1) has been more extensively studied than the other, which involves the addition of a "CR" carbene unit to a C=N (imine) bond. This reaction is often catalyzed by transition metals through coordination of the nitrene[4] or by Lewis acids through substrate activation.[5] In transition-metal-catalyzed olefin aziridination reactions, the most widely employed reaction (Scheme 1) has been nitrene transfer from (tosylimino)phenyliodinane (PhINTs).[7–9]

Scheme 1.

Many copper-based catalysts have been reported for nitrene-transfer reactions from PhINTs to alkenes, although they have rarely been structurally characterized.[4,10–14] Halfen et al. have systematically investigated[10] the structural and electronic factors that regulate the catalytic activity of copper complexes in such nitrene-transfer reactions. They used the complex $[Cu(i\text{Pr}_3\text{TACN})(O_2CCF_3)_2]$ to effect the near-quantitative aziridination of styrene derivatives. They also reported aziridination of olefins catalyzed by a series of square-based copper(II) complexes in which tetradentate pyridyl-appended diazacycloalkane ligands are meridionally coordinated.[13] In these complexes the axial coordination site(s) are either vacant or occupied by a readily displaced solvent or counterion, which facilitates the aziridination with the nitrene source PhINTs. The reactivity of the copper(II) complexes is significantly enhanced for aziridination of styrene when the ligand denticity is lowered from tetradentate to tridentate.[15] Very recently Vadernikov

[a] School of Chemistry, Bharathidasan University, Tiruchirappallli-620024, India
E-mail: palani51@sify.com; palanim51@yahoo.com
[b] Analytical Science Discipline, Central Salt and Marine Chemicals Research Institute, Bhavnagar 364 002, India
[c] Department of Chemistry, University of Neuchatel, Neuchatel, Switzerland

 © 2006 Wiley-VCH Verlag GmbH & Co. KGaA, Weinheim 

et al. have reported that coordinative unsaturation at copper is responsible for the very high catalytic activity of certain four-coordinate copper(II) chloride complexes of pyridine-based ligands.[16]

We decided to prepare copper(II) complexes of tridentate $N_3$ ligands and study them systematically to identify the key ligand structural and electronic properties for optimum copper catalyst performance. As the highly oxidized copper-nitrene species are suggested[10] to be stabilized by electron-rich and sterically hindered ligands, sterically hindering N–Me and quinolyl moieties were incorporated into the tridentate $N_3$ ligands (Scheme 2) chosen for the present study. The ring system of the ligand would provide resistance[13] towards oxidative degradation of the catalyst by the strongly oxidizing nitrene transfer agent PhINTs. The coordinative unsaturation as well as steric crowding around copper(II) in the present complexes is expected to lead to improved selectivity, reaction rates, and broad substrate tolerance. The X-ray crystal structures of two of the complexes were determined to establish the degree of coordinative unsaturation and distortion in the complexes. The solution structures of the complexes have been probed by employing spectroscopic and electrochemical methods to understand the effect of the ligand architecture on the copper(II) coordination geometry. All the complexes examined were found to be fast and efficient catalysts for the aziridination of styrene, cyclohexene, and cyclooctene when a high amount (5–10 equiv.) of olefin was treated with PhINTs (1 equiv.).

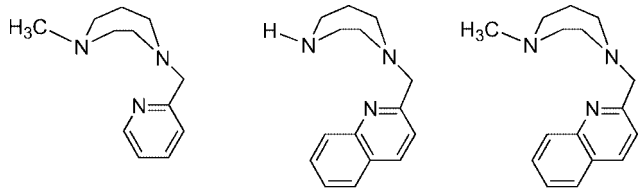


Scheme 2. Ligands employed for the present study.

## Results and Discussion

### Synthesis of Ligands and Complexes

The tridentate ligands L1–L3 were prepared as oils in good yields (50–70%) by stirring the appropriate diazacycloheptane (homopiperazine or *N*-methylhomopiperazine) with one equivalent of 2-picolyl chloride or 2-quinolyl chloride and two equivalents of triethylamine in ethanol at room temperature for three days. The copper(II) complexes of the ligands were prepared by the addition of either $CuCl_2{\cdot}H_2O$ or $Cu(ClO_4)_2{\cdot}6H_2O$ in methanol to a methanolic solution of the ligands; they were characterized by analytical and spectroscopic methods and studied as catalysts for aziridination reactions. The ligands occupy three coordination positions in the X-ray crystal structures of both **2** and **3**, with a chloride ion in the equatorial position. Conductivity studies revealed that complex **1** behaves as a 2:1 electrolyte (190 $\Omega^{-1}cm^2M^{-1}$) while **2** and **3** behave as 1:1 electrolytes (**2**, 98 and **3**, 86 $\Omega^{-1}cm^2M^{-1}$) in methanol solution, corresponding to dissociation of the axial chloride to give $[Cu(L)Cl]^+$ ions. The longer equatorial chloride can dissociate in solution in the presence of the substrates and facilitate aziridination reaction.

### Description of the Crystal Structures

An ORTEP view of the structures of complexes **2**·$CH_3CN$ and **3**, along with the atom numbering schemes, are shown in Figures 1 and 2 respectively. Selected bond lengths and bond angles relevant to the copper coordination spheres are given in Table 1. In the complex **2**·$CH_3CN$ copper(II) is bound to two chloride ions and two nitrogen atoms (N2 and N3) of the homopiperazine moiety and the nitrogen atom (N1) of the quinoline moiety of the tridentate ligand L2. The value of the structural index[17] $\tau$ (0.08) suggests that the pentacoordinate complex is very slightly distorted square pyramidal and the coordination geometry around copper(II) may be best described as trigonal-bipyramidal distorted square-based pyramidal (TBDSBP)[18] in which the square plane is constituted by the three nitrogen atoms (N1, N2, N3) of L2 and one chloride ion (Cl1) and the apical position occupied by the other chloride ion (Cl2). Two crystallographically independent complex molecules with the same chemical formula are present in the asymmetric unit cell of complex **3**. In both these molecules copper(II) is coordinated by three nitrogen atoms, two (N2 and N3) from the homopiperazine moiety and one (N1) from the quinoline moiety of ligand L3, and two chloride ions (Cl1 and Cl2), as in **2**·$CH_3CN$. The value of the structural index[17] $\tau$ (0.48) reveals that the coordination geometry around copper(II) in **3** is best described as TBDSBP in which the corners of the square plane are occupied by the three nitrogen atoms of L3 and one chloride ion (Cl1), and the apical position by the other chloride ion (Cl2). In fact, the coordination geometry lies exactly midway between trigonal-bipyramidal and square-pyramidal geometries. The value of the trigonality index $\tau$ for **3** is much higher than

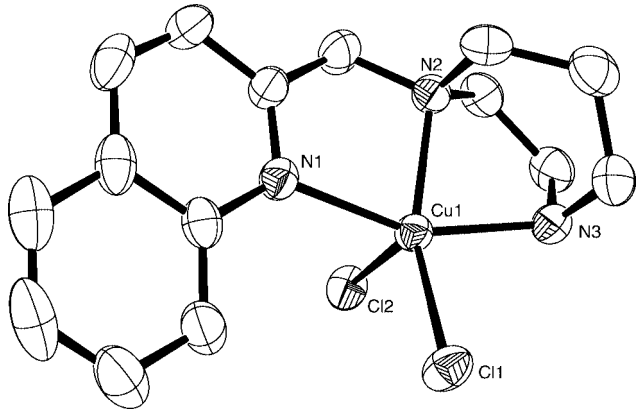


Figure 1. ORTEP drawing of $[Cu(L2)Cl_2]$ (**2**) showing the atom numbering scheme and the thermal motion ellipsoids (50% probability level).

 © 2006 Wiley-VCH Verlag GmbH & Co. KGaA, Weinheim 

that for **2**·$CH_3CN$, thus revealing that incorporation of the sterically hindering N–Me group in **3** leads to a greater geometrical constraint at copper(II). The Cu–$N_{amine}$ distances in both **2**·$CH_3CN$ and **3** are in the range expected[15] and, interestingly, they are longer in **3** (2.052, 2.068 Å) than those (2.036, 2.0392 Å) in **2**·$CH_3CN$, thus revealing that the lone pair orbitals of the N-Me group in **3** are not oriented exactly along the $d_{x^2-y^2}$ orbital of copper(II).[19] Further, the axial chloride ions in both **2**·$CH_3CN$ and **3** are located further away from the metal (2.456 Å in **2** and 2.462 Å in **3**) than the equatorial chloride ions (2.272 Å in **2** and 2.304 Å in **3**). This is obviously because of the presence of two electrons in the $d_{z^2}$ orbital of copper(II) in the square-based environments of both complexes. It is interesting to note that both **2**·$CH_3CN$ and **3** are monomeric, which is in contrast to the dimeric structure of the complex [(L4)Cu(μ-Cl)$_2$-Cu(L4)], where L4 is 5-methyl-1-(2-pyridylmethyl)-1,5-diazacyclooctane, the pyridine analogue of ligands L2 and L3. The incorporation of the sterically hindering quinolyl moiety in place of the pyridyl moiety in L4 and that of the ethylene linker instead of propylene one in the homopiperazine backbone of L4 prevent the dimerization of both **2** and **3**. We have previously shown[20] that incorporation of a sterically hindering $NMe_2$ group in the place of a pyridine donor enhances the Fe–O–C bond angle in iron(III) complexes of certain tetradentate monophenolate ligands from 128.5° to 136.1°. The equatorial chloride ion in **2**·$CH_3CN$ and **3** can be replaced by PhINTs, which leads to catalysis of aziridination reactions, as observed for copper(II) complexes of didentate ligands.[16]

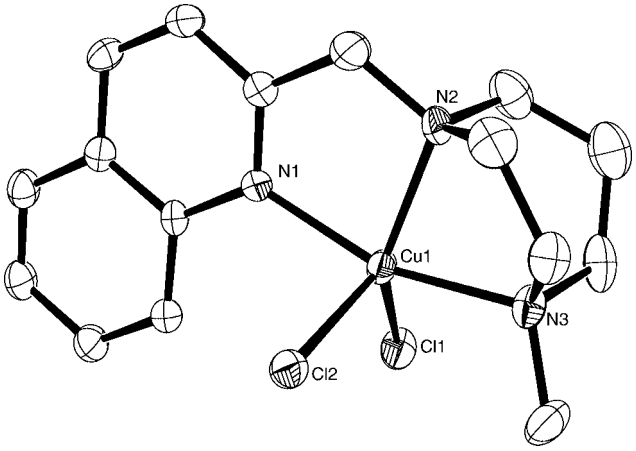


Figure 2. ORTEP drawing of [Cu(L3)$Cl_2$] (**3**) showing the atom numbering scheme and the thermal motion ellipsoids (50% probability level).

Table 1. Selected bond lengths [Å] and angles [°] for **2** and **3**.

| **2** | | **3** | |
|---|---|---|---|
| Cu(1)–N(1) | 2.135(2) | Cu(1)–N(1) | 2.039(2) |
| Cu(1)–N(2) | 2.0392(17) | Cu(1)–N(3) | 2.052(2) |
| Cu(1)–N(3) | 2.036(2) | Cu(1)–N(2) | 2.068(2) |
| Cu(1)–Cl(1) | 2.2722(9) | Cu(1)–Cl(1) | 2.3043(8) |
| Cu(1)–Cl(2) | 2.4556(9) | Cu(1)–Cl(2) | 2.4620(8) |
| | | Cu(2)–N(21) | 2.045(2) |
| | | Cu(2)–N(22) | 2.056(2) |
| | | Cu(2)–N(23) | 2.068(2) |
| | | Cu(2)–Cl(21) | 2.3183(8) |
| | | Cu(2)–Cl(22) | 2.4299(8) |
| N(1)–Cu(1)–N(2) | 81.19(6) | N(1)–Cu(1)–N(3) | 161.28(10) |
| N(1)–Cu(1)–N(3) | 154.90(7) | N(1)–Cu(1)–N(2) | 83.05(9) |
| N(2)–Cu(1)–N(3) | 76.59(7) | N(3)–Cu(1)–N(2) | 78.23(10) |
| Cl(1)–Cu(1)–N(1) | 103.67(5) | N(1)–Cu(1)–Cl(1) | 100.72(7) |
| Cl(1)–Cu(1)–N(2) | 149.96(5) | N(3)–Cu(1)–Cl(1) | 92.69(7) |
| Cl(1)–Cu(1)–N(3) | 90.23(5) | N(2)–Cu(1)–Cl(1) | 133.78(8) |
| Cl(2)–Cu(1)–N(1) | 93.78(4) | N(1)–Cu(1)–Cl(2) | 91.92(7) |
| Cl(2)–Cu(1)–N(2) | 101.96(5) | N(3)–Cu(1)–Cl(2) | 94.24(7) |
| Cl(2)–Cu(1)–N(3) | 102.04(5) | N(2)–Cu(1)–Cl(2) | 111.03(8) |
| Cl(1)–Cu(1)–Cl(2) | 107.19(2) | Cl(1)–Cu(1)–Cl(2) | 114.82(3) |
| | | N(21)–Cu(2)–N(22) | 83.36(9) |
| | | N(21)–Cu(2)–N(23) | 161.08(10) |
| | | N(22)–Cu(2)–N(23) | 78.23(10) |
| | | N(21)–Cu(2)–Cl(21) | 102.24(7) |
| | | N(22)–Cu(2)–Cl(21) | 131.95(8) |
| | | N(23)–Cu(2)–Cl(21) | 93.37(7) |
| | | N(21)–Cu(2)–Cl(22) | 92.38(7) |
| | | N(22)–Cu(2)–Cl(22) | 117.75(7) |
| | | N(23)–Cu(2)–Cl(22) | 92.33(8) |
| | | Cl(21)–Cu(2)–Cl(22) | 109.72(3) |

## Spectral Properties

The solid-state reflectance spectra of all the complexes show a broad ligand-field feature (540–850 nm) in the visible region, which appears to contain more than one band; this is typical of $Cu^{II}$ located in a square-based environment, as evidenced from the X-ray crystal structures of complexes **2** and **3** (Table 2). On dissolution in methanol, only one ligand-field feature is observed (640–760 nm, Figure 3) for all the complexes, which suggests changes in their coordination geometries such as dissociation of the axial chloride ion in solution. The ligand-field energies of complexes **2** and **3** are much lower, with higher molar absorptivities, than those of **1**, thereby indicating that the replacement of the pyridyl moiety in **1** by the bulky quinolyl moiety in **2** and **3** leads to an enhancement of the distortion in the square-pyramidal geometry towards trigonal bipyramidal. Further, the ligand-field energy of **3** is lower, and the molar absorptivity higher, than those of **2**, as expected from the weaker σ-coordination of N(3), as explained above, and due to the steric hindrance imposed by the N-Me group leading to a more distorted coordination geometry, as evident from the X-ray structures of the complexes. A similar decrease in ligand-field energy has been observed upon replacing an NHMe group by an $NMe_2$ group in the coordination sphere of copper(II) complexes of tridentate pyridine-based ligands.[19]

The polycrystalline EPR spectra of complexes **1** and **2** are axial while that of **3** is rhombic, which is consistent with the distorted square-based geometry found in the X-ray crystal structure of **3**. The frozen solution spectra (Figure 4) of all the complexes are axial [$g_{\|} > g_{\perp} > 2.0$, $G = (g_{\|} - 2)/(g_{\perp} - 2) = 3.0–4.3$],[21] which is usual for mononuclear tetragonal copper(II) complexes with a $d_{x^2-y^2}$ ground state.[22] Copper(II) complexes with a square-based $CuN_4$ coordination sphere exhibit $g_{\|}$ and $A_{\|}$ values of around

 © 2006 Wiley-VCH Verlag GmbH & Co. KGaA, Weinheim 

Table 2. Electronic and EPR spectroscopic data for the copper(II) complexes.

| Complexes | Electronic spectra[a] $\lambda_{max}$ [nm] ($\varepsilon_{max}$ [$M^{-1}cm^{-1}$]) | | EPR spectra[b] | |
|---|---|---|---|---|
| | Solid | Solution (in methanol) | Solid | Frozen[c] solution |
| $[Cu(L1)(H_2O)](ClO_4)_2$ (**1**) | 545–645 | 642 (150)<br>268 (34310)[d] | $g_\parallel$ 2.223<br>$g_\perp$ 2.109 | $g_\parallel$ 2.227<br>$A_\parallel$ 186<br>$g_\perp$ 2.066<br>$g_\parallel/A_\parallel$ 119<br>G 3.43 |
| $[Cu(L2)Cl_2]$ (**2**) | 650–750 | 730 (195)<br>270 (33280)[d]<br>235 (35845)[d]<br>203 (34710)[d] | $g_\parallel$ 2.198<br>$g_\perp$ 2.147 | $g_\parallel$ 2.225<br>$A_\parallel$ 146<br>$g_\perp$ 2.052<br>$g_\parallel/A_\parallel$ 152<br>G 4.32 |
| $[Cu(L3)Cl_2]$ (**3**) | 700–850 | 758 (270)<br>275 (27430)[d]<br>238 (36005)[d] | $g_3$ 2.162<br>$g_2$ 2.136<br>$g_1$ 2.078 | $g_\parallel$ 2.231<br>$A_\parallel$ 130<br>$g_\perp$ 2.077<br>$g_\parallel/A_\parallel$ 171<br>G 3.00 |

[a] Concentration: $2\times10^{-3}$ M for ligand-field and $2\times10^{-5}$ M for ligand-based transitions. [b] $A_\parallel$ in $10^{-4}$ $cm^{-1}$. [c] Methanol/acetone (4:1, v/v) glass at 77 K. [d] π–π* transitions within the ligand.

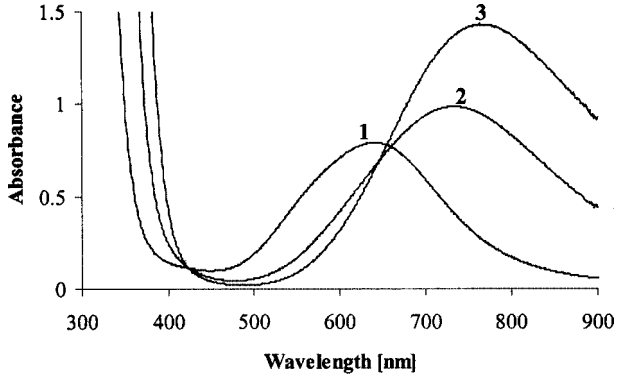


Figure 3. Electronic absorption spectra of complexes **1**–**3** in methanol solution. Concentration of the complexes: $5\times10^{-3}$ M.

2.200 and $200\times10^{-4}$ $cm^{-1}$, respectively. Replacement of a coordinated nitrogen in this chromophore by oxygen (solvent methanol) is expected to enhance the $g_\parallel$ value and decrease the $A_\parallel$ value. Thus, the $g_\parallel$ (2.225–2.231) and $A_\parallel$ (180–$130\times10^{-4}$ $cm^{-1}$) values of **1**–**3** are suggestive of the presence of a square-based $[Cu(N_3)Cl]^+$ chromophore.[19] Interestingly, the $A_\parallel$ values of **2** and **3** are much lower than that of **1**, which suggests that the coordination geometries in them are strongly distorted from planarity. In fact, the values of their $g_\parallel/A_\parallel$ quotient (152 cm for **2** and 171 cm for **3**) is higher than that for **1** (117 cm). This suggests a large deviation from a perfectly square-planar geometry ($g_\parallel/A_\parallel$ = 105–135 cm)[23] because of the incorporation of sterically demanding quinolyl moiety in **2** and **3** in place of the pyridyl moiety in **1**. Further, the $g_\parallel$ and $A_\parallel$ values of **2** are lower and higher, respectively, than those for **3**, and the $g_\parallel/A_\parallel$ value for **2** is lower than that for **3**. This reveals that the distortion from a square-based geometry in **3** is higher than that in **2** because of the sterically hindering N-Me substitution, which is consistent with the above X-ray structures and electronic spectral results.

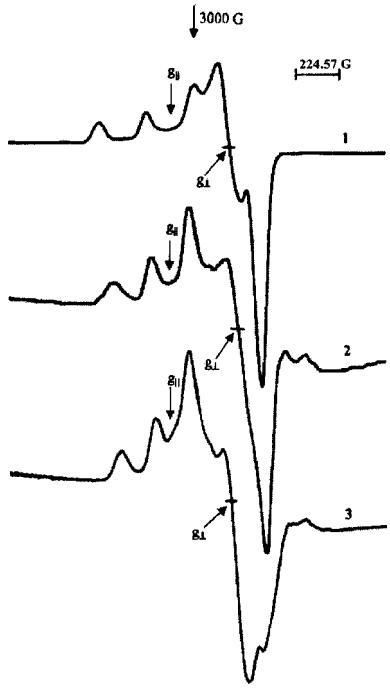


Figure 4. X-band EPR spectra of complexes **1**–**3** at 77 K in methanol/acetone (4:1 v/v) glass.

## Electrochemical Properties

The electrochemical data obtained for the present complexes in methanol solution using TBAP as supporting electrolyte are collected in Table 3. The cyclic (CV) and differential pulse voltammograms (DPV) were recorded using Pt as working electrode and Ag/AgCl as reference electrode. For all the complexes the $Cu^{II}$ to $Cu^{I}$ reduction ($E_{pc}$, –0.325 to –0.475 V) is associated with a reoxidation peak ($E_{pa}$, –0.244 to –0.318 V) in the reverse scan. The value of the limiting peak-to-peak separation ($\Delta E_p$ = 158–

 © 2006 Wiley-VCH Verlag GmbH & Co. KGaA, Weinheim 

Table 3. Electrochemical data[a] for copper(II) complexes at 25 ± 0.2 °C in methanol solution.

| Complexes | $E_{pc}$ [V] | $E_{pa}$ [V] | $E_{1/2}$ [V] CV | DPV[b] | $\Delta E_p$ [mV] | $i_{pa}/i_{pc}$ | $D$ [$10^{-6}$ cm$^2$ s$^{-1}$] |
|---|---|---|---|---|---|---|---|
| $[Cu(L1)(H_2O)](ClO_4)_2$ (**1**) | –0.476 | –0.318 | –0.397 | –0.378 | 158 | 0.6 | 3.4 |
| $[Cu(L2)Cl_2]$ (**2**) | –0.454 | –0.244 | –0.349 | –0.336 | 210 | 0.9 | 4.2 |
| $[Cu(L3)Cl_2]$ (**3**) | –0.326 | – | –0.164[c] | –0.252 | – | – | 5.8 |

[a] Potential measured vs. non-aqueous $Ag/AgNO_3$ reference electrode; add 0.544 V to convert to standard hydrogen electrode (SHE); $Fc/Fc^+$ couple: $E_{1/2}$ = 0.038 V (CV), $\Delta E_p$ = 88 mV; scan rate: 50 mV s$^{-1}$; supporting electrolyte: tetrabutylammonium perchlorate (0.1 M); complex concentration: $1 \times 10^{-3}$ M. [b] Differential pulse voltammetry (DPV); scan rate: 1 mV s$^{-1}$; pulse height: 50 mV. [c] Potential at half-height $E_{p1/2}$.

210 mV) is higher than that for the $Fc/Fc^+$ couple ($\Delta E_p$ = 88 mV) under identical conditions. This suggests that the heterogeneous electron-transfer process in the present complexes is far from reversible and that considerable stereochemical reorganization of the coordination sphere occurs on electron transfer. The $Cu^{II}/Cu^{I}$ redox potentials follow the trend **3** > **2** > **1** (Figure 5). This reveals the importance of the sterically hindering quinolyl moiety in destabilizing the $Cu^{II}$ form of **2**, thereby facilitating the electron transfer. Similarly, the incorporation of the sterically hindering and weakly σ-bonding N-Me group in **2** to obtain **3** further destabilizes the $Cu^{II}$ oxidation state, which is consistent with the X-ray structures of the complexes. Similar results have been observed by incorporating an $NMe_2$ group in the copper(II) complexes of certain pyridine-based linear $N_3$ ligands.[19]

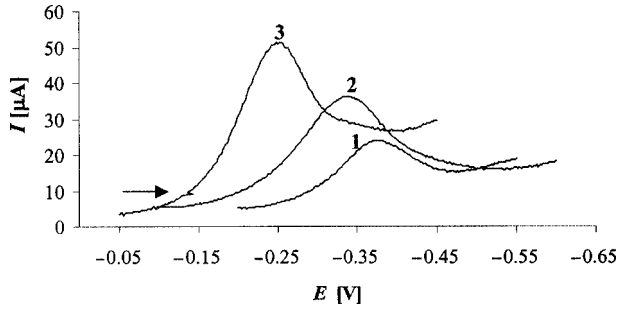


Figure 5. Differential pulse voltammograms of complexes **1**–**3** in methanol solution at 25 °C at a scan rate of 0.05 V s$^{-1}$. Complex concentration: 0.001 M.

### Application to Catalytic Olefin Aziridination Reactions

The newly synthesized copper(II) complexes **1**–**3** were examined for their ability to catalyze the aziridination of olefins, especially styrene, cyclohexene, and cyclooctene, using PhINTs as the nitrene source; the results are collected in Table 4. When a 10:1 olefin:PhINTs ratio was employed with a catalyst loading of 5 mol-%, all the complexes gave high yields (85–90%) for the aziridination of the most reactive olefin styrene. However, when the olefin:PhINTs ratio was decreased to 5:1, slightly lower yields (75–80%) were obtained. When this ratio was decreased from 5:1 to 1:1 as for **3**, the yield decreased further. A remarkable observation is the significantly accelerated rate of aziridination of styrene (within an hour) for complex **3**. The presence of labile ligands and the coordinative unsaturation around copper(II) promotes faster coordination of PhINTs to copper(II) (otherwise slow) and is responsible for the high yield and reduced reaction times. In fact, on treatment of **3** with excess PhINTs in acetonitrile solution, the ligand-field band is shifted from 799 to 794 nm with enhanced absorptivity, thus suggesting the coordination of PhINTs to copper(II). Further, the persistence of the blue or green color of the reaction mixtures after dissolution of PhINTs reveals that the resting state of the catalyst is always $Cu^{II}$. According to the very recently proposed mechanism for copper-catalyzed aziridination,[16] the coordination of =NTs to copper(II) is required for intramolecular electron transfer. This leads to the formation of PhI and a highly reactive copper-nitrene radical-like intermediate [$(L3)Cu^{II}$=NTs], which is then involved in consecutive nitrene transfer to olefin. Obviously, the steric crowding around copper(II) imposed by the bulky quinolyl moiety and the N-Me group (see above) of the tridentate ligand would stabilize this intermediate and facilitate the aziridination. Also, it would prevent any side reactions like recoordination of chloride. In fact, when aziridination was performed for complex **3** after the removal of two chloride ions by treatment with $AgNO_3$, the reaction time decreased further, as expected, but with no change in yield. It is interesting to note that the incorporation of a sterically hindering $NMe_2$ group in the place of a pyridine donor enhances the dioxygenase activity of iron(III) complexes of certain tetradentate monophenolate ligands.[20] No change in yield was observed with a decrease in the olefin:PhINTs ratio; however, the reaction becomes faster (completed within 30 min).

Aziridination of the less reactive cyclohexene was performed with 5 mol-% catalyst loading. When the olefin:PhINTs ratio was 5:1, all the complexes showed a good yield of more than 60%. It is remarkable that the yield of aziridine observed for cyclohexene is higher than those for other complexes available in the literature (except $[Cu(MeCN)_4]ClO_4$, 77%).[4] Also, and interestingly, no allylic sulfonamide insertion product was obtained. The complexes also catalyze the aziridination of the other less reactive olefin *cis*-cyclooctene, although the yield is very low (30–45%). When the olefin:PhINTs ratio was decreased from 10:1 to 5:1, the yield was also reduced. Again, complex **3** catalyzes the aziridination (within an hour) faster than the other two complexes.

 © 2006 Wiley-VCH Verlag GmbH & Co. KGaA, Weinheim 

Table 4. Results of catalytic aziridination studies using copper(II) complexes **1**–**3**.

| Olefin | Catalyst[a] | Equiv. of olefin | Yield [%][b] | Time [h] |
|---|---|---|---|---|
| | **1** | 10 | 90 | 3 |
| | | 5 | 80 | 2 |
| | **2** | 10 | 85 | 3 |
| | | 5 | 80 | 3 |
| | **3** | 10 | 85 | 1 |
| | | 5 | 75 | 1 |
| | | 4 | 84 | 1 |
| | | 2.5 | 53 | 0.5 |
| | | 1 | 18 | 0.5 |
| | **3** + 2 equiv. | 4 | 80 | 0.5 |
| | of $AgNO_3$ | 2.5 | 53 | 0.5 |
| | | 1 | 25 | 0.5 |
| | **1** | 5 | 64 | 3 |
| | **2** | 5 | 68 | 3 |
| | **3** | 5 | 60 | 3 |
| | **1** | 10 | 42 | 10 |
| | | 5 | 35 | 24 |
| | **2** | 10 | 38 | 6 |
| | | 5 | 35 | 6 |
| | **3** | 10 | 38 | 1 |
| | | 5 | 30 | 1 |

[a] 5 mol-% vs. PhINTs. [b] Isolated yields of *N*-tosylaziridine after purification with respect to 0.3 mM of PhI=NTs used.

## Conclusions

Copper(II) complexes of three new tridentate $N_3$ ligands have been isolated. Two of them have been structurally characterized to contain the meridionally coordinated ligand, and the incorporation of a sterically hindering quinolyl moiety and N-Me donor group in the ligand leads to a strong trigonal distortion of the copper(II) coordination geometries. All the complexes exhibit significant catalytic nitrene transfer reactivity with PhINTs towards three olefins. While good yields (above 80%) were obtained for the reactive olefin styrene, yields exceeding 60% were obtained for less reactive cyclohexene; however, lower yields (30–45%) were obtained for cyclooctene. The present findings confirm that both the degree of coordinative unsaturation and the steric congestion in copper-based systems are important factors that determine their catalytic activity. It is fascinating to note that the use of low-coordinate copper(II) species with distorted geometries as catalysts dramatically accelerates the aziridination (reaction times 0.5–1 h) for reactive as well as less reactive olefinic substrates. This finding could be expected to pave the way for the rational design of new and more active catalysts for aziridination and related group-transfer reactions.

## Experimental Section

**Materials and Methods:** $CuCl_2·2H_2O$, cyclohexene, triethylamine, (Merck, India), *p*-toluenesulfonamide, iodosobenzene diacetate (Merck, Germany), *tetra*-butylammonium bromide (G. F. Smith), *N*-methylhomopiperazine, homopiperazine, 2-picolylchloride hydrochloride, 2-quinolylchloride hydrochloride, $Cu(ClO_4)_2·6H_2O$, and *cis*-cyclooctene (Aldrich) were used as received. Styrene was distilled from KOH pellets at 25 °C under vacuum (0.3 Torr) and was stored at –20 °C. Anhydrous acetonitrile was used in catalytic aziridinations and was handled and stored under $N_2$. The iodinane PhINTs was prepared by a modified literature procedure and was stored in the dark.[7] *tetra*-Butylammonium perchlorate (TBAP) was prepared by the addition of sodium perchlorate to a hot ethanol solution of *tetra*-butylammonium bromide. The product was recrystallized from aqueous ethanol and was tested for the absence of bromide. $^1$H NMR spectra were obtained using a Bruker 200 MHz spectrometer at room temperature. $^1$H NMR chemical shifts are reported relative to TMS and are referenced to residual solvent peaks. Electronic absorption spectra were acquired using a Varian 300 spectrophotometer (200–900 nm). FTIR spectra (4000–400 $cm^{-1}$ range, KBr pellets) were recorded with a Jasco FT-IR spectrometer. EPR spectra were recorded with a JEOL JES-TE 100 X-band spectrometer, the field being calibrated with diphenylpicrylhydrazyl (dpph). The $g_0$ and $A_0$ values were estimated at ambient temperature and $g_\parallel$ and $A_\parallel$ at 77 K. The values of $g_\perp$ and $A_\perp$ were computed as $1/2(3g_0 - g_\parallel)$ and $1/2(3A_0 - A_\parallel)$ respectively. Electrochemical experiments were conducted using a EG & G PAR 273 potentiostat/galvanostat with EG & G M270 software, using a platinum sphere working electrode, an $Ag/AgNO_3$ reference electrode, and a platinum plate auxiliary electrode. Cyclic voltammograms were obtained in methanol using 0.1 M TBAP as supporting electrolyte. Elemental analyses were performed at Bharathiar University, Coimbatore. Conductivity measurements on methanolic solution of the complexes were made using an Elico conductivity bridge.

***Caution!*** Perchlorate salts of transition metal complexes containing organic ligands are potentially explosive and should be prepared in small quantities and handled with appropriate precautions. While no difficulties were encountered with the complexes reported herein, due caution should be exercised.

**4-Methyl-1-(pyrid-2-ylmethyl)-1,4-diazacycloheptane (L1):** An aqueous solution (5 mL) of NaOH (0.40 g, 10 mmol) was added dropwise to an aqueous solution (10 mL) of 2-picolyl chloride hydrochloride (0.82 g, 5 mmol) at 0 °C. An aqueous solution (10 mL) of *N*-methylhomopiperazine (0.57 g, 5 mmol) was then added to this mixture over 15 min. The mixture was stirred in a loosely sealed flask at room temperature for three days. The reaction mixture was then extracted with $CHCl_3$ (3 × 50 mL). The organic layer was washed with saturated sodium hydrogen carbonate solution, evaporated, and then dried ($Na_2SO_4$). The organic solvent was removed on a rotary evaporator to yield the crude product as a pale-yellow oil. The pure product was obtained by extracting the oil once again with ethyl acetate. The product obtained was used as such for the complex preparation. Yield: 0.58 g (56%). $C_{12}H_{19}N_3$ (205.16): calcd. C 70.20, H 9.33, N 20.47; found C 70.15, H 9.48, N 20.37. $^1$H NMR (200 MHz, $CDCl_3$): $\delta$ = 8.64–7.29 (m, 4 H), 3.95 (s, 2 H), 2.48 (m, 4 H), 2.36 (m, 4 H), 1.49 (quint, 2 H), 2.27 (br. s, 3 H) ppm. IR: $\tilde{\nu}$ = 3023 (m), 2983 (s), 2888 (w), 1467 (m), 1407 (s), 1240 (m), 941 (s), 779 (s) $cm^{-1}$.

**1-(Quinol-2-ylmethyl)-1,4-diazacycloheptane (L2):** The ligand L2 was synthesized by a slightly modified procedure that was reported for the preparation of the monosubstituted diazocyclooctane li-

 © 2006 Wiley-VCH Verlag GmbH & Co. KGaA, Weinheim 

gands.[24] Triethylamine (1.01 g, 10 mmol) was added to 2-quinolyl chloride hydrochloride (1.07 g, 5 mmol) in ethanol (25 mL) at 0 °C, and a solution of homopiperazine (2.00 g, 20 mmol) in ethanol (10 mL) was added slowly to this mixture with stirring. The whole mixture was refluxed for 2 h. The solution was stirred for 2 d at room temperature and the ethanolic solution was removed on a rotary evaporator to dryness. Water was added to the residue and the pH of the solution was adjusted to 10 with sodium carbonate. The solution was extracted with chloroform and the extracts were dried with sodium sulfate. The ligand was isolated as a yellow oil after rotary evaporation of the chloroform extracts. Yield: 0.75 g (61%). $C_{15}H_{19}N_3$ (241.16): calcd. C 74.65, H 7.94, N 17.41; found C 74.55, H 8.13, N, 17.32. $^1$H NMR (200 MHz, $CDCl_3$): $\delta$ = 8.02–7.36 (br. m, 6 H), 3.93 (s, 2 H), 2.65 (m, 2 H), 2.55 (m, 2 H), 2.45 (m, 2 H), 2.33 (m, 2 H), 1.51 (quint, 2 H), 2.91 (br. s, NH) ppm. IR: $\tilde{\nu}$ = 3432 (br), 3010 (s), 2884 (s), 1432 (s), 1230 (w), 760 (s), 629 (s) cm$^{-1}$.

**4-Methyl-1-(quinol-2-ylmethyl)-1,4-diazacycloheptane (L3):** A slightly different procedure was followed for the synthesis of L3. Triethylamine (1.01 g, 10 mmol) was added to 2-quinolyl chloride hydrochloride (1.07 g, 5 mmol) in ethanol (25 mL) at 0 °C. A solution of *N*-methylhomopiperazine (0.57 g, 5 mmol) in ethanol (10 mL) was added to this mixture slowly with stirring. The whole mixture was refluxed for 2 h and then stirred for 2 d at room temperature. The ethanolic solution was removed on a rotary evaporator to dryness, water was added to the residue, and the pH of the solution was adjusted to 10 with sodium carbonate. The solution was extracted with chloroform and the extracts were dried with sodium sulfate. The ligand was isolated as dark yellow oil after rotary evaporation of the chloroform extracts. Yield: 0.98 g (77%). $C_{16}H_{21}N_3$ (255.17): calcd. C 75.26, H 8.29, N 16.46; found C 75.33, H 8.15, N 16. 52. $^1$H NMR (200 MHz, $CDCl_3$): $\delta$ = 8.27–7.32 (br. m, 6 H), 3.98 (s, 2 H), 2.46 (m, 4 H), 2.36 (m, 4 H), 1.49 (quint, 2 H), 2.27 (br. s, 3 H) ppm. IR: $\tilde{\nu}$ = 3054 (s), 2981 (s), 2865 (s), 1459 (s), 1215 (w), 766 (s), 628 (s) cm$^{-1}$.

**[Cu(L1)(H$_2$O)](ClO$_4$)$_2$ (1):** A solution of L1 (0.21 g, 1 mmol) in methanol (15 mL) was treated with $Cu(ClO_4)_2 \cdot 6H_2O$ (0.37 g, 1 mmol) to obtain a deep-blue color. After 15 min of stirring, diethyl ether was allowed to diffuse into the solution. After a period of several days blue crystals of the product were deposited. Yield: 0.32 g (56%). $C_{12}H_{21}Cl_2CuN_3O_9$ (484.01): calcd. C 28.07, H 3.85, N 8.93; found C 28.11, H 3.78, N 8.98. IR: $\tilde{\nu}$ = 3451 (br), 2923 (w), 2869 (w), 1610 (s), 1089 (br, $ClO_4^-$), 890 (s), 626 (s, $ClO_4^-$) cm$^{-1}$.

**[Cu(L2)Cl$_2$] (2):** A procedure analogous to that used to prepare **1** was followed, using $CuCl_2 \cdot 2H_2O$ (0.17 g, 1 mmol) and L2 (0.24 g, 1 mmol) instead of L1. The pure product was isolated as blue crystals. Yield: 0.19 g (47%). $C_{15}H_{19}Cl_2CuN_3$ (374.04): calcd. C 47.94, H 5.10, N 11.18; found C 47.78, H 5.23, N 11.21. IR: $\tilde{\nu}$ = 3442 (br), 3235 (s), 2927 (s), 2884 (s), 1481 (w), 786 (s), 634 (s) cm$^{-1}$. X-ray diffraction quality crystals of **2**·$CH_3CN$ were obtained by the vapor diffusion of diethyl ether into a solution of the complex in acetonitrile.

**[Cu(L3)Cl$_2$] (3):** This complex was prepared by the addition of L3 (0.26 g, 1 mmol) in methanol (15 mL) to a methanolic solution of $CuCl_2 \cdot 2H_2O$ (0.17 g, 1 mmol) with stirring. After 15 min of stirring, the solution was layered with diethyl ether. Green crystals were deposited after two days. Yield: 0.26 g (65%). $C_{16}H_{21}Cl_2CuN_3$ (388.05): calcd. C 49.30, H 5.43, N 10.78; found C 49.42, H 5.38, N 10.71. IR: $\tilde{\nu}$ = 3442 (br), 3079 (w), 2981 (m), 2869 (m), 1610 (s), 782 (s), 634 (s) cm$^{-1}$. Suitable single crystals of **3** for X-ray diffraction were obtained by slow evaporation of the methanolic solution of the complex.

**Catalytic Aziridinations. Styrene:** Aziridinations were performed by stirring mixtures of PhINTs (0.3–0.4 mmol), styrene (10 to 1 equiv. vs. PhINTs), and the copper catalyst (5 mol% vs. PhINTs) in 2 mL of anhydrous $CH_3CN$ under a dry $N_2$ atmosphere as reported previously.[10] At the completion of the reactions, the clear, pale-green solutions were passed through a short column of neutral alumina to remove copper species, eluted with ethyl acetate, and the eluates were evaporated to yield oily residues. These crude product mixtures (of iodobenzene, 2-phenyl-1-tosylaziridine, and *p*-toluenesulfonamide) were treated with hexane to produce the crude aziridine products, which were recrystallized from hexane/diethyl ether mixtures at –20 °C. The 2-phenyl-1-tosylaziridine obtained was characterized by $^1$H NMR spectroscopy and the data were identical with those reported in the literature.[13]

**Cyclooctene:** Aziridinations were performed as described above by stirring mixtures of PhINTs (0.3–0.4 mmol), the olefin (10 to 5 equiv. vs. PhINTs), and the copper catalyst (5 mol-% vs. PhINTs) in 2 mL of anhydrous $CH_3CN$. At the completion of the reactions, the clear, pale-green solutions were passed through a short column of neutral alumina to remove copper species, eluted with ethyl acetate, and the eluates were evaporated to yield semi-solid residues. These crude product mixtures were treated with hexane, and the resultant mixtures were filtered to remove *p*-toluenesulfonamide. The filtrates were evaporated and dried overnight under vacuum to yield the pure aziridine products. $^1$H NMR spectroscopic data confirmed the formation of the aziridine.

**Cyclohexene:** Aziridinations were performed as described above by stirring mixtures of PhINTs (0.3–0.4 mmol), the olefin (5 equiv. vs. PhINTs), and the copper catalyst (5 mol-% vs. PhINTs) in 2 mL of anhydrous $CH_3CN$. At the end of the reaction, flash column chromatography (3 × 18 cm silica, 4:1 hexane/ethyl acetate) yielded the aziridine as a white crystalline solid. The *N*-(*p*-tolylsulfonyl)-7-azabicyclo-[4.1.0]heptane obtained was characterized by $^1$H NMR spectroscopy and the data were identical with those reported in the literature.[4e]

**X-ray Crystallography**: The single-crystal diffraction experiments for **2**·$CH_3CN$ were carried out on a Bruker SMART APEX CCD diffractometer at room temperature. The SMART[25] program was used for collecting frames of data, indexing reflections, and determining the lattice parameters; SAINT[25] was used for integration of the intensity of reflections and scaling; SADABS[25] was used for absorption correction, and the SHELXTL[25] program for space group and structure determination and least-squares refinements on $F^2$. The structure was solved by the heavy-atom method. Other non-hydrogen atoms were located in successive difference Fourier syntheses. The final refinement was performed by full-matrix least-squares. Most of the hydrogen atoms were located from the difference Fourier map and refined isotropically, except for the hydrogen atoms of the lattice acetonitrile molecule, which was placed at a geometrical position. For **3**, the intensity data were collected at 173 K on a Stoe Image Plate Diffraction System.[26] Image plate distance: 70 mm; φ oscillation scans: 0–200°; step: Δφ = 1.0°; exposure time: 3 min; 2$\theta$ range: 3.27–52.1°; $d_{min.}$–$d_{max.}$ = 12.45–0.81 Å. The structure was solved by direct methods using the programme SHELXS-97.[27] The refinement and all further calculations were carried out using SHELXL-97.[28] The H atoms were included in calculated positions and treated as riding atoms using the SHELXL default parameters. The non-H atoms were refined anisotropically, using weighted full-matrix least-squares on $F^2$. There are two independent molecules per asymmetric unit ($Z$ = 8, $Z'$ = 2). A multi-scan absorption correction was applied using the MULscanABS routine in PLATON;[29] transmission factors:

 © 2006 Wiley-VCH Verlag GmbH & Co. KGaA, Weinheim 

Table 5. Crystal data and structure refinement details for $[Cu(L2)Cl_2]$ (**2**) and $[Cu(L3)Cl_2]$ (**3**).

| | **2**·$CH_3CN$ | **3** |
|---|---|---|
| Empirical formula | $C_{15}H_{19}Cl_2CuN_3 \cdot C_2H_3N$ | $C_{16}H_{21}Cl_2CuN_3$ |
| Formula weight | 416.84 | 389.80 |
| Crystal system | monoclinic | monoclinic |
| Crystal size [mm] | $0.10 \times 0.16 \times 0.24$ | $0.27 \times 0.23 \times 0.23$ |
| Space group | $P2_1/C$ (no. 14) | $P2_1/n$ |
| $a$ [Å] | 13.641(4) | 16.6495(11) |
| $b$ [Å] | 11.138(3) | 10.7723(6) |
| $c$ [Å] | 12.613(3) | 18.9392(14) |
| $\alpha$ [°] | 90.000 | 90.000 |
| $\beta$ [°] | 107.966(4) | 105.767(8) |
| $\gamma$ [°] | 90 | 90 |
| $V$ [Å]$^3$ | 1822.9(8) | 3269.0(4) |
| $Z$ | 4 | 8 |
| $\lambda$ [Å] (Mo-$K_\alpha$) | 0.71073 | 0.71073 |
| $D_{calc}$ [g cm$^{-3}$] | 1.519 | 1.584 |
| Goodness-of-fit on $F^2$ | 1.032 | 1.040 |
| Number of reflections measured | 10552 | 25289 |
| Number of reflections used | 4231 | 6382 |
| Number of L.S. restraints | 0 | 0 |
| Number of refined parameters | 294 | 399 |
| Final $R$ indices [$I > 2\sigma(I)$] | | |
| $R_1$[a] | 0.0334 | 0.0332 |
| $wR_2$[b] | 0.0931 | 0.0837 |

[a] $R_1 = [\Sigma(||F_o| - |F_c||)/\Sigma|F_o|]$. [b] $wR_2 = \{[\Sigma[w(F_o^2 - F_c^2)^2]/\Sigma(wF_o^4)]^{1/2}\}$.

$T_{min.}/T_{max.}$ = 0.6675/0.7138. Relevant crystallographic information for **2** and **3** are summarized in Table 5.

CCDC-609006 (for **2**) and -609007 (for **3**) contain the supplementary crystallographic data for this paper. These data can be obtained free of charge from The Cambridge Crystallographic Data Center via www.ccdc.cam.ac.uk/data_request/cif.

## Acknowledgments

We sincerely thank the Council of Scientific and Industrial Research, New Delhi, for a Junior Research Fellowship to T. D. We also thank the Department of Science and Technology, New Delhi, for supporting this research (scheme no. SR/S1/IC-45/2003). We thank Dr. P. Sambasiva Rao, Pondicherry University, Pondicherry, for providing the EPR facilities and Prof. K. Natarajan, Bharathiar University, Coimbatore, for CHN analysis.

[1] R. J. B. Sweeney, *Chem. Soc. Rev.* **2002**, *31*, 247–258.
[2] a) D. Tanner, *Angew. Chem. Int. Ed. Engl.* **1994**, *33*, 599–619; b) W. H. Pearson, B. W. Lian, S. C. Bergmeier, in *Comprehensive Heterocyclic Chemistry II* (Ed.: A. Padwa), Pergamon Press, Oxford, U.K., **1996**, *1A*, pp. 1–60; c) K. M. L. Rai, A. Hassner, in *Comprehensive Heterocyclic Chemistry II* (Ed.: A. Padwa), Pergamon Press, Oxford, U.K., **1996**, *1A*, pp. 61–96.
[3] a) T. Fukuyama, L. Yang, *J. Am. Chem. Soc.* **1989**, *111*, 8303–8304; b) R. S. Coleman, J.-S. Kong, *J. Am. Chem. Soc.* **1998**, *120*, 3538–3539.
[4] a) D. A. Evans, M. M. Faul, M. T. Bilodeau, *J. Org. Chem.* **1991**, *56*, 6744–6746; b) S. Jain, B. Sain, *J. Mol. Catal. A* **2003**, *195*, 283–294; c) P. J. Perez, M. Brookhart, J. L. Templeton, *Organometallics* **1993**, *12*, 261–262; d) K. Guthikonda, J. Du Bois, *J. Am. Chem. Soc.* **2002**, *124*, 13672–13673; e) D. A. Evans, M. M. Faul, M. T. Bilodeau, *J. Am. Chem. Soc.* **1994**, *116*, 2742–2753; f) K. B. Hansen, N. S. Finney, E. N. Jacobsen, *Angew. Chem. Int. Ed. Engl.* **1995**, *34*, 676–678; g) P. Dauban, R. H. Dodd, *Tetrahedron Lett.* **1998**, *39*, 5739–5742.
[5] a) K. G. Rasmussen, K. A. Jørgensen, *J. Chem. Soc., Chem. Commun.* **1995**, 1401–1402; b) Z. Zhu, J. H. Espenson, *J. Org. Chem.* **1995**, *60*, 7090–7091; c) L. Casarrubios, J. A. Perez, M. Brookhart, J. L. Templeton, *J. Org. Chem.* **1996**, *61*, 8358–8359; d) M. F. Mayer, M. M. Hossain, *J. Org. Chem.* **1998**, *63*, 6839–6844; e) K. Juhl, R. G. Hazell, K. A. Jørgensen, *J. Chem. Soc., Perkin Trans. 1* **1999**, 2293–2298.
[6] a) P. Müller, in *Advances in Catalytic Processes* (Ed.: M. P. Doyle), JAI Press Inc., Greenwich, CT, USA, **1996**, vol. 2, pp. 113–151; b) Z. Li, K. R. Conser, E. N. Jacobsen, *J. Am. Chem. Soc.* **1993**, *115*, 5326–5327; c) D. A. Evans, M. M. Faul, M. T. Bilodeau, B. A. Anderson, D. M. Barnes, *J. Am. Chem. Soc.* **1993**, *115*, 5328–5329; d) K. Noda, N. Hosoya, R. Irie, Y. Ito, T. Katsuki, *Synlett* **1993**, 469–471; e) J. C. Antilla, W. D. Wulff, *J. Am. Chem. Soc.* **1999**, *121*, 5099–5100; f) T.-S. Lai, H.-L. Kwong, C.-M. Che, S.-M. Peng, *Chem. Commun.* **1997**, 2373–2374.
[7] Y. Yamada, T. Yamamoto, M. Okawara, *Chem. Lett.* **1975**, 361–362.
[8] a) P. Müller, C. Baud, Y. Jacquier, *Can. J. Chem.* **1998**, *76*, 738–750; b) P. Müller, C. Baud, Y. Jacquier, M. Moran, I. Nageli, *J. Phys. Org. Chem.* **1996**, *9*, 341–347.
[9] a) M. J. Sodergren, D. A. Alonso, P. G. Andersson, *Tetrahedron: Asymmetry* **1997**, *8*, 3563–3565; b) D. P. Albone, P. S. Aujla, P. C. Taylor, S. Challenger, A. M. Derrick, *J. Org. Chem.* **1998**, *63*, 9569–9571; c) P. Dauban, R. H. Dodd, *J. Org. Chem.* **1999**, *64*, 5304–5307; d) B. V. Meprathu, S. Diltz, P. J. Walsh, J. D. Protasiewicz, *Tetrahedron Lett.* **1999**, *40*, 5459–5460; e) A. V. Gontcharov, H. Liu, K. B. Sharpless, *Org. Lett.* **1999**, *1*, 783; f) A. N. Vedernikov, K. G. Caulton, *Org. Lett.* **2003**, *5*, 2591; g) A. N. Vedernikov, J. C. Huffman, K. G. Caulton, *Inorg. Chem.* **2002**, *41*, 6244–6248.
[10] J. A. Halfen, J. K. Hallman, J. A. Schultz, J. P. Emerson, *Organometallics* **1999**, *18*, 5435–5437.
[11] P. Comba, M. Merz, H. Pritzkow, *Eur. J. Inorg. Chem.* **2003**, 1711–1718.
[12] K. M. Gillespie, C. J. Sanders, P. O'Shaughnessy, I. Westmoreland, C. P. Thickitt, P. Scott, *J. Org. Chem.* **2002**, *67*, 3450–3458.

 © 2006 Wiley-VCH Verlag GmbH & Co. KGaA, Weinheim 

[13] J. A. Halfen, J. M. Uhan, D. C. Fox, M. P. Mehn, L. Que Jr, *Inorg. Chem.* **2000**, *39*, 4913–4920.
[14] a) J. Thorhauge, M. Roberson, R. G. Hazell, K. A. Jørgensen, *Chem. Eur. J.* **2002**, *8*, 1888; b) M. A. Mairena, M. M. Diaz-Requejo, T. R. Belderrain, M. C. Nicasio, S. Trofimenko, P. J. Perez, *Organometallics* **2004**, *23*, 253–256.
[15] J. A. Halfen, D. C. Fox, M. P. Mehn, L. Que Jr, *Inorg. Chem.* **2001**, *40*, 5060–5061.
[16] F. Mohr, S. A. Binfield, J. C. Fettinger, A. N. Vedernikov, *J. Org. Chem.* **2005**, *70*, 4833–4839.
[17] A. W. Addison, T. Nageswara Rao, J. Reedijk, J. van Rijn, G. C. Verschoor, *J. Chem. Soc., Dalton Trans.* **1984**, 1349–1356. [A structural index $\tau$ for these geometries, which has been defined as $\tau = (\beta - \alpha)/60$, with $\alpha$ and $\beta$ being the two largest coordination angles. In a perfect square-pyramidal geometry $\tau$ is 0, while it is 1 in a perfect trigonal-bipyramidal geometry].
[18] a) G. Murphy, P. Nagle, B. J. Murphy, B. J. Hathaway, *J. Chem. Soc., Dalton Trans.* **1997**, 2645–2652; b) G. Murphy, C. Murphy, B. Murphy, B. J. Hathaway, *J. Chem. Soc., Dalton Trans.* **1997**, 2653–2660; c) G. Murphy, C. O'Sullivan, B. Murphy, B. J. Hathaway, *Inorg. Chem.* **1998**, *37*, 240–248.
[19] A. Raja, V. Rajendiran, P. Uma Maheswari, R. Balamurugan, C. A. Kilner, M. A. Halcrow, M. Palaniandavar, *J. Inorg. Biochem.* **2005**, *99*, 1717–1732.
[20] M. Velusamy, R. Mayilmurugan, M. Palaniandavar, *Inorg. Chem.* **2004**, *43*, 6284–6293.
[21] a) M. Vaidyanathan, R. Viswanathan, M. Palaniandavar, T. Balasubramanian, P. Prabhaharan, T. P. Muthiah, *Inorg. Chem.* **1998**, *37*, 6418–6427; b) A. W. Addison, in *Copper Coordination Chemistry: Bio-chemical and Inorganic Perspectives* (Eds.: K. D. Karlin, J. Zubieta), Adenine Press, Guilderland, New York, **1983**, p. 109.
[22] L. Casella, *Inorg. Chem.* **1984**, *23*, 2781–2787.
[23] U. Sakaguchi, A. W. Addison, *J. Chem. Soc., Dalton Trans.* **1979**, 600–608.
[24] X.-H. Bu, M. Du, Z.-L. Shang, R.-H. Zhang, D.-Z. Liao, M. Shionoya, T. Clifford, *Inorg. Chem.* **2000**, *39*, 4190–4199.
[25] a) *SMART & SAINT Software Reference manuals*, version 5.0; Bruker AXS Inc., Madison, WI, **1998**; b) G. M. Sheldrick, *SADABS, software for empirical absorption correction*, University of Göttingen, Germany, **2000**; c) *SHELXTL Reference Manual*, version 5.1, Bruker AXS Inc., Madison, WI, **1998**.
[26] Stoe *IPDS Software*, Stoe & Cie GmbH, Darmstadt, Germany, **2000**.
[27] "*SHELXS-97 Program for Crystal Structure Determination*", G. M. Sheldrick, *Acta Crystallogr., Sect. A* **1990**, *46*, 467–473.
[28] G. M. Sheldrick, SHELXL-97, University of Göttingen, Germany, **1999**.
[29] A. L. Spek, *J. Appl. Crystallogr.* **2003**, *36*, 7–13.

Received: May 26, 2006
Published Online: September 22, 2006

 © 2006 Wiley-VCH Verlag GmbH & Co. KGaA, Weinheim 

DOI: 10.1002/ejic.200600838

# σ-Silane Ruthenium Complexes: The Crucial Role of Secondary Interactions

**Sébastien Lachaize[a] and Sylviane Sabo-Etienne*[a]**

**Keywords:** σ-Complexes / Ruthenium / Silanes / Hydrides / Coordination modes / Intramolecular interactions / Oxidative addition / Hypervalent compounds

*On pages 2118–2120 of the original article,[1] the references in Tables 1 and 2 are incorrect as a result of an inadvertent error during the revision of the article, and in Figure 6 on page 2121 of the same article,[1] the ligand L′ was omitted; the correct version of Tables 1 and 2 and Figure 6 are given.*

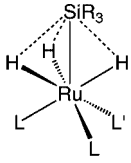


L, L' = phosphane, CO, σ-$H_2$
R = alkyl, aryl, alkoxy, amino or halogen

Figure 6. Schematic representation of a series of complexes of general formula $RuH_3(SiR_3)L_2L'$.

*The Authors*

[1] S. Lachaize, S. Sabo-Etienne, *Eur. J. Inorg. Chem.* **2006**, 2115–2127.

Received: September 6, 2006
Published Online: October 10, 2006

[a] Laboratoire de Chimie de Coordination du CNRS,
205 route de Narbonne, 31077 Toulouse Cedex 04, France
E-mail: sabo@lcc-toulouse.fr

 © 2006 Wiley-VCH Verlag GmbH & Co. KGaA, Weinheim 

Table 1. Selected NMR and IR data[a] for various silane and silyl ruthenium complexes.

| | Formula | $\delta = {}^{1}H$ [ppm] | $J_{SiH}$ [Hz] | $\delta = {}^{29}Si$ [ppm] | $\nu_{Ru-H-Si}$ [$cm^{-1}$] | $\nu_{Ru-H}$ [$cm^{-1}$] | Ref. |
|---|---|---|---|---|---|---|---|
| **2** | $RuH_2[(\eta^2\text{-}HSiMe_2)_2(C_6H_4)](PCy_3)_2$ | –7.74 (t)<br>–12.03 (m) | 65 | 4.8 | 1778 | 1969<br>1985 | [18,19] |
| **3a** | $RuH_2[(\eta^2\text{-}HSiMe_2)_2(CH_2)_2](PCy_3)_2$ | –8.21 (t)<br>–12.65 (m) | 70 | 12.2 | 1773 | 1981<br>2012 | [18] |
| **3b** | $RuH_2[(\eta^2\text{-}HSiMe_2)_2(CH_2)_2](PCy_3)(PPh_3)$ | –7.68 (t)<br>–11.10 (dd)<br>–11.47 (dd) | 64 | 14.7 | 1768 | <br>1989<br>2008 | [18] |
| **3c** | $RuH_2[(\eta^2\text{-}HSiMe_2)_2(CH_2)_2](PPh_3)_2$ | –7.60 (t)<br>–10.92 (m) | 64 | 16.4 | 1797 | 1961<br>1978 | [18] |
| **4** | $RuH_2[(\eta^2\text{-}HSiMe_2)_2(CH_2)_3](PCy_3)_2$ | –8.49 (t)<br>–12.17 (m) | 75 | –11.1 | 1803 | 1961<br>1994 | [18] |
| **5** | $RuH_2[(\eta^2\text{-}HSiMe_2)_2(OSiMe_2O)](PCy_3)_2$ | –9.14 (t)<br>11.20 (m) | 82 | 4.9 | 1798 | 1955<br>2045 | [18] |
| **6** | $RuH_2[(\eta^2\text{-}HSiMe_2)_2NH](PCy_3)_2$ | –8.36 (br.)<br>–8.62 (br.)<br>–9.93 (br.)<br>–10.76 (br.) | – | – | 1712 | <br>1972<br>2040 | [20] |
| **7** | $RuH_2[(\eta^2\text{-}HSiMe_2)_2O](PCy_3)_2$ | –8.1 (br.)<br>–8.5 (br.)<br>–9.4 (br.)<br>–10.2 (br.) | 22 (av.)[b] | –5.61 | 1699 | <br>1969<br>2045 | [18,19] |
| **8a** | $RuH_2[(\eta^2\text{-}HSiPh_2)_2O](PCy_3)_2$ (sym) | –7.67 (br.)<br>–9.70 (t) | 41 (av.)[b] | 4.80 | 1670 | 1976<br>2019 | [14,18] |
| **8b** | $RuH_2[(\eta^2\text{-}HSiPh_2)_2O](PCy_3)_2$ (non sym) | –7.08 (br.)<br>–8.11 (br.)<br>–8.99 (br. t)<br>–9.81 (br. t) | | | | | |
| **9a** | $RuH_2[(\eta^2\text{-}HSiPh_2)\text{–}O\text{–}(SiHPh_2)](PPh_3)_3$ | –8.97 (dt, 1 H)<br>–9.40 (br. t, 2 H) | 35 (av.)[b] | 11.7<br>–21.4 (free) | – | – | [14] |
| **9b** | $RuH_2[(\eta^2\text{-}HSiPh_2)\text{–}O\text{–}(Si(OH)Ph_2)](PPh_3)_3$ | –9.15 (m, 3 H) | – | – | – | – | [14] |
| **10** | $RuH_3(SiCl_2Me)(PPh_3)_3$ | –9.76 (m) | 39.7 (av.)[b] | 36.4 | – | 1961.5 | [21] |
| **11** | $RuH_3(SiPyr_3)(PPh_3)_3$ | –9.80 (m) | 47.4 (av.)[b] | 8.6 | – | 1960<br>1969 | [23] |
| **12a** | $RuH_3(SiMe_3)(PMe_3)_3$ | –10.18 (br. m) | – | –10.8 | – | 1887 (av.) | [27] |
| **12b** | $RuH_3(SiEt_3)(PMe_3)_3$ | –10.53 (br. m) | – | 12.7 | – | 1897 (av.) | [27] |
| **12c** | $RuH_3(SiMe_2CH_2SiMe_3)(PMe_3)_3$ | –10.15 (br. m) | 25 | –9.2<br>–0.9 (free) | – | 1898 (av.) | [22] |
| **13** | $RuH_2(\eta^2\text{-}HSiPh_3)(\eta^2\text{-}H_2)(PCy_3)_2$ | –8.3 (br. s) | 18 (av.)[b] | 5.7 | – | – | [28] |
| **14** | $RuH_2(\eta^2\text{-}HSiMe_2Cl)(\eta^2\text{-}H_2)(PCy_3)_2$ | –8.51 (br. s) | – | 38 | – | – | [29] |
| **15** | $RuH_2\{\eta^4\text{-}HSiMe_2(CH{=}CHMe)\}(PCy_3)_2$ | –8.77 (br.)<br>–9.46 (dt)<br>–12.46 (dt) | 105 | –11.3 | – | 1945<br>2021 | [32] |
| **16** | $RuCl(H)(\text{–}CH_2SiMe_2)(PMe_3)_3$ (*fac*) | –7.7 (dt) | 75.0 | –19.4 | 1615 | – | [33] |
| | $RuCl(H)(\text{–}CH_2SiMe_2)(PMe_3)_3$ (*mer*) | –6.0 (dt) | 77.5 | –19.8 | – | – | [33] |
| **17** | $RuH(\eta^2\text{-}HSiEt_3)\{(\eta^3\text{-}C_6H_8)PCy_2\}(PCy_3)$ | –9.54 (br. t)<br>–12.63 (dd) | 36.7<br>24.7 | – | – | – | [38] |
| **18** | $RuH(\eta^2\text{-}HSiMe_2Et)\{(\eta^3\text{-}C_6H_8)PCy_2\}(PCy_3)$ | –9.45 (ps t)<br>–12.46 (dd) | 40.1<br>24.1 | 5.0 | – | – | [37] |
| **19** | $RuH(\eta^2\text{-}HSiMe_2Cl)\{(\eta^3\text{-}C_6H_8)PCy_2\}(PCy_3)$ | –9.06 (ps t)<br>–11.98 (dd) | 37.3<br>24.1 | 46.2 | – | – | [29] |
| **20** | $Cp^*RuCl(\eta^2\text{-}HSiClMe_2)(P\mathit{i}Pr_3)$ | –9.65 (t) | 33.5 | – | 1916 | – | [35] |
| **21** | $[CpRuH(SiCl_3)(PMe_3)_2][B(3,5\text{-}(CF_3)_2C_6H_3)_4]$ | –9.87 (t) | 48 | 30.6 | – | – | [39] |
| **22** | $Ru_2H_4(\mu\text{-}\eta^2\text{:}\eta^2\text{:}\eta^2\text{:}\eta^2\text{-}SiH_4)(PCy_3)_4$ | –6.0 (br.)<br>–8.6 (br.) | 36 (av.)[b] | 290.2 | 1667 | 1911 | [40,41] |
| **23** | $Ru_2H_2[\mu\text{-}\eta^2\text{:}\eta^2\text{-}H_2Si(OMe)_2]_3(PCy_3)_2$ | –9.94 (br.) | 22 (av.)[b] | 85.7 | 1703 | 1899<br>2022 | [41] |
| **24** | $[Cp^*RuH]_2(\eta^2\text{:}\eta^2\text{-}H_2Si\mathit{t}Bu_2)$ | –6.15 (s)<br>–16.63 (s) | 75 | 75.5 | 1790 | – | [42] |
| **25a** | $[Cp^*Ru(CO)]_2(\eta^2\text{:}\eta^2\text{-}H_2Si\mathit{t}Bu_2)$ | –13.60 (s) | 22.4 | 186.2 | – | – | [42] |
| **25b** | $[Cp^*Ru(CO)]_2(\eta^2\text{:}\eta^2\text{-}HSi\mathit{t}Bu_2)H$ | –11.79 (s)<br>–14.40 (s) | 31.6 | 168.2 | – | – | [42] |
| **26a** | $[Cp^*Ru]_2(\mu\text{-}\eta^2\text{-}HSi\mathit{t}Bu_2)(\mu\text{-}\eta^2\text{-}HSiPhH)(\mu\text{-}H)H$ | –11.64 (s)<br>–12.84 (s)<br>–14.00 (s)<br>–16.46 (s) | 26<br><br>49<br> | – | 1813<br>1613<br><br> | 2054<br><br><br> | [42] |
| **26b** | $[Cp^*Ru]_2(\mu\text{-}\eta^2\text{-}HSi\mathit{t}Bu_2)(\mu\text{-}\eta^2\text{-}HSiEtH)(\mu\text{-}H)H$ | –12.32 (s)<br>–13.26 (s)<br>–14.29 (s)<br>–16.67 (s) | – | – | 1835<br>1659 | 2062<br><br><br> | [42] |

[a] NMR/IR data were obtained under the following conditions: **2**–**5**,**12**,**17**,**23**, $C_6D_6$, room temp./Nujol mull; **6**,**8**,**9a**,**22**, $C_7D_8$, 193 K/Nujol mull; **7**, $C_7D_8$, 178 K/Nujol mull; **9b**,**11**,**13**–**15**,**18**–**19**, $C_7D_8$, room temp./Nujol mull; **10**, $CD_2Cl_2$, room temp./KBr; **16**, $C_7D_8$, 301 K/Fluorolube; **20**, $C_7D_8$, 233 K/Nujol mull; **21**, $CD_2Cl_2$, 298 K; **24**–**26**, $C_7D_8$, 298 K/KBr. [b] $J_{SiH}$ values were determined at room temperature. Average values involving all the hydrides and dihydrogen ligand in the case of **13**.

 © 2006 Wiley-VCH Verlag GmbH & Co. KGaA, Weinheim 

Table 2. Selected interatomic distances [Å] for various silane and silyl ruthenium complexes.

| | Formula | Ru–Si | | Si–H | | Si···H | | Ref. |
|---|---|---|---|---|---|---|---|---|
| | | X-Ray | DFT[a] | X-Ray | DFT[a] | X-Ray | DFT[a] | |
| **2** | $RuH_2[(\eta^2\text{-}HSiMe_2)_2(C_6H_4)](PCy_3)_2$ | 2.425(1) | 2.425 | 1.84(2) | 1.848 | 2.22(2) | 2.253 | [18,19] |
| | | | | | | 2.18(2) | 2.253 | |
| | | 2.429(2) | 2.425 | 1.84(2) | 1.848 | 2.12(2) | 2.253 | |
| | | | | | | 2.21(2) | 2.253 | |
| **3a** | $RuH_2[(\eta^2\text{-}HSiMe_2)_2(CH_2)_2](PCy_3)_2$ | 2.428(1) | 2.441 | 1.73(3) | 1.853 | 2.27(3) | 2.22 | [18] |
| | | | | | | 2.13(3) | 2.329 | |
| | | 2.411(1) | 2.441 | 1.78(3) | 1.853 | 2.12(3) | 2.329 | |
| | | | | | | 2.31(3) | 2.22 | |
| **5** | $RuH_2[(\eta^2\text{-}HSiMe_2)_2(OSiMe_2O)](PCy_3)_2$ | 2.484(1) | 2.451 | 1.77(4) | 1.826 | 2.25(3) | 2.170 | [18] |
| | | | | | | 2.43(3) | 2.484 | |
| | | 2.434(1) | 2.447 | 1.81(3) | 1.839 | 2.32(3) | 2.426 | |
| | | | | | | 2.04(3) | 2.168 | |
| **6** | $RuH_2[(\eta^2\text{-}HSiMe_2)_2NH](PCy_3)_2$ | 2.395(2) | 2.416 | 1.93(5) | 1.922 | 2.35(6) | 2.510 | [20] |
| | | | | | | 2.25(6) | 2.191 | |
| | | 2.434(2) | 2.490 | 1.91(5) | 1.775 | 2.39(5) | 2.500 | |
| | | | | | | 2.09(6) | 2.367 | |
| **9b** | $RuH_2[(\eta^2\text{-}HSiPh_2)\text{–}O\text{–}(Si(OH)Ph_2)](PPh_3)_3$ | 2.356(2) | – | 1.97(5) | – | 2.03(5) | – | [14] |
| | | | | | | 2.07(5) | | |
| **10** | $RuH_3(SiCl_2Me)(PPh_3)_3$ | 2.2760(4) | – | – | – | 1.86(2) | – | [21] |
| | | | | | | 1.94(2) | | |
| | | | | | | 1.94(3) | | |
| **12a** | $RuH_3(SiMe_3)(PMe_3)_3$ | 2.376(1) | – | – | – | 2.13(5) | – | [27] |
| | | | | | | 2.18(5) | | |
| | | | | | | 2.23(5) | | |
| **12c** | $RuH_3(SiMe_2CH_2SiMe_3)(PMe_3)_3$ | 2.3774(8) | – | – | – | 2.00(4) | – | [22] |
| | | | | | | 2.09(4) | | |
| | | | | | | 2.05(5) | | |
| **12d** | $RuH_2(SiMe_2CH_2CH_2SiMe_2)(PMe_3)_3$ | 2.4682(9) | – | 1.81(4) | – | – | – | [22] |
| | | 2.4514(9) | | | | | | |
| **13** | $RuH_2(\eta^2\text{-}HSiPh_3)(\eta^2\text{-}H_2)(PCy_3)_2$ | 2.385(2) | 2.394 | 1.72(3) | 1.946 | 1.83(3) | 2.071 | [25] |
| | | | | | | 2.40(4) | 2.116 | |
| **15** | $RuH_2\{\eta^4\text{-}HSiMe_2(CH{=}CHMe)\}(PCy_3)_2$ | 2.498(2) | 2.499 | 1.59(8) | 1.658 | – | – | [32] |
| **16** | $RuCl(H)(\text{–}CH_2SiMe_2)(PMe_3)_3$ (*fac*) | 2.526(2) | – | 1.664 | – | – | – | [27] |
| **16** | $RuCl(H)(\text{–}CH_2SiMe_2)(PMe_3)_3$ (*mer*) | 2.468(2) | – | 1.557 | – | – | – | [27] |
| **18** | $RuH(\eta^2\text{-}HSiMe_2Et)\{(\eta^3\text{-}C_6H_8)PCy_2\}(PCy_3)$ | 2.418 (1) | 2.468 | – | 1.847 | – | 2.164 | [37] |
| **19**[b] | $RuH(\eta^2\text{-}HSiMe_2Cl)\{(\eta^3\text{-}C_6H_8)PCy_2\}(PCy_3)$ | 2.353 (2) | 2.398 | 1.91 (2) | 1.891 | 1.99(2) | 2.076 | [29] |
| **20** | $Cp^*RuCl(\eta^2\text{-}HSiClMe_2)(P\mathit{i}Pr_3)$ | 2.398(1) | 2.427 | 2.05 | 2.072 | – | – | [35] |
| **21** | $[CpRuH(SiCl_3)(PMe_3)_2]^+$ | 2.329(1) | – | 1.77(5) | – | – | – | [39] |
| **22** | $Ru_2H_4(\mu\text{-}\eta^2\text{:}\eta^2\text{:}\eta^2\text{:}\eta^2\text{-}SiH_4)(P\mathit{i}Pr_3)_4$ | 2.1875(4) | 2.229 | 1.69(3) | 1.685 | – | – | [41] |
| | | | | 1.73(3) | 1.685 | | | |
| **23** | $Ru_2H_2[\mu\text{-}\eta^2\text{:}\eta^2\text{-}H_2Si(OMe)_2]_3(PCy_3)_2$ | 2.456(3) | 2.486 | – | in the range | – | – | [41] |
| | | 2.364(3) | 2.398 | | 1.654–1.760 | | | |
| | | 2.408(3) | 2.551 | | | | | |
| | | 2.419(3) | 2.551 | | | | | |
| | | 2.355(3) | 2.400 | | | | | |
| | | 2.408(3) | 2.487 | | | | | |

[a] All the calculations were carried out at the B3LYP level of theory, except for compounds **2**, **6** (B3PW91) and **20** (BP86), by using the following model compounds: **2** $RuH_2[(\eta^2\text{-}HSiH_2)_2(C_6H_4)](PH_3)_2$, **3a** $RuH_2[(\eta^2\text{-}HSiH_2)_2(CH_2)_2](PH_3)_2$, **5** $RuH_2[(\eta^2\text{-}HSiH_2)_2(OSiH_2O)](PH_3)_2$, **6** $RuH_2[(\eta^2\text{-}HSiMe_2)_2NH](PCy_3)_2$, **13** $RuH_2(\eta^2\text{-}HSiH_3)(\eta^2\text{-}H_2)(PH_3)_2$, **15** $RuH_2\{\eta^4\text{-}HSiH_2(CH{=}CHMe)\}(PH_3)_2$, **18** $RuH(\eta^2\text{-}HSiMe_3)\{(\eta^3\text{-}C_6H_8)PH_2\}(PH_3)$, **19** $RuH(\eta^2\text{-}HSiMe_2Cl)\{(\eta^3\text{-}C_6H_8)PH_2\}(PH_3)$, **20** $Cp^*RuCl(\eta^2\text{-}HSiClMe_2)(P\mathit{i}Pr_3)$, **22** $Ru_2H_4(\mu\text{-}SiH_4)(PH_3)_4$, **23** $Ru_2H_2[\mu\text{-}H_2Si(OMe)_2]_3(PH_3)_2$. [b] Data for one isomer.

 © 2006 Wiley-VCH Verlag GmbH & Co. KGaA, Weinheim 

EurJIC
European Journal of Inorganic Chemistry

Issue 23/2006

Pages 4705–4948

*Papers available ahead of print in Early View at www.interscience.wiley.com*

*Earliest available Table of Contents:*
*Automatically, free of charge by e-mail through*
*www.interscience.wiley.com/alerts*

## COVER PICTURE

**The cover picture shows** the three-dimensional supramolecular arrangement of 1,10-phenanthroline (phen) residues in compound $(Hphen)_6[Ge_6(OH)_6(hedp)_6]\cdot 2(phen)\cdot 20H_2O$ (where $H_4$hedp stands for etidronic acid). Protonated organic residues, $Hphen^+$, π-π-stack along the [101] direction of the unit cell, which leads to the formation of columns that are interconnected through a series of weak C−H···π interactions with neighbouring 1,10-phenanthrolines. The resulting organic framework is highly porous and contains charge-balancing centrosymmetric hexameric anionic $[Ge_6(\mu_2\text{-}OH)_6(C_2H_4O_7P_2)_6]^{6-}$ moieties within the channels and a large number of highly disordered water molecules (total available volume of ca. 2462 Å$^3$ per unit cell). Details are discussed in the article by J. Rocha et al. on p. 4741 ff.

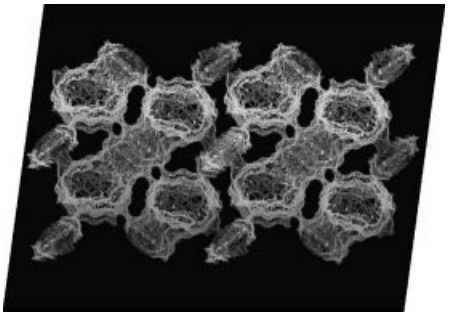

## MICROREVIEW

**Contents**

**4721** **A. Escuer, G. Aromí***

Azide as a Bridging Ligand and Magnetic Coupler in Transition Metal Clusters

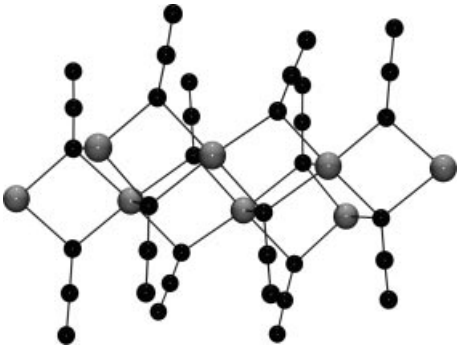

**Keywords:** Cluster compounds / Azides / Magnetic properties / Single-molecule magnets

 © 2006 Wiley-VCH Verlag GmbH & Co. KGaA, Weinheim 

# SHORT COMMUNICATION


**4737** **W.-Z. Chen, J. D. Protasiewicz, A. J. Shirar, T. Ren***

Dimerization of Diruthenium Coordination Compounds via Olefin Metathesis

**Keywords:** Olefin metathesis / Dimerization / Diruthenium compounds / ω-Alkene-α-carboxylate


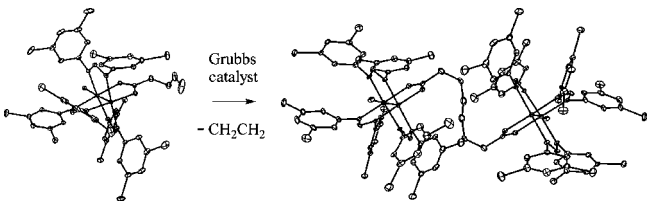


# FULL PAPERS


**4741** **L. Mafra, F. A. Almeida Paz, F.-N. Shi, R. A. Sá Ferreira, L. D. Carlos, T. Trindade, C. Fernandez, J. Klinowski, J. Rocha***

Crystal Structure, Solid-State NMR Spectroscopic and Photoluminescence Studies of Organic-Inorganic Hybrid Materials $(HL)_6[Ge_6(OH)_6(hedp)_6]\cdot 2(L)\cdot nH_2O$, L = hqn or phen

**Keywords:** Germanium / Organic−inorganic hybrid materials / Crystal structure / NMR spectroscopy / Photoluminescence


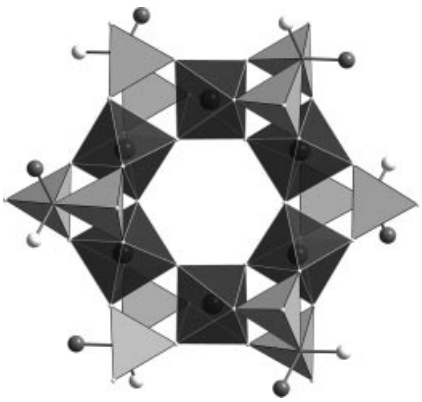


**4752** **S. González-Montiel, N. Andrade-López, V. García-Montalvo, J. A. Cogordan, J. G. Alvarado-Rodríguez***

Pentacoordination at Germanium by Transannular Bonding of Sulfur or Oxygen in an Eight-Membered Ring: An Experimental and Theoretical Study

**Keywords:** Germanium / Hypercoordinate compounds / Structure elucidation / Density functional theory / NBO analysis


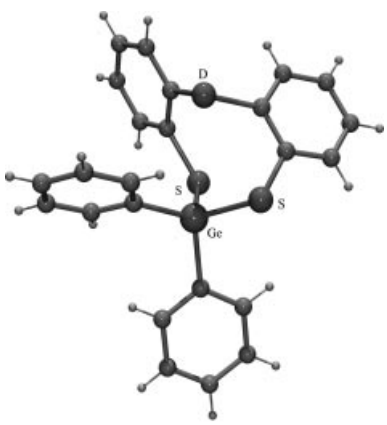


D = O, S


**4761** **V. Rosa, P. J. Gonzalez, T. Avilés,* P. T. Gomes, R. Welter,* A. C. Rizzi, M. C. G. Passeggi, C. D. Brondino***

Synthesis, Solid-State Structures, and EPR Spectroscopic Studies on Polycrystalline and Single-Crystal Samples of α-Diimine Cobalt(II) Complexes

**Keywords:** Cobalt(II) complexes / α-Diimine ligands / Single-crystal X-ray diffraction / EPR spectroscopy


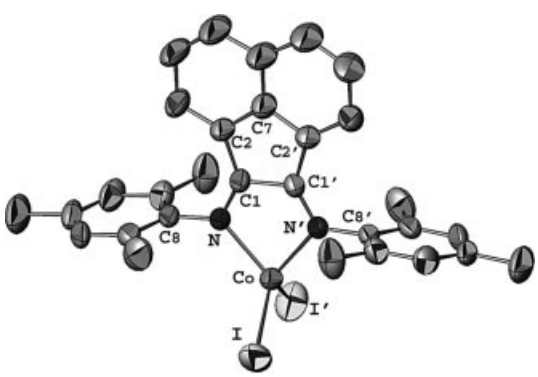

**4770** **C. von Hänisch,* D. Nikolova**

Synthesis and Characterisation of Molecular Bismuth Phosphorus Compounds Containing $Bi_2$ Units with Bi−Bi Single and Double Bonds

**Keywords:** Bismuth / Phosphorus / Double bonds

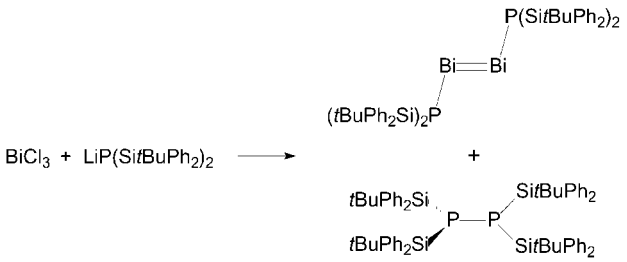


**4774** **Y. Guo, W. Meyer-Zaika, M. Muhler, S. Vukojević, M. Epple***

Cu/Zn/Al Xerogels and Aerogels Prepared by a Sol−Gel Reaction as Catalysts for Methanol Synthesis

**Keywords:** Heterogeneous catalysis / Copper / Zinc / Aluminum / Sol−gel processes / Mesoporous materials

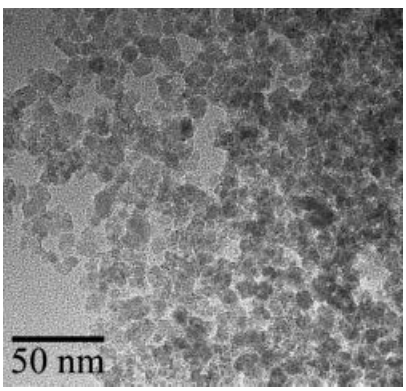


**4782** **R. Weiss, S. Vukojević, C. Baltes, R. N. d'Alnoncourt, M. Muhler, M. Epple***

Copper/Zinc L-Tartrates: Mixed Crystals and Thermolysis to a Mixture of Copper Oxide and Zinc Oxide That Is Catalytically Active in Methanol Synthesis

**Keywords:** Heterogeneous catalysis / Copper / Zinc / Thermochemistry

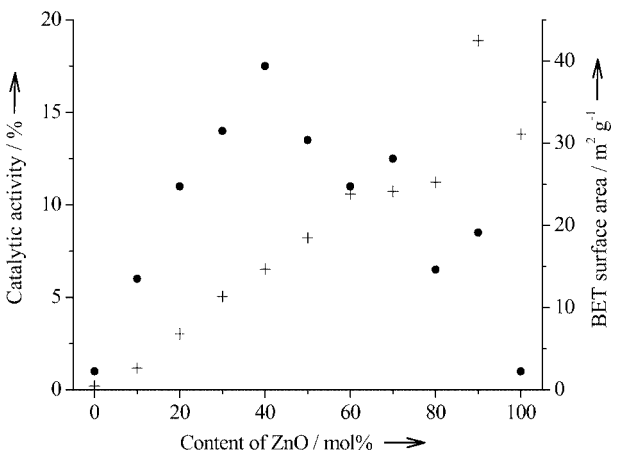


**4787** **L.-X. Yang, Y.-J. Zhu,* L. Li, L. Zhang, H. Tong, W.-W. Wang, G.-F. Cheng, J.-F. Zhu**

A Facile Hydrothermal Route to Flower-Like Cobalt Hydroxide and Oxide

**Keywords:** Cobalt hydroxide / Cobalt oxide / Materials science / Nanostructures / Solvothermal synthesis

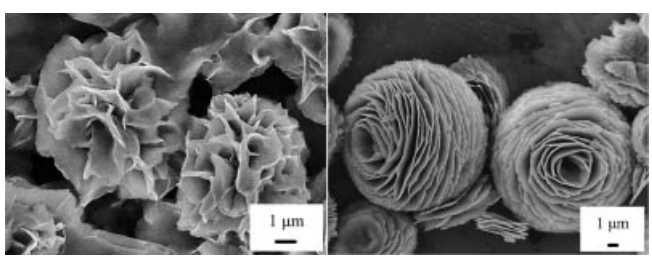


**4793** **P. I. Volkers, T. B. Rauchfuss,* S. R. Wilson**

Coordination Chemistry of 3-Mercapto-2-(mercaptomethyl)propanoic Acid (Dihydroasparagusic Acid) with Iron and Nickel

**Keywords:** Iron / Nickel / S ligands / Bridging ligands / Coordination modes

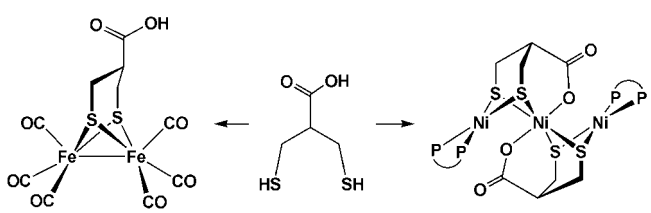



 © 2006 Wiley-VCH Verlag GmbH & Co. KGaA, Weinheim 

**4800** **J. A. W. Verhagen, C. Tock, M. Lutz, A. L. Spek, E. Bouwman***

Nickel Thiolate Complexes as Ligands for Copper and Zinc: Novel Additions to a Library of Binding Modes

**Keywords:** Nickel / Copper / Zinc / S ligands / Cluster compounds

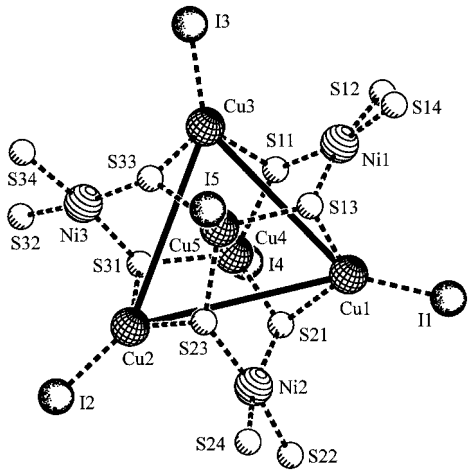


**4809** **S. V. Eliseeva,* M. Ryazanov,* F. Gumy, S. I. Troyanov, L. S. Lepnev, J.-C. G. Bünzli, N. P. Kuzmina**

Dimeric Complexes of Lanthanide(III) Hexafluoroacetylacetonates with 4-Cyanopyridine *N*-Oxide: Synthesis, Crystal Structure, Magnetic and Photoluminescent Properties

**Keywords:** Lanthanides / β-Diketonates / Luminescence / Thin films / Photophysics

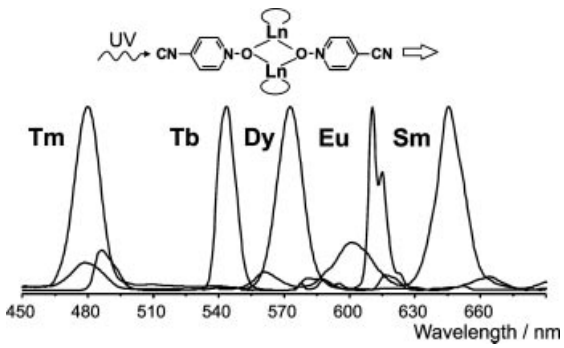


**4821** **E. Boanini, M. Fini, M. Gazzano, A. Bigi***

Hydroxyapatite Nanocrystals Modified with Acidic Amino Acids

**Keywords:** Hydroxyapatite / Amino acids / Nanocrystals

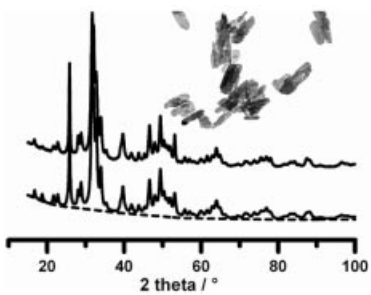


**4827** **H. Liu, J. Peng,* Z. Su, Y. Chen, B. Dong, A. Tian, Z. Han, E. Wang**

Synthesis and Structural Characterization of Sandwich-Type Keggin-γ-Lacunary Silicotungstates with an Open Wells−Dawson-Like Structure

**Keywords:** Polyoxometalates / Tungstosilicates / Keggin structures / Transition metals

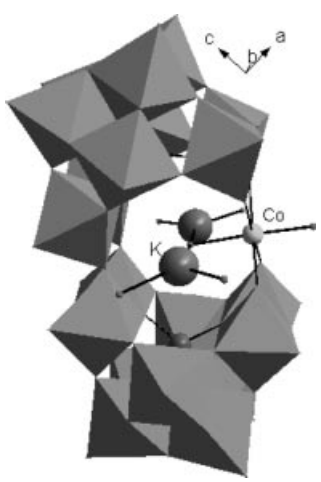


 © 2006 Wiley-VCH Verlag GmbH & Co. KGaA, Weinheim 

**4834** **C. N. Kato, Y. Kasahara, K. Hayashi, A. Yamaguchi, T. Hasegawa, K. Nomiya***

Syntheses, Characterization, and X-ray Crystal Structures of Mono-Lacunary Dawson Polyoxometalate-Based Organosilyl Complexes

**Keywords:** Silicon / Polyoxometalates / X-ray diffraction / Tungsten

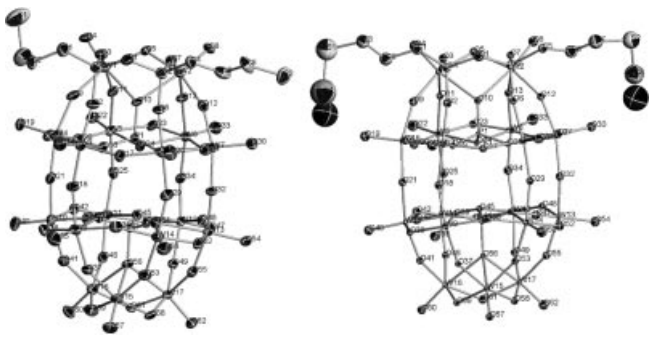

**4843** **Q.-Y. Liu, Y.-L. Wang, L. Xu***

Synthesis, Crystal Structures and Photoluminescent Properties of Three Novel Cadmium(II) Compounds Constructed from 5-Sulfoisophthalic Acid ($H_3SIP$)

**Keywords:** Cadmium compounds / Hydrothermal synthesis / Crystal structures / Photoluminescent properties

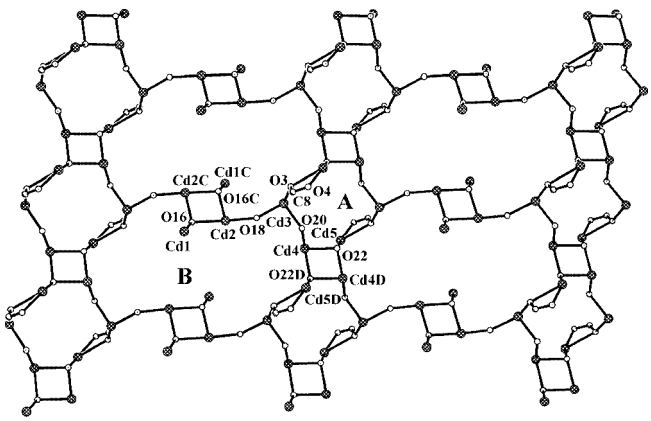


**4852** **Y. Zhou, C. Yue, D. Yuan, L. Chen, J. Chen, A. Lan, F. Jiang,* M. Hong**

Nickel-Organic Coordination Layers with Different Directional Cavities

**Keywords:** Nickel / Carboxylate ligands / Coordination polymers / Magnetic properties / Luminescence

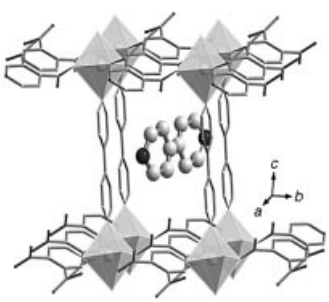


**4857** **J. A. Wright, A. A. Danopoulos,* W. B. Motherwell,* R. J. Carroll, S. Ellwood, J. Saßmannshausen**

"Pincer" N-Heterocyclic Carbene Complexes of Rhodium Functionalised with Pyridyl and Bipyridyl Donors

**Keywords:** Rhodium / Carbene ligands / Tridentate ligands / N ligands / Ligand design

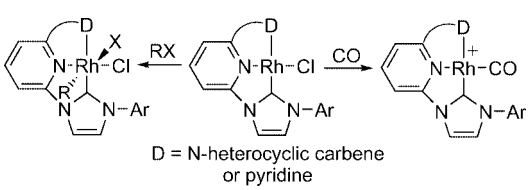


 © 2006 Wiley-VCH Verlag GmbH & Co. KGaA, Weinheim 

**4866** **J. M. Dou,* M. L. Liu, D. C. Li, D. Q. Wang**

Synthesis, Characterization, and Crystal Structure of Two Manganese Metallacrowns: 30-Metallacrown-10 and 18-Metallacrown-6 with Ligands Derived from 3-Hydroxy-2-naphthalenecarbohydrazide

**Keywords:** Metallacrowns / Manganese / Crystal structure / Supramolecular chemistry / Crown compounds

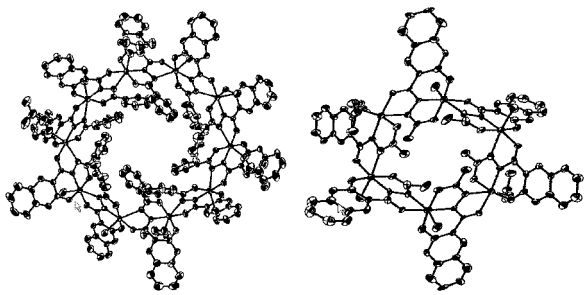

**4872** **M. J. Belousoff, B. Graham, B. Moubaraki, K. S. Murray, L. Spiccia***

Oxalato-Bridged Dinuclear Copper(II) Complexes of *N*-Alkylated Derivatives of 1,4,7-Triazacyclononane: Synthesis, X-ray Crystal Structures and Magnetic Properties

**Keywords:** Dinuclear copper(II) complexes / Oxalato bridges / *N*-Alkylated 1,4,7-triazacyclononane derivatives / X-ray structures / Antiferromagnetic coupling

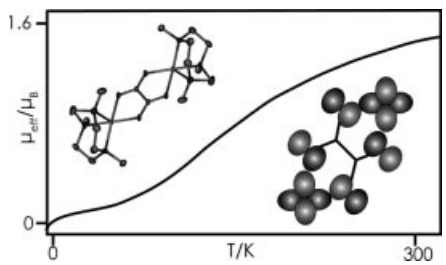


**4879** **A. Mukhopadhyay, S. Pal***

Intramolecular Apical C−H···M Interactions in Square-Planar Nickel(II) Complexes with Dianionic Tridentate Ligands and 2-Phenylimidazole

**Keywords:** Nickel(II) complexes / Square-planar complexes / Apical C−H···Ni interactions / X-ray structures / Theoretical calculations

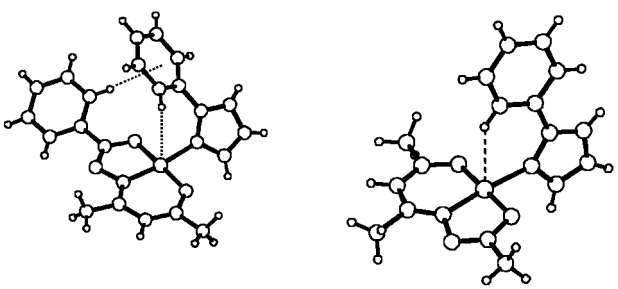

**4888** **N. Lah,* I. Leban, R. Clérac***

The Assembly of Dinuclear Alkoxo-Bridged $Cu^{II}$ Halide Complexes of Pyridine Alcohols To Form Tetranuclear and Polynuclear Compounds: Synthesis, Structure, and Magnetic Properties

**Keywords:** Pyridine alcohol ligands / Alkoxides / Copper(II) defect dicubanes / Copper(II) coordination polymers / X-ray structures / Magnetic properties

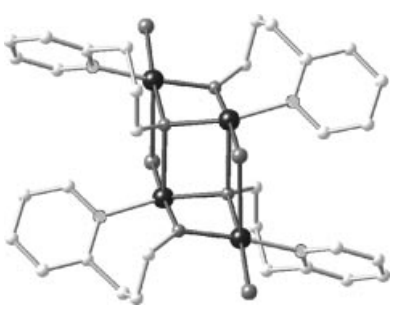

 © 2006 Wiley-VCH Verlag GmbH & Co. KGaA, Weinheim 

**4895** **C. Zhang, W.-H. Sun, Z.-X. Wang***

Cobalt and Nickel Complexes Bearing Pyrazolyliminophosphorane Ligands: Synthesis, Characterisation and Catalytic Ethylene Oligomerisation

**Keywords:** Cobalt / Nickel / Homogeneous catalysis / Ethylene / Oligomerisation

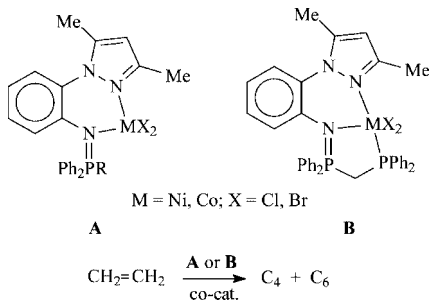


**4903** **S.-D. Bai, J.-P. Guo,* D.-S. Liu,* W.-Y. Wong**

Bulky-Hindrance-Controlled Ligand Transformation from Linked Bis(amidinate) to Linked Imido-Amidinate Promoted by a Mono(cyclopentadienyl)titanium Group

**Keywords:** Titanium / Bis(amidinate) / Bulky hindrance / Ligand transformation / Crystal structure / Steric hindrance

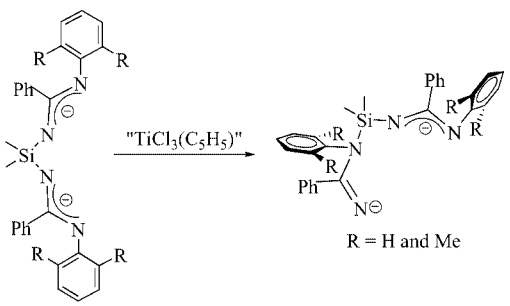


**4908** **T. A. Vanderah, T. Siegrist, M. W. Lufaso,* M. C. Yeager, R. S. Roth, J. C. Nino, S. Yates**

Phase Formation and Properties in the System $Bi_2O_3$:2$CoO_{1+x}$:$Nb_2O_5$

**Keywords:** Pyrochlore / Displacive disorder / Bismuth cobalt niobates / Bi−Co−Nb−O / Phase equilibria / Phase diagram / Dielectric properties / Magnetic properties

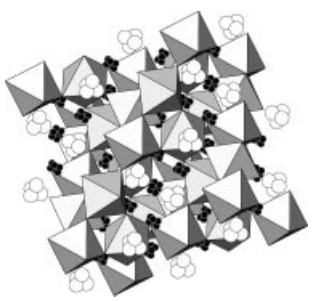

**4915** **H. Türkmen, O. Şahin, O. Büyükgüngör, B. Çetinkaya***

Silver, Palladium and Rhodium Complexes of Acenaphthylene-Anullated N-Heterocyclic Carbene Ligands: A Comparative Study

**Keywords:** N-Heterocyclic carbenes / Silver complexes / Thiones / Palladium complexes / Rhodium complexes / C−C coupling

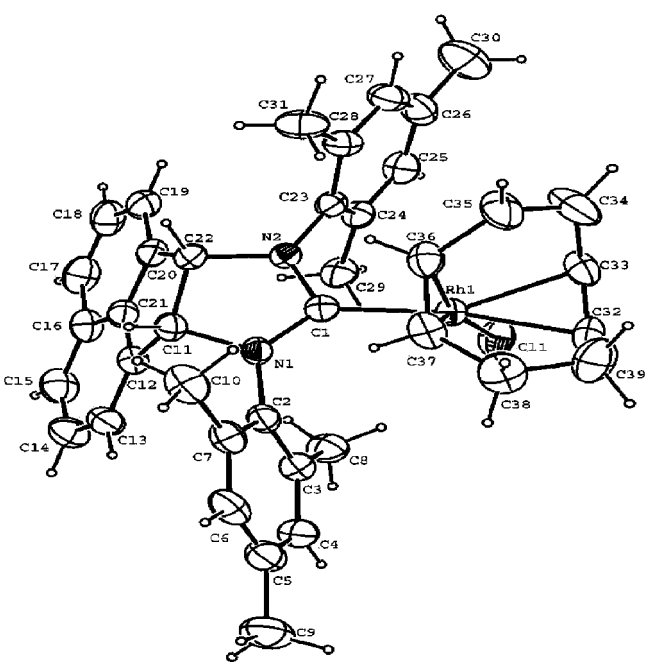


 © 2006 Wiley-VCH Verlag GmbH & Co. KGaA, Weinheim 

**4922** **U. Helmstedt, P. Lönnecke, J. Reinhold, E. Hey-Hawkins***

4-Thiolatobenzoato-Bridged Rhodium/Zirconium Complexes: 32-Membered Metallamacrocycles and Their Linear Dinuclear Counterparts

**Keywords:** Heterometallic complexes / Metallacycles / Bridging ligands / Metal−metal interactions / Rhodium / Zirconocenes / S,O ligands

Small cause – big effect!

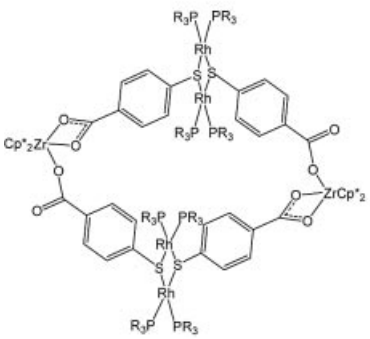

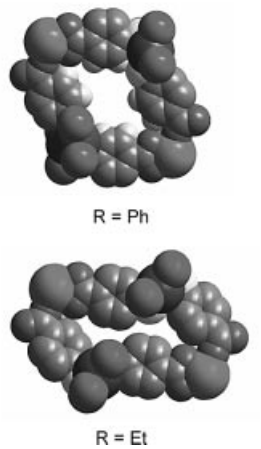


**4931** **W. Shi, X.-Y. Chen, N. Xu, H.-B. Song, B. Zhao, P. Cheng,* D.-Z. Liao, S.-P. Yan**

Synthesis, Crystal Structures, and Magnetic Properties of 2D Manganese(II) and 1D Gadolinium(III) Coordination Polymers with 1*H*-1,2,3-Triazole-4,5-dicarboxylic Acid

**Keywords:** Manganese / Gadolinium / Coordination polymers / Magnetic properties / N,O ligands

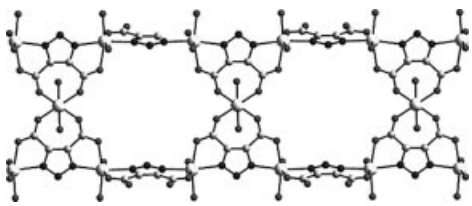

**4938** **P. Agnihotri, S. Patra, E. Suresh, P. Paul,* P. K. Ghosh***

Selective Precipitation of Alkaline Earth Metal Cations with Dipicrylamine Anion: Structure−Selectivity Correlation

**Keywords:** O ligands / Alkaline earth metals / Selectivity / Structure−selectivity correlation

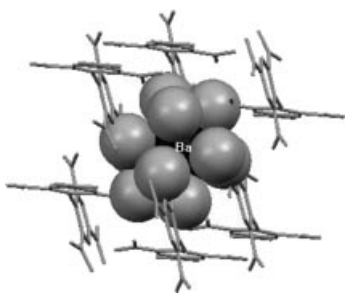


**RSS Feed**

Journal content prior to print publication can be found online on our Early View page at wwweurjic.org. Stay updated on the latest journal content by registering for our free e-mail alerts at http://interscience.wiley.com/alerts.

Keep up with the latest research with our RSS feed, which provides the titles, authors, and the Digital Object Identifiers (DOIs) of Early View articles, including links to the full texts. RSS is an XML-based format for sharing and distributing web content. To receive the RSS feed, just click on the orange feed icon at www.eurjic.org, or visit http://interscience.wiley.com/rss for more information.

DOI: 10.1002/ejic.200600552

# Azide as a Bridging Ligand and Magnetic Coupler in Transition Metal Clusters

**Albert Escuer[a] and Guillem Aromí*[a]**

**Keywords:** Cluster compounds / Azides / Magnetic properties / Single-molecule magnets

The synthesis of transition metal spin-clusters has become an important sub-discipline of coordination chemistry, especially since the discovery of single-molecule magnets (SMMs) in the early nineties. In this context, complexes with high spin-numbers and large anisotropy are particularly desired. The use of the azide ligand to act as a bridge and magnetic coupler within cages of paramagnetic ions has become increasingly common in this field, especially during the last five years, mainly because of the coordination versatility of this ligand, which is capable of bridging several metals in a variety of coordination modes, and its ability to induce ferromagnetic interactions. Several high-spin 3d metal aggregates have been prepared in this manner, a significant number of which behave as SMMs. This review covers the rapid progress made with this relatively recent synthetic approach by describing the structures and summarising the magnetic properties of the systems prepared in this manner. Some of the trends identified could serve as a privileged starting point for the further development of this promising area.
(© Wiley-VCH Verlag GmbH & Co. KGaA, 69451 Weinheim, Germany, 2007)

## Introduction

The synthesis of coordination polynuclear complexes has been stimulated to a large extent by the field of molecular magnetism.[1,2] Most of these species contain paramagnetic 3d ions and are thus susceptible to exhibiting large spin-numbers as a result of intramolecular magnetic exchange. Such high-spin molecules have been perceived as potential building blocks in the construction of molecule-based magnets. In this context, magnetic studies on the cluster $[Mn_{12}O_{12}(OAc)_{16}(H_2O)_4]$, hereafter referred to as $[Mn_{12}OAc]$ (**1**),[3] led to the discovery of single-molecule magnet (SMM) behaviour.[4,5] SMMs are molecular species capable of maintaining the orientation of their magnetisation fixed below a certain *blocking temperature*, $T_b$. This molecular property is caused by an energy barrier to the equilibration of the various spin angular momentum orientations, which is calculated as $S_T^2|D|$ (integer spin) or $(S_T^2 - 1/4)|D|$ (half-integer spin),[6] where $S_T$ is the total spin of the molecule at the ground state and $D$ is the zero-field splitting parameter gauging the axial anisotropy, which has

[a] Departament de Química Inorgànica and Institut de Nanociència i Nanotecnologia, Universitat de Barcelona,
Diagonal 647, 08028 Barcelona, Spain
Fax: +34-93-490-7725
E-mail: albert.escuer@qi.ub.es
guillem.aromi@qi.ub.es

*Albert Escuer was born in Lleida, Spain, in 1956. He completed both his BSc (1978) and PhD (1984) degrees at the Universitat de Barcelona, the latter under the supervision of Prof. J. Ribas. In 1986 he was a postdoc with Prof. Dante Gatteschi at the Universita degli Studi di Firenze (Italy). He became full professor of Inorganic Chemistry in 2003 and he is the current director of the Inorganic Chemistry Department of the Universitat de Barcelona. His research interests concern the study of coordination compounds with small bridging ligands, mainly pseudohalides, with particular interest in magnetochemistry. He is the author of more than 150 papers in international chemistry journals.*

*Dr. Guillem Aromí graduated in Chemistry from the Universitat de Barcelona and obtained his degree of Chemical Engineer at the European Higher Institute of Chemistry in Strasbourg. He received his PhD in 1999 from Indiana University, under the supervision of Prof. George Christou, and worked as a Postdoctoral fellow in the group of Prof. Jan Reedijk (Leiden University) and later in the group of Prof. Richard Winpenny (Manchester University). In 2003, he was awarded a Spanish Fellowship "Ramón y Cajal" to develop his research at the Universitat de Barcelona, where he currently works. His research interests are the development of synthetic strategies for the preparation of novel polynuclear coordination complexes, and the study of their magnetic properties. Dr. Aromí is a member of the International Advisory Board of the European Journal of Inorganic Chemistry.*

 © 2006 Wiley-VCH Verlag GmbH & Co. KGaA, Weinheim 

to be of the Ising type ($D < 0$). The search for new examples of SMMs has undoubtedly intensified efforts aimed at the preparation of more and different cluster coordination complexes,[7] possibly with high spin numbers and enhanced magnetoanisotropy.

The vast majority of these compounds have been prepared by the so-called method of "serendipitous self-assembly".[2] In this methodology, transition metal ions react with small bridging ligands (e.g. $O^{2-}$, $OH^-$, $OMe^-$, $Cl^-$, $N_3^-$) to form stable polynuclear arrays. Growth into infinite networks is blocked by terminal ligands that can either be monodentate (e.g. pyridine, alcohols, MeCN, carboxylic acids) or polydentate (e.g. bipyridine, 1,3-diketonates, picolinic acid). Additional bridging ligands are commonly included in the reaction system, and these, because of their versatility and varied coordination modes, have led to the formation of very diverse and large families of clusters. Among these categories of compounds are those containing carboxylates,[1] pyridones,[8] polyalcohols,[9] amino alcohols,[10] dipyridyl ketones,[11] etc. Of this important number of compounds, a relatively low percentage display spin ground-states larger than 5/2 (the maximum spin that can be achieved with a mononuclear d metal complex). This is, in part, true because antiferromagnetic interactions are more common than ferromagnetic ones.

Azide ligands have been widely employed in coordination chemistry, most of the time as part of 1-, 2- or 3D extended arrays or dinuclear complexes.[12] This research has allowed the discovery of magnetostructural correlations,[13,14] which have established, for example, that end-on $N_3^-$ ligands usually mediate ferromagnetic interactions, except in some recognized situations.[15] Moreover, this ligand has been shown to exhibit a wide variety of coordination modes (see below). For these reasons, the azide ligand constitutes a suitable entry into novel high-spin clusters, although this has been recognized only recently. Indeed, many members of the growing family of azide-bridged discrete polynuclear complexes display ferromagnetic interactions and large spin-numbers, of which an exceptionally large portion behave as SMMs. Interestingly, more than 80% of examples (containing four or more metal centres) have been reported during the last five years. It is thus clear that this category of com-

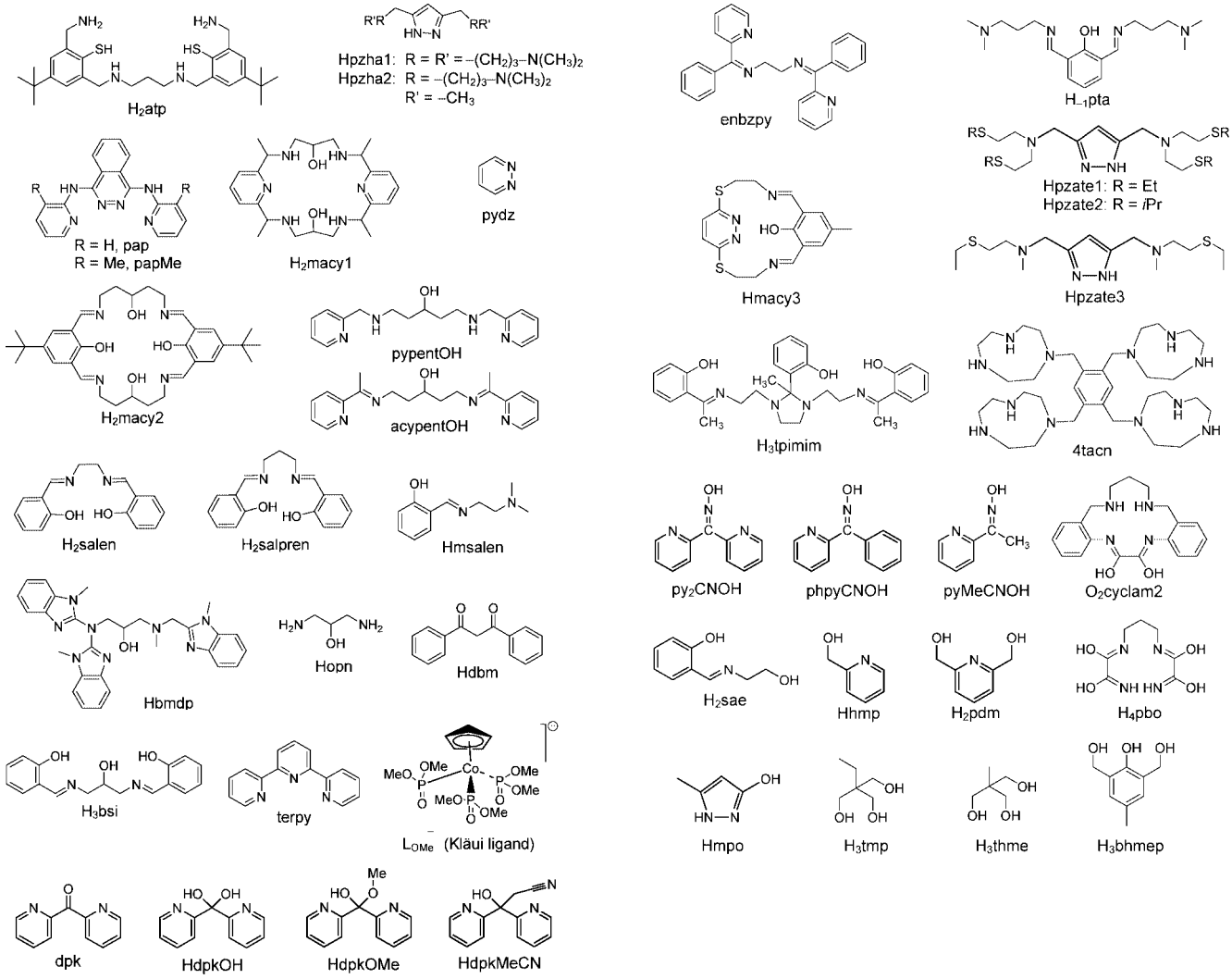


Scheme 1. Ligands discussed in this review.

 © 2006 Wiley-VCH Verlag GmbH & Co. KGaA, Weinheim 

pounds constitutes a large and promising field of open investigation in the search for magnetic clusters and SMMs. The area, however, is developing quite rapidly, and thus constitutes an excellent topic for a microreview, where the achievements made up to now are summarised while possible trends for future developments may be suggested. All the azide-bridged clusters containing four or more metal centres reported to date are gathered together in this account and organized, where possible, by structural types. The structures of the co-ligands of all the compounds reviewed are shown in Scheme 1. Structural descriptions are presented along with summaries and short discussions of their magnetic properties, where possible. A few compounds that are yet to be published have also been included in this compendium with the permission of the authors of their discovery.

## Structural Overview

A survey of the literature reveals that the metals most frequently observed as part of azide-bridged clusters are Ni and Cu, followed at a distance by Mn, Co and Fe. All nuclearities from four to ten have been observed, and there is then a large gap until the next observed metal count of nineteen. This number is then followed by twenty five and the highest nuclearity of thirty two. Of these topologies, the tetranuclear arrangement clearly dominates, making up about 70% of examples. Thus, most examples in the latter category can be analysed according to certain structural patterns, namely cyclic types (metallacrowns), linear arrays, cubanes and defective cubanes. Among all the complexes structurally characterised, about 10% behave as SMMs. Of the compounds reviewed, Cu derivatives are the most numerous, although most of their azide bridges are of the axial–equatorial type and consequently the intramolecular magnetic exchange is severely diminished. These compounds have, nevertheless, been included in this review for completeness. The clusters discussed in this review are listed in Table 1.

### Cyclic $M_4$ Clusters

The seven documented tetranuclear compounds with a cyclic topology (Figures 1 and 2) are $[Ni_4(atp)_2(pydz)_2(N_3)_2](BPh_4)_2$ (**1**),[16] $[Ni_4(pzha1)_2(N_3)_4](BPh_4)_2$ (**2**),[17,18] $[Ni_4(pzha2)_2(N_3)_4](X)_2$ (**3**; X = $ClO_4^-$, $BF_4^-$),[18] $[Cu_4(pap)_2(N_3)_8(MeOH)_2]$ (**4**),[19,20] $[Cu_4(papMe)_2(N_3)_4(H_2O)_2(NO_3)_2](NO_3)_2$ (**5**),[19] $[Mn_2(Hmacy1)(N_3)_2]_2(ClO_4)_2$ (**6**),[21] $[Cu_4(macy2)(N_3)_4]$ (**7**)[22] and $[Ni_4(N_3)_4(opn)_2(Hopn)_2](ClO_4)_2$ (**8**).[23] Of these, complexes **1**–**6** can be described as dimers of dinuclear units linked to each other by azide ligands where the co-ligand is playing the role of a dinucleating scaffold. The $N_3^-$ bridges linking the dimers are all of the end-to-end (EE) type (see Scheme 2), with the exception of **6**, where the end-on (EO) mode is observed. Presumably, EE coordination only occurs when the steric encumbrance prevents the EO mode from occurring, and this can be argued for complexes **1**–**6**. Complexes **7** and **8** are closer to true cycles rather than dimers-of-dimers.

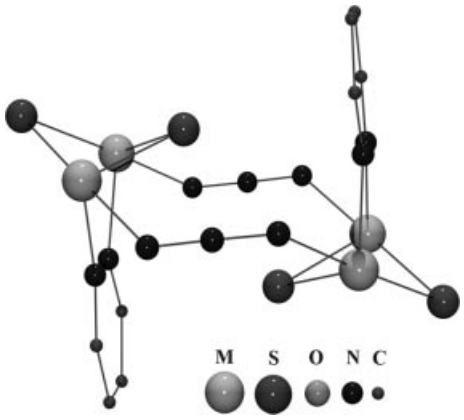


Figure 1. The core of $[Ni_4(atp)_2(pydz)_2(N_3)_2](BPh_4)_2$ (**1**) and the grey scale and size code of atoms used throughout the whole paper.

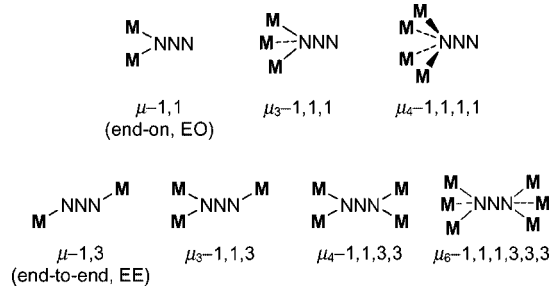


Scheme 2. Coordination modes observed for the azide ligand.

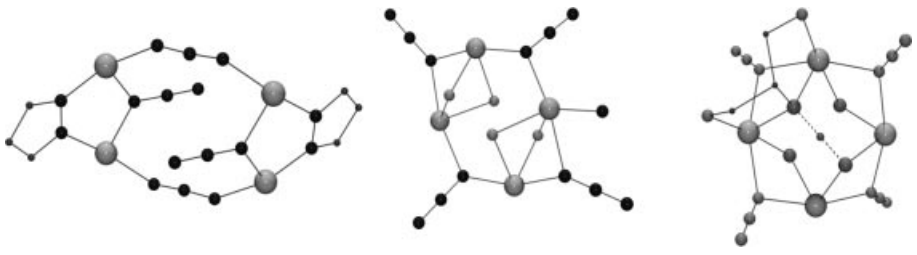

Figure 2. Several representative cores for cyclic $M_4$ azido clusters. Left: the $\mu_{1,3}$-azido-bridged dimer-of-dimers core of $[Ni_4(pzha1)_2(N_3)_4](BPh_4)_2$ (**2**), which is very similar to **3**, **4** and **5**. Centre: $\mu_{1,1}$-azido-bridged dimer-of-dimers core of $[Mn_2(Hmacy1)(N_3)_2]_2(ClO_4)_2$ (**6**). Right: true cyclic core of $[Ni_4(N_3)_4(opn)_2(Hopn)_2](ClO_4)_2$ (**8**) showing one of the H-bonds that helps to stabilize the structure (dashed bonds).

 © 2006 Wiley-VCH Verlag GmbH & Co. KGaA, Weinheim 

Table 1. List of all the clusters discussed in this review, including, in this order, formula, reference, ground spin state *S* (where known) and compound number used in the text.

| Complex | Lit. | *S* | |
|---|---|---|---|
| $[Ni_4(atp)_2(pydz)_2(N_3)_2](BPh_4)_2$ | [16] | 4 | **1** |
| $[Ni_4(pzha1)_2(N_3)_4](BPh_4)_2$ | [17,18] | 0 | **2** |
| $[Ni_4(pzha2)_2(N_3)_4](ClO_4)_2$ | [18] | 4 | **3a** |
| $[Ni_4(pzha2)_2(N_3)_4](BF_4)_2$ | [18] | 0 | **3b** |
| $[Cu_4(pap)_2(N_3)_8(MeOH)_2]$ | [19,20] | 0 | **4** |
| $[Cu_4(papMe)_2(N_3)_4(H_2O)_2(NO_3)_2](NO_3)_2$ | [19] | 0 | **5** |
| $[Mn_2(Hmacy1)(N_3)_2]_2(ClO_4)_2$ | [21] | 0 | **6** |
| $[Cu_4(macy2)(N_3)_4]$ | [22] | 0 | **7** |
| $[Ni_4(N_3)_4(opn)_2(Hopn)_2](ClO_4)_2$ | [23] | 4 | **8** |
| $[Fe_4(N_3)_6(pypentO)_2]$ | [27] | 0 | **9** |
| $[Fe_4(N_3)_4(acpypentO)_2]$ | [28] | 0 | **10** |
| $[Ni_4(pzha2)_2(N_3)_6]$ | [17] | 0 | **11** |
| $[Cu_4(msalen)_2(N_3)_2(H_2O)(MeOH)]$ | [33] | – | **12** |
| $[Cu_4(salen)_2(N_3)_4]$ | [29] | 0 | **13** |
| $[Cu_4(salpren)_2(N_3)_4(DMSO)_2]$ | [34] | – | **14** |
| $[Cu_4(bmdp)_2(OAc)_2(N_3)](ClO_4)_3$ | [35] | 0 | **15** |
| $[Cu_4(O_2cyclam1)_2(tmen)_2(N_3)](ClO_4)_3$ | [36] | – | **16** |
| $[Cu_4(acac)_2(phen)_4(N_3)_4(ClO_4)_2]$ | [37] | 2 | **17** |
| $[Ni_4(N_3)_4(dbm)_4(EtOH)_4]$ | [38,39] | 4 | **18** |
| $[Mn_4O_3(N_3)(OAc)_3(dbm)_3]$ | [40] | 9/2 | **19** |
| $[Ni_4(L_{OMe})_4(N_3)_4]$ | [43] | – | **20** |
| $[Co_4(L_{OMe})_4(N_3)_4]$ | [43] | – | **21** |
| $[Cu_4(bsi)_2(N_3)_2]$ | [44] | 0 | **22** |
| $[Ni_4(dpkOH)_2(dpkOCH_3)_2(N_3)_2(H_2O)_2](ClO_4)_4$ | [45] | 4 | **23** |
| $[Ni_4(dpkOH)_4(N_3)_4]$ | [46] | 4 | **24** |
| $[Ni_4(N_3)_8(enbzpy)_2]$ | [47] | 4 | **25** |
| $[Co_4(dpkOH)_4(N_3)_2(OBz)_2]$ | [48] | "2"[a] | **26** |
| $[Co_4(dpkOH)_4(N_3)_2(AcO)_2]$ | [49] | "2"[a] | **27** |
| $[Co_4(dpkOH)_2(dpkOCH_3)_2(N_3)_2(H_2O)_2](BF_4)_2$ | [50] | "2"[a] | **28** |
| $[Co_4(dpkOH)_2(dpkOMe)_2(N_3)_4]$ | [51] | "2"[a] | **29** |
| $[Mn_4(dpkOH)_2(dpkOMe)_2(N_3)_4]$ | [51] | 0 | **30** |
| $[Cu_4(macy3)_2(OEt)_2(N_3)_4]$ | [52] | 0 | **31** |
| $[Cu_4(pta)_2(N_3)_6](ClO_4)_4$ | [53] | 0 | **32** |
| $[Ni_4(pzate1)_2(N_3)_3(O_2CMe)](ClO_4)_2$ | [54] | 0 | **33** |
| $[Ni_4(pzate1)_2(N_3)_3(O_2CPh)](ClO_4)_2$ | [55] | 0 | **34** |
| $[Ni_4(pzate2)_2(N_3)_3(O_2CPh)](ClO_4)_2$ | [55] | 0 | **35** |
| $[Ni_4(pzate1)_2(N_3)_3(O_2CMe)_2](ClO_4)$ | [54] | 0 | **36** |
| $[Ni_4(pzate2)_2(N_3)_3(O_2CPh)_2](ClO_4)$ | [57] | 0 | **37** |
| $[Ni_4(pzate2)_2(N_3)_3(O_2CAda)_2](ClO_4)$ | [57] | 0 | **38** |
| $[Ni_4(pzate3)_2(N_3)(O_2CAda)_4](ClO_4)$ | [57] | 0 | **39** |
| $[Cu_4(tpimim)_2(N_3)]Cl$ | [58] | 0 | **40** |
| $[Mn_4O(N_3)(O_2Bz)_3(phpyCNO)_4]$ | [59] | 6 | **41** |
| $[Ni_4(SO_4)_2(N_3)_2(SH)_2(pyMeCNOH)_4]$ | [60] | – | **42** |
| $[Cu_4(4tacn)(N_3)_4](PF_6)$ | [61] | – | **43** |
| $[Ni_5(N_3)_4(phpyCNO)_4(O_2CH)_2(MeOH)_4]$ | [62] | 5 | **44a** |
| $[Ni_5(N_3)_4(phpyCNO)_4(O_2CCH_3)_2(MeOH)_4]$ | [62] | 5 | **44b** |
| $[Ni_5(N_3)_4(phpyCNO)_4(phpyCNOH)_4](ClO_4)_2$ | [63] | – | **45** |
| $[Cu_5(terpy)_2(N_3)_{10}]$ | [64] | $3 + 2 \times 1/2$[b] | **46** |
| $[KNi_6(CO_3)(N_3)_6(OAc)_3(dpkMeCN)_3]_2[K_2(H_2O)_2]$ | [65] | 6 | **47** |
| $Na_2[Ni_4Cu_2(dpa)_4(pbo)_2(H_2O)_2](ClO_4)_4$ | [68] | 0 | **48** |
| $[Cu_6(tmen)_6(N_3)_2(C_2O_4)_3(H_2O)_2](ClO_4)_4$ | [68] | 0 | **49** |
| $[Ni_7(AcO)_6(py_2CNO)_6(N_3)_2(H_2O)_2]$ | [70] | 3 | **50** |
| $[Ni_8Na_2(N_3)_{12}(OBz)_2(mpo)_4(Hmpo)_6(EtOAc)_6]$ | [71] | 8 | **51** |
| $[\{Mn_4O(sae)_4(N_3)(MeOH)\}_2(N_3)](N_3)$ | [72] | 0 | **52** |
| $[Ni_9(N_3)_2(AcO)_8(dpkO)_4]$ | [73] | 9 | **53** |
| $[Co_9(N_3)_2(AcO)_8(dpkO)_4]$ | [74] | "9/2"[a] | **54** |
| $[Fe_9(N_3)_2(AcO)_8(dpkO)_4]$ | [75] | 14 | **55** |
| $[Ni_{10}(tmp)_2(N_3)_8(acac)_6(MeOH)_6]$ | [76] | 10 | **56** |
| $[Mn_{10}O_4(N_3)_4(hmp)_{12}](N_3)_2$ | [77] | 22 | **57** |
| $[Mn_{10}O_4(N_3)_4(hmp)_{12}](ClO_4)_2$ | [77] | 22 | **58** |
| $[Mn_{19}O_8(N_3)_8(Hbhmep)_{12}(MeCN)_6]Cl_2$ | [78] | 83/2 | **59** |
| $[Mn_{25}O_{18}(OH)_2(N_3)_{12}(pdm)_6(pdmH)_6](Cl)_2$ | [79] | $51/2 \pm 1$[c] | **60** |
| $[Mn(bpy)_3]_{1.5}[Mn_{32}(thme)_{16}(bpy)_{24}(N_3)_{12}(OAc)_{12}](ClO_4)_{11}$ | [80] | 9 | **61** |
| $[Cu_4(O_2cyclam2)_4Mn_2(N_3)_4]$ | [86] | 0 | **62** |
| $[(\gamma\text{-}SiW_{10}O_{36})_2Mn_4(OH)_4(N_3)_2(H_2O)]^{10-}$ | [89] | 0 | **63** |
| $[(\gamma\text{-}SiW_{10}O_{36})_2Cu_4(N_3)_4]^{12-}$ | [89] | 2 | **64** |
| $[(\gamma\text{-}SiW_{10}O_{36})_2Cu_4(H_2O)_2(N_3)_4]^{12-}$ | [88] | 1 + 1[b] | **65** |
| $[(SiW_8O_{31})_3Cu_9(OH)_3(H_2O)_6(N_3)_4]^{10-}$ | [88] | 0 | **66** |

[a] Resulting from considering a effective spin of $S = 1/2$ for $Co^{II}$. [b] Resulting from uncoupled spins within the molecule. [c] Value subject to uncertainty of $\pm 1$.

 © 2006 Wiley-VCH Verlag GmbH & Co. KGaA, Weinheim 

### *[Ni$_4$(atp)$_2$(pydz)$_2$(N$_3$)$_2$](BPh$_4$)$_2$ (1)*

The core of complex **1** is shown in Figure 1.[16] It is a rectangular array resulting from the bridging by two $\mu_{1,3}$-$N_3^-$ ligands of two dinuclear [Ni$^{II}_2$] units, held together by a hexadentate aminothiophenolate ligand (atp), with the additional support of a pyridazine (pydz) group. This molecule forms from independent $[Ni_2(atp)_2]^+$ dinuclear complexes as a precursor of the higher nuclearity species upon reaction with $N_3^-$. It displays an $S = 4$ spin ground-state, which can be modelled as the result of ferromagnetic interactions through both type of bridges — the thiophenolato-pyridazine and the EE-azido. In the first case, it can be argued that the ferromagnetic coupling occurs because the Ni–S–Ni angle is close to 90°, whereas for the $N_3^-$ bridge, the observed Ni–N–N–N–Ni torsion angle of 76.4° (i.e. larger than 55°) is the cause of the ferromagnetism.[24–26]

### *[Ni$_4$(pzha1)$_2$(N$_3$)$_4$](BPh$_4$)$_2$ (2) and [Ni$_4$(pzha2)$_2$(N$_3$)$_4$](X)$_2$ (X = ClO$_4^-$, 3a; BF$_4^-$, 3b)*

Complexes **2** and **3** are similar to **1**, with each [Ni$^{II}_2$] moiety now supported by one polyaminopyrazolyl group (pzha, Scheme 1) and one $\mu_{1,1}$-$N_3^-$ ligand. Both dinuclear entities are connected by EE azide groups to complete the cyclic structure (Figure 2, left).[17,18] The spin ground-state, however, was found to be either $S = 0$ or $S = 4$. Fits of bulk magnetisation data were conducted by considering constants for the intra- and interdimer couplings. The first one was always found to be ferromagnetic, as expected from the influence of the EO azide bridge. The interactions through the EE azides, however, were found to be of either sign, depending on the value of the Ni–$N_3$–Ni torsion angle. Thus, torsion angles sufficiently close to 180° (as commonly encountered) facilitate antiferromagnetic coupling (as observed for **2** and **3b**, $S = 0$), whereas values close to 90° lead to ferromagnetic interactions (as seen for **3a**, $S = 4$).[24–26]

### *[Cu$_4$(pap)$_2$(N$_3$)$_8$(MeOH)$_2$] (4) and [Cu$_4$(papMe)$_2$(N$_3$)$_4$(H$_2$O)$_2$(NO$_3$)$_2$](NO$_3$)$_2$ (5)*

Complexes **4** and **5** are related[19,20] and their structure is analogous to those of **1**, **2** and **3**. The dinucleating ligand of both is a phthalazine aminopyridyl ligand (pap or papMe) with the Cu pairs also linked by EO $N_3^-$ ligands. The [Cu$^{II}_2$] dimers in **4** and **5** are linked to each other by EE $N_3^-$ groups and the difference between both complexes lies in the terminal ligands, which affect the charge of the complex, and the fact that **4** possesses two additional μ-MeOH molecules. The coupling in both complexes is antiferromagnetic, presumably because of the dominant influence of the phthalazine ligand. However, the magnetic data do not fit the Bleaney–Bowers equation satisfactorily and give unrealistic Weiss terms $\theta$. This was ascribed to the presence of a temperature-dependent $J$ value as a result of the possible variation of the Cu–N–Cu angle with temperature within the [Cu$^{II}_2$] groups. Possible exchange through the EE $N_3^-$ groups was not considered.

### *[Mn$_2$(Hmacy1)(N$_3$)$_2$]$_2$(ClO$_4$)$_2$ (6)*

Complex **6** is an [Mn$^{II}_2$]$_2$ species with each pair of metals assembled by one octadentate macrocycle (Scheme 1) containing amino, pyridyl and alcohol groups.[21] An EO $N_3^-$ bridge serves as an additional support of the intradimer connection (Figure 2, centre). Interestingly, both dimers are bridged here by $N_3^-$ ligands in the end-on form, instead of end-to-end. All Mn$^{II}$ ions in **6** are seven-coordinate, with a pentagonal bipyramidal geometry. Magnetic measurements show the overall coupling within **6** to be antiferromagnetic, thus indicating an $S = 0$ ground state. Although these results were not discussed in terms of the bridging ligands, it is conceivable that the alkoxide bridges cause a strong antiferromagnetic interaction within the dimers, which masks any possible (weaker) ferromagnetic pathway mediated by the $\mu_{1,1}$-$N_3^-$ links.

### *[Cu$_4$(macy2)(N$_3$)$_4$] (7)*

The large macrocyclic ligand in complex **7** (Scheme 1) keeps the tetranuclear cycle together by means of four alkoxide bridges, whereas two EE $N_3^-$ bridges support the link between two pairs of Cu$^{II}$ ions.[22] The coupling is antiferromagnetic due to the alkoxide bridges of the macrocycle.

### *[Ni$_4$(N$_3$)$_4$(opn)$_2$(Hopn)$_2$](ClO$_4$)$_2$ (8)*

Of the series of tetranuclear compounds with a cyclic arrangement, complex **8** is the only one that is square rather than rectangular (Figure 2, right).[23] All Ni$^{II}$ ions in this complex are equivalent and bridged by one EO azide group and the O atom of 1,3-diaminopropan-2-ol (Hopn). In fact, four diamino alcohol molecules share two of the hydroxy protons, which connect the four oxygen atoms pairwise through hydrogen bonds above and below the plane of the molecule. The $\chi_M T$ vs. $T$ curve of **8** ($\chi_M$ is the molar paramagnetic susceptibility) clearly indicates that the Ni···Ni interactions here are ferromagnetic and suggests an $S = 4$ ground state. When first published, complex **8** was the first azide-bridged, ferromagnetically coupled tetranuclear Ni$^{II}$ cluster ever synthesised. More than ten years after its discovery, ultra-low-temperature studies are underway to determine whether this complex behaves as an SMM.

## Linear M$_4$ Clusters

Of the nine reported clusters of this type, all but one can be described as two [M$^{II}_2$] dimers linked together by $N_3^-$ ligands in either an EO or an EE fashion. In all these cases, the dimers are kept together by polydentate ligands and the azide ligands complete the coordination and/or act as bridges between them.

### *[Fe$_4$(N$_3$)$_6$(pypentO)$_2$] (9) and [Fe$_4$(N$_3$)$_4$(acpypentO)$_2$] (10)*

Complexes **9**[27] and **10**[28] are analogous. Both consist of two [Fe$^{II}_2$] units mutually linked by two $\mu_{1,1}$-$N_3^-$ ligands. Each dimeric unit is held together by one pentadentate hydroxy/amine (**9**) or imine (**10**)/pyridyl ligand, supplemented

 © 2006 Wiley-VCH Verlag GmbH & Co. KGaA, Weinheim 

by another EO azide (Figure 3). Their magnetic behaviour is also very similar; in both cases the intradimer coupling is antiferromagnetic and the interdimer interaction ferromagnetic.

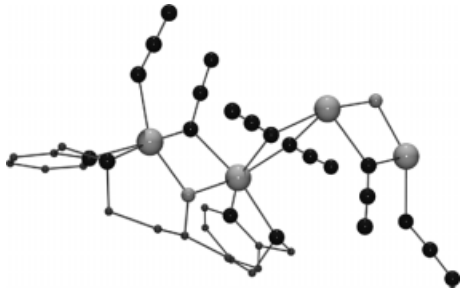

Figure 3. Plot of $[Fe_4(N_3)_6(pypentO)_2]$ (**9**). For clarity, only one of the pypentO ligands is represented.

### *[Ni$_4$(pzha2)$_2$(N$_3$)$_6$] (11)*

Compound **11** is very similar to complexes **2** and **3**, where the pyrazolyl $[Ni^{II}_2]$ units are now shifted so that the azide groups linking the dimers are in the very rare $\mu_{1,1,3}$ coordination mode.[17] As for **2** and **3**, the intradimer interactions are ferromagnetic due to the presence of EO azide ligands, whereas in this case the EE $N_3^-$ groups mediate antiferromagnetic coupling.

### *[Cu$_4$(msalen)$_2$(N$_3$)$_2$(H$_2$O)(MeOH)] (12), [Cu$_4$(salen)$_2$-(N$_3$)$_4$] (13) and [Cu$_4$(salpren)$_2$(N$_3$)$_4$(DMSO)$_2$] (14)*

These three complexes are related. They all consist of two dimers of $Cu^{II}$ formed by polydentate Schiff-base ligands (see Scheme 1) that are connected linearly through a pair of $\mu_{1,1}$-$N_3^-$ groups. Fitting of the magnetic susceptibility data from **13** yielded antiferromagnetic coupling constants for both Cu···Cu bridges.[29] This compound was claimed to be the first to exhibit antiferromagnetic coupling for the Cu–($\mu_{1,1}$-$N_3$)$_2$–Cu bridging mode. It needs to be pointed out, however, that such an interaction has been found several times before for this moiety, where some of the Cu–N bonds do not lie in equatorial positions.[30,31] In such cases the interaction is always very weak since the asymmetric bridge causes very little overlap between the magnetic orbitals of $Cu^{II}$ ($d_{x^2-y^2}$), contrary to the case where the bridge takes place through all basal positions.[32] The antiferromagnetic coupling in this complex was modelled theoretically on an experimental structure by means of density functional calculations,[15] although no explanation for this behaviour was offered. The magnetic analysis of complexes **12**[33] and **14**[34] was not provided.

### *[Cu$_4$(bmdp)$_2$(OAc)$_2$(N$_3$)](ClO$_4$)$_3$ (15) and [Cu$_4$(O$_2$cyclam1)$_2$(tmen)$_2$(N$_3$)](ClO$_4$)$_3$ (16)*

Complexes **15** and **16** are formed by two dimers of asymmetric dinucleating ligands, each featuring a coordinatively unsaturated $Cu^{II}$ that reacts selectively with one azido ligand to form $\mu_{1,3}$-$N_3^-$-linked tetranuclear complexes. In **15**,[35] the large ligand is based on 1,3-diaminopropan-2-ol and three *N*-methylbenzimidazole groups and this system shows weak ferromagnetic coupling, which could not be unambiguously assigned as either intra- or interdimeric coupling. In complex **16** (tmen = *N*,*N*,*N*′*N*′-tetramethylethylenediamine), the dinucleating ligand is a cyclic oxamide ligand. No magnetic properties were reported.[36]

### *[Cu$_4$(acac)$_2$(phen)$_4$(N$_3$)$_4$(ClO$_4$)$_2$] (17)*

This complex is a genuine linear tetranuclear array exclusively bridged by (single or double) $\mu$-$N_3^-$ ligands, with the remaining coordination sites saturated by chelating ligands [acetylacetonate (acac) and phenanthroline (phen)] or perchlorate.[37] Despite occurring through bridges of the axial–equatorial type, the coupling within this molecule is ferromagnetic and the ground state $S = 2$.

## $M_4$ Cubanes

The cubic arrangement is one of the most common structural motifs of tetranuclear coordination clusters {236 hits in the CCDC (version 5.27, August 2006) for the cubic $[M_4O_4]$ feature; M = first row transition metal}. Some of these have been found to act as SMMs (M = Ni, Mn, Fe, Co).[7] In most cases the cube is formed by four symmetrically equivalent metals and four monoatomic donors in a $\mu_3$-bridging mode, which are usually alkoxides, hydroxides or oxides. Because of its coordination versatility (Scheme 2), the $N_3^-$ group has also been found to act as a core ligand within cubane structures on a few occasions.

### *[Ni$_4$(N$_3$)$_4$(dbm)$_4$(EtOH)$_4$] (18)*

Complex **18** features four metals that are equivalent by idealised symmetry (Figure 4, top).[38,39] This compound was the first reported paramagnetic cluster containing $N_3^-$ ligands in the triply bridging mode, although many more examples have been reported since then (see below). These ligands are responsible for the weak ferromagnetic coupling that yields a spin ground state of $S = 4$. The peripheral ligation around the cubic core is completed by one chelating dibenzoylmethine ($dbm^-$) and one monodentate ethanol ligand on each $Ni^{II}$ ion.

### *[Mn$_4$O$_3$(N$_3$)(OAc)$_3$(dbm)$_3$] (19)*

Complex **19**[40] belongs to a group of cubane clusters with general formula $[Mn_4O_3X(OAc)_3(dbm)_3]$ that contain a distorted $[Mn^{III}_3Mn^{IV}XO_3]$ cubane core with a variable ligand X (X = $OH^-$, $OMe^-$, $F^-$, $Cl^-$, $Br^-$, $N_3^-$, $NCO^-$, $AcO^-$, $NO_3^-$, etc.)[40–42] along with a bridging $AcO^-$ that links each $Mn^{III}$ to a $Mn^{IV}$ ion and chelating ligands ($dbm^-$, on each $Mn^{III}$; Figure 4, bottom). Several features of these compounds make them good models of the $[Mn_4]$ complex of Photosystem II. Ferromagnetic coupling between the $Mn^{III}$ centres, together with the antiferromagnetic interaction within the $Mn^{IV}$···$Mn^{III}$ pairs, invariably confer the $S = 9/2$ spin ground state to all these clusters, which make up the second most important family of structurally related SMMs (after the $[Mn_{12}]$ complexes); complex **19** is the member of this family in which X = $N_3^-$. In this series of compounds, the X ligand consistently mediates ferromag-

 © 2006 Wiley-VCH Verlag GmbH & Co. KGaA, Weinheim 

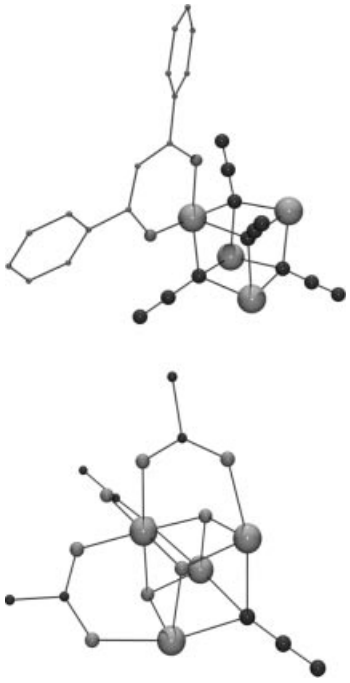

Figure 4. Top: core of $[Ni_4(N_3)_4(dbm)_4(EtOH)_4]$ (**18**), representative of the cubane systems with exclusively end-on azido bridges in the corners. One of the four dbm ligands is also shown. Bottom: core of $[Mn_4O_3(N_3)(OAc)_3(dbm)_3]$ (**19**), an unusual asymmetric cubane with only one azido bridge in one of the corners.

netic coupling between the metals it bridges, therefore replacement of any $\mu_3$-X ligand by azide does not imply the change to ferromagnetism observed for other families of complexes (see below).

### *$[Ni_4(L_{OMe})_4(N_3)_4]$ (20) and $[Co_4(L_{OMe})_4(N_3)_4]$ (21)*

Complexes **20** and **21** were obtained while studying the reactivity of the Kläui tripodal ligand $L_{OMe}$ (Scheme 1) with 3d transition metals[43] in an attempt to isolate adducts different from full-sandwich compounds $[M(L_{OMe})_2]$. Both clusters were obtained in the same manner, namely from the reaction of the labile mononuclear precursor $[M(L_{OMe})(NO_3)(acetone)]$ with $NaN_3$. The molecular structure of both complexes consists of a cubane with four $M^{II}$ metals and four $\mu_3$-$N_3^-$ ligands in the core, the hexacoordination around each metal being completed by a tripodal $L_{OMe}$ ligand. The magnetic properties of these compounds were not studied.

### *$[Cu_4(bsi)_2(N_3)_2]$ (22)*

This complex displays a very unconventional cubane structure with a $[Cu_4N_2O_2]$ core[44] where the N atoms belong to azide groups and the O donors are from alkoxides provided by a pentadentate Schiff-base ligand, which also serves to complete the peripheral ligation around $Cu^{II}$. The particularity of **22** within the category of cubanes is that it has two missing edges since these would be too long to consider them as bonds, which means that the cubane is open and the bridging N and O core atoms are $\mu$ and $\mu_3$, respectively. Magnetic measurements revealed that the coupling within the cubane core is dominated by antiferromagnetic interactions, which leads to a spin ground state of $S = 0$. This was modelled by considering three coupling constants describing single alkoxido, bis-alkoxido, and alkoxido/azide-bridged Cu···Cu pairs. The first two were found to be negative, as expected, whereas the mixed bridge was described as mediating ferromagnetic exchange, consistent with most instances involving EO azide.

### Defective Dicubane $M_4$ Arrangements

This topology has been described for ten complexes; three of $Ni^{II}$, four of $Co^{II}$, one of $Mn^{II}$ and two of $Cu^{II}$. Their formulae are $[Ni_4(dpkOH)_2(dpkOCH_3)_2(N_3)_2(H_2O)_2](ClO_4)_4$ (**23**),[45] $[Ni_4(dpkOH)_4(N_3)_4]$ (**24**),[46] $[Ni_4(N_3)_8(enbzpy)_2]$ (**25**),[47] $[Co_4(dpkOH)_4(N_3)_2(OBz)_2]$ (**26**),[48] $[Co_4(dpkOH)_4(N_3)_2(AcO)_2]$ (**27**),[49] $[Co_4(dpkOH)_2(dpkOCH_3)_2(N_3)_2(H_2O)_2](BF_4)_2$ (**28**),[50] $[Co_4(dpkOH)_2(dpkOMe)_2(N_3)_4]$ (**29**),[51] $[Mn_4(dpkOH)_2(dpkOMe)_2(N_3)_4]$ (**30**),[51] $[Cu_4(macy3)_2(OEt)_2(N_3)_4]$ (**31**)[52] and $[Cu_4(pta)_2(N_3)_6](ClO_4)_4$ (**32**).[53] The two latter complexes are best described as two dimers linked through very long axial bonds. In these, the magnetic behaviour is dominated by the coupling within the dimers, as imposed by the phenolate-based dinucleating ligands (very strongly antiferromagnetic). Seven of the remaining clusters (**23**, **24** and **26**–**30**) have been prepared using dipyridyl ketone (dpk) as reagent and exhibit a common skeleton in which the four metallic atoms are bridged by two end-on $\mu$-azide groups, two $\mu$-oxido and two $\mu_3$-oxido centres (Figure 5, top). The remaining coordination sites are occupied by four dpkOH or dpkOMe ligands and two monodentate terminal groups such as aquo, azido, acetato or benzoato. In contrast, although with the same metal topology, the skeleton of **25** contains only $N_3^-$ bridges (Figure 5, bottom) and is one of the rare examples of clusters with a mainly azide based core. Of the non-copper clusters, only **30** ($Mn^{II}$) shows an overall antiferromag-

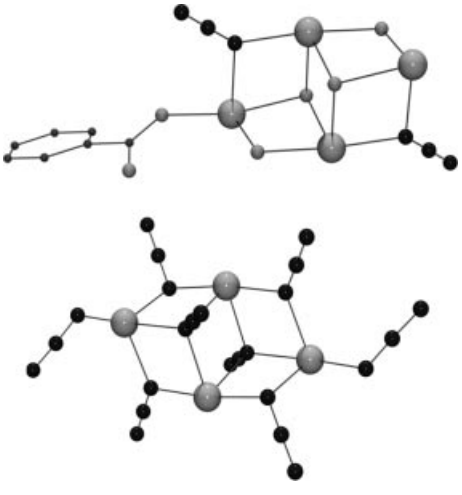

Figure 5. Top: core of compound $[Co_4(dpkOH)_4(N_3)_2(OBz)_2]$ (**26**). This core is common to compounds **23**, **24** and **26**–**30**, which differ in the counteranion or in the monodentate ligand. Bottom: end-on azido core of compound $[Ni_4(N_3)_8(enbzpy)_2]$ (**25**).

 © 2006 Wiley-VCH Verlag GmbH & Co. KGaA, Weinheim 

netic coupling with $S = 0$. The $Ni^{II}$ clusters all display ferromagnetic interactions due the EO-$N_3^-$ bridges and/or Ni–O–Ni angles close to 90°, which leads to an $S = 4$ ground state. This situation is analogous to the case of the $Co^{II}$ compounds. In these clusters, however, the analysis of the magnetic behaviour is complicated by the effect of spin-orbit coupling within the metals. Since at low temperature the $Co^{II}$ ions are better described as local $S_i = 1/2$ centres, the ground state of the $[Co_4]$ clusters can be considered as displaying a total $S = 2$ spin ground state with fairly large $g_{eff}$.

### Genuine $\mu_{1,1,3}$-$N_3^-$ Coordination in an $M_4$ Cluster

The group of complexes with general formula $[Ni_4(pzate\textit{n})_2(N_3)_3(O_2CR)](ClO_4)_2$ (R = Me, pzate1 **33**; R = Ph, pzate1 **34**; R = Ph, pzate2; **35**) were the first examples with azide in the $\mu_{1,1,3}$-bridging mode (Scheme 2).[54,55] They are described as two $[Ni_2]$ dimers of a pyrazole/amine-based ligand that are bridged asymmetrically by azide (seen in three different coordination modes) and carboxylate (Figure 6). Dominant antiferromagnetic interactions were observed for the three complexes, resulting in a diamagnetic ground state. Modelling of the bulk magnetisation data unveiled the presence of a combination of antiferromagnetic and ferromagnetic coupling (two $J$ constants of each type). The Ni···Ni pair bridged by two $\mu_{1,1}$-$N_3^-$ groups was assigned a moderate ferromagnetic constant in the three complexes, whereas weak ferromagnetic coupling was attributed to the pathway formed by a single $\mu_{1,3}$-$N_3^-$ ligand. The strongest antiferromagnetic coupling was ascribed to the link built by one $\mu_{1,1,3}$-azide and one pyrazolate, whereas the remaining single $\mu_{1,1,3}$-azide bridge was associated with the weakly antiferromagnetic constant. The last three assignments were made on the basis of the Ni–NNN–Ni torsion angles and the Ni–N–N angles. Indeed, observation of ferromagnetism within $Ni^{II}$ pairs as mediated by only one EE azide is very uncommon and requires these two angles to be close to 90° and larger than 155°, respectively.[16,56]

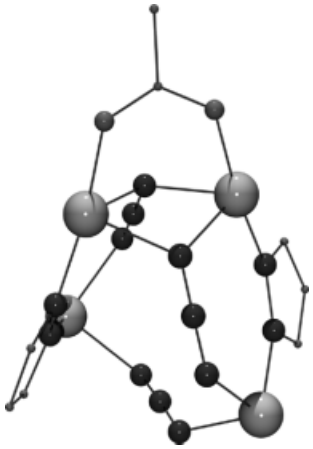

Figure 6. Core of compound $[Ni_4(pzate1)_2(N_3)_3(AcO)](ClO_4)_2$ (**33**), common to compounds **33**–**35**.

### Rare $\mu_{1,1,3,3}$-$N_3^-$ Coordination in an $M_4$ Cluster

The $\mu_{1,1,3,3}$ coordination mode (Scheme 2) was first observed in a group of compounds with formulae $[Ni_4(pzate\textit{n})_2(N_3)_3(O_2CR)_2](ClO_4)$ (pzate1: R = Me **36**, R = Ph **37**; pzate2: R = adamantyl **38**) and $[Ni_4(pzate3)_2(N_3)(O_2CR)_4](ClO_4)$ (R = adamantyl **39**). These complexes are $[Ni^{II}_4]$ rectangles with a central $\mu_4$-$N_3^-$ ligand, a pair of opposite sides occupied by bridging "pzate" ligands (Scheme 1) and the other pair of edges formed by either one $\mu$-$N_3^-$ and one $\mu$-$O_2CR^-$ (**36**, **37** and **38**; Figure 7), or by two bridging carboxylates (**39**).[54,57] Interestingly, the structural differences imposed by the bridging of these edges determine the disposition of the central azide ligand. Thus, in complexes of the former type the central azide caps the $Ni_4$ plane on one of its faces to form a sort of roof with $C_{2v}$ symmetry, whereas in complex **39** the metals form a flattened tetrahedron with the $\mu_4$-$N_3^-$ azide ligand inserted inside; this fragment displays $D_2$ symmetry. The magnetic properties of both types of complexes are marked by the coupling through the central azide, which is strongly antiferromagnetic along the edge spanned by the pyrazolate bridge (because of the EE azide) and ferromagnetic along the other edge (because of the EO mode of the $\mu_4$-$N_3^-$ ligand and reinforced by an additional EO azide in complexes **36**, **37** and **38**). The diagonal exchange is weakly ferromagnetic because of the large Ni–NNN–Ni torsion angle involved. The overall result is an $S = 0$ ground state for all complexes.

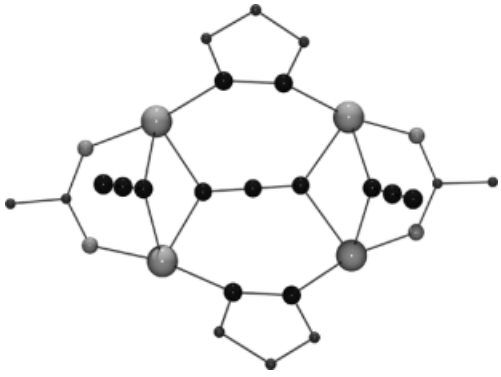

Figure 7. Core of compound $[Ni_4(pzate3)_2(N_3)_3(AcO)_2](ClO_4)$ (**36**), common to compounds **36**–**38**. Compound **39** shows a very similar core with coordination of a second carboxylate instead of the end-on azido ligands.

### *[Cu₄(tpimim)₂(N₃)]Cl (40)*

Complex **40** is the only $Cu^{II}$ species that contains azide in the $\mu_{1,1,3,3}$ mode.[58] As in complexes **36**–**39**, the central $\mu_4$-$N_3^-$ in **40** bridges a rectangle of four metals that now exhibits $C_{2h}$ symmetry. The metals spanned by two of the opposite edges are not supported by any additional ligand, while the other two sides are also spanned by two heptadentate tpimim ligands. Contrary to the Ni compounds with a central $\mu_4$-$N_3^-$ ligand, complex **40** exhibits very weak magnetic coupling. The likely reason for this is that the ligand is bound to $Cu^{II}$ at the apical positions and is thus

 © 2006 Wiley-VCH Verlag GmbH & Co. KGaA, Weinheim 

far from the magnetic orbitals. The interaction between the ions bridged by the tpimim ligand is weakly ferromagnetic, most probably because of the imidazolidine bridge, rather than the azide. The coupling mediated by EE azide pathways is, as usual, antiferromagnetic.

### A Tetrahedral and a Rectangular $M_4$ Cluster

The cluster $[Mn_4O(N_3)(O_2Bz)_3(phpyCNO)_4]$ (**41**)[59] shows a tetrahedral $[Mn^{IV}Mn^{II}_3O]^{8+}$ core (Figure 8) and is a rare example of a mixed-valent tetranuclear manganese complex exhibiting a $2e^-$ difference between oxidation states. There are four types of bridging ligands, including one $N_3^-$ group, which contributes to the ferromagnetic interaction between $Mn^{II}$ centres. The $Mn^{IV}$ ion is, in turn, coupled antiferromagnetically to the other three metals and this leads to a total spin ground state of $S = 6$, as shown by bulk magnetic measurements as well as EPR spectroscopy. The cluster $[Ni_4(SO_4)_2(N_3)_2(SH)_2(pyMeCNOH)_4]$ (**42**)[60] is a rectangle with two edges spanned by EO $\mu$-$N_3^-$ and the other two by $\mu$-$SH^-$ groups. The latter presumably originate from reduction of sulfate ligands. Two such ligands cap each face of the rectangle in an $\eta^2$:$\mu_4$-$SO_4^{2-}$ coordination mode and four pyridyl oxime ligands chelate the four metals to complete their octahedral coordination environment. No magnetic data are yet available for this compound.

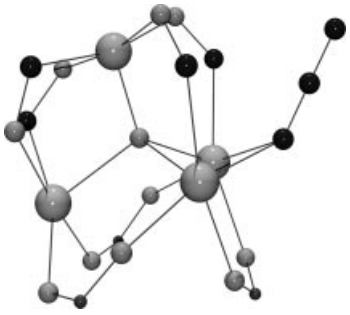

Figure 8. Core of compound $[Mn_4O(N_3)(O_2Bz)_3(phpyCNO)_4]$ (**41**).

### An $Mn_4$ Dimer of Separate Dimers

The compound $[Cu_4(4tacn)(N_3)_4](PF_6)$ (**43**)[61] is formed by a large ligand containing four tacn macrocycles (Scheme 1) that bind four $Cu^{II}$ ions, which are linked as two separate pairs through double $\mu$-$N_3^-$ bridges. As expected, ferromagnetic coupling operates within these pairs, whereas the presence of zero-field splitting and/or inter-pair interactions was modelled with a Curie–Weiss constant.

### Three Azido Bowties in $M_5$ Clusters

Azido-bridged clusters of five metals are much less common than tetranuclear complexes. Three Ni derivatives exhibit this nuclearity, namely $[Ni_5(N_3)_4(phpyCNO)_4(O_2CR)_2(MeOH)_4]$ (R = H **44a**, Me **44b**)[62] and $[Ni_5(N_3)_4(phpyCNO)_4(phpyCNOH)_4](ClO_4)_2$ (**45**).[63] These three compounds can be described as two $Ni^{II}$ triangles with a common vertex (a bowtie) linked by means of oximato and azido bridges in two different arrangements (Figure 9): **44a** and **44b** contain oximato bridges between the central and the peripheral $Ni^{II}$ atoms with $\mu_{1,1}$-azido and carboxylate bridges between the external cations and $\mu_{1,1,1}$ bridges at the centre of each triangle, whereas **45** has four $\mu_{1,1}$ bridges between the central and external $Ni^{II}$ atoms and the centres of the triangles are occupied by oximate $\mu_3$-(NO) bridges. The main difference in the preparation of these compounds is the presence in the reaction mixture of either a coordinating anion (carboxylate) or a non-coordinating one (perchlorate). Preliminary magnetic measurements indicate an $S = 5$ ground state for **44b** and **44b**. Moreover, the frequency dependence of the magnetisation has been observed for **44a**, which constitutes initial evidence that this compound behaves as an SMM. No magnetic data have been collected yet for complex **45**.

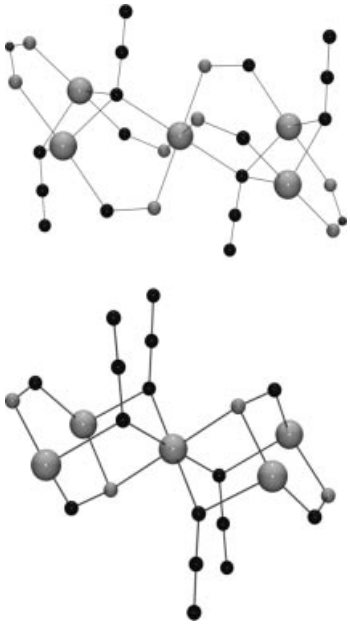

Figure 9. Core of compounds $[Ni_5(N_3)_4(phpyCNO)_4(O_2CH)_2(MeOH)_4]$ (**44**) (top) and $[Ni_5(N_3)_4(phpyCNO)_4(phpyCNO)_4](ClO_4)_2$ (**45**; bottom). It is noticeable that $N_3^-$ and oximate exchange their roles from one compound to the other.

### A Linear $Cu^{II}_5$ Arrangement

The compound $[Cu_5(terpy)_2(N_3)_{10}]$ (**46**; terpy = terpyridine) comprises a linear central trinuclear unit held together by two double $\mu$-$N_3^-$ bridges, with each external copper ion of this unit linked by a single EO azido ligand to a $[Cu(terpy)(N_3)]^+$ moiety.[64] Bulk magnetisation studies reveal that the peripheral $Cu^{II}$ centres essentially do not interact with the central unit, and the latter exhibits weak ferromagnetic coupling.

 © 2006 Wiley-VCH Verlag GmbH & Co. KGaA, Weinheim 

### $M_6$: The Largest Cycle

The only example of an azide-bridged cyclic cluster with six metals (Figure 10) is the complex $[KNi_6(CO_3)(N_3)_6(OAc)_3(dpkMeCN)_3]_2[K_2(H_2O)_2]$ (**47**).[65] It crystallises in the form of dimers of hexanuclear wheels that are connected through weak interactions to $K^+$ ions. Complex **47** is the only known metallacycle that is symmetrically bridged by $N_3^-$, besides complex **8** (see above). In addition to azide, the bridges within the cycle are completed by three *syn*,*syn*-OAc groups, which alternate with the μ-O atoms from three dpkMeCN$^-$ ligands, and by a central $\mu_6$-$CO_3^{2-}$ group. This compound exhibits intramolecular ferromagnetic coupling, as expected, which confers it the spin ground state $S = 6$. Fitting of the experimental data yielded the values $J_1 = 2.9$ and $J_2 = 25.4$ cm$^{-1}$, respectively, for the two types of bridge present (using the convention $H = \Sigma -J_{ij}S_iS_j$ for the exchange coupling). In both cases, the μ-$N_3^-$ bridge determines the ferromagnetic nature of the coupling. The strongest coupling is ascribed to the counter-complementarity effect[66] caused by the simultaneous presence of a μ-OAc$^-$ ligand. The other path involves an alkoxide bridge, which does not have the symmetry to cause this effect. $D$ was found to be positive (10.3 cm$^{-1}$) in this complex, which explains the lack of SMM behaviour.

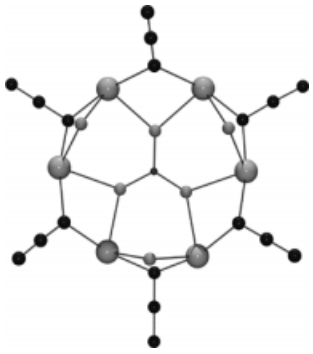

Figure 10. Core of one of the hexanuclear subunits of $[KNi_6(CO_3)(N_3)_6(OAc)_3(dpkMeCN)_3]_2[K_2(H_2O)_2]$ (**47**) showing the unusual $\mu_6$-carbonato anion in the centre of the complex.

### $M_6$: A Dimer of Trinuclear Units and a Trimer of Dinuclear Motifs

The complex $Na_2[Ni_4Cu_2(dpa)_4(pbo)_2(H_2O)_2](ClO_4)_4$ (**48**; dpa = 3,3′-diaminodipropylamine) consists of a hexanuclear cyclic structure in which the azido ligands bind two [NiCuNi] subunits (Figure 11, top). In spite of the heterometallic nature of the cycle, the azido bridges only link nickel atoms. Inside each trinuclear unit there is strong antiferromagnetic coupling via the oxamato ligands ($J_1$ = –101 cm$^{-1}$). The large Ni–$N_3$–Ni torsion angle justifies the low value for the interaction provided by the azido bridge ($J_2$ = –3.2 cm$^{-1}$ in the $H = \Sigma -J_{ij}S_iS_j$ convention), which results in an $S = 0$ ground state.[67]

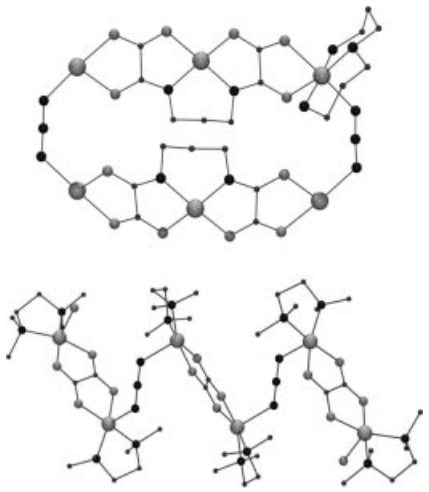

Figure 11. Top: plot of the dimer of trimers $Na_2[Ni_4Cu_2(dpa)_4(pbo)_2(H_2O)_2](ClO_4)_4$ (**48**). The copper atoms show a square-planar coordination whereas the Ni atoms in the corners exhibit an octahedral environment. For clarity, only one complete coordination sphere of the Ni atoms is shown. Bottom: plot of the trimer of dimers $[Cu_6(tmen)_6(N_3)_2(C_2O_4)_3(H_2O)_2](ClO_4)_4$ (**49**).

The hexanuclear complex $[Cu_6(tmen)_6(N_3)_2(C_2O_4)_3(H_2O)_2](ClO_4)_4$ (**49**; tmen = *N*,*N*,*N*′,*N*′-tetramethylethylenediamine)[68] is a rare combination of $[Cu_2(tmen)_2(C_2O_4)]^{2-}$ units connected by two EE $N_3^-$ groups, with both external metallic ions capped by $H_2O$ molecules (Figure 11, bottom). The magnetic behaviour of this linear cluster is governed by the strong antiferromagnetic coupling within the oxalate-bridged pairs, with the coupling through azide remaining negligible. Another hexanuclear cluster results from dimerisation of $[Cu_3]$ units bound to a trinucleating ligand, each of which features one pair of $Cu^{II}$ ions supported by μ-$N_3^-$.[69]

### $M_7$: An Unusual Nuclearity

There is only one compound with a nuclearity of seven containing azido bridges and it has the formula $[Ni_7(AcO)_6(py_2CNO)_6(N_3)_2(H_2O)_2]$ (**50**).[70] The compound consists of two pairs of $Ni^{II}$ triangular arrays fused through one edge and sharing the central cation (Figure 12). The four triangles are supported by four $\mu_3$-(NO) oximate bridges, and additional bridging is provided by two deprotonated oximate groups, six *syn*,*syn* acetate ligands and two EO azides, whereas peripheral coordination is completed by

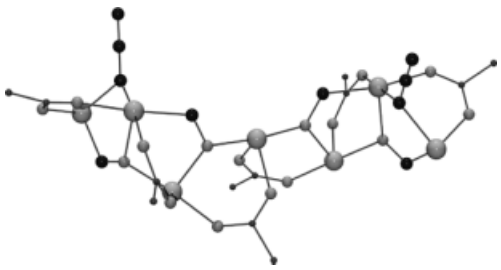

Figure 12. Core of $[Ni_7(AcO)_6(py_2CNO)_6(N_3)_2(H_2O)_2]$ (**50**).

 © 2006 Wiley-VCH Verlag GmbH & Co. KGaA, Weinheim 

two water molecules. Preliminary susceptibility measurements indicate an $S = 3$ ground state, which is greater than the expected value ($S = 1$) for a purely antiferromagnetic cluster and suggests the presence of ferromagnetic interactions between the nickel atoms bridged by the azido bridge; the remaining interactions remain antiferromagnetic.

### $M_8$: A Nickel-Based SMM

The SMM $[Ni_8Na_2(N_3)_{12}(OBz)_2(mpo)_4(Hmpo)_6(EtOAc)_6]$ (**51**; Figure 13)[71] was prepared in light of the benefits of using $N_3^-$ to dramatically increase the spin of metal clusters in a family of $[M_9]$ complexes (see below). Complex **51** features an $[Ni_8(N_3)_{12}]^{4+}$ core in the form of four "defective cubanes" bound to two additional peripheral $Ni^{II}$ ions. In addition, the complex contains two $Na^+$ ions. The bridging within this cluster is completed by two μ-$OBz^-$ groups and four pyrazolinolate ligands ($mpo^-$); terminal ligands saturate the remaining positions of the metals (six Hmpo and six EtOAc molecules). The presence of EO $N_3^-$ groups connecting all $Ni^{II}$ centres confers ferromagnetic character on this cluster and leads to an $S = 8$ spin ground state. Many high-spin clusters do not behave as SMMs because they do not possess magnetic anisotropy ($D \approx 0$) or because they are not of the Ising type ($D > 0$). In this case, however, $D = -0.07$ cm$^{-1}$, and the cluster exhibits slow relaxation of the magnetisation, as manifested by the presence of hysteresis loops at very low temperatures.

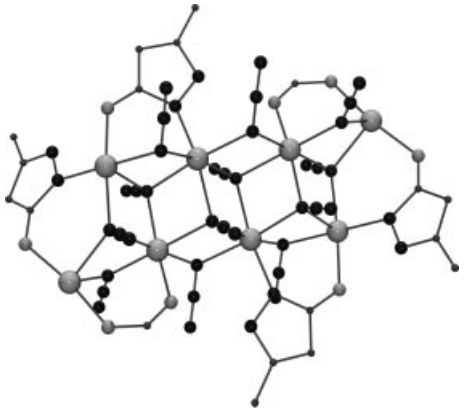

Figure 13. Plot of $[Ni_8Na_2(N_3)_{12}(OBz)_2(mpo)_4(Hmpo)_6(EtOAc)_6]$ (**51**). For clarity, only the bridging ligands are shown. Compound **51** is one of the few complexes in which the inner core contains exclusively end-on azido bridges.

### *[{Mn$_4$O(sae)$_4$(N$_3$)(MeOH)}$_2$(N$_3$)](N$_3$) (52)*

Complex **52** is the other only example of an azide-bridged cluster with a nuclearity of eight. The structure consists of two tetranuclear units linked to one other by a single $\mu_{1,3}$-$N_3^-$ ligand and held together by Schiff-base ligands (sae) and one EO azide.[72] The overall coupling within the cluster was found to be antiferromagnetic and no further discussion was offered.

### $M_9$: Activation of High Spin Numbers by Azide

The nuclearity of nine has been found for three analogous azide-containing complexes obtained with three different metals. These are $[Ni_9(N_3)_2(AcO)_8(dpkO)_4]$ (**53**),[73] $[Co_9(N_3)_2(AcO)_8(dpkO)_4]$ (**54**)[74] and $[Fe_9(N_3)_2(AcO)_8(dpkO)_4]$ (**55**).[75] The core of these compounds can be described as two square pyramids of metals with a common apex, the latter exhibiting (Figure 14) an unusual eight coordination environment ($MO_8$). Each doubly deprotonated $dpkO^{2-}$ ligand links up to five cations. The basal edges of each pyramid are spanned by a crown of four *syn*,*syn* acetate ligands and its square face is capped by one $\mu_4$-$N_3^-$ ligand. Azido ligands acting as a bridge between four cations are very unusual and these three compounds are currently the only examples of the monoatomic $\mu_{1,1,1,1}$ coordination mode for this ligand. The nickel and cobalt compounds are highly symmetric due to the presence of a crystallographic $C_4$ axis, whereas for the iron compound (**55**) the structure is the same but the symmetry is only idealised. In the three compounds, introduction of EO $N_3^-$ signifies the establishment of ferromagnetic interactions within both groups of four basal metals, thereby dramatically increasing

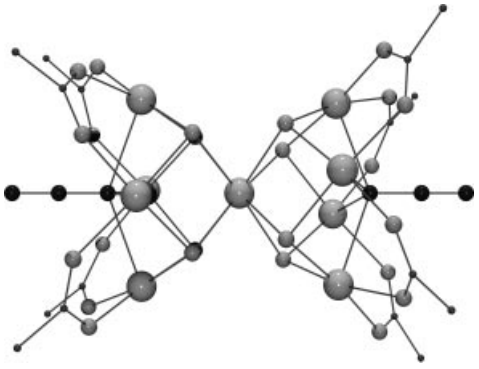

Figure 14. Core of compound $[Ni_9(N_3)_2(AcO)_8(dpkO)_4]$ (**53**). With minor differences besides the metals, this core is the same for **54** and **55**.

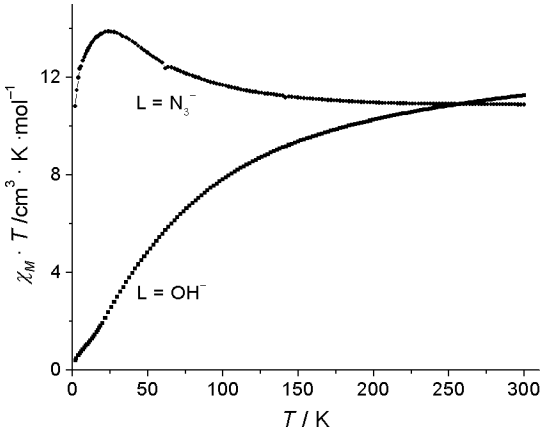


Figure 15. Plots of $\chi_M T$ vs. $T$ for complexes $[Ni_9(L)_2(AcO)_8(dpkO)_4]$ [L = $N_3^-$ (**53**) and the related compound with L = $OH^-$]. These compounds provide a good example of how end-on azido coordination can drastically modify the magnetic properties of clusters with the same skeleton.

 © 2006 Wiley-VCH Verlag GmbH & Co. KGaA, Weinheim 

the spin ground states ($S$ = 9 for **53**, $S$ = 14 for **55** and undetermined for **54** because of the spin-orbit coupling). These values are in sharp contrast to those observed for analogous clusters containing $OH^-$ bridges instead of $N_3^-$, where the coupling is systematically antiferromagnetic and the ground state is the equivalent to that of only the central metal (Figure 15). When studied under an ac magnetic field, complex **55** showed an SMM response, with frequency-dependent $\chi_M''$ signals (out-of-phase magnetic susceptibility) peaking between 2.34 and 2.00 K for frequencies varying between 1000 and 50 Hz. The energy barrier, $\Delta E$, calculated from these signals is 29 $cm^{-1}$.

### High-Spin Decanuclear Clusters

#### *[$Ni_{10}(tmp)_2(N_3)_8(acac)_6(MeOH)_6$] (56)*

This complex is an elegant example of one of the main messages of this review, which is that incorporation of azide within reaction schemes leading to coordination clusters is not only beneficial from a structural point of view but is potentially very convenient for changing the magnetic properties. Compound **56** originates from the reaction between $Ni(acac)_2$, the tripodal ligand $H_3$tmp and $NaN_3$ in methanol.[76] The structure (Figure 16, top) comprises a planar $[Ni_{10}O_{10}(N_3)_8]$ core where the oxygens originate from two $\mu_6$-$tmp^{3-}$ ligands and $acac^-$ groups. The latter appear in two coordination modes (terminal and bridging), whereas the $N_3^-$ ligands are all bridging ($\mu$ or $\mu_3$). Magnetic measurements show this compound to possess an $S$ = 10 spin ground state and large, Ising-type magnetoanisotropy, which converts it into the slowest relaxing Ni SMM known to date. This property is corroborated by the presence of temperature-dependent hysteresis loops of the magnetisation (Figure 17).

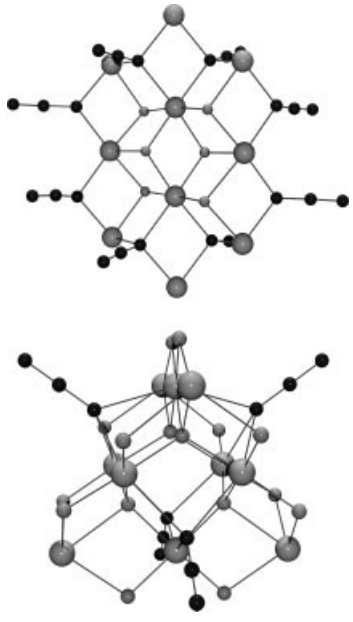

Figure 16. Top: core of $[Ni_{10}(tmp)_2(N_3)_8(acac)_6(MeOH)_6]$ (**56**). In a similar way to **51**, the core is formed by defective cubanes linked by end-on azido bridges. Bottom: core of $[Mn_{10}O_4(N_3)_4(hmp)_{12}](X)_2$ (**57**, **58**) in which the peripheral end-on azido bridges link the sub-sheets of Mn atoms.

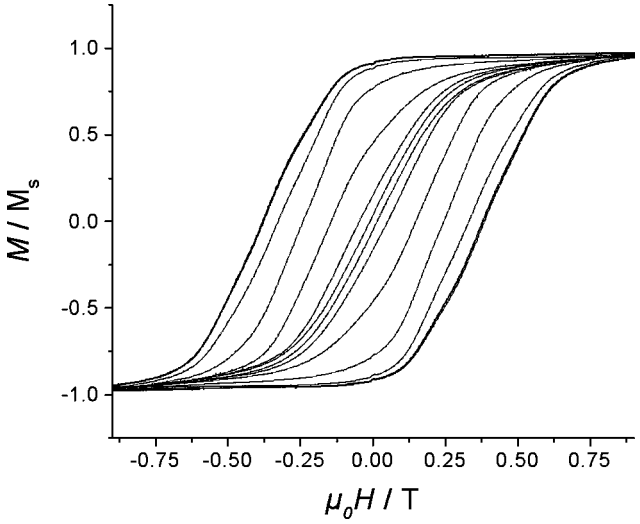


Figure 17. Single crystal magnetisation ($M$) vs. field ($H$) hysteresis loops for complex **56** at a field sweep rate of 0.002 $T s^{-1}$ and temperatures of 0.7, 0.6, 0.5, 0.4, 0.3, 0.2 and 0.04 K (the loops become wider with increasing temperature); the magnetisation is normalised to its saturation value.

#### *[$Mn_{10}O_4(N_3)_4(hmp)_{12}](X)_2$ ($X = N_3^-$ 57, $ClO_4^-$ 58)*

The very recently reported complexes **57** and **58**[77] display high symmetry (crystallographically imposed $T$) and each is formed by a central $[Mn^{III}]$ octahedron bridged by four $\mu_3$-$N_3^-$ ligands and four $\mu_4$-$O^{2-}$ atoms that also bind to four external $Mn^{II}$ ions (Figure 16, bottom). There are twelve $hmp^-$ ligands that ensure the bridging between the $Mn^{III}$ and $Mn^{II}$ centres as well as the peripheral ligation. The spin ground state in both clusters is $S$ = 22, the maximum possible, thanks to the ferromagnetic interaction induced by the azide ligands and by the $Mn^{III}$–O–$Mn^{II}$ connections with very acute angles. Given the high symmetry of the cluster, the total $D$ value is practically zero and therefore these compounds do not show SMM behaviour despite displaying one of the highest spin values ever observed for a molecular system.

### $M_{19}$: The Highest Ground Spin State ($S$ = 83/2)

The use of azide in combination with an oxide source and the polyalcohol $H_3$bhmep (Scheme 1) in a reaction with $MnCl_2$ led to the formation of the nonadecanuclear cluster $[Mn_{19}O_8(N_3)_8(Hbhmep)_{12}(MeCN)_6]Cl_2$ (**59**, Figure 18).[78] The presence of azide leads again to the maximum possible spin multiplicity for the cluster, leading to the highest molecular spin ground state ever observed ($S$ = 83/2). The small overall magnetic anisotropy, however, is the reason why hysteresis of the magnetisation is only observed below 0.5 K. Whether this behaviour at low temperature is ascribed to the SMM nature of **59** or is due to other reasons remains an open question.

 © 2006 Wiley-VCH Verlag GmbH & Co. KGaA, Weinheim 

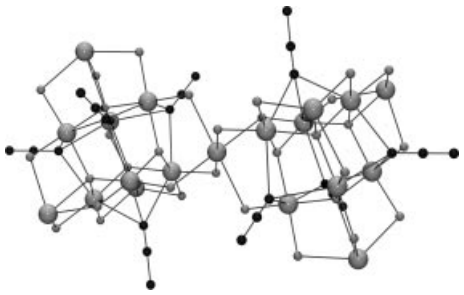

Figure 18. Core of $[Mn_{19}O_8(N_3)_8(Hbhmep)_{12}(MeCN)_6]Cl_2$ (**59**).

### The $M_{25}$ Cluster $[Mn_{25}O_{18}(OH)_2(N_3)_{12}(pdm)_6(pdmH)_6](Cl)_2$ (60)

Complex **60** is the second highest nuclearity cluster constructed to date with the help of azide ligands (Figure 19).[79] The composition of the metal ions is $6\,Mn^{II}$, $18\,Mn^{III}$ and $Mn^{IV}$. Of the twelve $N_3^-$ ligands, six are terminal and six bridge two metals each. The structure is held together by $\mu_4$-$O^{2-}$, $\mu_3$-$O^{2-}$ and $\mu_3$-$OH^-$ ions, with the help of Hpdm or $pdm^-$ ligands. The total spin of the cluster is postulated to be $51/2 \pm 1$, presumably as a result of a combination of ferro- and antiferromagnetic interactions. The SMM behaviour of **60** was proven through micro-squid measurements, which revealed the presence of low-temperature hysteresis loops of the magnetisation.

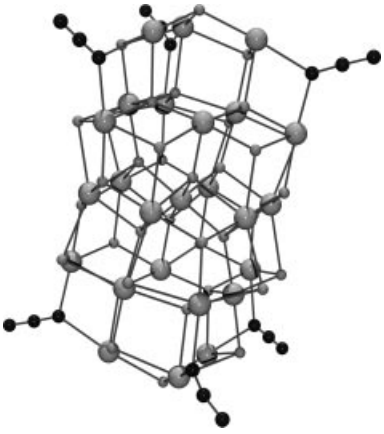

Figure 19. Core of $[Mn_{25}O_{18}(OH)_2(N_3)_{12}(pdm)_6(pdmH)_6](Cl)_2$ (**60**).

### $Mn_{32}$: A Truncated Cube

The largest manganese cluster containing bridging azides is $[Mn(bpy)_3]_{1.5}[Mn_{32}(thme)_{16}(bpy)_{24}(N_3)_{12}(OAc)_{12}](ClO_4)_{11}$ (**61**).[80] This spectacular cluster is made up of eight tetranuclear moieties, each cemented by the oxygen atoms of six tripodal $thme^{3-}$ ligands (Figure 20). These $[Mn_4]$ "stars" are located at the vertices of a cube and connected to each other through acetate and EO azide bridges. Chelating bpy helps to complete the coordination. A combination of weak ferro- and antiferromagnetic interactions leads to a spin ground state of close to 9 (or 10) with many low lying excited states, which precludes an accurate determination and characterisation of the spin ground state.

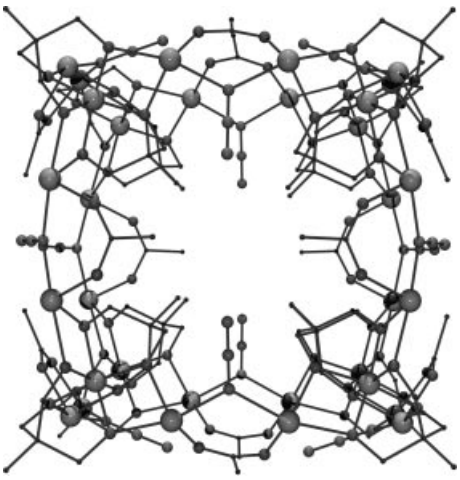

Figure 20. Core of $[Mn(bpy)_3]_{1.5}[Mn_{32}(thme)_{16}(bpy)_{24}(N_3)_{12}(OAc)_{12}](ClO_4)_{11}$ (**61**).

### Clusters with Heterometallic Azide Bridges

Compared with the plethora of homometallic azido systems reported to date, compounds in which the azido ligand acts as a bridge between two different paramagnetic centres (excluding different oxidation states of the same metallic atom) are extremely rare. The first such compound reported was an $[Ni_2Mn]$ triangular system containing $\mu_{1,1}$-azido bridges.[81] A few more examples of low nuclearity systems of this type have been reported recently, such as one [CuNi] dinuclear complex with $\mu_{1,1}$-azido bridges,[82] two trinuclear clusters, [FeCuFe] and [FeNiFe], linked by means of $\mu_{1,3}$-azido bridges[83,84] and two $\mu_{1,3}$ chain-like [NiMn] or [CoMn] alternating compounds.[85]

To the best of our knowledge, there is only one system with a nuclearity higher than four that contains heterometallic azido bridges, namely $[Cu_4(O_2cyclam2)_4Mn_2(N_3)_4]$ (**62**).[86] The asymmetric unit of this compound consists of a [CuMnCu] trinuclear unit in which the manganese atom is bridged to both copper atoms by means of oxamide bridges (Figure 21). Each $Cu^{II}$ ion is embedded within a macrocycle that is part of the oxamide moiety. The remaining coordination sites of the octahedral coordination sphere around manganese are occupied by two azido ligands. One of them acts as a terminal ligand whereas the second azido binds to the axial position of the square-pyramidal copper atom of

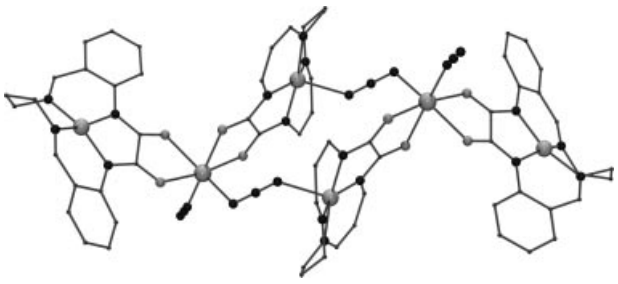

Figure 21. Plot of the structure of compound $[Cu_4(O_2cyclam2)_4Mn_2(N_3)_4]$ (**62**). Mn atoms exhibit hexacoordination whereas Cu atoms are coordinated only to the macrocyclic ligand.

 © 2006 Wiley-VCH Verlag GmbH & Co. KGaA, Weinheim 

a second trinuclear unit. The role of the azido bridges in the magnetism of **62** is marginal since these are coordinated to the axial sites of the copper atoms.

### Azido Clusters of Transition Metals and Polyoxometallates

A relatively new class of molecular magnetic materials is that whose members are prepared by using lacunary polyoxometallates (POMs) in combination with paramagnetic transition metal ions.[87] Recently, very interesting examples have been reported where the azide ligand has been employed as both bridge and magnetic coupler. Thus, the new cluster anions $[(\gamma\text{-}SiW_{10}O_{36})_2Mn_4(OH)_4(N_3)_2(H_2O)]^{10-}$ (**63**), $[(\gamma\text{-}SiW_{10}O_{36})_2Cu_4(N_3)_4]^{12-}$ (**64**), $[(\gamma\text{-}SiW_{10}O_{36})_2Cu_4(H_2O)_2(N_3)_4]^{12-}$ (**65**) and $[(SiW_8O_{31})_3Cu_9(OH)_3(H_2O)_6(N_3)_4]^{10-}$ (**66**) have been prepared,[88,89] and their magnetic properties analysed. The latter is especially remarkable because it features an unprecedented coordination mode for azide, namely $\mu_{1,1,1,3,3,3}$ (Scheme 2).[88]

### General Remarks about the Coordination by Azide

The above sections of this review have shown that the azido ligand is able to act as a bridge within high nuclearity clusters and can do so in a large variety of coordination modes. These are summarised in Scheme 2, and can be divided into two main groups: (i) modes in which the two ends of the ligand act as donors ($\mu_{1,3}$, $\mu_{1,1,3}$, $\mu_{1,1,3,3}$ or $\mu_{1,1,1,3,3,3}$), which need at least two metallic ions placed at more than 5 Å, and (ii) modes where the azido ligand acts as a monoatomic bridge ($\mu_{1,1}$, $\mu_{1,1,1}$ or $\mu_{1,1,1,1}$ modes) linking two or more metallic centres separated by about 3 Å.

EE $N_3^-$ bridges typically lie within the core of the cluster and are usually surrounded by other organic ligands, as can be seen in Figure 22, left. In contrast, EO azido bridges are attached to the metallic centres and point outwards approximately perpendicular to the surface of the cluster (Figure 22, right). In the latter case, the space requirement is minimal.

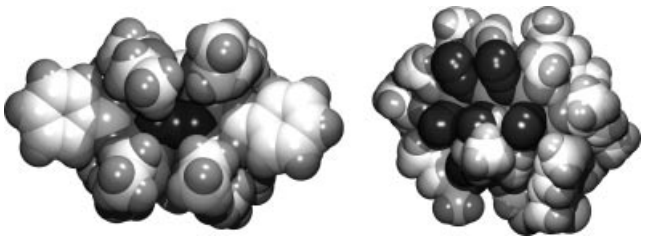

Figure 22. Left: space-filling diagram of complex **37**, emphasising the insertion of the EE $N_3^-$ ligand within the cluster. Right: space-filling diagram of complex **56**, showing the efficiency of EO $N_3^-$ in bridging metals with minimal space requirements.

EE is the most common coordination mode in extended systems such as chains, planes or 3D azido derivatives, whereas alternating $\mu_{1,3}/\mu_{1,1}$ compounds are not rare. However, coordination polymers with exclusively EO azido bridges are very scarce. In contrast, cluster azido chemistry is clearly dominated by EO coordination modes. Because of the similar stability of both coordination modes, the steric hindrance becomes one of the most determining factors favouring monoatomic coordination over EE modes.

Analysis of the structures reviewed above allows other trends regarding coordination by azide to be identified. It has been observed that single EO azido bridges are extremely rare, something that was known already from extended azido-based systems. Therefore, additional bridges always support the presence of $\mu\text{-}N_3^-$ groups. These are often the usual bridges found in cluster coordination chemistry, such as oxido, hydroxido, alkoxido, oximato or carboxylate groups (in addition to $N_3^-$ itself), which accommodate pairs of metals at M···M distances in the neighbourhood of 3 Å (Figure 23). Therefore, the core of most azido clusters reported to date is made up of such combinations of ligands. It must be pointed out, however, that a few prominent examples exist where the metallic core is held together almost exclusively by $N_3^-$ ligands, such as complexes **18** (cubane), **25** (double defective cubane), **46** (linear pentanuclear) and **51** ($Ni_8$).

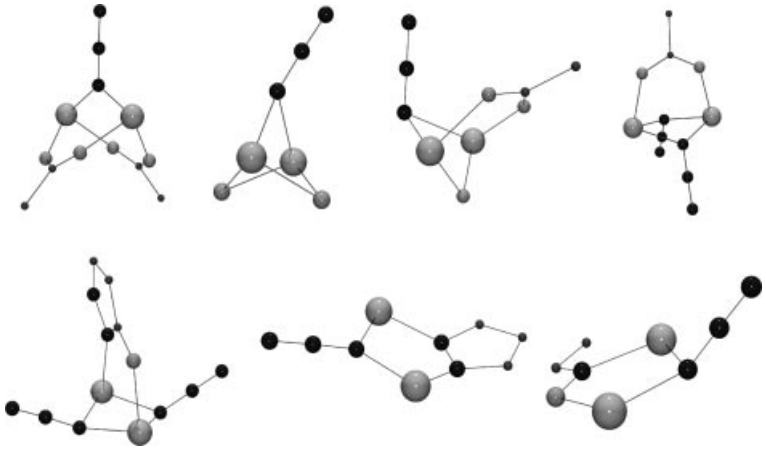

Figure 23. Several of the bridges encountered within the clusters of this review, involving the end-on azido ligand and at least a second bridge. Among the latter, the most common are oxido, hydroxido or carboxylato, but other bridges such as pyrazolato, pyrazolinolato or oximato are also not rare.

 © 2006 Wiley-VCH Verlag GmbH & Co. KGaA, Weinheim 

## Conclusions and Perspectives

The azide ligand has characteristics that render it very attractive for the synthesis of magnetic clusters. From a structural point of view it can participate in multiple bridges, very often in combination with other conventional ligands of cluster coordination chemistry (such as oxides or carboxylates). Magnetically, it usually induces ferromagnetic interactions that have yielded clusters with ground states ranging between $S = 4$ and 83/2. The unusually high number of compounds in this family that show SMM responses is also notable.

If we consider that the vast majority of these compounds have been synthesised in the last five years, we can suppose that the exploitation of this ligand for the synthesis of novel clusters with new and interesting properties relevant to SMM research is only in its infancy and that a very eventful and promising future lies ahead. We hope that this review will constitute an adequate reference for scientists eager to know about the state of this sub-discipline of magnetic cluster synthesis in its early stages. Given the speed at which this sub-area is developing, we are acutely aware that this account will soon become outdated.


[1] G. Aromí, S. M. J. Aubin, M. A. Bolcar, G. Christou, H. J. Eppley, K. Folting, D. N. Hendrickson, J. C. Huffman, R. C. Squire, H. L. Tsai, S. Wang, M. W. Wemple, *Polyhedron* **1998**, *17*, 3005–3020.
[2] R. E. P. Winpenny, *J. Chem. Soc., Dalton Trans.* **2002**, 1–10.
[3] T. Lis, *Acta Crystallogr., Sect. B* **1980**, *36*, 2042–2046.
[4] R. Sessoli, H. L. Tsai, A. R. Schake, S. Y. Wang, J. B. Vincent, K. Folting, D. Gatteschi, G. Christou, D. N. Hendrickson, *J. Am. Chem. Soc.* **1993**, *115*, 1804–1816.
[5] R. Sessoli, D. Gatteschi, A. Caneschi, M. A. Novak, *Nature* **1993**, *365*, 141–143.
[6] G. Christou, *Polyhedron* **2005**, *24*, 2065–2075.
[7] G. Aromí, E. K. Brechin, *Struct. Bonding (Berlin)* **2006**, *122*, 1–67.
[8] R. E. P. Winpenny, *Adv. Inorg. Chem.* **2001**, *52*, 1–111.
[9] L. F. Jones, D. M. Low, M. Helliwell, J. Raftery, D. Collison, G. Aromí, J. Cano, T. Mallah, W. Wernsdorfer, E. K. Brechin, E. J. L. McInnes, *Polyhedron* **2006**, *25*, 325–333.
[10] M. Murugesu, W. Wernsdorfer, K. A. Abboud, G. Christou, *Angew. Chem. Int. Ed.* **2005**, *44*, 892–896.
[11] G. S. Papaefstathiou, S. P. Perlepes, *Comments Inorg. Chem.* **2002**, *23*, 249–274.
[12] J. Ribas, A. Escuer, M. Monfort, R. Vicente, R. Cortés, L. Lezama, T. Rojo, *Coord. Chem. Rev.* **1999**, *195*, 1027–1068.
[13] S. S. Tandon, L. K. Thompson, M. E. Manuel, J. N. Bridson, *Inorg. Chem.* **1994**, *33*, 5555–5570.
[14] T. K. Karmakar, B. K. Ghosh, A. Usman, H. K. Fun, E. Riviere, T. Mallah, G. Aromí, S. K. Chandra, *Inorg. Chem.* **2005**, *44*, 2391–2399.
[15] S. Triki, C. J. Gómez-García, E. Ruiz, J. Sala-Pala, *Inorg. Chem.* **2005**, *44*, 5501–5508.
[16] B. Kersting, G. Steinfeld, D. Siebert, *Chem. Eur. J.* **2001**, *7*, 4253–4258.
[17] G. Leibeling, S. Demeshko, B. Bauer-Siebenlist, F. Meyer, H. Pritzkow, *Eur. J. Inorg. Chem.* **2004**, 2413–2420.
[18] S. Demeshko, G. Leibeling, S. Dechert, F. Meyer, *Dalton Trans.* **2006**, 3458–3465.
[19] C. L. Sheppard, S. S. Tandon, L. K. Thompson, J. N. Bridson, D. O. Miller, M. Handa, F. Lloret, *Inorg. Chim. Acta* **1996**, *250*, 227–239.
[20] S. S. Tandon, L. K. Thompson, D. O. Miller, *J. Chem. Soc., Chem. Commun.* **1995**, 1907–1908.
[21] S. Brooker, V. McKee, *J. Chem. Soc., Chem. Commun.* **1989**, 619–620.
[22] V. McKee, S. S. Tandon, *J. Chem. Soc., Dalton Trans.* **1991**, 221–230.
[23] J. Ribas, M. Monfort, R. Costa, X. Solans, *Inorg. Chem.* **1993**, *32*, 695–699.
[24] C. S. Hong, Y. Do, *Angew. Chem. Int. Ed.* **1999**, *38*, 193–195.
[25] M. Monfort, I. Resino, J. Ribas, H. Stoeckli-Evans, *Angew. Chem. Int. Ed.* **2000**, *39*, 191–193.
[26] P. S. Mukherjee, S. Dalai, E. Zangrando, F. Lloret, N. R. Chaudhuri, *Chem. Commun.* **2001**, 1444–1445.
[27] J. M. Clemente-Juan, C. Mackiewicz, M. Verelst, F. Dahan, A. Bousseksou, Y. Sanakis, J. P. Tuchagues, *Inorg. Chem.* **2002**, *41*, 1478–1491.
[28] A. K. Boudalis, J. M. Clemente-Juan, F. Dahan, J. P. Tuchagues, *Inorg. Chem.* **2004**, *43*, 1574–1586.
[29] S. Koner, S. Saha, K. I. Okamoto, J. P. Tuchagues, *Inorg. Chem.* **2003**, *42*, 4668–4672.
[30] G. De Munno, M. G. Lombardi, M. Julve, F. Lloret, J. Faus, *Inorg. Chim. Acta* **1998**, *282*, 82–89.
[31] R. Cortés, M. K. Urtiaga, L. Lezama, J. I. R. Larramendi, M. I. Arriortúa, T. Rojo, *J. Chem. Soc., Dalton Trans.* **1993**, 3685–3694.
[32] S. Koner, S. Saha, T. Mallah, K. Okamoto, *Inorg. Chem.* **2004**, *43*, 840–842.
[33] Z. L. You, H. L. Zhu, *Z. Anorg. Allg. Chem.* **2006**, *632*, 140–146.
[34] R. Kurtaran, K. C. Emregul, C. Arici, F. Ercan, V. J. Catalano, O. Atakol, *Synth. React. Inorg. Met.-Org. Chem.* **2003**, *33*, 281–296.
[35] J. H. Satcher, M. W. Droege, T. J. R. Weakley, R. T. Taylor, *Inorg. Chem.* **1995**, *34*, 3317–3328.
[36] J. K. Tang, O. Y. Yan, H. B. Zhou, Y. Z. Li, D. Z. Liao, Z. H. Jiang, S. P. Yan, P. Cheng, *Cryst. Growth Des.* **2005**, *5*, 813–819.
[37] A. M. Madalan, M. Noltemeyer, M. Neculai, H. W. Roesky, M. Schmidtmann, A. Muller, Y. Journaux, M. Andruh, *Inorg. Chim. Acta* **2006**, *359*, 459–467.
[38] M. A. Halcrow, J. S. Sun, J. C. Huffman, G. Christou, *Inorg. Chem.* **1995**, *34*, 4167–4177.
[39] M. A. Halcrow, J. C. Huffman, G. Christou, *Angew. Chem. Int. Ed. Engl.* **1995**, *34*, 889–891.
[40] M. W. Wemple, D. M. Adams, K. S. Hagen, K. Folting, D. N. Hendrickson, G. Christou, *J. Chem. Soc., Chem. Commun.* **1995**, 1591–1593.
[41] G. Aromí, S. Bhaduri, P. Artús, K. Folting, G. Christou, *Inorg. Chem.* **2002**, *41*, 805–817.
[42] G. Aromí, M. W. Wemple, S. J. Aubin, K. Folting, D. N. Hendrickson, G. Christou, *J. Am. Chem. Soc.* **1998**, *120*, 5850–5851.
[43] D. Q. Ma, S. Hikichi, M. Akita, Y. Moro-oka, *J. Chem. Soc., Dalton Trans.* **2000**, 1123–1134.
[44] Y. F. Song, C. Massera, O. Roubeau, P. Gamez, A. M. M. Lanfredi, J. Reedijk, *Inorg. Chem.* **2004**, *43*, 6842–6847.
[45] Z. E. Serna, L. Lezama, M. K. Urtiaga, M. I. Arriortúa, M. G. Barandika, R. Cortés, T. Rojo, *Angew. Chem. Int. Ed.* **2000**, *39*, 344–347.
[46] Z. E. Serna, M. G. Barandika, R. Cortés, M. K. Urtiaga, G. E. Barberis, T. Rojo, *J. Chem. Soc., Dalton Trans.* **2000**, 29–34.
[47] T. K. Karmakar, S. K. Chandra, J. Ribas, G. Mostafa, T. H. Lu, B. K. Ghosh, *Chem. Commun.* **2002**, 2364–2365.
[48] G. S. Papaefstathiou, A. Escuer, M. Font-Bardía, S. P. Perlepes, X. Solans, R. Vicente, *Polyhedron* **2002**, *21*, 2027–2032.
[49] S. P. Perlepes, **2006**, unpublished results.
[50] Z. E. Serna, M. K. Urtiaga, M. G. Barandika, R. Cortés, S. Martín, L. Lezama, M. I. Arriortúa, T. Rojo, *Inorg. Chem.* **2001**, *40*, 4550–4555.
[51] G. S. Papaefstathiou, A. Escuer, C. P. Raptopoulou, A. Terzis, S. P. Perlepes, R. Vicente, *Eur. J. Inorg. Chem.* **2001**, 1567–1574.
[52] S. S. Tandon, L. K. Thompson, J. N. Bridson, M. Bubenik, *Inorg. Chem.* **1993**, *32*, 4621–4631.


 © 2006 Wiley-VCH Verlag GmbH & Co. KGaA, Weinheim 

[53] J. Lorösch, H. Paulus, W. Haase, *Inorg. Chim. Acta* **1985**, *106*, 101–108.
[54] F. Meyer, P. Kircher, H. Pritzkow, *Chem. Commun.* **2003**, 774–775.
[55] F. Meyer, S. Demeshko, G. Leibeling, B. Kersting, E. Kaifer, H. Pritzkow, *Chem. Eur. J.* **2005**, *11*, 1518–1526.
[56] C. S. Hong, J. E. Koo, S. K. Son, Y. S. Lee, Y. S. Kim, Y. Do, *Chem. Eur. J.* **2001**, *7*, 4243–4252.
[57] S. Demeshko, G. Leibeling, W. Maringgele, F. Meyer, C. Mennerich, H. H. Klauss, H. Pritzkow, *Inorg. Chem.* **2005**, *44*, 519–528.
[58] P. K. Nanda, G. Aromí, D. Ray, *Chem. Commun.* **2006**, 3181–3183.
[59] C. J. Milios, S. Piligkos, A. R. Bell, R. H. Laye, S. J. Teat, R. Vicente, E. J. L. McInnes, A. Escuer, S. P. Perlepes, R. E. P. Winpenny, *Inorg. Chem. Commun.* **2006**, *9*, 638–641.
[60] S. P. Perlepes, **2006**, unpublished results.
[61] B. Graham, M. T. W. Hearn, P. C. Junk, C. M. Kepert, F. E. Mabbs, B. Moubaraki, K. S. Murray, L. Spiccia, *Inorg. Chem.* **2001**, *40*, 1536–1543.
[62] S. P. Perlepes, A. Escuer, **2006**, unpublished results.
[63] A. Escuer, G. Aromí, S. P. Perlepes, **2006**, unpublished results.
[64] J. D. Woodward, R. V. Backov, K. A. Abboud, D. Dai, H. J. Koo, M. H. Whangbo, M. W. Meisel, D. R. Talham, *Inorg. Chem.* **2005**, *44*, 638–648.
[65] M. L. Tong, M. Monfort, J. M. C. Juan, X. M. Chen, X. H. Bu, M. Ohba, S. Kitagawa, *Chem. Commun.* **2005**, 233–235.
[66] A. Escuer, R. Vicente, F. A. Mautner, M. A. S. Goher, *Inorg. Chem.* **1997**, *36*, 1233–1236.
[67] J. Tercero, C. Díaz, J. Ribas, M. Maestro, J. Mahía, H. Stoeckli-Evans, *Inorg. Chem.* **2003**, *42*, 3366–3373.
[68] R. Vicente, A. Escuer, X. Solans, M. Font-Bardía, *J. Chem. Soc., Dalton Trans.* **1996**, 1835–1838.
[69] K. D. Karlin, Q. F. Gan, A. Farooq, S. C. Liu, J. Zubieta, *Inorg. Chem.* **1990**, *29*, 2549–2551.
[70] S. P. Perlepes, **2006**, unpublished results.
[71] A. Bell, G. Aromí, S. J. Teat, W. Wernsdorfer, R. E. P. Winpenny, *Chem. Commun.* **2005**, 2808–2810.
[72] N. Hoshino, T. Ito, M. Nihei, H. Oshio, *Inorg. Chem. Commun.* **2003**, *6*, 377–380.
[73] G. S. Papaefstathiou, A. Escuer, R. Vicente, M. Font-Bardía, X. Solans, S. P. Perlepes, *Chem. Commun.* **2001**, 2414–2415.
[74] G. S. Papaefstathiou, S. P. Perlepes, A. Escuer, R. Vicente, M. Font-Bardía, X. Solans, *Angew. Chem. Int. Ed.* **2001**, *40*, 884–886.
[75] A. K. Boudalis, B. Donnadieu, V. Nastopoulos, J. Modesto Clemente-Juan, A. Mari, Y. Sanakis, J.-P. Tuchagues, S. P. Perlepes, *Angew. Chem. Int. Ed.* **2004**, *43*, 2266–2270.
[76] G. Aromí, S. Parsons, W. Wernsdorfer, E. K. Brechin, E. J. L. McInnes, *Chem. Commun.* **2005**, 5038–5040.
[77] T. C. Stamatatos, K. A. Abboud, W. Wernsdorfer, G. Christou, *Angew. Chem. Int. Ed.* **2006**, *45*, on line.
[78] A. M. Ako, I. J. Hewitt, V. Mereacre, R. Clérac, W. Wernsdorfer, C. E. Anson, A. K. Powell, *Angew. Chem. Int. Ed.* **2006**, *45*, 4926–4929.
[79] M. Murugesu, M. Habrych, W. Wernsdorfer, K. A. Abboud, G. Christou, *J. Am. Chem. Soc.* **2004**, *126*, 4766–4767.
[80] R. T. W. Scott, S. Parsons, M. Murugesu, W. Wernsdorfer, G. Christou, E. K. Brechin, *Angew. Chem. Int. Ed.* **2005**, *44*, 6540–6543.
[81] T. M. Rajendiran, C. Mathonière, S. Golhen, L. Ouahab, O. Kahn, *Inorg. Chem.* **1998**, *37*, 2651–2654.
[82] J. Suárez-Varela, I. B. Maimoun, E. Colacio, *Dalton Trans.* **2004**, 3938–3940.
[83] J. M. Domínguez-Vera, J. Suárez-Varela, K. Ben Maimoun, E. Colacio, *Eur. J. Inorg. Chem.* **2005**, 1907–1912.
[84] E. Colacio, J. P. Costes, J. M. Domínguez-Vera, I. Ben Maimoun, J. Suárez-Varela, *Chem. Commun.* **2005**, 534–536.
[85] M. L. Hernández, M. G. Barandika, M. K. Urtiaga, R. Cortés, L. Lezama, M. I. Arriortúa, *J. Chem. Soc., Dalton Trans.* **2000**, 79–84.
[86] S. B. Wang, G. M. Yang, R. F. Li, L. C. Li, D. Z. Liao, *Inorg. Chem. Commun.* **2004**, *7*, 1082–1085.
[87] B. Godin, Y. G. Chen, J. Vaissermann, L. Ruhlmann, M. Verdaguer, P. Gouzerh, *Angew. Chem. Int. Ed.* **2005**, *44*, 3072–3075.
[88] P. Mialane, A. Dolbecq, J. Marrot, E. Rivière, F. Secheresse, *Chem. Eur. J.* **2005**, *11*, 1771–1778.
[89] P. Mialane, C. Duboc, J. Marrot, E. Rivière, A. Dolbecq, F. Sécheresse, *Chem. Eur. J.* **2006**, *12*, 1950–1959.

Received: June 14, 2006
Published Online: November 3, 2006

 © 2006 Wiley-VCH Verlag GmbH & Co. KGaA, Weinheim 

DOI: 10.1002/ejic.200600831

# Dimerization of Diruthenium Coordination Compounds via Olefin Metathesis

**Wei-Zhong Chen,[a] John D. Protasiewicz,[b] Amanda J. Shirar,[a] and Tong Ren*[a]**

**Keywords:** Olefin metathesis / Dimerization / Diruthenium compounds / ω-Alkene-α-carboxylate

Diruthenium compounds containing an ω-alkene-α-carboxylate ligand, $Ru_2Cl[D(3,5\text{-}Cl_2Ph)F]_3[O_2C(CH_2)_nCH{=}CH_2]$ [$n$ = 1 (**1a**) and 2 (**1b**)], were prepared from the reactions between $Ru_2Cl[D(3,5\text{-}Cl_2Ph)F]_3(O_2CCH_3)$ [D(3,5-$Cl_2$Ph)F = *N*,*N*′-bis-(3,5-dicholorophenyl)formamidinate] and ω-alkene-α-carboxylic acids. Both compounds **1a** and **1b** undergo olefin cross-metathesis reactions catalyzed by $(Cy_3P)_2Cl_2Ru(=CHPh)$ to afford the dimerized compounds $[Ru_2Cl\{D(3,5\text{-}Cl_2Ph)F\}_3]_2[\mu\text{-}O_2C(CH_2)_nCH{=}CH(CH_2)_nCO_2]$ [$n$ = 1 (**2a**) and 2 (**2b**)]. Molecular structures of compounds **1a**/**1b** and **2a**/**2b** were established by X-ray diffraction studies, which revealed the formation of *trans* product only in the case of shorter tether (**2a**) and a mixture of *cis*-/*trans* isomers in the case of longer tether (**2b**).
(© Wiley-VCH Verlag GmbH & Co. KGaA, 69451 Weinheim, Germany, 2006)

## Introduction

Catalytic olefin metathesis, arguably one of the most important organic reactions discovered in the 20th century,[1] has found broad applications in organic and materials syntheses.[2,3] In comparison, there are only a limited number of applications of catalytic olefin metathesis in the synthesis of coordination and organometallic compounds.[4] Earlier studies by Rudler demonstrated that the W compounds of carbene ligands bearing alkene tails underwent ring-closing metathesis (RCM) with $WOCl_4/Ph_2SiH_2$ as the catalyst.[5] The RCM method was subsequently applied to the high-yield synthesis of Cu-templated [2]catenanes.[6] More recently, both the cross metathesis (CM) and RCM reactions have been utilized to prepare bridged metallocenes and pincer compounds.[7] The most noteworthy are the creative efforts from the laboratory of Gladysz in applying RCM to a variety of metal compounds with phosphane ligands bearing terminal alkene, which resulted in novel compounds including sterically shielded linear Pt–polyyne molecules and gyroscope-like molecules.[4,8]

Our laboratory has been developing methodologies to covalently modify diruthenium compounds at the ligand periphery, and Sonogashira and Suzuki cross couplings were successfully executed on N,N′-bridging ligands containing aryl iodo substituents.[9,10] Reported in this contribution is the synthesis of diruthenium compounds containing ω-alkenyl-α-carboxylate ligand, which subsequently undergoes cross metathesis reactions to afford a unique set of dimeric diruthenium compounds.

## Results and Discussion

Our approach began with the preparation of diruthenium compounds containing ω-alkene-α-carboxylate. $Ru_2[D(3,5\text{-}Cl_2Ph)F]_3(OAc)Cl$ [D(3,5-$Cl_2$Ph)F = *N*,*N*′-bis(3,5-dicholorophenyl)formamidinate][9,10] readily reacted with excess $HO_2C(CH_2)_nCH{=}CH_2$ ($n$ = 1, vinylacetic acid; $n$ = 2, 4-pentenoic acid) under reflux in THF/MeOH to afford the new compounds $Ru_2[D(3,5\text{-}Cl_2Ph)F]_3[\mu\text{-}O_2C(CH_2)_nCH{=}CH_2]Cl$ ($n$ = 1, **1a**; 2, **1b**) as purple crystalline materials, which were purified on silica column to ensure the complete removal of the unidentified by-products that might poison the metathesis catalyst. Although the paramagnetic nature of the compounds **1a/b** ($S$ = 3/2) prevents the recording of NMR spectra, both **1a** and **1b** were analyzed satisfactorily and characterized by single-crystal X-ray diffraction. Structural plots of molecules **1a** and **1b** are shown in Figure 1 and Figure 2, respectively, and the similarity in $Ru_2$ coordination spheres among **1a**, **1b** and $Ru_2[D(3,5\text{-}Cl_2Ph)F]_3(OAc)Cl$[9,10] is clear from the comparison of both the structural plots and key geometric parameters including the averaged Ru–N and Ru–O bond lengths. Interestingly, the lengths of terminal olefin, 1.29(2) Å for C3–C4 in **1a** and 1.356(9) Å for C4–C5 in **1b**, differ significantly, which may be attributed to the positional disorder caused by structural flexibility of terminal olefins. Also noteworthy is the averaged Ru–O distance for **1a/b** (ca. 2.05 Å), which is significantly longer than those of $Ru_2(O_2CR)_4Cl$ (2.02–2.03 Å)[11] due to the *trans* influence of D(3,5-$Cl_2$Ph)F ligand. Obviously, it is a concern whether such structural destabilization may translate into the lability

[a] Departments of Chemistry, Purdue University,
West Lafayette, Indiana 47907, USA
Fax: +1-765-494-0239
E-mail: tren@purdue.edu
[b] Departments of Chemistry, Case Western Reserve University,
Cleveland, Ohio 44106, USA
Supporting information for this article is available on the WWW under http://www.eurjic.org or from the author.

 © 2006 Wiley-VCH Verlag GmbH & Co. KGaA, Weinheim 

of ω-alkene-α-carboxylate during the metathesis reaction (Scheme 1).

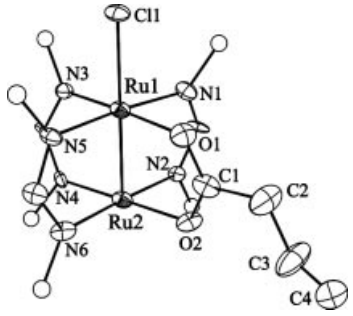


Figure 1. ORTEP plot of molecule **1a** at 40% probability level. All 3,5-$Cl_2$phenyl groups except for the *ipso*-carbon centers (shown as isotropic spheres) were removed for clarity. Selected bond lengths [Å] and angles [°]: Ru1–Ru2 2.321(2), Ru1–Cl1 2.382(3), Ru–N(av.) 2.060(11), Ru–O(av.) 2.051(9), C3–C4 1.29(2), C2–C3–C4 128(2).

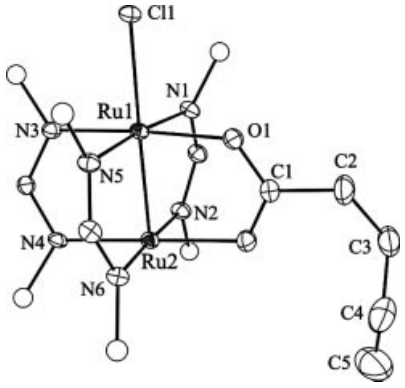


Figure 2. ORTEP plot of molecule **1b** at 40% probability level. All 3,5-$Cl_2$phenyl groups except for the *ipso*-carbon centers (shown as isotropic spheres) were removed for clarity. Selected bond lengths [Å] and angles [°]: Ru1–Ru2 2.3131(4), Ru1–Cl1 2.3828(8), Ru–N(av.) 2.064(4), Ru–O(av.) 2.056(4), C4–C5 1.356(9), C3–C4–C5 120.3(6).

Having incorporated ω-alkene-α-carboxylate into the coordination sphere of $Ru_2$ core, we were in position to investigate the feasibility of metathesis reactions. Compound **1a** was refluxed in $CH_2Cl_2$ in the presence of $(Cy_3P)_2Cl_2Ru(=CHPh)$ and a gradual build-up of a new compound **2a** was noted over a period of 5 d. The dimeric nature of **2a** was confirmed by both the observation of $[\mathbf{2a}\text{-}Cl_2]^+$ in MALDI-TOF-MS (2544) and a preliminary X-ray study, the latter of which revealed the *trans* configuration of the olefin bridge.[12] However, the conversion of **1a** to **2a** was only about 40% despite several additions of fresh catalyst during the course of reaction. In contrast, refluxing of compound **1b** under the same conditions resulted in a complete conversion of **1b** in 2 d to two new compounds that were similar in polarity ($R_f$ = 0.55 and 0.45 in THF/hexanes, 1:5, v/v) and yielded the same $[\mathbf{2b}\text{-}Cl]^+$ peak in ESI-MS (2606). The new compounds are obviously the *cis*/*trans* isomers, and the structural determination of the compound of $R_f$ = 0.45 (Figure 3) revealed a *trans* configuration of the olefin bond derived from the CM reaction. It is interesting to note that the cross metathesis of the coordinated vinyl acetate in

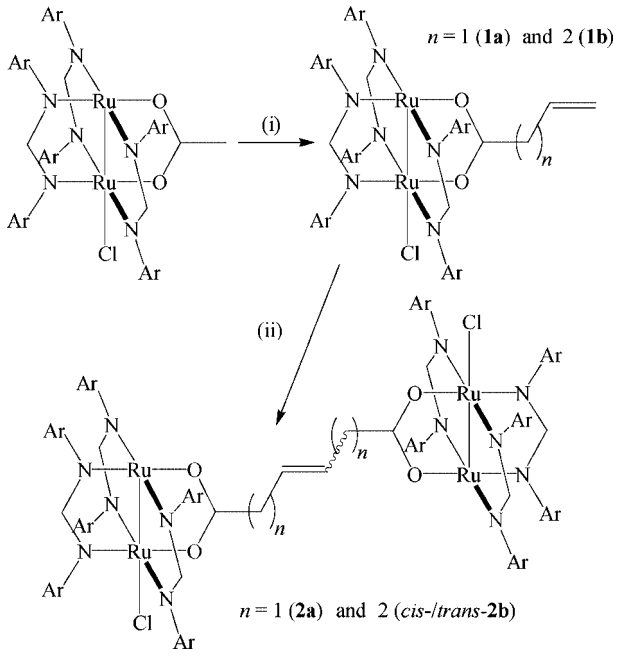


Scheme 1. (i) 10 equiv. $HOOC(CH_2)_nCH=CH_2$, THF/MeOH (1:1), reflux; ii) 5 mol-% $(Cy_3P)_2Cl_2Ru(=CHPh)$, $CH_2Cl_2$, reflux 2–5 d. Ar = 3,5-$Cl_2C_6H_3$.

**1a** was slow and gave the *trans* product only, while the reaction of the coordinated 4-pentenoate proceeded much faster and yielded a mixture of *cis*/*trans* products. Apparently, extension of the tether by a single methylene unit significantly reduces the steric strain imposed by the bulky diruthenium units between the during the CM reaction. Also critical is the use of chromatographically purified starting materials, as compounds **1** purified by recrystallization showed little or no reactivity under the same CM conditions. In comparison, the homo-dimerization reaction of acrylic acid was also classified as "slow" (15 h at 40 °C) with $(Cy_3P)(NHC)Cl_2Ru(=CHPh)$ as the catalyst.[13]

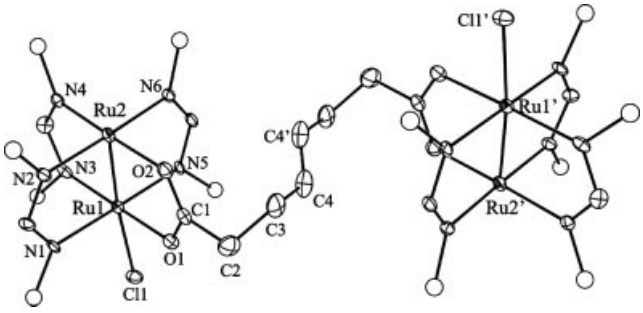


Figure 3. ORTEP plot of molecule *trans*-**2b** at 40% probability level. All 3,5-$Cl_2$phenyl groups except for the *ipso*-carbon centers (shown as isotropic spheres) were removed for clarity. Selected bond lengths [Å] and angles [°]: Ru1–Ru2 2.329(1), Ru1–Cl1 2.382(2), Ru–N(av.) 2.059(7), Ru–O(av.) 2.050(6), C4–C4′ 1.30(2), C3–C4–C4′ 111(1).

In the structure of *trans*-**2b**, there is a crystallographic inversion center that bisects the C4–C4′ bond and relates one half of the molecule to the other half. The structural features of the diruthenium unit in **2b** bear close resem-

 © 2006 Wiley-VCH Verlag GmbH & Co. KGaA, Weinheim 

blance to those of **1a/b**. Also obvious from Figure 3 is the formation of 1,8-dicarboxy-4-octene from the cross metathesis of **1b**.

When two identical metallic centers are tethered covalently, an obvious question is whether two centers are corporative (electronically coupled) or modular (electronically independent). To investigate the effect of dicarboxylate bridges, the redox properties of compounds **1a/b** and **2a/b** were examined with cyclic voltammetric (CV) measurements, and the CVs. of **1a** and **2a** are shown in Figure 4. Similar to the parent compound $Ru_2[D(3,5\text{-}Cl_2Ph)F]_3(OAc)Cl$, compound **1a** underwent a reversible oxidation (**A**) and a quasireversible reduction (**B**) in the potential window shown. The dimeric derivative **2a** displayed a nearly identical CV, except that the peak currents were roughly doubled. Similar comparison can be made between compounds **1b** and **2b**. Clearly, two diruthenium units remain modular in compounds **2**. Further corroborating the modular feature, both compounds **1** and **2** absorb intensely at 520 nm, and the molar extinction coefficients of the latter are about twice of that of the former (see supporting information).

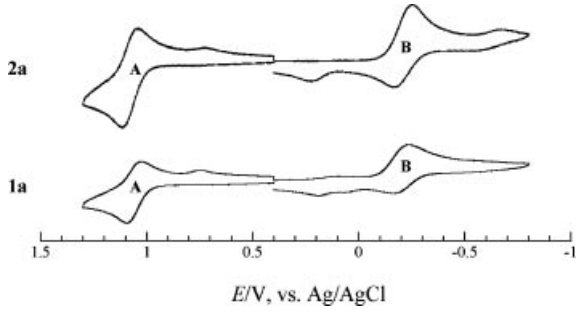


Figure 4. Cyclic voltammograms of **1a** and **2a** recorded in 0.20 M THF solution of $Bu_4NPF_6$ at a scan rate of 0.10 V/s.

## Conclusions

Formation of compounds **2a/b** from **1a/b** are the first examples of cross metathesis of coordinated ω-alkene-α-carboxylate to the best of our knowledge,[2] and represents a novel approach in applying olefin metathesis to inorganic chemistry. Supramolecules consisting of a pair of $Mo_2$ units linked by a dicarboxylate linker have been extensively studied by the laboratory of Cotton,[14] and supramolecules of $Ru_2$ units linked with both di-/tricarboxylates and other ditopic ligands have also been reported.[15] In most cases, the assemblies occur via the coordination to $M_2$ centers by pre-formed di-/tricarboxylate linkers. Clearly, the metathesis method developed here may be utilized as a novel alternative for the preparation of the $M_2$ supramolecules. In addition to the simple dimerization, we also envision the possibilities of macrocyclization through intra- and intermolecular metathesis and ring-opening polymerization based on $Ru_2$-containing scaffolds, which are being explored in our laboratory.

## Experimental Section

**General:** Vinylacetic acid and pentenoic acid were purchased from ACROS, silica gel was purchased from Merck, and $(Cy_3P)_2Cl_2Ru(=CHPh)$ was purchased from Aldrich. $Ru_2[D(3,5\text{-}Cl_2Ph)F]_3(OAc)Cl$ was prepared as reported earlier.[9] Magnetic susceptibility was measured at 294 K with a Johnson Matthey Mark-I Magnetic Susceptibility Balance. Elemental analysis was performed by Atlantic Microlab, Norcross, GA. Visible absorption spectra were recorded with a Cary300 UV/Vis spectrophotometer. Cyclic voltammograms were recorded in 0.2 M $(n\text{Bu})_4NPF_6$ solution (THF, $N_2$-degassed) with a CHI620A voltammetric analyzer with a glassy carbon working electrode (diameter 2 mm), a Pt-wire auxiliary electrode and a Ag/AgCl reference electrode. The concentration of diruthenium species was always 1.0 mM. The ferrocenium/ferrocene couple was observed at 0.582 V (vs. Ag/AgCl) under the experimental conditions.

**Preparation of $Ru_2[D(3,5\text{-}Cl_2Ph)F]_3(\mu\text{-}O_2CCH_2CH{=}CH_2)Cl$ (1a):** A mixture of $Ru_2[D(3,5\text{-}Cl_2Ph)F]_3(OAc)Cl$ (200 mg, 0.15 mmol), vinylacetic acid (10 equiv.), THF (20 mL) and methanol (20 mL) was refluxed in air overnight. The solvent was removed and the residue was washed repeatedly with $H_2O$ and hexanes. Further purification was carried out on a silica column (THF/hexanes, 1:5) to yield a purple crystalline material (170 mg, 81%). UV-Vis: $\lambda_{max}$ ($\varepsilon$, $M^{-1}cm^{-1}$) = 520 (11,200) nm. $C_{43}H_{26}Cl_{13}N_6O_2Ru_2{\cdot}THF$ (1393.84): calcd. C 40.50, H 2.46, N 6.03; found C 40.36, H 2.48, N 6.13. $\chi_{mol}$ (corrected) = $6.40{\cdot}10^{-3}$ emu, $\mu_{eff}$ = 3.90 BM. Cyclic voltammogram ($E_{1/2}$ [V], $\Delta E_p$ [V], $i_{backward}/i_{forward}$): **A**, 1.092, 0.066, 0.676, **B**, –0.208, 0.044, 0.704.

**Preparation of $Ru_2[D(3,5\text{-}Cl_2Ph)F]_3(\mu\text{-}O_2CCH_2CH_2CH{=}CH_2)Cl$ (1b):** Synthesis of **1b** was similar to that of **1a** with vinylacetic acid being replaced by pentenoic acid. Yield 87%. UV-Vis: $\lambda_{max}$ ($\varepsilon$, $M^{-1}cm^{-1}$) = 520 (10,400) nm. $C_{44}H_{28}Cl_{13}N_6O_2Ru_2$ (1335.76): calcd. C 39,56, H 2.11, N 6.29; found C 39.96; H 2.19, N 6.39. $\chi_{mol}$ (corrected) = $6.55{\cdot}10^{-3}$ emu, $\mu_{eff}$ = 3.95 BM. Cyclic voltammogram ($E_{1/2}$ [V], $\Delta E_p$ [V], $i_{backward}/i_{forward}$): **A**, 1.105, 0.065, 0.585; **B**, –0.215, 0.039, 0.742.

**Preparation of $[Ru_2[D(3,5\text{-}Cl_2Ph)F]_3]_2(\mu\text{-}O_2CCH_2CH{=}CH_2CH_2CO_2)Cl_2$ (2a):** $(Cy_3P)_2Cl_2Ru(=CHPh)$ (5 mol-%, 9 mg) was added to **1a** (300 mg) in 80 mL of dry $CH_2Cl_2$ . The resulting solution was refluxed under $N_2$ for 5 d. The reaction progress was monitored by TLC (THF/hexanes, 1:5, same below) and the product **2a** was detected; $R_f$ = 0.45 . The purification of **2a** was performed by a silica column chromatography (THF/hexanes, 1:7 to 1:5). Yield: 120 mg, 40%. MALDI-TOF-MS: $m/z$ = 2544, $[\mathbf{2a}\text{-}Cl_2]^+$. UV-Vis: $\lambda_{max}$ ($\varepsilon$, $M^{-1}cm^{-1}$) = 520 (22,800) nm. $C_{84}H_{56}Cl_{26}N_{12}O_4Ru_4{\cdot}THF$ (2687.51): calcd. C 39.33, H 2.10, N 6.25; found C 39.25, H 1.95, N 6.51. Cyclic voltammogram ($E_{1/2}$ [V], $\Delta E_p$ [V], $i_{backward}/i_{forward}$): **A**, 1.075, 0.061, 0.699; **B**, –0.212, 0.043, 0.715.

**Preparation of $[Ru_2[D(3,5\text{-}Cl_2Ph)F]_3]_2(\mu\text{-}O_2CCH_2CH_2CH{=}CH_2CH_2CH_2CO_2)Cl_2$ (*cis*-2b and *trans*-2b):** $(Cy_3P)_2Cl_2Ru(=CHPh)$ (5 mol-%, 10 mg) was added to **1b** (320 mg) in 80 mL of dry $CH_2Cl_2$. The resultant solution was refluxed under $N_2$ for 2 d. The metathesis products *cis*-**2b**/*trans*-**2b** with $R_f$ of 0.55 and 0.45, respectively, were detected. The compounds *cis*-**2b**/*trans*-**2b** were partially separated by a chromatography (THF/hexanes, 1:7 to 1:5). Combined yield: 191 mg, 60%.

**Data for *cis*-2b:** ESI-MS: $m/z$ = 2606, $[\mathbf{2b}\text{-}Cl]^+$. UV-Vis: $\lambda_{max}$ ($\varepsilon$, $M^{-1}cm^{-1}$) = 520 (23,100) nm. $C_{86}H_{52}Cl_{26}N_{12}O_4Ru_4{\cdot}THF$ (2715.57): calcd. C 39.81, H 2.23, N 6.19; found C 39.89, H 2.11, N 6.39.

 © 2006 Wiley-VCH Verlag GmbH & Co. KGaA, Weinheim 

Cyclic voltammogram ($E_{1/2}$ [V], $\Delta E_p$ [V], $i_{backward}/i_{forward}$): **A**, 1.073, 0.082, 0.536; **B**, –0.223, 0.074, 0.695.

**Data for *trans*-2b:** ESI-MS: $m/z$ = 2606, [**2b**-Cl]$^+$. Vis/NIR: $\lambda_{max}$ ($\varepsilon$, $M^{-1}cm^{-1}$) = 520 (22,400) nm. $C_{86}H_{52}Cl_{26}N_{12}O_4Ru_4$·THF (2715.57): calcd. C 39.81, H 2.23, N 6.19; found C 40.16, H 2.26, N 6.52. Cyclic voltammogram ($E_{1/2}$ [V], $\Delta E_p$ [V], $i_{backward}/i_{forward}$): **A**, 1.070, 0.071, 0.500; **B**, –0.220, 0.061, 0.726.

**X-ray Structural Studies:** Crystal data for **1a**·$C_6H_{14}$: $C_{49}H_{40}Cl_{13}N_6O_2Ru_2$, $M$ = 1407.86, triclinic, space group $P\bar{1}$, $a$ = 16.297(1) Å, $b$ = 16.413(1) Å, $c$ = 23.067(2) Å, $\alpha$ = 78.848(2)°, $\beta$ = 70.724(2)°, $\gamma$ = 74.988(3)°, $V$ = 5585.6(7) Å$^3$, $Z$ = 4, $D_c$ = 1.674 g cm$^{-3}$, $R_1$ = 0.0557 [$I > 2\sigma(I)$], $wR_2$ = 0.2139 (all data), $T$ = 100(2) [K]. **Crystal Data for 1b:** $C_{44}H_{28}Cl_{13}N_6O_2Ru_2$, $M$ = 1335.78, triclinic, space group $P\bar{1}$, $a$ = 11.5633(5) Å, $b$ = 14.8987(6) Å, $c$ = 15.7020(7) Å, $\alpha$ = 104.820(2)°, $\beta$ = 99.830(2)°, $\gamma$ = 94.748(2)°, $V$ = 2553.94(19) Å$^3$, $Z$ = 2, $D_c$ = 1.753 g cm$^{-3}$, $R_1$ = 0.034 [$I > 2\sigma(I)$], $wR_2$ = 0.080 (all data), $T$ = 150(1) K, Data were collected to a maximum $2\theta$ of 55.0°. **Crystal Data for *trans*-2b:** $C_{86}H_{60}Cl_{26}N_{12}O_4Ru_4$, $M$ = 2651.44, triclinic, space group $P\bar{1}$, $a$ = 11.8156(3) Å, $b$ = 17.4357(5) Å, $c$ = 24.9434(7) Å, $\alpha$ = 101.488(2)°, $\beta$ = 92.864(2)°, $\gamma$ = 92.053(2)°, $V$ = 5023.9(2) Å$^3$, $Z$ = 2, $D_c$ = 1.753 g cm$^{-3}$, $R_1$ = 0.0794 [$I > 2\sigma(I)$], $wR_2$ = 0.1938 (all data), $T$ = 100(2) K.

CCDC-616302 (for **1a**), -616285 (for **1b**) and -616303 (for *trans*-**2b**) contain the supplementary crystallographic data for this paper. These data can be obtained free of charge from The Cambridge Crystallographic Data Centre via www.ccdc.cam.ac.uk/data_request/cif.

**Supporting Information** (see also the footnote on the first page of this article): ORTEP plots of **1a**, **1b**, *trans*-**2b**, skeletal plot of *trans*-**2a**, Vis/NIR absorption spectra of compounds **1a** and **2a**, and CVs of compounds **1b** and **2b**.

## Acknowledgments

This work was supported by Purdue University (CHE 0242623/0553564) to T. R. and National Science Foundation (CHE0541766) to Case Western Reserve University for the purchase of an X-ray diffractometer).

[1] Y. Chauvin, *Angew. Chem. Int. Ed.* **2006**, *45*, 3740–3747; R. R. Schrock, *Angew. Chem. Int. Ed.* **2006**, *45*, 3748–3759; R. H. Grubbs, *Angew. Chem. Int. Ed.* **2006**, *45*, 3760–3765.
[2] *Handbook of Metathesis* (Ed.: R. H. Grubbs), Wiley-VCH, Weinheim, Germany, **2003**, vol. 1–3.
[3] D. Astruc, *New J. Chem.* **2005**, *29*, 42–56; N. M. Scott, S. P. Nolan, *Eur. J. Inorg. Chem.* **2005**, 1815–1828; B. Schmidt, *Eur. J. Org. Chem.* **2004**, 1865–1880.
[4] E. B. Bauer, J. A. Gladysz, in: *Handbook of Metathesis* (Ed.: R. H. Grubbs), Wiley-VCH, Weinheim, Germany, **2003**, vol. 2.
[5] C. Alvarez, A. Pacreau, A. Parlier, H. Rudler, *Organometallics* **1987**, *6*, 1057–1064.
[6] B. Mohr, M. Weck, J. P. Sauvage, R. H. Grubbs, *Angew. Chem. Int. Ed. Engl.* **1997**, *36*, 1308–1310.
[7] M. Ogasawara, T. Nagano, T. Hayashi, *J. Am. Chem. Soc.* **2002**, *124*, 9068–9069; J. Kuwabara, D. Takeuchi, K. Osakada, *Organometallics* **2005**, *24*, 2705–2712; K. Wedeking, Z. C. Mu, G. Kehr, J. C. Sierra, C. M. Lichtenfeld, S. Grimme, G. Erker, R. Fröhlich, L. F. Chi, W. C. Wang, D. Y. Zhong, H. Fuchs, *Chem. Eur. J.* **2006**, *12*, 1618–1628; H. P. Dijkstra, A. Chuchuryukin, B. Suijkerbuijk, G. P. M. van Klink, A. M. Mills, A. L. Spek, G. van Koten, *Adv. Synth. Catal.* **2002**, *344*, 771–780.
[8] J. M. Martin-Alvarez, F. Hampel, A. M. Arif, J. A. Gladysz, *Organometallics* **1999**, *18*, 955–957; J. Ruwwe, J. M. Martin-Alvarez, C. R. Horn, E. B. Bauer, S. Szafert, T. Lis, D. Hampel, P. C. Cagle, J. A. Gladysz, *Chem. Eur. J.* **2001**, *7*, 3931–3950; C. R. Horn, J. M. Martin-Alvarez, J. A. Gladysz, *Organometallics* **2002**, *21*, 5386–5393; J. Stahl, J. C. Bohling, E. B. Bauer, T. B. Peters, W. Mohr, J. M. Martin-Alvarez, F. Hampel, J. A. Gladysz, *Angew. Chem. Int. Ed.* **2002**, *41*, 1871–1876; L. de Quadras, F. Hampel, J. A. Gladysz, *Dalton Trans.* **2006**, 2929–2933; A. J. Nawara, T. Shima, F. Hampel, J. A. Gladysz, *J. Am. Chem. Soc.* **2006**, *128*, 4962–4963.
[9] W.-Z. Chen, T. Ren, *Inorg. Chem.* **2006**, *45*, 8156–8164.
[10] G.-L. Xu, T. Ren *Inorg. Chem.* **2006**, *45*, DOI: 10. 1021/ic060734y, W.-Z. Chen, T. Ren, *Organometallics* **2005**, *24*, 2660–2669; W.-Z. Chen, T. Ren, *Organometallics* **2004**, *23*, 3766–3768; G.-L. Xu, T. Ren, *Organometallics* **2005**, *24*, 2564–2566; T. Ren, *Organometallics* **2005**, *24*, 4854–4870.
[11] P. Angaridis, in: *Multiple Bonds between Metal Atoms*, 3rd ed. (Ed.: F. A. Cotton, C. A. Murillo, R. A. Walton), Springer Science and Business Media, Inc., New York, **2005**.
[12] Data collection on a crystal of **2a** revealed a triclinic cell of $a$ = 10.904, $b$ = 12.883, $c$ = 25.466 Å, $\alpha$ = 101.615, $\beta$ = 97.314, $\gamma$ = 106.175°, $V$ = 3299.6 Å$^3$, and the dimer of dimers framework. However, the quality of data set was poor and the least-squares refinement did not yield a structure of publishable figures of merit. See the supporting information for the plot of the preliminary structure.
[13] A. K. Chatterjee, T.-L. Choi, D. P. Sanders, R. H. Grubbs, *J. Am. Chem. Soc.* **2003**, *125*, 11360–11370; T.-L. Choi, A. K. Chatterjee, R. H. Grubbs, *Angew. Chem. Int. Ed.* **2001**, *40*, 1277–1279.
[14] F. A. Cotton, C. Lin, C. A. Murillo, *Acc. Chem. Res.* **2001**, *34*, 759–771; F. A. Cotton, J. P. Donahue, C. A. Murillo, *J. Am. Chem. Soc.* **2003**, *125*, 5436–5450; F. A. Cotton, J. P. Donahue, C. Lin, C. A. Murillo, *Inorg. Chem.* **2001**, *40*, 1234–1244.
[15] P. Angaridis, J. F. Berry, F. A. Cotton, C. A. Murillo, X. Wang, *J. Am. Chem. Soc.* **2003**, *125*, 10327–10334; P. Angaridis, J. F. Berry, F. A. Cotton, P. Lei, C. Lin, C. A. Murillo, D. Villagrán, *Inorg. Chem. Commun.* **2004**, *7*, 9–13; M. C. Barral, T. Gallo, S. Herrero, R. Jiménez-Aparicio, M. R. Torres, F. A. Urbanos, *Inorg. Chem.* **2006**, *45*, 3639–3647; A. Petitjean, F. Puntoriero, S. Campagna, A. Juris, J.-M. Lehn *Eur. J. Inorg. Chem*., DOI: 10.1002/ejic.200600466; J. L. Zuo, F. F. de Biani, A. M. Santos, K. Kohler, F. E. Kuhn, *Eur. J. Inorg. Chem.* **2003**, 449–452; J.-L. Zuo, E. Herdtweck, F. F. d. Biani, A. M. Santos, F. E. Kühn, *New J. Chem.* **2002**, *26*, 889–894.

Received: September 6, 2006
Published Online: October 23, 2006

 © 2006 Wiley-VCH Verlag GmbH & Co. KGaA, Weinheim 

DOI: 10.1002/ejic.200600680

# Crystal Structure, Solid-State NMR Spectroscopic and Photoluminescence Studies of Organic-Inorganic Hybrid Materials $(HL)_6[Ge_6(OH)_6(hedp)_6]\cdot 2(L)\cdot nH_2O$, L = hqn or phen[‡]

**Luís Mafra,[a] Filipe A. Almeida Paz,[a] Fa-Nian Shi,[a] Rute A. Sá Ferreira,[b] Luís D. Carlos,[b] Tito Trindade,[a] Christian Fernandez,[c] Jacek Klinowski,[d] and João Rocha*[a]**

**Keywords:** Germanium / Organic–inorganic hybrid materials / Crystal structure / NMR spectroscopy / Photoluminescence

Two germanium–$hedp^{4-}$ solids with heteroaromatic amines 8-hydroxyquinoline (hqn) and 1,10-phenanthroline (phen), $(HL)_6[Ge_6(OH)_6(hedp)_6]\cdot 2(L)\cdot nH_2O$ (L = hqn or phen), in **I** and **II** respectively, have been prepared and characterised by single-crystal XRD, thermogravimetry, FTIR and UV/Vis spectroscopy. The complex hydrogen-bond networks, particularly in compound **I**, have been studied by advanced high-resolution solid-state NMR spectroscopy that combines homonuclear recoupling techniques (two-dimensional $^1$H-$^1$H DQF and $^1$H-$^1$H RFDR MAS NMR) and combined rotation and multiple-pulse spectroscopy (two-dimensional $^1$H-$^1$H FS-LG, $^1$H-$^{31}$P FS-LG). The fine details of the crystal structure of **I** have been elucidated, mainly those involving the π–π stacking of 8-hydroxyquinoline and the relative orientation of adjacent such molecules. Compound **II** exhibits an emission from the lowest triplet-state energy (π–π* 0-phonon transition) of the aromatic rings at 320 nm (31250 $cm^{-1}$) from 14 K to room temperature. In contrast, the triplet emission of **I** at 530 nm (18868 $cm^{-1}$) is only detected at low temperature, because of thermally activated non-radiative mechanisms. The emission spectra of **I** and **II** display a lower-energy component with a larger life time, which results from the formation of an excimer state that originated from the π–π phenanthroline and hydroxyquinoline interactions, respectively.
(© Wiley-VCH Verlag GmbH & Co. KGaA, 69451 Weinheim, Germany, 2006)

## Introduction

Crystalline inorganic–organic hybrid materials have been the subject of much interest because of their structural diversity, interesting properties and potential applications in areas such as catalysis, magnetism, optics, medicine, electronics, photochemistry, gas storage, and coating films.[1–12] The organic components of these hybrid materials, until recently based mainly on carboxylic acid functional groups, are at present being replaced by phosphonic acid moieties because of their higher chelating versatility and ability to direct interesting structural topologies.[9,13,14] Examples of these organic chelating molecules include *N*-(phosphonomethyl)iminodiacetic acid ($H_4$pmida)[15] and 1-hydroxyethane-1,1-diphosphonic acid ($H_4$HEDP).[16–18]

In general, the $^1$H NMR spectra of solids suffer from homogeneous line broadening as a result of strong proton homonuclear dipolar couplings and the large concentration of protons in the materials. To circumvent this problem and to record high-resolution spectra, fast $^1$H MAS NMR techniques and Combined Rotation and Multiple-Pulse Sequences (CRAMPS) have been used. In organic materials,[19–22] hydrogen-bond networks have been much studied by solid-state $^1$H NMR spectroscopy, for example, by double-quantum filtered (DQF) NMR techniques.[21,23–26] However, advanced $^1$H NMR techniques have been much less applied to the study of complex inorganic-hybrid materials.[27–29]

Here, we wish to report the synthesis, single-crystal structure and photoluminescence properties of two germanium–$hedp^{4-}$ solids with heteroaromatic amines 8-hydroxyquinoline and 1,10-phenanthroline, $(HL)_6[Ge_6(OH)_6(hedp)_6]\cdot 2(L)\cdot nH_2O$ (L = hqn or phen), in **I** and **II**, respectively, which are involved in columnar π–π stacking interactions and exhibit complex hydrogen-bond networks. The materials have been further characterised by elemental analysis, thermogravimetry and FTIR, Raman and UV/Vis spectroscopy. High-resolution solid-state NMR spectroscopy has been used to study the complex hydrogen-bond networks, particularly in compound **I**. The combination of homonuclear recoupling techniques (2D $^1$H-$^1$H DQF,[30,31] 2D $^1$H-$^1$H

[‡] hedp, hqn and phen stand for 1-hydroxyethylidenediphosphonic acid, 8-hydroxyquinoline and 1,10-phenanthroline, respectively.

[a] Department of Chemistry, University of Aveiro, CICECO, 3810-193 Aveiro, Portugal
Fax: +351-234-370-084
E-mail: rocha@dq.ua.pt
[b] Department of Physics, University of Aveiro, CICECO, 3810-193 Aveiro, Portugal
[c] Laboratoire Catalyse et Spectrochimie (CNRS UMR 6506), ENSICAEN and Université de Caen-Basse Normandie, 14050 Caen, France
[d] Department of Chemistry, University of Cambridge, Lensfield Road, Cambridge CB2 1EW, UK

Supporting information for this article is available on the WWW under http://www.eurjic.org or from the author.

 © 2006 Wiley-VCH Verlag GmbH & Co. KGaA, Weinheim 

RFDR MAS NMR[32,33]) and CRAMPS[34] (2D $^1$H-$^1$H FS-LG, $^1$H-$^{31}$P FS-LG) provided a powerful means of characterising these organic–inorganic hybrid materials.

## Results and Discussion

### X-ray Crystallography

The hydrothermal reaction between germanium(IV) oxide, etidronic acid (or 1-hydroxyethylidenediphosphonic acid, $H_4$hedp, $C_2H_8O_7P_2$) and 8-hydroxyquinoline (hqn, $C_9H_7NO$) or 1,10-phenanthroline (phen, $C_{12}H_8N_2$), followed by slow evaporation at ambient temperature (Experimental Section), afforded highly crystalline materials, which were formulated as $(Hhqn)_6[Ge_6(OH)_6(hedp)_6]\cdot 2(hqn)\cdot 33H_2O$ (**I**) and $(Hphen)_6[Ge_6(OH)_6(hedp)_6]\cdot 2(phen)\cdot 20H_2O$ (**II**) on the basis of single-crystal X-ray diffraction (Table 1) in combination with thermogravimetry and solid-state NMR studies.

The main structural feature, common to both compounds, is the presence of the centrosymmetric hexameric anionic $[Ge_6(\mu_2\text{-}OH)_6(C_2H_4O_7P_2)_6]^{6-}$ moiety (Figure 1), which bears some similarity with the fragment present in materials reported recently.[35] This anionic moiety is composed of three crystallographically unique $Ge^{4+}$ centres [Ge(1), Ge(2) and Ge(3), Figure S2 in Supporting Information], each coordinated to two $hedp^{4-}$ residues (through the phosphonate moieties) and to two $\mu_2$-bridging hydroxy groups, and exhibits $\{GeO_6\}$ in a slightly distorted octahedral coordination geometry: for both compounds, all the Ge–O bonds are in the range 1.79 to 1.91 Å (Table S3 in Supporting Information); however, the *cis* and *trans* octahedral angles range from 85.2° to 95.3° and 174.2° to 179.3°, respectively (Table S4 in Supporting Information). The centrosymmetric hexameric anionic unit described here is different in a fundamental way from that previously reported by Seifullina and collaborators.[35] Indeed, while in compounds **I** and **II**, the centre of gravity of this anionic unit is located at an inversion centre (Table 1), which necessarily requires the presence of three crystallographically unique $Ge^{4+}$ centres, for the compounds reported by Seifullina et al., inversion arises as a combination of other symmetry elements, namely a twofold axis and a mirror plane (space group *C*2/m), and therefore only requires two single $Ge^{4+}$ centres.[35] Consequently, the $[Ge_6(\mu_2\text{-}OH)_6(C_2H_4O_7P_2)_6]^{6-}$ moiety present in compounds **I** and **II** is more distorted than its *C*2/*m* counterpart. A possible reason for this decrease in symmetry is the significant number of strong hydrogen bonds present in **I** and **II** that involve the phosphonate groups.

In both compounds, the $hedp^{4-}$ organic residues are chelating bridging ligands, linking neighbouring $Ge^{4+}$ centres through the two phosphonate groups, which coordinate the $Ge^{4+}$ centres in *cis* positions (Figure 1a). The Ge···Ge internuclear distances range from ca. 3.32 to 3.50 Å (Figure 1), which is in good accord with the values reported by Seifullina and collaborators[35] (ca. 3.39–3.50 Å). Because

Table 1. Crystal data and structure refinement information for compounds **I** and **II**.

| | **I** | **I** (after SQUEEZE) | **II** | **II** (after SQUEEZE) |
|---|---|---|---|---|
| Formula | $C_{84}H_{158}Ge_6N_8O_{89}P_{12}$ | – | $C_{108}H_{140}Ge_6N_{16}O_{68}P_{12}$ | – |
| Formula weight | 3511.36 | – | 3557.54 | – |
| Crystal system | Triclinic | – | Monoclinic | – |
| Space group | $P\bar{1}$ | – | $P2_1/n$ | – |
| *a* [Å] | 16.201(3) | – | 15.432(3) | – |
| *b* [Å] | 16.997(3) | – | 27.222(5) | – |
| *c* [Å] | 17.321(4) | – | 17.193(3) | – |
| *α* [°] | 61.09(3) | – | – | – |
| *β* [°] | 66.08(3) | – | 102.94(3) | – |
| *γ* [°] | 74.78(3) | – | – | – |
| Volume [Å$^3$] | 3803.4(13) | – | 7039(2) | – |
| *Z* | 1 | – | 2 | – |
| $D_c$ [g cm$^{-3}$] | 1.533 | – | 1.678 | – |
| $\mu$(Mo-$K_\alpha$) [mm$^{-1}$] | 1.402 | – | 1.507 | – |
| *F*(000) | 1802 | – | 3632 | – |
| Crystal size [mm] | 0.35 × 0.07 × 0.05 | – | 0.21 × 0.10 × 0.07 | – |
| Crystal type | yellow blocks | – | yellow needles | – |
| *θ* range [°] | 3.62 to 24.11 | 3.62 to 27.50 | 3.52 to 25.35 | 3.52 to 25.67 |
| Data completeness | 99.1% | 98.1% | 87.4% | 87.0% |
| Index ranges | $-18 \le h \le 18$ | $-20 \le h \le 21$ | $-18 \le h \le 18$ | $-18 \le h \le 18$ |
| | $-19 \le k \le 19$ | $-20 \le k \le 22$ | $-30 \le k \le 32$ | $-30 \le k \le 33$ |
| | $-19 \le l \le 19$ | $-22 \le l \le 22$ | $-15 \le l \le 20$ | $-15 \le l \le 20$ |
| Reflections collected | 30980 | 37902 | 24076 | 24554 |
| Independent reflections | 11985 ($R_{int}$ = 0.0594) | 17149 ($R_{int}$ = 0.0606) | 11271 ($R_{int}$ = 0.0535) | 11612 ($R_{int}$ = 0.0495) |
| Final *R* indices [$I > 2\sigma(I)$] | $R_1$ = 0.0836 | $R_1$ = 0.0639 | $R_1$ = 0.0930 | $R_1$ = 0.0952 |
| | $wR_2$ = 0.2269 | $wR_2$ = 0.1602 | $wR_2$ = 0.2192 | $wR_2$ = 0.2320 |
| Final *R* indices (all data) | $R_1$ = 0.1314 | $R_1$ = 0.1192 | $R_1$ = 0.1724 | $R_1$ = 0.1554 |
| | $wR_2$ = 0.2672 | $wR_2$ = 0.1774 | $wR_2$ = 0.2661 | $wR_2$ = 0.2564 |
| Largest diff. peak and hole | 1.133 and –1.086 e Å$^{-3}$ | – | 0.579 and –0.396 e Å$^{-3}$ | – |

 © 2006 Wiley-VCH Verlag GmbH & Co. KGaA, Weinheim 

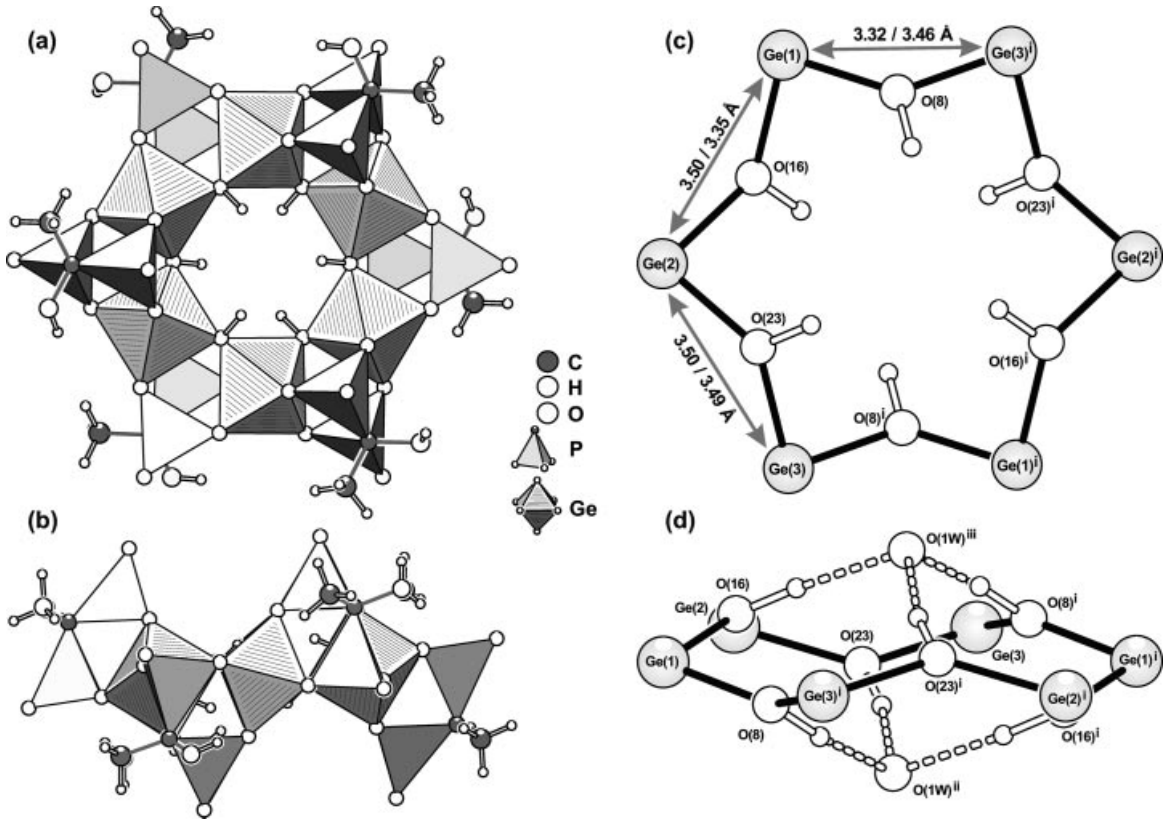


Figure 1. (a) and (b) Polyhedral representation of the hexameric anionic $[Ge_6(\mu_2\text{-}OH)_6(C_2H_4O_7P_2)_6]^{6-}$ moiety viewed from the top and from a lateral perspective. (c) and (d) Ball-and-stick representation of the internal $\{Ge_6(OH)_6\}$ hexagonal ring of the anionic $[Ge_6(OH)_6(C_2H_4O_7P_2)_6]^{6-}$ moieties. Hydrogen bonds with neighbouring O(1W) water molecules are represented as dashed lines. Selected bond lengths and angles are given in Tables S3 and S4 and the hydrogen bonding geometry in Tables S5 and S6 (Supporting Information). Symmetry codes used to generate equivalent atoms, **I**: (i) $1-x$, $2-y$, $2-z$; (ii) $x$, $y$, $1+z$; (iii) $1-x$, $2-y$, $1-z$.; **II**: (i) $1-x$, $1-y$, $2-z$; (ii) $x$, $-1+y$, $z$; (iii) $1-x$, $1-y$, $2-z$.

of steric hindrance, the six $hedp^{4-}$ ligands forming the anionic $[Ge_6(\mu_2\text{-}OH)_6(C_2H_4O_7P_2)_6]^{6-}$ moiety are distributed above and below the plane formed by the six $Ge^{4+}$ centres (Figure 1a and Figure 1b). An identical distribution also occurs for the six $\mu_2$-bridging hydroxy groups located and pointing towards the inner space of the hexameric moiety (Figure 1c and Figure 1d). Each one of the three $\mu_2$-OH groups from one side of the $\{Ge_6(OH)_6\}$ hexagonal ring interacts with a neighbouring water molecule of crystallisation (Figure 1d) through strong and highly directional O–H···O hydrogen bonds [average O···O internuclear distance and <(O–H···O) angle of 2.70 Å and 163°, respectively, for both compounds, Tables S5 and S6 in Supporting Information]. Within the dihydrated anionic $[Ge_6(\mu_2\text{-}OH)_6(C_2H_4O_7P_2)_6]^{6-}$ moiety, the O(1W)···O(1W) distances are ca. 3.18 and 3.31 Å for **I** and **II**, respectively. Interestingly, such an arrangement was reported by Seifullina et al. only for the material containing $[Mg(H_2O)_6]^{2+}$ cations, with a reported corresponding distance of ca. 3.17 Å.[35] The charge of the hexameric anionic $[Ge_6(\mu_2\text{-}OH)_6(C_2H_4O_7P_2)_6]^{6-}$ moieties is compensated by the presence of protonated 8-hydroxyquinoline ($Hhqn^+$, for **I**) or 1,10-phenanthroline ($Hphen^+$, for **II**) organic residues, which appear to be π–π stacked, thus leading to the formation of cationic columnar arrangements (Figures S3 and S4 in Supporting Information): while for **I**, the organic residues alternate in a hqn/$Hhqn^+$/$Hhqn^+$ fashion, for **II**, the rod-like columns are only formed by protonated phen residues. The location of these charge-balancing $H^+$ could only be unequivocally confirmed in the crystal structures by solid-state NMR spectroscopy (see below). This π–π stacking arrangement of organic molecules in both compounds seems to arise mainly as a result of the presence of the relatively large hexameric anionic unit. For example, the crystal structure of pure 1,10-phenanthroline does not contain any π–π interactions, and the stacking of adjacent molecules is instead driven by numerous weak C–H···π interactions.[36] For **I**, this particular feature led to significant and interesting photoluminescence properties, as will be discussed later.

Connections between neighbouring cationic columnar arrangements are mainly assured by weak C–H···π interactions with pairs of π–π-stacked organic molecules. While for compound **I**, this distribution generates organic layers (Figure S3 in Supporting Information), for **II**, the packing is much more efficient, which leads to a three-dimensional supramolecular arrangement of phen/$Hphen^+$ residues (Figure S4 in Supporting Information). Therefore, even though compound **II** has a significantly more available volume per unit cell, the volume accessible to solvent molecules (calculated by using Cerius$^2$ routines[42]) is approxi-

 © 2006 Wiley-VCH Verlag GmbH & Co. KGaA, Weinheim 

mately half of that for **I** (Figure S5 and Table S2 in Supporting Information). These supramolecular arrangements of organic residues closely interact with the hexameric anionic $[Ge_6(\mu_2\text{-}OH)_6(C_2H_4O_7P_2)_6]^{6-}$ moieties and water molecules of crystallisation through a series of strong hydrogen bonds (Tables S5 and S6 in Supporting Information), which will be discussed in more detail in the solid-state NMR section.

As suggested by thermogravimetry and previous studies on multi-dimensional coordination frameworks exhibiting

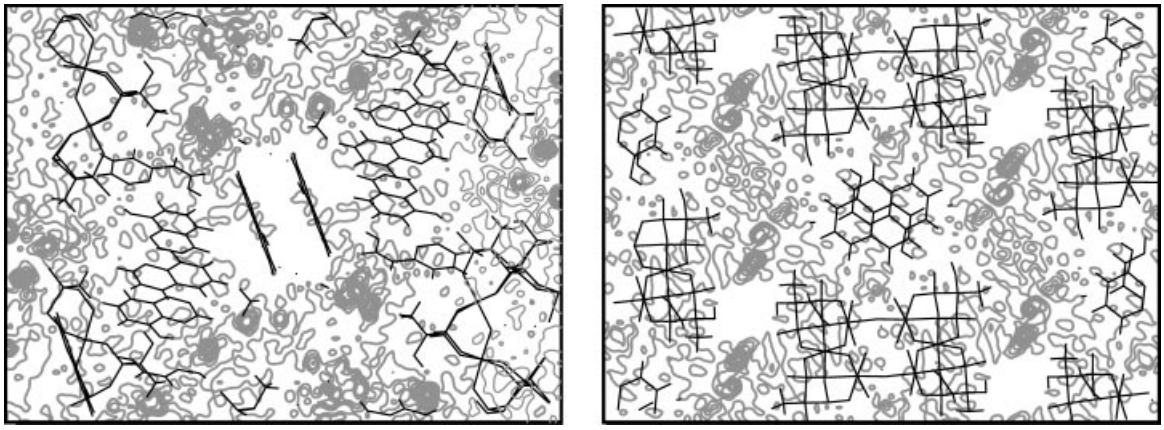

Figure 2. Contouring of difference Fourier SQUEEZE maps (grey) of compound **I** viewed parallel to the (left) *yz* and (right) *xy* planes.

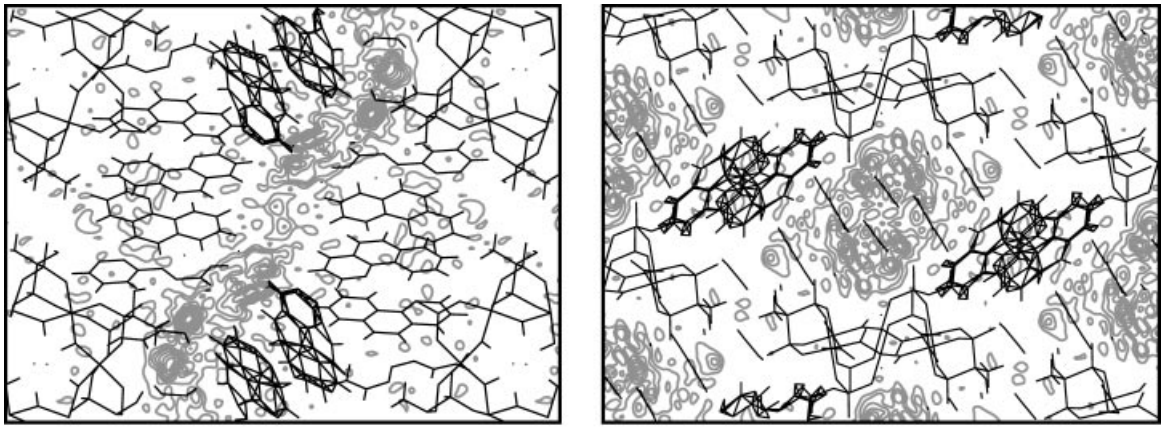

Figure 3. Contouring of difference Fourier SQUEEZE maps (grey) of compound **II** viewed parallel to the (left) *yz* and (right) *xy* planes.

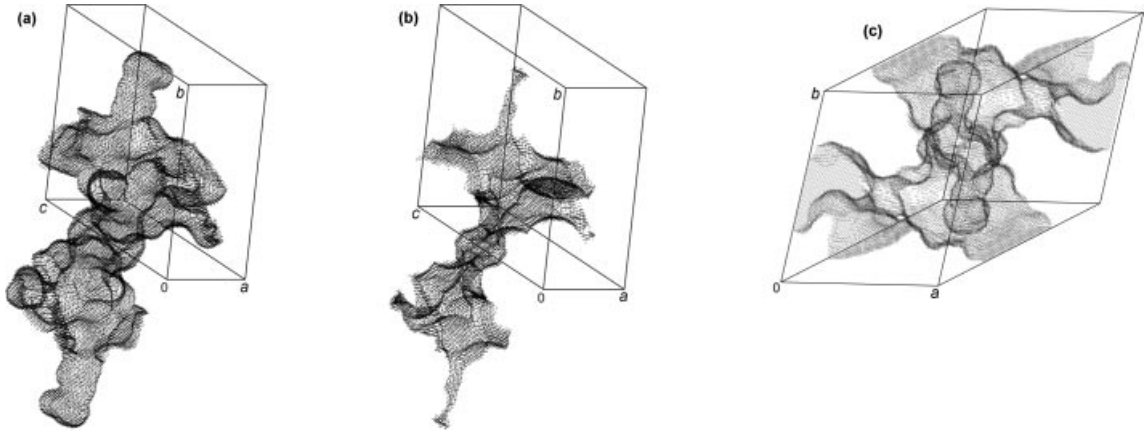


Figure 4. Solvent-accessible volumes of **I**. (a) Surface surrounding the large cavity centred at (–0.032 0.082 0.439). (b) The corresponding Ohashi volume representation showing all the points at 1.2 Å from the nearest van der Waals surface.[41] (c) Potential solvent-accessible volume inside the unit cell.

 © 2006 Wiley-VCH Verlag GmbH & Co. KGaA, Weinheim 

large channels,[37] it was clear that both compounds would contain a large number of highly disordered water molecules of crystallisation located within the voids, thus resulting in a significant spread-out electron density visible in the XRD data. Peak search routines of SHELXL are not designed to locate maxima in density ridges, which thus lead to additional difficulties during refinement and mask important structural features. SQUEEZE[38] subroutines included with the software package PLATON[39,40] were therefore employed to eliminate the contribution to the electron density of the water molecules of crystallisation present in the solvent-accessible area [except for the hydrogen-bonded O(1W) molecule, Figure 1c and Figure 1d]. Figure 2 and Figure 3 show the SQUEEZE contour maps for **I** and **II**, respectively, and emphasise the diffuse electron density present in some of the regions with solvent-accessible voids. For **I**, PLATON estimated that the unit cell has ca. 1363 Å$^3$ that is potentially accessible to the solvent (ca. 35.8% of the total volume) in a large cavity centred at (–0.032 0.082 0.439), with ca. 263 electrons per unit cell (Figure 4 and S5 in Supporting Information). For **II**, the unit cell only has ca. 1144 Å$^3$ that is potentially accessible to the solvent (ca. 16.3% of the total volume), which is distributed along two identical cavities centred at the special positions (0 0 0) and (1/2 1/2 1/2), with ca. 547 electrons per unit cell (Figure 5, S5 and S6 in Supporting Information). In all calculations, O(1W) was assumed to belong to the hybrid hydrogen-bonded frameworks.

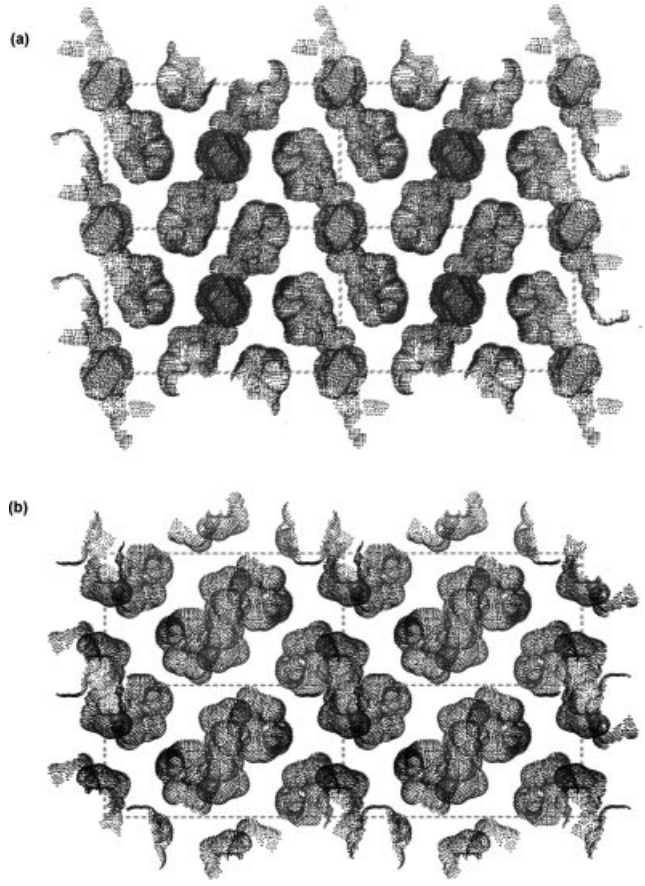


Figure 5. Perspective views along the (a) [100] and (b) [010] directions of the 2×2 unit cell packing of **II**, enhancing the shape of the two identical cavities centred at (0 0 0) and (1/2 1/2 1/2). Images created by generating Connolly surfaces (1.4 Å probe radius and 12.0 dot density) with the software package Cerius$^2$.[42]

## Solid-State NMR Spectroscopy

### *$^{13}$C CP MAS NMR Spectra*

The spectra of **I** and **II** exhibit similar features (Figure S1). The hexameric $[Ge_6(\mu_2\text{-}OH)_6(C_2H_4O_7P_2)_6]^{6-}$ moiety gives the following resonances for **I** and **II**, respectively: quaternary carbon atoms (C1, C3, C5) 70.9 and 71.3 ppm; methyl (C2, C4, C6) carbon atoms 18.6 and 19.9 ppm. This moiety has three crystallographically inequivalent quaternary and methyl carbon atoms, but three resonances are only clearly observed (as shoulders) in the quaternary carbon region of **I**. Above 100 ppm, resonances are assigned to the aromatic carbon atoms involved in the extensive columnar π–π stacking.

### *$^1$H Spectra: Hydrogen-Bonding Assignment*

The F1 projection of the $^1$H-$^1$H FS-LG and the $^1$H fast (30 kHz) MAS spectra (Figure 6) have similar resolution, and show up to 8 resolved peaks. However, a judicious choice of 2D F2 slices proves the presence of some 10 resonances (consider Figure 6c). The resonances ($H^a$-$H^c$) in the range 16.6–13.1 ppm are assigned to strong hydrogen bonds, because of their relatively high-frequency shifts (Table 2). Hydrogen-bonded systems involving carboxylic (C=O) and phosphonic (P=O) acids as electron donors (i.e. proton acceptors) were reported to resonate in the ranges 12–20 ppm and 11–17 ppm, respectively.[43] In **I**, the P=O groups are within the hydrogen-bonding distance of the OH groups of the 8-hydroxyquinoline (ArO–H) moieties ($r_{O\cdots O}$ = 2.61 Å). P=O groups involved in hydrogen bonds with OH residues have been reported to resonate at 11–12 ppm.[20,43] Resonance $H^c$ is tentatively attributed to ArO–H···O=P environments. Such hydrogen bonds (ArO–H···O=P) are likely to be stronger than other CO–H···O=P bonds[20] because the conjugated base ($ArO^-$) of the hydrogen donor (ArO–H) is weak, owing to aromatic ring stabilisation. When the acidity of a hydrogen-bonded OH group increases, its chemical shift also increases, and the resonance $H^c$ therefore appears at a chemical shift larger than 12 ppm.

The crystallographic N···O distance range (2.72–2.78 Å) suggests that the protonated nitrogen atom of 8-hydroxyquinoline is hydrogen-bonded to water molecules ($N^+$–H···$OH_2$). The presence of $N^+$–H groups involved in this type of interaction is likely because the charge of the anionic hexameric unit must be compensated by $H^+$. Protonation and hydrogen bonding result in a significant increase in the $^1$H chemical shift. Thus, the $H^a$ and $H^b$ resonances

 © 2006 Wiley-VCH Verlag GmbH & Co. KGaA, Weinheim 

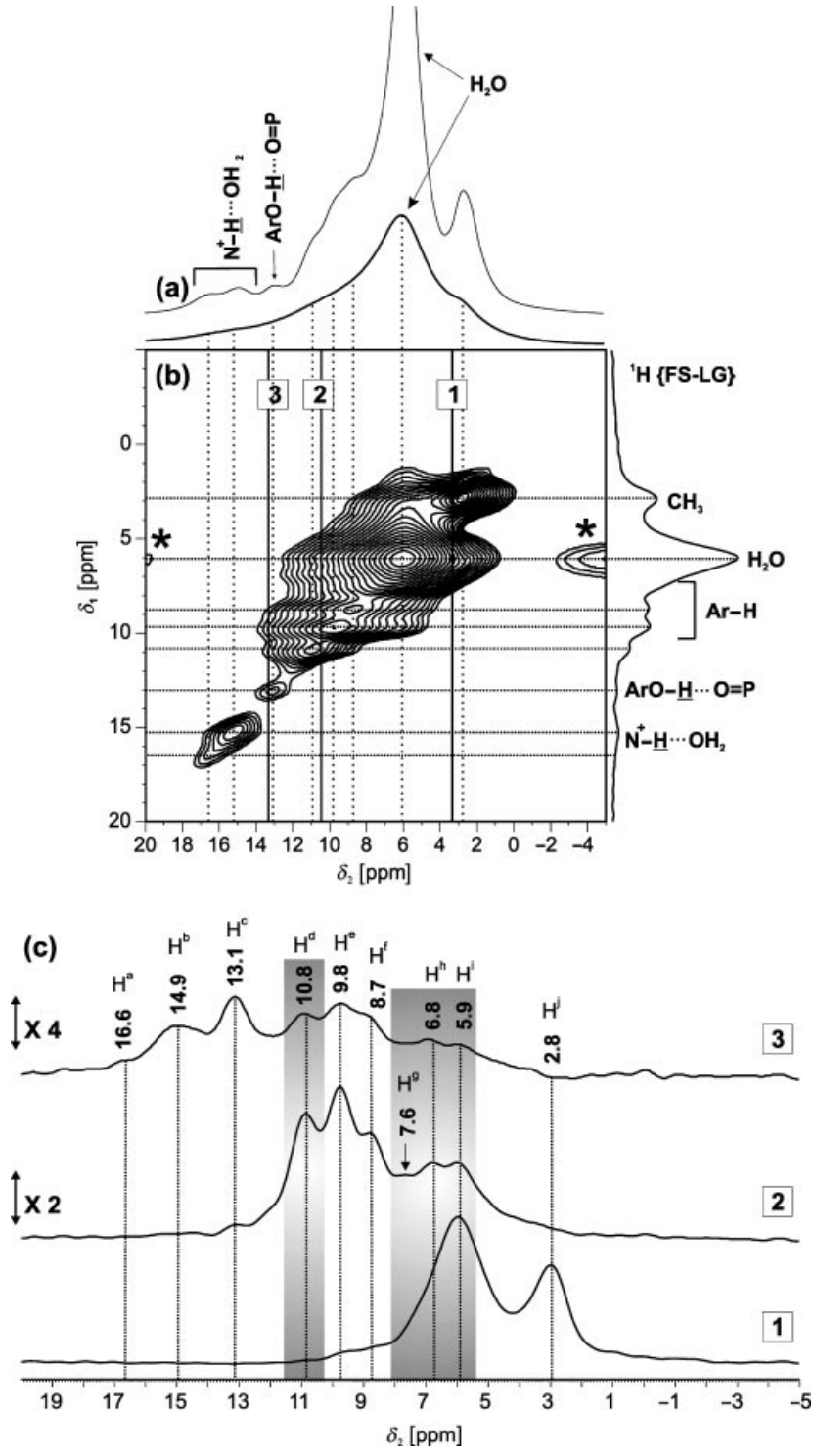


Figure 6. (a) $^1$H MAS and (b) 2D $^1$H-$^1$H FS-LG spectra of **I**. (c) F2 cross-sections of the $^1$H-$^1$H FS-LG spectrum of **I** taken at 3.4, 10.5 and 13.3 ppm. Asterisks depict spinning sidebands.

at $\delta$ = 16.6 and 14.9 ppm are tentatively assigned to $N^+$–H···$OH_2$ environments (and confirmed below by $^1$H-$^1$H DQF spectroscopy).

The $^1$H resonances $H^i$ and $H^j$ at ca. 5.9 and 2.8 ppm, respectively, are assigned to lattice water and $CH_3$ groups. The remaining $^1$H peaks between ca. 6 and 11 ppm cannot be assigned without information from other 2D techniques (see below).

The $^1$H-$^1$H FS-LG spectrum of **II** (Figure S8) displays fewer resonances than that of **I**. In particular, a peak is observed at ca. 15.1 ppm, which shows the presence of strong hydrogen bonds between the protonated nitrogen

 © 2006 Wiley-VCH Verlag GmbH & Co. KGaA, Weinheim 

Table 2. $^1H$ chemical shift assignment of **I**.

| $^1H$[a] | SQ $\delta_H$ [ppm] | DQ $\delta_H$ [ppm] | DQ coherences[b] |
|---|---|---|---|
| $ArN^+$–*H* ($H^a$) | 16.6 | 26.4 | $H^a\cdots H^e$ |
| $ArN^+$–*H* ($H^b$) | 14.9 | 24.7 | $H^b\cdots H^e$ |
| | | 22.5 | $H^b\cdots H^g$ |
| ArO–*H* ($H^c$) | 13.1 | 20.7 | $H^c\cdots H^g$ |
| CO–*H* ($H^d$) | 10.8 | 19.5 | $H^d\cdots H^f$ |
| | | 17.6 | $H^d\cdots H^h$ |
| | | 13.6 | $H^d\cdots H^j$ |
| Ar–*H* ($H^e$)[c] | 9.8 | 26.4 | $H^e\cdots H^a$ |
| | | 24.7 | $H^e\cdots H^b$ |
| Ar–*H* ($H^f$) | 8.7 | 16.3 | $H^f\cdots H^g$ |
| | | 11.5 | $H^f\cdots H^j$ |
| | | 19.5 | $H^f\cdots H^d$ |
| Ar–*H* ($H^g$)[c] | 7.6 | 16.3 | $H^g\cdots H^f$ |
| | | 20.7 | $H^g\cdots H^c$ |
| | | 22.5 | $H^g\cdots H^b$ |
| HO–*H* ($H^h$, $H^i$)[d] | 6.8, 5.9 | 8.7 | $H^i\cdots H^j$ |
| | | 17.6 | $H^h\cdots H^d$ |
| $CH_3$ ($H^j$) | 2.8 | 13.6 | $H^j\cdots H^d$ |
| | | 11.5 | $H^j\cdots H^f$ |

[a] Resonances observed in the $^1H$-$^1H$ FS-LG and $^1H$-$^1H$ DQF spectra are considered. [b] DQ coherences are not considered for the self-correlation peaks (diagonal peaks). [c] There is evidence of $H^e\cdots H^j$ and $H^g\cdots H^j$ correlations, but their observation is difficult (Figure 7b). [d] These $^1H$ resonances refer to the two resolved peaks ($H^h$ and $H^i$) observed in Figure 6, which are tentatively assigned to $H_2O$ protons.

[N(21)] of 1,10-phenanthroline and the P=O(6) groups of the anionic unit ($r_{N(21)\cdots O(14)}$ = 2.68 Å, Table S6). This supports the assignment of resonances $H^a$ and $H^b$ proposed above for compound **I**.

The presence of signals in the $^1H$-$^1H$ DQF spectrum (Figure 7b) reveals dipolar couplings between nuclei and allows the identification of mobile water molecules by comparison with the 30 kHz MAS $^1H$ NMR spectrum (Figure 7a). The latter is dominated by mobile water molecules located in the channels, which resonate at ca. 5.9 and 6.8 ppm for **I** and **II**, respectively (Figure 7a and S9a). This peak is suppressed in DQF experiments, simplifying the spectra (Figure 7b and S9b). In the following discussion, SQ coherences (Table 2) identified from $^1H$-$^1H$ FS-LG are taken into consideration in the study of the SQ-DQ correlations.

The Ar-H protons ($H^e$, $H^f$ and $H^g$, Scheme 1) are classed into three main groups on the basis of the chemical shifts of their resonances, which are expected in the order $\delta(H^e) > \delta(H^f) > \delta(H^g)$. In solution, pure 8-hydroxyquinoline resonates in the range 7.3–9.0 ppm, while for **I**, the chemical shifts range from 7.6 and 9.8 ppm. The identification of the Ar-H resonances was made possible by analysing the DQ frequency of the off-diagonal peaks (Figure 7b) that involve the hydrogen-bonded $^1H$ resonances ($H^a$, $H^b$ and $H^c$), which are well resolved.

In the 2D $^1H$-$^1H$ DQF spectrum, $H^e$ resonances exhibit strong off-diagonal correlations with those of $H^a$ and $H^b$ as these protons are in *ortho* positions (adjacent) and are thus relatively close (2.16–2.28 Å). DQ chemical shifts of ca. 26.4 (16.6 + 9.8) and 24.7 (14.9 + 9.8) ppm for $H^a$ and $H^b$, respectively, are observed. This evidence allows the assignment of

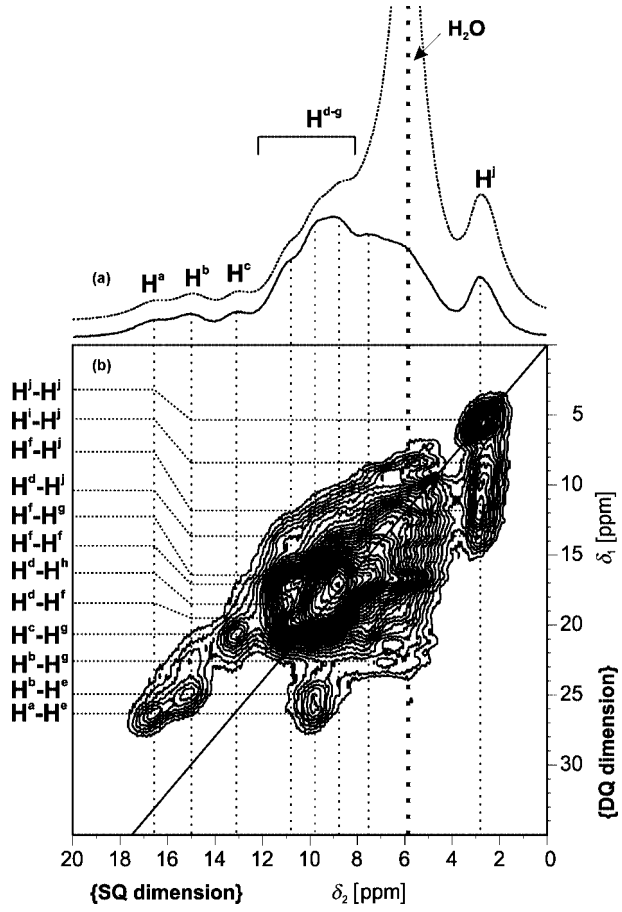


Figure 7. (a) $^1H$ MAS and (b) $^1H$-$^1H$ DQF MAS NMR spectra of **I**.

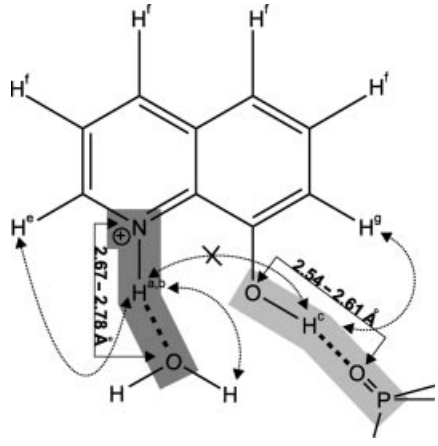


Scheme 1. Hydrogen bonds formed by 8-hydroxyquinoline in compound **I**. Dashed arrows show the interactions revealed by XRD (Table S5).

$H^a$ and $H^b$ to $N^+$–H···$OH_2$ bonds determined by XRD. In a similar way, the resonance at ca. 13.1 ppm ($H^c$) has a DQ frequency of ca. 20.7 ppm, which allows for the assignment of the peak at ca. 7.6 ppm to $H^g$, as this proton is also in an *ortho* position to $H^c$. Besides, $H^c$ is not correlated with $H^e$ because no DQ frequency appears at ca. 22.9 (13.1 + 9.8) ppm. Therefore, $H^c$ is not assigned to $N^+$–H protons in-

 © 2006 Wiley-VCH Verlag GmbH & Co. KGaA, Weinheim 

volved in hydrogen bonds with water; these latter protons ($H^a$ and $H^b$) have always shown to be correlated with $H^e$ (Scheme 1).

Because the peaks are hidden by neighbouring resonances, the correlations involving $H^f$ are harder to ascertain. The remaining peak in the aromatic region at 8.7 ppm is assigned to $H^f$. This is supported by the DQ self-correlation $H^f\cdots H^f$ peak at ca. 17.4 ppm in the DQ dimension. The assignment of DQ coherences involving $H^f\cdots H^g$ and $H^f\cdots H^e$ was not possible because of the lack of resolution.

We now consider the tentative assignment of the resonances of **I** at ca. 10.8 ($H^d$) and 6.8 ppm ($H^h$). The 2D $^1$H-$^1$H DQF spectrum suggests that these protons are close in space and lead to a DQ frequency of ca. 17.6 ppm ($H^d\cdots H^h$). In accord, XRD data reveals the presence of hydrogen bonds involving the $H^d$ protons of tertiary alcohol groups of $HEDP^{4-}$ and the $H^h$ protons of water molecules. Additionally, the $H^d$ protons ($\delta$ =10.8 ppm) exhibit another DQ frequency at 13.6 (10.8 + 2.8) ppm, showing the close proximity (<0.35 nm) between the CO–H and $CH_3$ groups. The spectrum also provides evidence for the proximity between the $CH_3$ protons ($H^j$) and 8-hydroxyquinoline because correlations with all the Ar-H ($H^e$, $H^f$ and $H^g$) resonances (Table 2 and Figure 3b) are observed.

As far as compound **II** is concerned, the main conclusion is that the high-frequency resonance (at $\delta$ = 15.1 ppm) may be assigned to $N^+$–H···O=P hydrogen bonds (Figure S9b). Indeed, **II** possesses only a single type of very short (1.86 Å) hydrogen bond.

The $^1$H-$^1$H exchange RFDR (Figure 8) and $^1$H-$^1$H DQF experiments provide complementary information — the former maps correlations involving both mobile and rigid species, while the latter maps only those involving the rigid species.

In **I**, the lattice water resonances ($H^i$) are correlated with all peaks even at low mixing times, revealing the presence of water molecules dispersed throughout the structure. On the other hand, at a mixing time of 0.53 ms (Figure 8a), the $CH_3$ ($H^j$) protons are not correlated with $H^a$, $H^b$ and $H^c$, thus supporting the DQF results and confirming that the $H^e$ protons are only near $H^a$ and $H^b$ (hydrogen bonds involving N–$H^+$–$OH_2$). Moreover, a clear correlation between $H^c$ and $H^g$ is observed. This pair of resonances ($H^c\cdots H^g$) is strongly correlated at low mixing times (Figure 8a), supporting the information given by $^1$H-$^1$H DQF spectroscopy (Figure 7b). The $^1$H-$^1$H RFDR spectrum of structure **II** is far less informative and will not be further discussed (Figure S10).

The $^1$H-$^1$H DQF spectrum of **I** also reveals important information on the spatial arrangement of the organic residues. Excellent reviews are available on the study of three-dimensional crystal packing based on ring-current effects arising from the aromatic π orbitals.[21,44,45] Moreover, the influence of ring currents on neighbouring molecules shifts the chemical shifts over a range of 2–5 ppm.[46] The Ar-H resonances ($H^e$, $H^f$ and $H^g$) of **I** are shifted to high frequency relative to the resonances of 8-hydroxyquinoline in solution, which may be due to either amine protonation or

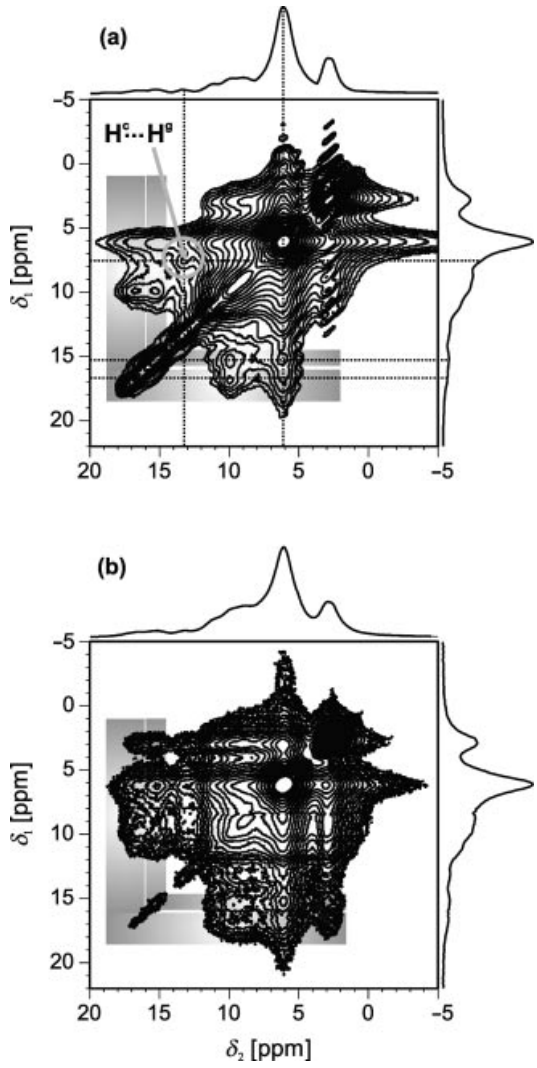


Figure 8. 2D $^1$H-$^1$H exchange RFDR spectra recorded with mixing times of (a) 0.53 ms and (b) 3.2 ms.

small ring-current effects caused by adjacent molecules. The relative orientation of adjacent 8-hydroxyquinoline molecules may be studied on the basis of the $^1$H-$^1$H DQF spectrum. The $H^b$ resonance shows an additional off-diagonal correlation at a DQ frequency of 22.5 ppm, clear evidence of spatial proximity between protons $H^b$ and $H^g$. Because the intra- and intermolecular distances between these protons are 5.3 and 3.2 Å, respectively, the SQ-DQ correlation is ascribed to the latter proton resonances. Moreover, the absence of diagonal peaks involving the resolved hydrogen bonds indicates that $H^a$, $H^b$ and $H^c$ are protons belonging to separate molecules (Figure 7b).

The $^1$H projection of the $^1$H-$^{31}$P FS-LG spectra of **I** (Figure S11) is better resolved than the F1 projection of the $^1$H-$^1$H FS-LG spectra (Figure 6b). Alternatively, the $^1$H-$^{31}$P FS-LG spectra are useful to probe the hydrogen bonds between the $HEDP^{4-}$ phosphonate group and the 8-hydroxyquinoline aromatic residues. At short contact times (0.2 ms), the $^1$H-$^{31}$P FS-LG $H^c$ resonances are slightly more

 © 2006 Wiley-VCH Verlag GmbH & Co. KGaA, Weinheim 

intense than those for $H^a$ and $H^b$, which indicates that the $H^c$ protons are hydrogen bonded to P=O groups, as mentioned above (Scheme 1).

### Photoluminescence Spectroscopy

Figure 9 shows the excitation spectrum of **I** recorded at 14 K. The spectrum consists of a broad band between 270 and 440 nm, assigned to aromatic ring π–π* transitions.[47] The excitation of **I** within such states leads to the observation of both a main band in the range 440 to 650 nm, peaking at 530 nm, and an emission component at higher wavelengths (Figure 9a). According to the crystal structures, the aromatic moieties have two distinct packing environments: columnar π···π stacking and adjacent molecules connected to the columns through weak C–H···π interactions. Hence, the former band may be assigned to the π–π* 0-phonon transition of the hydroquinoline adjacent rings,[47] which corresponds to a triplet-state energy of 18900 $cm^{-1}$, while the band at higher wavelengths is attributed to excimer formation through π···π hydroquinoline interactions. At room-temperature, no efficient emission could be detected, which indicates the presence of thermally activated non-radiative channels in **I**.

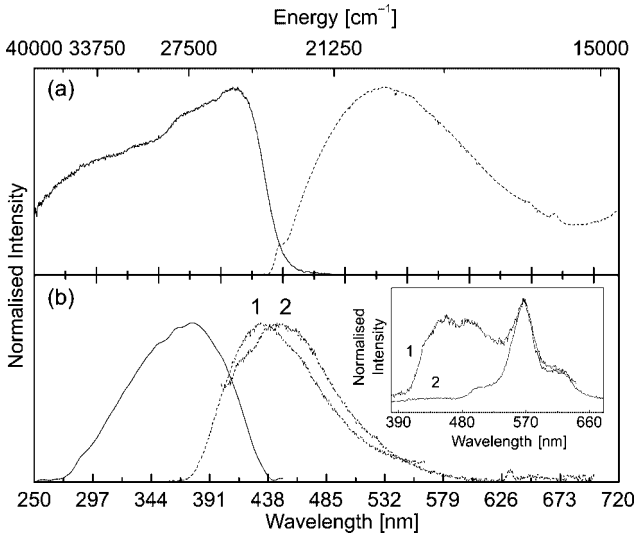


Figure 9. Excitation (solid line) and emission (dashed line) spectra of the complexes of (a) **I** and (b) **II** recorded at 14 K and room temperature, respectively. The excitation and emission spectra of **I** were monitored at 535 nm and excited at 408 nm, whereas for **II**, the monitoring wavelength was 490 nm and the excitation wavelengths were 330 nm (1) and 365 nm (2). The inset shows the time-resolved emission spectrum (14 K) of **II**, acquired with a starting delay of 0.05 ms and an acquisition window of 10.00 ms.

Figure 9b shows the room-temperature excitation spectra of **II** monitored at 490 nm. The spectrum displays a large broad band between 270 and 400 nm, peaking at 367 nm, ascribed to aromatic ring π–π* transitions.[48] The room-temperature reflectance spectrum (not shown) resembles the excitation spectra, displaying an absorption edge at 370 nm. This value is shifted to the red when compared with the singlet energy of the neutral 1,10-phenanthroline ligand (320 nm, 31250 $cm^{-1}$).[49] This energy difference is induced by the different local environment of 1,10-phenanthroline, in particular, the metal coordination and the packing of the complex in **II**.

Under UV excitation (Figure 9b), the emission of **II** consists of a large asymmetrical band between 380 and 550 nm. For excitation wavelengths in the range 270–370 nm, the emission energy peaks at 430 nm and does not depend on the excitation wavelength. For higher excitation wavelengths, a broadening and red-shift of the emission spectra are observed. The dependence on the excitation wavelength and the asymmetric shape of the emission suggest the appearance of a new emitting species, preferentially excited at higher wavelengths. As suggested for **I**, the presence of two distinct emission components may be due to the presence of two different packing environments for the 1,10-phenanthroline rings. The spectra acquired for excitation wavelengths between 270–370 nm may correspond to the preferential emission arising from the adjacent 1,10-phenanthroline rings. Like the excitation spectrum (Figure 9a), their emission energy is shifted with respect to that of the free 1,10-phenanthroline chromophore, whose lowest triplet-state energy (π–π* 0-phonon transition) peaks at 366 nm (27322 $cm^{-1}$);[50,51] however, the emission energy is very similar to that observed for $Gd(phen)_2Cl_3\cdot 2H_2O$[50], with a lowest triplet-state energy of 453 nm (22075 $cm^{-1}$).[52] The emission component at lower energy may be ascribed to the formation of an excimer through π···π phenanthroline interactions, as observed in 1,10-phenanthroline compounds with the same crystal packing of **II**.[50,51]

The presence of two distinct emissions in **II** was further established and investigated by time-resolved emission and lifetime measurements. These studies were performed at 14 K, since the room-temperature time-scale for the photoluminescence mechanisms is smaller than the detection limit of our equipment ($10^{-5}$ s). For lower excitation wavelengths, the spectrum consists of a structured broad band (inset in Figure 9b). Increasing the excitation wavelength results in a decrease in the relative intensity of the lower-wavelength-side of the spectra, which further indicates the presence of two distinct emitting species. Such an intensity decrease suggests that the time scale for the emission mechanisms of the emission component at lower wavelengths is smaller than that of the lower-wavelength emission. The short-lived emission is consistent with a monomer component, whereas the longer-lived and lower-energy emission is compatible with the formation of an excimer.[50,51,53] The excimer emission decay curve was monitored at 568 nm under 330 nm excitation wavelength (not shown). The decay curve is well reproduced by a single exponential function, which yields a lifetime of $4.33 \pm 0.11$ ms.

## Conclusions

Two germanium-$hedp^{4-}$ solids with heteroaromatic amines, 8-hydroxyquinoline (in **I**) and 1,10-phenanthroline (in **II**), have been prepared and characterised by single-crys-

 © 2006 Wiley-VCH Verlag GmbH & Co. KGaA, Weinheim 

tal XRD, thermogravimetry and FTIR and UV/Vis spectroscopy. High-resolution solid-state NMR spectroscopy has been used to study the complex hydrogen-bonded networks, particularly in compound **I**. Certain details of the crystal structure of **I** have been elucidated, mainly those involving the occurrence of π–π stacking of 8-hydroxyquinoline and the relative orientation of adjacent such molecules. It has been shown that the combination of homonuclear recoupling techniques (2D $^1$H-$^1$H DQF, 2D $^1$H-$^1$H RFDR MAS NMR) and CRAMPS techniques (2D $^1$H-$^1$H FS-LG, $^1$H-$^{31}$P FS-LG) provides a powerful toolbox for the characterisation of organic–inorganic hybrid materials.

Compound **II** displays an emission from the lowest triplet-state energy (π–π* 0-phonon transition) of the aromatic rings, which peaks at ca. 320 nm (31250 cm$^{-1}$) in the range 14 K to room temperature, whereas the triplet emission of complex **I** at ca. 530 nm (18868 cm$^{-1}$) is detected at low temperature. A long-lived and low-energy emission component, resulting from the formation of an excimer state and originating from π···π stacking of 1,10-phenanthroline and hydroxyquinoline residues, was observed for **I** and **II**, respectively.

## Experimental Section

**General:** Chemicals were readily available from commercial sources and were used as received without further purification. Elemental analyses for carbon, hydrogen and nitrogen were performed on a CHNS-932 Elemental Analyser instrument at the University of Aveiro. FTIR spectra were measured by using KBr disks (Aldrich, 99%, FTIR grade) on a Matson 7000 FTIR spectrometer. FT-Raman spectra were measured on a Bruker RFS 100 with a Nd:YAG coherent laser ($\lambda$ = 1064 nm). Thermogravimetric analyses (TGA) were carried out by using a Shimadzu TGA-50 instrument and Differential Scanning Calorimetry (DSC) analyses on a Shimadzu DSC-50 instrument with a heating rate of 5 °C/min under a nitrogen atmosphere with flow rate of 20 cm$^3$/min. PL and time-resolved spectra were recorded between 14 K and room temperature with a TRIAX 320 emission monochromator (Fluorolog-3, Jobin Yvon-Spex) coupled to an R928 Hamamatsu photomultiplier, using the front face acquisition mode.

**Synthesis of (Hhqn)$_6$[Ge$_6$(OH)$_6$(hedp)$_6$]·2(hqn)·33H$_2$O (I):** A suspension of 1-hydroxyethylidenediphosphonic acid (0.200 g, $H_4$hedp, $C_2H_8O_7P_2$, ≥97%, Fluka), germanium(IV) oxide amorphous (0.100 g, $GeO_2$, 99.99%, Aldrich), and 8-hydroxyquinoline (0.140 g, hqn, $C_9H_7NO$, 99%, Merck) in distilled water (ca. 12 g) was stirred thoroughly for 30 min at ambient temperature. The reactive mixture was transferred to a PTFE-lined stainless steel reaction vessel (ca. 40 cm$^3$), which was then placed inside an oven. The temperature was gradually increased to 120 °C and kept constant for 3 d, after which the vessel was cooled slowly to ambient temperature before opening. The resulting light-yellow phase was washed with distilled water, filtered and air dried at ambient temperature. The single-crystalline phase decomposes into a microcrystalline powder during this drying stage. Hence, (Hhqn)$_6$[Ge$_6$(OH)$_6$(hedp)$_6$]·2(hqn)·33H$_2$O samples suitable for single-crystal X-ray diffraction measurements were isolated while still wet directly from the autoclave mother liquor by slow evaporation at ambient temperature for 2 d. Elemental composition (based on single-crystal data for $C_{84}H_{158}Ge_6N_8O_{89}P_{12}$, $M_W$ 3511.36): calcd. C 28.73, N 3.20, H 4.54%; found C 28.87, N 3.08, H 4.51%. TGA data (mass losses): 20–86 °C: 14.2%; 86–155 °C: 3.3%; 155–210 °C: 2.3%; 210–400 °C: 5.5%. DSC peaks (endothermic processes): 76, 103, 184, 258 and 336 °C. Selected IR (KBr pellet) and Raman (in italics inside the parenthesis, cm$^{-1}$) data: $\nu$(HO–H/GeO–H/CO–H, with evidence of H-bonding) = 3430 vs/br., 3254 vs/br., 3093 vs/br. (*3116 w*); $\nu$(aromatic NH$^+$) = 2790 m/br.; $\nu$(C–H, aromatic) = 3093 br. (*3069 m*); $\nu_{as}$(C–H in –CH$_3$) = 2969 br. (*2979 w*, *2937 w*); $\nu_s$(C–H in –CH$_3$) = (*2875 w*); $\delta_s$(CO–H) and $\delta_{as}$(CH$_3$) = 1421 m, 1404 m; $\delta_s$(CH$_3$) = 1384 m (*1385 s*); $\nu$(N$^+$–H) = 2580 br.; $\delta$(–NH$^+$) = 1559 m; $\nu$(P=O) and $\nu$(C–O) = 1187 s and 1169 s (*1314*); $\nu$(C–C, skeletal vibrations) = 1603 m (*1606 m*); $\delta$(O–H, lattice water) = 1635 m (*1634 w*); $\nu$(C–N, heteroaromatic amines) and $\delta$(O–H, aromatic) = 1312 m (*1308 w*, *1279 w*); $\nu$(P–O) = 1010 vs (*1064 m*, *1038 w*); $\gamma$(C–C) = 488 w (*542 w*, *490 m*, *474 m*, *410 m*), various modes; $\gamma$(O–H, under H-bonding) = 976 br./vs; $\gamma$(C–H, aromatic) = 824 m (*716* vs); $\omega$(O–H, under H-bonding) = 583 br./m (*578*) cm$^{-1}$.

**Synthesis of (Hphen)$_6$[Ge$_6$(OH)$_6$(hedp)$_6$]·2(phen)·20H$_2$O (II):** A suspension of 1-hydroxyethylidenediphosphonic acid (0.200 g, $H_4$hedp, $C_2H_8O_7P_2$, ≥97%, Fluka), amorphous germanium(IV) oxide (0.240 g, $GeO_2$, 99.99%, Aldrich) and 1,10-phenanthroline monohydrate (0.190 g, phen, $C_{12}H_8N_2$·$H_2O$, ≥99.0%, Fluka) in distilled water (ca. 16 g) was stirred thoroughly for 30 min at ambient temperature. The reactive mixture was transferred to a PTFE-lined stainless steel reaction vessel (ca. 40 cm$^3$), which was then placed inside an oven. The temperature was gradually increased to 120 °C and kept constant for 3 d, after which the vessel was cooled slowly to ambient temperature before opening. The isolated microcrystalline light-brown phase was washed with distilled water, filtered and air-dried at ambient temperature. Single crystals of (Hphen)$_6$[Ge$_6$(OH)$_6$(hedp)$_6$]·2(phen)·20H$_2$O suitable for X-ray diffraction measurements were harvested from the autoclave mother liquor by slow evaporation at ambient temperature over 1 d. Elemental composition (based on single-crystal data for $C_{108}H_{140}Ge_6N_{16}O_{68}P_{12}$, $M_W$ 3557.54): calcd. C 36.46, N 6.33, H 3.97%; found C 35.47, N 5.46, H 4.20. TGA data (mass losses): 20–125 °C: 10.3%; 125–364 °C: 10.0%. Selected IR (KBr pellet) and Raman (in italics inside the parenthesis, cm$^{-1}$) data: $\nu$(HO–H/GeO–H/CO–H, with evidence of H-bonding) = 3389 vs/br., 3237 vs/br.; $\nu$(aromatic NH$^+$) = 2532 s/br.; $\nu$(C–H, aromatic) = 3062 m (*3066 m*); $\nu_{as}$(C–H in –CH$_3$) = 2932 m (*2990 w*, *2933 w*); $\nu_s$(C–H in –CH$_3$) = 2807 s, 2879 s (*2872 w*); $\delta_{as}$(CH$_3$) = 1452 m, 1469 m (*1452 s*, *1415* vs); $\delta_s$(CH$_3$) = 1373 w (*1373 m*); $\nu$(C–N, heteroaromatic amines) = 1316 m (*1316 w*); $\delta$(CO–H) = 1289 w (*1286 w*); $\nu$(N$^+$–H) = 2532 br.; $\delta$(–NH$^+$) = 1542 s; $\delta$(O–H, lattice water) = 1632 s/br. (*1629 w*); $\nu$(C–C, skeletal vibrations) = 1617 s, 1596 s (*1615 m*, *1596 m*); $\nu$(P=O) and $\nu$(C–O) = 1185 vs/br. (*1189 w*); $\nu$(P–O) = 1053 s (*1045 m*); $\gamma$(C–C) = 487 s, 461 s (*550 w*, *508 w*, *461 w*), various modes; $\gamma$(O–H, under H-bonding) = 971 vs/br., various modes; $\gamma$(C–H, aromatic) = 847 vs, 816 s (*848 w*); $\omega$(O–H, under H-bonding) = 620 vs, 592 vs, 568 vs, various modes (*598 w*) cm$^{-1}$.

CCDC-614629 and CCDC-614630 for **I** and **II** contain the supplementary crystallographic data for this paper. These data can be obtained free of charge from The Cambridge Crystallographic Data Centre via www.ccdc.cam.ac.uk/data_request/cif.

**Supporting Information** (see footnote on the first page of this article): Thermoanalytical and infrared results and detailed discussion are included. Technical and experimental details on the single-crystal X-ray diffraction, solid-state NMR spectroscopy and photoluminescence studies are also included. Additional structural drawings emphasizing the [Ge$_6$($\mu_2$-OH)$_6$($C_2H_4O_7P_2$)$_6$]$^{6-}$ moiety (and tables containing crystallographic bond lengths and angles), the or-

 © 2006 Wiley-VCH Verlag GmbH & Co. KGaA, Weinheim 

ganic frameworks and the solvent-accessible cavities are given. Results of a Cambridge Structural Database Survey for typical Ge–O–Ge bonds are presented. Tables summarising hydrogen-bonding geometries for the two compounds and additional NMR spectra [$^{13}C\{^1H\}$ RAMP-CP, $^1H$-$^1H$ FS-LG, $^1H$ MAS (for **II**), 2D $^1H$-$^1H$ RFDR (for **II**), $^1H$-$^{31}P$ FS-LG] are also included.

## Acknowledgments

We are grateful to FEDER, POCTI (Portugal) and to the Portuguese Foundation for Science and Technology (FCT) for their financial support and also to the Ph.D. and postdoctoral research grants Nos. SFRH/BD/13858/2003 (to L. M.) and SFRH/BPD/9309/2002 (to F.-N. S.), respectively.

[1] A. Clearfield, *Progress in Inorganic Chemistry Vol. 47* (Ed.: K. D. Karlin), New York, **1998**.
[2] G. Férey, *Chem. Mater.* **2001**, *13*, 3084.
[3] D. Hagrman, P. J. Hagrman, J. Zubieta, *Angew. Chem. Int. Ed.* **1999**, *38*, 3165.
[4] P. J. Hagrman, R. C. Finn, J. Zubieta, *Solid State Sci.* **2001**, *3*, 745.
[5] B. Moulton, M. J. Zaworotko, *Chem. Rev.* **2001**, *101*, 1629.
[6] J. L. C. Rowsell, O. M. Yaghi, *Angew. Chem. Int. Ed.* **2005**, *44*, 4670.
[7] C. Sanchez, G. J. D. A. A. Soler-Illia, F. Ribot, T. Lalot, C. R. Mayer, V. Cabuil, *Chem. Mater.* **2001**, *13*, 3061.
[8] E. W. Stein Sr, A. Clearfield, M. A. Subramanian, *Solid State Ionics* **1996**, *83*, 113.
[9] P. Ayyappan, O. R. Evans, B. M. Foxman, K. A. Wheeler, T. H. Warren, W. Lin, *Inorg. Chem.* **2001**, *40*, 5954.
[10] M. Eddaoudi, D. B. Moler, H. Li, B. Chen, T. M. Reineke, M. O'Keeffe, O. M. Yaghi, *Acc. Chem. Res.* **2001**, *34*, 319.
[11] M. Eddaoudi, O. M. Yaghi, H. Li, *J. Am. Chem. Soc.* **2000**, *122*, 1391.
[12] R. Murugavel, M. G. Walawalkar, M. Dan, C. N. R. Rao, H. W. Roesky, *Acc. Chem. Res.* **2004**, *37*, 763.
[13] B. Zhang, D. M. Poojary, A. Clearfield, *Inorg. Chem.* **1998**, *37*, 249.
[14] M. P. Jensen, J. V. Beitz, R. D. Rogers, K. L. Nash, *J. Chem. Soc., Dalton Trans.* **2000**, 3058–3064.
[15] D. M. Poojary, B. Zhang, A. Clearfield, *Angew. Chem. Int. Ed. Engl.* **1994**, *33*, 2324.
[16] E. N. Rizkalla, *Rev. Inorg. Chem.* **1983**, *5*, 233.
[17] J. Simon, D. A. Wilson, J. R. Garlich, D. E. Troutner (Dow Chemical Company), patent no. 899734, **1989**.
[18] K. L. Nash, J. Ferraro, R. D. Rogers, J. Zhang, *Inorg. Chim. Acta* **1998**, *269*, 211.
[19] A. E. Aliev, K. D. M. Harris, *Probing Hydrogen Bonding in Solids using Solid State NMR Spectroscopy*, Springer-Verlag Berlin, Berlin, **2004**.
[20] S. Pawsey, M. McCormick, S. De Paul, R. Graf, Y. S. Lee, L. Reven, H. W. Spiess, *J. Am. Chem. Soc.* **2003**, *125*, 4174–4184.
[21] I. Schnell, *Prog. Nucl. Magn. Reson. Spectrosc.* **2004**, *45*, 145–207.
[22] E. Brunner, U. Sternberg, *Prog. Nucl. Magn. Reson. Spectrosc.* **1998**, *32*, 21–57.
[23] G. R. Goward, M. F. H. Schuster, D. Sebastiani, I. Schnell, H. W. Spiess, *J. Phys. Chem. B* **2002**, *106*, 9322–9334.
[24] I. Schnell, S. P. Brown, H. Y. Low, H. Ishida, H. W. Spiess, *J. Am. Chem. Soc.* **1998**, *120*, 11784–11795.
[25] S. P. Brown, I. Schnell, J. D. Brand, K. Mullen, H. W. Spiess, *Phys. Chem. Chem. Phys.* **2000**, *2*, 1735–1745.
[26] I. Schnell, H. W. Spiess, *J. Magn. Reson.* **2001**, *151*, 153–227.
[27] L. Mafra, F. A. A. Paz, F. N. Shi, J. Rocha, T. Trindade, C. Fernandez, A. Makal, K. Wosniak, J. Klinowski, *Chem. Eur. J.* **2006**, *12*, 363–375.
[28] D. Massiot, B. Alonso, F. Fayon, F. Fredoueil, B. Bujoli, *Solid State Sci.* **2001**, *3*, 11–16.
[29] L. Mafra, J. Rocha, C. Fernandez, F. A. A. Paz, *J. Magn. Reson.* **2006**, *180*, 236–244.
[30] M. Feike, D. E. Demco, R. Graf, J. Gottwald, S. Hafner, H. W. Spiess, *J. Magn. Reson. Ser. A* **1996**, *122*, 214–221.
[31] I. Schnell, A. Watts, H. W. Spiess, *J. Magn. Reson.* **2001**, *149*, 90–102.
[32] A. E. Bennett, C. M. Rienstra, J. M. Griffiths, W. Zhen, P. T. Lansbury Jr, R. G. Griffin, *J. Chem. Phys.* **1998**, *108*, 9463–9479.
[33] A. E. Bennett, J. H. Ok, R. G. Griffin, S. Vega, *J. Chem. Phys.* **1992**, *96*, 8624–8627.
[34] A. Bielecki, A. C. Kolbert, M. H. Levitt, *Chem. Phys. Lett.* **1989**, *155*, 341–346.
[35] I. I. Seifullina, E. E. Martsinko, G. G. Aleksandrov, V. S. Sergienko, *Russ. J. Inorg. Chem.* **2004**, *49*, 844–852.
[36] S. Nishigaki, H. Yoshioka, K. Nakatsu, *Acta Crystallogr., Sect. B* **1978**, *34*, 875–879.
[37] F. A. A. Paz, J. Klinowski, *J. Phys. Org. Chem.* **2003**, *16*, 772–782.
[38] P. van der Sluis, A. L. Spek, *Acta Crysallogr., Sect. A* **1990**, *46*, 194–201.
[39] A. L. Spek, *J. Appl. Crystallogr.* **2003**, *36*, 7–13.
[40] A. L. Spek, *Acta Crystallogr., Sect. A* **1990**, *46*, C34.
[41] Y. Ohashi, K. Yanagi, T. Kurihara, Y. Sasada, Y. Ohgo, *J. Am. Chem. Soc.* **1981**, *103*, 5805–5812.
[42] *Cerius$^2$, Version, 4.2*, *Molecular Simulations Inc.*, San Diego, **2000**.
[43] R. K. Harris, P. Jackson, L. H. Merwin, B. J. Say, *J. Chem. Soc., Faraday Trans. 1* **1988**, *84*, 3649–3672.
[44] M. Umetsu, J. G. Hollander, J. Matysik, Z. Y. Wang, T. Adschiri, T. Nozawa, H. J. M. Groot, *J. Phys. Chem. B* **2004**, *108*, 2726–2734.
[45] J. S. Waugh, R. W. Fessenden, *J. Am. Chem. Soc.* **1957**, *79*, 846–849.
[46] A. Hoffmann, D. Sebastiani, E. Sugiono, S. Yun, K. S. Kim, H. W. Spiess, I. Schnell, *Chem. Phys. Lett.* **2004**, *388*, 164–169.
[47] D. Imbert, S. Comby, A.-S. Chauvin, J.-C. G. Bünzli, *Chem. Commun.* **2005**, 1432–1434.
[48] C.-J. Xua, F. Xiea, X.-Z. Guoa, H. Yang, *Spectrochim. Acta* **2005**, *61*, 2005–2008.
[49] H. Xin, M. Shi, X. C. Gao, Y. Y. Huang, Z. L. Gong, D. B. Nie, H. Cao, Z. Q. Bian, F. Y. Li, C. H. Huang, *J. Phys. Chem. B* **2004**, *108*, 10796–10800.
[50] R. Caballo, B. Covelo, C. Lodeiro, E. M. Vazquez-López, *CrystEngCommun* **2005**, *7*, 294–296.
[51] K. Hayashi, H. Akutsu, H. Ozaki, H. Sawai, *Chem. Commun.* **2004**, 1386–1387.
[52] B. Yan, H. Zhang, S. Wang, J. Ni, *J. Photochem. Photobiol. A* **1998**, *116*, 209–214.
[53] N. J. Turro, *Modern Molecular Photochemistry*, Benjamin/Cummings, Menlo Park, **1978**.

Received: July 20, 2006
Published Online: November 3, 2006

 © 2006 Wiley-VCH Verlag GmbH & Co. KGaA, Weinheim 

DOI: 10.1002/ejic.200600424

# Pentacoordination at Germanium by Transannular Bonding of Sulfur or Oxygen in an Eight-Membered Ring: An Experimental and Theoretical Study

**Simplicio González-Montiel,[a] Noemí Andrade-López,[a] Verónica García-Montalvo,[b] Juan Antonio Cogordan,[b] and José G. Alvarado-Rodríguez*[a]**

**Keywords:** Germanium / Hypercoordinate compounds / Structure elucidation / Density functional theory / NBO analysis

Treatment of $L_nGeCl_{4-n}$ with $D(C_6H_4SH)_2$ in the presence of *n*BuLi leads to the formation of the stable compounds $D(C_6H_4S)_2GeL_1L_2$ (for D = S, $L_1$ = Cl, $L_2$ = Ph, **1** and $L_1 = L_2$ = Ph, **3**; for D = O, $L_1$ = Cl, $L_2$ = Et, **4** and $L_1 = L_2$ = Ph, **5**). The $S(C_6H_4S)_2Ge(Ph)Br$ compound (**2**) has been synthesised by halogen exchange from **1** and potassium bromide. X-ray structure determinations of complexes **1**–**5** reveal that the germanium atom acts as an acceptor atom displaying an intramolecular transannular interaction with the chalcogen D atom. The geometry of the pentacoordinate Ge atom in the title compounds is described as distorted trigonal bipyramidal with a 64–31 % distortion displacement. The D→Ge (D = S, O) hypercoordinate interaction was studied by DFT methods using correlation consistent basis sets and relativistic ECP for Ge. NBO analysis showed that this interaction can be explained in terms of the interplay of covalent and Coulombic interactions.

(© Wiley-VCH Verlag GmbH & Co. KGaA, 69451 Weinheim, Germany, 2006)

## Introduction

In order to gain a deeper insight into the nature of the secondary bonding[1] and its relation with the hypercoordination phenomena of group 14 and 15 elements, a large variety of metallocanes of type **I** $D(CH_2CH_2E)_2A$ (D = NR′, O, S; E = O, S, $CH_2$; A = Ge, Sn, Pb, As, Sb or Bi) have been prepared and structurally characterised (Scheme 1).[2–8] In the solid state metallocanes usually exhibit a strong 1,5-transannular interaction between a Lewis acidic acceptor A and a basic donor D atom (D→A), where the coordination mode of the ligand $D(CH_2CH_2E)_2^{2-}$ is formally tridentate, leading to an increase in the coordination number of A. In these compounds the richness of the conformational diversity in the solid state and solution is supported by a wide variety of molecular structural features, for example bond lengths, bond angles, torsion angles and the central eight-membered ring conformation, as well as intermolecular interactions in the crystal.[2]

Crystallographic X-ray studies of the more constrained tricyclic systems of type **II**, known as dibenzometallocines $D(C_6H_4E)_2A$ (Scheme 1), have also shown a 1,5-transannular interaction. These compounds have been long studied in particular where D = S, E = O and A is a d block or light p block element (mainly phosphorus and silicon), meanwhile, with a softer donor atom such as D = E = S the chemistry is fully dominated by the d block metals.[9] In these transition metal complexes the transannular distance between the acidic metal centre and the thioether-like sulfur is usually quite short, suggesting the large capabilities of the $S(C_6H_4S)_2^{2-}$ as a tridentate ligand.

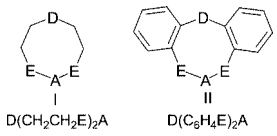


Scheme 1.

We have studied some monohalogenated dibenzometallocines $D(C_6H_4S)_2AHal$ (for A = Sb[5], D = S, Hal = Cl, Br, I; D = O, Hal = Cl; for A = As[10], D = S, Hal = Cl, Br, I) and have shown by means of X-ray crystallographic studies (and also DFT studies in the case of antimony) the acidic behaviour of the central atom, where the A acceptor experiences a structural change from pyramidal tricoordinate to $\psi$-trigonal-bipyramidal tetracoordinate. These results prompted us to extend the chemistry of the ligand $S(C_6H_4S)_2^{2-}$ to other p block heavier elements such as germanium(IV), where structural studies with similar ligands are scarce[11–14] and have mainly focused on metallocanes.[2–4]

Here we report an experimental and theoretical study of type **II** complexes with germanium as the acceptor atom. These compounds are good models for further understand-

[a] Centro de Investigaciones Químicas, Universidad Autónoma del Estado de Hidalgo,
Km. 4.5 Carretera Pachuca-Tulancingo, Pachuca, Hidalgo, C. P. 42076, México
E-mail: jgar@uaeh.edu.mx
[b] Instituto de Química, Universidad Nacional Autónoma de México, Circuito Exterior, Ciudad Universitaria, D. F. México, C. P. 04510, México

 © 2006 Wiley-VCH Verlag GmbH & Co. KGaA, Weinheim 

ing the nature of the D→Ge interaction. After the description of the synthesis of dibenzogermocines and the NMR spectroscopic and X-ray crystallographic data a theoretical study is presented and discussed.

## Results and Discussion

### Synthesis

The ligands $S(C_6H_4SH)_2$ and $O(C_6H_4SH)_2$ were prepared following the reported method.[9,15] The reaction of the corresponding organylgermanium(IV) in THF at 0 °C with the dilithium salt of the ligand, generated in situ from the dithiol and 2 equiv. of *n*BuLi, yielded the corresponding $Ge^{IV}$ complex (see Exp. Sect. for details). Treatment of $S(C_6H_4SLi)_2$ with $PhGeCl_3$ and $Ph_2GeCl_2$ yielded $S(C_6H_4S)_2GePhCl$ (**1**) and $S(C_6H_4S)_2GePh_2$ (**3**), respectively. $S(C_6H_4S)_2GePhBr$ (**2**) was synthesised from **1** by the treatment of excess KBr in a refluxing HBr/benzene mixture, giving **2** as colourless crystals. Treatment of $O(C_6H_4SLi)_2$ with $EtGeCl_3$ and $Ph_2GeCl_2$ yielded $O(C_6H_4S)_2GeEtCl$ (**4**) and $O(C_6H_4S)_2GePh_2$ (**5**), respectively (see Scheme 2).

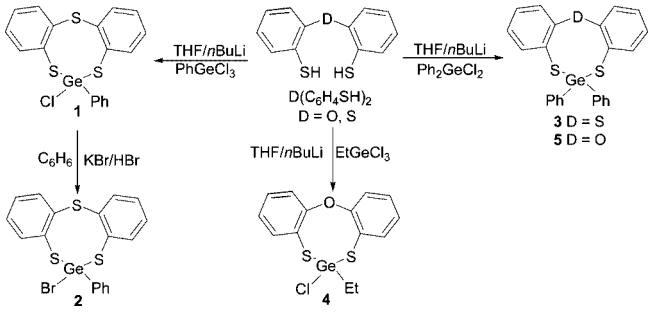


Scheme 2.

All complexes are air-stable, soluble in benzene, toluene, dichloromethane and chloroform, and insoluble in pentane, hexane and 2-propanol.

### Mass Spectra

FAB mass spectra for **1**, **2**, **3** and **5** and electron impact mass spectra for **4** exhibit a low intensity ion with the appropriate isotopic ratio representing the molecular ion ($M^{\cdot+}$); in all cases a basis peak corresponding to the fragment M–L [L = Cl (**1**), Br (**2**), Ph (**3** and **5**), Et (**4**)] is observed and assigned to the $D(C_6H_4S)_2GeL$ [L = Ph (**1**, **2**, **3** and **5**), and Cl (**4**)] tricyclic moiety, confirming the binding of germanium to the sulfur thiolate-like atoms. There are peaks corresponding to the $D(C_6H_4)_2S$ moiety [D = S (**1**, **2**, **3**); O (**4**, **5**)] in all the spectra. In the case of the diphenyl germanium complexes **3** and **5** the cluster peak at 229 *m*/*z* is assigned to the protonated $GePh_2$ fragment. No more peaks could be assigned.

### NMR Spectroscopy

NMR spectra of complexes **1**–**5** were recorded in a $CDCl_3$ solution at room temperature. Chemical shifts are relative to TMS. The assignments of these complexes were carried out by heteronuclear and homonuclear correlation two-dimensional experiments (HETCOR, COLOC and COSY).

$^1$H NMR spectra for complexes **1**–**5** each show four signals for the $DC_6H_4SGe$ moiety in an ABCD pattern, Table 1. In solution the two $DC_6H_4SGe$ halves are equivalent (see Scheme 3). In all complexes, the *ortho* proton 1-H is shifted towards high frequencies with respect to the free

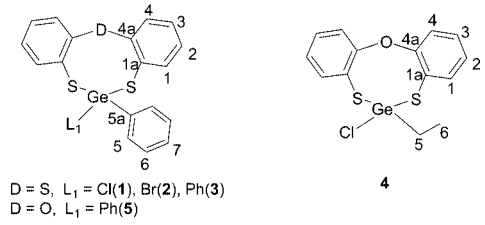


Scheme 3.

Table 1. $^1$H NMR chemical shifts ($\delta$ values [ppm]) for **1**–**5** in $CDCl_3$ at 25 °C.

| Compound | D | $L_1$ | 1-H | 2-H | 3-H | 4-H | 5-H | 6-H | 7-H |
|---|---|---|---|---|---|---|---|---|---|
| **1** | S | Cl | 7.65 | 7.27 | 7.16 | 7.44 | 7.81 | 7.40 | 7.40 |
| **2** | S | Br | 7.65 | 7.28 | 7.16 | 7.44 | 7.78 | 7.39 | 7.39 |
| **3** | S | Ph | 7.66 | 7.13 | 7.18 | 7.44 | 7.63 | 7.34 | 7.34 |
| **4** | O | Cl | 7.53 | 7.23 | 7.15 | 7.13 | 1.80 | 1.18 | – |
| **5** | O | Ph | 7.56 | 7.09 | 7.04 | 6.85 | 7.65 | 7.32 | 7.32 |

Table 2. $^{13}$C NMR chemical shifts ($\delta$ values [ppm]) for **1**–**5** in $CDCl_3$ at 25 °C.

| Compound | D | $L_1$ | C-1 | C-2 | C-3 | C-4 | C-1a | C-4a | C-5 | C-5a | C-6 | C-7 |
|---|---|---|---|---|---|---|---|---|---|---|---|---|
| **1** | S | Cl | 131.2 | 129.9 | 127.5 | 134.2 | 132.3 | 140.7 | 131.2 | 141.4 | 128.9 | 130.9 |
| **2** | S | Br | 131.2 | 129.9 | 127.5 | 134.3 | 132.3 | 140.7 | 131.1 | 141.9 | 128.9 | 132.1 |
| **3** | S | Ph | 134.3 | 127.4 | 128.3 | 134.9 | 137.4 | 139.8 | 133.2 | 138.2 | 128.5 | 130.0 |
| **4** | O | Cl | 132.6 | 127.7 | 125.8 | 120.2 | 126.2 | 152.7 | 23.1 | – | 8.3 | – |
| **5** | O | Ph | 133.7 | 127.5 | 124.6 | 120.6 | 126.6 | 154.8 | 133.6 | 136.4 | 128.4 | 130.1 |

 © 2006 Wiley-VCH Verlag GmbH & Co. KGaA, Weinheim 

neutral ligands.[9,15] In **4** and **5** the *ortho* proton, 4-H, is also observed at higher frequencies.

Proton decoupled $^{13}C$ spectra of complexes **1**–**3** and **5** display ten signals in the aromatic region, Table 2. In **4** the ethyl group is observed at low frequencies (23.1 and 8.3 ppm). In complexes **1**–**5** the values obtained for the variation of the chemical shift ($\Delta\delta$) with respect to the starting materials (free ligands and organogermanium chlorides) show the ipso carbon C-4a and the carbon C-4 at high frequencies; in these compounds the **1**–**3** complexes present large values of $\Delta\delta$. The $\Delta\delta$ value for the C-4a and C-4 in **1** are 8.2 and 4.0 ppm; in **2** they are 8.2 and 4.1 ppm; in **3** they are 7.3 and 4.7 ppm; in **4** they are 0.6 and 1.6 and in **5** they are 2.7 and 2.0 ppm, respectively. In the double phenylated **3** and **5** complexes the $\Delta\delta$ for the ipso carbon C5a presented the smallest values when compared to the diphenylgermanium dichloride ($\delta$ =3.7 ppm in **3** and 1.9 ppm in **5**). The data obtained suggest that the D→Ge transannular interaction in the complexes **3** and **5** is either very weak or completely lacking in solution.

### X-ray Structures of Compounds 1–5

The molecular structures in the crystalline solid state of **1**–**5** were determined by single-crystal X-ray diffraction analyses. The ORTEP drawings are depicted in Figure 1 and selected bond lengths, angles and torsion angles are

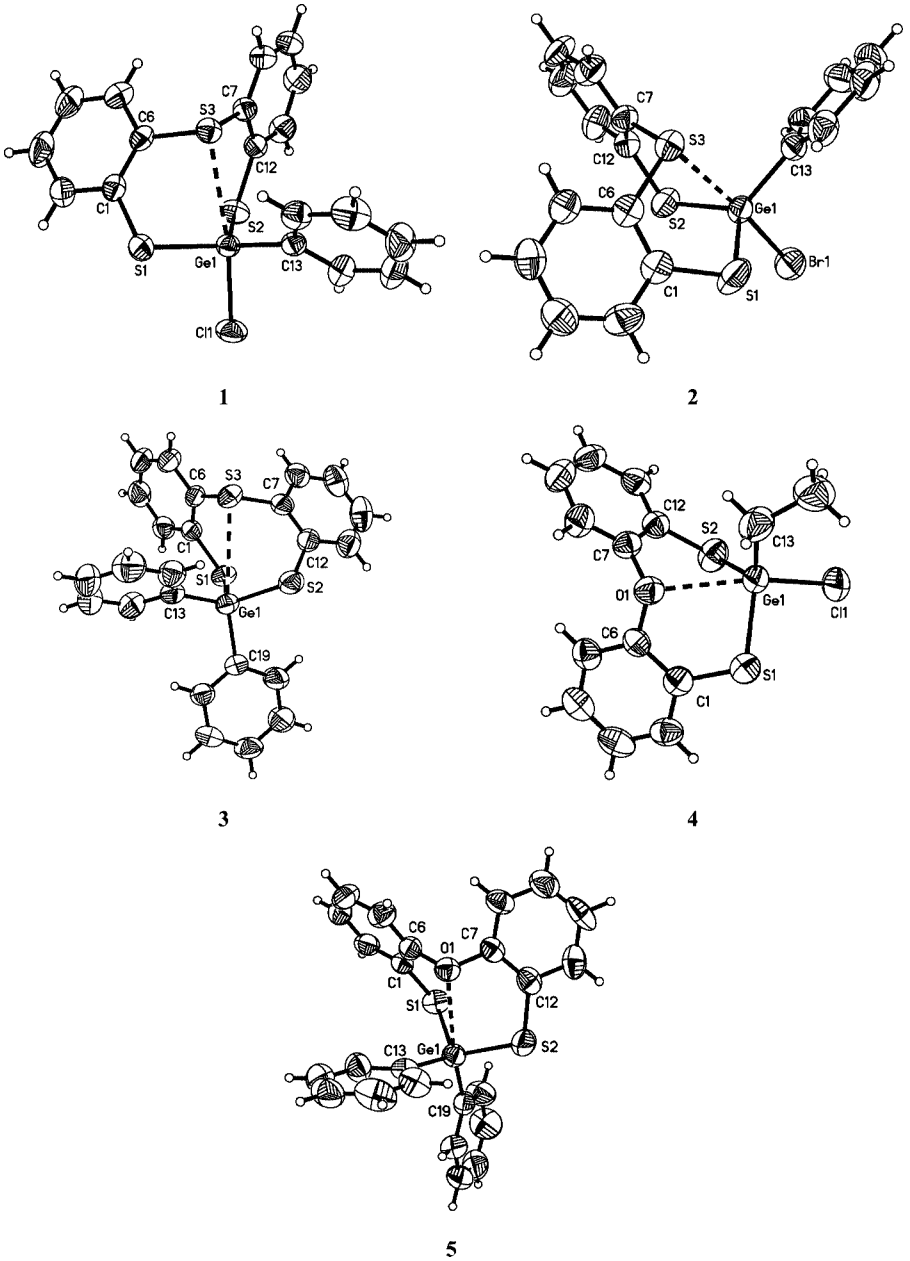


Figure 1. ORTEP diagrams of $S(C_6H_4S)_2GePhCl$ (**1**), $S(C_6H_4S)_2GePhBr$ (**2**), $S(C_6H_4S)_2GePh_2$ (**3**), $O(C_6H_4S)_2GeEtCl$ (**4**) and $O(C_6H_4S)_2GePh_2$ (**5**) (50% probability ellipsoids).

 © 2006 Wiley-VCH Verlag GmbH & Co. KGaA, Weinheim 

given in Table 3. In all compounds, there were no intermolecular interactions between non-hydrogen atoms that were separated by a distance shorter than the sum of their van der Waals radii. This essentially resulted in monomeric molecules.

Table 3. Selected bond lengths [Å] and bond angles [°] of $D(C_6H_4S)_2L_1GeL_2$.

| Compound | **1** | **2** | **3** | **4** | **5** |
|---|---|---|---|---|---|
| D | S | S | S | O | O |
| $L_1$ | Cl1 | Br1 | C19 | Cl1 | C19 |
| $L_2$ | C13 | C13 | C13 | C13 | C13 |
| D→Ge1 | 2.834(1) | 2.782(2) | 3.280(1) | 2.656(3) | 2.872(3) |
| Ge1–S1 | 2.236(1) | 2.228(2) | 2.235(1) | 2.231(1) | 2.229(1) |
| Ge1–S2 | 2.228(1) | 2.216(2) | 2.255(1) | 2.221(1) | 2.239(1) |
| Ge1–$L_1$ | 2.233(1) | 2.401(1) | 1.959(3) | 2.187(1) | 1.938(4) |
| Ge1–$L_2$ | 1.941(3) | 1.943(5) | 1.942(4) | 1.943(4) | 1.954(4) |
| D→Ge1–$L_1$ | 169.57(4) | 175.99(4) | 168.3(1) | 166.97(6) | 169.5(1) |
| S1–Ge1–S2 | 115.35(4) | 114.42(7) | 110.58(4) | 115.47(5) | 111.65(5) |
| S1–Ge1–$L_2$ | 120.5(1) | 120.89(2) | 112.3(1) | 115.0(1) | 113.8(1) |
| S2–Ge1–$L_2$ | 119.0(1) | 120.2(2) | 113.7(1) | 116.7(1) | 111.6(1) |
| $L_1$–Ge1–$L_2$ | 101.6(1) | 98.6(2) | 113.6(1) | 108.8(2) | 113.4(2) |
| S1–Ge1–$L_1$ | 98.47(4) | 97.03(5) | 100.6(1) | 98.6(1) | 100.8(1) |
| S2–Ge1–$L_1$ | 92.46(4) | 95.59(5) | 105.1(1) | 98.86(5) | 104.8(1) |
| C7–D–C6–C1 | 127.6(3) | 125.3(4) | 61.0(3) | 142.9(3) | 87.9(4) |
| C6–D–C7–C12 | –74.4(3) | –77.5(5) | –122.9(3) | –87.4(4) | –137.2(4) |
| S2–Ge1–S1–C1 | –31.1(1) | –40.3(2) | –97.7(1) | –33.0(1) | –94.0(1) |
| S1–Ge1–S2–C12 | 99.1(1) | 100.7(2) | 11.7(1) | 98.6(1) | 31.9(2) |

In all complexes, the Ge–S(thiolate) distances are in good agreement with those reported for eight-membered heterocycles and several other compounds containing germanium–sulfur bonds: 2.191(3) Å in $S(CH_2CH_2S)_2GeCl_2$,[16] 2.154(4)–2.217(4) Å in $O(CH_2CH_2S)_2GeCl_2$,[17] 2.216(1)–2.222(1) and 2.210(3)–2.236(3) Å in the spirocycles $\{O(CH_2CH_2S)_2\}_2Ge$ and $\{S(CH_2CH_2S)_2\}_2Ge$,[18] respectively, 2.111(1)–2.221(1) Å in the homoleptic Ge(S-4-$MeC_6H_4)_4$ compound,[19] but significantly shorter than the reported value in the spirocycle $\{PhP(C_6H_4S)_2\}_2Ge$ with a germanium atom in an octahedral local geometry [2.3429(12)–2.4000(10) Å].[11] The Ge–Cl distances in **1** and **4** are 6 and 4% longer, respectively, than that accepted as the common distance for Ge–Cl (2.10 Å in $GeCl_4$)[20] and similar to those found for $D(CH_2CH_2S)_2GeCl_2$ (D = O[17], S[16]); which are longer than that found in the 9,9-dichloro-9-germafluorene [2.1660(9) Å].[21] The Ge–Br distance is 4% longer than that observed for $GeBr_4$ (2.30 Å)[20] and intermediate between those found in $MeN(CH_2CH_2O)_2GeBr_2$ [2.4148(8) and 2.3215(9) Å].[4] The Ge–C distances are in good agreement with other compounds that contain germanium–carbon bonds.[12,22–24]

In addition to the expected bonding of the two sulfur atoms (thiolate-like) and the two exocyclic $L_1$ and $L_2$ ligands to germanium, a relatively short distance involving the transannular D and Ge atoms is observed (D = S in **1**, **2** and **3**; D = O in **4** and **5**). The S→Ge bond lengths in **1**, **2** and **3** are 2.834(1), 2.782(2) and 3.280(1) Å, respectively, which are 27, 24 and 46% longer than the covalent radii sum of Ge and S (2.24 Å)[25] but significantly shorter than the van der Waals radii sum (3.75 Å).[1,14] The magnitude of these distances is consistent with the existence of a secondary bonding.[1] These S→Ge distances in **1**, **2** and **3** are similar for the spirocycles $S(CH_2CH_2S)_2GeSO(C_2H_4)$ [2.842(1) Å],[2] $[S(CH_2CH_2S)_2]_2Ge$ [3.237(3) and 3.453(3) Å],[18] and $S(CH_2CH_2S)_2GeCl_2$ [3.01(3) Å],[16] and significantly longer than that reported for the spirocycle $[S(C_6H_4O)_2]_2Ge$ [2.447(1) Å].[14]

The O→Ge distances in **4** [2.656(3) Å] and **5** [2.872(3) Å] are significantly shorter than the van der Waals radii sum of Ge and O (3.47 Å)[1] and 41% and 53% longer than the covalent radii sum (1.88 Å),[2,25] respectively. The observed O→Ge bond lengths in **4** and **5** are significantly longer than those reported for $O(CH_2CH_2S)_2GeCl_2$ [2.36(1) and 2.39(1) Å],[17] for the spirocycles containing pentacoordinate germanium $O(CH_2CH_2S)_2GeSO(C_2H_4)$ [2.492(3) Å] and $O(CH_2CH_2S)_2GeS_2(C_2H_4)$ [2.616(1) Å], and shorter than those reported for the spiro compound containing hexacoordinate germanium $[O(CH_2CH_2S)_2]_2Ge$ displaying two crystallographic independent molecules in the solid state [2.914(3), 3.040(3), 2.955(3) and 2.946(3) Å][18]. If the transannular interaction (D→Ge) is taken into account, the geometry of the coordination sphere of the germanium atom can be described as trigonal bipyramidal (TBP), where the halogen (for **1**, **2** and **4**), carbon (for **3** and **5**) and D donor atoms (S for **1**, **2**, **3**, O for **4**, **5**) are in the axial positions, meanwhile the two thiolate-like sulfur and carbon atoms occupy equatorial positions.

Following the Holmes procedure based on the donor-acceptor atom bond length,[26–28] the degree of displacement at the Ge atom from tetrahedral to trigonal-bipyramidal geometry (TBP) was determined. Additionally and in order to evaluate the magnitude of the interaction based

Table 4. Comparison of D→Ge–$L_1$ geometrical bond parameters in complexes **1**–**5**; bond lengths [Å], bond angles [°], % TBP and Pauling bond order.

| Compound | D | $L_1$ | $L_2$ | D→Ge | D→Ge–L1 | % TBP | $\Delta d$[a] | BO[b] D→Ge |
|---|---|---|---|---|---|---|---|---|
| **1** | S | Cl | Ph | 2.834(1) | 169.57(4) | 60.7 | 0.594 | 0.1453 |
| **2** | S | Br | Ph | 2.782(2) | 175.99(4) | 64.1 | 0.542 | 0.1721 |
| **3** | S | Ph | Ph | 3.280(1) | 168.3(1) | 31.1 | 1.038 | 0.0343 |
| **4** | O | Cl | Et | 2.656(3) | 166.97(6) | 51.2 | 0.778 | 0.0799 |
| **5** | O | Ph | Ph | 2.872(3) | 169.5(1) | 37.6 | 0.992 | 0.0399 |

[a] Bond widening, $\Delta d = (d_{exp} - \Sigma r_{cov})$, according to standard bond lengths $d$(Ge S) 2.24, $d$(Ge O) 1.88.[1,2,14,25] [b] Mode of calculation $BO = 10^{-(1.41 \cdot \Delta d)}$.[29,30]

 © 2006 Wiley-VCH Verlag GmbH & Co. KGaA, Weinheim 

on the distances, the Pauling-type bond order, BO, for the transannular interactions (D→Ge) in all compounds was also calculated.[29,30] These results are reported in Table 4.

The TBP% for halogen compounds are larger than those for other compounds in the series, indicating the importance of attaching an electronegative ligand to germanium in order to expand its coordination number.

In all compounds the eight-membered ring conformation can be described as a twist boat ($C_1$ symmetry) according to the torsion angle data, where the double phenylated **3** and **5** compounds are most distorted when the TBP and BO order are smaller.

## Theoretical Study

In order to study the intramolecular interactions (D→Ge) we carried out theoretical calculations. Hence, each one of the compounds **1**–**5** was modelled with a GaussView visualizer,[31] followed by a geometry optimisation with the PM3 semi-empirical method[32]. A further geometry optimisation was carried out with density functional theory (DFT) using the hybrid B3LYP functional[33]. For our DFT computations we employed the relativistic Stuttgart-Dresden Effective Core Potential for Ge[34] along with its Triple-Zeta correlation consistent basis set[35]. For all the other atoms in compounds **1** to **5**, Dunning's Double-Zeta correlation consistent all electron basis set[36] was used. The basis sets we employed include polarisation and diffusion functions. Hereafter these calculations will be referred to as B3LYP ccSDDTZ. The computed bond orders, interatomic overlaps and charges reported herein were computed within the NBO approach.[37] All our calculations were carried out with the suite of programmes in Gaussian 03.[38]

## Theoretical Results and Discussion

All optimised molecular conformations for **1**–**5** are in good agreement when compared with those observed by X-ray crystallographic data. A selected set of bond lengths and bond and torsion angles is listed in Table 5. It is relevant to mention that we explored the two possible geometrical isomers for complexes **1**, **2** and **4**, i.e. those with the halogen ligand in an axial or in an equatorial position, where isomers that resemble the conformation determined by X-ray diffraction experiments were the most stable. These correspond to the lowest energy conformation of those obtained with the procedure previously outlined. A comparison between the X-ray and the computed D–Ge bond lengths shows a remarkable difference for compounds **1**, **2** and **3**. The largest difference is for compound **2** (≈0.39 Å), followed by that of compounds **1** and **3**, ≈0.32 Å and ≈0.05 Å respectively, whereas for compounds **4** and **5** we noticed that the distances O→Ge are ca. 0.13 Å and 0.07 Å larger than those obtained by X-ray spectroscopy at 298 K. The DFT calculations at the level employed reproduce well the experimental overall geometries; the observed differences in the geometrical parameters are not unusual[3] and may be due to the temperature of the diffraction experiments as well as the packing forces in the crystal.

## NBO Analysis

In Table 6 the computed Wiberg bond index values for a selected number of atoms in compounds **1**–**5** are reported. It is worth noting that this index has approximately the same value for all germanium–sulfur thiolate bonds. However, in **1**–**3** this bond index is bigger for the S(thiolate-

Table 5. Selected bond lengths [Å] and angles [°] for compounds **1**–**5**. **a** columns are data from X-ray characterisation. **b** columns are data obtained from B3LYP ccSDDTZ computations.

| Compound | **1a** | **1b** | **2a** | **2b** | **3a** | **3b** | **4a** | **4b** | **5a** | **5b** |
|---|---|---|---|---|---|---|---|---|---|---|
| D | S | S | S | S | S | S | O | O | O | O |
| L1 | Cl1 | Cl1 | Br1 | Br1 | C19 | C19 | Cl1 | Cl1 | C19 | C19 |
| L2 | C13 | C13 | C13 | C13 | C13 | C13 | C13 | C13 | C13 | C13 |
| D→Ge1 | 2.834(1) | 3.157 | 2.782(2) | 3.181 | 3.280(1) | 3.328 | 2.656(3) | 2.781 | 2.872(3) | 2.944 |
| Ge1–S1 | 2.236(1) | 2.278 | 2.228(2) | 2.280 | 2.235(1) | 2.281 | 2.231(1) | 2.272 | 2.229(1) | 2.286 |
| Ge1–S2 | 2.228(1) | 2.273 | 2.216(2) | 2.273 | 2.255(1) | 2.297 | 2.221(1) | 2.278 | 2.239(1) | 2.288 |
| Ge1–L1 | 2.233(1) | 2.215 | 2.401(1) | 2.377 | 1.959(3) | 1.970 | 2.187(1) | 2.210 | 1.938(4) | 1.966 |
| Ge1–L2 | 1.941(3) | 1.953 | 1.943(5) | 1.955 | 1.942(4) | 1.960 | 1.943(4) | 1.969 | 1.954(4) | 1.960 |
| D→Ge1–L1 | 169.57(4) | 169.79 | 175.99(4) | 169.69 | 168.3(1) | 170.32 | 166.97(6) | 169.89 | 169.5(1) | 168.40 |
| D→Ge1–S1 | 77.60(3) | 72.68 | 80.64(5) | 72.14 | 73.36(3) | 73.71 | 74.35(6) | 72.75 | 71.94(6) | 70.80 |
| D→Ge1–S2 | 80.76(3) | 76.42 | 82.45(5) | 76.01 | 68.78(3) | 69.61 | 75.17(6) | 73.40 | 71.98(6) | 69.56 |
| D→Ge1–L2 | 88.7(1) | 84.90 | 85.3(2) | 84.40 | 78.2(1) | 78.66 | 84.2(1) | 84.16 | 76.8(1) | 79.05 |
| S1–Ge1–L1 | 98.47(4) | 102.75 | 97.03(5) | 103.09 | 100.6(1) | 102.79 | 98.57(5) | 102.08 | 100.8(1) | 104.43 |
| S2–Ge1–L1 | 92.46(4) | 97.84 | 95.59(5) | 98.27 | 105.1(1) | 104.07 | 98.86(5) | 101.84 | 104.8(1) | 103.83 |
| S1–Ge1–S2 | 115.35(4) | 114.14 | 114.42(7) | 113.96 | 110.58(4) | 111.01 | 115.47(5) | 114.93 | 111.65(5) | 112.52 |
| S1–Ge1–L2 | 120.5(1) | 115.14 | 120.9(2) | 114.68 | 112.4(1) | 113.63 | 115.0(1) | 113.92 | 113.8(1) | 110.83 |
| S2–Ge1–L2 | 119.0(1) | 118.13 | 120.2(2) | 117.81 | 113.7(1) | 113.49 | 116.7(1) | 115.79 | 111.6(1) | 112.28 |
| L1–Ge1– L2 | 101.6(1) | 105.30 | 98.6(2) | 105.91 | 113. 6(1) | 110.90 | 108.8(2) | 105.94 | 113.4(2) | 112.52 |
| C6–D–C7 | 101.7(2) | 103.58 | 101.7(3) | 103.56 | 103.0(2) | 103.57 | 116.6(3) | 118.33 | 116.3(3) | 118.28 |
| S2–Ge1–S1–C1 | –31.1(1) | –19.40 | –40.3(2) | –18.33 | –97.7(1) | –95.25 | –33.0(1) | –29.68 | –94.0(1) | –91.76 |
| S1–Ge1–S2–C12 | 99.1(1) | 97.02 | 100.7(2) | 96.56 | 11.7(1) | 15.49 | 98.6(1) | 95.50 | 31.9(2) | 23.31 |

 © 2006 Wiley-VCH Verlag GmbH & Co. KGaA, Weinheim 

like)→Ge than for the S(thioether-like)→Ge interaction. A similar trend is exhibited by the O→Ge interaction in compounds **4** and **5**.

Table 6. NBO values of Wiberg bond index for a selected number of atoms in compounds **1**–**5**. Data from B3LYP ccSDDTZ computations.

| Compound | **1** | **2** | **3** | **4** | **5** |
|---|---|---|---|---|---|
| D | S | S | S | O1 | O1 |
| L1 | Cl1 | Br1 | C19 | Cl1 | C19 |
| L2 | C13 | C13 | C13 | C13 | C13 |
| D→Ge1 | 0.1080 | 0.1027 | 0.0594 | 0.0579 | 0.0357 |
| Ge1–S1 | 0.8308 | 0.8303 | 0.8561 | 0.8438 | 0.8478 |
| Ge1–S2 | 0.8506 | 0.8543 | 0.8185 | 0.8349 | 0.8350 |
| Ge1–L1 | 0.7757 | 0.8356 | 0.7233 | 0.7880 | 0.7326 |
| Ge1–L2 | 0.7154 | 0.7149 | 0.7260 | 0.7538 | 0.7292 |
| D–C6 | 1.0088 | 1.0091 | 1.0258 | 0.9120 | 0.9089 |
| D–C7 | 1.0201 | 1.0207 | 1.0121 | 0.9012 | 0.9245 |
| S1–C1 | 1.0557 | 1.0551 | 1.0628 | 1.0587 | 1.0587 |
| S2–C12 | 1.0634 | 1.0611 | 1.0558 | 1.0587 | 1.0565 |

To study the nature of this short Wiberg bond index, the computed overlap-weighted natural atomic orbital values are reported in Table 7. From this table it is possible to observe that compounds **1**–**3**, which contain the S→Ge interaction, have larger overlap values than compounds **4** and **5**, which contain the O→Ge interaction. It is important to observe that **3** and **5** exhibit the smallest overlap value in these two groups of molecules.

Table 7. NBO computed overlap-weighted natural atomic orbital values for compounds **1**–**5**. Data from computations with B3LYP cc-SDDTZ basis sets.

| Compound | **1** | **2** | **3** | **4** | **5** |
|---|---|---|---|---|---|
| D | S3 | S3 | S3 | O1 | O1 |
| L1 | Cl1 | Br1 | C19 | Cl1 | C19 |
| L2 | C13 | C13 | C13 | C13 | C13 |
| D→Ge1 | 0.1484 | 0.1429 | 0.0906 | 0.0877 | 0.0559 |
| Ge1–S1 | 0.7770 | 0.7728 | 0.7757 | 0.7880 | 0.7685 |
| Ge1–S2 | 0.7899 | 0.7885 | 0.7516 | 0.7810 | 0.7632 |
| Ge1–L1 | 0.7314 | 0.7899 | 0.7318 | 0.7389 | 0.7410 |
| Ge1–L2 | 0.7403 | 0.7336 | 0.7406 | 0.7614 | 0.7438 |

As a final element for our theoretical analysis we report, in Table 8, the charges obtained within the NBO procedure. It may be observed that the sulfur donor atoms in compounds **1**–**3** exhibit approximately the same positive charge, whereas the thiolate-like sulfur atoms roughly have the same negative charge. This may be a consequence of the different environments of the sulfur atoms in the dibenzotrithiagermocines: atoms S1 and S2 are dicoordinate and covalently bonded to a rather electropositive germanium atom while the S3 atom is bonded to a more electronegative carbon atom and also shares its electron density with the acidic germanium(IV) atom. The O1 atom in **4** and **5** has the same negative charge, according to the electronegativity of oxygen.

Table 8. Selected atom charges obtained within the NBO procedure for compounds **1**–**5**. Computations with B3LYP cc-SDDTZ basis sets.

| Compound | **1** | **2** | **3** | **4** | **5** |
|---|---|---|---|---|---|
| D | S3 | S3 | S3 | O1 | O1 |
| D | 0.30 | 0.30 | 0.30 | –0.56 | –0.56 |
| S1 | –0.13 | –0.13 | –0.13 | –0.12 | –0.13 |
| S2 | –0.11 | –0.11 | –0.16 | –0.11 | –0.15 |
| Ge3 | 1.28 | 1.19 | 1.40 | 1.29 | 1.40 |
| Cl1 | –0.41 | – | – | –0.41 | – |
| Br1 | – | –0.32 | – | – | – |
| C13 | –0.51 | –0.51 | –0.50 | –0.89 | –0.50 |
| C19 | – | – | –0.50 | – | –0.50 |

## Discussion

The calculated Wiberg bond index values in Table 6 show the existence of a bond interaction between the D→Ge (where D = S or O) in compounds **1** to **5**. The reported numerical values in Table 7 for the NAO overlap-weighted analysis confirm this bond possibility and give it a covalent like character. However, the reported atomic charges in Table 8 suggest the possibility of interatomic interactions with a Coulombic character.

We may conclude that the interaction S3→Ge in **1** and **2** has two components: one covalent and a second one with a Coulombic character. In these two compounds the interaction is dominated by a covalent interaction, which screens the positive–positive S3–Ge Coulomb interaction. This behaviour is enhanced by the halogen atom coordinated to Ge and its role in the Coulomb field within the molecule. Similar arguments may be given to the O1→Ge interaction in **4**. However, in this case, the negative charge on the oxygen donor atom increases the intensity of the Coulomb field making this the dominant part of this interaction.

In compounds **3** and **5** we have the opportunity to appreciate how this covalent-Coulombic dual character works. In this case we do not have halogen atoms to enhance the interchange. Hence S3→Ge in **3** has a more covalent than Coulombic character, whereas O1→Ge is dominated by a strong Coulomb interaction, which makes their intramolecular distances shorter supporting the results of the structural analyses in terms of our TBP and BO analyses for these complexes.

## Conclusions

In order to study the phenomena of hypercoordination in germanium heterocyclic compounds we have synthesised and fully structurally characterised five new dibenzogermocines **1**–**5** by employing tridentate $[D(C_6H_4S)_2]^{2-}$ ligands. All compounds exhibit a bipyramidal-trigonal local geometry of the germanium(IV) atom with intramolecular interactions D→Ge. Geometry optimisations at the DFT level of theory, using the hybrid functional B3LYP renders molecular conformations in good agreement to those determined by X-ray diffraction studies. An NBO analysis was carried out on this electron structure. The TBP and BO analysis

 © 2006 Wiley-VCH Verlag GmbH & Co. KGaA, Weinheim 

for the crystalline molecular structure and our NBO analysis show similar behaviour for the D→Ge interaction, which is enhanced by the presence of the halogen ligands.

## Experimental Section

**General Procedures:** All manipulations were performed under a dry, oxygen-free argon atmosphere using standard Schlenk techniques. Solvents were dried by standard methods and distilled prior to use. Melting points were determined with a Melt-Temp II instrument and are uncorrected. Spectra were recorded with the following instruments. Mass spectra: FAB-mass spectra were recorded with a JEOL JMS-AX505HA by using a Xe beam at 6 keV, with nitrobenzyl alcohol (NBA) as matrix. For EI, a Hewlett Packard 5989A mass spectrometer was used. Elemental analyses: Perkin–Elmer Series II CHNS/O Analyser. The IR spectra were record in the 4000-400 $cm^{-1}$ range with a Perkin–Elmer System 2000 FT-IR spectrometer, as KBr pellets. NMR: Jeol Eclipse 400 spectrometer; with the residual protio-solvent signal used as referenced for $^1H$ NMR spectra. $^{13}C\{^1H\}$ NMR spectra were referred through the solvent peaks. Chemical shifts are quoted on the $\delta$ scale (downfield shifts are positive) relative to tetramethylsilane ($^1H$, $^{13}C\{^1H\}$ NMR spectra). Spectra were recorded at 25 °C. $^1H$ NMR spectra; 399.78 MHz, $^{13}C\{^1H\}$ NMR spectra; 100.53 MHz. $S(C_6H_4SH)_2$[15] and $O(C_6H_4SH)_2$[9] were synthesised according to literature methods. $PhGeCl_3$, $Ph_2GeCl_2$, $EtGeCl_3$, *n*BuLi (1.6 M, in hexanes), KBr and HBr were purchased from Aldrich and Fluka and were used as supplied.

**$S(C_6H_4S)_2GePhCl$ (1):** *n*BuLi in hexanes (1.6 M, 5.5 mL, 8.8 mmol) was added to a solution containing $S(C_6H_4SH)_2$ (1.0 g, 4.0 mmol) in THF (40 mL) at 0 °C. After the solution was stirred for 30 min, a red solution resulted, $PhGeCl_3$ (0.66 mL, 4.0 mmol) was added via a syringe. The solution was kept overnight at room temperature. The colourless solution was refluxed for 4 h, and then the resultant heterogeneous reaction mixture was cooled to room temperature. The precipitate of LiCl was removed by filtration. Volatiles were removed under an argon flow to provide colourless crystals of **1**, which were washed with hexanes (40 mL) and filtered by suction. Yield: 1.50 g (86%). Mass spectrum (FAB+) *m*/*z* (rel int) = 434 (5) [$M^+$], 399 (50) [$M^+$ – Cl], 216 (45) [$M^+$ – Cl–PhSGe]. M.p. 201–203 °C. $S(C_6H_5S)_2GePhCl$: calcd. C 49.56, H 3.22; found C 49.76, H 3.20. $^1H$ NMR ($CDCl_3$): $\delta$ = 7.16 (ddd, $^3J_{3\text{-H},2\text{-H}} = {}^3J_{3\text{-H},4\text{-H}}$ = 7.74, $^4J_{3\text{-H},1\text{-H}}$ = 1.44 Hz, 2 H, 3-H), 7.27 (ddd, $^3J_{2\text{-H},1\text{-H}} = {}^3J_{2\text{-H},3\text{-H}}$ = 7.74, $^4J_{2\text{-H},4\text{-H}}$ = 1.44 Hz, 2 H, 2-H), 7.40 (m, 3 H, 6-H and 7-H), 7.44 (dd, $^3J_{4\text{-H},3\text{-H}}$ = 7.74, $^4J_{4\text{-H},2\text{-H}}$ = 1.44 Hz, 2 H, 4-H), 7.65 (dd, $^3J_{1\text{-H},2\text{-H}}$ = 7.74, $^4J_{1\text{-H},3\text{-H}}$ = 1.44 Hz, 2 H, 1-H), 7.81 (m, 2 H, 5-H) ppm. $^{13}C\{^1H\}$ NMR ($CDCl_3$): $\delta$ = 127.5, 128.9, 129.9, 130.9, 131.1, 131.2, 132.2, 134.2, 140.7, 141.5 ppm. IR (KBr pellet): $\tilde{\nu}$ = 3045, 1568, 1480, 1445, 1430, 1247, 1078, 1040, 1032, 851, 754, 733, 714, 689, 657 $cm^{-1}$.

**$S(C_6H_4S)_2GePhBr$ (2):** $S(C_6H_4S)_2GePhCl$ (**1**, 0.26 g, 0.60 mmol), KBr (0.18 g, 1.5 mmol) and HBr 48% (2 mL) were suspended in benzene (25 mL) and refluxed for 16 h. The water was removed from the resulting colourless solution by means of a Dean–Stark trap. The solution obtained was dried by means of a column of Celite and $Na_2SO_4$. The solution was left under an argon flow to provide colourless crystals of **2**, which were washed with hexanes (40 mL) and filtered by suction. Yield: 180 mg (63%). Mass spectrum (FAB+) *m*/*z* (rel int) = 478 (3) [$M^+$], 399 (50) [$M^+$ – Cl], 216 (20) [$M^+$ – Cl – PhSGe]. M.p. 197–199 °C. $S(C_6H_5S)_2GePhBr$: calcd. C 45.23, H 2.74; found C 45.96, H 2.74. $^1H$ NMR ($CDCl_3$): $\delta$ = 7.16 (ddd, $^3J_{3\text{-H},2\text{-H}} = {}^3J_{3\text{-H},4\text{-H}}$ = 7.68, $^4J_{3\text{-H},1\text{-H}}$ = 1.48 Hz, 2 H, 3-H), 7.27 (ddd, $^3J_{2\text{-H},1\text{-H}} = {}^3J_{2\text{-H},3\text{-H}}$ = 7.68, $^4J_{2\text{-H},4\text{-H}}$ = 1.48 Hz, 2 H, 2-H), 7.39 (m, 3 H, 6-H and 7-H), 7.44 (dd, $^3J_{4\text{-H},3\text{-H}}$ = 7.68, $^4J_{4\text{-H},2\text{-H}}$ = 1.48 Hz, 2 H, 4-H), 7.65 (dd, $^3J_{1\text{-H},2\text{-H}}$ = 7.68, $^4J_{1\text{-H},3\text{-H}}$ = 1.48 Hz, 2 H, 1-H), 7.78 (m, 2 H, 5-H) ppm. $^{13}C\{^1H\}$ NMR ($CDCl_3$): $\delta$ = 127.5, 128.9, 129.9, 130.9, 131.0, 132.1, 132.3, 134.3, 140.7,141.9 ppm. IR (KBr pellet): $\tilde{\nu}$ = 3050, 1568, 1445, 1442, 1249, 1081, 1039, 862, 735, 730, 710, 692 $cm^{-1}$.

**$S(C_6H_5S)_2GePh_2$ (3):** This compound was prepared in a similar fashion to compound **1**, with $S(C_6H_4SH)_2$ (0.42 g, 1.68 mmol), *n*BuLi in hexanes (1.6 M, 2.3 mL, 3.7 mmol) and $Ph_2GeCl_2$ (0.35 mL, 1.68 mmol). Colourless crystals were obtained. Yield: 0.50 g (63%). Mass spectrum (FAB+) *m*/*z* (rel int) = 476 (18) [$M^+$], 399 (base peak) [$M^+$ – Ph], 216 (65) [$M^+$ – Ph – Ph – SGe]. M.p. 126–128 °C. $S(C_6H_5S)_2Ph_2Ge$: calcd. C 60.66, H 3.82; found C 60.83, H 3.98. $^1H$ NMR ($CDCl_3$): $\delta$ = 7.13 (ddd, $^3J_{2\text{-H},1\text{-H}} = {}^3J_{2\text{-H},3\text{-H}}$ = 7.72, $^4J_{2\text{-H},4\text{-H}}$ = 1.44 Hz, 2 H, 2-H), 7.18 (ddd, $^3J_{3\text{-H},2\text{-H}} = {}^3J_{3\text{-H},4\text{-H}}$ = 7.72, $^4J_{3\text{-H},1\text{-H}}$ = 1.44 Hz, 2 H, 3-H), 7.34 (m, 6 H, 6-H and 7-H), 7.44 (dd, $^3J_{4\text{-H},3\text{-H}}$ = 7.72, $^4J_{4\text{-H},2\text{-H}}$ = 1.44 Hz, 2 H, 4-H), 7.63 (m, 4 H, 5-H), 7.66 (dd, $^3J_{1\text{-H},2\text{-H}}$ = 7.72, $^4J_{1\text{-H},3\text{-H}}$ = 1.44 Hz, 2 H, 1-H) ppm. $^{13}C\{^1H\}$ NMR ($CDCl_3$): $\delta$ = 127.4, 128.4, 128.5, 130.0, 133.2, 134.3, 134.9, 137.4, 138.2, 139.8 ppm. IR (KBr pellet): 3066, 3047, 1568, 1480, 1444, 1431, 1248, 1085, 1040, 859, 752, 734, 716, 693 $cm^{-1}$.

**$O(C_6H_4S)_2GeEtCl$ (4):** This compound was prepared in a similar fashion to compound **1**, with $O(C_6H_4SH)_2$ (0.92 g, 3.9 mmol), *n*BuLi in hexanes (1.6 M, 5.0 mL, 8.0 mmol) and $EtGeCl_3$ (0.5 mL, 3.9 mmol). The solid was filtered and recrystallised from *i*-PrOH. Colourless crystals were obtained. Yield: 0.20 g (28%). Mass spectrum (EI-MS, $CHCl_3$, 30 eV) *m*/*z* (rel int) = 370 (10) [$M^+$], 341 (20) [$M^+$ – Et], 305 (10) [$M^+$ – Et – Cl], 200 (base peak) [$M^+$ – Et–Cl–GeS]. M.p. 96–98 °C. $O(C_6H_4S)_2EtGeCl$: calcd. C 45.51, H 3.55; found C 45.80, H 3.55. $^1H$ NMR ($CDCl_3$): $\delta$ = 1.18 (t, $^3J_{6\text{-H},5\text{-H}}$ = 7.70 Hz, 3 H, 6-H), 1.80 (q, $^3J_{5\text{-H},6\text{-H}}$ = 7.70 Hz, 2 H, 5-H), 7.13 (dd, $^3J_{4\text{-H},3\text{-H}}$ = 7.70, $^4J_{4\text{-H},2\text{-H}}$ = 1.48 Hz, 2 H, 4-H), 7.15 (ddd, $^3J_{2\text{-H},1\text{-H}} = {}^3J_{2\text{-H},3\text{-H}}$ = 7.70, $^4J_{2\text{-H},4\text{-H}}$ = 1.48 Hz, 2 H, 2-H), 7.23 (ddd, $^3J_{3\text{-H},2\text{-H}} = {}^3J_{3\text{-H},4\text{-H}}$ = 7.70, $^4J_{3\text{-H},1\text{-H}}$ = 1.48 Hz, 2 H, 3-H), 7.53 (dd, $^3J_{1\text{-H},2\text{-H}}$ = 7.70, $^4J_{1\text{-H},3\text{-H}}$ = 1.48 Hz, 2 H, 1-H) ppm. $^{13}C\{^1H\}$ NMR ($CDCl_3$): $\delta$ = 8.3, 23.0, 120.2, 125.8, 126.2, 132.6, 152.7 ppm. IR (KBr pellet): 3061, 2958, 2923, 2868, 1564, 1462, 1440, 1210, 1061, 869, 799, 757, 732, 700 $cm^{-1}$.

**$O(C_6H_5S)_2GePh_2$ (5):** This compound was prepared in a similar fashion to compound **1**, with $O(C_6H_4SH)_2$ (0.39 g, 1.66 mmol), *n*BuLi in hexanes (1.6 M, 2.3 mL, 3.7 mmol) and $Ph_2GeCl_2$ (0.35 mL, 1.68 mmol). Colourless crystals were obtained. Yield: 0.20 g (26%). Mass spectrum (FAB+) *m*/*z* (rel int) = 460 (35) [$M^+$], 383 (base peak) [$M^+$ – Ph], 200 (95) [$M^+$ – Ph – PhGeS]. M.p. 105–107 °C. $O(C_6H_5S)_2Ph_2Ge$: calcd. C 62.78, H 3.95; found C 63.04, H 3.97. $^1H$ NMR ($CDCl_3$): $\delta$ = 6.85 (dd, $^3J_{4\text{-H},3\text{-H}}$ = 7.36, $^4J_{4\text{-H},2\text{-H}}$ = 1.80 Hz, 2 H, 4-H), 7.04 (ddd $^3J_{3\text{-H},2\text{-H}} = {}^3J_{3\text{-H},4\text{-H}}$ = 7.36, $^4J_{3\text{-H},1\text{-H}}$ = 1.80 Hz, 2 H, 3-H), 7.09 (ddd, $^3J_{2\text{-H},1\text{-H}} = {}^3J_{2\text{-H},3\text{-H}}$ = 7.36, $^4J_{2\text{-H},4\text{-H}}$ = 1.80 Hz, 2 H, 2-H), 7.32 (m, 6 H, 6-H and 7-H), 7.56 (dd, $^3J_{1\text{-H},2\text{-H}}$ = 7.36, $^4J_{1\text{-H},3\text{-H}}$ = 1.80 Hz, 2 H, 1-H), 7.65 (m, 4 H, 5-H[5]) ppm. $^{13}C\{^1H\}$ NMR ($CDCl_3$): $\delta$ = 120.6, 124.7, 126.6, 127.5, 128.4, 130.1, 133.6, 133.7, 136.4, 154.8 ppm. IR (KBr pellet): 3047, 3011, 1565, 1462, 1430, 1249, 1214, 1089, 1063, 870, 800, 763, 755, 733, 696, 669 $cm^{-1}$.

**X-ray Crystallography:** Suitable single crystals of the complexes **1**, **2**, **3** and **5** were grown by slow evaporation from a chloroform solution. Compound **4** was crystallised from *i*-PrOH. X-ray diffraction data on **1**–**5** were collected at room temperature on a CCD Smart 6000 diffractometer through the use of Mo-$K_\alpha$ radiation ($\lambda$ = 0.71073 Å, graphite monochromator). Data were integrated,

 © 2006 Wiley-VCH Verlag GmbH & Co. KGaA, Weinheim 

Table 9. Selected crystallographic data for compounds **1**–**5**.

| Compound | **1** | **2** | **3** | **4** | **5** |
|---|---|---|---|---|---|
| Empirical formula | $C_{18}H_{13}ClGeS_3$ | $C_{18}H_{13}BrGeS_3$ | $C_{24}H_{18}GeS_3$ | $C_{14}H_{13}ClGeOS_2$ | $C_{24}H_{18}GeOS_2$ |
| $M_r$ [g·mol$^{-1}$] | 433.50 | 477.96 | 475.15 | 369.40 | 459.09 |
| Crystal size [mm] | 0.6×0.2×0.1 | 0.6×0.13×0.08 | 0.5×0.3×0.13 | 0.12×0.26×0.60 | 0.17×0.23×0.48 |
| Crystal system | monoclinic | triclinic | monoclinic | monoclinic | triclinic |
| Space group | *P*21/*c* | $P\bar{1}$ | *P*21/*n* | *P*21/*n* | $P\bar{1}$ |
| $\rho_{calc}$ [Mg·m$^{-3}$] | 1.592 | 1.712 | 1.440 | 1.593 | 1.441 |
| Z | 4 | 2 | 4 | 4 | 2 |
| *a* [Å] | 9.7904(6) | 8.9753(9) | 10.8082(9) | 10.0723(9) | 9.3682(8) |
| *b* [Å] | 10.2618(7) | 9.836(1) | 14.626(1) | 11.301(1) | 9.3892(8) |
| *c* [Å] | 18.296(1) | 12.083(1) | 13.961(1) | 13.850(1) | 12.376(1) |
| *α* [°] | 90 | 79.655(2) | 90 | 90 | 85.188(2) |
| *β* [°] | 100.305(2) | 72.417(3) | 96.755(2) | 102.297(2) | 83.538(2) |
| *γ* [°] | 90 | 66.041(2) | 90 | 90 | 78.649(2) |
| *V* [Å$^3$] | 1808.5(2) | 927.3(2) | 2191.6(3) | 1540.3(2) | 1058.4(2) |
| *μ* [mm$^{-1}$] | 2.183 | 4.139 | 1.691 | 2.421 | 1.656 |
| *F*(000) | 872 | 472 | 968 | 744 | 468 |
| GoF | 0.909 | 0.963 | 0.811 | 0.837 | 0.930 |
| Abs. correction | SADABS | SADABS | SADABS | SADABS | SADABS |
| Reflections collected | 11696 | 6117 | 14261 | 10798 | 7098 |
| Unique reflections $R_{int}$ | 3540; 0.0467 | 3624; 0.0304 | 4296; 0.0568 | 3362; 0.0480 | 4167; 0.0289 |
| $R_1$, $wR_2$ [$I>2\sigma(I)$] | 0.0357, 0.0794 | 0.0440, 0.1144 | 0.0399, 0.0771 | 0.0426, 0.0892 | 0.0450, 0.0960 |
| $R_1$, $wR_2$ (all data) | 0.0566, 0.0851 | 0.0785, 0.1249 | 0.0800, 0.0859 | 0.0842, 0.0991 | 0.0770, 0.1168 |
| Large residuals [e·Å$^{-3}$] | 0.715/–0.427 | 0.592/–0.790 | 0.496/–0.268 | 0.646/–0.322 | 0.524/–0.260 |

scaled, sorted and averaged using the SMART software package. The structures were solved by direct methods, using SHELXTL NT Version 5.10 and refined by full-matrix least-squares against $F^2$.[39] An empirical absorption correction based on the multiple measurement of equivalent reflections was applied by using the programme SADABS.[40] The displacement parameters of non-hydrogen atoms were refined anisotropically. The positions of the hydrogen atoms were kept fixed with a common isotropic displacement parameter. Selected crystallographic data are given in Table 9.[41]

## Acknowledgments

J. A. C. wants to thank David Vazquez for the running of the computers and network at IQ-UNAM. We acknowledge DGSCA-UNAM for the generous allocation of CPU time. S. G. M. fully acknowledges the scholarship from CONACyT. This research was supported by CONACyT (Project 44009).

[1] N. W. Alcock, *Adv. Inorg. Chem. Radiochem.* **1972**, *15*, 1–58.
[2] R. Cea Olivares, V. García Montalvo, M. M. Moya Cabrera, *Coord. Chem. Rev.* **2005**, *249*, 859–872, and references cited therein.
[3] S. S. Karlov, E. K. Lermontova, M. V. Zabalov, A. A. Selina, A. V. Churakov, J. A. K. Howard, M. Yu. Antipin, G. S. Zaitseva, *Inorg. Chem.* **2005**, *44*, 4879–4886.
[4] S. S. Karlov, E. Kh. Yajuboca, E. V. Gauchenova, A. A. Selina, A. V. Churakov, J. A. K. Howard, D. A. Tyurin, J. Lorberth, G. S. Zaitseva, *Z. Naturforsch., Teil B* **2003**, *58*, 1165–1170.
[5] M. Beuter, U. Kolb, A. Zickgraf, E. Braeu, M. Bletz, M. Draeger, *Polyhedron* **1997**, *16*, 4005–4015.
[6] E. Braeu, A. Zickgraf, M. Draeger, E. Mocellin, M. Maeda, M. Takahashi, M. Takeda, C. Mealli, *Polyhedron* **1998**, *17*, 2655–2668.
[7] K. Jurkschat, J. Schilling, C. Mugge, A. Tzschach, J. Meunier Piret, M. van Meerssche, M. Gielen, R. Willem, *Organometallics* **1988**, *7*, 38–46.
[8] A. Zschunke, A. Tzschach, K. Jurkschat, *J. Organomet. Chem.* **1976**, *112*, 273–278.
[9] References cited in J. G. Alvarado Rodríguez, N. Andrade López, S. González Montiel, G. Merino, A. Vela, *Eur. J. Inorg. Chem.* **2003**, 3554–3561.
[10] J. G. Alvarado Rodríguez, N. Andrade López, S. González Montiel, *Eur. J. Inorg. Chem*. in press.
[11] M. Y. Chiang, L. Jing Wei, W. Feng Zeng, *Acta Crystallogr., Sect. C* **2005**, *61*, m84–m85.
[12] T. Thompson, S. D. Pastor, G. Rihs, *Inorg. Chem.* **1999**, *38*, 4163–4167.
[13] D. Pastor, V. Huang, D. NabiRahni, *Phosphorus, Sulfur Silicon Relat. Elem.* **1998**, *139*, 87–96.
[14] D. Pastor, V. Huang, D. NabiRhani, *Inorg. Chem.* **1997**, *36*, 5966–5968.
[15] D. Sellmann, D. Haussinger, *Eur. J. Inorg. Chem.* **1999**, 1715–1725.
[16] M. Draeger, *Chem. Ber.* **1975**, *108*, 1723–1730.
[17] M. Draeger, *Z. Anorg. Allg. Chem.* **1976**, *423*, 53–66.
[18] C. Deng Hai, C. Hung Cheh, U. Chuen Her, *Inorg. Chim. Acta* **1993**, *208*, 99–101.
[19] B. Kersting, B. Krebs, *Inorg. Chem.* **1994**, *33*, 3886–3892.
[20] J. E. Huheey, E. A. Keiter, R. L. Keiter, *Inorganic Chemistry: Principles of Structure and Reactivity*, 4th ed., Harper Collins College Publishers, New York, NY, **1993**, A30.
[21] Y. Liu, D. Ballweg, T. Müller, I. A. Guzei, R. W. Clark, R. West, *J. Am. Chem. Soc.* **2002**, *124*, 12174–12181.
[22] S. D. Pastor, A. R. Smith, G. Rihs, *Phosphorus Sulfur Silicon Relat. Elem.* **1996**, *115*, 169–177.
[23] K. Tani, S. Kato, T. Kanda, S. Inagaki, *Org. Lett.* **2001**, *3*, 655–657.
[24] A. K. Brisdon, I. R. Crossley, R. G. Pritchard, J. E. Warren, *Inorg. Chem.* **2002**, *41*, 4748–4755.
[25] W. W Porterfield, *Inorganic Chemistry: A Unified Approach*, 2nd ed., Academic Press, San Diego, Cal, **1993**, p. 214.
[26] A. Chandrasekaran, P. Sood, R. O. Day, R. R. Holmes, *Inorg. Chem.* **1999**, *38*, 3369–3376.
[27] N. V. Timosheva, A. Chandrasekaran, R. O. Day, R. R. Holmes, *Inorg. Chem.* **1998**, *37*, 3862–3867.
[28] D. J. Sherlock, A. Chandrasekaran, R. O. Day, R. R. Holmes, *Inorg. Chem.* **1997**, *36*, 5082–5089.
[29] L. Pauling, *The Nature of the Chemical Bond*, 3rd ed., Cornell University Press, Ithaca, NY, **1960**, p. 239.

 © 2006 Wiley-VCH Verlag GmbH & Co. KGaA, Weinheim 

[30] U. Kolb, M. Beuter, M. Gerner, M. Draeger, *Organometallics* **1994**, *13*, 4413–4425.
[31] *Gauss View Version 2.06*, Gaussian, Inc. Pittsburgh PA, USA.
[32] J. J. P. Stewart, *J. Comput. Chem.* **1989**, *10*, 209-220; J. J. P. Stewart, *J. Comput. Chem.* **1989**, *10*, 221–264.
[33] A. D. Becke, *J. Chem. Phys.* **1993**, *98*, 5648–5652.
[34] A. Bergner, M. Dolg, W. Kuechle, H. Stoll, H. Preuss, *Mol. Phys.* **1993**, *80*, 1431–1441.
[35] J. M. L. Martin, A. Sundermann, *J. Chem. Phys.* **2001**, *114*, 3408–3420.
[36] T. H. Dunning Jr., *J. Chem. Phys.* **1989**, *90*, 1007–1023.
[37] A. E. Reed, L. A. Curtiss, F. Weinhold, *Chem. Rev.* **1988**, *88*, 899–926.
[38] M. J. Frisch, G. W. Trucks, H. B. Schlegel, G. E. Scuseria, M. A. Robb, J. R. Cheeseman, J. A. Montgomery Jr., T. Vreven, K. N. Kudin, J. C. Burant, J. M. Millam, S. S. Iyengar, J. Tomasi, V. Barone, B. Mennucci, M. Cossi, G. Scalmani, N. Rega, G. A. Petersson, H. Nakatsuji, M. Hada, M. Ehara, K. Toyota, R. Fukuda, J. Hasegawa, M. Ishida, T. Nakajima, Y. Honda, O. Kitao, H. Nakai, M. Klene, X. Li, J. E. Knox, H. P. Hratchian, J. B. Cross, C. Adamo, J. Jaramillo, R. Gomperts, R. E. Stratmann, O. Yazyev, A. J. Austin, R. Cammi, C. Pomelli, J. W. Ochterski, P. Y. Ayala, K. Morokuma, G. A. Voth, P. Salvador, J. J. Dannenberg, V. G. Zakrzewski, S. Dapprich, A. D. Daniels, M. C. Strain, O. Farkas, D. K. Malick, A. D. Rabuck, K. Raghavachari, J. B. Foresman, J. V. Ortiz, Q. Cui, A. G. Baboul, S. Clifford, J. Cioslowski, B. B. Stefanov, G. Liu, A. Liashenko, P. Piskorz, I. Komaromi, R. L. Martin, D. J. Fox, T. Keith, M. A. Al-Laham, C. Y. Peng, A. Nanayakkara, M. Challacombe, P. M. W. Gill, B. Johnson, W. Chen, M. W. Wong, C. Gonzalez, J. A. Pople, *Gaussian 03, Revision B.05*, Gaussian, Inc., Pittsburgh PA, **2003**.
[39] G. M. Sheldrick, *SHEXTL 5.10*, Bruker AXS, Inc. Madison. WI. USA, **1998**.
[40] *SADABS: Area-Detector Absorption Correction Programme*, Siemens Industrial Automation, Inc. Madison, WI, **1996**.
[41] CCDC-605842, -605843, -605840, -605841, -605844 contain the supplementary crystallographic data for this paper. These data can be obtained free of charge from The Cambridge Crystallographic Data Centre via www.ccdc.cam.ac.uk/data_request/cif

Received: May 8, 2006
Published Online: October 10, 2006

 © 2006 Wiley-VCH Verlag GmbH & Co. KGaA, Weinheim 

DOI: 10.1002/ejic.200600448

# Synthesis, Solid-State Structures, and EPR Spectroscopic Studies on Polycrystalline and Single-Crystal Samples of α-Diimine Cobalt(II) Complexes

**Vítor Rosa,[a] Pablo J. Gonzalez,[a] Teresa Avilés,*[a] Pedro T. Gomes,[b] Richard Welter,*[c] Alberto C. Rizzi,[d] Mario C. G. Passeggi,[d,e] and Carlos D. Brondino*[d]**

**Keywords:** Cobalt(II) complexes / α-Diimine ligands / Single-crystal X-ray diffraction / EPR spectroscopy

Cobalt compounds of the general formula [$CoX_2$(α-diimine)], where X = Cl or I and the α-diimines are 1,4-diaryl-2,3-dimethyl-1,4-diaza-1,3-butadiene (Ar-DAB) and bis(aryl)-acenaphthenequinonediimine (Ar-BIAN) were synthesized by the direct reaction of the anhydrous cobalt salts $CoCl_2$ or $CoI_2$ and the corresponding α-diimine ligand in dried $CH_2Cl_2$. The synthesized compounds are [Co(Ph-DAB)$Cl_2$] (**1a**), [Co(*o*,*o*′,*p*-$Me_3C_6H_2$-DAB)$Cl_2$] (**1b**), and [Co(*o*,*o*′-$iPr_2C_6H_3$-DAB)$Cl_2$] (**1c**) with the ligands Ar-DAB, and also [Co(*o*,*o*′,*p*-$Me_3C_6H_2$-BIAN)$I_2$] (**2′b**) with the ligand Ar-BIAN. The crystal structures of all the compounds were solved by single-crystal X-ray diffraction. In all cases the cobalt atom is in a distorted tetrahedron, which is built up of two halide atoms and two nitrogen atoms of the α-diimine ligand. X-band EPR measurements of polycrystalline samples performed on compounds **1b**, **1c**, and **2′b** indicate a high-spin $Co^{II}$ ion ($S$ = 3/2) in an axially distorted environment. Single-crystal EPR experiments on compounds **1b** and **1c** allowed us to evaluate the orientation of the ***g*** tensor in the molecular frame.
(© Wiley-VCH Verlag GmbH & Co. KGaA, 69451 Weinheim, Germany, 2006)

## Introduction

Cobalt is a 3d transition metal element that has been extensively studied over the last decades. Interest in cobalt compounds arises from their participation in many different processes, from industrial and technological applications as catalysts to the essential role in several biological systems of central importance in nature.[1–5]

A large number of late transition metal complexes bearing α-diimine[6] ligands have been extensively studied in the commercial production of polyolefin from ethene and propene.[7,8] However, reports on cobalt complexes containing this type of ligands are still scarce.[9] Recently, some results from the insertion polymerization of ethylene have been reported using tetrahedral $Co^{II}$ complexes with related ligands.[10] α-Diimine ligands have also been the subject of different studies regarding the relative binding strengths,[11] as well as their reactivity with main group metals.[12]

[a] REQUIMTE/CQFB, Departamento de Química, FCT, Universidade Nova de Lisboa,
Caparica 2829-516, Portugal
E-mail: tap@dq.fct.unl.pt
[b] Centro de Química Estrutural, Instituto Superior Técnico, Av. Rovisco Pais, 1049-001 Lisboa, Portugal
[c] Laboratoire DECOMET, ILB Université Louis Pasteur 4, rue Blaise Pascal, 67000 Strasbourg, France
E-mail: welter@chimie.u-strasbg.fr
[d] Departamento de Física, Facultad de Bioquímica y Ciencias Biológicas, Universidad Nacional del Litoral, C.C. 242, 3000 Santa Fe, Argentina
E-mail: brondino@fbcb.unl.edu.ar
[e] INTEC, Universidad Nacional del Litoral, Güemes 3450, 3000 Santa Fe, Argentina

Less information exists about the magnetic properties of these types of compounds. The $Co^{II}$ ions can be present in two different spin configurations (high, $S$ = 3/2 or low, $S$ = 1/2), but in general they adopt the high-spin configuration when they are in distorted coordination environments. A large amount of work has focused on the study of the magnetic properties of $Co^{II}$ compounds in different coordination environments, some of them analyzing $Co^{II}$ in metalloproteins and compounds of biological interest.[13–19] Most of them have involved EPR spectroscopic studies on powder or frozen solutions and the evaluation of thermodynamic properties such as magnetic susceptibility and magnetization. In contrast, only a small amount of work related to high-spin $Co^{II}$ compounds having a low symmetry has been devoted to the study of the correlation between the principal values and directions of the ***g*** tensor.[20–24] This type of information, which can be only obtained from oriented single-crystal EPR spectroscopic experiments, is essential to understand the electronic and magnetic properties of the systems containing $Co^{II}$ ion complexes.

We report herein the synthesis and characterization of a series of $Co^{II}$ complexes of general formula [$CoX_2$(α-diimine)], where X = Cl or I and the α-diimines are 1,4-diaryl-2,3-dimethyl-1,4-diaza-1,3-butadiene (Ar-DAB) or bis(aryl)acenaphthenequinonediimine (Ar-BIAN), namely, [Co(Ph-DAB)$Cl_2$] (**1a**), [Co(*o*,*o*′,*p*-$Me_3C_6H_2$-DAB)$Cl_2$] (**1b**), [Co(*o*,*o*′-*i*$Pr_2C_6H_3$-DAB)$Cl_2$] (**1c**), and [Co(*o*,*o*′,*p*-$Me_3C_6H_2$-BIAN)$I_2$] (**2′b**). Their crystal structures were solved by single-crystal X-ray diffraction. Powder samples

 © 2006 Wiley-VCH Verlag GmbH & Co. KGaA, Weinheim 

of compounds **1b**, **1c**, and **2′b** were studied by EPR spectroscopy. Compounds **1b** and **1c** were also studied by single-crystal EPR spectroscopy. The EPR spectroscopic results obtained from both powder and single-crystal samples were correlated with the structures of the compounds.

## Results and Discussion

### General Characterization of the Compounds

The reaction of equimolar quantities of $CoX_2$, where X = Cl or I, and α-diimine ligands in dried $CH_2Cl_2$ at room temperature yields crystalline solids of compounds of the general formula [Co(α-diimine)$X_2$] in c.a. 75 to 85% yield (Scheme 1).

Elemental analyses, mass spectrometry, IR, X-ray, and EPR spectroscopy were used to characterize all of the synthesized compounds. The analytical data of the synthesized compounds are shown in Table 1.

The IR spectra of the cobalt complexes recorded as Nujol mulls display medium absorption bands in the region $\tilde{\nu}$ = 1643–1621 $cm^{-1}$, this is the absorption region for $\nu$(C=N). Bands assigned to C=N stretching vibrations of the free ligand were observed in the region $\tilde{\nu}$ = 1674–1633 $cm^{-1}$. The bands in the complexes are shifted to lower wavenumbers, which is a criterion for the coordination of both diimine nitrogen atoms of the α-diimine ligands to the cobalt(II) ion. Selected IR absorption bands are displayed in Table 2.

Table 2. Selected IR data in Nujol mulls (values of $\tilde{\nu}$ given in $cm^{-1}$).

| | Ar-DAB[a] | **1** | Ar-BIAN[a] | **2′** |
|---|---|---|---|---|
| **a** | 1633 | 1643 | | |
| **b** | 1637 | 1635 | 1674, 1650 | 1621 |
| **c** | 1639 | 1641 | | |

[a] Free ligands.

### Crystal Structure Descriptions

#### *Complex 1a*

The complex **1a** crystallizes in an orthorhombic space group $P2_12_12_1$. An ATOMS[25] view of the asymmetric unit of the crystal structure is shown in Figure 1. The cobalt atom is in a deformed tetrahedron, which is built up of two chloride atoms and two nitrogen atoms of the ligand [Co–Cl1: 2.214(1) Å; Co–Cl2: 2.210(1) Å; Co–N1: 2.043(4) Å;

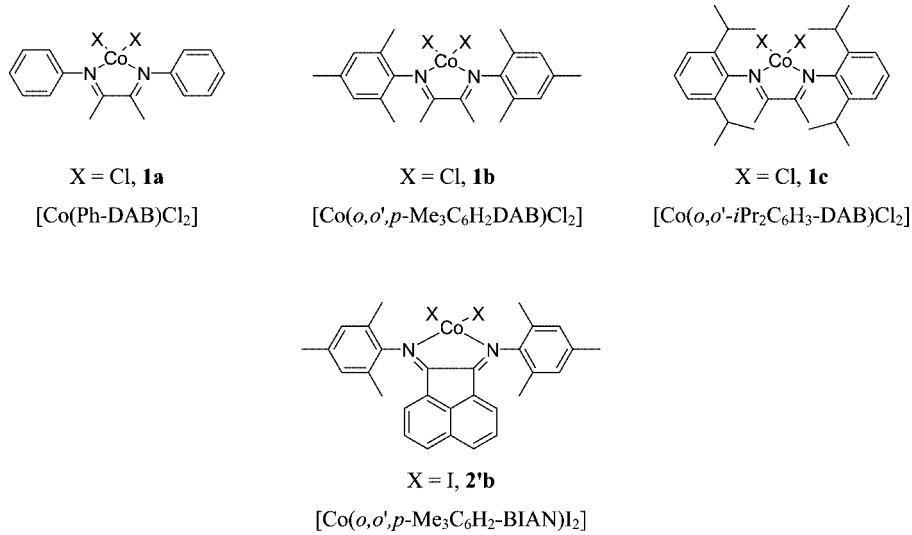


Scheme 1. Synthesized complexes.

Table 1. Analytical data.

| | Molecular mass [g mol$^{-1}$]; Molecular formula | MS(FAB) $m/z$[a] | Microanalysis (calcd.) [%] C | H | N | Color |
|---|---|---|---|---|---|---|
| **1a** | 366.15; $C_{16}H_{16}CoCl_2N_2$ | $[L_1 + H^+]$ 237 (77%); $[L_1CoL_1]^{2+}$ 265.5 (100%); $[CoL_1Cl]^+$ 330 (36%); $[L_1CoL_1Cl]^+$ 566 (71%) | 52.09 (52.48) | 4.34 (4.40) | 7.63 (7.65) | green |
| **1b** | 450.31; $C_{22}H_{28}CoCl_2N_2$ | $[L_2CoCl]^+$ 414.2 (97%) | 58.46 (58.68) | 6.42 (6.27) | 6.34 (6.22) | green |
| **1c** | 576.94; $C_{28}H_{40}CoCl_2N_2 \cdot 1/2CH_2Cl_2$ | $[CoL_3Cl]^+$ 498.3 (96%) | 60.63 (59.33) | 7.30 (7.16) | 5.16 (4.86) | green |
| **2′b** | 729.30; $C_{30}H_{28}CoI_2N_2$ | $[L_4 + H^+]$ 417.3 (16%); $[L_4Co\ I]^+$ 602.1 (30%) | 49.26 (49.41) | 4.16 (3.87) | 3.65 (3.84) | brown |

[a] Ligand 1,4-diaryl-2,3-dimethyl-1,4-diaza-1,3-butadiene (Ar-DAB); $L_1$: Ar = Ph; $L_2$: Ar = *o*,*o*′,*p*-$Me_3C_6H_2$; $L_3$: Ar = *o*,*o*′-*i*$Pr_2C_6H_3$; Ligand bis(aryl)acenaphthenequinonediimine (Ar-BIAN); $L_4$: Ar = *o*,*o*′,*p*-$Me_3C_6H_2N$.

 © 2006 Wiley-VCH Verlag GmbH & Co. KGaA, Weinheim 

Co–N2: 2.034(4) Å; Cl1–Co–Cl2: 119(1)°; N1–Co–N2: 80(1)°]. The [Co–N1–C1–C3–N2] plane is strictly planar [maximum deviation from least-squares plane is 0.007(5) Å] and makes an angle of 56(1)° with both phenyl groups ([C5–C10] and [C11–C16]). No hydrogen bonds have been found in this crystal structure.

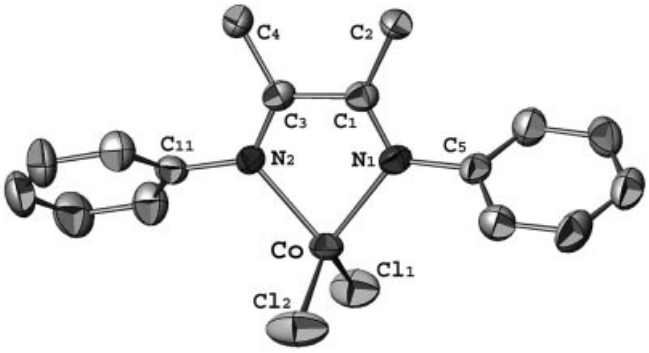


Figure 1. Molecular structure of complex **1a** (ATOMS view) with partial labeling scheme. The hydrogen atoms are omitted for clarity. The thermal ellipsoids enclose 50% of the electronic density.

### *Complex 1b*

The complex **1b** crystallizes in a monoclinic space group $P2_1/c$. An ATOMS view of the asymmetric unit of the crystal structure is shown in Figure 2. In this case again, the cobalt atom is in a deformed tetrahedron [Co–Cl1: 2.224(1) Å; Co–Cl2: 2.212(1) Å; Co–N1: 2.050(3) Å; Co–N2: 2.051(3) Å; Cl1–Co–Cl2: 113(1)°; N1–Co–N2: 80(1)°]. Two nonclassical intermolecular hydrogen bonds have been detected (PLATON software[26]) between C3 and Cl2 [H3B–CL2: 2.75(1) Å; C3–Cl2: 3.68(1) Å; C3–H3B–Cl2: 160(1)°] and C3 and Cl1 [H3C–CL1: 2.81(1) Å; C3–Cl1: 3.78(1) Å; C3–H3C–Cl1: 169(1)°]. The angle between both phenyl groups is 14(1)° and these groups are perpendicular to the central plane [Co–N1–C1–C2–N2] [maximum deviation from least-squares plane is 0.035(2) Å] with angles of 88(1)° and 90(1)°, respectively.

### *Complex 1c*

The complex **1c** crystallizes in an orthorhombic space group *Pnma*. An ATOMS view of the asymmetric unit of the crystal structure is shown in Figure 3. The deformed tetrahedral site around the Co atom is characterized by the following distances and angles: Co–Cl1: 2.197(2) Å; Co–Cl2: 2.201(1) Å; Co–N: 2.050(3) Å Cl1–Co–Cl2: 113(1)°; N1–Co–N2: 80(1)°. Compared to that observed in both the previous structures, the plane containing the Co atom is not well fitted by the least-squares planes calculation (SHELXL-97)[27] with a maximum deviation from the plane of 0.112(3) Å for both nitrogen atoms. This pseudo plane makes an angle of 87(1)° with both phenyl groups (identical by symmetry), the latter are tilted with an angle of 15(1)°, one compared to the other. At least two nonclassical intramolecular hydrogen bonds have been detected (PLATON software) between C9 and N [H9–N: 2.43(1) Å; C9–N: 2.94(1) Å; C9–H9–N: 111(1)°] and C12 and N [H12–N: 2.38(1) Å; C12–N: 2.88(1) Å; C12–H12–N: 110(1)°].

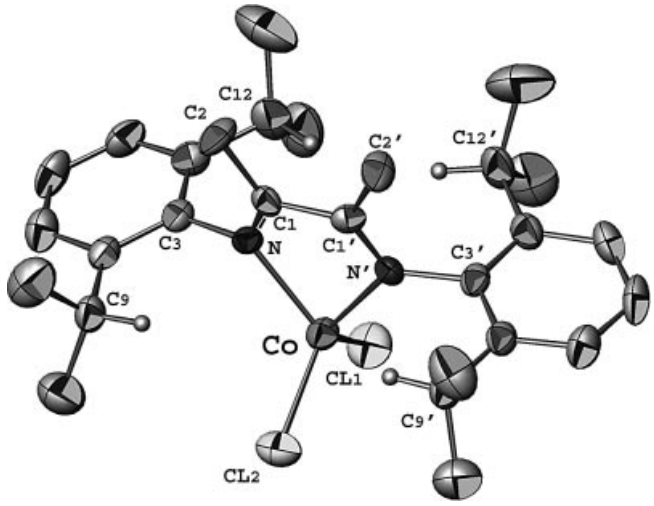


Figure 3. Molecular structure of complex **1c** (ATOMS view) with partial labeling scheme. The hydrogen atoms are omitted for clarity. The thermal ellipsoids enclose 50% of the electronic density. Operators for generating equivalent atoms: $x, y, -z+3/2$.

### *Complex 2′b*

The complex **2′b** crystallizes in an orthorhombic space group *Pcca*. An ATOMS view of the asymmetric unit of the crystal structure is shown in Figure 4. The deformed tetrahedral site around the Co atom is characterized by the

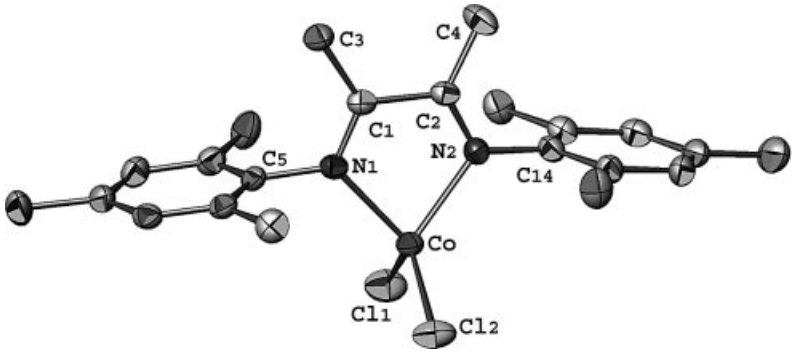


Figure 2. Molecular structure of complex **1b** (ATOMS view) with partial labeling scheme. The hydrogen atoms and the solvent molecules ($CH_2Cl_2$) are omitted for clarity. The thermal ellipsoids enclose 50% of the electronic density.

 © 2006 Wiley-VCH Verlag GmbH & Co. KGaA, Weinheim 

following distances and angles: Co–I: 2.509(1) Å; Co–N: 2.05(1) Å; I–Co–I′: 111(1)°; N–Co–N′: 82(1)°. The angle between both phenyl groups is 14(1)° and these groups make an angle of 85(1)° with the central plane [Co–N–C1–C1′-N′] [maximum deviation from least-squares plane is 0.001(4) Å]. It is important to note that the molecule of complex **2′b** is placed on a crystallographic mirror i.e. the following atoms are on the mirror (see Figure 4): Co, N, C8, C1, C2, C4, C5, C6, C7 and the corresponding equivalent atoms by the following symmetry operator: $-x$, $y$, $-z + 1/2$. No H bond has been detected in the case of this crystal structure. No H bond has been detected in the case of this molecular structure.

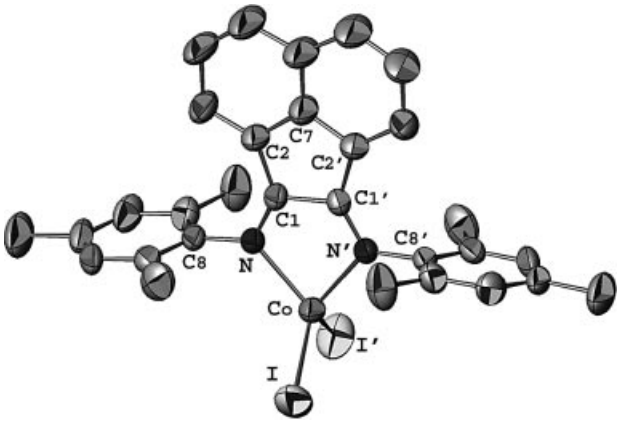


Figure 4. Molecular structure of complex **2′b** (ATOMS view) with partial labeling scheme. The hydrogen atoms and the solvent molecules ($CH_2Cl_2$) are omitted for clarity. The thermal ellipsoids enclose 50% of the electronic density. Operators for generating equivalent atoms: $-x$, $y$, $-z+1/2$.

## EPR Measurements

The X-band EPR spectra of polycrystalline samples of compounds **1b**, **1c**, and **2′b** and their simulations are shown in Figure 5. The peaks broaden at higher $T$ and disappear at ca. 50 K. The hyperfine structure expected for the 100% abundant $^{59}$Co isotope ($^{59}I = 7/2$) is not observed in any of the spectra of the powder samples. The values of the g factors $g_1$, $g_2$, and $g_3$ are given in Table 3 and are typical for $Co^{II}$ ions with a high spin $S = 3/2$ configuration.[17] The EPR spectrum obtained for compound **1a** (data not shown) is also compatible with a $Co^{II}$ ion in a high-spin configuration, however, a broad signal detected in the range 500–8000 Gauss and overlapping the $Co^{II}$ ion transitions precluded the interpretation.

In a purely tetrahedral environment, $Co^{II}$ has the orbital singlet $A_2$ at lowest energy,[13,14] and since $S = 3/2$, there is a fourfold spin degeneracy. As for compounds **1b**, **1c**, and **2′b** the sites are distorted, the fourfold spin degeneracy is lifted into two Kramers doublets. If the distortion is high enough ($>>kT$) to neatly separate both doublets and the experiments are performed at low temperatures, then the observed spectra can be assigned to transitions between the states of the lowest $S' = 1/2$ spin doublet, which is expected

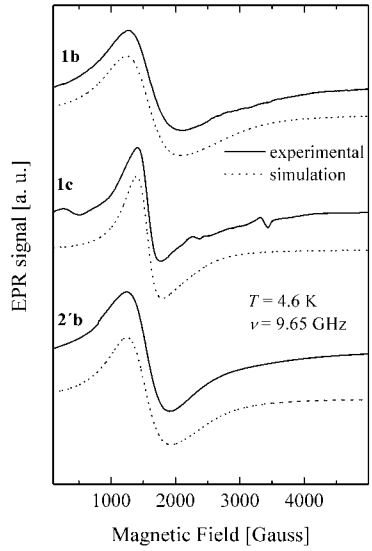


Figure 5. EPR spectra of powdered samples of compounds **1b**, **1c**, and **2′b** together with simulations. The EPR parameters obtained from simulation are given in Table 3. For compound **1c**, the peak at ≈3300 Gauss corresponds to $Cu^{II}$ impurities whereas the peak at ≈500 Gauss corresponds to a cavity background.

Table 3. EPR parameters obtained from powder and single-crystal samples for **1b**, **1c**, and **2′b**. Linewidths ($\Delta B$) are in Gauss. The components of the crystal $g$ tensors are expressed in the $abc^*$ ($c^* = a \times b$) and $abc$ coordinates system for compounds **1b** and **1c**, respectively. They were obtained by least-squares analyses of the single-crystal data.

| Compound | **1b** | **1c** | **2′b** |
|---|---|---|---|
| Powder sample | | | |
| $g_1$ | 4.83(5) | 4.85(5) | 4.87(5) |
| $g_2$ | 4.37(5) | 4.35(5) | 4.71(5) |
| $g_3$ | 2.58(9) | 3.12(9) | 3.08(9) |
| $\Delta B_1$ | 580(20) | 280(20) | 580(20) |
| $\Delta B_2$ | 680(20) | 280(20) | 480(20) |
| $\Delta B_3$ | 900(20) | 600(20) | 800(20) |
| Single crystal | | | |
| $g_{aa}$ | 2.66(2) | 4.47(1) | – |
| $g_{bb}$ | 4.83(1) | 3.12(2) | – |
| $g_{cc}$ | 4.32(1) | 4.71(1) | – |
| $g_{ac}$ | 1.51(4) | 0 | – |
| $g_{ab}$ | 0 | 0 | – |
| $g_{cb}$ | 0 | 0 | – |
| $g_{\parallel}$ | 2.58(2) | 3.12(2) | 3.08(9) |
| $g_{\perp}$ | 2.30(1) | 2.30(1) | 2.40(5) |
| E/D | 0.03 | 0.04 | 0.01 |

to be substantially populated.[28] The high anisotropy observed is also expected for $Co^{II}$ compounds with a distorted tetrahedral coordination.[29,30] Since the structural data do not show relevant chemical paths connecting the metal sites that could efficiently transmit exchange interactions, the principal $g$ values obtained from the powder spectra (Table 3) can be considered as corresponding to isolated $Co^{II}$ ions, in which the resonance lines may be broadened by dipolar interactions. The crystal lattice of all compounds consists of a 3D network of cobalt(II) ions, with closest

 © 2006 Wiley-VCH Verlag GmbH & Co. KGaA, Weinheim 

metal center distances in the range 6.4–8.4 Å. This could be the cause of the unobserved hyperfine structure in the EPR powder spectra.

Single-crystal EPR spectroscopic measurements were only performed on compounds **1b** and **1c** as the size of the crystals of compounds **1a** and **2′b** was not appropriate for the EPR spectroscopic experiments. In order to understand the single-crystal EPR spectroscopic experiment, it is important to first analyze the orientation of the Co sites as well as the symmetry operations relating them within the unit cell. The unit cell of compound **1b** contains four identical Co molecules, which are related by the symmetry operations of the space group $P2_1/c$ (Figure 6a). Co1 at the general position ($x$,$y$,$z$) is related to Co2 by a $C_{2b}$ rotation, as well as Co3 to Co4. Co1 and Co2 are related to Co3 and Co4, respectively, by an inversion. From the magnetic point of view, this compound can be assumed as having two magnetically nonequivalent molecules per unit cell, because the Co sites related by an inversion are indistinguishable for EPR spectroscopy.

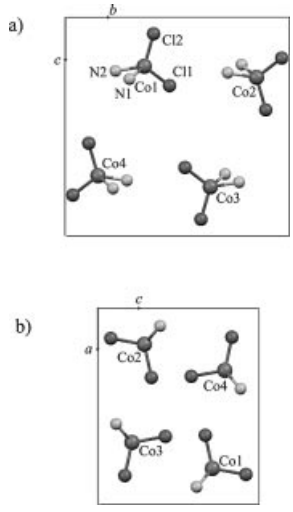


Figure 6. (a) Projection along $a$ of the four $Co^{II}$ ions and their ligands in the unit cell for compound **1b**. (b) Projection along $b$ of the four $Co^{II}$ ions and their ligands in the unit cell for compound **1c**.

Compound **1c** also has four identical Co molecules in the unit cell, related by the symmetry operations of the space group *Pnma* (Figure 6b). Co1 at the special position ($x$,1/4,$z$) is related to Co2, Co3, and Co4 by $C_{2b}$, $C_{2a}$, and $C_{2c}$ rotations, respectively. These operations determine that there are two $Co^{II}$ ion pairs magnetically equivalent per crystal plane, and also that the four Co sites are magnetically equivalent along the crystal $a$,$b$,$c$ axes. The Co molecule has a mirror plane defined by the $Co^{II}$ ion and the two Cl ligands, which is parallel to the *ca* plane. This particular local symmetry together with the space orientation of the Co molecules in the unit cell determines that the nonequivalent pairs of $Co^{II}$ ions are equivalent in the planes *ab* and *cb*.

Single-crystal EPR spectra were recorded with the magnetic field in three orthogonal crystal planes as explained in the experimental section. In all the planes and for the two compounds we observed one resonance line for all magnetic field orientations, except around the $b$ axis in the orthorhombic compound **1c**. In the planes *ab* and *cb* the signals become very broad around 90°, presumably because of a nonresolved hyperfine structure and therefore the position of the resonances in this zone could not be precisely evaluated. The position of the resonance line was obtained by least-squares fitting to a single Lorentzian line shape. Figure 7 shows the angular variation of the $g$ factor as a function of the magnetic field orientation for both compounds. The data in Figure 7 were least-squares fitted to a second rank tensor $g^2(\theta,\varphi) = \boldsymbol{h.g.g.h}$, in which $\boldsymbol{h} = \sin\theta\cos\varphi$, $\sin\theta\sin\varphi$, $\cos\theta$, is the magnetic field orientation, and $\boldsymbol{g}$ is the crystal $\boldsymbol{g}$ tensor defined as the average of the molecular $\boldsymbol{g}$ tensors of the nonequivalent $Co^{II}$ ions in the crystal lattice. The results are given in Table 3 and were used to obtain the solid lines in Figure 7. The overall symmetry of the evaluated $\boldsymbol{g}$ tensors follows the symmetry determined by the space group of each compound.

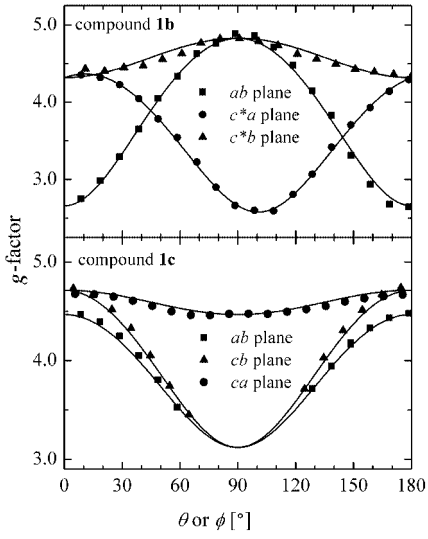


Figure 7. Angular variation of the $g$ factor obtained from oriented single-crystal EPR spectroscopic measurements of compounds **1b** and **1c** at 9.65 GHz and $T$ = 4.6 K. The solid lines in both plots were calculated with the components of the $\boldsymbol{g}^2$ tensor given in Table 3.

As discussed above, the angular variation of the $g$ factor in the orthorhombic compound **1c** can be associated with a single $Co^{II}$ ion in the planes *ab* and *cb*. By contrast, in the *ca* plane we would expect two resonance lines corresponding to the pairs Co1–Co2 and Co3–Co4. However, only one signal with a nearly isotropic angular variation was registered in this plane, which corresponds to the mirror Cl–Co–Cl plane. This fact can be due to either collapse by exchange interactions or resonance lines with similar $g$ factors. Taking into account that from the structural data we can discard the first possibility, the observed behavior can only be explained assuming two resonance lines with similar $g$ factors, which cannot be resolved by the EPR spectroscopic experiment at the X-band.

 © 2006 Wiley-VCH Verlag GmbH & Co. KGaA, Weinheim 

The orientation of the molecular ***g*** tensor for compound **1c** in the molecular frame can be evaluated from both the analysis of the geometry of coordination of the metal site and the EPR spectroscopic results. One eigenvector must correspond to the *b* crystal axis (0, 1, 0) because, as explained above, the planes *ab* and *cb* are associated with a single $Co^{II}$ ion and the angular variation of the *g* factor is symmetric around the *b* crystal axis ($g_3$ = 3.12). Thus, the two remaining eigenvectors must be in the Cl–Co–Cl plane. The Co molecule can be considered as having a local pseudo-$C_2$ symmetry axis (–0.760, 0, 0.650) determined by the intersection of the Cl–Co–Cl plane (parallel to the *ca* crystal plane) and the N–Co–N plane. This $C_2$ symmetry axis must correspond to another eigenvector. The direction of the third eigenvector is straightforward (0.650, 0, 0.760). The orientation of the ***g*** tensor is shown in Figure 8. This experiment allowed us to identify the eigenvalue along the *b* crystal axis, but not the remaining two eigenvalues because the single EPR line observed in the *ca* plane corresponds to two overlapping resonance lines associated with the pairs Co1–Co2 or Co3–Co4. However, they should correspond to the highest *g* values (4.35–4.85) of the ***g*** tensor obtained from the EPR powder spectra. Because of the above discussed nonequivalence of the cobalt ions in the *ca* plane both eigenvalues can be assigned to any of the $g_1$ and $g_2$ eigenvectors. The ***g***-tensor orientation of compound **1c** is similar to that determined in the pseudo-tetrahedral dichlorobis(triphenylphosphaneoxide)cobalt(II) compound.[21] This compound shows rhombic EPR spectra ($g_1$ = 5.67, $g_2$ = 3.69, $g_3$ = 2.16) with the two lowest *g* values approximately included in the Cl–Co–Cl plane. Compound **1c** presents a nearly axial signal, with the lowest *g* value ($g_3$) lying along the normal to the Cl–Co–Cl plane. The main structural difference between both compounds is that **1c** contains the stronger N ligands instead of O ligands. On the other hand, EPR spectroscopic studies performed on a square-pyramidal $Co^{II}$ complex showed that small deviations of the ideal $C_4$ site symmetry lead to important changes in the EPR spectroscopic properties of high-spin $Co^{II}$ ions.[22] Clearly, additional experimental work on a larger number of high spin $Co^{II}$ compounds with different structural characteristics is necessary to clarify how the different EPR spectroscopic properties can be correlated with differences in the coordination environment of the metal ion.

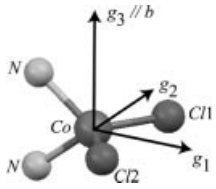


Figure 8. Orientation of the principal axes of the ***g*** tensor for the $Co^{II}$ site in compound **1c**. The direction cosines referring to the crystal axes are: (–0.760, 0, 0.650), (0.650, 0, 0.760), and (0, 1, 0) for $g_1$, $g_2$, and $g_3$ = 3.12, respectively. $g_1$ and $g_2$ can take either the values 4.35 and 4.85, respectively, or vice versa.

Structural data for compound **1b** show Co sites with coordination environments and space orientations similar to that of **1c**, but the local symmetry is lower (the local mirror plane cannot be defined in this case) and the Cl–Co–Cl plane is twisted by nearly 10° from the *cb* crystal plane (Figure 6a and b). The structural similarities are reflected in Figure 7: a nearly isotropic *g* factor was obtained in the plane *c***b*, and the lowest *g* value corresponds to a direction close to the normal of the Cl–Co–Cl plane. However, having nonresolved lines in the *ab* and *cb* planes precludes determining the ***g*** tensor associated with single $Co^{II}$ ions. Despite its lower symmetry, the coordination around $Co^{II}$ ions in both compounds shows no significant differences and we expect a ***g*** tensor orientation similar to that shown in Figure 8 for **1b**. Although we were not able to perform single-crystal EPR experiments on compounds **2′b**, the EPR spectroscopic data from powdered samples are similar for the three compounds. Consequently, we also expect similar ***g*** tensor orientation for the compounds in which I substitutes for Cl, but single-crystal experiments are necessary to confirm this hypothesis.

After this phenomenological assignment has been made, one wonders whether it might be possible to relate the highly anisotropic *g* factors corresponding to the effective $S' = 1/2$ of the lowest Kramers doublet with the distortions affecting the overall state of $S = 3/2$. The appropriate spin Hamiltonian within the $S = 3/2$ can be written as [Equation (1)]

$$H = \mu_B \mathbf{BgS} + \mathrm{D}\left(S_z^2 - \frac{1}{3}S(S+1)\right) + \mathrm{E}\left(S_x^2 - S_y^2\right) \quad (1)$$

where D and E are the axial and rhombic zero-field splitting parameters, respectively. The quantization axis *z* is assumed to be along the axial distortion. In principle, it is not required to assume that ***g*** will have its principal axes along any of these directions.

An effective Hamiltonian within the lowest $S' = 1/2$ (corresponding to either the originals $|3/2, \pm 3/2\rangle$ or the $|3/2, \pm 1/2\rangle$ states) Kramers doublet can be obtained under the form[31–34]

$\mathrm{H_{eff}} = \mu_B \mathbf{Bg'S'}$

If the ground state is that derived from to the original $|3/2, \pm 1/2\rangle$ doublet and if one assumes now that the principal axes of ***g*** coincide with that of the axial distortion such that $g_z = g_\parallel$ and $g_x = g_y = g_\perp$, one gets $g'_z = g_\parallel$ while $g'_x = 2g_\perp\left(1 - \frac{3}{2}\frac{\mathrm{E}}{\mathrm{D}}\right)$ and $g'_y = 2g_\perp\left(1 + \frac{3}{2}\frac{\mathrm{E}}{\mathrm{D}}\right)$. Note that $g'_x$, $g'_y$, and $g'_z$ correspond to $g_2$, $g_1$, and $g_3$, respectively, given in Table 3. The experimental data are not consistent with assigning the ground state to that derived from the original $|3/2, \pm 3/2\rangle$ doublet, in which $g'_z = 3g_\parallel$ while $g'_x \approx 0$ and $g'_y \approx 0$, which indicates a positive sign for the zero-field splitting parameter D. EPR data obtained from $Cs_3CoCl_5$ and $Cs_3CoBr_5$ complexes have been analyzed assuming a negative value for the D parameter,[35] and EPR spectroscopic results obtained from bis[dihydrobis(1-pyrazolyl)-

 © 2006 Wiley-VCH Verlag GmbH & Co. KGaA, Weinheim 

borato]$Co^{II}$ have been interpreted assuming transitions |3/2, ±3/2>.[36] In contrast, our EPR spectroscopic data indicate a |3/2, ±1/2> ground state, in line with both theoretical and experimental results obtained from other pseudotetrahedral $Co^{II}$ compounds.[20,21]

According to the previous discussion, adopting a coordinate system in which the $z$ axis lies along the $g_3$ direction (in compound **1c** this coincides with the crystal $b$ axis), leads to $g'_z = g_{\|}$. One can also estimate $g_\perp$ by using the other two eigenvalues obtained from the powder spectra, e.g. $g_\perp \cong (g'_x + g'_y)/4$. On the other hand, under the same assumptions, one gets

$$\left|\frac{E}{D}\right| = \frac{2\left|g'_x - g'_y\right|}{3\left(g'_x + g'_y\right)}$$

Table 3 shows these parameters obtained for the three compounds using this model. The results indicate a weak rhombic distortion for all the compounds.

## Conclusions

A series of cobalt(II) complexes of general formula [Co(α-diimine)$X_2$], **1a**, **1b**, **1c**, and **2′b**, have been synthesized by the direct reaction of equimolar quantities of the corresponding cobalt dihalide and the α-diimine ligand in dried $CH_2Cl_2$ in c.a. 75 to 85% yield. Single-crystal X-ray structural data for all compounds show in all cases that the cobalt atom is in a distorted tetrahedral coordination, which is built by two halide atoms and two nitrogen atoms of the α-diimine ligand. X-band EPR measurements in polycrystalline samples performed on **1b**, **1c**, and **2′b** indicate high-spin $Co^{II}$ ($S = 3/2$) in an axially distorted environment. The single-crystal EPR spectroscopic experiment allowed us to determine the ***g***-tensor orientation for a low symmetry $Co^{II}$ compound. Structural and EPR spectroscopic results suggest similar ***g***-tensor orientations for all the compounds and the electronic properties of the $Co^{II}$ ions seem to be independent of the type of halide coordinated to the metal site.

## Experimental Section

### General Procedures and Materials

All reactions and manipulations of solutions were performed under an argon atmosphere using Schlenk techniques. Solvents were reagent grade and were dried according to literature methods. $CoCl_2$ and $CoI_2$ were purchased from Aldrich and the α-diimine ligands were synthesized as described elsewhere.[37]

### Physical Methods

Infrared spectra were recorded as Nujol mulls on NaCl plates using a Mattson Satellite FTIR spectrometer. Elemental analyses were performed at the Analytical Services of the Laboratory of REQUIMTE. Mass spectra were recorded using an HP298S GC/MS system by the Mass Spectra Service of the Universitat Autònoma de Barcelona, Spain.

X-band CW EPR spectra of polycrystalline samples and single-crystal samples were taken at 4.6 K with a Bruker EMX spectrometer using a rectangular cavity with 100 kHz field modulation, and equipped with an Oxford continuous flow cryostat. The EPR parameters of powdered samples were obtained from spectral simulations using the program Simfonia (v. 1.25, Bruker Instruments Inc.). Powder samples for EPR spectroscopy were obtained by grinding single crystals.

The samples for the single-crystal EPR spectroscopic measurements were oriented by gluing the *cb* and *ca* faces of **1b** and **1c**, respectively, to a cleaved KCl cubic holder, which defines a set of orthogonal laboratory axes. The habit of the crystals was determined by measuring the angles between crystal faces using a goniometric microscope. The sample holder was introduced into a 4 mm OD quartz tube, and positioned in the center of the microwave cavity (see ref.[38] for details). The tubes were attached to a goniometer and the sample was rotated in steps of 10° with the magnetic field in three crystal planes.

### Synthesis of Complexes

**Synthesis of [Co(*o*,*o*′,*p*-$Me_3C_6H_2$-DAB)$Cl_2$] (1b):** A suspension of $CoCl_2$ (0.26 g, 2 mmol) in $CH_2Cl_2$ (20 mL) was treated with a yellow solution of *o*,*o*′,*p*-$Me_3C_6H_2$-DAB, (0.64 g, 2 mmol) in $CH_2Cl_2$ (30 mL), a color change was observed almost immediately from the blue of the initial suspension to green. The mixture was left stirring at room temperature for about 2 h until everything was dissolved. The solution was filtered, and concentrated by vacuum removal of the solvent. A green crystalline solid precipitated, which was separated by filtration, washed with diethyl ether (2 × 10 mL) and petroleum ether (2 × 10 mL), and then recrystallized from hot $CH_2Cl_2$. **1b** (0.76 g) was obtained in 85% yield.

Compounds **1a** and **1c** were obtained by this method. Yields obtained were between 75 and 85%. Compounds **1a**, **1b**, and **1c** are moisture sensitive.

**Synthesis of [Co(*o*,*o*′,*p*-$Me_3C_6H_2$-BIAN)$I_2$] (2′b):** A green suspension of $CoI_2$ (0.16 g, 0.5 mmol) in $CH_2Cl_2$ (20 mL) was treated with a red solution of *o*,*o*′,*p*-$Me_3C_6H_2$-BIAN (0.21 g, 0.5 mmol) in $CH_2Cl_2$ (30 mL). The mixture quickly turned to a red-wine color, and it was stirred overnight until everything was dissolved. After filtration of the solution the solvent was partially removed leaving a dark-red solid, which was separated by filtration, washed with petroleum ether (2 × 10 mL), and then recrystallised from $CH_2Cl_2$/petroleum ether. **2′b** (0.29 g) was obtained in 78% yield.

**Crystallography:** Single crystals of complexes **1a**, **1b**, **1c**, and **2′b** were mounted on a Nonius Kappa-CCD area detector diffractometer (Mo-$K_\alpha$ $\lambda$ = 0.71073 Å). The complete conditions of data collection (DENZO software) and structure refinements are given below. The cell parameters were determined from reflections taken from one set of 10 frames (1.0° steps in phi angle), each at 20 s exposure. The structures were solved by direct methods (SHELXS97) and refined against $F^2$ using the SHELXL97 software.[27] The absorption was not corrected. All non-hydrogen atoms were refined anisotropically. Hydrogen atoms were generated according to stereochemistry and refined using a riding model in SHELXL97. Some disorders have been fixed for solvent molecules in the case of **1b** and **2′b** complexes (for details, see the corresponding cif files). The fully-labeled ORTEP views have been deposited as supplementary materials. CCDC-297433–297436 contain the supplementary crystallographic data for this paper. These data can be obtained free of charge from The Cambridge Crystallographic Data Centre via www.ccdc.cam.ac.uk/data_request/cif.

**1a:** Green single crystal, dimension: 0.10 × 0.10 × 0.10 mm. $C_{16}H_{16}Cl_2CoN_2$, $M$ = 366.14 g mol$^{-1}$; orthorhombic; space group $P2_12_12_1$; $a$ = 10.5880(4) Å; $b$ = 8.2160(3) Å; $c$ = 19.1880(9) Å; $Z$ =

 © 2006 Wiley-VCH Verlag GmbH & Co. KGaA, Weinheim 

4; $D_{calcd.}$ = 1.457 g cm$^{-3}$; $\mu$(Mo-$K_\alpha$) = 1.342 mm$^{-1}$; a total of 14084 reflections; 2.20° < $\theta$ < 30.00°, 4806 independent reflections with 3211 having $I > 2\sigma(I)$; 191 parameters; final results: $R_1$ = 0.1149; $wR_2$ = 0.1256, Gof = 1.179, Flack $x$; 0.00(7), maximum residual electronic density = 0.614 e Å$^{-3}$.

**1b:** Green single crystal, dimension: 0.10 × 0.08 × 0.03 mm. $C_{22}H_{28}Cl_2CoN_2$, $CH_2CL_2$, $M$ = 535.22 g mol$^{-1}$; monoclinic; space group $P2_1/c$; $a$ = 12.686(5) Å; $b$ = 14.514(5) Å; $c$ = 14.180(5) Å; $\beta$ = 90.76(5)°; $Z$ = 4; $D_{calcd.}$ = 1.362 g cm$^{-3}$; $\mu$(Mo-$K_\alpha$) = 1.079 mm$^{-1}$; a total of 9800 reflections; 2.13° < $\theta$ < 29.98°, 7555 independent reflections with 4498 having $I > 2\sigma(I)$; 268 parameters; final results: $R_1$ = 0.0733; $wR_2$ = 0.2063, Gof = 1.037; maximum residual electronic density = 1.177 e Å$^{-3}$.

**1c:** Green single crystal, dimension: 0.13 × 0.10 × 0.08 mm. $C_{28}H_{40}Cl_2$ $CoN_2$, $M$ = 534.45 g mol$^{-1}$; orthorhombic; space group $Pnma$; $a$ = 10.4110(10) Å; $b$ = 12.707(2) Å; $c$ = 21.311(4) Å; $Z$ = 4; $D_{calcd.}$ = 1.259 g cm$^{-3}$; $\mu$(Mo-$K_\alpha$) = 0.816 mm$^{-1}$; a total of 33608 reflections; 1.91° < $\theta$ < 29.83°, 3965 independent reflections with 2385 having $I > 2\sigma(I)$; 154 parameters; final results: $R_1$ = 0.0614; $wR_2$ = 0.2027, Gof = 0.825, maximum residual electronic density = 0.324 e Å$^{-3}$.

**2′b:** Brown single crystal, dimension: 0.08 × 0.07 × 0.06 mm. $C_{30}H_{28}CoI_2N_2$, 0.2($C_4H_{10}O$), $M$ = 744.10 g mol$^{-1}$; orthorhombic; space group $Pcca$; $a$ = 16.769(3) Å; $b$ = 11.676(2) Å; $c$ = 18.313(3) Å; $Z$ = 4; $D_{calcd.}$ = 1.378 g cm$^{-3}$; $\mu$(Mo-$K_\alpha$) = 2.219 mm$^{-1}$; a total of 9862 reflections; 1.74° < $\theta$ < 30.04°, 5230 independent reflections with 3769 having $I > 2\sigma(I)$; 168 parameters; Final results: $R_1$ = 0.0710; $wR_2$ = 0.2249, Gof = 1.049, maximum residual electronic density = 1.424 e Å$^{-3}$.

## Acknowledgments

Work was supported by Fundação para a Ciência e Tecnologia (Project POCI/QUI/55519/2004) in Portugal and SEPCYT:PICT 2003-06-13872, CONICET PIP 02559/2000, and CAI+D-UNL in Argentina. V. R. thanks Fundação para a Ciência e Tecnologia for a Ph.D. grant (SFRH/BD/13777/2003). T. A. and R. W. thank CPU (France) and CRUP (Portugal) for the Portuguese-French Integrated Action-2006, N° F-27/07. A. C. R., M. C. G. P., and C. D. B. thank the Spanish Research Council (CSIC) for providing a free licence to the Cambridge Structural Database.[39] C. D. B. and M. C. G. P. are members of CONICET-Argentina.

[1] R. Crabtree, M. Mingos, *Comprehensive Organometallic Chemistry III: From Fundamentals to Applications*, (COMC-III), Elsevier, **2006**, and its predecessors COMC-II, 1995, and COMC, 1982.
[2] M. Kobayashi, S. Shimizu, *Eur. J. Biochem.* **1999**, *261*, 1–9.
[3] J. J. R. Fraústo da Silva, R. J. P. Williams, *The Biological Chemistry of the Elements. The Inorganic Chemistry of Life*, Clarendon Press, Oxford, **1991**.
[4] R. J. P. Williams, J. J. R. Fraústo da Silva, *The Natural Selection of the Chemical Elements*, Clarendon Press, Oxford, **1996**.
[5] S. J. Lippard, J. M. Berg, *Principles of Bioinorganic Chemistry*, University Science Books, Mill Valley, California, **1994**.
[6] G. van Koten, K. Vrieze, *Adv. Organomet. Chem.* **1982**, *21*, 151–190, and references therein.
[7] B. Rieger, L. Saunders Baugh, S. Kacker, S. Striegler, *Late Transition Metal Polymerization Catalysis*, Wiley-VCH, Weinheim **2003**.
[8] a) S. D. Ittel, L. K. Johnson, M. Brookhart, *Chem. Rev.* **2000**, *100*, 1169–1203; b) G. J. P. Britovsek, V. C. Gibson, D. F. Wass, *Angew. Chem. Int. Ed.* **1999**, *38*, 429–447; c) V. C. Gibson, S. K. Spitzmesser, *Chem. Rev.* **2003**, *103*, 283–315.
[9] a) M. C. Barral, E. Delgado, E. Gutierrez-Puebla, R. Jimenez-Aparicio, A. Monge, C. Delpino, A. Santos, *Inorg. Chim. Acta* **1983**, *74*, 101–107; b) H. Tom Dieck, M. Haarich, *J. Organomet. Chem.* **1985**, *291*, 71–87; c) M. J. Camazón, A. Alvarez-Valdés, J. R. Masaguer, M. C. Navarro-Ranninger, *Trans. Met. Chem.* **1986**, *11*, 334–336; d) Y. Doi, T. Fujita, JP Patent 10298225 (Mitsui Chemicals Inc., Japan) priority date April 25, **1997**; e) T. V. Laine, M. Klinga, A. Maaninen, E. Aitola, M. Leskelä, *Acta Chem. Scand.* **1999**, *53*, 968–973; f) M. Sieger, K. Hübler, T. Scheiring, T. Sixt, S. Zalis, W. Kaim, *Z. Anorg. Allg. Chem.* **2002**, *628*, 2360–2364; g) M. Sieger, M. Wanner, W. Kaim, D. J. Stufkens, T. L. Snoeck, S. Zalis, *Inorg. Chem.* **2003**, *42*, 3340–3346; h) U. El-Ayaan, A. A.-M. Abdel-Aziz, *Eur. J. Med. Chem.* **2005**, *40*, 1214–1221.
[10] a) T. V. Lainen, K. Lappalainen, J. Liimatta, E. Aitola, B. Löfgren, M. Leskelä, *Macromol. Rapid Commun.* **1999**, *20*, 487–491; b) M. Qian, M. Wang, B. Zhou, R. He, *Appl. Catal. A: Gen.* **2001**, *209*, 11–15; c) C. Bianchini, G. Mantovani, A. Meli, F. Migliacci, *Organometallics* **2003**, *22*, 2545–2547.
[11] a) M. Gasperini, F. Ragaini, *Organometallics* **2004**, *23*, 995; b) M. Gasperini, F. Ragaini, E. Gazzola, A. Caselli, P. Macchi, *Dalton Trans.* **2004**, 3376–3382; c) M. Gasperini, F. Ragaini, S. Cenini, *Organometallics* **2002**, *21*, 2950–2957.
[12] a) I. L. Fedushkin, N. M. Khvoinova, A. Y. Baurin, G. K. Fukin, V. K. Cherkasov, M. P. Bubnov, *Inorg. Chem.* **2004**, *43*, 7807–7815; b) I. L. Fedushkin, V. A. Chudakova, A. A. Skatova, N. M. Khvoinova, Y. A. Kurskii, T. A. Glukhova, G. K. Fukin, S. Dechert, M. Hummert, H. Shumann, *Z. Anorg. Allg. Chem.* **2004**, *630*, 501–507.
[13] A. Abragam, B. Bleaney. *Electron Paramagnetic Resonance of Transition Ions*, Clarendon Press, Oxford, **1970**.
[14] J. A. Weil, J. R. Bolton, J. E. Wertz, *Electron Paramagnetic Resonance. Elementary Theory and Practical Applications*, John Wiley & Sons, Inc., New York, **1994**.
[15] J. Zarembowitch, O. Kahn, *Inorg. Chem.* **1984**, *23*, 589–593.
[16] R. Carlin, *Magnetochemistry*, Springer, Berlin, **1986**.
[17] J. H. Pilbrow, *Transition Ion Electron Paramagnetic Resonance*, Clarendon Press, Oxford, **1990**.
[18] A. Goñi, L. M. Lezama, T. Rojo, M. E. Foglio, J. A. Valdivia, G. E. Barberis, *Phys. Rev. B* **1998**, *57*, 246–251.
[19] J. Krzystek, S. A. Zvyagin, A. Ozarowski, A. T. Fiedler, T. C. Brunold, J. Telser, *J. Am. Chem. Soc.* **2004**, *126*, 2148–2155.
[20] A. Bencini, D. Gatteschi, *Inorg. Chem.* **1977**, *16*, 2141–2142.
[21] A. Bencini, C. Benelli, D. Gatteschi, C. Zanchini, *Inorg. Chem.* **1979**, *18*, 2137–2140.
[22] A. Bencini, C. Benelli, D. Gatteschi, C. Zanchini, *Inorg. Chem.* **1979**, *18*, 2526–2528.
[23] L. C. Dickinson, J. C. W. Chien, *J. Am. Chem. Soc.* **1983**, *105*, 6481–6487.
[24] A. C. Rizzi, C. D. Brondino, R. Calvo, R. Baggio, M. T. Garland, E. E. Rapp, *Inorg. Chem.* **2003**, *42*, 4409–4416, and references therein.
[25] E. Dowty, (**1994**). *ATOMS*, Version 6.0, Shape Software, 521 Hidden Valley Road, Kingsport, TN 37663, USA.
[26] A. L. Spek, *J. Appl. Crystallogr.* **2003**, *36*, 7–13.
[27] G. M. Sheldrick, *SHELXL97*, University of Göttingen, Germany, **1997**.
[28] D. Pountney, M. Vasak, *Eur. J. Biochem.* **1992**, *209*, 335–341.
[29] O. Y. Gavel, S. A. Bursakov, J. J. Calvete, G. N. George, J. J. G. Moura, I. Moura, *Biochemistry* **1998**, *37*, 16225–16232.
[30] N. Bonander, T. Väangard, L. C. Tsai, V. Langer, H. Nar, L. Sjölin, *Proteins: Structure, Function and Genetics* **1997**, *27*, 385–394.
[31] C. A. Bates, J. M. Dixon, J. R. Fletcher, K. W. H. Stevens, *J. Phys. C (Proc. Phys Soc.)* **1968**, *1*, 859–871.
[32] K. W. H. Stevens, *J. Phys. C: Solid St. Phys.* **1970**, *3*, 2387–2391.
[33] M. C. G. Passeggi, *Phys. Stat. SolidiB* **1972**, *54*, 681–689.
[34] M. T. Werth, S.-F. Tang, G. Formicka, M. Zeppezauer, M. K. Johnson, *Inorg. Chem.* **1995**, *34*, 218–228.

 © 2006 Wiley-VCH Verlag GmbH & Co. KGaA, Weinheim 

[35] R. P. van Stapele, H. G. Beljers, P. F. Bongers, H. Zijlstra, *J. Chem. Phys.* **1966**, *44*, 3719–3725.
[36] L. J. Guggenberger, C. T. Prewitt, P. Meakin, S. Trofimenko, J. P. Jesson, *Inorg. Chem.* **1973**, *12*, 508–515.
[37] a) R. van Asselt, C. J. Elsevier, W. J. J. Smets, A. L. Spek, R. Benedix, *Recl. Trav. Chim. Pays-Bas* **1994**, *113*, 88–98; b) H. Tom Dieck, M. Svoboda, T. Grieser, *Z. Naturforsch., Teil B* **1981**, *36*, 823–832; c) M. Svoboda, H. Tom Dieck, *J. Organomet. Chem.* **1980**, *191*, 321–328.
[38] J. M. Schveigkardt, A. C. Rizzi, O. E. Piro, E. E. Castellano, R. Costa de Santana, R. Calvo, C. D. Brondino, *Eur. J. Inorg. Chem.* **2002**, 2913–2919.
[39] a) F. H. Allen, *Acta Crystallogr., Sect. B* **2002**, *58*, 380–388; b) I. J. Bruno, J. C. Cole, P. R. Edington, M. Kessler, C. F. Macrae, P. McCabe, J. Pearson, R. Taylor, *Acta Crystallogr., Sect. B* **2002**, *58*, 389–397.

Received: May 12, 2006
Published Online: October 5, 2006

 © 2006 Wiley-VCH Verlag GmbH & Co. KGaA, Weinheim 

DOI: 10.1002/ejic.200600474

# Synthesis and Characterisation of Molecular Bismuth Phosphorus Compounds Containing $Bi_2$ Units with Bi–Bi Single and Double Bonds

**Carsten von Hänisch*[a] and Donna Nikolova[a]**

**Keywords:** Bismuth / Phosphorus / Double bonds

The compound $[BiP(SiPh_2tBu)_2]_2$ (**1**), featuring a Bi–Bi double bond and two Bi–P single bonds, has been obtained from the reaction of $BiCl_3$ with the lithium phosphanide $LiP(SitBuPh_2)_2$. As a byproduct of this transmetallation/redox reaction the diphosphane $P_2(SitBuPh_2)_4$ (**2**) has been isolated. This compound shows a remarkably short P–P bond due to π interactions of the phosphorus atoms. The reaction of the dilithium phosphandiide $Li_2PSitBuPh_2$ with $BiCl_3$ yielded the bicyclic compound $[Bi_2(PSiPh_2tBu)_4]$ (**3**), exhibiting a Bi–Bi single bond. NMR studies of **3** show the availability of four different P atoms, as observed in the crystal structure.

(© Wiley-VCH Verlag GmbH & Co. KGaA, 69451 Weinheim, Germany, 2006)

## Introduction

Organobismuth compounds containing Bi–Bi bonds are of considerable interest because of their chemical and physical properties.[1] In contrast to the extensive investigation of dibismuthanes,[2] very few dibismuthenes are known as yet. The first evidence for a Bi–Bi double bond was observed in the compound (Tbt)Bi=Bi(Tbt),[3] where Tbt = 2,4,6-$[(Me_3Si)_2CH]_3C_6H_2$. The compounds $[BiC_6H_3$-2,6-$Mes_2]_2$ and $[BiC_6H_3$-2,6-$Trip_2]_2$ (Mes = 2,4,6-$Me_3C_6H_2$, Trip = 2,4,6-$iPr_3C_6H_2$), also featuring Bi–Bi double bonds, were obtained by Power et al.'s group.[4] On the other hand, the use of less bulky substituents expands the knowledge in the field of the homonuclear cyclic and polycyclic compounds of bismuth. A remarkable development in the last years is the synthesis of the first cyclo-$R_4Bi_4$ [R = $(Me_3Si)_2CH$][5] compound in equilibrium with the cyclo-$R_3Bi_3$ species. Parallel work described the isolation of $[(Me_3Si)_3Si]_4Bi_4$ and the bicycle $[(Me_3Si)_3Sn]_6Bi_8$.[6] Molecular compounds containing Bi–P bonds are still rare, and for that reason we investigate whether sterically demanding phosphanyl groups can be used for the synthesis of new polynuclear bismuth compounds. We report here on the synthesis and crystal structures of the new binuclear bismuth compounds $[BiP(SiPh_2tBu)_2]_2$ (**1**) and $[Bi_2(PSiPh_2tBu)_4]$ (**3**) as well as the diphosphane $P_2(SitBuPh_2)_4$ (**2**) (Scheme 1).

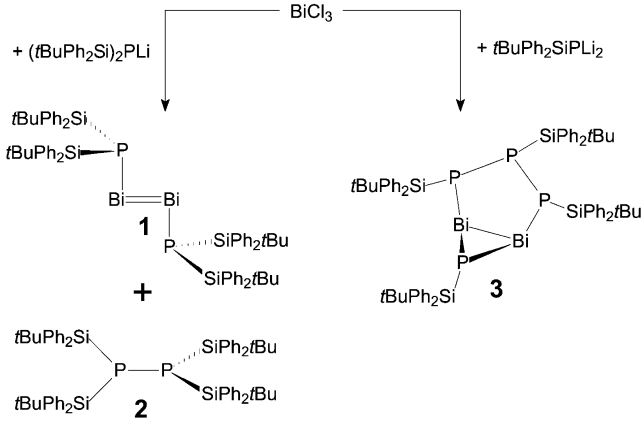


Scheme 1. Synthesis of compounds **1**–**3**.

## Results and Discussion

By reaction of $(tBuPh_2Si)_2PLi$ with $BiCl_3$ in molar ratio 3:1 the dibismuthene $[BiP(SiPh_2tBu)_2]_2$ (**1**) and the diphosphane $P_2(SiPh_2tBu)_4$ (**2**) were obtained. Compound **1** forms red crystals and crystallises in the triclinic space group $P\bar{1}$ with the centre of inversion located in the middle of the molecule (Figure 1). The X-ray investigation revealed that **1** exists as a binuclear complex. There are no significant intermolecular Bi···Bi contacts between the Bi atoms of adjacent molecules because of the large steric requirement of the $(tBuPh_2Si)_2P$ substituents. The molecule shows a *trans* conformation, a structural feature represented by the majority of the previously known organobismuth compounds with a Bi–Bi double bond.[3,4,7] In particular, *cis* forms of dibismuthenes have been described in tungsten pentacarbonyl complexes.[8] The bismuth atoms and the phosphorus atoms show a planar alignment. The Bi–Bi bond length is 282.1 pm, which is in the usual range for double bonds between bismuth atoms. Similar Bi–Bi bond lengths of 282.1 and 283.3 pm, for example, can be observed in $(TbtBi)_2$[3] and $(2,6\text{-}Mes_2C_6H_3Bi)_2$,[4] whereas in [RBi=BiR{W-

[a] Institut für Nanotechnologie, Forschungszentrum Karlsruhe, Postfach 3640, 76021 Karlsruhe, Germany
Fax: +49-7247-826368
E-mail: carsten.vonhaenisch@int.fzk.de


WILEY InterScience DISCOVER SOMETHING GREAT
© 2006 Wiley-VCH Verlag GmbH & Co. KGaA, Weinheim

$(CO)_5\}_2]$[8] (R = $Me_3CCH_2$, $Me_3SiCH_2$) these bonds are slightly longer (287.7–300.2 pm). The Bi–P bonds are 264.8 pm long. In the $Bi^{III}$ phosphide complex $[Bi(P_3tBu_3)_2]^-$, described by Wright and co-workers, the Bi–P bonds are between 263.0 and 291.1 pm long.[9] The Bi–Bi–P angle of 89.38° provides evidence for the very low tendency of bismuth to take part in hybridisation; the double bond is mostly composed from the orthogonally placed p orbitals.[10] Relatively wider Bi–Bi–C angles of 92.5° and 100.5° are observed in the structurally analogous dibismuthenes, mentioned above. One reason for the very low value of the Bi–Bi–P angle in **1** could be attractive interactions between Bi(1) and P(1′) [and Bi(1′) and P(1)]. The distances between these atoms are, at 386.5 pm, considerably shorter than the sum of the van der Waals radii (430 pm).

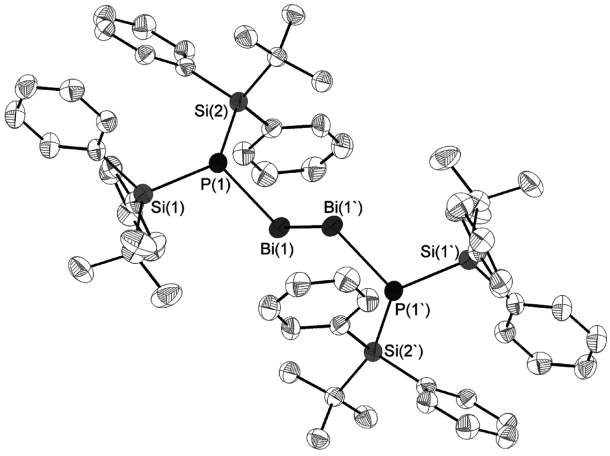


Figure 1. Molecular structure of **1** (ORTEP, thermal ellipsoids set at the 30% probability level). Hydrogen atoms are omitted for clarity. Selected bond lengths [pm] and angles [°]: Bi(1)–Bi(1′) 282.06(9), Bi(1)–P(1) 264.82(17), P(1)–Si(1) 227.3(3), P(1)–Si(2) 228.9(2); Bi(1′)–Bi(1)–P(1) 89.38(4), Bi(1)–P(1)–Si(1) 103.91(8), Bi(1)–P(1)–Si(2) 95.12(7), Si(1)–P(1)–Si(2) 110.78(9).

The $^{31}P\{^1H\}$ NMR spectrum of **1** in [$D_8$]THF displays one singlet at $\delta$ = –202.0 ppm. Compound **1** is stable in the solid but decomposes in THF solution within a few days, with formation of **2**, $(tBuPh_2Si)_2PH$, elemental bismuth as well as different oligophosphanes.

The second product of the transmetallation/redox reaction of $BiCl_3$ and $(tBuPh_2Si)_2PLi$ is the diphosphane **2**. It crystallises in the space group $P\bar{1}$ and is composed of two diorganophosphorus moieties, linked through a P–P single bond (Figure 2). Because of the steric effects of the bulky silyl groups, the geometry at each phosphorus atom is essentially planar (sum of bond angles: 353.8°) and the $P(SitBuPh_2)_2$ fragments show a twisted arrangement. An interesting aspect of the structure is the relatively short P–P bond length of 217.3 pm in comparison with the corresponding values in organophosphanes such as $P_2Ph_4$ (221.7 pm) and $tBu_4P_6$ (219.2–220.8 pm).[11,12] It seems that the twist structure and the almost planar environment of the phosphorus atoms is favourable for bond shortening due to some π bonding.[13] A similar explanation has recently been given for the short P–P bond in Hittorf's phosphorus.[14]

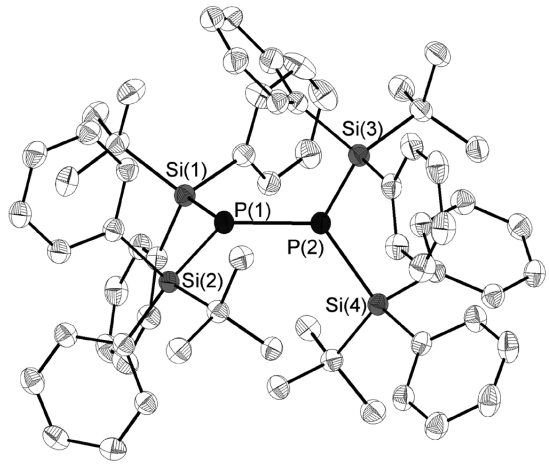


Figure 2. Molecular structure of **2** (ORTEP, thermal ellipsoids set at the 30% probability level). Hydrogen atoms are omitted for clarity. Selected bond lengths [pm] and angles [°]: P(1)–P(2) 217.31(13), P(1)–Si(1) 230.33(13), P(1)–Si(2) 231.16(15), P(2)–Si(3) 230.30(13), P(2)–Si(4) 231.12(14); P(1)–P(2)–Si(3) 108.62(5), P(1)–P(2)–Si(4) 125.36(5), P(2)–P(1)–Si(1) 108.55(6), P(2)–P(1)–Si(2) 124.81(6), Si(1)–P(1)–Si(2) 119.93(5), Si(3)–P(2)–Si(4) 119.36(5).

The reaction of $tBuPh_2SiPLi_2$ with $BiCl_3$ in molar ratio 3:2 affords the bicycle $[Bi_2(PSiPh_2tBu)_4]$ (**3**), which can be isolated in the form of red crystals. The compound crystallises in the triclinic space group $P\bar{1}$. It is constructed of five-membered $P_3Bi_2$ and three-membered $PBi_2$ rings sharing a common bridgehead (Figure 3). Of particular interest is the appearance of P–P and Bi–Bi single bonds in the molecule, obviously due to a reduction of the Bi atoms and corresponding oxidation of the P atoms. The central $Bi_2P_4$ unit features a nonplanar array; the plane through Bi(1), Bi(2), P(4) is virtually perpendicular to the $Bi_2P_3$ ring. Examination of the bond lengths and angles found in the bicyclic core of **3** indicates that there is a considerable amount of strain in this arrangement. The fold angles P(1)–Bi(1)–P(4) and P(3)–Bi(2)–P(4) are 82.65° and 103.36°, respectively. The comparatively large difference between these angles results from the manner of orientation of the sterically demanding silyl groups coordinated to P(1) and P(3). The $tBuPh_2Si$ substituent of P(1) is in *trans* position to the Bi(1)–P(4) bond, whereas the silyl group bonded to P(3) is in *cis* position to the Bi(2)–P(4) bond. The torsion angles Si(3)–P(3)–Bi(2)–P(4) and Si(1)–P(1)–Bi(1)–P(4) are 49.1° and 134.0° respectively. A similar structural pattern has been observed for the analogous antimony species $[Sb_2(PSiPh_2tBu)_4]$ in the course of our investigations.[15] The homonuclear bicyclic compound $tBu_4P_6$ reported by Baudler and co-workers however shows an all-*trans* arrangement of the *t*Bu groups.[12] The Bi–Bi bond is 294.1 pm and therefore shorter than the corresponding bond lengths in the structures of already known dibismuthanes, such as $Ph_4Bi_2$ (299.0 pm)[2a] and $(Me_3Si)_4Bi_2$ (303.5 pm).[2b] The bond shortening is possibly a conse-

 © 2006 Wiley-VCH Verlag GmbH & Co. KGaA, Weinheim 

quence of the fact that the $Bi_2$ moiety is bridged by the P(4) atom. The P–P and Bi–P bonds in **3** are 221.5 pm and 268.6 pm on average.

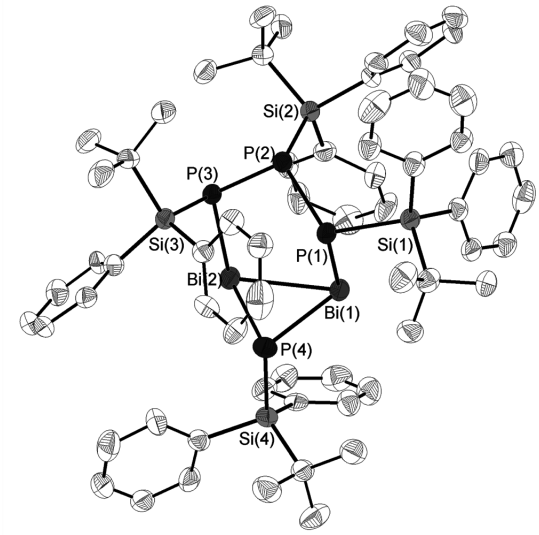


Figure 3. Molecular structure of **3** (ORTEP, thermal ellipsoids set at the 30% probability level). Hydrogen atoms are omitted for clarity. Selected bond lengths [pm] and angles [°]: Bi(1)–Bi(2) 294.2(2), Bi(1)–P(1) 266.3(6), Bi(1)–P(4) 269.2(6), Bi(2)–P(3) 269.3(6), Bi(2)–P(4) 269.5(6), P(1)–P(2) 221.9(8), P(2)–P(3) 221.2(7), P(1)–Si(1) 229.8(7), P(2)–Si(2) 232.0(8), P(3)–Si(3) 227.2(8), P(4)–Si(4) 227.7(9); Bi(1)–Bi(2)–P(4) 56.86(2), Bi(2)–Bi(1)–P(1) 90.26(2), Bi(2)–Bi(1)–P(4) 56.95(2), Bi(1)–P(4)–Bi(2) 66.19(4), Bi(1)–P(1)–P(2) 111.2(3), Bi(1)–P(3)–P(2) 113.1(2), P(1)–P(2)–P(3) 101.2(3), P(1)–Bi(1)–P(4) 82.65(8), P(3)–Bi(2)–P(4) 103.36(8).

The structure of **3** can be deduced from the $^{31}P\{^1H\}$ NMR spectrum, which shows, at room temperature, two triplet signals at $\delta$ = –77 ppm and $\delta$ = –265.5 ppm for the P(2) and P(4) atoms, respectively. An additional broad signal appears at $\delta$ = –115 ppm. At +70 °C two triplet signals and one doublet of doublets can be observed, which is consistent with chemically identical P(1) and P(3) atoms ($AM_2X$ spin system, $^1J_{P,P}$ = 400, $^2J_{P,P}$ = 87 Hz). At –50 °C the $^{31}P\{^1H\}$ NMR spectrum of **3** shows four multiplets, corresponding to four different P atoms, as observed in the crystal structure (Table 1).

As can be shown by the synthesis of compound **1**, sterically demanding disilylphosphanid ligands can be used for the kinetic stabilisation of unusual bonding situations. Hence they are an alternative to the frequently used bulky silyl or aryl groups such as $Si(SiMe_3)_3$ or 2,6-$Mes_2C_6H_3$. $R_3SiP$ fragments, however, can be used to build up binary polycycles, as can be seen from the synthesis of compound **3**.

## Experimental Section

All manipulations were carried out under rigorous exclusion of oxygen and moisture, using a Schlenk line and nitrogen atmosphere. Solvents were dried and freshly distilled before use. The starting material $t$BuPh$_2$SiPH$_2$ was prepared by LiCl-elimination reaction of $t$BuPh$_2$SiCl with [(dme)LiPH$_2$] in THF, in the manner described by us previously.[15] $BiCl_3$ was obtained from Aldrich and used as received. The $^{31}P$ NMR spectra were recorded with Bruker AC 250 and a Bruker Avance 300 spectrometers.

**($t$BuPh$_2$Si)$_2$PH:** This compound was isolated as a byproduct from the synthesis of $t$BuPh$_2$SiPH$_2$ and could be obtained as colourless crystals by recrystallisation of the distillation residue from *n*-pentane.[15] $C_{32}H_{39}PSi_2$ (510.81): calcd. C 75.24, H 7.70; found C 75.23, H 7.83. $^1H$ NMR ($C_6D_6$): $\delta$ = 1.21 [s, C(C$H_3$)$_3$, 18 H], 1.82 (d, P$H$, $^1J_{P,H}$ = 200.1 Hz, 1 H), 7.04 (m, *o*-Ph, 8 H), 7.10 (m, *p*-Ph, 4 H), 7.60 (m, *m*-Ph, 8 H) ppm. $^{13}C\{^1H\}$ NMR ($C_6D_6$): $\delta$ = 20.8 [d, $C(CH_3)_3$, $^2J_{P,C}$ = 12.4 Hz], 28.3 [d, C($CH_3$)$_3$, $^3J_{P,C}$ = 2.6 Hz], 127.7 (s, Ph), 129.3 (s, Ph), 134.7 (d, $J_{P,C}$ = 5.7 Hz, Ph), 136.8 (d, $J_{P,C}$ = 3.3 Hz, Ph) ppm. $^{29}Si\{^1H\}$ NMR ($C_6D_6$): $\delta$ = 4.9 (d, $^1J_{P,Si}$ = 36.6 Hz) ppm. $^{31}P$ NMR ($C_6D_6$): $\delta$ = –267 (d, $^1J_{P,H}$ = 200.1 Hz) ppm. IR (KBr): $\tilde{\nu}$ = 3071 (m), 3043 (m), 2964 (s), 2930 (s), 2892 (m), 2856 (s), 2295 (m), 1959 (w), 1896 (w), 1820 (w), 1776 (w),

Table 1. Crystallographic data of **1**–**3**.[16]

| | **1** | **2** | **3** |
|---|---|---|---|
| Empirical formula | $C_{64}H_{76}Bi_2P_2Si_4$ | $C_{64}H_{76}P_2Si_4{\cdot}2Et_2O$ | $C_{64}H_{76}Bi_2P_4Si_4$ |
| Space group | $P\bar{1}$ | $P\bar{1}$ | $P\bar{1}$ |
| Formula units | 1 | 2 | 2 |
| Temperature [K] | 200 | 200 | 200 |
| $a$ [pm] | 961.72(2) | 1403.6(3) | 1400.3(3) |
| $b$ [pm] | 1114.6(2) | 1644.3(3) | 1424.9(3) |
| $c$ [pm] | 1651.9(3) | 1748.4(4) | 2157.2(4) |
| $\alpha$ [°] | 71.52(3) | 66.97(3) | 106.36(3) |
| $\beta$ [°] | 87.71(3) | 69.99(3) | 92.13(3) |
| $\gamma$ [°] | 68.79(3) | 71.44(3) | 118.87(3) |
| Volume [Å$^3$] | 1560.0(5) | 3409.1(12) | 3539.0(12) |
| Density [g cm$^{-3}$] | 1.530 | 1.138 | 1.407 |
| $2\theta$ range [°] | 3–49 | 3–48 | 2–45 |
| Reflections measured | 9429 | 14639 | 17447 |
| Independent reflections | 5044 ($R_{int}$ = 0.0371) | 9570 ($R_{int}$ = 0.0254) | 8825 ($R_{int}$ = 0.0797) |
| Independent reflections with $F_o > 4\sigma(F_o)$ | 4593 | 7717 | 5634 |
| Parameters | 325 | 671 | 667 |
| $\mu$(Mo-$K_\alpha$) [mm$^{-1}$] | 5.798 | 0.177 | 5.158 |
| $R_1$ | 0.0474 | 0.0609 | 0.0739 |
| $wR_2$ (all data) | 0.1263 | 0.1738 | 0.1531 |
| Residual electron density [e Å$^{-3}$] | –1.957/1.063 | –0.862/1.29 | –2.91/1.92 |

 © 2006 Wiley-VCH Verlag GmbH & Co. KGaA, Weinheim 

1588 (w), 1567 (w), 1486 (w), 1470 (m), 1426 (s), 1389 (m), 1359 (m), 1309 (w), 1262 (w), 1188 (m), 1157 (w), 1102 (vs), 1028 (w), 1007 (m), 934 (m), 846 (w), 816 (s), 740 (s), 698 (vs), 620 (w), 597 (s), 561 (w), 518 (vs), 483 (s), 454 (s), 402 (m) $cm^{-1}$.

**1 and 2:** Butyllithium solution (0.37 mL, 1.6 M) was added to a solution of $(t\text{BuPh}_2\text{Si})_2\text{PH}$ (0.3 g, 0.59 mmol) in $Et_2O$ (10 mL) at 0 °C. After warming to room temperature, the solution of $(t\text{BuPh}_2\text{Si})_2\text{PLi}$ was added to a suspension of 0.06 g (0.2 mmol) $BiCl_3$ in 10 mL $Et_2O$ at –60 °C. Subsequently the red mixture was slowly warmed to room temperature while stirring and then agitated overnight. The solution was reduced to 5 mL in vacuo. After filtration and cooling to 0 °C red crystals of **1** were obtained within a few hours. Subsequent reduction of the volume to 3 mL in vacuo and cooling of the solution for two days yielded a second crystal fraction consisting of **1** and colourless crystals of **2**.

**1:** Yield: 0.12 g (41.7%). $C_{64}H_{76}Bi_2P_2Si_4$ (1437.56): calcd. C 53.47, H 5.33; found C 53.84, H 5.32. $^1$H NMR ([D$_8$]THF): $\delta$ = 1.21 (s, CC$H_3$, 36 H), 7.28 (m), 7.50 (m), 7.54 (m): SiPh (40 H) ppm. $^{29}$Si{$^1$H} NMR ([D$_8$]THF): $\delta$ = 13.9 (m) ppm. $^{31}$P{$^1$H} NMR ([D$_8$]THF): $\delta$ = –202.0 (s) ppm. IR (KBr): $\tilde{\nu}$ =3132 (w), 3049 (m), 2961 (s), 2928 (s), 2889 (m), 2855 (s), 1958 (w), 1895 (w), 1822 (w), 1587 (w), 1567 (w), 1468 (m), 1426 (s), 1388 (w), 1360 (w) 1309 (w), 1262 (m), 1188 (w), 1155 (vw), 1099 (vs), 1006 (m), 935 (w), 884 (w) 814 (s), 737 (s), 701 (vs), 593 (s), 523 (vs), 485 (m), 408 (w) $cm^{-1}$. UV/Vis: $\lambda$ ($\varepsilon$ in $L\,mol^{-1}\,cm^{-1}$) = 820 (shoulder, 100), 564 (2944), 466 nm (shoulder, 1180).

**2:** Yield: about 0.02 g after sorting by hand. No satisfying elemental analysis can be obtained because of co-crystallisation of compound **1**. $^1$H NMR ([D$_8$]toluene): $\delta$ = 1.20 (s, CC$H_3$, 36 H), 7.06 (m), 7.19 (m), 7.57 (m): SiPh (40 H) ppm. $^{29}$Si{$^1$H} NMR ([D$_8$]-toluene): $\delta$ = 8.1 (pseudo-t, $J_{PSi}$ = 18.2 Hz) ppm. $^{31}$P{$^1$H} NMR ([D$_8$]toluene): $\delta$ = –199.8 (s) ppm. MS (EI = 70 eV, 180 °C): *m*/*z* (%) = 1019 (22) [M$^+$], 961 (3.4) [M$^+$ – *t*Bu], 904 (4.4) [M$^+$ – 2 *t*Bu], 779 (21) [M$^+$ – Si*t*BuPh$_2$], 722 (36) [M$^+$ – Si*t*BuPh$_2$ – *t*Bu], 665 (37) [M$^+$ – Si*t*BuPh$_2$ – 2 *t*Bu], 453 (100) [M$^+$/2 – $C_4H_8$], 397 (100) [M$^+$/2 – 2 $C_4H_8$].

**3:** Butyllithium solution (1.1 mL, 1.6 M) was added to a solution of $t\text{BuPh}_2\text{SiPH}_2$ (0.24 g, 0.88 mmol) in $Et_2O$ 5 mL) at 0 °C. After stirring for 10 min, this solution was added to a suspension of $BiCl_3$ (0.19 g, 0.59 mmol) in Heptan (20 mL) at –70 °C. The reaction mixture was warmed up to room temperature and then stirred for an additional 16 h. Some of the solvent (20 mL) was removed in vacuo. The resulting black-green solution was filtered to remove the precipitated LiCl and elemental bismuth and cooled to –35 °C. Red crystals of **3** were obtained over a period of some days. Yield: 0.1 g (22.6%). $C_{64}H_{76}Bi_2P_4Si_4$ (1499.5): calcd. C 51.26, H 5.11; found C 51.63, H 5.30. $^1$H NMR ($C_6D_6$): $\delta$ = 1.36 (s, Si*t*Bu, 9 H), 1.39 (s, Si*t*Bu, 9 H), 1.52 (s, Si*t*Bu, 18 H), 6.86 (m), 7.15 (m), 7.36 (m), 7.58 (m), 7.80 (m), 8.06 (m): SiPh (40 H) ppm. $^{31}$P{$^1$H} NMR ([D$_8$]toluol, 70 °C): $\delta$ = –256.6 (t, $^2J_{PP}$ = 87 Hz), –113 (dd, $^1J_{PP}$ = 400 Hz, $^2J_{PP}$ = 87 Hz), –73.7 (t, $^1J_{PP}$ = 400 Hz) ppm. $^{31}$P{$^1$H} NMR ([D$_8$]toluol, –50 °C): –82.3 (m), –102.0 (m), –145.1 (m), –279.5 (m) ppm. IR (KBr): $\tilde{\nu}$ 3132 (w), 3068 (m), 3046 (m), 3013 (w), 2959 (s), 2925 (s), 2889 (m), 2854 (s), 1955 (w), 1890 (w), 1822 (w), 1719 (w), 1586 (w), 1565 (w), 1484 (w), 1468 (m), 1426 (s), 1389 (m), 1361 (m) 1303 (w), 1262 (m), 1192 (w), 1156 (vw), 1100 (vs), 1008 (m), 936 (w), 853 (w) 814 (s), 737 (s), 699 (vs), 620 (w), 595 (m), 516 (vs), 484 (s), 405 (m) $cm^{-1}$.

CCDC-606897 to -606899 contain the supplementary crystallographic data for this paper. These data can be obtained free of charge from The Cambridge Crystallographic Data Centre via www.ccdc.cam.ac.uk/data_request/cif.


[1] Review articles: a) H. J. Breunig, *Z. Anorg. Allg. Chem.* **2005**, *631*, 621–631; b) L. Balazs, H. J. Breunig, *Coord. Chem. Rev.* **2004**, *248*, 603–621.

[2] a) G. Balazs, H. J. Breuning, E. Lork, *Organometallics* **2002**, *21*, 2584–2586; b) A. J. Ashe, *Adv. Organomet. Chem.* **1990**, *30*, 77–97; c) F. Calderazzo, R. Poli, *J. Chem. Soc., Dalton Trans.* **1984**, 2365–2369; d) O. Mundt, G. Becker, M. Rössler, C. Witthauer, *Z. Anorg. Allg. Chem.* **1983**, *506*, 42–58.

[3] N. Tokitoh, Y. Arai, R. Okazaki, S. Nagase, *Science* **1997**, *277*, 78–80.

[4] B. Tramley, C. D. Sofield, M. M. Olmstead, P. P. Power, *J. Am. Chem. Soc.* **1999**, *121*, 3357–3367.

[5] H. J. Breunig, R. Rösler, E. Lork, *Angew. Chem.* **1998**, *110*, 3361–3363; *Angew. Chem. Int. Ed.* **1998**, *37*, 3175–3177.

[6] G. Linti, W. Köstler, *Z. Anorg. Allg. Chem.* **2002**, *628*, 63–66.

[7] L. Balazs, H. J. Breunig, E. Lork, *Angew. Chem.* **2002**, *114*, 2411–2414; *Angew. Chem. Int. Ed.* **2002**, *41*, 2309–2312.

[8] G. Balazs, L. Balazs, H. J. Breunig, E. Lork, *Organometallics* **2003**, *22*, 2919–2924.

[9] M. A. Beswick, N. Choi, A. D. Hopkins, Y. G. Lawson, M. McPartlin, A. Rothenberger, D. Stalke, A. E. H. Wheatley, D. S. Wright, *Angew. Chem.* **1999**, *111*, 3236–3238; *Angew. Chem. Int. Ed.* **1999**, *38*, 3053–3055.

[10] S. Nagase, in *The Chemistry of Organic Arsenic, Antimony and Bismuth Compounds* (Ed.: S. Patai), Wiley, New York, **1994**.

[11] A. Dashti-Mommertz, B. Neumüller, *Z. Anorg. Allg. Chem.* **1999**, *625*, 954–960.

[12] M. Baudler, Y. Aktalay, K. Tebbe, T. Heinlein, *Angew. Chem.* **1981**, *93*, 1020–1022; *Angew. Chem. Int. Ed. Engl.* **1981**, *11*, 967–969.

[13] Overlap of the p-type lone pair at one phosphorus atom with symmetry adapted *anti* bonding Si–P orbitals and/or empty d orbitals at the other phosphorus atom.

[14] M. Ruck, D. Hoppe, B. Wahl, P. Simon, Y. Wang, G. Seifert, *Angew. Chem.* **2005**, *117*, 7788–7792; *Angew. Chem. Int. Ed.* **2005**, *44*, 7616–7619.

[15] D. Nikolova, C. von Hänisch, *Eur. J. Inorg. Chem.* **2005**, 378–382.

[16] STOE-IPDS2 (Mo-$K_\alpha$ radiation, $\lambda$ = 0.71073 Å). The structures were solved by direct methods and refined by full-matrix least-squares techniques against $F^2$ (Bi, P, Si, C refined anisotropically, H atoms were calculated at ideal positions). Numerical absorption correction was applied for compound **1**.


Received: May 22, 2006
Published Online: October 13, 2006

 © 2006 Wiley-VCH Verlag GmbH & Co. KGaA, Weinheim 

DOI: 10.1002/ejic.200600550

# Cu/Zn/Al Xerogels and Aerogels Prepared by a Sol–Gel Reaction as Catalysts for Methanol Synthesis

Yanzhi Guo,[a] Wolfgang Meyer-Zaika,[a] Martin Muhler,[b] Sascha Vukojević,[c] and Matthias Epple*[a]

**Keywords:** Heterogeneous catalysis / Copper / Zinc / Aluminum / Sol–gel processes / Mesoporous materials

$ZnO/Al_2O_3$, $CuO/Al_2O_3$, and $CuO/ZnO/Al_2O_3$ xerogels and aerogels have been prepared by a sol–gel route using propylene oxide as gelation initiator. For aerogel preparation, the solvent was extracted with supercritical $CO_2$. Calcination of these xerogels and aerogels was followed by thermogravimetry (TG), and the microstructure of these calcined xerogels and aerogels was investigated by TEM, powder XRD, EXAFS, and nitrogen physisorption (BET, BJH). The oxide mixtures $CuO/Al_2O_3$ and $CuO/ZnO/Al_2O_3$ were also studied by temperature-programmed reduction (TPR), and their catalytic activity in the formation of methanol from $CO/CO_2/H_2$ synthesis gas was measured. The aerogels have a higher specific surface area and a higher Cu surface area than the corresponding xerogels, which results in a higher catalytic activity for methanol synthesis. The presence of ZnO significantly increases the catalytic activities of both the xerogel and the aerogel.

(© Wiley-VCH Verlag GmbH & Co. KGaA, 69451 Weinheim, Germany, 2006)

## Introduction

$Cu/ZnO/Al_2O_3$ catalysts are widely used for the industrial synthesis of methanol, for methanol reforming, and for the water-gas shift reaction, and have therefore been intensively investigated in the last few decades.[1–3] Various methods have been developed for the preparation of $Cu/ZnO/Al_2O_3$ catalysts. The differences in preparation methods, synthesis conditions, and pre-treatment have a considerable influence on the structure of the catalysts, which finally leads to disparities in the catalytic performance. It is generally accepted that a large specific Cu surface area leads to an active methanol synthesis catalyst.[1,4] In addition, the metal–support interaction plays a key role in this catalytic reaction.[1,2,5,6]

Catalyst preparation usually involves complex processes and the performance of the final product is very sensitive to rather subtle changes in the synthetic procedures.[7–11] Copper/zinc oxide nanocomposites are usually prepared by co-precipitation from aqueous solutions. Typically, a mixed solution of copper and zinc salts (frequently nitrates or acetates) is prepared and the precipitation of both carbonates is induced by the addition of sodium or ammonium carbonate whilst stirring, followed by drying and calcination.[8,9,12] The particle size and crystallinity of the products can be adjusted by varying the pH, the reactant concentrations, the stirring rate, the duration of precipitation and aging, and the calcination conditions.[13] Günter et al. have investigated binary Cu/ZnO catalysts with varying Cu/Zn molar ratios (90:10 to 10:90) and found that the precursor phase composition directly influences the resulting Cu microstructure and, in turn, the performance of the Cu/ZnO catalyst.[8] The effect of pH on the composition of the precursors and the activity of the $Cu/ZnO/Al_2O_3$ catalysts for methanol synthesis has been studied by Fang et al.,[14] and Deng et al. have prepared ultra-fine $Cu/ZnO/Al_2O_3$ catalysts by an oxalate gel co-precipitation.[15] The obtained catalysts show a high activity in methanol synthesis. A non-aqueous organometallic route has been developed by Fischer et al. and uniform copper/zinc nanoparticles ("nanobrass") were obtained with $[Cu\{OCH(Me)CH_2NMe_2\}_2]$ and $Et_2Zn$ as precursors.[16] Schüth et al. have reported that colloidal copper nanoparticles prepared by reduction of copper acetylacetonate with trialkylaluminum are highly active for quasi-homogeneous methanol synthesis.[17] We have reported the preparation of copper/zinc nanocomposites by the thermolysis of dimetallic copper/zinc cyanide coordination compounds under mild conditions.[18–21] For instance, the copper/zinc cyanide compound $[Zn\{Cu(CN)_3\}]$ was precipitated by both a batch-wise and a continuous synthesis method. Depending on the ligands in the complex and the thermolysis conditions, the activity towards methanol synthesis could be controlled.[21]

The sol–gel route can be considered as a very interesting way of preparing catalysts because of the possibility to con-

[a] Inorganic Chemistry, University of Duisburg–Essen, Universitaetsstrasse 5–7, 45117 Essen, Germany
Fax: +49-201-183-2621
E-mail: matthias.epple@uni-due.de
[b] Laboratory of Industrial Chemistry, Ruhr University Bochum, Universitaetsstrasse 150, 44801 Bochum, Germany
[c] Max-Planck-Institute for Coal Research, Kaiser-Wilhelm-Platz 1, 45470 Muelheim an der Ruhr, Germany

 InterScience © 2006 Wiley-VCH Verlag GmbH & Co. KGaA, Weinheim 

trol many variables involved in the synthesis.[22] Traditionally, the sol–gel method has involved the use of metal alkoxide precursors that readily undergo catalyzed hydrolysis and condensation to form a sol of metal oxide particles with nanoscale dimensions (1–100 nm).[22] This route has proven to be an efficient, easy, and successful approach for the preparation of $SiO_2$-, $Al_2O_3$-, and $ZrO_2$-based porous materials.[23] A novel sol–gel technique was recently developed for the preparation of transition and main-group metal oxide aerogels, xerogels, and nanocomposites.[24] This method involves the use of epoxides as gelation initiators in the preparation of porous metal oxides such as $Fe_2O_3$, $Al_2O_3$, and $Cr_2O_3$.[25,26] Here we report the sol–gel preparation and catalytic performance of Cu-, Zn-, and Al-based di- and trimetallic nanocomposites by this method.

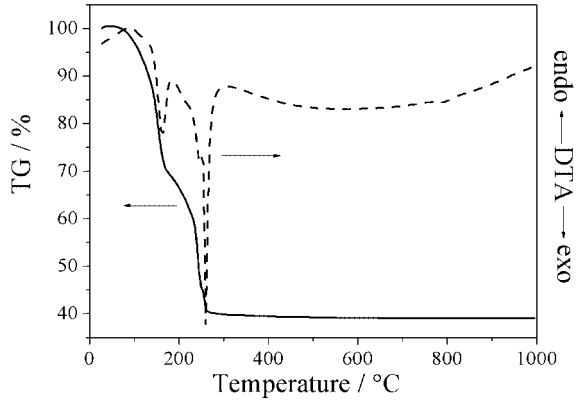


Figure 1. TG and DTA analysis of the Cu/Zn/Al dried xerogel (1:1:1) under dynamic oxygen atmosphere (5 $K\,min^{-1}$), leading to an intimate mixture of CuO, ZnO, and $Al_2O_3$.

## Results and Discussion

### Synthesis

Metal oxide aerogels and xerogels can be prepared directly from metal salts using epoxides as gelation initiators.[27,28] These initiators, which act as irreversible proton scavengers, induce the hydrolysis and condensation of hydrated metal cations. The initiators consume the protons from the hydrated metal species and enhance the sol–gel condensation reaction. The protonated epoxide is ultimately consumed during gelation by a ring-opening reaction with a suitable nucleophile. In this work, propylene oxide was used as gelation initiator and the gel formed within 30–60 min in ethanol solution. No shrinkage was observed either during the gelation process or in the drying process with supercritical carbon dioxide. However, shrinkage was observed after drying in air to a xerogel. As a result, the obtained oxide xerogels and aerogels exhibit very low densities, especially the latter. Different combinations of metals were realized.

### Thermolysis of the Zn/Al and Cu/Zn/Al Xerogels and Aerogels

The thermal decomposition of the air-dried xerogels and the aerogels to the corresponding oxides was studied by thermogravimetry (TG).[29] The decomposition behavior showed only a small dependence on the composition of the gel, i.e. the ratio of Cu/Zn/Al or the drying procedure (air-drying or extraction with supercritical $CO_2$). Figure 1 shows the TG and DTA curves of a Cu/Zn/Al air-dried xerogel (1:1:1) under dynamic oxygen atmosphere. The first peak is a broad endothermal one with a maximum at about 92 °C, which is probably due to the loss of residual volatile solvent (ethanol or water). The subsequent exothermal peaks at 160, 245, and 260 °C can be attributed to the oxidation of residual organic compounds, which is in good agreement with the literature.[28] The total weight loss is about 60%. A similar behavior has been observed for the other samples, although with slight temperature variations of the exothermal peaks.

### $ZnO/Al_2O_3$ Xerogels

TEM images of the calcined $ZnO/Al_2O_3$ xerogel with different Zn/Al ratios are shown in Figure 2. The particles in Figure 2a have a typical particle diameter of 10 nm. When the Zn/Al ratio was increased to 2:1, the homogeneity decreased, with particle sizes up to 30 nm (Figure 2b).

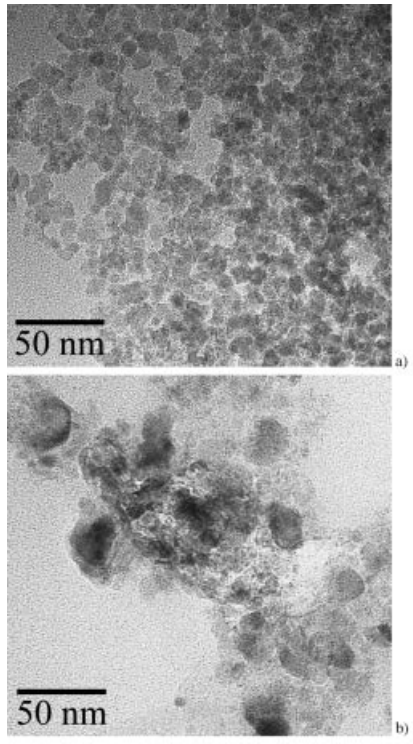


Figure 2. TEM images of $ZnO/Al_2O_3$ calcined xerogels (400 °C) with different Zn/Al molar ratios: a) Zn/Al = 1:2; b) Zn/Al = 2:1.

The structure of the sol–gel products depends on the type and concentration of the polyoxometalates present during the formation of the condensed gel.[26] The nature of these

 © 2006 Wiley-VCH Verlag GmbH & Co. KGaA, Weinheim 

transient species is determined by a number of synthesis parameters, such as the reaction pH, solvent, temperature, ionic strength of the solution, as well as the compositions in the case of mixed species. XRD studies showed that the crystallinity of the Zn/Al oxides is strongly affected by the Zn/Al ratio (Figure 3). $ZnO/Al_2O_3$ is X-ray amorphous for a Zn/Al ratio of 1:2, thus indicating the absence of long-range order. However, for a 2:1 ratio the crystallinity increases significantly, as indicated by peaks originating from ZnO nanocrystals corresponding to the presence of larger particles in the TEM image. The $Al_2O_3$ phase is always X-ray amorphous.

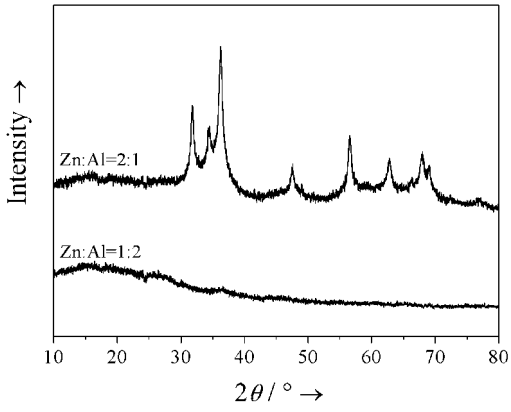


Figure 3. XRD patterns of $ZnO/Al_2O_3$ calcined xerogels (400 °C) with different Zn/Al molar ratio. All peaks in the upper diffractogram correspond to ZnO.

A closer look at the structure of the $ZnO/Al_2O_3$ calcined xerogel (400 °C) was obtained by EXAFS (Figure 4 and Table 1). In the Zn K-edge Fourier transform magnitudes, the first shell of Zn–O in ZnO is clearly present in both samples. The Zn–Zn shells at about 3 Å, however, are different for different Zn/Al ratios. For the sample with a Zn/Al ratio of 1:2 the Zn–Zn peak is almost invisible. The absence of Zn neighbors around Zn suggests a high structural disorder or a dispersion of ZnO in $Al_2O_3$ on the atomic scale. This dispersion can be beneficial when these $ZnO/Al_2O_3$ oxide mixtures are used as a support for metallic Cu catalysts in methanol synthesis. The Zn–Zn peak is much stronger for the 2:1 sample, thereby indicating the presence of ZnO nanocrystals; this is in good agreement with the XRD and the TEM results. In both cases, the coordination number of the Zn–Zn shell is much less than 12, which is the crystallographic coordination number of crystalline ZnO. We conclude that an appropriate concentration of $Al_2O_3$ can effectively disperse ZnO and inhibit the formation of crystalline ZnO.

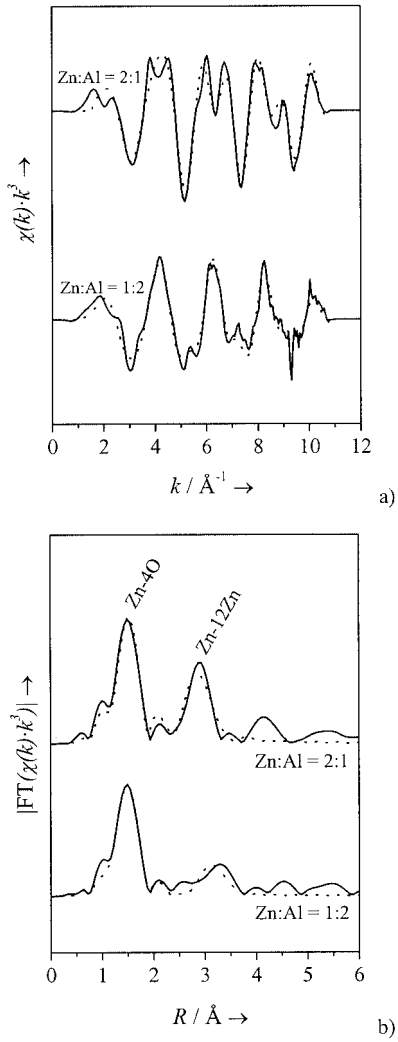


Figure 4. Zn K-edge EXAFS raw data (a) and Fourier transform magnitudes (b) of $ZnO/Al_2O_3$ calcined xerogels (400 °C) with different Zn/Al molar ratio. Solid line: experimental data; dotted line: fit data.

Nitrogen physisorption isotherms and the corresponding pore-size distributions of porous $ZnO/Al_2O_3$ samples are shown in Figure 5. The isotherms of both samples have significant hysteresis loops that are associated with the filling and emptying of mesopores by the condensate. $ZnO/Al_2O_3$ with a Zn/Al ratio of 1:2 has the smallest pore size and the narrowest distribution (Figure 5b). The pore sizes are in the range of 5–10 nm. With increasing Zn concentration, the pore size increases and the distribution is broadened considerably. When the Zn/Al ratio is 2:1 the pore sizes are in the range of 5–25 nm.

Table 1. Results of EXAFS fits of $ZnO/Al_2O_3$ calcined xerogels (Zn K-edge; 9659 eV).

| Zn/Al molar ratio | $R$(Zn–O) [Å] | $N$(Zn–O) | $\sigma^2$(Zn–O) [$Å^2 \times 10^3$] | $R$(Zn–Zn) [Å] | $N$(Zn–Zn) | $\sigma^2$(Zn–Zn) [$Å^2 \times 10^3$] |
|---|---|---|---|---|---|---|
| 1:2 | 1.95 | 3.5 | 7.7 | 3.52 | 0.6 | 1.97 |
| 2:1 | 1.96 | 3.7 | 6.1 | 3.21 | 7.3 | 13.2 |

 © 2006 Wiley-VCH Verlag GmbH & Co. KGaA, Weinheim 

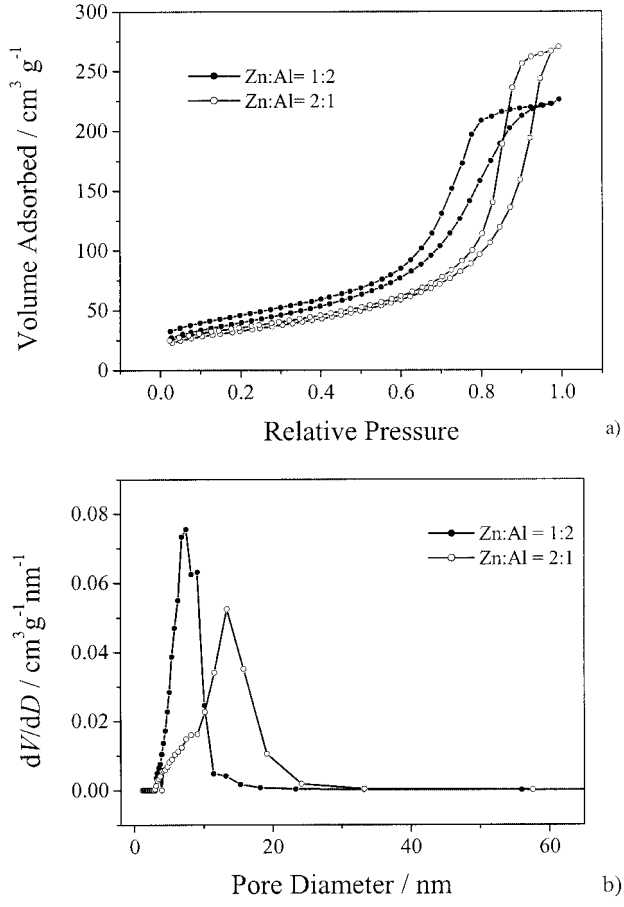


Figure 5. Nitrogen physisorption isotherms (a) and pore-size distribution (b) of $ZnO/Al_2O_3$ calcined xerogels (400 °C) with different Zn/Al ratios.

The BET surface area and the pore volume derived from nitrogen physisorption are listed in Table 2. An increase of the Zn concentration leads to a decrease of the BET surface area. A maximum surface area of 144 $m^2 g^{-1}$ was obtained for $ZnO/Al_2O_3$ with a Zn/Al ratio of 1:2, and this material also exhibits a smaller pore size and a narrower size distribution. The pore volume was found to be 0.42 $cm^3 g^{-1}$ for the sample with a Zn/Al ratio of 2:1. Baumann et al. have prepared $Al_2O_3$ aerogels by the same method and obtained a specific surface area of 289 $m^2 g^{-1}$, an average pore diameter of 32 nm, and pore volume of 2.6 $cm^3 g^{-1}$.[26] We conclude that the presence of Zn leads to smaller pores and a smaller specific surface area than with $Al_2O_3$ alone.

Table 2. BET surface area and pore volume of $ZnO/Al_2O_3$ calcined xerogels (400 °C).

| Zn/Al molar ratio | BET surface area [$m^2 g^{-1}$] | Pore volume [$cm^3 g^{-1}$] |
|---|---|---|
| 1:2 | 144 | 0.36 |
| 2:1 | 116 | 0.42 |

### Copper-Containing Xerogels and Aerogels (Cu/Al and Cu/Zn/Al Systems)

The industrial catalyst in methanol synthesis contains metallic copper, zinc oxide, and aluminum oxide, therefore the synthesis was extended to copper as the third component. Xerogels were obtained by simple drying in air. Aerogels were also prepared with these systems to obtain samples with a high specific surface area. Supercritical point drying of the wet gels with $CO_2$ gave highly porous, fluffy materials with an effective density of about 0.9 $g cm^{-3}$. The aerogels are blue and then turn black after calcination at 400 °C. The $Al_2O_3$ phase is X-ray amorphous in both the calcined xerogels and the aerogels. The XRD patterns of both the $CuO/Al_2O_3$ and the $CuO/ZnO/Al_2O_3$ calcined xerogels show strong CuO peaks, as shown in Figure 6a, with ZnO as a crystalline phase in the latter case. The ZnO peaks are weak, thereby indicating a good dispersion and a small crystallite size. The decrease of the CuO peak intensities can be attributed to an improved dispersion due to the presence of ZnO. Compared to the calcined xerogels, the calcined aerogels exhibit weaker CuO and ZnO contributions characterized by broad peaks (Figure 6b). We conclude that the dispersions of both Cu and Zn are improved by the drying process with supercritical $CO_2$.

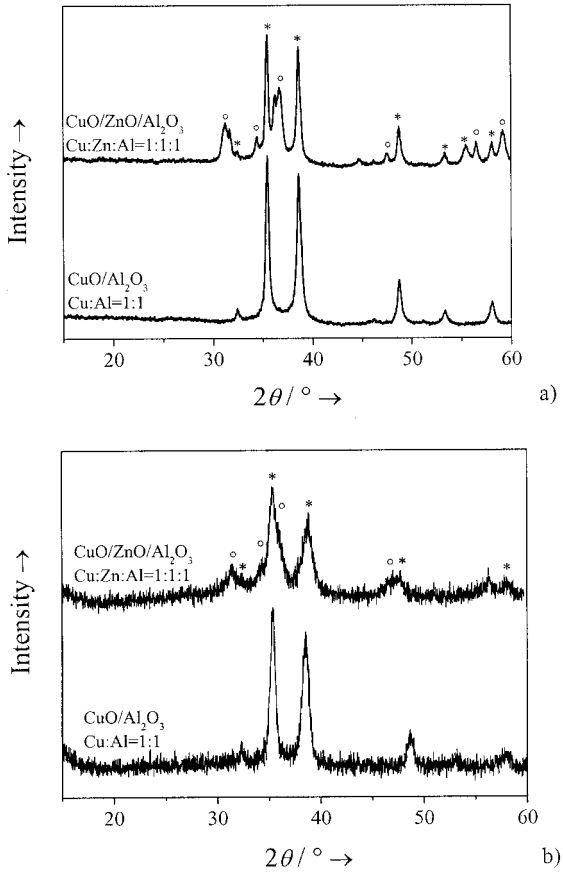


Figure 6. XRD patterns of $CuO/Al_2O_3$ and $CuO/ZnO/Al_2O_3$ calcined xerogels (a) and calcined aerogels (b). The marked peaks correspond to CuO (*) and ZnO (o), respectively.

Nitrogen physisorption of the $CuO/Al_2O_3$ and the $CuO/ZnO/Al_2O_3$ aerogels gave their pore-size distributions, which are broad in both cases (Figure 7). A narrow distribution in the range of 5–10 nm was obtained for the Zn/Al xerogel (see above). However, the Cu/Al aerogel gave a

 © 2006 Wiley-VCH Verlag GmbH & Co. KGaA, Weinheim 

distribution from 2 nm up to more than 30 nm. The presence of Zn narrows the pore-size distribution slightly and reduces the average pore size, as indicated by the shift of the peak maximum to smaller pore diameters.

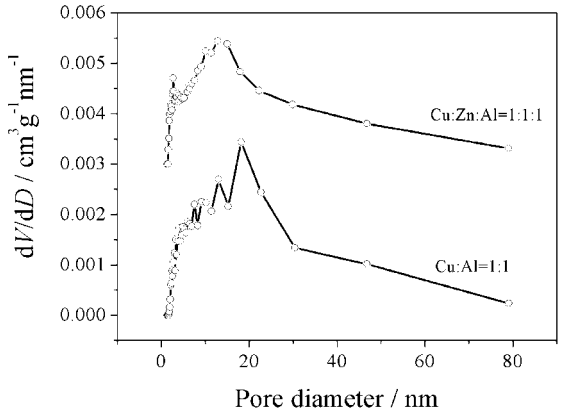


Figure 7. Pore-size distribution of $CuO/Al_2O_3$ and $CuO/ZnO/Al_2O_3$ calcined aerogels derived from nitrogen physisorption isotherms.

The CuO particle size and size distribution have a considerable influence on the reduction behavior.[30] For large CuO particles, the reduction of near-surface $Cu^{II}$ species can occur at lower temperature.[31] The reduction of the bulk then appears at higher temperature. For small particles, the reduction may be very fast so that separate peaks or shoulders cannot be observed. In addition, the reduction behavior becomes even more complex due to the presence of $CuZnO_x$[32] and $CuAl_2O_4$.[33]

The TPR spectra of the calcined $CuO/Al_2O_3$ xerogels and aerogels are shown in Figure 8. In both samples the reduction of CuO occurs in three steps, presumably due to intermediate phases like $Cu_2O$[34] and the broad particle-size distribution. The first reduction step of the xerogel is characterized by a broad shoulder. The reduction starts at about 140 °C for both aerogel and xerogel. The peak maximum of the aerogel appears at 176 °C, a lower temperature than that of the xerogel, for which it appears at 220 °C. The shift of the peak to higher temperature can be attributed to an increased particle size of CuO. The reduction of the $CuO/ZnO/Al_2O_3$ xerogel occurs in two steps, as indicated by a peak and a shoulder on the left-hand side (Figure 8c), although the aerogel gave only one peak (Figure 8d). The peak maxima appear at 166 °C and 197 °C for the aerogel and xerogel, respectively. The reduction temperature is lower than those of the corresponding $CuO/Al_2O_3$ aerogel (176 °C) and xerogel (220 °C), which can be attributed to an increased dispersion of CuO. Obviously, ZnO plays a key role in the dispersion of CuO by increasing the metal–support interaction. The intermediate phases during the reduction are clearly different with or without ZnO, as reflected by the different reduction behaviors. The CuO contents of the samples were derived from the TPR spectra. The results were found to be in good agreement with the results obtained by AAS elemental analysis (Table 3). This confirms that the reduction of CuO during TPR is com-

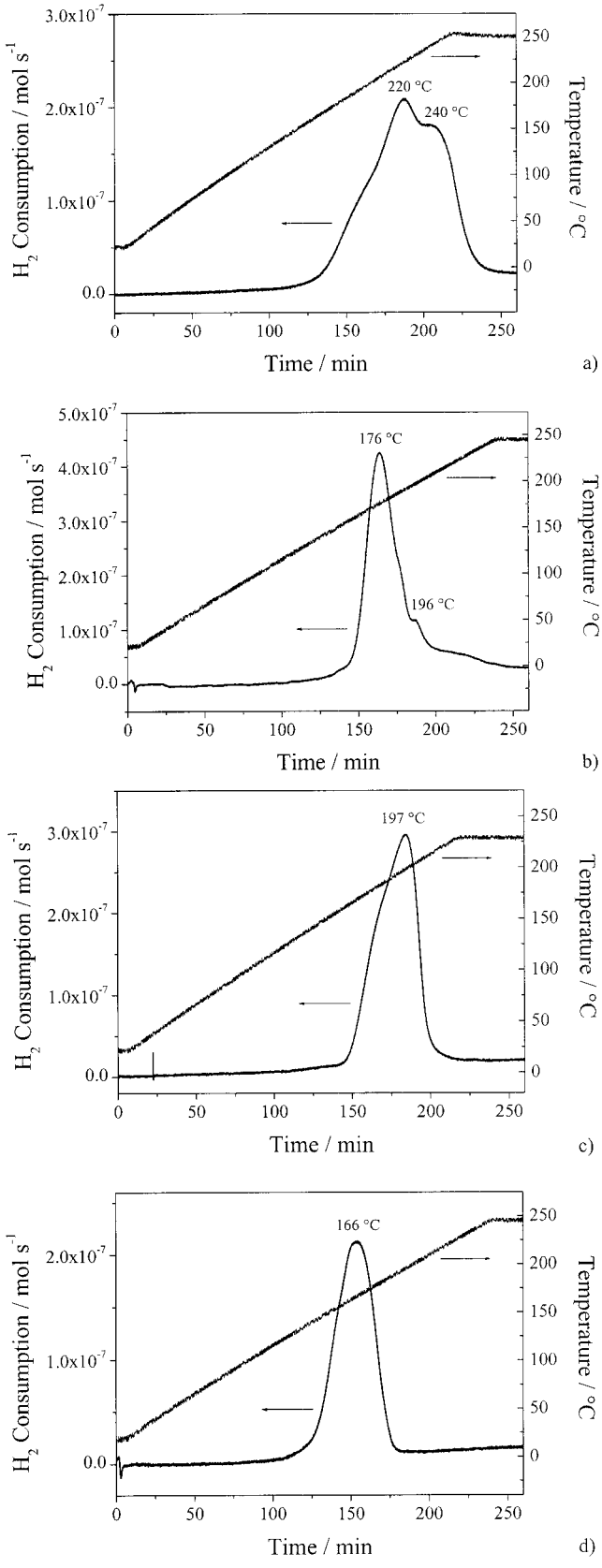


Figure 8. TPR patterns of $CuO/Al_2O_3$ (1:1) and $CuO/ZnO/Al_2O_3$ (1:1:1) calcined xerogels and aerogels at a heating rate of 1 K $min^{-1}$ in $H_2$/He: a) CuO/ZnO (1:1) xerogel; b) CuO/ZnO (1:1) aerogel; c) $CuO/ZnO/Al_2O_3$ (1:1:1) xerogel; d) $CuO/ZnO/Al_2O_3$ (1:1:1) aerogel.

 © 2006 Wiley-VCH Verlag GmbH & Co. KGaA, Weinheim 

Table 3. CuO contents in the $CuO/Al_2O_3$ and $CuO/ZnO/Al_2O_3$ samples.

| Samples | $CuO/Al_2O_3$ calcined xerogel | $CuO/Al_2O_3$ calcined aerogel | $CuO/ZnO/Al_2O_3$ calcined xerogel | $CuO/ZnO/Al_2O_3$ calcined aerogel |
|---|---|---|---|---|
| CuO [$g_{cat}^{-1}$] | Cu/Al = 1:1 | Cu/Al = 1:1 | Cu/Zn/Al = 1:1:1 | Cu/Zn/Al = 1:1:1 |
| by TPR | 50.9 wt-% | 52.7 wt-% | 39.3 wt-% | 34.2 wt-% |
| by AAS | 50.4 wt-% | 50.5 wt-% | 38.6 wt-% | 34.2 wt-% |

Table 4. BET surface area, Cu surface area and catalytic activity for methanol synthesis of Cu/Zn/Al calcined xerogels and aerogels.

| Sample | | BET surface area [$m^2 g^{-1}$] | Pore volume [$cm^3 g^{-1}$] | Specific Cu surface area [$m^2 g^{-1}$] | Catalytic activity in methanol synthesis[a] |
|---|---|---|---|---|---|
| $CuO/Al_2O_3$ | xerogel | 34 | – | 3.7 | 2.0% |
| (Cu/Al = 1:1) | aerogel | 222 | 1.03 | 5.2 | 4.0% |
| $CuO/ZnO/Al_2O_3$ | xerogel | 57 | – | 2.6 | 4.9% |
| (Cu/Zn/Al = 1:1:1) | aerogel | 175 | 0.85 | 6.0 | 22% |

[a] The activity of the industrial standard catalyst (ICI) was used as reference and set to 100%.

plete, and that the consumption of $H_2$ by other phases can be excluded.

### Catalytic Activities of Cu-Containing Xerogels and Aerogels

The specific surface area of the samples was determined by nitrogen physisorption. Different drying methods (air or supercritical $CO_2$) have a significant influence on the surface area (Table 4). The porous microstructure of the wet gel is better preserved by supercritical drying, resulting in a higher specific surface area. High specific pore volumes (as much as 1 $cm^3 g^{-1}$) were found, compared to about 0.4 $cm^3 g^{-1}$ for the $ZnO/Al_2O_3$ calcined xerogel (Table 2). The specific Cu surface area,[4] as determined by $N_2O$ reactive frontal chromatography, is given in Table 4. The higher Cu surface area of the Cu/Al or Cu/Zn/Al calcined xerogels leads to a higher catalytic activity, and both aerogels show a much higher activity in methanol synthesis than the corresponding xerogels. The presence of ZnO also improves the catalytic activities. In the 1:1 Cu/Al xerogels, the catalytic activity increases from 2.0% to 4.9% despite a smaller specific Cu surface area. The higher activity of the ternary aerogel can be attributed to a strong metal–support interaction, as supported by the XRD and TPR investigations. We note that the presence of $Zn^{2+}$ or $Cu^{2+}$ leads to a smaller specific surface area and a lower pore volume, but also to a smaller average pore size.

## Conclusions

A sol–gel route has been employed to prepare Cu/Zn/Al xerogels and aerogels with propylene oxide as gelation initiator. ZnO can be atomically dispersed in $Al_2O_3$ in xerogels in a wide range of Zn concentrations. A higher Cu dispersion is found in the aerogels than in the xerogels, which leads to a higher specific surface area, a higher Cu surface area, and a higher catalytic activity in methanol synthesis. The presence of ZnO increases the catalytic activities in both the xerogel and aerogel, which we attribute to a strong metal–support interaction. The sol–gel method is easy to apply and well suited to the preparation of binary or ternary catalysts for methanol synthesis.

## Experimental Section

**Preparation of $ZnO/Al_2O_3$, $CuO/Al_2O_3$, and $CuO/ZnO/Al_2O_3$ Xerogels and Aerogels:** $Cu(NO_3)_2 \cdot 3H_2O$ (Merck, 98%), $Zn(NO_3)_2 \cdot 6H_2O$ (Merck, 98%), and $Al(NO_3)_3 \cdot 9H_2O$ (Merck, 98%) were used as metal precursors, and propylene oxide (Acros, 99%) was used as gelation initiator.[20–22] Metal nitrates of different compositions were dissolved in absolute ethanol (typically 10–20 mL) to give a clear solution with a total metal ion concentration of 1 M. Propylene oxide was then added to the solution. The molar ratio of propylene oxide to the molar sum of the metal ions was 10:1. After stirring at room temperature for 10 min, the reaction mixture was transferred into a closed vessel. A wet gel formed within 30–60 min. This wet gel was allowed to age at room temperature for 24 h in the closed vessel and then soaked in a bath of absolute ethanol for 24 h to exchange the water from the pores of the gel. Note that the water is the water of crystallization of the starting salts. The exchange of water with ethanol was performed twice. The air-dried xerogel was then obtained by drying of the gel under air at room temperature for 5–6 d. For the preparation of an aerogel, the obtained wet gel was soaked in a bath of acetone for 24 h to exchange the ethanol and water from the pores. The exchange was repeated twice. A $CO_2$ critical point dryer (BAL-TEC, CPD 030) was then used to dry the wet gel. The acetone in the pores was extracted with liquid $CO_2$ 6–8 times at 10 °C and 5.0 MPa. After that, the temperature was increased to 40 °C and the pressure to 7.5 MPa to give supercritical $CO_2$. The autoclave was then depressurized over about 1 h to give the aerogel. For calcination, the air-dried xerogel or aerogel was heated to 400 °C at a rate of 3 K $min^{-1}$ under a dynamic air atmosphere in a tubular reactor to give an intimate mixture of CuO, ZnO, and $Al_2O_3$. The reactor was held at that temperature for 3 h, and then cooled to room temperature. After calcination, all copper-containing samples were black due to CuO formation and the other ones were white. Table 5 lists all prepared samples.

 © 2006 Wiley-VCH Verlag GmbH & Co. KGaA, Weinheim 

Table 5. Prepared samples of different compositions and molar ratios.

| Xerogel | $ZnO/Al_2O_3$ Zn/Al = 2:1 | $ZnO/Al_2O_3$ Zn/Al = 1:2 | $CuO/Al_2O_3$ Cu/Al = 1:1 | $CuO/ZnO/Al_2O_3$ Cu/Zn/Al = 1:1:1 |
|---|---|---|---|---|
| Aerogel | | | $CuO/Al_2O_3$ Cu/Al = 1:1 | $CuO/ZnO/Al_2O_3$ Cu/Zn/Al = 1:1:1 |

**Characterization:** Thermogravimetry was carried out with a Netzsch STA 409 TG-DTA/DSC instrument. Samples were heated from room temperature to 1000 °C at a rate of 5 K min$^{-1}$ under dynamic $O_2$ atmosphere at a flow rate of 50 mL min$^{-1}$. The structure of the resulting products was studied by TEM with a Philips CM 200 FEG instrument. Powder XRD was carried out at room temperature in transmission mode at the B2 beamline at HASYLAB with monochromatic radiation or with a Siemens D5000 instrument with Cu-$K_\alpha$ radiation. EXAFS was carried out at the E4 beamline at HASYLAB/DESY in transmission mode at 77 K. The programs SPLINE and XFIT[35] were used for quantitative data evaluation. Theoretical standards were computed with the program FEFF 6.01a.[36] The amplitude reduction factor, $S_o^2$, was fixed to 1. Variation parameters were the bond lengths, the coordination numbers, the Debye–Waller factors ($\sigma^2$), and the zero-energy correction ($E_o$). The specific surface area was determined by nitrogen physisorption at 77 K (BET method). The pore-size distribution was obtained using the BJH method from the desorption branch of the isotherms. Temperature-programmed reduction (TPR) was carried out for the calcined xerogels and aerogels. About 0.1 g of the sample was placed in a quartz reactor. The reduction was performed under flowing diluted $H_2$ (4.2 vol-% $H_2$ in He) by increasing the temperature to 240 °C at 1 K min$^{-1}$ and maintaining that temperature for 1 h. The active surface area of Cu was determined by $N_2O$ reactive frontal chromatography at 300 K.[37] Atomic absorption spectroscopy (AAS) was performed with a Thermo Electron Corporation instrument (M series) to determine the copper content of the samples.

**Catalytic Activity Measurements:** Catalytic measurements were performed in a high-throughput 49-parallel channel reactor.[38] The catalyst (100 mg diluted with 200 mg of quartz per well) was placed in a sample holder consisting of a stainless-steel cartridge closed at the bottom by a stainless-steel sinter metal frit. Prior to the catalytic measurements, the catalysts were reduced with $H_2$ at 245 °C according to the procedure for the commercial benchmark catalyst ICI Katalco 51-8. Before measuring the catalytic activity, all samples were equilibrated for 3 h (reaction pressure: 4.5 MPa; reaction temperature: 245 °C; analytic flow: 20 mL min$^{-1}$). The reaction gas consisted of 70 vol-% $H_2$, 24 vol-% CO, and 6 vol-% $CO_2$. A double GC system (HP GC 6890) equipped with a methanizer FID was used for online gas analysis. Oxo product separation ($H_3COH$, $HCOOCH_3$, $H_3CCOOCH_3$, $H_3CCH_2OH$) was carried out on a SuppelcoWAX 0.53 mm column and CO, $CO_2$, and $CH_4$ were separated on a Carboxen 1006 column. Methanol productivities for all measured samples were compared to the productivity of the industrial benchmark catalyst ICI Katalco 51-8.

## Acknowledgments

This work was supported by the Deutsche Forschungsgemeinschaft within the scope of the Collaborative Research Center SFB 558 ("Metal–substrate interactions in heterogeneous catalysis"). We thank HASYLAB at DESY (Hamburg) for generous allocation of synchrotron beam time. We thank F. Schüth, Mülheim/Ruhr, for helpful discussions and R. Naumann d'Alnoncourt for experimental assistance.

[1] C. Chauvin, J. Jaussey, J. C. Lavalley, H. Idriss, J. P. Hidermann, A. Kiennemann, P. Chaumette, P. Coutry, *J. Catal.* **1990**, *121*, 56–69.
[2] T. Ressler, B. L. Kniep, I. Kasatkin, R. Schlögl, *Angew. Chem.* **2005**, *117*, 4782–4785; *Angew. Chem. Int. Ed.* **2005**, *44*, 4704–4707.
[3] M. Saito, K. Murata, *Catal. Surv. Asia* **2004**, *8*, 285–294.
[4] G. E. Parris, K. Klier, *J. Catal.* **1986**, *97*, 374–384.
[5] P. L. Hansen, J. B. Wagner, S. Helveg, J. R. Rostrup-Nielsen, B. S. Clausen, H. Topsoe, *Science* **2002**, *295*, 2053–2055.
[6] J. B. Wagner, P. L. Hansen, A. M. Molenbroek, H. Topsoe, B. S. Clausen, S. Helveg, *J. Phys. Chem. B* **2003**, *107*, 7753–7758.
[7] R. Schlögl, *Angew. Chem.* **1993**, *105*, 403–405; *Angew. Chem. Int. Ed. Engl.* **1993**, *32*, 381–383.
[8] M. M. Günter, T. Ressler, B. Bems, C. Büscher, T. Genger, O. Hinrichsen, M. Muhler, R. Schlögl, *Catal. Lett.* **2001**, *71*, 37–44.
[9] B. Bems, M. Schur, A. Dassenoy, H. Junkes, D. Herein, R. Schlögl, *Chem. Eur. J.* **2003**, *9*, 2039–2052.
[10] H. Wilmer, M. Kurtz, K. Klementiev, O. Tkachenko, W. Grünert, O. Hinrichsen, A. Birkner, S. Rabe, K. Merz, M. Driess, C. Wöll, M. Muhler, *Phys. Chem. Chem. Phys.* **2003**, *5*, 4736–4742.
[11] B. L. Kniep, T. Ressler, A. Rabis, F. Girgsdies, M. Baenitz, F. Steglich, R. Schlögl, *Angew. Chem.* **2004**, *116*, 114–117; *Angew. Chem. Int. Ed.* **2004**, *43*, 112–115.
[12] M. Schur, B. Bems, A. Dassenoy, I. Kassatkine, J. Urban, H. Wilmes, O. Hinrichsen, M. Muhler, R. Schlögl, *Angew. Chem.* **2003**, *115*, 3945–3947; *Angew. Chem. Int. Ed.* **2003**, *42*, 3815–3817.
[13] M. Kurtz, H. Wilmer, T. Genger, O. Hinrichsen, M. Muhler, *Catal. Lett.* **2003**, *86*, 77–80.
[14] D. Fang, Z. Liu, Y. Yang, H. Zhang, J. Lin, *Shiyou Huagong* **2005**, *34*, 1032–1037; *Chem. Abstr.* **2006**, *145*, 175100.
[15] J. F. Deng, Q. Sun, Y. L. Zhang, S. Y. Chen, D. Wu, *Appl. Catal. A* **1996**, *139*, 75–85.
[16] J. Hambrock, M. K. Schroeter, A. Birkner, C. Woell, R. A. Fischer, *Chem. Mater.* **2003**, *15*, 4217–4222.
[17] S. Vukojević, O. Trapp, J. D. Grunwaldt, C. Kiener, F. Schüth, *Angew. Chem.* **2005**, *117*, 8192–8195; *Angew. Chem. Int. Ed.* **2005**, *44*, 7978–7981.
[18] Y. Guo, R. Weiss, M. Epple, *Eur. J. Inorg. Chem.* **2005**, 3072–3079.
[19] Y. Guo, R. Weiss, R. Boese, M. Epple, *Thermochim. Acta* **2006**, *446*, 101–105.
[20] R. Weiss, G. Jansen, R. Boese, M. Epple, *Dalton Trans.* **2006**, 1831–1835.
[21] R. Weiss, Y. Guo, S. Vukojević, L. Khodeir, R. Boese, F. Schüth, M. Muhler, M. Epple, *Eur. J. Inorg. Chem.* **2006**, 1796–1802.
[22] C. J. Brinker, G. W. Scherer, *Sol–Gel Science. The Physics and Chemistry of Sol–Gel Processing*, Academic Press, Boston, **1990**.
[23] J. Livage, M. Henry, C. Sanchez, *Prog. Solid State Chem.* **1988**, *18*, 259–341.
[24] A. E. Gash, T. M. Tillotson, J. H. Satcher, J. F. Poco, L. W. Hrubesh, R. L. Simpson, *Chem. Mater.* **2001**, *13*, 999–1007.
[25] A. E. Gash, T. M. Tillotson, J. H. Satcher Jr, L. W. Hrubesh, R. L. Simpson, *J. Non-Cryst. Solids* **2001**, *285*, 22–28.
[26] T. F. Baumann, A. E. Gash, S. C. Chinn, A. M. Sawvel, R. S. Maxwell, J. H. Satcher Jr, *Chem. Mater.* **2005**, *17*, 395–401.
[27] A. E. Gash, J. H. Satcher, R. L. Simpson, *Chem. Mater.* **2003**, *15*, 3268–3275.

 © 2006 Wiley-VCH Verlag GmbH & Co. KGaA, Weinheim 

[28] C. N. Chervin, B. J. Clapsaddle, H. W. Chiu, A. E. Gash, J. H. Satcher Jr, S. M. Kauzlarich, *Chem. Mater.* **2005**, *17*, 3345–3351.
[29] H. K. Cammenga, M. Epple, *Angew. Chem.* **1995**, *107*, 1284–1301; *Angew. Chem. Int. Ed. Engl.* **1995**, *34*, 1171–1187.
[30] J. Agrell, K. Hasselbo, K. Jansson, S. G. Järas, M. Boutonnet, *Appl. Catal. A* **2001**, *221*, 239–250.
[31] M. Turco, G. Bagnasco, U. Costantino, F. Marmottini, T. Montanari, G. Ramis, G. Busca, *J. Catal.* **2004**, *228*, 43–55.
[32] H. Wilmer, T. Genger, O. Hinrichsen, *J. Catal.* **2003**, *215*, 188–198.
[33] S. Velu, K. Suzuki, M. Okazaki, M. P. Kapoor, T. Osaki, F. Ohashi, *J. Catal.* **2000**, *194*, 373–384.
[34] M. M. Günter, T. Ressler, R. E. Jentoft, B. Bems, *J. Catal.* **2001**, *203*, 133–149.
[35] P. J. Ellis, H. C. Freeman, *J. Synchrotron Radiat.* **1995**, *2*, 190–195.
[36] E. A. Stern, M. Newville, B. Ravel, Y. Yacoby, D. Haskel, *Physica B* **1995**, *208–209*, 117–120.
[37] O. Hinrichsen, T. Genger, M. Muhler, *Chem. Eng. Technol.* **2000**, *11*, 956–959.
[38] C. Kiener, M. Kurtz, H. Wilmer, C. Hoffmann, H. W. Schmidt, J. D. Grunwaldt, M. Muhler, F. Schüth, *J. Catal.* **2003**, *216*, 110–119.

Received: June 14, 2006
Published Online: October 12, 2006

 © 2006 Wiley-VCH Verlag GmbH & Co. KGaA, Weinheim 

DOI: 10.1002/ejic.200600561

# Copper/Zinc L-Tartrates: Mixed Crystals and Thermolysis to a Mixture of Copper Oxide and Zinc Oxide That Is Catalytically Active in Methanol Synthesis

**Rainer Weiss,[a] Sascha Vukojević,[b] Christian Baltes,[b] Raoul Naumann d'Alnoncourt,[c] Martin Muhler,[c] and Matthias Epple*[a]**

**Keywords:** Heterogeneous catalysis / Copper / Zinc / Thermochemistry

The system consisting of copper/zinc L-tartrate mixed crystals has been systematically explored in the whole range from pure copper tartrate to pure zinc tartrate. Mixed crystal L-tartrates were prepared and their thermochemical behaviour under oxygen was investigated. Oxidic precatalysts (CuO/ZnO) for catalytic tests in methanol synthesis were prepared by mild thermolysis of the mixed tartrates in air at 300 °C. Catalytic tests were performed with a multi-channel parallel reactor. The catalytic activity shows a maximum at about equal amounts of copper and zinc whereas the specific surface area (BET surface) increases strongly when going from CuO to ZnO. This system offers a convenient, inexpensive route to CuO/ZnO precatalysts with adjustable compositions that avoids all other metals during preparation.
(© Wiley-VCH Verlag GmbH & Co. KGaA, 69451 Weinheim, Germany, 2006)

## Introduction

Methanol is the most important chemical base material due to its use as a solvent or as a parent compound for the industrial synthesis of higher organic compounds.[1] The industrial synthesis of methanol is typically carried out with synthesis gas containing $H_2$, CO and $CO_2$ with Cu/ZnO/$Al_2O_3$ as catalyst, which is prepared by reduction of a CuO/ZnO/$Al_2O_3$ precatalyst.[2–8] These oxide composites are usually prepared by thermolysis of co-precipitated hydroxycarbonate precatalysts in which all three metals are present.[9] Despite numerous experimental and theoretical studies, the catalytic processes on the surface of the bulk catalysts are not yet fully understood.[9–15] The activities of the obtained catalysts depend on many factors. To reduce the number of factors that influence the performance of the catalyst, the catalytic system is often limited to the system Cu/ZnO. Even then, the thermolysis temperature and pressure, the reduction temperature and the composition remain important external factors.[3–5,7,9,11,12,16] In the case of dinuclear complexes that contain both copper and zinc, the thermolysis is always complex due to the decomposition of the corresponding anions.[17,18] It was our goal to find a precursor that contains both metals in one solid phase (to achieve a good interaction in the final catalyst) and which can be decomposed at moderate temperature (to avoid sintering to larger crystals). Mixed copper/zinc L-tartrates turned out to be well suited for this purpose because their synthesis is straightforward and also because inorganic counterions like alkali metals or carbonate can be avoided.

## Results and Discussion

### Preparation

Metal L-tartrates (MTTs) with different ratios of Cu/Zn were prepared in aqueous solution by precipitation from copper acetate and zinc acetate with L-tartaric acid ($H_2TT$) [Equation (1)].

$$x\,Cu(OAc)_2 + y\,Zn(OAc)_2 + H_2TT \rightarrow Cu_xZn_yTT{\cdot}n\,H_2O + 2\,HOAc;\ x + y = 1 \text{ and } n \leq 3 \quad (1)$$

Note that the only counterion is acetate, which remains quantitatively in solution. At a final tartrate concentration of 0.05 M large single crystals were obtained after slow crystallisation. Unfortunately, these were always twinned and not suitable for single-crystal X-ray structure analysis. At a higher final tartrate concentration of 0.2 M a fast precipitation occurred and the product was obtained as a microcrystalline powder. These microcrystalline samples were used for all experiments described below. In all cases we obtained hydrates of the mixed tartrates in which the water

[a] Inorganic Chemistry, University of Duisburg-Essen, Universitaetsstrasse 5–7, 45117 Essen, Germany
Fax: +49-201-183-2621
E-mail: matthias.epple@uni-due.de
[b] Max-Planck-Institute for Coal Research, Kaiser-Wilhelm-Platz 1, 45470 Muelheim an der Ruhr, Germany
[c] Laboratory of Industrial Chemistry, Ruhr University Bochum, Universitaetsstrasse 150, 44801 Bochum, Germany

 InterScience © 2006 Wiley-VCH Verlag GmbH & Co. KGaA, Weinheim 

Table 1. Elemental analysis results of the anhydrous copper/zinc tartrates after removal of water of crystallisation at 130 °C. The molar fractions of Cu and Zn can be derived from the formulae in the last column. They correspond well to the expected molar fraction (first three columns).

| Sample | Expected [mol-%] | | Found [wt.-%] | | | | Calcd. [wt.-%] | Calculated formulae from elemental analysis (normalised to $C_4$) |
|---|---|---|---|---|---|---|---|---|
| | Cu | Zn | Cu | Zn | C | H | O | $C_4H_4O_6Cu_xZn_y$ |
| CuTT | 100 | 0 | 29.25 | 0.00 | 22.28 | 2.22 | 46.26 | $C_4H_{4.75}O_{6.24}Cu_1Zn_0$ |
| $Cu_{0.9}Zn_{0.1}TT$ | 90 | 10 | 26.86 | 2.62 | 22.06 | 2.20 | 46.28 | $C_4H_{4.75}O_{6.30}Cu_{0.92}Zn_{0.09}$ |
| $Cu_{0.8}Zn_{0.2}TT$ | 80 | 20 | 24.29 | 4.95 | 22.33 | 2.21 | 46.23 | $C_4H_{4.71}O_{6.22}Cu_{0.82}Zn_{0.18}$ |
| $Cu_{0.7}Zn_{0.3}TT$ | 70 | 30 | 22.11 | 7.47 | 22.46 | 2.16 | 45.81 | $C_4H_{4.59}O_{6.12}Cu_{0.75}Zn_{0.25}$ |
| $Cu_{0.6}Zn_{0.4}TT$ | 60 | 40 | 18.88 | 10.79 | 22.51 | 2.03 | 45.80 | $C_4H_{4.30}O_{6.11}Cu_{0.64}Zn_{0.35}$ |
| $Cu_{0.5}Zn_{0.5}TT$ | 50 | 50 | 15.21 | 14.96 | 22.28 | 2.00 | 45.55 | $C_4H_{4.28}O_{6.14}Cu_{0.51}Zn_{0.49}$ |
| $Cu_{0.4}Zn_{0.6}TT$ | 40 | 60 | 11.22 | 19.24 | 22.29 | 2.03 | 45.23 | $C_4H_{4.33}O_{6.10}Cu_{0.38}Zn_{0.63}$ |
| $Cu_{0.3}Zn_{0.7}TT$ | 30 | 70 | 8.42 | 22.18 | 22.20 | 2.00 | 45.21 | $C_4H_{4.30}O_{6.12}Cu_{0.29}Zn_{0.73}$ |
| $Cu_{0.2}Zn_{0.8}TT$ | 20 | 80 | 5.71 | 25.44 | 22.29 | 1.98 | 44.59 | $C_4H_{4.28}O_{6.01}Cu_{0.19}Zn_{0.84}$ |
| $Cu_{0.1}Zn_{0.9}TT$ | 10 | 90 | 2.95 | 28.47 | 22.30 | 2.01 | 44.28 | $C_4H_{4.30}O_{5.97}Cu_{0.10}Zn_{0.94}$ |
| ZnTT | 0 | 100 | 0.00 | 31.10 | 22.21 | 2.03 | 44.67 | $C_4H_{4.36}O_{6.04}Cu_0Zn_1$ |

loss starts at room temperature. In order to obtain anhydrous samples with a defined stoichiometry the products were fully dehydrated at 130 °C in air. Elemental analysis (Table 1) showed that the compositions of the samples were in good accordance with the intended composition, i.e. that all metal ions present in solution were also present in the same ratio in the precipitate. The Cu/Zn ratio was thereby easily controlled by variation of the ratio of copper/zinc in solution. Unfortunately, it was not possible to synthesise a ternary precursor that also contains aluminium by precipitation or crystallisation due to the high solubility of $Al_2TT_3$.

## Crystal Structures, Powder Diffraction Patterns and Precursor Morphology

The structures of the hydrates $ZnTT{\cdot}2.5\,H_2O$[19] and $CuTT{\cdot}3\,H_2O$[20] are both known. These compounds are not isostructural. No structural data are available in the literature for Cu/Zn tartrate mixed crystals. The crystal structures of anhydrous copper L-tartrate and zinc L-tartrate are also unknown. However, after the removal of water of crystallisation all precursor samples were still crystalline according to X-ray diffractometry. The diffraction patterns of copper and zinc L-tartrate are similar, but still distinguishable (Figure 1). The change between the two structures occurs around an equimolar ratio of copper/zinc. Because the single-crystal structures are not known, it is not possible to draw safe conclusions about the phases that are present. However, the powder diffractograms clearly indicate that two structurally different phases of dimetallic tartrate precursors are present, both of which contain copper and zinc in the same phase.

The morphology of the Cu/Zn dimetallic tartrates was studied by SEM (Figure 2). The particle shape depended on the ratio of the two metals, but all samples were microcrystalline, as also supported by the narrow X-ray diffraction peaks in Figure 1.

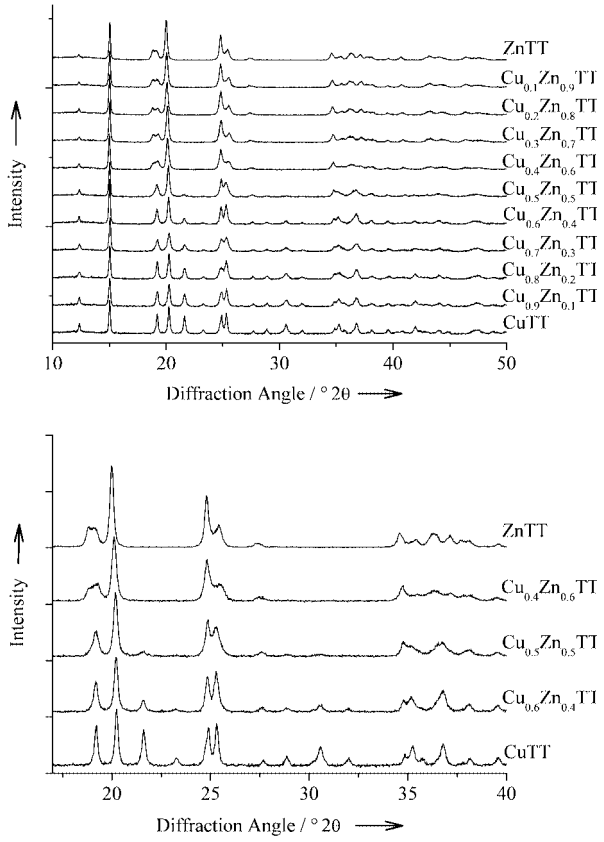


Figure 1. Powder diffraction patterns of the mixed Cu/Zn tartrates. Top: overview; bottom: magnification of selected samples.

## Thermogravimetric Analysis

Three MTT samples were heated to 500 °C under pure oxygen (50 mL min$^{-1}$) at 5 K min$^{-1}$. The thermolysis occurs in one step and is accompanied by sharp exothermic DTA peaks (Figure 3). Incidentally, the exothermic nature of the thermolysis (combustion) was clear from the observation that the sample glowed red in the furnace, even at 300 °C (autocatalytic oxidation by oxygen). The onset temperature

 © 2006 Wiley-VCH Verlag GmbH & Co. KGaA, Weinheim 

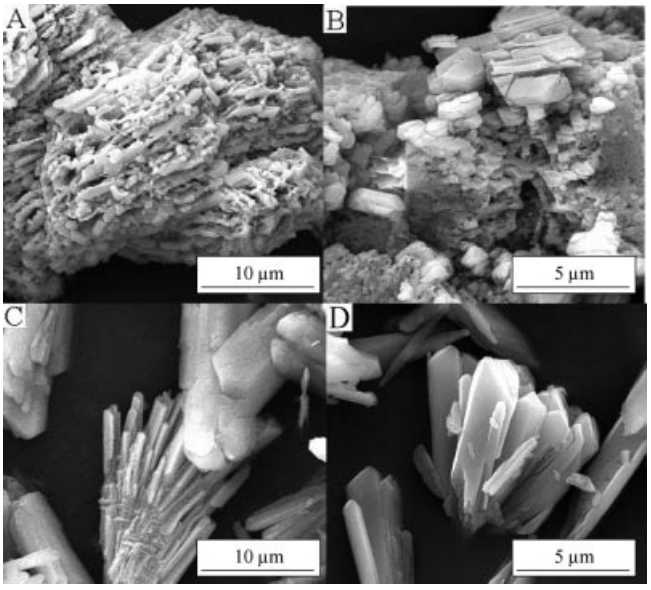


Figure 2. Scanning electron micrographs of the tartrates CuTT (A), $Cu_{0.7}Zn_{0.3}TT$ (B), $Cu_{0.3}Zn_{0.7}TT$ (C) and ZnTT (D).

of thermolysis increases with increasing zinc content. The mass increase above 250 °C for CuTT can be ascribed to an oxidation of the initially formed $Cu_2O$ to CuO. Interestingly, such a mass increase was not observed for $Cu_{0.5}Zn_{0.5}TT$, which means that this sample is directly converted into CuO/ZnO during the combustion step. The obtained final masses at 500 °C (CuTT: 36.7 wt.-%; $Cu_{0.5}Zn_{0.5}TT$: 38.4 wt.-%; ZnTT: 37.3 wt.-%) correspond well to the calculated masses (CuO from CuTT: 37.5 wt.-%; CuO/ZnO from $Cu_{0.5}Zn_{0.5}TT$: 37.8 wt.-%: ZnO from ZnTT: 38.1 wt.-%). The final products contained neither carbon nor hydrogen (by elemental analysis). The external morphology of the tartrate crystals is preserved in the assembly of the product crystals (Figure 4). Note that Schmid and Felsche have reported that the thermolysis of copper tartrate under inert gas (argon) leads to copper metal.[21]

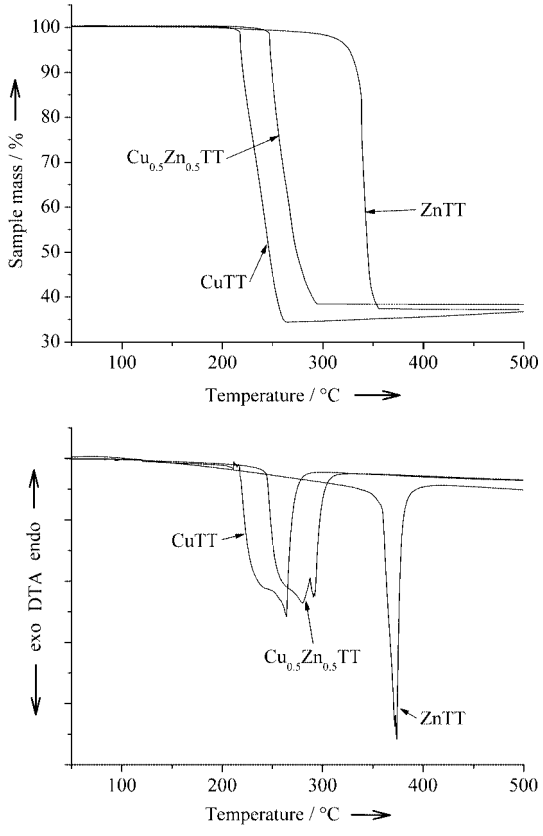


Figure 3. Top: Thermogravimetric measurements of CuTT, $Cu_{0.5}Zn_{0.5}TT$ and ZnTT under a dynamic oxygen atmosphere. Bottom: The mass loss is accompanied by sharp exothermic DTA peaks in all three cases, indicating local combustion processes.

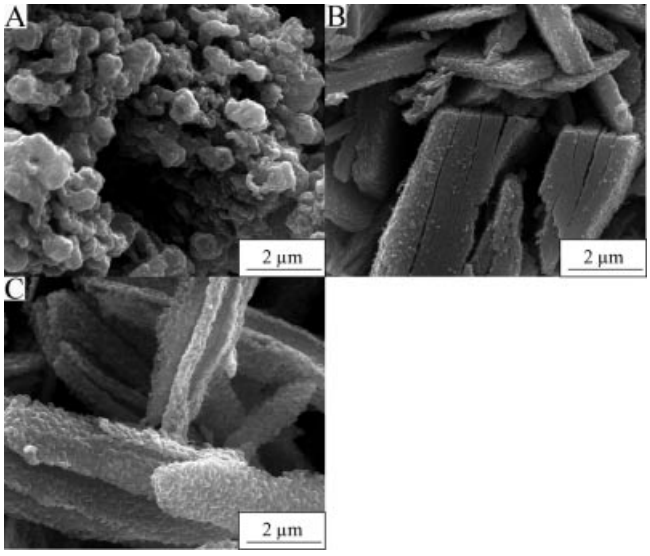


Figure 4. Scanning electron micrographs of the oxide samples obtained after thermogravimetry of CuTT (A), $Cu_{0.5}Zn_{0.5}TT$ (B) and ZnTT (C) under oxygen (500 °C). Note the preservation of the morphology of the original large crystals.

## Thermolysis in Air and Morphologic Studies

Larger amounts of the oxide samples for catalytic studies were prepared by thermolysis in air at 300 °C for 24 h, followed by slight mechanical grinding. Note that a thermolysis at 250 °C for 48 h gave very similar results. The lowermost temperature necessary for complete thermolysis was chosen in order to avoid sintering of the reaction products to larger crystals. Note that a small crystallite size is important for the catalytic performance.[22] A high specific copper surface area is also important for a good catalytic performance.[2,23] The diffraction pattern of the product from CuTT shows the presence of $Cu_2O$ and CuO. In contrast, all mixed oxide samples that contain copper contain only CuO and ZnO. ZnTT leads to ZnO after thermolysis (Figure 5). Under these conditions, the precursor morphology is better conserved and the surface of the former tartrate crystals is smoother (Figure 6).

 © 2006 Wiley-VCH Verlag GmbH & Co. KGaA, Weinheim 

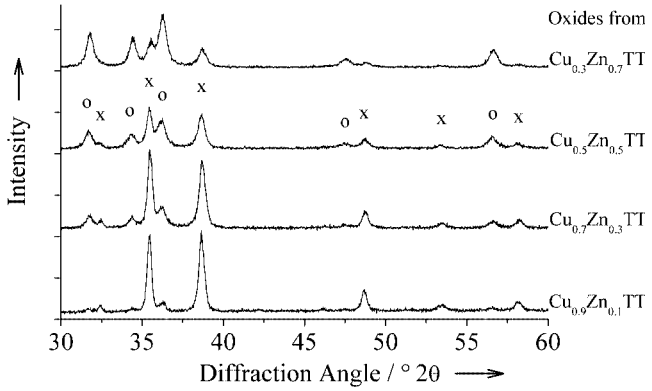


Figure 5. Powder diffraction patterns of oxide mixtures obtained by thermolysis in air at 300 °C (24 h) and containing CuO (x; tenorite; JCPDS no. 481548) and ZnO (o; wurtzite; JCDPS no. 361451).

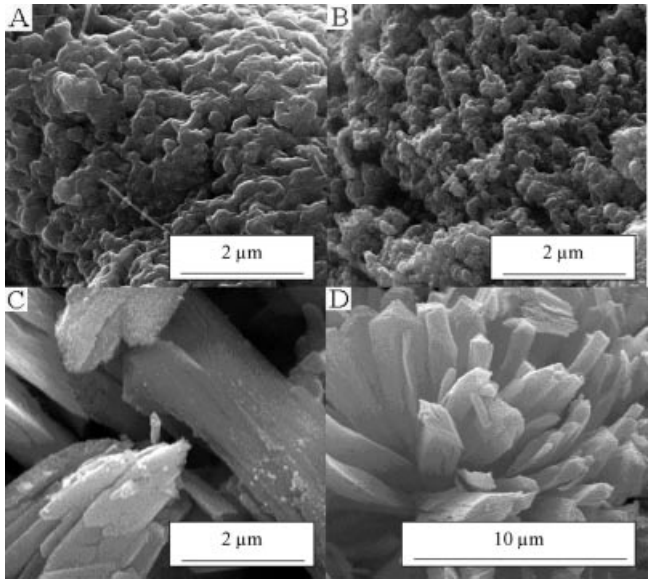


Figure 6. Scanning electron micrographs of the oxide samples obtained by thermolysis of CuTT (A), $Cu_{0.7}Zn_{0.3}TT$ (B), $Cu_{0.3}Zn_{0.7}TT$ (C) and ZnTT (D) in air at 300 °C (24 h).

### Catalytic Activity

The oxide samples were tested regarding their ability to catalyze the formation of methanol from synthesis gas (CO, $CO_2$ and $H_2$). The CuO/ZnO mixture was reduced directly in the catalytic reactor to Cu/ZnO with $H_2$. The Cu/Zn ratio had a remarkable influence on the catalytic activity, showing a clear maximum for an approximately equimolar ratio of Cu and Zn (Figure 7). Although the thermolysis was performed at moderate temperatures, the catalytic activities are low in comparison to an industrial benchmark catalyst (set to 100%). However, the maximum activity (17%) was of the order of a Cu/ZnO catalyst prepared from co-precipitated hydroxycarbonate (about 25%).[18] The specific surface area of the oxide precatalysts shows an almost linear increase, starting from almost zero (0.46 $m^2 g^{-1}$) for pure CuO up to 30–40 $m^2 g^{-1}$ for samples with high zinc content. The sample $Cu_{0.5}Zn_{0.5}TT$ was also subjected to temperature-programmed reduction (TPR) and to reactive frontal chromatography (RFC). The content of 50 mol-% Cu was confirmed by TPR. However, the specific copper surface area (by RFC) was only 0.34 $m^2 g^{-1}$ (note that the accuracy of values below 1 $m^2 g^{-1}$ is limited), which is surprisingly small given the considerable catalytic activity of this sample. For comparison, the specific copper surface area is 17.0 $m^2 g^{-1}$ for the aforementioned hydroxycarbonate-based catalyst and 23.4 $m^2 g^{-1}$ for the industrial reference catalyst.[18]

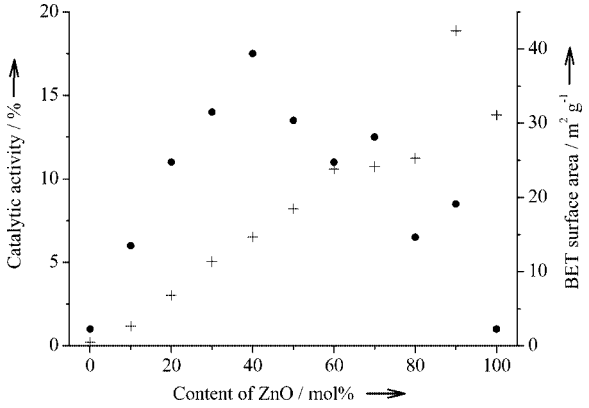


Figure 7. Catalytic activity of CuO/ZnO samples after thermolysis of mixed tartrates (300 °C; air; 24 h) after reduction to Cu/ZnO in situ in a multireactor with $H_2$, measured at 245 °C and 4.5 MPa (●; left scale). The activity of a technical methanol catalyst was set to 100%. The BET surface area of the oxide precatalysts (i.e. before reduction) is shown on the right (+).

A possible explanation for the lower activity compared to hydroxycarbonate-derived catalysts could be the fact that the thermolysis of the tartrates is associated with an exothermic effect, in contrast to the endothermic decomposition of hydroxycarbonates. This exothermic effect may lead to microscopic self-heating and thereby to a growth of oxide crystals. This is supported by the X-ray diffraction data (Figure 5), which show narrow peaks for the oxides, i.e. no nanocrystalline particles that would give rise to diffraction peak broadening. These CuO particles form the active centres of the final reduced catalyst (Cu on ZnO), and it is known that larger copper crystals are catalytically less active than smaller copper crystals.[2,22,23] This is corroborated by the small observed specific copper surface area for the 50:50 sample.

## Conclusions

Metal L-tartrates that contain both copper and zinc as a mixed crystal are well-suited precursors to prepare CuO/ZnO precatalysts that can then be reduced to Cu/ZnO, i.e. an active methanol catalyst. The maximum activity is found at about equimolar amounts of copper and zinc, although the specific surface area increases strongly with increasing zinc content. The presence of this activity maximum reflects the interplay between metal (Cu) and support (ZnO) and the necessity for a sufficiently high specific surface area. The preparation by precipitation easily allows control of the ratio of Cu/Zn in the precursor, and thereby of the catalytic

 © 2006 Wiley-VCH Verlag GmbH & Co. KGaA, Weinheim 

activity. Except for carbonate, other ions are avoided during the synthesis. This synthetic method presents an alternative to classical hydroxycarbonate precursors.

## Experimental Section

**General:** Deionised water was used for all preparations.

**Preparation of the Precursor Samples:** A solution of 50 mmol of copper acetate and/or zinc acetate in the appropriate ratio in 200 mL of water (55 °C) and a solution of 50 mmol of L-tartaric acid in 50 mL of water (room temperature) were prepared. The solution of the acid was rapidly poured into the solution of the metal acetates with vigorous stirring. Approximately 30 s after the addition, the precursor began to precipitate. The mixture was stirred at about 50 °C for another 15 min. After sedimentation of the precipitate, the precipitate was filtered and washed three times with water and then once with ethanol. The tartrates were first dried at 70 °C for 2 h and then at 130 °C for 12 h. With the exception of ZnTT, all products were obtained as fine powders. CuTT was slightly blue, ZnTT was white, and the mixed crystals showed a continuous row of intermediate colours.

**Catalytic Measurements:** Measurements were performed in a high-throughput 49-parallel channel reactor.[5] The samples (100 mg diluted with 200 mg of quartz per well) were placed in a sample holder consisting of a stainless-steel cartridge closed at the bottom by a stainless-steel sinter metal frit. Prior to the catalytic measurements, the catalysts were reduced with $H_2$ at 245 °C according to the procedure for the commercial benchmark catalyst ICI Katalco 51-8. Before measuring the catalytic activity, all samples were equilibrated for 3 h (reaction pressure: 4.5 MPa; reaction temperature: 245 °C; analytic flow: 20 mL min$^{-1}$). The reaction gas consisted of 70 vol% $H_2$, 24 vol% CO and 6 vol% $CO_2$. A double GC system (HP GC 6890) equipped with a methanizer FID was used for online gas analysis. Oxo product separation ($H_3COH$, $HCOOCH_3$, $H_3CCOOCH_3$, $H_3CCH_2OH$) was carried out on a SuppelcoWAX 0.53 mm column and CO, $CO_2$ and $CH_4$ were separated on a Carboxen 1006 column. Methanol productivities for all measured samples were compared to the productivity of the industrial benchmark catalyst ICI Katalco 51-8 [$P_{ICI}$ = 40 mol MeOH(kg$_{cat}$ h)$^{-1}$ at 245 °C and 4.5 MPa].

**Analytical Techniques:** Combined thermogravimetry-IR spectroscopy (TG-IR) was carried out with a Netzsch STA 209 TG-DTA/DSC instrument. Samples were heated from 30 to 500 °C at a rate of 5 K min$^{-1}$ under dynamic $O_2$ atmosphere (50 mL min$^{-1}$). Scanning electron microscopy images were recorded with an ESEM Quanta 400 instrument (FEI) on Au/Pd-sputtered samples. X-ray powder diffractometry was carried out in Bragg–Brentano mode with a Bruker AXS D8 Advance instrument with Cu-$K_\alpha$ radiation. Atomic absorption spectroscopy (AAS) was performed with a Thermo Electron Corporation instrument (M series) to determine the contents of copper and zinc in the samples. The contents of carbon and hydrogen were determined by standard combustion analysis with an EA 1110 (CE Instruments) instrument. The specific surface area was determined by nitrogen physisorption at 77 K (BET method) on the oxide precatalysts (i.e. CuO/ZnO). Temperature-programmed reduction (TPR) was carried out on the oxide product from the sample $Cu_{0.5}Zn_{0.5}$TT. About 0.1 g of this sample was placed in a quartz reactor. The reduction was performed under flowing diluted $H_2$ (4.2 vol% $H_2$ in He) by increasing the temperature to 240 °C at a rate of 1 K min$^{-1}$ and maintaining that temperature for 1 h. The active surface area of Cu was determined by $N_2O$ reactive frontal chromatography at 300 K on the same sample of $Cu_{0.5}Zn_{0.5}$TT.[24]

## Acknowledgments

This work was supported by the Deutsche Forschungsgemeinschaft within the scope of the Collaborative Research Center SFB 558 (metal–substrate interactions in heterogeneous catalysis). We are grateful to F. Schüth, Mülheim, for helpful discussions.

[1] J. M. Thomas, W. J. Thomas, *Principles and Practice of Heterogeneous Catalysis*, VCH, Weinheim, **1996**.
[2] C. Chauvin, J. Jaussey, J. C. Lavalley, H. Idriss, J. P. Hidermann, A. Kiennemann, P. Chaumette, P. Coutry, *J. Catal.* **1990**, *121*, 56–69.
[3] M. M. Günter, T. Ressler, B. Bems, C. Büscher, T. Genger, O. Hinrichsen, M. Muhler, R. Schlögl, *Catal. Lett.* **2001**, *71*, 37–44.
[4] B. Bems, M. Schur, A. Dassenoy, H. Junkes, D. Herein, R. Schlögl, *Chem. Eur. J.* **2003**, *9*, 2039–2052.
[5] C. Kiener, M. Kurtz, H. Wilmer, C. Hoffmann, H. W. Schmidt, J. D. Grunwaldt, M. Muhler, F. Schüth, *J. Catal.* **2003**, *216*, 110–119.
[6] G. J. Hutchings, J. C. Vedrine, in *Basic Principles in Applied Catalysis*, vol. 75 (Ed.: M. Baerns), Springer, New York, **2004**, pp. 217–258.
[7] B. L. Kniep, T. Ressler, A. Rabis, F. Girgsdies, M. Baenitz, F. Steglich, R. Schlögl, *Angew. Chem.* **2004**, *116*, 114–117; *Angew. Chem. Int. Ed.* **2004**, *43*, 112–115.
[8] M. Saito, K. Murata, *Catal. Surv. Asia* **2004**, *8*, 285–294.
[9] M. Schur, B. Bems, A. Dassenoy, I. Kassatkine, J. Urban, H. Wilmes, O. Hinrichsen, M. Muhler, R. Schlögl, *Angew. Chem.* **2003**, *115*, 3945–3947; *Angew. Chem. Int. Ed.* **2003**, *42*, 3815–3817.
[10] P. L. Hansen, J. B. Wagner, S. Helveg, J. R. Rostrup-Nielsen, B. S. Clausen, H. Topsoe, *Science* **2002**, *295*, 2053–2055.
[11] S. A. French, A. A. Sokol, S. T. Bromley, C. R. A. Catlow, P. Sherwood, *Top. Catal.* **2003**, *24*, 161–172.
[12] J. B. Wagner, P. L. Hansen, A. M. Molenbroek, H. Topsoe, B. S. Clausen, S. Helveg, *J. Phys. Chem. B* **2003**, *107*, 7753–7758.
[13] M. Kurtz, J. Strunk, O. Hinrichsen, M. Muhler, K. Fink, B. Meyer, C. Wöll, *Angew. Chem.* **2005**, *117*, 2850–2854; *Angew. Chem. Int. Ed.* **2005**, *44*, 2790–2794.
[14] T. Ressler, B. L. Kniep, I. Kasatkin, R. Schlögl, *Angew. Chem.* **2005**, *117*, 4782–4785; *Angew. Chem. Int. Ed.* **2005**, *44*, 4704–4707.
[15] S. Vukojević, O. Trapp, J. D. Grunwaldt, C. Kiener, F. Schüth, *Angew. Chem.* **2005**, *117*, 8192–8195; *Angew. Chem. Int. Ed.* **2005**, *44*, 7978–7981.
[16] I. Böttger, T. Schedel-Niedrig, O. Timpe, R. Gottschall, M. Hävecker, T. Ressler, R. Schlögl, *Chem. Eur. J.* **2000**, *6*, 1870–1876.
[17] Y. Guo, R. Weiss, M. Epple, *Eur. J. Inorg. Chem.* **2005**, 3072–3079.
[18] R. Weiss, Y. Guo, S. Vukojević, L. Khodeir, R. Boese, F. Schüth, M. Muhler, M. Epple, *Eur. J. Inorg. Chem.* **2006**, 1796–1802.
[19] L. K. Templeton, D. H. Templeton, D. Zhang, A. Zalkin, *Acta Crystallogr., Sect. C* **1985**, *41*, 363–365.
[20] F. Jian, P. Zhao, Q. Wang, *J. Coord. Chem.* **2005**, *58*, 1133–1138.
[21] R. L. Schmid, J. Felsche, *Thermochim. Acta* **1982**, *59*, 105–114.
[22] M. Kurtz, H. Wilmer, T. Genger, O. Hinrichsen, M. Muhler, *Catal. Lett.* **2003**, *86*, 77–80.
[23] G. E. Parris, K. Klier, *J. Catal.* **1986**, *97*, 374–384.
[24] O. Hinrichsen, T. Genger, M. Muhler, *Chem. Eng. Technol.* **2000**, *11*, 956–959.

Received: June 16, 2006
Published Online: October 12, 2006

 © 2006 Wiley-VCH Verlag GmbH & Co. KGaA, Weinheim 

DOI: 10.1002/ejic.200600553

# A Facile Hydrothermal Route to Flower-Like Cobalt Hydroxide and Oxide

Li-Xia Yang,[a,b] Ying-Jie Zhu,*[a] Liang Li,[a,b] Ling Zhang,[a,b] Hua Tong,[a,b] Wei-Wei Wang,[a,b] Guo-Feng Cheng,[a] and Jie-Fang Zhu[a]

**Keywords:** Cobalt hydroxide / Cobalt oxide / Materials science / Nanostructures / Solvothermal synthesis

Flower-like cobalt hydroxide [β-$Co(OH)_2$] consisting of nanosheet networks has been synthesized by a hydrothermal method from $Co(CH_3COO)_2{\cdot}4H_2O$ in mixtures of water and glycerol/ethylene glycol at 200 °C. The morphology and phase of the cobalt hydroxide can be controlled by adjusting the experimental parameters that include cobalt acetate concentration and the volume ratio of water to glycerol/ethylene glycol. The possible formation mechanism of flower-like cobalt hydroxide is discussed on the basis of experimental results. Cobalt oxide ($Co_3O_4$) flowers have also been obtained by thermal decomposition of cobalt hydroxide flowers in air at 400 °C. The products were characterized by powder XRD, TEM, selected-area electron diffraction (SAED), high resolution TEM (HRTEM), and field-emission SEM (FESEM).
(© Wiley-VCH Verlag GmbH & Co. KGaA, 69451 Weinheim, Germany, 2006)

## Introduction

Research into nanomaterials has increased recently due to their unique electrical, optical, magnetic, and catalytic characteristics in comparison with the bulk materials. Currently, inorganic architectures with a hierarchical structure based on nano units and their specific properties for applications are attracting much interest in materials chemistry.[1–5] For example, the mediator-template assembly of gold nanoparticles into size-controllable nanostructures has been reported.[1] The interesting morphological and optical properties of these nanoparticle assemblies could potentially be exploited for optical sensing applications.[1] CoPt nanopolypods derived from the assembly of nanorods have been synthesized by a simple and large-scale-applicable thermolytic reaction,[2] and high-order superstructures of zeolite doughnuts with nanoscale building blocks (sheet-like discs) have been synthesized by a synergic dual-template method in a one-pot reaction.[3] The controlled construction of primary building blocks into curved structures provides another challenge for materials synthesis because of their potential use in new technological applications.

Cobalt hydroxide [$Co(OH)_2$] has recently received increasing attention due to its important technological applications. For example, cobalt hydroxide is usually added to nickel hydroxide electrodes to enhance the electrode conductivity and chargeability,[6,7] and composite materials of cobalt hydroxide and ultra-stable Y zeolite molecular sieves have shown potential applications in electrochemical capacitors.[8] Cobalt hydroxide films show catalytic and reversible electrochromic properties.[9,10] In particular, Kurmoo has reported the incorporation of different anions into the interlayers of cobalt hydroxide to form organic magnetic materials.[11] The preparation of single-crystalline β-$Co(OH)_2$ nanosheets is easily achieved because of their intrinsic lamellar structures.[12–14] However, there are few reports on the formation of 3D β-$Co(OH)_2$ architectures assembled from nanostructures, except the butterfly-like nanocrystals of β-$Co(OH)_2$ prepared by an ethylenediamine-mediated route.[15] At present, the synthesis of β-$Co(OH)_2$ hierarchical nanostructures is still a big challenge for researchers.

Spinel cobalt oxide ($Co_3O_4$), which is an important p-type semiconductor, has potential applications in sensors, lithium-ion batteries, and catalysis.[16–19] Furthermore, $Co_3O_4$ nanoparticles show interesting magnetic and field-emission properties.[20,21] There have been some reports on the synthesis of cobalt oxide nanocubes, nanorods, nanotubes, hollow spheres, and nanoboxes.[22–27] However, to the best of our knowledge, there has been no report on the synthesis of $Co_3O_4$ flowers consisting of nanosheet building blocks.

Here we report a simple hydrothermal approach to the synthesis of two kinds of β-$Co(OH)_2$ flowers consisting of nanosheet building blocks by the hydrolysis of cobalt acetate in solvent mixtures containing a polyalcohol and deionized water. $Co_3O_4$ flowers are readily obtained by thermal decomposition of $Co(OH)_2$ flowers in air. These β-$Co(OH)_2$ and $Co_3O_4$ flowers are expected to have potential applications in sensors, batteries, and catalysis.

[a] State Key Laboratory of High Performance Ceramics and Superfine Microstructure, Shanghai Institute of Ceramics, Chinese Academy of Sciences,
Shanghai 200050, P. R. China
Fax: +86-21-5241-3122
E-mail: y.j.zhu@mail.sic.ac.cn
[b] Graduate School of Chinese Academy of Sciences, P. R. China

 © 2006 Wiley-VCH Verlag GmbH & Co. KGaA, Weinheim 

## Results and Discussion

The phase of the as-prepared sample was examined by XRD. Figure 1(a) shows the XRD pattern of sample 1 prepared in a mixture of water and glycerol. All diffraction peaks in this pattern can be indexed as a single phase of the hexagonal brucite-like β-$Co(OH)_2$, which is consistent with the values in the literature (JCPDS no. 74-1057). The typical FESEM micrographs shown in Figure 1b–d reveal that sample 1 consists of relatively uniform flower-like structures. Each flower-like structure is composed of a network of nanosheet building blocks. The sizes of these flowers are in the range 6–9 μm, and the thickness of the nanosheets is less than 100 nm. The above results demonstrate that β-$Co(OH)_2$ with a flower-like morphology can be produced using the present synthetic scheme.

It is believed that the physical and chemical properties of the solvent can influence the solubility, reactivity, and diffusion behavior of the reagents and the intermediate.[28] In our reaction system, the properties of the mixed solvents can be easily adjusted by varying the volume ratio of glycerol to water. The volume ratio of glycerol to water ($V_g/V_w$) has a great influence on the formation of the product. As discussed above, a single phase of hexagonal β-$Co(OH)_2$ was obtained when $V_g/V_w$ was 1:3 (sample 1). When $V_g/V_w$ was adjusted to 1:6.5, however, a mixture of $Co_3O_4$ and β-$Co(OH)_2$ was obtained at 200 °C after 10.5 h [sample 2, Figure 2(a)]. When the reaction time was prolonged to 24.5 h (sample 3), a single phase of β-$Co(OH)_2$ was obtained (Figure 2b), thus indicating that glycerol can act as a reducing agent to reduce $Co^{3+}$ to $Co^{2+}$, which results in the transformation of $Co_3O_4$ to $Co(OH)_2$. Compared with the reaction with $V_g/V_w$ = 1:3, it takes a relatively longer time to form a single phase of β-$Co(OH)_2$ when using less glycerol. We also studied the effect of cobalt acetate concentration on the product, with a constant $V_g/V_w$ ratio of 1:3. When the amount of cobalt acetate was decreased to 0.100 g, a single phase of β-$Co(OH)_2$ with a pink color was still obtained (sample 4). However, if more cobalt acetate was used (1.000 g, sample 5), the product was blue, similar to that of α-$Co(OH)_2$, although the XRD pattern (Figure 2c) cannot be indexed to that of α-$Co(OH)_2$.

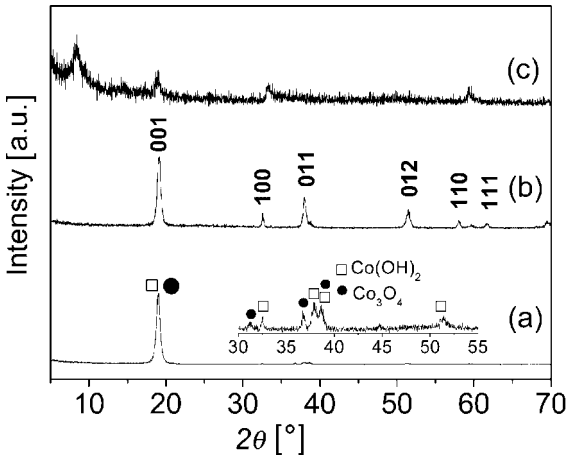


Figure 2. XRD patterns of different samples prepared by hydrothermal treatment at 200 °C: (a) sample 2; (b) sample 3; (c) sample 5.

In order to understand the formation process of β-$Co(OH)_2$ flowers, the morphologies of samples 3 and 4 were also examined by FESEM. When using less cobalt acetate (sample 4, Figure 3a), imperfect flowers assembled from

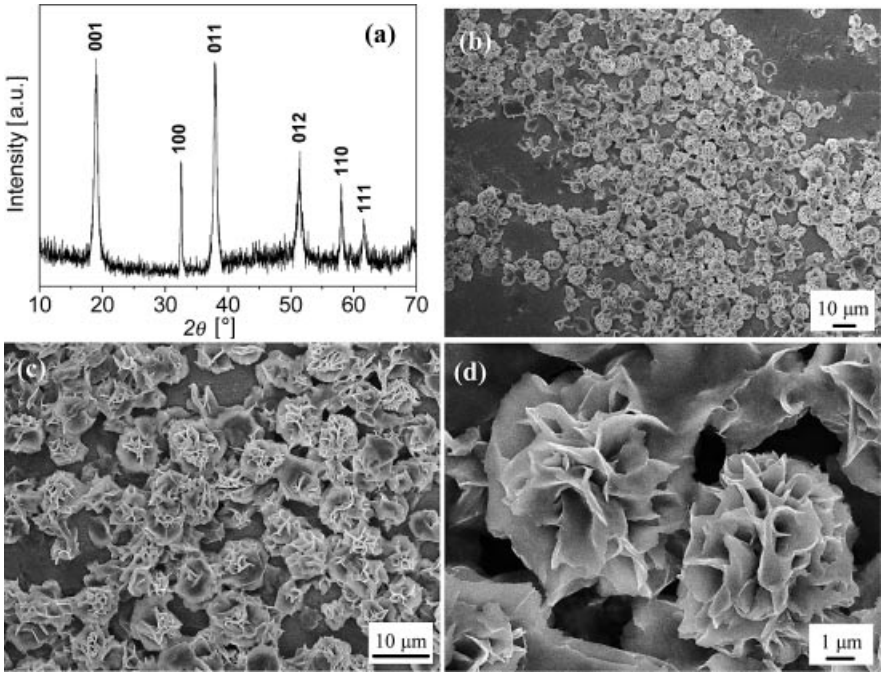


Figure 1. (a) XRD pattern of the obtained β-$Co(OH)_2$ (sample 1); (b–d) FESEM micrographs of β-$Co(OH)_2$ flowers (sample 1) at different magnifications.

 © 2006 Wiley-VCH Verlag GmbH & Co. KGaA, Weinheim 

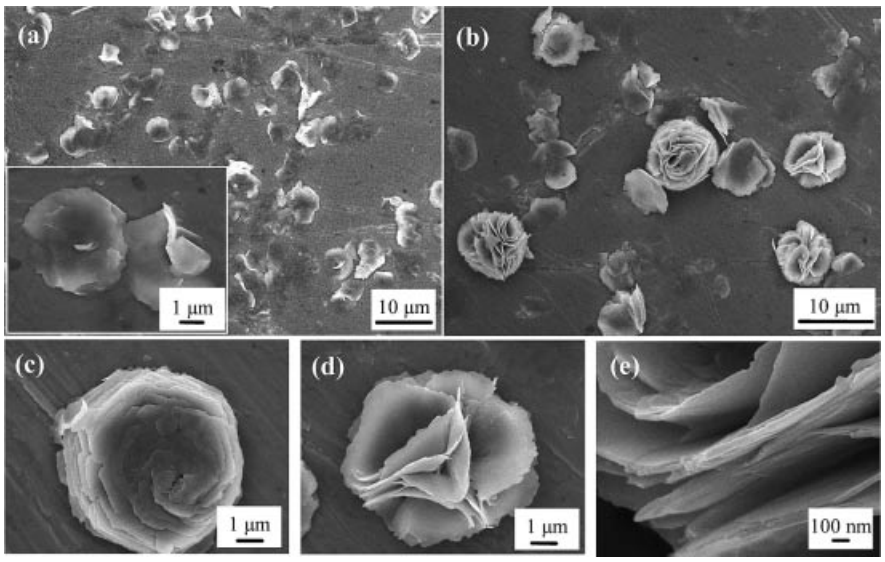


Figure 3. (a) FESEM micrograph of sample 4; (b) FESEM micrograph of sample 3; (c) and (d) FESEM micrographs of single flowers in sample 3; (e) a magnified FESEM micrograph of a flower in sample 3.

nanosheets were observed with dimensions below 7.5 μm, along with a few single nanosheets. The number of petals in these flowers is less than those in sample 1, as shown in Figure 3a. Upon decreasing the volume of glycerol, sample 3 shows a mixed morphology of nanosheets and flowers. Two kinds of flowers are observed, as shown in Figures 3c and 3d, which show that one kind of flower consists of flat nanosheets and the other of curved nanosheets. The morphology in Figure 3c was not observed in sample 1, so we suggest that it is due to the lower volume of glycerol used. The thickness of the nanosheets in the flowers was estimated to be below 50 nm (Figure 3e).

Ethylene glycol (EG) was also used as a co-solvent to substitute glycerol in order to understand the formation mechanism of the β-$Co(OH)_2$ flowers. The same experimental conditions as for the formation of sample 1 were adopted except for the use of EG instead of glycerol, and a mixture of β-$Co(OH)_2$ and $Co_3O_4$ was obtained, thereby illustrating that EG cannot completely reduce $Co^{3+}$ to $Co^{2+}$ at 200 °C after 10.5 h. A single phase of β-$Co(OH)_2$ was obtained upon increasing the volume ratio of EG to water and prolonging the reaction time to 20.5 h (sample 6, Figure 4a). Surprisingly, a different kind of flower was observed, as shown in the FESEM micrographs of sample 6 (Figure 4). The β-$Co(OH)_2$ flowers look like carnations consisting of curved nanosheet building blocks. These carnations have sizes in the range 5–15 μm.

On the basis of the above results, we can propose a formation mechanism for the β-$Co(OH)_2$ flowers. First, the hydrolysis of cobalt acetate results in the formation of $OH^-$ ions ($CH_3COO^- + H_2O \rightarrow CH_3COOH + OH^-$), which provide a basic environment for the formation of cobalt hydroxide. Sheet-like $Co(OH)_2$ forms as a general morphology due to its layered structure. In addition, glycerol/EG can act as a reducing agent. In the absence of glycerol or EG, only $Co_3O_4$ nanocubes are obtained. $Co_3O_4$ is formed by the oxidation of β-$Co(OH)_2$ by oxygen in the autoclave and is then reduced by glycerol/EG to form a single phase of β-$Co(OH)_2$. Besides acting as a reducing agent, glycerol/EG could coordinate to the cobalt ions to form complexes in solution,[29,30] which decreases the free $Co^{2+}$ concentration in solution and results in the slow generation of β-$Co(OH)_2$. This coordination between cobalt ions and glycerol/EG may be favorable for the formation of the flower nuclei,

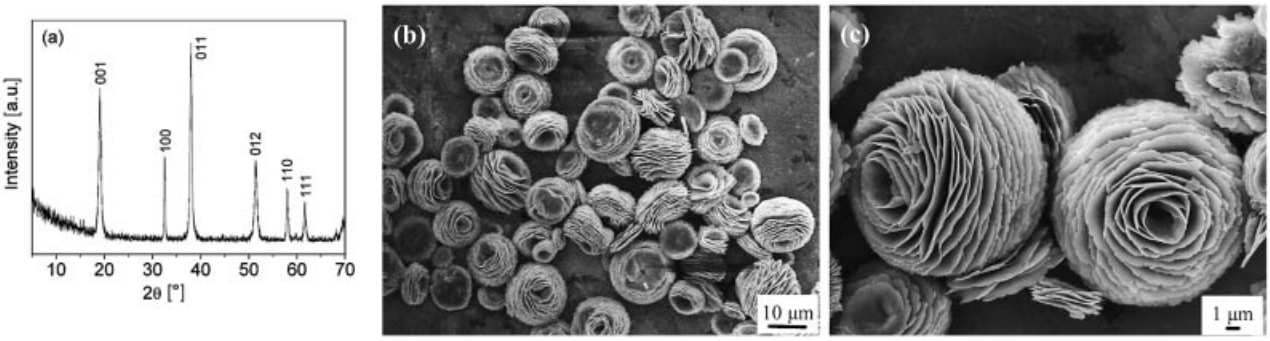


Figure 4. (a) XRD pattern of sample 6; (b) and (c) FESEM micrographs of sample 6 at different magnifications.

 © 2006 Wiley-VCH Verlag GmbH & Co. KGaA, Weinheim 

resulting in the formation of flower-like β-$Co(OH)_2$. Furthermore, glycerol helps to generate a highly viscous and stable mixture solution, which favors the stable growth of nanosheets and the formation of β-$Co(OH)_2$ flowers with nanosheets as building blocks. As discussed above, a higher $V_g/V_w$ ratio favors the formation of flowers consisting of curved nanosheets instead of those with flat nanosheets (samples 1 and 3), thus indicating that the higher viscosity caused by glycerol can prohibit the aggregation of nanosheets and promotes the formation of flowers with curved nanosheets. Qian et al.[31] have reported the synthesis of copper nanowires by a complex-surfactant-assisted hydrothermal reduction process in a mixture of water and glycerol. The high viscosity shows a good effect on prohibiting the aggregation of copper particles and results in a relatively stable suspension. One of the keys to the formation of these flower structures is the use of cobalt acetate as the cobalt source without the addition of any base. The slower hydrolysis of acetate and the complexation of cobalt ions with glycerol/EG are favorable for the formation of these superstructures. In the presence of glycerol, when NaOH is added to the solution (sample 7), only irregular nanosheets are formed (Figure 5). Although glycerol provides a viscous environment, the introduction of a strong base (NaOH) could accelerate the reaction and prevent the formation of flowers. However, in the presence of EG, the viscosity is not as high as with glycerol, therefore the nanosheets tend to self-assemble to reduce the surface energy in the mixture of EG and water, and follows a layer-by-layer growth style so that hierarchical carnation structures are formed.

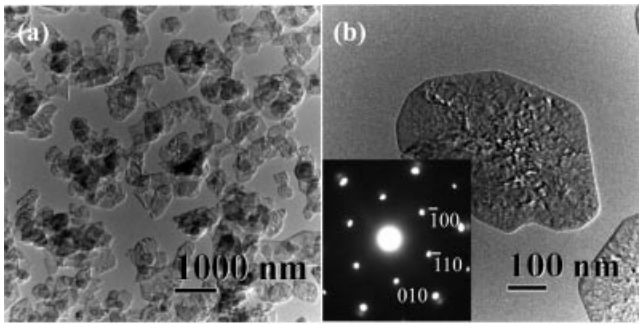


Figure 5. (a, b) TEM micrographs of the obtained β-$Co(OH)_2$ nanosheets of sample 7; the inset of (b) is the corresponding SAED pattern.

TEM was used to study the crystal structure of β-$Co(OH)_2$. Figure 6a shows a single nanosheet of sample 4. The SAED pattern (Figure 6b) of this nanosheet exhibits a hexagonal symmetry, thus indicating that the surface of the nanosheet is the $(00\bar{1})$ plane of β-$Co(OH)_2$, and the direction along the thickness of the obtained β-$Co(OH)_2$ is $[00\bar{1}$; the *c* axis of hexagonal β-$Co(OH)_2$]. The SAED pattern changes rapidly under electron irradiation to give another set of diffraction patterns that are close to the original one that show elongated diffraction spots rather than bright dots, thereby indicating the coexistence of two different species (Figure 6c). The inner set of hexagonal diffraction spots is still due to β-$Co(OH)_2$, and the outer set of diffraction spots corresponds to CoOOH. The electron beam is also along the $[00\bar{1}]$ direction of hexagonal CoOOH (JCPDS no. 26-1107). A similar SAED pattern has been reported for a mixture of β-$Co(OH)_2$ and CoOOH.[32] The diffraction pattern of β-$Co(OH)_2$ vanishes after prolonged irradiation by the electron beam and another set of SAED patterns (Figure 6d) is obtained, which shows the coexistence of CoOOH and $Co_3O_4$. The diffraction dots indicated by the white arrows show a hexagonal symmetry and can be indexed to the SAED pattern of a cubic $Co_3O_4$ phase (JCPDS no. 80-1541) with the incident electron beam along the [111] direction. This phenomenon implies that the thin β-$Co(OH)_2$ nanosheets synthesized using the current method are not stable under electron beam irradiation and that prolonged exposure of the sample to the electron beam during the TEM observation will destroy the structure of β-$Co(OH)_2$, resulting in the formation of $Co_3O_4$ nanoparticles with sizes of 1–4 nm, as shown in the high-resolution TEM (HRTEM) image of Figure 6e. The interplanar dis-

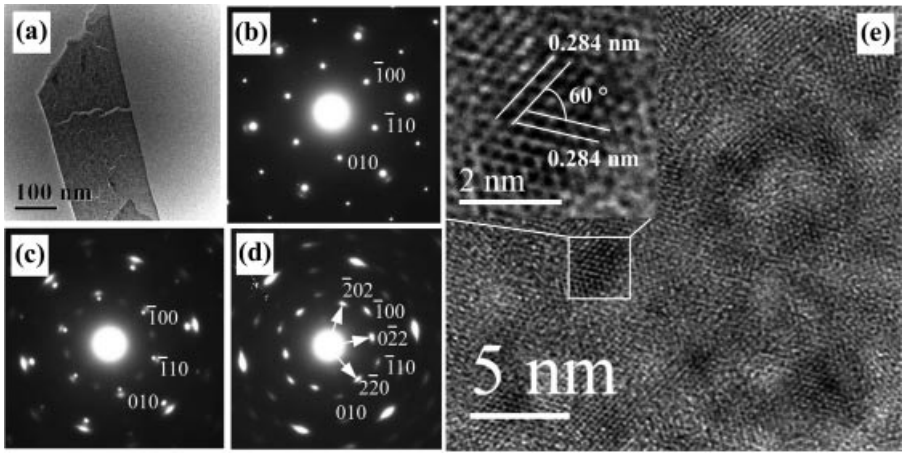


Figure 6. (a) TEM micrograph of an individual β-$Co(OH)_2$ nanosheet of sample 4; (b–d) the corresponding SAED patterns taken at different irradiation times; (e) HRTEM image taken of the individual nanosheet corresponding to the SAED pattern of (d).

 © 2006 Wiley-VCH Verlag GmbH & Co. KGaA, Weinheim 

tance of the crystal fringes with an angle of 60° is 2.84 nm, which is consistent with the $(\bar{2}02)$ and $(0\bar{2}2)$ planes of a cubic $Co_3O_4$ phase.

$Co_3O_4$ is obtained by thermal conversion of the β-$Co(OH)_2$ flower precursor at 400 °C after 3 h. Figure 7 shows the XRD pattern of the product. All the diffraction peaks can be indexed to a single phase of a cubic $Co_3O_4$, which matches well with the reported data (JCPDS no. 80-1541). No peaks from the β-$Co(OH)_2$ precursor are observed in the XRD pattern, thus indicating the complete transformation of β-$Co(OH)_2$ to $Co_3O_4$.

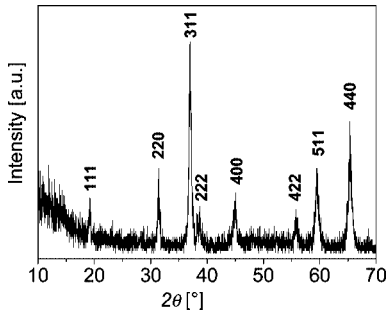


Figure 7. XRD pattern of $Co_3O_4$ (sample C1).

After the thermal conversion from β-$Co(OH)_2$ to $Co_3O_4$, the two kinds of flower-like morphology of β-$Co(OH)_2$ were almost sustained and $Co_3O_4$ flowers were obtained. In addition, a few single nanosheets were also observed, as shown in Figure 8a,b. A single nanosheet is shown in Figure 8c, from which one can see that the surface of this nanosheet is not smooth. The SAED pattern of this nanosheet, which was taken by focusing the incident electron beam along the [111] zone axis, reveals a single crystal structure that can be indexed to cubic $Co_3O_4$, consistent with the XRD results. The HRTEM image of the nanosheet shows that the spacing between clear lattice fringes with an angle of 60° is 0.284 nm, which is consistent with the $(\bar{2}02)$ and $(0\bar{2}2)$ planes of a cubic $Co_3O_4$.

## Conclusions

We have demonstrated a facile strategy to synthesize two kinds of β-$Co(OH)_2$ flowers consisting of nanosheets as the building unit. Glycerol or ethylene glycol serves as a co-solvent and also a reducing agent in this reaction system. Both the volume ratio of glycerol/EG to water and the concentration of cobalt acetate affect the phase and morphology of the product. $Co_3O_4$ flowers can be obtained by a simple thermal conversion of the β-$Co(OH)_2$ flower precursor in air; the flower-like morphology can be preserved during the thermal conversion process. β-$Co(OH)_2$ nanosheets are not stable under electron beam irradiation and are transformed into CoOOH and $Co_3O_4$. This simple synthetic method, which does not use any surfactant or template, may be extended to the synthesis of other materials with novel morphologies.

## Experimental Section

All reagents were of analytical grade and were purchased and used as received without further purification. In a typical procedure, cobalt acetate [$Co(CH_3COO)_2{\cdot}4H_2O$] (0.25 g) was dissolved in a mixture of deionized water and glycerol (30 mL) with a volume ratio

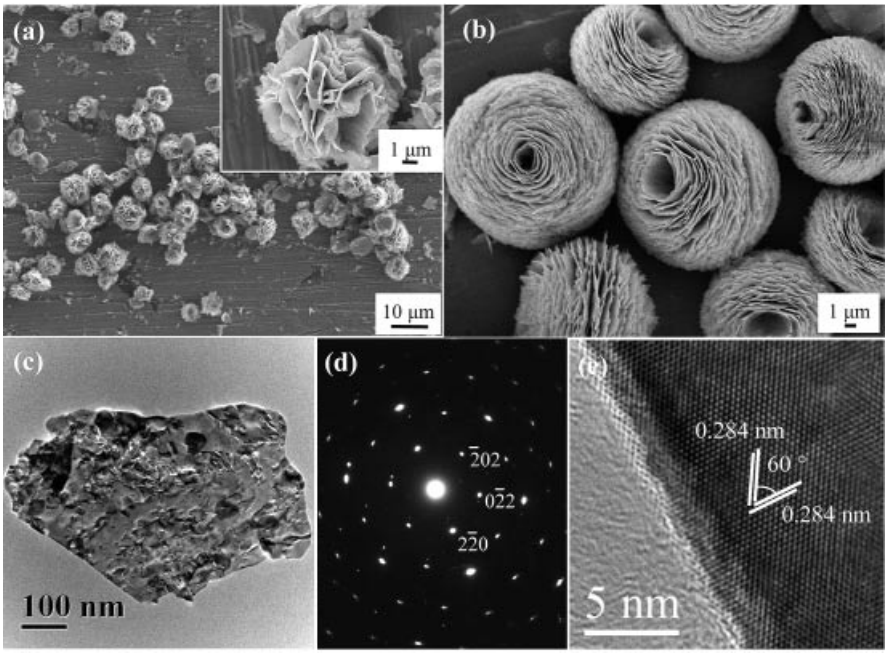


Figure 8. (a) FESEM micrograph of $Co_3O_4$ (sample C1); (b) FESEM micrograph of $Co_3O_4$ (sample C6); (c) TEM micrograph of an individual nanosheet (sample C1) and (d) the corresponding SAED pattern; (e) HRTEM image of this individual $Co_3O_4$ nanosheet.

 © 2006 Wiley-VCH Verlag GmbH & Co. KGaA, Weinheim 

Table 1. Detailed experimental parameters for the synthesis of some typical samples (at 200 °C for all samples).

| Sample | Reaction system | Time [h] | Phase | Morphology |
|---|---|---|---|---|
| 1 | 0.25 g $Co(CH_3COO)_2{\cdot}4H_2O$ + 7.5 mL glycerol + 22.5 mL $H_2O$ | 10.5 | β-$Co(OH)_2$ | flowers |
| 2 | 0.25 g $Co(CH_3COO)_2{\cdot}4H_2O$ + 4 mL glycerol + 26 mL $H_2O$ | 10.5 | β-$Co(OH)_2$ + $Co_3O_4$ | – |
| 3 | 0.25 g $Co(CH_3COO)_2{\cdot}4H_2O$ + 4 mL glycerol + 26 mL $H_2O$ | 24.5 | β-$Co(OH)_2$ | flowers and nanosheets |
| 4 | 0.10 g $Co(CH_3COO)_2{\cdot}4H_2O$ + 7.5 mL glycerol + 22.5 mL $H_2O$ | 10.5 | β-$Co(OH)_2$ | imperfect flowers |
| 5 | 1.00 g $Co(CH_3COO)_2{\cdot}4H_2O$ + 7.5 mL glycerol + 22.5 mL $H_2O$ | 10.5 | unknown | – |
| 6 | 0.25 g $Co(CH_3COO)_2{\cdot}4H_2O$ + 20 mL ethylene glycol + 10 mL $H_2O$ | 20.5 | β-$Co(OH)_2$ | carnations |
| 7 | 0.25 g $Co(CH_3COO)_2{\cdot}4H_2O$ + 7.5 mL glycerol + 17.5 mL $H_2O$ + 5 mL NaOH (1 M) | 10.5 | β-$Co(OH)_2$ | nanosheets |

of 3:1 at room temperature, and the solution was then transferred into a Teflon-lined, 40-mL autoclave and maintained at 200 °C for 10.5 h. It was then cooled to room temperature. This sample was denoted as sample 1. The product was then collected by centrifugation and washed with deionized water and absolute ethanol repeatedly, then dried in air at 60 °C. The detailed experimental parameters for the synthesis of some typical samples are listed in Table 1. $Co_3O_4$ samples were obtained by thermal decomposition of β-$Co(OH)_2$ flowers (samples 1 and 6) in a tubular oven at 400 °C after 3 h in air. The obtained $Co_3O_4$ samples are denoted as samples C1 and C6, respectively.

Powder XRD data were collected on a Rigaku D/max 2550 V X-ray diffractometer with high-intensity Cu-$K_\alpha$ radiation ($\lambda$ = 1.54178 Å) and a graphite monochromator. The morphology was studied with a JEOL JSM-6700F field emission scanning electron microscope (FESEM). TEM, SAED, and HRTEM images were obtained using a JEOL JEM-2100F field emission transmission electron microscope.

## Acknowledgments

Financial support from the National Natural Science Foundation of China (50472014), the Chinese Academy of Sciences under the Program for Recruiting Outstanding Overseas Chinese (Hundred Talents Program), and the Fund for Innovation Research from the Shanghai Institute of Ceramics is gratefully acknowledged. This work was also supported by the Program of the Shanghai Postdoctoral Scientific Research Foundation (05R214148), the Opening Project of the State Key Laboratory of High Performance Ceramics and Superfine Microstructure (SKL200506SIC), Shanghai Institute of Ceramics, Chinese Academy of Sciences.

[1] M. M. Maye, I. I. S. Lim, J. Luo, Z. Rab, D. Rabinovich, T. B. Liu, C. J. Zhong, *J. Am. Chem. Soc.* **2005**, *127*, 1519–1529.
[2] V. Tzitzios, D. Niarchos, M. Gjoka, N. Boukos, D. Petridis, *J. Am. Chem. Soc.* **2005**, *127*, 13756–13757.
[3] G. Hu, D. Ma, L. Liu, M. Cheng, X. H. Bao, *Angew. Chem. Int. Ed.* **2004**, *43*, 3452–3456.
[4] M. Mo, J. C. Yu, L. Z. Zhang, S. K. A. Li, *Adv. Mater.* **2005**, *17*, 756–760.
[5] B. Liu, S. H. Yu, L. Li, Q. Zhang, F. Zhang, K. Jiang, *Angew. Chem. Int. Ed.* **2004**, *43*, 4745–4750.
[6] W. Y. Li, S. Y. Zhang, J. Chen, *J. Phys. Chem. B* **2005**, *109*, 14025–14032.
[7] J. Ismail, M. F. Ahmed, P. V. Kamath, *J. Power Sources* **1993**, *41*, 223–230.
[8] L. Cao, F. Xu, Y. Y. Liang, H. L. Li, *Adv. Mater.* **2004**, *16*, 1853–1857.
[9] M. Dinamani, P. V. Kamath, *J. Appl. Electrochem.* **2000**, *30*, 1157–1161.
[10] N. Ozer, D. G. Chen, T. Buyuklimanli, *Sol. Energy Mater. Sol. Cells* **1998**, *52*, 223–230.
[11] M. Kurmoo, *Chem. Mater.* **1999**, *11*, 3370–3378.
[12] Y. L. Hou, H. Kondoh, M. Shimojo, T. Kogure, T. Ohta, *J. Phys. Chem. B* **2005**, *109*, 19094–19098.
[13] Z. P. Liu, R. Z. Ma, M. Osada, K. Takada, T. Sasaki, *J. Am. Chem. Soc.* **2005**, *127*, 13869–13874.
[14] Y. C. Zhu, H. L. Li, Y. Koltypin, A. Gedanken, *J. Mater. Chem.* **2002**, *12*, 729–733.
[15] J. T. Sampanthar, H. C. Zeng, *J. Am. Chem. Soc.* **2002**, *124*, 6668–6675.
[16] W. Y. Li, L. N. Xu, J. Chen, *Adv. Funct. Mater.* **2005**, *15*, 851–857.
[17] Y. M. Kang, M. S. Song, J. H. Kim, H. S. Kim, M. S. Park, J. Y. Lee, H. K. Liu, S. X. Dou, *Electrochim. Acta* **2005**, *50*, 3667–3673.
[18] J. Jansson, A. E. C. Palmqvist, E. Fridell, M. Skoglundh, L. Österlund, P. Thormählen, V. Langer, *J. Catal.* **2002**, *211*, 387–397.
[19] S. Fujita, K. Suzuki, T. Mori, *Catal. Lett.* **2003**, *86*, 139–144.
[20] C. Nethravathi, S. Sen, N. Ravishankar, M. Rajamathi, C. Pietzonka, B. Harbrecht, *J. Phys. Chem. B* **2005**, *109*, 11468–11472.
[21] T. Yu, Y. W. Zhu, X. J. Xu, Z. X. Shen, P. Chen, C. T. Lim, J. T. L. Thong, C. H. Sow, *Adv. Mater.* **2005**, *17*, 1595–1599.
[22] T. He, D. R. Chen, X. L. Jiao, Y. L. Wang, Y. Z. Duan, *Chem. Mater.* **2005**, *17*, 4023–4030.
[23] R. Xu, H. C. Zeng, *J. Phys. Chem. B* **2003**, *107*, 926–930.
[24] Y. K. Liu, G. H. Wang, C. K. Xu, W. Z. Wang, *Chem. Commun.* **2002**, 1486–1487.
[25] X. Y. Shi, S. B. Han, R. J. Sanedrin, F. Zhou, M. Selke, *Chem. Mater.* **2002**, *14*, 1897–1902.
[26] T. He, D. R. Chen, X. L. Jiao, Y. Y. Xu, Y. X. Gu, *Langmuir* **2004**, *20*, 8404–8408.
[27] T. He, D. R. Chen, X. L. Jiao, Y. L. Wang, *Adv. Mater.* **2006**, *18*, 1078–1082.
[28] Z. P. Liu, J. B. Liang, S. Li, S. Peng, Y. T. Qian, *Chem. Eur. J.* **2004**, *10*, 634–640.
[29] E. W. Radoslovich, M. Raupach, P. G. Slade, R. M. Taylor, *Aust. J. Chem.* **1970**, *23*, 1963–1971.
[30] N. Chakroune, G. Viau, S. Ammar, N. Jouini, P. Gredin, M. J. Vaulay, F. Fiévet, *New J. Chem.* **2005**, *29*, 355–361.
[31] Z. P. Liu, Y. Yang, J. B. Liang, Z. K. Hu, S. Li, S. Peng, Y. T. Qian, *J. Phys. Chem. B* **2003**, *107*, 12658–12661.
[32] L. Q. Zhang, A. K. Dutta, G. Jarero, P. Stroeve, *Langmuir* **2000**, *16*, 7095–7100.

Received: June 15, 2006
Published Online: October 10, 2006

 © 2006 Wiley-VCH Verlag GmbH & Co. KGaA, Weinheim 

DOI: 10.1002/ejic.200600636

# Coordination Chemistry of 3-Mercapto-2-(mercaptomethyl)propanoic Acid (Dihydroasparagusic Acid) with Iron and Nickel

**Phillip I. Volkers,[a] Thomas B. Rauchfuss,*[a] and Scott R. Wilson[a]**

**Keywords:** Iron / Nickel / S ligands / Bridging ligands / Coordination modes

The first transition-metal complexes bearing the natural product dihydroasparagusic acid, $(HSCH_2)_2CHCO_2H$, as a ligand are reported. Various coordination modes and nuclearities are demonstrated for the chelating ligand by a series of iron and nickel complexes. $Fe_2[(SCH_2)_2CHCO_2H](CO)_6$ retains carbonyl substitution reactivity typical of $Fe_2(SR)_2(CO)_6$ complexes, yet carboxy coordination to $Fe^I$ was unobserved. Coupling of the carboxylic acid with amines yields the corresponding amides $Fe_2[(SCH_2)_2CHC(O)NHR](CO)_6$ (R = Et, gly–*O*–*t*Bu). $Fe_2[(SCH_2)_2CHCO_2H](CO)_4(PMe_3)_2$ catalyzes $H_2$ production, but no better than unfunctionalized alkyl dithiolate analogs. Reactions of the ligand with $NiCl_2$(dppe) afforded mono-, di-, and trinuclear complexes. Noteworthy is $Ni_3[(SCH_2)_2CHCO_2]_2(dppe)_2$, which features an octahedrally coordinated $Ni^{II}$ center linked to a pair of square-planar $Ni^{II}$ centers.
(© Wiley-VCH Verlag GmbH & Co. KGaA, 69451 Weinheim, Germany, 2006)

## Introduction

The coordination properties of the natural product dihydroasparagusic acid,[1] $(HSCH_2)_2CHCO_2H$, has received little attention.[2] This compound has long been known, is prepared easily, and offers the possibility of serving as a functionalized bridging dithiolate ligand.[3,4] Our interest in exploring its coordination properties was motivated by the occurrence of propanedithiolate or the isosteric 2-azapropane-1,3-dithiolate as a cofactor in the iron hydrogenases.[5–7]

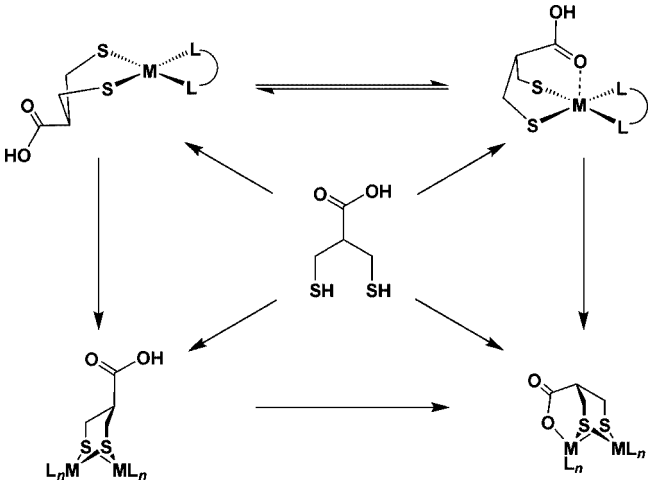


Scheme 1. General coordination modes for $(HSCH_2)_2CHCO_2H$.

In considering the coordinating properties of asparagusic acid, one can anticipate several motifs: *S*,*S*-bidentate; *S*,*S*,*O*-tridentate; and dinuclear derivatives of each of these (Scheme 1). Examples of such coordination modes are presented here using iron and nickel platforms. We were particularly interested in the possibility that the carboxylic acid functionality in $Fe_2[(SCH_2)_2CHCO_2H](CO)_{6-x}L_x$ would permit attachment of functionality, affect electrocatalytic $H_2$ production,[8,9] or lead to more robust linkages between metal atoms.

## Results and Discussion

### I. Complexes with Iron

#### *$Fe_2[(SCH_2)_2CHCOOH](CO)_6$*

The air-stable parent complex, hereafter $Fe_2$(aspH)$(CO)_6$, was synthesized in 43% yield by the reaction of $Fe_3(CO)_{12}$ and dihydroasparagusic acid, $(HSCH_2)_2$CHCOOH ($aspH_3$). The preparation was more conveniently conducted in the presence of $NEt_iPr_2$, followed by acidification to produce $Fe_2$(aspH)$(CO)_6$. Crystallographic characterization of $Fe_2$(aspH)$(CO)_6$ verified the anticipated $Fe_2(SR)_2(CO)_6$ core and demonstrated hydrogen-bonding interactions between pairs of carboxyl groups (Figure 1, Table 1). The carboxylic acid occupies an equatorial position on the cyclohexane-like $FeS_2C_3$ ring, projecting orthogonally with respect to the Fe–Fe vector.

$Fe_2$(aspH)$(CO)_6$ undergoes the transformations expected for a carboxylic acid (Scheme 2). Amide-bond formation with $EtNH_2$ was effected using a phosphonium-based coup-

[a] Department of Chemistry, University of Illinois, 601 S. Goodwin Ave., Urbana, IL 61801, USA

 © 2006 Wiley-VCH Verlag GmbH & Co. KGaA, Weinheim 

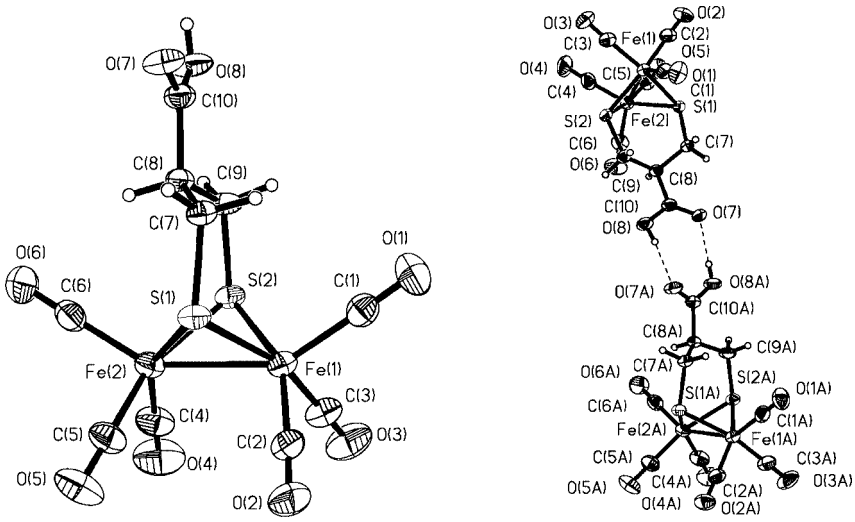


Figure 1. Left: structure of $Fe_2(aspH)(CO)_6$ with thermal ellipsoids set at the 50% probability level. Right: structure of the hydrogen-bonded dimer of $Fe_2(aspH)(CO)_6$. Selected distances [Å] and angles [°]: Fe(1)–Fe(2) 2.5130(8), Fe(1)–C(1) 1.813(2), Fe(1)–C(2) 1.803(2), Fe(1)–C(3) 1.811(2), Fe(1)–S(1) 2.2485(8), Fe(1)–S(2) 2.2535(7), Fe(2)–C(4) 1.794(2), Fe(2)–C(5) 1.797(2), Fe(2)–C(6) 1.808(2), Fe(2)–S(2) 2.2529(7), Fe(2)–S(1) 2.2554(7), O(7)–C(10) 1.216(2), O(8)–C(10) 1.314(2); S(1)–Fe(1)–S(2) 85.21(3), S(2)–Fe(2)–S(1) 85.06(3).

Table 1. Selected crystallographic data for iron-containing asparagusic complexes.

| | $Fe_2(aspH)(CO)_6$ | $Fe_2[(SCH_2)_2CHCONHEt](CO)_6$ | $Fe_2[(SCH_2)_2CHCONHCH_2CO_2tBu](CO)_6$ |
|---|---|---|---|
| Empirical formula | $C_{10}H_6Fe_2O_8S_2$ | $C_{12}H_{11}Fe_2NO_7S_2$ | $C_{16}H_{17}Fe_2NO_9S_2$ |
| Formula mass | 429.97 | 457.04 | 543.13 |
| $T$ [K] | 193(2) | 193(2) | 193(2) |
| $\lambda$ [Å] | 0.71073 | 0.71073 | 0.71073 |
| Crystal system | monoclinic | monoclinic | monoclinic |
| Space group | $C2/c$ | $P2_1/c$ | $P2_1/c$ |
| $a$ [Å] | 23.521(8) | 14.267(3) | 11.623(2) |
| $b$ [Å] | 9.672(3) | 13.792(3) | 16.309(3) |
| $c$ [Å] | 14.383(5) | 9.307(2) | 24.543(4) |
| $\alpha$ [°] | 90 | 90 | 90 |
| $\beta$ [°] | 113.389(5) | 106.954(4) | 95.558(3) |
| $\gamma$ [°] | 90 | 90 | 90 |
| $V$ [Å$^3$] | 3003.3(17) | 1751.8(7) | 4630.2(14) |
| $Z$ | 8 | 4 | 8 |
| $\rho$ (calcd.) [g/cm$^3$] | 1.902 | 1.733 | 1.558 |
| $\mu$ (Mo-$K_\alpha$) [mm$^{-1}$] | 2.244 | 1.926 | 1.477 |
| $F$(000) | 1712 | 920 | 2208 |
| Crystal size [mm] | $0.44 \times 0.40 \times 0.16$ | $0.44 \times 0.09 \times 0.05$ | $0.34 \times 0.26 \times 0.20$ |
| $\theta$ range [°] | 1.89–28.27 | 2.10–28.31 | 1.76–25.38 |
| Reflections collected | 14606 | 17196 | 36784 |
| Independent reflections | 3668 [$R$(int) = 0.0357] | 4292 [$R$(int) = 0.0671] | 8492 [$R$(int) = 0.0573] |
| Absorption correction | integration | integration | integration |
| Max./min. transmission | 0.7170/0.4373 | 0.9099/0.4495 | 0.7641/0.6190 |
| Goodness-of-fit on $F^2$ | 1.03 | 0.875 | 0.918 |
| Final $R$ indices [$I > 2\sigma(I)$] | $R_1$ = 0.0274 | $R_1$ = 0.0368 | $R_1$ = 0.0330 |
| | $wR_2$ = 0.0665 | $wR_2$ = 0.0646 | $wR_2$ = 0.0643 |
| $R$ indices (all data) | $R_1$ = 0.0389 | $R_1$ = 0.0844 | $R_1$ = 0.0651 |
| | $wR_2$ = 0.0709 | $wR_2$ = 0.0727 | $wR_2$ = 0.0716 |
| Largest diff. peak/hole [e·Å$^{-3}$] | 0.308/–0.365 | 0.533/–0.322 | 0.321/–0.240 |

ling agent. The crystallographic characterization of $Fe_2[(SCH_2)_2CHCONHEt](CO)_6$ confirms the structure (Figure 2, Table 1). The amide substituent is again equatorial with respect to the cyclohexane-like $FeS_2C_3$ ring and the nitrogen is planar. The occurrence of two identical splitting patterns in the $^1$H NMR spectrum is attributed to *cisoid* and *transoid* rotamers of the amide, consistent with restricted rotation about the C(O)–N bond. Coupling of $Fe_2(aspH)(CO)_6$ with glycine *tert*-butyl ester afforded the corresponding amido ester $Fe_2[(SCH_2)_2CHCONHCH_2CO_2tBu](CO)_6$, which exhibited crystallographic features akin to those in the ethyl derivative (Figure 3, Table 1). Again, two rotamers were observed in the $^1$H NMR spectrum.

 © 2006 Wiley-VCH Verlag GmbH & Co. KGaA, Weinheim 

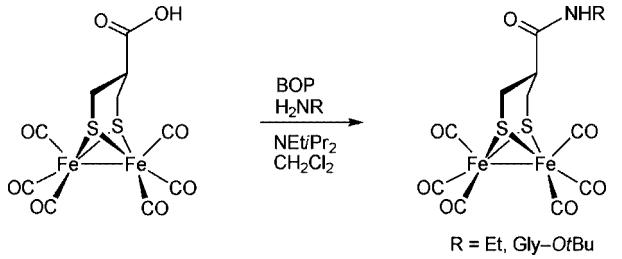


Scheme 2. Synthetic route for amide-bond derivatization of $Fe_2(aspH)(CO)_6$.

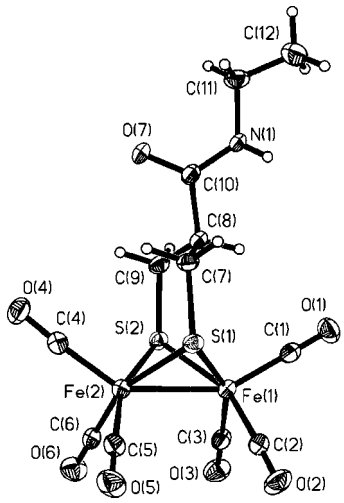


Figure 2. Structure of $Fe_2[(SCH_2)_2CHCONHEt](CO)_6$ with thermal ellipsoids set at the 50% probability level. Selected distances [Å] and angles [°]: Fe(1)–Fe(2) 2.5167(8), Fe(1)–C(1) 1.800(3), Fe(1)–C(2) 1.797(3), Fe(1)–C(3) 1.801(3), Fe(1)–S(1) 2.2542(9), Fe(1)–S(2) 2.2574(8), Fe(2)–C(4) 1.795(3), Fe(2)–C(5) 1.799(3), Fe(2)–C(6) 1.807(3), Fe(2)–S(1) 2.2497(9), Fe(2)–S(2) 2.2522(9); S(1)–Fe(1)–S(2) 85.07(3), S(1)–Fe(2)–S(2) 85.30(3).

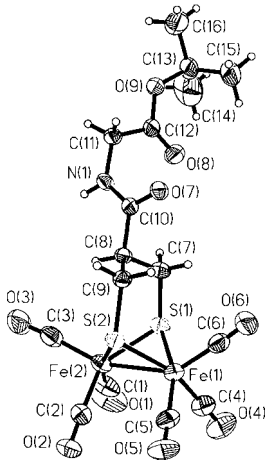


Figure 3. Structure of $Fe_2[(SCH_2)_2CHCONHCH_2CO_2tBu](CO)_6$ with thermal ellipsoids set at the 50% probability level. Selected distances [Å] and angles [°]: Fe(1)–Fe(2) 2.5141(7), C(1)–Fe(2) 1.791(3), C(2)–Fe(2) 1.795(3), C(3)–Fe(2) 1.806(4), C(4)–Fe(1) 1.801(3), C(5)–Fe(1) 1.798(3), C(6)–Fe(1) 1.797(3), S(1)–Fe(1) 2.2567(8), S(1)–Fe(2) 2.2574(9), S(2)–Fe(1) 2.2532(8), S(2)–Fe(2) 2.2676(8); S(2)–Fe(1)–S(1) 85.32(3), S(1)–Fe(2)–S(2) 84.96(3).

### *Acid-Base Properties*

Although only poorly soluble in MeOH, $Fe_2(aspH)(CO)_6$ was found to dissolve upon addition of $Et_3N$, indicative of the formation of $Et_3NH[Fe_2(asp)(CO)_6]$. The $\nu_{CO}$ region in the solution IR spectrum of this deprotonated compound exhibited negligible shifts relative to $Fe_2(aspH)(CO)_6$, indicating minor electronic influence of the pendant carboxy/carboxylate group on the diiron unit. The easy deprotonation of $Fe_2(aspH)(CO)_6$ interfered with experiments aimed at its decarbonylation using $Me_3NO$.[10] Rather than the usual red-to-purple color change observed upon decarbonylation of $Fe_2(SR)_2(CO)_6$,[9] solutions deposited a brown precipitate, presumably of $Me_3NOH[Fe_2(asp)(CO)_6]$.

### *Substitution Reactions of $Fe_2(aspH)(CO)_6$*

Upon heating in the presence of excess $PMe_3$, $HNEtiPr_2[Fe_2(asp)(CO)_6]$ converted readily into $HNEtiPr_2[Fe_2(asp)(CO)_4(PMe_3)_2]$. The $^{31}P$ NMR spectrum of the product showed two equally intense singlets, indicating the nonequivalency imposed by the pendant carboxylate group. IR measurements in the $\nu_{CO}$ region indicate that this salt is very similar electronically to related derivatives, e.g. $Fe_2(S_2C_3H_6)(CO)_4(PMe_3)_2$.[11]

Substitution of the CO ligands in $Fe_2(aspH)(CO)_6$ by cyanide was also explored. IR spectroscopic measurements in the $\nu_{CO}$ region established that the first equivalent of $CN^-$ deprotonated the carboxylic acid. The prevalence of monosubstituted product, $[Fe_2(asp)(CN)(CO)_5]^{2-}$ ($\nu_{CN,CO}$ = 2091, 2028, 1974, 1952, 1914), shows that the pendant carboxylate group inhibits a second cyanide ion from attacking the unsubstituted iron center. When the carboxylic acid was first deprotonated with an amine base, followed by treatment with 1 equiv. of $CN^-$, we again obtained the monosubstituted product. Upon heating in the presence of an additional equivalent of $CN^-$, $[Fe_2(asp)(CN)(CO)_5]^{2-}$ converted into the dicyanide derivative, $[Fe_2(asp)(CN)_2(CO)_4]^{3-}$, as established by IR spectroscopy ($\nu_{CN,CO}$ = 2074, 1960, 1919, 1880).

### *Electrochemical Studies*

Cyclic voltammetry studies showed that MeCN solutions of $Fe_2(aspH)(CO)_6$ reduce at –1.20 and –1.96 V vs. Ag/AgCl, corresponding to $Fe^IFe^I/Fe^0Fe^I$ and $Fe^0Fe^I/Fe^0Fe^0$ couples, respectively.[12] Addition of 1–4 equiv. of HOAc caused an increase in the cathodic current at ca. –1.8 V, characteristic of catalytic $H_2$ production.[12] The electrocatalytic properties do not, however, differ significantly from analogous $Fe_2(S_2C_3H_6)(CO)_6$. In a confirmatory experiment, a 1:1 mixture of $Fe_2(aspH)(CO)_6$ and $Fe_2(S_2C_3H_6)(CO)_6$ in acetonitrile was analyzed electrochemically. The mixture displayed reduction events at –1.20 and –1.96 V, indicating that the two compounds had overlapping reduction events. Similarly, electrochemical analyses of $Fe_2(aspH)(CO)_4(PMe_3)_2$ and HOAc or HOTs showed catalytic $H_2$ production at –1.86 or –1.21 V, respectively, typical of $Fe_2(S_2C_xH_{2x})(CO)_4(PMe_3)_2$ species.[12,13]

 © 2006 Wiley-VCH Verlag GmbH & Co. KGaA, Weinheim 

## II. Complexes with Nickel

### *Ni(aspH)(dppe)*

Treatment of $NiCl_2$(dppe) with a solution of $aspH_3$ and base yielded orange mononuclear Ni(aspH)(dppe) (Scheme 3).[14,15] The crystallographic characterization of Ni(aspH)(dppe) confirmed the expected square-planar coordination and intermolecular hydrogen bonding (Figure 4, Table 2). The six-membered chelate ring adopts a twist-boat conformation, which projects the carboxylic acid away from the metal center. Ni(aspH)(dppe) was only slightly soluble in MeOH; however, the salt resulting from treatment of Ni(aspH)(dppe) with $NEt_3$ was found to dissolve in both MeOH and $CH_2Cl_2$.

### *$[Ni_2(aspH)(dppe)_2]^{2+}$ and $Ni_3(asp)_2(dppe)_2$*

These di- and trinuclear species[16] were initially obtained as byproducts of the synthesis of Ni(aspH)(dppe). $[Ni_2(aspH)(dppe)_2]Cl_2$ (Scheme 3) was identified by ESI-MS, and its $^{31}P$ NMR spectrum displays two doublets. Isolation of the dinuclear dication was attempted by forming its $BPh_4^-$ salt. Surprisingly, the $^{31}P$ NMR spectrum displays only one, albeit broad, resonance for the inequivalent phosphane ligands. The dinuclear product was identified again by ESI-MS and a preliminary X-ray crystallographic analysis as its $BPh_4^-$ salt. The salt was unstable as a solid under $N_2$.

Upon standing, solutions of Ni(aspH)(dppe) and $[Ni_2(aspH)(dppe)_2](Cl)_2$ deposited crystals of the trinuclear spe-

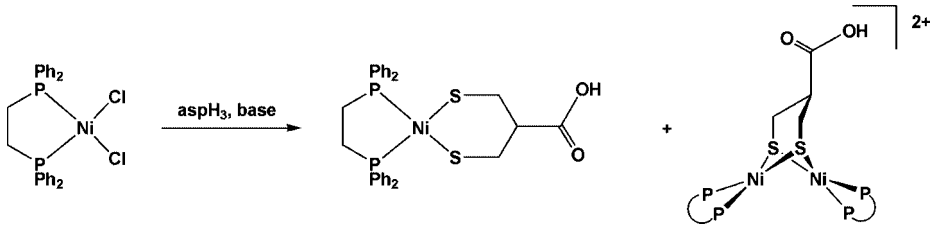


Scheme 3. Synthetic route to Ni(aspH)(dppe) and $[Ni_2(aspH)(dppe)_2]^{2+}$.

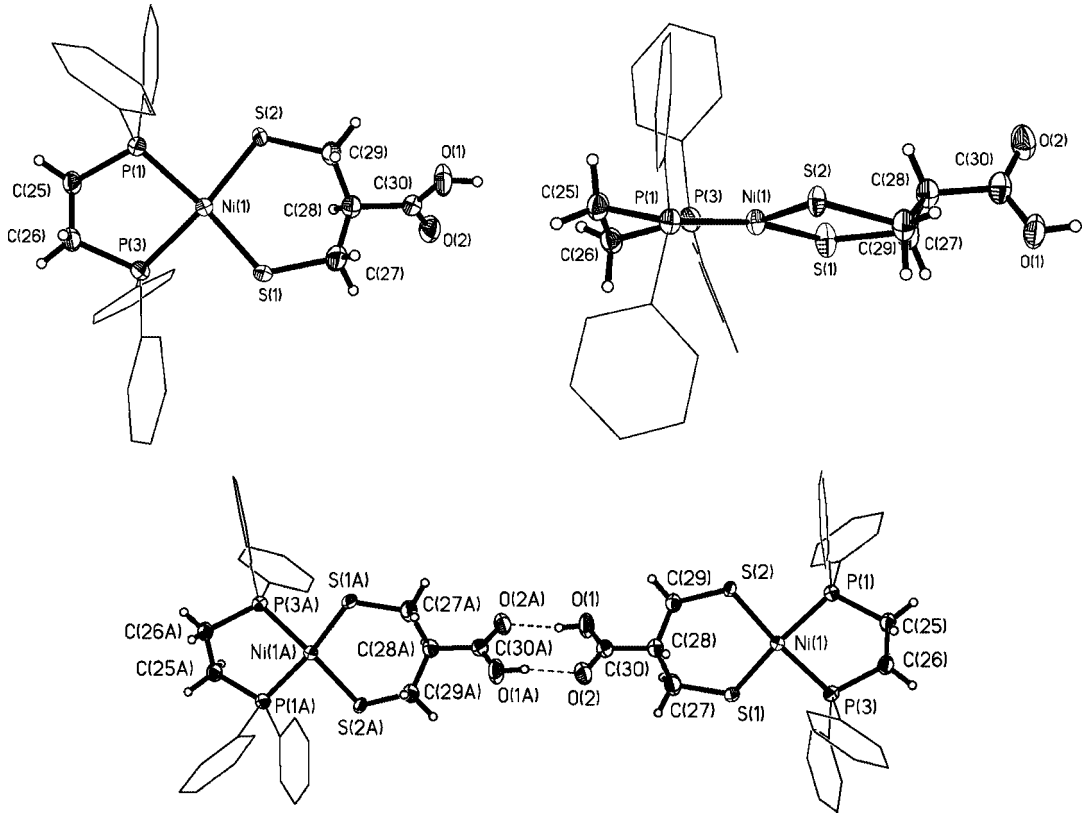


Figure 4. Top left: structure of Ni(aspH)(dppe) with thermal ellipsoids set at the 50% probability level. Top right: orthogonal view of Ni(aspH)(dppe). Bottom: structure of the hydrogen-bonded dimer of Ni(aspH)(dppe). Phenyl ellipsoids and phenyl hydrogen atoms are omitted for clarity. Selected distances [Å] and angles [°]: S(1)–Ni(1) 2.149(5), S(2)–Ni(1) 2.197(4), P(1)–Ni(1) 2.1772(6), P(3)–Ni(1) 2.1743(6); S(1)–Ni(1)–P(3) 87.76(10), S(1)–Ni(1)–P(1) 168.17(14), P(3)–Ni(1)–P(1) 86.51(2), S(1)–Ni(1)–S(2) 101.30(11), P(3)–Ni(1)–S(2) 165.84(11), P(1)–Ni(1)–S(2) 86.40(9).

 © 2006 Wiley-VCH Verlag GmbH & Co. KGaA, Weinheim 

Table 2. Selected crystallographic data for nickel-containing asparagusic complexes.

| | Ni(aspH)(dppe) | $Ni_3(asp)_2(dppe)_2$ |
|---|---|---|
| Empirical formula | $C_{30}H_{30}NiO_2P_2S_2$ | $C_{62}H_{61}NNi_3O_4P_4S_4$ |
| Formula mass | 607.31 | 1312.37 |
| $T$ [K] | 193(2) | 193(2) |
| $\lambda$ [Å] | 0.71073 | 0.71073 |
| Crystal system | monoclinic | triclinic |
| Space group | $P2_1/n$ | $P\bar{1}$ |
| $a$ [Å] | 11.242(2) | 10.6763(5) |
| $b$ [Å] | 14.418(3) | 11.3329(6) |
| $c$ [Å] | 17.256(3) | 12.3295(7) |
| $\alpha$ [°] | 90 | 76.447(3) |
| $\beta$ [°] | 92.569(3) | 85.874(2) |
| $\gamma$ [°] | 90 | 79.774(2) |
| $V$ [Å$^3$] | 2794.2(9) | 1426.49(13) |
| $Z$ | 4 | 1 |
| $\rho$ (calcd.) [g/cm$^3$] | 1.444 | 1.528 |
| $\mu$ (Mo-$K_\alpha$) [mm$^{-1}$] | 0.985 | 1.288 |
| $F$(000) | 1264 | 680 |
| Crystal size [mm] | $0.38 \times 0.33 \times 0.22$ | $0.22 \times 0.14 \times 0.09$ |
| $\theta$ range [°] | 1.84–25.34 | 1.70–30.00 |
| Reflections collected | 20742 | 44467 |
| Independent reflections | 5113 | 8302 |
| | [$R$(int) = 0.0275] | [$R$(int) = 0.0239] |
| Absorption correction | integration | integration |
| Max./min. transmission | 0.8425/0.6397 | 0.8983/0.7746 |
| Goodness-of-fit on $F^2$ | 1.044 | 1.039 |
| Final $R$ indices [$I > 2\sigma(I)$] | $R_1$ = 0.0289 | $R_1$ = 0.0255 |
| | $wR_2$ = 0.0685 | $wR_2$ = 0.0649 |
| $R$ indices (all data) | $R_1$ = 0.0366 | $R_1$ = 0.0324 |
| | $wR_2$ = 0.0715 | $wR_2$ = 0.0689 |
| Largest diff. peak/hole [e·Å$^{-3}$] | 0.277/–0.236 | 0.402/–0.307 |

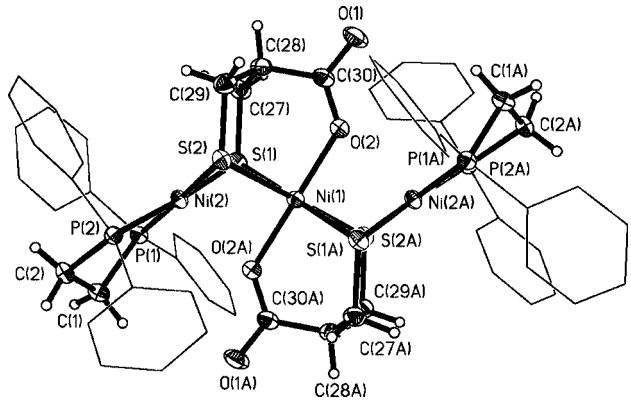


Figure 5. Structure of $Ni_3(asp)_2(dppe)_2$ with thermal ellipsoids set at the 50% probability level. The solvent molecules, phenyl ellipsoids, and phenyl hydrogen atoms are omitted for clarity. Selected distances [Å] and angles [°]: Ni(1)–O(2) 2.0172(15), Ni(1)–O(2A) 2.0172(15), Ni(1)–S(2A) 2.4424(5), Ni(1)–S(2) 2.4424(5), Ni(1)–S(1A) 2.4528(5), Ni(1)–S(1) 2.4528(5), Ni(1)–Ni(2A) 2.8423(3), Ni(2)–P(1) 2.1529(6), Ni(2)–P(2) 2.1670(6), Ni(2)–S(2) 2.2280(5), Ni(2)–S(1) 2.2350(6); O(2)–Ni(1)–O(2A) 180.0, O(2)–Ni(1)–S(2A) 89.43(5), O(2A)–Ni(1)–S(2A) 90.57(5), O(2)–Ni(1)–S(2) 90.57(5), O(2A)–Ni(1)–S(2) 89.43(5), S(2A)–Ni(1)–S(2) 180.000(19), O(2)–Ni(1)–S(1A) 87.98(4), O(2A)–Ni(1)–S(1A) 92.02(4), S(2A)–Ni(1)–S(1A) 81.724(17), S(2)–Ni(1)–S(1A) 98.276(17), O(2)–Ni(1)–S(1) 92.02(4), O(2A)–Ni(1)–S(1) 87.98(4), S(2A)–Ni(1)–S(1) 98.276(17), S(2)–Ni(1)–S(1) 81.724(17), S(1A)–Ni(1)–S(1) 180.0, O(2)–Ni(1)–Ni(2A) 58.05(4), O(2A)–Ni(1)–Ni(2A) 121.95(4), S(2A)–Ni(1)–Ni(2A) 49.158(13), S(2)–Ni(1)–Ni(2A) 130.842(13), S(1A)–Ni(1)–Ni(2A) 49.260(13), S(1)–Ni(1)–Ni(2A) 130.740(13), P(1)–Ni(2)–P(2) 87.32(2), P(1)–Ni(2)–S(2) 177.96(2), P(2)–Ni(2)–S(2) 90.71(2), P(1)–Ni(2)–S(1) 90.23(2), P(2)–Ni(2)–S(1) 175.79(2), S(2)–Ni(2)–S(1) 91.71(2), Ni(2)–S(1)–Ni(1) 74.514(11), Ni(2)–S(2)–Ni(1) 74.831(11).

cies analyzing as $Ni_3(asp)_2(dppe)_2$ (Scheme 4). The conversion was accelerated by exposure to air, and FD-MS of the resulting supernatant revealed formation of $dppeO_2$. Crystallographic analysis (Figure 5, Table 2) confirmed a trimetallic complex featuring an unusual Ni(μ-SR)$_2$Ni(μ-SR)$_2$Ni motif.[17–20] Unlike the well-precedented $L_2$Ni(μ-SR)$_2$Ni(μ-SR)$_2$NiL$_2$ motif, the central nickel atom in $Ni_3(asp)_2(dppe)_2$ is octahedral, being bound also to the two carboxylate ligands with Ni–O distances of 2.0 Å (Figure 5). The terminal nickel centers are square-planar and low-spin. The terminal Ni$^{II}$ centers are more tightly bonded to the sulfur atoms (2.22–2.23 Å), whereas the interior nickel center exhibits longer bonds to the sulfur atoms (2.44–2.45 Å), reflecting its higher coordination number. Insolubility of the crystals precluded further analysis of, and reactivity experiments on, the trinuclear species.

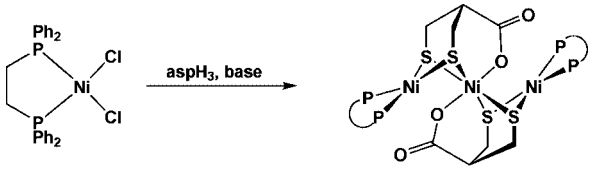


Scheme 4. Synthetic route to $Ni_3(asp)_2(dppe)_2$.

## Summary

The first transition-metal complexes bearing the chelating ligand asparagusic acid are reported. Electronically, the pendant carboxyl group does not perturb the *S*,*S* coordination to metal centers, as evidenced by IR and CV studies. The ligand enables straightforward derivatization to be performed on the pendant carboxyl group. Substitution chemistry at the metal centers is also retained, but in the case of $Fe_2(aspH)(CO)_6$ the reactions are slower than the related propanedithiolate complex. In general, the bulk of the dithiolate backbone strongly influences the rates of substitution at the underlying $Fe(CO)_3$ units. The dithiolate–carboxylate can serve as a bridging tridentate chelate by binding a pair of metal centers through *S*,*S*,*O* ligation.

Pickett, Darensbourg, and our group have demonstrated the utility of pendant coordinating groups in modeling the active site of the Fe $H_2$-ases.[21–23] Such pendant ligands, however, were always soft, being phosphanes, thioethers, or alkenes. In the case of $Fe_2(aspH)(CO)_6$ or its amides, we observed no evidence of coordination of the hard oxygen ligands to Fe$^{I}$. Furthermore, we observed no indication that the carboxylic acid or its anion usefully influence the catalytic chemistry of the related $Fe_2(aspH)(CO)_4(PMe_3)_2$ complexes. This lack of an effect is consistent with a mechanism whereby catalysis is localized on the region between the two iron centers.

 © 2006 Wiley-VCH Verlag GmbH & Co. KGaA, Weinheim 

## Experimental Section

**General:** Nylon syringe filters (0.2 μm) were acquired from Nalgene. (Benzotriazol-1-yloxy)tris(dimethylamino)phosphonium hexafluorophosphate (BOP) was acquired from ChemImpex Intl. All other chemicals were acquired from Aldrich and used without further purification. Solvents were dried by distillation or were dispensed through two 1-m columns of activated alumina. Solvents were further purified by degassing with a nitrogen purge. Reactions were performed under purified nitrogen using either standard Schlenk techniques or a glove box.

**Dihydroasparagusic Acid [3-Mercapto-2-(mercaptomethyl)propanoic Acid]:** The free ligand was prepared based on the method of Singh and Whitesides.[4] After concentrating the EtOAc extract, the dithiol was extracted into hexane and subsequent slow evaporation of solvent yielded white crystals in 54% yield based on 2-(bromomethyl)propenoic acid.

**$Fe_2(aspH)(CO)_6$:** NEt*i*Pr$_2$ (921 μL, 5.29 mmol) was added to a THF solution (20 mL) of 3-mercapto-2-(mercaptomethyl)propanoic acid (805 mg, 5.29 mmol). An additional 45 mL of THF was added followed by $Fe_3(CO)_{12}$ (2.421 g, 4.81 mmol). Gas evolution commenced immediately, and the color of the solution changed from green-black to yellow-red, concomitant with the formation of a yellow precipitate. The mixture was refluxed for 2.25 h. The resulting dark red solution was filtered in air through a pad of Celite; removal of the solvent gave a red oil. The product was extracted into MeOH, and this extract was filtered again through Celite and concentrated in vacuo. The residue was taken up in 15 mL of $CH_2Cl_2$, treated with trifluoroacetic acid (600 μL, 8.08 mmol), and chromatographed on silica gel, eluting with MeCN/$CH_2Cl_2$ (1:7, v:v). The second red band was collected and concentrated in vacuo to give a red crystalline product. Yield: 888 mg (43%). $C_{10}H_6Fe_2O_8S_2$ (429.98): calcd. C 27.93, H 1.41; found C 27.79, H 1.13. $^1$H NMR (500 MHz, $CD_3OD$): $\delta$ = 2.92 (dd, 2 H, SC*H*H), 2.16 (br., 1 H, C*H*COO), 1.81 (dd, 2 H, SCH*H*) ppm. The solid product decomposed at 118 °C. IR (MeOH): $\nu_{CO}$ = 2076 (vs), 2037 (vs), 1997 (vs), 1730 (m, monomer), 1710 (m, dimer) cm$^{-1}$. FD-MS: *m*/*z* = 429.8 [M$^+$], 373.8 [M$^+$ – 2 CO].

**Alternative Synthesis of $Fe_2(aspH)(CO)_6$:** A mixture of $Fe_3(CO)_{12}$ (5.00 g, 9.92 mmol) and 3-mercapto-2-(mercaptomethyl)propanoic acid (1.51 g, 9.92 mmol) in toluene (100 mL) was heated at 80 °C for 30 min, resulting in a red solution and a fine orange precipitate. The cooled reaction mixture was filtered through a pad of Celite, and the filtrate was concentrated to dryness. The product was extracted with MeCN and was filtered through a nylon membrane (0.2 μm). The solvent was removed to afford a red powder. Single crystals were grown by cooling a concentrated $CH_2Cl_2$ solution to –20 °C. Yield: 1.55 g (36%).

**$Fe_2[(SCH_2)_2CHC(O)NHEt](CO)_6$:** (Benzotriazol-1-yloxy)tris(dimethylamino)phosphonium hexafluorophosphate (103 mg, 0.233 mmol) was added to a solution of $Fe_2(aspH)(CO)_6$ (100 mg, 0.233 mmol) in $CHCl_3$ (5 mL) followed by $H_2$Net (17 μL, 0.2114 mmol). After stirring for 2 min, the coupling reaction was initiated upon addition of NEt*i*Pr$_2$ (55 μL, 0.317 mmol). The reaction was monitored by TLC. After 21 h, the reaction solution was concentrated in vacuo before being chromatographed on silica gel, eluting with MeOH/$CH_2Cl_2$ (5:95, v:v). The first red band was collected, and solvent removal by rotary evaporation yielded an orange powder. Single crystals were grown from a MeOH solution that was cooled to –20 °C. Yield: 30 mg (31%). $C_{12}H_{11}Fe_2NO_7S_2$ (457.05): calcd. C 31.54, H 2.43, N 3.06; found C 32.76, H 2.51, N 3.37. $^1$H NMR (400 MHz, $CDCl_3$): $\delta$ = 3.21 (dq, 2 H, NC$H_2$), 2.66 (dd, 2 H, SC$H_a$), 1.85 [m, 3 H, SC$H_b$ and $(SCH_2)_2$C*H*], 1.11 (t, 3 H, NCH$_2$C$H_3$) ppm. IR (MeOH): $\nu_{CO}$ = 2076 (vs), 2037 (vs), 1997 (vs), 1660 [m, C(O)N], 1563 (w, C–N stretch coupled to N–H deformation), 1310 (w, C–N) cm$^{-1}$. FD-MS: *m*/*z* = 456.9 (100) [M$^+$], 428.9 (23) [M$^+$ – CO], 400.8 (80%, M$^+$ – 2 CO).

**$Fe_2[(SCH_2)_2CHCONHCH_2CO_2tBu](CO)_6$:** [BOP]$PF_6$ (123 mg, 0.279 mmol) was added to a solution of $Fe_2(aspH)(CO)_6$ (120 mg, 0.279 mmol) in $CH_2Cl_2$ (5 mL) followed by the addition of Gly–*Ot*Bu·HCl (42 mg, 0.211 mmol). Addition of NEt*i*Pr$_2$ (110 μL, 0.63 mmol) and stirring for 2 h produced a clear, dark red solution. A concentrated $CH_2Cl_2$ solution was chromatographed on silica gel, eluting with MeOH/$CH_2Cl_2$ (5:95, v:v). Evaporation of solvent from the first red-orange band yielded a red-orange solid. Single crystals were grown by layering a $CH_2Cl_2$ solution of the compound with hexane followed by cooling to –20 °C. Yield: 38 mg (28%). $C_{16}H_{17}Fe_2NO_9S_2$ (543.14): calcd. C 35.38, H 3.15, N 2.58; found C 35.31, H 3.18, N 2.89. $^1$H NMR (500 MHz, $CDCl_3$): $\delta$ = 5.81 (t, 1 H, N*H*), 3.84 (d, 2 H, NC$H_2$), 2.71 (dd, 2 H, SCH*H*), 1.91 (m, 3 H, SC*H*H and C*H*CO), 1.46 [s, 9 H, C(C$H_3$)$_3$] ppm. IR (MeOH): $\nu_{CO}$ = 2075 (m), 2036 (vs), 1997 (s), 1748 [w, C(O)-OCMe$_3$], 1668 [w, NC(O), amide I]; 1558 (w, C–N and N–H, amide II) cm$^{-1}$. FD-MS: *m*/*z* = 542.9 [M$^+$], 487 [M$^+$ – 2 CO].

**Ni(aspH)(dppe):** NaOMe (2 equiv.) in MeOH (40 mL) was added to a mixture of $NiCl_2$(dppe) (835 mg, 1.58 mmol) and asp$H_3$ (240 mg, 1.58 mmol) in MeOH (40 mL). The immediately resulting dark red solution yielded a bright orange precipitate after 1 h. After 4 h, volatiles were removed in vacuo. The residue was washed with 3 × 5 mL of MeOH to remove $[Ni_2(\mu,\mu'\text{-aspH})(dppe)_2]^{2+}$ and other impurities, leaving a bright orange powder. Yield: 577 mg (60%). Single crystals were grown by layering a $CH_2Cl_2$ solution of the compound with $Et_2O$. $C_{30}H_{30}NiO_2P_2S_2$ (607.34): calcd. C 59.33, H 4.98; found C 59.06, H 4.93. $^1$H NMR (500 MHz, $CDCl_3$): $\delta$ = 10.30 (br. s, 1 H, COO*H*), 7.83–7.79 and 7.55–7.46 (m, 20 H, PC$_6H_5$), 3.10 [quint, 1 H, $(SCH_2)_2$C*H*], 2.79–2.64 (m, 4 H, SC$H_2$), 2.18 (d, 4 H, PC$H_2$) ppm. $^{31}$P NMR (202 MHz, $CDCl_3$): $\delta$ = 57.92 (s). FD-MS: *m*/*z* = 606.1 [M$^+$ – H], 398 [dppe].

**$[Ni_2(aspH)(dppe)_2](X)_2$ (X = Cl$^-$, $BPh_4^-$):** NaOMe (2 equiv.) in MeOH (5 mL) was added to a mixture of $NiCl_2$(dppe) (200 mg, 0.379 mmol) and asp$H_3$ (58 mg, 0.379 mmol) in MeOH (5 mL). The solvent was removed in vacuo from the resulting clear, dark red solution after 5.5 h. $^{31}$P NMR (202 MHz, $CD_3CN$): $\delta$ = 59.889 [s, 1 P, $NiCl_2$(dppe)], 57.738 [s, 1 P, Ni(aspH)(dppe)], 53.149 and 53.028 (d, 9 P, $[Ni_2(aspH)(dppe)_2]^{2+}$), 50.470 and 50.349 (d, 9 P, $[Ni_2(aspH)(dppe)_2]^{2+}$) ppm. ESI-MS: *m*/*z* (%) = 1099.4 (100) [{$[Ni_2(aspH)(dppe)_2]Cl$}$^+$], 1063.1 (2) $[Ni_2(asp)(dppe)_2]^+$, 532.3 (12) $[Ni_2(aspH)(dppe)_2]^{2+}$. The product was extracted into 5 mL of MeOH, filtered through a pad of Celite, and treated with a solution of $NaBPh_4$ (140 mg, 0.40791 mmol) in MeOH (3 mL). The resulting yellow-orange precipitate was washed with 15 mL MeOH and dried in vacuo. Yield: 173 mg (27%). Single crystals were grown from an acetone solution layered with methanol. $^{31}$P NMR (202 MHz, $CD_3CN$): $\delta$ = 57.46 (br. s) ppm. ESI-MS: *m*/*z* (%) = 1063.3 (10) $[Ni_2(asp)(dppe)_2]^+$, 532.0 (100) $[Ni_2(aspH)(dppe)_2]^{2+}$.

**$Ni_3(asp)_2(dppe)_2$:** A mixture of $NiCl_2$(dppe) (100 mg, 0.18939 mmol) and asp$H_3$ (28.8 mg, 0.18939 mmol) in MeCN (15 mL) in air was treated with $NEt_3$ (79.2 μL, 0.56817 mmol). Upon standing for 3 h, a crystalline black precipitate began forming. After 1 d, the supernatant was decanted. The extremely dark maroon crystalline solid was collected and dried in air. Yield: 59 mg (74%). $C_{60}H_{58}Ni_3P_4O_4S_4$ (1271.35): calcd. C 56.68, H 4.60; found C 56.41, H 4.48.

 © 2006 Wiley-VCH Verlag GmbH & Co. KGaA, Weinheim 

**Crystallography:** Data were collected at –80 °C with a Siemens Platform/CCD automated diffractometer. Data processing was performed with SAINT PLUS version 6.22. Structures were solved by direct methods and refined using full-matrix least squares on $F^2$ using Bruker SHELXTL version 6.10. Methyl, carboxyl, and amide H atom thermal parameters were assigned as 1.5× those of the adjacent atom. Remaining hydrogen atoms were fixed in idealized positions with thermal parameters 1.2× those of the attached carbon atoms. CCDC-613254 [$Fe_2$(aspH)$(CO)_6$], -613255 {$Fe_2$[$(SCH_2)_2$CHCONHEt]$(CO)_6$}, -613256 {$Fe_2$[$(SCH_2)_2$-CHCONHCH$_2$CO$_2$*t*Bu]$(CO)_6$}, -613252 [Ni(aspH)(dppe)], and -613253 [$Ni_3(asp)_2(dppe)_2$] contain the supplementary crystallographic data for this paper. These data can be obtained free of charge from The Cambridge Crystallographic Data Centre via www.ccdc.cam.ac.uk/data_request/cif.

## Acknowledgments

P. I. V. thanks Dr. Danica P. Galonic for helpful discussions. This research was supported by the National Institutes of Health.

[1] H. Yanagawa, T. Kato, Y. Kitahara, N. Takahashi, Y. Kato, *Tetrahedron Lett.* **1972**, *13*, 2549–2552.
[2] Y. Tsuneo, S. Kikuo (Sumitomo Chemical Co., Ltd., Japan), *Jpn. Kokai Tokkyo Koho* **1985**, JP60011494U.
[3] H. Yanagawa, T. Kato, H. Sagami, Y. Kitahara, *Synthesis* **1973**, 607–608.
[4] R. Singh, G. M. Whitesides, *J. Am. Chem. Soc.* **1990**, *112*, 1190–1197.
[5] Y. Nicolet, A. L. de Lacey, X. Vernède, V. M. Fernandez, E. C. Hatchikian, J. C. Fontecilla-Camps, *J. Am. Chem. Soc.* **2001**, *123*, 1596–1601.
[6] Y. Nicolet, B. J. Lemon, J. C. Fontecilla-Camps, J. W. Peters, *Trends Biochem. Sci.* **2000**, *25*, 138–143.
[7] Y. Nicolet, C. Piras, P. Legrand, C. E. Hatchikian, J. C. Fontecilla-Camps, *Structure* **1999**, *7*, 13–23.
[8] F. Gloaguen, J. D. Lawrence, T. B. Rauchfuss, *J. Am. Chem. Soc.* **2001**, *123*, 9476–9477.
[9] F. Gloaguen, J. D. Lawrence, M. Schmidt, S. R. Wilson, T. B. Rauchfuss, *J. Am. Chem. Soc.* **2001**, *123*, 12518–12527.
[10] Y. Shvo, E. Hazum, *J. Chem. Soc., Chem. Commun.* **1975**, 829–830.
[11] X. Zhao, I. P. Georgakaki, M. L. Miller, J. C. Yarbrough, M. Y. Darensbourg, *J. Am. Chem. Soc.* **2001**, *123*, 9710–9711.
[12] D. Chong, I. P. Georgakaki, R. Mejia-Rodriguez, J. Sanabria-Chinchilla, M. P. Soriaga, M. Y. Darensbourg, *Dalton Trans.* **2003**, 4158–4163.
[13] F. Gloaguen, J. D. Lawrence, T. B. Rauchfuss, M. Benard, M.-M. Rohmer, *Inorg. Chem.* **2002**, *41*, 6573–6582.
[14] T. B. Rauchfuss, D. M. Roundhill, *J. Am. Chem. Soc.* **1975**, *97*, 3386–3392.
[15] Q. Wang, A. C. Marr, A. J. Blake, C. Wilson, M. Schroeder, *Chem. Commun.* **2003**, 2776–2777.
[16] S. S. Oster, R. J. Lachicotte, W. D. Jones, *Inorg. Chim. Acta* **2002**, *330*, 118–127.
[17] P. V. Rao, S. Bhaduri, J. Jiang, D. Hong, R. H. Holm, *J. Am. Chem. Soc.* **2005**, *127*, 1933–1945.
[18] J. A. W. Verhagen, M. Beretta, A. L. Spek, E. Bouwman, *Inorg. Chim. Acta* **2004**, *357*, 2687–2693.
[19] D. M. Roundhill, *Inorg. Chem.* **1980**, *19*, 557–560.
[20] K. Issleib, D. Wienbeck, *Z. Anorg. Allg. Chem.* **1978**, *440*, 5–21.
[21] M. Razavet, S. J. Borg, S. J. George, S. P. Best, S. A. Fairhurst, C. J. Pickett, *Chem. Commun.* **2002**, 700–701.
[22] X. Zhao, Y.-M. Hsiao, C.-H. Lai, J. H. Reibenspies, M. Y. Darensbourg, *Inorg. Chem.* **2002**, *41*, 699–708.
[23] J. D. Lawrence, H. Li, T. B. Rauchfuss, *Chem. Commun.* **2001**, 1482–1483.

Received: July 6, 2006
Published Online: October 19, 2006

 © 2006 Wiley-VCH Verlag GmbH & Co. KGaA, Weinheim 

DOI: 10.1002/ejic.200600645

# Nickel Thiolate Complexes as Ligands for Copper and Zinc: Novel Additions to a Library of Binding Modes

**Johanna A. W. Verhagen,[a] Christian Tock,[a] Martin Lutz,[b] Anthony L. Spek,[b] and Elisabeth Bouwman*[a]**

**Keywords:** Nickel / Copper / Zinc / S ligands / Cluster compounds

The reactivity of the two nickel complexes [Ni(xbsms)] and [Ni(bsms)$_2$] [H$_2$xbsms = α,α′-bis(4-mercapto-3,3-dimethyl-2-thiabutyl)-*o*-xylene; Hbsms = 4-mercapto-3,3-dimethyl-1-phenyl-2-thiabutane] towards copper iodide and zinc bromide has been investigated. The reactions yield novel aggregates of higher nuclearity with topologies that are different from previous reports; the nickel complexes in all cases can be considered as didentate S ligands. The X-ray structure of the novel octanuclear cluster [{Ni(bsms)$_2$}$_3$(CuI)$_5$] shows a unique arrangement in which the *cis*-NiS$_2$S′$_2$ units act as didentate ligands to a trigonal-bipyramidal array of five Cu$^{I}$ ions. The tetranuclear structure of [{Ni(xbsms)CuI}$_2$] shows unprecedented asymmetric bridging of the thiolate sulfur atoms, with one of the thiolate groups binding to one copper ion and the other one μ$_3$-bridging to two copper ions. The complex is located on a crystallographic twofold axis and the complex in a single crystal is enantiomerically pure. The trinuclear complex [Ni$_2$(bsms)$_3$ZnBr$_3$] is formed as a result of dissociation of the didentate bsms ligand from part of the mononuclear complex and reassembly to form a dinuclear core to which the ZnBr$_3^-$ unit is coordinated to a single thiolate sulfur atom. A complex of stoichiometry [Ni$_3$(xbsms)$_2$-(ZnBr$_3$)$_2$] has also been isolated and a structure proposal based on spectroscopic properties is given. All complexes have been characterised by analytical and spectroscopic methods.
(© Wiley-VCH Verlag GmbH & Co. KGaA, 69451 Weinheim, Germany, 2006)

## Introduction

It is now generally accepted that the A-cluster of acetyl-coenzyme-A-synthase/CO-dehydrogenase (ACS/CODH) in its active state contains a dinuclear nickel site bound to an iron–sulfur cluster.[1] However, due to the earlier reports of Cu- or Zn-containing structures,[2,3] attempts to synthesise structural models of the A-cluster have resulted in reports of several new heteronuclear clusters.[4–11] In most of these investigations, discrete mononuclear nickel complexes of tetradentate N$_2$S$_2$ ligands have been used as building blocks, and their reactivity towards transition metals such as Fe, Ni, Cu, Zn, Ag, Pd and Hg have been studied. The nickel complexes can be considered to react as didentate S ligands. A wealth of structures has become available, and a range of possible bridging modes for the thiolate sulfur atoms have been reported.[7] The two *cis*-thiolate sulfur atoms in the parent nickel complex may form single bridges to two different metal ions in, for example, Ni$_3$Cu$_2$, Ni$_3$Ag$_2$ or Ni$_3$Zn$_2$ clusters[4,10,12,13] or Ni$_4$Pd$_2$ paddle wheels;[10,14] they can act as a chelating ligand to one metal ion to form discrete NiCu or NiNi dinuclear complexes[4,5,8,11] or linear trinuclear Ni$_3$ or Ni$_2$Cu complexes;[8,15] or they may bind to four different metal ions through μ$_3$-S bridges in larger Ni$_2$Cu$_4$ aggregates.[16] The nuclearity of the cluster and type of aggregate that is formed is largely dependent on the stoichiometry of the reactants and the presence or absence of coordinating anions. In all of these clusters the nickel ion in the parent complex remains divalent and low-spin in a square-planar geometry. However, when using flexible ligands that allow for different geometries, in a reaction with low-valent metal centres the nickel ion may be reduced and expelled from the ligand[17,18] or it may result in clusters in which the nickel centre is coordinated by the ligand in a tetrahedral geometry and in which additional metal–metal bonds are formed.[19,20]

Numerous Cu$^{I}$ thiolate clusters have been reported. Homoleptic Cu$^{I}$ clusters with monodentate thiolate ligands have been reported as [Cu$_4$(SR)$_4$] in a square-planar or cubane arrangement, as [Cu$_4$(SR)$_6$] in a tetrahedral or adamantane arrangement, or as clusters of varying stoichiometry such as [Cu$_5$(SR)$_6$], [Cu$_5$(SR)$_7$], [Cu$_6$(SR)$_6$], [Cu$_8$(SR)$_8$], [Cu$_8$(SR)$_{12}$] and [Cu$_{12}$(SR)$_{12}$].[21] In addition, some Cu$^{I}$ clusters containing dithiolate ligands have been reported.[22] The central cores in these homoleptic clusters are remarkably similar to the heteronuclear clusters that can be obtained with the nickel complexes, in which the [NiN$_2$S$_2$] group acts as a didentate sulfur ligand.

[a] Leiden Institute of Chemistry, Gorlaeus Laboratories, Leiden University,
P. O. Box 9502, 2300 RA Leiden, The Netherlands
Fax: +31-71-527-4550
E-mail: bouwman@chem.leidenuniv.nl
[b] Bijvoet Center for Biomolecular Research, Crystal and Structural Chemistry, Utrecht University,
Utrecht, The Netherlands

 © 2006 Wiley-VCH Verlag GmbH & Co. KGaA, Weinheim 

Earlier we have synthesised nickel complexes as models for hydrogenases by making use of various ligands containing oxygen, nitrogen and sulfur donor atoms.[23–25] The reactivity of these nickel complexes with various iron sources has resulted in novel compounds, in some cases of surprising composition.[17–19] Recently, we have reported the mononuclear complexes [Ni(bsms)$_2$] and [Ni(xbsms)] in which the nickel ion is in an $S_4$ coordination environment [$H_2$xbsms = α,α′-bis(4-mercapto-3,3-dimethyl-2-thiabutyl)-*o*-xylene; Hbsms = 4-mercapto-3,3-dimethyl-1-phenyl-2-thiabutane].[26] The reactivity of these mononuclear complexes towards nickel and iron has been studied and the trinuclear nickel complexes [$Ni_3$(bsms)$_4$]($BF_4$)$_2$ and [$Ni_3$(xbsms)$_2$]($BF_4$)$_2$ have been reported.[15,27]

The reactivity of these complexes towards copper(I) and zinc(II) salts has now been investigated, resulting in a number of novel aggregates with unprecedented structures that are described below.

## Results

### Reactivity Studies

The reactivity of the mononuclear $NiS_4$ complex [Ni(xbsms)] towards $FeCl_2$, [$Fe_2(CO)_9$] and [$Fe(CO)_2(NO)_2$] appeared to be very similar to that reported for $NiN_2S_2$ complexes,[28] with the nickel complex acting as a monodentate or didentate chelating ligand to iron. Despite the *trans* orientation of the two didentate ligands in [Ni(bsms)$_2$] a similar reactivity towards $FeCl_2$ has been observed;[15] in aggregation reactions with nickel or iron the two ligands tend to rearrange to form a nickel complex with the *cis*-dithiolate conformation required for further binding. The reactivity of the mononuclear complexes [Ni(xbsms)] and [Ni(bsms)$_2$] has now been investigated in reactions with $ZnBr_2$, $ZnCl_2$ and CuI, with acetonitrile as the solvent and in 1:1 molar ratios; interesting new products of unexpected stoichiometries have been obtained (Scheme 1). The reactivity of the complexes towards $ZnBr_2$ and $ZnCl_2$ appeared to be similar as analogous products were obtained; only the results of the reactions with $ZnBr_2$ are reported.

Reactions of the related trinuclear nickel complexes [$Ni_3$(xbsms)$_2$]($BF_4$)$_2$ and [$Ni_3$(bsms)$_4$]($BF_4$)$_2$ with either CuI or $ZnBr_2$ did not generate any new compounds of different stoichiometries. The trinuclear complexes appeared to be relatively inert, and the starting materials could be recovered from most of the reactions.

### Structures of the Complexes

#### *Structure of [{Ni(bsms)$_2$}$_3$(CuI)$_5$] (1)*

The asymmetric unit contains two independent molecules of [{Ni(bsms)$_2$}$_3$(CuI)$_5$] together with four acetone molecules and two diethyl ether molecules. The differences between the two independent molecules are very small, therefore the detailed geometry of only one of them is discussed. An ORTEP projection of the structure of [{Ni(bsms)$_2$}$_3$(CuI)$_5$] is shown in Figure 1. Another projection showing the coordination environment of the nickel and copper centres is given in Figure 2. Crystal data are given in the Experimental Section and selected bond lengths and angles are summarised in Table 1. Three square-planar nickel(II) centres, three trigonal-planar copper(I) ions and two tetrahedrally coordinated copper(I) ions constitute the octanuclear cluster. The nickel ions have an $S_2S'_2$ coordination, with the coordination environment consisting of two didentate bsms ligands that bind through the thiolate groups in the *cis* positions. The trigonal-planar copper ions have an $S_2I$ coordination environment and the tetrahedral copper ions are in an $S_3I$ coordination environment.

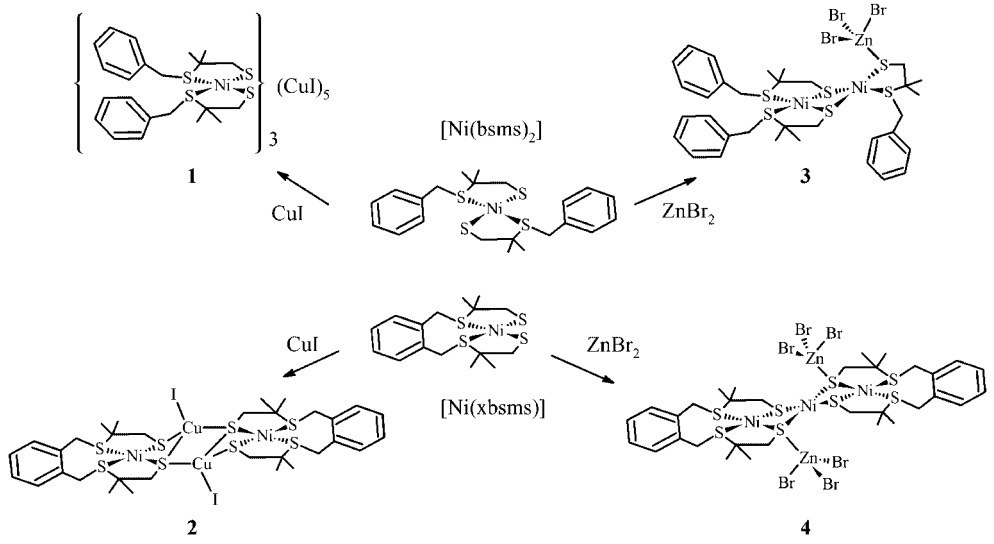


Scheme 1. Synthesis of the novel clusters.

 © 2006 Wiley-VCH Verlag GmbH & Co. KGaA, Weinheim 

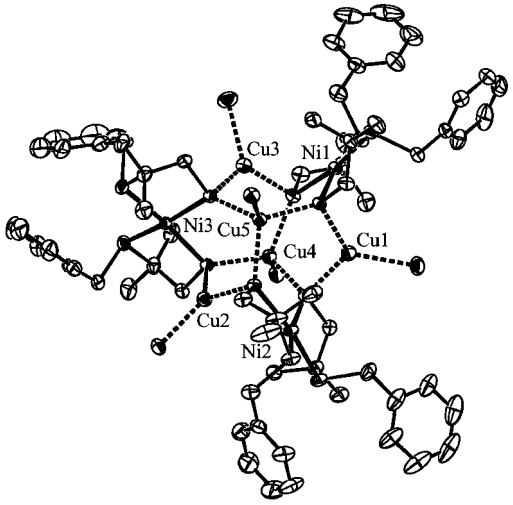


Figure 1. Displacement ellipsoid plot of one of the independent molecules of $[\{Ni(bsms)_2\}_3(CuI)_5]$ (**1**), drawn at the 50% probability level. Hydrogen atoms and the solvent molecules have been omitted and copper surroundings are indicated by dashed bonds for clarity.

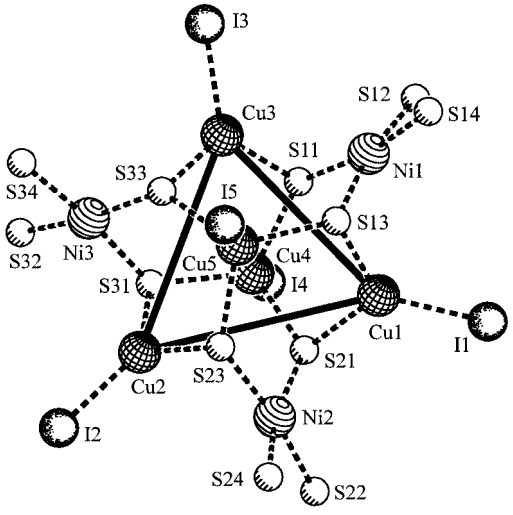


Figure 2. Projection of the central core and the coordination environment of the copper and nickel centres in **1**. View approximately along the pseudo-threefold axis of the trigonal bipyramid; the trigonal plane is indicated by solid lines.

The five copper ions are clustered in a trigonal-bipyramidal array, with the three trigonal-planar copper ions in the equatorial plane and the tetrahedral copper ions at the apices. The $NiS_2S'_2$ units are each capping two edges of the trigonal bipyramid with two $\mu_3$-bridging thiolate groups that each connect two copper ions with one nickel ion; each nickel complex thus binds to four different copper ions. Each nickel dithiolate complex bridges two equatorial copper ions to form a giant twelve-membered $Ni_3Cu_3S_6$ ring. The tetrahedral copper ions are coordinated to three thiolate groups, each from a different $NiS_2S'_2$ unit, thus capping the 12-membered crown on both sides, and as a result creating a cage. All thiolate sulfur atoms use three lone pairs in a distorted tetrahedral geometry in binding to one nickel ion and two copper ions. Finally, the coordination environment of each copper ion is completed by one iodide ion.

Table 1. Selected bond lengths [Å] and angles [°] in $[\{Ni(bsms)_2\}_3(CuI)_5]$ (**1**).

| | | | |
|---|---|---|---|
| Cu(4)···Cu(5) | 4.2012(12) | Cu(1)···Cu(4) | 3.5855(12) |
| Cu(1)···Ni(1) | 3.1381(13) | Ni(1)···Ni(2) | 6.1880(15) |
| Ni(1)–S(11) | 2.1868(17) | Ni(1)–S(12) | 2.2010(19) |
| Ni(1)–S(13) | 2.1970(18) | Ni(1)–S(14) | 2.1966(18) |
| Cu(1)–S(13) | 2.2481(18) | Cu(4)–S(11) | 2.3252(18) |
| Cu(1)–S(21) | 2.2775(18) | Cu(4)–S(21) | 2.3548(18) |
| Cu(1)–I(1) | 2.4903(10) | Cu(4)–S(31) | 2.3354(18) |
| | | Cu(4)–I(4) | 2.5801(9) |
| S(13)–Cu(1)–S(21) | 110.34(7) | S(11)–Ni(1)–S(12) | 91.64(7) |
| S(13)–Cu(1)–I(1) | 130.85(5) | S(11)–Ni(1)–S(13) | 91.15(6) |
| S(21)–Cu(1)–I(1) | 118.73(5) | S(11)–Ni(1)–S(14) | 169.77(8) |
| S(11)–Cu(4)–S(21) | 106.79(6) | S(12)–Ni(1)–S(13) | 169.19(8) |
| S(11)–Cu(4)–S(31) | 115.73(7) | S(12)–Ni(1)–S(14) | 87.84(7) |
| S(11)–Cu(4)–I(4) | 105.31(5) | S(13)–Ni(1)–S(14) | 91.25(7) |
| S(21)–Cu(4)–S(31) | 104.64(7) | Cu(1)–S(13)–Cu(5) | 112.11(7) |
| S(21)–Cu(4)–I(4) | 113.42(5) | Cu(1)–S(13)–Ni(1) | 89.81(6) |
| S(31)–Cu(4)–I(4) | 111.11(5) | Cu(5)–S(13)–Ni(1) | 129.75(8) |

The molecule lacks crystallographic symmetry elements and therefore every nickel centre and every copper centre is unique. However, the molecule contains an approximate, non-crystallographic threefold rotation axis running through the apical copper ions that makes the differences between the three nickel ions, the three equatorial copper ions $Cu_{eq}$ and the two tetrahedrally coordinated copper ions $Cu_{ap}$ very small. The nickel–thiolate distances vary from 2.082(17) to 2.1861(18) Å, and are comparable to the distances found in the starting complex $[Ni(bsms)_2]$, and the nickel–thioether distances are 2.1966(18)–2.2108(19) Å, slightly longer than those in $[Ni(bsms)_2]$.[26] The $Cu_{eq}$–thiolate distances vary from 2.2328(19) to 2.2775(18) Å, whereas the $Cu_{ap}$–thiolate distances are slightly longer and vary from 2.3204(18) to 2.3548(18) Å. The $Cu_{eq}$–iodide distances are 2.4860(10)–2.4903(10) Å and the $Cu_{ap}$–iodide distances are 2.5775(9)–2.5801(9) Å. Because of the rigid conformation of the complex the nickel centres have a tetrahedral distortion with a dihedral angle varying from 12.09(10) to 18.44(10)° between the planes S(n1)–Ni(n)–S(n2) and S(n3)–Ni(n)–S(n4). The geometry around the $Cu_{eq}$ ions deviates only slightly from planarity and the angles around the tetrahedral $Cu_{ap}$ ions are in the range 104.64(7)–115.73(7)°.

The intramolecular Cu···Cu contacts vary from 3.4668(13) to 5.3666(14) Å, with the shortest distances between the apical and equatorial copper ions. The distances between the nickel centres range from 6.0776(15) to 6.3023(14) Å.

Although the nickel(II) ions in the solid structure have a significant tetrahedral distortion, in solution the $Ni^{II}$ ions are in a low-spin state, as shown by NMR experiments. In the $^1H$ NMR spectrum of the complex in $[D_6]$DMSO only one set of relatively sharp signals is observed for the ligand, thus confirming its rather symmetrical structure in solution.

### *Structure of [{Ni(xbsms)CuI}$_2$] (2)*

A projection of the structure of $[\{Ni(xbsms)CuI\}_2]$ is shown in Figure 3. Crystal data are given in the Experimen-

 © 2006 Wiley-VCH Verlag GmbH & Co. KGaA, Weinheim 

tal Section and selected bond lengths and angles are given in Table 2. The compound crystallises in the trigonal space group $P3_221$. The disordered solvent contained in this crystal structure was modelled as diffuse electron density (see Experimental Section). One tetranuclear complex contains two nickel(II) centres in square-planar surroundings and two copper(I) ions in a tetrahedral geometry. The complex is located on an exact, crystallographic twofold rotation axis and the complex in a single crystal is enantiomerically pure, with clockwise rotation along the positive *c*-axis. Because of the symmetry the compound can be considered as being a dimer of a heterodinuclear nickel-copper complex. The nickel centres have an $S_2S'_2$ coordination sphere consisting of two thiolate sulfur atoms in enforced *cis* positions and two thioether sulfur atoms. These nickel ions are in a square-planar geometry with a small tetrahedral distortion defined by a dihedral angle of 5.44(7)° between the planes Ni(1)–S(6)–S(9) and Ni(1)–S(16)–S(19). The bonds of the thioether sulfur atoms and the thiolate sulfur atoms to Ni are slightly longer than in the parent nickel complex [Ni(xbsms)][26] but are still unexceptional. Both thiolate sulfur atoms of the $NiS_4$ unit are bound as a chelating ligand to a single copper ion with one short Cu(2)–S(6) distance of 2.3010(12) Å and one long Cu(2)–S(16) distance of 2.6229(9) Å. The latter thiolate S(16) is the one that binds to the symmetry-related copper ion Cu(2a), with a short copper–thiolate distance of 2.2929(9) Å, and is therefore $\mu_3$-bridging between both copper ions and one nickel ion. The copper centres additionally have one coordinated iodide ion and are therefore in a tetrahedral $S_3I$ coordination environment. The tetranuclear molecules are arranged in a helical motif around a $3_2$ screw axis in the crystallographic *c* direction by π–π stacking of the xbsms ligands (Figure 4). The geometric centres of the stacking phenyl rings are 3.636(3) Å apart and the phenyl rings have a dihedral angle of 2.0(3)°. Large, solvent-accessible channels are located along this $3_2$ screw axis (see Experimental Section).

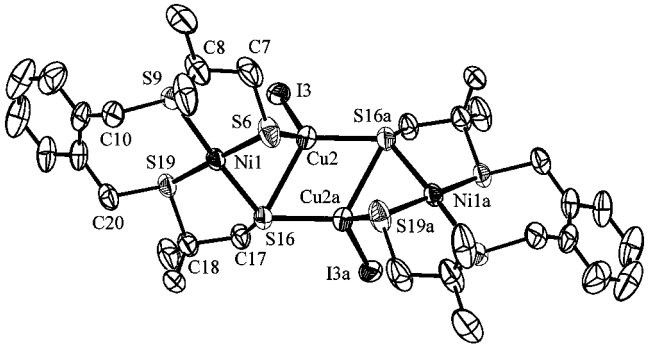


Figure 3. Displacement ellipsoid plot of [{Ni(xbsms)CuI}$_2$] (**2**), drawn at the 50% probability level. Hydrogen atoms and solvent molecules have been omitted for clarity.

The NMR spectra of **2** were obtained in $CDCl_3$ at room temperature and at 238 K. Due to the presence of the twofold rotation axis, only one set of ligand signals is expected for the tetranuclear complex. The $^1$H NMR spectrum recorded at room temperature displays signals that are broadened and only two $CH_2$ resonances can be discerned: one for the ethylene bridges and one for the xylyl-$CH_2$ groups. Furthermore, only one resonance is observed for all four methyl groups. This indicates that both sides of one ligand and both protons on a $CH_2$ group are chemically equivalent in solution on the NMR timescale at room temperature. After cooling the sample to 238 K, the spectrum is sharpened and four doublets are observed for the eight $CH_2$ protons and two singlets are observed for the four methyl groups. In addition, the protons within a $CH_2$ group show COSY and NOESY cross-peaks. This indicates that even at low temperature both sides of one ligand are still chemically equivalent: C7 and C17, C10 and C20, and C8 and C18 are mutually equivalent. So, in solution the asymmetry of the crystal structure is apparently released. Full assignment of the resonance signals could be made from the COSY and NOESY NMR spectra at 238 K. The signal of one of the benzylic protons has shifted 1.8 ppm downfield to $\delta$ = 5.6 ppm as compared to that in the parent nickel complex. This rather large shift is comparable to the shift of the signal of one benzylic proton in [Ni(xbsms)Fe(CO)$_4$].[28] From

Table 2. Selected bond lengths [Å] and angles [°] in [Ni(xbsms)-CuI]$_2$ (**2**).

| | | | |
|---|---|---|---|
| Ni(1)···Cu(2) | 2.7496(6) | Cu(2)···Cu(2)[a] | 2.5671(9) |
| Ni(1)–S(6) | 2.1956(11) | Cu(2)–S(6) | 2.3010(12) |
| Ni(1)–S(9) | 2.1936(10) | Cu(2)–S(16) | 2.6229(9) |
| Ni(1)–S(16) | 2.1983(10) | Cu(2)–I(3) | 2.5301(5) |
| Ni(1)–S(19) | 2.2024(10) | Cu(2)–S(16)[a] | 2.2929(9) |
| S(6)–Ni(1)–S(9) | 89.94(4) | S(6)–Cu(2)–S(16) | 76.12(4) |
| S(6)–Ni(1)–S(16) | 87.77(4) | S(6)–Cu(2)–I(3) | 122.38(4) |
| S(6)–Ni(1)–S(19) | 174.57(4) | S(6)–Cu(2)–S(16)[a] | 114.86(4) |
| S(9)–Ni(1)–S(16) | 176.73(4) | S(16)–Cu(2)–I(3) | 111.18(3) |
| S(9)–Ni(1)–S(19) | 92.35(4) | S(16)–Cu(2)–S(16)[a] | 117.23(3) |
| S(16)–Ni(1)–S(19) | 89.73(4) | I(3)–Cu(2)–S(16)[a] | 111.00(3) |

[a] Symmetry position: $x - y$, $-y$, $1/3 - z$.

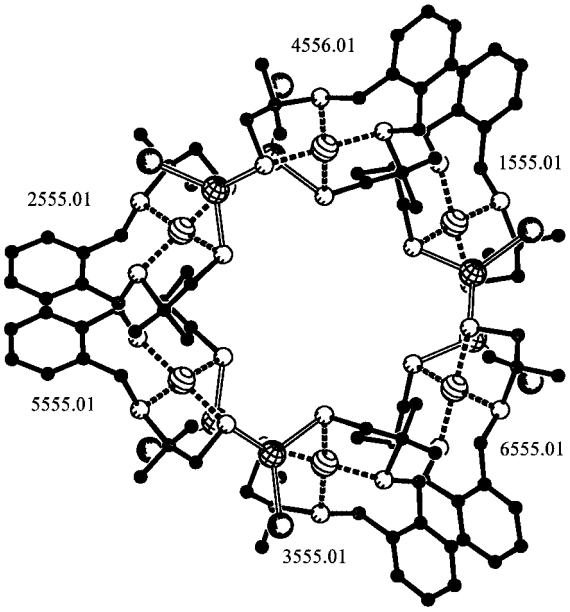


Figure 4. Stacking plot of [{Ni(xbsms)CuI}$_2$] (**2**), including the ARU numbers. View along the $3_2$ screw axis.

 © 2006 Wiley-VCH Verlag GmbH & Co. KGaA, Weinheim 

the crystal structure, however, no apparent interactions can be discerned that may be responsible for this downfield shift; the shortest Ni···benzylic-H distance is 3.27 Å, and an iodine–H interaction of 3.1 Å is present.

### *Structure of [$Ni_2(bsms)_3ZnBr_3$] (3)*

A projection of the structure of [$Ni_2(bsms)_3ZnBr_3$] is shown in Figure 5. Crystal data are given in the Experimental Section and selected bond lengths and angles in Table 3. The asymmetric unit contains the trinuclear complex [$Ni_2(bsms)_3ZnBr_3$] and two molecules of acetone. The trinuclear complex is built up from two nickel(II) centres with square-planar surroundings and a tetrahedral zinc(II) ion. Ni(1) has an $S_2S'_2$ coordination environment originating from two bsms ligands, with the two thiolate sulfur atoms in *cis* positions. The square-planar coordination of this nickel ion has a small tetrahedral distortion, with an interplanar angle of 4.7(3)°. Both thiolate sulfur atoms are bridging to the second nickel ion, Ni(2), which is in an $S_3S'$ coordination environment consisting of the already mentioned bridging thiolate sulfur atoms and an additional didentate bsms ligand. The Ni(2) ion is also in a rather perfect square-planar geometry with a small tetrahedral distortion and a dihedral angle of only 2.9(2)°. The thiolate sulfur atom of this third bsms ligand is bridging between Ni(2) and the zinc(II) ion, which has an $SBr_3$ coordination environment. The bond lengths to nickel are similar to those in the parent nickel complex [Ni(bsms)$_2$] and are unexceptional.[26]

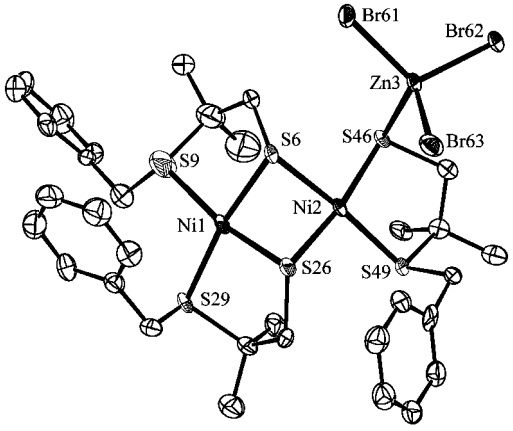


Figure 5. Displacement ellipsoid plot of [$Ni_2(bsms)_3ZnBr_3$] (**3**), drawn at the 50% probability level. Hydrogen atoms and solvent molecules are omitted for clarity.

Table 3. Selected bond lengths [Å] and angles [°] in [$Ni_2(bsms)_3ZnBr_3$] (**3**).

| | | | |
|---|---|---|---|
| Ni(1)···Ni(2) | 2.864(3) | Ni(2)···Zn(3) | 3.616(3) |
| Ni(1)–S(6) | 2.162(4) | Zn(3)–S(46) | 2.414(4) |
| Ni(1)–S(9) | 2.211(5) | Zn(3)–Br(61) | 2.379(2) |
| Ni(1)–S(26) | 2.147(4) | Zn(3)–Br(62) | 2.406(2) |
| Ni(1)–S(29) | 2.192(4) | Zn(3)–Br(63) | 2.402(2) |
| Ni(2)–S(6) | 2.211(4) | Ni(2)–S(46) | 2.175(4) |
| Ni(2)–S(26) | 2.212(4) | Ni(2)–S(49) | 2.192(4) |
| S(6)–Ni(1)–S(9) | 87.27(17) | S(26)–Ni(2)–S(46) | 170.85(16) |
| S(6)–Ni(1)–S(26) | 80.93(15) | S(26)–Ni(2)–S(49) | 97.36(16) |
| S(6)–Ni(1)–S(29) | 170.60(17) | S(46)–Ni(2)–S(49) | 91.77(15) |
| S(9)–Ni(1)–S(26) | 168.03(18) | S(46)–Zn(3)–Br(61) | 111.74(11) |
| S(9)–Ni(1)–S(29) | 101.04(17) | S(46)–Zn(3)–Br(62) | 100.99(11) |
| S(26)–Ni(1)–S(29) | 90.88(15) | S(46)–Zn(3)–Br(63) | 106.19(12) |
| S(6)–Ni(2)–S(26) | 78.45(15) | Br(61)–Zn(3)–Br(62) | 112.93(9) |
| S(6)–Ni(2)–S(46) | 92.46(16) | Br(61)–Zn(3)–Br(63) | 109.66(9) |
| S(6)–Ni(2)–S(49) | 175.01(15) | Br(62)–Zn(3)–Br(63) | 114.86(8) |

The NMR spectroscopic results confirm the diamagnetic properties of the complex, with two square-planar low-spin nickel(II) centres and a zinc(II) ion, which is retained in solution. Quite unexpectedly, only a single set of resonances is discernible for the three ligands, which makes the spectrum quite similar to the $^1$H NMR spectrum of [Ni(bsms)$_2$].

### *Structure of [$Ni_3(xbsms)_2(ZnBr_3)_2$] (4)*

A structure proposal based on elemental analysis and IR, NMR and ligand-field spectroscopy is shown in Figure 6. The structure proposal is based on the known type of trinuclear complexes of the form $[Ni_3(xbsms)_2]^{2+}$, which are composed of a zig-zag chain of three square planes similar to that reported for $[Ni_3(bsms)_4]^{2+}$.[15] This arrangement leaves space for two $ZnBr_3$ units to coordinate above and below the trinuclear complex, similar to the binding observed in [$Ni_2(bsms)_3ZnBr_3$]. The $^1$H NMR spectrum of this compound again shows only one set of sharp signals, in agreement with a symmetrical structure and square-planar surrounding for the nickel(II) ions. The coordination of the $ZnBr_3$ groups apparently has a stabilizing effect on the fluxionality of the nickel ions as no sharp NMR spectrum could be obtained for the parent trinuclear complex, even at low temperature.[27]

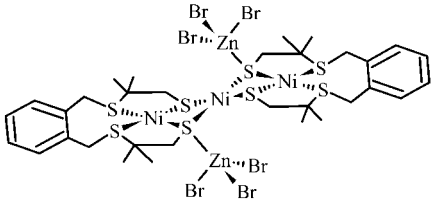


Figure 6. Proposed structure of [$Ni_3(xbsms)_2(ZnBr_3)_2$] (**4**).

## UV/Vis/NIR Spectroscopy of the Complexes

The square-planar surrounding of the nickel(II) ions in all of the mixed-metal complexes discussed above is reflected in their ligand-field spectra. The UV/Vis/NIR data are presented in Table 4. The nickel–copper complexes are black solids that yield brown solutions both in chloroform and in acetonitrile. These complexes show a very broad absorption band in the solid state with the diffuse reflectance technique. The nickel–zinc complexes are brown solids that also yield brown solutions in both chloroform and acetonitrile. [$Ni_3(xbsms)_2(ZnBr_3)_2$] (**4**) dissolves very poorly in chloroform and therefore the ligand-field data of this complex are only given for acetonitrile. For [$Ni_2(bsms)_3ZnBr_3$] (**3**), the differences in the ligand-field spectra of a solution in chloroform and a solution in acetonitrile are very small,

 © 2006 Wiley-VCH Verlag GmbH & Co. KGaA, Weinheim 

Table 4. Electronic absorption maxima for the NiCu and NiZn complexes.

| | $\tilde{\nu}$ [$10^3$ $cm^{-1}$] ($\varepsilon$ [$M^{-1}$ $cm^{-1}$]) | | |
|---|---|---|---|
| | Solid state[a] | Chloroform | Acetonitrile |
| $[\{Ni(bsms)_2\}_3(CuI)_5]$ (**1**) | 21.2 | 22.6 ($14\times10^3$) | |
| | | 28.0 ($14\times10^3$) | 26.2 (sh) |
| | | | 34.4 (sh) |
| | | 38.1 ($62\times10^3$) | 40.3 ($107\times10^3$) |
| | | | 47.6 ($255\times10^3$) |
| $[\{Ni(xbsms)CuI\}_2]$ (**2**) | | 14.5 (sh) | 14.5 (300) |
| | 21.0 | 20.6 (2400) | 21.8 (630) |
| | | 26.2 (3100) | 30.0 (sh) |
| | | 35.6 ($14\times10^3$) | 35.1 ($13\times10^3$) |
| | | | 40.3 ($20\times10^3$) |
| $[Ni_2(bsms)_3ZnBr_3]$ (**3**) | 15.1 | | 13.6 (120) |
| | 20.2 | 19.3 (sh) | 20.4 (sh) |
| | 24.1 | 25.0 (2200) | 25.8 (4500) |
| | | 34.4 (sh) | 34.4 (sh) |
| | | 36.7 ($12\times10^3$) | 37.2 ($21\times10^3$) |
| $[Ni_3(xbsms)_2(ZnBr_3)_2]$ (**4**) | 19.5 | | 19.7 (6600) |
| | 23.2 | | 23.4 ($19\times10^3$) |
| | 30.2 | | |
| | 37.5 | | 36.2 ($54\times10^3$) |

[a] Diffuse reflectance.

thus indicating that solvent coordination does not take place in this case. Coordination of acetonitrile cannot be excluded for the nickel–copper complexes $[\{Ni(xbsms)CuI\}_2]$ and $[\{Ni(bsms)_2\}_3(CuI)_5]$. The d–d transitions of the nickel centres in all complexes are at slightly lower energy and the ligand-to-metal charge-transfer transitions are at higher energy compared with the starting complexes $[Ni(bsms)_2]$ and [Ni(xbsms)] (see Table 4).[26] These changes are just the opposite to the shifts in energy in ligand field for the $[\{NiLFeX_2\}_2]$ complexes $[\{Ni(xbsms)FeCl_2\}_2]$, $[\{Ni(xbsms)FeBr_2\}_2]$ and $[\{Ni(xbsms)FeI_2\}_2]$.[28] Apparently, the somewhat softer CuI and $ZnBr_3$ units accept more electron density from the thiolate sulfur atoms.

## Discussion

The ability of $[NiN_2S_2]$ complexes to act as a ligand to other metal ions has long been recognized, but intense efforts to study the binding of mononuclear $[NiN_2S_2]$ to transition metal ions were triggered by the publication of the X-ray structure of ACS. Many examples of the versatile binding of nickel dithiolate complexes − as compared with "normal" didentate sulfur ligands − have now been reported. As the reactivity of the mononuclear $NiS_4$ complexes [Ni(xbsms)] and $[Ni(bsms)_2]$ towards iron sources is rather similar to that of $NiN_2S_2$ complexes, the unique products formed with copper and zinc salts were quite unexpected. Regarding the $NiS_4$ complexes as dithiolate ligands makes the novel octanuclear compound $[\{Ni(bsms)_2\}_3(CuI)_5]$ a $[Cu_5("S_2")_3]$ cluster. Numerous $Cu^I$ thiolate clusters have been reported; however, only two clusters have been reported with a related $Cu_5(SR)_6$ arrangement.[29] The copper centres in these complexes are also in a trigonal-bipyramidal array, each axial–equatorial edge of which is bridged by a thiolate sulfur atom. However, the copper ions do not have additional halogen ions coordinated and the Cu···Cu distances are much smaller and are more likely to indicate a metal–metal interaction.

The rearrangement of the didentate ligands in $[\{Ni(bsms)_2\}_3(CuI)_5]$ to form *cis*-planar nickel complexes would imply that a similar structure could possibly be obtained from [Ni(xbsms)]. However, the resulting complex $[\{Ni(xbsms)CuI\}_2]$ is obviously different and, as similar reaction conditions were applied in the two syntheses, the resulting dissimilar structures must be a consequence of packing effects. The reported[6,16] complex $[\{Ni(N_2S_2)\}_3(CuBr)_2]$ may be regarded as being derived from the present $Ni_3Cu_5$ complex by removal of the three equatorial CuI units. Structures have been reported of $[\{Ni(N_2S_2)\}_2Cu_2]^{2+}$, which have the same nickel/copper ratio as $[\{Ni(xbsms)CuI\}_2]$ but which do not contain coordinated halides and in which the sulfur binding is different.[5,7]

The reaction of $NiN_2S_2$ complexes with copper and zinc halides has been shown to result in similar structures in some cases,[12] although different topologies have also been reported.[7] Our new nickel–zinc complexes $[Ni_2(bsms)_3ZnBr_3]$ and $[Ni_3(xbsms)_2(ZnBr_3)_2]$ are noticeably different from these earlier reported structures, and are also quite different from each other, as a result of dissociation of the didentate bsms ligand from part of the mononuclear complex and re-assembly to form a dinuclear core similar to that of the nickel ethanedithiolate compound $[Ni_2(edt)_3]$.[30] The binding of the $ZnBr_3^-$ group to one thiolate sulfur atom is similar to the binding observed in the dinuclear complex $[Ni(N_2S_2)ZnCl_2(dmf)]$.[7] The proposed structure of the pentanuclear complex of general formula $[Ni_3(xbsms)_2(ZnBr_3)_2]$ is based on the assumption of a similar binding of the $ZnBr_3^-$ groups; binding at two sides of the trinuclear core is proposed for reasons of steric bulk and the existence of a symmetrical structure as indicated by NMR spectroscopy.

 © 2006 Wiley-VCH Verlag GmbH & Co. KGaA, Weinheim 

The structures of the products of the reactions of the mononuclear complexes [Ni(xbsms)] and [Ni(bsms)$_2$] with copper and zinc salts are remarkably different from those that have been reported earlier, and the reactivity of these products as well as that of the trinuclear nickel complexes also differ from the analogous $NiN_2S_2$ compounds. A study[6] of the reactivity of the complexes [{Ni($N_2S_2$)}$_3$($ZnCl_2$)]$^{2+}$, [{Ni($N_2S_2$)}$_3$($CuBr_2$)] and [{Ni($N_2S_2$)}$_2$Ni]$^{2+}$ towards nickel, copper and zinc salts resulted in a qualitative ranking of metal ion affinity by the nickel dithiolate ligand, i.e. $Zn^{2+} < Ni^{2+} < Cu^{+}$. With this in mind the nickel–zinc complexes [$Ni_2$(bsms)$_3$$ZnBr_3$] and [$Ni_3$(xbsms)$_2$($ZnBr_3$)$_2$] have been tested for their reactivity towards $Ni(BF_4)_2$ and CuI. Both complexes show no reactivity towards $Ni(BF_4)_2$ and only the starting complexes were recovered after 24 h. The complex [$Ni_2$(bsms)$_2$$ZnBr_3$], however, does show reactivity towards CuI; this reaction again gives the stable octanuclear cluster [{Ni(bsms)$_2$}$_3$($CuI)_5$]. The complex [$Ni_3$(xbsms)$_2$($ZnBr_3$)$_2$] does not show reactivity towards CuI, which may be related to the low solubility of this complex. The trinuclear nickel complexes appear to be comparatively inert, and from most of the reactions only the starting materials could be recovered.

## Conclusions

Four new heteronuclear aggregates of various composition have been synthesised and characterised by using the $NiS_4$ compounds [Ni(xbsms)] and [Ni(bsms)$_2$] as a ligand for copper and zinc salts. Despite the similar reactivity of these two complexes towards iron salts, the products of the reactions with CuI and $ZnBr_2$ are diverse. The novel octanuclear structure of [{Ni(bsms)$_2$}$_3$($CuI)_5$] shows a unique arrangement of copper and nickel centres, with a central trigonal-bipyramidal array of copper ions to which the three $NiS_2S'_2$ units act as capping ligands. This remarkable complex represents another important example of the structural versatility possible for the reaction products of nickel dithiolate complexes as ligands to other transition metal ions. The tetranuclear structure [{Ni(xbsms)CuI}$_2$] shows unprecedented asymmetric bridging of the thiolate sulfur atoms, with one of the thiolate groups binding to one copper ion and the other one $\mu_3$-bridging to two copper ions. The trinuclear complex [$Ni_2$(bsms)$_3$$ZnBr_3$] is formed as a result of dissociation of the didentate bsms ligand from part of the mononuclear complex and reassembly to form the dinuclear core. The *trans* binding of the didentate ligand in the starting complex [Ni(bsms)$_2$] appears not to limit its ability to bind to other transition metal ions as a chelating ligand; it does, however, result in the formation of new, unexpected aggregates. The formation of these cluster compounds as opposed to the desired dinuclear complexes emphasises the importance of the site isolation in metalloenzymes and the difficulty of controlling the product formation in vitro.

## Experimental Section

**Chemicals:** All preparations were carried out in reagent-grade solvents. All chemicals used in the syntheses were obtained from Acros or Aldrich and were used without further purification. The complexes were synthesised under argon using standard Schlenk techniques. Solvents were deoxygenated and dried with molecular sieves. The synthesis of [Ni(bsms)$_2$] and [Ni(xbsms)] has been reported earlier.[26]

**Physical Measurements:** IR spectra were recorded with a Perkin–Elmer FT-IR Paragon 1000 spectrophotometer equipped with a golden-gate ATR device, using the reflectance technique (4000–300 cm$^{-1}$; resolution 4 cm$^{-1}$). Elemental analyses were carried out with a Perkin–Elmer series II CHNS/O analyzer 2400. Metal analyses were performed with a Perkin–Elmer 3100 atomic absorption (AAS) and flame emission spectrometer using a linear calibration method. Due to the presence of variable amounts of solvent encapsulated in the complexes, some of the analytical data may be considered not satisfactory. Ligand-field spectra were obtained with a Perkin–Elmer Lambda 900 spectrophotometer. The diffuse reflectance technique, with MgO as a reference, was used for the solid compounds. Ligand-field spectra of the solutions were obtained with the solvent in the reference beam. NMR spectra were recorded with a Bruker WM 300 MHz spectrometer or a Jeol FX-200 Teqmac. $^1$H and $^{13}$C chemical shifts are quoted in ppm relative to tetramethylsilane (TMS).

**[{Ni(bsms)$_2$}$_3$($CuI)_5$] (1):** A solution of CuI (0.072 g, 0.38 mmol) in 80 mL of $CH_3CN$ was added to a solution of [Ni(bsms)$_2$] (0.18 g, 0.37 mmol) in 170 mL of $CH_3CN$, and the solution was stirred for 20 h. The solvent was then evaporated and the crude product was recrystallised from acetone/diethyl ether. Dark-red crystals suitable for X-ray diffraction were formed in a yield of 0.146 g (75%). IR: $\tilde{\nu}_{max}$ = 2960 m, 2907 m, 1495 m, 1454 m, 1386 m, 1368 m, 1256 w, 1228 w, 1199 w, 1139 m, 1083 m, 1071 m, 1028 w, 955 w, 925 w, 889 w, 772 m, 696 vs, 668 m, 476 m cm$^{-1}$. $^1$H NMR (300.13 MHz, [$D_6$]dmso, 298 K): $\delta$ = 7.31 (m, 30 H, Ph), 3.68 (s, 12 H, Ph-C$H_2$-S), 2.26 [s, 12 H, C($CH_3$)$_2$-C$H_2$-S], 1.21 (s, 36 H, C$H_3$) ppm. $C_{66}H_{90}Cu_5I_5Ni_3S_{12}$ (2396.5): calcd. C 33.08, H 3.79, Cu 13.26, Ni 7.35, S 16.05; found C 33.25, H 4.17, Cu 13.05, Ni 7.71, S 15.44.

**[{Ni(xbsms)CuI}$_2$] (2):** CuI (0.19 g, 1.0 mmol) in 80 mL of $CH_3CN$ was slowly added to a solution of [Ni(xbsms)] (0.4 g, 1.0 mmol) in 100 mL of $CH_3CN$, and the solution was stirred for 23 h. After evaporation of the solvent, the product was recrystallised from dmf/diethyl ether in a yield of 0.46 g (78%). Dark-red crystals suitable for X-ray diffraction were obtained. IR: $\tilde{\nu}_{max}$ = 2963 m, 2926 m, 1676 m, 1660 vs, 1497 m, 1454 m, 1437 m, 1382 m,1362 m, 1253 m, 1227 m, 1190 w, 1134 m, 1079 s, 956 m, 890 m, 768 s, 759 m, 743 w, 691 s, 668 s, 660 m, 606 m, 579 w, 488 m, 462 m cm$^{-1}$. $^1$H NMR (300.13 MHz, $CDCl_3$, 238 K): $\delta$ = 7.28 (m, 4 H, $C^{23}$-*H*, $C^{26}$-*H*), 7.18 (m, 4 H, $C^{24}$-*H*, $C^{25}$-*H*), 5.65 (d, $^2J$ = 12.4 Hz, 4 H, $C^{10/20}$*H*H), 3.55 (d, $^2J$ = 12.4 Hz, 4 H, $C^{10/20}$H*H*), 2.84 (d, $^2J$ = 12.9 Hz, 4 H, $C^{7/17}$H*H*), 2.45 (d, $^2J$ = 12.9 Hz, 4 H, $C^{7/17}$*H*H), 1.74 (s, 12 H, C$H_3$), 1.48 (s, 12 H, C$H'_3$) ppm; see Figure 3 for numbering scheme. $C_{32}H_{48}Cu_2I_2Ni_2S_8$ (1187.5): calcd. C 32.37, H 4.07, Cu 10.70, Ni 9.89, S 21.60; found C 33.24, H 4.45, Cu 10.55, Ni 9.86, S 18.94.

**[$Ni_2$(bsms)$_3$$ZnBr_3$] (3):** $ZnBr_2$ (0.23 g, 1.0 mmol) in 50 mL of $CH_3CN$ was added to a solution of [Ni(bsms)$_2$] (0.50 g, 1.04 mmol) in 200 mL of $CH_3CN$. The solution changed colour from light brown to dark brown and was stirred for 19 h. The solvent was evaporated and the obtained product was recrystallised from acetone/hexane. A yield of 0.48 g of red crystals suitable for X-ray diffraction was obtained (80%). IR: $\tilde{\nu}_{max}$ = 2957 w, 2920 w, 1601 w, 1495 m, 1463 m, 1455 m, 1417 m, 1385 w, 1362 m, 1264 m, 1240 m, 1221 m, 1195 m, 1141 m, 1082 m, 1070 m, 1030 w, 953 m, 879 w, 806 m, 767 s, 736 w, 699 vs, 668 w, 620 w, 585 w, 528 m, 487 s,

 © 2006 Wiley-VCH Verlag GmbH & Co. KGaA, Weinheim 

Table 5. Crystal and structure-refinement data for [{Ni(bsms)$_2$}$_3$(CuI)$_5$] (**1**), [{Ni(xbsms)CuI}$_2$] (**2**) and [Ni$_2$(bsms)$_3$ZnBr$_3$] (**3**).

| Complex | **1** | **2** | **3** |
|---|---|---|---|
| Empirical formula | $C_{66}H_{90}Cu_5I_5Ni_3S_{12}$ $(C_3H_6O)_2$ $(C_4H_{10}O)_{0.9}$ | $C_{32}H_{48}Cu_2I_2Ni_2S_8$ + disordered solvent | $C_{33}H_{45}Br_3Ni_2S_6Zn$ $(C_3H_6O)_2$ |
| Formula mass | 2579.41 | 1187.48[a] | 1172.73 |
| Crystal colour | dark red | dark red | red |
| Crystal dimensions [mm] | 0.42 × 0.27 × 0.09 | 0.15 × 0.15 × 0.42 | 0.03 × 0.42 × 0.48 |
| Crystal system | triclinic | trigonal | triclinic |
| Space group | $P\bar{1}$ (no. 2) | $P3_221$ (no. 154) | $P\bar{1}$ (no. 2) |
| $a$ [Å] | 14.5217(19) | 13.0141(1) | 10.249(3) |
| $b$ [Å] | 14.5596(6) | 13.0141(1) | 11.549(3) |
| $c$ [Å] | 46.735(4) | 26.9539(2) | 21.388(7) |
| $\alpha$ [°] | 98.451(7) | 90 | 104.28(3) |
| $\beta$ [°] | 97.003(9) | 90 | 96.52(2) |
| $\gamma$ [°] | 93.656(6) | 120 | 97.44(2) |
| $V$ [Å$^3$] | 9667.3(16) | 3953.49(5) | 2404.9(12) |
| $Z$ | 4 | 3 | 2 |
| $D_{calcd.}$ [Mg m$^{-3}$] | 1.772 | 1.496[a] | 1.620 |
| $\mu$ [mm$^{-1}$] | 3.545 | 3.006[a] | 4.054 |
| Absorption correction | analytical | multi-scan | analytical |
| Absorption correction range | 0.36–0.81 | 0.45–0.63 | 0.11–0.83 |
| $(\sin\theta/\lambda)_{max}$ [Å$^{-1}$] | 0.61 | 0.61 | 0.48 |
| No. of measured reflns | 100932 | 62695 | 19594 |
| No. of independent reflns | 34944 | 5001 | 4453 |
| $R_1$[b]/$wR_2$[c] [$I > 2\sigma(I)$] | 0.0465/0.0965 | 0.0253/0.0609 | 0.0726/0.1814 |
| $R_1$[b]/$wR_2$[c] (all refl.) | 0.0691/0.1050 | 0.0284/0.0619 | 0.0831/0.1904 |
| $S$[d] | 1.162 | 1.104 | 1.110 |
| No. of refined parameters | 1873 | 212 | 489 |
| No. of restraints | 195 | 0 | 300 |
| Flack $x$ parameter | – | 0.008(14) | – |

[a] Derived parameters do not contain the contribution of the disordered solvent. [b] $R = \Sigma(||F_o| - |F_c||)/\Sigma|F_o|$. [c] $wR_2 = \{\Sigma[w(F_o^2 - F_c^2)^2]/\Sigma[w(F_o^2)^2]\}^{1/2}$. [d] $S = \{\Sigma[w(F_o^2 - F_c^2)^2]/(n - p)\}^{1/2}$.

411 w, 328 m cm$^{-1}$. $^1$H NMR (300.13 MHz, [D$_6$]dmso, 298 K): $\delta$ = 7.49 (m, 6 H, Ph-*ortho*-H), 7.34 (m, 6 H, Ph-*meta*-H), 7.28 (m, 3 H, Ph-*para*-H), 4.04 (s, 6 H, Ph-C*H*$_2$-S), 2.25 [s, 6 H, C(CH$_3$)$_2$-C*H*$_2$-S], 1.42 (s,18 H, C*H*$_3$) ppm. $C_{33}H_{45}Br_3Ni_2S_6Zn$ (1056.6): calcd. C 37.51, H 4.29, Ni 11.11, S 18.21, Zn 6.19; found: calcd. C 37.92, H 4.41, Ni 11.61, S 17.13, Zn 6.67.

**[Ni$_3$(xbsms)$_2$(ZnBr$_3$)$_2$] (4):** ZnBr$_2$ (0.23 g, 1.0 mmol) in 50 mL of CH$_3$CN was slowly added to a solution of [Ni(xbsms)] (0.4 g, 1.0 mmol) in 100 mL of CH$_3$CN. The colour changed from dark green to dark brown and the solution was stirred for 20 h. A pale-brown product (0.415 g) was collected by filtration and recrystallised from dmf/diethyl ether. After 2 d, a brown precipitate was collected by filtration in a yield of 0.11 g (22%). IR: $\tilde{\nu}_{max}$ = 2960 m, 2925 m, 1647 vs, 1490 w, 1456 m, 1436 m, 1383 s, 1371 s, 1252 m, 1137 m, 1115 m, 1088 m, 957 w, 865 w, 774 s, 688 m, 658 m, 606 w, 492 w, 467 w cm$^{-1}$. $^1$H NMR (300.13 MHz, [D$_6$]dmso, 298 K): $\delta$ = 7.34 (m, 8 H, Ph), 4.10 (s, 8 H, Ph-C*H*$_2$-S), 2.00 [s, 8 H, C(CH$_3$)$_2$-C*H*$_2$-S], 1.65 (s, 24 H, C*H*$_3$) ppm. $C_{32}H_{48}Br_6Ni_3S_8Zn_2$ (1475.6) + DMF: calcd. C 27.15, H 3.58, N 0.90, Ni 11.37, S 16.56, Zn 8.44; found C 28.19, H 3.66, N 1.10, Ni 11.82, S 16.81, Zn 8.40.

**Crystal Structure Determinations:** X-ray intensities were measured with a Nonius KappaCCD diffractometer with rotating anode and graphite monochromator ($\lambda$ = 0.71073 Å) at a temperature of 150(2) K. Numerical data and details of the data collection and refinement are presented in Table 5. The structures were solved by direct methods (SHELXS-97[31] for compounds **1** and **3**; SIR-97[32] for compound **2**) and refined with SHELXL97 against $F^2$ of all reflections.[31] Non-hydrogen atoms were refined freely with anisotropic displacement parameters; hydrogen atoms were refined as rigid groups. Molecular illustrations, structure checking and calculations were performed with the PLATON package.[33] CCDC-612515 (**1**), -612516 (**2**), and -612517 (**3**) contain the supplementary crystallographic data for this paper. These data can be obtained free of charge from the Cambridge Crystallographic Data Centre via www.ccdc.cam.ac.uk/data_request/cif. **1:** The diethyl ether solvent molecule was refined with an occupancy of 0.9. **2:** The crystal structure contains large, solvent-accessible channels along the $3_2$ screw axis (1078.9 Å$^3$ per unit cell) filled with disordered solvent molecules. Their contribution to the structure factors was secured by back Fourier transformation using the SQUEEZE routine of the program PLATON,[33] amounting to 267 electrons in the unit cell. **3:** The crystal appeared to be non-merohedrally twinned with a 180° rotation about *uvw* = [100] as the twin operation. Additionally, there was a large anisotropic mosaicity about *hkl* = (100) present. The intensity data were evaluated with EvalCCD.[34] The twin refinement[35] resulted in a twin fraction of 0.331(3).

## Acknowledgments

These investigations were supported in part (M. L. and A. L. S.) by the Netherlands Foundation for Chemical Research, with financial aid from the Netherlands Organisation of Scientific Research (CW-NWO). C. T. (University of Strasbourg) was involved in the project through the Socrates student exchange programme. The authors thank Prof. Dr. Jan Reedijk for stimulating discussions.

[1] C. L. Drennan, T. I. Doukov, S. W. Ragsdale, *J. Biol. Inorg. Chem.* **2004**, *9*, 511–515.

[2] T. I. Doukov, T. M. Iverson, J. Seravalli, S. W. Ragsdale, C. L. Drennan, *Science* **2002**, *298*, 567–572.

 © 2006 Wiley-VCH Verlag GmbH & Co. KGaA, Weinheim 

[3] C. Darnault, A. Volbeda, E. J. Kim, P. Legrand, X. Vernede, P. A. Lindahl, J. C. Fontecilla-Camps, *Nat. Struct. Biol.* **2003**, *10*, 271–279.
[4] R. Krishnan, J. K. Voo, C. G. Riordan, L. Zahkarov, A. L. Rheingold, *J. Am. Chem. Soc.* **2003**, *125*, 4422–4423.
[5] R. C. Linck, C. W. Spahn, T. B. Rauchfuss, S. R. Wilson, *J. Am. Chem. Soc.* **2003**, *125*, 8700–8701.
[6] M. L. Golden, M. Rampersad, J. H. Reibenspies, M. Y. Darensbourg, *Chem. Commun.* **2003**, 1824–1825.
[7] P. V. Rao, S. Bhaduri, J. Jiang, R. H. Holm, *Inorg. Chem.* **2004**, *43*, 5833–5849.
[8] T. C. Harrop, M. M. Olmstead, P. K. Mascharak, *J. Am. Chem. Soc.* **2004**, *126*, 14714–14715.
[9] R. Krishnan, C. G. Riordan, *J. Am. Chem. Soc.* **2004**, *126*, 4484–4485.
[10] A. J. Amoroso, S. S. M. Chung, D. J. E. Spencer, J. P. Danks, M. W. Glenny, A. J. Blake, P. A. Cooke, C. Wilson, M. Schröder, *Chem. Commun.* **2003**, 2020–2021.
[11] Q. Wang, A. J. Blake, E. S. Davies, E. J. L. McInnes, C. Wilson, M. Schröder, *Chem. Commun.* **2003**, 3012–3013.
[12] M. L. Golden, C. M. Whaley, M. V. Rampersad, J. H. Reibenspies, R. D. Hancock, M. Y. Darensbourg, *Inorg. Chem.* **2005**, *44*, 875–883.
[13] T. Konno, M. Usami, M. Hirotsu, T. Yoshimura, T. Kawamoto, *Chem. Commun.* **2004**, 2296–2297.
[14] M. L. Golden, S. P. Jeffery, M. L. Miller, J. H. Reibenspies, M. Y. Darensbourg, *Eur. J. Inorg. Chem.* **2004**, 231–236.
[15] J. A. W. Verhagen, M. Beretta, A. L. Spek, E. Bouwman, *Inorg. Chim. Acta* **2004**, *357*, 2687–2693.
[16] M. L. Miller, S. A. Ibrahim, M. L. Golden, M. Y. Darensbourg, *Inorg. Chem.* **2003**, *42*, 2999–3007.
[17] E. Bouwman, R. K. Henderson, A. L. Spek, J. Reedijk, *Eur. J. Inorg. Chem.* **1999**, 217–219.
[18] V. E. Kaasjager, R. K. Henderson, E. Bouwman, M. Lutz, A. L. Spek, J. Reedijk, *Angew. Chem. Int. Ed.* **1998**, *37*, 1668–1670.
[19] M.-C. Chalbot, A. M. Mills, A. L. Spek, G. J. Long, E. Bouwman, *Eur. J. Inorg. Chem.* **2003**, 453–457.
[20] Q. Wang, J. E. Barclay, A. J. Blake, E. S. Davies, D. J. Evans, A. C. Marr, E. J. L. McInnes, J. McMaster, C. Wilson, M. Schröder, *Chem. Eur. J.* **2004**, *10*, 3384–3396.
[21] D. R. Winge, C. T. Dameron, G. N. George, I. J. Pickering, I. G. Dance, in *Bioinorganic Chemistry of Copper* (Eds.: K. D. Karlin, Z. Tyeklár), Chapman & Hall, New York **1993**, vol. 1, p. 110–123.
[22] M. Baumgartner, H. Schmalle, E. Dubler, *Inorg. Chim. Acta* **1993**, *208*, 135–143.
[23] V. E. Kaasjager, E. Bouwman, S. Gorter, J. Reedijk, C. A. Grapperhaus, J. H. Reibenspies, J. J. Smee, M. Y. Darensbourg, A. Derecskei-Kovacs, L. M. Thomson, *Inorg. Chem.* **2002**, *41*, 1837–1844.
[24] V. E. Kaasjager, J. van den Broeke, R. K. Henderson, W. J. J. Smeets, A. L. Spek, W. L. Driessen, E. Bouwman, J. Reedijk, *Inorg. Chim. Acta* **2001**, *316*, 99–104.
[25] V. E. Kaasjager, L. Puglisi, E. Bouwman, W. L. Driessen, J. Reedijk, *Inorg. Chim. Acta* **2000**, *310*, 183–190.
[26] J. A. W. Verhagen, D. D. Ellis, M. Lutz, A. L. Spek, E. Bouwman, *J. Chem. Soc., Dalton Trans.* **2002**, 1275–1280.
[27] J. A. W. Verhagen, Ph.D. Thesis, Leiden University, Leiden, **2004**.
[28] J. A. W. Verhagen, M. Lutz, A. L. Spek, E. Bouwman, *Eur. J. Inorg. Chem.* **2003**, 3968–3974.
[29] G. A. Bowmaker, G. R. Clark, J. K. Seadon, *Polyhedron* **1984**, *3*, 535–544.
[30] C. P. Rao, J. R. Dorfman, R. H. Holm, *Inorg. Chem.* **1986**, *25*, 428–439.
[31] G. M. Sheldrick, University of Göttingen, Germnay, **1997**.
[32] A. Altomare, M. C. Burla, M. Camalli, G. L. Cascarano, C. Giacovazzo, A. Guagliardi, A. G. G. Moliterni, G. Polidori, R. Spagna, *J. Appl. Crystallogr.* **1999**, *32*, 115–119.
[33] A. L. Spek, *J. Appl. Crystallogr.* **2003**, *36*, 7–13.
[34] A. J. M. Duisenberg, L. M. J. Kroon-Batenburg, A. M. M. Schreurs, *J. Appl. Crystallogr.* **2003**, *36*, 220–229.
[35] R. Herbst-Irmer, G. M. Sheldrick, *Acta Crystallogr., Sect. B* **1998**, *54*, 443–449.

Received: July 10, 2006
Published Online: October 10, 2006

 © 2006 Wiley-VCH Verlag GmbH & Co. KGaA, Weinheim 

DOI: 10.1002/ejic.200600673

# Dimeric Complexes of Lanthanide(III) Hexafluoroacetylacetonates with 4-Cyanopyridine *N*-Oxide: Synthesis, Crystal Structure, Magnetic and Photoluminescent Properties

**Svetlana V. Eliseeva,*[a] Mikhail Ryazanov,*[a,b] Frédéric Gumy,[c] Sergey I. Troyanov,[a] Leonid S. Lepnev,[d] Jean-Claude G. Bünzli,[c] and Natalia P. Kuzmina[a]**

**Keywords:** Lanthanides / β-Diketonates / Luminescence / Thin films / Photophysics

A series of new mixed-ligand lanthanide complexes $[Ln(hfa)_3(4\text{-cpyNO})]_2$ ($Ln = Sm^{III}$–$Ho^{III}$ and $Tm^{III}$; $hfa^-$ = hexafluoroacetylacetonate; 4-cpyNO = 4-cyanopyridine *N*-oxide) have been synthesised by treating the corresponding lanthanide hexafluoroacetylacetonates with 4-cpyNO (molar ratio 1:1) in chloroform. Single-crystal X-ray analysis revealed that $[Tb(hfa)_3(4\text{-cpyNO})]_2$ and $[Ho(hfa)_3(4\text{-cpyNO})]_2$ are isostructural and are comprised of two types of symmetrically independent dimetallic molecules. Within a dimer, the eight-fold-coordinated metal atoms are bridged by two 4-cpyNO ligands through the oxygen atoms of the *N*-oxide groups. The magnetic susceptibility data for the $Gd^{III}$ and $Tb^{III}$ complexes indicate the presence of weak antiferromagnetic interactions within the dimetallic $Ln_2O_2$ units. The thermal stability of the $[Ln(hfa)_3(4\text{-cpyNO})]_2$ adducts was studied by thermogravimetric analysis and their volatility estimated from sublimation experiments under reduced pressure. The photoluminescent properties were measured for solid samples upon excitation at 330–360 nm. The mixed-ligand complexes of $Sm^{III}$, $Eu^{III}$, $Tb^{III}$, $Dy^{III}$ and $Tm^{III}$ exhibit metal-centred luminescence in the entire visible spectral range with characteristic pink, red, green, yellow and blue emission, respectively. The introduction of ancillary 4-cpyNO molecules into the coordination sphere of the lanthanide(III) ions was found to significantly affect their luminescence quantum yields. $[Eu(hfa)_3(4\text{-cpyNO})]_2$ thin films on quartz substrates were obtained by the vacuum evaporation technique and their photoluminescent properties were found to be enhanced when compared with those of the bulk samples. This suggests that these dimers could be good candidates for the fabrication of emitting layers for light-emitting diodes.

(© Wiley-VCH Verlag GmbH & Co. KGaA, 69451 Weinheim, Germany, 2006)

## Introduction

Luminescent lanthanide complexes with organic ligands are of great interest since they can be used, for instance, as light-converting optical materials, light-emitting layers in electroluminescent (EL) devices,[1] contrast agents for magnetic resonance imaging[2] and luminescent probes in biology.[3] Such coordination compounds are chemically stable and provide a versatile tool for tuning their spectroscopic properties both by choosing the appropriate lanthanide ions as well as by changing the characteristics of the organic ligands, such as by introducing suitable substituents/atoms or conjugated π-electron fragments.[4,5]

The aim of this work is to develop and test highly luminescent lanthanide(III) complexes that can be utilized for fabricating light-emitting thin films. Lanthanide tris(β-diketonate) chelates are among the most investigated $Ln^{III}$ coordination compounds as they exhibit sharp emission bands in the visible and near-infrared spectral ranges. These compounds usually crystallise with solvent molecules, which are detrimental to their photophysical properties. To overcome the solvent-quenching problem, an additional β-diketonate ligand can be introduced to give anionic lanthanide(III) complexes, or, alternatively, neutral chromophoric ligands may be used as ancillary ligands to saturate the inner coordination sphere of the metal ion. In the latter case, the sensitisation of lanthanide luminescence can be additionally improved when the ancillary ligand possesses suitable energy levels to provide an effective intramolecular energy transfer from the ligand to the lanthanide ion.[5] For further

[a] Lomonosov Moscow State University, Department of Chemistry,
Leninskie Gory, 119992 Moscow, Russia
Fax: +7-495-939-0998
E-mail: eliseeva@inorg.chem.msu.ru
[b] Max-Planck Institut für Festkörperforschung
Heisenbergstr. 1, 70569 Stuttgart, Germany
Fax: +49-711-689-1091
E-mail: m.ryazanov@fkf.mpg.de
[c] École Polytechnique Fédérale de Lausanne (EPFL), Laboratory of Lanthanide Supramolecular Chemistry,
BCH 1405, 1015 Lausanne, Switzerland
Fax: +41-21-693-9825
E-mail: jean-claude.bunzli@epfl.ch
[d] Lebedev Physical Institute of Russian Academy of Sciences, Vavilov Luminescence Laboratory,
Leninsky Prospect 53, 119991 Moscow, Russia
Fax: +7-495-938-2251
E-mail: lepn@sci.lebedev.ru

Supporting information for this article is available on the WWW under http://www.eurjic.org or from the author.

 © 2006 Wiley-VCH Verlag GmbH & Co. KGaA, Weinheim 

potential application of luminescent complexes as emitting layers, for example in organic light-emitting diodes, it is interesting and useful to investigate their photoluminescent properties in thin films. It is well known that the luminescence of lanthanide(III) ions, especially $Eu^{III}$, is very sensitive to the local micro-environment of the ion.[6] As a consequence, the packing of the molecules in the crystal structure, the sample form (solid/powder, thin film or solution) and even the deposition method of thin films (vacuum evaporation, spin-coating, etc.) may have a significant influence on the luminescence lifetimes and quantum yields. However, only a few studies have been devoted to this question.[7]

In this paper, we report the synthesis, structural study and thermal analysis of the new mixed-ligand lanthanide(III) complexes $[Ln(hfa)_3(4\text{-cpyNO})]_2$ (Ln = $Sm^{III}$–$Ho^{III}$, $Tm^{III}$) with 4-cyanopyridine *N*-oxide as a bridging ligand to link the metal atoms into dimetallic molecular species. The luminescent and magnetic properties of these compounds were studied and the effect of introducing the ancillary 4-cpyNO ligands on their luminescence characteristics is discussed. Furthermore, in order to assess the potential of the dimeric complexes for light-emitting layers in electroluminescent devices, thin films of $[Eu(hfa)_3(4\text{-cpyNO})]_2$ were obtained by the vacuum evaporation technique and their photoluminescent properties compared with those of the bulk samples.

## Results and Discussion

### Synthesis and Characterisation

The reaction of 4-cyanopyridine *N*-oxide with an equimolar amount of $[Ln(hfa)_3(H_2O)_2]$ in chloroform yields air-stable complexes $[Ln(hfa)_3(4\text{-cpyNO})]_2$ (Ln = $Sm^{III}$–$Ho^{III}$, and $Tm^{III}$), which were isolated as colourless ($Gd^{III}$, $Tb^{III}$), pale yellow ($Sm^{III}$, $Eu^{III}$, $Ho^{III}$ and $Dy^{III}$) or pale aquamarine ($Tm^{III}$) polycrystalline precipitates by removing part of the solvent at low pressure. The formation of the mixed-ligand lanthanide adducts was confirmed by elemental analysis and IR spectroscopy. The IR spectra of all the complexes obtained are similar, exhibiting C=O and C=C absorption bands in the region 1700–1500 $cm^{-1}$ that are typical of lanthanide chelate complexes containing fluorinated β-diketonate ligands.[8] The characteristic bands due to the terminal C≡N group and pyridine *N*-oxide C–H vibrations of the 4-cpyNO ligand appear in the ranges 2300–2200 $cm^{-1}$ and 3200–3000/900–600 $cm^{-1}$, respectively. The

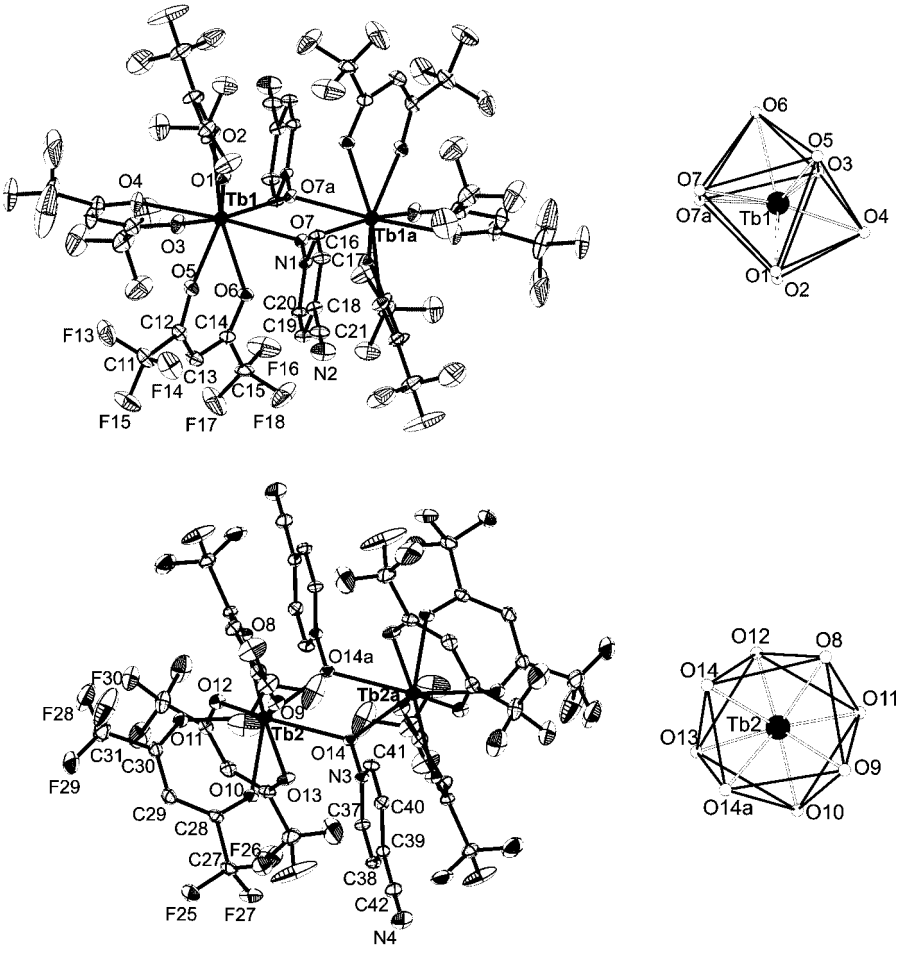


Figure 1. Molecular structures of the centrosymmetric LnL-1 and LnL-2 species in the crystal structure of $[Tb(hfa)_3(4\text{-cpyNO})]_2$ with coordination polyhedra around the metal atoms outlined (30% probability level ellipsoids). Hydrogen atoms omitted for clarity.

 © 2006 Wiley-VCH Verlag GmbH & Co. KGaA, Weinheim 

assignment of the bands at 1300–1100 $cm^{-1}$ is difficult due to overlap of the ν(N–O) and ν(C–F) vibrations. The absence of absorption between 3600 and 3200 $cm^{-1}$ implies that these compounds contain no water molecules.

### Crystal and Molecular Structures

Single crystals of $[Tb(hfa)_3(4\text{-cpyNO})]_2$ and $[Ho(hfa)_3(4\text{-cpyNO})]_2$ were obtained from chloroform, and their structures were determined by X-ray crystallography (see Experimental Section for further details). Both compounds are isostructural, crystallising in the monoclinic space group $P2_1/c$ with $Z = 4$. The crystal structure consists of two types of symmetrically independent centrosymmetric dimetallic $[Ln(hfa)_3(4\text{-cpyNO})]_2$ molecules, hereafter referred to as LnL-1 and LnL-2, which differ from each other mainly in the coordination geometry of the lanthanide atoms (vide infra). Perspective views of the molecules, with the $LnO_8$ polyhedra outlined, are given in Figure 1 for the $Tb^{III}$ derivative. Selected bond lengths and angles are summarised in Table 1. Within a dimer, the metal ions are eight-coordinated by oxygen atoms from two bridging μ-4-cpyNO ligands and from three $hfa^-$ anions, which act as didentate chelating ligands. The bridging LnOOLn(a) core is completely planar due to the presence of an inversion centre. Intramolecular Ln···Ln separations across the Ln–O–Ln(a) vary in the range 3.99–4.13 Å (Table 1). A detailed analysis of the molecular geometry[9,10] reveals that the metal atoms in LnL-1 have a distorted bicapped trigonal-prismatic (BCTP) coordination environment, whereas those in LnL-2 have square-antiprismatic (SAP) coordination (cf. Table 2). In the BCTP polyhedron, the trigonal faces are formed by atoms O1, O5, O7 and O2, O3, O7a, respectively, while the O4 and O6 atoms cap two quadrilateral faces of the trigonal prism. The dihedral angle between the trigonal planes is 18.4°. In the SAP polyhedron, the square faces are delimited by atoms O10, O11, O12, O13 and O8, O9, O14, O14a, respectively, with the dihedral angle between the corresponding planes being 2.8°. The different coordination patterns observed are likely due to steric effects. The planar 4-cpyNO units in LnL-1 are arranged nearly perpendicular relative to the bridging $Ln_2O_2$ plane ($\phi = 86.4°$), thus minimizing the steric hindrance of the β-diketonate ligands. These units become more twisted toward the $hfa^-$ ligands ($\phi = 80.7°$) in the LnL-2 molecules, leading to distortion of the oxygen atoms along a pathway from SAP to BCTP. It is interesting to note a structural difference between $[Tb(hfa)_3(4\text{-cpyNO})]_2$ and a related adduct of $Eu^{III}$ hexafluoroacetylacetonate with pyridine *N*-oxide, namely $[Eu_2(hfa)_6(pyNO)_3]$:[11] the crystal structure of the latter also contains dimetallic species, although the metal atoms are nine-coordinate and are bridged by three μ-pyNO ligands.

A regular deviation in the mean values of the Ln–O(β-diketonate) bond lengths and O–Ln–O angles is found when comparing the $Tb^{III}$ and $Ho^{III}$ structures (2.38–2.33 Å and 72.4–73.0°, respectively), consistent with a decreasing size of the metal atom. The Ln–O distances for the neutral 4-cpyNO ligands are longer than those for the anionic $hfa^-$ ligands, ranging from 2.416 to 2.435 Å ($Tb^{III}$) and from 2.372 to 2.393 Å ($Ho^{III}$).

The symmetrically independent LnL-1 and LnL-2 molecules in the crystal structure of $[Ln(hfa)_3(4\text{-cpyNO})]_2$ are interconnected by weak intermolecular CH···N hydrogen bonds (Table 1) and lone-pair–π interactions between the 4-cpyNO species to form two-dimensional molecular assemblies in the *ac* plane (Figure 2). In the $Tb^{III}$ complex, the substituted pyridine *N*-oxide fragments of LnL-1 and LnL-2 are aligned almost orthogonally to each other, with the nitrile N atoms being either involved in hydrogen bonding with the CH groups of neighbouring 4-cpyNO species [C(H)···N = 3.22 Å] or directed towards the pyridine ring of the neighbours with a distance to its centre of 3.54 Å.

Table 1. Selected bond lengths [Å] and angles [°] in the crystal structures[a] of $[Tb(hfa)_3(4\text{-cpyNO})]_2$ and $[Ho(hfa)_3(4\text{-cpyNO})]_2$.

| | $[Tb(hfa)_3(4\text{-cpyNO})]_2$ | | $[Ho(hfa)_3(4\text{-cpyNO})]_2$ | |
|---|---|---|---|---|
| | TbL-1 | TbL-2 | HoL-1 | HoL-2 |
| Ln···Ln | 4.065(3) | 4.129(3) | 3.991(5) | 4.050(5) |
| Ln–O1(O8) | 2.354(3) | 2.347(3) | 2.312(5) | 2.304(5) |
| Ln–O2(O9) | 2.348(3) | 2.365(3) | 2.306(5) | 2.325(5) |
| Ln–O3(O10) | 2.306(4) | 2.332(3) | 2.267(5) | 2.294(5) |
| Ln–O4(O11) | 2.352(4) | 2.367(4) | 2.323(6) | 2.329(5) |
| Ln–O5(O12) | 2.343(4) | 2.340(4) | 2.298(5) | 2.301(5) |
| Ln–O6(O13) | 2.442(3) | 2.399(3) | 2.418(5) | 2.353(5) |
| Ln–O7(O14) | 2.435(3) | 2.433(3) | 2.378(5) | 2.382(5) |
| Ln–O7a(O14a) | 2.416(3) | 2.429(3) | 2.372(5) | 2.393(5) |
| N1–O7 (N3–O14) | 1.357(5) | 1.365(4) | 1.348(7) | 1.348(7) |
| H17···N4[b] [CH···N] | 2.462(1) | | 2.430(1) | |
| C39···N2 | 3.248(1) | | 3.149(1) | |
| Ln–O7–Ln1a (Ln–O14–Ln1a) | 113.9(1) | 116.3(1) | 114.3(2) | 116.0(2) |
| O1–Ln–O2 (O8–Ln–O9) | 73.6(1) | 72.2(1) | 74.5(2) | 72.9(2) |
| O3–Ln–O4 (O10–Ln–O11) | 73.2(1) | 72.6(1) | 74.0(2) | 73.2(2) |
| O5–Ln–O6 (O12–Ln–O13) | 70.9(1) | 72.0(1) | 71.3(2) | 72.1(2) |
| O7–Ln–O7a (O14–Ln–O14a) | 66.1(1) | 63.7(1) | 65.7(2) | 64.0(2) |
| N1–O7–Ln (N3–O14–Ln) | 122.0(2) | 122.9(2) | 122.4(4) | 123.7(4) |
| C17–H17···N4 | 138.7(2) | | 133.7(2) | |
| C21–N2···C39 | 178.1(1) | | 178.8(2) | |

[a] Atom labels referring to the LnL-2 molecules are displayed in round prentheses. [b] Code of symmetry operations: $1 - x$, $1 - y$, $-z$.

Table 2. Observed and ideal dihedral angles for eight-coordinate complexes.

| Polyhedral complexes | Angles [°] |
|---|---|
| Ideal dodecahedron | 29.5, 29.5, 29.5, 29.5 |
| Ideal square antiprism | 0, 0, 52.4, 52.4 |
| Ideal bicapped trigonal prism | 0, 21.8, 48.2, 48.2 |
| $[Tb(hfa)_3(4\text{-cpyNO})]_2$ | |
| TbL-1 | 2.4, 16.0, 43.3, 47.2 |
| TbL-2 | 1.2, 6.0, 46.9, 50.6 |
| $[Ho(hfa)_3(4\text{-cpyNO})]_2$ | |
| HoL-1 | 3.1, 16.4, 42.3, 47.2 |
| HoL-2 | 1.4, 4.7, 47.4, 51.0 |

 © 2006 Wiley-VCH Verlag GmbH & Co. KGaA, Weinheim 

The latter suggests interactions between nitrogen lone pairs and the π-electrons of the pyridine system. The CN groups are located substantially off the ring's centre axis so that the angle, $\alpha$, between the line pointing towards the centre of the pyridine ring and its face amounts to about 66° (see Figure 2). According to ab initio studies on the interaction of water with hexafluorobenzene,[12] a similar off-axis geometry is also favourable for this system and is likely to result from optimisation of the electrostatic interactions.

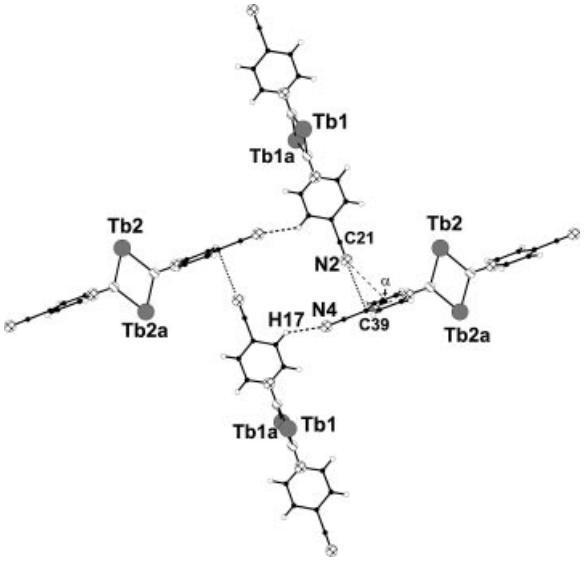


Figure 2. Packing of 4-cpyNO entities in the crystal structure of $[Tb(hfa)_3(4\text{-cpyNO})]_2$.

## Magnetic Properties

The short metal–metal distances (3.99–4.13 Å) within the $[Ln(hfa)_3(4\text{-cpyNO})]_2$ complexes make these compounds interesting for a study of the magnetic exchange interactions between the paramagnetic centres. We have recently reported the magnetic properties of a related dimeric manganese(II) complex, $[Mn(hfa)_2(4\text{-cpyNO})]_2$, which exhibits weak ferromagnetic coupling at low temperatures.[13] Here, temperature-dependent studies of the magnetic susceptibility ($\chi_m$) are presented for the gadolinium(III) and terbium(III) complexes. The former compound was found to be isostructural with the $Tb^{III}$ derivative, as evidenced by X-ray powder diffraction experiments.

The temperature dependence of the $\chi_m T$ product for $[Gd(hfa)_3(4\text{-cpyNO})]_2$ combined with a plot of $\chi_m^{-1}$ vs. $T$ is shown in Figure 3. At room temperature, the $\chi_m T$ value is about 15.7 $cm^3 mol^{-1} K$, close to that expected for two non-interacting $Gd^{III}$ ions (15.75 $cm^3 mol^{-1} K$). Upon cooling, it remains almost constant until 70 K. At lower temperatures, $\chi_m T$ passes through a small maximum at 40 K before decreasing to a value of 14.96 $cm^3 mol^{-1} K$ at 2 K. This characteristic drop in $\chi_m T$ is indicative of weak antiferromagnetic $Gd^{III}$–$Gd^{III}$ interactions within the dimeric molecules. A quantitative analysis of the magnetic data has been carried out using Equation (1) derived from the isotropic spin Hamiltonian $H = -JS_{Gd1} \cdot S_{Gd2}$, where $J$ is the exchange coupling parameter and $S_{Gd1}$ and $S_{Gd2}$ are the spin operators associated with the interacting spin centres ($S_{Gd1} = S_{Gd2} = 7/2$).

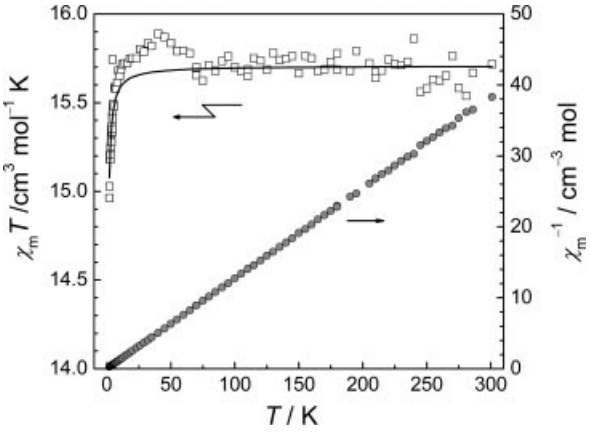


Figure 3. Temperature dependence of $\chi_m T$ (open squares) and $\chi_m^{-1}$ (filled circles) for $[Gd(hfa)_3(4\text{-cpyNO})]_2$; the solid line represents the best-fit calculated values.

$$\chi_m T = \frac{2Ng^2\mu_B^2}{k} \frac{140+91e^{7x}+55e^{13x}+30e^{18x}+14e^{22x}+5e^{25x}+e^{27x}}{15+13e^{7x}+11e^{13x}+9e^{18x}+7e^{22x}+5e^{25x}+3e^{27x}+e^{28x}}, x = -J/kT \quad (1)$$

Least-squares fitting of the experimental data with Equation (1) leads to the following parameters: $J$ = –0.010(1) $cm^{-1}$ and $g$ = 1.99. The good agreement between the observed and calculated values is reflected by a small value of the $R$ factor ($R = 2.7 \times 10^{-5}$), defined as $\Sigma[(\chi_m T)_{calc} - (\chi_m T)_{obs}]^2/\Sigma[(\chi_m T)_{obs}]^2$. The weak antiferromagnetic coupling between the $Gd^{III}$ ions in $[Gd(hfa)_3(4\text{-cpyNO})]_2$ is further evidenced by the $\chi_m^{-1}(T)$ data, which obey a Curie–Weiss law in the whole temperature range studied (Figure 3), thereby yielding an effective magnetic moment, $\mu_{eff}$, of 15.80(1) $\mu_B$ (per formula unit) and a negative Curie–Weiss temperature, $\theta$, of –0.3(1) K.

For $[Tb(hfa)_3(4\text{-cpyNO})]_2$, the room-temperature $\chi_m T$ value of 23.3 $cm^3 mol^{-1} K$ remains almost unchanged in the 70–300 K region, and compares very well with the expected value for two magnetically isolated $Tb^{III}$ ions (23.6 $cm^3 mol^{-1} K$). Upon decreasing the temperature below about 70 K, the $\chi_m T$ vs. $T$ curve begins to decrease abruptly, and exhibits a change in slope at 40 K. The dramatic drop of $\chi_m T$ from 23.3 to 11.54 $cm^3 mol^{-1} K$ at 2 K is mainly due to the crystal-field splitting of the $Tb^{III}$ ground state because of strong spin-orbit coupling, and could be indicative of a weak intramolecular antiferromagnetic coupling between the metal ions at low temperatures. The high-temperature data ($T > 100$ K) can be fitted to the Curie–Weiss law to yield an effective magnetic moment and a negative Curie–Weiss parameter of 19.3 $\mu_B$ per formula unit and –2(1) K, respectively.

 © 2006 Wiley-VCH Verlag GmbH & Co. KGaA, Weinheim 

### Thermal Analyses and Vacuum Sublimation

The thermogravimetric analysis of $[Ln(hfa)_3(4\text{-cpyNO})]_2$ revealed a similar thermal behaviour for all the compounds studied. Figure 4 illustrates the weight loss for the $Gd^{III}$ derivative. A single-step weight loss occurs in the range 190–280 °C, indicating that the lanthanide hexafluoroacetylacetonate adducts with 4-cyanopyridine *N*-oxide are thermally stable up to 190 °C. The total weight loss (ca. 92%) is much higher than that calculated for thermal decomposition of the complex into non-volatile gadolinium(III) oxyfluoride (ca. 79%) or $Gd_2O_3$ (ca. 80%), thus indicating partial sublimation of the sample under atmospheric pressure.

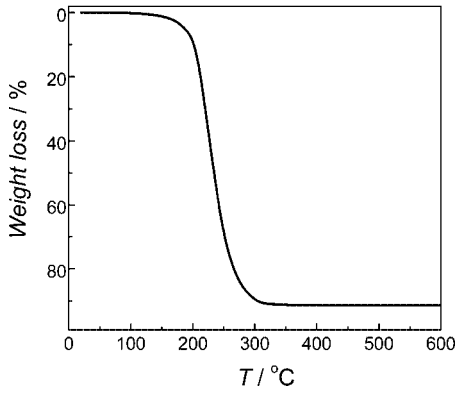


Figure 4. Thermogravimetric analysis under nitrogen for $[Gd(hfa)_3(4\text{-cpyNO})]_2$.

The vacuum sublimation experiments conducted at low pressure ($10^{-2}$ Torr) showed that all samples are quantitatively sublimed intact at 200–220 °C according to the elemental analysis and mass spectrometric studies.[14] This allowed us to obtain good-quality thin films of the $[Eu(hfa)_3(4\text{-cpyNO})]_2$ dimer (thickness 414 ± 1 nm) by vacuum evaporation at a pressure of $10^{-6}$ Torr.

### Photophysical Properties

The luminescence of lanthanide complexes upon excitation into the ligand absorption band arises from f–f transitions from the radiative level of $Ln^{III}$ to their lower-lying states. It should be emphasised that transitions between the f-states are formally parity-forbidden (Laporte's rule), which, in turn, results in long radiative lifetimes (up to the millisecond timescale) and line-like emission bands.[15,16] The excited levels of $Ln^{III}$ ions are usually populated as a result of energy transfer from the triplet level of the organic ligand, which is formed by rapid intersystem crossing. The excited level of the lanthanide(III) ion is further deactivated either radiatively with emission of light or non-radiatively by energy degradation to the vibrations of surrounding molecular groups. So, the intensity of lanthanide luminescence is determined by the ratio of the rates of radiative and non-radiative processes at all stages of the energy transfer.[17] While the emission colour and the shape of luminescence spectrum mainly depend on the electronic nature of the lanthanide ion, the energy of the triplet states of coordinated ligands plays an important role in the efficiency of the energy transfer: they should lie close to the resonant levels of the lanthanide ion but sufficiently high to prevent back energy-transfer.[18] Quenching mechanisms induced by the presence of solvent molecules in the first coordination sphere or by ligand-to-metal charge transfer (LMCT) states can also strongly influence the lanthanide luminescence.[17,19] Thus, in order to investigate the energy matching between the triplet state of the ligand and the luminescent level of the corresponding lanthanide ion, we recorded the phosphorescence spectra of solid samples of $[Gd(NO_3)_3(4\text{-cpyNO})]$, $[Gd(hfa)_3(H_2O)_2]$ and the mixed-ligand complex $[Gd(hfa)_3(4\text{-cpyNO})]_2$ at 77 K. The phosphorescence spectra of $[Gd(hfa)_3(H_2O)_2]$ and $[Gd(NO_3)_3(4\text{-cpyNO})]$ present broad bands with maxima at around 468 (21370) and 525 nm (19048 $cm^{-1}$), respectively (Figure 5). A small feature at 480 nm (20830 $cm^{-1}$) is also observed for the latter compound. The energies of zero-phonon transition of the triplet $^3\pi\pi^*$ states of the hexafluoroacetylacetonate and 4-cyanopyridine *N*-oxide ligands were thus estimated to be at around 21930 (456) and 20830 $cm^{-1}$ (480 nm), respectively. The phosphorescence spectrum of $[Gd(hfa)_3(4\text{-cpyNO})]_2$ exhibits a broad band characterised by two maxima of almost equal intensity at about 460 (21740) and 485 nm (20620 $cm^{-1}$), with a shoulder at about 515 nm (19420 $cm^{-1}$), i.e., it resembles the superposition of the phosphorescence spectra of the organic ligands (Figure 5). Therefore, in the mixed-ligand dimetallic complexes $[Ln(hfa)_3(4\text{-cpyNO})]_2$, the energy transfer originates from both $hfa^-$ and 4-cpyNO ligands. Figure 6 displays the energy diagram of the ligand triplet states and selected electronic levels of the lanthanide ions; the corresponding calculated energy gaps are listed in Table 3. According to empirical rules proposed for an optimal ligand-to-metal energy transfer $-2500 < \Delta E(^3\pi\pi^* - {}^5D_0) < 3500$ $cm^{-1}$ for $Eu^{III}$

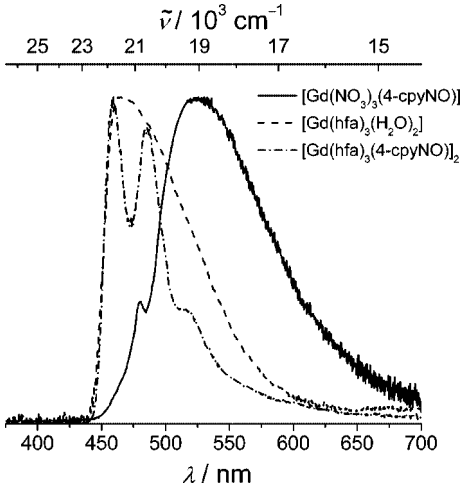


Figure 5. Phosphorescence spectra of $[Gd(NO_3)_3(4\text{-cpyNO})]$, $[Gd(hfa)_3(H_2O)_2]$ and $[Gd(hfa)_3(4\text{-cpyNO})]_2$ under excitation at 337 nm; $T$ = 77 K.

 © 2006 Wiley-VCH Verlag GmbH & Co. KGaA, Weinheim 

Table 3. Energy gaps [$cm^{-1}$] between the triplet states of hexafluoroacetylacetonate ($^3\pi\pi^*_{hfa}$) or 4-cyanopyridine *N*-oxide ($^3\pi\pi^*_{4\text{-cpyNO}}$) and the $^4G_{5/2}$(Sm), $^5D_0$(Eu), $^5D_4$(Tb), $^4F_{9/2}$(Dy), $^1G_4$(Tm) luminescent levels of lanthanide(III) ions.

| Triplet state | $\Delta E(^3\pi\pi^*–^4G_{5/2})$ | $\Delta E(^3\pi\pi^*–^5D_0)$ | $\Delta E(^3\pi\pi^*–^5D_4)$ | $\Delta E(^3\pi\pi^*–^4F_{9/2})$ | $\Delta E(^3\pi\pi^*–^1G_4)$ |
|---|---|---|---|---|---|
| $^3\pi\pi^*_{hfa}$ | 4030 | 4630 | 1430 | 930 | 530 |
| $^3\pi\pi^*_{4\text{-cpyNO}}$ | 2930 | 3530 | 330 | –170 | –570 |

ions and $2500 < \Delta E(^3\pi\pi^* - {}^5D_4) < 4000\ cm^{-1}$ for $Tb^{III}$ ions[20] – both the $hfa^-$ and 4-cpyNO ligands are best suited for the sensitisation of europium(III) and possibly samarium(III) luminescence. For the other Ln ions under investigation, the triplet states of the organic ligands are very close in energy to the lanthanide luminescent levels or even below, thus increasing the probability of back energy-transfer processes.

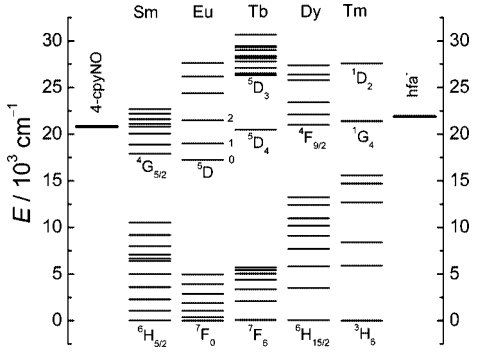


Figure 6. Energy diagram of the triplet states of the organic ligands and some energy levels of the lanthanide ions. The main luminescent and fundamental levels of the Ln ions are labelled.

To determine the influence of the substitution of water molecules by 4-cyanopyridine *N*-oxide on the photophysical properties, we compared the characteristics of solid samples of the parent $[Ln(hfa)_3(H_2O)_2]$ complexes with those of the mixed-ligand adducts $[Ln(hfa)_3(4\text{-cpyNO})]_2$.

The excitation spectra of $[Tb(hfa)_3(H_2O)_2]$ and $[Tb(hfa)_3(4\text{-cpyNO})]_2$ are very similar in shape (Figure 7) and exhibit broad bands up to 460 nm (21740 $cm^{-1}$), with two maxima at around 270 (37040) and 350 nm (28570 $cm^{-1}$) and two shoulders at 400 (25000) and 435 nm (22989 $cm^{-1}$), respectively. The excitation spectra of the europium(III) complexes are quite different from those of the terbium(III) derivatives and from each other (Figure 7). The excitation spectrum of $[Eu(hfa)_3(H_2O)_2]$ features a broad band ranging up to 400 nm (25000 $cm^{-1}$) with a maximum at around 300 nm (33333 $cm^{-1}$) and two weak shoulders at 330 (30303) and 360 nm (27778 $cm^{-1}$). In the excitation spectrum of $[Eu(hfa)_3(4\text{-cpyNO})]_2$, the intensity of the shoulders at 330 and 360 nm is larger, and they merge into a broad band extending up to 440 nm (22727 $cm^{-1}$) with a maximum at 275 nm (36363 $cm^{-1}$). Moreover, all of the excitation spectra display the characteristic bands of the metal-centred transitions at 377 and 486 nm for $Tb^{III}$, assigned to $^5D_3 \leftarrow {}^7F_6$ and $^5D_4 \leftarrow {}^7F_6$ transitions, and at 464 and 534 nm for $Eu^{III}$, corresponding to $^5D_2 \leftarrow {}^7F_0$ and $^5D_1 \leftarrow {}^7F_0$ transitions, respectively. However, the intensities of the f–f transitions are much weaker than the excitation bands of the organic ligands, thus indicating a good sensitisation of the metal-centred luminescence in these complexes through the ligand levels. As a result, under ligand excitation the $Tb^{III}$ and $Eu^{III}$ complexes $[Ln(hfa)_3(H_2O)_2]$ and $[Ln(hfa)_3(4\text{-cpyNO})]_2$ show bright green and red luminescence due to the $^5D_4 \rightarrow {}^7F_J$ ($J$ = 6–0) and $^5D_0 \rightarrow {}^7F_J$ ($J$ = 0–4) transitions,

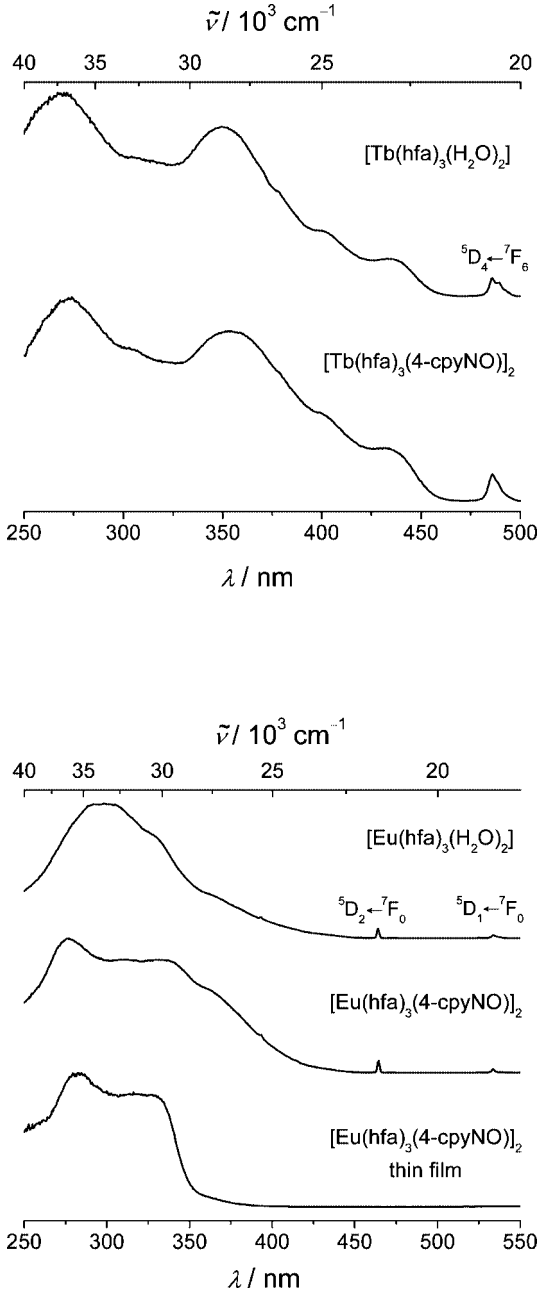


Figure 7. Excitation spectra of $[Ln(hfa)_3(H_2O)_2]$ and mixed-ligand $[Ln(hfa)_3(4\text{-cpyNO})]_2$ complexes (Ln = $Eu^{III}$, $Tb^{III}$) at 295 K.

 © 2006 Wiley-VCH Verlag GmbH & Co. KGaA, Weinheim 

respectively (Figure 8). No broad-band emission is observed from the triplet states of the organic ligands, thus reflecting an efficient ligand-to-metal energy transfer. The integral intensities of the $^5D_0 \rightarrow {}^7F_J$ ($J$ = 0–4, $Eu^{III}$) and $^5D_4 \rightarrow {}^7F_J$ ($J$ = 6–0, $Tb^{III}$) transitions are compared in Table 4. The emission spectra and relative integral intensities of the $Tb^{III}$ complexes are essentially identical, in agreement with the fact that the terbium(III) emission bands are less sensitive to changes in the first coordination sphere of the metal centre than those of europium(III). For the $Eu^{III}$ derivatives, the intensity of the hypersensitive $^5D_0 \rightarrow {}^7F_{2,4}$ transitions is larger for $[Eu(hfa)_3(4\text{-cpyNO})]_2$ than for $[Eu(hfa)_3(H_2O)_2]$ (Figure 8), and this is also true for the other transitions, thus implying that the introduction of the ancillary ligand increases the nephelauxetic effect. Further, the emission spectra of both complexes show only one peak for the $^5D_0 \rightarrow {}^7F_0$ transition, which points to approximately the same chemical environment around the europium(III) ions. The substitution of water molecules by 4-cyanopyridine *N*-oxide leads to an approximately threefold increase in the lifetime of the Eu ($^5D_0$) level (Table 5). This can be explained by elimination of the non-radiative deactivation pathway through O–H vibrations, as reported previously for many hydrated lanthanide(III) β-diketonates.[5] The improvement in the luminescent properties upon introduction of 4-cpyNO is further substantiated by the determination of the absolute quantum yields ($Q^L_{Ln}$) for solid samples of the $Eu^{III}$ and $Tb^{III}$ complexes (cf. Table 5). The greatest effect is observed for $Eu^{III}$ compounds, with an approximately tenfold enhancement in $Q^L_{Ln}$, while the quantum yield of the corresponding $Tb^{III}$ dimer increases only by a factor of 2. This result is in agreement with the evaluated energy gaps between the luminescent levels of $Eu^{III}$ and $Tb^{III}$ ions and the triplet state of 4-cpyNO (vide supra, Table 3).

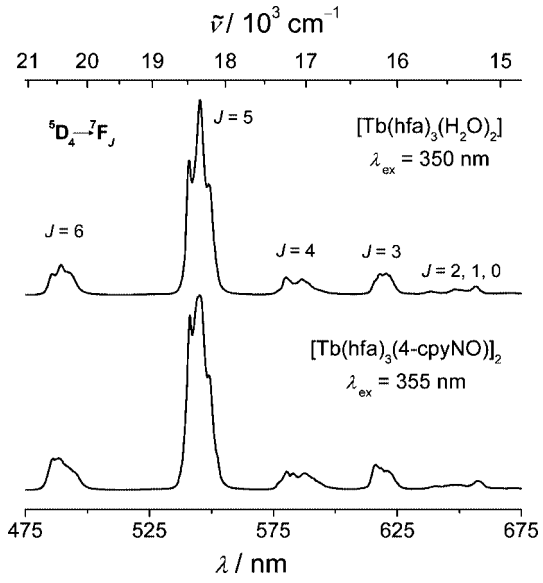


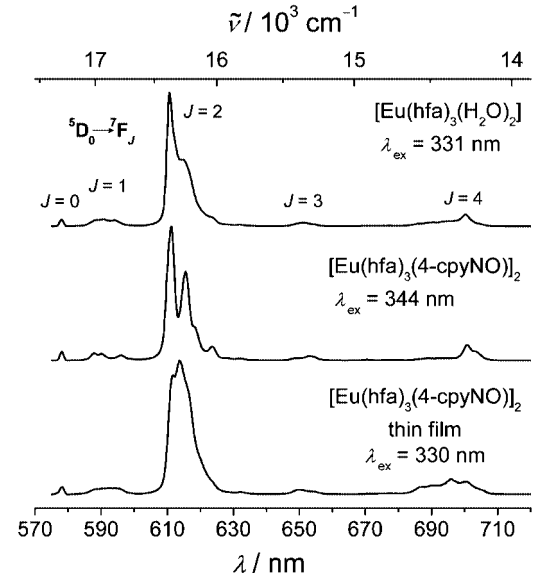


Figure 8. Emission spectra of $[Ln(hfa)_3(H_2O)_2]$ and mixed-ligand $[Ln(hfa)_3(4\text{-cpyNO})]_2$ complexes (Ln = $Eu^{III}$, $Tb^{III}$) under ligand excitation at 295 K.

Table 4. Integral intensities of the $^5D_0 \rightarrow {}^7F_J$ and $^5D_4 \rightarrow {}^7F_J$ transitions for the $Eu^{III}$ and $Tb^{III}$ complexes at 295 K relative to the $^5D_0 \rightarrow {}^7F_1$ and $^5D_4 \rightarrow {}^7F_5$ transitions, respectively.

| | $\int_{0-0}$ | $\int_{0-1}$ | $\int_{0-2}$ | $\int_{0-3}$ | $\int_{0-4}$ |
|---|---|---|---|---|---|
| $[Eu(hfa)_3(H_2O)_2]$ | 0.17 | 1.00 | 14.30 | 0.38 | 1.72 |
| $[Eu(hfa)_3(4\text{-cpyNO})]_2$ | 0.24 | 1.00 | 17.00 | 0.54 | 2.16 |
| $[Eu(hfa)_3(4\text{-cpyNO})]_2$, thin film | 0.23 | 1.00 | 17.95 | 0.42 | 2.42 |
| | $\int_{4-6}$ | $\int_{4-5}$ | $\int_{4-4}$ | $\int_{4-3}$ | $\int_{4-2,1,0}$ |
| $[Tb(hfa)_3(H_2O)_2]$ | 0.22 | 1.00 | 0.11 | 0.08 | 0.04 |
| $[Tb(hfa)_3(4\text{-cpyNO})]_2$ | 0.23 | 1.00 | 0.11 | 0.08 | 0.04 |

For lanthanide(III) complexes, the efficiency of the overall ligand-to-metal energy transfer ($\eta_{sens}$) can be estimated from Equation (2),[21] where $Q^L_{Ln}$ is the overall quantum yield upon ligand excitation, $\eta_{et}$ is the efficiency of the $^3\pi\pi^*$–Ln energy transfer, $\eta_{isc}$ is the efficiency of the intersystem crossing, $Q^{Ln}_{Ln}$ is the intrinsic quantum yield upon direct excitation of the lanthanide(III) ion, $\tau_{obs}$ is the observed lifetime and $\tau_{rad}$ is the radiative lifetime (i.e. the lifetime in the absence of any non-radiative process).

As the intensity of the purely magnetic dipole transition ($^5D_0 \rightarrow {}^7F_1$) for europium(III) is independent of the chemical environment around the metal ion, the intrinsic quantum yield may be estimated from Equation (3),[21] where $A_{MD,0}$ = 14.65 $s^{-1}$ is the spontaneous emission probability of the magnetic dipole $^5D_0 \rightarrow {}^7F_1$ transition, $n$ is the refractive index, $I_{tot}$ is the integrated emission of the $^5D_0 \rightarrow {}^7F_J$ ($J$ = 0–4) transitions and $I_{MD}$ is the integrated emission of the $^5D_0 \rightarrow {}^7F_1$ transition.

From the data obtained (Table 5), it can be concluded that the substitution of water molecules by 4-cpyNO leads to a 3.4-fold increase in the intrinsic quantum yield (from

 © 2006 Wiley-VCH Verlag GmbH & Co. KGaA, Weinheim 

Table 5. Observed and radiative luminescence lifetimes, intrinsic and absolute (±10%) quantum yields, and sensitisation efficiency of $[Ln(hfa)_3(H_2O)_2]$ and $[Ln(hfa)_3(4\text{-cpyNO})]_2$ (Ln = $Eu^{III}$, $Tb^{III}$) at 295 K.[a]

| Compound | $\tilde{\nu}/\lambda_{em}$ [$cm^{-1}$/nm] | $\tau_{obs}$ [ms] | $\tau_{rad}$ [ms] | $Q^{Eu}_{Eu}$ [%] | $Q^{L}_{Ln}$ [%] | $\eta_{sens}$ [%] |
|---|---|---|---|---|---|---|
| $[Eu(hfa)_3(H_2O)_2]$ | 16375/610.7 | 0.22 ± 0.01 | 1.13 | 19 | 2.6 | 13 ± 2 |
| $[Eu(hfa)_3(4\text{-cpyNO})]_2$ | 16359/611.3 | 0.61 ± 0.01 | 0.95 | 65 | 25.7 | 40 ± 6 |
| $[Eu(hfa)_3(4\text{-cpyNO})]_2$, thin film | 16359/611.3 | 0.74 ± 0.03 | 0.90 | 82 | [b] | 31 ± 5[c] |
| $[Tb(hfa)_3(H_2O)_2]$ | 18349/544.0 | 0.53 ± 0.04[d] | [b] | [b] | 26.7 | [b] |
| $[Tb(hfa)_3(4\text{-cpyNO})]_2$ | 18349/544.0 | 0.44 ± 0.05[d] | [b] | [b] | 49.3 | [b] |

[a] $\tau_{rad}$, $Q^{Eu}_{Eu}$ and $\eta_{sens}$ were calculated under the assumption that refractive indices are the same for thin film and solid samples, and equal to 1.5109 for $[Eu(hfa)_3(4\text{-cpyNO})]_2$ and 1.51 for $[Eu(hfa)_3(H_2O)_2]$. [b] Not determined. [c] Calculated under the assumption that the overall quantum yield is the same as for the solid sample. [d] $\tau_{obs}$ is almost the same upon excitation of either ligand or terbium(III) levels.

$$Q^{L}_{Ln} = \eta_{sens} Q^{Ln}_{Ln} = \eta_{et}\eta_{isc} Q^{Ln}_{Ln} = \eta_{et}\eta_{isc} \cdot \frac{\tau_{obs}}{\tau_{rad}}, \quad (2)$$

$$Q^{Eu}_{Eu} = \tau_{obs} A_{MD,0} n^3 \cdot \frac{I_{tot}}{I_{MD}}, \quad (3)$$

19 to 65%) and to a 3.1-fold enhancement (from 13 to 40%) of $\eta_{sens}$, respectively. Thus, the ancillary ligand significantly contributes to the overall sensitisation process of the $Eu^{III}$ complexes and, additionally, removes part of the quenching processes. In the case of the $Tb^{III}$ compounds, the lifetimes measured upon excitation of either the ligand or the $Tb^{III}$ ion are almost the same, within experimental errors, the lifetime of the mixed-ligand $[Tb(hfa)_3(4\text{-cpyNO})]_2$ dimer being only slightly shorter than that of the parent $[Tb(hfa)_3(H_2O)_2]$ (Table 5). This can be traced back to a larger energy gap displayed by this ion, which means that the contribution of the water molecules to the non-radiative de-excitation processes is smaller than for europium(III).[20,22] Additionally, a lower energy of the triplet state in the mixed-ligand complex relative to the luminescent $Tb^{III}$ levels (Table 3) allows a more efficient back-transfer process, which means that the improvement found in the quantum yield upon binding the ancillary ligand for this ion is entirely due to better sensitisation efficiency.

In the excitation spectrum of a thin film of $[Eu(hfa)_3(4\text{-cpyNO})]_2$, the shoulder feature at 360 nm (27778 $cm^{-1}$) disappears when compared with the bulk sample (cf. Figure 6), thereby displaying a better correspondence with the reflectance/absorption spectra. This can be explained by the very strong absorption up to 330 nm in the bulk $[Eu(hfa)_3(4\text{-cpyNO})]_2$, which leads to absorption of the incident light only by the near-surface region of the sample while excitation higher than 330 nm will be absorbed throughout the bulk sample. The photoluminescence spectra of the thin film are very similar to those of the bulk sample (cf. Figure 8). On the other hand, the integral intensity of the hypersensitive $^5D_0 \rightarrow {}^7F_{2,4}$ transitions (cf. Table 4) is larger for the thin film than for the bulk sample and this is also the case for the observed luminescence lifetimes and evaluated intrinsic quantum yields (cf. Table 5). These results can be attributed to the higher order of packing of the $[Eu(hfa)_3(4\text{-cpyNO})]_2$ dimers in the thin film than in the bulk solid sample, which, in turn, results in a decrease in the energy transfer rate constants and in a longer luminescence lifetime.

The effect of the mixed-ligand complex formation with 4-cyanopyridine *N*-oxide on the luminescent properties has also been studied for the $Sm^{III}$, $Dy^{III}$ and $Tm^{III}$ hexafluoroacetylacetonates. The excitation of both $[Ln(hfa)_3(H_2O)_2]$ and $[Ln(hfa)_3(4\text{-cpyNO})]_2$ (Ln = $Sm^{III}$, $Dy^{III}$, $Tm^{III}$) into the ligand-centred band (337 nm) results in characteristic line-like emissions of the corresponding lanthanide ion (Figure 9 and Figures S2 and S3 in the Supporting Information). The luminescence spectra of $[Ln(hfa)_3(H_2O)_2]$ and $[Ln(hfa)_3(4\text{-cpyNO})]_2$ for a given lanthanide ion display the same features. It should be noted that no emission from the lowest triplet state of the ligands has been observed, which reflects the existence of a $^3\pi\pi^*$–Ln energy transfer. The samarium(III) and dysprosium(III) complexes exhibit pink and yellow emission due to $^4G_{5/2} \rightarrow {}^6H_J$ ($J$ = 5/2, 7/2, 9/2, 11/2) and $^4F_{9/2} \rightarrow {}^6H_J$ ($J$ = 13/2, 11/2, 9/2) transitions, with the most intense bands centred at 647 ($^4G_{5/2} \rightarrow {}^6H_{9/2}$) and 573 nm ($^4F_{9/2} \rightarrow {}^6H_{11/2}$), respectively. The excitation spectra of $[Ln(hfa)_3(H_2O)_2]$ and $[Ln(hfa)_3(4\text{-cpyNO})]_2$ (Ln = $Sm^{III}$ and $Dy^{III}$) are very similar in shape (Figure S1 in the Supporting Information) and present two broad bands around 270 (37000) and 350 nm (28500 $cm^{-1}$), respectively, which match the corresponding features in the reflectance spectra (see Figure S4 in the Supporting Information). This confirms that the energy transfer takes place from the organic ligands to the lanthanide ions. The excitation spectra also display features corresponding to the metal-centred transitions at around 363 ($^4D_{3/2} \leftarrow {}^6H_{5/2}$), 377 ($^6P_{7/2} \leftarrow {}^6H_{5/2}$), 405 ($^6P_{3/2} \leftarrow {}^6H_{5/2}$) and 420 nm ($^6P_{5/2}$, $^4P_{5/2} \leftarrow {}^6H_{5/2}$) for $Sm^{III}$, and around 365 ($^4M_{9/2} \leftarrow {}^6H_{15/2}$), 389 ($^4F_{7/2} \leftarrow {}^6H_{15/2}$), 434 ($^4G_{11/2} \leftarrow {}^6H_{15/2}$), 454 ($^4I_{15/2} \leftarrow {}^6H_{15/2}$) and 474 nm ($^4F_{9/2} \leftarrow {}^6H_{15/2}$) for the $Dy^{III}$ derivative. The $[Tm(hfa)_3(H_2O)_2]$ and $[Tm(hfa)_3(4\text{-cpyNO})]_2$ samples were found to be luminescent only at 77 K. Excitation in the ligand absorption band (337 nm) results in blue luminescence with a maximum at 480 nm, which can be assigned to the $^1G_4 \rightarrow {}^3H_6$ transition. The substitution of water molecules in $[Ln(hfa)_3(H_2O)_2]$ (Ln = $Sm^{III}$, $Dy^{III}$, $Tm^{III}$) by 4-cyanopyridine *N*-oxide leads to a decrease of both the luminescence intensity and quantum yields. When compared with the

 © 2006 Wiley-VCH Verlag GmbH & Co. KGaA, Weinheim 

parent hydrated compounds, the relative quantum yields, $Q_{rel}^{Ln,L}$, of the mixed-ligand $Sm^{III}$ and $Dy^{III}$ complexes are $0.55 \pm 0.06$ and $0.50 \pm 0.05$, respectively. The most drastic decrease occurs for the $Tm^{III}$ adduct, leading to a $Q_{rel}^{Ln,L}$ value of $0.19 \pm 0.02$. This is probably due to multi-phonon deactivation of the excited states for the respective lanthanide ions by the N–O vibrations of 4-cyanopyridine *N*-oxide. The efficacy of this quenching process is inversely proportional to the energy gap between the emitting state and the ground state manifold: the larger the energy gap, the lower the non-radiative rate constant will be as the number of phonons necessary to bridge the gap increases in this case.[22] So, this quenching is more significant for $Sm^{III}$, $Dy^{III}$ and $Tm^{III}$ than for $Eu^{III}$ or $Tb^{III}$ because the energy gaps between the luminescent state and ground-state manifold are not large for the former (7400 for $Sm^{III}$, 7850 for $Dy^{III}$ and 5800 $cm^{-1}$ for $Tm^{III}$) when compared with the values for $Eu^{III}$ or $Tb^{III}$ (12300 and 14800 $cm^{-1}$, respectively). Although the main vibrations of the N–O bonds in 4-cpyNO are not too energetic (around 1280 $cm^{-1}$), they contribute substantially to the quenching process: approximately 6, 6, and 4–5 phonons are required to bridge the energy gap of $Sm^{III}$, $Dy^{III}$ and $Tm^{III}$, respectively. Moreover, in the mixed-ligand $Dy^{III}$ and $Tm^{III}$ complexes, poor luminescence sensitisation may be caused by poorly matched energy gaps between the triplet state of the ancillary ligand and the luminescent levels of these ions (Table 3).

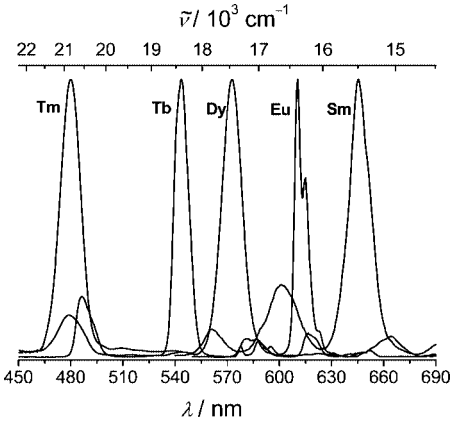


Figure 9. Emission spectra of mixed-ligand dimeric complexes $[Ln(hfa)_3(4\text{-cpyNO})]_2$ (Ln = $Tm^{III}$, $Tb^{III}$, $Dy^{III}$, $Eu^{III}$, $Sm^{III}$) under ligand excitation (see also Figure S3).

## Conclusions

The reaction of lanthanide hexafluoroacetylacetonates $[Ln(hfa)_3(H_2O)_2]$ (Ln = $Sm^{III}$–$Ho^{III}$, and $Tm^{III}$) with 4-cyanopyridine *N*-oxide in a 1:1 ratio results in the formation of $[Ln(hfa)_3(4\text{-cpyNO})]_2$ dimers in which the two metal ions are separated by about 3.99–4.13 Å. The magnetic studies reveal weak antiferromagnetic exchange interactions between neighbouring metal centres within the dimeric $[Gd(hfa)_3(4\text{-cpyNO})]_2$ units. The substitution of water molecules in the parent hydrated complexes $[Ln(hfa)_3(H_2O)_2]$ by 4-cpyNO has a large effect on the luminescence properties. Such a combination of organic ligands is able to sensitize the metal-centred luminescence of $Sm^{III}$, $Eu^{III}$, $Tb^{III}$, $Dy^{III}$ and $Tm^{III}$ ions that emit pink, red, green, yellow and blue light, respectively, i.e. within the entire spectral visible range. The introduction of the ancillary ligand leads to substantial and varying changes in the luminescence quantum yields. The greatest effect occurs for $[Eu(hfa)_3(4\text{-cpyNO})]_2$, with a tenfold increase in the absolute quantum yield (from 2.6 to 25.7%) with respect to the hydrated complex. On the other hand, a decrease in the quantum yield is observed for $Sm^{III}$, $Dy^{III}$ and $Tm^{III}$ dimers with respect to the hydrated chelates. The $[Ln(hfa)_3(4\text{-cpyNO})]_2$ dimers are thermally stable up to 190 °C and can be quantitatively sublimed at 200 °C under reduced pressure ($10^{-2}$ Torr), thus opening the way to the production of luminescent thin films, as demonstrated here with $Eu^{III}$. Both the luminescence lifetime and intrinsic quantum yield of $Eu^{III}$ are higher in thin films than in the solid sample, while the sensitisation efficacy remains approximately the same. In conclusion, high volatility, good thermal stability and efficient luminescent properties make the mixed-ligand $[Ln(hfa)_3(4\text{-cpyNO})]_2$ complexes, especially the $Eu^{III}$ and $Tb^{III}$ derivatives, good candidates for emitting layers in light-emitting diodes.

## Experimental Section

**Reagents and Physical Methods:** The commercially available starting reagents Hhfa (Merck) and 4-cyanopyridine *N*-oxide (Aldrich) were of analytical grade and used as received. Lanthanide nitrate hydrates $Ln(NO_3)_3 \cdot xH_2O$ were obtained by treating the respective lanthanide oxides $Ln_2O_3$ (99.998%) with concentrated nitric acid, followed by evaporation of the excess acid. For the synthesis of $[Ln(hfa)_3(H_2O)_2]$ (Ln = $Sm^{III}$–$Ho^{III}$, and $Tm^{III}$) the procedure described in ref.[23] was used. Elemental analysis (C, H, N) was performed by the Microanalytical Service of the Centre for Drug Chemistry (Moscow, Russia). The lanthanide content was determined by titrimetric analysis.[24] IR spectra were recorded in Nujol mull or hexachlorobutadiene between KBr plates in the range 4000–400 $cm^{-1}$ using a Perkin–Elmer 1600 FT-IR spectrometer. Thermogravimetric analyses were performed with a Q-1500 thermal analyzer under nitrogen, at a heating rate of 10 °C $min^{-1}$. Isothermal dynamic sublimation experiments were run with samples (ca. 100 mg) placed into glass test tubes at 20–220 °C and a pressure of $10^{-2}$ Torr for periods of about 30 min. Weight loss was essentially 100%. The homogeneous sublimate was collected in the cold part of the tube and analysed.

**Syntheses:** All lanthanide(III) hexafluoroacetylacetonate adducts $[Ln(hfa)_3(4\text{-cpyNO})]_2$ (Ln = $Sm^{III}$–$Ho^{III}$, $Tm^{III}$) were synthesised in a similar way. A typical preparation procedure is as follows: 4-Cyanopyridine *N*-oxide (60 mg, 0.5 mmol) was added to a solution of $[Ln(hfa)_3(H_2O)_2]$ (0.5 mmol) in chloroform (20 mL). The resulting mixture was then stirred at room temperature for 1 h. Further evaporation of the solvent under low pressure yielded a colourless ($Gd^{III}$, $Tb^{III}$), pale yellow ($Sm^{III}$, $Eu^{III}$, $Ho^{III}$ and $Dy^{III}$) or pale aquamarine ($Tm^{III}$) polycrystalline precipitate, which was filtered off and dried in air. Yield: 80–90%.

$C_{42}H_{14}F_{36}N_4O_{14}Sm_2$ (1783.3): calcd. C 28.25, H 0.78, N 3.14, Sm 16.8; found C 28.0, H 0.8, N 3.2, Sm 16.7. IR: $\tilde{\nu}$ = 3140 m, 3106 m,

 © 2006 Wiley-VCH Verlag GmbH & Co. KGaA, Weinheim 

3076 m, 2262 w, 1650 vs, 1612 m, 1560 s, 1534 s, 1490 s, 1394 w, 1350 m, 1324 m, 1258 br. s, 1210 br. s, 1144 br. s, 1098 s, 950 w, 852 s, 802 s, 772 w, 740 s, 724 s, 660 s, 586 s, 558 m, 528 w, 488 w, 456 br. w $cm^{-1}$.

$C_{42}H_{14}Eu_2F_{36}N_4O_{14}$ (1786.5): calcd. C 28.19, H 0.78, Eu 17.0, N 3.13; found C 28.43, H 0.89, Eu 16.9, N 3.38. IR: $\tilde{\nu}$ = 3132 m, 3102 m, 3078 m, 2258 w, 1660 vs, 1650 s, 1612 m, 1562 s, 1538 s, 1498 s, 1464 s, 1448 m, 1440 m, 1394 w, 1350 m, 1324 m, 1254 br. s, 1218 br. s, 1148 br. s, 1108 s, 1100 s, 950 w, 860 m, 850 s, 806 s, 770 w, 742 m, 734 m, 660 s, 588 s, 560 w, 554 w, 528 w, 486 w, 474 w, 456 w $cm^{-1}$.

$C_{42}H_{14}F_{36}Gd_2N_4O_{14}$ (1797.0): calcd. C 28.03, H 0.78, Gd 17.5, N 3.11; found C 27.89, H 0.79, Gd 17.3, N 3.07. IR: $\tilde{\nu}$ = 3132 m, 3102 m, 3080 m, 2260 w, 1660 vs, 1650 s, 1612 m, 1562 s, 1538 s, 1500 s, 1446 s, 1446 m, 1394 w, 1350 m, 1324 m, 1268 s, 1254 br. s, 1146 br. s, 1216 br. s, 1108 s, 1100 s, 952 w, 862 m, 850 s, 804 s, 770 w, 742 m, 734 m, 662 s, 588 s, 560 w, 554 w, 528 w, 488 w, 476 w, 456 w $cm^{-1}$.

$C_{42}H_{14}F_{36}N_4O_{14}Tb_2$ (1800.4): calcd. C 27.97, H 0.78, N 3.11, Tb 17.6; found C 27.71, H 0.74, N 3.05, Tb 17.5. IR: $\tilde{\nu}$ = 3134 m, 3102 m, 3080 m, 2262 w, 1658 vs, 1650 s, 1612 m, 1562 s, 1358 s, 1502 s, 1464 s, 1442 m, 1396 w, 1352 m, 1268 s, 1254 br. s, 1216 br. s, 1146 br. s, 1100 s, 974 w, 952 w, 862 m, 850 s, 804 s, 770 w, 742 m, 734 m, 662 s, 588 s, 562 w, 528 w, 490 w, 476 w, 456 w $cm^{-1}$.

$C_{42}H_{14}Dy_2F_{36}N_4O_{14}$ (1807.5): calcd. C 27.86, H 0.77, Dy 18.0, N 3.09; found C 28.50, H 0.81, Dy 17.9, N 3.17. IR: $\tilde{\nu}$ = 3142 m, 3106 m, 3080 m, 2256 w, 1652 br. s, 1616 m, 1564 s, 1540 s, 1506 s, 1492 s, 1466 s, 1442 m, 1394 w, 1354 m, 1256 br. s, 1212 br. s, 1146 br. s, 1100 s, 1038 m, 980 w, 952 w, 852 s, 806 s, 772 w, 734 m, 722 m, 660 s, 588 s, 564 w, 528 w, 494 w, 480 w, 458 w $cm^{-1}$.

$C_{42}H_{14}F_{36}Ho_2N_4O_{14}$ (1812.4): calcd. C 27.78, H 0.77, Ho 18.2, N 3.09; found C 27.95, H 0.82, Ho 18.2, N 3.12. IR: $\tilde{\nu}$ = 3140 m, 3104 m, 3080 m, 2260 w, 1664 s, 1652 s, 1612 m, 1564 s, 1538 s, 1506 s, 1490 s, 1482 s, 1448 m, 1354 m, 1338 m, 1265 s, 1250 br. s, 1216 br. s, 1146 br. s, 1102 s, 952 w, 864 m, 850 s, 804 s, 773 w, 742 m, 734 m, 662 s, 588 s, 560 w, 527 w, 496 w, 480 w, 454 w $cm^{-1}$.

$C_{42}H_{14}F_{36}N_4O_{14}Tm_2$ (1820.4): calcd. C 27.66, H 0.77, Tm 18.6, N 3.07; found C 27.68, H 0.79, Tm 18.6, N 3.12. IR: $\tilde{\nu}$ = 3138 m, 3104 m, 3082 m, 2262 w, 1664 s, 1652 s, 1612 m, 1564 s, 1538 s, 1506 s, 1490 s, 1482 s, 1466 s, 1448 m, 1354 m, 1338 m, 1270 s, 1254 br. s, 1216 br. s, 1146 br. s, 1102 s, 952 w, 864 m, 852 s, 804 s, 770 w, 742 m, 734 m, 662 s, 588 s, 560 w, 528 w, 496 w, 482 w, 454 w $cm^{-1}$.

The monomeric complex $[Gd(NO_3)_3(4\text{-cpyNO})]$ was prepared in ethanol by a similar procedure as described above for $[Ln(hfa)_3(4\text{-cpyNO})]_2$. Yield: 90%. $C_6H_4GdN_5O_{10}$ (463.38): calcd. Gd 33.9; found Gd 33.9. IR: $\tilde{\nu}$ = 3116 m, 3084 m, 3062 m, 3032 m, 2246 m, 1648 m, 1620 m, 1488 m, 1456 m, 1438 m, 1378 m, 1324 s, 1238 s, 1222 m, 1180 m, 1110 w, 1044 w, 1032 m, 974 w, 864 m, 858 m, 818 w, 734 m, 634 br. w, 584 w, 560 m, 478 w, 462 w, 436 w $cm^{-1}$.

**Data Collection and Structural Refinement:** Single crystals suitable for X-ray analysis were obtained by recrystallisation of the crude products from chloroform. Diffraction data were collected with an image-plate diffractometer (Stoe IPDS) for the $Tb^{III}$ complex and with a four-circle CCD diffractometer (Stoe STADI4) for the $Ho^{III}$ derivative, using graphite-monochromated Mo-$K_\alpha$ radiation ($\lambda$ = 0.71073 Å). The structures were solved by direct methods (SHELXS-97)[25] and refined anisotropically for all non-hydrogen atoms by employing full-matrix least squares on $F^2$ (SHELXL-97).[26] The hydrogen atoms were included in the calculated positions and refined in a riding mode. Crystallographic data and some details of data collection and structure refinement are listed in Table 6. CCDC-612981 and -612982 contain the supplementary crystallographic data for this paper. These data can be obtained free of charge from The Cambridge Crystallographic Data Centre via www.ccdc.cam.ac.uk/data_request/cif.

**Diffuse Reflectivity Spectra:** UV/Vis reflectance spectra for solid samples of $Sm^{III}$, $Dy^{III}$ and $Tm^{III}$ complexes (Figure S4 in the Supporting Information) were recorded with a Lambda 35 spectrophotometer (Perkin–Elmer). The absorption spectra (absorption coefficient $\alpha$ over scattering coefficient $\sigma$ as a function of wavelength) were extracted from the diffuse reflectance spectra of the "infinitely thick" powder samples ($R_\infty$), using the Kubelka–Munk function, $\frac{\alpha}{\sigma} = \frac{(1-R_\infty)^2}{2R_\infty}$. Plots of the corresponding Kubelka–Munk functions are shown in Figure S5.

Table 6. Crystallographic data and some details of data collection and structure refinement for $[Ln(hfa)_3(4\text{-cpyNO})]_2$ complexes (Ln = $Tb^{III}$, $Ho^{III}$).

| | $[Tb(hfa)_3(4\text{-cpyNO})]_2$ | $[Ho(hfa)_3(4\text{-cpyNO})]_2$ |
|---|---|---|
| Empirical formula | $C_{42}H_{14}F_{36}N_4O_{14}Tb_2$ | $C_{42}H_{14}F_{36}N_4O_{14}Ho_2$ |
| Formula mass | 1800.42 | 1812.44 |
| Crystal system | monoclinic | monoclinic |
| Space group | $P2_1/c$ (no. 14) | $P2_1/c$ (no. 14) |
| $a$ [Å] | 18.918(4) | 18.636(5) |
| $b$ [Å] | 18.552(4) | 18.110(5) |
| $c$ [Å] | 17.420(3) | 17.099(5) |
| $\beta$ [°] | 92.90(3) | 93.95(3) |
| $V$ [Å$^3$] | 6106(2) | 5757(3) |
| $Z$ | 4 | 4 |
| $\rho_{calcd.}$ [g cm$^{-3}$] | 1.959 | 2.091 |
| $T$ [K] | 293(2) | 160(2) |
| Crystal size [mm] | 0.25 × 0.20 × 0.16 | 0.60 × 0.40 × 0.25 |
| Absorption coefficient $\mu$ [cm$^{-1}$] | 24.68 | 29.10 |
| Reflections collected | 41843 | 9740 |
| Data/parameters | 12937/883 | 9740/883 |
| $R_1$ [$I > 2\sigma(I)$] | 0.0356 | 0.0474 |
| $\omega R_2$ (all data) | 0.0881 | 0.1004 |
| Goodness-of-fit on $F^2$ | 0.842 | 1.087 |

 © 2006 Wiley-VCH Verlag GmbH & Co. KGaA, Weinheim 

**Luminescence Measurements:** Solid samples were ground into fine powders prior to the luminescence measurements. Excitation and photoluminescence spectra of $Sm^{III}$ and $Dy^{III}$ adducts were recorded at 295 K with a Perkin–Elmer LS-55 luminescence spectrometer ($\lambda_{ex}$ = 337 nm, xenon lamp). Luminescence spectra of $Gd^{III}$ and $Tm^{III}$ complexes were measured at 77 K with a multichannel spectrometer S2000 (Ocean Optics) utilizing a nitrogen laser LGI-21 ($\lambda_{ex}$ = 337 nm) as an excitation source. The luminescence data (excitation spectra, lifetimes and absolute quantum yields) of $Eu^{III}$ and $Tb^{III}$ derivatives were recorded at 295 K with a Fluorolog FL3-22 spectrofluorimeter from Horiba–Jobin–Yvon–Spex; to prevent saturation of the signal in photon-counting mode, the emission bandpass was set to 1 nm. Excitation spectra were measured by monitoring the characteristic $^4G_{5/2}\rightarrow{}^6H_{9/2}$, $^5D_0\rightarrow{}^7F_2$, $^5D_4\rightarrow{}^7F_5$ and $^4F_{9/2}\rightarrow{}^6H_{11/2}$ transitions for $Sm^{III}$, $Eu^{III}$, $Tb^{III}$ and $Dy^{III}$, respectively. Luminescence lifetimes ($\tau_{obs}$) of the $Eu^{III}$ compounds were determined by excitation of the $^5D_2$ level (466 nm, 21459 $cm^{-1}$) and monitoring the $^5D_0\rightarrow{}^7F_2$ transition, while those of the $Tb^{III}$ complexes were measured by excitation of either the $Tb^{III}$ ion or the ligand and monitoring the $^5D_4\rightarrow{}^7F_5$ transition. Lifetimes are the averages of at least three independent measurements. All luminescence decays proved to be perfect single exponential functions. All excitation and luminescence spectra were corrected by the instrumental functions. Electronic transitions were assigned by comparing the measured spectra with those reported by Elyashevich[27] and in other previous studies.[28] Luminescence quantum yields of $[Ln(hfa)_3(H_2O)_2]$ and $[Ln(hfa)_3(4\text{-cpyNO})]_2$ (Ln = $Eu^{III}$, $Tb^{III}$) were determined for solid samples by excitation into the ligand absorption band, according to the absolute method of Wrighton.[29] Each sample was measured several times under slightly different experimental conditions. Relative quantum yields, $Q_{rel}^{Ln,L}$, of $Sm^{III}$, $Dy^{III}$ and $Tm^{III}$ chelates $[Ln(hfa)_3(4\text{-cpyNO})]_2$ were calculated relative to the respective $[Ln(hfa)_3(H_2O)_2]$ complexes (at the same excitation wavelength and experimental geometry), using Equation (4), where $Q$ is the quantum yield, $R$ is the amount of reflected excitation radiation, $\phi$ is the integrated area of the corrected luminescence spectra and the indexes $x$ and $r$ correspond to $[Ln(hfa)_3(4\text{-cpyNO})]_2$ and $[Ln(hfa)_3(H_2O)_2]$, respectively. For comparison reasons, $Q_r$ was set to 1. The estimated error for the luminescence quantum yields is ±10%.

$$Q_{rel}^{Ln,L} = \frac{Q_x}{Q_r} = \left(\frac{1-R_r}{1-R_x}\right)\left(\frac{\phi_x}{\phi_r}\right) \quad (4)$$

**Refractive Index and Thickness of Thin Films:** Thin films of $[Eu(hfa)_3(4\text{-cpyNO})]_2$ were deposited on quartz substrates by the thermal evaporation method in a vacuum chamber ($P \approx 10^{-6}$ Torr, Leybold Heraeus). The refractive index ($n$) and layer thickness ($d$) were measured with a Filmetric F20 Thin Film Analyzer. The results are averages of at least three measurements. $[Eu(hfa)_3(4\text{-cpyNO})]_2$ (thin film): $n = 1.511 \pm 0.002$, $d = 414 \pm 1$ nm.

**Magnetic Measurements:** Magnetic susceptibility data (2–300 K) for polycrystalline samples of $[Ln(hfa)_3(4\text{-cpyNO})]_2$ (Ln = $Gd^{III}$, $Tb^{III}$) were collected with a SQUID magnetometer using a Quantum Design MPMS instrument with applied DC magnetic fields of 200 and 1000 Oe, respectively. The experimental data were corrected for the sample holder contribution and for diamagnetism of the constituent atoms estimated from Pascal's increments.[30]

**Supporting Information** (see footnote on the first page of this article): Reflection, excitation and photoluminescence spectra.

## Acknowledgments

We are grateful to Prof. Ritta Szymczak and Dr. Marek Baran (Institute of Physics, Polish Academy of Sciences) for the magnetic measurements, Mr. Andrei A. Vaschenko (Lebedev Physical Institute of Russian Academy of Sciences) for his assistance in obtaining thin-film samples, and the Russian Foundation for Basic Research (RFBR, grants 05-03-33090, 04-02-17040) for financial support.

[1] J. Kido, Y. Okamoto, *Chem. Rev.* **2002**, *102*, 2357–2368 and references cited therein.
[2] S. Faulkner, S. J. A. Pope, B. P. Burton-Pye, *Appl. Spectrosc. Rev.* **2005**, *40*, 1–31 and references cited therein.
[3] V. W. W. Yam, K. K. W. Lo, *Coord. Chem. Rev.* **1999**, *184*, 157–240 and references cited therein.
[4] J.-C. G. Bünzli, C. Piguet, *Chem. Soc. Rev.* **2005**, *34*, 1048–1077.
[5] K. Binnemans, in *Handbook on the Physics and Chemistry of Rare Earths* (Eds.: K. A. Gschneidner Jr, J.-C. G. Bünzli, V. K. Pecharsky), Elsevier, Amsterdam, **2005**, vol. 35, chapter 225.
[6] J.-C. G. Bünzli, in *Lanthanide Probes in Life, Chemical and Earth Sciences. Theory and Practice* (Eds.: J.-C. G. Bünzli, G. R. Choppin), Elsevier, Amsterdam, Oxford, New York, Tokyo, **1989**, chapter 7.
[7] See for example: P. Lenaerts, A. Storms, J. Mullens, J. D′Haen, C. Görller-Walrand, K. Binnemans, K. Driesen, *Chem. Mater.* **2005**, *17*, 5194–5201; S. W. Magennis, A. J. Ferguson, T. Bryden, T. S. Jones, A. Beeby, I. D. W. Samuel, *Synth. Met.* **2003**, *138*, 463–469; R. Reisfeld, T. Saraidarov, M. Pietraszkiewicz, S. Lis, *Chem. Phys. Lett.* **2001**, *349*, 266–270; H. Suzuki, Y. Hattori, T. Iizuka, K. Yuzawa, N. Matsumoto, *Thin Solid Films* **2003**, *438–439*, 288–293.
[8] K. Nakanishi, *IR Spectroscopy and Structure of Organic Compounds*, Mir, Moscow, **1965** (in Russian).
[9] E. L. Muetterties, L. J. Guggenberger, *J. Am. Chem. Soc.* **1974**, *96*, 1748–1756.
[10] M. G. B. Drew, *Coord. Chem. Rev.* **1977**, *24*, 179–275.
[11] V. A. Petrov, W. J. Marshall, V. V. Grushin, *Chem. Commun.* **2002**, 520–521.
[12] J. P. Gallivan, D. A. Dougherty, *Org. Lett.* **1999**, *1*, 103–105.
[13] M. Ryazanov, S. Troyanov, M. Baran, R. Szymczak, N. Kuzmina, *Polyhedron* **2004**, *23*, 879–883.
[14] I. P. Malkerova, A. S. Alikhanyan, S. V. Eliseeva, N. P. Kuzmina, *Russ. J. Inorg. Chem.*, in press.
[15] S. I. Weissman, *J. Chem. Phys.* **1942**, *10*, 214–217.
[16] N. Sabbatini, M. Guardigli, J.-M. Lehn, *Coord. Chem. Rev.* **1993**, *123*, 201–228.
[17] See for example: G. F. de Sá, O. L. Malta, C. D. Donega, A. M. Simas, R. L. Longa, P. A. Santa-Cruz, E. F. da Silva, *Coord. Chem. Rev.* **2000**, *196*, 165–195; F. R. Conçalves e Silva, O. L. Malta, C. Reinhard, H. U. Güdel, C. Piguet, J. E. Moser, J.-C. G. Bünzli, *J. Phys. Chem. A* **2002**, *106*, 1670–1677; F. R. Conçalves e Silva, R. L. Longo, O. L. Malta, C. Piguet, J.-C. G. Bünzli, *Phys. Chem. Chem. Phys.* **2000**, *2*, 5400–5403.
[18] See for example: M. Latva, H. Takalo, V. M. Mukkala, C. Matachescu, J.-C. Rodriguez-Ubis, J. Kankare, *J. Lumin.* **1997**, *75*, 149–169; F. Gutierrez, C. Tedeschi, L. Maron, J. P. Daudey, R. Poteau, J. Azema, P. Tisnes, C. Picard, *Dalton Trans.* **2004**, 1334–1347; H. J. Kim, J. E. Lee, Y. S. Kim, N. G. Park, *Opt. Mater.* **2002**, *21*, 181–186.
[19] S. Petoud, J.-C. G. Bünzli, T. Glanzman, C. Piguet, Q. Xiang, R. P. Thummel, *J. Lumin.* **1999**, *82*, 69–79.
[20] J.-C. G. Bünzli, in *Spectroscopic Properties of Rare-Earths in Optical Materials* (Eds.: G. Liu, B. Jacquier), Springer-Verlag, Berlin, **2005**, chapter 11.
[21] A.-S. Chauvin, F. Gumy, D. Imbert, J.-C. G. Bünzli, *Spectrosc. Lett.* **2004**, *37*, 517–532.

 © 2006 Wiley-VCH Verlag GmbH & Co. KGaA, Weinheim 

[22] A. Beeby, I. M. Clarkson, R. S. Dickins, S. Faulkner, D. Parker, L. Royle, A. S. de Sousa, J. A. G. Williams, M. Woods, *J. Chem. Soc., Perkin Trans. 2* **1999**, 493–503.
[23] M. F. Richardson, W. F. Wagner, D. E. Dands, *J. Inorg. Nucl. Chem.* **1968**, *30*, 1275–1289.
[24] R. Prshibil, *Complexones in Chemical Analysis*, Mir, Moscow, **1955** (in Russian).
[25] G. M. Sheldrick, *SHELXS 97, Program for the Solution of Crystal Structures*, University of Göttingen, Germany, **1997**.
[26] G. M. Sheldrick, *SHELXL 97, Program for the Refinement of Crystal Structures*, University of Göttingen, Germany, **1997**.
[27] M. A. Elyashevich, *Spectra of Rare-Earth Elements*, Gosteht-eoretizdat, Moscow, **1953** (in Russian).
[28] See for example: W. T. Carnall, P. R. Fields, K. Rajnak, *J. Chem. Phys.* **1968**, *49*, 4424–4442; W. T. Carnall, P. R. Fields, K. Rajnak, *J. Chem. Phys.* **1968**, *49*, 4443–4446; W. T. Carnall, P. R. Fields, K. Rajnak, *J. Chem. Phys.* **1968**, *49*, 4447–4449; W. T. Carnall, P. R. Fields, K. Rajnak, *J. Chem. Phys.* **1968**, *49*, 4450–4455.
[29] M. S. Wrighton, D. S. Ginley, D. L. Morse, *J. Phys. Chem.* **1974**, *78*, 2229–2233; N. C. Greenham, I. D. W. Samule, G. R. Hayes, R. T. Philips, Y. A. R. R. Kessener, S. C. Moratti, A. B. Holmes, R. H. Friend, *Chem. Phys. Lett.* **1995**, *241*, 89–96; J. C. de Mello, H. F. Wittmann, R. H. Friend, *Adv. Mater.* **1997**, *9*, 230–232.
[30] R. L. Carlin, *Magnetochemistry*, Springer-Verlag, Berlin, **1986**.
Received: July 18, 2006
Published Online: October 18, 2006

 © 2006 Wiley-VCH Verlag GmbH & Co. KGaA, Weinheim 

DOI: 10.1002/ejic.200600423

# Hydroxyapatite Nanocrystals Modified with Acidic Amino Acids

**Elisa Boanini,[a] Milena Fini,[b] Massimo Gazzano,[c] and Adriana Bigi*[a]**

**Keywords:** Hydroxyapatite / Amino acids / Nanocrystals

HA-aspartic acid (HA-ASP) and HA-glutamic acid (HA-GLU) composite nanocrystals were synthesized in aqueous medium. The relative amino acid content, determined through HPLC analysis, increases with the amino acid concentration in solution up to a maximum of about 7.8 wt.-% for HA-ASP and 4.3 wt.-% for HA-GLU composites. The dimensions of the composite nanocrystals decrease on increasing the amino acid content. The line profile analysis of the X-ray diffraction reflections was performed using: (i) the Scherrer method, (ii) the Warren–Averbach approach, and (iii) the Rietveld refinement. The results indicate that the broadening of the diffraction peaks is partly due to the decrease of crystallite size on increasing amino acid content, and even more to the simultaneous increase of microstrain. The different extent of structural disorder induced by the two amino acids, in agreement with their different incorporation, suggests a greater affinity of aspartic acid for hydroxyapatite structure.

(© Wiley-VCH Verlag GmbH & Co. KGaA, 69451 Weinheim, Germany, 2006)

## Introduction

The idea of mimicking designs from nature and adopting the same strategies as those utilized by living organisms to produce functional structures has entered into many areas of applied science, most notably the synthesis of new materials.[1] The biomimetic strategy is based on the principle that nucleation and growth of inorganic crystals in biological environments occurs in the presence of biological macromolecules, which may be linked to structural organic matrices or secreted as soluble polyelectrolytes in the mineralization environment.[2,3] Control occurs through specific or nonspecific interactions of biological macromolecules with the charged surfaces of the growing inorganic crystals.[3–5] This has prompted a number of studies on the preparation of hydroxyapatite nanocrystals in the presence of biomolecules.[6–8] Proteins and macromolecules, which are most active in the mediation of biologically directed mineral growth, contain amino acid residues, specifically regions rich in carboxylates, that interact with mineral surfaces.[9–11] In bone, nucleation and growth of apatite crystals involve proteins containing high amounts of aspartic and glutamic acid residues.[12] Both glutamic and aspartic acids have been reported to induce osteoblast differentiation and to increase extracellular mineralization.[13–15]

[a] Department of Chemistry "G. Ciamician", University of Bologna,
Via Selmi 2, 40126 Bologna, Italy
Fax: +39-51-2099456
E-mail adriana.bigi@unibo.it
[b] Experimental Surgery Department, Research Institute Codivilla Putti, Rizzoli Orthopaedic Institute,
Bologna, Italy
[c] ISOF-CNR, c/o Department of Chemistry "G. Ciamician", Bologna, Italy

We have recently demonstrated the possibility of synthesizing hydroxyapatite, $Ca_{10}(PO_4)_6(OH)_2$ (HA), containing aspartic acid (HA-ASP) and HA containing glutamic acid (HA-GLU), and we have verified that the presence of the acidic amino acids in the composite nanocrystals favours osteoblast proliferation and promotes their metabolism and differentiation.[16] Understanding how these amino acids interact with HA structure, and clarifying their role in the control of the properties of the HA crystals is of interest both for the development of biomaterials suitable to repair the skeletal system, as well as for a better understanding of the natural processes. To this aim, we have carried out a structural, morphological and chemical investigation of hydroxyapatite nanocrystals synthesized in the presence of increasing amounts of aspartic acid and of glutamic acid.

## Results and Discussion

### Sample Characterization

The powder X-ray diffraction patterns of the products synthesized in the presence of L-aspartic acid or L-glutamic acid indicate that they are constituted of hydroxyapatite as a unique crystalline phase. However, glutamic acid, and even more so aspartic acid, provokes a broadening of the diffraction peaks, which increases on increasing the amino acid concentration in solution, as is appreciable in the patterns shown in Figure 1. The reduction of the degree of crystallinity is confirmed by the results of the FT-IR absorption analysis. In fact, the FT-IR spectra of the products obtained in the presence of increasing concentration of amino acid show a decrease of the relative intensity of the absorption bands at 3572 and 630 $cm^{-1}$, caused by $OH^-$

 © 2006 Wiley-VCH Verlag GmbH & Co. KGaA, Weinheim InterScience 

stretching and libration mode, respectively (Figure 2). Moreover, the spectra of HA samples prepared in the presence of an amino acid display, other than the bands characteristic of the hydroxide and phosphate groups, several absorption bands in the range 1700–1400 $cm^{-1}$, which are indicative of the presence of the amino acids, as can be observed for sample HA-GLU 0.20 in part b of Figure 2. This region of the spectra is quite different from that present in the previously reported spectra of mechanical mixtures containing HA and ASP or GLU, which display a number of bands due to the two discrete components of the mixture.[16] In particular, the broad absorption band centred at 1568 $cm^{-1}$ (1591 $cm^{-1}$ in the HA-ASP spectra) can be attributed to glutamic acid (aspartic acid). The small shift with respect to the position characteristic of the carboxylic stretching band in the free amino acids is in agreement with an increase of the C–O bond length due to interaction with the apatitic phase.[17] Table 1 reports the relative amount of amino acid determined through HPLC and expressed as wt.-% of the solid product. The relative quantity of amino acid in the crystals increases with the amino acid concentration in solution up to a maximum of about 7.8 wt.-% for HA-ASP and 4.3 wt.-% for HA-GLU composites. Aspartic acid incorporation into HA nanocrystals is always greater than that of glutamic acid, suggesting a greater affinity of aspartic acid for hydroxyapatite structure. Amino acid incorporation does not significantly affect the stoichiometry of hydroxyapatite as it can be deduced also from the Ca/P molar ratio of the composites which assumes a mean value of $1.68 \pm 0.03$, very close to the stoichiometric value of 1.67, independently from the amino acid content. On the contrary, the dimensions of the crystals are strongly affected by the presence of both aspartic and glutamic acid. In Figure 3, a TEM micrograph of HA crystals is compared with that of HA-amino acid composite crystals. Hydroxyapatite is constituted of platelet-shaped crystals with mean dimensions up to about 200 × 40 nm, elongated along a direction parallel to the crystallographic *c*-axis (Figure 3, a), whereas composite nanocrystals display definitely smaller dimensions (Figure 3, b–d). The dimensions decrease on increasing the amino acid content, in agreement with the reduction of the degree of crystallinity. Furthermore, the crystals with higher amino acid content, which display mean dimensions of about 50 × 10 nm, should be also extremely thin as they appear very transparent to the electron beam. In a previous study on the interaction of poly-L-aspartate with HA, we verified a remarkable increase of the length/width ratio of the composite crystallites, in agreement with a preferential adsorption of the polyamino acid on the crystal faces parallel to the *c*-axis.[18] At variance, the significant reduction of the dimensions along all the three directions induced by ASP and GLU suggests a nonspecific interaction with the HA crystal faces, and it might be interpreted as indicating

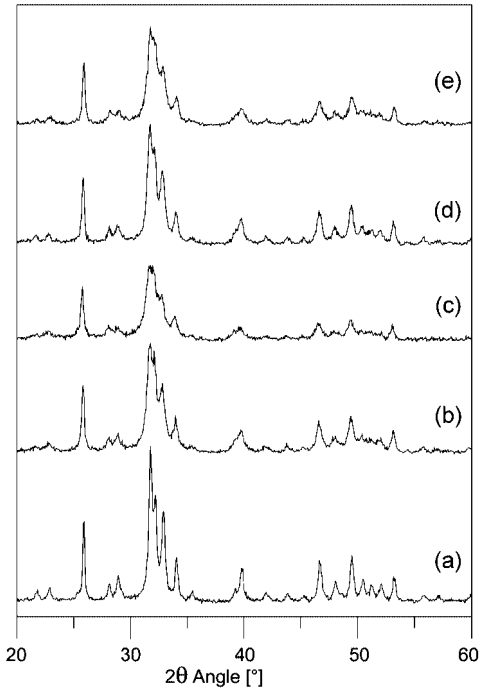


Figure 1. Powder X-ray diffraction patterns of hydroxyapatite synthesized in the absence of amino acid (a); in the presence of aspartic acid 0.10 M (b) and 0.20 M (c) and in the presence of glutamic acid 0.10 M (d) and 0.20 M (e).

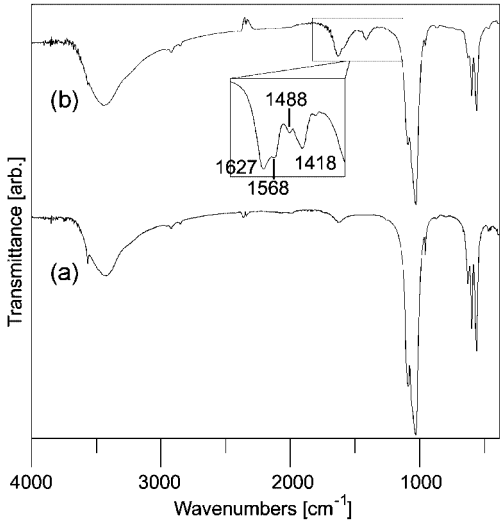


Figure 2. FT-IR adsorption spectra of the HA samples prepared in the absence of amino acid (a) and in the presence of glutamic acid 0.20 M (b). The absorption bands in the zoomed range 1700–1400 $cm^{-1}$ can be attributed to glutamic acid.

Table 1. Amount of amino acid associated to the inorganic phase evaluated through HPLC and expressed as wt.-% of the solid product.

| Amino acid concentration in solution [M] | Aspartic acid content [wt.-%] | Glutamic acid content [wt.-%] |
|---|---|---|
| 0 | – | – |
| 0.05 | 3.14 | 1.17 |
| 0.10 | 4.28 | 2.50 |
| 0.15 | 5.35 | 3.30 |
| 0.20 | 7.80 | 4.30 |

 © 2006 Wiley-VCH Verlag GmbH & Co. KGaA, Weinheim 

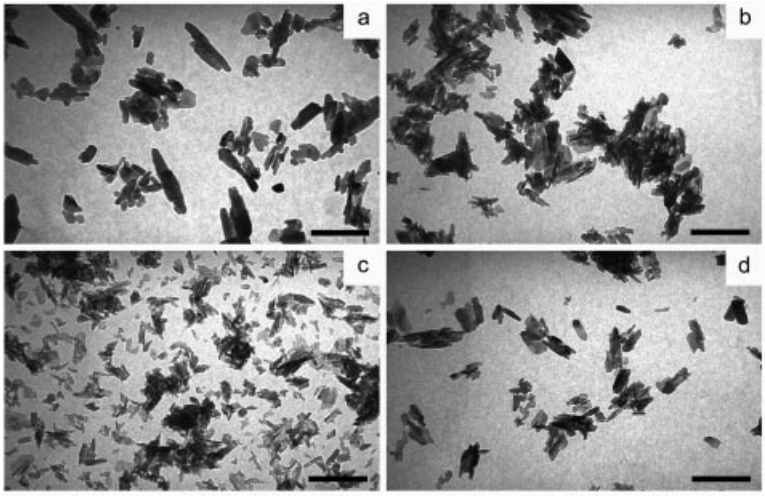


Figure 3. TEM micrographs of HA crystals synthesized in the absence of amino acid (a); in the presence of aspartic acid 0.10 M (b) and 0.20 M (c) and in the presence of glutamic acid 0.20 M (d). Scale-bar = 200 nm.

that the presence of the amino acids provokes an increase of the nucleation rate that, as a consequence, leads to a growth reduction.[15] Aspartic and glutamic acid seem to exert a similar control on crystal dimensions, as can be deduced from the comparison of Figure 3 (parts b and d).

In agreement with the crystal dimensions, the values of the specific surface area, determined applying the Brunauer–Emmett–Teller (BET) theory and reported in Table 2 increases as a function of amino acid content, up to 114 $m^2 g^{-1}$, which represents a very high value for synthetic platelet-like hydroxyapatite crystals.

Table 2. Surface areas of hydroxyapatite samples synthesized in the presence of different amino acid concentrations in solution.

| Sample | Surface area [$m^2 g^{-1}$] |
|---|---|
| HA | 60 |
| HA-ASP 0.10 | 84 |
| HA-ASP 0.20 | 114 |
| HA-GLU 0.10 | 78 |
| HA-GLU 0.20 | 86 |

## Crystallographic Investigation

Line profile analysis has been applied in order to investigate the line broadening increase observed in the XRD patterns of the samples synthesized in the presence of increasing amounts of amino acid (Figure 1).

A qualitative estimation of the size of coherently scattering domains (i.e., the crystallite size) as derived from the Scherrer equation, on the hypothesis of negligible microstrain, is reported in Table 3. $\tau_{002}$ is related to the mean crystallite size along the *c*-axis whereas $\tau_{310}$ refers to the mean crystal size along a direction perpendicular to it.

Table 3. Coherent lengths ($\tau_{hkl}$) of the perfect crystalline domains in the direction normal to 002 and to 310 planes calculated using the Scherrer method.

| Sample | $\tau_{002}$ [nm] | $\tau_{310}$ [nm] |
|---|---|---|
| HA | 44.3(9) | 22.4(6) |
| HA-ASP 0.05 | 38.9(7) | 17.0(3) |
| HA-ASP 0.10 | 35.8(3) | 15.5(2) |
| HA-ASP 0.15 | 35.2(3) | 14.8(3) |
| HA-ASP 0.20 | 29.8(4) | 11.3(3) |
| HA-GLU 0.05 | 43.8(9) | 19.9(3) |
| HA-GLU 0.10 | 35.8(6) | 15.2(2) |
| HA-GLU 0.15 | 34.6(3) | 14.7(3) |
| HA-GLU 0.20 | 33.7(3) | 12.0(3) |

The crystal sizes decrease as the aspartic or glutamic acid content increases. The contraction appears to be greater along the direction orthogonal to the *c*-axis, similarly to what was previously found for poly-L-aspartate.[18] The comparison with the data reported in Table 1 indicates that GLU incorporation provokes a greater contraction of crystal size.

In general, the nature of imperfections responsible for the broadening of the diffraction peaks could be due to (i) a reduction of the crystallite domains, (ii) the occurrence of still large domains but with lattice spacings that differ one from another, and (iii) the presence of elastic deformations and stacking faults inside the domains. In order to evaluate the relative contribution of crystallite size and microstrain to the diffraction peak broadening, some selected samples were submitted to the Warren–Averbach analysis. The analysis was performed on two pairs of reflections (002/004 and 111/222). The results are reported in Table 4. Since only two pairs of peaks were analysed, the results are rather semi-quantitative. However, the data clearly show that both amino acids provoke a reduction of the mean crystallite size, without significant differences along the two investigated directions.

 © 2006 Wiley-VCH Verlag GmbH & Co. KGaA, Weinheim 

Table 4. Microstructural parameters calculated using Warren–Averbach analysis.

| Sample | 002/004 | | | | 111/222 | | | |
|---|---|---|---|---|---|---|---|---|
| | $\langle D \rangle_s$ (nm) | $\langle D \rangle_v$ (nm) | $\langle \varepsilon_L^2 \rangle^{\frac{1}{2}}$ ($\times 10^3$) | $\left\langle \varepsilon^2_{\frac{\langle D \rangle_V}{2}} \right\rangle^{\frac{1}{2}}$ ($\times 10^3$) | $\langle D \rangle_s$ (nm) | $\langle D \rangle_v$ (nm) | $\langle \varepsilon_L^2 \rangle^{\frac{1}{2}}$ ($\times 10^3$) | $\left\langle \varepsilon^2_{\frac{\langle D \rangle_V}{2}} \right\rangle^{\frac{1}{2}}$ ($\times 10^3$) |
| HA | 38.7 | 28.6 | 1.34 | 1.57 | 27.7 | 26.4 | 0.97 | 0.93 |
| HA-ASP 0.10 | 18.7 | 21.9 | 1.36 | 1.56 | 17.0 | 18.0 | 1.21 | 1.71 |
| HA-ASP 0.20 | 11.3 | 11.6 | 1.33 | 2.55 | 9.8 | 10.4 | 1.43 | 2.81 |
| HA-GLU 0.10 | 18.6 | 22.4 | 1.33 | 1.78 | 16.9 | 17.9 | 1.33 | 1.76 |
| HA-GLU 0.20 | 14.7 | 18.7 | 1.59 | 2.73 | 9.7 | 12.1 | 1.53 | 2.82 |

$\langle D \rangle_s$, $\langle D \rangle_v$ are the mean sizes of crystallites weighed on the surface or volume

$\langle \varepsilon_L^2 \rangle^{\frac{1}{2}}$ is the root of mean-square lattice strain

Furthermore, all the composites show an increase of the microstrain parameters indicating that the incorporation of both amino acids provokes a significant decrease of crystal perfection, which is more evident for HA-GLU composites. The parameters obtained for the 111/222 planes are larger than those for the 002/004 planes suggesting a smaller amount of stacking faults along the *c*-axis. These data can be used to interpret the different results obtained with the Scherrer analysis. The Scherrer formula gives proper values of the mean crystallite size along the investigated direction only for strain-free samples. In spite of the different reflections analyzed by the Warren–Averbach method, the results clearly indicate that the microstrain contribution is smaller along the 00*l* direction than along the direction orthogonal to it. As a consequence, $\tau_{310}$ appeared more affected than $\tau_{002}$ simply because of the neglected microstrain contribution.

In order to verify the possible structural modifications, a full profile fitting was performed on XRD patterns of the two composites at the highest amino acid content (samples HA-ASP 0.20 and HA-GLU 0.20). The main steps of the procedure are reported in the experimental section and a comparison between the experimental and calculated pattern, as obtained at the end of the process, is reported in Figure 4 for the HA-aspartic acid sample. The final discrepancy factors *Rp* = 0.044, *Rwp* = 0.058 and *Rp* = 0.049, *Rwp* = 0.064 were achieved for HA-ASP 0.20 and HA-GLU 0.20, respectively. The results indicate that the cell parameters of the HA-amino acid composites are still the same as a stoichiometric HA [HA *a* = 0.9424(1) nm, *c* = 0.6880(1) nm; HA-ASP 0.20 *a* = 0.9427(7) nm, *c* = 0.6877(8) nm; HA-GLU 0.20 *a* = 0.9425(4) nm, *c* = 0.6884(4) nm]. The presence of an appreciable amorphous fraction in the samples has to be excluded, because leaving variable the integrated intensity of a bell-shaped curve superimposed on the background did not allow a better convergence. The Debvin program takes into account the anisotropy of the crystallite dimensions that can be used as variable parameters.[19] A good agreement index is reached when the mean value of the crystallite dimensions along the *c*-axis is almost double respect to the values along *a* and *b*, in agreement with the results of the Scherrer and Warren–Averbach analysis. No significant variation of the atomic positions and occupancy factors was detected, whereas an increase of about 20% in the thermal parameters seems to indicate an increased general disorder in the structure of the composites.

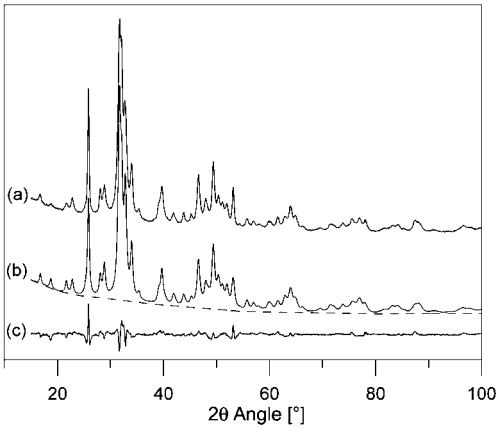


Figure 4. Comparison between the observed (a) and the calculated (b) powder diffraction patterns of HA-ASP 0.20. The dotted line is the background, while the line at the bottom (c) is the difference curve.

## Conclusions

Composite HA-ASP and HA-GLU nanocrystals have been synthesized at different amino acid content. The presence of the amino acids in the reaction solution does not inhibit nucleation of HA, but reduces the growth of the composite nanocrystals in agreement with the increase of the surface area on increasing amino acid content. TEM images confirm the reduction of dimensions, which does not modify the morphology of the composite nanocrystals. Accordingly, the results of the structural analyses showed a major contribution from microstrain to the broadening of the diffraction peaks for both HA-ASP and HA-GLU. However, glutamic acid induces a greater disorder in the HA structure, most likely because of its bigger size, which

 © 2006 Wiley-VCH Verlag GmbH & Co. KGaA, Weinheim 

could justify the greater affinity of aspartic acid for HA suggested by its greater incorporation into the composite nanocrystals.

## Experimental Section

The synthesis of hydroxyapatite was carried out under $N_2$ using a $Ca(NO_3)_2{\cdot}4H_2O$ (50 mL, 1.08 M) solution at pH adjusted to 10 with $NH_4OH$. The solution was heated at 90 °C and a $(NH_4)_2HPO_4$ solution (50 mL, 0.65 M), pH 10 adjusted with $NH_4OH$, was added dropwise whilst stirring. The precipitate was maintained in contact with the reaction solution for 5 h at 90 °C whilst stirring, then centrifuged at 10000 rpm for 10 min and repeatedly washed with $CO_2$-free distilled water. The product was dried at 37 °C overnight.

Hydroxyapatites at different amino acid contents were obtained by adding L-aspartic acid or L-glutamic acid (SIGMA) to the phosphate solution, before adjusting the pH to 10 with $NH_4OH$. The tested concentrations were 0.05, 0.10, 0.15 and 0.20 M.

X-ray diffraction analysis was carried out by means of a PANalytical X'Pert PRO powder diffractometer. Cu-$K_\alpha$ radiation was used (40 mA, 40 kV). The $2\theta$ range was from 10 to 60° at a scanning speed of 0.75°min$^{-1}$. In order to evaluate the coherence lengths of the crystals and to perform the line profile analysis, further X-ray powder data were collected in step scanning mode with a fixed counting time of 10 s for each 0.030°/step.

For FT-IR adsorption analysis, the powdered samples (1 mg) were carefully mixed with KBr (250 mg, infrared grade) and pelletized under a pressure of 10 tons for 2 min. The pellets were analyzed with a Nicolet FT 205 IR spectrophotometer to collect 32 scans in the range 4000–400 cm$^{-1}$ at a resolution of 4 cm$^{-1}$.

Amino acid contents were determined by means of HPLC, following a procedure reported elsewhere.[20] Briefly, to the starting solution containing the amino acid in HCl ($10^{-2}$ M) was added an equal volume of borate buffer (0.2 M, pH 8) and then 9-fluorenylmethyl chloroformate (FMOC-Cl) solution (in $CH_3CN$). At the end of the time allowed for derivatization (typically 1 min), excess 1-aminoamantadine (ADAM) was added to prevent hydrolysis of excess FMOC-Cl to FMOC-OH. Before injection sample solutions were filtered through Teflon filters (0.2-μm porosity). Compounds were separated on a 250 × 4 mm i.d. 5-μm Purospher column from Merck. The HPLC pump was a Varian 9012 and the injection valve a Rheodyne 7525 equipped with a 13.2 μL calibrated loop. Compounds were detected with a Hewlett–Packard 1040 diode array detector. Data were acquired and processed with an HP 9000 Chemstation.

Calcium and phosphorus contents were determined by means of a Dionex DX100 chromatography system equipped with a Dionex CD20 conductivity detector. Powders were previously dissolved in HCl (0.1 M). The chromatographic data were collected and processed with the Dionex Peaknet 5.1 program.

For TEM investigations, a small amount of powder was dispersed in ethanol and submitted to ultrasonication. A drop of the calcium phosphate suspension was transferred onto holey carbon foils supported on conventional copper microgrids. A Philips CM 100 transmission electron microscope operating at 80 kV was used.

The surface area was measured using a Carlo Erba Sorpty 1750 BET analyser using constant volume $N_2$ absorption with desorption at 100 °C.

**Line Profile Analysis**

**Scherrer Analysis:** The line broadening of the 002 and 310 reflections was used to evaluate the length of the coherent domains ($\tau_{hkl}$) along the *c*-axis and along a direction perpendicular to it. $\tau_{hkl}$ values were calculated from the widths at half maximum intensity ($\beta_{1/2}$) using the Scherrer equation (1)[21]

$$\tau_{hkl} = \frac{k\,\lambda}{\beta_{1/2}\cos\theta} \quad (1)$$

where $\lambda$ is the wavelength, $\theta$ the diffraction angle and $K$ a constant depending on crystal habit (chosen as 0.9). The silicon standard peak 111 was used to evaluate the instrumental broadening.

**Warren–Averbach Analysis:** The Warren–Averbach approach[21] was applied with the aim to separate the line broadening due to size effect from the strain contribution. The analysis was performed on two couples of reflections (002/004 and 111/222) by using the WinFit program.[22] A strain free $LaB_6$ NIST sample was used to take into account the instrumental broadening.

**Rietveld Refinement Analysis:** The DEBVIN program,[23] essentially implemented on the Rietveld routine,[24] was used to refine the structures of HA and HA-amino acid composites. The same space group ($P6_3$/m, *n*. 176), cell parameters, atomic positions and thermal parameters as those of the initial structural model of HA were introduced.[25] The background was treated as an empirical segmented line where the heights of the seven nodes are free variables. The peaks were fitted by using a Pearson VII function. Half width of the diffraction peaks as a function of $2\theta$ was evaluated by the formulation of the Caglioti model.[26] Rietveld refinement was performed in several stages, the parameters obtained in each step being deferred in the following one. In the first cycles the scale factor and the background were refined. Refinement of the other parameters is in the following order: zero shift, profile parameters, asymmetry parameter and cell parameters. Refinements of the occupancy factors and of the coordinates were tested at the latest stages of the procedure, starting with those of the two metal sites. In the last refinement cycles the overall thermal parameter was released together with the other 14 variables.

## Acknowledgments

This research was carried out with the financial support of MIUR (FIRB RBNE01458S_004), and the University of Bologna (Funds for Selected Research Topics).

[1] S. Mann, *Biomineralization. Principles and Concepts in Bioinorganic Materials Chemistry*, Oxford University Press, Oxford, **2001**.
[2] A. L. Boskey, *Calcif. Tissue Int.* **1998**, *63*, 179–182.
[3] L. Addadi, J. Moradian-Oldak, H. Furedi-Milhofer, S. Weiner, A. Veis, in *Chemistry and Biology of Mineralized Tissues* (Eds.: H. Slavkin, P. Price), Elsevier, The Netherlands, **1992**, pp. 153–162.
[4] A. Berman, L. Addadi, A. Kvick, L. Laiserovitz, M. Nelson, S. Weiner, *Science* **1990**, *250*, 664–667.
[5] S. Mann, B. R. Heywood, S. Rajam, J. D. Birchall, *Nature* **1988**, *394*, 692–695.
[6] R. Gonzalez-McQuire, J. Y. Chane-Ching, E. Vignaud, A. Lebugle, S. Mann, *J. Mater. Chem.* **2004**, *14*, 2277–2281.
[7] S. Tanaka, N. Shiba, M. Senna, *Sci. Technol. Adv. Mater.* **2006**, *7*, 226–228.
[8] S. Teng, J. Shi, B. Peng, L. Chen, *Compos. Sci. Technol.* **2006**, *66*, 1532–1538.

 © 2006 Wiley-VCH Verlag GmbH & Co. KGaA, Weinheim 

[9] C. S. Sikes, M. L. Yeung, A. P. Wheeler, in *Surface Reactive Peptides and Polymers: Discovery and Commercialization* (Eds.: C. S. Sikes, A. P. Wheeler), ACS Symposium Series XIII, ACS Books, Washington, DC, **1991**, p. 444.
[10] A. George, L. Bannon, B. Sabsay, J. W. Dillon, J. Malone, A. Veis, N. A. Jenkins, D. J. Gilbert, N. G. Copeland, *J. Biol. Chem.* **1996**, *271*, 32869–32873.
[11] S. R. Qiu, A. Wierzbicki, C. A. Orme, A. M. Cody, J. R. Hoyer, G. H. Nancollas, S. Zepeda, J. J. De Yoreo, *Proc. Natl. Acad. Sci. USA* **2004**, *101*, 1811–1815.
[12] G. K. Hunter, C. L. Kyle, H. A. Goldberg, *Biochem. J.* **1994**, *300*, 723–728.
[13] E. Hinoi, T. Takarada, Y. Yoneda, *J. Pharmacol. Sci.* **2004**, *94*, 215–220.
[14] D. J. Mason, *Eur. Cells Mater.* **2004**, *7*, 12–26.
[15] S. Sarig, *Bone* **2004**, *35*, 108–113.
[16] E. Boanini, P. Torricelli, M. Gazzano, R. Giardino, A. Bigi, *Biomaterials* **2006**, *27*, 4428–4433.
[17] A. Barth, *Prog. Biophys. Mol. Biol.* **2000**, *74*, 141–173.
[18] A. Bigi, E. Boanini, M. Gazzano, M. A. Kojdecki, K. Rubini, *J. Mater. Chem.* **2004**, *14*, 274–279.
[19] R. Millini, G. Perego, S. Brückner, *Mater. Sci. Forum* **1991**, *79–82*, 239–244.
[20] D. Melucci, M. Xie, P. Reschiglian, G. Torsi, *Chromatographia* **1999**, *49*, 317–320.
[21] H. P. Klug, L. E. Alexander, *X-ray Diffraction Procedures for Polycrystalline and Amorphous Materials*, Wiley Interscience, New York, **1974**.
[22] S. Krumm, Proceedings of the XIIIth Conference on Clay Mineralogy and Petrology, Praha, in *Acta Universitatis Carolinae Geologica*, **1994**, *38*, 253–261.
[23] A. Immirzi, *Acta Crystallogr., Sect. B* **1980**, *36*, 2378–2385; S. Brückner, *Chim. Ind.* **1988**, *70*, 48–53; S. V. Meille, S. Brückner, J. B. Lando, *Polymer* **1989**, *30*, 786–792.
[24] H. M. Rietveld, *J. Appl. Crystallogr.* **1969**, *2*, 65–67.
[25] M. I. Kay, R. A. Young, A. S. Posner, *Nature* **1964**, *204*, 1050–1052.
[26] G. Caglioti, A. Paoletti, F. P. Ricci, *Nucl. Instrum.* **1958**, *3*, 223–228.

Received: May 8, 2006
Published Online: October 5, 2006

 © 2006 Wiley-VCH Verlag GmbH & Co. KGaA, Weinheim 

DOI: 10.1002/ejic.200600717

# Synthesis and Structural Characterization of Sandwich-Type Keggin-γ-Lacunary Silicotungstates with an Open Wells–Dawson-Like Structure

**Hongsheng Liu,[a] Jun Peng,*[a] Zhongnin Su,[a] Yanhui Chen,[a] Baoxia Dong,[a] Aixiang Tian,[a] Zhangang Han,[a] and Enbo Wang[a]**

**Keywords:** Polyoxometalates / Tungstosilicates / Keggin structures / Transition metals

Three novel $[\gamma\text{-}SiW_{10}O_{36}]^{8-}$ dimers, $[\{K(H_2O)\}_2\{(\mu_3\text{-}H_2O)M(H_2O)\}(\gamma\text{-}Si_2W_{20}O_{70})]^{8-}$ (M = $Mn^{2+}$, **1**; $Co^{2+}$, **2**; $Ni^{2+}$, **3**), are isolated from an aqueous acidic medium without isomerization, which is different from most reactions of $[\gamma\text{-}SiW_{10}O_{36}]^{8-}$ with first-row transition metals. They are isomorphous and crystallize in the orthorhombic system, space group *Pnma*. These species are the first examples of imidazole–potassium mixed salts of Keggin-γ-type dimers having an analogous open structure related to the Wells–Dawson anionic cluster.

(© Wiley-VCH Verlag GmbH & Co. KGaA, 69451 Weinheim, Germany, 2006)

## Introduction

Polyoxometalates (POMs), a well-known, large, and unique class of inorganic polynuclear compounds, are the focus of numerous interdisciplinary projects in recent years owing to their special redox properties and tunable structure variety. This research area, as summarized in a vivid meeting review by Kögerler and Cronin, has undergone "an important transition from classical inorganic chemistry towards the chemistry of "smart", "functional materials"".[1] Among thousands of POM compounds, the metastable lacunary polyoxotungstates, such as Keggin-type 9-series $[AW_9O_{34}]^{n-}$ (A = P, Si,···), 10-series $[\gamma\text{-}AW_{10}O_{36}]^{8-}$, 11-series $[AW_{11}O_{39}]^{8-}$, and Wells–Dawson-type $[P_2W_{15}O_{56}]^{12-}$, $[P_2W_{17}O_{61}]^{10-}$, and so on, bearing an analogy with porphyrin, have drawn increasing attention as structural fragments or building blocks due to their versatility to generate unexpected species with surprising structures and multiple properties, which include catalytic, medicinal, magnetic, electronic, and optical properties.[2] Especially, mono- and trivacant α- and β-Keggin polyoxoanions have been studied for many years and are in general understood.[3] On the contrary, investigation of the divacant γ-Keggin polyoxoanion $[\gamma\text{-}SiW_{10}O_{36}]^{8-}$ (γ-$SiW_{10}$), first reported by Hervé et al.,[4] is less perhaps due to its poor stability in aqueous solution. However, extensive studies on γ-$SiW_{10}$ are prompted by very interesting results that have been reported in recent years,[5–20] from which three kinds of derivatives, **I**, **II**, and **III** symbolized in Scheme 1, can be summarized. Derivative **I** represents the derivatives in which the γ-$SiW_{10}$ anion accommodates the two vacant positions to two transition-metal atoms or other groups to generate the complete or modified γ- or β- Keggin anions; derivative **II** represents the sandwich-type derivatives in which two γ-$SiW_{10}$ subunits associate together by additional bridges; derivative **III** represents oligomeric derivatives in which the γ-$SiW_{10}$ anions are isomerized and polymerized by transition metal ions.

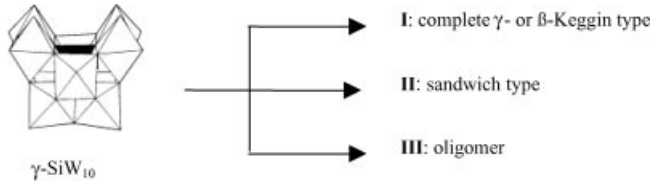


Scheme 1. Three kinds of derivatives synthesized from the precursor $[\gamma\text{-}SiW_{10}O_{36}]^{8-}$ anion.

Kortz and co-workers carried out a systematical study on the reaction of γ-$SiW_{10}$ anions with first-row transition metals from which they isolated a series of isomerized oligomers ranging in size from dimers to tetramers. They found that the dilacunary precursor isomerized easily in an aqueous acidic medium upon heating and in the presence of first-row transition metal ions, unlike the 9-series and 2:18-series whose structures could be preserved in the sandwich-type products. Accordingly, sandwich-type γ-$SiW_{10}$ dimers are still a challenge to obtain for POM chemists. Up to now, only Pope's group has reported a sandwich-type γ-$SiW_{10}$ dimer that was isolated as a cesium salt.[13] In our efforts to modify POM clusters,[21] we obtained three novel compounds with the $[\gamma\text{-}SiW_{10}O_{36}]^{8-}$ fragment preserved. Herein we report the syntheses and structural characterization of them. They possess an open Wells–Dawson-like

[a] Key Laboratory of Polyoxometalate Science of Ministry of Education, Faculty of Chemistry, Northeast Normal University,
Changchun 130024, P. R. China
E-mail: jpeng@nenu.edu.cn

Supporting information for this article is available on the WWW under http://www.eurjic.org or from the author.

 © 2006 Wiley-VCH Verlag GmbH & Co. KGaA, Weinheim 

structure in which two γ-$SiW_{10}$ subunits are directly associated to each other in an eclipsed fashion. To the best of our knowledge, this type of structure that is constructed from γ-$SiW_{10}$ has not yet been reported until now. From a structure point of view, only [α-$Si_2W_{18}O_{66}$][22] was an analog.

## Results and Discussion

### Synthesis

The title compounds were isolated from an acidic solution containing γ-$SiW_{10}$, transition-metal cations, and imidazole under gentle conditions, illustrated by the reaction:

$$2\,[\gamma\text{-}SiW_{10}O_{36}]^{8-} + 4\,H^+ + 2\,K^+ + M^{2+} + 2\,H_2O \rightarrow [\{K(H_2O)\}_2(\mu_3\text{-}H_2O)M(H_2O)(\gamma\text{-}Si_2W_{20}O_{70})]^{8-}$$

It deserves to be mentioned that the γ-silicodecatungstate is a metastable species and easily isomerizes to α- or β-species, such as α-dodecasilicotungstates and β-undecasilicotungstates.[18] Therefore, a key problem is to inhibit its decomposition and isomerization during the reaction process in order to keep the anionic skeleton intact. Slight changes in the reaction conditions, such as temperature or pH, may influence the final products. The synthetic conditions of the compounds reported from precursor $K_8[\gamma\text{-}SiW_{10}O_{36}]$ are collected in Table 3. From Table 3 it can be found that lower or higher pH values ($3 > pH > 5$), elevated temperatures (≥50 °C), and long reaction times (≥30 min) are favorable for the decomposition and reassembly or isomerization of γ-$SiW_{10}$, whereas the presence of an organic solvent or bigger cations such as $K^+$, $Rb^+$, and $Cs^+$ would increase the stability of the γ-$SiW_{10}$ skeleton.[25–27] In the preparation process we controlled the reaction temperature to a maximum of 45 °C and the pH wave to not more than ±0.3. It is worthy to mention that imidazole–potassium mixed salts are obtained but only two $K^+$ ions are included in the crystal structures of the compounds even though excessive amounts of $K^+$ ions are present in the reaction solution.

The role of the $K^+$ ion in the reaction is conjectured as illustrated in Scheme 2: two $K^+$ ions occupy the pseudosymmetrical position in front of the aperture of the structure.[4] Because of the strong coordinative tendency of $K^+$ to bind to the open facial oxygen atoms,[22] two γ-$SiW_{10}$ subunits combine through them. The insertion of transition metal ions and the interjunction of two γ-$SiW_{10}$ subunits would enhance the coordination of $K^+$ to the surrounding oxo ligands, which would lead to stability of the open Wells–Dawson-like structure.

Additionally, the simulative and experimental powder X-ray diffraction patterns of **1** and **2** are coincident as well, which confirms that the as-prepared compounds are pure (see Figure S3).

### Structure Description

Compounds **1**, **2**, and **3** are isomorphic and are isolated as imidazole salts of the γ-$SiW_{10}$ derivative. The anion is a dimer of $[\gamma\text{-}SiW_{10}O_{36}]^{8-}$ subunits that are jointed together by two adjacent terminal oxygen atoms Od′ (Od′, initially marked by Hervé[4]) corner-shared with two pairs of edge-shared $WO_6$ octahedra from two parent $[\gamma\text{-}SiW_{10}O_{36}]^{8-}$ anions (see Figure 1 and Figure S1).

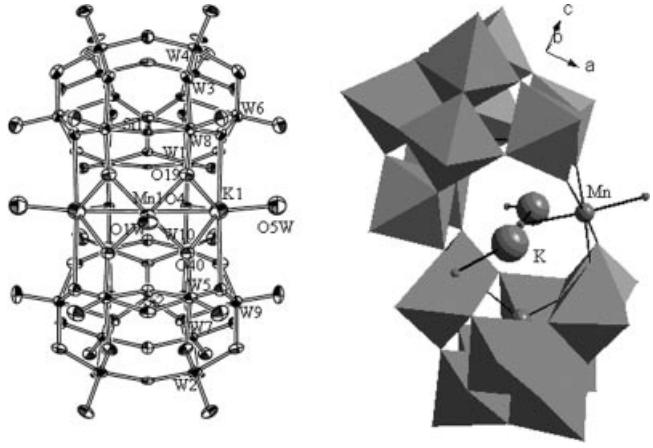


Figure 1. Structure of anion in **1**: the ORTEP view showing the atom-labeling scheme with 50% thermal ellipsoids (left); combined polyhedral/ball and stick representation (right), tungsten–oxygen octahedra, Si (big ball), oxygen (small ball), potassium (labeled), manganese (labeled). All hydrogen atoms are omitted for clarity.

In **1**, eight open facial bridging Ob atoms (four in each γ-$SiW_{10}$ subunit), two oxygen atoms of the W–Od′–W junctions (shared between two γ-$SiW_{10}$ subunits) and the remaining four Od′ atoms (two in each γ-$SiW_{10}$ subunit), totaling fourteen oxygen atoms, delimit the open "mouth". The four Od′ atoms of the edge-shared $WO_6$ octahedral dimer in the hatch of the [γ-$Si_2W_{20}O_{70}$] cluster are strongly basic to form active sites, either for protonation or for coordination,[23] which is a characteristic reminiscent of porphyrin. One $Mn^{II}$ ion is coordinated by the four Od′ atoms like sharp incisors biting a $Mn^{II}$ ion. Perpendicular to the plane of the $MnOd'_4$, two $H_2O$ molecules coordinate to the $Mn^{II}$ center to complete an octahedral coordination environment

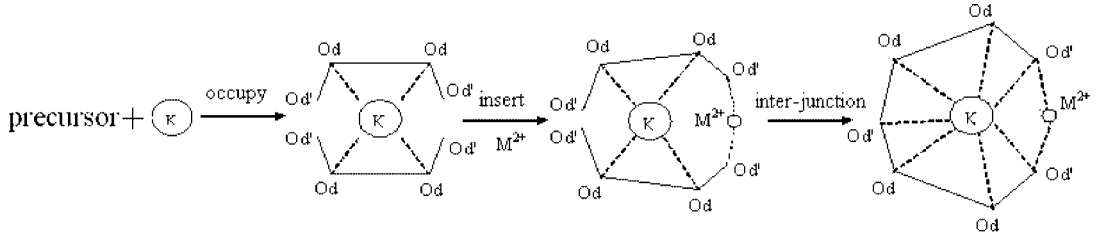


Scheme 2. Illustration of possible role of $K^+$ ions in the formation of the open Wells–Dawson-like structure.

 © 2006 Wiley-VCH Verlag GmbH & Co. KGaA, Weinheim 

of $Mn^{II}$, one towards the outside (O2W) and the other towards the inside (O1W). Interestingly, the "internal" $H_2O$, acting as a tri-bridge $H_2O$ ($\mu_3$-$H_2O$), links two $K^+$ ions in the middle point of the $K^+$-to-$K^+$ line; thus, a T-type connection composed of $K^+$, $\mu_3$-$H_2O$ and $Mn^{II}$ is formed (see Figure 2a). In fact, two $K^+$ ions are located separately on the two parotids of the "mouth", each bonding to seven oxygen atoms; thus, a nine-coordination sphere of the $K^+$ ion is accomplished by the coordination of the inside $\mu_3$-$H_2O$ and the outside $H_2O$ molecules (see Figure 2b). The K–OW bond lengths are in the range 2.80(6)–2.84(2) Å, and seven K–O bond lengths [2.96(1)–3.13(1) Å] correspond to the range (2.76–3.22 Å) reported by Hervé.[22] The W1–O4–W10 angle of the junctions is 135.1° and the bond lengths are1.85(1) Å and 2.02(1) Å, respectively, which is in the normal range for corner W–O–W bridges in each subunit (See Figure S2 for the coordination spheres of **2** and **3**).

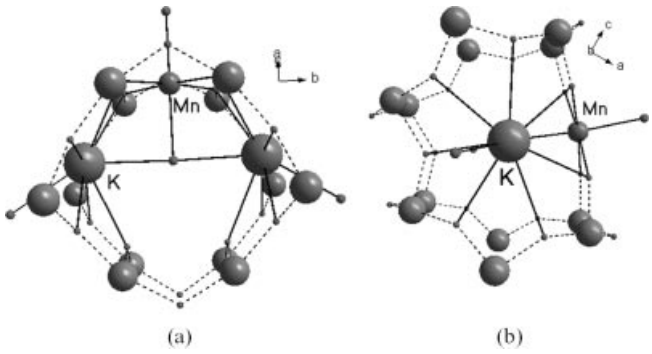


Figure 2. Coordination spheres of $K^+$ and $Mn^{2+}$ in compound **1**: (a) viewed along the normal direction of the ∇ K–M–K plane, (b) viewed along the line of K–$OW_{int}$–K, tungsten (big ball), oxygen (small ball), potassium (labeled), manganese (labeled).

It is interesting to make a comparison with the filling manners of the "mouths" for the $[\gamma\text{-}Si_2W_{20}O_{70}]$ and $[\alpha\text{-}Si_2W_{18}O_{66}]$ clusters. The "mouth" of $[\alpha\text{-}Si_2W_{18}O_{66}]$ seems to be more open than that of $[\gamma\text{-}Si_2W_{20}O_{70}]$. In the former, there exist several filling manners of the "mouth" or "pocket", such as $K_3$, KCo, and $KCo_2$, whereas in the latter the filling manners seem to be more regular, as only $K_2M$ (M = $Mn^{II}$, $Co^{II}$, or $Ni^{II}$) is found.

Selected bond lengths and angles of compounds **1**, **2**, and **3** are listed in Table 1 along with those of the $[\gamma\text{-}SiW_{10}O_{36}]^{8-}$ precursor for comparison. From Table 1 we can see that the bond lengths of Si–Oa ($W_2$ diad) (the oxygen atom belongs to a ditungstic group) are longer in compounds **1**, **2**, and **3** than those of the $[\gamma\text{-}SiW_{10}O_{36}]^{8-}$ precursor, whereas those of Si–Oa ($W_3$ triad) (the oxygen atom belongs to a tritungstic group) are shorter, that is, the Si–Oa bond lengths go to an average value that is close to 1.63 Å for $[\alpha\text{-}SiW_{12}O_{40}]^{4-}$.[1] This would enhance the stability of **1**. Other W–O bond lengths are within their normal values, except for the longer W10–Od (O31) and W10/W1–Od′ (O4) bonds which are the junctions of the two $SiW_{10}$ subunits (see Table S1). The corresponding bond lengths and bond angles of the transition metal in the hatches of $[\gamma\text{-}Si_2W_{20}O_{70}]$ for **1**, **2**, and **3** are listed in Table 2 along with those of $[\alpha\text{-}Si_2W_{18}O_{66}]$ for comparison. The average bond lengths of M–Od′ are 2.12 Å for **1**, 2.05 Å for **2**, and 2.03 Å for **3**, and the W–O–W bond angles of the junctions are smaller than that of $[\alpha\text{-}Si_2W_{18}O_{66}]$.

The anion packing diagram in the unit cell of **1** viewed down the *b* axis is given in Figure 3a. There are four anions labeled as A, A*, B, and B*. The two adjacent anions A and A* or B and B* are, respectively, related by an inversion center and associated with each other in a "mouth-to-mouth" manner by imidazole molecules with the Mn···Mn distance of 8.37 Å. Anions A* and B arrange in a "head-to-head" manner on the same plane, and B* and A run in this manner on another plane (Figure 3b). Thus A*···B···A*···B and B*···A···B*···A form zigzag chains along the *a* axis, respectively, and further extend into a 2D structure along the *c* axis by hydrogen bonding with Im

Table 1. Selected bond length ranges [Å] for **1**, **2**, and **3**.

| Bond length | $[\{K(H_2O)\}_2\{(\mu_3\text{-}H_2O)M(H_2O)\}(\gamma\text{-}Si_2W_{20}O_{70})]^{8-}$ | | | $[\gamma\text{-}SiW_{10}O_{36}]^{8-}$[4] |
|---|---|---|---|---|
| | **1** (M = $Mn^{II}$) | **2** (M = $Co^{II}$) | **3** (M = $Ni^{II}$) | |
| W–Oa | 2.22(1)–2.36(1) | 2.21(10)–2.36(1) | 2.21(1)–2.35(1) | 2.21(5)–2.34(4) |
| W–Ob/Oc | 1.76(1)–2.16(1) | 1.78(1)–2.14(1) | 1.78(1)–2.14(1) | 1.73(5)–2.25(5) |
| W–Od | 1.71(1)–1.88(2) | 1.71(1)–1.88(1) | 1.70(1)–1.84(1) | 1.67(5)–1.77(4) |
| W–Od′ | 1.76(1)–2.02(1) | 1.78(1)–1.98(1) | 1.78(1)–1.96(1) | 1.70(5)–1.79(4) |
| Si–Oa ($W_2$ diad) | 1.62(1)–1.63(1) | 1.59(1)–1.62(1) | 1.60(1)–1.64(1) | 1.54(5)–1.59(5) |
| Si–Oa ($W_3$ triad) | 1.65(1)–1.65(1) | 1.64(1)–1.65(1) | 1.64(1)–1.64(1) | 1.68(4)–1.68(4) |

Table 2. Comparison of the corresponding bond length [Å] and bond angle [°] of metal polyhedrons.

| Bond length/angle | $[\gamma\text{-}Si_2W_{20}O_{70}]$ in **1**–**3** | | | $[\alpha\text{-}Si_2W_{18}O_{66}]$[22] |
|---|---|---|---|---|
| | **1** (M = $Mn^{II}$) | **2** (M = $Co^{II}$) | **3** (M = $Ni^{II}$) | 1Co–K |
| K–O | 2.97(1)–3.13(1) | 2.94(1)–3.09(1) | 2.93(1)–3.08(1) | 2.76–3.22 |
| K–OW(inside) | 2.80(6) | 2.75(9) | 2.77(1) | |
| K–OW(outside) | 2.84(2) | 2.59(5)–2.67(4) | 2.58(6)–2.61(7) | 2.669–3.162 (for K9 and K11) |
| M–OW(inside) | 2.43(1) | 2.22(1) | 2.192(1) | |
| M–OW(outside) | 2.29(2) | 2.09(2) | 2.04(1) | |
| M–Od′ | 2.12(1)–2.12(1) | 2.04(1)–2.05(1) | 2.02(1)–2.03(1) | |
| W–O–W junction | 135.1(6) | 136.4(6) | 136.6(7) | 147.7–148.2 |

 © 2006 Wiley-VCH Verlag GmbH & Co. KGaA, Weinheim 

Table 3. Comparison of the synthetic conditions from precursor $K_8[\gamma\text{-}SiW_{10}O_{36}]$.

| Compound[a] | pH | $T$ [°C] | $t$ | Ref. |
|---|---|---|---|---|
| **I** a) $[(C_4H_9)_4N]_4[(SiO_4)W_{10}Mn^{III}{}_2O_{36}H_6]$ | 3.8–4.5 | – | 5 min | [5] |
| **I** b) $Cs_5[\gamma\text{-}SiO_4W_{10}O_{32}(OH)Cr_2(OOCCH_3)_2(OH_2)_2]$ | 4.8 | 80 | 30 min | [6] |
| **I** c) $[(n\text{-}C_4H_9)_4N]_{3.5}H_{2.5}[\gamma\text{-}SiW_{10}\{Fe(OH_2)\}_2O_{38}]$ | 3.9 | – | 5 min | [7] |
| **I** d) $Cs_4H_2\text{-}\gamma(1,2)\text{-}[SiV_2W_{10}O_{40}]$ | – | – | few min | |
| **I** d) $Cs_6\text{-}\beta(8,12)\text{-}[SiV_2W_{10}O_{40}]$ | 6.5–6.8 | – | 4 h | [8] |
| **I** d) $Cs_6\text{-}\beta(3,8)\text{-}[SiV_2W_{10}O_{40}]$ | 8.0–8.3 | – | 10 min | |
| **I** e) $(Bu_4N)_3H[\gamma\text{-}SiW_{10}O_{36}(RSi)_2O]$ | $CH_3CN$/HCl | – | 6 h | [9] |
| **I** f) $(NEt_4)_6[\gamma\text{-}SiW_{10}Mo_2S_2O_{38}]$ | DMF | 50 | 30 min | [10] |
| **I** g) $(NBu_4)_3K[\gamma\text{-}SiW_{10}O_{36}(HPO)_2]$ | $CH_3CN$/HCl | – | overnight | [11] |
| **I** h) $[(CH_3)_2NH_2]_5[\beta\text{-}SiFe_2W_{10}O_{36}(OH)_2(H_2O)Cl]$ | 1.7 | – | 5 min | [12] |
| **II** a) $Cs_9H[(PhSnOH_2)_2(\gamma\text{-}SiW_{10}O_{36})_2]$ | – | – | rapid | [13a] |
| **II** b) $K_xNa_{12-x}[\{SiM_2W_9O_{34}(H_2O)\}_2]^{12-}$ (M = $Mn^{2+}$,$Cu^{2+}$,$Zn^{2+}$) | 4.8 | 90 | 40 min | [14] |
| **III** a) $K_{12}[\{\beta\text{-}SiNi_2W_{10}O_{36}(OH)_2(H_2O)\}_2]$ | 4.8 | 50 | 45 min | [15] |
| **III** b) $K_{24}[\{\beta\text{-}Ti_2SiW_{10}O_{39}\}_4]$ | 2 | 80 | 1 h | [16] |
| **III** c) $Na_5[Co_6(H_2O)_{30}\{Co_9Cl_2(OH)_3(H_2O)_9(\beta\text{-}SiW_8O_{31})_3\}]$ | 5.5 | 50 | 30 min | [17] |
| **III** d) $Cs_4K_{11}[(\beta_2\text{-}SiW_{11}MnO_{38}OH)_3]$ | 3.9 | – | 15 min | [18] |
| **III** e)$K_{10}Na_{12}[\{Co_3(B\text{-}\beta\text{-}SiW_9O_{33}(OH))[B\text{-}\beta\text{-}SiW_8O_{29}(OH)_2]\}_2]$ | 4.8 | 50 | 30 min | [19] |
| **III** f) $Rb_6H_3[Si_2W_{23}O_{77}(OH)]$ | $HClO_4$ | – | 1 h | [20] |

[a] **I**: complete γ- or β-Keggin-type **II**: sandwich-type **III**: oligomer.

molecules. There are significant contacts between oxo groups of the anions and imidazole molecules along the *b* axis, which leads to a linear chain of the anions with a straight linkage of K···K···K (see Figure 4). Imidazole and water molecules fill in the space among the anions.

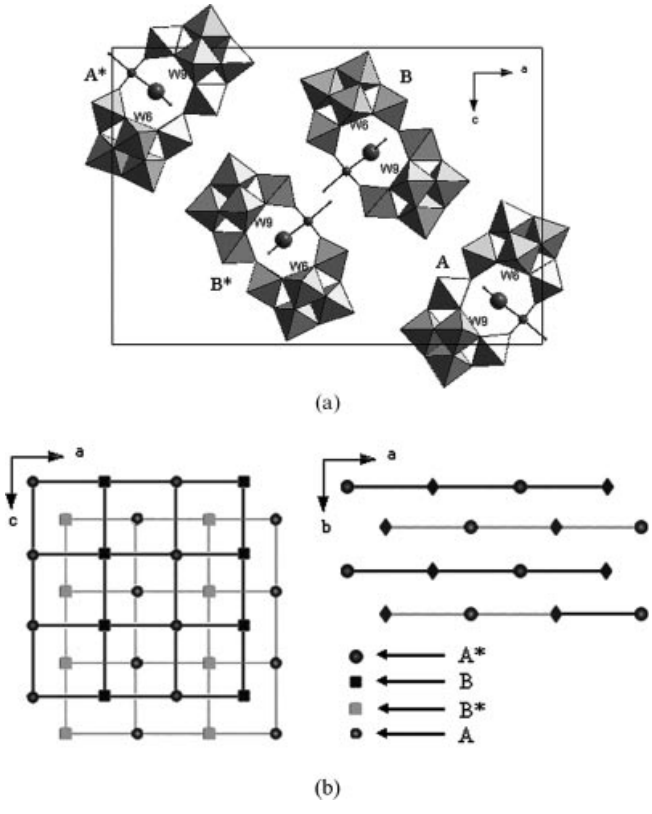


Figure 3. Schematic representation of the relative locations of the polyanions. (a) Packing diagram in **1** viewed along the *b* axis. (b) 3D supramolecular network based on the topology of anion–anion position.

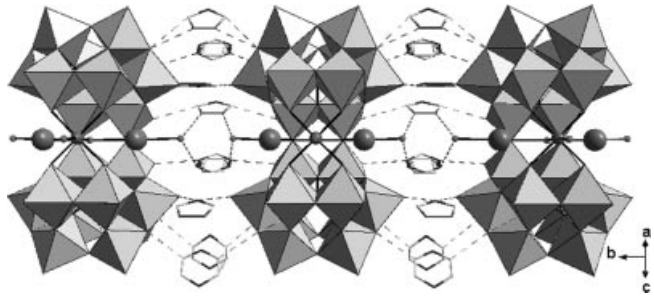


Figure 4. View of the connection between the polyanions and Im molecules through hydrogen bonding. All water molecules are omitted for clarity.

Because compounds **2** and **3** are isomorphs of **1**, structural descriptions for them are omitted. The difference between them is that the outer $H_2O$ molecule that is coordinated to the $K^+$ ion is disordered with an occupancy factor of 50% for both **2** and **3**. Additionally, there exists other disordered water and imidazole molecules in the crystal structures of these three complexes.

The assignment of the oxidation state of Mn is based on bond valence sum (BVS) calculations,[24] which gives a value of 2.064 and indicates the +2 oxidation state. The inside O atom and the outside O atom of the Mn–O bonds have much lower BVS values, 0.180 and 0.252, which suggests that they are water ligands (O1W and O2W). The BVS values of the bridge and terminal oxygen atoms show that they are not protonated. While in the acidic condition, the N atom of imidazole is easily protonated and leads to the formation of the stable salts. Thus, including $K^+$ and $M^{II}$, the anionic structure can be written as $[\{K(H_2O)\}_2\{(\mu_3\text{-}H_2O)M(H_2O)\}(Si_2W_{20}O_{70})]^{8-}$ (M = $Mn^{2+}$, $Co^{2+}$ or $Ni^{2+}$). Overall, the anions have an ideal symmetry of $C_{2v}$.

 © 2006 Wiley-VCH Verlag GmbH & Co. KGaA, Weinheim 

### IR Spectra

The infrared spectra of **1**, **2**, and **3**, measured in the range 400–1000 $cm^{-1}$, show characteristic absorptive peaks for the γ-anion at ca. 993 $cm^{-1}$ for $\nu_{as}$(W–Od), 940 $cm^{-1}$ for $\nu_{as}$(Si–Oa), 895 and 861 $cm^{-1}$ for $\nu_{as}$(W–Ob–W), 780 and 741 $cm^{-1}$ for $\nu_{as}$(W–Oc–W), which indicates the retention of the γ-tungstosilicate framework (see Figure S4).[6] In comparison with the $\nu_{as}$(W–O–W) in γ-$SiW_{10}$, the splitting of the corresponding bands in the range 700–850 $cm^{-1}$ is weakened in the title compounds and is due to the coordination of the transition metal ion, as in the case of the monosubstituted tungstosilicate. Additionally, the vibration bands in the range 1000–1200 $cm^{-1}$ are assigned to those of imidazole and around 620 $cm^{-1}$ to those of the M–O bonds.

### Thermogravimetric(TG) Analysis

The TG curve for **1** is divided into three stages. The first weight loss of 3.05% in the temperature range 45–180 °C corresponds to the release of crystal water and is in good agreement with the calculated value of 3.1%. The successive weight loss of the second step (5.68%) from 200 °C to 350 °C and the third step (7.93%) from 520 °C to 750 °C is ascribed to the release of imidazole and structural water, respectively, which is around the combined calculated value of 13.16%. No weight loss occurs above 750 °C. TG for **2** (see Figure S5) is similar to that of **1**.

### Cyclic Voltammetry (CV)

The CV behaviors of **1**, **2**, and **3** are similar (see Figure 5). Each CV curve shows two pairs of redox peaks with $E_1$ = –582 mV and $E_2$ = –685 mV for **1**, $E_1$ = –581 mV and $E_2$ = –688 mV for **2**, and $E_1$ = –570 mV and $E_2$ = –675 mV for **3**, where $E$ = ($E$pa + $E$pc)/2, in 0.5 M KAc/HAc buffer (pH 3.9). The anodic-to-cathodic peak potential difference for each pair of redox waves is ca.30 mV and the peak-to-peak distance between $E_1$ and $E_2$ is ca. 100 mV for each compound, which shows a similar electrochemical behavior to that of the parent γ-$SiW_{10}$, except that the half-wave potentials shift positively. These can be reasonably explained by the global charges of the polyanions. Both of the anions, [{$K(H_2O)$}$_2$($\mu_3$-$H_2O$)$M(H_2O)$(γ-$Si_2W_{20}O_{70}$)]$^{8-}$ and [γ-$SiW_{10}O_{36}$]$^{8-}$, are in the –8 charge state, while the anion volume of the former is double that of the latter, which leads to less electronic density on the anion global.

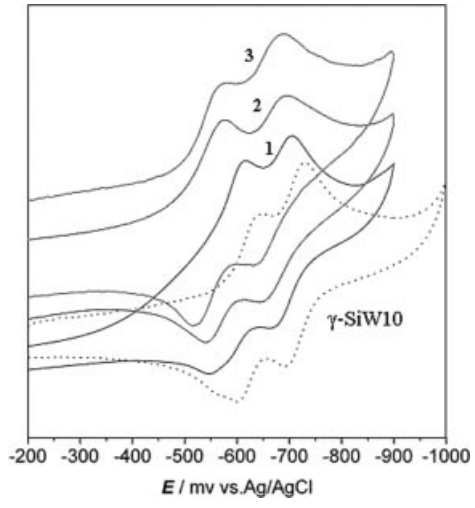


Figure 5. The cyclic voltammogram (glassy-carbon working electrode, scan-rate 50 mV $s^{-1}$, 0.5 M KAc–HAc, pH = 3.9) of compounds **1**, **2**, and **3** and precursor γ-$SiW_{10}$.

## Conclusions

In summary, three novel compounds based on γ-$SiW_{10}$ subunits have been isolated in acidic solutions. They are successful examples of the γ-$SiW_{10}$ derivative possessing an open Wells–Dawson-like sandwich structure with $K^+$ and $M^{II}$ ions symmetrically enchased in the hatch of the (γ-$SiW_{10}$)$_2$ dimer, giving the compound structural aesthetics. To check if the solid structure is stable in solution without the dissociation of the potassium cations, electrophoresis of compound **1** was carried out. The analytical result of the anodic area indicates that the potassium cations are attached to the polyoxo dimers and move towards the anode direction. This fact supports the polyanion structure formulated by [{$K(H_2O)$}$_2${($\mu_3$-$H_2O$)$M(H_2O)$}(γ-$Si_2W_{20}O_{70}$)]$^{8-}$ and that the solid structure of the dimeric anions is maintained in the solution without the dissociation of the potassium cations, under the tested pH of 3.6.

This new crystal structure suggests that the skeleton of the unstable species γ-$SiW_{10}$ could also be maintained by carefully controlling the reaction conditions. The functions of potassium and transition-metal ions in the reactions of γ-$SiW_{10}$ are not clearly understood yet and attempts to clarify them still represent a challenge. Kortz and co-workers have emphasized the crucial role of potassium ions in the synthesis medium, especially in the order of addition of the solid KCl.[13] The title compounds were isolated under similar reaction conditions to those reported by Kortz and coworkers. However, they obtained full potassium salts and we obtained imidazole–potassium mixed salts of Keggin-γ-type dimers. Besides the presence of imidazole, the difference in the order of addition of the solid KCl perhaps is the reason why mixed salts were crystallized in our case. Kortz's and our synthetic investigations both lead to the conclusion that the formation of the dimers is highly sensitive to pH and temperature variations.

The filling style in the "mouth" of the [γ-$Si_2W_{20}O_{70}$] is perhaps less random than those of the [α-$Si_2W_{18}O_{66}$] because of the feature of the opening. The external $H_2O$ ligand that is coordinated to $M^{II}$ is likely to improve the catalytic activity and would be a further derivative of the polytungstates. We will attempt to modify the framework so as to obtain more unexpected species with interesting structure and properties.

 © 2006 Wiley-VCH Verlag GmbH & Co. KGaA, Weinheim 

## Experimental Section

**Materials and Methods:** The precursor $K_8[\gamma\text{-}SiW_{10}O_{36}]\cdot 12H_2O$ was prepared according to the literature[28] and its purity was confirmed by infrared spectroscopy and cyclic voltammetry. All other reagents were used as purchased without further purification. Elemental analyses were carried out with a Plasma-Spec(I) ICP emission spectrometer for W, Si, and transition metal elements and with a PE-3030 atomic absorption spectrophotometer for K. To carry out the elemental analysis measurements, the samples were dissolved in water by assistance of $H_2O_2$ as these imidazole salts have poor solubility in water. Infrared spectra were recorded with an Alpha Centaurt FTIR spectrometer in the 4000–400 $cm^{-1}$ region. X-ray powder diffraction (XRPD) patterns were recorded with a Siemens D5005 diffractometer with Cu-$K_\alpha$($\lambda$ = 1.5418 Å) radiation. Thermogravimetry was carried out with a Perkin–Elmer TGA-7 instrument in flowing $N_2$ with a heating rate of 10 °C $min^{-1}$ up to 800 °C. Electrochemical data were obtained with a CHI 660 Electrochemical Workstation connected to a Digital-586 personal computer under $N_2$ gas, with the use of a conventional three-electrode system.

**Synthesis of $(HIm)_8[\{K(H_2O)\}_2\{(\mu_3\text{-}H_2O)Mn(H_2O)\}(Si_2W_{20}O_{70})]\cdot 10H_2O$(Im = imidazole) (1):** Solid $MnSO_4\cdot 2H_2O$ (0.076 g, 0.41 mmol) was added with stirring to a solution of imidazole (0.55 g, 2.3 mmol) dissolved in water (20 mL). Glacial acetic acid was then added dropwise until pH 3.6 was reached. To the resulting solution, $K_8[\gamma\text{-}SiW_{10}O_{36}]\cdot 12H_2O$ (0.226 g, 0.075 mmol) dissolved in water (2 mL) was immediately added, followed by the addition of solid KCl (2–3 g, ca. 30 mmol). Finally, the yellow solution was cooled to room temperature and filtered through a fine frit. Prism-like yellow crystals were obtained after 3 d from the filtrate. Yield: 0.142 g (65% based on $\gamma\text{-}SiW_{10}$). IR (KBr pellet): 1093, 1049, 993, 950, 894, 861, 781, 741, 621, 555 $cm^{-1}$. $C_{24}H_{35.76}K_2MnN_{16}O_{84}Si_2W_{20}$ (5758.57): calcd. W 63.22, Si 0.96, Mn 0.94, K, 1.34; found W 63.09, Si 0.92, Mn 0.96, K 1.30.

**Synthesis of $(HIm)_8[\{K(H_2O)\}_2\{(\mu_3\text{-}H_2O)Co(H_2O)\}(Si_2W_{20}O_{70})]\cdot 9H_2O$ (2):** The synthesis of **2** followed a similar procedure to that of compound **1**, except $Co(NO_3)_2\cdot 6H_2O$ (0.058 g, 0.20 mmol) was used instead of $MnSO_4\cdot 2H_2O$. The reaction solution was heated to 45 °C with stirring for 15 min and filtered for lustration. Prism-like rosy crystals were obtained after ca.6 d from the filtrate. Yield: 0.113 g (52% based on $\gamma\text{-}SiW_{10}$). IR (KBr pellet): 1098, 1051, 998, 952, 897, 863, 778, 743, 622, 549 $cm^{-1}$. $C_{24}H_{31.5}K_2CoN_{16}O_{83}Si_2W_{20}$ (5742.26): calcd. W 63.92, Si 0.97, Co 1.02, K 1.36; found W 63.73, Si 0.94, Co 1.09, K 1.32.

**Synthesis of $(HIm)_8[\{K(H_2O)\}_2\{(\mu_3\text{-}H_2O)Ni(H_2O)\}(Si_2W_{20}O_{70})]\cdot 9H_2O$ (3):** The synthesis of **3** followed a similar procedure to that of compound **2**, except $NiSO_4\cdot 6H_2O$ (0.105 g, 0.40 mmol) was used instead of $Co(NO_3)_2\cdot 6H_2O$. Prism-like slight green crystals were obtained after six months. Yield: 0.022 g (10% based on $\gamma\text{-}SiW_{10}$). IR (KBr pellet): 1091, 1049, 995, 951, 895, 861, 781, 739, 626, 554 $cm^{-1}$. $C_{24}H_{26}K_2NiN_{16}O_{83}Si_2W_{20}$ (5736.70): calcd. W 64.3, Si 0.97, Ni 1.03, K 1.36; found W 64.05, Si 0.92, Ni 0.98, K 1.29.

**X-ray Crystallography:** Single-crystals of **1** (0.37 × 0.11 × 0.10 mm), **2** (0.24 × 0.07 × 0.05 mm), and **3** (0.35 × 0.12 × 0.05 mm) were taken directly from the mother liquor and immediately cooled to 193(2) K on a Bruker SMART CCD diffractometer with graphite-monochromated Mo-$K_\alpha$ radiation ($\lambda$ = 0.71703 Å). Semi-empirical absorption correction based on symmetry equivalent reflections was applied. A total of 53450 reflections for **1** were collected, of which 9634 were unique ($R_{(int)}$ = 0.0531), a total of 52611 reflections for **2** were collected, of which 9454 reflections were unique ($R_{(int)}$ = 0.0516), and a total of 58285 reflections for **3** were collected, of which 10568 reflections were unique ($R_{(int)}$ = 0.1003) ($1.52 < \theta < 25.01°$). The structures were solved by direct methods and difference Fourier techniques and refined by the full-matrix least-squares method on the basis of $F^2$. Structure solution, refinement, and generation of publication materials were performed with the use of the SHELXTL crystallographic software package.[29] Some C and N atoms and some water molecules were not anisotropically refined to solve disorder. The hydrogen atoms of imidazole and water were geometrically placed and refined with the use of a riding model. However, some hydrogen atoms have not been included in the final refinement because of the presence of some disordered imidazole and water. Crystallographic data are summarized in Table 4. Atomic coordinates and isotropic displacement parameters for the anions of **1**, **2**, and **3** are listed in Tables S2, S3, and S4. CCDC-294280 for **1**, -294279 for **2**, and -604702 for **3** contain the supplementary crystallographic data for this paper. These data can be obtained free of charge from The Cambridge Crystallographic Data Centre via www.ccdc.cam.ac.uk/data_request/cif.

**Supporting Information** (see footnote on the first page of this article): Tables of atomic coordinates and isotropic displacement parameters, figures showing coordination spheres of $K^+$ and $M^{2+}$ for

Table 4. Crystal data and structure refinement for **1**, **2**, and **3**.

| | **1** | **2** | **3** |
|---|---|---|---|
| Empirical formula | $C_{48}H_{71.52}K_4Mn_2N_{32}O_{168}Si_4W_{40}$ | $C_{48}H_{63}Co_2K_4N_{32}O_{166}Si_4W_{40}$ | $C_{48}H_{52}K4N_{32}Ni_2O_{166}Si_4W_{40}$ |
| Formula mass | 11517.13 | 11484.52 | 11444.93 |
| Space group | *Pnma* | *Pnma* | *Pnma* |
| *a* [Å] | 33.1566(14) | 32.9856(15) | 32.947(2) |
| *b* [Å] | 13.6167(6) | 13.5564(6) | 13.5430(10) |
| *c* [Å] | 22.9345(10) | 22.9521(11) | 22.9577(16) |
| *V* [Å$^3$] | 10354.5(8) | 10263.4(8) | 10243.8(12) |
| *Z* | 2 | 2 | 2 |
| $D_{calcd.}$ [g $cm^{-3}$] | 3.694 | 3.716 | 3.711 |
| *T* [K] | 193(2) | 193(2) | 193(2) |
| $\lambda$ [Å] | 0.71073 | 0.71073 | 0.71073 |
| $\mu$ [$mm^{-1}$] | 22.447 | 22.684 | 22.748 |
| GOF | 1.058 | 1.059 | 1.026 |
| Final $R_1$[a] [$I > 2\sigma(I)$] | 0.0529 | 0.0483 | 0.0564 |
| Final $wR_2$[b] [$I > 2\sigma(I)$] | 0.1478 | 0.1350 | 0.1689 |

[a] $R_1 = \Sigma||F_o|-|F_c||/|F_o|$. [b] $wR_2 = \{\Sigma[w(F_o^2-F_c^2)^2]/\Sigma[w(F_o^2)^2]\}^{0.5}$.

 © 2006 Wiley-VCH Verlag GmbH & Co. KGaA, Weinheim 

compounds **2** and **3**, XRD, IR, TG, and X-ray crystallographic data of compounds **1**, **2** and **3**.

## Acknowledgments

This work was supported by the National Natural Science Foundation of China (No. 20671016).

[1] a) M. T. Pope, *Heteropoly and Isopoly Oxometalates*, Springer, Berlin, **1983**; b) P. Kögerler, L. Cronin, *Angew. Chem. Int. Ed.* **2005**, *44*, 844–846.

[2] a) M. T. Pope, A. Müller, *Angew. Chem. Int. Ed. Engl.* **1991**, *30*, 34–48; b) Y. Nakagawa, K. Uehara, N. Mizuno, *Inorg. Chem.* **2005**, *44*, 14–16; c) T. Hayashi, A. Kishida, N. Mizuno, *Chem. Commun.* **2000**, 381–382; d) K. Kamata, K. Yonehara, Y. Sumida, K. Yamaguchi, S. Hikichi, N. Mizuno, *Science* **2003**, *300*, 964–966; e) Y. Nishiyama, Y. Nakagawa, N. Mizuno, *Angew. Chem. Int. Ed.* **2001**, *40*, 3639–3641.

[3] a) S. Bareyt, S. Piligkos, B. Hasenknopf, P. Gouzerh, E. Lacote, S. Thorimbert, M. Malacria, *J. Am. Chem. Soc.* **2005**, *127*, 6788–6794; b) L. H. Bi, U. Kortz, *Inorg. Chem.* **2004**, *43*, 7961–7962.

[4] J. Canny, A. Tézé, R. Thouvenot, G. Hervé, *Inorg. Chem.* **1986**, *25*, 2114–2119.

[5] X.-Y. Zhang, C. J. O'Connor, G. B. Jameson, M. T. Pope, *Inorg. Chem.* **1996**, *35*, 30–34.

[6] K. Wassermann, H. J. Lunk, R. Palm, J. Fuchs, N. Steinfeldt, R. Stösser, M. T. Pope, *Inorg. Chem.* **1996**, *35*, 3273–3279.

[7] C. Nozaki, I. Kiyoto, Y. Minai, M. Misono, N. Mizuno, *Inorg. Chem.* **1999**, *38*, 5724–5729.

[8] J. Canny, R. Thouvenot, A. Tézé, G. Hervé, M. Leparulo-Loftus, M. T. Pope, *Inorg. Chem.* **1991**, *30*, 976–981.

[9] C. R. Mayer, I. Fournier, R. Thouvenot, *Chem. Eur. J.* **2000**, *6*, 105–110.

[10] E. Cadot, V. Béreau, B. Marg, S. Halut, F. Sécheresse, *Inorg. Chem.* **1996**, *35*, 3099–3106.

[11] C. R. Mayer, P. Herson, R. Thouvenot, *Inorg. Chem.* **1999**, *38*, 6152–6158.

[12] B. Botar, Y. V. Geletii, P. Kogerler, D. G. Musaev, K. Morokuma, I. A. Weinstock, C. L. Hill, *Dalton Trans.* **2005**, 2017–2021.

[13] a) F. Xin, M. T. Pope, *Inorg. Chem.* **1996**, *35*, 5693–5695; b) F. Xin, M. T. Pope, G. J. Long, U. Russo, *Inorg. Chem.* **1996**, *35*, 1207–1213; c) During the preparation of this paper, three potassium salts of decatungstosilicate dimers were reported: B. S. Bassil, M. H. Dickman, M. Reicke, U. Kortz, B. Keitab, L. Nadjo, *Dalton Trans.* **2006**, 4253. DOI: 10.1039/b606911h.

[14] U. Kortz, S. Isber, M. H. Dickman, D. Ravot, *Inorg. Chem.* **2000**, *39*, 2915–2922.

[15] U. Kortz, Y. P. Jeannin, A. Tézé, G. Hervé, S. Isber, *Inorg. Chem.* **1999**, *38*, 3670–3675.

[16] F. Hussain, B. S. Bassil, L. H. Bi, M. Reicke, U. Kortz, *Angew. Chem. Int. Ed.* **2004**, *43*, 3485–3488.

[17] B. S. Bassil, S. Nellutla, U. Kortz, A. C. Stowe, J. van Tol, N. S. Dalal, B. Keita, L. Nadjo, *Inorg. Chem.* **2005**, *44*, 2659–2665.

[18] U. Kortz, S. Matta, *Inorg. Chem.* **2001**, *40*, 815–817.

[19] B. S. Bassil, U. Kortz, A. S. Tigan, J. M. Clemente-Juan, B. Keita, P. de Oliveira, L. Nadjo, *Inorg. Chem.* **2005**, *44*, 9360–9368.

[20] A. Tézé, M. Michelon, G. Hervé, *Inorg. Chem.* **1997**, *36*, 5666–5669.

[21] a) J. Peng, W. Z. Li, E. B. Wang, Q. L. Bai, *J. Chem. Soc., Dalton Trans.* **2001**, 3668–3671; b) J. Peng, H. Y. Ma, Z. G. Han, B. X. Dong, W. Z. Li, J. Lu, E. B. Wang, *Dalton Trans.* **2003**, 3850–3855.

[22] N. Leclerc-Laronze, J. Marrot, G. Hervé, *Inorg. Chem.* **2005**, *44*, 1275–1281.

[23] D. G. Musaev, K. Morokuma, Y. V. Geletii, C. L. Hill, *Inorg. Chem.* **2004**, *43*, 7702–7708.

[24] I. D. Brown, D. Altermatt, *Acta Crystallogr., Sect. B* **1985**, *41*, 244–247.

[25] A. Tézé, J. Canny, L. Gurban, R. Thouvenot, G. Hervé, *Inorg. Chem.* **1996**, *35*, 1001–1005.

[26] N. Leclerc-Laronze, J. Marrot, G. Hervé, *Inorg. Chem.* **2003**, *42*, 5857–5862.

[27] T. M. Anderson, W. A. Neiwert, C. L. Hill, *Inorg. Chem.* **2004**, *43*, 7353–7358.

[28] A. Tézé, G. Hervé, *Inorg. Synth.* **1990**, *27*, 85–88.

[29] G. M. Sheldrick, *SHELXS-97, Program for Crystal Structure Solution*, University of Göttingen, Germany, **1997**.

Received: August 1, 2006
Published Online: October 12, 2006

 © 2006 Wiley-VCH Verlag GmbH & Co. KGaA, Weinheim 

DOI: 10.1002/ejic.200600479

# Syntheses, Characterization, and X-ray Crystal Structures of Mono-Lacunary Dawson Polyoxometalate-Based Organosilyl Complexes

Chika Nozaki Kato,[a] Yuhki Kasahara,[a] Kunihiko Hayashi,[a] Asuka Yamaguchi,[a] Takeshi Hasegawa,[a] and Kenji Nomiya*[a]

**Keywords:** Silicon / Polyoxometalates / X-ray diffraction / Tungsten

The syntheses and crystal structures of a series of organosilyl polyoxotungstate derivatives with the Dawson monovacant phosphotungstate $[\alpha_2\text{-}P_2W_{17}O_{61}]^{10-}$ are described. The polyoxometalates $(Me_2NH_2)_5H[\alpha_2\text{-}P_2W_{17}O_{61}\{O[Si(CH_2)_3SH]_2\}]\cdot 6H_2O$ ($Me_2NH_2$-**1**), $(Me_2NH_2)_6[\alpha_2\text{-}P_2W_{17}O_{61}\{O[Si(CH_2)_3SCN]_2\}]\cdot 3H_2O$ ($Me_2NH_2$-**2**), and $(Me_2NH_2)_6[\alpha_2\text{-}P_2W_{17}O_{61}\{O(SiPh)_2\}]\cdot 4H_2O$ ($Me_2NH_2$-**3**) were obtained as analytically pure, homogeneous yellow crystals by the reaction of monolacunary Dawson polyoxotungstate with $HS(CH_2)_3Si(OMe)_3$, $NCS(CH_2)_3Si(OEt)_3$, and $PhSiCl_3$, respectively, in an HCl/water/acetonitrile mixed solution or a water/acetonitrile mixed solution, followed by crystallization from water in the dark. Single-crystal X-ray structure analyses revealed that the four-coordinate –Si–O–Si– bonding of the organosilyl groups $\{O[Si(CH_2)_3SH]_2\}$, $\{O[Si(CH_2)_3SCN]_2\}$, and $\{O(SiPh)_2\}$ is attained through four oxygen atoms in the mono-lacunary site of the polyanion, resulting in an overall $C_1$ symmetry for $Me_2NH_2$-**1** and $Me_2NH_2$-**2** and $C_s$ symmetry for $Me_2NH_2$-**3**. In the molecular structures of $Me_2NH_2$-**1** and $Me_2NH_2$-**2**, a unique configuration of the organosilyl groups is observed in the solid state, i.e. the equatorial and axial bonding of each of the two $HS(CH_2)Si$ moieties in the $\{O[Si(CH_2)_3SH]_2\}$ group for $Me_2NH_2$-**1** and the two $NCS(CH_2)_3Si$ moieties oriented in a *syn* fashion in the $\{O[Si(CH_2)_3SCN]_2\}$ group for $Me_2NH_2$-**2**. The characterization of $Me_2NH_2$-(**1**–**3**) was accomplished by elemental analysis, TG/DTA, and FT-IR, solution ($^1H$, $^{13}C$, and $^{31}P$) NMR, and solid-state $^{13}C$ NMR spectroscopy.

(© Wiley-VCH Verlag GmbH & Co. KGaA, 69451 Weinheim, Germany, 2006)

## Introduction

Polyoxometalates (POMs) have attracted considerable attention because of their extreme versatility and unique range of properties, including catalytic and biological activities and/or photo- and electrochromism.[1] The introduction of organic groups into POMs is an efficient technology to significantly increase the number of organic–inorganic hybrid compounds and thus to improve their properties. For example, organostannyl derivatives such as $[TW_{11}O_{39}(SnCH_2CH_2X)]^{n-}$ [T (isomer) = Si (α), Ge (α), Ga (a mixture of α and β); X = COOH, $COOCH_3$, $CONH_2$, CN; *n* = 5,6],[2] $[\alpha\text{-}XW_{11}O_{39}(SnR)]^{n-}$ [X = P, As, Si; R = Me, *n*Bu, Ph, $CH_2C_6H_5$, $(CH_2)_3Br$, $(CH_2)_4Cl$, $(CH_2)_{11}CH_3$, $(CH_2)_6Br$, $C_{27}H_{45}$, CN; *n* = 5,6],[3] $[\alpha_2\text{-}X_2W_{17}O_{61}(SnR)]^{7-}$ [X = P, As; R = Me, *n*Bu, Ph, $(CH_2)_{11}CH_3$],[3] $[\alpha_2\text{-}P_2W_{17}O_{61}(SnCH_2R)]^{7-}$ (R = $CH_2COOH$, $CH_2COOEt$, $CH{=}CH_2$, $CH_2CHO$),[4] $[\alpha_1\text{-}P_2W_{17}O_{61}(SnCH_2R)]^{7-}$ (R = $CH_2COOH$, $CH_2COOEt$, $CH_2COOMenthyl$),[4] $[(\beta\text{-}APW_9O_{34})_2(RSnOH)_3]^{12-}$ (R = Ph, Bu),[5] $[\alpha\text{-}P_2W_{15}O_{59}(RSn)_3]^{9-}$ (R = Ph, Bu),[5] $[SiW_9O_{37}(RSn)_3]^{7-}$ (R, isomer: Ph, α; *n*Bu, α; Ph, β; *n*Bu, β),[6] and $[(SiW_9O_{34})_2(RSnOH)_3]^{14-}$ (R, isomer: Ph, α; *n*Bu, α; Ph, β; *n*Bu, β),[6] and $[(\gamma\text{-}SiW_{10}O_{36})_2(PhSnOH)_2]^{10-}$;[7] organophosphonyl derivatives such as $[\alpha\text{-}A\text{-}PW_9O_{34}(RPO)_2]^{5-}$ (R = Et, *n*Bu, *t*Bu, allyl, Ph),[8] $[\alpha\text{-}T^{n+}W_{11}O_{39}(PhPO)_2]^{(8-n)-}$ (T = $P^{5+}$, $Si^{4+}$),[9] $[\alpha\text{-}PW_{11}O_{39}(PhPO)][PhPO(OH)]^{4-}$,[9] $[\gamma\text{-}SiW_{10}O_{36}(RPO)_2]^{4-}$ [R = H, Et, *n*Bu, *t*Bu, $C_2H_4COOH$, Ph],[10] and $[\gamma\text{-}H_2\{(SiW_{10}O_{36})[O{=}PCH_2(C_6H_4)_nCH_2P{=}O]\}_2]^{6-}$;[11] organogermanyl derivatives such as $[TW_{11}O_{39}\{GeCH_2CH_2X\}]^{n-}$ [T (isomer) = Si (α), Ge (α), Ga (a mixture of α and β); X = COOH, $COOCH_3$, $CONH_2$, CN; *n* = 5, 6];[2] and organosilyl derivatives such as $[\alpha\text{-}SiW_{11}O_{40}(SiR)_2]^{4-}$ [R = $C_2H_5$, $CH{=}CH_2$, $C_{10}H_{21}$, Ph, $NC(CH_2)_3$, $C_3H_5$],[12] $[\alpha_2\text{-}P_2W_{17}O_{61}\{O(SiR)_2\}]^{6-}$ {R = $C_6H_5$, 4-$[(C_2H_5O)_2P(=O)CH_2]$-$C_6H_4$, $C_3H_6SH$},[13,14] $[\gamma\text{-}PW_{10}O_{36}(t\text{BuSiOH})_2]^{3-}$,[15] $[\gamma\text{-}PW_{10}O_{36}(t\text{BuSiO})_2(SiMe_2)]^{3-}$,[15] $[\gamma\text{-}SiW_{10}O_{36}(RSiO)_4]^{4-}$ [R = Ph, $CH_2{=}C(CH_3)CO_2(CH_2)_3$],[16] $[\alpha\text{-}A\text{-}PW_9O_{34}(t\text{BuSiO})_3(SiR)]^{3-}$ [R = H, $CH_3$, Et, $CH{=}CH_2$, $CH_2\text{-}CH{=}CH_2$, $(CH_2)_4CH{=}CH_2$, $CH_2CH_2CH_2Cl$],[17,18] $[\alpha\text{-}A\text{-}TW_9O_{34}(R_2Si)_3]^{n-}$ (T = Si, P; R = Me, Ph; *n* = 3,4),[18] $[\alpha\text{-}A\text{-}PW_9O_{34}(t\text{BuSiOH})_3]^{3-}$,[18] $[\alpha\text{-}B\text{-}AsW_9O_{33}(t\text{BuSiOH})_3]^{3-}$,[18] $[\alpha\text{-}B\text{-}AsW_9O_{33}(t\text{BuSiO})_3(RSi)]^{3-}$,[18] $[\alpha\text{-}A\text{-}TW_9O_{34}(RSiO)_3(RSi)]^{n-}$ (T = Si, P; R = H, Me, $C_2H_3$, Et, *n*Bu; *n* = 3,4),[19,20] and $[\gamma\text{-}SiW_{10}O_{36}\{O(SiC_3H_6SH)_2\}]^{4-}$[21] have been reported. In particular, $[\alpha_2\text{-}P_2W_{17}O_{61}\{O(SiC_3H_6SH)_2\}]^{6-}$

[a] Department of Materials Science, Faculty of Science, Kanagawa University,
Tsuchiya 2946, Hiratsuka, Kanagawa 259-1293, Japan
Fax: +81-463-58-9684
E-mail: nomiya@kanagawa-u.ac.jp

Supporting information for this article is available on the WWW under http://www.eurjic.org or from the author.

 © 2006 Wiley-VCH Verlag GmbH & Co. KGaA, Weinheim 

and $[\gamma\text{-}SiW_{10}O_{36}\{O(SiC_3H_6SH)_2\}]^{4-}$ are intriguing examples of the use of organic moieties having an –SH group grafted to the lacunary sites of $[\alpha_2\text{-}P_2W_{17}O_{61}]^{10-}$ and $[\gamma\text{-}SiW_{10}O_{36}]^{8-}$ to derive new nanoscale hybrid systems in which covalent linkages between the polyoxometalate species and chlorobenzyl-functionalized polymer nanoparticles or gold nanoparticles are formed through the thiol groups. Although various types of complexes with organic groups have been prepared, the molecular structures of only a few complexes have been determined by X-ray crystallography. These include $[(\beta\text{-A-}PW_9O_{34})_2(PhSnOH)_3]^{12-}$,[5] $[\alpha\text{-}P_2W_{15}O_{59}(PhSn)_3]^{9-}$,[5] $[\beta\text{-}SiW_9O_{37}(PhSn)_3]^{7-}$,[6] $[(\alpha\text{-}SiW_9O_{34})_2(BuSnOH)_3]^{14-}$,[6] $[\alpha\text{-}PW_{11}O_{39}(PhPO)_2]^{3-}$,[9] $[\gamma\text{-}PW_{10}O_{36}(t\text{BuSiOH})_2]^{3-}$,[15] $[\alpha\text{-A-}PW_9O_{34}(t\text{BuSiO})_3(SiCH_2\text{-}CH{=}CH_2)]^{3-}$,[17] and $[\alpha\text{-A-}PW_9O_{34}(RSiO)_3(RSi)]^{3-}$ (R = $C_2H_3$, $CH_3$, $C_2H_5$).[18,20] In particular, X-ray crystal structure analyses of Dawson POM-based organic–inorganic hybrid compounds are crucial for polyoxoanion crystallography because of the difficulty in crystallizing them.

In this study, we report a series of Dawson-type POM-based organosilyl complexes containing $\{O[Si(CH_2)_3SH]_2\}$, $\{O[Si(CH_2)_3SCN]_2\}$, and $\{O(SiPh)_2\}$ groups, and the X-ray crystal structure analyses of $(Me_2NH_2)_5H[\alpha_2\text{-}P_2W_{17}O_{61}\{O[Si(CH_2)_3SH]_2\}]\cdot 6H_2O$ ($Me_2NH_2$-**1**), $(Me_2NH_2)_6[\alpha_2\text{-}P_2W_{17}O_{61}\{O[Si(CH_2)_3SCN]_2\}]\cdot 3H_2O$ ($Me_2NH_2$-**2**), and $(Me_2NH_2)_6[\alpha_2\text{-}P_2W_{17}O_{61}\{O(SiPh)_2\}]\cdot 4H_2O$ ($Me_2NH_2$-**3**). We describe their syntheses, characterization, and the molecular structures of compounds $Me_2NH_2$-(**1**–**3**) in complete detail.

## Results and Discussion

### Syntheses, Characterization, and Molecular Structures of a Series of the Dawson-Type POM-Based Organosilyl Compounds $Me_2NH_2$-(1–3)

The three compounds $Me_2NH_2$-(**1**–**3**) containing organosilyl groups were formed by direct reaction of the organosilyl precursors [$RSiX_3$; R = $HS(CH_2)_3$, $NCS(CH_2)_3$, and Ph; X = OMe, OEt, or Cl] with the mono-lacunary Dawson POM $[\alpha_2\text{-}P_2W_{17}O_{61}]^{10-}$ in an HCl/water/acetonitrile mixed solution or a water/acetonitrile mixed solution at room temperature in air, followed by crystallization from water in the dark. The formation of $Me_2NH_2$-(**1**–**3**) is given by the ionic balance shown in Equations (1), (2), and (3) in which the hydrolysis of Si–X bonds occurs upon addition of acid; the electrophilic organosilyl moieties then attack the lacunary surface sites of polyoxometalates.[13]

$$RSi(X)_3 + 3\ H_2O \rightarrow RSi(OH)_3 + 3\ XH \quad [R = HS(CH_2)_3,\ NCS(CH_2)_3;\ X = OMe,\ OEt] \quad (1)$$

$$[\alpha_2\text{-}P_2W_{17}O_{61}]^{10-} + 2\ RSi(OH)_3 + 4\ H^+ \rightarrow [\alpha_2\text{-}P_2W_{17}O_{61}\{O(SiR)_2\}]^{6-} + 5\ H_2O \quad (2)$$

$$[\alpha_2\text{-}P_2W_{17}O_{61}]^{10-} + 2\ PhSiCl_3 + H_2O \rightarrow [\alpha_2\text{-}P_2W_{17}O_{61}\{O(SiPh)_2\}]^{6-} + 2\ H^+ + 6\ Cl^- \quad (3)$$

The crystal structures of $Me_2NH_2$-**1** (Figure 1), $Me_2NH_2$-**2** (Figure 2), and $Me_2NH_2$-**3** (Figure 3) are composed of the mono-lacunary Dawson POM unit "$\alpha_2\text{-}P_2W_{17}O_{61}$" and the $\{O[Si(CH_2)_3SH]_2\}$, $\{O[Si(CH_2)_3SCN]_2\}$, and $\{O(SiPh)_2\}$ groups, respectively. Each silyl group is linked to two tungsten atoms located in two different positions of the mono-lacunary site through the bonding of four oxygen atoms O(2), O(3), O(6), and O(7) for $Me_2NH_2$-**1** and $Me_2NH_2$-**2**, which have $C_1$ symmetry for the polyanions **1** and **2**, and O(2), O(3), O(2A), and O(3A) for $Me_2NH_2$-**3**, which has $C_s$ symmetry for polyanion **3**. $Me_2NH_2$-**1** and $Me_2NH_2$-**2** were found as a set of enantiomeric pairs in the unit cell, as shown in Figures 1 and 2, respectively. The lengths of the Si–O bonds coordi-

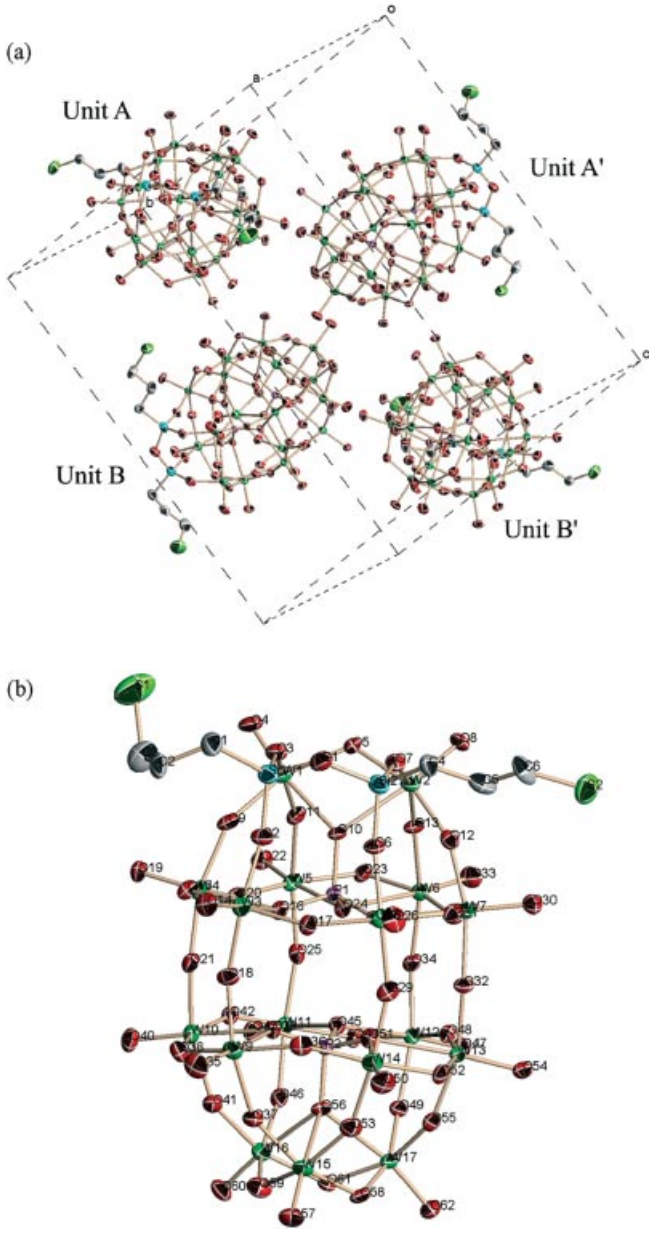


Figure 1. (a) The solid-state packing of $Me_2NH_2$-**1** ($Z$ = 4) and (b) the molecular structure of $Me_2NH_2$-**1** with 50% probability ellipsoids. In (a), units (A, A′) and (B, B′) represent different sets of enantiomeric pairs. The molecular structure of unit A is depicted in (b).

 © 2006 Wiley-VCH Verlag GmbH & Co. KGaA, Weinheim 

nated to the four oxygen atoms in the lacunary site are in the range 1.611(12)–1.650(13) Å (average 1.64 Å) for $Me_2NH_2$-**1**, 1.608(12)–1.647(13) Å (1.63 Å) for $Me_2NH_2$-**2**, and 1.613(8)–1.651(8) Å (1.63 Å) for $Me_2NH_2$-**3** (see Tables 1, 2, and 3, respectively, and Tables S1–S3 in the Supporting Information). These values are similar to those of $[\gamma\text{-}PW_{10}O_{36}(t\text{BuSiOH})_2]^{3-}$ (1.62–1.70 Å)[15] and $[\alpha\text{-A-}PW_9O_{34}(t\text{BuSiO})_3(SiCH_2\text{-}CH{=}CH_2)]^{3-}$ (1.59–1.65 Å),[17] which have a similar tetrahedral environment of the silicon atom. On the other hand, the W–O lengths in the vacant site are in the range 1.873–1.919 Å [W(1)–O(3), W(2)–O(7), W(3)–O(2), and W(8)–O(6)] for $Me_2NH_2$-**1**, 1.889–1.912 Å [W(1)–O(3), W(2)–O(7), W(3)–O(2), and W(8)–O(6)] for $Me_2NH_2$-**2**, and 1.898–1.914 Å [W(1)–O(3) and W(2)–O(2)] for $Me_2NH_2$-**3**; these bonds are longer than those to the terminal oxygen in $[\alpha_2\text{-}P_2W_{17}O_{61}]^{10-}$ (ca. 1.7 Å).[22] Thus, the W–O lengths of the terminal oxygen in the vacant site of $[\alpha_2\text{-}P_2W_{17}O_{61}]^{10-}$ are stretched by the binding of the organosilyl groups. In contrast, the W–O lengths in the $W_3$ cap and the two $W_6$ belts, i.e. W–$O_t$ ($O_t$: terminal oxygen), W–$O_e$ ($O_e$: edge-sharing oxygen), W–$O_c$ (W belt) ($O_c$: corner-sharing oxygen), and W–$O_a$ ($O_a$: oxygen coordinated to the P atom) are in the normal range.[1b,22] The Si–O–Si bond angles for $Me_2NH_2$-(**1**–**3**) are 126.3(9)°, 124.7(8)°, and 127.4(7)°, respectively, which means they are much smaller than that of $[\alpha\text{-A-}PW_9O_{34}(t\text{BuSiO})_3(SiCH_2\text{–}CH{=}CH_2)]^{3-}$ (173.7°).[17]

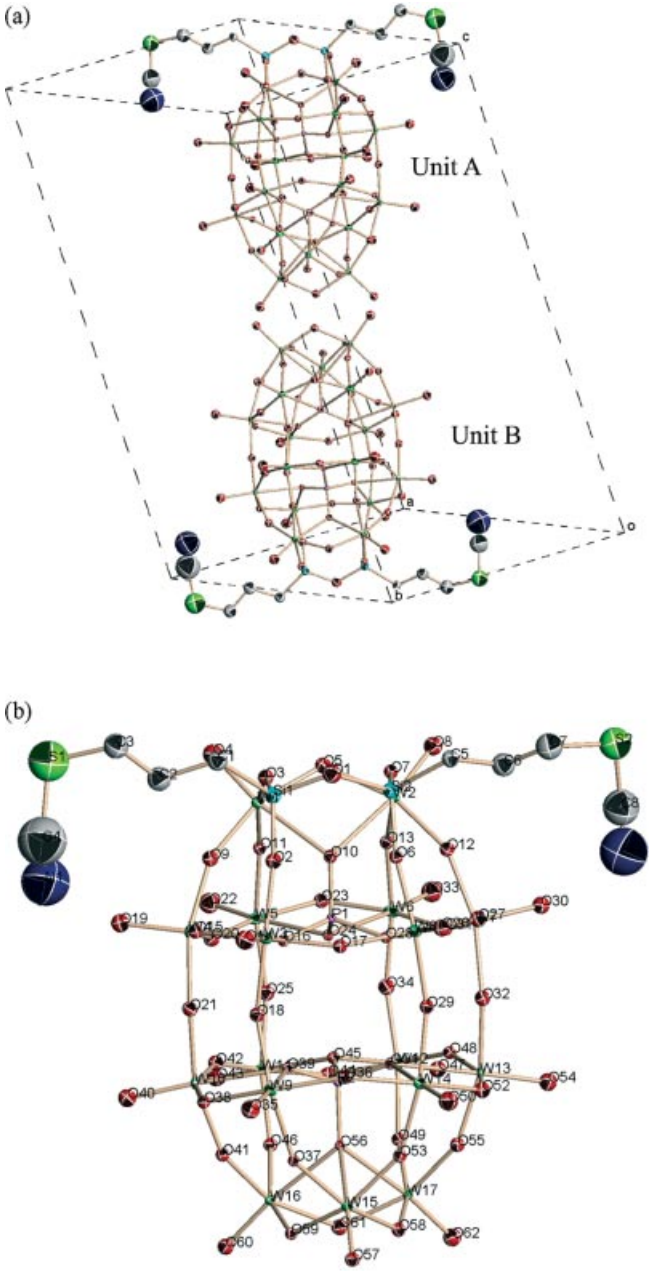


Figure 2. (a) The solid-state packing of $Me_2NH_2$-**2** ($Z$ = 2) and (b) the molecular structure of $Me_2NH_2$-**2** with 50% probability ellipsoids. In (a), (A, B) represents an enantiomeric pair. The molecular structure of unit A is depicted in (b).

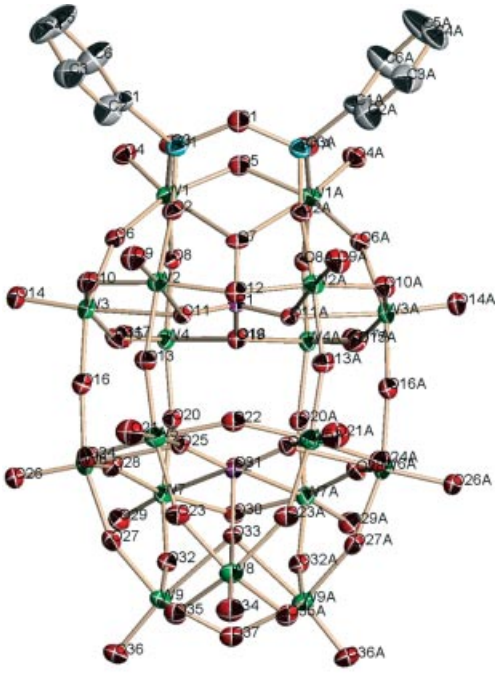

Figure 3. Molecular structure of $Me_2NH_2$-**3** with 50% probability ellipsoids.

With regard to the $\{O[Si(CH_2)_3SH]_2\}$ group of $Me_2NH_2$-**1**, it was noted that one of the two $HS(CH_2)_3Si$ moieties in this group is oriented in the equatorial direction while the other is oriented in the axial bonding direction. This unique configuration was found three times by X-ray crystallography. The Si–C bond lengths are in the range 1.86–1.87 Å and are slightly shorter than those of $[\gamma\text{-}PW_{10}O_{36}(t\text{Bu-SiOH})_2]^{3-}$ (1.94–1.97 Å).[15] The bond angles of the left $HS(CH_2)_3Si$ moiety [Si(1)–C(1)–C(2), C(1)–C(2)–C(3), and C(2)–C(3)–S(1)] are larger than those of the right moiety [Si(2)–C(4)–C(5), C(4)–C(5)–C(6), C(5)–C(6)–S(2)], as shown in Table 1. In the case of the $\{O[Si(CH_2)_3SCN]_2\}$ group of $Me_2NH_2$-**2**, the two $NCS(CH_2)_3Si$ moieties are oriented in a *syn* fashion. This configuration was also found twice by X-ray crystallography. The Si–C bond lengths are in the range 1.84–1.89 Å and are similar to those of $Me_2NH_2$-**1**. The S(1)–C(4) distance [1.97(6) Å] is somewhat longer than that of S(2)–C(8) [1.71(4) Å]. The bond angles

 © 2006 Wiley-VCH Verlag GmbH & Co. KGaA, Weinheim 

Table 1. Selected bond lengths [Å] and angles [°] for $Me_2NH_2$-**1** around the $\{O[Si(CH_2)_3SH]_2\}$ group.

| Bond lengths | | | |
|---|---|---|---|
| Si(1)–O(1) | 1.637(15) | C(2)–C(3) | 1.48(3) |
| Si(1)–O(2) | 1.632(12) | C(3)–S(1) | 1.81(3) |
| Si(1)–O(3) | 1.649(14) | C(4)–C(5) | 1.58(3) |
| Si(1)–C(1) | 1.86(2) | C(5)–C(6) | 1.52(3) |
| Si(2)–O(1) | 1.631(14) | C(6)–S(2) | 1.85(2) |
| Si(2)–O(6) | 1.611(12) | W(1)–O(3) | 1.919(13) |
| Si(2)–O(7) | 1.650(13) | W(2)–O(7) | 1.908(12) |
| Si(2)–C(4) | 1.869(19) | W(3)–O(2) | 1.873(11) |
| C(1)–C(2) | 1.55(3) | W(8)–O(6) | 1.887(11) |
| **Bond angles** | | | |
| O(1)–Si(1)–O(2) | 106.8(7) | Si(1)–O(1)–Si(2) | 126.3(9) |
| O(2)–Si(1)–O(3) | 109.8(7) | Si(1)–O(2)–W(3) | 168.2(8) |
| O(3)–Si(1)–O(1) | 106.8(7) | Si(1)–O(3)–W(1) | 142.6(7) |
| O(1)–Si(1)–C(1) | 109.9(8) | Si(2)–O(6)–W(8) | 168.1(8) |
| O(2)–Si(1)–C(1) | 110.2(8) | Si(2)–O(7)–W(2) | 143.2(7) |
| O(3)–Si(1)–C(1) | 113.0(9) | Si(1)–C(1)–C(2) | 114.2(14) |
| O(1)–Si(2)–O(6) | 107.4(7) | C(1)–C(2)–C(3) | 118.2(19) |
| O(6)–Si(2)–O(7) | 110.7(7) | C(2)–C(3)–S(1) | 114.9(18) |
| O(7)–Si(2)–O(1) | 106.6(7) | Si(2)–C(4)–C(5) | 105.9(13) |
| O(1)–Si(2)–C(4) | 113.5(8) | C(4)–C(5)–C(6) | 107.9(17) |
| O(6)–Si(2)–C(4) | 108.2(8) | C(5)–C(6)–S(2) | 107.0(15) |
| O(7)–Si(2)–C(4) | 110.4(8) | | |

Table 2. Selected bond lengths [Å] and angles [°] for $Me_2NH_2$-**2** around the $\{O[Si(CH_2)_3SCN]_2\}$ group.

| Bond lengths | | | |
|---|---|---|---|
| Si(1)–O(1) | 1.632(13) | S(1)–C(4) | 1.97(6) |
| Si(1)–O(2) | 1.627(12) | N(1)–C(4) | 1.15(6) |
| Si(1)–O(3) | 1.608(12) | C(5)–C(6) | 1.48(3) |
| Si(1)–C(1) | 1.84(2) | C(6)–C(7) | 1.45(3) |
| Si(2)–O(1) | 1.647(13) | C(7)–S(2) | 1.77(3) |
| Si(2)–O(6) | 1.630(11) | S(2)–C(8) | 1.71(4) |
| Si(2)–O(7) | 1.629(12) | C(8)–N(2) | 1.10(5) |
| Si(2)–C(5) | 1.890(18) | W(1)–O(3) | 1.905(11) |
| C(1)–C(2) | 1.56(3) | W(2)–O(7) | 1.889(10) |
| C(2)–C(3) | 1.50(3) | W(3)–O(2) | 1.912(11) |
| C(3)–S(1) | 1.77(3) | W(8)–O(6) | 1.893(11) |
| **Bond angles** | | | |
| O(1)–Si(1)–O(2) | 106.2(7) | Si(1)–O(3)–W(1) | 145.3(7) |
| O(2)–Si(1)–O(3) | 111.2(6) | Si(2)–O(6)–W(8) | 169.0(7) |
| O(3)–Si(1)–O(1) | 108.8(7) | Si(2)–O(7)–W(2) | 143.9(7) |
| O(1)–Si(1)–C(1) | 110.3(8) | Si(1)–C(1)–C(2) | 113.7(13) |
| O(2)–Si(1)–C(1) | 115.1(8) | C(1)–C(2)–C(3) | 111.1(17) |
| O(3)–Si(1)–C(1) | 105.1(8) | C(2)–C(3)–S(1) | 114.2(16) |
| O(1)–Si(2)–O(6) | 107.9(6) | C(3)–S(1)–C(4) | 107(2) |
| O(6)–Si(2)–O(7) | 108.1(6) | S(1)–C(4)–N(1) | 150(6) |
| O(7)–Si(2)–O(1) | 108.1(7) | Si(2)–C(5)–C(6) | 113.9(13) |
| O(1)–Si(2)–C(5) | 112.4(7) | C(5)–C(6)–C(7) | 112.1(18) |
| O(6)–Si(2)–C(5) | 110.0(7) | C(6)–C(7)–S(2) | 119.1(18) |
| O(7)–Si(2)–C(5) | 110.3(7) | C(7)–S(2)–C(8) | 101.6(16) |
| Si(1)–O(1)–Si(2) | 124.7(8) | S(2)–C(8)–N(2) | 166(4) |
| Si(1)–O(2)–W(3) | 172.9(8) | | |

of the left $NCS(CH_2)_3Si$ moiety [Si(1)–C(1)–C(2) and C(1)–C(2)–C(3)] are similar to those of the right moiety [Si(2)–C(5)–C(6) and C(5)–C(6)–C(7)]; however, the C(2)–C(3)–S(1), C(3)–S(1)–C(4), and particularly, S(1)–C(4)–N(1) bond angles are quite different from those of C(6)–C(7)–S(2), C(7)–S(2)–C(8), and S(2)–C(8)–N(2), respectively, as shown in Table 2. For the $\{O(SiPh)_2\}$ group of $Me_2NH_2$-**3**, the Si–C bond length is 1.85 Å, which is similar to those of $Me_2NH_2$-**1** and $Me_2NH_2$-**2**, as shown in Table 3.

Table 3. Selected bond lengths [Å] and angles [°] for $Me_2NH_2$-**3** around the $\{O(SiPh)_2\}$ group.

| Bond lengths | | | |
|---|---|---|---|
| Si(1)–O(1) | 1.634(6) | C(3)–C(4) | 1.40(2) |
| Si(1)–O(2) | 1.613(8) | C(4)–C(5) | 1.37(2) |
| Si(1)–O(3) | 1.651(8) | C(5)–C(6) | 1.38(2) |
| Si(1)–C(1) | 1.847(11) | C(6)–C(1) | 1.395(19) |
| Si(1A)–O(1) | 1.634(6) | W(1)–O(3) | 1.914(7) |
| C(1)–C(2) | 1.394(18) | W(2)–O(2) | 1.898(8) |
| C(2)–C(3) | 1.42(2) | | |
| **Bond angles** | | | |
| O(1)–Si(1)–O(2) | 108.2(5) | C(1)–C(2)–C(3) | 119.9(14) |
| O(2)–Si(1)–O(3) | 111.5(4) | C(2)–C(3)–C(4) | 119.4(14) |
| O(3)–Si(1)–O(1) | 106.2(5) | C(3)–C(4)–C(5) | 119.7(13) |
| O(1)–Si(1)–C(1) | 108.4(5) | C(4)–C(5)–C(6) | 120.7(16) |
| O(2)–Si(1)–C(1) | 111.8(5) | C(5)–C(6)–C(1) | 121.5(15) |
| O(3)–Si(1)–C(1) | 110.5(5) | Si(1)–O(1)–Si(1A) | 127.4(7) |
| C(2)–C(1)–C(6) | 118.5(12) | Si(1)–O(2)–W(2) | 170.7(5) |
| C(2)–C(1)–Si(1) | 118.0(10) | Si(1)–O(3)–W(1) | 139.9(5) |
| C(6)–C(1)–Si(1) | 123.5(10) | | |

The bond valence sums (BVS) for $Me_2NH_2$-(**1**–**3**),[23] calculated on the basis of the observed bond lengths, are in the range 5.950–6.232 (average 6.12), 6.017–6.359 (6.18), and 6.105–6.289 (6.16) for the 17 W atoms, respectively, those of the two P atoms are in the range 4.833–4.877 (average 4.86), 4.908–5.127 (5.02), and 4.901–4.933 (4.92), respectively, and those of the 62 O atoms are in the range 1.618–2.166 (average 1.90), 1.635–2.172 (1.96), and 1.717–2.174 (1.95), respectively. These values correspond reasonably well to the formal valences $W^{6+}$, $P^{5+}$, and $O^{2-}$, respectively (see Tables S4–S6 in the Supporting Information).

The crystal structures of $Me_2NH_2$-(**1**–**3**) are consistent with the elemental analyses, TG/DTA data, and FTIR, solution NMR ($^1H$, $^{13}C$, and $^{31}P$), and solid-state $^{13}C$ NMR spectra. The elemental analyses had to be performed for compounds $Me_2NH_2$-(**1**–**3**) after drying them at room temperature at $10^{-3}$–$10^{-4}$ Torr overnight before the results were consistent with the compositions $(Me_2NH_2)_5H[\alpha_2$-$P_2W_{17}O_{61}\{O[Si(CH_2)_3SH]_2\}]$, $(Me_2NH_2)_6[\alpha_2$-$P_2W_{17}O_{61}$-$\{O[Si(CH_2)_3SCN]_2\}]$, and $(Me_2NH_2)_6[\alpha_2$-$P_2W_{17}O_{61}$-$\{O(SiPh)_2\}]$, respectively. The TG/DTA measurements performed under atmospheric conditions showed a weight loss of 2.38%, 1.27%, and 1.62%, with an endothermic point at 67, 37, and 86 °C, respectively; these values correspond to the presence of 6, 3, and 4 water molecules, respectively, due to both the intrinsic water of hydration and the water adsorbed from the atmosphere. Thus, the number of hydrated water molecules in compounds $Me_2NH_2$-(**1**–**3**) is 6, 3, and 4, respectively.

The FTIR spectra of compounds $Me_2NH_2$-(**1**–**3**) measured as a KBr disk are shown in Figure 4. The spectral patterns of these compounds are similar to those of $[\alpha_2$-$P_2W_{17}O_{61}]^{10-}$ (1086, 1054, 1016, 940, 885, 811, 741, 601, 527, and 467 $cm^{-1}$) rather than those of $[\alpha$-$P_2W_{18}O_{62}]^{6-}$ (1088, 1040, 956, 925, and 713 $cm^{-1}$). The additional bands observed at 2566 and 2154 $cm^{-1}$ in the case of compounds

 © 2006 Wiley-VCH Verlag GmbH & Co. KGaA, Weinheim 

$Me_2NH_2$-**1** and $Me_2NH_2$-**2** were assigned to the SH and SCN moieties, respectively.[24]

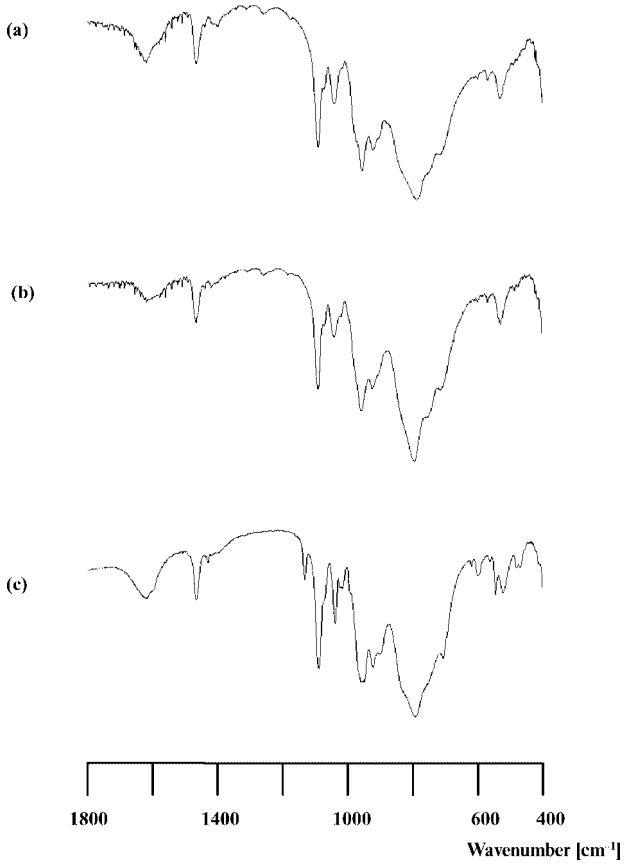


Figure 4. FTIR spectra, measured as KBr disks, in the polyoxoanion region (1800–400 $cm^{-1}$) of (a) $Me_2NH_2$-**1**, (b) $Me_2NH_2$-**2**, and (c) $Me_2NH_2$-**3**.

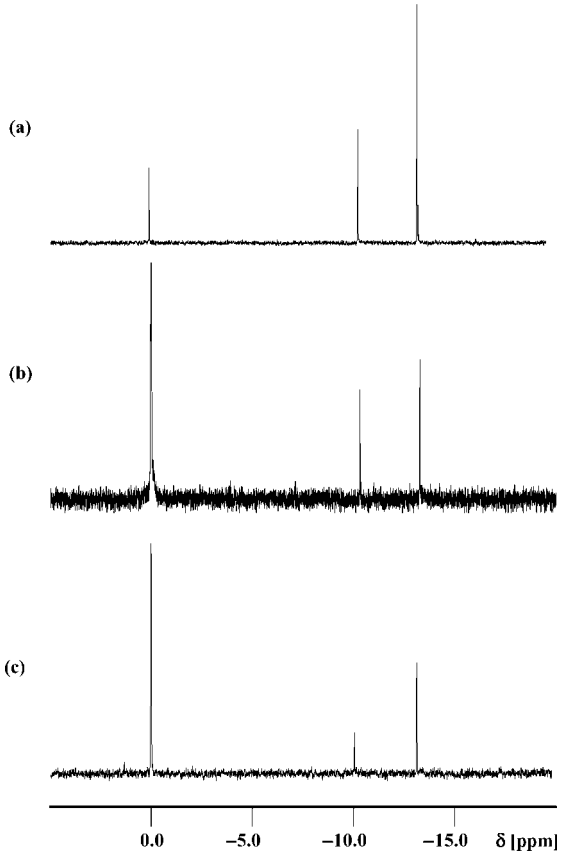


Figure 5. $^{31}P$ NMR spectra in $D_2O$ of (a) $Me_2NH_2$-**1**, (b) $Me_2NH_2$-**2**, and (c) $Me_2NH_2$-**3**.

The $^{31}P$ NMR spectra of compounds $Me_2NH_2$-(**1**–**3**) in $D_2O$ at about 25 °C show a clear two-line spectrum at $\delta$ = –10.52 and –13.50 ppm, $\delta$ = –10.33 and –13.28 ppm, and $\delta$ = –10.21 and –13.29 ppm, respectively, thereby confirming their purity and homogeneity (see Figure 5). The downfield resonance was assigned to the phosphorus closest to the organosilyl sites and the upfield resonance to the phosphorus closer to the $W_3$ cap.

The $^1H$ NMR spectra of $Me_2NH_2$-**1** and $Me_2NH_2$-**2** in $D_2O$ at about 25 °C show signals at $\delta$ = 0.93–1.03, 1.95–1.96, and 2.72–2.77 ppm and $\delta$ = 1.04–1.10, 2.18–2.21, and 3.28–3.31 ppm, respectively, arising from the two $–(CH_2)_3–$ groups in the $\{O[Si(CH_2)_3SH]_2\}$ and $\{O[Si(CH_2)_3SCN]_2\}$ groups, respectively (Table 4). For $Me_2NH_2$-**3**, $^1H$ signals assigned to the two phenyl groups in the $\{O(SiPh)_2\}$ moiety are observed at $\delta$ = 7.53–7.94 ppm. The $^{13}C$ NMR spectra of $Me_2NH_2$-**1** and $Me_2NH_2$-**2** in $D_2O$ at about 25 °C show signals at $\delta$ = 13.2, 29.1, and 29.9 ppm and $\delta$ = 12.8, 26.1, and 38.4 ppm, respectively, which can also be assigned to the two $–(CH_2)_3–$ groups in the $\{O[Si(CH_2)_3SH]_2\}$ and $\{O[Si(CH_2)_3SCN]_2\}$ groups, respectively (Table 4). The $^{13}C$ NMR spectrum of $Me_2NH_2$-**2** also shows a signal at $\delta$ = 117.9 ppm due to the SCN group. For $Me_2NH_2$-**3**, $^{13}C$ signals due to the two phenyl groups are observed at $\delta$ = 131.1–137.3 ppm. In aqueous solution, the two $HS(CH_2)_3$-Si moieties in the $\{O[Si(CH_2)_3SH]_2\}$ group and the two $NCS(CH_2)_3Si$ moieties in the $\{O[Si(CH_2)_3SCN]_2\}$ group cannot be distinguished by $^1H$ and $^{13}C$ NMR spectroscopy.

Table 4. Solution $^1H$ and $^{13}C$ NMR spectroscopic data for compounds $Me_2NH_2$-(**1**–**3**).

| | $^1H$ [$\delta$, ppm] | $^{13}C$ [$\delta$, ppm] |
|---|---|---|
| $Me_2NH_2$-**1** | 0.93–1.03 (H1) | 13.2 (C1) |
| | 1.95–1.96 (H2) | 29.1 (C3) |
| | 2.72–2.77 (H3) | 29.9 (C2) |
| | 2.80 ($Me_2NH_2$) | 37.6 ($Me_2NH_2$) |
| $Me_2NH_2$-**2** | 1.04–1.10 (H1) | 12.8 (C1) |
| | 2.18–2.21(H2) | 26.1 (C2) |
| | 3.28–3.31 (H3) | 38.4 (C3) |
| | 2.81 ($Me_2NH_2$) | 37.4 ($Me_2NH_2$) |
| | | 117.9 (S*C*N) |
| $Me_2NH_2$-**3** | 7.53–7.94 (Ph) | 131.1–137.3 (Ph) |
| | 2.76 ($Me_2NH_2$) | 37.6 ($Me_2NH_2$) |

In order to determine the configuration of the two $HS(CH_2)_3Si$ moieties in the $\{O[Si(CH_2)_3SH]_2\}$ group and the two $NCS(CH_2)_3Si$ moieties in the $\{O[Si(CH_2)_3SCN]_2\}$ group in the bulk samples, we measured the solid-state $^{13}C$

 © 2006 Wiley-VCH Verlag GmbH & Co. KGaA, Weinheim 

NMR spectra for $Me_2NH_2$-**1** and $Me_2NH_2$-**2** (see Figure 6). In the spectrum of $Me_2NH_2$-**1**, C1 appears as two signals at $\delta$ = 12.7 ppm and 14.3 ppm; this is because of the different configuration, i.e. the equatorial and axial bonding of each of the two $HS(CH_2)_3Si$ moieties in the $\{O[Si(CH_2)_3SH]_2\}$ group. The C2 and C3 signals could not be identified owing to broadening of the signals. For $Me_2NH_2$-**2**, a broadening of the C1 signal is observed because of the somewhat different configurations of the two $NCS(CH_2)_3Si$ moieties, which are in a *syn* fashion in the $\{O[Si(CH_2)_3SCN]_2\}$ group (Scheme 1). The C3 signal could not be distinguished because of overlap with the $Me_2NH_2$ signal. These results are consistent with the X-ray structures and suggest that the configuration of the organosilyl groups of $Me_2NH_2$-**1** and $Me_2NH_2$-**2** observed by X-ray crystallography represents the solid structure of the bulk samples; these structures are not maintained in aqueous solution because of the mobility and/or flexibility of organosilyl groups that have straight-chain carbon structures.

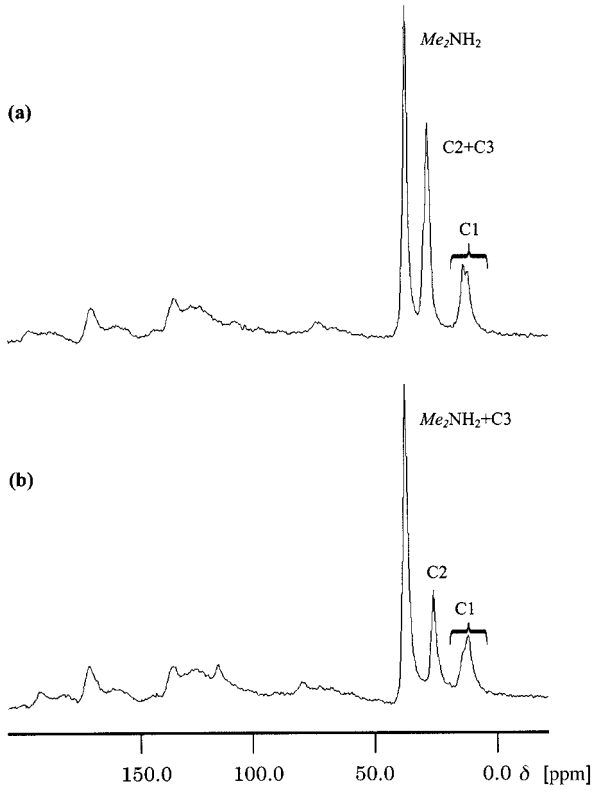


Figure 6. Solid-state $^{13}C$ NMR spectra of (a) $Me_2NH_2$-**1** and (b) $Me_2NH_2$-**2**.

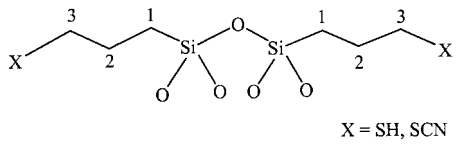


Scheme 1. Drawings of the $\{O[Si(CH_2)_3SH]_2\}$ and $\{O[Si(CH_2)_3SCN]_2\}$ groups.

## Conclusions

A series of organosilyl complexes with the Dawson mono-lacunary phosphotungstate $[\alpha_2\text{-}P_2W_{17}O_{61}]^{10-}$ is presented. We have successfully obtained single crystals of the water-soluble dimethylammonium salts $(Me_2NH_2)_5H[\alpha_2\text{-}P_2W_{17}O_{61}\{O[Si(CH_2)_3SH]_2\}]\cdot 6H_2O$, $(Me_2NH_2)_6[\alpha_2\text{-}P_2W_{17}O_{61}\{O[Si(CH_2)_3SCN]_2\}]\cdot 3H_2O$, and $(Me_2NH_2)_6[\alpha_2\text{-}P_2W_{17}O_{61}\{O(SiPh)_2\}]\cdot 4H_2O$ by treating the organosilyl precursors $HS(CH_2)_3Si(OMe)_3$, $NCS(CH_2)_3Si(OEt)_3$, and $PhSiCl_3$, respectively, with the mono-lacunary polyoxoanion. The characterization of compounds $Me_2NH_2$-(**1**–**3**) has been accomplished by X-ray structure analyses, elemental analysis, TG/DTA, and FTIR and solution ($^1H$, $^{13}C$, and $^{31}P$) and solid-state $^{13}C$ NMR spectroscopy. The crystal structures of $Me_2NH_2$-(**1**–**3**) reveal that each silyl group is linked to two tungsten atoms that are located in two different positions of the mono-lacunary site by the bonding of four oxygen atoms for $Me_2NH_2$-**1** and $Me_2NH_2$-**2** with $C_1$ symmetry and $Me_2NH_2$-**3** with the $C_s$ symmetry. The organosilyl groups with straight-chain carbon structures bound to the vacant site of $[\alpha_2\text{-}P_2W_{17}O_{61}]^{10-}$ have unique configurations, i.e. equatorial and axial bonding for each of the two $HS(CH_2)_3Si$ moieties in the $\{O[Si(CH_2)_3SH]_2\}$ group of $Me_2NH_2$-**1** and the two $NCS(CH_2)_3Si$ moieties oriented in a *syn* fashion in the $\{O[Si(CH_2)_3SCN]_2\}$ group of $Me_2NH_2$-**2**. Although these unique configurations are not maintained in aqueous solution, the crystal structures of these compounds represent the solid structures of the bulk samples. To the best of our knowledge, the X-ray crystal structures of compounds $Me_2NH_2$-(**1**–**3**) are the first examples of the molecular structures of Dawson-type polyoxometalate-based organosilyl complexes. Preliminary experiments show that it is possible to graft these polyoxometalates onto polymers.

## Experimental Section

**Materials:** $K_{10}[\alpha_2\text{-}P_2W_{17}O_{61}]\cdot 19H_2O$ was prepared as described in the literature.[25] The number of solvated water molecules was determined by TG/DTA analysis. All reagents and solvents (acetonitrile, ethanol, methanol, and diethyl ether) were obtained from commercial sources and used as received. $HS(CH_2)_3Si(OMe)_3$, $NCS(CH_2)_3Si(OEt)_3$, and $PhSiCl_3$ were obtained from Azmax.

**Instrumentation/Analytical Procedures:** Elemental analyses were carried out with a Perkin–Elmer 2400 CHNS Elemental Analyzer II (Kanagawa University) and Mikroanalytisches Labor Pascher (Remagen, Germany). The samples were dried at room temperature at $10^{-3}$–$10^{-4}$ Torr overnight before analysis. IR spectra were recorded with a Jasco 4100 FT-IR spectrometer in KBr disks at room temperature. Thermogravimetric (TG) and differential thermal analyses (DTA) data were acquired using a Rigaku Thermo Plus 2 series TG/DTA TG 8120 instrument. TG/DTA measurements were performed in air with a temperature ramp of 4 °C per minute between 20 and 500 °C. The $^1H$ (399.65 MHz), $^{13}C\{^1H\}$ (100.40 MHz), and $^{31}P\{^1H\}$ NMR (161.70 MHz) spectra in solution were recorded in 5-mm outer diameter tubes with a JEOL JNM-EX 400 FT-NMR spectrometer equipped with a JEOL EX-400 data-processing system. $^1H$ and $^{13}C\{^1H\}$ NMR spectra of the

 © 2006 Wiley-VCH Verlag GmbH & Co. KGaA, Weinheim 

complexes were measured in $D_2O$ solution with reference to internal DSS or TSP [sodium 2,2,3,3-[$D_4$]3-(trimethylsilyl)propionate]. Chemical shifts are reported as positive for resonances downfield of DSS or TSP ($\delta$ = 0 ppm). The $^{31}P\{^1H\}$ NMR spectra were referenced to an external standard of 25% $H_3PO_4$ in $H_2O$ in a sealed capillary. Chemical shifts are reported as negative on the $\delta$ scale with resonances upfield of $H_3PO_4$ ($\delta$ = 0 ppm). Solid-state $^{13}C$ NMR spectra were recorded at 300 MHz with a JEOL JNM-ECP 300 FT-NMR spectrometer equipped with a JEOL ECP-300 data-processing system. The chemical shifts are referenced to $C_6(CH_3)_6$ and are reported to be positive on the $\delta$ scale with resonances upfield of the methyl group of $C_6(CH_3)_6$ ($\delta$ = 17.4 ppm).

**Synthesis and Crystallization of $(Me_2NH_2)_5H[\alpha_2$-$P_2W_{17}O_{61}$-$\{O[Si(CH_2)_3SH]_2\}]\cdot 6H_2O$ ($Me_2NH_2$-1):** $K_{10}[\alpha_2$-$P_2W_{17}O_{61}]\cdot 19H_2O$ (5.00 g, 1.00 mmol) was added to a colorless clear solution of $HS(CH_2)_3Si(OMe)_3$ (380 μL, 2.00 mmol [$d$ = 1.056]) dissolved in a mixture of water (50 mL) and $CH_3CN$ (150 mL), and the pH was adjusted to 1.8 with 1 M aqueous HCl. After stirring for 30 min, the solution was evaporated to a volume of about 30 mL on a rotary evaporator at 30 °C. $Me_2NH_2Cl$ (5.5 g, 67.5 mmol) was then added to the resulting pale-yellow clear solution. Hereafter, the experiments were performed in the dark because the precipitate is sensitive to light. A yellow-white precipitate was formed, which was collected on a membrane filter (JG, 0.2 μm), and washed with methanol (3 × 30 mL) and diethyl ether (3 × 30 mL). At this stage, the crude dimethylammonium salt was obtained in 4.15 g yield. A portion of this crude product (0.5 g) was dissolved in aqueous HCl (4 mL of 6 M solution) in a water bath at about 60 °C. The clear yellow solution was then slowly evaporated at room temperature in the dark. After 2 d, clear yellow granular crystals were formed. The crystals were obtained in 14.8% (0.070 g scale) yield based on $(Me_2NH_2)_5H[\alpha_2$-$P_2W_{17}O_{61}\{O[Si(CH_2)_3SH]_2\}]\cdot 6H_2O$. $Me_2NH_2$-**1** is very soluble in acetonitrile and dimethyl sulfoxide, soluble in water, and insoluble in methanol, ethanol, acetone, ethyl acetate, dichloromethane, and diethyl ether. The solid sample gradually changes to blue upon exposure to light and is slightly hygroscopic. $(Me_2NH_2)_5H[\alpha_2$-$P_2W_{17}O_{61}\{O[Si(CH_2)_3SH]_2\}]\cdot xH_2O$ ($x$ = 0), $C_{16}H_{55}N_5O_{62}P_2W_{17}S_2Si_2$ (4617.1): calcd. C 4.16, H 1.20, N 1.52, P 1.34, S 1.39, Si 1.22, W 67.69; found C 3.52 (3.97) [3.88], H 1.14 (1.24), N 1.35 (1.39), P 1.30, S 1.29, Si 1.32, W 67.6. The values in round and square brackets are the 2nd and 3rd data, respectively, which were measured at Kanagawa University. A weight loss of 2.21% was observed during the course of overnight drying at room temperature at $10^{-3}$–$10^{-4}$ Torr before the analyses, which suggests the presence of between five and six weakly solvated or adsorbed water molecules. TG/DTA under atmospheric conditions: a weight loss of 2.38% with an endothermic point at 67 °C was observed below 137 °C; calcd. 2.29% for $x$ = 6 in $(Me_2NH_2)_5H[\alpha_2$-$P_2W_{17}O_{61}\{O[Si(CH_2)_3SH]_2\}]\cdot xH_2O$. IR (KBr disk): $\tilde{\nu}$ = 2571 (m) [SH], 1623 (s), 1507 (w), 1465 (s), 1437 (w), 1412 (w), 1399 (w), 1374 (w), 1362 (w), 1339 (w), 1308 (w), 1254 (w), 1173 (w), 1088 (vs), 1069 (w), 1038 (s), 953 (s), 920 (m), 783 (vs, br.), 714 (w), 596 (w), 565 (w), 526 (m), 486 (w), 476 (w), 431 (w), 419 (w) $cm^{-1}$. $^1H$ NMR (22.6 °C, $D_2O$): $\delta$ = 0.93–1.03 (H1), 1.95–1.96 (H2), 2.72–2.77 (H3), 2.80 ($Me_2NH_2$) ppm. $^{13}C$ NMR (25.4 °C, $D_2O$): $\delta$ = 13.2 (C1), 29.1 (C3), 29.9 (C2), 37.6 ($Me_2NH_2$) ppm. $^{31}P$ NMR (23.3 °C, $D_2O$): $\delta$ = –10.52, –13.50 ppm. The $^{183}W$ NMR measurement in $D_2O$ was unsuccessful because the concentration of $Me_2NH_2$-**1** in aqueous solution was insufficient. Solid-state $^{13}C$ NMR: $\delta$ = 12.7 (C1), 14.3 (C1), 28.8 (C2, C3), 37.8 ($Me_2NH_2$) ppm.

**Synthesis and Crystallization of $(Me_2NH_2)_6[\alpha_2$-$P_2W_{17}O_{61}$-$\{O[Si(CH_2)_3SCN]_2\}]\cdot 3H_2O$ ($Me_2NH_2$-2):** $K_{10}[\alpha_2$-$P_2W_{17}O_{61}]\cdot 19H_2O$ (5.00 g, 1.00 mmol) was added to a colorless clear solution of $NCS(CH_2)_3Si(OEt)_3$ (767 μL, 3.00 mmol [$d$ = 1.03]) dissolved in a mixture of water (50 mL) and $CH_3CN$ (150 mL), and the pH was adjusted to 1.8 with 1 M aqueous HCl. After stirring for 30 min, the solution was evaporated to a volume of about 30 mL on a rotary evaporator at 30 °C. $Me_2NH_2Cl$ (5.0 g, 61.3 mmol) was then added to this pale-yellow clear solution. Hereafter, the experiments were performed in the dark because the precipitate is sensitive to light. A yellow-white precipitate was formed, which was collected on a membrane filter (JG, 0.2 μm) and washed with ethanol (3 × 30 mL) and diethyl ether (3 × 30 mL). At this stage the crude dimethylammonium salt was obtained in 4.31 g yield. A portion of this crude product (0.5 g) was dissolved in water (9.5 mL) in a water bath at about 80 °C and then cooled to about 25 °C. After 1 d, the crude crystalline precipitate was removed by filtering through a folded filter paper (Watman #2). The resulting clear pale-yellow solution was slowly evaporated at room temperature in the dark. After 6 d, pale-yellow plate crystals were formed. The crystals were obtained in 17.8% (0.085 g scale) yield based on $(Me_2NH_2)_6[\alpha_2$-$P_2W_{17}O_{61}\{O[Si(CH_2)_3SCN]_2\}]\cdot 3H_2O$. $Me_2NH_2$-**2** is soluble in water, dimethyl sulfoxide, and acetonitrile, while it is insoluble in methanol, ethanol, ethyl acetate, and diethyl ether. The solid sample gradually became blue upon exposure to light and is slightly hygroscopic. $(Me_2NH_2)_6[\alpha_2$-$P_2W_{17}O_{61}\{O[Si(CH_2)_3SCN]_2\}]\cdot xH_2O$ ($x$ = 0), $C_{20}H_{60}N_8O_{62}P_2W_{17}Si_2S_2$ (4712.2): calcd. C 5.10, H 1.28, N 2.38, P 1.31, S 1.36, Si 1.19, W 66.32; found C 5.03, H 1.27, N 2.40, P 1.29, S 1.27, Si 1.33, W 66.2. A weight loss of 1.55% was observed during the course of overnight drying at room temperature and $10^{-3}$–$10^{-4}$ Torr before the analyses, which suggests the presence of between four and five weakly solvated or adsorbed water molecules. TG/DTA under atmospheric conditions: a weight loss of 1.27% with an endothermic point at 37 °C was observed below 140 °C; calcd. 1.13% for $x$ = 3 in $(Me_2NH_2)_6[\alpha_2$-$P_2W_{17}O_{61}\{O(SiC_3H_6SCN)_2\}]\cdot xH_2O$. The number of solvated or adsorbed water molecules determined by TG/DTA was slightly different from that measured by Pascher (Germany) because the TG/DTA data are dependent on the conditions before analysis. Here, we used three water molecules for the X-ray crystal analysis. IR (KBr disk): $\tilde{\nu}$ = 2154 (m) [SCN], 1616 (m), 1465 (m), 1437 (w), 1418 (w), 1305 (w), 1257 (w), 1182 (w), 1089 (vs), 1069 (w), 1038 (m), 955 (vs), 922 (w), 794 (vs, br.), 710 (w), 669 (w), 597 (w), 584 (w), 566 (w), 526 (m), 484 (w), 472 (w) $cm^{-1}$. $^1H$ NMR (24.5 °C, $D_2O$): $\delta$ = 1.04–1.10 (H1), 2.18–2.21 (H2), 3.28–3.31 (H3), 2.81 ($Me_2NH_2$) ppm. $^{13}C$ NMR (25.5 °C, $D_2O$): $\delta$ = 12.8 (C1), 26.1(C2), 38.4 (C3), 37.4 ($Me_2NH_2$), 117.9 (S*C*N) ppm. $^{31}P$ NMR (23.6 °C, $D_2O$): $\delta$ = –10.33, –13.28 ppm. The $^{183}W$ NMR measurement in $D_2O$ was unsuccessful because the concentration of $Me_2NH_2$-**2** in aqueous solution was insufficient. Solid-state $^{13}C$ NMR: $\delta$ = 12.31 (sh) (C1), 26.41 (C2), 38.16 ($Me_2NH_2$, C3) ppm.

**Synthesis and Crystallization of $(Me_2NH_2)_6[\alpha_2$-$P_2W_{17}O_{61}\{O$-$(SiPh)_2\}]\cdot 4H_2O$ ($Me_2NH_2$-3):** $Me_2NH_2$-**3** was synthesized by a modification of the reported method.[13] $K_{10}[\alpha_2$-$P_2W_{17}O_{61}]\cdot 19H_2O$ (5.00 g, 1.00 mmol) was added to a colorless clear solution of $C_6H_5SiCl_3$ (325 μL, 2.00 mmol [$d$ = 1.28]) dissolved in a mixture of water (50 mL) and $CH_3CN$ (250 mL) and stirred for 1 h. The solution was evaporated to about 40 mL on a rotary evaporator at 30 °C. The pale-yellow suspension was filtered through a membrane filter (JG, 0.2 μm), and the resulting pale-yellow clear filtrate was re-evaporated to about 35 mL in a water bath at about 80 °C. After filtration through a membrane filter (JG, 0.2 μm), $Me_2NH_2Cl$ (5.5 g, 67.5 mmol) was added to the pale-yellow filtrate. Hereafter, the experiments were performed in the dark because the powder formed is sensitive to light. A white precipitate and yellow oil were formed. After stirring in the dark for 10 min in a water bath at

 © 2006 Wiley-VCH Verlag GmbH & Co. KGaA, Weinheim 

about 80 °C, the solution was cooled to room temperature. A yellow-white precipitate was formed, which was collected on a membrane filter (JG, 0.2 μm), and washed with ethanol (3 × 10 mL) and diethyl ether (3 × 30 mL). At this stage the crude dimethylammonium salt was obtained in 3.62 g yield. A portion of this crude product (2.00 g) was dissolved in water (50 mL) in a water bath at 80 °C and filtered through a folded filter paper while the solution was hot. The pale-yellow clear filtrate was slowly evaporated at room temperature in the dark. After 3 d, yellow granular crystals were formed. The crystals were obtained in 37.0% (0.74 g scale) yield based on $(Me_2NH_2)_6[\alpha_2\text{-}P_2W_{17}O_{61}\{O(SiPh)_2\}]\cdot 4H_2O$. $Me_2NH_2$-**3** is very soluble in acetonitrile and dimethyl sulfoxide, soluble in water, acetone, and methanol, slightly soluble in ethanol, and insoluble in diethyl ether. The solid sample gradually became blue upon exposure to light and is slightly hygroscopic. $(Me_2NH_2)_6[\alpha_2\text{-}P_2W_{17}O_{61}\{O(SiPh)_2\}]\cdot xH_2O$ ($x$ = 0), $C_{24}H_{58}N_6O_{62}Si_2P_2W_{17}$ (4666.1): calcd. C 6.18, H 1.25, N 1.80, P 1.33, Si 1.20, W 66.98; found C 6.15, H 1.23, N 1.81, P 1.29, Si 1.31, W 66.5. A weight loss of 1.91% was observed during the course of overnight drying at room temperature and $10^{-3}$–$10^{-4}$ Torr before the analyses, which suggests the presence of between five and six weakly solvated or adsorbed water molecules. TG/DTA under atmospheric conditions: a weight loss of 1.62% with an endothermic point at 83 °C was observed below 201 °C; calcd. 1.52% for $x$ = 4 in $(Me_2NH_2)_6[\alpha_2\text{-}P_2W_{17}O_{61}\{O(SiPh)_2\}]\cdot xH_2O$. The number of solvated or adsorbed water molecules determined by TG/DTA was slightly different from that measured by Pascher (Germany) because the TG/DTA data are dependent on the conditions before analysis. Here, we used four water molecules for the X-ray crystal analysis. IR (KBr disk): $\tilde{\nu}$ = 1617 (s), 1507 (w), 1466 (s), 1430 (w) [PhSi], 1133 (m) [PhSi], 1091 (vs), 1040 (s), 1026 (m), 1017 (m), 960 (s), 952 (s), 925 (m), 904 (w), 795 (vs, br.), 710 (w), 622 (w), 603 (m), 566 (w), 549 (m), 526 (m), 484 (m), 474 (w), 445 (w), 441 (w), 436 (w), 418 (w) $cm^{-1}$. $^1H$ NMR (23.0 °C, $D_2O$): $\delta$ = 2.76 ($Me_2NH_2$), 7.53–7.94 (Ph) ppm. $^{13}C$ NMR (25.7 °C, $D_2O$): $\delta$ = 37.6 ($Me_2NH_2$) 131.1–137.3 ppm (Ph). $^{31}P$ NMR (22.2 °C, $D_2O$): $\delta$ = –10.21, –13.29 ppm.

**X-ray Crystallography:** Crystals of compounds $Me_2NH_2$-(**1**–**3**) were covered with liquid paraffin to prevent their degradation. The crystal sizes were 0.11 × 0.11 × 0.07 mm, 0.10 × 0.09 × 0.03 mm, and 0.20 × 0.11 × 0.03 mm, respectively. Data collection was carried out with a Bruker SMART APEX CCD diffractometer at 90 K. The intensity data were automatically corrected for Lorentz and polarization effects during integration. The structure was obtained by direct methods (SHELXS-97),[26] followed by a subsequent difference Fourier calculation, and refined by the full-matrix least-squares procedure (SHELXL-97).[27] Absorption correction was performed with SADABS (empirical absorption correction).[28]

**Crystal Data for $Me_2NH_2$-1:** $C_{10}H_{42}N_2O_{68}P_2S_2Si_2W_{17}$, $M$ = 4586.15, monoclinic, space group $P2_1/n$, $a$ = 15.100(4), $b$ = 21.373(5), $c$ = 24.498(6) Å, $\alpha$ = 90°, $\beta$ = 92.511(4)°, $\gamma$ = 90°, $V$ = 7898(3) Å$^3$, $Z$ = 4, $D_c$ = 3.857 Mg m$^{-3}$, $\mu$(Mo-$K_\alpha$) = 24.871 mm$^{-1}$. $R_1$ = 0.0727, $wR_2$ = 0.1554 (for all data). $R_{int}$ = 0.0579, $R_1$ = 0.0562, $wR_2$ = 0.1447, GOF = 1.071 [92569 total reflections, 19693 unique reflections with $I > 2\sigma(I)$]. The maximum and minimum residual densities (12.244 and –2.629 e Å$^{-3}$) were located at 1.34 Å from O1 and 0.58 Å from W9, respectively.

**Crystal Data for $Me_2NH_2$-2:** $C_{20}H_{66}N_8O_{65}P_2S_2Si_2W_{17}$, $M$ = 4766.50, triclinic, space group $P\bar{1}$, $a$ = 13.2879(12), $b$ = 13.3218(12), $c$ = 26.190(2) Å, $\alpha$ = 80.868(2)°, $\beta$ = 80.562(2)°, $\gamma$ = 66.9000(10)°, $V$ = 4183.8(7) Å$^3$, $Z$ = 2, $D_c$ = 3.784 Mg m$^{-3}$, $\mu$(Mo-$K_\alpha$) = 23.483 mm$^{-1}$. $R_1$ = 0.0796, $wR_2$ = 0.1803 (for all data). $R_{int}$ = 0.1890, $R_1$ = 0.0612, $wR_2$ = 0.1637, GOF = 0.983 [59851 total reflections, 20747 unique reflections where $I > 2\sigma(I)$]. The maximum and minimum residual densities (10.686 and –4.776 e Å$^{-3}$) were located at 1.34 Å from O1 and 0.97 Å from W13, respectively.

**Crystal Data for $Me_2NH_2$-3:** $C_{22}H_{58}N_5O_{66}P_2Si_2W_{17}$, $M$ = 4692.30, orthorhombic, space group $Pnma$, $a$ = 20.894(4), $b$ = 20.413(4), $c$ = 18.939(3) Å, $\alpha$ = 90°, $\beta$ = 90°, $\gamma$ = 90°, $V$ = 8077(3) Å$^3$, $Z$ = 4, $D_c$ = 3.859 Mg m$^{-3}$, $\mu$(Mo-$K_\alpha$) = 24.274 mm$^{-1}$. $R_1$ = 0.0534, $wR_2$ = 0.1168 (for all data). $R_{int}$ = 0.0736, $R_1$ = 0.0386, $wR_2$ = 0.1026, GOF = 1.080 [108211 total reflections, 10317 unique reflections where $I > 2\sigma(I)$]. The maximum and minimum residual densities (6.824 and –1.646 e Å$^{-3}$) were located at 1.34 Å from O1 and 1.57 Å from O26, respectively.

For compound $Me_2NH_2$-**1**, 17 tungsten atoms, two phosphorus atoms, two silicon atoms, six carbon atoms, and two sulfur atoms were clearly identified. For compound $Me_2NH_2$-**2**, 17 tungsten atoms, two phosphorus atoms, two silicon atoms, eight carbon atoms, two nitrogen atoms, and two sulfur atoms were clearly identified. For compound $Me_2NH_2$-**3**, 17 tungsten atoms, two phosphorus atoms, two silicon atoms, and twelve carbon atoms were clearly identified. However, the resolution obtained for the structure of the salt was limited by the poor quality of the available crystals and by the considerable disorder of the countercations and the solvent of crystallization. These features are common in POM crystallography.[29]

CCDC-604936, -604937, and -604938 [$Me_2NH_2$-(**1**–**3**), respectively] contain the supplementary crystallographic data for this paper. These data can be obtained free of charge from The Cambridge Crystallographic Data Centre via www.ccdc.cam.ac.uk/data_request/cif.

**Supporting Information** (see the footnote on the first page of this article): The bond lengths, bond angles, and bond valence sums for compounds $Me_2NH_2$-(**1**–**3**) (Tables S1–S6).

## Acknowledgments

This work was supported by Grant-in Aid for Scientific Research (C) no. 18550062 and a High-Tech Research Center Project, both from the Ministry of Education, Culture, Sports, Science and Technology, Japan.

[1] a) M. T. Pope, *Heteropoly and Isopoly Oxometalates*, Springer-Verlag, Berlin, **1983**; b) M. T. Pope, A. Müller, *Angew. Chem. Int. Ed. Engl.* **1991**, *30*, 34–48; c) *Polyoxometalates: From Platonic Solids to Ant-Retrociral Activity* (Eds.: M. T. Pope, A. Müller), Kluwer Academic Publishers, Dordrecht, The Netherlands, **1994**; d) *Chem. Rev.* **1998**, *98*, 1–390 (special issue on polyoxometalates; C. L. Hill, guest editor).
[2] G. Sazani, M. T. Pope, *Dalton Trans.* **2004**, 1989–1994.
[3] a) F. Zonnevijlle, M. T. Pope, *J. Am. Chem. Soc.* **1979**, *101*, 2731–2732; b) G. S. Chorghade, M. T. Pope, *J. Am. Chem. Soc.* **1987**, *109*, 5134–5138; c) W. H. Knoth, *J. Am. Chem. Soc.* **1979**, *101*, 2211–2213.
[4] S. Bareyt, S. Piligkos, B. Hasenknopf, P. Gouserh, E. Laeôte, S. Thorimbert, M. Malacria, *J. Am. Chem. Soc.* **2005**, *127*, 6788–6794.
[5] F. Xin, M. T. Pope, *Organometallics* **1994**, *13*, 4881–4886.
[6] F. Xin, M. T. Pope, G. J. Long, U. Russo, *Inorg. Chem.* **1996**, *35*, 1207–1213.
[7] F. Xin, M. T. Pope, *Inorg. Chem.* **1996**, *35*, 5693–5695.
[8] C. R. Mayer, R. Thouvenot, *J. Chem. Soc., Dalton Trans.* **1998**, 7–13.
[9] G. S. Kim, K. S. Hagen, C. L. Hill, *Inorg. Chem.* **1992**, *31*, 5316–5324.
[10] C. R. Mayer, P. Herson, R. Thouvenot, *Inorg. Chem.* **1999**, *38*, 6152–6158.

 © 2006 Wiley-VCH Verlag GmbH & Co. KGaA, Weinheim 

[11] C. R. Mayer, M. Hervè, H. Lavanant, J.-C. Blais, F. Sécheresse, *Eur. J. Inorg. Chem.* **2004**, 973–977.
[12] a) P. Judeinstein, C. Deprun, L. Nadjo, *J. Chem. Soc., Dalton Trans.* **1991**, 1991–1997; b) W. H. Knoth, *J. Am. Chem. Soc.* **1979**, *101*, 759–760.
[13] C. R. Mayer, C. Roch-Marchal, H. Lavanant, R. Thouvenot, N. Sellier, J.-C. Blais, F. Sécheresse, *Chem. Eur. J.* **2004**, *10*, 5517–5523.
[14] C. Cannizzo, C. R. Mayer, F. Sécheresse, C. Larpent, *Adv. Mater.* **2005**, *17*, 2888–2892.
[15] A. Mazeaud, Y. Dromzee, R. Thouvenot, *Inorg. Chem.* **2000**, *39*, 4735–4740.
[16] C. R. Mayer, R. Thouvenot, T. Lalot, *Macromolecules* **2000**, *33*, 4433–4437.
[17] D. Agustin, C. Coelho, A. Mazeaud, P. Herson, A. Proust, R. Thouvenot, *Z. Anorg. Allg. Chem.* **2004**, *630*, 2049–2053.
[18] A. Maseaud, N. Ammari, F. Robert, R. Thouvenot, *Angew. Chem. Int. Ed. Engl.* **1996**, *35*, 1961–1964.
[19] N. Ammari, G. Hervè, R. Thouvenot, *New J. Chem.* **1991**, *15*, 607–608.
[20] J. Niu, M. Li, J. Wang, *J. Organomet. Chem.* **2003**, *675*, 84–90.
[21] C. R. Mayer, S. Neveu, V. Cabuil, *Angew. Chem. Int. Ed.* **2002**, *41*, 501–503.
[22] Y. Sakai, A. Shinohara, K. Hayashi, K. Nomiya, *Eur. J. Inorg. Chem.* **2006**, 163–171.
[23] a) I. D. Brown, D. Altermatt, *Acta Crystallogr., Sect. B* **1985**, *41*, 244–247; b) I. D. Brown, R. D. Shannon, *Acta Crystallogr., Sect. A* **1973**, *29*, 266–282; c) I. D. Brown, *Acta Crystallogr., Sect. B* **1992**, *48*, 553–572; d) I. D. Brown, *Appl. Cryst.* **1996**, *29*, 479–480.
[24] R. M. Silverstein, G. C. Bassler, T. C. Morrill, *Spectrometric Identification of Organic Compounds*, 5th ed., John Wiley & Sons, Inc., New York, **1991**.
[25] D. K. Lyon, W. K. Miller, T. Novet, P. J. Domaille, E. Evitt, D. C. Johnson, R. G. Finke, *J. Am. Chem. Soc.* **1991**, *113*, 7209–7221.
[26] G. M. Sheldrick, *Acta Crystallogr., Sect. A* **1990**, *46*, 467–473.
[27] G. M. Sheldrick, SHELXL-97, *Program for Crystal Structure Refinement*, University of Göttingen, Germany, **1997**.
[28] G. M. Sheldrick, SADABS, University of Göttingen, Germany, **1996**.
[29] a) K. Nomiya, M. Takahashi, K. Ohsawa, J. A. Widegren, *J. Chem. Soc., Dalton Trans.* **2001**, 2872–2878; b) T. J. R. Weakley, R. G. Finke, *Inorg. Chem.* **1990**, *29*, 1235–1241; c) Y. Lin, T. J. R. Weakley, B. Rapko, R. G. Finke, *Inorg. Chem.* **1993**, *32*, 5095–5101; d) T. Yamase, T. Ozeki, H. Sakamoto, S. Nishiya, A. Yamamoto, *Bull. Chem. Soc. Jpn.* **1993**, *66*, 103–108; e) K. Nomiya, M. Takahashi, J. A. Widegren, T. Aizawa, Y. Sakai, N. C. Kasuga, *J. Chem. Soc., Dalton Trans.* **2002**, 3679–3685.

Received: May 23, 2006
Published Online: October 12, 2006

 © 2006 Wiley-VCH Verlag GmbH & Co. KGaA, Weinheim 

DOI: 10.1002/ejic.200600532

# Synthesis, Crystal Structures and Photoluminescent Properties of Three Novel Cadmium(II) Compounds Constructed from 5-Sulfoisophthalic Acid ($H_3SIP$)

**Qing-Yan Liu,[a] Yu-Ling Wang,[b] and Li Xu*[a]**

**Keywords:** Cadmium compounds / Hydrothermal synthesis / Crystal structures / Photoluminescent properties

Hydrothermal reactions of $Cd(NO_3)_2$ and $NaH_2SIP$ (5-sulfoisophthalic acid monosodium salt) at pH = 2 and 7 produce $[Cd_2(\mu_2\text{-}OH_2)_2(HSIP)_2(H_2O)_6]$ (**1**) and $[Cd_5(\mu_2\text{-}OH)_2(\mu_3\text{-}OH)_2(SIP)_2(H_2O)_5]_n$ (**2**), respectively. A similar hydrothermal reaction in the presence of dpp [1,3-bis(4-pyridyl)propane] yields $\{[Cd_3(SIP)_2(dpp)_6]\cdot 4(H_2O)\}_n$ (**3**). Single-crystal X-ray diffraction reveals that compound **1** has a discrete dinuclear structure with the $[Cd_2(\mu_2\text{-}OH_2)_2]$ unit. Polymer **2** features an inorganic layer, which has centrosymmetric 12- and 24-membered rings composed of chair-shaped $[Cd_4(\mu_3\text{-}OH)_2]$ units and $Cd(\mu_2\text{-}OH)_2(CO_2)$ units, and is interconnected by SIP into a 3D framework. Complex **3** contains a 1D ladder-like $[Cd_4(SIP)_4]_n$ unit with four cadmium atoms co-planar, which is interconnected by dpp into a 2D nanosized layered structure. In the solid state, compounds **1** and **3** exhibit blue-violet photoluminescence with maxima at 436 and 409 nm upon excitation at 342 and 350 nm, respectively. However, compound **2** shows photoluminescence with the maximum at 306 nm upon excitation at 270 nm.

(© Wiley-VCH Verlag GmbH & Co. KGaA, 69451 Weinheim, Germany, 2006)

## Introduction

The design and construction of metal–organic frameworks (MOFs) has been one of the most active areas of materials research in recent years. The intense interest in these materials is driven by their potential applications as functional materials (catalysis, magnetism, electric conductivity and nonlinear optics) and intriguing structural diversities.[1–4] Assembly of these metal–organic coordination polymers allows for a wide choice of various parameters including diverse electronic properties and coordination geometries of the metal ions as well as versatile functions of organic ligands.[5–7] Consequently, a wide variety of coordination architectures with interesting structures and desired properties have been prepared through judicious choice of organic ligands and metal ions.[8–11] Recently, 5-sulfoisophthalic acid ($H_3SIP$) has been successfully used to investigate the lanthanide contraction effect[12] and the coordination polymer chemistry of a main group metal

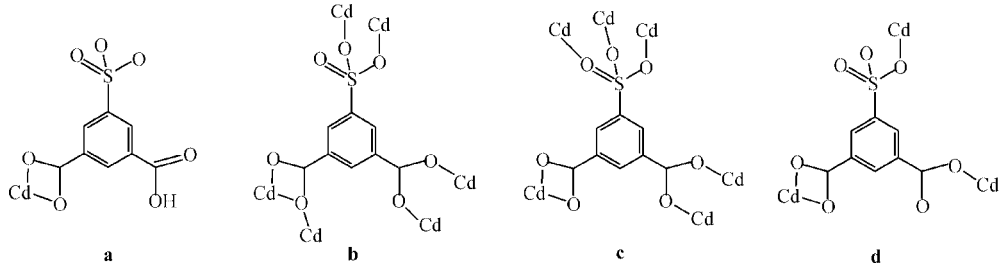


Scheme 1. Coordination modes of 5-sulfoisophthalic acid observed in compounds **1**–**3**.

[a] State Key Laboratory of Structural Chemistry, Fujian Institute of Research on the Structure of Matter, Chinese Academy of Sciences,
Fuzhou, Fujian 350002, P. R. China
Fax: +86-591-83705045
E-mail: xli@fjirsm.ac.cn
qyliu@fjirsm.ac.cn
[b] College of Chemistry and Chemical Engineering, Jiangxi Normal University,
Nanchang, Jiangxi 330022, P. R. China
Fax: +86-791-8120387
E-mail: ylwangchem@gmail.com

($Pb^{2+}$),[13] because of its multiple coordinating modes and the sensitivity of the sulfonate group to the surrounding chemical environment. In this contribution, SIP will serve as a probe to examine the coordination polymer chemistry of the late transition metal $Cd^{2+}$. Three novel (SIP)Cd compounds, $[Cd_2(\mu_2\text{-}OH_2)_2(HSIP)_2(H_2O)_6]$ (**1**), $[Cd_5(\mu_2\text{-}OH)_2(\mu_3\text{-}OH)_2(SIP)_2(H_2O)_5]_n$ (**2**) and $\{[Cd_3(SIP)_2(dpp)_6]\cdot 4(H_2O)\}_n$ (**3**), will be described with regard to syntheses, crystal structures, and IR spectroscopic and photolumines-

 © 2006 Wiley-VCH Verlag GmbH & Co. KGaA, Weinheim 

cent properties. Two unprecedented bridging coordination modes of SIP (Scheme 1, **b** and **c**) are observed in polymer **2**.

## Results and Discussion

### Preparation of the Compounds

Hydrothermal synthesis is widely employed to produce new materials with diverse structural architectures, but is still a kind of black box. This method can minimise the problems associated with ligand solubility and enhance the reactivity of reactants in favour of efficient molecular building during the crystallisation process. There are a variety of hydrothermal parameters such as reaction time, temperature, pH value, templates and molar ratio of reactants, and small changes in one or more of these parameters can have a profound influence on the final reaction outcome. Compounds **1** and **2**, with very different structures, were obtained from similar reactions but at different pH values, indicating that the hydrothermal reaction outcome of the Cd/$H_3$SIP system is pH-dependent. We also notice that N-containing auxiliary ligands such as dpp [1,3-bis(4-pyridyl)-propane] are also able to tune the framework structures. At a ratio of Cd/SIP/dpp = 3:2:6, the 2D polymer **3** is formed. Reducing the corresponding ratio to 3:2:2 results in the 1D compound $\{[Cd(SIP)(dpp)(H_2O)_3]\cdot 0.5Cd(H_2O)_6\cdot 5H_2O\}_n$,[14] indicating that the reaction products are ratio-dependent. The preparative reactions were carried out at different temperatures (140 °C, 160 °C and 180 °C) to examine the temperature dependence of their solid structures. X-ray diffraction analyses of these reaction products indicate that the same results were obtained under these reaction temperatures although the purity and yields were slightly different, indicative of the thermodynamic nature of the hydrothermal reactions.[15]

### Crystal Structure of $[Cd_2(\mu_2\text{-}OH_2)_2(HSIP)_2(H_2O)_6]$ (1)

The dinuclear structure of **1** is shown in Figure 1; it has a crystallographically imposed $C_{2h}$ symmetry, which has the $C_2$ axis passing through O7 and O7A (for symmetry code see Table 1). The two $Cd^{II}$ atoms are linked by two bridging water molecules to form the rhomboidal $[Cd_2(\mu_2\text{-}OH_2)_2]$ core with a Cd–O distance of 2.412(1) Å and O(7)–Cd(1)–O(7A) bond angle of 75.48(8)°. Each cadmium ion is bonded to two bridging water molecules, three terminal water molecules and one $HSIP^{2-}$ dianion through the chelating carboxylate group. The Cd–O distances range from 2.412(1) to 2.567(3) Å, which is consistent with those found in comparable structures.[16–19] The uncoordinated carboxylate group is protonated for charge balance, as suggested by the strong absorption at 1710 $cm^{-1}$.[20] As shown in Figure 2a, a 3D supramolecular framework is formed through three types of hydrogen bonds between (a) coordinated water molecules and sulfonate oxygen atoms [O(7)···O(5B) 2.732(2) Å, O(8)···O(6C) 2.832(2) Å and O(9)···O(6D) 2.808(2) Å]; (b) coordinated water molecules and carboxylate oxygen atoms [O(9)···O(4B) 2.867(3) Å]; and (c) a carboxylate group and a carboxylate oxygen atom [O(3)···O(2E) 2.581(3) Å]. Of particular interest is the infinite tape formed by hydrogen bonds between the $[Cd_2(\mu_2\text{-}OH_2)_2(H_2O)_2]$ units and the sulfonate groups along the crystallographic *b* axis (Figure 2b). The hydrogen-bonded tape features an eight-membered ring [the bridging $H_2O(7)$, O(5) and their equivalents], which is nearly perpendicular to the $[Cd_2(\mu_2\text{-}OH_2)_2]$ plane (95.7°). The tape is strengthened by the O(8)···O(6C) hydrogen bonds, as shown in Figure 2b. The 3D supramolecular structures are further stabilised by π–π interactions between the parallel aromatic rings in an off-set fashion with a face-to-face distance of 3.44(2) Å and a centre-to-centre distance of 3.66(3) Å. This indicates that noncovalent interactions can play a crucial role in constructing the whole packing.

### Crystal Structure of $[Cd_5(\mu_2\text{-}OH)_2(\mu_3\text{-}OH)_2(SIP)_2(H_2O)_5]_n$ (2)

Compound **2** contains five unique $Cd^{II}$ ions, four of which are six-coordinate and one [Cd(3)] five-coordinate.

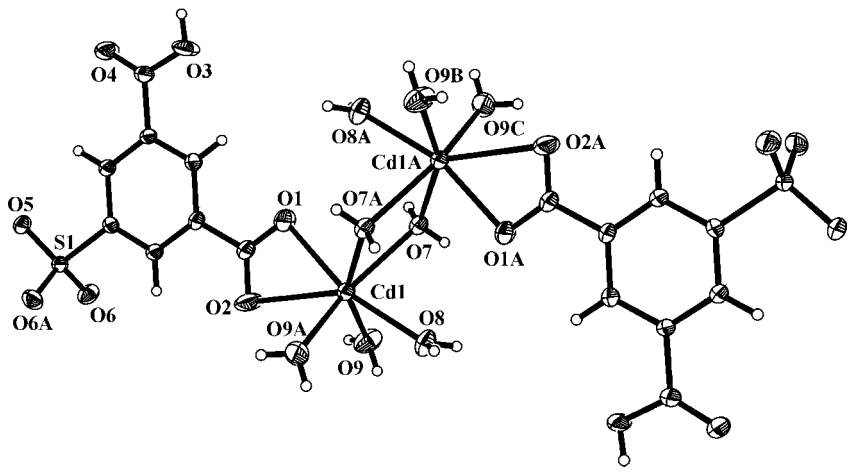


Figure 1. ORTEP drawing of **1** with 40% probability displacement ellipsoids. Hydrogen atoms are shown as small spheres of arbitrary radii.

 © 2006 Wiley-VCH Verlag GmbH & Co. KGaA, Weinheim 

As shown in Figure 3, Cd(1) has a distorted octahedral coordination geometry with the equatorial positions taken up by one chelating carboxylate group [O(10A) and O(11A)], one monodentate carboxylate oxygen atom [O(1)] and one $\mu_3$-hydroxy oxygen atom [O(16)]. The axial positions are occupied by one water molecule [O(15)] and one sulfonate oxygen atom [O(5B)] from the third SIP ligand. The angles formed by the equatorial atoms range from 54.97(9)° [O(10A)–Cd(1)–O(11A)] to 118.75(9)° [O(1)–Cd(1)–O(16)], indicative of a serious distortion of the [$CdO_6$] octahedron. Cd(5) has a similar coordination environment to that of Cd(1). Cd(2) also has a distorted [$CdO_6$] octahedral coordination geometry in which a pair of symmetrically related $\mu_3$-hydroxy oxygen atoms [O(16) and O(16C)], a $\mu_2$-hydroxy oxygen atom [O(18)] and a sulfonate oxygen atom [O(6B)] form the equatorial plane. The water molecule [O(17)] and the carboxylate oxygen atom [O(2)] occupy the apical positions. The coordination environment of Cd(4) is similar to that of Cd(2) but the terminal water molecule [O(21)] is located at the equatorial plane and the $\mu_2$-hydroxy oxygen atom [O(20)] occupies the apical position. The Cd(3) atom is coordinated by one $\mu_2$-hydroxy oxygen atom [O(18)], a sulfonate oxygen atom [O(12)] and one carboxylate oxygen atom [O(3)] in an equatorial plane, and the other $\mu_2$-hydroxy oxygen atom [O(20)] and the water molecule [O(19)] in the apical positions to complete its trigonal-bipyramidal coordination environment. The Cd–O distances range from 2.182(3) to 2.517(2) Å, as listed in Table 1. Two crystallographically unique SIP ligands exhibit two different coordination modes (Scheme 1, **b** and **c**). One SIP (**b**) acts as a hexadentate ligand with the bidentate sulfonate and carboxylate groups, and one $\mu_2$-$\eta^2$:$\eta^1$ carboxylate group (one oxygen atom bridges two metal atoms, the other connects one metal atom and the carboxylate group coordinates to two metal atoms). The other SIP ligand also adopts a hexadentate bridging coordination mode through its one bidentate carboxylate group, one chelate carboxylate group and the tridentate sulfonate group. To the best of our knowledge,

Table 1. Selected bond lengths [Å] and bond angles [°] of **1**–**3**.[a]

| | | | |
|---|---|---|---|
| Compound **1** | | | |
| Cd(1)–O(1) | 2.265(2) | Cd(1)–O(2) | 2.567(3) |
| Cd(1)–O(7) | 2.4121(13) | Cd(1)–O(8) | 2.284(2) |
| Cd(1)–O(9) | 2.2683(18) | | |
| O(1)–Cd(1)–O(2) | 52.45(8) | O(1)–Cd(1)–O(7) | 83.93(5) |
| O(1)–Cd(1)–O(8) | 163.71(9) | O(1)–Cd(1)–O(9) | 107.82(6) |
| O(7)–Cd(1)–O(7A) | 75.48(8) | O(9)–Cd(1)–O(7) | 85.73(7) |
| O(9)–Cd(1)–O(8) | 81.13(6) | O(7)–Cd(1)–O(8) | 83.21(5) |
| O(9)–Cd(1)–O(2) | 78.00(6) | O(2)–Cd(1)–O(8) | 143.84(8) |
| O(7)–Cd(1)–O(2) | 123.84(4) | O(9)–Cd(1)–O(9A) | 108.51(11) |
| Cd(1)–O(7)–Cd(1A) | 104.52(8) | | |
| Compound **2** | | | |
| Cd(1)–O(1) | 2.258(3) | Cd(1)–O(15) | 2.327(3) |
| Cd(1)–O(16) | 2.198(2) | Cd(1)–O(10A) | 2.405(3) |
| Cd(1)–O(11A) | 2.317(3) | Cd(1)–O(5B) | 2.445(2) |
| Cd(2)–O(2) | 2.315(3) | Cd(2)–O(16) | 2.276(2) |
| Cd(2)–O(16C) | 2.260(2) | Cd(2)–O(17) | 2.398(4) |
| Cd(2)–O(18) | 2.200(3) | Cd(2)–O(6B) | 2.412(2) |
| Cd(3)–O(3) | 2.260(2) | Cd(3)–O(12) | 2.432(2) |
| Cd(3)–O(18) | 2.201(3) | Cd(3)–O(19) | 2.287(3) |
| Cd(3)–O(20) | 2.182(3) | Cd(4)–O(13) | 2.416(2) |
| Cd(4)–O(20) | 2.237(2) | Cd(4)–O(21) | 2.276(3) |
| Cd(4)–O(22) | 2.286(2) | Cd(4)–O(9E) | 2.345(2) |
| Cd(4)–O(22D) | 2.235(2) | Cd(5)–O(14) | 2.517(2) |
| Cd(5)–O(22) | 2.193(2) | Cd(5)–O(23) | 2.279(3) |
| Cd(5)–O(8E) | 2.270(2) | Cd(5)–O(3F) | 2.507(2) |
| Cd(5)–O(4F) | 2.309(3) | | |
| O(1)–Cd(1)–O(16) | 118.75(9) | O(1)–Cd(1)–O(11A) | 82.70(9) |
| O(10A)–Cd(1)–O(11A) | 54.97(9) | O(16)–Cd(1)–O(10A) | 101.87(9) |
| O(15)–Cd(1)–O(16) | 97.29(10) | O(15)–Cd(1)–O(1) | 99.84(12) |
| O(15)–Cd(1)–O(10A) | 85.45(13) | O(15)–Cd(1)–O(11A) | 93.96(11) |
| O(5B)–Cd(1)–O(1) | 90.71(9) | O(5B)–Cd(1)–O(16) | 79.69(8) |
| O(5B)–Cd(1)–O(10A) | 84.97(11) | O(5B)–Cd(1)–O(11A) | 84.72(10) |
| O(16C)–Cd(2)–O(16) | 81.20(8) | O(6B)–Cd(2)–O(16) | 174.23(9) |
| O(18)–Cd(2)–O(6B) | 90.15(11) | O(16C)–Cd(2)–O(18) | 93.27(11) |
| O(2)–Cd(2)–O(16) | 78.61(9) | O(2)–Cd(2)–O(16C) | 92.43(9) |
| O(2)–Cd(2)–O(18) | 108.43(11) | O(2)–Cd(2)–O(6B) | 82.08(9) |
| O(17)–Cd(2)–O(16) | 90.06(15) | O(17)–Cd(2)–O(16C) | 100.81(16) |
| O(17)–Cd(2)–O(18) | 84.41(15) | O(17)–Cd(2)–O(6B) | 84.14(15) |
| O(3)–Cd(3)–O(12) | 103.64(8) | O(3)–Cd(3)–O(18) | 129.41(11) |
| O(12)–Cd(3)–O(18) | 121.49(11) | O(19)–Cd(3)–O(3) | 78.58(9) |
| O(19)–Cd(3)–O(12) | 73.32(9) | O(19)–Cd(3)–O(18) | 92.68(11) |
| O(20)–Cd(2)–O(3) | 92.98(9) | O(20)–Cd(3)–O(12) | 98.00(9) |
| O(20)–Cd(3)–O(18) | 101.49(11) | O(13)–Cd(4)–O(21) | 82.07(10) |
| O(13)–Cd(4)–O(22) | 100.35(8) | O(22D)–Cd(4)–O(21) | 92.43(9) |
| O(22D)–Cd(4)–O(22) | 83.20(8) | O(22)–Cd(4)–O(20) | 100.88(9) |
| O(13)–Cd(4)–O(20) | 82.62(9) | O(22D)–Cd(4)–O(20) | 110.23(9) |
| O(21)–Cd(4)–O(20) | 88.06(10) | O(22)–Cd(4)–O(9E) | 79.23(8) |
| O(13)–Cd(4)–O(9E) | 77.61(9) | O(22D)–Cd(4)–O(9E) | 89.83(9) |
| O(21)–Cd(4)–O(9E) | 92.88(10) | O(3F)–Cd(5)–O(4F) | 54.08(8) |
| O(4B)–Cd(5)–O(8E) | 83.71(9) | O(3F)–Cd(5)–O(22) | 97.64(8) |
| O(8E)–Cd(5)–O(22) | 120.34(9) | O(14)–Cd(5)–O(3F) | 79.74(8) |
| O(14)–Cd(5)–O(4F) | 85.51(9) | O(14)–Cd(5)–O(22) | 78.12(8) |
| O(14)–Cd(5)–O(8E) | 87.58(9) | O(23)–Cd(5)–O(3F) | 94.46(11) |
| O(23)–Cd(5)–O(4F) | 97.71(11) | O(23)–Cd(5)–O(22) | 94.77(10) |
| O(23)–Cd(5)–O(8E) | 102.12(11) | Cd(1)–O(16)–Cd(2) | 105.56(9) |
| Cd(1)–O(16)–Cd(2C) | 124.45(11) | Cd(2)–O(16)–Cd(2C) | 98.80(8) |
| Cd(2)–O(18)–Cd(3) | 142.54(16) | Cd(3)–O(20)–Cd(4) | 111.16(11) |
| Cd(4)–O(22)–Cd(5) | 105.06(9) | Cd(4)–O(22)–Cd(4D) | 96.80(8) |
| Cd(5)–O(22)–Cd(4D) | 121.22(10) | Cd(3)–O(3)–Cd(5F) | 121.56(10) |

Table 1. *(continued)*.

| | | | |
|---|---|---|---|
| Compound **3** | | | |
| Cd(1)–O(5) | 2.317(2) | Cd(1)–N(1) | 2.372(3) |
| Cd(1)–N(3) | 2.338(3) | Cd(2)–O(1) | 2.302(2) |
| Cd(2)–O(3B) | 2.539(2) | Cd(2)–O(4B) | 2.346(2) |
| Cd(2)–N(5) | 2.300(3) | Cd(2)–N(4C) | 2.351(3) |
| Cd(2)–N(6D) | 2.356(3) | | |
| N(1)–Cd(1)–N(3) | 82.75(10) | N(1)–Cd(1)–N(3A) | 97.25(10) |
| N(1)–Cd(1)–O(5) | 90.22(9) | N(3)–Cd(1)–O(5) | 95.57(9) |
| N(1A)–Cd(1)–O(5) | 89.78(9) | N(3A)–Cd(1)–O(5) | 84.43(9) |
| O(1)–Cd(2)–N(5) | 129.70(9) | O(1)–Cd(2)–O(4B) | 84.90(8) |
| O(3B)–Cd(2)–O(4B) | 53.47(7) | N(5)–Cd(2)–O(3B) | 91.42(8) |
| N(6D)–Cd(2)–O(1) | 86.42(10) | N(6D)–Cd(2)–O(3B) | 83.31(9) |
| N(6D)–Cd(2)–O(4B) | 83.89(9) | N(6D)–Cd(1)–N(5) | 91.61(10) |
| N(4C)–Cd(2)–O(1) | 84.90(8) | N(4C)–Cd(2)–O(3B) | 85.97(9) |
| N(4C)–Cd(2)–O(4B) | 84.37(9) | N(4C)–Cd(1)–N(5) | 95.33(10) |
| N(4C)–Cd(2)–O(6D) | 167.37(10) | | |

[a] Symmetry transformation for equivalent atoms: Compound **1**: A: *–x*, *–y* + 1, *–z* + 2. Compound **2**: A: *x* + 1, *y*, *z* – 1; B: *–x*, *–y* + 2, *–z* + 1; C: *–x* – 1, *–y* + 3, *–z* + 1; D: *–x*, *–y* + 2, *–z* + 2; E: *–x* – 1, *–y* + 3, *–z* + 2; F: *–x* – 1, *–y* + 2, *–z* + 2. Compound **3**: A: *–x* – 1, *–y* + 1, *–z* + 1; B: *x* – 1, *y*, *z*; C: *–x* – 1, *–y*, *–z* + 1; D: *x*, *y* + 1, *z*.

 © 2006 Wiley-VCH Verlag GmbH & Co. KGaA, Weinheim 

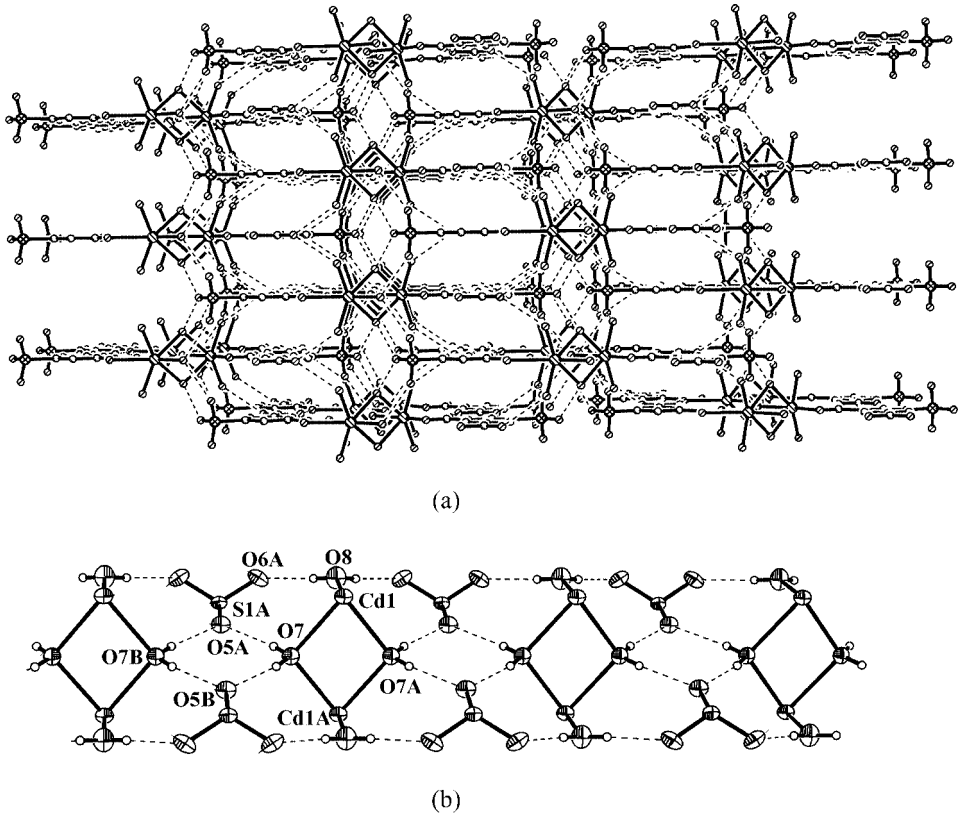


Figure 2. (a) 3D porous supramolecular open framework of **1** viewed along the *c* axis. (b) $[Cd_2(\mu_2\text{-}OH_2)_2]$ cores bridged by sulfonate groups through hydrogen bonds to form a 1D tape.

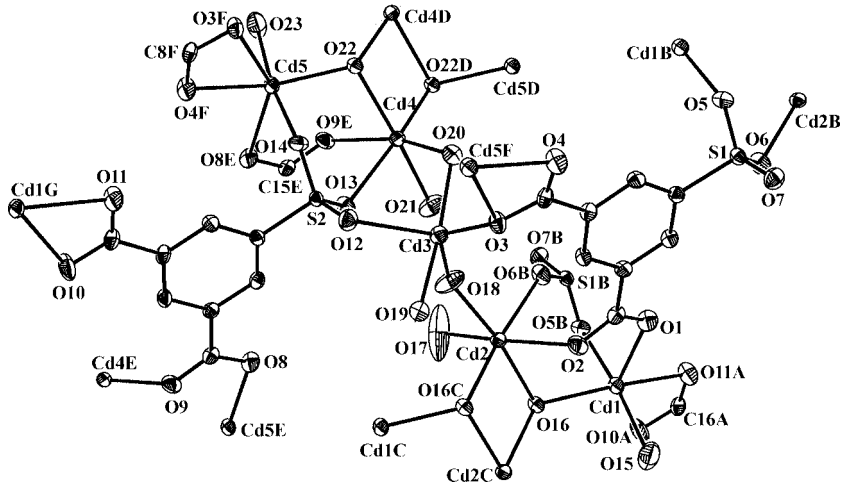


Figure 3. ORTEP drawing of **2** with 40% probability displacement ellipsoids.

neither type of coordination mode of the SIP ligands is observed in the reported SIP complexes.

The 3D framework structure shown in Figure 4a is constructed by inorganic oxide layers pillared by the SIP ligands, reminiscent of reported metal biphosphonate compounds.[21,22] The inorganic oxide layer contains two types of chair-like $[Cd_4(\mu_3\text{-}OH)_2]$ cluster units formed by Cd(1)/Cd(2) and Cd(4)/Cd(5), respectively, and features two types of centrosymmetric rings: 12-membered (A) and 24-membered (B). As shown in Figure 4b, each $\mu_3$-hydroxy group (O16) as a metal linker bridges the neighbouring three Cd atoms to generate a chair-shaped tetranuclear $[Cd_4(\mu_3\text{-}OH)_2]$ cluster with Cd(2), O(16) and their equivalents related by an inversion centre defining a plane and with the two Cd(1) atoms above and below the $[Cd_2(\mu_3\text{-}OH)_2]$ plane. The Cd(1)–O(16), Cd(2)–O(16) and Cd(2C)–O(16) distances are 2.198(2), 2.276(2) and 2.260(2) Å, respectively, with surrounding angles of 105.56(9)°, 124.45(11)° and 98.80(8)° for Cd(1)–O(16)–Cd(2), Cd(1)–O(16)–Cd(2C) and Cd(2)–O(16)–Cd(2C), respectively. The chair-shaped

 © 2006 Wiley-VCH Verlag GmbH & Co. KGaA, Weinheim 

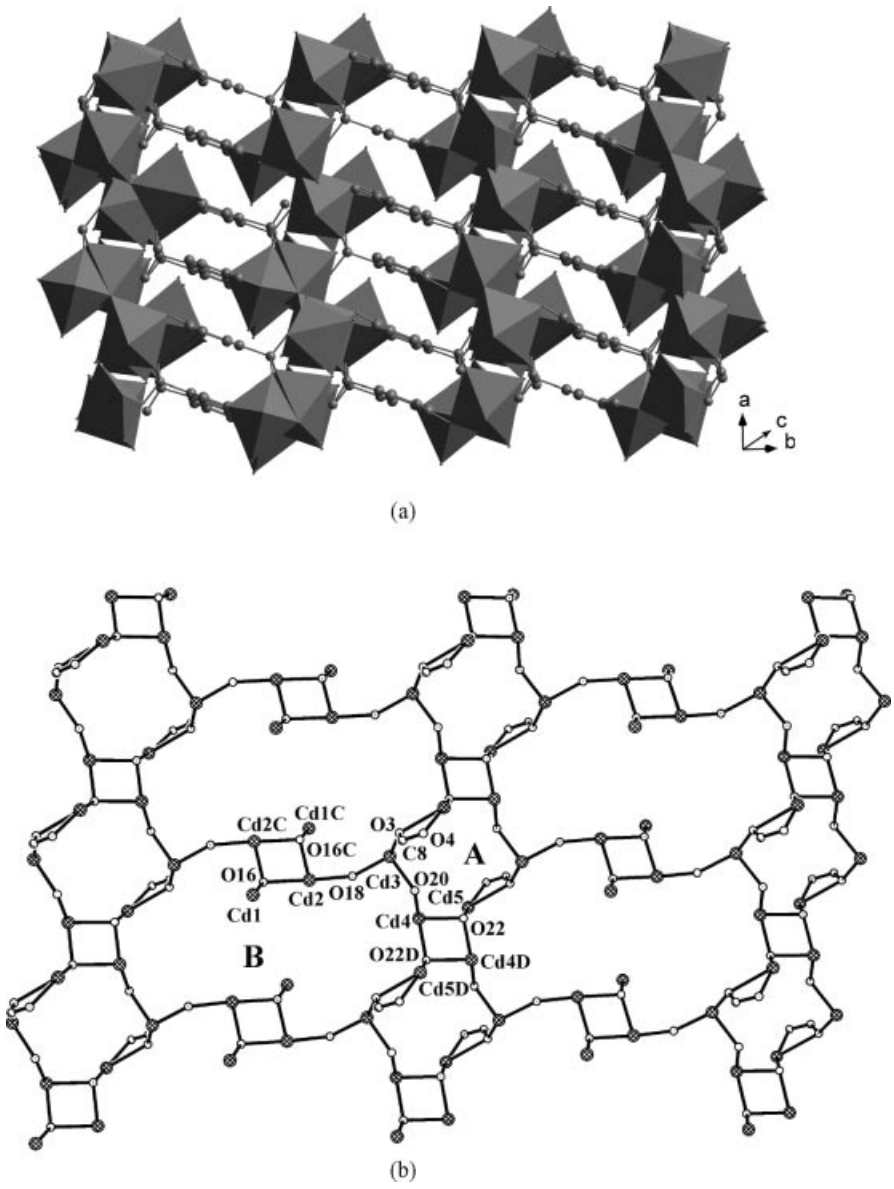


Figure 4. (a) 3D structure of **2** (the polyhedral presentation indicates the coordination environments for the Cd centre). (b) Perspective view of the 2D metal–oxide inorganic layer featuring the chair-shaped $[Cd_4(\mu_3\text{-}OH)_2]$ clusters and two types of large rings.

$[Cd_4(\mu_3\text{-}OH)_2]$ cluster formed by Cd(4)/Cd(5) has a similar geometry to that of the $[Cd_4(\mu_3\text{-}OH)_2]$ cluster formed by Cd(1)/Cd(2), with Cd(5)–O(22), Cd(4)–O(20) and Cd(4)–O(22) bond lengths of 2.193(2), 2.286(2) and 2.237(2) Å, respectively, and surrounding angles of 105.06(9)°, 121.22(10)° and 96.80(8)° for Cd(4)–O(22)–Cd(5), Cd(5)–O(22)–Cd(4D) and Cd(4)–O(22)–Cd(4D), respectively. There are several compounds containing a chair-shaped tetranuclear cadmium cluster,[23–25] but those with two capping $\mu_3$-OH groups are rare. It is even more interesting that the $[Cd_4(\mu_3\text{-}OH)_2]$ cluster units are interconnected by the $Cd(3)(\mu_2\text{-}OH)_2(CO_2)$ unit into an unusual inorganic oxide layer. Although cadmium cluster units have been known to be present in coordination polymers,[6,26–28] such cluster-based inorganic layers as subunits of a coordination polymer are still scarce. The layer has a 12-membered ring (A) with approximate dimensions of $3.8 \times 4.9$ Å$^2$, which is composed of Cd(3), Cd(4) and Cd(5) atoms and their equivalents linked by two $\mu_3$-OH, two $\mu_2$-OH and two carboxylate groups. It also contains a large 24-membered ring (B) with approximate dimensions of $4.7 \times 14.3$ Å$^2$. The inorganic oxide layer is linked by the carboxylate and sulfonate groups of the SIP ligands to form a 3D pillared framework.

### Crystal Structure of $\{[Cd_3(SIP)_2(dpp)_6]\cdot 4(H_2O)\}_n$ (3)

As shown in Figure 5, **3** contains two crystallographically independent cadmium ions; Cd(1) lies on the crystallographic inversion centre. Both $Cd^{2+}$ ions are octahedrally coordinated but their coordination environments are different. Cd(1) is coordinated to four equatorial pyridine ni-

 © 2006 Wiley-VCH Verlag GmbH & Co. KGaA, Weinheim 

trogen atoms [Cd–N = 2.372(3) and 2.338(3) Å] in a square-planar arrangement and two apical sulfonate oxygen atoms from two *trans*-SIP ligands [Cd–O = 2.317(2) Å]. Cd(2) is coordinated by one chelating and one monodentate carboxylate group from two different SIP ligands, and one pyridine nitrogen atom in equatorial positions with Cd–O distances of 2.346(2), 2.539(2) and 2.302(2) Å, respectively, and a Cd–N distance of 2.300(3) Å. The axial positions are taken up by two other pyridine nitrogen atoms, with Cd–N distances of 2.351(3) and 2.356(3) Å. As illustrated in Figure 6, the SIP ligands interconnect the $Cd^{2+}$ ions in coordination mode **d** (Scheme 1) into an infinite ladder structure along the *a* axis, which features the cyclic $[Cd_4(SIP)_4]$ unit with dimensions of $7.5 \times 12.8$ Å$^2$. It is interesting that the four Cd ions [Cd(1), Cd(2), Cd(1A) and Cd(2A)] are co-planar. The 1D ladder can also conveniently be regarded as resulting from two antiparallel $[Cd(SIP)]_n$ single chains bridged by Cd(1) (Figure 6).

Compound **3** contains one monodentate [N(1)···N(2)] and two bridging dpp ligands [N(3)···N(4) and N(5)···N(6)]. The flexible dpp ligand can adopt several conformations based on the orientations of the $CH_2$ groups, such as *TT*, *TG*, *GG* and *GG′* (*T* = *trans*; *G* =*gauche* ), with quite different N···N separations (6.7–10.1 Å).[29,30] In the present case, the monodentate dpp has a conformation of *TG* with an N···N distance of 8.9 Å and the bridging ones adopt *TT* conformation with an N···N separation of 9.5 Å. The 1D ladders are connected by the bridging dpp ligands to form a 2D nanolayer with a thickness of about 1.5 nm, as shown in Figure 7; the cavity is filled in by the monodentate dpp.

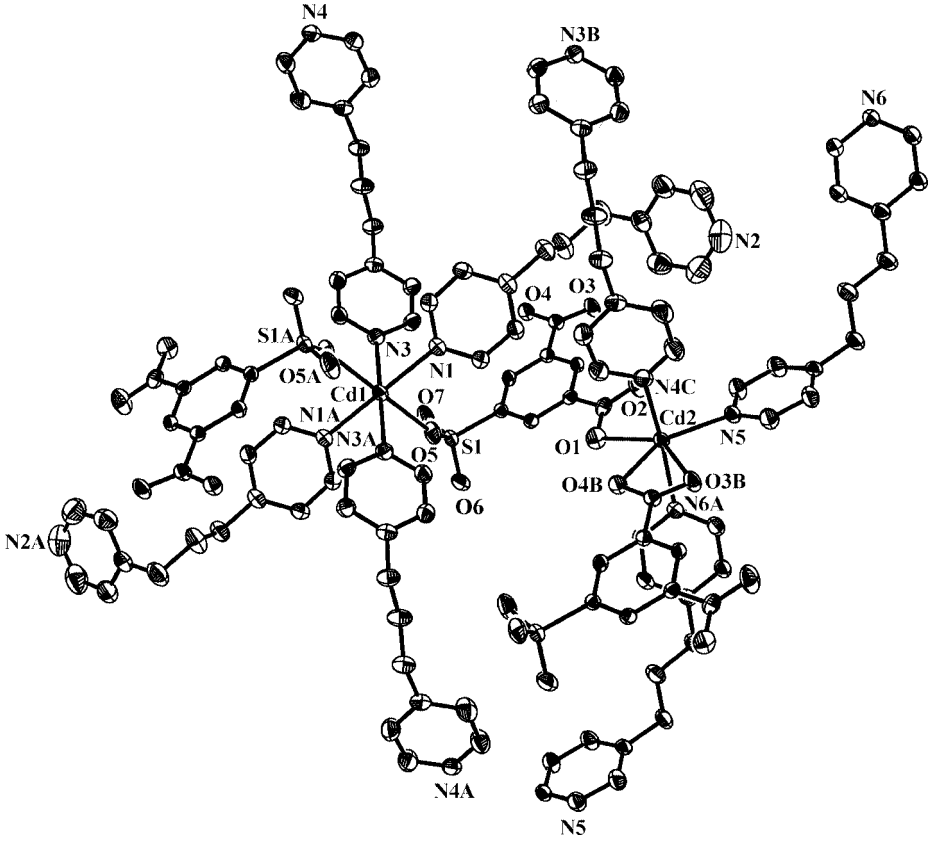


Figure 5. ORTEP drawing of **3** with 35% probability displacement ellipsoids.

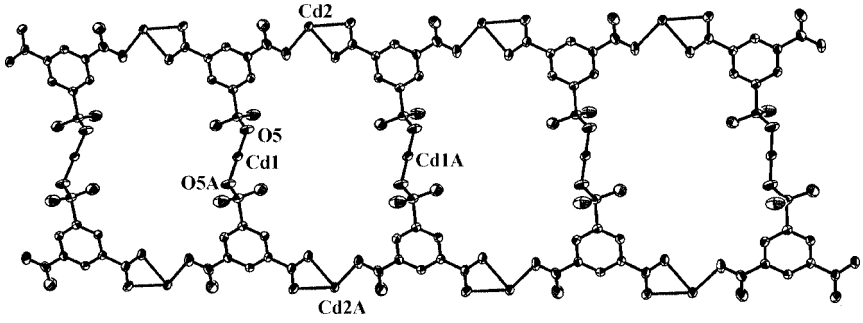


Figure 6. 1D ladder structure in compound **3** featuring the cyclic $[Cd_4(SIP)_4]$ unit.

 © 2006 Wiley-VCH Verlag GmbH & Co. KGaA, Weinheim 

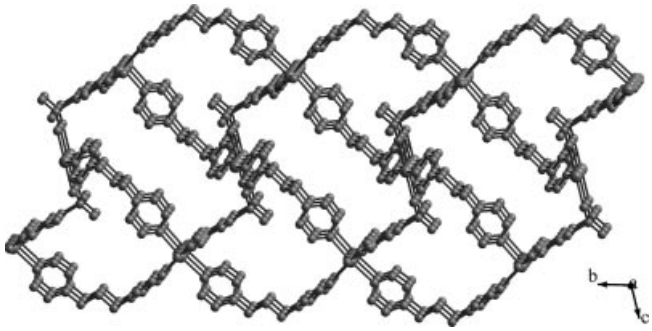

Figure 7. Perspective view of the 2D structure of **3**. Lattice water molecules and monodentate dpp molecules omitted for clarity.

### FTIR Spectra

The FTIR spectra of **1** and **3** exhibit broad absorptions centred at 3498 and 3399 $cm^{-1}$ for **1** and **3**, respectively, because of the existence of water molecules in the structures. The O–H stretching vibrations of the water molecules and hydroxy group in **2** appear at 3435 and 3159 $cm^{-1}$. The IR spectra of **1**–**3** display the typical stretching bands of carboxylate groups between 1400 and 1622 $cm^{-1}$. The characteristic band at 1710 $cm^{-1}$ in **1** is attributable to the protonated carboxylate group of $H_3SIP$ ligand. The absorptions in the region 1000–1230 $cm^{-1}$ in **1**–**3** are typical for the sulfonate groups. The strong absorptions at about 620 $cm^{-1}$ in **1**–**3** can be assigned to the S–O stretching vibrations.

### Photoluminescent Properties

Metal–organic frameworks (MOFs) are promising photoluminescent materials because of their high thermal stability, and structure- and metal-dependent emission. The combination of organic linkers and metal centres in coordination polymers provides an efficient route to a new type of photoluminescent materials with potential applications as light-emitting diodes (LEDs). The $d^{10}$ metal compounds have been shown to exhibit interesting photoluminescent properties.[31–33] In the present work, we have examined the photoluminescent properties of **1**–**3** and the free $H_3SIP$ ligand in the solid state at room temperature. Free $NaH_2SIP$ displays a photoluminescent emission at 320 nm upon excitation at 286 nm.[17] Compound **1** exhibits a broad photoluminescent emission centred at 436 nm upon excitation at 342 nm and **3** displays an emission at 409 nm upon excitation at 350 nm (Figure 8). The emissions of **1** (436 nm) and **3** (409 nm) occur at much longer wavelengths than that of the free ligand (320 nm). Such a large bathochromic shift indicates that the aromatic rings of the ligand effectively interact with the metal ion and/or with each other through π-stacking interactions, as described above. In other words, the π-electrons of the aromatic rings are delocalised over the $Cd^{2+}$ ion and/or the neighbouring ligand. With the above concerns in mind, the fluorescence emission of **1** may tentatively be assigned to the formation of the $[Cd_2(\mu_2\text{-}OH_2)_2]$ cluster, which compares to our recently reported (SIP)lead compound.[13] The emission peak of **3** at 409 nm, which is similar to that of the analogue $\{[Cd(SIP)(H_2O)_3]\cdot 0.5(H_2en)(H_2O)\}_n$[17] (412 nm), can be assigned to ligand-to-metal charge transfer (LMCT). This is consistent with the fact that the $Cd^{II}$ or $Zn^{II}$ coordination complexes with aromatic carboxylate ligands may possess an LMCT photoluminescent property.[34–36] In the case of **2**, the emission at 306 nm upon excitation at 270 nm is similar to that of the free $H_3SIP$ ligand. This indicates that the emission band of **2** is an intraligand transition. The further lifetime measurements at room temperature of each emission maximum give results of 0.61, 18 and 0.56 ns for compounds **1**, **2** and **3**, respectively. The lifetime of **2** is significantly longer than those of **1** and **3**. This is consistent with the fact that metal hydroxide (or oxide) clusters usually have longer emission lifetimes[35] because the $\mu_2/\mu_3$-OH ligands can tighten the whole framework and thus result in weaker vibrations. These observations clearly reveal the structure-dependent photoluminescent properties of coordination polymers.

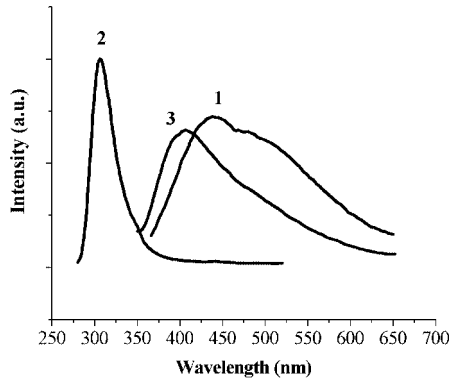


Figure 8. Solid-state emission photoluminescent spectra of **1**–**3** at room temperature.

## Conclusions

In conclusion, hydrothermal reactions of the $Cd/H_3SIP$ system are pH-dependent. Incomplete deprotonation of the $H_3SIP$ ligand occurs under acidic conditions, leading to lowered connectivity of the SIP ligand and the formation of the discrete dinuclear compound **1**. The ligand is fully deprotonated under neutral or basic conditions, accompanied by the formation of the hydroxy-bridged cadmium clusters **2**. In **2**, the chair-like $[Cd_4(\mu_3\text{-}OH)_2]$ cluster units are interconnected by the $[Cd(\mu_2\text{-}OH)_2(CO_2)]$ unit into an unprecedented inorganic oxide layer, which is pillared by the $SIP^{3-}$ ligand into a 3D framework structure. Two unprecedented coordination modes are observed in compound **2**. The addition of the auxiliary ligand dpp leads to the 2D structure of **3** containing a cyclic $[Cd_4(SIP)_4]$ unit with the Cd atoms co-planar. Compounds **1**–**3** display different photoluminescent emissions at room temperature, indicating structure-dependent photoluminescent properties of the Cd/SIP coordination polymers and thus potential application in LED technology.

 © 2006 Wiley-VCH Verlag GmbH & Co. KGaA, Weinheim 

## Experimental Section

**General Remarks:** All chemicals were purchased commercially and used without further purication, including 5-sulfoisophthalic acid monosodium salt (Alfa) and 1,3-bis(4-pyridyl)propane (Acros). Elemental analyses were carried out with an Elementar Vario EL III analyser and IR spectra (KBr pellets) were recorded with a Perkin–Elmer Spectrum One. Fluorescent spectra were measured at room temperature with an Edinburgh FL-FS90 TCSPC system. All complexes were synthesised by a hydrothermal method under autogenous pressure.

**Synthesis of $[Cd_2(\mu\text{-}OH_2)_2(HSIP)_2(H_2O)_6]$ (1):** A mixture of $Cd^{II}$ nitrate tetrahydrate (0.0616 g, 0.2 mmol), 5-sulfoisophthalic acid monosodium salt (0.0536 g, 0.2 mmol), triethylamine (0.01 mL) and water (15 mL) (pH = 2) was heated at 160 °C for 4 d. Colourless plate-like crystals of **1** were obtained when cooling to room temperature at 5 °C/h. The crystals were recovered by filtration, washed with distilled water and dried in air (yield: 0.05 g, 63% based on Cd). $C_{16}H_{24}Cd_2O_{22}S_2$ (857.27): calcd. C 22.33, H 2.81; found C 22.31, H 2.76. IR (KBr pellet): $\tilde{\nu}$ = 3498 s, 1710 s, 1622 s, 1580 w, 1552 s, 1436 w, 1371 s, 1231 s, 1187 s, 1118 s, 1047 s, 999 w, 857 w, 768 m, 731 w, 673 m, 624 m, 580 w $cm^{-1}$.

**Synthesis of $[Cd_5(\mu_2\text{-}OH)_2(\mu_3\text{-}OH)_2(SIP)_2(H_2O)_5]_n$ (2):** A mixture of $Cd^{II}$ nitrate tetrahydrate (0.0616 g, 0.2 mmol), 5-sulfoisophthalic acid monosodium salt (0.0536 g, 0.2 mmol), triethylamine (0.05 mL) and water (15 mL) (pH = 7) was heated at 160 °C for 4 d. Colourless prism-like crystals of **2** were obtained when cooling to room temperature at 5 °C/h. The crystals were recovered by filtration, washed with distilled water and dried in air (yield: 0.013 g, 11% based on Cd). $C_{16}H_{20}Cd_5O_{23}S_2$ (1206.44): calcd. C 15.82, H 1.66; found C 15.76, H 1.63. IR (KBr pellet): $\tilde{\nu}$ = 3435 s, 3159 s, 1615 s, 1569 w, 1553 m, 1400 s, 1216 w, 1182 s, 1106 m, 1044 s, 858 w, 833 w, 707 w, 673 m, 620 m, 447 w $cm^{-1}$.

**Synthesis of $\{[Cd_3(SIP)_2(dpp)_6]\cdot 4(H_2O)\}_n$ (3):** A mixture of $Cd^{II}$ nitrate tetrahydrate (0.0231 g, 0.075 mmol), 5-sulfoisophthalic acid monosodium salt (0.0134 g, 0.05 mmol), 1,3-bis(4-pyridyl)propane (0.0297 g, 0.15 mmol), triethylamine (0.01 mL) and water (15 mL) was heated at 160 °C for 4 d. Colourless rod-like crystals of **3** were obtained when cooling to room temperature at 5 °C/h. The crystals were recovered by filtration, washed with distilled water and dried in air (yield: 0.023 g, 46% based on Cd). $C_{94}H_{98}Cd_3N_{12}O_{18}S_2$ (2085.16): calcd. C 54.02, H 4.73, N 8.05; found C 54.03, H 4.71, N 8.02. IR (KBr pellet): $\tilde{\nu}$ = 3399 s, 2943 s, 1612 s, 1560 w, 1502 w, 1428 s, 1364 s, 1224 m, 1199 m, 1103 m, 1068 w, 1042 m, 1015 m, 925 w, 846 w, 811 m, 781 w, 728 m, 624 m, 576 w, 515 w, 448 w $cm^{-1}$.

**X-ray Crystallographic Study:** X-ray diffraction data of compounds **1**–**3** were collected with a Rigaku Mercury CCD diffractometer equipped with graphite-monochromated Mo-$K_a$ radiation ($\lambda$ = 0.71073 Å). CrystalClear software was used for data reduction and empirical absorption correction.[37] The structures were solved by the direct methods and successive Fourier difference syntheses, and refined by the full-matrix least-squares method on $F^2$ (SHELXTL Version 5.1[38]). The H atoms bonded to C atoms and N atoms were assigned to calculated positions and refined using a riding model [C–H = 0.93 Å, $U_{iso}$(H) = 1.2$U_{iso}$(C); N–H = 0.89 Å, $U_{iso}$(H) = 1.2$U_{iso}$(N)]; H atoms bonded to O atoms were located from difference maps except for one lattice water oxygen atom of compound **3**, which could not be located. The $R_1$ values are defined as $R_1 = \Sigma||F_o| - |F_c||/\Sigma|F_o|$ and $wR_2 = \{\Sigma[w(F_o^2 - F_c^2)^2]/\Sigma[w(F_o^2)^2]\}^{1/2}$. Details of the crystal parameters, data collection and refinement are summarised in Table 2, and selected bond lengths and bond

Table 2. Crystallographic data for compounds **1**–**3**.

| | **1** | **2** | **3** |
|---|---|---|---|
| Empirical formula | $C_{16}H_{24}Cd_2O_{22}S_2$ | $C_{16}H_{20}Cd_5O_{23}S_2$ | $C_{94}H_{98}Cd_3N_{12}O_{18}S_2$ |
| Formula mass | 857.27 | 1206.44 | 2085.16 |
| Temperature [K] | 293(2) | 293(2) | 293(2) |
| Crystal size [mm] | 0.40 × 0.28 × 0.05 | 0.38 × 0.30 × 0.20 | 0.45 × 0.25 × 0.10 |
| Crystal system | monoclinic | triclinic | triclinic |
| Space group | *C*2/*m* | $P\bar{1}$ | $P\bar{1}$ |
| *Z* | 2 | 2 | 1 |
| *a* [Å] | 23.104(6) | 8.16570(10) | 10.2233(15) |
| *b* [Å] | 6.8756(11) | 12.0452(2) | 12.842(2) |
| *c* [Å] | 8.7315(18) | 15.2366(3) | 19.073(3) |
| *α* [°] | 90 | 78.749(5) | 101.562(4) |
| *β* [°] | 107.007(14) | 85.824(6) | 99.637(5) |
| *γ* [°] | 90 | 72.229(5) | 104.124(6) |
| *V* [Å$^3$] | 1326.4(5) | 1399.56(4) | 2316.5(6) |
| $D_{calcd.}$ [g/cm$^3$] | 2.146 | 2.863 | 1.495 |
| $\mu$ [mm$^{-1}$] | 1.860 | 3.988 | 0.801 |
| Measured reflections | 5133 | 10722 | 18047 |
| Independent reflections | 1645 | 6286 | 10479 |
| Observed reflections [$I > 2\sigma(I)$] | 1581 | 5828 | 9017 |
| Parameters | 136 | 464 | 584 |
| *F*(000) | 848 | 1144 | 1066 |
| Completeness [%] | 99.7 | 97.8 | 98.5 |
| 2$\theta$ range [°] | 3.10–27.49 | 3.19–27.48 | 3.06–27.48 |
| *h*/*k*/*l* ranges | –29/29 | –10/10 | –13/12 |
| | –8/8 | –9/15 | –13/16 |
| | –6/11 | –18/19 | –24/24 |
| $R_{int}$ | 0.0258 | 0.0164 | 0.0225 |
| $R_1$ (obsd. refl.) | 0.0208 | 0.0267 | 0.0439 |
| $wR_2$ (all refl.) | 0.0550 | 0.0705 | 0.0980 |
| Largest diff. peak/hole [e/Å$^3$] | 0.390/–0.728 | 1.798/–1.372 | 1.246/–0.598 |

 © 2006 Wiley-VCH Verlag GmbH & Co. KGaA, Weinheim 

angles are listed in Table 1. CCDC-609221 to -609223 (for **1**–**3**) contain the supplementary crystallographic data for this paper. These data can be obtained free of charge from The Cambridge Crystallographic Data Centre via www.ccdc.cam.ac.uk/data_request/cif.

## Acknowledgments

We gratefully acknowledgement the financial support of the "One Hundred Talents Program" of the Chinese Academy of Sciences and the National Science Foundation of China (Grant No. 20473092).

[1] B. Moulton, M. J. Zaworotko, *Chem. Rev.* **2001**, *101*, 1629–1658.
[2] O. R. Evans, R. Xiong, Z. Wang, G. K. Wong, W. Lin, *Angew. Chem.* **1999**, *111*, 557–559; *Angew. Chem. Int. Ed.* **1999**, *38*, 536–538.
[3] M. Eddaoudi, D. B. Moler, H. L. Li, B. L. Chen, T. M. Reineke, M. O'Keeffe, O. M. Yaghi, *Acc. Chem. Res.* **2001**, *34*, 319–330.
[4] C. D. Wu, W. B. Lin, *Angew. Chem. Int. Ed.* **2005**, *44*, 1958–1961.
[5] S. Kitagawa, R. Kitaura, S. I. Noro, *Angew. Chem. Int. Ed.* **2004**, *43*, 2334–2375.
[6] O. R. Evans, W. B. Lin, *Acc. Chem. Res.* **2002**, *35*, 511–522.
[7] C. N. R. Rao, S. Natarajan, R. Vaidhyanathan, *Angew. Chem. Int. Ed.* **2004**, *43*, 1466–1496.
[8] J. P. Zhang, Y. Y. Lin, X. C. Huang, X. M. Chen, *J. Am. Chem. Soc.* **2005**, *127*, 5495.
[9] G. H. Li, Z. Shi, X. M. Liu, Z. M. Dai, S. H. Feng, *Inorg. Chem.* **2004**, *43*, 6884–6886.
[10] Y. M. Song, T. Zhou, X. S. Wang, X. N. Li, R. G. Xiong, *Cryst. Growth Des.* **2006**, *6*, 14–17.
[11] X. H. Bu, M. L. Tong, H. Chang, S. Kitagawa, S. R. Batten, *Angew. Chem. Int. Ed.* **2004**, *43*, 192–195.
[12] Q. Y. Liu, L. Xu, *Eur. J. Inorg. Chem.* **2005**, 3458–3466.
[13] Q. Y. Liu, L. Xu, *Eur. J. Inorg. Chem.* **2006**, 1620–1628.
[14] Q. Y. Liu, L. Xu, *CrystEngComm* **2005**, *7*, 87–89.
[15] R. M. Barrer, *Hydrothermal Chemistry of Zeolite*, Academic Press, London, **1982**.
[16] Z. M. Sun, J. G. Mao, Y. Q. Sun, H. Y. Zeng, A. Clearfield, *Inorg. Chem.* **2004**, *43*, 336–341.
[17] Q. Y. Liu, L. Xu, *Inorg. Chem. Commun.* **2005**, *8*, 401–405.
[18] J. Tao, X. Yin, Z. B. Wei, R. B. Huang, L. S. Zheng, *Eur. J. Inorg. Chem.* **2004**, 125–133.
[19] X. Li, R. Cao, W. H. Bi, D. Q. Yuan, D. F. Sun, *Eur. J. Inorg. Chem.* **2005**, 3156–3166.
[20] L. J. Bellamy, *The Infrared Spectra of Complex Molecules*, Wiley, New York, **1958**.
[21] E. V. Bakhmutova, X. Ouyang, D. G. Medvedev, A. Clearfield, *Inorg. Chem.* **2003**, *42*, 7046–7051.
[22] Z. M. Sun, J. G. Mao, Y. Q. Sun, H. Y. Zeng, A. Clearfield, *New J. Chem.* **2003**, *27*, 1326–1330.
[23] M. Weidenbruch, M. Herrndorf, A. Schäfer, S. Pohl, W. Saak, *J. Organomet. Chem.* **1989**, *361*, 139–145.
[24] S. Boulmaaz, R. Papiernik, L. G. H. Vaissermann, J. C. Daran, *Polyhedron* **1992**, *11*, 1331–1336.
[25] D. C. Liles, M. McPartlin, P. A. Tasker, H. C. Lip, L. F. Lindoy, *J. Chem. Soc., Chem. Commun.* **1976**, 549–551.
[26] W. B. Lin, Z. Y. Wang, L. Ma, *J. Am. Chem. Soc.* **1999**, *121*, 11249–11250.
[27] X. Xue, X. S. Wang, L. Z. Wang, R. G. Xiong, B. F. Abrahams, X. Z. You, Z. L. Xue, C. M. Che, *Inorg. Chem.* **2002**, *41*, 6544–6546.
[28] S. Lulin′ski, I. Madura, J. Serwatowski, J. Zachara, *Inorg. Chem.* **1999**, *38*, 4937–4941.
[29] L. Carlucci, G. Ciani, D. W. v. Gudenberg, D. M. Proserpio, *Inorg. Chem.* **1997**, *36*, 3812–3813.
[30] M. F. Tabellion, S. R. Seidel, A. M. Arif, P. J. Stang, *J. Am. Chem. Soc.* **2001**, *123*, 11982–11990.
[31] P. C. Ford, A. Vogler, *Acc. Chem. Res.* **1993**, *26*, 220–226.
[32] C. M. Che, S. W. Lai, *Coord. Chem. Rev.* **2005**, *249*, 1296–1309.
[33] R. Bertoncello, M. Bettinelli, M. Casarin, A. Gulino, E. Tondello, A. Vittadini, *Inorg. Chem.* **1992**, *31*, 1558–1565.
[34] G. A. Crosby, R. G. Highland, K. A. Truesdell, *Coord. Chem. Rev.* **1985**, *64*, 41–52.
[35] S. L. Zheng, J. H. Yang, X. L. Yu, X. M. Chen, W. T. Wong, *Inorg. Chem.* **2004**, *43*, 830–838.
[36] B. Valeur, *Molecular Fluorescence: Principles and Applications*, Wiley-VCH, Weinheim, **2002**.
[37] *CrystalClear*, version 1.3, Rigaku Corp., **2000**.
[38] G. M. Sheldrick, *SHELXS 97*, *Program for Crystal Structure Solution*, University of Göttingen, **1997**.

Received: June 8, 2006
Published Online: October 19, 2006

 © 2006 Wiley-VCH Verlag GmbH & Co. KGaA, Weinheim 

DOI: 10.1002/ejic.200600539

# Nickel-Organic Coordination Layers with Different Directional Cavities

Youfu Zhou,[a] Chengyang Yue,[a] Daqiang Yuan,[a] Lian Chen,[a] Jiutong Chen,[a] Anjian Lan,[a] Feilong Jiang,*[a] and Maochun Hong[a]

**Keywords:** Nickel / Carboxylate ligands / Coordination polymers / Magnetic properties / Luminescence

The two new metal-organic coordination frameworks $[Ni_2(pydc)_2(4,4'\text{-bpy})(H_2O)_4]_n\cdot 0.5n(4,4'\text{-bpy})2H_2O$ (**1**) and $[Ni_2(pydc)_2(2,2'\text{-bpy})_2(H_2O)_2]_n\cdot 2nH_2O$ (**2**) ($H_2$pydc = pyridine-3,4-dicarboxylic acid; bpy = bipyridine) have been synthesised under hydrothermal conditions and characterised by single-crystal X-ray diffraction analysis. The structure of **1** contains parallel rectangular channels that accommodate large 4,4′-bpy guests while that of **2** contains vertical channels coordinated to 2,2′-bpy ligands. Their magnetic analyses show that they exhibit different magnetic interactions. The red shifts of the peak in their emission spectra relative to those of the the free ligands could be attributable to the metal–ligand coordination.

(© Wiley-VCH Verlag GmbH & Co. KGaA, 69451 Weinheim, Germany, 2006)

## Introduction

Recently, there has been much effort devoted to developing coordination frameworks with special and accessible cavities for use in catalysis, separations, sensors and electronics.[1,2] The assembly of pre-selected building blocks represents a new approach to the formation of novel frameworks, and multidentate carboxylate ligands are widely adopted for the construction of coordination frameworks owing to their rich coordination modes.[3–5] Another common ligand is bipyridyl, which not only acts as a space filler but also provides potential π–π stacking interactions that increase the stability of the framework. It is interesting that mixed ligands can be combined to construct a great variety of frameworks, such as two-dimensional (2D) layers and three-dimensional (3D) networks, including channel-like, interpenetrating and host–guest structures. To the best of our knowledge, 2D layers with parallel channels filled with guests have seldom been reported. In addition, the effect of co-ligands on the final structures is less common. Pyridine-3,4-dicarboxylate (pydc) ligands containing different donor atoms in the 1-, 3- and 4-positions are expected to form more diverse coordination frameworks.[6,7] To investigate the cooperation between pydc and co-ligands, we have explored their assembly with transitional metal ions. Here we report the syntheses, crystal structures and magnetic and photophysical properties of two polymeric complexes with interesting frameworks, namely $[Ni_2(pydc)_2(4,4'\text{-bpy})(H_2O)_4]_n\cdot 0.5n(4,4'\text{-bpy})2H_2O$ (**1**) and $[Ni_2(pydc)_2(2,2'\text{-bpy})_2(H_2O)_2]_n\cdot 2nH_2O$ (**2**) (bpy = bipyridine).

[a] The State Key Laboratory of Structural Chemistry, Fujian Institute of Research on the Structure of Matter, Chinese Academy of Sciences,
Fuzhou 350002, China
Fax: +86-591-8371-4946
E-mail: fjiang@fjirsm.ac.cn

Supporting information for this article is available on the WWW under http://www.eurjic.org or from the author.

## Results and Discussion

The hydrothermal reaction of $NiCl_2\cdot 6H_2O$, $H_2$pydc and 4,4′-bpy or 2,2′-bpy in a molar ratio of about 1:1:1 yielded green crystals of **1** or **2**, respectively. X-ray single-crystal analysis revealed that the structure of **1** consists of 2D layers with parallel channels, which are stacked by hydrogen bonding. Each $Ni^{II}$ ion is six-coordinate with two N atoms from 4,4′-bpy and pydc ligands [Ni–N = 2.087(6)–2.105(7) Å] and four O atoms from two terminal water molecules and two pydc monodentate carboxylate groups [Ni–O = 2.046(5)–2.130(5) Å], which provide a distorted octahedral coordination geometry (Figure 1). Four pairs of $Ni^{II}$ ions are linked by 4,4′-bpy ligands that act as four edges, which are further linked by four three-connecting pydc ligands in a *syn-syn* bis-monodentate mode to form a cubane-like building block (Figure 2). These building blocks are extended through the Ni–O bonds to form a 2D double-layered framework. Consequently, this gives rise to novel parallel rectangular channels ($11.99\times 7.92$ Å$^2$) along the *a* axis (Figure 3). It is interesting that 4,4′-bpy acts not only as a bridging linker but also as a guest that is accommodated within each channel in a stacked arrangement. There are π–π stacking interactions between the pyridyl rings of adjacent 4,4′-bpy guests, with a face-to-face distance of 3.263 Å; this distance consolidates the stacking. The dihedral angle between the mean plane of the pyridyl rings and the transect plane of the channel is 59.0°. The 2D layers are stacked by hydrogen bonding between the oxygen atoms of the lattice water, coordinated water and carboxylate groups. However, van der Waals interactions are not

 © 2006 Wiley-VCH Verlag GmbH & Co. KGaA, Weinheim 

observed between the 4,4′-bpy guests and the channels – the closest distance is 5.66 Å.

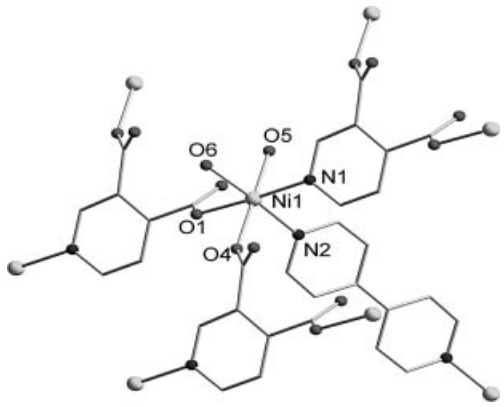


Figure 1. Coordination environments of $Ni^{II}$ atoms in compound **1**.

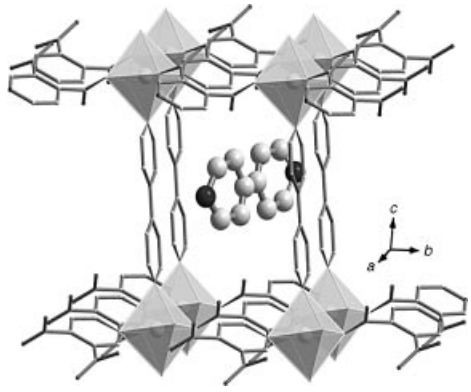


Figure 2. Cubane-like building block in **1** showing the Ni coordination octahedra and 4,4′-bpy guests.

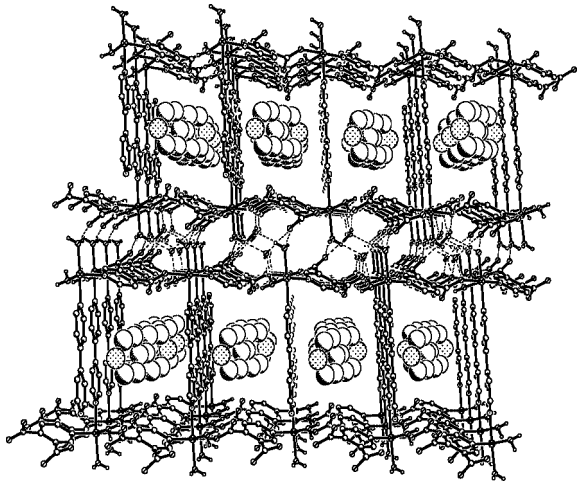

Figure 3. Packing structure of compound **1** along the *a* axis.

In compound **2**, two independent $Ni^{II}$ ions are both in distorted octahedral coordination geometries. Each of them is coordinated by three N atoms from 2,2′-bpy and pydc ligands [Ni–N = 2.058(5)–2.128(5) Å] and by three O atoms from a coordinated water molecule and two pydc carboxylate groups [Ni–O = 2.069(5)–2.094(5) Å] (Figure 4). The two independent $Ni^{II}$ ions are both bridged by two pydc ligands by *anti-syn* bis-monodentate carboxylate groups, which results in two types of binuclear units ($Ni1\cdots Ni1^{i}$ = 5.330 Å and $Ni2\cdots Ni2^{ii}$ = 5.581 Å; symmetry codes: *i*: 1 – *x*, 1 – *y*,1 – *z*; *ii*: 2 – *x*, –*y*, –*z*). Furthermore, every four binuclear units are connected through their pydc spacers alternately to form a large rectangular grid (7.3 × 10.3 $Å^2$), as shown in Figure 5. Each $Ni^{II}$ ion is attached by a chelating bpy ligand within the rectangular grid. There are π–π stacking interactions between the 2,2′-bpy pyridyl rings and the pydc aromatic rings, with face-to-face distances of 3.03–3.40 Å. The rectangular grids stretch to a 2D layer parallel to the *bc* plane in a tiled manner. The interlayer free water molecules are hydrogen bonded to the O atoms of the pydc carboxylate groups or coordinated water molecules in the adjacent layers (Figure 6). These 2D layers are stacked along the *c* axis into a 3D supramolecular architecture through hydrogen bonding.

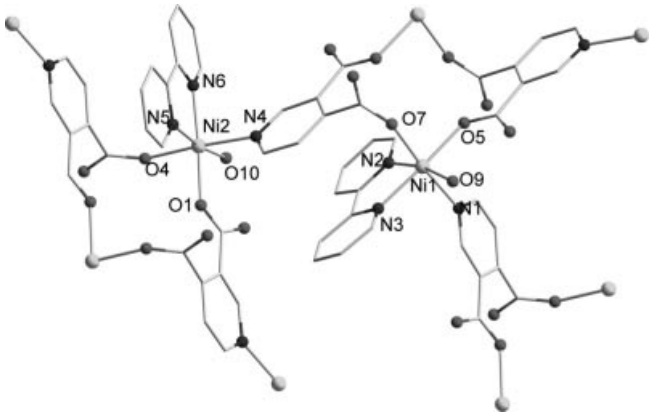


Figure 4. Coordination environments of the $Ni^{II}$ atoms in compound **2**.

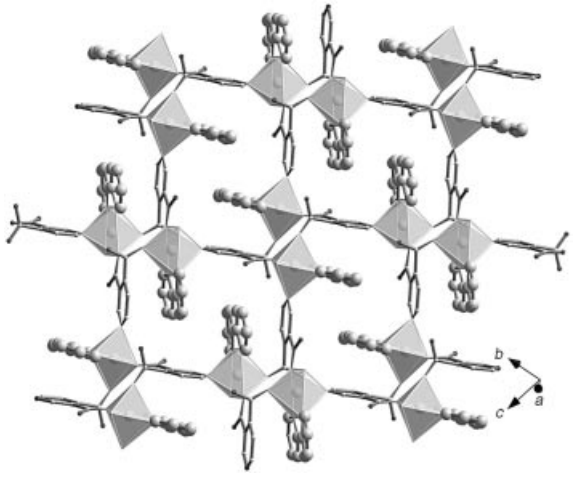


Figure 5. View of the 2D layer in compound **2**.

To investigate their thermal stabilities, thermogravimetric analyses (TGA) of **1** and **2** were carried out at a heating rate of 10 °C $min^{-1}$ under $N_2$. Compound **1** shows a two-

 © 2006 Wiley-VCH Verlag GmbH & Co. KGaA, Weinheim 

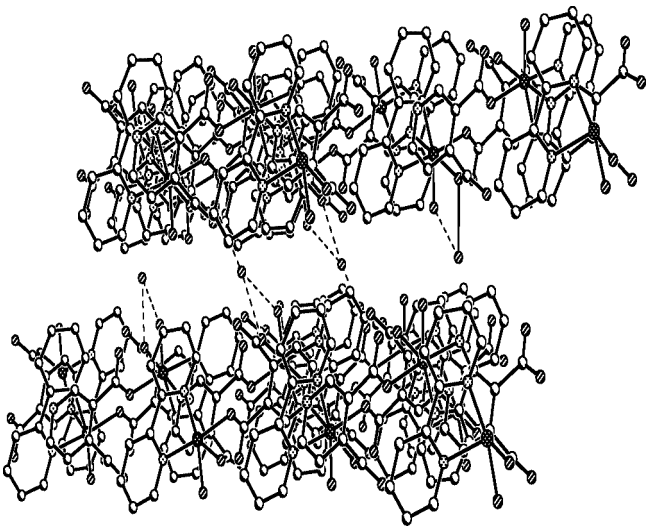

Figure 6. Packing structure of compound **2**.

step weight loss between 150 and 400 °C. The first weight loss between 150 and 230 °C cannot be distinguished clearly from the second one as the coordinated water molecules are involved in the dehydration process (observed: 14.36%; expected: 13.68%), thus implying that the big guest molecules (4,4′-bpy) cannot depart freely without the collapse of the coordination channels. The second step between 230 and 400 °C is assigned to the decomposition of organic ligands in a continuous fashion. The thermal behaviour of compound **2** shows a two-step weight loss between 145 and 430 °C. The first weight loss between 145 and 200 °C corresponds to the dehydration process (observed: 8.4%; expected: 8.6%). The second step between 290 and 430 °C is also assigned to the decomposition of organic ligands.

Temperature-dependent magnetic susceptibilities of compounds **1** and **2** were measured between 5 and 300 K (Figure 7). At room temperature, $\chi_m T$ is 2.03 $cm^3 mol^{-1} K$ for **1** and 2.14 for **2**, which is slightly higher than the expected value of 2.00 $cm^3 mol^{-1} K$ for two uncoupled spin-only $Ni^{II}$ ions ($S$ = 1/2, $g$ = 2). For **1**, $\chi_m T$ is almost constant from 300 K to 36 K, then increases as the temperature is lowered and reaches a maximum value of 2.14 $cm^3 mol^{-1} K$ at 12 K. Finally, it decreases to 1.75 $cm^3 mol^{-1} K$ at 5 K, which shows that there may be both weak ferromagnetic interactions and single-ion zero-field-splitting (D) of isolated $Ni^{II}$ ions. For **2**, the observed $\chi_m T$ value decreases slightly to 1.95 $cm^3 mol^{-1} K$ from 300 K to 40 K, and then quickly decreases to 1.11 $cm^3 mol^{-1} K$ at 5 K, which suggests that the global features of **2** are characteristic either of weak antiferromagnetic intramolecular interactions and/or of the presence of single-ion zero-field-splitting of isolated $Ni^{II}$ ions. In view of the complicated 2D structures of **1** and **2**, it is very difficult, even impossible, to estimate the magnitude of the magnetic coupling in this system. Therefore, two different simple treatments were carried out by using the Fisher model [Equation (1)] or by using the D parameter [Equation (2)] considering only a simple $Ni^{II}$ ion.[8,9]

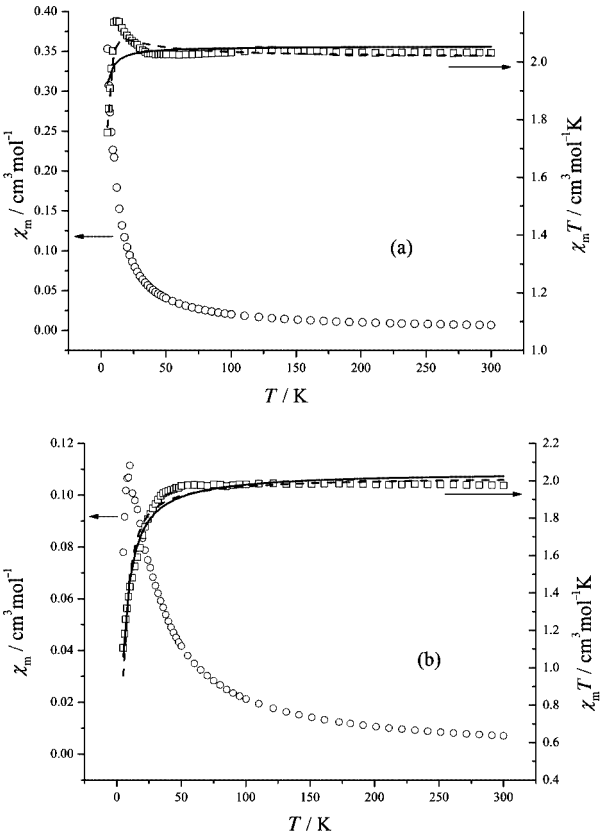


Figure 7. Plots of $\chi_m$ (○) and $\chi_m T$ (□) vs. $T$ for **1** (a) and **2** (b) (dotted lines are the best fit with parameter $D$ and solid lines the best fit with coupling parameter $J$).

$$\chi_m = \frac{\chi_{chain}}{1-(2zJ'\times\chi_{chain})/N\beta^2 g^2}$$
$$\chi_{chain} = \frac{Ng^2\beta^2 S(S+1)}{3kT}\frac{1+u}{1-u}$$
$$u = \coth\left[\frac{JS(S+1)}{kT}\right] - \left[\frac{kT}{JS(S+1)}\right] \quad (1)$$

$$\chi_m = \frac{2Ng^2\beta^2}{3k(T-\theta)}\left[\frac{2kT/D - 2kT\exp(-D/kT)/D + \exp(-D/kT)}{1+2\exp(-D/kT)}\right] \quad (2)$$

where the molecular field approximation ($zJ'$) for interchain interactions and a Weiss-like temperature correction ($\theta'$) are applied to account for intermolecular exchange effects between $Ni^{II}$ ions.

The best fit of the experimental data to Equations (1) and (2) yields $g$ = 2.09, $J$ = –0.17 $cm^{-1}$, $zJ'$ = –0.07 $cm^{-1}$ and $R = 6.3\times10^{-4}$ ($R = \Sigma[(\chi_m T)_{obsd} - (\chi_m T)_{calcd}]^2/\Sigma[(\chi_m T)_{obsd}]^2$), or $g$ = 2.01, $D$ = 11.58, $\theta$ = 3.22 and $R = 1.6\times10^{-4}$ for **1**; and $g$ = 2.05, $J$ = –1.76 $cm^{-1}$, $zJ'$ = –0.03 $cm^{-1}$ and $R = 2.0\times10^{-3}$, or $g$ = 2.01, $D$ = 20.26, $\theta$ = –8.57 and $R = 1.9\times10^{-3}$ for **2**. As expected, the fit is not very good, although we can conclude that compound **1**

 © 2006 Wiley-VCH Verlag GmbH & Co. KGaA, Weinheim 

exhibits a weak ferromagnetic interaction and **2** exhibits a weak antiferromagnetic interaction between $Ni^{II}$ ions.

The fluorescence spectra of compounds **1** and **2** in the solid state were measured at room temperature. The emission spectra of the two compounds are almost the same, as shown in Figure 8. Upon excitation at $\lambda = 427$ nm they produce intense orange fluorescence peaks at 600 nm and 602 nm, respectively, which are assigned to the metal-to-ligand charge transfer (MLCT) states.[10] As free $H_2$pydc exhibits a weak luminescence at around 490 nm in the solid state at room temperature, and free 2,2′-bpy and 4,4′-bpy display a weak luminescence at around 530 and 486 nm,[11,12] respectively, the red shifts and the luminescent enhancement for both **1** and **2** may be attributed to the coordination between the ligands and $Ni^{II}$.[11]

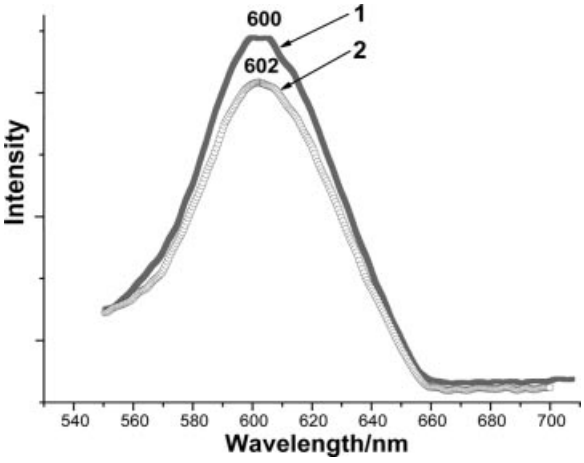


Figure 8. Fluorescent emission ($\lambda_{ex}$ = 427 nm) spectra of compounds **1** and **2** at room temperature.

## Conclusions

In summary, the assembly of $NiCl_2$, pydc and bipyridyl ligands results in two 2D layered coordination frameworks with different directional cavities. It is interesting that one structure contains parallel rectangular channels that accommodate large 4,4′-bpy guests whereas the other contains vertical channels with coordinated 2,2′-bpy ligands. The magnetic analyses show the presence of magnetic interactions. Excitation of compounds **1** and **2** produces an intense orange fluorescence.

## Experimental Section

**General:** All commercially available chemicals were of reagent grade and were used as received. Elemental analyses were determined with an Elemental Vario ELIII elemental analyzer. IR spectra were measured as KBr pellets with a Perkin–Elmer Spectrum One FTIR spectrometer in the range 200–4000 $cm^{-1}$. Thermogravimetric analyses were carried out with a Netzsch STA 449C unit from 30 to 900 °C at a heating rate of 10 °C $min^{-1}$ under nitrogen. Variable-temperature (5.0–300.0 K) magnetic susceptibility measurements were carried out in an external field of 10.0 kG with a Quantum Design PPMS model 6000 magnetometer. Fluorescent analyses were performed with a Perkin–Elmer LS55 luminescence spectrometer.

**Synthesis of 1:** A mixture of $NiCl_2 \cdot 6H_2O$ (71 mg, 0.30 mmol), $H_2$pydc (50 mg, 0.30 mmol) and 4,4′-bpy (47 mg, 0.30 mmol) in $H_2O$ (10 mL) was heated to 170 °C for 4 d. After cooling to room temperature, green crystals of **1** were collected by filtration, washed with distilled water and dried to afford a yield of 41% (41.56 mg) based on Ni. $C_{24}H_{22}N_4Ni_2O_{12}$ (675.84): calcd. C 42.65, H 3.28, N 8.29; found C 42.28, H 3.72, N 8.43. IR (KBr pellet): $\tilde{\nu}$ = 3286 (m), 1626 (s), 1574 (s), 1552 (s), 1489 (m), 1404 (s), 1223 (m), 1174 (m), 987 (m), 683 (m), 606 $cm^{-1}$ (m).

**Synthesis of 2:** A mixture of $Ni(OAc)_2 \cdot 4H_2O$ (0.25 mmol), $H_2$pydc (0.25 mmol) and bpy (0.25 mmol) in $H_2O$ (10.0 mL) was heated to 170 °C for 4 d and then cooled at a rate of 5 °C $h^{-1}$ to room temperature. Green plate-like crystals of **2** were isolated in 45% yield (46.80 mg) based on Ni. $C_{34}H_{30}N_6Ni_2O_{12}$ (832.06): calcd. C 49.08, H 3.63, N 10.10; found C 49.01, H 3.48, N 10.02. IR (KBr pellet): $\tilde{\nu}$ = 3444 (m), 3124 (m), 1614 (s), 1568 (s), 1477 (m), 1444 (m), 1390 (s), 1194 (w), 1026 (w), 827 (m), 768 (m), 683 (m), 656 $cm^{-1}$ (w).

**X-ray Crystallography:** Intensity data for compounds **1** and **2** were measured on a Siemens Smart CCD diffractometer with graphite-monochromated Mo-$K_\alpha$ radiation ($\lambda$ = 0.71073 Å) at 173 K. Empirical absorption corrections were applied by using the SADABS program for the Siemens area detector. The structures were solved by direct methods and all calculations were performed with the SHELXL-97 program. The metal atoms were found in the electron density map, and subsequent difference Fourier syntheses gave all the coordinates of the non-hydrogen atoms, which were refined anisotropically. All hydrogen atoms were added in the riding model and refined isotropically with C–H = 0.96 Å.

**Crystal Data for Compound 1:** Triclinic, space group $P\bar{1}$, $a$ = 7.0457(3) Å, $b$ = 7.9225(4) Å, $c$ = 16.3125(1) Å, $\alpha$ = 78.445(2)°, $\beta$ = 77.782(3)°, $\gamma$ = 75.833(3)°, $V$ = 852.20(6) $Å^3$, $Z$ = 2, $T$ = 293(2) K, $D_c$ = 1.539 g $cm^{-3}$, $\mu$(Mo-$K_\alpha$) = 1.179 $mm^{-1}$, $F$(000) = 407, 2969 independent reflections ($R_{int}$ = 0.0476) with $2\theta \leq 50.18°$. Refinement of 247 parameters converged at final $R_1$ [for selected data with $I > 2\sigma(I)$] = 0.0694, $wR_2$ = 0.2095 and $S$ = 1.107.

**Crystal Data for Compound 2:** Triclinic, space group $P\bar{1}$, $a$ = 11.5331(8) Å, $b$ = 12.0447(8) Å, $c$ = 14.4712(9) Å, $\alpha$ = 71.811(2)°, $\beta$ = 69.716(2)°, $\gamma$ = 68.285(2)°, $V$ = 1712.3(2) $Å^3$, $Z$ = 2, $T$ = 293(2) K, $D_c$ = 1.614 g $cm^{-3}$, $\mu$(Mo-$K_\alpha$) = 1.175 $mm^{-1}$, $F$(000) = 856, 5946 independent reflections ($R_{int}$ = 0.0491) with $2\theta \leq 50°$. Refinement of 511 parameters converged at final $R_1$ [for selected data with $I > 2\sigma(I)$] = 0.0640, $wR_2$ = 0.1679 and $S$ = 0.987.

CCDC-232641 (**1**) and -290754 (**2**) contain the supplementary crystallographic data for this paper. These data can be obtained free of charge from The Cambridge Crystallographic Data Centre via www.ccdc.cam.ac.uk/data_request/cif.

**Supporting Information** (see footnote on the first page of this article): TGA curves for compounds **1** and **2**.

## Acknowledgments

This work was financially supported by the Nation Natural Science Foundation of China (20571074) and the Natural Science Foundation of Fujian province. We thank Professor Jiutong Chen for technical assistance and discussions.

[1] M. Yaghi, H. L. Li, C. Davis, D. Richardson, T. L. Groy, *Acc. Chem. Res.* **1998**, *31*, 474; M. Fujita, *Chem. Soc. Rev.* **1998**, *27*,

 © 2006 Wiley-VCH Verlag GmbH & Co. KGaA, Weinheim 

417; P. J. Hagrman, D. Hagrman, J. Zubieta, *Angew. Chem. Int. Ed.* **1999**, *38*, 2639.
[2] B. E. Abrahams, P. A. Jackson, R. Robson, *Angew. Chem.* **1998**, *110*, 2801; *Angew. Chem. Int. Ed.* **1998**, *37*, 2656; M. Eddaoudi, J. Kim, J. B. Wachter, H. K. Chae, M. O'Keeffe, O. M. Yaghi, *J. Am. Chem. Soc.* **2001**, *123*, 4368; M. J. Zaworotko, *Chem. Soc. Rev.* **1994**, *23*, 283; J. S. Miller, A. J. Epstein, *Chem. Commun.* **1998**, 1319.
[3] C. J. Kepert, T. J. Prior, M. J. Rosseinsky, *J. Am. Chem. Soc.* **2000**, *122*, 5158; F. A. Cotton, L. M. Daniels, C. Lin, C. A. Murillo, *Chem. Commun.* **1999**, 841; T. J. Prior, M. J. Rosseinsky, *Chem. Commun.* **2001**, 1222; T. J. Prior, M. J. Rosseinsky, *Chem. Commun.* **2001**, 495; S. S. Y. Chui, S. M. F. Lo, J. P. H. Charmant, A. G. Orpen, L. D. Williams, *Science* **1999**, *283*, 1148.
[4] J. Lu, A. Mondal, B. Moulton, M. J. Zaworotko, *Angew. Chem. Int. Ed.* **2001**, *40*, 2113; O. M. Yaghi, H. Li, T. L. Groy, *J. Am. Chem. Soc.* **1996**, *118*, 9096; O. M. Yaghi, C. E. Davis, G. Li, H. Li, *J. Am. Chem. Soc.* **1997**, *119*, 2861.
[5] M. J. Plater, A. J. Roberts, J. Marr, E. E. Lachowski, R. A. Howie, *J. Chem. Soc., Dalton Trans.* **1998**, 797; J. C. Dai, X. T. Wu, Z. Y. Fu, S. M. Hu, W. X. Du, C. P. Cui, L. M. Wu, H. H. Zhang, R. Q. Sun, *Chem. Commun.* **2002**, 12.
[6] Z. Y. Fu, S. M. Hu, J. C. Dai, J. J. Zhang, X. T. Wu, *Eur. J. Inorg. Chem.* **2003**, 2670; W. Chen, Q. Yue, C. Chen, H. M. Yuan, W. Xu, J. S. Chen, S. N. Wang, *Dalton Trans.* **2003**, 28.
[7] M. L. Tong, S. Kitagawa, H. C. Chang, M. Ohba, *Chem. Commun.* **2004**, 418; X. Wang, C. Qin, E. Wang, Y. Li, C. Hu, L. Xu, *Chem. Commun.* **2004**, 378.
[8] Kahn, *Molecular Magnetism*, VCH, Weinheim, **1993**.
[9] X. S. Tan, D. F. Xiang, W. X. Tang, K. B. Yu, *Polyhedron* **1997**, *16*, 1411; S. R. Marshall, C. D. Incarvito, J. L. Manson, A. L. Rheingold, J. S. Miller, *Inorg. Chem.* **2000**, *39*, 1969; S. Konar, E. Zangrando, M. G. B. Drew, J. Ribas, N. Ray Chaudhuri, *Dalton Trans.* **2004**, 260.
[10] N. R. M. Simpson, M. D. Ward, A. F. Morales, F. Barigelletti, *J. Chem. Soc., Dalton Trans.* **2002**, 2449; A. C. Bhasikuttan, M. Suzuki, S. Nakashima, T. Okada, *J. Am. Chem. Soc.* **2002**, *124*, 8398.
[11] Y. F. Zhou, D. Q. Yuan, B. L. Wu, R. H. Wang, M. C. Hong, *New J. Chem.* **2004**, *28*, 1590.
[12] L. Y. Zhang, G. F. Liu, S. L. Zheng, B. H. Ye, X. M. Zhang, X. M. Chen, *Eur. J. Inorg. Chem.* **2003**, 2965.

Received: June 9, 2006
Published Online: October 2, 2006

 © 2006 Wiley-VCH Verlag GmbH & Co. KGaA, Weinheim 

DOI: 10.1002/ejic.200600559

# "Pincer" N-Heterocyclic Carbene Complexes of Rhodium Functionalised with Pyridyl and Bipyridyl Donors

**Joseph A. Wright,[a] Andreas A. Danopoulos,*[a] William B. Motherwell,*[b] Robert J. Carroll,[b] Simon Ellwood,[c] and Jörg Saßmannshausen[d]**

**Keywords:** Rhodium / Carbene ligands / Tridentate ligands / N ligands / Ligand design

The "pincer"-type carbene complexes Rh(C–N–C)Cl and Rh(C–N–N)Cl [C–N–C = 3,3′-diaryl-1,1′-pyridine-2,6-diylbis-(imidazol-2-ylidene), C–N–N = 1-aryl-3-(2,2′-bipyridin-6-yl)-imidazol-2-ylidene] have been prepared and characterised by spectroscopic and diffraction methods. They bind CO to give cationic complexes but are inert to $H_2$. Both oxidatively add $CH_2Cl_2$ to give octahedral $Rh^{III}$ complexes. Theoretical calculations provide insight into the bonding of the Rh(C–N–C)Cl and Rh(C–N–N)Cl complexes.

(© Wiley-VCH Verlag GmbH & Co. KGaA, 69451 Weinheim, Germany, 2006)

## Introduction

Since the development of the first route to free N-heterocyclic carbenes (NHCs),[1] ligands based around the stabilised-carbene core have become a major focus of research activity. Interest in N-heterocyclic carbene (NHC) metal complexes is now expanding to the study of new versatile ligand topologies with "classical" functional groups, which have shown promising spectator characteristics.[2] One of these is the "pincer" architecture, which provides a preorganised backbone capable of blocking meridional or pseudo-meridional coordination sites of the metal atom, leaving the remaining available for catalysis.[3] "Pincer" phosphane, amine, amide, imine, thioether and oxazoline complexes have been extensively studied and show very useful properties,[4] for example, unusually high thermal and air stability, stabilisation of uncommon oxidation states, stabilisation of unstable fragments on the metal atom, helical chirality and catalytic activity.

As part of our ongoing studies involving the use of the versatile "pincer" ligand 3,3′-diaryl-1,1′-pyridine-2,6-diylbis(imidazol-2-ylidene) (C–N–C),[5] we now report the formation and reactivity of rhodium(I) and rhodium(III) species based on this ligand system. We also detail the synthesis of a novel bipyridylcarbene ligand (C–N–N) and the formation of the derived rhodium complexes.

## Results and Discussion

### (C–N–C)$Rh^{I}$ and -$Rh^{III}$ Complexes

Interaction of the free carbene **1** with $[Rh(alkene)_2Cl]_2$ (alkene = ethene, cyclooctene) in THF at either room temperature or –78 °C gave a rapid colour change from orange to deep purple (Scheme 1).

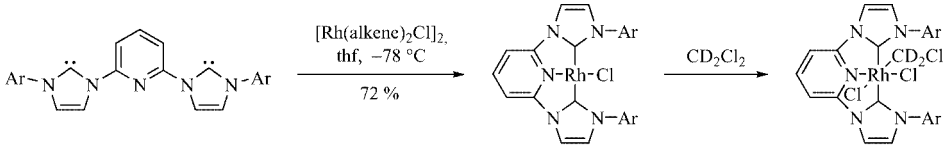


Scheme 1. Synthesis of rhodium complexes **2** and **3** (alkene = $C_2H_4$, $C_8H_{14}$; Ar = 2,6-*i*$Pr_2C_6H_3$).

Following removal of the solvent, a deep purple microcrystalline solid was obtained, which was sparingly soluble in benzene but readily re-dissolved in THF. The planar symmetry of the complex was supported by NMR spectroscopy. The proton spectrum in [$D_8$]THF showed two doublets at δ = 1.15 and 1.44 ppm (12 H each), along with a single septet at δ = 3.06 ppm (4 H), supporting the pres-

[a] School of Chemistry, University of Southampton, Highfield, Southampton, SO17 1BJ, UK
[b] Christopher Ingold Laboratories, University College London, 20 Gordon Street, London, WC1H 0AJ, UK
[c] Quest International, Kennington Road, Ashford, Kent, TN24 0LT, UK
[d] TU Graz, Institute for Chemistry and Technology of Organic Materials, Stremayrgasse 16/I, 8010 Graz, Austria
E-mail: ad1@soton.ac.uk

Supporting information for this article is available on the WWW under http://www.eurjic.org or from the author.

 © 2006 Wiley-VCH Verlag GmbH & Co. KGaA, Weinheim 

ence of equivalent isopropyl groups on the bulky DiPP [2,6-(diisopropyl)phenyl] groups. The $^{13}C\{^1H\}$ NMR spectrum also is in agreement with a symmetric structure; however, the $C_{NHC}$ signal was not observed. Crystals of **2** suitable for X-ray diffraction were grown by slow diffusion of petroleum ether into a THF solution of the complex (Figure 1).

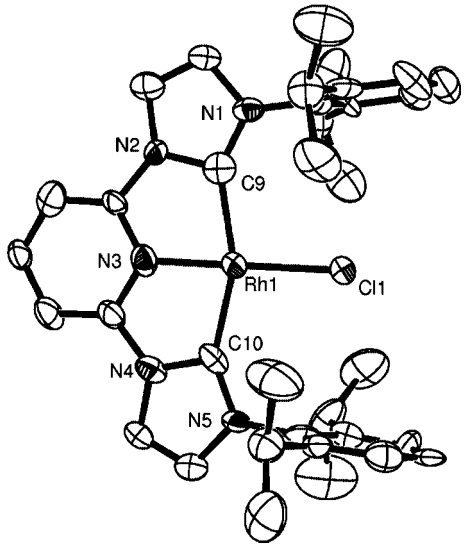


Figure 1. ORTEP representation of the structure of **2** showing 50% probability ellipsoids with hydrogen atoms omitted for clarity. Selected bond lengths [Å] and angles [°] with estimated standard deviations: Rh(1)–Cl(1) 2.331(3), Rh(1)–N(3) 1.955(8), Rh(1)–C(9) 2.001(10), Rh(1)–C(10) 1.979(9); N(3)–Rh(1)–Cl(1) 178.4(3), N(3)–Rh(1)–C(9) 78.5(4), N(3)–Rh(1)–C(10) 79.4(4), C(9)–Rh(1)–Cl(1) 101.2(3), C(10)–Rh(1)–Cl(1) 100.8(3).

The coordination sphere around the metal atom is essentially square-planar. The rhodium centre lies 0.027(4) Å out of the mean plane defined by the coordinating atoms. The Rh–$C_{NHC}$ bond lengths [2.001(10) and 1.979(9) Å] are typical for rhodium(I)–$C_{NHC}$ bond lengths. Complex **2** constitutes the first structurally characterised dicarbene complex of $Rh^I$ in which the coordination sphere is comprised of non-π-acidic ligands. The synthesis of the analogous [(C–N–C)Rh(CO)]($PF_6$), where C–N–C = 3,3′-dialkyl-1,1′-pridine-2,6-diylbis(imidazol-2-ylidene) (alkyl = methyl, ethyl, benzyl) has been recently reported, together with reactivity studies towards the oxidative addition of methyl iodide.[6] In addition, (C–N–C)$RhBr_3$ has been prepared by reaction of the corresponding imidazolium salt with $[Rh(COD)Cl]_2$ and triethylamine in acetonitrile.[7]

Dissolution of complex **2** in $CD_2Cl_2$ initially gave a purple solution, which became yellow within a few minutes. The NMR spectra of this solution showed a lowering of the molecular symmetry of the new complex compared to **2**. It comprised two signals for the methine groups (integrating for 2 H each), along with four signals for the methyl groups of the *i*Pr groups (each integrating for 6 H). However, the signals assigned to the pyridine and imidazol-2-ylidene backbones retained the same appearance as in the starting material. These changes are in line with oxidative addition to the metal centre and consistent with the structure proposed for **3** in Scheme 1. On standing, crystals of **3** formed from the $CD_2Cl_2$ solution, and these were suitable for a single-crystal diffraction study (Figure 2).

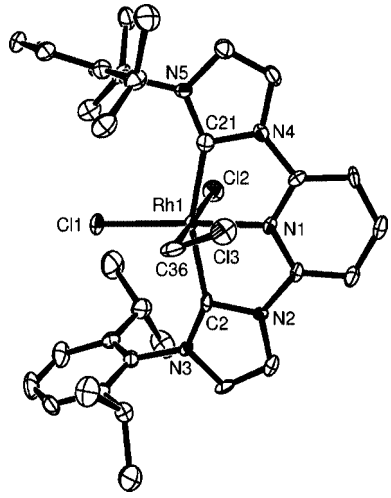


Figure 2. ORTEP representation of the structure of **3** showing 50% probability ellipsoids with hydrogen atoms and one molecule of $CD_2Cl_2$ omitted for clarity. Selected bond lengths [Å] and angles [°] with estimated standard deviations: Rh(1)–Cl(1) 2.3656(15), Rh(1)–Cl(2) 2.5164(16), Rh(1)–C(36) 2.075(6), Rh(1)–N(1) 1.978(4), Rh(1)–C(21) 2.034(6), Rh(1)–C(2) 2.040(6); N(1)–Rh(1)–Cl(1) 177.68(15), N(1)–Rh(1)–C(21) 79.1(2), N(1)–Rh(1)–C(2) 79.2(2), C(36)–Rh(1)–Cl(2) 177.22(19).

Complex **3** adopts an unsymmetrical distorted octahedral geometry, with the tridentate "pincer" occupying meridional sites with the remaining sites being occupied by two *cis*-chlorine atoms and the $CH_2Cl$ group. The Rh–$C_{NHC}$ bond lengths in complexes **2** and **3** are the same within the observed esds [averages of 1.990(13) and 2.037(8) Å, respectively]. However, the rhodium–chloride distances for the chloride ion bound *trans* to $N_{pyridine}$ are significantly different: the Rh–$N_{pyridine}$ bond in **3** [2.3656(15) Å] is longer than that in **2** [2.331(3) Å]. This is presumably due to the more crowded environment around the metal atom in the octahedral complex **3**. The two Rh–Cl distances in **3** are also significantly different from each other: the Cl ion *trans* to the $CD_2Cl$ group is approximately 0.15 Å further from the Rh atom than that *trans* to the $N_{pyridine}$ atom.

Complex **2** showed oxidative reactivity with a range of alkyl halides and pseudohalides. For example, addition of methyl iodide, 1,1,1-trichloroethane, benzyl chloride or methyl triflate to **2** in THF led to colour changes from purple to light yellow. The time taken for these reactions varied from seconds ($CH_3I$) to overnight (1,1,1-trichloroethane), presumably due to the differing reactivity of the C–halide bond. The NMR spectra of all products demonstrated the same lowering of symmetry as seen in **3**, although additional changes were also seen which could not be readily assigned. Addition of phosgene to **2** also gave a rapid and clean oxidative addition, leading to a stable unsymmetrical product. Complex **2** also reacted very fast with oxygen both in solution and in the solid state; the organometallic product from the oxidation has not been characterised.

 © 2006 Wiley-VCH Verlag GmbH & Co. KGaA, Weinheim 

In contrast to the rapid reactions observed with alkyl halides and oxygen, complex **2** was unreactive towards other potential reagents for oxidative addition. No reaction was observed with triethylsilane, phenyldiazomethane or PhS=CHPh.[4e] In all cases, $^1$H NMR spectra indicated that the starting material was unchanged. Similarly, no reactivity was seen with benzene (heating solutions of the complex in $C_6D_6$ in a sealed system to over 150 °C or exposure of the solution to UV light). Attempts to derivatise **2** by substitution of the chloride ion with organolithium compounds and Grignard reagents under various conditions were likewise unsuccessful.

### Reactivity with CO

Hydroformylation is a major industrial process, and (phosphane)rhodium complexes are widely used for the formation of short-chain ($C_2$ to $C_5$) aldehydes under these conditions.[8] However, some phosphane complexes are unsuitable for use with other substrates due to thermal degradation. The development of novel rhodium-based hydroformylation catalysts for heavier alkenes ($C_8$ and higher) remains a challenge. As a probe for potential hydroformylation activity, the reactivity of **2** towards synthesis gas and carbon monoxide was studied (Scheme 2).

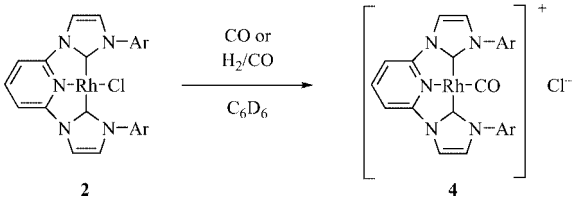


**2** **4**

Scheme 2. Reaction of complex **2** with CO (Ar = 2,6-*i*Pr$_2$C$_6$H$_3$).

Bubbling a mixture of $H_2$/CO (1:1) through a $C_6D_6$ solution of **3** resulted in a fast irreversible colour change from purple to pink. Evaporation of the solvent from the mixture gave a light pink, air-stable complex **4** which is noticeably more soluble in $C_6D_6$ than the parent complex. $^1$H NMR spectra indicate that the products obtained with CO and CO/$H_2$ are identical; as a confirmation of this, no reaction was observed with hydrogen gas alone. The $^1$H or $^{13}$C{$^1$H} NMR spectra of **4** show the same symmetry to **2**. However, in the $^1$H NMR spectrum, a significant change occurs in the shift of one of the imidazole backbone signals (from $\delta$ = 8.15 ppm to $\delta$ = 10.42 ppm on coordination of CO). The electrospray mass spectrum of **4** shows a single signal at *m*/*z* = 662.5, consistent with an adduct of the (pincer)rhodium core and CO. Complex **4** also shows only a single IR stretch at 1968 cm$^{-1}$. This compares with 1982 cm$^{-1}$ reported for [Rh(C–N–C)(CO)](PF$_6$) and 1980 cm$^{-1}$ for [Rh(P–N–P)(CO)]Cl {P–N–P = 2,6-bis[(diphenylphosphanyl)methyl]-pyridine}.[6,9] Attempts to grow single crystals of **4** were unsuccessful, and anion exchange also failed to give useful products.

Whilst the reactivity of **4** with carbon monoxide was rapid, the high stability of the product indicated possible problems in hydroformylation. NMR-scale addition of ethene to **2** showed no reaction. The hydroformylation activity was investigated using synthesis gas and styrene. No reaction was observed under a range of conditions, and a pink-coloured solution was recovered. Thus, it seems likely that under hydroformylation conditions an irreversible coordination of CO occurs to give **4**, whilst **2** will not bind alkenes or hydrogen.

### Bipyridyl NHC Ligands

Even though the C–N–C ligand **1** is considered a strong σ-donor, its limitations became apparent from the inactivity of **2** in hydroformylation which could be ascribed to the low lability of the Rh–$C_{NHC}$ bond hindering the formation of coordinatively unsaturated catalytic sites. In addition, due to the strong σ-donating ability of the NHC donors, **1** may be better suited for the stabilisation of Rh$^{III}$ rather than the promotion of Rh$^{I}$–Rh$^{III}$ catalytic cycles. Therefore, we decided to explore the chemistry of alternative "pincer" ligand designs by replacing one of the NHC donors of the C–N–C system with another classical donor. Whilst there is clearly a large range of potential ligands which could be constructed around this motif, we have concentrated on an NHC–bipyridyl system **7** (Scheme 4). Recently, Milstein has reported nonsymmetrical pincer-type ligands bearing phosphane and amine wingtips.[10]

The necessary bromide **4** is available in three steps from commercially available 2,2′-bipyridine.[11,12] Quaternisation of **4** with the imidazole **5** (Scheme 3) proceeds smoothly in the melt at 160 °C, giving moderate yields of the desired imidazolium bromide after purification and azeotropic drying. In contrast to the pincer imidazolium salts of the C–N–C type, deprotonation of **6** could not be readily achieved under the standard conditions[5a] which involved the reaction with KN(SiMe$_3$)$_2$ in THF at –30 °C, followed by addition of toluene (to precipitate the KBr formed in the reaction). This method gave only low yields of **7** (less than 5%). As an alternative to deprotonation, we explored the reductive deprotonation of the imidazolium salt with potassium metal, which has recently been used for the preparation of IMes from (IMesH)$^+$Cl$^-$.[13] This methodology, when applied to the preparation of **7**, resulted in improved isolated yields (ca. 30%) allowing the study of the coordination chemistry of **7**. The structure of **7** was also determined crystallographically (Figure 3).

In common with other free-carbene solid-state structures,[14] the free-carbene and pyridine rings adopt a *trans* arrangement. The three donor-atom-containing rings are virtually coplanar, with interplane angles of 3.3(2)° (carbene–pyridine) and 2.7(2)° (pyridine–pyridine). The single "wingtip" aromatic ring is nearly perpendicular to the rest of the ligand, with an interplane angle of 84.64(11)° between this and the imidazol-2-ylidene ring.

The imidazolium salt **6** has also been successfully used for the synthesis of the (carbene)silver complex **8** in good yields, by the reaction with $Ag_2O$ in dichloromethane in

 © 2006 Wiley-VCH Verlag GmbH & Co. KGaA, Weinheim 

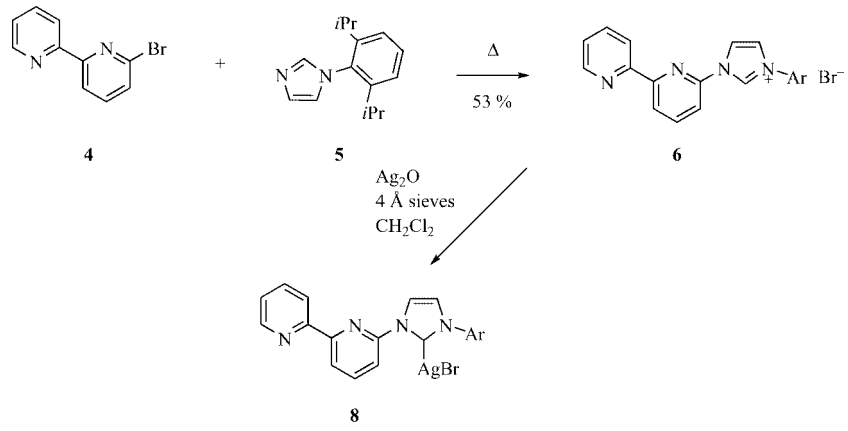


4 5 6 8

Scheme 3. Formation of the "bipy" salt **6** and attempt to deprotonate (Ar = 2,6-*i*Pr$_2$C$_6$H$_3$).

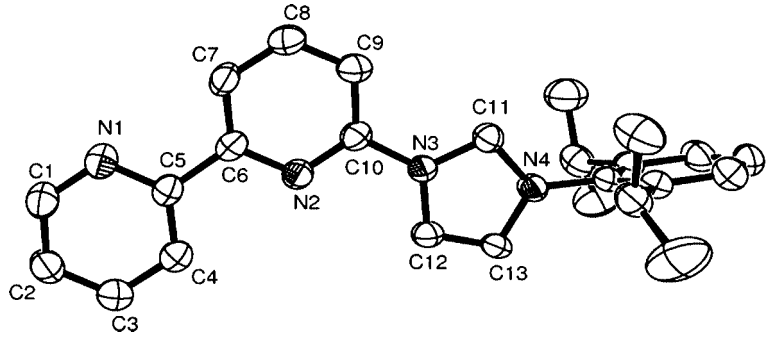


Figure 3. ORTEP representation of the structure of **7** showing 50% probability ellipsoids with hydrogen atoms omitted for clarity. Selected bond lengths [Å] and angles [°] with estimated standard deviations: C(11)–N(4) 1.361(3), C(11)–N(3) 1.375(3), C(5)–C(6) 1.486(4),C(10)–N(3) 1.427(3); N(4)–C(11)–N(3) 101.3(2).

the presence of molecular sieves (4 Å). The (carbene)silver complex was characterised by spectroscopic (NMR and MS) and analytical methods.

The Rh(C–N–N)X [X = Cl (**9b**), Br (**9a**)] complexes have been synthesised by two different routes on the basis of either the reaction of **6** with [(COD)Rh(OMe)]$_2$ (**9b**) or the reaction of **7** with [(COE)$_2$RhCl]$_2$ (**9a**) (Scheme 4).

The green, very air-sensitive complex was characterised by analytical and spectroscopic methods. Even though it is sparingly soluble in non-chlorinated solvents, meaningful $^1$H NMR spectra of **9a** were recorded in [D$_8$]THF. The appearance of peaks assignable to the *i*Pr groups of the DiPP group supports the presence of a plane of symmetry in the molecule. However, the poor solubility of **9a** prevented the collection of strong $^{13}$C{$^1$H} NMR spectroscopic data even after prolonged acquisition times. It is interesting to note that silver transmetallation reactions, which have been commonly used for the synthesis of NHC–Rh complexes were not successful here due to the reactivity of the initially formed Rh$^I$ product with dichloromethane which is the

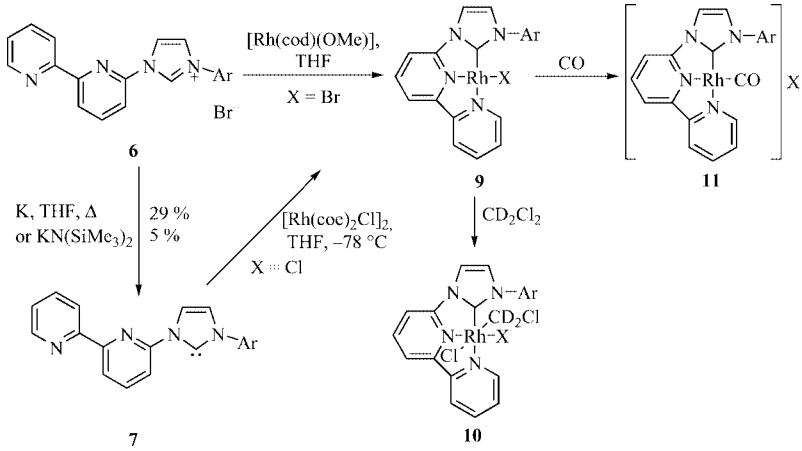


6 9 11 7 10

Scheme 4. Generation of free carbene **7** and complexes **9a** and **9b** (Ar = 2,6-*i*Pr$_2$C$_6$H$_3$; **9a**: X = Br; **9b**: X = Cl).

 © 2006 Wiley-VCH Verlag GmbH & Co. KGaA, Weinheim 

commonly used solvent in reactions of this type (vide infra). The structure of the complex was unequivocally established crystallographically (Figure 4).

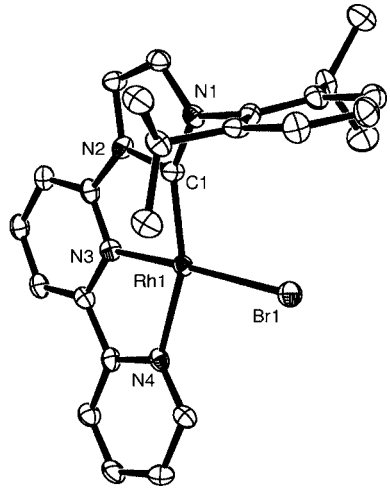


Figure 4. ORTEP representation of the structure of **9a** showing 50% probability ellipsoids with hydrogen atoms omitted for clarity. Selected bond lengths [Å] and angles [°] with estimated standard deviations: C(1)–Rh(1) 1.957(6), N(3)–Rh(1) 1.941(5), N(4)–Rh(1) 2.116(5), Br(1)–Rh(1) 2.4904(8); N(3)–Rh(1)–Br(1) 172.26(14), C(1)–Rh(1)–Br(1) 104.30(17), N(4)–Rh(1)–Br(1) 97.27(13).

The rhodium centre adopts a distorted square-planar geometry, with the rhodium atom being 0.034(2) Å out of the plane of the donor atoms. The terminal pyridine nitrogen atom N(4) is approx. 0.15 Å further from the metal centre than N(3). The Rh–$C_{NHC}$ bonds [1.957(6) Å] are slightly shorter than those reported for **2**. In comparison to the recently reported blue Rh(terpy)Cl,[15] the corresponding Rh–$N_{pyridine}$ bonds in **9a** are longer.

### Reactivity of 9a

The replacement in complex **2** of one NHC by the poorer σ-donating pyridine group to give **9** is expected to reduce the electron density on the metal atom. However, it should be more electron-rich than the metal atom in Rh(terpy)Cl.[15] In the latter, $Rh^{I}$ has been classified as electron-rich on the basis of the oxidation potential of the complex, as measured by CV and DFT calculations. Complex **9a** reacts easily with dichloromethane at room temperature giving rise to the oxidative addition adduct **10** (Scheme 4), which was characterised by NMR spectroscopy in a way analogous to **3**. It also reacts fast with CO (1 bar, room temperature). The NMR spectra of the product suggest the formation of the CO adduct **11** (Scheme 4). The $^{1}H$ NMR spectrum of **11** shows a number of changes in the aromatic region, but significantly retains the single pair of doublets in the *i*Pr region: as before, this indicates retention of the plane of symmetry in the product. The CO adduct appears to be stable, and in contrast to **9a** it can be exposed to air and chlorinated solvents without degradation.

Attempts to carry out hydroformylation using **9** were not successful. Addition of $CO/H_2$ to a solution of the complex (0.2 mol-%) and styrene in toluene gave a rapid colour change to light orange. After 3 h at 70 °C under 9 bar of $CO/H_2$, analysis of the reaction mixture by GC-MS showed no hydroformylation products.

### Theoretical Studies of Complexes 2 and 9b

In order to obtain a further insight into the bonding in the new (pincer)$Rh^{I}$ complexes we performed DFT studies on **2** and **9b**. No symmetry restriction was imposed on the molecules. The Rh(C–N–C) and Rh(C–N–N) substructures in the calculated optimised geometries of **2-dft** and **9b-dft** are in very good agreement with those observed in the crystal structures (see Supporting Information). Only the bulky DiPP substituent is slightly dislocated, presumably due to crystal-packing effects.

The HOMO orbital of both complexes has $d_{z^2}$ character. As expected, the LUMO of both **2-dft** and **9b-dft** reside on the π* system of the pyridine ligand, with some contribution of the metal atom. The HOMO–LUMO gap for **2-dft** of 2.92 eV is marginally larger than the gap for **9b-dft** (2.49 eV). For comparison, these values are much larger than the values reported for Rh(terpy)Cl (1.04 eV).[15] It is therefore plausible that this difference may lead to different reactivity of **2** and **9b** compared with Rh(terpy)Cl. This point is being investigated further in our laboratory.

For complex **2-dft**, the HOMO-1 has predominantly Cl($p_\pi$)/Rh($d_{zx}$) character, with some contribution of the pyridine ligand (see Supporting Information for plots of the orbitals). HOMO-2 is of similar character with some contribution from the NHC ligand to the Rh($d_{xy}$) atom. HOMO-3 is predominantly on the metal atom [Rh($d_{yz}$)] and HOMO-4 is predominantly on the DiPP ligands and the chloride ion.

For complex **9b-dft**, similar observations can be made: HOMO-1 is predominately of Cl($p_\pi$)/Rh($d_{zx}$) character, with some contribution of the pyridine ligand *trans* to the chloride ion. HOMO-2 is of similar character as HOMO-2 of **2-dft**; however, the pyridine ligand *trans* to the NHC is less involved in the molecular orbital. HOMO-3 is again similar to HOMO-3 of **2-dft**; again the pyridine ligand *trans* to the NHC is not involved in the molecular orbital. HOMO-4 is predominately on the DiPP ligand.

The electronic environment in the complexes was further investigated by Natural Bonding Orbital (NBO) analysis. In **2-dft**, the lone pair of the pyridine nitrogen atom is donating into an empty orbital of the Rh atom. One of the NHC ligands is donating into an empty orbital of the Rh atom and into the antibonding orbital of the other Rh–$C_{NHC}$ bond. However, unexpectedly, backdonation occurs from a filled $d_{yz}$ orbital of the metal atom to antibonding orbitals of both the NHC and the pyridine ligand. For complex **9b-dft**, similar observations have been made. The lone pairs of the pyridine nitrogen atoms are donating into an empty d-orbital of the metal atom. The nitrogen atom *trans* to the NHC is donating into the carbene–metal antibonding orbital. A smaller contribution to this bonding is made by the

 © 2006 Wiley-VCH Verlag GmbH & Co. KGaA, Weinheim 

nitrogen atom on the other pyridine ligand. As with **2-dft**, a filled d-orbital of the metal atom is donating into an C–N antibonding orbital of the NHC. Backdonation from a different filled d-orbital of the metal atom to the pyridine ligand *trans* to the chloride ion is also observed. Orbital representation of the NBO analysis for both complexes are detailed in the Supporting Information.

As expected, the LUMO of both **2-dft** and **9b-dft** reside on the π* system of the pyridine ligand, with some contribution of the metal atom. The higher-lying virtual orbitals of **2-dft** and **9b-dft** are almost exclusively localised on the ligands. Exceptions are the LUMO+6 of **2-dft** and LUMO+5 of **9b-dft**, which are metal-based. Metal-based high-lying LUMOs have been observed before, notably for the complex Rh(terpy)Cl (LUMO+5).[15]

## Conclusions

Highly reactive electron-rich $Rh^{I}$ complexes with the pyridine-based dicarbene and bipyridyl-based monocarbene rigid tridentate pincers and without any π-acidic co-ligands have been prepared and characterised by spectroscopic and diffraction methods. The complexes easily undergo oxidative addition reactions of C–halide bonds, but are resistant to oxidative addition of other less polar bonds (H–H, Si–H, C–H, etc.). The $Rh^{III}$ products obtained are extremely stable. The complexes also form stable adducts with the π-acidic CO, which are resistant to further reactions by alkenes, $H_2$, $O_2$, etc. The use of the new complexes as hydroformylation catalysts is hampered by rigid structures and stabilisation of the higher oxidation states by the strongly σ-donating ligand system. However, these "σ-loaded" rigid pincers may prove useful co-ligands in the stabilisation of higher oxidation states.

## Experimental Section

**General Methods:** Solvents were dried by standard methods[16] and either used directly or stored in ampoules with molecular sieves (4 Å). All air- or moisture-sensitive reactions were carried out under dry nitrogen using standard Schlenk techniques or in an M. Braun glove box. NMR spectroscopic data were recorded with Bruker AMX-300 and DPX-400 spectrometers, operating at 300 and 400 MHz ($^1$H), respectively. The spectra were referenced internally using the signal from the residual protio solvent ($^1$H) or the signals of the solvent ($^{13}$C). Mass spectra (electrospray ionisation) were obtained from acetonitrile solutions with a VG Biotec platform. The calculated isotopic envelopes agree well with the experimentally observed patterns. Commercial chemicals were from Acros, Aldrich, Lancaster and Avocado; the light petroleum ether had boiling range of 40–60 °C. The following starting materials were prepared as described in the literature: 3,3′-Bis(2,6-diisopropylphenyl)-1,1′-pyridine-2,6-diylbis(imidazol-3-ium) dibromide,[5b] 6-bromo-2,2′-bipyridine,[11,12] 3-(2,6-diisopropylphenyl)-1*H*-imidazole,[17] bis[μ-chlorobis(η$^2$-cyclooctene)rhodium(I)],[18] bis[μ-chlorobis(η$^2$-ethene)rhodium(I)][19] and bis[μ-methoxybis(η$^2$-cyclooctene)rhodium(I)].[20]

**3,3′-Bis(2,6-diisopropylphenyl)-1,1′-pyridine-2,6-diylbis(imidazol-2-ylidene) (1):** The synthesis was carried out by an improved version of the previously published procedure.[5b] Thus, the corresponding bis(imidazolium) salt (CH–N–CH)$Br_2$ (Ar = 2,6-*i*$Pr_2C_6H_3$) (6.89 g, 9.93 mmol) was suspended in THF (100 mL) in a large Schlenk tube, and cooled to –78 °C. A solution of potassium bis(trimethylsilyl)amide (4.32 g, 21.6 mmol) in THF (100 mL) was cooled to –78 °C and added to the salt suspension. The reaction mixture was warmed to room temperature overnight, the solvent evaporated and the residue dissolved in toluene (100 mL). The dark-brown solution was filtered through a pad of Celite®, and the volume reduced to ca. 20 mL. Dilution with petroleum ether (40 mL) led to the precipitation of the product, which was filtered off, washed with petroleum ether and dried under vacuum to yield a cream-colored solid (4.09 g, 77%). $^1$H NMR (300 MHz, $C_6D_6$, 25 °C): $\delta$ = 1.20 (d, $J$ = 6.9 Hz, 12 H, Me), 1.29 (d, $J$ = 6.8 Hz, 6 H, Me), 3.01 [sept, $J$ = 6.9 Hz, 4 H, *C*H(CH$_3$)$_2$], 6.73 (d, $J$ = 1.7 Hz, 1 H, imidazole backbone), 7.16 (t, $J$ = 8.0 Hz, 1 H, central CH of pyridine), 7.25 (d, $J$ = 7.5 Hz, 4 H, aromatic CH), 7.35 (d, $J$ = 6.9 Hz, 1 H, aromatic CH), 7.38 (d, $J$ = 6.9 Hz, 1 H, aromatic CH), 8.17 (d, $J$ = 1.7 Hz, 2 H, imidazole backbone), 8.54 (d, $J$ = 8.0 Hz, 2 H, outer 2×CH of pyridine) ppm. $^{13}$C NMR (75.45 MHz, $C_6D_6$, 25 °C): $\delta$ = 24.0 (Me), 24.4 (Me), 28.6 [*C*H(CH$_3$)$_2$], 111.7 (aromatic CH), 116.3 (aromatic CH), 122.8 (aromatic CH), 123.8 (aromatic CH), 129.3 (aromatic CH), 138.7 (aromatic C), 140.7 (aromatic C), 146.2 (aromatic CH), 152.6 (aromatic C), 220.4 (carbene) ppm.

**3,3′-Dimesityl-1,1′-pyridine-2,6-diylbis(imidazol-2-ylidene) (1b):** This was prepared according to a similar route to **1** from the salt (CH–N–CH)$Br_2$ (Ar = mesityl) (2.78 g, 4.00 mmol) and potassium bis(trimethylsilyl)amide (1.68 g, 8.42 mmol). After the reaction, the crude solid was dissolved in benzene (60 mL) and worked up as for **1**. This gave the product as a cream-colored solid (1.07 g, 60%). $^1$H NMR (300 MHz, $C_6D_6$, 25 °C): $\delta$ = 2.12 (s, 12 H, Me), 2.14 (s, 6 H, Me), 6.44 (d, $J$ = 1.4 Hz, 2 H, imidazole backbone), 6.79 (s, 4 H, aromatic CH), 7.09 (t, $J$ = 7.6 Hz, 1 H, central CH of pyridine), 8.11 (d, $J$ = 1.4 Hz, 2 H, imidazole backbone), 8.54 (d, $J$ = 7.6 Hz, 2 H, outer 2×CH of pyridine) ppm. $^{13}$C (75.45 MHz, $C_6D_6$, 25 °C): $\delta$ = 18.1 (Me), 21.0 (Me), 111.5 (aromatic CH), 116.5 (aromatic CH), 119.7 (aromatic CH), 129.0 (aromatic C), 129.2 (aromatic C), 130.4 (aromatic CH), 135.3 (aromatic C), 138.9 (aromatic C), 140.7 (aromatic CH), 152.69 (carbene) ppm.

**[3,3′-Bis(2,6-diisopropylphenyl)-1,1′-pyridine-2,6-diylbis(imidazol-2-ylidene)]chlororhodium(I) (2):** A solution of carbene **1** (162 mg, 0.305 mmol) in THF (10 mL) was added to a suspension of bis[μ-chlorobis(η$^2$-ethene)rhodium(I)] (60 mg, 0.154 mg) in THF (5 mL), leading to an immediate colour change to dark purple. The solution was stirred under an oil bubbler for 90 min, before evaporation of the solvent. The residue was washed with petroleum ether (2×5 mL) to leave a dark purple solid (124 mg, 61%). Layering of a THF solution of this residue with an equal volume of petroleum ether led to the formation of X-ray quality crystals. $^1$H NMR (300 MHz, $C_6D_6$, 25 °C): $\delta$ = 1.14 (d, $J$ = 7.0 Hz, 12 H, Me), 1.44 (d, $J$ = 6.8 Hz, 12 H, Me), 3.06 [sept, $J$ = 6.9 Hz, 4 H, C*H*(CH$_3$)$_2$], 6.08 (d, $J$ = 8.1 Hz, 2 H, pyridyl CH), 6.42 (d, $J$ = 2.0 Hz, 2 H, imidazole backbone), 6.83 (d, $J$ = 2.0 Hz, 2 H, imidazole backbone), 7.19 (d, $J$ = 7.3 Hz, 4 H, aromatic CH), 7.33 (t, $J$ = 7.3 Hz, 2 H, aromatic CH), 7.45 (t, $J$ = 8.1 Hz, 1 H, pyridyl CH) ppm. $^{13}$C NMR (75.45 MHz, [D$_8$]THF, 25 °C): $\delta$ = 24.3 (Me), 24.5 (Me), 29.3 (Me), 104.8 (aromatic CH), 114.3 (aromatic CH), 123.7 (aromatic CH), 125.6 (aromatic CH), 126.8 (aromatic CH), 129.4 (aromatic CH), 137.3 (aromatic C), 146.3 (aromatic C), 152.7 (aromatic C) ppm; carbene signal not observed. $C_{35}H_{41}ClN_5Rh$ (670.10): calcd. C 62.73, H 6.17, N 10.45; found C 62.65, H 6.05, N 10.25.

**3,3′-Bis(2,6-diisopropylphenyl)-1,1′-pyridine-2,6-diylbis(imidazol-2-ylidene)dichloro(chloromethyl)rhodium(III) (3):** Dissolution of the

 © 2006 Wiley-VCH Verlag GmbH & Co. KGaA, Weinheim 

rhodium(I) complex **2** (ca. 15 mg) in $CD_2Cl_2$ (0.75 mL) led to a rapid colour change from purple to light yellow. Upon standing, light yellow crystals suitable for X-ray diffraction formed in quantitative yield. $^1$H NMR (300 MHz, $CD_2Cl_2$, 25 °C): $\delta$ = 0.96 (d, $J$ = 7.0 Hz, 6 H, Me), 1.11 (d, $J$ = 6.8 Hz, 6 H, Me), 1.15 (d, $J$ = 6.8 Hz, 6 H, Me), 1.21 (d, $J$ = 6.5 Hz, 6 H, Me), 2.55 [sept, $J$ = 6.7 Hz, 2 H, C*H*$(CH_3)_2$], 3.36 [sept, $J$ = 6.7 Hz, 2 H, C*H*$(CH_3)_2$], 7.07 (d, $J$ = 2.4 Hz, 2 H, imidazole backbone), 7.15 (d, $J$ = 7.6 Hz, 2 H, aromatic CH), 7.19 (d, $J$ = 8.1 Hz, 2 H, aromatic CH), 7.35 (t, $J$ = 7.6 Hz, 2 H, aromatic CH), 7.49 (dm, $J$ = 8.1 Hz, 2 H, pyridyl CH), 7.85 (d, $J$ = 2.4 Hz, 2 H, imidazole backbone), 8.12 (t, $J$ = 8.1 Hz, 1 H, pyridyl CH) ppm. $^{13}$C (75.45 MHz, $CD_2Cl_2$, 25 °C): $\delta$ = 22.9 (Me), 23.0 (Me), 26.0 (Me), 26.3 (Me), 28.4 [*C*H$(CH_3)_2$], 28.5 [C*H*$(CH_3)_2$], 68.1 ($CD_2Cl$) 106.1 (aromatic CH), 116.2 (aromatic CH), 123.3 (aromatic CH), 124.2 (aromatic CH), 126.3 (aromatic CH), 130.1 (aromatic CH), 134.4 (aromatic C), 141.3 (aromatic C), 145.2 (aromatic CH), 147.8 (aromatic C), 162.8 (aromatic C) ppm, carbene not observed.

**1-(2,2′-Bipyridin-6-yl)-3-(2,6-diisopropylphenyl)-3*H*-imidazol-1-ium Bromide (6):** 6-Bromo-2,2′-bipyridine (1.40 g, 5.95 mmol) and 1-(2,6-diisopropylphenyl)imidazole (1.46 g, 6.38 mmol) were placed in a glass ampoule which was sealed under vacuum. This was completely immersed in an oil bath at 150 °C for 6 d. After cooling to room temperature, the ampoule was opened and the brown residue was dissolved in dichloromethane. After evaporation of the solvent, the product was stirred with diethyl ether at 0 °C for several hours, the solvent removed by filtration and the solid dried in vacuo. This gave the product as a brown solid (2.27 g, 82%). $C_{25}H_{27}BrN_4$ (463.42): calcd. C 64.79, H 5.87, N 12.09; found C 64.31, H 5.98, N 11.92. $^1$H NMR (300 MHz, $CDCl_3$, 25 °C): $\delta$ = 1.19 (d, $J$ = 6.6 Hz, 6 H, Me), 1.32 (d, $J$ = 6.6 Hz, 6 H, Me), 2.46 [sept, $J$ = 6.6 Hz, 2 H, C*H*$(CH_3)_2$], 7.37 (d, $J$ = 7.5 Hz, 2 H, aromatic CH), 7.42 (br. s, 1 H, pyridyl CH), 7.59 (t, $J$ = 7.9 Hz, 1 H, aromatic CH), 7.68 (br. s, 1 H, pyridyl CH), 8.25 (t, $J$ = 7.9 Hz, 2 H, pyridyl CH), 8.62–8.75 (m, 3 H, pyridyl CH), 9.33 (d, $J$ = 7.9 Hz, 1 H, pyridyl CH), 9.37 (br. s, 1 H, imidazole backbone), 11.30 (s, 1 H, imidazolium salt) ppm. $^{13}$C NMR (74.45 MHz, $CDCl_3$, 25 °C): $\delta$ = 24.0 (Me), 24.1 (Me), 28.6 [*C*H$(CH_3)_2$], 116.9 (aromatic CH), 121.2 (aromatic CH), 123.5 (aromatic CH), 124.5 (aromatic CH), 125.5 (aromatic CH), 125.6 (aromatic CH), 129.8 (aromatic C), 131.9 (aromatic CH), 136.2 (aromatic CH), 142.2 (aromatic CH), 144.8 (aromatic C), 145.6 (aromatic C) ppm. MS (ESI+): $m/z$ = 155.0, 367.3, 170.0, 182.1, 196.1, 213.1, 352.2, 383.3 [$M^+$].

**1-(2,2′-Bipyridin-6-yl)-3-(2,6-diisopropylphenyl)imidazol-2-ylidene (7):** The salt **6** (1.02 g, 2.21 mmol) and potassium bis(trimethylsilyl)amide (0.56 g, 2.81 mmol) were stirred under nitrogen and cooled to –78 °C. Pre-cooled THF (35 mL) was added, and the solution stirred at low temperature for 1 h. It was warmed to –30 °C, then left to stand overnight. After evaporation of the solvent, the product was filtered through Celite® as a solution in toluene (20 mL). Reduction to a volume of 2 mL was followed by addition of petroleum ether (10 mL); cooling to –30 °C gave the product as a brown solid (36 mg, 4%). Better yields are obtained as follows: Potassium metal (348 mg, 8.9 mmol) was added to **6** (3.00 g, 5.25 mmol) in THF (120 mL) and the mixture heated to reflux overnight. After cooling to room temperature, the solution was filtered through Celite® and the solvent removed in vacuo. The solid residue was dissolved in toluene (70 mL), the solution filtered and the volume reduced to ca. 15 mL. After addition of petroleum ether (50 mL), the product was crystallised at –30 °C. Filtration and washing with petroleum ether (20 mL) gave the carbene as a brown solid (586 mg, 29%). $^1$H NMR (300 MHz, $C_6D_6$, 25 °C): $\delta$ = 1.13 (d, $J$ = 6.9 Hz, 6 H, Me), 1.22 (d, $J$ = 6.8 Hz, 6 H, Me), 2.94 [sept, $J$ = 6.9 Hz, 2 H, C*H*$(CH_3)_2$], 6.66 (d, $J$ = 1.6 Hz, 1 H, imidazole backbone CH), 6.74 (ddd, $J$ = 1.1, 4.7, 7.4 Hz, 1 H, aromatic CH), 7.19–7.32 (m, 5 H, aromatic CH), 8.28 (d, $J$ = 1.7 Hz, 1 H, imidazole backbone CH), 8.48–8.56 (m, 3 H, aromatic CH), 8.66 (d, $J$ = 8.2 Hz, 1 H, aromatic CH) ppm. $^{13}$C NMR (75.45 MHz, $C_6D_6$, 25 °C): $\delta$ = 22.82 (Me), 23.17 (Me), 27.36 [*C*H$(CH_3)_2$], 113.80 (aromatic CH), 115.13 (aromatic CH), 117.63 (aromatic CH), 119.61 (aromatic CH), 121.56 (aromatic CH), 122.55 (aromatic CH), 127.07 (aromatic CH), 127.98 (aromatic CH), 135.19 (aromatic CH), 138.07 (aromatic CH), 145.01 (aromatic C), 148.27 (aromatic CH), 152.34 (aromatic C), 153.46 (aromatic C), 154.98 (aromatic C) ppm; carbene carbon signal not observed. X-ray quality colourless crystals were obtained by cooling solutions of **7** in toluene/petroleum ether (50:50) at –30 °C.

**[1-(2,2′-Bipyridin-6-yl)-3-(2,6-diisopropylphenyl)imidazol-2-ylidene]-silver(I) Bromide (8):** The imidazolium salt **6** (1.00 g, 2.16 mmol), molecular sieves (4 Å) (ca. 5 g) and $Ag_2O$ were suspended in the dark in $CH_2Cl_2$ (30 mL) and the mixture refluxed overnight. After cooling to room temperature, the solution was filtered through Celite® and the solvent removed in vacuo. The product was obtained as a pale brown solid (881 mg, 71%). $C_{25}H_{26}AgBrN_4$ (570.3): calcd. C 52.65, H 4.59, N 9.82; found C 52.15, H 4.44, N 9.68. $^1$H NMR (300 MHz, $CDCl_3$, 25 °C): $\delta$ = 1.21 (d, $J$ = 6.6 Hz, 6 H, Me), 1.34 (d, $J$ = 6.6 Hz, 6 H, Me), 2.57 [sept, $J$ = 6.6 Hz, 2 H, C*H*$(CH_3)_2$], 7.24 (br. s, 1 H, imidazole backbone CH), 7.36 (d, $J$ = 8.0 Hz, 2 H, aromatic CH), 7.43 (m, 1 H, aromatic CH), 7.54 (t, $J$ = 8.0 Hz, 1 H, central aromatic CH), 8.12 (t, $J$ = 7.4 Hz, 1 H, aromatic CH), 8.26 (br. s, 1 H, imidazole backbone CH), 8.30 (d, $J$ = 8.1 Hz, 2 H, aromatic CH), 8.61 (m, 2 H, aromatic CH), 8.78 (br. s, 1 H, aromatic CH) ppm. $^{13}$C NMR (75.45 MHz, $CDCl_3$, 25 °C): $\delta$ = 24.40 (Me), 24.50 (Me), 28.40 [*C*H$(CH_3)_2$], 115.07 (aromatic CH), 119.94 (aromatic CH), 121.18 (aromatic CH), 124.38 (aromatic CH), 124.50 (aromatic CH), 128.18 (aromatic C), 128.90 (aromatic C), 130.75 (aromatic CH), 140.36 (aromatic CH), 145.52 (aromatic C), 149.36 (aromatic CH), 172.20 (s, carbene) ppm. MS ($ES^+$): $m/z$ = 871.5 [carbene$_2$$Ag^+$].

**[1-(2,2′-Bipyridin-6-yl)-3-(2,6-diisopropylphenyl)imidazol-2-ylidene]-rhodium(I) Halide [Halide = Br (9a), Cl (9b)]:** The salt **6** (93 mg, 0.20 mmol) was suspended in THF (5 mL) and cooled to –78 °C, and a solution of bis[μ-methoxybis(η$^2$-cyclooctene)rhodium(I)] (49 mg, 0.10 mmol) in THF (5 mL) at –78 °C was added. The solution was warmed to room temperature and became red, then brown and finally dark green. A small amount of solid was filtered off, and the solution diluted with petroleum ether (15 mL). The resulting precipitate was filtered off, dissolved in THF (5 mL) and layered with petroleum ether (5 mL). Cooling to –30 °C gave green crystals of the title compound suitable for X-ray diffraction. $C_{25}H_{26}BrN_4Rh$ (565.32): calcd. C 53.12, H 4.64, N 9.91; found C 52.78, H 4.42, N 9.73. $^1$H NMR ([D$_8$]THF): $\delta$ = 1.13 (d, $J$ = 6.9 Hz, 6 H, Me), 1.21 (d, $J$ = 6.8 Hz, 6 H, Me), 3.00 [sept, $J$ = 6.9 Hz, 2 H, C*H*$(CH_3)_2$], 7.20 (m, 3 H, aromatic CH), 7.35 (t, $J$ = 8.2 Hz, 1 H, aromatic CH), 7.44 (d, $J$ = 8.0 Hz, 1 H, aromatic CH), 7.71 (d, $J$ = 8.0 Hz, 1 H, aromatic CH), 7.76 ("t", $J$ = 6.0 Hz, 1 H, aromatic CH), 8.10 (m, 2 H, aromatic CH), 8.21 (d, $J$ = 8.0 Hz, 1 H, aromatic CH), 8.26 (t, $J$ = 8.0 Hz, 1 H, aromatic CH), 9.47 (d, 1 H, imidazole backbone CH) ppm. The chloride analogue **9b** can be obtained as green powder by the reaction of **7** generated in situ with $[Rh(COE)_2Cl]_2$ in THF at room temperature for 2 h. It exhibits identical NMR spectroscopic data to **9a**. $C_{25}H_{26}ClN_4Rh$ (520.9): calcd. C 57.65, H 5.03, N 10.76; found C 57.12, H 4.87, N 10.61.

**Oxidative Addition Adduct 10 of 9a with $CD_2Cl_2$:** Addition of $CD_2Cl_2$ to a solid sample of **9a** initially gave a dark green solution,

 © 2006 Wiley-VCH Verlag GmbH & Co. KGaA, Weinheim 

but this rapidly became brown (ca. 5 min.). The product of this reaction was the oxidative addition complex **10**. Yield quantitative. $^1$H NMR (300 MHz, $CD_2Cl_2$, 25 °C): $\delta$ = 1.05 (d, $J$ = 6.9 Hz, 3 H, Me), 1.17 (d, $J$ = 6.8 Hz, 3 H, Me), 1.30 (d, $J$ = 6.8 Hz, 3 H, Me), 1.35 (d, $J$ = 6.8 Hz, 3 H, Me), 2.66 [sept, $J$ = 6.8 Hz, 1 H, C*H*-$(CH_3)_2$], 3.47 [sept, $J$ = 6.6 Hz, 1 H, C*H*$(CH_3)_2$], 7.08 (d, $J$ = 2.2 Hz, 1 H, imidazole backbone CH), 7.33 (ddd, $J$ = 1.1, 7.7, 14.3 Hz, 2 H, 2 aromatic CH), 7.52 (t, $J$ = 7.8 Hz, 1 H, aromatic CH), 7.64 (m, 1 H, aromatic CH), 7.63 (t, $J$ = 6.5 Hz, 1 H, aromatic CH), 7.76 (d, $J$ = 8.1 Hz, 1 H, aromatic CH), 8.00 (m, 2 H, aromatic CH), 8.05 (dd, $J$ = 1.3, 7.8 Hz, 1 H, aromatic CH), 8.11 (t, $J$ = 8.1 Hz, 1 H, aromatic CH), 8.19 (d, $J$ = 7.9 Hz, 1 H, aromatic CH), 9.14 (d, $J$ = 4.8 Hz, 1 H, aromatic CH) ppm. $^{13}$C NMR (75.45 MHz, $CD_2Cl_2$, 25 °C): $\delta$ = 23.28 (Me), 23.59 (Me), 26.28 (Me), 26.80 (Me), 28.92 [*C*H$(CH_3)_2$], 28.99 [*C*H$(CH_3)_2$], 112.05 (aromatic CH), 117.37 (aromatic CH), 119.17 (aromatic CH), 123.92 (aromatic CH), 124.12 (aromatic CH), 124.85 (aromatic CH), 126.71 (aromatic CH), 128.31 (aromatic CH), 131.01 (aromatic CH), 134.94 (aromatic C), 139.47 (aromatic CH), 140.60 (aromatic CH), 146.01 (aromatic C), 148.25 (aromatic C), 150.90 (aromatic C), 152.04 (aromatic C), 155.90 (aromatic C) ppm; carbene and $CD_2Cl$ signals not observed. MS (ESI+): $m/z$ = 570.9 [$M^+$ – HCl], 611.9 [$M^+$ – HCl + MeCN].

**Reaction of 9a with CO:** To a green solution of **9a** in THF was bubbled CO for 1 min. The colour changed to dark red-orange within 5 min and a pink precipitate appeared after sometime which was isolated by filtration and dried. Yield: 45%. $^1$H NMR (300 MHz, $CD_2Cl_2$, 25 °C): $\delta$ = 1.05 (d, $J$ = 6.9 Hz, 3 H, Me), 1.17 (d, $J$ = 6.8 Hz, 3 H, Me), 1.30 (d, $J$ = 6.8 Hz, 3 H, Me), 1.35 (d, $J$ = 6.8 Hz, 3 H, Me) 2.66 [sept, $J$ = 6.8 Hz, 1 H, C*H*$(CH_3)_2$], 3.47 [sept, $J$ = 6.8 Hz, 1 H, C*H*$(CH_3)_2$], 7.33 (ddd, $J$ = 1.1, 7.7, 14.3 Hz, 2 H, aromatic), 7.52 (t, $J$ = 7.8 Hz, 1 H, aromatic), 7.63 (t, $J$ = 6.5 Hz, 1 H, aromatic), 7.76 (d, $J$ = 8.1 Hz, 1 H, aromatic), 8.00 (m, 2 H, aromatic), 8.05 (dd, $J$ = 1.3, 7.8 Hz, 1 H, aromatic), 8.11 (t, $J$ = 8.1 Hz, 1 H, aromatic), 8.19 (d, $J$ = 7.9 Hz, 1 H, aromatic) 9.14 (d, $J$ = 4.8 Hz, 1 H, aromatic) ppm. $^{13}$C NMR (75.45 MHz, $CD_2Cl_2$, 25 °C): $\delta$ = 23.80 (Me), 24.45 (Me), 28.47 [*C*H$(CH_3)_2$], 114.46 (aromatic CH), 118.79 (aromatic CH), 120.58 (aromatic CH), 124.08 (aromatic CH), 124.35 (aromatic CH), 124.41 (aromatic CH), 128.01 (aromatic CH), 130.99 (aromatic CH), 134.18 (aromatic C), 140.53 (aromatic CH), 144.77 (aromatic CH), 145.66 (aromatic C), 152.24 (aromatic C), 154.29 (aromatic CH), 154.97 (aromatic C), 156.09 (aromatic C) ppm.

**X-ray Crystallography:** A summary of the crystal data, data collection and refinement for compounds **2**, **3**, **7**, and **9a** are given in Table 1. All data sets were collected with an Enraf–Nonius Kappa CCD area detector diffractometer, fitted with an FR591 rotating anode (Mo-$K_\alpha$ radiation) and an Oxford Cryosystems low-temperature device, operating in $\omega$-scanning mode with $\psi$- and $\omega$-scans to fill the Ewald sphere. Data collection and reduction were carried out using the software packages Collect, Scalepack, and Denzo.[21] The crystals were mounted on a glass fibre with silicon grease from Fomblin vacuo oil. In all cases refinement was carried out by full-matrix least-squares methods using SHELXL-97[22] within the WinGX program suite.[23] All non-hydrogen atoms were refined using anisotropic thermal parameters, and hydrogen atoms were added using a riding model. CCDC-607971 (**2**), -607972 (**3**), -607973 (**7**) and -607974 (**9a**) contain the supplementary crystallographic data for this paper. These data can be obtained free of charge from The Cambridge Crystallographic Data Centre via www.ccdc.cam.ac.uk/data_request/cif.

**Computational Details:** DFT calculations were carried out using the GAUSSIAN03[24] program package, running on a Mandriva Linux Dual-Opteron. Geometries have been fully optimised without symmetry constraints, involving the functional combinations according to Becke[25] (hybrid) and Lee, Yang, Parr[26] (denoted B3LYP), with the corresponding valence basis set for Rh (Stuttgart-Dresden, keyword SDD in Gaussian) and standard 6-31G* basis set for C, H, N and Cl (denoted as ECP1).[27] The stationary points were characterised as minima by analytical harmonic frequency (zero imaginary frequency), which were used without scaling for zero-point and thermal corrections. MOLDEN[28] was used for the chemical representation of the calculated compounds, and NBO-View[29] for the representation of the orbitals. Tables of Cartesian coordinates of all calculated structures are available as Supporting Information in $x$, $y$, $z$ format.

Table 1. Summary of crystallographic data for **2**, **3**, **7**, and **9a**.

| | **2** | **3** | **7** | **9a** |
|---|---|---|---|---|
| Empirical formula | $C_{35}H_{41}ClN_5Rh$ | $C_{36}H_{43}Cl_3N_5Rh{\cdot}CH_2Cl_2$ | $C_{25}H_{26}N_4$ | $C_{25}H_{26}BrN_4Rh$ |
| Formula mass | 670.09 | 839.94 | 382.50 | 565.32 |
| Crystal description | purple block | light yellow prism | orange prism | dark green plate |
| Crystal dimensions [mm] | 0.10×0.17×0.20 | 0.06×0.06×0.20 | 0.12×0.12×0.18 | 0.02×0.06×0.10 |
| Crystal system | tetragonal | monoclinic | monoclinic | triclinic |
| Space group | $P\bar{4}2_1c$ | $P2_1/c$ | $P2_1/n$ | $P\bar{1}$ |
| $a$ [Å] | 20.1073(9) | 11.2296(2) | 8.5183(11) | 7.9185(12) |
| $b$ [Å] | 20.1073(9) | 18.5984(5) | 10.7315(11) | 8.5368(12) |
| $c$ [Å] | 16.5070(12) | 18.2031(5) | 23.237(3) | 17.452(3) |
| $\alpha$ [°] | 90 | 90 | 90 | 86.492(5) |
| $\beta$ [°] | 90 | 95.905(2) | 92.215(5) | 79.947(4) |
| $\gamma$ [°] | 90 | 90 | 90 | 72.753(4) |
| $V$ [Å$^3$] | 6673.8(6) | 3781.59(16) | 2122.6(4) | 1109.3(3) |
| $Z$ | 8 | 4 | 4 | 2 |
| $T$ [K] | 120(2) | 120(2) | 120(2) | 120(2) |
| $\mu$ [mm$^{-1}$] | 0.623 | 0.839 | 0.072 | 2.591 |
| No. of data collected | 19201 | 24805 | 13277 | 15065 |
| No. of unique data | 6775 | 3812 | 4754 | 4870 |
| $R_{int}$ | 0.0901 | 0.0883 | 0.0914 | 0.1160 |
| $R_1$ [$I>2\sigma(I)$] | 0.0935 | 0.0399 | 0.0856 | 0.0618 |
| $wR_2$ (all data) | 0.1979 | 0.0979 | 0.1730 | 0.1470 |

 © 2006 Wiley-VCH Verlag GmbH & Co. KGaA, Weinheim 

**Supporting Information** (see footnote on the first page of this article): Tables of cartesian coordinates (*x*, *y*, *z* format) of all calculated structures, HOMO/LUMO and selected NBO graphical respresentations.

## Acknowledgments

We thank ICI Plc (Quest International) for generous support and Professor M. B. Hursthouse for the provision of X-ray facilities.

[1] A. Arduengo, R. L. Harlow, M. Kline, *J. Am. Chem. Soc.* **1991**, *113*, 361–363.
[2] a) W. A. Herrmann, *Angew. Chem. Int. Ed.* **2002**, *41*, 1290–1309; b) D. S. Clyne, J. Jin, E. Genest, J. C. Gallucci, T. V. RajanBabu, *Org. Lett.* **2000**, *2*, 1125–1128 (binaphthyl-substituted NHCs); c) B. Bildstein, M. Malaun, G. Opromolla, P. Zanello, *Organometallics* **1999**, *18*, 4325–4336 (ferrocenyl-substituted NHCs); d) J. C. Garrison, R. S. Simons, J. M. Talley, C. Wesdemiotis, C. A. Tessier, W. J. Youngs, *Organometallics* **2001**, *20*, 1276–1278; e) M. V. Baker, B. W. Skelton, A. White, C. C. Williams, *J. Chem. Soc., Dalton Trans.* **2001**, 111–120 (cyclophane-substituted NHCs).
[3] M. Albrecht, G. van Koten, *Angew. Chem. Int. Ed.* **2001**, *40*, 3750–3781, and references therein.
[4] For recent selected references, see: a) M. Gerisch, J. R. Krumper, R. G. Bergman, T. D. Tilley, *J. Am. Chem. Soc.* **2001**, *123*, 5818–5819; b) F. Guerin, D. H. McConville, J. J. Vittal, *Organometallics* **1996**, *15*, 5586–5590; c) B. L. Small, M. Brookhart, A. M. Bennett, *J. Am. Chem. Soc.* **1998**, *120*, 404–4050; d) G. J. P. Britovsek, V. C. Gibson, B. S. Kimberley, P. J. Maddox, S. J. McTavish, G. A. Solan, A. J. P. White, D. J. Williams, *Chem. Commun.* **1998**, 849–850; e) M. Gandelman, B. Rybtchinski, N. Ashkenazi, R. M. Gauvin, D. Milstein, *J. Am. Chem. Soc.* **2001**, *123*, 5372–5373.
[5] a) A. A. Danopoulos, S. Winston, W. B. Motherwell, *Chem. Commun.* **2002**, 1376–1377; b) A. A. Danopoulos, A. A. D. Tulloch, S. Winston, G. Eastham, M. B. Hursthouse, *Dalton Trans.* **2003**, 1009–1015; c) A. A. Danopoulos, N. Tsoureas, J. A. Wright, M. E. Light, *Organometallics* **2004**, *23*, 166–168; d) A. A. Danopoulos, J. A. Wright, W. B. Motherwell, S. Ellwood, *Organometallics* **2004**, *23*, 4807–4810; e) A. A. Danopoulos, J. A. Wright, W. B. Motherwell, *Chem. Commun.* **2005**, 784–786.
[6] J. M. Wilson, G. J. Sunley, H. Adams, A. Haynes, *J. Organomet. Chem.* **2005**, *690*, 6089–6095.
[7] M. Poyatos, E. Mas-Marzá, J. A. Mata, M. Sanaú, E. Peris, *Eur. J. Inorg. Chem.* **2003**, 1215–1221.
[8] a) P. N. W. M. van Leeuwen, C. Claver, *Rhodium Catalysed Hydroformylation*, Kluwer, Dordrecht, **2000**; b) C. D. Frohling, C. W. Kohlpaintner, in *Applied Homogeneous Catalysis with Organometallic Compound*s (Eds.: B. Cornils, W. A. Herrmann), VCH, Weinheim, **1996**, vol. 1, pp. 27–104.
[9] G. Vassapolo, P. Giannocarro, C. F. Nobile, A. Sacco, *Inorg. Chim. Acta* **1981**, *48*, 125–128.
[10] E. Poverenov, G. Leitus, J. W. Shimon, D. Milstein, *Organometallics* **2005**, *24*, 5937–5944.
[11] T. Norrby, A. Börje, L. Zhang, B. Åkermark, *Acta Chem. Scand.* **1998**, *52*, 77–85.
[12] J. S. Field, R. J. Haines, C. J. Perry, S. H. Sookraj, *S. Afr. J. Chem.* **1993**, *46*, 70–74.
[13] B. Gorodetsky, T. Ramnial, N. R. Branda, J. A. C. Clyburne, *Chem. Commun.* **2004**, 1972–1973.
[14] A. A. Danopoulos, S. Winston, W. B. Motherwell, *Chem. Commun.* **2002**, 1376–1377.
[15] B. C. de Pater, H.-W. Frühauf, K. Vrieze, R. de Gelder, E. J. Baerends, D. McCormack, M. Lutz, A. L. Spek, F. Hartl, *Eur. J. Inorg. Chem.* **2004**, 1675–1686.
[16] W. L. F. Armarego, D. D. Perrin, *Purification of Laboratory Chemicals*, 4th ed., Butterworth-Heinemann, Oxford, **1996**.
[17] A. L. Johnson, *US Patent* **1972**, 3637731.
[18] A. van der Ent, A. L. Onderdelinden, *Inorg. Synth.* **1990**, *28*, 90–92.
[19] R. Cramer, *Inorg. Synth.* **1990**, *28*, 86–88.
[20] R. Uson, L. A. Oro, J. A. Cabeza, *Inorg. Synth.* **1985**, *23*, 126–130.
[21] a) R. W. W. Hooft, COLLECT data collection software, Nonius B. V., **1998**; b) SCALEPACK, DENZO: Z. Otwinoski, W. Minor, *Methods Enzymol.* **1997**, *276*, 307–326.
[22] G. M. Sheldrick, *Programs for Crystal Structure Analysis*, University of Göttingen, Germany, **1997**.
[23] L. J. Farrugia, *J. Appl. Crystallogr.* **1999**, *32*, 837–838.
[24] M. J. Frisch, G. W. Trucks, H. B. Schlegel, G. E. Scuseria, M. A. Robb, J. R. Cheeseman, J. A. Montgomery Jr, T. Vreven, K. N. Kudin, J. C. Burant, J. M. Millam, S. S. Iyengar, J. Tomasi, V. Barone, B. Mennucci, M. Cossi, G. Scalmani, N. Rega, G. A. Petersson, H. Nakatsuji, M. Hada, M. Ehara, K. Toyota, R. Fukuda, J. Hasegawa, M. Ishida, T. Nakajima, Y. Honda, O. Kitao, H. Nakai, M. Klene, X. Li, J. E. Knox, H. P. Hratchian, J. B. Cross, V. Bakken, C. Adamo, J. Jaramillo, R. Gomperts, R. E. Stratmann, O. Yazyev, A. J. Austin, R. Cammi, C. Pomelli, J. W. Ochterski, P. Y. Ayala, K. Morokuma, G. A. Voth, P. Salvador, J. J. Dannenberg, V. G. Zakrzewski, S. Dapprich, A. D. Daniels, M. C. Strain, O. Farkas, D. K. Malick, A. D. Rabuck, K. Raghavachari, J. B. Foresman, J. V. Ortiz, Q. Cui, A. G. Baboul, S. Clifford, J. Cioslowski, B. B. Stefanov, G. Liu, A. Liashenko, P. Piskorz, I. Komaromi, R. L. Martin, D. J. Fox, T. Keith, M. A. Al-Laham, C. Y. Peng, A. Nanayakkara, M. Challacombe, P. M. W. Gill, B. Johnson, W. Chen, M. W. Wong, C. Gonzalez, J. A. Pople, *Gaussian03*, Gaussian, Inc., Pittsburgh, PA, **2004**.
[25] A. D. Becke, *J. Chem. Phys.* **1993**, *98*, 5648–5652.
[26] C. Lee, W. Yang, R. G. Parr, *Phys. Rev. B* **1988**, *37*, 785–789.
[27] W. J. Hehre, R. Ditchfield, J. A. Pople, *J. Chem. Phys.* **1972**, *56*, 2257–2261.
[28] G. Schaftenaar, J. H. Noordik, *J. Comput.-Aided Mol. Des.* **2000**, *14*, 123–134.
[29] E. D. Glendening, J. K. Badenhoop, A. E. Reed, J. E. Carpenter, J. A. Bohmann, C. M. Morales, F. Weinhold, *NBO 5.G.*, Theoretical Chemistry Institute, University of Wisconsin, Madison, USA, **2001**.

Received: June 16, 2006
Published Online: October 5, 2006

 © 2006 Wiley-VCH Verlag GmbH & Co. KGaA, Weinheim 

DOI: 10.1002/ejic.200600565

# Synthesis, Characterization, and Crystal Structure of Two Manganese Metallacrowns: 30-Metallacrown-10 and 18-Metallacrown-6 with Ligands Derived from 3-Hydroxy-2-naphthalenecarbohydrazide

**Jianmin Dou,*[a] Mingli Liu,[a] Dacheng Li,[a] and Daqi Wang[a]**

**Keywords:** Metallacrowns / Manganese / Crystal structure / Supramolecular chemistry / Crown compounds

Two manganese metallacrowns $[Mn_{10}(pnhz)_{10}(DMF)_4(H_2O)_6]\cdot10.5H_2O\cdot MeOH\cdot DMF$ (**1**) and $[Mn_6(anhz)_6(DMF)_2(H_2O)_4]\cdot6DMF$ (**2**), ($H_3$pnhz = 3-hydroxy-*N*-phenyl-2-naphthalenecarbohydrazide, $H_3$anhz = *N*-acyl-3-hydroxy-2-naphthalenecarbohydrazide) have been prepared by the reactions of two pentadentate ligands, $H_3$anhz and $H_3$pnhz, with the corresponding manganese(II) salt, respectively, and characterized by elemental analysis, IR spectra, and X-ray single-crystal diffraction analysis. Complex **1** has an $[Mn–N–N]_{10}$ skeleton with two kinds of $Mn^{III}$ centers in an ···AABAB··· alignment, and the metallic centers exhibit a ···ΔΛΔΛ··· chiral configuration alignment. Adjacent molecules are linked by four intermolecular H bonds to form a 1D infinite chain structure. This is the first 1D supramolecular sample of a metallacrown formed by weak interactions. Complex **2** shows an $[Mn–N–N]_6$ skeleton with two kinds of $Mn^{III}$ centers in a ···BAA··· alignment. The successive manganese centers possess a ···ΔΛΔΛ··· chiral configuration alignment.
(© Wiley-VCH Verlag GmbH & Co. KGaA, 69451 Weinheim, Germany, 2006)

## Introduction

Since the first metallacrown (MC) [9-MC-3] was synthesized and confirmed by Pecoraro and coworkers[1] in 1989, this kind of metallic macrocyclic complex has received considerable attention in supramolecular chemistry, self-assembly, host–guest chemistry, and molecular recognition. Interest in the metallacrowns stems not only from their high symmetry and aesthetic molecular frameworks, but also from their magnetic properties and selective recognitions to cations and anions, along with the potential applications in chemically modified electrodes and liquid-crystal precursors.[2–10] At present, the groups of metallacrowns mainly include: (1) metallacrowns with a $[M–N–O]_n$ repeating linkage. This type of metallacrown can be synthesized by multidentate ligands such as hydroxamic,[11] ketonoxime,[11a,12] and aminohydroxamic acids[13] and their cyclic size has been enlarged from 9-MC-3 to 24-MC-8,[1,14–18] including several inverse metallacrowns.[2,19–21] (2) Metallacrowns with the $[M–N–N]_n$ repeating linkage, for example, azametallacrown, which can be synthesized by multidentate ligands such as *N*-substituted salicylhydrazide, salicylhydrazone, or 2-pyridinecarbaldehyde hydrazone. Their cyclic size has been developed from 18-MC-6 to 36-MC-12.[22–24] During the studies of the design of azametallacrowns, *N*-acyl-substituted salicylhydrazide ligands have often been used. In the last two years, the factors that control the ring size and nuclearity of azametallacrowns[25–26] have been investigated; the result shows that the nature of the *N*-acyl substituent group can influence the size and nuclearity of the macrocycle complex. Two- and three-dimensional networks can be constructed[27] if an *exo*-bidentate ligand is employed in the synthesis of azametallacrowns. To the best of our knowledge, only one azametallacrown prepared from a hydrazide that was derived from 3-hydroxy-2-naphthoic acid has been reported.[28] In this current work, we have synthesized two kinds of ligands that contain the 3-hydroxy-2-naphthyl, the *N*-acetyl-3-hydroxy-2-naphthalenecarbohydrazide, and the 3-hydroxy-*N*-phenyl-2-naphthalenecarbohydrazide groups and two azametallacrowns $[Mn_{10}(pnhz)_{10}(DMF)_4(H_2O)_6]\cdot10.5H_2O\cdot MeOH\cdot DMF$ (**1**) and $[Mn_6(anhz)_6(DMF)_2(H_2O)_4]\cdot6DMF$ (**2**) with the use of these two ligands, respectively.

## Results and Discussion

### Complex 1

Complex **1** was obtained by the reaction of manganese acetate tetrahydrate in methanol with $H_3$pnhz in DMF in a 1:1 molar ratio.[29] The crystallographic data is summarized in Table 1. The structure of complex **1** is illustrated in Figure 1. X-ray structural analysis shows that complex **1** has a planar decanuclear thirty-membered ring core. In the man-

[a] Department of Chemistry, Liaocheng University, Liaocheng 252059, P. R. China
Fax: +86-635-8239121
E-mail: jmdou@lctu.edu.cn

 © 2006 Wiley-VCH Verlag GmbH & Co. KGaA, Weinheim 

Table 1. Crystallographic data for the structure of complexes **1** and **2**.

| | | |
|---|---|---|
| Empirical formula | $C_{195}H_{178}Mn_{10}N_{25}O_{50.50}$ | $C_{102}H_{118}Mn_6N_{20}O_{30}$ |
| Formula weight | 4229.03 | 2433.88 |
| $T$ [K] | 298(2) | 298(2) |
| Wavelength [Å] | 0.71073 | 0.71073 |
| Crystal system | Triclinic | Triclinic |
| Space group | $P\bar{1}$ | $P\bar{1}$ |
| $a$ [Å] | 15.616(11) | 12.755(16) |
| $b$ [Å] | 20.340(14) | 15.278(19) |
| $c$ [Å] | 21.510(15) | 17.50(2) |
| $\alpha$ [°] | 99.599(12) | 69.12(2) |
| $\beta$ [°] | 106.661(12) | 71.75(2) |
| $\gamma$ [°] | 101.254(13) | 76.55(3) |
| Volume [Å$^3$] | 6237(7) | 2998(6) |
| $Z$ | 1 | 1 |
| $D_{calcd.}$ [g/cm$^3$] | 1.126 | 1.348 |
| $\mu$(Mo-$K_\alpha$) [mm$^{-1}$] | 3.892 | 2.058 |
| $F$(000) | 15246 | 1260 |
| Crystal size [mm] | 0.38 × 0.31 × 0.12 | 0.33 × 0.30 × 0.26 |
| $\theta$ range for data collection [°] | 1.85 to 25.01 | 1.92 to 25.01 |
| Limiting indices | $-17 \le h \le 18$, $-24 \le k \le 18$, $-25 \le l \le 25$ | $-10 \le h \le 15$, $-18 \le k \le 17$, $-20 \le l \le 18$ |
| Reflections collected/unique | 32431/21451 [$R$(int) = 0.0847] | 14763/10167 [$R$(int) = 0.1876] |
| Completeness to $\theta$ = 25.0 [%] | 97.5 | 96.2 |
| Absorption correction | Semi-empirical from equivalents | Semi-empirical from equivalents |
| Max. and min. transmission | 0.6523 and 0.3194 | 0.6167 and 0.5499 |
| Refinement method | Full-matrix least-squares on $F^2$ | Full-matrix least-squares on $F^2$ |
| Data/restraints/parameters | 21451/487/1330 | 10167/360/770 |
| Goodness-of-fit on $F^2$ | 0.943 | 0.873 |
| $R_1$, $wR_2$ [$I > 2\sigma(I)$] | 0.1066, 0.2550 | 0.1193, 0.2242 |
| $R_1$, $wR_2$ (all data) | 0.2614, 0.3757 | 0.3573, 0.3354 |
| Largest diff. peak and hole [e·Å$^{-3}$] | 1.012 and –0.594 | 0.790 and –0.541 |

ganese complex, a crystallographic centrosymmetric [-Mn–N–N-]$_{10}$ unit is exhibited with 5.001 Å, 4.934 Å, 4.886 Å, 4.937 Å, and 4.907 Å for the neighboring Mn···Mn distances which are consistent with 4.906(1)–4.986(2) Å for the corresponding distances in $[Mn(C_{14}H_9N_2O_3)(CH_3OH)]_{10}\cdot 5CH_2Cl_2\cdot 16CH_3OH\cdot H_2O$.[6] The average angle of the successive manganese ions is 136.91° and it is comparable to the interior angle of 144° in an n-decagon. The size or dimension and even the depth of the cavity of the 30-MC-10 in this communication exceeds those of the previous 30-MC-10 in ref.[6] The size of the cavity in the metallacrown is measured between the opposite carbon atoms: 13.206 Å for C5···C5#1, 8.987 Å for C77···C77#1, 12.335 Å for C23···C23#1, 9.830 Å for C41···C41#1, and 12.014 Å for C59···C59#1. The approximate dimensions of the oval-shaped cavity are about 7.948 Å in diameter at the entrance, approximately 16.4 Å at its largest diameter at the center of the cavity, and around 7.3703 Å in depth, which is large enough to capture some neutral molecules. So the solvent hydrate molecule (O25) is drawn in the cavity at a depth of 0.9061 Å during the self-assembly.

All manganese centers have a $N_2O_4$ geometry but in two different environments. The trivalent anionic nphz$^{3-}$ acts as a pentadentate ligand chelate for two adjacent manganese atoms in a back-to-back mode by five atoms. One phenolate oxygen atom, one carbonyl oxygen atom (phenyl end), and one hydrazide nitrogen atom bind to one manganese ion; the residual carbonyl oxygen atom (naphthyl end) and the hydrazide nitrogen atom coordinate to the neighboring metal ions as illustrated in Scheme 1. Therefore, the ligands around the Mn$^{III}$ ion are forced into a propeller configuration owing to the meridional coordination of the adjacent ligand to this metal ion. The other vertex position of each octahedral geometry is occupied by either a $H_2O$ molecule or a DMF molecule, which forms two kinds of Mn centers and the geometric environments of them are named A and B, respectively. In each octahedral geometry around Mn$^{III}$, the mean axial distance of Mn–O/N is approximately 0.38 Å longer than the mean value of the basal distances. The typical Jahn–Teller elongation along the $z$ axis of Mn$^{III}$ ions that possess the high-spin d$^4$ orbit was also found in several Mn$^{III}$ complexes.[7,26] Finally, the successive Mn$^{III}$ centers show an environment with the ···AABAB··· alignment and with an alternating ···ΔΛΔΛ··· chiral configuration.[32]

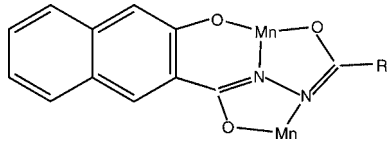


Scheme 1.

Metallocrown 30-MC-10 forms a 1D chain structure through hydrogen bond interactions that are formed by a noncovalent force. Each coordinated O8 interacts with two DMF molecules through H bonds, and the O atoms in the DMF molecules further interact with O8#1 in an adjacent molecule also through H bonds. Therefore, the adjacent metallacrown molecules are linked together by two DMF molecules by four such H bonds to form a 1D chain struc-

 © 2006 Wiley-VCH Verlag GmbH & Co. KGaA, Weinheim 

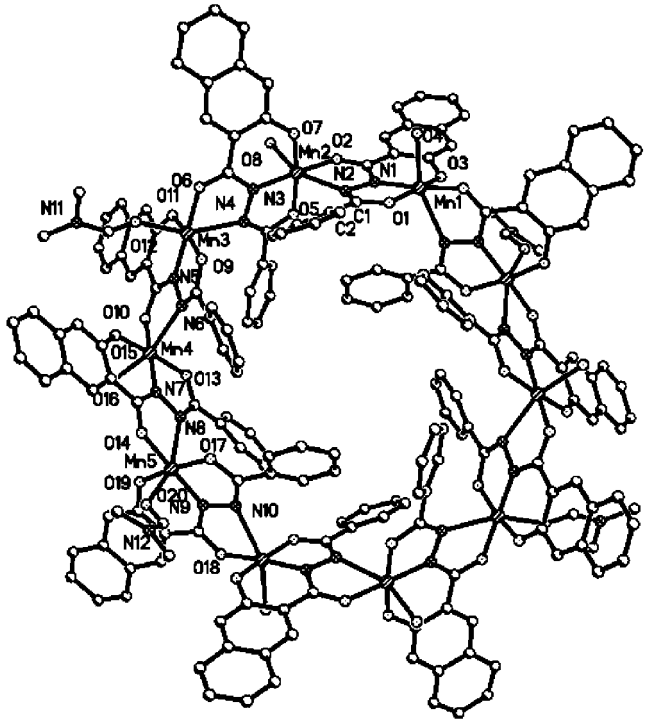


Figure 1. Molecular structure of complex **1**. All the solvent molecules have been omitted for clarity. Selected bond lengths [Å]: Mn1–O3 1.819(8) Mn1–O1 1.888(7), Mn1–N1 1.947(8), Mn1–O18#1 1.975(6), Mn1–O4 2.174(9), Mn1–N10#1 2.338(9), Mn2–O7 1.854(7), Mn2–O5 1.887(7), Mn2–O2 1.922(7), Mn2–N3 1.922(8), Mn2–O8 2.242(8), Mn2–N2 2.400(8), Mn3–O11 1.830(7), Mn3–O9 1.902(7), Mn3–N5 1.935(8), Mn3–O6 1.988(7), Mn3–O12 2.233(10), Mn3–N4 2.327(9), Mn4–O15 1.808(8), Mn4–O13 1.888(7), Mn4–N7 1.917(8), Mn4–O10 1.960(7), Mn4–O16 2.250(9), Mn4–N6 2.300(9), Mn5–O19 1.846(8), Mn5–O17 1.886(8), Mn5–N9 1.915(9), Mn5–O14 1.934(7), Mn5–O20 2.241(10), Mn5–N8 2.377(8). Selected bond angles [°]: O4–Mn1–N10#1 155.4(3), N1–Mn1–O18#1 170.6(3), O3–Mn1–O1 169.1(3), O7–Mn2–O5 170.5(3), O2–Mn2–N3 170.5(3), O8–Mn2–N2 155.1(3), O12–Mn3–N4 154.8(4), N5–Mn3–O6 173.5(3), O11–Mn3–O9 170.7(3), N7–Mn4–O10 172.0(3), O16–Mn4–N6 155.9(3), O15–Mn4–O13 171.5(3), O19–Mn5–O17 170.8(3), O20–Mn5–N8 156.1(3), N9–Mn5–O14 171.6(3).

ture as illustrated in Figure 2. The H bond lengths are 2.785(18) Å and 3.026(18) Å for O8···O21#2 and O8···O21#3, respectively. Among all of the azametallacrowns reported, no supramolecule has been formed by H bonds.

### Complex 2

The reaction of manganese 2,4-pentanedionate in methanol with $H_3$anhz in DMF gives rise to the single-crystal of complex **2**; its crystallographic data is listed in Table 1. The X-ray structural analysis shown in Figure 3 reveals that complex **2** is a hexanuclear manganese azametallacrown with a $[Mn–N–N]_6$ unit. Different from previous analogues which either possess pseudo $C_{3i}$[23] or crystallographic $C_{3i}$ symmetry,[22] this 18-MC-6 is a crystallographic $C_{2i}$ symmetric molecule.

The two kinds of $Mn^{III}$ centers both reside in the octahedral geometries of the complex that is composed of $N_2O_4$: five atoms from two dianionic anhz$^{3-}$ and one O atom occupy one axial site from either $H_2O$ (A-environment for the $Mn^{III}$ center) or DMF (B-environment for the $Mn^{III}$ center). The mean axial distances [mean value 2.183 Å for Mn(A)–O and 2.221 Å for Mn(A)–N; 2.177(10) Å for Mn(B)–O and 2.247(12) Å for Mn(B)–N] are all about 0.30 Å longer than the average basal bond lengths for each $Mn^{III}$ center, which indicates that the elongation of the octahedrons takes place in the axial direction due to the Jahn–Teller distortion of the high-spin $d^4$ $Mn^{III}$ ion. The pentadentate ligands anhz$^{3-}$ not only bridge the adjacent manganese ions by -N–N-, but also forces the stereochemistry of the metal ions into a propeller configuration because of the meridional coordination of the neighboring ligands. As a result, the complex exhibits a combination of the ···BAA··· environment with the ···ΔΛΔΛ··· chiral configuration. The Mn···Mn distances fall in the range of 4.843–4.856 Å and Mn···Mn···Mn angles of 113.4–115.81°. Metallacrown **2** measures about 1.95 nm in diameter and 1.3 nm in thick-

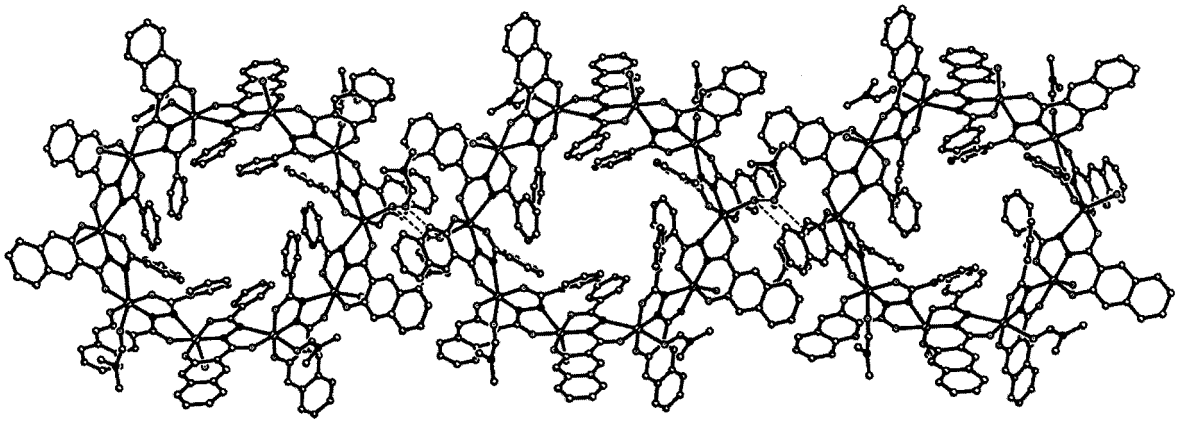

Figure 2. The 1D chain that is formed by intermolecular H bonds with the use of 30-MC-10 as a building block. H bond data [Å]: O8···O21#1 2.785(18), O8–H8A···O21#1 121.4; O8···O21#2 3.026(18), O8–H8B···O21#2 139.1. #1: $x$, $y+1$, $z$; #2: 2 $–x$, 1 $–y$, 1 $–z$.

 © 2006 Wiley-VCH Verlag GmbH & Co. KGaA, Weinheim 

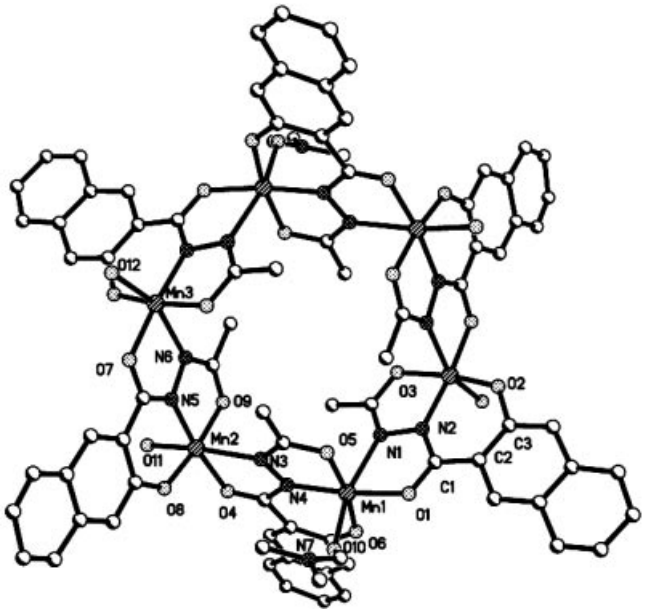


Figure 3. The molecular structure of complex **2**; all of the noncoordinated solvent molecules are removed for clarity. Selected bond lengths [Å]: Mn1–O6 1.818(10), Mn1–O5 1.919(11), Mn1–N4 1.934(12), Mn1–O1 1.953(10), Mn1–O10 2.177(10), Mn1–N1 2.247(12), Mn2–O8 1.838(11), Mn2–O9 1.887(10), Mn2–N5 1.933(12), Mn2–O4 1.941(10), Mn2–O11 2.157(12), Mn2–N3 2.249(14), Mn3–O2#1 1.821(11), Mn3–O3#1 1.910(10), Mn3–N2#1 1.91 6(11), Mn3–O7 1.960(9), Mn3–N6 2.194(13), Mn3–O12 2.209(12). Selected bond angles [°]: O6–Mn1–O5 170.3(5), N4–Mn1–O1 173.0(5), O10–Mn1–N1 160.0(5), N5–Mn2–O4 172.1(5), O11–Mn2–N3 164.0(5), O8–Mn2–O9 171.0(4), N6–Mn3–O12 155.1(5), N2#1–Mn3–O7 172.3(5), O2#1–Mn3–O3#1 170.6(5).

ness. Complex **2** possesses an empty cavity in the center of the metallacrown. Although the geometry and the chirality of the metallic center is similar to some reported 18-MC-6.[22] However, complex **2** possesses a larger cavity due to the heavier head of the 3-hydroxy-2-naphthyl groups and the paddle configuration. The size of the cavity, measured between the opposite carbon atoms, is 6.982 Å (C13···C13#1), 6.399 Å (C26···C26#1), and 6.370 Å (C39···C39#1). For the oval-shaped cavity, the minimum diameter is approximately 4.66 Å at the entrance and the maximum diameter is about 9.612 Å at the center of the cavity.

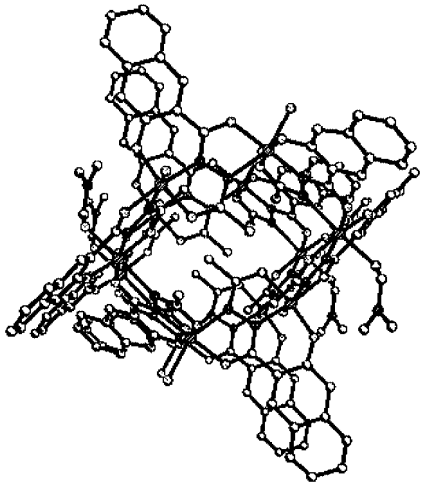

Figure 4. Crystal packing structure of complex **2**.

The crystal packing structure of complex **2** shows that the hexanuclear cluster is aligned approximately along the crystallographic *c* axis. The cavities of the clusters in the crystal structure are also aligned and one-dimensional channels are formed which is shown in Figure 4.

### Magnetism Properties

Temperature-dependent magnetic susceptibility measurements on polycrystalline samples of the title complex indicate that the complex exhibits significant antiferromagnetic coupling between manganese centers. At 300 K, the molar effective magnetic moment ($\mu_{eff}$) is equal to 4.26 $\mu_B$, which is slightly smaller than the expected value for one isolated high-spin $Mn^{III}$ center with $S = 2$ ($\mu_{eff} = 4.90\ \mu_B$). If the sample is cooled, the value decreases gradually until the temperature is about 50 K, and then the value of $\mu_{eff}$ falls rapidly. The antiferromagnetic coupling is further confirmed by a negative Weiss constant –14.85 K, which is calculated with the use of the data within $T > 50$ K and with the use of the Curie–Weiss law $\chi_m^{-1}(T) = C/(T-\theta)$. Only the coupling of the neighboring ($J_1$) and near-neighboring centers ($J_2$) are considered and interactions between the paramagnetic centers in other positions are omitted because of the long distances (Figure 5).

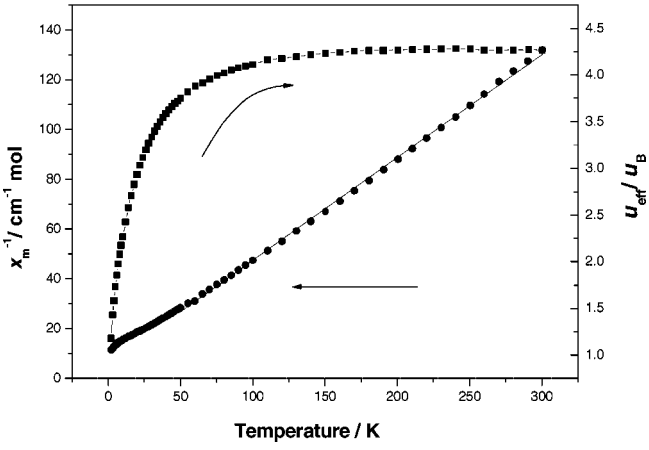


Figure 5. Plots of the effective magnetic moment ($\mu_{eff}$) and the inverse susceptibility $\chi_m^{-1}$ versus temperature for complex **1**. The square and round points represent $\mu_{eff}$ and $\chi_m^{-1}$ data and the line through the round points represents the fitting curve according to the Curie–Weiss law.

## Conclusions

Two azametallacrowns, 18-MC-6 and 30-MC-10, that contain the naphthalene group have been synthesized by introducing $H_3$anhz and $H_3$anhz as the supporting ligands.

 © 2006 Wiley-VCH Verlag GmbH & Co. KGaA, Weinheim 

Both crown compounds are found to possess larger cavities than those found in the corresponding metallacrowns reported previously, which indicates the higher probability that complex **1** can be used as a host to accept some ions or neutral molecules. This probability is realized by 30-MC-10 in which one cavity was able to capture a hydrate molecule. Because of the existence of free DMF in the system, a 1D chain of 30-MC-10 was assembled successfully, which is the first example of an azametallacrown supramolecule that is formed by noncovalent force.

## Experimental Section

**Materials and General Methods:** The ligands $H_3$pnhz and $H_3$anhz were prepared as described in ref.[29] All other chemicals were commercially purchased and used without further purification. Elemental analyses (C, H, and N) were performed with a Perkin–Elmer 2400II analyzer. FTIR spectra of the complex were measured with a Nicolet-460 FTIR spectrometer in the range of 4000–400 $cm^{-1}$.

**Synthesis of Complex 1:** A solution of $H_3$pnhz (0.15 mmol, 0.046 g) in DMF (20 mL) was added to a solution of manganese acetate tetrahydrate (0.15 mmol, 0.030 g) in methanol (20 mL) at room temperature. The reaction mixture was then stirred for 3 h. The resultant dark red solution was left open to air to generate a dark red block crystal after about twenty days. Yield 0.12 g, 18.9%. M.p. >300 °C (dec.). $C_{195}H_{178}Mn_{10}N_{25}O_{50.50}$ (4229.03): calcd. C 55.60, H 4.18; found C 55.81, H 4.20. FTIR (KBr): 2929(w), 1654(vs), 1626(s), 1592(s), 1515(s), 1454(m), 1360(m), 1341(w), 1262(w), 1145(w), 1103(w), 918(w), 874(m), 801(m), 705(m) $cm^{-1}$.

**Synthesis of Complex 2:** A solution of $H_3$anhz (0.25 mmol, 0.062 g) in DMF (15 mL) was added to a solution of diacetylacetone manganese (0.25 mmol, 0.064 g) in a mixture of MeOH/$CHCl_3$ (1:1; 20 mL), and the reaction mixture was then stirred for two hours. The red–brown clear solution obtained after filtration was left open to air to afford a kind of dark red column crystal after one day. Yield 0.08 g. M.p. >300 °C (dec.) $C_{102}H_{118}Mn_6N_{20}O_{30}$ (2433.88): calcd. C 50.29, H 4.85; found C 50.11, H 5.07. FTIR (KBr): 2924(w), 1652(vs), 1627(vs), 1594(s), 1518(vs), 1454(m), 1381(vs), 1337(s), 1264(m), 1229(m), 800(m), 751(m), 659(m) $cm^{-1}$.

**X-ray Crystallography:** Data was collected with a Bruker SMART 1000 CCD diffractometer with the use of Mo-$K_\alpha$ radiation. Empirical absorption corrections were applied following the procedure of Sadabs.[30] The structures were solved by direct method and expanded with the use of difference Fourier techniques with the SHELXL-97 program[31] and refined anisotropically for all nonhydrogen atoms by full-matrix least-squares calculations on $F^2$ with the use of the SHELXTL program package. Hydrogen atoms were placed geometrically and with $U_{iso}$ constrained to be 1.2 (1.5 for methyl groups and hydroxy) times $U_{eq}$ of the carrier atom. CCDC-279967 and -282855 contain the supplementary crystallographic data for this paper. These data can be obtained free of charge from The Cambridge Crystallographic Data Centre via www.ccdc.cam.ac.uk/data_request/cif.

## Acknowledgments

This work was financially supported by the National Natural Science Foundation of China (20671048).

[1] V. L. Pecoraro, *Inorg. Chim. Acta* **1989**, 171–176.
[2] V. L. Pecoraro, A. J. Stemmler, B. R. Gibney, J. J. Bodwin, H. Wang, J. W. Kampf, A. Barwinski, *Prog. Inorg. Chem.* **1997**, *45*, 83–177.
[3] R. W. Saalfrank, N. F. Hampel, H. D. Stachel, *Angew. Chem. Int. Ed. Engl.* **1996**, *35*, 2209–2210.
[4] A. D. Cutland, R. G. Malkani, J. W. Kampf, V. L. Pecoraro, *Angew. Chem. Int. Ed.* **2000**, *39*, 2689–2692.
[5] M. L. Lehaire, R. Scopelliti, H. Piotrowski, K. Severin, *Angew. Chem. Int. Ed.* **2002**, *41*, 1488–1508.
[6] S. X. Liu, S. B. Lin, Z. C. Lin, C. Lin, J. Q. Huang, *Angew. Chem. Int. Ed.* **2001**, *40*, 1084–1087.
[7] D. Gaynor, Z. A. Starikoca, S. Ostrovsky, W. Haase, K. B. Nolan, *Chem. Commun.* **2002**, 506–507.
[8] J. L. Bodwin, V. Pecoraro, *Inorg. Chem.* **2000**, *39*, 3434–3435.
[9] A. D. Noord, J. W. Kamlpf, V. L. Pecoraro, *Angew. Chem. Int. Ed.* **2002**, *41*, 4667–4670.
[10] a) J. A. Johnson, J. W. Kampf, V. L. Pecoraro, *Angew. Chem. Int. Ed.* **2003**, *42*, 546–549; b) M. S. Lah, V. L. Pecoraro, *Comments Inorg. Chem.* **1990**, *11*, 59–84.
[11] a) C. Dendrinou-Samara, G. Psomas, L. Iordanidis, V. Tangoulis, D. P. Kessissoglou, *Chem. Eur. J.* **2001**, *7*, 5041–5051; b) C. Dendrinou-Samara, L. Alevizopoulou, L. Iordanidis, E. Samaras, D. P. Kessissoglou, *J. Inorg. Biochem.* **2002**, *89*, 89–96.
[12] G. Psomas, C. Dendrinou-Samara, M. Alexiou, A. Tsohos, C. P. Raptopoulou, A. Terzis, D. P. Kessissoglou, *Inorg. Chem.* **1998**, *37*, 6556–6557.
[13] a) . A. J. Stemmler, A. Barwinski, M. J. Baldwin, V. Young, V. L. Pecoraro, *J. Am. Chem. Soc.* **1996**, *118*, 11962–11963; b) . M. Careri, F. Dallavalle, M. Tegoni, I. Zagnoni, *J. Inorg. Biochem.* **2003**, *93*, 174–180.
[14] M. S. Lah, M. L. Kirk, W. Hatfield, V. L. Pecoraro, *J. Chem. Soc., Chem. Commun.* **1989**, 1606–1608.
[15] A. D. Cutland, J. A. Halfen, J. W. Kampf, V. L. Pecoraro, *J. Am. Chem. Soc.* **2001**, *123*, 6211–6212.
[16] M. Tegoni, F. Dallavalle, B. Belosi, M. Remelli, *Dalton Trans.* **2004**, 1329–1333.
[17] B. R. Gibney, D. P. Kessissoglou, J. W. Kampf, V. L. Pecoraro, *Inorg. Chem.* **1994**, *33*, 4840–4849.
[18] C. Dendrnou-samara, C. M. Zaleski, A. Evagorou, J. W. Kampf, V. L. Pecoraro, D. P. Kessissoglou, *Chem. Commun.* **2003**, 2668–2669.
[19] M. Alexiou, C. Dendrinou-Samara, C. P. Raptopoulou, A. Terzis, D. P. Kessissoglou, *Inorg. Chem.* **2002**, *41*, 4732–4738.
[20] A. J. Stemmler, J. W. Kampf, V. L. Pecoraro, *Inorg. Chem.* **1995**, *34*, 2271–2272.
[21] J. L. Song, J. G. Mao, H. Y. Zeng, R. K. Kremer, Z. C. Dong, *Inorg. Chem. Commun.* **2003**, *6*, 891–895.
[22] B. Li, D. D. Han, G. Z. Cheng, Z. P. Ji, *Inorg. Chem. Commun.* **2005**, *8*, 216–218.
[23] S. Lin, S. X. Liu, J. Q. Huang, C. C. Lin, *J. Chem. Soc., Dalton Trans.* **2002**, 1595–1601.
[24] a) R. P. John, K. Lee, M. S. Lah, *Chem. Commun.* **2004**, 2660–2661; b) B. Kwak, H. Rhee, S. Park, M. S. Lah, *Inorg. Chem.* **1998**, *37*, 3599–3602; c) B. Kwak, H. Rhee, M. S. Lah, *Polyhedron* **2000**, *19*, 1985–1994; d) S. Lin, S. X. Liu, B. Z. Lin, *Chin. J. Inorg. Chem.* **2002**, *18*, 1205–1210; e) S. Lin, S. X. Liu, B. Z. Lin, *Inorg. Chim. Acta* **2002**, *328*, 69–73; f) J. Song, D. Moon, M. S. Lah, *Bull. Korean Chem. Soc.* **2002**, *23*, 708–714.
[25] S. Lin, S. X. Liu, Z. Chen, B. Z. Lin, S. Gao, *Inorg. Chem.* **2004**, *43*, 2222–2224.
[26] R. P. John, K. Lee, B. J. Kim, B. J. Suh, H. Rhee, M. S. Lah, *Inorg. Chem.* **2005**, *44*, 7109–7121.
[27] D. Moon, J. Song, B. J. Kin, B. J. Suh, M. S. Lah, *Inorg. Chem.* **2004**, *43*, 8230–8232.
[28] D. D. Han, G. Z. Cheng, Z. P. Ji, B. G. Zhang, *Wuhan Univ. J. Nat. Sci.* **2004**, *9*, 93–95.
[29] a) G. J. M. Fernandez, M. R. Patiño-Maya, R. A. Toscano, L. Velasco, M. Otero-López, M. Aguilar-Martinez, *Polyhedron*

 © 2006 Wiley-VCH Verlag GmbH & Co. KGaA, Weinheim 

**1997**, *16*, 4371–4378; b) . A. J. Bard, L. R. Faulkner, *Electrochemical Methods – Fundamentals and Applications*, John Wiley, New York, **1980**; c) K. A. Abboud, C. G. Ortiz, R. C. Palenik, G. J. Palenik, *Acta Crystallogr., Sect. C* **1997**, *53*, 1322–1323.
[30] G. M. Sheldrick, *SADABS. Program for Empirical Absorption Correction of Area Detector Data*, University of Göttingen, Germany, **1996**.
[31] G. M. Sheldrick, *SHELXL-97. Program for Crystal Structure Analysis*, University of Göttingen, Göttingen, Germany, **1997**.
[32] a) A. Caneschi, A. Cornia, S. J. Lippard, *Angew. Chem. Int. Ed. Engl.* **1995**, *34*, 467–469; b) K. A. Jensen, *Inorg. Chem.* **1970**, *9*, 1–5; c) H. N. Dogan, S. Rollas, H. Erdeniz, *Il Farmaco* **1998**, *53*, 462–467.

Received: June 18, 2006
Published Online: October 10, 2006

 © 2006 Wiley-VCH Verlag GmbH & Co. KGaA, Weinheim 

DOI: 10.1002/ejic.200600570

# Oxalato-Bridged Dinuclear Copper(II) Complexes of *N*-Alkylated Derivatives of 1,4,7-Triazacyclononane: Synthesis, X-ray Crystal Structures and Magnetic Properties

**Matthew J. Belousoff,[a] Bim Graham,[a][‡] Boujemaa Moubaraki,[a] Keith S. Murray,[a] and Leone Spiccia*[a]**

**Keywords:** Dinuclear copper(II) complexes / Oxalato bridges / *N*-Alkylated 1,4,7-triazacyclononane derivatives / X-ray structures / Antiferromagnetic coupling

The synthesis, X-ray crystal structure and magnetic properties of two oxalato-bridged dinuclear $Cu^{II}$ complexes, $[L\text{-}Cu(\mu\text{-}ox)Cu\text{-}L](ClO_4)_2$, where ox = oxalate and L = 1,4,7-trimethyl-1,4,7-triazacyclononane ($Me_3$tacn) or 1-benzyl-4,7-dimethyl-1,4,7-triazacyclononane ($BzMe_2$tacn) are reported, as well as the X-ray crystal structure of the mononuclear complex, $[Cu(Me_3tacn)(OH_2)_2](ClO_4)_2$, which features an extended H-bonding network between the ligand and the perchlorate counterions. The crystal structures of the dinuclear complexes both feature a centrosymmetric complex cation in which the two copper centres exist in a distorted square-pyramidal geometry, with each end capped by a facially coordinated "tacn" unit, and are bridged by an oxalate anion. Variable-temperature magnetic susceptibility measurements revealed strong antiferromagnetic interactions between the $Cu^{II}$ centres, with 2*J* values of ca. –300 $cm^{-1}$, even though the Cu···Cu separation is very long, viz. 5.18 Å ($BzMe_2$tacn) and 5.47 Å ($Me_3$tacn). The separation for the $Me_3$tacn complex is the longest separation reported for this type of $Cu^{II}$ complex. No pattern could be detected between the *J* values and structural features for 21 oxalato-bridged complexes.

(© Wiley-VCH Verlag GmbH & Co. KGaA, 69451 Weinheim, Germany, 2006)

## Introduction

The magnetic properties of copper(II) complexes have been an attractive area of research. This is due to the fact that copper(II) ($d^9$) has a single unpaired electron and therefore can be used as a model system for probing the nature of magnetic exchange interactions between single unpaired electrons on two or more metal centres, and, in particular, how this interaction is mediated by the ligands that bridge the metal centres.[1–3] Hydroxo-bridged metal complexes, in which the metal atoms are linked by single-atom bridges, have been most widely studied. The data that have been obtained have been used to develop empirical correlations of the strength of magnetic coupling with key structural descriptors of the Cu–OH–Cu bridging unit(s).[4–6] Further, theoretical analyses have been undertaken in an effort to develop a molecular orbital view of coupling in these complexes.[7,8]

Oxalato-bridged complexes have also been of interest[9–15] since, in this case, the $Cu^{II}$ centres are linked by multi-atom bridges, yet they can exhibit quite strong antiferromagnetic interactions even when the $Cu^{II}$ centres are separated by more than 5 Å.[2] Whilst most of these complexes exhibit antiferromagnetic coupling, the strength of this interaction can vary from very weak [2*J* value (exchange constant) close to 0 $cm^{-1}$] to very strong (2*J* value up to –400 $cm^{-1}$). The strength of the antiferromagnetic interaction has been proposed to be related to the "square of the overlap between the magnetic orbitals located on each copper(II)".[1] In the case of the oxalato-bridged copper(II) complexes it is the overlap of the $d_{x^2-y^2}$ and the σ-bonding orbitals on the oxygen atoms of the oxalato bridge that determines the strength of the interaction.

The ligand 1,4,7-triazacyclonone (tacn) is a particularly well-studied aza-macrocycle that uses three N-donor atoms to bind to the copper atom, forming highly stable complexes. Copper(II)–tacn complexes exhibit well-defined coordination polyhedra, consistently adopting either distorted octahedral or square-pyramidal geometries. The proposal by Kahn et al. that the extent of spin coupling in dinuclear complexes could be "tuned" by changing the $Cu^{II}$ coordination sphere that supports the oxalato bridge[1] led us to investigate the effect of geometric constraints introduced by the tacn macrocycle on the extent of magnetic interaction between the metal centres in oxalato-bridged dinuclear copper(II) complexes. Herein we report the synthesis, X-ray crystal structure and magnetic properties of two new oxalato-bridged copper(II) complexes of *N*-alkylated tacn

[a] School of Chemistry, Monash University, Victoria, 3800, Australia
Fax: +61-3-99054597
E-mail: leone.spiccia@sci.monash.edu.au
[‡] Current address: Department of Medicinal Chemistry, Victorian College of Pharmacy, Monash University, 381 Royal Parade, Parkville, Victoria, 3052, Australia

 © 2006 Wiley-VCH Verlag GmbH & Co. KGaA, Weinheim 

macrocycles ($Me_3$tacn = 1,4,7-trimethyl-1,4,7-triazacyclononane and $BzMe_2$tacn = 1-benzyl-4,7-dimethyl-1,4,7-triazacyclononane) and, for comparison, the X-ray crystal structure of $[Cu(Me_3tacn)(OH_2)_2](ClO_4)_2$ (**C1**).

## Results and Discussion

$[Cu_2(Me_3tacn)(\mu\text{-ox})](ClO_4)_2$ (**C2**) was prepared by treating the diaqua mononuclear precursor, $[Cu(Me_3tacn)(OH_2)_2](ClO_4)_2$ (**C1**),[16] with 1 equiv. of sodium oxalate (see Scheme 1). Careful concentration of the solution to dryness and recrystallisation from a mixture of methanol/ethanol (1:1) produced analytically pure blue crystals. The IR spectrum of **C2** reveals the characteristic stretching modes of the oxalato ligand at 1648 $cm^{-1}$ ($\upsilon_{asym}$) and 1467 $cm^{-1}$ ($\upsilon_{sym}$), which are typical for bridging oxalato ligands.[17] The solution UV/Vis spectrum shows the electronic d→d transitions expected for square-pyramidal copper(II) complexes at 1100 nm ($\varepsilon_{max}$ = 68 $M^{-1}cm^{-1}$) and 636 nm ($\varepsilon_{max}$ = 118 $M^{-1}cm^{-1}$).[18] Band maxima are also observed at 333 nm ($\varepsilon_{max}$ = 4160 $M^{-1}cm^{-1}$), 282 nm ($\varepsilon_{max}$ = 11100 $M^{-1}cm^{-1}$) and 195 nm ($\varepsilon_{max}$ = 11400 $M^{-1}cm^{-1}$), which could result from either charge transfer or ligand π→π* transitions.

The synthesis of $[Cu_2(BzMe_2tacn)(\mu\text{-ox})](ClO_4)_2$ (**C3**) involved first the formation of the precursor mononuclear copper(II) complex in an aqueous methanolic solution, which was then treated with sodium oxalate to yield the desired dinuclear complex as analytically pure blue crystals (see Scheme 1). The IR spectrum of **C3** again shows the expected stretching modes from the oxalato ligand at 1654 $cm^{-1}$ ($\upsilon_{asym}$) and 1466 $cm^{-1}$ ($\upsilon_{sym}$). The electronic spectrum exhibits two d→d transitions at 1090 nm ($\varepsilon_{max}$ = 67 $M^{-1}cm^{-1}$) and 644 nm ($\varepsilon_{max}$ = 110 $M^{-1}cm^{-1}$), which again suggests that the copper(II) centre exists in a square-pyramidal geometry in solution.[18] A strong band at 284 nm ($\varepsilon_{max}$ = 9100 $M^{-1}cm^{-1}$) could be an MLCT or a π→π* transition within the ligand.

### X-ray Crystal Structure Determinations

The X-ray crystal structure of **C1** reveals a mononuclear complex, in which the distorted octahedral copper(II) coordination sphere is occupied by three nitrogen donors from the $Me_3$tacn ligand, two oxygen atoms from ligated water and a distant oxygen atom from a perchlorate counteranion (see Figure 1). There is significant elongation in the axial direction of the coordination polyhedron, viz. the Cu(1)–N(1) bond is 0.19 Å longer than the Cu–N distances in the basal plane and for the weakly interacting perchlorate anion the Cu(1)–O(1) distance is 2.519(3) Å. All other bond lengths and angles are in the expected range for $(tacn)Cu^{II}$ complexes (see Table 1).

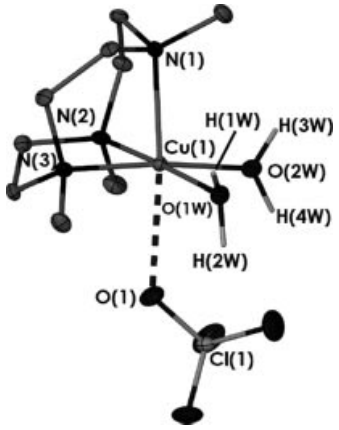


Figure 1. Thermal ellipsoid plot of **C1** (drawn at 50% probability). Dashed line indicates a weak interaction; some hydrogen atoms and a perchlorate anion have been omitted for clarity.

The hydrogen-bonding network formed by the hydrogen atoms from the coordinated water molecules and the perchlorate anions is particularly interesting. Each coordinated water molecule hydrogen-bonds to different perchlorate anions, which in turn hydrogen-bond to water molecules coordinated to different complexes (Table 2). This forms infinite two-dimensional layered sheets (see Figure 2).

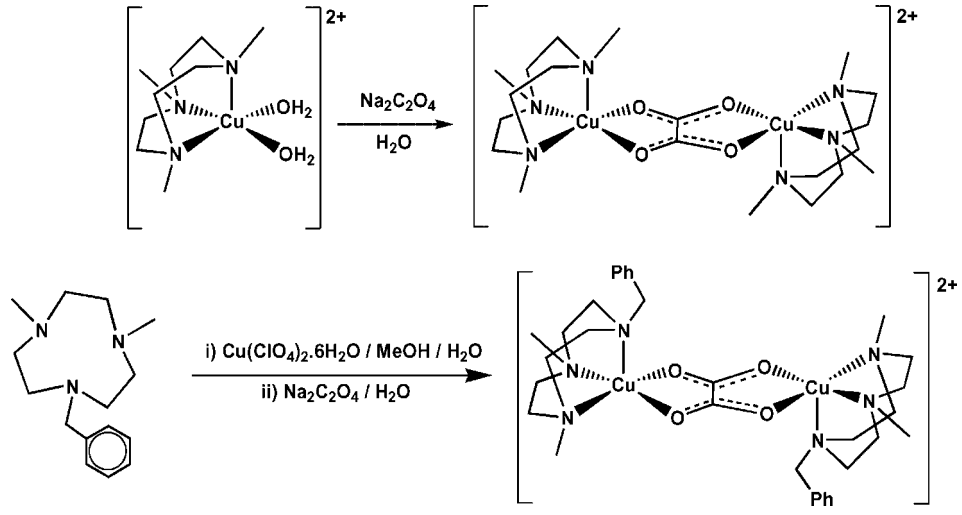


Scheme 1. Synthesis of oxalato-bridged copper(II) complexes.

 © 2006 Wiley-VCH Verlag GmbH & Co. KGaA, Weinheim 

Table 1. Selected bond lengths [Å] and angles [°] for **C1** (esd in parentheses).

| | | | |
|---|---|---|---|
| Cu(1)–O(1W) | 2.004(2) | O(1W)–Cu(1)–N(2) | 176.56(8) |
| Cu(1)–N(2) | 2.031(2) | O(1W)–Cu(1)–O(2W) | 85.98(8) |
| Cu(1)–O(2W) | 2.044(2) | N(2)–Cu(1)–O(2W) | 92.24(9) |
| Cu(1)–N(3) | 2.063(2) | O(1W)–Cu(1)–N(3) | 95.42(8) |
| Cu(1)–N(1) | 2.218(2) | N(2)–Cu(1)–N(3) | 86.02(8) |
| Cu(1)–O(1) | 2.519(3) | O(2W)–Cu(1)–N(3) | 173.53(8) |
| | | O(1W)–Cu(1)–N(1) | 98.24(8) |
| | | N(2)–Cu(1)–N(1) | 84.98(8) |
| | | O(2W)–Cu(1)–N(1) | 101.06(8) |
| | | N(3)–Cu(1)–N(1) | 85.01(8) |

Table 2. Hydrogen bonds for **C1** [Å and °] (esd in parentheses).

| D–H···A | *d*(D–H) | *d*(H···A) | *d*(D···A) | <(DHA) |
|---|---|---|---|---|
| O(2W)–H(3W)···O(6)[a] | 0.93(1) | 1.84(1) | 2.760(3) | 167(3) |
| O(1W)–H(1W)···O(7)[b] | 0.94(1) | 1.85(2) | 2.749(3) | 159(3) |
| O(2W)–H(4W)···O(2)[c] | 0.93(1) | 2.12(2) | 2.919(3) | 144(3) |
| O(2W)–H(4W)···O(4) | 0.93(1) | 2.50(3) | 3.108(3) | 123(3) |
| O(1W)–H(2W)···O(3)[d] | 0.93(1) | 1.97(3) | 2.729(3) | 137(4) |
| O(1W)–H(2W)···O(4) | 0.94(1) | 2.62(4) | 3.219(3) | 122(3) |

Symmetry transformations used to generate equivalent atoms: [a] $-x, -y + 1, -z + 1$. [b] $-x + 1, -y + 1, -z + 1$. [c] $-x, -y + 1, -z + 2$. [d] $-x + 1, -y + 1, -z + 2$.

The structure of **C2**, shown in Figure 3, reveals a dinuclear copper(II) complex featuring two capping $Me_3$tacn ligands and a bridging oxalato ligand that binds through all four of its oxygen atom. The complex is centrosymmetric, half existing in the asymmetric unit (ASU), with the other half generated by crystallographic symmetry. The metal centres at each end of the complex exist in a highly distorted geometry because of the geometric constraints introduced by the tacn macrocycle and the bridging oxalato ligand (see Table 3). The degree of distortion is highlighted by the three quite different Cu–N distances, which, in a five-coordinate complex, would be indicative of distortion away from square-pyramidal towards trigonal-bipyramidal geometry. An oxygen atom from a perchlorate anion is oriented in the direction of the vacant axial position of the copper(II) coordination polyhedron [Cu–O distance of 2.808(5) Å]. This distance is much longer than that in **C1**, probably because of the distortion of the coordination polyhedron beyond the usual tetragonal elongation. Whether the solid-state $Cu^{II}$ geometry is best described as distorted octahedral (6-coordinate) or distorted square-pyramidal (5-coordinate) is therefore debatable. With respect to the oxalato bridge, the two apical tacn nitrogen atoms in each dinuclear complex adopt a *trans* configuration. The two copper

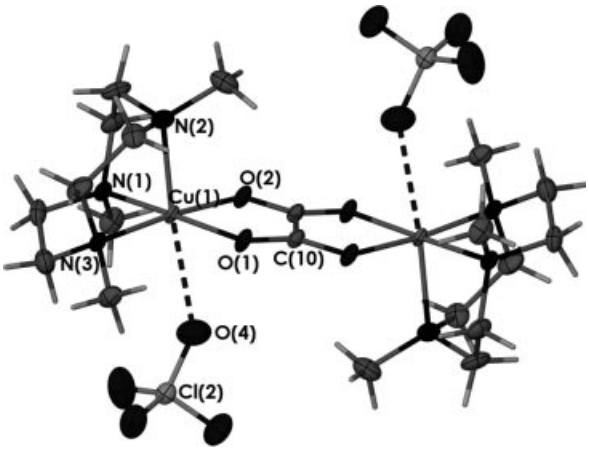


Figure 3. Thermal ellipsoid plot of **C2** (drawn at 50% probability). Dashed lines indicate a weak coordination bond.

Table 3. Selected bond lengths [Å] and angles [°] for **C2** (esd in parentheses).

| | | | |
|---|---|---|---|
| Cu(1)···Cu(1)[a] | 5.467(3) | O(1)–Cu(1)–N(1) | 175.7(1) |
| Cu(1)–O(1) | 2.026(2) | O(1)–Cu(1)–O(2) | 81.3(1) |
| Cu(1)–O(2) | 2.091(2) | N(1)–Cu(1)–O(2) | 95.4(1) |
| Cu(1)–N(1) | 2.052(3) | O(1)–Cu(1)–N(3) | 99.5(1) |
| Cu(1)–N(3) | 2.141(3) | N(1)–Cu(1)–N(3) | 83.4(1) |
| Cu(1)–N(2) | 2.248(3) | O(2)–Cu(1)–N(3) | 173.6(1) |
| Cu(1)–O(4) | 2.808(5) | O(1)–Cu(1)–N(2) | 96.9(1) |
| O(1)–C(10) | 1.316(4) | N(1)–Cu(1)–N(2) | 86.3(1) |
| O(2)–C(10)[a] | 1.289(4) | O(2)–Cu(1)–N(2) | 97.5(1) |
| C(10)–O(2)[a] | 1.289(4) | N(3)–Cu(1)–N(2) | 88.7(1) |
| C(10)–C(10)[a] | 1.554(6) | | |

Symmetry transformations used to generate equivalent atoms: [a] $-x + 1/2, -y + 1/2, -z$.

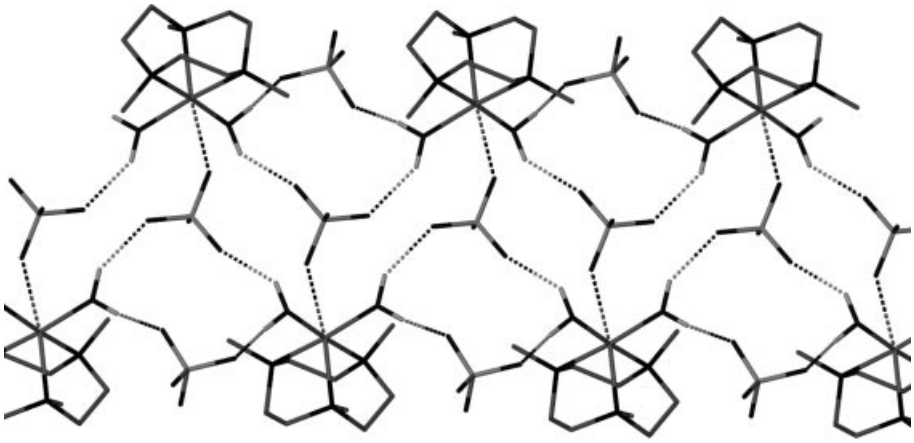

Figure 2. Infinite two-dimensional sheets formed by hydrogen-bonding interactions (dotted lines) in **C1**.

 © 2006 Wiley-VCH Verlag GmbH & Co. KGaA, Weinheim 

atoms are separated by 5.467(3) Å, and the Cu–O(ox) distances of 2.026(2) and 2.091(2) Å indicate that the two pairs of stronger and weaker binding oxygen atoms adopt a *trans* configuration.

A least-squares analysis of the plane of the oxalato ligand and the O(1)–Cu(1)–O(2) plane reveals that the $CuN_2O_2$ basal unit does not lie in the same plane as the oxalato ligand (see Figure 7). The dihedral angle created by the intersection of these two planes [$\varphi$ = 4.8(3)°] means that there is a "step" between the two coordination spheres, perhaps reducing the overlap of the $d_{x^2-y^2}$ and the σ-bonding orbitals on the oxalato ligand (vide infra).

This structure is broadly similar to that found for $[Cu_2(tacn)_2(\mu\text{-ox})](ClO_4)_2$ by Zhang et al.,[19] but there are significant differences in that the Cu–O distances in **C2** are slightly longer and give rise to a Cu···Cu separation that is 0.291 Å longer in **C2** than in the tacn counterpart. One reason for this could be that extensive H-bonding involving the secondary nitrogen atoms was found in the tacn complex, which cannot be formed by the alkylated ligand in **C2**.

The overall structure of **C3** is similar to that of **C2**, the main difference being that $BzMe_2$tacn ligands cap the ends of the complex instead of $Me_3$tacn (see Figure 4). The tertiary nitrogen atom with the benzyl pendant arm occupies an apical position and, as in **C2**, this Cu–N distance is longer (by 0.24 Å) than the two in the basal plane (see Table 4), and the two apical positions are oriented *trans* with respect to the oxalato bridge. The $\varphi$ angle (see Figure 7) in **C3** is much larger [12.2(1)°] and the two copper(II) centres are closer to each other [Cu–Cu distance 5.178(11) Å]. A further significant difference is that the oxalato ligand in **C3** binds much more strongly and the bridging unit is more symmetric, viz. all the Cu–O distances [1.9908(11) and 1.9982(11) Å] are identical, while in **C2**, these distances are quite different [2.026(2) and 2.091(2) Å]. In contrast to **C2**, the two Cu–N(tacn) distances in the equatorial plane are identical (av. 2.205 Å), while those in **C2** differ by 0.09 Å (Table 3). It may have been anticipated that the $BzMe_2$tacn ligand in **C3** would have been more likely to induce structural asymmetry. The more symmetric $Cu^{II}$ coordination sphere allows for a closer approach of the weakly interacting perchlorate counterion [Cu(1)–O(3) distance of 2.648(13) Å is a little shorter than the corresponding bond in **C2**].

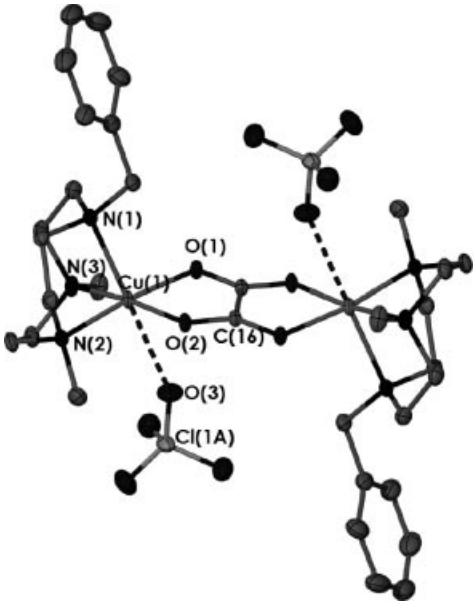


Figure 4. Thermal ellipsoid plot of **C3** (drawn at 50% probability, dashed lines indicate a weak interaction, hydrogen atoms omitted for clarity).

Table 4. Selected bond lengths [Å] and angles [°] for **C3** (esd in parentheses).

| | | | |
|---|---|---|---|
| Cu(1)···Cu(1)[a] | 5.178(1) | O(1)–Cu(1)–O(2) | 83.98(4) |
| Cu(1)–O(1) | 1.991(1) | O(1)–Cu(1)–N(2) | 173.65(5) |
| Cu(1)–O(2) | 1.998(1) | O(2)–Cu(1)–N(2) | 93.43(5) |
| Cu(1)–N(2) | 2.022(1) | O(1)–Cu(1)–N(3) | 95.75(5) |
| Cu(1)–N(3) | 2.028(1) | O(2)–Cu(1)–N(3) | 172.35(5) |
| Cu(1)–N(1) | 2.265(1) | N(2)–Cu(1)–N(3) | 86.05(5) |
| Cu(1)–O(3) | 2.648(1) | O(1)–Cu(1)–N(1) | 102.12(5) |
| O(2)–C(16) | 1.257(2) | O(2)–Cu(1)–N(1) | 102.38(5) |
| O(1)–C(16)[a] | 1.254(2) | N(2)–Cu(1)–N(1) | 84.09(5) |
| C(16)–O(1)[a] | 1.254(2) | N(3)–Cu(1)–N(1) | 85.17(5) |
| C(16)–C(16)[a] | 1.538(3) | | |

Symmetry transformations used to generate equivalent atoms: [a] $-x + 2, -y, -z + 1$.

## Magnetic Properties

Variable-temperature magnetic susceptibility studies were carried out on powdered samples of **C2** and **C3** to determine the nature and strength of the magnetic exchange interactions between the copper(II) centres in these oxalato-bridged dinuclear complexes. The measurements were performed in the 4.2–300 K temperature range with an applied field of 1 T. Plots of the magnetic moment vs. temperature for **C2** and **C3** are given in Figures 5 and 6, respectively.

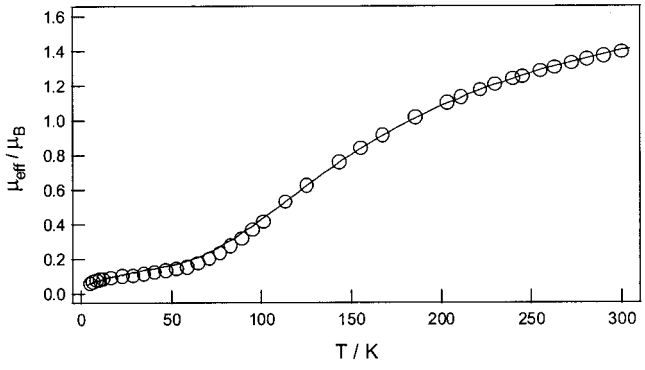


Figure 5. Plot of $\mu_{eff}$ (per Cu) vs. temperature for **C2**. The solid line is the best fit using the parameters: $g$ = 2.17, $Na$ = $60 \times 10^{-6}$ cm$^3$ mol$^{-1}$, $J$ = –159 cm$^{-1}$, monomer = 0.3%.

Figure 5 shows that the magnetic moment of **C2** decreases substantially from 1.43 $\mu_B$ (per Cu) at 300K to 0.08 $\mu_B$ at 4.2 K. This is indicative of a strong antiferromagnetic interaction between the $Cu^{II}$ centres. The data were modelled using a $-2J\bar{S}_1\cdot\bar{S}_2$ Bleaney–Bowers approach,[20] by fitting to the susceptibility Equation (1), where all the sym-

 © 2006 Wiley-VCH Verlag GmbH & Co. KGaA, Weinheim 

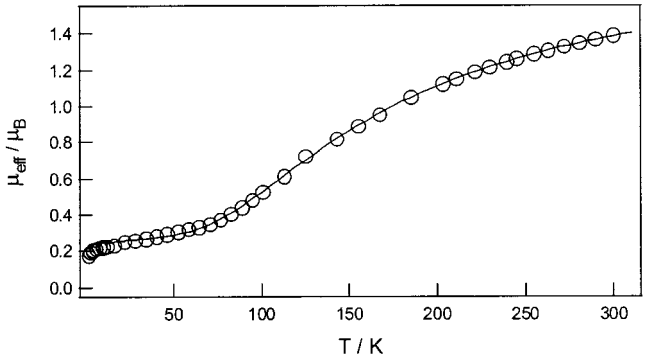


Figure 6. Plot of $\mu_{eff}$ (per Cu) vs. temperature for **C3**. The solid line is the best-fit using the parameters: $g$ = 2.03, $N\alpha$ = $60\times10^{-6}$ cm$^3$ mol$^{-1}$, $J$ = –147 cm$^{-1}$, monomer = 1.8%.

bols have their usual meaning. The best fit parameters for **C2** are $g$ = 2.17, $N\alpha$ (temperature independent paramagetism) = $60\times10^{-6}$ cm$^3$ mol$^{-1}$, $J$ = –159 cm$^{-1}$, with a monomer impurity of 0.3%.

$$\chi_M = \frac{Ng^2\beta^2}{kT}\left[\frac{2}{3+\exp\left(\frac{-2J}{kT}\right)}\right] + N\alpha \qquad (1)$$

For **C3**, the magnetic moment drops from 1.39 $\mu_B$ (per Cu) at 300 K to 0.21 $\mu_B$ at 4.2 K (Figure 6). This also indicates strong antiferromagnetic coupling. The data were fitted using the same approach as for **C2** to yield the best-fit parameters of $g$ = 2.03, $N\alpha$ = $60\times10^{-6}$ cm$^3$ mol$^{-1}$, $J$ = –147 cm$^{-1}$, monomer impurity of 1.8%.

### Magnetostructural Correlations

There has been much work aimed at determining how molecular structure influences the extent of magnetic interaction between metal centres with all types of bridging motifs.[1–5,9,10,12,13,15,19,21–25] Until recently, predictions of the extent of magnetic interactions in dinuclear copper(II) complexes have been largely based upon observations of how certain geometrical features influence magnetism. For example, Hoffmann et al.[26] determined that the coupling constant, $J$, for a d$^9$ metal complex is given by Equation (2), where $|\varepsilon_S - \varepsilon_A|^2$ is the splitting energy between the singly occupied molecular orbitals and $K_{ab}$, $J_{aa}$ and $J_{ab}$ are the two-electron integrals involving the localised orthogonal orbitals involved in the magnetic interaction.

$$2J = 2K_{ab} - \frac{|\varepsilon_S - \varepsilon_A|^2}{(J_{aa} - J_{ab})} \qquad (2)$$

Computational studies by Ruiz et al.[8,27] have led to the more general conclusion that the strength of antiferromagnetic coupling in oxalato-bridged dinuclear complexes is determined predominantly by two main geometrical factors: the out-of-plane displacement of the copper ion ($h_{Cu}$), and the dihedral angle between the plane of the oxalato ligand and the basal coordination plane ($\varphi$) (see Figure 7).

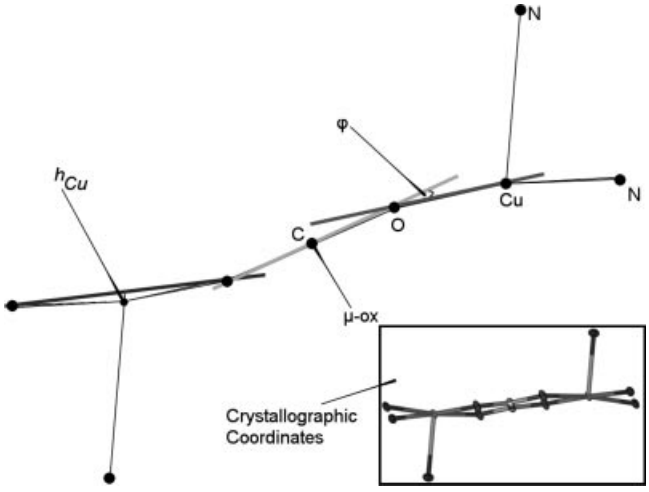


Figure 7. Representation of the core geometry of the complex cation structural motif showing the angle ($\varphi$) between the plane of the oxalato ligand and the O–Cu–O plane.

A compilation of structural and magnetic properties of related oxalato-bridged copper(II) complexes can be found in Table 5. Curiously, $[Cu_2(tacn)_2(\mu\text{-ox})](ClO_4)_2$, which has

Table 5. Selected magneto-structural parameters for oxalato-bridged Cu$^{II}$ complexes of the type $[(L)Cu(\mu\text{-ox})Cu(L)]X_2$.[a]

| L | X | $\varphi$ [°][b] | $h_{Cu}$ [Å][c] | $d_{Cu-Cu}$ [Å] | $2J$ [cm$^{-1}$] | Ref. |
|---|---|---|---|---|---|---|
| $Me_3$tacn | $ClO_4$ | 4.8(3) | 0.08 | 5.467(3) | –318 | this work |
| $BzMe_2$tacn | $ClO_4$ | 12.2(1) | 0.12 | 5.178(11) | –294 | this work |
| tacn | $ClO_4$ | 1.2/3.1 | 0.043/0.049 | 5.176 | –41 | [19] |
| phen | $NO_3$ | 16.9 | 0.27 | 5.158(1) | –330 | [28] |
| bdpm | $ClO_4$ | 2.2 | 0.3293 | 5.194 | –102 | [19] |
| bipy | $NO_3$ | 3.2 | 0.16 | 5.154(1) | –386 | [1] |
| bipy | $ClO_4$ | 12.0 | 0.18 | 5.150(1) | –376 | [12] |
| bipy | $BF_4$ | 10.4 | 0.16 | 5.144(1) | –378 | [12] |
| dpa | $NO_3$ | 7.2 | 0.08 | 5.22 | –305 | [24] |
| tmen | $ClO_4$ | 8.4 | 0.18 | 5.147/5.167 | –385.4 | [1] |
| deen | $ClO_4$ | 3.9 | n/r | n/r | –300 | [29] |
| mpz | $PF_6$ | 13.9 | 0.24 | n/r | –402 | [30] |
| mpz | $NO_3$ | 2.1 | 0.06 | n/r | –312 | [30] |
| mpz | $NO_3$ | n/r | 0.12 | 5.217 | –284 | [31] |
| dpp | $NO_3$ | 7.3 | 0.16 | 5.171(1) | –312 | [9] |
| bpz | Cl | 4.9 | 0.10/0.09 | 5.134(2) | –345 | [9] |
| $Pz_2CPh_2$ | Cl | 20.3 | 0.39 | 5.212 | –364 | [14] |
| $Pz_2CPh_2$ | $NO_3$ | 18.7 | 0.35 | 5.161 | –344 | [14] |
| $Pz_2CPh_2$ | $ClO_4$ | 2.6 | 0.26 | n/r | –424 | [14] |
| $Pz^{3m}{}_2CPh_2$ | $NO_3$ | 23.6 | 0.34 | 5.178 | –378 | [14] |

[a] Abbreviations: $Me_3$tacn = 1,4,7-trimethyl-1,4,7-triazacyclononane; $BzMe_2$tacn = 1-benzyl-4,7-dimethyl-1,4,7-triazacyclononae, tacn = 1,4,7-triazacyclononane; phen = 1,10-phenanthroline; bdpm = bis(3,5-dimethylpyrazol-1-yl)methane; bipy = 2,2′-bipyridine; dpa = 2,2′-dipyridylamine; tmen = *N*,*N*,*N*′,*N*′-tetramethylethylenediamine; deen = *N*,*N*-diethylethane-1,2-diamine; mpz = 4-methoxy-2-(5-methoxy-3-methylpyrazol-1-yl)-6-methylpyrimidine; dpp = 2,3-bis(2-pyridyl)pyrazine; bpz = 2,2′-bipyrazine; $Pz_2CPh_2$ = diphenyldipyrazolylmethane; $Pz^{3m}{}_2CPh_2$ = diphenylbis(3-methylpyrazolyl)methane; n/r = not reported. [b] Dihedral angle between the mean oxalato plane and the basal coordination plane. [c] Distance of the copper atom from the basal plane.

 © 2006 Wiley-VCH Verlag GmbH & Co. KGaA, Weinheim 

a very similar bridging motif to both **C2** and **C3**, exhibits relatively weak antiferromagnetic coupling.[19] Both **C2** and **C3**, which have similar $J$ values, have larger $\varphi$ and $h_{Cu}$ values than the parent tacn complex but this difference does not account for the large difference in the $J$ value. In $[Cu_2(tacn)_2(\mu\text{-ox})](ClO_4)_2$, quite strong hydrogen bonding exists between the secondary amine group of the tacn ligand and oxalato oxygen atoms [N–H···O = 2.138(3) Å] on adjacent dinuclear complex units. This could withdraw electron density from the σ-bonding orbitals of the oxalato bridge, hence weakening the strength of orbital overlap with the magnetic orbitals on the copper(II) centre.

The data in Table 5 also indicate that the strength of antiferromagnetic coupling in **C2** and **C3** is similar to that found in many of the other complexes. The strength of the antiferromagnetic coupling in **C2** is of interest as this complex features the longest Cu···Cu distance (by ca. 0.2 Å) reported so far for these types of complexes. However, as can be seen from the collected structural and coupling data, there seems to be no correlation between the extent of coupling and any particular set of geometric parameters. This is clearly highlighted by the fact that **C2** and **C3** have a similar $2J$ value, but have a 7° diffence in the $\varphi$ angle, and 0.04 Å difference in $h_{Cu}$.

## Conclusions

This work has shown that *N*-alkylation of the tacn macrocycle significantly increases the strength of antiferromagnetic coupling in oxalato-bridged dinuclear copper(II) complexes to the extent that in $[Cu_2(Me_3tacn)_2(\mu\text{-ox})](ClO_4)_2$ strong coupling has been observed over a Cu···Cu distance (5.46 Å) that is 0.2 Å longer than in any other related oxalato-bridged $Cu^{II}$ complex.

## Experimental Section

**Materials and Reagents:** All solvents and reagents used were of reagent or analytical grade and used as purchased. Distilled $H_2O$ was used throughout. $[Cu(Me_3tacn)(OH_2)_2](ClO_4)_2$ (**C1**) was prepared according to Fry et al.[16] 1-Benzyl-4,7-dimethyl-1,4,7-triazacyclononane was prepared according to a previously reported method.[6]

**Instrumentation:** UV/Vis spectra were recorded in acetonitrile using a Varian Cary 5G spectrophotometer. IR spectra were recorded using a Perkin–Elmer FTIR 1600 series spectrometer at 4.0 $cm^{-1}$ resolution, using KBr discs. CHN microanalyses were carried out by the Campbell Microanalytical Laboratory, University of Otago, New Zealand. Magnetic susceptibilities were measured on samples of ca. 20 mg in mass using a Quantum Design MPMS 5 Squid instrument. Diamagnetic corrections were made for the gelatine capsule sample holder and for ligands using Pascal's constants.

***Caution:*** Although no problems were encountered in this work, transition metal perchlorates are potentially explosive and should be prepared in small quantities and handled with care.

**Synthesis of $[Cu_2(Me_3tacn)(\mu\text{-ox})](ClO_4)_2$ (C2):** A solution of $Na_2C_2O_4$ (0.096 g, 0.70 mmol) in $H_2O$ (5 mL) was added to a solution of $[Cu(Me_3tacn)(OH_2)_2](ClO_4)_2$ (0.30 g, 0.64 mmol) in $H_2O$ (10 mL). The resulting solution was heated at reflux for 1 h. The solution was then concentrated to dryness and residues were dissolved in a hot solution of MeOH/EtOH (1:1). The resulting blue solution was then filtered while hot and the filtrate slowly cooled to yield deep-blue crystals that were suitable for X-ray crystallography. Yield: 0.21 g (86%). $C_{20}H_{42}Cl_2Cu_2N_6O_{12}$ (756.58): calcd. C 31.8, H 5.6, N 11.1; found C 32.0, H 5.6, N 11.1. IR (selected bands; KBr disk): $\tilde{\nu}$ = 2996 (w), 2965 (m), 2924 (s), 1648 (s), 1467 (s), 1352 (m), 1300 (m), 1145 (s), 1078 (br. s), 1015 (s), 1006 (s), 894 (m), 786 (m), 746 (w) $cm^{-1}$. UV/Vis (MeCN): $\lambda_{max}$ ($\varepsilon_{max}$) = 1100 (68), 636 (118), 333 (4160), 282 (11100), 195 (11400 $M^{-1}cm^{-1}$) nm.

**Synthesis of $[Cu_2(BzMe_2tacn)(\mu\text{-ox})](ClO_4)_2$ (C3):** 1-Benzyl-4,7-dimethyl-1,4,7-triazacyclononane (0.21 g, 0.85 mmol) was dissolved in MeOH/$H_2O$ (1:1) (10 mL) and a solution of $Cu(ClO_4)_2{\cdot}6H_2O$ (0.32 g, 0.87 mmol) in $H_2O$ (5 mL) was slowly added to this solu-

Table 6. Crystallographic data.

| | C1 | C2 | C3 |
|---|---|---|---|
| Empirical formula | $C_9H_{25}Cl_2CuN_3O_{10}$ | $C_{20}H_{42}Cl_2Cu_2N_6O_{12}$ | $C_{32}H_{50}Cl_2Cu_2N_6O_{12}$ |
| $M$ [g mol$^{-1}$] | 469.76 | 756.58 | 908.78 |
| Crystal system | monoclinic | monoclinic | monclinic |
| Space group | $P2_1/n$ | $C2/c$ | $P2_1/n$ |
| $a$ [Å] | 8.5463(17) | 25.593(5) | 7.7961(4) |
| $b$ [Å] | 13.713(3) | 7.7096(15) | 19.0662(9) |
| $c$ [Å] | 14.741(3) | 16.222(3) | 13.0878(7) |
| $\beta$ [°] | 91.08(3) | 93.13(3) | 99.742(3) |
| $V$ [Å$^3$] | 1727.2(6) | 3196.1(11) | 1917.31(17) |
| $Z$ | 4 | 4 | 2 |
| $T$ [K] | 123(2) | 123(2) | 123(2) |
| $\lambda$ [Å] | 0.71073 | 0.71073 | 0.71073 |
| $D_c$ [g cm$^{-3}$] | 1.806 | 1.572 | 1.574 |
| $\mu$ (Mo-$K_\alpha$) [mm$^{-1}$] | 1.630 | 1.562 | 1.317 |
| No. data measured | 20597 | 18296 | 29838 |
| Unique data ($R_{int}$) | 4109 (0.0792) | 3583 (0.0507) | 6884 (0.0264) |
| Observed data [$I > 2(\sigma)$I] | 3034 | 2899 | 5669 |
| Final $R_1$, $wR_2$ (obsd. data) | 0.0383,[a] 0.0739[b] | 0.0462,[a] 0.1075[b] | 0.0351,[a] 0.0889[b] |
| Final $R_1$, $wR_2$ (all data) | 0.0682, 0.0809 | 0.0628, 0.1158 | 0.0470, 0.0960 |
| $\rho_{min}$, $\rho_{max}$ [e Å$^{-3}$] | –0.604, 0.481 | –0.441, 1.111 | –0.869, 0.989 |

[a] $R = \Sigma(|F_o| - |F_c|)/\Sigma|F_o|$. [b] $R' = [\Sigma w(|F_o| - |F_c|)^2/\Sigma F_o^2]^{1/2}$, where $w = [\sigma^2(F_o)]^{-1}$.

 © 2006 Wiley-VCH Verlag GmbH & Co. KGaA, Weinheim 

tion. The resulting mixture was then stirred at room temperature for 1 h and filtered. A solution of $Na_2C_2O_4$ (0.11 g, 0.84 mmol) in $H_2O$ (5 mL) was added to the filtrate. The mixture was allowed to stand at room temperature and crystals suitable for X-ray diffraction crystallography grew directly from the solution. Yield 0.21 g (54%). $C_{32}H_{50}Cl_2Cu_2N_6O_{12}$ (908.78): calcd. C 42.3, H 5.6, N 9.3; found C 42.6, H 5.6, N 9.4. IR (selected bands; KBr disk): $\tilde{\nu}$ = 2936 (m), 2851 (m), 1654 (s), 1466 (m), 1355 (w), 1315 (w), 1087 (s), 997 (m), 898 (w), 782 (m), 727 (m), 701 (m), 637 (m), 623 (m), 490 (w) $cm^{-1}$. UV/Vis (MeCN): $\lambda_{max}$ ($\varepsilon_{max}$) = 1090 (67), 644 (110), 284 (9100 $M^{-1}cm^{-1}$) nm.

**X-ray Crystallography:** Intensity data for blue crystals of **C1** (0.15×0.15×0.11 mm), **C2** (0.3×0.1×0.1 mm) and **C3** (0.30×0.10×0.09 mm) were measured at 123 K with a Nonius Kappa CCD (Bruker Kappa Apex II for **C3**) fitted with graphite-monochromated Mo-$K_\alpha$ radiation (0. 71073 Å). The data were collected to a maximum $2\theta$ value of 55° (60° for **C3**) and processed using the Bruker–Nonius software. Crystal parameters and details of the data are summarised in Table 6. The structures were solved by direct methods and expanded using standard Fourier routines in the SHELX-97 software package.[32,33] All hydrogen atoms were placed in idealised positions and all non-hydrogen atoms were refined anisotropically. The water hydrogen atoms in **C1** were located on the Fourier difference map but restraints were placed upon them during refinement. The perchlorate anion in **C3** is disordered over two distinct positions, and the chlorine atoms as well as two of the perchlorate oxygen atoms had their site occupancy refined against each other. CCDC-605826 (for **C1**), -605827 (for **C2**) and -605828 (for **C3**) contain the supplementary crystallographic data for this paper. These data can be obtained free of charge from The Cambridge Crystallographic Data Centre via www.ccdc.cam.ac.uk/data_request/cif.


[1] M. Julve, M. Verdaguer, O. Kahn, A. Gleizes, M. Philoche-Levisalles, *Inorg. Chem.* **1983**, *22*, 368.
[2] O. Kahn, *Inorg. Chim. Acta* **1982**, *62*, 3.
[3] O. Kahn, J. Galy, Y. Journaux, J. Jaud, I. Morgenstern-Badarau, *J. Am. Chem. Soc.* **1982**, *104*, 2165.
[4] M. F. Charlot, S. Jeannin, O. Kahn, J. Lucrece-Abaul, *Inorg. Chem.* **1979**, *18*, 1675.
[5] V. H. Crawford, H. W. Richardson, J. R. Wasson, D. J. Hodgson, W. E. Hatfield, *Inorg. Chem.* **1976**, *15*, 2107.
[6] M. J. Belousoff, M. B. Duriska, B. Graham, S. R. Batten, B. Moubaraki, K. S. Murray, L. Spiccia, *Inorg. Chem.* **2006**,*45*, 3746.
[7] H. Hu, Y. Liu, D. Zhang, C. Liu, *Theochem* **2001**, *546*, 73.
[8] E. Ruiz, P. Alemany, S. Alvarez, J. Cano, *J. Am. Chem. Soc.* **1997**, *119*, 1297.
[9] J. Carranza, H. Grove, J. Sletten, F. Lloret, M. Julve, P. E. Kruger, C. Eller, D. P. Rillema, *Eur. J. Inorg. Chem.* **2004**, 4836.
[10] O. Castillo, I. Muga, A. Luque, J. M. Gutierrez-Zorrilla, J. Sertucha, P. Vitoria, P. Roman, *Polyhedron* **1999**, *18*, 1235.
[11] T. R. Felthouse, E. J. Laskowski, D. N. Hendrickson, *Inorg. Chem.* **1977**, *16*, 1077.
[12] A. Gleizes, M. Julve, M. Verdaguer, J. A. Real, J. Faus, X. Solons, *J. Chem. Soc., Dalton Trans.* **1992**, 3209.
[13] P. Gomez-Saiz, J. Garcia-Tojal, M. Maestro, J. Mahia, L. Lezama, T. Rojo, *Eur. J. Inorg. Chem.* **2003**, 2123.
[14] J. L. Shaw, G. T. Yee, G. Wang, D. E. Benson, C. Gokdemir, C. J. Ziegler, *Inorg. Chem.* **2005**, *44*, 5060.
[15] Z. Smekal, J. Kamenicek, P. Klasova, G. Wrzeszcz, Z. Sindelar, P. Kopel, Z. Zak, *Polyhedron* **2002**, *21*, 1203.
[16] F. Fry, A. J. Fischmann, M. J. Belousoff, L. Spiccia, J. Brugger, *Inorg. Chem.* **2005**, *44*, 941.
[17] K. Nakamoto, *Infrared and Raman Spectra of Inorganic and Coordination Compounds*, 4th ed., John Wiley & Sons, New York, **1986**.
[18] F. A. Cotton, G. Wilkinson, C. A. Murillo, M. Bochmann, *Advanced Inorganic Chemistry*, 6th ed., Wiley-Interscience, New York, **1999**.
[19] L. Zhang, B. Wei-Ming, S.-P. Yan, Z.-H. Jiang, D.-Z. Liao, G.-L. Wang, *Polyhedron* **2000**, *19*, 1105.
[20] B. Bleaney, K. D. Bowers, *Proc. R. Soc. London, Ser. A* **1952**, *214*, 451.
[21] Y.-M. Lee, H.-C. Jung, S.-N. Choi, N. H. Hur, *J. Kor. Chem. Soc.* **2000**, *44*, 166.
[22] W.-G. Lu, Y.-F. Pan, C.-H. Peng, *Wuji Huaxue Xuebao* **2005**, *21*, 709.
[23] P. S. Mukherjee, T. K. Maji, S. Koner, G. Rosair, N. R. Chaudhuri, *Ind. J. Chem. Sect. A* **2001**, *40A*, 451.
[24] S. Youngme, N. Chaichit, P. Gunnasoot, P. Kongsaeree, I. Mutikainen, O. Roubeau, J. Reedijk, U. Turpeinen, *Inorg. Chim. Acta* **2003**, *353*, 119.
[25] S. Youngme, P. Gunnasoot, N. Chaichit, C. Pakawatchai, *Transition Met. Chem.* **2004**, *29*, 840.
[26] P. J. Hay, J. C. Thibeault, R. Hoffmann, *J. Am. Chem. Soc.* **1975**, *97*, 4884.
[27] J. Cano, P. Alemany, S. Alvarez, M. Verdaguer, E. Ruiz, *Chem. Eur. J.* **1998**, *4*, 476.
[28] A. Bencini, A. C. Fabretti, C. Zanchini, P. Zanini, *Inorg. Chem.* **1987**, *26*, 1445.
[29] R. Vincente, J. Escuer, J. Ferretjans, H. Stoecklis-Evans, X. Solons, M. Font-Bardia, *J. Chem. Soc., Dalton Trans.* **1997**, 167.
[30] L. Soto, J. Garcia, E. Escriva, J. P. Legros, J. P. Tuchagues, F. Dahan, A. Fuertes, *Inorg. Chem.* **1989**, *28*, 3378.
[31] L. S. Tuero, J. Garcia-Lozano, E. E. Molto, M. B. Borja, F. Dahan, J. P. Tuchagues, J. P. Legros, *J. Chem. Soc., Dalton Trans.* **1991**, 2619.
[32] G. M. Sheldrick, *SHELXL-97*, University of Göttingen, Germany, **1997**.
[33] G. M. Sheldrick, *SHELXS-97*, University of Göttingen, Germany, **1997**.


Received: June 19, 2006
Published Online: October 13, 2006

 © 2006 Wiley-VCH Verlag GmbH & Co. KGaA, Weinheim 

DOI: 10.1002/ejic.200600594

# Intramolecular Apical C–H···M Interactions in Square-Planar Nickel(II) Complexes with Dianionic Tridentate Ligands and 2-Phenylimidazole

**Abhik Mukhopadhyay[a] and Samudranil Pal*[a]**

**Keywords:** Nickel(II) complexes / Square-planar complexes / Apical C–H···Ni interactions / X-ray structures / Theoretical calculations

Two square-planar ternary nickel(II) complexes [Ni(bhac)(phim)] (**1**) and [Ni(ahac)(phim)] (**2**) with O,N,O-donor Schiff bases [acetylacetone benzoylhydrazone ($H_2$bhac) and acetylacetone acetylhydrazone ($H_2$ahac)] and $sp^2$ N-donor 2-phenylimidazole (phim) as the ancillary ligand have been synthesised and characterised by analytical, spectroscopic, magnetic and electrochemical methods. The solid-state structures of both complexes have been determined by X-ray crystallography. The asymmetric unit of **1** contains a single complex molecule while that of **2** contains four complex molecules with different conformations. The molecular structures of both complexes reveal that one of the two *ortho* C–H groups of the pendant phenyl ring of the phim ligand is very close to the metal centre at the apical site indicating the presence of an intramolecular C–H···Ni interaction. In the structures of **1** and **2**, the shape of the C–H···Ni interaction is determined by the twisting of the phim ligand and the extent of orthogonality between the planes containing the chelate rings formed by the tridentate ligand and the imidazole ring. A survey of the reported X-ray structures of similar $d^8$ metal ion complexes containing intramolecular C–H···M interactions has been performed for comparison with the structural features of **1** and **2**. The optimised molecular structures of **1** and **2** generated by calculations based on the density functional method are compared with the experimental structures. Calculations also reveal that the four molecules present in the asymmetric unit of **2** are very close in energy. Theoretical studies and the down-field shift of the proton resonance on cooling in the NMR spectra suggest three-centre four-electron hydrogen-bond character of the observed apical C–H···Ni interaction in **1** and **2**.

(© Wiley-VCH Verlag GmbH & Co. KGaA, 69451 Weinheim, Germany, 2006)

## Introduction

The long standing interest in the interaction of transition metal ions with proximate C–H fragments is primarily due to the C–H activation processes involved in many catalytic reactions. Such interactions have been scrutinised intensively for a better understanding of their structural and bonding features.[1–12] The C–H···M interaction in coordinatively unsaturated and electron-deficient (16-electron) species is called an agostic interaction or agostic bond where the filled C–H σ orbital interacts with an empty metal orbital. In these agostic interactions, generally the C–H fragment is side-on to the metal ion. This T-shape of the agostic C–H···M interaction facilitates the involvement of the filled metal dπ orbital and the empty C–H σ* orbital in back bonding. However, the nature of the apical C–H···M interactions in square-planar 16-electron complexes of $d^8$ metal ions is not very clear.[9–12] In such species, these interactions can be agostic bond (three-centre two-electron) as well as non-classical hydrogen bond (three-centre four-electron) in character because of the availability of the empty orbital as well as the lone pair of electrons on the metal ion. Such apical C–H···M interactions in square-planar $d^8$ systems have been described as weakly agostic bonds, nonclassical hydrogen bonds and also as repulsive because of the filled metal $d_{z^2}$ and C–H σ-orbitals.[2,12–14] Compared with the agostic interaction the nonclassical hydrogen bond is not common in metal complexes. For a metal centre to participate as the proton acceptor in a hydrogen bond, it is essential for it to be electron rich. Examples of such complexes occur mostly with $d^8$ and $d^{10}$ metal centres. It has been demonstrated that such hydrogen bonds can facilitate the oxidative addition of H–X to a metal centre.[15]

Herein we report two square-planar nickel(II) complexes with the tridentate Schiff bases $H_2$bhac and $H_2$ahac and the monodentate 2-phenylimidazole as the ancillary ligand. The deprotonated Schiff bases ($bhac^{2-}$ and $ahac^{2-}$) satisfy the +2 charge on the metal ion and three coordination sites. The $sp^2$ N atom of the neutral 2-phenylimidazole (phim) occupies the fourth coordination site and completes the $N_2O_2$ square plane around the metal ion. The ancillary ligand 2-phenylimidazole has been specifically chosen so that one of the two *ortho* C–H groups of the phenyl ring can be in close proximity with the metal ion at the apical site. The complexes, [Ni(bhac)(phim)] (**1**) and [Ni(ahac)(phim)] (**2**),

[a] School of Chemistry, University of Hyderabad, Hyderabad 500 046, India
Fax: +91-40-2301-2460
E-mail: spsc@uohyd.ernet.in

Supporting information for this article is available on the WWW under http://www.eurjic.org or from the author.

 © 2006 Wiley-VCH Verlag GmbH & Co. KGaA, Weinheim 

have been characterised by analytical, magnetic, spectroscopic and electrochemical measurements. The X-ray structures of **1** and **2** indeed reveal the presence of an apical C–H···M interaction in both complex molecules. We have examined the reported structures of the square-planar $d^8$ systems with similar intramolecular C–H···M interactions available in the Cambridge Structural Database for a comparison with the structural features of **1** and **2**. Calculations based on density functional methods have been performed to understand the molecular conformations and the nature of the C–H···Ni interaction observed in the X-ray structures of **1** and **2**. Variable temperature NMR spectroscopic measurements have been carried out to probe the nature of this interaction in solution.

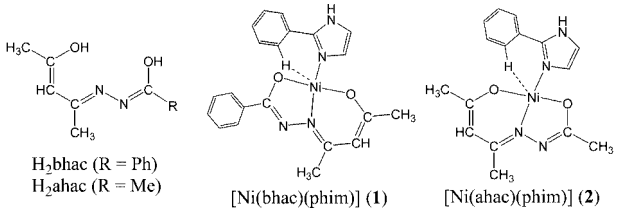


## Results and Discussion

### Synthesis and Some Properties

The reactions of 1 equiv. each of $Ni(O_2CCH_3)_2{\cdot}4H_2O$, the Schiff bases ($H_2$bhac and $H_2$ahac) and 2-phenylimidazole in boiling methanol afford the dark brown complexes in moderate to good yields. Elemental analysis data are consistent with the molecular formula [Ni(bhac)(phim)] (**1**) and [Ni(ahac)(phim)] (**2**). Both **1** and **2** are electrically nonconducting in methanol solutions. The complexes are diamagnetic and NMR spectroscopically active. Thus in each complex, the nickel ion is in the +2 oxidation state and the coordination geometry around the metal centre is square planar.

The infrared spectra of **1** and **2** do not display any band assignable to the amide or secondary amine N–H stretch.[16] Several sharp weak bands observed in the range 2900–3150 $cm^{-1}$ are likely to be due to the C–H stretches. The absence of any band for the N–H group of the ancillary ligand phim is consistent with its involvement in strong intermolecular hydrogen bonding (vide infra). Free $H_2$bhac and $H_2$ahac display the amide C=O stretch[17] near ≈1675 $cm^{-1}$. The absence of any such band in the spectra of **1** and **2** indicates complete deprotonation of the Schiff bases in the complexes. Thus in both complexes, the dianionic tridentate ligands ($bhac^{2-}$ and $ahac^{2-}$) act as the enolate-O, the imine-N and the deprotonated amide-O donor. A strong band observed near 1590 $cm^{-1}$ might involve the C=N stretches.[18,19]

The electronic spectra were collected using methanol solutions of the complexes. Both complexes display several absorptions. For **1** the absorption bands are in the range 565–234 nm and those for **2** are within 425–235 nm. The density functional calculations show that in both **1** and **2** the lowest unoccupied molecular orbital (LUMO) is primarily localised on the ancillary ligand phim and the highest occupied molecular orbital (HOMO) is composed of d and p orbitals of the metal and coordinated O atoms, respectively. The spectra of the free Schiff bases and 2-phenylimidazole in methanol solutions display a single absorption in the range 250–215 nm. Thus the absorptions observed for **1** and **2** are possibly due to the metal-to-ligand and inter- or intra-ligand charge-transfer transitions.

Electron transfer properties of **1** and **2** have been investigated by cyclic voltammetry using acetonitrile solutions of the complexes. Both **1** and **2** display an irreversible oxidation response at 0.69 and 0.71 V, respectively. The current height of this response is comparable with known one-electron redox processes under identical conditions.[19,20] No such response is observed for the deprotonated Schiff bases and 2-phenylimidazole under the same conditions. The iron(III) and copper(II) complexes with $bhac^{2-}$ show metal-centred oxidation responses in the potential range 0.4–0.8 V.[21–23] Therefore, the oxidation responses observed for **1** and **2** are assigned to a $Ni^{II} \rightarrow Ni^{III}$ process. The nature of the HOMO in both complexes also supports this assignment. The irreversible nature of the response suggests that in each case the corresponding oxidised species is unstable on the cyclic voltammetry time scale.

### Description of X-ray Structures and C–H···Ni Interactions

The molecular structures of **1** and **2** are depicted in Figure 1. Bond parameters associated with the metal ions are listed in Table 1. The asymmetric unit of **1** contains one complex molecule while that of **2** contains four complex molecules. In each molecule, the enolate-O, the imine-N and the deprotonated amide-O donor tridentate ligand and the imine-N donor monodentate phim form a $N_2O_2$ square plane around the metal centre. There is no deviation of the metal centre from the $N_2O_2$ square plane. The Ni–O(enolate), Ni–N(imine), Ni–O(amide) and Ni–N(imidazole) bond lengths are comparable with those observed in nickel-

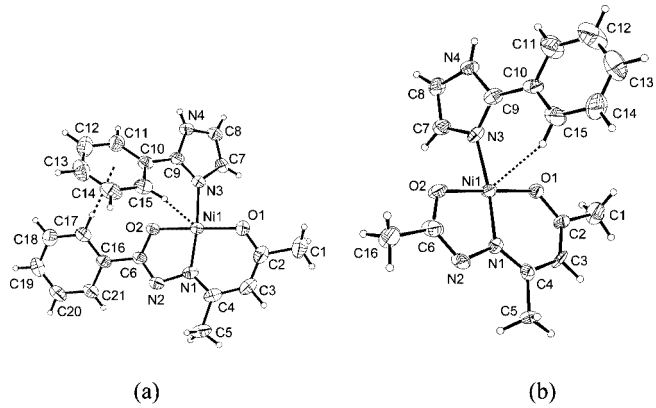


Figure 1. Molecular structures of (a) [Ni(bhac)(phim)] (**1**) and (b) [Ni(ahac)(phim)] (**2**) with the atom labelling scheme. All non-hydrogen atoms are represented by their 40% probability thermal ellipsoids.

 © 2006 Wiley-VCH Verlag GmbH & Co. KGaA, Weinheim 

(II) complexes having the same coordinating atoms.[24–26] The average N–C and C–O bond lengths in the –N=C(O⁻)– fragments[21–26] and the C–C and C–O bond lengths in the –C=C(O⁻)– fragments[21–24] are consistent with the enolate form of both amide and acetylacetone moieties of the tridentate ligands.

Table 1. Selected bond lengths [Å] and bond angles [°] for **1** and **2**.

| | [Ni(bhac)(phim)] (**1**) | | |
|---|---|---|---|
| Ni(1)–O(1) | 1.8195(17) | Ni(1)–O(2) | 1.8443(16) |
| Ni(1)–N(1) | 1.8269(18) | Ni(1)–N(3) | 1.9136(18) |
| O(1)–Ni(1)–O(2) | 175.76(7) | O(1)–Ni(1)–N(1) | 96.15(7) |
| O(1)–Ni(1)–N(3) | 89.07(7) | O(2)–Ni(1)–N(1) | 84.13(7) |
| O(2)–Ni(1)–N(3) | 91.08(7) | N(1)–Ni(1)–N(3) | 172.37(8) |
| | [Ni(ahac)(phim)] (**2**) | | |
| Molecule 1 | | | |
| Ni(1)–O(1) | 1.829(5) | Ni(1)–O(2) | 1.851(5) |
| Ni(1)–N(1) | 1.826(6) | Ni(1)–N(3) | 1.923(6) |
| O(1)–Ni(1)–O(2) | 178.3(2) | O(1)–Ni(1)–N(1) | 95.6(3) |
| O(1)–Ni(1)–N(3) | 91.4(2) | O(2)–Ni(1)–N(1) | 84.0(2) |
| O(2)–Ni(1)–N(3) | 89.0(2) | N(1)–Ni(1)–N(3) | 173.0(3) |
| Molecule 2 | | | |
| Ni(2)–O(3) | 1.818(5) | Ni(2)–O(4) | 1.852(5) |
| Ni(2)–N(5) | 1.821(7) | Ni(2)–N(7) | 1.909(6) |
| O(3)–Ni(2)–O(4) | 177.8(2) | O(3)–Ni(2)–N(5) | 96.0(3) |
| O(3)–Ni(2)–N(7) | 90.3(3) | O(4)–Ni(2)–N(5) | 83.8(3) |
| O(4)–Ni(2)–N(7) | 89.8(3) | N(5)–Ni(2)–N(7) | 173.6(3) |
| Molecule 3 | | | |
| Ni(3)–O(5) | 1.820(5) | Ni(3)–O(6) | 1.855(5) |
| Ni(3)–N(9) | 1.820(6) | Ni(3)–N(11) | 1.918(6) |
| O(5)–Ni(3)–O(6) | 178.3(3) | O(5)–Ni(3)–N(9) | 95.6(3) |
| O(5)–Ni(3)–N(11) | 89.4(3) | O(6)–Ni(3)–N(9) | 84.3(3) |
| O(6)–Ni(3)–N(11) | 90.5(3) | N(9)–Ni(3)–N(11) | 174.2(3) |
| Molecule 4 | | | |
| Ni(4)–O(7) | 1.832(6) | Ni(4)–O(8) | 1.853(5) |
| Ni(4)–N(13) | 1.838(6) | Ni(4)–N(15) | 1.928(7) |
| O(7)–Ni(4)–O(8) | 179.6(3) | O(7)–Ni(4)–N(13) | 96.0(3) |
| O(7)–Ni(4)–N(15) | 89.4(3) | O(8)–Ni(4)–N(13) | 83.7(3) |
| O(8)–Ni(4)–N(15) | 91.0(3) | N(13)–Ni(4)–N(15) | 173.5(3) |

In **1**, the tridentate ligand $bhac^{2-}$ is not planar because of the twisting of the phenyl ring plane along the C6–C16 bond (Figure 1). The dihedral angle between the phenyl ring plane and the plane constituted by the rest of the atoms in $bhac^{2-}$ is 25.56(8)°. It is also interesting to note that one of the two *ortho* C–H groups of the phenyl ring of $bhac^{2-}$ is involved in a C–H···π interaction with the phenyl ring of the ancillary ligand phim (Figure 1). The H···Cg distance and the C–H···Cg angle are 2.962 Å and 153°, respectively. Possibly this C–H···π interaction is primarily responsible for the twisting of the phenyl ring plane of $bhac^{2-}$ along the C6–C16 bond. The O1–Ni1–N3–C9 torsion angle ($\theta$) is 48.9° (Table 2). Thus the chelate forming fragment (O1,O2,N1,N2,C1–C6) of $bhac^{2-}$ and the metal coordinated imidazole ring plane are not orthogonal (Figure 1). The phim moiety is not planar because of the twisting of the imidazole ring plane and the phenyl ring plane along the C9–C10 bond (Figure 1). The extent of twisting ($\psi$) is measured by taking the average of the N3–C9–C10–C15 and N4–C9–C10–C11 torsion angles. The value of $\psi$ is calculated as 35.8°. As a result an *ortho* C–H group of the phim phenyl ring is close to the metal centre at the apical site (Figure 1). The Ni···H and Ni···C distances and the Ni···H–C angle are 2.79(2), 3.321(3) Å and 116.8(2)°, respectively (Table 2).

The bond lengths and bond angles of the four molecules present in the asymmetric unit of **2** are very similar (Table 1). However, the orthogonality ($\theta$) between the chelate forming fragment of $ahac^{2-}$ and the metal coordinated imidazole ring plane and the twisting of phim ($\psi$) differ significantly. The $\theta$ and $\psi$ values are in the ranges 72.9–91.6° and 1.6–21.6°, respectively (Table 2). Most importantly in two molecules the orientation of the phim phenyl ring with respect to the {Ni(ahac)} plane is on one side and in the other two molecules it is on the other side (Figure 2). As in **1**, one of the two *ortho* C–H groups of the phim phenyl ring is close to the metal centre at the apical site in each of the four molecules. The Ni···H and Ni···C distances and the C–H···Ni angles are within 2.42–2.69 Å, 3.20–3.36 Å, and 130.1–142.2°, respectively (Table 2).

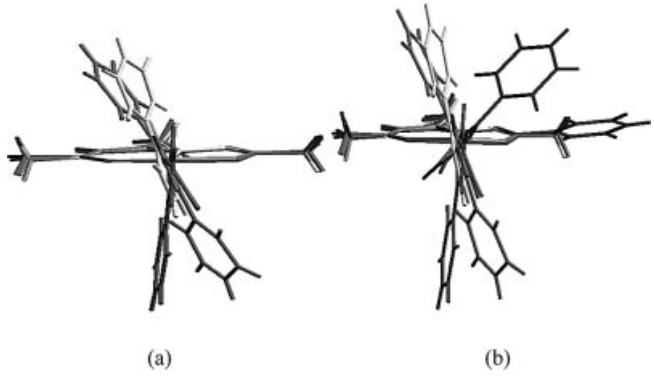


Figure 2. Overlay diagrams of (a) the four molecules present in the asymmetric unit of [Ni(ahac)(phim)] (**2**), and (b) the molecule of [Ni(bhac)(phim)] (**1**) and the four molecules of [Ni(ahac)(phim)] (**2**).

Table 2. Structural parameters related to C–H···Ni interactions and molecular conformations of **1** and **2**.

| Parameters | [Ni(bhac)(phim)] (**1**) | | [Ni(ahac)(phim)] (**2**) | | | | |
|---|---|---|---|---|---|---|---|
| | Experimental | Calculated | Experimental | | | | Calculated |
| | | | Molecule 1 | Molecule 2 | Molecule 3 | Molecule 4 | |
| Ni···H distance [Å] | 2.79(2) | 2.48 | 2.54 | 2.42 | 2.47 | 2.69 | 2.51 |
| Ni···C distance [Å] | 3.321(3) | 3.26 | 3.288(9) | 3.207(9) | 3.236(12) | 3.364(11) | 3.23 |
| C–H···Ni angle [°] | 116.8(2) | 125 | 137.7 | 142.2 | 139.3 | 130.1 | 127 |
| $\psi$[a] [°] | 35.8 | 28 | 12.9 | 1.6 | 11.3 | 21.6 | 27 |
| $\theta$[b] [°] | 48.9 | 56 | 73.1 | 91.6 | 76.4 | 72.9 | 58 |

[a] Average of N3–C9–C10–C15 and N4–C9–C10–C11 torsion angles. [b] O1–Ni–N3–C9 torsion angle.

 © 2006 Wiley-VCH Verlag GmbH & Co. KGaA, Weinheim 

The following trends are very clear from the above observations on the molecular structures of **1** and **2**. In **1**, only one complex molecule is present in the asymmetric unit and both the phenyl ring and the imidazole ring planes of phim are tilted toward the phenyl ring of the benzoyl fragment of $bhac^{2-}$ (Figure 1). In spite of being weak in nature we believe that the intramolecular C–H···π interaction plays a major role in restricting the phim moiety from taking random orientations and a single conformation of it is stabilized in **1**. Because of the replacement of the phenyl group of $bhac^{2-}$ by a methyl group in $ahac^{2-}$ the C–H···π interaction of the type observed in **1** is not possible in **2**. Complex **2** crystallises with four molecules in the asymmetric unit and the phim moieties are randomly oriented on both sides of the plane containing the {Ni(ahac)} moiety. Thus the lack of the C–H···π interaction facilitates free rotation of phim about the Ni–N(imidazole) bond. In addition, the imidazole plane in **2** is closer to the orthogonal arrangement with the plane containing the two chelate rings ($\theta$ = 72.9–91.6°) compared with that in **1** ($\theta$ = 48.9°). This difference is also likely to be because of the C–H···π interaction in **1**. The internal twisting of phim in **1** ($\psi$ = 35.8°) is significantly larger than that in **2** ($\psi$ = 1.6–21.6°). Possibly this difference is also partly due to the intramolecular C–H···π interaction in **1**. Despite the differences in the $\theta$ and $\psi$ values one of the two *ortho* C–H groups of the phim phenyl ring is near to the apical position of the metal ion in all the structures. In this context, it may be noted that the crystal structure of the protonated 2-phenylimidazole ($Hphim^{+}$) is known.[27] Here the $\psi$ value is 22.32°. Thus in all probability significantly different twisting of phim in **1** and **2** compared with that in $Hphim^{+}$ is due to the intramolecular C–H···π and C–H···Ni interactions observed in the present complex molecules.

A close scrutiny of the structural parameters (Table 2) related to the C–H···Ni interactions and the molecular conformations of **1** and **2** reveals the following. The longer the Ni···H distance the shorter the C–H···Ni angle. There is a satisfactory linear correlation between the Ni···H distance and the C–H···Ni angle (Figure S1, Supporting Information). The values of the Ni···H distances and the corresponding C–H···Ni angles strongly depend on the molecular conformations. In general, the Ni···H distance increases and the C–H···Ni angle decreases with the increase of the twisting ($\psi$) of phim and the decrease of the orthogonality ($\theta$) between the imidazole ring plane and the plane containing the two chelate forming fragments of the tridentate ligands (Table 2). The Ni···H distance is linearly related to the $\psi$ values as well as $\theta$ values with opposite slopes (Figure S1). Thus a large twist of the phim ligand forces a T-shape of the C–H···Ni interaction with an increase in the Ni···H distance, while a small twist of the phim ligand makes the C–H···Ni interaction more linear with a decrease in the Ni···H distance. It is clear from the above facts that the geometrical arrangement of the C–H···Ni interaction largely depends on the twist of the phim ligand in **1** and **2**. A detailed theoretical study reported previously has supported the idea that the axial M···H interactions in $d^8$ metal ion complexes are mainly repulsive in nature.[10] But a minor attractive contribution to the C–H···M interaction can not be ruled out in the present complexes. The Ni···H distances in both complexes and shorter Ni···H distances in **2** compared with that in **1**, unaided and unhindered by any geometrical constraint in the former, substantiate this idea.

### Intermolecular Hydrogen Bonds and Self-Assembly of 1 and 2

Both complex molecules contain the imidazole N–H group and metal coordinated O atoms, which are conventional hydrogen-bond donors and acceptors, respectively. In the crystal lattice, the molecules of each of the two complexes are involved in intermolecular N–H···O hydrogen bonding interactions involving the imidazole N–H groups and the metal coordinated amide O atoms of the tridentate ligands. In the case of **1**, the N···O distance and the N–H···O angle are 2.856(3) Å and 160(2)°, respectively. There are some variations in the geometrical parameters related to the N–H···O interactions for the four molecules present in the asymmetric unit of **2**. The N···O distances are in the range 2.788(8)–2.846(9) Å and the N–H···O angles are within 148–163°. In each case, self-assembly of the complex molecules through these intermolecular N–H···O hydrogen bonds leads to a one-dimensional supramolecular structure in the crystal lattice (Figure 3).

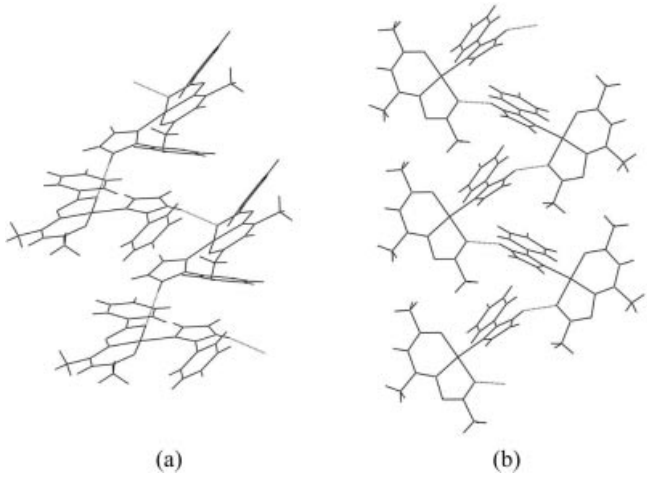


Figure 3. One-dimensional ordering of (a) [Ni(bhac)(phim)] (**1**) and (b) [Ni(ahac)(phim)] (**2**) through intermolecular N–H···O hydrogen bonds.

### Survey of the $d^8$ Metal Ion Complexes with Intramolecular C–H···M Interactions

The molecular structures of **1** and **2** show that the Ni···H distance, the C–H···Ni angle and hence the shape (T or linear) of the C–H···Ni interaction largely depend on the twisting ($\psi$) of 2-phenylimidazole (vide supra). The Ni···H distance is linearly related with $\psi$ and the C–H···Ni angle (Figure S1). To verify whether the trends observed for **1** and **2** are general or not we have performed a Cambridge Structural Database (version 5.26) search for $d^8$ metal ion com-

 © 2006 Wiley-VCH Verlag GmbH & Co. KGaA, Weinheim 

plexes having intramolecular C–H···M interactions. The search was based on the following criteria: (i) the metal ion is always coordinated to a N atom that is bonded to the atom X (elements of groups 14–16), (ii) X is connected to an unsubstituted/substituted phenyl ring by a single bond, (iii) the phenyl ring *ortho* C–H at the $\delta$ position is involved in the C–H···M interaction, (iv) the M···H separation is in the range 2.0–3.0 Å, (v) the $N_\alpha$–$X_\beta$–$C_\gamma$ angle is within 110–140°, (vi) the $N_\alpha$–$X_\beta$–$C_\gamma$–$C_\delta$ torsion angle ($\psi$) is in the range 0–180° and (vii) structures with *R* factors > 10 are excluded. The number of hits obtained was 44. Selected structural parameters of these 44 X-ray structures are listed in Table 3.

Table 3. Structural data for the intramolecular C–H···M interaction in $d^8$ metal ion complexes.

| Refcode | $M^{II}$ | M···H dist. [Å] | C–H···M angle [°] | $\psi$ [°] |
|---|---|---|---|---|
| COPGET | $Ni^{II}$ | 2.668 | 125.102 | 33.573 |
| DAWGUD | $Ni^{II}$ | 2.885 | 102.297 | 85.365 |
| ERURAK | $Ni^{II}$ | 2.885 | 94.712 | 87.400 |
| ERUREO | $Ni^{II}$ | 2.733 | 109.016 | 77.854 |
| FAKVIW | $Ni^{II}$ | 2.894 | 93.133 | 85.339 |
| GIGVEX10 | $Ni^{II}$ | 2.859 | 107.358 | 88.293 |
| IFAFIE | $Ni^{II}$ | 2.476 | 136.801 | 12.763 |
| KIYQUE | $Ni^{II}$ | 2.792 | 129.004 | 36.500 |
| KOHHAQ | $Ni^{II}$ | 2.810 | 128.477 | 55.681 |
| LOKZOA | $Ni^{II}$ | 2.919 | 101.781 | 88.010 |
| LUQJOW | $Ni^{II}$ | 2.833 | 90.816 | 86.319 |
| MIYQEQ | $Ni^{II}$ | 2.607, 2.972 | 123.717, 99.198 | 31.403, 31.403 |
| NOKVOY | $Ni^{II}$ | 2.663 | 105.555 | 77.495 |
| QOZROM | $Ni^{II}$ | 2.353 | 140.411 | 14.618 |
| RORHUB | $Ni^{II}$ | 2.869 | 90.055 | 86.797 |
| SENHIC | $Ni^{II}$ | 2.874 | 114.987 | 75.856 |
| SOSVAX | $Ni^{II}$ | 2.786 | 90.748 | 37.947 |
| SOSVAX10 | $Ni^{II}$ | 2.786 | 90.750 | 37.948 |
| TISPEQ | $Ni^{II}$ | 2.844 | 111.106 | 77.368 |
| TISPIU | $Ni^{II}$ | 2.967 | 108.425 | 82.605 |
| VETPEP | $Ni^{II}$ | 2.979 | 97.906 | 90.369 |
| BABDIS | $Pd^{II}$ | 2.703 | 119.125 | 73.137 |
| BECGEV | $Pd^{II}$ | 2.949 | 117.971 | 70.944 |
| CAPVOE | $Pd^{II}$ | 2.585, 2.732 | 125.092, 115.835 | 15.776, 1.934 |
| DAGGUN | $Pd^{II}$ | 2.946 | 112.824 | 15.596 |
| DUHYUA | $Pd^{II}$ | 2.783 | 102.092 | 43.831 |
| DUNWAK | $Pd^{II}$ | 2.944 | 99.833 | 45.921 |
| EFODEI | $Pd^{II}$ | 2.884 | 107.519 | 31.598 |
| HAPNIV | $Pd^{II}$ | 2.926 | 115.268 | 16.080 |
| HOZNUF | $Pd^{II}$ | 2.880, 2.836 | 100.278, 96.338 | 85.396, 84.995 |
| JEDDIF | $Pd^{II}$ | 2.865 | 102.679 | 79.360 |
| KIMXOT | $Pd^{II}$ | 2.871 | 132.141 | 54.848 |
| LANBIL | $Pd^{II}$ | 2.968 | 108.260 | 79.553 |
| LIJHUH | $Pd^{II}$ | 2.946 | 106.715 | 88.674 |
| NINMAY | $Pd^{II}$ | 2.933, 2.744 | 119.920, 128.876 | 69.726, 62.872 |
| NOKGUP | $Pd^{II}$ | 2.823 | 108.391 | 57.224 |
| SUGWEW | $Pd^{II}$ | 2.596 | 133.835 | 54.013 |
| TURKIA | $Pd^{II}$ | 2.679 | 122.982 | 68.115 |
| UGIKOK | $Pd^{II}$ | 2.983, 2.953, 2.843 | 110.515, 114.306, 122.513 | 14.014, 10.811, 3.029 |
| XODPEL | $Pd^{II}$ | 2.815 | 107.154 | 48.564 |
| YIYHIX | $Pd^{II}$ | 2.833 | 117.149 | 72.866 |
| ZODQOY | $Pd^{II}$ | 2.868 | 101.858 | 86.739 |
| HAPZPT10 | $Pt^{II}$ | 2.966 | 90.958 | 68.292 |
| HIXJUT | $Pt^{II}$ | 2.854, 2.976 | 125.650, 131.625 | 12.480, 33.951 |

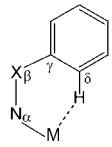


In the structures collected in Table 3, the mean M···H distance increases in the order $Ni^{II} < Pd^{II} < Pt^{II}$. These values are 2.795, 2.841 and 2.932 Å for $Ni^{II}$, $Pd^{II}$ and $Pt^{II}$, respectively. This order is expected as the van der Waals radius increases in the order $Ni^{II} < Pd^{II} < Pt^{II}$.[10] In contrast to the structures of **1** and **2**, there is no readily apparent relationship between the M···H distance and the $N_\alpha$–$X_\beta$–$C_\gamma$–$C_\delta$ torsion angle ($\psi$). However, the scattergram of $\psi$ against the M···H distance (Figure 4a) shows the prevailing trend of long M···H distances for large $\psi$ values. On the other hand, the M···H distance generally increases with the decrease of the C–H···M angle (Figure 4b) as observed for **1** and **2**. In other words, the C–H···M interaction becomes more T-shaped with the increase of the M···H distance.

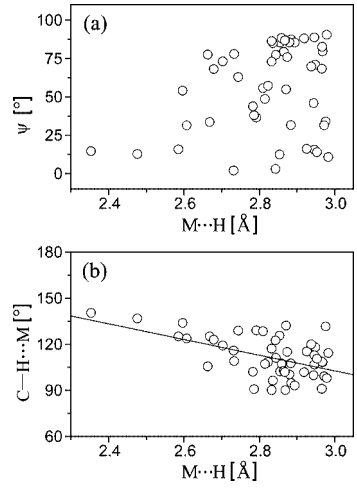


Figure 4. Scattergrams of (a) $\psi$ (see text for definition) vs. M···H distance and (b) C–H···M angle vs. M···H distance. The straight line in (b) represents the least-squares fit.

## Computational Results

Calculations based on density functional methods have been performed for structural optimisations of **1** and **2**. Each of the two complex molecules was computed as a complete system to consider all steric and electronic factors of the tridentate ligand ($bhac^{2-}$ or $ahac^{2-}$) and of the monodentate ancillary ligand 2-phenylimidazole (phim). In both cases, the atomic coordinates of the molecules obtained in the crystal structures were used as the starting points and references for geometry optimisation. The calculated structural parameters related to the C–H···Ni interaction and the molecular conformations are listed in Table 2.

 © 2006 Wiley-VCH Verlag GmbH & Co. KGaA, Weinheim 

In the case of **1**, the overall conformation of the molecule in the optimised structure is comparable with that found in the solid-state X-ray structure. With regard to the molecular conformation the only major difference between the optimised and the experimental structures is in the dihedral angle between the phenyl ring plane and the plane containing the rest of the atoms of the $bhac^{2-}$ ligand. In the optimised structure the whole tridentate ligand is essentially planar. It may be noted that the X-ray structure of **1** shows an intramolecular C–H···π interaction between the phenyl ring of $bhac^{2-}$ and that of phim (vide supra). It is very likely that this interaction is responsible for the nonplanarity of $bhac^{2-}$ in the experimental structure. For the present level of calculation we could not reproduce the C–H···π interaction in the optimised geometry. The calculated geometrical parameters indicate a more linear C–H···Ni interaction compared with that in the experimental structure (Table 2).

The same optimised molecular structure is obtained from the X-ray structural coordinates of the four molecules present in the asymmetric unit of **2**. The optimised molecule of **2** is very similar to that of **1** with regard to the Ni···H distance, C–H···Ni angle and $\psi$ and $\theta$ values (Table 2). However, this optimised structure is rather different when compared with the structures of the four molecules obtained in the X-ray structure of **2**. In general, the twisting of phim ($\psi$) is much less, the imidazole ring plane and the plane containing the two chelate rings are more orthogonal ($\theta$) and the Ni···H–C interaction is more linear in the experimental structures than those in the optimised structure (Table 2).

The dependence of the conformational energies of **1** and **2** on the twisting ($\psi$) of phim has been analysed by performing single point energy calculations by varying $\psi$ from 0 to 90°. The experimental structures of **1** and molecule 1 of **2** are used for these calculations. The relative energies ($\Delta E$) with respect to the lowest energy (at $\psi \approx 35°$ for **1** and $\psi \approx 15°$ for **2**) are plotted against the $\psi$ values (Figure 5). For **1** it is a symmetric well-like plot. On the other hand, for **2** below 20° the change in energy is very low compared with that above 20°. The energy increases by only 0.20 kcal mol$^{-1}$ due to the gradual decrease of $\psi$ from 20 to 0°. The small increase of energy indicates the absence of any significant steric or electronic constraint for the twisting of the phim in this range of $\psi$. For this reason, it is very likely that four molecules with $\psi$ values in the range 1.6–21.6° have been found in the asymmetric unit of **2**.

The nature of the C–H···Ni interaction in **1** and **2** has been examined by several computational methods. In a three-centre four-electron C–H···M interaction, the interacting hydrogen atom should have a more positive charge compared with the other hydrogen atoms that are away from the metal centre. The natural population analysis[28] shows that the charge on the *ortho*-hydrogen atom of the phim phenyl ring, which is at the apical site of the metal centre, is more positive (by +0.009e and +0.010e for **1** and **2**, respectively) compared with the charge on the other *ortho*-hydrogen atom of the same phenyl ring. The nickel(II) centre has an empty d orbital as well as a lone pair. Thus it can also accept electrons from the filled C–H σ orbital. The delocalisation energies for the C–H σ donation to the metal calculated through natural bond orbital analysis[28] are 0.58 and 0.63 kcal mol$^{-1}$ for **1** and **2**, respectively. These delocalisation energies are insignificant compared with those obtained for strong agostic interactions and are comparable with C–H···M hydrogen-bonding interactions.[29,30] The "atoms in molecules" theory[31] has also been used for further probing of the topological properties of the C–H···Ni interaction in **1** and **2**. The values obtained for the electron densities ($\rho_b$ = 0.011 and 0.012 a.u. for **1** and **2**, respectively) and the Laplacians ($\nabla^2\rho_b$ = 0.039 and 0.041 a.u. for **1** and **2**, respectively) at the bond critical points are well within the range reported for C–H···M interactions that are hydrogen bonds in character.[30,32–35]

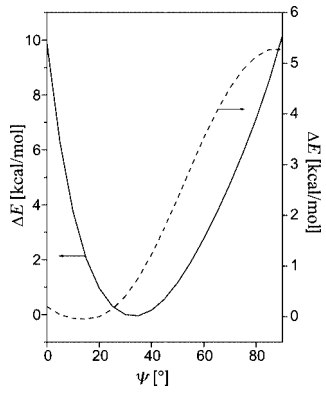


Figure 5. Relative energies of [Ni(bhac)(phim)] (**1**) (–) and [Ni(ahac)(phim)] (**2**) (----) as a function of twist angles ($\psi$) of 2-phenylimidazole (phim).

## Proton NMR Spectroscopic Studies

NMR spectroscopy is a useful tool for the diagnosis of the agostic or hydrogen-bond character of C–H···M interactions in square-planar $d^8$ metal ion complexes. The proton resonance shifts to an up-field position for agostic interactions while it shifts down-field for hydrogen-bond interactions compared with that of the free C–H group.[9,11,36] The room temperature proton NMR spectra were recorded using $(CD_3)_2CO$ solutions of **1** and **2**. The protons of the two methyl groups of the acetylacetone fragment in **1** appear as two singlets at $\delta$ = 1.47 and 2.20 ppm. The singlet observed at $\delta$ = 5.07 ppm is assigned to the –CH= group proton. The imidazole N-H proton resonates as a doublet at $\delta$ = 8.87 ppm ($J$ = 8 Hz). The multiplet observed in the range $\delta$ = 7.2–7.6 ppm is likely to be due to the imidazole ring C-H and aromatic protons. The absence of any cross-coupled peak in the 2D NMR spectrum of **1** indicates that the C–H···π interaction is probably absent in the solution state. In addition to all the above signals a broad singlet is observed at $\delta$ = 12.07 ppm. This down-field signal is attributed to the *ortho*-C-H proton of the phim phenyl ring, which is proximal to the metal centre. It may be noted that the free phim or the Schiff bases do not show any resonance in this region. The protons of the three methyl groups of

 © 2006 Wiley-VCH Verlag GmbH & Co. KGaA, Weinheim 

ahac$^{2-}$ in **2** are observed as three singlets at $\delta$ = 2.01, 2.11 and 2.27 ppm. The proton of the –CH= group resonates as a singlet at $\delta$ = 5.51 ppm. A broad singlet at $\delta$ = 8.89 ppm is assigned to the imidazole N-H proton. As observed for **1** the signal from the phim phenyl ring *ortho* C-H proton, close to the apical site of the metal centre, appears down-field ($\delta$ = 11.63 ppm) as a broad singlet. The multiplet in the range $\delta$ = 7.1–7.8 ppm corresponds to the imidazole ring C-H and the rest of the aromatic protons in the molecule.

We have recorded the NMR spectra of both complexes in the temperature range 20 to –80 °C and monitored the broad singlet observed at $\delta$ = 12.07 and 11.63 ppm for **1** and **2**, respectively. In each case, the signal becomes sharper and is shifted further down-field on cooling (Figure 6). The shifts are 0.75 and 0.90 ppm for **1** and **2**, respectively. The observation of the down-field signal and its behaviour on lowering the temperature suggest that the C–H···Ni interaction present in the solid-state structures of both **1** and **2** is also present in solution and it is essentially hydrogen bond in character.

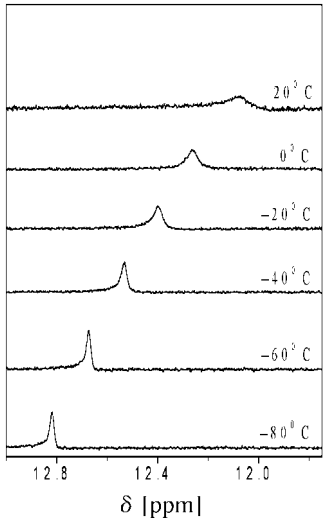


Figure 6. Temperature dependence of the down-field signal in the proton NMR spectrum of [Ni(bhac)(phim)] (**1**).

## Conclusions

The tridentate O,N,O-donor benzoyl- and acetylhydrazone of acetylacetone ($H_2$bhac and $H_2$ahac) and monodentate N-donor 2-phenylimidazole (phim) yielded square-planar nickel(II) complexes [Ni(bhac)(phim)] (**1**) and [Ni(ahac)(phim)] (**2**). X-ray crystal structures reveal that the asymmetric unit of **1** contains a single molecule while that of **2** contains four molecules with different conformations. The conformation of **1** is significantly different compared with that of any of the four molecules of **2**. Perhaps the intramolecular C–H···π interaction present in **1** is one of the factors for this difference. In each of **1** and **2**, one of the two *ortho* hydrogen atoms of the phim phenyl ring is very close to the metal centre at the apical site suggesting an intramolecular C–H···Ni interaction. The shape of the C–H···Ni interaction depends on the twisting ($\psi$) of the phim and the extent of the orthogonality ($\theta$) between the plane containing the chelate rings and the imidazole plane. The observed trends are compared with the structures of similar species reported in the literature. Theoretically optimised structures of both **1** and **2** are very similar. Energy calculations were performed by varying $\psi$ from 0 to 90° for both **1** and **2**. The conformer of **1** having a $\psi$ value of ≈35° (experimental $\psi$ = 35.8°) is at the lowest energy and the plot of the relative energies ($\Delta E$) of various conformers against $\psi$ provides a reasonably symmetric well-type curve. For **2** the lowest energy conformer has a $\psi$ value of ≈20°. However, the energy change is very little below $\psi$ = 20°. This observation explains the presence of four molecules having $\psi$ in the range 1.6–21.6° in the asymmetric unit of **2**. Theoretical investigations suggest that a hydrogen-bond description of the C–H···Ni interaction in both **1** and **2** is more appropriate. In the NMR spectra of **1** and **2**, the appearance of this interacting proton at down-field and further down-field shifts, because of the lowering of the temperature, substantiates the hydrogen-bond character of this interaction.

## Experimental Section

**Materials:** The Schiff bases $H_2$bhac and $H_2$ahac were prepared by condensation reactions of acetylacetone with benzoylhydrazine and acetylhydrazine, respectively.[21] All other chemicals and solvents used in this work were of analytical grade, available commercially and were used without further purification.

**Physical Measurements:** Microanalytical (C, H, N) data were obtained with a Thermo Finnigon Flash EA1112 series elemental analyser. Infrared spectra were collected by using KBr pellets with a Jasco-5300 FT-IR spectrophotometer. A Shimadzu 3101-PC UV/Vis/NIR spectrophotometer was used to record the electronic spectra. The proton NMR spectra were recorded with a Bruker 400 MHz spectrometer. Solution electrical conductivities were measured with a Digisun DI-909 conductivity meter. A Sherwood Scientific balance was used for magnetic susceptibility measurements. A CH-Instruments model 620A electrochemical analyser was used for cyclic voltammetric experiments with acetonitrile solutions of the complexes containing tetrabutylammonium perchlorate (TBAP) as the supporting electrolyte. The three electrode measurements were carried out at 298 K under a dinitrogen atmosphere with a platinum disc working electrode, a platinum wire auxiliary electrode and an Ag/AgCl reference electrode.

### Synthesis of the Complexes

**[Ni(bhac)(phim)] (1):** A dry methanol solution (15 cm$^3$) of Ni$(O_2CCH_3)_2{\cdot}4H_2O$ (125 mg, 0.5 mmol) was added to a dry methanol solution (10 cm$^3$) of $H_2$bhac (110 mg, 0.5 mmol) and 2-phenylimidazole (72 mg, 0.5 mmol). The resulting deep brown mixture was kept under reflux for 2 h and then evaporated on a steam bath to approximately half of the original volume. The brown needles that separated after cooling to room temperature were collected by filtration, washed with a little ice-cold methanol and finally dried in air. The yield obtained was 160 mg (76%). A single crystal suitable for X-ray structure determination was selected from this material. $NiC_{21}H_{20}N_4O_2$ (419.12): calcd. C 60.18, H 4.81, N 13.37; found C 59.95, H 4.78, N 13.24. Electronic spectroscopic data in $CH_3OH$:

 © 2006 Wiley-VCH Verlag GmbH & Co. KGaA, Weinheim 

$\lambda_{max}$ ($\varepsilon$) = 565 sh (94), 380 (14200), 366 sh (12700), 267 (19800), 234 sh (21100) nm.

**[Ni(ahac)(phim)] (2):** A dry methanol solution (15 $cm^3$) of Ni-$(O_2CCH_3)_2{\cdot}4H_2O$ (125 mg, 0.5 mmol) was added to a dry methanol solution (10 $cm^3$) of $H_2$ahac (70 mg, 0.5 mmol) and 2-phenylimidazole (72 mg, 0.5 mmol), and the mixture was kept under reflux for 2 h. A brown crystalline material was deposited on the wall of the round-bottomed flask along the surface of the solvent and formed a ring. The reaction mixture was cooled to room temperature and the almost colourless and clear mother liquor was removed carefully by using a dropper. The crystalline material was collected after drying in air. The yield obtained was 110 mg (62%). A single crystal suitable for X-ray structure determination was selected from this material. $NiC_{16}H_{18}N_4O_2$ (357.05): C 53.82, H 5.08, N 15.69; found C 53.54, H 4.86, N 15.47. Electronic spectroscopic data in $CH_3OH$: $\lambda_{max}$ ($\varepsilon$) = 425 sh (370), 358 sh (3500), 344 (4700), 330 sh (4400), 267 (18400), 235 sh (18600) nm.

**X-ray Crystallography:** Complexes **1** and **2** crystallise in the space groups $C2/c$ and $P2_1/c$, respectively. Unit cell parameters and the intensity data were obtained with a Bruker-Nonius SMART APEX CCD single-crystal diffractometer, equipped with a graphite monochromator and a Mo-$K_\alpha$ fine-focus sealed tube ($\lambda$ = 0.71073 Å) operated at 2.0 kW. The detector was placed at a distance of 6.0 cm from the crystal. Data were collected at 298 K with a scan width of 0.3° in $\omega$ and an exposure time of 30 sec/frame. The SMART software was used for data acquisition and the SAINT-Plus software was used for data extraction.[37] In each case, an absorption correction was performed with the help of the SADABS programme.[38] The structures were solved by direct methods and refined on $F^2$ by full-matrix least-squares procedures. In both structures, all non-hydrogen atoms were refined with anisotropic thermal parameters. Hydrogen atoms were added at idealised positions by using a riding model. For **1** the hydrogen atoms were refined isotropically while for **2** they were not refined. The SHELX-97 programmes[39] of the WinGX package[40] were used for structure solution and refinement. The ORTEX6a[41] and Platon[42] packages were used for molecular graphics. Significant crystallographic data for **1** and **2** are summarised in Table 4.

Table 4. Selected crystallographic data for **1** and **2**.

| Complex | [Ni(bhac)(phim)] (**1**) | [Ni(ahac)(phim)] (**2**) |
|---|---|---|
| Empirical formula | $C_{21}H_{20}N_4O_2Ni$ | $C_{16}H_{18}N_4O_2Ni$ |
| Formula mass [g$mol^{-1}$] | 419.12 | 357.05 |
| Crystal system | monoclinic | monoclinic |
| Space group | $C2/c$ | $P2_1/c$ |
| $a$ [Å] | 43.532(3) | 24.450(2) |
| $b$ [Å] | 11.8872(9) | 8.5337(7) |
| $c$ [Å] | 7.6363(6) | 33.518(3) |
| $\beta$ [°] | 99.3510(10) | 108.985(2) |
| $V$ [$Å^{-3}$] | 3899.1(5) | 6613.2(9) |
| $Z$ | 8 | 16 |
| $\mu$ [$mm^{-1}$] | 1.019 | 1.188 |
| Reflections collected | 19894 | 49271 |
| Reflections unique | 3853 | 8643 |
| Reflections [$I \geq 2\sigma(I)$] | 3013 | 4844 |
| Parameters | 333 | 841 |
| $R_1$, $wR_2$ [$I \geq 2\sigma(I)$] | 0.0361, 0.0889 | 0.0713, 0.1155 |
| $R_1$, $wR_2$ (all data) | 0.0488, 0.0970 | 0.1408, 0.1375 |
| GOF on $F^2$ | 0.913 | 1.025 |
| Largest peak, hole [e$Å^{-3}$] | 0.388, –0.201 | 0.400, –0.332 |

CCDC-294281 and CCDC-294282 contain the supplementary crystallographic data for **1** and **2**, respectively. These data can be obtained free of charge from the Cambridge Crystallographic Data Centre via www.ccdc.cam.ac.uk/data_request/cif.

**Computational Methods:** DFT calculations for **1** and **2** were performed at the B3LYP/6-311G(d,p) level.[43–45] The starting points of the geometry optimisations were the X-ray structural coordinates of the single molecule of **1** and of the four independent molecules of **2** found in the corresponding asymmetric units. The Gaussian 03[46] suite of programmes was used for all calculations.

**Supporting Information** (see footnote on the first page of this article): Plots of C–H···Ni angles, $\psi$ and $\theta$ (see text for definitions) against the Ni···H distances for **1** and **2** (Figure S1).

## Acknowledgments

Financial support for this work was provided by the Council of Scientific and Industrial Research (CSIR) [Grant No. 01(1880)/03/EMR-II]. A. Mukhopadhyay thanks the CSIR for a research fellowship. We thank B. Pathak and T. S. Thakur for helpful discussions on the theoretical calculations. All calculations were done using the computational facility at the Centre for Modelling, Simulation and Design, University of Hyderabad. X-ray crystallographic studies were performed at the National Single Crystal Diffractometer Facility, School of Chemistry, University of Hyderabad (funded by the Department of Science and Technology). We thank the University Grants Commission for the facilities provided under the UPE and CAS programmes.

[1] M. Brookhart, M. L. H. Green, *J. Organomet. Chem.* **1983**, *250*, 395.
[2] J.-Y. Saillard, R. J. Hoffman, *J. Am. Chem. Soc.* **1984**, *106*, 2006.
[3] M. Brookhart, M. L. H. Green, L. L. Wong, *Prog. Inorg. Chem.* **1988**, *36*, 1.
[4] R. H. Crabtree, D. G. Hamilton, *Adv. Organomet. Chem.* **1988**, *28*, 299.
[5] A. D. Ryabov, *Chem. Rev.* **1990**, *90*, 403.
[6] R. H. Crabtree, *Angew. Chem. Int. Ed. Engl.* **1993**, *32*, 789.
[7] A. J. Canty, G. van Koten, *Acc. Chem. Res.* **1995**, *28*, 406.
[8] D. Braga, F. Grepioni, E. Tedesco, K. Biradha, G. R. Desiraju, *Organometallics* **1997**, *16*, 1846.
[9] W. Yao, O. Eisenstein, R. H. Crabtree, *Inorg. Chim. Acta* **1997**, *254*, 105.
[10] T. W. Hambley, *Inorg. Chem.* **1998**, *37*, 3767.
[11] M. J. Calhorda, *Chem. Commun.* **2000**, 801.
[12] L. Brammer, *Dalton Trans.* **2003**, 3145.
[13] A. Albinati, P. S. Pregosin, F. Wombacher, *Inorg. Chem.* **1990**, *29*, 1812.
[14] M. Bortolin, U. E. Bucher, H. Rüegger, L. M. Venanzi, A. Albinati, F. Lianza, S. Trofimenko, *Organometallics* **1992**, *11*, 2514.
[15] T. Hascall, M.-H. Baik, B. M. Bridgewater, J. H. Shin, D. G. Churchill, R. A. Friesner, G. Parkin, *Chem. Commun.* **2002**, 2644.
[16] W. Kemp, *Organic Spectroscopy*, Macmillan, Hampshire, **1987**, pp. 62–66.
[17] K. Nakamoto, *Infrared and Raman Spectra of Inorganic and Coordination Compounds*, Wiley, New York, **1986**, pp. 241–242.
[18] S. Das, S. Pal, *J. Organomet. Chem.* **2004**, *689*, 352.
[19] S. G. Sreerama, S. Pal, *Inorg. Chem.* **2005**, *44*, 6299.
[20] S. G. Sreerama, S. Pal, *Eur. J. Inorg. Chem.* **2004**, 4718.
[21] N. R. Sangeetha, C. K. Pal, P. Ghosh, S. Pal, *J. Chem. Soc., Dalton Trans.* **1996**, 3293.
[22] S. Das, G. P. Muthukumaragopal, S. N. Pal, S. Pal, *New J. Chem.* **2003**, *27*, 1102.
[23] S. Das, S. Pal, *J. Mol. Struct.* **2005**, *741*, 183.

 © 2006 Wiley-VCH Verlag GmbH & Co. KGaA, Weinheim 

[24] A. Mukhopadhyay, G. Padmaja, S. N. Pal, S. Pal, *Inorg. Chem. Commun.* **2003**, *6*, 381.
[25] A. Mukhopadhyay, S. Pal, *Polyhedron* **2004**, *23*, 1997.
[26] G. V. Karunakar, N. R. Sangeetha, V. Susila, S. Pal, *J. Coord. Chem.* **2000**, *50*, 51.
[27] D. R. Trivedi, A. Ballabh, P. Dastidar, *CrystEngComm* **2003**, *5*, 358.
[28] A. E. Reed, L. A. Curtiss, F. Weinhold, *Chem. Rev.* **1988**, *88*, 899.
[29] R. B. Cracknell, A. G. Orpen, J. L. Spencer, *J. Chem. Soc., Chem. Commun.* **1984**, 326.
[30] T. S. Thakur, G. R. Desiraju, *Chem. Commun.* **2006**, 552.
[31] R. F. W. Bader, *Atom in Molecules, A Quantum Theory*, The Clarendon Press, Oxford, **1990**.
[32] U. Koch, P. L. A. Popelier, *J. Phys. Chem.* **1995**, *99*, 9747.
[33] P. L. A. Popelier, G. Logothetis, *J. Organomet. Chem.* **1998**, *555*, 101.
[34] S. Pillet, G. Wu, V. Kulsomphob, B. G. Harvey, R. D. Ernst, P. Coppens, *J. Am. Chem. Soc.* **2003**, *125*, 1937.
[35] C.-S. Liu, P.-Q. Chen, E.-C. Yang, J.-L. Tian, X.-H. Bu, Z.-M. Li, H.-W. Sun, Z. Lin, *Inorg. Chem.* **2006**, ASAP article.
[36] A. J. Canty, G. van Koten, *Acc. Chem. Res.* **1995**, *28*, 406.
[37] *SMART V5.630 and SAINT-plus V6.45*, Bruker-Nonius Analytical X-ray Systems Inc., Madison, WI, USA, **2003**.
[38] G. M. Sheldrick, *SADABS Program for area detector absorption correction*, University of Göttingen, Göttingen, Germany, **1997**.
[39] G. M. Sheldrick, *SHELX-97 Structure Determination Software*, University of Göttingen, Göttingen, Germany, **1997**.
[40] L. J. Farrugia, *J. Appl. Crystallogr.* **1999**, *32*, 837.
[41] P. McArdle, *J. Appl. Crystallogr.* **1995**, *28*, 65.
[42] A. L. Spek, *PLATON A Multipurpose Crystallographic Tool*, Utrecht University, Utrecht, The Netherlands, **2002**.
[43] A. D. Becke, *J. Chem. Phys.* **1993**, *98*, 5648.
[44] C. Lee, W. Yang, R. G. Parr, *Phys. Rev. B* **1988**, *37*, 785.
[45] T. H. Dunning Jr, P. J. Hay, *Modern Theoretical Chemistry* (Ed.: H. F. Schaefer III), Plenum, New York, **1976**, pp. 1–28.
[46] M. J. Frisch et al., *Gaussian 03 Revision B05*, Gaussian Inc., Pittsburgh, PA, **2004**.

Received: June 24, 2006
Published Online: October 10, 2006

 © 2006 Wiley-VCH Verlag GmbH & Co. KGaA, Weinheim 

DOI: 10.1002/ejic.200600596

# The Assembly of Dinuclear Alkoxido-Bridged $Cu^{II}$ Halide Complexes of Pyridine Alcohols To Form Tetranuclear and Polynuclear Compounds: Synthesis, Structure, and Magnetic Properties

**Nina Lah,*[a] Ivan Leban,[a] and Rodolphe Clérac*[b]**

**Keywords:** Pyridine alcohol ligands / Alkoxido ligands / Copper(II) defect dicubanes / Copper(II) coordination polymers / X-ray structures / Magnetic properties

Reaction of $CuX_2$ (X = Cl, Br) with pyridine alcohol ligands [2-(hydroxymethyl)pyridine = Hhmp, 2-(hydroxyethyl)pyridine = Hhep and 2-(hydroxypropyl)pyridine = Hhpp] affords a series of new $Cu^{II}$ alkoxide complexes with a similar $Cu_2O_2$ structural motif: a dinuclear complex, $[Cu_2(hpp)_2Br_2]$ (**1**), two tetranuclear compounds, $[Cu_4(hpp)_4Br_4]$ (**2**) and $[Cu_4(hpp)_4Cl_4]$ (**3**), and polynuclear chains, $[Cu_2(hep)_2Cl_2]_n$ (**4**) and $[Cu_2(Hhmp)_2Cl_4]_n$ (**5**). The dinuclear complex **1** represents the basic building unit of the four other materials. In this family of compounds, the pyridine alcohol type ligands (Hhmp, Hhep, or Hhpp) provide the two alkoxido functions that bridge the $Cu^{II}$ centers. The tetranuclear analogues exhibit an unusual structure of the defect dicubane-like type with two missing vertices. The one-dimensional polymers **4** and **5** are composed of $Cu_2O_2$ dinuclear units interlinked through bridging chlorido ligands to form infinite chains. The analysis of the magnetic susceptibility measurements indicates the presence of strong antiferromagnetic coupling between the $S = 1/2$ $Cu^{II}$ metal ions through the bis(alkoxido) bridge.

(© Wiley-VCH Verlag GmbH & Co. KGaA, 69451 Weinheim, Germany, 2006)

## Introduction

The aggregation of small well-defined coordination building blocks to form larger architectures is one of the major trends of research in coordination chemistry.[1–4] $Cu^{II}$ complexes are particularly popular since the metal ion is paramagnetic and affords easy formation of polynuclear clusters. Dinuclear $Cu^{II}$ complexes have often been used as models to study the magnetic-exchange interactions and as building blocks for the construction of polynuclear compounds with interesting magnetic properties.[5] Among them, $Cu^{II}$ carboxylates with a paddle-wheel structure and doubly bridged dinuclear complexes containing hydroxido alkoxido or halide bridging ligands have drawn considerable interest.[6] Our quest has been the preparation of new complexes based on the dinuclear $[Cu_2(OR)_2X_2]$ core. This motif consists of two copper atoms bridged by two alkoxido oxygen atoms from alkoxypyridine-type ligands. Moreover, each of the $Cu^{II}$ metal ions displays a pseudo-square-planar coordination geometry completed by two halogen anions in *trans* positions (Scheme 1, I) and by the pyridine function of the chosen ligand. The tendency of copper ions to accept

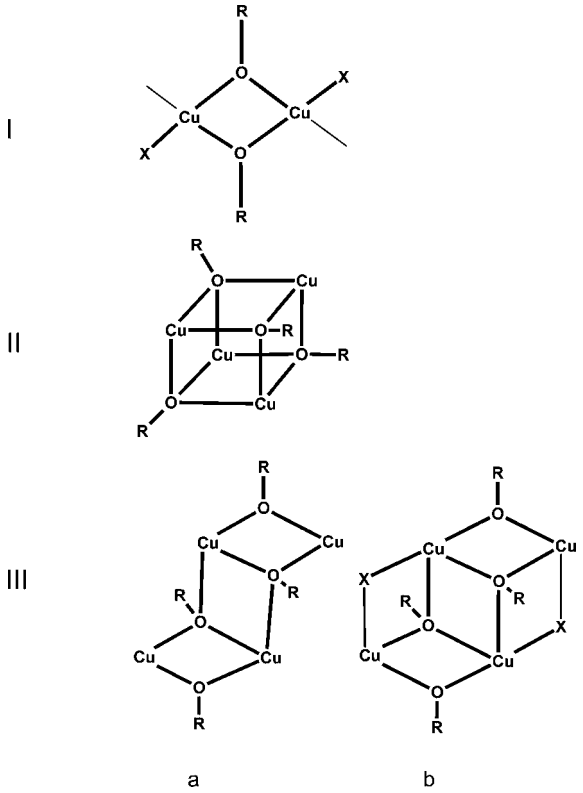


Scheme 1. The $[Cu_2(OR)_2X_2]$ structural core (I) and the tetranuclear species of cubane type (II), stepped-cubane type (IIIa) and "defect dicubane type" (IIIb).

[a] University of Ljubljana, Faculty of Chemistry and Chemical Technology,
Aškerčeva 5, 1000 Ljubljana, Slovenia
Fax: +386-1-2419-220
E-mail: nina.lah@fkkt.uni-lj.si
[b] Centre de Recherche Paul Pascal CNRS-UPR-8641,
115 Avenue Dr. A Schweitzer, 33600 Pessac, France
E-mail: clerac@crpp-bordeaux.cnrs.fr

 © 2006 Wiley-VCH Verlag GmbH & Co. KGaA, Weinheim 

a fifth ligand at the axial coordination site and the ability of alkoxido ligands to participate in bridging allow for the possibility of associating these dinuclear units into discrete oligonuclear and polynuclear compounds. The assembly of two dinuclear units leads to two types of tetranuclear aggregates: the cubane type (Scheme 1, II) and the so-called stepped-cubane type (Scheme 1, IIIa). Both types are known in $Cu^{II}$ alkoxide chemistry. While abundant structural data on cubane-type complexes is available in the literature,[7] the stepped cubanes appear much less frequently,[8] particularly, compounds that contain a halide ligand as one of the equatorial ligands of the copper centers in the dinuclear core. Upon association of the type I dinuclear units (Scheme 1), one of the two terminal halogenide ligands of each dimeric unit bridges neighboring $Cu_2(OR)_2$ building blocks to give rise to an unusual structural type (Scheme 1, IIIb). The resulting complex may be envisioned as an arrangement of two fused cubes, each missing one apex. It is worth noting that as far as we know, only one structurally characterized $[Cu_4(OR)_4X_4]$ species of this type has been reported in the literature.[9]

Although a considerable amount of research is currently focused on the rational design of premeditated architectures and complexes, it is often difficult, if not impossible, to answer the question why one complex is obtained rather than another. Progress in understanding self-assembly processes is likely to be developed by studying the aggregation of relatively simple and small building units. Herein we report on the preparation and structural characterization of copper(II) complexes that have the $Cu_2(OR)_2X_2$ core with three simple chelating pyridine-based alkoxido ligands (Scheme 2): 2-(hydroxymethyl)pyridine (Hhmp), 2-(hydroxyethyl)pyridine (Hhep), and 2-(hydroxypropyl)-pyridine (Hhpp). Five new compounds are presented, spanning diverse architectures from dinuclear $[Cu_2(hpp)_2Br_2]$ to two tetranuclear complexes with a dicubane-type structure, ($[Cu_4(hpp)_4Br_4]$ and $[Cu_4(hpp)_4Cl_4]$), and two polymeric chain compounds with the composition $[Cu_2(hep)_2Cl_2]_n$ and $[Cu_2(Hhmp)_2Cl_4]_n$. In addition to the synthesis and the structural characterization, the magnetic properties of the $Cu_2(OR)_2X_2$ core will be discussed.

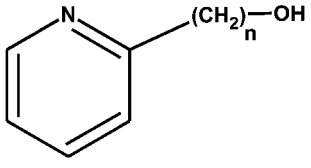


*n* = 1; 2-(hydroxymethyl) pyridine (Hhmp)
*n* = 2; 2-(hydroxyethyl) pyridine (Hhep)
*n* = 3; 2-(hydroxypropyl) pyridine (Hhpp)

Scheme 2. Pyridine alcohol ligands discussed in this work.

## Results and Discussion

Simple pyridine-based alcohols such as 2-(hydroxymethyl)- (Hhmp), 2-(hydroxyethyl)- (Hhep) and 2-(hydroxypropyl)pyridine (Hhpp) have the ability to act as chelating and/or bridging ligands in their neutral and ionic forms, where the OH groups are deprotonated. Surprisingly, these simple commercially available substances have not been employed widely as ligands in coordination chemistry. Only in recent years, the simplest one from the above homologue series, Hhmp, has been used in manganese chemistry to obtain new single-molecule magnets (SMMs) or extended networks of SMMs.[10] Among the structurally characterized $Cu^{II}$ complexes based on the ligands listed above, the compounds with (hydroxymethyl)pyridine (Hhmp) prevail. The search through the Cambridge Structural Database (CSD) revealed six structures containing Hhmp and $Cu^{II}$ metal ions.[11] All of these examples are mononuclear species with six-coordinate $Cu^{II}$ centers to which Hhmp binds as a chelating ligand. In addition, it is worth noting that there is only one report on a structure with the anionic hmp ligand that adopts a chelating-bridging mode, which results in a tetranuclear complex $[Cu_4(hmp)_4(CH_3COO)_4]$ of a cubane type.[12] Structures with Hhep/hep and Hhpp/hpp appear even less frequently. Two $Cu^{II}$ mononuclear complexes with Hhep have been found in the CSD, while no example seems to exist with the ligand in its deprotonated form.[13] Only one mononuclear compound with Hhpp and one dinuclear example with the ligand in its deprotonated form (hpp) have been reported so far on the basis of a CSD search.[14]

We have carried out the syntheses by using simple bromide and chloride copper(II) salts ($CuX_2$ with X = Br, Cl) with Hhmp, Hhep, and Hhpp in methanol, ethanol, or a mixture of both alcohols. While the reactions with Hhep and Hhpp lead to the deprotonation of the ligand and thus alkoxido-bridged complexes (**1**–**4**), the Hhmp ligands stay protonated in **5**. The origin of this difference and the mechanism that assists the deprotonation of the coordinated alcohol in the case of the Hhep and Hhpp ligands is not clear. We have no explanation for the formation of alkoxido-bridged rather than hydroxido-bridged complexes, since the metal salts were not dried and water was not excluded from the reaction mixture. Analogically, the deprotonation of Hhmp under similar reaction conditions was expected even if the chelating mode of Hhmp coordination is apparently favored over the bridging mode. Indeed, this tendency to form five-membered chelating rings for the Hhmp ligand is also reflected in the CSD and in the occurrence of structures containing Hhmp.

### Structural Descriptions

#### *Dinuclear Complex $[Cu_2(hpp)_2Br_2]$ (1)*

Compound **1** represents the smallest complex in terms of nuclearity in this study (Figure 1). It consists of two copper atoms doubly bridged by chelating μ-hpp ligands. The remaining sites of the distorted square-planar environment around the copper centers are occupied by two bromido ligands that are arranged in a *trans* fashion. The two copper atoms are symmetry related by an inversion center and are separated by 3.0642(5) Å. The μ-O bridge is asymmetrical

 © 2006 Wiley-VCH Verlag GmbH & Co. KGaA, Weinheim 

with Cu–O distances of 1.9179(13) and 1.9489(13) Å and a Cu–O–Cu angle of 104.8°. Basic geometric parameters, relevant to the Cu coordination sphere, are summarized in Table 1. There are no covalent interactions between the dimeric units.

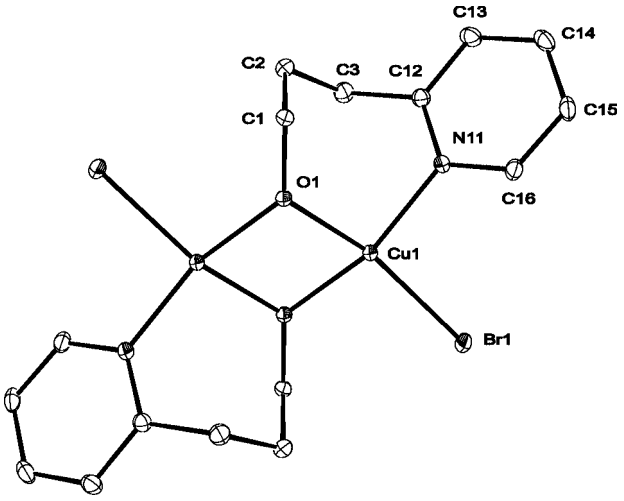


Figure 1. View of a centrosymmetric dinuclear unit in **1** (30% probability thermal ellipsoids). Only the atoms of the asymmetric unit are labeled.

Table 1. Selected bond lengths [Å] and angles [°] for **1**.[a]

| | |
|---|---|
| Cu1–O1 | 1.9489(13) |
| Cu1–N11 | 2.0011(16) |
| Cu1–Br1 | 2.3753(3) |
| Cu1–O1$^{i}$ | 1.9179(13) |
| Cu1–Cu1$^{i}$ | 3.0642(5) |
| Cu1–O1–Cu1$^{i}$ | 104.82(6) |

[a] Symmetry code: (i) $-x+2$, $-y+1$, $-z+1$.

### *Tetramers [Cu$_4$(hpp)$_4$Br$_4$] (2) and [Cu$_4$(hpp)$_4$Cl$_4$] (3)*

The basic molecular motif of these two materials is similar and is composed of four copper centers arranged to form a planar "rhombic" geometry (Scheme 1, IIIb). These tetranuclear complexes can be described as two [Cu$_2$(hpp)$_2$X$_2$] (with X: Br or Cl) dinuclear units, one lying on top of the other and slipped with respect to each other. One of the two bridging hpp oxygen atoms of each dinuclear unit is triply bridging and connects the two [Cu$_2$(hpp)$_2$X$_2$] moieties to form a stepped-cubane-type geometry. The tetranuclear aggregate is further stabilized by two halogen bridges inducing the "defect dicubane type" geometry: a pair of uncompleted cubes connected by a common Cu$_2$O$_2$ face. The bromido complex **2** crystallizes in a noncentrosymmetric space group $P2_1$ with the whole tetranuclear molecule as the asymmetric unit (Figure 2). The geometry of the two dinuclear moieties is essentially the same as can be seen from bond lengths and angles given in Table 2. The copper centers, which are doubly bridged by alkoxido oxygen atoms, are separated by 3.0421(9) and 3.0464(9) Å, while the distances between the copper atoms belonging to different dinuclear units are longer. Those involving $\mu_3$-O- and μ-Br-bridged Cu atoms are 3.6003(9) and 3.6113(9) Å for the Cu1–Cu3 and Cu4–Cu2 pairs, respectively. The ($\mu_3$-O)$_2$-bridged pair of copper atoms (Cu1 and Cu2) is separated by 3.3555(8) Å. The chloride analogue **3** crystallizes in the space group $P2_1/n$ with an inversion center located in the center of the Cu$_2$($\mu_3$-O)$_2$ plane (Figure 3). Thus, the asymmetric unit here is composed only of a dimeric half of the tetranuclear complex [Cu$_2$(hpp)$_2$X$_2$]. The geometry of this dinuclear unit (Table 2) is similar to that of the bromido analogue. Again, the bridging alkoxido group from one [Cu$_2$(hpp)$_2$X$_2$] motif coordinates to the copper ions of the other moiety, thereby becoming a $\mu_3$ ligand. Additionally, two chlorido bridges consolidate the tetranuclear core to form a centrosymmetric complex with a IIIb topology (Scheme 1), as presented in Figure 3. In these aggregates, two types of Cu$^{II}$ ions with a square-pyramidal coordination sphere can be distinguished: (i) Cu1 and Cu2 in **2** or Cu2 in **3** possess a CuXNO$_3$ environment with a basal plane occupied by a triply bridging hmp oxygen atom, a halogen ion, a pyridine-type nitrogen atom, and μ-O atom from a chelating hmp. The apical site is occupied by a $\mu_3$-O atom from the neighboring dinuclear unit. The remaining

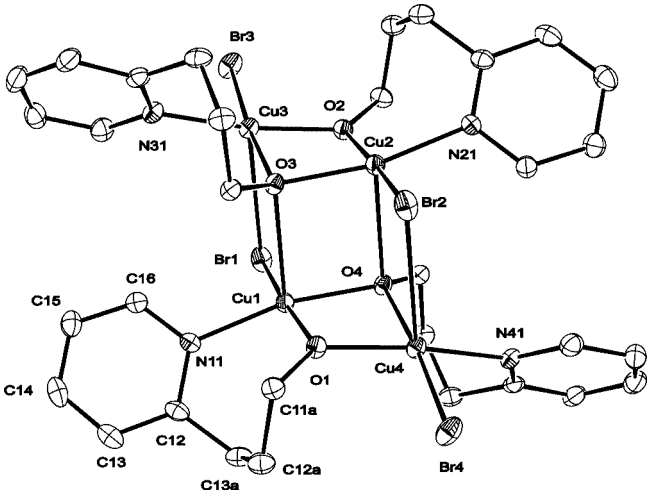


Figure 2. Structural representation of **2** (30% probability thermal ellipsoids).

Table 2. Selected bond lengths [Å] and angles [°] for the tetranuclear compounds **2** and **3**.[a]

| **2** | | | | **3** | |
|---|---|---|---|---|---|
| Cu2–Cu3 | 3.0421(9) | Cu1–Cu4 | 3.0464(9) | Cu1–Cu2 | 3.0438(3) |
| Cu2–O2 | 1.934(4) | Cu1–O1 | 1.941(4) | Cu1–O1b | 1.9071(12) |
| Cu2–O3 | 1.979(4) | Cu1–O4 | 1.972(4) | Cu1–O1a | 1.9791(12) |
| Cu2–Br2 | 2.4023(10) | Cu1–Br1 | 2.4105(9) | Cu1–Cl1 | 2.2474(5) |
| Cu2–N21 | 2.022(5) | Cu1–N11 | 2.021(5) | Cu1–N11 | 2.0093(15) |
| Cu3–O2 | 1.896(4) | Cu4–O1 | 1.907(4) | Cu2–O1a | 1.9293(12) |
| Cu3–O3 | 2.003(4) | Cu4–O4 | 1.984(4) | Cu2–O1b | 1.9891(12) |
| Cu3–Br3 | 2.4087(9) | Cu4–Br4 | 2.4105(9) | Cu2–Cl2 | 2.2553(5) |
| Cu3–N31 | 2.002(5) | Cu4–N41 | 2.004(5) | Cu2–N21 | 2.0227(15) |
| Cu2–O4 | 2.536(4) | Cu1–O3 | 2.512(4) | Cu1–Cl2$^{i}$ | 3.0035(6) |
| Cu3–Br1 | 3.1102(10) | Cu4–Br2 | 3.1667(10) | | |
| Cu3–O2–Cu2 | 105.2(2) | Cu1–O1–Cu4 | 104.7(2) | Cu1–O1a–Cu2 | 100.18(5) |
| Cu3–O3–Cu2 | 99.63(17) | Cu1–O4–Cu4 | 100.72(18) | Cu1–O1b–Cu2 | 105.01(6) |

[a] Symmetry code: (i) $-x$, $-y$, $-z$.

 © 2006 Wiley-VCH Verlag GmbH & Co. KGaA, Weinheim 

two copper centers, Cu3 and Cu4 in **2** or Cu1 in **3**, possess a $CuX_2NO_2$ geometry. The equatorial plane is formed by a μ-O atom from a bridging hmp ligand, a halogen ion, a pyridine-type nitrogen atom, and a $\mu_3$-O atom from a chelating hmp. The axial site is occupied by a halogen ion from the adjacent dinuclear unit. It is worth noting that the assembly of two alkoxido-bridged dicopper units usually results in a compact cube-like complex, particularly when the dinuclear unit contains halide ligands. To the best of our knowledge, there is only one structure known, $[Cu_4(M3)_2(\mu_3\text{-}OMe)_2(\mu\text{-}Cl)_2Cl_2]$, that contains the $[Cu_4(\mu\text{-}OR)_2(\mu_3\text{-}OR)_2(\mu\text{-}X)_2X_2]$ tetranuclear defect dicubane core.[9] However, the arrangement of the bridging and terminal halogenide ligands in the present tetranuclear complexes differ from that observed in the reported structure. In **2** and **3**, the basic dinuclear moiety contains halogen ions located in a *trans* fashion, whereas in the aforementioned complex, the Cl ions are coordinated to the $Cu^{II}$ centers in *cis* positions. The $[Cu_4(M3)_2(\mu_3\text{-}OMe)_2(\mu\text{-}Cl)_2Cl_2]$ complex contains two different alkoxido ligands: $\mu_3$-bridging methoxy groups and a tridentate macrocyclic ligand (M3) that offers a μ-bridging phenoxo group and occupies, by its two nitrogen atoms, the two (*cis*) equatorial positions of each of the copper metal ions. This peculiar macrocyclic ligand geometry thus prevents the chlorido ligands from adopting *trans* positions.

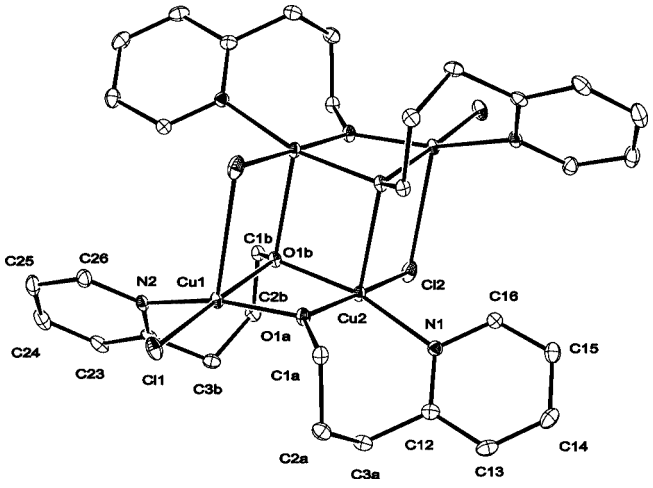


Figure 3. Structural representation of a centrosymmetric tetranuclear core of **3** (30% probability thermal ellipsoids).

### *Polymer $[Cu_2(hep)_2Cl_2]_n$ (4)*

In **4**, the centrosymmetric dimeric units (Figure 4, Table 3) assemble through weak interactions arising from two bridging chlorido ligands to form a linear chain shown in Figure 5. The distance between the copper centers within the alkoxido dimer is 3.0833(4) Å, whereas the distance between the copper centers that are doubly bridged by μ-Cl is longer: 3.8080(5) Å. The consecutive bridging planes ($Cu_2O_2$ and $Cu_2Cl_2$) are twisted with respect to each other and the dihedral angle is 77.93(5)°. The overall structure may be compared to the one observed in the complex $[Cu(nhep)Cl]_2$ containing 1-(2-hydroxyethyl)pyrazole (nhep) as the alkoxido bridging ligand.[15] In this compound, the basic dinuclear unit has no center of symmetry but connects through weak inter-dimer interactions arising from two bridging chlorido ligands to form polynuclear chains with di-μ-O and di-μ-Cl bridges, as described here.

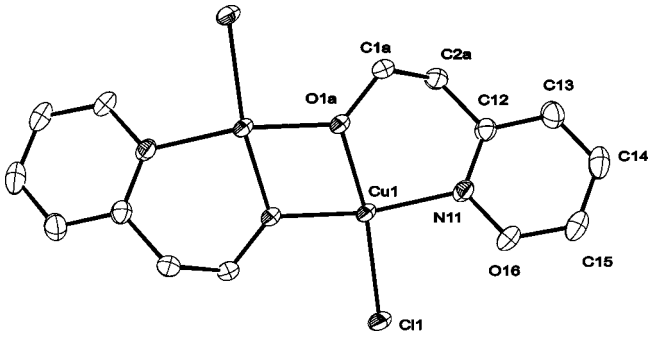


Figure 4. Structural representation of a centrosymmetric dinuclear core in **4** (30% probability thermal ellipsoids).

Table 3. Selected bond lengths [Å] and angles [°] for polynuclear compounds **4** and **5**.[a]

| **4** | | **5** | |
|---|---|---|---|
| Cu1–O1a | 1.9349(14) | Cu1–Cl2 | 2.2418(5) |
| Cu1–O1a$^{i}$ | 1.9434(14) | Cu1–Cl2$^{iii}$ | 2.9415(6) |
| Cu1–N11 | 2.0211(18) | Cu1–N11 | 1.9957(17) |
| Cu1–Cl1 | 2.2597(6) | Cu1–O1 | 1.9959(16) |
| Cu1–Cl1$^{ii}$ | 2.9413(7) | Cu1–Cl1 | 2.2607(6) |
| | | Cu1–O1$^{iv}$ | 2.9073(16) |
| Cu1–Cu1$^{i}$ | 3.0833(4) | Cu1–Cu1$^{iii}$ | 3.8641(5) |
| Cu1–Cu1$^{ii}$ | 3.8080(5) | Cu1–Cu1$^{iv}$ | 3.9191(5) |
| Cu1–O1a–Cu1$^{i}$ | 105.31(7) | | |

[a] Symmetry codes: (i) $-x+1$, $-y$, $-z+1$, (ii) $-x+2$, $-y$, $-z+1$, (iii) $-x$, $-y$, $-z+2$, (iv) $-x+1$, $-y$, $-z+2$.

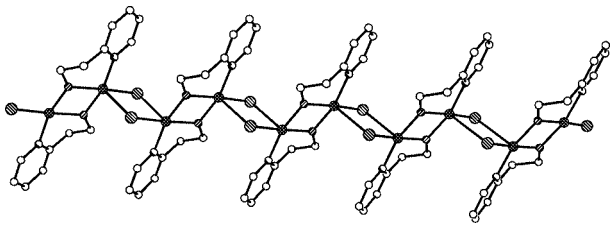

Figure 5. The one-dimensional chain structure of **4**.

### *Polymer $[Cu_2(Hhmp)_2Cl_4]_n \cdot 2nCH_3OH$ (5)*

Complex **5** contains 2-(hydroxymethyl)pyridine (Hhmp) in its protonated form. The polymeric chain is built up from centrosymmetric dinuclear $[Cu_2Hhmp_2Cl_4]$ units presented in Figure 6. The two Cu atoms, separated by 3.8641(5) Å, are doubly bridged by two chlorido ligands. The bridge is far from symmetrical with Cu1–Cl2 and Cu1–Cl2* (with *: $-x$, $-y$ $-z+2$) distances of 2.2418(5) and 2.9415(6) Å, respectively, and a Cu1–Cl2–Cu1* bridging angle of 95.45°. The Hhmp ligand binds to a single Cu metal ion within the dimer in a chelating manner [Cu1–N11: 1.9957(17) Å and Cu1–O1: 1.9959(16) Å]. The fifth coordination site is occupied by a terminal chlorido ligand at a distance of 2.2607(6) Å. Additionally, copper ions show rather weak in-

 © 2006 Wiley-VCH Verlag GmbH & Co. KGaA, Weinheim 

teractions with the Hhmp oxygen atom from a neighboring dimer with a distance between Cu1 and O1* (with *: $-x+1$, $-y$ $-z+2$) of 2.9073(16) Å. As a result of this weak interaction, infinite chains are formed in which $[Cu_2Hhmp_2Cl_4]$ dimers are further doubly bridged by Hhmp oxygen atoms as illustrated by Figure 7. The inter-dimer Cu–Cu separation is 3.9191(5) Å. The consecutive bridging planes $Cu_2Cl_2$ and $Cu_2O_2$ are almost perpendicular to each other [dihedral angle of 88.34(5)°]. Topologically, the chain structure of compound **5** is related to that of **4**. Its formation may as well be described as $[Cu_2Hhmp_2Cl_2]$ dimers connected into chains through μ-Cl ligands. Because Hhmp exists in **5** in the neutral form, such a chain would bear a positive charge. Thus, an additional terminal chlorido ligand is bound to each copper atom to compensate for the charge and complete the six-coordinate geometry of the Cu centers. The compound crystallizes as methanol solvate with two solvate molecules per dimeric unit. Both alcohols, Hhmp and methanol, are involved in hydrogen-bond interactions [O1–O2* with *: $-x+1$, $-y$, $-z+2$ = 2.583(2) Å; O2–Cl1* with *: $x+1$, $y$, $z$ = 3.090(2) Å].

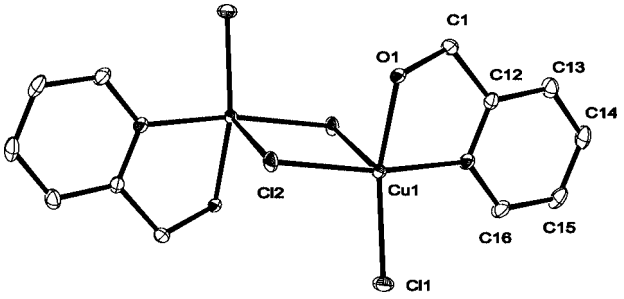


Figure 6. Structural representation of the centrosymmetric dinuclear unit in **5** (30% probability thermal ellipsoids).

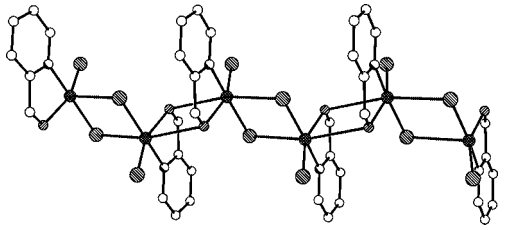

Figure 7. The one-dimensional chain structure of **5**.

### Magnetic Behavior

The variable temperature magnetic susceptibility measurements for compound **1** are shown in Figure 8 as an $\chi T$ vs. $T$ plot. By lowering the temperature, the $\chi T$ product that reaches 0.06 $cm^3\,K\,mol^{-1}$ at room temperature continuously decreases down to 130 K. Below 130 K, the compound displays a diamagnetic ground state. This magnetic behavior is typically observed for dinuclear $Cu^{II}$ complexes that possess a strong intracomplex antiferromagnetic interaction. A simple dinuclear Heisenberg $S = 1/2$ model[16] has been used to fit the magnetic susceptibility (Figure 8) by considering the following spin Hamiltonian: $H = -2J\ \{S_{Cu1}\cdot S_{Cu2}\}$ (where $S_{Cu1}$ and $S_{Cu2}$ are the spin operators with $S_{Cu1} = S_{Cu2} = 1/2$). The best set of parameters obtained for **1** by using the above model is: $J/k_B = -580(20)$ K, $g = 2.1(1)$ and $\rho = 0.002$ [this $\rho$ parameter has been added to the model in order to take into account a residual paramagnetic Curie component as $\chi = (1-\rho)\,\chi_{dimer} + \rho C_{S=1/2}/T$]. From a magnetic point of view, all the other compounds, **2**, **3**, and **4**, can be described as $CuO_2Cu$ dinuclear complexes by considering only the magnetic interactions through the bis(alkoxido) bridge. The assembly of these dinuclear units takes place through the axial sites of each copper ion and thus the bis(chlorido) bridge is likely to be much weaker. Therefore, the magnetic susceptibility of compounds **2**, **3**, and **4** can be modeled by using the above-described magnetic Heisenberg approach (Figure 8). The best set of parameters obtained by using this model is: $J/k_B = -586(20)$ K, $g = 2.3(1)$, $\rho = 0.026$ for **2**, $J/k_B = -641(25)$ K, $g = 2.2(1)$, $\rho = 0.021$ for **3**, and $J/k_b = -850(30)$ K, $g = 2.1(1)$, $\rho = 0.02$ for **4**. It is worth noting that similar magnetic behavior and antiferromagnetic interactions have been found for bis(alkoxido) dinuclear copper(II) complexes.[9,15] The present compounds thus possess a diamagnetic ground state that is the only thermally populated state above 130 K.

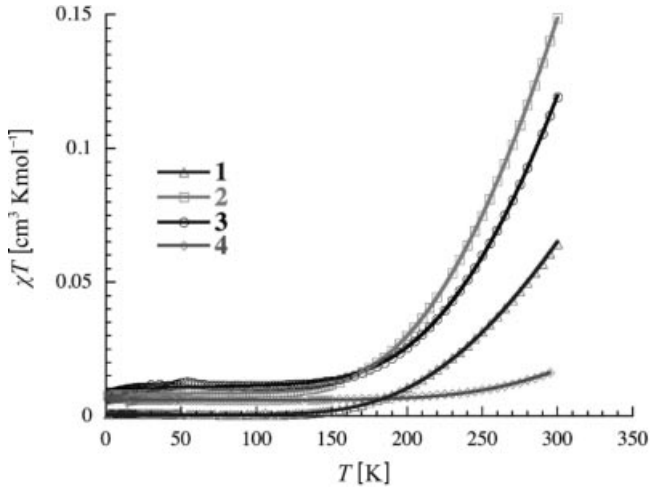


Figure 8. $\chi T$ vs. $T$ data (where $\chi = M/H$) for compound **1**, **2**, **3**, and **4** measured at 1000 Oe. The solid lines are the best fits obtained with the Heisenberg model described in the text.

## Concluding Remarks

The reactions of copper(II) halides with three pyridine alcohol ligands afforded a series of new complexes based on a dinuclear $Cu_2(OR)_2X_2$ core. Among them, two tetranuclear compounds (**2**, **3**) exhibit a defect dicubane structure with two missing vertices, which is rarely observed in $Cu^{II}$ alkoxide chemistry. As shown by the magnetic properties of **1**, this dinuclear $Cu_2(OR)_2X_2$ building block possesses a singlet ground state and thus induces all the resulting complexes based on this unit to also exhibit a diamagnetic ground state. The paramagnetic triplet state is thermally populated above 130 K for all the reported mate-

 © 2006 Wiley-VCH Verlag GmbH & Co. KGaA, Weinheim 

rials. The existence of neutral and deprotonated forms of the coordinated ligands warrants further investigation on the reaction conditions necessary for ligand deprotonation.

## Experimental Section

**General Procedures and Materials:** All manipulations were carried out under ambient conditions by using commercial grade solvents. Chemicals were used as received (Aldrich) without further purification.

**Synthesis**

**$[Cu_2(hpp)_2Br_2]$ (1):** $CuBr_2$ (0.11 g) was dissolved in a mixture of methanol (10.0 mL) and ethanol (10.0 mL). On adding the disodium salt of succinic acid (0.05 g), a blue product precipitated. After the addition of 2-(hydroxypropyl)pyridine (0.13 mL), the mixture was heated to boiling and then cooled to ambient temperature. The remaining blue product was filtered off. Slow cooling of the green filtrate to 5 °C gave bluish-green plate-like crystals of **1**. Yield: 0.023 g (16%). $C_{16}H_{20}Br_2Cu_2N_2O_2$ (559.24): calcd. C 34.36, H 3.60, N 5.01; found C 34.55, H 3.76, N 4.95.

**$[Cu_4(hpp)_4Br_4]$ (2):** $CuBr_2$ (0.11 g) was dissolved in methanol (9.0 mL) and 2-(hydroxypropyl)pyridine (0.13 mL) was added. Slow cooling of the resulting olive-green solution to 5 °C gave grass-green rod-like crystals. Yield: 0.067 g (48%). $C_{32}H_{40}Br_4Cu_4N_4O_4$ (1118.48): calcd. C 34.36, H 3.60, N 5.01; found C 34.57, H 3.72, N 4.90.

**$[Cu_4(hpp)_4Cl_4]$ (3):** $CuCl_2{\cdot}2H_2O$ (0.11 g) was dissolved in methanol (10 mL). 2-(Hydroxypropyl)pyridine (0.13 mL) was then added whilst stirring. Upon ligand addition, the color of the solution changed from light blue to olive green. Green crystals precipitated on standing overnight at ambient conditions. Yield: 0.073 g (62%). $C_{32}H_{40}Cl_4Cu_4N_4O_4$ (940.68): calcd. C 40.85, H 4.29, N 5.96; found C 40.89 H, 4.39, N 5.81.

**$[Cu_2(hep)_2Cl_2]_n$ (4):** $CuCl_2{\cdot}2H_2O$ (0.11 g) was dissolved in methanol (15 mL). 2-(Hydroxyethyl)pyridine (0.13 mL) was then added whilst stirring. Upon ligand addition, the color of the solution changed from light blue to grass green. Green crystals precipitated on standing overnight at room temperature. Yield: 0.078 g (27%). $C_{14}H_{16}Cl_2Cu_2N_2O_2$ (442.28): calcd. C 38.02, H 3.65, N 6.33; found C 38.16, H 3.74, N 6.21.

**$[Cu_2(Hhmp)_2Cl_4]_n{\cdot}2nCH_3OH$ (5):** $CuCl_2{\cdot}2H_2O$ (0.11 g) was dissolved in methanol (10 mL). 2-(Hydroxymethyl)pyridine (0.20 mL) was then added whilst stirring. Upon ligand addition, the color of the solution changed from light blue to grass green. On standing at room temperature, a green microcrystalline product precipitated, which was then filtered off. The mother liquor was cooled slowly to 5 °C, which resulted in the precipitation of grass-green elongated blocks, unstable in air.

**Physical Measurements:** Elemental analyses were measured at the Faculty of Chemistry and Chemical Technology, University of Ljubljana with a Perkin–Elmer 240 C, H, N analyzer. IR spectra were recorded with a Perkin–Elmer 2000 spectrometer. Spectra can be obtained from authors upon request. Magnetic susceptibility measurements were obtained with the use of a Quantum Design SQUID MPMS-XL magnetometer. Measurements were performed on finely ground crystalline samples: 25.13 mg (**1**), 13.48 mg (**2**), 32.14 mg (**3**), and 25.73 mg (**4**) over the temperature range 1.8–300 K. The magnetic data were corrected for the sample holder, and the diamagnetic contribution calculated from Pascal's constants.[17] The presence of ferromagnetic impurities has been systematically checked by measuring the magnetization as a function of the field at 100 K. No presence of ferromagnetic impurities was seen in **1**, **3**, and **4**. For **2**, the susceptibility obtained at 100 K from the $M$ vs. $H$ data has been used to correct the extrinsic ferromagnetic contribution. Physical characterizations of **5** have not been possible because of its high instability in air.

**Crystallography:** X-ray single-crystal data were collected with a Nonius Kappa CCD diffractometer with graphite monochromated Mo-$K_\alpha$ radiation ($\lambda$ = 0.71073 Å) at 150 K for compounds **1**, **3**, and **5** and at 293 K for compounds **2** and **4**. The data were processed by using DENZO and SCALEPACK.[18] The structures were solved by direct methods implemented in the SHELX-97 package[19] and refined by a full-matrix least-squares method on $F^2$ against all reflections by using the same program. Hydrogen atoms were placed in geometrically calculated positions and were refined using a riding model, except those of the alcohol groups in compound **5**, which were found from a Fourier difference map and freely refined. Compound **2** crystallizes in the noncentrosymmetric space group $P2_1$. The value of the Flack parameter 0.495(12) indicates possible racemic twinning. Crystallographic data are listed in Table 4. CCDC-602082, -602083, -602084, -611672, and -611673 contain the supplementary crystallographic data for this paper. These data

Table 4. Crystallographic data for compounds **1**–**5**.

| | **1** | **2** | **3** | **4** | **5** |
|---|---|---|---|---|---|
| Empirical formula | $C_{16}H_{20}Br_2Cu_2N_2O_2$ | $C_{32}H_{40}Br_4Cu_4N_4O_4$ | $C_{32}H_{40}Cl_4Cu_4N_4O_4$ | $C_{14}H_{16}Cl_2Cu_2N_2O_2$ | $C_{14}H_{18}Cl_4Cu_2NO_4$ |
| Formula mass [g mol$^{-1}$] | 559.24 | 1118.48 | 940.68 | 442.28 | 551.24 |
| Space group | $P2_1/a$ | $P2_1$ | $P2_1/n$ | $P\bar{1}$ | $P2_1/n$ |
| $Z$ | 2 | 2 | 2 | 1 | 2 |
| $T$ [K] | 150 | 293 | 150 | 293 | 150 |
| $a$ [Å] | 9.9878(2) | 9.5570(10) | 9.25380(10) | 6.19550(10) | 6.87280(10) |
| $b$ [Å] | 8.83220(10) | 17.2949(2) | 16.8305(2) | 8.0167(2) | 14.9500(2) |
| $c$ [Å] | 10.1894(2) | 11.89280(10) | 11.61430(10) | 8.5418(2) | 10.4520(2) |
| $\alpha$ [°] | | | | 89.7300(10) | |
| $\beta$ [°] | 95.2740(10) | 104.658(2) | 104.899(10) | 79.2820(10) | 104.7518(7) |
| $\gamma$ [°] | | | | 70.0321(10) | |
| $V$ [Å$^3$] | 895.05(3) | 1841.80(4) | 1748.07(9) | 390.994(15) | 1038.53(3) |
| $\mu$ (Mo-$K_\alpha$) [mm$^{-1}$] | 6.851 | 6.659 | 2.750 | 3.067 | 2.584 |
| $d_{calcd.}$ [g cm$^{-3}$] | 2.075 | 2.017 | 1.787 | 1.878 | 1.763 |
| $R_1$, $wR_2$ [$I > 2\sigma(I)$] | 0.0200, 0.0486 | 0.0377, 0.0938 | 0.0231, 0.0587 | 0.0240, 0.0572 | 0.0263, 0.0596 |

 © 2006 Wiley-VCH Verlag GmbH & Co. KGaA, Weinheim 

can be obtained free of charge from The Cambridge Crystallographic Data Centre via www.ccdc.cam.ac.uk/data_request/cif.

## Acknowledgments

We are grateful to the Slovenian Ministry of Higher Education, Science and Technology for financial support through research grant P1–175–103. R.C. thanks MAGMANet (NMP3-CT-2005–515767), the CNRS, the University of Bordeaux 1, and the Conseil Régional d′Aquitaine for financial support.

[1] L. K. Thompson, *Coord. Chem. Rev.* **2002**, *233–234*, 193–206.
[2] J. L. Stuart, *Chem. Soc. Rev.* **2003**, *32*, 276–288.
[3] C. Janiak, *Dalton Trans.* **2003**, 2781–2804.
[4] M. O'Keeffe, M. Eddaoudi, L. Hailian, T. Reineke, O. M. Yaghi, *J. Solid State Chem.* **2000**, *152*, 3–20.
[5] See for example: a) V. Zelenak, A. Orendacova, I. Cisarova, J. Cernak, O. V. Kravchyna, J. Park, M. Orendac, A. G. Anders, A. Feher, M. W. Meisel, *Inorg. Chem.* **2006**, *45*, 1774–1782; b) U. P. Chaudrhuri, L. R. Whiteaker, L. Yang, R. P. Houser, *Dalton Trans.* **2006**, 1902–1908; c) S. Laborda, R. Clérac, C. E. Anson, A. K. Powell, *Inorg. Chem.* **2004**, *43*, 5931–5943; d) M. Murugesu, R. Clérac, C. E. Anson, A. K. Powell, *Chem. Commun.* **2004**, 1598–1599; e) M. Murugesu, P. King, R. Clérac, C. E. Anson, A. K. Powell, *Chem. Commun.* **2004**, 740–741; f) M. Murugesu, R. Clérac, C. E. Anson, A. K. Powell, *Inorg. Chem.* **2004**, *43*, 7269–7271; g) M. Murugesu, R. Clérac, C. E. Anson, A. K. Powell, *J. Phys. Chem. Solids* **2004**, *65*, 667–676.
[6] a) R. E. P. Winpenny, *Chem. Soc. Rev.* **1998**, *27*, 447–452; b) L. K. Thompson, *Coord. Chem. Rev.* **2002**, 193–206; c) J. Mrozinski, *Coord. Chem. Rev.* **2005**, 2534–2548; d) A. Rodriguez-Fortea, P. Alemany, S. Alvarez, E. Ruiz, *Chem. Eur. J.* **2001**, *7*, 627–637; e) M. R. Sundberg, R. Uggla, M. Melnik, *Polyhedron* **1996**, *15*, 1157–1163.
[7] Illustrated by some examples: a) B. Gustaffson, M. Hakansson, G. Westman, S. Jagner, *J. Organomet. Chem.* **2003**, *649*, 204–208; b) U. Turpeinen, O. Orama, I. Mutikainen, R. Hamalainen, *Z. Kristallogr.* **1996**, *211*, 867–869; c) R. Mergehenn, L. Merz, W. Haase, *J. Chem. Soc., Dalton Trans.* **1980**, 1703–1709; d) J. K. Eberhardt, T. Glaser, R.-D. Hoffman, R. Frohlich, E.-U. Wurthwein, *Eur. J. Inorg. Chem.* **2005**, 1175–1181; e) H. Oshio, Y. Saito, T. Ito, *Angew. Chem. Int. Ed. Engl.* **1997**, *36*, 2673–2675; f) R. Wegner, M. Gottschaldt, H. Gorls, E.-G. Jager, D. Klemm, *Chem. Eur. J.* **2001**, *7*, 2143–2157; g) A. Mukherjee, R. Raghunathan, M. K. Saha, M. Nethaji, S. Ramasesha, A. R. Chakravarty, *Chem. Eur. J.* **2005**, *11*, 3087–3096.
[8] Illustrated by some examples: a) M. Koikawa, H. Yamashita, T. Tokii, *Inorg. Chim. Acta* **2004**, *357*, 2635–2642; b) A. Bencini, A. Dei, C. Sangregorio, F. Totti, M. G. F. Vaz, *Inorg. Chem.* **2003**, *42*, 8065; c) D. Christodoulou, C. George, L. K. Keefer, *J. Chem. Soc., Chem. Commun.* **1993**, 937–939; d) W. Bidell, V. Shklover, H. Berke, *Inorg. Chem.* **1992**, *31*, 5561–5571.
[9] S. S. Tandon, L. K. Thompson, J. N. Bridson, M. Bubenik, *Inorg. Chem.* **1993**, *32*, 4621–4631.
[10] a) J. Yoo, A. Yamaguchi, M. Nakano, J. Krzystek, W. E. Streib, L. C. Brunel, H. Hishimoto, G. Christou, D. N. Hendrickson, *Inorg. Chem.* **2001**, *40*, 4604–4616; b) E. C. Yang, N. Harden, W. Wernsdorfer, L. Zakhrov, E. K. Brechin, A. L. Rheingold, G. Christou, D. N. Hendrickson, *Polyhedron* **2003**, *22*, 1857–1863; c) D. N. Hendrickson, G. Christou, H. Ishimoto, J. Yoo, E. K. Brechin, A. Yamaguchi, E. M. Rumberger, S. M. J. Aubin, Z. Sun, G. Aromí, *Polyhedron* **2001**, *20*, 1479–1488; d) L. Lecren, Y.-G. Li, W. Wernsdorfer, O. Roubeau, H. Miyasaka, R. Clérac, *Inorg. Chem. Commun.* **2005**, *8*, 626–630; e) L. Lecren, O. Roubeau, C. Coulon, Y.-G. Li, X. F. Le Golf, W. Wernsdorfer, H. Miyasaka, R. Clérac, *J. Am. Chem. Soc.* **2005**, *127*, 17353–17363; f) L. Lecren, W. Wernsdorfer, Y.-G. Li, O. Roubeau, H. Miyasaka, R. Clérac, *J. Am. Chem. Soc.* **2005**, *127*, 11311–11317; g) J. Yoo, J. W. Wernsdorfer, E.-C. Yang, M. Nakano, A. L. Rheingold, D. N. Hendrickson, *Inorg. Chem.* **2005**, *44*, 3377–3379; h) H. Miyasaka, K. Nakata, L. Lecren, C. Coulon, Y. Nakazawa, T. Fujisaki, K.-I. Sugiura, M. Yamashita, R. Clérac, *J. Am. Chem. Soc.* **2006**, *128*, 3770–3783.
[11] a) J. Moncol, M. Mudra, P. Lonnecke, M. Koman, M. Melnik, *J. Coord. Chem.* **2004**, *57*, 1065–1078; b) V. T. Yilmaz, S. Guney, O. Andac, W. T. A. Harrison, *Polyhedron* **2002**, *21*, 2393–2402; c) N. N. Hoang, F. Valach, M. Dunaj-Jurco, M. Melnik, *Acta Crystallogr., Sect. C* **1992**, *48*, 443–445; d) J. Moncol, J. Kalinakova, J. Svorec, M. Kleinova, M. Koman, D. Hudecova, M. Melnik, M. Mazur, M. Valko, *Inorg. Chim. Acta* **2004**, *357*, 3211–3222; e) F. He, D. Liu, *Acta Crystallogr., Sect. E* **2005**, *61*, m1350–1351; f) M. Mudra, J. Moncol, P. Lonnecke, M. Melnik, CSD reference code: ACEJAU01.
[12] W. Choong, N. C. Stephenson, *Cryst. Struct. Commun.* **1975**, *4*, 275–280.
[13] a) S. Hamamci, V. T. Yilmaz, C. Thöne, *Acta Crystallogr., Sect. E* **2004**, *60*, m159–161; b) V. T. Yilmaz, S. Hamamci, C. Thöne, *J. Coord. Chem.* **2003**, *56*, 787–795.
[14] V. T. Yilmaz, S. Hamamci, O. Andac, C. Thöne, W. T. A. Harrison, *Transition Met. Chem.* **2003**, *28*, 676–681.
[15] S. Tanase, E. Bouwman, W. L. Driessen, J. Reedijk, R. de Gelder, *Inorg. Chim. Acta* **2003**, *355*, 458–461.
[16] B. Bleaney, K. D. Bowers, *Proc. R. Soc. London* **1952**, A214.
[17] E. A. Boudreaux, L. N. Mulay (Eds), *Theory and Applications of Molecular Paramagnetism*; John Wiley & Sons: New York, **1976**.
[18] Z. Otwinowski, W. Minor, *Methods Enzymol.* **1996**, *276*, 307.
[19] G. M. Sheldrick, *SHELX-97*, *Program for Crystal Structure Solution and Refinement*, University of Göttingen: Göttingen, Germany, **1997**.

Received: June 26, 2006
Published Online: October 13, 2006

 © 2006 Wiley-VCH Verlag GmbH & Co. KGaA, Weinheim 

DOI: 10.1002/ejic.200600651

# Cobalt and Nickel Complexes Bearing Pyrazolyliminophosphorane Ligands: Synthesis, Characterisation and Catalytic Ethylene Oligomerisation Behaviour

**Cheng Zhang,[a] Wen-Hua Sun,[b] and Zhong-Xia Wang*[a]**

**Keywords:** Cobalt / Nickel / Homogeneous catalysis / Ethylene / Oligomerisation

Treatment of 1-(2′-azidophenyl)-3,5-dimethylpyrazole (**1**) with $Ph_2PR$ (R = Ph, Me) and $(Ph_2P)_2CH_2$, respectively, affords the pyrazolyliminophosphoranes **2**, **3** and **4**. Reaction of **2** or **3** with $[NiCl_2(dme)]$ or $NiBr_2$ yields the N,N-chelate nickel complexes **5**–**8**, and with $CoCl_2$ complexes **9** and **10**. Reaction of **4** with $[NiCl_2(dme)]$, $NiBr_2$ and $CoCl_2$, respectively, affords the N,N,P-chelate complexes **11**–**13**. Compounds **2**–**4** were characterised by $^1H$, $^{13}C$, $^{31}P$ NMR and IR spectroscopy and elemental analysis, while complexes **5**–**13** were characterised by IR spectroscopy and elemental analysis. The structures of complexes **5**, **9** and **12** were further characterised by single-crystal X-ray diffraction techniques. Complexes **5**–**13** are active catalysts for ethylene oligomerisation upon activation with alkylaluminium derivatives ($Et_2AlCl$, MAO or MMAO). These complexes exhibit good to high catalytic activities (up to $3.54 \times 10^6$ g mol$^{-1}$ h atm for the nickel complexes and $5.48 \times 10^5$ g mol$^{-1}$ h atm for the cobalt complexes). The effects of varying ethylene pressure, temperature and aluminium co-catalyst/Ni or Co ratios with complexes **5**, **9**, **11** and **12** are reported.
(© Wiley-VCH Verlag GmbH & Co. KGaA, 69451 Weinheim, Germany, 2006)

## Introduction

Ethylene oligomerisation to form linear α-olefins has become a topic of considerable interest in both academia and industry as these oligomers are used as co-monomers with ethylene and for the preparation of a variety of important compounds such as detergents, synthetic lubricants, additives for high-density polyethylene production and surfactants.[1] Late transition metal complexes have demonstrated potential as catalysts for ethylene oligomerisation. A representative example is the nickel catalysts in the Shell higher olefin process (SHOP).[2] Other late transition metal complexes have also proved to be active. These complexes are supported by extensive didentate and tridentate ligands, including N,N,[3] N,P,[1,4] N,O,[5] P,O,[6] P,P,[7] N,N,P,[8] N,N,N,[1b,3b,9] N,P,N[10] and P,N,P[11] ligands. Recently, chelating nitrogen ligands featuring iminophosphorane moieties have attracted considerable attention. Examples include **I**–**V** (Scheme 1).[3a–3d,12] Some of the late transition metal complexes with these ligands exhibit ethylene polymerisation or oligomerisation activities in the presence of appropriate co-catalysts. Pyrazole-based ligands have also received extensive attention in recent years for the preparation of olefin polymerisation catalysts, including poly(pyrazolyl)borates, didentate bis-pyrazolyl ligands and mixed donor ligands.[1b,4f,9b,13] Our aim was to examine a set of new ligands that combine pyrazolyl and iminophosphorane units for late transition metals relevant for catalysis of ethylene polymerisation or oligomerisation. Herein we report the synthesis, characterisation and catalytic performance for ethylene oligomerisation of cobalt and nickel complexes bearing pyrazolyliminophosphorane ligands.

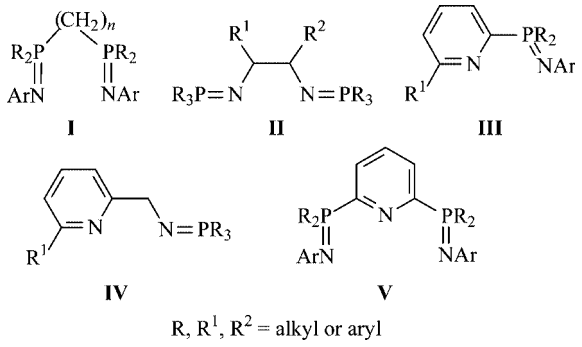


Scheme 1.

## Results and Discussion

### Synthesis and Characterisation of Compounds 2–13

Compound **1** was prepared according to a literature method.[4f,14] Syntheses of ligands **2**–**4** and cobalt and nickel complexes **5**–**13** are summarised in Scheme 2. Treatment of **1** with one equivalent of phosphane $Ph_2PR$ (R = Ph or Me) or $Ph_2PCH_2PPh_2$ yielded iminophosphoranes **2**–**4** in high yields. Reaction of **2** or **3** with $MX_2$ (M = Ni, X

[a] Department of Chemistry, University of Science and Technology of China,
Hefei, Anhui 230026, P. R. China
[b] Key Laboratory of Engineering Plastics, Institute of Chemistry, The Chinese Academy of Sciences,
Beijing 100080, P. R. China

 © 2006 Wiley-VCH Verlag GmbH & Co. KGaA, Weinheim 

= Br; M = Co, X = Cl) or [$NiCl_2$(dme)] afforded complexes **5**–**10** in good to excellent yields. A similar reaction between **4** and the metal halides gave complexes **11**–**13**. Compounds **2**–**4** are yellow (**2** and **4**) or orange (**3**) solids and were fully characterised by $^1H$, $^{13}C$ and $^{31}P$ NMR spectroscopy and elemental analyses. Complexes **5**–**13** are blue (**5**–**10** and **13**), purple (**11**) or yellow (**12**) crystals or powder. Complexes **5** and **7**–**13** are air stable and complex **6** forms an $H_2O$ adduct after being exposed to air for a long period. These complexes are paramagnetic and were characterised by IR spectroscopy and elemental analyses, as well as by single-crystal X-ray diffraction techniques (for **5**, **9** and **12**).

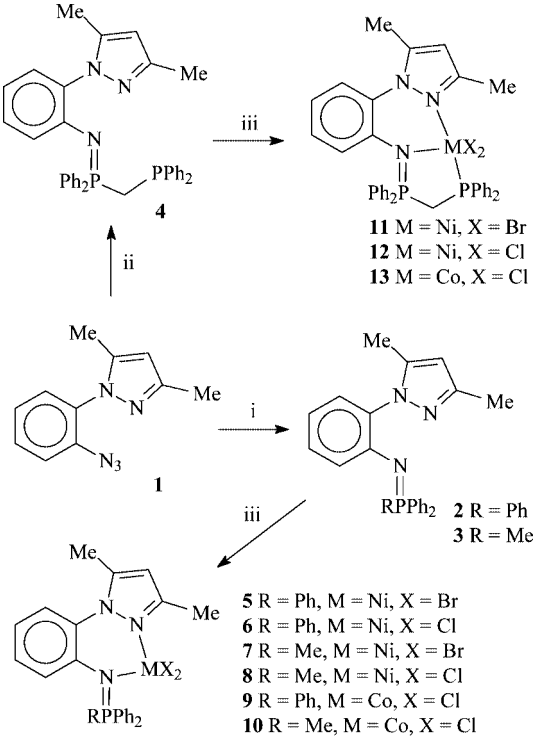


Scheme 2. Synthesis of compounds **2**–**13**. Reagents and conditions: i) $Ph_2PR$ (R = Ph, Me), $CH_2Cl_2$, room temperature, 12 h; ii) $Ph_2PCH_2PPh_2$, $CH_2Cl_2$, room temperature, 12 h; iii) $MX_2$ (M = Ni, X = Br; M = Co, X = Cl) or [$NiCl_2$(dme)], thf, room temperature, 15 h.

The structure of **5** is presented in Figure 1. Crystalline **5** is monomeric. Its Ni atom is four coordinate and has a distorted tetrahedral geometry. The N1–C19–C24–N2 atoms lie in the same plane. The N1–Ni1–N3–N2 atoms are also approximately co-planar, with a torsion angle of 4°. The six-membered metallacycle shows a boat conformation. The Ni1–N1 distance of 2.002(6) Å is longer than those found in [{2-[$Ph_2P$=N($C_6H_3Me_2$-2′,6′)]-6-($SiMe_3$)-$C_5H_3N$}$NiBr_2$] [1.996(8) Å] and [{2-($Ph_3P$=$NCH_2$)-6-$MeC_5H_3N$}$NiBr_2$] [1.983(3) Å].[3c] The Ni1–N3 distance of 2.007(6) Å is close to that in [{1-(2′-$Ph_2PC_6H_4$)-3,5-$Me_2C_3HN_2$}$NiCl_2$] [2.003(4) Å],[4f] but slightly shorter than those found in [{NH(1-$CH_2CH_2$-3,5-$Me_2$-$C_3HN_2)_2$}$NiCl_2$] [2.069(2) and 2.0334(19) Å, respectively].[1b] The two Ni–Br bond lengths are very similar and are typical for this class of compounds.[3c,15] The P–N distance of 1.624(6) Å is normal for metal-coordinated iminophosphoranes.[3b,16]

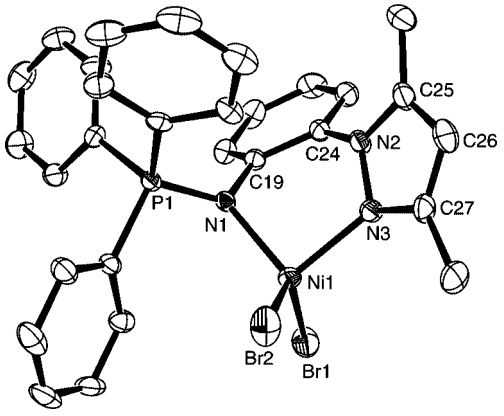


Figure 1. ORTEP drawing of complex **5** (thermal ellipsoids at 30% probability). Selected bond lengths [Å] and angles [°]: Ni(1)–N(1) 2.002(6), Ni(1)–N(3) 2.007(6), Ni(1)–Br(1) 2.3614(13), Ni(1)–Br(2) 2.3743(13), P(1)–N(1) 1.624(6), N(1)–C(19) 1.421(9), N(2)–N(3) 1.388(8), N(2)–C(24) 1.434(9), C(19)–C(24) 1.412(10); N(1)–Ni(1)–N(3) 92.2(2), N(1)–Ni(1)–Br(1) 104.75(17), N(3)–Ni(1)–Br(1) 108.5(2), N(1)–Ni(1)–Br(2) 113.81(16), N(3)–Ni(1)–Br(2) 106.71(18), Br(1)–Ni(1)–Br(2) 125.71(6), C(19)–N(1)–Ni(1) 113.3(4), P(1)–N(1)–Ni(1) 124.4(3), C(27)–N(3)–Ni(1) 127.4(5), N(2)–N(3)–Ni(1) 118.3(4), C(19)–N(1)–P(1) 121.5(5), N(3)–N(2)–C(24) 119.1(6).

The structure of **9** is shown in Figure 2. Crystalline **9** is monomeric and the Co centre is in a distorted tetrahedral environment. Like complex **5**, the six-membered metallacycle also exists in a boat conformation in the solid state. The Co–N distance (av. 2.045 Å) is close to that in [{$CH_2$($Ph_2P$=NPh)$_2$}$CoCl_2$] (av. 2.032 Å).[3b] The Co–Cl

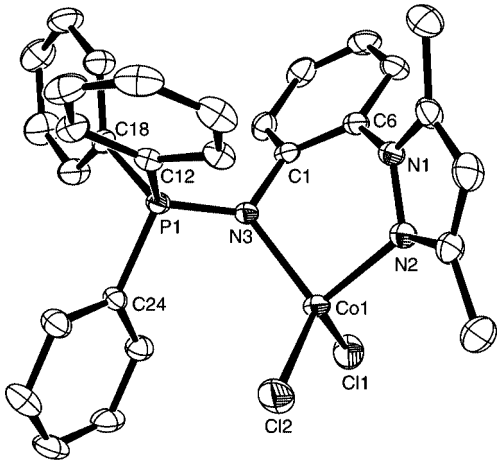


Figure 2. ORTEP drawing of complex **9** (thermal ellipsoids at 30% probability). Selected bond lengths [Å] and angles [°]: Co(1)–N(2) 2.052(2), Co(1)–N(3) 2.038(2), Co(1)–Cl(1) 2.2376(10), Co(1)–Cl(2) 2.2476(10), P(1)–N(3) 1.610(2), N(1)–N(2) 1.385(3), N(1)–C(6) 1.435(4), C(1)–C(6) 1.401(4), N(3)–C(1) 1.427(3); N(3)–Co(1)–N(2) 91.54(9), N(3)–Co(1)–Cl(1) 108.60(7), N(2)–Co(1)–Cl(1) 113.27(8), N(3)–Co(1)–Cl(2) 115.95(7), N(2)–Co(1)–Cl(2) 107.75(8), Cl(1)–Co(1)–Cl(2) 117.01(4), N(1)–N(2)–Co(1) 117.84(18), C(1)–N(3)–Co(1) 111.62(17), N(2)–N(1)–C(6) 119.4(2), C(1)–N(3)–P(1) 122.10(18), C(1)–N(3)–Co(1) 111.62(17), P(1)–N(3)–Co(1) 125.55(13).

 © 2006 Wiley-VCH Verlag GmbH & Co. KGaA, Weinheim 

distances [2.2376(10) and 2.2476(10) Å, respectively] are within the normal range for four-coordinate Co complexes.[3b,3c,17]

Single crystals of complex **12** suitable for X-ray crystallography were grown from toluene. The molecular structure of complex **12** is presented in Figure 3. Complex **12** is monomeric and co-crystallises with one toluene molecule. The coordination geometry around the nickel atom is distorted trigonal bipyramidal in which the P1–Ni1–N3 angle is 167.57(9)° as a result of the strain imposed by the five- and six-membered chelate rings. The N1–Ni1–Cl1–Cl2 atoms are nearly co-planar. The N1–C26–P2–Ni1 atoms are also approximately in the same plane, the sum of the angles around N1 being 359.92°. The Ni–N distance (av. 2.063 Å) is slightly longer than that in complex **5** and comparable to those in [{NH(1-$CH_2CH_2$-3,5-$Me_2C_3HN_2$)$_2$}$NiCl_2$] [2.069(2) and 2.0334(19) Å, respectively].[1b] Both P1 and P2 exhibit distorted tetrahedral geometries. The Ni1–P1 distance of 2.4001(11) Å is longer than that in [{1-(2′-$Ph_2PC_6H_4$)-3,5-$Me_2C_3HN_2$}$NiCl_2$] [2.281(2) Å],[4f] but still within the normal range.[8]

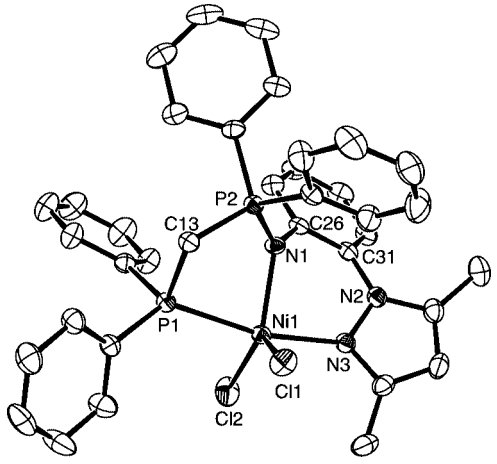


Figure 3. ORTEP drawing of complex **12** (thermal ellipsoids at 30% probability). Selected bond lengths [Å] and angles [°]: Ni(1)–N(1) 2.066(3), Ni(1)–N(3) 2.060(3), Ni(1)–Cl(2) 2.3012(11), Ni(1)–Cl(1) 2.3187(11), Ni(1)–P(1) 2.4001(11), P(2)–N(1) 1.603(3), P(1)–C(13) 1.842(3), P(2)–C(13) 1.806(3), N(2)–N(3) 1.377(4), N(2)–C(31) 1.424(5), N(1)–C(26) 1.405(4), C(26)–C(31) 1.412(5); N(1)–Ni(1)–N(3) 87.00(11), N(1)–Ni(1)–Cl(2) 129.22(9), N(3)–Ni(1)–Cl(2) 92.76(9), N(1)–Ni(1)–Cl(1) 102.94(9), N(3)–Ni(1)–Cl(1) 94.35(9), Cl(2)–Ni(1)–Cl(1) 127.65(5), N(1)–Ni(1)–P(1) 80.64(8), N(3)–Ni(1)–P(1) 167.57(9), Cl(2)–Ni(1)–P(1) 96,05(4), Cl(1)–Ni(1)–P(1) 87.20(4), P(2)–N(1)–Ni(1) 118.82(15), C(26)–N(1)–Ni(1) 114.9(2), C(26)–N(1)–P(2) 126.2(2), N(2)–N(3)–Ni(1) 122.8(2), C(13)–P(1)–Ni(1) 99.02(12), N(1)–P(2)–C(13) 106.93(15).

## Catalytic Properties of Complexes 5–13 for Ethylene Oligomerisation

We initially examined the catalytic activities of complexes **5**–**10** using $Et_2AlCl$ as activator; the results are displayed in Table 1. At an Al/metal molar ratio of 300 and 20 °C under 1 atm of ethylene the cobalt complexes **9** and **10** are inactive, whereas complexes **5**–**8** catalyse the dimerisation and trimerisation of ethylene with high activity ($2.09 \times 10^5$ to $1.86 \times 10^6$ g mol$^{-1}$ h; entries 3 and 11–13 in Table 1). The influence of the Al/Ni ratio, the reaction temperature and ethylene pressure was investigated for complex **5**. At 20 °C under 1 atm of ethylene, when the ratio of Al to Ni was 300 complex **5** showed the highest catalytic activity ($1.34 \times 10^6$ g mol$^{-1}$ h atm). Variation of the reaction temperature also influences the catalytic activity and product distribution. Thus, with a rise of the temperature from 20 °C to 40 °C and finally to 55 °C the catalytic activity of **5** gradually decreased and the proportion of $C_6$ component increased (entries 3, 7 and 8 in Table 1). At 0 °C the catalytic activity of **5** was close to that at 40 °C. However, the proportion of $C_6$ component at 0 °C was far lower than that at 40 °C (entry 3 in Table 1). This decrease of catalytic activity with a rise of temperature may be attributable to the lower solubility of ethylene and the decomposition of the active sites at higher temperature. The catalytic activities of complexes **6** and **7** at 20 °C under 1 atm of ethylene and with a 300:1 Al/Ni molar ratio ($7.67 \times 10^5$ and $2.09 \times 10^5$ g mol$^{-1}$ h atm, respectively) are lower than that of complex **5**. Complex **8** exhibits the highest catalytic activity ($1.86 \times 10^6$ g mol$^{-1}$ h atm). Enhancement of the ethylene pressure does not increase the catalytic activity of **5** in unit pressure (entry 10 in Table 1). Comparison of the catalytic

Table 1. Ethylene oligomerisation with **5**–**8**.[a]

| Entry | Complex | Al/Ni | *P* [atm] | Time [h] | *T* [°C] | Activity[b] | $C_4$ [%][c] | $C_6$ [%][c] |
|---|---|---|---|---|---|---|---|---|
| 1 | **5** | 50 | 1 | 0.5 | 20 | 2.24 | 67.3 | 32.7 |
| 2 | **5** | 200 | 1 | 0.5 | 20 | 7.99 | 82.1 | 17.9 |
| 3 | **5** | 300 | 1 | 0.5 | 20 | 13.4 | 78.8 | 21.2 |
| 4 | **5** | 400 | 1 | 0.5 | 20 | 7.30 | 73.4 | 26.6 |
| 5 | **5** | 600 | 1 | 0.5 | 20 | 7.09 | 54.1 | 45.9 |
| 6 | **5** | 300 | 1 | 0.5 | 0 | 5.50 | 74.0 | 26.0 |
| 7 | **5** | 300 | 1 | 0.5 | 40 | 5.64 | 13.3 | 86.7 |
| 8 | **5** | 300 | 1 | 0.5 | 55 | 2.86 | 5.4 | 94.6 |
| 9 | **5** | 300 | 1 | 1 | 20 | 14.3 | 76.9 | 23.1 |
| 10 | **5** | 300 | 10 | 0.5 | 20 | 71.3 | 79.2 | 20.8 |
| 11 | **6** | 300 | 1 | 0.5 | 20 | 7.67 | 64.7 | 35.3 |
| 12 | **7** | 300 | 1 | 0.5 | 20 | 2.09 | 77.8 | 22.2 |
| 13 | **8** | 300 | 1 | 0.5 | 20 | 18.6 | 72.1 | 27.9 |

[a] Conditions: 5 μmol of pre-catalyst, $Et_2AlCl$ as co-catalyst, 30 mL of toluene (120 mL of toluene with 10 atm of ethylene). [b] $10^5$ g mol$^{-1}$ h. [c] Weight percent determined by GC analysis.

 © 2006 Wiley-VCH Verlag GmbH & Co. KGaA, Weinheim 

Table 2. Ethylene oligomerisation with complexes **11** and **12**.[a]

| Entry | Complex | Al/Ni | *P* [atm] | Time [h] | *t* [°C] | Activity[b] | $C_4$ [%][c] | $C_6$ [%][c] |
|---|---|---|---|---|---|---|---|---|
| 1 | **11** | 50 | 1 | 0.5 | 20 | 1.80 | 76.6 | 23.4 |
| 2 | **11** | 200 | 1 | 0.5 | 20 | 2.12 | 78.8 | 21.2 |
| 3 | **11** | 300 | 1 | 0.5 | 20 | 2.97 | 61.0 | 39.0 |
| 4 | **11** | 500 | 1 | 0.5 | 20 | 2.63 | 57.4 | 42.6 |
| 5 | **11** | 700 | 1 | 0.5 | 20 | 2.23 | 61.8 | 38.2 |
| 6 | **11** | 300 | 1 | 0.5 | 0 | 2.38 | 80.5 | 19.5 |
| 7 | **11** | 300 | 1 | 0.5 | 40 | 3.54 | 72.2 | 27.8 |
| 8 | **11** | 300 | 1 | 0.5 | 60 | 1.07 | 68.0 | 32.0 |
| 9 | **11** | 300 | 1 | 1 | 20 | 1.41 | 50.4 | 49.6 |
| 10 | **11** | 300 | 10 | 0.5 | 40 | 8.52 | 76.2 | 23.8 |
| 11 | **12** | 300 | 1 | 0.5 | 20 | 2.85 | 70.5 | 29.5 |
| 12 | **12** | 300 | 1 | 0.5 | 40 | 2.53 | 62.0 | 38.0 |
| 13 | **12** | 300 | 1 | 0.5 | 0 | 2.42 | 68.9 | 31.1 |
| 14 | **12** | 300 | 1 | 0.5 | 60 | 1.88 | 66.0 | 34.0 |

[a] Conditions: 5 μmol of pre-catalyst, $Et_2AlCl$ as co-catalyst, 30 mL of toluene (120 mL of toluene when determined at 10 atm). [b] $10^6$ g mol$^{-1}$ h. [c] Weight percent determined by GC analysis.

activities of complexes **5**–**8** showed that under the same conditions the activity order is **8** > **5** > **6** > **7**. Unfortunately, it is difficult to establish a relationship between the catalytic activities and the electronic and steric effects of the groups attached to the phosphorus and nickel atoms from these results.

It has been reported that the nickel complexes of N,N,P-tridentate ligands **VI** show high catalytic activity for ethylene oligomerisation in the presence of $EtAlCl_2$.[8] We therefore added a $Ph_2P$ group to the *P*-methyl of ligand **3** to construct the new N,N,P tridentate ligand **4**. The nickel complexes of the ligand (**11** and **12**) show high catalytic activity for ethylene oligomerisation in the presence of $Et_2AlCl$ (Table 2). In each case the reaction produced a mixture of $C_4$ and $C_6$ species. The quantity of aluminium co-catalyst affected the outcome of the reaction. For complex **11**, enhancement of the Al/Ni molar ratio from 50:1 to 300:1 gave an increase in catalytic activity. With further augmentation of the Al/Ni ratio the catalytic activity gradually decreased (entries 1–5 in Table 2). The effect of reaction temperature was also studied. The reaction was carried out at 0, 20, 40 and 60 °C, and the results showed that the highest catalytic activity was achieved at 40 °C. It seems that in this example the lowering of ethylene solubility at higher temperature is not the main factor affecting the catalytic activity of **11**. It was also noted that prolonging the reaction time led to a decrease of catalytic activity and an increase of the $C_6$ fraction in the products. This increase of the proportion of $C_6$ component may be due to co-oligomerisation of $C_4$ accumulated in the reaction vessel. The influence of pressure was similar to that with complex **5**. Thus, an increase of ethylene pressure did not obviously

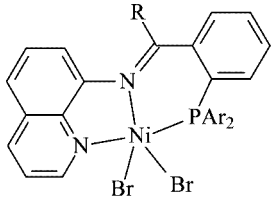


**VI**

Table 3. Ethylene oligomerisation with complexes **9**, **10** and **13**.[a]

| Entry | Complex | Co-catalyst | Al/Co | Activity[b] | $C_4$ [%][c] | $C_6$ [%][c] |
|---|---|---|---|---|---|---|
| 1 | **9** | MAO | 300 | very low | | |
| 2 | **9** | MAO | 500 | 2.56 | 82.7 | 17.3 |
| 3 | **9** | MAO | 800 | 3.18 | 20.7 | 79.3 |
| 4 | **9** | MAO | 1000 | 3.85 | 27.9 | 72.1 |
| 5 | **9** | MAO | 1500 | 4.51 | 16.9 | 83.1 |
| 6 | **9** | MAO | 1800 | 5.62 | 19.1 | 80.9 |
| 7 | **9** | MAO | 2400 | 8.60 | 21.0 | 79.0 |
| 8 | **10** | MAO | 2400 | 7.01 | 16.9 | 83.1 |
| 9 | **13** | MAO | 2400 | 7.12 | 22.6 | 77.4 |
| 10 | **9** | MMAO | 300 | 15.5 | 97.6 | 2.4 |
| 11 | **9** | MMAO | 500 | 24.2 | >99 | |
| 12 | **9** | MMAO | 800 | 26.0 | >99 | |
| 13 | **9** | MMAO | 1000 | 27.3 | >99 | |
| 14 | **9** | MMAO | 1500 | 52.3 | >99 | |
| 15 | **9** | MMAO | 2000 | 53.3 | >99 | |
| 16 | **10** | MMAO | 2000 | 54.8 | >99 | |
| 17 | **13** | MMAO | 2000 | 33.6 | >99 | |

[a] Conditions: 5 μmol of pre-catalyst, 20 °C, 30 mL of toluene, 1 atm of ethylene, 0.5 h. [b] $10^4$ g mol$^{-1}$ h. [c] Weight percent determined by GC analysis.

 © 2006 Wiley-VCH Verlag GmbH & Co. KGaA, Weinheim 

enhance the catalytic activity of **11** in unit pressure (entry 10 in Table 2). For complex **12**, the highest activity was observed at 20 °C and 1 atm of ethylene in the presence of 300 equiv. of $Et_2AlCl$.

In addition, compared with the nickel complexes with didentate ligands **5**–**8**, complexes **11** and **12** exhibit higher catalytic activity under similar reaction conditions.

The nature of the aluminium co-catalyst affects the catalytic properties of the pre-catalysts greatly. As we mentioned above, the cobalt complexes are inactive for ethylene oligomerisation with $Et_2AlCl$ as co-catalyst. However, they showed good catalytic activities for ethylene oligomerisation with MAO or MMAO as activator (Table 3). Complexes **9**, **10** and **13** showed similar catalytic activities when MAO was used as co-catalyst (Al/Co = 2400) at 20 °C under 1 atm of ethylene. The catalytic reaction yielded a mixture of $C_4$ and $C_6$ species.

When MMAO was used as co-catalyst, **13** revealed lower activity than **9** and **10**. However, each of complexes **9**, **10** and **13** exhibits higher activities than that with MAO as activator under similar reaction conditions. We also tested the effect of the Al/Co ratio for complex **9**. Increase of the MAO/Co or MMAO/Co ratio resulted in an enhancement of catalytic activities (entries 1–7 and 10–15 in Table 3). An important feature of the cobalt complex/MMAO systems was the selectivity: in each case the reaction gave almost single $C_4$ species.

## Conclusions

We have synthesised and characterised a set of novel N,N and N,N,P chelating ligands and their nickel and cobalt complexes. Upon activation with $Et_2AlCl$, the nickel complexes reveal high catalytic activity for the dimerisation and trimerisation of ethylene under the optimal conditions, whereas the cobalt complexes are inactive. When activated with MAO or MMAO the cobalt complexes exhibit high catalytic activities. It was also observed that the catalytic activity of complex **9** increases with an increase of the Al/Co ratio. When activated with MMAO, the cobalt complexes show high selectivity, forming almost single $C_4$ species. Investigation of the action of the ligands revealed that the nickel complexes with the tridentate ligand have a higher catalytic activity than those with didentate ligands when activated with $Et_2AlCl$. However, the cobalt complexes with tridentate ligands exhibit lower activity than those with didentate ligands when activated with MMAO. When MAO was used as activator, the cobalt complexes with either tridentate or didentate ligands show similar catalytic activity.

## Experimental Section

**General Procedure:** All air- or moisture-sensitive manipulations were performed under dry $N_2$ using standard Schlenk and vacuum-line techniques. Solvents were distilled under $N_2$ over sodium/benzophenone (toluene, *n*-hexane, thf and $Et_2O$) or $CaH_2$ ($CH_2Cl_2$) and degassed prior to use. NMR spectra were recorded with a Bruker av300 spectrometer at ambient temperature (300 MHz for $^1H$, 75.5 MHz for $^{13}C$ and 121.5 MHz for $^{31}P$). The chemical shifts of $^1H$ and $^{13}C$ NMR spectra are referenced to internal solvent resonances; the $^{31}P$ NMR spectra are referenced to external 85% $H_3PO_4$. IR spectra were recorded with a Bruker VECTOR-22 spectrometer. Elemental analyses were performed by the Analytical Centre of the University of Science and Technology of China. GC analyses were performed with a Carlo Erba Strumentazione gas chromatograph equipped with a flame ionisation detector and a 30 m (0.25 mm i.d., 0.25 μm film thickness) DM-1 silica capillary column. High purity ethylene was purchased from Beijing Yanshan Petrochemical Co. and used as received. Methylaluminoxane (MAO, 1.46 M in toluene) and modified methylaluminoxane (MMAO, 1.93 M in heptane) were purchased from Akzo Nobel Corp. $Et_2AlCl$ was purchased from Fluka as a 1.90 M solution in hexane. 3,5-Dimethyl-1-(2′-azidophenyl)pyrazole and [$NiCl_2$(dme)] were prepared according to literature methods.[4f,14,18]

**Preparations**

**1-{*o*-($Ph_3PN$)$C_6H_4$}-3,5-$Me_2C_3HN_2$ (2):** A solution of **1** (2.09 g, 9.8 mmol) in $CH_2Cl_2$ (20 mL) was added to a stirred solution of $PPh_3$ (2.57 g, 9.8 mmol) in $CH_2Cl_2$ (10 mL) at room temperature and the mixture was stirred overnight. Volatiles were removed in vacuo and the residue was dissolved in diethyl ether. Filtration of the solution and concentration of the filtrate afforded **2** as a yellow powder (3.95 g, 90.2%), m.p. 126–127 °C. $^1H$ NMR ($CDCl_3$): $\delta$ = 2.02 (s, 3 H, $CH_3$), 2.25 (s, 3 H, $CH_3$), 5.89 (s, 1 H, CH), 6.42 (d, $J$ = 7.8 Hz, 1 H, $C_6H_4$), 6.58 (t, $J$ = 7.5 Hz, 1 H, $C_6H_4$), 6.81 (dt, $J$ = 7.5, 8.1 Hz, 1 H, $C_6H_4$), 7.14–7.20 (m, 1 H, $C_6H_4$), 7.25–7.31 (m, 6 H, Ph), 7.35–7.39 (m, 3 H, Ph), 7.47–7.54 (m, 6 H, Ph) ppm. $^{13}C$ NMR ($CDCl_3$): $\delta$ = 11.8, 13.9, 104.0, 117.1, 122.1 (d, $J$ = 9.4 Hz), 128.5 (d, $J$ = 12.1 Hz), 128.7, 130.5, 131.6 (d, $J$ = 2.7 Hz), 131.8, 132.6 (d, $J$ = 9.8 Hz), 134.5, 134.8, 141.7, 147.5 ppm. $^{31}P$ NMR ($CDCl_3$): $\delta$ = –3.56 ppm. IR: $\tilde{\nu}$ = 3049 $cm^{-1}$ w, 3017 vw, 2960 vw, 2925 w, 1591 m, 1548 m, 1496 vs, 1472 s, 1460 s, 1438 s, 1378 m, 1366 m, 1343 vs, 1314 m, 1288 m, 1164 w, 1137 w, 1109 vs, 1054 m, 1033 m, 1020 m, 997 m, 930 w, 780 m, 768 m, 764 s, 718 vs, 694 s, 657 w, 648 w. $C_{29}H_{26}N_3P$ (447.511): calcd. C 77.83, H 5.85, N 9.39; found C 77.50, H 5.87, N 9.49.

**1-{*o*-($Ph_2MePN$)$C_6H_4$}-3,5-$Me_2C_3HN_2$ (3):** This compound was prepared using a similar method to that for **2**. Reaction of $Ph_2PMe$ (1.67 g, 8.4 mmol) with **1** (1.78 g, 8.4 mmol) in $CH_2Cl_2$ (30 mL) gave orange crystals of **3** (2.74 g, 84.5%), m.p. 86–87 °C. $^1H$ NMR ($CDCl_3$): $\delta$ = 1.96 (d, $J$ = 12.6 Hz, 3 H, $CH_3$), 2.21 (s, 3 H, $CH_3$), 2.32 (s, 3 H, $CH_3$), 5.93 (s, 1 H, CH), 6.54 (d, $J$ = 8.1 Hz, 1 H, $C_6H_4$), 6.71 (t, $J$ = 7.2 Hz, 1 H, $C_6H_4$), 6.95–7.01 (m, 1 H, $C_6H_4$), 7.24–7.27 (m, 1 H, $C_6H_4$), 7.32–7.49 (m, 6 H, Ph), 7.57–7.63 (m, 4 H, Ph) ppm. $^{13}C$ NMR ($CDCl_3$): $\delta$ = 11.9, 13.8, 14.0 (d, $J$ = 62.4 Hz), 104.2, 117.4, 123.0 (d, $J$ = 10.9 Hz), 128.6 (d, $J$ = 12 Hz), 128.8 (d, $J$ = 3.8 Hz), 131.2 (d, $J$ = 9.8 Hz), 131.5 (d, $J$ = 2.9 Hz), 134.7, 135.0, 141.7, 147.6, 147.9 ppm. $^{31}P$ NMR ($CDCl_3$): $\delta$ = –2.14 ppm. IR: $\tilde{\nu}$ = 3051 $cm^{-1}$ m, 3039 m, 2951 w, 2915 m, 1591 s, 1549 m, 1499 vs, 1427 s, 1436 s, 1417 m, 1358 vs, 1316 m, 1289 m, 1276 m, 1160 w, 1116 s, 1055 m, 1033 m, 1022 m, 998 w, 927 vw, 879 m, 869 m, 768 m, 753 s, 741 s, 732 s, 711 m, 692 s, 648 m. $C_{24}H_{24}N_3P$ (385.441): calcd. C 74.79, H 6.27, N 10.90; found C 74.69, H 6.29, N 11.16.

**1-[*o*-{$Ph_2PCH_2P(Ph)_2N$}$C_6H_4$]-3,5-$Me_2C_3HN_2$ (4):** A solution of **1** (3.33 g, 15.6 mmol) in $CH_2Cl_2$ (20 mL) was added to a stirred solution of $Ph_2PCH_2PPh_2$ (6.01 g, 15.6 mmol) in $CH_2Cl_2$ (10 mL) at 0 °C and the mixture was stirred overnight at room temperature. Volatiles were removed in vacuo and the residue was dissolved in

 © 2006 Wiley-VCH Verlag GmbH & Co. KGaA, Weinheim 

diethyl ether (20 mL). Filtration of the solution and concentration of the filtrate produced **4** as a yellow powder (7.36 g, 82.7%), m.p. 130–131 °C. $^1$H NMR ($CDCl_3$): $\delta$ = 2.13 (s, 3 H, $CH_3$), 2.25 (s, 3 H, $CH_3$), 3.07 (d, $J$ = 12.5 Hz, 2 H, $CH_2$), 5.81 (s, 1 H, CH), 6.38 (d, $J$ = 8.0 Hz, 1 H, $C_6H_4$), 6.64 (t, $J$ = 7.6 Hz, 1 H, $C_6H_4$), 6.80–6.85 (m, 1 H, $C_6H_4$), 7.11–7.24 (m, 15 H, Ph, $C_6H_4$), 7.32 (d, $J$ = 7.1 Hz, 2 H, Ph), 7.47–7.53 (m, 4 H, Ph) ppm. $^{13}$C NMR ($CDCl_3$): $\delta$ = 12.0, 13.9, 29.6 (dd, $J$ = 61.8, 70.8 Hz), 104.2, 117.4, 123.3 (d, $J$ = 10.3 Hz), 128.4, 128.49, 128.54, 128.65, 128.75, 131.5, 131. 9 (d, $J$ = 9.1 Hz), 132.7, 133.0, 134.6, 134.9, 142.0, 147.5 ppm. $^{31}$P NMR ($CDCl_3$): $\delta$ = –1.98 (d, $J$ = 51.9 Hz), –31.42 (d, $J$ = 52.6 Hz) ppm. IR: $\tilde{\nu}$ = 3054 cm$^{-1}$ m, 2923 m, 1595 m, 1547 m, 1498 vs, 1468 s, 1433 s, 1365 vs, 1357, 1309 w, 1289 w, 1182 vw, 1155 vw, 1118 m, 1060 w, 1022 m, 998 w, 930 vw, 798 w, 778 m, 765 w, 735 vs, 694 s, 643 w. $C_{36}H_{33}N_3P_2$ (569.615): calcd. C 75.91, H 5.84, N 7.38; found C 75.79, H 5.91, N 7.68.

**[{1-[*o*-($Ph_3PN$)$C_6H_4$]-3,5-$Me_2C_3HN_2$}$NiBr_2$] (5):** A solution of **2** (0.552 g, 1.23 mmol) in thf (10 mL) was added to a suspension of $NiBr_2$ (0.270 g, 1.23 mmol) in thf (10 mL) and the mixture was stirred overnight at room temperature. The solvent was then removed under vacuum and the residue was dissolved in $CH_2Cl_2$. The solution was filtered and the filtrate was concentrated to about 3 mL. Toluene was added to the solution to give **5** as a blue powder (0.693 g, 93.6%), m.p. 311–312 °C. IR (KBr): $\tilde{\nu}$ = 3055 cm$^{-1}$ w, 3047 w, 2958 vw, 2922 w, 1590 w, 1549 m, 1497 m, 1483 m, 1438 vs, 1366 m, 1279 m, 1263 vs, 1232 m, 1187 w, 1125 m, 1107 vs, 1058 w, 1047 m, 1005 m, 993 s, 811 s, 783 m, 753 s, 741 m, 721 s, 694 s, 667 w, 622 w. $C_{29}H_{26}Br_2N_3NiP$ (666.01): calcd. C 52.29, H 3.93, N 6.31; found C 52.34, H 3.88, N 6.48.

**[{1-[*o*-($Ph_3PN$)$C_6H_4$]-3,5-$Me_2C_3HN_2$}$NiCl_2$] (6):** A solution of **2** (0.407 g, 0.91 mmol) in thf (10 mL) was added to a stirred suspension of [$NiCl_2$(dme)] (0.200 g, 0.91 mmol) in thf (10 mL) at room temperature and the mixture was stirred overnight at room temperature. The volatiles were removed under vacuum and the residue was dissolved in $CH_2Cl_2$ (10 mL). The solution was filtered and the filtrate was concentrated to about 2 mL. Hexane was added to the solution to give **6** as a blue powder (0.477 g, 90.8%), m.p. 275–276 °C. IR (KBr): $\tilde{\nu}$ = 3065 cm$^{-1}$ w, 2970 vw, 2926 vw, 1591 m, 1549 m, 1497 s, 1487 s, 1437 vs, 1389 w, 1368 m, 1283 m, 1263 s, 1233 m, 1188 w, 1140 w, 1110 s, 1048 m, 1029 w, 994 m, 812 s, 783 m, 756 s, 744 m, 723 s, 695 s, 678 w, 612 w. $C_{29}H_{26}Cl_2N_3NiP$ (577.11): calcd. C 60.35, H 4.75, N 7.28; found C 60.39, H 4.64, N 7.29.

**[{1-[*o*-($Ph_2MePN$)$C_6H_4$]-3,5-$Me_2C_3HN_2$}$NiBr_2$] (7):** A solution of **3** (0.278 g, 0.72 mmol) in thf (10 mL) was added to a stirred suspension of $NiBr_2$ (0.158 g, 0.72 mmol) in thf (10 mL) at room temperature and the mixture was allowed to stir overnight. The solvent was then removed under vacuum and the residue was dissolved in $CH_2Cl_2$. The solution was filtered and the filtrate was concentrated to about 2 mL. Toluene was added to yield blue crystals of **7**·$CH_2Cl_2$ (0.427 g, 86.1%), m.p. 239–240 °C. IR (KBr): $\tilde{\nu}$ = 3056 cm$^{-1}$ w, 2987 w, 2916 w, 1593 m, 1550 m, 1499 s, 1453 m, 1437 s, 1419 m, 1389 w, 1373 w, 1298 m, 1272 s, 1236 m, 1160 w, 1117 vs, 1061 w, 1047 w, 1010 s, 996 s, 894 s, 799 w, 781 m, 743 vs, 716 w, 693 s, 667 s, 615 w. $C_{24}H_{24}Br_2N_3NiP$·$CH_2Cl_2$ (688.88): calcd. C 43.59, H 3.80, N 6.10; found C 43.72, H 3.82, N 6.17.

**[{1-[*o*-($Ph_2MePN$)$C_6H_4$]-3,5-$Me_2C_3HN_2$}$NiCl_2$] (8):** A solution of **3** (0.321 g, 0.83 mmol) in thf (10 mL) was added to a stirred suspension of [$NiCl_2$(dme)] (0.183 g, 0.83 mmol) in thf (10 mL) at room temperature and the mixture was allowed to stir overnight. The volatiles were then removed under vacuum and the residue was dissolved in $CH_2Cl_2$. The solution was filtered and the filtrate was concentrated to about 2 mL. Toluene was added to give **8**·$CH_2Cl_2$·0.3THF as a blue powder (0.414 g, 80.2%), m.p. 117–118 °C. IR (KBr): $\tilde{\nu}$ = 3052 cm$^{-1}$ w, 2986 w, 2915 w, 1594 m, 1556 m, 1499 s, 1487 m, 1450 m, 1437 s, 1390 m, 1374 m, 1302 m, 1274 s, 1238 m, 1150 w, 1114 vs, 1067 m, 1010 s, 998 s, 897 s, 866 w, 801 m, 786 m, 780 m, 749 vs, 729 s, 695 s, 668 w, 616 w. $C_{24}H_{24}Cl_2N_3NiP$·$CH_2Cl_2$·0.3THF (621.60): calcd. C 50.62, H 4.61, N 6.76, found C 50.82, H 4.51, N 7.10.

**[{1-[*o*-($Ph_3PN$)$C_6H_4$]-3,5-$Me_2C_3HN_2$}$CoCl_2$] (9):** A solution of ligand **2** (0.432 g, 0.96 mmol) in thf (10 mL) was added to a stirred suspension of $CoCl_2$ (0.125 g, 0.96 mmol) in thf (10 mL) at room temperature and the mixture was allowed to stir overnight. The solvent was then removed under vacuum and the residue was dissolved in $CH_2Cl_2$. The solution was filtered and the filtrate was concentrated to about 2 mL. Hexane was added to give **9** as a blue powder (0.535 g, 96.4%), m.p. 268–269 °C. IR (KBr): $\tilde{\nu}$ = 3057 cm$^{-1}$ w, 2958 vw, 2922 w, 2853 vw, 1590 m, 1549 m, 1496 s, 1484 s, 1438 vs, 1389 w, 1366 m, 1313 w, 1278 m, 1260 vs, 1232 s, 1188 w, 1158 vw, 1138 w, 1125 s, 1108 vs, 1048 m, 1027 w, 1006 m, 992 s, 807 s, 781 s, 753 s, 742 m, 721 s, 694 s, 666 m, 645 w, 621 m. $C_{29}H_{26}Cl_2CoN_3P$ (577.35): calcd. C 60.33, H 4.54, N 7.28; found C 60.34, H 4.53, N 7.55.

**[{1-[*o*-($Ph_2MePN$)$C_6H_4$]-3,5-$Me_2C_3HN_2$}$CoCl_2$] (10):** A solution of **3** (0.326 g, 0.85 mmol) in thf (10 mL) was added to a stirred suspension of $CoCl_2$ (0.110 g, 0.85 mmol) in thf (10 mL) at room temperature and the mixture was allowed to stir overnight. The solvent was then removed under vacuum and the residue was dissolved in $CH_2Cl_2$. The solution was filtered and the filtrate was concentrated to about 2 mL. Toluene was added to produce blue crystals of **10**·1.5$C_7H_8$ (0.404 g, 72.7%), m.p. 125–126 °C. IR (KBr): $\tilde{\nu}$ = 3053 cm$^{-1}$ w, 2985 w, 2914 w, 1592 m, 1552 m, 1498 s, 1484 m, 1437 s, 1423 m, 1388 w, 1371 m, 1302 m, 1272 s, 1236 m, 1161 w, 1144 w, 1113 s, 1064 m, 998 s, 949 w, 898 s, 798 w, 777 m, 749 s, 728 m, 695 m, 666 w, 614 w. $C_{24}H_{24}Cl_2CoN_3P$·1.5$C_7H_8$ (653.49): calcd. C 63.41, H 5.55, N 6.43; found C 63.24, H 5.47, N 6.52.

**[{1-[*o*-($Ph_2PCH_2PPh_2N$)$C_6H_4$]-3,5-$Me_2C_3HN_2$}$NiBr_2$] (11):** A solution of **4** (0.524 g, 0.92 mmol) in thf (10 mL) was added to a suspension of $NiBr_2$ (0.201 g, 0.92 mmol) in thf (5 mL) at room temperature with stirring and the mixture was allowed to stir for 4 h. The solvent was then removed under vacuum and the residue was dissolved in $CH_2Cl_2$ (10 mL). The solution was filtered and the filtrate was concentrated to about 4 mL. Hexane (10 mL) was added to produce purple microcrystals of **11** (0.693 g, 95.6%), m.p. 225–226 °C. An analytically pure sample was obtained by recrystallisation from a mixture of dmf and benzene. IR (KBr): $\tilde{\nu}$ = 3052 cm$^{-1}$ m, 3016 w, 2987 w, 2960 vw, 2816 w, 1590 m, 1553 m, 1499 vs, 1484 s, 1454 s, 1436 vs, 1389 m, 1366 m, 1298 s, 1241 m, 1190 w, 1160 m, 1114 vs, 1047 m, 997 s, 804 s, 782 vs, 741 vs, 725 s, 691 vs, 642 w, 615 w. $C_{36}H_{33}Br_2N_3NiP_2$·THF·$C_6H_6$ (938.33): calcd. C 57.54, H 4.93, N 5.96; found C 57.24, H 4.82, N 5.83.

**[{1-[*o*-($Ph_2PCH_2PPh_2N$)$C_6H_4$]-3,5-$Me_2C_3HN_2$}$NiCl_2$] (12):** A solution of **4** (0.337 g, 0.59 mmol) in thf (10 mL) was added to a stirred suspension of [$NiCl_2$(dme)] (0.130 g, 0.59 mmol) in thf (10 mL) and the mixture was stirred overnight at room temperature. The volatiles were then removed under vacuum and the residue was dissolved in $CH_2Cl_2$. The solution was filtered and the filtrate was concentrated to about 2 mL. Toluene was added to produce yellow crystals of **12**·THF (0.379 g, 83.3%), m.p. 180–181 °C. IR (KBr): $\tilde{\nu}$ = 3055 cm$^{-1}$ w, 3028 w, 2963 w, 2904 w, 1590 m, 1556 m, 1496 s, 1486 s, 1447 m, 1435 vs, 1371 m, 1291 s, 1241 m, 1142 m, 1112 s, 1058 m, 1028 w, 996 s, 802 m, 782 s, 770 s, 739 s, 720 s, 693 s, 616 w. $C_{36}H_{33}Cl_2N_3NiP_2$·THF (771.32): calcd. C 62.29, H 5.36, N 5.45;

 © 2006 Wiley-VCH Verlag GmbH & Co. KGaA, Weinheim 

Table 4. Details of the X-ray structure determinations of complexes **5**, **9** and **12**.

| | **5** | **9** | **12·$C_7H_8$** |
|---|---|---|---|
| Empirical formula | $C_{29}H_{26}Br_2N_3NiP$ | $C_{29}H_{26}Cl_2CoN_3P$ | $C_{43}H_{41}Cl_2N_3NiP_2$ |
| Formula mass | 666.03 | 577.33 | 791.34 |
| Crystal system | orthorhombic | orthorhombic | monoclinic |
| Space group | *Pbca* | *Pbca* | $P2_1/c$ |
| $a$ [Å] | 18.168(4) | 16.597(2) | 14.793(2) |
| $b$ [Å] | 16.691(4) | 18.007(2) | 13.929(2) |
| $c$ [Å] | 18.302(4) | 18.198(2) | 20.250(3) |
| $\alpha$ [°] | 90 | 90 | 90 |
| $\beta$ [°] | 90 | 90 | 109.793(3) |
| $\gamma$ [°] | 90 | 90 | 90 |
| $V$ [Å$^3$] | 5550(2) | 5438.5(12) | 3926.2(11) |
| $Z$ | 8 | 8 | 4 |
| $D_{calcd.}$ [g cm$^{-3}$] | 1.594 | 1.410 | 1.339 |
| $F(000)$ | 2672 | 2376 | 1648 |
| $\mu$ [mm$^{-1}$] | 3.660 | 0.910 | 0.746 |
| $\theta$ range for data collection [°] | 2.00 to 26.40 | 2.01 to 27.19 | 1.46 to 25.95 |
| No. of reflns. collected | 29235 | 29912 | 20646 |
| No. of independent reflns. ($R_{int}$) | 5662 ($R_{int}$ = 0.0652) | 5876 ($R_{int}$ = 0.0681) | 7598 ($R_{int}$ = 0.0569) |
| No. of data / restraints / parameters | 5662 / 0 / 327 | 5876 / 0 / 327 | 7598 / 0 / 463 |
| Goodness of fit on $F^2$ | 1.125 | 1.050 | 1.013 |
| Final $R$ indices[a] [$I > 2\sigma(I)$] | $R_1$ = 0.0615<br>$wR_2$ = 0.1973 | $R_1$ = 0.0415<br>$wR_2$ = 0.0806 | $R_1$ = 0.0484,<br>$wR_2$ = 0.1092 |
| $R$ indices (all data) | $R_1$ = 0.0964<br>$wR_2$ = 0.2185 | $R_1$ = 0.0899<br>$wR_2$ = 0.0997 | $R_1$ = 0.0960,<br>$wR_2$ = 0.1353 |
| Largest diff. peak and hole [e Å$^{-3}$] | 1.082 and –0.803 | 0.364 and –0.384 | 0.778 and –0.431 |

[a] $R_1 = \Sigma||F_o| - |F_c||/\Sigma|F_o|$; $wR_2 = [\Sigma w(F_o^2 - F_c^2)^2/\Sigma w(F_o^4)]^{1/2}$.

found C 62.60, H 5.16, N 5.35. Single crystals suitable for X-ray diffraction analysis were obtained by recrystallisation of **12** from toluene (thf was removed from **12**·THF under vacuum prior to recrystallisation).

**[{1-[*o*-($Ph_2PCH_2PPh_2N$)$C_6H_4$]-3,5-$Me_2C_3HN_2$}$CoCl_2$] (13):** A solution of **4** (0.482 g, 0.85 mmol) in thf (10 mL) was added to a suspension of $CoCl_2$ (0.110 g, 0.85 mmol) in thf (10 mL) at room temperature with stirring. The volatiles were then removed under vacuum and the residue was dissolved in $CH_2Cl_2$. The solution was filtered and the filtrate was concentrated to about 2 mL. Toluene was added to produce blue crystals of **13**·0.75$C_7H_8$ (0.567 g, 86.8%), m.p. 129–130 °C. IR (KBr): $\tilde{\nu}$ = 3052 cm$^{-1}$ m, 3021 m, 2950 m, 2924 m, 2902 m, 1590 s, 1572 w, 1556 s, 1495 s, 1481 s, 1467 s, 1435 vs, 1372 s, 1361 s, 1301 s, 1267 vs, 1239 s, 1189 w, 1158 w, 1139 s, 1111 vs, 1057 s, 1044 s, 1028 m, 991 vs, 938 w, 922 w, 825 w, 800 s, 782 vs, 769 vs, 739 vs, 717 vs, 694 vs, 662 s, 638 m, 616 m. $C_{36}H_{33}Cl_2CoN_3P_2$·0.75$C_7H_8$ (768.56): calcd. C 64.46, H 5.11, N 5.46; found C 64.24, H 5.16, N 5.41.

**X-ray Crystallography:** Crystals were mounted in Lindemann capillaries under $N_2$. Diffraction data were collected on a Siemens CCD area detector at 294(2) K with graphite-monochromated Mo-$K_\alpha$ radiation ($\lambda$ = 0.71073 Å). A semi-empirical absorption correction was applied to the data. The structures were solved by direct methods using SHELXS-97[19] and refined against $F^2$ by full-matrix least-squares using SHELXL-97.[20] Crystal data and experimental details of the structure determinations are listed in Table 4.
CCDC-606680 (for **5**), -606681 (for **9**) and -617850 (for **12**) contain the supplementary crystallographic data for this paper. These data can be obtained free of charge from The Cambridge Crystallographic Data Centre via www.ccdc.cam.ac.uk/data_request/cif.

**General Procedure for Ethylene Oligomerisation:** The oligomerisation with 1 atm of ethylene was carried out in a Schlenk tube. Thus, the pre-catalyst (5 μmol) was added to a dried Schlenk tube and then the tube was back-filled three times with $N_2$ and twice with ethylene. Toluene (30 mL) was added to the tube and then the appropriate co-catalyst solution was added with a syringe. The reaction mixture was vigorously stirred at the given temperature under 1 atm of ethylene. After the desired period of time (30 or 60 min), the reaction was terminated by adding 10% HCl solution (30 mL). About 1 mL of the organic layer was dried with anhydrous $Na_2SO_4$ for GC analysis. Ethanol (100 mL) was added to the remaining solution; no polymer was observed.

The oligomerisation with 10 atm of ethylene was carried out in a stainless-steel autoclave (250 mL capacity) equipped with a gas ballast through a solenoid valve for continuous feeding of ethylene at constant pressure. Toluene (120 mL) containing the pre-catalyst was transferred into the fully dried reactor under $N_2$ atmosphere. The required amount of co-catalyst was injected into the reactor with a syringe. Once the desired temperature had been reached the reactor was pressurised to 10 atm. After stirring for 30 min, the reaction was quenched and worked-up using the same procedure as described above for the reaction at 1 atm.

## Acknowledgments

This work was supported by the National Natural Science Foundation of China (grant no. 20272056). Z. X. W. thanks Professors H.-B. Song and H.-G. Wang for the single-crystal X-ray structure determinations.

[1] a) F. Speiser, P. Braunstein, L. Saussine, *Acc. Chem. Res.* **2005**, *38*, 784–793; b) N. Ajellal, M. C. A. Kuhn, A. D. G. Boff, M. Hörner, C. M. Thomas, J.-F. Carpentier, O. L. Casagrande, Jr., *Organometallics* **2006**, *25*, 1213–1216.
[2] W. Keim, F. H. Kowalt, R. Goddard, C. Krüger, *Angew. Chem. Int. Ed. Engl.* **1978**, *17*, 466–472.
[3] a) M. Sauthier, F. Leca, R. F. de Souza, K. Bernardo-Gusmão, L. F. T. Queiroz, L. Toupet, R. Réau, *New J. Chem.* **2002**, *26*,

 © 2006 Wiley-VCH Verlag GmbH & Co. KGaA, Weinheim 

630–635; b) S. Al-Benna, M. J. Sarsfield, M. Thornton-Pett, D. L. Ormsby, P. J. Maddox, P. Brès, M. Bochmann, *J. Chem. Soc., Dalton Trans.* **2000**, 4247–4257; c) L. P. Spencer, R. Altwer, P. Wei, L. Gelmini, J. Gauld, D. W. Stephan, *Organometallics* **2003**, *22*, 3841–3854; d) K. V. Axenov, M. Leskelä, T. Repo, *J. Catal.* **2006**, *238*, 196–205; e) G. J. P. Britovsek, V. C. Gibson, D. F. Wass, *Angew. Chem. Int. Ed.* **1999**, *38*, 428–447; f) V. C. Gibson, S. K. Spitzmesser, *Chem. Rev.* **2003**, *103*, 283–316; g) S. Plentz-Meneghetti, P. J. Lutz, J. Kress, *Organometallics* **1999**, *18*, 2734–2737; h) W.-H. Sun, D. Zhang, S. Zhang, S. Jie, J. Hou, *Kinet. Catal.* **2006**, *47*, 278–283.

[4] a) M. E. Bluhm, C. Folli, O. Walter, M. Döring, *J. Mol. Catal. A* **2005**, *229*, 177–181; b) F. Speiser, P. Braunstein, L. Saussine, *Organometallics* **2004**, *23*, 2633–2640; c) F. Speiser, P. Braunstein, L. Saussine, *Organometallics* **2004**, *23*, 2625–2632; d) D. Sirbu, G. Consiglio, S. Gischig, *J. Organomet. Chem.* **2006**, *691*, 1143–1150; e) S. I. Pascu, K. S. Coleman, A. R. Cowley, M. L. H. Green, N. H. Rees, *New J. Chem.* **2005**, *29*, 385–397; f) A. Mukherjee, U. Subramanyam, V. G. Puranik, T. P. Mohandas, A. Sarkar, *Eur. J. Inorg. Chem.* **2005**, 1254–1263; g) Z. Weng, S. Teo, L. L. Koh, T. S. A. Hor, *Angew. Chem. Int. Ed.* **2005**, *44*, 7560–7564; h) W.-H. Sun, Z. Li, H. Hu, B. Wu, H. Yang, N. Zhu, X. Leng, H. Wang, *New J. Chem.* **2002**, *26*, 1474–1478.

[5] a) J. Hou, W.-H. Sun, D. Zhang, L. Chen, W. Li, D. Zhao, H. Song, *J. Mol. Catal. A* **2005**, *231*, 221–233; b) Y. Chen, G. Wu, G. C. Bazan, *Angew. Chem. Int. Ed.* **2005**, *44*, 1108–1112; c) F. Speiser, P. Braunstein, L. Saussine, *Inorg. Chem.* **2004**, *43*, 4234–4240; d) S. Wu, S. Lu, *Appl. Catal.A* **2003**, *246*, 295–301.

[6] a) J. Heinicke, M. Z. He, A. Dal, H. F. Klein, O. Hetche, W. Keim, U. Florke, H. J. Haupt, *Eur. J. Inorg. Chem.* **2000**, 431–440; b) Z. J. A. Komon, X. Bu, G. C. Bazan, *J. Am. Chem. Soc.* **2000**, *122*, 12379–12380; c) J. M. Malinoski, M. Brookhart, *Organometallics* **2003**, *22*, 5324–5335; d) P. Kuhn, D. Sémeril, C. Jeunesse, D. Matt, M. Neuburger, A. Mota, *Chem. Eur. J.* **2006**, *12*, 5210–5219.

[7] a) J. N. L. Dennett, A. L. Gillon, K. Heslop, D. J. Hyett, J. S. Fleming, C. E. Lloyd-Jones, A. G. Orpen, P. G. Pringle, D. F. Wass, *Organometallics* **2004**, *23*, 6077–6079; b) C. Bianchini, L. Gonsalvi, W. Oberhauser, D. Sémeril, P. Brüggeller, R. Gutmann, *Dalton Trans.* **2003**, 3869–3875; c) M. Lejeune, D. Sémeril, C. Jeunesse, D. Matt, F. Peruch, P. J. Lutz, L. Ricard, *Chem. Eur. J.* **2004**, *10*, 5354–5360.

[8] J. Hou, W.-H. Sun, S. Zhang, H. Ma, Y. Deng, X. Lu, *Organometallics* **2006**, *25*, 236–244.

[9] a) W.-H. Sun, S. Jie, S. Zhang, W. Zhang, Y. Song, H. Ma, J. Chen, K. Wedeking, R. Fröhlich, *Organometallics* **2006**, *25*, 666–677; b) A. R. Karam, E. L. Catarí, F. López-Linares, G. Agrifoglio, C. L. Albano, A. Díaz-Barrios, T. E. Lehmann, S. V. Pekerar, L. A. Albornoz, R. Atencio, T. González, H. B. Ortega, P. Joskowics, *Appl. Catal. A* **2005**, *280*, 165–173; c) M. J. Overett, R. Meijboom, J. R. Moss, *Dalton Trans.* **2005**, 551–555; d) K. P. Tellmann, V. C. Gibson, A. J. P. White, D. J. Williams, *Organometallics* **2005**, *24*, 280–286; e) R. Schmidt, M. B. Welch, R. D. Knudsen, S. Gottfried, H. G. Alt, *J. Mol. Catal. A* **2004**, *222*, 17–25; f) B. L. Small, M. J. Carney, D. M. Holman, C. E. O'Rourke, J. A. Halfen, *Macromolecules* **2004**, *37*, 4375–4386.

[10] F. Speiser, P. Braunstein, L. Saussine, *Dalton Trans.* **2004**, 1539–1545.

[11] a) M. Bluhm, O. Walter, M. Döring, *J. Organomet. Chem.* **2005**, *690*, 713–721; b) D. S. McGuinness, P. Wasserscheid, W. Keim, C. Hu, U. Englert, J. T. Dixon, C. Grove, *Chem. Commun.* **2003**, 334–335; c) D. S. McGuinness, P. Wasserscheid, D. H. Morgan, J. T. Dixon, *Organometallics* **2005**, *24*, 552–556; d) M. Wang, X. Yu, Z. Shi, M. Qian, K. Jin, J. Chen, R. He, *J. Organomet. Chem.* **2002**, *645*, 127–133.

[12] a) L. LePichon, D. W. Stephan, X. Gao, Q. Wang, *Organometallics* **2002**, *21*, 1362–1366; b) J. D. Masuda, P. Wei, D. W. Stephan, *Dalton Trans.* **2003**, 3500–3505; c) H.-R. Wu, Y.-H. Liu, S.-M. Peng, S.-T. Liu, *Eur. J. Inorg. Chem.* **2003**, 3152–3159.

[13] S. D. Ittel, L. K. Johnson, *Chem. Rev.* **2000**, *100*, 1169–1204.

[14] a) D. S. C. Black, G. B. Deacon, G. L. Edwards, *Aust. J. Chem.* **1991**, *44*, 1771–1781; b) J. M. Lindley, I. M. McRobbie, O. Meth-Cohn, H. Suschitzky, *J. Chem. Soc., Perkin Trans. 1* **1980**, 982–994.

[15] X. Tang, D. Zhang, S. Jie, W.-H. Sun, J. Chen, *J. Organomet. Chem.* **2005**, *690*, 3918–3928.

[16] a) M. T. Reetz, E. Bohres, R. Goddard, *Chem. Commun.* **1998**, 935–936; b) M. Sauthier, J. Forniés-Cámer, L. Toupet, R. Réau, *Organometallics* **2000**, *19*, 553–562.

[17] L. Wang, W.-H. Sun, L. Han, Z. Li, Y. Hu, C. He, C. Yan, *J. Organomet. Chem.* **2002**, *650*, 59–64.

[18] F. A. Cotton, *Inorg. Synth.* **1971**, *13*, 160–162.

[19] G. M. Sheldrick, *Acta Crystallogr. Sect. A* **1990**, *46*, 467–473.

[20] G. M. Sheldrick, *SHELXL97, Programs for structure refinement*; University of Göttingen, Germany, **1997**.

Received: July 12, 2006
Published Online: October 18, 2006

 © 2006 Wiley-VCH Verlag GmbH & Co. KGaA, Weinheim 

DOI: 10.1002/ejic.200600658

# Bulky-Hindrance-Controlled Ligand Transformation from Linked Bis(amidinate) to Linked Imido-Amidinate Promoted by a Mono(cyclopentadienyl)titanium Group

**Sheng-Di Bai,[a] Jian-Ping Guo,*[a] Dian-Sheng Liu,*[a] and Wai-Yeung Wong[b]**

**Keywords:** Titanium / Bis(amidinate) / Bulky hindrance / Ligand transformation / Crystal structure / Steric hindrance

A novel class of silyl-linked bis(amidinate) ligands [$SiMe_2$-{NC(Ph)N(2,6-$R_2$Ph)Li}$_2$] [**L$^1$** (R = H), **L$^2$** (R = Me), and **L$^3$** (R = *i*Pr)] reacted with $TiCl_3(C_5H_5)$ to produce the half-sandwich titanium complexes **1**, **2**, and **3**. The molecular structures of **1**–**3** were confirmed successfully by X-ray crystallography. An unprecedented intramolecular ligand transformation from the linked bis(amidinate) configuration to the linked imido-amidinate configuration took place in the cases of **L$^1$** and **L$^2$**. It was found that the rearrangement process was related to the steric hindrance of the terminal substituents.
(© Wiley-VCH Verlag GmbH & Co. KGaA, 69451 Weinheim, Germany, 2006)

## Introduction

Both cyclopentadienyl and amidinate ligands have been extensively studied for decades because of their high adaptability to a wide variety of metals in coordination chemistry. The corresponding metal complexes have shown remarkable utility as homogeneous catalysts for olefin polymerization.[1,2] As a further step, systematic investigations on the metal compounds with a mixed-ligand environment containing these two types of ancillary ligands have been carried out in the past few years, involving the new generation of Ziegler–Natta catalysts, carbon mono- or dioxide reactants, and Kharasch reaction catalysts.[3–9] These merits have made the chemistry of half-sandwich compounds an attractive research field. On the other hand, much attention has recently been paid to metal compounds incorporated with the linked bis(amidinate) ligands, as these unique dianionic ligands have the advantage of affording dinuclear complexes or mononuclear complexes analogous to "ansa-metallocenes", leading to valuable geometric structures and properties. Nevertheless, there have been few reports on linked bis(amidinate) half-sandwich compounds.[4a,9]

A novel class of linked bis(amidinate) ligands (**L$^1$**, **L$^2$**, and **L$^3$**) were developed in our laboratory. They displayed close contact between the two amidinate moieties; that is in contrast to other common examples reported in the literature.[10] We next attempted the preparation of the half-sandwich derivatives from the reactions of ligands with $TiCl_3(C_5H_5)$. It was found, to our surprise, that in the cases of the substituents attached to the terminal nitrogen atoms, which were less bulky, the N–C–N–Si–N–C–N backbone of these dianionic ligands could be transformed to a new class of linked imido-amidinate ligands. We believe that the metal center of mono(cyclopentadienyl)titanium complexes promoted the rearrangement reaction.

[a] Institute of Modern Chemistry, Shanxi University, Taiyuan, Shanxi 030006, P. R. China
Fax: +86-351-7011743
E-mail: guojp@sxu.edu.cn
[b] Department of Chemistry, Hong Kong Baptist University, Waterloo Road, Kowloon Tong, Hong Kong, P. R. China

## Result and Discussion

### Synthesis and Structural Characterization

The analogous silyl-linked bis(amidinate) ligands **L$^1$**, **L$^2$**, and **L$^3$** were prepared in our previous work. They demonstrated a trend of increasing steric hindrance by variation of the 2,6-substituents of the corresponding phenyl analogue. Treatment of **L$^1$** with 1 equiv. of $TiCl_3(C_5H_5)$ in thf gave, after extraction with $CH_2Cl_2$ and crystallization, compound **1** as red crystals in 82% yield. Complexes **2** and **3** were prepared under similar synthetic procedures in yields of 48% and 65%, respectively (Scheme 1). These half-sandwich titanium compounds were characterized by NMR spectroscopy, elemental analysis, and single-crystal X-ray diffraction analysis.

The molecular structure of **1** is shown in Figure 1 and the key bonding parameters are listed in Table 1. The ligand coordinating to the titanium center does not keep the configuration in **L$^1$**. The original linked bis(amidinate) ligand was expected to coordinate to the metal center in a tetradentate mode. However, the ligand is tridentate in compound **1**. On both sides of the silyl bridge, the two amidinate moieties exhibit different coordination styles to the Ti ion. One is chelating and the other is monodentate. Moreover, the latter one adopts the opposite direction involving a phenyl migration from N4 to N3. It gives a new imido

 © 2006 Wiley-VCH Verlag GmbH & Co. KGaA, Weinheim 

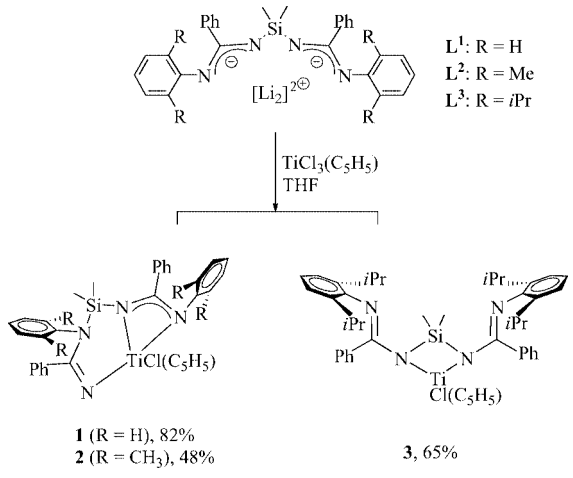


Scheme 1.

group [demonstrated by N3–C22 being 1.385(4) Å and N4–C22 being 1.288(4) Å]. On the other hand, the five-membered skeleton of N4–C22–N3–Si1–N2 displays analogous structural features, with an N2–Ti1–N4 angle of 84.70(13)°, as in some reported titanium β-diketiminates, such as [(Ar)NC(CH$_3$)CHC(CH$_3$)N(Ar)]Ti=NAr(OTf).[11] The Ti–N$_{imido}$ bond [1.847(3) Å] is much shorter than the Ti–N$_{amidinate}$ bonds [2.220(3) and 2.111(3) Å]. The "unsymmetrical" distribution of the two N–C–N moieties leads to a difference of 0.09 Å between the silyl bridge and the neighboring nitrogen atoms on either side.

Compound **2** was derived from **L$^2$**, which was more bulky than **L$^1$**, by introducing 2,6-dimethyl groups onto the terminal phenyl rings. Complex **2** is almost isostructural to **1** except for the presence of additional methyl groups. Structural analysis indicates that the increased steric bulk ascribed to the methyl groups plays no role in differentiating

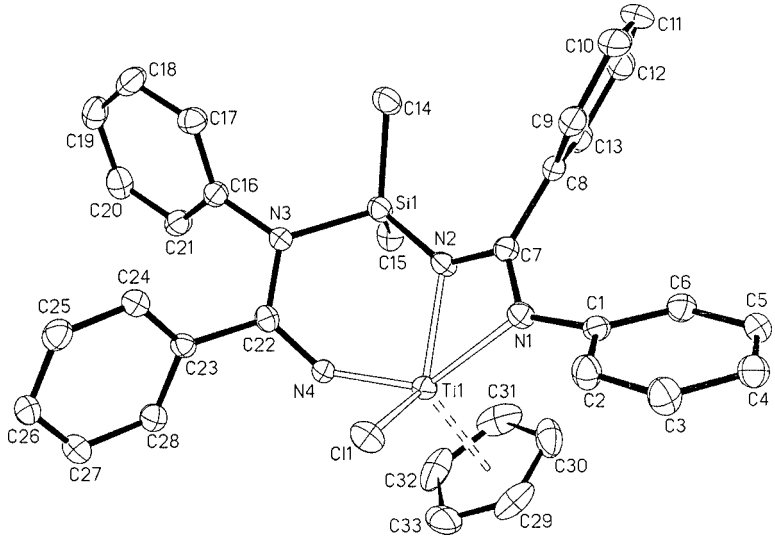


Figure 1. ORTEP drawing (30% probability level) of the molecular structure of compound **1**. Hydrogen atoms are omitted for clarity.

Table 1. Selected bond lengths [Å] and bond angles [°] for compounds **1**, **2**, and **3**.

| **1** | | **2** | | **3** | |
|---|---|---|---|---|---|
| Ti(1)–N(1) | 2.220(3) | Ti(1)–N(1) | 2.352(3) | Ti(1)–N(2) | 1.900(3) |
| Ti(1)–N(2) | 2.111(3) | Ti(1)–N(2) | 2.061(3) | Ti(1)–N(3) | 1.911(3) |
| Ti(1)–N(4) | 1.847(3) | Ti(1)–N(4) | 1.840(3) | Ti(1)–Cl(1) | 2.2921(14) |
| Ti(1)–Cl(1) | 2.362(3) | Ti(1)–Cl(1) | 2.3392(11) | Ti(1)–Cp(centroid) | 2.027 |
| Ti(1)–Cp(centroid) | 2.050 | Ti(1)–Cp(centroid) | 2.043 | N(1)–C(13) | 1.284(5) |
| N(1)–C(7) | 1.313(4) | N(1)–C(9) | 1.297(4) | N(2)–C(13) | 1.397(4) |
| N(2)–C(7) | 1.349(4) | N(2)–C(9) | 1.344(4) | Si(1)–N(2) | 1.790(3) |
| Si(1)–N(2) | 1.709(3) | Si(1)–N(2) | 1.709(3) | Si(1)–N(3) | 1.791(3) |
| Si(1)–N(3) | 1.799(3) | Si(1)–N(3) | 1.794(3) | N(3)–C(22) | 1.388(4) |
| N(3)–C(22) | 1.385(4) | N(3)–C(26) | 1.381(4) | N(4)–C(22) | 1.278(5) |
| N(4)–C(22) | 1.288(4) | N(4)–C(26) | 1.282(4) | N(2)–Ti(1)–N(3) | 83.26(13) |
| N(2)–Ti(1)–N(1) | 60.91(12) | N(2)–Ti(1)–N(1) | 59.54(10) | Cl(1)–Ti(1)–Cp(centroid) | 116.4 |
| N(4)–Ti(1)–N(2) | 84.70(13) | N(4)–Ti(1)–N(2) | 84.46(12) | C(21)–Si(1)–C(20) | 116.9(2) |
| Cl(1)–Ti(1)–Cp(centroid) | 116.6 | Cl(1)–Ti(1)–Cp(centroid) | 116.9 | N(1)–C(13)–N(2) | 116.8(3) |
| N(1)–C(7)–N(2) | 111.2(3) | N(1)–C(9)–N(2) | 113.3(3) | N(2)–Si(1)–N(3) | 90.01(14) |
| N(2)–Si(1)–N(3) | 105.97(15) | N(2)–Si(1)–N(3) | 105.76(13) | N(4)–C(22)–N(3) | 118.1(3) |
| N(4)–C(22)–N(3) | 122.5(3) | N(4)–C(26)–N(3) | 121.5(3) | | |
| C(22)–N(4)–Ti(1) | 137.0(2) | C(26)–N(4)–Ti(1) | 143.7(3) | | |

 © 2006 Wiley-VCH Verlag GmbH & Co. KGaA, Weinheim 

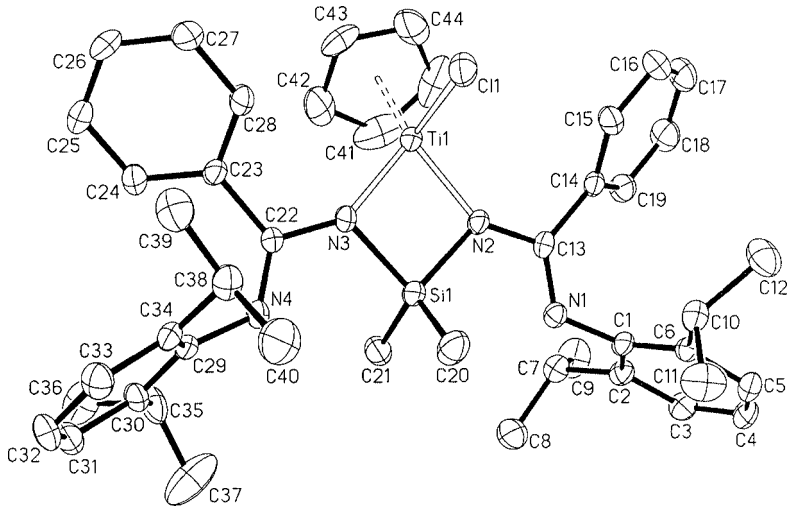


Figure 2. ORTEP drawing (30% probability level) of the molecular structure of compound **3**. Hydrogen atoms are omitted for clarity.

the configuration of **2** from that of **1**. However, the sterically more demanding isopropyl groups do make compound **3** saliently different from **1** and **2**. The ligand framework of **3** (Figure 2) is identical to that of ligand $\mathbf{L^3}$. It should be pointed out that the ligand of **3** adopts the diamido configuration rather than the linked bis(amidinate) configuration. The Ti–$N_{amido}$ bonds in **3** are much shorter than the Ti–$N_{amidinato}$ bonds in **1** and **2**. The two terminal nitrogen atoms have no bonding contacts with the metal center and they are converted into imino groups. The resulting diamido ligand bites the titanium ion at a right angle and it exhibits a planar Ti–N–Si–N tetragonal core. The tetragonal square is perpendicular to another coincident plane composed of C20–Si1–C21 and Cl1–Ti1–Cp(centroid) (with a dihedral angle of 89.8°).

### Intramolecular Rearrangement Reaction

The tetradentate bonding mode between the ligands and the Ti center is not preferred because the common electron count of the titanium ion is 12 or 14. Apparently, the steric bulk of the terminal group plays an important role in the determination of the resulting configuration of compounds **1**, **2**, and **3**. In the absence of sterically demanding substituents, such as in $\mathbf{L^1}$ and $\mathbf{L^2}$, one amidinate moiety of the ligand tends to take the end-contact mode rather than the general chelating mode in order to obtain 14 outer electrons for the Ti ion. The initial terminal nitrogen atom is linked to a phenyl group, which decreases the electronegativity of that N atom and the bond strength of the corresponding N–Ti edge. Comparatively, N4 in **1** or **2** becomes an imido nitrogen atom after rearrangement and the new N–Ti bond is greatly reinforced. These factors in combination drive the ligand transformation process in **1** and **2**.

The proposed mechanism for the formation of **1** and **2** is outlined in Scheme 2. Combination of the linked bis(amidinate) ligands and titanium salt gives the expected compounds with the tetradentate coordination environment (**a**). Induced by the electronically deficient metal center, one amidinate moiety is polarized, and its C–N double bond is located at the outer position because of the electronic withdrawal from the aromatic group. The electronically rich imino nitrogen atom then attacks the silicon atom (**b**). It forms an N–C–N–Si four-membered ring and a notable five-coordinate silicon transition state. The original N–Si bond is then weakened (**c**). Rearrangement is completed after electron transfer to form an imido group (**d**). It should be pointed out that the N–C–N–Si–N–C–N fragment in

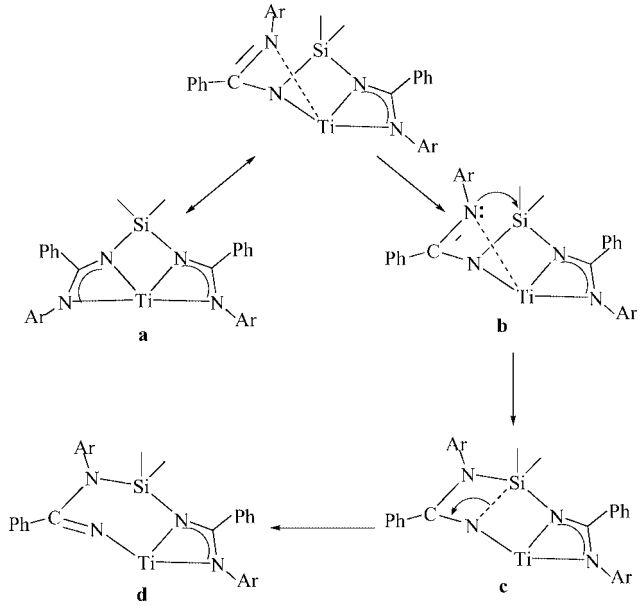


Scheme 2.

 © 2006 Wiley-VCH Verlag GmbH & Co. KGaA, Weinheim 

these ligands is quite flexible. The intramolecular N–Si coupling could be fulfilled without shielding from sterically demanding substituents. This is the crucial step for the transformation. On the contrary, the isopropyl groups in **L³** are bulky enough to stop that terminal N atom from being bonded to the Ti center or approaching the silyl bridge. This gives compound **3** with the ligand remaining intact and the Ti center with 12 outer electrons.

## Conclusions

A novel intramolecular rearrangement of linked bis(amidinate) ligands was demonstrated. It was promoted by the active titanium ion but could be tuned by the bulky hindrance of terminal substituents. We are currently exploring the reactions between the ligands and other metal salts so as to investigate the generalization of this type of chemical transformation.

## Experimental Section

**General Procedures:** All reactions were carried out under nitrogen in flame-dried Schlenk-type glassware on a dual-manifold Schlenk line. Solvents were dried prior to use. The ligand transfer reagents **L¹**, **L²**, and **L³** were prepared according to the reported methods.[10] $TiCl_3(C_5H_5)$ was prepared according to literature procedures.[12] $^1H$ and $^{13}C$ NMR spectra were recorded with a Bruker DRX-300 spectrometer. Elemental analyses were performed with a Vario EL-III instrument. Melting points were taken with a Sanyo Gallenkamp Variable Heater.

**Preparation of 1:** A solution of **L¹** (1.88 mmol) in thf (20 mL) was added to a solution of $TiCl_3(C_5H_5)$ (0.41 g, 1.88 mmol) in thf (10 mL) at 0 °C. The red solution was stirred at room temperature for 12 h and then concentrated under vacuum. The residue was extracted with $CH_2Cl_2$ (20 mL) and the solution filtered. The filtrate was concentrated to give compound **1** as red crystals. Yield: 1.05 g (82%); m.p. 171–172 °C. $^1H$ NMR (300 MHz, $CDCl_3$): $\delta$ = 7.61–6.99 (m, 20 H, phenyl), 6.67, 6.50, 6.13 (t, 5 H, Cp), 0.57, –0.47 (d, 6 H, Si*Me*$_2$) ppm. $^{13}C$ NMR (75 MHz, $CDCl_3$): $\delta$ = 174.7, 163.4 (N-*C*-N), 148.9–125.9 (phenyl), 120.5, 118.9, 116.7 (Cp), 4.7, 2.9 (Si*Me*$_2$) ppm. $C_{33}H_{31}ClN_4SiTi{\cdot}CH_2Cl_2$ (679.98): calcd. C 60.06, H 4.89, N 8.24; found C 59.82, H 4.90, N 8.18.

**Preparation of 2:** A solution of **L²** (2.51 mmol) in thf (20 mL) was added to a solution of $TiCl_3(C_5H_5)$ (0.55 g, 2.51 mmol) in thf (10 mL) at 0 °C. The red solution was stirred at room temperature for 12 h and then concentrated under vacuum. The residue was extracted with $CH_2Cl_2$ (20 mL) and the solution filtered. The filtrate was concentrated to give compound **2** as red crystals. Yield: 0.79 g (48%); m.p. 179–180 °C. $^1H$ NMR (300 MHz, $CDCl_3$): $\delta$ = 7.60–6.68 (m, 16 H, phenyl), 6.55, 6.48 (d, 5 H, Cp), 2.74–2.04 (m, 12 H, methyl), 0.70, –0.24, –0.95 (t, 6 H, Si*Me*$_2$) ppm. $^{13}C$ NMR (75 MHz, $CDCl_3$): $\delta$ = 179.3, 17.6, 168.5 (N-*C*-N), 149.8–124.2 (phenyl), 120.6, 117.1 (Cp), 27.1–24.9 (methyl), 9.5, 4.5 (Si*Me*$_2$) ppm. $C_{37}H_{39}ClN_4SiTi{\cdot}(CH_2Cl_2)_{0.25}$ (672.37): calcd. C 66.54, H 5.92, N 8.33; found C 66.89, H 5.97, N 8.31.

**Preparation of 3:** A solution of **L³** (1.55 mmol) in thf (20 mL) was added to a solution of $TiCl_3(C_5H_5)$ (0.34 g, 1.55 mmol) in thf (10 mL) at 0 °C. The red solution was stirred at room temperature for 12 h and then concentrated under vacuum. The residue was extracted with $CH_2Cl_2$ (20 mL) and the solution filtered. The filtrate was concentrated to give compound **3** as red crystals. Yield: 0.77 g (65%); m.p. 186–187 °C. $^1H$ NMR (300 MHz, $CDCl_3$): $\delta$ = 7.50–6.87 (m, 16 H, phenyl), 6.44, 5.83 (d, 5 H, Cp), 3.49, 2.78 (d, 4 H, *CH* of *i*Pr), 1.36–0.86 (m, 24 H, methyl of *i*Pr), 0.56, 0.18, (d, 6 H, Si*Me*$_2$) ppm. $^{13}C$ NMR (75 MHz, $CDCl_3$): $\delta$ = 166.7 (N-*C*-N), 143.8–123.6 (phenyl), 117.5 (Cp), 28.6, 27.8, 25.1, 22.8 (*i*Pr on phenyl), 2.3, –0.6 (Si*Me*$_2$) ppm. $C_{45}H_{55}ClN_4SiTi$ (763.37): calcd. C 70.80, H 7.26, N 7.34; found C 70.41, H 7.25, N 7.27.

**X-ray Crystallography:** Single crystals of **1**, **2**, and **3** suitable for X-ray diffraction studies were obtained by crystallization from $CH_2Cl_2$. X-ray diffraction data were collected using graphite-monochromated Mo-$K_\alpha$ radiation ($\lambda$ = 0.71073 Å) with a Bruker Smart Apex CCD diffractometer, equipped with an Oxford Cryosystems CRYOSTREAM device. The collected frames were processed with the proprietary software SAINT and an absorption correction was applied (SADABS) to the collected reflections.[13,14] The structures of these molecules were solved by direct methods and ex-

Table 2. Crystal data and refinement results for compounds **1**, **2**, and **3**.

| | **1** | **2** | **3** |
|---|---|---|---|
| Empirical formula | $C_{34}H_{33}Cl_3N_4SiTi$ | $C_{37}H_{39}ClN_4SiTi$ | $C_{45}H_{55}ClN_4SiTi$ |
| Formula mass | 679.98 | 651.16 | 763.37 |
| Crystal system | monoclinic | monoclinic | monoclinic |
| Space group | $P2_1/c$ (no. 14) | $P2_1/n$ (no. 14) | $P2_1/n$ (no. 14) |
| $a$ [Å] | 11.000(9) | 11.4269(19) | 18.187(6) |
| $b$ [Å] | 15.650(19) | 24.534(4) | 9.818(3) |
| $c$ [Å] | 19.278(17) | 12.329(2) | 24.152(8) |
| $\beta$ [°] | 102.70(6) | 103.438(2) | 96.464(6) |
| $V$ [Å$^3$] | 3237(5) | 3361.9(10) | 4285(3) |
| $Z$ | 4 | 4 | 4 |
| $F$(000) | 1408 | 1368 | 1624 |
| $D_{calcd.}$ [g cm$^{-3}$] | 1.395 | 1.286 | 1.183 |
| $\mu$(Mo-$K_\alpha$) [mm$^{-1}$] | 0.580 | 0.402 | 0.325 |
| Reflections collected | 13119 | 13786 | 20142 |
| Unique reflections | 5696 | 5864 | 7544 |
| Observed reflections | 3774 | 4109 | 4490 |
| *Gof* (for $F^2$) | 0.951 | 1.030 | 1.029 |
| $R_1$, $wR_2$ [$I > 2\sigma(I)$] | 0.0580, 0.1090 | 0.0605, 0.1184 | 0.0645, 0.1415 |
| $R_1$, $wR_2$ (all data) | 0.0927, 0.1203 | 0.0913, 0.1296 | 0.1182, 0.1670 |
| Largest diff. peak/hole [e Å$^{-3}$] | 0.492/–0.344 | 0.465/–0.286 | 0.445/–0.281 |

 © 2006 Wiley-VCH Verlag GmbH & Co. KGaA, Weinheim 

panded by standard difference Fourier syntheses using the software SHELXTL.[15] Structure refinements were made on $F^2$ using the full-matrix least-squares technique. All non-hydrogen atoms were refined with anisotropic displacement parameters. Hydrogen atoms were placed in their idealized positions and allowed to ride on the respective parent atoms. Pertinent crystallographic data and other experimental details are summarized in Table 2. CCDC-295090 (for **1**), -295091 (for **2**), and -295092 (for **3**) contain the supplementary crystallographic data for this paper. These data can be obtained free of charge from The Cambridge Crystallographic Data Centre via www.ccdc.cam.ac.uk/data_request/cif.

## Acknowledgments

This work was supported by grants from the Natural Science Foundation of China (20472046 to D.-S. L. and 50443001 to J.-P. G.).

[1] a) A. Togni, R. L. Halterman, *Metallocenes*, Wiley-VCH Verlag GmbH, Weinheim, Germany, **1998**; b) S. Arndt, J. Okuda, *Chem. Rev.* **2002**, *102*, 1953–1976; c) Y. Qian, J. Huang, M. D. Bala, B. Lian, H. Zhang, H. Zhang, *Chem. Rev.* **2003**, *103*, 2633–2690.

[2] a) J. Barker, M. Kilner, *Coord. Chem. Rev.* **1994**, *133*, 219–300; b) F. T. Edelmann, *Coord. Chem. Rev.* **1994**, *137*, 403–481.

[3] a) A. N. Chernega, R. Gómez, M. L. H. Green, *J. Chem. Soc., Chem. Commun.* **1993**, 1415–1417; b) R. Gómez, R. Duchateau, A. N. Chernega, J. H. Teuben, F. T. Edelmann, M. L. H. Green, *J. Organomet. Chem.* **1995**, *491*, 153–158; c) C.-T. Chen, L. H. Doerrer, V. C. Williams, M. L. H. Green, *J. Chem. Soc., Dalton Trans.* **2000**, 967–974.

[4] a) J. R. Babcock, C. Incarvito, A. L. Rheingold, J. C. Fettinger, L. R. Sita, *Organometallics* **1999**, *18*, 5729–5732; b) Y. Zhang, L. R. Sita, *Chem. Commun.* **2003**, 2358–2359; c) Y. Zhang, R. J. Keaton, L. R. Sita, *J. Am. Chem. Soc.* **2003**, *125*, 8746–8747; d) Y. Zhang, E. K. Reeder, R. J. Keaton, L. R. Sita, *Organometallics* **2004**, *23*, 3512–3520; e) M. B. Harney, R. J. Keaton, L. R. Sita, *J. Am. Chem. Soc.* **2004**, *126*, 4536–4537; f) Y. Zhang, L. R. Sita, *J. Am. Chem. Soc.* **2004**, *126*, 7776–7777.

[5] a) P. J. Stewart, A. J. Blake, P. Mountford, *J. Organomet. Chem.* **1998**, *564*, 209–214; b) A. E. Guiducci, A. R. Cowley, M. E. G. Skinner, P. Mountford, *J. Chem. Soc., Dalton Trans.* **2001**, 1392–1394; c) C. L. Boyd, E. Clot, A. E. Guiducci, P. Mountford, *Organometallics* **2005**, *24*, 2347–2367.

[6] a) H. Kondo, Y. Yamaguchi, H. Nagashima, *J. Am. Chem. Soc.* **2001**, *123*, 500–501; b) H. Kondo, K. Matsubara, H. Nagashima, *J. Am. Chem. Soc.* **2002**, *124*, 534–535; c) H. Nagashima, M. Gondo, S. Masuda, H. Kondo, Y. Yamaguchi, K. Matsubara, *Chem. Commun.* **2003**, 442–443; d) Y. Motoyama, M. Gondo, S. Masuda, Y. Iwashita, H. Nagashima, *Chem. Lett.* **2004**, *33*, 442–443; e) J. Terasawa, H. Kondo, T. Matsumoto, K. Kirchner, Y. Motoyama, H. Nagashima, *Organometallics* **2005**, *24*, 2713–2721.

[7] W. J. van Meerendonk, K. Schröder, E. A. C. Brussee, A. Meetsma, B. Hessen, J. H. Teuben, *Eur. J. Inorg. Chem.* **2003**, 427–432.

[8] A. Xia, H. M. El-Kaderi, M. J. Heeg, C. H. Winter, *J. Organomet. Chem.* **2003**, *682*, 224–232.

[9] a) J. R. Hagadorn, M. J. McNevin, *Organometallics* **2003**, *22*, 609–611; b) J. R. Hagadorn, M. J. McNevin, G. Wiedenfeld, R. Shoemaker, *Organometallics* **2003**, *22*, 4818–4824; c) M. J. McNevin, J. R. Hagadorn, *Inorg. Chem.* **2004**, *43*, 8547–8554; d) J. R. Hagadorn, *Chem. Commun.* **2001**, 2144–2145.

[10] S.-D. Bai, J.-P. Guo, D.-S. Liu, *Dalton Trans.* **2006**, 2244–2250; and for examples of other kinds of linked bis(amidinate)compounds, see: a) H. A. Jenkins, D. Abeysekera, D. A. Dickie, J. A. C. Clyburne, *J. Chem. Soc., Dalton Trans.* **2002**, 3919–3922; b) J. Grundy, M. P. Coles, P. B. Hitchcock, *J. Organomet. Chem.* **2002**, *662*, 178–187; c) C.-T. Chen, L. H. Rees, A. R. Cowley, M. L. H. Green, *J. Chem. Soc., Dalton Trans.* **2001**, 1761–1767; d) C.-T. Chen, C.-A. Huang, Y.-R. Tzeng, B.-H. Huang, *Dalton Trans.* **2003**, 2585–2590; e) J.-F. Li, L.-H. Weng, X.-H. Wei, D.-S. Liu, *J. Chem. Soc., Dalton Trans.* **2002**, 1401–1405; f) J.-F. Li, S.-P. Huang, L.-H. Weng, D.-S. Liu, *Eur. J. Inorg. Chem.* **2003**, 810–813; g) H. Kawaguchi, T. Matsuo, *Chem. Commun.* **2002**, 958–959; h) J. R. Hagadorn, J. Arnold, *Angew. Chem.* **1998**, *110*, 1813–1815; *Angew. Chem. Int. Ed.* **1998**, *37*, 1729–1731; i) G. D. Whitener, J. R. Hagadorn, J. Arnold, *J. Chem. Soc., Dalton Trans.* **1999**, 1249–1255; j) J. R. Babcock, C. Incarvito, A. L. Rheingold, J. C. Fettinger, L. R. Sita, *Organometallics* **1999**, *18*, 5729–5732; k) S. Bambirra, A. Meetsma, B. Hessen, J. H. Teuben, *Organometallics* **2001**, *20*, 782–785.

[11] a) F. Basuli, J. C. Huffman, D. J. Mindiola, *Inorg. Chem.* **2003**, *42*, 8003–8010; b) F. Basuli, B. C. Bailey, J. Tomaszewski, J. C. Huffman, D. J. Mindiola, *J. Am. Chem. Soc.* **2003**, *125*, 6052–6053.

[12] R. D. Gorsich, *J. Am. Chem. Soc.* **1958**, *80*, 4744–4744.

[13] *SAINT*, *Reference Manual*, Siemens Energy and Automation, Madison, WI, **1994–1996**.

[14] G. M. Sheldrick, *SADABS*, *Empirical Absorption Correction Program*, University of Göttingen, Germany, **1997**.

[15] G. M. Sheldrick, *SHELXTL™*, *Reference Manual*, version 5.1, Siemens, Madison, WI, **1997**.

Received: July 13, 2006
Published Online: October 5, 2006

 © 2006 Wiley-VCH Verlag GmbH & Co. KGaA, Weinheim 

DOI: 10.1002/ejic.200600661

# Phase Formation and Properties in the System $Bi_2O_3$:$2CoO_{1+x}$:$Nb_2O_5$

**Terrell A. Vanderah,[a] Theo Siegrist,[b] Michael W. Lufaso,*[a][‡] Margaret C. Yeager,[a] Robert S. Roth,[a] Juan C. Nino,[c] and Samantha Yates[c]**

**Keywords:** Pyrochlore / Displacive disorder / Bismuth cobalt niobates / Bi–Co–Nb–O / Phase equilibria / Phase diagram / Dielectric properties / Magnetic properties

Subsolidus phase relations have been determined for the Bi–Co–Nb–O system in air (750–925 °C). Ternary compound formation was limited to pyrochlore ($A_2B_2O_6O'$), which formed a substantial solid solution region at Bi-deficient stoichiometries (relative to $Bi_2Co_{2/3}Nb_{4/3}O_7$) suggesting that about 8 to 25 % of the A sites are occupied by Co. X-ray powder diffraction data confirmed that all Bi–Co–Nb–O pyrochlores exhibit displacive behavior. A structural refinement of the pyrochlore $Bi_{1.56}Co_{0.96}Nb_{1.48}O_7$ using single-crystal X-ray diffraction data is reported with the A and O′ atoms displaced (0.34 Å and 0.45 Å, respectively) from ideal positions to 96g sites and 32e sites, respectively [$Fd\bar{3}m$ (#227), $a$ = 10.551(1) Å]. The displacive structural behavior is similar to that found in analogous Bi–M–Nb–O pyrochlores (M = Zn, Fe, Mn). Bi–Co–Nb–O pyrochlores exhibited overall paramagnetic behavior with negative Curie–Weiss temperature intercepts indicating weak antiferromagnetic interactions. At 250 K and 1 MHz the relative dielectric permittivity of the pyrochlore 0.4400:0.2100:0.3500 $Bi_2O_3$:$2CoO_{1+x}$:$Nb_2O_5$ was ca. 115 with tan $\delta$ = 0.06; however, at lower frequencies the sample was conductive. Low-temperature dielectric relaxation such as that observed for $Bi_{1.5}Zn_{0.92}Nb_{1.5}O_{6.92}$ and other bismuth-based pyrochlores was not observed. Consideration of bond lengths, effective magnetic moments, and dielectric properties suggests that the average oxidation state of Co in the pyrochlore phases is close to but slightly higher than 2.0.
(© Wiley-VCH Verlag GmbH & Co. KGaA, 69451 Weinheim, Germany, 2006)

## Introduction

Multiferroic ceramics which exhibit magnetoelectric effects display coupling between cooperative phenomena such as ferroelectricity and ferromagnetism, and have attracted considerable attention owing to their scientific and practical interest.[1] The possibility of manipulating the magnetic or dielectric properties of a single material by an applied electric or magnetic field, respectively, opens up entirely new device applications in microelectronics and data storage.[2–4] Only a few compounds are known to exhibit these properties,[3,5,6] including several Fe-[3,7] and Mn-containing[8–12] complex oxides. Currently, however, single-phase materials with magnetoelectric responses sufficiently robust for practical exploitation are not known. The present study of the $Bi_2O_3$–$2CoO_{1+x}$–$Nb_2O_5$ system was undertaken to characterize the formation and properties of ternary compounds that form from strongly polarizable ($Bi_2O_3$, $Nb_2O_5$) and magnetic ($CoO_{1+x}$) components.

[a] National Institute of Standards and Technology, Materials Science & Engineering Laboratory,
Gaithersburg, MD 20899, USA
[b] Bell Laboratories, Lucent Technologies,
Murray Hill, NJ 07974, USA
[c] University of Florida, Department of Materials Science & Engineering,
Gainesville, FL 32611-6400, USA
[‡] University of North Florida, Department of Chemistry & Physics,
Jacksonville, FL 32224, USA

## Results and Discussion

### Phase Formation

The results of the phase-equilibrium study are presented in Figure 1. In the Co–Nb–O subsystem the $Co^{2+}$ compounds $CoNb_2O_6$ and $Co_4Nb_2O_9$ were observed.[13] The $CoO$:$Nb_2O_5$ intergrowth phases reported to form at molar ratios of 1:7, 1:18, and 1:34, respectively,[13,14] were difficult to equilibrate and exhibited highly complex X-ray powder diffraction patterns related to that of $Nb_2O_5$ (as expected); this region of the phase diagram is depicted to obey the phase rule but was not investigated in detail. Phase-equilibria information for the $Bi_2O_3$–$CoO_{1+x}$ system has not, to the best of our knowledge, been reported. In the present study only a single phase of the sillenite-type was observed to form at $Bi_{25}CoO_{40-\delta}$.[15,16] Specimens equilibrated at 0.500:0.500 and 0.333:0.667 $Bi_2O_3$:$2CoO_{1+x}$ (800 °C) were mixtures of the sillenite phase and $Co_3O_4$ – the former composition formed considerable liquid at 850 °C, the latter at 900 °C. Giant electric polarization has been predicted for $BiCoO_3$ using first-principles methods;[17] however, the synthesis of this phase has not, to the best of our knowledge, been reported. The binary Bi–Nb–O phases observed were in general agreement with the comprehensive study reported by Roth[18] except for the high-$Bi_2O_3$ (≥0.75 mol fraction) region, represented in Figure 1 as a "fluorite" solid solution extending from 75:25 $Bi_2O_3$:$Nb_2O_5$ ($Bi_3Nb_2O_7$)

 © 2006 Wiley-VCH Verlag GmbH & Co. KGaA, Weinheim 

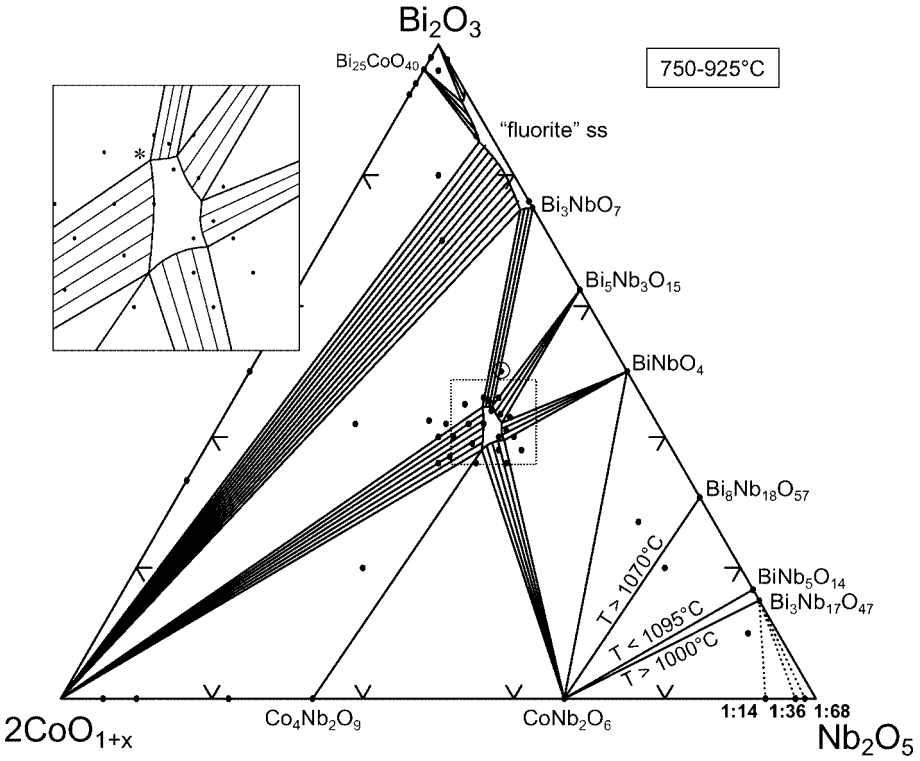


Figure 1. Subsolidus phase equilibrium diagram in air for the $Bi_2O_3$:$2CoO_{1+x}$:$Nb_2O_5$ system. Black dots denote the compositions of specimens prepared in the study; concentrations are on a molar fraction basis. Ternary phase formation is limited to pyrochlore, which forms an appreciable solid solution near the center of the diagram (enlarged in the inset). The "pyrochlore-like" composition $Bi_2Co_{2/3}Nb_{4/3}O_7$ (open circle) is not included in the solid solution region, but rather forms a three-phase mixture of $Bi_3NbO_7$, pyrochlore, and $Bi_5Nb_3O_{15}$. The limiting compositions of the pyrochlore field suggested by the present data are (inset: clockwise beginning with the cusp marked with an asterisk) $Bi_2O_3$:$2CoO_{1+x}$:$Nb_2O_5$ = 0.446:0.220:0.334 [$Bi_{1.79}Co_{0.88}Nb_{1.34}O_7$, $a$ = 10.580(1) Å], 0.448:0.205:0.347 [$Bi_{1.78}Co_{0.81}Nb_{1.38}O_7$, $a$ = 10.589(1) Å], 0.422:0.205:0.373 [$Bi_{1.65}Co_{0.80}Nb_{1.46}O_7$, $a$ = 10.571(1) Å], 0.395:0.215:0.390 [$Bi_{1.53}Co_{0.83}Nb_{1.51}O_7$, $a$ = 10.556(1) Å], and 0.380:0.253:0.367 [$Bi_{1.51}Co_{1.00}Nb_{1.46}O_7$, $a$ = 10.544(1) Å] (all formulas assume $Co^{2.2+}$). The temperature-dependent joins between $CoNb_2O_6$ and the binary Bi–Nb–O phases are consistent with established $Bi_2O_3$–$Nb_2O_5$ phase relations. The compound $BiCoO_3$ was not observed under the conditions of this study.

to 93:7 $Bi_2O_3$:$Nb_2O_5$. This region has received considerable attention as it forms a series of structurally complex, modulated superstructures[19–23] with variable and potentially useful dielectric properties.[24,25] Reported differences in the detailed phase relations in this region likely arise from kinetic effects, variations in synthesis (especially cooling methods), and/or differences in characterization methods (e.g. X-ray or electron diffraction). For example, the present study, in agreement with early studies,[18] did not find a sillenite-type compound at the composition $Bi_{12}Nb_{0.29}O_{20-x}$.[20] This specimen was a mixture of monoclinic $Bi_2O_3$ and the fluorite-type solid solution after repeated heatings at 700 °C for a total of 414 h; however, a different heat treatment may have resulted in the metastable body-centered cubic form of $Bi_2O_3$ (sillenite-type)[26] instead of the monoclinic polymorph.

Ternary phase formation in the $Bi_2O_3$:$2CoO_{1+x}$:$Nb_2O_5$ system was found to be limited to pyrochlore, which forms an appreciable solid solution region (Figure 1). During synthesis, the pyrochlore phase formed early in partially reacted samples and was readily purified within the single-phase region, suggesting high thermodynamic stability. Numerous descriptions can be found for the pyrochlore crystal structure, $^{VIII}A_2{}^{VI}B_2O_7$, which is unusual in that it can be considered as two relatively independent interpenetrating networks of [$BO_6$] octahedra sharing all vertices and [$O'A_4$] tetrahedra in an *anti*-cristobalite-type arrangement.[27–30] The formula is often written as ($A_2O'$)($B_2O_6$) or $A_2B_2O_6O'$ to emphasize this interesting structural character and distinguish the two networks. The larger A-cations are eight-fold (= 6+2) coordinated by six oxygen atoms in puckered rings formed by the $B_2O_6$ network plus two O′ oxygen atoms above and below in the $A_2O'$ network. The structure inherently facilitates non-stoichiometry as the $A_2O'$ network can be partially occupied, or in some cases completely absent; furthermore, numerous non-oxide and halide pyrochlores are known. In addition to extensive compositional ranges, pyrochlores exhibit a remarkable variety of exploitable physical properties, hence the considerable technical importance of this class of solids.[29]

Bi–Co–Nb–O pyrochlores have been previously reported to form at the stoichiometries $Bi_2Co_{2/3}Nb_{4/3}O_7$,[31] $Bi_2Co_3Nb_2O_{12+y}$, $Bi_2Co_4Nb_2O_{13+y}$, and $Bi_2CoNb_2O_{9+y}$;[32] however, under the conditions of the present study none of these compositions are included in the pyrochlore single-phase field: Composition $Bi_2Co_{2/3}Nb_{4/3}O_7$ formed a three-

 © 2006 Wiley-VCH Verlag GmbH & Co. KGaA, Weinheim 

phase mixture as described in Figure 1; $Bi_2Co_3Nb_2O_{12+y}$ and $Bi_2Co_4Nb_2O_{13+y}$ both occur in three-phase fields consisting of pyrochlore, $CoO/Co_3O_4$, and a small amount of $CoNb_2O_6$;[33] and the stoichiometry $Bi_2CoNb_2O_{9+y}$ resulted in a three-phase mixture of pyrochlore, $BiNbO_4$, and a small amount of $CoNb_2O_6$. As shown on the diagram (Figure 1), Bi–Co–Nb–O pyrochlores form thermodynamically stable mixtures with the $Bi_3NbO_7$ solid solution, $Bi_5Nb_3O_{15}$, $BiNbO_4$, $CoNb_2O_6$, $Co_4Nb_2O_9$, and $CoO/Co_3O_4$. Compositions, nominal formulas, and refined unit cell parameters for single-phase Bi–Co–Nb–O pyrochlores (all dull dark greenish gray in color) prepared in the present study are given in Table 1.[34] The trends in unit cell parameters show a strong dependence on Bi concentration.

Table 1. Compositions, nominal formulas, and unit cell parameters (*a*, space group $Fd\bar{3}m$, #227) for single-phase pyrochlore specimens prepared in this study. These compositions correspond to the points within the five-sided pyrochlore region shown in Figure 1.[34]

| $Bi_2O_3$:$2CoO_{1+x}$:$Nb_2O_5$ | Nominal formula ($Co^{2.2+}$) | *a* [Å] |
|---|---|---|
| 0.4400:0.2100:0.3500 | $Bi_{1.744}Co_{0.8324}Nb_{1.387}O_7$ | 10.580(1) |
| 0.4200:0.2300:0.3500 | $Bi_{1.672}Co_{0.9158}Nb_{1.394}O_7$ | 10.566(1) |
| 0.4000:0.2200:0.3800 | $Bi_{1.562}Co_{0.8594}Nb_{1.484}O_7$ | 10.556(1) |

Observed, indexed X-ray powder diffraction data for the pyrochlore with composition 0.4400:0.2100:0.3500 $Bi_2O_3$:$2CoO_{1+x}$:$Nb_2O_5$ are given in Table 2. As noted previously,[29] the 442 reflection, forbidden for an ideal pyrochlore structure, was easily observed in this pattern and in *all* patterns of pyrochlore and pyrochlore-containing specimens prepared in this study. The 442 reflection was also observed in precession photos of single crystals. Similar to the Bi–Zn–Nb–O pyrochlores,[29,35] the observation of this diagnostic reflection indicates the presence of displacements from ideal crystallographic sites. The consistent observation of this reflection indicates that *all* Bi–Co–Nb–O pyrochlores exhibit positional displacements. Furthermore, the stoichiometric location of the pyrochlore phase field, as also found for the analogous Bi–M–Nb–O systems (M = Zn,[29] Fe,[36] Mn[37]), occurs at substantially lower Bi concentrations than conventional formulations placing only Bi on the A sites and the smaller M/Nb cations on the B sites. The pyrochlore field includes compositions with "excess" B cations that require mixing of some Co on the A sites with $Bi^{3+}$, as found for Zn in *all* Bi–Zn–Nb–O pyrochlores.[29] The limiting compositions observed for the pyrochlore field (Figure 1) suggest that the Co concentration on the A sites can range from ca. 8 to 25%,[38] which is comparable to the analogous ranges observed for other Bi–M–Nb–O pyrochlores with Co replaced by Zn (≈ 16 to 26%),[29] Fe (ca. 4 to 15%),[36] and Mn (ca. 14 to 30%).[37]

Table 2. Observed X-ray powder diffraction data for the pyrochlore with composition $Bi_2O_3$:$2CoO_{1+x}$:$Nb_2O_5$ = 0.4400:0.2100:0.3500 [space group $Fd\bar{3}m$, #227, *a* = 10.580(1) Å]. The nominal pyrochlore formula is $Bi_{1.744}Co_{0.8324}Nb_{1.387}O_7$; however, the actual O′ occupancy factor and precise Co oxidation state are uncertain.

| *h* | *k* | *l* | $2\theta_{obsd.}$ | $I_{obsd.}$ | $2\theta_{calcd.}$ | $\Delta 2\theta$ | $d_{obsd.}$ |
|---|---|---|---|---|---|---|---|
| 1 | 1 | 1 | 14.482 | 7 | 14.490 | 0.007 | 6.1112 |
| 2 | 2 | 0 | 23.757 | <1 | 23.769 | 0.012 | 3.7423 |
| 3 | 1 | 1 | 27.945 | 8 | 27.948 | 0.003 | 3.1902 |
| 2 | 2 | 2 | 29.217 | 100 | 29.218 | 0.001 | 3.0541 |
| 4 | 0 | 0 | 33.863 | 35 | 33.865 | 0.002 | 2.6450 |
| 3 | 3 | 1 | 37.007 | 11 | 37.008 | 0.001 | 2.4272 |
| 3 | 3 | 3 | 44.460 | 4 | 44.461 | 0.001 | 2.0361 |
| 4 | 4 | 0 | 48.644 | 50 | 48.646 | 0.002 | 1.8703 |
| 5 | 3 | 1 | 51.037 | 4 | 51.030 | –0.007 | 1.7881 |
| 4 | 4 | 2 | 51.810 | 1 | 51.808 | –0.003 | 1.7632 |
| 6 | 2 | 0 | 54.854 | 2 | 54.838 | –0.016 | 1.6723 |
| 5 | 3 | 3 | 57.056 | <1 | 57.038 | –0.018 | 1.6129 |
| 6 | 2 | 2 | 57.763 | 46 | 57.759 | –0.004 | 1.5948 |
| 4 | 4 | 4 | 60.583 | 13 | 60.589 | 0.006 | 1.5271 |
| 7 | 1 | 1 | 62.666 | 1 | 62.660 | –0.006 | 1.4813 |
| 6 | 4 | 2 | 66.036 | <1 | 66.030 | –0.005 | 1.4136 |
| 5 | 5 | 3 | 67.999 | <1 | 68.010 | 0.011 | 1.3775 |

## Structural Refinement of the Pyrochlore Phase

The highly symmetrical ideal pyrochlore structure $A_2B_2O_6O'$ crystallizes in space group $Fd\bar{3}m$ with A and B cations on two special positions (16d, 16c) and oxygen atoms on two sites, 48f (O) and 8b (O′), resulting in a single positional variable (*x* for the 48f-site oxygen atoms in the $B_2O_6$ octahedral network). As expected, this model resulted in anomalously large thermal parameters for the A-site cations and the O′ oxygen atoms in an initial refinement using single-crystal X-ray diffraction data [$R_f$(obsd.) = 0.325, $R_w$(obsd.) = 0.237]. The disordered structure was therefore modeled assuming static displacements of the A and O′ atoms, similar to the analogous Bi–M–Nb–O pyrochlores (M = Zn,[35] Fe,[36] Mn[37]) whose structures were refined using neutron powder diffraction data. The Bi:Co:Nb ratio of the single crystal was fixed at a stoichiometry inferred from the refined unit cell parameter of ground crystals [*a* = 10.551(1) Å] taken from the same batch. This value, compared to that for the single-phase pyrochlore powder from which the crystals were grown [*a* = 10.580(1) Å] indicates reduced Bi concentrations in the crystals. When compared to the unit cell parameters obtained for other single-phase pyrochlores (Table 1) and for the limiting compositions of the phase field (cusps, Figure 1), the metal stoichiometry extrapolated for the single crystal was 39.0:24.0:37.0 Bi:Co:Nb. The oxygen content of the crystal was calculated by assuming an average Co oxidation state of 2+, for simplicity, and the O′ sites were assumed to be filled, resulting in an overall formula of $Bi_{1.56}Co_{0.96}Nb_{1.48}O_7$ for the crystals, with fully occupied metal positions.

The refinement of the positional parameters for the disordered metal sites was carried out assuming displacements of the $A_2O'$ network, as found for a number of other pyrochlores.[29,35–37,39–42] Refinement with only Bi displaced gave residuals for observed reflections of $R_f$ = 0.116 and $R_w$ = 0.072 – improved results were obtained when O′ was also displaced. The A site Bi/Co metals were displaced to six partially filled 96g sites; however, the corresponding 96g position for O′ was not stable, and difference Fourier maps consistently showed peaks at and around the ideal 8b site (5/8, 1/8, 1/8). Refinement of the O′ isotropic thermal pa-

 © 2006 Wiley-VCH Verlag GmbH & Co. KGaA, Weinheim 

Table 3. Refined positional parameters *x*, *y*, *z* and $B_{iso}$ for pyrochlore-type $Bi_{1.56}Co_{0.44}(Co_{0.52}Nb_{1.48})O_7$ at ambient temperature using single-crystal X-ray diffraction data [space group $Fd\bar{3}m$, #227, $a$ = 10.551(1) Å]; $R_f$(obsd.) = 0.109, $R_w$(obsd.) = 0.0704.[a]

| Atom | Position | *x* | *y* | *z* | $B_{iso}$ [Å$^2$] | Occ. |
|---|---|---|---|---|---|---|
| Bi/Co | 96g | 0.5082(15) | 0.5082 | 0.4701(18) | 2.66(21) | 0.1300/0.0367 |
| Nb/Co | 16c | 0 | 0 | 0 | 1.46(3) | 0.74/0.26 |
| O | 48f | 1/8 | 1/8 | 0.3218(14) | 1.8(4) | 1.00 |
| O′ | 32e | 0.150(7) | 0.150 | 0.650 | 4.9(24) | 0.25 |

[a] E.S.D. values. refer to the last digit printed.

rameter diverged, so a displaced position using the 32e site was chosen. Other combinations were not stable. The O′ oxygen position was refined assuming a total contribution of 8 oxygen atoms, hence the occupancy factor of 0.25. The final refinement results are given in Table 3 and illustrated in Figure 2. In the present study, the scattering was dominated by the much heavier Bi and Nb atoms, resulting in limited definition of the displaced oxygen O′ positions. In addition, the disorder on the A and B metal sites hampered a proper refinement of the scale factor due to strong correlations with occupancy parameters. Furthermore, the oxidation state of Co (and therefore oxygen content) and the level of vacancies (if any) on the A and O′ sites were uncertain.[43]

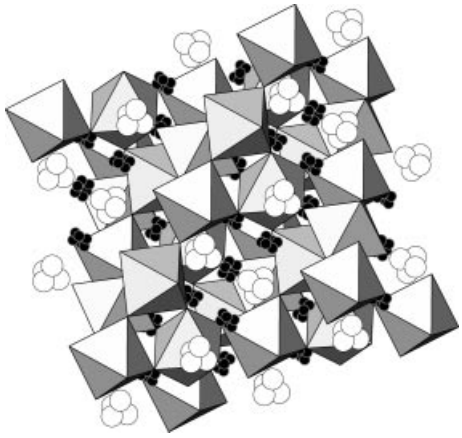

Figure 2. Crystal structure of the pyrochlore $Bi_{1.56}Co_{0.96}Nb_{1.48}O_7$ illustrating the displacive disorder of the $A_2O'$ network (Table 3). The vertex-linked polyhedra represent the octahedral $B_2O_6$ = $(Co,Nb)_2O_6$ network. The puckered rings of black spheres represent the six equivalent, partially filled 96g sites for the A-site Bi/Co cations; the tetrahedral clusters of larger white spheres denote the four possible positions for O′ oxygens displaced to the 32e sites. The results indicate that the A-site cations are displaced 0.34 Å from the ideal 16d position, while O′ oxygen atoms on 32e sites are displaced 0.45 Å from the high-symmetry 8b position.

The [(Co,Nb)$O_6$] octahedra in the $B_2O_6$ network are nearly regular, with metal–oxygen distances of 2.01(1) Å (×6), and O–B–O angles deviating about 3.7° from 90°. The observed bond valence sums calculated about this site[44] using the $R_o$ parameters for $Nb^{5+}$ and $Co^{2+}$ are 4.55 v.u. and 2.52 v.u., respectively. The bonds are therefore longer than expected for Nb–O, suggesting that Co is predominantly present in the 2+ oxidation state, which has a larger sixfold ionic radius (0.745 Å, HS) than $Nb^{5+}$ (0.64 Å) (whereas $Co^{3+}$ is smaller at 0.61 Å, HS).[45] The observed and theoretical bond valence sums for the Nb/Co site using the occupancy factors in Table 3 and assuming the presence of $Nb^{5+}$/$Co^{2+}$ are 4.03 v.u. and 4.22 v.u., respectively, which are in reasonable agreement given the uncertainties in composition. The A-site Bi/Co metal positions and associated O′ positions are displacively disordered, therefore the A-site coordination sphere is variable. Observed Bi/Co–O distances range from 2.05(5) Å up to 2.96(1) Å. Of these, the distances to the octahedral framework O atoms tend to be longer, ranging from 2.34(1) Å to 2.96(1) Å (with an average of 2.66 Å). The distances between Bi/Co and the displaced O′(32e) atoms are shorter (with an average 2.34 Å) and include the shortest values of 2.05(5) Å, 2.15(5) Å (2x), and 2.25(7) Å (2×), which could reasonably accommodate the smaller Co cations. The equivalent isotropic displacement parameter obtained for the Bi/Co site corresponds to a mean-square displacement of 0.2 Å, as compared with the displacement of 0.34 Å from the ideal site. Similarly, the large displacement parameter for O′ corresponds to a mean-square displacement of 0.25 Å whereas the displacement from the ideal site is 0.45 Å. These values suggest that the large thermal parameters reflect disorder on these sites rather than thermal motion.

The displacive model in Table 3 for the Bi–Co–Nb–O pyrochlore is similar to that reported for a Bi–Fe–Nb–O pyrochlore[36] wherein the A-site cations were displaced 0.43 Å to 96g sites with O′ displaced 0.29 Å to 32e sites. The considerably larger O′ displacement in the Co system (0.45 Å) may reflect the higher concentration of smaller B-type ions on the A sites (≈ 22% compared to <10% in the Fe system). Displacive models for analogous Bi–Zn–Nb–O[35] and Bi–Mn–Nb–O[37] pyrochlores also displaced A sites to 96g sites (0.39 Å and 0.36 Å, respectively), but O′ was displaced differently, to 96g sites (0.46 Å for Zn, 0.33 Å for Mn). Differences in the details of the structural displacements are not unexpected, since the local crystal chemistry and any short-range correlations should be affected by different concentrations of small B-type ions on the A sites as well as variations in the concentrations of vacancies on both the A sites and the O′ sites.

## Magnetic Properties of Pyrochlore Phases

Magnetic data obtained for three different single-phase Bi–Co–Nb–O pyrochlore samples indicated qualitatively similar properties. The field dependence of the magnetization confirmed that all samples were overall paramagnetic in nature. The temperature dependence of the magnetic susceptibility, and its inverse, for the pyrochlore with com-

 © 2006 Wiley-VCH Verlag GmbH & Co. KGaA, Weinheim 

position 0.4000:0.2200:0.3800 $Bi_2O_3$:$2CoO_{1+x}$:$Nb_2O_5$ are shown in Figure 3. Above 100 K the inverse magnetic susceptibility was linear and that range was fit to the Curie Weiss law; the results are given in Table 4. For all three compounds, the extrapolation of the linear fits indicated small negative temperature intercepts, suggesting the presence of weak antiferromagnetic cooperative interactions. All of the observed effective magnetic moments calculated from the slopes of the Curie–Weiss fits are higher than the high-spin, spin-only values expected for $Co^{2+}$ ($3d^7$, $S$ = 3/2, 3.87 $\mu\beta$) and $Co^{3+}$ ($3d^6$, S = 2, 4.90 $\mu\beta$), suggesting considerable unquenched orbital contributions, as observed for other Co-containing pyrochlores.[46] Given the range of values previously reported for high-spin $Co^{2+}$ (4.6–5.2 $\mu\beta$/Co) and high-spin $Co^{3+}$ (5.1–5.7 $\mu\beta$/Co)[47] compounds, the observed effective moments for the pyrochlore phases are consistent with the presence of divalent, or mixed divalent-trivalent Co. Slight curvature is observed in the magnetization vs. field data at 10 K (Figure 3, inset). The complex magnetic behavior exhibited by the Bi–Co–Nb–O pyrochlores is

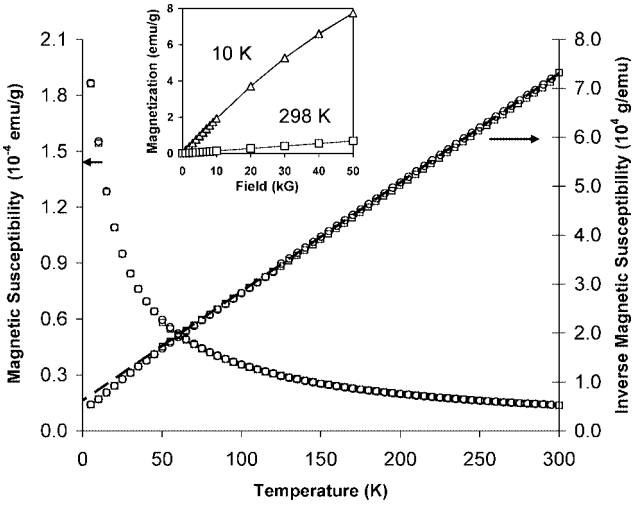


Figure 3. Temperature dependence of the zero-field-cooled (circles) and field-cooled (squares) mass susceptibility and inverse mass susceptibility for the single-phase pyrochlore 0.4000:0.2200:0.3800 $Bi_2O_3$:$2CoO_{1+x}$:$Nb_2O_5$ at an applied field of 50 kG. The inset shows the field dependence of the magnetization measured at 10 K (triangles) and 298 K (squares). (Lines are present to guide the eye.) Slight curvature is observed in the low-temperature data. (Units: To convert susceptibility values in emu/g to SI units $m^3$/kg, multiply by $4\pi/10^3$. To convert field values in Oe (or G) to SI units A/m, multiply by $10^3/4\pi$. Magnetization values in emu/g units are numerically equal to SI units of $A\,m^2$/kg.[48]).

Table 4. Magnetic data for single-phase Bi–Co–Nb–O pyrochlore specimens listed in Table 1. The observed effective moments ($\mu_{eff}$/mol Co) and temperature-axis intercepts ($\theta$, K) were obtained from linear fits of the inverse susceptibility data in the temperature range 100–300 K.

| Composition $Bi_2O_3$:$2CoO_{1+x}$:$Nb_2O_5$ | $\mu_{eff}$/mol Co [$\mu\beta$] | $\theta$ [K] |
|---|---|---|
| 0.4400:0.2100:0.3500 | 5.1 | –35 |
| 0.4000:0.2200:0.3800 | 5.1 | –26 |
| 0.4200:0.2300:0.3500 | 5.0 | –35 |

not unexpected given the triangular symmetry of the metal lattices which results in geometric magnetic frustration.[49–50] Pyrochlore compounds are known to exhibit a wide range of cooperative magnetic properties and, for example, are of significant interest as "spin-ice" systems.[51–53]

### Dielectric Properties of the Pyrochlore Phase

The relative permittivity (corrected for 10% porosity) and dielectric loss as a function of temperature and frequency for the single-phase pyrochlore with composition 0.4400:0.2100:0.3500 $Bi_2O_3$:$2CoO_{1+x}$:$Nb_2O_5$ are shown in Figure 4. The upturns in the data above 250 K indicate that the sample becomes predominantly conductive, and the onset of conductivity is frequency dependent. For example, at 250 K and 1 MHz the sample is still insulating and exhibits a relative permittivity of ca. 115 and tan $\delta$ = 0.06, yet at 10 kHz tan $\delta$ is greater than 0.2, indicating conductivity. This behavior is in sharp contrast with previously reported bismuth based pyrochlores for which dielectric relaxation is observed.[36,54] The temperature- and frequency-dependent behavior observed is consistent with interfacial polarization mediated by the presence of multivalent Co ions – similar properties were observed for pyrochlores in the Bi–Mn–Nb–O system.[37]

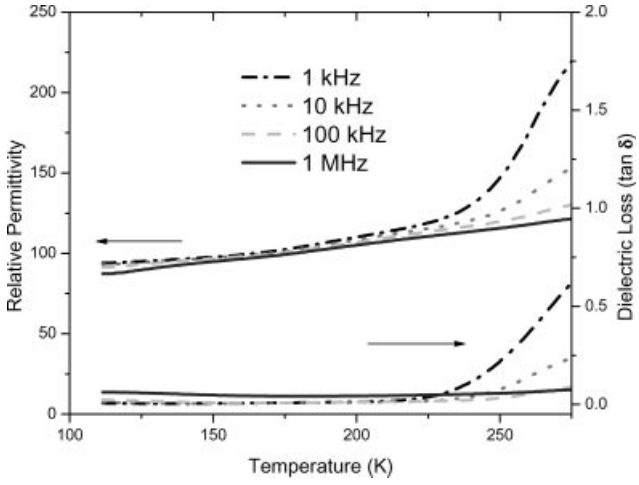


Figure 4. Relative dielectric permittivity (corrected for porosity) and dielectric loss for the single-phase pyrochlore with composition 0.4400:0.2100:0.3500 $Bi_2O_3$:$2CoO_{1+x}$:$Nb_2O_5$ at frequencies of 10 kHz, 100 kHz and 1 MHz. The sample is predominantly conductive at temperatures above 250 K and the onset of conductivity is frequency dependent; these effects likely reflect the presence of mixed-valent $Co^{2+/3+}$.

## Conclusions

Subsolidus phase relations have been determined for the Bi–Co–Nb–O system in air using specimens equilibrated at 750–925 °C. Ternary phase formation was limited to pyrochlore, which forms a considerable solid solution region at stoichiometries that are "Bi-deficient" compared to conven-

 © 2006 Wiley-VCH Verlag GmbH & Co. KGaA, Weinheim 

tional $A_2B_2O_7$-type formulations with Bi on the A sites and Co/Nb on the B sites. The location of the pyrochlore field suggests that approximately 8 to 25% of the A sites can be occupied by Co. All Bi–Co–Nb–O pyrochlores form with positional displacements off ideal crystallographic positions, as also found for analogous Bi–M–Nb–O pyrochlores with M = Zn, Fe, and Mn. A structural refinement of the pyrochlore $Bi_{1.56}Co_{0.96}Nb_{1.48}O_7$ using single–crystal X-ray diffraction data is reported with displacements in the $A_2O'$ network. Bi–Co–Nb–O pyrochlores exhibited overall paramagnetic behavior with weak antiferromagnetic interactions; observed effective moments were consistent with the presence of $Co^{2+}$ or $Co^{2+/3+}$ mixtures; however, the observed bond lengths suggest that Co is present predominantly as the larger 2+ ion. Measurements of relative dielectric permittivity and dielectric loss between 110 and 450 K indicated conductive, frequency-dependent properties consistent with the presence of mixed-valent Co. In contrast to $Bi_{1.5}Zn_{0.92}Nb_{1.5}O_{6.92}$, no low-temperature dielectric relaxation was observed. The Bi–Co–Nb–O pyrochlores form thermodynamically stable mixtures with the $Bi_3NbO_7$ solid solution, $Bi_5Nb_3O_{15}$, $BiNbO_4$, $CoNb_2O_6$, $Co_4Nb_2O_9$, and $CoO/Co_3O_4$.

## Experimental Section

Forty-seven polycrystalline specimens (3–4 g each) were prepared in air by solid-state reactions using $Bi_2O_3$ (99.999%), $Co_3O_4$ (99.9985%, pre-analyzed by X-ray powder diffraction), and $Nb_2O_5$ (99.999%). Prior to each heating, each sample was mixed by grinding with an agate mortar and pestle for 15 min, pelletized, and placed on a bed of sacrificial powder of the same composition supported on alumina ceramic. After an initial calcinations overnight at 800 °C (below the m.p. of $Bi_2O_3$, 825 °C) multiple 1–3 d heatings (with intermediate grinding and re-pelletizing) were carried out at 875–925 °C.[55] Samples were furnace-cooled to ca. 700 °C and then air-quenched on the bench-top. Metastable melting in non-equilibrated ternary specimens (an initial problem owing to large differences in the melting points of $Bi_2O_3$, $CoO_x$, and $Nb_2O_5$) was avoided by soaking samples at 875 °C for 1–3 d for the second heating, followed by a third heating at 925 °C for 2–3 d. Equilibrium was presumed when no further changes could be detected in the weakest peaks observed in the X-ray powder diffraction patterns. A eutectic in the ternary system may occur near 42:40:18 $Bi_2O_3$:$2CoO_{1+x}$:$Nb_2O_5$, which formed liquid at 900 °C. $Bi_2O_3$ volatilization was observed above the solidus by thermogravimetric analysis, but was not detectable in the subsolidus study. Pyrochlore-type crystals were easily obtained by heating a single-phase polycrystalline specimen (composition 0.4400:0.2100:0.3500 $Bi_2O_3$:$2CoO_{1+x}$:$Nb_2O_5$) in a Pt capsule (sealed by welding) to 1300 °C, followed by slow cooling (4 °C/h) to below the freezing point (≈1160 °C). The crystals exhibited conchoidal fracture and were obtained as brown-black shards.

Phase assemblages were ascertained using the disappearing phase method[56,57] and X-ray powder diffraction data obtained with a Philips[58] diffractometer equipped with incident Soller slits, a theta-compensating slit and graphite monochromator, and a scintillation detector. Samples were mounted in welled glass slides. Patterns were collected at ambient temperatures using Cu-$K_\alpha$ radiation over the range 3–70° 2$\theta$ with a 0.02° 2$\theta$ step size and a 2 s count time. Intensity data measured as relative peak heights above background were obtained using the DATASCAN software package, and processed using JADE. For unit cell refinements, observed 2$\theta$ line positions were first corrected using SRM 660, $LaB_6$,[59] as an external calibrant. Lattice parameters were refined using JADE (2$\theta$ values, Cu-$K_{\alpha1}$ = 1.540593 Å).

Preliminary characterization of pyrochlore-type single crystals was carried out using the precession camera method (Zr-filtered Mo-$K_\alpha$ radiation) to assess quality, cell parameter, and space group. Data for structural refinement were collected with an Oxford Diffraction Xcalibur 2 CCD diffractometer with graphite-monochromated Mo-$K_\alpha$ radiation. Due to the strong absorption coefficient of 50.2 $mm^{-1}$, several small crystals with approximate dimensions 0.03 mm × 0.04 mm × 0.04 mm were chosen, and measurements included 2$\theta$ angles up to 100°. However, large absorption corrections were still required and limited the range of observable reflections. Further details of the crystal-structure investigation may be obtained from the Fachinformationzentrum Karlsruhe, 76344 Eggenstein-Leopoldshafen, Germany, on quoting the depository number CSD-416601.

Magnetic properties were characterized with a Quantum Design SQUID magnetometer and single-phase polycrystalline samples. Magnetization was measured as a function of temperature between 2 K and 300 K after cooling in the absence of an applied field (zero-field cooled, ZFC) and while cooling in a magnetic field (field-cooled, FC) of 50 kG between 2 K and 300 K. In addition, measurements at 10 K and at 298 K were carried out to determine the field dependence of the magnetization in applied fields between 0 and 50 kG.

Dielectric properties were evaluated using pellets prepared from single-phase powders mixed with 2 wt.-% PVA (polyvinyl alcohol) to assist forming. Mixtures were ground using a mortar and pestle, sieved (300 μm mesh), and then dried at 120 °C for 5 min. Approximately 0.6 g of the mixture was uniaxially pressed into a disk (ca. 1 mm thick, ca. 10 mm diameter) using a pressure of ca. 180 MPa. The green pellets were then sintered in air at 975 °C for 4 h. The density of the sintered samples was measured in water using Archimedes's principle and compared to the theoretical density of the material. Gold/palladium electrodes (ca. 75 nm thick) were sputtered onto the top and bottom surfaces to form parallel plate capacitors. The complex dielectric permittivity was measured between 1 kHz and 1 MHz using an Agilent 4284 LCR meter. The sample temperature was controlled with a programmable 9023 Delta Design for measurements between 110 and 450 K.

## Acknowledgments

We thank L. P. Cook for thermogravimetric analyses, N. Swanson for graphical representation of the phase diagram data, and R. Drew and R. D. Shull for assistance with magnetic measurements. M. C. Y. was supported in part by the National Science Foundation's Research Experience for Undergraduates (REU) program, Division of Materials Research.

[1] N. A. Spaldin, M. Fiebig, *Science* **2005**, *309*, 391–392.
[2] V. E. Wood, A. E. Austin, in: *Magnetoelectric Interaction Phenomena in Crystals* (Eds.: A. J. Freeman, H. Schmid), Gordon and Breach, London, **1975**.
[3] N. A. Hill, *J. Phys. Chem. B* **2000**, *104*, 6694–6709, and references therein.
[4] P. Baettig, N. A. Spaldin, *Appl. Phys. Lett.* **2005**, *86*, 012505 (article number), and references therein.

 © 2006 Wiley-VCH Verlag GmbH & Co. KGaA, Weinheim 

[5] D. V. Efremov, J. Van Den Brink, D. I. Khomskii, *Nat. Mater.* **2004**, *3*, 853–856.
[6] N. A. Spaldin, W. E. Pickett, *J. Solid State Chem.* **2003**, *176*, 615–632.
[7] C. Ederer, N. A. Spaldin, *Phys. Rev. B* **2005**, *71*, 060401 (article number) and references cited therein.
[8] T. Kimura, S. Kawamoto, I. Yamada, M. Azuma, M. Takano, Y. Tokura, *Phys. Rev. B* **2003**, *67*, 180401 (article number), and references therein.
[9] B. B. Van Aken, T. T. M. Palstra, A. Filippetti, N. A. Spaldin, *Nature* **2004**, *3*, 164–170, and references therein.
[10] M. Kenzelmann, A. B. Harris, S. Jonas, C. Broholm, J. Schefer, S. B. Kim, C. L. Zhang, S. W. Cheong, O. P. Vajk, J. W. Lynn, *Phys. Rev. Lett.* **2005**, *95*, 087206 (article number), and references therein.
[11] O. P. Vajk, M. Kenzelmann, J. W. Lynn, S. B. Kim, S. W. Cheong, *Phys. Rev. Lett.* **2005**, *94*, 087601 (article number), and references therein.
[12] M. Azuma, K. Takata, T. Saito, S. Ishiwata, Y. Shimakawa, M. Takano, *J. Am. Chem. Soc.* **2005**, *127*, 8889–8892.
[13] *Phase Equilibria Diagrams* (formerly Phase Diagrams for Ceramists), The American Ceramic Society, Westerville, Ohio; Figs, 6:6391, EC-096.
[14] A. Burdese, M. Lucco-Borlera, P. Rolando, *Atti Accad. Sci. Torino, Cl. Sci. Fis., Mater. Nat.* **1964**, *99*, 565–575.
[15] A. Ramanan, J. Gopalakrishnan, *Indian J. Chem. Sect. A* **1985**, *24*, 594.
[16] N. Rangavittal, T. N. Guru Row, C. N. R. Rao, *Eur. J. Solid State Inorg. Chem.* **1994**, *31*, 409.
[17] Y. Uratani, T. Shishidou, F. Ishii, T. Oguchi, *Japn. J. Appl. Phys.* **2005**, *44*, 7130–7133.
[18] R. S. Roth, J. L. Waring, *J. Res. Natl. Bur. Stand.* **1962**, *66A*, 451.
[19] R. L. Withers, C. D. Ling, S. Schmid, *Z. Kristallogr.* **1999**, *214*, 296–304.
[20] C. D. Ling, R. L. Withers, S. Schmid, J. G. Thompson, *J. Solid State Chem.* **1998**, *137*, 42.
[21] M. Valant, B. Jancar, U. Pirnat, D. Suvorov, *J. Eur. Ceram. Soc.* **2005**, *25*, 2829–2834.
[22] U. Pirnat, M. Valant, B. Jancar, D. Suvorov, *Chem. Mater.* **2005**, *17*, 5155–5160.
[23] C. D. Ling, M. Johnson, *J. Solid State Chem.* **2004**, *177*, 1838–1846.
[24] M. Valant, D. Suvorov, *J. Am. Ceram. Soc.* **2003**, *86*, 939.
[25] M. Valant, D. Suvorov, *J. Am. Ceram. Soc.* **2004**, *87*, 1056–1061.
[26] E. M. Levin, R. S. Roth, *J. Res. Natl. Bur. Stand.* **1964**, *68A*, 189–195.
[27] A. F. Wells, *Structural Inorganic Chemistry*, Clarendon Press, Oxford, 4th edition, **1975**, p. 499.
[28] M. A. Subramanian, G. Aravamudan, G. V. S. Rao, *Prog. Solid State Chem.* **1983**, *15*, 55.
[29] T. A. Vanderah, I. Levin, M. W. Lufaso, *Eur. J. Inorg. Chem.* **2005**, *14*, 2895–2901, and references therein.
[30] R. L. Withers, W. Somophon, V. P. Ting, Y. Liu, Q. Zhou, B. J. Kennedy, *J. Solid State Chem.*, in press (**2006**).
[31] G. A. Smolenskii, V. A. Isupov, G. I. Golovshchifova, A. G. Tutov, *Inorg. Mater.* **1976**, *12*, 255–258.
[32] I. V. Piir, D. A. Prikhodko, S. V. Ignatchenko, A. V. Schukariov, *Solid State Ionics* **1997**, *101–103*, 1141–1146.
[33] More accurately, these points occur within the four-phase compatibility volume ($Bi_2O_3$–CoO–$Co_3O_4$–$CoNb_2O_6$). The relations in the four-component system actually studied here ($Bi_2O_3$–CoO–$Co_3O_4$–$Nb_2O_5$) have been projected onto a ternary slice (Figure 1) to simplify presentation of the results.
[34] Although the metal ratios given here are precise, the actual populations on the A and B sites depend on the O′ occupancy factor and Co oxidation state(s), which are uncertain and which may vary in each pyrochlore. Expressions for the structural formulas for the pyrochlore phases are therefore ambiguous. For purposes of comparison, the formulas have been normalized to seven oxygens (full occupancy of the O′ site) and assume an average oxidation state of 2.2+ for Co; the reasons for the latter assumption are described in the text.
[35] I. Levin, T. G. Amos, J. C. Nino, T. A. Vanderah, C. A. Randall, M. T. Lanagan, *J. Solid State Chem.* **2002**, *168*, 69.
[36] M. W. Lufaso, T. A. Vanderah, I. M. Pazos, I. Levin, J. C. Nino, V. Provenzano, P. K. Schenck, submitted to *J. Solid State Chem.*.
[37] T. A. Vanderah, M. W. Lufaso, A. U. Adler, I. Levin, J. C. Nino, V. Provenzano, P. K. Schenck, *J. Solid State Chem.*, in press.
[38] Estimated by assuming a range of average Co oxidation states from 2.0+ to 2.5+, and full occupancy of the O' site; the latter assumption results in maximum estimates for $Co_{A\ site}$ concentrations and minimum estimates for A-site vacancy concentrations.
[39] M. Ganne, K. Toyama, *Mater. Res. Bull.* **1975**, *10*, 1313.
[40] M. Avdeev, M. K. Haas, J. D. Jorgensen, R. J. Cava, *J. Solid State Chem.* **2002**, *169*, 24.
[41] L. Q. Li, B. J. Kennedy, *Chem. Mater.* **2003**, *15*, 4060.
[42] Ismunandar, T. Kamiyama, K. Oikawa, A. Hoshikawa, B. J. Kennedy, Y. Kubota, K. Kato, *Mater. Res. Bull.* **2004**, *39*, 553.
[43] These results should be considered as an approximation of the disordered structure; the large differences in X-ray scattering factors suggests that neutron diffraction techniques may yield a more detailed picture of the structural disorder.
[44] N. E. Brese, M. O'Keeffe, *Acta Crystallogr., Sect. B* **1991**, *47*, 192–197, with updated $R_o$ parameters http://www.ccp14.ac.uk/ccp/web-mirrors/i_d_brown/.
[45] R. D. Shannon, *Acta Crystallogr., Sect. A* **1976**, *32*, 751.
[46] M. K. Haas, R. J. Cava, M. Avdeev, J. J. Jorgensen, *Phys. Rev. B* **2002**, *66*, 094429.
[47] R. L. Carlin, Magnetochemistry, Springer-Verlag, Berlin, **1986**, chapter 4.
[48] R. B. Goldfarb, *Concise Encyclopedia of Superconducting and Magnetic Materials* (Ed.: J. Evetts), Pergamon Press, Oxford, **1992**, p. 256..
[49] J. E. Greedan, *J. Mater. Chem.* **2001**, *11*, 37.
[50] K. Ramesha, L. Sebastian, B. Eichhorn, J. Gopalakrishnan, *J. Mater. Chem.* **2003**, *13*, 2011.
[51] A. P. Ramirez, A. Hayashi, R. J. Cava, R. Siddharthan, B. S. Shastry, *Nature* **1999**, *399*, 333.
[52] R. Siddharthan, B. S. Shastry, A. P. Ramirez, A. Hayashi, R. J. Cava, S. Rosenkranz, *Phys. Rev. Lett.* **1999**, *83*, 1854.
[53] G. D. Blundred, C. A. Bridges, M. J. Rosseinsky, *Angew. Chem. Int. Ed.* **2004**, *43*, 3562.
[54] J. C. Nino, H. J. Youn, M. T. Lanagan, C. A. Randall, *J. Mater. Res.* **2002**, *17*, 1178.
[55] Exceptions: specimens with Bi contents at least 70 mol-% were not heated above 750 °C (to avoid melting and decomposition of sillenite-type phases), and those with Bi contents less than 30 mol-% were heated at higher final temperatures, 950–1300 °C, to achieve equilibrium more quickly.
[56] C. G. Bergeron, S. H. Risbud, *Introduction to Phase Equilibria in Ceramics*, American Ceramic Society, Westerville, **1984**.
[57] C. S. Barrett, *Structure of Metals*, McGraw-Hill, New York, **1943**, chapter X, 1st edition.
[58] Certain commercial equipment and software are identified in order to adequately specify the experimental procedure; recommendation or endorsement by the National Institute of Standards and Technology is not therein implied.
[59] C. R. Hubbard, Y. Zhang, R. L. McKenzie, *Certificate of Analysis, SRM 660*, National Institute of Standards and Technology, Gaithersburg, MD, 20899, **1989**.

Received: July 13, 2006
Published Online: October 5, 2006

 © 2006 Wiley-VCH Verlag GmbH & Co. KGaA, Weinheim 

DOI: 10.1002/ejic.200600545

# Silver, Palladium and Rhodium Complexes of Acenaphthylene-Anullated N-Heterocyclic Carbene Ligands: A Comparative Study

**Hayati Türkmen,[a] Onur Şahin,[b] Orhan Büyükgüngör,[b] and Bekir Çetinkaya*[a]**

**Keywords:** N-Heterocyclic carbenes / Silver complexes / Thiones / Palladium complexes / Rhodium complexes / C–C coupling

The newly prepared carbene precursor 1,3-dimesitylacenaphtho[1,2-*d*]imidazolinium chloride, (NHC–H)Cl, **3**, could be readily converted into the NHC-silver(I) complex, **4**, which is an efficient carbene transfer agent and has been used to synthesise thione **5**, *trans*-[$PdCl_2(NHC)_2$], **6** and [RhCl(NHC)(COD)], **7**. All compounds synthesised were characterised by elemental analysis, NMR spectroscopy and the molecular structures of the thione **5** and complex **7** were determined by X-ray crystallography. Complex **7** was converted into *cis*-[$RhCl(NHC)(CO)_2$] and the electron donating properties and *trans* influence of the NHC ligand were compared with nonanullated counterparts. The catalytic activity in the Heck reaction of **6** and the in situ formed palladium complex was evaluated. The activity of the in situ formed complexes for the Heck coupling of alkenes was high.

(© Wiley-VCH Verlag GmbH & Co. KGaA, 69451 Weinheim, Germany, 2006)

## Introduction

Owing to their bonding versatility and the relative ease with which their electronic and steric properties can be modified, increasing attention has been focused on using imidazole-based N-heterocyclic carbene (NHC) compounds as ancillary ligands for a number of transition metal mediated catalytic reactions.[1–4] Their donating properties are superior to those of the most basic phosphanes. The ability of NHCs to coordinate to metal centres makes them excellent candidates for the design of well-defined catalysts. In a recent study, we observed that the variation of *p*-substituents on the phenyl ring of 1,3-diarylimidazolin-2-ylidenepalladium(II) complexes has a significant influence on the catalytic behaviour of the Suzuki coupling of NHC-Pd complexes.[5] Increasing knowledge of the chemical properties of ligands and complexes derived from them has led to a growing demand for systems with more and more complex structures. Anullated NHCs have attracted increasing attention in recent years since the introduction of carbo- and heterocyclic groups may give an opportunity for better control of the stability of the active species and improve catalytic activity. In this context, benzo-, pyrido-, naphtha- and quinoxalino-anullated imidazol-2-ylidenes have been reported.[6] These studies have demonstrated that the electron density at $C^2$ varies with the π donor/acceptor properties of the anullated rings. The 4,5-positions of the imidazolidine ring seem to be ideally suited for substitution since they are quite far from the catalytically active metal site. Therefore, we focused on the design of an acenaphthylene-anullated NHC ligand to modify the environment of the metal centre. Model studies showed that the tetracyclic ring system is highly strained. Our main aim was to determine how these properties are reflected in the electron donating properties of its complexes.

## Results and Discussion

### Preparation of Ligand Precursor 3, Thione 5 and NHC Complexes 6–8

The general route to the targeted NHC ligand precursor and metal complexes is shown in Scheme 1. The amine **2** was readily synthesised in good yield as a red, crystalline solid by means of the reduction of the corresponding imine **1** which served as a chelating ligand for several transition metal complexes.[7] Cyclisation of **2** with $CH(OEt)_3$ in the presence of one equiv. of $NH_4Cl$ gave the diazolinium salt **3**. For the sake of comparison, the 4,5-dimethyl-1,3-dimesityl imidazolinium salt and related compounds (**4′**–**8′**) were also prepared (Scheme 2).

Treatment of **3** with NaO*t*Bu or NaH/NaO*t*Bu resulted in the deprotonation of the imidazolinium salt. However, attempted isolation of the free carbene failed. These precursor salts were subsequently deprotonated using basic silver oxide. Silver(I) NHC complexes are easy to make and can be used as air- and moisture-stable carbene transfer agents.[8] Such silver(I) NHC complexes with coordinating halides are well known to oligomerise by means of silver-silver interactions, bridging halides or carbenes[9] and they

[a] Department of Chemistry, Ege University
35100 Bornova-Izmir, Turkey
[b] Department of Physics, Ondokuz Mayıs University
55139 Samsun, Turkey

 © 2006 Wiley-VCH Verlag GmbH & Co. KGaA, Weinheim 

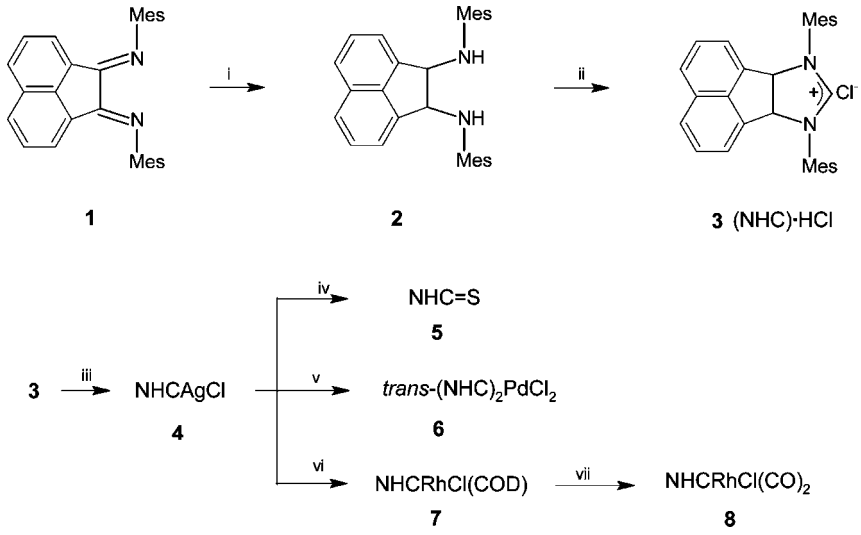


Scheme 1. i) $NaCNBH_3$, MeOH; ii) $NH_4Cl$, $HC(OEt)_3$; iii) $Ag_2O$, $CH_2Cl_2$; iv) $S_8$, $CH_2Cl_2$; v) $PdCl_2(CNCH_3)_2$, $CH_2Cl_2$; vi) $[RhCl(COD)]_2$, $PhCH_3$; vii) CO, $CH_2Cl_2$.

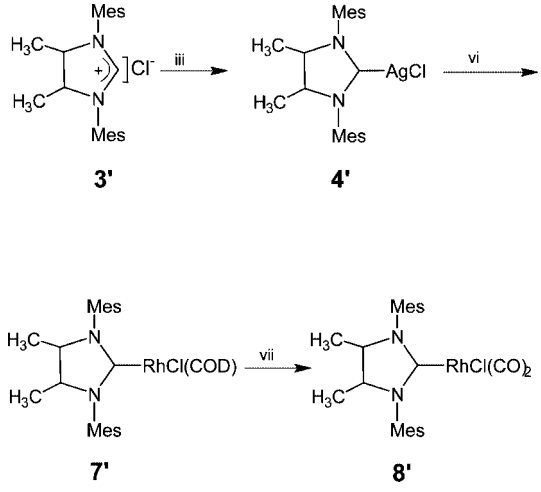


Scheme 2. iii) $Ag_2O$, $CH_2Cl_2$; vi) $[RhCl(COD)]_2$, $PhCH_3$; vii) CO, $CH_2Cl_2$.

have been characterised by $^1H$ and $^{13}C$ NMR spectroscopy.

The clearest spectroscopic evidence identifying **4** as a silver NHC complex is the appearance of a highly deshielded $^{13}C$ NMR signal for $C_{carb}$ at $\delta$ = 205.5 ppm [dd, $^1J_{^{109}Ag,C}$ = 221.9, $^1J_{^{107}Ag,C}$ = 255.4 Hz]. The chemical shift and splitting pattern is consistent with the monomeric structure of **4**.[10] By comparison, the dimers consisting of $(NHC)_2Ag^+$ cations and $AgX_2^-$ anions or $(NHC–Ag–\mu–X)_2$ structures display $C_{carb}$ singlets due to partial dissociation and monomer/dimer equilibrium in solution. Ionic $(NHC)_2Ag^+$ complexes exhibit smaller $J_{^{107,109}Ag,C}$ coupling constants (180–190 and 200–215 Hz).[9] The chemical shift is also indicative of the donating nature of the carbene in the carbene–Ag interaction (Scheme 1).

Despite its large coupling constant, complex **4** is a good carbene transfer agent. Interaction of **4** with elemental sulfur readily afforded the thione **5**. This thione is a stable crystalline substance, the structure of which was elucidated by NMR spectroscopy and X-ray analysis. The most important peak in the $^{13}C$ NMR spectrum is the peak corresponding to C=S at $\delta$ = 179.6 ppm. X-ray diffraction analysis of **5** allowed us to draw some conclusions about the structure of **5**. The structure and the atom numbering scheme are shown in Figure 1. Very few cyclic thiones with bulky substituents at the N atoms of the NHC ligand have been reported[8] and this appears to be the first such compound with an anullated group.

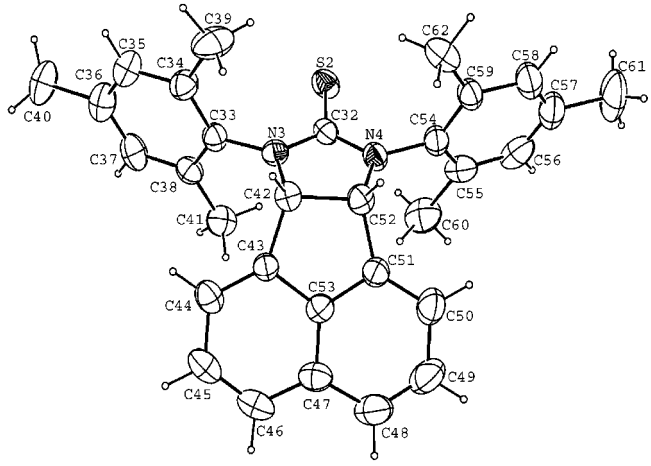


Figure 1. Molecular structure of **5**. Selected bond lengths [Å] and bond angles [°]: C32–S2 1.661(6), C32–N3 1.357(7), C32–N4 1.344(6), C33–N3 1.357(7), C54–N4 1.442(5), C42–C52 1.553(5); N3–C32–N4 108.6(5), N3–C32–S2 124.9(4), N4–C32–S2 126.5(4).

Crystallographic data for the structural analysis of **5** are given in Table 3. An ORTEP representation of the structure is shown in Figure 1 and selected bond lengths and angles are listed in the caption. The C(1)–S(1) bond length of 1.661 Å in **5** compares well with known C(32)–S(2) bond lengths in derivatives of imidazolidin-2-thiones.[8,11]

The reaction of the Ag complex **4** with palladium species bearing weakly coordinated $CH_3CN$ ligands yielded the disubstituted carbene complexes **6**. The *trans* configuration of

 © 2006 Wiley-VCH Verlag GmbH & Co. KGaA, Weinheim 

the carbene ligands was confirmed by $^{13}C$ NMR spectroscopy in which the $C_2$ signal occurs at $\delta$ = 198.9 ppm, a value typical for *trans* carbene complexes.[12] At room temperature, the $^1H$ NMR spectrum of **6** shows that the NHC ligands are nonequivalent. Four signals can be observed at 1.22, 1.27, 2.25 and 2.33 ppm for each $CH_3$ group in the 2,6-positions of the aryl ring. This indicates that there is hindered rotation around the Pd–$C_{carb}$ bond arising from the bulky phenyl substituent on the NHC ligand. The $Pd^{II}$ carbene complex **6** and the in situ formed complexes between **3** and $Pd(OAc)_2$ were tested as catalysts in C–C coupling reactions.

In a similar fashion to that described for **6**, the reaction between **4** and the dimer $[RhCl(COD)]_2$ in boiling toluene generates the monocarbene complex **7**. The $^1H$ NMR spectrum shows singlets at $\delta$ = 1.46, 1.86, 2.53 and 2.82 ppm for the *o*-Me groups and 6.90, 6.99, 7.01 and 7.11 ppm for the *m*-protons of the mesityl groups, respectively, presumably because of the restricted rotation around the Rh–$C_{carb}$ bond.[13] The detection of a doublet at $\delta$ = 213.7 ppm in the $^{13}C$ NMR spectrum together with a characteristic $J_{103Rh,13C}$ coupling of 48.8 Hz indicated the formation of the proposed complex. Further information was obtained from the crystal structure of [RhCl(NHC)(COD)], **7**, presented in Figure 2.

The single-crystal X-ray diffraction study of complex **7** confirmed the square-planar coordination geometry of the rhodium atom. The structure is represented in Figure 2 and selected bond lengths and angles are listed in the caption. The structural parameters of **7** are similar to those in other rhodium carbene complexes. The rhodium-carbene distance Rh(1)–C(1) [2.047(3) Å] is slightly longer than that observed in saturated analogues (2.003 Å), which may reflect the steric hindrance. However, the distance Rh(1)–Cl(1) [2.3768(9) Å] lies within the expected range.[14] The N(1)–C(1)–N(2) angle of 107.6° is close to that of thione **5** but slightly larger than that reported for [RhCl(SIMes)(COD)].[15] The difference in the *trans* influences of the carbene and the chloride ligands leads to different C=C bond lengths in the coordinated COD ligand: C32–C33 1.355(6) Å and C36–C37 1.385(6) Å.

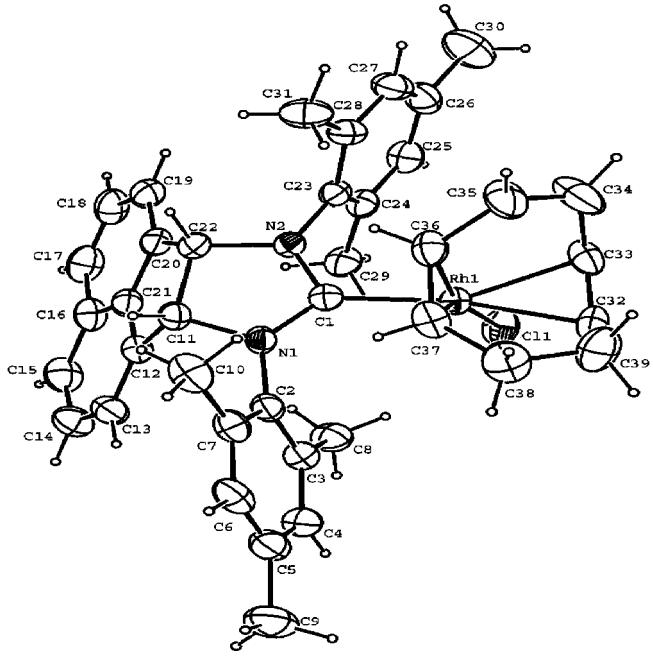


Figure 2. Structure of one molecule of **7** in the crystal. Selected bond lengths [Å] and bond angles [°]: C1–Rh1 2.047(3), C1–N1 1.357(4), C1–N2 1.341(4), C2–N1 1.427(4), C11–N1 1.476(4), C11–C22 1.538(5), C22–N2 1.488(4), C23–N2 1.435(4), C32–Rh1 2.219 (3), C32–C33 1.355(6), C33–Rh1 2.181(4), C36–Rh1 2.114(3), C36–C37 1.385(6), C37–Rh1 2.106(3), Cl1–Rh1 2.376(9); N1–C1–N2 107.6(3), N1–C1–Rh1 128.9(2), N2–C1–Rh1 122.7(2), N1–C11–C12 116.4(3), N1–C11–C22 102.3(2), N2–C22–C11 102.1(2), N2–C22–C20 114.9(3), C1–Rh1–Cl1 96.63(8).

The C–O stretching frequencies of *cis*-$[RhCl(CO)_2(NHC)]$ are considered as an excellent measure for the σ donor/π acceptor properties of the NHC ligands.[15] Therefore, we synthesised complexes of the type **8/8′** by replacing the COD ligand with excess CO. The IR spectra of **8/8′** revealed two bands corresponding to symmetric and asym-

Table 1. Selected NMR and IR spectroscopic data for **4/4′**–**8/8′**.

| Complex | $\delta$ [ppm] | Appearance of signal | $J_{M,C}$ | $\tilde{\nu}$(CO) sym | $\tilde{\nu}$ (CO) asym | Ref. |
|---|---|---|---|---|---|---|
| (IMes)AgCl | 185.0 | dd | 270/234 | – | – | [7b] |
| (SIMes)AgCl | 207.5 | dd | 256/222 | – | – | [7b] |
| **4** | 205.5 | dd | 256/222 | – | – | this work |
| **4′** | 206.0 | dd | 255/223 | – | – | this work |
| $(IMes)_2PdCl_2$ | 171.2 | s | – | – | – | [17] |
| $(SIMes)_2PdCl_2$ | 199.2 | s | – | – | – | [5] |
| **6** | 198.9 | s | – | – | – | this work |
| **6′** | 196.7 | s | – | – | – | [5] |
| (IMes)RhCl(COD) | 183.7 | d | 52 | – | – | [19] |
| (SIMes)RhCl(COD) | 211.9 | d | 47 | – | – | [15] |
| **7** | 213.7 | d | 49 | – | – | this work |
| **7′** | 212.5 | d | 48 | – | – | this work |
| $(IMes)RhCl(CO)_2$ | – | – | – | 2076 | 2006 | [15] |
| $(SIMes)RhCl(CO)_2$ | 205.7 | d | 41 | 2081 | 1996 | [15] |
| **8** | 206.5 | d | 42 | 2074 | 1988 | this work |
| **8′** | 206.8 | d | 42 | 2078 | 1994 | this work |

 © 2006 Wiley-VCH Verlag GmbH & Co. KGaA, Weinheim 

metric vibrations. A comparison of IR data compiled for *cis*-[RhCl(CO)$_2$(NHC)] complexes of NHCs in Table 1 shows that acenaphthylene-anullated NHCs are stronger donors than corresponding nonanullated analogues bearing the imidazole skeleton.

### Catalytic Arylation of Alkenes

We were interested in exploring the influence of substituents located at the 4,5-positions of the imidazolidine ring. Consequently, we tested in situ formed complexes [by use of 3 mol-% Pd(OAc)$_2$ and 3 mol-% **3**] and preformed **6** for activity in the Heck reaction[16] using a set of standard substrates, under standard reaction conditions in terms of solvent, temperature and base (Table 2).

Table 2. The Heck reaction catalysed by in situ formed [**3** + Pd(OAc)$_2$] or preformed complex **6**.[a]

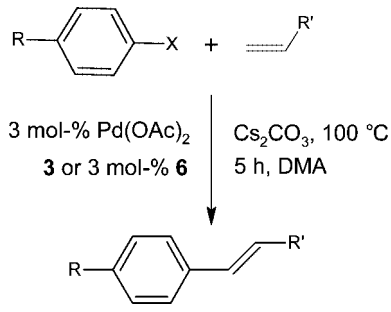


| Entry | Cat | R | R′ | X | Yield (%) |
|---|---|---|---|---|---|
| 1 | **3** | Me | COO*n*Bu | Br | 80 |
| 2 | **6** | Me | COO*n*Bu | Br | 30 |
| 3 | **3** | Me | Ph | Br | 86 |
| 4 | **6** | Me | Ph | Br | 33 |
| 5 | **3** | Me(O)C | Ph | Br | 89 |
| 6 | **6** | Me(O)C | Ph | Br | 35 |
| 7 | **3** | Me(O)C | Ph | Cl | 38 |
| 8 | **6** | Me(O)C | Ph | Cl | 10 |
| 9 | **3′** | Me(O)C | COO*n*Bu | Br | 67 |
| 10 | **3** | Me(O)C | COO*n*Bu | Br | 80 |
| 11 | SIMesHCl | Me(O)C | COO*n*Bu | Br | 62 |

[a] Reactions conditions: 1.0 mmol of the aryl halide, 1.5 mmol of olefin, 1.5 mmol $Cs_2CO_3$, 3 mL DMA, 100 °C, 5 h. GC yields (diethylene glycol dibutyl ether used as internal standard, average of two runs).

The coupling of 4-bromoacetophenone or 4-bromotoluene with alkenes was found to proceed in good yield in the presence of 3% of in situ formed catalyst (entries 1, 3 and 5). In the presence of preformed catalyst **6**, deactivated aryl bromides and activated 4-chloroacetophenone were less reactive under the same reaction conditions (entries 2, 4 and 6). The electron-donating capability of the substituents located at the 4,5-positions of the imidazolidine ring appear to play a role in the complex's catalytic activity. Thus, yields of 80%, 67% and 62% were achieved with complexes formed in situ between Pd(OAc)$_2$ and the salts **3**, **3′** and SIMesHCl, respectively, under identical conditions (entries 9–11). Clearly, acenapthene anullation has an unexpected effect of increasing the complex reactivity. This is somewhat surprising, since there is no conjugation between the imidazoline and naphthalene rings.

## Conclusions

In order to further extend the possibilities of ligand tuning and the scope of NHC based catalysts, anullation of the imidazole ring by acenaphthylene was studied. Thione **5** and the transition metal complexes **6**–**8** of the anullated NHC ligand were easily obtainable from the silver-NHC complex **4** which was prepared from the salt **3** and $Ag_2O$. Silver is readily replaced by other metals to give, for example, $Pd^{II}$ and $Rh^{I}$ complexes in high yield. A comparison of NMR and IR spectroscopic data indicates that the new carbene seems to range between saturated and unsaturated imidazol-2-ylidene in terms of its electronic properties. A preliminary study has indicated that the in situ formed palladium complex is an active catalyst for arylation of alkenes.

The greater rigidity of the NHC complexes afforded by the tetracyclic imidazole framework exemplified by **6**–**8** can be anticipated to provide selective transformations. Investigations along these lines are in progress.

## Experimental Section

**General:** All manipulations were carried out in vacuo using Schlenk techniques. Anhydrous solvents were either distilled from appropriate drying agents or purchased from Merck and were degassed prior to use by purging with dry argon. The solvents were then kept over molecular sieves. All other reagents were commercially available and were used as received.

NMR spectra were recorded at 297 K on a Varian Mercury AS 400 instrument at 400 MHz ($^1$H) or 100.56 MHz ($^{13}$C). Elemental analyses were carried out by the analytical service of TUBITAK with a Carlo–Erba Strumentazione Model 1106 instrument. FTIR Spectra were recorded on a Perkin–Elmer Spectrum 100 series instrument. Compound **1** was prepared according to the literature.[18] The structural characterisations of **1′**, **2′**, **3′** and **6′** are given elsewhere.[5]

### Starting Materials

**1,2-Bis(mesitylamino)acenaphthylene (2):** A suspension of **1** (2250 mg, 5.4 mmol) in MeOH (50 mL) was treated at room temperature under argon with $NaCNBH_3$ (2050 mg, 32.6 mmol) in portions of 1 g over a period of 20 min. To the resultant mixture was added bromocresol green and then 0.1 N HCl was added until the colour changed from green to yellow. The solution was stirred for 20 h and heated subsequently for 4 h under reflux. The mixture was then cooled to room temperature and 0.1 N KOH (10 mL), $H_2O$ (100 mL) and $CH_2Cl_2$ (50 mL) were added. The aqueous phase was washed with $CH_2Cl_2$ several times. After this step, the $CH_2Cl_2$ washings were combined and dried with $MgSO_4$. The solvent was concentrated and then methanol was added. The precipitate was separated and washed with methanol. Drying under vacuum provided NMR spectroscopically pure off-white crystals of **2**. Yield: 1.82 g, 81%. M.p. 156–157 °C. $C_{30}H_{32}N_2$ (420.59): calcd. C 85.67, H 7.67, N 6.66; found C 86.10, H 7.82, N 6.93. $^1$H NMR (400 MHz, $CDCl_3$, 297 K): $\delta$ = 2.18 (s, 12 H, $H^{12,13}$), 2.31 (s, 6 H, $H^{14}$), 3.84 (s, 2 H, NH), 5.31 (s, 2 H, $H^{4,5}$), 6.86 (s, 2 H, $H^{8,10}$),

 © 2006 Wiley-VCH Verlag GmbH & Co. KGaA, Weinheim 

6.96 (d, $J$ = 1.6 Hz, 2 H, $H^{16}$), 7.39 (t, $J$ = 1.9 Hz, 2 H, $H^{17}$), 7.68 (d, $J$ = 2 Hz, 2 H, $H^{18}$) ppm. $^{13}C$ NMR (100 MHz, $CDCl_3$, 297 K): $\delta$ = 19.1 ($C^{12,13}$), 20.9 ($C^{14}$), 62.4 ($C^{4,5}$), 120.5 ($C^{16}$), 124.3 ($C^{18}$), 128.2 ($C^{17}$), 129.3 ($C^{8,10}$), 129.9 ($C^{7-11}$), 130.9 ($C^{19}$), 131.6 ($C^{9}$), 135.8 ($C^{20}$), 142.4 ($C^{6}$), 144.4 ($C^{15}$) ppm.

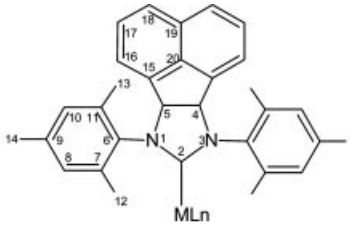


M = Ag, Pd, Rh

Ln = others

**1,3-Dimesitylacenaphtho[1,2-*d*]imidazolinium Chloride (3):** A mixture of **2** (1170 mg, 2.78 mmol), triethyl orthoformate (10 mL) and ammonium chloride (150 mg, 2.84 mmol) was heated in a distillation apparatus until the ethanol distillation ceased. The temperature of the reaction mixture reached 130 °C. After cooling to room temp., ether (30 mL) was added. A colourless solid precipitated which was collected by filtration. Purification was achieved by repeated recrystallisations from ethanol/ether. Yield: 1.20 g, 93%. M.p. 393–395 °C. $C_{31}H_{31}N_2Cl$ (467.05): calcd. C 79.72, H 6.69, N 6.00; found C 79.10, H 7.02, N 6.13. $^1H$ NMR (400 MHz, $CDCl_3$, 297 K): $\delta$ = 1.56, 2.34 (s, 12 H, $H^{12,13}$), 2.68 (s, 6 H, $H^{14}$), 6.61 (s, 2 H, $H^{4,5}$), 6.86 (d, $J$ = 1.8 Hz, 2 H, $H^{16}$), 6.88 (s, 2 H, $H^{8,10}$), 7.08 (s, 2 H, $H^{8,10}$), 7.48 (t, $J$ = 1.9 Hz, 2 H, $H^{17}$), 7.89 (d, $J$ = 2.2 Hz, 2 H, $H^{18}$), 10.21 (s, 1 H, $H^2$) ppm. $^{13}C$ NMR (100 MHz, $CDCl_3$, 297 K): $\delta$ = 18.5, 19.1 ($C^{12,13}$), 21.4 ($C^{14}$), 70.6 ($C^{4,5}$), 122.3 ($C^{16}$), 126.9 ($C^{18}$), 128.7 ($C^{17}$), 129.1 ($C^{8}$), 130.4 ($C^{10}$), 130.7 ($C^{19}$), 131.9 ($C^{9}$), 135.4 ($C^{20}$), 136.3 ($C^{7}$), 136.4 ($C^{11}$), 137.5 ($C^{6}$), 140.8 ($C^{15}$), 159.3 ($C^{2}$) ppm.

**Chloro(1,3-dimesitylacenaphtho[1,2-*d*]imidazolin-2-ylidene)silver(I) (4):** A suspension of **3** (470 mg, 1 mmol) and an equivalent amount of $Ag_2O$ in dichloromethane (50 mL) was stirred at room temperature for 24 h with exclusion of light. The colour of the suspension gradually changed from black to colorless. The suspension was then filtered, washed with dichloromethane and dried under vacuum to give a white solid. 0.52 g, 90%. M.p. 363–365 °C. $C_{31}H_{30}AgClN_2$ (573.90): calcd. C 64.88, H 5.27, N 4.88; found C 65.02, H 5.33, N 4.99. $^1H$ NMR (400 MHz, $CDCl_3$, 297 K): $\delta$ = 1.50, 2.35 (s, 12 H, $H^{12,13}$), 2.49 (s, 6 H, $H^{14}$), 6.09 (s, 2 H, $H^{4,5}$), 6.83 (d, $J$ = 1.8 Hz, 2 H, $H^{16}$), 6.88, 7.08 (s, 4 H, $H^{8,10}$), 7.44 (q, 2 H, $H^{17}$), 7.82 (d, $J$ = 2.0 Hz, 2 H, $H^{18}$) ppm. $^{13}C$ NMR (100 MHz, $CDCl_3$, 297 K): $\delta$ = 18.4, 18.7 ($C^{12,13}$), 21.3 ($C^{14}$), 71.1, 71.3 ($C^{4,5}$), 121.8 ($C^{16}$), 126.0 ($C^{18}$), 128.5 ($C^{17}$), 130.3 ($C^{8}$), 130.4 ($C^{10}$), 131.8 ($C^{19}$), 134.0 ($C^{9}$), 135.2 ($C^{20}$), 136.9 ($C^{7}$), 137.2 ($C^{11}$), 138.7 ($C^{6}$), 139.1 ($C^{15}$), 205.5 (2d, $^1J_{^{13}C,^{107,109}Ag}$ = 221.9, 255.4 Hz, $C^2$) ppm.

**Chloro(1,3-dimesityl-4,5-dimethylimidazolidin-2-ylidene)silver(I) (4′):** Yield: 0.39 mg, 82%. M.p. 368–370 °C (dec.). $C_{23}H_{30}AgClN_2$ (477.82): calcd. C 57.81, H 6.33, N 5.86; found C 64.86, H 5.38, N 5.00. $^1H$ NMR (400 MHz, $CDCl_3$, 297 K): $\delta$ = 1.17–1.13 [s, 6 H, $NCH(CH_3)CH(CH_3)N$], 1.96 (s, 6 H, $p$-$CH_3$), 2.03, 2.01 (s, 12 H, $o$-$CH_3$), 4.01–3.98 [m, 2 H, $NCH(CH_3)CH(CH_3)N$], 7.13, 7.10 (s, 4 H, Mes) ppm. $^{13}C$ NMR (100 MHz, $CDCl_3$, 297 K): $\delta$ = 18.0, 17.8, [$NCH(CH_3)CH(CH_3)N$], 20.1, 19.9 ($o$-$CH_3$), 19.7 ($p$-$CH_3$), 52.3, 52.1 [$NCH(CH_3)CH(CH_3)N$], 127.8, 131.0, 131.3, 137.4, 138.1, 138.2, (Mes), 206.0 (2d, $^1J_{^{13}C,^{107,109}Ag}$ = 223.0, 255.0 Hz, $C^2$) ppm.

**1,3-Dimesitylacenaphtho[1,2-*d*]imidazole-2-thione (5):** A mixture of the silver complex **4** (570 mg, 1 mmol) and sulfur (32 mg, 1 mmol) was suspended in dichloromethane (50 mL) and stirred for 24 h at room temperature. After removal of silver chloride by filtration, the solution was concentrated in vacuo and hexane was added to afford white crystals of **5**. Yield: 0.40 g, 87%. M.p. 323–325 °C. $C_{31}H_{30}N_2S$ (462.64): calcd. C 80.48, H 6.54, N 6.06; found C 79.12, H 6.83, N 5.98. $^1H$ NMR (400 MHz, $CDCl_3$, 297 K): $\delta$ = 1.40, 2.26 (s, 12 H, $H^{12,13}$), 2.42 (s, 6 H, $H^{14}$), 6.23 (s, 2 H, $H^{4,5}$), 6.71 (d, $J$ = 1.8 Hz, 2 H, $H^{16}$), 6.91 (s, 2 H, $H^{8,10}$), 7.11 (s, 2 H, $H^{8,10}$), 7.42 (t, $J$ = 1.9 Hz 2 H, $H^{17}$), 7.85 (d, $J$ = 2.1 Hz, 2 H, $H^{18}$) ppm. $^{13}C$ NMR (100 MHz, $CDCl_3$, 297 K): $\delta$ = 18.4, 18.5 ($C^{12,13}$), 21.5 ($C^{14}$), 67.2 ($C^{4,5}$), 122.0 ($C^{16}$), 125.7 ($C^{18}$), 128.3 ($C^{17}$), 129.9 130.0 ($C^{10}$), 132.1 ($C^{19}$), 133.5 ($C^{9}$), 135.9 ($C^{11}$), 137.6 ($C^{7}$), 138.5 ($C^{6}$), 138.8 ($C^{15}$), 179.6 ($C^{2}$) ppm.

**Dichloro(1,3-dimesitylacenaphtho[1,2-*d*]imidazolin-2-ylidene)-palladium(II) (6):** $PdCl_2(MeCN)_2$ (260 mg, 1 mmol) and **4** (1140 mg, 2 mmol) were stirred in dichloromethane (50 mL) at 60 °C for 24 h in a sealed ampoule. The resultant mixture was filtered and the solvent was removed to yield a cream-colored solid. The solid was purified by crystallisation from $CH_2Cl_2$ layered with ethanol. 0.87 g, 84%. M.p. 390–392 °C. $C_{62}H_{60}Cl_2N_4Pd$ (1038.49): calcd. C 71.71, H 5.82, N 5.40; found C 71.79, H 5.88, N 4.96. $^1H$ NMR (400 MHz, $CDCl_3$, 297 K): $\delta$ = 1.22, 1.27, 2.25, 2.33 (s, 24 H, $H^{12,13}$), 2.49 (s, 12 H, $H^{14}$), 5.68 (d, $J$ = 1.3 Hz 4 H, $H^{4,5}$), 6.67 (t, $J$ = 1.7 Hz, 4 H, $H^{16}$), 6.73, 6.79, 6.86, 6.94 (s, 8 H, $H^{8,10}$), 7.28 (q, 4 H, $H^{17}$), 7.65 (q, 4 H, $H^{18}$) ppm. $^{13}C$ NMR (100 MHz, $CDCl_3$, 297 K): $\delta$ = 19.7, 19.8, 20.3, 20.4 ($C^{12,13}$), 21.5 ($C^{14}$), 71.0 ($C^{4,5}$), 122.0 ($C^{16}$), 125.3 ($C^{18}$), 128.0 ($C^{17}$), 129.9, 129.6 ($C^{8,10}$), 131.5 ($C^{19}$), 134.6,134.8 ($C^{9}$), 136.5, 136.6, 136.7 ($C^{7,11}$), 137.4, 137.5 ($C^{20}$), 138.9, 139.0 ($C^{6}$), 139.4, 139.5 ($C^{15}$), 198.9 ($C^{2}$) ppm.

**Chloro($\eta^4$-1,5-cylooctadiene)(1,3-dimesitylacenaphtho[1,2-*d*]-imidazolin-2-ylidene)rhodium(I) (7):** A suspension of $[RhCl(COD)]_2$ (250 mg, 0.5 mmol) and silver complex **4** (570 mg, 1 mmol) in toluene (10 mL) was stirred for 4 h at 100 °C. The resultant yellowish suspension was cooled to room temperature, filtered through celite and the yellow filtrate was concentrated. Addition of hexane (10 mL) precipitated a yellow powder, which was collected and dried in vacuo. Crystals of **7** suitable for X-ray analysis were obtained by crystallisation from $CH_2Cl_2/C_2H_5OH$. 0.59 g, 87%. M.p. 363–365 °C. $C_{39}H_{42}ClN_2Rh$ (677.12): calcd. C 69.18, H 6.25, N 4.14; found C 69.12, H 6.33, N 4.08. $^1H$ NMR (400 MHz, $CDCl_3$, 297 K): $\delta$ = 1.35–1.73 (m, 8 H, COD-$CH_2$), 1.46, 1.86, 2.53, 2.82 (s, 12 H, $H^{12,13}$), 2.23 (s, 6 H, $H^{14}$), 3.40 (d, $J$ = 0.7 Hz, 2 H, COD-CH), 4.40 (t, $J$ = 1 Hz, 2 H, COD-CH), 5.92, 6.00 (s, 2 H, $H^{4,5}$), 6.78 (d, $J$ = 1.8 Hz, 1 H, $H^{16}$), 6.84 (d, $J$ = 1.8 Hz, 1 H, $H^{16}$), 6.90, 6.99, 7.01, 7.11 (s, 4 H, $H^{8,10}$), 7.38 (m, 2 H, $H^{17}$), 7.74 (t, $J$ = 2.2 Hz, 2 H, $H^{18}$) ppm. $^{13}C$ NMR (100 MHz, $CDCl_3$, 297 K): $\delta$ = 19.3, 19.5, 20.6, 21.3 ($C^{12,13}$), 21.4, 21.5 ($C^{14}$), 28.3, 28.4, 32.7, 32.8 (COD-$CH_2$), 67.3 (d, $J$ = 14.5 Hz, COD-CH), 68.0 (d, $J$ = 13.7 Hz, COD-CH), 71.1, 71.4 ($C^{4,5}$), 96.2 (d, $J$ = 6.9 Hz, COD-CH), 97.5 96.2 (d, $J$ = 6.9 Hz, COD-CH), 121.9, 122.2 ($C^{16}$), 125.6, 125.7 ($C^{18}$), 128.1, 128.2 ($C^{17}$), 128.7, 128.9, 130.4 130.6 ($C^{8-10}$), 131.6, 131.8 ($C^{19}$), 134.5, 135.0 ($C^{9}$), 135.3, 137.3 ($C^{11}$), 137.6, 138.0 ($C^{7}$), 138.1, 138.3 ($C^{6}$), 139.7, 139.8 ($C^{15}$), 213.7 (d, $^1J$ = 48.8 Hz, Rh-$C^2$) ppm.

**(Chloro)($\eta^4$-1.5-cylooctadiene)(1,3-dimesityl-4,5-dimethylimidazolidin-2-ylidene)rhodium(I) (7′):** Yield: 0.20 g, 70%. M.p. 210–212 °C (dec.). $C_{31}H_{42}ClN_2Rh$ (581.07): calcd. C 64.08, H 7.29, N 4.82; found C 63.89, H 7.08, N 4.96. $^1H$ NMR (400 MHz, $CDCl_3$, 297 K): $\delta$ = 1.17, 1.18, 1.19, 1.20 [s, 6 H, $NCH(CH_3)CH(CH_3)N$], 1.31–1.35 (m, 1 H, COD-$CH_2$), 1.58–1.56 (m, 3 H, COD-$CH_2$),

 © 2006 Wiley-VCH Verlag GmbH & Co. KGaA, Weinheim 

1.64–1.66 (m, 3 H, COD-$CH_2$), 1.93–2.71, (m, 19 H, COD-$CH_2$, *p*-$CH_3$, *o*-$CH_3$), 3.13–3.17 (m, 1 H, COD-CH), 3.36–3.37 (m, 1 H, COD-CH), 3.76–3.81, 3.86–3.91 [m, 2 H, NCH($CH_3$)CH($CH_3$)N], 4.36–4.38 (m, 1 H, COD-CH), 4.51–4.42 (m, 1 H, COD-CH), 7.06, 7.01, 6.95, 6.89 (s, 4 H, Mes) ppm. $^{13}$C NMR (100 MHz, $CDCl_3$, 297 K): $\delta$ = 18.8, 18.9, [NCH($CH_3$)CH($CH_3$)N], 19.0, 20.3 (*p*-$CH_3$), 21.0, 21.2, 21.3, 21.4, (*o*-$CH_3$), 27.0, 29.6, 32.4 (COD-$CH_2$), 65.4 (d, *J* = 14.5 Hz, COD-CH=CH), 66.0, 66.7 [NCH($CH_3$)CH($CH_3$)-N], 70.2 (d, *J* = 14.5 Hz, COD-CH=CH), 96.6, 98.1, (d, *J* = 6.9 Hz, COD-CH=CH), 128.6, 128.9, 130.3, 130.4, 135.0, 135.2, 135.7, 136.8, 137.7, 137.8, 138.9, 139.5 (Mes), 212.5 (d, *J* = 48.0 Hz, Rh-$C^2$) ppm.

**(Chloro)(dicarbonyl)(1,3-dimesitylacenaphtho[1,2-*d*]imidazolin-2-ylidene)rhodium(I) (8):** Compound **7** (50 mg, 73 μmol) was dissolved in $CH_2Cl_2$ in a Schlenk flask and carbon monoxide was bubbled through the solution for 50 min. The reaction mixture was stirred at room temperature for 1.5 h and then concentrated to dryness giving a cream powder. Yield 40 mg, 86%. $C_{33}H_{32}ClN_2O_2Rh$ (624.96): calcd. C 63.42, H 4.84, N 4.48; found C 63.54, H 5.00, N 4.52. $^1$H NMR (400 MHz, $CDCl_3$, 297 K): $\delta$ = 1.50, 2.30 (s, 12 H, $H^{12,13}$), 2.62 (s, 6 H, $H^{14}$), 6.03 (s, 2 H, $H^{4,5}$), 6.78 (d, *J* = 1.8 Hz, 2 H, $H^{16}$), 6.84, 7.00 (s, 4 H, $H^{8,10}$), 7.36 (t, *J* = 1.8 Hz 2 H, $H^{17}$), 7.74 (d, *J* = 2.1 Hz, 2 H, $H^{18}$) ppm. $^{13}$C NMR (100 MHz, $CDCl_3$, 297 K): $\delta$ = 19.3, 19.6 ($C^{12,13}$), 21.4 ($C^{14}$), 71.4 ($C^{4,5}$), 122.1 ($C^{16}$), 125.9 ($C^{18}$), 128.4 ($C^{17}$), 129.7 ($C^{10}$), 130.4 ($C^{19}$), 131.8 ($C^9$), 133.8 ($C^{11}$), 136.6 ($C^7$), 138.7 ($C^6$), 138.9 ($C^{15}$), 183.6 [d, CO, $^1J_{^{103}Rh,^{13}C}$ = 76 Hz], 185.3 [d, CO, $^1J_{^{103}Rh,^{13}C}$ = 52.4 Hz], 206.5 [d, $^1J_{^{103}Rh,^{13}C}$ = 42 Hz, Rh-$C^2$] ppm. IR (KBr): $\tilde{\nu}$ = 2074, 1988 (CO) cm$^{-1}$.

**Chloro(dicarbonyl)(1,3-dimesityl-4,5-dimethylimidazolidin-2-ylidene)rhodium(I) (8′):** Yield: 41.9 mg, 92%. M.p. 149–151 °C (dec.). $C_{25}H_{30}ClN_2O_2Rh$ (528.87): calcd. C 56.77, H 5.72, N 5.30; found: C 56.86, H 5.65, N 5.33. $^1$H NMR (400 MHz, $CDCl_3$, 297 K): $\delta$ = 1.13 –1.27 [s, 6 H, NCH($CH_3$)CH($CH_3$)N], 1.99 (s, 6 H, *p*-$CH_3$), 2.05, 2.13 (s, 12 H, *o*-$CH_3$), 3.98–4.01 [m, 2 H, NCH($CH_3$)-CH($CH_3$)N], 7.11, 7.20 (s, 4 H, Mes) ppm. $^{13}$C NMR (100 MHz, $CDCl_3$, 297 K): $\delta$ = 18.0, 18.2, [NCH($CH_3$)CH($CH_3$)N],19.9 (*p*-$CH_3$), 20.9, 21.4 (*o*-$CH_3$), 53.1, 53.3 [NCH($CH_3$)CH($CH_3$)N], 128.9, 130.3, 130.4, 137.8, 138.9, 139.5 (Mes), 182.8 [d, CO, $^1J_{^{103}Rh,^{13}C}$ = 73.3 Hz], 185.0 [d, CO, $^1J_{^{103}Rh,^{13}C}$ = 52.5 Hz], 206.7 [d, $^1J_{^{103}Rh,^{13}C}$ = 41.4 Hz, Rh-$C^2$] ppm. IR (KBr): $\tilde{\nu}$ = 2078, 1994 (CO) cm$^{-1}$.

**General Procedure for Heck Coupling Reactions:** A two-necked 25 mL flask fitted with a reflux condenser was charged with aryl halide (1.0 mmol), olefin (1.5 mmol), $Cs_2CO_3$ (1.5 mmol), diethylene glycol dibutyl ether (internal standard), DMA (3 mL) and 3 mol-% of in situ formed catalyst or preformed complex **6**. The mixture, under an atmosphere of argon, was placed in a preheated oil bath (100 °C) and stirred for 5 h. The conversion was monitored by gas chromatography.

**X-ray Structural Analyses of 5 and 7:** Crystals of thione **5** suitable for X-ray analysis were obtained from a dichloromethane solution layered with hexane. Similarly, we obtained crystals of **7**, suitable for X-ray analysis, from $CH_2Cl_2$ layered with EtOH.

A colourless single-crystal of **5** and a yellow crystal of **7** suitable for data collection were mounted on glass fibres and data collection was performed on a STOE IPDS II diffractometer with graphite monochromated Mo-$K_\alpha$ radiation at 296 K. The structures were solved by direct-methods using SHELXS-97[20] and refined by full-matrix least-squares methods on $F^2$ using SHELXL-97[21] from within the WINGX[22,23] suite of software. All non-hydrogen atoms were refined with anisotropic parameters. Hydrogen atoms bonded to carbon were placed in calculated positions (C–H = 0.93–0.98 Å) and treated using a riding model with *U* = 1.2 times the *U* value of the parent atom for CH, $CH_2$ and $CH_3$. Molecular diagrams were created using ORTEP-III.[24] Geometric calculations were performed with Platon.[25] Atomic coordinates and equivalent isotropic displacement parameters are listed in Table 3.

Table 3. Crystal data and structural refinements for **5** and **7**.

| | $C_{31}H_{30}N_2S$ | $C_{39}H_{40}ClN_2Rh$ |
|---|---|---|
| Formula weight | 462.63 | 675.09 |
| Temperature [K] | 296 | 296 |
| Wavelength [Å] | 0.71073 | 0.71073 |
| Crystal system | orthorhombic | monoclinic |
| Space group | $Pna2_1$ | $P2_1/c$ |
| Unit cell dimensions | | |
| *a* [Å] | 19.5086(7) | 9.0872(6) |
| *b* [Å] | 7.1186(3) | 17.0953(7) |
| *c* [Å] | 37.5917(15) | 21.0906(11) |
| $\alpha$ [°] | 90 | 90 |
| $\beta$ [°] | 90 | 93.293 (5) |
| $\gamma$ [°] | 90 | 90 |
| Volume [Å$^3$] | 5220.5(4) | 3271.0(3) |
| *Z* | 8 | 4 |
| Calculated density [Mg m$^{-3}$] | 1.177 | 1.371 |
| Absorption coefficient [mm$^{-1}$] | 0.145 | 0.634 |
| *F*(000) | 1968 | 1399.8 |
| Crystal size [mm] | 0.34 × 0.42 × 0.50 | 0.33 × 0.21 × 0.12 |
| $\theta$ range for data collection [°] | 1.50 to 24.07 | 1.53 to 27.19 |
| Independent reflection | 8204 | 6422 |
| Collected reflection | 35086 | 29998 |
| Absorption correction | integration | integration |
| $T_{min}$ | 0.9389 | 0.8788 |
| $T_{max}$ | 0.9685 | 0.9294 |
| $R_{int}$ | 0.1013 | 0.047 |
| $\theta_{max}$ [°] | 24.11 | 26 |
| *h* | –22 to 22 | –11 to 11 |
| *k* | –8 to 8 | –21 to 24 |
| *l* | –42 to 42 | –25 to 26 |
| Refinement method | full-matrix least-squares on $F^2$ | |
| $wR(F^2)$ | 0.1161 | 0.0912 |
| Goodness-of-fit on $F^2$ | 0.920 | 0.939 |
| Final *R* indices [$I > 2\sigma(I)$] | $R_1$ = 0.047 | $R_1$ = 0.0359 |
| *R* indices (all data) | $R_1$ = 0.076 | $R_1$ = 0.0598 |
| $(\Delta/\sigma)_{max}$ | 0.292 | 0.000 |
| $\Delta\rho_{max}$ [e Å$^{-3}$] | 0.132 | 0.404 |
| $\Delta\rho_{min}$ [e Å$^{-3}$] | –0.196 | –0.325 |

CCDC-610151 and -610150 contain the supplementary crystallographic data for this paper. These data can be obtained free of charge from The Cambridge Crystallographic Data Centre via www.ccdc.cam.ac.uk/data_request/cif.

## Acknowledgments

Financial support from Ege university (Project: 03-BIL-015 and 05-FEN-020) is gratefully acknowledged. The authors wish to acknowledge the Faculty of Arts and Sciences, Ondokuz Mayıs University, Turkey, for the use of the Stoe IPDS-II diffractometer (purchased from grant No. F279 of the University Research Fund).

[1] D. Bourissou, O. Guerret, F. P. Gabbai, G. Bertrand, *Chem. Rev.* **2000**, *100*, 39–91.

 © 2006 Wiley-VCH Verlag GmbH & Co. KGaA, Weinheim 

[2] a) M. C. Perry, K. Burgess, *Tetrahedron: Asymmetry* **2003**, *14*, 951–961; b) V. Cesar, S. Bellemin-Laponnaz, L. H. Gade, *Chem. Soc. Rev.* **2004**, *33*, 619–636.
[3] W. A. Herrmann, *Angew. Chem. Int. Ed.* **2002**, *41*, 1290–1309.
[4] a) N. Gürbüz, I. Özdemir, S. Demir, B. Çetinkaya, *J. Mol. Cat. A: Chem.* **2004**, *209*, 23–28; b) I. Özdemir, B. Yiğit, B. Çetinkaya, D. Ülkü, M. N. Tahir, C. Arıcı, *J. Organomet. Chem.* **2001**, *633*, 27–32.
[5] H. Türkmen, B. Çetinkaya, *J. Organomet. Chem*. **2006**, *691*, 3749–3759.
[6] a) C. Metallinos, F. B. Barrett, J. L. Chaytor, M. E. A. Heska, *Org. Lett*. **2004**, *6*, 3641–3644; b) S. Saravanakumar, M. K. Kindermann, J. Heinicke, M. Köckerling, *Chem. Commun.* **2006**, 640–642; c) S. Saravanakumar, A. I. Oprea, M. K. Kindermann, P. G. Jones, J. Heinicke, *Chem. Eur. J.* **2006**, *12*, 3143–3154; d) W. A. Hermann, D. Baskakov, E. Herdtweck, S. D. Hoffmann, T. Bunlaksananusorn, F. Rampf, L. Rodefeld, *Organometallics* **2006**, *25*, 2449–2456; e) F. E. Hahn, M. Foth, *J. Organomet. Chem.* **1999**, *585*, 241–245; f) F. E. Hahn, L. Wittenbecher, R. Boese, D. Blaser, *Chem. Eur. J.* **1999**, *5*, 1931–1935; g) F. E. Hahn, L. Wittenbecher, D. L. Van, R. Fröhlich, *Angew. Chem. Int. Ed.* **2000**, *39*, 541–543; h) F. E. Hahn, M. Paas, D. L. Van, T. Lügger, *Angew. Chem. Int. Ed.* **2003**, *42*, 5243–5246; i) F. E. Hahn, V. Langenhahn, N. Meier, T. Lügger, W. P. Felhammer, *Chem. Eur. J.* **2003**, *9*, 704–712; j) F. E. Hahn, M. Paas, D. L. Van, R. Fröhlich, *Chem. Eur. J.* **2005**, *11*, 5080–5085; k) F. E. Hahn, T. V. Fehren, T. Lügger, *Inorg. Chim. Acta* **2005**, *358*, 4137–4144; l) F. E. Hahn, C. Holtgrewe, T. Pape, M. Martin, E. Sola, L. A. Oro, *Organometallics* **2005**, *24*, 2203–2209; m) F. E. Hahn, V. Langenhahn, T. Lügger, T. Pape, D. L. Van, *Angew. Chem. Int. Ed.* **2005**, *44*, 3759–3763; n) F. E. Hahn, *Angew. Chem. Int. Ed.* **2006**, *45*, 1348–1352.
[7] a) S. D. Ittel, L. K. Johnson, M. Brookhart, *Chem. Rev.* **2000**, *100*, 1169–1203; b) P. D. Fremont, N. M. Scott, E. D. Stevens, T. Ramnial, O. C. Lightbody, C. L. B. Macdonald, J. A. C. Clyburne, C. D. Abernethy, S. P. Nolan, *Organometallics* **2005**, *24*, 6301–6309.
[8] a) M. Paas, B. Wibbeling, R. Fröhlich, F. E. Hahn, *Eur. J. Inorg. Chem.* **2006**, 158–162; b) H. M. J. Wang, I. J. B. Lin, *Organometallics* **1998**, *17*, 972–975.
[9] J. C. Garrison, W. J. Youngs, *Chem. Rev.* **2005**, *105*, 3978–4008.
[10] K. Weigl, K. Kohler, S. Dechert, F. Meyer, *Organometallics* **2005**, *24*, 4049–4056.
[11] H. Karabıyık, M. E. Günay, M. Aygün, B. Çetinkaya, C. Kazak, *J. Chem. Crystallog.*, in press.
[12] a) D. S. McGuinness, K. J. Cavell, *Organometallics* **2000**, *19*, 741–748; b) H. V. Huynh, J. H. H. Ho, T. C. Neo, L. L. Koh, *J. Organomet. Chem.* **2005**, *690*, 3854–3860.
[13] K. H. Park, S. Y. Kim, S. U. Son, Y. K. Chung, *Eur. J. Org. Chem.* **2003**, 4341–4345.
[14] a) M. E. Günay, M. Aygün, A. Kartal, B. Çetinkaya, E. Kendi, *Cryst. Res. Technol.* **2006**, *41*, 615–621; b) W. Gil, T. Lis, A. M. Trzeciak, J. J. Ziolkowski, *Inorg. Chim. Acta* **2006**, *359*, 2835–2841.
[15] a) W. A. Herrmann, J. Schütz, G. D. Frey, E. Herdtweck, *Organometallics* **2006**, *25*, 2437–2448; b) M. Alcarazo, R. Fernandez, E. Alvarez, J. M. Lassaletta, *J. Organomet. Chem.* **2005**, *690*, 5979–5988; c) Y. Canac, S. Conejero, B. Donnadieu, W. W. Schoeller, G. Bertrand, *J. Am. Chem. Soc.* **2005**, *127*, 7312–7313; d) A. R. Chianese, X. W. Li, M. C. Janzen, J. W. Faller, R. H. Crabtree, *Organometallics* **2003**, *22*, 1663–1667; e) V. Lavallo, Y. Canac, A. De Hope, B. Donnadieu, G. Bertrand, *Angew. Chem. Int. Ed.* **2005**, *44*, 7236–7239; f) K. Denk, P. Sirch, W. A. Herrmann, *J. Organomet. Chem.* **2002**, *649*, 219–224.
[16] a) U. Christmann, R. Vilar, *Angew. Chem. Int. Ed.* **2005**, *44*, 366–374; b) R. B. Bedford, C. S. J. Cazin, D. Holder, *Coord. Chem. Rev.* **2004**, *248*, 2283–2321.
[17] H. Lebel, M. K. Janes, A. B. Charette, S. P. Nolan, *J. Am. Chem. Soc.* **2004**, *126*, 5046–5047.
[18] a) G. A. Grasa, R. Singh, E. D. Stevens, S. P. Nolan, *J. Organomet. Chem.* **2003**, *687*, 269–279; b) G. Reeske, C. R. Hoberg, N. J. Hill, A. H. Cowley, *J. Am. Chem. Soc.* **2006**, *128*, 2800–2801.
[19] P. A. Evans, E. W. Baum, A. N. Fazal, M. Pink, *Chem. Commun.* **2005**, 63–65.
[20] G. M. Sheldrick, *SHELXS-97 – A Program for Automatic Solution of Crystal Structures*, Univ. of Göttingen, Germany, **1997**.
[21] G. M. Sheldrick, *SHELXL-97 – A Program for Crystal Structure Refinement*, Univ. of Göttingen, Germany, **1997**.
[22] L. J. Farrugia, *WINGX – A Windows Program for Crystal Structure Analysis*, University of Glasgow, **1998**.
[23] L. J. Farrugia, *J. Appl. Cryst.* **1999**, *30*, 837–838.
[24] L. J. Farrugia, *Appl. Crystallogr.* **1997**, *30*, 565.
[25] A. L. Spek, *PLATON – A Multipurpose Crystallographic Tool*, Utrecht, Utrecht University, The Netherlands, **2005**.

Received: June 13, 2006
Published Online: October 2, 2006

 © 2006 Wiley-VCH Verlag GmbH & Co. KGaA, Weinheim 

DOI: 10.1002/ejic.200600549

# 4-Thiolatobenzoato-Bridged Rhodium/Zirconium Complexes: 32-Membered Metallamacrocycles and Their Linear Dinuclear Counterparts

**Ulrike Helmstedt,[a] Peter Lönnecke,[a][‡] and Joachim Reinhold,[b][‡‡] and Evamarie Hey-Hawkins*[a]**

**Keywords:** Heterometallic complexes / Metallacycles / Bridging ligands / Metal–metal interactions / Rhodium / Zirconocenes / S,O ligands

The heterometallic dinuclear complex $[Cp^*_2Zr(Me)\{(\mu\text{-}OOCC_6H_4S)Rh(PEt_3)_3\}]$ (**3**) is readily obtained by methane elimination in the reaction of $[Rh(SC_6H_4COOH)(PEt_3)_3]$ with $[Cp^*_2ZrMe_2]$ in a 1:1 ratio. Complex **3** reacts with 1 equiv. of water to give $[Cp^*_2Zr(OH)\{(\mu\text{-}OOCC_6H_4S)Rh(PEt_3)_3\}]$ (**4**), a rare example of a terminal hydroxo complex of a zirconocene. Complexes **3** and **4** are isotypic. The influence of the zirconocene group on the properties of the rhodium complex was evaluated with $^{31}P$ NMR spectroscopy, cyclic voltammetry and DFT calculations. $[Cp^*_2ZrMe_2]$ reacts with $[\{Rh(\mu\text{-}SC_6H_4COOH)(PPh_3)_2\}_2]$ (even in a 1:1 ratio at room temperature) or with $[Rh(SC_6H_4COOH)(PEt_3)_3]$ (in a 1:2 ratio at elevated temperature) to give 32-membered metallamacrocycles containing four rhodium and two zirconium atoms, in which each zirconocene group bridges two $\{Rh(SC_6H_4COO)(PR_3)_2\}_2$ units [R = Ph (**5**), Et (**6**)]. The only significant structural difference in **5** and **6** is the presence of two different isomers, in which the bridging thiolato ligands occupy either the *exo* or the *endo* position of the $Rh_2S_2$ ring. However, this small difference has a significant influence on the size of the macrocyclic cavity.

(© Wiley-VCH Verlag GmbH & Co. KGaA, 69451 Weinheim, Germany, 2006)

## Introduction

Interest in early/late heterobimetallics (ELHBs) has strongly increased in the last few decades.[1] The reasons for this are mainly the elucidation of mechanisms of enzymes whose active centres include more than one metal centre,[2] the explanation of the strong metal–support interaction phenomenon in heterogeneous catalysis[3] and the applicability of cooperative effects between different metal centres for catalysts[4] and magnetic materials.[5] Of special interest for these applications is the investigation of metal–metal interactions. These can be achieved either by direct contact of the metal centres within the compounds[6] or with the help of bridging ligands which allow electronic interactions through π-conjugated bridges.[7]

To elucidate the influence of the second metal centre, it is useful to compare the properties of the heterometallic complexes with those of their mononuclear precursors. Therefore, the preferred synthesis of ELHBs starts with the preparation of a monometallic complex, which is then employed as a so-called metalloligand to coordinate the second metal centre. To selectively coordinate the first metal centre to one coordination site of a di- or multifunctional, potentially bridging ligand, different concepts are known from the literature, for example exploitation of the chelate effect[8] or the use of donor atoms with different coordination behaviour[9] according to the hard and soft acids and bases concept of Pearson.[10]

We have previously employed S,O ligands, such as mercaptocarboxylic acids, which show high bonding selectivity in the synthesis of heterometallic complexes[11] if they cannot bind in a chelating fashion.[12] By changing the bridging ligand from saturated mercaptocarboxylic acids to unsaturated ones, we have now extended our studies to the 4-thiolatobenzoate dianion and have already prepared several rhodium(I) complexes of 4-thiolatobenzoic acid.[13] The special feature of these complexes is the free carboxyl group, which allows further coordination to a second metal ion. For this, we chose zirconocene derivatives, which are known to form stable carboxylato complexes.[14]

## Results and Discussion

The reaction of the metalloligands $[\{Rh(SC_6H_4COOH)(PPh_3)_2\}_2]$ (**1**)[13] and $[Rh(SC_6H_4COOH)(PEt_3)_3]$ (**2**)[13] with $[Cp^*_2ZrMe_2]$ ($Cp^* = C_5Me_5$) yielded the mono- and bis(carboxylato) complexes of the zirconocenes, depending on the stoichiometry and the reactivity of the starting materials. At room temperature, **2** gives only the monosubstitution product (Scheme 1), while disubstitution is achieved at ele-

[a] Institut für Anorganische Chemie, Universität Leipzig, Johannisallee 29, 04103 Leipzig, Germany
E-mail: hey@rz.uni-leipzig.de
[b] Institut für Physikalische und Theoretische Chemie, Universität Leipzig, Johannisallee 29, 04103 Leipzig, Germany
[‡] Crystal structure determinations
[‡‡] DFT calculations

 © 2006 Wiley-VCH Verlag GmbH & Co. KGaA, Weinheim 

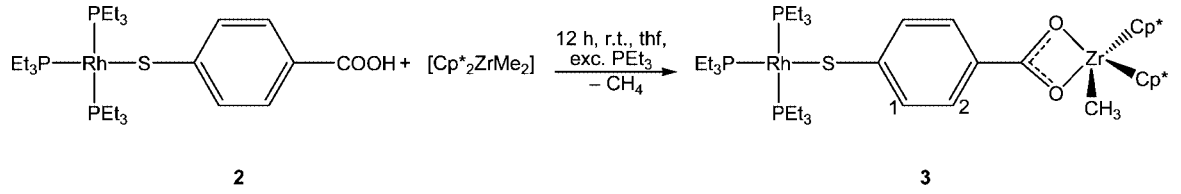


**2** **3**

Scheme 1.

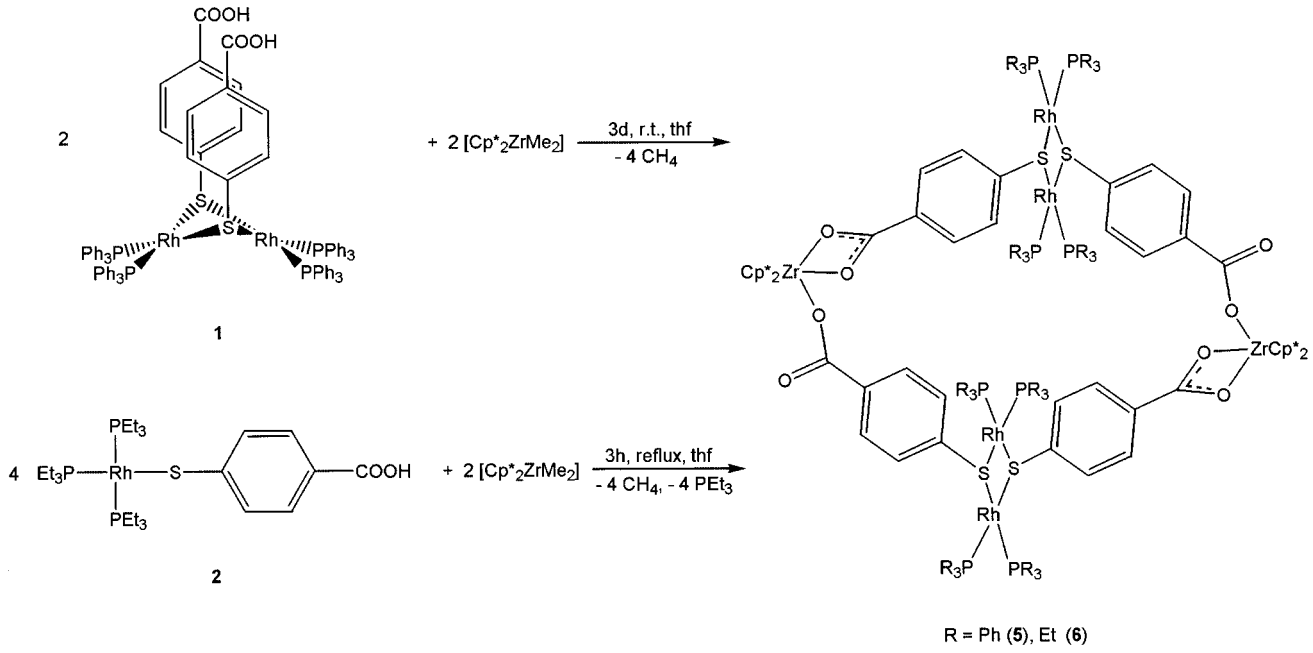


Scheme 2.

vated temperatures. In contrast, **1** readily reacts with the zirconocene derivative even at room temperature with elimination of 2 equiv. of methane (Scheme 2). Purification of the highly air- and moisture-sensitive complexes was facilitated by the fact that only methane was produced as byproduct.

### Mono(carboxylato)zirconocene Complexes

As shown previously, **2** dimerises in solution with phosphane dissociation (Scheme 3). To stabilise the monomeric form, an excess of triethylphosphane must be used. Complex **2** reacts with 1 equiv. of $[Cp^*_2ZrMe_2]$ in the presence

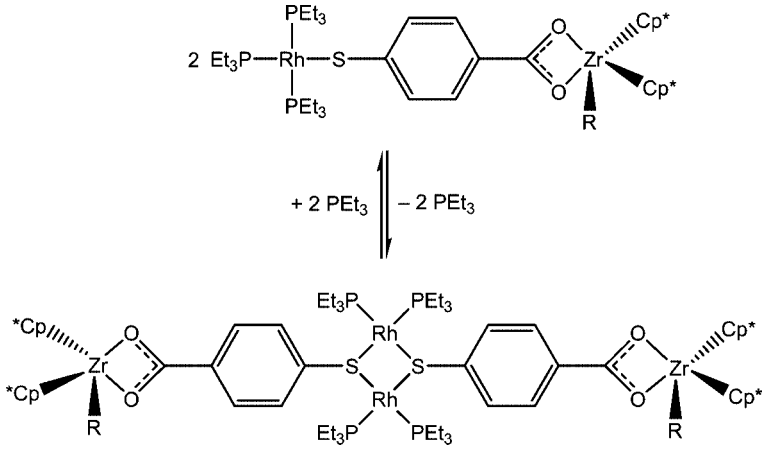


Scheme 3. R = Me (**3**) or OH (**4**).

 © 2006 Wiley-VCH Verlag GmbH & Co. KGaA, Weinheim 

of an excess of $PEt_3$ to yield [Cp*$_2$Zr(Me){(μ-$O_2CC_6H_4S$)-Rh($PEt_3$)$_3$}] (**3**) exclusively. Complex **3** could be isolated as orange crystals; the molecular structure in the solid state is shown in Figure 1.

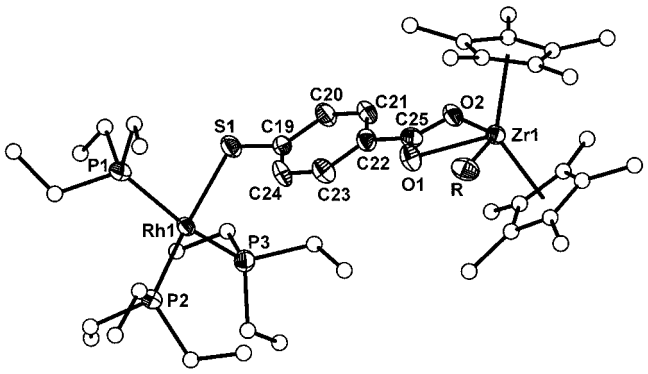


Figure 1. View of the molecular structure of [Cp*$_2$Zr(Me){(μ-$O_2CC_6H_4S$)Rh($PEt_3$)$_3$}] (**3**) (R = Me) and [Cp*$_2$Zr(OH){(μ-$O_2CC_6H_4S$)Rh($PEt_3$)$_3$}] (**4**) (R = OH). Hydrogen atoms are omitted for clarity. Thermal ellipsoid level 50%. The atoms not shown as ellipsoids are the carbon atoms of the coligands. Selected bond lengths [pm] and bond angles [°] for **3**: Zr1–O1 230.3(4), Zr1–O2 227.1(4), Zr1–C46 226.9(8), O1–C25 126.3(8), O2–C25 126.9(7), Rh1–S1 241.4(2), Rh1–P1 230.5(2), Rh1–P2 224.7(2), Rh1–P3 232.7(2); O1–Zr1–O2 56.6(2), O1–Zr1–C46 73.8(3), O1–C25–O2 117.9(6), S1–Rh1–P1 82.93(6), S1–Rh1–P2 166.98(7), S1–Rh1–P3 83.94(6), P1–Rh1–P2 96.76(6), P2–Rh1–P3 101.05(6), P1–Rh1–P3 153.70(7), Rh1–S1–C19 104.8(2). Selected bond lengths [pm] and bond angles [°] for **4**: Zr1–O1 229.5(5), Zr1–O2 228.6(5), Zr1–O3 207.8(6), O1–C25 128(1), O2–C25 124.8(9), Rh1–S1 241.4(2), Rh1–P1 231.0(2), Rh1–P2 225.0(3), Rh1–P3 232.6(3); O1–Zr1–O2 56.4(2), O1–Zr1–O3 76.8(2), O1–C25–O2 117.6(8), S1–Rh1–P1 83.06(9), S1–Rh1–P2 167.39(9), S1–Rh1–P3 84.25(9), P1–Rh1–P2 96.39(9), P2–Rh1–P3 100.64(9), P3–Rh1–P1 154.79(9), Rh1–S1–C19 106.2(3).

Complex **3** crystallises in the monoclinic space group $P2_1/c$ with four molecules per unit cell. The rhodium atom is coordinated by three triethylphosphane and one thiolato ligand in a tetrahedrally distorted square-planar fashion [S1–Rh1–P2 166.98(7)°, P1–Rh1–P3 153.70(7)°]. The carboxylato group coordinates in a bidentate mode, resulting in the zirconium atom being an 18-valence-electron species. The two oxygen atoms, the carbon atom of the methyl group and the zirconium atom are coplanar. The plane defined by Zr1, O1 and O2 forms an angle of 9.12° with the plane of the aromatic ring. The bond lengths C25–O1 [126.3(8) pm] and C25–O2 [126.9(7) pm] as well as Zr1–O1 [230.3(4) pm] and Zr1–O2 [227.1(4) pm] are similar, and this indicates delocalisation of the lone pair of electrons. This is supported by the IR spectrum (KBr), which shows symmetric and asymmetric COO vibrations at 1561 and at 1420 $cm^{-1}$ instead of discrete C=O and C–O vibrations.

By treating a solution of **3** with 1 equiv. of water, the methyl group can be exchanged selectively with an OH group to form [Cp*$_2$Zr(OH){(μ-$OOCC_6H_4S$)Rh($PEt_3$)$_3$}] (**4**), a rare example of a terminal hydroxo complex of a zirconocene. Stabilisation by the sterically bulky Cp* ligands prevents dimerisation with formation of oxo bridges, which usually occurs with elimination of water,[15] as first described by Hillhouse et al.[16] and Bortolin et al.[17] Complex **4** is the first heteroleptic carboxylato hydroxo complex structurally characterised by X-ray crystallography. Pellny et al. reported the NMR spectroscopic observation of the compounds [Cp*$_2$Zr(OH){OOC–C($SiMe_3$)=CHPh}] and [Cp*$_2$Zr(OH){OOC–CPh=CH($SiMe_3$)}], but could not isolate them.[18] Yellow needle-like crystals of **4** were structurally characterised by X-ray crystallography. Complex **4** crystallises isotypic to **3** (Figure 1).

The short Zr–O bond length of 207.8 pm corresponds to those in other structurally characterised compounds of this kind.[17,19] The O3···O1 distance of 272.1 pm seems to indicate the presence of a hydrogen bond between them. As the C46···O1 distance in **3** is also only 274.6 pm, it appears that the two atoms are forced into close proximity due to the high steric demand of the Cp* rings. The steric crowding is also apparent from the deviation of the methyl groups from the $C_5$ ring plane where the two rings are in close proximity.

The OH stretching vibration (3658 $cm^{-1}$) has very low intensity but could be observed in the IR spectra of a KBr pellet and of a single crystal. The intensities of OH vibrations reported in the literature also differ.[19a,19b]

In the $^1$H NMR spectrum, the signals of the protons of the aromatic ring of the 4-thiolatobenzoate ligand (AA′BB′ spin system) are broader than the other signals. This indicates hindered rotation of the $SC_6H_4COOZr(R)Cp^*_2$ group (R = Me, OH) and prevents simulation of the spectra to determine the coupling constants. As can be observed with the help of $^{31}$P NMR spectroscopy, **3** and **4** dimerise in solution with dissociation of 1 equiv. of $PEt_3$ per rhodium atom, as already described for **2** (Scheme 3). The equilibrium can be shifted towards the monomer by adding an excess of triethylphosphane.

### Bis(carboxylato)zirconocene Complexes

Treatment of **1** with [Cp*$_2$Z$rMe_2$] in a 1:1 ratio as well as of **2** with [Cp*$_2$Z$rMe_2$] in a 2:1 ratio results in the formation of compounds of the type [(Cp*$_2$Zr{(μ-$O_2CC_6H_4S$)-Rh($PR_3$)$_2$}$_2$)$_2$] [R = Ph (**5**), R = Et (**6**)]. In the solid state both compounds reveal a nearly identical molecular structure, that is, a 32-membered macrocycle containing two dimeric $Rh_2(SR)_2$ units, as observed in metalloligand **1**, which are deprotonated and bridged by two zirconocene groups (Scheme 2).

Both compounds crystallise in the triclinic space group $P\bar{1}$, and one molecule in the unit cell is located on a crystallographic centre of inversion (Figures 2 and 3). Co-crystallisation of 12 molecules of thf (two of them disordered) for **5** and one molecule of diethyl ether for **6** is observed per unit cell.

The typical bonding mode for zirconocene bis(carboxylato) complexes[20,24–26] is also observed in **5** and **6**: one carboxylato ligand coordinates in a bidentate fashion and the other in a monodentate one. All coordinating oxygen atoms are coplanar with the zirconium atom. In contrast to **3** and

 © 2006 Wiley-VCH Verlag GmbH & Co. KGaA, Weinheim 

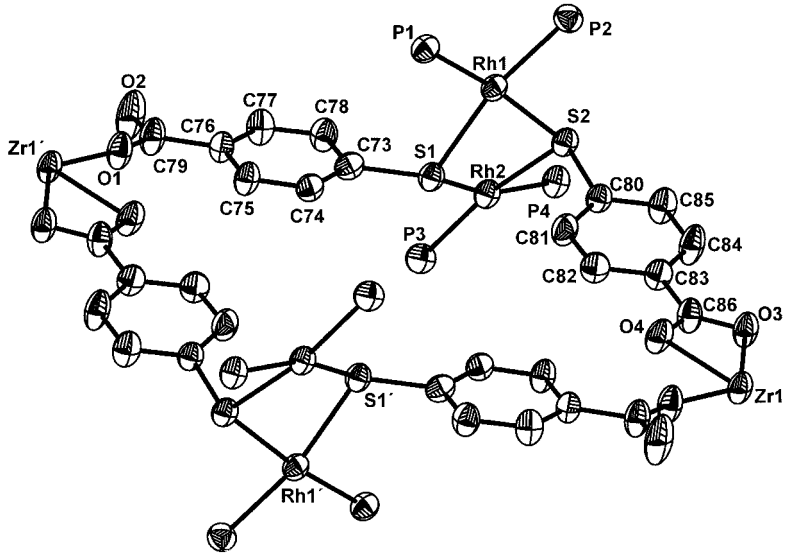


Figure 2. View of the molecular structure of $[(Cp^*_2Zr\{(\mu\text{-}O_2CC_6H_4S)Rh(PPh_3)_2\}_2)_2]$ (**5**). Thermal ellipsoid level 50%. Hydrogen atoms and the carbon atoms of the coligands and thf molecules are omitted for clarity. Selected bond lengths [pm] and bond angles [°]: Zr1–O1 207.1(2), Zr1–O3 232.2(2), Zr1–O4 223.9(2), Rh1–S1 244.12(9), Rh1–S2 237.73(9), Rh1–P1 228.0(1), Rh1–P2 224.3(1), Rh2–S1 236.72(9), Rh2–S2 239.41(9), Rh2–P3 224.8(1), Rh2–P4 226.6(1), C79–O1 129.9(4), C79–O2 122.4(4), C86–O3 126.9(4), C86–O4 127.5(4); O3–Zr1–O4 56.94(8), S1–Rh1–S2 78.76(3), P1–Rh1–S1 96.64(3), P1–Rh1–P2 94.36(4), S1–Rh2–S2 79.91(3), P3–Rh2–S1 99.75(3), P3–Rh2–P4 98.13(4), (S1–Rh1–S2)/(S1–Rh2–S2) 146.46(5).

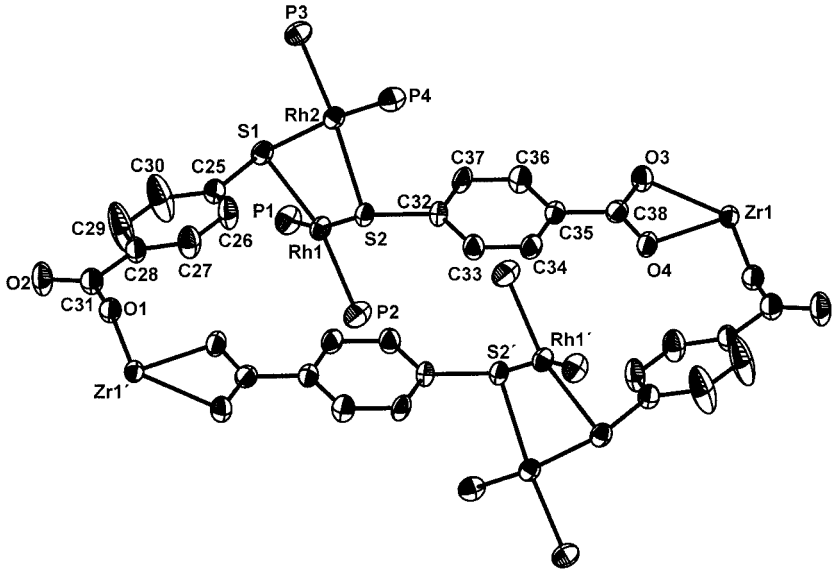


Figure 3. View of the molecular structure of $[(Cp^*_2Zr\{(\mu\text{-}O_2CC_6H_4S)Rh(PEt_3)_2\}_2)_2]$ (**6**). Thermal ellipsoid level 50%. Diethyl ether, hydrogen atoms and the carbon atoms of the coligands are omitted for clarity. Selected bond lengths [pm] and bond angles [°]: Zr1–O1 206.9(3), Zr1–O3 236.1(3), Zr1–O4 222.2(3), Rh1–S1 239.8(1), Rh1–S2 241.3(1), Rh1–P1 224.3(1), Rh1–P2 226.5(1), Rh2–S1 240.6(1), Rh2–S2 242.2(1), Rh2–P3 224.5(1), Rh2–P4 224.5(1), C31–O1 131.2(5), C31–O2 121.9(5), C38–O3 126.3(5), C38–O4 127.6(5); O3–Zr1–O4 56.6(2), S1–Rh1–S2 81.47(4), P1–Rh1–S1 85.33(4), P1–Rh1–P2 102.08(5), S1–Rh2–S2 81.47(4), P3–Rh2–S1 93.40(4), P3–Rh2–P4 97.69(5), (S1–Rh1–S2)/(S1–Rh2–S2) 145.50(5).

**4**, the Zr–O bond lengths of the bidentate ligand differ by 8 pm (**5**) and 14 pm (**6**) and are thus indicative of the strain imposed by the macrocycle. This is also supported by the IR spectrum (KBr), in which the COO vibration is observed at 1633 $cm^{-1}$ (**5**) and 1635 $cm^{-1}$ (**6**), which are in between the values for a C=O bond [1678 $cm^{-1}$ for $HSC_6H_4(C{=}O)$-OH] and a symmetric vibration of the COO group as expected for unstrained molecules {e.g. 1561 $cm^{-1}$ for $[Cp^*_2Zr(Me)\{(\mu\text{-}O_2CC_6H_4S)Rh(PEt_3)_3\}]$ (**3**) and $[Cp^*_2Zr(OH)\{(\mu\text{-}O_2CC_6H_4S)Rh(PEt_3)_3\}]$ (**4**)}. The position of the asymmetric COO vibration could not be identified because of overlap with other bands.

 © 2006 Wiley-VCH Verlag GmbH & Co. KGaA, Weinheim 

In both compounds, the $Rh_2S_2$ ring is puckered and shows an *anti* conformation. The angle between the S–Rh–S planes is 147° for **5** and 146° for **6**. The only considerable difference is that in **5** the thiolato ligands occupy the *exo* position of the $Rh_2S_2$ ring, and the *endo* position in **6**. This has a crucial influence on the size and shape of the macrocyclic cavity (Figure 4). For **5** the cavity is rhombohedral with internal edges of 470 and 331 pm, while in **6**, because of the different conformation of the $Rh_2S_2$ ring and the different orientation of the arylene bridges, the cavity is divided into two smaller cavities with dimensions of $87 \times 380$ pm.

The cavity is shielded by coligands, as shown exemplarily for **6** in Figure 5. Thus, the solvent molecules are not located inside the cavity. Figure 5 also shows that the 32-membered rings are almost planar, with the exception of

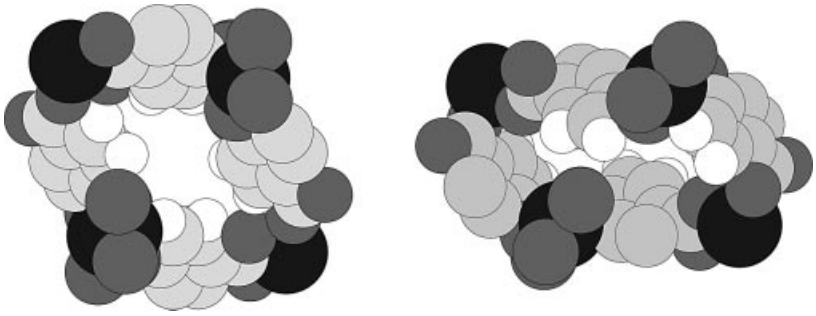

Figure 4. Space-filling model of the macrocycles **5** (left) and **6** (right). The carbon atoms of the coligands and those hydrogen atoms that do not influence the size of the cavities are omitted for clarity. The metal atoms are black, the heteroatoms (oxygen, sulfur and phosphorus) grey, the carbon atoms light grey and the hydrogen atoms white.

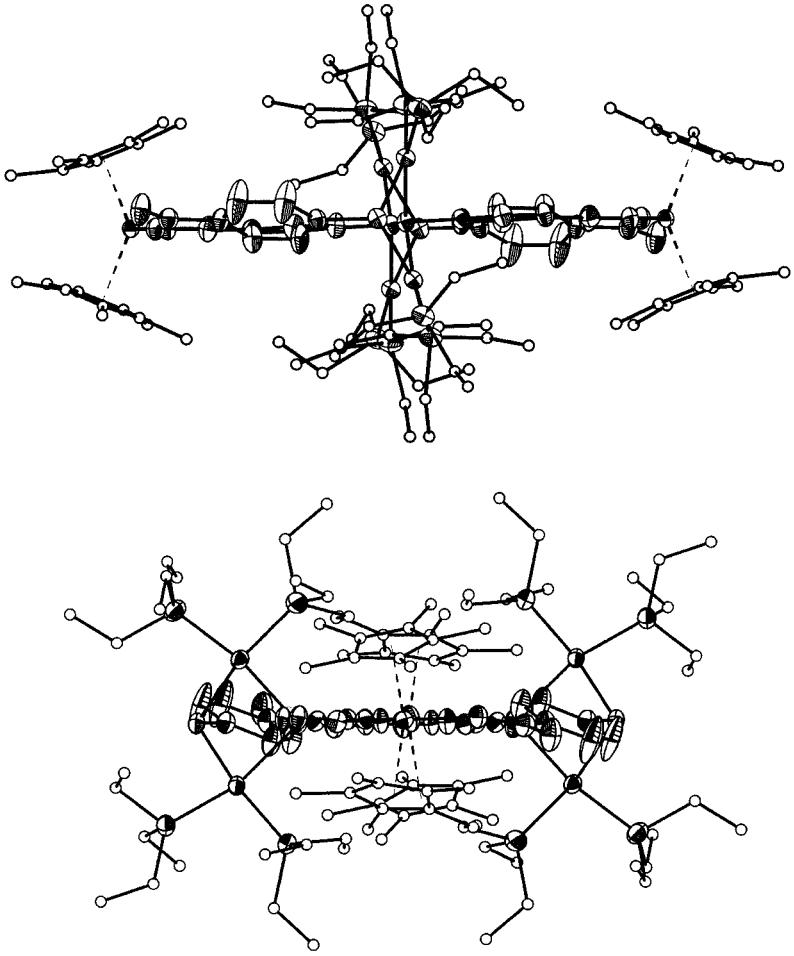

Figure 5. View of the molecular structure of $[(Cp^*_2Zr\{(\mu\text{-}O_2CC_6H_4S)Rh(PEt_3)_2\}_2)_2]$ (**6**). Thermal ellipsoid level 50%. Hydrogen atoms and $Et_2O$ have been omitted for clarity. The atoms not shown as ellipsoids are the carbon atoms of the coligands. Top: View along the axis through the $Rh_2S_2$ rings. Bottom: View along the axis through the zirconocene groups.

 © 2006 Wiley-VCH Verlag GmbH & Co. KGaA, Weinheim 

the aromatic rings of two of the bridging thiolatobenzoato ligands.

The solubility of **5** and **6** in common organic solvents (*n*-hexane, toluene, thf, $Et_2O$, $CH_3CN$, dmf and dmso) is very low. A sufficient concentration for $^{31}P\{^1H\}$ NMR studies was achieved solely for **5** in thf. At room temperature, a very broad signal is observed at $\delta$ = 38 ppm, which splits into two broad doublets ($\delta$ =37.7 ppm, $^1J_{P\text{-}Rh}$ = 153 Hz, $PPh_3$ of isomer 1, and 38.4 ppm, $^1J_{P\text{-}Rh}$ = 149 Hz, $PPh_3$ of isomer 2) on cooling the sample to –100 °C. Considering that fluxional behaviour of zirconocene bis(carboxylato) complexes in solution is known from the literature[12b] (one of the ligands coordinates alternatingly in a mono- or bidentate fashion) and that dynamic behaviour, that is exchange between different conformers of the $Rh_2S_2$ ring, could be observed for **1**,[13] one could consider different isomers in solution. However, because of solvent restrictions, the sample could not be cooled down sufficiently to achieve fine splitting and to gain deeper insights into the species present in solution.

### Comparison of the Spectroscopic and Electrochemical Properties of 2 and 3

Information about the change in electron density at the rhodium atom after introduction of the second metal centre can be obtained by comparing the spectroscopic and electrochemical properties of the monometallic complex $[Rh(SC_6H_4COOH)(PEt_3)_3]$ (**2**)[13] and the corresponding heterometallic complex $[Cp^*_2Zr(Me)\{(\mu\text{-}O_2CC_6H_4S)\text{-}Rh(PEt_3)_3\}]$ (**3**). For this purpose, the $^{31}P$ NMR chemical shifts of the phosphorus nuclei of the phosphane ligands, the oxidation potentials (Table 1) and the wavelengths of the S–Rh charge-transfer bands of **2** and **3** (Figure 6) were compared.

Table 1. Anodic peak potentials vs. SCE, $^{31}P$ NMR shifts of the phosphorus nucleus *trans* ($\delta_{trans}$) and *cis* ($\delta_{cis}$) to the thiolato ligand and the lowest energy UV/Vis absorption bands.

| Compound | $E_{pa}$ [V] | $\delta_{trans}$ [ppm] | $\delta_{cis}$ [ppm] | $\lambda_{max}$ [nm] |
|---|---|---|---|---|
| **2** | 1.28 | 26.7 | 12.1 | 337 |
| **3** | 1.32 | 28.4 | 13.5 | 358 |

After introduction of the zirconium atom as the second metal centre, the $^{31}P$ chemical shifts of the phosphorus nuclei *cis* and *trans* to the thiolato ligand are shifted to lower field by 1.4 and 1.7 ppm, respectively. This indicates a weak electron-withdrawing character of the Lewis-acidic zirconium atom. This is also shown by a 40-mV shift of the oxidation potential of **3** compared to **2**. The oxidation is irreversible, as known for other rhodium(I) complexes.[21] The observation of a small cathodic peak at –0.72 V in both cases proposes a following chemical reaction and the reduction of its reaction product.

The DFT calculations were carried out for the model compounds $[Rh(SC_6H_4COOH)(PMe_3)_3]$ (for **2**) and $[Cp_2ZrCH_3\{(\mu\text{-}OOCC_6H_4S)Rh(PMe_3)_3\}]$ (for **3**; Cp = $C_5H_5$). According to these calculations for both model compounds, the highest occupied molecular orbitals (HOMO) have both sulfur lone pair and rhodium d character. The HOMO itself is mainly sulfur-centred with some rhodium contribution. The lowest unoccupied molecular orbitals (LUMO) correspond to the σ* orbitals of the almost square-planar coordination sphere of the rhodium(I) centre.

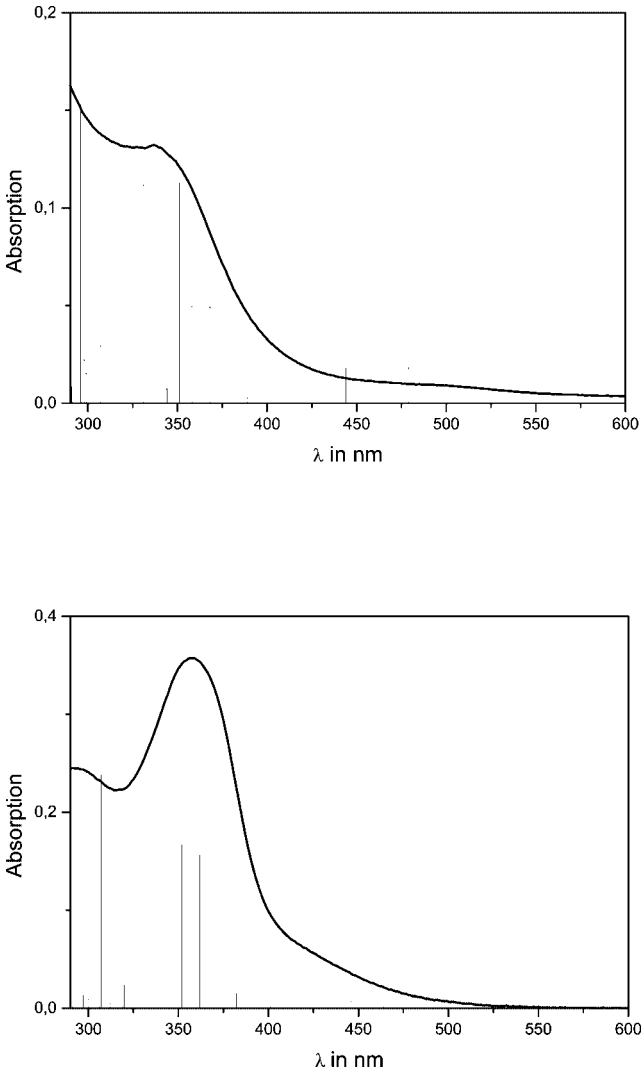


Figure 6. Comparison of the observed UV/Vis spectra of **2** (top) and **3** (bottom) in thf with the calculated transitions (line spectra).

The UV/Vis spectra of **2** and **3** are dominated by one broad band at 337 nm for **2** and 358 nm for **3**. TD-DFT studies show that for both model compounds this band can be assigned to several HOMO-to-LUMO excitations (Figure 6). Cp→Zr charge transfer processes, usually reported for the UV/Vis spectra of zirconocene complexes,[22] seem to play no role for **3**. They are calculated to be of too high energy and too low oscillator strength to be observable in the spectrum.

 © 2006 Wiley-VCH Verlag GmbH & Co. KGaA, Weinheim 

## Conclusions

While [Cp*$_2$ZrMe$_2$] reacts with [Rh(SC$_6$H$_4$COOH)(PEt$_3$)$_3$] to give selectively either the 1:1 or the 2:4 product, [Cp*$_2$Zr(Me){(μ-OOCC$_6$H$_4$S)Rh(PEt$_3$)$_3$}] (**3**) or [(Cp*$_2$Zr{(μ-O$_2$CC$_6$H$_4$S)Rh(PEt$_3$)$_2$}$_2$)$_2$] (**6**), the reaction with [{Rh(μ-SC$_6$H$_4$COO)(PPh$_3$)$_2$}$_2$] (more labile phosphane ligands) gives exclusively the 2:4 product, [(Cp*$_2$Zr{(μ-O$_2$CC$_6$H$_4$S)Rh(PPh$_3$)$_2$}$_2$)$_2$] (**5**).

Complex **3** reacts with 1 equiv. of water to yield [Cp*$_2$Zr(OH){(μ-OOCC$_6$H$_4$S)Rh(PEt$_3$)$_3$}] (**4**), a rare example of a terminal hydroxo complex of a zirconocene. Complexes **3** and **4** are isotypic in the solid state. The introduction of the Lewis-acidic zirconium atom in **3** has a weak electron-withdrawing effect on the rhodium centre.

The hexanuclear complexes **5** and **6** consist of 32-membered metallacycles in which two zirconocene groups bridge two {Rh(SC$_6$H$_4$COO)(PR$_3$)$_2$}$_2$ units [R = Ph (**5**), Et (**6**)]. The main structural difference in **5** and **6** is the presence of two different isomers, in which the bridging thiolato ligands occupy either the *exo* or the *endo* position of the Rh$_2$S$_2$ ring, which has, however, a significant influence on the size of the macrocyclic cavity.

## Experimental Section

**General Remarks:** All reactions were performed under nitrogen using standard Schlenk techniques. Solvents were dried with the appropriate drying agents and distilled under nitrogen. K(Hmba) (H$_2$mba = 4-mercaptobenzoic acid),[13] [RhCl(PPh$_3$)$_3$],[23] [RhCl(PEt$_3$)$_3$][24] and [Cp*$_2$ZrMe$_2$][25] were prepared according to literature procedures. Complexes **1** and **2** were prepared in situ; their synthesis and spectroscopic data are given in ref.[13] NMR spectra were recorded with a Bruker AVANCE DRX 400 ($^1$H NMR 400.13 MHz, $^{13}$C NMR 100.3 MHz, $^{31}$P NMR 161.97 MHz); Si(CH$_3$)$_4$ was used as internal standard in the $^1$H NMR spectra. All heteronuclei spectra were referenced to Si(CH$_3$)$_4$ with the Ξ scale.[26] NMR spectra of **3** and **4** were measured in the presence of excess PEt$_3$. IR spectra were recorded with an FTIR spectrometer Perkin–Elmer Spektrum 2000 (KBr) in the range of 350–4000 cm$^{-1}$; a single crystal of **4** was measured with a Perkin–Elmer AutoImage microscope system with a diamond cell. The elemental composition was determined with a Hereaus CHN-O-S Analyzer. The melting points were determined in sealed capillaries (under nitrogen) using a Gallenkamp apparatus and are uncorrected. Cyclovoltammetry experiments were performed in an airtight three-electrode cell attached to a Schlenk line. The working electrode was a platinum disc electrode (diameter 2 mm), the counter electrode a platinum sheet and a silver wire was used as pseudoreference electrode. The working electrode was polished on alumina according to standard procedures. The measurements were performed in $5 \times 10^{-3}$ M solutions of the substances in thf containing 0.1 mol of [*n*Bu$_4$N]BF$_4$ per L. The potentials were referenced to the ferrocene/ferrocenium redox couple ($E_{1/2}$ = 0.54 V vs. saturated calomel electrode). UV/Vis spectra were recorded with a Perkin–Elmer UV/Vis/NIR spectrometer Lambda 900.

**(Methyl-1κ*C*)bis(pentamethylcyclopentadienyl-1κ$^5$*C*)(μ-4-thiolatobenzoato-1κ$^2$*O*:2κ*S*)tris(triethylphosphane-2κ*P*)zirconiumrhodium (3):** Complex **2** was prepared in situ by adding a solution of [RhCl(PEt$_3$)$_3$] (243 mg, 0.5 mmol) and PEt$_3$ (1 mL) in thf (15 mL) to a suspension of K(Hmba) (100 mg, 0.5 mmol) in thf (10 mL) at 0 °C. The suspension was warmed to room temperature over 1 h and was then stirred for 16 h. The red solution was filtered and added to a solution of [Cp*$_2$ZrMe$_2$] (194 mg, 0.5 mmol) in thf (5 mL). After stirring at room temperature overnight, the solvent was removed in vacuo and the resulting red solid was washed with cold diethyl ether (2 mL) and cold *n*-hexane (2 mL). Recrystallisation from *n*-hexane/PEt$_3$ gave 380 mg (77%) of orange needles. M.p. 175–180 °C (dec.). C$_{46}$H$_{82}$O$_2$P$_3$RhSZr (986.26): calcd. C 56.02, H 8.38; found C 55.75, H 8.45. $^1$H NMR ([D$_8$]thf): δ = –0.26 (s, 3 H, ZrC*H*$_3$), 1.20, 1.38, 1.94 [each m, 45 H, P(C$_2$*H*$_5$)$_3$], 1.94 [s, 30 H, C$_5$(C*H*$_3$)$_5$], 7.59 [m, 2 H, A part of the AA′BB′ spin system, H$^1$ in O$_2$CC$_6$H$_4$S (for numbering, see Scheme 1)], 8.04 (m, 2 H, B part of the AA′BB′ spin system, H$^2$ in O$_2$CC$_6$H$_4$S) ppm. $^{13}$C{$^1$H} NMR ([D$_8$]thf): δ = 1.7 (Zr*C*H$_3$), 9.5 [2×P(CH$_2$*C*H$_3$)$_3$]$^\dagger$, 10.0 [P(CH$_2$*C*H$_3$)$_3$], 11.6 [C$_5$(*C*H$_3$)$_5$], 18.8 [2×P(*C*H$_2$CH$_3$)$_3$]$^\dagger$, 22.7 [d, $^1J_{C,P}$ = 34.6 Hz, P(*C*H$_2$CH$_3$)$_3$], 118.1 [*C*$_5$(CH$_3$)$_5$], 123.8 (S*C*), 127.9 (*C*$^1$ in O$_2$CC$_6$H$_4$S), 132.7 (C$^2$ in O$_2$CC$_6$H$_4$S), 164.6 (*C*CO$_2$), 181.6 (C*C*O$_2$) ppm ($^\dagger$coupling constants $J_{A\text{-}X}$, $J_{A'\text{-}X}$ and $J_{M\text{-}X}$ of the AA′MX spin system could not be simulated because of low resolution). $^{31}$P{$^1$H} NMR ([D$_8$]thf): δ = 13.5 [dd, $^1J_{P\text{-}Rh}$ = 137.4 Hz, $^2J_{P\text{-}P}$ = 38.6 Hz, 2 P, P(C$_2$H$_5$)$_3$], 28.4 [dt, $^1J_{P\text{-}Rh}$ = 160.4, $^2J_{P\text{-}P}$ = 38.6 Hz, 1 P, P(C$_2$H$_5$)$_3$] ppm. IR (KBr): ṽ = 2960 s, 2908 s, 2890 m, 1583 s, 1561 w, 1494 m, 1420 s (sh), 1377 m, 1290 w, 1262 w (sh), 1168 w, 1078 m (sh), 1030 s (sh), 869 m, 847 w, 806 w (br), 775 m, 763 m, 732 w, 703 m, 677 w, 617 w, 552 m, 481 w cm$^{-1}$.

**(Hydroxo-1κ*O*)bis(pentamethylcyclopentadienyl-1κ$^5$*C*)-(μ-4-thiolatobenzoato-1κ$^2$*O*:2κ*S*)tris(triethylphosphane-2κ*P*)zirconiumrhodium (4):** Complex **3** was prepared as described above from [RhCl(PEt$_3$)$_3$] (162 mg, 0.33 mmol), PEt$_3$ (1 mL), K(Hmba) (67 mg, 0.35 mmol) and [Cp*$_2$ZrMe$_2$] (129 mg, 0.33 mmol). The resulting red solid was dissolved in *n*-hexane (5 mL) which contained H$_2$O (6 μL, 0.33 mmol) and PEt$_3$ (1 mL). The solution was refluxed for 15 min and the solvent evaporated in vacuo until the solution became slightly cloudy. Light orange crystals (209 mg, 64%) were obtained at room temperature from this mixture. C$_{45}$H$_{80}$O$_3$P$_3$RhSZr (988.19): calcd. C 54.69, H 8.16; found C 54.39, H 8.32. $^1$H NMR (C$_6$D$_6$): δ = 1.20, 1.39, 1.88 [each m, 45 H, P(C$_2$*H*$_5$)$_3$], 1.91 [s, 30 H, C$_5$(C*H*$_3$)$_5$], 3.47 [s (br), 1 H, ZrO*H*], 7.45 (m, 2 H, A part of the AA′BB′ spin system, H$^1$ in O$_2$CC$_6$H$_4$S), 8.10 (m, 2 H, B part of the AA′BB′ spin system, H$^2$ in O$_2$CC$_6$H$_4$S) ppm. $^{13}$C{$^1$H} NMR (C$_6$D$_6$): δ = 9.0 [2×P(CH$_2$*C*H$_3$)$_3$]$^\dagger$, 10.8 [P(CH$_2$*C*H$_3$)$_3$], 11.9 [C$_5$(*C*H$_3$)$_5$], 17.6 [2×P(*C*H$_2$CH$_3$)$_3$]$^\dagger$, 21.4 [d, $^1J_{C\text{-}P}$ = 34.5 Hz, P(*C*H$_2$CH$_3$)$_3$], 118.7 [*C*$_5$(CH$_3$)$_5$], 123.8 (S*C*, overlapped by solvent signal), 124.5 (C$^1$ in O$_2$CC$_6$H$_4$S), 131.8 (C$^2$ in O$_2$CC$_6$H$_4$S), 163.3 (*C*CO$_2$), 180.5 (C*C*O$_2$) ppm ($^\dagger$coupling constants $J_{A\text{-}X}$, $J_{A'\text{-}X}$ and $J_{M\text{-}X}$ of the AA′MX spin system could not be simulated because of low resolution). $^{31}$P{$^1$H} NMR (C$_6$D$_6$): δ = 14.2 [dd, $^1J_{P\text{-}Rh}$ = 136.6 Hz, $^2J_{P\text{-}P}$ = 38.6 Hz, 2 P, P(C$_2$H$_5$)$_3$], 28.4 [dt, $^1J_{P\text{-}Rh}$ = 162.5 Hz, $^2J_{P\text{-}P}$ = 38.4 Hz, 1 P, P(C$_2$H$_5$)$_3$] ppm. IR (KBr): ṽ = 3658 w, 2960 m, 2924 m, 2908 m, 2874 m, 1583 m, 1561 m, 1494 m, 1420 s (sh), 1377 w, 1306 w (br), 1260 w (br), 1169 w, 1078 m (sh), 1030 m (sh), 869 m, 848 w, 805 w (br), 775 m, 763 m, 733 w, 702 w, 616 w, 552 w (sh) cm$^{-1}$.

**Bis[bis(pentamethylcyclopentadienyl-1κ$^5$*C*)(μ-4-thiolatobenzoato-1κ$^2$*O*:2κ*S*)bis(triphenylphosphane-2κ*P*)zirconiumdirhodium] (5):** A solution of [RhCl(PPh$_3$)$_3$] (167 mg, 0.18 mmol) in thf (50 mL) was added to a suspension of K(Hmba) (27 mg, 0.18 mmol) in thf (50 mL). The mixture was heated to 50 °C for 4 h. The resulting orange solution was filtered and added to a solution of [Cp*$_2$ZrMe$_2$] (35.2 mg, 0.09 mmol) in thf (5 mL). After standing at room temperature for 3 d (stirring resulted in the precipitation of impure product), the solvent was removed in vacuo and the brown residue was washed with cold thf (0.5 mL) and *n*-hexane (2 mL).

 © 2006 Wiley-VCH Verlag GmbH & Co. KGaA, Weinheim 

Table 2. Crystallographic data for **3**, **4**, **5**·12thf and **6**·$Et_2O$.

| | **3** | **4** | **5**·12thf | **6**·$Et_2O$ |
|---|---|---|---|---|
| Empirical formula | $C_{46}H_{82}O_2P_3RhSZr$ | $C_{45}H_{80}O_3P_3RhSZr$ | $C_{260}H_{292}O_{20}P_8Rh_4S_4Zr_2$ | $C_{120}H_{206}O_9P_8Rh_4S_4Zr_2$ |
| $M_r$ | 986.22 | 988.19 | 4707.02 | 2762.93 |
| $T$ [K] | 213(2) | 213(2) | 243(2) | 213(2) |
| $\lambda$ [pm] | 71.073 | 71.073 | 71.073 | 71.073 |
| Crystal system | monoclinic | monoclinic | triclinic | triclinic |
| Space group | $P2_1/c$ | $P2_1/c$ | $P\bar{1}$ | $P\bar{1}$ |
| $a$ [pm] | 931.91(8) | 932.52(6) | 1732.7(1) | 1418.35(9) |
| $b$ [pm] | 3155.1(3) | 3160.6(2) | 1854.2(1) | 1564.7(1) |
| $c$ [pm] | 1706.3(1) | 1695.1(2) | 2044.1(1) | 1822.6(1) |
| $\alpha$ [°] | 90 | 90 | 86.354(1) | 66.950(1) |
| $\beta$ [°] | 90.833(1) | 90.083(9) | 76.425(1) | 86.797(1) |
| $\gamma$ [°] | 90 | 90 | 67.987(1) | 67.515(1) |
| $V$ [nm$^3$] | 5.0163(7) | 4.9961(7) | 5.9161(7) | 3.4180(4) |
| $Z$ | 4 | 4 | 1 | 1 |
| $\rho_{calcd.}$ [g cm$^{-3}$] | 1.306 | 1.314 | 1.321 | 1.342 |
| $\mu$ [mm$^{-1}$] | 0.707 | 0.712 | 0.509 | 0.822 |
| $F(000)$ | 2080 | 2080 | 2456 | 1442 |
| Crystal size [mm] | 0.60 × 0.10 × 0.08 | 0.20 × 0.10 × 0.05 | 0.60 × 0.30 × 0.30 | 0.30 × 0.30 × 0.05 |
| $\theta$ range [°] | 1.76–26.39 | 1.76–24.10 | 1.83–28.40 | 1.54–28.32 |
| $h$, $k$, $l$ collected | $-11 \le h \le 11$ | $-10 \le h \le 9$ | $-21 \le h \le 22$ | $-18 \le h \le 18$ |
| | $-38 \le k \le 39$ | $-36 \le k \le 36$ | $-24 \le k \le 16$ | $-20 \le k \le 20$ |
| | $-21 \le l \le 21$ | $-16 \le l \le 19$ | $-26 \le l \le 24$ | $-22 \le l \le 24$ |
| Measured reflections | 36561 | 19408 | 37232 | 24670 |
| Unique reflections | 10148 | 7733 | 27376 | 12941 |
| Restraints/parameters | 0/518 | 0/507 | 352/1347 | 7/682 |
| *Gof* (all data) | 1.582 | 0.597 | 0.935 | 1.093 |
| Final $R$ indices | $R_1 = 0.0931$ | $R_1 = 0.0470$ | $R_1 = 0.0479$ | $R_1 = 0.0499$ |
| $[I > 2\sigma(I)]$ | $wR_2 = 0.1391$ | $wR_2 = 0.1004$ | $wR_2 = 0.1065$ | $wR_2 = 0.0978$ |
| $R$ indices | $R_1 = 0.1010$ | $R_1 = 0.1237$ | $R_1 = 0.1011$ | $R_1 = 0.0716$ |
| (all data) | $wR_2 = 0.1410$ | $wR_2 = 0.1126$ | $wR_2 = 0.1248$ | $wR_2 = 0.1046$ |
| $\Delta\rho$(max/min) [e Å$^{-3}$] | 0.795/–1.229 | 1.044/–0.576 | 1.184/–0.664 | 0.853/–0.379 |

Recrystallisation from thf gave 146 mg (42%) of red crystals. M.p. 198–202 °C (dec.). $C_{212}H_{196}O_8P_8Rh_4S_4Zr_2$ (3842.04): calcd. C 66.27, H 5.14; found C 65.85, H 5.32. $^1$H NMR ([D$_8$]thf, $T$ = 300 K): $\delta$ = 1.73–1.78 (br., 60 H, $C_5Me_5$), 7.00–8.00 [br., 136 H, $P(C_6H_5)_3$ + $O_2CC_6H_4S$] ppm. $^{31}P\{^1H\}$ NMR ([D$_8$]thf): $T$ = 300 K: $\delta \approx$ 38 (br. d, $P$Ph$_3$); $T$ = 173 K: 37.7 (br. d, $^1J_{P\text{-}Rh}$ = 153 Hz, $P$Ph$_3$ of isomer 1), 38.4 (br. d, $^1J_{P\text{-}Rh}$ = 149 Hz, $P$Ph$_3$ of isomer 2) ppm. IR (KBr): $\tilde{\nu}$ = 3050 m, 3000 w, 1633 m, 1585 m, 1495 m, 1481 m, 1432 s, 1380 w, 1306 s, 1262 m, 1170 w, 1135 w, 1091 m (sh), 1027 m, 1016 m, 872 w, 848 w, 805 w, 775 w, 740 m, 694 s, 619 w, 534 m, 522 s, 492 w, 458 w, 437 w cm$^{-1}$.

**Bis[bis(pentamethylcyclopentadienyl-1κ$^5$*C*)(μ-4-thiolatobenzoato-1κ$^2$*O*:2κ*S*)bis(triethylphosphane-2κ*P*)zirconiumdirhodium] (6):** [RhCl(PEt$_3$)$_3$] (162 mg, 0.33 mmol) was dissolved in thf (7 mL) and added to a suspension of K(Hmba) (67 mg, 0.35 mmol) in thf (7 mL) at 0 °C. The suspension was warmed to room temperature over 1 h and then stirred for 16 h. The red solution was filtered, treated with a solution of [Cp*$_2$ZrMe$_2$] (65 mg, 0.17 mmol) in thf (5 mL) and heated to reflux for 3 h. After cooling, the solvent was reduced to half its volume. Vapour diffusion with diethyl ether yielded dark red crystals (170 mg, 37%), which were washed with *n*-hexane and dried in vacuo. M.p. 239–242 °C (dec.). $C_{116}H_{196}O_8P_8Rh_4S_4Zr_2$ (2688.97): calcd. C 51.81, H 7.35; found C 51.28, H 7.69. IR (KBr): $\tilde{\nu}$ = 2958, 2908, 2873, 1635, 1585, 1494, 1429, 1392, 1379, 1301, 1261, 1169, 1136, 1094, 1032, 873, 848, 807, 766, 730, 702, 658, 622, 549, 515, 480, 413 cm$^{-1}$.

**X-ray Crystallography:** X-ray data were collected with a Siemens CCD Smart diffractometer for **3**, **5** and **6**, and with a Stoe IPDS1 for **4** using graphite-monochromated Mo-$K_\alpha$ radiation ($\lambda$ = 0.71073 Å). Absorption correction was performed with the program SADABS[27] for **3**, **5** and **6**, and numerically for **4**. Structure solution and refinement were performed with WinGX,[28] SHELXS-97 and SHELXL-97.[29] All non-hydrogen atoms were refined anisotropically; most hydrogen atoms were refined in calculated positions. Visualisation was carried out with the program DIAMOND. The crystallographic data are summarised in Table 2. CCDC-609917 (for **3**), -609918 (for **4**), -609915 (for **5**) and -609916 (for **6**) contain the supplementary crystallographic data for this paper. These data can be obtained free of charge from the Cambridge Crystallographic Data Centre via www.ccdc.cam.ac.uk/data_request/cif.

**DFT Calculations:** The calculations were carried out with the Gaussian03 program package[30] using B3LYP[31] hybrid functionals. For the metal atoms, effective core potentials were used;[32] the outer core electrons were considered explicitly. For the coordinating atoms, the standard 6-31g(d) basis set was used.[33] The calculations of the ultraviolet spectra were performed with time-dependent density functional theory based on the optimised ground-state structure for **2** and on the experimental structure for **3**.

## Acknowledgments

U. H. thanks the Studienstiftung des Deutschen Volkes for a PhD grant. Support from the Graduiertenkolleg 378 (DFG) and a generous donation of $RhCl_3$ from Umicore AG & Co KG are gratefully acknowledged.

[1] D. W. Stephan, *Coord. Chem. Rev.* **1989**, *95*, 41–107.
[2] R. H. Holm, P. Kennepohl, E. I. Solomon, *Chem. Rev.* **1996**, *96*, 2239–2314.

 © 2006 Wiley-VCH Verlag GmbH & Co. KGaA, Weinheim 

[3] S. J. Tauster, *Acc. Chem. Res.* **1987**, *20*, 389–394.
[4] a) M. A. Rida, A. K. Smith in *Modern Coordination Chemistry – The Legacy of J. Chatt* (Eds.: J. J. Leigh, N. Winterton), Royal Society of Chemistry, Cambridge, UK, **2002**, pp. 154–161; b) F. Senocq, C. Randrianalimanana, A. Thorez, P. Kalck, R. Choukroun, D. Gervais, *J. Chem. Soc., Chem. Commun.* **1984**, 1376–1377; c) R. Choukroun, D. Gervais, J. Jaud, P. Kalck, F. Senocq, *Organometallics* **1986**, *5*, 67–71; d) W. Partenheimer, Amoco Corp., USA, Patent US 4992580.
[5] O. Kahn, *Adv. Inorg. Chem.* **1995**, *43*, 179–259.
[6] R. M. Bullock, C. P. Casey, *Acc. Chem. Res.* **1987**, *20*, 167–173.
[7] a) S. Back, T. Stein, W. Frosch, I. Wu, J. Kralik, M. Büchner, G. Huttner, G. Rheinwald, H. Lang, *Inorg. Chim. Acta* **2001**, *325*, 94–102; b) H. Plenio, D. Burth, *Organometallics* **1996**, *15*, 4054–4062.
[8] S. Fritzsche, P. Lönnecke, T. Höcher, E. Hey-Hawkins, *Z. Anorg. Allg. Chem.* **2006**, *632*, 2256.
[9] a) R. Ruiz, J. Fans, F. Lloret, M. Julve, J. Journaux, *Coord. Chem. Rev.* **1999**, *193–95*, 1069–1117; b) P. Chaudhuri, *Coord. Chem. Rev.* **2003**, *243*, 143–190.
[10] R. G. Pearson, *Chemical Hardness – Application From Molecules to Solids*, Wiley-VCH, Weinheim, **1997**.
[11] a) B. Wenzel, P. Lönnecke, E. Hey-Hawkins, *Eur. J. Inorg. Chem.* **2002**, 1761–1764; b) B. Wenzel, P. Lönnecke, E. Hey-Hawkins, *Z. Anorg. Allg. Chem.* **2003**, *629*, 1596–1600.
[12] a) B. Wenzel, P. Lönnecke, E. Hey-Hawkins, *Organometallics* **2002**, *21*, 2070–2077; b) B. Wenzel, P. Lönnecke, M. Stender, E. Hey-Hawkins, *J. Chem. Soc., Dalton Trans.* **2002**, 478–480; c) B. Wenzel, P. Lönnecke, E. Hey-Hawkins, *Z. Anorg. Allg. Chem.* **2002**, *628*, 1925–1929.
[13] U. Helmstedt, P. Lönnecke, E. Hey-Hawkins, *Inorg. Chem*., in press.
[14] E. Hey-Hawkins, *Chem. Rev.* **1994**, *94*, 1661–1717.
[15] G. Hidalgo, M. A. Pellinghelli, P. Royo, R. Serrano, A. Tiripicchio, *J. Chem. Soc., Chem. Commun.* **1990**, 1118–1120.
[16] G. L. Hillhouse, J. E. Bercaw, *J. Am. Chem. Soc.* **1984**, *106*, 5472–5478.
[17] R. Bortolin, V. Patel, I. Munday, N. J. Taylor, A. J. Carty, *J. Chem. Soc., Chem. Commun.* **1985**, 456–458.
[18] P.-M. Pellny, V. V. Burlakov, W. Baumann, A. Spannenberg, U. Rosenthal, *Z. Anorg. Allg. Chem.* **1999**, *625*, 910–918.
[19] a) W. A. Howard, G. Parkin, *Polyhedron* **1993**, *12*, 1253–1256; b) W. A. Howard, G. Parkin, *J. Am. Chem. Soc.* **1994**, *116*, 606–615; c) W. A. Howard, T. M. Trnka, M. Waters, G. Parkin, *J. Organomet. Chem.* **1997**, *528*, 95–121; d) B. D. Santassiero, E. J. Moore, *Acta Crystallogr., Sect. C: Cryst. Struct. Commun.* **1988**, *44*, 433–435.
[20] a) T. Koch, S. Blauock, E. Hey-Hawkins, M. Galan-Ferres, D. Plat, M. S. Eisen, *J. Organomet. Chem.* **2000**, *595*, 126–133; b) H. Dorn, S. A. A. Shah, E. Parisini, M. Noltemeyer, H.-G. Schmidt, H. W. Roesky, *Inorg. Chem.* **1996**, *35*, 7181–7184.
[21] a) J. Forniés-Cámer, A. M. Masdeu-Bultó, C. Claver, C. Tejel, M. A. Ciriano, C. J. Cardin, *Organometallics* **2002**, *21*, 2609–2618; b) M. F. C. Guedes da Silva, A. M. Trzeciak, J. J. Ziólkowski, A. J. L. Pombeiro, *J. Organomet. Chem.* **2001**, *620*, 174–181.
[22] a) U. Wieser, F. Schnaper, H. H. Brintziger, N. T. Makela, H. R. Knuttila, M. Leskela, *Organometallics* **2002**, *21*, 541–545; b) X. Wang, L. Chen, A. Endou, M. Kubo, A. Miyamato, *J. Organomet. Chem.* **2003**, *678*, 156–165; c) C. E. Zachmanoglou, A. Docrat, B. M. Brandow, J. E. Bercaw, C. N. Jardine, M. Lyall, J. C. Green, J. B. Keister, *J. Am. Chem. Soc.* **2002**, *124*, 9525–9546.
[23] J. A. Osborn, F. H. Jardin, J. F. Young, G. Wilkinson, *J. Chem. Soc. A* **1996**, 1711–1732.
[24] G. M. Intille, *Inorg. Chem.* **1972**, *11*, 695–702.
[25] a) J. M. Manriquez, J. E. Bercaw, *J. Am. Chem. Soc.* **1974**, *96*, 6229–6230; b) J. M. Manriquez, D. R. McAlister, E. Rosenberg, A. M. Shiller, K. L. Williamson, S. I. Chan, J. E. Bercaw, *J. Am. Chem. Soc.* **1978**, *100*, 3078–3083; c) J. M. Manriquez, D. R. McAlister, R. D. Sanner, J. E. Bercaw, *J. Am. Chem. Soc.* **1978**, *100*, 2716–2723.
[26] *NMR Nomenclature. Nuclear Spin Properties and Conventions for Chemical Shifts* (IUPAC Recommendations 2001): R. H. Harris, E. D. Becher, S. M. Cabral de Menezes, R. Goodfellow, P. Granger, *Concepts Magn. Reson.* **2002**, *14*, 326–346.
[27] G. M. Sheldrick, *SADABS – A Program for Empirical Absorption Correction*, University of Göttingen, **1998**.
[28] *WinGX – Suite for Small-Molecule Single-Crystal Crystallography*: L. J. Farrugia, *J. Appl. Crystallogr.* **1999**, *32*, 837–838.
[29] G. M. Sheldrick, *SHELXS97*, *SHELXL97 – Programs for Crystal Structure Analysis*, Release 97-2, University of Göttingen, **1998**.
[30] M. J. Frisch, G. W. Trucks, H. B. Schlegel, G. E. Scuseria, M. A. Robb, J. R. Cheeseman, J. A. Montgommery Jr, T. Vreven, K. N. Kudin, J. C. Burant, J. M. Millam, S. S. Iyengar, J. Tomasi, V. Barone, B. Mennucci, M. Cossi, G. Scalmani, N. Rega, G. A. Petersson, H. Nakatsuji, M. Hada, M. Ehara, K. Toyota, R. Fukuda, J. Hasegawa, M. Ishida, T. Nakajima, Y. Honda, O. Kitao, H. Nakai, M. Kleene, X. Li, J. E. Knox, H. P. Hratchian, J. B. Cross, C. Adamo, J. Jaramillo, R. Gomperts, R. E. Stratmann, O. Yazyev, A. J. Austin, R. Cammi, C. Pomelli, J. W. Ochterski, P. Y. Ayala, K. Morokuma, G. A. Voth, P. Salvador, J. J. Dannenberg, V. G. Zakrzewski, S. Dapprich, A. D. Daniels, M. C. Strain, O. Farkas, D. K. Malick, A. D. Rabuck, K. Raghavachari, J. B. Foresman, J. V. Ortiz, Q. Cui, A. G. Baboul, S. Clifford, J. Cioslowski, B. B. Stefanov, G. Liu, A. Liashenko, P. Piskorz, I. Komaromi, R. L. Martin, D. J. Fox, T. Keith, M. A. Al-Laham, C. Y. Peng, A. Nanyakkara, M. Challacombe, P. M. W. Gill, B. Johnson, W. Chen, M. W. Wong, C. Gonzalez, J. A. Pople, *Gaussian03*, Revision C.02, Gaussian, Inc., Pittsburgh, PA, **2003**.
[31] a) A. D. Becke, *J. Chem. Phys.* **1993**, *98*, 5648–5652; b) C. Lee, W. Yang, R. G. Parr, *Phys. Rev. B: Condens. Matter* **1988**, *37*, 785–789; c) S. J. Vosko, L. Wilk, M. Nusair, *Can. J. Phys.* **1980**, *58*, 1200–1211.
[32] a) P. J. Hay, W. R. Wadt, *J. Chem. Phys.* **1985**, *82*, 270–283; b) W. R. Wadt, P. J. Hay, *J. Chem. Phys.* **1985**, *82*, 284–298; c) P. J. Hay, W. R. Wadt, *J. Chem. Phys.* **1985**, *82*, 299–310.
[33] W. J. Hehre, L. Radom, P. v. R. Schleyer, J. Pople, *Ab initio Molecular Orbital Theory*, Wiley, New York, **1986**.

Received: June 14, 2006
Published Online: October 12, 2006

 © 2006 Wiley-VCH Verlag GmbH & Co. KGaA, Weinheim 

DOI: 10.1002/ejic.200600632

# Synthesis, Crystal Structures, and Magnetic Properties of 2D Manganese(II) and 1D Gadolinium(III) Coordination Polymers with 1*H*-1,2,3-Triazole-4,5-dicarboxylic Acid

**Wei Shi,[a] Xiao-Yan Chen,[a] Na Xu,[a] Hai-Bin Song,[b] Bin Zhao,[a] Peng Cheng,*[a] Dai-Zheng Liao,[a] and Shi-Ping Yan[a]**

**Keywords:** Manganese / Gadolinium / Coordination polymers / Magnetic properties / N,O ligands

Two new coordination polymers, namely $[\{Mn_3(tda)_2(H_2O)_6\}\cdot 6H_2O]_n$ (**1**) and $[\{Gd(H_2O)_4(Htda)\}\cdot(H_2tda)\cdot H_2O]_n$ (**2**) ($H_3tda$ = 1*H*-1,2,3-triazole-4,5-dicarboxylic acid), have been prepared and characterized by IR spectroscopy, elemental analysis, and single-crystal X-ray diffraction. Polymer **1** is a novel 2D stair-like coordination polymer, while **2** is a 1D chain. Temperature-dependent magnetic measurements indicate the existence of antiferromagnetic interactions in both **1** and **2**.

(© Wiley-VCH Verlag GmbH & Co. KGaA, 69451 Weinheim, Germany, 2006)

## Introduction

The design and construction of architectures with appealing topologies have been attracting considerable attention in supramolecular chemistry and crystal engineering in recent years.[1] Among them, the use of metal ions as nodes and bridging ligands as spacers has had a large impact on the building of coordination polymers with novel structures and is expected to lead to the development of exploitable properties such as magnetism, molecular sensors, luminescent materials, absorption materials, and so on.[2] Although many intriguing complexes have been well documented as 1D chains[3] and ladders,[4] 2D grids,[5] 3D frameworks, and helical staircase networks[6] in previous studies, the rational design of specific complexes with the above-mentioned properties is still a challenge for chemists.

The selection of polydentate organic compounds as ligands is a key point in the design and assembly of the expected complexes. In our previous studies, pyridine-2,6-dicarboxylic acid, pyridine-2,5-dicarboxylic acid, pyridine-2,4,6-tricarboxylic acid, and related derivatives have been employed for the construction of novel structures with dimensionalities from discrete to 3D, and with useful properties such as luminescence.[7] This type of ligand is based on the six-membered aromatic ring of pyridine with carboxylic groups in different sites as substituents. As a continuation of this work, we focus our attention here on the ligand based on the five-membered heterocycle dicarboxylic derivative $H_3tda$ ($H_3tda$ = 1*H*-1,2,3-triazole-4,5-dicarboxylic acid). The molecular structure of this ligand is shown in Scheme 1. Most studies of $H_3tda$ with metal ions are in the solution state,[8] and only two examples of rhodium(II) and copper(II) complexes with crystal structures of this ligand have been reported as far as we know.[9]

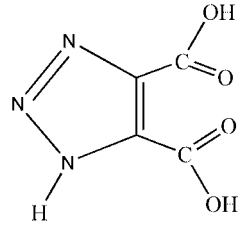


Scheme 1.

In this contribution, two coordination polymers, namely $[\{Mn_3(tda)_2(H_2O)_6\}\cdot 6H_2O]_n$ (**1**) and $[\{Gd(H_2O)_4(Htda)\}\cdot(H_2tda)\cdot H_2O]_n$ (**2**), are reported. The metal ions manganese(II) and gadolinium(III) were used for magnetic studies for two reasons: (a) they possess the highest spin ground state in transition metal ions and lanthanide metal ions ($^6A_{1g}$ for $Mn^{II}$ and $^8S_{7/2}$ for $Gd^{III}$), and always show important magnetic behaviors; (b) the first-order orbital moment of these two metal ions is completely quenched by the ligand field so that the magnetic behavior can be effectively analyzed with the expression derived from the pure spin Hamiltonian. Both of the complexes were characterized by IR spectroscopy, elemental analysis, and single-crystal X-ray diffraction. Polymer **1** is a novel stair-like 2D network based on trinuclear isosceles triangular Mn3 secondary building units, while **2** is a 1D coordination polymer. Tem-

[a] Department of Chemistry, Nankai University, Tianjin, 300071, P. R. China
Fax: +86-22-2350-2458
E-mail: pcheng@nankai.edu.cn
[b] State Key Laboratory of Elemento-Organic Chemistry, Nankai University, Tianjin 300071, P. R. China

 © 2006 Wiley-VCH Verlag GmbH & Co. KGaA, Weinheim 

perature-dependent magnetic measurements show that there are antiferromagnetic interactions in both **1** and **2**.

## Results and Discussion

### Description of the Structure

#### *[{Mn$_3$(tda)$_2$(H$_2$O)$_6$}·6H$_2$O]$_n$ (1)*

Polymer **1** crystallizes in the orthorhombic space group *Pmna* with two crystallographically independent $Mn^{II}$ ions in the crystal lattice, as shown in Figure 1. Mn1 lies in a distorted octahedral environment. The equatorial plane contains O1 and O1A [Mn1–O1(O1A) 2.219(2) Å] from the carboxylate groups and O3 and O3A [Mn1–O3(O3A) 2.139(3) Å] from coordinated water molecules. N1 and N1A [Mn1–N1 2.240(3) Å] from the $tda^{3-}$ ligand occupy the axial direction with an N1–Mn1–N1A angle of 162.22(14)°. Mn2 lies in a centrosymmetrical octahedral environment, which is completed by O2, O2A, O2B, and O2C [Mn2–O2 2.158(2) Å] from the carboxylate groups in the equatorial plane and O4 and O4A [Mn2–O4 2.190(4) Å] from the coordinated water molecules in the axial positions. O2, O2A, O2B, and O2C are perfectly coplanar, and O4, Mn2, and O4A are completely co-linear. The $tda^{3-}$ ligand exhibits an unusual hexadentate binding mode, chelating three $Mn^{II}$ ions. It should be noted that all the atoms of every $tda^{3-}$ ligand are essentially coplanar. The maximum deviation from the plane containing N1, N2, and N1A is 0.07 Å, with an average value of 0.00 Å. This suggests that a conjugated $\pi_{11}^{14}$ bond delocalized over both the triazole ring and the carboxylate groups may exist in the structure. The Mn1···Mn1A and Mn1···Mn2 distances are 6.579(6) and 6.190(5) Å, respectively. As shown in Figure 2 (a), every $tda^{3-}$ ligand further bridges two crystallographically identical Mn1 ions to form a 1D chain in the *a* direction. Furthermore, these chains are linked through the Mn2 ions coordinated to the carboxylate groups of $tda^{3-}$ in the *c* direction to form a 1D ladder-like structure comprising Mn6 coordination rings. Importantly, the molecular planes of the $tda^{3-}$ anions in the 1D chain are perpendicular to each other, and the 1D ladders are further assembled into a novel 2D stair-like network in which the plane of every ladder is also perpendicular (Figure 2, b). This particular supramolecular structure is rather rare among known molecular

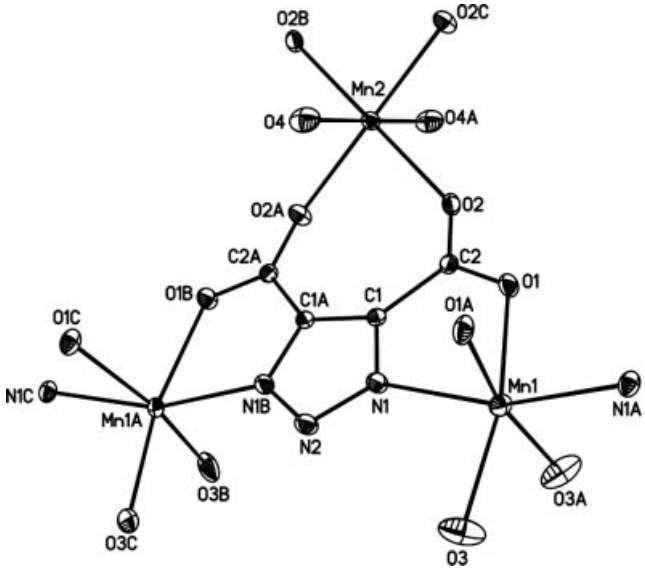


Figure 1. The molecular unit of **1**. Hydrogen bonds and lattice water molecules have been omitted for clarity.

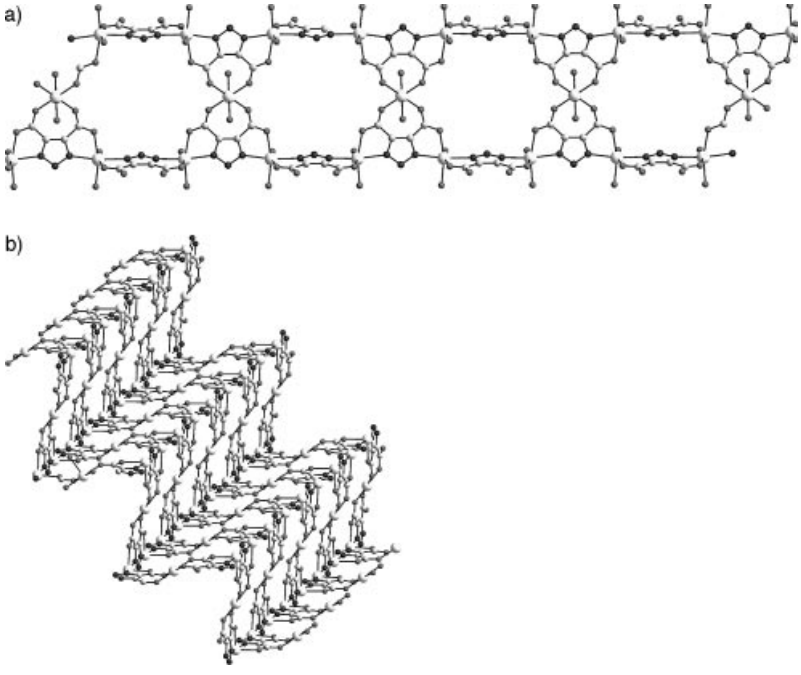


Figure 2. (a) The ladder like structure of **1** viewed along the *a* axis. (b) The 2D stair-like structure of **1**. Water molecules coordinated to the $Mn^{II}$ ions have been omitted for clarity.

 © 2006 Wiley-VCH Verlag GmbH & Co. KGaA, Weinheim 

frameworks.[10] In the crystal, the 2D networks are connected by hydrogen bonds to form a 3D supramolecular architecture containing 1D channels along the *b* direction, as shown in Figure 3.

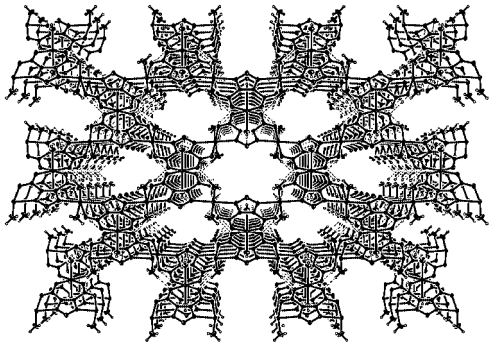

Figure 3. The 3D supramolecular architecture of **1** viewed down the *b* axis. Lattice water molecules in the channel have been omitted for clarity.

### *[{Gd(H$_2$O)$_4$(Htda)}·(H$_2$tda)·H$_2$O]$_n$ (2)*

Polymer **2** crystallizes in the monoclinic space group *C*2/*c*. There is only one crystallographically independent Gd$^{III}$ ion in the crystal lattice. As shown in Figure 4 this Gd$^{III}$ ion is eight-coordinate, with three oxygen atoms and one nitrogen atom from the Htda$^{2-}$ ligand and four water molecules, which together form a square-antiprismatic coordination environment. The Gd–N bond length is 2.582(5) Å, and that of Gd–O is in the range 2.318(4)–2.437(4) Å, with an average value of 2.379(4) Å. Every Htda$^{2-}$ ligand links two Gd$^{III}$ ions to form a 1D zigzag chain in the *b* direction, as shown in Figure 5. Moreover, the 1D zigzag chains are linked by intermolecular hydrogen bonds between the nitrogen atoms in the triazole ring and the oxygen atoms of the carboxylate groups to form 2D layers. These layers are further linked through the counterions of H$_2$tda$^-$ and lattice water molecules into a 3D supramolecular network, as shown in Figure 6.

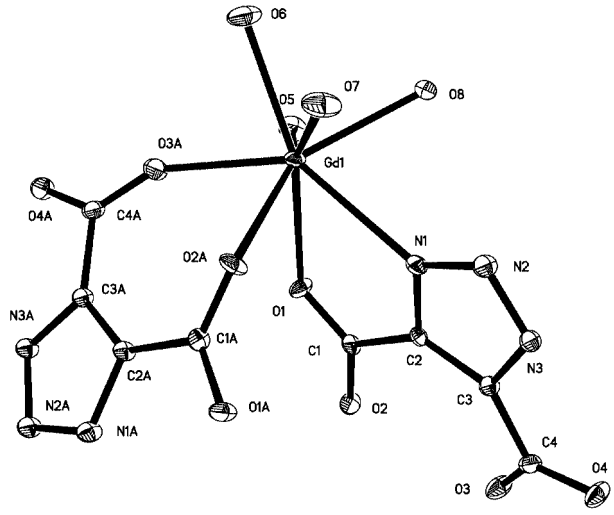


Figure 4. Diagram showing the coordination environment of the Gd$^{III}$ ion in **2**. Hydrogen atoms have been omitted for clarity.

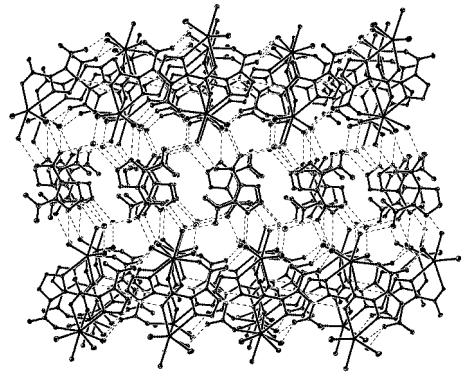

Figure 6. The 3D supramolecular architecture of **2** linked through the counterions of Htda$^-$. Dotted lines represent hydrogen bonding interactions.

The coordination modes of **1** and **2** are shown in Scheme 2. The proton in the 1-position in the triazole ring plays an important role in the formation of the two different coordination modes. For charge neutralization, it is suggested that the ligand is completely deprotonated, existing as tda$^{3-}$ in **1**. The nitrogen atoms in the 1- and 3-positions in the triazole ring become identical from a chemical viewpoint and the tda$^{3-}$ ligand therefore has $C_2$ symmetry. In **2**, the ligand is only doubly deprotonated (at the carboxylate groups) therefore it exists as Htda$^{2-}$ and only has $C_1$ sym-

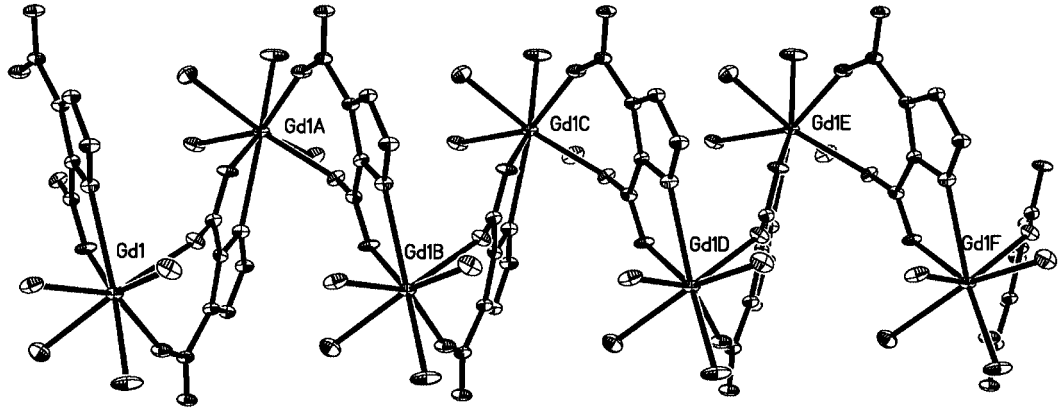


Figure 5. Diagram showing the 1D zigzag chain of **2**. Hydrogen atoms have been omitted for clarity.

 © 2006 Wiley-VCH Verlag GmbH & Co. KGaA, Weinheim 

metry. The different symmetries of the ligands result in different coordination modes.

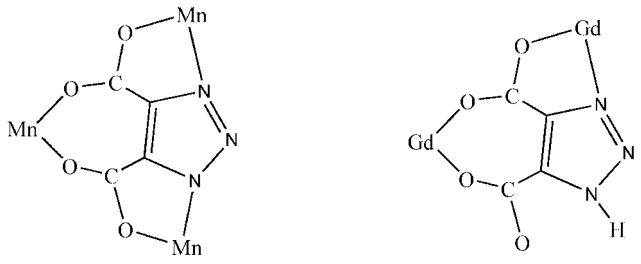


Scheme 2.

### Infrared Spectra

The main features in the IR spectra of both **1** and **2** mainly concern the carboxylate groups and the triazole rings. In **1**, a very strong band appears at around 1595 $cm^{-1}$ due to the antisymmetric stretching ($\nu_{as}$) of the carboxylate group; the symmetrical stretching ($\nu_s$) band of this group appears at 1470 and 1445 $cm^{-1}$, respectively. The difference between $\nu_{as}$ and $\nu_s$ is lower than 200 $cm^{-1}$, which indicates the $\mu_{1,3}$-bridging mode of the carboxylate group to the metal ion, in agreement with the X-ray crystal analysis.[11] In **2**, the $\nu_{as}$ and $\nu_s$ absorptions appear at 1631 and 1380 $cm^{-1}$, respectively. The bands at 1499, 1464, 1016, and 781 $cm^{-1}$ may be attributed to the $\nu$(C–N) stretching of the triazole ring.

### Magnetic Properties

In order to understand the magnetic interactions between the paramagnetic ions via the $H_3$tda ligand in such 1D and 2D structures, the magnetic susceptibilities ($\chi_M$) of both compounds were measured on a Quantum Design MPMS-5S SQUID magnetometer in a field of 1000 Oe. The plots of $\chi_M$ and $\mu_{eff}$ vs. $T$ are shown in Figures 7 and 8 for **1** and **2**, respectively. For **1**, the magnetic susceptibilities were measured in the temperature range from 2 to 300 K. The room-temperature value of 10.23 $\mu_B$ for $\mu_{eff}$ is close to the value of 10.25 $\mu_B$, which is the spin-only value expected for three free $Mn^{II}$ ions with isotropic $g$ = 2.00. As the temperature decreases, the value of $\mu_{eff}$ decreases smoothly, and below 50 K it decreases abruptly to a minimum of 3.52 $\mu_B$ at 2 K. This curve is in agreement with an antiferromagnetic coupling between the $Mn^{II}$ ions. An analytical expression of magnetic susceptibilities for this kind of 2D $Mn^{II}$ complex is not available and only an approximate approach based on both the structural and magnetic data can be performed.[12] Here, we first use the Curie–Weiss law to analyze the experimental data. The best fit gives a Curie constant, $C$, of 4.57 emu K $mol^{-1}$ and a Weiss constant, $\theta$, of –15.47 K, which is consistent with the $\mu_{eff}$ vs. $T$ curve for the antiferromagnetic interactions in **1**. Secondly, based on the crystal data, there are two main pathways (Mn–O–C–O–Mn and Mn–N–N–N–Mn) to transfer the magnetic interactions. By considering that the isosceles triangular Mn3 unit is the basic building block, the expression derived from the Hamiltonian $H = -2J_1S_2(S_1 + S_3) - 2J_2S_1S_3$ (where $J_1$ is the coupling constant between Mn1 and Mn2, and $J_2$ is the coupling constant between Mn1 and Mn1A; see Figure 1 and Scheme 3) was used to fit the data.[13] Because the trinuclear units further assemble into a 2D structure, a $\theta$ parameter was considered to correct the possible secondary effects such as the interactions between the Mn3 units and/or the zero-field splitting of the $Mn^{II}$ ion.[13] The least-squares fit gives $J_1$ = –17.99 $cm^{-1}$, $J_2$ = –9.3 $cm^{-1}$, $\theta$ = –3.9 K, and $g$ = 2.00, with an agreement factor, $R$, of $9.54 \times 10^{-4}$ ($R = \Sigma(\chi_{obsd} - \chi_{calcd})^2/\Sigma(\chi^2_{obsd})$. The $J_1$ value of **1** is obviously larger than other single carboxylato-bridged $Mn^{II}$ complexes, such as $[\{Mn(bipy)_2(H_2O)\}_2\{(CH_3)_3NCH_2CO_2\}](ClO_4)_4 \cdot 2H_2O$ ($g$ = 1.97, $J$ = –0.193 $cm^{-1}$) and $[Mn(MCPA)_2(H_2O)_2]_n$ (MCPA = 2-methyl-4-chlorophenoxyacetic acid; $g$ = 1.90, $J$ = –0.30 $cm^{-1}$).[14] The reason for this may be that the delocalized electrons not only appear around the carboxylate groups but also reside on the $tda^{3-}$

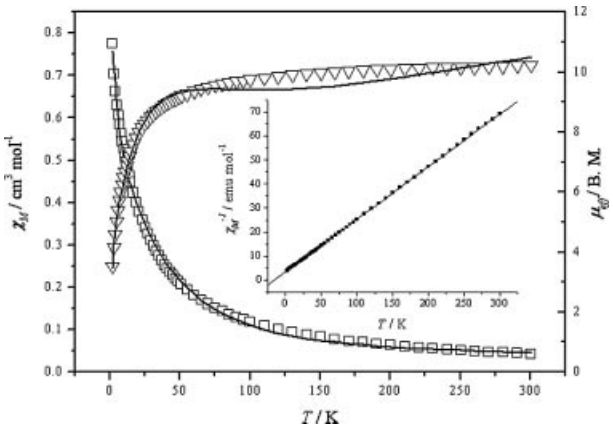


Figure 7. Plots of $\chi_M$ (□) and $\mu_{eff}$ (∇) vs. the temperature for **1**; the solid line represents the best fit. Inset: the Curie–Weiss fit.

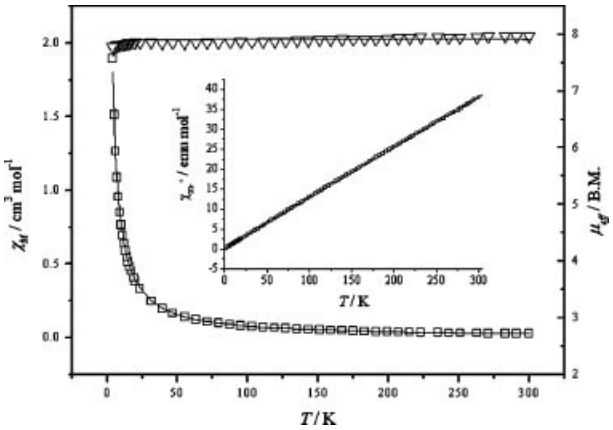


Figure 8. Plots of $\chi_M$ (□) and $\mu_{eff}$ (∇) vs. the temperature for **2**; the solid line represents the best fit.

 © 2006 Wiley-VCH Verlag GmbH & Co. KGaA, Weinheim 

anion, which enhances the capability for magnetic exchange. By comparing the $J_1$ and $J_2$ values, the ability of triazole for magnetic exchange is seen to be smaller than that of the carboxylate group. These results indicate that the $tda^{3-}$ anion is a favorable bridging ligand for magnetic exchange of paramagnetic metal ions.

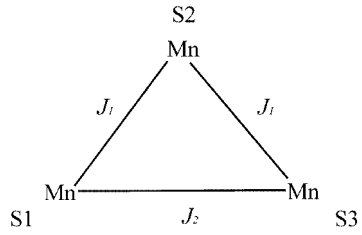


Scheme 3.

Since the $Gd^{III}$ ion in **2** lies in the $^8S_{7/2}$ singlet ground state and does not possess a first-order orbital moment, its magnetic properties are amenable to a rather simple analysis based on a spin-only Hamiltonian. The $\mu_{eff}$ value of **2** at room temperature is 7.97 $\mu_B$, which compares well with the theoretical value of 7.94 $\mu_B$ for one isolated $Gd^{III}$ ion with an isotropic $g$ value of 2.00. The $\mu_{eff}$ value remains almost constant with a decrease of temperature to 2 K, which indicates that the interactions transferred through the $H_3tda$ ligand are very weak. The Curie–Weiss fit for the experimental data gives a Curie constant of 7.89 emu K $mol^{-1}$ and a Weiss constant of –0.85 K. The theoretical $\chi_m$ is given by the following expression, which is based on the spin Hamiltonian $H = -J\sum S_i S_{i+1}$ with the quantum numbers $S_{Gd} = 7/2$:[15]

$$\chi_M = \frac{N\beta^2 g^2 S(S+1)}{3kT} \cdot \frac{1+u}{1-u}$$

$$u = \coth\left[\frac{JS(S+1)}{kT}\right] - \left[\frac{kT}{JS(S+1)}\right]$$

Least-squares fitting of the experimental data leads to $J = -0.10$ $cm^{-1}$, $g = 2.00$, and an agreement factor, $R$, of $6.9 \times 10^{-4}$. These results indicate a very weak antiferromagnetic interaction between the $Gd^{III}$ ions. The magnitude of $J$ is small but is of the same order as other $Gd^{III}$ complexes.[16] The reason for this may be that the 4f electrons lie closer to the metal center than the 5d and 6s electrons and are less influenced by the surrounding environment.

A qualitative interpretation of the magnetic interactions in such metal ions with half-filled orbitals can be made by the well-known Kahn model. The exchange integral ($J$) can be decomposed into two terms, one involving ferromagnetic ($J_F$) and the other antiferromagnetic contributions ($J_{AF}$).[17] The value of $J_{AF}$ is proportional to the square of the integral overlap and is always much larger in magnitude than $J_F$. Since the orbitals of $Mn^{II}$ and $Gd^{III}$ ions are both half-filled such that the electron cloud is completely symmetrical, the nonzero overlap integral of the magnetic orbitals of $Gd^{III}$ or $Mn^{II}$ would result in an antiferromagnetic interaction.

### EPR Spectra

The manganese(II) ion has an $S = 5/2$ electronic spin, and $^{55}Mn$ has a high natural abundance of 100% and an $I = 5/2$ nuclear spin. The X-band EPR spectra of **1** in both the solid state and dmso solution were recorded at room temperature. Only broad bands centered at $g \approx 2.00$ were observed, and no hyperfine pattern could be resolved. This may be due to the strong antiferromagnetic between manganese(II) ions and/or the resonance from the zero-field splitting.[13]

### Theoretical Investigation of $tda^{3-}$

As mentioned in the crystal structure discussion, a conjugated $\pi_{11}^{14}$ bond may exist in the $tda^{3-}$ anion as all its atoms are almost coplanar. A charge density distribution calculation was performed on $tda^{3-}$ at the DFT/B3LYP/6-311G* level using the Gaussian 98 program.[18] The atomic coordinates for input were taken from the crystal data. The calculation result shows that the three negative charges are almost averagely delocalized over the whole $tda^{3-}$ anion, which indicates the existence of a conjugated $\pi_{11}^{14}$ bond.

## Conclusions

We have synthesized two new coordination polymers with 1*H*-1,2,3-triazole-4,5-dicarboxylic acid. The results show that **1** is a novel 2D stair-like coordination polymer based on trinuclear isosceles triangular Mn3 secondary building units, while **2** exists as a 1D chain. Although temperature-dependent magnetic measurements indicate only antiferromagnetic interactions in both **1** and **2**, the interesting structures with variable coordination modes of $H_3tda$ indicate that further studies of this ligand should be made, especially for the construction of 3d–4f complexes.

## Experimental Section

**General Remarks:** All reagents and solvents employed were commercially available and used as received without further purification. $H_3tda$ was synthesized according to the literature method.[19]

**Synthesis of $[\{Mn_3(tda)_2(H_2O)_6\}\cdot 6H_2O]_n$ (1):** A mixture of $Mn(ClO_4)_2\cdot 6H_2O$ (0.145 g, 0.40 mmol), $H_3tda$ (0.156 g, 1.0 mmol), and $H_2O$ (8 mL) was put in a 20-mL acid digestion bomb and heated at 150 °C for three days. The colorless crystals obtained were collected after washing with water (2 × 5 mL) in a yield of 52% (92 mg). $C_8H_{24}Mn_3N_6O_{20}$ (689.15): calcd. C 13.94, H 3.51, N 12.19; found C 14.31, H 3.77, N 12.55.

**Synthesis of $[\{Gd(H_2O)_4(Htda)\}\cdot(H_2tda)\cdot H_2O]_n$ (2):** A mixture of $Mn(ClO_4)_2\cdot 6H_2O$ (0.091 g, 0.25 mmol), $H_3tda$ (0.039 g, 0.25 mmol), $Gd(ClO_4)_3\cdot 6H_2O$ (0.282 g, 0.25 mmol), and $H_2O$ (15 mL) was refluxed in a 100-mL round-bottomed flask for 2 h. The precipitate was filtered off and the filtrate was left to stand at room temperature. Slow concentration of the resulting solution under ambient conditions led to the formation of colorless single crystals of **2** as the only solid with a yield of 86% (68 mg). Without the admixture of $Mn(ClO_4)_2\cdot 6H_2O$ under the same conditions only

 © 2006 Wiley-VCH Verlag GmbH & Co. KGaA, Weinheim 

Table 1. Crystal data and structure refinement for **1** and **2**.

| | **1** | **2** |
|---|---|---|
| Empirical formula | $C_8H_{24}N_6O_{20}Mn_3$ | $C_8H_{13}N_6O_{13}Gd$ |
| $M_r$ | 689.15 | 558.49 |
| Temperature [K] | 293(2) | 294(2) |
| Crystal system | orthorhombic | monoclinic |
| Space group | *Pmna* | *C*2/*c* |
| *a* [Å] | 13.158(4) | 35.000(10) |
| *b* [Å] | 7.446(2) | 6.860(2) |
| *c* [Å] | 12.255(4) | 14.179(4) |
| *α* [°] | 90 | 90 |
| *β* [°] | 90 | 98.183(5) |
| *γ* [°] | 90 | 90 |
| *V* [Å$^3$] | 1200.6(6) | 3369.4(17) |
| *Z* | 2 | 8 |
| $D_{calcd.}$ [mg m$^{-3}$] | 1.906 | 2.202 |
| $\mu$ [mm$^{-1}$] | 1.655 | 4.022 |
| $\theta$ [°] | 2.27–25.00 | 1.18–26.57 |
| Index ranges | $-15 \le h \le 15$ | $-33 \le h \le 44$ |
| | $-8 \le k \le 8$ | $-8 \le k \le 8$ |
| | $-14 \le l \le 9$ | $-17 \le l \le 17$ |
| Reflections collected | 5795 | 8853 |
| Independent reflections | 1112, *R*(int) = 0.0445 | 3497, [*R*(int) = 0.0470] |
| Max, min transmission | 1.000000 and 0.749560 | 1.000000 and 0.525940 |
| Data/restraints/parameters | 1112/9/97 | 3497/5/262 |
| Goodness-of-fit on $F^2$ | 1.076 | 1.052 |
| $R_1$, $wR_2$ [$I > 2\sigma(I)$] | 0.0354, 0.0850 | 0.0420, 0.1052 |
| $R_1$, $wR_2$ (all data) | 0.0501, 0.0920 | 0.0549, 0.1116 |
| Largest diff. peak and hole [e Å$^{-3}$] | 0.413 and –0.485 | 2.209 and –2.211 |

a powder sample of **2** was obtained, as confirmed by IR spectroscopy, elemental analyses, and PXRD. $C_8H_{13}GdN_6O_{13}$ (545.48): calcd. C 17.21, H 2.35, N 15.05; found C 16.85, H 2.42, N 15.19.

**Physical Techniques:** C, H, and N analyses were obtained at the Institute of Elemental Organic Chemistry, Nankai University. The FT-IR spectra were measured with a Bruker Tensor 27 Spectrometer on KBr disks. Variable-temperature magnetic susceptibilities were measured on a Quantum Design MPMS-5S SQUID magnetometer. Diamagnetic corrections were made with Pascal's constants for all the constituent atoms.

Table 2. Selected bond lengths [Å] and angles [°] for **1** and **2**.

| **1**[a] | | | |
|---|---|---|---|
| Mn1–O3 | 2.139(3) | Mn1–N1 | 2.240(3) |
| Mn1–O1 | 2.219(2) | Mn2–O2 | 2.158(2) |
| Mn2–O4 | 2.190(4) | | |
| O3A–Mn1–O3 | 88.57(17) | O2A–Mn2–O2 | 91.35(12) |
| O3A–Mn1–O1 | 91.87(11) | O1–Mn1–O1A | 90.87(14) |
| O3–Mn1–O1 | 166.39(10) | O3–Mn1–N1A | 98.49(11) |
| O1–Mn1–N1 | 72.26(9) | O1–Mn1–N1A | 95.04(9) |
| O1A–Mn1–N1 | 95.04(9) | O3A–Mn1–N1 | 98.49(11) |
| N1A–Mn1–N1 | 162.22(14) | O2–Mn2–O4A | 92.96(9) |
| O2C–Mn2–O2B | 88.65(12) | | |
| | **2**[b] | | |
| Gd1–O3A | 2.318(4) | Gd1–O8 | 2.394(4) |
| Gd1–O7 | 2.347(5) | Gd1–O5 | 2.420(4) |
| Gd1–O2A | 2.365(4) | Gd1–O1 | 2.437(4) |
| Gd1–O6 | 2.372(5) | Gd1–N1 | 2.582(5) |
| O7–Gd1–O6 | 74.75(18) | O8–Gd1–O1 | 106.43(16) |
| O7–Gd1–O8 | 82.06(18) | O5–Gd1–O1 | 73.33(16) |
| O6–Gd1–O8 | 81.82(18) | O7–Gd1–N1 | 80.27(18) |
| O7–Gd1–O5 | 146.87(17) | O6–Gd1–N1 | 146.51(16) |
| O6–Gd1–O5 | 78.22(18) | O8–Gd1–N1 | 72.86(16) |
| O8–Gd1–O5 | 75.42(17) | O5–Gd1–N1 | 114.82(17) |
| O7–Gd1–O1 | 137.39(16) | O1–Gd1–N1 | 63.73(14) |
| O6–Gd1–O1 | 146.95(15) | | |

[a] A: $-x + 1/2$, $y$, $-z + 1/2$; B: $x$, $-y + 1$, $-z$; C: $-x + 1$, $-y + 1$, $-z$. [b] A: $-x + 1/2$, $y + 1/2$, $-z + 1/2$.

**X-ray Crystallographic Studies:** The structural determinations of **1** and **2** were performed by single-crystal XRD analyses. Determinations of the unit cell and data collection were performed with Mo-$K_\alpha$ radiation ($\lambda$ = 0.71073 Å) on a Bruker Smart 1000 diffractometer equipped with a CCD camera. The ω–φ scan technique was employed. Crystal parameters and structure refinements for **1** and **2** are summarized in Table 1. Selected bond lengths and angles are listed in Table 2.

The structures were solved primarily by direct methods and Fourier difference techniques and refined by the full-matrix least-squares method. The computations were performed with the SHELXL-97 program.[20] All non-hydrogen atoms were refined anisotropically. The hydrogen atoms were set in calculated positions and refined as riding atoms with a common fixed isotropic thermal parameter.

CCDC-290628 (for **1**) and -287164 (for **2**) contain the supplementary crystallographic data for this paper. These data can be obtained free of charge from The Cambridge Crystallographic Data Centre via www.ccdc.cam.ac.uk/data_request/cif.

## Acknowledgments

This work was supported by the National Natural Science Foundation of China (grant nos. 90501002 and 20425103), the NSF of Tianjin (grant no. 06YFJZJC009000), and the State Key Project of Fundamental Research of MOST (2005CCA01200), P. R. China.

[1] a) J. M. Lehn, *Supramolecular Chemistry*, VCH, Weinheim, **1995**, chap. 9; b) P. J. Hagrman, D. Hagrman, J. Zubieta, *Angew. Chem. Int. Ed.* **1999**, *38*, 2638–2684; c) S. S. Chui, S. M. F.

 © 2006 Wiley-VCH Verlag GmbH & Co. KGaA, Weinheim 

Lo, J. P. H. Charmant, A. G. Orpen, I. D. Williams, *Science* **1999**, *283*, 1148–1150; d) H. Li, M. Eddaoudi, M. O'Keeffe, O. M. Yaghi, *Nature* **1999**, *402*, 276–279; e) M. Albrecht, M. Luta, A. L. Spek, G. van Koten, *Nature* **2000**, *406*, 970–974; f) R. Owen, W. Lin, *Acc. Chem. Res.* **2002**, *35*, 511–522.

[2] a) D. W. Bruce, D. O'Hare *Inorganic Materials*, Wiley, Chichester, UK, **1992**; b) O. Kahn, *Molecular Magnetism*, VCH, New York, **1993**; c) E. Holder, B. M. W. Langeveld, U. S. Schubert, *Adv. Mater.* **2005**, *17*, 1109–1121; d) J. C. G. Bunzli, G. R. Choppin, *Lanthanide Probes in Life, Chemical and Earth Sciences*, Elsevier, New York, **1989**; e) B. Valeur, *Molecular Fluorescence: Principles and Applications*, Wiley-VCH, **2001**; f) M. Eddaoudi, D. B. Moler, H. L. Li, B. L. Chen, T. M. Reineke, M. O'Keeffe, O. M. Yaghi, *Acc. Chem. Res.* **2001**, *34*, 319–330.

[3] a) D. M. Shin, I. S. Lee, Y. A. Lee, Y. K. Chung, *Inorg. Chem.* **2003**, *42*, 2977–2982; b) M. A. Withersby, A. J. Blake, N. R. Champness, P. Hubberstey, W. S. Li, M. Schröder, *Angew. Chem. Int. Ed. Engl.* **1997**, *36*, 2327–2329; c) A. S. Batsanov, M. J. Begley, P. Hubberstey, J. Stroud, *J. Chem. Soc., Dalton Trans.* **1996**, 1947–1957.

[4] a) M. A. Withersby, A. J. Blake, N. R. Champness, P. A. Cooke, P. Hubberstey, W. S. Li, M. Schröder, *Inorg. Chem.* **1999**, *38*, 2259–2266; b) K. Nomiya, H. Yokoyama, *J. Chem. Soc., Dalton Trans.* **2002**, 2483–2490.

[5] a) D. M. Shin, I. S. Lee, Y. K. Chung, M. S. Lah, *Inorg. Chem.* **2003**, *42*, 5459–5461; b) K. Mitsurs, M. Shimamura, S. I. Noro, S. Minakoshi, A. Asami, K. Seki, S. Kitagawa, *Chem. Mater.* **2000**, *12*, 1288–1299; c) L. Carlucci, G. Ciani, D. M. Proserpio, *J. Chem. Soc., Dalton Trans.* **1999**, 1799–1804; d) C. He, B. G. Zhang, C. Y. Duan, J. H. Li, Q. J. Meng, *Eur. J. Inorg. Chem.* **2000**, 2549–2554.

[6] a) M. Eddaoudi, J. Kim, N. Rosi, D. Vodak, J. Wachter, M. O'Keeffe, O. M. Yaghi, *Science* **2002**, *295*, 469–472; b) C. D. Wu, C. Z. Lu, H. H. Zhuang, J. S. Huang, *J. Am. Chem. Soc.* **2002**, *124*, 3836–3837; c) T. M. Reineke, M. Eddaoudi, D. Moler, M. O'Keeffe, O. M. Yaghi, *J. Am. Chem. Soc.* **2000**, *122*, 4843–4844; d) R. B. Stuart, R. Richard, *Angew. Chem. Int. Ed.* **1998**, *37*, 1460–1494.

[7] a) B. Zhao, P. Cheng, Y. Dai, C. Cheng, D. Z. Liao, S. P. Yan, Z. H. Jiang, G. L. Wang, *Angew. Chem. Int. Ed.* **2003**, *42*, 934–936; b) B. Zhao, P. Cheng, X. Y. Chen, C. Cheng, W. Shi, D. Z. Liao, S. P. Yan, Z. H. Jiang, *J. Am. Chem. Soc.* **2004**, *126*, 3012–3013; c) B. Zhao, X. Y. Chen, P. Cheng, D. Z. Liao, S. P. Yan, Z. H. Jiang, *J. Am. Chem. Soc.* **2004**, *126*, 15394–15395; d) B. Zhao, H. L. Gao, X. Y. Chen, P. Cheng, W. Shi, D. Z. Liao, S. P. Yan, Z. H. Jiang, *Chem. Eur. J.* **2006**, *12*, 149–158; e) H. L. Gao, C. Cheng, B. Ding, W. Shi, H. B. Song, P. Cheng, D. Z. Liao, S. P. Yan, Z. H. Jiang, *J. Mol. Struct.* **2005**, *738*, 105–111; f) H. L. Gao, L. Yi, B. Ding, H. S. Wang, P. Cheng, D. Z. Liao, S. P. Yan, *Inorg. Chem.* **2006**, *45*, 481–483.

[8] a) L. D. Hansen, B. D. West, E. J. Baca, C. L. Blank, *J. Am. Chem. Soc.* **1968**, *90*, 6588–6592; b) A. D. Robertis, C. Foti, A. Gianguzza, *J. Chem. Res. S* **1995**, *7*, 288–289; c) F. Capitan, F. Salinas, E. J. Alonso, *Anal. Quim.* **1973**, *69*, 1133–1139; d) F. Capitan, F. Salinas, E. J. Alonso, *Bol. Soc. Quim. Peru* **1973**, *39*, 1–14.

[9] a) C. Net, J. C. Bayon, P. Esteban, *Inorg. Chem.* **1993**, *32*, 5313–5321; b) J. R. Olson, M. Yamauchi, *Inorg. Chim. Acta* **1985**, *99*, 121–128.

[10] L. Zhang, P. Cheng, L. F. Tang, L. H. Weng, Z. H. Jiang, D. Z. Liao, S. P. Yan, G. L. Wang, *Chem. Commun.* **2000**, 717–718.

[11] K. Nakamoto, *Infrared and Raman Spectra of Inorganic and Coordination Compounds*, 4th ed., Wiley Press, **1986**.

[12] a) E. Q. Gao, Y. F. Yue, S. Q. Bai, Z. He, S. W. Zhang, C. H. Yan, *Chem. Mater.* **2004**, *16*, 1590–1596; b) B. Bitschnau, A. Egger, A. Escuer, F. A. Mautner, B. Sodin, R. Vicente, *Inorg. Chem.* **2006**, *45*, 868–876.

[13] R. L. Carlin, *Magnetochemistry*, Springer-Verlag, Berlin, **1986**.

[14] a) X. M. Chen, Y. X. Tong, Z. T. Xu, T. C. W. Mak, *J. Chem. Soc., Dalton Trans.* **1995**, 4001–4004; b) V. Tangoulis, G. Psomas, C. Dendrinou-Samara, C. P. Raptopoulou, A. Terzis, D. P. Kessissoglou, *Inorg. Chem.* **1996**, *35*, 7655–7660.

[15] M. E. Fisher, *Am. J. Phys.* **1964**, *32*, 343–346.

[16] M. Hernandez-Molina, C. Ruiz-Perez, T. Lopez, F. Lloret, M. Julve, *Inorg. Chem.* **2003**, *42*, 5456–5458.

[17] O. Kahn, M. F. Charlot, *Nouv. J. Chim.* **1980**, *4*, 567–576.

[18] M. J. Frisch, G. W. Trucks, H. B. Schlegel, G. E. Scuseria, M. A. Robb, J. R. Cheeseman, V. G. Zakrzewski, J. A. Montgomery, Jr., R. E. Stratmann, J. C. Burant, S. Dapprich, J. M. Millam, A. D. Daniels, K. N. Kudin, M. C. Strain, O. Farkas, J. Tomasi, V. Barone, M. Cossi, R. Cammi, B. Mennucci, C. Pomelli, C. Adamo, S. Clifford, J. Ochterski, G. A. Petersson, P. Y. Ayala, Q. Cui, K. Morokuma, D. K. Malick, A. D. Rabuck, K. Raghavachari, J. B. Foresman, J. Cioslowski, J. V. Ortiz, A. G. Baboul, B. B. Stefanov, G. Liu, A. Liashenko, P. Piskorz, I. Komaromi, R. Gomperts, R. L. Martin, D. J. Fox, T. Keith, M. A. Al-Laham, C. Y. Peng, A. Nanayakkara, M. Challacombe, P. M. W. Gill, B. Johnson, W. Chen, M. W. Wong, J. L. Andres, C. Gonzalez, M. Head-Gordon, E. S. Replogle, J. A. Pople, *Gaussian 98, Revision A.9*, Gaussian, Inc., Pittsburgh PA, **1998**.

[19] L. E. Hinkel, G. O. Richards, O. Thomas, *J. Chem. Soc.* **1937**, 1432–1437.

[20] a) G. M. Sheldrick, *SHELXS 97, Program for the Solution of Crystal Structures*, University of Göttingen, Germany, **1997**; b) G. M. Sheldrick, *SHELXL 97, Program for the Refinement of Crystal Structures*, University of Göttingen, Germany, **1997**.

Received: July 4, 2006
Published Online: October 2, 2006

 © 2006 Wiley-VCH Verlag GmbH & Co. KGaA, Weinheim 

DOI: 10.1002/ejic.200600666

# Selective Precipitation of Alkaline Earth Metal Cations with Dipicrylamine Anion: Structure–Selectivity Correlation

**Pragati Agnihotri,[a] Subrata Patra,[a] Eringathodi Suresh,[a] Parimal Paul,*[a] and Pushpito K. Ghosh*[a]**

**Keywords:** O ligands / Alkaline earth metals / Selectivity / Structure–selectivity correlation

Salts of dipicrylamine anion and alkaline earth metal ions are highly soluble in water, unlike the salts formed with $K^+$, $Rb^+$, and $Cs^+$. We report here that when $DPA^-$ is added to a solution containing $Mg^{2+}$, $Ca^{2+}$, $Sr^{2+}$, and $Ba^{2+}$, $Ba^{2+}$ can be precipitated out with high yield and selectivity by optimizing the concentrations. When $[DPA^-] = 0.17$ M and the molar ratio of each metal ion to $DPA^-$ is 1:1, $Sr^{2+}$ and $Ba^{2+}$ are precipitated out in about 90% overall yield (with respect to $DPA^-$) and 85% selectivity of $Ba^{2+}$. Salts of $Mg^{2+}$ and $Ca^{2+}$ are virtually absent. Single-crystal XRD of the pure $Sr^{2+}$ and $Ba^{2+}$ compounds has been performed. Layered structures are observed with clear evidence that the salts exist in the form of complexes with the composition $[M(DPA)_2(H_2O)_4]$. This is different to the case of alkali metal ions, where the complexes have no coordinated water molecules. The $Ba^{2+}$ complex has a more compact layered structure than the $Sr^{2+}$ complex, with reduced exposure of the polar entities. As a result it would be expected to have relatively lower solubility in water, which would account for its selective precipitation over the $Sr^{2+}$ complex. That it is legitimate to rationalize the precipitation behavior from the structure deduced by single crystal XRD is verified due to the close similarity between the experimental powder XRD data of the precipitate and the simulated powder XRD pattern obtained from the single-crystal data.

(© Wiley-VCH Verlag GmbH & Co. KGaA, 69451 Weinheim, Germany, 2006)

## Introduction

Dipicrylamine (2,2′,4,4′,6,6′-hexanitrodiphenylamine, DPA) possesses some interesting structural features (Figure 1), namely six nitro groups that are flexible and can interact and adjust in the space and partial delocalization of the resultant charge mediated by the aromatic rings that facilitates coordination of the oxygen atoms with suitable metal ions. Recently, crystal structures of DPA and a computational study on the intermolecular interactions observed in the crystal structure have been reported.[1] The crystal structures of some of its organic salts have also been reported.[2] $DPA^-$ has been used for quantitative estimation of potassium by Winkel and Mass.[3] It has also been used for the recovery of $K^+$ from seawater,[4] and recovery of $Cs^+$ from radioactive waste.[5,6] Studies have also been conducted with a mixture of cations (e.g. $K^+$, $Rb^+$, and $Cs^+$) and $DPA^-$ to assess the relative selectivity of the metal ion.[7] In spite of the voluminous reports on the utility of $DPA^-$, little is known about the factors that control its selectivity towards different alkali and alkaline earth metal ions. We recently undertook a systematic study with $Na^+$, $K^+$, $Rb^+$, and $Cs^+$ to understand the factors that control the selective precipitation behavior.[8] By applying this reaction to the complex sea bittern system, highly pure and concentrated aqueous KCl could be extracted and the same KCl solution could be utilized in a novel process for the preparation of potassium sulfate.[9]

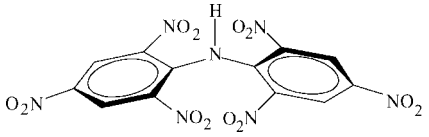

Figure 1. Structure of dipicrylamine (DPA).

Alkaline earth metal ions are dicationic ($Mg^{2+}$, $Ca^{2+}$, $Sr^{2+}$, and $Ba^{2+}$) and their hydration enthalpies (–459.1, –376.9, –344.9, and –311.9 kcal mol$^{-1}$, respectively) are significantly higher than those of the alkali metal ions ($Na^+$: –97, $K^+$: –77, $Rb^+$: –70, and $Cs^+$: –63 kcal mol$^{-1}$). Because of this difference in ionic charge and hydration enthalpy, their structural network and selective precipitation properties are expected to be significantly different from that of

[a] Analytical Science Division, Central Salt and Marine Chemicals Research Institute, G. B. Marg, Bhavnagar 364002, India
E-mail: ppaul@csmcri.org
pkghosh@csmcri.org

Supporting information for this article is available on the WWW under http://www.eurjic.org or from the author.

 © 2006 Wiley-VCH Verlag GmbH & Co. KGaA, Weinheim 

the alkali metal ions. Herein, we report our study on the selective precipitation of $Ba^{2+}$ in high yield from a solution containing the $DPA^-$ anion and an equimolar mixture of $Mg^{2+}$, $Ca^{2+}$, $Sr^{2+}$, and $Ba^{2+}$. This precipitation is induced at high concentrations (ca. 0.15–0.50 M) of $DPA^-$. We have also isolated single crystals of the $Sr^{2+}$ and $Ba^{2+}$ salts of $DPA^-$ to deduce their structures and to unravel the causes underlining this selective precipitation.

## Results and Discussion

### Ion Selectivity

Ion selectivity was determined by analyzing the concentrations of metal ions in the precipitate formed upon addition of 1 mL of an aqueous solution containing $Mg^{2+}$, $Sr^{2+}$, and $Ba^{2+}$ (0.5 M each) to 2 mL of an aqueous solution containing 0.25 M $Ca(DPA)_2$ to yield the overall composition: 0.333 M $DPA^-$ and 0.166 M each of the four metal ions prior to precipitation. The relative proportions of metal ions in the precipitate were assayed by ion chromatography using a reference standard for the purpose of comparison (Figure 2). The tiny peaks corresponding to $Mg^{2+}$ and $Ca^{2+}$ in the ion chromatogram of the precipitate are possibly due to entrapped impurities in the solid (such impurities can remain since washing was avoided to prevent re-dissolution of the precipitate). The molar percentages of $Sr^{2+}$ and $Ba^{2+}$ in the precipitate were 24.1 and 75.9, respectively, while the total molar yield, i.e. sum of the molar yields of $Sr(DPA)_2$ and $Ba(DPA)_2$, was 91% with respect to $DPA^-$ taken up. When all of the concentrations in the solution were halved, the molar percentages of $Sr^{2+}$and $Ba^{2+}$ in the precipitate were 15.0 and 84.9, respectively, while the total molar yield remained virtually constant at 90%. In other words, there was higher recovery of $Ba^{2+}$ (76% in the latter case relative to 69% in the former case) with enhanced selectivity (84.9% in the latter case relative to 75.9% in the former case). This encouraging trend suggests that further increases in recovery and selectivity of $Ba^{2+}$ are possible, although such optimization studies were not carried out. It has been shown previously that understanding of the structures of the solid-state complexes obtained with alkali metal ions can provide valuable insight into their solubility characteristics and precipitation behavior. To extend this understanding to the present system, $Sr^{2+}$and $Ba^{2+}$ complexes of $DPA^-$ were synthesized and structurally characterized.

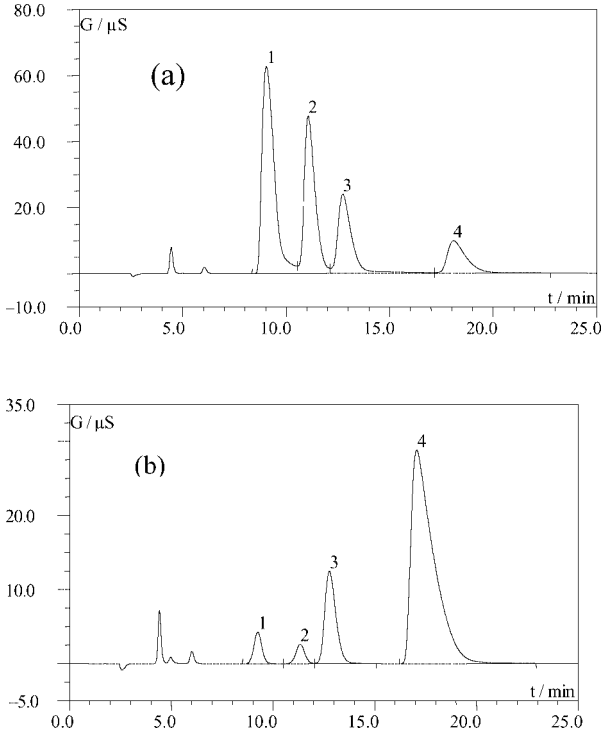


Figure 2. Ion chromatograms of (a) a standard solution containing $MgCl_2$, $CaCl_2$, $SrCl_2$, and $BaCl_2$ (20 ppm each); 1 ($Mg^{2+}$): 9.037, 2 ($Ca^{2+}$): 11.067, 3 ($Sr^{2+}$): 12.740, 4 ($Ba^{2+}$): 18.090 min; and (b) the precipitate separated from the mixture containing 0.17 M of each metal ion; 1 ($Mg^{2+}$): 9.247, 2 ($Ca^{2+}$): 11.333, 3 ($Sr^{2+}$): 12.777, 4 ($Ba^{2+}$): 17.070 min. The tiny peaks of $Mg^{2+}$ and $Ca^{2+}$ found in (b) are probably due to trace amounts of these ions trapped in the precipitate as it was not washed with water to avoid dissolution of the complexes.

### Synthesis of Complexes

$Sr^{2+}$and $Ba^{2+}$ complexes of $DPA^-$ were synthesized by adding an aqueous solution of 0.2 M $Ca(DPA)_2$ to a 0.2 M aqueous solution of the respective chloride salt ($SrCl_2$ and $BaCl_2$), as described in the Experimental Section. The $Sr^{2+}$ complex was partially precipitated during the reaction, and a second crop of the precipitate was obtained when the volume of the filtrate was reduced; even so, the yield was only 72%. In the case of the $Ba^{2+}$ complex, precipitation was nearly instantaneous and almost quantitative (92%), even without recourse to evaporation, which is clearly indicative of its lower solubility than the $Sr^{2+}$ complex. C, H, and N analyses corresponded to the compositions $[Sr(DPA)_2(H_2O)_4]$ (**1**) and $[Ba(DPA)_2(H_2O)_4]$ (**2**). X-ray quality single crystals of **1** and **2** were grown by slow evaporation of dilute aqueous solutions of the complexes at room temperature, and the molecular structures were established by single-crystal X-ray diffraction (see below). To verify whether the bulk precipitates are structurally similar to the single crystals, powder XRD patterns of the bulk precipitates were recorded and compared to those obtained from the single-crystal X-ray data by simulation. The close similarity between the experimental and simulated diffractograms of both **1** and **2** (Figure 3) led us to conclude that the former are indeed structurally similar to the latter and, therefore, understanding of the crystal structures may provide vital information about the solubility/selectivity trend.

 © 2006 Wiley-VCH Verlag GmbH & Co. KGaA, Weinheim 

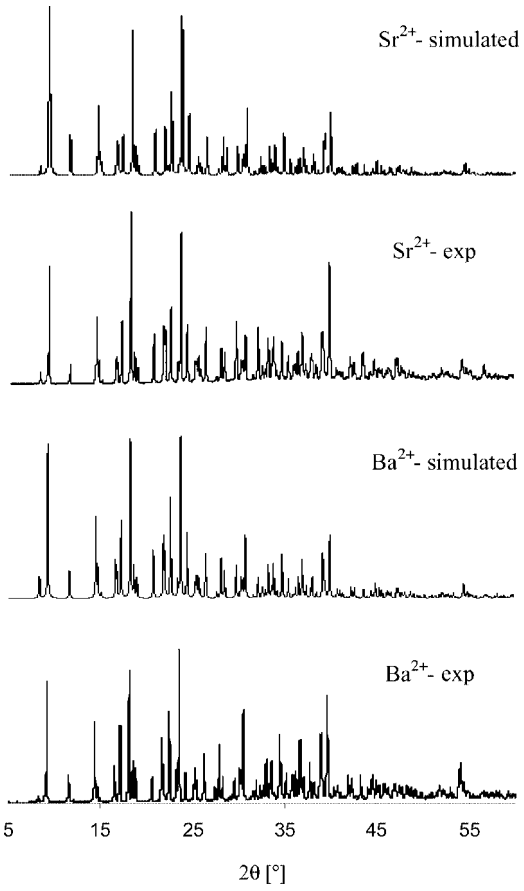


Figure 3. Experimental powder XRD data of bulk precipitates of $Sr^{2+}$ and $Ba^{2+}$ salts of $DPA^-$ vs. XRD patterns simulated from the single-crystal X-ray data of the corresponding crystalline salts grown from the bulk precipitates.

## Crystal Structures

### *[Sr(DPA)$_2$(H$_2$O)$_4$] (1)*

This molecule crystallizes in the acentric space group $P322_1$ – the $Sr^{2+}$ atom possesses a twofold symmetry. The $Sr^{2+}$ ion, which occupies a special position, is coordinated to ten oxygen atoms, six oxygen atoms from the nitro groups of four symmetry-related $DPA^-$ moieties and four oxygen atoms from water molecules. An ORTEP view of the binding of $DPA^-$ to the metal ion is available as Supporting Information (Figure S1). Interactions between the $DPA^-$ anion and the metal ions generate a layered, one-dimensional network, as depicted in Figure 4. The Sr···Sr distance is 9.401 Å, and the angle subtended by the metal ions within the layer is 113.89°. The Sr···O distances are in the range 2.785(2)–2.852(2) Å, and the average Sr···O distance is 2.810(2) Å (Table 1). The oxygen atoms of the coordinated water molecules interact even more strongly with the metal ion [Sr···O13 = 2.534(2) and Sr···O14 = 2.595(2) Å]. The Sr···O distances observed from the structural data (Table 1) are in close agreement with the reported values.[10] The phenyl rings of $DPA^-$ in the complex are almost orthogonal to each other, and the mean plane distortion between them is 75.55°. The coordinated *o*-nitro groups N1–O1/O2 and N5–O7/O8 are rotated by 11.98° and 30.66°, respectively, with respect to the phenyl rings to which they are attached. The uncoordinated *o*-nitro groups N3–O5/O6 and N7–O11/O12 also show significant rotation (88.56° and 19.55°, respectively) from the respective phenyl rings (C1–C6 and C7–C12) to which they are attached. The *p*-nitro groups N2–O3/O4 and N6–O9/O10 are almost in the same plane with respect to the phenyl rings C1–C6 and C7–C12 (deviation 0.82° and 0.54°). It appears that these rotations are self-optimized in order to make effective coordination with the metal ion to propagate the doubly bridged $Sr^{2+}$-$DPA^-$ corrugated network.

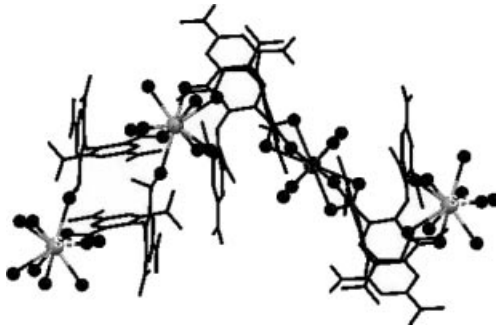

Figure 4. Mercury diagram depicting the adjacent corrugated layered network created by linking of $Sr(H_2O)_4$ units and $DPA^-$.

Table 1. Metal–oxygen distances [Å] for **1** and **2**.

| Compound **1**[a] | | | |
|---|---|---|---|
| Sr(1)–O(14)#1 | 2.5340(19) | Sr(1)–O(7)#3 | 2.785(2) |
| Sr(1)–O(14) | 2.534(2) | Sr(1)–O(2)#1 | 2.792(2) |
| Sr(1)–O(13)#1 | 2.5945(19) | Sr(1)–O(2) | 2.792(2) |
| Sr(1)–O(13) | 2.5945(18) | Sr(1)–O(1)#1 | 2.8523(16) |
| Sr(1)–O(7)#2 | 2.785(2) | Sr(1)–O(1) | 2.8523(17) |
| Compound **2**[b] | | | |
| Ba–O(14)#1 | 2.791(2) | Ba–O(3)#2 | 2.991(2) |
| Ba–O(14) | 2.791(2) | Ba–O(3)#3 | 2.991(2) |
| Ba–O(13)#1 | 2.845(2) | Ba–O(1)#4 | 2.993(2) |
| Ba–O(13) | 2.845(2) | Ba–O(1)#5 | 2.993(2) |
| Ba–O(7)#1 | 3.051(2) | Ba–O(2)#4 | 3.120(2) |
| Ba–O(7) | 3.051(2) | Ba–O(2)#5 | 3.120(2) |

[a] #1: $x - y, -y, -z + 7/3$; #2: $-x + y, -x, z + 1/3$, #3: $y, x, -z + 2$, #4 $-y, x - y, z - 1/3$. [b] #1: $x + 1, -y + 1, -z + 2$; #2: $x + 2, -y, -z + 2$; #3: $x - 1, y + 1, z$; #4: $x - 1, y, z$; #5: $-x + 2, -y + 1, -z + 2$.

The molecular packing shows strong intermolecular O–H···O interactions. The hydrogen atoms of the symmetrically disposed coordinated water molecules (H131 and H132 attached to O13, and H141 and H142 attached to O14) on either side act as donors and participate in H-bonding with the nitro oxygen atoms O5, O9, O3, and O12 to bridge the adjacent corrugated layers into a two-dimensional H-bonded network. The nitro oxygen atom O10 is also involved in an intermolecular C–H···O interaction with the phenyl hydrogen H4. Details of the hydrogen-bonding parameters are given in Table 2.

 © 2006 Wiley-VCH Verlag GmbH & Co. KGaA, Weinheim 

Table 2. Hydrogen-bonding parameters for **1** and **2**.

| D–H···A | *d*(D···A) [Å] | <D–H···A [°] |
|---|---|---|
| | Compound **1**[a] | |
| O(13)–H(131)···O(5)#1 | O(13)···O(5) = 2.089(4) | O(13)–H(131)···O(5) = 152 |
| O(13)–H(132)···O(9)#2 | O(13)···O(9) = 2.944(4) | O(13)–H(131)···O(5) = 145 |
| O(14)–H(141)···O(3)#3 | O(14)···O(3) = 2.920(4) | O(14)–H(141)···O(3) = 151 |
| O(14)–H(142)···O(12)#4 | O(14)···O(12) = 3.085(4) | O(14)–H(142)···O(12) = 174 |
| C(4)–H(4)···O(10)#5 | C(4)···O(10) = 3.221(4) | C(4)–H(4)···O(10) = 134 |
| | Compound **2**[b] | |
| O(13)–H(131)···O(8)#1 | O(13)···O(8) = 3.145(3) | O(13)-(131)···O(8) = 150(4) |
| O(13)–H(132)···O(9)#2 | O(13)···O(9) = 2.901(4) | O(13)-(131)···O(9) = 170(5) |
| O(14)–H(141)···O(11)#3 | O(14)···O(11) = 3.024(4) | O(14)–H(141)···O(11) = 138(6) |
| O(14)–H(141)···O(4)#4 | O(14)···O(4) = 3.109(3) | O(14)–H(141)···O(4) = 140(6) |
| O(14)–H(142)···O(10)#5 | O(14)···O(10) = 3.060(3) | O(14)–H(142)···O(10) = 159(5) |

[a] #1: *y*, –1 + *x*, 2 – *z*; #2: 1 + *y*, *x*, 2 – *z*; #3: –1 + *x*, –1 + *y*, *z*; #4: *y*, –1 + *x*, 2 – *z*; #5: 1 + *x*, 1 + *y*, *z*. [b] #1: *x*, *y*, *z*; #2: *x*, –1 + *y*, *z*; #3: –1 + *x*, *y*, 1 + *z*; #4: 2 – *x*, –*y*, 2 – *z*; #5: 1 – *x*, 2 – *y*, 2 – *z*.

### *[Ba(DPA)$_2$(H$_2$O)$_4$] (2)*

The metal ion in compound **2** sits on a center of symmetry and can accommodate twelve coordinating atoms (eight nitro oxygen atoms from six surrounding DPA$^-$ moieties and four oxygen atoms from coordinated water molecules). An ORTEP view of the binding of DPA$^-$ to the metal ion is available as Supporting Information (Figure S2). The Ba···O distances involving the nitro oxygen atoms are in the range 2.991–3.120 Å (Table 1; average Ba···O = 3.0386 Å). The Ba···O distances involving O13 and O14 of the water molecules are 2.845 and 2.791 Å, respectively, which are in close agreement with the reported values.[11] The Ba···O interaction involving the nitro oxygen atoms O1, O2, and O3 creates a layered doubly bridged architecture in the *ab* plane. However, an additional short contact formed by the nitro oxygen O7 from either side bridges the neighboring layers and extends the layered motif into a two-dimensional sheet-like arrangement, as depicted in Figure 5. The Ba···Ba distance within the coordination network is 9.189 and 6.635 Å along the *a* and *b* axes, respectively. The mean plane distortion between the phenyl rings of DPA$^-$ is 71.78°, which is 3.77° less than that in complex **1**. The coordinated *o*-nitro groups N1–O1/O2 and N5–O7/O8 are rotated with respect to the phenyl rings to which they are attached by 15.49° and 10.06°, respectively, whereas the coordinated *p*-nitro group N2–O3/O4 shows a comparatively smaller rotation (4.68°) with respect to the phenyl ring C1–C6. The uncoordinated *o*-nitro groups N3–O5/O6 and N7–O11/O12 and the *p*-nitro group N6–O9/10 make angles of 29.17°, 5.39°, and 4.35° with respect to the phenyl rings to which they are attached.

Analysis of the molecular packing reveals that both the hydrogen atoms from all the coordinated symmetry-related water molecules act as donors and are involved in intra- and intermolecular O–H···O interactions with the nitro oxygen atoms. Details of the hydrogen-bonding parameters are given in Table 2. These intermolecular H-bonding interactions not only connect the adjacent two-dimensional sheets but also stabilize the network in the crystal lattice.

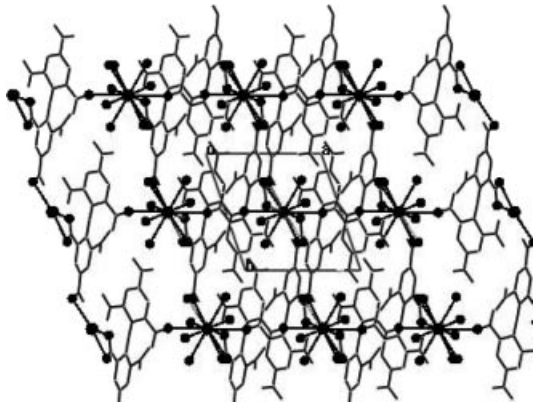

Figure 5. Packing diagram (Mercury) viewed down the *c* axis showing the two-dimensional coordination networks in complex **2**.

### Structure–Selectivity Correlation

Competitive precipitation of a metal ion from a mixture of cations determines selectivity. $Sr^{2+}$ and $Ba^{2+}$ complexes with DPA$^-$ have identical compositions, therefore selective precipitation of a particular complex should be related to the structural arrangement in the solid state, which can profoundly influence the solubility in water. As can be seen from the single-crystal structures of **1** and **2**, these structures are held in place by M···O and C–H···O interactions that form an extended network. From the packing diagrams it is clear that the metal ions are encapsulated in the cavities at regular intervals in the structural network. This self-assembled system reduces the solubility of the complex, and consequently precipitation occurs. Space-filling models of the respective cavities comprising the metal ion and metal-bound oxygen atoms have been generated from the packing diagrams of **1** and **2** (Figure 6 and Figure 7, respectively). The ten oxygen atoms around $Sr^{2+}$ and the twelve oxygen atoms around $Ba^{2+}$ form near-spherical cavities, the approximate diameter of which can be determined from the average distance between the *trans* oxygen atoms having O–M–O angles ≤ 150°. The approximate diameters of the

 © 2006 Wiley-VCH Verlag GmbH & Co. KGaA, Weinheim 

cavities thus obtained are 5.43 and 6.08 Å for $Sr^{2+}$ and $Ba^{2+}$, respectively. These diameters qualitatively follow the order of the ionic sizes of these cations (2.26 and 2.68 Å for $Sr^{2+}$ and $Ba^{2+}$, respectively).[12] $Mg^{2+}$and $Ca^{2+}$, with ionic sizes of 1.30 and 1.98 Å, respectively, may be too small to fit in this cavity and make the significant M···O interactions needed to form a stable assembly, provided a similar structure were to apply in their case also. Alternative structures with smaller cavity sizes are, of course, possible with a lower number of ligands around the metal ion with reduced steric hindrance. However, due to the lack of a sufficient number of M···O and intermolecular C–H···O interactions for such an arrangement, it may not be possible to form the stable assembly essential for precipitation. In the case of alkali metal ions, $Na^+$, which has a smaller ionic size (1.94 Å), does not precipitate out in the presence of $DPA^-$ either due to the lack of formation of a supramolecular network. However, $K^+$, $Rb^+$, and $Cs^+$, which have ionic sizes of 2.66, 2.94, and 3.34 Å, respectively, precipitate out spontaneously in the presence of $DPA^-$.[8] Therefore, the size of the cation is an important factor for the formation of the network structure and thus precipitation.

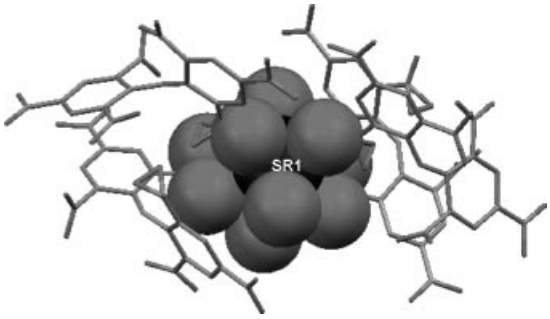


Figure 6. Space-filling model (Mercury diagram) of the cavity comprising the $Sr^{2+}$ ion and metal-bound oxygen atoms.

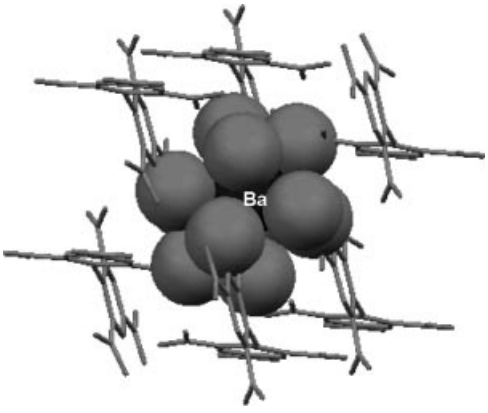


Figure 7. Space-filling model (Mercury diagram) of the cavity comprising the $Ba^{2+}$ ion and metal-bound oxygen atoms.

There can be variations in solubility even for complexes exhibiting a network structure. Reduced exposure of the metal ion and the polar groups of the ligand to water (by tying these up internally in the structure) would lead to reduced solubility and, consequently, more favorable precipitation. In the $Ba^{2+}$ complex, the metal ion is twelve coordinate, unlike in the case of the $Sr^{2+}$ complex in which the coordination number is 10. Moreover, analysis of the packing diagram shows that H-bonding interactions connect the adjacent two-dimensional sheets, which makes the structure more compact than that of the $Sr^{2+}$ complex and reduces the possibility of contact between the polar groups of the ligand and/or coordinated water molecules with the solvent (water). The higher expected stability of the network (Figure 5), coupled with the expectation of reduced solubility due to the reasons above, leads to its higher selectivity over $Sr^{2+}$. Even so, the above solid complexes are much more "exposed" to the solvent than the earlier complexes reported for alkali metal ions ($K^+$, $Rb^+$, $Cs^+$), both in terms of their networked structure and also in terms of their microenvironment, which contains four coordinated water molecules.

Hydration enthalpy is another factor to consider. The hydration enthalpies of $Mg^{2+}$, $Ca^{2+}$, $Sr^{2+}$, and $Ba^{2+}$ are –459.1, –376.9, –344.9, and –311.9 kcal mol$^{-1}$, respectively.[13] Therefore, the displacement of water from the hydrated ions is least facile for $Mg^{2+}$ and most facile for $Ba^{2+}$. This would promote complex formation with $DPA^-$ in the case of $Ba^{2+}$, which, in turn, would allow formation of the network structure required for precipitation. A similar trend was also observed for the alkali metal ions $Na^+$, $K^+$, $Rb^+$, and $Cs^+$. However, that the other factors alluded to above are also critically important is evident from the fact that $Na^+$, despite a much lower hydration enthalpy (–97 kcal mol$^{-1}$) than $Sr^{2+}$ and $Ba^{2+}$, does not form a complex whereas the latter ions do. Moreover, the charge of the cation is also expected to play an important role in complexation. The doubly positive charge on the alkaline earth metal ions obviously attracts $O^{\delta-}$ of the ligand more strongly than monovalent cations. This stronger interaction partially compensates the opposite force due to the high hydration enthalpy of the cations in the complexation process.

## Conclusion

We conclude from the present study that precipitation of alkaline earth metal ions with $DPA^-$ requires the formation of stable assemblies. Simple salts such as $Ca(DPA)_2$, which are unable to form network structures, are highly soluble in water. Formation of such an assembly primarily depends on the ionic size, hydration enthalpy, and ionic charge. Ionic size should be such that the metal ion can fit into the cavity and provide the strong M···O interactions needed to form a stable complex. A smaller ionic size, typically ≤2.0 Å − the ionic sizes of $Mg^{2+}$, $Ca^{2+}$, and $Na^+$ are 1.30, 1.98, and 1.94 Å, respectively − is unfavorable for formation of this assembly. The possibility of complex formation decreases for cations having the same charge with increasing hydration enthalpy. With a mixture of cations, the selectivity depends on the ease of complex formation and the consequent structures of the assemblies: the lower the exposure of the metal ion and polar groups of the ligand to the sol-

 © 2006 Wiley-VCH Verlag GmbH & Co. KGaA, Weinheim 

vent (water), the higher the selectivity to precipitation. Taking both the alkali and alkaline earth metal ions jointly, the selectivity towards precipitation in the presence of $DPA^-$ follows the overall trend: $Cs^+ > Rb^+ > K^+ > Ba^{2+} > Sr^{2+} >> Na^+, Ca^{2+}, Mg^{2+}$.

## Experimental Section

**Materials:** Dipicrylamine was purchased from National Chemical Co., India, and was used as received. AR grade $MgCl_2$, $SrCl_2$, $BaCl_2$, and CaO were obtained from S. D. Fine Chemicals. Doubly distilled water was used for the preparation of all complexes.

**Instrumentation:** Elemental analyses (C, H, N) were performed on a model 2400 Perkin–Elmer elemental analyzer. Cation concentration was measured with a Dionex 500 ion chromatograph. X-ray powder diffraction data were collected with a Philips X' Pert MPD system with Cu-$K_\alpha$ radiation. Single-crystal structures were determined with a Bruker SMART APEX (CCD) diffractometer.

**Competitive Precipitation Study with $DPA^-$:** $Ca(DPA)_2$ was obtained by stoichiometric reaction of CaO and DPA in an aqueous medium; this compound is highly soluble in water. The $Sr^{2+}$ complex was found to be less soluble in water and the $Ba^{2+}$ complex is the least soluble among these salts. For the competitive precipitation study an aqueous solution of $Ca(DPA)_2$ was added to a solution containing equimolar amounts of $Mg^{2+}$, $Sr^{2+}$, and $Ba^{2+}$. In a typical experiment, an aqueous solution (2 mL) of $Ca(DPA)_2$ (0.25 M), obtained by the reaction of CaO (0.5 mmol) and DPA (1.0 mmol), was added to a solution (1 mL) containing a mixture of $MgCl_2$, $SrCl_2$, and $BaCl_2$ (0.5 M with respect to each metal ion). The reaction mixture was then stirred for 30 min at room temperature, and the orange precipitate thus obtained was isolated by filtration on a frit and dried in vacuo overnight to yield 488 mg (91%) of a solid with a similar powder XRD pattern to that of $[M(DPA)_2(H_2O)_4]$ (M = Ba, Sr). The precipitate was not washed with water to avoid possible dissolution of some of it. The concentrations of metal ions in the precipitate were assessed by ion chromatography. The solubility of the $Sr^{2+}$ complex in water is significant, therefore, the amount of this complex in the precipitate obtained from the mixture of cations should decrease upon decreasing the concentration of the metal ion in the reaction mixture. Therefore, another set of experiments was conducted under similar experimental conditions, with the exception of the concentration of the metal ions – in this case 4 mL of a solution containing 0.5 mmol of each metal ion (0.125 M) was used. Yield: 485 mg (90%) with respect to $DPA^-$.

To estimate the relative concentrations of metal ions in the precipitate, a standard solution containing chloride salts of $Mg^{2+}$, $Ca^{2+}$, $Sr^{2+}$, and $Ba^{2+}$ (20 ppm each) was analyzed by ion chromatography on an Ion Pac CS12 (2 mm) analytical column with 20 mM methylsulfonic acid as eluent (flow rate: 0.25 mL min$^{-1}$). Subsequently, 7.4 mg of the precipitate obtained above was dissolved in 10 mL of Milli-Q (Millipore Corporation) water and filtered through 0.2-μm filter paper. Peaks were obtained at the same retention times as above suggesting that the $[M(DPA)_2(H_2O)_4]$ complexes dissociate under dilute conditions to yield the fully hydrated ions as in the case of solutions made from the simple chloride salts. Analytical results (in mol-%) obtained for the first experiment (0.333 M of each metal ion): $Ba^{2+}$: 75.9; $Sr^{2+}$: 24.0; $Mg^{2+}$ and $Ca^{2+}$: traces; for the second experiment (0.17 M of each metal ion): $Ba^{2+}$: 84.9; $Sr^{2+}$: 15.0; $Mg^{2+}$ and $Ca^{2+}$: traces.

**Synthesis of Metal Salts of $DPA^-$**

**$[Sr(DPA)_2(H_2O)_4]$ (1):** Solid CaO (1.1 mmol, 61.7 mg) was added to DPA (2 mmol, 878 mg) suspended in water (5 mL). After 10 min of stirring at room temperature, the dark-red solution was filtered, and the filtrate containing $Ca(DPA)_2$ was added dropwise to an aqueous solution (5 mL) of $SrCl_2{\cdot}6H_2O$ (1 mmol, 266.6 mg). The reaction mixture was stirred for 1 h, during which some of the $Sr^{2+}$ complex precipitated. The compound was separated by filtration, and the filtrate was allowed to evaporate to dryness at room temperature. After 2 d another crop of microcrystalline complex was obtained. Combined yield: 0.72 g (70%). X-ray quality crystals were obtained by slow evaporation (ca. two weeks) of an aqueous solution of the complex. $C_{24}H_{16}N_{14}O_{28}Sr$ (1036.1): calcd. C 27.82, H 1.56, N 18.93; found C 28.10, H 1.45, N 18.62.

**$[Ba(DPA)_2(H_2O)_4]$ (2):** This compound was synthesized following the same procedure as that described for complex **1**, except $BaCl_2{\cdot}4H_2O$ was used in place of $SrCl_2{\cdot}6H_2O$. In this case almost the entire amount of compound was precipitated during stirring, and the filtrate was not processed further to obtain another crop. Yield: 1.0 g (92%). X-ray quality crystals were obtained following the same method as that described for compound **1**. $C_{24}H_{16}BaN_{14}O_{28}$ (1085.8): calcd. C 26.54, H 1.49, N 18.06; found C 26.29, H 1.36, N 17.91.

**X-ray Crystallography:** Crystal data collection and refinement parameters for complexes **1** and **2** are given in Table 3. Data sets were obtained on a Bruker Smart Apex diffractometer with a CCD area detector using graphite-monochromated Mo-$K_\alpha$ radiation ($\lambda$ = 0.71073 Å) at 100 K. Data frames were processed using the Bruker SAINT program.[14] Intensities were corrected for Lorentz, polarization, and decay effects, and an absorption correction was applied using SADABS.[15] The structure was solved by direct methods using SHELXS-97[16] and refined on $F^2$ using SHELXL-97.[17] The non-hydrogen atoms were located directly by successive difference Fourier calculations, and anisotropic full-matrix refinement of all atoms was carried out using SHELXL-97 until convergence was reached, which showed no significant peaks in the difference Fourier map. H-atoms attached to the phenyl rings of the DPA moiety in both the complexes were calculated on the basis of geometric criteria and were treated with a riding model in subsequent refine-

Table 3. Summary of crystallographic data for **1** and **2**.

| Compound | **1** | **2** |
|---|---|---|
| Formula | $C_{12}H_8N_7O_{14}Sr_{0.5}$ | $C_{12}H_8Ba_{0.50}N_7O_{14}$ |
| Formula weight | 518.06 | 542.92 |
| $a$ [Å] | 12.1812(6) | 9.1889(15) |
| $b$ [Å] | 12.1812(6) | 9.6352(16) |
| $c$ [Å] | 21.8380(16) | 11.697(2) |
| $\alpha$ [°] | 90.00 | 76.106(3) |
| $\beta$ [°] | 90.00 | 72.734(3) |
| $\gamma$ [°] | 120.000 | 68.376(3) |
| $Z$ | 6 | 2 |
| $V$ [Å$^3$] | 2806.2(3) | 909.3(3) |
| Crystal system | trigonal | triclinic |
| Space group | $P322_1$ | $P\bar{1}$ |
| $\lambda$ [Å] | 0.71073 | 0.71073 |
| $\rho_{calcd.}$ [g cm$^{-3}$] | 1.839 | 1.983 |
| Abs coefficient, $\mu$ [cm$^{-1}$] | 15.68 | 12.23 |
| $F$(000) | 1560 | 538 |
| Temperature [K] | 100(2) | 100(2) |
| Reflns collected/unique/$R$(int) | 16369/4417/0.0291 | 5510/3990/0.0103 |
| GOF on $F^2$ | 0.683 | 1.041 |
| $R_1/wR_2$ [$I > 2\sigma(I)$] | 0.0302/0.0762 | 0.0264/0.0710 |
| $R_1/wR_2$ (all data) | 0.0364/0.0790 | 0.0264/0.0710 |

 © 2006 Wiley-VCH Verlag GmbH & Co. KGaA, Weinheim 

ments using the SHELXL default parameters. Hydrogen atoms attached to the water oxygen atoms in both the complexes were located from the difference Fourier map. In the case of **1**, water hydrogen atoms were kept fixed and included only in the structure factor calculation whereas in **2** they were refined isotropically. Molecular graphics of the crystal structures were generated using ORTEP, PLATON, and Mercury.[18–20]

CCDC-610046 and -610047 (for **1** and **2**, respectively) contain the supplementary crystallographic data for this paper. These data can be obtained free of charge from The Cambridge Crystallographic Data Centre via www.ccdc.cam.ac.uk/data_request/cif.

**Powder X-ray Data Collection:** Powder X-ray data of the bulk precipitates of **1** and **2** were collected at room temperature in continuous scan mode in the $2\theta$ range 5–60° with a step size of 0.02° $2\theta$ and a count time of 4 s per step. Powder XRD patterns of **1** and **2** were also obtained by simulation from the single-crystal X-ray data using the Mercury program.[20]

**Supporting Information** (see footnote on the first page of this article): ORTEP views of complexes **1** (Figure S1) and **2** (Figure S2).

## Acknowledgments

We are grateful to the Department of Science and Technology (DST), Government of India, for financial support. We also thank CSIR, New Delhi, for generous support towards infrastructures and core competency development. P.A. gratefully acknowledges CSIR for their award of a Senior Research Fellowship. We thank Dr. (Mrs.) P. Bhatt for the powder XRD measurements.

[1] K. Wozniak, P. R. Mallinson, C. C. Wilson, E. Hovestreydt, E. Grech, *J. Phys. Chem. A* **2002**, *106*, 6897.
[2] a) K. Wozniak, H. He, J. Klinowski, W. Jones, E. Grech, *J. Phys. Chem.* **1994**, *98*, 13755; b) M. L. Kundu, J. N. Kapoor, S. K. Ghosh, *Proc. Indian Acad. Sci. (Chem. Sci.)* **1982**, *91*, 65.
[3] A. Winkel, D. I. H. Maas, *Angew. Chem.* **1936**, *49*, 827.
[4] a) J. Kielland, *Patent*, **1940**, No. Au 109552 19400110; **1941**, No. DE 715199 19411120; b) J. Kielland, W. Fleischer, *Patent*, **1940**, No. AU 112196 19401219; c) E. Berner, J. Kielland, *Patent*, **1942**, No. DE 726545 19420903; d) F. Massazza, B. Riva, *Ann. Chim. (Rome)* **1958**, *48*, 664; e) F. Massazza, B. Riva, *Ann. Chim. (Rome)* **1961**, *51*, 645; f) J. N. Kapoor, J. M. Sarkar, *Technology (Sindri, India)* **1966**, *3*, 177; g) S.-K. Chu, C.-T. Liaw, *Huaxue* **1969**, *4*, 106; h) J. Kielland, *Chem. Ind. (London)* **1971**, 1309; i) M. Y. Bakr, A. A. Zatout, *Chem. Econ. Eng. Rev.* **1979**, *11*, 31.
[5] V. Kourim, J. Krtil, *Proceedings of the UN International Conference on the Peaceful Uses of Atomic Energy*, 2nd meeting, Geneva, **1958**, *28*, 139.
[6] J. Rais, P. Selucky, *Patent*, **1973**, No. CZXXA9 CS 149403 19730715.
[7] L. A. Bray, E. C. Martin, R. L. Moore, W. A. Richland, *U.S. At. Energy Commun.* **1962**, *##HW-SA-2620*, 8.
[8] E. Suresh, P. Agnihotri, B. Ganguly, P. Bhatt, P. S. Subramanian, P. Paul, P. K. Ghosh, *Eur. J. Inorg. Chem.* **2005**, 2198.
[9] P. Paul, P. K. Ghosh, K. J. Langalia, P. S. Subramanian, E. Suresh, S. Patra, P. Agnihotri, *Patent (applied, PCT and USA)*, **2005**, Application No. 0312NF2005.
[10] P. D. Beer, P. A. Gale, Z. Chen, M. G. B. Drew, J. A. Heath, M. I. Ogden, H. R. Powell, *Inorg. Chem.* **1997**, *36*, 5880.
[11] G. Mezei, R. G. Raptis, *New J. Chem.* **2003**, *27*, 1399.
[12] C. J. Pedersen, *J. Am. Chem. Soc.* **1967**, *89*, 7017.
[13] F. A. Cotton, W. Wilkinson, *Advanced Inorganic Chemistry, A comprehensive Text*, 3rd Ed., **1979**, pp. 198 and 645.
[14] Bruker Analytical X-ray Instruments, Inc., Madison, WI.
[15] G. M. Sheldrick, University of Göttingen, Göttingen, Germany, **1996**.
[16] G. M. Sheldrick, *SHELXS97, a program for crystal structure solution*, University of Göttingen, Germany, **1997**.
[17] G. M. Sheldrick, *SHELXL97, a program for crystal structure refinement*, University of Göttingen, Germany, **1997**.
[18] C. K. Johnson, *ORTEP II, Report ORNL-5138*, Oak Ridge National Laboratory, Oak Ridge, TN, **1976**.
[19] A. L. Spek, *PLATON-97*, University of Utrecht, Utrecht, The Netherlands, **1997**.
[20] *Mercury 1.3*, Supplied with Cambridge Structural Database CCDC, Cambridge, U. K., **2003–2004**.

Received: July 14, 2006
Published Online: October 12, 2006

 © 2006 Wiley-VCH Verlag GmbH & Co. KGaA, Weinheim 

EurJIC
European Journal of Inorganic Chemistry

Issue 24/2006

Pages 4949–5184

*Papers available ahead of print in Early View at www.interscience.wiley.com*

*Earliest available Table of Contents:*
*Automatically, free of charge by e-mail through*
*www.interscience.wiley.com/alerts*

## COVER PICTURE

**The cover picture shows** the constellation scorpio (lat. scorpius), which symbolises the heteroscorpionate ligands described in the article. To the left, a complex bearing such a heteroscorpionate ligand is fixed on a solid phase. In the back, another ligand with a linker for immobilisation is approaching the resin. The IR spectra (from bottom to top) correspond to a homogenous tricarbonylmanganese complex, the solid phase, a control experiment and a tricarbonyl complex grafted on the solid phase. The $A_1$ and two E bands prove the facial coordination of the ligands and the fixation of the ligand on the solid phase. Details are discussed in the article by N. Burzlaff et al. on p. 4989 ff.

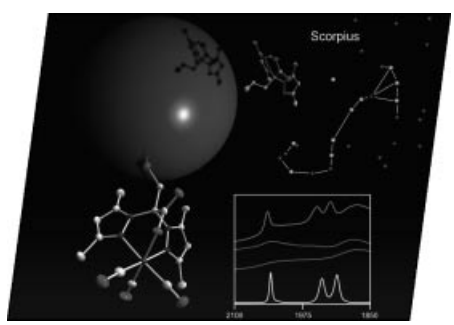


## MICROREVIEW

Contents

**4963** **N. Guillou,* C. Livage, G. Férey**

Cobalt and Nickel Oxide Architectures in Metal Carboxylate Frameworks: From Coordination Polymers to 3D Inorganic Skeletons

**Keywords:** Cobalt / Nickel / Organic–inorganic hybrids / Solvothermal synthesis / Microporous materials

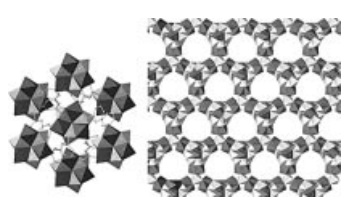

 © 2006 Wiley-VCH Verlag GmbH & Co. KGaA, Weinheim 

# SHORT COMMUNICATIONS


**4979** **C. S. Chin,* M.-S. Eum, S. y. Kim, C. Kim, S. K. Kang**

New Type of Photoluminescent Iridium Complex: Novel Synthetic Route for Cationic *trans*-Bis(2-phenylpyridinato)iridium(III) Complex

**Keywords:** Isomerization / Iridium / Photoluminescence / Synthetic methods / Bis(ppy) complex


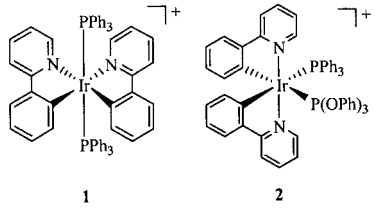



**4983** **M. A. Carreon,* V. V. Guliants,* L. Yuan, A. R. Hughett, A. Dozier, G. A. Seisenbaeva, V. G. Kessler**

Mesoporous Nanocrystalline Mixed Metal Oxides from Heterometallic Alkoxide Precursors: Cobalt−Nickel Oxide Spinels for Propane Oxidation

**Keywords:** Mesoporous Co−Ni oxides / Oligomeric surfactants / Nanocrystalline spinels / Thermal stability / Hydrocarbon combustion


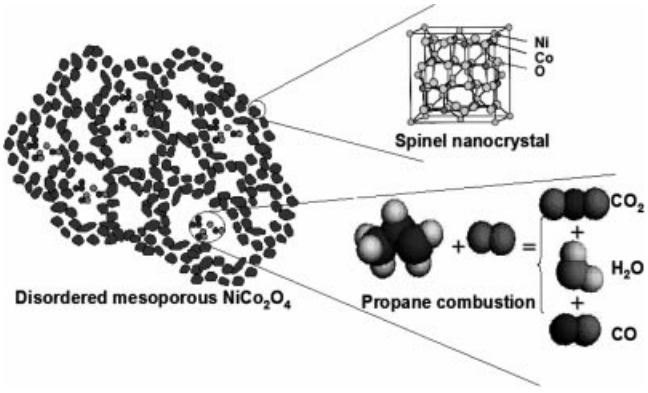


# FULL PAPERS


**4989** **E. Hübner, T. Haas, N. Burzlaff***

Synthesis and Transition Metal Complexes of Novel *N*,*N*,*O* Scorpionate Ligands Suitable for Solid Phase Immobilisation

**Keywords:** Solid phase / Immobilisation / Tripodal ligands / *N*,*N*,*O* ligands / Tricarbonyl complexes


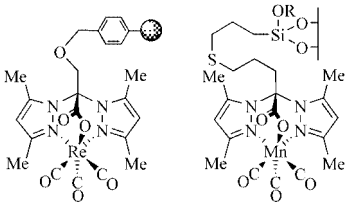



**4998** **H.-W. Lerner,* M. Bolte, K. Schurz, N. Wiberg, G. Baum, D. Fenske, J. W. Bats, M. Wagner**

Chemical and Structural Features of $NMe_2Et$ Adducts of the Silanimines $Me_2Si{=}NSitBu_3$ and $tBu_2Si{=}NSiCltBu_2$

**Keywords:** Silanimines / Amines / Donor adduct / Wittig reaction / Stevens rearrangement


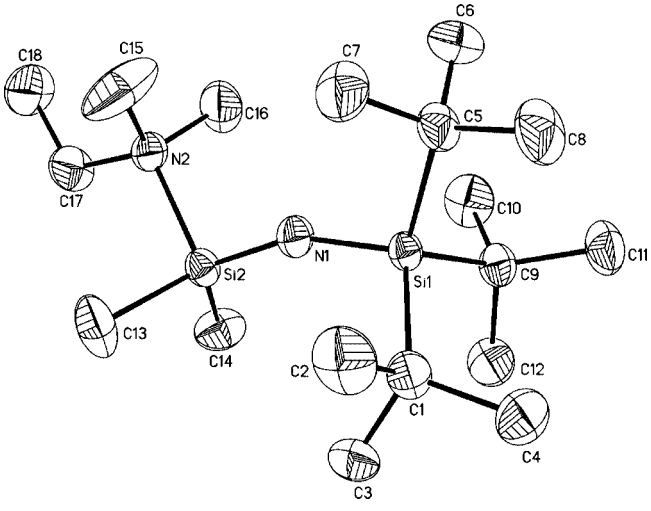

**5006** **H. Fukumoto, K. Mashima***

π-Conjugated α,ω-Diphenylpolyene Complexes of RuClCp* Fragment(s) in $\eta^4$-*s*-*cis* Conformation

**Keywords:** π-Conjugated polyenes / Coordination modes / Fluxionality / Multinuclear complexes / Ruthenium

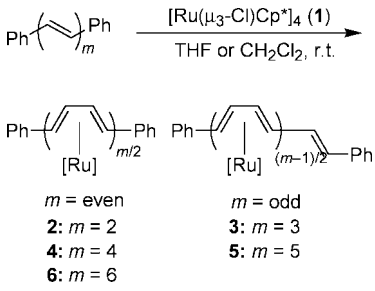


**5012** **M. Nomura, M. Geoffroy, P. Adkine, M. Fourmigué***

Neutral, Radical [CpNi(dithiolene)] Complexes with Flexible, Nonplanar Seven-Membered Rings: [CpNi{$S_2C_2S_2(CH_2)_2X$}] (X = $CH_2$, $CF_2$, C=$CH_2$, S, C=O)

**Keywords:** Nickel / S ligands / Radicals / Metallacycles / Magnetic properties

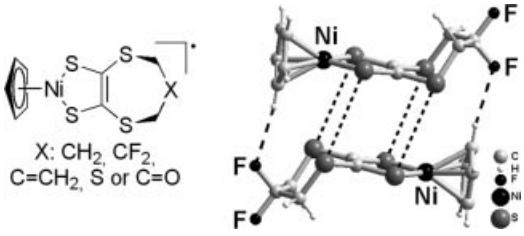


**5022** **H. P. Gupta, M. S. Kumar, S. Upreti, A. J. Elias***

Synthesis of Methyl Metallocenecarboxylates [{$\eta^4$-$Ph_{4-n}(SiMe_3)_nC_4$}Co{$\eta^5$-$MeOC(O)C_5H_4$}] (*n* = 1, 2) and Their Desilylation Reactions: Structural Studies and Conversion to Metallocenecarboxylic Acids and Their Alcohol Derivatives

**Keywords:** Cobalt / Alkynes / Desilylation / Metallocenes / Carboxylic acids

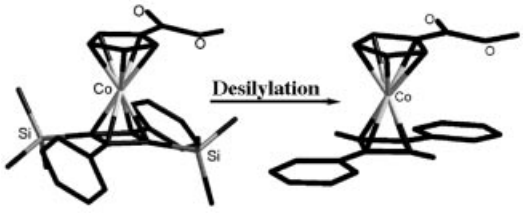


**5033** **M. F. Anderlund, J. Högblom, W. Shi, P. Huang, L. Eriksson, H. Weihe, S. Styring, B. Åkermark, R. Lomoth,* A. Magnuson***

Redox Chemistry of a Dimanganese(II,III) Complex with an Unsymmetric Ligand: Water Binding, Deprotonation and Accumulative Light-Induced Oxidation

**Keywords:** Manganese / Bioinorganic chemistry / Ligand exchange / EPR spectroscopy / IR spectroscopy

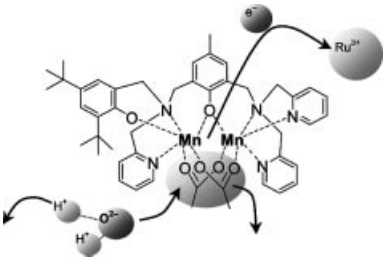


**5048** **L. Weber,* J. Förster, H.-G. Stammler, B. Neumann**

Contribution to the Reactivity of *N*,*N*′-Diaryl-1,4-diazabutadienes Aryl−N=CH−CH=N−Aryl (Aryl = 2,6-Dimethylphenyl; 2,4,6-Trimethylphenyl) Towards Boron Trichloride

**Keywords:** Diazabutadienes / Diazaboroles / Aminoboranes / Structures / Boron

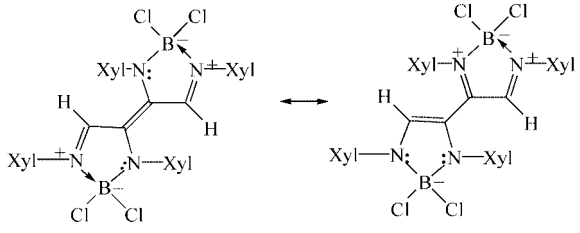


 © 2006 Wiley-VCH Verlag GmbH & Co. KGaA, Weinheim 

**5057** **V. A. de la Peña O'Shea,* M. C. Álvarez-Galván, J. M. Campos-Martin, N. N. Menéndez, J. D. Tornero, J. L. G. Fierro***

Surface and Structural Features of Co-Fe Oxide Nanoparticles Deposited on a Silica Substrate

**Keywords:** Cobalt / Iron / Oxides / Metal−metal interactions / Materials science

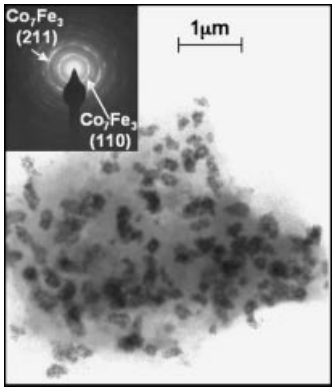


**5069** **I. Nowik,* R. H. Herber**

Computational Determination of Iron Hyperfine Interactions in Organometallics Using Small Transverse External Magnetic Fields

**Keywords:** Mössbauer spectroscopy / Metallocenes / Quadrupole splitting / Magnetic hyperfine field / External magnetic field perturbation / Iron

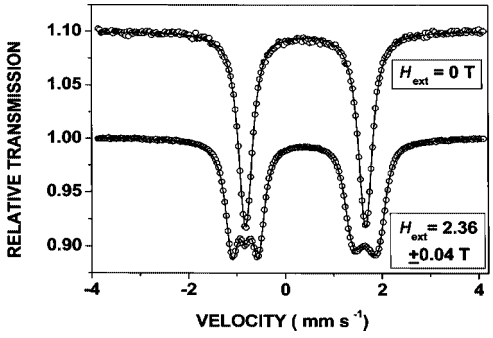


**5076** **Y. Canac, G. E. Aniol, S. Conejero, B. Donnadieu, G. Bertrand***

A Facile Synthesis of Carbamoylsilanes, -boranes and -phosphane Oxides − Isolation of the First Uncomplexed Carbamoylborane

**Keywords:** Carbenes / Rearrangement / Boron / Silicon

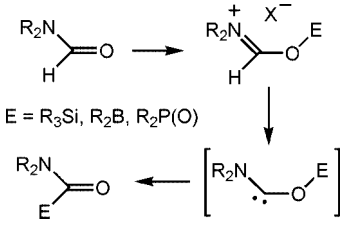


**5081** **F. Liang, H. W. Schmalle, H. Berke***

μ-Coordination Chemistry of NO Ligands: Adducts of *trans*-Mo(dmpe)$_2$(Cl)(NO) with Lithium Salts

**Keywords:** Coordination polymers / Bridging ligands / Phosphane ligands / Lithium / Molybdenum

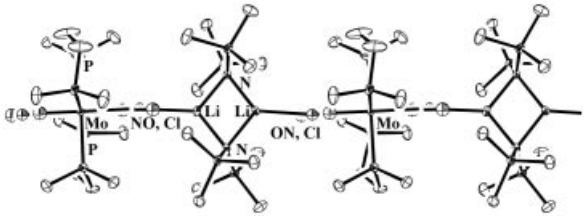


**5089** **U. Patel, H. B. Singh,* R. J. Butcher**

Synthesis and Characterization of Some New 22-Membered Chalcogenoaza Macrocycles and Their Co$^{II}$ and Ni$^{II}$ Complexes

**Keywords:** Cobalt / Magnetic properties / N ligands / Selenium / Tellurium

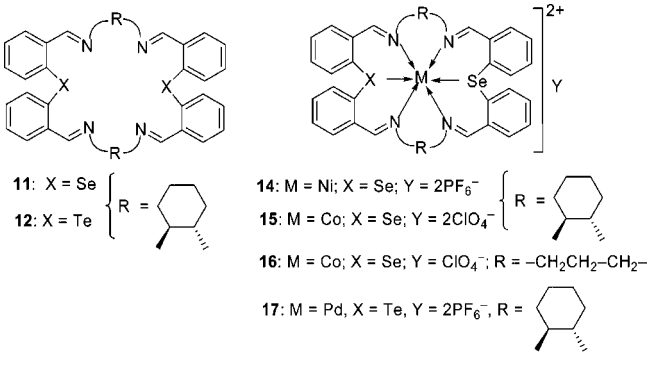


 © 2006 Wiley-VCH Verlag GmbH & Co. KGaA, Weinheim 

**5098** **E. Madej, A. Katafias,* P. Kita,* J. Eriksen, O. Mønsted***

Kinetics and Mechanism of Ligand Substitution in Some Chromium(III) Tetraaza Macrocyclic Complexes in Acidic Media: Differences in Reactivity Between *cis* and *trans* Isomers

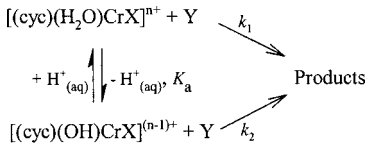


**Keywords:** Chromium / Structure−activity relationships / Ligand substitution / Macrocyclic complexes / Kinetics

**5106** **M. Gómez,* P. Gómez-Sal, J. M. Hernández**

New Bis(silyl)cyclopentadienidoniobium and -tantalum Complexes: X-ray Crystal Structures of [NbCp^Cl$_4$] and [NbCp^Cl$_4$(CNAr)] [Cp^ = $\eta^5$-C$_5$H$_3$(SiClMe$_2$)(SiMe$_3$); Ar = 2,6-Me$_2$C$_6$H$_3$]

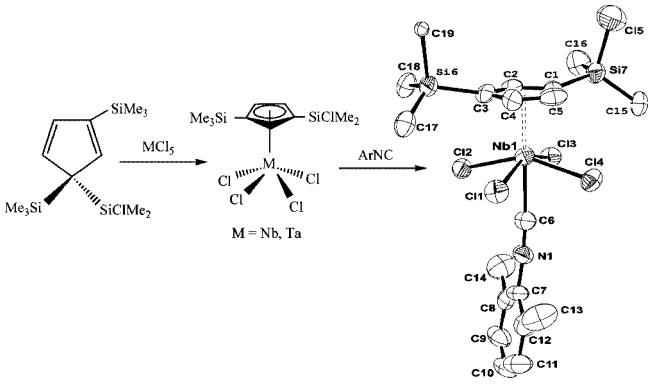


**Keywords:** Niobium / Tantalum / Cyclopentadienyl complexes

**5115** **E. Aznar, S. Ferrer,* J. Borrás, F. Lloret, M. Liu-González, H. Rodríguez-Prieto, S. García-Granda**

Coordinative Versatility of Guanazole [3,5-Diamino-1,2,4-triazole]: Synthesis, Crystal Structure, EPR, and Magnetic Properties of a Dinuclear and a Linear Trinuclear Copper(II) Complex Containing Small Bridges and Triazole Ligands

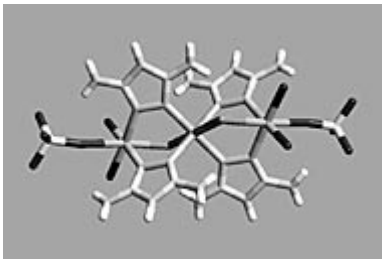

**Keywords:** Copper / 1,2,4-Triazole ligands / Polynuclear compounds / X-ray structures / Magnetic properties

**5126** **L.-K. Yan, Z. Dou, W. Guan, S.-Q. Shi, Z.-M. Su***

A DFT Study on the Electronic and Redox Properties of [PW$_{11}$O$_{39}$(ReN)]$^{n-}$ ($n$ = 3, 4, 5) and [PW$_{11}$O$_{39}$(OsN)]$^{2-}$

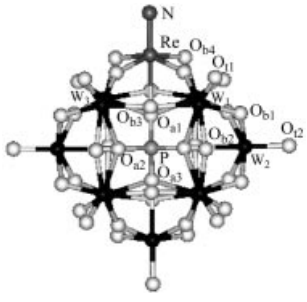


**Keywords:** Electronic properties / DFT / Nitrido-functionalized / Polyoxometalates / Redox properties

**5130** **L.-P. Sun, S.-Y. Niu,* J. Jin, G.-D. Yang, L. Ye**

Synthesis, Structure and Surface Photovoltage of a Series of Ni$^{II}$ Coordination Polymers

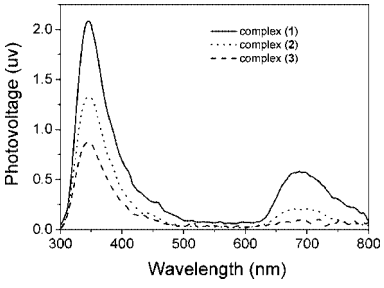


**Keywords:** Coordination polymers / Nickel / Hydrogen bonds / Surface photovoltage spectroscopy

 © 2006 Wiley-VCH Verlag GmbH & Co. KGaA, Weinheim 

**5138** **F. Dornhaus, M. Bolte, H.-W. Lerner, M. Wagner***

A Comparative Study of Chalcogenated Phosphanylborohydrides $[EPR_2BH_3]^-$ (R = Ph, *t*Bu) and Triorganophosphane Chalcogenides $EPPh_2CH_3$ (E = O, S, Se, Te)

**Keywords:** P ligands / Boranes / Ligand design / Chalcogens / Isoelectronic analogues

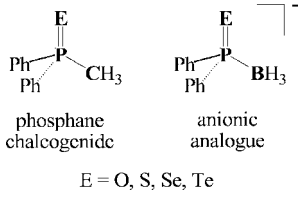


**5148** **J. Guadalupe Lopez Cortes, O. Ramon, S. Vincendeau, D. Serra, F. Lamy, J.-C. Daran, E. Manoury,* M. Gouygou***

New Chiral Ferrocene-Bridged Phosphole–Phosphane Ligands

**Keywords:** Ferrocenes / Phospholes / P,P ligands / Asymmetric catalysis / X-ray diffraction

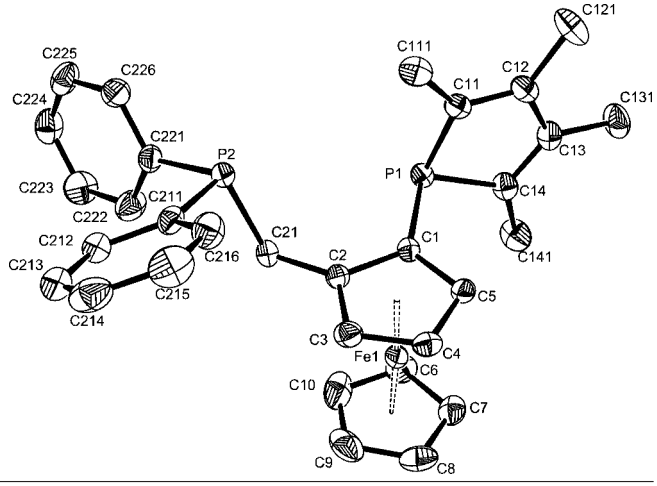


**5158** **T. Tekeste, H. Vahrenkamp***

"Inhibition" of the Enzyme Model $Tp^{Ph,Me}Zn$–OH by Diketo Compounds

**Keywords:** Zinc / Bioinorganic chemistry / Enzyme inhibition / Diketo compounds

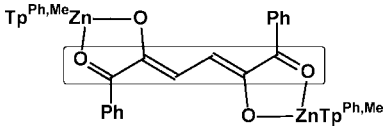


**5165** **Index 2006**

*The editorial staff and the publishers thank all readers, authors, referees, and advertisers for their interest and support over the past year and wish them all a happy new year.*

 © 2006 Wiley-VCH Verlag GmbH & Co. KGaA, Weinheim 

DOI: 10.1002/ejic.200600663

# Cobalt and Nickel Oxide Architectures in Metal Carboxylate Frameworks: From Coordination Polymers to 3D Inorganic Skeletons

**Nathalie Guillou,*[a] Carine Livage,[a] and Gérard Férey[a]**

**Keywords:** Cobalt / Nickel / Organic–inorganic hybrids / Solvothermal synthesis / Microporous materials

This microreview is devoted to the synthesis and properties of nickel and cobalt polycarboxylates, which are classified in terms of the geometries of the organic moieties. It is divided into three main sections — dicarboxylates, tricarboxylates and tetra- and hexacarboxylates — and discusses the extreme diversity of these architectures. Numerous topologies can be obtained, ranging from coordination polymers to 3D inorganic skeletons. This microreview begins with the widely studied cobalt succinate system, for which, to date, seven compounds have been reported. Then, examples from malonate to pimelate illustrate the influence of the length of the organic ligand, whereas examples from fumarate to diphenate illustrate the effects of rigidity and complexity. In the same way, examples from trimesate to mellitate show the effects of "multiconnecting" organic partners. These latter seem to disadvantage metal oxide condensation, since the two 3D inorganic frameworks contain linear dicarboxylate ions. On the other hand, 3D nickel oxide skeletons seem to be easier to synthesise than cobalt ones. Moreover, under similar hydrothermal conditions, using cobalt and nickel generally leads to different architectures.

(© Wiley-VCH Verlag GmbH & Co. KGaA, 69451 Weinheim, Germany, 2006)

## Introduction

The wide utility of zeolites in the domains of catalysis, gas separation and ion-exchange has provoked widespread interest in new families of nanoporous materials.[1] Moreover, the opportunity to combine the exciting functionality of transition metal compounds, such as magnetic, electronic conductivity and optical properties, with the porosity of zeolites has become very attractive.[2] The first examples of 3D open frameworks incorporating transition metals were alumino- and gallophosphates substituted by metal ions in the skeleton; those based on cobalt were found to be some of the most promising catalysts.[3] Pure 3D metal phosphates were then synthesised and our first investigations with nickel showed that it could generate microporous materials with novel 3D M–O–M connectivities with face-, edge- and/or corner-sharing polyhedra that present interesting catalytic properties and good thermal stability.[4] The use of phosphate usually reduces electronic interactions and the preparation technique is, most of the time, a limiting factor for obtaining large pores. Indeed, metal phosphates are usually obtained by a templating method, therefore the removal of organic cationic templates generally leads to the collapse of the network. New synthetic approaches avoiding templating agents were therefore developed, with the use of donor ligands that can be part of the framework.[2] In this respect, the ability of carboxylates to strongly connect cobalt and nickel is very fruitful for building new architectures and often leads to a readily accessible porosity as well as physical properties that are usually encountered in dense solids.

The aim of this microreview is to focus on the structural variety and properties of nickel and cobalt polycarboxylates. The diversity of these organic partners offers a great potential to modulate structural architectures and the use of hydrothermal conditions considerably enlarges the range of possible arrangements arising from a metal and an organic molecule. Moreover, the electronic properties of cobalt and nickel significantly extend the potential applications of this type of compounds, especially in the field of porous magnetic materials. Although their ionic radii are similar, nickel and cobalt generally form different architectures. For $Ni^{2+}$ ($d^7$) the ligand-field stabilisation energies strongly favour octahedral coordination, whereas for $Co^{2+}$ ($d^8$) the tetrahedral environment is less disadvantaged.

The field of porous hybrid solids is very topical and is, of course, much wider. The use of oxalate, monocarboxylates or other organic linkers containing N-donor ligands (solely or in addition to carboxylates) will not be tackled here. For an overall overview of porous hybrid materials, we refer the reader to the reviews of Rao et al.,[5] which is devoted to metal carboxylates with open architectures, and of Kitagawa et al.,[6] which deals with functional porous coordination polymers.

The carboxylates presented in this review are classified in terms of the geometries of the organic partners. The first

[a] Institut Lavoisier, UMR CNRS 8180, Université de Versailles St-Quentin-en-Yvelines,
45 Avenue des Etats-Unis, 78035 Versailles, France
E-mail: nathalie.guillou@uvsq.fr

 © 2006 Wiley-VCH Verlag GmbH & Co. KGaA, Weinheim 

section is devoted to dicarboxylates and begins with the widely explored succinates. The influence of length, rigidity and complexity of the organic moieties is then presented. The second and the third parts are devoted to tricarboxylates and tetra- and hexacarboxylates, respectively.

## Dicarboxylates

### The Case of Succinate

The best characterised system of transition metal polycarboxylates is the cobalt succinate family. Altogether, seven phases containing cobalt, succinate, water and hydroxide have been discovered, mainly by varying the reaction temperature. The first of the series, $[Co(H_2O)_4(C_4H_4O_4)]$ (**1**), which is obtained at room temperature, was first identified in the Sixties[7] and is constructed from chains of cobalt octahedra bridged by succinate ions.[8] Upon increasing the temperature, inorganic condensation occurs to form edge-sharing octahedral trimers linked by carboxylates into the one-dimensional polymer $[Co(H_2O)_2(C_4H_4O_4)]$ (**2**).[9] A higher degree of condensation occurs under hydrothermal conditions, leading to the formation of open networks with extended M–O–M connectivity. $[Co_5(OH)_2(C_4H_4O_4)_4]$ (MIL-9, **3**), synthesised by Livage et al.,[10] is a nice example of a 2D metal oxide framework pillared by an organic moiety in a 3D coordination polymer. It is constructed from zig-zag layers of edge-sharing cobalt octahedra that generate 12-membered ring cavities with a lozenge shape (Figure 1, a). Half of the succinates are localised within the windows and the other half act as bridges between the sheets. In a more dilute medium, $[Co_4(OH)_2(H_2O)_2(C_4H_4O_4)_3{\cdot}2H_2O]$ (MIL-16, **4**) is formed.[11] It contains a 2D oxide network with 14-membered ring windows (Figure 1, b) and can easily be described as parallel "helicoidal" chains (light grey) connected by tetrameric units of co-planar octahedra (dark grey). Occluded and coordinated water can be removed from this compound in a reversible process. $[Co_6(OH)_2(C_4H_4O_4)_5{\cdot}H_2O]$ (**5**), synthesised by Long et al., is three-dimensional.[12] It presents layers similar to those of MIL-16 with the same helicoidal chains (light grey) but with the tetramers being replaced by dimers of edge-sharing square pyramids (dark grey, Figure 1, c). Four deprotonated succinates are located around the layers, although only one acts as a pillar. The originality of this compound lies in the presence of penta- and hexacoordinate metal centres, which are rather rare in the family of cobalt carboxylates. Forster et al. have recently demonstrated that these five compounds, and also **8**, which was previously obtained with nickel and is described below, can be obtained from the same starting mixture simply by varying the temperature.[9,13] The overall dimensionality of the materials, as well as the degree of M–O–M condensation, increases with temperature. The compounds present chains up to 125 °C, then the inorganic skeleton is two-dimensional, and above 190 °C a 3D overall dimensionality is observed (see Figure 2).[13]

Changing the solvent to a methanol/water mixture, at room temperature, leads to $[Co_3(OH)_2(H_2O)_4(C_4H_4O_4)_2{\cdot}6H_2O]$ (**6**).[14] This hybrid presents an interesting architec

*Nathalie Guillou studied Materials Sciences in Brittany at the University of Rennes, where she obtained her PhD in Chemistry in 1994 under the supervision of Daniel Louër in the "Powder Crystallography and Reactivity of solids" group. She worked on cerium nitrates as precursors of nanocrystalline oxides. In 1995 she joined the Technical University of Darmstadt, as a postdoctoral research fellow, to work on nanostructured materials. Since October 1996, she has held a permanent position as Chargée de Recherche CNRS at the Institut Lavoisier of Versailles. Her current research interests focus on hybrid organic–inorganic porous materials and their structural determination by powder X-ray diffraction.*

*Carine Livage studied chemistry in the University of Orsay (Paris XI) and received her Ph.D. degree in 1991 working on the synthesis of molecular conductors and their characterisation under the supervision of Dr. Patrick Batail in the Laboratoire de physique des solides. (1991–1993). She undertook postdoctoral research in the group of Professor Lisa Klein in the Department of Ceramics of Rutgers University (New Jersey, USA) on the solution syntheses of ferroelectric thin films. She joined the Department of Chemistry of the University of Versailles in 1993 as an associate professor. Her field of research is mainly directed toward the synthesis and characterisation of porous transition metal hybrids.*

*Gérard Férey was born in Normandy, France, in 1941. After education in Caen, he became Professor at Le Mans University and moved to Versailles in 1996 to create the Institut Lavoisier. After a long period dedicated to magnetic inorganic fluorides, he is currently interested in the field of inorganic and hybrid porous solids in which he develops a global approach to these phases, from synthesis to applications through the mechanisms of reaction and prediction of structures. He is now Professor at the Institut Universitaire de France and member of the French Academy of Sciences.*

 © 2006 Wiley-VCH Verlag GmbH & Co. KGaA, Weinheim 

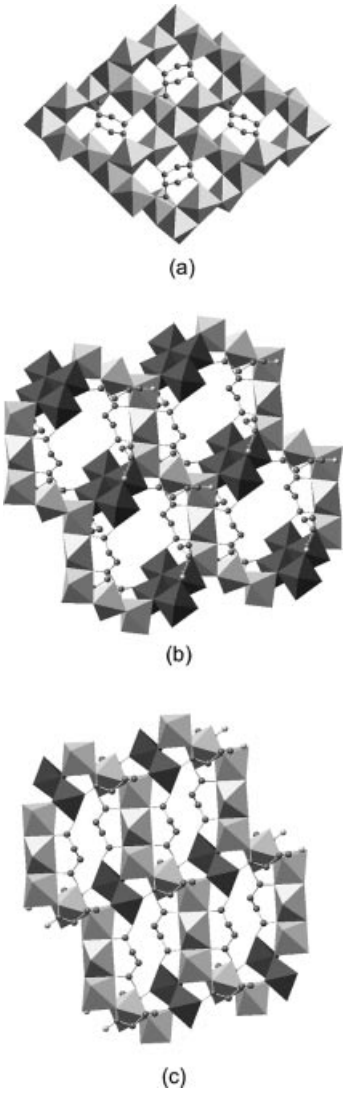


Figure 1. (a) Polyhedral representation of the 12-membered ring cavities lined by organic moieties in MIL-9 (**3**); (b) polyhedral view of MIL-16 (**4**) showing the connectivity between cobalt octahedra within the tetrameric unit (dark grey) and the helicoidal chain (light grey); (c) polyhedral view of **5** showing the connectivity between dimers of square pyramids (dark grey) and the helicoidal chain (light grey).

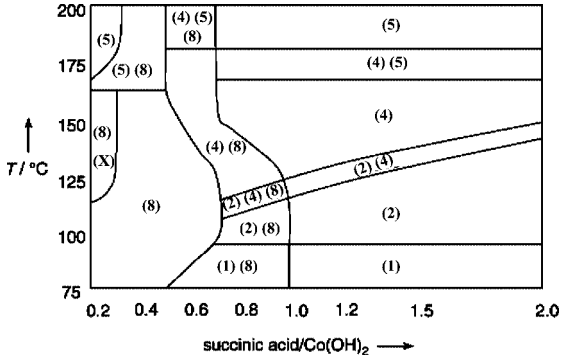


Figure 2. Crystallisation diagram in the succinate system (reproduced with permission from A. K. Cheetham[13]). The phases are indicated by their number code. The phase labelled X is still unknown.

ture that is often encountered with rigid linkers. Its structure can be described as metal oxide chains linked by the organic moiety into a 3D architecture with lozenge-shaped tunnels (see Figure 7). This topology bears a striking resemblance to a vanadium terephthalate isolated by Barthelet et al.[15]

As shown by these few examples, metal organic frameworks obtained with cobalt often exhibit interesting open architectures, although metal oxide condensation is most of the time "classical" with edge- or corner-sharing polyhedra. The architectures obtained hydrothermally with nickel, even though its radius and electronegativity are nearly identical to those of cobalt, are often different and the inorganic condensation more diverse. To date, two nickel succinate compounds have been described. Forster and Cheetham obtained the first metal carboxylate to present a three-dimensional oxide network, namely $[Ni_7(OH)_2(C_4H_4O_4)_6(H_2O)_2 \cdot 2H_2O]$ (**7**).[16] Its structure can be described as layers of edge-sharing octahedra constructed from circular 12-rings surrounded by six truncated triangular 15-rings (Figure 3, a). The three-dimensionality is ensured by "isolated" corner-sharing octahedra (dark grey in the inset of Figure 3, a). This arrangement leads to a remarkable honeycomb framework with 1D pores lined by succinate anions. $[Ni_7(OH)_6(C_4H_4O_4)_4(H_2O)_3 \cdot 7H_2O]$ (MIL-73, **8**), which is obtained under similar synthetic conditions, presents hybrid layers constructed from corrugated chains of nickel oxide connected by succinate ions (Figure 3, b).[17] The inorganic chains are made from hexanuclear metallic octahedral units (light grey) connected by a seventh octahedron (dark grey).

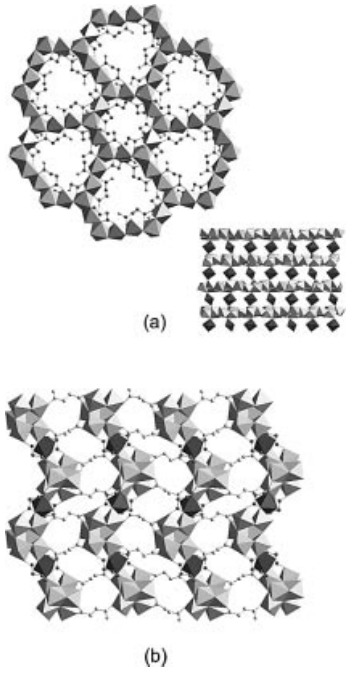


Figure 3. (a) View of a single nickel oxide layer in **7**; connection of the layers through isolated corner-sharing octahedra (dark grey) is shown in the inset; (b) view of one hybrid layer of **8**, where hexanickel units (light grey) are connected to bridging Ni octahedra (dark grey). Decorating succinate ions are represented in dark grey and bridging ones in light grey.

 © 2006 Wiley-VCH Verlag GmbH & Co. KGaA, Weinheim 

This hexameric unit is unusual and is built up from a dimer of face-sharing octahedra grafted onto a tetramer formed by two edge-sharing dimers connected by their corners. A pseudo-3D framework is formed due to the presence of strong hydrogen bonds between adjacent layers. This arrangement presents hydrated channels, where water molecules can be easily removed and reabsorbed. An isostructural phase has recently been obtained with cobalt using high-throughput synthesis.[18] Its structure, as determined by X-ray single crystal diffraction, confirmed the accuracy of the ab initio structural investigation of the nickel analogue, in spite of its high complexity due to the large number of independent atoms.

### Changing the Length of the Aliphatic Chain

The reaction of malonic acid with transition metal ions has been reported, but most of the time in the presence of an additional co-ligand such as 2,2′-bipyrimidine.[19] One 2D cobalt malonate, **9**, which is isostructural with a nickel compound, has been obtained by Delgado et al.[20] Its structure consists of "isolated" metal octahedra connected through bridging carboxylate groups to four other metal centres (see Figure 4) to form layers with a pseudo square geometry.

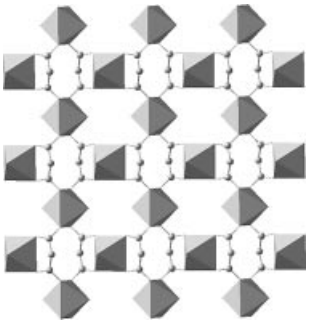

Figure 4. View of a layer of **9** showing the interconnection of metal octahedra through malonate ions.

Two compounds have been reported with glutaric acid: one with cobalt and the other with nickel. $[Co(C_5H_6O_4)]$ (**10**), reported by Lee et al.,[21] is a 3D coordination polymer constructed from cobalt tetrahedra linked by glutarate anions. Its topology will be described below (Figure 6, b) with that of its pimelic acid analogue MIL-36.[26] Cubic $[Ni_{20}(H_2O)_8(C_5H_6O_4)_{20}\cdot 40H_2O]$ (MIL-77, **11**), reported by us, presents an amazing chiral three-dimensional metal oxide network.[22] Its skeleton can be described as helices of edge-sharing octahedra connected to four parallel neighbouring ones through a nickel octahedron (dark grey in Figure 5, a). This induces the formation of perpendicular helices and generates corrugated 20-membered rings (Figure 5, b), which intersect to construct very large crossing tunnels in the [111] direction (Figure 5, c). The oxide framework is walled by two independent glutarate anions: the first one (light grey) is located on the twofold axis and the second one (dark grey) on the threefold one, with a statistical occupancy of 2/3. The nickel environments present bridging water molecules, and the tunnels contain disordered water molecules which can easily be removed by heating, leading to a porous compound (346 $m^2 g^{-1}$). MIL-77 is also a pure ferromagnet at low temperature. More recently, the adaptability of this 3D inorganic skeleton has been proved by obtaining the same topology with 3-methylglutaric acid.[23] The main difference between MIL-77 and this compound is the position of the second organic molecule. Unfortunately, this has drastic consequences for the porosity — its surface area is about half that of MIL-77.

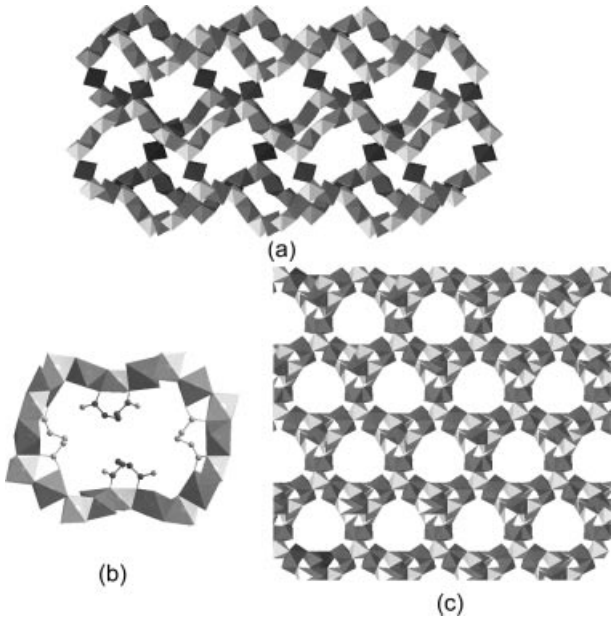


Figure 5. Views of the structure of MIL-77 (**11**): (a) view of six helices connected by nickel octahedra (dark grey); (b) polyhedral view of a corrugated 20- membered ring with the two independent glutarate ions; (c) view of the nickel oxide tunnels down [111].

Two compounds are obtained at room temperature upon increasing the aliphatic chain length by one carbon: $[Ni(H_2O)_4(C_6H_8O_4)]$ (**12**),[24] which presents a 1D metal-organic chain and layered $[Co_2(H_2O)_6(C_6H_8O_4)_2\cdot 4H_2O]$ (**13**).[25] The latter is constructed from corner-sharing octahedral chains where $Co(H_2O)_6$ shares its *trans*-$H_2O$ molecules with two neighbouring $[CoO_4(H_2O)_2]$ polyhedra (Figure 6, a). These chains are connected by adipates to generate the 2D open network.

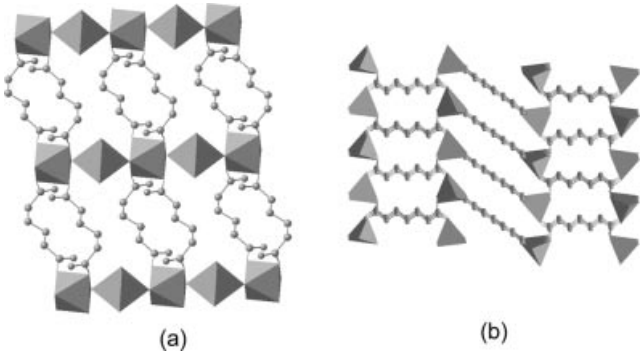


Figure 6. (a) View of a layer of **13** showing inorganic chains bound by adipate ions; (b) view of the 3D coordination polymer MIL-36 (**14**).

 © 2006 Wiley-VCH Verlag GmbH & Co. KGaA, Weinheim 

With pimelic acid, only $[Co(C_7H_{10}O_4)]$ (MIL-36, **14**) has been reported in the literature.[26] It is a 3D coordination polymer built up from cobalt tetrahedra where Co–$CO_2$–Co linkages give rise to infinite two-dimensional networks linked by the aliphatic chains. Therefore, hydrophobic carbon chains form the "walls" of two types of channels and act as spacers to generate an open structure (Figure 6, b). This type of arrangement has also been observed with adipate linkers.[27]

### Using Unsaturated Chains

The use of fumaric acid leads to the formation of $[M_3(OH)_2(H_2O)_4(C_4H_2O_4)_2{\cdot}2H_2O]$ (**15**) with both cobalt and nickel, but with totally different synthetic procedures: the nickel compound was obtained under hydrothermal conditions[28] whereas its cobalt analogue was synthesised at 50 °C.[29] Their structure consists of chains of metal octahedra connected by fumarate ions to form a 3D framework (Figure 7). A remarkable feature is the presence of perpendicular intersecting tunnels. These have a large lozenge shape down the *a* axis and are delineated by four walls of fumarate-linked nickel oxide chains (Figure 7, a). The tunnels down the *b* axis are delimited by the space between two fumarate pillars (Figure 7, b). The repeating structural motif in the metal oxide chain is a trimer consisting of two edge-sharing octahedra linked by a $\mu_3$-OH to a vertex of a third one (Figure 7, c). The carboxylic functions are bidentate and bridge successive metal atoms of the chains. It is interesting to note that the same topology can also be obtained with succinic acid.[14] The main difference concerns the aperture of the lozenge tunnels, which is more open in the case of the succinate. The cavity located at the intersection of the two perpendicular tunnels contains one water molecule for the fumarate and three for the succinate. Two other 1D compounds have been synthesised by Konar et al. simultaneously in the same batch: *cis*-$[Co(H_2O)_4(C_4H_2O_4){\cdot}2H_2O]$ (**16**) and *trans*-$[Co(H_2O)_4(C_4H_2O_4)]$ (**17**).[30] Both structures are built up from isolated cobalt octahedra linked by carboxylate in a bis-monodendate fashion. With acetylenedicarboxylic acid, only $[M(H_2O)_4(C_4O_4){\cdot}2H_2O]$ (**18**) (M = Co, Ni) has been described.[31] Heating it to 100 °C leads to $[M(H_2O)_2(C_4O_4)]$ (**19**). This latter solid presents a metal organic framework where octahedra are connected by dicarboxylate ligands into a compact 3D network.

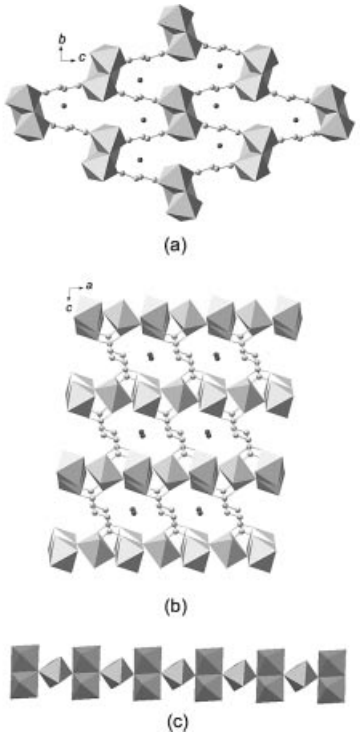


Figure 7. (a) View of the structure of **15** along *a* showing the lozenge-shaped tunnel topology; (b) view of the tunnels of **15** along the *b* axis; (c) the inorganic chain encountered in **6** and **15**.

### Using Carboxylates Containing One Cycle

Two 3D compounds, namely $[Co_2(OH)_2(1,4\text{-BDC})]$ (**20**)[32,33] and $[Co(H_2O)_2(1,4\text{-BDC})]$ (**21**)[33] have been isolated with 1,4-benzenedicarboxylic acid (1,4-$H_2$BDC; also known as terephthalic acid). Compound **20** is built up from inorganic layers where two types of parallel tilted chains of edge-sharing octahedra are linked by OH bridges (Figure 8, a). The cobalt atoms of the light-grey chain are surrounded in the equatorial plane by four terephthalate oxygen atoms and in the apical positions by two OH groups, whereas those of the dark-grey chain are coordinated to four OH groups in the equatorial plane and two carboxylate oxygens. The layers are then connected together through terephthalate into a 3D architecture. The second coordination polymer, **21**, was obtained hydrothermally. Its structure

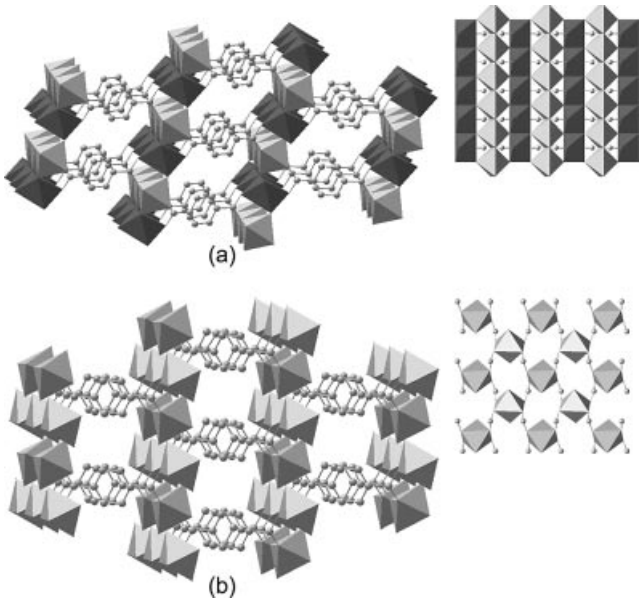


Figure 8. (a) Polyhedral view of the structure of **20** constructed from cobalt hydroxide layers (shown as inset) pillared by terephthalate ions; (b) polyhedral representation of the coordination polymer **21** with layers of a pseudo square symmetry shown as the inset.

 © 2006 Wiley-VCH Verlag GmbH & Co. KGaA, Weinheim 

presents isolated cobalt octahedra bridged by carboxylates into layers with a pseudo square symmetry (Figure 8, b). As for **20**, these layers are connected through terephthalate into a 3D network.

With 1,3-benzenedicarboxylic acid (1,3-$H_2$BDC; isophthalic acid) only one compound, namely [$Na_3${$Co_6O$(OH)(1,3-BDC)$_6$}·$H_2O$] (MIL-104, **22**), has been reported.[34] Its structure is constructed from an unprecedented hexanuclear octahedral "cluster". The hexameric cobalt unit may be viewed as the association of two trimers connected through six $\mu_2$-O vertices, each trimer being composed of octahedra sharing a central $\mu_3$-O atom (Figure 9, a). The octahedra are highly distorted due to the chelating mode of one of the carboxylate groups. Indeed, the "bite" of the rigid acid group is too short for a cobalt octahedral coordination, therefore the angle is very narrow and Co–O distances are longer than usual. The architecture is a classical metal organic framework (MOF), with each hexamer joined by isophthalate ions to six neighbouring ones and serving as an octahedral node of a cuboid net (Figure 9, b). The small cavities left free by the hexamer packing are occupied by sodium cations. Each hexanuclear cluster is connected to six sodium ions to form a larger "super octahedron". In terms of "scale chemistry",[35] the topology is the same as that found for $ReO_3$, with {$Na_6Co_6O_{26}$} units as giant octahedra.

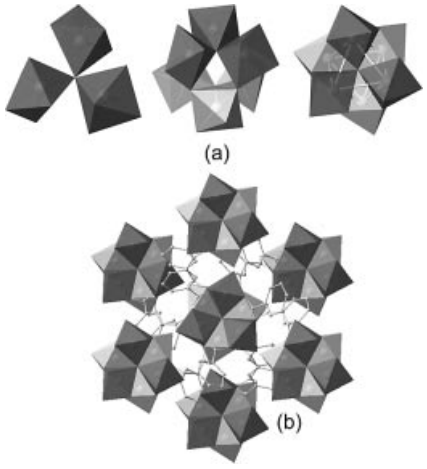


Figure 9. (a) Schematic representation of the hexameric unit of MIL-104 (**22**) showing its octahedral geometry; (b) projection of the structure showing the connection of one unit to six neighbouring ones that lie at the corners of an octahedron.

[$Co_3(OH)_2(C_8H_4O_4)_2$] (**23**) has been obtained hydrothermally with phthalic acid.[36] Its 2D structure consists of inorganic layers of edge-sharing octahedra which generate eight-membered ring cavities (Figure 10). Phthalate ions are grafted onto the layers within the window and organic part is localised up and down the inorganic layer.

One cobalt compound [$Co(C_8H_8O_4)$], (**24**) has been reported with 4-cyclohexene-1,2-dicarboxylic acid.[37] The originality of its structure lies in the tetrahedral coordination of the metal, which is less common than octahedral

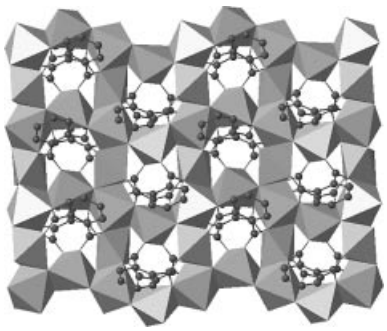

Figure 10. Polyhedral representation of **23** showing the eight-membered ring cavities lined by organic moieties.

under hydrothermal conditions. It is interesting to note that the starting material was the *cis* form of the dicarboxylic acid whereas the resulting compound presents the *trans* one. Such changes are not unusual under hydrothermal conditions.[38] The structure is formed from isolated distorted tetrahedra linked by carboxylates into layers (see Figure 11). Two facing tetrahedra are first doubly bridged by carboxylates to form dimers, which are then bridged by the second carboxylate function to construct ribbons. These chains are connected through the organic moiety into a 2D network. As for the phthalate compound, the organic moiety is localised on the surface of the layer. As shown by these two last examples, the presence of a hydrophobic region opposite the carboxylate groups favours lamellar systems.

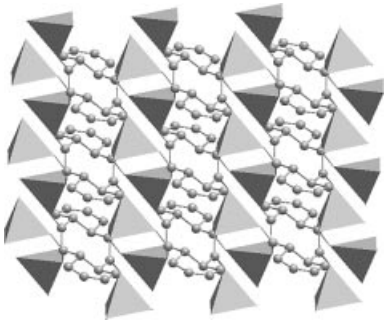

Figure 11. View of a layer of **24** showing the connection of cobalt tetrahedra by organic moieties.

The compound [$Co_5(OH)_8$(CHDC)·$4H_2O$] (**25**) has been synthesised hydrothermally from 1,4-cyclohexanedicarboxylic acid ($H_2$CHDC).[39] Although the starting material was a mixture of *cis* and *trans* $H_2$CHDC, this compound is formed only with the *trans* conformation. Its structure is based on metal–hydroxide octahedral–tetrahedral layers pillared by dicarboxylate ions. These layers are closely related to the brucite type but with one out of every four octahedra removed and replaced by two tetrahedra above and below the layer (Figure 12). Each tetrahedron shares three corners with octahedra and the cobalt coordination is completed by unidentate carboxylate groups of CHDC pillars. A 3D framework is thus formed that contains channels filled with water. The dehydration–rehydration process is reversible,

 © 2006 Wiley-VCH Verlag GmbH & Co. KGaA, Weinheim 

thereby conferring to this hybrid some porous properties. Removal of the water molecules leads to a shift of the layers combined with a tilt and a rotation of the organic moieties and a shortening of the interlayer space of about 1 Å (Figure 12). Moreover, this material presents a spontaneous ferrimagnetic magnetisation around 60 K, a temperature that is among the highest observed for this kind of compounds.

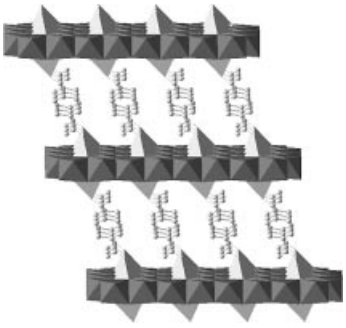

Figure 12. Polyhedral representation of $[Co_5(OH)_8(CHDC)]$, the anhydrous form of **25**; tetrahedra are represented in light grey and octahedra in dark grey.

### Use of More Complex Aromatic Carboxylates

The coordination polymer $[Co(H_2O)_2(C_{10}H_6O_4)]$ (**26**) has been obtained hydrothermally with 4-carboxycinnamic acid.[40] Its structure presents the same topology as that described for its analogue obtained with terephthalic acid (**21**).[33] With 1,4-naphthalenedicarboxylic acid, one 3D hybrid compound, namely $[Co(C_{12}H_6O_4)]$ (**27**), has been obtained by Maji et al. (Figure 13, a).[41] Its structure is similar to that of the fumarates (**15**),[28,29] with chains of metal octahedra connected by an organic moiety into a 3D framework. The main difference between this structure and those previously described is the topology of the chain, which here is zig-zag and is only constructed from edge-sharing cobalt octahedra (Figure 13, c).

With 2,6-naphthalenedicarboxylic acid, only a 1D compound, namely $[M(H_2O)_4(C_{12}H_6O_4)]$ (**28**), has been reported with both cobalt and nickel. It is constructed from chains of isolated metal octahedra bridged by organic ions.[42]

Two compounds have been isolated under hydrothermal conditions using 1,1′-biphenyl-2,2′-dicarboxylic acid.[43] $[M(H_2O)_4(C_{14}H_8O_4)]$ (**29**) presents chains of isolated cobalt or nickel octahedra bridged by dicarboxylate ions. Nevertheless, a peculiar geometry of the organic moiety allows the formation of a chain with an interesting helical geometry (Figure 14, a). $[Co_6(OH)_2(H_2O)_4(C_{14}H_8O_4)_5]$ (**30**) is also 1D but with an infinite M–O–M connectivity. Its metal oxide chain is constituted of pentameric units of edge-sharing octahedra connected to its neighbour by a corner-sharing tetrahedron (Figure 14, b). The pentameric unit has a cross shape made of two linear trimers sharing a central octahedron.

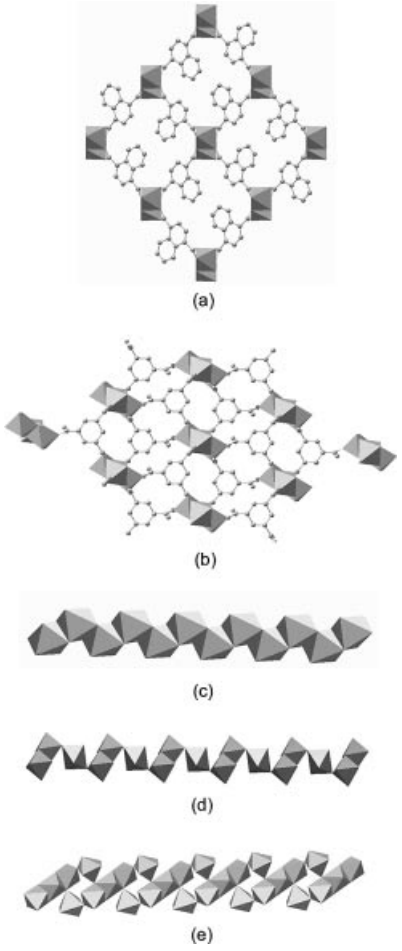


Figure 13. (a) View of the structure of **27** showing the lozenge-shaped tunnel topology; (b) view of the structure of **39** derived from the lozenge-shaped tunnel topology; (c) inorganic chain of **27** constructed from edge-sharing cobalt octahedra; (d) view of the chain of **39** with dimers of edge-sharing octahedra connected through a third octahedron by $\mu_2$-$OH_2$; (e) view of the chain of **42** with linear trimers bridged through corner-sharing octahedra.

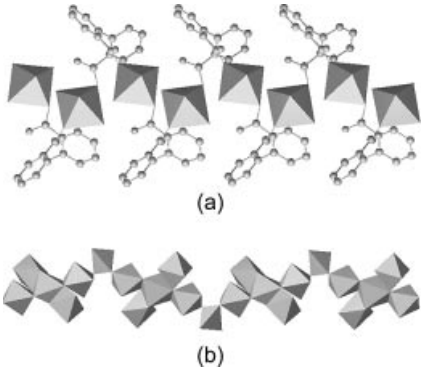


Figure 14. (a) View of a hybrid chain of **29** showing an interesting helical geometry; (b) representation of the oxide chain of **30** constructed from pentameric units of edge-sharing octahedra connected by a corner-sharing tetrahedron.

## Tricarboxylates

Rigid, triangular 1,3,5-benzenetricarboxylic acid ($H_3BTC$), commonly named trimesic acid, has been exten-

 © 2006 Wiley-VCH Verlag GmbH & Co. KGaA, Weinheim 

sively used to construct hybrid porous materials.[44] With cobalt and nickel, Yaghi et al. have reported the 1D polymer $[M_3(H_2O)_{12}(BTC)_2]$ (**31**) under hydrothermal conditions.[45] This compound, constructed from zig-zag chains of isolated octahedra connected through trimesate ions, can reversibly liberate eleven aqua ligands. The metal atoms at the centre of the sinusoid are surrounded by four water molecules in an equatorial plane, and the coordination environment is completed by two unidentate carboxylate ions (Figure 15, a). One side of the sinusoid is occupied by dangling carboxylate ions and the other one is taken up by metal octahedra. Compound **31** can also been obtained by thermal treatment of $[M_3(H_2O)_{14}(BTC)_2{\cdot}4H_2O]$,[46,47] the structure of which can be described as the juxtaposition of molecular motifs composed of three isolated octahedra linearly connected by two unidentate carboxylate ions. $[NaCo_3(OH)(H_2O)_{11}(BTC)_2{\cdot}1.5\,H_2O]$ (**32**) is another example of a 1D compound which has been synthesised at room temperature from trimesic acid.[47] Its structure consists of trinuclear units of *cis* edge-sharing metal octahedra, $\{Co_3O_6(\mu_3\text{-}OH)(\mu_2\text{-}OH_2)_2(H_2O)_5\}$, surrounded by three bridging carboxylate functions and connected by trimesate ions to construct the chains (Figure 15, b).

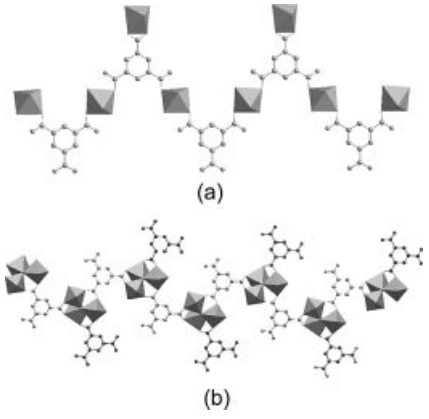


Figure 15. (a) View of a hybrid chain of **31** with isolated octahedra; (b) view of a hybrid chain of **32** showing trimers of edge-sharing octahedra.

$[Ni_3(H_2O)_8(BTC)_2]$ (**33**), a 2D compound obtained by us under hydrothermal conditions, is also constructed from $\{Ni_3O_8(\mu_2\text{-}OH_2)_2(H_2O)_6\}$ trimers.[48] These trimers are linear, with corner-sharing octahedra connected by $\mu_2$-$H_2O$ molecules, the stability of which is reinforced by the closeness of an unprotonated carboxylate and strong hydrogen bonds. Each trimer is surrounded by six carboxylate ions, two of which bridge the central nickel octahedron to its neighbour while the other four are unidentate (Figure 16, a). Six bridging trimesates connect each trimer to six neighbouring ones to construct an infinite 2D pseudo-hexagonal network. The planes are interpenetrated and positioned to favour π–π interactions (Figure 16, b). These planes can also be described as "double layers" of parallel organic rings connected through trimers.

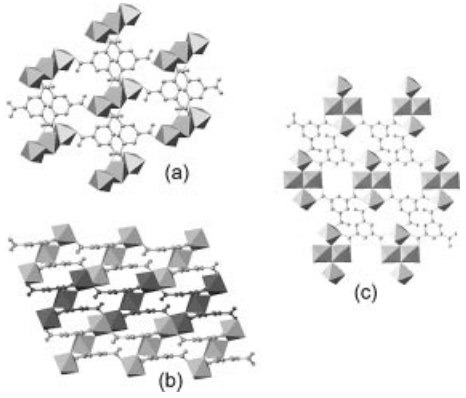


Figure 16. (a) Projection of the structure of **33** showing one nickel cluster connected to six equivalent ones; (b) view of the stacking of the layers of **33** dominated by π–π interactions; (c) view of the structure of **34** showing one nickel cluster connected to six equivalent ones.

$[Ni_2F(H_2O)_4(BTC){\cdot}2H_2O]$ (**34**) has been obtained by incorporating hydrofluoric acid into the starting hydrothermal mixture,[49] which is rather common for the synthesis of weakly soluble main group cations.[2] Its structure is very similar to that of **33** previously described and presents "double layers" of parallel organic rings, although here they are connected through tetrameric $\{Ni_4O_{10}(\mu_3\text{-}F)_2(H_2O)_8\}$ clusters, where the four nickel octahedra are connected by two $\mu_3$-F atoms. Each tetramer is also connected to six neighbours through bridging trimesate ions (Figure 16, c). Four bridging carboxylates are in a planar arrangement in the tetramer, whereas the two additional monodentate ones are localised above and below this plane, which is here nearly parallel to the benzene rings.

$[Co_3(H_2O)_6(BTC)(HBTC)(H_2BTC){\cdot}2H_2O]$ (**35**) is also layered and its construction is dominated by π–π interactions with a mean interlayer distance of 3.4 Å.[50] The cobalt atoms have distorted octahedral environments, with carboxylate oxygen atoms in the four equatorial positions and water molecules in the apical ones. Distortion of the octahedra is due to the chelating connecting mode of one carboxylate. Due to this important distortion, only one carboxylate at a time can bind the metal in a chelating way and the metal environment is completed by monodentate ligands. The organic moiety acts as a triangular connector for the cobalt octahedra and presents the three states of protonation, which indicates that protonation depends not only on the pH of the medium but mostly upon condensation. This connection leads to the formation of a nearly planar infinite net with a pseudo-threefold symmetry that presents triangular cavities made from three cobalt octahedra and three trimesate ions (Figure 17, a), half of which are occupied by water molecules. The solid is formed by the stacking of six types of layers that are chemically identical but shifted (Figure 17, b). The only compound synthesised with trimesic acid that presents a 3D open structure is $[K\{Co_3(BTC)(HBTC)_2\}{\cdot}5H_2O]$, (**36**).[50] Its structure is based on sinusoidal chains of cobalt octahedra whose

 © 2006 Wiley-VCH Verlag GmbH & Co. KGaA, Weinheim 

period is strongly correlated to the geometry of the organic molecule (Figure 17, c). The chains are connected to four other parallel sinusoids through two types of perpendicular carboxylates, leading to a 3D structure with rectangular tunnels. The oxide chains are constructed from dimeric units of edge-sharing octahedra that are connected by a vertex-sharing octahedron. The cobalt atoms of the dimer are surrounded by the organic moiety in a strongly distorted environment due to the chelating mode of one carboxylate. The protonated carboxylate group of HBTC points toward the centre of the channels delineated by four sinusoidal metal oxide chains connected by trimesate ions. Water molecules and potassium (in half occupancy) are located inside these rectangular tunnels (Figure 17, d).

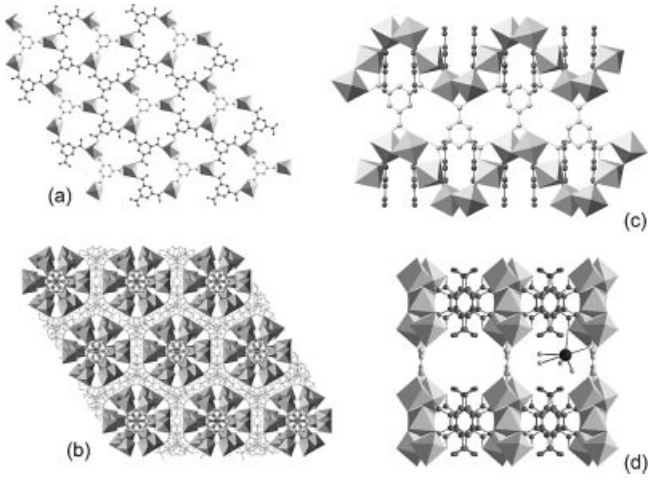


Figure 17. (a) Projection of one layer showing the triangular cavities in **35**; (b) projection of six equivalent layers in **35**; (c) projection of the structure of **36** showing the sinusoidal chains of cobalt octahedra; (d) view of two rectangular channels delineated by four cobalt and trimesate ions with a disordered potassium cation in **36**.

By changing the position of the carboxylate groups and using 1,2,3-benzenetricarboxylic acid (1,2,3-$H_3$BTC), two compounds have been obtained by Gutschke et al.[51] Both compounds, $[Co_2(OH)(H_2O)(1,2,3\text{-BTC})\cdot H_2O]$ (**37**) and $[Co_2(OH)(H_2O)(1,2,3\text{-BTC})]$ (**38**), are constructed from inorganic chains presenting a Δ topology. In **37**, the chains are constructed from corner-sharing polyhedra, with a backbone where cobalt octahedra and tetrahedra alternate and on which pendant trigonal-bipyramids are grafted (Figure 18, a). These metal oxide strips run perpendicularly but never intersect. The connection of a chain to the orthogonal ones by carboxylate forms an amazing 3D network (Figure 18, b). In **38**, *trans* corner-sharing octahedra build the backbone of the chain, on which tetrahedra are attached by sharing edges with octahedra (Figure 18, c). Parallel chains are connected through the organic moiety to construct a 2D framework.

With *cis,cis*-cyclohexane-1,3,5-tricarboxylic acid ($H_3$CTC), one 3D hybrid compound with both cobalt and nickel, namely $[M_3(H_2O)_4(CTC)_2\cdot 5H_2O]$ (**39**), has been synthesised hydrothermally by Kumagai et al.[52] It presents a

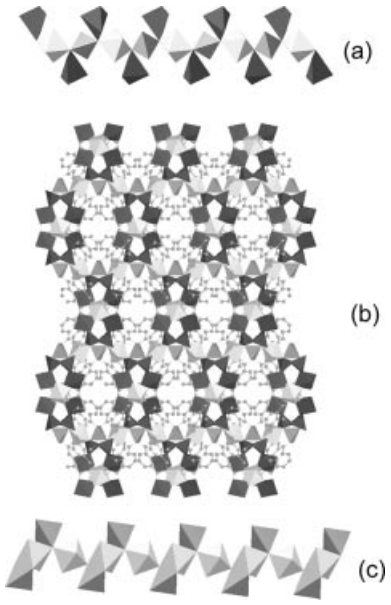


Figure 18. (a) View of the inorganic chain presenting a Δ topology in **37** with a backbone constructed from cobalt octahedra (light grey) and tetrahedra (medium grey), on which pendant trigonal bipyramids (dark grey) are grafted; (b) view of the structure of **37** showing the linking of the polyhedra by the organic moieties; (c) view of the inorganic chain presenting a Δ topology in **38** with a backbone constructed from cobalt octahedra (light grey), on which tetrahedra (medium grey) are grafted.

structure derived from the lozenge-shaped tunnel topology with inorganic chains connected by the organic moiety. The four oxide chains in this compound are all connected through two central tricarboxylates (Figure 13, b) in one lozenge, and are slightly different to those reported previously. Dimers of edge-sharing octahedra are connected through a third octahedron which shares its *trans* vertices with two neighbouring dimers through a $\mu_2$-$OH_2$ (Figure 13, d).

## Tetra- and Hexacarboxylates

The three compounds synthesised hydrothermally with 1,2,4,5-benzenetetracarboxylic (pyromellitic) acid ($H_4$PM) have 3D architectures. $[Co_2(H_2O)_4(PM)\cdot 2H_2O]$ (**40**) and $[Co_2(PM)]$ (**41**) have been reported by Kumagai et al.[53] Compound **40** is a coordination polymer built up from cobalt octahedra bridged by carboxylates to construct layers with a pseudo square geometry similar to that observed in **20**. These layers are connected through organic moieties into a 3D network which presents cavities filled with water molecules. Compound **41** is formed from edge-sharing cobalt octahedra chains connected by pyromellitates.

$[Co_5(OH)_2(H_2O)_4(PM)_2]$ (**42**) has been synthesised by Gutschke et al. simply by increasing the reaction temperature.[54] Its 3D structure is very similar to that of the fumarates (Figure 7) and presents, once again,

 © 2006 Wiley-VCH Verlag GmbH & Co. KGaA, Weinheim 

lozenge-shaped tunnels with chains of cobalt octahedra connected by the organic moiety. Nevertheless, the topology of the oxide chain is really original, with parallel linear trimers of edge-sharing octahedra bridged by two corner-sharing octahedra (Figure 13, e).

With benzenehexacarboxylic (mellitic) acid ($H_6$MLT), only one 2D compound has been reported, namely $[Ni_4(OH)_2(H_2O)_6(MLT)]$ (**43**).[55] Its structure consists of inorganic chains generated by dimers of edge-sharing octahedra connected through a $\mu_3$-OH group. These chains are further bridged by mellitates to construct corrugated layers.

## Concluding Remarks

Although it is difficult to predict structures on the basis of the ligand and metal chosen, the results presented here allow us to draw some conclusions. This review reveals the extreme diversity of the cobalt and nickel oxide architectures obtained by the use of carboxylate ligands: "from coordination polymers to 3D inorganic skeletons". One of the reasons for the richness of these systems relates first to the electronic structure of $Co^{2+}$ ($d^7$) and $Ni^{2+}$ ($d^8$). Moreover, at variance with what is observed in templated metallophosphates[56] and metal organic frameworks based on $Cu^{2+}$ and $Zn^{2+}$,[57] in which the number of secondary building units (SBUs) is rather limited, the systems based on $Co^{2+}$ and $Ni^{2+}$ are, in terms of SBUs, extremely rich and diverse, and almost all structures present their own polyhedral building blocks. In the inorganic framework, one indeed observes monomeric moieties, in tetrahedral (Co) and octahedral (Ni, Co) coordination, along with dimers, trimers, tetramers, pentamers and hexamers with polyhedra sharing either vertices, edges or faces, as well as their connections into chains, layers and 3D networks (Figure 19). This diversity implies much more numerous possibilities of connection with the organic moieties, which are also numerous as shown in this review. Therefore, the exploration of the richness of these systems is still in its infancy, although careful attention must be paid to the experimental conditions as, besides the already shown effect of temperature and its influence on the condensation of the oligomers, the pH of the reaction mixture is also very important for the reactivity of these cations.

In terms of topologies, some of them are represented by one member, such as the remarkable honeycomb oxide framework with 1D pores of $[Ni_7(OH)_2(C_4H_4O_4)_6(H_2O)_2 \cdot 2H_2O]$, whereas others appear regularly, with rigid or flexible organic molecules and with di- or tetracarboxylates. This is the case for the lozenge-shaped tunnel topology with inorganic chains connected by organic bridges. This architectural type is observed with both cobalt and nickel and has been obtained with dicarboxylates ions as diverse as small fumarate and cumbersome naphthalene-1,4-dicarboxylate and 1,2,4,5-benzenetetracarboxylate. These few examples demonstrate how much the oxide backbone can adopt diverse M–O–M connectivities to adapt to the organic moiety. More recently, this family has been enlarged with a new member obtained with 1,4-cyclohexanedicarboxylate, which presents the same chains as those observed with fumarate or succinate.[58,59] It is obvious that metal oxide condensation in solution is favoured by an increase of temperature. Nevertheless, it is interesting to note the counter-example of 1,4-cyclohexanedicarboxylate, which demonstrates the high complexity of these systems.[58] Indeed, simply by increasing the temperature from 140 to 170 °C, the lozenge-shaped tunnel topology is replaced by a layered compound constructed from remarkable hexanuclear prismatic nickel clusters (Figure 19l) connected through the organic moiety.

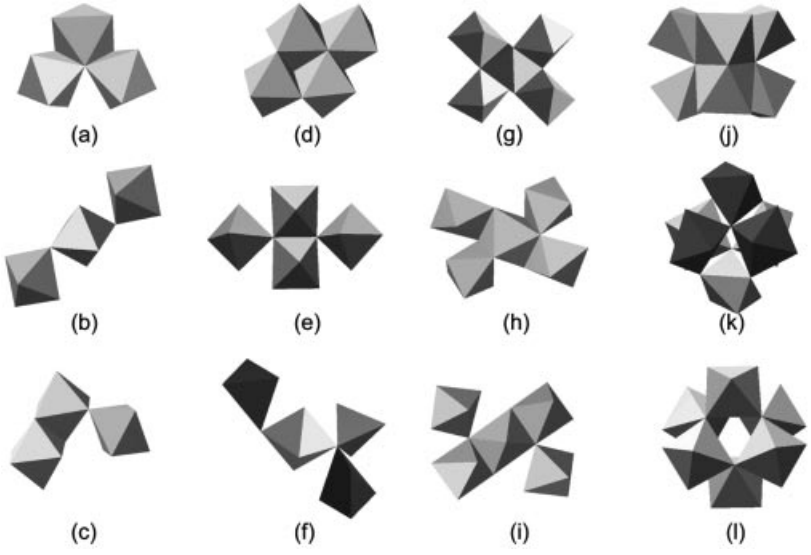


Figure 19. View of a few of the oligomers encountered in nickel and cobalt carboxylates: isolated trimers in **32** (a) or **33** (b) and the trimer of the inorganic chain of **39** (c); tetramers of the 2D oxide framework of MIL-16 (**4**, d), of the coordination polymer **34** (e), of the chain of **37** (f); pentamers of the inorganic layer of MIL-9 (**3**, g), of the oxide chains of **30** (h) and **42** (i); hexamers of the inorganic chains of MIL-73 (**8**, j) and those encountered in the coordination polymers MIL-104 (**22**, k) and $[Ni_6(OH)_6(C_8H_{10}O_4)_3(H_2O)_6 \cdot 2H_2O]$ (l) reported recently.[58]

 © 2006 Wiley-VCH Verlag GmbH & Co. KGaA, Weinheim 

The topology of the extended inorganic network depends strongly on the geometry and connectivity of the organic partner. Inorganic condensation is favoured with small flexible organic molecules such as succinate but disfavoured with large and/or rigid ones. Glutarate is at the interface, since it allows the formation of an amazing 3D inorganic skeleton[22] as well as the construction of a metal organic framework with isolated tetrahedra.[21] With longer linear carboxylates, the final organisation is driven by weak interactions (hydrophobic) between alkyl chains.

In water, the use of rigid organic partners with benzene rings disfavours the formation of an extended oxide network and, most of the time, 3D coordination polymers or layered compounds dominated by π–π interactions are obtained. The example of the trimesate system illustrates the competition between covalent linkages and π–π interactions, which seems to be the decisive factor in the final architecture, well. It is difficult to draw rules from just two examples, but "multiconnecting" organics also seem to disadvantage oxide condensation. Indeed, the two 3D oxide frameworks have been synthesised with linear dicarboxylate ions. In both cases, the organic partner lines the oxide skeleton and is flexible enough to act as a chelate ligand for one metal via the oxygen atoms of neighbouring carboxylate groups. All modes of coordination of the organic moieties observed in the compounds described here are represented below. Only three coordination modes are present in the two 3D inorganic skeletons (modes c, i and f in Scheme 1). Mode a is mostly observed for 1D compounds with metal–organic chains, whereas mode d is present in several metal–organic frameworks (MOF). Others, such as modes b, e, g, h and j have been observed only once to date and seem to be rather scarce.

For tricarboxylates (see Scheme 2), the number of connecting modes is higher than the number of compounds and only one mode (j) has been observed in two compounds.

The connecting modes of tetra- and hexacarboxylates (Scheme 3) are also diverse and their number corresponds to that of described compounds. The ratio (number of metal atoms)/(number of organic moieties) (M/org) is given in Table 1 and varies from 1/2 for 1D compounds with metal–organic chains to 5 for **25**, which is constructed from hydroxide layers linked by organic pillars.[39] In the two 3D oxide frameworks, M/org is equal, or very close (7/6), to one.

Under hydrothermal conditions, the reactivity of cobalt and nickel is very different and similar synthetic conditions most of the time lead to totally different structural types. Isostructural compounds can sometimes be isolated but often under very distinct experimental procedures, as illustrated by the example of MIL-73, which is obtained hydrothermally with nickel and under reflux with cobalt. Under "basic" hydrothermal conditions it seems to be easier to isolate 3D inorganic skeletons with nickel than with cobalt. On the other hand, 2D oxide frameworks are very common with cobalt, whereas none have been isolated with nickel and polycarboxylates yet. Whereas only structures containing octahedra are reported for nickel carboxylates, the cobalt environment is more diverse, with the presence of tetrahedra and pentacoordinate metal. This is easily understandable in light of the coordinational flexibility of cobalt, which is higher than that of nickel due to its field anisotropy. On the other hand, the growth of nickel crystallites is most of the time limited compared to cobalt, therefore nickel compounds generally need structural determinations from powder diffraction data.

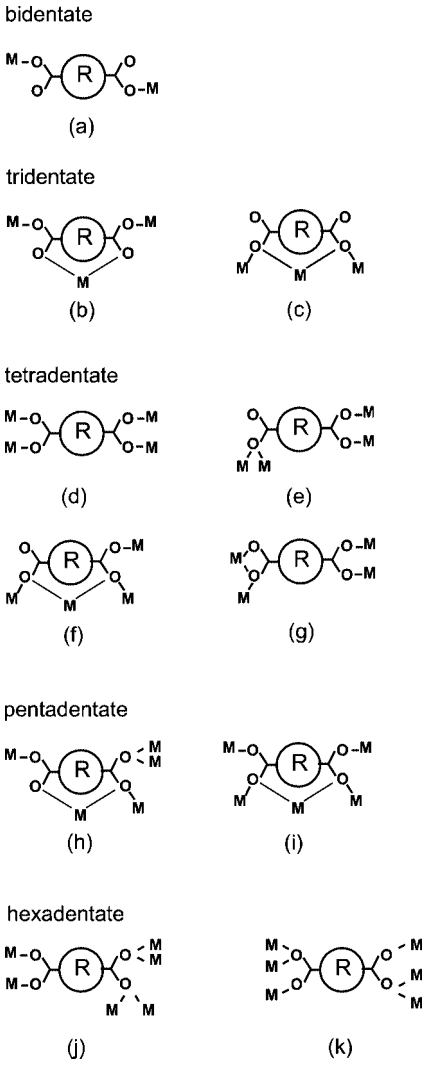


Scheme 1. Modes of coordination of the dicarboxylate ions observed in compounds **1**–**30**.

It is also interesting to comment here on the success of Neeraj et al. in the synthesis of sodalite networks based on cobalt and squarate,[60a] an organic moiety which is not so far from carboxylates. The six four-membered $Al_2Si_2$ rings of the sodalite cage are replaced here by the four-membered squarate (C4) rings, and are now linked by 12 cobalt octahedra instead of oxygen atoms. This organisation has already been encountered for a few other metal ions,[60b–60d] particularly nickel,[60b] and is therefore certainly a thermodynamically stable topology.

 © 2006 Wiley-VCH Verlag GmbH & Co. KGaA, Weinheim 

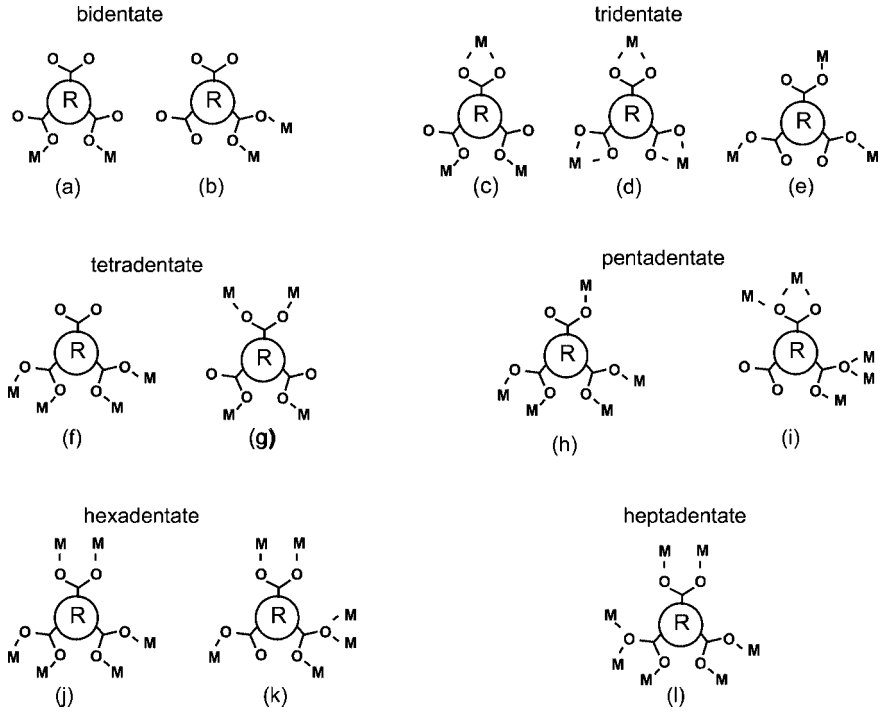


Scheme 2. Modes of coordination of the tricarboxylate ions observed in compounds **31**–**39**.

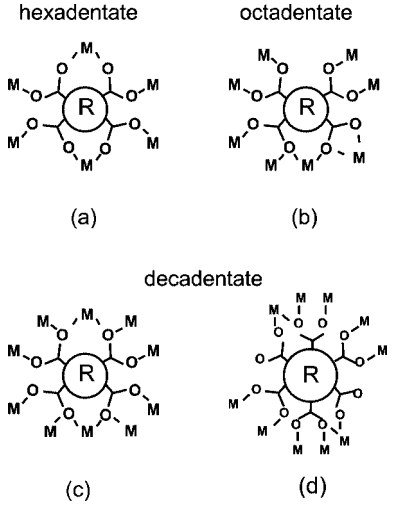


Scheme 3. Modes of coordination of the tetra- and hexacarboxylate ions observed in compounds **40**–**43**.

Magnetic measurements have been undertaken for most of the listed compounds and show diverse and usually extremely complicated behaviours, with competition between antiferromagnetic (AF) and ferromagnetic (F) interactions. This can be explained by the diversity of the inorganic networks and, of course, by their complexity. It is usual to have several independent metal centres, in a single architecture, showing various bond lengths and angles and sometimes, with cobalt, different geometries.

It is well known that connections with large M–O–M angles favour antiferromagnetic superexchange whereas connections with angles close to 90° favour ferromagnetic interactions,[61] although the M–O–C–O–M pathway should also be taken into account as well as the weak coupling between metal assemblies via organic bridges. The complexity of the M–O–M connectivity, as illustrated by MIL-73, in which octahedra are linked by faces, edges and corners, means that compounds often present interactions with different signs and strengths and are often frustrated. The only porous 3D oxide network described as a pure ferromagnet, MIL-77, is cubic with two independent octahedrally nickel atoms connected by sharing edges.

The two compounds with a lozenge-shaped topology and the same inorganic backbone, namely **15** and $[Ni_3(OH)_2(trans\text{-}C_8H_{10}O_4)_2(H_2O)_4{\cdot}4H_2O]$, both present a ferrimagnetic behaviour, with a lower critical temperature for the second compound, which may be due to the difference of the organic moieties.[59] $[Ni_3(OH)_2(cis\text{-}C_8H_{10}O_4)_2(H_2O)_4{\cdot}2H_2O]$ has also been synthesised recently by Kurmoo et al. and can be described as being formed from the same oxide chains but connected by a *cis*-1,4-cyclohexanedicarboxylate instead of a *trans* one.[59] It also exhibits a ferrimagnetic ordering that reversibly transforms into a ferromagnetic one upon partial dehydration, thus showing once again the complexity of the interaction pathways.

It is also not unusual that isostructural compounds obtained with cobalt and nickel display different dominant magnetic interactions[20,52] — antiferromagnetic for cobalt compounds and ferromagnetic for their nickel analogues.

Finally, the numerous nickel and cobalt carboxylates presented above illustrate the variety of structural architectures. Taking into account their great diversity, carboxylates

 © 2006 Wiley-VCH Verlag GmbH & Co. KGaA, Weinheim 

Table 1. Cobalt and nickel polycarboxylates.

| Organic acid | Compound | M/org[a] | Dim.[b] | Synthesis | Mode[c] | Metal oxide connectivity | Magnetic interactions | Ref. |
|---|---|---|---|---|---|---|---|---|
| Succinic acid | $Co(H_2O)_4(C_4H_4O_4)$ (**1**) | 1/1 | 0–1 | room temp. | 1–a | isolated octahedra | not given | [8] |
| | $Co(H_2O)_2(C_4H_4O_4)$ (**2**) | 1/1 | 0–1 | 100 °C | 1–cd | trimers of edge-sharing octahedra | not given | [9] |
| | $Co_5(OH)_2(C_4H_4O_4)_4$ (**3**) MIL-9 | 5/4 | 2–3 | hydrothermal 180 °C | 1–hj | edge-sharing octahedra | ferrimagnetic $T < 10$ K | [10] |
| | $Co_4(OH)_2(H_2O)_2(C_4H_4O_4)_3 \cdot 2H_2O$ (**4**) MIL-16 | 4/3 | 2–2 | hydrothermal 180 °C | 1–ef | edge-sharing octahedra | ferrimagnetic $T < 10$ K | [11] |
| | $Co_6(OH)_2(C_4H_4O_4)_5 \cdot H_2O$ (**5**) | 6/5 | 2–3 | hydrothermal 180 °C | 1–di | $CoO_5$ and $CoO_6$ polyhedra | antiferromagnetic $T < 26$ K | [12] |
| | $Co_3(OH)_2(H_2O)_4(C_4H_4O_4)_2 \cdot 6H_2O$ (**6**) | 3/2 | 1–3 | room temp. | 1–d | edge-/corner-sharing octahedra | not given | [14] |
| | $Ni_7(OH)_2(C_4H_4O_4)_6(H_2O)_2 \cdot 2H_2O$ (**7**) | 7/6 | 3–3 | hydrothermal 150 °C | 1–fi | edge-/corner -sharing octahedra | paramagnetic | [16] |
| | $M_7(OH)_6(C_4H_4O_4)_4(H_2O)_3 \cdot 7H_2O$ (**8**) M = Ni, Co MIL-73 | 7/4 | 1–2 | hydrothermal 180 °C (Ni) under reflux (Co) | 1–di | edge-/face-sharing octahedra | ferrimagnetic $T < 20$ K | [17] |
| Malonic acid | $M_2(H_2O)_4(C_3H_2O_4)_2$ (**9**) M = Ni, Co | 1/1 | 0–2 | 60 °C | 1–b | isolated octahedra | weak antiferromagnetic $T < 15$ K (Co), very weak ferromagnetic $T < 7.5$ K (Ni) | [20] |
| Glutaric acid | $Co(C_5H_6O_4)$ (**10**) | 1/1 | 0–3 | hydrothermal 180 °C | 1–d | isolated tetrahedra | antiferromagnetic $T < 14$ K | [21] |
| | $Ni_{20}(H_2O)_8(C_5H_6O_4)_{20} \cdot 40H_2O$ (**11**) MIL-77 | 1/1 | 3–3 | solvothermal 180 °C (water/ethanol) | 1–ci | edge-sharing octahedra | pure ferromagnet $T_c \approx 4$ K | [22] |
| Adipic acid | $Ni(H_2O)_4(C_6H_8O_4)$ (**12**) | 1/1 | 0–1 | room temp. | 1–a | isolated octahedra | paramagnetic | [24] |
| | $Co_2(H_2O)_6(C_6H_8O_4)_2 \cdot 4H_2O$ (**13**) | 1/1 | 1–2 | room temp. | 1–a | corner-sharing octahedra | not given | [25] |
| Pimelic acid | $Co(C_7H_{10}O_4)$ (**14**) MIL-36 | 1/1 | 0–3 | hydrothermal 180 °C | 1–d | isolated tetrahedra | antiferromagnetic $T < 20$ K | [26] |
| Fumaric acid | $M_3(OH)_2(H_2O)_4(C_4H_2O_4)_2 \cdot 2H_2O$ (**15**) M = Ni, Co | 3/2 | 1–3 | hydrothermal 170 °C (Ni) 50 °C (Co) | 1–d | edge-/corner-sharing octahedra | ferrimagnetic $T < 20$ K (Ni) paramagnetic (Co) | [28][29] |
| | *cis*-$Co(H_2O)_4(C_4H_2O_4) \cdot 2H_2O$ (**16**) | 1/1 | 0–1 | room temp. | 1–a | isolated octahedra | not given | [30] |
| | *trans*-$Co(H_2O)_4(C_4H_2O_4)$ (**17**) | 1/1 | 0–1 | room temp. | 1–a | isolated octahedra | paramagnetic | [29][30] |
| Acetylene-dicarboxylic acid | $M(H_2O)_4(C_4O_4) \cdot 2H_2O$ (**18**) M = Ni, Co | 1/1 | 0–1 | room temp. | 1–a | isolated octahedra | not given | [31] |
| | $M(H_2O)_2(C_4O_4)$ (**19**) M = Ni, Co | 1/1 | 0–3 | by heating **18** at 100 °C | 1–d | isolated octahedra | antiferromagnetic $T < 50$ K (Co and Ni) | [31] |
| Terephthalic acid | $Co_2(OH)_2(C_8H_4O_4)$ (**20**) | 2/1 | 2–3 | 80 °C | 1–k | edge-/corner-sharing octahedra | antiferromagnetic $T < 48$ K | [32][33] |
| | $Co(H_2O)_2(C_8H_4O_4)$ (**21**) | 1/1 | 0–3 | hydrothermal 120 °C | 1–d | isolated octahedra | paramagnetic with AF coupling | [33] |
| Isophthalic acid | $Na_3Co_6O(OH)(C_8H_4O_4)_6 \cdot H_2O$ (**22**) MIL-104 | 1/1 | 0–3 | solvothermal 180 °C (water/ethanol) | 1–g | hexamers of corner-sharing octahedra | antiferromagnetic $T < 50$ K | [34] |
| Phthalic acid | $Co_3(OH)_2(C_8H_4O_4)_2$ (**23**) | 3/2 | 2–2 | hydrothermal 200 °C | 1–k | edge-sharing octahedra | not given | [36] |
| 4-Cyclohexene-1,2-dicarboxylic acid | $Co(C_8H_8O_4)$ (**24**) | 1/1 | 0–2 | hydrothermal 180 °C | 1–d | isolated tetrahedra | not given | [37] |
| 1,4-Cyclohexane-dicarboxylic acid | $Co_5(OH)_8(C_8H_{10}O_4) \cdot 4H_2O$ (**25**) | 5/1 | 2–3 | hydrothermal 170 °C | 1–a | edge-sharing octahedra and corner-sharing tetrahedra | ferrimagnetic $T < 60.5$ K | [39] |
| 4-Carboxycinnamic acid | $Co(H_2O)_2(C_{10}H_6O_4)$ (**26**) | 1/1 | 0–3 | hydrothermal 120 °C | 1–d | isolated octahedra | paramagnetic | [40] |

 © 2006 Wiley-VCH Verlag GmbH & Co. KGaA, Weinheim 

Table 1. *(continued)*

| Organic acid | Compound | M/org[a] | Dim.[b] | Synthesis | Mode[c] | Metal oxide connectivity | Magnetic interactions | Ref. |
|---|---|---|---|---|---|---|---|---|
| 1,4-Naphthalene-dicarboxylic acid | $Co(C_{12}H_6O_4)$ (**27**) | 1/1 | 1–3 | hydrothermal 170 °C | 1–k | edge-sharing octahedra | intrachain: ferromagnetic interchain: antiferromagnetic $T_c$ = 5.5 K | [41] |
| 2,6-Naphthalene-dicarboxylic acid | $M(H_2O)_4(C_{12}H_6O_4)$ (**28**) M = Ni, Co | 1/1 | 0–1 | room temp. | 1–a | isolated octahedra | not given | [42] |
| Diphenic acid | $M(H_2O)_4(C_{14}H_8O_4)$ (**29**) M = Ni, Co | 1/1 | 0–1 | hydrothermal 170 °C | 1–a | isolated octahedra | (Co) paramagnetic (Ni) paramagnetic with F (intrachain) and AF (interchain) couplings | [43a] |
| | $Co_6(OH)_2(H_2O)_4(C_{14}H_8O_4)_5$ (**30**) | 6/5 | 1–1 | hydrothermal 170 °C | 1–dei | edge-sharing octahedra and corner-sharing tetrahedra | paramagnetic with AF coupling | [43b] |
| Trimesic acid ($H_3BTC$) | $M_3(H_2O)_{12}(BTC)_2$ (**31**) M = Ni, Co | 3/2 | 0–1 | hydrothermal 140 °C | 2–ac | isolated octahedra | not given | [45] |
| | $NaCo3(OH)(H_2O)_{11}(BTC)_2 \cdot 1.5H_2O$ (**32**) | 3/2 | 0–1 | room temp. | 2–bf | trimers of edge-sharing octahedra | not given | [47] |
| | $Ni_3(H_2O)_8(BTC)_2$ (**33**) | 3/2 | 0–2 | solvothermal 180 °C | 2–g | trimers of corner-sharing octahedra | paramagnetic with F coupling | [48] |
| | $Ni_2F(H_2O)_4(BTC) \cdot 2H_2O$ (**34**) | 2/1 | 0–2 | hydrothermal 150 °C | 2–h | tetramers of edge and corner-sharing octahedra | not given | [49] |
| | $Co_3(H_2O)_6(BTC)(HBTC)$-$(H_2BTC) \cdot 2H_2O$ (**35**) | 1/1 | 0–2 | hydrothermal 180 °C | 2–de | isolated octahedra | paramagnetic with AF coupling | [50] |
| | $K[Co_3(BTC)(HBTC)_2] \cdot 5H_2O$ (**36**) | 1/1 | 1–3 | hydrothermal 180 °C | 2–ij | edge-/corner-sharing octahedra | paramagnetic | [50] |
| 1,2,3-Benzenetricarboxylic acid (1,2,3-$H_3BTC$) | $Co_2(OH)(H_2O)(1,2,3\text{-}BTC) \cdot H_2O$ (**37**) | 2/1 | 1–3 | hydrothermal 200-220 °C | 2–j | corner-sharing octahedra, trigonal bipyramids, and tetrahedra | paramagnetic with AF coupling – spin frustration | [51] |
| | $Co_2(OH)(1,2,3\text{-}BTC)$ (**38**) | 2/1 | 1–2 | hydrothermal 200-220 °C | 2–l | tetrahedra sharing edge with octahedra and corner-sharing octahedra | ferrimagnetic $T < 40$ K | [51] |
| *cis*,*cis*-Cyclohexane-1,3,5-tricarboxylic acid ($H_3CTC$) | $M_3(H_2O)_4(CTC)_2 \cdot 5H_2O$ (**39**) M = Ni, Co | 3/2 | 1–3 | hydrothermal 170 °C | 2–k | edge-/corner-sharing octahedra | (Co) dominant antiferromagnetic tending towards ferrimagnetic at low temp. (Ni) mostly ferromagnetic | [52] |
| 1,2,4,5-Benzenetetra-carboxylic or pyromellitic acid ($H_4PM$) | $Co_2(H_2O)_4(PM) \cdot 2H_2O$ (**40**) | 2/1 | 0–3 | hydrothermal 110 °C | 3–b | isolated octahedra | paramagnetic | [53] |
| | $Co_2(PM)$ (**41**) | 2/1 | 1–3 | hydrothermal 170 °C | 3–a | edge-sharing octahedra | antiferromagnetic $T_N$ = 16 K ferromagnetic $T < 13$ K | [53] |
| | $Co_5(OH)_2(H_2O)_4(PM)_2$ (**42**) | 5/2 | 1–3 | hydrothermal 190 °C | 3–c | edge-/corner-sharing octahedra | not given | [54] |
| Benzenehexacarboxylic or mellitic acid ($H_6MLT$) | $Ni_4(OH)_2(H_2O)_6(MLT)$ (**43**) | 4/1 | 1–2 | hydrothermal 170 °C | 3–d | edge-/corner-sharing octahedra | paramagnetic with AF coupling | [55] |

[a] The "M/org" column refers to the ratio number of metal ions/number of organic moieties. [b] The first number in the "Dim." column refers to the M–O–M dimensionality and the second refers to the total dimensionality. [c] The "mode" column refers to the mode of coordination of the polycarboxylate ions (see Schemes 1–3).

 © 2006 Wiley-VCH Verlag GmbH & Co. KGaA, Weinheim 

are the partners of choice for constructing novel materials with interesting properties such as porosity, chirality or magnetism. Thus, much still remains to be understood in this field, although it is clear that very simple organic partners can lead to the most remarkable frameworks.


[1] a) A. Corma, *Chem. Rev.* **1997**, *97*, 2373–2419; b) M. E. Davis, *Chem. Eur. J.* **1997**, *3*, 1745–1750; c) J. M. Thomas, *Sci. Am.***1992**, *266*, 112–118; d) J. M. Thomas, *Angew. Chem. Int. Ed. Engl.* **1994**, *33*, 913–937.
[2] A. K. Cheetham, G. Férey, T. Loiseau, *Angew. Chem. Int. Ed.* **1999**, *38*, 3268–3292.
[3] P. Feng, X. Bu, G. D. Stucky, *Nature* **1997**, *388*, 735–740.
[4] N. Guillou, Q. Gao, P. M. Forster, J.-S. Chang, M. Noguès, S.-E. Park, G. Férey, A. K. Cheetham, *Angew. Chem. Int. Ed. Engl.* **2001**, *40*, 2831–2834.
[5] C. N. R. Rao, S. Natarajan, R. Vaidhyanathan, *Angew. Chem. Int. Ed.* **2004**, *43*, 1466–1496.
[6] S. Kitagawa, R. Kitaura, S.-I. Noro, *Angew. Chem. Int. Ed. Engl.* **2004**, *43*, 2334–2375.
[7] M. Le Van, G. Périnet, R. Lafont, *C. R. Acad. Sci. Paris* **1969**, *268*, 406–408.
[8] C. Livage, C. Egger, G. Férey, *Chem. Mater.* **2001**, *13*, 410–414.
[9] P. M. Forster, A. R. Burbank, C. Livage, G. Férey, A. K. Cheetham, *Chem. Commun.* **2004**, 368–369.
[10] C. Livage, C. Egger, M. Noguès, G. Férey, *J. Mater. Chem.* **1998**, *8*, 2743–2747.
[11] C. Livage, C. Egger, G. Férey, *Chem. Mater.* **1999**, *11*, 1546–1550.
[12] L.-S. Long, X.-M. Chen, M.-L. Tong, Z.-G. Sun, Y.-P. Ren, R.-B. Huang, L.-S. Zheng, *J. Chem. Soc., Dalton Trans.* **2001**, 2888–2890.
[13] P. M. Forster, N. Stock, A. K. Cheetham, *Angew. Chem. Int. Ed.* **2005**, *44*, 7608–7611.
[14] Y.-Q. Zheng, J.-L. Lin, *Z. Kristallogr. NCS* **2001**, *216*, 139–140.
[15] K. Barthelet, J. Marrot, D. Riou, G. Férey, *Angew. Chem. Int. Ed.* **2002**, *41*, 281–284.
[16] P. M. Forster, A. K. Cheetham, *Angew. Chem. Int. Ed.* **2002**, *41*, 457–459.
[17] N. Guillou, C. Livage, W. van Beek, M. Noguès, G. Férey, *Angew. Chem. Int. Ed.* **2003**, *42*, 644–647.
[18] P. M. Forster, A. R. Burbank, M. C. O'Sullivan, N. Guillou, C. Livage, G. Férey, N. Stock, A. K. Cheetham, *Solid State Sci.* **2005**, *7*, 1549–1555.
[19] Y. Rodríguez-Martín, M. Hernández-Molina, F. S. Delgado, J. Pasán, C. Riuz-Pérez, J. Sanchiz, F. Lloret, M. Julve, *CrystEngComm* **2002**, *4*, 522–535.
[20] F. S. Delgado, M. Hernández-Molina, J. Sanchiz, C. Riuz-Pérez, Y. Rodríguez-Martín, T. López, F. Lloret, M. Julve, *CrystEngComm* **2004**, *6*, 106–111.
[21] E. W. Lee, Y. J. Kim, D.-Y. Jung, *Inorg. Chem.* **2002**, *41*, 501–506.
[22] N. Guillou, C. Livage, M. Drillon, G. Férey, *Angew. Chem. Int. Ed.* **2003**, *42*, 5314–5317.
[23] N. Guillou, C. Livage, J. Chaigneau, G. Férey, *Powder Diffr.* **2005**, *20*, 288–293.
[24] E. G. Bakalbassis, M. Korabik, A. Michailides, J. Mrozinski, C. Raptopoulou, S. Skoulika, A. Terzis, D. Tsaousis, *J. Chem. Soc., Dalton Trans.* **2001**, 850–857.
[25] Y.-Q. Zheng, J.-L. Lin, A.-Y. Pan, *Z. Anorg. Allg. Chem.* **2000**, *626*, 1718–1720.
[26] C. Livage, C. Egger, M. Noguès, G. Férey, *C. R. Acad. Sci. Ser. IIc* **2001**, *4*, 221–226.
[27] C. Livage, C. Egger, G. Férey, *Second International Conference on Inorganic Materials*, September 13–16, **2000**, Santa Barbara, USA, P166.
[28] a) S. Konar, P. S. Mukherjee, E. Zangrando, F. Lloret, N. R. Chaudhuri, *Angew. Chem. Int. Ed.* **2002**, *41*, 1561–1563; b) N. Guillou, S. Pastre, C. Livage, G. Férey, *Chem. Commun.* **2002**, 2358–2359.
[29] Y.-Q. Zheng, H.-Z. Xie, *J. Solid State Chem.* **2004**, *177*, 1352–1358.
[30] S. Konar, E. Zangrando, N. R. Chaudhuri, *Inorg. Chim. Acta* **2003**, *355*, 264–271.
[31] a) I. Pantenburg, U. Ruschewitz, *Z. Anorg. Allg. Chem.* **2002**, *628*, 1697–1702; b) F. Hohn, H. Billetter, I. Pantenburg, U. Ruschewitz, *Z. Naturforsch., Teil B* **2002**, *57*, 1375–1381.
[32] Z.-L. Huang, M. Drillon, N. Masciocchi, A. Sironi, J.-T. Zhao, P. Rabu, P. Panissod, *Chem. Mater.* **2000**, *12*, 2805–2812.
[33] M. Kurmoo, H. Kumagai, M. A. Green, B. W. Lovett, S. J. Blundell, A. Ardavan, J. Singleton, *J. Solid State Chem.* **2001**, *159*, 343–351.
[34] C. Livage, N. Guillou, J. Chaigneau, P. Rabu, M. Drillon, G. Férey, *Angew. Chem. Int. Ed.* **2005**, *44*, 2–6.
[35] G. Férey, *J. Solid State Chem.* **2000**, *152*, 37–48.
[36] S.-Y. Yang, L.-S. Long, R.-B. Huang, L.-S. Zheng, S. W. Ng, *Acta Crystallogr., Sect. C* **2003**, *59*, 456–458.
[37] D. S. Kim, P. M. Forster, G. Diaz de Delgado, S.-E. Park, A. K. Cheetham, *Dalton Trans.* **2004**, 3365–3369.
[38] Y. J. Kim, D.-Y. Jung, *Chem. Commun.* **2002**, 908–909.
[39] M. Kurmoo, H. Kumagai, S. M. Hughes, C. J. Kepert, *Inorg. Chem.* **2003**, *42*, 6709–6722.
[40] H. Kumagai, Y. Oka, K. Inoue, M. Kurmoo, *J. Chem. Soc., Dalton Trans.* **2002**, 3442–3446.
[41] T. K. Maji, W. Kaneko, M. Ohba, S. Kitagawa, *Chem. Commun.* **2005**, 4613–4615.
[42] J. A. Kaduk, J. A. Hanko, *J. Appl. Crystallogr.* **2001**, *34*, 710–714.
[43] a) J.-M. Rueff, S. Pillet, N. Claiser, G. Bonaventure, M. Souhassou, P. Rabu, *Eur. J. Inorg. Chem.* **2002**, 895–900; b) J.-M. Rueff, S. Pillet, G. Bonaventure, M. Souhassou, P. Rabu, *Eur. J. Inorg. Chem.* **2003**, 4173–4178.
[44] H. Li, M. Eddaoudi, M. O'Keeffe, O. Yaghi, *Nature* **1999**, *402*, 276–279.
[45] O. M. Yaghi, H. Li, T. L. Groy, *J. Am. Chem. Soc.* **1996**, *118*, 9096–9101.
[46] C. Daiguebonne, A. Deluzet, M. Camara, K. Boubekeur, N. Audrebrand, Y. Gérault, C. Baux, O. Guillou, *Cryst. Growth Des.* **2003**, *3*, 1015–1020.
[47] D. Cheng, M. A. Khan, R. P. Houser, *Cryst. Growth Des.* **2004**, *4*, 599–604.
[48] C. Livage, N. Guillou, J. Chaigneau, P. Rabu, *Mater. Res. Bull.* **2006**, *41*, 981–986.
[49] P. M. Forster, D. S. Kim, A. K. Cheetham, *Solid State Sci.* **2005**, *7*, 594–602.
[50] C. Livage, N. Guillou, J. Marrot, G. Férey, *Chem. Mater.* **2001**, *13*, 4387–4392.
[51] S. O. H. Gutschke, D. J. Price, A. K. Powell, P. T. Wood, *Angew. Chem. Int. Ed.* **2001**, *40*, 1920–1923.
[52] H. Kumagai, M. Akita-Tanaka, K. Inoue, M. Kurmoo, *J. Mater. Chem.* **2001**, *11*, 2146–2151.
[53] H. Kumagai, C. J. Kepert, M. Kurmoo, *Inorg. Chem.* **2002**, *41*, 3410–3422.
[54] S. O. H. Gutschke, D. J. Price, A. K. Powell, P. T. Wood, *Eur. J. Inorg. Chem.* **2001**, 2739–2741.
[55] H. Kumagai, Y. Oka, M. Akita-Tanaka, K. Inoue, *Inorg. Chim. Acta* **2002**, *332*, 176–180.
[56] G. Férey, *J. Fluorine Chem.* **1995**, *72*, 187–193.
[57] a) M. Eddaoudi, D. B. Moler, H. Li, B. Chen, T. M. Reineke, M. O'Keeffe, O. M. Yaghi, *Acc. Chem. Res.* **2001**, *34*, 319–330; b) J. Kim, B. Chen, T. M. Reineke, H. Li, M. Eddaoudi, D. B. Moler, M. O'Keeffe, O. M. Yaghi, *J. Am. Chem. Soc.* **2001**, *123*, 8239–8247.
[58] J. Chen, M. Ohba, D. Zhao, W. Kenako, S. Kitagawa, *Cryst. Growth Des.* **2006**, *6*, 664–668.


 © 2006 Wiley-VCH Verlag GmbH & Co. KGaA, Weinheim 

[59] M. Kurmoo, H. Kumagai, M. Akita-Tanaka, K. Inoue, S. Takagi, *Inorg. Chem.* **2006**, *45*, 1627–1637.
[60] a) S. Neeraj, M. L. Noy, C. N. R. Rao, A. K. Cheetham, *Solid State Sci.* **2002**, *4*, 1231–1236; b) A. Weiss, E. Riegler, C. Robl, *Z. Naturforsch., Teil B* **1986**, *41*, 1329–1332; c) A. Weiss, E. Riegler, C. Robl, *Z. Naturforsch., Teil B* **1986**, *41*, 1333–1336; d) C. R. Lee, C. C. Wang, Y. Wang, *Acta Crystallogr., Sect. B* **1996**, *52*, 966–975.
[61] J. B. Goodenough, *Magnetism and the Chemical Bond*, Wiley, New York, **1963**.

Received: July 14, 2006
Published Online: November 6, 2006

 © 2006 Wiley-VCH Verlag GmbH & Co. KGaA, Weinheim 

DOI: 10.1002/ejic.200600888

# New Type of Photoluminescent Iridium Complex: Novel Synthetic Route for Cationic *trans*-Bis(2-phenylpyridinato)iridium(III) Complex

**Chong Shik Chin,*[a] Min-Sik Eum,[a] Song yi Kim,[a] Choongil Kim,[a] and Sung Kwon Kang[b]**

**Keywords:** Isomerization / Iridium / Photoluminescence / Synthetic methods / Bis(ppy) complex

A new type of iridium(III) complex [*trans*-Ir(ppy)$_2$(PPh$_3$)$_2$]$^+$ (**1**) has been prepared by a novel synthetic method and its structural and photoluminescent characteristics have been compared with those of the *cis* analogue, [*cis*-Ir(ppy)$_2$(PPh$_3$)-(P(OPh)$_3$)]$^+$ (**2**) which has also been newly prepared in this study.

(© Wiley-VCH Verlag GmbH & Co. KGaA, 69451 Weinheim, Germany, 2006)

## Introduction

Studies on iridium(III) complexes of 2-phenylpyridinato (ppy) and related ligands have been extensively carried out as their characteristic luminescent properties seem to be utilizable in the display industry.[1] There are three different types of compounds reported thus far: tris-ppy complexes, *fac*- and *mer*-Ir(ppy)$_3$;[1c,2] bis-ppy complexes, *cis*-Ir(ppy)$_2$(L)(L′);[3] and mono-ppy complexes, *trans,cis*-Ir(ppy)(PR$_3$)$_2$(L)(L′) [*trans*-(PR$_3$)$_2$, *cis*-(L)(L′)].[1a] Emission characteristics such as $\lambda_{max}$, $\Phi_{PL}$, and $\tau$ are somewhat successfully controlled by modifying the ppy ligand and by introducing diverse ancillary ligands (L and L′).[1–4]

There has been no report of *trans*-Ir(ppy)$_2$(L)(L′) containing two ppy ligands *trans* to each other probably because of the lack of the established synthetic procedures, although these *trans* bis-ppy complexes are expected to show emission properties that are comparable with those of *cis*-Ir(ppy)$_2$(L)(L′); the properties may also be tunable by modifying the ppy ligand and by varying ancillary ligands. The *trans*-M(ppy)$_2$ moiety is only observed in four-coordinate Pt(ppy)$_2$[5,6] and Pd(ppy)$_2$,[6] which also emit strongly in the visible region.

We now report the synthesis of new complexes [*trans*-Ir(ppy)$_2$(PPh$_3$)$_2$]$^+$ (**1**) with the two nitrogen atoms *cis* to each other and [*cis*-Ir(ppy)$_2$(PPh$_3$){P(OPh)$_3$}]$^+$ (**2**) and their emission characteristics.

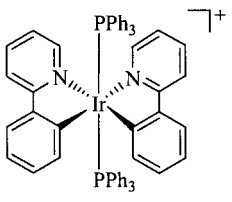


**1**

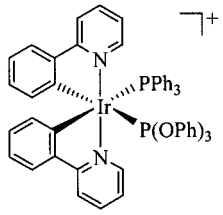


**2**

## Results and Discussion

### Synthesis

Complex **1**, [*trans*-Ir(ppy)$_2$(PPh$_3$)$_2$]$^+$(OTf), is synthesized in high yield following the procedure depicted in Equation (1) where the ppy ligands are added to the metal one by one. Complex **3** was chosen as the starting material because of its unique reactivity that results from the four equatorial ligands (H)$_2$(MeCN)$_2$. These equatorial ligands can be readily replaced by two anionic hydrocarbyls and two other neutral ligands.[7] The mono-ppy complex [Ir(ppy)-(H)(NCMe)(PPh$_3$)$_2$]$^+$ (**4**) has to be isolated in good purity for the next step (**4**→**5**) to obtain **1** in high purity and yield. An analogous mono-ppy complex [Ir(ppy)(H)(OC-Me$_2$)(PPh$_3$)$_2$]$^+$ was previously prepared.[8] The two ligands (H)(MeCN) of **3** are readily replaced with one ppy ligand to give complex **4** by facile dissociation of the MeCN ligand along with H$_2$ evolution. Complex **4**, however, does not react further with ppyH in refluxing toluene. The reaction mixture of **4** and ppyH in C$_3$H$_7$OC$_2$H$_4$OH (b.p. 150 °C) heated at reflux affords **1** with unknown materials, whereas the reaction in refluxing C$_2$H$_5$OC$_2$H$_4$OH (b.p. 133 °C) gives a stable complex [*trans*-Ir(ppy)(ppyH)(H)(PPh$_3$)$_2$]$^+$ (**6**) [Equation (2)] which does not undergo further reaction. Replacement of the labile MeCN ligand by ppyH was also

[a] Chemistry Department, Sogang University,
Seoul 121-742, Korea
Fax: +82-2-701-0967
E-mail: cschin@sogang.ac.kr
[b] Chemistry Department, Choong-Nam University,
Daegeon 305-764, Korea

Supporting information for this article is available on the WWW under http://www.eurjic.org or from the author.

 © 2006 Wiley-VCH Verlag GmbH & Co. KGaA, Weinheim 

observed in the reaction of $[Ir^{I}(NCMe)(CO)(PPh_3)_2]^+$ at 25 °C to give $[Ir^{I}(CO)(ppyH)(PPh_3)_2]^+$ which undergoes oxidative addition of ppyH to produce $[Ir(ppy)(H)(CO)(PPh_3)_2]^+$ at the elevated temperature.[9] Insertion of a bulky alkyne into the Ir–H bond of **4** makes abstraction of the bulky alkenyl ligand, –CH=CH–*p*-$C_6H_4CH_3$, of **5** facile to give **1**. Alkyne insertion into the Ir–H bond of **6** has not been observed yet. Formation of stable hydrocarbon $CH_2$=CH–*p*-$C_6H_4CH_3$ may facilitate the production of **1** from **5**. Attempts to replace one $PPh_3$ of **1** with $P(OPh)_3$ to prepare [*trans*-$Ir(ppy)_2(PPh_3)\{P(OPh)_3\}]^+$ have been unsuccessful thus far.

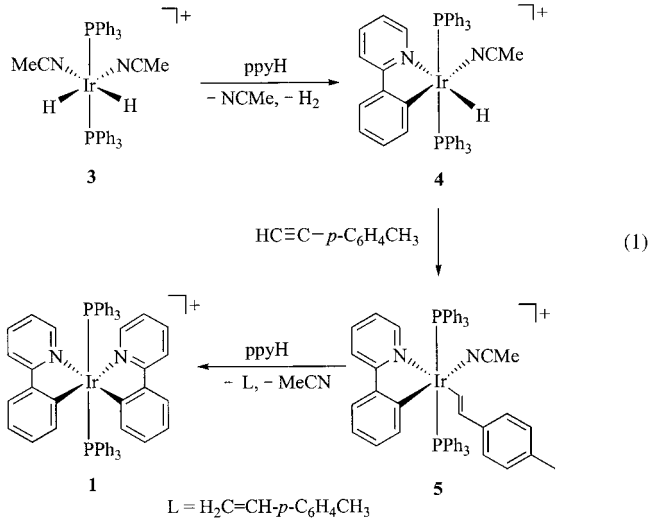


**3** **4** (1) **1** **5**

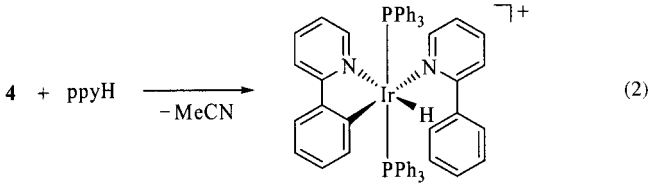


(2) **6**

Complex **2**, [*cis*-$Ir(ppy)_2(PPh_3)\{P(OPh)_3\}]^+$(OTf), has been synthesized [Equation (3)] in order to compare its properties with those of **1**. Attempts to prepare [*cis*-$Ir(ppy)_2(PPh_3)_2]^+$ have been unsuccessful, probably because $PPh_3$ is too large for the *cis*-$Ir(ppy)_2$ moiety to have two $PPh_3$ in the *cis* position[10] (see below for the crystal structure of **2**). Although monophosphorus ligand complexes such as *cis*-$Ir(ppy)_2(PR_3)(X)$ (X = Cl, CN; R = Ph, *n*Bu, OPh)[3c] have been previously prepared, no report of a bis(phosphorus base ligand) complex such as [*cis*-$Ir(ppy)_2(PR_3)\{P(OPh)_3\}]^+$ (**2**) has been made.

Complexes **1**$F_2$, **1**$F_2$Me, **2**$F_2$, and **2**$F_2$Me have also been prepared by the same procedures shown in Equations (1) and (3) to investigate the effects that modification of the ppy ligand would have on the emission characteristics of complexes **1** and **2**.

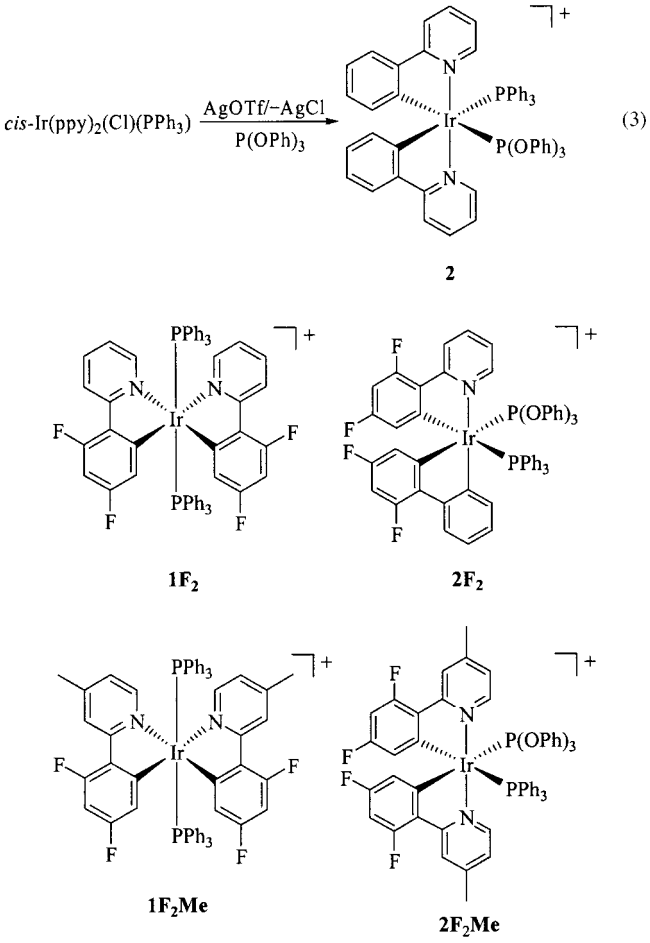


(3)

Newly prepared complexes **1**, **1**$F_2$, **1**$F_2$Me, **2**, **2**$F_2$, **2**$F_2$Me, **4**, **5**, and **6** have been unambiguously characterized by detailed spectral ($^1$H-, $^{13}$C-, $^{31}$P NMR, IR, TOF mass) and elemental analysis data and also crystal X-ray diffraction data analysis for **1** and **2**. Assignment of the spectral signals is mostly straightforward (see Supporting Information for spectra and detailed assignments).

## Crystal Structures

Figures 1 and 2 show the two nitrogen atoms that are *cis* to each other in *trans*-isomer **1** but *trans* to each other in *cis*-isomer **2**. Figure 2 shows the two ppy groups being pushed away from the two phosphorus ligands, which results in a notable difference between the two Ir–N distances (2.089 and 2.042 Å) and the N–Ir–N bond angle (164°), which is far smaller than 180°. It seems less likely for *cis*-bis(ppy) complex **2** to maintain two bulky $PPh_3$ groups in the *cis* position without severe steric hindrance. Density function theory calculations suggest that the HOMO of $Ir(ppy)_3$,[1c,11] $Ir(ppy)_2L_2$,[1f,11] and $Pt(ppy)L_2$[12] involve dπ-orbitals of the metal and whose energy level is closely related to the bond lengths between the metal and the ligands. Both Ir–N and Ir–C distances for **1** are very close to those of *fac*-$Ir(ppy)_3$ and *fac*-$Ir(tpy)_3$ (see Table 1) where all N

 © 2006 Wiley-VCH Verlag GmbH & Co. KGaA, Weinheim 

atoms are *trans* to the C atoms. The Ir–N distances are longer in *trans* complex **1** than those in *cis* complexes **2** and *cis*-Ir(tpy)$_2$(P–P) (Table 1). The Ir–P [phosphite, P(OPh)$_3$] distances are shorter than those in Ir–P [phosphane, PPh$_3$, (PPh$_2$CH$_2$)$_2$BPh$_2$] (see Table 1).

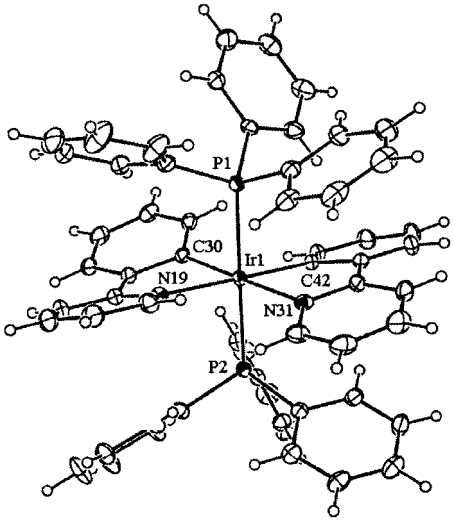


Figure 1. ORTEP drawing of [*trans*-Ir(ppy)$_2$(PPh$_3$)$_2$]$^+$ (**1**) with thermal ellipsoids drawn at the 50% probability level. Selected bond lengths [Å]: Ir1–C42 = 2.050(5); Ir1–C30 = 2.052(5); Ir1–N31 = 2.160(4); Ir1–N19 = 2.168(4); Ir1–P2 = 2.3802(12); Ir1–P1 = 2.3891(12). Selected bond angles [°]: C30–Ir–N31 = 178.99(16); C42–Ir–N19 = 178.81(17); P1–Ir–P2 = 179.19(4).

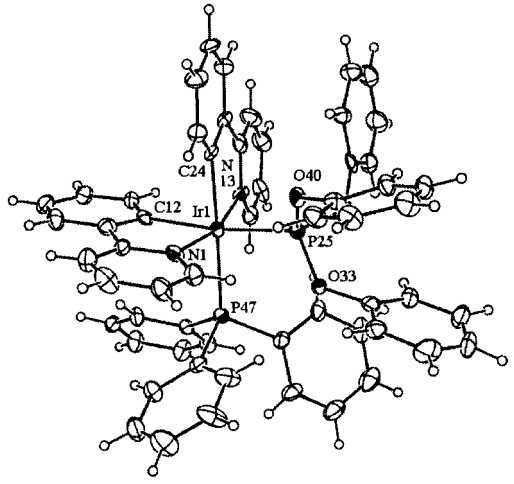


Figure 2. ORTEP drawing of [*cis*-Ir(ppy)$_2$(PPh$_3$){P(OPh)$_3$}]$^+$ (**2**) with thermal ellipsoids drawn at the 50% probability level. Selected bond lengths [Å]: Ir–N1 = 2.089(11); Ir–N13 = 2.042(11); Ir–C12 = 2.072(13); Ir–C24 = 2.071(12); Ir–P25 = 2.307(3); Ir–P47 = 2.433(3). Selected bond angle [°]: N1–Ir–N13 = 164.3(4); C12–Ir–P25 = 169.3(4); C24–Ir–P47 = 177.0(4).

### Emission Spectral Data

Both *trans*- and *cis*- complexes (**1** and **2**, respectively) display relatively strong emission in the green–blue color region (see $\lambda_{max}$ in Table 2). *trans*-Bis(PPh$_3$) complex **1** shows the $\lambda_{max}$ emission at a somewhat longer wavelength than that of *cis*-(PPh$_3$)[P(OPh)$_3$] complex **2**. This small difference in $\lambda_{max}$ may be due to the P(OPh)$_3$ in **2** since *cis*-Ir(ppy)$_2$-X(PPh$_3$) complexes show their emission at longer wavelengths than do *cis*-Ir(ppy)$_2$X[P(OPh)$_3$] complexes.[3c]

Table 2. Photoluminescence spectroscopic data in degassed MeCN at 25 °C for [*trans*-Ir(ppy)$_2$(PPh$_3$)$_2$]$^+$ (**1**), [*trans*-Ir(F$_2$ppy)$_2$-(PPh$_3$)$_2$]$^+$ (**1**F$_2$), [*trans*-Ir(F$_2$Meppy)$_2$(PPh$_3$)$_2$]$^+$ (**1**F$_2$Me), [*cis*-Ir-(ppy)$_2$(PPh$_3$){P(OPh$_3$}]$^+$ (**2**), [*cis*-Ir(F$_2$ppy)$_2$(PPh$_3$)$_2$]$^+$ (**2**F$_2$) and [*cis*-Ir(F$_2$Meppy)$_2$ (PPh$_3$)$_2$]$^+$ (**2**F$_2$Me). [Ir] = 1·10$^{-5}$ M.

| Complex | $\lambda_{max}$ [nm] | $\Phi_{PL}$ | $\tau$ [μs] |
|---|---|---|---|
| **1** | 470, 497 | 0.24 | 4.4 |
| **1**F$_2$ | 452, 479 | 0.36 | 4.8 |
| **1**F$_2$Me | 450, 475 | 0.37 | 3.5 |
| **2** | 458, 488 | 0.18 | 0.31 |
| **2**F$_2$ | 444, 473 | 0.91 | 2.8 |
| **2**F$_2$Me | 442, 470 | 0.72 | 2.9 |

It is well-established that $\lambda_{max}$ emission bands for *cis*-Ir(ppy)$_2$(L)(L′) are shifted to shorter wavelengths when the ppy ligand is F-substituted on the phenyl ring and Me-substituted on the pyridyl ring.[1c,g,3b,4] It is noticed that the blueshifts, which result from the exchange of a ppy ligand to either a F$_2$ppy or F$_2$Meppy ligand, are greater for the *trans* complexes (**1**, **1**F$_2$, **1**F$_2$Me) than they are for the *cis* complexes (**2**, **2**F$_2$, **2**F$_2$Me) (see Table 2). It is also noticed that quantum yields are significantly larger for F$_2$ppy (**1**F$_2$) and F$_2$Meppy (**1**F$_2$Me) complexes than for ppy (**1**) complexes. A striking increase in $\Phi_{PL}$ is observed when the ppy ligand of **2** is replaced with either a F$_2$ppy or F$_2$Meppy ligand (Table 2).

In conclusion, a new type of iridium(III) complex [*trans*-Ir(ppy)$_2$(PPh$_3$)$_2$]$^+$ (**1**) has been prepared by a novel synthetic method and its structural and photoluminescent characteristics have been compared with those of the *cis* analogue, [*cis*-Ir(ppy)$_2$(PPh$_3$){P(OPh)$_3$}]$^+$ (**2**), which has also been newly prepared in this study. No significant differences have been found for their photoluminescent properties because of the geometric differences between *trans*-**1** and *cis*-**2**. Sky

Table 1. Structural and Photoemission data for [*trans*-Ir(ppy)$_2$(PPh$_3$)$_2$]$^+$ (**1**), [*cis*-Ir(ppy)$_2$(PPh$_3$){P(OPh)$_3$}]$^+$ (**2**) and related complexes.

| Complex | Ir–C [Å] | Ir–N [Å] | Ir–P [Å] | $\lambda_{max}$ [nm] |
|---|---|---|---|---|
| [*trans*-(ppy)$_2$Ir(PPh$_3$)$_2$]$^+$ (**1**) | 2.050, 2.052 | 2,160, 2.168 | 2.380, 2.389 | 470, 497 |
| [*cis*-(ppy)$_2$Ir(PPh$_3$){P(OPh)$_3$}]$^+$ (**2**) | 2.072, 2.071 | 2.089, 2.042 | 2.307, 2.433 | 458, 488 |
| *fac*-Ir(ppy)$_3$[1d] | 2.035 | 2.167 | | 545 |
| *fac*-Ir(tpy)$_3$[a],[1c] | 2.024 | 2.132 | | 510 |
| *mer*-Ir(tpy)$_3$[a],[1c] | 2.076, 2.086, 2.020[c] | 2.151,[d] 2.044, 2.065 | | 512 |
| *cis*-(tpy)$_2$Ir(P–P)[a,b],[1f] | 2.047, 2.057 | 2.082, 2.083 | 2.420, 2.431 | 468 |

[a] tpy = 2-(*p*-tolyl)pyridinato. [b] P–P = (PPh$_2$CH$_2$)$_2$BPh$_2$. [c] *trans* to N. [d] *trans* to C.

 © 2006 Wiley-VCH Verlag GmbH & Co. KGaA, Weinheim 

blue color emission can be obtained by replacing the ppy ligands of **1** or **2**, which produce greenish–blue light, with either $F_2$ppy or $F_2$Meppy ligands. New synthetic methods are currently under investigation to replace the $PPh_3$ axial ligand of **1** with a variety of ligands to prepare [*trans*-$Ir(ppy)_2(L)(L')]^{+,0}$ (L, L′ = neutral or anionic C, N, P, O-base) which would show diverse luminescent characteristics. Finally, we wish this study to open a new research field that deals with light emitting iridium complexes containing two ppy ligands and related cyclometalated ligands *trans* to each other.

**Supporting Information** (see footnote on the first page of this article): $^1$H-, $^{13}$C-, $^{31}$P NMR spectra for **1**–**6**. Experimental details with $^1$H-, $^{13}$C-, $^{31}$P NMR, FTIR, TOF-Mass spectral and EA data. PL decay diagrams. CCDC-617305 (**1**) and -617304 (**2**) contain the supplementary crystallographic data for this paper. These data can be obtained free of charge from The Cambridge Crystallographic Data Centre via www.ccdc.cam.ac.uk/data_request/cif.

## Acknowledgments

The authors wish to thank the Korea Research Foundationfor their financial support of this study through the Basic Science Research Institute program grant No. 2005–015-C00222and Prof. B. Lee, Physics Dept., Sogang Univ. for the loan of the apparatus for measurements of PL lifetime.

[1] a) N. Herron, N. S. Radu, E. M. Smith, Y. Wang, *US Patent* **2005**/0048312 A1; b) S. Lamansky, M. E. Thompson, V. Adamovich, P. I. Djurovich, C. Adachi, M. A. Baldo, S. R. Forrest, R. Kwong, *US Patent* **2002**/0182441 A1; c) A. B. Tamayo, B. D. Alleyne, P. I. Djurovich, S. Lamansky, I. Tsyba, N. N. Ho, R. Bau, M. E. Thompson, *J. Am. Chem. Soc.* **2003**, *125*, 7377–7387; d) J. Breu, P. Stössel, S. Schrader, A. Starukhin, W. J. Finkenzeller, H. Yersin, *Chem. Mater.* **2005**, *17*, 1745–1752; e) M. K. Nazeeruddin, R. Humphrey-Baker, D. Berner, S. Rivier, L. Zuppiroli, M. Graetzel, *J. Am. Chem. Soc.* **2003**, *125*, 8790–8797; f) J. Li, P. I. Djurovich, B. D. Alleyne, M. Yousufuddin, N. N. Ho, J. C. Thomas, J. C. Peters, R. Bau, M. E. Thompson, *Inorg. Chem.* **2005**, *44*, 1713–1727.

[2] K. A. King, P. J. Spellane, R. J. Watts, *J. Am. Chem. Soc.* **1985**, *107*, 1431–1432.

[3] a) W. J. Finkenzeller, P. Stößel, H. Yersin, *Chem. Phys. Lett.* **2004**, *397*, 289–295; b) C. Adachi, R. C. Kwong, P. I. Djurovich, V. Adamovich, M. A. Baldo, M. E. Thompson, S. R. Forrest, *Appl. Phys. Lett.* **2001**, *79*, 2082–2084; c) C.-L. Lee, R. R. Das, J.-J. Kim, *Curr. Appl. Phys.* **2005**, *5*, 309–313; d) Q. Zhao, S. Liu, M. Shi, C. Wang, M. Yu, L. Li, F. Li, T. Yi, C. Haung, *Inorg. Chem.* **2006**, *45*, 6152–6160.

[4] a) C.-H. Yang, K.-H. Fang, C.-H. Chen, I.-W. Sun, *Chem. Commun.* **2004**, 2232–2233; b) R. Ragni, E. A. Plummer, K. Brunner, J. W. Hofstraat, F. Babudri, G. M. Farinola, F. Naso, L. De Cola, *J. Mater. Chem.* **2006**, *16*, 1161–1170; c) T. Tsuzuki, N. Shirasawa, T. Suzuki, S. Tokito, *Adv. Mater.* **2003**, *15*, 1455–1458.

[5] a) L. Chassot, E. Müller, A. von Zelewsky, *Inorg. Chem.* **1984**, *23*, 4249–4253; b) M. Maestri, D. Sandrini, V. Balzani, L. Chassot, P. Jolliet, A. von Zelewsky, *Chem. Phys. Lett.* **1985**, *122*, 375–379; c) L. Chassot, A. von Zelewsky, *Inorg. Chem.* **1987**, *26*, 2814–2818.

[6] P. Jolliet, M. Gianini, A. von Zelewsky, G. Bernadinelli, H. Stoeckli-Evans, *Inorg. Chem.* **1996**, *35*, 4883–4888.

[7] a) C. S. Chin, H. Lee, S. Noh, H. Park, M. Kim, *Organometallics* **2003**, *22*, 2119–2123; b) C. S. Chin, M. Kim, H. Lee, S. Noh, K. M. Ok, *Organometallics* **2002**, *21*, 4785–4793.

[8] X. Li, T. Vogel, C. D. Incarvito, R. H. Crabtree, *Organometallics* **2005**, *24*, 62–76.

[9] F. Neve, M. Ghedini, G. De Munno, A. Crispini, *Organometallics* **1991**, *10*, 1143–1148.

[10] [*cis*-$Ir(ppy)_2(PPh_2Me)_2]^+$ will be reported elsewhere.

[11] P. J. Hay, *J. Phys. Chem. A* **2002**, *106*, 1634–1641.

[12] J. Brooks, Y. Babayan, S. Lamansky, P. I. Djurovivh, I. Tsyba, R. Bau, M. E. Thompson, *Inorg. Chem.* **2002**, *41*, 3055–3066.

Received: September 4, 2006
Published Online: November 6, 2006

 © 2006 Wiley-VCH Verlag GmbH & Co. KGaA, Weinheim 

DOI: 10.1002/ejic.200600747

# Mesoporous Nanocrystalline Mixed Metal Oxides from Heterometallic Alkoxide Precursors: Cobalt–Nickel Oxide Spinels for Propane Oxidation

**Moises A. Carreon,*[a] Vadim V. Guliants,*[b] Li Yuan,[b] Andrew R. Hughett,[b] Alan Dozier,[c] Gulaim A. Seisenbaeva,[d] and Vadim G. Kessler[d]**

**Keywords:** Mesoporous Co–Ni oxides / Oligomeric surfactants / Nanocrystalline spinels / Thermal stability / Hydrocarbon combustion

Uniform nanocrystalline mesoporous mixed cobalt–nickel spinel phases displaying unimodal pores in the 7–12 nm range and relatively high specific surface areas up to 83 $m^2$/g were prepared by a novel low temperature synthesis approach in which the desired metal oxide stoichiometries were introduced on a molecular level by reacting heterometallic alkoxide precursors in the presence of supramolecular liquid crystalline phases. The resultant phases, composed mainly of ca. 8–11 nm uniform cobalt–nickel spinel nanoparticles, were highly promising as low-temperature hydrocarbon combustion catalysts investigated in a model reaction of propane oxidation.
(© Wiley-VCH Verlag GmbH & Co. KGaA, 69451 Weinheim, Germany, 2006)

## Introduction

Since the discovery of periodic mesoporous silicas[1] there has been a great interest in developing new materials with diverse compositions, properties and functionalities.[2] In particular, cobalt and nickel oxides are important materials for current technologies. These materials find applications as heterogeneous catalysts, sensors, electrochromic, electrical and optoelectronic devices.[3] Cobalt-based catalysts are of great interest in the field of heterogeneous catalysis. In the oxidized state they are active catalysts for the total combustion of organic molecules.[4] In combination with Mo or W dispersed on an alumina support, they are precursors of sulfided catalysts for hydrosulfurization;[5] and after prereduction, they are highly efficient Fischer–Tropsch synthesis catalysts.[6] The Co–Fe–O system has been used as a catalyst for low-temperature oxidation of phenol into nontoxic compounds,[7] while NiO was investigated as a catalyst for the oxidation of CO.[8] It is well documented that spinels containing transition-metal ions function as efficient catalysts in a number of heterogeneous processes, such as CO oxidation,[9] catalytic combustion of hydrocarbons[10] and selective oxidation and reduction of organic molecules.[11] In particular, Co- and Ni-based mixed oxides including spinels are frequently used as highly efficient hydrocarbon combustion and partial oxidation catalysts.[12]

In the past, cobalt–nickel oxide spinels have been prepared by diverse synthetic routes, such as co-precipitation,[13a,13b] sol-gel[13c,13d] carbonate decomposition,[13c] cryochemical,[13b] spray-pyrolysis.[13b,13e] However, these synthesis approaches have shown poor control over composition and crystal-size homogeneity. Chi et al.[13a] prepared hexagonal $NiCo_2O_4$ spinels (ca. 200 nm) by a co-precipitation method. Although the particle sizes became uniform at calcination temperatures above 400 °C, NiO was present as secondary phase. Lapham and Tseung[13b] reported the synthesis of $NiCo_2O_4$ spinels by several synthesis methods, including co-precipitation, salts decomposition, cryochemical and spray-pyrolysis. Although spinel crystal sizes in the order of 5–16 nm were obtained, these phases were composed of non-homogeneous particles with poorly crystalline structures. Furthermore, the presence of undesirable phases such as NiO, $Co_3O_4$ and $NiCoO_2$ confirmed metal oxide segregation. Attempts to synthesize $NiCo_2O_4$ spinels employing sol-gel chemistry have led to poorly crystalline phases with the presence of undesirable NiO, $Co_3O_4$.[13c,13d]

Herein, we present the novel soft chemical synthesis of mesoporous nanocrystalline cobalt–nickel spinel by the self-assembly of heterometallic alkoxides in the presence of supramolecular liquid crystalline phases. The use of heterometallic alkoxide precursors allows one to incorporate the desired metal oxide stoichiometries. This novel soft-chemistry approach affords desired bulk compositions in nanocrystalline mixed metal oxides under mild conditions, which prevents metal oxide segregation and eliminates the need for high synthesis temperatures commonly required for so-

[a] Department of Chemical and Biological Engineering, University of Colorado Boulder,
Boulder, CO 80309-0424, USA
E-mail: Moises.Carreon@colorado.edu
[b] Department of Chemical and Materials Engineering, University of Cincinnati,
Cincinnati, OH 45221-0012, USA
[c] Department of Chemical and Materials Engineering, University of Kentucky,
Lexington, KY 40506-0046, USA
[d] Department of Chemistry, Swedish University of Agricultural Sciences,
Box 7015, 75007, Uppsala, Sweden

 © 2006 Wiley-VCH Verlag GmbH & Co. KGaA, Weinheim 

lid-state reactions. The resultant mesophases were investigated in the model reaction of propane oxidation.

## Results and Discussion

Several promising synthesis strategies to overcome the limited thermal stability of mesostructured mixed transition-metal oxides have been recently reviewed.[14] One of these strategies was adopted in this work, i.e. the elimination of strong electrostatic interactions at the inorganic–organic interface by directing the synthesis by weak hydrogen-bonding interactions, and consequently improving the thermal stability of the final mesostructure.[14a] This was accomplished by using the non-ionic oligomeric surfactant Brij-35 as a structure-directing agent. As inorganic source, an heterometallic single-source precursor $(Ni_{0.33}Co_{0.67})$-(OMe)(acac)(MeOH) was used for the synthesis of mesoporous nanocrystalline cobalt–nickel oxide spinels. 1-Butanol was chosen as a solvent due to its relatively hydrophobic nature, which promotes an enhanced phase separation between the template and the inorganic phase leading to a better defined mesostructure with robust inorganic walls.[15]

The mesoscopic order of the as-synthesized mixed oxide mesophase was confirmed by SAXS. The SAXS pattern of the as-synthesized mesoporous Co–Ni oxide phases (Figure 1) showed a single broad peak at a *d* spacing of ca. 13.5 nm suggesting the formation of a wormhole mesostructure. Upon calcination at 350, 400 and 450 °C, the low $2\Theta$ angle peak disappeared and the amorphous walls of the as-synthesized mesophase began to crystallize. In spite of the low $2\Theta$ angle peak disappearance for the calcined samples, highly porous mesostructures were observed as confirmed by porosimetry studies. The nitrogen adsorption–desorption isotherms and BJH pore-size distributions on the basis of the adsorption branches of the $N_2$ isotherms for mesoporous Co–Ni oxide phases calcined at different temperatures are shown in Figure 2. The sample calcined at 350 °C showed a type IV isotherm representative of mesoporous solids with an H2 hysteresis loop, suggesting the presence of ink-bottle-shaped or cage-type pores.[16] It had a specific surface area of ca. 83 $m^2/g$ with average unimodal pore diameter of 7 nm. The sample calcined at 400 °C also showed a type IV isotherm with an H2 hysteresis loop. It possessed a specific surface area of ca. 35 $m^2/g$ with average unimodal pore diameter of 11.5 nm. Higher calcination temperature led to the collapse of the mesoporous structure as shown in part c of Figure 2. This sample calcined at 450 °C shows only a specific surface area of ca. 12 $m^2/g$ with disordered random pore-size distribution, indicating the formation of a nonmesoporous structure. The moderate alkaline conditions employed in our synthesis near the isoelectric point of both hydroxo systems, i.e. pH ca. 8 for $Co^{3+}$ and pH ca. 8–10 for $Ni^{2+}$,[17] enhanced the condensation of the Co and Ni ions at the micellar interface. Furthermore, the synthesis conditions near the isoelectric point were favorable for the mesostructural organization of the Co–Ni–O species enabling the formation of heterometallic sol particles. The enhancement in cross-linking of the inorganic framework may be in part responsible for the thermal stability of these mesophases. Furthermore, the TEM image of the thermally stable mesoporous Co–Ni oxide phase shown in Figure 3 confirmed the presence of highly porous nanostructured aggregates. An average pore diameter of ca. 7–8 nm can be observed in agreement with the nitrogen porosimetry data.

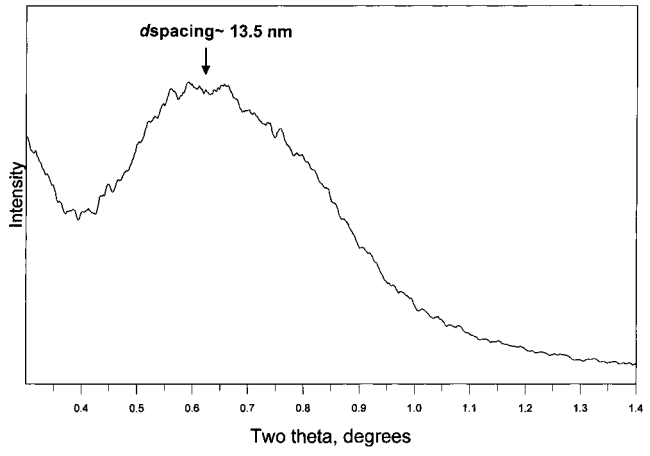


Figure 1. SAXS pattern of the as-synthesized mesoporous Co–Ni oxide phase.

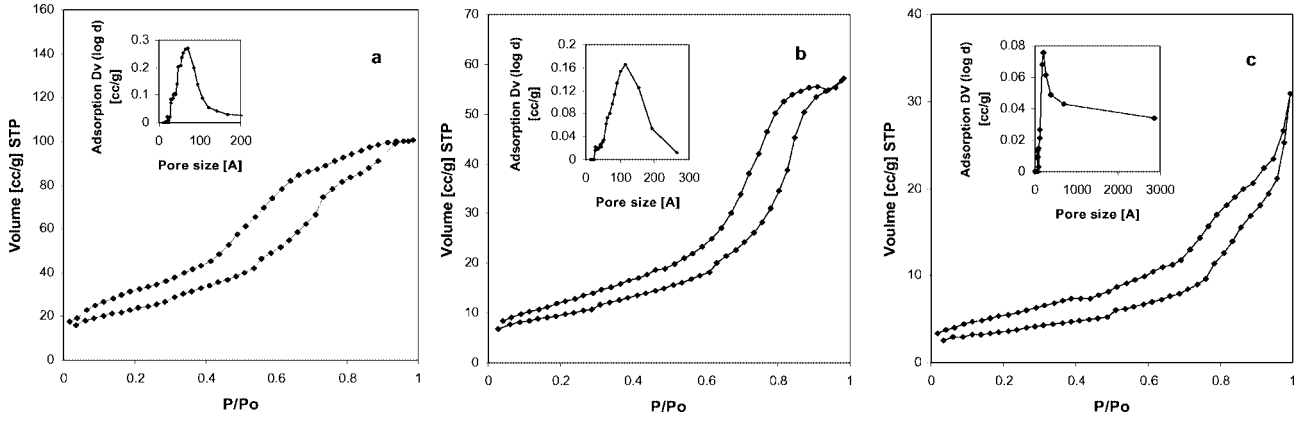


Figure 2. Nitrogen adsorption-desorption isotherms and pore size distribution of mesoporous nanocrystalline cobalt–nickel oxides calcined at (a) 350 °C, (b) 400 °C and (c) 450 °C.

 © 2006 Wiley-VCH Verlag GmbH & Co. KGaA, Weinheim 

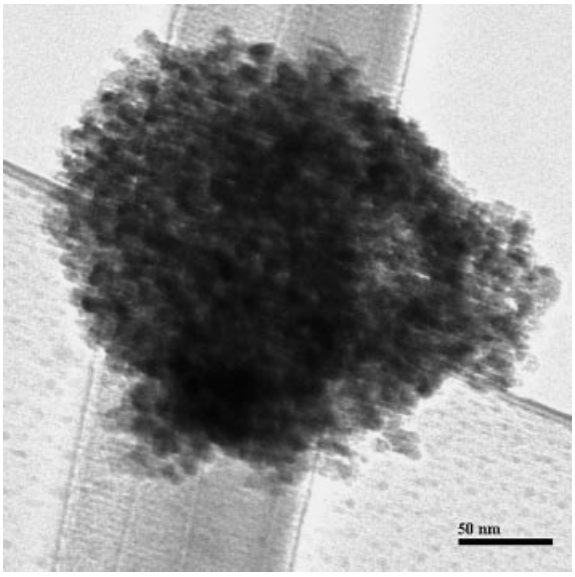


Figure 3. TEM image of mesoporous nanocrystalline cobalt–nickel oxide spinel calcined at 350 °C.

These uniform mesoporous nanostructures were composed of $NiCo_2O_4$ and NiO nanocrystals. Despite the crystallization of amorphous walls upon calcination, the composition of the spinel phase remained essentially the same as that of the original heterometallic alkoxide precursor. Table 1 summarizes the textural properties and spinel average crystal size of the mesoporous cobalt–nickel oxide phases at different calcination temperatures. Figure 4 shows the PXRD patterns of the cobalt–nickel oxide phases as a function of calcination temperature, whereas Table 2 summarizes their compositional and structural properties. The structural properties of the uniform nanocrystalline mesoporous phases were determined using Topas profile fitting software.[18] These findings indicated that the spinel content remained practically unchanged at 81–84% for samples calcined at 350 °C and 400 °C, whereas the nanoparticle size increased from 8.4 nm to 11.1 nm, respectively, due to progressive crystal growth. A remarkable change in compositional and structural properties is evident for the sample calcined at 450 °C. This particular sample contained only 73% of 20.6 nm spinel nanocrystals. The excessive crystal growth at higher calcination temperatures was responsible

Table 1. Selected textural properties and spinel average crystal size of mesoporous nanocrystalline cobalt–nickel oxides as a function of calcination temperature.

| Sample | Average pore size [nm] | Specific surface area [$m^2$/g] | $NiCo_2O_4$ particle size [nm] |
|---|---|---|---|
| mesoporous/350 °C | 7.0 | 83.8 | 8.4 |
| mesoporous/400 °C | 11.5 | 35.0 | 11.1 |
| mesoporous/450 °C | – | 12.1 | 20.6 |

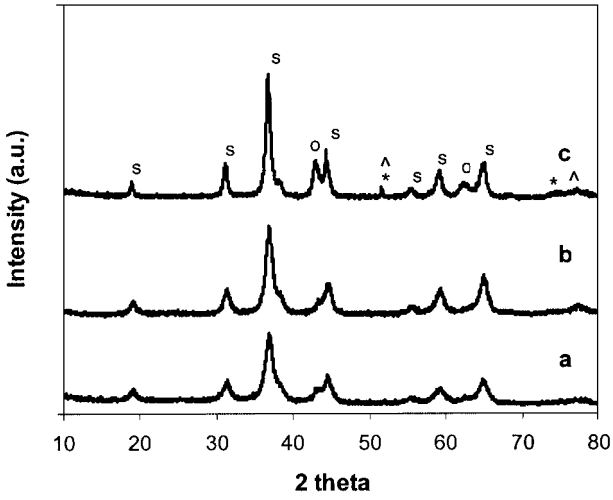


Figure 4. PXRD patterns of mesoporous nanocrystalline cobalt–nickel oxides calcined at (a) 350 °C, (b) 400 °C and (c) 450 °C. s = $NiCo_2O_4$, o = NiO, * = Ni, ^ = Co.

Table 2. Compositional and structural parameters of mesoporous nanocrystalline cobalt–nickel oxides as a function of calcination temperature.

| *T* [°C] | Phase | Phase content [wt.-%] | Lattice parameter [Å] | Volume [$Å^3$] | Mean domain size [nm] | Lattice disorder, $e_0$[a] |
|---|---|---|---|---|---|---|
| 350 | $NiCo_2O_4$ *Fd3 m* | 81.1 | 8.14 | 539 | 8.4 | 0.22 |
| | NiO *Fm3m* | 17.1 | 4.19 | 73.1 | 9.7 | 0.70 |
| | Ni,Co *Fm3m* | 0.80 | 3.54 | 44.3 | 19.4 | 0.01 |
| 400 | $NiCo_2O_4$ *Fd3m* | 83.8 | 8.13 | 538 | 11.1 | 0.12 |
| | NiO *Fm3m* | 15.8 | 4.19 | 71.0 | 14.2 | 0.95 |
| | Ni,Co *Fm3m* | 0.40 | 3.54 | 44.4 | 19.5 | 0.00 |
| 450 | $NiCo_2O_4$ *Fd3m* | 73.2 | 8.13 | 537 | 20.6 | 0.19 |
| | NiO *Fm3m* | 25.8 | 4.21 | 74.4 | 18.8 | 0.43 |
| | Ni,Co *Fm3m* | 1.0 | 3.54 | 44.4 | 20.5 | 0.00 |

[a] The lattice disorder (measured as an average strain, $e_0$) is directly related to the atomic disorder of the metals in the lattice.

 © 2006 Wiley-VCH Verlag GmbH & Co. KGaA, Weinheim 

Table 3. Catalytic properties of dense Co–Ni–O spinel and mesoporous Co–Ni–O oxides in propane combustion at 280 °C. Feed: 6.3 vol.-% propane, 9.4 vol.-% $O_2$ and balance He.

| Catalyst | $C_3$ conversion mol-% | $S(CO)$[a] mol-% | $S(CO_2)$ mol-% | $C_3$ combustion rate nanomol/$m^2$s |
|---|---|---|---|---|
| dense spinel | 11 | 79 | 21 | 1.76 |
| mesoporous/350 °C | 59 | 37 | 63 | 1.40 |
| mesoporous/400 °C | 64 | 31 | 69 | 3.59 |
| mesoporous/450 °C | 9 | 29 | 71 | 1.42 |

[a] $S$ = selectivity.

for the mesostructure collapse. Traces of Ni and Co metals were also detected in all three mesoporous samples.

The morphological changes of the uniform mesoporous mixed Co–Ni oxide phases as a function of calcination temperature are shown in Figure 5. The sample calcined at 350 °C was very uniform containing spheroidal ca. 8.4-nm spinel nanoparticles. The sample calcined at 400 °C contained spheroidal ca. 11.1-nm spinel nanoparticles as well as rhombohedral crystals of some minority phase, probably NiO. Excessive growth of spinel nanocrystals within the channel walls of the inorganic framework led to the formation of well-defined hexagonal and rhombohedral 20-nm spinel nanocrystals which disrupted the mesoporous structure.

The CH analysis (Robertson Microlit Laboratories) indicated that only 0.42, 0.66 and 0.30% C remained in the 350, 400 and 450 °C calcined mesoporous Co–Ni oxide phases, respectively.

Table 3 shows representative catalytic properties of the uniform mesoporous Co–Ni oxides and a dense Co–Ni oxide spinel in propane combustion. The mesoporous catalysts calcined at 350 and 400 °C were much more active in propane combustion than the dense spinel and mesoporous catalyst calcined at 450 °C. These catalysts showed a high degree of propane conversion to CO and $CO_2$ at the same gas space velocity indicating that these mesoporous Co–Ni oxides contained a higher number of active surface sites, whereas the catalytic behavior of the mesoporous Co–Ni oxide calcined at 450 °C was similar to that of the dense spinel, confirming that the former phase was no longer mesoporous. The catalytic data were further analyzed in terms of propane combustion rate normalized by the surface areas of these model catalysts. Some variation of the propane combustion rate was observed (Table 3) suggesting that the nature of the active surface sites was largely unaffected by the self-assembly process. Moreover, the mesoporous catalysts calcined at 350 and 400 °C were significantly more selective to $CO_2$ than CO as compared to the dense spinel phase, which is highly desirable for catalytic combustion applications. We believe that the mesoporous samples showed superior catalytic behavior not only due to their greater surface areas and mesoporous structure, but also because of the relatively small size of the spinel crystallites. In particular, the higher combustion rate observed for the mesoporous sample calcined at 400 °C suggests the existence of optimal crystallite size in the nanoscale regime. Furthermore, the presence of mesoporous channels enhanced the diffusion of reactant and product molecules and improved the mass-transfer characteristics of Co–Ni–O spinels.

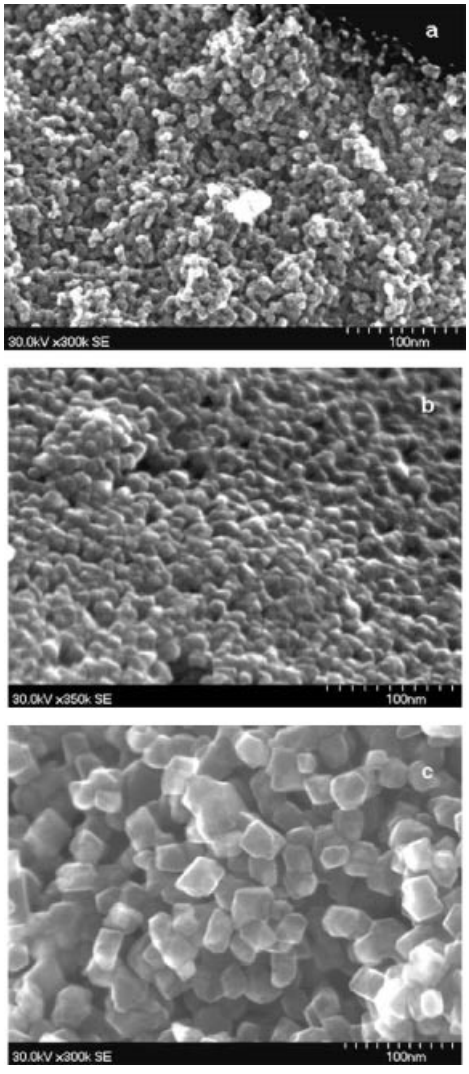


Figure 5. High resolution SEM images of mesoporous nanocrystalline cobalt–nickel oxides calcined at (a) 350 °C, (b) 400 °C and (c) 450 °C.

## Conclusions

Uniform nanocrystalline mesoporous cobalt–nickel oxide spinels were prepared by employing a heterometallic

 © 2006 Wiley-VCH Verlag GmbH & Co. KGaA, Weinheim 

alkoxide precursor and oligomeric alkyl-ethylene oxide surfactant as a structure-directing agent. These resultant mesoporous phases displayed unimodal pores in the 7–12 nm range and relatively high specific surface areas up to 83 $m^2$/g. The mesoporous phases were composed mainly of ca. 8–11 nm Co–Ni–O spinel nanocrystals. These nanocrystalline uniform cobalt–nickel oxides were studied as catalysts in the combustion of propane, showing higher propane conversion to CO and $CO_2$ as compared to a conventional dense spinel. This improved catalytic behavior may be related to their morphological and structural advantages such as larger surface area and mesoporous structure, and to the relatively small size of the spinel crystallites. Furthermore, this soft chemistry method is highly promising for the general synthesis of nanocrystalline and mesoporous mixed metal oxides with desired bulk stoichiometries from heterometallic alkoxide precursors in the presence of supramolecular liquid crystalline phases.

## Experimental Section

**Synthesis of the Heterometallic Single-Source Alkoxide Precursor:** The heterometallic single-source precursor $(Ni_{0.33}Co_{0.67})$(OMe)(acac)(MeOH) was obtained as follows. Na (2.517 g, 109 mmol) was refluxed in a solution of anhydrous toluene (50 mL), 2-methoxyethanol (12.5 mL, 164 mmol) and acetylacetone (5.5 mL). A mixture anhydrous $CoCl_2$ (4.934 g, 36.5 mmol) and $Ni(NH_3)_6Cl_2$ (4.209 g, 18.2 mol) was added to the above solution under vigorous stirring. The resultant heterogeneous mixture was refluxed for 2 h, diluted with additional 20 mL of toluene and refluxed again for another 2 h. The voluminous sediment of NaCl was precipitated overnight and the purple solution transferred into a separate flask and the solvents evaporated to dryness leaving a viscous purple liquid. It was dissolved then in 50 mL of anhydrous MeOH. The formation of purple red prismatic crystals started almost immediately. The mixture was left overnight in a freezer at –30 °C and the solid product was then separated by decantation, washed with 5 mL of cold MeOH and dried in vacuo. The purity of the resultant heterometallic Co–Ni alkoxide was confirmed by elemental analysis and IR. Yield: 9.124 g (76%). $(Ni_{0.33}Co_{0.67})$(OMe)(acac)(MeOH) (221.04): calcd. C 38.0, H 6.4; found C 37.6, H 6.3. IR: $\tilde{\nu}$ = 3221 (s br), 1603 (vs br), 1515 (s), 1397 (s), 1255 (m), 1193 (w), 1124 (w), 1045 (s), 1033 (sh), 1014 (m), 922 (m), 765 (m), 636 (w), 571 (m), 554 (m), 435 (s), 416 (s) $cm^{-1}$. This heterometallic Co–Ni alkoxide was used as inorganic precursor.

**Synthesis of Mesoporous Nanocrystalline Cobalt–Nickel Oxide Spinels:** The mesoporous nanocrystalline cobalt–nickel oxide spinels were prepared as follows. The synthesized heterometallic single-source alkoxide precursor (see above) was dissolved in 1-butanol (Aldrich, 99.9%) and heated at 70 °C. Separately, the oligomeric alkyl-ethylene oxide surfactant Brij-35 $[C_{12}H_{25}(OCH_2CH_2)_{23}OH$, Aldrich] was dissolved in butanol and then added to the inorganic precursor solution. This solution was stirred at room temperature for 3 h, and then precipitated with $NH_4OH$ 1 M (Fisher Chemicals) at pH = 8.0–9.0. The resultant grayish slurry was aged in an open Petri dish at 50 °C for 2 d, and then dried at 90 °C for 1 d to yield brownish powders upon evaporation. The as-synthesized powders were calcined at 350 °C, 400 °C and 450 °C to remove the template and increase crosslinking of the inorganic framework. Typical synthesis compositions on weight basis were 1-butanol:surfactant = 21–26; precursor:surfactant = 0.55–0.60; precursor:solvent = 0.023–0.026. The surfactant volume fraction expressed as $V_{template}/(V_{template} + V_{inorganic})$ was kept constant at Ø = 0.20–0.25. A reference sample of dense Co–Ni oxide spinel was also prepared as described above, but without the addition of the structure directing agent. This dense phase was calcined at 450 °C.

**Characterization:** The nitrogen adsorption–desorption isotherms were measured with a TRI-STAR 3000 porosimeter. The pore-size distributions were calculated from the adsorption branch of the isotherm using the BJH method. The PXRD was measured with a Siemens D5000 diffractometer using high power Ni-filtered Cu-$K_\alpha$ radiation with $\lambda$ = 1.54178 Å source operating at 50 kV/35 mA. High-resolution SEM analysis was performed with Hitachi S-5200 (30 kV, 10 mA). The samples for SEM were deposited onto carbon film-supported 200 mesh copper grids. The SAXS pattern was collected in a Hi-Star area two-dimensional multiwire proportional counter detector (BRUKER AXS GADDS system, $\lambda$ = 1.5418 Å). The TEM image was captured with a GATAN multi-scan digital camera mounted on a JEOL 2010F. The TEM sample was prepared by depositing a small amount of powder on a lacey carbon 200 mesh copper TEM grid. Propane oxidation was conducted at 350–450 °C using a feed of 6.3 vol.-% propane, 9.4 vol.-% oxygen and balance He and ca. 0.1 g of catalyst packed in a 3/8"-quartz tubular microreactor in a programmable oven. The flow rate was 4.2 $cm^3$/min in all cases. An HP 5890II gas chromatograph equipped with an FID and TCD was employed for the reaction product analysis. The carbon balances agreed within 5 mol%.

## Acknowledgments

This research was supported by the National Science Foundation under NSF CAREER Award CTS#0238962 to V. V. Guliants. The authors thank Dr. Srebri Petrov (Chemistry Department, University of Toronto) for his help in collecting the SAXS and XRD data.

[1] a) C. T. Kresge, M. E. Leonowicz, W. J. Roth, J. C. Vartulli, J. S. Beck, *Nature* **1992**, *359*, 710; b) J. S. Beck, J. C. Vartulli, W. J. Roth, M. E. Leonowicz, C. T. Kresge, K. D. Schmitt, C. T. W. Chu, D. H. Olson, E. W. Sheppard, S. B. McCullen, J. B. Higgins, J. L. Schlenker, *J. Am. Chem. Soc.* **1992**, *114*, 10834.
[2] a) J. Y. Ying, C. P. Mehnert, M. S. Wong, *Angew. Chem. Int. Ed.* **1999**, *111*, 58; b) C. J. Brinker, *Curr. Opin. Solid State Mater. Sci.* **1996**, *1*, 798; c) P. Behrens, *Angew. Chem.* **1996**, *108*, 561; *Angew. Chem. Int. Ed. Engl.* **1996**, *35*, 515; d) G. J. A. A. Soler-Illia, C. Sanchez, B. Lebeau, J. Patarin, *Chem. Rev.* **2002**, *102*, 4093.
[3] D. N. Srivastava, N. Perkas, G. A. Seisenbaeva, Y. Koltypin, V. G. Kessler, A. Gedanken, *Ultrason. Sonochem.* **2003**, *10*, 1.
[4] M. Machida, K. Eguchi, H. Arai, *J. Catal.* **1989**, *120*, 377.
[5] H. Topsoe, B. S. Clausen, F. E. Massoth, *Hydrotreating Catalysis*, Springer-Verlag, Berlin, **1996**.
[6] E. Iglesia, S. C. Reyes, R. J. Madon, S. L. Soled, *Adv. Catal.* **1993**, *39*, 221.
[7] S. Christoskova, M. Stoyanova, M. Georgieva, *Appl. Catal. A* **2001**, *208*, 243.
[8] V. L. Budarin, V. Diyuk, L. Matzui, L. Vovchenko, T. Tsvetkova, M. Zakharenko, *J. Therm. Anal. Calorim.* **2000**, *62*, 345.
[9] J. Ghose, K. S. R. C. Murthy, *J. Catal.* **1996**, *162*, 359.
[10] N. Guilhaume, M. Primet, *J. Chem. Soc., Faraday Trans.* **1994**, *90*, 1541.
[11] J. P. Jacobs, A. Maltha, J. G. H. Reintjes, J. Drimal, V. Ponec, H. H. Brongersma, *J. Catal.* **1994**, *147*, 294.

 © 2006 Wiley-VCH Verlag GmbH & Co. KGaA, Weinheim 

[12] a) N. Bahlawane, E. F. Rivera, K. Kohse-Hoinghaus, A. Brechling, U. Kleineberg, *Appl. Catal. B* **2004**, *53*, 245; b) I. Yuranov, N. Dunand, L. Kiwi-Minsker, A. Renken, *Appl. Catal. B* **2002**, *36*, 183; c) S. Liu, L. Xu, S. Xie, Q. Wang, G. Xiong, *Appl. Catal. A* **2001**, *211*, 145.
[13] a) B. Chi, J. Li, Y. Han, Y. Chen, *Int. J. Hydrogen Energy* **2004**, *29*, 605; b) D. P. Lapham, A. C. C. Tseung, *J. Mater. Sci.* **2004**, *39*, 251; c) J. F. Marco, J. R. Gancedo, M. Gracia, J. L. Gautier, E. Rios, F. J. Berry, *J. Solid State Chem.* **2000**, *153*, 74; d) M. El Baydi, S. K. Tiwari, R. N. Singh, J. L. Rehspringer, P. Chartier, J. F. Koenig, G. Poillerat, *J. Solid State Chem.* **1995**, *116*, 157; e) P. Nkeng, J. F. Koenig, J. L. Gautier, P. Chartier, G. Poillerat, *J. Electroanal. Chem.* **1996**, *402*, 81.
[14] a) M. A. Carreon, V. V. Guliants, *Eur. J. Inorg. Chem.* **2005**, *1*, 27; b) A. Taguchi, F. Schuth, *Microporous Mesoporous Mater.* **2005**, *77*, 1.
[15] S. Y. Choi, M. Mamak, N. Coombs, N. Chopra, G. A. Ozin, *Adv. Funct. Mater.* **2004**, *14*, 335.
[16] K. S. W. Sing, D. H. Everett, R. A. W. Haul, L. Moscou, R. A. Pierroti, J. Rouquerol, J. Siemieniewska, *J. Pure Appl. Chem.* **1985**, *57*, 603.
[17] G. A. Parks, *Chem. Rev.* **1965**, *65*, 177.
[18] Topas, v 2.1. User's Manual, Bruker-AXS, Karlsruhe, Germany, **2003**.

Received: August 9, 2006
Published Online: November 3, 2006

 © 2006 Wiley-VCH Verlag GmbH & Co. KGaA, Weinheim 

DOI: 10.1002/ejic.200600835

# Synthesis and Transition Metal Complexes of Novel *N*,*N*,*O* Scorpionate Ligands Suitable for Solid Phase Immobilisation

**Eike Hübner,[a] Thomas Haas,[b] and Nicolai Burzlaff*[a]**

**Keywords:** Solid phase / Immobilisation / Tripodal ligands / *N*,*N*,*O* ligands / Tricarbonyl complexes

Introduction of an allyl or a hydroxymethyl group to bis(3,5-dimethylpyrazol-1-yl)acetic acid (**1**) at the bridging carbon atom leads to the new tripodal *N*,*N*,*O* ligands 2,2-bis(3,5-dimethylpyrazol-1-yl)pent-4-enoic acid (Hbdmpzpen) (**2**) and 2,2-bis(3,5-dimethylpyrazol-1-yl)-3-hydroxypropionic acid (Hbdmpzhp) (**3**). These ligands exhibit similar chemical behaviour to that of **1**, but they have the additional possibility to be immobilised to a solid phase. Esterification of the hydroxymethyl linker of **3** yields 2,2-bis(3,5-dimethylpyrazol-1-yl)-3-acetatopropionic acid (Hbdmpzap) (**4**). The molecular structures of **2**, **3** and **4** all exhibit intramolecular hydrogen bridges. Introduction of a hydroxymethyl group to methyl bis(3,5-dimethylpyrazol-1-yl)acetate (**5**) yields methyl 2,2-bis(3,5-dimethylpyrazol-1-yl)-3-hydroxypropionate (Mebdmpzhp) (**6**), which can be immobilised on Merrifield polymer to yield modified resin **P**-**6**. To investigate the reactivity of these new ligands, manganese and rhenium complexes of **2**, **3** and **4** have been studied. The molecular structures of the two manganese complexes [Mn(bdmpzpen)(CO)$_3$] (**7**) and [Mn(bdmpzap)(CO)$_3$] (**8**) have been confirmed by single-crystal X-ray structure determination. Saponification of polymer resin **P**-**6** and subsequent reaction with [ReBr(CO)$_5$] yields rhenium tricarbonyl complexes anchored on Merrifield polymer (**P**-Re). Solid phase immobilisation of the [Mn(bdmpzpen)(CO)$_3$] (**7**) and [Re(bdmpzpen)(CO)$_3$] (**9**) complexes on 3-mercaptopropyl functionalised silica is initialised by AIBN. The tripodal coordination of manganese and rhenium in these functionalised Merrifield resins (**P**-Re) and silica (**S**-Mn, **S**-Re) is proven by a single A$_1$ and two E signals in the IR spectra that are typical for unsymmetrical "piano stool" type carbonyl complexes.

(© Wiley-VCH Verlag GmbH & Co. KGaA, 69451 Weinheim, Germany, 2006)

## Introduction

Bis(pyrazol-1-yl)acetic acids have proved to be a versatile class of *N*,*N*,*O* ligands, structurally related to the well-known hydrotris(pyrazol-1-yl)borate (Tp). Different synthetic routes for achiral, chiral and enantiopure bis(pyrazol-1-yl)acetic acids have been developed since their introduction to coordination chemistry in 1999 by A. Otero.[1,2] A broad spectrum of transition metal complexes bearing these ligands revealed their behaviour as weak electron-donating ligands in inorganic chemistry,[2a,2c] which often behave almost identically to Tp ligands. Typical examples are the manganese and rhenium tricarbonyl complexes [Mn(bdmpza)(CO)$_3$] and [Re(bdmpza)(CO)$_3$] [bdmpza: bis(3,5-dimethylpyrazol-1-yl)acetate].[2a] Furthermore, model complexes with iron(II) and zinc(II) show their potential to mimic the active site of metalloenzymes with a 2-His-1-carboxylate motif.[2b,2e–2g]

Fixation of these ligands on a solid phase is of particular interest, especially with regard to the potential use as catalysts with easy work up or to achieve dedicated structural environments with sterically less hindered ligands. Most methods used for immobilisation of ligands or transition metal complexes introduce a linker group to the ligand which connects the ligand through stable covalent bonds to the solid material.[3] Isolated double bonds as in allyl or acryl groups open up a broad field of methods available to immobilise the ligand.[4,5] Common examples are copolymerisation, metathesis reactions and especially radical-induced carbon–sulfur bond formations.[5] Recent investigations on structurally related bis(oxazoline) ligands have shown the feasibility of immobilising such ligands while maintaining catalytic activity of the resulting immobilised complexes.[5b] Alternatively, a hydroxymethyl linker would allow solid phase fixation by esterification or ether synthesis.

## Results and Discussion

We found bis(3,5-dimethylpyrazol-1-yl)acetic acid (Hbdmpza) (**1**) to be a convenient starting material for linker modified ligands, which is accessible from dibromo- or dichloroacetic acid in a one-step synthesis.[2a,2b] Deprotonation of the remaining hydrogen at the bridging carbon atom in **1** with excess LDA in THF at –80 °C and subse-

[a] Institute of Inorganic Chemistry, University of Erlangen-Nürnberg,
Egerlandstraße 1, 91058 Erlangen, Germany
Fax: +49-9131-85-27387
E-mail: burzlaff@chemie.uni-erlangen.de
[b] Department of Chemistry, University of Konstanz, Fach M728, 78457 Konstanz, Germany

 © 2006 Wiley-VCH Verlag GmbH & Co. KGaA, Weinheim 

quent alkylation with allyl bromide leads to 2,2-bis(3,5-dimethylpyrazol-1-yl)pent-4-enoic acid (Hbdmpzpen) (**2**) (Scheme 1). Similar modifications of tris(pyrazolyl)methane ligands with various bases such as *n*BuLi or LiN[Si(CH$_3$)$_3$]$_2$ have been reported recently by D. L. Reger et al.[6]

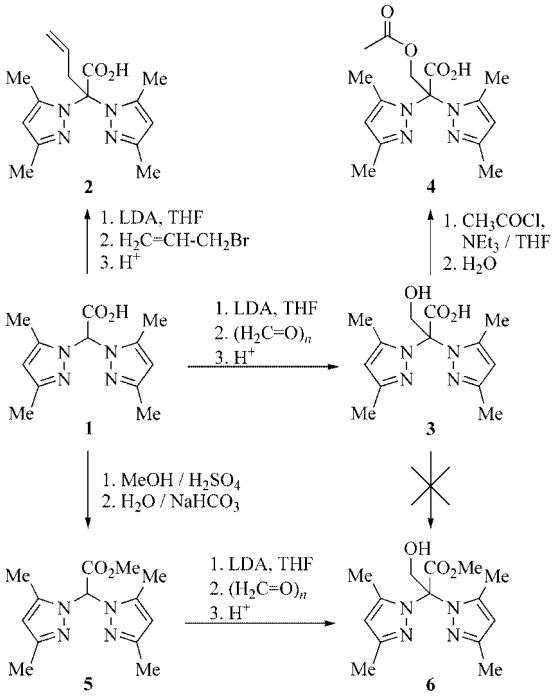


Scheme 1.

Despite heating under reflux, no reaction of the deprotonated carboxylate group with allyl bromide is observed, although this is a well-known reaction, for example in the case of fluoroacetic acid.[7] Thus, the asymmetric carboxylate IR band (THF) is found at 1729 cm$^{-1}$. The molecular structure of **2** (Figure 1) was determined by X-ray crystallography, which revealed an intramolecular hydrogen bridge [d(O1–N11) = 2.504(2) Å] between the carboxylate and the pyrazolyl group. The $^1$H and $^{13}$C NMR spectroscopic data of resulting ligand **2** are almost identical to those of **1**, except for the lack of a $^1$H NMR resonance of the bridging CH group and the additional allyl resonances. This is consistent with a $C_s$ symmetry in solution.

A quite similar reaction with paraformaldehyde instead of allyl bromide yields 2,2-bis(3,5-dimethylpyrazol-1-yl)-3-hydroxypropionic acid (Hbdmpzhp) (**3**) (Scheme 1).

Again, the result of an X-ray structure determination of **3** exhibits an intramolecular hydrogen bond [d(O3–N21) = 2.715(3) Å], in this case between the hydroxy and the pyrazolyl group (Figure 2).

According to the NMR spectroscopic data, the molecular structure exhibits $C_s$ symmetry in solution as well. The IR band (KBr) at 1752 cm$^{-1}$ is assigned to the carboxylate signal. In solution, two IR bands occur for the carboxylate group (THF, 1750 and 1716 cm$^{-1}$), which indicates that there is hydrogen bonding between the carboxylate group and the OH-linker.

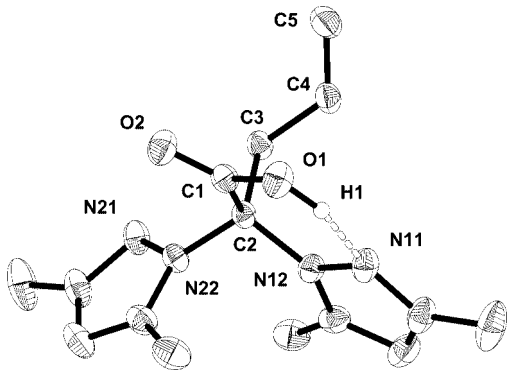


Figure 1. Molecular structure of 2,2-bis(3,5-dimethylpyrazol-1-yl)-pent-4-enoic acid (**2**); thermal ellipsoids are drawn at the 50% probability level. Selected bond lengths [Å] and angles [°]: d(C1–O1) = 1.3194(18), d(C1–O2) = 1.2058(17), d(O1–N11) = 2.504(2), ∠(N12,C2,N22)=108.09(11).

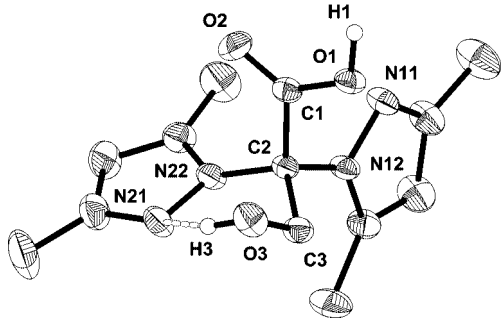


Figure 2. Molecular structure of 2,2-bis(3,5-dimethylpyrazol-1-yl)-3-hydroxypropionic acid (**3**); thermal ellipsoids are drawn at the 50% probability level. Selected bond lengths [Å] and angles [°]: d(C1–O1) = 1.320(3), d(C1–O2) = 1.201(3), d(C3–O3) = 1.414(3), d(O3–N21) = 2.715(3), ∠(N12,C2,N22) = 109.6(2).

Because the linker groups are introduced at the bridging carbon atom, this concept may be extended to homochiral bis(pyrazol-1-yl)acetic acids, which we reported on recently,[2h,2i] without breaking the chirality or chiral induction.

Besides direct solid phase fixation, the functional OH-group of **3** may be used for further modifications. Possible applications would be linking biomolecules by esterification or the addition of new linking groups. Esterification with acetyl chloride at the OH-linker (Scheme 1) leads to **4** and provides a heteroscorpionate ligand with the protected OH-linker.

The intramolecular hydrogen group is found in the X-ray structure, too, [d(O1–N21) = 2.478(3) Å] between the carboxylic acid and the pyrazole nitrogen (Figure 3).

On the other hand, ligand **3** may be modified at the carboxylate donor instead of the OH-linker. This is necessary depending on the applied procedure of solid phase fixation (see below) to prevent the carboxylate donor from acting as a linking group. Although the most obvious protecting group is methyl ester **6** (Scheme 1), direct esterification of **5** results in 2,2-bis(3,5-dimethylpyrazol-1-yl)-1-ethanol caused by decarboxylation. Therefore, methyl ester **6** is synthesised by esterification of **1** in a first step and subsequent

 © 2006 Wiley-VCH Verlag GmbH & Co. KGaA, Weinheim 

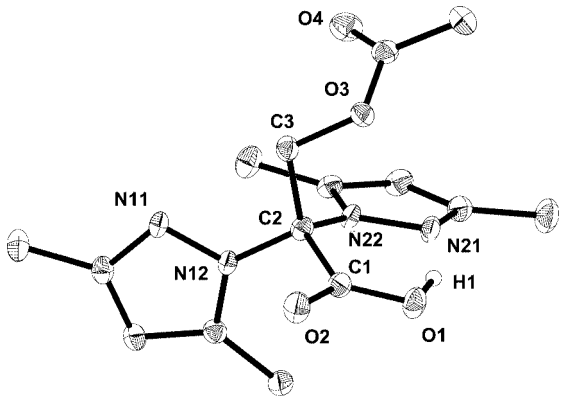


Figure 3. Molecular structure of 2,2-bis(3,5-dimethylpyrazol-1-yl)-3-acetatopropionic acid (**4**); thermal ellipsoids are drawn at the 50% probability level. Selected bond lengths [Å] and angles [°]: d(C1–O1) = 1.306(3), d(C1–O2) = 1.203(3), d(O1–N21) = 2.478(3), ∠(N12,C2,N22)=108.72(18).

reaction of **5** with LDA and paraformaldehyde to **6** (Scheme 1).

To study the potential of these new ligands, **2**, **3**, **4** and **6**, in coordination chemistry and to examine their chemical behaviour, tricarbonyl complexes with manganese and rhenium were synthesised. The general synthesis of such tricarbonyl metal complexes starts from $[MnBr(CO)_5]$ and $[ReBr(CO)_5]$, respectively, and leads after reaction with potassium bis(pyrazol-1-yl)carboxylates to the corresponding tricarbonyl complexes.[2a]

To verify tripodal binding of the solid-bound ligand, manganese and rhenium complexes of ligand **4**, which bears the acetyl protected OH-linker, were synthesised accordingly (Scheme 2). The protected OH linker in **4** acts as model for the solid phase bound ligand.

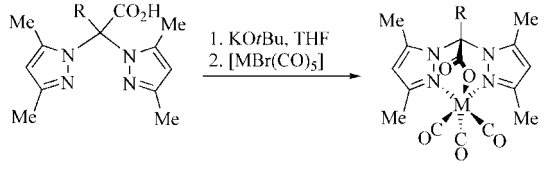


Scheme 2.

In contrast to **3**, ligand **4** reacts with the metal carbonyls as it is well known for the heteroscorpionate ligand Hbdmpza.[2a] This is also observed with allyl-functionalised ligand **2** (Scheme 2).

The formation of tricarbonyl complexes **7** to **10** can be monitored by IR spectroscopy during the reaction. The presence of the tricarbonyl complexes is indicated by a single $A_1$ and two E signals typical for unsymmetrical "piano stool" type carbonyl complexes[2a] [**7**: $\tilde{\nu}$(CO) = 2033, 1939 and 1911 $cm^{-1}$; **9**: $\tilde{\nu}$(CO) = 2023, 1915 and 1892 $cm^{-1}$; **8**: $\tilde{\nu}$(CO) = 2034, 1940 and 1913 $cm^{-1}$; **10**: $\tilde{\nu}$(CO) = 2024, 1918 and 1894 $cm^{-1}$]. These IR absorptions are in good agreement with those of the complexes $[M(bdmpza)(CO)_3]$ (M = Mn, Re) we reported on earlier and prove the desired $\kappa^3$-*N,N,O* coordination of the ligands.[2a] The IR bands at 1687 (**7**), 1697 (**9**), 1692 (**8**) and 1702 (**10**) $cm^{-1}$ are assigned to the asymmetric carboxylate vibration $\tilde{\nu}_{asym}(CO_2^-)$. Complexes **8** and **10** show an additional IR signal at 1761 and 1762 $cm^{-1}$, respectively, which was assigned to the asymmetric carboxylate vibration in the acetyl residue. The complexes are also confirmed by the $[M + H]^+$ peaks in the FAB and FD mass spectra. In the case of **7**, in accordance with $[Mn(bdmpza)(CO)_3]$, the $^1H$ NMR spectra consists of broad signals without clear couplings. Nevertheless, the signals can be assigned unambiguously. Also the $^1H$ and $^{13}C$ NMR spectra of **9** show a clear set of signals for the coordinated bdmpzpen ligand. The carboxylate group shows a $^{13}C$ NMR resonance at $\delta$ = 164.5 ppm. Two $^{13}C$ NMR resonances are observed for the carbonyl ligands of complexes **7** and **9** (**7**: 220.6 ppm, 222.4 ppm, **9**: 195.7 ppm, 196.0 ppm).

Finally, X-ray structure analyses of **7** (Figure 4) and **8** (Figure 5) doubtless reveal the $\kappa^3$-*N,N,O* coordination of tripodal *N,N,O* ligands **2** and **4**. Complex **8** crystallised in a chiral conformation with the acetyl protected linker group positioned between one pyrazole donor and the carboxylate donor (Figure 5 and Scheme 3). Both possible enantiomers are found in the cell because of the space group P-1.

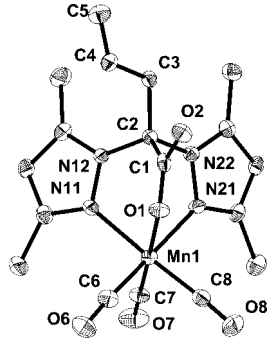


Figure 4. Molecular structure of $[Mn(bdmpzpen)(CO)_3]$ (**7**); thermal ellipsoids are drawn at the 50% probability level. Selected bond lengths [Å] and angles [°]: d(C1–O1) = 1.266(5), d(C1–O2) = 1.233(4), d(Mn1–N11) = 2.049(3), d(Mn1–N21) = 2.090(3), d(Mn1–O1) = 1.993(3), d(Mn1–C6) = 1.813(4), d(Mn1–C7) = 1.805(4), d(Mn1–C8) = 1.817(4), d(C6–O6) = 1.153(5), d(C7–O7) = 1.149(5), d(C8–O8) = 1.149(5), ∠(N11,Mn1,C8) = 175.15(16), ∠(N21,Mn1,C6) = 176.41(15), ∠(O1,Mn1,C7) = 175.61(14), ∠(N11,Mn1,O1) = 83.72(12), ∠(N21,Mn1,O1) = 85.02(12), ∠(N21,Mn1,C7) = 91.77(15), ∠(N11,Mn1,C7) = 93.09(16), ∠(N11,Mn1,N21) = 86.22(12).

Thus, the coordination of the new ligands is not hindered by the additional linker groups at the bridging carbon atom. Coordination of the linker to the metal centre instead of the carboxylate donor does not take place in the case of **2**. The position of the allyl group in **7** (Figure 3), as well as of the acetyl group in **8**, indicate its ability to act as a linking group to solid phase. The agreement of the bond lengths and angles of **7** and **8** with those of the previously reported $[Mn(bdmpza)(CO)_3]$[2a] implies similar ligand properties of **2**, **3** and **4** in comparison to those of **1**.

Both complexes $[Mn(bdmpzap)(CO)_3]$ (**8**) and $[Re(bdmpzap)(CO)_3]$ (**10**) exhibit an AB system in the $^1H$ NMR spectrum for the -$CH_2O$- protons because of the chi-

 © 2006 Wiley-VCH Verlag GmbH & Co. KGaA, Weinheim 

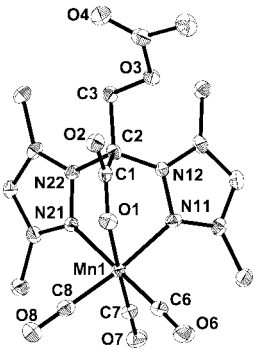


Figure 5. Molecular structure of [Mn(bdmpzap)$(CO)_3$] (**8**); thermal ellipsoids are drawn at the 50% probability level. Selected bond lengths [Å] and angles [°]: d(C1–O1) = 1.263(4), d(C1–O2) = 1.226(4), d(Mn1–N11) = 2.037(3), d(Mn1–N21) = 2.060(3), d(Mn1–O1) = 1.999(3), d(Mn1–C6) = 1.809(4), d(Mn1–C7) = 1.786(4), d(Mn1–C8) = 1.808(5), d(C6–O6) = 1.150(4), d(C7–O7) = 1.157(5), d(C8–O8) = 1.152(5), ∠(N11,Mn1,C8) = 173.26(16), ∠(N21,Mn1,C6) = 176.70(17), ∠(O1,Mn1,C7) = 177.21(15), ∠(N11,Mn1,O1) = 84.22(11), ∠(N21,Mn1,O1) = 86.51(11), ∠(N21,Mn1,C7) = 92.22(15) ∠(N11,Mn1,C7) = 93.19(16), ∠(N11,Mn1,N21) = 84.39(12).

Scheme 3. Dynamic interconversion of the two enantiomers of complexes **8** and **10**. The Newman projection shows the view along the C3–C2 axis. The numbering was carried out according to Figure 5.

rality described above. These AB systems, as well as the signals of the two methyl groups, are rather broad due to a dynamic interconversion of the two possible enantiomers (Scheme 3). This dynamic interconversion might also explain why rather weak $^{13}C$ NMR spectroscopic data were obtained for manganese and rhenium complexes **8** and **10**.

In the case of OH-functionalised ligand **3**, the IR spectra of the manganese and the rhenium compounds indicate the formation of at least two species because several bands for the CO signals appear. This is backed by NMR spectra, which shows more than one set of signals for the methyl groups of the pyrazole donors. Furthermore, the NMR signals are broadened and especially the carboxylate group is not clearly visible in the IR spectra. Although we could not solve this problem in detail, this might indicate a dynamic equilibrium in which either the carboxylate donor or the hydroxo linker coordinates towards the metal centre. A related dynamic behaviour was reported recently by W. Kläui and coworkers.[8] After binding the hydroxymethyl linker to solid phase, this part of the molecule will presumably act no longer as a donor towards the metal centre as shown in complex **8**. Thus, this behaviour will not interfere with the future use of ligands **3** or **6** as a solid-bound *N*,*N*,*O* ligand.

## Solid Phase Binding

The purpose of our efforts, as mentioned above, is to bind monoanionic *N*,*N*,*O* ligands to various solid phases. This solid phase fixation of the ligands and their complexes should strongly affect their chemical properties. For instance, the formation of bisligand complexes [$ML_2$] as well as the autoxidation or dimerisation of complexes should be prevented.

Chloromethylated resin, so called Merrifield polymer, is one of the most popular solid phase supports. Thus, we used this resin in our first attempt to bind linker modified bis(pyrazol-1-yl)acetic acids to a solid phase. Primarily, Merrifield polymer was designed to bind carboxylic acids. Thus, we had to use the ester methyl 2,2-bis(3,5-dimethylpyrazol-1-yl)-3-hydroxypropionate (**6**) instead of the 2,2-bis(3,5-dimethylpyrazol-1-yl)-3-hydroxypropionic acid (**3**). Fixation on the resin is achieved by nucleophilic substitution of the benzylic chlorine for the deprotonated OH-linker of **6** (Scheme 4). The best result was obtained by using a mixture of KO*t*Bu, 18-crown-6 and CsBr in this reaction. To verify the functionalisation of the polymer, elemental analyses of solid phase samples were accomplished. Determination of the nitrogen content does not only prove the binding of ligand **6** to the solid phase, but also enables the calculation of the degree of functionalisation (Table 1). Usually, an occupancy of more than 20% of the theoretical sites was achieved. Subsequent saponification of functionalised Merrifield resin **P-6** with $H_2O$/NaOH/THF leads to the targeted monoanionic *N*,*N*,*O* functionalised solid phase. Further reaction with [$ReBr(CO)_5$] afforded polymer mounted tricarbonyl rhenium complex **P**-Re (Scheme 4). A similar reaction with [$MnBr(CO)_5$] has not been successful so far.

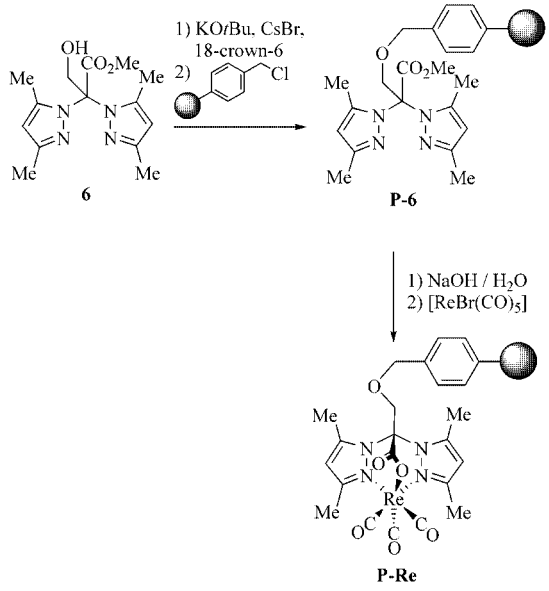


Scheme 4.

The IR spectra of **P**-Re exhibits a single $A_1$ and two E signals [$\tilde{\nu}$(CO) = 2022, 1915 and 1890 $cm^{-1}$] (Figure 6c). The location of these signals is almost identical to those of the complex [Re(bdmpzap)$(CO)_3$] (**10**) (Figure 6a) which we described above. An additional signal at 1964 $cm^{-1}$ is caused by the Merrifield polymer (Figure 6b and Fig-

 © 2006 Wiley-VCH Verlag GmbH & Co. KGaA, Weinheim 

Table 1. Occupancy of the functionalised solid phases **P-6**, **S-2**, **S**-Mn and **S**-Re.

| Solid phase | Linker [mmol g$^{-1}$] | Functionalised solid phase | Nitrogen content [%] | Ligand/ complex [mmol g$^{-1}$] | Occupancy of sites [%] |
|---|---|---|---|---|---|
| Merrifield polymer | 1.1 | **P-6** | 1.26 | 0.23 | 21 |
| Mercaptopropyl silica | 0.98 | **S-2** | 0.97 | 0.17 | 18 |
| Mercaptopropyl silica[a] | 0.98 | **S**-Mn | 0.20 | 0.036 | 4 |
| Mercaptopropyl silica[b] | 0.98 | **S**-Mn-II | 0.35 | 0.063 | 6 |
| Mercaptopropyl silica[a] | 0.98 | **S**-Re | 0.23 | 0.041 | 4 |
| Mercaptopropyl silica[b] | 0.98 | **S**-Re-II | 0.44 | 0.078 | 8 |

[a] After 8 h. [b] After 48 h.

ure 6c). A control experiment with unfunctionalised methyl bis(3,5-dimethylpyrazol-1-yl)acetate (**5**) showed no occupancy of the polymer sites and subsequently no $A_1$ and E signals but a typical IR spectrum of Merrifield polymer (Figure 6b). Therefore, the results of our experiments prove a solid phase fixation of the ligand and the resulting tricarbonyl complex as well as a facial coordination of rhenium(I) by the monoanionic *N,N,O* tripod ligand.

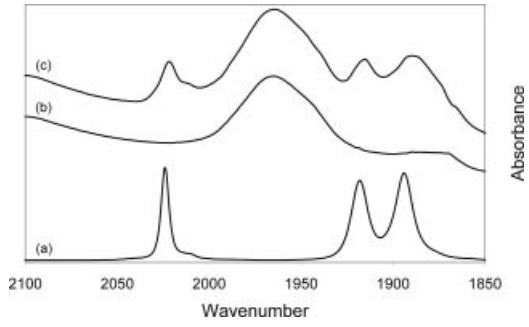


Figure 6. IR spectra of (a) [Re(bdmpzap)(CO)$_3$] (**10**) (THF), (b) Merrifield polymer (THF) and (c) **P**-Re – the rhenium tricarbonyl complex anchored on Merrifield polymer (THF).

Unfortunately, the solvents compatible to reactions with Merrifield polymer are quite limited. Especially, reactions in water are almost impossible. To overcome this limitation for future applications, the fixation on silica solid phase can be achieved by mercaptopropyl functionalised silica. Immobilisation of chelating *N,N* ligands bearing allyl linker groups on such functionalised silica has been reported recently by Mayoral et al.[5b] Following a similar procedure, 2,2-bis(3,5-dimethylpyrazol-1-yl)pent-4-enoic acid (**2**) was immobilised by a radical induced reaction with mercaptopropyl silica in the presence of azobisisobutyronitrile (AIBN). An analysis of the nitrogen content of resulting silica **S-2** showed an occupancy of more than 17% of the mercaptopropyl sites (Table 1). Unfortunately, the mercaptopropyl functionalised silica itself as well as the modified silica **S-2** can undergo complexation with [MnBr(CO)$_5$] and [ReBr(CO)$_5$]. After reaction with [ReBr(CO)$_5$], both silica exhibit various rather broad IR signals, which could be assigned to signals of various carbonyl species.

In an attempt to overcome this problem we tried to immobilise the [Mn(bdmpzpen)(CO)$_3$] (**7**) and [Re(bdmpzpen)(CO)$_3$] (**9**) complexes themselves. On following this approach, complexes **7** and **9** were grafted onto mercaptopropyl silica in the presence of AIBN (Scheme 5).

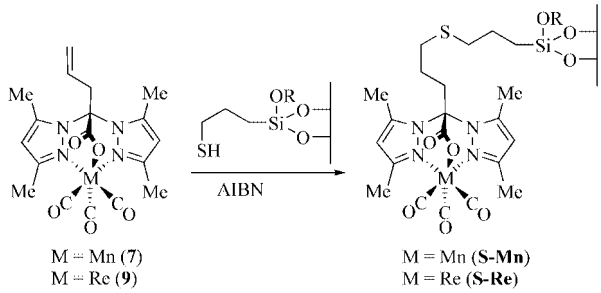


Scheme 5.

Elemental analyses of resulting silica samples **S**-Mn and **S**-Re were accomplished to determine the nitrogen content. The deduced occupancy of mercaptopropyl sites by the tricarbonyl complexes add up to 3.6% (**S**-Mn) and 4.2% (**S**-Re) (Table 1). IR spectra of silica phases **S**-Mn and **S**-Re show signals that can be assigned to the $A_1$ and E signals of the grafted manganese and rhenium tricarbonyl complexes [**S**-Mn: $\tilde{\nu}$(CO) = 2039, 1948 and 1923 cm$^{-1}$ (Figure 7d); **S**-Re: $\tilde{\nu}$(CO) = 2027, 1920 and 1905 cm$^{-1}$ (Figure 7f)]. A longer reaction time (48 h) results in higher occupancies

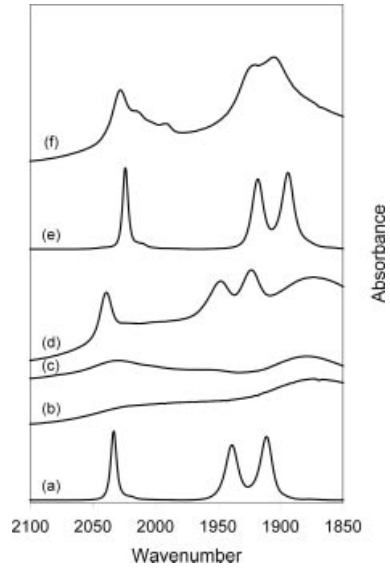


Figure 7. IR spectra of (a) [Mn(bdmpzpen)(CO)$_3$] (**7**) (THF), (b) mercaptopropyl silica (Nujol), (c) control experiment with [Mn(bdmpza)(CO)$_3$], (d) manganese tricarbonyl complex **7** immobilised on silica (**S**-Mn) (Nujol), (e) [Re(bdmpzpen)(CO)$_3$] (**9**) (THF) and (f) rhenium tricarbonyl complex **9** immobilised on silica (**S**-Re) (Nujol).

 © 2006 Wiley-VCH Verlag GmbH & Co. KGaA, Weinheim 

[6.4% (**S**-Mn-II) and 8.0% (**S**-Re-II)], but caused also obscure IR spectra probably due to degradation of the carbonyl complexes or a further reaction with surrounding non innocent free SH-groups.

Neither the IR spectra of the mercaptopropyl functionalised silica (Figure 7b) nor that of a control experiment with the unfunctionalised complex [Mn(bdmpza)$(CO)_3$] (Figure 7c) show any signals in this region. Thus, these results prove an immobilisation of manganese and rhenium tricarbonyl complexes on silica through a *N*,*N*,*O* tripod ligand with an allyl linker.

## Conclusions

In conclusion, modifications to the in coordination chemistry well-established ligand Hbdmpza (**1**) led to the new functionalised ligands 2,2-bis(3,5-dimethylpyrazol-1-yl)pent-4-enoic acid (**2**) and 2,2-bis(3,5-dimethylpyrazol-1-yl)-3-hydroxypropionic acid (**3**) bearing an allyl or an hydroxymethyl linker for solid phase fixation. These ligands, or their protected analogues, provide similar coordination properties as **1**, proven by the synthesis of various transition metal carbonyl complexes. By way of well-known solid phase coupling reactions, **2** and **3** have been grafted on silica and on Merrifield polymer. The degree of functionalisation of the solid phase can be determined by elemental analysis. Furthermore, we were able to prove the typical tripodal monoanionic *N*,*N*,*O* binding behaviour by the characteristic IR spectra of immobilised tricarbonyl complexes.

## Experimental Section

**General Remarks:** All operations were carried out under an inert gas atmosphere by using conventional Schlenk techniques. Solvents were freshly distilled and degassed prior to use from appropriate drying agents. The yields refer to analytically pure substances and were not optimised. IR spectra were recorded with a Biorad FTS 60 spectrometer or a Varian Excalibur FTS-3500 FTIR spectrometer in $CaF_2$ cuvettes (0.2 mm) or in Nujol. $^1H$ and $^{13}C$ NMR spectra were measured with Bruker AC 250 MHz, Varian Inova 400 MHz or Bruker DPX300 instruments. $\delta$ values are measured relative to TMS or the deuterated solvent. Mass spectra were recorded with a modified Finnigan MAT 312 instrument by using either EI or FAB technique with 3-nitrobenzyl alcohol as matrix for complexes **7** and **9** and glycerine/NaI as matrix for ligands **2** and **3** or were recorded on a Jeol JMS-700 instrument using FD technique. Elemental analyses were measured with a Heraeus CHN-O-Rapid, Euro EA 3000 (Euro Vector) and EA 1108 (Carlo Erba) ($\sigma \pm 1$% of the measured content). A modified Siemens P4 diffractometer and a STOE IPDS II diffractometer were used for X-ray structure determination. Chemicals were used as purchased without further purification. Chloromethylated resin, "Merrifield polymer" [polystyrene-divinylbenzene, 1% cross linking, 1.1 mmol Cl $g^{-1}$, 200–400 mesh (Fluka)] and 3-mercaptopropyl functionalised silica [0.98 mmol S $g^{-1}$ (Aldrich)] were used as purchased. Both solid phases were evacuated for 2 h ($10^{-2}$ mbar) and flushed with dry nitrogen prior to use. Bis(3,5-dimethylpyrazol-1-yl)acetic acid (**1**) was synthesised as described earlier but starting from dichloroacetic acid instead of dibromoacetic acid and with a reaction time of 72 h.[2b] [$ReBr(CO)_5$], [$MnBr(CO)_5$] and [Mn(bdmpza)$(CO)_3$] were synthesised according to the literature.[2a,9a,9b] Solid phase fixation on mercaptopropyl silica was achieved according to the literature.[5b]

**Synthesis of 2,2-Bis(3,5-dimethylpyrazol-1-yl)pent-4-enoic Acid (2):** A solution of Hbdmpza (**1**) (3.30 g, 13.3 mmol) in dry THF (200 mL) was treated with LDA (≈ 1.8 M in heptane/THF/ethylbenzene, 23.0 mL, 41.4 mmol) at –80 °C. The solution was warmed up to –40 °C over a period of 2 h and was stirred for 1 h at –40 °C. Allyl bromide (9.00 mL, 12.6 g, 104 mmol) was added, and the mixture was warmed up to ambient temperature. The solution was heated under reflux for 30 min and then stirred overnight. The solvent was removed in vacuo, and the residue was dissolved in water. The aqueous solution was acidified with dilute HCl to pH 7–8 and extracted with pentane ($1 \times 100$ mL) to remove impurities. The aqueous solution was further acidified to pH 4 and **2** precipitated immediately. The crude mixture was extracted with pentane ($4 \times 200$ mL) and the combined organic layers were dried with $Na_2SO_4$ and concentrated in vacuo. Product **2** was recrystallised from pentane in colourless blocks suitable for X-ray structure determination. Yield: 1.68 g (5.82 mmol, 44%). M.p. 84–86 °C. $^1H$ NMR (400 MHz, $CDCl_3$, 25 °C): $\delta$ = 1.71 [d, $J_{H,H}$ = 0.4 Hz (through space), 6 H, $C^5$-$CH_3$], 2.27 (s, 6 H, $C^3$-$CH_3$), 3.57 (dd, $^3J_{H,H}$ = 7.5 Hz, $^4J_{H,H}$ = 1.0 Hz, 2 H, $CH_2$), 5.09 (ddt, $^3J_{H,H}$ = 16.9 Hz, $^2J_{H,H}$ = 1.6 Hz, $^4J_{H,H}$ = 1.2 Hz, 1 H, =$CH_{2,allyl}$), 5.10 (ddt, $^3J_{H,H}$ = 10.2 Hz, $^2J_{H,H}$ = 1.6 Hz, $^4J_{H,H}$ = 0.8 Hz, 1 H, =$CH_{2,allyl}$), 5.59 [dddt, $^3J_{H,H}$ = 16.3 Hz, $^3J_{H,H}$ = 10.8 Hz, $^3J_{H,H}$ = 7.4 Hz, $J_{H,H}$ = 1.1 Hz (through space), 1 H, =$CH_{allyl}$], 5.87 (s, 2 H, $H_{pz}$) ppm. $^{13}C$ NMR (100.5 MHz, $CDCl_3$, 25 °C): $\delta$ = 10.7 ($C^5$-$CH_3$), 13.2 ($C^3$-$CH_3$), 44.0 ($CH_2$), 80.9 ($C_{bridge}$), 108.7 ($C_{pz}$-H), 121.2 (=$CH_{2,allyl}$), 129.3 ($CH_{allyl}$), 141.5 ($C^5_{pz}$), 146.3 ($C^3_{pz}$), 168.7 ($CO_2H$) ppm. IR (THF): $\tilde{\nu}$ = 1729 ($CO_2H$), 1563 (C=N) $cm^{-1}$. FAB-MS: *m*/*z* (%) = 311 (18) $[M + Na]^+$, 289 (28) $[M + H]^+$, 193 (28) $[M - pz]^+$, 149 (100) $[M - pz - CO_2H]^+$, 95 (62) $[pz]^+$. $C_{15}H_{20}N_4O_2$ (288.35): calcd. C 62.48, H 6.99, N 19.43; found C 62.46, H 6.81, N 18.91.

**Synthesis of 2,2-Bis(3,5-dimethylpyrazol-1-yl)-3-hydroxypropionic Acid (3):** A solution of Hbdmpza (**1**) (3.30 g, 13.3 mmol) in dry THF (200 mL) was treated with LDA (≈ 1.8 M in heptane/THF/ethylbenzene, 23.0 mL, 41.4 mmol) at –80 °C and warmed up to –40 °C over a period of 2 h. After 1 h at –40 °C, paraformaldehyde (4.00 g, 132 mmol) was added. The mixture was warmed up to ambient temperature and finally heated under reflux for 60 min and stirred overnight. The solvent was removed in vacuo, the residue was dissolved in water and washed with pentane (200 mL). The aqueous phase was acidified with dilute HCl (pH 2) and extracted with diethyl ether ($4 \times 200$ mL). The combined diethyl ether layers were dried ($Na_2SO_4$) and concentrated under reduced pressure. Product **3** was recrystallised from diethyl ether. Yield: 2.12 g (7.62 mmol, 57%). M.p. 119–121 °C. $^1H$ NMR (400 MHz, $CDCl_3$, 25 °C): $\delta$ = 1.72 (s, 6 H, $C^5$-$CH_3$), 2.29 (s, 6 H, $C^3$-$CH_3$), 4.43 (s, 2 H, $HOCH_2$) 5.96 (s, 2 H, $H_{pz}$) ppm. $^{13}C$ NMR (100.5 MHz, $CDCl_3$, 25 °C): $\delta$ = 10.6 ($C^5$-$CH_3$), 13.2 ($C^3$-$CH_3$), 68.8 ($CH_2$-OH), 81.5 ($C_{bridge}$), 108.5 ($C_{pz}$-H), 143.1 ($C^5_{pz}$), 148.0 ($C^3_{pz}$), 168.9 ($CO_2H$) ppm. IR (KBr): $\tilde{\nu}$ = 1752 ($CO_2H$), 1561 (C=N) $cm^{-1}$. FAB-MS: *m*/*z* (%) = 300 (18) $[M + Na]^+$, 217 (100) $[M - CO_2H - OH]^+$, 203 (100) $[M - CO_2H - CH_2OH]^+$. $C_{13}H_{18}N_4O_3$ (278.31): calcd. C 56.10, H 6.52, N 20.13; found C 56.62, H 6.75, N 19.91.

**Synthesis of 2,2-Bis(3,5-dimethylpyrazol-1-yl)-3-acetatopropionic Acid (4):** To a solution of Hbdmpzhp (**3**) (1.00 g, 3.60 mmol) in dichloromethane (100 mL), excess $NEt_3$ (4.00 mL, 2.92 g,

 © 2006 Wiley-VCH Verlag GmbH & Co. KGaA, Weinheim 

28.9 mmol) was added. Acetyl chloride (0.64 mL, 0.71 g, 9.00 mmol) was then added dropwise under continuous stirring. The mixture was stirred for 1 d. Water (20 mL) was added slowly and the two-phased mixture was vigourously stirred for 3 h. The solvents were removed in vacuo. The slurry residue was dissolved in water, acidified with dilute HCl (pH 2) and extracted with diethyl ether (4 × 200 mL). The combined organic layers were dried ($Na_2SO_4$) and concentrated under reduced pressure to the oily residue of **4**. Product **4** was recrystallised from acetone in colourless blocks suitable for X-ray structure determination. Yield: 612 mg (2.65 mmol, 53%). M.p. 107–109 °C. $^1$H NMR ($CDCl_3$, 300 MHz, 25 °C): $\delta$ = 1.74 (s, 6 H, $C^5$-$CH_3$), 1.97 (s, 3 H, $CH_3CO$), 2.27 (s, 6 H, $C^3$-$CH_3$), 5.32 (s, 2 H, OCO-$CH_2$-), 5.93 (s, 2 H, $H_{pz}$) ppm. $^{13}$C NMR ($CDCl_3$, 75.5 MHz, 25 °C): $\delta$ = 10.6 ($C^5$-$CH_3$), 13.2 ($C^3$-$CH_3$), 20.4 ($CH_3$-CO), 66.6 ($CH_2$-O), 78.3 ($C_{bridge}$), 108.8 ($C_{pz}$-H), 142.0 ($C^5{}_{pz}$), 147.2 ($C^3{}_{pz}$), 167.9 (COOH), 169.4 ($CH_3CO$) ppm. IR (THF): $\tilde{\nu}$ = 1759 ($CO_2H$), 1718 ($CH_3CO$), 1565 (C=N) cm$^{-1}$. FD-MS: *m*/*z* (%) = 322 (100) [M + H]$^+$, 276 (60) [M + H – $CO_2$H]$^+$, 234 (28) [M + H – $CO_2H$ – $CH_3CO$]$^+$. $C_{15}H_{20}N_4O_4$ (320.35): calcd. C 56.24, H 6.29, N 17.49; found C 56.59, H 6.47, N 17.89.

**Synthesis of Methyl 2,2-Bis(3,5-dimethylpyrazol-1-yl)acetate (5):** To a solution of Hbdmpza (**1**) (1.00 g, 4.03 mmol) in excess methanol (100 mL), conc. $H_2SO_4$ (0.15 mL, 0.28 g, 2.86 mmol) was added and stirred at ambient temperature for 3 d. The solvent was removed in vacuo and diethyl ether (200 mL) was added to the residue. The organic phase was extracted with a saturated aqueous solution of $NaHCO_3$ and dried with $Na_2SO_4$. The organic layer was concentrated in vacuo to a yellow crystalline powder of **5**. Recrystallisation from petroleum ether/ethyl acetate (3:1) yielded colourless blocks suitable for X-ray structure determination. Yield: 887 mg (3.38 mmol, 84%). M.p. 117–119 °C. $^1$H NMR ($CDCl_3$, 300 MHz, 25 °C): $\delta$ = 2.11 (s, 6 H, $C^5$-$CH_3$), 2.19 (s, 6 H, $C^3$-$CH_3$), 3.89 (s, 3 H, $OCH_3$), 5.85 (s, 2 H, $H_{pz}$), 6.95 (s, 1 H, $H_{bridge}$) ppm. $^{13}$C NMR ($CDCl_3$, 75.5 MHz, 25 °C): $\delta$ = 11.0 ($C^5$-$CH_3$), 13.5 ($C^3$-$CH_3$), 53.4 ($OCH_3$), 73.0 ($C_{bridge}$), 107.6 ($C_{pz}$-H), 141.3 ($C^5{}_{pz}$), 148.5 ($C^3{}_{pz}$), 165.3 (COOH) ppm. IR (THF): $\tilde{\nu}$ = 1771 ($CO_2H$), 1561 (C=N) cm$^{-1}$. FD-MS: *m*/*z* (%) = 263 (100) [M + H]$^+$. $C_{13}H_{18}N_4O_2$ (262.31): calcd. C 59.51, H 6.92, N 21.37; found C 59.88, H 7.20, N 21.11.

**Synthesis of Methyl 2,2-Bis(3,5-dimethylpyrazol-1-yl)-3-hydroxypropionate (6):** A solution of Mebdmpza (**5**) (0.75 g, 2.86 mmol) in dry THF (100 mL) was treated with LDA (≈ 1.8 M in heptane/THF/ethylbenzene, 1.8 mL, 3.24 mmol) at –80 °C and warmed up to –40 °C over a period of 2 h. After 1 h at –40 °C, paraformaldehyde (0.90 g, 27.0 mmol) was added. The mixture was warmed up to ambient temperature and finally heated under reflux for 60 min and stirred overnight. The solvent was removed in vacuo, the residue was dissolved in water and extracted with diethyl ether (3 × 150 mL). The combined diethyl ether layers were dried ($Na_2SO_4$) and concentrated under reduced pressure. Recrystallisation from hexane/acetone (1:1) yielded **6** as colourless blocks. Yield: 0.63 g (2.16 mmol, 76%). M.p. 116–118 °C. $^1$H NMR (300 MHz, $CDCl_3$, 25 °C): $\delta$ = 1.69 (s, 6 H, $C^5$-$CH_3$), 2.20 (s, 6 H, $C^3$-$CH_3$), 3.98 (s, 3 H, $OCH_3$), 4.65 (d, $^3J_{H,H}$ = 7.5 Hz, 2 H, $OCH_2$), 5.34 (t, $^3J_{H,H}$ = 7.5 Hz, 1 H, OH), 5.86 (s, 2 H, $H_{pz}$) ppm. $^{13}$C NMR (75.5 MHz, $CDCl_3$, 25 °C): $\delta$ = 11.2 ($C^5$-$CH_3$), 13.9 ($C^3$-$CH_3$), 53.9 ($OCH_3$), 66.7 ($CH_2$-OH), 84.3 ($C_{bridge}$), 108.8 ($C_{pz}$-H), 142.5 ($C^5{}_{pz}$), 148.3 ($C^3{}_{pz}$), 166.3 ($CO_2$R) ppm. IR (THF): $\tilde{\nu}$ = 1762 ($CO_2$Me), 1562 (C=N) cm$^{-1}$. FD-MS: *m*/*z* (%) = 292 (100) [M]$^+$, 234 (12) [M + H –$CO_2$Me]$^+$. $C_{14}H_{20}N_4O_3$ (292.34): calcd. C 57.52, H 6.90, N 19.17; found C 57.85, H 7.05, N 19.59.

**Synthesis of [Mn(bdmpzpen)(CO)$_3$] (7):** To Hbdmpzpen (**2**) (176 mg, 0.610 mmol) in dry THF (30 mL), KO*t*Bu (68.0 mg, 0.610 mmol) was added, and the reaction mixture stirred at ambient temperature for 30 min. [$MnBr(CO)_5$] (167 mg, 0.610 mmol) was added, and the reaction mixture was heated under reflux and controlled by IR on a regular basis. After 12 h, the reaction was complete, and the solution was filtered. The filtrate was concentrated in vacuo, washed with water (2 × 1 mL) and dried in vacuo. Recrystallisation from $CHCl_3$ yielded yellow crystals suitable for X-ray structure determination. Yield: 119 mg (0.28 mmol, 46%). M.p. 194–198 °C. $^1$H NMR (250 MHz, $CDCl_3$, 25 °C): $\delta$ = 2.53 (br., 12 H, $CH_3$), 3.83 (br., 2 H, $CH_2$), 5.04 (br., 1 H, =$CH_{2,allyl}$), 5.25 (br., 1 H, =$CH_{2,allyl}$), ≈ 5.75 (br., partly covered, 1 H, =$CH_{allyl}$), 5.98 (br., 2 H, $H_{pz}$) ppm. $^{13}$C NMR (62.9 MHz, $CDCl_3$, 25 °C): $\delta$ = 15.3 ($CH_3$), 16.2 ($CH_3$), 35.6 ($CH_2$), 111.8 ($C_{pz}$-H), 117.7 (=$CH_{2,allyl}$), 128.0 ($CH_{allyl}$), 143.3 ($C_{pz}$), 153.8 ($C_{pz}$), 220.6 (CO), 222.4 (CO) ppm. IR (THF): $\tilde{\nu}$ = 2033 (s, C=O), 1939 (s, C=O), 1911 (s, C=O), 1687 (m, $CO_2^-$) cm$^{-1}$. FAB-MS: *m*/*z* (%) = 427 (70) [M + H]$^+$, 343 (36) [M – 3 CO]$^+$, 299 (100) [M – 3 CO – $CH_2CH=CH_2$]$^+$. $C_{18}H_{19}N_4O_5Mn$ (426.31): calcd. C 50.71, H 4.49, N 13.14; found C 50.77, H 4.60, N 13.08.

**Synthesis of [Re(bdmpzpen)(CO)$_3$] (9):** To Hbdmpzpen (**2**) (176 mg, 0.610 mmol) in dry THF (30 mL), KO*t*Bu (68.0 mg, 0.610 mmol) was added, and the reaction mixture was stirred at ambient temperature for 30 min. [$ReBr(CO)_5$] (250 mg, 0.610 mmol) was added, and the reaction mixture was heated under reflux and controlled by IR on a regular basis. After 24 h, the reaction was complete, and the solution was filtered. The filtrate was concentrated in vacuo, washed with water (2 × 1 mL) and dried in vacuo. Recrystallisation from acetone yielded colourless crystals suitable for X-ray structure determination. Yield: 139 mg (0.25 mmol, 41%). M.p. 228–230 °C. $^1$H NMR (250 MHz, $CDCl_3$, 25 °C): $\delta$ = 2.53 (s, 6 H, $CH_3$), 2.57 (s, 6 H, $CH_3$), 3.97 (br., 2 H, $CH_2$), 5.27 (dtd, $^3J_{H,H}$ = 16.5 Hz, $^4J_{H,H}$ = 1.8 Hz, $^2J_{H,H}$ = 0.6 Hz, 1 H, =$CH_{2,allyl}$), 5.28 (dtd, $^3J_{H,H}$ = 12.0 Hz, $^4J_{H,H}$ = 1.8 Hz, $^2J_{H,H}$ = 0.6 Hz, 1 H, =$CH_{2,allyl}$), 5.71 (ddt, $^3J_{H,H}$ = 17.7 Hz, $^3J_{H,H}$ = 10.4 Hz, $^3J_{H,H}$ = 4.6 Hz, 1 H, =$CH_{allyl}$), 6.03 (s, 2 H, $H_{pz}$) ppm. $^{13}$C NMR (62.9 MHz, $CDCl_3$, 25 °C): $\delta$ = 16.3 ($CH_3$), 16.4 ($CH_3$), 36.2 ($CH_2$), 84.8 ($C_{bridge}$), 111.7 ($C_{pz}$-H), 118.3 (=$CH_{2,allyl}$), 132.5 ($CH_{allyl}$), 143.7 ($C_{pz}$), 154.4 ($C_{pz}$), 164.5 ($CO_2^-$), 195.7 (CO), 196.0 (CO) ppm. IR (THF): $\tilde{\nu}$ = 2023 (s, C=O), 1915 (s, C=O), 1892 (s, C=O), 1697 (m, $CO_2^-$) cm$^{-1}$. FAB-MS: *m*/*z* (%) = 559 (100) [M + H]$^+$, 531 (47) [M – CO]$^+$, 473 (97) [M – 3 CO]$^+$, 435 (38) [M – 3 CO – $CH_2CH=CH_2$]$^+$. $C_{18}H_{19}N_4O_5Re$ (557.57): calcd. C 38.77, H 3.43, N 10.05; found C 38.41, H 3.19, N 9.81.

**Synthesis of [Mn(bdmpzap)(CO)$_3$] (8):** To Hbdmpzap (**4**) (320 mg, 1.00 mmol) in dry THF (50 mL), KO*t*Bu (112 mg, 1.00 mmol) was added, and the reaction mixture was stirred at ambient temperature for 30 min. [$MnBr(CO)_5$] (275 mg, 1.00 mmol) was added, and the reaction mixture was heated under reflux and controlled by IR on a regular basis. After 12 h the reaction was complete, and the solution was filtered. The filtrate was concentrated in vacuo, washed with water (2 × 2 mL) and dried in vacuo. Recrystallisation from $CH_2Cl_2$ yielded yellow crystals suitable for X-ray structure determination. Yield: 340 mg (0.74 mmol, 74%). M.p. 174–176 °C. $^1$H NMR (400 MHz, $CDCl_3$, 25 °C): $\delta$ = 2.05 (s, 3 H, $CH_3CO$), 2.42 (s, 6 H, $CH_3$), 2.51 (br., 6 H, $CH_3$), 5.04, 5.67 (AB system, br. coupling not resolved, 2 H, $CH_2O$), 5.95 (br., 2 H, $H_{pz}$) ppm. $^{13}$C NMR (100.5 MHz, $CDCl_3$, 25 °C): $\delta$ = 15.0 ($CH_3$), 15.3 ($CH_3$), 20.7 ($CH_3$), 61.0 ($CH_2O$), 81.4 ($C_{bridge}$), 111.9 ($C_{pz}$-H), 143.2 ($C_{pz}$), 154.0 ($C_{pz}$), 165.2 ($CO_2$), 169.6 ($O_2CCH_3$), 220.0 (2 × CO), 222.3 (CO) ppm. IR (THF): $\tilde{\nu}$ = 2034 (s, C=O), 1940 (s, C=O), 1913 (s, C=O), 1761 (m, $CH_3CO$), 1692 (m, $CO_2^-$) cm$^{-1}$. FD-MS: *m*/*z* (%) = 458 (100) [M]$^+$, 416 (18) [M + H – $CH_3CO$]$^+$. $C_{18}H_{19}N_4O_7Mn$

 © 2006 Wiley-VCH Verlag GmbH & Co. KGaA, Weinheim 

(458.31): calcd. C 47.16, H 4.18, N 12.23; no suitable elemental analysis was obtained.

**Synthesis of [Re(bdmpzap)(CO)$_3$] (10):** To Hbdmpzap (**4**) (247 mg, 0.77 mmol) in dry THF (50 mL), KO*t*Bu (86 mg, 0.77 mmol) was added, and the reaction mixture was stirred at ambient temperature for 30 min. [ReBr(CO)$_5$] (313 mg, 0.77 mmol) was added, and the reaction mixture was heated under reflux and controlled by IR on a regular basis. After 20 h, the reaction was complete, and the solution was filtered. The filtrate was concentrated in vacuo, washed with water (2 × 2 mL) and diethyl ether (2 × 2 mL) and dried in vacuo. Yield: 305 mg (0.52 mmol, 52%). M.p. 233–236 °C. $^1$H NMR (400 MHz, $CDCl_3$, 25 °C): $\delta$ = 2.05 (s, 3 H, $CH_3CO$), 2.46 (s, 12 H, $CH_3$), 5.11, 5.73 (AB system, $J_{AB}$ = 9.6 Hz, 2 H, $CH_2O$), 5.98 (br., 1 H, $H_{pz}$), 6.03 (br., 1 H, $H_{pz}$) ppm. $^{13}$C NMR (100.5 MHz, $CDCl_3$, 25 °C): $\delta$ = 15.3 ($CH_3$), 16.4 ($CH_3$), 20.8 ($CH_3$), 61.6 ($CH_2O$), 82.9 ($C_{bridge}$), 111.8 ($C_{pz}$-H), 143.2 ($C_{pz}$), 154.5 ($C_{pz}$), 163.5 ($CO_2$), 169.5 ($O_2CCH_3$), 195.5 (2 × CO), 195.5 (CO) ppm. IR (THF): $\tilde{\nu}$ = 2024 (s, C=O), 1918 (s, C=O), 1894 (s, C=O), 1762 (m, $O_2CCH_3$), 1702 (m, $CO_2^-$) cm$^{-1}$. FD-MS: *m*/*z* (%) = 591 (100) $[M + H]^+$. $C_{18}H_{19}N_4O_7Re$ (589.58): calcd. C 36.67, H 3.25, N 9.50; found C 37.12, H 3.34, N 9.14.

**Solid Phase Fixation of Methyl 2,2-Bis(3,5-dimethylpyrazol-1-yl)-3-hydroxypropionate (P-6):** A suspension of a chloromethylated resin [0.45 g, loading 1.1 mmol g$^{-1}$, 0.50 equiv.], Mebdmpzhp (**6**) (439 mg, 1.5 mmol), KO*t*Bu (112 mg, 1.0 mmol), 18-crown-6 (264 mg, 1.0 mmol) and CsBr (212 mg, 1.0 mmol) in dry THF was heated under reflux for 48 h under a nitrogen atmosphere. The suspension was filtered through a sintered glass filter with suction and washed thoroughly with THF, methanol and water and the remaining polymer was dried in vacuo. The content of ligand on the polymer is determined by elemental analysis to 0.23 mmol g$^{-1}$.

**Ester Hydrolysis of Methyl 2,2-Bis(3,5-dimethylpyrazol-1-yl)-3-hydroxypropionate on Solid Phase – Polymer P-3:** To a suspension of **P-6** (0.45 g) and NaOH (40 mg, 1.0 mmol) in THF (50 mL), excess water (1 mL, 1 g, 55.5 mmol) was added, and the suspension was heated under reflux for 12 h. The suspension was filtered through a sintered glass filter with suction and washed thoroughly with THF, water and again THF and the remaining polymer **P-3** with the deprotonated and solid phase bound ligand **3** was dried in vacuo.

**Polymer Bound Rhenium Tricarbonyl Complexes:** A suspension of polymer **P-3** (90 mg) in THF and [Re(CO)$_5$Br] (0.25 mmol, 102 mg) was heated under reflux for 48 h, filtered through a sintered glass filter with suction and washed thoroughly with THF, water, methanol and dichloromethane. IR (THF): $\tilde{\nu}$ = 2022 (CO), 1915 (CO), 1890 (CO) cm$^{-1}$.

**Solid Phase Fixation of 2,2-Bis(3,5-dimethylpyrazol-1-yl)pent-4-enoic Acid (S-2):** A suspension of mercaptopropyl silica [0.5 g, loading 0.98 mmol g$^{-1}$, 0.49 equiv.], Hbdmpzpen (**2**) (141 mg, 0.49 mmol) and azobisisobutyronitrile (10 mg, 0.06 mmol) in dry chloroform was heated at reflux for 48 h under a nitrogen atmosphere. The suspension was filtered through a sintered glass filter with suction and washed thoroughly with dichloromethane, toluene and methanol and the remaining silica was dried in vacuo. The procedure was repeated once. The content of ligand on the silica is determined by elemental analysis to 0.17 mmol g$^{-1}$.

**Silica Bound Manganese Tricarbonyl Complexes:** A suspension of mercaptopropyl silica [0.20 g, loading 0.98 mmol g$^{-1}$, 0.20 equiv.],

Table 2. Details of the structure determination for **2**, **3**, **4**, **7** and **8**.

| | **2** | **3** | **4** | **7** | **8** |
|---|---|---|---|---|---|
| Empirical formula | $C_{15}H_{20}N_4O_2$ | $C_{13}H_{18}N_4O_3$ | $C_{15}H_{20}N_4O_4$ | $C_{18}H_{19}MnN_4O_5$ | $C_{18}H_{19}MnN_4O_7$ |
| Formula mass | 288.35 | 278.31 | 320.35 | 426.31 | 458.31 |
| Crystal colour/habit | colourless block | colourless block | colourless block | yellow block | yellow block |
| Crystal system | triclinic | monoclinic | orthorhombic | orthorhombic | triclinic |
| Space group | $P\bar{1}$ | $P2_1/c$ | $P2_12_12_1$ | *Pbca* | $P\bar{1}$ |
| *a* [Å] | 8.369(5) | 12.167(5) | 8.6376(17) | 12.924(7) | 6.8735(12) |
| *b* [Å] | 9.351(6) | 8.099(3) | 10.996(2) | 14.337(5) | 11.4738(18) |
| *c* [Å] | 10.774(6) | 15.854(7) | 16.882(3) | 20.167(8) | 13.423(2) |
| $\alpha$ [°] | 86.45(6) | 90.00 | 90.00 | 90.00 | 104.165(12) |
| $\beta$ [°] | 88.14(4) | 108.41(4) | 90.00 | 90.00 | 103.862(13) |
| $\gamma$ [°] | 67.44(4) | 90.00 | 90.00 | 90.00 | 100.881(13) |
| *V* [Å$^3$] | 777.1(8) | 1482.2(10) | 1603.4(6) | 3737(3) | 961.5(3) |
| $\theta$ [°] | 2.64–27.00 | 2.71–26.99 | 3.37–29.29 | 2.02–26.99 | 3.45–25.56 |
| *H* | –3 to 10 | –15 to 0 | –11 to 11 | –16 to 16 | –8 to 8 |
| *K* | –9 to 11 | –10 to 0 | –15 to 15 | –18 to 0 | –13 to 13 |
| *L* | –13 to 13 | –19 to 19 | –23 to 23 | –13 to 25 | –16 to 16 |
| *F*(000) | 308 | 592 | 680 | 1760 | 472 |
| *Z* | 2 | 4 | 4 | 8 | 2 |
| $\mu$ (Mo-$K_\alpha$) [mm$^{-1}$] | 0.085 | 0.091 | 0.098 | 0.745 | 0.737 |
| Crystal size [mm] | 0.5 × 0.5 × 0.5 | 0.5 × 0.4 × 0.3 | 0.2 × 0.15 × 0.1 | 0.5 × 0.4 × 0.3 | 0.4 × 0.23 × 0.1 |
| $D_{calcd.}$ [g cm$^{-3}$], *T* [K] | 1.232, 188(2) | 1.247, 188(2) | 1.327, 100(2) | 1.516, 188(2) | 1.583, 100(2) |
| Reflections collected | 3539 | 3380 | 30272 | 4382 | 11953 |
| Indep. reflections | 3342 | 3219 | 2467 | 4077 | 3585 |
| Obsd. refl. (>2$\sigma I$) | 2878 | 1930 | 2146 | 2488 | 2554 |
| Parameter | 194 | 187 | 211 | 253 | 271 |
| Weight parameter *a* | 0.0583 | 0.0768 | 0.0434 | 0.0417 | 0.0354 |
| Weight parameter *b* | 0.2387 | 0.3199 | 0.6164 | 2.1574 | 0.0096 |
| $R_1$ (obsd.) | 0.0425 | 0.0632 | 0.0486 | 0.0570 | 0.0590 |
| $R_1$ (overall) | 0.0494 | 0.1172 | 0.0612 | 0.1161 | 0.0990 |
| $wR_2$ (obsd.) | 0.1112 | 0.1404 | 0.0975 | 0.1045 | 0.0908 |
| $wR_2$ (overall) | 0.1174 | 0.1674 | 0.1016 | 0.1253 | 0.0996 |
| Diff. peak/hole [e/Å$^3$] | 0.309/–0.225 | 0.285/–0.328 | 0.235/–0.265 | 0.371/–0.454 | 0.377/–0.406 |

 © 2006 Wiley-VCH Verlag GmbH & Co. KGaA, Weinheim 

[Mn(bdmpzpen)$(CO)_3$] (**2**) (85 mg, 0.20 mmol) and azobisisobutyronitrile (10 mg, 0.06 mmol) in dry chloroform was heated at reflux for 8 h under a nitrogen atmosphere. The suspension was filtered through a sintered glass filter with suction and washed thoroughly with dichloromethane, THF, toluene and methanol and the remaining yellow silica was dried in vacuo. The content of ligand on the silica is determined by elemental analysis to 0.036 mmol $g^{-1}$. A longer reaction time of 48 h leads to a content of 0.063 mmol $g^{-1}$. IR (nujol): $\tilde{\nu}$ = 2039 (CO), 1948 (CO), 1923 (CO) $cm^{-1}$.

**Silica Bound Rhenium Tricarbonyl Complexes:** A suspension of mercaptopropyl silica [0.20 g, loading 0.98 mmol $g^{-1}$, 0.20 equiv.], [Re(bdmpzpen)$(CO)_3$] (**9**) (112 mg, 0.20 mmol) and azobisisobutyronitrile (10 mg, 0.06 mmol) in dry chloroform was heated under reflux for 8 h under a nitrogen atmosphere. The suspension was filtered through a sintered glass filter with suction and washed thoroughly with dichloromethane, THF, toluene and methanol and the remaining silica was dried in vacuo. The content of ligand on the silica is determined by elemental analysis to 0.041 mmol $g^{-1}$. A longer reaction time of 48 h leads to a content of 0.078 mmol $g^{-1}$. IR (nujol): $\tilde{\nu}$ = 2027 (CO), 1920 (CO), 1905 (CO) $cm^{-1}$.

**X-ray Structure Determinations:** Single crystals of **2**, **3**, **4**, **7** and **8** were mounted with Paratone-N or glue on a glass fibre. A modified Siemens P4-Diffractometer and a STOE IPDS II diffractometer were used for data collection (graphite monochromator, Mo-$K_\alpha$ radiation, $\lambda$ = 0.71073 Å). The structures were solved by using direct methods and refined with full-matrix least-squares against $F^2$ {Siemens SHELX-97}.[10] A weighting scheme was applied in the last steps of the refinement with $w = 1/[\sigma^2(F_o^2) + (aP)^2 + bP]$ and $P = [2F_c^2 + \max(F_o^2,0)]/3$. Most hydrogen atoms were included in their calculated positions and refined in a riding model. The protons of carboxylic acids (**2**–**4**) were found and their coordinates were refined freely. All details and parameters of the measurements are summarised in Table 2. The structure pictures were prepared with the program Diamond 2.1e.[11] CCDC-232648 (for **2**), CCDC-289443 (for **3**), CCDC-619381 (for **4**), CCDC-289442 (for **7**) and CCDC-619380 (for **8**) contain the supplementary crystallographic data for this paper. These data can be obtained free of charge from The Cambridge Crystallographic Data Centre via www.ccdc.cam.ac.uk/data_request/cif.

## Acknowledgments

Generous financial support by the Deutsche Forschungsgemeinschaft (SFB 583) is gratefully acknowledged.

[1] a) A. Otero, J. Fernández-Baeza, J. Tejeda, A. Antiñolo, F. Carrillo-Hermosilla, E. Díez-Barra, A. Lara-Sánchez, M. Fernández-López, M. Lanfranchi, M. A. Pellinghelli, *J. Chem. Soc., Dalton Trans.* **1999**, 3537–3539; b) A. Otero, J. Fernández-Baeza, J. Tejeda, A. Antiñolo, F. Carrillo-Hermosilla, E. Díez-Barra, A. Lara-Sánchez, M. Fernández-López, *J. Chem. Soc., Dalton Trans.* **2000**, 2367–2374; c) A. Otero, J. Fernández-Baeza, A. Antiñolo, F. Carrillo-Hermosilla, J. Tejeda, E. Díez-Barra, A. Lara-Sánchez, L. Sánchez-Barba, I. López-Solera, M. R. Ribeiro, J. M. Campos, *Organometallics* **2001**, *20*, 2428–2439; d) A. Otero, J. Fernández-Baeza, A. Antiñolo, J. Tejeda, A. Lara-Sánchez, L. Sánchez-Barba, M. T. Expósito, A. M. Rodríguez, *Dalton Trans.* **2003**, 1614–1619.

[2] a) N. Burzlaff, I. Hegelmann, B. Weibert, *J. Organomet. Chem.* **2001**, *626*, 16–23; b) A. Beck, B. Weibert, N. Burzlaff, *Eur. J. Inorg. Chem.* **2001**, 521–527; c) N. Burzlaff, I. Hegelmann, *Inorg. Chim. Acta* **2002**, *329*, 147–150; d) A. López-Hernández, R. Müller, H. Kopf, N. Burzlaff, *Eur. J. Inorg. Chem.* **2002**, 671–677; e) I. Hegelmann, A. Beck, C. Eichhorn, B. Weibert, N. Burzlaff, *Eur. J. Inorg. Chem.* **2003**, 339–347; f) A. Beck, A. Barth, E. Hübner, N. Burzlaff, *Inorg. Chem.* **2003**, *42*, 7182–7188; g) R. Müller, E. Hübner, N. Burzlaff, *Eur. J. Inorg. Chem.* **2004**, 2151–2159; h) I. Hegelmann, N. Burzlaff, *Eur. J. Inorg. Chem.* **2003**, 409–411; i) L. Peters, N. Burzlaff, *Polyhedron* **2004**, *23*, 245–251.

[3] For recent reviews, see: a) M. Tada, Y. Iwasawa, *Chem. Commun.* **2006**, 2833–2844; b) B. M. L. Dioos, I. F. J. Vankelecom, P. A. Jacobs, *Adv. Synth. Catal.* **2006**, *348*, 1413–1446.

[4] R. A. Findeis, L. H. Gade, *Dalton Trans.* **2003**, 249–254.

[5] a) J. M. Fraile, J. I. García, J. A. Mayoral, A. J. Royo, *Tetrahedron: Asymmetry* **1996**, *7*, 2263–2276; b) M. I. Burguete, J. M. Fraile, J. I. García, E. García-Verdugo, C. I. Herrerías, S. V. Luis, J. A. Mayoral, *J. Org. Chem.* **2001**, *66*, 8893–8901.

[6] D. L. Reger, T. C. Grattan, *Synthesis* **2003**, 350–356.

[7] D. Appleton, A. B. Duguid, S.-K. Lee, Y.-J. Ha, H.-J. Ha, F. J. Leeper, *J. Chem. Soc., Perkin Trans. 1* **1998**, *1*, 89–101.

[8] W. Kläui, M. Berghahn, W. Frank, G. J. Reiß, T. Schönherr, G. Rheinwald, H. Lang, *Eur. J. Inorg. Chem.* **2003**, 2059–2070.

[9] a) D. Vitali, F. Calderazzo, *Gazz. Chim. Ital.* **1972**, *102*, 586–596; b) E. W. Abel, G. Wilkinson, *J. Chem. Soc.* **1959**, 1501–1505.

[10] G. M. Sheldrick, SHELX-97, Program for Crystal Structure Analysis, University of Göttingen, Göttingen, Germany, **1997**.

[11] K. Brandenburg, M. Berndt, Diamond – Visual Crystal Structure Information System, Crystal Impact GbR, Bonn, Germany, **1999**; for Software Review, see: W. T. Pennington, *J. Appl. Crystallogr.* **1999**, *32*, 1028–1029.

Received: September 7, 2006
Published Online: November 17, 2006

 © 2006 Wiley-VCH Verlag GmbH & Co. KGaA, Weinheim 

DOI: 10.1002/ejic.200600614

# Chemical and Structural Features of $NMe_2Et$ Adducts of the Silanimines $Me_2Si{=}NSi\mathit{t}Bu_3$ and $\mathit{t}Bu_2Si{=}NSiCl\mathit{t}Bu_2$

**Hans-Wolfram Lerner,*[a] Michael Bolte,[a] Klaus Schurz,[b] Nils Wiberg,[b] Gerhard Baum,[c] Dieter Fenske,[c] Jan W. Bats,[d] and Matthias Wagner[a]**

**Keywords:** Silanimines / Amines / Donor adduct / Wittig reaction / Stevens rearrangement

In contrast to $\mathit{t}Bu_2SiN(Li)SiX\mathit{t}Bu_2$ (X = Cl, *t*Bu), the silyl amide $Me_2SiClN(Li)Si\mathit{t}Bu_3$ is unstable towards LiCl elimination, which means that the silanimine donor adduct $Me_2Si{=}NSi\mathit{t}Bu_3{\cdot}NMe_2Et$ can be synthesized in high yield from the reaction of $Me_2SiClN(H)Si\mathit{t}Bu_3$ with *n*BuLi in the presence of $NMe_2Et$. The silanimine adduct $\mathit{t}Bu_2Si{=}NSiCl\mathit{t}Bu_2{\cdot}NMe_2Et$, with bulky *t*Bu substituents at the unsaturated Si center, is accessible by treating the donor-free silanimine $\mathit{t}Bu_2Si{=}NSiCl\mathit{t}Bu_2$ with $NMe_2Et$. X-ray quality crystals of the silanimine amine adduct $Me_2Si{=}NSi\mathit{t}Bu_3{\cdot}NMe_2Et$ (monoclinic, $P2_1/n$) were grown from pentane at –25 °C. During thermolysis of the adducts $Me_2Si{=}NSi\mathit{t}Bu_3{\cdot}NMe_2Et$ and $\mathit{t}Bu_2Si{=}NSiCl\mathit{t}Bu_2{\cdot}NMe_2Et$ in $NMe_2Et$ as solvent a Stevens rearrangement takes place to produce $EtN(Me)CH_2SiMe_2N(H)Si\mathit{t}Bu_3$ and $EtN(Me)CH[Me_2SiN(H)Si\mathit{t}Bu_3]_2$, and $EtN(Me)CH_2Si\mathit{t}Bu_2N(H)SiCl\mathit{t}Bu_2$, respectively. In contrast, the thermolysis of $Me_2Si{=}NSi\mathit{t}Bu_3{\cdot}NMe_2Et$ in vacuo gives the silanimine dimer $(Me_2SiNSi\mathit{t}Bu_3)_2$ (monoclinic, $P2_1/n$) in 80 % yield. The benzophenone imine $Ph_2C{=}NSi\mathit{t}Bu_3$ (triclinic, $P\bar{1}$) was obtained from the Wittig-like reaction of $Me_2Si{=}N{-}Si\mathit{t}Bu_3$ with $Ph_2CO$.

(© Wiley-VCH Verlag GmbH & Co. KGaA, 69451 Weinheim, Germany, 2006)

## Introduction

Ab initio calculations have shown that the silanimine $H_2Si{=}NSiH_3$ possesses an almost linear Si–N–Si skeleton with a short Si=N double bond and a short Si–N single bond.[1] Moreover, these calculations reveal a negative charge of 1.71 on the N center of $H_2Si{=}NSiH_3$. It is interesting to note that in the solid state the stable, substituted silanimine $\mathit{t}Bu_2Si{=}N{-}Si\mathit{t}Bu_3$, which contains bulky *t*Bu groups,[2] features nearly the same Si=NSi skeleton as that calculated for $H_2Si{=}NSiH_3$. Obviously only electronic effects, namely the difference in electronegativity between Si and N, determine the molecular structure of this type of silanimine (Scheme 1).

Silanimines are highly reactive compounds therefore their syntheses should be carried out under mild conditions. We have found that at low temperature in the weakly polar solvent $Bu_2O$ the reaction of the silyl azide $\mathit{t}Bu_2SiClN_3$ with the silanides $\mathit{t}Bu_3SiNa$ and $\mathit{t}Bu_2PhSiNa$, respectively, in a 1:1 stoichiometry, leads cleanly to the silanimines $\mathit{t}Bu_2Si{=}NSi\mathit{t}Bu_3$ [**1a**(*t*Bu)] and $\mathit{t}Bu_2Si{=}NSiPh\mathit{t}Bu_2$ [**1a**(Ph)].[2,3] In contrast, when $\mathit{t}Bu_2ClSiN_3$ is treated with $\mathit{t}Bu_3SiNa$ in the polar solvent tetrahydrofuran, the sodium amide $\mathit{t}Bu_2Si{-}ClN(Na)Si\mathit{t}Bu_3$ is formed rather than the silanimine **1a**(*t*Bu).[4] As reported earlier, LiCl elimination of silyl amides can also be carried out at higher temperatures in vacuo to give silanimines.[5] As we noted previously, the silanimine $\mathit{t}Bu_2Si{=}NSiCl\mathit{t}Bu_2$ [**1a**(Cl)] can be synthesized by a [3+2] cycloreversion reaction.[6] Surprisingly, in the thermolysis of the silatetrazoline **2**(Cl) the silanimine **1a**(Cl) and the silyl azide $\mathit{t}Bu_3SiN_3$ are produced, as shown in Scheme 2.[6,7]

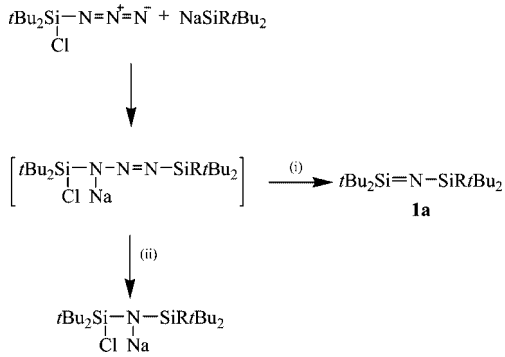


Scheme 1. (i) $–N_2$, –NaCl, $Bu_2O$ (R = *t*Bu, Ph); (ii) $–N_2$, thf (R = *t*Bu).

[a] Institut für Anorganische Chemie, Johann Wolfgang Goethe-Universität Frankfurt am Main,
Max-von-Laue-Straße 7, 60438 Frankfurt am Main, Germany
Fax: +49-69-798-29260
E-mail: lerner@chemie.uni-frankfurt.de
[b] Department Chemie, Ludwig-Maximilians-Universität München,
Butenandtstr. 5–13 (Haus D), 81377 München, Germany
[c] Institut für Anorganische Chemie, Universität Karlsruhe,
Engesserstraße, Geb. Nr. 30.45, 76128 Karlsruhe, Germany
[d] Institut für Organische Chemie, Johann Wolfgang Goethe-Universität Frankfurt am Main,
Max-von-Laue-Straße 7, 60438 Frankfurt am Main, Germany

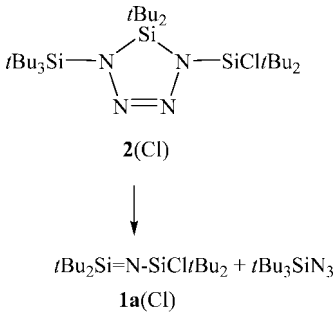


Scheme 2.

In this paper, the syntheses and thermolysis reactions of the silanamine aminates Me$_2$Si=NSi*t*Bu$_3$·NMe$_2$Et and *t*Bu$_2$Si=NSiCl*t*Bu$_2$·NMe$_2$Et are described. We also report the crystal structures of the silanimine aminate Me$_2$Si=NSi*t*Bu$_3$·NMe$_2$Et, the silanimine dimer (Me$_2$SiN-Si*t*Bu$_3$)$_2$, the benzophenone imine Ph$_2$C=NSi*t*Bu$_3$, and the silylamine *t*Bu$_2$SiClN(H)Si*t*Bu$_3$.

## Results and Discussion

### Syntheses

The silyl amides *t*Bu$_2$SiClN(Li)SiX*t*Bu$_2$ (X = Cl, *t*Bu) can be cleanly prepared from the precursor silylamines *t*Bu$_2$SiClN(H)SiX*t*Bu$_2$ (X = Cl, *t*Bu) [**3**(Cl), **3**(*t*Bu)] and alkyllithium reagents like MeLi or *n*BuLi. The NMR spectra of *t*Bu$_2$SiClN(Li)SiX*t*Bu$_2$ (X = Cl, *t*Bu) reveal that elimination of LiCl does not take place in the presence of thf or Et$_2$O at ambient or lower temperatures, whereas the silyl amide Me$_2$SiClN(Li)Si*t*Bu$_3$ eliminates LiCl at low temperature in Et$_2$O. An important factor influencing LiCl elimination of these silyl amides appears to be the degree of steric crowding around the unsaturated silicon center. In earlier reports we described the synthesis of several donor adducts of the silanimines **1a**(*t*Bu) and Me$_2$Si=NSi*t*Bu$_3$ (**1b**),[8,9] and we found that donor adducts of the silanimines **1a**(*t*Bu) and **1b** can be generated by reaction of the silyl amides *t*Bu$_2$SiClN(Li)Si*t*Bu$_3$ and Me$_2$SiClN(Li)Si*t*Bu$_3$, respectively, with CF$_3$SO$_3$SiMe$_3$.[8,9] In this paper we describe a synthesis that does not require CF$_3$SO$_3$SiMe$_3$ by which the silanimine aminate **1b**·NMe$_2$Et can be produced in large amounts. The silanimine amine adduct **1b**·NMe$_2$Et was synthesized from the reaction of Me$_2$SiClN(H)Si*t*Bu$_3$ with *n*BuLi in the presence of NMe$_2$Et at –78 °C in Et$_2$O. X-ray quality crystals of **1b**·NMe$_2$Et (monoclinic, $P2_1/n$) were grown from a pentane solution at –25 °C (Scheme 3). The adduct of silanimine **1a**(Cl) with NMe$_2$Et, which possesses a bulky *t*Bu substituent at the unsaturated Si center, is accessible by treating the donor-free silanimine **1a**(Cl) with NMe$_2$Et.

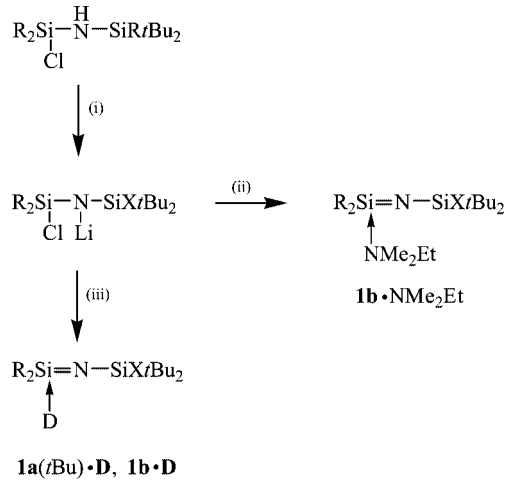


Scheme 3. (i) +RLi, –RH; (ii) +NMe$_2$Et, –LiCl (R = Me, X = *t*Bu); (iii) +CF$_3$SO$_3$SiMe$_3$, +D (D = thf, Et$_2$O, NEt$_3$), –Me$_3$SiCl, –CF$_3$SO$_3$Li (R = Me, *t*Bu; X = *t*Bu).

### Reactivity of Me$_2$Si=NSi*t*Bu$_3$·NMe$_2$Et and *t*Bu$_2$Si=NSiCl*t*Bu$_2$·NMe$_2$Et

Thermolysis of the donor-free silanimines **1a**(Cl), **1a**(*t*Bu), and **1a**(Ph) in [D$_6$]benzene at ambient temperature gave the compounds **4**(Cl), **4**(*t*Bu), and **4**(Ph), respectively, as isolable products (Scheme 4).[6,10] The formation of these products can be explained by an ene reaction of isobutene with two molecules of the silanimine. Obviously, the *t*Bu-substituted silanimines **1a**(Cl), **1a**(*t*Bu), and **1a**(Ph) are the source of isobutene at ambient temperature. Thus, these silanimines undergo a β-elimination reaction to form isobutene, which reacts twice with the undegraded silanimines to give the corresponding ene reaction products.

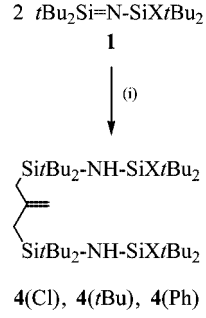


Scheme 4. (i) +CH$_2$=C(CH$_3$)$_2$ (X = Cl, *t*Bu, Ph).

In contrast to the degradation reaction of donor-free silanimines **1a**(Cl), **1a**(*t*Bu), and **1a**(Ph), during thermolysis of the silanimine amine adducts **1a**(Cl)·NMe$_2$Et and **1b**·NMe$_2$Et in dimethylethylamine as solvent a Stevens rearrangement takes place to produce EtN(Me)CH$_2$Si-Me$_2$N(H)Si*t*Bu$_3$ [**5**(Me,*t*Bu)] and EtN(Me)CH[Me$_2$SiN(H)-Si*t*Bu$_3$]$_2$ [**6**(Me,*t*Bu)], and EtN(Me)CH$_2$Si*t*Bu$_2$N(H)-SiCl*t*Bu$_2$ [**5**(*t*Bu,Cl)], respectively. A similar reaction was observed in the thermolysis of the pyridine adduct of **1a**(Ph).[11] It is interesting to note that the thermolysis reaction of **1b**·NMe$_2$Et leads to two products [80% **5**(Me,*t*Bu) and 20% **6**(Me,*t*Bu) in NMe$_2$Et; 10% **5**(Me,*t*Bu) and 90%

 © 2006 Wiley-VCH Verlag GmbH & Co. KGaA, Weinheim 

**6**(Me,*t*Bu) in [$D_6$]benzene; Scheme 5]. The thermolysis of **1b**·$NMe_2Et$ in vacuo gives the silanimine dimer ($Me_2SiN$-$SitBu_3$)$_2$ (**1b$_2$**) in 80% yield. The silylamines **5**(Me,*t*Bu) and **6**(Me,*t*Bu) were produced as side products in this reaction, as shown in Scheme 5. The silanimine dimer **1b$_2$** was characterized by X-ray crystallography (see below).

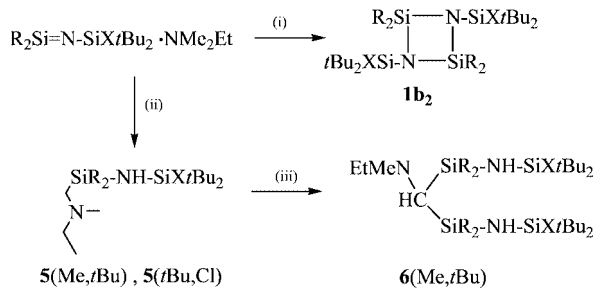


Scheme 5. (i) in vacuo (R = Me, X = *t*Bu); (ii) R = Me, X = *t*Bu; R = *t*Bu, X = Cl; (iii) +$Me_2SiNSitBu_3$ (R = Me, X = *t*Bu).

Generally, the reactivity of the silanimine–$NMe_2Et$ adducts of **1a**(Cl) and **1b** resemble those of the corresponding donor-free silanimines. In earlier reports we discussed the reactivity of the silanimines **1a**(Cl) and **1b** in detail.[6,8] In contrast to the reaction of **1a**(*t*Bu) with benzophenone, in which a stable silanimine adduct is formed due to steric hindrance,[12] the silanimine **1b**·$NMe_2Et$ reacts with benzophenone to produce benzophenone imine **8**, via the oxaazasilacyclobutane **7**, by a Wittig-like reaction, as depicted in Scheme 6. The benzophenone imine **8** was obtained in 53% yield. X-ray quality crystals of this compound were obtained by sublimation at 105 °C/0.001 mbar.

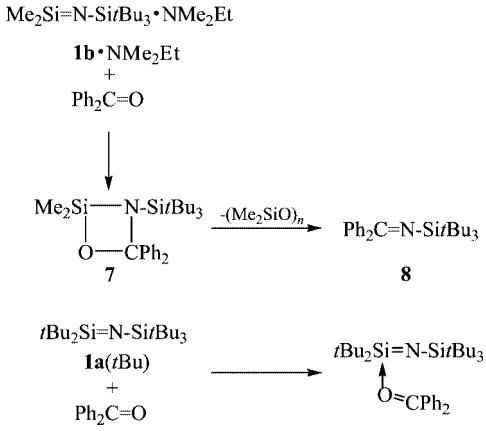


Scheme 6.

## NMR Spectra

When considering the $^{29}Si$ NMR spectra of the silanimines of the type $R_2Si(1)=NSi(2)R_3$ and their donor adducts, certain general trends can be observed. As is to be expected for the unsaturated Si centers of silanimines, the $^{29}Si$ signals of these nuclei are shifted extremely downfield whereas the silanimine donor adducts show signals for the unsaturated Si center that are shifted upfield, as listed in Table 1. Due to anisotropy effects the signals of both Si atoms of $R_2Si(1)=NSi(2)R_3$ are shifted upfield. The linearity of the silanimine $R_2Si(1)=NSi(2)R_3$ skeleton [Si(1)–N–Si(2) angle] is therefore recognizable by the $^{29}Si$ NMR shift of the Si(2) center. If a strong donor is coordinated to the silanimine the skeleton deviates more from linearity than if a weak one is bonded. In this case, the signal of the Si(2) center will be shifted further downfield than the Si(2) signal of a weak adduct. Therefore, the strength of a silanimine donor can be measured by the $^{29}Si$ NMR shift of Si(2) of these adducts. In contrast to **1b**, the silanimines **1a**(Cl) and **1a**(*t*Bu) form weaker adducts with $NMe_2Et$ than with thf.[6,9] As shown in Table 1, this trend can also be seen in their $^{29}Si$ NMR spectra.

Table 1. $^{29}Si$ NMR shifts (in $C_6D_6$ if not indicated otherwise) of silanimines $R_2Si(1)=NSi(2)R_3$.

| | $\delta^{29}$Si(1) | $\delta^{29}$Si(2) | Ref. |
|---|---|---|---|
| $tBu_2Si(1)=NSi(2)tBu_3$ | 78.4 | –7.7 | [2] |
| $tBu_2Si(1)=NSi(2)PhtBu_2$ | 81.8 | –13.1 | [3] |
| $tBu_2Si(1)=NSi(2)CltBu_2$ | 3.0 | 3.0 | [6] |
| $Me_2Si(1)=NSi(2)tBu_3$·$NMe_2Et$ | –8.9 | –10.3 | – |
| $tBu_2Si(1)=NSi(2)CltBu_2$·$NMe_2Et$ | –3.4 | –6.4 | – |
| $Me_2Si(1)=NSi(2)tBu_3$·THF | –4.4 | –11.1 | [2] |
| $tBu_2Si(1)=NSi(2)tBu_3$·THF | 1.1 | –14.7 | [2] |
| $tBu_2Si(1)=NSi(2)CltBu_2$·THF | 2.9 | –5.2 | [6] |
| $Me_2Si(1)=NSi(2)tBu_3$·$Et_2O$ | –1.5[a] | –11.1[a] | [8] |
| $tBu_2Si(1)=NSi(2)CltBu_2$·$Et_2O$ | –0.2[a] | –6.5[a] | [6] |

[a] Recorded in $Et_2O$.

It is interesting to note that in contrast to the NMR spectra of the donor-free silanimine **1a**(Cl),[6] which reveal only one signal set for both silyl groups, the NMR spectra of its $NMe_2Et$ complex show signals that can be assigned to two different silyl groups.

## Structure of $Me_2Si=NSitBu_3$·$NMe_2Et$

Figure 1 shows the molecular structure of the silanimine amine adduct **1b**·$NMe_2Et$ (monoclinic, $P2_1/n$); selected bond lengths and angles are listed in the figure caption.

As shown in Table 2, the silanimine amine adduct **1b**·$NMe_2Et$ has an Si–N–Si angle smaller than 180° and smaller than those in the donor-free silanimines **1a**(*t*Bu), and **1a**(Ph) and in the corresponding thf adduct **1b**·thf [**1a**(*t*Bu): Si–N–Si 177.8(2)°; **1a**(Ph): Si–N–Si 168.34(16)° and 172.95(18)°; **1b**·thf: Si–N–Si 161.0(6)° and 161.5(6)°; **1b**·$NMe_2Et$: Si–N–Si 156.44(10)°]. The Si=N double bond in **1b**·$NMe_2Et$ [1.6036(13) Å] is somewhat longer than those of the donor-free silanimines **1a**(*t*Bu) and **1a**(Ph) and the corresponding thf adduct **1b**·thf [**1a**(*t*Bu): Si=N 1.568(3) Å; **1a**(Ph): Si=N 1.573(3) Å; **1b**·thf: Si=N 1.574(10) and 1.588(9) Å]. As depicted in Table 2, the N–Si single bonds in the silanimines **1a**(*t*Bu), **1a**(Ph), and in the silanimines adducts **1b**·$NMe_2Et$ and **1b**·thf, however, are remarkably shorter than those found in related supersilylated nitrogen compounds [e.g. **1b$_2$**, **3**(*t*Bu), and **8**; Table 3]. Due to the higher Lewis acidity of silanimines in comparison to that of silenes, the distance between the unsaturated Si center

 © 2006 Wiley-VCH Verlag GmbH & Co. KGaA, Weinheim 

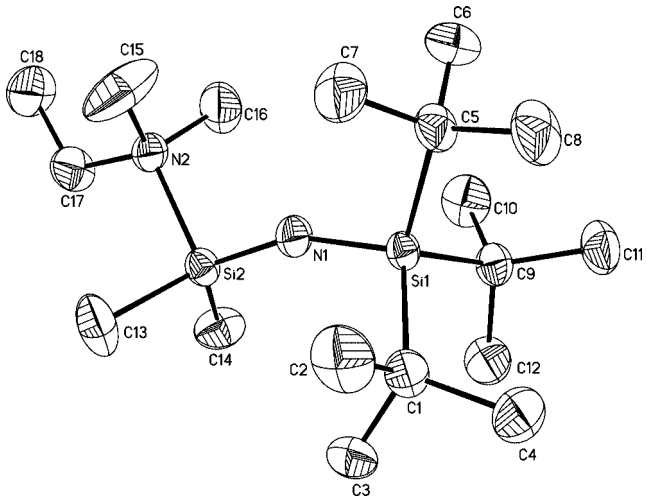


Figure 1. Thermal ellipsoid plot of $Me_2Si{=}NSi\textit{t}Bu_3{\cdot}NMe_2Et$ (**1b**·$NMe_2Et$) showing the atomic numbering scheme. The displacement ellipsoids are drawn at the 50% probability level. Selected bond lengths [Å] and angles [°]: Si(1)–N(1) 1.6600(13), Si(1)–C(1) 1.951(2), Si(1)–C(5) 1.954(2), Si(1)–C(9) 1.956(2), N(1)–Si(2) 1.6036(13), Si(2)–C(14) 1.868(2), Si(2)–C(13) 1.868(2), Si(2)–N(2) 1.9694(14); N(1)–Si(1)–C(1) 110.06(7), N(1)–Si(1)–C(5) 107.52 (7), C(1)–Si(1)–C(5) 110.15 (8), N(1)–Si(1)–C(9) 110.05(7), C(1)–Si(1)–C(9) 109.55(8), C(5)–Si(1)–C(9) 109.49(7), Si(2)–N(1)–Si(1) 156.44(10), N(1)–Si(2)–C(14) 119.27(10), N(1)–Si(2)–C(13) 119.38 (9), N(1)–Si(2)–N(2) 105.13 (6), C(14)–Si(2)–N(2) 101.73(8), C(13)–Si(2)–N(2) 102.11(10), C(16)–N(2)–Si(2) 107.97(12), C(15)–N(2)–Si(2) 107.4(2), C(17)–N(2)–Si(2) 112.98(11), N(2)–C(17)–C (18) 117.3 (2).

and the amine N atom in **1b**·$NMe_2Et$ (1.969 Å) is shorter than that in the adduct $Me_2Si{=}C(SiMe_2Ph)_2{\cdot}NMe_2Et$ (1.988 Å).[13]

### Structure of the Silanimine Dimer ($Me_2SiNSi\textit{t}Bu_3)_2$

X-ray quality crystals of the silanimine dimer ($Me_2SiNSi\textit{t}Bu_3)_2$ (**1b$_2$**) were grown from a benzene solution at ambi-

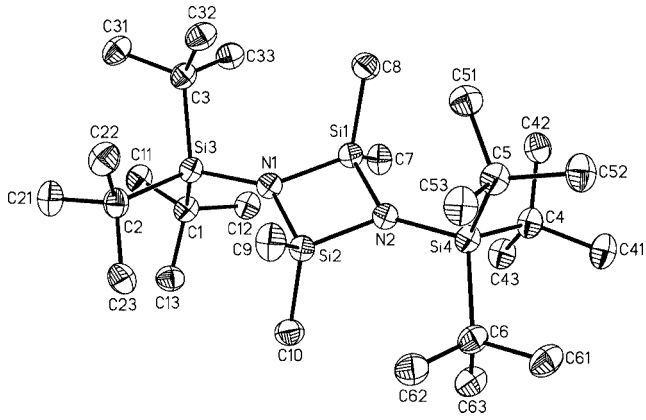


Figure 2. Thermal ellipsoid plot of the silanimine dimer ($Me_2SiNSi\textit{t}Bu_3)_2$ (**1b$_2$**) showing the atom numbering scheme. The displacement ellipsoids are drawn at the 50% probability level. Selected bond lengths [Å] and angles [°]: N(1)–Si(2) 1.764(2), N(1)–Si(3) 1.774(2), N(1)–Si(1) 1.778(2), N(2)–Si(2) 1.761(2), N(2)–Si(1) 1.774(2), N(2)–Si(4) 1.775(2), Si(1)–C(8) 1.866(3), Si(1)–C(7) 1.873(3), Si(1)–Si(2) 2.4690(9), Si(2)–C(10) 1.867(3), Si(2)–C(9) 1.868(3), Si(3)–C(3) 1.950(3), Si(3)–C(2) 1.959(3), Si(3)–C(1) 1.961(3), Si(4)–C(4) 1.950(3), Si(4)–C(5) 1.955(3), Si(4)–C(6) 1.956(3); Si(2)–N(1)–Si(3) 133.53(12), Si(2)–N(1)–Si(1) 88.38(9), Si(3)–N(1)–Si(1) 137.98(12), Si(2)–N(2)–Si(1) 88.60(9), Si(2)–N(2)–Si(4) 132.76(12), Si(1)–N(2)–Si(4) 138.42(12), N(2)–Si(1)–N(1) 91.07(9), N(2)–Si(1)–C(8) 115.47(11), N(1)–Si(1)–C(8) 116.19(11), N(2)–Si(1)–C(7) 115.82(11), N(1)–Si(1)–C(7) 116.13(11), C(8)–Si(1)–C(7) 102.84(13), C(8)–Si(1)–Si(2) 128.81(9), C(7)–Si(1)–Si(2) 128.35(10), N(2)–Si(2)–N(1) 91.95(10), N(2)–Si(2)–C(10) 113.80(11), N(1)–Si(2)–C(10) 110.43(11), N(2)–Si(2)–C(9) 111.06(11), N(1)–Si(2)–C(9) 113.78(11), C(10)–Si(2)–C(9) 113.95(13), C(10)–Si(2)–Si(1) 122.43(9), C(9)–Si(2)–Si(1) 123.62(10), N(1)–Si(3)–C(3) 106.58(11), N(1)–Si(3)–C(2) 112.06(10), C(3)–Si(3)–C(2) 108.62(11), N(1)–Si(3)–C(1) 110.50(10), C(3)–Si(3)–C(1) 110.47(11), C(2)–Si(3)–C(1) 108.59(11), N(2)–Si(4)–C(4) 107.12(10), N(2)–Si(4)–C(5) 110.42(10), C(4)–Si(4)–C(5) 110.06(11), N(2)–Si(4)–C(6) 111.54(11), C(4)–Si(4)–C(6) 108.80(11), C(5)–Si(4)–C(6) 108.88(11).

Table 2. Bond lengths [Å] and angles [°] of silanimines.

| | **1b**·$NMe_2Et$ | **1b**·thf[2] | **1a**(Ph)[11] | **1a**($\textit{t}$Bu)[2] | $H_2Si{=}NSiH_3$[1] |
|---|---|---|---|---|---|
| Si=N | 1.6036(13) | 1.588(9)/1.574(10) | 1.573(2)/1.573(3) | 1.568(3) | 1.549[a] |
| Si–N | 1.6600(13) | 1.654(9)/1.667(10) | 1.695(2)/1.690(3) | 1.695(3) | 1.688[a] |
| Si–N–Si | 156.44(10) | 161.5(5)/161.0(6) | 168.34(16)/172.95(18) | 177.8(2) | 175.6[a] |

[a] Calculated.

Table 3. Bond lengths [Å] and angles [°] of supersilylated nitrogen compounds (av. = average value).

| | N–Si$\textit{t}Bu_3$ | N–$SiR_2$ | Si–N–E (E = Si, C, N, M) | Si–$C_{\textit{t}Bu}$ (av.) |
|---|---|---|---|---|
| $(\textit{t}Bu_3SiNSiMe_2)_2$ (**1b$_2$**) | 1.775(2) av. | 1.769(2) av. | 135.67(12) av. | 1.955(3) |
| $\textit{t}Bu_3SiN(H)ClSi\textit{t}Bu_2$ [**3**($\textit{t}$Bu)] | 1.729(6) av. | 1.694(7) av. | 160.5(5) av. | 1.931(8) |
| $\textit{t}Bu_3SiN{=}CPh_2$ (**8**) | 1.721(4) av. | – | 154.3(3) av. | 1.922(4) |
| $\textit{t}Bu_2Si{=}NSi\textit{t}Bu_3{\cdot}\textit{t}BuMe_2SiN_3$[7] | 1.815(2) av. | 1.789(2) av. | 153.0(3) av. | 1.940(3) |
| $O(\textit{t}Bu_2SiHNSi\textit{t}Bu_3)_2$[14] | 1.750(1) | 1.772(1) | 157.13(6) | 1.947(3) |
| $\textit{t}Bu_3SiN(H)SiMesCH_2C_6H_2Me_2$[15] | 1.770(8) | 1.729(8) | 145.5(5) | 1.866(12) |
| $\textit{t}Bu_3SiNC\textit{t}Bu^+$ [16] | 1.822 | – | 179.0 | 1.902 |
| $\textit{t}Bu_3SiN(H)N(H)Si\textit{t}Bu_3$[17] | 1.760(3) | – | 120.6(2) | 1.932(3) |
| $\textit{t}Bu_3SiN(H)N{=}NSi\textit{t}Bu_3$[18] | 1.790(8) av. | – | 124.9(7) av. | 1.95(1) |
| $\textit{t}Bu_3SiN(SnMe_3)N{=}NSi\textit{t}Bu_3$[18] | 1.82(2) av. | – | 119.1(15) av. | 1.922(4) |
| $\textit{t}Bu_3SiNHM$[19] (M = Ti, V, Zr, Ta, W) | 1.723(9)–1.758(4) | – | 160.9(3)–166.6(5) | 1.92(1)–1.94(1) |
| $\textit{t}Bu_3SiNM_2$[19] (M = Ti, V, Zr, Ta, W) | 1.719(14)–1.778(3) | – | 164.1(2)–176.3(2) | 1.93(3)–1.95(1) |

 © 2006 Wiley-VCH Verlag GmbH & Co. KGaA, Weinheim 

ent temperature. It crystallizes in the monoclinic space group $P2_1/n$. As depicted in Figure 2, the central core of **1b$_2$** is a planar four-membered ring. The corners of this four-membered ring are alternately occupied by two Si and two N atoms [Si–N–Si (av) 88.49(9)°; N–Si–N 91.51(10)°]. The Si–N bond lengths of **1b$_2$** are longer than those of the silanimines **1a**(*t*Bu), **1a**(Ph), **1b**·thf, and **1b**·$NMe_2Et$, and those of the silylamine **3**(*t*Bu) (see Tables 2 and 3).

### Structure of the Benzophenone Imine $Ph_2C{=}NSitBu_3$

X-ray quality crystals of the benzophenone imine **8** were obtained by sublimation at 105 °C/0.001 mbar. It crystallizes in the triclinic space group $P\bar{1}$. It is interesting to note that the solid-state structure features three independent molecules in the asymmetric unit. As depicted in Figure 3, the C=N–Si skeleton deviates much more from linearity [C–N–Si 154.6(3)°, 154.9(3)°, and 153.5(3)°] than the Si=N–Si skeleton of **1a**(*t*Bu). The structure of **8** contains a C=N double bond [1.253(4), 1.263(5), and 1.261(5) Å] and, in comparison with the silanimine **1a**(*t*Bu), a longer Si–N single bond, as shown in Tables 2 and 3 [**1a**(*t*Bu): N–Si*t*Bu$_3$ 1.695(3) Å; **8**: N–Si*t*Bu$_3$ 1.722(3), 1.720(3), and 1.721(4) Å; Figure 3].

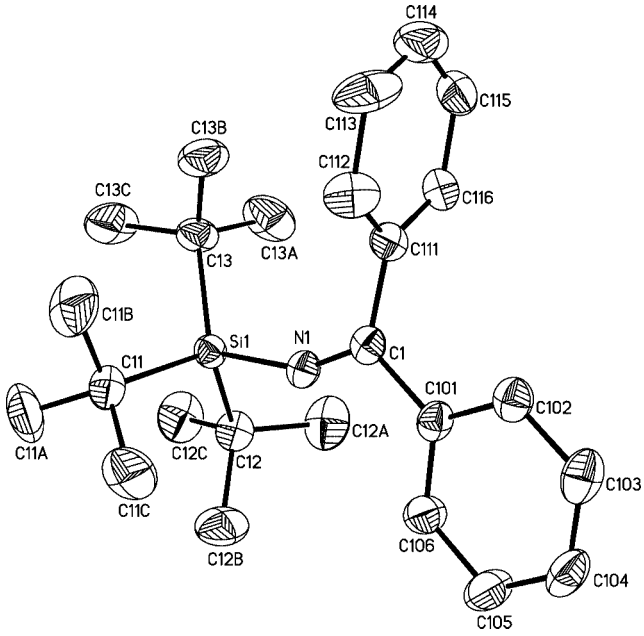


Figure 3. Thermal ellipsoid plot of one of three independent molecules in the asymmetric unit of $Ph_2C{=}NSitBu_3$ (**8**) showing the atom numbering scheme. The displacement ellipsoids are drawn at the 50% probability level. Selected bond lengths [Å] and angles [°]: Si(1)–N(1) 1.722(3), Si(1)–C(11) 1.919(4), Si(1)–C(13) 1.922(4), Si(1)–C(12) 1.929(4), N(1)–C(1) 1.253(4), C(1)–C(101) 1.510(5), C(1)–C(111) 1.512(5); N(1)–Si(1)–C(11) 102.30(18), N(1)–Si(1)–C(13) 116.02(18), C(11)–Si(1)–C(13) 112.1(2), N(1)–Si(1)–C(12) 101.14(18), C(11)–Si(1)–C(12) 113.6(2), C(13)–Si(1)–C(12) 111.1(2), C(1)–N(1)–Si(1) 154.6(3), N(1)–C(1)–C(101) 119.8(4), N(1)–C(1)–C(111) 123.9(4), C(101)–C(1)–C(111) 116.2(4).

### Structure of the Silylamine $tBu_2SiClN(H)Sitbu_3$

The solid-state structure of the silylamine $tBu_2SiClN(H)$-Si*t*Bu$_3$ [**3**(*t*Bu)] (triclinic, $P\bar{1}$) shows two symmetrically independent molecules in the unit cell. As shown in Table 3, **3**(*t*Bu) possesses Si–N–Si angles of 164.2(5)° and 158.5(5)°, respectively, which can be compared to the values for **1a**(*t*Bu) [177.8(2)°], **1a**(Ph) [172.95(18)°], **1b**·thf [161.0(6)° and 161.5(6)°], and **1b**·$NMe_2Et$ [156.44(10)°]. The Si(Cl)–N bond [av. 1.694(7) Å] in **3**(*t*Bu) lies in the range of the N–Si*t*Bu$_3$ bond lengths for the supersilyl-substituted silanimines **1a**(*t*Bu), **1a**(Ph), **1b**·thf, and **1b**·$NMe_2Et$ but is shorter than the Si–N single bonds of the silanimine dimer **1b$_2$** and the benzophenone imine **8** (Table 3). On the other hand, the length of the N–Si*t*Bu$_3$ bond in **3**(*t*Bu) is similar to those found in the silanimine dimer **1b$_2$** and the benzophenone imine **8**. Both molecules of **3**(*t*Bu) show large thermal displacements, resulting in distorted structural parameters and a large difference density. The molecular structure of **3**(*t*Bu) shows that the N–H groups are extremely shielded by the *t*Bu groups and are not involved in hydrogen bonding (Figure 4 and Table 4).

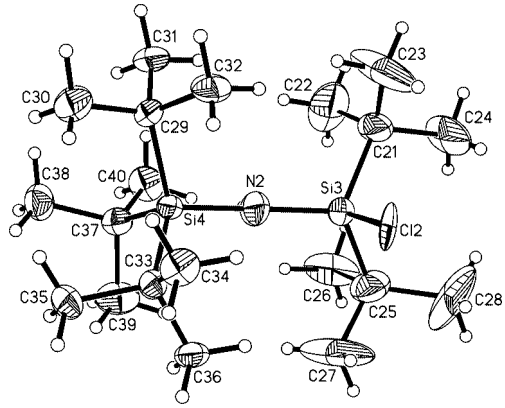


Figure 4. Thermal ellipsoid plot of one of the two independent molecules in the asymmetric unit of the silylamine $tBu_2SiClN(H)$ Si*t*Bu$_3$ [**3**(*t*Bu)]. The displacement ellipsoids are drawn at the 30% probability level. Selected bond lengths [Å] and angles [°]: Si(4)–N(2) 1.733(6), Si(4)–C(29) 1.918(7), Si(4)–C(33) 1.925(7), Si(4)–C(37) 1.935(8), Cl(2)–Si(3) 2.293(3) Si(3)–N(2) 1.679(7), Si(3)–C(25) 1.851(9), Si(3)–C(21) 1.908(9); Si(3)–N(2)–Si(4) 164.2(5), N(2)–Si(4)–C(29) 109.5(3), N(2)–Si(4)–C(33) 111.2(3), C(29)–Si(4)–C(33) 110.8(3), N(2)–Si(4)–C(37) 102.8(4), C(29)–Si(4)–C(37) 110.5(3), C(33)–Si(4)–C(37) 111.9(3), N(2)–Si(3)–C(25) 114.6(4), N(2)–Si(3)–C(21) 112.3(4), C(25)–Si(3)–C(21) 114.3(5), N(2)–Si(3)–Cl(2) 101.9(3), C(25)–Si(3)–Cl(2) 105.1(4), C(21)–Si(3)–Cl(2) 107.3(5).

## Conclusions

In summary, we have shown that in contrast to $tBu_2SiN$-(Li)Si*X*t*Bu*$_2$ (X = Cl, *t*Bu), the silyl amide $Me_2SiClN(Li)$-Si*t*Bu$_3$ is unstable towards LiCl elimination, which means that the silanimine aminate **1b**·$NMe_2Et$ can be synthesized in high yield from the reaction of $Me_2SiClN(H)Sitbu_3$ with *n*BuLi in the presence of $NMe_2Et$. The silanimine adduct **1a(Cl)·NMe$_2$Et**, which possesses the bulky *t*Bu substituent

 © 2006 Wiley-VCH Verlag GmbH & Co. KGaA, Weinheim 

Table 4. Crystallographic data and further details of the structure determination of **1b**·$NMe_2Et$, **1b$_2$**, **3**(*t*Bu), and **8**.

| | **1b**·$NMe_2Et$ | **1b$_2$** | **3**(*t*Bu) | **8** |
|---|---|---|---|---|
| Empirical formula | $C_{18}H_{44}N_2Si_2$ | $C_{28}H_{66}N_2Si_4$ | $C_{20}H_{46}ClNSi_2$ | $C_{25}H_{37}NSi$ |
| Color | colorless | colorless | colorless | yellow |
| Formula weight | 344.73 | 543.19 | 392.21 | 379.65 |
| Crystal system | monoclinic | monoclinic | triclinic | triclinic |
| Space group | $P2_1/n$ | $P2_1/n$ | $P\bar{1}$ | $P\bar{1}$ |
| $a$ [Å] | 10.431(2) | 8.8953(4) | 8.7999(18) | 8.4950(10) |
| $b$ [Å] | 17.361(2) | 25.2188(9) | 15.954(7) | 16.830(2) |
| $c$ [Å] | 12.664(2) | 14.8096(7) | 18.366(6) | 26.592(3) |
| $\alpha$ [°] | 90 | 90 | 94.16(3) | 105.598(4) |
| $\beta$ [°] | 97.80(2) | 90.632(4) | 100.41(3) | 97.122(4) |
| $\gamma$ [°] | 90 | 90 | 98.26(4) | 101.089(4) |
| $V$ [Å$^3$], $Z$ | 2272.1(6), 4 | 3322.0(2), 4 | 2496.8(14), 4 | 3530.9(7), 6 |
| $D_{calcd.}$ [Mg m$^{-3}$] | 1.008 | 1.086 | 1.043 | 1.071 |
| $\mu$(Mo-$K_\alpha$) [mm$^{-1}$] | 0.157 | 0.198 | 0.253 | 0.109 |
| $F$(000) | 776 | 1216 | 872 | 1248 |
| Crystal size [mm$^3$] | 0.4 × 0.4 × 0.8 | 0.49 × 0.29 × 0.27 | 0.50 × 0.19 × 0.10 | 0.31 × 0.14 × 0.12 |
| Diffractometer | Stoe-IPDS-II | Stoe-IPDS-II | Siemens Smart CCD | Siemens Smart CCD |
| $\theta$-range [°] | 2.00–28.00 | 1.59–25.35 | 1.13–30.73 | 0.81–25.03 |
| Index ranges | $-13 \le h \le 10$ | $-10 \le h \le 10$ | $-12 \le h \le 12$ | $-10 \le h \le 10$ |
| | $0 \le k \le 21$ | $-30 \le k \le 30$ | $-22 \le k \le 22$ | $-20 \le k \le 20$ |
| | $-15 \le l \le 16$ | $-17 \le l \le 17$ | $-27 \le l \le 28$ | $-31 \le l \le 31$ |
| No. of reflections collected | 6319 | 82992 | 31799 | 34387 |
| No. of independent reflections | 4619 | 6085 | 13016 | 12390 |
| $R$(int) | 0.0203 | 0.1395 | 0.0787 | 0.1345 |
| Absorption correction | empirical | empirical | empirical | empirical |
| No. of data/restraints/parameter | 4619/0/375 | 6085/0/307 | 13016/0/433 | 12390/0/730 |
| Goodness of fit on $F^2$ | 1.063 | 1.104 | 1.772 | 0.958 |
| Final $R$ indices [$I > 2\sigma(I)$], $R_1$, $wR_2$ | 0.0351, 0.0940 | 0.0565, 0.1431 | 0.1502, 0.3527 | 0.0763, 0.1171 |
| Largest diff. peak/hole [e Å$^{-3}$] | 0.276/–0.203 | 0.474/–0.371 | 2.045/–0.700 | 0.241/–0.271 |

on the unsaturated Si center, is accessible by treating the donor-free silanimine **1a**(Cl) with $NMe_2Et$.

In contrast to the degradation reaction of the donor-free silanimines **1a**(Cl), **1a**(*t*Bu), and **1a**(Ph), a Stevens rearrangement takes place in the thermolysis of the silanimine amine adducts **1a**(Cl)·$NMe_2Et$ and **1b**·$NMe_2Et$ in dimethylethylamine to produce $EtN(Me)CH_2SiMe_2N(H)SitBu_3$ and $EtN(Me)CH[Me_2SiN(H)SitBu_3]_2$, and $EtN(Me)CH_2Si$-$tBu_2N(H)SiCltBu_2$, respectively. The thermolysis of **1b**·$NMe_2Et$ in vacuo gives the silanimine dimer **1b$_2$** in 80% yield. In contrast to the reaction of **1a**(*t*Bu) with benzophenone, in which a stable silanimine adduct is formed, the silanimine amine complex **1b**·$NMe_2Et$ reacts with benzophenone to produce benzophenone imine **8**, via oxaazasilacyclobutane **7**, by a Wittig-like reaction. Due to the anisotropy effect the $^{29}$Si NMR spectra of silanimines of the type $R_2Si(1){=}NSi(2)R_3$ reveal upfield-shifted signals for both Si nuclei, therefore the linearity of the silanimine skeleton can be determined from the $^{29}$Si shift of the Si(2) center.

## Experimental Section

**General Remarks:** All experiments were carried out under dry nitrogen or argon with strict exclusion of air and moisture using standard Schlenk techniques. $tBu_2Si{=}NSiCltBu_2$,[6] $tBu_2SiFH$,[20] $tBu_2SiClH$,[20] and $Me_2SiClN(H)SitBu_3$[8] were prepared according to literature procedures. All other starting materials were purchased from commercial sources and used without further purification. The solvents were distilled from sodium/benzophenone (benzene, toluene, tetrahydrofuran, diethyl ether) or Na/Pb alloy (pentane, hexane, heptane) prior to use. $C_6D_6$ was dried with molecular sieves and stored under dry nitrogen. The NMR spectra were recorded with a Jeol FX 90, a Jeol GSX 270, a Bruker AM 250, a Bruker DPX 250, or a Bruker Avance 400 spectrometer. The $^{29}$Si NMR spectra were recorded using the INEPT pulse sequence with empirically optimized parameters for polarization transfer from the *t*Bu substituents.

**Synthesis of $tBu_2SiClN(H)SitBu_3$ [3(*t*Bu)]:** This compound was prepared according to a literature procedure.[4] X-ray quality crystals of **3**(*t*Bu) were grown from benzene at ambient temperature. Selected data: thermal decomposition of **3**(*t*Bu) occurs at 113 °C. $^1$H NMR ($C_6D_6$, internal TMS): $\delta$ = 1.19 (s, 18 H, $tBu_2SiCl$), 1.21 (s, 27 H, $tBu_3Si$) ppm. $^{13}C\{^1H\}$ NMR ($C_6D_6$, internal TMS): $\delta$ = 23.6 (3 C, $CMe_3$), 24.5 (2 C, $CMe_3$), 29.3 (6 C, $CMe_3$), 31.3 (9 C, $CMe_3$) ppm. $^{29}Si\{^1H\}$ NMR ($C_6D_6$, external TMS): $\delta$ = 8.4 ($SitBu_3$), 16.0 ($SiCltBu_3$) ppm. $C_{20}H_{46}ClNSi$ (392.22): calcd. C 61.25, H 11.82, N 3.57; found C 62.02, H 12.05, N 3.18. EI MS: *m*/*z* (%) 334 (100) $[M - tBu]^+$.

**Synthesis of $tBu_2Si(H)NH_2$:** $tBu_2SiClH$ (10.05 g, 56.2 mmol) was added to 10 mL of liquid $NH_3$ at –60 °C and stirred for 6 h. After heating to room temperature the reaction product was distilled at 93 °C/100 Torr: Yield: 5.72 g (68%). $^1$H NMR ($C_6D_6$, internal TMS): $\delta$ = 0.97 (s, 18 H, $tBu_2Si$), 4.03 (br., HSi) ppm. $^{13}C\{^1H\}$ NMR ($C_6D_6$, internal TMS): $\delta$ = 18.9 ($CMe_3$), 27.7 ($CMe_3$) ppm. $^{29}Si\{^1H\}$ NMR ($C_6D_6$, external TMS): $\delta$ = 7.1 ppm ($SitBu_2$). $C_8H_{21}NSi$ (159.35): calcd. C 60.30, H 13.28, N 8.78; found C 59.13, H 13.14, N 8.02. EI MS: *m*/*z* (%) 159 (13) $[M]^+$, 102 (100) $[M - tBu]^+$.

**Synthesis of $tBu_2Si(H)N(H)SiHtBu_2$:** A mixture of $LiNH_2$ (4.60 g, 200 mmol) and $tBu_2SiFH$ (16.20 g, 100 mmol) in tetrahydrofuran (100 mL) was refluxed for 24 h. After addition of methanol

 © 2006 Wiley-VCH Verlag GmbH & Co. KGaA, Weinheim 

(40 mL), all volatile compounds were removed in vacuo and the residue was extracted into 150 mL of pentane. After filtration, the solvent was removed in vacuo to give $t$Bu$_2$Si(H)N(H)SiH$t$Bu$_2$ as a colorless oil: Yield: 10.93 g (72%). B.p. 58 °C/0.01 mbar. $^1$H NMR ($C_6D_6$, internal TMS): $\delta$ = 1.07 (s, 36 H, $t$Bu$_2$Si), 4.23 (d, HSi) ppm. $^{13}$C{$^1$H} NMR ($C_6D_6$, internal TMS): $\delta$ = 20.6 (*C*Me$_3$), 28.5 (C*Me$_3$*) ppm. $^{29}$Si{$^1$H} NMR ($C_6D_6$, external TMS): $\delta$ = 7.0 ppm (Si$t$Bu$_2$). $C_{16}H_{39}NSi_2$ (301.67): calcd. C 63.70, H 13.03, N 4.64; found C 63.04, H 12.95, N 4.72. EI MS: *m*/*z* (%) 301 (5) [M]$^+$, 244 (100) [M – $t$Bu]$^+$.

***Note:*** $t$Bu$_2$Si(H)N(H)SiH$t$Bu$_2$ can also be synthesized from $t$Bu$_2$Si(H)NHLi and $t$Bu$_2$SiFH in tetrahydrofuran by heating.

**Synthesis of $t$Bu$_2$SiClN(H)SiCl$t$Bu$_2$ [3(Cl)]:** A mixture of *N*-chlorosuccinimide (23.79 g, 178.1 mmol) and $t$Bu$_2$Si(H)N(H)SiH$t$Bu$_2$ (9.775 g, 32.4 mmol) in $CCl_4$ (75 mL) was refluxed for 48 h. After filtration, the solvent was removed in vacuo and the obtained solid reaction product was sublimed at 60 °C/10$^{-4}$ Torr: Yield: 9.36 g (80%). $^1$H NMR ($C_6D_6$, internal TMS): $\delta$ = 1.12 (s, 36 H, $t$Bu$_2$Si) ppm. $^{13}$C{$^1$H} NMR ($C_6D_6$, internal TMS): $\delta$ = 23.4 (*C*Me$_3$), 28.1 (C*Me$_3$*) ppm. $^{29}$Si{$^1$H} NMR ($C_6D_6$, external TMS): $\delta$ = 17.9 ppm (Si$t$Bu$_2$). $C_{16}H_{37}Cl_2NSi_2$ (370.56): calcd. C 51.86, H 10.06, N 3.78; found C 50.74, H 9.89, N 3.42. EI MS: *m*/*z* (%) 369 (1) [M]$^+$, 312 (100) [M – $t$Bu]$^+$.

**Synthesis of the Silanimine Adduct $t$Bu$_2$Si=NSiCl$t$Bu$_2$·NMe$_2$Et [1a(Cl)·NMe$_2$Et]:** NMe$_2$Et (2 mL) was added to a solution of $t$Bu$_2$Si=NSiCl$t$Bu$_2$ (0.8 mmol) in 5 mL of benzene. After removing all volatile compounds in vacuo **1a**(Cl)·NMe$_2$Et was obtained as a colorless solid. $^1$H NMR ($C_6D_6$, internal TMS): $\delta$ = 1.18 (s, 18 H, $t$Bu$_2$SiCl), 1.46 (s, 18 H, $t$Bu$_2$Si), 0.63 (t, $^3J$ = 7.2 Hz, 3 H, CH$_3$), 2.89 (q, $^3J$ = 7.2 Hz, 2 H, NCH$_2$), 2.11 (s, 6 H, NMe$_2$) ppm. $^{13}$C{$^1$H} NMR ($C_6D_6$, internal TMS): $\delta$ = 9.7 (CH$_3$), 25.3 (*C*Me$_3$), 25.7 (*C*Me$_3$), 30.3 (C*Me$_3$*), 31.8 (C*Me$_3$*), 44.8 (NCH$_2$), 52.9 (NMe$_2$) ppm. $^{29}$Si{$^1$H} NMR ($C_6D_6$, external TMS): $\delta$ = –6.4 (SiCl$t$Bu$_2$), –3.4 (Si$t$Bu$_2$) ppm.

**Synthesis of the Silanimine Adduct Me$_2$Si=NSi$t$Bu$_3$·NMe$_2$Et (1b·NMe$_2$Et):** *n*BuLi (7.89 mmol) in hexane (5.1 mL) was added to a solution of Me$_2$SiClN(H)Si$t$Bu$_3$ (2.43 g, 7.89 mmol) and 10 mL of NMe$_2$Et in 50 mL of Et$_2$O at –78 °C and stirred for 4 h. After heating to room temperature the volatile compounds were removed in vacuo and the solid reaction product was extracted into 30 mL of pentane. After filtration, single crystals of **1b**·NMe$_2$Et were obtained from the pentane filtrate at –25 °C. Yield: 1.47 g (54%). $^1$H NMR ($C_6D_6$, internal TMS): $\delta$ = 0.12 (s, 6 H Me$_2$Si), 0.32 (t, 3 H, CH$_3$), 1.45 (s, 27 H, $t$Bu$_3$Si), 1.77 (s, 6 H, NMe$_2$), 2.50 (q, 2 H, NCH$_2$) ppm. $^{13}$C{$^1$H} NMR ($C_6D_6$, internal TMS): $\delta$ = 1.9 (Me$_2$Si), 6.5 (CH$_3$), 24.5 (*C*Me$_3$), 32.1 (C*Me$_3$*), 41.5 (NCH$_2$), 51.0 (NMe$_2$) ppm. $^{29}$Si{$^1$H} NMR ($C_6D_6$, external TMS): $\delta$ = –8.9 (Me$_2$Si), –10.3 (Si$t$Bu$_3$) ppm.

**Synthesis of the Silanimine Dimer (Me$_2$SiNSi$t$Bu$_3$)$_2$ (1b$_2$):** Compound **1b**·NMe$_2$Et (0.608 g, 1.76 mmol) was heated at 120 °C in vacuo (0.01 mbar) for 4 h, then the obtained solid was extracted into 10 mL of benzene. **1b$_2$** was crystallized from this solution at ambient temperature. Yield: 0.382 g (80%). The NMR spectra of the mother liquid show the signals of **1b$_2$** and small signals which can be assigned to **5**(Me,*t*Bu) and **6**(Me,*t*Bu). Selected data for **1b$_2$**: m.p. 268 °C. $^1$H NMR ($C_6D_6$, internal TMS): $\delta$ = 0.79 (s, 12 H Me$_2$Si), 1.23 (s, 54 H, $t$Bu$_3$Si) ppm. $^{13}$C{$^1$H} NMR ($C_6D_6$, internal TMS): $\delta$ = 12.1 (Me$_2$Si), 23.8 (*C*Me$_3$), 32.6 (C*Me$_3$*) ppm. $^{29}$Si{$^1$H} NMR ($C_6D_6$, external TMS): $\delta$ = 7.4 (Me$_2$Si), 4.6 (Si$t$Bu$_3$) ppm. $C_{28}H_{66}N_2Si_4$ (543.18): calcd. C 61.91, H 12.95, N 5.16; found C 61.28, H 12.62, N 5.09.

**Thermolysis of the Silanimine Adduct Me$_2$SiNSi$t$Bu$_3$·NMe$_2$Et (1b·NMe$_2$Et):** A solution of **1b·NMe$_2$Et** (0.168 g, 0.487 mmol) in 0.8 mL of NMe$_2$Et was heated at 135 °C for 30 h. The NMR ($^1$H, $^{13}$C, $^{29}$Si) spectra showed the signals of **5**(Me,*t*Bu) (80%) and **6**(Me,*t*Bu) (20%). After removing all volatile compounds at room temp. and 0.001 mbar, colorless **5**(Me,*t*Bu) was distilled at 70 °C/0.001 mbar from the obtained mixture. Analytically pure **6**(Me,*t*Bu) remained as the distillation residue.

**5(Me,*t*Bu):** $^1$H NMR ($C_6D_6$, internal TMS): $\delta$ = 0.26 (s, 6 H Me$_2$Si), 0.96 (t, $^1J$ = 7.1 Hz, 3 H, CH$_3$), 1.20 (s, 27 H, $t$Bu$_3$Si), 1.74 (s, 2 H, SiCH$_2$N), 2.15 (s, 3 H, NCH$_3$), 2.30 (q, $^1J$ = 7.1 Hz, 2 H, NCH$_2$) ppm. $^{13}$C{$^1$H} NMR ($C_6D_6$, internal TMS): $\delta$ = 3.64 (Me$_2$Si), 13.3 (CH$_3$), 23.0 (*C*Me$_3$), 30.7 (C*Me$_3$*), 45.4 (NCH$_3$), 50.2 (NCH$_2$Si), 55.7 (NCH$_2$) ppm. $^{29}$Si{$^1$H} NMR ($C_6D_6$, external TMS): $\delta$ = –3.7 (Me$_2$Si), 6.4 (Si$t$Bu$_3$) ppm. $C_{18}H_{44}N_2Si_2$ (344.74): calcd. C 62.71, H 12.87, N 8.13; found C 63.01, H 12.14, N 8.52. EI MS: *m*/*z* (%) 344 (7) [M]$^+$, 287 (100) [M – $t$Bu]$^+$.

**6(Me,*t*Bu):** M.p. 116 °C. $^1$H NMR ($C_6D_6$, internal TMS): $\delta$ = 0.41 (s, 6 H MeSi), 0.44 (s, 6 H MeSi), 1.06 (t, $^1J$ = 7.1 Hz, 3 H, CH$_3$), 1.20 (s, 54 H, $t$Bu$_3$Si), 1.76 (s, 1 H, Si$_2$CHN), 2.49 (s, 3 H, NCH$_3$), 2.81 (q, $^1J$ = 7.1 Hz, 2 H, NCH$_2$) ppm. $^{13}$C{$^1$H} NMR ($C_6D_6$, internal TMS): $\delta$ = 6.1 (MeSi), 6.2 (MeSi), 14.7 (CH$_3$), 23.0 (*C*Me$_3$), 30.9 (C*Me$_3$*), 44.0 (NCH$_3$), 53.6 (NCHSi$_2$), 54.0 (NCH$_2$) ppm. $^{29}$Si{$^1$H} NMR ($C_6D_6$, external TMS): $\delta$ = –1.6 (Me$_2$Si), 6.7 (Si$t$Bu$_3$) ppm. $C_{32}H_{77}N_3Si_4$ (616.33): calcd. C 62.36, H 12.60, N 6.80; found C 62.00, H 12.83, N 6.65. EI MS: *m*/*z* (%) 615 (3) [M]$^+$, 558 (100) [M – $t$Bu]$^+$.

***Remark:*** A solution of **1b**·NMe$_2$Et (0.025 g, 0.073 mmol), 0.1 mL of NMe$_2$Et and 1 mL of $C_6D_6$ was heated at 120 °C for 24 h. The NMR ($^1$H, $^{13}$C, $^{29}$Si) spectra showed the signals of **5**(Me,*t*Bu) (10%) and **6**(Me,*t*Bu) (90%).

**Thermolysis of the Silanimine Adduct $t$Bu$_2$Si=NSiCl$t$Bu$_2$·NMe$_2$Et [1a(Cl)·NMe$_2$Et]:** A solution of **1a**(Cl)·NMe$_2$Et (0.5 mmol) in 2 mL of NMe$_2$Et was stored for 2 weeks at ambient temperature. The NMR ($^1$H, $^{13}$C, $^{29}$Si) spectra showed only the signals of **5**(*t*Bu,Cl). $^1$H NMR ($C_6D_6$, internal TMS): $\delta$ = 0.96 (t, $^1J$ = 7.33 Hz, 3 H, CH$_3$), 1.14 (s, 18 H, $t$Bu$_2$Si), 1.23 (s, 18 H, $t$Bu$_2$Si), 2.06 (s, 3 H, NCH$_3$), 2.15 (q, $^1J$ = 7.33 Hz, 2 H, NCH$_2$), 2.35 (s, 2 H, SiCH$_2$N) ppm. $^{13}$C{$^1$H} NMR ($C_6D_6$, internal TMS): $\delta$ = 13.1 (CH$_3$), 23.3 (*C*Me$_3$), 23.6 (*C*Me$_3$), 28.7 (C*Me$_3$*), 29.5 (C*Me$_3$*), 39.2 (NCH$_2$Si), 45.1 (NCH$_3$), 53.7 (NCH$_2$) ppm. $^{29}$Si{$^1$H} NMR ($C_6D_6$, external TMS): $\delta$ = 17.5 ($t$Bu$_2$SiCl), 0.6 (Si$t$Bu$_2$) ppm. EI MS: *m*/*z* (%) 334 (43) [M – $t$Bu]$^+$, 166 (100) [Me$_2$SiNHSiClMe$_2$]$^+$.

***Note:*** A solution of **1a**(Cl)·NMe$_2$Et (0.134 g, 0.329 mmol) in 0.6 mL of $C_6D_6$ was stored at ambient temperature for a week. The NMR ($^1$H, $^{13}$C, $^{29}$Si) spectra showed the signals of **5**(*t*Bu,Cl).

**Reaction of the Silanimine Adduct Me$_2$Si=NSi$t$Bu$_3$·NMe$_2$Et (1b·NMe$_2$Et) with Ph$_2$CO:** A solution of Ph$_2$C=O (0.275 g, 1.50 mmol) in 10 mL of Et$_2$O was added to a solution of **1b**·NMe$_2$Et (0.520 g, 1.51 mmol) in 10 mL of Et$_2$O at –78 °C. The NMR ($^1$H, $^{13}$C, $^{29}$Si) spectra showed the signals of Ph$_2$C=NSi$t$Bu$_3$ (**8**) and other compounds containing Me$_2$SiO groups.[8] After removing all volatile compounds in vacuo (0.001 mbar), single crystals of **8** were obtained by sublimation at 105 °C/0.001 mbar. Yield: 0.301 g (53%). M.p. 98 °C. $^1$H NMR ($C_6D_6$, internal TMS): $\delta$ = 1.18 (s, 27 H, $t$Bu$_3$Si), 7.08 (m, 6 H, *o*/*p*-Ph), 7.387 (m, 4 H, *m*-Ph) ppm. $^{13}$C{$^1$H} NMR ($C_6D_6$, internal TMS): $\delta$ = 23.7 (*C*Me$_3$), 30.9 (C*Me$_3$*), 128.26 (*m*/*o*-Ph), 128.29 (*m*/*o*-Ph), 129.3 (*p*-Ph), 143.3 (*i*-Ph), 170.3 (C=N) ppm. $^{29}$Si{$^1$H} NMR ($C_6D_6$, external TMS): $\delta$ = –4.9 ppm (Si$t$Bu$_3$). $C_{19}H_{39}NSi_2$ (379.66): calcd. C 79.01, H 9.81, N 3.69; found C 78.54, H 9.65, N 3.72. EI MS: *m*/*z* (%) 322 (100)

 © 2006 Wiley-VCH Verlag GmbH & Co. KGaA, Weinheim 

$[M - tBu]^+$. IR: $\nu_{C=N}$ = 1692 $cm^{-1}$. UV/Vis: $\lambda_{max}$ = 401 nm ($\varepsilon_{401}$ = 7.48 $M^{-1}cm^{-1}$).

**Lithiation of $tBu_2SiClN(H)SiXtBu_2$ (X = Cl, *t*Bu) [3(Cl), 3(*t*Bu)]:** A solution of RLi [X = Cl(thf): RLi = 3.16 mmol of *n*BuLi in 2 mL of hexane and 10 mL of thf; X = Cl(thf): RLi = 1.93 mmol of MeLi in 3 mL of $Et_2O$; X = Cl($Et_2O$): RLi = 1.05 mmol of *n*BuLi in 0.7 mL of hexane and 10 mL of $Et_2O$] was added to a solution of $tBu_2SiClN(H)SiXtBu_2$ (in 10 mL of thf, X = Cl, 1.162 g, 3.14 mmol; in 6 mL of thf, X = *t*Bu, 0.756 g, 1.93 mmol; in 10 mL $Et_2O$, X = Cl, 0.385 g, 1.05 mmol) at –78 °C. After removing the solvent, the silylated amides $tBu_2SiClN(Li)SiXtBu_2$ (X = Cl, *t*Bu) were obtained as colorless solids. The NMR spectra of the reaction solution showed only the signals of the silylated amides $tBu_2SiClN(Li)SiXtBu_2$ (X = Cl, *t*Bu).

**$tBu_2SiClNLi(thf)SiCltBu_2$:** $^1H$ NMR ($C_6D_6$, internal TMS): $\delta$ = 1.32 (m, 4 H, $CH_2$), 1.36 (s, 36 H, $tBu_2Si$), 3.47 (m, 4 H $OCH_2$). $^{13}C\{^1H\}$ NMR ($C_6D_6$, internal TMS): $\delta$ = 24.8 ($CMe_3$), 25.2 ($CH_2$), 28.9 ($CMe_3$), 68.7 ($OCH_2$) ppm. $^{29}Si\{^1H\}$ NMR ($C_6D_6$, external TMS): $\delta$ = 4.8 ppm ($SitBu_2$).

**$tBu_2SiClNLi(thf)SitBu_3$:** $^1H$ NMR ($C_6D_6$, internal TMS): $\delta$ = 1.17 (m, 4 H, $CH_2$), 1.32 (s, 27 H, $tBu_3Si$), 1.44 (s, 18 H, $tBu_2Si$), 3.35 (s, 8 H $OCH_2$) ppm.

**$tBu_2SiCl$-NLi($Et_2O$)$SiCltBu_2$:** $^1H$ NMR ($C_6D_6$, internal TMS): $\delta$ = 0.904 (t, 6 H, $CH_3$), 1.315 (s, 36 H, $tBu_2Si$), 3.181 (q, 4 H $OCH_2$) ppm. $^{13}C\{^1H\}$ NMR ($C_6D_6$, internal TMS): $\delta$ = 14.8 ($CH_3$), 24.8 ($CMe_3$), 29.0 ($CMe_3$), 65.8 ($OCH_2$) ppm. $^{29}Si\{^1H\}$ NMR ($C_6D_6$, external TMS): $\delta$ = 5.5 ppm ($SitBu_2$).

***Note:*** Treatment of one equivalent of $tBu_2SiClN(Li)SiXtBu_2$ (X = Cl, *t*Bu) with one equivalent of MeOH leads quantitatively to the formation of **3**(Cl) and **3**(*t*Bu).

**X-ray Crystallographic Study:** Data collection was performed with either a Stoe-IPDS-II diffractometer or a Siemens CCD three-circle diffractometer. Empirical absorption correction was performed with MULABS[21] and SADABS,[22] structure solution by direct methods,[23] and structure refinement by full-matrix least-squares on $F^2$ with SHELXL-97.[24] Hydrogen atoms were placed at ideal positions and refined with fixed isotropic displacement parameters using a riding model.

CCDC-602102 (for **1b**·$NMe_2Et$), -602101 (for **1b$_2$**), -609530 [for **3**(*t*Bu)], and -609686 (for **8**) contain the supplementary crystallographic data for this paper. These data can be obtained free of charge from The Cambridge Crystallographic Data Centre via www.ccdc.cam.ac.uk/data_request/cif.


[1] P. von Ragué Schleyer, P. D. Stout, *J. Chem. Soc., Chem. Commun.* **1986**, 1373–1374.
[2] N. Wiberg, K. Schurz, G. Reber, G. Müller, *J. Chem. Soc., Chem. Commun.* **1986**, 591–592.
[3] H.-W. Lerner, S. Scholz, M. Bolte, *Z. Anorg. Allg. Chem.* **2001**, *627*, 1638–1642.
[4] P. Karampatses, *PhD Thesis*, München, Germany, **1985**.
[5] M. Hesse, U. Klingebiel, *Angew. Chem. Int. Ed. Engl.* **1986**, *25*, 649–650.
[6] H.-W. Lerner, N. Wiberg, J. W. Bats, *J. Organomet. Chem.* **2005**, *690*, 3898–3907.
[7] H.-W. Lerner, N. Wiberg, K. Polborn, *Z. Naturforsch., Teil B* **2002**, *57*, 1199–1206.
[8] N. Wiberg, K. Schurz, *J. Organomet. Chem.* **1988**, *341*, 145–163.
[9] N. Wiberg, K. Schurz, *Chem. Ber.* **1988**, *121*, 581–589.
[10] H.-W. Lerner, *PhD Thesis*, München, Germany, **1994**.
[11] J. Niesmann, U. Klingebiel, M. Schäfer, R. Boese, *Organometallics* **1998**, *17*, 947–953.
[12] N. Wiberg, K. Schurz, G. Müller, J. Riese, *Angew. Chem. Int. Ed. Engl.* **1988**, *27*, 935–936.
[13] N. Wiberg, K.-S. Joo, K. Polborn, *Chem. Ber.* **1993**, *126*, 67–69.
[14] N. Wiberg, E. Kuhnel, K. Schurz, H. Borrmann, A. Simon, *Z. Naturforsch., Teil B* **1988**, *43*, 1075–1086.
[15] M. Weidenbruch, B. Brand-Roth, S. Pohl, W. Saak, *J. Organomet. Chem.* **1989**, *379*, 217–222.
[16] M. Ichinohe, H. Fukui, A. Sekiguchi, *Chem. Lett.* **2000**, *126*, 600.
[17] H.-W. Lerner, N. Wiberg, M. Bolte, H. Nöth, J. Knizek, *Z. Naturforsch., Teil B* **2002**, *57*, 177–182.
[18] N. Wiberg, P. Karampatses, E. Kuhnel, M. Veith, V. Huch, *Z. Anorg. Allg. Chem.* **1988**, *562*, 91–101.
[19] Cambridge Structural Database (CSD, version 5.27, updated May 2006): F. H. Allen, *Acta Crystallogr. Sect. B* **2002**, *58*, 380.
[20] N. Wiberg, K. Amelunxen, H.-W. Lerner, H. Schuster, H. Nöth, I. Krossing, M. Schmidt-Amelunxen, T. Seifert, *J. Organomet. Chem.* **1997**, *542*, 1–18.
[21] R. H. Blessing, *Acta Crystallogr. Sect. A* **1995**, *51*, 33.
[22] G. M. Sheldrick, SADABS, University of Göttingen, Germany, **2000**.
[23] G. M. Sheldrick, *Acta Crystallogr. Sect. A* **1990**, *46*, 467.
[24] G. M. Sheldrick, *SHELXL-97, A Program for the Refinement of Crystal Structures*, University of Göttingen, Germany, **1997**.


Received: June 29, 2006
Published Online: October 31, 2006

 © 2006 Wiley-VCH Verlag GmbH & Co. KGaA, Weinheim 

DOI: 10.1002/ejic.200600620

# π-Conjugated α,ω-Diphenylpolyene Complexes of RuClCp* Fragment(s) in $\eta^4$-*s*-*cis* Conformation

**Hiroki Fukumoto[a] and Kazushi Mashima*[b]**

**Keywords:** π-Conjugated polyenes / Coordination modes / Fluxionality / Multinuclear complexes / Ruthenium

π-Conjugated polyene complexes of the general formula $(RuClCp^{\star})_n$(polyene) [**2**: $n$ = 1, polyene = 1,4-diphenylbuta-1,3-diene; **3**: $n$ = 1, polyene = 1,6-diphenylhexa-1,3,5-triene; **4**: $n$ = 2, polyene = 1,8-diphenylocta-1,3,5,7-tetraene; **5**: $n$ = 2, polyene = 1,10-diphenyldeca-1,3,5,7,9-pentaene; **6**: $n$ = 3, polyene = 1,12-diphenyldodeca-1,3,5,7,9,11-hexaene], in which each ruthenium(II) atom has $Cp^{\star}$ ($Cp^{\star}$ = $\eta^5$-$C_5Me_5$) and chlorido ligands, were prepared by treating [Ru($\mu_3$-Cl)-$Cp^{\star}$]$_4$ (**1**) with the corresponding α,ω-diphenylpolyenes. All diene units of the complexes were fully metalated by the coordination of "RuClCp$^{\star}$" fragments in an $\eta^4$-*s*-*cis* conformation.
(© Wiley-VCH Verlag GmbH & Co. KGaA, 69451 Weinheim, Germany, 2006)

## Introduction

One-dimensional π-conjugated polyenes are excellent supporting ligands to which plural transition metals can coordinate, and their metal complexes are expected to show unique properties on the basis of an extended pπ–dπ conjugated organometallic system.[1] Their physical properties are thus controlled by not only the number of transition metals bound to the polyene ligand but also their coordination features such as nuclearity (mono-,[2,3] di-,[4] or polynuclear[5]), stereochemistry (*syn* and *anti* for polynuclear complexes), and fluxionality[6,7] (metal migration on a polyene). Moreover, ancillary ligands on a metal center also play an important role in controlling the structure and properties of π-conjugated polyene complexes. We have recently reported the systematic preparation of α,ω-diphenylpolyene complexes bearing $Ru(acac)_2$ (acac = acetylacetonato) fragments, which coordinate to all diene units of the polyene in an $\eta^4$-*s*-*trans* fashion,[8a] resulting in the full metalation of all diene units of the polyenes. In contrast, ruthenium fragments with Cp* (Cp* = $C_5Me_5$) and chlorido ligands prefer to coordinate to a diene moiety of diene and tetraene in an $\eta^4$-*s*-*cis* fashion revealed by our previous work.[8b] The selectivity of coordination mode originating from the difference of ancillary ligands on a ruthenium center has attracted interest. Furthermore, "RuClCp*" fragments as well as "$Ru(acac)_2$"[8a] and "$Fe(CO)_3$"[7] fragments are also expected to move on a π-conjugated polyene with an odd number of olefinic parts such as triene and pentaene. As an extension of our continuing interest in this area, we have investigated the complexation of the "RuClCp*" fragment with longer polyenes. Here, we report the synthesis of a series of α,ω-diphenylpolyene complexes (polyene = di-, tri-, tetra-, penta-, and hexaene) bearing RuClCp* fragments and their structural features.

## Results and Discussion

The reaction of α,ω-diphenylpolyenes with [Ru($\mu_3$-Cl)-Cp*]$_4$ (**1**)[2g] in THF or dichloromethane at room temperature gave the corresponding chlorido($\eta^5$-pentamethylcyclopentadienyl)ruthenium(II) complexes of the general formula $(RuClCp^*)_n$(polyene) [**2**: $n$ = 1, polyene = 1,4-diphenylbuta-1,3-diene; **3**: $n$ = 1, polyene = 1,6-diphenylhexa-1,3,5-triene; **4**: $n$ = 2, polyene = 1,8-diphenylocta-1,3,5,7-tetraene; **5**: $n$ = 2, polyene = 1,10-diphenyldeca-1,3,5,7,9-pentaene; **6**: $n$ = 3, polyene = 1,12-diphenyldodeca-1,3,5,7,9,11-hexaene] in modest yields [Equation (1)]. Among them, the diene and tetraene complexes **2** and **4** had previously been prepared and characterized.[8b] Both complexes are stable to air and moisture in the solid state, but are not stable in solution. Complexes **3**, **5**, and **6** are soluble in dichloromethane and chloroform, and are slightly soluble in THF. The treatment of **1** with longer polyenes such as 1,14-diphenyltetradeca-1,3,5,7,9,11,13-heptaene and 1,16-diphenylhexadeca-1,3,5,7,9,11,13,15-octaene did not yield any products because of the low solubility of heptaene and octaene ligands in any common organic solvent.

In the obtained complexes, RuClCp* fragments coordinated in an $\eta^4$-*s*-*cis* fashion to all diene units of the polyenes. The $^1$H NMR spectra of all complexes (except **2**) showed signals of the outer protons of coordinated diene

[a] Chemical Resources Laboratory, Tokyo Institute of Technology, 4259, Nagatsuta, Midori-ku, Yokohama 226-8503, Japan
[b] Department of Chemistry, Graduate School of Engineering Science, Osaka University,
Toyonaka, Osaka 560-8531, Japan
Fax: +81-6-6850-6296
E-mail: mashima@chem.es.osaka-u.ac.jp

 InterScience © 2006 Wiley-VCH Verlag GmbH & Co. KGaA, Weinheim 

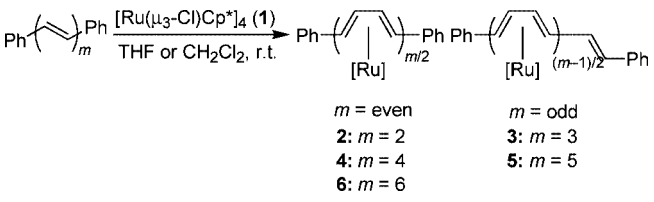


(1)

units in the range of δ = 2.5–4.0 ppm. Siganls of the inner protons of the *s*-*cis* diene moieties are observed at δ ≈ 5 ppm, with a smaller coupling constant ($^3J$ = 5.9 Hz),[2] in sharp contrast to those ($^3J$ = 7–8 Hz) observed for $\eta^4$-*s*-*trans*-diene[3] complexes of $Ru(acac)_2$ fragments.

The conformation of a diene moiety around a ruthenium center can be explained by the electron influence of ancillary ligands.[1b] Some (diene)ruthenium complexes, $Ru(acac)_2(\eta^4$-1,3-diene),[3f] TpRuCl($\eta^4$-1,3-diene),[3h] and $[Ru(NH_3)_4(\eta^4$-1,3-diene)]$^{2+}$,[3i] prefer the *s*-*trans* mode, presumably because the electronic deficiency around the ruthenium center of each fragment, as compared with the "RuClCp*" fragment, is compensated for by electron donation from the *s*-*trans*-diene ligand. In addition, the overall stereochemistry at a ruthenium center may influence the conformation mode. The above *s*-*trans*-diene complexes have a hexacoordinate octahedral structure when the *s*-*trans*-diene moiety is regarded as a bidentate chelating ligand. In the case of RuClCp*($\eta^4$-1,3-diene), the regular octahedral structure of the $Ru^{II}$ complex is deviated by a bulky tridentate Cp* ligand. Thus, the diene moiety of the polyene complexes prefers the *s*-*cis* coordination.

UV/Vis spectroscopic data of **2**–**6** together with those of $\eta^4$-*s*-*trans*-polyene complexes with $Ru(acac)_2$ fragments[8a] are summarized in Table 1. The absorption maxima of **2**–**6** shift to a longer wavelength as the number of diene units of the polyene ligand increases, indicating that the π-conjugated system along the polyene chain is kept even after the dπ orbital of the RuClCp* fragment is incorporated in the pπ orbital of the polyene, consistent with the results of the X-ray analysis of **4**.[8b] In contrast, we observed that $\eta^4$-*s*-*trans*-polyene complexes containing $Ru(acac)_2$ fragments have almost the same absorption maxima because their π-conjugation systems are separated into individual diene units due to the structural deformation of ruthenium-coordinated diene units. These UV/Vis data also suggest that ancillary ligands (Cp* or acac) on a ruthenium center can control not only their structural shape, such as the metal coordination mode (*s*-*cis* or *s*-*trans* for diene complexation), but also the planarity of the polyene backbone.

Table 1. UV/Vis spectroscopic data of (polyene)ruthenium complexes, [Ru](α,ω-diphenylpolyene) in $CH_2Cl_2$.

| Diphenylpolyene | $\lambda_{max}$/nm (ε/M cm$^{-1}$) | |
|---|---|---|
| | [Ru] = RuClCp* | [Ru] = $Ru(acac)_2$ |
| Butadiene | 481 (5900) (**2**) | 325 (1300)[a] |
| Hexatriene | 492 (6800) (**3**) | 340 (21000)[b] |
| Octatetraene | 518 (11400) (**4**) | 340 (2600)[a] |
| Decapentaene | 525 (16500) (**5**) | 343 (35000)[b] |
| Dodecahexaene | 525 (–) (**6**)[c] | 340 (43000)[b] |

[a] Ref.[8b] [b] Ref.[8a] [c] Because of the low solubility of **6**, we could not estimate the ε value.

The $^1$H NMR spectra of **2**, **4**, and **6** displayed no peaks assignable to the uncoordinated olefinic protons in the range of δ = 6–7 ppm, indicating that polyenes with an even number of olefinic parts are fully metalated.[8] For **4**, we attempted to carry out the reaction of a tetraene ligand with 1 equiv. of **1** to obtain a mononuclear complex; however, no partly metalated olefinic parts with one ruthenium fragment was observed, and a mixture of **4** and a free tetraene was detected by NMR analysis. Likewise, the reaction of **1** with a hexaene gave **6**, without any complexes, having one or two ruthenium fragments. For the multinuclear complexes **4** and **6**, there are several possible *syn* and *anti* isomers owing to the relative face selection of sequential metal coordination across the polyene ligand. For the tetraene complex **4**, an *anti* structure of two RuClCp* fragments coordinated to a tetraene has been revealed by X-ray analysis.[8b] The $^1$H NMR spectrum of the trinuclear hexaene complex **6** in $CDCl_3$ showed only one set of six olefinic protons together with two methyl protons (1:2 ratio) of Cp*

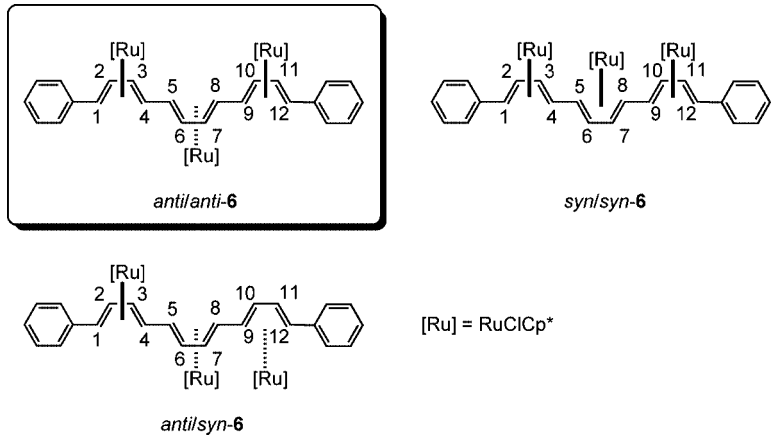


Scheme 1.

 © 2006 Wiley-VCH Verlag GmbH & Co. KGaA, Weinheim 

ligands, suggesting that **6** may have a $C_2$ axis or a mirror plane passing through the central ruthenium atom and the center of the hexaene ligand. For **6**, four isomers are possible, which are categorized into three types: *syn*/*syn*-, *anti*/*anti*-, and *anti*/*syn*- (= *syn*/*anti*-) **-6**, as depicted in Scheme 1. On the basis of the $^1$H NMR spectrum of **6**, the structurally unsymmetrical isomer *anti*/*syn*-**6** is excluded. Furthermore, *syn*/*syn*-**6** is also ruled out because of steric repulsion among the three bulky RuClCp* fragments. Thus, it is reasonably conceivable that **6** has an *anti*/*anti* structure.

In contrast to those of **4** and **6**, the $^1$H NMR spectrum of the triene complex **3** exhibited six signals of magnetically nonequivalent nuclei: four peaks in the range of δ = 3.3–5.4 ppm were from olefinic protons of the diene part bound to a ruthenium atom and the other two signals observed at δ ≈ 6.5 ppm were assignable to noncoordinating olefin protons. The RuClCp* fragment coordinated in an *s*-*cis* fashion to a diene part of the triene, as judged from a typical coupling constant ($^3J$ = 5.9 Hz) between the inner protons $H^2$ and $H^3$ (signals observed at $\delta$ = 5.28 and 4.90 ppm).[2] The coupling constants $J_{4,5}$ (10.3 Hz) and $J_{5,6}$ (15.6 Hz) further indicated that the C(3)–C(4)–C(5)–C(6) sequence is *s*-*trans*.

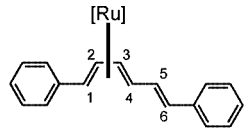


**3**

[Ru] = RuClCp*

The dinuclear pentaene complex **5** was isolated as a mixture of two isomers: **5a** (major, 90%) and **5b** (minor, 10%). In the 2D COSY and NOESY spectra of **5** (Figures 1 and 2), 10 signals of magnetically nonequivalent nuclei assignable to the major isomer **5a** revealed that two ruthenium fragments coordinated to two neighboring diene moieties (1,2,3,4-$\eta^4$ and 5,6,7,8-$\eta^4$ coordination); five peaks due to the minor isomer **5b** indicated that two ruthenium fragments coordinated at separated positions (1,2,3,4-$\eta^4$ and 7,8,9,10-$\eta^4$ coordination).

There are four (= $2^2$) possible structures of complex **5**: two *syn* and two *anti* isomers are schematically depicted in Scheme 2. When the pentaene ligand reacted with **1**, it is assumed that there were two partly metalated intermediates (1,2,3,4-$\eta^4$-**7** and 3,4,5,6-$\eta^4$-**7**). For the latter intermediate,

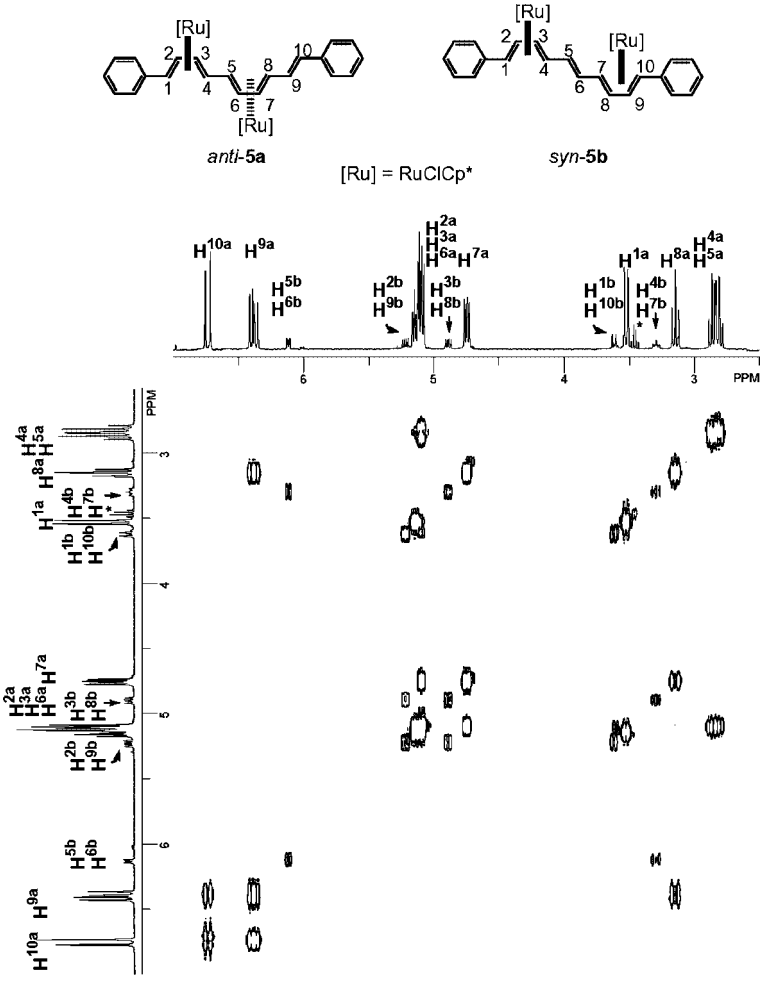


Figure 1. The 2D COSY spectrum of **5** in $CDCl_3$ at 30 °C. Peaks marked with * are due to solvent impurities.

 © 2006 Wiley-VCH Verlag GmbH & Co. KGaA, Weinheim 

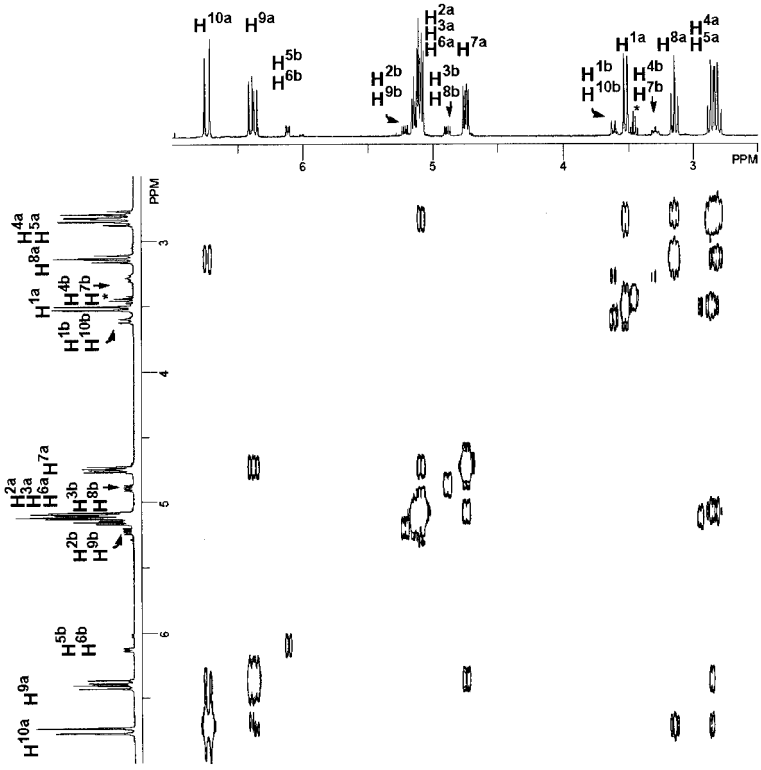


Figure 2. The 2D NOESY spectrum of **5** in $CDCl_3$ at 30 °C. Peaks marked with * are due to solvent impurities.

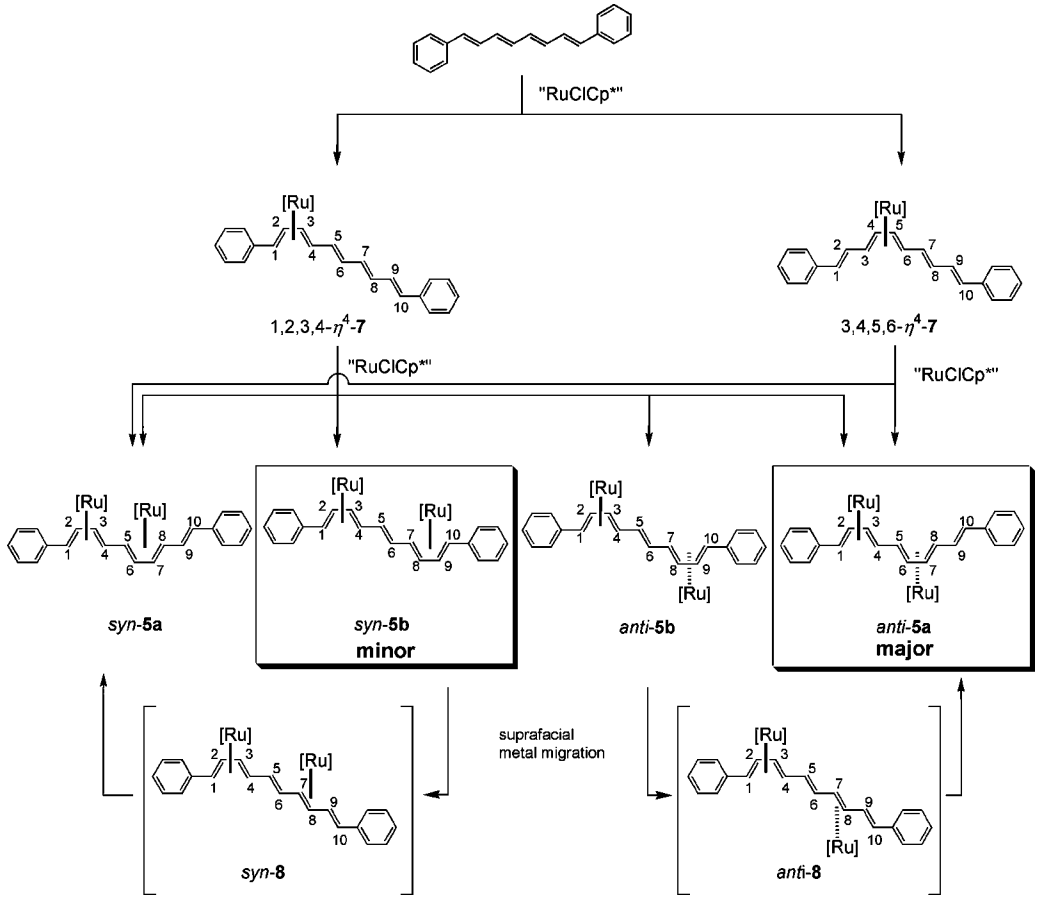


Scheme 2.

 © 2006 Wiley-VCH Verlag GmbH & Co. KGaA, Weinheim 

one diene part [C(7)–C(8)–C(9)–C(10)] remained intact and was applicable to the coordination of another RuClCp* fragment, giving *anti*-**5a** and *syn*-**5a**. On the other hand, the former one has a triene part, to which the coordination of another ruthenium fragment affords four possible isomers (*anti*-**5a**, *syn*-**5a**, *anti*-**5b**, and *syn*-**5b**). Among these isomers, *syn*-**5a** was ruled out because of steric repulsion between the two Cp* rings. Thus, the structure of the major isomer **5a** was concluded to be *anti*-**5a**. In contrast, from the $^1$H NMR spectrum of **5b**, the stereochemistry of the minor product **5b** could not be determined because two possible isomers (*anti*-**5b** and *syn*-**5b**) displayed the same signals (magnetically equivalent nuclei) due to the inversion at the center of C(5)–C(6) in the pentaene ligand for *anti*-**5b**, and the $C_2$ axis passing through the center of the pentaene backbone for *syn*-**5b**.[8a]

The minor product **5b** remained even at elevated temperatures; the percentage of **5b** did not change on heating the chloroform solution of **5**, indicating that either *syn*-**5b** or *anti*-**5b** is thermodynamically stable. As shown in Scheme 2, the major isomer *anti*-**5a** was also produced by the migration of an RuClCp* fragment of *anti*-**5b** via the $\eta^2$-intermediate *anti*-**8**, based on the assumption that a ruthenium fragment suprafacially moved over the pentaene ligand. On the other hand, the suprafacial migration of a ruthenium fragment on *syn*-**5b** did not proceed via *syn*-**8**, because of the steric congestion between two RuClCp* fragments of *syn*-**5a**. Thus, *syn*-**5b** was observed as the minor product and its percentage did not change. Scheme 3 depicts an example of metal migration on a polyene ligand for a trienal complex of the iron compound $Fe(CO)_3$(7-phenyl-2,4,6-heptatrienal). An isomer with an iron fragment at neighboring positions of a phenyl group has been isomerized to another isomer with an iron fragment at neighboring positions of an electron-withdrawing formyl group through the migration of a tricarbonyliron fragment over a trienal ligand.[7b] Accordingly, it is concluded that the treatment of **1** with a pentaene ligand finally gives *anti*-**5a** and *syn*-**5b** as major and minor products, respectively.

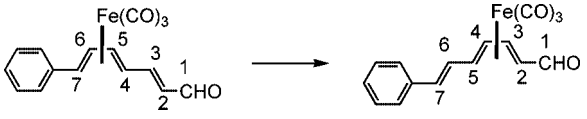


Scheme 3.

## Conclusions

We demonstrated that the ruthenium fragment RuClCp* coordinates in an *s-cis* fashion to α,ω-diphenylpolyenes to afford the corresponding polyene complexes **2**–**6**, in sharp contrast to the case of $\eta^4$-*s-trans*-polyene complexes with $Ru(acac)_2$ fragments. All diene units were fully metalated with RuClCp* fragments. We also found that the coordination of RuClCp* fragments maintains a long π-conjugation system along the polyene chain in comparison with $\eta^4$-*s-trans*-polyene complexes with $Ru(acac)_2$ fragments, as revealed by UV/Vis spectroscopy. We also discussed the structures of pentaene and hexaene complexes on the basis of the bulkiness of RuClCp* moieties: the hexaene complex **6** was assumed to have *anti*/*anti* geometry. The pentaene complex **5** was isolated as a mixture of two isomers: **5a** (major) and **5b** (minor). The RuClCp* fragment of one minor isomer, *anti*-**5b**, suprafacially moved over the pentaene backbone to afford the major isomer *anti*-**5a**, and the other isomer, *syn*-**5b**, remained as the minor product. This supports our previous conclusion that ancillary ligands (Cp* or acac) on a ruthenium center play an important role in controlling their structural shape, such as the metal coordination mode (*s-cis* or *s-trans* for diene complexation) and planarity of the polyene backbone.

## Experimental Section

**General Procedure:** All manipulations involving air- and moisture-sensitive organometallic compounds were carried out using standard Schlenk techniques under argon. THF, hexane, toluene, and diethyl ether were dried and deoxygenated by distillation from sodium/benzophenone ketyl under argon. Dichloromethane was purified by distillation after drying with $CaH_2$. 1,6-Diphenyl-1,3,5-hexatriene was purchased from Aldrich Chemical Co., Inc.; $[Ru(\mu_3\text{-}Cl)Cp^*]_4$,[2g] 1,10-diphenyl-1,3,5,7,9-decapentaene,[9] and 1,12-diphenyl-1,3,5,7,9,11-dodecahexaene[9] were prepared according to literature procedures. The preparation of **2** and **4** has already been reported.[8b] NMR [$^1$H (400 MHz)] spectra were measured using a JEOL JNM-GSK400 spectrometer. The assignments of the $^1$H NMR peaks of some complexes were aided by 2D COSY and NOESY spectra. Other spectra were recorded using the following instruments: IR: Jasco FTIR-120 and Hitachi 295; low- and high-resolution MS: JEOL SX-102. UV/Vis: Jasco Ubest-30 and Shimadzu UV-265FS. Elemental analyses were performed with a Perkin–Elmer 2400 instrument at the Faculty of Engineering Science, Osaka University. All melting points were measured in sealed tubes and are not corrected.

### Synthetic Procedures

**Complex 3:** 1,6-Diphenyl-1,3,5-hexatriene (0.092 g, 0.40 mmol) was added to a solution of $[Ru(\mu_3\text{-}Cl)Cp^*]_4$ (**1**) (0.120 g, 0.11 mmol) in THF (50 mL) at 25 °C. The color of the reaction mixture turned bright red, and then red solids precipitated. After the reaction mixture was stirred for 3 h, the red precipitates were collected and washed with hexane (5 mL). Recrystallization from dichloromethane afforded **3** (0.12 g, 60% yield) as red microcrystals, m.p. 220–230 °C (dec.). $^1$H NMR ($CDCl_3$, 30 °C): $\delta$ = 7.17–7.52 (m, 10 H, $C_6H_5$), 6.82 (d, $J_{5,6}$ = 15.6 Hz, 1 H, H$^6$), 6.44 (dd, $J_{4,5}$ = 10.3 Hz, 1 H, H$^5$), 5.28 (dd, $J_{1,2}$ = 10.7 and $J_{2,3}$ = 5.9 Hz, 1 H, H$^2$), 4.90 (dd, $J_{3,4}$ = 10.7 Hz, 1 H, H$^3$), 3.68 (d, 1 H, H$^1$), 3.40 (dd, 1 H, H$^4$), 1.36 (s, 15 H, $C_5Me_5$) ppm. UV/Vis ($CH_2Cl_2$): $\lambda_{max}$ ($\varepsilon$) = 492 nm (6800 L mol$^{-1}$ cm$^{-1}$). MS (FAB): *m*/*z* = 504 [M$^+$]. $C_{28}H_{31}ClRu$ (504.07): calcd. C 66.72, H 6.20; found C 66.43, H 6.30.

**Complex 5:** 1,10-Diphenyl-1,3,5,7,9-decapentaene (0.170 g, 0.60 mmol) was added to a dichloromethane (50 mL) solution of **1** (0.350 g, 0.32 mmol), and the reaction mixture was stirred at room temperature for 3 h. After removing insoluble impurities by centrifugation, the resulting red solution was concentrated to approximately 5 mL and kept at –20 °C, affording **5** (0.26 g, 52% yield) as red microcrystals, m.p. 190–200 °C (dec.). Major isomer (*anti*-**5a**): $^1$H NMR ($CDCl_3$, 30 °C): $\delta$ = 7.10–7.50 (m, 10 H, $C_6H_5$), 6.74 (d,

 © 2006 Wiley-VCH Verlag GmbH & Co. KGaA, Weinheim 

$J_{9,10}$ = 15.6 Hz, 1 H, $H^{10}$), 6.38 (dd, $J_{8,9}$ = 10.3 Hz, 1 H, $H^9$), 5.15 (dd, $J_{1,2}$ = 10.3 and $J_{2,3}$ = 5.9 Hz, 1 H, $H^2$), 5.14 (dd, $J_{3,4}$ = 9.3 Hz, 1 H, $H^3$), 5.10 (dd, $J_{6,7}$ = 5.9 and $J_{5,6}$ = 9.3 Hz, 1 H, $H^6$), 4.75 (dd, $J_{7,8}$ = 10.3 Hz, 1 H, $H^7$), 3.52 (d, 1 H, $H^1$), 3.15 (t, 1 H, $H^8$), 2.85 (dd, $J_{4,5}$ = 10.3 Hz, 1 H, $H^4$), 2.81 (dd, 1 H, $H^5$), 1.53 (s, 15 H, $C_5Me_5$), 1.31 (s, 15 H, $C_5Me_5$) ppm. Minor isomer (*syn*-**5b**): $^1$H NMR ($CDCl_3$, 30 °C): $\delta$ = 7.10–7.50 (m, 10 H, $C_6H_5$), 6.12 (m, 2 H, $H^5$ and $H^6$), 5.21 (dd, $J_{2,3}$ and $J_{8,9}$ = 5.9, $J_{1,2}$ and $J_{9,10}$ = 10.7 Hz, 2 H, $H^2$ and $H^9$), 4.89 (dd, $J_{3,4}$ and $J_{7,8}$ = 10.3 Hz, 2 H, $H^3$ and $H^8$), 3.62 (d, 2 H, $H^1$ and $H^{10}$), 3.15 (m, 2 H, $H^4$ and $H^7$), 1.32 (s, 30 H, $C_5Me_5$) ppm. UV/Vis ($CH_2Cl_2$): $\lambda_{max}$ ($\varepsilon$) = 525 nm (16000 L mol$^{-1}$ cm$^{-1}$). MS (FAB): *m*/*z* = 556 [$M^+$ – RuCp*Cl]. $C_{42}H_{50}Cl_2Ru_2$ (827.89): calcd. C 60.92, H 6.09; found: C 60.44, H 5.90.

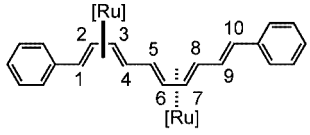


*anti*-**5a**

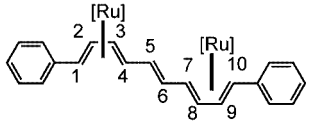


*syn*-**5b**

[Ru] = RuClCp*

**Complex 6:** A reaction mixture of **1** (0.0820 g, 0.075 mmol) and 1,12-diphenyl-1,3,5,7,9,11-dodecahexaene (0.0310 g, 0.10 mmol) in $CH_2Cl_2$ (30 mL) was stirred at 25 °C for 3 h to give a red precipitate. The precipitate was filtered and then washed with hexane (5 mL). Recrystallization from dichloromethane afforded **6** (0.043 g, 38% yield) as red microcrystals, m.p. 195–200 °C (dec.). $^1$H NMR ($CDCl_3$, 30 °C): $\delta$ = 7.12–7.46 (m, 10 H, $C_6H_5$), 5.15 (dd, 2 H, $H^2$ and $H^{11}$), 5.09 (dd, $J_{2,3}$ and $J_{10,11}$ = 5.9 Hz, 2 H, $H^3$ and $H^{10}$), 5.01 (dd, $J_{6,7}$ = 4.4 and $J_{5,6}$ and $J_{7,8}$ = 9.3 Hz, 2 H, $H^6$ and $H^7$), 3.53 (d, $J_{1,2}$ and $J_{11,12}$ = 10.7 Hz, 2 H, $H^1$ and $H^{12}$), 2.91 (dd, $J_{3,4}$ and $J_{9,10}$ = 10.3 and $J_{4,5}$ and $J_{8,9}$ = 9.8 Hz, 2 H, $H^4$ and $H^9$), 2.69 (dd, 2 H, $H^5$ and $H^8$), 1.52 (s, 15 H, $C_5Me_5$), 1.32 (s, 30 H, $C_5Me_5$) ppm. UV/Vis ($CH_2Cl_2$): $\lambda_{max}$ = 525 nm. MS (FAB): *m*/*z* = 547 [$M^+$ – 2 Cp*RuCl – Cl]. The low solubilities of both the complex and 1,12-diphenyl-1,3,5,7,9,11-dodecahexaene prevented the separation of the polyene by repeated crystallizations, and an elemental analysis of the complexes could not be performed.

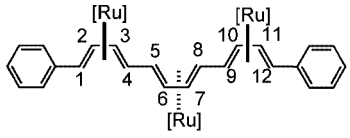


**6**

[Ru] = RuClCp*

## Acknowledgments

This research was supported by a Grant-in-Aid for Scientific Research from the Ministry of Education, Culture, Sports, Science and Technology, Japan.

[1] For reviews see: a) A. Nakamura, *Bull. Chem. Soc. Jpn.* **1995**, *68*, 1515–1521; b) K. Mashima, A. Nakamura, *J. Organomet. Chem.* **2002**, *663*, 5–12.

[2] a) G. M. Smith, H. Suzuki, V. W. D. Sonnenberger, T. J. Marks, *Organometallics* **1986**, *5*, 549–561; b) G. Erker, T. Mühlenbernd, R. Benn, A. Rufińska, *Organometallics* **1986**, *5*, 402–404; c) Y. Kai, N. Kanehisa, N. Miki, N. Kasai, K. Mashima, H. Yasuda, A. Nakamura, *Chem. Lett.* **1982**, 1277–1280; d) K. Mashima, H. Sugiyama, K. Kanehisa, Y. Kai, H. Yasuda, A. Nakamura, *J. Am. Chem. Soc.* **1994**, *116*, 6977–6978; e) K. Mashima, H. Sugiyama, A. Nakamura, *J. Chem. Soc., Chem. Commun.* **1994**, 1581–1582; f) T. Okamoto, H. Yasuda, A. Nakamura, Y. Kai, N. Kanehisa, N. Kasai, *J. Am. Chem. Soc.* **1988**, *110*, 5008–5017; g) P. J. Fagan, W. S. Mahoney, J. C. Calabrese, I. D. Williams, *Organometallics* **1990**, *9*, 1843–1852.

[3] a) M. Dahlmann, G. Erker, R. Fröhlich, O. Meyer, *Organometallics* **1999**, *18*, 4459–4461; b) Y. Kai, N. Kanehisa, K. Miki, N. Kasai, K. Mashima, K. Nagasuna, H. Yasuda, A. Nakamura, *J. Chem. Soc., Chem. Commun.* **1982**, 191–192; c) H. C. Strauch, G. Erker, R. Fröehlich, *Organometallics* **1998**, *17*, 5746–5757; d) L.-S. Wang, J. C. Fettinger, R. Poli, *J. Am. Chem. Soc.* **1997**, *119*, 4453–4464; e) A. D. Hunter, P. Legzdins, C. R. Nurse, F. W. B. Einstein, A. C. Willis, *J. Am. Chem. Soc.* **1985**, *107*, 1791–1792; f) R. D. Ernst, E. Melendez, L. Stahl, M. L. Ziegler, *Organometallics* **1991**, *10*, 3635–3642; g) E. Melendez, R. Ilarraza, G. P. A. Yap, A. L. Rheingold, *J. Organomet. Chem.* **1996**, *522*, 1–7; h) C. Gemel, K. Mereiter, R. Schmid, K. Kirchner, *Organometallics* **1997**, *16*, 2623–2626; i) T. Sugaya, A. Tomita, H. Sago, M. Sano, *Inorg. Chem.* **1996**, *35*, 2692–2694.

[4] a) H. E. Sasse, M. L. Ziegler, *Z. Anorg. Allg. Chem.* **1972**, *392*, 167–172; b) G. S. Lewandos, S. A. R. Knox, A. G. Orpen, *J. Chem. Soc., Dalton Trans.* **1987**, 2703–2707; c) M. Tachikawa, J. Shapley, R. C. Haltiwanger, C. G. Pierpont, *J. Am. Chem. Soc.* **1976**, *98*, 4651–4652; d) C. G. Pierpont, *Inorg. Chem.* **1978**, *17*, 1976–1980; e) T. Murahashi, N. Kanehisa, Y. Kai, T. Otani, H. Kurosawa, *Chem. Commun.* **1996**, 825–826; f) T. Murahashi, T. Otani, E. Mochizuki, Y. Kai, H. Kurosawa, *J. Am. Chem. Soc.* **1998**, *120*, 4536–4537.

[5] a) T. Murahashi, E. Mochizuki, Y. Kai, H. Kurosawa, *J. Am. Chem. Soc.* **1999**, *121*, 10660–10661; b) J. C. Zhong, M. Munakata, T. Kuroda-Sowa, M. Maekawa, Y. Suenaga, H. Konaka, *Inorg. Chim. Acta* **2001**, *322*, 150–156.

[6] a) A. Nakamura, N. Hagihara, *Bull. Chem. Soc. Jpn.* **1959**, *32*, 880–881; b) F. A. Cotton, D. L. Hunter, *J. Am. Chem. Soc.* **1976**, *98*, 1413–1417; c) T. A. Albright, P. Hofmann, R. Hoffmann, C. P. Lillya, P. A. Dobosh, *J. Am. Chem. Soc.* **1983**, *105*, 3396–3411; d) M. A. Bennett, M. Bown, D. C. R. Hockless, J. E. McGrady, H. W. Schranz, R. Stranger, A. C. Willis, *Organometallics* **1998**, *17*, 3784–3797.

[7] a) H. W. Whitlock, Y. N. Chuah, *J. Am. Chem. Soc.* **1965**, *87*, 3605–3608; b) H. W. Whitlock, C. Reich, W. D. Woessner, *J. Am. Chem. Soc.* **1971**, *93*, 2483–2492; c) H. W. Whitlock, R. L. Markezich, *J. Am. Chem. Soc.* **1971**, *93*, 5290–5291; H. W. Whitlock, R. L. Markezich, *J. Am. Chem. Soc.* **1971**, *93*, 5291–5293.

[8] a) H. Fukumoto, K. Mashima, *Organometallics* **2005**, *24*, 3932–3938; b) K. Mashima, H. Fukumoto, K. Tani, M. Haga, A. Nakamura, *Organometallics* **1998**, *17*, 410–414.

[9] C. W. Spangler, R. K. McCoy, A. A. Dembek, L. S. Sapochak, B. D. Gates, *J. Chem. Soc., Perkin Trans. 1* **1989**, 151–154.

Received: June 30, 2006
Published Online: October 31, 2006

 © 2006 Wiley-VCH Verlag GmbH & Co. KGaA, Weinheim 

DOI: 10.1002/ejic.200600649

# Neutral, Radical [CpNi(dithiolene)] Complexes with Flexible, Nonplanar Seven-Membered Rings: [CpNi{$S_2C_2S_2(CH_2)_2X$}] (X = $CH_2$, $CF_2$, C=$CH_2$, S, C=O)

**Mitsushiro Nomura,[a] Michel Geoffroy,[b] Prashant Adkine,[b] and Marc Fourmigué*[a]**

**Keywords:** Nickel / S ligands / Radicals / Metallacycles / Magnetic properties

Neutral, radical [CpNi(dithiolene)] complexes fused with seven-membered rings, formulated as [CpNi{$S_2C_2S_2(CH_2)_2$-X}] (X = $CH_2$, $CF_2$, C=$CH_2$, S), have been synthesized in 30–60 % yields from the reactions of nickelocene with the corresponding neutral, square-planar, (dithiolene)nickel complexes [Ni{$S_2C_2S_2(CH_2)_2X$}$_2$]. [CpNi{$S_2C_2S_2(CH_2)_2X$}] (X = C=O) was prepared from nickelocene and [1,3]dithiolo[4,5-*b*][1,4]dithiepine-2,6-dione under thermal or photochemical conditions. All complexes exhibit reversible oxidation and reduction waves to the cation and anion form, respectively. The terminal groups (X) in the seven-membered ring shift their redox potentials to anodic potentials in the following order: $CF_2$ > C=O > S > C=$CH_2$ > $CH_2$. The singlet EPR responses of [CpNi{$S_2C_2S_2(CH_2)_2$(X)}] appear at $g \approx 2.0514$–$2.0529$ in dichloromethane solution at room temperature. An NIR absorption is observed at $\lambda_{max} \approx 798$–$848$ nm ($\varepsilon \approx 1700$–$2400$ $M^{-1}$ $cm^{-1}$) in dichloromethane solution. The X-ray structures of the five complexes show two-legged piano-stool geometries around the central nickel atom (formally $Ni^{III}$) and strong distortions from planarity of the seven-membered $C_2S_2(CH_2)_2X$ rings. In the solid state, those radical ($S$ = 1/2) species adopt either one-dimensional alternating chain-like motifs (X = $CH_2$, C=$CH_2$, S) or dimeric entities characterized by a singlet–triplet magnetic behavior (X = $CF_2$, C=O).
(© Wiley-VCH Verlag GmbH & Co. KGaA, 69451 Weinheim, Germany, 2006)

## Introduction

(Dithiolene)nickel complexes are currently being extensively investigated from the viewpoint of optical,[1] magnetic,[2] and conductivity studies.[3] Most of these studies involve square-planar bis(dithiolene) complexes,[4] although several mono(dithiolene)nickel complexes formulated as [Ni(dithiolene)$L_2$] have been described where L is an imine or a phosphane.[5] Heteroleptic complexes involving dithiolene and $\eta^5$-cyclopentadienido (Cp) ligands are also known with various Cp/dithiolene ratios and different metal centers.[6] Among them, different series of paramagnetic complexes such as the $d^1$ cation [$Cp_2$Mo(dithiolene)]$^+$ have shown a wide variety of magnetic behaviors, ranging from uniform spin chains to spin ladders or antiferromagnetic ground states.[7] In this respect, the half-metallocene (dithiolene)nickel complexes formulated as [CpNi(dithiolene)] are particularly attractive since they are neutral radical ($S$ = 1/2) species. We have recently investigated the synthesis and electronic properties of a variety of such [CpNi(dithiolene)] complexes, which are characterized by very attractive features such as a strong NIR absorption or a highly delocalized spin density.[8] Among them, [CpNi($S_2C_2R_2$)] complexes bearing simple substituents (R = CN, COOMe, $CF_3$, Ph, and Me) have been synthesized by several dithiolene transfer reactions from the square-planar nickel complex [Ni($S_2C_2R_2$)$_2$] to [$Cp_2$Ni].[8b] Complexes involving 1,2-dithiolato ligands fused with five-membered rings, such as [CpNi(dmit)],[9] [CpNi(dmid)], and [CpNi(dsit)] (dmit = 1,3-dithiol-2-thione-4,5-dithiolato; dmid = 1,3-dithiol-2-one-4,5-dithiolato; dsit = 1,3-dithiol-2-thione-4,5-diselenolato) exhibit a set of three-dimensional intermolecular interactions in the solid state that stabilize an ordered 3D antiferromagnetic ground state.[8a]

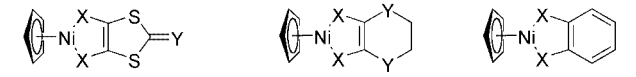


We also recently reported the CpNi(dithiolene) and -(diselenolene) complexes fused with a six-membered ring such as benzene, 5,6-dihydro-1,4-dithiine, or 5,6-dihydro-1,4-diselenine rings, as in [CpNi(dddt)], [CpNi(dsdt)], [CpNi(ddds)], [CpNi(bdt)], and [CpNi(bds)] (dddt = 5,6-dihydro-1,4-dithiine-2,3-dithiolato; ddds = 5,6-dihydro-1,4-dithiine-2,3-diselenolato; dsdt = 5,6-dihydro-1,4-diselenine-2,3-dithiolato; bdt = 1,2-benzenedithiolato; bds = 1,2-benzenediselenolato).[8c] Efficient synthetic methods were developed, and structural and magnetic investigation revealed, besides the recurrent dithiolene/dithiolene interactions, an original antiferromagnetic interaction mediated by

[a] Sciences Chimiques de Rennes, UMR 6226 CNRS – Université Rennes,
1, Campus de Beaulieu, 35042 Rennes cedex, France
Fax: +33-2-2323-6732
E-mail: marc.fourmigue@univ-rennes1.fr
[b] Department of Physical Chemistry, University of Geneva, 30 Quai Ernest Ansermet, 1211 Geneva, Switzerland

 © 2006 Wiley-VCH Verlag GmbH & Co. KGaA, Weinheim 

Cp···Cp overlap. We wanted to further develop these attractive series by also investigating *nonplanar* dithiolate ligands as the added flexibility in the dithiolene ligand could provide novel association patterns in the solid state for such neutral radical complexes. We report here the synthesis and electronic, structural, and magnetic properties of five paramagnetic complexes formulated as [CpNi{$S_2C_2S_2(CH_2)_2X$}] (X = $CH_2$, $CF_2$, C=$CH_2$, S, and C=O).

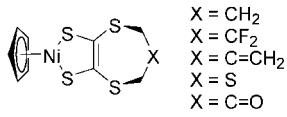


Square-planar bis(dithiolene)nickel complexes have been described with such dithiolato ligands fused with a $C_2S_2(CH_2)_2X$ seven-membered motif, all of which exhibit strong distortions from planarity, as reported for X = $CH_2$,[10] $CF_2$,[11] C=$CH_2$,[12] and S.[13] We wanted to investigate how those distortions might modify the electronic absorptions, crystal structures, and solid-state properties of the radical [CpNi(dithiolene)] complexes. Within this series, the dithiolato ligands where X = $CF_2$ and S can be considered as isosteric, as are those where X = C=$CH_2$ and C=O. It is therefore interesting to compare their solid-state structures to evaluate the precise role played by every X moiety in the definition of the pertinent intermolecular interactions that control their organization in the solid state. We report here the syntheses, structures, and properties of these novel complexes, which will be referred to as follows according to the nature of X: [CpNi($CH_2$)], [CpNi($CF_2$)], [CpNi(C=$CH_2$)], [CpNi(S)] and [CpNi(C=O)].

## Results and Discussion

### Syntheses and Molecular Properties

Faulmann et al. have reported the serendipitous formation of [CpNi(dmit)] from the reaction of [$Cp_2Ni$]($BF_4$) with Na[Ni(dmit)$_2$].[9] We have found that this complex can also be obtained in good yields from the reaction of neutral [$Cp_2Ni$] with the neutral square-planar nickel complexes [Ni(dithiolene)$_2$]$^0$.[8] Accordingly, the reaction of [$Cp_2Ni$] with [Ni($CH_2$)$_2$]$^0$, [Ni($CF_2$)$_2$]$^0$, [Ni(C=$CH_2$)$_2$]$^0$, and [Ni($S_2$)]$^0$ at 80 °C affords the corresponding [CpNi(dithiolene)] complexes in good to fair yields: [CpNi($CH_2$)] (54%), [CpNi($CF_2$)] (41%), [CpNi(C=$CH_2$)] (30%), and [CpNi(S)] (61%) (see Scheme 1 and Entries 1–4 in Table 1).

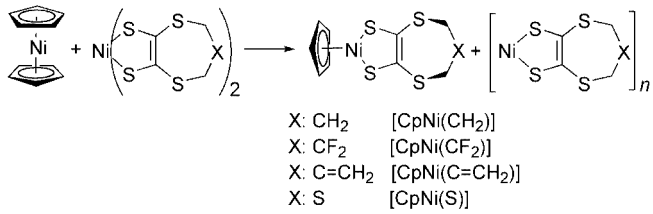


Scheme 1.

The corresponding square-planar dithiolene complex [Ni(C=O)$_2$]$^0$ could not be prepared in a similar manner because of the complete insolubility of the anionic precursor ($Bu_4N$)[Ni(C=O)$_2$], which also does not react directly with [$Cp_2Ni$]($BF_4$) (Faulmann method) for the same reason (Entry 5). We therefore envisioned alternative routes involving thermal or photochemical reactions starting from the corresponding 1,3-dithiol-2-one derivative [1,3]dithiolo-[4,5-*b*][1,4]dithiepine-2,6-dione (**1**) (Scheme 2). Its reaction with [$Cp_2Ni$] at 110 °C or whilst being irradiated for 24 h indeed afforded [CpNi(C=O)], but only in 9% yield. King has also reported the synthesis of [CpNi(tfd)] [tfd = bis-(trifluoromethyl)-1,2-ethenedithiolate] from the reaction of [CpNi(CO)]$_2$ with bis(trifluoromethyl)-1,2-dithiete [$S_2C_2(CF_3)_2$].[14] Accordingly, we performed the reaction of the 1,3-dithiol-2-one **1** with 0.5 equiv. of [CpNi(CO)]$_2$ at 110 °C for 6 h to obtain [CpNi(C=O)] in a slightly improved yield of 15%. Note that 1,2-dithioketones have been postulated as plausible intermediates in these thermal and photochemical reactions of 1,3-dithiol-2-ones.[15] All five complexes are air-stable compounds that are soluble in typical organic solvents (dichloromethane, toluene, acetone, and thf). Their solubility decreases upon addition of *n*-hexane.

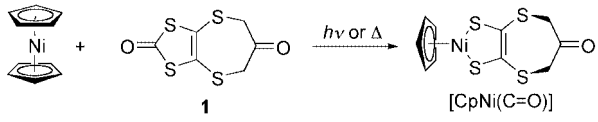


Scheme 2.

Table 1. Syntheses of CpNi(dithiolene) complexes.

| Entry | Dithiolene source | CpNi source | Molar ratio | Solvent | Temperature | Time [h] | Product | Yield [%][a] |
|---|---|---|---|---|---|---|---|---|
| 1 | [Ni($CH_2$)$_2$] | [$Cp_2Ni$] | 1:1 | toluene | 80 °C | 2 | [CpNi($CH_2$)] | 54 |
| 2 | [Ni($CF_2$)$_2$] | [$Cp_2Ni$] | 1:1 | toluene | 80 °C | 2 | [CpNi($CF_2$)] | 41 |
| 3 | [Ni(C=$CH_2$)$_2$] | [$Cp_2Ni$] | 1:1 | toluene | 80 °C | 2 | [CpNi(C=$CH_2$)] | 30 |
| 4 | [Ni($S_2$)] | [$Cp_2Ni$] | 1:1 | toluene | 80 °C | 2 | [CpNi(S)] | 61 |
| 5 | [Ni(C=O)$_2$]$^{-}$[b] | [$Cp_2Ni$]($BF_4$) | 1:1 | MeOH | reflux | 2 | –[c] | 0 |
| 6 | **1** | [$Cp_2Ni$] | 1:1 | toluene | reflux | 24 | [CpNi(C=O)] | 9 |
| 7 | **1** | [$Cp_2Ni$] | 1:1 | toluene | *hν* | 24 | [CpNi(C=O)] | 9 |
| 8 | **1** | [CpNi(CO)]$_2$ | 2:1 | toluene | reflux | 6 | [CpNi(C=O)] | 15 |

[a] Yield of isolated product. [b] As $Bu_4N^+$ salt. [c] No reaction.

 © 2006 Wiley-VCH Verlag GmbH & Co. KGaA, Weinheim 

In the reaction shown in Scheme 1, some mono(dithiolene)nickel oligomers, formulated as $[Ni\{S_2C_2S_2(CH_2)_2(X)\}]_n$ (X = $CH_2$, $CF_2$), were obtained as by-products (4–5% yields). The by-products were identified as hexamers ($n$ = 6) by TOF mass spectrometry.[16] The other oligomers (X = C=$CH_2$, S) could not be isolated by column chromatography as their solubility is too low. We consider that this dithiolene transfer reaction using [Ni(dithiolene)$_2$] is different from that using $(R_4N)_2$[Zn(dithiolene)$_2$].[17] Although the Zn complex can provide both dithiolene ligands, the Ni complex can release only one of two dithiolene ligands and the remaining [Ni(dithiolene)] moiety then oligomerizes.

Characteristic cyclic voltammograms (CVs) of the [CpNi(dithiolene)] complexes $[CpNi\{S_2C_2S_2(CH_2)_2X\}]$ are shown in Figure 1, and the redox potentials of the five complexes (vs. $Fc/Fc^+$), together with their $\Delta E$ and $\Delta E_p$ values, are collected in Table 2. The CVs show reversible, well-defined oxidation and reduction waves.

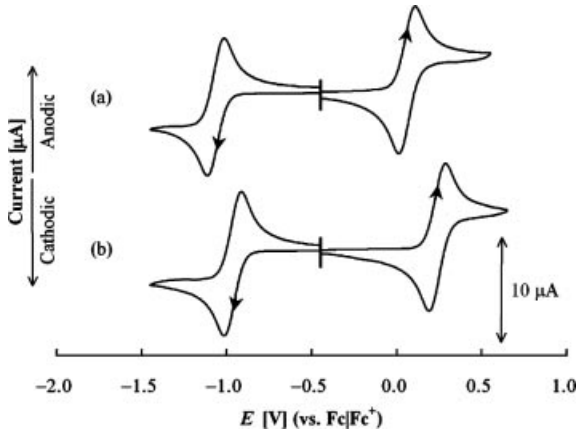


Figure 1. Cyclic voltammograms of (a) [CpNi($CH_2$)] and (b) [CpNi($CF_2$)] ($v$ = 100 mV s$^{-1}$, working electrode 1.6 mm in diameter, Pt disk) in dichloromethane solution containing $Bu_4NPF_6$ (0.1 M).

The nature of the terminal X group in the seven-membered ring shifts their redox potentials to anodic potentials in the following order: $CF_2$ > C=O > S > C=$CH_2$ > $CH_2$. A similar tendency is also found for the redox potentials [$E_{1/2}$(–2/–1) and $E_{1/2}$(–1/0)] of the corresponding square-planar nickel complexes $[Ni\{S_2C_2S_2(CH_2)_2(X)\}_2]^n$ ($n$ = –2, –1, 0).

The EPR spectra of the five complexes were measured in dichloromethane solution at room temperature. Singlet signals were found for [CpNi($CH_2$)] ($g$ = 2.0514), [CpNi($CF_2$)] ($g$ = 2.0529), [CpNi(C=$CH_2$)] ($g$ = 2.0518), [CpNi(S)] ($g$ = 2.0524), and [CpNi(C=O)] ($g$ = 2.0525). These $g$ values are almost identical to those of the other CpNi(dithiolene) complexes ($g$ = 2.041–2.054),[8] and are smaller then those of the CpNi(diselenolene) complexes ($g$ = 2.088–2.095).[8c] Note also that the $g$ values of the isoelectronic (17-electron) cobalt complexes $[CpCo(tfd)]^-$ ($g$ = 2.454)[18] and $[CpCo(mnt)]^-$ ($g \approx 2.5$)[19] are larger, thus demonstrating that the 17-electron Co(dithiolene) complexes have a large spin contribution on the metal center (formal $Co^{II}$), while the spin density of the nickel complex is largely delocalized on the ligands.[8]

The UV/Vis/NIR absorption spectra (Figure 2) exhibit a characteristic NIR absorption centered at ca. 800–850 nm. Their maximum absorption wavelengths ($\lambda_{max}$) and molar absorption coefficients ($\varepsilon$) are summarized in Table 3. Interestingly, the $\lambda_{max}$ evolution with the nature of X follows the electrochemical series identified above, with the lowest energy absorption observed with the most electron-rich dithiolato ligands.

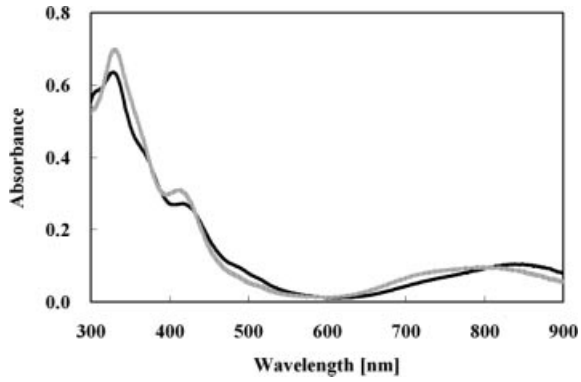


Figure 2. UV/Vis/NIR spectra of [CpNi($CH_2$)] (black line) and [CpNi($CF_2$)] (grey line) in dichloromethane solution ($c$ = $5 \times 10^{-5}$ M).

Table 2. Redox potentials (vs. $Fc/Fc^+$) of CpNi(dithiolene) complexes.

| | $E_{1/2}$ (red) [V][a] | $\Delta E$ [mV] | $\Delta E_p$ [mV] | $E_{1/2}$ (ox) [V] | $\Delta E$ [mV] | $\Delta E_p$ [mV] | Ref. |
|---|---|---|---|---|---|---|---|
| [CpNi(dddt)] | –1.06 | 72 | 106 | –0.02 | 74 | 106 | [8c] |
| [CpNi($CH_2$)] | –1.08 | 70 | 100 | +0.07 | 68 | 92 | this work |
| [CpNi(C=$CH_2$)] | –1.05 | 72 | 100 | +0.12 | 72 | 100 | this work |
| [CpNi(S)] | –1.02 | 70 | 98 | +0.19 | 72 | 98 | this work |
| [CpNi(C=O)] | –0.98 | 68 | 104 | +0.22 | 68 | 98 | this work |
| [CpNi($CF_2$)] | –0.98 | 72 | 102 | +0.25 | 72 | 98 | this work |
| [CpNi(bdt)] | –1.00 | 68 | 92 | +0.30 | 72 | 88 | [8c] |
| [CpNi(dmit)] | –0.72 | _[b] | 100 | +0.28 | _[b] | 100 | [8c] |
| [CpNi(mnt)] | –0.64 | _[b] | _[b] | +0.79[c] | _[b] | _[b] | [8b] |

[a] $E_{1/2} = (E_p + E_{p/2})/2$, $\Delta E = |E_p - E_{p/2}|$, $\Delta E_p = |E_{pa} - E_{pc}|$. [b] Not available. [c] Irreversible.

 © 2006 Wiley-VCH Verlag GmbH & Co. KGaA, Weinheim 

Table 3. UV/Vis/NIR data of CpNi(dithiolene) complexes and reference compounds.

| | $\lambda_{max}$ [nm] | $\varepsilon$ [$M^{-1}cm^{-1}$] | Ref. |
|---|---|---|---|
| [CpNi(dddt)] | 1012 | 4700 | [8c] |
| [CpNi(dmit)] | 967 | 6000 | [8c] |
| [CpNi(dsit)] | 948 | 3200 | [8c] |
| [CpNi($S_2C_2Ph_2$)] | 846 | 2900 | [8b] |
| [CpNi($S_2C_2Me_2$)] | 835 | 2600 | [8b] |
| [CpNi($CH_2$)] | 848 | 2100 | this work |
| [CpNi($C{=}CH_2$)] | 840 | 2400 | this work |
| [CpNi(S)] | 823 | 1800 | this work |
| [CpNi(C=O)] | 806 | 1700 | this work |
| [CpNi($CF_2$)] | 798 | 2000 | this work |
| [CpNi(bdt)] | 722 | 2600 | [8c] |
| [CpNi(mnt)] | 698 | 2000 | [8b] |
| [CpNi{$S_2C_2(CO_2Me)_2$}] | 695 | 1500 | [8b] |

### Solid-State Structural and Magnetic Properties

X-ray structure determinations were performed for the five new CpNi(dithiolene) complexes, which are not isostructural despite their closely related molecular structures: [CpNi($CH_2$)] (triclinic, $P\bar{1}$), [CpNi($CF_2$)] (orthorhombic, *Pbca*), [CpNi($C{=}CH_2$)] (monoclinic, $P2_1$), [CpNi(S)] (monoclinic, $P2_1/c$), and [CpNi(C=O)] (monoclinic, $P2_1/n$). The ORTEP drawings are shown in Figures 3 and 4.

Selected bond lengths and bond angles are summarized in Tables 4 and 5, respectively. The Ni–S bond lengths are ca. 2.12 Å and are therefore similar to those of the other CpNi(dithiolene) complexes (Table 4) but slightly shorter than in monoanionic square-planar bis(dithiolene) complexes such as $[Ni(CH_2)_2]^-$,[10a] $[Ni(CF_2)_2]^-$,[11a] $[Ni(C{=}CH_2)_2]^-$,[12a] and $[Ni(S)_2]^-$[13] (ca. 2.14 Å). Similarly, we observe that the C–S and C=C distances are slightly shorter and slightly longer, respectively, in the [CpNi(dithiolene)] complexes than in the anionic Ni(dithiolene)$_2^-$ complexes. Since both types of complexes are formally $Ni^{III}$ $d^7$ species, the evolution of the bond lengths within the dithiolato ligand gives an indication of its contribution to the SOMO (singly occupied molecular orbital) of the complexes. Indeed, the two-electron oxidation of the dithiolato ligand leads to the corresponding dithioketone species, thus implying that partial oxidation of this ligand results in a shortening of the C–S bonds and associated lengthening of the C=C bond of the metallacycle. The fact that these trends are more marked in the [CpNi(dithiolene)] com-

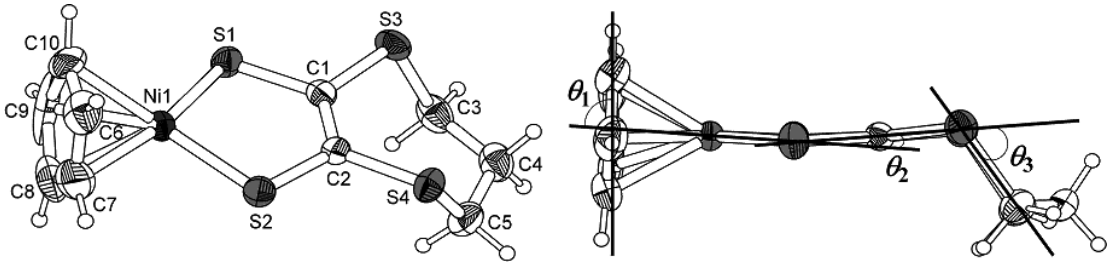


Figure 3. Left: ORTEP drawing of [CpNi($CH_2$)], thermal ellipsoids are drawn at 50% probability level. Right: a side view showing the definition of the three folding angles reported in Table 6; $\theta_1$ is the dihedral angle [°] between the Cp and $NiS_2$ mean planes, $\theta_2$ represents the small folding of the metallacycle along the S···S hinge, and $\theta_3$ the large folding of the seven-membered ring along the S···S hinge.

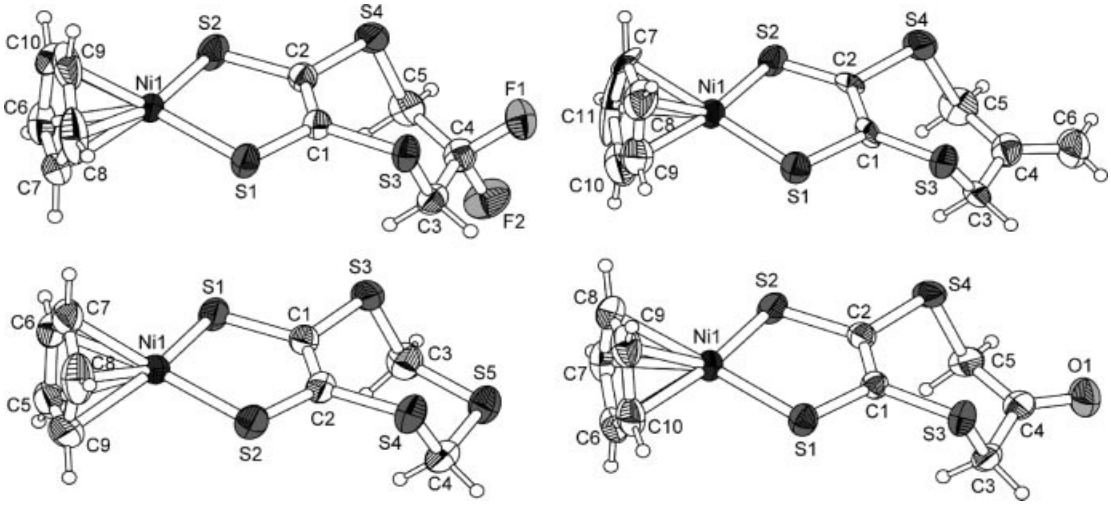


Figure 4. ORTEP drawings of [CpNi($CF_2$)] (top left), [CpNi($C{=}CH_2$)] (top right), [CpNi(S)] (bottom left) and [CpNi(C=O)] (bottom right). Thermal ellipsoids are drawn at the 50% probability level.

 © 2006 Wiley-VCH Verlag GmbH & Co. KGaA, Weinheim 

Table 4. Selected bond lengths [Å] of CpNi(dithiolene) and square-planar Ni(dithiolene)$_2$ complexes.

| | Ni1–S1 | Ni1–S2 | S1–C1 | S2–C2 | C1–C2 | Ref. |
|---|---|---|---|---|---|---|
| [CpNi($CH_2$)] | 2.1242(10) | 2.1242(10) | 1.725(3) | 1.726(3) | 1.358(5) | this work |
| ($NEt_4$)[Ni($CH_2$)$_2$] | 2.141(1) | 2.145(1) | 1.728(2) | 1.729(2) | 1.351(3) | [10a] |
| [CpNi($CF_2$)] | 2.1195(9) | 2.1314(9) | 1.724(3) | 1.725(3) | 1.349(4) | this work |
| ($NBu_4$)[Ni($CF_2$)$_2$] | 2.1450(10) | 2.1494(11) | 1.734(4) | 1.741(4) | 1.338(5) | [11a] |
| [CpNi(C=$CH_2$)] | 2.128(4) | 2.129(4) | 1.807(11) | 1.636(10) | 1.387(6) | this work |
| ($NBu_4$)[Ni(C=$CH_2$)$_2$] | 2.143(2) | 2.130(2) | 1.726(7) | 1.729(7) | 1.356(8) | [12a] |
| [CpNi(S)] | 2.1209(7) | 2.1337(8) | 1.729(3) | 1.733(3) | 1.356(4) | this work |
| ($NBu_4$)[Ni(S)$_2$] | 2.141 | 2.139 | 1.716 | 1.712 | 1.377 | [13] |
| [CpNi(C=O)] | 2.1244(9) | 2.1258(9) | 1.729(3) | 1.732(3) | 1.357(4) | this work |
| [CpNi(dddt)] | 2.125(2) | 2.127(2) | 1.711(10) | 1.744(9) | 1.336(13) | [8c] |
| [CpNi(bdt)] | 2.1205(13) | 2.1280(13) | 1.731(5) | 1.740(4) | 1.410(6) | [8c] |
| [CpNi(dmit)] | 2.138(2) | 2.133(2) | 1.706(8) | 1.716(7) | 1.36(1) | [9] |
| [CpNi(mnt)] | 2.1255(8) | 2.1282(8) | 1.715(3) | 1.725(3) | 1.354(4) | [8b] |

Table 5. Selected bond angles and dihedral angles [°] of CpNi(dithiolene) complexes.

| | S1–Ni1–S2 | Ni–S1–C1 | Ni1–S2–C2 | $\theta_1$ | $\theta_2$ | $\theta_3$ | Ref. |
|---|---|---|---|---|---|---|---|
| [CpNi($CH_2$)] | 92.42(4) | 103.97(11) | 103.85(11) | 89.3 | 7.7 | 61.32 | this work |
| [CpNi($CF_2$)] | 92.58(3) | 103.78(10) | 103.45(10) | 89.8 | 5.0 | 66.77 | this work |
| [CpNi(C=$CH_2$)] | 92.51(4) | 104.4(4) | 103.4(3) | 89.8 | 7.5 | 63.65 | this work |
| [CpNi(S)] | 92.74(3) | 103.77(10) | 103.67(10) | 87.3 | 5.1 | 63.09 | this work |
| [CpNi(C=O)] | 93.03(3) | 103.42(10) | 103.64(11) | 86.2 | 2.4 | 64.48 | this work |
| [CpNi(dddt)] | 92.42(9) | 103.4(3) | 103.7(3) | 86.9 | 1.0, 4.3 | – | [8c] |
| [CpNi(bdt)] | 93.93(5) | 103.71(15) | 103.61(15) | 84.9 | 2.7, 5.0 | – | [8c] |
| [CpNi(dmit)] | 94.97(8) | 100.8(3) | 100.9(3) | 86.5 | 4.0 | – | [9] |
| [CpNi(mnt)] | 94.61(3) | 101.7(1) | 101.7(1) | 89.9 | 1.4 | – | [8b] |

plexes than in the corresponding square-planar bis(dithiolene) ones clearly indicates a stronger participation of the dithiolato ligand in the SOMO.

These complexes adopt typical two-legged piano-stool geometries. The dihedral angle $\theta_1$ between the Cp and $NiS_2$ mean planes (see Figure 3) is close to 90°, a geometry comparable to that of 16-electron $CpCo^{III}$,[20] $CpRh^{III}$,[21] $CpIr^{III}$,[22] and ($\eta^6$-arene)$Ru^{II}$[23] dithiolene complexes. The $NiS_2C_2$ metallacycle is not perfectly planar but is slightly folded along the S···S hinge with $\theta_2$ values of between 2 and 8°, as is also observed with the complexes with dithiolato ligands fused with rigid five- (dmit, dmid) or six-membered (dddt, bdt) rings.[8] Furthermore, the dihedral angles ($\theta_3$ in Figure 3) between the C1–C2–S3–S4 and S3–S4–C3–C5 mean planes are found in the range 61–67° (Table 5).

The solid-state organization of the complexes differs strongly from one to the other. Considering that these molecules are radicals ($S$ = 1/2), with the spin density largely delocalized on the nickel atom, the dithiolene ligand, and the cyclopentadienido ring,[8c] their crystal structure can be analyzed in the light of possible paths for direct exchange magnetic interactions based on short contacts between the sulfur atoms of the dithiolene ligands and eventually between the Cp rings. Applying this procedure to the parent [CpNi($CH_2$)] complex first reveals (Figure 5) that the only short intermolecular contact involves the sulfur atoms of the metallacycles, affording chains running along the *c*-axis with two similar S···S intermolecular distances of 3.80 and 3.83 Å.

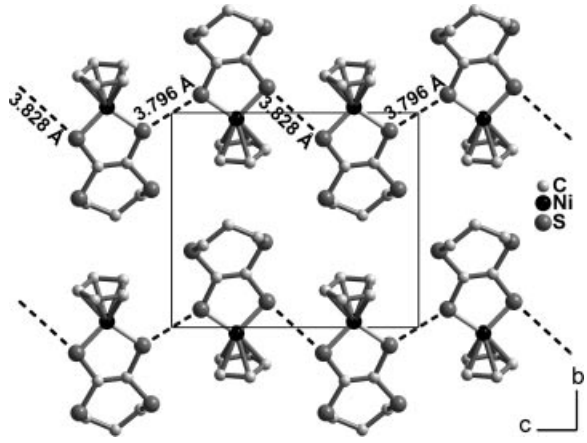


Figure 5. Projection view of the unit cell of [CpNi($CH_2$)] along the *a*-axis showing the chain motif.

As shown in Figure 6, a similar chain motif is also identified in [CpNi(C=$CH_2$)], which gives rise, for symmetry reasons, to a uniform chain structure with equivalent S···S distances of a slightly shorter 3.75 Å.

On the other hand, a projection view of [CpNi(S)] along the *b*-axis of the structure (Figure 7) does not reveal any short intermolecular contacts; the metallacycles are almost perpendicular to each other and the shortest S···S intermolecular distance of 4.0 Å involves the sulfur atom of the thioether moiety. All other S···S contacts exceed 4.5 Å.

However, looking at the stacking of the radical complexes in the perpendicular direction (along the monoclinic

 © 2006 Wiley-VCH Verlag GmbH & Co. KGaA, Weinheim 

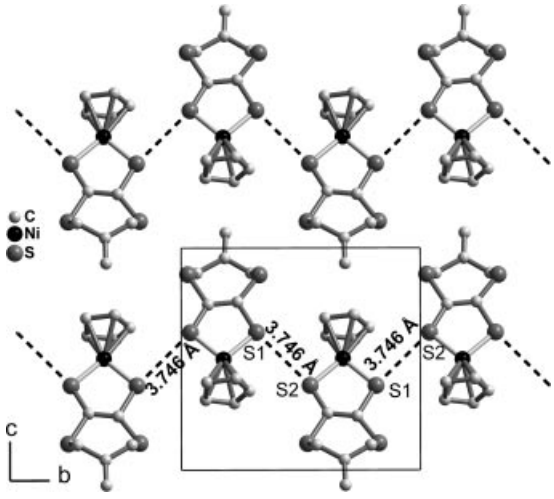


Figure 6. Projection of the unit cell of [CpNi(C=$CH_2$)] along the *a*-axis showing the uniform chain motif running along the *b*-axis.

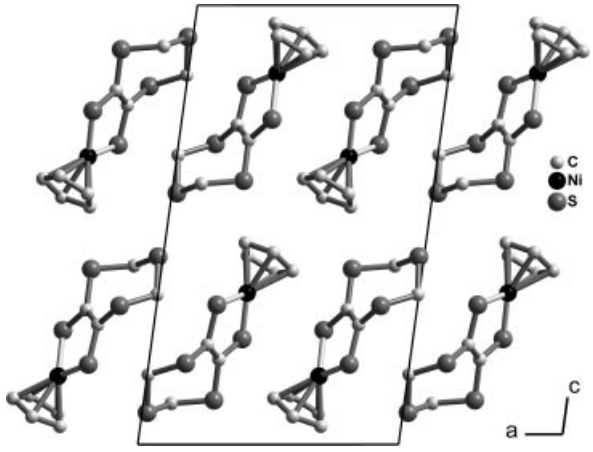


Figure 7. Projection view of [CpNi(S)] along the *b*-axis.

*b*-axis, Figure 8), the complexes form uniform chains that are characterized by a set on S···S intermolecular distances of between 3.69 and 4.06 Å that involve not only the sulfur atoms of the metallacycle, as already observed above in [CpNi($CH_2$)] and [CpNi(C=$CH_2$)], but also the outer sulfur atoms of the seven-membered metallacycle.

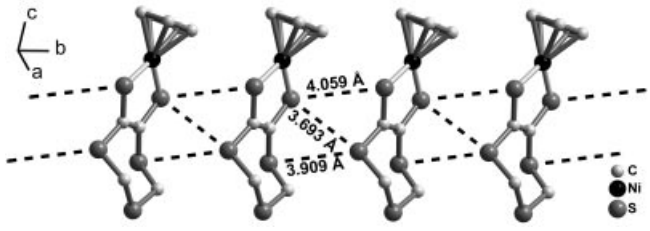


Figure 8. View of the chain-like structure of [CpNi(S)].

It is therefore expected from this structural analysis that [CpNi(S)] most probably experiences weaker antiferromagnetic interactions than the other two derivatives, as indeed observed from the temperature dependence of their magnetic susceptibility. As shown in Figure 9, all three exhibit a smooth maximum at low temperatures, characteristic of a Bonner–Fischer-type behavior of a Heisenberg uniform chain.[24] The molar susceptibility can be properly fitted in the whole temperature range (2–300 K) to the expression $\chi = \chi_0 + (1 - \rho)\cdot 0.375/T + \rho\cdot\chi_{BF}$, where $\chi_0$ is a temperature-independent value, $(1 - \rho)\cdot 0.375/T$ ($\chi_C$) represents a contribution of paramagnetic defaults (Curie tail), and $\rho\cdot\chi_{BF}$ is the contribution of the uniform chain; this also takes into account the *g* value of the different complexes determined from the solution EPR measurements (see above). *J*/*k* values of –39.2(3), –21.4(1), and –6.3(1) K, that is 27.2, 14.8, and 4.4 $cm^{-1}$, were found for [CpNi($CH_2$)], [CpNi(C=$CH_2$)], and [CpNi(S)], respectively, with Curie tail contributions not exceeding 0.4% of $S = 1/2$ species. Note that for [CpNi($CH_2$)] the chain is not really uniform from a structural point of view (Figure 5). However, attempts to use an alternating chain model to fit the data, even with a weak alternation, were unsuccessful.

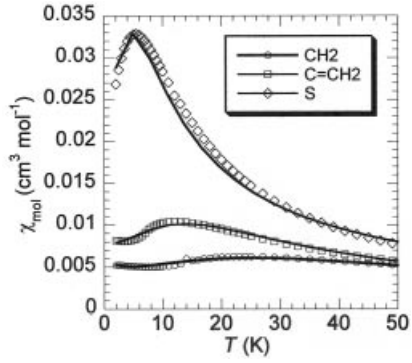


Figure 9. Temperature dependence of the magnetic susceptibility in [CpNi($CH_2$)], [CpNi(C=$CH_2$)], and [CpNi(S)]. Solid lines are fits to the uniform spin-chain model (see text).

The situation is completely different in the two other complexes, thereby illustrating the flexibility and adaptability of these series. As shown in Figure 10, [CpNi($CF_2$)] molecules are organized into layers perpendicular to the *c*-axis.

Within these layers, inversion-centered dyadic motifs are identified, which are most probably stabilized by two, almost linear, C–H···F hydrogen bonds (Figure 11). Similar C–H···F hydrogen bonds, although weak, have been shown to play a crucial role in halogenated molecules in the solid state.[25] Their geometrical characteristics [H···F = 2.508 Å, C(–H)···F = 3.430(6) Å, C–H···F = 171.5°] compare favorably with those described, for example, in *p*-difluorobenzene, whose H···F distances have been reported to be 2.49 Å,[26] as well as in several tetrathiafulvalene derivatives incorporating the very same seven-membered motif.[27]

This dyadic motif, with the $CH_2CF_2CH_2$ moiety bent away from the neighboring molecule, allows for an almost perfect eclipsed overlap between the planar $C_2S_4$ moieties of both complexes, although with large S···S distances of

 © 2006 Wiley-VCH Verlag GmbH & Co. KGaA, Weinheim 

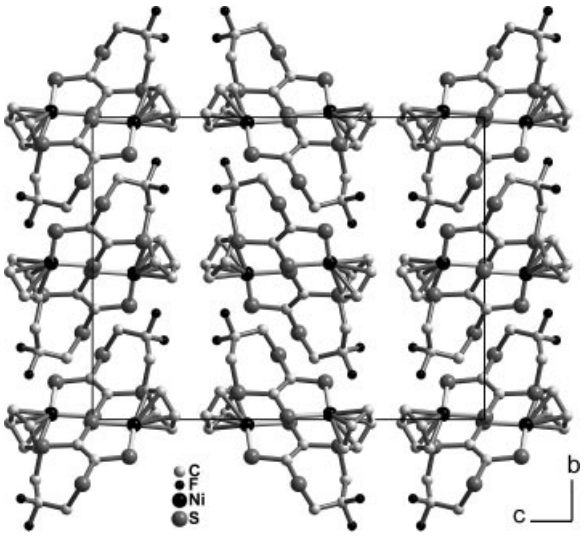


Figure 10. Projection view of the unit cell of [CpNi($CF_2$)] along the *a*-axis.

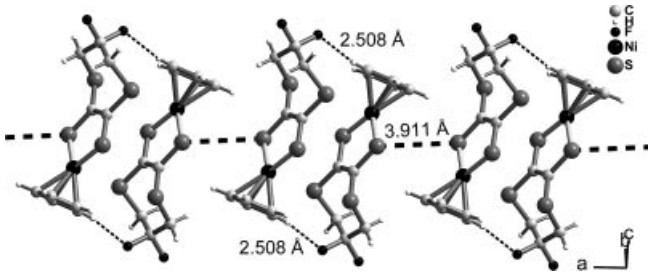


Figure 11. View of the solid-state organization of [CpNi($CF_2$)] showing the C–H···F hydrogen bonds and the shortest S···S intermolecular interactions.

between 4.06 and 4.10 Å. A notably shorter S···S contact [3.911(1) Å], which furthermore involves the sulfur atoms of the metallacycles, connects these dyads together and offers a more efficient path for direct magnetic exchange interactions. The temperature dependence of the magnetic susceptibility of [CpNi($CF_2$)] (Figure 12) confirms this analysis and the associated singlet–triplet behavior. Indeed, the susceptibility goes through a maximum upon cooling and decreases abruptly, as expected for a singlet ground state. It can be properly fitted to the expression $\chi = \chi_0 + (1 - \rho)\cdot 0.375/T + \rho\cdot\chi_{ST}$, where $\chi_0$ is a temperature-independent value, $(1 - \rho)\cdot 0.375/T$ the contribution of a small fraction of Curie-type magnetic defaults, and $\rho\cdot\chi_{ST}$ the contribution of the dyads with:

$$\chi_{ST} = [(Ng^2\beta^2)/k]\cdot\{1/[3 + \exp(-J/kT)]\}$$

This affords a $J_{CF_2}/k$ value of –11.9(1) K (8.3 $cm^{-1}$) with a Curie tail contribution of 3% of $S = 1/2$ magnetic defaults, thus demonstrating that at S···S distances of ca. 4 Å the overlap interaction is indeed very weak, as already noted above in the chain behavior of [CpNi(S)].

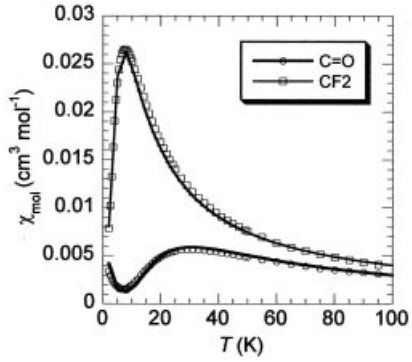


Figure 12. Temperature dependence of the magnetic susceptibility in [CpNi(C=O)] and [CpNi($CF_2$)]. Solid lines are fits to the singlet–triplet model (see text).

In [CpNi(C=O)], a similar singlet–triplet behavior is observed, although with much stronger interactions since the fit of the magnetic data, performed as described above for [CpNi($CF_2$)], affords a $J_{CO}/k$ value of –50.6(4) K (35.2 $cm^{-1}$), together with a Curie tail contribution of 2.3% of $S = 1/2$ species.

A projection view of the unit cell of [CpNi(C=O)] is shown in Figure 13. A close observation of the solid-state organization in the structure of [CpNi(C=O)] also shows the presence of inversion-centered dyadic motifs (Figure 14), with a complex set of S···S short distances between 3.69 and 4.02 Å within columns of dyads running along the *b*-axis. Such a magnetic system is related to spin ladder systems with a singlet state as ground state, as also observed experimentally from the temperature dependence of the susceptibility. However, no analytical model is available to fit the behavior of such a complex interaction network. Therefore, the singlet–triplet fit described above can only be considered as an estimation of the strongest interaction.

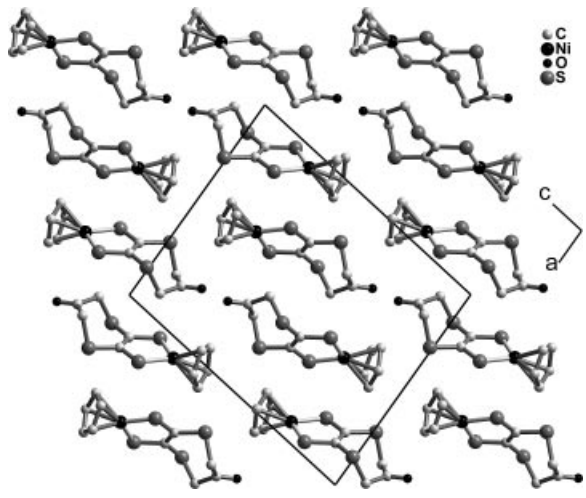


Figure 13. Projection view of the unit cell of [CpNi(C=O)].

 © 2006 Wiley-VCH Verlag GmbH & Co. KGaA, Weinheim 

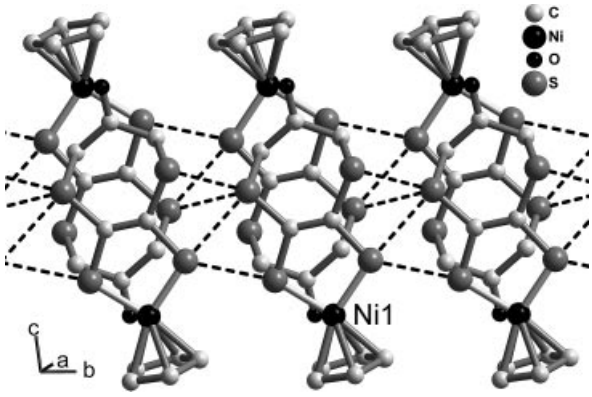


Figure 14. Shortest S···S intermolecular contacts (dotted lines) in [CpNi(C=O)].

## Conclusions

The regular evolution of the electrochemical and absorption properties experimentally observed here in solution with the order $CF_2 > C=O > S > C=CH_2 > CH_2$ offers an attractive series, particularly when it comes to evaluating the origin of the NIR absorption band in these complexes. Theoretical calculations are under way to determine the nature of the transitions involved in this absorption band. The diversity of structural and magnetic behaviors encountered in this isosteric series of radical complexes demonstrates that the nature of the terminal group has a strong influence on the solid-state organization, which complements earlier observations. Indeed, while the S/Se substitution in the metallacycle was found to afford isostructural compounds as in the dithiolene/diselenolene pairs [CpNi(dmit)] vs. [CpNi(dsit)],[8a] [CpNi(dddt)] vs. [CpNi(ddds)],[8c] and [CpNi(bdt)] vs. [CpNi(bds)],[8c] a limited modification of the dithiolate ligand affecting the side heterocycle strongly modifies their crystal structure, as already observed in the following pairs, which are not isostructural: [CpNi(dmit)] vs. [CpNi(dmid)][8a] or [CpNi(dddt)] vs. [CpNi(dsdt)].[8c] More generally, the strong folding of the dithiolato ligand in the five complexes hinders the face-to-face overlap on the ligand, thus favoring one-dimensional spin chains through side-by-side interactions between sulfur atoms of the metallacycles.

## Experimental Section

**General Remarks:** All reactions were carried out under argon by means of standard Schlenk techniques. All solvents for chemical reactions were dried and distilled from Na/benzophenone (for toluene) or $CaH_2$ (for methanol) before use. The square-planar (dithiolene)nickel complexes [Ni(pddt)$_2$],[10] [Ni($F_2$pddt)$_2$],[11] [Ni(dpdt)$_2$],[12] and [Ni(dtdt)$_2$][13] were synthesized according to literature methods. [1,3]Dithiolo[4,5-*b*][1,4]dithiepine-2,6-dione[28] and [$Cp_2$Ni]($BF_4$)[29] were also prepared according to literature methods. [$Cp_2$Ni] and [CpNi(CO)]$_2$ were obtained from Strem Chemicals and Aldrich Chemicals, respectively. Silica gel (Silica gel 60) was obtained from Merck, Ltd. TOF mass spectra were recorded with a Bruker Daltonics MALDI-TOF BIFLEX III mass spectrometer. UV/Vis and NIR spectra were recorded with a Hitachi Model UV-2500PC and a Perkin Elmer Model Lambda 19 UV/Vis/NIR spectrometer, respectively. Elemental analyses were performed by the "Service d'Analyse du CNRS" at Gif/Yvette, France. UV irradiation for the photoreaction was performed with a high-pressure Hg lamp (Applied Photophysics, Ltd).

**General Procedure for the Synthesis of [CpNi($CH_2$)], [CpNi($CF_2$)], [CpNi(C=$CH_2$)], and [CpNi(S)]:** A toluene solution of [$Cp_2$Ni] (38 mg, 0.2 mmol) and the square-planar dithiolene complex [Ni(dithiolene)$_2$] (0.2 mmol) was heated at 80 °C for 2 h. After removal of the solvent under reduced pressure, the residue was extracted and separated by column chromatography (silica gel; dichloromethane/*n*-hexane, 1:1 v/v). The product was further purified by recrystallization (*n*-hexane/dichloromethane) to afford the corresponding CpNi(dithiolene) complexes: [CpNi($CH_2$)] (black needles, 34.4 mg, 54% yield); [CpNi($CF_2$)] (black plates, 29 mg, 41% yield); [CpNi(C=$CH_2$)] (black needles, 19.8 mg, 30% yield); [CpNi(S)] (dark-green blocks, 41 mg, 61% yield). Details are summarized in Table 2. In the reactions of [Ni($CH_2$)$_2$] and [Ni($CF_2$)$_2$] with [$Cp_2$Ni], the mono(dithiolene)nickel oligomers [Ni($CH_2$)]$_n$ and [Ni($CF_2$)]$_n$ were also obtained by column chromatography (silica gel; dichloromethane). These brown products (a few mg) were identified as hexamers ($n$ = 6).

**[CpNi($CH_2$)]:** TOF-MS (EI$^+$, 1.3 kV): $m/z$ = 317 [M$^+$], 275 [M$^+$ – ($CH_2$)$_3$]. UV/Vis/NIR ($CH_2Cl_2$): $\lambda_{max}$ ($\varepsilon$) = 848 nm (2100 $M^{-1}cm^{-1}$), 417 (5400), 329 (13000), 271 (12000). $C_{10}H_{11}NiS_4$ (318.15): calcd. C 37.75, H 3.48, S 40.32; found C 37.80, H 3.27, S 40.15.

**[CpNi($CF_2$)]:** TOF-MS (EI$^+$, 1.3 kV): $m/z$ = 353 [M$^+$]. UV/Vis/NIR ($CH_2Cl_2$): $\lambda_{max}$ ($\varepsilon$) = 798 nm (2000 $M^{-1}cm^{-1}$), 411 (6400), 330 (15000), 264 (13000). $C_{10}H_9F_2NiS_4$ (354.13): calcd. C 33.92, H 2.56, S 36.22; found C 34.02, H 2.83, S 36.14.

**[CpNi(C=$CH_2$)]:** TOF-MS (EI$^+$, 1.3 kV): $m/z$ = 329 [M$^+$], 301 [M$^+$ – ($CH_2$)$_2$], 275 [M$^+$ – ($CH_2$)$_2$C=$CH_2$]. UV/Vis/NIR ($CH_2Cl_2$): $\lambda_{max}$ ($\varepsilon$) = 840 nm (2400 $M^{-1}cm^{-1}$), 419 (6500), 327 (15000), 266 (12000). $C_{11}H_{11}NiS_4$ (330.16): calcd. C 40.02, H 3.36, S 38.85; found C 40.22, H 3.65, S 38.56.

**[CpNi(S)]:** TOF-MS (EI$^+$, 1.3 kV): $m/z$ = 335 [M$^+$]. UV/Vis/NIR ($CH_2Cl_2$): $\lambda_{max}$ ($\varepsilon$) = 823 nm (1800 $M^{-1}cm^{-1}$), 418 (5900), 321 (14000). $C_9H_9NiS_5$ (336.19): calcd. C 32.15, H 2.70, S 47.69; found C 32.24, H 2.55, S 47.79.

**Synthesis of [CpNi(C=O)]. (a) Thermal Conditions:** A solution of [$Cp_2$Ni] (94 mg, 0.5 mmol) and [1,3]dithiolo[4,5-*b*][1,4]dithiepine-2,6-dione (118 mg, 0.5 mmol) was heated in refluxing toluene for 24 h. Silica gel was then added to the solution to oxidize remaining [$Cp_2$Ni] in the reaction mixture. The solvent was removed under reduced pressure, and the residue was separated by column chromatography (silica gel; dichloromethane/*n*-hexane, 1:1 v/v) to afford [CpNi(C=O)] as a black solid (15 mg, 9% yield). The same reaction performed with 2 equiv. of [1,3]dithiolo[4,5-*b*][1,4]dithiepine-2,6-dione and a shorter reaction time (6 h) afforded 25 mg of [CpNi(C=O)] in a slightly improved 15% yield. **(b) Photochemical Conditions:** A toluene solution (300 mL) of [$Cp_2$Ni] (57 mg, 0.3 mmol, $c = 1.0 \times 10^{-3}$ M) and [1,3]dithiolo[4,5-*b*][1,4]dithiepine-2,6-dione (71 mg, 0.3 mmol, $c = 1.0 \times 10^{-3}$ M) was irradiated with a high-pressure Hg lamp (400 W) for 24 h. A black precipitate was filtered off, and the solvent removed under reduced pressure. The reaction mixture was separated by column chromatography (silica gel; dichloromethane/*n*-hexane, 1:1 v/v) to afford [CpNi(C=O)] as a black solid (15 mg, 9% yield).

**[CpNi(C=O)]:** TOF-MS (EI$^+$, 1.3 kV): $m/z$ = 331 [M$^+$], 275 [M$^+$ – ($CH_2$)$_2$C=O]. UV/Vis/NIR ($CH_2Cl_2$): $\lambda_{max}$ ($\varepsilon$) = 806 nm (1700 $M^{-1}cm^{-1}$), 416 (5600), 325 (13000), 264 (11000). $C_{10}H_9NiOS_4$

 © 2006 Wiley-VCH Verlag GmbH & Co. KGaA, Weinheim 

Table 6. Crystallographic data of CpNi(dithiolene) complexes.[a]

| | [CpNi($CH_2$)] | [CpNi($CF_2$)] | [CpNi(C=$CH_2$)] | [CpNi(S)] | [CpNi(C=O)] |
|---|---|---|---|---|---|
| Empirical formula | $C_{10}H_{11}NiS_4$ | $C_{10}H_9F_2NiS_4$ | $C_{11}H_{11}NiS_4$ | $C_9H_9NiS_5$ | $C_{10}H_9NiOS_4$ |
| Formula mass [g mol$^{-1}$] | 318.14 | 354.12 | 330.15 | 336.17 | 332.12 |
| Crystal system | triclinic | orthorhomic | monoclinic | monoclinic | monoclinic |
| Space group | $P\bar{1}$ (no. 2) | *Pbca* (no. 61) | $P2_1$ (no. 4) | $P2_1/c$ (no. 14) | $P2_1/n$ (no. 14) |
| *a* [Å] | 5.5452(8) | 9.3407(9) | 5.6953(11) | 10.9076(10) | 12.8566(15) |
| *b* [Å] | 9.9075(15) | 14.8645(12) | 11.1493(16) | 6.1650(4) | 6.1488(5) |
| *c* [Å] | 11.4352(16) | 19.2204(15) | 10.484(2) | 18.5748(16) | 15.4174(17) |
| *α* [°] | 89.756(18) | – | – | – | – |
| *β* [°] | 85.714(17) | – | 99.54(2) | 97.731(11) | 97.012(14) |
| *γ* [°] | 86.397(18) | – | – | – | – |
| *V* [Å$^3$] | 625.24(16) | 2668.7(4) | 656.5(2) | 1237.72(18) | 1209.7(2) |
| *T* [K] | 293(2) | 293(2) | 293(2) | 293(2) | 293(2) |
| *Z* | 2 | 8 | 2 | 4 | 4 |
| $D_{calcd.}$ [g cm$^{-3}$] | 1.690 | 1.763 | 1.670 | 1.804 | 1.824 |
| $\mu$ [mm$^{-1}$] | 2.182 | 2.075 | 2.081 | 2.372 | 2.270 |
| Total reflections | 6053 | 22010 | 6450 | 9122 | 8817 |
| Absorption correction | multi-scan | gaussian | multi-scan | multi-scan | gaussian |
| Independent reflections ($R_{int}$) | 2239 (0.0395) | 2581 (0.0772) | 2526 (0.0475) | 2351 (0.0313) | 2260 (0.0471) |
| Reflections [$I > 2\sigma(I)$] | 1872 | 1690 | 1646 | 1794 | 1503 |
| $R_1$, $wR_2$ [$I > 2\sigma(I)$] | 0.0343, 0.0918 | 0.0306, 0.0540 | 0.0277, 0.0445 | 0.0275, 0.0694 | 0.0270, 0.0455 |
| $R_1$, $wR_2$ (all data) | 0.0442, 0.0969 | 0.0631, 0.0608 | 0.0594, 0.0498 | 0.0396, 0.0756 | 0.0568, 0.0501 |
| Goodness-of-fit | 1.055 | 0.882 | 0.845 | 0.737 | 0.849 |

[a] $R_1 = \Sigma||F_o| - |F_c||/\Sigma|F_o|$; $wR_2 = [\Sigma w(F_o^2 - F_c^2)^2/\Sigma wF_o^4]^{1/2}$.

(332.13): calcd. C 36.16, H 2.73, S 38.62; found C 35.98, H 2.65, S 38.43.

**CV Measurements:** All electrochemical measurements were performed under argon. Solvents for electrochemical measurements were dried over molecular sieves (4 Å) before use. A platinum wire served as a counter electrode, and the reference electrode (Ag/AgCl) was corrected for junction potentials by being referenced internally to the ferrocene/ferrocenium ($Fc/Fc^+$) couple. A stationary platinum disk (1.6 mm in diameter) was used as working electrode. A Model CV-50W instrument from BAS Co. was used for cyclic voltammetry (CV) measurements. CVs were measured in 1 mM dichloromethane solutions of complexes containing 0.1 M tetrabutylammonium hexafluorophosphate ($Bu_4NPF_6$) at 25 °C.

**EPR Measurements:** EPR spectra were recorded with a Bruker ESP 300 spectrometer (X-band) equipped with a variable-temperature attachment from 1 mM dichloromethane solutions of complexes. Optimizations and simulations of the frozen solution spectra were carried out with a program, based on the Levenberg–Marquardt least-squares fit, which compares the position of the experimental resonance lines with those calculated by second-order perturbation theory.

**X-ray Diffraction Studies:** Single crystals of [CpNi(dithiolene)] complexes were obtained by recrystallization from dichloromethane solution and then vapor diffusion of *n*-hexane into these solutions. A crystal was mounted on the top of a thin glass fiber. Data were collected with a Stoe Imaging Plate Diffraction System (IPDS) with graphite-monochromated Mo-$K_\alpha$ radiation ($\lambda$ = 0.71073 Å) at room temperature. Structures were solved by direct methods (SHELXS-97) and refined (SHELXL-97)[30] by full-matrix least-squares methods, as implemented in the WinGX software package.[31] Absorption corrections were applied. Hydrogen atoms were introduced at calculated positions (riding model), included in structure factor calculations, and not refined. Crystallographic data of complexes are summarized in Table 6. CCDC-614018 {[CpNi(C=$CH_2$)]}, -614019 {[CpNi($CF_2$)}, -614020 {[CpNi($CH_2$)]}, -614021 {[CpNi(C=O)]} and -614022 {[CpNi(S)]} contain the supplementary crystallographic data for this paper. These data can be obtained free of charge from The Cambridge Crystallographic Data Centre via www.ccdc.cam.ac.uk/data_request/cif.

## Acknowledgments

We thank Prof. Masatsugu Kajitani (Sophia University) for his help with the CV measurements. We also thank the Ministère de la Recherche (France) for a postdoctoral grant (to M. N.) and the CNRS (France) and the National Swiss Foundation for financial support.

[1] a) S. D. Cummings, R. Eisenberg, *Prog. Inorg. Chem.* **2003**, *52*, 315; b) H. Kisch, *Coord. Chem. Rev.* **1993**, *125*, 155.
[2] a) A. T. Coomber, D. Beljonne, R. H. Friend, J. L. Bredas, A. Charlton, N. Robertson, A. E. Underhill, M. Kurmoo, P. Day, *Nature* **1996**, *380*, 144; b) C. Faulmann, P. Cassoux, *Prog. Inorg. Chem.* **2003**, *52*, 399.
[3] a) P. Cassoux, L. Valade, H. Kobayashi, A. Kobayashi, R. A. Clark, A. E. Underhill, *Coord. Chem. Rev.* **1991**, *110*, 115; b) R.-M. Olk, B. Olk, W. Dietzsch, R. Kirmse, E. Hoyer, *Coord. Chem. Rev.* **1992**, *117*, 99; c) R. Kato, *Chem. Rev.* **2004**, *104*, 5319; d) G. Matsubayashi, M. Nakano, H. Tamura, *Coord. Chem. Rev.* **2002**, *226*, 143.
[4] a) C. L. Beswick, J. M. Schulman, E. I. Stiefel, *Prog. Inorg. Chem.* **2003**, *52*, 55; b) G. N. Schrauzer, *Acc. Chem. Res.* **1969**, *2*, 72 and references cited therein.
[5] a) W. Paw, S. D. Cummings, M. A. Mansour, W. B. Connick, B. K. Geiger, R. Eisenberg, *Coord. Chem. Rev.* **1998**, *171*, 125; b) J. A. Zuleta, J. M. Bevilacqua, R. Eisenberg, *Coord. Chem. Rev.* **1991**, *111*, 237; c) J. A. Zuleta, M. S. Burberry, R. Eisenberg, *Coord. Chem. Rev.* **1990**, *97*, 47.
[6] M. Fourmigué, *Coord. Chem. Rev.* **1998**, *178*, 823 and references cited therein.
[7] M. Fourmigué, *Acc. Chem. Res.* **2004**, *37*, 179.
[8] a) M. Fourmigué, N. Avarvari, *Dalton Trans.* **2005**, 1365; b) M. Nomura, R. Okuyama, C. Fujita-Takayama, M. Kajitani, *Organometallics* **2005**, *24*, 5110; c) M. Nomura, T. Cauchy, M. Geoffroy, P. Adkine, M. Fourmigué, *Inorg. Chem.* **2006**, *45*, 8194.

 © 2006 Wiley-VCH Verlag GmbH & Co. KGaA, Weinheim 

[9] C. Faulmann, F. Delpech, I. Malfant, P. Cassoux, *J. Chem. Soc., Dalton Trans.* **1996**, 2261.
[10] a) R. D. Bereman, H. Lu, *Inorg. Chim. Acta* **1993**, *204*, 53; b) U. Geiser, S. F. Tytko, T. J. Allen, H. H. Wang, A. M. Kini, J. M. Williams, *Acta Crystallogr., Sect. C* **1991**, *47*, 1164.
[11] a) O. J. Dautel, M. Fourmigué, *Inorg. Chem.* **2001**, *40*, 2083; b) O. J. Dautel, M. Fourmigué, E. Canadell, P. Auban-Senzier, *Adv. Funct. Mater.* **2002**, *12*, 693.
[12] a) A. Charlton, A. E. Underhill, A. Kobayashi, H. Kobayashi, *J. Chem. Soc., Dalton Trans.* **1995**, 1285; b) A. Charlton, A. E. Underhill, K. M. A. Malik, M. B. Hursthouse, T. Jørgensen, J. Becher, *Synth. Met.* **1995**, *68*, 221.
[13] a) R. Kato, H. Kobayashi, A. Kobayashi, Y. Sasaka, *Bull. Chem. Soc. Jpn.* **1986**, *59*, 627; b) C. Faulmann, A. Errami, B. Donnadieu, I. Malfant, J.-P. Legros, P. Cassoux, C. Rovira, E. Canadell, *Inorg. Chem.* **1996**, *35*, 3856.
[14] R. B. King, *J. Am. Chem. Soc.* **1963**, *85*, 1587.
[15] a) W. Kusters, P. De Mayo, *J. Am. Chem. Soc.* **1974**, *96*, 3502; b) W. Schroth, H. Bahn, R. Zschernitz, *Z. Chem.* **1973**, *13*, 424; c) R. Schulz, A. Schweig, K. Hartke, J. Koester, *J. Am. Chem. Soc.* **1983**, *105*, 4519.
[16] TOF MS (no matrix): *m/z* = 1518 $[Ni\{S_2C_2S_2(CH_2)_3\}]_6$ $[M^+]$ and 1734 $[Ni\{S_2C_2S_2(CH_2)_2(CF_2)\}]_6$ $[M^+]$.
[17] T. B. Rauchfuss, *Prog. Inorg. Chem.* **2003**, *52*, 1.
[18] R. E. Dessy, F. E. Stary, R. B. King, M. Waldrop, *J. Am. Chem. Soc.* **1966**, *88*, 471.
[19] J. A. McCleverty, T. A. James, E. J. Wharton, *Inorg. Chem.* **1969**, *8*, 1340.
[20] a) C. Takayama, M. Kajitani, T. Sugiyama, A. Sugimori, *J. Organomet. Chem.* **1998**, *563*, 161; b) M. Fourmigué, V. Perrocheau, *Acta Crystallogr., Sect. C* **1997**, *53*, 1213.
[21] K. Kawabata, M. Nakano, H. Tamura, G. Matsubayashi, *J. Organomet. Chem.* **2004**, *689*, 405.
[22] G.-X. Jin, M. Herberhold, A. L. Rheingold, *New J. Chem.* **1998**, *22*, 1035.
[23] a) K. Mashima, H. Kaneyoshi, S. Kaneko, A. Mikami, K. Tani, A. Nakamura, *Organometallics* **1997**, *16*, 1016; b) M. Nomura, M. Fujii, K. Fukuda, T. Sugiyama, Y. Yokoyama, M. Kajitani, *J. Organomet. Chem.* **2005**, *690*, 1627.
[24] O. Kahn, *Molecular Magnetism*, VCH, Weinheim, **1993**, chapter 11.
[25] G. R. Desiraju, T. Steiner, in *The Weak Hydrogen Bond*, Oxford University Press, New York, **1999**.
[26] V. R. Thalladi, H.-C. Weiss, D. Bläser, R. Boese, A. Nangia, G. R. Desiraju, *J. Am. Chem. Soc.* **1998**, *120*, 8702.
[27] a) O. J. Dautel, M. Fourmigué, *J. Org. Chem.* **2000**, *65*, 6479; b) O. J. Dautel, M. Fourmigué, E. Canadell, *Chem. Eur. J.* **2001**, *7*, 2635.
[28] M. R. Bryce, G. J. Marshallsay, *Tetrahedron Lett.* **1991**, *32*, 6033.
[29] J. S. Miller, J. C. Calabrese, H. Rommelmann, S. R. Chittipeddi, J. H. Zhang, W. M. Reiff, A. J. Epstein, *J. Am. Chem. Soc.* **1987**, *109*, 769.
[30] SHELX97, Program for Crystal Structure Analysis (release 97-2). G. M. Sheldrick, **1998**.
[31] L. J. Farrugia, *J. Appl. Crystallogr.* **1999**, *32*, 837.

Received: July 11, 2006
Published Online: October 31, 2006

 © 2006 Wiley-VCH Verlag GmbH & Co. KGaA, Weinheim 

DOI: 10.1002/ejic.200600672

# Synthesis of Methyl Metallocenecarboxylates [{η⁴-Ph$_{4-n}$(SiMe$_3$)$_n$C$_4$}Co{η⁵-MeOC(O)C$_5$H$_4$}] (*n* = 1, 2) and Their Desilylation Reactions: Structural Studies and Conversion to Metallocenecarboxylic Acids and Their Alcohol Derivatives

**Hanuman P. Gupta,[a] M. Senthil Kumar,[a] Shailesh Upreti,[a] and Anil J. Elias*[a]**

**Keywords:** Cobalt / Alkynes / Desilylation / Metallocenes / Carboxylic acids

The reaction of (2-phenylethynyl)trimethylsilane (Me$_3$SiC≡CPh) with [{η⁵-MeOC(O)C$_5$H$_4$}Co(PPh$_3$)$_2$] generated in situ results in the exclusive formation of two isomers of methyl metallocenecarboxylates, namely [{*trans*-η⁴-Ph$_2$(Me$_3$Si)$_2$C$_4$}Co{η⁵-MeOC(O)C$_5$H$_4$}] (**1**) and [{*cis*-η⁴-Ph$_2$(Me$_3$Si)$_2$C$_4$}Co{η⁵-MeOC(O)C$_5$H$_4$}] (**2**). The reaction of [{η⁵-MeOC(O)C$_5$H$_4$}Co(PPh$_3$)(Me$_3$SiC≡CPh)] with PhC≡CPh yields the methyl metallocenecarboxylate [{η⁴-Ph$_3$(Me$_3$Si)C$_4$}Co{η⁵-MeOC(O)C$_5$H$_4$}] (**3**) along with [{η⁴-Ph$_4$C$_4$}Co{η⁵-MeOC(O)C$_5$H$_4$}] (**4**). The reactions of **1**, **2** and **3** with Bu$_4$NF in dmso results in the desilylated complexes [(*trans*-η⁴-Ph$_2$H$_2$C$_4$)Co{η⁵-MeOC(O)C$_5$H$_4$}] (**5**), [(*cis*-η⁴-Ph$_2$H$_2$C$_4$)Co{η⁵-MeOC(O)C$_5$H$_4$}] (**6**) and [(η⁴-Ph$_3$HC$_4$)Co{η⁵-MeOC(O)C$_5$H$_4$}] (**7**), respectively. Compounds **5**, **6** and **7** yield the carboxylic acids [(*trans*-η⁴-Ph$_2$H$_2$C$_4$)Co{η⁵-HOC(O)C$_5$H$_4$}] (**8**), [(*cis*-η⁴-Ph$_2$H$_2$C$_4$)Co{η⁵-HOC(O)C$_5$H$_4$}] (**9**) and [(η⁴-Ph$_3$HC$_4$)Co{η⁵-HOC(O)C$_5$H$_4$}] (**10**) upon treatment with KO*t*Bu in dmso. Reduction of **5** and **7** with LiAlH$_4$ in thf gives the alcohol complexes [(*trans*-η⁴-Ph$_2$H$_2$C$_4$)Co(η⁵-HOCH$_2$C$_5$H$_4$)] (**11**) and [(η⁴-Ph$_3$HC$_4$)Co(η⁵-HOCH$_2$C$_5$H$_4$)] (**12**) in good yields. Compounds **1**–**7** and **11** were characterized structurally. These structural studies show interesting variations in the orientations of the cyclobutadiene-bound phenyl groups when the silyl groups are systematically removed from the cyclobutadiene moiety.

(© Wiley-VCH Verlag GmbH & Co. KGaA, 69451 Weinheim, Germany, 2006)

## Introduction

Stable metallocenecarboxylic acids and their alcohol derivatives are excellent precursors for a host of organometallic molecules with a wide range of potential applications. The most well-known among these is ferrocenecarboxylic acid, which, for example, is widely used in the design and development of electrochemical biosensors for monitoring of glucose and lactate,[1] in electrochemical DNA sensors,[2] in the design of stable electroactive multi(ferrocenyl)stannoxane clusters,[3] and as a reagent for the synthesis of prochiral ferrocene catalysts bearing oxazoline substituents.[4] Unlike ferrocenecarboxylic acid, whose rich chemistry has been well documented, the chemistry of other metallocenecarboxylic acids is still being developed. Among these, (η⁵-carboxycyclopentadienyl)(η⁴-tetraphenylcyclobutadiene)cobalt, a highly stable cyclobutadienylcobaltocenecarboxylic acid, has shown great promise in terms of stability and reactivity.[5,6] Cobalt(I) oxazoline palladacycles (COP) such as COP-OAc and COP-Cl, which are commercially available and are prepared from this carboxylic acid, effectively promote the asymmetric rearrangement of allylic trichloroacetimidates and *N*-(4-methoxyphenyl)trifluoroacetimidates, which provides easy access to allylic amines and allylic alcohols of high enantiomeric purity.[7,8] Pioneering work by Richards and co-worker has simplified the preparation of this carboxylic acid by the generation of [{MeOC(O)C$_5$H$_4$}Co(PPh$_3$)$_2$] in situ instead of the older and more expensive method involving [CpCo(CO)$_2$].[9,10] However, it has been observed that the steric bulkiness of the tetraphenylcyclobutadiene moiety of [(η⁴-Ph$_4$C$_4$)Co(η⁵-C$_5$H$_4$COOH)] significantly influences the nature of the products formed from its reactions, often reducing its reactivity in comparison to ferrocenecarboxylic acid.[11] We were interested in reducing the steric bulkiness of the tetraphenylcyclobutadiene part of this complex by systematically replacing the phenyl substituents with hydrogen atoms so as to fine-tune its reactivity while maintaining its high stability and accessibility. The method adopted was to initially make metallocenes containing a varying number of phenyl and trimethylsilyl groups on the cyclobutadiene moiety and then removing the silyl groups.

An added interest in this study stems from the difference in reactivity of the cobalt-bound cyclopentadienyl and cyclobutadienyl groups. Rosenblum and co-workers have shown that for the parent complex, (η⁵-cyclopentadienyl)(η⁴-cyclobutadiene)cobalt, the hydrogen atoms of the

[a] Department of Chemistry, Indian Institute of Technology Delhi,
Hauz Khas, New Delhi 110016, India
Fax: +91-11-2658-1102
E-mail: eliasanil@gmail.com

 © 2006 Wiley-VCH Verlag GmbH & Co. KGaA, Weinheim 

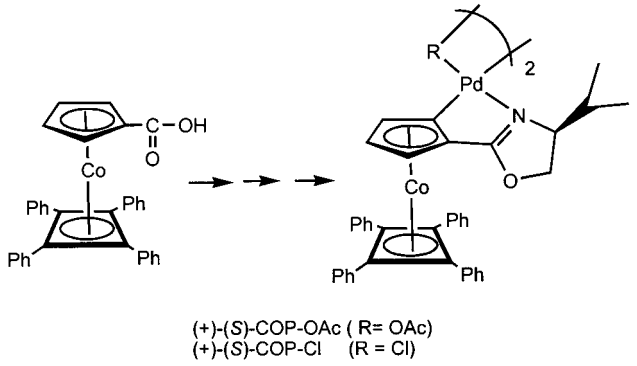


(+)-(*S*)-COP-OAc ( R= OAc)
(+)-(*S*)-COP-Cl (R = Cl)

cyclobutadiene ring are more reactive towards electrophilic substitution reactions than those of the cyclopentadiene ring.[12] In this paper we describe our efforts to prepare examples of sterically less hindered ($\eta^5$-cyclopentadienyl)($\eta^4$-phenylcyclobutadiene)cobalt-based carboxylic esters, carboxylic acids and their alcohols derivatives with varying numbers of hydrogen atoms and phenyl groups bound to the cyclobutadiene unit. Structural studies on the silylated and desilylated metallocenes indicate interesting orientational changes of the phenyl groups around the cyclobutadiene moiety upon removal of the trimethylsilyl groups.

## Results and Discussion

The generation of [$\eta^5$-MeOC(O)$C_5H_4$]Co($PPh_3$)$_2$ in situ was carried out by the preparation of [(methoxycarbonyl)-cyclopentadienyl]sodium from cyclopentadienylsodium and dimethyl carbonate followed by the reaction with chloridotris(triphenylphosphane)cobalt. The alkyne, (2-phenylethynyl)trimethylsilane, was then added to this solution of [{$\eta^5$-MeOC(O)$C_5H_4$}Co($PPh_3$)$_2$] in the required molar ratio.

It has been observed that the reaction of the half-sandwich complex [CpCo(CO)$_2$] with disubstituted acetylenes differs significantly from that of the phosphane complex [CpCo($PPh_3$)$_2$].[13] Thus, while the former results in the formation of cobaltocenes having $\eta^5$-cyclopentadienide and $\eta^4$-cyclobutadiene groups often along with another metallocene having a carbonyl-inserted $\eta^4$-cyclopentenone moiety, the latter has often been found to form $PPh_3$-stabilized cobaltocyclopentadiene metallacycles along with ($\eta^5$-cyclopentadienyl)($\eta^4$-cyclobutadiene)cobaltocenes. It is of interest to note that in all the reactions that were carried out in the present study using (2-phenylethynyl)trimethylsilane, no $PPh_3$-stabilized cobaltocyclopentadiene metallacycles were found to form. The reaction of equimolar amounts of [CoCl($PPh_3$)$_3$] with [(methoxycarbonyl)cyclopentadienyl]-sodium in a mixture of thf and toluene followed by the reaction with 2 equiv. of (2-phenylethynyl)trimethylsilane under reflux conditions resulted in the formation of the *cis* and *trans* isomers of [$\eta^5$-(methoxycarbonyl)cyclopentadienyl]($\eta^4$-diphenylbis(trimethylsilyl)cyclobutadiene)-cobalt, [{*trans*-$\eta^4$-$Ph_2(Me_3Si)_2C_4$}Co{$\eta^5$-MeOC(O)-$C_5H_4$}] (**1**) and [{*cis*-$\eta^4$-$Ph_2(Me_3Si)_2C_4$}Co{$\eta^5$-MeOC(O)-$C_5H_4$}] (**2**) (Scheme 1).

Compounds **1** and **2** were formed in a ca. 3:1 ratio and were purified by column chromatography. While the *trans* isomer crystallized readily from the mixture, purification and crystallization of the *cis* isomer proved time-consuming. Pure crystals of **2** (15%) were isolated by repeated fractional crystallization after removal of **1** (41%) from the mixture. Spectral studies and a crystal-structure analysis of **1** and **2** confirmed their identity.

With a view to preparing complexes having one or three phenyl groups on the cyclobutadiene ring, a different strategy was adopted. The stoichiometry of the reagents and the reaction parameters were controlled so as to synthesize a cobalt complex having only one $Me_3SiC{\equiv}CPh$ moiety coordinated to it in situ. It was expected that this complex would react with another equivalent of PhC≡CPh or $Me_3SiC{\equiv}CSiMe_3$ to yield the expected complexes. However, the equimolar reaction of [CoCl($PPh_3$)$_3$] with [(methoxycarbonyl)cyclopentadienyl]sodium and (2-phenylethynyl)trimethylsilane followed by the reaction with 1 equiv. of diphenylacetylene did not result in the monosilylated product **3**, but gave **1** along with the tetraphenylcyclobutadienyl derivative **4**. From independent studies it was observed that the intermediate complex having one acetylene moiety is formed in only around 50% yield. Changing the stoichiometry of the reactants by halving the amounts of (2-phenylethynyl)trimethylsilane followed by the reaction with diphenylacetylene gave the triphenyl(trimethylsilyl)cyclobutadienyl-substituted complex **3** along with the tetraphenylcyclobutadienyl derivative **4** (Scheme 2). Similar attempts to prepare metallocenes containing three trimethylsilyl groups bound to the cyclobutadiene ring by the reaction of [CpCo($PPh_3$)(PhC≡$CSiMe_3$)] with $Me_3SiC{\equiv}CSiMe_3$ were found not to proceed, even under reflux conditions in toluene.

Compounds **1**–**3** were found to readily undergo desilylation when treated with $Bu_4NF$ in dmso at 70 °C for 24 h, resulting in *cis* and *trans* isomers of diphenyl- (**5**, **6**) and triphenyl-substituted (**7**) cyclobutadienyl complexes (Scheme 3). The yields of the products varied from 87 to

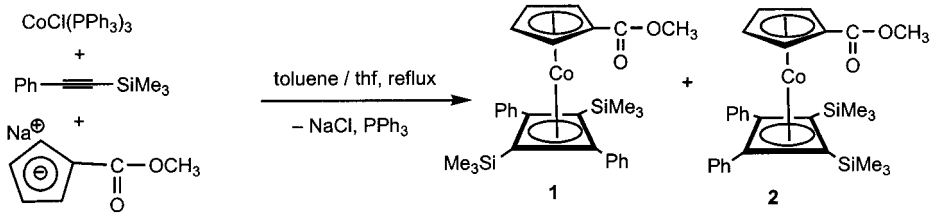


Scheme 1.

 © 2006 Wiley-VCH Verlag GmbH & Co. KGaA, Weinheim 

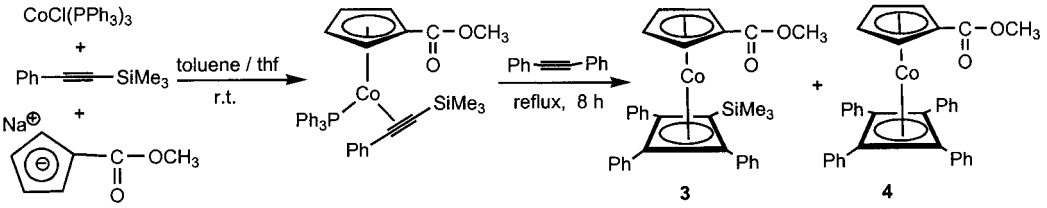


Scheme 2.

93%. The silylated and desilylated methyl esters have $^{13}C$ NMR chemical shifts in the range $\delta$ = 166.12–167.25 ppm for the ester group.

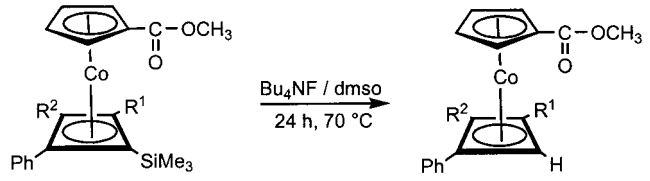


| | | | |
|---|---|---|---|
| $R^1$ = Ph, $R^2$ = $SiMe_3$ | **1** | $R^1$ = Ph, $R^2$ = H | **5** |
| $R^1$ = $SiMe_3$, $R^2$ = Ph | **2** | $R^1$ = H, $R^2$ = Ph | **6** |
| $R^1$ = $R^2$ = Ph | **3** | $R^1$ = $R^2$ = Ph | **7** |

Scheme 3.

We observed that high yields of desilylated products were obtained by using tetrabutylammonium fluoride as the desilylating reagent. Compounds **5**–**7** are quite stable to hydrolysis and were purified by column chromatography on silica gel. The $^1H$ NMR spectra of these complexes clearly show the presence of the cyclobutadienyl protons. For complexes **5** and **7**, for example, the cyclobutadienyl proton signals are observed at $\delta$ = 4.96 and 5.02 ppm, while for the *cis* isomer **6** they are observed at $\delta$ = 4.47 ppm. It is of interest to note that the signal for the cyclobutadiene protons is observed at $\delta$ = 3.66 ppm for the parent unsubstituted complex,[12] and at $\delta$ = 4.04 ppm for tricarbonyl(cyclobutadiene)iron.[14] The deshielding of the cyclobutadiene protons in **5** and **7** is possibly due to the anisotropy effect of the phenyl groups on both sides of the cyclobutadiene-bound hydrogen atoms. The cyclopentadienyl hydrogen atoms appear as a set of two peaks, one in the range $\delta$ = 4.60–4.88 ppm and the other in the range $\delta$ = 5.24–5.33 ppm. The molecular ion peaks in the FAB mass spectra of complexes **5**–**7** also confirm their identity.

Esters **5**–**7** were converted into the corresponding carboxylic acids **8**–**10** by treatment with potassium *tert*-butoxide in dmso at room temperature (Scheme 4). The yields of the carboxylic acids varied from 78 to 85%. The IR spectra of the carboxylic acids **8**–**10** show the acid carbonyl stretching bands at 1658, 1671 and 1674 $cm^{-1}$, respectively, while those for the corresponding esters are observed at 1708, 1706 and 1714 $cm^{-1}$, respectively. The $^1H$ NMR spectra also show similar variations in the cyclopentadienyl peaks ($\delta$ = 4.60–4.88 and 5.24–5.33 ppm for the esters and $\delta$ = 4.71–4.75 and 5.18–5.40 ppm for the carboxylic acids). The $^{13}C$ NMR spectra of the complex ($\eta^5$-carboxycyclopentadienyl)($\eta^4$-tetraphenylcyclobutadiene)cobalt show a chemical shift of $\delta$ = 191.1 ppm for the carboxylic acid carbon atom,[9] and the carboxylic acid carbon atoms of the acid complexes **8**, **9** and **10** show $^{13}C$ chemical shifts in the range $\delta$ = 192.26–193.45 ppm. Mass spectral analysis also further confirms the identity of the carboxylic acids. Due to the difficulty in growing suitable crystals, structural analysis of these complexes could not be performed.

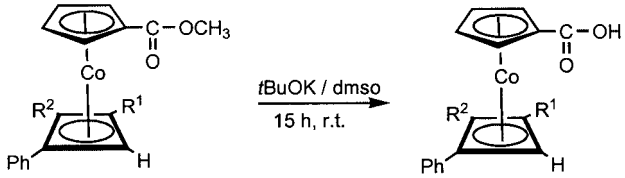


| | | | |
|---|---|---|---|
| $R^1$ = Ph, $R^2$ = H | **5** | $R^1$ = Ph, $R^2$ = H | **8** |
| $R^1$ = H, $R^2$ = Ph | **6** | $R^1$ = H, $R^2$ = Ph | **9** |
| $R^1$ = $R^2$ = Ph | **7** | $R^1$ = $R^2$ = Ph | **10** |

Scheme 4.

The carboxylates **5** and **7** were reduced to the corresponding alcohols **11** and **12** by treatment with lithium aluminium hydride in diethyl ether at room temperature (Scheme 5). The stable alcohols were obtained in 69 and 86% yield, respectively, as crystalline solids and were purified by column chromatography. The identity of the *trans*-diphenyl-substituted alcohol **11** was further confirmed by single-crystal X-ray structural analysis. Reduction of the carboxylate **6** could not be carried out as the quantity needed for the reaction was not available due to the poor yield of its precursor complex **2**.

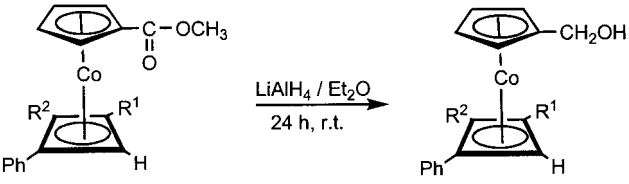


| | | | |
|---|---|---|---|
| $R^1$ = Ph, $R^2$ = H | **5** | $R^1$ = Ph, $R^2$ = H | **11** |
| $R^1$ = $R^2$ = Ph | **7** | $R^1$ = $R^2$ = Ph | **12** |

Scheme 5.

## Electrochemical Studies of Complexes 1–12

Cyclic voltammetric studies on complexes **1**–**12** were carried out using a 0.005 M solution of each complex in 0.1 M tetrabutylammonium perchlorate as supporting electrolyte in dichloromethane solution. Compounds **1**–**3** and **5**–**12** show a quasi-reversible redox couple in the potential range

 © 2006 Wiley-VCH Verlag GmbH & Co. KGaA, Weinheim 

0.0–1.5 V at a scan rate of 0.1 $Vs^{-1}$ in the positive direction. Interestingly, under identical measurement conditions the voltammogram of the tetraphenylcyclobutadienyl ester [($\eta^4$-$Ph_4C_4$)Co{$\eta^5$-$MeOC(O)C_5H_4$}] shows an almost reversible redox couple while that of the tetraphenyl acid [($\eta^4$-$Ph_4C_4$)Co{$\eta^5$-$HOC(O)C_5H_4$}] shows a fully reversible redox couple. The $E_{1/2}$ values given in Table 1 were calculated by averaging the anodic and cathodic potential of the respective redox couple with respect to the ferrocene/ferrocenium redox couple. On increasing the number of cycles, the height of both the anodic and cathodic peaks decreases, although this reduction is minimal after the second cycle; this indicates partial decomposition of the complex at the electrode surface. It is interesting to note that on going from the silylated complexes **1**, **2** and **3** to the desilylated complexes **5**, **6** and **7** there is a negative shift in $E_{1/2}$ values. From the desilylated complexes **5**, **6** and **7** to the carboxylic acids (**8**, **9** and **10**) and alcohols (**11** and **12**) a further negative shift in $E_{1/2}$ values is observed. This indicates that the system is more electroactive towards oxidation on going from silylated complexes through desilylated complexes to carboxylic acids and their alcohol derivatives. The $E_{1/2}$ value for complex **4**, which bears four phenyl rings on the cyclobutadiene ring, is 0.570 V. On removing the phenyl rings one by one, the $E_{1/2}$ values decrease and oxidation becomes easier.

Table 1. Cyclic voltammetric data of complexes **1**–**12**.

| Entry | Complex | $E_{1/2}$ vs. $Fc/Fc^+$ [V] |
|---|---|---|
| 1 | **1** | 0.587 |
| 2 | **2** | 0.589 |
| 3 | **3** | 0.637 |
| 4 | **4** | 0.570 |
| 5 | **5** | 0.433 |
| 6 | **6** | 0.494 |
| 7 | **7** | 0.539 |
| 8 | **8** | 0.368 |
| 9 | **9** | 0.382 |
| 10 | **10** | 0.415 |
| 11 | **11** | 0.287 |
| 12 | **12** | 0.416 |

### Structural Studies on Complexes 1–7 and 11

Detailed structural analysis were carried out on the silylated and desilylated carboxylates **1**–**7** and the alcohol **11** as there is only a preliminary communication available in the literature on the structures of the *cis*- and *trans*-metallocenes [$CpCo\{(Me_3Si)_2Ph_2C_4\}$], which contain unsubstituted cyclopentadienyl rings.[15] The crystal structures of complexes **1**–**7** and **11** are given in Figures 1, 2, 3, 4, 5, 6, 7 and 8, respectively. Selected bond lengths and angles are given in Tables 2 and 3 and details of data collection, solution and crystal parameters are given in the Experimental Section. The structural studies on complexes **1**–**7** indicate no significant variation in the structure and orientation of the ester-substituted cyclopentadienyl group. However, on comparing structures of complexes **1**–**3** with those of **5**–**7**, the structural changes associated with the cyclobutadiene ring and its substituents were found to be quite significant. As such, the four phenyl rings of the tetraphenylcyclobutadiene ring of **4** are displaced at angles of 37.39°, 48.44°, 29.25° and 60.49° with respect to the cyclobutadiene ring. A comparison of **4** with the corresponding carboxylic acid also shows that the relative orientation of the phenyl rings with

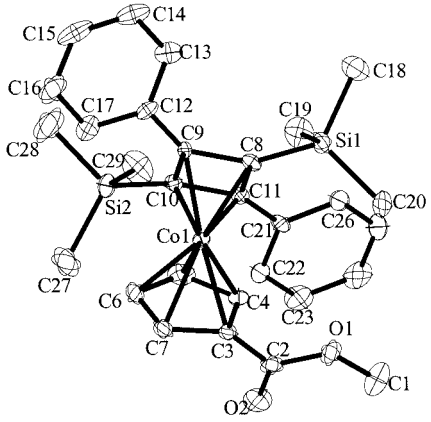


Figure 1. Thermal ellipsoid view of complex **1** with 30% probability ellipsoids (H atoms omitted for clarity).

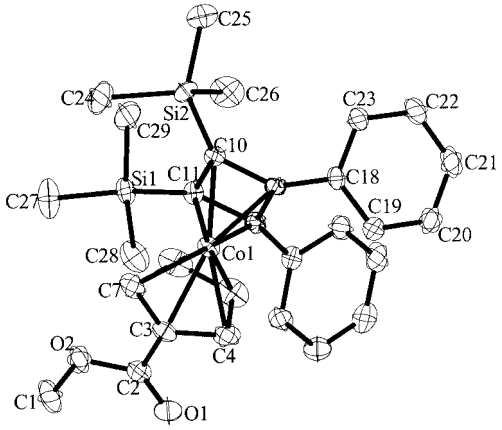


Figure 2. Thermal ellipsoid view of complex **2** with 30% probability ellipsoids (H atoms omitted for clarity).

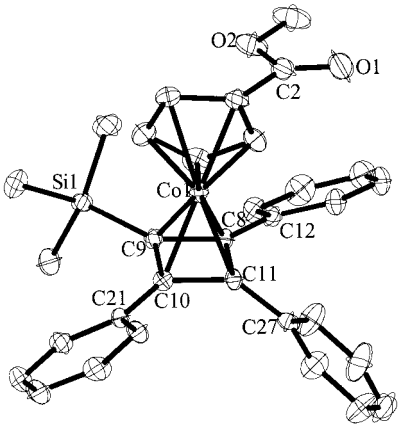


Figure 3. Thermal ellipsoid view of complex **3** with 30% probability ellipsoids (H atoms omitted for clarity).

 © 2006 Wiley-VCH Verlag GmbH & Co. KGaA, Weinheim 

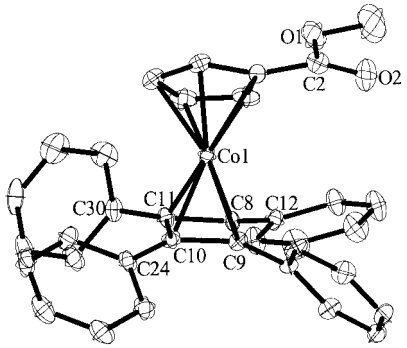


Figure 4. Thermal ellipsoid view of complex **4** with 30% probability ellipsoids (H atoms omitted for clarity).

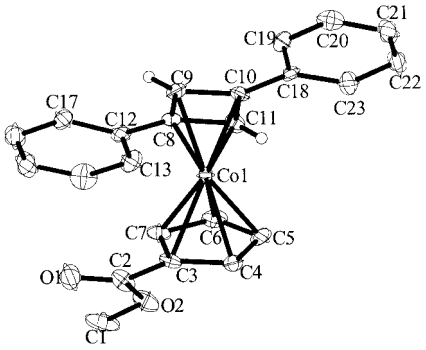


Figure 5. Thermal ellipsoid view of complex **5** with 30% probability ellipsoids (all H atoms, except those of the cyclobutadiene moiety, omitted for clarity).

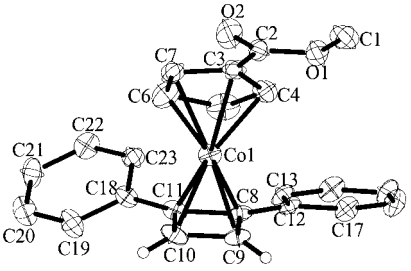


Figure 6. Thermal ellipsoid view of complex **6** with 30% probability ellipsoids (all H atoms, except those of the cyclobutadiene moiety, omitted for clarity).

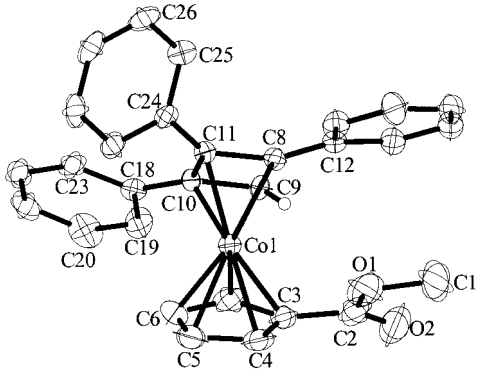


Figure 7. Thermal ellipsoid view of complex **7** with 30% probability ellipsoids (all H atoms, except those of the cyclobutadiene moiety, omitted for clarity).

respect to the cyclobutadiene ring varies significantly from 7.05° to 89.20°.[11] It was therefore of interest to see whether desilylation, which results in lower crowding around the cyclobutadiene ring, will affect the orientation of the phenyl groups in complexes **5**–**7**. In addition, complex **4** is a propeller-type molecule, and such complexes show promise in the design of molecular devices. This study therefore provides information on structural changes at the molecular level accompanying the removal of substituents that are akin to the blades of such propeller-type molecules.

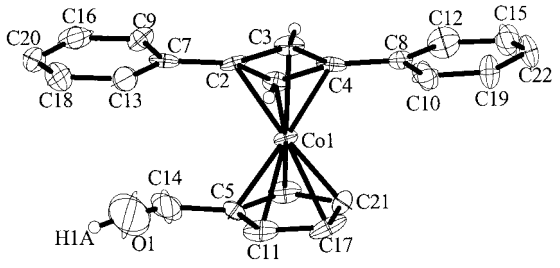


Figure 8. Thermal ellipsoid view of complex **11** with 30% probability ellipsoids (all H atoms, except those of the cyclobutadiene moiety, omitted for clarity).

On comparing the structures of complexes **1**–**3** with their desilylated analogues **5**–**7** it can be seen that, basically, two noticeable structural changes occur. The phenyl groups, which are pushed away from the plane of the cyclobutadienyl ring in complexes **1**–**3**, tend to come close to the plane of the cyclobutadiene ring in complexes **5**–**7**. More interestingly, however, the phenyl groups rotate and take up orientations which tend to align with the planarity of the cyclobutadiene ring. Both these structural changes indicate a tendency to gain better π-delocalization of the phenyl groups with the metal-coordinated cyclobutadiene ring (Scheme 6).

The angle ($\theta$) between the mean plane of the cyclobutadiene ring and the mean plane of a substituted phenyl ring represents the extent of deviation of the phenyl rings from the plane of the cyclobutadiene ring. For complex **1**, which has a *trans* orientation of two phenyl substituents, the values of $\theta$ are 32.68° and 43.97°. The corresponding desilylated complex **5** has $\theta$ reduced to 5.34° and 3.09° (5.45° and 2.15° for the other crystallographically independent structure in the unit cell). For the *cis*-oriented complex **2**, the values of $\theta$ are 63.14° and 43.98°, which are reduced to 24.75° and 12.45° for the desilylated complex **6**. Similarly for the triphenyl(trimethylsilyl)cyclobutadiene complex **3**, the $\theta$ values are 34. 26°, 31.47° and 64.19°, which are reduced in complex **7** to 14.14°, 12.26° and 54.13° respectively (13.97°, 12.26° and 53.98° for the other crystallographically independent structure in the unit cell). These results clearly indicate that removing the steric crowding around the cyclobutadiene unit tends to make the phenyl groups become more aligned to the cyclobutadiene ring.

The other interesting difference observed on comparing complexes **1**–**3** with complexes **5**–**7** is the distortion from planarity observed for the exocyclic cyclobutadiene–phenyl bonds. Although the bond connecting the phenyl ring to the cyclobutadiene ring should ideally lie in the same plane

 © 2006 Wiley-VCH Verlag GmbH & Co. KGaA, Weinheim 

Table 2. Selected bond lengths [Å] and angles [°] for complexes **1**–**4**.

| | | | |
|---|---|---|---|
| Compound **1** | | | |
| Co(1)–C(9) | 1.972(5) | Co(1)–C(8) | 2.005(5) |
| Co(1)–C(3) | 2.069(5) | Si(1)–C(8) | 1.866(6) |
| Si(1)–C(20) | 1.868(8) | O(1)–C(1) | 1.446(10) |
| O(1)–C(2) | 1.336(7) | O(2)–C(2) | 1.195(9) |
| C(2)–C(3) | 1.47(1) | C(3)–C(7) | 1.418(9) |
| C(9)–C(12) | 1.458(9) | C(12)–C(13) | 1.379(10) |
| C(11)–C(12) | 1.467(9) | | |
| C(17)–C(12)–C(13) | 117.5(7) | C(13)–C(12)–C(9) | 120.9(6) |
| C(12)–C(9)–C(8) | 133.3(5) | C(8)–Si(1)–C(18) | 109.4(4) |
| C(9)–C(8)–C(11) | 88.2(5) | C(10)–Co(1)–C(6) | 117.9(3) |
| C(6)–C(7)–C(3) | 107.9(6) | C(7)–C(3)–C(2) | 123.0(6) |
| O(2)–C(2)–O(1) | 123.1(7) | C(2)–O(1)–C(1) | 115.2(6) |
| Compound **2** | | | |
| Co(1)–C(9) | 1.999(4) | Co(1)–C(11) | 1.982(3) |
| Co(1)–C(3) | 2.069(6) | Si(1)–C(11) | 1.864(5) |
| Si(1)–C(27) | 1.863(4) | C(1)–O(2) | 1.447(4) |
| C(2)–O(1) | 1.199(3) | C(2)–O(2) | 1.331(4) |
| C(2)–C(3) | 1.467(4) | C(3)–C(4) | 1.426(4) |
| C(11)–C(10) | 1.487(4) | C(9)–C(18) | 1.473(4) |
| C(8)–C(12) | 1.481(3) | | |
| C(25)–Si(2)–C(26) | 108.92(11) | C(26)–Si(2)–C(10) | 110.23(8) |
| Si(2)–C(10)–C(9) | 131.81(12) | C(10)–C(9)–C(18) | 135.28(14) |
| C(9)–C(18)–C(23) | 120.57(15) | C(11)–C(10)–C(9) | 89.36(12) |
| C(11)–Co(1)–C(7) | 118.31(7) | C(7)–C(3)–C(2) | 127.75(16) |
| C(7)–C(3)–C(4) | 108.29(16) | O(2)–C(2)–O(1) | 123.40(17) |
| Compound **3** | | | |
| Co(1)–C(8) | 2.000(3) | Co(1)–C(3) | 2.073(4) |
| Si(1)–C(18) | 1.866(2) | Si(2)–C(9) | 1.868(4) |
| C(9)–C(10) | 1.475(3) | C(10)–C(21) | 1.468(3) |
| C(3)–C(7) | 1.421(3) | C(3)–C(2) | 1.464(4) |
| O(2)–C(2) | 1.337(4) | O(2)–C(1) | 1.448(4) |
| C(2)–O(1) | 1.208(4) | C(21)–C(22) | 1.395(3) |
| C(8)–C(12) | 1.465(3) | C(11)–C(27) | 1.501(3) |
| C(1)–O(2)–C(2) | 116.77(18) | O(2)–C(2)–O(1) | 124.57(21) |
| O(2)–C(2)–C(3) | 111.31(18) | C(2)–C(3)–C(7) | 127.12(18) |
| C(7)–C(3)–C(4) | 107.60(16) | C(7)–C(3)–C(4) | 107.60(16) |
| C(7)–Co(1)–C(9) | 112.25(7) | C(10)–C(9)–C(8) | 88.32(12) |
| C(10)–C(9)–Si(1) | 135.06(12) | C(9)–C(10)–C(21) | 135.46(14) |
| Compound **4** | | | |
| Co(1)–C(8) | 1.994(3) | Co(1)–C(3) | 2.074(3) |
| O(1)–C(1) | 1.446(6) | O(1)–C(2) | 1.343(4) |
| O(2)–C(20) | 1.194(4) | C(2)–C(3) | 1.450(4) |
| C(3)–C(4) | 1.420(4) | C(10)–C(11) | 1.462(3) |
| C(11)–C(30) | 1.472(3) | C(31)–C(32) | 1.375(5) |
| C(8)–C(12) | 1.458(3) | C(10)–C(24) | 1.375(5) |
| C(9)–C(18) | 1.473(3) | | 1.458(3) |
| C(1)–O(1)–C(2) | 115.81(31) | O(1)–C(2)–O(2) | 123.13(29) |
| O(1)–C(2)–C(3) | 111.12(25) | C(2)–C(3)–C(7) | 128.05(24) |
| C(7)–C(3)–C(4) | 107.23(22) | C(7)–Co(1)–C(8) | 122.97(10) |
| C(11)–C(8)–C(9) | 90.07(18) | C(30)–C(11)–C(10) | 134.06(21) |

Table 3. Selected bond lengths [Å] and angles [°] for complexes **5**–**7** and **11**.

| | | | |
|---|---|---|---|
| Compound **5** | | | |
| Co(1)–C(11) | 1.969(8) | Co(1)–C(10) | 1.978(6) |
| Co(1)–C(3) | 2.062(5) | O(2)–C(1) | 1.452(8) |
| C(2)–O(2) | 1.326(8) | C(2)–O(1) | 1.201(8) |
| C(2)–C(3) | 1.471(7) | C(11)–C(8) | 1.434(8) |
| C(8)–C(12) | 1.478(7) | C(4)–C(5) | 1.430(8) |
| C(10)–C(18) | 1.446(6) | C(10)–C(11) | 1.446(9) |
| C(1)–O(2)–C(2) | 115.67(5) | O(2)–C(2)–O(1) | 123.5(5) |
| O(1)–C(2)–C(3) | 125.1(5) | C(7)–C(3)–C(4) | 108.6(5) |
| C(3)–Co(1)–C(8) | 115.0(2) | C(9)–C(8)–C(11) | 90.2(4) |
| C(13)–C(12)–C(8) | 120.3(5) | C(17)–C(12)–C(13) | 119.0(5) |
| Compound **6** | | | |
| Co(1)–C(9) | 1.968(3) | Co(1)–C(8) | 1.981(2) |
| Co(1)–C(3) | 2.045(3) | O(1)–C(1) | 1.445(4) |
| O(1)–C(2) | 1.335(4) | O(2)–C(2) | 1.196(4) |
| C(2)–C(3) | 1.464(4) | C(3)–C(7) | 1.422(4) |
| C(9)–C(10) | 1.430(4) | C(11)–C(18) | 1.471(4) |
| C(8)–C(9) | 1.458(4) | C(8)–C(12) | 1.453(3) |
| C(1)–O(1)–C(2) | 115.77(23) | O(1)–C(2)–O(2) | 123.12(26) |
| O(2)–C(2)–C(3) | 124.58(28) | C(2)–C(3)–C(7) | 124.16(27) |
| C(7)–C(3)–C(4) | 107.33(25) | C(7)–Co(1)–C(11) | 112.59(12) |
| C(10)–C(11)–C(8) | 88.97(22) | C(18)–C(11)–C(10) | 131.98(25) |
| Compound **7** | | | |
| C(1)–O(1) | 1.474(6) | O(1)–C(2) | 1.294(5) |
| O(2)–C(2) | 1.187(5) | C(3)–C(2) | 1.497(5) |
| C(3)–C(4) | 1.406(4) | Co(1)–C(3) | 2.050(3) |
| Co(1)–C(8) | 1.992(3) | C(11)–C(8) | 1.463(3) |
| C(9)–C(8) | 1.444(4) | C(10)–C(18) | 1.452(3) |
| C(11)–C(24) | 1.473(3) | | |
| C(1)–O(1)–C(2) | 111.69(34) | O(1)–C(2)–O(2) | 126.69(41) |
| O(2)–C(2)–C(3) | 123.43(35) | C(2)–C(3)–C(7) | 130.33(30) |
| C(4)–C(3)–C(7) | 108.19(29) | C(10)–C(11)–C(8) | 89.42(19) |
| C(10)–C(9)–C(8) | 91.03(20) | C(9)–C(8)–C(12) | 134.00(26) |
| C(9)–C(10)–C(18) | 132.96(22) | C(10)C(18)C(19) | 120.56(21) |
| Compound **11** | | | |
| O(1)–C(14) | 1.231(34) | C(14)–C(5) | 1.548(24) |
| C(11)–C(5) | 1.441(22) | Co(1)–C(5) | 2.066(14) |
| Co(1)–C(4) | 1.966(12) | C(1)–C(4) | 1.486(14) |
| C(4)–C(8) | 1.467(16) | C(2)–C(7) | 1.470(15) |
| O(1)–C(14)–C(5) | 105.4(17) | C(14)–C(5)–C(11) | 136.2(14) |
| C(6)–C(5)–C(11) | 106.3(10) | C(5)–Co(1)–C(2) | 113.37(44) |
| C(4)–C(1)–C(2) | 89.4(8) | C(3)–C(4)–C(1) | 89.2(8) |
| C(2)–C(7)–C(13) | 121.0(10) | | |

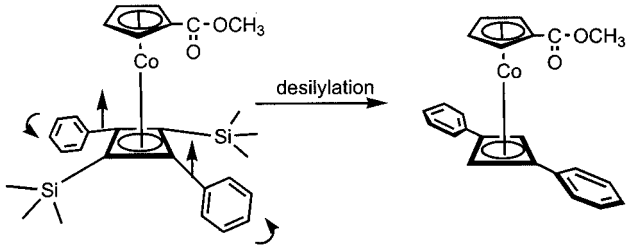


Scheme 6.

as that of the cyclobutadiene ring, what is observed is that all the exocyclic bonds from the cyclobutadiene ring to the phenyl groups are displaced at an angle ($\phi$) to the plane of the cyclobutadiene ring with the displacement directed away from the cyclopentadienylcobalt moiety. The value of $\phi$ varies from 167.50° to 177.11° for the phenyl substituents. A comparison of the silylated metallocenes **1**–**3** and desilylated metallocenes **5**–**7** indicates that this distortion decreases upon desilylation, with the angles coming closer to 180°. The values of $\phi$ for complex **1** are 172.54° and 175.48° which become 176.14° and 177.11° in **5** upon desilylation. For **2**, the values of $\phi$ are 174.36° and 167.50°, which in-

 © 2006 Wiley-VCH Verlag GmbH & Co. KGaA, Weinheim 

creases to 174.56° and 173.44° for complex **6**. A similar, while minor, increase is seen when $\phi$ is compared for complexes **3** and **7**.

Both these structural variations clearly indicate that, in the absence of steric repulsion, the phenyl groups would prefer to lie aligned with the plane of the cyclobutadiene ring, which possibly helps to extend the aromatic conjugation between the phenyl rings and the cobalt-bound cyclobutadienyl ring. We have also observed that these variations in structural parameters are not affected by the orientation of the ester groups on this ring. This study provides a good comparison to the structure of biphenyl.[16] In the case of biphenyl, the two phenyl groups do not lie in the same plane due to the *ortho* effect of the hydrogen atoms. Such an effect does not exist in the case of complexes such as **5**. It has also been reported that the C–C bond connecting the two phenyl rings in biphenyl is 1.507 Å. In the case of complexes **1**–**4**, the bond length between the cyclobutadiene and phenyl groups varies from 1.458(3) to 1.501(3) Å, while for complexes **5**–**7** and **11** the same distance varies from 1.444(7) to 1.486(8) Å, which is between those of a carbon–carbon single and double bond.

The crystal structure of the alcohol complex **11** is quite similar to that of complex **5**, with the values of $\theta$ being 1.19° and 6.01°. This indicates that both the phenyl groups and the cyclobutadiene ring are almost in the same plane, further increasing their aromatic conjugation. The hydroxy group of the complex is disordered and the oxygen atom has two independent crystallographic positions (occupancy factors of 0.8 and 0.2).

## Conclusions

In conclusion, we have described a method to prepare examples of sterically less hindered and stable carboxylic acid analogues of [($\eta^5$-Cp)Co($\eta^4$-$C_4Ph_4$)] and their alcohol derivatives by desilyation, de-esterification and reduction of the trimethylsilyl-derived metallocenecarboxylates. The carboxylic acids are potential reagents for preparing catalysts such as cobalt(I) oxazoline palladacycles and a host of other similar catalysts and reagents with less steric bulkiness than [($\eta^5$-Cp)Co($\eta^4$-$C_4Ph_4$)] on the cyclobutadiene ring. The silylated and desilylated carboxylates have been structurally characterized and this study provides an opportunity to compare structural changes around the cyclobutadiene moiety accompanying the desilylation reactions. It has been observed that two major structural changes occur upon desilylation of the silylated esters: the phenyl groups rotate around their bonds to the cyclobutadiene ring and also bend towards the plane of the cyclobutadiene ring, tending to become more aligned and parallel to its plane. This possibly helps to extend the delocalization of electron density of the phenyl groups to that of the cobalt-bound cyclobutadiene ring. Further work exploring the chemistry of these new metallocenecarboxylic acids and their alcohol derivatives is in progress.

## Experimental Section

**General Remarks:** All manipulations of the complexes were carried out using standard Schlenk techniques under nitrogen. Toluene and thf were freshly distilled from sodium benzophenone ketyl under nitrogen before use. The sodium salt of (methoxycarbonyl)cyclopentadiene,[9] chloridotris(triphenylphosphane)cobalt[17] and (2-phenylethynyl)trimethylsilane[18] were prepared according to literature procedures. Diphenylacetylene, dimethyl carbonate and triphenylphosphane (Aldrich) were used as received. $^1$H and $^{13}$C{$^1$H} NMR spectra were recorded with a Bruker Spectrospin DPX-300 NMR spectrometer at 300 and 75.47 MHz, respectively. IR spectra in the range 4000–250 cm$^{-1}$ were recorded with a Nicolet Protége 460 FT-IR spectrometer as KBr pellets. Elemental analyses were carried out with a Carlo Erba CHNSO 1108 elemental analyzer. Mass spectra were recorded in the FAB mode using a JEOL SX 102/DA-6000 mass spectrometer and in the electrospray mode with a Micromass Quattro II triple quadrupole mass spectrometer.

**Electrochemical Studies:** All electrochemical measurements were performed with a basic electrochemistry system CHI 604A, using a three-electrode configuration of a Pt working electrode (0.1 mm diameter), a commercially available Ag/AgCl electrode as the reference electrode and a Pt mesh electrode as the counter electrode. Half-wave potentials were measured as the average of the cathodic and anodic peak potentials. The voltammograms were recorded in $CH_2Cl_2$ containing 0.1 M tetrabutylammonium perchlorate as the supporting electrolyte, and the potential was scanned from 0 to +1.5 V at various scan rates. Ferrocene gave a reversible single redox couple with $E_{1/2}$ at 652 mV under the same experimental conditions.

**Preparation of [{*trans*-$\eta^4$-$Ph_2(Me_3Si)_2C_4$}Co{$\eta^5$-MeOC(O)$C_5H_4$}] (1) and [{*cis*-$\eta^4$-$Ph_2(Me_3Si)_2C_4$}Co{$\eta^5$-MeOC(O)$C_5H_4$}] (2):** A solution of chloridotris(triphenylphosphane)cobalt(I) (5.06 g, 5.73 mmol) in toluene (30 mL) was added to a solution of [(methoxycarbonyl)cyclopentadienyl]sodium (0.84 g, 5.73 mmol) in thf (10 mL). The resulting red solution was stirred for 0.5 h and then added to (2-phenylethynyl)trimethylsilane (2.00 g, 11.5 mmol). The solution turned dark brown on stirring at room temperature for 0.5 h. The resulting mixture was heated at reflux for 8 h and then cooled to room temperature. The solvent was removed in vacuo and the residue dissolved in hexane and filtered to give a yellow filtrate. This was concentrated and cooled to partially remove triphenylphosphane by fractional crystallization. The residue was chromatographed on silica gel using a mixture of hexane and ethyl acetate as eluent to give a mixture of **1** and **2**. Compound **1** (1.20 g, 41%) crystallized readily upon cooling the solution and complex **2** (0.42 g 15%) was isolated by repeated fractional crystallization of the remaining solution.

**[{*trans*-$\eta^4$-$Ph_2(Me_3Si)_2C_4$}Co{$\eta^5$-MeOC(O)$C_5H_4$}] (1):** M.p. 95 °C. $^1$H NMR (300 MHz, $CDCl_3$): $\delta$ = 3.18 (s, 3 H, $CH_3$), 4.77 (s, 2 H, CpH), 5.41 (s, 2 H, CpH), 7.07 (m, 6 H, PhH), 7.16 (m, 4 H, PhH), 0.02 (s, 18 H, $SiMe_3$) ppm. $^{13}$C NMR (75 MHz, $CDCl_3$): $\delta$ = 0.8 ($SiMe_3$), 60.0 (COMe), 69.8, 82.0 ($C_4$ ring), 82.7, 86.6, 90.9 (CpC), 126.3, 127.5, 128.9, 137.3 (Ph-C), 166.1 (C=O) ppm. IR (KBr): $\tilde{\nu}$ = 3396 m, 3095 w, 2951 s, 2896 m, 1706 vs, 1596 w, 1495 vs, 1467 s, 1362 s, 1288 vs, 1245 vs, 1194 s, 1140 vs, 1068 m, 1026 m, 969 m, 843 vs, 761 vs, 694 vs, 602 w, 560 w, 509 w, 443 w cm$^{-1}$. MS (FAB): *m*/*z* = 530 [M$^+$], 531 [M + 1], 499 [M$^+$ – $OCH_3$], 407 [M$^+$ – $CpCo_2Me$] 515 [M$^+$ – $CH_3$], 356 [M$^+$ – $PhCCSiMe_3$]. $C_{29}H_{35}CoO_2Si_2$ (530.15): calcd. C 65.63, H 6.65; found C 65.59, H 6.52.

**[*cis*-$\eta^4$-$Ph_2(Me_3Si)_2C_4$]Co{$\eta^5$-MeOC(O)$C_5H_4$}] (2):** M.p. 80 °C. $^1$H NMR (300 MHz, $CDCl_3$): $\delta$ = 3.10 (s, 3 H, $CH_3$), 4.81 (s, 2 H,

 © 2006 Wiley-VCH Verlag GmbH & Co. KGaA, Weinheim 

CpH), 5.14 (s, 2 H, CpH), 6.97 (m, 6 H, PhH), 7.03 (m, 4 H, PhH), 0.01 ($SiMe_3$) ppm. $^{13}C$ NMR (75 MHz, $CDCl_3$): $\delta$ = 0.8 ($SiMe_3C$), 51.0 (COOMeC), 67.9, 82.0 ($C_4$ ring), 82.7, 87.1, 90.4 (CpC), 126.4, 127.5, 129.0, 135.7 (PhC), 166.2 (C=O) ppm. IR, (KBr): $\tilde{\nu}$ = 3054 m, 3021 w, 2954 s, 2896 m, 1710 vs, 1599 w, 1467 vs, 1439 s, 1369 s, 1287 vs, 1248 vs, 1192 s, 1147 vs, 1064 m, 1028 m, 970 m, 839 vs, 772 vs, 695 vs, 633 w, 616 w, 509 w $cm^{-1}$. MS (FAB): *m*/*z* = 530 [$M^+$], 531 [$M^+$ + 1], 529 [$M^+$ – 1], 498 [$M^+$ – $OCH_3$], 514 [$M^+$ – $CH_3$], 457 [$M^+$ – $SiMe_3$], 356 [$M^+$ – $PhCCSiMe_3$], 407 [$M^+$ – $CpCO_2Me$]. $C_{29}H_{35}CoO_2Si_2$ (530.15): calcd. C 65.63, H 6.65; found C 65.57, H 6.60.

**Preparation of [{η⁴-Ph₃(Me₃Si)C₄}Co{η⁵-MeOC(O)C₅H₄}] (3) and [(η⁴-Ph₄C₄)Co{η⁵-MeOC(O)C₅H₄}] (4):** A solution of chloridotris-(triphenylphosphane)cobalt(I) (5.16 g, 5.84 mmol) in toluene (30 mL) was added to a solution of [(methoxycarbonyl)cyclopentadienyl]sodium (0.86 g, 5.85 mmol) in thf (5 mL). The resulting red solution was stirred at room temperature for 0.5 h and then a solution of (2-phenylethynyl)trimethylsilane (0.61 g, 3.50 mmol) in toluene was added and stirred at room temperature for 1 h to give a brown solution. A solution of diphenylacetylene (1.04 g, 5.85 mmol) in toluene was added and the resulting mixture was stirred at room temperature for 10 min and thereafter refluxed for 8 h and cooled to room temperature. The solvent was removed in vacuo and the residue suspended in 20% ethyl acetate in hexane and filtered. The filtrate was concentrated and chromatographed on silica gel, eluting with a hexane/ethyl acetate mixture (2% ethyl acetate) to give a yellow solution, which upon slow cooling gave crystals of **3** (0.52 g, 29%). On increasing the polarity of the eluent (10% ethyl acetate) a dark yellow solution was obtained, which on cooling gave crystals of **4** (0.76 g, 24%). The physical and spectral properties of **4** were found to agree well with those reported in the literature.[9]

**[{η⁴-Ph₃(Me₃Si)C₄}Co{η⁵-MeOC(O)C₅H₄}] (3):** M.p. 75 °C. $^1H$ NMR (300 MHz, $CDCl_3$): $\delta$ = 0.27 (s, 9 H, $SiMe_3$), 3.33 (s, 3 H, $CH_3$), 4.94 (s, 2 H, CpH), 5.37 (s, 2 H, CpH), 7.28–7.34 (m, 9 H, PhH), 7.47–7.48 (m, 6 H, PhH) ppm. $^{13}C$ NMR (75 MHz, $CDCl_3$): $\delta$ = 1.1 ($SiMe_3$), 51.1 ($CO_2Me$), 63.1, 82.5 ($C_4$ ring), 83.6, 84.3, 86.9 (CpC), 135.9, 135.1, 129.6, 129.0, 128.0, 127.7, 126.7, 126.5 (PhC), 167.2 (C=O) ppm. IR (KBr): $\tilde{\nu}$ = 3051 m, 3020 w, 2950 m, 1717 vs, 1596 m, 1495 m, 1469 m, 1444 m, 1364 m, 1280 vs, 1250 s, 1229 m, 1145 s, 1066 w, 826 s, 768 s, 694 s, 585 s $cm^{-1}$. MS (FAB): *m*/*z* = 534 [$M^+$], 335 [$M^+$ + 1], 356 [$M^+$ – PhCCPh], 411 [$M^+$ – $CpCO_2Me$], 360 [$M^+$ – $PhCCSiMe_3$], 503 [$M^+$ – $OCH_3$]. $C_{32}H_{31}CoO_2Si$ (534.14): calcd. C 71.89, H 5.84; found C 71.80, H 5.90.

**General Procedure for the Desilylation of Compounds 1–3:** The silylated cobalt complex (1.0 mmol) and a slight excess of tetrabutylammonium fluoride (1 M solution in thf) were dissolved in dmso (10 mL) and the mixture was stirred at 70 °C under nitrogen for 24 h. The product was extracted with ethyl acetate, and the solution was washed repeatedly with water to remove any trace of dmso. The ethyl acetate solution was dried with anhydrous $MgSO_4$ and concentrated to give a dark yellow powder, which was chromatographed on silica gel with an appropriate eluent.

**[{*trans*-η⁴-Ph₂H₂C₄}Co{η⁵-MeOC(O)C₅H₄}] (5):** Chromatographed on silica gel with hexane as eluent to give 0.36 g (93%) of **5**. M.p. 122 °C. $^1H$ NMR (300 MHz, $CDCl_3$): $\delta$ = 3.20 (s, 3 H, $CH_3$), 4.96 (s, 2 H, $C_4$ ring), 4.60 (s, 2 H, CpH), 5.39 (s, 2 H, CpH), 7.19 (m, 6 H, PhH), 7.17 (m, 4 H, PhH) ppm. $^{13}C$ NMR (75 MHz, $CDCl_3$): $\delta$ = 51.1 (OMeC), 54.8, 76.1 ($C_4$ ring), 81.7, 84.1, 86.1 (CpC), 124.5, 126.1, 128.4, 136.3 (PhC), 166.7 (C=O) ppm. IR (KBr): $\tilde{\nu}$ = 3086 w, 3055 m, 2952 m, 1708 vs, 1594 s, 1501 s, 1468 vs, 1393 m 1358 m, 1282 vs, 1197 s, 1143 vs, 1067 m, 1022 s, 967 s, 902 s, 817 s, 764 vs, 691 vs. 663 m, 538 m, 480 s $cm^{-1}$. MS (FAB): *m*/*z* = 386 [$M^+$], 387[$M^+$ + 1], 355 [$M^+$ – $OCH_3$], 263 [$M^+$ – $CpCO_2Me$]. $C_{23}H_{19}CoO_2$ (386.07): calcd. C 71.51, H 4.96; found C 71.63, H 4.92.

**[{*cis*-η⁴-Ph₂H₂C₄}Co{η⁵-MeOC(O)C₅H₄}] (6):** Chromatographed on silica gel with hexane as eluent to give 0.35 g (92%) of **6**. M.p. 70 °C. $^1H$ NMR (300 MHz, $CDCl_3$): $\delta$ = 3.36 (s, 3 H, $CH_3$), 4.88 (s, 2 H, CpH), 5.24 (s, 2 H, CpH), 4.46 (s, 2 H, $C_4$ ring), 7.24–7.26 (m, 6 H, PhH), 7.38 (m, 4 H, PhH) ppm. $^{13}C$ NMR (75 MHz, $CDCl_3$): $\delta$ = 51.22 ($CH_3$), 58.2, 77.4 ($C_4$ ring), 82.6 (CpC), 83.1, 86.2 (CpC), 124.6, 126.6, 128.3, 136.7 (PhC), 167.2 (C=O) ppm. IR (KBr): 3059 m, 29469 m, 1706 vs, 1597 w, 1567 w, 1499 w, 1458 s, 1359 m, 1278 vs, 1187 m, 1135 vs, 1024 w, 961 m, 893 m, 827 m, 766 vs, 694 vs, 576 vs, 523 m $cm^{-1}$. MS (FAB): *m*/*z* = 386 [$M^+$], 387 [$M^+$ + 1], 355 [$M^+$ – $OCH_3$], 263 [$M^+$ – $CpCO_2Me$]. $C_{23}H_{19}CoO_2$ (386.07): calcd. C 71.51, H 4.96; found C 71.58, H 4.85.

**[(η⁴-Ph₃HC₄)Co{η⁵-MeOC(O)C₅H₄}] (7):** Chromatographed on silica gel with hexane as eluent to give 0.33 g (87%) of **7**. M.p. 180 °C. $^1H$ NMR (300 MHz, $CDCl_3$): $\delta$ = 3.21 (s, 3 H, $CH_3$), 4.67 (s, 2 H, CpH), 5.02 (s, 1 H, $C_4$ ring), 5.33 (s, 2 H, CpH), 7.7 (m, 2 H, PhH), 7.34 (m, 3 H, PhH), 7.24–7.18 (m, 10 H, PhH) ppm. $^{13}C$ NMR (75 MHz, $CDCl_3$): $\delta$ = 51.1 ($CH_3C$), 54.6, 76.1, 77.9 ($C_4$ ring), 85.7, 84.9, 82.9 (CpC), 125.9, 126.3, 127.0, 128.1, 128.3, 130.1, 135.4, 136.2 (PhC), 166.2 (C=O) ppm. IR (KBr): 3080 w, 2948 w, 2362 w, 1714 vs, 1595 m, 1500 s, 1467 s, 1363 m, 1281 vs, 1187 s, 1139 vs, 1067 w, 1026 w, 967 w, 825 w, 764 vs, 692 vs, 608 w, 582 w $cm^{-1}$. MS (FAB): *m*/*z* = 462 [$M^+$], 463 [$M^+$ + 1], 339 [$M^+$ – $CpCO_2Me$]. $C_{29}H_{23}CoO_2$ (462.40): calcd. C 75.32, H 5.01; found C 75.24, H 5.15.

**General Procedure for the De-esterification of Compounds 5–7:** A mixture of 1.0 mmol of the ester and potassium *tert*-butoxide (1.68 g, 15 mmol) in 10 mL of dmso was stirred at room temperature for 15 h and then quenched with 2 M HCl (20 mL). After extraction with ethyl acetate, the organic phase was separated and dried with $MgSO_4$. The solvent was removed in vacuo and the residue was column-chromatographed on silica gel with an appropriate eluent to give the carboxylic acid complex.

**[*trans*-(η⁴-Ph₂H₂C₄)Co(η⁵-C₅H₄COOH)] (8):** Chromatographed on silica gel with 20% EtOAc/chloroform as eluent to give 0.31 g (84%) of **8** as an orange crystalline solid. M.p. 165 °C. $^1H$ NMR (300 MHz, $CDCl_3$): $\delta$ = 4.75 (br. s, 2 H, CpH), 5.06 (s, 2 H, $C_4$ ring), 5.40 (br. s, 2 H, CpH), 7.10–7.20 (m, 10 H, PhH) ppm. $^{13}C$ NMR (75 MHz, $CDCl_3$): $\delta$ = 54.2, 76.1 ($C_4$ ring), 85.3, 86.8, 92.5 (CpC), 124.8, 126.2, 128.6, 135.9 (PhC), 193.1 (COOH) ppm. IR (KBr): $\tilde{\nu}$ = 3053 m, 3023 m, 2912 m, 1659 vs, 1596 m, 1495 m, 1448 s, 1365 m, 1296 m, 1184 w, 1118 w, 1034 vs, 966 s, 758 vs, 695 vs, 541 s $cm^{-1}$. MS (FAB): *m*/*z* = 371 [$M^+$ – 1], 370 [$M^+$ – 2], 369 [$M^+$ – 3], 263 [$M^+$ – $CpCO_2Me$]. $C_{22}H_{17}CoO_2$ (372.05): calcd. C 70.97, H 4.60; found C 71.05, H 4.65.

**[*cis*-(η⁴-Ph₂H₂C₄)Co(η⁵-C₅H₄COOH)] (9):** Chromatographed on silica gel with 20% EtOAc/chloroform as eluent to give 0.29 g (78%) of **9** as an orange crystalline solid. M.p. 188 °C. $^1H$ NMR (300 MHz, $CDCl_3$): $\delta$ = 4.48 (s, 2 H, $C_4$ ring), 4.75 (s, 2 H, CpH), 5.18 (s, 2 H, CpH), 7.21–7.33 (s, 10 H, PhH) ppm. $^{13}C$ NMR (75 MHz, $CDCl_3$): $\delta$ = 58.3, 77.4 ($C_4$ ring), 86.4, 87.1, 92.2 (CpC), 126.2, 128.1, 128.6, 136.2 (PhC), 192.2 (COOH) ppm. IR (KBr): $\tilde{\nu}$ = 2927 w, 2625 w, 1674 vs, 1599 m,1480 w, 1421 m, 1354 w, 1295 vs, 1165 w, 1122 w, 1021 w, 947 m, 761 s, 694 s $cm^{-1}$. MS (ESI): *m*/*z* = 371 [$M^+$ – 1], 325 [$M^+$ – COOH]. $C_{22}H_{17}CoO_2$ (372.30): calcd. C 70.97, H 4.60; found C 71.07, H 4.69.

**[(η⁴-Ph₃HC₄)Co(η⁵-C₅H₄COOH)] (10):** Chromatographed on silica gel with 20% EtOAc/chloroform as eluent to give 0.38 g (85%)

 © 2006 Wiley-VCH Verlag GmbH & Co. KGaA, Weinheim 

of **10** as an orange crystalline solid. M.p. 180 °C. $^1$H NMR (300 MHz, $CDCl_3$): $\delta$ = 4.71 (br. s, 2 H, CpH), 5.02 (s, 1 H, $C_4$ ring), 5.27 (br. s, 2 H, CpH), 7.10–7.71 (m, 15 H, PhH) ppm. $^{13}$C NMR (75 MHz, $CDCl_3$): $\delta$ = 54.7, 76.0, 78.0 ($C_4$ ring), 86.4, 86.8, 92.2 (CpC), 125.0, 126.1, 127.2, 128.1, 128.5, 130.1, 135.2, 136.3 (PhC), 193.4 (C=O) ppm. IR (KBr): 3053 m, 2634 m, 2561 m, 2360 m, 1671 vs, 1598 m, 1480 vs, 1404 w, 1358 m, 1301 vs, 1166 s, 1023 w, 916 w, 823 w, 753 vs, 690 vs, 572 m cm$^{-1}$. MS (FAB): *m*/*z* = 448 [M$^+$], 449 [M$^+$ + 1], 431 [M$^+$ – OH], 339 [M$^+$ – $CpCO_2Me$]. $C_{28}H_{21}CoO_2$ (448.08): calcd. C 75.00, H 4.72; found C 75.09, H 4.65.

**General Procedure for the Reduction:** A 50-mL, two necked, round-bottomed flask was charged with $LiAlH_4$ (0.19 g, 5.0 mmol) and 30 mL of dry diethyl ether under nitrogen. The ester complex (1.0 mmol) was then added and the resulting mixture was stirred at room temperature for 24 h. The reaction was quenched by adding 25 mL of ethyl acetate and stirring for 0.5 h. After that solution was filtered through Whatman 40 filter paper, the solvent was evaporated and the residue was chromatographed on silica gel with a suitable eluent.

**[*trans*-($\eta^4$-$Ph_2H_2C_4$)Co($\eta^5$-$C_5H_4CH_2OH$)] (11):** Chromatographed on silica gel with chloroform as eluent to give 0.27 g (69%) of complex **11**. M.p. 95 °C. $^1$H NMR (300 MHz, $CDCl_3$): $\delta$ = 1.48 (s, 1 H, OH), 3.87 (s, 2 H, $OCH_2$), 4.39 (s, 2 H, $C_4$ ring H), 4.72 (s, 2 H, CpH), 4.86 (s, 2 H, CpH), 7.13 (s, 10 H, PhH) ppm. IR (KBr): $\tilde{\nu}$ = 3558 vs, 3056 m, 2921 s, 2856 s, 1592 s, 1499 s, 1447 s, 1394 m, 13639 w, 1262 w,1180 w, 1103 w, 1049 vs,1017 vs, 810 vs, 764 vs, 691 vs cm$^{-1}$. MS (FAB): *m*/*z* = 358 [M$^+$], 359 [M$^+$ + 1], 341 [M$^+$ – OH], 263 [M$^+$ – $CpCH_2OH$]. $C_{22}H_{19}CoO$ (358.07): calcd. C 73.74, H 5.34; found C 73.69, H 5.45.

**[($\eta^4$-$Ph_3HC_4$)Co($\eta^5$-$C_5H_4CH_2OH$)] (12):** Chromatographed on silica gel with chloroform as eluent to give 0.37 g (86%) of complex **12**. $^1$H NMR (300 MHz, $CDCl_3$): $\delta$ = 1.55 (s, 1 H, OH), 3.9 (s, 2 H, $OCH_2$), 4.97 (s, 2 H, CbH), 4.54 (s, 2 H, CpH), 4.78 (s, 2 H, CpH), 7.1–7.72 (m, 15 H, PhH). IR (KBr): $\tilde{\nu}$ = 3530 s, 3054 m, 2922 m, 1595 s, 1499 s, 1444 m, 1322 w, 1231 m, 1178 w, 1066 w,1000 vs, 818 s, 760 vs, 693 vs, 582 w cm$^{-1}$. MS (FAB): *m*/*z* = 435[M$^+$ + 1], 417[M$^+$ – OH]. $C_{28}H_{23}CoO$ (434.10): calcd. C 77.41, H 5.34; found C 77.55, H 5.24.

**X-ray Crystallographic Study:** Suitable crystals of complexes **1**–**7** and **11** were obtained by slow concentration of their saturated solutions in ethyl acetate/hexane solvent mixtures. Details of data collection and solution and crystal parameters are given in Tables 4 and 5. Single-crystal diffraction studies were carried out with a Bruker SMART APEX CCD diffractometer with an Mo-$K_\alpha$ ($\lambda$ = 0.71073 Å) sealed-tube radiation source. All crystal structures were solved by direct methods. The program SAINT (version 6.22) was used for integration of the intensity of reflections and scaling. The program SADABS was used for absorption correction.[19] The crystal structures were solved and refined using the SHELXTL (version 6.12) package.[20] All hydrogen atoms were included in idealized positions, and a riding model was used. Non-hydrogen atoms were refined with anisotropic displacement parameters. Because of the poor crystal quality of complex **1**, higher 2$\theta$ reflections were omitted to bring the value of the residual factor down. The oxygen atom of the alcohol group present in the cyclopentadienyl ring of complex **11** shows disorder and occupies two crystallographically independent positions which could be located from the additional residual electron density observed in the difference map. The site occupancy factors were refined with the help of the free variable

Table 4. X-ray crystallographic data for complexes **1**–**4**.

| | **1** | **2** | **3** | **4** |
|---|---|---|---|---|
| Empirical formula | $C_{29}H_{35}CoO_2Si_2$ | $C_{29}H_{35}CoO_2Si_2$ | $C_{32}H_{31}CoO_2Si$ | $C_{35}H_{27}CoO_2$ |
| Formula mass | 530.68 | 530.6 | 534.62 | 538.50 |
| Crystal system | orthorhombic | triclinic | triclinic | monoclinic |
| Space group | *Pbca* | $P\bar{1}$ | $P\bar{1}$ | $P2_1/n$ |
| *T* [K] | 298(2) | 298(2) | 298(2) | 298(2) |
| *a* (Å | 10.6624(11) | 9.256(2) | 9.1247(19) | 10.8340(15) |
| *b* [Å] | 20.098(2) | 9.381(2) | 11.255(2) | 16.982(2) |
| *c* [Å] | 26.255(3) | 16.219(5) | 13.342(3) | 14.279(2) |
| *a* [°] | 90 | 96.700(5) | 91.538(3) | 90 |
| *β* [°] | 90 | 98.844(4) | 101.728(3) | 92.587(2) |
| *γ* [°] | 90 | 91.188(3) | 92.523(3) | 90 |
| *V* [Å$^3$] | 5626.3(10) | 1381.0(6) | 1339.4(5) | 2624.4(6) |
| *Z* | 8 | 2 | 2 | 4 |
| $D_{calcd.}$ [g cm$^{-3}$] | 1.253 | 1.276 | 1.326 | 1.363 |
| $\mu$ [mm$^{-1}$] | 0.718 | 0.731 | 0.709 | 0.685 |
| $T_{max}/T_{min}$ | 0.927/0.826 | 0.939/0.907 | 0.941/0.849 | 0.929/0.859 |
| $\theta$ range [°] | 2.17–23.25 | 2.23–28.26 | 2.22–24.55 | 2.23–25.38 |
| Index ranges | $-11 \le h \le 11$ | $-11 \le h \le 11$ | $-11 \le h \le 11$ | $-13 \le h \le 13$ |
| | $-21 \le k \le 21$ | $-11 \le k \le 11$ | $-13 \le k \le 13$ | $-20 \le k \le 20$ |
| | $-28 \le l \le 28$ | $-19 \le l \le 19$ | $-16 \le l \le 16$ | $-17 \le l \le 17$ |
| Refl. collected | 40499 | 13657 | 13369 | 25438 |
| Refl. unique | 3690 | 5115 | 4985 | 25438 |
| Refl. observed | 3572 | 4829 | 4602 | 4435 |
| Restraint/parameters | 0/314 | 0/314 | 0/329 | 0/344 |
| Goodness of fit on $F^2$ | 1.446 | 1.076 | 1.065 | 1.199 |
| $R_1[I > 2\sigma(I)]$[a] | 0.0868 | 0.0309 | 0.0318 | 0.0479 |
| $wR_2$ (all data)[b] | 0.2027 | 0.0870 | 0.0882 | 0.1226 |
| $(\Delta\rho)_{max}/(\Delta\rho)_{min}$ | 0.555/–0.662 | 0.239/–0.381 | 0.299/–0.201 | 0.312/–0.392 |
| $\lambda$ [Å] | 0.71073 | 0.71073 | 0.71073 | 0.71073 |

[a] $R_1 = \Sigma||F_o| - |F_c||/\Sigma|F_o|$. [b] $wR_2 = \Sigma w(F_o^2 - F_c^2)^2/\Sigma[(F_o^2)^2]^{1/2}$.

 © 2006 Wiley-VCH Verlag GmbH & Co. KGaA, Weinheim 

Table 5. X-ray crystallographic data for complexes **5**–**7** and **11**.

| | **5** | **6** | **7** | **11** |
|---|---|---|---|---|
| Empirical formula | $C_{23}H_{19}CoO_2$ | $C_{23}H_{19}CoO_2$ | $C_{29}H_{23}CoO_2$ | $C_{22}H_{19}CoO$ |
| Formula mass | 386.31 | 386.31 | 462.40 | 358.30 |
| Crystal system | monoclinic | orthorhombic | orthorhombic | monoclinic |
| Space group | $P2_1$ | $P2$ | $Pcca$ | $P2_1$ |
| $T$ [K] | 273(2) | 273(2) | 273(2) | 273(2) |
| $a$ [Å] | 5.818(3) | 8.5776(12) | 41.122(5) | 10.463(5) |
| $b$ [Å] | 27.822(12) | 10.7107(15) | 10.7107(15) | 7.535(4) |
| $c$ [Å] | 10.967(5) | 19.950(3) | 10.0060(13) | 11.911(6) |
| $\alpha$ [°] | 90 | 90 | 90 | 90 |
| $\beta$ [°] | 91.226(8) | 90 | 90 | 113.528(7) |
| $\gamma$ [°] | 90 | 90 | 90 | 90 |
| $V$ [Å$^3$] | 1774.8(14) | 1832.8(5) | 4480.9(10) | 856.0(7) |
| $Z$ | 4 | 4 | 8 | 2 |
| $D_{calcd.}$ [g cm$^{-3}$] | 1.446 | 1.400 | 1.371 | 1.390 |
| $\mu$ [mm$^{-1}$] | 0.975 | 0.950 | 0.790 | 1.006 |
| $T_{max}/T_{min}$ | 0.927/0.888 | 0.872/0.816 | 0.500/0.391 | 0.913/0.863 |
| $\theta$ range [°] | 2.37–25.50 | 2.16–24.49 | 2.81–25.0 | 2.20–25.00 |
| Index ranges | $-7 \le h \le 7$ | $-10 \le h \le 10$ | $-48 \le h \le 48$ | $-12 \le h \le 12$ |
| | $-33 \le k \le 33$ | $-12 \le k \le 12$ | $-12 \le k \le 12$ | $-8 \le k \le 8$ |
| | $-13 \le l \le 13$ | $-24 \le l \le 24$ | $-11 \le l \le 11$ | $-14 \le l \le 14$ |
| Refl. collected | 17235 | 18108 | 39929 | 7793 |
| Refl. unique | 3362 | 3402 | 3936 | 1637 |
| Refl. observed | 3024 | 3208 | 3267 | 1571 |
| Restraint/parameters | 1/471 | 0/236 | 0/290 | 1/217 |
| Goodness of fit on $F^2$ | 1.017 | 1.140 | 1.064 | 1.137 |
| $R_1[I > 2\sigma(I)]$[a] | 0.0517 | 0.0339 | 0.0442 | 0.0974 |
| $wR_2$ (all data)[b] | 0.1194 | 0.0859 | 0.1120 | 0.2344 |
| $(\Delta\rho)_{max}/(\Delta\rho)_{min}$ | 0.653/–0.671 | 0.472/–0.328 | 0.517/–0.241 | 2.135/–1.089 |
| $\lambda$ [Å] | 0.71073 | 0.71073 | 0.71073 | 0.71073 |

[a] $R_1 = \Sigma||F_o| - |F_c||/\Sigma|F_o|$. [b] $wR_2 = \Sigma w(F_o^2 - F_c^2)^2/\Sigma[(F_o^2)^2]^{1/2}$.

PART instruction.[20] CCDC-614825, -614826, -614827, -614828, -614829, -614830, -614831 and -614832 (**1**–**7** and **11**, respectively) contain the supplementary crystallographic data for this paper. These data can be obtained free of charge from The Cambridge Crystallographic Data Centre via www.ccdc.cam.ac.uk/data_request/cif.

## Acknowledgments

The authors wish to thank the Council of Scientific and Industrial Research (CSIR), India, and the Department of Science and Technology (DST), India, for financial assistance in the form of research grants and IIT, Delhi, for an equipment grant. We acknowledge DST-FIST and IITD for funding of the single-crystal X-ray diffraction facility at IIT. We thank Dr. N. G. Ramesh, IIT, for valuable discussions. We thank Mr. N. K. Nautiyal and Mr. J. P. Singh of the Department of Chemistry, IIT, and Prof. P. S. Verma, University of Rajasthan, for assistance in spectral and electroanalytical measurements. Thanks are due to SAIF, CDRI Lucknow, for mass spectral and analytical measurements.

[1] a) D. M. Georganopoulou, R. Carley, D. A. Jones, M. G. Boutelle, *Faraday Discuss.* **2000**, *116*, 291–303; b) N. Adanyi, M. Toth-Markus, E. E. Szabo, M. Varadi, M. P. Sammartiono, M. Tomasetti, L. Campanella, *Anal. Chim. Acta* **2004**, *501*, 219–225; c) N. Ganesan, A. P. Gadre, M. Paranjape, J. F. Currie, *Anal. Biochem.* **2005**, *343*, 188–191.

[2] a) A. Hess, N. Metzler-Nolte, *Chem. Commun.* **1999**, *10*, 885–886; b) K. Eiko, M. Mizuta, T. Terada, M. Seikine, *J. Org. Chem.* **2005**, *70*, 10311–10315; c) K. Mukumoto, T. Nojima, S. Takenank, *Tetrahedron* **2005**, *61*, 11705–11715; d) M. Yang, I. Gao, P. He, Y. Fang, *Fenxi Huaxue* **2005**, *33*, 1469–1472; *Chem. Abstr.* **2005**, *144*, 66222.

[3] a) V. Chandrasekhar, K. Gopal, S. Nagendran, P. Singh, A. Steiner, S. Zacchini, J. F. Bickley, *Chem. Eur. J.* **2005**, *11*, 5437–5448; b) V. Chandrasekhar, V. Baskar, R. Boomishankar, K. Gopal, S. Zacchini, J. F. Bickley, A. Steiner, *Organometallics* **2003**, *22*, 3710–3716; c) V. Chandrasekhar, S. Nagendran, S. Bansal, M. A. Kozee, D. R. Powell, *Angew. Chem. Int. Ed.* **2000**, *39*, 1833–1835.

[4] a) W. Bauer, K. Polborn, W. Beck, *J. Organomet. Chem.* **1999**, *579*, 269–279; b) Y. Nishibayashi, K. Segawa, Y. Arkawa, K. Ohe, M. Hidai, S. Uemura, *J. Organomet. Chem.* **1997**, *545*, 381–398; c) C. J. Richards, A. W. Mulvaney, *Tetrahedron: Asymmetry* **1996**, *7*, 1419–1430.

[5] a) G. Jones, C. J. Richards, *Tetrahedron: Asymmetry* **2004**, *15*, 653–664; b) D. C. D. Butler, C. J. Richards, *Organometallics* **2002**, *21*, 5433–5436; c) G. Jones, C. J. Richards, *Organometallics* **2001**, *20*, 1251–1254; d) G. Jones, D. C. D. Butler, C. J. Richards, *Tetrahedron Lett.* **2000**, *41*, 9351–9354.

[6] J. Kang, T. H. Kim, K. H. Yew, W. K. Lee, *Tetrahedron: Asymmetry* **2003**, *14*, 415–418.

[7] a) C. E. Anderson, L. E. Overman, *J. Am. Chem. Soc.* **2003**, *125*, 12412–12413; b) S. F. Kirsch, L. E. Overman, M. P. Watson, *J. Org. Chem.* **2004**, *69*, 8101–8104; c) S. F. Kirsch, L. E. Overman, *J. Am. Chem. Soc.* **2005**, *127*, 2866–2867.

[8] R. S. Prasad, C. E. Anderson, C. J. Richards, L. E. Overman, *Organometallics* **2005**, *24*, 77–81.

[9] A. M. Stevens, C. J. Richards, *Organometallics* **1999**, *18*, 1346–1348.

[10] S. T. Mabrouk, M. D. Rausch, *J. Organomet. Chem.* **1996**, *523*, 111–117.

[11] M. Senthil Kumar, S. Upreti, H. P. Gupta, A. J. Elias, *J. Organomet. Chem.*, in press.

 © 2006 Wiley-VCH Verlag GmbH & Co. KGaA, Weinheim 

[12] M. Rosenblum, B. North, D. Wells, W. P. Giering, *J. Am. Chem. Soc.* **1972**, *94*, 1239–1246.
[13] a) J. A. Varela, C. Saa, *Chem. Rev.* **2003**, *103*, 3787–3801; b) D. K. MacFarland, R. Gorodetzer, *J. Chem. Educ.* **2005**, *82*, 109–110; c) M. D. Rausch, R. A. Genetti, *J. Org. Chem.* **1970**, *35*, 3888–3897; d) Y. Wakatsuki, O. Nomura, K. Kitaura, K. Morokuma, H. Yamazaki, *J. Am. Chem. Soc.* **1983**, *105*, 1907–1912; e) K. Yasafuku, H. Yamazaki, *J. Organomet. Chem.* **1977**, *127*, 197–207; f) H. Yamazaki, Y. Wakatsuki, *J. Organomet. Chem.* **1977**, *132*, 157–167.
[14] M. Rosenblum, C. Gatsonis, *J. Am. Chem. Soc.* **1967**, *89*, 5074–5075.
[15] C. Kabuto, J. Hayashi, H. Sakurai, Y. Kitahara, *J. Organomet. Chem.* **1972**, *43*, C23–C25.
[16] G. B. Robertson, *Nature* **1961**, *191*, 593–594.
[17] Y. Wakatsuki, H. Yamazaki, *Inorg. Synth.* **1989**, *26*, 189–200.
[18] H. Sakurai, J. Hayashi, *J. Organomet. Chem.* **1972**, *39*, 365–370.
[19] G. M. Sheldrick, **1996**, unpublished work based on the method described in: R. H. Blessing, *Acta Crystallogr., Sect. A* **1995**, S1–S33.
[20] a) G. M. Sheldrick, *Acta Crystallogr., Sect. A* **1990**, *46*, 467–473; b) G. M. Sheldrick, *SHELXTL-NT*, version 6.12, reference manual, University of Göttingen, Germany, **2000**.

Received: July 18, 2006
Published Online: October 18, 2006

 © 2006 Wiley-VCH Verlag GmbH & Co. KGaA, Weinheim 

DOI: 10.1002/ejic.200600676

# Redox Chemistry of a Dimanganese(II,III) Complex with an Unsymmetric Ligand: Water Binding, Deprotonation and Accumulative Light-Induced Oxidation

**Magnus F. Anderlund,[a] Joakim Högblom,[b] Wei Shi,[a] Ping Huang,[a] Lars Eriksson,[c] Högni Weihe,[d] Stenbjörn Styring,[a] Björn Åkermark,[e] Reiner Lomoth,*[a] and Ann Magnuson*[a]**

**Keywords:** Manganese / Bioinorganic chemistry / Ligand exchange / EPR spectroscopy / IR spectroscopy

A dinuclear manganese complex {[$Mn_2^{II,III}$L(μ-$OAc)_2$]-$ClO_4$} has been synthesised, where L is the dianion of 2-{[bis-(pyrid-2-ylmethyl)amino]methyl}-6-{[(3,5-di-*tert*-butyl-2-hydroxybenzyl)(pyrid-2-ylmethyl)amino]methyl}-4-methylphenol, an unsymmetric binucleating ligand with two coordinating phenol groups. The two manganese ions, with a Mn–Mn distance of 3.498 Å, are bridged by the two bidentate acetate ligands and the 4-methylphenolate group of the ligand, resulting in a $N_3O_3$ and $N_2O_4$ donor set of $Mn^{II}$ and $Mn^{III}$, respectively. Electrochemically [$Mn_2^{II,III}$L(μ-$OAc)_2$]$^+$ is reduced to [$Mn_2^{II,II}$L(μ-$OAc)_2$] at $E_{1/2}(1)$ = –0.53 V versus $Fc^{+/0}$ and oxidised to [$Mn_2^{III,III}$L(μ-$OAc)_2$]$^{2+}$ at $E_{1/2}(2)$ = 0.38 V versus $Fc^{+/0}$. All three redox states have been characterised by EPR, IR and UV/Vis spectroscopy. Subsequent oxidation of [$Mn_2^{II,III}$L(μ-$OAc)_2$]$^{2+}$ [$E_{1/2}(3)$ = 0.75 V vs. $Fc^{+/0}$] in dry acetonitrile results in an unstable primary product with a lifetime of about 100 ms. At high scan rates quasireversible voltammetric behaviour is found for all three electrode processes, with particularly slow electron transfer for the II,III/II,II [$k°(1)$ = 0.002 cm s$^{-1}$] and III,III/II,III [$k°(2)$ = 0.005 cm s$^{-1}$] couples, which can be rationalised in terms of major distortions of the $Mn^{III}$ centres. In aqueous media the bridging acetates are replaced by water-derived ligands. Deprotonation of these stabilises higher valence states, and photo-induced oxidation of the manganese complex results in a $Mn_2^{III,IV}$L complex with oxo or hydroxo bridging ligands, which is further oxidised to an EPR-silent product. These results demonstrate that a larger number of metal-centred oxidations can be compressed in a narrow potential range if build up of charge is avoided by charge-compensating reactions.
(© Wiley-VCH Verlag GmbH & Co. KGaA, 69451 Weinheim, Germany, 2006)

## Introduction

The utilisation of solar energy for fuel production, through a molecular system for artificial photosynthesis, is an attractive solution to the need for renewable energy.[1] In natural photosynthesis, solar energy is used to extract electrons from water.[2] Photo-induced charge separation in the Photosystem II (PSII) reaction centre leads to oxidation of the water-oxidising complex (WOC), a catalyst consisting of a protein-bound cluster with four manganese ions and one calcium ion.[3,4] After four consecutive one-electron transfer events, the WOC retrieves four electrons from water and releases molecular oxygen.[3,5] During catalysis, the WOC cycles through five redox states.[6,7] The manganese ions are mostly in the $Mn^{III}$ oxidation state or higher, and several of the intermediates involve manganese-centred oxidation.[7–9]

Synthetic manganese complexes have been extensively studied as model systems for the WOC but functional mimics that are able to evolve molecular oxygen from water are very few in number.[10,11] They require electrochemical oxidation at highly anodic potentials or strong chemical oxidants. In the latter case the formation of the important Mn-oxo intermediate often relies on oxygen atom transfer from the oxidant rather than from water.[11]

In our work towards artificial photosynthesis, we pursue supramolecular complexes in which the Mn portion undergoes accumulative oxidation by *light-induced* charge separation.[12–14] With the ultimate goal of photochemical water splitting, this requires Mn complexes that can un-

[a] Department of Photochemistry and Molecular Science, Uppsala University,
P. O. Box 523, 75120 Uppsala, Sweden
E-mail: ann.magnuson@fotomol.uu.se
reiner.lomoth@fotomol.uu.se
[b] Department of Biochemistry, Department of Chemistry, Lund University,
P. O. Box 124, 22100 Lund, Sweden
[c] Division of Structural Chemistry, Arrhenius Laboratories, Stockholm University,
10691 Stockholm, Sweden
[d] Department of Chemistry, University of Copenhagen,
Universitetsparken 5, 2100 Copenhagen, Denmark
[e] Department of Organic Chemistry, Arrhenius Laboratories, Stockholm University,
10691 Stockholm, Sweden
Supporting information for this article is available on the WWW under http://www.eurjic.org or from the author.

 © 2006 Wiley-VCH Verlag GmbH & Co. KGaA, Weinheim 

dergo four oxidation steps within the thermodynamic limit of the photo-oxidant. On the other hand, all stored oxidation equivalents need to be sufficiently oxidising, with an average potential of 0.8 V (at pH 7), to be capable of driving the catalytic oxidation of water.[15] In the WOC all four single-electron oxidations of the $Ca(Mn)_4$ cluster occur within an interval of only 0.25–0.3 V at potentials close to the limit (ca. 1 V vs. NHE[15]) given by the oxidising $Tyr_Z$ radical. This compression of oxidation potentials is a result of charge-compensating deprotonation reactions and it is evident that a suitable mechanism for charge compensation is a central feature in the design of synthetic mimics.

In previous studies we could show that oxidation of the manganese dimer $[Mn_2(bpmp)(\mu\text{-}OAc)_2]^+$[16] in the presence of water involves exchange of the bridging acetates for water-derived ligands that are increasingly deprotonated in higher oxidation states.[17,18] The resulting charge compensation stabilises higher valence states and thereby allows for three metal-centred oxidations, from the $Mn_2^{II,II}$ dimer to a $Mn_2^{III,IV}$ species, to be driven by photo-generated $Ru^{II\text{-}I}(bpy)_3$.[13,17,19,20] The binding of water, deprotonation of bridging ligands and accumulative, light-induced oxidation of $[Mn_2(bpmp)(\mu\text{-}OAc)_2]^+$ mimic important aspects of the catalytic complex in PSII and we therefore set out to investigate modifications of the structural motif. With consideration to the prevalence of high-valent manganese species and the high O/N ratio in the ligand sphere of the $Ca(Mn)_4$ complex in PSII, we synthesised analogous dinuclear manganese complexes, with an increased number of phenolic ligand functions. In $[Mn_2(bhpp)(\mu\text{-}OAc)_2]^+$[19,21] two additional phenol groups of the bhpp ligand result in an oxygen-to-nitrogen ratio of 4:2. Compared to $[Mn_2(bpmp)(\mu\text{-}OAc)_2]^+$ with O/N = 3:3, the potentials for the manganese redox couples are lowered substantially and the oxidation equivalents stored on $[Mn_2(bhpp)(\mu\text{-}OAc)_2]^+$ are on average not sufficiently oxidising with respect to water oxidation.

In the present study we report a new di-μ-acetato-bridged dinuclear manganese complex, **5** ($[Mn_2L(\mu\text{-}OAc)_2]^+$), with an unsymmetric ligand molecule, L = 2-{[bis(pyrid-2-ylmethyl)amino]methyl}-6-{[(3,5-di-*tert*-butyl-2-hydroxybenzyl)(pyrid-2-ylmethyl)amino]methyl}-4-methylphenol. With a $N_3O_3/N_2O_4$ coordination sphere, the new complex is an intermediate between the $[Mn_2(bpmp)(\mu\text{-}OAc)_2]^+$ and $[Mn_2(bhpp)(\mu\text{-}OAc)_2]^+$ complexes. We chose to synthesise an unsymmetric ligand, as we anticipated that a compromise between the need for high valent Mn states and sufficiently high redox potentials could be accomplished with the intermediate O/N ratio. Here we present the synthesis and characterisation of the new manganese complex and its redox properties in anhydrous and partially aqueous solutions, including photo-oxidation studies.

Unsymmetric ligands have previously been used to a limited extent for coordinating manganese, mainly for mimicking the active site of manganese catalases,[22–25] or to support the formation of heterobinuclear metal complexes.[22,26] As a novelty in the present study, photo-oxidation of complex **5** generates products beyond the $Mn_2^{III,IV}$ level, which is not the case with $[Mn_2(bpmp)(\mu\text{-}OAc)_2]$, while the potentials are above those of $[Mn_2(bhpp)(\mu\text{-}OAc)_2]^+$. The favourable behaviour of the novel complex can be attributed to the combination of the flexible bridging motif that is inherent to this type of complex and the intermediate O/N ratio of the chelating ligand. These findings point to the intricate balance of donor properties in the set of permanent and flexible ligands that will be needed for functional mimics of the WOC suitable for photo-induced water oxidation.

## Results and Discussion

### Synthesis and Characterisation

#### *Synthesis*

The synthesis route for the preparation of compound **5** is described in Scheme 1. The synthesis of the unsymmetrical ligand $H_2L$ (**4**) is based on the unsymmetrical phenol **1**.[27] Compound **2** was obtained by letting phenol **1** react with 1 equiv. of (3,5-di-*tert*-butyl-2-hydroxybenzyl)(2-pyridylmethyl)amine[21] and 2 equiv. of $Et_3N$ in $CH_2Cl_2$ under reflux. Compound **3** was then obtained by reduction of **2** with $NaBH_4$ in methanol and thereafter chlorinated with $SOCl_2$ in dry $CH_2Cl_2$.

The unsymmetrical ligand $H_2L$ (**4**) is produced by amination by nucleophilic attack on the benzylic chloride in **3** with bis-picolylamine[28] and $Et_3N$ in $CH_2Cl_2$ under reflux. The yield was excellent in the first two steps (95.1 and 97.5%) but only moderate in the last step (67.4%), possibly because of steric hindrance of the two *tert*-butyl groups on the phenol.

The complexation of $H_2L$ with $MnOAc_3{\cdot}2H_2O$ in ethanol under argon affords the stable dimanganese(II,III) complex **5** after addition of $NaClO_4{\cdot}H_2O$ in 52% yield. We have not been able to isolate any $Mn_2^{III,III}$ complex under these conditions. The reduction of $Mn^{III}$ to $Mn^{II}$ was possibly done by the solvent or by disproportionation of $Mn^{III}$ to $MnO_2$ and $Mn^{II}$ in the presence of water. Though we have not detected any $MnO_2$, we cannot rule out that colloidal $MnO_2$ was present in the solution after the complexation. However, the slow and well-behaved crystal growth, as well as the purity of the crystals established by elemental analysis, indicates that any impurities in the mother liquor were successfully removed prior to characterisation of **5**.

#### *X-ray Structure Determination*

The crystal structure of **5** (Figure 1) is of a monovalent cation, counterbalanced with a perchlorate ion (not shown). The displacement parameters of the perchlorate are heavily anisotropic, in agreement with a weakly coordinated perchlorate ion, and there are no ordered solvent molecules present in the structure. The manganese ions are bridged by the oxygen in the central 4-methylphenolate and the two bidentate acetates. The slightly distorted octahedral coordination of Mn(1) is completed by the two pyridyl nitrogen

 © 2006 Wiley-VCH Verlag GmbH & Co. KGaA, Weinheim 

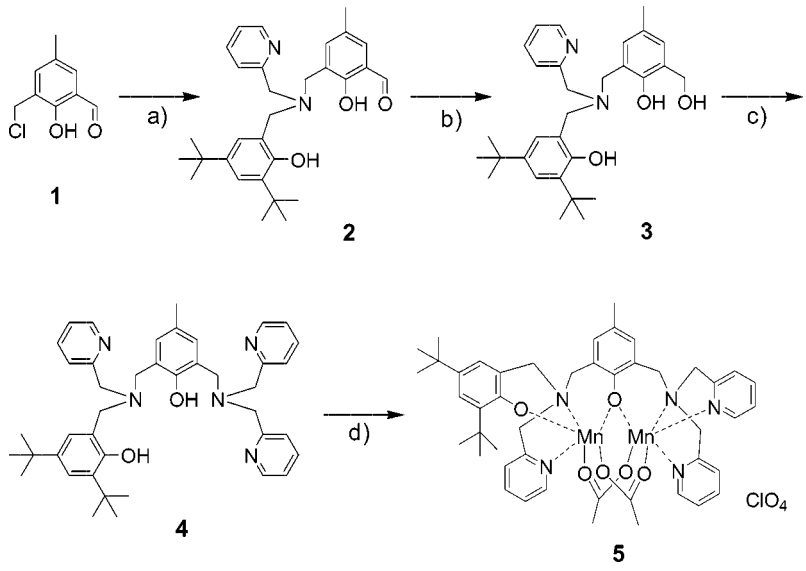


Scheme 1. Reaction conditions are as follows: (a) (3,5-di-*tert*-butylbenzyl-2-hydroxy)(2-pyridylmethyl)amine, $CH_2Cl_2$, reflux; (b) $NaBH_4$, MeOH, room temperature; (c) 1. $SOCl_2$, $CH_2Cl_2$, 2. DPA, $Et_3N$, $CH_2Cl_2$, reflux; (d) $MnOAc_3{\cdot}2H_2O$, EtOH, 60 °C, $NaClO_4{\cdot}H_2O$.

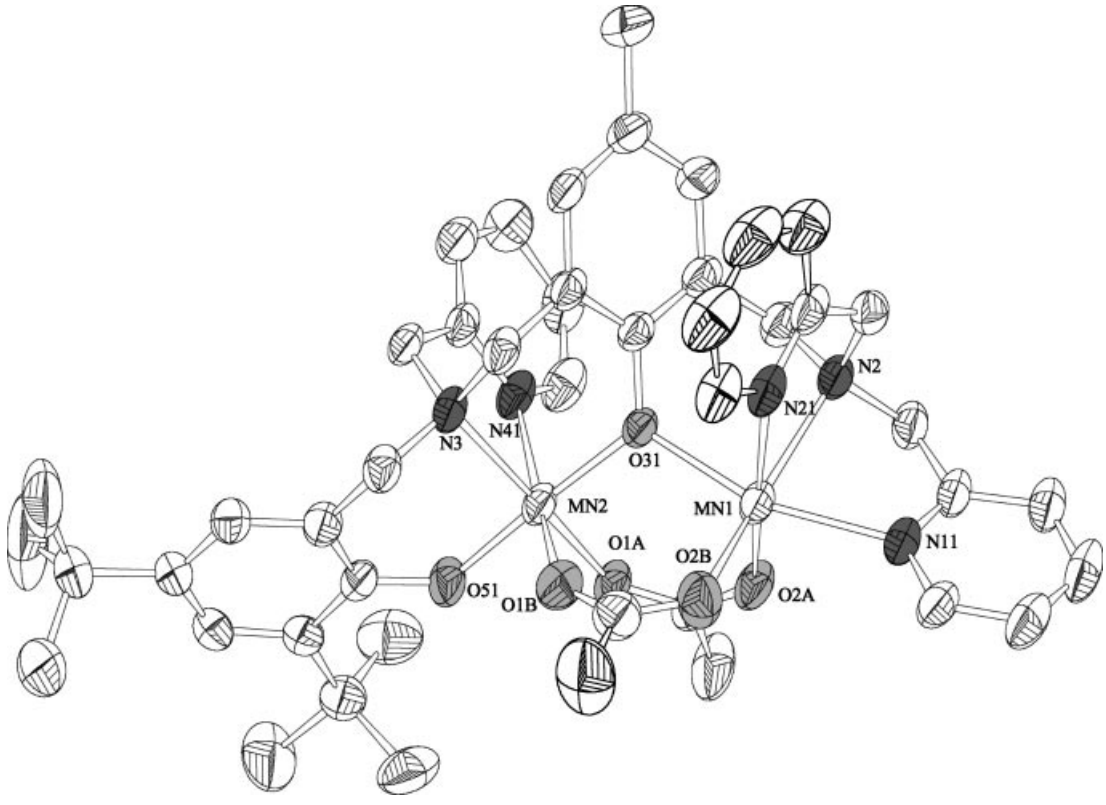


Figure 1. ORTEP view (30% probability ellipsoids) of **5** with atomic numbering for all non-hydrogen atoms. The hydrogen atoms were geometrically placed and shown as small circles of arbitrary radii. Figure drawn by Diamond.

atoms and one amine nitrogen atom of one branch of the ligand, resulting in a $N_3O_3$ ligand sphere. The oxygen atom from the *tert*-butyl-substituted phenolate coordinates Mn(2) in a *trans* position to the bridging phenolate group. The $N_2O_4$ coordination sphere of Mn(2) is completed by the pyridyl and amine nitrogens.

Selected bond lengths and angles are found in Table 1. Bond valence calculations gave 2.1 for Mn(1) and 3.2 for Mn(2) in agreement with the different donor sets and coordination symmetries of the two manganese ions.[29]

Mn(2) has a more distorted octahedral geometry, consistent with its assignment as $Mn^{III}$. For Mn(2), the shortest

 © 2006 Wiley-VCH Verlag GmbH & Co. KGaA, Weinheim 

Table 1. Selected bond lengths [Å] and angles [°] for **5**. The distances and angles given describe the coordination polyhedron around each Mn and the orientation of the two polyhedrons with respect to each other.

| | | | |
|---|---|---|---|
| Mn1···Mn2 | 3.4985(15) | Mn1–O31–Mn2 | 116.95(18) |
| Mn1–O2b | 2.089(5) | Mn2–O51 | 1.820(4) |
| Mn1–O2a | 2.127(4) | Mn2–O31 | 1.922(4) |
| Mn1–O31 | 2.179(4) | Mn2–O1a | 1.972(4) |
| Mn1–N11 | 2.255(5) | Mn2–N3 | 2.114(4) |
| Mn1–N21 | 2.280(5) | Mn2–O1b | 2.154(5) |
| Mn1–N2 | 2.317(5) | Mn2–N41 | 2.266(6) |
| O2B–Mn1–O2A | 99.6(2) | O51–Mn2–O31 | 177.1(2) |
| O2B–Mn1–O31 | 100.98(19) | O51–Mn2–O1A | 86.47(18) |
| O2A–Mn1–O31 | 88.28(15) | O31–Mn2–O1A | 92.05(16) |
| O2B–Mn1–N11 | 102.2(2) | O51–Mn2–N | 89.93(18) |
| O2A–Mn1–N11 | 86.06(17) | O31–Mn2–N3 | 91.96(17) |
| O31–Mn1–N11 | 156.78(19) | O1A–Mn2–N3 | 169.45(18) |
| O2B–Mn1–N21 | 91.0(2) | O51–Mn2–O1B | 89.5(2) |
| O2A–Mn1–N21 | 169.2(2) | O31–Mn2–O1B | 88.16(19) |
| O31–Mn1–N21 | 87.68(15) | O1A–Mn2–O1B | 97.3(2) |
| N11–Mn1–N21 | 93.77(18) | N3–Mn2–O1B | 92.57(19) |
| O2B–Mn1–N2 | 164.6(2) | O51–Mn2–N41 | 96.5(2) |
| O2A–Mn1–N2 | 94.82(18) | O31–Mn2–N41 | 86.05(18) |
| O31–Mn1–N2 | 84.88(16) | O1A–Mn2–N41 | 92.22(19) |
| N11–Mn1–N2 | 73.20(19) | N3–Mn2–N41 | 78.33(19) |
| N21–Mn1–N2 | 74.9(2) | O1B–Mn2–N41 | 169.02(19) |

Mn–O bond length is that of the *tert*-butyl-substituted phenoxyl (O51), and the bridging phenoxyl provides the second shortest Mn–O bond length. Thus, in contrast to the coordination sphere of Mn(1), the two bridging acetate ligands provide the longest Mn–O bonds. A similar, although less enhanced, effect was also observed for the $Mn^{III}$ ion in the $[Mn_2^{II,III}(bpmp)(\mu\text{-}OAc)_2]^{2+}$ structure.[16] The ligand sphere of Mn(2) is therefore very compressed along the O–Mn–O axis, which is 0.21 Å shorter than the corresponding molecular axis of the $Mn^{III}$ ion in $[Mn_2^{II,III}(bpmp)(\mu\text{-}OAc)_2]^{2+}$. The O–Mn–N axis formed by the pyridyl nitrogen and the carboxyl oxygen *trans* to it is quite long, making the Mn(2) coordination even more distorted, consistent with the Jahn–Teller effects that are common for $Mn^{III}$ complexes. The Mn–Mn distance is 3.498 Å, and the $Mn^{II}$–O–$Mn^{III}$ angle is 116.95°, which is in the range of other $Mn_2^{II,III}$ complexes.[16,25,30]

In conclusion, the crystal structure shows that the terminal phenoxyl in one branch of the ligand favours coordination of $Mn^{III}$ over $Mn^{II}$, and that its axial position introduces an unusually large distortion away from octahedral symmetry.

### *Magnetic Susceptibility*

The experimentally determined magnetic susceptibilities in the temperature range 4.45–301 K are shown in Figure 2. At room temperature, the effective magnetic moment is 7.20, which is slightly lower than the value 7.68 expected for a $Mn^{II}Mn^{III}$ dimer in which the metals are weakly antiferromagnetically interacting. The magnetic moment decreased smoothly from 298 K to 50 K, and then more abruptly down to 3 K. This behaviour is expected for an antiferromagnetically coupled $Mn_2^{II,III}$ complex with moderate exchange coupling.[16,30] At the lowest temperatures the magnetic moment was 1.79, which compares well with the value 1.73 expected for an $S = 1/2$ ground state.

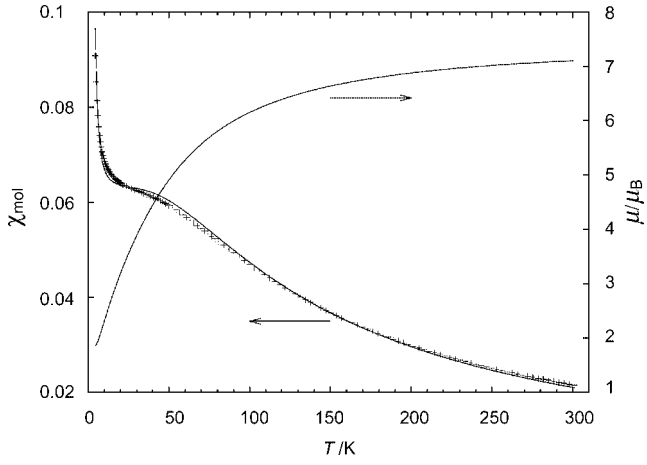


Figure 2. The magnetic susceptibility (+) and a fitted curve based on Equation (1) (solid line) in CGS units, as well as the effective magnetic moment as a function of temperature.

For known $Mn_2^{II,III}$ complexes the exchange coupling between the two manganese ions is rather weak, compared to that in $Mn_2^{III,IV}$ complexes, and typically ranges between about 0 and 10 $cm^{-1}$.[25,30,31] When analysing the susceptibility data for **5**, it proved impossible to satisfactorily interpret the magnetic susceptibilities in terms of an isotropic spin Hamiltonian (Model 1 in Table 2). As the zero-field splitting parameter $D$ of $Mn^{III}$ is often of the same order of magnitude as the exchange coupling $J$, the Hamiltonian was augmented with a term accounting for the magnetic anisotropy of the $Mn^{III}$ ion,

$$H = J\,\hat{\mathbf{S}}_2\cdot\hat{\mathbf{S}}_3 + \mu_B\mathbf{B}\cdot\mathbf{g}\cdot(\hat{\mathbf{S}}_2 + \hat{\mathbf{S}}_3) + D_3[\hat{\mathbf{S}}^2_{3z} - \frac{1}{3}S(S+1)] \quad (1)$$

Table 2. Results from fitting magnetic susceptibility data. Models 1 and 2 refer to Equation (1) without and with the third term, respectively.

| | Model 1 | Model 2 |
|---|---|---|
| $J$ [$cm^{-1}$] | $11.0 \pm 0.05$ | $10.9 \pm 0.3$ |
| $D_3$ [$cm^{-1}$] | – | $3.35 \pm 0.4$ |
| TIP ($\times 10^{-12}$) | $-5.05 \pm 1.19$ | $-3.95 \pm 4.97$ |
| Curie ($\times 10^{-11}$) | $4.04 \pm 1.90$ | $25 \pm 4.5$ |
| $\chi^2$ | 131.9 | 100 |
| $f$-test | – | 0.07 |
| No. of fit parameters | 3 | 4 |
| Degrees of freedom | 137 | 136 |
| No. of points | 140 | 140 |

In Equation (1) the subscripts refer to the oxidation numbers of the metal ions. By inclusion of the last term in Equation (1), the following parameters were obtained: $J = 10.9 \pm 0.3$ $cm^{-1}$ and $D_3 = 3.35$ $cm^{-1}$ (Model 2 in Table 2). The relatively large and positive zero-field parameter $D_3$ reflects to some degree the coordination geometry of the

 © 2006 Wiley-VCH Verlag GmbH & Co. KGaA, Weinheim 

$Mn^{III}$ ion. Six-coordinated $Mn^{III}$ complexes with distorted octahedral coordination typically display $D$ values of –3 to –4 $cm^{-1}$. However, deviations occur, for example, when the ligand field has low symmetry in the equatorial plane, as in **5**, and the increased rhombicity of the ZFS parameters can lead to a change in sign to positive values of $D$.[32]

### *IR Spectroscopy*

The IR spectrum of **5** in a KBr pellet was recorded between 4000 and 400 $cm^{-1}$ (Supporting information). Based on characteristic frequencies the following assignments are suggested in agreement with the composition of the complex: 3062 (w, $\nu$C–H, aryl); 2952, 2867 (m, $\nu$C–H, alkyl); 1590 (s, $\nu_a$C–O, carboxylate); 1441 (s, $\nu_s$C–O, carboxylate); 1477, 1435 (s, $\nu$C–C, aryl); 1094 (s, $\nu_a$Cl–O, perchlorate); 623 (m, $\delta_a$Cl–O, perchlorate) $cm^{-1}$.

The IR spectrum of **5** in [$D_3$]acetonitrile solution (Supporting Information) is identical to the solid state spectrum, which provides strong evidence that the di-μ-acetato bridging structure established for crystalline **5** is maintained in anhydrous acetonitrile solution.

### *EPR Spectroscopy*

The EPR spectrum of **5** in anhydrous acetonitrile is shown in Figure 3, spectrum a. The spectrum recorded at 4 K shows the $Mn_2^{II,III}$ $S$ = 1/2 ground-state EPR signal, centred at $g$ = 2 and displaying 16–20 hyperfine-lines, with a peak split of 110–140 gauss. The mixed-valence forms of dinuclear manganese complexes, $Mn_2^{II,III}$ and $Mn_2^{III,IV}$, are known to display similar ground-state EPR signals in the $g$ = 2 region at cryogenic temperatures.[33] The acetato-bridged $Mn_2^{II,III}$ complexes normally show a weaker exchange coupling than μ-oxo-bridged $Mn_2^{III,IV}$ complexes, because of less orbital overlap between the Mn ions. The excited $S$ = 3/2 and $S$ = 5/2 states in the $Mn_2^{II,III}$ complexes will then give rise to transitions at low field, at relatively low temperatures (5–20 K). Thus, when the temperature was raised from 4 K to 5–11 K, the first excited state ($S$ = 3/2) gave rise to a signal at $g$ = 5.4 (Figure 3, inset).

The spectrum from complex **5** (Figure 3, a) could be simulated assuming an effective spin of $S$ = 1/2, and using the spin Hamiltonian

$$\hat{H} = \beta\,\hat{\mathbf{S}}\cdot\mathbf{g}\cdot\mathbf{B} + \hat{\mathbf{I}}_1\cdot\mathbf{A}_1\cdot\hat{\mathbf{S}} + \hat{\mathbf{I}}_2\cdot\mathbf{A}_2\cdot\hat{\mathbf{S}} \quad (2)$$

(A full account of the EPR simulation parameters at both X- and Q-bands, as well as simulated spectra, was published by Huang et al.[34]) The obtained hyperfine tensors showed considerable anisotropy,[35] which could be explained by a significant Jahn–Teller distortion of $Mn^{III}$, taking into account the unexpected positive sign of the zero-field parameter $D$. These spectroscopic properties are a direct result of the rhombic distortion of the $Mn^{III}$ coordination sphere.

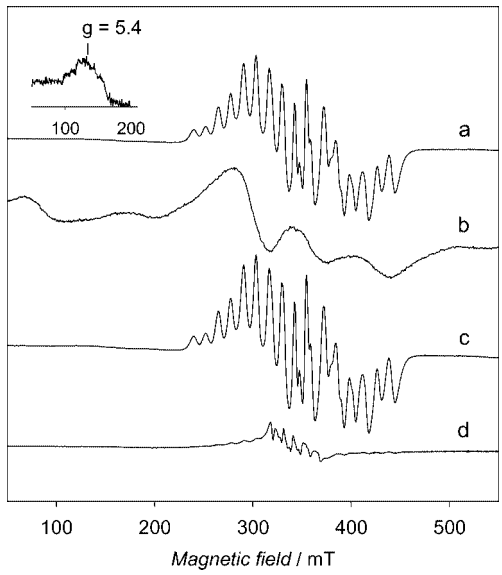


Figure 3. EPR spectra recorded by exposing **5** to controlled potentials. (a) After applying –0.08 V to the sample solution. The spectrum arises from the $S$ = 1/2 ground spin state of the $Mn_2^{II,III}$ complex. No current was recorded at this potential. (b) After reduction at –0.93 V a spectrum typical of a weakly coupled $Mn_2^{II,II}$ complex is observed. (c) Recovery of the $Mn_2^{II,III}$ complex after reoxidation at –0.08 V of the sample giving spectrum b. (d) After oxidation at 0.57 V. The spectrum can be identified as a remaining fraction (5%) of $Mn_2^{II,III}$ complexes, still present after bulk electrolysis. In the centre of the spectrum, a six-line signal from monomeric $Mn^{II}$ can be distinguished, corresponding to less than 2% of the manganese. Spectrometer settings: microwave frequency, 9.6 GHz; modulation amplitude, 10 G; microwave power spectrum a and c, 20 mW; in spectrum b, 2 mW; temperature in spectra a, c and d, 4 K; in spectrum b, 12 K. Insert: the signal at $g$ = 5 arising from the excited $S$ = 3/2 spin state of **5**, observed at $T > 5$ K.

## Redox Properties in Anhydrous Media

### *Electrochemistry*

The redox behaviour of **5** in acetonitrile was studied by cyclic voltammetry (CV), differential pulse voltammetry (DPV) and controlled potential electrolysis. The products of the oxidation and reduction processes were characterised by EPR spectroscopy and UV/Vis and IR spectroelectrochemisty. The electrochemical data are compiled in Table 3. All potentials are referenced versus ferrocene as redox standard and about 0.4 V should be added to these values in order to compare them with potentials in aqueous solution versus NHE.[36]

Voltammograms of **5** in acetonitrile solution (Figure 4) showed reversible to quasireversible CV waves for reduction at $E_{1/2}$ = –0.53 V (1) and oxidation at $E_{1/2}$ = 0.38 V versus $Fc^+/Fc^0$ (2) while further oxidation was irreversible on the normal CV time scale ($v$ = 0.100 $V\,s^{-1}$). At higher scan rates on a microelectrode, the second oxidation gave rise to a quasireversible CV wave with the half-wave potential $E_{1/2}$ = 0.75 V (3) in good agreement with the DPV peak potential. Chemical reversibility was obtained for scan rates of $v \geq$ 10 $V\,s^{-1}$ and a lower limit of the lifetime of the product of the second oxidation of about 100 ms (at room tempera-

 © 2006 Wiley-VCH Verlag GmbH & Co. KGaA, Weinheim 

Table 3. Electrochemical data for $[Mn_2L(\mu\text{-}OAc)_2]^+$ in acetonitrile.

| Redox process | (1) | (2) | (3) |
|---|---|---|---|
| Mn ox. states | II,III/II,II | III,III/II,III | –[a] |
| $E_{1/2}$[b] [V] | –0.535 | 0.380 | 0.755 |
| $\Delta E_p(0.1)$[c,d] [mV] | 70 | 100 | –[e] |
| $\Delta E_p(100)$[c,f] [mV] | 580 | 495 | 190 |
| $k^\circ$[f,g] [$10^{-3}$ cm s$^{-1}$] | 2 | 5 | 100 |

[a] Not assigned. [b] Half-wave potential ± 0.02 V vs. ferrocene/ferrocenium. [c] Peak split (scan rate in volts per second). [d] Glassy carbon electrode. [e] Irreversible at 0.1 V s$^{-1}$. [f] Pt microdisk electrode. [g] Apparent standard rate constant from digital simulation of cyclic voltammograms taking $\alpha = 0.5$ and $D = 1 \times 10^{-5}$ cm$^2$ s$^{-1}$.

ture) could be estimated. The reduction and the first oxidation of **5** are one-electron processes as evidenced by coulometry during controlled potential electrolysis at –0.93 and 0.57 V, respectively. We could not obtain reliable coulometric data for the second oxidation because of the instability of the product, but the voltammetric peak heights suggested the assignment to a one-electron process.[37]

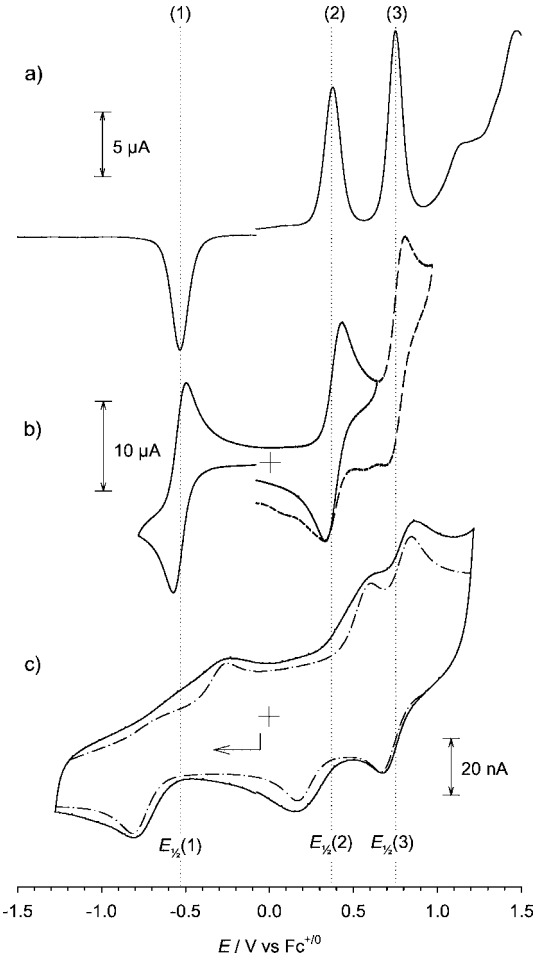


Figure 4. Voltammograms of **5** (1 mM) in acetonitrile with $(n\text{-}C_4H_9)_4N{\cdot}ClO_4$ (0.1 M) as supporting electrolyte. (a) Differential pulse voltammogram (step potential 5 mV, modulation amplitude 25 mV, modulation time 50 ms, interval time 100 ms, glassy carbon disk, 3 mm). (b) Cyclic voltammograms ($v = 0.100$ V s$^{-1}$, glassy carbon disk, 3 mm). (c) Cyclic voltammogram ($v = 100$ V s$^{-1}$, Pt microdisk, 25 μm) and digital simulation (– · –) with the parameters from Table 1.

The electrode processes (1) and (2) exhibited much larger CV peak splits at high scan rates than process (3) (Figure 4). This strongly non-Nernstian behaviour is indicative of slow heterogeneous electron transfer. We could obtain the standard rate constants $k^\circ$ to a close approximation by digital simulations (Figure 4, c) using a model of three quasireversible waves and the parameters given in Table 3. Neglecting work terms, the standard rate constant for a heterogeneous electron transfer reaction is given by

$$k^\circ = Z_{het}\left\{e^{-\lambda/(4kT)}\right\} \quad (3)$$

where $Z_{het}$ is the collision factor and $\lambda$ is the reorganisation energy.[38] For **5** we obtain

$$Z_{het} = (RT/2\pi M)^{1/2} = 2.2 \times 10^3 \text{ cm s}^{-1} \quad (4)$$

($M = 883$ g mol$^{-1}$) and can estimate approximate reorganisation energies of 1.4, 1.3 and 1.0 eV for the electrode processes (1), (2) and (3), respectively. The contribution of the solvent reorganisation can be estimated as $\lambda_{solv} \leq 0.3$ eV.[39] This would indicate that the electrode reactions, in particular (1) and (2), are associated with large inner reorganisation energies of $\lambda_i \approx 1$ eV. A similar estimate of $\lambda_i$ based on crystallographic data for the II,III/II,II couple of $[Mn_2(bpmp)(\mu\text{-}OAc)_2]^{2+/+}$ has been presented and can explain the unusually slow electron transfer observed in electron transfer dyads and triads that involve manganese complexes as donor units.[14,40] For the $Mn^{II}/Mn^{III}$ couples this can be attributed to the Jahn–Teller distortion associated with the high-spin $d^4$ configuration of the $Mn^{III}$ centre. The significantly smaller reorganisation energy for the second oxidation implies that the coordination geometry changes are less pronounced between $Mn^{III}$ and $Mn^{IV}$ or that this process is a ligand-based rather than a metal-centred oxidation.

### *Spectroscopic Characterisation of the Oxidation and Reduction Products*

The one-electron reduction product was prepared by bulk electrolysis at –0.93 V. Its EPR spectrum (Figure 3b) is typical for a weakly antiferromagnetically coupled $Mn_2^{II,II}$ complex and the reduction of **5** can be attributed to the metal-centred process (5).

$$[Mn_2^{II,III}L(\mu\text{-}OAc)_2]^+ + e^- \rightarrow [Mn_2^{II,II}L(\mu\text{-}OAc)_2] \quad (5)$$

$Mn_2^{II,II}$ is an integral spin system, where the diamagnetic ($S = 0$) ground state dominates at liquid He temperatures and accordingly we did not detect any EPR signals at 4 K. Weakly coupled $Mn_2^{II,II}$ complexes are, on the other hand, known to display EPR-active excited states at temperatures above about 7 K, similar to that in Figure 3, spectrum b.[41] We therefore conclude that the spectrum in Figure 3 (b), which was recorded at 12 K, originates from a superposition of one or more excited spin states from $Mn_2^{II,II}$ with $S = 1, 2, \ldots$. When $[Mn^{II}{}_2L(\mu\text{-}OAc)_2]$ was reoxidised by elec-

 © 2006 Wiley-VCH Verlag GmbH & Co. KGaA, Weinheim 

trolysis at –0.08 V, the $Mn_2^{II,III}$ spectrum of **5** was quantitatively recovered (Figure 3, c), confirming the stability of $[Mn^{II}{}_2L(\mu\text{-}OAc)_2]$.

The one-electron oxidation product was produced by bulk electrolysis at 0.57 V. The product is EPR-silent and the spectrum only showed a residual (5%) of the original $Mn_2^{II,III}$ signal (Figure 3, d). $Mn_2^{III,III}$, which is an integral spin system, might produce EPR-active states at higher temperatures, but so far no EPR signals from this valence state in either parallel or perpendicular mode EPR at X-band frequencies have been found by us or other researchers. Therefore, the EPR-silent product of the first oxidation can be assigned to$[Mn_2^{III,III}L(\mu\text{-}OAc)_2]^{2+}$ according to equation (6).

$$[Mn_2^{II,III}L(\mu\text{-}OAc)_2]^{+} \rightarrow [Mn_2^{III,III}L(\mu\text{-}OAc)_2]^{2+} + e^- \quad (6)$$

After reduction of $[Mn_2^{III,III}L(\mu\text{-}OAc)_2]^{2+}$at –0.08 V about 95% of the original $Mn_2^{II,III}$ signal was recovered (not shown). A slow degradation reaction of $[Mn_2^{III,III}L(\mu\text{-}OAc)_2]^{2+}$ resulted in the release of minor amounts of monomeric $Mn^{II}$ that could be observed in the spectra of the oxidised and re-reduced material (2% and 5% of the total Mn respectively), where it gave rise to the weak EPR signal around $g = 2$ with six hyperfine lines at a separation of about 100 gauss (Figure 4, d).

The short-lived primary product of the second oxidation could not be prepared by bulk electrolysis. After electrolysis at 0.82 V a significant amount of monomeric $Mn^{II}$ was observed by EPR, obscuring any other paramagnetic species that might be present in the solution (not shown). The instability of the oxidised complex on longer timescales can be attributed to oxidative degradation of the ligand, as evidenced by the release of monomeric $Mn^{II}$ ions. This reaction might be triggered either by a transiently formed high-valent metal centre (7a) or by direct ligand oxidation (7b).

$$[Mn_2^{III,III}L(\mu\text{-}OAc)_2]^{2+} \rightarrow [Mn_2^{III,IV}L(\mu\text{-}OAc)_2]^{3+} + e^- \quad (7a)$$

$$[Mn_2^{III,III}L(\mu\text{-}OAc)_2]^{2+} \rightarrow [Mn_2^{III,III}L^{\cdot}(\mu\text{-}OAc)_2]^{3+} + e^- \quad (7b)$$

### *UV/Vis Spectroelectrochemistry*

The electronic absorption spectra of $[Mn_2L(\mu\text{-}OAc)_2]^{n+}$ ($n = 0, 1, 2$) in the UV and visible range are shown in Figure 5 and Table 4. The spectra after one-electron reduction and one-electron oxidisation of **5** were obtained by spectroelectrochemistry. The spectral changes induced by reduction and the first oxidation were fully reversible and isosbestic points (221, 242, 260, 306, 332 nm) were maintained in the course of the reduction (Figure 5, left panel). In the $Mn_2^{II,II}$ state the complex displayed basically no visible absorption as metal-to-ligand charge transfer (MLCT) bands of $Mn^{II}$ complexes are usually of low intensity. The visible absorption bands of the $Mn_2^{II,III}$ and $Mn_2^{III,III}$ states (Figure 5, right panel) can be attributed to ligand-to-metal charge transfer (LMCT) transitions from multiple donor functions to the $Mn^{III}$ centres. No additional band of the mixed-valence complex could be detected including the near infrared spectrum ($\leq$ 2700 nm). With a free energy change of $\Delta G° \approx 0.5$ eV for the metal-to-metal charge transfer (8) and $\lambda > 1$ eV per metal centre, the intervalence charge transfer transitions might be superimposed on the LMCT bands in the UV/Vis range.

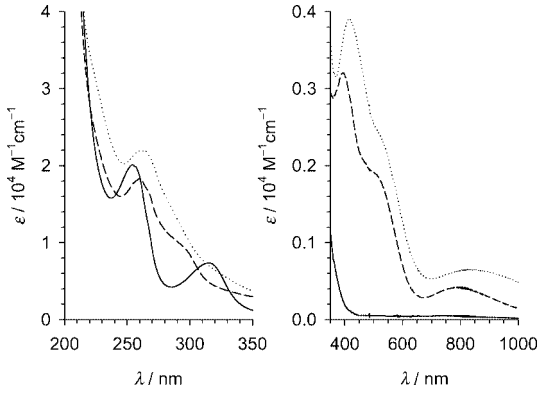


Figure 5. Electronic spectra of $[Mn_2L(\mu\text{-}OAc)_2]$ (–), $[Mn_2L(\mu\text{-}OAc)_2]^{+}$ (– –) and $[Mn_2L(\mu\text{-}OAc)_2]^{2+}$ (· · ·) in acetonitrile with $(n\text{-}C_4H_9)_4N{\cdot}ClO_4$ (0.1 M).

Table 4. UV/Vis absorption data of $[Mn_2L(\mu\text{-}OAc)_2]^{n+}$ in acetonitrile.

| $n$ | Mn oxidation state | $\lambda_{max}$ [nm] ($\varepsilon$ [$M^{-1}cm^{-1}$]) |
|---|---|---|
| 0 | II,II | 202 (61200), 253 (20100), 315 (7350) |
| 1 | II,III | 260 (18300), 393 (3200), 795 (420) |
| 2 | III,III | 262 (22000), 417 (3900), 830 (650) |

$$[(N)_3Mn^{II}(\mu\text{-}O\text{-}\phi)(\mu\text{-}OAc)_2Mn^{III}(N)_2(O)] \rightarrow [(N)_3Mn^{III}(\mu\text{-}O\text{-}\phi)(\mu\text{-}OAc)_2Mn^{II}(N)_2(O)] \quad (8)$$

Upon the second oxidation the optical absorption above 377 nm and below 310 nm was bleached and an increasing absorption was initially observed between these wavelengths. The isosbestic points were, however, not maintained and a pure spectrum of the initial product could not be obtained.

Scheme 2 compares the redox properties of **5** to those of the symmetric analogues $[Mn_2(bpmp)(\mu\text{-}OAc)_2]^{+}$ and $[Mn_2(bhpp)(\mu\text{-}OAc)_2]^{+}$ with $(N_3O_3)_2$ and $(N_2O_4)_2$ donor sets, respectively.[17,21] It illustrates the stabilisation of high-valent metal centres by the increasing number of oxygen donors. For the unsymmetric complex the mixed $(N_3O_3)/(N_2O_4)$ donor set results in localisation of and an extended stability to the mixed-valence $Mn_2^{II,III}$ state, with a free energy of comproportionation of $\Delta G_c = -88$ kJ mol$^{-1}$ [$K_c = \exp(\Delta E_{1/2}F/RT) = 5.49 \times 10^{15}$ at 293 K] as compared to –54.0 and –34.7 kJ mol$^{-1}$ in the $(N_3O_3)_2$ and $(N_2O_4)_2$ ana-

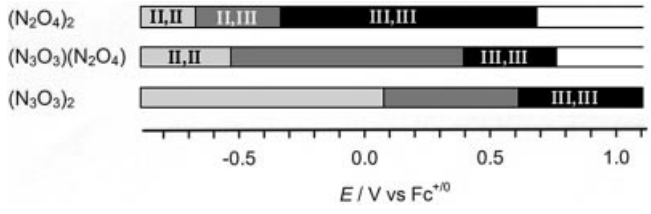


Scheme 2.

 © 2006 Wiley-VCH Verlag GmbH & Co. KGaA, Weinheim 

logues, respectively. For **5**, as for the symmetric analogues, no metal oxidation state higher than $Mn_2^{III,III}$ could be obtained by bulk electrolysis in nonaqueous solvents, and the second oxidation of **5** resulted in a short-lived product that could not be characterised. This demonstrates the general problem that several accumulative oxidations without charge compensation will be spread over a large potential range, placing the potentials for generating the higher metal oxidation states so high that oxidative degradation of the complexes is inevitable.

### *IR Spectroelectrochemistry*

IR spectra of the isovalent complexes $[Mn_2^{II,II}L(\mu\text{-}OAc)_2]$ and $[Mn_2^{III,III}L(\mu\text{-}OAc)_2]^{2+}$ (see Supporting Information) were obtained by spectroelectrochemistry that gave fully reversible absorption changes for reduction and oxidation of **5**. For the $\nu_{as}$ mode of the acetate ligands only a minor shift to higher frequency is observed upon reduction, while oxidation results in a broader, less symmetric $\nu_{as}$ band. The absorption between 1440 and 1440 $cm^{-1}$ can be assigned to the $\nu_s$ mode of the acetate ligands superimposed on absorptions of the binucleating ligand. The spectral changes induced by reduction and oxidation suggest a shift towards higher frequency in the II,II state and to lower frequency in the III,III state. The same trend has been found for the $Mn_2(bpmp)(\mu\text{-}OAc)_2$ complex[18] and the values of $\Delta\tilde{\nu} = \tilde{\nu}_{as} - \tilde{\nu}_s$ of about 120, 170 and 220 $cm^{-1}$ would be in agreement with bridging coordination of the acetate in all three oxidation states.

## Redox Properties in Partially Aqueous Media

In previous studies of $[Mn_2(bpmp)(\mu\text{-}OAc)_2]^+$ and $[Mn_2(bhpp)(\mu\text{-}OAc)_2]^+$, we have shown that complexes in higher oxidation states can be generated in partially aqueous solutions.[17–19] For $[Mn_2(bpmp)(\mu\text{-}OAc)_2]^+$ we could show that the exchange of acetate bridges for water-derived ligands ($H_2O$, $OH^-$, $O^{2-}$) accounts for the changes in redox behaviour in the presence of water. We were able to identify the products of the ligand exchange reactions and could demonstrate that increasing deprotonation of water-derived ligands provides the charge compensation needed for the stabilisation of high metal oxidation states.[18] In this way a di-μ-oxo-bridged dimer $[Mn_2^{III,IV}(bpmp)(\mu\text{-}O)_2]^{2+}$ can be obtained by three-electron oxidation of $[Mn_2^{II,II}(bpmp)(\mu\text{-}OAc)_2]^+$ that cannot be oxidised beyond the $Mn_2^{III,III}$ state, in its original di-μ-acetato form.

It could be anticipated that similar ligand exchange processes might take place in **5**. We therefore wanted to investigate the extent of these processes in **5**, and if complexes with oxidation states higher than $Mn_2^{III,III}$ could be formed from **5** as a result of ligand exchange in aqueous media.

### *IR Spectroscopy*

The exchange of acetate ligands for water-derived ligands was monitored by IR spectroscopy in $CD_3CN/D_2O$ mixtures (Figure 6, a). With increasing water concentration the sharp absorption peak arising from the acetate ligands ($\nu_{as}$, 1590 $cm^{-1}$, $\varepsilon$ = 4170 $M^{-1}cm^{-1}$) is depleted and replaced by the broader and weaker $\nu_{as}$ band of free acetate ions that can be observed at lower frequency (1574 $cm^{-1}$, $\varepsilon$ = 840 $M^{-1}cm^{-1}$).[18] The ratio of free versus bound acetate approaches unity, indicating that on average only one acetate per molecule of **5** is lost, even for the highest water concentration (inset in Figure 6, a). Assuming that the absorption changes represent a uniform reaction, this indicates that either all complexes have lost one acetate or half of them have lost both ligands. The dependence of the acetate concentration on the water content (Figure 6, b) is in good agreement with (9), with an equilibrium constant $K_9$ = $7.6 \times 10^{-5}$ $M^{-1}$ (Figure 6, c), while other obvious possibilities (10, 11) are not in agreement with the IR data.

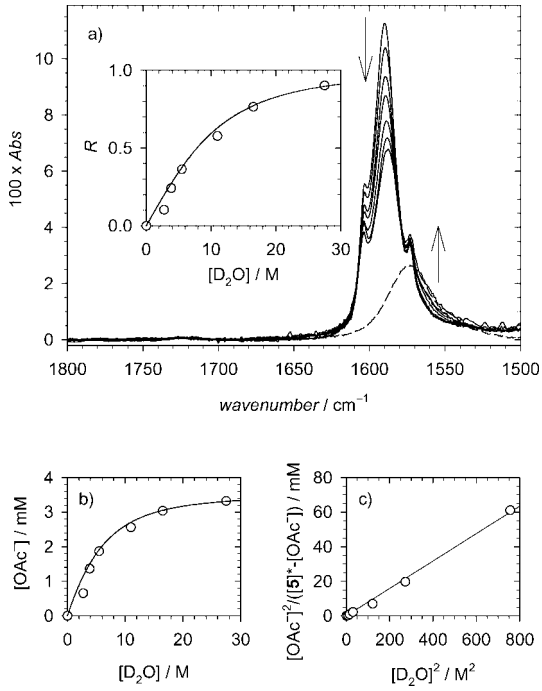


Figure 6. (a) IR spectra of **5** (3.5 mM) in $[D_3]$acetonitrile and $[D_3]$-acetonitrile/water ($D_2O$) mixtures. Arrows indicate direction of absorbance changes for increasing $D_2O$ concentration. Dashed line is the spectrum of ionic acetate (3.5 mM as NaOAc). Inset: ratio $R$ = $[OAc^-]/[M\text{-}OAc]$ of ionic vs. coordinated acetate as a function of water concentration. (b) Absolute concentration of ionic acetate and (c) plot according to Reaction (9) with a slope of $K_9$ = $7.6 \times 10^{-5}$ $M^{-1}$. [Lines in (a) inset and (b) are computed with this value of $K_9$.]

$$[Mn_2L(\mu\text{-}OAc)_2]^+ + 2H_2O \leftrightarrows [Mn_2L(\mu\text{-}OAc)(H_2O)_2]^{2+} + OAc^- \quad (9)$$

$$[Mn_2L(\mu\text{-}OAc)_2]^+ + H_2O \leftrightarrows [Mn_2L(\mu\text{-}OAc)(\mu\text{-}H_2O)]^{2+} + OAc^- \quad (10)$$

$$[Mn_2L(\mu\text{-}OAc)_2]^+ + 2H_2O \leftrightarrows [Mn_2L(\mu\text{-}H_2O)_2]^{3+} + 2OAc^- \quad (11)$$

In summary, the IR data suggest that one of the acetate bridges is lost more readily and is replaced by two terminal aquo ligands while the second acetate remains coordinated to the Mn centres even at the highest water concentrations. In this respect **5** behaves differently from the bpmp ana-

 © 2006 Wiley-VCH Verlag GmbH & Co. KGaA, Weinheim 

logues where the $Mn_2^{II,II}$ complex, which has the same charge as **5**, as well as the $Mn_2^{II,III}$ complex, in the same valence state as **5**, release both acetate ligands under comparable conditions.[18] Another difference between **5** and $[Mn_2(bpmp)(\mu\text{-}OAc)_2]^{2+}$ is the protonation state of the water-derived ligands. For the bpmp complex it was observed that the reaction of the $Mn_2^{II,III}$ state with water results in free acetate as well as acetic acid, which can be rationalised in terms of deprotonation of the water-derived ligands, resulting in the formation of oxo- and hydroxo bridges. In the case of **5** the absence of acetic acid hence implies that the aquo ligands are less acidic and remain protonated when bound to the $Mn_2^{II,III}$ complex. It is therefore likely that the water-derived ligands are terminal and not bridging in this valence state, although the formation of bridging aqueous ligands cannot be ruled out.

### *Electrochemistry*

The effect of the ligand exchange reactions on the redox behaviour of **5** was studied by cyclic voltammetry in different acetonitrile/water mixtures (Figure 7). With lower water concentration (1% v:v, 0.55 M) the ligand exchange equilibrium is largely on the left hand side and the magnitude of the first oxidation wave (2) is identical to dry acetonitrile solution (Figure 7, a and b). Also the reversibility of this wave (2) as well as the magnitude and reversibility of the reduction wave (1) (not shown) are unaffected. This indicates that under these conditions **5** does not react with water to a sizeable extent neither in the initial $Mn_2^{II,III}$ nor in the $Mn_2^{III,III}$ or $Mn_2^{II,II}$ forms.

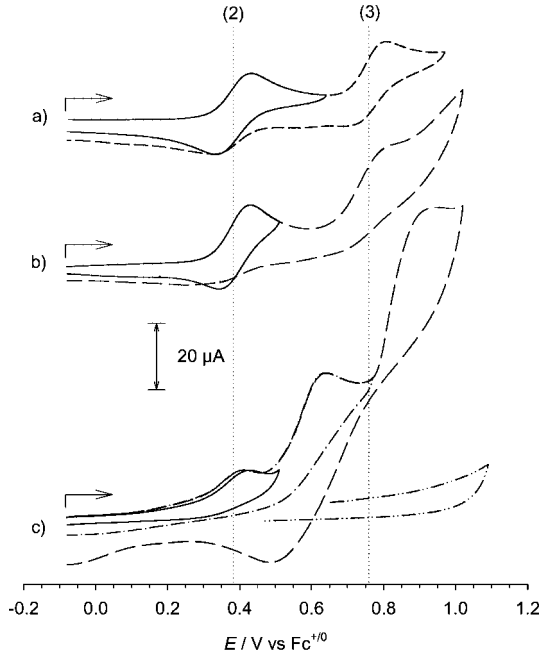


Figure 7. Cyclic voltammograms ($v$ = 0.100 V s$^{-1}$, first scans) of **5** (1 mM) with ($n$-$C_4H_9)_4N{\cdot}ClO_4$ (0.1 M) as supporting electrolyte. (a) Anhydrous acetonitrile. (b) Acetonitrile with 1% water (v:v). (c) Acetonitrile with 10% water (v:v). The dashed and dotted line shows the solvent background with 10% water.

With higher water concentration (10% v:v, 5.5 M) the first oxidation wave (2) is already depleted and fully irreversible while the second oxidation wave (3) of the original complex is absent (Figure 7, c). This shows that with the increased water content more than half of the complexes react with water already in the initial $Mn_2^{II,III}$ state, and the more reactive $Mn_2^{III,III}$ state is converted completely by the ligand exchange reactions. The additional anodic peaks around 0.6 and 0.9 V can be attributed to the oxidation of the products from the ligand exchange reactions. The first attempts to investigate the ligand exchanged oxidation products by EPR spectroscopy after bulk electrolysis of **5** in partially aqueous solutions were unsuccessful however. We therefore sought information on the oxidation products from IR spectroscopy, which benefits from more rapid electrochemical conversion in the thin-layer cell employed for IR spectroelectrochemistry.

### *IR Spectroelectrochemistry*

Figure 8 shows the IR absorption changes induced by oxidation of **5** in acetonitrile solution with 10% water. Electrolysis at the potential of the first oxidation (0.47 V vs. $Fc^{+/0}$) generates acetic acid (1725, 1380 and 1300 cm$^{-1}$) as well as free acetate ions with their absorption band (1575 cm$^{-1}$) partly cancelled by the bleach of the acetate ligand band (1590 cm$^{-1}$). This is in line with the notion that higher oxidation states are more reactive towards water (see Electrochemistry) and demonstrates that the water-derived ligands are at least partly deprotonated upon oxidation of the Mn centres. Subsequent oxidation at 0.72 V versus $Fc^{+/0}$ transforms the remaining acetate ligands as well as the acetate released in the previous oxidation step into acetic acid. This shows that the product(s) generated in the second oxidation wave peaking at 0.6 V do not carry any acetate ligands and that the water-derived ligands are further deprotonated.

Therefore, it can be concluded that the most oxidised products are oxo- ore hydroxo-bridged complexes. For $[Mn_2^{II,II}(bpmp)(\mu\text{-}OAc)_2]^+$ we showed that $[Mn_2^{III,IV}(bpmp)(\mu\text{-}O)_2]^{2+}$ was formed close to the potential of the III,III/II,III couple of the parent complex. The product was identified by rapid on-line transfer of the electrolysis products to a mass spectrometer.[18] The same product complex was also detected by EPR spectroscopy after light-induced oxidation of $[Mn_2^{II,II}(bpmp)(\mu\text{-}OAc)_2]^+$ via $[Ru^{III}(bpy)_3]^{3+}$ and rapid freezing of the products.[17,19] With the increased O/N ratio of complex **5** we anticipated that product complexes at least at the $Mn_2^{III,IV}$ level or even higher might be formed with the $Ru^{III}$ oxidant ($E_{1/2}$ = 0.90 V vs. $Fc^{+/0}$) and be detected by a combination of photo-oxidation and EPR spectroscopy.

### *EPR Spectroscopy of Photo-Oxidised Samples*

The oxidant $[Ru^{III}(bpy)_3]^{3+}$ was generated by oxidative quenching of photoexcited $[Ru^{II}(bpy)_3]^{2+}$. The sacrificial electron acceptor $[Co^{III}(NH_3)_5Cl]^{2+}$ avoids electron recombination, and thereby allows for accumulative oxidation of the manganese complex. To dissolve a sufficient amount of

 © 2006 Wiley-VCH Verlag GmbH & Co. KGaA, Weinheim 

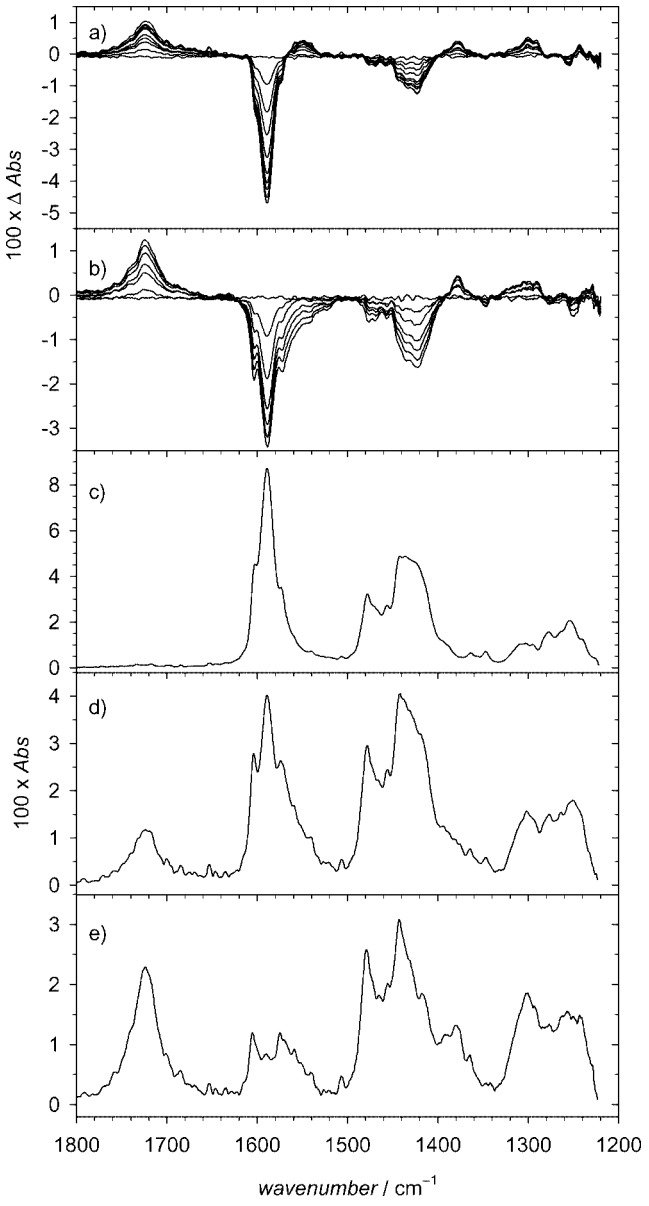


Figure 8. IR spectroelectrochemistry of **5** (3.5 mM) in [$D_3$]acetonitrile with 5.5 M water ($D_2O$). Absorbance changes upon oxidation at 0.47 V vs. $Fc^{+/0}$ (a) and subsequent oxidation at 0.72 V vs. $Fc^{+/0}$ (b). Spectra before oxidation (c) and after exhaustive oxidation at 0.47 V (d) and 0.72 V (e).

the acceptor, a high water content (1:1 water/acetonitrile) was needed for these measurements. The results from the IR spectra demonstrate that under these conditions each complex loses one of the acetate ligands already in the initial $Mn_2^{II,III}$ state. When **5** was dissolved in the reaction mixture, the 17 hyperfine lines in the $Mn_2^{II,III}$ EPR spectrum were broadened, and a signal with less-resolved hyperfine structure dominated the spectrum of the starting material (Figure 9, spectrum a). However, the integrated area of the spectrum was almost the same as for the well-resolved $Mn_2^{II,III}$ spectrum in acetonitrile (the magnitude of the EPR signal corresponds to about 80% of the nominal concentration), which indicates that essentially the entire sample remained in the original valence state. This demonstrates that even at this very high water content the major part of the material prevails as coupled $Mn_2^{II,III}$ dimers, and the broadened hyperfine structure can be attributed to strain effects due to accessibility to the bulk solution.

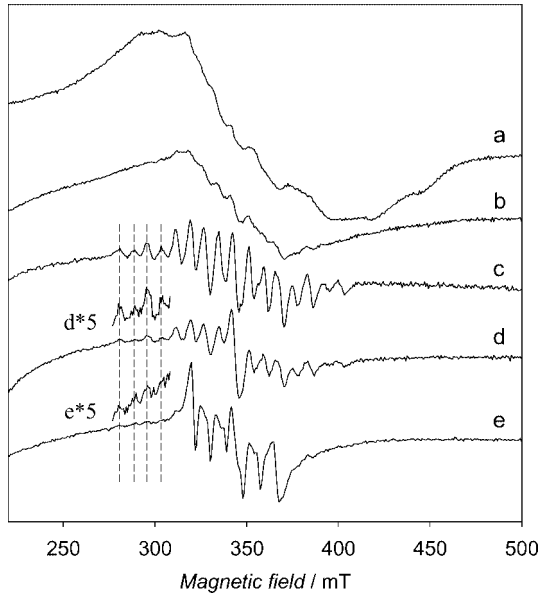


Figure 9. EPR spectra of **5** (0.5 mM) exposed to a variable number of laser flashes at 20 °C in the presence of $[Ru^{II}(bpy)_3]^{2+}$ (4 mM) and $[Co^{III}(NH_3)_5Cl]^{2+}$ (8 mM) in acetonitrile/aqueous solution (1:1 v/v). The spectra were recorded from the same sample, exposed to 0 (a), 20 (b), 100 (c), 180 (d) and 380 (e) laser flashes. In spectra d and e the magnified parts on the low-field side show the remaining presence of the EPR signal from $Mn_2^{III,IV}$. Spectrometer settings as in Figure 4.

Upon illumination with an increasing number of laser flashes, the initial EPR signal from $Mn_2^{II,III}$ decreased successively (Figure 10). To ensure accurate quantification of $Mn_2^{II,III}$, all measurements were made at 4 K, where all complexes are in the $S = 1/2$ ground state.[36] The simultaneously increasing EPR signal from the reduced electron acceptor $[Co^{II}(NH_3)_x(H_2O)_y]^{2+}$ ($g = 5$, not shown but cf. Huang et al.[17]) showed that the depletion of the $Mn_2^{II,III}$ signal is due to oxidation with the photogenerated $[Ru^{III}(bpy)_3]^{3+}$.

After 40 flashes a new signal at $g = 2$ appeared (Figure 9, spectrum c). It bears the typical signatures of a $S = 1/2$ ground state of a strongly coupled $Mn_2^{III,IV}$ complex, being about 2300 gauss wide and displaying 16 hyperfine lines with a spacing of 75–80 gauss.[34,42] The hyperfine splitting arises because of strong antiferromagnetic coupling typical of di-μ-oxo- or di-μ-hydroxo-bridged $Mn_2^{III,IV}$ dimers. For $[Mn_2(bpmp)(\mu\text{-}OAc)_2]^+$ we could demonstrate that the aquo and hydroxo complexes formed by ligand exchange in the lower oxidation states were ultimately transformed into the di-μ-oxo complex upon oxidation to the $Mn_2^{III,IV}$ level.[18] With the additional phenolate donor ligand in **5**, a μ-oxo-μ-hydroxo complex is the most probable structure for this oxidation state.

 © 2006 Wiley-VCH Verlag GmbH & Co. KGaA, Weinheim 

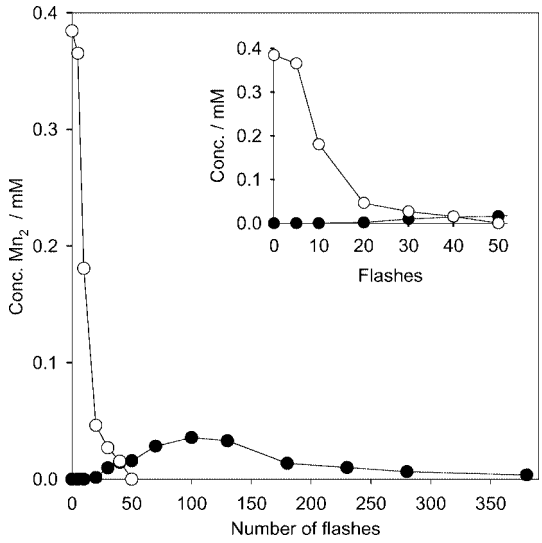


Figure 10. Flash-dependent concentrations of $Mn_2^{II,III}$ (–○–) and $Mn_2^{III,IV}$ (–●–). The data are obtained after quantification of $Mn_2^{II,III}$ and $Mn_2^{III,IV}$ from EPR spectra similar to those in Figure 7. All $Mn_2^{II,III}$ is quantitatively oxidised after 50 flashes, and the maximum observed amount of $Mn_2^{III,IV}$ appears after 100 flashes. The intermediate, $Mn_2^{III,III}$, cannot be observed by EPR. The inset shows a magnification of the data obtained between flashes 0 and 50, to highlight the lag phase in formation of $Mn_2^{III,IV}$.

Oxidation of the $Mn_2^{II,III}$ complexes to the $Mn_2^{III,IV}$ product with the one-electron photo-oxidant $Ru^{III}(bpy)_3$ should proceed via intermediates at the $Mn_2^{III,III}$ level. These are expected to be EPR-silent and not observable by EPR, which explains the lag phase between complete disappearance of the $Mn_2^{II,III}$ EPR spectrum and the maximum intensity of the $Mn_2^{III,IV}$ EPR signal (Figure 10). After 40 flashes, approximately equal concentrations of the $Mn_2^{II,III}$ and $Mn_2^{III,IV}$ species coexist in the reaction solution mixture, demonstrating that the high oxidation state in the $Mn_2^{III,IV}$ species possesses the desired stability. If we assume that the potential of the III,III/II,III couple of the species we observe under the experimental conditions of flash photolysis is similar to that of the di-μ-acetato complex (0.38 V vs. $Fc^{+/0}$), we can assume a similar potential for the III,IV/III,III couple of the $Mn_2^{III,IV}$ species. We made an analogous estimation of potentials for $[Mn_2(bpmp)(\mu\text{-}OAc)_2]^+$, where the mass spectrometry data indicated formation of $[Mn_2^{III,IV}(bpmp)(\mu\text{-}O)_2]^{2+}$ at potentials close to the III,III/II,III couple of the parent complex.[18] This compression of multiple redox reactions in a narrow potential range, which is a consequence of the ligand exchange reactions, indicates that disproportionation of III,III intermediates might contribute to the formation of the $Mn_2^{III,IV}$ species.

The $Mn_2^{III,IV}$ species reached a maximum concentration of about 10% relative to the initial $Mn_2^{II,III}$ signal before it started to decrease after about 100 flashes (Figure 10). The $Mn_2^{III,IV}$ spectrum was not immediately replaced by any other EPR-active species, suggesting that the $Mn_2^{III,IV}$ complex was further oxidised to an EPR-silent product. This could be either a $Mn_2^{IV,IV}$ complex or a $Mn_2^{III,IV}L^{\cdot}$ form with a ligand-based radical strongly coupled to the metal. Subsequent oxidation could also account for the relatively low yield of $Mn_2^{III,IV}$ species. When the $Mn_2^{III,IV}$ signal was almost fully depleted, a weak radical signal could be observed (Figure 9, in the centre of spectrum d) that was about 70 G wide (peak-to-trough) and had enhanced relaxation properties, as a consequence of being close to a paramagnetic metal centre. It is similar to the radical spectrum observed upon oxidation of the analogous $[Mn_2(bhpp)(OAc)_2]$ complex[21] and most likely arises from the oxidised *tert*-butyl-substituted phenol group. If it is the case that further oxidation of the $Mn_2^{III,IV}$ species results in formation of $Mn_2^{III,IV}L^{\cdot}$, the detected radical signal might arise from a minor fraction of the product where the oxidised phenol ligand has been detached from the manganese, while the major fraction with the radical coordinated to the metal centre is EPR-silent. The disappearance of the $Mn_2^{III,IV}$ EPR species cannot be explained by disintegration of the complexes, as that usually results in the release of monomeric $Mn^{II}$. In contrast, only a small quantity of $Mn^{II}$ (about 2% of the total Mn concentration) was released according to its EPR signal consisting of six lines at $g = 2$ (Figure 9, spectrum e).[43]

In summary, the results of photo-oxidation show that oxidation of **5** in partly aqueous solution generates a $Mn_2^{III,IV}$ complex, most likely with a di-μ-oxo or di-μ-oxo/hydroxo bridging motif replacing the acetate ligands. In addition, our data indicate that further photoinduced oxidation of this complex might result in a $Mn_2^{IV,IV}$ or $Mn_2^{III,IV}$-$L^{\cdot}$ product.

## Conclusions

The unsymmetric ligand in the mixed-valent manganese complex **5** ($[Mn_2^{II,III}L(\mu\text{-}OAc)_2]ClO_4$) provides, together with the bridging acetates, a $N_3O_3$ and a $N_2O_4$ donor set to the $Mn^{II}$ and $Mn^{III}$ centres respectively. Compared to the symmetric ligand analogues bpmp[16] and bhpp,[21] the unsymmetric ligand provides an intermediate O/N ratio and substantially stabilises the mixed-valence state, where the higher-valent metal ion is localised in the $N_3O_3$ environment. The pseudo-octahedral coordination geometry is largely distorted and conversion to the isovalent states is associated with large inner reorganisation energies resulting in slow electron transfer reactions.

Complex **5** displays two oxidation processes in nonaqueous solvents, where charge accumulation precludes the formation of stable oxidation states beyond the $Mn_2^{III,III}$ state. This situation changes in aqueous media where the acetate bridges of **5** are replaced by water-derived ligands. These provide charge compensation by deprotonation upon oxidation of the metal centres.[18,44] As a result, the potential interval for accumulative oxidations becomes more compressed, so that three metal-centred oxidation processes can be driven by $[Ru^{III}(bpy)_3]^{3+}$ ($E_{1/2}$ = 1.27 V vs. NHE). Moreover, the ability to acquire water-derived ligands is an essen-

 © 2006 Wiley-VCH Verlag GmbH & Co. KGaA, Weinheim 

tial characteristic of any functional model for the water-oxidising complex in PSII.

The product of the photoinduced oxidation is a $Mn_2^{III,IV}$ complex, which can be further oxidised to, most likely, a $Mn_2^{IV,IV}$ complex. The high-valent complexes are oxo- or hydroxo-bridged, which is supported by the EPR spectrum observed for the $Mn_2^{III,IV}$ complex, which is consistent with a strongly antiferromagnetically coupled complex.

These results demonstrate that four, possibly five, manganese valence states can be sustained in the same binucleating ligand, as the build-up of charge can be balanced because of the flexibility of the bridging motif. Water oxidation in PSII is believed to involve at least $Mn^{IV}$ or even $Mn^{V}$ to provide sufficiently electrophilic oxo ligands that can engage in O–O bond formation.[5,7,45] Compared to the related $[Mn_2(bpmp)(OAc)_2]^+$ we note that the increased O/N ratio of **5** stabilises higher valence states, which results in oxidation of the ligand exchange products beyond the $Mn_2^{III,IV}$ level. This is a significant improvement in view of prospective biomimetic water oxidation catalysts. It is however important to note that there is an unavoidable trade-off between stabilising higher oxidation states and maintaining sufficient oxidising potential. For the $Mn_2^{III,IV}$ complex derived from **5** the estimated oxidation potential of the III,IV/III,III couple is probably comparable to the III,III/II,III couple of the parent complex (≈0.4 V vs. $Fc^{+/0}$, ≈0.8 V vs. NHE). This suggests that all oxidation products derived from **5** are within a desirable potential range with respect to the average potential of 0.81 V versus NHE (at pH 7) required for water oxidation. Thus, the O/N ratio in **5** seems to create close to an optimal balance between oxidising potential and valence state stabilisation.

## Experimental Section

**Materials:** 2-(Chloromethyl)-6-formyl-4-methylphenol,[27] dipicolylamine[28] and (3,5-di-*tert*-butyl-2-hydroxybenzyl)(2-pyridylmethyl)amine[21] were prepared according to the literature procedures. Dichloromethane and triethylamine were distilled under argon over sodium/benzophenone and calcium hydride, respectively. Column chromatography was performed using silica gel (60–80 mesh). All other reagents were of reagent grade quality and used as received. $^1$H NMR spectra were recorded with a Varian 400-MHz spectrometer.

**2-{[(3,5-Di-*tert*-butyl-2-hydroxybenzyl)(pyrid-2-ylmethyl)amino]-methyl}-6-formyl-4-methylphenol (2):** (3,5-Di-*tert*-butyl-2-hydroxybenzyl)(pyrid-2-ylmethyl)amine (1.64 g, 5.0 mmol) and triethylamine (0.62 g, 6.1 mmol) in $CH_2Cl_2$ (15 mL) under argon were added to a solution of 2-(chloromethyl)-6-formyl-4-methylphenol (**1**) (1.03 g, 5.6 mmol) in $CH_2Cl_2$ (15 mL). The reaction mixture was refluxed overnight under argon. The reaction was poured into water and extracted with $CH_2Cl_2$. The combined organic phases were dried with anhydrous sodium sulfate, filtered and evaporated under reduce pressure. The residue was purified by column chromatography, eluting with $CH_2Cl_2$/MeOH, 97:3. Yield 1.84 g (95%). $^1$H NMR ($CDCl_3$): $\delta$ = 1.26 (s, 9 H), 1.42 (s, 9 H), 2.28 (s, 3 H), 3.77 (s, 2 H), 3.79 (s, 2 H), 3.84 (s, 2 H), 6.86 (d, 1 H), 7.16–7.20 (m, 2 H), 7.28–7.34 (m, 3 H), 7.65 (dt, 1 H), 8.56 (dd, 1 H), 9.95 (s, 1 H), 10.9 (s broad, 2 H) ppm.

**2-{[(3,5-Di-*tert*-butyl-2-hydroxybenzyl)(pyrid-2-ylmethyl)amino]-methyl}-6-(hydroxymethyl)-4-methylphenol (3):** Complex **2** (0.94 g, 2.0 mmol) was dissolved in methanol (20 mL) and treated with sodium borohydride (0.17 g, 4.4 mmol). The reaction was stirred at room temperature overnight. The solution was evaporated under reduced pressure and the residue was dissolved in water, acidified to pH 2–3 and stirred for 1 h. The pH was adjusted to 7–8 with sodium hydrogen carbonate and then extracted with dichloromethane. The combined organic phases were washed with brine, dried with anhydrous sodium sulfate and filtered. Evaporation under reduced pressure of the solvent afforded 0.92 g of **3** (97%). $^1$H NMR ($CDCl_3$): $\delta$ = 1.27 (s, 9 H), 1.41 (s, 9 H), 2.24 (s, 3 H), 3.77 (s, 2 H), 3.78 (s, 2 H), 3.85 (s, 2 H), 4.68 (s, 2 H), 6.84 (d, 1 H), 8.90 (d, 1 H), 6.96 (d, 1 H), 7.17 (d, 1 H), 7.22 (d, 1 H), 7.32 (dt, 1 H), 7.74 (dt, 1 H), 8.86 (dd, 1 H), 10.80 (s broad, 2 H) ppm.

**2-{[Bis(pyrid-2-ylmethyl)amino]methyl}-6-{[(3,5-di-*tert*-butyl-2-hydroxybenzyl)(pyrid-2-ylmethyl)amino]methyl}-4-methylphenol, $H_2L$ (4):** Complex **3** (2.27 g, 4.8 mmol) was dissolved in freshly distilled thionyl chloride (5 mL) and $CH_2Cl_2$ (30 mL). The solution was stirred at room temperature for 2.5 h and then distilled under reduced pressure. The residue was dissolved in $CH_2Cl_2$ and washed with a cooled sodium hydrogen carbonate solution. The organic phase was dried with anhydrous sodium sulfate, filtered and evaporated under reduced pressure. The residue was dissolved in $CH_2Cl_2$ and added to a solution of bis-picolylamine (0.95 g, 4.8 mmol) and triethylamine (1.03 g, 10 mmol) and refluxed overnight under argon. The solution was washed with brine and dried with anhydrous sodium sulfate. After filtration and evaporation under reduced pressure the crude product was purified by column chromatography on silica gel, eluting with $CH_2Cl_2$/MeOH, 95:5. Yield 2.10 g (67%). $^1$H NMR ($CDCl_3$): $\delta$ = 1.25 (s, 9 H), 1.38 (s, 9 H), 2.19 (s, 3 H), 3.73 (s, 2 H), 3.79 (s, 2 H), 3.82 (s, 2 H), 3.83 (s, 2 H), 3.86 (s, 4 H), 6.79 (d, 1 H), 6.84 (d, 1 H), 6.96 (d, 1 H), 7.06–7.15 (m, 4 H), 7.34 (d, 2 H), 7.42 (d, 2 H), 7.51–7.59 (m, 3 H), 8.49 (d, 1 H), 8.58 (d, 1 H), 10.90 (s broad, 2 H) ppm.

**$Mn_2L(OAc)_2{\cdot}ClO_4$ (5):** $Mn(OAc)_3{\cdot}(H_2O)_2$ (1.04 g, 3.9 mmol) was added to an ethanol solution (9 mL) of **4** (1.05 g, 1.6 mmol) in one portion. The dark red-brown solution was heated to 60 °C under argon for 20 min. A solution of $NaClO_4{\cdot}H_2O$ (0.58 g, 4.1 mol) in ethanol/water (3:1, 4 mL) was added dropwise and the reaction solution was slowly cooled to room temperature and then stored in a freezer (–18 °C) for 48 h. The dark red-brown microcrystalline solid was filtered and washed with cooled ethanol and diethyl ether. The solid was recrystallised from ethanol/hexane to give 0.79 g dark red-brown rod-like crystals (yield 52%) suitable for X-ray diffraction. ESI-MS: (*m*/*z*) (%) = 883.3354 $[M - ClO_4]^+$. $C_{46}H_{55}N_5O_6Mn_2^+$ (883.2913): found C 56.03, H 5.71, N 7.08, Cl 3.48, Mn 11.05. $C_{46}H_{55}Mn_2N_5O_6{\cdot}ClO_4$: calcd. C 56.19, H 5.64, N 7.12, Cl 3.61, Mn 11.17.

**X-ray Crystallography:** Single crystal X-ray diffraction patterns were recorded with a Stoe IPDS diffractometer on a rotating anode Mo-radiation source ($\lambda$ = 0.71073 Å) with &phis; scans of 1° width. The total rotation range was 200°. The sample-detector distance was 70 mm and with the diameter of the image plate being 180 mm this gave max $2\theta \approx 52°$. Measuring further out in $2\theta$ proved to give very little significant extra data. Suitable single crystals were chosen from the crystallisation (see "Synthesis" above) and were mounted and measured inside sealed glass capillaries with mother liquor surrounding the crystals. Crystals that were simply glued to a glass pin ceased to diffract after a few minutes. Indexing, cell refinements and integration of reflection intensities were performed with STOE IPDS software (Stoe & Cie GmbH, Darmstadt). Numerical ab-

 © 2006 Wiley-VCH Verlag GmbH & Co. KGaA, Weinheim 

sorption correction was performed with the program X-RED (Stoe & Cie GmbH, Darmstadt) and the crystal shape was verified with the program X-SHAPE (Stoe & Cie GmbH, Darmstadt) using multiple measurements of symmetry equivalent reflections. The structure was solved by direct methods using SHELXS97 giving electron density maps where most non-hydrogen atoms could be resolved.[46] The rest of the non-hydrogen atoms were located from difference electron density maps and the structure model was refined with full-matrix least-squares calculations on $F^2$ using the program SHELXL97-2.[47] All non-hydrogen atoms were refined with anisotropic displacement parameters and the hydrogens, which were placed at geometrically calculated positions and let to ride on the atoms they were bonded to, were given isotropic displacement parameters calculated as $\xi \cdot U_{eq.}$ for the non-hydrogen atoms with $\xi = 1.5$ for methyl H atoms ($-CH_3$) and $\xi = 1.2$ for methylenic ($-CH_2-$) and aromatic H atoms.

Only 39.2% of the reflections fulfilled the significance criterion $I > 2\sigma(I)$, thus the residual values calculated from all reflection are larger than those calculated from the significant reflections.

CCDC-256953 contains the supplementary crystallographic data for this paper. These data can be obtained free of charge from The Cambridge Crystallographic Data Centre via www.ccdc.cam.ac.uk/data_request/cif.

**Magnetic Susceptibility:** The magnetic susceptibility in the temperature range 4–300 K was measured on a powder sample of **5** at a magnetic field of 1.35 T using a Faraday balance. Correction for diamagnetism was made using Pascal's constants.

**Electrochemistry:** All solutions were prepared from dry acetonitrile (Merck, spectroscopy grade, dried with MS 3 Å) with 0.1 M tetrabutylammonium perchlorate that had been dried in a vacuum at 353 K (Fluka, electrochemical grade) as the supporting electrolyte. Before all measurements, oxygen was removed by bubbling the stirred solutions with solvent-saturated argon and the samples were kept under argon during measurements. Cyclic voltammetry, differential pulse voltammetry and controlled potential electrolysis were carried out using an Autolab PGSTAT 100 potentiostat with a GPES 4.9 electrochemical interface (Eco Chemie). The working electrode was a glassy carbon disc (diameter 3 mm, freshly polished) for voltammetry, a Pt disk microelectrode (CH Instruments, diameter 25 μm, freshly polished with alumina 0.3 μm) for fast voltammetry or a platinum grid for bulk electrolysis. A platinum spiral in a compartment separated from the bulk solution by a fritted disk was used as the counter electrode. The reference electrode was a nonaqueous $Ag/Ag^+$ electrode (CH Instruments, 0.01 M $AgNO_3$ in acetonitrile) with a potential of –0.08 V versus the ferrocenium/ferrocene ($Fc^+/Fc$) couple in acetonitrile as an external standard. All potentials reported here are versus the $Fc^+/Fc$ couple, which is obtained by adding –0.08 V to the potentials measured versus the $Ag/Ag^+$ electrode. No compensation for $iR$ drop has been made. With a specific conductivity of $\kappa > 0.01\ S\,cm^{-1}$ of the electrolyte the resistance for the microelectrode ($r = 12.5$ μm) is $R = 1/(4\kappa r) < 20$ kΩ With voltammetric peak currents $i < 100$ nA, the $iR$ drop is negligible (<2 mV) in the microelectrode measurements. Digital simulations of the cyclic voltammograms have been performed with GPES 4.9 software (Eco Chemie). The simulated voltammograms have been composed from the faradic current of a quasireversible and a two-component quasireversible model superimposed on a linear nonfaradic background. The heterogeneous electron transfer rate constants are reported as apparent standard rate constants without corrections for double-layer effects.

**UV/Vis Spectroscopy:** The electronic absorption spectrum was recorded with a UV/Vis-NIR spectrophotometer (Varian CARY 2400) between 200 and 2700 nm. Spectroelectrochemical measurements were made in a OTTLE-type quartz cell with an optical path length of 1 mm. A platinum grid with a size of $10 \times 30\ mm^2$ and 400 meshes per $cm^2$ was used as the working electrode. The counter and reference electrodes were of the same type as described in the electrochemistry paragraph. Samples were bubbled for 20 min with solvent-saturated argon and transferred to the argon-flushed cell with the argon stream. The spectra were recorded with a UV/Vis diode array spectrophotometer (Hewlett Packard 8435) with the background collected on electrolyte solution in the potential free OTTLE cell.

**IR Spectroscopy:** IR absorption spectra were recorded at a resolution of $1\ cm^{-1}$ with a Bruker FTIR spectrometer (IFS 66v/S) with the sample as a KBr pellet or as solution in a liquid-sample cell (Bruker A140) between $CaF_2$ windows and with a path length of 125 μm. The solutions were prepared in $CD_3CN$ (Aldrich, 99.8 atom-% D) or mixtures of $CD_3CN$ with $D_2O$ (Aldrich, 99 atom-% D).

The ratio of free versus coordinated acetate ($R = [OAc^-]/[M\text{-}OAc]$) was determined from the absorbance at $1590\ cm^{-1}$ $\{Abs_{1590} = d(\varepsilon_{OAc^-}[OAc^-] + \varepsilon_{M\text{-}OAc}[M\text{-}OAc]) = d\varepsilon[OAc]\}$ as

$$R = (\varepsilon_{M\text{-}OAc} - \varepsilon)/(\varepsilon - \varepsilon_{OAc^-})$$

where $\varepsilon$ is a formal extinction coefficient and $[OAc] = 2 \times [\mathbf{5}]$ is the total acetate concentration. The concentration of free acetate is then given by

$$[OAc^-] = \{1 - 1/(R + 1)\}[OAc]$$

For Reaction (9) the equilibrium constant is defined as

$$K_9 = \{[Mn_2L(OAc)(H_2O)_2]\ [OAc^-])/([Mn_2L(OAc)_2]\ [H_2O]^2\} = [OAc^-]^2/\{([\mathbf{5}] - [OAc^-])\ [H_2O]^2\}$$

and was determined from a plot of $[OAc^-]^2/([\mathbf{5}] - [OAc^-])$ over $[H_2O]^2$.

IR spectroelectrochemical measurements were performed on solutions of **5** in $CD_3CN$ or $CD_3CN/D_2O$ with $KPF_6$ (0.1 M). The spectra were recorded in a thin-layer cell equipped with $CaF_2$ windows and an optical path length of 90 μm. The working electrode was a carbon fibre mesh (49% open area) and the counter electrode was a Pt cylinder concentric with the working electrode. The reference electrode was of the same type as described for electrochemistry and connected to the cell by a salt bridge (0.5 M $KPF_6$ in $CD_3CN$). $CD_3CN$, $D_2O$ and $KPF_6$ were purchased from Sigma Aldrich. $CD_3CN$ was dried with molecular sieves (3 Å) prior to use and $KPF_6$ was dried overnight at 353 K in vacuo.

**EPR Spectroscopy:** The electrochemical preparation of EPR samples was performed by bulk electrolysis of 1-mM solutions at controlled potentials. After electrolysis, 250-μL samples were taken with an argon-filled syringe via a septum from the electrolysis vessel and transferred to argon-flushed EPR tubes. The samples were immediately frozen and kept in liquid nitrogen. X-band EPR measurements were performed at cryogenic temperatures with a Bruker E500 ELEXSYS spectrometer equipped with a $TE_{102}$ resonator, an Oxford Instruments ESR 900 flow cryostat and an ITC 503 temperature controller.

For flash photolysis, a 1-mM solution of **5** in dry acetonitrile was mixed at a 1:1 ratio with an aqueous solution containing tris(2,2′-bipyridyl)dichloro-ruthenium(II) hexahydrate ($[Ru^{II}(bpy)_3]^{2+}$) (8 mM), and penta-aminechlorocobalt(III) chloride ($[Co^{III}(NH_3)_5Cl]^{2+}$) (16 mM), as described previously.[32] The solution was transferred to EPR tubes and the samples were immediately frozen in an ethanol/dry ice bath ($T = 198$ K) and then frozen at 77 K. All

 © 2006 Wiley-VCH Verlag GmbH & Co. KGaA, Weinheim 

sample mixing and handling took place under dim red light and inert atmosphere, and care was taken to minimise the interval between mixing and freezing of the samples (mix–freeze time < 1 min). Laser flashes from a frequency doubled Spectra Physics DCR 3G Nd:YAG laser at 5 Hz and 532 nm (6 ns pulse width, about 250 mJ flash$^{-1}$) were given at room temperature to the pre-thawed EPR samples. The incident laser light was adjusted with lenses to cover the entire EPR sample volume. After the designated number of flashes, the sample was frozen in an ethanol/dry ice bath within 2 s and then quickly transferred to liquid $N_2$ until further use. X-band EPR spectra were recorded before and after flash illumination of the EPR samples. Evaluation of the change in $Mn_2^{II,III}$ concentration was done by double integration of the ground-state EPR signal at 4 K, and comparison with a reference $Mn_2^{II,III}$ spectrum from a known concentration of **5** in acetonitrile. To quantify the formation of $Mn_2$(III,IV) we used $Mn_2^{III,IV}(bpy)_4(\mu\text{-}O)_2$ as spectroscopic reference.[48] The concentration of $Mn_2^{III,IV}(bpy)_4(\mu\text{-}O)_2$ in acetonitrile was determined by UV/Vis spectrophotometry, using the extinction coefficient $\varepsilon = 900\ M^{-1}cm^{-1}$ at $\lambda$ = 687 nm. Simulations of EPR spectra were made using the Xsophe-Sophe-Xepr-View® software suite from Bruker GmbH.

**Supporting Information** (see footnote on the first page of this article): Figure S1 shows IR spectroelectrochemistry of **5**. IR spectra of **5** in KBr, and of the isovalent products $[Mn_2^{II,II}L(\mu\text{-}OAc)_2]$ and $[Mn_2^{III,III}L(\mu\text{-}OAc)_2]^{2+}$ in [$D_3$]acetonitrile solution. Selected crystallographic data not shown in Table 1.

## Acknowledgments

This work was supported by grants from the Swedish Energy Agency, The Knut and Alice Wallenberg Foundation, The Swedish Research Council, NEST-STRP SOLAR-H (EU contract no. 516510), The Royal Swedish Academy of Sciences (A. M.), the Carl Trygger Foundation (A. M.), the Swedish Foundation for Strategic Research (M. F. A.) and Stiftelsen Bengt Lundqvists minne (P. H.).

[1] IR spectroelectrochemistry of **5**: a) J. H. Alstrum-Acevedo, M. Kyle Brennaman, T. J. Meyer, *Inorg. Chem.* **2005**, *44*, 6802–6827; b) S. Chakraborty, T. J. Wadas, H. Hester, R. Schmehl, R. Eisenberg, *Inorg. Chem.* **2005**, *44*, 6865–6878.

[2] a) J. H. A. Nugent (Ed.), *Special Issue on Photosynthetic Water Oxidation*, *BBA-Bioenergetics*, Elsevier, Amsterdam, **2001**, p. 1503; b) J. Barber, *BBA-Bioenergetics* **2004**, *1655*, 123–132.

[3] a) B. A. Diner, G. T. Babcock, in *Oxygenic Photosynthesis: The Light Reactions* (Eds.: D. R. Ort, C. F. Yocum), Kluwer Academic Publishers, Dordrecht, **1996**, pp. 213–247; b) J. Barber, *Curr. Opin. Struct. Biol.* **2002**, *12*, 523–530; c) R. D. Britt, in *Oxygenic Photosynthesis: The Light Reactions* (Eds.: D. R. Ort, C. F. Yocum), Kluwer Academic Publishers, Dordrecht, **1996**, pp. 137–164.

[4] a) K. N. Ferreira, T. M. Iverson, K. Maglaoui, J. Barber, S. Iwata, *Science* **2004**, *303*, 1831–1838; b) B. Loll, J. Kern, W. Saenger, A. Zouni, J. Biesiadka, *Nature* **2005**, *438*, 1040–1044.

[5] W. C. Hoganson, G. T. Babcock, *Science* **1997**, *277*, 1953–1956.

[6] a) B. Kok, B. Forbush, M. McGloin, *Photochem. Photobiol.* **1970**, *11*, 457–475; b) B. Forbush, B. Kok, M. McGloin, *Photochem. Photobiol.* **1971**, *14*, 307–321.

[7] M. Haumann, P. Liebisch, C. Müller, M. Barra, M. Grabolle, H. Dau, *Science* **2005**, *310*, 1019–1021.

[8] a) S. Mukhopadhyay, S. K. Mandal, S. Bhaduri, W. H. Armstrong, *Chem. Rev.* **2004**, *104*, 3981–4026; b) J. H. Robblee, R. M. Cinco, V. K. Yachandra, *BBA-Bioenergetics* **2001**, *1503*, 7–23; c) H. Dau, L. Iuzzolino, J. Dittmer, *BBA-Bioenergetics* **2001**, *1503*, 24–39; d) D. Kuzek, R. J. Pace, *BBA-Bioenergetics* **2001**, *1503*, 123–137.

[9] M. Haumann, C. Müller, P. Liebisch, L. Iuzzolino, J. Dittmer, M. Grabolle, T. Neisius, W. Meyer-Klaucke, H. Dau, *Biochemistry* **2005**, *44*, 1894–1908.

[10] a) Y. Naruta, M. Sasayama, T. Sasaki, *Angew. Chem. Int. Ed. Engl.* **1994**, *33*, 1839–1841; b) M. Watkinson, A. Whiting, C. A. McAuliffe, *J. Chem. Soc., Chem. Commun.* **1994**, *18*, 2141–2142; c) W. Ruettinger, M. Yagi, K. Wolf, S. Bernasek, G. C. Dismukes, *J. Am. Chem. Soc.* **2000**, *122*, 10353–10357.

[11] a) J. Limburg, J. S. Vrettos, L. M. Liable-Sands, A. C. Rheingold, R. H. Crabtree, G. W. Brudvig, *Science* **1999**, *283*, 1524–1527; b) A. K. Poulsen, A. Rompel, C. J. McKenzie, *Angew. Chem. Int. Ed.* **2005**, *44*, 6916–6920.

[12] a) L. Sun, H. Berglund, R. Davydov, T. Norrby, L. Hammarström, P. Korall, A. Börje, C. Philouze, K. Berg, A. Tran, M. Andersson, G. Stenhagen, J. Mårtensson, M. Almgren, S. Styring, B. Åkermark, *J. Am. Chem. Soc.* **1997**, *119*, 6996–7004; b) A. Magnuson, Y. Frapart, M. Abrahamsson, O. Horner, B. Åkermark, L. Sun, J.-J. Girerd, L. Hammarström, S. Styring, *J. Am. Chem. Soc.* **1999**, *121*, 89–96; c) L. Sun, L. Hammarström, B. Åkermark, S. Styring, *Chem. Soc. Rev.* **2001**, *30*, 36–49.

[13] L. Sun, M. Raymond, A. Magnuson, D. LeGourrierec, M. Tamm, M. Abrahamsson, P. Huang Kenéz, J. Mårtensson, G. Stenhagen, L. Hammarström, S. Styring, S. Åkermark, *J. Inorg. Biochem.* **2000**, *78*, 15–22.

[14] M. Borgström, N. Shaikh, O. Johansson, M. F. Anderlund, S. Styring, B. Åkermark, A. Magnuson, L. Hammarström, *J. Am. Chem. Soc.* **2005**, *127*, 17504–17515.

[15] a) I. Vass, S. Styring, *Biochemistry* **1991**, *30*, 830–839; b) C. Tommos, G. T. Babcock, *BBA-Bioenergetics* **2000**, *1458*, 199–219; c) P. Geijer, F. Morvaridi, S. Styring, *Biochemistry* **2001**, *40*, 10881–10891; d) R. Radmer, G. Cheniae, *Top. Photosynthesis* **1977**, *2*, 303–348.

[16] a) bpmp = 2,6-bis{[*N*,*N*-bis(2-pyridinemethyl)amino]methyl}-4-methylphenol; b) H. Diril, H. R. Chang, M. J. Nilges, X. H. Zhang, J. A. Potenza, H. J. Schugar, S. S. Isied, D. N. Hendrickson, *J. Am. Chem. Soc.* **1989**, *111*, 5102–5114.

[17] P. Huang, A. Magnuson, R. Lomoth, M. Abrahamsson, M. Tamm, L. Sun, B. van Rotterdam, J. Park, L. Hammarström, B. Åkermark, S. Styring, *J. Inorg. Biochem.* **2002**, *91*, 159–172.

[18] G. Eilers, C. Zettersten, L. Nyholm, L. Hammarström, R. Lomoth, *Dalton Trans.* **2005**, 1033–1041.

[19] P. Huang, J. Högblom, M. F. Anderlund, L. Sun, A. Magnuson, S. Styring, *J. Inorg. Biochem.* **2004**, *98*, 733–745.

[20] bpy = 2,2-bipyridine.

[21] a) bhpp = 2,6-bis{[(2-hydroxy-3,5-di-*tert*-butylbenzyl)(2-pyridylmethyl)amino]methyl}-4-methylphenol; b) R. Lomoth, P. Huang, J. Zheng, L. Sun, L. Hammarström, B. Åkermark, S. Styring, *Eur. J. Inorg. Chem.* **2002**, 2965–2974.

[22] C. Higushi, H. Sakiyama, H. Okawa, R. Isobe, D. E. Fenton, *J. Chem. Soc., Dalton Trans.* **1994**, *7*, 1097–1103.

[23] B. C. Dave, R. S. Czernuszewicz, *Inorg. Chim. Acta* **1998**, *281*, 25–35.

[24] P. Karsten, A. Neves, A. J. Bortoluzzi, J. Strahle, C. Maichle-Mossmer, *Inorg. Chem. Commun.* **2002**, *5*, 434–438.

[25] a) L. Dubois, D.-F. Xiang, X.-S. Tan, J. Pécault, P. Jones, S. Baudron, L. LePape, J.-M. Latour, C. Baffert, S. Chardon-Noblat, M.-N. Collomb, A. Deronzier, *Inorg. Chem.* **2003**, *42*, 750–760; b) L. Dubois, R. Caspar, L. Jacquamet, P.-E. Petit, M. F. Charlot, C. Baffert, M.-N. Collomb, A. Deronzier, J.-M. Latour, *Inorg. Chem.* **2003**, *42*, 4817–4827.

[26] a) C. Fraser, L. Johnston, A. L. Rheingold, B. S. Haggerty, J. K. Williams, J. Whelan, B. Bosnich, *Inorg. Chem.* **1992**, *31*, 1835–1844; b) R. Hotzelmann, K. Wieghardt, U. Florke, H. J. Haupt, D. C. Weatherburn, J. Bonvoisin, G. Blondin, J.-J. Girerd, *J. Am. Chem. Soc.* **1992**, *114*, 1681–1696; c) P. Karsten, A. Neves, A. J. Bortoluzzi, M. Lanznaster, V. Drago, *Inorg. Chem.* **2002**, *41*, 4624–4626.

 © 2006 Wiley-VCH Verlag GmbH & Co. KGaA, Weinheim 

[27] E. Lambert, B. Chabut, S. Chardon-Noblat, A. Deronzier, G. Chottard, A. Bousseksou, J. Tuchagues, J. Laugier, M. Bardet, J. M. Latour, *J. Am. Chem. Soc.* **1997**, *119*, 9424–9437.
[28] M. Lubben, B. L. Feringa, *J. Org. Chem.* **1994**, *59*, 2227–2233.
[29] I. D. Brown, D. Altermatt, *Acta Crystallogr., Sect. B: Struct. Sci.* **1985**, *41*, 244–247.
[30] a) R. M. Buchanan, K. J. Oberhausen, J. F. Richardson, *Inorg. Chem.* **1988**, *27*, 971–973; b) H.-R. Chang, S. K. Larsen, P. D. W. Boyd, C. G. Pierpont, D. N. Hendrickson, *J. Am. Chem. Soc.* **1988**, *110*, 4565–4576.
[31] H. Diril, H.-R. Chang, X. Zhang, S. K. Larsen, J. A. Potenza, C. G. Pierpont, H. J. Schugar, S. S. Isied, D. N. Hendrickson, *J. Am. Chem. Soc.* **1987**, *109*, 6207–6208.
[32] G. Aromi, J. Telser, A. Ozarowski, L.-C. Brunel, H.-M. Stoeckli-Evans, J. Krzystek, *Inorg. Chem.* **2005**, *44*, 187–196.
[33] a) S. R. Cooper, G. C. Dismukes, M. P. Klein, M. Calvin, *J. Am. Chem. Soc.* **1978**, *100*, 7248–7252; b) M. Zheng, S. V. Khangulov, G. C. Dismukes, V. V. Barynin, *Inorg. Chem.* **1994**, *33*, 382–387; c) J. S. Bashkin, A. R. Schake, J. B. Vincent, H.-R. Chang, Q. Li, J. C. Huffman, G. Christou, D. N. Hendrickson, *J. Chem. Soc., Chem. Commun.* **1988**, *11*, 700–702; d) G. C. Dismukes, J. E. Sheats, J. A. Smegal, *J. Am. Chem. Soc.* **1987**, *109*, 7202–7203.
[34] P. Huang, N. Shaikh, M. Anderlund, S. Styring, L. Hammarström, *J. Inorg. Biochem.* **2006**, *100*, 1139–1146.
[35] In ref.[34] the spin Hamiltonian $\hat{H} = \beta\,\hat{\mathbf{S}}\cdot\mathbf{g}\cdot\mathbf{B} + \hat{\mathbf{I}}_1\cdot\hat{\mathbf{A}}_1\cdot\hat{\mathbf{S}} + \hat{\mathbf{I}}_2\cdot\hat{\mathbf{A}}_2\cdot\hat{\mathbf{S}}$ was used, resulting in the hyperfine parameters $A_{1,x} = 171\times10^{-4}\ \mathrm{cm}^{-1}$, $A_{1,y} = 148\times10^{-4}\ \mathrm{cm}^{-1}$, $A_{1,z} = 261\times10^{-4}\ \mathrm{cm}^{-1}$ and $A_{2,x} = 55\times10^{-4}\ \mathrm{cm}^{-1}$, $A_{2,y} = 90\times10^{-4}\ \mathrm{cm}^{-1}$, $A_{2,z} = 122\times10^{-4}\ \mathrm{cm}^{-1}$ for manganese 1 and 2 respectively.
[36] a) This is based on the potential of the $[Ru(bpy)_3]^{3/2+}$ couple that is considered to be largely solvent independent and amounts to 0.90 V versus $Fc^{+/0}$ in acetonitrile (1.27 V vs. NHE in water). Potentials in nonaqueous solvents are frequently measured and reported versus the aqueous SCE. This introduces unknown junction potentials, however, and a comparison of such data with potentials obtained in other solvents like water is not meaningful even if the potentials are formally given versus the same reference electrode like SCE or NHE. Independent of this problem, electrochemical potentials are intrinsically solvent dependent and any comparison between data in different solvents can only be approximate; b) I. Rubinstein, A. J. Bard, *J. Am. Chem. Soc.* **1981**, *103*, 512–516.
[37] Electrolysis at 0.92 V appears to be a multielectron process presumably because of the oxidation of degradation products.
[38] R. A. Marcus, *J. Chem. Phys.* **1965**, *43*, 679–701.
[39] a) The outer reorganisation energy of the electrode reaction in acetonitrile solutions ($n = 1.344$, $\varepsilon = 35.94$) was estimated from $\lambda_o = [e^2/(8\pi\varepsilon_o)](1/r - 1/R)(1/n^2 - 1/\varepsilon)$ where $r \approx 5$ Å is the molecular radius and $R(\geq 2r)$ is the distance between the molecule and its image charge; b) A. J. Bard, L. R. Faulkner, in *Electrochemical Methods: Fundamentals and Applications*, 2nd ed., Wiley, New York, **2001**.
[40] M. L. A. Abrahamsson, H. Berglund Baudin, A. Tran, C. Philouze, K. E. Berg, M. K. Raymond-Johansson, L. Sun, B. Åkermark, S. Styring, L. Hammarström, *Inorg. Chem.* **2002**, *41*, 1534–1544.
[41] a) P. J. Pessiki, S. V. Khangulov, G. C. Dismukes, *J. Am. Chem. Soc.* **1994**, *116*, 891–897; b) S. V. Khangulov, P. J. Pessiki, V. V. Barynin, D. E. Ash, G. C. Dismukes, *Biochemistry* **1995**, *34*, 2015–2025; c) T. Howard, J. Telser, V. J. DeRose, *Inorg. Chem.* **2000**, *39*, 3379–3385; d) S. Blanchard, G. Blondin, E. Rivière, M. Nierlich, J.-J. Girerd, *Inorg. Chem.* **2003**, *42*, 4568–4578.
[42] K.-O. Schäfer, R. Bittl, W. Zweygart, F. Lendzian, G. Haselhorst, T. Weyhermüller, K. Wieghardt, W. Lubitz, *J. Am. Chem. Soc.* **1998**, *120*, 13104–13120.
[43] Formation of colloidal $MnO_2$ was not observed by visual inspection but cannot be excluded.
[44] a) J. E. Sheats, R. S. Czernuszewitcz, G. C. Dismukes, A. L. Rheingold, V. Petrouleas, J.-A. Stubbe, W. H. Armstrong, R. H. Beer, S. J. Lippard, *J. Am. Chem. Soc.* **1987**, *109*, 1435–1444; b) E. M. Boelrijk, S. V. Khangulov, C. G. Dismukes, *Inorg. Chem.* **2000**, *39*, 3009–3019.
[45] J. Limburg, J. S. Vrettos, H. Chen, J. C. de Paula, R. H. Crabtree, G. W. Brudvig, *J. Am. Chem. Soc.* **2001**, *123*, 423–430.
[46] G. M. Sheldrick, *Acta Crystallogr., Sect. A: Found. Crystallogr.* **1990**, *46*, 467–473.
[47] G. M. Sheldrick, *Computer Program for the Refinement of Crystal Structures*, University of Göttingen, **1997**.
[48] R. Manchanda, G. W. Brudvig, R. H. Crabtree, *New J. Chem.* **1994**, *18*, 561–568.

Received: July 19, 2006
Published Online: October 27, 2006

 © 2006 Wiley-VCH Verlag GmbH & Co. KGaA, Weinheim 

DOI: 10.1002/ejic.200600728

# Contribution to the Reactivity of *N*,*N*′-Diaryl-1,4-diazabutadienes Aryl–N=CH–CH=N–Aryl (Aryl = 2,6-Dimethylphenyl; 2,4,6-Trimethylphenyl) Towards Boron Trichloride

**Lothar Weber,*[a] Jan Förster,[a] Hans-Georg Stammler,[a] and Beate Neumann[a]**

**Keywords:** Diazabutadienes / Diazaboroles / Aminoboranes / Structures / Boron

The reaction of Aryl–N=CH–CH=N–Aryl (**3a**: Aryl = 2,6-$Me_2C_6H_3$; **3b**: Aryl = 2,4,6-$Me_3C_6H_2$) with 2 equiv. $BCl_3$ in a toluene/hexane mixture at –50 °C led to an inseparable mixture of borolium salts [Aryl–N$^a$=CH–CH=N(Aryl)$BCl_2$($N^a$–$B$)]$^+BCl_4^-$ (**4a**: Aryl = 2,6-$Me_2C_6H_3$; **9a**: Aryl = 2,4,6-$Me_3C_6H_2$) and [Aryl–N$^a$=CH–C(Cl)=N(Aryl)$BCl_2$($N^a$–$B$)]$^+BCl_4^-$ (**4b**: Aryl = 2,6-$Me_2C_6H_3$; **9b**: Aryl = 2,4,6-$Me_3C_6H_2$) and the bicyclic species [HC$^a$=N(Aryl)$BCl_2$N(Aryl)–C$^b$=($C^a$–$C^b$)]$_2$ (**5**: Aryl = 2,6-$Me_2C_6H_3$; **10**: Aryl = 2,4,6-$Me_3C_6H_2$). Sodium amalgam reduction of borolium salts **4a**,**b** and **9a**,**b** afforded inseparable mixtures of the diazaboroles 2,6-$Me_2C_6H_3N^aCH$=CR–N$^b$(2,6-$Me_2C_6H_3$)BCl($N^a$–$B$) (**1**: R = H; **6**: R = Cl) and 2,4,6-$Me_3C_6H_2N^aCH$=CR–N$^b$(2,4,6-$Me_3C_6H_2$)BCl($N^a$–$B$) (**2**: R = H; **11**: R = Cl). In order to obtain pure **1** and **2**, diazabutadienes **3a** and **3b** were slowly combined with 2 equiv. $BCl_3$ in the same solvents at –78 °C. The acyclic adducts $Cl_3BN$(Aryl)=CH–CH=N(Aryl)$BCl_3$ (**7a**: Aryl = 2,6-$Me_2C_6H_3$; **7b**: Aryl = 2,4,6-$Me_3C_6H_2$) were reduced with sodium amalgam to furnish the aminoboranes $Cl_2BN$(Aryl)CH=CH–N(Aryl)$BCl_2$ (**8**: Aryl = 2,6-$Me_2C_6H_3$; **12**: Aryl = 2,4,6-$Me_3C_6H_2$). Stirring solutions of **8** and **12** in the presence of $CaH_2$ cleanly gave the diazaboroles **1** and **2**, respectively. The novel compounds were characterized by elemental analyses and $^1$H-, $^{11}$B-, $^{13}$C NMR and mass spectra. The molecular structures of **1**, **4a**, **5** and **8** were elucidated by single X-ray diffraction analyses.

(© Wiley-VCH Verlag GmbH & Co. KGaA, 69451 Weinheim, Germany, 2006)

## Introduction

The synthesis and reactivity of 1,3-dialkyl-2-halo-2,3-dihydro-1*H*-1,3,2-diazaboroles **I** as well as their molecular structures have been thoroughly investigated and documented in the literature.[1–12] More recently, the electrochemical and optophysical properties of such compounds have attracted our interest. The electrochemical oxidation of 1,3-di-*tert*-butyl-2,3-dihydro-1*H*-1,3,2-diazaboroles by cyclic voltammetry displays clean but irreversible waves, and the oxidation potentials $E_{ox,1/2}$ vary strongly with the substitution pattern at the boron atom.[13] Diazaboroles that are functionalized at the boron center by thienyl-, dithienyl- or biphenyl groups are highly luminescent, emitting bright blue light upon UV irradiation.[14,15] With respect to this, we planned to extend the scope of our diazaboroles to representatives with aryl groups at both ring nitrogen atoms.

In an early paper, we described the preparation of heterocycle **II** by treatment of diacetyldianil with methylboron dibromide and subsequent reduction of the obtained borolium salt with an excess of sodium amalgam.[3]

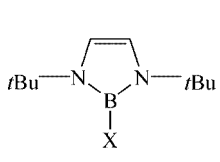


**I**

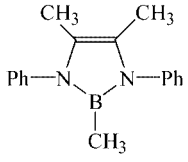


**II**

Later this route was followed to synthesize the 2-chloro-1,3-dixylyl-2,3-dihydro-1*H*-1,3,2-diazaborole (**1**).[10] An alternative route to **1** and to the corresponding 2-bromo derivative was based on the reduction of the corresponding diazabutadiene with lithium metal and the cyclocondensation of the dilithiated species with $BX_3$ (X = Cl, Br).[10] In this contribution we report on the reaction of *N*,*N*′-diaryl-1,4-diazabutadienes with $BCl_3$. It was found that the reactivity of the *N*,*N*′-diaryl-1,4-diazabutadienes towards $BCl_3$ is far less straightforward than that of *N*,*N*′-di-*tert*-butyl-1,4-diazabutadiene.

## Results and Discussion

For the synthesis of **1**, it was obvious to follow the procedure that we previously elaborated.[10] In only one instance did the combination of diazabutadiene **3a** with two molar equivalents of boron trichloride in a mixture of toluene and hexane at –50 °C and subsequent stirring for 15 h

[a] Fakultät für Chemie der Universität Bielefeld,
Universitätsstrasse 25, 33615 Bielefeld, Germany
Fax: +49-521-106-6146
E-mail: lothar.weber@uni-bielefeld.de


InterScience
© 2006 Wiley-VCH Verlag GmbH & Co. KGaA, Weinheim

at 20 °C lead to the precipitation of the burgundy-red borolium salt **4a** in about 70% yield. In all the other cases, however, a black solid precipitated, which was identified as an inseparable mixture of **4a** and its analogue **4b** with a chlorine substituent at a ring carbon atom (about 30% yield). After filtration, the mother liquor was placed for 14 d at +4 °C, and compound **5** separated as deep red crystals in 18% yield. When the supernatant solution was decanted and concentrated to one-third of its volume, impure diazaborole **6** was isolated after storing this solution for 2 d at –4 °C. Recrystallization from pentane led to a few crystals of pure compound **6**, which is chlorinated at the C=C double bond.

The usual reduction of the mixture of **4a** and **4b** with sodium amalgam in hexane afforded an inseparable mixture of the diazaboroles **1** and **6**. A **1**/**6** ratio of 10:1 was determined by $^1$H NMR spectroscopy. Although the reaction of pure salt **4a** gave a sample of pure **1** in one case, this synthetic pathway was discarded because of its poor reproducibility (Scheme 1).

Slow combination (4–5 h) of a toluene solution of **3a** with a cold (–78 °C) solution of $BCl_3$ in pentane in a molar ratio of 1:2 gave a precipitate of the red-brown adduct **7a** (60% yield). A slurry of this material in *n*-pentane was treated with sodium amalgam at 20 °C. From the supernatant solution, the acyclic doubly borylated (*E*)-*N*,*N*′-diaminoethene **8** was isolated as colorless crystals in about 70% yield. Stirring a solution of **8** in pentane in the presence of $CaH_2$ led to cyclization and the formation of diazaborole **1** (46% yield) (Scheme 2).

The reaction of diazabutadiene **3b** with 2 equiv. $BCl_3$ at –50 °C in a toluene/hexane mixture was performed analogously. A 1:1 mixture of the borolium salts **9a** (R = H) and **9b** (R = Cl) precipitated as a black solid (about 20% yield).

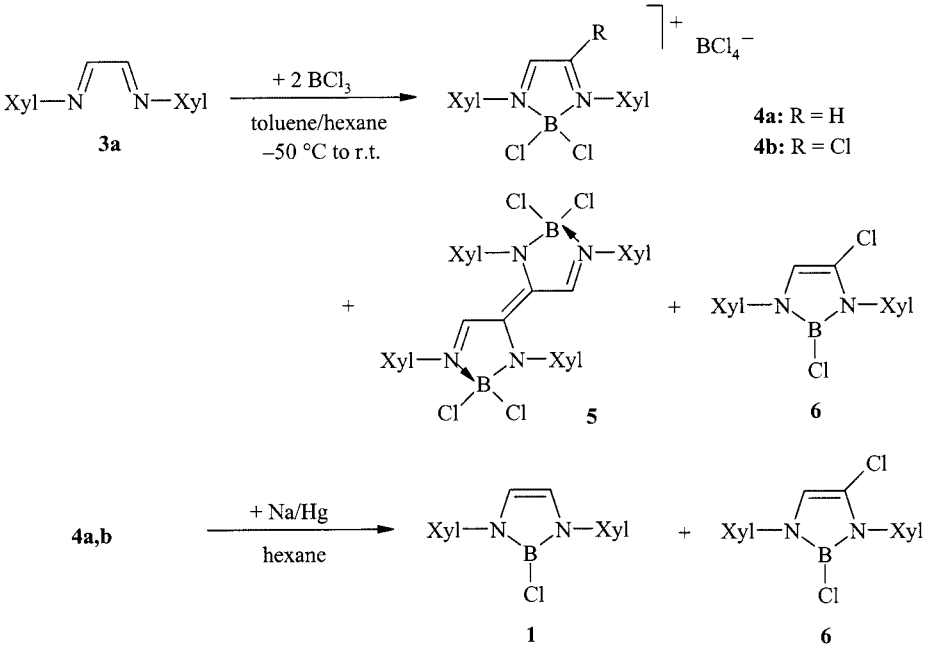


Scheme 1.

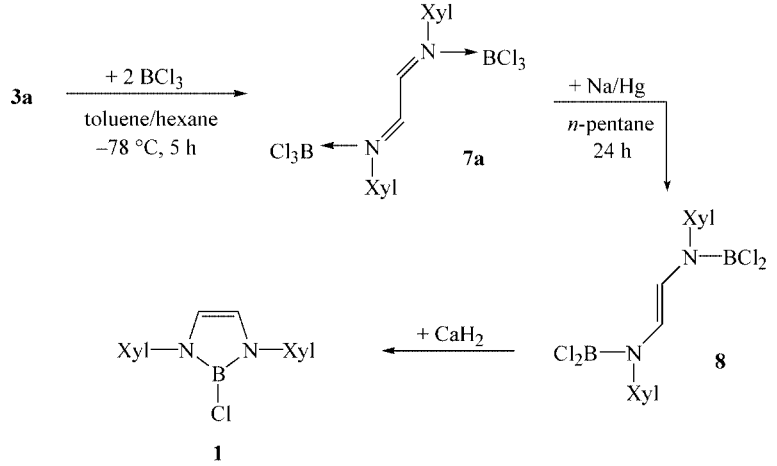


Scheme 2.

 © 2006 Wiley-VCH Verlag GmbH & Co. KGaA, Weinheim 

The mother liquor was concentrated and stored at +4 °C for 14 d, after which product **10** separated as deep green crystals in 14% yield (Scheme 3).

In the $^{11}B$ NMR spectrum of the mother liquor, a small singlet at $\delta$ = 21.8 ppm indicates small amounts of a 1,3,2-diazaborole. Its isolation, however, failed. The reduction of **9a**,**b** with sodium amalgam led to an inseparable mixture of the diazaboroles **2** and **11**. The generation of pure **2** first required the preparation of the violet adduct **7b** from the reaction of **3b** and 2 equiv. $BCl_3$ at –78 °C for 4–5 h (70% yield). The sodium amalgam reduction of **7b** afforded the acyclic aminoborane **12**, which upon treatment with $CaH_2$ cyclized to **2** in 54% yield (Scheme 4).

In order to suppress undesired side reactions at the carbon atom of the heterocycle, diacetyl[bis(2,6-dimethylphenylimine)] **13** was subjected to reaction with 2 equiv. $BCl_3$ in *n*-hexane. The green borolium salt **14** (yield 63%) was reduced with sodium amalgam to furnish, near quantitatively, the expected diazaborole **15** (Scheme 5).

Because of the pronounced thermolability of the 2-chloro-1,3,2-diazaborole **15**, this compound was converted immediately into the more stable 2-cyano-1,3,2-diazaborole **16** by reaction with silver cyanide in acetonitrile (Scheme 5).

The $^{11}B$ NMR spectra of the borolium salts show singlets ($\delta$ = 7.7 ppm) in the typical region for tetracoordinate boron atoms. For the tetracoordinate boron atoms in the binuclear compounds **5** and **10**, singlets are observed at $\delta$ = 8.6 and 8.5 ppm, respectively. The 2-chloroboroles **1**, **2**, **6** and **11** give rise to $^{11}B$ NMR signals at $\delta$ = 21.1–21.8 ppm. An influence of the Cl substituent at the C=C bond is not visible. In the $^{11}B$ NMR spectra of 2-cyanoborole **16**, the $^{11}B$ resonance appears as a singlet at $\delta$ = 13.5 ppm. The $^{11}B$ NMR resonances of the acyclic aminodichloroboranes **8** and **12** are at $\delta$ = 32.5 ppm. The signals for the ring protons

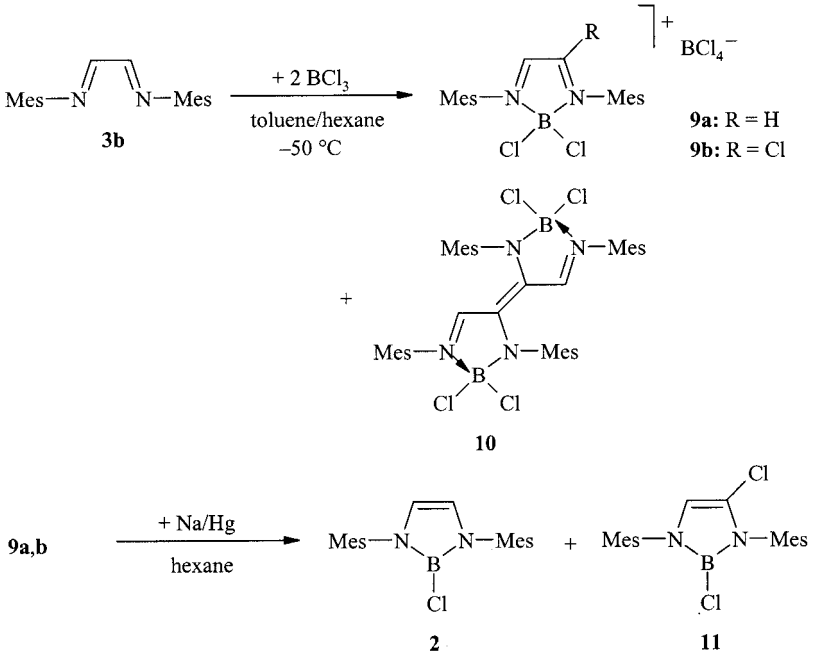


Scheme 3.

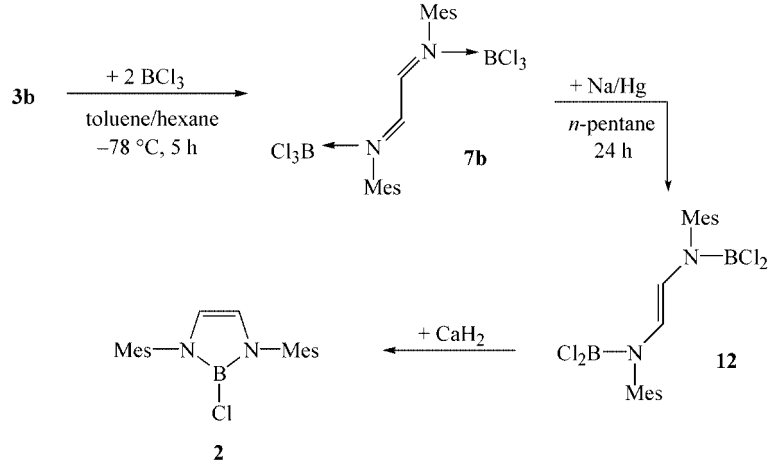


Scheme 4.

 © 2006 Wiley-VCH Verlag GmbH & Co. KGaA, Weinheim 

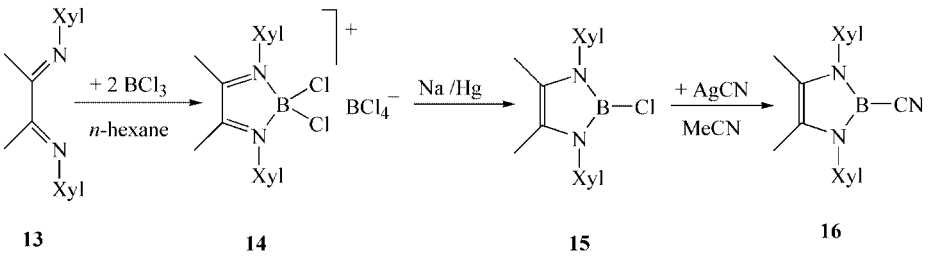


Scheme 5.

in the diazaboroles **1**, **2**, **6** and **11** are observed in the range from 5.51 to 5.93 ppm. The protons at the 1,6-diazahexatriene backbone of **5** and **10** are assigned as singlets at $\delta$ = 6.85 ppm. In the (*E*)-configured diaminoethenes **7** and **12**, the protons at the double bond give rise to singlets at $\delta$ = 6.40 ppm.

In the $^{13}C\{^1H\}$ NMR spectra of diazaboroles **1** and **2**, singlets at $\delta$ = 117.7 and 117.8 ppm, respectively, are assigned to the identical carbon atoms of the C=C group of the rings. The corresponding carbon atoms in the chlorinated derivative **6** give rise to two singlets at $\delta(^{13}C)$ = 113.7 and 126.8 ppm. The carbon atoms of the $N_2C_4$ backbone of **5** and **10** are attributed to singlets at $\delta$ = 161.3 and 170.3 ppm, respectively.

## X-ray Structural Analysis of 1

Single crystals of **1** were grown from the crude reaction mixture at +4 °C. The molecular structure of **1** (Figure 1, Table 1) features a planar 1,3,2-diazaborole ring with two almost orthogonally oriented *ortho*-xylyl substituents at the nitrogen atoms (interplanar angle between the heterocycle and arene ring $\varphi$ = 82.2°). A $C_2$ axis bisects the molecule along the B(1)–Cl(1) vector. The bond length B(1)–Cl(1) [1.768(2) Å] is close to the sum of the covalent radii of bo-

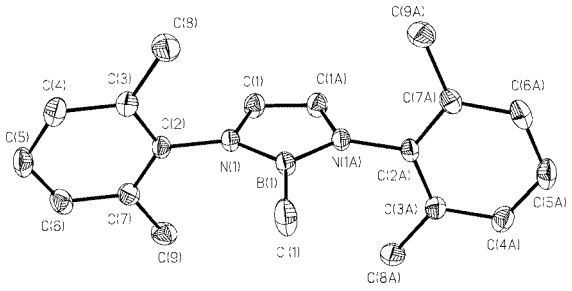


Figure 1. Molecular structure of **1** in the crystal; H atoms have been omitted for clarity. Selected bond lengths [Å] and angles [°]: B(1)–Cl(1) 1.768(2), B(1)–N(1) 1.419(1), N(1)–C(1) 1.401(2), C(1)=C(1A) 1.349(2), N(1)–C(2) 1.433(2); N(1)–B(1)–N(1A) 106.9(1), N(1)–B(1)–Cl(1) 126.6(1), B(1)–N(1)–C(1) 107.2(1), B(1)–N(1)–C(2) 130.3(1), C(1)–N(1)–C(2) 122.5(1), N(1)–C(1)–C(1A) 109.4(1).

Table 1. Crystal data and collection parameters.

| | **1** | **4a** | **5** | **8** |
|---|---|---|---|---|
| Empirical formula | $C_{18}H_{20}BClN_2$ | $C_{18}H_{20}B_2Cl_6{\cdot}0.5C_7H_8$ | $C_{36}H_{38}B_2Cl_4N_4$ | $C_{18}H_{20}B_2Cl_4N_2$ |
| $M_r$ [mg mol$^{-1}$] | 310.62 | 544.75 | 690.12 | 427.78 |
| Crystal dimensions [mm] | 0.30 × 0.12 × 0.06 | 0.24 × 0.17 × 0.04 | 0.15 × 0.15 × 0.14 | 0.30 × 0.30 × 0.24 |
| Crystal system | monoclinic | monoclinic | monoclinic | monoclinic |
| Space group | *C*2/*c* | *C*2/*c* | *P*2$_1$/*n* | *P*2$_1$/*n* |
| *a* [Å] | 14.5730(4) | 26.9130(6) | 10.3100(3) | 7.54300(10) |
| *b* [Å] | 7.4850(2) | 10.7970(2) | 14.8210(3) | 14.4950(2) |
| *c* [Å] | 16.6840(4) | 17.6110(3) | 11.4650(4) | 10.1860(2) |
| $\beta$ [°] | 114.9510(16) | 90.8770(12) | 93.6320(14) | 109.3190(10) |
| *V* [Å$^3$] | 1650.02(7) | 5116.80(17) | 1748.39(9) | 1050.98(3) |
| *Z* | 4 | 8 | 2 | 2 |
| $\rho_{calcd}$ [mg m$^{-3}$] | 1.250 | 1.414 | 1.311 | 1.352 |
| $\mu$ [mm$^{-1}$] | 0.229 | 0.685 | 0.371 | 0.568 |
| *F*(000) | 656 | 2232 | 720 | 440 |
| $\Theta$ [°] | 3–30 | 3–27.5 | 3–27.5 | 3–30 |
| Collected reflections | 22930 | 49724 | 21040 | 28834 |
| Unique reflections | 2417 | 5848 | 4002 | 3061 |
| *R*(int) | 0.043 | 0.052 | 0.040 | 0.030 |
| Refined parameters | 141 | 293 | 262 | 120 |
| Gof | 1.035 | 1.020 | 1.017 | 1.045 |
| $R_F$ [$I > 2\sigma(I)$] | 0.0402 | 0.0311 | 0.0354 | 0.0261 |
| $wR_F^2$ [all data] | 0.1125 | 0.0788 | 0.0923 | 0.0708 |
| $\Delta\rho_{max/min}$ [e Å$^{-3}$] | 0.281/–0.352 | 0.279/–0.248 | 0.274/–0.265 | 0.327/–0.310 |
| Remarks | – | disorder of toluene on an inversion centre | disorder of hydrogens at C(17) and C(18) | – |
| CCDC number | 616595 | 616596 | 616597 | 616598 |

 © 2006 Wiley-VCH Verlag GmbH & Co. KGaA, Weinheim 

ron (0.81 Å) and chlorine (0.99 Å)[16] and compares well with the corresponding value in solid $B_2Cl_4$ (1.75 Å).[17] Atomic distances and valence angles within the diazaborole ring are in good agreement with the corresponding data for XylN[a]–CH=CH–N[b](Xyl)BI(*N[a]–B*)[10] and need no particular discussion at this point.

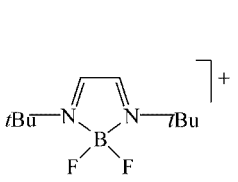


**III**

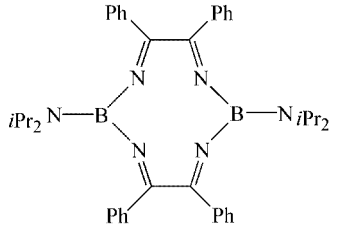


**IV**

## X-ray Structural Analysis of 4a

Red plates of **4a** suitable for an X-ray diffraction study (Table 1) were grown from the toluene/hexane mother liquor after removal of solid **4a**. The analysis features a planar diazaborolium cation [sum of bond angles 539.3°(1)], in addition to a tetrachloroborate anion (Figure 2).

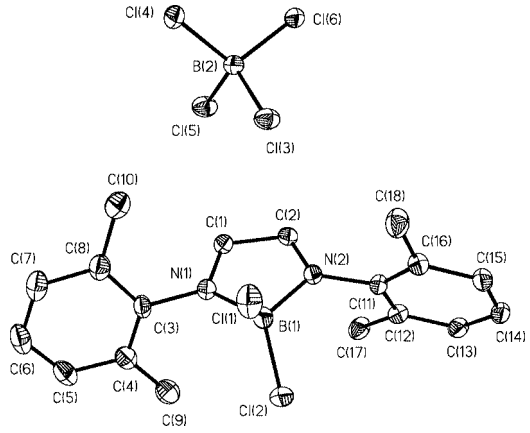


Figure 2. Molecular structure of **4a** in the crystal; H atoms have been omitted for clarity. Selected bond lengths [Å] and angles [°]: B(1)–Cl(1) 1.813(2), B(1)–Cl(2) 1.791(2), B(2)–Cl(3) 1.872(2), B(2)–Cl(4) 1.830(2), B(2)–Cl(5) 1.844(2), B(2)–Cl(6) 1.866(2), B(1)–N(1) 1.615(2), B(1)–N(2) 1.594(2), N(1)=C(1) 1.276(2), N(1)–C(3) 1.462(2), N(2)=C(2) 1.279(2), N(2)–C(11) 1.464(2), C(1)–C(2) 1.477(2); N(1)–B(1)–N(2) 95.8(1), B(1)–N(1)–C(1) 110.7(1), B(1)–N(1)–C(3) 127.4(1), B(1)–N(2)–C(2) 111.5(1), B(1)–N(2)–C(11) 125.9(1), C(1)–N(1)–C(3) 121.2(1), C(2)–N(2)–C(11) 121.7(1), N(1)–C(1)–C(2) 110.7(1), N(2)–C(2)–C(1) 110.6(1), Cl(1)–B(1)–Cl(2) 113.3(1), B(2)–Cl(3–6) 107.4(1)–111.2(1).

There are no bonding contacts between the cation and the anion. The bond lengths B(1)–Cl(1) [1.813(2) Å] and B(1)–Cl(2) [1.791(2) Å] are slightly shorter than the B–Cl bonds in $BCl_4^-$, which range from 1.830(2) to 1.872(2) Å. The boron–nitrogen bond lengths [B(1)–N(1) 1.615(2) Å, B(1)–N(2) 1.594(2) Å] slightly exceed the average value for the B–N single bond (1.59 Å) found in aminoboranes[18] and compare well with the corresponding bond lengths in cation **III** [1.607(3) and 1.611(3) Å].[19]

In 1,3,2-diazaboroles B–N bond lengths range from 1.40 to 1.45 Å. The endocyclic C–N bond lengths [C(1)–N(1) 1.276(2) Å, C(2)–N(2) 1.279(2) Å] are characteristic for double bonds and compare well with those in the cyclic ketiminoborane **IV** [1.273(3)–1.277(2) Å].[20]

The carbon–carbon bond length in the cation [1.477(2) Å] indicates a bond order of unity, whereas in diazaboroles, double bonds [1.362(8) Å in **1**] are typical. In comparison with **1** [106.9(4)°], the angle at the boron atom is compressed to 95.8(1)°, whereas the endocyclic angles B(1)–N(1)–C(1) [110.7(1)°], B(1)–N(1)–C(2) [111.5(1)°], N(1)–C(1)–C(2) [110.7(1)°] and N(2)–C(2)–C(1) [110.6(1)°] are slightly more obtuse than that in **1** [107.2(1), 109.4(1)°].

## X-ray Structural Analysis of 5

The X-ray analysis (Figure 3, Table 1) discloses a molecule in which two planar $BN_2C_2$ rings (sum of angles 539.7°) are fused by an elongated C(1)–C(1A) multiple bond [1.398(3) Å] ($C{=}C_{calcd.}$ = 1.33 Å) with an inversion center in the middle of the bond. The bond C(1)–N(1) [1.387(2) Å] is between the double bond N(2)=C(2) [1.300(2) Å] on the one hand and the single bonds N(1)–C(3) [1.440(2) Å] and N(2)–C(11) [1.447(2) Å] on the other hand. The distance C(1)–C(2) [1.437(2) Å] corresponds to a single bond.

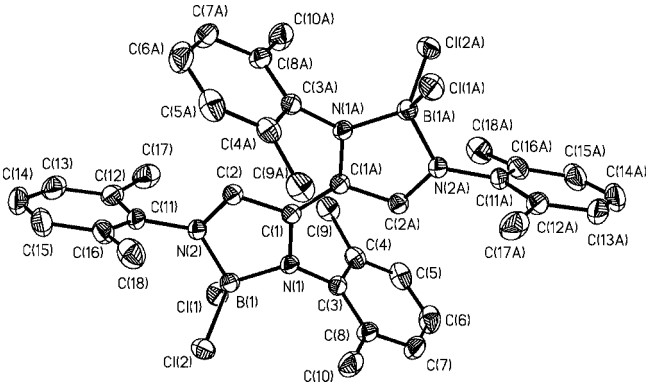


Figure 3. Molecular structure of **5** in the crystal. Selected bond lengths [Å] and angles [°]: B(1)–Cl(1) 1.840(2), B(1)–Cl(2) 1.878(2), B(1)–N(1) 1.518(2), B(1)–N(2) 1.576(2), N(1)–C(1) 1.387(2), N(1)–C(3) 1.440(2), N(2)=C(2) 1.300(2), N(2)–C(11) 1.447(2), C(1)–C(2) 1.437(2), C(1)=C(1A) 1.398(3); Cl(1)–B(1)–Cl(2) 106.6(1), N(1)–B(1)–N(2) 98.5(1), B(1)–N(1)–C(1) 111.4(1), B(1)–N(2)–C(2) 110.2(1), B(1)–N(1)–C(3) 125.4(1), B(1)–N(2)–C(11) 129.1(1), N(1)–C(1)–C(2) 107.0(1), N(1)–C(1)–C(1A) 128.7(2), N(2)–C(2)–C(1) 112.6(1), C(2)–N(2)–C(11) 120.3(1).

The boron–nitrogen bond B(1)–N(1) [1.518(2) Å] reflects a single bond between a tetracoordinate boron atom and an $sp^2$-hybridized nitrogen atom. It is markedly shorter than the coordinative bond B(1)–N(2) [1.576(2) Å]. The B–Cl bond lengths [1.840(2) and 1.878(2) Å] are longer than

 © 2006 Wiley-VCH Verlag GmbH & Co. KGaA, Weinheim 

those in ring **4** [1.791(2) and 1.813(2) Å] and compare with the B–Cl bond lengths in the $BCl_4^-$ ion.

The shortening of bond N(1)–C(1) and the elongation of bond C(1)=C(1A) are consistent with an extensive delocalization of charge as indicated by the two limiting formulae (Scheme 6).

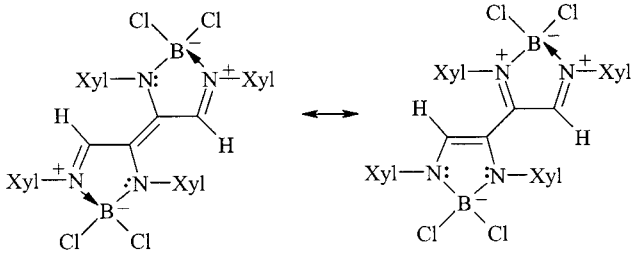

Scheme 6.

The xylyl rings are oriented in a near perpendicular fashion to the plane defined by the two heterocycles, with interplanar angles of $\varphi$ = 99.3° at N(1) and $\varphi$ = 88.1° at N(2). The angle B(1)–N(1)–N(2) [98.5(1)°] is markedly more acute than those in 1,3,2-diazaboroles [cf. 106.9(1) in **1**]. The angles B(1)–N(1)–C(1) [111.4(1)°] and B(1)–N(2)–C(2) [110.2(1)°] compare with those in the chloroborolium cation of **4a** [110.7(1) and 111.5(1)°] and are slightly more obtuse than that in diazaborole **1** [107.2(1)°]

## X-ray Structural Analysis of 8

Single crystals of **8**, suitable for an X-ray structural study, were grown from a toluene/hexane mixture at 4 °C. The analysis shows the features of a planar 2,5-diaza-1,6-dibora-hexa-1,3,5-triene with an inversion center in the middle of the C=C bond (Figure 4, Table 1). The planes of the two xylyl substituents at the nitrogen atoms are perpendicularly oriented to the plane of the chain ($\varphi$ = 85.8°). The chlorine atoms at the boron are located in the plane of the molecule and feature single bonds with lengths of 1.766(1) and 1.767(1) Å. The B–N bond length of 1.395(1) Å is consistent with a double bond, as is the central bond length C(1)–C(1A) of 1.333(2) Å. The distances N(1)–C(1) [1.422(1) Å] and N(1)–C(2) [1.451(1) Å] reflect single bonds.

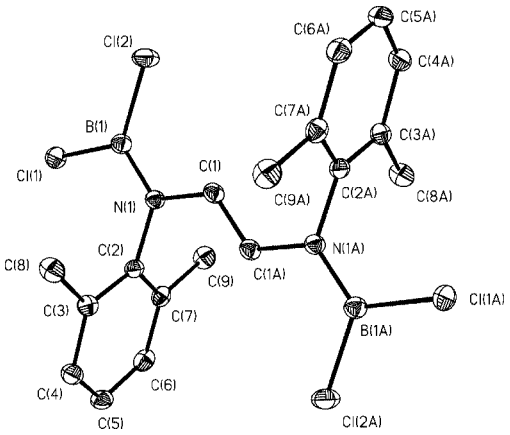


Figure 4. Molecular structure of **8** in the crystal; H atoms have been omitted for clarity. Selected bond lengths [Å] and angles [°]: B(1)–Cl(1) 1.766(1), B(1)–Cl(2) 1.767(1), B(1)–N(1) 1.395(1), N(1)–C(1) 1.422(1), N(1)–C(2) 1.451(1), C(1)=C(1A) 1.333(2); Cl(1)–B(1)–Cl(2) 118.1(1), Cl(1)–B(1)–N(1) 120.2(8), Cl(2)–B(1)–N(1) 121.7(1), B(1)–N(1)–C(1) 123.2(1), B(1)–N(1)–C(2) 121.1(1), C(1)–N(1)–C(2) 115.7(1), N(1)–C(1)–C(1A) 123.2(1).

In going from diazaboroles with various alkyl substituents at the ring atoms to xylyl and mesityl units, the generation of diazaboroles with one chlorine atom at the C=C bond was unexpected. In the case of compound **15** in which the double bond is substituted by two methyl groups, such a behavior could not be observed. Here, a recent paper on the reactivity of $BCl_3$ towards glyoxal[bis(2,6-diisopropylphenylimine)] by Mair et al. seems relevant.[21] He postulated the initial formation of a borolium salt **V**, the cation of which undergoes a twofold nucleophilic attack by chloride ions to eventually yield the trichlorinated diazaborolidine **VII** (Scheme 7). If, in our case, transient diazaborolidines are dehydrochlorinated by a base, diazaboroles such as **6** and **11** would be the products. It is conceivable that the carbon chlorination of diaryldiazabutadienes is favored by bulky arene groups.

The initial step in the formation of **5** and **10** is most likely the electrophilic attack of one immonium carbon atom of **4a** or **9a** at the C=C bond of **6** or **11** to give intermediate **VIII**. Elimination of HCl leads to cation **IX**, which finally adds a chloride ion at the tricoordinate boron atom to yield products **5** or **10** (Scheme 8).

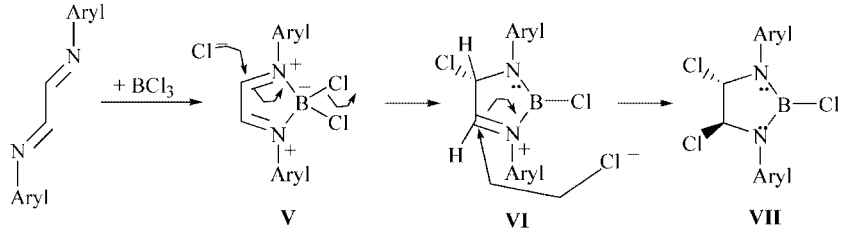


Aryl = 2,6-*i*Pr$_2$C$_6$H$_3$

Scheme 7.

 © 2006 Wiley-VCH Verlag GmbH & Co. KGaA, Weinheim 

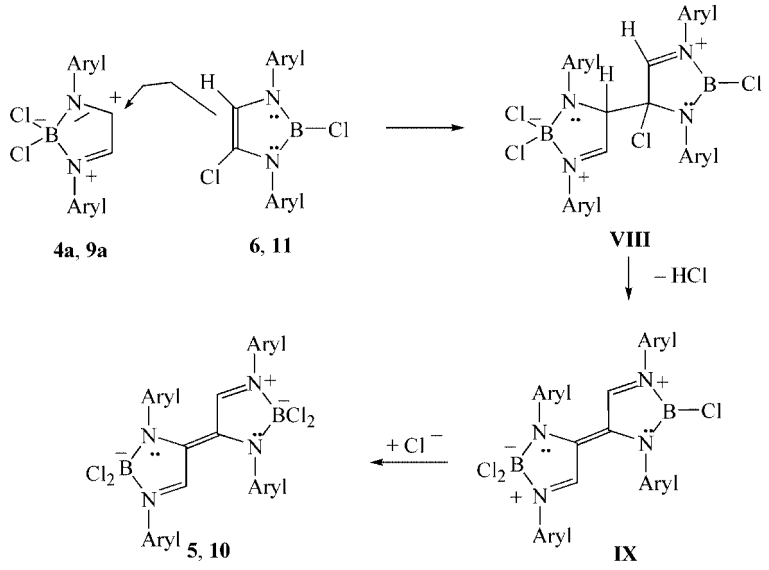


Scheme 8.

## Conclusions

The extension of methodologies for the synthesis of 1,3-dialkyl-2,3-dihydro-1*H*-1,3,2-diazaboroles to the construction of 1,3-diaryl-2,3-dihydro-1*H*-1,3,2-diazaboroles is not straightforward. The direct combination of *N*,*N*′-diaryl-1,4-diazabutadienes with 2 equiv. boron trichloride and the reduction of the obtained borolium salts by sodium amalgam invariably afforded mixtures of singly and doubly chlorinated products. Thus, a detour to pure 2-chloro-1,3-diaryl-2,3-dihydro-1*H*-1,3,2-diazaboroles was developed. Reaction of the components at –78 °C gave a 1:2 adduct, the reduction of which furnished aminoboranes $Cl_2BN(Aryl)$-$CH{=}CHN(Aryl)BCl_2$. Cyclization of these molecules to 2-chloro-1,3,2-diazaboroles was effected by solid calcium hydride.

## Experimental Section

**General:** All experiments were performed under dry, oxygen-free dinitrogen by using standard Schlenk techniques. Solvents were dried with appropriate drying agents and freshly distilled under $N_2$ before use. The following compounds were prepared according to literature procedures: $2,6\text{-}Me_2C_6H_3N{=}CHCH{=}NC_6H_3Me_2$-2,6 (**3a**)[22], $2,4,6\text{-}Me_3C_6H_2N{=}CHCH{=}NC_6H_2Me_3$-2,4,6 (**3b**)[23] and $2,6\text{-}Me_2C_6H_3N{=}C(Me)C(Me){=}NC_6H_3Me_2$-2,6 (**13**).[24,25] $^1H$, $^{11}B$ and $^{13}C$ NMR spectra were recorded at ambient temperature in $C_6D_6$ except for **5** and **10**, which were investigated in $CD_2Cl_2$ with a Bruker AM Avance DRX 500 instrument ($^1H$: 500.13 MHz; $^{11}B$: 160.46 MHz; $^{13}C$: 125.75 MHz). The spectra were referenced versus $SiMe_4$ ($^1H$, $^{13}C$) and $BF_3{\cdot}OEt_2$ ($^{11}B$) standards. Boron trichloride, glyoxal, 2,6-dimethylaniline and 2,4,6-trimethylaniline were purchased commercially.

**Reaction of Glyoxal-bis(2,6-dimethylphenylimine) (3a) with Boron Trichloride:** A solution of **3a** (18.2 g, 69.0 mmol) in a mixture of toluene (300 mL) and hexane (100 mL) was added over 4.5 h to a chilled solution (–50 °C) of boron trichloride (16.4 g, 140.0 mmol) in hexane (250 mL). After stirring at –50 °C for another hour, it was warmed up to ambient temperature and stirring was continued for 15 h. A microcrystalline solid was filtered off, washed with hexane and dried in vacuo to give 11.0 g of a mixture of borolium salts **4a** and **4b**. The filtrate was stored for 14 d at +4 °C, and dark red crystals of **5** (4.2 g, 18%) separated. In the supernatant liquid, the presence of a 1,3,2-diazaborole was evidenced by $^{11}B$ NMR spectroscopy ($\delta$ = 21.6 ppm). The filtrate was concentrated to 30% of its volume and stored for 2 d at –4 °C, from which crystals of impure **6** were formed. Recrystallization from pentane yielded a few crystals of pure **6**.

In only one case did the reaction of **3a** and $BCl_3$ cleanly afford the burgundy red borolium salt **4a** in about 70% yield. A slurry of the borolium salts **4a** and **4b** (11.0 g) in a mixture of toluene (150 mL) and hexane (300 mL) was treated with sodium amalgam (300 g of a 1% alloy) and vigorously stirred for 20 h. The solution was decanted, filtered, and the solvents evaporated to dryness to give 4.8 g of an inseparable mixture of **1** and **6**. If the solution, after having been separated from mercury, was kept for 14 d at +4 °C, a few crystals of pure **1**[10] could be separated.

**1:** $^1H$ NMR: $\delta$ = 2.17 (s, 12 H, $CH_3$), 5.85 (s, 2 H, HC=N), 6.99 (m, 6 H, aryl-H) ppm. $^{13}C\{^1H\}$ NMR: $\delta$ = 18.1 (s, $CH_3$), 117.7 (s, HC=N), 127.3 (s, *p*-aryl-C), 135.8 (s, *o*-aryl-C), 139.9 (s, *i*-aryl-C) ppm. $^{11}B\{^1H\}$NMR: $\delta$ = 21.1 (s) ppm. EI-MS: *m*/*z* (%) = 310 (100) [$M^+$].

**6:** $^1H$ NMR: $\delta$ = 2.11 (s, 6 H, $CH_3$), 2.16 (s, 6 H, $CH_3$), 5.75 (s, 1 H, HC=N), 6.98 (m, 6 H, aryl-H) ppm. $^{13}C\{^1H\}$ NMR: $\delta$ = 18.02 (s, $CH_3$), 18.05 (s, $CH_3$), 113.7 (s, HC=N), 126.6 (s, ClC=N), 127.2 (s, *p*-aryl-C), 127.7 (s, *p*-aryl-C), 127.9 (s, *m*-aryl-C), 129.1 (s, *m*-aryl-C), 135.5 (s, *o*-aryl-C), 136.7 (s, *o*-aryl-C), 138.9 (s, *i*-aryl-C), 138.5 (s, *i*-aryl-C) ppm. $^{11}B\{^1H\}$ NMR: $\delta$ = 21.6 (s) ppm. EI-MS: *m*/*z* (%) = 344.1 (100) [$M^+$], 309.1 (79) [$M^+$ – Cl]. $C_{18}H_{19}BCl_2N_2$ (345.06): calcd. C 62.65, H 5.55, N 8.12; found C 62.67, H 5.44, N 8.15.

**5:** $^1H$ NMR: $\delta$ = 2.24 (s, 12 H, $CH_3$), 2.45 (s, 12 H, $CH_3$), 6.85 (s, 2 H, HC=N), 7.15 (m, 12 H, aryl-H) ppm. $^{13}C\{^1H\}$ NMR: $\delta$ = 19.1 (s, $CH_3$), 19.7 (s, $CH_3$), 128.9 (s, *p*-aryl-C), 129.2 (s, *p*-aryl-C), 130.9 (s, *m*-aryl-C), 133.7 (s, *o*-aryl-C), 136.8 (s, *o*-aryl-C), 137.7 (s, *i*-aryl-C), 139.1 (s, *i*-aryl-C), 161.3 (s, HC=N) ppm. $^{11}B\{^1H\}$ NMR: $\delta$ = 8.6 (s) ppm. EI-MS: *m*/*z* (%) = 688.2 (2) [$M^+$], 652.2 (100)

 © 2006 Wiley-VCH Verlag GmbH & Co. KGaA, Weinheim 

[$M^+$ – Cl], 618.2 (82) [$M^+$ – 2 Cl]. $C_{36}H_{38}B_2Cl_4N_4$ (690.12): calcd. C 62.65, H 5.55, N 8.12; found C 62.71, H 5.38, N 8.09. Because of the poor solubility, no reliable NMR spectra of the borolium salts **4a**,**b** were obtained.

**(*E*)-$Cl_2$B(*o*-Xyl)N–CH=CH–N(*o*-Xyl)B$Cl_2$ (8):** A solution of **3a** (5.29 g, 20.0 mmol) in toluene (100 mL) was added dropwise over 4–5 h to a chilled solution (–78 °C) of $BCl_3$ (4.67 g, 40 mmol) in pentane (75 mL). Immediately after the addition, the red-brown precipitate of the adduct **7a** was collected by filtration and dried at $10^{-3}$ bar. Reduction of the adduct was effected by treatment with sodium amalgam (100 g of a 1% alloy) in pentane (150 mL) over 24 h. The supernatant liquid was separated and concentrated to about 100 mL. Storage overnight at +4 °C afforded colorless crystals of **8** (5.13 g, 60%). $^1$H NMR: $\delta$ = 1.99 (s, 12 H, $CH_3$), 6.40 (s, 2 H, NCH=), 6.92 (m, 6 H, aryl-H) ppm. $^{13}$C{$^1$H} NMR: $\delta$ = 17.3 (s, $CH_3$), 120.5 (s, NCH=), 128.3 (s, *p*-aryl-C), 129.3 (s, *m*-aryl-C), 134.6 (s, *o*-aryl-C), 139.3 (s, *i*-aryl-C) ppm. $^{11}$B{$^1$H} NMR: $\delta$ = 32.6 (s) ppm. EI-MS: *m*/*z* (%) = 428.0 (100) [$M^+$], 395.2 (6) [$M^+$ – Cl], 310.1 (73) [$M^+$ – $BCl_3$]. $C_{18}H_{20}B_2Cl_4N_2$ (427.79): calcd. C 50.54, H 4.71, N 6.55; found C 50.26, H 4.82, N 6.43. Because of the low solubility of **7a**, no useful NMR spectra were obtained.

**Cyclization of 8 to 1:** A sample of **8** (0.50 g, 1.2 mmol) was dissolved in hexane (50 mL). $CaH_2$ (0.05 g) was added, and the slurry was stirred at ambient temperature for 48 h. It was filtered, and the filtrate concentrated to 10 mL and stored at –4 °C, after which crystalline **1** (0.175 g, 46%) separated.

**Reaction of Glyoxal-bis(2,4,6-trimethylphenylimine) (3b) with Boron Trichloride:** Analogously to the reaction of **3a** with $BCl_3$, a solution of **3b** (14.55 g, 50.0 mmol) in a mixture of toluene (200 mL) and hexane (50 mL) was combined with a chilled solution (–50 °C) of $BCl_3$ (11.8 g, 100.0 mmol) in hexane (250 mL) over a period of 4.5 h. Stirring was continued for 1 h at –50 °C and then for 15 h at 20 °C. The microcrystalline black precipitate was filtered off and dried (5.6 g of a mixture of salts **9a** and **9b**). Storage of the mother liquor for 2 weeks at +4 °C afforded dark green crystals of **10** (2.7 g, 14%). Sodium amalgam (200 g of a 1% alloy) was added to a slurry of the borolium salts (5.6 g) in a mixture of toluene (100 mL) and hexane (200 mL). The mixture was vigorously stirred for 20 h. The organic phase was decanted, and the solvents were removed in vacuo. An inseparable 4:1 mixture (2.4 g) of **2** and **11** as a white powder was obtained.

**10:** $^1$H NMR: $\delta$ = 2.17 (s, 18 H, $CH_3$), 2.29 (s, 6 H, $CH_3$), 2.36 (s, 12 H, $CH_3$), 6.85 (s, 2 H, =CHN), 6.93 (s, 4 H, aryl-H), 6.98 (s, 4 H, aryl-H) ppm. $^{13}$C{$^1$H} NMR: $\delta$ = 18.6 (s, $CH_3$), 20.5 (s, $CH_3$), 20.6 (s, $CH_3$), 129.4, 130.1, 131.2, 133.0, 134.2, 135.1, 136.0, 136.3, 138.6, 139.0 (10 s, aryl-C), 161.2 (s, =CHN) ppm. $^{11}$B{$^1$H} NMR: $\delta$ = 8.5 (s) ppm. EI-MS: *m*/*z* (%) = 744.2 (2) [$M^+$], 710.3 (100) [$M^+$ – Cl], 674.4 (66) [$M^+$ – 2 Cl]. $C_{40}H_{46}B_2Cl_4N_4$ (746.27): calcd. C 64.32, H 6.21, N 7.51; found C 64.30, H 6.11, N 7.52.

**2 and 11:** $^{11}$B{$^1$H} NMR: $\delta$ = 21.8 (s) ppm. This mixture was not analyzed further. Because of the poor solubility, no reliable NMR spectra of the borolium salts **9a**,**b** were obtained.

**(*E*)-$Cl_2$B(Mes)N–CH=CH–N(Mes)B$Cl_2$ (12):** By analogy to the preparation of **8**, compounds **3b** (5.84 g, 20.0 mmol) and $BCl_3$ (4.67 g, 40 mmol) were combined in a toluene/pentane mixture at –78 °C over 4–5 h. A violet precipitate was filtered off and dried at $10^{-3}$ mbar. Sodium amalgam reduction of this solid (150 g, 1% Na/Hg) was effected in pentane (150 mL) for 24 h. Concentration of the organic phase to about 100 mL and storage of the liquid overnight at +4 °C afforded colorless crystals of **12** (5.93 g, 65%). $^1$H NMR: $\delta$ = 2.03 (s, 12 H, *o*-$CH_3$), 2.04 (s, 6 H, *p*-$CH_3$), 6.50 [s, 2 H, NC(H)=C], 6.75 (s, 4 H, aryl-H) ppm. $^{13}$C{$^1$H} NMR: $\delta$ = 17.3 (s, *o*-$CH_3$), 20.9 (s, *p*-$CH_3$), 120.9 (s, CH=CH), 130.1 (s, *m*-aryl-C), 134.2 (s, *o*-aryl-C), 136.9 (s, *p*-aryl-C), 137.8 (s, *i*-aryl-C) ppm. $^{11}$B{$^1$H} NMR: $\delta$ = 32.6(s) ppm. EI-MS: *m*/*z* (%) = 338 (100) [$M^+$ – $BCl_3$]. $C_{20}H_{24}B_2Cl_4N_2$ (455.85): calcd. C 52.69, H 5.33, N 6.14; found C 52.63, H 5.35, N 6.13.

**Cyclization of 12 to 2:** A mixture of **12** (0.50 g, 1.1 mmol), $CaH_2$ (0.05 g) and hexane (50 mL) was stirred at 25 °C for 48 h and then filtered, and the filtrate was concentrated to 10 mL. Crystallization at –4 °C afforded pure **2** (0.20 g, 54%). $^1$H NMR: $\delta$ = 2.13 (s, 6 H, *p*-aryl-$CH_3$), 2.19 (s, 12 H, *o*-aryl-$CH_3$), 5.92 [s, 2 H, NC(H)=C], 6.79 (m, 4 H, aryl-H) ppm. $^{13}$C{$^1$H} NMR: $\delta$ = 18.0 (s, *o*-aryl-$CH_3$), 20.9 (s, *p*-aryl-$CH_3$), 117.8 (s, N–CH), 129.2 (s, *m*-aryl-C), 135.3 (s, *o*-aryl-C), 136.4 (s, *p*-aryl-C), 137.4 (s, *i*-aryl-C) ppm. $^{11}$B{$^1$H} NMR: $\delta$ = 21.9 (s) ppm. EI-MS: *m*/*z* (%) = 338.2 (100) [$M^+$]. $C_{20}H_{24}BClN_2$ (338.68): calcd. C 70.93, H 7.14, N 8.27; found C 70.68, H 7.20, N 8.16.

**Xyl–N$^a$C(CH$_3$)=C(CH$_3$)–N$^b$(Xyl)BCN(*N$^a$*–*B*) (16):** A solution of **13** (6.80 g, 23.0 mmol) in hexane (250 mL) was added dropwise over 4.5 h to a chilled solution (–50 °C) of $BCl_3$ (5.39 g, 46.0 mmol) in hexane (250 mL). Stirring was continued for 1 h at –50 °C and 15 h at ambient temperature. Green borolium salt **14** (7.6 g, 63%) was filtered off and dried at $10^{-1}$ bar. The slurry of the salt in hexane (350 mL) was reduced with sodium amalgam (150 g of a 1% alloy, 20 h). Decanting of the organic phase was followed by evaporation to dryness to afford crude **15** (4.5 g, 98.6%) as a light grey powder. A sample of solid AgCN (3.2 g, 24.0 mmol) was added to a solution of **15** in acetonitrile (350 mL), and the mixture was stirred for 20 h at 20 °C. It was filtered, and the filtrate was concentrated, after which **16** (3.10 g, 41.0%) was obtained. $^1$H NMR: $\delta$ = 1.44 [s, 6 H, =C($CH_3$)N], 2.03 (s, 12 H, aryl-$CH_3$), 6.99 (m, 6 H, aryl-H) ppm. $^{13}$C{$^1$H} NMR: $\delta$ = 9.8 [s, =C(*C*H$_3$)N], 17.9 (s, aryl-$CH_3$), 121.2 [s, *C*($CH_3$)=*C*($CH_3$)], 127.6 (s, *p*-aryl-C), 128.2 (s, BCN), 128.5 (s, *m*-aryl-C), 135.6 (s, *o*-aryl-C), 138.1 (s, *i*-aryl-C) ppm. $^{11}$B{$^1$H} NMR: $\delta$ = 13.5 (s) ppm. EI-MS: *m*/*z* (%) = 329.2 (100) [$M^+$], 314.2 (12) [$M^+$ – $CH_3$]. $C_{21}H_{24}BN_3$ (329.24): calcd. C 76.61, H 7.35, N 12.76; found C 76.59, H 7.42, N 12.65.

**15:** $^1$H NMR: $\delta$ = 1.57 [s, 6 H, =C($CH_3$)N], 2.15 (s, 12 H, aryl-$CH_3$), 7.02 (s, 6 H, aryl-H) ppm. $^{13}$C{$^1$H} NMR: $\delta$ = 10.2 [s, =C(*C*H$_3$)N], 18.2 (s, aryl-$CH_3$), 118.9 [s, =*C*($CH_3$)N], 127.2 (s, *p*-aryl-C), 128.3 (s, *m*-aryl-C), 136.6 (s, *o*-aryl-C), 138.6 (s, *i*-aryl-C) ppm. $^{11}$B{$^1$H} = 21.3 (s) ppm. EI-MS: *m*/*z* = 338.2 [$M^+$].

**X-ray Structural Analyses:** Crystal data were measured on a Nonius Kappa CCD-diffractometer and are given in Table 1. CCDC-616595 (**1**), -616596 (**4a**), -616597 (**5**) and -616598 (**8**) contain the supplementary crystallographic data for this paper. These data can be obtained free of charge from The Cambridge Crystallographic Data Centre via www.ccdc.cam.ac.uk/data_request/cif.

[1] J. S. Meriam, K. Niedenzu, *J. Organomet. Chem.* **1973**, *51*, C1–C2.
[2] K. Niedenzu, J. S. Meriam, *Z. Anorg. Allg. Chem.* **1974**, *406*, 251–259.
[3] L. Weber, G. Schmid, *Angew. Chem.* **1974**, *86*, 519; *Angew. Chem. Int. Ed. Engl.* **1974**, *13*, 467.
[4] G. Schmid, J. Schulze, *Chem. Ber.* **1977**, *110*, 2744.
[5] G. Schmid, J. Schulze, *Angew. Chem.* **1977**, *89*, 258–259; *Angew. Chem. Int. Ed. Engl.* **1977**, *16*, 246.
[6] G. Schmid, J. Schulze, *Chem. Ber.* **1981**, *114*, 495–504.
[7] G. Schmid, M. Polk, R. Boese, *Inorg. Chem.* **1990**, *29*, 4421–4429.
[8] G. Schmid, J. Lehr, M. Polk, R. Boese, *Angew. Chem.* **1991**, *103*, 1029–1031; *Angew. Chem. Int. Ed. Engl.* **1991**, *30*, 1015.

 © 2006 Wiley-VCH Verlag GmbH & Co. KGaA, Weinheim 

[9] L. Weber, E. Dobbert, H.-G. Stammler, B. Neumann, R. Boese, D. Bläser, *Chem. Ber./Recueil* **1997**, *130*, 705–710.
[10] L. Weber, E. Dobbert, R. Boese, M. T. Kirchner, D. Bläser, *Eur. J. Inorg. Chem.* **1998**, 1145–1152.
[11] L. Weber, E. Dobbert, H.-G. Stammler, B. Neumann, R. Boese, D. Bläser, *Eur. J. Inorg. Chem.* **1999**, 491–497.
[12] Review: L. Weber, *Coord. Chem. Rev.* **2001**, *215*, 39–77.
[13] L. Weber, I. Domke, W. Greschner, K. Miqueu, A. Chrostowska, P. Baylère, *Organometallics* **2005**, *24*, 5455–5463.
[14] L. Weber, I. Domke, C. Schmidt, T. Braun, H.-G. Stammler, B. Neumann, *Dalton Trans.* **2006**, 2127–2135.
[15] L. Weber, V. Werner, I. Domke, H.-G. Stammler, B. Neumann, *Dalton Trans.* **2006**, 3777–3784.
[16] A. F. Holleman, E. Wiberg, *Lehrbuch der Anorganischen Chemie*, 91st–100th ed., W. de Gruyter, Berlin, **1985**, p. 133.
[17] N. N. Greenwood, A. Earnshaw, *Chemie der Elemente*, 1st ed., VCH, Weinheim, **1988**, p. 249.
[18] P. Paetzold, *Adv. Inorg. Chem.* **1987**, *31*, 123.
[19] L. Weber, I. Domke, J. Kahlert, H.-G. Stammler, B. Neumann, *Eur. J. Inorg. Chem.* **2006**, 3419–3424.
[20] N. Weis, H. Pritzkow, W. Siebert, *Eur. J. Inorg. Chem.* **1999**, 7–9.
[21] F. S. Mair, R. Manning, R. C. Pritchard, J. E. Warren, *Chem. Commun.* **2001**, 1136–1137.
[22] H. tom Dieck, M. Svoboda, T. Greiser, *Z. Naturforsch., B: Chem. Sci.* **1981**, *36*, 823–832.
[23] M. B. Abrams, B. L. Scott, R. T. Baker, *Organometallics* **2000**, *19*, 4944–4956.
[24] H. tom Dieck, I. W. Renk, *Chem. Ber.* **1971**, *104*, 92–109.
[25] H. Bock, H. tom Dieck, *Chem. Ber.* **1967**, *100*, 228–246.

Received: August 4, 2006
Published Online: October 24, 2006

 © 2006 Wiley-VCH Verlag GmbH & Co. KGaA, Weinheim 

DOI: 10.1002/ejic.200600778

# Surface and Structural Features of Co-Fe Oxide Nanoparticles Deposited on a Silica Substrate

Víctor A. de la Peña O'Shea,*[a,b] M. Consuelo Álvarez-Galván,[a] José M. Campos-Martin,[a] Nieves N. Menéndez,[c] Jesús D. Tornero,[c] and José L. G. Fierro*[a]

**Keywords:** Cobalt / Iron / Oxides / Metal–metal interactions / Materials science

Mono- and dimetallic cobalt- and iron oxide nanoparticles deposited on the surface of a silica substrate have been prepared by an impregnation technique. Both the bulk and surface structures of these particles have been characterised by different physical and chemical techniques. The results provided by X-ray diffraction, Mössbauer and X-ray photoelectron spectroscopy show the formation of separate $Co_3O_4$ and $Fe_2O_3$ nanoparticles in oxide samples, but in no case were cobalt–iron mixed oxides detected. Quantitative data also showed that the dispersion degree of cobalt- and iron oxides is rather low. It was also observed that pretreatment of the supported metal oxide nanoparticles under a hydrogen atmosphere does not promote the formation of a metal–support interaction, although a cobalt–iron interaction is observed in the dimetallic systems. The diffraction patterns and photoelectron and Mössbauer spectra of these dimetallic samples provide conclusive proof for the formation of both metallic $Co^0$ and iron-cobalt ($Co_7Fe_3$) alloy phases in the hydrogen-reduced samples. It was also found that the crystallite size of the alloyed $Co_7Fe_3$ phase increases with increasing iron content, i.e. 11 and 23 nm for samples containing 1 % and 5 % Fe added to the base Co sample, respectively, while that of $Co^0$ was constant (10 nm).

(© Wiley-VCH Verlag GmbH & Co. KGaA, 69451 Weinheim, Germany, 2006)

## Introduction

Nowadays, composite materials give rise to numerous studies with a view to improving their mechanical, thermal, optical and other properties, which hold promise for novel technological applications. Transition metal oxides are being widely used, and Fe-Co materials are of particular interest in catalytic reactions such as the Fischer–Tropsch synthesis (FTS),[1–6] methanol decomposition,[7–9] $NH_3$ synthesis,[10] carbon nanotube synthesis.[11–13] Furthermore, their interesting magnetic properties[14] suggest that they will have many applications in magneto-optical recording media, displays and devices such as wave-guides, insulators, modulators and switches.[15–17]

This fact has provoked several reports in which these mixtures are prepared by different synthetic methods such as sol–gel,[18,19] co-precipitation,[20] plasma coating,[21] sintering[22] and thermal decomposition.[23] Co- and/or Fe-supported systems prepared by wetness- or incipient wetness impregnation methods from nitrate precursors have also been reported.[6,14] Dimetallic catalysts prepared by the incipient wetness method show reactivities different from that of equivalent Fe- or Co single-metal catalysts, thus indicating that the intimate interaction between Fe and Co is important.[24,25] A synthesis of iron-cobalt nanoparticles dispersed in a silica matrix has also been reported, and the authors noted the formation of magnetic cobalt ferrite nanocomposites, $Co_3O_4$ and ferrihydrite or Co-Fe alloys, depending on the Fe and Co precursors.[19] Fe/Co catalyst mixtures have been prepared on several supports, including alumina,[24] carbon,[26,27] zirconia[28] and titania.[14,25,29,30]

A viable methodology that has been developed for controlling the property of a metal is that of alloying.[31–35] Three structures have been found for the metal in the iron-cobalt alloy, depending on the synthesis temperature and the subsequent thermal treatment: a bcc structure, an α-Mn-like structure and a fcc structure that appears after thermal treatment.[36,37] The bcc and fcc structures are classical structures for iron- and cobalt-based alloys. These alloys exhibit outstanding properties, particularly the cobalt-enriched composites. Indeed, these latter are active in the FTS and favour the formation of olefins without producing high amounts of $CO_2$[4,38] and alcohol production.[6]

A large body of work has been developed over the past decades on the performance of supported cobalt catalysts, especially with regard to the effect of promoters,[39–43] sup-

[a] Instituto de Catálisis y Petroleoquímica, CSIC, Cantoblanco, 28049 Madrid, Spain
[b] Departament de Química Inorgànica, Universitat de Barcelona, C/Martí i Franquès 1–11, 08028 Barcelona, Spain
Fax: +34-93-490-7725
E-mail: victor@ qi.ub.es
[c] Universidad Autónoma de Madrid, Cantoblanco, 28049 Madrid, Spain

 © 2006 Wiley-VCH Verlag GmbH & Co. KGaA, Weinheim 

ports[44–46] and preparation[47–52] methods. Cobalt catalysts produce high yields of long-chain alkenes in the FTS. They are also characterised by a low ability to yield oxygenates. In addition, cobalt catalysts exhibit considerable stability in the metallic state.

Iron is the other active phase that is most often used in the hydrogenation reactions of carbon oxides. It is know that several forms of iron (iron, iron carbides, iron oxide) exist in iron-based catalysts when subjected to FTS, and there are many studies dealing with the role of iron phases in the FTS.[53–55] Iron catalysts used in CO hydrogenation are usually promoted to obtain a high stability and catalytic activity. These systems produce higher yields of oxygenated products and can perform the water gas-shift reaction. The incorporation of cobalt and iron phases onto a support substrate results in substantial changes in both activity and product distribution as, when used together, they do not simply give the additive properties (activity, selectivity) expected from knowledge of the properties of the individual metals. These dimetallic CoFe catalysts proved to be much more attractive in terms of alcohol formation and give rise to the production of ethanol and propanol, depending on the iron content.[6] Taking this into account, the possible interaction of cobalt and iron, in the form of cobalt ferrite or alloys, when used together as active phases for catalytic reactions such as FTS or as a possible magnetic composite should be studied by different characterisation techniques.

In light of the above, the present work was undertaken with the aim of analysing the effect of the incorporation of both cobalt and iron species supported on a silica matrix on the structural, textural and morphological characteristics relative to the properties shown by the monometallic systems. In particular, emphasis is placed on the formation of CoFe intermetallic compounds after catalyst activation. Some clues to the nature of the bulk and surface structures generated on the silica-supported cobalt-iron catalysts were obtained by XRD, X-ray photoelectron spectroscopy (XPS), Mössbauer spectroscopy and temperature-programmed reduction (TPR). The synergism between cobalt and iron, two FT active metals, will be explored in a subsequent work that will consider whether the above metals, when used together, give the additive properties (activity and selectivity) expected of the individual metals or not.

## Results and Discussion

### Chemical Composition and Textural Properties

The chemical composition of the oxide samples was determined by ICP-AES; results are compiled in Table 1. These results indicate that cobalt- and/or iron loadings are close to the nominal values. The BET specific areas and pore volumes of the fresh metal oxide loaded samples and the bare $SiO_2$ support, also summarised in Table 1, indicate that incorporation of cobalt and/or iron onto the $SiO_2$ substrate leads to a drop in both specific area and pore volume. A decrease in the BET area of around 20–30% is found upon incorporation of iron and cobalt, and a similar drop is found for the other two dimetallic (CoFe10/1-c and CoFe10/5-c) samples. The pore-size distributions of the metal-oxide-loaded samples and $SiO_2$ reference are displayed in Figure 1. The pore-size distributions of the samples do not change upon incorporation of cobalt- and/or iron oxides during the preparation step. The simultaneous drop in BET area and pore volume and the almost unchanged pore distribution of the metal-oxide-loaded sam-

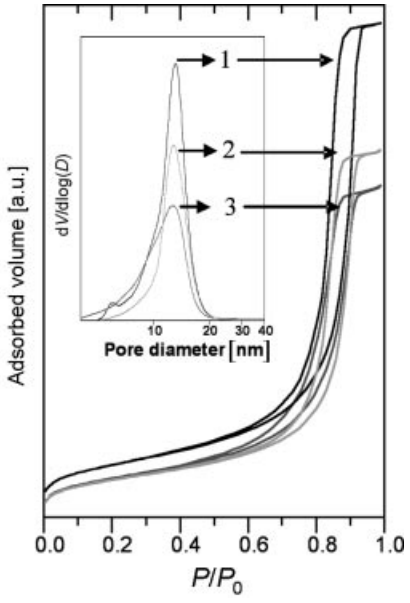


Figure 1. Pore distribution for the (1) support, (2) CoFe10/5-c and (3) Co10-c.

Table 1. Elemental analysis and textural characteristics of the $CoFe/SiO_2$ system.

| | Elemental analysis | | | | $N_2$ adsorption | |
|---|---|---|---|---|---|---|
| | Metal loading (% Co) | | Metal loading (% Fe) | | | |
| Catalyst | nominal | ICP | nominal | ICP | $S_{BET}$ [$m^2 g^{-1}$] | $V_{ads}$ [$cm^3 g^{-1}$] |
| $SiO_2$ | – | – | – | – | 289 | 1.19 |
| $SiO_2$-c | – | – | – | – | 300 | 1.18 |
| Co10-c | 10 | 10.2 | – | – | 219 | 0.80 |
| Fe10-c | – | – | 10 | 10.2 | 216 | 0.93 |
| CoFe10/5c | 10 | 9.3 | 5 | 5.1 | 221 | 0.96 |
| CoFe10/1c | 10 | 9.4 | 1 | 0.9 | 210 | 0.88 |

 © 2006 Wiley-VCH Verlag GmbH & Co. KGaA, Weinheim 

ples point to a preferential location of big cobalt- and/or iron oxide particles in the interparticle voids between silica particles. Thus, the decrease in the pore volume as a result of pore locking does not change the pore-size distribution and is in accordance with the greater decrease in pore volume, which is higher than the weight fraction of deposited metal phases. However, deposition of very small metal oxide particles within the smallest pores of silica, and more specifically for the Co10-c sample, cannot be ruled out.

## Crystalline Structure

### *Calcined Samples*

The crystal structures of the supported cobalt and iron phases of oxide samples were determined by X-ray diffraction (Figure 2A). The monometallic Co10-c sample displays sharp and narrow diffraction lines that fit very well with that of $Co_3O_4$ spinel (JCPDS card 78-1970).[56] The obtained lattice parameter for this phase is $a$ = 8.088 Å, which is similar to that obtained for the cobalt oxide spinel phase. A broad band centred at about 22° 2$\theta$ belongs to the amorphous structure of silica. A detailed examination of the spectrum was done to ensure that no other crystalline Co-containing phases, such as $Co_2SiO_4$, had developed. As $Co_3O_4$ and $CoSiO_4$ species have similar interplanar distances, differentiation between both compounds is not easy unless they are very well crystallised. It should be emphasised that formation of a crystalline $Co_2SiO_4$ phase is only possible upon calcination of the impregnate at temperatures substantially higher than that (773 K) employed in this work.[57] Note that the formation of a cobalt-oxide–silica interacting layer cannot be ruled out from this XRD pattern.

The diffraction pattern of the calcined Fe10-c sample shows all the lines of crystalline $Fe_2O_3$[58,59] (JCPDS card 85-0599), together with the broad feature of silica at about 22° 2$\theta$ (see above). No peaks of any other iron-containing compound are observed.

The XRD patterns of calcined CoFe10/5-c and CoFe10/1-c samples are also included in Figure 2A. Both samples show diffraction lines that correspond to the $Fe_2O_3$ phase; these lines, as expected, are more intense in the sample with a higher Fe loading (CoFe10/5-c). Some of the $Fe_2O_3$ lines are overlapped by those of the $Co_3O_4$ spinel,[58,60] and the rather low intensity of the lines corresponding to $Fe_2O_3$ indicates the low crystallinity of the $Fe_2O_3$ particles. A weak interaction between $Fe_2O_3$ and $Co_3O_4$ phases is possible and could affect the crystallinity of the iron oxide particles without producing any modification in the structure of the oxides. These results indicate that the two oxides remain as separate phases at the scale of the XRD technique, which is above 3–4 nm. The lattice parameters found for the dimetallic systems CoFe10/5-c and CoFe10/1-c are $a$ = 8.090 and 8.089 Å, respectively, and are very similar to that of $Co_3O_4$, which indicates that a CoFe mixed composite has not been formed. The presence of a mixed cobalt–iron oxide phase would give a higher value of the lattice parameter.

The mean particle size of the supported cobalt- and/or iron oxides was calculated from the Scherrer equation by selecting the most intense diffraction line for each oxide — the crystal planes (311) for $Co_3O_4$ and (220) for $Fe_2O_3$ — and by assuming a spherical geometry for the oxide particles. The results compiled in Table 2 reveal that the larger size corresponds to $Co_3O_4$ particles in the monometallic catalyst (21 nm), while it is slightly reduced (17 nm) for the parent Fe10-c sample. It can also be seen that the size of the $Co_3O_4$ particles decreases upon adding iron, and this drop is even more marked for sample CoFe10/5-c. Finally,

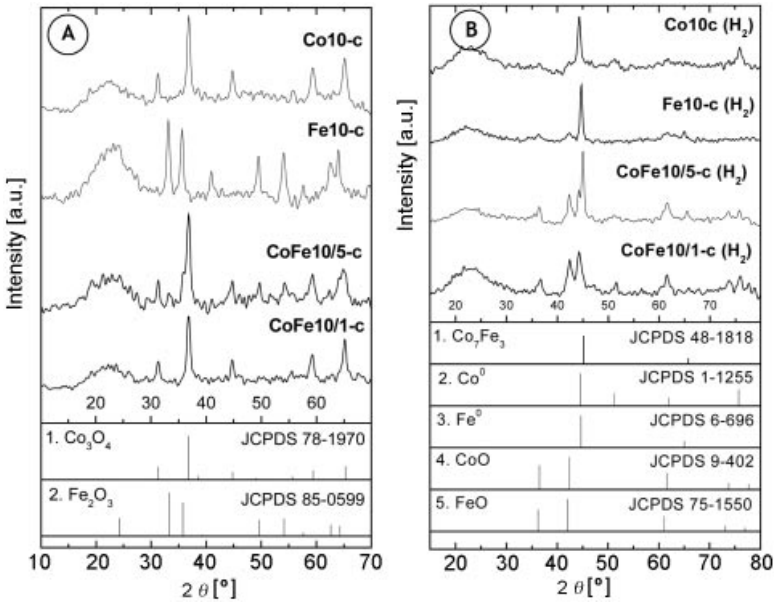


Figure 2. X-ray diffraction pattern of Co/Fe($SiO_2$): (A) calcined, (B) after $H_2$ reduction at 773 K.

 © 2006 Wiley-VCH Verlag GmbH & Co. KGaA, Weinheim 

no attempt was made to calculate the size of the iron oxide particles in the CoFe10/1-c sample because of the extreme broadening of the $Fe_2O_3$ diffraction lines. This fact indicates that the particle size should be below 5 nm, which is the limit for applying the Scherrer equation.

Table 2. Crystallite size of supported nanoparticles for the calcined and reduced systems.

| Sample | XRD phases | $2\theta$ [°] | Crystal size [nm] |
|---|---|---|---|
| Co10-c | $Co_3O_4$ | 44.38 | 21 |
| Fe10-c | $Fe_2O_3$ | 44.75 | 18 |
| CoFe10/5-c | $Co_3O_4$ | 44.22 | 14 |
| | $Fe_2O_3$ | 45.03 | 14 |
| CoFe10/1-c | $Co_3O_4$ | 44.33 | 17 |
| | $Fe_2O_3$ | 42.49 | – |
| Co10-c ($H_2$) | $Co^0$ | 44.38 | 17 |
| Fe10-c ($H_2$) | $Fe^0$ | 44.75 | 22 |
| CoFe10/5-c ($H_2$) | $Co^0$ | 44.22 | 10 |
| | $Fe_3Co_7$ | 45.03 | 23 |
| CoFe10/1-c ($H_2$) | $Co^0$ | 44.33 | 10 |
| | $Fe_3Co_7$ | 42.49 | 11 |

### *Reduced Samples*

The pattern of the Co10-c sample reduced in $H_2$ at 773 K shows diffraction lines belonging to the (111), (220) and (311) planes of the fcc $Co^0$ crystallites (JCPDS card 1-1255). The lattice parameter found for cubic $Co^0$ is $a$ = 3.541 Å. No hexagonal structure is observed because the reduction temperature is too high to achieve this type of crystal structure. The diffraction lines of CoO are still observed, which indicates than the cobalt phase has not been reduced completely, although their intensity is lower than that of the oxide sample. A broad feature at about 22° $2\theta$ arising from the amorphous silica substrate is also found.

The reduction profile of the Fe10-c sample is shown in Figure 2B. Diffraction lines of metallic α-Fe (JCPDS card 6-696) and FeO (JCPDS card 75-1150) are observed, although the intensity of the peaks of the latter phase is weak. The absence of hematite ($Fe_2O_3$) or magnetite ($Fe_3O_4$) phases indicates that the reduction is in the final stage. The lattice parameter found for this species is $a$ = 2.863 Å.

The diffraction profiles of the dimetallic CoFe10/5-c and CoFe10/1-c samples are also displayed in Figure 2B. Besides the species found in the monometallic samples, new diffraction lines belonging to a FeCo phase are observed. These new peaks — the most intense one in both diffraction patterns occurrs at $2\theta \approx 45°$ — correspond to the (110) plane of the $Co_7Fe_3$ alloy (JCPDS card 48-1818) with a bcc crystal structure. This indicates that most of the cobalt and iron phases are involved in this alloy. Some additional peaks observed in both reduced samples can be indexed to metallic Co and cobalt oxide, although apparently no lines for a metallic iron phase are present. This fact could be due to an overlapping of these lines with those assigned to cobalt and to the $Co_7Fe_3$ alloy, since the ionic radii are very similar. The intensity of the main diffraction line characteristic of the alloy in the reduced CoFe10/1-c sample is lower than that of metallic $Co^0$, which contrasts with the proportion obtained for the reduced CoFe10/5-c sample and is in accordance with the relative proportions of Co and Fe in this sample. Both metallic species found in the dimetallic systems present very similar lattice parameters. The following lattice parameters are found for both systems: $a$ = 2.842 Å, which corresponds to $Co^0$, and $a$ = 3.541 Å, which corresponds to the CoFe alloy.

The mean particle size was determined by X-ray line broadening according to the Scherrer equation (Table 2). For this calculation, the (111) plane of metallic Co, the (110) plane for metallic Fe and the (110) plane for the Co-Fe alloy phases were selected. A comparison of the crystallite sizes for both reduced and calcined samples shows an increase in crystallite phase during the reduction because of sintering of the metal phase. In addition, the extent of sintering is higher in Fe10-c than in Co10-c. For the dimetallic catalysts, an increase in alloy particle size is observed in CoFe10/5-c. Finally, the crystallite size of $Co^0$ in both dimetallic samples is similar but lower than for Co10-c, which suggests that alloy formation inhibits the sintering of $Co^0$ particles.

## Morphology and Phase Distribution

### *Calcined Samples*

The morphology of the samples was studied by electron microscopy and line profile analysis (LPA). The LPA technique allows the determination of the catalyst surface topology as well as the active-phase disposition, the metallic particle size and the surface state of the support. Figures 3A and 3C show SEM micrographs of cobalt, while Figures 3B and 3D display micrographs of monometallic silica-supported samples taken at two different magnifications. No differences were found for these two types of samples. The surface is made up of particles of irregular shape and size ranging from 2 to 25 μm. The particles are delimited by well-defined faces formed by laminar exfoliation (A and B). Higher magnification images (C and D) indicate

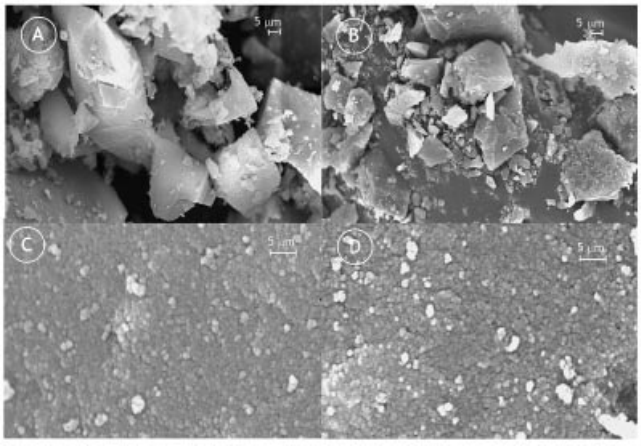


Figure 3. SEM images of calcined Co10-c (A and C) and Fe10-c (B and D).

 © 2006 Wiley-VCH Verlag GmbH & Co. KGaA, Weinheim 

the presence of uniformly developed spherical particles, about 0.2 μm in size, with compact packing. The SEM micrographs of the dimetallic samples do not show any differences with respect to those of the monometallic samples.

The LPA analysis indicates a very irregular profile for silicon, with holes and protuberances of different sizes, depths and heights. However, the profile belonging to cobalt is more homogeneous and is consistent with a well-dispersed phase. Similarly, LPA analysis of the monometallic Fe10-c sample shows a silicon profile resembling that of the cobalt counterpart (Co10-c), although the iron profile reflects a wider size distribution of the iron oxide particles. In addition, the LPA profiles for the dimetallic CoFe10/5-c and CoFe10/1-c samples indicate that both cobalt and iron profiles are more homogeneous than in the monometallic ones, thereby suggesting a better distribution of the $Co_3O_4$ and $Fe_2O_3$ phases across the surface.

The cobalt and iron mono- and dimetallic systems were also analysed by TEM with the aim of determining the form, shape and distribution of the particles on the silica support. The TEM images of Co10-c show spherical particles with non-uniform sizes within each $SiO_2$ particle. The same is true for other $SiO_2$ particles. The size of the cobalt oxide particles falls between 0.1 and 1 μm (Figure 4A). Riva et al.[61] have performed a TEM analysis of silica-supported cobalt oxides and found that metal oxide particles form spherical aggregates both inside and on the surface of silica particles, with non-uniform sizes and a mean diameter of between 0.3 and 0.5 μm. On the contrary, the micrograph of Fe10-c shows that iron oxide particles are not spherical as in the case of Co10-c (Figure 4B). In addition, non-uniform aggregates, with sizes ranging from 0.1 to 1 μm, are formed on each silica particle. Elemental analysis was also performed on individual particles, and the results indicated that they are mainly made up of iron and oxygen. XRD, XPS and Mössbauer spectroscopy revealed $Fe_2O_3$ to be the only phase present. Finally, the TEM images of CoFe10/5-c and CoFe10/1-c revealed that the particle size diminishes with respect to the monometallic samples, which is in good agreement with the Mössbauer data.

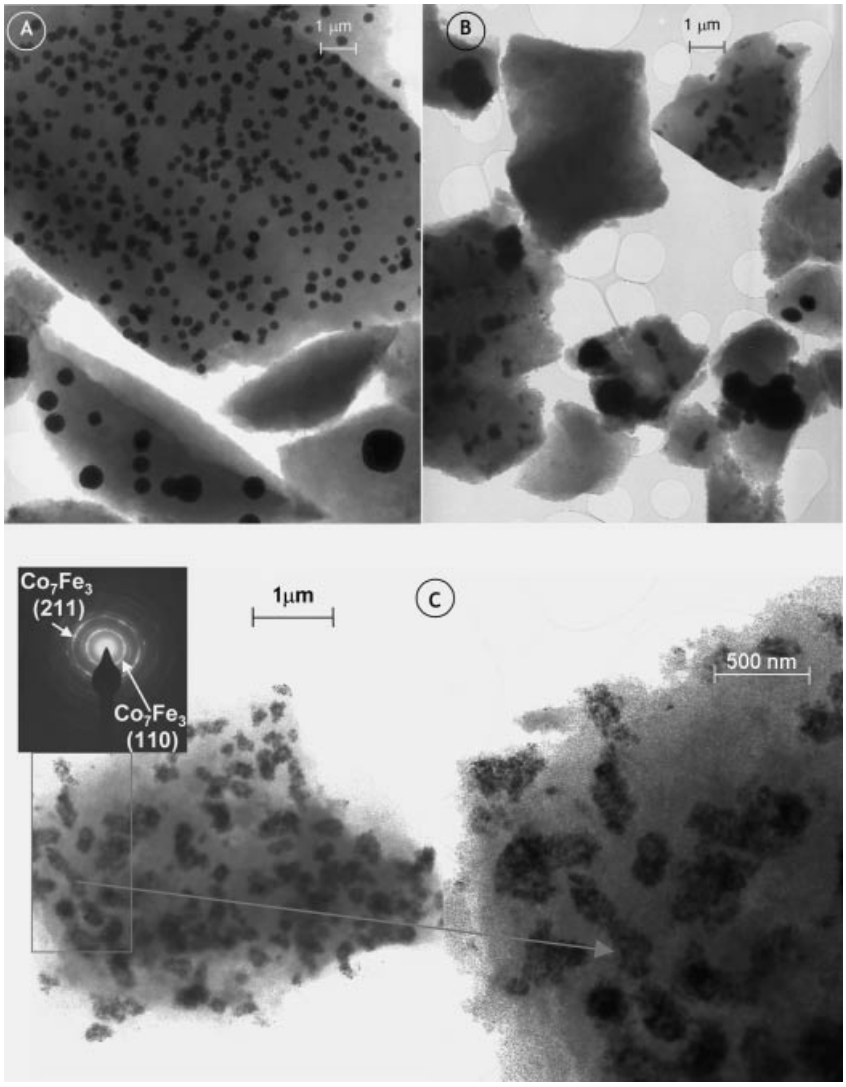


Figure 4. TEM images of (A) Co10-c and (B) Fe10-c; (C) TEM images of CoFe10/5-c reduced in $H_2$ at 773 K, with a high resolution image on the right. Inset: the electron diffraction pattern.

 © 2006 Wiley-VCH Verlag GmbH & Co. KGaA, Weinheim 

### *Reduced Samples*

Co10-c, Fe10-c and dimetallic samples reduced in hydrogen at 773 K were analysed by TEM with the aim of comparing the size, shape and distribution of the metal particles with respect to the fresh counterparts. The TEM images of Co10-c show that the size and shape of some particles remain unchanged upon reduction. In addition, a certain fraction of particles lose their spherical form and form other non-uniform aggregates. The reduced Fe10-c sample behaves similarly. The TEM image of reduced CoFe10/5-c displayed in Figure 4B reveals that the particles present an irregular shape and appear better dispersed on the silica substrate. Electron nanodiffraction taken on a large particle (Figure 4B) confirms the formation of an iron-cobalt alloy. This phase was also confirmed by XRD, XPS and Mössbauer spectroscopy.

## Bulk Structures of Iron-Containing Catalysts (Mössbauer Spectroscopy)

### *Oxide Samples*

The bulk structure of iron-containing catalysts was revealed by Mössbauer spectroscopy, and both the chemical state and relative abundance of iron and cobalt at the catalyst surface was determined by photoelectron spectroscopy. The iron-containing samples were characterised by Mössbauer spectroscopy with the aim of determining the local environment of the iron species and their concentration. Only the two calcined Fe10-c and CoFe10/5-c samples were analysed by this technique. The other dimetallic sample (CoFe10/1-c), which contains a much lower amount of iron (1 wt.-%), was not studied since its signal is too weak to get reliable information. Figure 5A displays the Mössbauer spectrum of sample Fe10-c. It includes two components: a paramagnetic doublet assigned to highly dispersed $Fe^{3+}$ and a magnetic sextet related to iron(III) oxide particles with a particle size larger than that responsible for the doublet. The hyperfine field corresponding to the sextet (50.4 T) is lower than that of bulk α-$Fe_2O_3$ (51.5 T).[62,63] This fact points to the presence of small α-$Fe_2O_3$ particles with a diameter of between 7 and 12 nm.[64] α-$Fe_2O_3$ species are the only species detected by Mössbauer analysis of the calcined Fe10-c sample, in agreement with the XRD pattern analysis presented above. The isomer shift ($\delta$), quadrupolar shift ($QS$), quadrupolar magnetic field ($H_{hf}$) and weight concentration of each species were measured and are reported in Table 3. It can be seen that α-$Fe_2O_3$ crystallites form the major phase (71%), while the proportion of $Fe^{3+}$ nanoparticles is substantially lower (29%). In addition, these results indicate that the dispersion degree of the major phase (α-$Fe_2O_3$) is rather low.

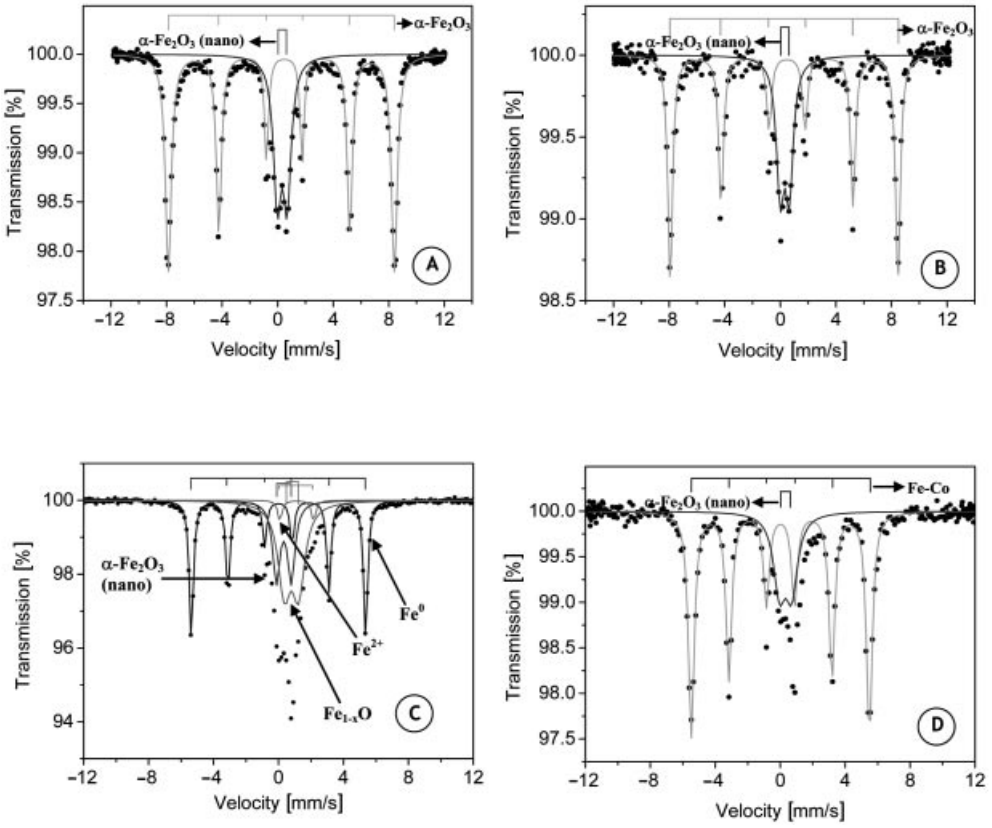


Figure 5. Mössbauer spectra of calcined (A) Fe10-c and (B) CoFe10/5-c; Mössbauer spectra of (C) Fe10-c and (D) CoFe10/5-c reduced in $H_2$ at 773 K.

 © 2006 Wiley-VCH Verlag GmbH & Co. KGaA, Weinheim 

Table 3. Mössbauer parameters for the systems Fe10-c and CoFe10/5-c calcined and reduced with $H_2$ at 773 K.

| Sample | Components | $\delta$ [mm s$^{-1}$] | $QS$ [mm s$^{-1}$] | $H_{hf}$ [T] | % |
|---|---|---|---|---|---|
| Fe10-c | α-$Fe_2O_3$ | 0.37 | 0.21 | 50.4 | 71 |
| | α-$Fe_2O_3$ (nano-size) | 0.33 | 0.71 | – | 29 |
| CoFe10/5-c | α-$Fe_2O_3$ | 0.37 | 0.21 | 50.7 | 69 |
| | α-$Fe_2O_3$ (nano-size) | 0.32 | 0.71 | – | 31 |
| Fe10-c ($H_2$) | α-Fe | 0.00 | 0.01 | 33.2 | 39 |
| | α-$Fe_2O_3$ (nano-size) | 0.33 | 0.92 | – | 20 |
| | $Fe_{1-x}O$ | 0.79 | 0.87 | – | 38 |
| | $Fe^{2+}$ ($Fe_2SiO_4$) | 1.12 | 2.07 | – | 3 |
| CoFe10/5-c ($H_2$) | Co-Fe | 0.01 | 0.01 | 33.9 | 76 |
| | α-$Fe_2O_3$ (nano-size) | 0.32 | 0.71 | – | 24 |

The Mössbauer spectrum of the calcined CoFe10/5-c sample (Figure 5B) is quite similar to that of the monometallic Fe10-c sample. The appearance of a sextet suggests the presence of ferromagnetic particles that correspond to iron(III) oxide, while the doublet ($\delta$ = 0.32 mm s$^{-1}$, $QS$ = 0.71 mm s$^{-1}$) is characteristic of highly dispersed $Fe^{3+}$ ions, thus revealing the existence of nanometre-sized particles (5–10 nm). From the data collected in Table 3, it can be inferred that the proportion of α-$Fe_2O_3$ and nano-sized $Fe^{III}$ oxide particles in the calcined CoFe10/5-c sample is similar to that found in monometallic Fe10-c.

### *Reduced Samples*

The local environment of the iron atoms in $H_2$-reduced iron-containing samples was revealed by Mössbauer spectroscopy. The Mössbauer spectrum of Fe10-c after reduction with hydrogen at 773 K for 2 h is displayed in Figure 5C. This spectrum can be fitted by four components: (i) a magnetic sextet that corresponds to α-Fe, (ii) a paramagnetic doublet due to small iron oxide particles (α-$Fe_2O_3$) similar to the one found in the calcined sample, and (iii) two paramagnetic doublets corresponding to $Fe^{2+}$ species. It should be emphasised that one of these latter doublets has a low isomer shift, which suggests that the $Fe^{2+}$ ions have a low coordination number (tetrahedral coordination), while the other doublet has an isomer shift characteristic of octahedral coordination.[65,66] No magnetic component belonging to $Fe_3O_4$ was found after hydrogen reduction. This observation agrees with previous studies by Yuen et al.[67] and Weilers et al.[68] Thus, for hydrogen-reduced silica-supported iron samples, Yuen et al.[54] observed the presence of two doublets corresponding to $Fe^{2+}$ species with different coordination environments: an inner doublet attributed to low-coordinate cations strongly interacting with the substrate and an external doublet assigned to high-coordinate $Fe^{2+}$ cations present in highly dispersed iron oxide particles. A somewhat different interpretation of these two doublets was proposed by Bjerne et al.[69] These authors suggested that both components correspond to superficial iron silicates with different symmetry (tetrahedral and octahedral environment). The Mössbauer parameters found in the $H_2$-reduced Fe10-c sample are collected in Table 3 and are similar to the ones reported by these authors. The assignment of the parameters was done on the basis of studies by Cagnoli et al.[70] and Hobson et al.,[66] in which the doublet with $\delta$ = 0.76 mm s$^{-1}$ and $\Delta QS$ = 0.98 mm s$^{-1}$ was assigned to small FeO crystallites supported on the $SiO_2$ substrate. For the second doublet, the large differences between the obtained quadrupole shift and the one reported in the literature for $Fe_{1-x}O$ species suggests the existence of $Fe^{2+}$ particles interacting strongly with the support. The quadrupole shift of this second doublet is similar to that reported in the literature for different $Fe_2SiO_4$ species.[71,72] Indeed, the reduction of these iron silicate species to iron metal [Equation (1)] is extremely difficult and hence requires high temperatures.

$$Fe_2SiO_4 + H_2 \rightarrow 2\,Fe + SiO_2 + H_2O \quad (1)$$

Figure 5D depicts the Mössbauer spectrum of the CoFe10/5-c sample reduced under hydrogen at 773 K for 2 h. The Mössbauer spectrum of this sample arises from the convolution of a magnetic sextet and a paramagnetic doublet. The values of the hyperfine field ($H$) obtained for the sextet points to the appearance of the CoFe alloy. Johnson et al.[73] have collected a sequence of values for different CoFe alloys between 34.6 and 35.6 T. The value of the hyperfine field (33.9 T) found for the $H_2$-reduced CoFe10/5-c sample is similar to that reported by other authors.[74,75] The paramagnetic doublet can be assigned to small $Fe_2O_3$ particles highly dispersed on the silica surface. In favour of this assignment is the work of Huang et al.,[76] who proposed that this paramagnetic doublet arises from iron(III) particles exchanged with the silica, which are, indeed, very difficult to reduce.

## Surface Structures

### *Oxide Samples*

The chemical state and relative abundance of cobalt- and/or iron oxides at the silica surface were determined by photoelectron spectroscopy. Figure 6A shows the energy region corresponding to the Co $2p_{3/2}$ core levels in calcined Co10-c. This peak can be resolved, after curve-fitting procedures, into two components belonging to the $Co^{2+}$ and $Co^{3+}$ ions present in the two samples. From this comparison, it is evident that the $Co_3O_4$ spinel phase is present in the sample Co10-c. The first peak at 780.0 eV can be ascribed to $Co^{3+}$ in an octahedral environment, while that at 782.5 eV can be assigned to $Co^{2+}$ ions in a tetrahedral environment.[57] Similarly, the XP spectrum of the Fe $2p_{3/2}$ core level of calcined Fe10-c is displayed in Figure 6B. This suggests that hematite ($Fe_2O_3$) is the only species present in the calcined Fe10-c sample.

Figures 6C and 6D show the energy regions corresponding to the Co $2p_{3/2}$ and Fe 2p3/2 core-levels of the calcined CoFe10/5-c sample. The similarity between the peak posi-

 © 2006 Wiley-VCH Verlag GmbH & Co. KGaA, Weinheim 

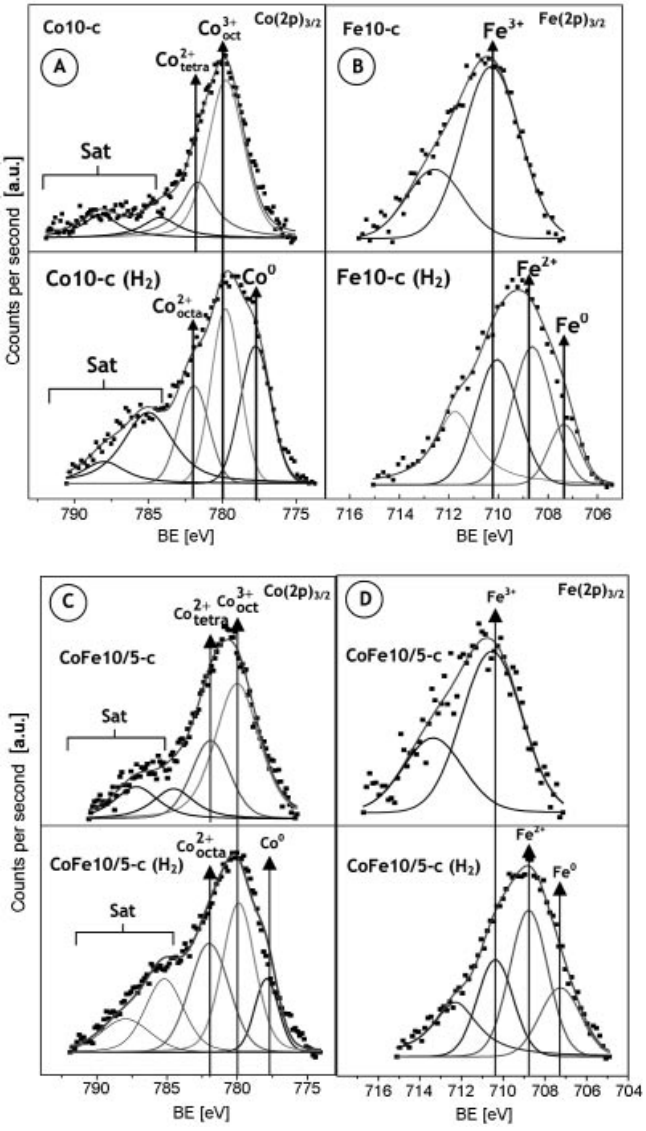


Figure 6. XPS profiles of (A) Co10-c, (B) Fe10-c and (C and D) CoFe10/5-c calcined and reduced with $H_2$ at 773 K.

tions and line profiles in the Co $2p_{3/2}$ and Fe $2p_{3/2}$ regions for the calcined CoFe10/5-c sample and those of the respective Co10-c and Fe10-c monometallic samples is an indication that the cobalt- and iron oxide phases are the same as in the monometallic systems, that is, $Co_3O_4$ and $Fe_2O_3$ are the only phases detected. As is the case with Co10-c, a shift in the binding energy of the Co $2p_{3/2}$ peak of CoFe10/5 is observed relative to bulk $Co_3O_4$ because of the presence of metal–substrate interactions. As the binding energies of the Co $2p_{3/2}$ and Fe $2p_{3/2}$ levels for CoFe10/5-c are practically the same as those found for the monometallic samples, it can be inferred that the Co–Fe interaction in the calcined sample, if any, is very weak. Finally, it should be emphasised that both CoFe10/5-c and CoFe10/1-c were analysed but the signal-to-noise ratio in the Fe $2p_{3/2}$ region for the latter sample was too low to be measured accurately and hence no further attention was paid to this level.

### *Reduced Samples*

The chemical state of the elements and their relative abundances on the catalyst surface after reduction were revealed by photoelectron spectroscopy. Figure 6A depicts the Co $2p_{3/2}$ peaks of Co10-c after reduction. The calcined Co10-c sample shows two components: one associated with $Co^{3+}$ in an octahedral position and the other assigned to $Co^{2+}$ in the tetrahedral position of the $Co_3O_4$ spinel.[77,78] Upon reduction with $H_2$, three components are observed: octahedral $Co^{3+}$ ions present in an unreduced $Co_3O_4$ phase,[57,77] octahedral $Co^{2+}$ ions in CoO[79–81] and $Co^0$.[81–83] Figure 6B shows the Fe $2p_{3/2}$ core-level spectrum of Fe10-c after reduction. The fresh sample exhibits one component assigned to $Fe^{3+}$ ($Fe_2O_3$), whereas the reduced sample displays three components, one due to $Fe^{3+}$ in a non-reduced $Fe_2O_3$[84] phase, the second due to $Fe^{2+}$ (FeO),[85,86] and the third due to metallic iron.[84,87]

Figure 6C shows the Co $2p_{3/2}$ and Fe $2p_{3/2}$ regions of CoFe10/5-c. Some differences are observed for the reduced samples. Although the profiles of the dimetallic and monometallic samples are similar, the binding energies of the $Co^0$ and $Fe^0$ species are different, which suggests that a Co-Fe alloy is formed in the dimetallic samples. It is apparent from the binding energies that the reduction of iron oxide is facilitated in the presence of cobalt,[88] while the reduction of cobalt oxide in close interaction with iron oxide is partly inhibited. This observation agrees with the results reported in the literature[89] and is consistent with the TPR data. Table 4 shows the metal/support surface ratios. An increase in the amount of surface metallic phase is observed for the dimetallic catalyst after reduction.

Table 4. Surface metal/Si ratios obtained by XPS.

| Sample | Oxide | | $H_2$ reduced (773 K) | |
|---|---|---|---|---|
| | Co/Si | Fe/Si | Co/Si | Fe/Si |
| Co10-c | 0.01 | – | 0.01 | – |
| Fe10-c | – | 0.01 | – | 0.01 |
| CoFe10/5-c | 0.01 | 0.01 | 0.02 | 0.02 |

## Redox Properties

An insight into the structure of the supported metal oxide phase can be derived from programmed reduction experiments. The reduction profile of Co10-c and a bulk $Co_3O_4$ reference are shown in Figure 7A. The reduction profile of Co10-c shows two peaks that are similar to those observed in the bulk $Co_3O_4$ oxide. These profiles point to a two-step reduction process: the first one involving low $H_2$ consumption starts at about 475 K and overlaps with the more intense second one whose maximum is placed at about 630 K. Thus, the reduction of $Co_3O_4$ can be described by the reduction of $Co^{3+}$ ions present in the spinel structure to $Co^{2+}$ [Equation (2)], with the subsequent structural change to CoO, followed by the reduction of CoO to metallic cobalt [Equation (3)].[90–92]

 © 2006 Wiley-VCH Verlag GmbH & Co. KGaA, Weinheim 

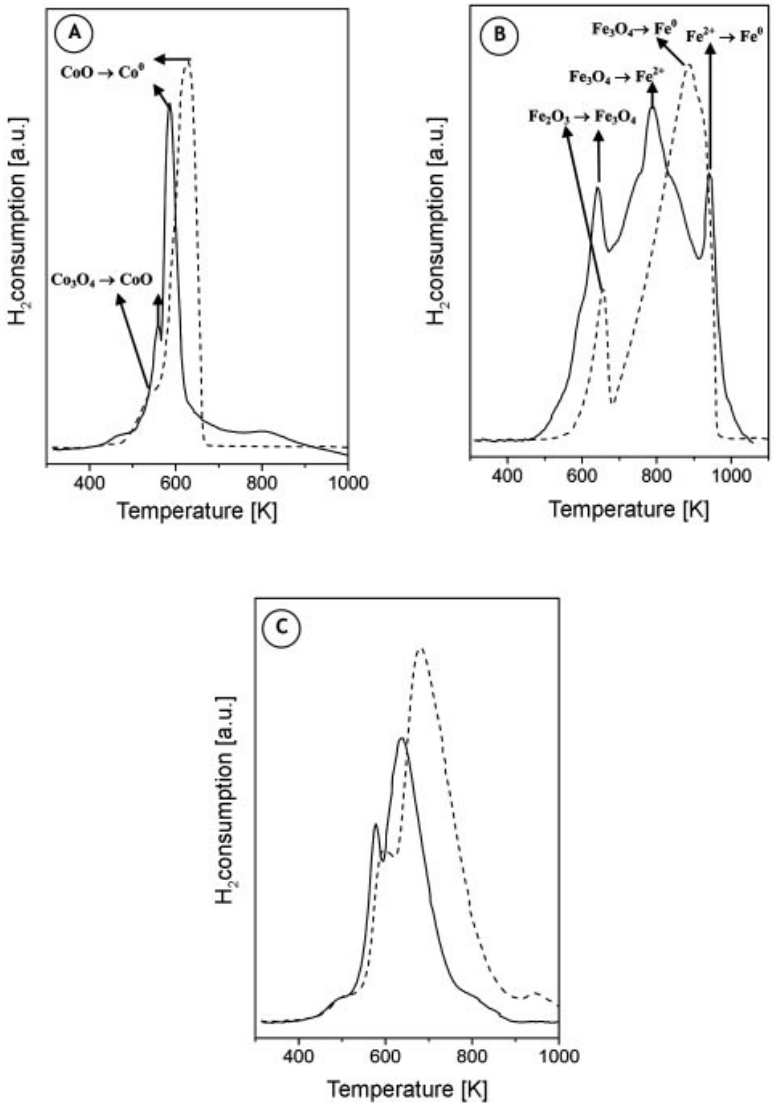


Figure 7. A comparison of the TPR profiles: (A) $Co_3O_4$ (dashed line) vs. Co10-c (solid line); (B) $Fe_2O_3$ (dashed line) vs. Fe10-c (solid line); (C) CoFe101/5-c (dashed line) and CoFe10/1-c (solid line).

$$Co_3O_4 + H_2 \rightarrow 3\,CoO + H_2O \quad (2)$$

$$3\,CoO + 3\,H_2 \rightarrow 3\,Co + 3H_2O \quad (3)$$

The reduction profile of Co10-c shows a very intense peak, which includes contributions at 558 and 587 K, associated to the two reduction steps found in bulk $Co_3O_4$, although shifted to lower temperatures as a consequence of lower crystallite sizes of supported phase. Deconvolution of the reduction peak into two components reveals that the ratio between the hydrogen consumption for the first peak and the second peak is 1:3, which is consistent with the two-step reduction depicted in Equations (2) and (3) and agrees with literature findings.[93–98] $H_2$ consumption still continues in the range 770–1000 K, and then tends to increase again at higher temperature. The broad $H_2$ consumption peak in the range 770–1000 K could reasonably be attributed to the reduction of cobalt species placed in the internal cavities of the support, where the reduction process should be limited by $H_2O$ diffusion through the pores.[90,93] This interpretation is supported by the XPS results, which point to a low surface concentration of $Co^{2+}$. The hydrogen consumption between 950 and 1000 K could be due to the reduction of a cobalt silicate phase, which could not be detected by other techniques. Therefore, the similarity of the reduction profiles for Co10-c and bulk $Co_3O_4$ up to 770 K can be taken as an indication that most of the cobalt oxide species in Co10-c interact weakly with the silica substrate.

Figure 7B shows the reduction profiles of calcined Fe10-c and bulk $Fe_2O_3$ as reference. The reduction of bulk hematite ($\alpha$-$Fe_2O_3$) occurs via magnetite ($Fe_3O_4$) and wustite (FeO) to zero-valent metallic iron.[99,100] FeO formation is not observed as wustite is a metastable phase below 843 K[99,100] and disproportionates into $Fe_3O_4$ and $Fe^0$. Two well-defined peaks are observed in the $Fe_2O_3$ reduction profile: the first is narrow, with a maximum at 654 K, and the

 © 2006 Wiley-VCH Verlag GmbH & Co. KGaA, Weinheim 

second is wider and asymmetric, with a maximum at 886 K. Thus, the two-stage reduction of $Fe_2O_3$ can be described by Equations (4) and (5).

$$3\,Fe_2O_3 + H_2 \rightarrow 3\,Fe_3O_4 \quad (4)$$

$$Fe_3O_4 + 4\,H_2 \rightarrow 3\,Fe + 4H_2O \quad (5)$$

FeO formation is not detected under the reduction conditions employed in this work. However, the reduction profile of Fe10-c exhibits three peaks arising from the reduction of iron species through the consecutive steps $Fe_2O_3 \rightarrow Fe_3O_4 \rightarrow FeO \rightarrow Fe^0$ according to Equations (6), (7) and (8).[99]

$$3\,Fe_2O_3 + H_2 \rightarrow 3\,Fe_3O_4 \quad (6)$$

$$Fe_3O_4 + H_2 \rightarrow 2\,FeO \quad (7)$$

$$FeO + H_2 \rightarrow 2\,Fe + H_2O \quad (8)$$

The similarity in reduction temperatures for both bulk $Fe_2O_3$ and Fe10-c suggests a weak metal–support interaction in the first reduction stage, as for Co10-c. The only major difference between them is the absence of the reduction stage of magnetite to wustite.

The reduction profiles of mono- and dimetallic cobalt samples were also recorded and are compared in Figure 7C. Quantitative analysis of these reduction profiles is difficult because the iron oxide reduction steps are overshadowed by the cobalt oxide ones. Nevertheless an interaction between both oxides can be inferred from the changes in the reduction of both iron- and cobalt oxides. It appears that the cobalt oxide reduction is inhibited by iron oxide — this is more evident for CoFe10/5-c — while the iron oxide reduction is favoured by the presence of cobalt oxide. As can be seen by Mössbauer spectroscopy, a CoFe alloy is formed in this sample upon reduction. Thus, it is likely that this interaction between both metal oxides is responsible for alloy formation.

An important observation for all reduction profiles is that $H_2$ consumption continues above 1100 K. As mentioned above, the species that are reduced at high temperature could be metallic silicates, i.e. $Co_2SiO_4$ and $Fe_2SiO_4$, or ionic species placed inside the support cavities.

## Conclusions

A detailed analysis of the data derived from mono- and dimetallic silica-supported cobalt-iron systems has allowed us to draw the following conclusions: (i) the textural properties of the supported oxide phases are not influenced by the calcination of the oxide precursors; (ii) the results obtained by XRD, XPS and Mössbauer spectroscopy do not show the development of a cobalt–iron interaction in the calcined oxides — the dimetallic systems only show separate $Co_3O_4$ and $Fe_2O_3$ phases and in no case are cobalt–iron mixed oxides detected. The quantitative data also show that the dispersion degree of the cobalt- and iron oxides is very low; (iii) pre-treatment of the supported cobalt oxide nanoparticles under a hydrogen atmosphere does not promote the formation of a metal–support interaction; (iv) a cobalt–iron interaction is observed in dimetallic systems after reduction, and as a result of this interaction, the reducibility of cobalt oxide is partly inhibited while that of iron oxide follows an opposite trend. The XRD patterns and photoelectron and Mössbauer spectra are conclusive for the formation of an iron-cobalt alloy in the hydrogen-reduced samples.

## Experimental Section

**Catalyst Preparation:** Silica-supported cobalt- and/or iron oxides were prepared by the wetness impregnation method on a silica carrier (Grace Davison; specific surface area of 310 $m^2 g^{-1}$, pore volume of 1.22 $m^2 g^{-1}$) with aqueous solutions of cobalt nitrate [$Co(NO_3)_2 \cdot 6H_2O$, Merck reagent grade] and iron nitrate [$Fe(NO_3)_3 \cdot 9H_2O$, Merck reagent grade]. Monometallic cobalt and iron catalysts were prepared by the appropriate concentration of the above salts to achieve a final metal amount of 10 wt.-%. These samples are labelled Co10-c and Fe10-c, respectively. Two dimetallic FeCo-supported catalysts containing a fixed amount of cobalt (10 wt.-%) and different amounts of Fe (1 and 5 wt.-%, labelled CoFe10/1-c and CoFe10–5c, respectively) were prepared by simultaneous impregnation with a solution containing both cobalt and iron salts. All impregnates were dried at 393 K overnight and calcined at 773 K under flowing air for 2 h.

**Catalyst Characterisation:** The cobalt content of the catalyst was determined by the ICP technique using a Perkin–Elmer Optima 3300 DV apparatus. Specific areas were calculated using the BET method from the nitrogen adsorption isotherms, recorded at the temperature of liquid nitrogen using a Micromeritics apparatus (model ASAP-2000) with a value of 0.162 $nm^2$ for the cross-sectional area of the $N_2$ molecule adsorbed at 77 K. Samples were degassed at 423 K prior to adsorption measurements.

The powder XRD patterns of the precursor and calcined samples were recorded with a Seifert 3000 P diffractometer using nickel-filtered Cu-$K_{\alpha 1}$ ($\lambda$ = 0.15406 nm) radiation. A scanning step of 0.02° was taken between 5 and 80° Bragg angles.

Temperature-programmed reduction (TPR) experiments were carried out with a Micromeritics TPD/TPR 2900 apparatus equipped with a thermal conductivity detector. Reduction profiles were obtained by passing a 10% $H_2$/Ar flow at a rate of 50 mL (STP) per minute through the sample (weight about 30 mg). The temperature was increased from 300 to 1273 K at a rate of 10 K $min^{-1}$, and the amount of hydrogen consumed was determined as a function of temperature. Under these conditions, the line profile and peak position can be measured accurately. The effluent gas was passed through a cold trap placed before the TCD in order to remove water from the exit stream of the reactor.

SEM images were recorded with an ISI DS-130 microscope coupled to a solid-state Si/Li Kevex detector and a SUN SparcStation 5 for acquiring and processing energy-dispersive X-ray (EDX) spectra. Powder samples were converted into flat pellets and coated with a thin graphite layer to prevent the accumulation of static charge derived from the electron beam. Transmission electron micrographs were recorded with a Fei Tecnai G30 microscope. The acceleration voltage was set at 200 kV. The powdered sample was first suspended in acetone, after which a drop of the suspension was deposited on a copper grid covered with a fine carbon film evaporated under vacuum.

 © 2006 Wiley-VCH Verlag GmbH & Co. KGaA, Weinheim 

Surface analysis was carried out with a VG Escalab 200R electron spectrometer equipped with an Mg-$K_\alpha$ X-ray source and a hemispherical electron analyser. The powder samples were pressed in 8-mm-diameter copper troughs and then mounted on a sample rod placed in a pre-treatment chamber and heated under vacuum at 373 K for 1 h prior to being moved into the analysis chamber. The base pressure in the analysis chamber was maintained below $4 \times 10^{-9}$ mbar during data acquisition. The area under analysis was about 2.4 $mm^2$, and the pass energy of the analyser was set at 50 eV, for which the resolution as measured by the full width at half maximum (FWHM) of the Au $4f_{7/2}$ core level was 1.7 eV. The binding energies were referenced to the C 1s peak at 284.9 eV due to adventitious carbon. Data processing was performed with the *XPS peak* program, the spectra were decomposed with the least-squares fitting routine provided with the software with Gaussian/Lorentzian (90/10) product function and after subtracting a Shirley background. Atomic fractions were calculated using peak areas normalised on the basis of sensitivity factors.[101]

Mössbauer spectra were recorded in a sinusoidal mode using a transmission spectrometer with a $^{57}$Co/Rh source. Spectral analyses were performed by non-linear fit using the NORMOS[102] program, and energy calibrations were accomplished with an α-Fe (6 μm) foil.

## Acknowledgments

A fellowship (VPO) granted by the Repsol-YPF Foundation is acknowledged. This work was partly supported by the MCYT (Spain; projects MAT2001-2215-C03-01 and ENE2004-07345-C03-01/ALT).

[1] S. L. González-Cortés, S. M. A. Rodulfo-Baechler, A. Oliveros, J. Orozco, B. Fontal, A. J. Mora, G. Delgado, *React. Kinet. Catal. Lett.* **2002**, *75*, 3.
[2] A. J. Dalai, N. N. Bakhshi, M. N. Esmail, *Fuel Process. Technol.* **1997**, *51*, 219.
[3] F. Tihay, A. C. Roger, G. Pourroy, A. Kiennemann, *Energy Fuels* **2002**, *16*, 1271.
[4] F. Tihay, A. C. Roger, A. Kiennemann, G. Pourroy, *Catal. Today* **2000**, *58*, 263.
[5] C. Cabet, A. C. Roger, A. Kiennemann, S. Lakamp, G. Pourroy, *J. Catal.* **1998**, *173*, 64.
[6] V. A. de la Peña O'Shea, N. N. Menéndez, J. D. Tornero, J. L. G. Fierro, *Catal. Lett.* **2003**, *88*, 123.
[7] L. Pettersson, K. Sjöström, *Combust. Sci. Technol.* **1991**, *80*, 265.
[8] J. Agrell, B. Lindstroem, L. J. Pettersson, S. Jaras, *Catalysis* **2002**, *16*, 67.
[9] E. Manova, T. Tsoncheva, D. Paneva, I. Mitov, K. Tenchev, L. Petrov, *Appl. Catal. A* **2004**, *222*, 119.
[10] S. Hagen, R. Barfod, R. Fehrmann, C. J. H. Jacobsen, H. T. Teunissen, I. Chorkendorff, *J. Catal.* **2003**, *214*, 327.
[11] Z. Kóya, I. Vesseléyi, K. Lázár, J. Kiss, I. Kiricsi, *IEEE Trans. Nanotechnol.* **2004**, *3*, 73.
[12] N. Nagaraju, A. Fonesca, Z. Konya, J. B. Nagy, *J. Mol. Catal. A* **2000**, *181*, 57.
[13] K. Hernadi, A. Fonseca, J. B. Nagy, B. Bernaerts, A. A. Lucas, *Carbon* **1996**, *34*, 1249.
[14] D. J. Duvenhage, N. J. Coville, *Appl. Catal. A* **2005**, *289*, 231.
[15] M. Sugimoto, *J. Am. Ceram. Soc.* **1999**, *82*, 269.
[16] G. Bate, *J. Magn. Magn. Mater.* **1999**, *100*, 413.
[17] R. C. Pedroza, S. W. da Silva, M. G. Soler, P. P. C. Sartoratto, D. R. Rezende, P. C. Morais, *J. Magn. Magn. Mater.* **2005**, *289*, 139.
[18] X. Huang, Z. Chen, *Solid State Commun.* **2004**, *132*, 845.
[19] A. Corrias, M. Casula, G. Ennas, S. Marras, G. Navarra, G. Mountjoy, *J. Phys. Chem. B* **2003**, *107*, 3030.
[20] *Chemierohstoffe aus Kohle* (Eds.: C. D. Fröhning, H. Kölbel, M. Ralek, W. Rottig, F. Schnur, H. Schulz J. Falbe), G. Thieme Verlag, Stuttgart, **1977**, p. 247.
[21] A. K. Dalai, N. N. Bakhshi, M. N. Esmail, *Ind. Eng. Chem. Res.* **1992**, *31*, 1449.
[22] M. E. Dry, in *Catalysis Science and Technology* (Eds.: J. R. Anderson, M. Boudart), Springer, Berlin, **1981**, p. 159.
[23] S. Zwart, R. Snel, *J. Mol. Catal.* **1985**, *30*, 305.
[24] T. V. Reshetenko, L. B. Avdeeva, A. A. Khassin, G. N. Kustova, V. A. Ushakov, E. M. Moroz, A. N. Shmakov, V. V. Kriventsov, D. I. Kochubey, Y. T. Pavlyukhin, A. L. Chuvilin, Z. R. Ismagilov, *Appl. Catal. A* **2004**, *268*, 127.
[25] D. J. Duvenhage, N. J. Coville, *J. Mol. Catal. A* **2005**, *235*, 230.
[26] S. Hagen, R. Barfod, R. Fehrmann, C. J. H. Jacobsen, H. T. Teunissen, I. Chorkendorff, *J. Catal.* **2003**, *214*, 327.
[27] C. Pham-Huu, N. Keller, C. Estournes, G. Ehret, M. J. Ledoux, *Chem. Commun.* **2002**, 1882.
[28] Y. Bi, A. K. Dalai, *Can. J. Chem. Eng.* **2003**, *81*, 230.
[29] D. Banerjee, D. K. Chakrabarthy, *Indian J. Technol.* **1992**, *30*, 81.
[30] H. Arai, K. Mitsuishi, T. Seiyama, *Chem. Lett.* **1984**, 1291.
[31] G. Ennas, M. F. Casula, A. Falqui, D. Gatteschi, G. Marongiu, G. Piccaluga, C. Sangregorio, G. Pinna, *J. Non-Cryst. Solids* **2001**, *239*, 1.
[32] M. F. Casula, A. Corrias, G. Paschina, *J. Mater. Chem.* **2002**, *12*, 1505.
[33] A. Corrias, M. F. Casula, A. Falqui, G. Paschina, *J. Sol-Gel Sci. Technol.* **2004**, *31*, 83.
[34] A. Hutlova, D. Niznansky, J. Plocek, J. Bursik, J.-L. Rehspringer, *J. Sol-Gel Sci. Technol.* **2003**, *26*, 473.
[35] T. Caillot, G. Pourroy, D. Stuerga, *J. Solid State Chem.* **2004**, *177*, 3843.
[36] A. Malats i Riera, G. Pourroy, P. Poix, *J. Alloys Compd.* **1993**, *202*, 113.
[37] G. Pourroy, S. Läkamp, S. Vilminot, *J. Alloys Compd.* **1996**, *244*, 90.
[38] F. Tihay, G. Pourroy, M. Richard-Plouet, A. C. Roger, A. Kiennemann, *Appl. Catal. A* **2001**, *206*, 29.
[39] G. Jacobs, T. K. Das, Y. Zhang, J. Li, G. Racoillet, B. H. Davis, *Appl. Catal. A* **2002**, *233*, 263.
[40] J. Panpranot, J. G. Goodwin Jr, A. Sayari, *J. Catal.* **2002**, *211*, 530.
[41] S. Sun, K. Fujimoto, Y. Yoneyama, N. Tsubaki, *Fuel* **2002**, *81*, 1583.
[42] G. W. Huber, C. H. Bartholomew, *Stud. Surf. Sci. Catal.* **2001**, *136*, 283.
[43] S. Ali, B. Chen, J. G. Goodwin, *J. Catal.* **1995**, *157*, 35.
[44] R. L. Chin, D. M. Hercules, *J. Phys. Chem.* **1982**, *86*, 360.
[45] H. M. Bruce, G. Baker, *Appl. Catal. A* **1995**, *123*, 23.
[46] E. Coulter, A. G. Sault, *J. Catal.* **1995**, *154*, 56.
[47] S. Sun, L. Fan, K. Fujimoto, *Chem. Lett.* **1999**, *28*, 343.
[48] E. Iglesia, S. C. Reyes, R. J. Madon, S. T. Soled, *Adv. Catal.* **1993**, *39*, 221.
[49] E. Iglesia, S. L. Soled, R. A. Fiato, G. H. A. Via, *J. Catal.* **1993**, *143*, 345.
[50] R. C. Reuel, C. H. Bartholomew, *J. Catal.* **1985**, *85*, 63–77.
[51] R. C. Reuel, C. H. Bartholomew, *J. Catal.* **1985**, *85*, 78–88.
[52] B. A. Sexton, A. E. Hughes, T. W. Turney, *J. Catal.* **1986**, *97*, 390.
[53] D. B. Bukur, K. Okabe, M. P. Rosynek, C. Li, D. Wang, K. R. P. M. Rao, G. P. Huffman, *J. Catal.* **1995**, *155*, 535.
[54] C. S. Kuivila, P. C. Stair, J. B. Butt, *J. Catal.* **1989**, *118*, 299–311.
[55] B. H. Davis, *Catal. Today* **2003**, *84*, 83.
[56] B. K. Sharma, M. P. Sharma, S. Kumar, S. K. Roy, S. K. Roy, S. Badrinarayanan, S. R. Sainkar, A. B. Mandale, S. K. Date, *Appl. Catal. A* **2001**, *211*, 203.

 © 2006 Wiley-VCH Verlag GmbH & Co. KGaA, Weinheim 

[57] B. Ernst, A. Bensaddik, L. Hilarie, P. Chaumette, A. Kinneman, *Catal. Today* **1998**, *39*, 329.
[58] F. P. Larkins, A. Z. Khan, *Appl. Catal.* **1989**, *47*, 209.
[59] K. Jothimurugesan, J. G. Goodwin Jr, K. Santosh, K. Ganwal, J. J. Spivey, *Catal. Today* **2000**, *58*, 355.
[60] D. J. Duvenhage, N. J. Coville, *Appl. Catal. A* **1997**, *15*, 43.
[61] R. Riva, H. Miessner, R. Vitali, G. del Piero, *Appl. Catal. A* **2000**, *196*, 111.
[62] H. M. Gager, M. C. Hobson, *Catal. Rev. Sci. Eng.* **1975**, *11*, 117.
[63] X. Gao, J. Shen, Y. Shia, Y. Chen, *J. Chem. Soc., Faraday Trans.* **1993**, *89*, 1079.
[64] A. M. van der Kraan, *Phys. Status Solidi A* **1973**, *18*, 215.
[65] M. C. Hobson Jr, H. M. Gager, *J. Colloid Interface Sci.* **1970**, *34*, 357.
[66] M. C. Hobson, A. D. Campbell, *J. Catal.* **1967**, *8*, 294.
[67] S. Yuen, Y. Chen, J. E. Kubsh, J. A. Dumesic, N. Topsøe, H. Topsøe, *J. Phys. Chem.* **1982**, *86*, 3022.
[68] A. F. H. Wielers, A. H. J. M. Dock, C. E. C. A. Hop, J. W. Geus, A. M. van der Kraan, *J. Catal.* **1989**, *117*, 1.
[69] S. C. Bjerne, H. Topsøe, S. Mørup, *Appl. Catal.* **1989**, *48*, 327.
[70] M. V. Cagnoli, S. G. Marchetti, N. G. Gallegos, A. M. Alvarez, A. C. Mercader, A. A. Yeramian, *J. Catal.* **1989**, *123*, 21.
[71] W. Kündig, J. A. Cape, R. H. Lindquist, G. J. J. Constabaris, *Appl. Phys.* **1967**, *38*, 947.
[72] G. M. Bancroft, A. G. Maddock, R. G. Burns, *Geochim. Cosmochim. Acta* **1967**, *31*, 2219.
[73] C. E. Johnson, M. S. Ridout, T. E. Cranshaw, P. E. Madsen, *Phys. Rev. Lett.* **1961**, *6*, 450.
[74] J. P. Pinheiro, P. Gadelle, C. Jeandey, J. L. Oddou, *J. Phys. Chem. Solids* **2001**, *62*, 1023.
[75] R. M. Stanfield, W. N. Delgass, *J. Catal.* **1981**, *72*, 37.
[76] Y. Y. Huang, J. R. Anderson, *J. Catal.* **1975**, *40*, 143.
[77] B. Ernst, S. Libs, P. Chaumette, A. Kiennemann, *Appl. Catal. A* **1999**, *189*, 145.
[78] A. Bensaddik, B. Ernst, F. Garin, G. Maire, A. Kiennemann, *J. Phys. IV* **1996**, *6*, 645.
[79] B. J. Tan, K. J. Klabunde, P. M. A. Sherdwood, *J. Am. Chem. Soc.* **1991**, *113*, 855.
[80] T. J. Chuang, C. R. Brundle, D. W. Rice, *Surf. Sci.* **1976**, *59*, 413.
[81] Y. Okomoto, T. Imanaka, S. Teranishi, *J. Catal.* **1980**, *65*, 44.
[82] B. K. Sharma, M. P. Sharma, S. Kuma, S. K. Roy, S. Badrinarayana, S. R. Sainkar, A. B. Mandale, S. Date, *Appl. Catal. A* **2001**, *211*, 203.
[83] J. Łojewska, W. Makowski, T. Tyszewski, R. Dziembaj, *Catal. Today* **2001**, *69*, 409.
[84] J. P. Baltrus, J. R. Dile, M. A. McDonald, M. F. Zarochak, *Appl. Catal.* **1989**, *48*, 199.
[85] M. Oku, K. J. Hirokawa, *Appl. Phys.* **1979**, *50*, 6303.
[86] J. B. Lambert, L. Xue, J. M. Weydert, J. H. Winter, *Archaeometry* **1990**, *32*, 47.
[87] R. V. Siriwardene, J. M. Cook, *J. Colloid Interface Sci.* **1985**, *108*, 414.
[88] D. D. Hawnm, B. M. Dekoven, *Surf. Interface Anal.* **1987**, *10*, 63.
[89] D. J. Duvenhage, N. J. Coville, *Appl. Catal. A* **2002**, *233*, 63.
[90] Y. Okamoto, T. Nagata, T. Adachi, T. Imanaka, K. Inamura, T. Takyu, *J. Chem. Phys.* **1991**, *95*, 310.
[91] G. J. Haddad, J. G. Goodwin, *J. Catal.* **1995**, *157*, 56.
[92] E. van Steen, G. S. Sewell, R. A. Makhothe, H. Micklethwaite, H. Manstein, M. de Lange, C. T. O'Connor, *J. Catal.* **1996**, *162*, 220.
[93] D. G. Castner, P. R. Watson, I. Y. Chan, *J. Phys. Chem.* **1990**, *94*, 819.
[94] M. P. Rosynek, C. A. Polanky, *Appl. Catal.* **1991**, *73*, 97.
[95] L. B. Backman, A. Rautiainen, A. O. I. Krause, M. Lindblad, *Catal. Today* **1998**, *43*, 11.
[96] S. Bessell, *Appl. Catal. A* **1993**, *96*, 253.
[97] J. G. Choi, *Catal. Lett.* **1995**, *35*, 291.
[98] H. Ming, B. G. Baker, *Appl. Catal. A* **1995**, *123*, 23.
[99] A. J. H. M. Kock, H. M. Fortuin, J. W. Geus, *J. Catal.* **1985**, *96*, 261.
[100] X. Gao, J. Shen, Y. Hsia, Y. Chen, *J. Chem. Soc., Faraday Trans.* **1993**, *89*, 1079.
[101] C. D. Wagner, L. E. Davis, M. V. Zeller, J. A. Taylor, R. H. Raymond, L. H. Gale, *Surf. Interface Anal.* **1981**, *3*, 211.
[102] R. A. Brand, *Nucl. Instrum. Methods Phys. Res., Sect. B* **1987**, *28*, 398.

Received: August 23, 2006
Published Online: October 24, 2006

 © 2006 Wiley-VCH Verlag GmbH & Co. KGaA, Weinheim 

DOI: 10.1002/ejic.200600779

# Computational Determination of Iron Hyperfine Interactions in Organometallics Using Small Transverse External Magnetic Fields

**Israel Nowik*[a] and Rolfe H. Herber[a]**

**Keywords:** Mössbauer spectroscopy / Metallocenes / Quadrupole splitting / Magnetic hyperfine field / External magnetic field perturbation / Iron

A number of organometallic and related iron-containing compounds have been examined by transmission $^{57}$Fe Mössbauer spectroscopy in modest (0–2.4 T) magnetic fields in order to determine the sign of the quadrupole-splitting hyperfine parameter ($QS$) as well as the internal magnetic field in derived paramagnetic solids. A computer program has been developed to extract these parameters from the spectroscopic data. The sign of the $QS$ is found to be positive in the neutral ferrocenoid solids and negative in the derived cationic complexes. The internal hyperfine field makes a positive contribution in the cationic ferrocenoids and a negative contribution in $FeF_2$ and $Fe(phen)_2(SCN)_2$.
(© Wiley-VCH Verlag GmbH & Co. KGaA, 69451 Weinheim, Germany, 2006)

## Introduction

Diamagnetic and paramagnetic iron compounds may display $^{57}$Fe Mössbauer spectra composed of a pure quadrupole doublet. The quadrupole splitting ($QS$) of this doublet is given by:

$$QS = \tfrac{1}{2}\, e^2qQ(1 + \tfrac{1}{3}\eta^2)^{1/2}$$

where $e^2qQ$ is the quadrupole interaction and $\eta$ is the value of the electric field gradient anisotropy [$\eta = (\mathbf{V}_{xx} - \mathbf{V}_{yy})/\mathbf{V}_{zz}$]. It is well known that magnetic fields acting on the Mössbauer absorber nuclei will change the spectra in such a way that the sign of the quadrupole interaction can be obtained. However, perturbations that will yield definite and readily observable results require magnetic fields above 2 T. Such measurements have been carried out in the past and the underlying theory has been worked out to various degrees of approximation.[1]

Here we present a theoretical treatment for the case of an applied magnetic field perpendicular to the γ-ray. The theory contains the diagonalization of the full Hamiltonian for any orientation of the local electric field gradient (EFG) main axis to the magnetic field. For powder samples an averaging over all possible random orientations is performed, taking into account the anisotropy of the Mössbauer recoil-free fraction. A computer program has been developed that uses this theory to least-square fit the simulated spectra to the experimental spectra, yielding the sign of the quadrupole interaction even for the low applied magnetic fields available in most laboratories. In addition to the value of the quadrupole interaction and $\eta$, the spectra yield the effective magnetic field acting on the nucleus. In paramagnetic compounds this is not necessarily equal to the applied magnetic field, and yields the value and sign of the induced magnetic internal hyperfine field. For axial cases ($\eta = 0$) the analysis also yields the mean square vibrational anisotropy parameter $N = k^2(\langle x^2_{par}\rangle - \langle x^2_{per}\rangle)$.[2] If the samples studied contain texture effects, the theory will take this into account and determine the fraction aligned in the plane of the absorber. The method is applied to the study of powders of diamagnetic and paramagnetic iron-containing organometallics.

[a] Racah Institute of Physics, The Hebrew University, Jerusalem 91904, Israel
E-mail: nowik@vms.huji.ac.il

### Theory

We have chosen the laboratory coordinate system ($x$, $y$, $z$) in which the γ-ray is along the "$x$" axis, and the magnetic field is in the plane of the absorber, along the "$z$" axis. The orientation of the randomly distributed axial EFG is along ($\sin\theta\cos\phi$, $\sin\theta\sin\phi$, $\cos\theta$), defined as the local coordinate system $z'$ axis (see Figure 1). For calculating the Mössbauer nuclear level energies and transition probabilities the quantization axis is chosen to be that of the magnetic field, the laboratory "$z$" axis. This simplifies the considerations of the absorption line intensities' dependence on the direction of the γ-ray.

Thus the Hamiltonian $\mathbf{H}$ for the $^{57}$Fe excited level ($I = 3/2$) has the general, non-axial quadrupole form (1):

$$\mathbf{H} = g_{exc}H_{eff}I_z + (e^2qQ/12)[3I_{z'}^2 - I(I+1) + \eta(I_{x'}^2 - I_{y'}^2)] \quad (1)$$

Here the magnetic term is defined in the laboratory system, whereas the quadrupole interaction is in the local coordinate system. In the case of axial symmetry, when $\eta = 0$, the calculation of the matrix elements of the quadrupole

 © 2006 Wiley-VCH Verlag GmbH & Co. KGaA, Weinheim 

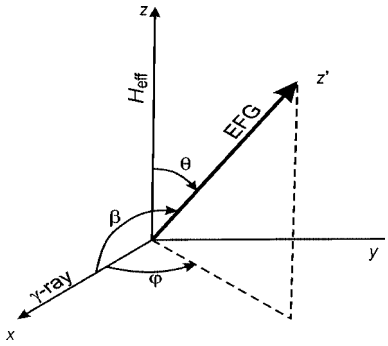


Figure 1. The experimental layout in the laboratory coordinate system. The γ-ray is in the $z = 0$ plane; its direction is chosen to be the $x$ axis so that the absorber is in the $x = 0$ plane.

interaction term in the laboratory coordinate system becomes very simple. The formulas for the matrix elements have all been calculated.[3] The Hamiltonian matrix is real symmetric, and its eigenvalues and eigenvectors do not depend on the angle $\phi$, as is also obvious from the symmetry of the experimental situation shown in Figure 1. Thus the diagonalization of this Hamiltonian and that of the ground state (in the particular choice of quantization axis chosen here, no diagonalization is required for the ground state, $I = ½$) yields the energies $E_{exc}(i)$ ($i = 1, 4$) and $E_{gr}(j)$ ($j = 1, 2$) and the corresponding wave functions $|\psi_{exc},i\rangle$ and $|\psi_{gr},j\rangle$, where all depend on $H_{eff}$, $eqQ$, and $\theta$. These wave functions are mixtures of pure $|I,m\rangle$ nuclear wave functions. The nuclear transition probabilities for the nuclear magnetic dipole transition operator $T_q$, where $q = \Delta m = -1, 0, 1$ corresponding to the $\Delta m = 0$ and $\Delta m = \pm 1$ pure nuclear transitions, is given by: $|\langle\psi_{exc},i|T_q|\psi_{gr},j\rangle|^2$. The matrix elements $\langle m_{ex}|T_q|m_{gr}\rangle$ are proportional to the Clebsch–Gordan coefficients yielding the 3:2:1 line intensities for a normal magnetic powder Mössbauer spectrum. As our quantization $z$ axis is at an angle $\pi/2$ relative to the γ-ray, the γ-ray is along an arbitrary chosen "$x$" axis, and the electric field gradient $z'$ axis is at angle $\beta$ [$\cos(\beta) = \sin(\theta)\cos(\phi)$] relative to the γ-ray, the total $T_{ij}$ intensity, considering angular dependence of the various nuclear transitions, will be given by the equations in ref.[4] or ref.[5], which leads to (2):

$$T_{ij}(\theta, \phi) = \Sigma_{q=-1,0,1} |\langle\psi_{exc}, i|T_q|\psi_{gr}, j\rangle|^2 P_q \exp(-N\cos^2\beta) \quad (2)$$

Here the constants $P_q$ are: $P_0 = 1$ and $P_{\pm 1} = ½$. The exponent $\exp(-N\cos^2\beta)$ reflects the anisotropy in the recoil-free fraction defined earlier.[2] The Mössbauer spectrum for a perfect powder sample is now given by the double integral over all orientations of the EFG, namely (3):

$$S_P(\omega) = (1/4\pi)\int_{0\to\pi} \sin\theta\, d\theta\, \Sigma_{i,j} L[\omega, \Gamma, E_{ij}(\theta)] \int_{0\to 2\pi} T_{ij}(\theta, \phi)\, d\phi \quad (3)$$

where $L(\omega, \Gamma, E)$ is the Lorentzian Mössbauer absorption line shape, and $\omega$ and $\Gamma$ are the γ-ray energy and the natural absorption line width, respectively. In the case of non-axial symmetry ($\eta \neq 0$), the full Hamiltonian of Equation (1) has to be diagonalized and then the energies and wave functions depend on all three Euler angles of the transformation between the local and the laboratory coordinate system, which makes the situation more complicated and will be discussed below.

### The Texture Effect

If intentionally (or unintentionally) the crystallites in the absorber holder are aligned in the plane, namely their local $z'$ axis (Figure 1) is randomly distributed in the $x = 0$ absorber plane, the calculation of the expected Mössbauer spectrum is simplified. In the present case the angle $\phi$ is fixed to the value ½π, which means that in Equation (2) we have to replace $\phi$ by ½π ($\cos\phi = 0$), and the formula for the final spectrum (3) takes the form (4):

$$S_{Tex}(\omega) = (1/\pi)\int_{0\to\pi} \Sigma_{i,j} L[\omega, \Gamma, E_{ij}(\theta)]\, T_{ij}(\theta)\, d\theta \quad (4)$$

If the texture effect is partial, then the observed experimental spectrum is a superposition of Equations (3) and (4), namely (5):

$$S_{Total}(\omega) = a\, S_P(\omega) + (1 - a)\, S_{Tex}(\omega) \quad (5)$$

Thus if a texture effect is present it adds only one extra parameter ($a$) to the least-square fitting procedure.

### Non-Axial Quadrupole Interactions

In the general case where $\eta \neq 0$ in Equation (1) one has to transform the electric field gradient second-order tensor expressed as a diagonal matrix ($\mathbf{V}_{x'x'}$, $\mathbf{V}_{y'y'}$, $\mathbf{V}_{z'z'}$) in the local ($x'$, $y'$, $z'$) coordinate system into the ($x$, $y$, $z$) laboratory coordinate system by three Eulerian angles ($\phi$, $\theta$, $\psi$),[6] and one obtains a nondiagonal, though symmetric, matrix ($\mathbf{V}_{ij}$). Then it is necessary to calculate all the matrix elements of the Hamiltonian in Equation (1), which is now a complex, Hermitian matrix. The quadrupole Hamiltonian has now its more general form (6):

$$\mathbf{H}_Q = ½\, \Sigma_{ij}\, \mathbf{V}_{ij}\, Q_{ij} \quad (6)$$

where the nuclear operators are:[7] $Q_{ij} = ½\,(I_i\, I_j + I_j\, I_i) - {}^1/_3\, \delta_{ij}\, I(I + 1)$

If we identify $\mathbf{V}'_{z'z'}$ with $e^2qQ/12$ and $\mathbf{V}$ as the rotational second-order tensor matrix transform of $\mathbf{V}'$, then the matrix elements of $\mathbf{H}_Q$ are as shown in (7):

$$\begin{aligned}
&\langle m\,|\mathbf{H}_Q|\,m\rangle = \mathrm{V}_{zz}\,(3m^2 - I(I+1)) \\
&\langle m+1\,|\mathbf{H}_Q|\,m\rangle = (\mathbf{V}_{xz} - i\mathbf{V}_{yz})\,(2m+1)\,(I(I+1) - m(m+1))^{½} \\
&\langle m+2\,|\mathbf{H}_Q|\,m\rangle = ½\,(\mathbf{V}_{xx} - \mathbf{V}_{yy} - 2i\mathrm{V}_{xy})\,((I(I+1) - \\
&\qquad m(m+1))\,((I(I+1) - (m+1)(m+2)))^{½}
\end{aligned} \quad (7)$$

After diagonalization of the total Hamiltonian it is possible to calculate the associated spectra and average out over all possible orientations of the electric field gradient ($z'$ axis in Figure 1). Here an additional averaging over the angle $\psi$ has to be performed. The angle between the quantization axis and γ-ray is still $\pi/2$. The anisotropy in the recoil-free fraction is now non-axial and the parameter $N$ is not enough to represent the real situation. However we include this term in the program, as it is better than to ignore

 © 2006 Wiley-VCH Verlag GmbH & Co. KGaA, Weinheim 

it completely. The angle $\beta$ between the local $z'$ axis and the $\gamma$-ray is still $\cos(\beta) = \sin(\theta)\cos(\phi)$, as is obvious from Figure 1. This procedure was converted to two computer programs. One program is very simple, used only for $\eta = 0$, and works very fast (five least-square fit iterations with eight free parameters and 400 points on the unit sphere), within less than a second on an HP AlphaServer DS20E computer. The other program, used for $\eta \neq 0$, also works well, though it consumes much more (several minutes) computing time than the former. In order to test the programs, simulated spectra for various $\eta$ values (keeping a positive quadrupole interaction QS = 2.5 mm s$^{-1}$ and $H_{ext}$ = 2.4 T) have been calculated and are shown in Figure 2. One observes that for $\eta = 1$ the spectrum is symmetric and for $\eta = 3$ the spectrum is identical to the $\eta = 0$ case but with a negative quadrupole interaction. These observations are in agreement with those expected theoretically, and thus show that the program yields correct results.

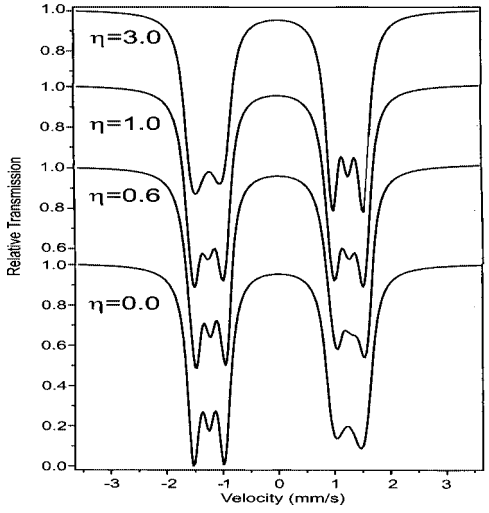


Figure 2. Mössbauer spectra simulations, for various $\eta$ values, employing the program described in the text.

### Paramagnetic Compounds

In the case of paramagnetic compounds, the effective magnetic field ($H_{eff}$) acting on the nucleus is not equal to the external magnetic field ($H_{ext}$). $H_{ext}$ can be accurately measured by a diamagnetic compound situated with identical geometry in the field. The unpaired electrons, which produce a fluctuating magnetic field averaged to zero in the absence of an external field, contribute in the presence of an external field at a temperature $T$ the additional term $H_p$ given by (8):

$$H_p = H_{hf}\, B_S(g\mu_B S H_{ext}/kT) \quad (8)$$

where $g\mu_B S$ is the total magnetic moment of the ground state of the magnetic ion ($\mu_B$ is the Bohr magneton and $g$ is the gyromagnetic factor), $B_S$ is the spin S Brillouin function, and $H_{hf}$ is the hyperfine magnetic field produced by this electronic state. For $\mu_B H_{ext}/kT << 1$, one can write the simple approximate relation (9):

$$H_p = [g\mu_B(S + 1)H_{hf}/3kT]H_{ext} \quad (9)$$

Namely, the effective field acting on the nucleus is given now by (10):

$$H_{eff} = \{1 + [g\mu_B(S + 1)H_{hf}/3kT]\}H_{ext} \quad (10)$$

In the cases where the magnetic ion has a ground-state Kramers doublet with an effective spin $S = ½$, common in the magnetic organometallics, formula (10) obtains the form (11):

$$H_{eff} = [1 + (g_{eff}\mu_B S H_{hfa}/kT)]H_{ext} \quad (11)$$

where in powders $g_{eff} = {}^1/_3\, g_{\parallel} + {}^2/_3\, g_{\perp}$ and $H_{hfa}$ is a similar average of $H_{hf}$. Thus a measurement of a paramagnetic compound in an external magnetic field may yield the average value of $H_{hf}$ with its sign (12):

$$H_{hfa} = (kT/g_{eff}\mu_B S H_{ext})(H_{eff} - H_{ext}) \quad (12)$$

In strongly covalent systems, such as diamagnetic organometallics, $H_{hf}$ can be very large and positive. Indeed we observe, for example, in paramagnetic octamethylferrocenium tetrafluoroborate ($OMFc^+BF_4^-$) and decamethylferrocenium hexafluorophosphate ($DMFc^+PF_6^-$), that $H_{eff}$ is much larger than $H_{ext}$, as will be discussed below.

## Results and Discussion

As a test case for the procedure, a sample of $FeF_2$, containing an impurity (probably $FeF_3{\cdot}3H_2O \approx 10\%$), whose hyperfine interaction parameters are known,[8,9] has been studied. The spectra in zero external magnetic field and in an external field of 2.13 T are displayed in Figure 3. Using the known starting parameters (isomer shift, quadrupole interaction, and saturation magnetic hyperfine field) of both

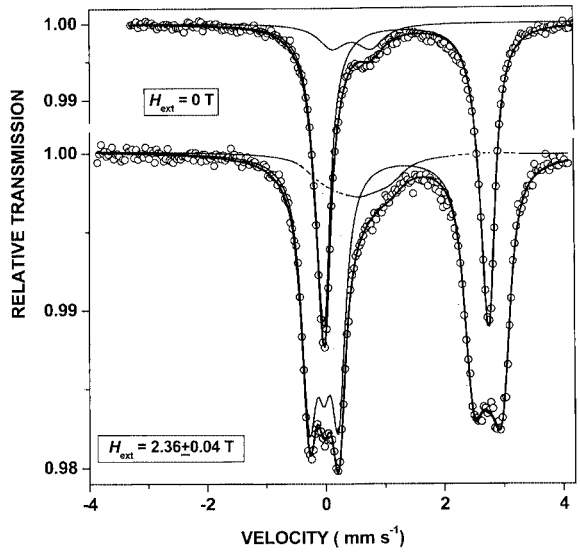


Figure 3. Mössbauer spectra of (predominantly) $FeF_2$ in $H_{ext}$ = 0 (upper trace) and $H_{ext}$ = 2.36 T (lower trace). The solid curve represents the program least-square fit, yielding the parameters given in Table 1.

 © 2006 Wiley-VCH Verlag GmbH & Co. KGaA, Weinheim 

Table 1. The hyperfine interaction parameters obtained from the Mössbauer spectra in zero external magnetic field (1) and in a field of 2.13 or 2.35 T (2).

| Compound | IS1 ($mm\,s^{-1}$) | QS1 ($mm\,s^{-1}$) | $\Gamma$1 ($mm\,s^{-1}$) | IS2 ($mm\,s^{-1}$) | QS2 ($mm\,s^{-1}$) | $\eta$ | $\Gamma$2 ($mm\,s^{-1}$) | $H_{eff}$ (T) | $H_{hf}$ sign (T) |
|---|---|---|---|---|---|---|---|---|---|
| OMFc | 0.413(3) | 2.512(3) | 0.299(2) | 0.411(3) | 2.505(3) | | 0.284(4) | 2.13(5) | 0 |
| $OMFc^+BF_4^-$ | 0.40(2) | –0.21(2) | 0.32(5) | 0.40(2) | –0.21 | | 0.32 | 2.32(9) | 38 P |
| DMFc | 0.420(5) | 2.478(5) | 0.339(2) | 0.412(9) | 2.473(9) | | 0.302(2) | 2.36(4) | 0 |
| $DMFc^+PF_6^-$ | 0.411(6) | –0.272(6) | 0.485(6) | 0.416(6) | –0.240(6) | | 0.420(10) | 2.59(14) | 46 P |
| $Fe(phen)_2(SCN)_2$ | 0.951(2) | 2.669(2) | 0.30(1) | 0.976(3) | –2.587(3) | 0.2(1) | 0.33(1) | 2.07(2) | –28 N |
| $FeF_2$[a] | 1.35 | 2.826 | 0.29 | 1.35 | 2.81 | 0.6(1) | 0.29 | 2.14 | –20 N |
| $Na_2Fe[(CN)_5NO]\cdot 2H_2O$ | –0.273(10) | 1.711(1) | 0.337(4) | –0.275(5) | 1.713(5) | 0.5(1) | 0.302(4) | 2.332 | |

[a] Contains 10% impurity, probably $FeF_3\cdot 3H_2O$.

$FeF_2$ and $FeF_3\cdot 3H_2O$ (averaged over the two phases[9]), we obtain, from the computer least-square fit, the solid curve shown in the lower trace of Figure 3. The fit to the experimental spectrum is quite satisfactory, and the numerical data, including the hyperfine parameters $\eta$, $H_{eff}$, and $H_{hf}$, are summarized in Table 1. It is noted that $\eta$ of $FeF_2$ is determined to relatively good precision. As both compounds have significant ionic character in the iron–ligand bonding, the magnetic hyperfine fields are negative, and the effective field acting on the metal atom nuclei is smaller than the external field.

Turning next to the application of this methodology to the study of primarily covalent iron organometallics, a typical application of transverse magnetic field measurements to decamethylferrocene is summarized graphically in Figure 4. The upper ME spectrum is in zero applied field and yields the parameters $IS = 0.420 \pm 0.003\ mm\,s^{-1}$ and $QS = +2.478 \pm 0.004\ mm\,s^{-1}$ in good agreement with the previously published values.[10] The line width ($\Gamma$, FWHM) = $0.339 \pm 0.002\ mm\,s^{-1}$ is slightly broadened from its theoretical value because of the effect of the long (38 cm) source drive rod. The lower spectrum is that recorded with the same sample in a transverse applied field. The hyperfine parameters obtained from the least-square fit to the above outlined theoretical calculations are: $IS = 0.412 \pm 0.009\ mm\,s^{-1}$, $\Gamma = 0.302 \pm 0.002\ mm\,s^{-1}$, $QS = +2.473 \pm 0.009\ mm\,s^{-1}$, $H_{ext} = 2.36 \pm 0.04$ T, $\eta \leq 0.02$, and $N \leq 0.05$. It is immediately obvious from the lower trace that the peak at negative velocities consists of three lines, while the peak at positive velocities is composed of an asymmetric doublet. Comparing these results with those of Collins and Travis[1] (for ferrocene), it is clear (even visually) that the QS is positive in DMFc, as it is in ferrocene itself.

In order to test the sensitivity of the computer program in determining the sign of the quadrupole interaction, we repeated the measurement in external fields of 0.81, 1.34, 1.86, and 2.34 T. In the case of the lowest field, one notices in Figure 5 that the sign cannot be determined visually, or by measuring the line width of the two components. However the computer program least-square fit yields quite a large difference in $\chi^2$ values between assumed positive and negative quadrupole interactions, with QS consistently positive. An obvious extension of these results is to the paramagnetic decamethyl ferricinium tetrafluoroborate ($DMFc^+BF_4^-$). In zero field, the resonance spectrum consists of a broadened absorption line, which can be fitted to a spin relaxation model calculation and corresponds to IS = $0.401 \pm 0.006\ mm\,s^{-1}$ and QS = $-0.272 \pm 0.006\ mm\,s^{-1}$. This spectrum is shown in the upper trace of Figure 6. When

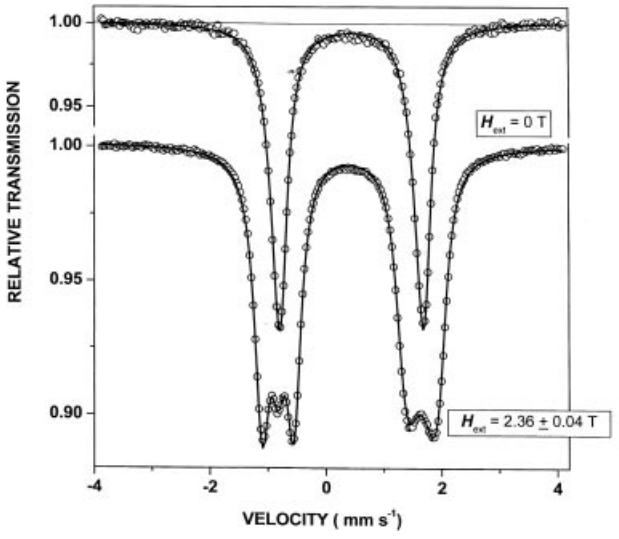


Figure 4. Mössbauer spectra of decamethylferrocene, in $H_{ext} = 0$ (upper trace) and $H_{ext} = 2.36$ T (lower trace). The solid curve represents the program least-square fit, yielding the parameters given in Table 1.

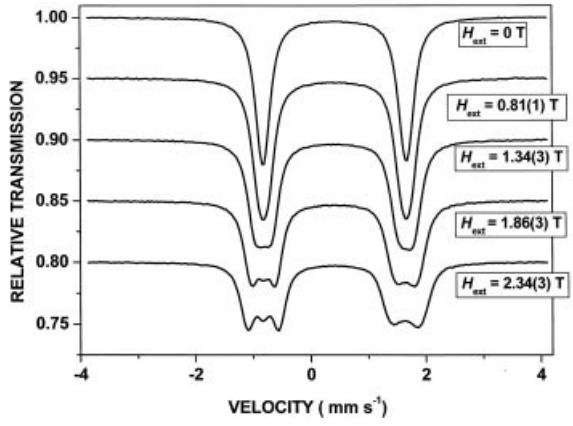


Figure 5. Mössbauer spectra of decamethylferrocene in a series of external magnetic field values. The ordinate offsets were arbitrarily fixed at 5% but all spectra were accumulated under identical conditions.

 © 2006 Wiley-VCH Verlag GmbH & Co. KGaA, Weinheim 

this sample is examined in a transverse magnetic field the resonance line is broadened to give an asymmetric doublet, as shown in the lower trace of Figure 6. The internal field is $H_{eff} = 2.58 \pm 0.03$ T. The value of the QS was frozen to its zero-field value of –0.272 mm s$^{-1}$. The negative sign of the quadrupole interaction is derived not only from the zero-field spectrum (Figure 6), but also from the fact that the $\chi^2$ value of the computer fit is consistently smaller for a negative value of this parameter than for a positive value also in the in-field spectrum. It should be noted that $H_{eff}$ for the cationic complex, under identical conditions, is larger than that observed for the neutral complex by ≈0.19 T, which, according to Equation (12), leads to a positive value for the internal magnetic hyperfine field, $H_{hf} \approx +38$ T.

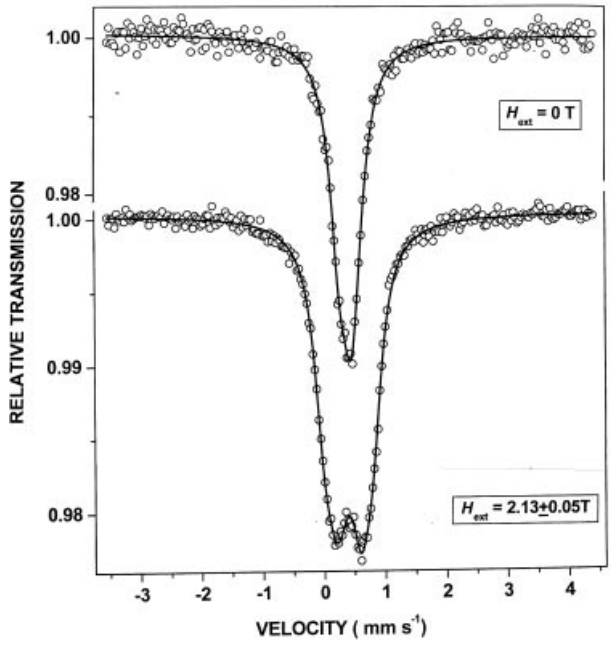


Figure 6. Mössbauer spectra of decamethylferrocenium tetrafluoroborate ($DMFc^+BF_4^-$), in $H_{ext} = 0$ (upper trace) and $H_{ext} = 2.36$ T (lower trace). The solid curve represents the program least-square fit, yielding the parameters given in Table 1.

A comparable set of experiments has been carried out with $^{57}$Fe OMFc and $^{57}$Fe $OMFc^+BF_4^-$, and the parameters extracted from the corresponding Mössbauer spectra are included in Table 1. As in the case of the DMFc complexes, the QS parameter is clearly positive in the neutral compound and negative in the cationic homologue.

We observe in paramagnetic $OMFc^+BF_4^-$ that $H_{eff}$ is significantly larger than $H_{ext}$, and yields a magnetic hyperfine field $H_{hf}$ (assuming that $g_{eff}\mu_B S$ is about 1 $\mu_B$) of about +40 T. Such large positive hyperfine fields have been previously observed and interpreted as due to orbital contributions to the hyperfine field.[11,12] Once $H_{hf}$ is estimated, one can use this value for the analysis of the zero external field Mössbauer spectra from which spin relaxation rates can be derived, using a simple spin ½ up down formula.[13] The reduced hyperfine interaction parameters from the least-square fitting of the various Mössbauer spectra are all summarized in Table 1.

The above experiments were carried out on $^{57}$Fe-enriched ferrocenoid complexes in which the shape of the electric field around the metal atom is expected to be oblate, because of the $C_{5v}$ symmetry of the ring ligands.

These measurements have been further extended to an iron complex in which the shape of the electric field around the metal atom is expected to be prolate, of which $Fe(phen)_2(SCN)_2$ (phen = 1,10 phenanthroline) is a representative example. This compound has been extensively studied by Mössbauer effect spectroscopy[14,20] in view of its interesting high spin–low spin transition at ca. 175 K. At room temperature the iron is in a high-spin state and has an effective moment of ca. 5 $\mu_B$, indicating the presence of four unpaired electrons ($S = 2$). The two SCN ligands occupy *cis* positions, and hence the asymmetry parameter $\eta \neq 0$. These experiments were carried out with natural abundance iron, so that relatively long data acquisition times (up to 72 h) were required to record statistically significant data. The brass sample cavity in this case was $0.4 \times 0.4 \times 1$ cm$^3$, and typically holds 0.7–1.0 mmol of solid. As before, the pole piece gap was 0.6 cm. A typical data set is summarized graphically in Figure 7, where again the zero-field resonance spectrum is shown in the upper trace, and the in-field absorbance in the lower. Although the magnetic splitting is smaller than that observed in the ferrocenoid complexes, it is clear that in an applied field of $2.36 \pm 0.04$ T the absorbance at negative velocities is due to an asymmetric doublet, while that at positive velocities arises from a triplet, in agreement with the existence of a negative QS. The least-square fit analysis yields the hyperfine interaction parameters given in Table 1. The striking result is that in the present case, $H_{eff}$ is smaller (!) than the external field,

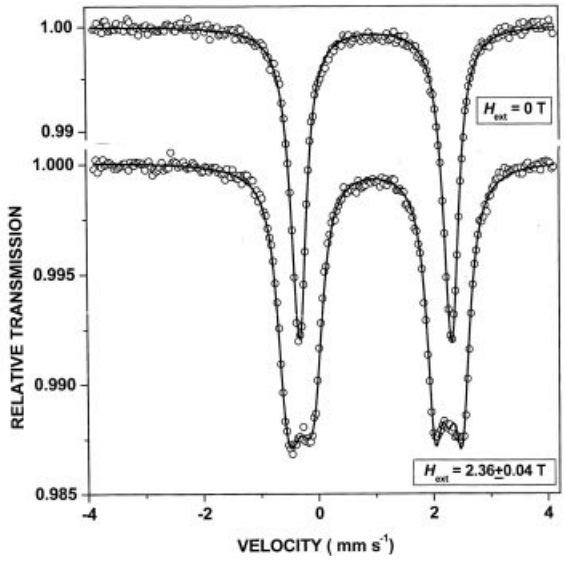


Figure 7. Mössbauer spectra of bis(phenanthroline)bis(thiocyanato)iron(II), in $H_{ext} = 0$ (upper trace) and $H_{ext} = 2.36$ T (lower trace). The solid curve represents the program least-square fit, yielding the parameters given in Table 1.

 © 2006 Wiley-VCH Verlag GmbH & Co. KGaA, Weinheim 

namely the induced internal hyperfine field is negative and leads according to Equation (10) to the value of $H_{hf} \approx -28$ T.

An example of a compound in which $\eta$ is expected to be equal or close to zero is provided by $Na_2Fe[(CN)_5NO]\cdot 2H_2O$, SNP, which has again been thoroughly investigated by Mössbauer techniques,[15,21] in part because of its interesting optical properties and ease of preparation of high-purity single crystals. An early high-precision study of very thin samples has been published by Grant et al.[16] Single-crystal X-ray diffraction studies[17] have shown that the local site symmetry is $C_{4v}$ and the space group is $P_{nnm}$ and $\eta \leq 0.04$. A magnetic field experiment carried out on a finely crushed powder sample is summarized graphically in Figure 8 and the derived hyperfine parameters are included in Table 1. From Figure 8 it is evident that the quadrupole splitting ($1.713 \pm 0.005$ mm s$^{-1}$ at room temperature) is positive, in consonance with the results reported by Grant.[18] The $\eta$ value obtained from the data processed by the $\eta \neq 0$ program is 0.5, although the $\chi^2$ value is not very much smaller than for $\eta = 0$.

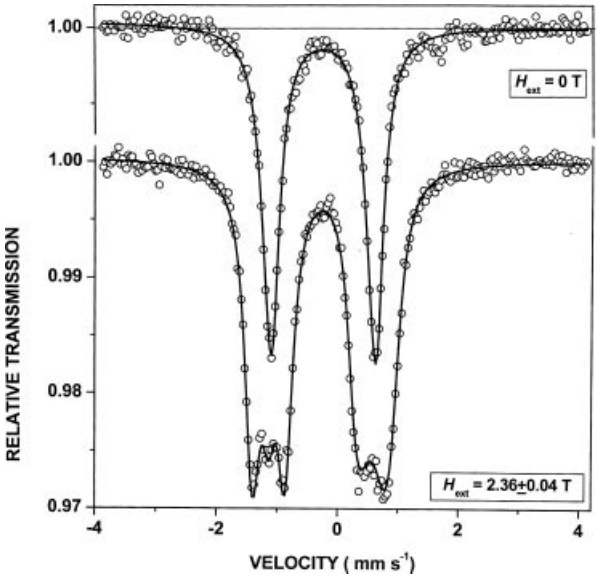


Figure 8. Mössbauer spectra of sodium nitroprusside dihydrate [$Fe^{II}$ in $H_{ext} = 0$ (upper trace) and $H_{ext} = 2.36$ T (lower trace)]. The solid curve represents the program least-square fit, yielding the parameters given in Table 1.

## Conclusions

Using a standard laboratory electromagnet having 3-cm pole pieces and operating at about 7 A, in conjunction with transmission Mössbauer spectroscopy it has been possible to determine the sign of the quadrupole splitting in a series of organometallic iron compounds at room temperature. In addition, the application of a complete diagonalization program of the full Hamiltonian for powder samples averaging over all possible random orientations makes it possible to extract the internal hyperfine field in both diamagnetic and paramagnetic complexes. While the use of enriched ($^{57}$Fe) samples reduces the required data acquisition time, even natural abundance samples employing in the order of 1 mmol of iron complex permits the acquisition of statistically reliable parameter information in reasonable data-acquisition times. The quadrupole splitting is positive in diamagnetic complexes such as OMFc, DMFc, and Fe(phen)$_2$(SCN)$_2$ (as it is in ferrocene itself), and negative in the associated one-electron oxidation products. In addition, corresponding data are presented for $FeF_2$.

## Experimental Section

A sample of natural abundance $FeF_2$, produced by microwave irradiation of $Fe(NO_3)_3\cdot 9H_2O$ in the presence of $BMIBF_4$,[8,19] was generously made available to us by Prof. A. Gedanken of Bar Ilan University and used as received. Samples of $^{57}$Fe-enriched decamethylferrocene (DMFc), decamethylferrocenium hexafluorophosphate ($DMFc^+PF_6^-$), octamethylferrocene (OMFc), and octamethylferrocinium tetrafluoroborate ($OMFc^+BF_4^-$) were generously made available by Prof. H. S. Schottenberger of the University of Innsbruck. Bis(phenanthroline)bis(thiocyanato)iron(II) [Fe(phen)$_2$(SCN)$_2$] was prepared by literature methods[9] and its purity was checked by FTIR measurements. Sodium nitroprusside [$Na_2Fe(CN)_5NO\cdot 2H_2O$][10] was taken from high-purity single-crystal material. All solids were ground with Pyrex powder and mixed with BN to assure the absence of texture-induced asymmetry in the spectra. The powdered enriched $Fe^{57}$ samples were transferred to a rectangular brass holder of 6 mm width and 2 mm thickness (unless otherwise noted), having a sample cavity of 0.08 cm$^3$, which will hold (typically) about 0.4–0.6 mmol of an organometallic solid. The sample space was windowed with 5 N Al foil and the holder assembly clamped between the pole pieces of an electromagnet. The DC electromagnet used in this study was a Newport Instruments model 369 having gap-adjustable shaped pole faces, which allowed variable field intensities to be investigated. The standard pole piece gap was 0.6 cm. Normal operating conditions were 55 V and 6–7 A at room temperature. The Mössbauer effect measurements were carried out in transmission geometry, with the 100 mCi $^{57}$Co (Rh) source mounted on a 38 cm long stainless steel tube driven by a standard triangular wave velocity drive. As was noted above, this arrangement leads to only a small (less than 0.05 mm s$^{-1}$) broadening of the resonance lines. Spectrometer calibration was effected in magnet geometry ($H = 0$) by standard α-Fe absorption, and all IS are reported with respect to the centroid of this spectrum.

Data analysis was effected in the usual manner, by the above-described programs. These computer programs are available upon request from the corresponding author.

## Acknowledgments

The authors are indebted to Prof. H. Schottenberger for providing samples of the enriched compounds examined in this study, and to O. Levy for the preparation of high-purity Fe(phen)$_2$(SCN)$_2$.

[1] R. L. Collins, J. C. Travis in *Mössbauer Effect Methodology* (Ed.: I. J. Gruverman), Plenum Press, New York, **1967**, vol. 3, p. 123, and references therein.
[2] V. I. Goldanskii, E. F. Makarov in *Chemical Applications of Mössbauer Spectroscopy* (Eds.: V. I. Goldanskii, R. H. Herber), Academic Press, **1968**, p. 105.
[3] E. Matthias, W. Schneider, R. M. Steffen, *Phys. Rev.* **1962**, *125*, 261.

 © 2006 Wiley-VCH Verlag GmbH & Co. KGaA, Weinheim 

[4] W. T. Oosterhuis, G. Lang, *Phys. Rev.* **1969**, *178*, 439.
[5] J. P. Zory, *Phys. Rev. A: At. Mol. Opt. Phys.* **1965**, *140*, 1401.
[6] H. Goldstein (Ed.), *Classical Mechanics*, Addison-Wesley, **1956**, pp. 107–109.
[7] S. Ofer, I. Nowik, S. G. Cohen, in *Chemical Applications of Mössbauer Spectroscopy* (Eds.: V. I. Goldanskii, R. H. Herber), Academic Press, **1968**, p. 442.
[8] G. K. Wertheim, H. J. Guggenheim, D. N. E. Buchanan, *Phys. Rev.* **1967**, *169*, 465–470; A. R. Champion, R. W. Vaughan, H. G. Drickamer, *J. Chem. Phys.* **1967**, *47*, 2583.
[9] D. G. Karraker, P. K. Smith, *Inorg. Chem.* **1992**, *31*, 1118–1120.
[10] R. H. Herber, I. Nowik, V. Kahlenberg, H. Kopacka, H. Schottenberger, *Eur. J. Inorg. Chem.* **2006**, 3255–3260.
[11] K. Ono, M. Shinohara, A. Ito, N. Sakai, M. Suenaga, *Phys. Rev. Lett.* **1970**, *24*, 770.
[12] H. Andres, E. L. Baminaar, J. M. Smith, N. A. Eckert, P. L. Holland, E. Münck, *J. Am. Chem. Soc.* **2002**, *124*, 3012.
[13] I. Nowik, H. H. Wickman, *Phys. Rev. Lett.* **1966**, *17*, 949–951.
[14] P. Gütlich in *Chemical Mössbauer Spectroscopy* (Ed.: R. H. Herber), Plenum Press, New York, **1984**, ch. 2, pp. 27ff and references cited therein; W. M. Reiff, G. J. Long, *Inorg. Chem.* **1974**, *13*, 2150–2153.
[15] See the discussion, in: N. N. Greenwood, T. C. Gibb, *Mössbauer Spectroscopy*, Chapman Hall Ltd., London, **1971**, pp. 90 and 182–187.
[16] R. W. Grant, R. M. Housley, U. Gonser, *Phys. Rev.* **1969**, *178*, 523–530.
[17] P. T. Manorahan, W. C. Hamilton, *Inorg. Chem.* **1963**, *2*, 1043–1047.
[18] R. W. Grant in *Mössbauer Effect Methodology* (Ed.: I. J. Gruverman), Plenum Press, New York, **1966**, vol. 2, pp. 23–38.
[19] D. S. Jacob, L. Bitton, J. Grinblat, I. Felner, Y. Koltypin, A. Gedanken, *Chem. Mater.* **2006**, *181*, 3162–3168.
[20] E. König, K. Madeja, *Inorg. Chem.* **1967**, *6*, 48–55 and refs. therein; P. Ganguli, P. Gütlich, E. W. Müller, *J. Chem. Soc., Dalton Trans.* **1981**, 441–446; W. A. Baker, H. M. Bobonich, *Inorg. Chem.* **1964**, *3*, 1184–1188.
[21] R. W. Grant, R. M. Housley, U. Gonser, *Phys. Rev.* **1969**, *178*, 523–530; R. M. Housley, R. W. Grant, U. Gonser, *Phys. Rev.* **1969**, *178*, 514.

Received: August 23, 2006
Published Online: October 27, 2006

 © 2006 Wiley-VCH Verlag GmbH & Co. KGaA, Weinheim 

DOI: 10.1002/ejic.200600799

# A Facile Synthesis of Carbamoylsilanes, -boranes and -phosphane Oxides – Isolation of the First Uncomplexed Carbamoylborane

Yves Canac,[a] Greg E. Aniol,[a] Salvador Conejero,[a] Bruno Donnadieu,[a] and Guy Bertrand*[a]

**Keywords:** Carbenes / Rearrangement / Boron / Silicon

*C*-(Trimethylsilyloxy)-, *C*-(triisopropylsilyloxy)-, *C*-(diphenylboryloxy), *C*-[bis(diisopropylamino)boryloxy]- and *C*-(di-*tert*-butylphosphoryloxy)-*N*,*N*-diisopropylaldiminium salts are readily prepared in good to excellent yields from either diisopropylformamide or (chloromethylene)diisopropylammonium chloride. Deprotonation of these aldiminium salts leads to transient (amino)(oxy)carbenes, which cleanly rearrange to carbamoyl derivatives. This synthetic methodology gives access to sterically hindered carbamoylsilanes, -boranes and phosphane oxides that are hardly accessible by other routes. (© Wiley-VCH Verlag GmbH & Co. KGaA, 69451 Weinheim, Germany, 2006)

Although first described over 30 years ago,[1] the carbamoylsilanes **A** remain difficult to prepare. Most of the known synthetic routes[2] have a rather limited scope of application and/or proceed in low to medium yields. The most powerful preparative methods are the low-temperature metalation/silylation of the corresponding *N*,*N*-dialkylformamide,[3] and the *trans*-silylation of carbamoylsilanes with the desired silyl chloride.[4] These synthetic routes, however, are inefficient when bulky substrates are involved. Despite the difficulties associated with their synthesis, carbamoylsilanes have found various synthetic applications.[4,5] In the boron series, the *B*-complexed carbamoylboranes **B**[6] have been known for a long time, and have even been described as potent cytotoxic agents in different cancer cells,[7] but so far no examples of free carbamoylboranes **C** have been reported. Even with bulky aryl groups at the boron atom, Cunico et al. have shown that carbamoylboranes spontaneously dimerize to give the six-membered heterocycles **D**[8] (Scheme 1).

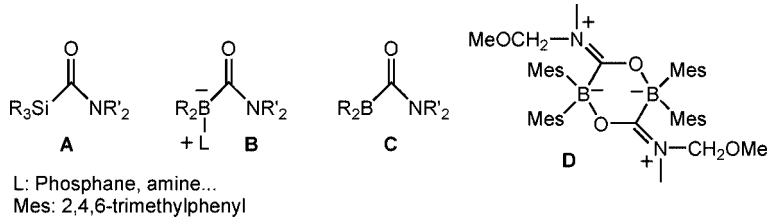


Scheme 1.

Here we describe a general route for the high-yield synthesis of carbamoyl derivatives, which include sterically relatively hindered carbamoylsilanes, as well as the first example of a noncomplexed carbamoylborane. The latter has been characterized by a single-crystal X-ray diffraction study. To further demonstrate the broad scope of application of our synthetic methodology, the preparation of a carbamoylphosphane oxide[9] is also described.

Moss et al.[10] have shown that the (phenylcarbonyloxy)-carbenes **E** quickly rearrange to 1,2-diketones, due to the carbanion-like attack of the carbene lone pair at the electrophilic carbonyl group (Scheme 2). Accordingly, any nucleophilic carbenes,[11] featuring an electrophilic center in β-position should rearrange as well. In contrast with most carbenes,[12] highly nucleophilic transient and even stable aminocarbenes[13] are readily accessible, and therefore our synthetic strategy towards carbamoyl derivatives is based on

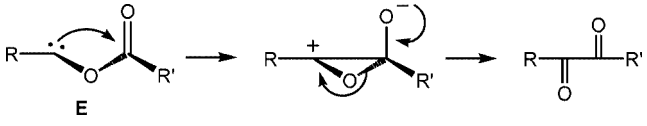


Scheme 2.

[a] UCR-CNRS Joint Research Chemistry Laboratory (UMI 2957), Department of Chemistry, University of California Riverside, CA 92521-0403, USA
Fax: +1-951-827-2725
E-mail: gbertran@mail.ucr.edu

 © 2006 Wiley-VCH Verlag GmbH & Co. KGaA, Weinheim 

the rearrangement of the appropriately substituted aminocarbenes.

The classical precursors for aminocarbenes are the corresponding aldiminium salts. The desired silyloxy derivative **1a** was readily obtained in 89% yield by treatment of diisopropylformamide with 1 equiv. of trimethylsilyl trifluoromethanesulfonate at –78 °C. Subsequent deprotonation of **1a** with lithium bis(trimethylsilyl)amide (LiHMDS) in THF quickly occurred at –78 °C, and after work up the carbamoylsilane **2a** was isolated in 93% yield (Scheme 3). The overall yield for this two-step process (83%) is comparable to that obtained using the metalation/silylation route (81%).[3b] To demonstrate the potential synthetic utility of this new route, we extended our approach to the triisopropylsilyl analogue **2b**, which was reported to be not accessible by the other routes due to steric hindrance.[4] Using triisopropylsilyl trifluoromethanesulfonate, the aldiminium salt **1b** was obtained in 67% yield, and after subsequent deprotonation with LiHMDS, **2b** was isolated in 96% yield. All attempts to spectroscopically characterize the initially formed aminocarbene ($i$Pr$_2$N–C–OSi$i$Pr$_3$) failed; unsurprisingly the rearrangement to the carbamoyl isomer is not sensitive to the steric bulk.

We then turned our attention to the group 13 carbamoyl derivatives. Treatment of diisopropylformamide with 1 equiv. of chlorodiphenylborane in diethyl ether at room temperature led, after workup, to the iminium salt **1c** in 95% yield. Deprotonation of **1c** with the lithium salt of 2,2,6,6-tetramethylpiperidine occurred at –78 °C in THF. After purification by chromatography on silica gel and recrystallization in hexane at –20 °C, the derivative **3c** was isolated as white crystals (70% yield, m.p. 261–263 °C). Compound **3c** displayed a broad signal at $\delta$ = 1.8 ppm in the $^{11}$B NMR spectrum, consistent with a tetracoordinate boron atom possessing anionic character. Despite the poor quality of the crystals, a single-crystal X-ray diffraction study showed that **3c** has a structure similar to the previously reported compound **D**.[8] Taking advantage of the possibility of using sterically hindered substrates, we investigated the possibility of preparing an isolable uncomplexed carbamoylborane. We chose diisopropylamino substituents at the boron atom, their π-donating properties also imparting electronic protection to the molecule. The iminium salt **1d** was prepared in 96% yield by the reaction of diisopropylformamide with 1 equiv. of chlorobis(diisopropylamino)borane in the presence of a stoichiometric amount of silver trifluoromethanesulfonate. As expected, deprotonation of **1d** with LiHMDS in THF afforded the carbamoylborane **2d**, which after recrystallization was obtained as thermally highly stable colorless crystals in 75% yield (m.p. 228–230 °C). The $^{11}$B NMR spectrum of **2d** exhibits a signal at $\delta$ = 29.2 ppm, which is in agreement with a tricoordinate boron atom possessing two amino groups. The $^{13}$C NMR spectrum shows the presence of a signal at rather low field ($\delta$ =190.0 ppm) consistent with an amide-type carbon atom substituted by an electron-withdrawing group. The single-crystal X-ray diffraction study confirms the monomeric nature of the carbamoyl borane **2d** (Figure 1). As expected, N1, C1, B1, N2 and N3 are in a perfectly planar environment, which demonstrates the interaction of N1 with the carbonyl group, and N2 and N3 with the boron center. It is noteworthy that all attempts to characterize the putative carbene intermediate here also failed, even when the deprotonation reaction was monitored by NMR spectroscopy at –78 °C.

In order to broaden the scope of this synthetic methodology, we also prepared the phosphane oxide substituted iminium salt **1e** (84% yield) by treatment of (chloromethylene)diisopropylammonium chloride with 1 equiv. of $t$Bu$_2$P(O)OSiMe$_3$. Deprotonation of **1e** with LiHMDS in

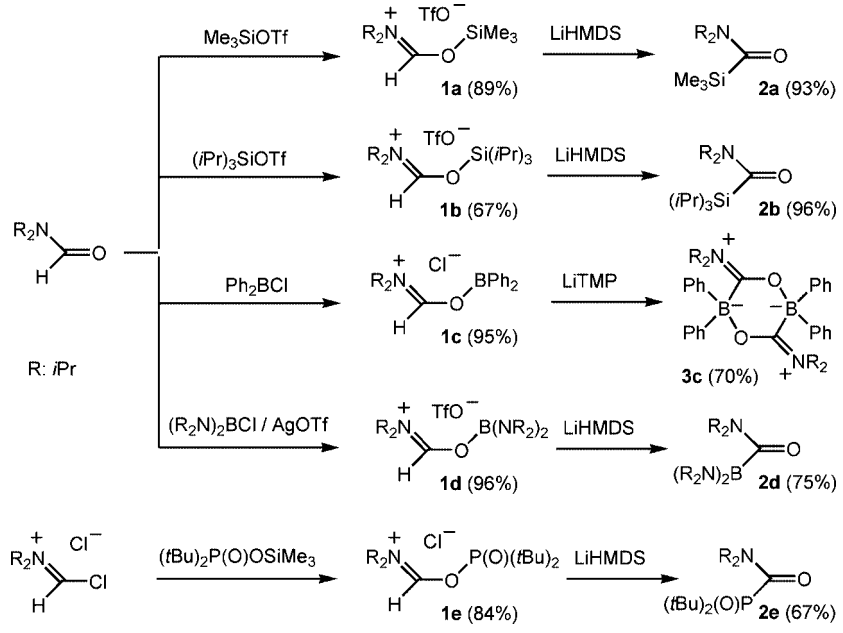


Scheme 3.

 © 2006 Wiley-VCH Verlag GmbH & Co. KGaA, Weinheim 

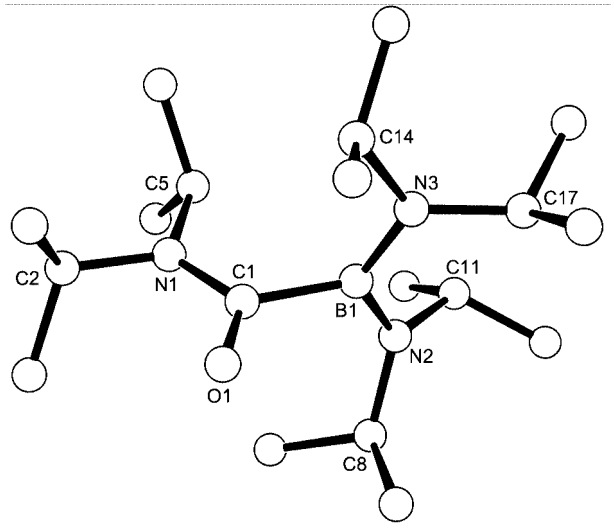


Figure 1. Molecular view of the crystal structure of **2d** (H atoms omitted). Selected bond lengths [Å] and angles [°]: B1–N2 1.4394(17), B1–N3 1.4223(17), B1–C1 1.6185(18), C1–O1 1.2449(14), C1–N1 1.3644(15); N3–B1–N2 124.35(11), N3–B1–C1 116.22(11), N2–B1–C1 119.31(11), O1–C1–N1 121.04(11), O1–C1–B1 118.54(10), N1–C1–B1 120.43(10), C1–N1–C5 120.89(10), C1–N1–C2 121.91(10), C5–N1–C2 117.07(10), B1–N2–C11 122.20(10), B1–N2–C8 122.68(10), C11–N2–C8 114.98(10), B1–N3–C17 120.08(10), B1–N3–C14 118.84(10), C17–N3–C14 120.33(10).

THF afforded the carbamoylphosphane oxide **2e**, which was isolated in 67% yield (Scheme 3).

This work is a new demonstration of the usefulness of the readily available aminocarbenes in organic synthesis. Moreover, the ready availability of these carbamoyl derivatives should favour their use for various synthetic applications.

## Experimental Section

**General:** All manipulations were performed under argon using standard Schlenk techniques. Dry, oxygen-free solvents were employed. $^{1}$H, $^{13}$C, $^{31}$P and $^{11}$B NMR spectra were recorded with Varian Inova 300, 500 and Bruker Avance 300 spectrometers. The high purity of all isolated products have been confirmed by multinuclear NMR spectroscopy.

***N*,*N*-Diisopropyl-*C*-(trimethylsilyloxy)aldiminium Salt 1a:** $Me_3Si$-OTf (0.69 mL, 3.9 mmol) was added dropwise to a solution of diisopropylformamide (0.56 mL, 3.9 mmol) in $CH_2Cl_2$ (10 mL) at –78 °C. The suspension was warmed to room temperature and stirred for 30 min. After evaporation of the solvent, the solid residue was washed with $Et_2O$ (15 mL) to afford aldiminium salt **1a** as a white solid (1.21 g, 89%). $^{1}$H NMR ($CD_3CN$, 25 °C): $\delta$ = 0.47 [s, 9 H, Si(C$H_3$)$_3$], 1.37 (d, $^{3}J$ = 6.9 Hz, 12 H, CHC$H_3$), 4.14 (m, 2 H, C$H$CH$_3$), 8.11 (s, 1 H, C$H$) ppm. $^{13}$C NMR ($CD_3CN$, 25 °C): $\delta$ = –0.3 [Si(*C*H$_3$)$_3$], 20.0 (CH*C*H$_3$), 21.2 (CH*C*H$_3$), 51.5 (*C*HCH$_3$), 56.9 (*C*HCH$_3$), 120.9 (q, $^{1}J$ = 319.5 Hz, *C*F$_3$SO$_3$), 164.6 (*C*H) ppm.

**(Diisopropylcarbamoyl)trimethylsilane (2a):** A 1:1 mixture of LiHMDS/aldiminium salt **1a** (7.4 mmol) was cooled to –78 °C and THF (20 mL) was added. The suspension was warmed to room temperature and stirred for 30 min. After evaporation of the solvent, the solid residue was washed with hexane (30 mL). Extraction with $CH_2Cl_2$ (15 mL) gave, after concentration, a white solid (1.39 g, 93%). The physical and spectroscopic data are identical to those reported previously.[3b]

***N*,*N*-Diisopropyl-*C*-(triisopropylsilyloxy)aldiminium Salt 1b:** $i$Pr$_3$Si-OTf (2.0 mL, 7.7 mmol) was added dropwise at –78 °C to a solution of diisopropylformamide (1.12 mL, 7.7 mmol) in $CH_2Cl_2$ (20 mL). The suspension was warmed to room temperature and stirred for 2 h. After evaporation of the solvent, the solid residue was washed with $Et_2O$ (20 mL) to afford aldiminium salt **1b** as a white solid (2.25 g, 67%). $^{1}$H NMR ($CDCl_3$, 25 °C): $\delta$ = 1.11 [d, $^{3}J$ = 7.2 Hz, 18 H, Si(CHC$H_3$)$_3$], 1.39 (d, $^{3}J$ = 7.2 Hz, 6 H, CHC$H_3$), 1.42 (d, $^{3}J$ = 7.2 Hz, 6 H, CHC$H_3$), 1.48 [sept, $^{3}J$ = 7.2 Hz, 3 H, Si(C$H$CH$_3$)$_3$], 4.09 (sept, $^{3}J$ = 7.2 Hz, 1 H, C$H$CH$_3$), 4.52 (m, 1 H, C$H$CH$_3$), 8.70 (s, 1 H, C$H$) ppm. $^{13}$C NMR ($CDCl_3$, 25 °C): $\delta$ = 11.6 [Si(*C*HCH$_3$)$_3$], 17.2 [Si(CH*C*H$_3$)$_3$], 19.7 (CH*C*H$_3$), 20.9 (CH*C*H$_3$), 50.0 (*C*HCH$_3$), 56.4 (*C*HCH$_3$), 120.9 (q, $^{1}J_{CF}$ = 319.0 Hz, *C*F$_3$SO$_3$), 163.5 (*C*H) ppm.

**(Diisopropylcarbamoyl)triisopropylsilane (2b):** A 1:1 mixture of LiHMDS/aldiminium salt **1b** (1.1 mmol) was cooled to –78 °C and THF (10 mL) was added. The suspension was warmed to room temperature and stirred for 30 min. After evaporation of the solvent and extraction with $CH_2Cl_2$ (10 mL), a white solid was isolated (0.31 g, 96%). $^{1}$H NMR ([D$_8$]THF, 25 °C): $\delta$ = 1.11 [d, $^{3}J$ = 6.8 Hz, 18 H, Si(CHC$H_3$)$_3$], 1.19 (d, $^{3}J$ = 6.6 Hz, 6 H, CHC$H_3$), 1.25 [m, 3 H, Si(C$H$CH$_3$)$_3$], 1.40 (d, $^{3}J$ = 6.8 Hz, 6 H, CHC$H_3$), 3.35 (sept, $^{3}J$ = 6.8 Hz, 1 H, C$H$CH$_3$), 3.92 (sept, $^{3}J$ = 6.6 Hz, 1 H, C$H$CH$_3$) ppm. $^{13}$C NMR ([D$_8$]THF, 25 °C): $\delta$ = 13.9 [Si(*C*HCH$_3$)$_3$], 19.7 [Si(CH*C*H$_3$)$_3$], 21.3 (CH*C*H$_3$), 22.1 (CH*C*H$_3$), 46.9 (*C*HCH$_3$), 49.5 (*C*HCH$_3$), 186.0 (*C*) ppm.

***C*-(Diphenylboryloxy)-*N*,*N*-diisopropylaldiminium Salt 1c:** A $Et_2O$ solution (10 mL) of diisopropylformamide (0.58 mL, 4.0 mmol) was added at –78 °C to a $Et_2O$ solution (10 mL) of chlorodiphenylborane (0.70 mL, 4.0 mmol), and the suspension was stirred at room temperature for 12 h. After filtration, the solid residue was washed with $Et_2O$ (20 mL) to afford aldiminium salt **1c** as a white solid (1.25 g, 95%). $^{1}$H NMR ($CDCl_3$, 25 °C): $\delta$ = 1.46 (d, $^{3}J$ = 6.9 Hz, 6 H, CHC$H_3$), 1.57 (d, $^{3}J$ = 6.6 Hz, 6 H, CHC$H_3$), 3.93 (sept, $^{3}J$ = 6.6 Hz, 1 H, C$H$CH$_3$), 4.41 (sept, $^{3}J$ = 6.9 Hz, 1 H, C$H$CH$_3$), 7.30–7.42 and 7.63–7.67 (m, 10 H, $H_{ar}$), 8.48 (s, 1 H, C$H$) ppm. $^{13}$C NMR ($CDCl_3$, 25 °C): $\delta$ = 20.1 (CH*C*H$_3$), 22.7 (CH*C*H$_3$), 48.6 (*C*HCH$_3$), 52.7 (*C*HCH$_3$), 126.5 ($C_{ar}$), 127.5 ($C_{ar}$), 128.5 ($C_{ar}$), 132.3 ($C_{ar}$), 165.6 (*C*H) ppm. $^{11}$B NMR ($CDCl_3$, 25 °C): $\delta$ = 11.6 ppm.

**Carbamoylborane Dimer 3c:** A 1:1 mixture of TMPLi/aldiminium salt **1c** (1.0 mmol) was cooled to –78 °C and THF (10 mL) was added. The suspension was warmed to room temperature and stirred for 30 min. After evaporation of the solvent under vacuum, purification by chromatography on silica gel (hexane/ethyl acetate) gave a solid residue, which was recrystallized at –20 °C from hexane (0.20 g, 70%, m.p. 261–263 °C). $^{1}$H NMR ($CDCl_3$, 25 °C): $\delta$ = 0.45 (d, $^{3}J$ = 6.3 Hz, 12 H, CHC$H_3$), 1.16 (d, $^{3}J$ = 6.3 Hz, 12 H, CHC$H_3$), 3.20 (sept, $^{3}J$ = 6.6 Hz, 2 H, C$H$CH$_3$), 4.05 (sept, $^{3}J$ = 6.9 Hz, 2 H, C$H$CH$_3$), 7.15–7.27 and 7.41–7.45 (m, 20 H, $H_{ar}$) ppm. $^{13}$C NMR ($CDCl_3$, 25 °C): $\delta$ = 19.3 (CH*C*H$_3$), 21.1 (CH*C*H$_3$), 48.3 (*C*HCH$_3$), 53.4 (*C*HCH$_3$), 126.7 ($C_{ar}$), 127.2 ($C_{ar}$), 127.3 ($C_{ar}$), 127.9 ($C_{ar}$), 132.2 ($C_{ar}$), 134.3 ($C_{ar}$), 144.9 ($C_{ar}$), 147.4 ($C_{ar}$), 198.8 (*C*) ppm. $^{11}$B NMR ($CDCl_3$, 25 °C): $\delta$ = 1.8 ppm.

***C*-[Bis(diisopropylamino)boryloxy]-*N*,*N*-diisopropylaldiminium Salt 1d:** A $CH_2Cl_2$ solution (10 mL) of AgOTf (2.03 g, 7.9 mmol) was added at –78 °C to a $CH_2Cl_2$ solution (10 mL) of diisopropylformamide (1.15 mL, 7.9 mmol) and chlorobis(diisopropylamino)borane (2.03 mL, 7.9 mmol). The suspension was then stirred at room temperature for 12 h. After filtration and evaporation of the sol-

 © 2006 Wiley-VCH Verlag GmbH & Co. KGaA, Weinheim 

vent, the solid residue was washed with $Et_2O$ (30 mL) to afford **1d** as a white solid (3.70 g, 96%). $^1H$ NMR ($CDCl_3$, 25 °C): $\delta$ = 1.16 (d, $^3J$ = 6.5 Hz, 24 H, CHC$H_3$), 1.48 (d, $^3J$ = 7.0 Hz, 6 H, CHC$H_3$), 1.53 (d, $^3J$ = 7.0 Hz, 6 H, CHC$H_3$), 3.44 (sept, $^3J$ = 6.5 Hz, 4 H, C*H*CH$_3$), 4.33 (sept, $^3J$ = 7.0 Hz, 1 H, C*H*CH$_3$), 4.63 (sept, $^3J$ = 7.0 Hz, 1 H, C*H*CH$_3$), 8.70 (s, 1 H, C*H*) ppm. $^{13}C$ NMR ($CDCl_3$, 25 °C): $\delta$ = 19.6 (CH*C*H$_3$), 22.9 (CH*C*H$_3$), 23.8 (CH*C*H$_3$), 46.4 (*C*HCH$_3$), 50.9 (*C*HCH$_3$), 53.0 (*C*HCH$_3$), 120.9 (q, $^1J$ = 319.5 Hz, *C*F$_3$SO$_3^-$), 164.6 (*C*H) ppm. $^{11}B$ NMR ($CDCl_3$, 25 °C): $\delta$ = 27.7 ppm.

**Bis(diisopropylamino)(diisopropylcarbamoyl)borane (2d):** A 1:1 mixture of LiHMDS/aldiminium salt **1d** (5.0 mmol) was cooled to –78 °C and THF (20 mL) was added. The suspension was then warmed to room temperature and stirred for 30 min. After evaporation of the solvent and extraction with $Et_2O$ (40 mL), a solid residue was obtained. After washing with hexane (10 mL) and extraction with $CH_2Cl_2$ (30 mL), evaporation of the solvent gave a white solid that was recrystallized from $Et_2O$ at –20 °C to give **2d** as colorless crystals (1.27 g, 75%, m.p. 228–230 °C). $^1H$ NMR ($CDCl_3$, 25 °C): $\delta$ = 1.20 (d, $^3J$ = 6.9 Hz, 18 H, CHC$H_3$), 1.23 (d, $^3J$ = 7.2 Hz, 12 H, CHC$H_3$), 1.45 (d, $^3J$ = 6.9 Hz, 6 H, CHC$H_3$), 3.28 (sept, $^3J$ = 6.9 Hz, 1 H, C*H*CH$_3$), 3.53 (sept, $^3J$ = 7.2 Hz, 4 H, C*H*CH$_3$), 3.86 (sept, $^3J$ = 6.9 Hz, 1 H, C*H*CH$_3$) ppm. $^{13}C$ NMR ($CDCl_3$, 25 °C): $\delta$ = 20.3 (CH*C*H$_3$), 21.1 (CH*C*H$_3$), 24.6 (CH*C*H$_3$), 25.0 (CH*C*H$_3$), 45.0 (*C*HCH$_3$), 48.2 (*C*HCH$_3$), 49.7 (*C*HCH$_3$), 190.0 (*C*) ppm. $^{11}B$ NMR ($CDCl_3$, 25 °C): $\delta$ = 29.2 ppm.

***C*-(Di-*tert*-butylphosphoryloxy)-*N*,*N*-diisopropylaldiminium Salt 1e:** A $CH_3CN$ solution (10 mL) of di-*tert*-butyl(trimethylsilyloxy)phosphane oxide (0.50 g, 2.0 mmol) was added at –78 °C to a $CH_3CN$ solution (10 mL) of (chloromethylene)diisopropylammonium chloride (0.37 g, 2.0 mmol). The suspension was stirred at room temperature for 3 h. After evaporation of the solvent, the solid residue was washed with $Et_2O$ (15 mL) to afford **1e** as a white solid (0.55 g, 84%). $^{31}P$ NMR ($CDCl_3$, 25 °C): $\delta$ = +87.8 ppm. $^1H$ NMR ($CDCl_3$, 25 °C): $\delta$ = 1.35 [d, $^3J$ = 15.9 Hz, 18 H, C(C$H_3$)$_3$], 1.47 (d, $^3J$ = 6.6 Hz, 6 H, CHC$H_3$), 1.54 (d, $^3J$ = 6.3 Hz, 6 H, CHC$H_3$), 4.30 (sept, $^3J$ = 6.6 Hz, 1 H, C*H*CH$_3$), 5.18 (sept, $^3J$ = 6.3 Hz, 1 H, C*H*CH$_3$), 9.38 (d, $^3J$ = 6.6 Hz, 1 H, C*H*) ppm. $^{13}C$ NMR ($CDCl_3$, 25 °C): $\delta$ = 20.4 (CH*C*H$_3$), 20.6 (CH*C*H$_3$), 26.1 [C(*C*H$_3$)], 37.5 [d, $^1J$ = 67.9 Hz, *C*(CH$_3$)], 51.4 (*C*HCH$_3$), 59.0 (*C*HCH$_3$), 162.0 (*C*H) ppm.

**Di-*tert*-butyl(diisopropylcarbamoyl)phosphane Oxide (2e):** A 1:1 mixture of LiHMDS/salt **1e** (1.0 mmol) was cooled to –78 °C and THF (10 mL) was added. The suspension was warmed to room temperature and stirred for 20 min. After evaporation of the solvent and extraction with hexane (10 mL), a solid residue was obtained (0.19 g, 67%). $^{31}P$ NMR ($CDCl_3$, 25 °C): $\delta$ = +52.3 ppm. $^1H$ NMR ($CDCl_3$, 25 °C): $\delta$ = 1.17 (d, $^3J$ = 6.3 Hz, 6 H, CHC$H_3$), 1.32 [d, $^3J$ = 14.1 Hz, 18 H, C(C$H_3$)$_3$], 1.41 (d, $^3J$ = 6.3 Hz, 6 H, CHC$H_3$), 3.43 (sept, $^3J$ = 6.3 Hz, 1 H, C*H*CH$_3$), 5.80 (m, 1 H, C*H*CH$_3$) ppm. $^{13}C$ NMR ($CDCl_3$, 25 °C): $\delta$ = 19.9 (CH*C*H$_3$), 20.8 (CH*C*H$_3$), 26.9 [C(*C*H$_3$)], 36.5 [d, $^1J$ = 57.6 Hz, *C*(CH$_3$)], 46.6 (*C*HCH$_3$), 47.6 (*C*HCH$_3$), 169.2 (d, $^1J$ = 97.0 Hz, *C*) ppm.

**Crystal Structure Determination of Carbamoylborane 2d:** A Bruker X8-APEX X-ray diffraction instrument with Mo radiation was used for data collection. All data frames were collected at low temperatures ($T$ = 100 K) using an $\omega/\varphi$-scan mode (–0.5° $\omega$-scan width, hemisphere of reflections) and integrated using a Bruker SAINTPLUS software package. The intensity data were corrected for Lorentzian polarization. Absorption corrections were performed using the SADABS program. A Sir92 software package was used for direct methods of phase determination and structure refinement. Atomic coordinates, isotropic and anisotropic displacement parameters of all the non-hydrogen atoms were refined by means of a full-matrix least-squares procedure on $F^2$. All hydrogen atoms were included in the refinement in calculated positions riding on the atoms to which they were attached. Drawings of molecules were performed using ORTEP 3. Crystal and structure parameters of **2d**: size 0.38 × 0.20 × 0.09 mm, triclinic, space group $P\bar{1}$, $a$ = 9.7141(6) Å, $b$ = 12.2962(7) Å, $c$ = 18.7798(12) Å, $\alpha$ = 92.122(4)°, $\beta$ = 101.343(4)°, $\gamma$ = 93.291(4)°, $V$ = 2193.1(2) Å$^3$, $\rho_{calcd.}$ = 1.028 g/cm$^3$, $2\theta_{max}$ = 55.76°, Mo radiation ($\lambda$ = 0.71073 Å), temperature = 100(2)° K, reflections collected = 33410, independent reflections = 10433, $R_{int}$ = 0.0301, absorption coefficient $\mu$ = 0.062 mm$^{-1}$; max/min transmission = 0.9945/0.9769, 457 parameters were refined and converged at $R_1$ = 0.0457, $wR_2$ = 0.1132, with intensity $I > 2\sigma(I)$, the final difference map was 0.986–0.337 e·Å$^{-3}$. CCDC-618399 contains the supplementary crystallographic data for this paper. These data can be obtained free of charge from The Cambridge Crystallographic Data Centre via www.ccdc.cam.ac.uk/data_request/cif.

## Acknowledgments

We are grateful to the NIH (R01 GM 68825) for financial support of this work.

[1] G. J. D. Peddle, R. W. Walsingham, *J. Chem. Soc. D* **1969**, 462.
[2] a) J. E. Baldwin, A. E. Derome, P. D. Riordan, *Tetrahedron* **1983**, *39*, 2989; b) A. Orita, K. Ohe, S. Murai, *Organometallics* **1994**, *13*, 1533; c) A. Orita, K. Ohe, S. Murai, *J. Organomet. Chem.* **1994**, *474*, 23.
[3] a) R. F. Cunico, *Tetrahedron Lett.* **2001**, *42*, 1423; b) R. F. Cunico, J. Chen, *Synth. Commun.* **2003**, *33*, 1963.
[4] R. F. Cunico, A. R. Motta, *J. Organomet. Chem.* **2006**, *691*, 3109.
[5] a) R. F. Cunico, R. K. Pandey, J. X. Chen, A. R. Motta, *Synlett* **2005**, 3157; b) R. F. Cunico, R. K. Pandey, *J. Org. Chem.* **2005**, *70*, 9048; c) R. F. Cunico, R. K. Pandey, *J. Org. Chem.* **2005**, *70*, 5344; d) J. X. Chen, R. K. Pandey, R. F. Cunico, *Tetrahedron Asymmetry* **2005**, *16*, 941; e) R. F. Cunico, A. R. Motta, *Org. Lett.* **2005**, *7*, 771; f) J. X. Chen, R. F. Cunico, *J. Org. Chem.* **2004**, *69*, 5509; g) R. F. Cunico, B. C. Maity, *Org. Lett.* **2003**, *5*, 4947; h) J. X. Chen, R. F. Cunico, *Tetrahedron Lett.* **2003**, *44*, 8025; i) R. F. Cunico, B. C. Maity, *Org. Lett.* **2002**, *4*, 4357; j) J. X. Chen, R. F. Cunico, *Tetrahedron Lett.* **2002**, *43*, 8595; k) R. F. Cunico, *Tetrahedron Lett.* **2002**, *43*, 355.
[6] a) B. F. Spielvogel, F. U. Ahmed, K. W. Morse, A. T. McPhail, *Inorg. Chem.* **1984**, *23*, 1776; b) C. K. Sood, A. Sood, B. F. Spielvogel, J. A. Yousef, B. Burnham, I. H. Hall, *J. Pharm. Sci.* **1991**, *80*, 1133; c) C. H. Sutton, M. W. Baize, L. J. Todd, *Inorg. Chem.* **1994**, *33*, 4221; d) G. Rana, K. Vyakaranam, B. F. Spielvogel, S. J. Li, C. Zheng, J. A. Maguire, N. S. Hosmane, *Inorg. Chim. Acta* **2003**, *342*, 255.
[7] a) I. H. Hall, C. J. Gilbert, A. T. McPhail, K. W. Morse, K. Hassett, B. F. Spielvogel, *J. Pharm. Sci.* **1985**, *74*, 755; b) I. H. Hall, C. O. Starnes, B. F. Spielvogel, P. Wisian-Neilson, M. K. Das, L. Wojnowich, *J. Pharm. Sci.* **1979**, *68*, 685; c) B. Burnham, S. Y. Chen, A. Sood, B. F. Spielvogel, I. H. Hall, *Pharmazie* **1995**, *50*, 779.
[8] R. F. Cunico, C. Zheng, *Inorg. Chem. Commun.* **2002**, *5*, 1066.
[9] a) P. Beudaert, V. Lamare, J. F. Dozol, L. Troxler, G. Wipff, *J. Chem. Soc., Perkin Trans. 2* **1999**, 2515; b) C. Boehme, G. Wipff, *Inorg. Chem.* **2002**, *41*, 727; c) R. N. Kapoor, P. Guillory, L. Schulte, F. Cervantes-Lee, I. Haiduc, L. Parkanyi, K. H. Pannell, *Appl. Organomet. Chem.* **2005**, *19*, 510.
[10] R. A. Moss, S. Xue, W. Liu, K. Krogh-Jespersen, *J. Am. Chem. Soc.* **1996**, *118*, 12588.

 © 2006 Wiley-VCH Verlag GmbH & Co. KGaA, Weinheim 

[11] For a recent discussion on carbenephilicity: R. A. Moss, *Acc. Chem. Res.* **2006**, *39*, 267.
[12] For general reviews on carbene chemistry: a) R. A. Moss, M. S. Platz, M. Jones Jr, (Eds.), *Reactive Intermediate Chemistry*, Wiley, New York, **2004**; b) U. H. Brinker (Ed.), *Advances in Carbene Chemistry*, JAI, Greenwich, CT, **2001**.
[13] For reviews on aminocarbenes: a) F. E. Hahn, *Angew. Chem.* **2006**, *118*, 1374; *Angew. Chem. Int. Ed.* **2006**, *45*, 1348; b) N. M. Scott, S. P. Nolan, *Eur. J. Inorg. Chem.* **2005**, 1815; c) E. Peris, R. H. Crabtree, *Coord. Chem. Rev.* **2004**, *248*, 2239; d) C. M. Crudden, D. P. Allen, *Coord. Chem. Rev.* **2004**, *248*, 2247; e) V. César, S. Bellemin-Laponnaz, L. H. Gade, *Chem. Soc. Rev.* **2004**, *33*, 619; f) D. Enders, T. Balensiefer, *Acc. Chem. Res.* **2004**, *37*, 534; g) W. Kirmse, *Angew. Chem.* **2004**, *116*, 1799; *Angew. Chem. Int. Ed.* **2004**, *43*, 1767; h) R. W. Alder, M. E. Blake, M. E. Chaker, J. N. Harvey, F. Paolini, J. Schütz, *Angew. Chem.* **2004**, *116*, 6020; *Angew. Chem. Int. Ed.* **2004**, *43*, 5896; i) Y. Canac, M. Soleilhavoup, S. Conejero, G. Bertrand, *J. Organomet. Chem.* **2004**, *689*, 3857; j) D. Bourissou, O. Guerret, F. P. Gabbaï, G. Bertrand, *Chem. Rev.* **2000**, *100*, 39.

Received: August 29, 2006
Published Online: October 23, 2006

 © 2006 Wiley-VCH Verlag GmbH & Co. KGaA, Weinheim 

DOI: 10.1002/ejic.200600482

# μ-Coordination Chemistry of NO Ligands: Adducts of *trans*-Mo(dmpe)$_2$(Cl)-(NO) with Lithium Salts

**Fupei Liang,[a] Helmut W. Schmalle,[b] and Heinz Berke*[b]**

**Keywords:** Coordination polymers / Bridging ligands / Phosphane ligands / Lithium / Molybdenum

Reaction of *trans*-Mo(dmpe)$_2$(Cl)(NO) (**1**) [dmpe = bis(dimethylphosphanyl)ethane] with lithium triethylborohydride and lithium bis(trimethylsilyl)amide affords the adducts [Mo(dmpe)$_2$(Cl)(NO)(LiHBEt$_3$)]$_n$ (**2**) and {Mo(dmpe)$_2$(Cl)-(NO)[LiN(SiMe$_3$)$_2$]$_2$}$_n$ (**3**), respectively, and the reaction of **1** with *n*-butyllithium and iodomethane generates the complex [Mo(dmpe)$_2$(Cl)(NO)]$_3$(LiI)$_2$ (**4**). Complexes **2**–**4** have been characterized by elemental analysis, IR spectroscopy, NMR spectroscopy, and single-crystal X-ray diffraction analysis. The structure of **2** shows an infinite one-dimensional "zigzag" chain constructed from an alternating arrangement of Mo(dmpe)$_2$(Cl)(NO) and LiHBEt$_3$ moieties, whereas the structure of **3** exhibits an infinite linear chain generated by the alternating arrangement of the Mo(dmpe)$_2$(Cl)(NO) moiety and the dimeric [LiN(SiMe$_3$)$_2$]$_2$ unit. In both compounds, the Mo(dmpe)$_2$(Cl)(NO) moieties act as bridging ligands by coordination of the nitrosyl oxygen atom and the chlorine atom to the lithium ions. Complex **4** displays a discrete structure formed by two separate monomeric LiI units that are bridged by the nitrosyl oxygen atoms of three Mo(dmpe)$_2$-(Cl)(NO) moieties. The chlorine atoms of **4** are not involved in coordination.
(© Wiley-VCH Verlag GmbH & Co. KGaA, 69451 Weinheim, Germany, 2006)

Transition metal nitrosyl complexes have received considerable attention for many years due to their potential applications as catalysts in organic synthesis and small molecule activation.[1,2] Our interest in this field lies mainly in the chemistry of nitrosyl hydrido transition metal complexes. In this context a series of compounds of manganese,[3] rhenium,[4] chromium,[5] tungsten,[6] and molybdenum[7] have been synthesized and explored in particular with regard to hydride-transfer chemistry. It has been found that the nitrosyl group exhibits versatile functions in such compounds. It can stabilize the different oxidation states of the metal center,[1,8] and it can induce quite strong hydridic polarization by the "nitrosyl effect"; thus the nitrosyl group promotes the activation of the metal–hydrogen bond.[9] Additionally, the nitrosyl group can show a certain amount of Lewis base behavior by interacting with Lewis acids at the oxygen atom site.[8,10]

The nitrosyl ligand/Lewis acid interactions have been found to sometimes play a key role in organic (organometallic) syntheses and reactions. For example, the catalytic oxidation of alcohols by a cobalt nitro/nitrosyl couple with the use of molecular oxygen as an oxidant was found to be facilitated by Lewis acids such as $BF_3{\cdot}Et_2O$ or $LiPF_6$.[11] The effects of the Lewis acids in the reaction were attributed to their interactions with nitro and nitrosyl ligands. In dinitrosyl complexes Re(H)(NO)$_2$(PR$_3$)$_2$ (R = *i*Pr, Cy), one nitrosyl group was found to be capable of coordinating to one or two $BF_3$ molecules, and the interaction of a second $BF_3$ molecule caused the bending of the nitrosyl group; thus, a new coordination site in the metal sphere is provided.[12] The coordination of the nitrosyl group to the lithium ions in the compounds [Cp*Mo(NO)(CH$_2$SiMe$_3$)-(=CHSiMe$_3$)]$_2$[Li$_2$(THF)$_3$], [($\eta^5$,$\eta^1$-C$_5$Me$_4$CH$_2$)Mo(NO)-(CH$_2$Si- Me$_3$)$_2$][Li(THF)$_3$], and {[Cp*Mo(NO)(CH$_2$SiMe$_3$)$_2$]-[Li(THF)]}$_2$ was thought to further stabilize the corresponding anionic complexes thus facilitating the isolations of these species.[13] Despite the apparent significance of coordinated nitrosyl ligand/Lewis acid interactions, studies on such interactions are relatively rare[14] in contrast to the rich chemistry of the Lewis basicity of coordinated carbonyl ligands.[15] We describe here the isolation and structural characterization of the compounds formed by *trans*-Mo-(dmpe)$_2$(Cl)(NO) (**1**) [dmpe = bis(dimethylphosphanyl)-ethane] with lithium reagents. To the best of our knowledge, fully structurally characterized adducts formed by neutral nitrosyl complexes with metal ions by the coordination of bound nitrosyl have not yet been reported.

## Results

### Preparation and Characterization of 2, 3, and 4

#### *Complex 2*

Treatment of **1** with 1 equiv. of lithium triethylborohydride in diethyl ether did not provide the product of a H/Cl

[a] School of Chemistry and Chemical Engineering, Guangxi Normal University,
Guilin 541004, P. R. China
[b] Anorganisch-Chemisches Institut der Universität Zürich,
Winterthurerstrasse190, 8057 Zürich, Switzerland

 © 2006 Wiley-VCH Verlag GmbH & Co. KGaA, Weinheim 

metathetical reaction, but the polymeric **1**/$LiHBEt_3$ adduct of $[Mo(dmpe)_2(Cl)(NO)LiHBEt_3]_n$ (**2**), [Equation (1)] which was isolated as yellow crystals in 88% yield after slow evaporation of the solvent at room temperature. Complex **2** is apparently stable enough to resist hydride formation and no further conversion was observed even under forced reaction conditions, for example, the application of up to 5 equiv. of lithium triethylborohydride and heating to 50 °C for two days. Complex **2** has been characterized by IR spectroscopy, NMR spectroscopy, elemental analysis, and a single-crystal X-ray diffraction study. The IR spectrum of **2** in a Nujol mull shows a nitrosyl stretching band at 1486 $cm^{-1}$, which is 52 $cm^{-1}$ lower in energy than the corresponding nitrosyl band of **1** ($\nu_{NO}$ = 1538 $cm^{-1}$ in Nujol). The lowering of the nitrosyl stretching frequency typically indicates the coordination of the $O_{NO}$ atom to the lithium ion. The $^1$H- and $^{13}C\{^1H\}$ NMR spectra of **2** in $C_6D_6$ display all of the resonances that correspond to the $Mo(dmpe)_2(Cl)(NO)$ and $LiHB(C_2H_5)_3$ moieties. The chemical shifts of the $^1$H-, $^{13}$C-, and $^{31}$P NMR resonances for the $Mo(dmpe)_2(Cl)(NO)$ moiety in **2** are similar to those exhibited by **1**. The fact that the $^7$Li NMR spectrum shows a singlet at 2.1 ppm and that the $^{11}$B NMR spectrum displays a broad singlet at $\delta$ = –2.76 ppm further confirms the presence of the $LiHB(C_2H_5)_3$ moiety in the molecule. The elemental analysis is in good agreement with the composition of a 1:1 adduct of $Mo(dmpe)_2(Cl)(NO)$ and $LiHBEt_3$.

$$z{\cdot}x\ Mo(dmpe)_2(Cl)(NO) + z{\cdot}y LiX \rightarrow \{[Mo(dmpe)_2(Cl)(NO)]_x(LiX)_y\}_z$$
**2**: $x = y = 1$; $z = \infty$; X = $HBEt_3$
**3**: $x = 1$; $y = 2$; $z = \infty$; X = $N(SiMe_3)_2$
**4**: $x = 3$; $y = 2$; $z = 1$; X = I (1)

### *Complex 3*

The reaction of **1** with lithium bis(trimethylsilyl)amide in diethyl ether produced $\{Mo(dmpe)_2(Cl)(NO)[LiN(SiMe_3)_2]_2\}_n$ (**3**) with a 1:2 ratio of **1** and $LiN(SiMe_3)_2$ [Equation (1)]. It is found that this ratio is independent on the initially employed amounts of lithium bis(trimethylsilyl)amide. Treatment of **1** with an equimolar amount or with 2 equiv. of $LiN(SiMe_3)_2$ always resulted in **3**. In a typical reaction, **3** was isolated as yellow crystals in a yield of 84%. Once it has been isolated **3** is difficult to redissolve in diethyl ether, but is readily soluble in THF. Dissolution of the complex in chlorinated solvents such as $CH_2Cl_2$ and $HCCl_3$ resulted in immediate decomposition. In the IR spectrum of **3** (in Nujol) the nitrosyl stretching band appears at 1489 $cm^{-1}$. This value is 49 $cm^{-1}$ lower than that of precursor **1** ($\nu_{NO}$ = 1538 $cm^{-1}$). The decrease in the nitrosyl stretching frequency is again indicative of the coordination of the $O_{NO}$ atom. The $^1$H NMR spectrum of **3** in $[D_8]$THF displays two multiplets at $\delta$ = 1.68 and 1.55 ppm and two singlets at 1.48 and 1.43 ppm, which correspond to the resonances of the methylene and methyl groups of the dmpe ligands, respectively. The signal for the $SiMe_3$ moieties is observed as a singlet at $\delta$ = –0.16 ppm. The $^{13}$C- and $^{31}$P NMR spectra for the $Mo(dmpe)_2(Cl)(NO)$ moiety are similar to those exhibited by **1**. The $^{13}$C NMR resonance for the $SiMe_3$ group appears as a singlet at 6.2 ppm. In the $^7$Li NMR spectrum, a singlet is found at $\delta$ = 4.26 ppm, which, together with its resemblance to the $^1$H- and $^{13}$C NMR spectra of **1**, may imply dissociation of **3** in THF.

### *Complex 4*

To extend the scope of these investigations, the capability of **1** to form adducts with inorganic lithium salts has also been probed. According to literature reports, lithium halides form an extremely variable and structurally diverse family of complexes with simple nitrogen- or oxygen-containing ligands.[16] However, compounds of lithium halides with complexes as ligands have been reported only in rare instances.[17] An in situ generation of the lithium halide has been proven to be superior for the syntheses of its adducts.[16] Thus, the reactions of a **1**/*n*BuLi mixture with *n*BuCl, $SiMe_3Cl$, and *n*BuBr were investigated. They failed to produce any **1**/LiCl or **1**/LiBr adduct. However, a unique **1**/LiI adduct could be prepared from the reaction of **1**/*n*BuLi with MeI. In a typical batch, complex **1** (0.061 mmol) in toluene (2 mL) was mixed with equimolar amounts of *n*BuLi and iodomethane in that order. The final mixture was left undisturbed at room temperature. Overnight, well-defined crystals of a **1**/LiI adduct $[Mo(dmpe)_2(Cl)(NO)]_3(LiI)_2$ (**4**) precipitated from the solution [Equation (1)], which was isolated in 70% yield. Complex **4** has been characterized by elemental analysis, IR and NMR spectroscopy. The elemental analysis is consistent with the composition of a 3:2 **1**/LiI adduct stoichiometry. The IR spectrum of **4** in Nujol mull displays a nitrosyl band at 1449 $cm^{-1}$, which is 89 $cm^{-1}$ lower than that of precursor **1**. It is worth noting that the decrease in the $\nu_{NO}$ vibration of **4** appears at significantly higher wavenumbers than those observed for **2** and **3**, which is presumably caused by the bridging mode of the nitrosyl oxygen (vide infra). The $^1$H NMR spectrum of **4** in $CD_2Cl_2$ exhibits resonances for the methylene and methyl groups of the dmpe ligands as a multiplet at $\delta$ = 1.51 ppm and as a singlet at $\delta$ = 1.42 ppm. The $^{13}$C NMR spectrum is similar to that exhibited by precursor **1**. The signals for the methylene and the methyl carbon atoms appear at $\delta$ = 29.8 ppm (quintet) and 15.3 and 14.6 ppm (two quintets), respectively. The $^{31}$P NMR spectrum displays a singlet at $\delta$ = 34.6 ppm and in the $^7$Li NMR spectrum a singlet is observed at $\delta$ = 3.28 ppm.

## Structures of 2, 3, and 4

### *Structure of 2*

The molecular structure of **2** has been established by X-ray diffraction analysis. Suitable crystals were obtained by the slow evaporation of a diethyl ether solution. An ORTEP representation of the molecule is shown in Figure 1 and reveals the NO group and chlorine atom disorder. Selected bond lengths and bond angles are listed in Table 1. The striking feature of the structure of **2** is its infinite one-di-

 © 2006 Wiley-VCH Verlag GmbH & Co. KGaA, Weinheim 

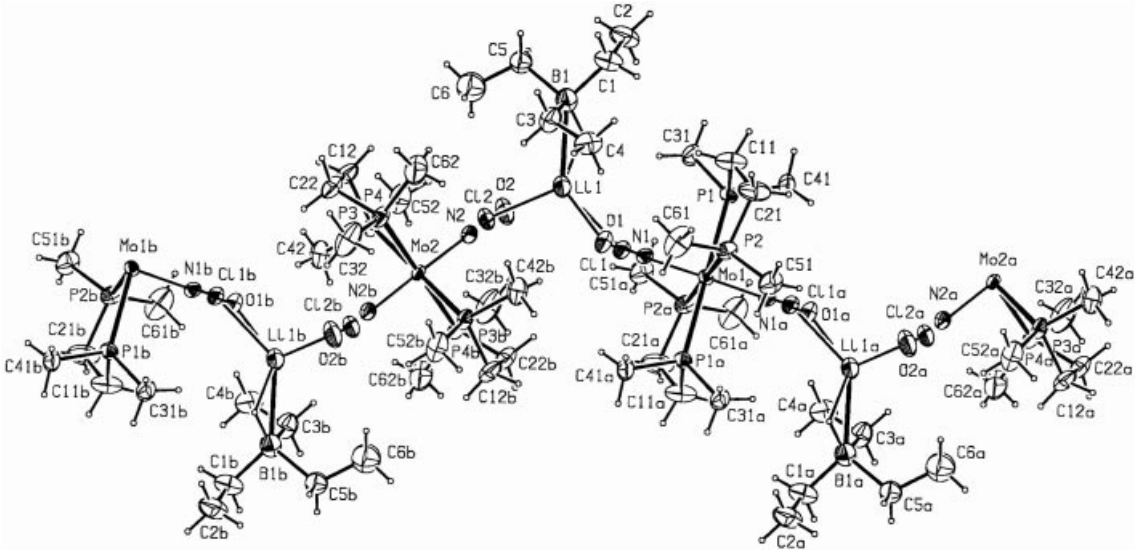


Figure 1. ORTEP plot of the structure of **2**. Displacement ellipsoids are drawn with 50% probability. The chloride and NO group display positional disorder.

mensional "zigzag" chain. The $Mo(dmpe)_2(Cl)(NO)$ moiety acts as a bridging "complex ligand", and two adjacent $LiHB(C_2H_5)_3$ moieties are $O_{NO}$ and Cl connected to the Li atoms by the $Mo(dmpe)_2(Cl)(NO)$ moieties. The two $LiHB(C_2H_5)_3$ moieties on the two sides of a $Mo(dmpe)_2(Cl)(NO)$ molecule create an inversion at the Mo atom center. Infinite repetition of these motifs build a polymeric chain of alternating $Mo(dmpe)_2(Cl)(NO)$ and $LiHB(C_2H_5)_3$ units. The lithium ion of **2** is tricoordinated by oxygen and furthermore by one chlorine and a hydrogen atom. The coordination geometry at the Li center can be described as pseudopyramidal where the three bond angles at the Li center are O1–Li1–H1, Cl2–Li1–H1, and O1–Li1–Cl2 with the values 120.2(9)°, 125.5(9)°, and 103.9(3)°, respectively. The Li1–H1 distance of 1.76(3) Å is comparable to that in the $(LiH)_\infty$ lattice (av. 1.78 Å)[18], but shorter than those found for the complexes containing $Li(\mu_2\text{-}H)_2B$ or $Li(\mu_2\text{-}H)_3B$ bridges (ca. 1.90–2.20 Å).[19] The B1–Li1 distance of 2.420(5) Å is similar to that in $LiBH_4{\cdot}3(py)$ [2.401(7) Å].[20] The O1–Li1 distance of 1.944(6) Å and the Cl2–Li1 distance of 2.329(4) Å are in the normal ranges of O–Li and Cl–Li bond lengths in organolithium compounds.[17] The coordination geometry around Mo is close to that of parent complex **1**, which becomes particularly evident from a comparison of the Mo–P bond lengths and P–Mo–P angles. The Mo1–N1 bond length of 1.832(5) Å and the Mo2–N2 bond length of 1.826(5) Å are shorter than that found in **1** (1.851(4) Å[7b]), whereas the N1–O1 and N2–O2 bond lengths of 1.229(6) and 1.230(5) Å are longer than the N–O distance of 1.187(4) Å in **1**. The shortening of the Mo–N bond and the lengthening of the N–O bond can be explained by the lithium induced enhancement of the Mo→NO back-bonding. The average Mo–Cl bond length is close to that of **1**. The N1–O1–Li1 and Mo2–Cl2–Li1 linkages show a certain extent of bending [145.1(6)° and 156.76(13)°, respectively], which is presumably due to the steric interaction between neighboring $Mo(dmpe)_2(Cl)(NO)$ and $B(C_2H_5)_3$ moieties.

Table 1. Selected bond lengths [Å] and bond angles [°] of **2**.

| Bond lengths | | Bond angles | |
|---|---|---|---|
| Mo1–N1 | 1.832(5) | N1–Mo1–P1 | 87.44(13) |
| Mo1–Cl1 | 2.5088(19) | N1–Mo1–P2 | 92.47(16) |
| Mo1–P1 | 2.4598(5) | Cl1–Mo1–P1 | 91.37(4) |
| Mo1–P2 | 2.4601(5) | Cl1–Mo1–P2 | 86.92(5) |
| N1–O1 | 1.229(6) | Mo1–N1–O1 | 178.4(7) |
| O1-Li1 | 1.944(6) | N1–O1–Li1 | 145.1(6) |
| Li1–H1 | 1.76(3) | O1–Li1–H1 | 120.2(9) |
| Li1–B1 | 2.420(5) | O1–Li1–Cl2 | 103.9(3) |
| B1–H1 | 1.23(2) | Cl2–Li1–H1 | 125.5(9) |
| Mo2–N2 | 1.826(5) | P1–Mo1–P2 | 80.223(18) |
| Mo2–Cl2 | 2.4759(18) | N2–Mo2–P3 | 90.77(15) |
| Mo2–P3 | 2.4573(5) | N2–Mo2–P4 | 85.32(15) |
| Mo2–P4 | 2.4550(5) | P3–Mo2–P4 | 80.90(2) |
| N2–O2 | 1.230(5) | Cl2–Mo2–P3 | 88.37(5) |
| Cl1–Li1 | 2.443(4) | Cl2–Mo2–P4 | 93.48(5) |
| Cl2–Li1 | 2.329(4) | Mo2–Cl2–Li1 | 156.76(13) |
| B1–C1 | 1.624(4) | Mo2–N2–O2 | 174.1(5) |
| B1–C3 | 1.659(3) | C1–B1–C3 | 110.3(2) |
| B1–C5 | 1.735(8)[a] | C1–B1–C5 | 98.1(3) |
| B1–C7 | 1.618(5)[a] | C3–B1–C5 | 105.9(3) |

[a] C(5) and C(7) represent split positions of a disordered ethyl group.

### *Structure of 3*

The molecular structure of **3**, established by single-crystal X-ray crystallographic analysis, is arranged as an infinite linear chain as shown in Figure 2. The molecular chain can be viewed as being composed of alternating $Mo(dmpe)_2(Cl)(NO)$ moieties and dimeric $[LiN(SiMe_3)_2]_2$ units. Two neighboring units of the dimeric $[LiN(SiMe_3)_2]_2$ part are thus linked by the "complex ligand" of $Mo(dmpe)_2(Cl)(NO)$ acting as a bridging unit. The complex $LiN(SiMe_3)_2$ has previously been reported to be trimeric.[21] The

 © 2006 Wiley-VCH Verlag GmbH & Co. KGaA, Weinheim 

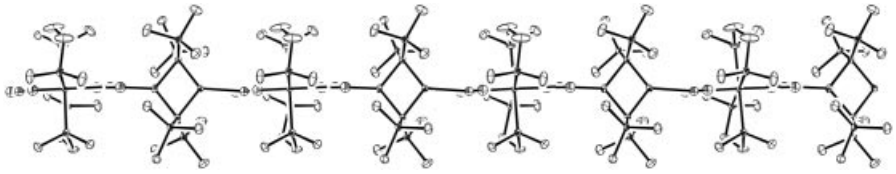

Figure 2. One-dimensional chain structure of **3**. The hydrogen atoms have been omitted for clarity.

solvated species $[Li(Et_2O)N(SiMe_3)_2]_2$[22] and $[Li(THF)N(SiMe_3)_2]_2$[23] were found to be dimeric. Figure 3 displays the asymmetric unit of the structure of **3**. In the dimeric $[LiN(SiMe_3)_2]_2$ unit, each lithium ion possesses a triangular-coordination geometry built up from two nitrogen atoms of the amides and one $O_{NO}$ or a chlorine atom of the $Mo(dmpe)_2(Cl)(NO)$ moiety. The average Li–N distances are 2.034(4) Å for Li1 and 2.053(4) Å for Li2 (Table 2). They are comparable to those distances found in some symmetric dimeric lithium amides such as $[Li\{HN(iPr)_2\}N\text{-}1\text{-}c\text{-}C_6H_9Ph]_2$ (Li–N = 2.05 Å),[24] $[Li(THF)HMCTS]_2$ (Li–N = 2.04 Å),[25] $[Li(THF)NSiMe_3HMCTS]_2$ (Li–N = 2.04 Å)[26] etc. and are in the same range as for $[Li(THF)N(SiMe_3)_2]_2$[23] [2.025(9) Å] and for $[Li(Et_2O)N(SiMe_3)_2]_2$[22] [2.055(5) Å]. However, both bond lengths are longer than those observed in trimeric $[LiN(SiMe_3)_2]_3$ [Li–N = 2.00(2) Å],[21] which is presumably due to the higher coordination number of the Li ion and the bridging mode of the $[N(SiMe_3)_2]^-$ ligand in **3**. The average Li–N–Li angle of 75.76(16)° and N–Li–N angle of 104.24(17)° are similar to related bond angles observed in $[Li(Et_2O)N(SiMe_3)_2]_2$[22] and $[Li(THF)N(SiMe_3)_2]_2$.[23] Because of enhanced Mo→NO back-bonding in the $Mo(dmpe)_2(Cl)(NO)$ moiety of **3**, the average Mo–N bond length of 1.753(6) Å is 0.098 Å shorter and the average N–O bond length of 1.253(7) Å is 0.066 Å longer than the corresponding ones in **1**. The coordination of the chloride ligand to the lithium center does not induce a significant change in the Mo–Cl bond length [2.4937(15) Å in **3** versus 2.4881(14) Å in **1**], which may indicate only a weak interaction of the chlorine atom with the lithium center. In contrast to **2**, the N–O–Li and Mo–Cl–Li linkages are almost straight with average bond angles of 171.8(4)° and 172.94(12)°, which provokes the chain structure of **3**, composed of an MoCl–Li–Li–O–N–Mo backbone, to be linear overall as shown in Figure 2.

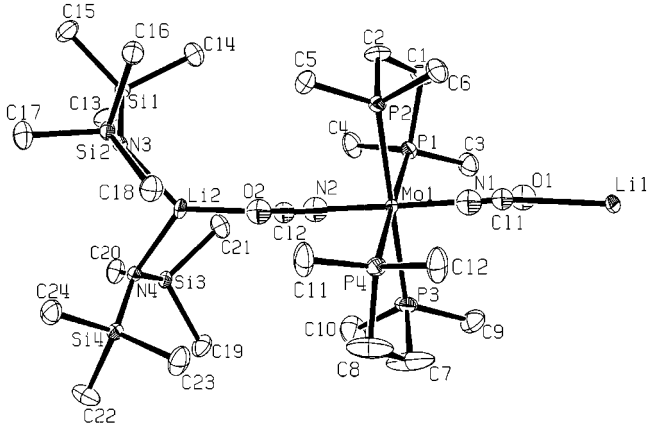


Figure 3. The asymmetrical unit of **3**. Displacement ellipsoids are drawn with 50% probability. The chloride ion and nitrosyl group show disorder.

Table 2. Selected bond lengths [Å] and bond angles [°] of **3**.

| Bond lengths | | Bond angles | |
|---|---|---|---|
| Mo1–N1 | 1.747(5) | N1–Mo1–P1 | 86.89(17) |
| Mo1–N2 | 1.758(6) | N1–Mo1–P2 | 91.30(17) |
| Mo1–Cl1 | 2.4966(14) | N1–Mo1–P3 | 88.23(17) |
| Mo1–Cl2 | 2.4907(16) | N1–Mo1–P4 | 91.34(17) |
| Mo1–P1 | 2.4749(6) | Cl2–Mo1–P1 | 93.75(3) |
| Mo1–P2 | 2.4628(6) | Cl2–Mo1–P2 | 89.06(3) |
| Mo1–P3 | 2.4572(7) | Cl2–Mo1–P3 | 91.41(4) |
| Mo1–P4 | 2.4707(7) | Cl2–Mo1–P4 | 88.03(3) |
| N1–O1 | 1.204(7) | Mo1–N1–O1 | 176.0(5) |
| N2–O2 | 1.301(7) | Mo1–N2–O2 | 175.8(4) |
| O1–Li1 | 1.975(6) | P1–Mo1–P2 | 80.56(2) |
| O2–Li2 | 1.866(6) | P3–Mo1–P4 | 80.74(2) |
| Cl1–Li1 | 2.426(4) | N1–O1–Li1 | 170.0(4) |
| Cl2–Li1 | 2.435(4) | N2–O2–Li2 | 173.5(4) |
| Li1–N3 | 2.040(4) | Mo1–Cl1–Li1 | 171.43(11) |
| Li1–N4 | 2.027(4) | Mo1–Cl2–Li2 | 174.45(12) |
| Li2–N3 | 2.051(4) | O1–Li1–N3 | 121.2(2) |
| Li2–N4 | 2.054(4) | O1–Li1–N4 | 133.8(2) |
| Li1–Li2 | 2.509(5) | N3–Li1–N4 | 104.92(17) |
| N3–Si1 | 1.702(2) | Cl2–Li2–N3 | 130.9(2) |
| N3–Si2 | 1.700(2) | Cl2–Li2–N4 | 125.53(19) |
| N4–Si3 | 1.702(2) | N3–Li2–N4 | 103.56(17) |
| N4–Si4 | 1.701(2) | Li1–N3–Li2 | 75.65(16) |
| | | Li1–N4–Li2 | 75.87(16) |

### *Structure of 4*

An ORTEP plot of **4** is shown in Figure 4. Selected bond lengths and bond angles are listed in Table 3. As shown in Figure 4, complex **4** can be formulated as $\{[Mo(dmpe)_2(Cl)(NO)]_3(LiI)_2\}$ with a 2:3 Li/Mo stoichiometry. Its structure can be described as two unique LiI units that are bridged by the nitrosyl oxygen atoms of three "$Mo(dmpe)_2(Cl)(NO)$ ligands". For LiI-containing adducts 1:1 (Li:ligand), 1:2, and 1:3 monomers,[27] 1:1 and 1:2 dimers,[28] a 1:1 tetramer,[29] and ion-pair coordinated species[30] have been reported. A 2:3 adduct of LiI with 2,4,6-trimethylpyridine (tmpy) was found in fact to be a tetramer with the formulation $[(LiI)_4(tmpy)_6]$.[31] In dimers and higher agglomerates the iodine anion usually acts as a bridging ligand. The observation of the 2:3 stoichiometry and the structural feature of the donor-connected LiI monomers in **4** is quite unusual. To the best of our knowledge, only the case of a $[(LiBr)_2(HMPA)_3(toluene)_{0.5}]$ molecule (HMPA = hexamethylphosphoramide)[32] provides further analogy.

 © 2006 Wiley-VCH Verlag GmbH & Co. KGaA, Weinheim 

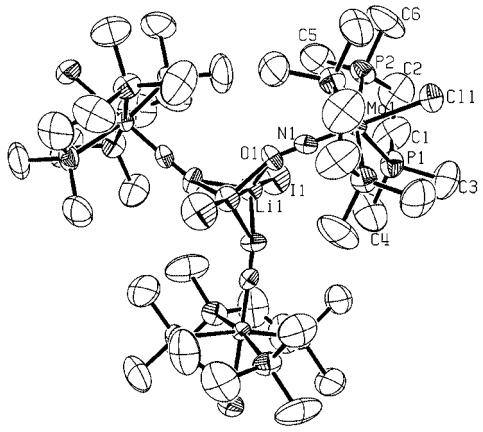


Figure 4. ORTEP plot of the structure of **4**. Displacement ellipsoids are drawn with 50% probability. Labeling of symmetry-related atoms is not shown (symmetry operations: $i_1 = x, y, -z+1/2$, $i_2 = -y+1, x-y, z$; $i_3 = -x+y+1, -x+1, z$).

Table 3. Selected bond lengths [Å] and bond angles [°] of **4**.[a]

| Bond lengths | | Bond angles | |
|---|---|---|---|
| Mo1–N1 | 1.780(7) | N1–Mo1–P1 | 93.85(14) |
| Mo1–P1 | 2.4466(17) | N1–Mo1–P2 | 96.98(13) |
| Mo1–P2 | 2.4551(17) | P1–Mo1–P2 | 80.06(6) |
| Mo1–Cl1 | 2.574(3) | Cl1–Mo1–P1 | 86.36(6) |
| N1–O1 | 1.234(8) | Cl1–Mo1–P2 | 82.80(6) |
| O1–Li1 | 2.040(10) | N1–O1–Li1 | 137.7(4) |
| I1–Li1 | 2.622(16) | Li1–O1–Li($i_1$) | 71.4(8) |
| Li1-Li($i_1$) | 2.38(3) | O1–Li1–O($i_2$) | 89.4(5) |
| | | O1–Li1–I1 | 125.7(4) |

[a] Symmetry transformations used to generate equivalent atoms: $i_1 = x, y, -z+1/2$; $i_2 = -y+1, x-y, z$; $i_3 = -x+y+1, -x+1, z$).

Unlike the three-coordinate Li ion in **2** and **3**, the lithium cation of **4** is tetra-coordinated in a pseudotetrahedral geometry and has one iodine atom and three oxygen atoms of the three "Mo(dmpe)$_2$(Cl)(NO) ligands" attached. In agreement with the higher coordination number of the Li ion in **4**, the O–Li distance of 2.040(10) Å is significantly longer than those observed in **2** and **3** [1.944(6) Å and 1.921(6) Å, respectively]. The I–Li bond length of 2.622(16) Å is particularly short compared with other tetra-coordinated LiI complexes (usually in the range of 2.70 to 2.95 Å[27–31]). The transannular Li–Li "contact" is 2.38(3) Å, which is also particularly short [the shortest Li–Li distance reported in LiI complexes is 3.575(6) Å[29] and in **3** it is 2.509(5) Å]. The observation of unusually short Li–halide and Li–Li distances in **4** is similar to that of the structurally analogous complex [(LiBr)$_2$(HMPA)$_3$-(toluene)$_{0.5}$].[32] In this context, it is noteworthy that the Li–Li distances in both complexes are very close [2.36(3) Å in the LiBr complex]. The Mo–P bond lengths of **4** do not differ significantly from the bond of precursor **1**. However, related Cl–Mo–P bond angles are smaller than those exhibited by **1**, which indicating further bending of the dmpe ligands towards the chlorine side. This bending is apparently due to the mutual repulsion of the three "Mo-(dmpe)$_2$(Cl)(NO) ligands". As a consequence of this bending, the Mo–Cl bond lengths increase distinctly from 2.4881(14) Å in **1** to 2.574(3) Å in **4**.

## Discussion

The reactions of halide-containing transition metal complexes with organic lithium reagents normally afford metathetical products.[7] However, the reaction of **1** with the reagents LiHBEt$_3$, LiN(SiMe$_3$)$_2$, and *n*BuLi led to lithium reagent/**1** adduct formation. This result can be attributed to a relatively strong donicity of the $O_{NO}$ atom in **1** induced by strongly σ-donating dmpe ligands, which cause charge accumulation on the molybdenum center and concomitantly strong electron transfer to the NO group.

Compounds **2**, **3**, and **4** show different **1**/Li ratios and various structural features. Compound **2** exhibits an infinite one-dimensional "zigzag" chain with a 1:1 ratio of **1**/LiHBEt$_3$, whereas compound **3** displays an infinite linear chain with a 1:2 ratio of **1** and LiN(SiMe$_3$)$_2$. The strong bridging ability of the N(SiMe$_3$)$_2^-$ anion eases formation of a polymeric structure for the LiN(SiMe$_3$)$_2$ part. In addition, this is the main reason for **3** to adopt a higher **1**/Li ratio as compared to **1**. In **2** and **3**, complex **1** acts as a bridging ligand by coordinating the $O_{NO}$ and Cl atoms. The capability of the Cl atom to participate in the coordination can be ascribed to the strong Lewis acidic property and high reactivity of the Li$^+$ ion in LiHBEt$_3$ and LiN(SiMe$_3$)$_2$. In contrast to **2** and **3**, complex **4** forms a structure of distinct molecules with a 3:2 **1**/Li ratio. The chlorine atom of **4** is not involved in coordination. The fact that **4** prefers a small unit structure may be ascribed to the relatively small size of the iodine counterion in comparison with the bulky organic anions of **2** and **3** and the competition between the oxygen and iodine bridges. As a result, the $O_{NO}$ atom of **4** adopts a $\mu_2$-bridging coordination mode rather than a terminal mode as in **2** and **3**, which allows for the formation of distinct molecular units in **4**.

The adducts formed from LiHBEt$_3$ and donor ligands have rarely been reported, and although the compounds formed from LiN(SiMe$_3$)$_2$ and LiI with ligands containing O- or N-donor atoms have been well documented, those with a metal complex as a ligand are not. The three compounds described here represent the first examples of lithium adducts with a complex as a ligand. The work documents not only excellent Lewis basicity of the NO ligand, but also shows the great structural diversity that such μ-NO complexation may lead to.

## Conclusions

In summary, the reactions of the chloride complex Mo(dmpe)$_2$(Cl)(NO) (**1**) with the lithium reagents LiHB(C$_2$H$_5$)$_3$, LiN(SiMe$_3$)$_2$, and the mixture of *n*BuLi/MeI did not provide the usual products of a H/Cl metathetical reaction, but rather afforded the adducts of **1** with lithium salts because of the coordination of the nitrosyl group to the lithium ion. A relatively strong donicity of the bound

 © 2006 Wiley-VCH Verlag GmbH & Co. KGaA, Weinheim 

nitrosyl group in **1** is indicated, which may be attributed, for the most part, to the effect of the strongly σ-donating dmpe ligands. The two dmpe ligands cause charge accumulation on the molybdenum center and thus enhance the electron density on the nitrosyl oxygen atom. The resulting propensity to act as a σ donor for the nitrosyl oxygen atom may also have implications on the reactivity of **1**, as for instance in the conversion of **1** to the corresponding borohydride $Mo(dmpe)_2(HBH_3)(NO)$, where the isolation of the borohydride proved to be troublesome presumably because of the adduct formation with the alkaline element borohydride starting material.[7b]

## Experimental Section

All reactions and manipulations were carried out under an atmosphere of dry nitrogen with the use of conventional Schlenk techniques or a glove box. Solvents were dried by standard methods and freshly distilled under an atmosphere of nitrogen before use. *trans*-$Mo(dmpe)_2(Cl)(NO)$ (**1**) was prepared as described previously.[7b] Other reagents were purchased from Fluka or Aldrich. NMR spectra were recorded with the following spectrometers: Varian Gemini-300 instrument for $^1$H-, $^{13}$C-, $^{31}$P-, and $^{11}$B NMR; Bruker DRX-500 instrument for $^7$Li NMR. $\delta(^1H)$ and $\delta(^{13}C)$ are relative to $SiMe_4$, $\delta(^{31}P)$ is relative to 85% $H_3PO_4$, $\delta(^{11}B)$ is relative to $BF_3{\cdot}OEt_2$, and $\delta(^7Li)$ is relative to $LiClO_4$ in $H_2O$. IR spectra were recorded with a Biorad FTS-45 instrument. Elemental analyses were performed with a Leco CHN(S)-932 instrument.

**$[Mo(dmpe)_2(Cl)(NO)LiHB(C_2H_5)_3]_n$ (2):** A lithium triethylborohydride solution (0.13 mL, 1.0 M solution in THF) was added to a solution of **1** (0.055 g, 0.12 mmol) in diethyl ether (15 mL). The mixture was stirred for 3 h and then left undisturbed at room temperature to allow the solvent to evaporate. Slow evaporation of the diethyl ether for 3 d provided **2** as yellow crystals that were suitable for an X-ray diffraction study. Yield: 0.060 g (88%). IR (Nujol): $\tilde{\nu}$ = 1486 (NO) cm$^{-1}$. $^1$H NMR (300.1 MHz, $C_6D_6$): $\delta$ = 1.43 (m, 4 H, $PCH_2$), 1.24 (m, 4 H, $PCH_2'$), 1.32 (s, 12 H, PMe), 1.28 (s, 12 H, PMe′), 1.21 [t, $^3J_{H,H}$ = 7.2 Hz, 9 H, Me of $B(C_2H_5)_3$], 0.85 [m, 6 H, $CH_2$ of $B(C_2H_5)_3$] ppm. $^{13}C\{^1H\}$ NMR (75.4 MHz, $C_6D_6$): $\delta$ = 29.5 (quint, $^1J_{C,P}$ = 9.7 Hz, $PCH_2$), 15.0 (quint, $^1J_{C,P}$ = 5.0 Hz, PMe), 14.5 (quint, $^1J_{C,P}$ = 5.0 Hz, PMe′), 15.5 [br., $CH_2$ of $B(C_2H_5)_3$], 11.2 [br., Me of $B(C_2H_5)_3$] ppm. $^{31}P\{^1H\}$ NMR (121.5 MHz, $C_6D_6$): $\delta$ = 34.6 (s) ppm. $^{11}$B NMR (96.2 MHz, $C_6D_6$): $\delta$ = –2.76 (s, br) ppm. $^7$Li NMR (194.4 MHz, $C_6D_6$): $\delta$ = 2.10 (s) ppm. $C_{18}H_{48}BClLiMoNOP_4$ (567.63): calcd. C 38.08, H 8.54, N 2.47; found C 38.33, H 8.17, N 2.44.

**$\{Mo(dmpe)_2(Cl)(NO)[LiN(SiMe_3)_2]_2\}_n$ (3):** A mixture of **1** (0.022 g, 0.048 mmol) and lithium bis(trimethylsilyl)amide (0.017 g, 0.102 mmol) was dissolved in diethyl ether (15 mL) and the resulting solution was stirred for 3 h. The solvent was then evaporated slowly at room temperature for 4 d to afford **3** as yellow crystals. Yield: 0.032 g (84%). IR (Nujol): $\tilde{\nu}$ = 1489 (NO) cm$^{-1}$. $^1$H NMR (300.1 MHz, [D$_8$]THF): $\delta$ = 1.68 (m, 4 H, $PCH_2$), 1.55 (m, 4 H, $PCH_2'$), 1.48 (s, 12 H, PMe), 1.43 (s, 12 H, PMe′), –0.16 (s, 36 H, $SiMe_3$) ppm. $^{13}C\{^1H\}$ NMR (75.4 MHz, [D$_8$]THF): $\delta$ = 30.6 (quint, $^1J_{C,P}$ = 10 Hz, $PCH_2$), 15.0 (quint, $^1J_{C,P}$ = 5.0 Hz, PMe), 14.8 (quint, $^1J_{C,P}$ = 5.0 Hz, PMe′), 6.2 (s, $SiMe_3$) ppm. $^{31}P\{^1H\}$ NMR (121.5 MHz, [D$_8$]THF): $\delta$ = 36.3 (s) ppm. $^7$Li NMR (194.4 MHz, [D$_8$]THF): $\delta$ = 4.26 (s) ppm. $C_{24}H_{68}ClLi_2MoN_3OP_4Si_4$ (796.34): calcd. C 36.19, H 8.62, N 5.28; found C 36.52, H 8.40, N 5.31.

**$[Mo(dmpe)_2(Cl)(NO)]_3(LiI)_2$ (4):** A butyllithium solution (0.038 mL, 0.061 mmol, 1.6 M solution in hexane) and iodomethane (3.8 μL, 0.061 mmol) were added to a solution of **1** (0.028 g

Table 4. Crystallographic data and structure refinement parameters for **2**, **3**, and **4**.

| | **2** | **3** | **4** |
|---|---|---|---|
| Formula | $C_{18}H_{48}BClLiMoNOP_4$ | $C_{24}H_{68}ClLi_2MoN_3OP_4Si_4$ | $C_{36}H_{96}Cl_3I_2Li_2Mo_3N_3O_3P_{12}$ |
| *Fw* | 567.59 | 796.32 | 1652.65 |
| Color | yellow | yellow | orange |
| Crystal dimensions [mm] | 0.37 × 0.28 × 0.16 | 0.35 × 0.22 × 0.18 | 0.32 × 0.25 × 0.22 |
| Temperature [K] | 173(2) | 123(2) | 183(2) |
| Crystal system | monoclinic | monoclinic | hexagonal |
| Space group (No.) | $P2_1/n$ (14) | $P2_1/n$ (14) | $P6_3/m$ (176) |
| *a* [Å] | 9.0226(4) | 12.3360(7) | 14.8449(8) |
| *b* [Å] | 21.0532(13) | 18.9211(10) | 14.8449(8) |
| *c* [Å] | 15.9680(7) | 19.4073(10) | 18.3676(9) |
| *α* [°] | 90 | 90 | 90 |
| *β* [°] | 105.029(5) | 106.848(6) | 90 |
| *γ* [°] | 90 | 90 | 120 |
| V [Å$^3$] | 2929.4(3) | 4335.4(4) | 3505.4(3) |
| *Z* | 4 | 4 | 2 |
| $D_{calcd.}$ [g cm$^{-3}$] | 1.287 | 1.220 | 1.566 |
| Abs. coeff. [mm$^{-1}$] | 0.767 | 0.643 | 1.829 |
| *F*(000) | 1192 | 1688 | 1652 |
| 2*θ* Scan range [°] | 5.62 < 2*θ* < 60.58 | 5.08 < 2*θ* < 60.58 | 5.46 < 2*θ* < 55.98 |
| No. of unique data | 8134 | 12831 | 2899 |
| No. of data obsd [$I > 2\sigma(I)$] | 4922 | 9053 | 1418 |
| Abs. corr. | numerical | numerical | numerical |
| Solution method | Patterson | Patterson | Patterson |
| No. of parameters refined | 292 | 375 | 107 |
| *R*, $wR_2$ [%] all data | 5.74, 4.52 | 6.00, 8.65 | 9.51, 11.22 |
| $R_1$, $wR_2$ (obsd.) [%][a] | 2.85, 4.35 | 3.78, 8.32 | 5.13, 10.63 |
| Goodness of fit | 1.028 | 1.019 | 1.028 |

[a] $R_1 = \Sigma(F_o - F_c) / \Sigma F_o$; $I > 2\sigma(I)$; $wR_2 = \{\Sigma w(F_o^2 - F_c^2)^2 / \Sigma w(F_o^2)^2\}^{1/2}$.

 © 2006 Wiley-VCH Verlag GmbH & Co. KGaA, Weinheim 

(0.061 mmol) in toluene (ca. 2 mL). The mixture was stirred to obtain a homogeneous solution and then stood undisturbed at room temperature overnight. Large orange crystals of **4** were obtained. Yield: 0.023 g (70%). IR (Nujol): $\tilde{\nu}$ = 1449 (NO) $cm^{-1}$. $^1H$ NMR (300.1 MHz, $CD_2Cl_2$): $\delta$ = 1.51 (m, 8 H, $PCH_2$), 1.42 (s, 24 H, PMe) ppm. $^{13}C\{^1H\}$ NMR (75.4 MHz, $CD_2Cl_2$): $\delta$ = 29.8 (quint, $^1J_{C,P}$ = 9.6 Hz, $PCH_2$), 15.3 (quint, $^1J_{C,P}$ = 4.7 Hz, PMe), 14.6 (quint, $^1J_{C,P}$ = 4.7 Hz, PMe′) ppm. $^{31}P\{^1H\}$ NMR (121.5 MHz, $CD_2Cl_2$): $\delta$ = 34.6 (s) ppm. $^7Li$ NMR (194.4 MHz, $CD_2Cl_2$): $\delta$ = 3.28 (s) ppm. $C_{36}H_{96}Cl_3I_2Li_2Mo_3N_3O_3P_{12}$ (1652.73): calcd. C 26.16, H 5.87, N 2.54; found C 26.29, H 6.11, N 2.71.

**X-ray Crystal Structure Analyses:** The X-ray diffraction data were collected at 173(2) K (**2**), 123(2) K (**3**), and 183(2) K (**4**) with the use of an imaging plate detector system (Stoe IPDS) with graphite monochromated Mo-$K_\alpha$ radiation. A total of 180, 167, and 167 images were exposed at constant times of 4.00, 3.00, and 2.80 min/image for compounds **2**, **3**, and **4**, respectively. The crystal-to-image distances were set to 50, 50, and 60 mm, respectively. The corresponding $\theta_{max}$ values were 30.29°, 30.29°, and 27.99°, respectively. $\phi$-oscillation (**2**, **3**) or rotation scan modes (**4**) were selected for the $\phi$ increments of 1.0°,1.2°, and 1.2° per exposure in each case. Total exposure times for the three compounds were 25, 20, and 19 hours, respectively. After integrations and corrections for Lorentz and polarization effects, a total of 8000 reflections were selected out of the whole limiting sphere for the cell-parameter refinements. A total of 30218, 49957, and 33867 reflections were collected, of which 8134, 12831, and 2899 reflections were unique ($R_{int}$ = 4.74%, 4.93%, and 4.90%); data reduction and numerical absorption corrections used 15, 18, and 17 indexed crystal faces.[33] The structures were solved by the Patterson method with the use of the program SHELXS-97,[34] and they were refined with SHELXL-97.[35] The X-ray data collections and the processing parameters are given in Table 4.

CCDC-606806 -606808 (for **2**, **3**, and **4**) contain the supplementary crystallographic data for this paper. These data can be obtained free of charge from The Cambridge Crystallographic Data Centre via www.ccdc.cam.ac.uk/data_request/cif.

## Acknowledgments

Financial support from the Swiss National Science Foundation and the Funds from the University of Zurich are gratefully acknowledged.

[1] G. B. Richter-Addo, P. Legzdins, *Metal Nitrosyls*, Oxford University Press, New York, **1992**.
[2] W. Macyk, A. Franke, G. Stochel, *Coord. Chem. Rev.* **2005**, *249*, 2437.
[3] D. Nietlispach, H. W. Bosch, H. Berke, *Chem. Ber.* **1994**, *127*, 2403.
[4] a) H. U. Hund, U. Ruppli, H. Berke, *Helv. Chim. Acta* **1993**, *76*, 963; b) D. Nietlispach, D. Veghini, H. Berke, *Helv. Chim. Acta* **1994**, *77*, 2197; c) S. Feracin, T. Bürgi, V. I. Bakhmutov, I. Eremenko, E. V. Vorontsov, A. B. Vimenits, H. Berke, *Organometallics* **1994**, *13*, 4194; d) V. I. Bakhmutov, T. Bürgi, P. Burger, U. Ruppli, H. Berke, *Organometallics* **1994**, *13*, 4203; e) H. Jacobsen, K. Heinze, A. Llamazares, H. W. Schmalle, G. Artus, H. Berke, *J. Chem. Soc., Dalton Trans.* **1999**, 1717; f) A. Llamazares, H. W. Schmalle, H. Berke, *Organometallics* **2001**, *20*, 5277.
[5] A. A. H. van der Zeijden, T. Bürgi, H. Berke, *Inorg. Chim. Acta* **1992**, *201*, 131.
[6] a) A. A. H. van der Zeijden, C. Sontag, H. W. Bosch, V. Shklover, H. Berke, D. Nanz, W. von Philipsborn, *Helv. Chim. Acta* **1991**, *74*, 1194; b) A. A. H. van der Zeijden, V. Shklover, H. Berke, *Inorg. Chem.* **1991**, *30*, 4393; c) A. A. H. van der Zeijden, H. W. Bosch, H. Berke, *Organometallics* **1992**, *11*, 563; d) A. A. H. van der Zeijden, H. W. Bosch, H. Berke, *Organometallics* **1992**, *11*, 2051; e) J. Höck, H. Jacobsen, H. W. Schmalle, G. R. J. Artus, T. Fox, J. I. Amor, F. Bäth, H. Berke, *Organometallics* **2001**, *20*, 1533; f) Z. Chen, H. W. Schmalle, T. Fox, H. Berke, *Dalton Trans.* **2005**, 580.
[7] a) F. Liang, H. Jacobsen, H. W. Schmalle, T. Fox, H. Berke, *Organometallics* **2000**, *19*, 1950; b) F. Liang, H. W. Schmalle, T. Fox, H. Berke, *Organometallics* **2003**, *22*, 3382; c) F. Liang, H. W. Schmalle, H. Berke, *Inorg. Chem.* **2004**, *43*, 993; d) Y. Zhao, H. W. Schmalle, T. Fox, O. Blacque, H. Berke, *Dalton Trans.* **2006**, 73.
[8] D. G. Gusev, A. Llamazares, G. Artus, H. Jacobsen, H. Berke, *Organometallics* **1999**, *18*, 75.
[9] a) H. Berke, P. Burger, *Comments Inorg. Chem.* **1994**, *16*, 279; b) H. Jacobsen, H. Berke, "Hydridicity of Transition Metals and its Implications for Reactivity" in *Recent Advances in Hydride Chemistry* (Eds.: R. Poli, M. Peruzzi), Elsevier, **2001**.
[10] a) N. V. Belkova, E. S. Shubina, A. V. Ionidis, L. M. Epstein, H. Jacobsen, A. Messmer, H. Berke, *Inorg. Chem.* **1997**, *36*, 1522; b) A. Messmer, H. Jacobsen, H. Berke, *Chem. Eur. J.* **1999**, *5*, 3341.
[11] B. S. Tovrog, S. E. Diamond, F. Mares, A. Szalkiewicz, *J. Am. Chem. Soc.* **1981**, *103*, 3522.
[12] A. Llamazares, G. Artus, H. Berke, manuscript in preparation.
[13] a) P. Legzdins, S. F. Sayers, *Organometallics* **1996**, *15*, 3907; b) P. Legzdins, S. F. Sayers, *Chem. Eur. J.* **1997**, *3*, 1579; c) P. Legzdins, K. J. Ross, S. F. Sayers, S. J. Rettig, *Organometallics* **1997**, *16*, 190.
[14] a) G. B. Richter-Addo, P. Legzdings, *Chem. Rev.* **1988**, *88*, 991; b) F. Bottomley, "Reactions of Nitrosyls" in *Reactions of Coordinated Ligands* (Ed.: P. S. Braterman), Plenum, New York, **1989**, vol. 2, p. 115.
[15] a) C. P. Horwitz, D. F. Shriver, *Adv. Organomet. Chem.* **1984**, *23*, 219; b) D. F. Shriver, *J. Organomet. Chem.* **1975**, *94*, 259; c) M. Y. Darensbourg, *Prog. Inorg. Chem.* **1985**, *33*, 221.
[16] R. Snaith, D. S. Wright, "Complexes of Inorganic Lithium Salts" in *Lithium Chemistry: A Theoretical and Experimental Overview* (Eds.: A.-M. Sapse, P. von Ragué Schleyer), John Wiley & Sons, **1995**, p. 227.
[17] W. N. Setzer, P. von Ragué Schleyer, *Adv. Organomet. Chem.* **1985**, *24*, 353.
[18] E. Zintl, A. Z. Harder, *Phys. Chem. Sect. B* **1935**, *28*, 478.
[19] a) J. Hooz, S. Akiyama, F. J. Cedar, M. J. Bennett, R. M. Tuggle, *J. Am. Chem. Soc.* **1974**, *96*, 274; b) C. Eaborn, M. N. A. El-Kheli, P. B. Hitchcock, J. D. Smith, *J. Chem. Soc., Chem. Commun.* **1984**, 1673; c) D. R. Armstrong, W. Clegg, H. M. Colquhoun, J. A. Daniels, R. E. Mulvey, I. R. Stephenson, K. Wade, *J. Chem. Soc., Chem. Commun.* **1987**, 630; d) H. H. Giese, T. Habereder, J. Knizek, H. Nöth, M. Warchhold, *Eur. J. Inorg. Chem.* **2001**, 1195.
[20] H.-H. Giese, T. Habereder, H. Nöth, W. Ponikwar, S. Thomas, M. Warchhold, *Inorg. Chem.* **1999**, *38*, 4188.
[21] a) V. D. Mootz, A. Zinnius, B. Böttcher, *Angew. Chem.* **1969**, *81*, 398; b) R. D. Gogers, J. L. Atwood, R. Grüning, *J. Organomet. Chem.* **1978**, *157*, 229.
[22] a) M. F. Lappert, M. J. Slade, A. Singh, *J. Am. Chem. Soc.* **1983**, *105*, 302; b) L. M. Engelhardt, A. S. May, C. L. Raston, A. H. White, *J. Chem. Soc., Dalton Trans.* **1983**, 1671.
[23] L. M. Engelhardt, B. S. Jolly, P. C. Junk, C. L. Raston, B. W. Skelton, A. H. White, *Aust. J. Chem.* **1986**, *39*, 1337.
[24] R. A. Wanat, D. B. Collum, G. V. Duyne, J. Clardy, R. T. DePue, *J. Am. Chem. Soc.* **1986**, *108*, 3415.
[25] M. Haase, G. M. Sheldrick, *Acta Crystallogr., Sect. C* **1986**, *42*, 1009.
[26] E. Egert, U. Kliebisch, U. Klingebiel, D. Z. Schmidt, *Z. Anorg. Allg. Chem.* **1987**, *548*, 89.

 © 2006 Wiley-VCH Verlag GmbH & Co. KGaA, Weinheim 

[27] a) C. L. Raston, B. W. Skelton, C. R. Whitaker, A. H. White, *J. Chem. Soc., Dalton Trans.* **1988**, 987; b) C. L. Raston, B. W. Skelton, C. R. Whitaker, A. H. White, *Aust. J. Chem.* **1988**, *41*, 341; c) H. Giffel, B. Neumuller, E. Fluck, *Z. Anorg. Allg. Chem.* **1993**, *619*, 1682.
[28] a) C. L. Raston, C. R. Whitaker, A. H. White, *J. Chem. Soc., Dalton Trans.* **1988**, 991; b) C. L. Raston, B. W. Skelton, C. R. Whitaker, A. H. White, *Aust. J. Chem.* **1988**, *41*, 1925; c) C. L. Raston, C. R. Whitaker, A. H. White, *Inorg. Chem.* **1989**, *28*, 163.
[29] C. Doriat, R. Baum, E. Köppe, G. Stösser, H. Köhnlein, H. Schnöckel, *Inorg. Chem.* **2000**, *39*, 1534.
[30] E. Fischer, H.-U. Hummel, *Z. Anorg. Allg. Chem.* **1997**, *623*, 483.
[31] C. L. Raston, W. T. Robinson, B. W. Skelton, C. R. Whitaker, A. H. White, *Aust. J. Chem.* **1990**, *43*, 1163.
[32] D. Barr, M. J. Doyle, R. E. Mulvey, P. R. Raithby, D. Reed, R. Snaith, D. S. Wright, *J. Chem. Soc., Chem. Commun.* **1989**, 318.
[33] Stoe IPDS software for data collection, cell refinementm, and data reduction. Version 2.87–2.92. Stoe & Cie, Darmstadt, Germany **1997**–**1999**.
[34] SHELXS-97: G. M. Sheldrick, *Acta Crystallogr., Sect. A* **1990**, *46*, 467.
[35] SHELXL-97: G. M. Sheldrick, *Program for the Refinement of Crystal Structures*. University of Göttingen, Germany, **1997**.

Received: May 24, 2006
Published Online: October 27, 2006

 © 2006 Wiley-VCH Verlag GmbH & Co. KGaA, Weinheim 

DOI: 10.1002/ejic.200600495

# Synthesis and Characterization of Some New 22-Membered Chalcogenoaza Macrocycles and Their $Co^{II}$ and $Ni^{II}$ Complexes

**Upali Patel,[a] Harkesh B. Singh,*[a] and Ray J. Butcher[b]**

**Keywords:** Cobalt / Magnetic properties / N ligands / Selenium / Tellurium

The [2+2] cyclocondensation of bis(*o*-formylphenyl)chalcogenides (**9**, **10**) with *trans*-1,2-diaminocyclohexane affords novel macrocyclic ligands **11** and **12** in very good yields. Crystals of **11** are triclinic, space group $P\bar{1}$ with $a$ = 11.4037(11), $b$ = 11.8184(12), $c$ = 14.6835(14) Å, $Z$ = 4 and those of **12** are triclinic, space group $P\bar{1}$ with $a$ = 11.2692(9), $b$ = 12.8612(11), $c$ = 15.2439(12) Å and $Z$ = 2. Reduction of **11** with sodium borohydride affords macrocycle **13**. The coordination chemistry of **11** has been studied with the "hard" metal ions $Ni^{II}$ and $Co^{II}$. Reaction of $NiCl_2{\cdot}6H_2O$ with one molar equivalent of **11** in refluxing methanol followed by addition of $NH_4PF_6$ affords $Ni^{II}$ complex **14**. The assignment of an octahedral geometry to **14** follows from its paramagnetism ($\mu_{eff}$ = 2.50 $\mu_B$) and UV/Vis spectrum and was further confirmed by single-crystal X-ray diffraction studies. The crystal structure of **14** consists of a distorted octahedral nickel center coordinated by two selenium and four nitrogen atoms. Complex **14**: hexagonal, space group $P6_1$, $a$ = 17.0747(16), $b$ = 17.0747(16), $c$ = 29.958(4) Å, $Z$ = 6. $Co^{II}$ complexes **15** and **16** of selenaaza macrocycles were prepared by the reaction of $Co(ClO_4)_2{\cdot}6H_2O$ with **11** and **3**, respectively. Complex **16**: monoclinic, space group $C_2$, $a$ = 17.160(2), $b$ = 10.9660(14), $c$ = 9.4941(12) Å, $Z$ = 2. The cyclic voltammograms of **15** and **16** in MeCN solution show well-behaved quasi-reversible couples.

(© Wiley-VCH Verlag GmbH & Co. KGaA, 69451 Weinheim, Germany, 2006)

## Introduction

Over the last decade mixed-donor chalcogen (N, O, S, Se, Te) macrocycles have attracted considerable attention.[1–7] Among them, the chalcogenoaza macrocycles containing heavier chalcogens (Se, Te) have been less studied. Our group has been involved in the synthesis and complexation studies of Schiff base selenaaza and telluraaza macrocycles **1**–**5**.[6,7] Interestingly, Schiff base macrocycle **2** shows a tendency to undergo transmetalation with $Pt^{II}$ and $Hg^{II}$ cations,[6a] and **1** hydrolyzed with $Pd^{II}$ cation leads to cleavage of the macrocycle.[6b] Macrocycles **5** and **6** exhibit contrasting ligating behavior with $Pd^{II}$ and $Pt^{II}$. Thus, macrocycle **5** forms a 23-membered metallamacrocycle on ligation with $Pt^{II}$ where oxidative addition of the C–Se bond to the $Pt^{II}$ center occurs to form a hexacoordinate $Pt^{IV}$ complex.[7c] The synthesis and structure of complexes of $Hg_2^{2+}$ and $Pb^{II}$ with 28-membered selenaaza macrocycle **4** have also been reported.[7d] There are limited examples of $Ni^{II}$ complexes of mixed-donor selenaaza macrocycles,[7b,7e] and there are no reports on the structures of $Co^{II}$ complexes of selenaethers or selenaaza macrocycles in the literature. However, two examples of structurally characterized $Co^{III}$ complexes of selenamacrocycles have been reported. The $Co^{III}$ complex of sarcophagine theme, with an N3Se3 donor (**7**), has been obtained from the reaction of $CoCl_3$ with $\{MeC[CH_2Se(CH_2)_2{-}NH_2]_3\}$ in HCHO and $MeNO_2$.[5] The complex $[CoX_2([16]aneSe_4)]PF_6$ (X = Br) (**8**) has been prepared by the reaction of $CoX_2$ (X = Cl, Br, I) with $[16aneSe_4]$ and $NH_4PF_6$, where the original $Co^{II}$ has been oxidized to $Co^{III}$.[8] Here we report the synthesis and characterization of some new 22-membered selenaaza and telluraaza macrocycles derived from *trans*-1,2-diaminocyclohex-

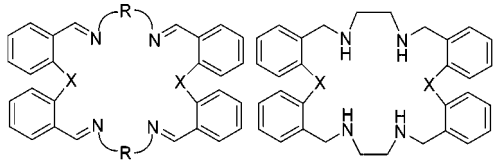

**1**: X = Se, R = -$CH_2CH_2$-
**2**: X = Te, R = -$CH_2CH_2$-
**3**: X = Se, R = -$CH_2CH_2CH_2$-
**4**: X = Se, R = -$CH_2CH_2$-N-$CH_2CH_2$-

**5**: X = Se
**6**: X = Te

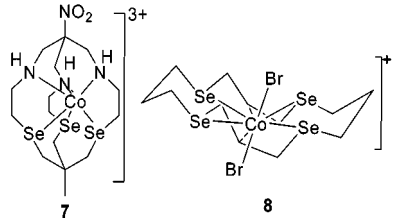

**7** **8**

[a] Department of Chemistry, Indian Institute of Technology Bombay,
Mumbai, 400 076, India
Fax: +91-22-2572-3480
E-mail: chhbsia@chem.iitb.ac.in
[b] Department of Chemistry, Howard University,
Washington, DC 20059, USA

 © 2006 Wiley-VCH Verlag GmbH & Co. KGaA, Weinheim 

ane, which imposes some rigidity on the macrocycle ring, and the coordination properties of the selenaaza macrocycles towards $Co^{II}$ and $Ni^{II}$. Although we have earlier reported the synthesis of a $Co^{II}$ complex with **1**, our attempts to characterize the complex by single crystal structure determination were unsuccessful.[7b] Now we report the first X-ray structural characterization of a $Co^{II}$ complex with a selenaaza macrocycle and its detailed magnetic properties. The coordination behavior of the telluraaza macrocycles with $Pd^{II}$ is also studied.

## Results and Discussion

Compounds **3**,[7b] **9**,[7a] and **10**[6a] were synthesized by the reported procedures. Ligands **11** and **12** were obtained in good yield by the stoichiometric reaction of bis(*o*-formylphenyl) chalcogenides **9** and **10** with *trans*-1,2-diaminocyclohexane as white and yellow solids, respectively (Scheme 1). Reduction of Schiff-base ligand **11** with an excess amount of sodium borohydride in ethanol afforded tetraamino derivative **13** as a white solid in good yield (Scheme 1). All these ligands were characterized by elemental analysis, IR-, $^1$H-, $^{13}$C-, and $^{77}$Se/$^{125}$Te NMR spectroscopy, and ESI mass spectrometry. Both of the Schiff-base ligands (**11**, **12**) were also characterized by single-crystal X-ray crystallography.

For ligand **11**, broadening of the $^1$H- and $^{13}$C NMR signals was observed at room temperature; hence the spectra were recorded at –50 °C. There were no significant changes in the $^1$H NMR spectrum even at –50 °C. However, the $^{13}$C NMR spectrum shows two sets of well-resolved peaks at low temperature, which may be due to the fluxional behavior of **11**.

The observation of single signals in the $^{77}$Se NMR spectra of the macrocycles **11** and **13** confirmed the equivalence of the selenium atoms. The $^{77}$Se NMR signals are observed at $\delta$ = 404 and 340 ppm for **11** and **13**, respectively. These values are comparable to the corresponding values for 22-membered selenaaza Schiff base **1** and reduced derivative **5**.[7b] Ligand **12** exhibits the $^{125}$Te NMR signal at $\delta$ = 581 ppm.

### Crystal Structures of 11 and 12

An ORTEP view of **11** is shown in Figure 1 and selected bond lengths and angles are listed in Table 1. The compound crystallizes in the triclinic crystal system with the space group $P\bar{1}$. N1A and N2A are intramolecularly coordinated to Se1 and Se2, respectively, making the geometry around selenium T-shaped. The Se1···N1A and Se2···N2A bond lengths (2.816 and 2.782 Å, respectively) are only slightly longer than the Se···N distance observed for 22-membered selenaaza macrocycles **1** and **5**[7b,7e] (2.723 and 2.729 Å, respectively). The Se1···N1B and Se2···N2B the distances (4.409 and 4.322 Å, respectively) are longer than the sum of the van der Waals radii (3.5 Å) and indicate no intramolecular interaction. Surprisingly, the transannular Se···Se distance (5.881 Å) is longer than that in **1** (3.808 Å).[7b] The bond angles C1A–Se1–C1B and C20A–Se2–C20B are 97.79(13)° and 97.10(13)°, respectively, and are smaller than those of macrocycle **1** [100.2(3)°].

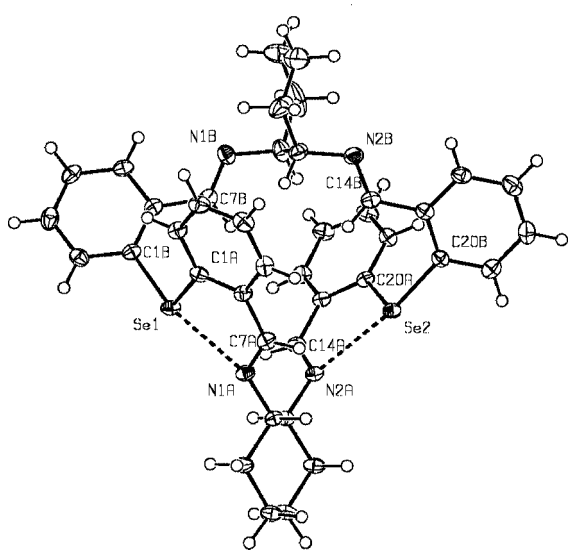


Figure 1. ORTEP diagram of **11**.

An ORTEP view of compound **12** is represented in Figure 2 and selected bond lengths and angles are listed in Table 2. Similar to macrocycle **11**, only one of the nitrogen atoms is coordinated to each tellurium in **12**. The

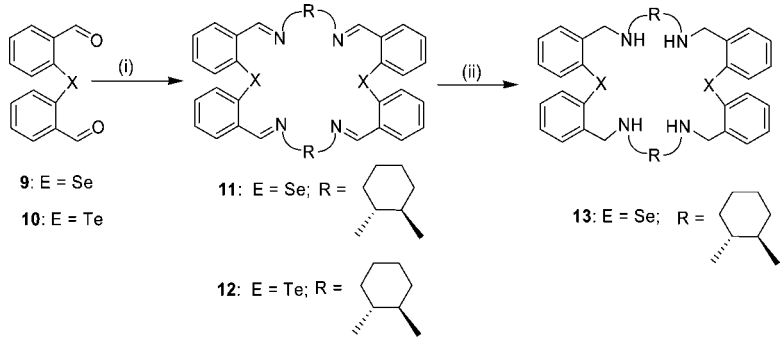


Scheme 1. Reagents: (i) *trans*-1,2-diaminocyclohexylamine, $CH_3CN$; (ii) $NaBH_4$, EtOH, reflux.

 © 2006 Wiley-VCH Verlag GmbH & Co. KGaA, Weinheim 

Table 1. Significant bond lengths [Å] and angles [°] for **11**.

| | | | |
|---|---|---|---|
| Se1–C1A | 1.917(3) | Se1–C1B | 1.927(3) |
| Se2–C20A | 1.921(3) | Se2–C20B | 1.932(3) |
| N1A–C7A | 1.259(4) | N2A–C14A | 1.263(4) |
| C1A–Se1–C1B | 97.79(13) | C20A–Se2–C20B | 97.10(13) |

Te2···N2B#2 and Te2#2···N2B bond lengths are 2.662 and 2.667 Å, respectively, and are similar to the Te···N bond length of 2.701 Å in **2**.[6a] The Te2#2···N1B#2 (4.707 Å) and Te2···N1B (4.708 Å) distances indicate no intramolecular interaction. The transannular Te···Te distance (4.904 Å) is comparable to that observed for the 22-membered telluraza macrocycle **2** (4.979 Å)[6a] and longer than the sum of the van der Waals radii (4 Å). The C1B–Te2–C20B#2 bond angle is 94.49°, which is comparable to that observed for telluraaza macrocycle **2**. The packing diagram shows hydrogen bonding between the macrocyclic N atom and the H of solvent dichloromethane.

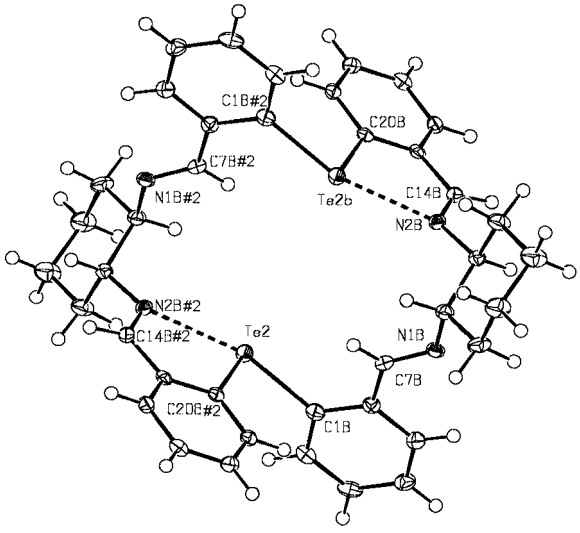


Figure 2. ORTEP diagram of **12**.

Table 2. Significant bond lengths [Å] and angles [°] for **12**.[a]

| | | | |
|---|---|---|---|
| Te1–C1A | 2.117(3) | Te2–C1B | 2.166(3) |
| Te1–C20A#1 | 2.156(3) | Te2–C20B#2 | 2.109(2) |
| Te2–N1B | 4.708 | Te2#2–N2B | 2.667 |
| Te2–N2B#2 | 2.667 | Te2#2–N1B#2 | 4.707 |
| C1A–Te1–C20A#1 | 94.73(10) | C20B#2–Te2–C1B | 94.49(9) |

[a] Symmetry transformations: #1: $-x + 1, -y + 1, -z$; #2: $-x + 1, -y + 1, -z + 1$.

## Complexation

With the objective of synthesizing metal complexes, macrocycles **11**, **3**, and **12** were treated with the transition metal ions $Ni^{II}$, $Co^{II}$, and $Pd^{II}$ in a 1:1 molar ratio to afford complexes **14**, **15**, **16**, and **17**.

### *Complex 14*

Refluxing equimolar amounts of ligand **11** and $NiCl_2·6H_2O$ in a 1:1 ratio and subsequent addition of ammonium hexafluorophosphate gave reddish-brown, air-stable complex **14** (Scheme 2). The IR spectrum of **14** shows the presence of the $PF_6^-$ anion [$\nu$(P–F) = 848, $\delta$(F–P–F) = 565 $cm^{-1}$] and also displays the characteristic $\nu$(C=N) stretching frequency at 1627 $cm^{-1}$, which is shifted slightly compared with the $\nu$(C=N) of free ligand **11** (1642 $cm^{-1}$). The electronic spectrum (UV/Vis) of complex **14** was recorded at room temperature in $CH_3CN$. It shows four bands at 218 (12752), 348 (613), 450 (123) and 850 nm (50 $M^{-1}cm^{-1}$), which can be assigned to the intraligand π–π* and $^3A_{2g}\rightarrow{}^3T_{1g(P)}$, $^3A_{2g}\rightarrow{}^3T_{2g}$, and $^3A_{2g}\rightarrow{}^3T_{1g(F)}$ transitions, respectively.[9] The assignment of an octahedral geometry to complex **14** [Ni(**11**)]$(PF_6)_2$ follows from its paramagnetism ($\mu_{eff}$ = 2.50 $\mu_B$), which indicates an $n = 2$, $S = 1$ high-spin complex with two unpaired electrons. This was further confirmed by single-crystal X-ray studies (vide infra). As expected for octahedral $Ni^{II}$ complexes, complex **14** is ESR silent.[10,11]

The structure of **14** (Figure 3) shows that $Ni^{II}$ occupies the macrocycle cavity and is bonded to all four nitrogen and two selenium donors to complete the distorted octahedral geometry [Ni–N2A = 2.052(5), Ni–N1B = 2.086(5), Ni–N1A = 2.059(5), Ni–N2B = 2.095(5), Ni–Se2 = 2.508(10), and Ni–Se1 = 2.510(10) Å; Table 3]. The average Ni–Se distance (2.509 Å) is comparable to the average Ni–Se distance (2.52 Å) observed for [Ni(**1**)]$(PF_6)_2$ but smaller than the average Ni–Se distances in [Ni(**3**)]$(PF_6)_2$[7b] (2.568 Å) and

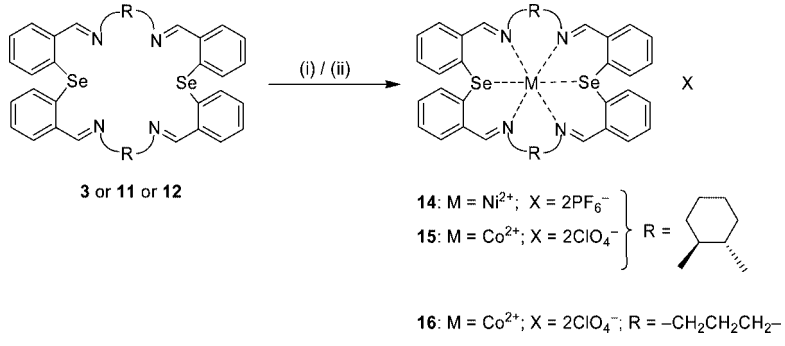


Scheme 2. Reagents: (i) $NiCl_2·6H_2O$, $NH_4PF_6$, MeOH; (ii) $Co(ClO_4)_2·6H_2O$, $CH_3CN$.

 © 2006 Wiley-VCH Verlag GmbH & Co. KGaA, Weinheim 

$[Ni(\mathbf{5})](PF_6)_2$ (2.618 Å).[7e] The C1A–Se1–C1B angle [98.3(3)°] differs slightly from that of the ligand (97.79°). The angles around the central metal atom lie in the range 77.8(2)–101.54(19)° for those involving mutually *cis* donor atoms and 165.22(14)–179.12(17)° for the mutually *trans* donor atoms, thereby deviating only slightly from those expected for a regular octahedral geometry.

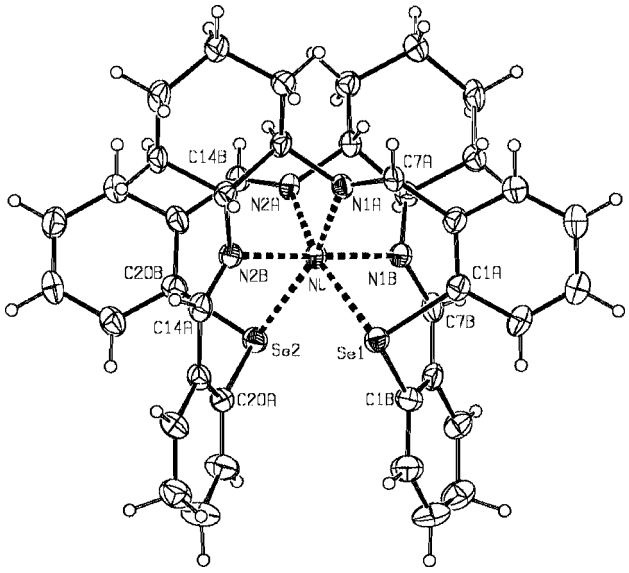


Figure 3. ORTEP diagram of **14** ($PF_6$ anion and H atoms have been omitted for clarity).

Table 3. Significant bond lengths [Å] and angles [°] for **14**.

| | | | |
|---|---|---|---|
| Ni–N2A | 2.052(5) | Ni–N1B | 2.086(5) |
| Ni–N1A | 2.059(5) | Ni–N2B | 2.095(5) |
| Ni–Se2 | 2.5089(10) | Ni–Se1 | 2.5105(10) |
| Se1–C1B | 1.909(7) | Se1–C1A | 1.944(7) |
| Se2–C20B | 1.923(7) | Se2–C20A | 1.933(6) |
| N1A–C7A | 1.275(8) | N2A–C14B | 1.267(8) |
| C1B–Se1–C1A | 98.3(3) | C20B–Se2–C20A | 98.0(3) |

### *Complex 15*

The reaction of ligand **11** and $Co(ClO_4)_2{\cdot}6H_2O$ in a 1:1 ratio afforded brown complex **15**. Complex **15** is soluble in $CH_3CN$ and acetone but decomposes in DMSO. The IR spectrum shows the $\nu$(C=N) band shifted from 1642 to 1617 $cm^{-1}$, thus implying the coordination of all the imine nitrogens to the metal. The molecular ion peak is not observed in the ESI mass spectrum of the complex, although the peaks at $m/z$ = 894 and 795 correspond to $[M - ClO_4]^+$ and $[M - 2ClO_4]^+$, respectively, and confirm the formation of complex **15**. The bands at 222 (15162) and 356 nm (1487) in the UV/Vis spectrum can be assigned to intraligand π–π* transitions and the band at around 546 nm (218) is due to the $^4T_{1g(F)} \rightarrow {}^4T_{1g(P)}$ transitions. The cyclic voltammogram in acetonitrile solution reveals a quasireversible wave at $E_{1/2}$ = 0.236 V versus saturated calomel electrode (SCE) with a $\Delta E$ value of 0.070 V.

### *Complex 16*

$Co^{II}$ complex **16** was synthesized similarly with a 1:1 ratio of ligand **3** and $Co(ClO_4)_2{\cdot}6H_2O$ in acetonitrile. This complex is also soluble in acetone and acetonitrile but decomposes in DMSO. The elemental analysis data of complex **16** suggest the formation of a 1:1 product. The IR spectroscopic measurements show that the $\nu$(C=N) absorption of **16** has shifted from 1642 to 1627 $cm^{-1}$. In the ESI mass spectrum the highest recorded peak for complex **16** is found at $m/z$ = 814 and can be assigned to $[\mathbf{16} - ClO_4]^+$,which confirms the formation of the complex. The cyclic voltammetric study shows a well-behaved, quasireversible redox wave with $E_{1/2}$ = 0.249 V versus saturated calomel electrode (SCE) and a $\Delta E$ value of 0.062 V. The UV/Vis spectrum of **16** consists of three bands at 224 (18141), 354 (1734), 546 nm (285) due to π–π* and d–d transitions. The structure was confirmed by X-ray crystallographic studies.

Selected bond lengths and angles are given in Table 4 and the ORTEP diagram is shown in Figure 4. The complex crystallizes in the triclinic system with space group $C_2$. The $Co^{II}$ ion is bound to the hexadentate macrocycle **3** by two selenium donors and four nitrogen donors. The notable feature of this structure is the $Co^{II}$–Se intermolecular interaction: the $Co^{II}$–Se distances [Co–Se1 = 2.593(6), Co–Sea = 2.593(6) Å] are longer then the $Co^{III}$–Se distance (2.340 Å) observed in the structure of macrobicyclic cage $[CoL]^{3+}$ (L = 8-methyl-1-nitro-6,10,19-triselena-3,13,16-triazabicyclo-[6.6.6]icosane) (**7**).[5] The angles around the central metal atom lie in the range 84.22(9)–98.89(18)° for those involving mutually *cis* donor atoms and 171.12(9)–174.6(2)° for those mutually *trans* donor atoms. Thus, they do not deviate greatly from the values of 90° and 180° expected for a regular octahedron. The Co–N bond lengths are Co–N1 = 2.128(3), Co–N1#1 = 2.129(3), Co–N2#1 = 2.157(3), and Co–N2 = 2.157(3) Å. The Se–C distances [Se–C17#1 = 1.927(4), Se–C1 = 1.928(3), C17–Se#1 = 1.927(4) Å] are comparable to the parent ligand and are close to the sum of the Pauling covalent radii for selenium (1.17 Å) and an $sp^2$-hybridized carbon (0.74 Å). The C–Se–C angle [C17#1–Se–C1 = 96.56(15)°, C17#1–Se–C = 97.44(11)°] deviate slightly from the C–Se–C angle (97.44°) in the ligand.

Table 4. Significant bond lengths [Å] and angles [°] for **16**.

| | | | |
|---|---|---|---|
| Co–N1 | 2.128(3) | Co–N1#1 | 2.129(3) |
| Co–N1#1 | 2.129(3) | Co–N2#1 | 2.157(3) |
| Co–N2 | 2.157(3) | C17–Se#1 | 1.927(4) |
| Co–Se | 2.5931(6) | Co–Se#1 | 2.5931(6) |
| Se–C17#1 | 1.927(4) | Se–C1 | 1.928(3) |
| N1–C7 | 1.290(5) | N2–C11 | 1.262(6) |
| C17#1–Se–C1 | 96.56(15) | | |

 © 2006 Wiley-VCH Verlag GmbH & Co. KGaA, Weinheim 

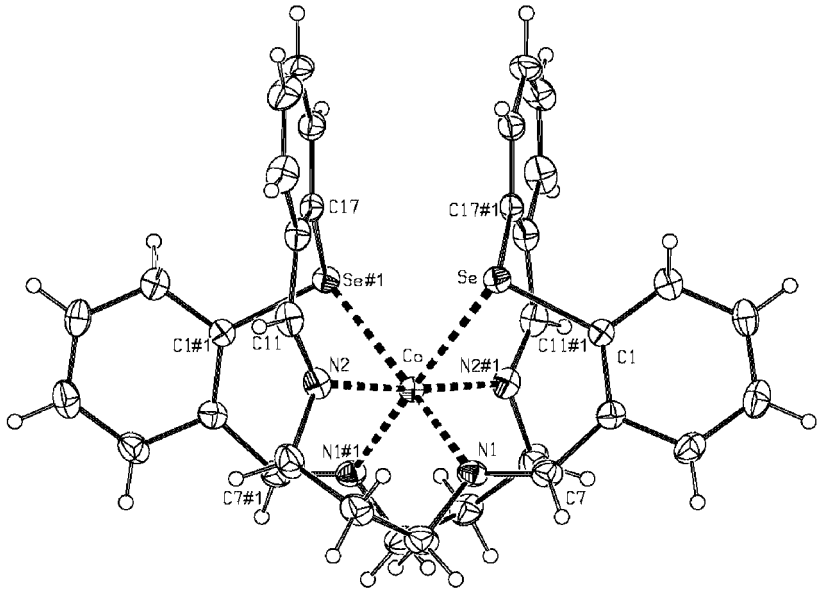


Figure 4. ORTEP diagram of **16** ($ClO_4$ has been omitted for clarity).

### *Complex 17*

The reaction of **12** with $[PdCl_2(C_6H_5CN)_2]$ followed by the addition of an excess amount of ammonium hexafluorophosphate afforded yellow complex **17** (Scheme 3). The elemental analysis data suggest the formation of a 1:1 ligand/metal complex. The $^1H$ NMR spectrum exhibits two sets of signals for each kind of proton. Two singlets at $\delta$ = 8.5 and 9.0 ppm are observed for the imine protons, with one singlet being shifted downfield from $\delta$ = 8.5 ppm (for the parent imine proton) to $\delta$ = 9.0 ppm. The N-C*H*-$CH_2$ protons also appear as two singlets, with one of these singlets being shifted downfield relative to the parent compound. The $^{13}C$ NMR spectrum also shows two sets of signal. The $^{125}Te$ NMR signal of complex **17** at $\delta$ = 751 ppm is shifted downfield relative to the parent compound ($\delta$ = 581 ppm), which indicates that tellurium is coordinated to the palladium. All NMR spectroscopic data confirm the coordination of the two imine nitrogens and two telluriums to palladium to form a square-planar geometry around it,[6c] which explains the two sets of signals, one for the coordinated part and another for the uncoordinated part. In the ESI mass spectrum the peaks at *m*/*z* = 934 and 1085 correspond to $[M - 2PF_6]^+$ and $[M - PF_6]^+$ and confirm the formation of complex **17**.

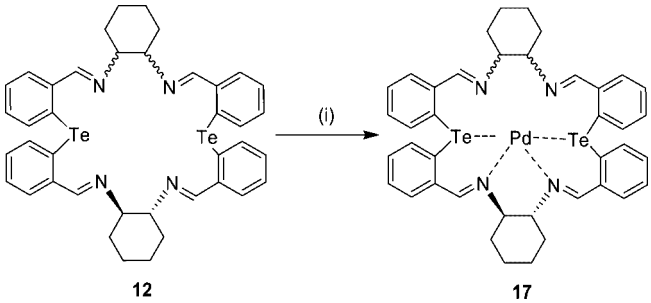


Scheme 3. Reagents: (i) $[PdCl_2(C_6H_5CN)_2]$, $CHCl_3/CH_2Cl_2$.

### Magnetic Properties and ESR Data of 15 and 16

The thermal dependence of the molar magnetic susceptibility ($\chi_M$) vs. *T* plot and the $\mu_{eff}$ vs. *T* plot are shown in the Figure 5. The molar magnetic susceptibility ($\chi_M$) increases with a decrease in temperature, as expected for normal paramagnetic samples. The magnetic moment measurement in the temperature range 4 K ($\mu_{eff}$ = 1.3 $\mu_B$) to 300 K ($\mu_{eff}$ = 2.3 $\mu_B$) implies that compound **15** is a low-spin $Co^{II}$ complex ($t_{2g}^6 e_g^1$) with one unpaired electron.

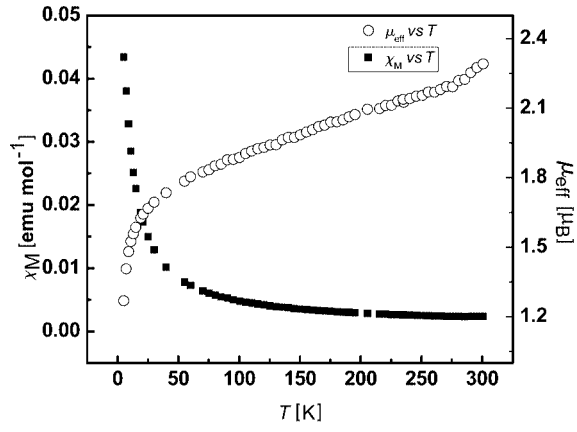


Figure 5. Magnetic properties of **15**: $\chi_M$ vs. *T* plot and $\mu_{eff}$ vs. *T* plot.

The distinct axial-type EPR spectrum of complex **15** is shown in Figure 6 ($g_1 = g_2 = 2.19$, $g_3 = 2.03$). The complex does not show a clear EPR signal at 298 K, which may be due to spin-lattice relaxation of the $Co^{II}$ ion in an octahedral field at room temperature.[12] However, the signal starts developing from 268 K downwards (shown in Figure 6). The hyperfine splitting due to $^{57}Co$ ($I$ = 5/2) is not seen even at 77 K.

 © 2006 Wiley-VCH Verlag GmbH & Co. KGaA, Weinheim 

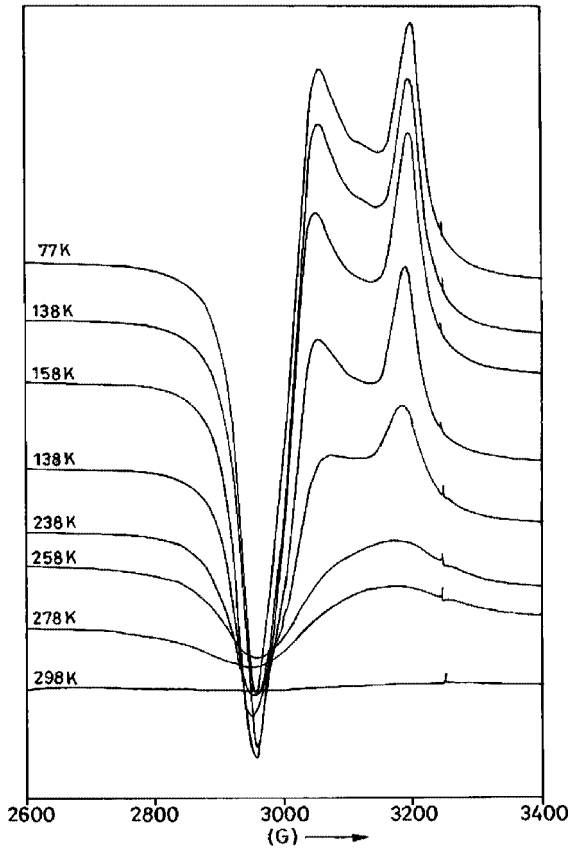


Figure 6. ESR spectra of **15** at variable temperature.

The variable-temperature magnetic susceptibility measurements for **16** were performed on powdered samples between 4 and 300 K. The $\chi_M$ vs. $T$ and $\mu_{eff}$ = 2.84 $(\chi_M T)^{1/2}$ vs. $T$ plots are shown in Figure 7. The molar magnetic susceptibility ($\chi_M$) of **16** increases with a decrease in temperature, as expected for normal paramagnetic samples. The magnetic moment of **16** shows an $\mu_{eff}$ value ranging from 4.0 to 4.9 $\mu_B$, which is higher than that expected for high-spin $Co^{II}$ ($t_{2g}^4 e_g^2$) with three unpaired electrons ($\mu_s$ = 3.8 $\mu_B$) and indicates the presence of an orbital contribution. However, these values are in good agreement with those observed for $Co^{II}$ ions in a distorted octahedral arrangement.

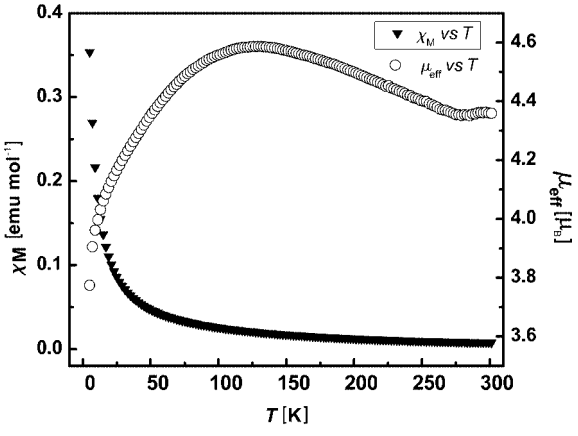


Figure 7. Magnetic properties of **16**: $\chi_M$ vs. $T$ plot and $\mu_{eff}$ vs. $T$ plot.

The complex does not show any EPR signal at 298 K, which may be due to spin lattice relaxation.[12] However, it starts growing from 218 K and the intensity increases appreciably with a further lowering in temperature (Figure 8). At 77 K it shows a clear axial-type EPR spectrum, with $g_1$ = $g_2$ = 2.19, and $g_3$ = 2.03. The expected signal at around $g$ = 5 could not be resolved, even at 77 K.

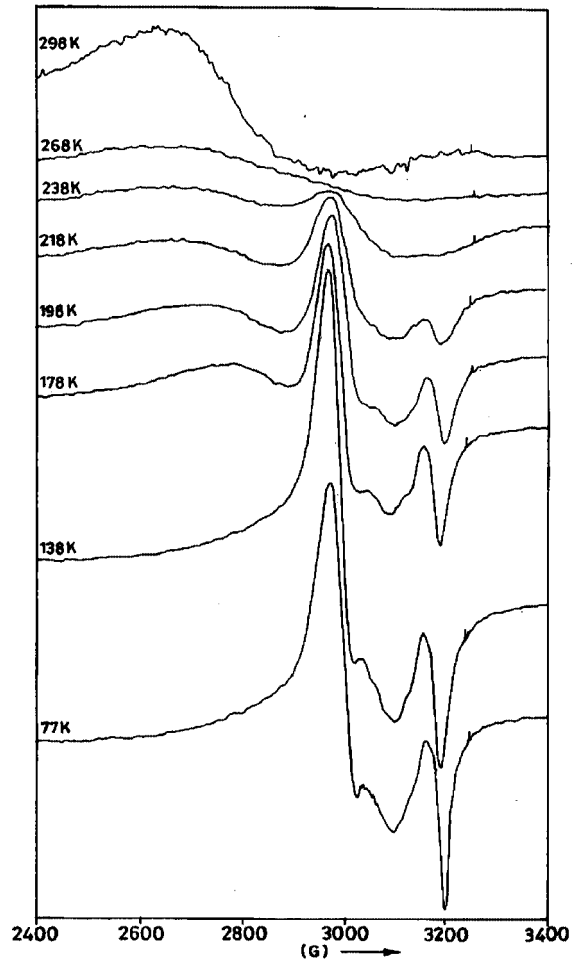


Figure 8. ESR spectra of **16** at variable temperature.

## Conclusions

The crystal structures of macrocycles **11** and **12** confirm the formation of 22-membered selenaaza and telluraaza macrocycles incorporating a 1,2-cyclohexane bridge. The replacement of an ethylene bridge with a cyclohexane bridge leads to a significant change in the cavity size. The Se···Se transannular distance for **11** is 5.881 Å, compared with 3.808 Å for **1**, whereas comparison of **2** with **12** indicates a stronger Te···N interaction in **12**. Ligands **3** and **11** both stabilize $Co^{II}$ ion and, as expected, **16** has a longer $Co^{II}$–Se distance than the $Co^{III}$–Se bond length. Surprisingly, $Co^{II}$ complex **15** is low-spin whereas **16** is high-spin; both show ESR signals at low temperatures.

 © 2006 Wiley-VCH Verlag GmbH & Co. KGaA, Weinheim 

## Experimental Section

**General:** Bis(*o*-formylphenyl)selenide,[7a] bis(*o*-formylphenyl)telluride,[6a] ligand **3**, [7b] and $[PdCl_2(C_6H_5CN)_2]$[13] were prepared by reported procedures. Air-sensitive reactions were carried out under an inert atmosphere. Solvents were purified by standard techniques and were freshly distilled prior to use. *trans*-1,2-Diaminocyclohexane was obtained from Aldrich and used as such; 1,3-diaminopropane was reagent grade and was dried and distilled prior to use. Melting points were recorded in capillary tubes and are uncorrected. IR spectra were recorded as KBr pellets on a Perkin–Elmer precisely FTIR spectrometer. Electronic absorption spectra were obtained in $CHCl_3/CH_3CN$ at 25 °C in a 1-cm quartz cuvette with a JASCO V-570 spectrophotometer. $^1H$-, $^{13}C$-, $^{77}Se$-, and $^{125}Te$ NMR spectra were recorded with a Varian VXR 300S or Varian 400 MHz spectrometer. Chemical shifts cited were referenced to TMS ($^1H$, $^{13}C$) as internal or $SeMe_2$ ($^{77}Se$) or $TeMe_2$ ($^{125}Te$) as external standard. Elemental analyses were performed with a Carlo–Erba model 1106 elemental analyzer. ESI mass spectra were recorded at room temperature with a Q-Tof micro (YA-105) mass spectrometer. Variable-temperature magnetic susceptibility data in the temperature range 4–300 K for a polycrystalline sample of **15** and **16** were measured with a Quantum design MPMS squid magnetometer equipped with a closed-cycle cryostat (Air products). $Hg[Co(NCS)_4]$ was used as a standard. Experimental susceptibility data were corrected for diamagnetic contributions. The magnetic moments at various temperatures were calculated by using the expression $2.84(\chi_M T)^{1/2}$. The magnetic susceptibility of **14** was determined at room temperature on a Faraday balance and standardized with mercury tetracyanocobaltate(II) [$\chi = 16.44 \times 10^{-6}\ cm^3\,mol^{-1}$]. The molar susceptibilities were corrected for diamagnetism with the use of Pascal's constants. The effective magnetic moments were calculated by using the expression $\mu_{eff} = 2.84(\chi_M T)^{1/2}$. The ESR measurements for **14**, **15**, and **16** (powder sample) were performed with a Varian model 109CE-line X-band spectrometer fitted with a quartz Dewar for measurements at 77 K and at variable temperature. Cyclic voltammetry experiments were performed with a Scanning Potentiostat EG and G PARC Model 362 instrument, which consists of a one-compartment cell with platinum working and counter electrodes and a standard calomel as reference electrode. Tetrabutylammonium tetrafluoroborate (Aldrich) was used as the supporting electrolyte. All solutions were purged with nitrogen before the CV data were recorded. Measurements were conducted in 0.1 M $NBu_4BF_4$ in acetonitrile with a sample concentration 0.05 mM. Ferrocene was taken as standard.

**Synthesis of Schiff-Base Macrocycle 11:** A solution of bis(*o*-formylphenyl)selenide (**9**; 0.313 g, 1 mmol) in acetonitrile (100 mL) was added dropwise to a stirred solution of *trans*-1,2-diaminocyclohexane (0.114 g, 1 mmol) in acetonitrile (200 mL) over a period of five to six hours. The mixture was stirred overnight and the precipitated white powder was filtered off. The solvent was evaporated under reduced pressure and the compound obtained was washed with acetonitrile two or three times. Crystals were grown from a chloroform/hexane mixture. Yield: 0.30 g (76%). M.p. 197–99 °C. $^1H$ NMR (299.9 MHz, $CDCl_3$, –50 °C): $\delta$ = 1.41–2.0 (m, $NCHCH_2CH_2$, 16 H), 3.50 (s, 4 H, $NCHCH_2$), 8.49 (s, 4 H, CH=N), 6.9–7.8 (m, 16 H, Ar-*H*) ppm. $^{13}C$ NMR (100.5 MHz, $CDCl_3$, room temp.): $\delta$ = 23.6, 31.8, 73.7, 126.9, 130.1, 130.1, 135.2, 136.9, 161.1 ppm; all peaks are broad). $^{13}C$ NMR (75.4 MHz, $CDCl_3$, –50 °C): $\delta$ = 20.5, 24.1, 26.3, 32.5, 71.8, 75.2, 124.6, 127.9, 129.6 (t), 130.4, 131.7, 133.4, 135.1, 136.5, 136.8, 138.8, 160.1, 161.6 ppm. $^{77}Se$ NMR (57.2 MHz, $CDCl_3$): $\delta$ = 404 ppm. IR (KBr): $\tilde{\nu}$ = 1641 $cm^{-1}$ $\nu$(C=N). UV/Vis ($CH_2Cl_2$): $\lambda_{max}$ ($\varepsilon$, $M^{-1}\,cm^{-1}$) = 240 (12938), 332 nm (1869). ESI-MS ($CHCl_3$): *m*/*z* (%) = 737 (100) $[M]^+$. $C_{40}H_{40}N_4Se_2$: calcd. C 65.40, H 5.48, N 7.62; found C 65.20, H 5.51, N 7.51.

**Synthesis of Schiff-Base Macrocycle 12:** A solution of bis(*o*-formylphenyl)telluride (**10**; 0.398 g, 1 mmol) in acetonitrile was added dropwise to a stirred solution of *trans*-1,2-diaminocyclohexane (0.114 g, 1 mmol) in acetonitrile (200 mL) over a period of five to six hours. The mixture was stirred overnight and the precipitated white powder was filtered off. The solvent was evaporated under reduced pressure and the compound obtained was washed with acetonitrile two or three times. Yield: 0.28 g (57%). M.p. 200–202 °C. $^1H$ NMR (399.99 MHz, $CDCl_3$): $\delta$ = 1.45–1.90 (m, 16 H, $NCHCH_2CH_2$), 3.63 (s, 4 H, $NCHCH_2$), 7.09–8.01 (m, Ar-H, 16 H), 8.53 (s, 4 H, N=CH) ppm. $^{13}C$ NMR (100.5 MHz, $CDCl_3$): $\delta$ = 58.1, 126.3, 130.1, 132.9, 138.5, 144.5, 166.7, 167.3 ppm. $^{125}Te$ NMR (94.78 MHz, $CDCl_3$): $\delta$ = 581 ppm. IR (KBr): $\tilde{\nu}$ = 1637 $cm^{-1}$ $\nu$(C=N). UV/Vis ($CH_2Cl_2$): $\lambda_{max}$ ($\varepsilon$, $M^{-1}\,cm^{-1}$) = 368 (16676), 332 nm (2541). ESI-MS ($CHCl_3$): *m*/*z* (%) = 832 (100) $[M]^+$. $C_{40}H_{40}N_4Te_2$: calcd. C 57.74, H 4.84, N 6.73; found C 57.88, H 5.20, N 7.18.

**Synthesis of Reduced Macrocycle 13:** An excess of $NaBH_4$ was added, in small portions, to a suspension of **11** (0.734 g, 1 mmol) in ethanol, and the reaction mixture was stirred for 4 h at room temperature, after which time it was heated at reflux for 3–4 h. The excess of ethanol was removed under reduced pressure. Water was added to the residue and the product was extracted with chloroform and kept over sodium sulfate. It was filtered and the solvents evaporated to dryness. The residue was used for characterization. Colour: white. Yield: 0.49 g (66%). M.p. 240–242 °C. $^1H$ NMR (399.99 MHz, $CDCl_3$): $\delta$ = 1.0 (br. s, 4 H, $CH_2NH$), 1.2 (m, 8 H, $CHCH_2CH_2$), 1.7 (m, 8 H, $CHCH_2CH_2$), 2.3 (m, 4 H, NCH), 3.9 (dd, *J* = 13.4 Hz, 8 H, $NCH_2$), 6.95–7.25 (m, 16 H) ppm. $^{13}C$ NMR (75.43 MHz, $CDCl_3$): $\delta$ = 30.1, 50.4, 24.4, 58.2, 126.2, 127.6, 129.1, 129.9, 130.9, 140.8 ppm. $^{77}Se$ NMR (57.2 MHz, $CDCl_3$): $\delta$ = 340 ppm. IR (KBr): $\tilde{\nu}$ = 3300, 3277, 3165, 3053, 1460 (N-H bending). ESI-MS: *m*/*z* = 743 $[M]^+$. $C_{40}H_{48}N_4Se_2$: calcd. C 64.69, H 6.51, N 7.54; found C 64.52, H 6.93, N 7.29.

**Synthesis of Complex 14:** Schiff-base ligand **11** (0.245 g, 0.33 mmol) was added to a two-necked, round-bottomed flask along with methanol (20 mL). After stirring for some time, $NiCl_2{\cdot}6H_2O$ (0.08 g, 0.33 mmol) was added and the mixture refluxed for one hour, the color of the reaction mixture changing to a clear reddish-brown. An excess of ammonium hexafluorophosphate was then added. The reddish-brown precipitate formed was filtered off and washed with methanol. Complex **14** was recrystallized as reddish-brown needles by slow diffusion of diethyl ether into a MeCN solution. Yield: 0.30 g (84%). M.p. 250–252 °C (dec.). IR (KBr): $\tilde{\nu}$ = 2935, 1627, 1291, 848, 766, 586 $cm^{-1}$. UV/Vis (MeCN): $\lambda_{max}$ ($\varepsilon$, $M^{-1}\,cm^{-1}$) = 218 (12752), 348 (613), 450 (123), 850 nm (50). $\mu_{eff}$ = 2.5 $\mu_B$. ESI-MS: *m*/*z* (%) = 793 (100) $[M - 2PF_6]^+$, 939 (50) $[M - PF_6]^+$. $C_{40}H_{40}F_{12}N_4NiP_2Se_2$: calcd. C 44.35, H 3.72, N 5.17; found C 44.59, H 3.48, N 5.25.

**Synthesis of Complex 15:** $Co(ClO_4)_2{\cdot}6H_2O$ (0.12 g, 0.33 mmol) was added to a suspension of ligand **11** (0.25 g, 0.33 mmol) in acetonitrile. The color of the reaction mixture changed from light brown to dark brown, and after stirring for 4–5 h a clear brown solution had formed. The reaction mixture was stirred overnight and was then filtered and evaporated to 15 mL. It was kept as such for crystallization, which produced a black, crystalline compound. Yield: 0.23 g (68%). IR (KBr): $\tilde{\nu}$ = 1617 $cm^{-1}$ $\nu$(C=N), 1591, 1092, 624. UV/Vis ($CH_3CN$): $\lambda_{max}$ ($\varepsilon$, $M^{-1}\,cm^{-1}$) = 222 (15162), 356 (1487), 546 nm (218). ESI-MS: *m*/*z* (%) = 795 (50) $[M - 2ClO_4]^+$, 894 (20)

 © 2006 Wiley-VCH Verlag GmbH & Co. KGaA, Weinheim 

$[M - ClO_4]^+$. $C_{40}H_{40}Cl_2CoN_4O_8Se_2$: calcd. C 48.41, H 4.06, N 5.64; found C 48.29, H 4.14, N 5.94.

**Synthesis of Complex 16:** $Co(ClO_4)_2 \cdot 6H_2O$ (0.10 g, 0.33 mmol) was added to a suspension of ligand **3** (0.22 g, 0.33 mmol) in acetonitrile (60 mL) and stirred for overnight. The solution was then filtered and evaporated to 20 mL. Diethyl ether was added to this solution to induce crystallization. The brown, crystalline product that separated was used for characterization. Yield: 0.20 g (65%). UV/Vis ($CH_3CN$): $\lambda_{max}$ ($\varepsilon$, $M^{-1}cm^{-1}$) = 224 (18141), 354 (1734), 546 nm (285). ESI-MS: *m/z* (%) = 814 (50) $[M - 2ClO_4]^+$. $C_{34}H_{32}Cl_2CoN_4O_8Se_2$: calcd. C 44.76, H 3.53, N 6.14; found C 44.58, H 3.12, N 6.24.

**Synthesis of Complex 17:** $[PdCl_2(C_6H_5CN)_2]$ (0.13 g, 0.33 mmol) in dichloromethane (10 mL) was added dropwise to a chloroform (10 mL) solution of **12** (0.33 mmol, 0.28 g). On stirring for 2 h, a yellow solution formed. After stirring for a further 2 h the yellow solution was evaporated and the residue was dissolved in methanol (5 mL), to which an excess of $NH_4PF_6$ was added. The yellow product formed was washed with diethyl ether and recrystallized from acetonitrile. Yield: 0.24 g (58%). M.p. 260–62 °C (dec.). $^1H$ NMR (399.99 MHz, $CD_3CN$): $\delta$ = 1.4–2.5 (m, 16 H, NCHC$H_2$C$H_2$), 3.6 (d, $J$ = 8.9 Hz, 2 H, NC$H$C$H_2$), 4.0 (d, $J$ = 3.9 Hz, 2 H, NC$H$C$H_2$), 7.0 (d, $J$ = 7.8 Hz, 2 H), 7.32 (t, $J$ = 7.8 Hz, 2 H), 7.4 (m, 4 H), 7.55 (m, 4 H), 7.92 (d, $J$ = 7.4 Hz, 2 H), 8.2 (d, $J$ = 7.4 Hz, 2 H), 8.5 (s, 2 H, C$H$=N), 9.0 (s, 2 H, C$H$=N) ppm. $^{13}C$ NMR (100.5 MHz, $CD_3CN$): $\delta$ = 25.4, 25.6, 31.9, 33.6, 68.5, 75.3, 119.4, 122.2, 132.1, 132.8, 134.1, 135.2, 135.3, 135.8, 137.2, 138.9, 139.2, 140.6, 162.4, 168.9 ppm. $^{125}Te$ NMR (94.87 MHz, $CD_3CN$): $\delta$ = 751 ppm. UV/Vis ($CH_3CN$): $\lambda_{max}$ ($\varepsilon$, $M^{-1}cm^{-1}$) = 218 (17794), 304 (5044), 394 nm (1583). ESI-MS ($CH_3CN$): *m/z* (%) = 939 (20) $[M - 2PF_6]^+$, 957 (70) $[M - 2PF_6 + H_2O]^+$, 1085 (50) $[M - PF_6]^+$.

**X-ray Crystallographic Studies:** The diffraction measurements for the ligands as well as the complexes were performed at room temperature with a "Bruker P4" diffractometer with graphite-monochromated Mo-$K_\alpha$ radiation ($\lambda$ = 0.71073 Å). The data were corrected for Lorentz, polarization, and absorption effects The structures were determined by routine heavy-atom and Fourier methods by using SHELXS 97[14] and refined by full-matrix least-squares with the non-hydrogen atoms anisotropic and hydrogen with fixed isotropic thermal parameters of 0.07 Å by means of the SHELXL 97[15] program. The hydrogens were partially located from difference electron-density maps and the rest were fixed at predetermined positions. Scattering factors were from common sources.[16] Some details of data collection and refinement are given in Tables 5 and 6.

Table 5. Crystallographic data for compound **11** and **12**.

| | **11** | **12** |
|---|---|---|
| Empirical formula | $C_{20}H_{20}N_2Se$ | $C_{41}H_{42}Cl_2N_4Te_2$ |
| *Fw* | 367.34 | 916.89 |
| Crystal system | triclinic | triclinic |
| Space group | $P\bar{1}$ | $P\bar{1}$ |
| *a* [Å] | 11.4037(11) | 11.2692(9) |
| *b* [Å] | 11.8184(12) | 12.8612(11) |
| *c* [Å] | 14.6835(14) | 15.2439(12) |
| $\alpha$ [°] | 73.693(2) | 66.6600(10) |
| $\beta$ [°] | 87.145(3) | 75.1630(10) |
| $\gamma$ [°] | 64.196(2) | 73.4570(10) |
| *V* [Å$^3$] | 1703.9(3) | 1918.7(3) |
| *Z* | 4 | 2 |
| $D_{calcd.}$ [mg m$^{-3}$] | 1.432 | 1.587 |
| Temp [K] | 103(2) | 103(2) |
| $\theta$ range [°] | 2.10–27.84 | 1.86–28.33 |
| Abs. coeff. [mm$^{-1}$] | 2.205 | 1.694 |
| Final $R(F)$ $[I > 2\sigma(I)]$[a] | 0.0448 | 0.0278 |
| $wR(F^2)$ indices $[I > 2\sigma(I)]$ | 0.1177 | 0.0629 |
| Data/restraints/parameters | 7181/0/416 | 8969/0/443 |
| Goodness of fit on $F^2$ | 1.086 | 1.046 |

[a] Definitions: $R(F_o) = \sum||F_o| - |F_c||/\sum|F_o|$ and $wR(F_o^2) = \{\sum[w(F_o^2 - F_c^2)^2]/\sum[w(F_c^2)^2]\}^{1/2}$.

Table 6. Crystallographic data for Compound **14** and **16**.

| | **14** | **16** |
|---|---|---|
| Empirical formula | $C_{40}H_{42}F_{12}N_4NiP_2Se_2$ | $C_{34}H_{32}Cl_2CoN_4O_8Se_2$ |
| *Fw* | 1085.35 | 912.39 |
| Crystal system | hexagonal | monoclinic |
| Space group | $P6_1$ | $C_2$ |
| *a* [Å] | 17.0747(16) | 17.160(2) |
| *b* [Å] | 17.0747(16) | 10.9660(14) |
| *c* [Å] | 29.958(4) | 9.4941(12) |
| $\alpha$ [°] | 90 | 90 |
| $\beta$ [°] | 90 | 104.351(2) |
| $\gamma$ [°] | 120 | 90 |
| *V* [Å$^3$] | 7564.0(14) | 1730.8(4) |
| *Z* | 6 | 2 |
| $D_{calcd.}$ [mg m$^{-3}$] | 1.430 | 1.751 |
| Temp [K] | 293(2) | 293(2) |
| $\lambda$ [Å] | 0.71073 | 0.71073 |
| $\theta$ range [°] | 1.54–28.93 | 2.21–28.32 |
| Abs. coeff. [mm$^{-1}$] | 1.967 | 2.812 |
| Obsd. reflections $[I > 2\sigma(I)]$ | 57207 | 6330 |
| Final $R(F)$ $[I > 2\sigma(I)]$[a] | 0.0545 | $R_1$ = 0.0321 |
| $wR(F^2)$ indices $[I > 2\sigma(I)]$ | 0.1486 | $wR_2$ = 0.0778 |
| Data/restraints/parameters | 12299/1/550 | 3873/1/232 |
| Goodness of fit on $F^2$ | 1.030 | 1.066 |

[a] Definitions: $R(F_o) = \sum||F_o| - |F_c||/\sum|F_o|$ and $wR(F_o^2) = \{\sum[w(F_o^2 - F_c^2)^2]/\sum[w(F_c^2)^2]\}^{1/2}$.

CCDC-604888 (**11**), -604889 (**12**), -604890 (**14**) and -604891 (**16**) contain the supplementary crystallographic data for this paper. These data can be obtained free of charge from The Cambridge Crystallographic Data Centre via www.ccdc.cam.ac.uk/data_request/cif.

## Acknowledgments

We are grateful to the Department of Science and Technology (DST), New Delhi, and the Council of Science and Industrial Research (CSIR), New Delhi, for funding this work. Additional help from the Sophisticated Analytical Instrumentation Facility (SAIF), Indian Institute of Technology (IIT), Bombay, for 300 MHz NMR spectroscopy is also acknowledged. We are grateful to Prof. G. K. Lahiri for useful discussions regarding the magnetic susceptibility data and ESR. Prof. G. Mugesh (IISC Bangalore) and Prof. A. K. Nigam (TIFR, Bombay) are gratefully acknowledged for their help in recording the magnetic susceptibility data.

[1] a) C. Bornet, R. Amardeil, P. Meunier, J. C. Daran, *J. Chem. Soc., Dalton Trans.* **1999**, 1039; b) J. L. Li, J. B. Meng, Y. M. Wang, J. T. Wang, T. Matsuura, *J. Chem. Soc., Perkin Trans. 1* **2001**, 1140; c) M. Iwaoka, S. Tomoda, *J. Am. Chem. Soc.* **1994**, *116*, 4463; d) A. Mazouz, J. Bodiguel, P. Meunier, B. Gautheron, *Phosphorus Sulfur Silicon Relat. Elem.* **1991**, *61*, 247; e) A. Mazouz, P. Meunier, M. M. Kubicki, B. Hanquet, R. Amardeil, C. Bornet, A. Zahidi, *J. Chem. Soc., Dalton Trans.* **1997**, 1043; f) X. Zeng, X. Han, L. Chen, Q. Li, F. Xu, X. He, Z. Zhang, *Tetrahedron Lett.* **2001**, *43*, 131.

 © 2006 Wiley-VCH Verlag GmbH & Co. KGaA, Weinheim 

[2] a) K. Kobayashi, H. Izawa, K. Yamaguchi, E. Horn, N. Furukawa, *Chem. Commun.* **2001**, 1428; b) M. J. Hesford, W. Levason, M. L. Matthews, G. Reid, *Dalton Trans.* **2003**, 2852.
[3] a) R. J. Batchelor, F. W. B. Einstein, I. D. Gay, J. H. Gu, S. Mehta, B. M. Pinto, X. M. Zhou, *Inorg. Chem.* **2000**, *39*, 2558; b) M. J. Hesford, W. Levason, M. L. Matthews, S. D. Orchard, G. Reid, *Dalton Trans.* **2003**, 2434.
[4] S. Muralidharan, M. Hojjatie, M. Firestone, H. Freiser, *J. Org. Chem.* **1989**, *54*, 393.
[5] R. Bhula, A. P. Arnold, G. J. Gainsford, W. G. Jackson, *Chem. Commun.* **1996**, 143.
[6] a) S. C. Menon, H. B. Singh, R. P. Patel, S. K. Kulshereshtha, *J. Chem. Soc., Dalton Trans.* **1996**, 1203; b) S. C. Menon, A. Panda, H. B. Singh, R. J. Butcher, *Chem. Commun.* **2000**, 143; c) S. C. Menon, A. Panda, H. B. Singh, R. P. Patel, S. K. Kulshereshtha, W. L. Darby, R. J. Butcher, *J. Organomet. Chem.* **2004**, *689*, 1452.
[7] a) A. Panda, S. C. Menon, H. B. Singh, R. J. Butcher, *J. Organomet. Chem.* **2001**, *623*, 87; b) A. Panda, S. C. Menon, H. B. Singh, C. P. Morley, R. Bachman, T. M. Cocker, R. J. Butcher, *Eur. J. Inorg. Chem.* **2005**, *6*, 1114; c) S. Panda, H. B. Singh, R. J. Butcher, *Chem. Commun.* **2004**, 322; d) S. Panda, H. B. Singh, R. J. Butcher, *Inorg. Chem.* **2004**, *43*, 8532; e) S. Panda, H. B. Singh, R. J. Butcher, *Eur. J. Inorg. Chem.* **2006**, *7*, 172.
[8] a) W. Levason, J. J. Quirk, G. Reid, *J. Chem. Soc., Dalton Trans.* **1996**, 3713.
[9] F. A. Cotton, G. Wilkinson *Advanced Inorganic Chemistry, A Comprehensive Text*, Wiley Eastern Limited, 3rd ed., India, **1993**, p. 894.
[10] a) M. Schröder, *Encyclopedia of Inorganic Chemistry* (Ed.: R. B. King), Wiley, New York, **1994**, vol. 5, p. 2395; b) L. Sacconi, F. Mani, A. Benicini, *Comprehensive Coordination Chemistry* (Eds.: G. Wilkinson, R. D. Gillard, J. A. McCleverty), Pergamon, **1987**, vol. 5, p. 55.
[11] P. B. Ayscough, *Electron Spin Resonance Chemistry*, Methuen and Co. Ltd., **1967**.
[12] J. A. Weil, J. R. Bolton, E. Wertz, *Electron Spin Resonance, Elementary Theory and Practical Applications*, 2nd ed., Wiley, New York, **1994**.
[13] J. R. Doyle, P. E. Slade, H. B. Jonassen, *Inorg. Synth.* **1960**, *6*, 218.
[14] G. M. Sheldrick, SHELXS 97, *Program for the Solution of Crystal Structures*, University of Göttingen, Germany, **1990**.
[15] G. M. Sheldrick, SHELXL 97, *Program for Refining Crystal Structures*, University of Göttingen, Germany, **1997**.
[16] D. T Cromer; J. T. Waber *International Tables for X-ray Crystallography*, Kynoch Press, Birmingham, **1974**, vol. IV, p. 99 and p. 149.

Received: May 29, 2006
Published Online: October 27, 2006

 © 2006 Wiley-VCH Verlag GmbH & Co. KGaA, Weinheim 

DOI: 10.1002/ejic.200600627

# Kinetics and Mechanism of Ligand Substitution in Some Chromium(III) Tetraaza Macrocyclic Complexes in Acidic Media: Differences in Reactivity Between *cis* and *trans* Isomers

**Edyta Madej,[a] Anna Katafias,*[a] Przemysław Kita,*[a] Jette Eriksen,[b] and Ole Mønsted*[b]**

**Keywords:** Chromium / Structure–activity relationships / Ligand substitution / Macrocyclic complexes / Kinetics

Thiocyanate anation of the macrocyclic complexes *cis*-$[Cr(cyc\mathit{b})(OH_2)_2]^{3+}$ and *trans*-$[Cr(cyc\mathit{a})(OH_2)_2]^{3+}$ (cyc*b* and cyc*a* are *rac*- and *meso*-5,5,7,12,12,14-hexamethyl-1,4,8,11-tetraazacyclotetradecane, respectively), and mercury(II)-induced aquation of the product thiocyanato-*N* complexes, has been studied in acidic solution. The rate retardation with an increase of the acid concentration for both types of reactions follows the rate expression $k_{obs} = (k_1 + k_2K_a/[H^+_{(aq)}])/(1 + K_a/[H^+_{(aq)}])$, corresponding to parallel reaction paths through aqua and hydroxo complexes. Some general trends in the differences in reactivity between the two geometrical isomers have been observed and are discussed.
(© Wiley-VCH Verlag GmbH & Co. KGaA, 69451 Weinheim, Germany, 2006)

## Introduction

Recent advances in the elucidation of the mechanisms of ligand-substitution reactions in solution have been reviewed in a series of articles.[1] The chemistry of transition metal complexes of macrocyclic ligands is an area that has attracted considerable interest in recent years.[2–6] These complexes exhibit a range of characteristic properties that are frequently so markedly different from those of their acyclic analogues that the special, but not very informative, label "macrocyclic effects" has been introduced to describe the differences.

Cyclic tetraaza ligands are among the more readily available macrocyclic ligands, and these ligands have been coordinated to most metal ions of the periodic table. Macrocyclic ligands are usually robustly bound, even to metal ions otherwise characterized as "labile", but knowledge of their ability to modify reactivities at the coordination positions not occupied by the macrocyclic ligand is very sparse for most metal ions.

Base hydrolysis of *cis*-$[Cr(cyc\mathit{b})(OH)X]^+$- and *trans*-$[Cr(cyc\mathit{a})(OH)X]^+$-type species ($X^-$ = $Cl^-$, $NCS^-$, or $N_3^-$), leading to liberation of the X ligand and formation of the dihydroxo complexes, has been studied previously.[7] These processes occur without any stereochemical changes or aquation of the macrocyclic amine ligand, even at higher temperatures and in strongly basic solution. However, they are markedly influenced by the composition of the ionic medium, and this has been rationalized by a competitive ion-pair formation between hydroxide ions and the anion of the supporting electrolyte.

The aim of the present work is to gain further insight into the mechanism of ligand substitution in this type of complexes in acidic media by comparison of the reactivity of the two geometrical isomers in two types of reactions, namely anation of the diaqua complexes *cis*-$[Cr(cyc\mathit{b})(OH_2)_2]^{3+}$ and *trans*-$[Cr(cyc\mathit{a})(OH_2)_2]^{3+}$ by thiocyanate and mercury(II)-induced aquation of the thiocyanato ligand by formation of the heterodinuclear ions *cis*-$[(cyc\mathit{b})(H_2O)Cr\text{-}NCS\text{-}Hg]^{4+}$ and *trans*-$[(cyc\mathit{a})(H_2O)Cr\text{-}NCS\text{-}Hg]^{4+}$.

## Results and Discussion

### Characteristics of the Systems Studied

Direct structural investigations on chromium(III) complexes of the ligands cyc*a*[8] and cyc*b*[9] (Scheme 1), as well as other types of evidence, point towards structures of the diaqua complexes with two equivalent water ligands. Consequently, substitution of a water ligand with another monodentate ligand will give only one product. For the thiocyanato ligand, this has previously been demonstrated by isolation of solutions of aquathiocyanato-type complexes formed by thiocyanate anation of *cis*-$[Cr(cyc\mathit{b})(OH_2)_2]^{3+}$ and *trans*-$[Cr(cyc\mathit{a})(OH_2)_2]^{3+}$, in which only one isomer was present.[7]

[a] Faculty of Chemistry, N. Copernicus University, 87-100 Toruń, Poland
E-mail: katafias@chem.uni.torun.pl
pkita@chem.uni.torun.pl
[b] Department of Chemistry, University of Copenhagen, 2100 Copenhagen Ø, Denmark
E-mail: omm@kiku.dk
Supporting information for this article is available on the WWW under http://www.eurjic.org or from the author.

 © 2006 Wiley-VCH Verlag GmbH & Co. KGaA, Weinheim 

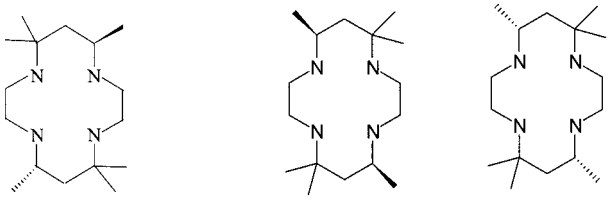


Scheme 1.

The thiocyanato ligand in these complexes is sufficiently robustly coordinated for complexation of mercury(II) to the uncoordinated sulfur atom of the thiocyanato ligand to be studied free from complications due to aquation of this ligand. Preliminary results demonstrated that anation of the diaqua complexes by thiocyanate and mercury(II)-assisted aquation of the monothiocyanato-*N* derivatives proceed, for both the macrocyclic ligands studied, according to Equations (1) and (2):

$$[Cr(cyc)(OH_2)_2]^{3+} + NCS^- \rightarrow [Cr(cyc)(OH_2)(NCS)]^{2+} + H_2O \quad (1)$$

$$[Cr(cyc)(OH_2)(NCS)]^{2+} + Hg^{II} + H_2O \rightarrow [Cr(cyc)(OH_2)_2]^{3+} + Hg(SCN)^+_{aq} \quad (2)$$

Complete retention of configuration is observed in these reaction sequences and the possible aquation of the macrocyclic ligand does not interfere with the reactions under the conditions applied in the present work. This conclusion is based on the results of chromatographic separations and electronic spectra of the eluted chromium(III) species.

The value of the formation constant, at 298 K, for mercury(II) complexation to cationic complexes is usually between $10^3$ and $10^4$ $M^{-1}$, and for complexation to anionic complexes usually somewhat higher[10,11] (frequently over $10^5$ $M^{-1}$). The values found for the present cationic macrocyclic complexes (Table 1) are similar, $3.9 \times 10^3$ $M^{-1}$ for the *trans* and $8.5 \times 10^3$ $M^{-1}$ for the *cis* isomer. The complexation reactions are both significantly exothermic (with small negative entropies of reaction), as expected for the interaction between a "soft" metal center and a "soft" ligand.

The macrocyclic chromium(III) complexes were further characterized by their acid/base properties; the acidity constants determined for the aquathiocyanato and the diaqua complexes are presented in Table 2. It can be seen that the acidity constants for the monothiocyanato 2+ complexes are over one order of magnitude lower than those of the diaqua 3+ complexes, which is as expected from the overall charge variation of the complexes. A direct titrimetric determination of the acidity constants for the dinuclear Cr–NCS–$Hg^{4+}$ species was not possible because of the need for a large excess of mercury(II), which exhibits similar acid/base properties to the investigated complexes.[12] In the hydrogen concentration range selected for kinetic measurements, deprotonation of the aqua complexes is stoichiometrically unimportant.

### Kinetics of the Mercury(II)-Induced Aquation Reaction

Mercury(II) aquaion is known to efficiently induce aquation of both halide and pseudo-halide ligands in robust classical complexes[13] as well as in organometallic species.[14] A rate enhancement of up to four orders of magnitude[10,11] has been observed for thiocyanato ligand aquation due to coordination of mercury(II) to the uncoordinated sulfur atom of this ligand. Examples are known, however, of mercury(II) causing rate retardation by coordination at another available position and not at the ligand which is the leaving group.[15]

The mercury(II)-induced aquation reactions of the present macrocyclic complexes have been studied in the presence of an excess of mercury(II) sufficient to transform the aquathiocyanatochromium(III) reagents into [$Cr^{III}$–NCS–$Hg^{II}$]-type complexes with a degree of conversion exceeding 95%. This guarantees independence of the observed rate constant on the mercury(II) concentration. The two macrocyclic thiocyanatochromium(III) complexes aquate, with a rate that decreases with an increase in acid concentration, as shown in Figure 1.

Table 1. Equilibrium constants ($K_{Hg}$ at 298 K) and reaction enthalpies ($\Delta_r H°$) for mercury(II) complexation to aquathiocyanato complexes of two macrocyclic chromium(III) complexes in 2.0 M (Na/H)$ClO_4$. Standard deviations are given in parentheses.

| Chromium(III) complex | $K_{Hg}$ (298 K) [$M^{-1}$] | $\Delta_r H°$ [kJ mol$^{-1}$] | $\Delta_r S°$ [J K$^{-1}$ mol$^{-1}$] |
|---|---|---|---|
| *trans*-[Cr(cyc*a*)$(OH_2)(NCS)]^{2+}$ | $3.90(10) \times 10^3$ | –28.5(10) | –27(3) |
| *cis*-[Cr(cyc*b*)$(OH_2)(NCS)]^{2+}$ | $8.5(2) \times 10^3$ | –25.0(10) | –9(3) |

Table 2. Acidity constants, $K_{a1}$, for monoaqua complexes at 298 K and 313 K, $K_{a1}$ and $K_{a2}$ for diaqua complexes at 298 K, and reaction enthalpies, $\Delta_r H°$, determined by acid/base titrations in 1.0 M NaBr. Standard deviations are given in parentheses.

| Complex | –log($K_a$/M) (298 K) | –log($K_a$/M) (313 K) | $\Delta_r H°$ [kJ mol$^{-1}$] |
|---|---|---|---|
| *trans*-[Cr(cyc*a*)$(OH_2)_2]^{3+}$ | 2.44(3) | | 29(8) |
| | 6.929(12) | | 38(2) |
| *trans*-[Cr(cyc*a*)$(OH_2)(NCS)]^{2+}$ | 3.817(8) | 3.70(4)[a] | 24(3) |
| *cis*-[Cr(cyc*b*)$(OH_2)_2]^{3+}$ | 3.490(8) | | 29.4(10) |
| | 7.112(6) | | 41.7(13) |
| *cis*-[Cr(cyc*b*)$(OH_2)(NCS)]^{2+}$ | 5.298(5) | 4.91(2)[a] | 30(7) |

[a] Noticeable decomposition during titration. The $\Delta_r H°$ values given are those from Table 4.

 © 2006 Wiley-VCH Verlag GmbH & Co. KGaA, Weinheim 

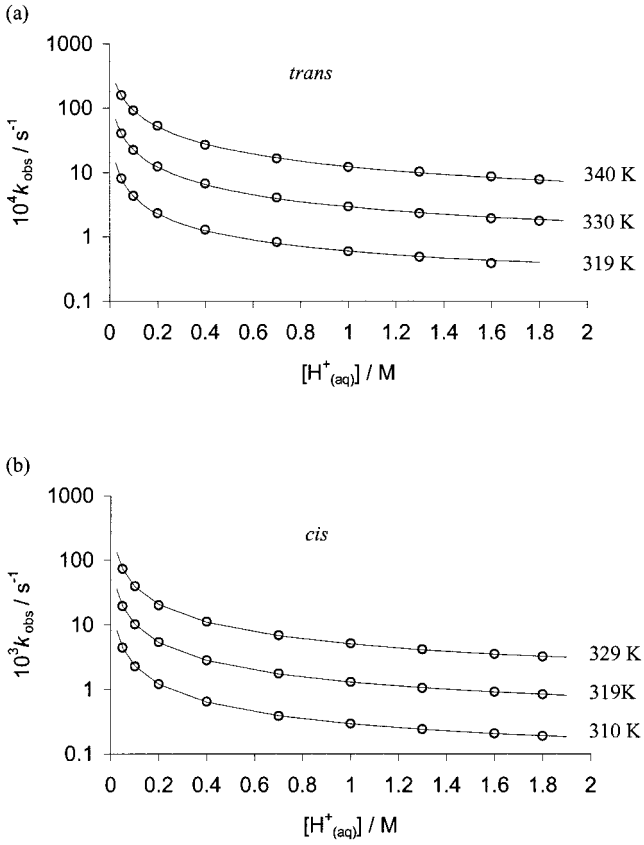


Figure 1. Pseudo-first-order rate constants for aquation of *trans*-[(cyc*a*)($H_2O$)Cr-NCS-Hg]$^{4+}$ (a) and *cis*-[(cyc*b*)($H_2O$)Cr-NCS-Hg]$^{4+}$ (b) complexes as a function of the hydrogen ion concentration in 2.0 M (H/Na)$ClO_4$; [$Hg^{II}$] = 25 mM.

The observed pseudo-first-order rate constant, $k_{obs}$, vs. [$H^+_{(aq)}$] data can be reproduced by Equation (3) which is derived by assuming a fast protolytic equilibrium step followed by the parallel substitution of the thiocyanato-*S*–mercury(II) ion from the aqua and the hydroxo forms of the reagents, as shown in Scheme 2.

$$k_{obs} = (k_1 + k_2 \cdot K_a/[H^+_{(aq)}])/(1 + K_a/[H^+_{(aq)}]) \quad (3)$$

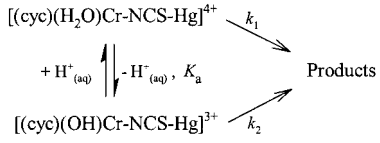


Scheme 2.

Non-linear regression analysis was used to give the parameters in Table 3. The data in this table show that the values of the rate constants and the acid dissociation constants are obtained with significant errors despite the good fit of the data to the theoretical equation. This is mainly caused by the relatively narrow range of hydrogen ion concentrations that had to be used.

The values of the acidity constants, $K_a$, for both isomers of [Cr(cyc)($H_2O$–NCS–Hg)]$^{4+}$-type (see Table 3) seem to be reasonable and are remarkably higher than those for the [Cr(cyc)($H_2O$)(NCS)]$^{2+}$-type isomers (Table 2), as can be expected due to the higher charge of the cationic complexes. However, the acidity constants for the *trans*- and *cis*-thiocyanato ions differ significantly (about 30 times), whereas the values for the mercury(II) derivatives are very similar.

The reactivity comparison of the *cis* and the *trans* isomers in the aqua ($k_1$) and hydroxo ($k_2$) forms is based on the two parameters in Equation (3). The $k_1$ and $k_2$ values at 298 K for the *cis* isomer are about 20 times higher than for the *trans* one in spite of the higher value of the activation energy. The $k_2/k_1$ quotient is a measure of the labilizing effect of $OH^-$ *trans* and *cis* to the leaving ligand. These values are similar for both isomers — about 1330 for the *cis* and about 1000 for the *trans* species. The rate constant increase due to deprotonation of the coordinated water molecule is larger for the studied macrocyclic complexes than for many other chromium(III) complexes; [$Cr(H_2O)_5(OH)]^{2+}$, for example, exchanges its water molecule only 75 times faster than [$Cr(H_2O)_6]^{3+}$.[1] The significant uncertainties in the activation parameters make mechanistic con-

Table 3. Rate constants ($k_1$ and $k_2$ at 298 K and 323 K), acidity constants ($K_a$ at 298 K and 323 K), activation energies ($E_a$) and reaction enthalpies ($\Delta_r H°$) for mercury(II)-induced aquation of two macrocyclic chromium(III) complexes in 2.0 M (Na/H)$ClO_4$ [see Scheme 2 and Equation (3)]. Standard deviations are given in parentheses.[a]

| *trans*-[Cr(cyc*a*)($OH_2$)(NCS)]$^{2+}$ | 298 K | 323 K | $E_a$ or $\Delta_r H°$ [kJ mol$^{-1}$] |
|---|---|---|---|
| $k_1$ [s$^{-1}$] | $6(2)\times10^{-7}$ | $2.0(2)\times10^{-5}$ | 113(11) |
| $k_2K_a$ [M$^{-1}$ s$^{-1}$] | $1.19(2)\times10^{-6}$ | $8.5(2)\times10^{-5}$ | 137(2) |
| $k_2$ [s$^{-1}$] | $6(2)\times10^{-4}$ | $9.9(12)\times10^{-3}$ | 89(8) |
| –log($K_a$/M) | 2.72(18) | 2.06(6) | 48(9) |
| *cis*-[Cr(cyc*b*)($OH_2$)(NCS)]$^{2+}$ | 298 K | 323 K | $E_a$ or $\Delta_r H°$ [kJ mol$^{-1}$] |
| $k_1$ [s$^{-1}$] | $9.8(6)\times10^{-6}$ | $4.66(12)\times10^{-4}$ | 124(2) |
| $k_2K_a$ [M$^{-1}$ s$^{-1}$] | $3.42(6)\times10^{-5}$ | $1.831(13)\times10^{-3}$ | 127.5(7) |
| $k_2$ [s$^{-1}$] | $1.3(2)\times10^{-2}$ | $4.4(3)\times10^{-1}$ | 114(7) |
| –log($K_a$/M) | 2.57(9) | 2.38(3) | 14(8) |

[a] It should be noted that the functional form of the mathematical equation used to interpret the data does not allow a particularly well-defined separation of the $k_2$ and the $K_a$ parameters for the present set of data. Consequently, the significantly better defined parameter product $k_2K_a$ is also given in the table.

 © 2006 Wiley-VCH Verlag GmbH & Co. KGaA, Weinheim 

siderations difficult, although the rate enhancement is accompanied by a lowering of the activation energy (Table 3) rather than the increase observed if the mechanism changes from $I_a$ to $I_d$ as the result of the deprotonation. Remarkably, the $k_1$ rate constants for the studied macrocyclic complexes are three to four orders of magnitude lower than those for other $Cr^{III}$–NCS–Hg type species that are thought to be very inert.[10,11] Thus, the "kinetic macrocyclic effect" manifests itself first of all in the extreme inertness of both geometrical isomers and in a strong reactivity difference between the aqua and the hydroxo forms of the complexes.

### Kinetics of the Anation Reaction

Both *cis*-$[Cr(cyc\textit{b})(OH_2)_2]^{3+}$ and *trans*-$[Cr(cyc\textit{a})(OH_2)_2]^{3+}$ isomers undergo slow anation by thiocyanate in acidic media to give the corresponding monothiocyanato complexes. At lower temperatures — 298–318 K for the *cis* and 308–328 K for the *trans* complex — the reaction is so slow that it can be conveniently studied by applying an initial rate analysis. The pseudo-zero-order rate constants, $k^{(0)}$, were found to be proportional to the chromium(III) concentration, and were converted to pseudo-first-order rate constants, $k^{(1)}$, with [Equation (4)].

$$k^{(1)} = k^{(0)}/[Cr^{III}] \quad (4)$$

These constants depend on the thiocyanate and hydrogen ion concentrations, as demonstrated in Figures 2 and 3. For thiocyanate concentrations below 0.1 M, the pseudo-first-order rate constant is proportional to the thiocyanate concentration, whereas at higher thiocyanate concentrations a non-linear behaviour is seen. In the simple anation model two parameters — the encounter complex formation constant $Q$ and the rate constant $k$ — describe the reaction of a particular reagent. However, the non-linear kinetics of the reaction observed at higher $NCS^-$ concentration (Figure 3) does not allow for the separation of these parameters and are ignored in the following discussion.

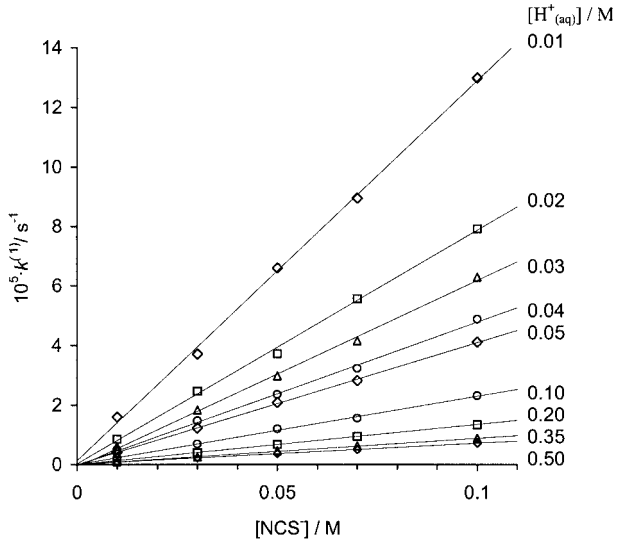


Figure 2. Pseudo-first-order rate constants for anation of *cis*-$[Cr(cyc\textit{b})(H_2O)_2]^{3+}$ as a function of the thiocyanate concentration in 1.0 M (H/Na)(Br/NCS); $T$ = 298 K.

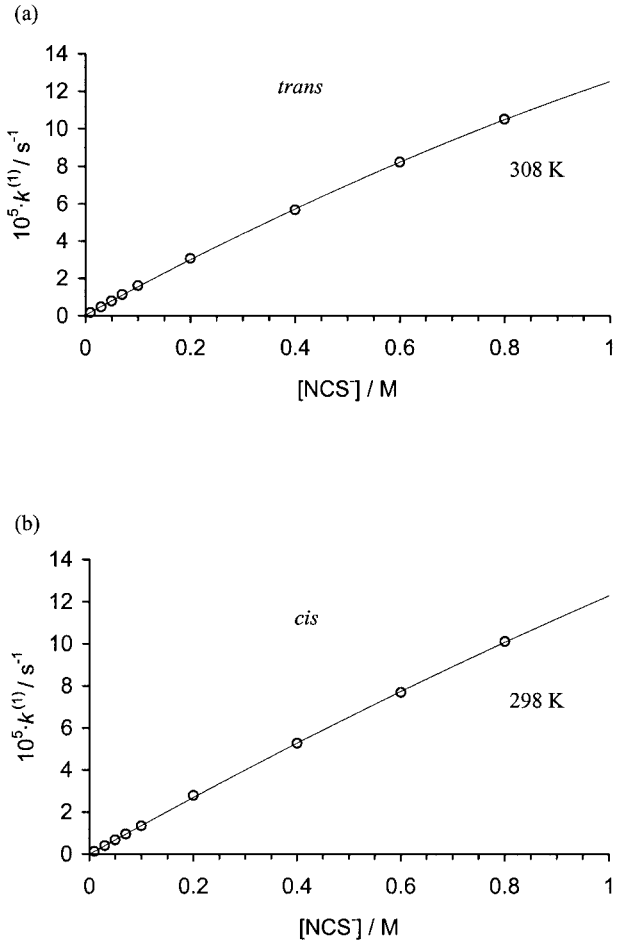


Figure 3. Pseudo-first-order rate constants for anation of *trans*-$[Cr(cyc\textit{a})(H_2O)_2]^{3+}$ (a) and *cis*-$[Cr(cyc\textit{b})(H_2O)_2]^{3+}$ (b) as a function of the thiocyanate concentration in 1.0 M (H/Na)(Br/NCS); $[H^+_{(aq)}]$ = 0.2 M.

At higher temperatures — 318–338 K for the *cis* and 328–348 K for the *trans* complex — reactions were monitored under pseudo-first-order conditions with thiocyanate in substantial excess over the chromium(III) reagent. Under such conditions the reactions are of first order, and the pseudo-first-order rate constant is proportional to the thiocyanate concentration, in agreement with the results at lower temperatures. Ignoring the data demonstrating deviations from linearity at thiocyanate concentrations higher than 0.1 M, the reactions are found to be of second order, first order in complex and first order in thiocyanate, corresponding to the second-order anation rate constant, $k_{an}$, given by Equation (5) where $k_{an}$ can be interpreted, in terms of a simple anation model, as the product of the encounter complex formation constant $Q$ and the rate constant $k$ [Equation (6)] if the pre-equilibrium step is shifted to the left.

 © 2006 Wiley-VCH Verlag GmbH & Co. KGaA, Weinheim 

$$k_{an} = k^{(1)}/[NCS^-] \quad (5)$$

$$M\text{-}OH_2 + X \overset{Q}{\rightleftharpoons} MOH_2, X \xrightarrow{k} MX \quad (6)$$

The hydrogen ion concentration dependence of the second-order rate constant is shown in Figure 4. The significant rate retardation at high acidities can be rationalized in terms of the reaction given in Scheme 3, which shows parallel reaction paths by water ligand substitution in the diaqua and the aquahydroxo complexes and gives the expression in Equation (7) for the second-order anation rate constant.

$$k_{an} = (k_1 + k_2 \cdot K_a/[H^+_{(aq)}])/(1 + K_a/[H^+_{(aq)}]) \quad (7)$$

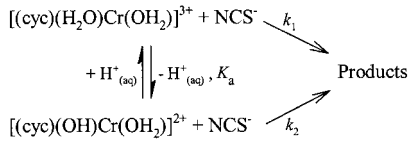


Scheme 3.

The parameters obtained by combining the rate data for all the kinetic experiments are given in Table 4. The validity of the proposed reaction scheme can be verified by comparison of the kinetically determined acidity constants, $K_a$, with those determined independently by titration experiments (see Table 2). A very good agreement of these two sets of parameters supports the correctness of the postulated reaction model.

The data in Table 4 show that, as in the case of the aquation, the values of the rate constants and the acid dissociation constants have been determined with significant errors.

The results obtained for the anation demonstrate, as for the aquation, a higher reactivity of the *cis* isomer; the ratio of $k_1$ for the *cis* and *trans* isomers is about 7 whereas the same ratio for $k_2$ is even higher at about 380. Deprotonation of the coordinated water molecule increases the reactivity, as in the case of the aquation, although the extent of this effect is different for the isomers: the $k_2/k_1$ quotient is about 1100 for the *cis* but only around 20 for the *trans* isomer. However, it should be noted that the $k_1$ and $k_2$ parameters are composite quantities, interpreted in terms of a simple

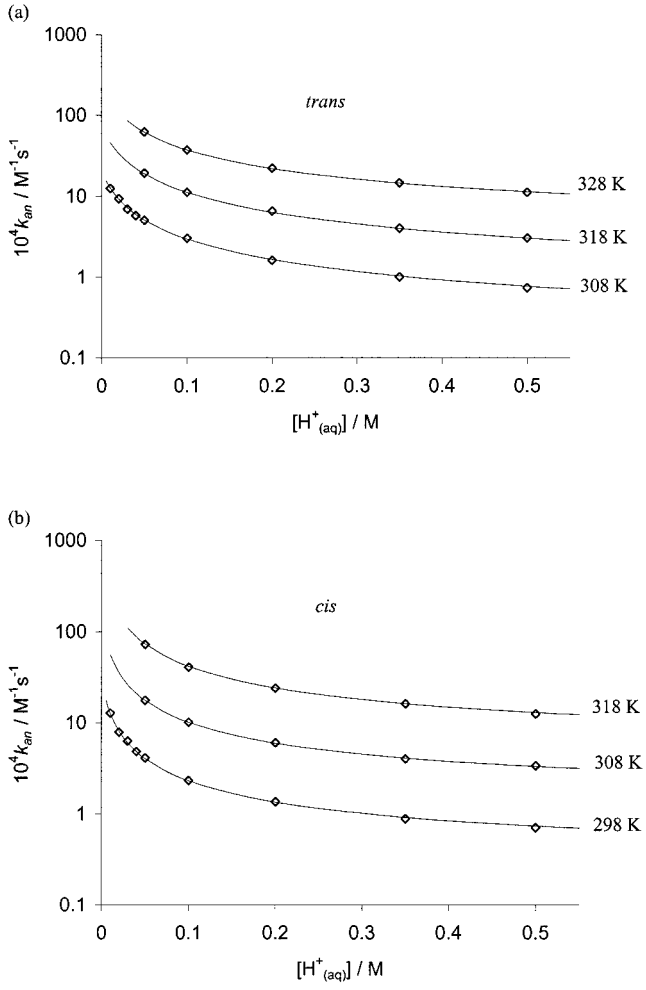


Figure 4. Pseudo-second-order rate constants for the anation of *trans*-$[Cr(cyc\mathit{a})(H_2O)_2]^{3+}$ (a) and *cis*-$[Cr(cyc\mathit{b})(H_2O)_2]^{3+}$ (b) complexes by $NCS^-$ as a function of $[H^+_{(aq)}]$; $I$ = 1.0 M (H/Na)(Br/NCS).

Table 4. Rate constants ($k_1$ and $k_2$ at 298 K and 323 K), acidity constants ($K_a$ at 298 K and 323 K), activation energies ($E_a$) and reaction enthalpies ($\Delta_r H°$) for thiocyanate anation of two macrocyclic chromium(III) complexes in 1.0 M (Na/H)(Br/NCS) [see Scheme 3 and Equation (7)]. Standard deviations are given in parentheses.[a]

| *trans*-$[Cr(cyc\mathit{a})(OH_2)_2]^{3+}$ | 298 K | 323 K | $E_a$ or $\Delta_r H°$ [kJ mol$^{-1}$] |
|---|---|---|---|
| $k_1$ [s$^{-1}$] | $6.5(9) \times 10^{-6}$ | $2.61(18) \times 10^{-4}$ | 119(6) |
| $k_2K_a$ [M$^{-1}$ s$^{-1}$] | $4.92(14) \times 10^{-6}$ | $2.42(4) \times 10^{-4}$ | 124.9(8) |
| $k_2$ [s$^{-1}$] | $1.25(6) \times 10^{-3}$ | $2.95(8) \times 10^{-2}$ | 101.3(12) |
| $-\log(K_a/M)$ | 2.40(3) | 2.084(16) | 23.6(15) |
| *cis*-$[Cr(cyc\mathit{b})(OH_2)_2]^{3+}$ | 298 K | 323 K | $E_a$ or $\Delta_r H°$ [kJ mol$^{-1}$] |
| $k_1$ [s$^{-1}$] | $4.2(3) \times 10^{-5}$ | $9.4(11) \times 10^{-4}$ | 100(5) |
| $k_2K_a$ [M$^{-1}$ s$^{-1}$] | $1.73(5) \times 10^{-5}$ | $9.38(13) \times 10^{-3}$ | 128.0(8) |
| $k_2$ [s$^{-1}$] | $4.8(11) \times 10^{-2}$ | 1.03(8) | 98(7) |
| $-\log(K_a/M)$ | 3.44(11) | 3.04(4) | 30(8) |

[a] It should be noted that the functional form of the mathematical equation used to interpret the data does not allow a particularly well-defined separation of the $k_2$ and the $K_a$ parameters for the set of data for the *cis* isomer. Consequently, the significantly better defined parameter product $k_2K_a$ is also given in the table.

 © 2006 Wiley-VCH Verlag GmbH & Co. KGaA, Weinheim 

anation model, as the product of the encounter complex formation constant $Q$ and the rate constant $k$ [see Equation (6)].

The significant uncertainties in the apparent activation parameters for the anation make them almost unusable for mechanistic considerations.

## Summary and Conclusions

Data for the presently investigated reactions, supplemented with base hydrolysis data for complexes of the same macrocyclic ligands,[7] are shown in the form of a linear free energy relationship at 298 K in Figure 5. The same trend in the relative rates is observed for the *cis* and the *trans* series of complexes, with the *trans* complexes reacting between 6.5 and 38 times slower than the *cis* complexes. The linearized correlation in Figure 5 corresponds to the rate constant relationship $k_{cis} \approx 20\,k_{trans}$, or to a difference in the free energy of activation of about 8 kJ mol$^{-1}$. Regrettably, the activation parameters are not accurate enough to separate the free energy into well-defined enthalpy and entropy contributions.

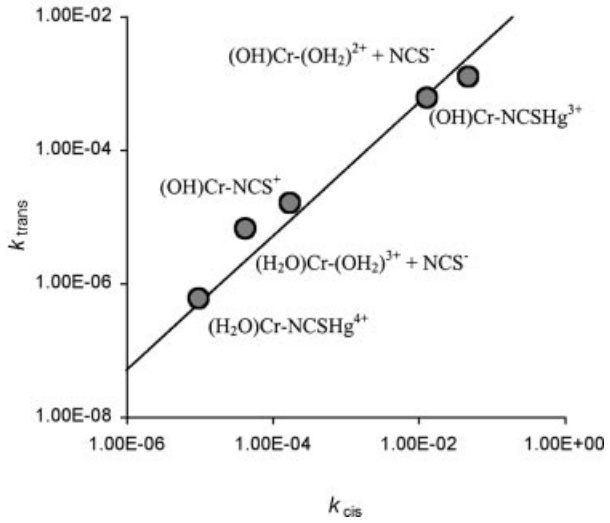


Figure 5. Correlation between free energies of activation for reactions of *cis*-Cr(cyc*b*) and *trans*-Cr(cyc*a*) complexes at 298 K. The data are from this work and from ref.[7] Rate constants are given in units of s$^{-1}$ or M$^{-1}$ s$^{-1}$ according to the type of reaction. The line drawn corresponds to $k_{cis} \approx 20\,k_{trans}$.

Some other general trends are worth pointing out explicitly. For example, the exceptional inertness and stereorigidity is a characteristic feature of the studied macrocyclic complexes. An increased acidity of the water ligands coordinated to the macrocyclic complexes with a highly hydrophobic coordination sphere is also seen. For the present complexes, this manifests itself in dominating reactivity contributions from deprotonated complexes, even in strongly acidic solution. The strong increase in reactivity caused by the coordinated water molecule deprotonation may be correlated with a lowering of the energy of activation. Regrettably, however, the present data are not accurate enough to determine whether this is the only effect operating. This effect is practically non-directional for the aquation but, unexpectedly, is much stronger in the *cis* position for the anation. The general reactivity pattern of the present reactions follows that normally seen for complexes of chromium(III) involving slow substitution processes of and by thiocyanate ligands.

## Experimental Section

**Materials:** *cis*-[Cr(cyc*b*)(OH$_2$)$_2$]Br$_3$·2H$_2$O was prepared according to a literature method;[16] *trans*-[Cr(cyc*a*)(OH$_2$)$_2$]Br$_3$·3H$_2$O was prepared analogously;[16] *cis*-[Cr(cyc*b*)(OH$_2$)(NCS)]$^{2+}$ and *trans*-[Cr(cyc*a*)(OH$_2$)(NCS)]$^{2+}$ complexes were prepared and characterised in solution as described previously.[7] Sephadex SP C-25 ($Na^+$,$H^+$) was used for chromatographic separations. Other chemicals were the best available commercial grades. For all solutions doubly distilled water was used.

**Determination of the Formation Constant for the Cr$^{III}$–NCS–Hg$^{II}$ Complexes:** Equilibrium constants, $K_{Hg}$, for reactions of the type shown in Equation (8) were determined spectrophotometrically at $\lambda$ = 312 nm for the *cis* isomer and at $\lambda$ = 309 nm for the *trans* isomer, using a Perkin–Elmer Lambda-20 spectrophotometer.

$$[Cr(cyc)(OH_2)(NCS)]^{2+}_{(aq)} + Hg^{2+}_{(aq)} \rightleftharpoons [Cr(cyc)(OH_2)(NCS\text{-}Hg)]^{4+}_{(aq)} \quad (8)$$

Spectra were taken immediately after mixing of the reactants, and effects of subsequent aquation reactions were not observed during the time of the experiments. A decrease of the thiocyanatochromium(III) charge-transfer bands with an increase of the mercury(II) concentration was observed for both isomers. An example is shown in Figure S1 (see Supporting Information). The equilibria in Equation (8) were examined at three temperatures (293.7–330.1 K) at a hydrogen ion concentration of 0.5 M and an ionic strength of 2.0 M maintained by the addition of $NaClO_4$. The concentration of the chromium(III) species was about 0.4 mM and the mercury(II) concentration was varied between 0.1 and 2.5 mM. The equilibrium constants, $K_{Hg}$, were calculated from Equation (9) which is derived from the relevant mass-action expressions in Equation (10) where [C] = [S] + [P], P = [Cr(cyc)(OH$_2$)(NCS–Hg)]$^{4+}_{(aq)}$, S = [Cr(cyc)-(OH$_2$)(NCS)]$^{2+}_{(aq)}$, [P] = $(A_i - A_s)/\Delta\varepsilon$, $\Delta\varepsilon = \varepsilon_p - \varepsilon_s$, assuming $\varepsilon_p$ = 0. The results are given in Table 1.

$$A_i = \frac{[Hg^{2+}_{(aq)}]_i \varepsilon_s K_{Hg} + A_s K_{Hg} + \varepsilon_s + \sqrt{K_{Hg}^2([Hg^{2+}_{(aq)}]_i \varepsilon_s + A_s)^2 + 2K_{Hg}([Hg^{2+}_{(aq)}]_i \varepsilon_s^2 - A_s \varepsilon_s) + \varepsilon_s^2}}{2K_{Hg}} \quad (9)$$

 © 2006 Wiley-VCH Verlag GmbH & Co. KGaA, Weinheim 

$$K = \frac{[P]}{([C]-[P])([Hg^{2+}_{(aq)}]_i - [P])} \quad (10)$$

**Identification of Reaction Products:** Stoichiometric studies of the aquation of the $Cr^{III}$–NCS–$Hg^{II}$ complexes were carried out to 95% conversion and anation of the diaqua isomers by thiocyanate to 5% conversion. The reaction mixtures were chromatographed and the chromium(III) species were eluted with 0.1–0.5 M $HClO_4$. The complexes were identified by their UV/Vis spectra. Chromium concentrations were determined by atomic absorption spectrometry using a Varian ABQ-20 instrument.

**Mercury(II)-Assisted Aquation Kinetics:** These reactions were monitored spectrophotometrically using a Shimadzu UV-1601 PC spectrophotometer equipped with a Shimadzu CPS-240A digital temperature controller. Absorbance/time data were collected at $\lambda$ = 270 nm for the *cis* isomer and at $\lambda$ = 265 nm for the *trans* isomer; the decrease of absorbance was up to 0.4. The kinetic experiments covered the temperature range 298–329 K for the *cis* and 298–340 K for the *trans* isomer and the hydrogen ion concentration range 0.02–1.8 M, giving half-lives of the reactions of between 6 and 18000 s. The chromium(III) concentration was kept at 0.25 mM in most of the experiments but was varied in the range 0.2–0.5 mM. The concentration of mercury(II) necessary for greater than 95% transformation of the starting complexes into the dinuclear compounds was kept at 25 mM in most experiments but was varied in the concentration range 0.02–0.1 M. The ionic strength was maintained constant at 2.0 M by the addition of $NaClO_4$. Reactions were initiated by injecting a portion of the stock complex solution (0.2 mL) into a thermostatted solution (1.8 mL) containing all other components. Kinetic runs were repeated three times, five times at the lowest $H^+_{(aq)}$ concentration. The pseudo-first-order rate constants, $k_{obs}$, were calculated by standard non-linear regression analysis from the absorbance, $A_{obs}$, vs. time, $t$, data using the formula $A_{obs} \approx A_{calc} = A_0 + A_1 \cdot e^{-k_{obs} \cdot t}$. Data up to four half-lives were used for the rate-constant calculations. The obtained rate constants were practically independent of the chromium(III) concentration and independent of mercury(II) concentrations at levels above 0.02 M. The average reproduction in the final calculations to give the rate constants and activation parameters of Table 3 was about 1.0% for the *cis* reagent and 3.6% for the *trans* reagent.

**Thiocyanate Anation Kinetics:** The thiocyanate anation reactions were monitored spectrophotometrically at $\lambda$ = 310 nm using Perkin–Elmer Lambda 18 and Lambda 20 spectrophotometers, with cell holders thermostatted with a Perkin–Elmer or a Julabo F-25 thermostat. The ionic strength was kept constant at 1.0 M with $H^+$, $Na^+$, $Br^-$ and $NCS^-$. Kinetic measurements at the lower temperatures were done by applying an initial rate method, under pseudo-zero-order conditions, where the increase of absorbance was recorded up to less than 5% of the conversion degree. Absorbance changes for the *trans* isomer are shown in Figure S2 in the Supporting Information. The absorbance changes for the *cis* complex are analogous to those seen for the *trans* complex, as could be expected. The experiments covered the temperature range 298–318 K for the *cis* and 308–328 K for the *trans* complex and the concentration ranges $[Cr^{III}]$ = 5–15 mM, $[NCS^-]$ = 0.01–0.8 M and $[H^+_{(aq)}]$ = 0.01–0.5 M. The reactions were initiated by injection of a stock NaNCS solution (0.1 mL) into a thermostatted solution (1.9 mL) containing all other components. All kinetic runs were repeated three times. The pseudo-zero-order rate constants, $k_{obs}^{(0)}$, were calculated by linear regression analysis from the absorbance, $A$, vs. time, $t$, data using the expression $A_{obs} \approx A_{calc} = A_0 + k_{obs}^{(0)} \cdot \varepsilon_{310} \cdot t$, where $\varepsilon_{310}$ is the molar absorption coefficient for the complexes. The pseudo-first-order rate constants $k^{(1)}$, calculated as $k_{obs}^{(0)}/[Cr^{III}] = k^{(1)}$, are directly proportional to the thiocyanate concentration at $[NCS^-] << 0.1$ M. The kinetic parameters obtained in this way are, of course, strongly dependent on the accuracy of the determination of the reactant concentrations and accurate determination of the molar absorption coefficients for the examined complexes. However, a good agreement between the values found by this method at lower temperatures and by the experimental approach described below for the higher temperatures was obtained. Kinetic measurements at these latter conditions were performed under conventional pseudo-first-order conditions with $[Cr^{III}]$ (0.1 mM) << $[NCS^-]$ (0.035–0.1 M). These experiments covered the temperature range 318–338 K for the *cis* and 328–348 K for the *trans* complex and the hydrogen ion concentration range 0.002–0.1 M. The reactions were initiated by injection of a stock solution of the complex (0.1 mL) into a thermostatted solution (3.0 mL) containing all other components. The pseudo-first-order rate constants, $k_{obs}^{(1)}$, were calculated by non-linear regression from the absorbance, $A_{obs}$, vs. time, $t$, data using the formula $A_{obs} \approx A_{calc} = A_0 + A_1 \cdot e^{-k_{obs}^{(1)} \cdot t}$. At higher thiocyanate concentrations a deviation from the linear behaviour is seen. The pseudo-first-order rate constants at the lower thiocyanate concentrations were converted into second-order rate constants, and these data are the basis for the average rate constants and activation parameters listed in Table 4. The reproduction of the individual rate constants in this final calculation was about 4.7% for the *cis* reagent and 3.6% for the *trans* reagent.

**Determination of Acidity Constants:** Acidity constants were determined by potentiometric titrations at 298 and 313 K. The ionic strength was kept constant at 1.0 M by the addition of NaBr. The results are given in Table 2.

**Supporting Information** (see footnote on the first page of this article): Spectral changes accompanying the addition of mercury(II) to *cis*-$[Cr(cyc\textit{b})(H_2O)(NCS)]^{2+}$ and anation of *trans*-$[Cr(cyc\textit{a})(OH_2)_2]^{3+}$ by thiocyanate.

## Acknowledgments

This work was supported financially by the Polish State Committee for Scientific Research through grant no. 7 T09A 056 20.

[1] L. Helm, A. E. Merbach, *Chem. Rev.* **2005**, *105*, 1923–1959; D. T. Richens, *Chem. Rev.* **2005**, *105*, 1961–2002; F. P. Rotzinger, *Chem. Rev.* **2005**, *105*, 2003–2037.
[2] V. Alexander, *Chem. Rev.* **1995**, *95*, 273–342.
[3] Special issues: *Coord. Chem. Rev.* **1996**, *148*; *Coord. Chem. Rev.* **1998**, *174*.
[4] E. Graf, M. W. Hosseini, *Coord. Chem. Rev.* **1998**, *178–180*, 1193–1209.
[5] M. Meyer, V. Dahaoni-Gindrey, C. Lecomte, R. Gillard, *Coord. Chem. Rev.* **1998**, *178–180*, 1313–1405.
[6] J. Nelson, V. McKee, G. Morgan, *Prog. Inorg. Chem.* **1998**, *47*, 167–316.
[7] E. Madej, P. Kita, O. Mønsted, *J. Chem. Soc., Dalton Trans.* **2002**, 2361–2365.
[8] R. Temple, D. A. House, W. T. Robinson, *Acta Crystallogr., Sect. C* **1984**, *40*, 1789–1791.
[9] E. Bang, O. Mønsted, *Acta Chem. Scand.* **1984**, *A38*, 281–287.
[10] J. Chatłas, P. Kita, *Pol. J. Chem.* **1986**, *60*, 741–747.
[11] S. Kaizaki, P. Kita, J. Wiśniewska, N. Sakagami, *Transition Met. Chem.* **1998**, *23*, 511–515.
[12] I. Ahlberg, *Acta Chem. Scand.* **1962**, *16*, 887.

 © 2006 Wiley-VCH Verlag GmbH & Co. KGaA, Weinheim 

[13] R. Banerjee, *Coord. Chem. Rev.* **1985**, *68*, 145–167.
[14] P. Kita, R. B. Jordan, *Inorg. Chem.* **1985**, *24*, 2701–2702.
[15] Ö. Gröning, A. M. Sargeson, R. J. Deeth, L. I. Elding, *Inorg. Chem.* **2000**, *39*, 4286–4294.
[16] J. Eriksen, O. Mønsted, *Acta Chem. Scand.* **1983**, *A37*, 579–584.

Received: July 3, 2006
Published Online: October 31, 2006

 © 2006 Wiley-VCH Verlag GmbH & Co. KGaA, Weinheim 

DOI: 10.1002/ejic.200600633

# New Bis(silyl)cyclopentadienidoniobium and -tantalum Complexes: X-ray Crystal Structures of [NbCp^Cl$_4$] and [NbCp^Cl$_4$(CNAr)] [Cp^ = η$^5$-C$_5$H$_3$(SiClMe$_2$)(SiMe$_3$); Ar = 2,6-Me$_2$C$_6$H$_3$]

**Manuel Gómez,*[a] Pilar Gómez-Sal,[a] and José Manuel Hernández[a]**

**Keywords:** Niobium / Tantalum / Cyclopentadienyl complexes

The [bis(silyl)cyclopentadienido]tetrachloroniobium and -tantalum complexes [MCp^Cl$_4$] [Cp^ = η$^5$-C$_5$H$_3$(SiClMe$_2$)(SiMe$_3$); M = Nb **3**, Ta **4**] were synthesized by reaction of the pentachlorides MCl$_5$ with C$_5$H$_3$(SiClMe$_2$)(SiMe$_3$)$_2$ (**1**). Although the Lewis acidity of tetrachloro complexes **3** and **4** is lower than that of the pentahalides, two adducts [M{η$^5$-C$_5$H$_3$(SiClMe$_2$)(SiMe$_3$)}Cl$_4$(CNAr)] (Ar = 2,6-Me$_2$C$_6$H$_3$; M = Nb **5**, Ta **6**) have been isolated by reaction with ArNC. Complexes **3** and **4** react with *tert*-butylamine or lithium amides to afford the dichloroimido and amidochloroimido complexes [M{η$^5$-C$_5$H$_3$(SiClMe$_2$)(SiMe$_3$)}Cl$_2$(NR)] (R = *t*Bu, M = Nb **7**, Ta **8**; R = Me, M = Nb **9**) and [Ta{η$^5$-C$_5$H$_3$(SiClMe$_2$)(SiMe$_3$)}Cl(NH*t*Bu)(N*t*Bu)] (**10**), respectively. In addition, **7** and **8** can be prepared by treatment of the pentachlorides with [C$_5$H$_3$(SiMe$_2$NH*t*Bu)(SiMe$_3$)$_2$] (**2**) by elimination of **1**. The tetrachloro compound **3** reacts with four equivalents of *t*BuNH$_2$ to give the constrained-geometry derivative [Nb{η$^5$-C$_5$H$_3$(SiMe$_2$N*t*Bu-κ*N*)(SiMe$_3$)}Cl(N*t*Bu)] (**11**), whereas the treatment of toluene solutions of **3** and **4** with H$_2$NCH$_2$CH$_2$NH$_2$ in the presence of triethylamine leads to the trichloro complexes [M{η$^5$-C$_5$H$_3$(SiMe$_2$NCH$_2$CH$_2$NH$_2$-κ$^2$*N*,*N*)(SiMe$_3$)}Cl$_3$] (M = Nb **12**, Ta **13**). All the reported complexes were studied by IR and NMR spectroscopy and the molecular structures of complexes **3** and **5** were determined by X-ray diffraction methods.

(© Wiley-VCH Verlag GmbH & Co. KGaA, 69451 Weinheim, Germany, 2006)

## Introduction

Mono- and bis(cyclopentadienido) complexes of early transition metals with silyl-substituted cyclopentadienido rings have been extensively used as reagents in organic synthesis and also as precursors to prepare soluble Ziegler–Natta-type olefin polymerization catalysts.[1] The presence of different substituents in the cyclopentadienido moiety modifies the steric and electronic requirements of the central metal atom, particularly when such substituents contain reactive functional groups. Thus, when chlorine is present in these silyl groups the complex offers a new reactivity center that allows their fixation on silica supports and the cyclopentadienido ring loses its exclusive role as an ancillary ligand. In the last few years various studies have been published regarding the comparative reactivity between the Si–Cl and M–Cl bonds of different chlorosilylcyclopentadienido complexes[2] that have been used as versatile starting compounds in significant synthetic strategies for constrained-geometry catalysts[2d,3] with bidentate η$^5$-silylcyclopentadienido-η$^1$-amido ligands.

The imido group is a strong π-donor ligand that is useful for stabilizing high-valent metal complexes.[4] It is isolobal with the cyclopentadienido moiety[5] and therefore provides group 5 metal complexes that are isoelectronic with the group 4 metallocenes that are extensively used as Ziegler–Natta catalysts. Furthermore, the easy modification of the steric and electronic properties of the imido ligand by varying its alkyl moiety make this type of compound very versatile. For these reasons a rich chemistry of imido group 5 metal complexes has been reported in the last few years.[6]

As part our interest in the structure–reactivity relationship analysis in group 5 metal monocyclopentadienido compounds, we report here the synthesis of new bis(silyl)-cyclopentadienidoniobium and -tantalum complexes and the results obtained in the study of the simultaneous aminolysis of Si–Cl and M–Cl bonds. In addition, the molecular structures of complexes **3** and **5**, as determined by X-ray diffraction methods, are reported.

## Results and Discussion

The synthesis of C$_5$H$_3$(SiClMe$_2$)(SiMe$_3$)$_2$ (**1**) was effected by treatment of a tetrahydrofuran suspension of the lithium salt [Li{C$_5$H$_3$(SiMe$_3$)$_2$}][7] with dichlorodimethylsilane at –78 °C (Scheme 1). After work-up, **1** was obtained as a yellow oil which can be stored in the dark under an inert atmosphere for several weeks (yield 85%) and was identified by $^1$H NMR spectroscopy (see Experimental Section) as an equilibrium mixture of isomers in which 1-(chlorodimethyl-

[a] Departamento de Química Inorgánica, Universidad de Alcalá de Henares, Campus Universitario,
28871 Alcalá de Henares, Spain
Fax: +34-91-885-46-83
E-mail: manuel.gomez@uah.es

 © 2006 Wiley-VCH Verlag GmbH & Co. KGaA, Weinheim 

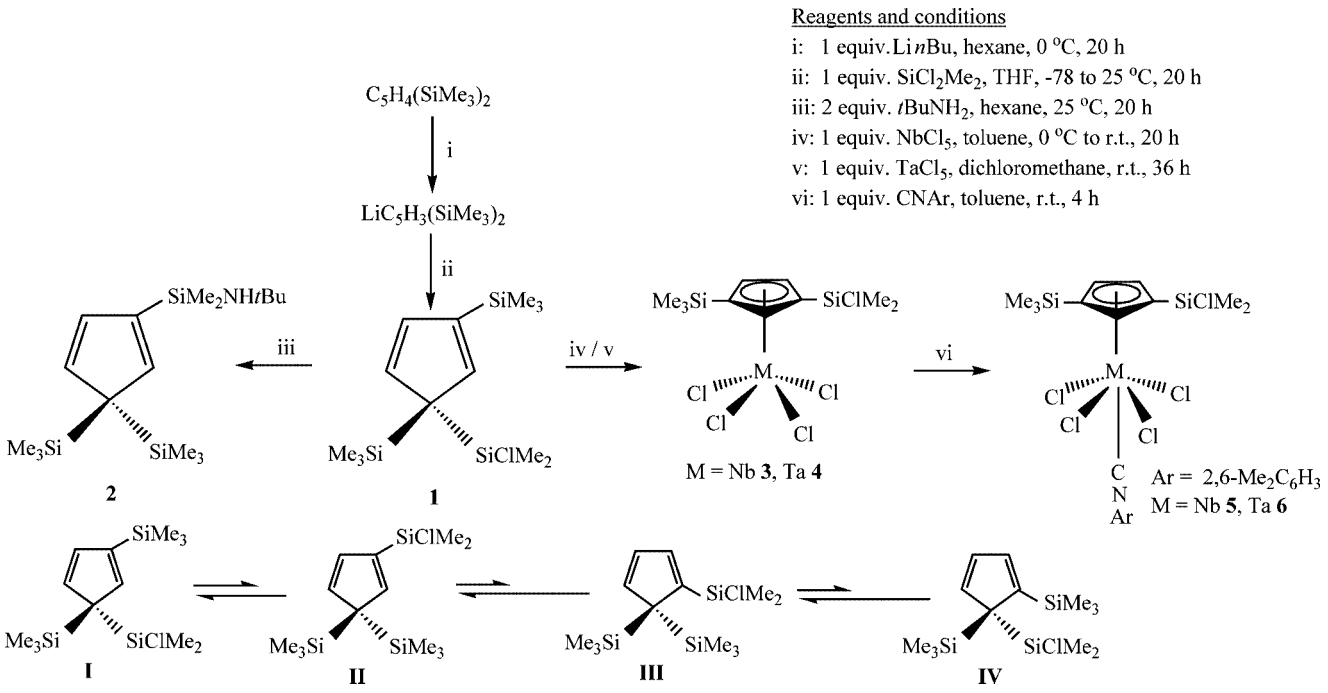


Scheme 1.

silyl)-1,3-bis(trimethylsilyl)cyclopentadiene (**I**) and 1,1-bis-(trimethylsilyl)-3-(chlorodimethylsilyl)cyclopentadiene (**II**) are the major components in a 3:2 ratio, as usually occurs in all cyclopentadienes of the type $C_5H_3X_2Y$.[8]

The precursor $C_5H_3(SiMe_2NHtBu)(SiMe_3)_2$ (**2**) was prepared in good yields (90%) as an orange oil by treatment of **1** with two equivalents of *tert*-butylamine in hexane at room temperature. Compound **2** was characterized by NMR spectroscopy as essentially the only product of the reaction.

Compound **1** reacts with one equivalent of the pentachlorides $MCl_5$ (M = Nb, Ta) in toluene (M = Nb) or dichloromethane (M = Ta) at 0 °C (M = Nb) or room temperature (M = Ta) to give the corresponding monocyclopentadienido complexes $[M\{\eta^5\text{-}C_5H_3(SiClMe_2)(SiMe_3)\}Cl_4]$ (M = Nb **3**, Ta, **4**) with elimination of $SiClMe_3$. The red (M = Nb) and green (M = Ta) compounds were isolated in 90 and 70% yield, respectively, upon cooling their solutions to –20 °C. Both tetrachloro complexes **3** and **4** show a Lewis acidic character and adducts $[M\{\eta^5\text{-}C_5H_3(SiMe_3)(SiClMe_2)\}Cl_4(CNAr)]$ (Ar = 2,6-$Me_2C_6H_3$; M = Nb **5**, Ta, **6**) can be isolated by addition of one equivalent of 2,6-$Me_2C_6H_3NC$ to their toluene solutions.

The molecular structure and atom-labeling scheme of **3** are shown in Figure 1, while the most relevant geometrical parameters are summarized in Table 1. In the solid state, this complex presents a dimeric structure with the two half moieties related by a symmetric center and the niobium atoms bonded through two asymmetrically bridging chlorine atoms. The coordination sphere of the niobium atom

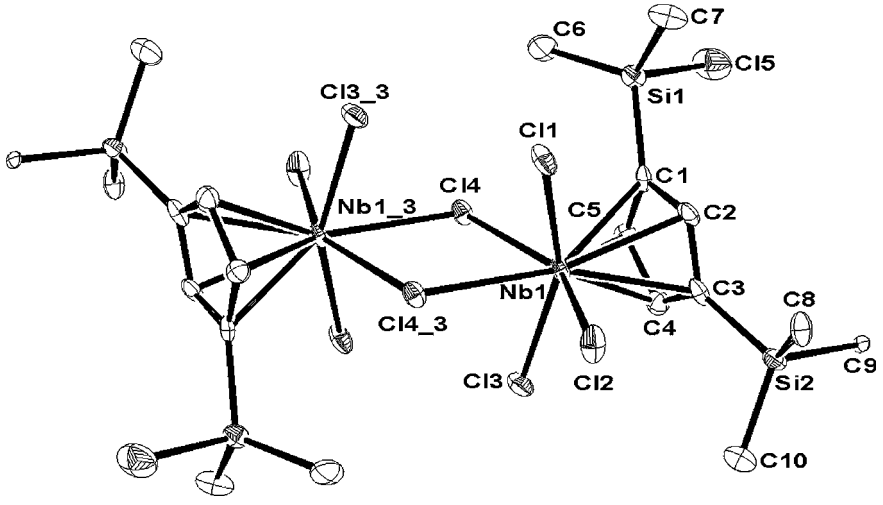


Figure 1. ORTEP drawing of compound **3** with thermal ellipsoids at the 50% probability level.

 © 2006 Wiley-VCH Verlag GmbH & Co. KGaA, Weinheim 

Table 1. Selected bond lengths [Å] and angles [°] for compound **3**.[a]

| | | | |
|---|---|---|---|
| Nb(1)–Cl(1) | 2.380(2) | Nb(1)–Cl(2) | 2.3765(19) |
| Nb(1)–Cl(3) | 2.401(2) | Nb(1)–Cl(4) | 2.4808(18) |
| Nb(1)–Cl(4)#1 | 2.764(2) | Cl(4)–Nb(1)#1 | 2.764(2) |
| Nb(1)–C(1) | 2.443(7) | Nb(1)–C(2) | 2.422(8) |
| Nb(1)–C(3) | 2.480(8) | Nb(1)–C(4) | 2.457(8) |
| Nb(1)–C(5) | 2.426(8) | Nb(1)–Cp(1) | 1.235 |
| Si(2)–C(3) | 1.894(8) | Si(1)–C(1) | 1.885(8) |
| Si(2)–C(8) | 1.869(8) | Cl(5)–Si(1) | 2.072(3) |
| Si(2)–C(9) | 1.922(7) | Si(1)–C(6) | 1.832(9) |
| Si(2)–C(10) | 1.848(9) | Si(1)–C(7) | 1.847(9) |
| Cp(1)–Nb(1)–Cl(1) | 102.99 | Cp(1)–Nb(1)–Cl(2) | 108.17 |
| Cp(1)–Nb(1)–Cl(3) | 103.39 | Cp(1)–Nb(1)–Cl(4) | 103.17 |
| Cl(2)–Nb(1)–Cl(1) | 87.23(8) | Cl(2)–Nb(1)–Cl(3) | 86.43(8) |
| Cl(1)–Nb(1)–Cl(3) | 153.54(7) | Cl(1)–Nb(1)–Cl(4) | 86.65(7) |
| Cl(2)–Nb(1)–Cl(4) | 148.61(7) | Cl(3)–Nb(1)–Cl(4) | 85.50(7) |
| Cl(4)–Nb(1)–Cl(4)#1 | 71.90(6) | Nb(1)–Cl(4)–Nb(1)#1 | 108.10(6) |
| C(6)–Si(1)–Cl(5) | 108.6(4) | C(1)–Si(1)–Cl(5) | 99.7(3) |
| Cp(1)–Nb(1)–Cl(4)#1 | 175.03 | | |

[a] Cp(1) is the centroid of C(1)–C(5); symmetry operation #1: $-x + 2, -y + 1, -z$.

can be described as elongated octahedral, with the cyclopentadienido ring and a chlorine atom in the apical positions and with four chlorine atoms in the equatorial plane. The niobium atom is located 0.6 Å above the equatorial plane.[6d,6f,9,10] The Nb–$Cl_{equatorial}$ bond lengths range from 2.375(2) to 2.482(2) Å, with the largest distance corresponding to the chlorine atom implicated in the bridging system that is also bonded at the apical position of the symmetry-related niobium atom, although in this case with a larger distance of 2.763(2) Å. The Cp–Nb–$Cl(4)_{apical}$ angle and the Nb–Cp distance are 175.03° and 1.235 Å, respectively, both of which are in the normal range. A similar asymmetric bridge has been described for the complexes $[\{(NbCl_2)_2(\mu\text{-}O)(\mu\text{-}Cl)_2\}\{(\eta^5\text{-}C_5H_4)_2(Me_2SiOSiMe_2)\}]$[6c] and $[\{Nb(\eta^5\text{-}C_5H_4SiMe_3)Cl_2\}_2(\mu\text{-}O)(\mu\text{-}Cl)_2]$,[11] although in these cases a bridging oxygen atom is also present.

The two silicon atoms of the substituents in the cyclopentadienido ring [Si(1) and Si(2)] are located above the Cp plane by 0.37 and 0.39 Å, respectively, and the chlorine atom is perpendicular to this plane. This position for the chlorine atom has been described in other complexes containing a $C_5H_4(SiClMe_2)$ ring.[12] It is relevant to note that no other similar structures with a disubstituted Cp ring have been described.

A view of the molecular structure of complex **5** is shown in Figure 2 together with the atom-numbering scheme. Selected bond lengths and angles are given in Table 2. The Cp^ ring is bound to the niobium atom in a nearly symmetric $\eta^5$-fashion with the distance between the metal and the centroid of the ring being 2.137 Å and with the two silicon atoms of the substituents Si(6) and Si(7) located 0.31 Å above the ring plane. The isocyanide ligand is linearly bound to the niobium atom, the values of the Nb–C(6) bond length and of the Nb–C(6)–N(1) and C(6)–N(1)–C(7) angles being 2.215(13) Å and 176.3(11)° and 175.2(13)°, respectively; the length of the N(1)–C(6) bond [1.192(15) Å] is in agreement with a triple bond.[6,13] The coordination around the niobium atom is completed by four chlorine atoms with Nb–Cl bond lengths ranging from 2.412(3) to 2.442(3) Å. Complex **5** is pseudo-octahedral if the centroid of the Cp^ ring is considered as occupying a coordination site, although the niobium atom is displaced by 0.60 Å from the mean equatorial plane passing through the four chlorine atoms toward the cyclopentadienido ring.

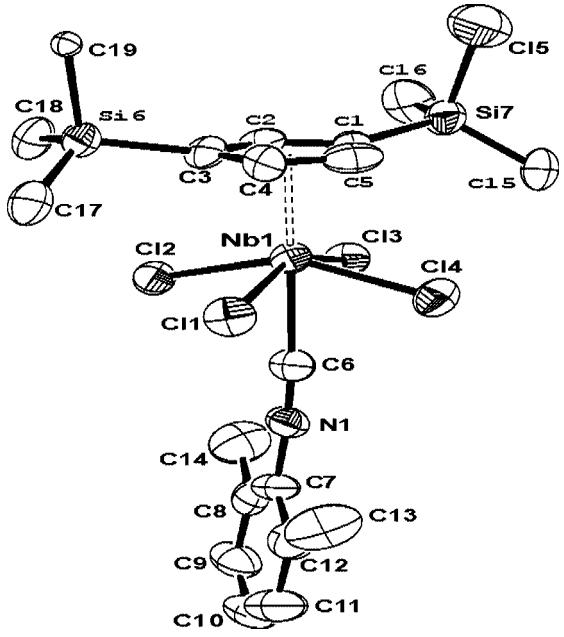


Figure 2. ORTEP drawing of compound **5** with thermal ellipsoids at the 50% probability level.

The comparative reactivity of the two different types of Si–Cl and M–Cl bonds present in the starting tetrachloro complexes **3** and **4** was studied in reactions with amines and amides. Related studies with chlorocyclopentadienidotitanium[3g,3h,14] and -niobium[2d] derivatives led to the formation of constrained monomeric cyclic species containing the pendant amido group of the cyclopentadienido ligand coordinated to the metal center. The dichloroimido complexes $[MCp^{\wedge}Cl_2(NR)]$ [$Cp^{\wedge} = \eta^5\text{-}C_5H_3(SiClMe_2)(SiMe_3)$; R =

 © 2006 Wiley-VCH Verlag GmbH & Co. KGaA, Weinheim 

Table 2. Selected bond lengths [Å] and angles [°] for compound **5**.[a]

| | | | |
|---|---|---|---|
| Nb(1)–Cl(1) | 2.412(3) | Nb(1)–Cl(2) | 2.418(3) |
| Nb(1)–Cl(3) | 2.442(3) | Nb(1)–Cl(4) | 2.430(3) |
| Nb(1)–C(6) | 2.215(13) | Nb(1)–C(1) | 2.458(10) |
| Nb(1)–C(2) | 2.431(11) | Nb(1)–C(3) | 2.485(11) |
| Nb(1)–C(4) | 2.475(11) | Nb(1)–C(5) | 2.444(12) |
| Si(6)–C(3) | 1.894(12) | Si(7)–C(1) | 1.897(11) |
| Si(6)–C(17) | 1.861(13) | Si(7)–Cl(5) | 2.064(6) |
| Si(6)–C(18) | 1.852(13) | Si(7)–C(15) | 1.809(13) |
| Si(6)–C(19) | 1.955(10) | Si(7)–C(16) | 1.897(11) |
| Cp(1)–Nb(1) | 2.137 | C(6)–N(1) | 1.192(15) |
| C(6)–Nb(1)–Cl(1) | 76.2(3) | C(6)–Nb(1)–Cl(2) | 74.5(4) |
| C(6)–Nb(1)–Cl(3) | 75.2(3) | C(6)–Nb(1)–Cl(4) | 76.2(4) |
| Cl(1)–Nb(1)–Cl(2) | 87.31(12) | Cl(1)–Nb(1)–Cl(4) | 86.93(12) |
| Cl(1)–Nb(1)–Cl(3) | 151.39(12) | Cl(2)–Nb(1)–Cl(4) | 150.68(11) |
| Cl(2)–Nb(1)–Cl(3) | 84.74(11) | Cl(4)–Nb(1)–Cl(3) | 86.74(11) |
| Cp(1)–Nb(1)–N(1) | 178.56 | Cp(1)–Nb(1)–Cl(1) | 104.44 |
| Cp(1)–Nb(1)–Cl(2) | 104.33 | Cp(1)–Nb(1)–Cl(3) | 104.11 |
| Cp(1)–Nb(1)–Cl(14) | 105.03 | Nb(1)–C(1)–N(1) | 176.3(11) |
| C(6)–N(1)–C(7) | 175.2(13) | | |

[a] Cp is the centroid of C(1)–C(5).

*t*Bu, M = Nb **7**, Ta, **8**; R = Me, M = Nb **9**] were isolated in good yields upon treatment of **3** and **4** with one equivalent of the appropriate lithium amide (see Scheme 2). Complex **7** also can be prepared with two equivalents of *tert*-butylamine, whereas the treatment of **4** with 1.5 equivalents of LiNH*t*Bu leads to the amidochloroimido complex [Ta{η$^5$-$C_5H_3(SiMe_3)(SiClMe_2)$}Cl(NH*t*Bu)(N*t*Bu)] (**10**). The formation of the imido complexes **7**–**10** takes place with elimination of LiCl and HCl but the Si–Cl bond of the cyclopentadienido ring remaining unaltered.

Alternatively, the reaction of **2** with niobium and tantalum pentachlorides in a 1:1 ratio leads to the dichloroimido compounds **7** and **8**, respectively, by elimination of HCl, cyclopentadiene **1**, and a mixture of other, unidentified products.

Partial substitution of the chloride moieties occurs upon treatment of a hexane solution of **3** with four equivalents of $tBuNH_2$ (Scheme 3) and leads to the constrained-geometry complex [Nb{η$^5$-$C_5H_3(SiMe_3)(SiMe_2N$*t*Bu-κ*N*)}Cl(N*t*Bu)] (**11**) with evolution of HCl. Furthermore, the addition of

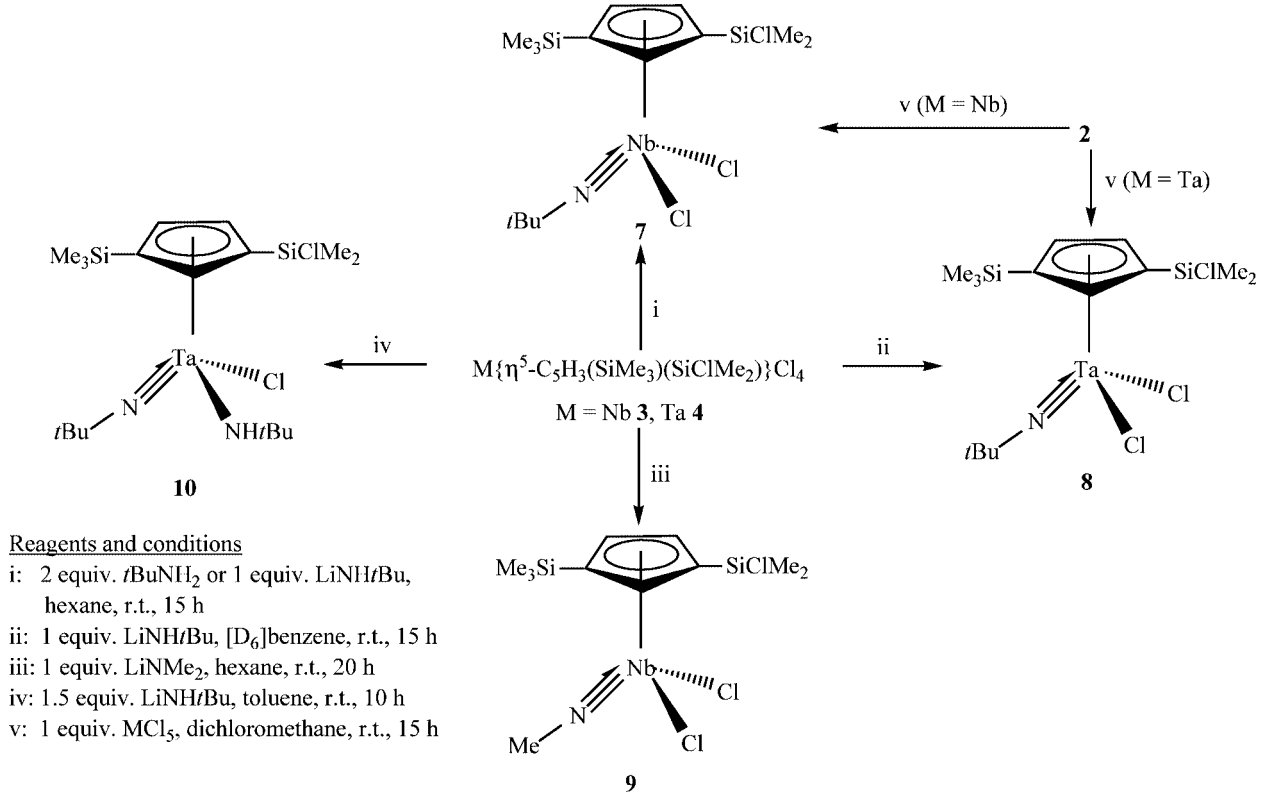


Scheme 2.

 © 2006 Wiley-VCH Verlag GmbH & Co. KGaA, Weinheim 

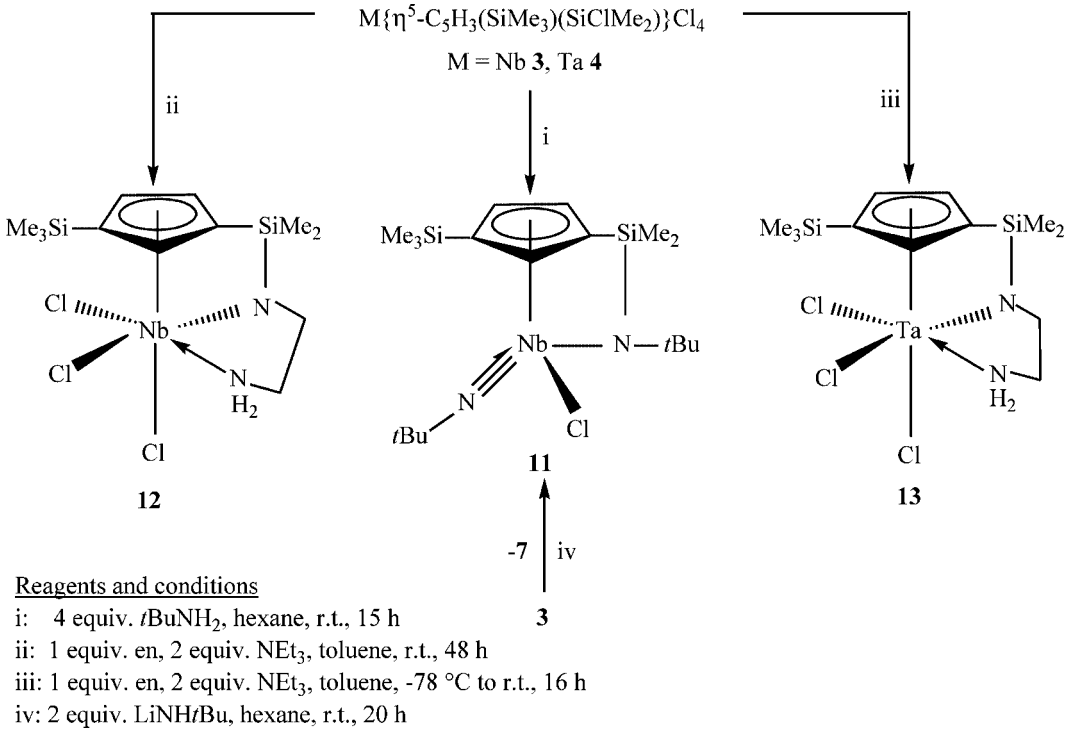


Scheme 3.

one equivalent of ethylenediamine and two equivalents of $NEt_3$ to toluene solutions of the tetrachloro complexes **3** and **4** gives, after separation of the ammonium salt formed, the pseudo-octahedral trichloro species $[M\{\eta^5\text{-}C_5H_3(SiMe_3)[SiMe_2N(CH_2)_2NH_2\text{-}\kappa^2N,N\}Cl_3]$ (M = Nb **12**, Ta **13**). However, a mixture of complexes **7** and **11** was obtained upon treatment of **3** with two equivalents of LiNH*t*Bu.

Complexes **3**–**13** are soluble in most organic solvents, including saturated hydrocarbons. They are extremely air- and moisture-sensitive, so rigorously dried solvents and handling under dry inert atmosphere were found to be imperative for successful preparations. Their spectroscopic data (see Experimental Section) are in agreement with the proposed structures. The IR spectra show the characteristic absorptions for a cyclopentadienido ring ($\nu_{C-H} \approx 839\ cm^{-1}$)[15] and the trimethylsilyl substituent [$\delta_s(CH_3) \approx 1254\ cm^{-1}$].[6f,15] Complexes **5** and **6** show $\nu_{C\equiv N}$[6a,13] at around 2221 $cm^{-1}$, whereas the imido complexes show the $\nu_{M=N}$[6,15,16] IR absorption at about 1348 $cm^{-1}$. The M–C, M–N, and N–H stretching vibrations are observed at $\tilde{\nu} \approx$ 469,[6a,17] 594,[6d] and 3248 $cm^{-1}$,[6a,18] respectively.

The $^1H$ NMR spectra of complexes **3** and **4** show the expected resonances for the methyl groups bonded to silicon. Three broad multiplets corresponding to an ABC spin system are observed for the cyclopentadienido ring protons. These assignments were confirmed by the $^{13}C\{^1H\}$ NMR spectra. The NMR spectroscopic data of adducts **5** and **6** are in agreement with the expected behavior for pseudo-octahedral compounds[6a,13] with the cyclopentadienido ring and the isocyanide ligand mutually *trans*. The *o*-methylphenyl isocyanide groups are equivalent and, in addition, three and five resonances for the $C_5H_3(SiClMe_2)(SiMe_3)$ ring protons and carbons are observed, respectively.

Although the structures of complexes **7**–**10** in the solid state have not been determined, we assume them to be monomers that are pseudo-tetrahedral and isostructural with other half-sandwich imido group 5 metal derivatives.[6b,6d,6e] Their formulation as dichloroimido complexes is supported by analytical and spectroscopic data (see Experimental Section) according to the behavior expected for three-legged piano-stool species.

Complex **11** is a disymmetric molecule due to the enantiotopic faces of the cyclopentadienido ring and the niobium atom. Its $^1H$ NMR spectrum shows a singlet for the equivalent methyl protons of the $SiMe_3$ substituent, two singlets for the inequivalent methyl groups bonded to the silicon in the $SiClMe_2$ moiety, and three low-field multiplets for the ring protons due to the presence of the chiral niobium center. In addition, three methylsilyl resonances, two N*t*Bu signals, and five ring carbon resonances appear in the $^{13}C\{^1H\}$ NMR spectrum.

The trichloro complexes **12** and **13** show a similar NMR behavior to that discussed above for **11**, and all these *ansa* compounds exhibit a characteristic $^{13}C$ signal due to the ring carbon $C^1$–$SiClMe_2$ [$\delta$ = 110 (**11**), 106 (**12**), 105.2 ppm (**13**)], which is shifted upfield with respect to the other ring carbon resonances.[3h,19]

## Conclusions

The tetrachlorobis(silyl)cyclopentadienidoniobium and -tantalum complexes $[M\{\eta^5\text{-}C_5H_3(SiClMe_2)(SiMe_3)\}Cl_4]$

 © 2006 Wiley-VCH Verlag GmbH & Co. KGaA, Weinheim 

(M = Nb **3**, Ta **4**) have been prepared by a conventional reaction between $MCl_5$ and $C_5H_3(SiClMe_2)(SiMe_3)_2$ (**1**). Its Lewis acid character has been established by reaction with isocyanides to give $[M\{\eta^5\text{-}C_5H_3(SiClMe_2)(SiMe_3)\}Cl_4L]$ (M = Nb **5**, Ta **6**; L = 2,6-$Me_2C_6H_3NC$), while in the presence of stoichiometric amounts of amines or lithium amides the dichloroimido and amidochloroimido complexes $[M\{\eta^5\text{-}C_5H_3(SiClMe_2)(SiMe_3)\}Cl_2(NR)]$ (R = *t*Bu, M = Nb **7**, Ta **8**; R = Me, M = Nb **9**) and $[Ta\{\eta^5\text{-}C_5H_3(SiClMe_2)(SiMe_3)\}Cl(NH\textit{t}Bu)(N\textit{t}Bu)]$ (**10**), respectively, are isolated. In addition, the constrained-geometry niobium derivative $[Nb\{\eta^5\text{-}C_5H_3(SiMe_2N\textit{t}Bu\text{-}\kappa\textit{N})(SiMe_3)\}Cl(N\textit{t}Bu)]$ (**11**) can be prepared by treatment of the tetrachloro compound with four equivlents of $\textit{t}BuNH_2$, whereas with ethylenediamine the pseudo-octahedral trichloro complexes $[M\{\eta^5\text{-}C_5H_3(SiMe_2NCH_2CH_2NH_2\text{-}\kappa^2\textit{N},\textit{N})(SiMe_3)\}Cl_3]$ (M = Nb **12**, Ta **13**) were obtained.

## Experimental Section

**General:** All reactions and manipulations were carried out under argon using standard Schlenk-tube and globe-box techniques. Solvents were refluxed in the presence of an appropriate drying agent and distilled and degassed prior use: [$D_6$]benzene and hexane (Na/K alloy), [D]chloroform (NaH), tetrahydrofuran (Na/benzophenone), dichloromethane ($P_2O_5$), and toluene (Na). Bis(trimethylsilyl)cyclopentadienide[7d] was synthesized as described previously, while LiNH*t*Bu was prepared by treatment of $\textit{t}BuNH_2$ with Li*n*Bu. Reagent-grade chemicals were purchased from commercial sources and used without further purification: $SiClMe_3$, $SiCl_2Me_2$, $\textit{t}BuNH_2$, $TaCl_5$, Li*n*Bu (1.6 M in hexanes), $LiNMe_2$, $NEt_3$, and $H_2N\text{–}(CH_2)_2\text{–}NH_2$ from Aldrich, and $NbCl_5$ from Fluka. Infrared spectra were recorded with a Perkin–Elmer Spectrum 2000 spectrophotometer (4000–400 $cm^{-1}$) with samples as KBr pellets. $^1H$ and $^{13}C\{^1H\}$ NMR spectra were recorded with a "Unity 300" or a "Mercury VX 300" (Varian NMR Systems) spectrometer; chemical shifts are referenced to the $^1H$ ($\delta$ = 7.15 and 7.24 ppm) and $^{13}C$ ($\delta$ = 128 and 77 ppm) residual resonances of [$D_6$]benzene and [$D_1$]-chloroform, respectively. Microanalyses (C,H,N) were performed with a LECO CHNS 932 microanalyzer.

**$[C_5H_3(SiClMe_2)(SiMe_3)_2]$ (1):** A 1.6 M hexane solution of Li*n*Bu (62.5 mL, 100 mmol) was added dropwise at 0 °C to a solution of freshly distilled $C_5H_4(SiMe_3)_2$ (21.02 g, 100 mmol) in hexane (400 mL). The reaction mixture was slowly warmed to room temperature and stirred for 20 h to afford a white precipitate, which, after filtration, was washed with hexane (2 × 100 mL), dried under vacuum, and identified as $LiC_5H_3(SiMe_3)_2$ (19.45 g, 90.00 mmol, 90%).

A suspension of $LiC_5H_3(SiMe_3)_2$ (19.45 g, 90.00 mmol) in tetrahydrofuran (300 mL) was treated with $SiCl_2Me_2$ (10.92 mL, 90.00 mmol) at –78 °C. The reaction mixture was then warmed to room temperature and stirred for 20 h. After filtration, the solvent was removed by evaporation under vacuum and the residue extracted with hexane (2 × 100 mL). The solvent was again removed to give a yellow oil, which was characterized as compound **1** (23.18 g, 80.00 mmol, 85%). $^1H$ NMR ([$D_6$]benzene, 25 °C): **I** (*major*): $\delta$ = 6.85 (m, 1 H, $C_5H_3$), 6.81 (m, 1 H, $C_5H_3$), 6.49 (m, 1 H, $C_5H_3$), 0.24 (s, 9 H, $SiMe_3$), 0.19 (s, 3 H, $SiClMe_2$), 0.16 (s, 3 H, $SiClMe_2$), 0.07 ppm (s, 9 H, $SiMe_3$); **II** (*minor*): $\delta$ = 6.95 (m, 1 H, $C_5H_3$), 6.90 (m, 1 H, $C_5H_3$), 6.46 (m, 1 H, $C_5H_3$), 0.54 (s, 6 H, $SiClMe_2$), –0.04 ppm (s, 18 H, $SiMe_3$). $^{13}C\{^1H\}$ NMR ([$D_6$]benzene, 25 °C): **I** (*major*): $\delta$ = 147.3 ($C^3$), 143.2, 136.7, 135.2, 71.5 (br., $C^1$ of $C^5$ ring), 1.8, 1.4 ($SiClMe_2$), –0.77 ($SiMe_3$), –0.83 ppm ($SiMe_3$); **II** (*minor*): $\delta$ = 147.1 ($C^3$), 137.5, 135.3, 133.6, 71.5 (br., $C^1$ of $C^5$ ring), 2.7 ($SiClMe_2$), –0.7 ppm ($SiMe_3$). $^{29}Si$ NMR ([$D_6$]-benzene, 25 °C): **I** (*major*): $\delta$ = 19.7 ($SiClMe_2$), –1.0 ($SiMe_3$), –10.4 ppm ($SiMe_3$); **II** (*minor*): $\delta$ = 14.4 ($SiClMe_2$), –1.9 ppm ($SiMe_3$).

**$[C_5H_3(SiMe_2NH\textit{t}Bu)(SiMe_3)_2]$ (2):** A solution of **1** (10.00 g, 33.00 mmol) in hexane (150 mL) was treated with *tert*-butylamine (4.83 g, 66.00 mmol) at room temperature. The reaction mixture was stirred for 20 h and then the resulting suspension was filtered. The solvent was evaporated to dryness to give an orange oil, which was identified as compound **2**. Yield: 7.95 g (90%). $^1H$ NMR ([$D_6$]-benzene, 25 °C): $\delta$ = 7.00 (m, 1 H, $C_5H_3$), 6.85 (m, 1 H, $C_5H_3$), 6.51 (m, 1 H, $C_5H_3$), 1.17 (s, 9 H, *t*Bu), 0.36 (s, 6 H, $SiMe_2NH\textit{t}Bu$), –0.02 ppm (s, 18 H, $SiMe_3$); N*H* signal not detected. $^{13}C\{^1H\}$ NMR ([$D_6$]benzene, 25 °C): $\delta$ = 146.7 ($C^3$), 145.3, 136.2, 135.3, 60 ($C^1$ of $C^5$ ring), 49.6 ($CMe_3$), 33.9 ($CMe_3$), 2.0 ($SiMe_2$), –0.5 ppm ($SiMe_3$).

**$[Nb\{\eta^5\text{-}C_5H_3(SiClMe_2)(SiMe_3)\}Cl_4]$ (3):** Compound **1** (2.24 g, 7.40 mmol) was added to a suspension of $NbCl_5$ (2.00 g, 7.40 mmol) in toluene (150 mL) at 0 °C. The reaction was slowly warmed at room temperature and stirred for 20 h. After filtration, the resulting solution was concentrated to about 25 mL and cooled to –20 °C to give a dark red microcrystalline solid which was characterized as **3**. Yield: 3.10 g (90%). IR (KBr): $\tilde{\nu}$ = 3091 $cm^{-1}$ w, 1397 m, 1262 vs, 1089 m, 839 vs, 488 vs, 455 s. $^1H$ NMR ([$D_1$]chloroform, 25 °C): $\delta$ = 7.49 (br., 1 H, $C_5H_3$), 7.41 (br., 1 H, $C_5H_3$), 7.20 (br., 1 H, $C_5H_3$), 0.92 (s, 6 H, $SiClMe_2$), 0.43 ppm (s, 9 H, $SiMe_3$). $^{13}C\{^1H\}$ NMR ([$D_1$]chloroform, 25 °C): $\delta$ = 146.6 ($C^1$), 139.7 ($C^3$), 134, 133.6, 133.2 ($C_5H_3$), 1.9 ($SiClMe_2$), –0.6 ppm ($SiMe_3$). $C_{10}H_{18}Cl_5NbSi_2$ (464.60): calcd. C 25.85, H 3.90; found C 25.78, H 3.63.

**$[Ta\{\eta^5\text{-}C_5H_3(SiClMe_2)(SiMe_3)\}Cl_4]$ (4):** A mixture of equimolar amounts of **1** (2.53 g, 8.36 mmol) and freshly sublimed $TaCl_5$ (3.00 g, 8.36 mmol) in dichloromethane (200 mL) was stirred at room temperature for 36 h in a sealed ampoule. After the ampoule was opened, the suspension was filtered and the resulting green solution was concentrated to about 25 mL and cooled to –20 °C to give **4** as a green microcrystalline solid. Yield: 3.23 g (70%). IR (KBr): $\tilde{\nu}$ = 3093 $cm^{-1}$ w, 1393 m, 1252 vs, 1093 s, 831 vs, 497 vs, 455 s. $^1H$ NMR ([$D_1$]chloroform, 25 °C): $\delta$ = 7.32 (m, 1 H, $C_5H_3$), 7.23 (m, 1 H, $C_5H_3$), 7.00 (m, 1 H, $C_5H_3$), 0.91 (s, 6 H, $SiClMe_2$), 0.42 ppm (s, 9 H, $SiMe_3$). $^{13}C\{^1H\}$ NMR ([$D_1$]chloroform, 25 °C): $\delta$ = 142.5 ($C^1$), 131.6 ($C^3$), 131.1, 130.9, 130.8 ($C_5H_3$), 2.0 ($SiClMe_2$), –0.5 ppm ($SiMe_3$). $C_{10}H_{18}Cl_5Si_2Ta$ (552.64): calcd. C 21.73, H 3.28; found C 21.65, H 3.13.

**$[M\{\eta^5\text{-}C_5H_3(SiClMe_2)(SiMe_3)\}Cl_4(CNAr)]$ [Ar = 2,6-$Me_2C_6H_3$; M = Nb (5), Ta (6)]:** 2,6-$Me_2C_6H_3NC$ (0.17 g, 1.30 mmol) was added to a toluene (70 mL) solution of **3** (0.60 g, 1.30 mmol) or **4** (0.72 g, 1.30 mmol) under rigorously anhydrous conditions. The mixture was stirred for 4 h and then filtered. Concentration and cooling of the filtrate gave **5** and **6** as rose (**5**) and green (**6**) microcrystalline solids.

**5:** Yield: 0.70 g (90%). IR (KBr): $\tilde{\nu}$ = 3100 $cm^{-1}$ w, 2957 m, 2218 s, 1625 m, 1473 m, 1401 m, 1255 vs, 1089 s, 842 vs, 484 vs, 455 vs. $^1H$ NMR ([$D_1$]chloroform, 25 °C): $\delta$ = 7.52 (t, $^3J_{H,H}$ = 2.1 Hz, 1 H, $C_5H_3$), 7.41 (t, $^3J_{H,H}$ = 2.1 Hz, 1 H, $C_5H_3$), 7.21 (t, $^3J_{H,H}$ = 2.1 Hz, 1 H, $C_5H_3$), 7.25 (t, $^3J_{H,H}$ = 7.8 Hz, 1 H, *p*-$C_6H_3$), 7.11 (d, $^3J_{H,H}$ = 7.8 Hz, 2 H, *m*-$C_6H_3$), 2.54 (s, 6 H, $C_6H_3Me_2NC$), 0.95 (s, 3 H, $SiClMe_2$), 0.88 (s, 3 H, $SiClMe_2$), 0.41 ppm (s, 9 H, $SiMe_3$).

 © 2006 Wiley-VCH Verlag GmbH & Co. KGaA, Weinheim 

$^{13}C\{^1H\}$ NMR ([D$_1$]chloroform, 25 °C ): $\delta$ = 195 (*C*N), 142.4, 139.2, 139, 138.4, 136.8 ($C_5H_3$), 130.5 ($C^{2,6}$), 129 ($C^1$), 128.1 ($C^{3,5}$), 125.3 ($C^4$, $C_6H_3Me_2NC$), 18.4 ($C_6H_3Me_2NC$), 3.02, 2.97 (SiCl*Me*$_2$), 0.03 ppm (Si*Me*$_3$). $C_{19}H_{27}Cl_5NNbSi_2$ (595.775): calcd. C 38.30, H 4.57, N 2.35; found C 38.49, H 4.65, N 2.30.

**6:** Yield: 0.62 g (70%). IR (KBr): $\tilde{\nu}$ = 3098 cm$^{-1}$ w, 2954 m, 2223 s, 1629 s, 1474 m, 1403 m, 1252 vs, 1091 s, 840 vs, 490 vs, 457 s. $^1H$ NMR ([D$_1$]chloroform, 25 °C): $\delta$ = 7.23 (t, 1 H), 7.20 (t, 1 H), 6.88 (t, $^3J_{H,H}$ = 2.1 Hz, 1 H, $C_5H_3$), 7.10 (m, 3 H, $C_6H_3Me_2NC$), 2.52 (s, 6 H, $C_6H_3Me_2NC$), 0.99 (s, 3 H, SiCl*Me*$_2$), 0.88 (s, 3 H, SiCl*Me*$_2$), 0.41 ppm (s, 9 H, Si*Me*$_3$). $C_{19}H_{27}Cl_5NSi_2Ta$ (683.817): calcd. C 33.37, H 3.98, N 2.05; found C 33.17, H 3.83, N 2.00.

**[Nb{η$^5$-C$_5$H$_3$(SiClMe$_2$)(SiMe$_3$)}Cl$_2$(N*t*Bu)] (7):** Complex **7** can be prepared by two synthetic methods.

**Method A:** *t*BuNH$_2$ (0.07 g, 0.96 mmol) was added under rigorously anhydrous conditions to a solution of **3** (0.22 g, 0.48 mmol) in hexane (50 mL) and the reaction mixture was stirred for 15 h. The solution was filtered and the solvent reduced to dryness to give an orange oil which was identified as **7**.

**Method B:** A solution of LiN*H*t*Bu (0.04 g, 0.48 mmol) in hexane (15 mL) was added to a solution of **3** (0.22 g, 0.48 mmol) in hexane (50 mL) at room temperature. The reaction mixture was stirred for 15 h. Filtration of the supernatant solution from the solid, followed by concentration to dryness, produced **7** as an orange oil. Yield: 0.16 g (70%). IR (KBr): $\tilde{\nu}$ = 3190 cm$^{-1}$ w, 2973 m, 1404 m, 1359 m, 1254 vs, 1084 vs, 840 vs, 503 vs, 459 m. $^1H$ NMR ([D$_6$]benzene, 25 °C): $\delta$ = 7.04 (m, 1 H, $C_5H_3$), 6.49 (m, 1 H, $C_5H_3$), 6.45 (m, 1 H, $C_5H_3$), 1.13(s, 9 H, N*t*Bu), 0.59 (s, 6 H, SiCl*Me*$_2$), 0.21 ppm (s, 9 H, Si*Me*$_3$). $^{13}C\{^1H\}$ NMR ([D$_6$]benzene, 25 °C ): $\delta$ = 130 ($C^1$), 129.3 ($C^3$), 124.4, 122.1, 121.6 ($C_5H_3$), 70.2 [N(*C*Me$_3$)], 30.5 [N(C*Me*$_3$)], 3.6, 3.1 (SiCl*Me*$_2$), 0.02 ppm (Si*Me*$_3$). $C_{14}H_{27}Cl_3NNbSi_2$ (464.814): calcd. C 36.18, H 5.85, N 3.01; found C 35.93, H 5.96, N 2.90.

**[Ta{η$^5$-C$_5$H$_3$(SiClMe$_2$)(SiMe$_3$)}Cl$_2$(N*t*Bu)] (8):** LiN*H*t*Bu (0.003 g, 0.040 mmol) was added to a solution of **4** (0.20 g, 0.40 mmol) in [D$_6$]benzene (0.7 mL) in a valved NMR tube under rigorously anhydrous conditions. The reaction was monitored by $^1H$ NMR spectroscopy until no further changes were observed. The final spectrum was indicative of complete transformation of the starting material and confirmed the formation of **8** in quantitative yield. Evaporation of the solvent gave **8** as a yellow oil. Yield: 0.17 g (75%). $^1H$ NMR ([D$_6$]benzene, 25 °C): $\delta$ = 7.03 (m, 1 H, $C_5H_3$), 6.42 (m, 2 H, $C_5H_3$), 1.20 (s, 9 H, N*t*Bu), 0.58 (s, 3 H, SiCl*Me*$_2$), 0.56 (s, 3 H, SiCl*Me*$_2$), 0.2 ppm (s, 9 H, Si*Me*$_3$). $^{13}C\{^1H\}$ NMR ([D$_6$]benzene, 25 °C): $\delta$ = 127 ($C^1$), 127.3, 122.3, 121.6, 121.2 ($C_5H_3$), 66.6 [N(*C*Me$_3$)], 32.1 [N(C*Me*$_3$)], 3.4, 3.0 (SiCl*Me*$_2$), –0.1 ppm (Si*Me*$_3$). $C_{14}H_{27}Cl_3NNbSi_2$ (552.86): calcd. C 30.42, H 4.92, N 2.53; found C 30.44, H 4.71, N 2.37.

**Reaction of C$_5$H$_3$(SiMe$_2$NH*t*Bu)(SiMe$_2$) (2) with MCl$_5$ (M = Nb, Ta):** $C_5H_3$(SiMe$_2$NH*t*Bu)(SiMe$_2$) (0.63 g, 1.85 mmol) was added to a suspension of $NbCl_5$ (0.50 g, 1.85 mmol) in dichloromethane (80 mL) and the reaction mixture stirred for 15 h. After filtration, the volatiles were removed under vacuum to give a yellow oil, which was identified as a mixture of **1** and **7** by $^1H$ NMR spectroscopy. With $TaCl_5$ a mixture of **1** and **8** was identified by $^1H$ NMR spectroscopy.

**[Nb{η$^5$-C$_5$H$_3$(SiClMe$_2$)(SiMe$_3$)}Cl$_2$(NMe)] (9):** A mixture of **3** (0.30 g, 0.64 mmol) and $LiNMe_2$ (0.03 g, 0.64 mmol) was dissolved in hexane (50 mL) under rigorously anhydrous conditions. The reaction mixture was stirred for 20 h at room temperature and then filtered. The filtrate was evaporated to dryness and the residue extracted with hexane (2 × 10 mL). Concentration and cooling of the filtrate produced **9** as a brown solid. Yield: 0.10 g (37%). $^1H$ NMR ([D$_6$]benzene, 25 °C): $\delta$ = 6.85 (m, 1 H, $C_5H_3$), 6.34 (m, 1 H, $C_5H_3$), 6.27 (m, 1 H, $C_5H_3$), 3.31(s, 3 H, N*Me*), 0.55 (s, 3 H, SiCl*Me*$_2$), 0.53 (s, 3 H, SiCl*Me*$_2$), 0.17 ppm (s, 9 H, Si*Me*$_3$). $^{13}C\{^1H\}$ NMR ([D$_6$]benzene, 25 °C): $\delta$ = 129.5, 122.7, 122.5, 122.1, 121.6 ($C_5H_3$), 54.3 (N*Me*), 3.2, 2.7 (SiCl*Me*$_2$), –0.3 ppm (Si*Me*$_3$). $C_{11}H_{21}Cl_3NSi_2Ta$ (422.733): calcd. C 31.25, H 5.01, N 3.31; found C 31.12, H 4.94, N 3.25.

**[Ta{η$^5$-C$_5$H$_3$(SiClMe$_2$)(SiMe$_3$)}Cl(NH*t*Bu)(N*t*Bu)] (10):** A toluene (15 mL) solution of LiN*H*t*Bu (0.06 g, 0.81 mmol) was slowly added to a solution of **4** (0.30 g, 0.54 mmol) in toluene (60 mL) and the reaction mixture was stirred overnight. The resulting suspension was filtered and the solvent evaporated to dryness. The residue was extracted with hexane (2 × 10 mL) and the solution was concentrated and cooled to –20 °C to give an oily yellow product which was characterized as **10**. Yield: 0.09 g (30%). IR (KBr): $\tilde{\nu}$ = 3083 cm$^{-1}$ w, 1403 m, 1358 s, 1261 vs, 1085 vs, 840 vs, 633 m, 504 s, 548 m. $^1H$ NMR ([D$_1$]chloroform, 25 °C): $\delta$ = 8.09 (br., 1 H, N*H*t*Bu), 7.05 (m, 1 H, $C_5H_3$), 6.79 (m, 2 H, $C_5H_3$), 1.24 (s, 18 H, NH*t*Bu + N*t*Bu), 0.74 (s, 3 H, SiCl*Me*$_2$), 0.72 (s, 3 H, SiCl*Me*$_2$), 0.31 ppm (s, 9 H, Si*Me*$_3$). $^{13}C\{^1H\}$ NMR ([D$_1$]chloroform, 25 °C): $\delta$ = 134.8, 127.8, 127.3, 121.6, 121.2 ($C_5H_3$), 66.6 (N*C*Me$_3$), 53.2 (NH*C*Me$_3$), 32.1 (NHC*Me*$_3$ + NC*Me*$_3$), 3.4 (SiCl*Me*$_2$), 2.9 (SiCl*Me*$_2$), –0.1 ppm (Si*Me*$_3$). $C_{18}H_{37}Cl_2N_2Si_2Ta$ (589.53): calcd. C 36.67, H 6.33, N 4.75; found C 36.47, H 6.43, N 4.57.

**[Nb{η$^5$-C$_5$H$_3$(SiMe$_2$N*t*Bu-κ*N*)(SiMe$_3$)}Cl(N*t*Bu)] (11):** A solution of **3** (0.22 g, 0.48 mmol) in hexane (50 mL) was treated with *t*BuNH$_2$ (0.14 g, 1.92 mmol). The mixture was stirred at room temperature for 15 h and then filtered. Solvent was removed from the resulting solution to give **11** as a yellow oil. Yield: 0.14 g (60%). IR (KBr): $\tilde{\nu}$ = 3196 cm$^{-1}$ w, 1448 m, 1359 s, 1250 vs, 1081 vs, 841 vs, 633 m, 499 m. $^1H$ NMR ([D$_6$]benzene, 25 °C): $\delta$ = 7.09 (m, 1 H, $C_5H_3$), 6.64 (m, 1 H, $C_5H_3$), 6.50 (m, 1 H, $C_5H_3$), 1.19 (s, 9 H, *t*Bu), 1.03 (s, 9 H, *t*Bu), 0.48 (s, 3 H, Si*Me*$_2$), 0.42 (s, 3 H, Si*Me*$_2$), 0.27 ppm (s, 9 H, Si*Me*$_3$). $^{13}C\{^1H\}$ NMR ([D$_6$]benzene, 25 °C): $\delta$ = 137.3 ($C^1$), 123.1, 122.2, 122.1, 110 ($C^3$, $C_5H_3$), 49.9, 48.5 (N*C*Me$_3$), 33.8, 30.6 (NC*Me*$_3$), 2.9, 2.7 (Si*Me*$_2$), 0.15 ppm (Si*Me*$_3$). $C_{18}H_{36}ClN_2NbSi_2$ (465.03): calcd. C 46.49, H 7.80, N 6.02; found C 46.38, H 7.69, N 5.92.

**Reaction of [Nb{η$^5$-C$_5$H$_3$(SiClMe$_2$)(SiMe$_3$)}Cl$_4$] (3) with LiN*H*t*Bu:** LiN*H*t*Bu (0.07 g, 0.86 mmol) was added to a solution of **3** (0.20 g, 0.43 mmol) in hexane (30 mL). The reaction mixture was stirred for 20 h and the solvent was then completely removed under vacuum. The resulting oily brown product was characterized as a mixture of complexes **7** and **11** by $^1H$ NMR spectroscopy.

**[Nb{η$^5$-C$_5$H$_3$(SiMe$_2$NCH$_2$CH$_2$NH$_2$-κ$^2$*N*,*N*)(SiMe$_3$)}Cl$_3$] (12):** A solution of **3** (1.40 g, 3.00 mmol) in toluene (150 mL) was treated at room temperature with a solution of ethylenediamine (0.18 g, 3.00 mmol) and triethylamine (0.61 g, 6.00 mmol) in toluene (20 mL). The reaction mixture was stirred for 48 h and the solvent was evaporated to dryness. The resulting yellow residue was washed with cool hexane (2 × 5 mL) and the solid was dried in vacuo and identified as **12**. The result was similar when **3** was treated with 2 equiv. of ethylenediamine. Yield: 1.00 g (75%). IR (KBr): $\tilde{\nu}$ = 3249 cm$^{-1}$ m, 3072 w, 1448 w, 1259 vs, 1248 vs, 1089 s, 836 vs, 553 s, 493 m. $^1H$ NMR ([D$_6$]benzene, 25 °C): $\delta$ = 6.94 (m, 1 H, $C_5H_3$), 6.86 (m, 2 H, $C_5H_3$), 4.60 (br, 2 H, $CH_2CH_2NH_2$), 3.27 (m, 2 H, $NCH_2CH_2$), 2.68 (m, 2 H, $NCH_2CH_2$), 0.51 (s, 9 H, Si*Me*$_3$), 0.08 (s, 3 H, Si*Me*$_2$), 0.05 ppm (s, 3 H, Si*Me*$_2$). $^{13}C\{^1H\}$ NMR ([D$_6$]-benzene, 25 °C): $\delta$ = 140.8 ($C^1$), 133.4, 130.1, 130, 106 [$C^3$, $C_5H_3$(SiMe$_2$NCH$_2$CH$_2$NH$_2$)(SiMe$_3$)], 59.7 (N*C*H$_2$CH$_2$), 45.4 (NCH$_2$*C*H$_2$),

 © 2006 Wiley-VCH Verlag GmbH & Co. KGaA, Weinheim 

Table 3. Crystal data and structure refinement for **3** and **5**.[a]

| | **3** | **5** |
|---|---|---|
| Formula | $C_{10}H_{18}Cl_5NbSi_2$ | $C_{19}H_{27}Cl_5NNbSi_2$ |
| *Fw* | 464.58 | 595.76 |
| *T* [K] | 170(2) | 200(2) |
| $\lambda$ (Mo-$K_\alpha$) [Å] | 0.71073 | 0.71073 |
| Crystal system, space group | monoclinic, $P2_1/n$ | monoclinic, $P2_1/a$ |
| *a* [Å] | 7.0559(8) | 12.936(2) |
| *b* [Å] | 12.0123(13) | 10.1328(8) |
| *c* [Å] | 20.8380(15) | 20.959(3) |
| $\beta$ [°] | 92.751(6) | 106.01(1) |
| *V* [Å$^3$] | 1764.1(3) | 2640.8(6) |
| *Z* | 4 | 4 |
| $\rho_{calcd}$ [g cm$^{-3}$] | 1.749 | 1.498 |
| $\mu$ [mm$^{-1}$] | 1.557 | 1.060 |
| *F*(000) | 928 | 1208 |
| Crystal size [mm] | 0.4 × 0.4 × 0.3 | 0.43 × 0.23 × 0.2 |
| $\theta$ range [deg] | 5.05 to 27.50 | 3.03 to 26.02 |
| Index ranges | $-9 \le h \le 9$ | $-15 \le h \le 15$ |
| | $-15 \le k \le 15$ | $-11 \le k \le 12$ |
| | $25 \le l \le 27$ | $-25 \le l \le 25$ |
| No. of data collected | 21029 | 14858 |
| No. of unique data [$I > 2\sigma(I)$] | 3914 [*R*(int) = 0.2754] | 5147 [*R*(int) = 0.2309] |
| Absorption correction | none | semiempirical from equivalents |
| Max. and min. transmission | | 1.446 and 0.774 |
| Parameters refined | 158 | 248 |
| Goodness-of-fit on $F^2$ | 1.133 | 1.086 |
| Final *R* indices [$I > 2\sigma(I)$] | $R_1$ = 0.0827 | $R_1$ = 0.0924 |
| | $wR_2$ = 0.1986 | $wR_2$ = 0.1997 |
| *R* indices (all data) | $R_1$ = 0.0990 | $R_1$ = 0.2300 |
| | $wR_2$ = 0.2072 | $wR_2$ = 0.2798 |
| Largest diff. peak and hole [e Å$^{-3}$] | 1.602 and –2.254 | 1.544 and –1.364 |

[a] $R_1 = \Sigma||F_o| - |F_c||/[\Sigma|F_o|]$; $wR_2 = \{[\Sigma w(F_o^2 - F_c)^2]/[\Sigma w(F_o^2)^2]\}^{1/2}$.

0.05 (Si*Me*$_3$), –3.9 (Si*Me*$_2$), –5.4 ppm (Si*Me*$_2$). $^{29}$Si NMR ([D$_6$]-benzene, 25 °C): $\delta$ = –3.9 (*Si*Me$_3$), –12.3 ppm (*Si*Me$_2$). $C_{12}H_{24}Cl_3N_2NbSi_2$ (451.78): calcd. C 31.90, H 5.35, N 6.20; found C 32.00, H 5.32, N 5.73.

**[Ta{η$^5$-C$_5$H$_3$(SiMe$_2$NCH$_2$CH$_2$NH$_2$-κ$^2$*N*,*N*)(SiMe$_3$)}Cl$_3$] (13):** A solution of ethylenediamine (0.039 g, 0.65 mmol) and triethylamine (0.13 g, 1.30 mmol) in toluene (10 mL) was slowly added to a solution of **4** (0.36 g, 0.65 mmol) in toluene (50 mL) at –78 °C. The reaction mixture was warmed to room temperature and stirred for 16 h. The volatiles were removed in vacuo and the residue was extracted with hexane (2 × 10 mL). The resulting solution was concentrated and cooled to –20 °C to afford **11** as a pale-yellow crystalline solid. Yield: 0.15 g (40%). IR (KBr): $\tilde{\nu}$ = 3247 cm$^{-1}$ br. s, 3073 w, 1443 w, 1248 vs, 1089 s, 847 vs, 556 s, 492 m. $^1$H NMR ([D$_6$]benzene, 25 °C): $\delta$ = 6.79 (d, $^3J_{H,H}$ = 2.1 Hz, 1 H, C$_5H_3$), 6.67 (d, $^3J_{H,H}$ = 2.1 Hz, 2 H, C$_5H_3$), 4.28 (br, 2 H, CH$_2$CH$_2$N*H*$_2$), 3.54 (m, 2 H, C*H*$_2$CH$_2$NH$_2$), 2.63 (m, 2 H, CH$_2$C*H*$_2$NH$_2$), 0.51 (s, 9 H, Si*Me*$_3$), 0.12 (s, 3 H, Si*Me*$_2$), 0.09 ppm (s, 3 H, Si*Me*$_2$). $^{13}$C{$^1$H} NMR ([D$_6$]benzene, 25 °C): $\delta$ = 131.3 (*C*$^1$), 129.3, 126.4, 125.6, 105.2 (*C*$^3$, *C*$_5$H$_3$), 55.4, 45.3 (*C*H$_2$*C*H$_2$NH$_2$), 1.4 (Si*Me*$_3$), 0.4 (Si*Me*$_2$), 0.2 ppm (Si*Me*$_2$). $^{29}$Si NMR ([D$_6$]benzene, 25 °C): $\delta$ = –4.5 (*Si*Me$_3$), –13.2 ppm (*Si*Me$_2$). $C_{12}H_{24}Cl_3N_2Si_2Ta$ (539.82): calcd. C 26.70, H 4.48, N 5.19; found C 26.55, H 4.33, N 5.25.

**X-ray Structure Determination of 3 and 5:** Crystallographic and experimental details of the crystal structure determinations are given in Table 3. Suitable crystals of complexes **3** and **5** were covered with mineral oil and mounted in the N$_2$ stream of a Bruker-Nonius Kappa CCD diffractometer; data were collected using graphite monochromated Mo-$K_\alpha$ radiation ($\lambda$ = 0.71073 Å). Data collections were performed at low temperature (see Table 3), in the case of compound **3** with an exposure time of 8 s per frame (5 sets; 391 frames) and for compound **5** with an exposure time of 36 s per frame (5 sets; 240 frames). Raw data were corrected for Lorenz and polarization effects.

Both structures were solved by direct methods, completed by the subsequent difference Fourier techniques, and refined by full-matrix least-squares on $F^2$ with SHELXL-97.[20] Anisotropic thermal parameters were used in the last cycles of refinement for the non hydrogen atoms. The hydrogen atoms were included from geometrical calculations and refined using a riding model. All the calculations were made using the WINGX system.[21]

CCDC-613239 (for **3**) and -613240 (for **5**) contain the supplementary crystallographic data for this paper. These data can be obtained free of charge from The Cambridge Crystallographic Data Centre via www.ccdc.cam.ac.uk/data_request/cif.

## Acknowledgments

We thank the MEC (project CTQ 2006-04540/BQU), the CAM (project S-0505/PPQ/0328-02), and the Universidad de Alcalá (project GC 2005/94) for their financial support of this research.

[1] a) H. Brintzinger, D. Fischer, R. Mülhaupt, B. Rieger, R. Waymouth, *Angew. Chem. Int. Ed. Engl.* **1995**, *34*, 1143–1170; b) T. Cuenca, P. Royo, *Coord. Chem. Rev.* **1999**, *193–195*, 447–498; c) V. C. Gibson, S. K. Spitzmesser, *Chem. Rev.* **2003**, *103*, 283–315.

[2] a) B. Royo, P. Royo, L. M. Cadenas, *J. Organomet. Chem.* **1998**, *551*, 293–297; b) R. Gómez, P. Gómez-Sal, A. Martín, A. Núñez, P. A. del Real, P. Royo, *J. Organomet. Chem.* **1998**, *564*,

 © 2006 Wiley-VCH Verlag GmbH & Co. KGaA, Weinheim 

93–100; c) M. I. Alcalde, P. Gómez-Sal, A. Martín, P. Royo, *Organometallics* **1998**, *17*, 1144–1150; d) M. I. Alcalde, P. Gómez-Sal, P. Royo, *Organometallics* **1999**, *18*, 546–554; e) F. J. de la Mata, P. Giner, P. Royo, *J. Organomet. Chem.* **1999**, *572*, 155–161.

[3] a) J. Okuda, T. Eberle, T. P. Spaniol, *Chem. Ber./Recueil* **1997**, *130*, 209; b) Y.-X. Chen, T. J. Marks, *Organometallics* **1997**, *16*, 3649–3657; c) L. Schwink, P. Knochel, T. Eberle, J. Okuda, *Organometallics* **1998**, *17*, 7–9; d) J. Cano, P. Royo, H. Jacobsen, O. Blacque, H. Berke, E. Herdtweck, *Eur. J. Inorg. Chem.* **2003**, 2463–2474; e) A. B. Vázquez, P. Royo, *J. Organomet. Chem.* **2003**, *671*, 172–178; f) . O. Buitrago, G. Jimenez, T. Cuenca, *J. Organomet. Chem.* **2003**, *683*, 70–76; g) A. B. Vázquez, P. Royo, E. Herdtweck, *J. Organomet. Chem.* **2003**, *683*, 155–164; h) M. Sudupe, J. Cano, P. Royo, E. Herdtweck, *Eur. J. Inorg. Chem.* **2004**, 3074–3083.

[4] D. E. Wigley, *Prog. Inorg. Chem.* **1994**, *42*, 239.

[5] a) D. S. Williams, M. H. Schofield, R. R. Schrock, *Organometallics* **1993**, *12*, 4560–4571; b) V. C. Gibson, *J. Chem. Soc., Dalton Trans.* **1994**, 1607–1618.

[6] a) M. Gómez, P. Gómez-Sal, M. P. Nicolás, P. Royo, *J. Organomet. Chem.* **1995**, *491*, 121–125; b) A. Castro, M. V. Galakhov, M. Gómez, P. Gómez-Sal, A. Martín, P. Royo, *J. Organomet. Chem.* **1998**, *554*, 185–194; c) M. I. Alcalde, P. Gómez-Sal, A. Martín, P. Royo, *Organometallics* **1998**, *17*, 1144–1150; d) A. Castro, M. V. Galakhov, M. Gómez, F. Sánchez, *J. Organomet. Chem.* **1999**, *580*, 161–168; e) M. I. Alcalde, M. P. Gómez-Sal, P. Royo, *Organometallics* **1999**, *18*, 546–554; f) A. Castro, M. V. Galakhov, M. Gómez, P. Gómez-Sal, A. Martín, F. Sánchez, *J. Organomet. Chem.* **2000**, *595*, 36–53.

[7] a) A. M. Cardoso, R. J. H. Clark, S. Moorhouse, *J. Chem. Soc., Dalton Trans.* **1980**, 1156–1160; b) J. M. Rozell, P. R. Jones, *Organometallics* **1985**, *4*, 2206–2210; c) M. Gómez, P. Royo, J. M. Selas, *J. Organomet. Chem.* **1986**, *314*, 131–138; d) T. K. Panda, M. T. Gamer, P. W. Roesky, *Organometallics* **2003**, *22*, 877–878.

[8] P. Jutzi, *Chem. Rev.* **1986**, *86*, 983–996 and references cited therein.

[9] A. Castro, M. V. Galakhov, M. Gómez, P. Gómez-Sal, A. Martín, F. Sánchez, P. Velasco, *Eur. J. Inorg. Chem.* **2000**, 2047–2054.

[10] a) M. V. Galakhov, M. Gómez, G. Jiménez, P. Royo, M. A. Pellinghelli, A. Tiripicchio, *Organometallics* **1995**, *14*, 1901–1910; b) M. V. Galakhov, M. Gómez, G. Jiménez, P. Royo, M. A. Pellinghelli, A. Tiripicchio, *Organometallics* **1995**, *14*, 2843–2854.

[11] A. M. Andreu, F. A. Jalón, A. Otero, P. Royo, A. M. Manotti Lanfredi, A. Tiripicchio, *J. Chem. Soc., Dalton Trans.* **1987**, 953–956.

[12] R. Kempe, A. Spannenberg, *Z. Kristallogr. New Cryst. Struct.* **1997**, *212*, 478.

[13] M. I. Alcalde, J. de la Mata, M. Gómez, P. Royo, M. A. Pellinghelli, A. Tiripicchio, *Organometallics* **1994**, *13*, 462–467.

[14] S. Ciruelos, T. Cuenca, R. Gómez, P. Gómez-Sal, A. Manzanero, P. Royo, *Organometallics* **1996**, *15*, 5577–5585.

[15] a) F. A. Cotton, T. J. Marks, *J. Am. Chem. Soc.* **1969**, *91*, 7281–7285; b) A. Castro, M. V. Galakhov, M. Gómez, P. Gómez-Sal, A. Martín, *Eur. J. Inorg. Chem.* **2002**, 1336–1342.

[16] D. N. Williams, J. P. Mitchell, A. D. Poole, U. Siemeling, W. Clegg, D. C. R. Hockless, P. A. O'Neil, V. C. Gibson, *J. Chem. Soc., Dalton Trans.* **1992**, 739–751.

[17] M. I. Alcalde, J. de la Mata, M. Gómez, P. Royo, F. Sánchez, *J. Organomet. Chem.* **1995**, *492*, 151–155.

[18] R. M. Silverstein, G. C. Bassler, T. C. Morril, *Spectrometric Identification of Organic Compounds*, Wiley, New York, **1974**.

[19] C. S. Bajgur, W. R. Tikannen, J. L. Petersen, *Inorg. Chem.* **1985**, *24*, 2539–2546.

[20] G. M. Sheldrick, *SHELX-97, Program for Crystal Structure Analysis*, University of Göttingen, Germany, **1998**.

[21] L. J. Farrugia, *J. Appl. Crystallogr.* **1999**, *32*, 837.

Received: July 4, 2006
Published Online: October 27, 2006

 © 2006 Wiley-VCH Verlag GmbH & Co. KGaA, Weinheim 

DOI: 10.1002/ejic.200600711

# Coordinative Versatility of Guanazole [3,5-Diamino-1,2,4-triazole]: Synthesis, Crystal Structure, EPR, and Magnetic Properties of a Dinuclear and a Linear Trinuclear Copper(II) Complex Containing Small Bridges and Triazole Ligands

**Elena Aznar,[a] Sacramento Ferrer,*[a] Joaquín Borrás,[a] Francesc Lloret,[a] Malva Liu-González,[b] Héctor Rodríguez-Prieto,[c] and Santiago García-Granda[c]**

**Keywords:** Copper / 1,2,4-Triazole ligands / Polynuclear compounds / X-ray structures / Magnetic properties

New complexes with guanazole (3,5-diamino-1,2,4-triazole = Hdatrz), $[Cu_2(Hdatrz)_2(\mu\text{-}OH_2)(H_2O)_4(SO_4)](SO_4)\cdot 3.5H_2O$ (**1**) and $[Cu_3(Hdatrz)_4(\mu\text{-}Cl)_2(H_2O)_4(SO_4)_2]\cdot 11.4H_2O$ (**2**), have been prepared and structurally characterized. Complex **1** is a noncentrosymmetric dinuclear compound in which the copper(II) ions are bridged by two triazole ligands and one $\mu$-$OH_2$ molecule, with a Cu(1)···Cu(2) distance of 3.4945(8) Å. The chromophores are $Cu(1)N_2O_2O'$ (square pyramidal), and $Cu(2)N_2O_2O'O''$ (octahedral). Complex **2** has a linear trinuclear copper(II) structure, with two crystallographically independent copper(II) atoms. Neighboring copper(II) ions are linked by two triazole ligands and one slightly asymmetric chlorido bridge. The intratrimeric Cu(1)···Cu(2) distance is 3.5602 (4) Å. Cu(2), the central copper, is coordinated to $N_4Cl_2$ (octahedral) while Cu(1), the terminal copper, is coordinated to $N_2O_2ClO'$ (also octahedral). Magnetic susceptibility measurements (2–300 K) are in accordance with the dinuclear (**1**) and trinuclear (**2**) nature of these compounds. The best-fit parameters, obtained with the Hamiltonian $\mathbf{H} = -J\Sigma_{i<j}\mathbf{S}_i\mathbf{S}_j$, are as follows: $g = 2.10(1)$ and $J = -94.3(2)$ cm$^{-1}$ for **1**; and $g_{central} = 2.12(1)$, $g_{peripheral} = 2.07(1)$, and $J = -89.9(3)$ cm$^{-1}$ for **2**. Compound **1**, which has an unprecedented *folded* bridging $\{Cu(N\text{–}N)_2Cu\}$ system, exhibits a magnetic exchange comparable to that of related *planar* compounds. Comparison of the magneto-structural properties of **2** with those of analogous linear trinuclear compounds has made a first approach to the relative magnitude of the *J* value possible. The Q-band powder spectra, which were recorded in a range from 4 K to room temperature, are in agreement with the magnetic susceptibility measurements.
(© Wiley-VCH Verlag GmbH & Co. KGaA, 69451 Weinheim, Germany, 2006)

## Introduction

A variety of coordination compounds with 3,5-disubstituted 1,2,4-triazoles as ligands coordinating to transition-metal ions have been reported.[1–3] The interesting magnetic properties of the coordination compounds of iron(II) and copper(II) with 1,2,4-triazole ligands have been investigated extensively; among these, polynuclear (1,2,4-triazole)-iron(II) compounds have been found to show spin-crossover behavior.[4–7] These ligands allow for two general bridging modes, one involving only triazole bridges and another also containing either small bridging anions, such as $Cl^-$, $F^-$, $NCS^-$, $N_3^-$ or $OH^-$, or small bridging molecules such as $H_2O$.[1]

Even though guanazole (3,5-diamino-1,2,4-triazole = Hdatrz) (Figure 1) is a simple molecule and an inexpensive chemical, only nine X-ray structures of complexes of this triazole have been documented to date and, to the best of our knowledge, none with $Cu^{II}$ have been reported thus far. There is a similar lack of publications concerning the related unsubstituted 1,2,4-triazole ligand. In the latter case, the scarcity of structures has been attributed in part to the fact that the ligand often immediately produces a microcrystalline, insoluble precipitate with transition-metal ions.[1] The structures described for guanazole include one mononuclear compound with $Pt^{II}$;[8] two two-dimensional polymers: one with $Cd^{II}$[9] and one with $Mn^{II}$;[10] two cyclic trinuclear compounds of $Pd^{II}$;[11,12] and four linear trinuclear compounds with $[M_3\{(H)datrz\}_6L_6]$ (L = $H_2O$ or

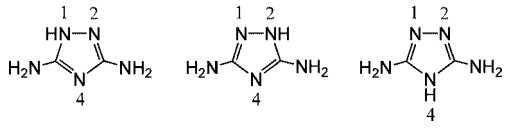

Figure 1. Tautomers of guanazole [Hdatrz].

[a] Departament de Química Inorgànica, Universitat de València, Vicent Andrés Estellés s/n, 46100 Burjassot, Valencia, Spain
E-mail: Sacramento.Ferrer@uv.es
[b] S.C.S.I.E. – Rayos X, Universitat de València, Vicent Andrés Estellés s/n, 46100 Burjassot, Valencia, Spain
[c] Departamento de Química Física y Analítica, Universidad de Oviedo, Julián Clavería 8, 33006 Oviedo, Spain

 © 2006 Wiley-VCH Verlag GmbH & Co. KGaA, Weinheim 

$NCS^-$) units: one with Co(II,III)[13] and three with $Ni^{II}$.[14–16] No dinuclear structures have been reported. It has been suggested that, because the substituents in position 3 and 5 are apparently capable of forming hydrogen bonds, the linking of metal ions by triple bridges is preferred.[1,17]

In the aforementioned structures, guanazole is known to coordinate in three different ways, either unidentate through *N*1, or bridging-bidentate through *N*1,*N*2 or *N*2,*N*4. Moreover, Hdatrz can occur in three different chemical forms, namely neutral (in most cases), anionic (with deprotonation at *N*4),[13] or cationic (with protonation at *N*2).[8] Especially interesting is the compound $[Co_3(datrz)_2(Hdatrz)_4(H_2O)_6]Cl_3{\cdot}9H_2O$, which includes mixed valences of cobalt ions and triazole/triazolate mixed ligand bridges.[13] Thus, in spite of its apparent simplicity, guanazole is quite a versatile ligand. As a result, we have found that the reaction solution often affords a mixture of compounds.

In this paper, we report on the isolation of two $Cu^{II}$ compounds of Hdatrz with different nuclearity, one dinuclear (**1**) and the other linear trinuclear (**2**). Both compounds present double-triazole bridges and an additional small bridge, which is water in the case of **1** or chlorido in the case of **2**. Both compounds also contain the neutral *N*1,*N*2-bidentate ligand guanazole. We describe here the structural and spectroscopic characterization of these compounds, as well as the study of their magnetic properties in the context of related compounds.

## Results and Discussion

### Crystal Structure of $[Cu_2(Hdatrz)_2(\mu\text{-}OH_2)(H_2O)_4(SO_4)](SO_4){\cdot}3.5H_2O$ (1)

The structure of complex **1** is made up of dinuclear cations, one sulfate anion per cation, and non-coordinated water molecules, one of which is located on a symmetry site. There is one O(7) lattice water molecule per four $Cu^{II}$ ions. An ORTEP view of the structure, together with its numbering scheme, is depicted in Figure 2. Selected bond lengths and angles are presented in Table 1.

Table 1. Selected bond lengths [Å] and bond angles [°] for **1**.

| | | | |
|---|---|---|---|
| Cu(2)–N(1b) | 2.005(4) | Cu(1)···Cu(2) | 3.4945(8) |
| Cu(2)–N(2a) | 1.986(5) | Cu(1)–N(2b) | 1.988(3) |
| Cu(2)–O(1) | 1.976(5) | Cu(1)–N(1a) | 1.988(5) |
| Cu(2)–O(2) | 2.000(4) | Cu(1)–O(3) | 1.968(5) |
| Cu(2)–O(11) | 2.425(4) | Cu(1)–O(4) | 1.995(5) |
| Cu(2)–O(5) | 2.382(5) | Cu(1)–O(5) | 2.474(4) |
| | | | |
| O(5)–Cu(2)–N(1b) | 81.8(2) | O(5)–Cu(1)–N(2b) | 82.5(2) |
| O(5)–Cu(2)–N(2a) | 90.0(2) | O(5)–Cu(1)–N(1a) | 90.6(2) |
| O(5)–Cu(2)–O(11) | 169.3(2) | O(5)–Cu(1)–O(3) | 96.2(2) |
| O(5)–Cu(2)–O(1) | 98.7(2) | O(5)–Cu(1)–O(4) | 89.7(2) |
| O(5)–Cu(2)–O(2) | 94.4(2) | N(1b)–Cu(2)–N(2a) | 93.3(2) |
| Cu(1)–O(5)–Cu(2) | 92.0(2) | N(2a)–Cu(2)–O(2) | 87.2(2) |
| Cu(1)–N(1a)–N(2a) | 119.9(3) | N(1b)–Cu(2)–O(1) | 93.8(2) |
| Cu(1)–N(2b)–N(1b) | 121.0(3) | O(11)–Cu(2)–O(1) | 84.8(2) |
| Cu(2)–N(2a)–N(1a) | 123.3(3) | O(11)–Cu(2)–O(2) | 95.9(2) |
| Cu(2)–N(1b)–N(2b) | 121.7(3) | O(11)–Cu(2)–N(2a) | 87.7(2) |
| N(2b)–Cu(1)–N(1a) | 91.4(2) | O(11)–Cu(2)–N(1b) | 87.9(2) |
| N(2b)–Cu(1)–O(4) | 89.1(2) | O(1)–Cu(2)–O(2) | 86.3(2) |
| N(1a)–Cu(1)–O(3) | 88.0(2) | | |
| O(3)–Cu(1)–O(4) | 91.4(2) | | |

In the dinuclear unit, the two copper centers, which are crystallographically independent, are bridged by two neutral guanazole ligands and one water molecule. The coordination environment around Cu(1) is distorted square pyramidal, with two triazole N atoms and two water O atoms in equatorial positions and the bridging water O atom in the axial position [Cu(1)–O(5) = 2.474(4) Å]. The second $Cu^{II}$ has a similar environment, but it is octahedrally coordinated; the second axial coordination position is achieved by one sulfate O atom [Cu(2)–O(5) = 2.382(5), Cu(2)–O(11) = 2.425(4) Å]. The observed Cu–N distances, ranging from 1.986(5) to 2.005(4) Å, are common for dinuclear *N*1,*N*2-

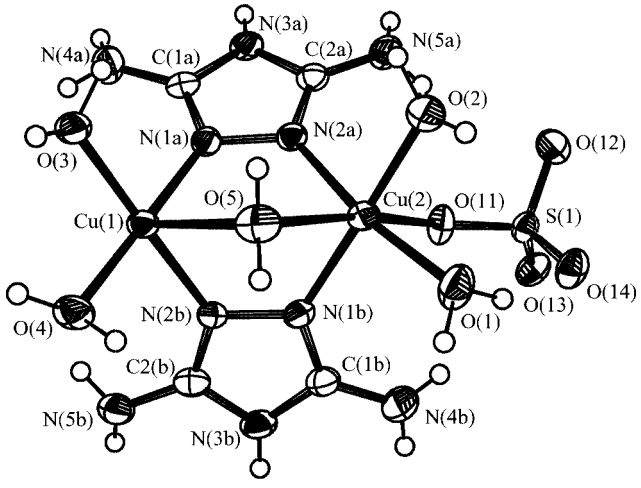


a

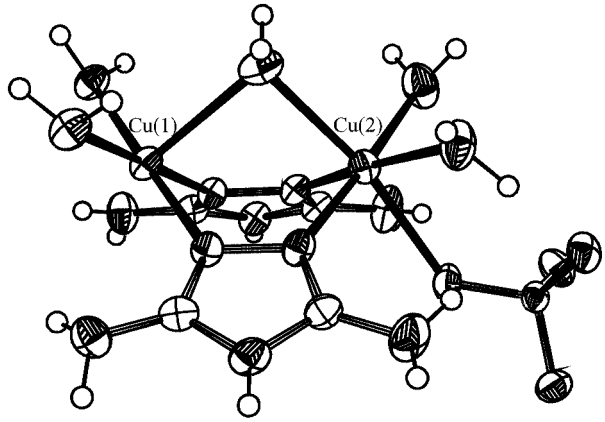


b

Figure 2. ORTEP drawing of **1** showing the atomic labeling system (a) and the noncoplanarity of the $\{Cu(N–N)_2Cu\}$ framework (b).

 © 2006 Wiley-VCH Verlag GmbH & Co. KGaA, Weinheim 

triazole-bridged $Cu^{II}$ compounds[1,18,19] and comparable to the Cu–O water distances, which range from 1.968(5) to 2.000(4) Å. Cu(1) and Cu(2) are displaced from their corresponding equatorial planes by 0.0104(7) Å and 0.0416(9) Å, respectively. The two equatorial planes are almost perpendicular; the dihedral angle between them measures 80.3(2)°.

The two Cu–O(5) distances differ slightly. The angle Cu(1)–O(5)–Cu(2) is 92.0(2)°. The combination of both bridges gives rise to a Cu···Cu′ distance of 3.4945(8)°. This distance is significantly shorter than that found in double-triazole-bridged $Cu^{II}$ compounds without a third bridge. For example, the Cu···Cu′ distances compiled by Slangen et al.[18] and Ferrer et al.[19] for dimeric compounds oscillate between 4.085(1) and 3.854(6) Å, which indicates that the μ-$OH_2$ causes the bridging system to fold. It must be taken into account, however, that since the referred compounds all contain *N*,*N*-bridging ligands with N/O-chelating substituents that form five/six-membered chelate rings, the situation is not strictly comparable with that of our structure. In the triazole bridge, the Cu–N–N angles of **1**, which range from 119.9(3) to 123.3(3)°, also differ clearly from those of the aforementioned dimeric $Cu^{II}$ structures, all of which have at least one Cu–N–N angle larger than 128°; besides, those with five-membered chelating rings all have at least two Cu–N–N angles close to 135°.[18,19]

On the other hand, as will be discussed in the next section, the Cu···Cu′ distance of **1** is shorter than the equivalent distance in the analogous linear trinuclear structure of **2** [3.5602(4) Å], which also has an additional small bridge, but a different donor atom size ($O_{H_2O}$ in **1**; $Cl^-$ in **2**).

Another difference between **1** and the dinuclear $Cu^{II}$ complexes mentioned in the literature is that in the latter the {Cu–$(N–N)_2$–Cu} framework is nearly planar,[17] whereas in **1** this group of atoms deviates significantly from planarity (the N atoms deviate from the least-squares plane by 0.8–0.9 Å). In fact, in the double-triazole bridging system of **1**, the dihedral angle between the planes defined by [Cu(1),N(1a),N(2a),Cu(2)] and [Cu(1),N(2b),N(1b),Cu(2)] is 64.3(1)° (Figure 2b).

Complex **1** is, to the best of our knowledge, the second example of a binuclear compound with two bridging triazoles and one bridging oxygen atom. The first example reported, the Cd compound $[Cd_2(deatrz)_2(H_2O)Br_4]$ (deatrz = 3,5-diethyl-4-amino-1,2,4-triazole), forms a 1D chain through hydrogen-bonding contacts.[20] This complex has a Cd···Cd′ distance of 3.819 Å.[21]

Finally, complex **1** presents strong intermolecular hydrogen bonds between the bridging water molecule and the sulfate anions: O(5)–H(w5a)···O(23) (from the non-coordinated sulfate) [2.874(9) Å, 148(5)°] and O(5)–H(w5b)···$O(14^{\#})$ [from the coordinated sulfate of a different asymmetric unit; $O(14^{\#})$ is generated by the symmetry operation: $x - 1/2, -y + 1/2 + 1, + z - 1/2$] [2.723(4) Å, 161(5)°]. Such contacts should play an important role in the stabilization of the structure.

### Crystal Structure of $[Cu_3(Hdatrz)_4(\mu\text{-}Cl)_2(H_2O)_4(SO_4)_2]\cdot 11.4H_2O$ (2)

The structure of complex **2** consists of discrete trinuclear entities and randomly placed water of crystallization. The fractional number of water molecules arises from the fact that 2 out of the 7 crystallographically different crystallization water molecules found in the structure do not have a 100% occupancy factor; actually, that of O(5) is 40%, while that of O(9) is only 30%. An ORTEP projection of the structure and the atom-labeling scheme are given in Figure 3. Selected bond lengths and angles are listed in Table 2.

In the linear trinuclear units the metal ions are bridged by two neutral guanazole ligands and one chloride anion. The central copper atom, located at the inversion center, exhibits a tetragonally distorted coordination afforded by four nitrogen atoms from the bridging *N*1,*N*2-triazole ligands and the two bridging chloride anions. Because the copper is situated at the inversion center, the nitrogen atoms are in a nearly regular square, with Cu(2)–N distances of 2.024(3) and 2.003(3) Å. Again, these distances are within

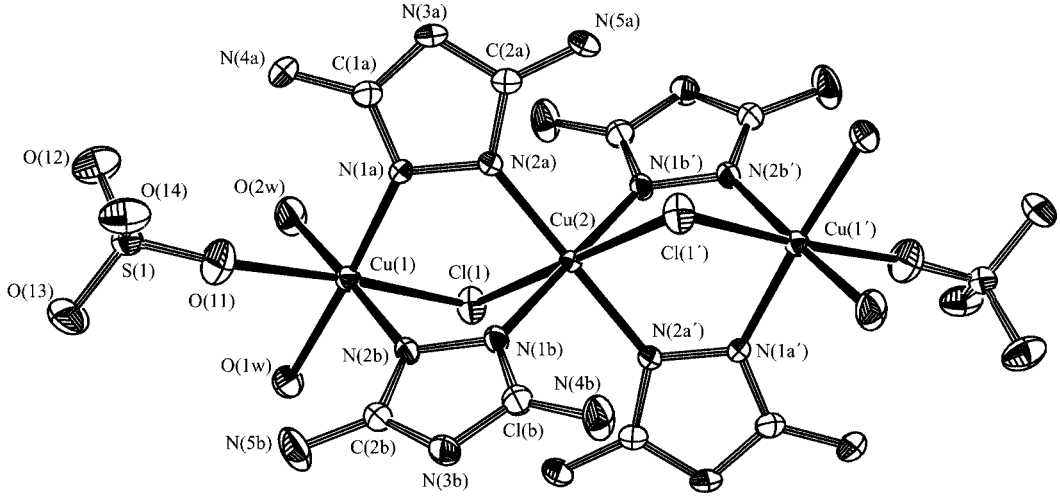


Figure 3. ORTEP drawing of **2** showing the atomic labeling system. H atoms have been omitted for clarity.

 © 2006 Wiley-VCH Verlag GmbH & Co. KGaA, Weinheim 

Table 2. Selected bond lengths [Å] and bond angles [°] for **2**.[a]

| | | | |
|---|---|---|---|
| Cu(1)···Cu(2) | 3.5602(4) | Cu(1)–N(2b) | 1.987(3) |
| Cu(1)···Cu(1′) | 7.120(8) | Cu(1)–N(1a) | 1.955(3) |
| | | Cu(1)–O(1w) | 2.003(3) |
| Cu(2)–N(1b) | 2.024(3) | Cu(1)–O(2w) | 1.977(3) |
| Cu(2)–N(2a) | 2.003(3) | Cu(1)–O(11) | 2.511(3) |
| Cu(2)–Cl(1) | 2.785(2) | Cu(1)–Cl(1) | 2.624(2) |
| | | | |
| Cl(1)–Cu(2)–N(1b) | 87.91(9) | Cl(1)–Cu(1)–N(2b) | 89.25(9) |
| Cl(1)–Cu(2)–N(2a) | 88.03(9) | Cl(1)–Cu(1)–N(1a) | 92.22(9) |
| Cl(1)–Cu(2)–Cl(1′) | 180.00(0) | Cl(1)–Cu(1)–O(11) | 176.19(8) |
| Cl(1)–Cu(2)–N(1b′) | 92.09(9) | Cl(1)–Cu(1)–O(1w) | 92.30(9) |
| Cl(1)–Cu(2)–N(2a′) | 91.97(9) | Cl(1)–Cu(1)–O(2w) | 90.26(10) |
| Cu(1)–Cl(1)–Cu(2) | 82.28(3) | N(2b)–Cu(1)–O(1w) | 89.1(2) |
| Cu(1)–N(1a)–N(2a) | 122.0(3) | N(1a)–Cu(1)–O(2w) | 91.0(2) |
| Cu(1)–N(2b)–N(1b) | 122.3(2) | N(2b)–Cu(1)–N(1a) | 91.7(2) |
| Cu(2)–N(2a)–N(1a) | 123.1(2) | O(1w)–Cu(1)–O(2w) | 88.2(2) |
| Cu(2)–N(1b)–N(2b) | 122.0(2) | N(1a)–Cu(1)–O(1w) | 175.4(2) |
| N(1b)–Cu(2)–N(2a) | 89.4(2) | N(2b)–Cu(1)–O(2w) | 177.2(2) |
| N(1b)–Cu(2)–Cl(1) | 87.91(9) | N(2b)–Cu(1)–O(11) | 90.00(2) |
| N(2a)–Cu(2)–Cl(1) | 88.03(9) | N(1a)–Cu(1)–O(11) | 91.55(2) |
| N(2a)–Cu(2)–N(1b′) | 90.6(2) | O(1w)–Cu(1)–O(11) | 83.96(2) |
| | | O(2w)–Cu(1)–O(11) | 90.30(2) |

[a] Primed atoms are generated by $-x, -y, -z$.

the normal range for *N*1,*N*2-bridging 1,2,4-triazole ligands.[1,18,19,22] The two chloride anions act as axial ligands at semi-coordinating distances [Cu(2)–Cl(1) = 2.785(2) Å]; the distance from the bridging chloride to the terminal metal ion is comparable [Cu(1)–Cl(1) = 2.624(2) Å]. Thus, the chlorido bridge, with a Cu(1)–Cl(1)–Cu(2) angle of 82.28(3)°, is rather symmetrical.

The chlorido bridging system of **2** is different from that found in the analogous compound reported by van Koningsbruggen et al., $[Cu_3(H_2ahmt)_6Cl_4]Cl_2$ [$H_2$ahmt = 4-amino-3,5-bis(hydroxymethyl)-1,2,4-triazole] (compound **6**, Table 3), in which not only are the μ-$Cl^-$ located at equatorial instead of axial positions in the environment of the central $Cu^{II}$, but also the bridging distances are very asymmetric [Cu(1)–Cl(1) = 2.296(1), Cu(2)–Cl(1) = 2.688(1) Å].[22] This situation is probably related to the steric hindrance produced by bulkier substituents on the ring of the $H_2$ahmt ligand. In contrast, **2** is more comparable with the compound described by Keij and co-workers, $[Cu_3(tmtz)_8F_2](BF_4)_4{\cdot}2H_2O$ [tmtz = 3,4,5-trimethyl-1,2,4-triazole] (**7**), although the latter has one $F^-$ instead of one $Cl^-$ bridge [Cu(1)–F(1) = 2.20(1), Cu(2)–F(1) = 1.91(1) Å].[23]

The terminal copper ions of **2** are hexacoordinated by two nitrogen atoms from bridging triazole ligands and two oxygen atoms from two water molecules, all in equatorial positions, and by the bridging chloride anion and an oxygen atom from a sulfate anion in apical positions [Cu(1)–O(1) = 2.511(3) Å]. The Cu(1)(terminal)–N distances [1.995(3), 1.987(3) Å] are slightly shorter that the Cu(2)(central)–N distances [2.003(3), 2.024(3) Å], but it can be considered that the $H_2$datrz ligands also bridge the copper(II) ions in an almost symmetrical way, as evidenced by the close values of the Cu–N–N angles, which range from 122.0(3) to 123.1(2)°, and those of the N–Cu–N angles, with values of 89.4(2) and 91.7(2)°. The Cu–N–N–Cu torsion angles [–4.2(4) and –9.4(4) Å], indicate that the triazole ligands tend to twist out of the equatorial plane formed by the two $Cu^{II}$ ions involved.

The equatorial coordination planes around Cu(1) and Cu(2) form a dihedral angle of 79.0(1)°. Thus, they are almost perpendicular, as was also observed in the dimeric structure of **1**. The dihedral angle between the least-squares planes through the triazole rings linking Cu(1) and Cu(2) measures 55.7(2) Å (Figure 3).

The Cu(1)–Cu(2) distance is 3.5602(4) Å, which is similar to that found in related linear trinuclear double-μ-*N*1,*N*2-triazole-bridged $Cu^{II}$ complexes with an additional small bridging anion such as $Cl^-$ [3.5426(1), 3.620(3), and 3.5682(5) Å, for complexes **3**, **4**, and **6**, respectively][22,24] or $N_3^-$ [3.5034(6) Å for **5**],[25] but longer than that of the analogous complex with an $F^-$ bridge [3.362(3) Å for **7**].[23] This is probably due to the small size of the $F^-$ ion (Table 3). It should be noted that the Cu···Cu′ separation in **2** is shorter than that in triple-μ-*N*1,*N*2-triazole-bridged copper(II) compounds, such as $[Cu_3(metrz)_6(H_2O)_4](CF_3SO_3)_6{\cdot}4H_2O$ (metrz = 3-methyl-4-ethyl-1,2,4-triazole) [3.719(7) Å][26] or $[Cu(hyetrz)_3](ClO_4)_2{\cdot}3H_2O$ [hyetrz = 4-(2-hydroxyethyl)-1,2,4-triazole] [3.853(2) and 3.829(2) Å].[27] This indicates that, when the third triazole is replaced by monatomic bridges, the Cu···Cu′ distance tends to shorten, as previously reported[25,27] and, indeed, as expected due to the larger size of the third bridge.

Table 3. Magnetic and structural parameters in linear trinuclear double-(μ-*N*1,*N*2-triazole)-bridged $Cu^{II}$ complexes with a small additional bridge.

| Complex[a] | Cu(2)···Cu(1) [Å] | Cu(2)–A[b]–Cu(1) [°] | Cu(1)–N(1a) Cu(1′)–N(1a′) [Å] | Cu(1)–N(2b) Cu(1′)–N(2b′) [Å] | Cu(2)–N(1b) Cu(2)–N(1b′) [Å] | Cu(2)–N(2a) Cu(2)–N(2a′) [Å] | *J* [$cm^{-1}$] | Ref. |
|---|---|---|---|---|---|---|---|---|
| $[Cu_3(Hdatrz)_4Cl_2(H_2O)_4(SO_4)_2]{\cdot}11.4H_2O$ (**2**) | 3.5602(4) | 82.28(3) | 1.995(3) | 1.987(3) | 2.024(3) | 2.00(3) | –89.9 | this work |
| $[Cu_3(attn)_2Cl_2(H_2O)_2]Cl_4{\cdot}4H_2O$ (**3**) | 3.5426(1) | 84.013(9) | 2.023(1) | 2.003(1) | 2.040(1) | 1.985(1) | –75.1 | [24] |
| $[Cu_3(attn)_2Cl_2(ZnCl_4)_2]$ (**4**) | 3.620(3) | 80.6(1) | 1.98(1) | 1.99(1) | 2.04(1) | 1.98(1) | –70.9 | [24] |
| $[Cu(atrz)_2(N_3)](NO_3)$ (**5**) | 3.5034(6) | 104.05(12) | 2.402(3) | 2.008(3) | 2.011(3) | 2.029(3) | –35.4 | [25] |
| $[Cu_3(H_2ahmt)_6Cl_4]Cl_2$ (**6**) | 3.5682(5) | 91.09(4) | 1.966(3) | 2.079(4) | 2.023(3) | 2.554(3) | –33.8 | [22] |
| $[Cu_3(tmtz)_8F_2](BF_4)_4{\cdot}2H_2O$ (**7**) | 3.362(3) | – | 2.24(2) | 2.01(1) | 2.05(1) | 2.04(1) | – | [23] |

[a] Hdatrz = 3,5-diamino-1,2,4-triazole; attn = 1,9-bis(3-aminotriazol-5-yl)3,7-dithianonane; atrz = 4-amino-1,2,4-triazole; $H_2$ahmt = 4-amino-3,5-bis(hydroxymethyl)-1,2,4-triazole; tmtz = 3,4,5-trimethyl-1,2,4-triazole. [b] A = $Cl^-$, $N(N_3^-)$, $F^-$.

 © 2006 Wiley-VCH Verlag GmbH & Co. KGaA, Weinheim 

We have carried out a review of the literature in order to compare more systematically some structural parameters of **2** with those of analogous compounds. Several linear trinuclear coordination compounds of this type, i.e. containing *two* 1,2,4-triazole ligands bridging through *N*1,*N*2 atoms and either a halogen anion or a second small bridging anion, have been previously reported: (a) three $Co^{II}$ compounds with $F^-$[28,29] or *N*-bridging $NCS^-$ ligands,[30] (b) three $Ni^{II}$–*N*($NCS^-$) compounds,[30–32] (c) one Mn(II,III,II) complex with hydroxido bridges,[33] (d) two $Cd^{II}$ compounds containing $Cl^-$[20] or *N*,*N*-isothiocyanato bridges,[20] and (e) a few $Cu^{II}$ compounds (Table 3). The first structurally characterized (triazole)copper(II) compound to include μ-chloride ions was [{Cu(Htrz)$Cl_2$}$_\infty$], but it consists of an infinite chain with two $Cl^-$ and a *single* triazole ligand per pair of copper atoms instead of one $Cl^-$ and two triazole ligands.[34] To the best of our knowledge, only five $Cu^{II}$ compounds strictly comparable to **2** as regards bridging systems have been published to date (all have been mentioned above): one containing μ-fluoride anions (**7**),[23] three with chlorido bridges (**3**, **4**, and **6**; of which **3** and **4** have an unusual chelating tetradentate triazole ligand), and one in which the small bridging anion is the azido $N_3^-$ group (**5**).[25] Table 3 lists several structural parameters, including coordination distances, which will be considered in the magnetism section.

## Magnetic Properties

### *Magnetic Properties of 1*

Figure 4 displays the magnetic behavior of **1** in the form of a $\chi_M T$ and $\chi_M$ vs. *T* plot, where $\chi_M$ is the magnetic susceptibility per two $Cu^{II}$ ions. Upon cooling, the $\chi_M T$ values decrease continuously from room temperature (0.73 $cm^3 \cdot mol^{-1} \cdot K$) until they vanish at 20 K. The $\chi_M$ curve shows a maximum at 90 K. This behavior is characteristic of an antiferromagnetic interaction between $Cu^{II}$ ions with a singlet spin ground state.

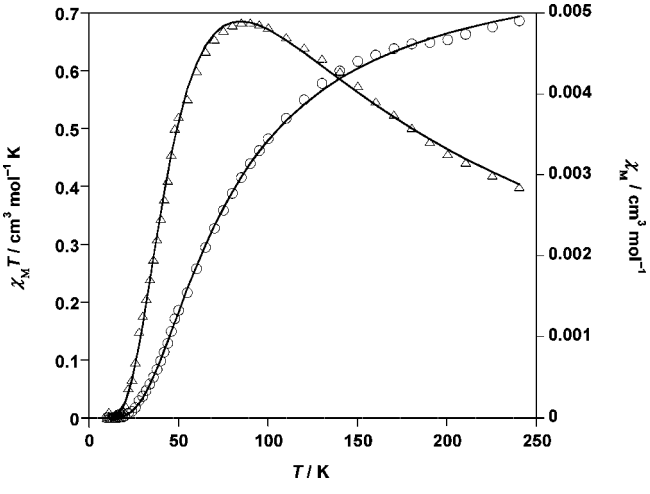


Figure 4. Thermal dependence of $\chi_M T$ (○) and $\chi_M$ (Δ) for **1** (solid lines represent theoretical curves, see text).

The magnetic data have been interpreted in accordance with the actual dinuclear nature of the complex by using the spin Hamiltonian $\mathbf{H} = -J\mathbf{S}_1\mathbf{S}_2$, from which the following susceptibility equation can be derived [Equation (1)]:

$$\chi_M = \frac{2N\beta^2 g^2}{kT} \frac{1}{3 + \exp(-\frac{J}{kT})} \quad (1)$$

Assuming that the *g* factors for both $Cu^{II}$ atoms are identical, the fit of the magnetic data with this expression results in $g = 2.10(1)$ and $J = -94.3(2)$ $cm^{-1}$.

From the molecular structure, it could be concluded that the magnetic exchange occurs via the $d_{x^2-y^2}$ orbitals on the $Cu^{II}$ ions that overlap with the σ orbitals of the nitrogen atoms of the triazole bridges, which are placed at equatorial positions. Exchange interaction through the pathway provided by the large axial bonding (through the μ-$OH_2$) can be expected to have little relevance (see Figure 2b) because of the low unpaired electron density along de $d_{z^2}$ orbital in the octahedral coordination around the copper atoms. In principle, then, at least from a magnetic point of view, compound **1** could be compared to related bis(μ-triazole)-bridged $Cu^{II}$ complexes.

Although the literature contains many examples of copper(II) complexes with bridging triazole or triazolate functionalities, only 15 acyclic complexes with metal centers bridged by two triazole-triazolate units have been structurally characterized to date,[18,19,36–42] and for only 10 of these has a magnetic study been performed; Table 4 offers a compilation of these studies.[18,19,35–39,41] As a first attempt at establishing magneto-structural correlations, Haasnoot and co-workers,[18] working with a set of compounds, concluded that Cu–$N_{trz}$–$N_{trz}$ angles of 134–135° in symmetrically doubly bridged systems lead to the largest possible coupling, with $|J| \approx 240$ $cm^{-1}$. Table 4, however, shows that, taken separately, neither the symmetry nor the Cu–$N_{trz}$–$N_{trz}$ angles allow for a prediction of the magnitude of the exchange coupling. The last two compounds in Table 4, both of which exhibit fairly symmetrical {Cu–N–N}$_2$ frameworks, present the lowest $|J|$ values. Moreover, in spite of its smaller Cu–$N_{trz}$–$N_{trz}$ angles, compound **1** displays an absolute value for *J* that is larger than that for [Cu(daat)-($NO_3$)($H_2O$)]$_2$. In this context, and with the aim of determining the factors that dominate the magnetic interaction, we carried out several DFT calculations. Trials with models including fixed Cu–N distances and variable bridging angles turned out to be unsuccessful in that they could not reproduce the trend of the experimental *J* values. In fact, the only conclusion was that the bridging angles are related with, but do not determine, the *J* value, as we had already deduced from Table 4. On the other hand, it should be noticed that, as mentioned above, in all the previously reported complexes, the [$Cu_2L_2$] unit is planar; compound **1** is the only described instance of a folded dicopper(II) complex with acyclic triazole ligands.[43] In a series of closely related dicobalt(II) complexes, a decrease in magnetic exchange interactions was observed for folded dico-

 © 2006 Wiley-VCH Verlag GmbH & Co. KGaA, Weinheim 

Table 4. Magnetic and structural parameters in the $\{Cu–N–N\}_2$ ring for dinuclear double-(μ-*N*1,*N*2-triazole)-bridged copper(II) compounds.[18,19].

| Compound[a] | N(1a)–Cu(1)–N(2b) [°][b] | Cu(2)–N(2a)–N(1a) [°][b] | Cu(1)–N(1a)–N(2a) [°][b] | Cu···Cu′ [Å] | $-J$[c] [$cm^{-1}$] | Ref. |
|---|---|---|---|---|---|---|
| $[Cu(bpt)(CF_3SO_3)(H_2O)]_2$ | 90.2(1) | 134.7(2) | 135.0(2) | 4.085(1) | 236 | [35] |
| $[Cu(aamt)Br(H_2O)]_2Br_2·2H_2O·CH_3OH$ | 92.1(1) | 134.2(2) | 133.7(2) | 4.0694(7) | 220 | [36] |
| $Cu_2(ibdpt)_2(ClO_4)_4(MeCN)$ | 92.7(2) | 133.8(3) | 133.5(3) | 4.070(1) | 210[d] | [41] |
| $[Cu(aamt)(H_2O)_2]_2(SO_4)_2·4H_2O$ | 91.9(4) | 135.1(8) | 132.9(8) | 4.088(3) | 194 | [37] |
| $[Cu^{II}(maamt)(Cu^{I}Cl_3)]_2$ | – | 133.0(4) | 133.9(3) | 4.048(1) | 156 | [39] |
| $[Cu_2(pt)_2(4,4'\text{-bpy})(NO_3)_2(H_2O)_2]·4H_2O$ | 95.5(1) | 139.4(2) | 125.2(2) | 4.0198(7) | 102 | [38] |
| $[Cu_2(pt)_2(SO_4)(H_2O)_3]·3H_2O$ | 94.7(2) | 139.8(3) | 124.9(3) | 4.0265(8) | 98 | [18] |
| $[Cu_2(pt)_2(Hpz)_2(NO_3)_2(H_2O)_2]$ | 96.5(2) | 139.6(3) | 123.9(3) | 3.974(1) | 98 | [38] |
| $[Cu_2(pt)_2(Meim)_2(NO_3)_2(H_2O)_2]·4H_2O$ | 95.4(1) | 138.7(2) | 125.8(2) | 4.022(1) | 96 | [38] |
| $[Cu_2(Hdatrz)_2(\mu\text{-}OH_2)(H_2O)_4(SO_4)](SO_4)·3.5H_2O$ (**1**) | 92.4(2) | 122.2(3) | 120.8(3) | 3.495(8) | 94 | this work |
| $[Cu(daat)(NO_3)(H_2O)]_2$ | 102.8(5) | 128.0(8) | 129.2(8) | 3.832(1) | 72 | [19] |

[a] bpt = 3,5-bis(pyridin-2-yl)-1,2,4-triazolate; aamt = 4-amino-3,5-bis(aminomethyl)-1,2,4-triazole; ibdpt = 4-isobutyl-3,5-bis(2-pyridyl)-4*H*-1,2,4-triazole; maamt = 4-amino-3,5-bis[(*N*-methylamino)methyl]-1,2,4-triazole; pt = 3-pyridin-2-yl-1,2,4-triazolate; 4,4′-bpy = bipyridine; Hpz = pyrazole; Meim = *N*-methylimidazole; daat = 3,5-bis(acetylamino)-1,2,4-triazolate. [b] Averaged values. [c] Values from literature adapted according to definition used in this work [see Equation (1)]. [d] Measurements performed on partially desolvated sample (and in the presence of some monomeric impurities).

balt(II) complexes as compared to their planar analogues.[43,44] This behavior is reasonable since the distortion leads to less overlap between the magnetic orbitals of the metal centers and the σ orbital of the ligand. In contrast, compound **1** exhibits larger coupling than the planar $[Cu(daat)(NO_3)(H_2O)]_2$ compound, thereby excluding coplanarity as a main factor in the magnitude of the interaction. In summary, several parameters seem to influence the magnetic exchange in the double-triazole-bridged dinuclear compounds; more examples are needed to derive a clear magneto-structural relationship.

### *Magnetic Properties of 2*

The magnetic behavior of **2** is depicted in Figure 5 in the form of a $\chi_M T$ vs. $T$ plot, where $\chi_M$ is the magnetic susceptibility per three $Cu^{II}$ ions. At room temperature, the $\chi_M T$ value is 1.00 $cm^3·mol^{-1}·K$. Upon cooling, the $\chi_M T$ values decrease, reaching a plateau with a value of 0.43 $cm^3·mol^{-1}·K$ at approximately 25 K. This behavior is characteristic for compounds with an overall antiferromagnetic interaction between the $Cu^{II}$ ions, which induces a spin doublet ground state.

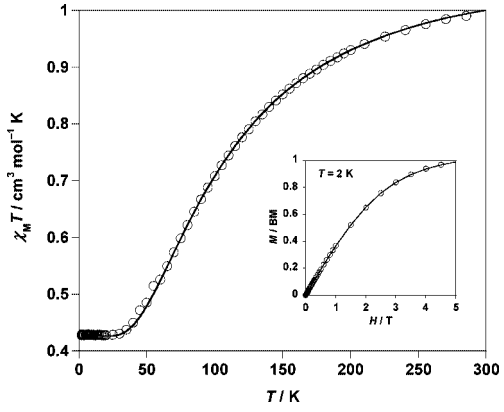


Figure 5. Thermal dependence of $\chi_M T$ for **2** (the solid line represents the theoretical curve, see text). The inset displays the magnetization curve at 2 K for **2** (the solid line is drawn to guide the eye).

In order to obtain the relevant magnetic parameters, the experimental data have been fitted by using Equation (2), derived from the spin Hamiltonian $\mathbf{H} = -J(\mathbf{S}_1\mathbf{S}_2 + \mathbf{S}_2\mathbf{S}_3)$, where $\mathbf{S}_1$ and $\mathbf{S}_3$ correspond to the peripheral $Cu^{II}$ ions ($g_1 = g_3 = g_p$) and $\mathbf{S}_2$ to the central one ($g_2 = g_c$).

$$\chi_M = \frac{N\beta^2}{4kT}\frac{g_{1/2,1}^2 + g_{1/2,0}^2\exp(\frac{J}{kT}) + 10g_{3/2,1}^2\exp(\frac{3J}{2kT})}{1+\exp(\frac{J}{kT})+2\exp(\frac{3J}{2kT})} \quad (2)$$

where:

$$g_{1/2,1} = \frac{4g_p - g_c}{3}$$
$$g_{3/2,1} = \frac{2g_p + g_c}{3} \quad (3)$$
$$g_{1/2,0} = g_c$$

The exchange constant between the terminal copper ions is assumed to be negligible. This assumption is justified from the study of the triple triazole-bridged $Fe^{II}$–$Fe^{II}$–$Fe^{II}$[45] and $Co^{II}$–$Co^{III}$–$Co^{II}$[13] trinuclear clusters, in which the central metal ion is diamagnetic, and no magnetic interactions are detected between the paramagnetic terminal ions. Moreover, these interactions only affect the relative position of the excited spin doublet with respect to the ground spin doublet and the excited spin quartet. The effect of these interactions on magnetic properties, if any, is insignificant.[46,47]

The best-fit parameters obtained were: $J = -89.9(3)$ $cm^{-1}$, $g_{central} = 2.12(1)$, and $g_{peripheral} = 2.07(1)$. The $J$ value of **2** is thus very similar to that observed for the dinuclear compound **1**, as could be expected from the identical nature of the main bridge and the similar distortion of the cores (the dihedral angles between the equatorial $Cu^{II}$ planes are 80° in **1** and 79° in **2**).

 © 2006 Wiley-VCH Verlag GmbH & Co. KGaA, Weinheim 

Selected magneto-structural data for the known linear trinuclear $Cu^{II}$ compounds with double μ-triazole bridges and an additional small bridge are listed in Table 3. Two groups of compounds can be established from the magnitude of the exchange: (a) those with $J$ values around –75 $cm^{-1}$ (compounds **2**–**4**), and (b) those with $J$ values close to –34 $cm^{-1}$ (compounds **5** and **6**). This trend in the $J$ values can be understood on the basis of simple orbital symmetry considerations (see Figure 6) and also by taking into account that the magnitude of the antiferromagnetic coupling, $J_{AF}$, is proportional to the overlap integral between the magnetic orbitals.[48]

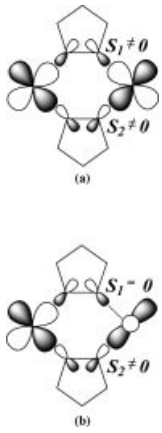


Figure 6. Orbital models for the triazole bridging system.

For compounds **2**–**4** (Figure 6a), in which both triazole bridges are located at equatorial positions as deduced from the coordination distances (see Table 3), the unpaired electron on each $Cu^{II}$ ion is in a $d_{x^2-y^2}$ type magnetic orbital, where the $x$ and $y$ axes are roughly described by the copper–$N_{triazole}$ bonds. Both magnetic orbitals exhibit good sigma overlap on each side of the bridge. As for compounds **5** and **6** (Figure 6b), only one triazole bridge is at an equatorial position (see coordination distances in Table 3). As a consequence, one of the magnetic orbitals (that corresponding to the axial site) is reversed and thus perpendicular to the triazole ring, whereas the other magnetic orbital remains coplanar. Because of the relative orientation of these magnetic orbitals, the interaction only occurs through one side of the bridge. The experimental $J$ values for both groups of compounds, that is, around –75 $cm^{-1}$ for **2**–**4** and around –34 $cm^{-1}$ for **5** and **6**, are in agreement with this simple orbital model.

## Spectroscopic Properties

### *IR Spectra*

The IR spectrum of guanazole has already been studied in detail by Desseyn et al.[9] and Kumar et al.[49] The assignment of the main peaks of the ligand and complexes **1** and **2** is indicated in the experimental section. Especially noteworthy is the fact that the IR spectra of both compounds are almost indistinguishable; this is related to the similarity in the coordination of the ligand and to the presence of similar IR-active groups such as uncoordinated and/or monocoordinated sulfate and coordinated and uncoordinated water molecules in both **1** and **2**. A minor difference is observed in the first band of the spectrum (at around 3400 $cm^{-1}$), which appears at a higher frequency in **1** than in **2**. This could be attributed to the vibrations of the μ-$OH_2$ bridge. Characteristic absorbances in agreement with both coordinated ($C_{3v}$ symmetry) and uncoordinated sulfate can be appreciated in the spectra of both complexes.[50]

### *Electronic Spectra*

The UV/Vis spectra of both compounds, recorded by using solid samples (diffuse-reflectance technique), show asymmetric bands centered at around 700 nm (**1**) and 710 nm (**2**). This feature is in agreement with the presence of two different chromophores in each complex and with the distorted tetragonal (square-pyramidal or octahedral) geometry of the copper(II) ions present in the two structures.[51] Furthermore, a clearly distinguishable maximum is observed at ca. 400 nm (**1**) and ca. 415 nm (**2**), which could be attributed either to a charge-transfer band or, in the case of **1**, to the high-energy absorption for copper(II) dimers frequently present in this region of the spectra.[19,35,52,53]

### *EPR Spectra*

Powder EPR spectra of the complexes have been recorded at room temperature at the X-band frequencies (0–5000 G), and from room temperature to 4 K at the Q-band frequencies (0–15000 G). To exclude the presence of impurities, different measurements were performed with samples obtained by powdering single crystals from different preparations. Figure 7 (for **1**) and Figure 8 (for **2**) exhibit selected Q-band spectra.

The room-temperature X-band EPR spectrum of **1** exhibits a very weak half-field ($\Delta M_s = \pm 2$) signal, centered at 1550 G, typical of a spin-coupled binuclear copper(II) system with significant population at the triplet state. An isotropic $\Delta M_s = \pm 1$ transition is also observed at $g = 2.16$. As for the Q-band frequencies, the room-temperature spectrum of **1** can be described either as inverted axial or as slightly rhombic (Figure 7a). No signal corresponding to the forbidden transition (around 4000 G) could be detected. At lower temperatures, the spectrum becomes progressively more resolved. At 30 K (Figure 7b), the spectrum shows an anisotropic signal at 10910 G and a signal at 11960 G, which can be assigned to one of the perpendicular and parallel transitions, respectively, of the excited triplet state ($S = 1$).[51] Finally, as expected, the spectrum vanishes below 30 K because of the antiferromagnetic interaction in the dimer, which leads to a diamagnetic $S = 0$ state.

The exchange interaction parameter $J$ can be determined from the temperature variation of the EPR absorption lines. The relative intensity of the absorption is expressed by Equation (3):[54]

$$R \propto (1/T)\,[(e^{-J/kT})/(1 + 3\,e^{-J/kT})] \quad (3)$$

 © 2006 Wiley-VCH Verlag GmbH & Co. KGaA, Weinheim 

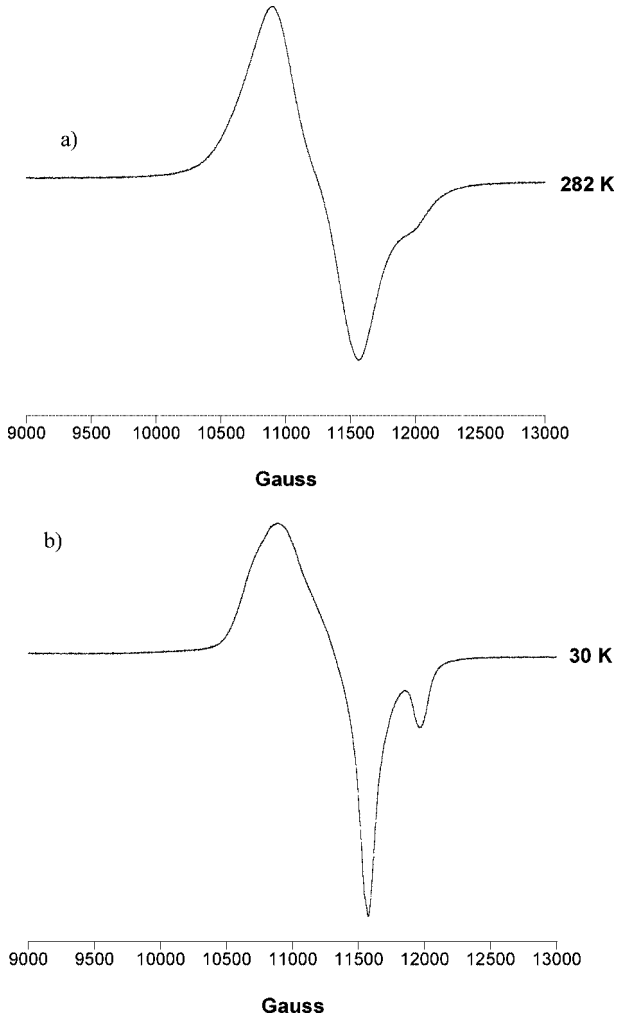


Figure 7. EPR for **1** at (a) 282 K and (b) 30 K.

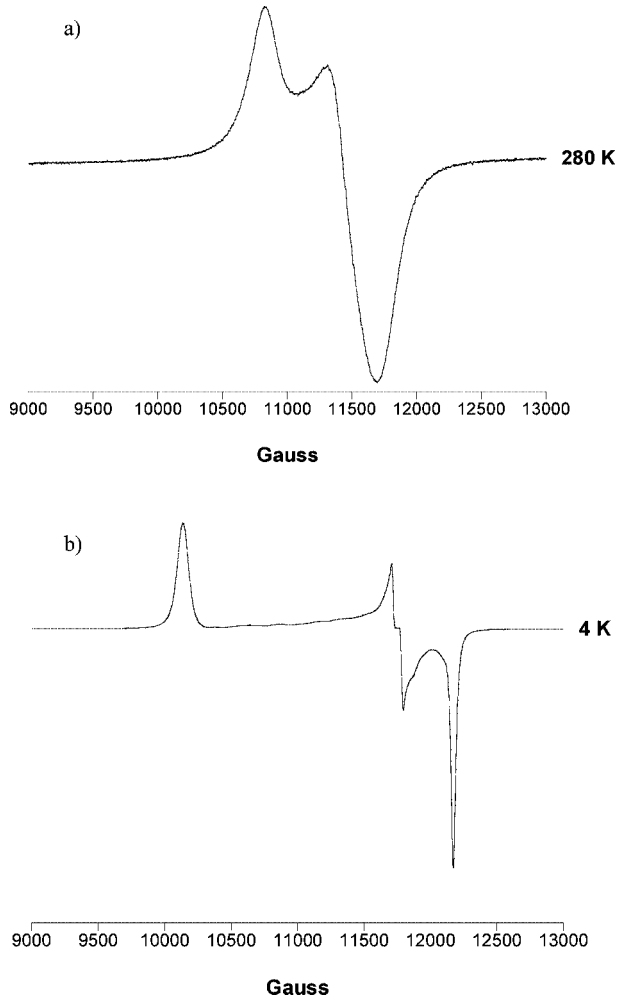


Figure 8. EPR for **2** at (a) 280 K and (b) 4 K.

This approach was applied to compound **1**. A value of $-J = 89\ cm^{-1}$ was obtained, which is very close to the value calculated from the magnetic measurements [$J = -94.3(2)\ cm^{-1}$].

For **2**, the X-band EPR spectrum recorded at room temperature is isotropic, with a signal centered at $g = 2.13$. The room temperature Q-band spectrum is axial (Figure 8a). At lower temperatures, the signals become better defined and the spectra are rhombic. Figure 8b displays the spectrum at 4 K; it is clearly rhombic, with signals at $g_3 = 2.39$, $g_2 = 2.07$, and $g_1 = 2.00$, which is in agreement with both the stereochemistry of the copper(II) ions[51] and the spin doublet ground state.[55]

## Concluding Remarks

Control of appropriate conditions for synthesis has permitted the isolation of two $Cu^{II}$ compounds of guanazole, **1** and **2**, with different nuclearity. To the best of our knowledge, these compounds represent the first structurally characterized $Cu^{II}$ compounds of this ligand. In both cases, the guanazole acts in its neutral form through its *N*1,*N*2-bidentate bridging mode. While compound **1** is dimeric, **2** is a linear trinuclear complex. The two copper atoms in **1**, and the two nearest copper atoms in **2**, are linked by double triazole bridges and by a third, small $H_2O$ (in **1**) or $Cl^-$ (in **2**) bridge. Compound **1** is the second reported case of a compound that uses triazole ligands together with $\mu$-$OH_2$ as bridges.[21]

For both compounds, a significant antiferromagnetic interaction of similar magnitude [$J = -94.3(2)\ cm^{-1}$ (**1**), $J = -89.9(3)\ cm^{-1}$ (**2**)] has been observed. This is in agreement with the similarity of the bridging triazole systems, which comprise the main exchange pathways. Compound **1** has presented us with the opportunity of testing the influence of a nonplanar $\{Cu(N–N)_2Cu\}$ framework on the magnitude of the AF exchange. For its part, compound **2** exhibits one of the largest magnetic exchange constants found in linear trinuclear double/triple-triazole bridged $Cu^{II}$ complexes to date; this has likewise been rationalized for the first time in terms of simple orbital symmetry models.

 © 2006 Wiley-VCH Verlag GmbH & Co. KGaA, Weinheim 

## Experimental Section

**Instrumentation:** Elemental analyses were performed with a CE EA 1110 CHNS instrument. Infrared spectra were recorded with a Mattson Satellite FT-IR spectrophotometer from 4000 to 400 $cm^{-1}$ by using KBr disks. Ligand field spectra were obtained from 800 to 200 nm with a Shimadzu 2101-PC UV/Vis instrument, by using the diffuse-reflectance technique, with Nujol mulls. EPR spectra of powdered samples were collected on a Bruker ELEXSYS spectrometer at variable temperature operating at Q-band frequencies, and at room temperature operating at X-band frequencies. Magnetic susceptibility measurements of polycrystalline samples were measured over the temperature range 2–300 K with a Quantum Design SQUID magnetometer by using an applied magnetic field of 1000 G. Diamagnetic corrections of the constituent atoms were estimated from Pascal's constants. Experimental susceptibilities were also corrected for the temperature-independent paramagnetism [$-60 \times 10^{-6}$ $cm^3 \cdot mol^{-1}$ per copper(II)] and for the magnetization of the sample holder.

**Chemicals:** The guanazole ligand (Hdatrz) was obtained from Janssen Chimica. The 3,5-diacetylamino-1,2,4-triazole ligand (Hdaatrz) was prepared as indicated by van den Bos[56] and recrystallized from boiling water. Copper salts and solvents of high purity were commercially available and used as such.

**Synthesis of $[Cu_2(Hdatrz)_2(\mu\text{-}OH_2)(H_2O)_4(SO_4)](SO_4)\cdot 3.5H_2O$ (1):** (a) Copper(II) sulfate (6 mmol, 1.52 g) and Hdaatrz (1 mmol, 0.14 g) were mixed in water (40 mL) with continuous stirring. The resulting green solution was allowed to stand at room temperature. In about one month, a precipitate appeared which was filtered off, and the resulting solution was kept in the freezer. After about six months, large, green, hexagonal prism-shaped crystals of **1** (ca. 0.23 g, 70%) were observed together with a few smaller, lighter green crystals. Crystals of **1** were manually isolated on filter paper. One of those crystals was selected for X-ray measurements. The X-ray analysis revealed that Hdaatrz, in the presence of a high proportion of aqueous copper(II) [$Cu^{II}$:Hdaatrz is 6:1], had undergone hydrolysis to form a (guanazole)copper(II) compound. (b) Single crystals of **1** could also be obtained directly from guanazole as follows: Copper(II) sulfate (1 mmol, 0.25 g) was added to a hot aqueous solution of guanazole (1 mmol, 0.10 g, in 30 mL) with continuous stirring (so that the ratio $Cu^{II}$: guanazole is 1:1). A precipitate was immediately formed, which was separated by filtration. The resulting green solution was allowed to stand at room temperature. After ca. one month, single crystals of **1** (ca. 0.10 g, 30%) appeared together with other brownish green, needle-shaped crystals. Crystals of **1** were manually isolated on filter paper. The synthesis from guanazole (b) gave a lower yield than that from Hdaatrz (a).

**Synthesis of $[Cu_3(Hdatrz)_4(\mu\text{-}Cl)_2(H_2O)_4(SO_4)_2]\cdot 11.4H_2O$ (2):** Copper(II) sulfate (0.5 mmol, 0.13 g) was mixed with a hot aqueous solution of guanazole (1 mmol, 0.10 g, in 30 mL) with continuous stirring. A precipitate was formed immediately. Then, copper(II) chloride (3 mmol, 0.51 g) was added to the suspension, and the precipitate was redissolved (so that the ratio $Cu^{II}$:Hdatrz was 3.5:1). The resulting brownish green solution was allowed to stand in the freezer. After less than one week, large, dark green, prism-shaped crystals of **2** (ca. 0.10 g, 70%) were observed and isolated on filter paper. These crystals, however, are unstable at room temperature and turn to powder after ca. one hour after being taken out of the freezer, due to water loss (as indicated by the corresponding elemental analysis). So, all analyses and measurements had to be performed directly after isolation of the crystals.

**Analysis:** For **1**: $C_4H_{27}Cu_2N_{10}O_{16.5}S_2$ (670.56): calcd. C 7.16, H 4.06, N 20.89, S 9.56; found C 7.37, H 4.20, N 21.02, S 10.01 (on the sample synthesized by method b). Crystals of **1** from synthesis (a) were only analyzed by X-ray diffraction (Table 5). For **2**: $C_4H_{25.4}Cl_1Cu_{1.5}N_{10}O_{11.7}S_1$ (563.76): calcd. C 8.52, H 4.54, N 24.85, S 5.69; found C 8.27, H 4.85, N 24.46, S 5.70.

**Spectroscopy**

$\tilde{\nu}_{max}$ for Hdatrz: [$\upsilon(N\text{–}H)_{NH,NH_2}$] 3398 (m), 3368 (sh), 3312 (m), 3237 (w); [$\upsilon$(C=N)/ring stretching vibrations + $\delta(N\text{–}H)_{NH,NH_2}$] 1628 (vs), 1582–1563 (split,s), 1489 (s), 1417 (s); other peaks: 1346 (m), 1152 (w), 1126 (w), 1064 (m), 1015 (w), 808 (m), 727 (w), 647–616 (broad,m), 539 (w) $cm^{-1}$.

$\lambda_{max}$ (solid sample, diffuse-reflectance technique) for **1**: ca. 400, ca. 700 nm; $\tilde{\nu}_{max}$ for **1**: [$\upsilon(O\text{–}H)_{H2O}$ + $\upsilon(N\text{–}H)_{NH,NH_2}$] 3426 (m); [$\upsilon$(C=N)/ring stretching vibrations + $\delta(N\text{–}H)_{NH,NH_2}$] 1705 (sh), 1663–1644(split,s); [$\upsilon_3(SO_4)$] 1187 (sh), 1115 (vs); [$\upsilon_4(SO_4)$] 620 (m) $cm^{-1}$.

$\lambda_{max}$ (solid sample, diffuse-reflectance technique) for **2**: 415, ca. 710 nm; $\tilde{\nu}_{max}$ for **2**: [$\upsilon(O\text{–}H)_{H2O}$ + $\upsilon(N\text{–}H)_{NH,NH_2}$] 3407–3315(br,m); [$\upsilon$(C=N)/ring stretching vibrations + $\delta(N\text{–}H)_{NH,NH_2}$] 1647 (vs); [$\upsilon_3(SO_4)$] 1195 (w), 1115 (s), 1061 (sh); [$\upsilon_4(SO_4)$] 624 (m) $cm^{-1}$.

**Crystal Structure Determination:** Crystallographic data for **1** and **2** are summarized in Table 5. One light green (**1**) and one dark green (**2**) prism-shaped crystal were selected. That of **2** was mounted with Vaseline on a capillary. Throughout the experiment Cu-$K_\alpha$ (**1**) or Mo-$K_\alpha$ (**2**) was used with a graphite crystal monochromator on a Nonius Kappa-CCD [$\lambda$ = 1.54184 Å (**1**); $\lambda$ = 0.71073 Å (**2**)] single-crystal diffractometer. Unit cell dimensions were determined from the angular settings of 4343 (**1**) and 3966 (**2**) reflections with $\theta$ between 0.883° to 70.076° (**1**) and 0.998° to 27.485° (**2**), and refined with the programs HKL Denzo and Scalepack.[57] Space groups were determined to be monoclinic $C2/c$ (**1**) or triclinic $P\bar{1}$ (**2**), from systematic absences (**1**) or from structure determination (**2**). Crystal-detector distance was fixed at 30 mm, and a total of 1732 (**1**)/183 (**2**) images were collected by using the oscillation method, with scan angle per frame 2° oscillation and 5 s exposure time per image. The data collection strategy was calculated with the program Collect.[58] Structure **1** was solved by using DIRDIF;[59] structure **2** by using SIR97;[60] isotropic least-squares refinements on $F^2$ were made by using SHELX97;[61] during the final stages of refinements on $F^2$ the positional parameters and the anisotropic thermal parameters of the non-H atoms were refined. Some hydrogen atoms were located by Fourier difference synthesis and the rest were geometrically placed. H atoms on triazole N atoms were found in a Fourier map for **1** and geometrically placed in **2**. The final difference Fourier map for **1** showed the highest peaks of 2.055 e $A^{-3}$ at 1.41 Å from O(24) and of 1.89 e $A^{-3}$ at 1.25 Å from O(21); the rest of them were lower than 0.67 e $A^{-3}$, the deepest hole being –1.109 e $A^{-3}$ at 0.62 Å from Cu(1). The same map for **2** showed the highest peak of 1.044 e $A^{-3}$ at 0.7 Å from O(5w) and the deepest hole of –0.723 e $A^{-3}$ at 0.14 Å from H(6a). Figure 1 and Figure 2, made with ORTEP,[62] show the atomic numbering schemes. Atomic scattering factors were taken from ref.[63]. Geometrical calculations were made with PARST.[64] CCDC-293618 (**1**) and CCDC-293619 (**2**) contain the supplementary crystallographic data for this paper. These data can be obtained free of charge from The Cambridge Crystallographic Data Centre via www.ccdc.cam.ac.uk/data_request/cif.

 © 2006 Wiley-VCH Verlag GmbH & Co. KGaA, Weinheim 

Table 5. Crystallographic data and structure refinement for compounds **1** and **2**.[a]

| Compound | **1** | **2** |
|---|---|---|
| Empirical formula | $C_4H_{27}Cu_2N_{10}O_{16.5}S_2$ | $C_4H_{25.4}Cu_{1.5}N_{10}O_{11.7}S_1Cl_1$ |
| Formula weight | 670.56 | 563.76 |
| Temperature [K] | 293(2) | 293(2) |
| Wavelength [Å] | 1.54184 | 0.71073 |
| Crystal system, space group | monoclinic, *C*2/c | triclinic, $P\bar{1}$ |
| *a* [Å] | 19.0944(4) | 10.2780(2) |
| *b* [Å] | 21.3853(4) | 10.5110(2) |
| *c* [Å] | 14.4018(3) | 11.4020(2) |
| *α* [°] | | 77.6520(12) |
| *β* [°] | 129.8510(10) | 63.3760(10) |
| *γ* [°] | | 81.7600(10) |
| Volume [Å$^3$] | 4514.78(16) | 1074.11(3) |
| *Z*, calculated density [Mg/m$^3$] | 8, 1.973 | 2, 1.743 |
| Absorption coefficient [mm$^{-1}$] | 4.962 | 1.791 |
| *F*(000) | 2744 | 579 |
| Crystal size [mm] | $0.20 \times 0.15 \times 0.08$ | $0.32 \times 0.25 \times 0.20$ |
| *θ* range for data collection [°] | 3.66 to 69.54 | 2.03 to 27.48 |
| Index ranges | $0 \le h \le 23$, $0 \le k \le 25$, $-17 \le l \le 13$ | $-13 \le h \le 13$, $-13 \le k \le 12$, $-14 \le l \le 11$ |
| Reflections collected/unique | 4251/4251 | 7843/4879 |
| Refinement method | full-matrix least squares on $F^2$ | full-matrix least squares on $F^2$ |
| Data/restraints/parameters | 4251/25/416 | 4879/2/296 |
| Goodness-of-fit on $F^2$ | 1.048 | 1.068 |
| Final *R* indices [$I > 2\sigma(I)$] ($R_1$, $wR_2$) | 0.0597, 0.1612 | 0.0451, 0.1225 |
| *R* indices (all data) ($R_1$, $wR_2$) | 0.0643, 0.1676 | 0.0620, 0.1358 |
| Largest diff. peak and hole [e·Å$^{-3}$] | 2.055 and –1.109 | 1.044 and –0.723 |

[a] GOOF = $\{\Sigma[w(F_o^2 - F_c^2)^2]/(n-p)\}^{1}/_{2}$, $R_1 = \Sigma||F_o| - |F_c||/\Sigma|F_o|$, $wR_2 = \{\Sigma[w(F_o^2 - F_c^2)^2]/\Sigma[w(F_o^2)^2]\}^{1}/_{2}$, $w = 1/[\sigma^2(F_o^2) + (aP)^2 + bP]$, where $P = [\max(F_o^2,0) + 2F_c^2]/3$; $a = 0.1163$, $b = 18.2879$ for **1** and $a = 0.0678$, $b = 2.2442$ for **2**.

## Acknowledgments

Authors E. A., S. F., J. B., and M. L.-G. are grateful to MCyT (grant CTQ2004–03735/BQU), and authors H. R.-P. and S. G.-G. to MCyT (grant BQU2003–05093) and FICYT (grant PR-01-GE-4) for financial support.

[1] J. G. Haasnoot, *Coord. Chem. Rev.* **2000**, *200–202*, 131.
[2] a) M. H. Klingele, S. Brooker, *Coord. Chem. Rev.* **2003**, *241*, 119; b) U. Beckmann, S. Brooker, *Coord. Chem. Rev.* **2003**, *245*, 17.
[3] J. P. Zhang, Y.-Y. Lin, X.-C. Huang, X.-M. Chen, *J. Am. Chem. Soc.* **2005**, *127*, 5495.
[4] P. Gütlich, A. Hauser, H. Spiering, *Angew. Chem. Int. Ed. Engl.* **1994**, *33*, 2024.
[5] L. G. Lavrenova, S. V. Larionov, *Koord. Khim.* **1998**, *24*, 403.
[6] P. J. van Koningsbruggen, *Top. Curr. Chem.* **2004**, *233*, 123.
[7] M. Klingele, B. Moubaraki, J. D. Cashion, K. S. Murray, S. Brooker, *Chem. Commun.* **2005**, 987.
[8] A. C. Fabretti, *J. Crystallogr. Spectrosc. Res.* **1992**, *22*, 523.
[9] H. O. Desseyn, A. C. Fabretti, W. Malavasi, *J. Crystallogr. Spectrosc. Res.* **1990**, *20*, 355.
[10] A. C. Fabretti, A. Giusti, R. Sessoli, *Inorg. Chim. Acta* **1993**, *205*, 53.
[11] S. R. Grap, L. G. Kuz′mina, O. Y. Burtseva, M. A. Porai-Koshits, A. P. Kurbakova, I. A. Efimenko, *Zh. Neorg. Khim.* **1991**, *36*, 1427.
[12] S. R. Grap, L. G. Kuz′mina, M. A. Porai-Koshits, A. P. Kurbakova, I. A. Efimenko, *Koord. Khim.* **1993**, *19*, 566.
[13] L. Antolini, A. C. Fabretti, D. Gatesschi, A. Giusti, R. Sessoli, *Inorg. Chem.* **1991**, *30*, 4858.
[14] L. Antolini, A. C. Fabretti, D. Gatesschi, A. Giusti, R. Sessoli, *Inorg. Chem.* **1990**, *29*, 143.
[15] T. B. Brill, A. L. Rheingold, M. B. Allen, *Private Communication, CCD.* **1996**, NADHAB.
[16] Y. B. Brill, A. L. Rheingold, A. M. Allen, *Private Communication, CCD.* **1996**, NADPAJ.
[17] Recently, during the process of the revision of this manuscript, a 3D $Cu^I$–guanazole compound, synthesized under solvothermal conditions, has been structurally characterized: $[(H_3O)_2(H_2O)_4][\{Cu_6(datrz)_6\}\{(Cu_4I_4)_2O\}]$; see Q. G. Zhai, C.-Z. Lou, S.-M. Chen, X.-J. Xu, W.-B. Yang, *Inorg. Chem. Commun.* **2006**, *9*, 819.
[18] P. M. Slangen, P. J. van Koningsbruggen, K. Goubitz, J. G. Haasnoot, J. Reedijk, *Inorg. Chem.* **1994**, *33*, 1121.
[19] S. Ferrer, P. J. van Koningsbruggen, J. G. Haasnoot, J. Reedijk, H. Kooijman, A. L. Spek, L. Lezama, A. M. Arif, J. S. Miller, *J. Chem. Soc., Dalton Trans.* **1999**, 4269.
[20] L. Yi, B. Zhao, P. Cheng, D.-Z. Liao, S.-P. Yan, Z.-H. Jiang, *Inorg. Chem.* **2004**, *43*, 33.
[21] After submission of this manuscript, the authors were informed of three new dinuclear structures of $Ni^{II}$ with one water and two triazole bridges: a) J.-H. Zhou, R.-M. Cheng, Y. Song, Y.-Z. Li, Z. Yu, X.-T. Chen, X.-Z. You, *Polyhedron* **2006**, *25*, 2426; b) P. Ren, B. Ding, W. Shi, Y. Wang, T. Lu, P. Cheng, *Inorg. Chim. Acta* **2006**, *359*, 3824.
[22] P. J. van Koningsbruggen, J. W. van Hal, R. A. G. de Graaff, J. G. Haasnoot, J. Reedijk, *J. Chem. Soc., Dalton Trans.* **1993**, 2163.
[23] S. F. Keij, Ph. D. Thesis, Leiden University, The Netherlands, **1990**.
[24] R. Prins, M. Biagini-Cingi, M. Drillon, R. A. G. de Graff, J. Haasnoot, A.-M. Manotti-Lanfredi, P. Rabu, J. Reedijk, F. Ugozzoli, *Inorg. Chim. Acta* **1996**, *248*, 35.
[25] J.-C. Liu, D.-G. Fu, J.-Z. Zhuang, C.-Y. Duan, X.-Z. You, *J. Chem. Soc., Dalton Trans.* **1999**, 2337.
[26] a) W. Vreugdenhil, J. G. Haasnoot, J. Reedijk, J. S. Wood, *Inorg. Chim. Acta* **1990**, *167*, 109; b) W. Vreugdenhil, Ph. D. Thesis, Leiden University, The Netherlands, **1987**.

 © 2006 Wiley-VCH Verlag GmbH & Co. KGaA, Weinheim 

[27] Y. Garcia, P. J. van Koningsbruggen, G. Bravic, P. Guionneau, D. Chasseau, G. L. Cascarano, J. Moscovici, K. Lambert, A. Michalowicz, O. Kahn, *Inorg. Chem.* **1997**, *36*, 6357.
[28] F. J. Rietmeijer, G. A. van Albada, R. A. G. de Graaff, J. G. Haasnoot, J. Reedijk, *Inorg. Chem.* **1985**, *24*, 3597.
[29] F. J. Rietmeijer, J. G. Haasnoot, A. J. Den Hartog, J. Reedijk, *Inorg. Chim. Acta* **1986**, *113*, 147.
[30] Q. Zhao, H. Li, A. Chen, R. Fang, *Inorg. Chim. Acta* **2002**, *336*, 142.
[31] G. A. van Albada, R. A. G. de Graaff, J. Haasnoot, J. Reedijk, *Inorg. Chem.* **1984**, *23*, 1404.
[32] J.-C. Liu, Y. Song, J.-Z. Zhuang, X.-Z. You, X.-Y. Huang, Z.-X, *Jiegou Huaxue* **2000**, *19*, 81.
[33] J.-C. Liu, Y. Xu, C.-Y. Duan, S.-L. Wang, F.-L. Liao, J.-Z. Zhuang, X.-Z. You, *Inorg. Chim. Acta* **1999**, *295*, 229.
[34] J. A. J. Jarvis, *Acta Crystallogr.* **1962**, *15*, 964.
[35] R. Prins, P. J. Birker, J. G. Haasnoot, G. C. Verschoor, J. Reedijk, *Inorg. Chem.* **1985**, *24*, 4128.
[36] W. M. E. Koomen-van-Oudenniel, R. A. G. de Graaff, J. G. Haasnoot, R. Prins, J. Reedijk, *Inorg. Chem.* **1989**, *28*, 1128.
[37] P. J. van Koningsbruggen, J. G. Haasnoot, R. A. G. de Graaff, J. Reedijk, S. Slingerland, *Acta Crystallogr., Sect. C: Cryst. Struct. Commun.* **1992**, *48*, 1923.
[38] P. M. Slangen, P. J. van Koningsbruggen, J. G. Haasnoot, J. Jansen, S. Gorter, J. Reedijk, H. Kooijman, W. J. J. Smeets, A. L. Spek, *Inorg. Chim. Acta* **1993**, *212*, 289.
[39] P. J. van Koningsbruggen, J. G. Haasnoot, H. Kooijman, J. Reedijk, A. L. Spek, *Inorg. Chem.* **1997**, *36*, 2487.
[40] O. Castillo, U. García-Couceiro, A. Luque, Juan P. García-Terán, P. Román, *Acta Crystallogr. Sect. E: Struct. Rep. Online* **2004**, *60*, m9-m11, DOI: 10.1107/S1600536803027119.
[41] M. H. Klingele, P. D. Boyd, B. Moubaraki, K. S. Murray, S. Brooker, *Eur. J. Inorg. Chem.* **2005**, 910.
[42] M. H. Klingele, P. D. Boyd, B. Moubaraki, K. S. Murray, S. Brooker, *Eur. J. Inorg. Chem.* **2006**, 573.
[43] For the first example of a structurally characterized triazolate-containing *macrocyclic* copper compound, see: C. V. Depree, U. Beckmann, K. Heslop, S. Brooker, *Dalton Trans.* **2003**, 3071.
[44] U. Beckmann, S. Brooker, C. V. Depree, J. D. Ewing, B. Moubaraki, K. S. Murray, *Dalton Trans.* **2003**, 1308.
[45] G. Vos, R. A. G. de Graaff, J. Haasnoot, A. M. van der Kraan, P. de Vaal, J. Reedjik, *Inorg. Chem.* **1984**, *23*, 2905.
[46] Y. Journaux, J. Sletten, O. Kahn, *Inorg. Chem.* **1986**, *25*, 439.
[47] R. Veit, J.-J. Girerd, O. Kahn, F. Robert, Y. Jeannin, *Inorg. Chem.* **1986**, *25*, 4175.
[48] O. Kahn, in *Magneto-Structural Correlations in Exchange Coupled Systems* (Eds.: D. Gatteschi, O. Kahn, R. D. Willet), NATO Advanced Study Institute Series, Reidel, Dordrecht, **1984**, vol. C140.
[49] V. K. Kumar, G. Keresztury, T. Sundius, R. J. Xavier, *Spectrochim. Acta, Part A* **2005**, *61*, 261.
[50] K. Nakamoto in *Infrared and Raman Spectra of Inorganic and Coordination Compounds: Part B: Applications in Coordination, Organometallic and Bioinorganic Chemistry*, 5th ed., John Wiley and Sons, New York, **1997**.
[51] B. J. Hathaway, D. E. Billing, *Coord. Chem. Rev.* **1970**, *5*, 143.
[52] J. Reedijk, D. Knetsch, B. Nieuwenhuisje, *Inorg. Chim. Acta* **1971**, *5*, 568.
[53] K. Nonoyama, H. Ojima, M. Nonoyama, *Inorg. Chim. Acta* **1984**, *84*, 13.
[54] J. R. Wasson, C.-I. Shyr, C. Trapp, *Inorg. Chem.* **1968**, *7*, 469.
[55] L. Banci, A. Bencini, D. Gatteschi, *Inorg. Chem.* **1983**, *22*, 2681.
[56] B. G. van den Bos, *Recl. Trav. Chim. Pays-Bas* **1960**, *79*, 836.
[57] Z. Otwinowski, W. Minor, *DENZO-SCALEPACK–Processing of X-ray Diffraction Data Collected in Oscillation Mode, Methods in Enzymology, Volume 276: Macromolecular Crystallography, Part A* (Eds.: C. W. Carter Jr., R. M. Sweet), Academic Press, New York, **1997**, pp. 307–326.
[58] *COLLECT*, Nonius BV, Delft, The Netherlands, **2000**.
[59] P. T. Beurskens, G. Beurskens, R. de Gelder, S. García-Granda, R. O. Gould, R. Israel, J. M. M. Smits, *The DIRDIF-99 Program System – Technical Report of the Crystallography Laboratory*, University of Nijmegen, The Netherlands, **1999**.
[60] *SIR97*: A. Altomare, M. C. Burla, M. Camalli, G. L. Cascarano, C. Giacovazzo, A. Guagliardi, A. G. G. Moliterni, G. Polidori, R. Spagna, *J. Appl. Crystallogr.* **1999**, *32*, 115.
[61] G. M. Sheldrick, *SHELX97–Programs for Crystal Structure Analysis* (Release 97–2), University of Göttingen, Germany, **1997**.
[62] *ORTEP3 for Windows*:L. J. Farrugia, *J. Appl. Crystallogr.* **1997**, *30*, 565.
[63] *International Tables for X-ray Crystallography* (Ed.: T. Hahn), Kluwer Academic Publishers, Dordrecht, The Netherlands, **1995**, vol. A.
[64] a) M. Nardelli, *Comput. Chem.* **1983**, *7*, 95; b) M. Nardelli, *Comput. Chem.* **1995**, *28*, 659.

Received: July 31, 2006
Published Online: November 3, 2006

 © 2006 Wiley-VCH Verlag GmbH & Co. KGaA, Weinheim 

DOI: 10.1002/ejic.200600720

# A DFT Study on the Electronic and Redox Properties of $[PW_{11}O_{39}(ReN)]^{n-}$ ($n$ = 3, 4, 5) and $[PW_{11}O_{39}(OsN)]^{2-}$

Li-Kai Yan,[a] Zhuo Dou,[a] Wei Guan,[a] Shao-Qing Shi,[a] and Zhong-Min Su*[a]

**Keywords:** Electronic properties / DFT / Nitrido-functionalized / Polyoxometalates / Redox properties

DFT calculations were carried out to investigate the electronic and redox properties of nitrido-functionalized polyoxometalate species, $[PW_{11}O_{39}(ReN)]^{n-}$ ($n$ = 3, 4, 5) and $[PW_{11}O_{39}(OsN)]^{2-}$. The rhenium- and osmium-nitrido effectively modify the electronic properties. The LUMOs in fully oxidized $[PW_{11}O_{39}(ReN)]^{3-}$ and $[PW_{11}O_{39}(OsN)]^{2-}$ are mainly concentrated on the Re and Os centers. The high-valent transition metals Re and Os modify the components and energies of the LUMO. The LUMO energies of $[PW_{11}O_{39}(ReN)]^{3-}$ and $[PW_{11}O_{39}(OsN)]^{2-}$ are lower than that of related Keggin $[PW_{12}O_{40}]^{3-}$. In addition, Re centers will prefer to accept the electrons in the first and second reduced process of fully oxidized $[PW_{11}O_{39}(ReN)]^{3-}$.

(© Wiley-VCH Verlag GmbH & Co. KGaA, 69451 Weinheim, Germany, 2006)

## Introduction

Polyoxometalates (POMs) are anionic clusters of discrete structure commonly based on molybdenum or tungsten oxides.[1–3] Most POMs possess an extensive and reversible redox chemistry and some contain multiple unpaired d-electrons that make them useful in several fields including catalysis, material science, and magnetochemistry.

One of the important applications of POMs is based on their potential to act as an electron acceptor, which leads to the possibility of the formation of charge-transfer or electron donor-acceptor materials with interesting electronic and magnetic properties.[4,5] Over the past few years, research on POMs has greatly expanded to investigate functionalized POMs by the incorporation or coordination of organic or organometallic moieties to produce novel systems.[6–9] The modification and functionalization of POMs have provided the means to more fully exploit these desirable attributes. Rhenium is known to incorporate into Keggin structures by virtue of its appropriate radius and ability to form short terminal M=O bonds.[10] Three nitrido-functionalized polyoxometalate species, $(n\text{Bu}_4\text{N})_4[PW_{11}O_{39}(OsN)]$, $(n\text{Bu}_4\text{N})_4[PW_{11}O_{39}(ReN)]$, and $(n\text{Bu}_4\text{N})_3[PW_{11}O_{39}(ReN)]$, which feature the incorporation of $[Os^{VI}{\equiv}N]^{3+}$, $[Re^{VI}{\equiv}N]^{3+}$, and $[Re^{VII}{\equiv}N]^{4+}$ fragments into the framework of a Keggin-type heteropolyanion were reported by Maatta.[11] It is the first time that rhenium- and osmium-nitrido were inserted into the polyoxometalate. Several questions drew our attention. First, how does the rhenium- or osmium-nitrido modify the structural and electronic properties? Second, how are the redox properties of POMs modified by the rhenium-nitrido segment? Third, does the rhenium atom prefer to accept an electron when the $[PW_{11}O_{39}(ReN)]^{3-}$ is reduced? Following our investigations of the electronic properties, bonding nature, stabilities, and nonlinear optical properties of POMs,[12–16] density functional theory (DFT), which has been proven to be a significant tool for understanding and rationalizing the electronic and magnetic properties of polyanions,[17–26] was employed to pursue the questions mentioned above. Our main objective was to investigate the effect of high-valent metal nitrido on the electronic and redox properties of POMs.

### Methodology

All calculations reported in this work were carried out with the ADF2005.01 program.[27] The local density approximation (LDA) characterized by the Vosko–Wilk–Nusair (VWN)[28] parameterization for correlation was used. Becke[29]and Perdew[30] gradient corrections were used for the exchange and correlation energy, respectively. Triple-ζ plus polarization Slater basis sets were used to describe the electrons of main group elements (O, C, H) and the valence electrons of all transitional-metal atoms (Re, Os, W). The internal or core electrons (1s–4d for Re, Os, W) were frozen and described by single Slater functions. The relativistic effects were taken into account by means of the zero-order regular approximation (ZORA).[31] The integration parameter in the molecular calculations, which determines the precision of the numerical integral, was set to 5.0. The default optimization convergence criteria in the ADF were used.

[a] Institute of Functional Material Chemistry, Department of Chemistry, Northeast Normal University,
Changchun 130024, P.R. China
Fax: +86-431-5684009
E-mail: zmsu@nenu.edu.cn

Supporting information for this article is available on the WWW under http://www.eurjic.org or from the author.

 © 2006 Wiley-VCH Verlag GmbH & Co. KGaA, Weinheim 

For purposes of comparison, calculations were also carried out on $[PW_{12}O_{40}]^{3-}$. A short-hand notation is used for the polyanions, without oxygen atoms and anion charge, and it specifies the number of blue electrons as well as the substituted transition metal oxidation states (e.g. $[PW_{12}O_{40}]^{3-}$ = $PW_{12}$, $[PW_{11}O_{39}(ReN)]^{3-}$ = $PW_{11}ReN$, and $[PW_{11}O_{39}(ReN)]^{4-}$ = $PW_{11}ReN1e$, where e specifies the electrons which the polyanion accepted).

## Results and Discussion

### The Effect of the Rhenium- or Osmium-Nitrido Segment on Geometrical Structure

The Keggin anion is made of an assembly of 12 $MO_6$ octahedrons sharing their corners or edges with a central $XO_4$ tetrahedron. The metal–oxygen bonds in the Keggin framework can be divided into three sets according to whether their oxygen atoms are tetrahedral ($O_a$), bridging ($O_b$), or terminal ($O_t$). From the point-of-view of structure, the transition metals Re and Os are inserted into a lacunary position of $PW_{12}$. At the same time, Re and Os link to the nitrogen atom instead of the terminal oxygen atom ($O_t$). Figure 1 shows the optimized structure of $PW_{11}ReN$, and other structures in this article are all similar to it.

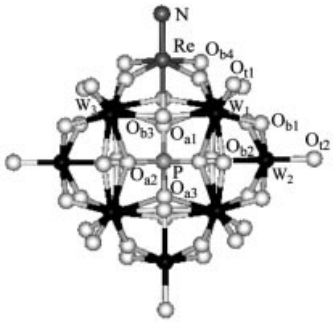


Figure 1. The calculation model $PW_{11}ReN$.

Some selected bond lengths are listed in Table 1. Compared with $PW_{12}$, the bonds in $PW_{11}ReN$ are lengthened, while the bonds in $PW_{11}OsN$ are shortened. The calculated atomic radii[32] of tungsten, rhenium, and osmium are 1.93, 1.88, and 1.85 Å, respectively. The $PW_{11}OsN$ is contracted when the osmium-nitrido segment substitutes the W=O unit because the radius of $Os^{VIII}$ is smaller than that of $W^{VI}$. Although the radius of $Re^{VII}$ is slightly smaller than that of $W^{VI}$, the cluster size of $PW_{11}ReN$ is enlarged. This may be due to the slightly weak interaction between Re and its adjacent atoms compared with related bonds in $PW_{12}$. As Poblet demonstrated that the reduction of a fully oxidized anion is accompanied by an expansion of the geometry,[33] the bonds in single- and double-electron reduced polyanions of $PW_{11}ReN$ are elongated. So, the reduced polyanions are loosened by adding reduced electrons. The lengthening of the bond would lead to a weakening of the bond strength, and then the electronic properties would be changed.

Table 1. Selected bond lengths [Å] of systems.

| | $PW_{12}$ | $PW_{11}ReN$ | $PW_{11}ReN1e$ | $PW_{11}ReN2e$ | $PW_{11}OsN$ |
|---|---|---|---|---|---|
| $W_1$–$O_{b1}$ | 1.938 | 1.941 | 1.958 | 1.969 | 1.922 |
| $W_1$–$O_{b2}$ | 1.938 | 1.943 | 1.979 | 1.975 | 1.909 |
| $W_3$–$O_{b3}$ | 1.932 | 1.932 | 1.936 | 1.936 | 1.936 |
| $W_1$–$O_{t1}$ | 1.725 | 1.726 | 1.735 | 1.746 | 1.720 |
| $W_2$–$O_{t2}$ | 1.725 | 1.726 | 1.734 | 1.744 | 1.719 |
| P–$O_{a1}$ | 1.555 | 1.554 | 1.553 | 1.553 | 1.562 |
| P–$O_{a2}$ | 1.555 | 1.556 | 1.558 | 1.560 | 1.555 |
| P–$O_{a3}$ | 1.555 | 1.558 | 1.561 | 1.563 | 1.555 |
| W(Re, Os)–P | 3.608 | 3.619 | 3.654 | 3.655 | 3.573 |
| Re(Os)–N | | 1.678 | 1.680 | 1.686 | 1.676 |
| Re(Os)–$O_{b4}$ | | 1.930 | 1.982 | 1.985 | 1.900 |

### Electronic Properties of Fully Oxidized $PW_{11}ReN$ and $PW_{11}OsN$

For fully oxidized polyanions, one of the remarkable properties concerns redox behavior. The molecular orbital distribution will give reasonable information about the redox properties of $PW_{11}Re$ and $PW_{11}Os$. In order to investigate the effect of the rhenium- or osmium-nitrido segment on the electronic properties of polyanions, the frontier molecular orbitals (FMO) of $PW_{12}$, $PW_{11}ReN$, and $PW_{11}OsN$ are compared. For Keggin anion $PW_{12}$, the ground-state configuration is typical of a fully oxidized polyanion for which the highest molecular orbital (HOMO) delocalizes over oxo-ligands, and the lowest molecular orbital (LUMO) delocalizes over the d-shells of tungsten atoms with some antibonding participation of oxygen orbitals (Figure 2).[24] The LUMO is a doubly degenerate orbital of symmetry $e$, and the LUMO+1 is a triply degenerate orbital of symmetry $t_1$.

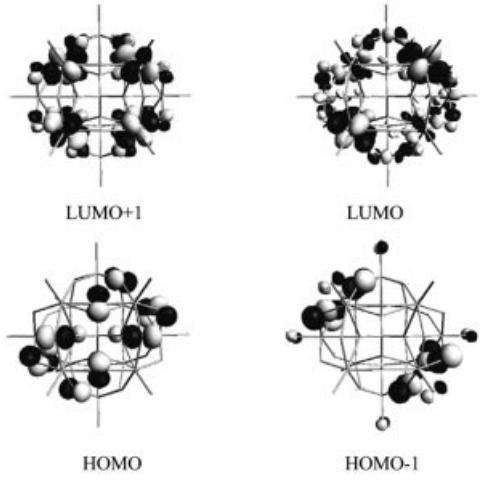


Figure 2. The molecular orbitals of $PW_{12}$.

The doubly degenerate HOMO and LUMO in $PW_{12}$ split into two orbitals of symmetry $a'$ and $a''$ in $PW_{11}ReN$ and $PW_{11}OsN$. The HOMO in $PW_{11}ReN$ is mainly delocalized over the bridge oxygen atoms, but the nitrogen atom has a contribution (6.58%; Figure 3). The LUMO is quite different from that of $PW_{12}$ and is mainly localized on the Re atom (39.76%), although there is some contribution from

 © 2006 Wiley-VCH Verlag GmbH & Co. KGaA, Weinheim 

the tungsten atoms (16.46%). The LUMO+1 in $PW_{11}ReN$ concentrates on the tungsten and bridge oxygen atoms, which is similar to the LUMO in $PW_{12}$. It can be proposed that the rhenium-nitrido segment mainly modifies the unoccupied orbitals and the redox properties would be modified as the redox property of a polyanion depends on the energy and compositions of the LUMO. The LUMO energy and the HOMO–LUMO energy gap are lower than that of $PW_{12}$ (Figure 4), so the electron transition between HOMO and LUMO is much easier.

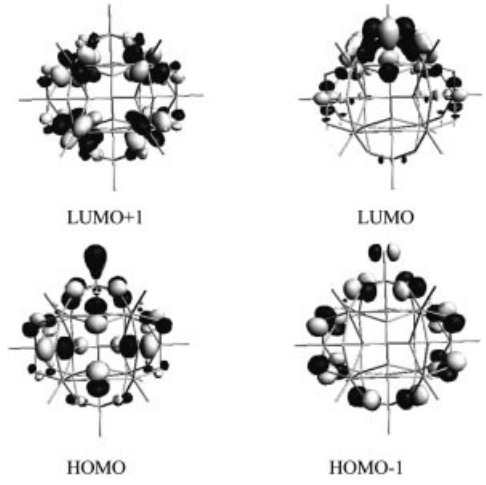


Figure 3. The molecular orbitals of $PW_{11}ReN$.

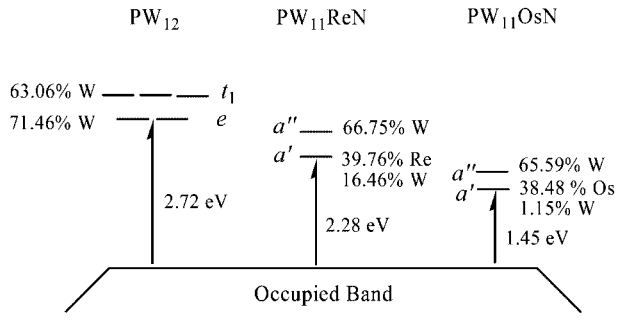


Figure 4. The energy level of $PW_{12}$, $PW_{11}Re$, and $PW_{11}Os$.

Let us now consider the osmium–nitrido substituted derivative $PW_{11}OsN$. The FMOs are presented in Figure 5. Here, the situation is somewhat different. The HOMO and HOMO-1 for $PW_{11}OsN$ are similar to $PW_{12}$, whereas the lowest metal orbitals are mainly localized on osmium (38.48%), and the contribution of tungsten atoms is only 1.15%. The d-osmium orbitals are lower in energy than the tungsten orbitals and strong competition between the osmium and tungsten orbitals would occur; $PW_{11}OsN$ tends to have a lower HOMO–LUMO energy gap and LUMO energy as presented in Figure 4.

The question we are now concerned with is whether tungsten or high-valent transition-metal Re or Os accept the extra electrons when the cluster is reduced. Taking $PW_{11}Re$ as an example, we investigated the reduction process in detail. It is known that the redox properties depend on the energy and composition of the LUMO, as the

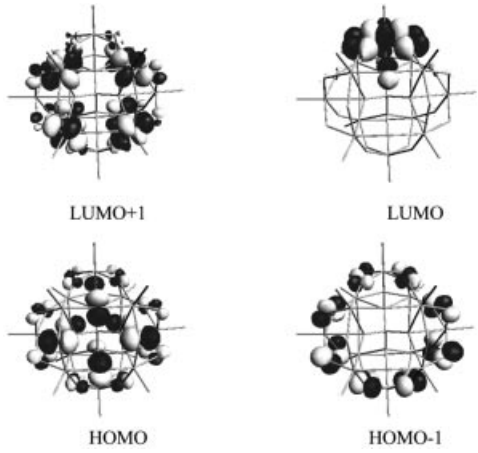


Figure 5. The molecular orbitals of $PW_{11}OsN$.

LUMO formally delocalizes over the metal atoms, which determine the redox properties of POMs.[21]

The LUMO of $PW_{11}Re$ is composed of 39.76% Re and 16.46%W contributions. It is more likely that Re will prefer to accept extra electrons when the cluster is reduced. In order to investigate the reduced center, the reduced species $PW_{11}Re1e$ and $PW_{11}Re2e$ were calculated. Table 2 shows the spin density for two reduced species of $PW_{11}Re$, which indicates that the extra electron in the monoreduced $PW_{11}Re1e$ localizes on the Re center with a 0.67 spin alpha electron. This suggests that $PW_{11}Re^{VII}$ is reduced to $PW_{11}Re^{VI}$ when the cluster accepts one electron.

Table 2. Spin density (α-β) for $PW_{11}Re1e$ and $PW_{11}Re2e$.

| | $PW_{11}ReN1e$ | $PW_{11}ReN2e$ |
|---|---|---|
| Re | 0.6700 | 0.6533 |
| W | 0.0008~0.0456 | 0.0081~0.1618 |

The LUMO in monoreduced $PW_{11}Re1e$ has a participation of Re orbitals (35.23%), and the contribution of tungsten increases to 27.36% (Figure 6). The spin density analysis indicates that 65% of the spin density is localized over the Re center and the rest of the spin density is delocalized over the polar tungsten atoms. The HOMO is entirely localized over the oxygen atoms. The additional electron mainly goes to the sphere of Re and $PW_{11}Re^{VI}N$ would be reduced to $PW_{11}Re^{V}N$. In addition, the LUMO in $PW_{11}Re2e$ has a little participation of the Re orbitals (1.91%). So, this suggests that the first and second reduced process of $PW_{11}ReN$ is $Re^{VII} \rightarrow Re^{VI} \rightarrow Re^{V}$, which is in agreement with the experimental investigation.[11]

## Conclusions

The effect of rhenium or osmium-nitrido on the electronic and redox properties of POMs was investigated by means of density functional calculations. The above results can be summarized in three principal conclusions: (1) Re and Os mainly modified the unoccupied orbitals of $[PW_{11}O_{39}(ReN)]^{3-}$ and $[PW_{11}O_{39}(OsN)]^{2-}$, especially the

 © 2006 Wiley-VCH Verlag GmbH & Co. KGaA, Weinheim 

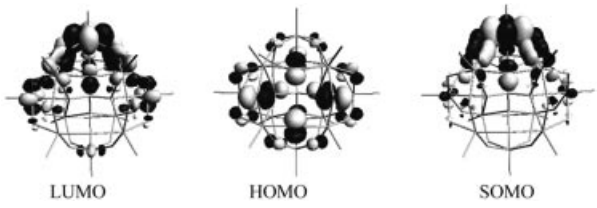


Figure 6. The molecular orbitals of $PW_{11}ReN1e$.

LUMO. The LUMO of fully oxidized $[PW_{11}O_{39}(ReN)]^{3-}$ is quite different from that of $[PW_{12}O_{40}]^{3-}$ and is localized on the Re atom, and the tungsten atoms also contribute to some extent. The LUMO of $[PW_{11}O_{39}(OsN)]^{2-}$ is mainly localized on osmium, and the contribution from the tungsten atoms is quite small. (2) Compared to Keggin $[PW_{12}O_{40}]^{3-}$, the LUMO energy in $[PW_{11}O_{39}(ReN)]^{3-}$ and $[PW_{11}O_{39}(OsN)]^{2-}$ is lower than that of $[PW_{12}O_{40}]^{3-}$, and the electron transition between HOMO and LUMO of nitrido-functionalized polyoxometalate species $[PW_{11}O_{39}(OsN)]^{2-}$ and $[PW_{11}O_{39}(ReN)]^{3-}$ is much easier compared with that of Keggin $[PW_{12}O_{40}]^{3-}$. (3) The Re center prefers to accept the extra electrons in the first and second reduced process of $PW_{11}ReN$, so the reduced process is $[PW_{11}O_{39}(Re^{VII}N)]^{3-} \rightarrow [PW_{11}O_{39}(Re^{VI}N)]^{4-} \rightarrow [PW_{11}O_{39}(Re^{V}N)]^{5-}$.

**Supporting Information** (see footnote on the first page of this article): Cartesian coordinates for the BP/TZP optimized $[PW_{11}O_{39}(ReN)]^{3-}$, $[PW_{11}O_{39}(ReN)]^{4-}$, $[PW_{11}O_{39}(ReN)]^{5-}$, $[PW_{11}O_{39}(OsN)]^{2-}$, and $[PW_{12}O_{40}]^{3-}$ structures.

## Acknowledgments

The authors gratefully acknowledge the financial support from the National Natural Science Foundation of China (Project Nos. 20573016 and 20373009) and the Science Foundation for Young Teachers of Northeast Normal University (111494017). We are also pleased to thank Yuhe Kan for computational support.

[1] M. T. Pope, *Heteropoly and Isopoly Oxometalates*, Springer, Berlin, **1983**.
[2] M. T. Pope, A. Müller, *Angew. Chem. Int. Ed. Engl.* **1991**, *30*, 34–48.
[3] C. L. Hill, *Chem. Rev.* **1998**, *98*, 1–2.
[4] T. Yamase, *Chem. Rev.* **1998**, *98*, 307–326.
[5] E. Coronado, C. J. Gómez-García, *Chem. Rev.* **1998**, *98*, 273–296.
[6] L. H. Bi, M. H. Dickman, U. Kortz, I. Dix, *Chem. Commun.* **2005**, 3962–3964.
[7] L. Xu, M. Lu, B. B. Xu, Y. G. Wei, Z. H. Peng, D. R. Powell, *Angew. Chem. Int. Ed.* **2002**, *41*, 4129–4132.
[8] R. Neumann, *Prog. Inorg. Chem.* **1998**, *47*, 317–320.
[9] X. Zhang, K. Sasaki, C. L. Hill, *J. Am. Chem. Soc.* **1996**, *118*, 4809–4816.
[10] M. J. Abrams, C. E. Costello, S. N. Shaikh, J. Zubieta, *Inorg. Chim. Acta* **1991**, *180*, 9–11.
[11] H. Kwen, S. Tomlinson, E. A. Maatta, C. Dablemont, R. Thouvenot, A. Proust, P. Gouzerh, *Chem. Commun.* **2002**, 2970–2971.
[12] L. K. Yan, Z. M. Su, W. Guan, M. Zhang, G. H. Chen, L. Xu, E. B. Wang, *J. Phys. Chem. B* **2004**, *108*, 17337–17343.
[13] L. K. Yan, G. C. Yang, W. Guan, Z. M. Su, R. S. Wang, *J. Phys. Chem. B* **2005**, *109*, 22332–22336.
[14] W. Guan, L. K. Yan, Z. M. Su, E. B. Wang, X. H. Wang, *Int. J. Quantum Chem.* **2006**, *106*, 1860–1864.
[15] L. K. Yan, Z. M. Su, K. Tan, M. Zhang, L. Y. Qu, R. S. Wang, *Int. J. Quantum Chem.* **2005**, *105*, 37–42.
[16] W. Guan, L. K. Yan, Z. M. Su, S. X. Liu, M. Zhang, *Inorg. Chem.* **2005**, *44*, 100–107.
[17] M. M. Rohmer, M. Bénard, J. P. Blaudeau, J. M. Maestre, J. M. Poblet, *Coord. Chem. Rev.* **1998**, *178–180*, 1019–1049.
[18] M. M. Rohmer, J. Devemy, R. Wiest, M. Benard, *J. Am. Chem. Soc.* **1996**, *118*, 13007–13014.
[19] J. M. Maestre, J. M. Poblet, C. Bo, N. C. Pastor, P. G. Romero, *Inorg. Chem.* **1998**, *37*, 3444–3446.
[20] X. Lopez, J. M. Maestre, C. Bo, J. M. Poblet, *J. Am. Chem. Soc.* **2001**, *123*, 9571–9576.
[21] J. M. Maestre, X. Lopez, C. Bo, J. M. Poblet, N. Casan-Pastor, *J. Am. Chem. Soc.* **2001**, *123*, 3749–3758.
[22] J. M. Maestre, X. Lopez, C. Bo, J. M. Poblet, *Inorg. Chem.* **2002**, *41*, 1883–1888.
[23] J. M. Poblet, X. Lopez, C. Bo, *Chem. Soc. Rev.* **2003**, *32*, 297–308.
[24] X. López, C. Bo, J. M. Poblet, *J. Am. Chem. Soc.* **2002**, *124*, 12574–12582.
[25] A. J. Bridgeman, G. Cavigliasso, *Inorg. Chem.* **2002**, *41*, 3500–3507.
[26] A. J. Bridgeman, G. Cavigliasso, *J. Phys. Chem. A* **2003**, *107*, 4568–4577.
[27] Chemistry with ADF: G. te Velde, F. M. Bickelhaupt, S. J. A. van Gisbergen, C. Fonseca Guerra, E. J. Baerends, J. G. Snijders, T. Ziegler, *J. Comput. Chem.* **2001**, *22*, 931; C. Fonseca Guerra, J. G. Snijders, G. te Velde, E. J. Baerends, *Theor. Chem. Acc.* **1998**, *99*, 391; *ADF2005.01*, SCM, Theoretical Chemistry, Vrije Universiteit, Amsterdam, The Netherlands.
[28] S. H. Vosko, L. Wilk, M. Nusair, *Can. J. Phys.* **1980**, *58*, 1200.
[29] A. D. Becke, *Phys. Rev. A* **1988**, *38*, 3098–3100.
[30] J. P. Perdew, *Phys. Rev. B* **1986**, *33*, 8822–8824.
[31] C. Chang, M. Pelissier, M. Durand, *Phys. Scr.* **1986**, *34*, 394; E. van Lenthe, E. J. Baerends, J. G. Snijders, *J. Chem. Phys.* **1993**, *99*, 4597–4610; E. van Lenthe, E. J. Baerends, J. G. Snijders, *J. Chem. Phys.* **1994**, *101*, 9783–9792; E. van Lenthe, R. van Leeuwen, E. J. Baerends, J. G. Snijders, *Int. J. Quantum Chem.* **1996**, *57*, 281–293.
[32] E. Clementi, D. L. Raimondi, W. P. Reinhardt, *J. Chem. Phys.* **1963**, *38*, 2686–2689.
[33] J. Gracia, J. M. Poblet, J. A. Fernandez, J. Autschbach, L. P. Kazansky, *Eur. J. Inorg. Chem.* **2006**, *6*, 1149–1154.

Received: August 2, 2006
Published Online: October 19, 2006

 © 2006 Wiley-VCH Verlag GmbH & Co. KGaA, Weinheim 

DOI: 10.1002/ejic.200600721

# Synthesis, Structure and Surface Photovoltage of a Series of $Ni^{II}$ Coordination Polymers

Li-Ping Sun,[a] Shu-Yun Niu,*[a] Jing Jin,[a] Guang-Di Yang,[b] and Ling Ye[b]

**Keywords:** Coordination polymers / Nickel / Hydrogen bonds / Surface photovoltage spectroscopy

Three novel $Ni^{II}$ coordination polymers $[Ni_2(HCOO)_4(H_2O)_4]_n$ (**1**), $[Na_2Ni(btec)(H_2O)_8]_n$ (**2**; $H_4$btec = 1,2,4,5-benzenetetracarboxylic acid) and $[\{Ni(pdc)(H_2O)_2\}\cdot H_2O]_n$ (**3**; $H_2$pdc = pyridine-2,5-dicarboxylic acid) have been hydrothermally synthesized and their structures determined by single-crystal X-ray diffraction. The formate groups in complex **1** bridge the $Ni^{II}$ ions to form a infinite 3D structure. Complex **2** also possesses a infinite 3D structure and the coordination environment of the $Ni^{II}$ ion is a perfect octahedron. Complex **3** is a 2D infinite coordination polymer. The surface photovoltage spectra of complexes **1**–**3** indicate that they all show three positive surface photovoltage (SPV) responses in the range of 300–800 nm and all show p-type semiconductor characteristics. Although the intensities of the SPV responses are obviously different, this can mainly be attributed to the difference of their structures. The field-induced surface photovoltage spectra (FISPS) of complexes **1**–**3** confirm their p-type semiconductor characteristics.
(© Wiley-VCH Verlag GmbH & Co. KGaA, 69451 Weinheim, Germany, 2006)

## Introduction

Metal–organic coordination polymers are receiving ever increasing attention owing to their potential applications in functional materials for use in fields such as magnetism, catalysis, electrical conductivity, optical materials, host–guest chemistry, and biomimetic chemistry.[1–5] The design and synthesis of the coordination polymers have therefore undergone rapid development in the areas of coordination and supramolecular chemistry.[6–9] Carboxylate groups often play an important role in the construction of polynuclear complexes as they can adapt many types of bridging pattern, e.g. *syn-syn*, *anti-anti*, *syn-anti* and mono-monodentate and mono-didentate etc.,[10–12] which result in a variety of structural frameworks. They can also act as both donors and acceptors of hydrogen bonds depending on whether the carboxylic O atoms are deprotonated or not.[13] The existence of a variety of hydrogen bonds therefore enriches the function of a coordination supramolecule.

The energy gaps of some transition metal coordination polymers with unique structures are sometimes in the region of those of semiconductors, which means that they can show semiconductor characteristics and can therefore be regarded as a kind of inorganic–organic hybrid semiconductor. The detection of the surface charge behavior and photoelectric properties of the coordination polymers would therefore allow further research on the function of these coordination polymers. To date, reports on this aspect have focused mainly on coordination complexes with phthalocyanines or porphyrins as ligands;[14–17] there are few reports on the coordination polymers.[18] Surface photovoltage spectroscopy (SPS) is a highly sensitive tool that can be used to investigate the photophysics of photogenerated species or excited states without any sample contamination or destruction.[19,20] This technique has been used to investigate photoelectric processes such as charge transfer and photocatalysis.[21] On the basis of the principle of SPS, Wang et al. have developed a field-induced surface photovoltage spectroscopy (FISPS) technique,[22,23] which they have used to investigate the photoelectric properties of semiconductors under the effect of an external electric field. We have also attempted to detect the surface charge behavior of coordination polymers with semiconductor characteristics using these techniques. In this paper we report the synthesis, structure, and surface photovoltage properties of three $Ni^{II}$ coordination polymers. The three complexes all contain carboxylic groups as the basic building unit. Their similarities and differences in the structures are beneficial when it comes to exploring the relationship between the structural and photoelectric properties.

[a] School of Chemistry and Chemical Engineering, Liaoning Normal University,
Dalian 116029, P. R. China
E-mail: syniu@sohu.com
[b] Key Lab of Supramolecular Structure and Materials of Ministry of Education, Jilin University,
Changchun 130023, P. R. China
Supporting information for this article is available on the WWW under http://www.eurjic.org or from the author.

## Result and Discussion

### Synthesis and General Discussion

The synthesis of complex **1** is intriguing. The ligand in complex **1** is a formate, which was not added as one of the

 © 2006 Wiley-VCH Verlag GmbH & Co. KGaA, Weinheim 

starting materials. The starting materials *o*-phthalic acid and 2,2′-bipyridyl do not take part in the coordination. The synthetic procedure involves dmf and $H_2O$ as solvents, and we think the formate group comes from dmf. This phenomenon has been reported previously,[24] and it has long been known that dmf can be hydrolyzed to formate and dma and that the rate of this process increases under basic conditions. We repeated the synthesis of complex **1** in the absence of dmf and obtained the complex [Ni(*o*-phthalate)(2,2′-bipyridyl)($H_2O$)]·$H_2O$, which further confirms the involvement of dmf in the synthesis of complex **1**.

The synthesis of complex **2** is also interesting. The original purpose of adding NaOH was to deprotonate and to adjust the pH. However, the $Na^+$ ions not only balance the charge but also participate in coordination.

## Structure Descriptions

The crystal data and structure refinement of complexes **1**–**3** are summarized in the Experimental Section; selected bond lengths and angles are listed in Table 1.

### $[Ni_2(HCOO)_4(H_2O)_4]_n$ (1)

The single-crystal X-ray diffraction analysis revealed that complex **1** exhibits a infinite 3D framework structure whose building unit is $[Ni_2(HCOO)_4(H_2O)_4]$ (Figure 1). There are two kinds of crystallographically independent $Ni^{II}$ ions. Ni1 is coordinated by six O atoms from six different formate O atoms, with O1, O1d, O3, and O3d atoms comprising the equatorial plane. The Ni1–O1 and Ni1–O3 bond lengths are 2.058(2) and 2.104(2) Å, respectively. The O1–Ni1–O1d and O3–Ni1–O3d bond angles are both 180°, and the O1–Ni1–O3 and O1d–Ni1–O3 bond angles are 92.98(8)° and 87.02(8)°, respectively. O2 and O2e occupy the apical positions. The Ni1–O2 bond length of 2.039(2) Å and the O2–Ni1–O2e bond angle of 180° mean that the coordination environment of Ni1 is a perfect octahedron. The other crystallographically independent Ni2 ion is also six coordinate, with two O atoms from two bridging formate O atoms and the other four O atoms from four coordinated water molecules. The formate groups in the crystal adopt an *anti-anti* coordination mode that links the Ni1 ions into a 1D infinite chain. The Ni1 ions of adjacent chains are further con-

Table 1. Selected bond lengths [Å] and angles [°] for complexes **1**–**3**.[a]

| | | | | | |
|---|---|---|---|---|---|
| **1** | | | | | |
| Ni(1)–O(2)$^{i}$ | 2.039(2) | Ni(1)–O(3) | 2.104(2) | Ni(2)–O(6)$^{ii}$ | 2.067(2) |
| Ni(1)–O(2) | 2.039(2) | Ni(1)–O(3)$^{i}$ | 2.104(2) | Ni(2)–O(6) | 2.067(2) |
| Ni(1)–O(1) | 2.058(2) | Ni(2)–O(5) | 2.026(2) | Ni(2)–O(4) | 2.099(2) |
| Ni(1)–O(1)$^{i}$ | 2.058(2) | Ni(2)–O(5)$^{ii}$ | 2.026(2) | Ni(2)–O(4)$^{ii}$ | 2.099(2) |
| O(2)$^{i}$–Ni(1)–O(2) | 180.00(8) | O(2)$^{i}$–Ni(1)–O(3)$^{i}$ | 87.28(8) | O(6)$^{ii}$–Ni(2)–O(6) | 180.0 |
| O(2)$^{i}$–Ni(1)–O(1) | 90.52(8) | O(2)–Ni(1)–O(3)$^{i}$ | 92.72(8) | O(5)–Ni(2)–O(4) | 89.57(11) |
| O(2)–Ni(1)–O(1) | 89.48(8) | O(1)–Ni(1)–O(3)$^{i}$ | 87.02(8) | O(5)$^{ii}$–Ni(2)–O(4) | 90.43(11) |
| O(2)$^{i}$–Ni(1)–O(1)$^{i}$ | 89.48(8) | O(1)$^{i}$–Ni(1)–O(3)$^{i}$ | 92.98(8) | O(6)$^{ii}$–Ni(2)–O(4) | 90.71(7) |
| O(2)–Ni(1)–O(1)$^{i}$ | 90.52(8) | O(3)–Ni(1)–O(3)$^{i}$ | 180.0 | O(6)–Ni(2)–O(4) | 89.29(7) |
| O(1)–Ni(1)–O(1)$^{i}$ | 180.00(5) | O(5)–Ni(2)–O(5)$^{ii}$ | 180.0 | O(5)–Ni(2)–O(4)$^{ii}$ | 90.43(11) |
| O(2)$^{i}$–Ni(1)–O(3) | 92.72(8) | O(5)–Ni(2)–O(6)$^{ii}$ | 89.34(9) | O(5)$^{ii}$–Ni(2)–O(4)$^{ii}$ | 89.57(11) |
| O(2)–Ni(1)–O(3) | 87.28(8) | O(5)$^{ii}$–Ni(2)–O(6)$^{ii}$ | 90.66(9) | O(6)$^{ii}$–Ni(2)–O(4)$^{ii}$ | 89.29(7) |
| O(1)–Ni(1)–O(3) | 92.98(8) | O(5)–Ni(2)–O(6) | 90.66(9) | O(6)–Ni(2)–O(4)$^{ii}$ | 90.71(7) |
| O(1)$^{i}$–Ni(1)–O(3) | 87.02(8) | O(5)$^{ii}$–Ni(2)–O(6) | 89.34(9) | O(4)–Ni(2)–O(4)$^{ii}$ | 180.0 |
| **2** | | | | | |
| Ni(1)–O(2) | 2.075(2) | Ni(1)–O(1)$^{iii}$ | 2.0767(15) | Ni(1)–O(1)$^{v}$ | 2.0767(15) |
| Ni(1)–O(2)$^{iii}$ | 2.075(2) | Ni(1)–O(1) | 2.0767(15) | Ni(1)–O(1)$^{iv}$ | 2.0767(15) |
| Na(1)–O(3) | 2.332(2) | Na(1)–O(3)$^{vi}$ | 2.332(2) | Na(1)–O(4)$^{vi}$ | 2.402(2) |
| Na(1)–O(5)$^{vi}$ | 2.5705(19) | | | | |
| O(2)–Ni(1)–O(2)$^{iii}$ | 180.0 | O(1)$^{iii}$–Ni(1)–O(1) | 180.0 | O(2)–Ni(1)–O(1)$^{v}$ | 85.95(5) |
| O(2)–Ni(1)–O(1)$^{iii}$ | 94.05(5) | O(2)–Ni(1)–O(1)$^{iv}$ | 94.05(5) | O(2)$^{iii}$–Ni(1)–O(1)$^{v}$ | 94.05(5) |
| O(2)$^{iii}$–Ni(1)–O(1)$^{iii}$ | 85.95(5) | O(2)$^{iii}$–Ni(1)–O(1)$^{iv}$ | 85.95(5) | O(1)$^{iii}$–Ni(1)–O(1)$^{v}$ | 86.86(9) |
| O(2)–Ni(1)–O(1) | 85.95(5) | O(1)$^{iii}$–Ni(1)–O(1)$^{iv}$ | 93.14(9) | O(1)–Ni(1)–O(1)$^{v}$ | 93.14(9) |
| O(2)$^{iii}$–Ni(1)–O(1) | 94.05(5) | O(1)–Ni(1)–O(1)$^{iv}$ | 86.86(9) | O(1)$^{iv}$–Ni(1)–O(1)$^{v}$ | 180.0 |
| O(3)–Na(1)–O(3)$^{vi}$ | 180.00(9) | O(3)$^{vi}$–Na(1)–O(4)$^{vi}$ | 83.10(8) | O(3)$^{vi}$–Na(1)–O(5)$^{vi}$ | 79.06(9) |
| O(3)–Na(1)–O(4)$^{vi}$ | 96.90(8) | O(3)–Na(1)–O(5)$^{vi}$ | 100.94(9) | O(4)$^{vi}$–Na(1)–O(5)$^{vi}$ | 92.17(9) |
| **3** | | | | | |
| Ni(1)–O(1) | 2.0340(15) | Ni(1)–O(3) | 2.0350(15) | Ni(1)–O(2) | 2.1064(15) |
| Ni(1)–O(7) | 2.0344(16) | Ni(1)–N(1) | 2.0843(17) | Ni(1)–O(4) | 2.1110(14) |
| O(1)–Ni(1)–O(7) | 97.48(7) | O(3)–Ni(1)–N(1) | 79.63(6) | O(1)–Ni(1)–O(4) | 86.71(6) |
| O(1)–Ni(1)–O(3) | 173.04(6) | O(1)–Ni(1)–O(2) | 86.74(7) | O(7)–Ni(1)–O(4) | 92.28(6) |
| O(7)–Ni(1)–O(3) | 88.08(7) | O(7)–Ni(1)–O(2) | 89.46(6) | O(3)–Ni(1)–O(4) | 97.28(6) |
| O(1)–Ni(1)–N(1) | 94.47(7) | O(3)–Ni(1)–O(2) | 89.14(6) | N(1)–Ni(1)–O(4) | 93.74(6) |
| O(7)–Ni(1)–N(1) | 166.90(6) | N(1)–Ni(1)–O(2) | 85.88(7) | O(2)–Ni(1)–O(4) | 173.39(6) |

[a] Symmetry transformations used to generate equivalent atoms: i: $-x + 1, -y, -z + 1$; ii: $-x + 2, -y + 1, -z + 1$; iii: $-x, -y, -z - 2$; iv: $-x, y, -z - 2$; v: $x, -y, z$; vi: $-x + 1/2, -y + 1/2, -z - 1$.

 © 2006 Wiley-VCH Verlag GmbH & Co. KGaA, Weinheim 

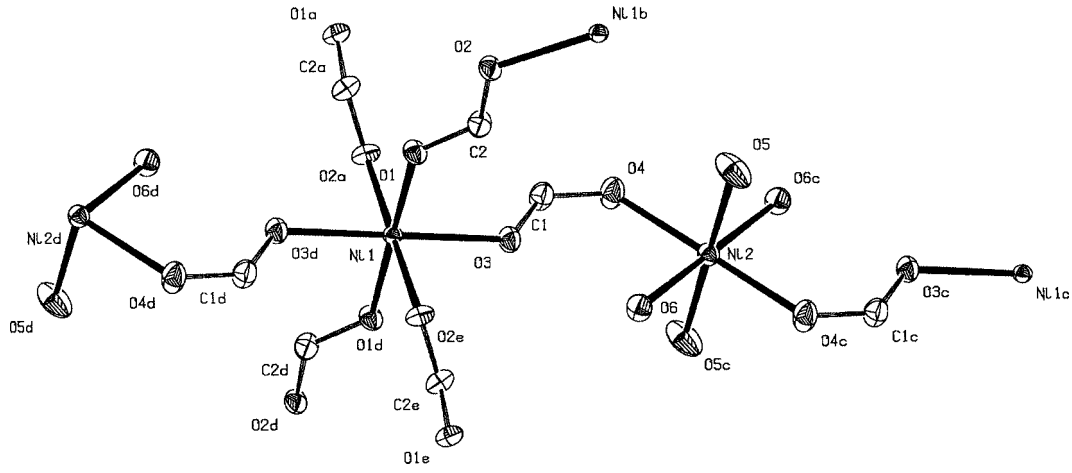


Figure 1. The ORTEP structure of complex **1** (30% probability thermal ellipsoids) showing the asymmetric unit.

nected to another 1D infinite chain along the perpendicular direction with the same mode, which means that the Ni1 ions are linked into a 2D layer in the *bc* plane (Figure 2). The coplanarity of this 2D layer is very good, and the Ni2 ions array regularly between the 2D layers. The formate groups, which lie between the Ni1 and Ni2 ions, connect these ions in a *syn-anti* mode to form a 1D infinite chain. This 1D infinite chain is perpendicular to the 2D layer, and the 2D layers are further connected into a infinite 3D structure (Figure 3). When projected along the *a* axis, it can clearly be seen that every four Ni1 ions form a rhombic hole. The sides of each rhombus are 5.808 Å and they extend infinitely along the *a* axis. The Ni2 ions lie between the holes (Figure 4).

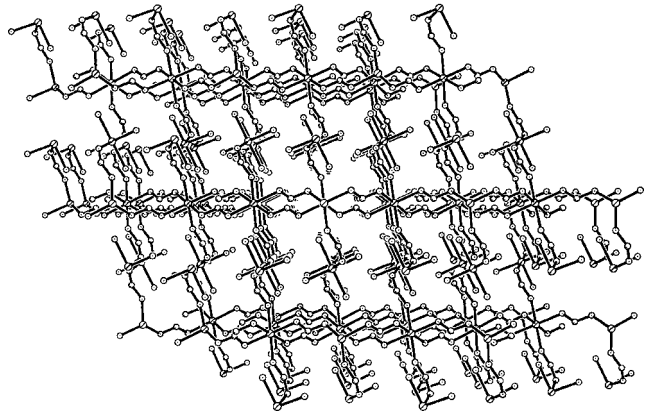

Figure 3. The 3D structure of complex **1**.

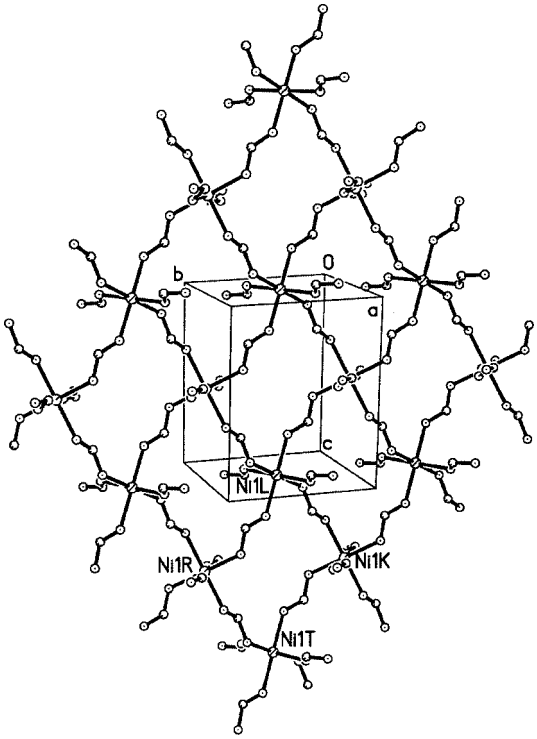


Figure 2. The 2D layer structure of Ni1 ions in complex **1**.

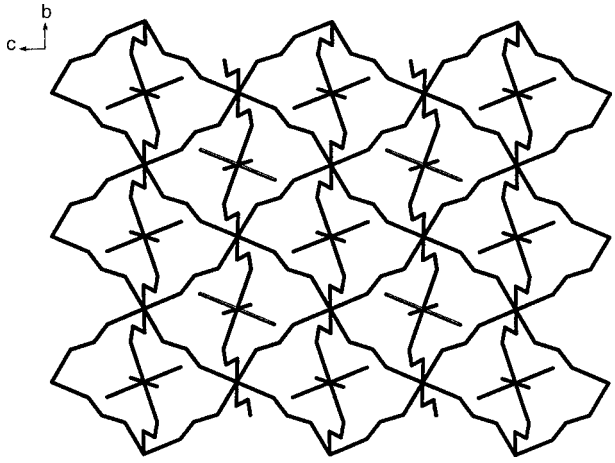


Figure 4. A projection of complex **1** along the *a* axis showing the Ni2 ions lying between the Ni1 holes.

### $[Na_2Ni(btec)(H_2O)_8]_n$ (2)

Complex **2** possesses a infinite 3D structure and its building unit is $[Na_2Ni(btec)(H_2O)_8]$ (Figure 5). Each $Ni^{II}$ ion is coordinated by six O atoms and its coordination environment is a perfect octahedron. Four O atoms (O1, O1A, O1B, O1C) are from four different btec groups, and these

 © 2006 Wiley-VCH Verlag GmbH & Co. KGaA, Weinheim 

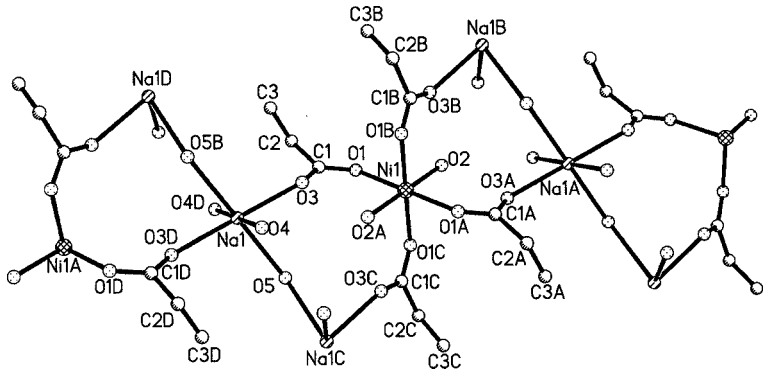


Figure 5. The building unit of complex **2**.

comprise the equatorial plane. The Ni–O1 bond length is 2.0767(15) Å and the O1A–Ni1–O1 and O1B–Ni1–O1C bond angles are all 180°. The O1–Ni1–O1B and O1–Ni1–O1C bond angles are 86.86(9)° and 93.14(9)°, respectively. The other two O atoms (O2, O2A) are from two coordinated water molecules and they occupy the apical positions of the octahedron. The Ni–O2 bond length is 2.075(2) Å and the O2–Ni–O2A bond angle is 180°.

The $Na^{I}$ ion is coordinated by six O atoms. Two O atoms are from two btec groups and four O atoms from four coordinated water molecules, all of which comprise the distorted octahedral coordination environment of $Na^{I}$. In the crystal, each btec group coordinates to four different $Ni^{II}$ ions through the four deprotonated carboxylic O atoms in a monodentate manner. Thus, the $Ni^{II}$ ions are connected to two perpendicular 1D chains in the *bc* plane. The coplanarity of the *bc* layer is very good. The *o*- and *m*-carboxylate moieties of each btec group separately link the different $Ni^{II}$ ions and form two kinds of multi-membered rings. The Ni1G–Ni1H (along the *c* axis) and Ni1H–Ni1B (along the *b* axis) distances are 6.086 and 9.488 Å, respectively (Figure 6). The $Na^{I}$ ions array along the *bc* plane and link two $Ni^{II}$ ions in the adjacent layer through the carboxylate group, which means that the 2D layers are further connected to form an infinite 3D structure (Figure 7). In addition, there are a lot of hydrogen bonds in the crystal. There are interactions between the coordinated water molecules and coordinated water molecules [O2–H···O5 2.808(3), O4–H···O4 3.145(6) Å] as well as coordinated carboxylate O atoms [O4–H···O3 3.098(3), O2–H···O3 2.608(2), O4–H···O1 3.098(3) Å]. These hydrogen bonds increase the stability of the structure.

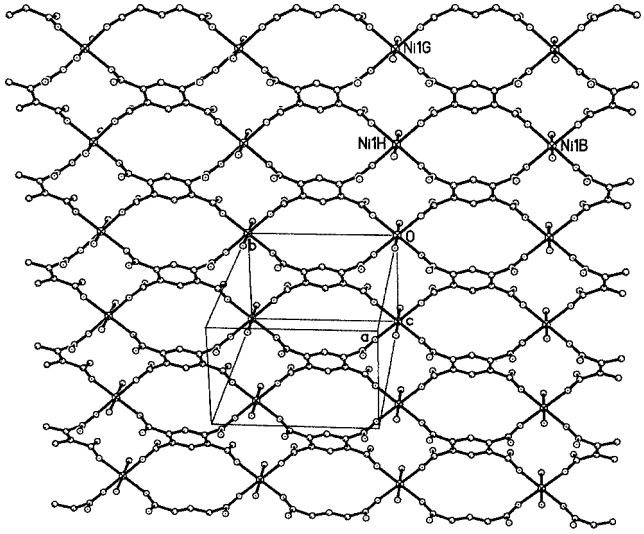


Figure 6. The 2D infinite layered structure of $Ni^{II}$ ions in complex **2**.

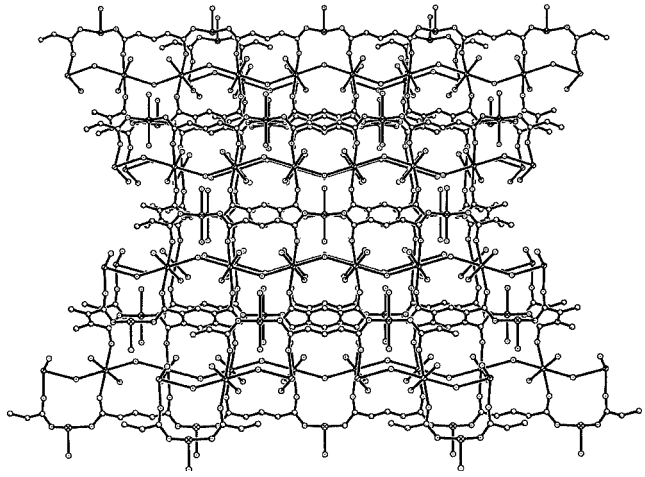

Figure 7. The 3D structure of complex **2**.

### $[\{Ni(pdc)(H_2O)_2\}\cdot H_2O]_n$ (3)

The structure of complex **3** has been reported previously by Min, Dongwon et al.,[25] therefore here we place more emphasis on its SPS and FISPS properties. Complex **3** is a 2D infinite coordination polymer and its asymmetric unit is $[\{Ni(pdc)(H_2O)_2\}\cdot H_2O]$. Each $Ni^{II}$ ion is coordinated by five O atoms and one N atom. One O atom and one N atom are from the same pdc group; the other four O atoms are from two different pdc groups and two coordinated water molecules (Figure 8). The coordination geometry around the $Ni^{II}$ ion is a distorted octahedron. The equatorial plane is defined by O2, O7, O4, and N1 and the apical position is occupied by O3 and O1. The O3–Ni–O1 bond

 © 2006 Wiley-VCH Verlag GmbH & Co. KGaA, Weinheim 

angle is 173.04(6)°. In the crystal, the pdc group plays a bridging role: the α-carboxylate O atom together with the pyridine N atom coordinate to one $Ni^{II}$ ion and the other carboxylate O atom coordinates to another $Ni^{II}$ ion in a monodentate mode. The $Ni^{II}$ ions are linked into a 1D infinite chain along the *a* axis. Each β-carboxylate O atom of the pdc group binds to one $Ni^{II}$ ion in a monodentate mode to form a zigzag chain along the *b* axis, so complex **3** is further connected into a 2D waved structure (Figure 9). There are five kinds of O–H···O hydrogen bonds in the crystal. These are the interactions between the coordinated water molecules and coordinated carboxylic O atoms [O7–H···O4 2.687(12), O1–H···O3 2.696(2) Å] as well as the uncoordinated carboxylic O atom [O1–H···O5 2.726(2) Å]. The other three types of hydrogen bond are between the lattice water molecule and the coordinated water molecule [O7–H···O6 2.625(3) Å], the coordinated carboxylic O atom [O6–H···O2 2.904(3) Å], and the uncoordinated carboxylic O atom [O6–H···O5 3.051(3) Å]. Complex **3** is further connected into a 3D web by hydrogen bonds (Figure 10).

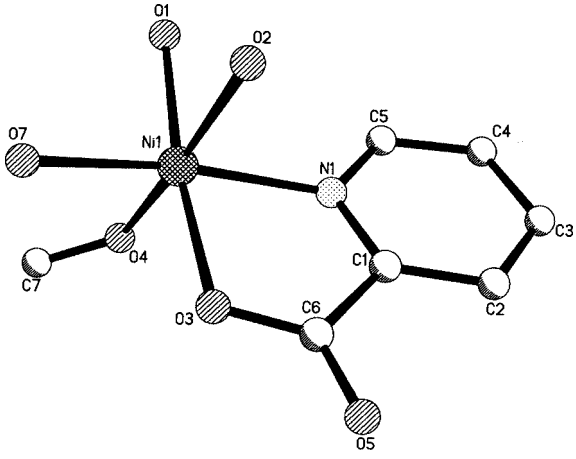


Figure 8. The asymmetric unit of complex **3**.

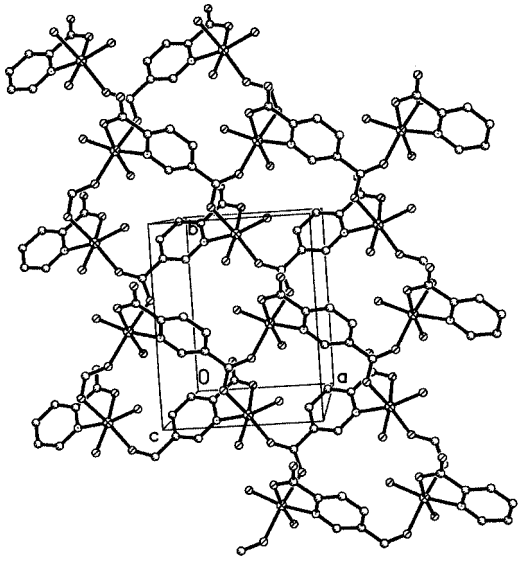


Figure 9. The 2D infinite structure of complex **3**.

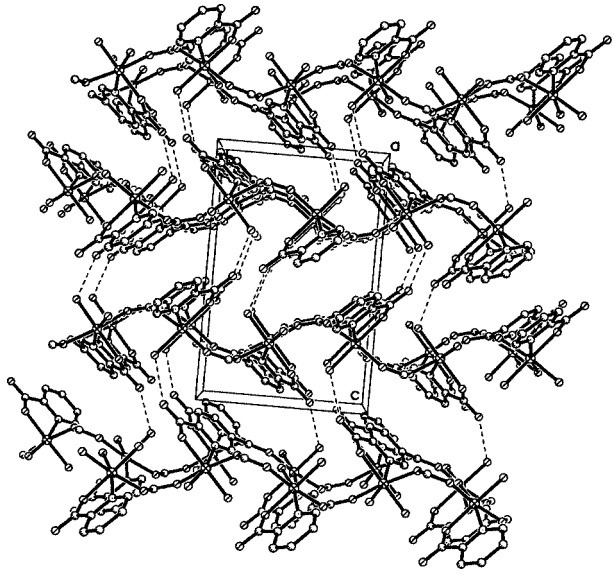


Figure 10. The 3D structure of complex **3**. Dotted lines indicate hydrogen bonds.

### Surface Photovoltage Spectra of Complexes

Surface photovoltage spectra were measured with a solid junction photovoltaic cell (ITO/sample/ITO) in the range 300–800 nm. A signal detected by SPS is equivalent to the change in the surface potential barrier on illumination ($\delta V_s$), which is given by the equation

$$\delta V_s = V_s' - V_s°$$

where $V_s°$ and $V_s'$ are the surface potential barriers before and after illumination, respectively. As far as band-to-band transitions are concerned, a positive response of SPV ($\delta V_s > 0$) means that the sample is characterized as a p-type semiconductor, whereas a negative response means that the sample is an n-type semiconductor. The magnitude of the surface potential barrier depends on the number of surface net charges. Figures 11 and 12 show the SPS spectra of complexes **1** and **3**, respectively. The SPS spectrum of complex **2** is similar to that of complex **1**. The SPV responses at 300–500 nm show some overlap, but they can be separated by treating them with the program Origin 7.0[26]. Complexes **1**–**3** all show three positive SPV responses in the range 300–800 nm, which indicates that they all have p-type semiconductor characteristics. The response bands at $\lambda_{max}$ = 342 nm can be attributed to an LMCT (ligand to metal charge transfer) transition. In contrast with a previous report,[18] the LMCT bands are blue-shifted. The complexes reported here are mainly coordinated by O atoms, in contrast to the other complexes, which are mainly coordinated by N atoms,[18] therefore, as the electronegativity of oxygen is larger than that of nitrogen, more energy is needed to produce the LMCT, which means that the LMCT band is blue-shifted. The responses at $\lambda_{max}$ = 392 (**1**), 387 (**2**), and 396 nm (**3**) can be assigned to the d→d* transition of $Ni^{II}$ [$^3A_{2g}\rightarrow{}^3T_{1g}$ ($^3P$)], and the response bands between 600 and

 © 2006 Wiley-VCH Verlag GmbH & Co. KGaA, Weinheim 

800 nm can be attributed to the d→d* transition of $Ni^{II}$ [$^3A_{2g}\rightarrow{}^3T_{1g}$ ($^3F$); Table 2]. The surface photovoltage spectra of complexes **1**–**3** match their absorption spectra.

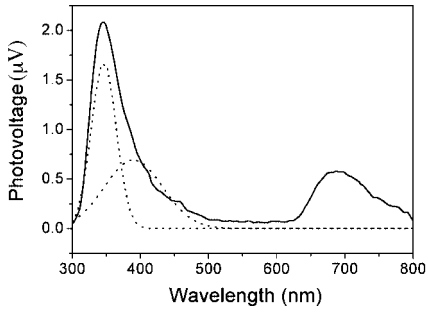


Figure 11. The surface photovoltage spectrum of complex **1**. The dotted lines are the peaks obtained after treatment with Origin 7.0.

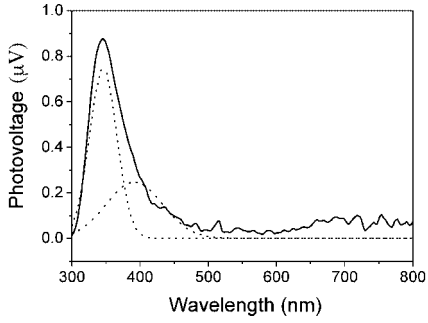


Figure 12. The surface photovoltage spectrum of complex **3**. The dotted lines are the peaks obtained after treatment with Origin 7.0.

Table 2. Assignment of the surface photovoltage spectra.

| | $\lambda_{max}$ [nm] | $\lambda_{max}$ [nm] | $\lambda_{max}$ [nm] |
|---|---|---|---|
| **1** | 342 | 392 | 690 |
| **2** | 342 | 387 | 700 |
| **3** | 342 | 396 | 689 |
| Assignment | LMCT | $^3A_{2g}\rightarrow{}^3T_{1g}(^3P)$ | $^3A_{2g}\rightarrow{}^3T_{1g}(^3F)$ |

Comparing the SPV responses of complexes **1**–**3** (Figure 13), it can be seen that without the external electric field the values of the three complexes' response bands are the same, although their intensities are obviously different; complex **1** is the strongest and complex **3** is the weakest. This intensity difference is mainly due to the differences in their structures. Complex **1** is an infinite 3D coordination polymer where the coordination environment of Ni1 is a perfect octahedron. The 2D layer which is formed by two perpendicularly 1D infinite chains is beneficial to the conduction of electrons or holes. Furthermore, another Ni 1D chain which is perpendicular to this 2D layer also provides a transmission passage for the electrons or holes, which means that more electrons diffuse to the surface, resulting in an increase of the SPV response intensities. Complex **2** possesses a infinite 3D structure and the coordination environment of $Ni^{II}$ ion is a perfect octahedron. The planarity of the 2D layer in complex **2** is very good therefore this 2D planar structure is also beneficial to transfer the electrons or holes. Another 1D infinite chain plumbing to the 2D layer intermingles $Na^I$ ions, which may also have certain effects on the transfer of electrons and holes. The intensity of the SPV in complex **2** is lower than that in complex **1**. In complex **3**, the irregularly spaced structure affects the transport of electrons or holes therefore the SPV response's intensity is the weakest. In addition, the types of bonds in the crystal have different effects when it comes to transferring electrons or holes. Complexes **1**–**3** all possess infinite 3D structures. Among them, the 3D structures of complexes **1** and **2** are formed by coordination bonds, whereas in complex **3** the 2D structure is formed by coordination bonds and the 2D layer is further connected into a 3D structure by hydrogen bonds. As hydrogen bonds are weak, their ability to transfer electrons or holes is much lower than that of coordination bonds, therefore the intensity of the SPV of complex **3** is lower than that of complexes **1** and **2**. Moreover, in the range 600–800 nm, it can be seen that the SPV response band of complexes **1** and **2** is a sine wave, whereas the response band of complex **3** shows obvious splitting. These phenomena are mainly attributed to the different symmetries of the $Ni^{II}$ coordination environments: the coordination environment of $Ni^{II}$ in complexes **1** and **2** is a perfect octahedron, whereas in complex **3** it is a distorted octahedron.

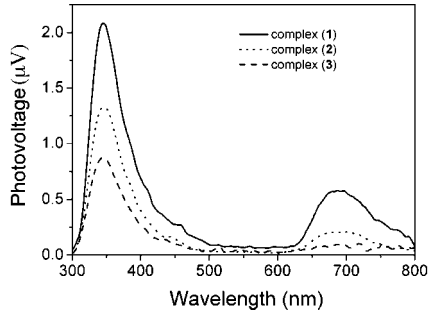


Figure 13. A comparative SPS diagram of complexes **1**–**3**.

## FISPS of Complexes

FISPS can determine the direction of the built-in field and the mobile direction of photogeneration carriers. If we apply a positive electric field (the illuminated surface is positive) vertically to the p-type semiconductor surface, whose direction is the same as the direction of the built-in field, the separation efficiency of the photogeneration carriers is increased and the intensity of SPV response increases in the original direction. If a negative electric field, whose direction is opposite to that of the built-in field, is applied, the separation efficiency of the photogenerated carriers reduces and the intensity of the SPV response is weakened, even in the reverse direction. In contrast to p-type semiconductors, the SPV response intensity of n-type semiconductors increases as a negative field is applied and reduces as a positive electric field is applied. The FISP spectrum of complex **1** is given in Figure 14; those of complexes **2** and **3** are analogous with complex **1**. The responses in the range 300–500 nm in all three complexes increase linearly with a posi-

 © 2006 Wiley-VCH Verlag GmbH & Co. KGaA, Weinheim 

tive electric field, which shows that the direction of this external electric field is consistent with the built-in field. This enhances the separation efficiency of the photoexcited electron–hole pairs and results in an increase of the surface potential, thus confirming that complexes **1**–**3** have p-type semiconductor characteristics.

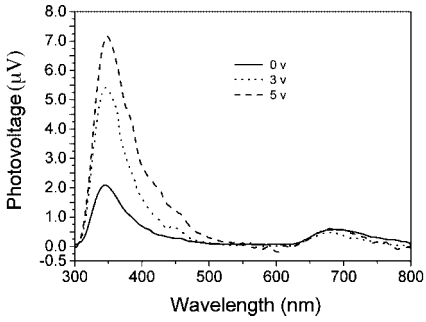


Figure 14. The FISP spectrum of complex **1**. The intensities of the SPV response increase linearly with the external positive electric field.

## Conclusion

Three $Ni^{II}$ coordination polymers have been synthesized by hydrothermal methods. Complexes **1** and **2** are both infinite 3D coordination polymers and complex **3** possesses a 2D infinite structure. The surface photovoltage spectra of complexes **1**–**3** show that they all have three positive responses in the range 300–800 nm and all take on p-type semiconductor characteristics. However, the intensities of the SPV response bands are obviously different, mainly due to their different structures. The coordination environment of the $Ni^{II}$ ion affects the shape of the SPV responses, and the FISP spectra confirm the p-type semiconductor characteristics of complexes **1**–**3**.

## Experimental Section

**Materials and Methods:** All reagents were of A.R. grade. IR spectra were recorded in the range 220–4000 $cm^{-1}$ with a JASCO FT-IR/480 spectrophotometer with KBr pellets. The elemental composition of the complexes was determined with a PE-240C analyzer and a TLASMA-II ICP instrument. SPS and FISPS measurements were conducted with the sample in a sandwich cell (ITO/sample/ITO) with the light source-monochromator-lock-in detection technique. All the measurements were performed under atmospheric pressure and at ambient temperature.

**$[Ni_2(HCOO)_4(H_2O)_4]_n$ (1):** A solution of $NiSO_4{\cdot}6H_2O$ (0.26 g, 1 mmol) in water (10 mL) was added to a solution of *o*-phthalic acid (0.17 g, 1 mmol) in water (10 mL), and 2,2′-bipyridyl (0.08 g, 0.5 mmol) and 5 mL of dmf were added to the above solution. The solution was then transferred into a Parr Teflon®-lined stainless steel vessel, which was sealed and heated to 100 °C for 5 d. After cooling to room temperature, the solution was filtered. Green crystals of complex **1** were obtained by leaving the solution to evaporate at room temperature for about one month. $C_4H_{12}Ni_2O_{12}$ (369.56): calcd. C 13.00, H 3.27, Ni 31.77; found C 13.25, H 3.31, Ni 31.53. IR (KBr): $\tilde{\nu}$ = 3360 $cm^{-1}$, 3277, 3206 ($\nu_{OH}$); 1574 ($\nu_{asCOO}$); 1378 ($\nu_{sCOO}$); 889, 850, 771 ($\delta_{C-H}$); 566, 357, 311 ($\nu_{Ni-O}$).

**$[Na_2Ni(btec)(H_2O)_8]_n$ (2):** A solution of $NiSO_4{\cdot}6H_2O$ (0.26 g, 1 mmol) in water (10 mL) was added to a solution of $H_4$btec (0.13 g, 0.5 mmol) and NaOH (0.08 g, 2 mmol) in water (10 mL), and NaSCN (0.08 g, 1 mmol) and 5 mL of dmf were added to the above solution. The mixture was then transferred into a Parr Teflon®-lined stainless steel vessel, which was sealed and heated to 100 °C for 5 d. After cooling to room temperature, green crystals of complex **2** were collected. $C_{10}H_{18}Na_2NiO_{16}$ (498.93): calcd. C 24.07, H 3.64, Na 9.22, Ni 11.77; found C 24.23, H 3.73, Na 9.03, Ni 11.59. IR (KBr): $\tilde{\nu}$ = 3595 $cm^{-1}$, 3415 ($\nu_{OH}$); 3029 ($\nu_{ArC-H}$); 1592 ($\nu_{asCOO}$); 1392 ($\nu_{sCOO}$); 1633, 1500, 1439 ($\nu_{ArC\cdots C}$); 1332 ($\delta_{O-H}$); 1145, 974, 912 ($\nu_{C-C,C-O}$); 854, 811, 765, 705 ($\delta_{C-H}$); 537 ($\nu_{Na-O}$), 475 ($\nu_{Ni-O}$).

Table 3. Crystallographic data for complexes **1**–**3**.

| | **1** | **2** | **3** |
|---|---|---|---|
| Empirical formula | $C_4H_{12}Ni_2O_{12}$ | $C_{10}H_{18}Na_2NiO_{16}$ | $C_7H_9NNiO_7$ |
| Formula weight | 369.56 | 498.93 | 277.86 |
| Temperature | 293(2) | 293(2) | 293(2) |
| Wavelength [Å] | 0.71073 | 0.71073 | 0.71073 |
| Crystal system | monoclinic | monoclinic | orthorhombic |
| Space group | $P2_1/c$ | $C2/m$ | $P2_12_12_1$ |
| Unit cell dimensions | | | |
| $a$ [Å] | 8.600(5) | 15.698(10) | 7.300(3) |
| $b$ [Å] | 7.068(6) | 9.488(7) | 9.289(4) |
| $c$ [Å] | 9.219(6) | 6.086(3) | 14.075(6) |
| $\alpha$ [°] | 90 | 90 | 90 |
| $\beta$ [°] | 97.44(3) | 93.21(3) | 90 |
| $\gamma$ [°] | 90 | 90 | 90 |
| Volume [$Å^3$] | 555.6(7) | 905.1(10) | 954.4(7) |
| $Z$ | 2 | 2 | 4 |
| $D_c$ [$g\,cm^{-3}$] | 2.209 | 1.831 | 1.934 |
| $F$(000) | 376 | 512 | 568 |
| Goodness-of-fit on $F^2$ | 1.105 | 1.066 | 1.044 |
| Final $R$ indices [$I > 2\sigma(I)$] | $R_1$ = 0.0323, $wR_2$ = 0.0941 | $R_1$ = 0.0291, $wR_2$ = 0.0816 | $R_1$ = 0.0195, $wR_2$ = 0.0505 |
| $R$ indices (all data) | $R_1$ = 0.0349, $wR_2$ = 0.0957 | $R_1$ = 0.0298, $wR_2$ = 0.0822 | $R_1$ = 0.0202, $wR_2$ = 0.0507 |
| Data/restraints/parameters | 1270/0/85 | 1093/2/81 | 2317/0/169 |
| Absolute structure parameter | – | – | 0.013(11) |

 © 2006 Wiley-VCH Verlag GmbH & Co. KGaA, Weinheim 

**$[\{Ni(pdc)(H_2O)_2\}\cdot H_2O]_n$ (3):** A solution of $NiSO_4\cdot 6H_2O$ (0.26 g, 1 mmol) in water (10 mL) was added to a solution of $H_2pdc$ (0.16 g, 1 mmol) and NaOH (0.08 g, 2 mmol) in water (10 mL). The mixture was then transferred into a Parr Teflon®-lined stainless steel vessel, which was sealed and heated to 160 °C for 5 d. After cooling to room temperature, green crystals of complex **3** were collected. $C_7H_9NNiO_7$ (277.86): calcd. C 30.26, H 3.26, N 5.04, Ni 21.13; found C 30.53, H 3.40, N 5.25, Ni 20.95. IR (KBr): $\tilde{\nu}$ = 3587 $cm^{-1}$, 3447, 3264, 3187 ($\nu_{OH}$); 3071 ($\nu_{ArC-H}$); 1581, 1549 ($\nu_{asCOO}$); 1394, 1363 ($\nu_{sCOO}$); 1661, 1602, 1479 ($\nu_{ArC\cdots C}$); 1289 ($\nu_{C-N}$); 1182, 1145, 1039 ($\nu_{C-C,C-O}$); 829, 772, 695 ($\delta_{C-H}$); 544, 527 ($\nu_{Ni-N}$); 446, 368, 314 ($\nu_{Ni-O}$).

**X-ray Crystallographic Study:** Crystallographic data for complexes **1** and **2** were collected on a Rigaku R-AXIS-RAPID diffractometer using graphite-monochromated Mo-$K_\alpha$ radiation ($\lambda$ = 0.71073 Å) at 293 K. Crystal data for complex **3** was collected on a Smart APEX II CCD diffractometer using graphite-monochromated Mo-$K_\alpha$ radiation ($\lambda$ = 0.71073 Å) at 293 K. Further details are given in Table 3. All data were corrected for Lorentz polarization factors and empirical absorption. The structures were solved by direct methods and refined by full-matrix least-squares calculations on $F^2$ using the SHELXTL 97 program. All non-hydrogen atoms were refined anisotropically. Hydrogen atoms were found by mixed methods. Selected bond lengths and angles for complexes **1**–**3** are listed in Table 1.

CCDC-615921 (for **1**), -615922 (for **2**) and -615923 (for **3**) contain the supplementary crystallographic data for this paper. These data can be obtained free of charge from The Cambridge Crystallographic Data Centre via www.ccdc.cam.ac.uk/data_request/cif.

**Supporting Information** (see also the footnote on the first page of this article): In the Supporting Information, there include three correlated structure figures of complexes **1** and **2**, the IR and UV/Vis spectra of complexes **1**–**3**, the SPS spectrum of complex **2** and the FISPS spectra of complexes **2** and **3**.

## Acknowledgments

This work was supported by the National Natural Science Foundation of China (nos. 20571037 and 90201018).

[1] B. Moulton, M. J. Zaworotko, *Chem. Rev.* **2001**, *101*, 1629–1658.
[2] A. Katz, M. E. Davis, *Nature* **2000**, *403*, 286–289.
[3] M. Tominaga, S. Tashiro, M. Aoyagi, *Chem. Commun.* **2002**, 2038–2039.
[4] W. Y. Sun, T. Kusukawa, M. Fujita, *J. Am. Chem. Soc.* **2002**, *124*, 11570–11571.
[5] E. Y. Choi, Y. U. Kwon, *Inorg. Chem. Commun.* **2004**, *7*, 942–945.
[6] S. R. Batten, R. Robson, *Angew. Chem. Int. Ed.* **1998**, *37*, 1460–1494.
[7] R. Sekiya, S. Nishikiori, *Chem. Eur. J.* **2002**, *8*, 4803–4810.
[8] Y. Q. Guo, D. R. Xiao, E. B. Wang, Y. Lu, J. Lü, X. X. Xu, L. Xu, *J. Solid State Chem.* **2005**, *178*, 776–781.
[9] P. J. Hagrman, D. Hagrman, J. Zubieta, *Angew. Chem. Int. Ed.* **1999**, *38*, 2638–2684.
[10] G. B. Deacon, R. J. Phillips, *Coord. Chem. Rev.* **1980**, *33*, 227–250.
[11] M. Melnik, *Coord. Chem. Rev.* **1981**, *36*, 1–44.
[12] M. Kato, Y. Nuto, *Coord. Chem. Rev.* **1988**, *92*, 45–83.
[13] R. H. Wang, F. L. Jiang, L. Han, Y. Q. Gong, Y. F. Zhou, M. C. Hong, *J. Mol. Struct.* **2004**, *699*, 79–84.
[14] D. J. Wang, J. Zhang, T. S. Shi, B. H. Wang, X. Z. Cao, T. J. Li, *J. Photochem. Photobiol. A* **1996**, *93*, 21–25.
[15] Q. L. Zhang, D. J. Wang, J. J. Xu, J. Cao, J. Z. Sun, M. Wang, *Mater. Chem. Phys.* **2003**, *82*, 525–528.
[16] U. Weiler, T. Mayer, W. Jaegermann, C. Kelting, D. Schlettwein, S. Makarov, D. Wöhrle, *J. Phys. Chem. B* **2004**, *108*, 19398–19403.
[17] T. Uekermann, D. Schlettwein, N. I. Jaeger, *J. Phys. Chem. B* **2001**, *105*, 9524–9532.
[18] L. P. Sun, S. Y. Niu, J. Jin, G. D. Yang, L. Ye, *Inorg. Chem. Commun.* **2006**, *9*, 679–682.
[19] T. F. Xie, D. J. Wang, L. J. Zhu, C. Wang, T. J. Li, *J. Phys. Chem. B* **2000**, *104*, 8177–8181.
[20] A. Kokler, J. Gruner, R. H. Friend, K. Mullen, V. Scherf, *Chem. Phys. Lett.* **1995**, *243*, 456–461.
[21] J. S. Kim, B. Lagel, E. Moons, N. Johansson, I. D. Baikie, W. R. Salaneck, R. H. Friend, F. Cacialli, *Synth. Met.* **2000**, *311*, 111–112.
[22] J. Zhang, D. J. Wang, T. S. Shi, B. H. Wang, J. Z. Sun, T. J. Li, *Thin Solid Films* **1996**, *284/285*, 596–599.
[23] H. F. Mao, H. J. Tian, Q. F. Hou, H. J. Xu, *Thin Solid Films* **1997**, *300*, 208–212.
[24] X. Y. Wang, L. Gan, S. W. Zhang, S. Gao, *Inorg. Chem.* **2004**, *43*, 4615–4625.
[25] D. W. Min, S. S. Yoon, C. Y. Lee, W. S. Han, S. W. Lee, *Bull. Korean Chem. Soc.* **2001**, *22*, 1041–1044.
[26] Y. A. Cao, Q. J. Meng, W. S. Yang, J. H. Yao, Y. C. Shu, W. Wang, G. H. Chen, *Colloids Surf., A* **2005**, *262*, 181–186.

Received: August 2, 2006
Published Online: October 31, 2006

 © 2006 Wiley-VCH Verlag GmbH & Co. KGaA, Weinheim 

DOI: 10.1002/ejic.200600753

# A Comparative Study of Chalcogenated Phosphanylborohydrides $[EPR_2BH_3]^-$ (R = Ph, *t*Bu) and Triorganophosphane Chalcogenides $EPPh_2CH_3$ (E = O, S, Se, Te)

**Franz Dornhaus,[a] Michael Bolte,[a] Hans-Wolfram Lerner,[a] and Matthias Wagner*[a]**

**Keywords:** P ligands / Boranes / Ligand design / Chalcogens / Isoelectronic analogues

Chalcogenation of the phosphanylborohydrides $K(PPh_2BH_3)$ and $K(PtBu_2BH_3)$ with $N_2O$, $S_8$, $Se_\infty$, and $Te_\infty$ leads to the corresponding species $K(EPR_2BH_3)$ in excellent yield (E = O–Te; R = Ph, *t*Bu). The parent systems as well as all the chalcogen derivatives have been structurally characterised as their 18-crown-6 adducts by X-ray crystallography. In the case of $[K(18\text{-c-}6)][EPPh_2BH_3]$ the anionic ligand binds to the $K^+$ ion through both its E atom and its $BH_3$ substituent. Significantly larger K–B distances together with shorter K–E contacts are observed in the sterically more congested *tert*-butyl derivatives $[K(18\text{-c-}6)][EPtBu_2BH_3]$. Based on a comparison of characteristic NMR parameters (e.g. $^1J_{P,B}$, $^1J_{P,C}$) of $K(EPPh_2BH_3)$ and $EPPh_2CH_3$, we come to the conclusion that the formal replacement of $CH_3^+$ by $BH_3$ leads to a significant increase in the p character of the E–P bond, which therefore indicates that $[PPh_2BH_3]^-$ is better suited to direct electron density towards an acceptor atom than its triorganophosphane congener $PPh_2CH_3$. In line with this interpretation, displacement experiments between $K(PPh_2BH_3)$ and $EPPh_2CH_3$ (E = S–Te) resulted in the quantitative formation of $K(EPPh_2BH_3)$ and $PPh_2CH_3$.

(© Wiley-VCH Verlag GmbH & Co. KGaA, 69451 Weinheim, Germany, 2006)

## Introduction

Organophosphanes are among the most abundant ligands in coordination chemistry,[1] therefore much effort is still devoted to the design of improved phosphane ligand systems with customised steric and electronic properties. Of particular importance is a targeted tuning of the Lewis basicity of the phosphorus atom in triorganophosphanes ($PR_3$) by careful variation of the R substituents. For example, aryl substituents result in phosphanes of medium donor strength (cf. $PPh_3$), while more electron-releasing alkyl substituents lead to an increased σ-donor ability (cf. $PEt_3$).[2] Given this background, it is interesting to explore whether replacement of an alkyl side-chain by the even less electronegative $BH_3$ fragment further promotes the capability of the phosphorus centre to deliver charge density to a coordinated acceptor atom. So far, the chemistry of such phosphanylborohydrides $[PR_2BH_3]^-$ has not been systematically developed, although a number of publications already exist that clearly prove the potential of phosphanylborohydrides in areas as diverse as the synthesis of polymeric materials containing group 13 and group 15 elements,[3] the preparation of chiral organophosphanes,[4–7] general coordination chemistry,[8–10] and homogeneous catalysis.[11] Our group has recently reported an assessment of the relative Lewis basicities of $[PPh_2BH_3]^-$, $PPh_2CH_3$ and $PPh_2H$ towards the Lewis acids $H^+$, $[CH_3]^+$ and $BH_3$.[12] In the corresponding adducts the ligands were treated as σ-donors and effects of π-backbonding, which, if present, are only relevant in the $BH_3$ adducts,[13] were neglected. The situation changes when triorganophosphane chalcogenides ($EPR_3$) and chalcogenated phosphanylborohydrides $[EPR_2BH_3]^-$ are included in the discussion. Especially in the case of phosphane oxides, the great stability of the OP group is most likely derived from multiple bonding. A nowadays widely accepted description of the multiple bond in the phosphoryl fragment suggests a donor–acceptor interaction between the electron lone-pair on phosphorus and the oxygen atom (σ-bond) superimposed by a transfer of electron density from two filled 2p orbitals on oxygen to a set of antibonding orbitals of e symmetry on the $PR_3$ fragment (π-bonds; *negative hyperconjugation*[14]).[15] Other theories, however, explain the short, strong and highly polar O–$PR_3$ bond by means of σ donation from P to O, which leads to a pronounced charge separation of the form $^-O\text{-}^+PR_3$ and, in turn, strengthens and shortens the O–P bond due to electrostatic attraction.[16,17]

The purpose of this paper is to compare the structural and NMR spectroscopic properties of compounds $[EPR_2BH_3]^-$ with those of related triorganylphosphane chalcogenides. Electronegative groups on phosphorus are known[18] to increase the degree of multiple bonding in $OPR_3$ compounds and it is therefore interesting to unveil

[a] Institut für Anorganische Chemie, Johann Wolfgang Goethe-Universität Frankfurt am Main,
Max-von-Laue-Strasse 7, 60438 Frankfurt, Germany
Fax: +49-69-798-29260
E-mail: Matthias.Wagner@chemie.uni-frankfurt.de

 © 2006 Wiley-VCH Verlag GmbH & Co. KGaA, Weinheim 

the influence of the electropositive $BH_3$ substituent on the electron distribution within the $[EPR_2BH_3]^-$ framework. Since it is well-known that a delicate interplay exists between steric and electronic effects in phosphane ligands,[2] we have chosen methylbis(phenyl)phosphane ($PPh_2CH_3$) and bis(phenyl)phosphanylborohydride $[PPh_2BH_3]^-$ for our comparative studies since these two compounds are largely isostructural. To elucidate the consequences of steric bulk on the ligand properties of phosphanylborohydrides the *tert*-butyl derivative $[PtBu_2BH_3]^-$ was also included in our investigation.

## Results and Discussion

### Syntheses

The phosphanylborohydrides $K(PR_2BH_3)$ [R = Ph (**1**), *t*Bu (**6**); Scheme 1] are readily accessible by deprotonation of the corresponding phosphane–borane adducts $HPR_2BH_3$ with potassium hydride in thf. Stirring of thf solutions of $K(PR_2BH_3)$ under an atmosphere of dry nitrous oxide leads to the clean formation of $K(OPR_2BH_3)$ (**2**, **7**). Complexes of the heavier chalcogens (**3**–**5** and **8**–**10**) were obtained upon treatment of $K(PR_2BH_3)$ with elemental sulfur, grey selenium or tellurium in thf (Scheme 1). In all cases, the yields were high. The molecules contain a P–B bond and there is no migration of $BH_3$ from the phosphorus to the chalcogen atom. Similar to this, secondary phosphane oxides also prefer $R_2(O)PH$ structures over the tautomeric forms $R_2POH$.[18] $R_2(O)PH$ compounds are weak acids and the proton on phosphorus can be removed with appropriate bases. In most transformations the resulting $[R_2(O)P:]^-$ intermediates react with electrophiles at the phosphorus site, thus preserving the phosphoryl group in the product. Consequently, our derivatives $K(OPR_2BH_3)$ (**2**, **7**) may be viewed as Lewis acid–base adducts between $BH_3$ and $K[R_2(O)P:]$. The O, S and Se derivatives **2**–**4** and **7**–**9** are reasonably stable towards air and moisture. Exposure of the Te derivatives **5** and **10** to water, however, instantaneously leads to the liberation of elemental tellurium together with the formation of $HPR_2BH_3$. The compounds also lose tellurium upon contact with silicone grease. It is interesting to note that **5**, even though it is not a very stable compound, can be synthesised, isolated and structurally characterised. This stands in marked contrast to the related triorganophosphane telluride $TePPh_2CH_3$, which forms only as minor component in a dynamic equilibrium when the phosphane $PPh_2CH_3$ is treated with tellurium in thf solution. Since this result already indicates phosphanylborohydrides $[PR_2BH_3]^-$ to be stronger Lewis bases than their triorganylphosphane counterparts, it prompted us to investigate whether a displacement reaction occurs between $K(PPh_2BH_3)$ (**1**) and the chalcogenides $EPPh_2CH_3$ (E = O, S, Se; **12**–**14**). Indeed, in situ $^{31}P$ NMR spectroscopy revealed quantitative transfer of the E atom from **13** and **14** to the phosphanylborohydride **1** in thf solution. In the case of **1**/**14**, the exchange of the selenium atom proceeds instantaneously at room temp., whereas sulfur transfer from **13** to **1** requires heating of the reaction mixture to 65 °C for 18 h. Under the same conditions an equimolar mixture of **1** and **12** remains unchanged. We believe that the reaction between **1** and **12**, even though thermodynamically favourable, is prevented by a high activation barrier.

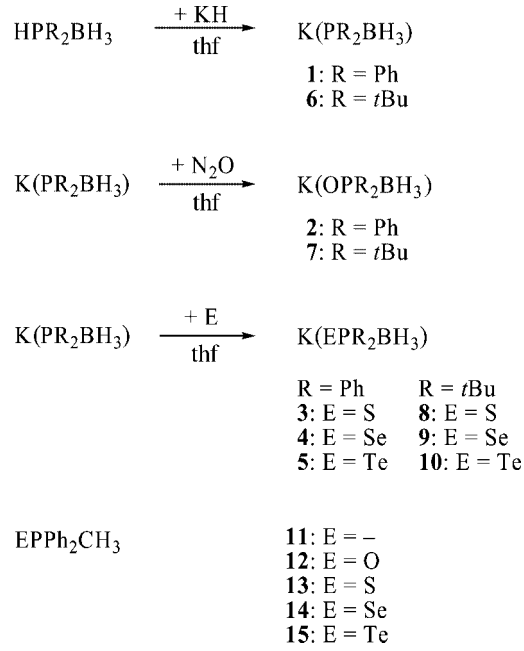


Scheme 1. Synthesis of the potassium phosphanylborohydrides **1** and **6** and their chalcogenation to **2**–**5** and **7**–**10**, along with the numbering scheme of the related methylbis(phenyl)phosphane **11** and its chalcogenides **12**–**15**.

The IR stretching frequency of the EP bond is a useful characteristic of compounds $K(EPR_2BH_3)$ (R = Ph, *t*Bu). Unfortunately, it was not possible to unambiguously assign the band of the EP stretch in the fingerprint region of the IR spectrum of any of the molecules under investigation here.

### X-ray Crystallography

X-ray quality crystals of the 18-crown-6 adducts **1**$^c$–**5**$^c$ were obtained by gas-phase diffusion of diethyl ether onto solutions containing **1**–**5** and equimolar amounts of 18-crown-6. Single-crystals of the adducts **6**$^c$–**10**$^c$ were grown by cooling their concentrated solutions in diethyl ether to –30 °C. Neutral methylbis(phenyl)phosphane oxide (**12**) was crystallised by allowing its hot, saturated, hexane solution to cool to room temp. Crystallographic data for compounds **1**$^c$–**10**$^c$ and **12** are given in the Experimental Section; selected bond lengths and angles are compiled in Table 1.

Each $K^+$ ion in **1**$^c$–**10**$^c$ is bonded to the six oxygen atoms of one 18-crown-6 ligand and to one chalcogenophosphorylic anion. In most cases, short K···B distances indicate $K^+$ coordination of the $BH_3$ substituent in addition to K–E adduct formation (Table 1; E = O, S, Se, Te). According to Edelstein's correlation[19] of metal···boron distances as a measure of the denticity of borohydride groups, values of

 © 2006 Wiley-VCH Verlag GmbH & Co. KGaA, Weinheim 

Table 1. Key structural parameters of compounds **1**$^{c}$–**10**$^{c}$ and **12**. In cases where the EPB fragment is disordered over two positions (E = O, S, Se, Te), the structural parameters of the molecule at the position with higher occupancy are given.

| | | P–E [Å] | P–B [Å] | P–C[a] [Å] | C–P–C′ [°] | K–P/E [Å] | K···B [Å] | K–E–P [°] |
|---|---|---|---|---|---|---|---|---|
| **1**$^{c}$ | $[K(18\text{-c-}6)][PPh_2BH_3]$ | – | 1.960(6) | 1.843(6) | 101.2(2) | 3.320(2) | 3.162 | – |
| **2**$^{c}$ | $[K(18\text{-c-}6)][OPPh_2BH_3]$ | 1.514(1) | 1.908(2) | 1.832(1) | 100.4(1) | 2.742(1) | 3.583 | 104.2(1) |
| **3**$^{c}$ | $[K(18\text{-c-}6)][SPPh_2BH_3]$ | 1.987(4) | 1.972(5) | 1.822(9) | 101.9(4) | 3.365(4) | 3.273 | 89.7(1) |
| **4**$^{c}$ | $[K(18\text{-c-}6)][SePPh_2BH_3]$ | 2.182(1) | 1.907(6) | 1.828(2) | 102.3(1) | 3.491(1) | 3.266 | 87.6(1) |
| **5**$^{c}$ | $[K(18\text{-c-}6)][TePPh_2BH_3]$ | 2.398(1) | 1.921(6) | 1.830(2) | 102.5(1) | 3.680(1) | 3.408 | 85.2(1) |
| **6**$^{c}$ | $[K(18\text{-c-}6)][PtBu_2BH_3]$ | – | 1.956(12)[b] | 1.882(12)[b] | 109.7(5)[b] | 4.92/4.94 | 3.029/3.133 | – |
| **7**$^{c}$ | $[K(18\text{-c-}6)][OPtBu_2BH_3]$ | 1.525(2) | 1.932(4) | 1.879(2) | 110.8(1) | 2.524(2) | 4.683 | 149.5(1) |
| **8**$^{c}$ | $[K(18\text{-c-}6)][SPtBu_2BH_3]$ | 2.011(1) | 1.948(2) | 1.880(2) | 111.0(1) | 3.297(1) | 3.751 | 96.2(1) |
| **9**$^{c}$ | $[K(18\text{-c-}6)][SePtBu_2BH_3]$ | 2.161(1) | 1.982(3) | 1.882(3) | 111.0(2) | 3.413(1) | 4.114 | 97.3(1) |
| **10**$^{c}$ | $[K(18\text{-c-}6)][TePtBu_2BH_3]$ | 2.412(1) | 2.141(2) | 1.889(2) | 111.1(1) | 3.796(1) | 3.698 | 83.2(1) |
| **12** | $OPPh_2CH_3$ | 1.494(2) | – | 1.808(3)[c] | 105.1(1)[d] | – | – | – |

[a] Mean value. [b] Mean value of the two crystallographically independent molecules. [c] P–C(phenyl). [d] C(phenyl)–P–C′(phenyl).

$1.6 \pm 0.1$ and $1.36 \pm 0.06$ Å are estimated for the ionic radii of didentate and tridentate borohydride ligands, respectively. Deduction of an effective ionic radius of a unidentate $BH_4^-$ group is less straightforward, however, mainly because of the greater flexibility of the M–H–B linkage (cf. $r(BH_4^-)$ = 2.23 Å in $[Fe(\eta^1\text{-}BH_4)H(dmpe)_2]$;[20] $r(BH_4^-)$ = 1.92 Å in $[Cu(\eta^1\text{-}BH_4)(PPh_2Me)_3]$[20,21]). However, it has been suggested that if subtraction of the metal ionic radius from the M···B distance in a tetrahydroborate complex gives a value of 1.8 Å or greater, it is likely that the $BH_4^-$ ligand is unidentate.[20] These data lead to the conclusion that K···B distances of about 3.5, 3.25 and 3.01 Å are to be expected for mono-, di and tridentate coordination modes, respectively (ionic radius of octacoordinate $K^+$ = 1.65 Å[22]).

We start our discussion of the molecular structures with a comparison of the two parent phosphanylborohydrides $[K(18\text{-c-}6)][PPh_2BH_3]$ (**1**$^{c}$; Figure 1) and $[K(18\text{-c-}6)][PtBu_2BH_3]$ (**6**$^{c}$; Figure 2) which differ substantially in the steric demand of their organyl substituents. The K–P contact in compound **1**$^{c}$ amounts to 3.320(2) Å and is thus significantly shorter than the sum (3.55 Å) of the van der Waals radius of phosphorus (1.9 Å[23]) and the ionic radius of $K^+$ [angle K–P–B = 68.1(2)°]. The corresponding K···B distance (3.162 Å) suggests an additional $\eta^2$-coordination of the $BH_3$ fragment. In contrast to **1**$^{c}$, the K–P distances of 4.92 and 4.94 Å in **6**$^{c}$ (two crystallographically independent molecules in the asymmetric unit) and K–B–P angles of 149° and 166° clearly exclude any bonding interaction between $K^+$ and the electron lone-pair at phosphorus. Similar to **1**$^{c}$, **6**$^{c}$ features short K···B contacts in the solid state (3.133 and 3.029 Å). In one of the two molecules, K–B coordination is therefore somewhere between $\eta^2$ and $\eta^3$, whereas the second ion-pair is linked by an $\eta^3$-coordinated $BH_3$ fragment. The differences between the solid-state

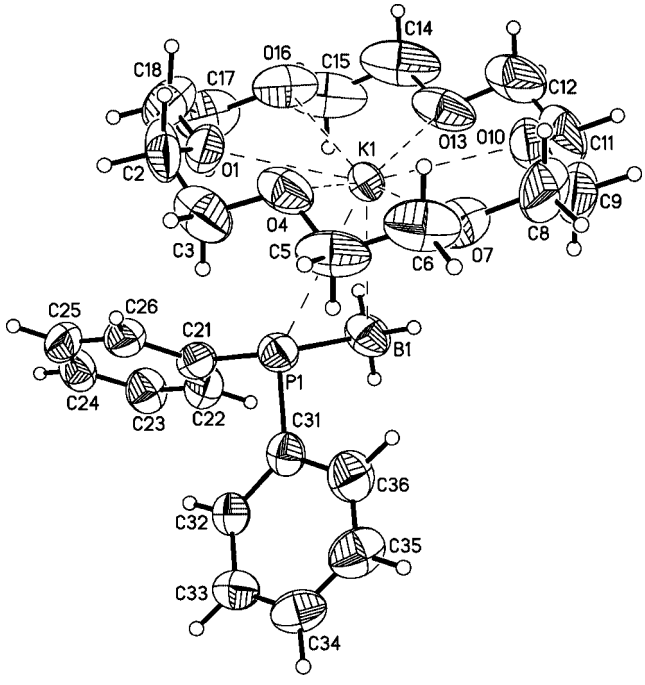


Figure 1. Molecular structure and numbering scheme of compound **1**$^{c}$; thermal ellipsoids shown at the 50% probability level.

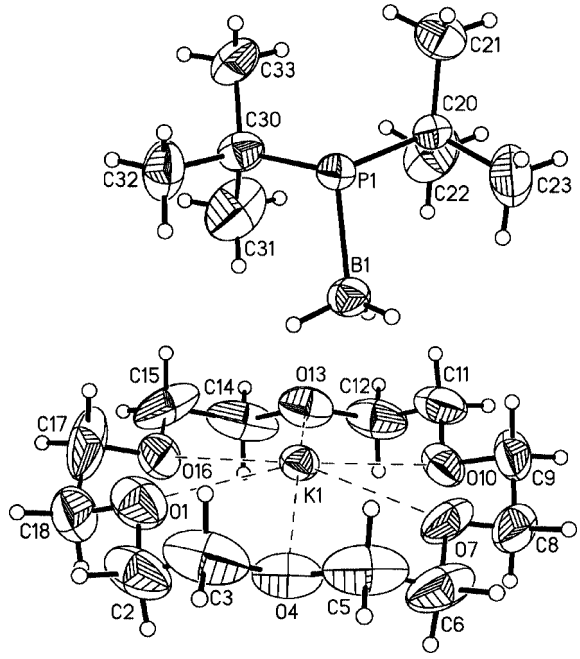


Figure 2. Molecular structure and numbering scheme of compound **6**$^{c}$; thermal ellipsoids shown at the 50% probability level. Only one of the two crystallographically independent $[K(18\text{-c-}6)][PtBu_2BH_3]$ units is shown.

 © 2006 Wiley-VCH Verlag GmbH & Co. KGaA, Weinheim 

structures of **1**[c] and **6**[c] clearly originate from the fact that the bulky *tert*-butyl substituents in the latter compound force the phosphorus centre away from the $[K(18\text{-c-}6)]^+$ plane.

The $[EPPh_2BH_3]^-$ anions of **2**[c]–**5**[c] all coordinate to the $K^+$ ion through both their chalcogen atom and their $BH_3$ groups ($\eta^2$ in the case of the sulfur and selenium derivatives **3**[c] and **4**[c], $\eta^1$ mode in the case of the oxygen and tellurium derivatives **2**[c] and **5**[c]; cf. K···B distances in Table 1). Replacement of phenyl by *tert*-butyl substituents (**7**[c]–**10**[c]) leads to longer K···B distances but shorter K–E bonds (the only exception is the K–Te bond of **10**[c], which is somewhat longer than the K–Te bond in **5**[c]). Provided that the steric requirements are met, as in the case of **2**[c]–**5**[c], it is thus apparent that $BH_3$ coordination to the $K^+$ ion can successfully compete with chalcogen binding. Even though the steric demand of two *tert*-butyl substituents in **7**[c]–**10**[c] precludes the close approach between $K^+$ and B required for the formation of 3c–2e KHB bonds, we nevertheless assume a significant electrostatic attraction between the negative partial charge residing on the $BH_3$ unit and the $K^+$ cation in the *tert*-butyl derivatives as well. As representative examples the molecular structures of $[K(18\text{-c-}6)][OPPh_2BH_3]$ (**2**[c]), $[K(18\text{-c-}6)][OPtBu_2BH_3]$ (**7**[c]), $[K(18\text{-c-}6)][TePPh_2BH_3]$ (**5**[c]) and $[K(18\text{-c-}6)][TePtBu_2BH_3]$ (**10**[c]) are shown in Figures 3, 4, 5 and 6, respectively.

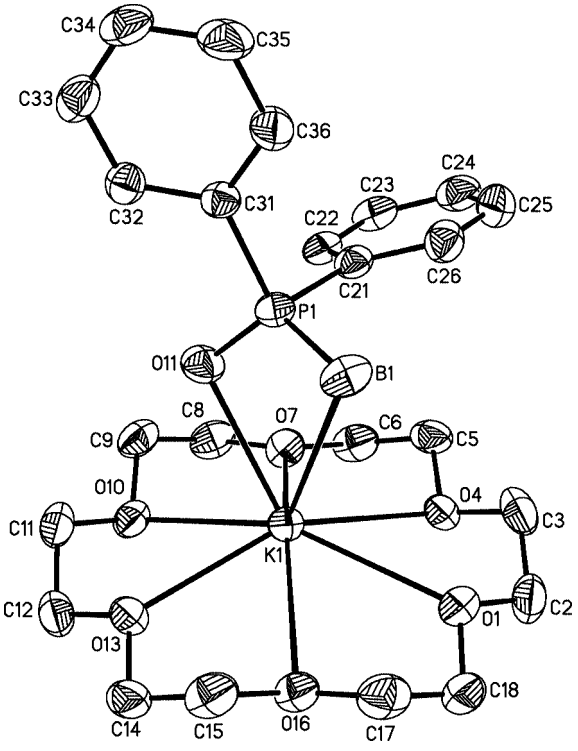


Figure 3. Molecular structure and numbering scheme of compound **2**[c]; thermal ellipsoids shown at the 50% probability level; hydrogen atoms omitted for clarity.

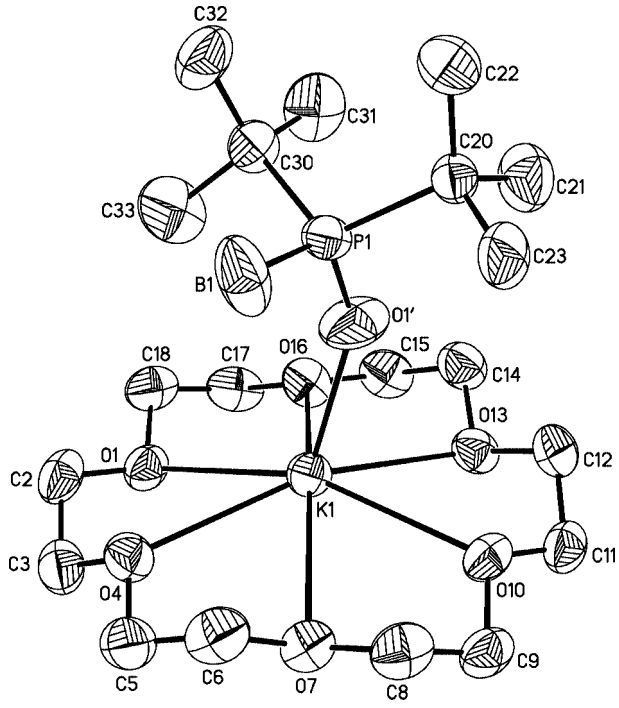


Figure 4. Molecular structure and numbering scheme of compound **7**[c]; thermal ellipsoids shown at the 50% probability level; hydrogen atoms omitted for clarity.

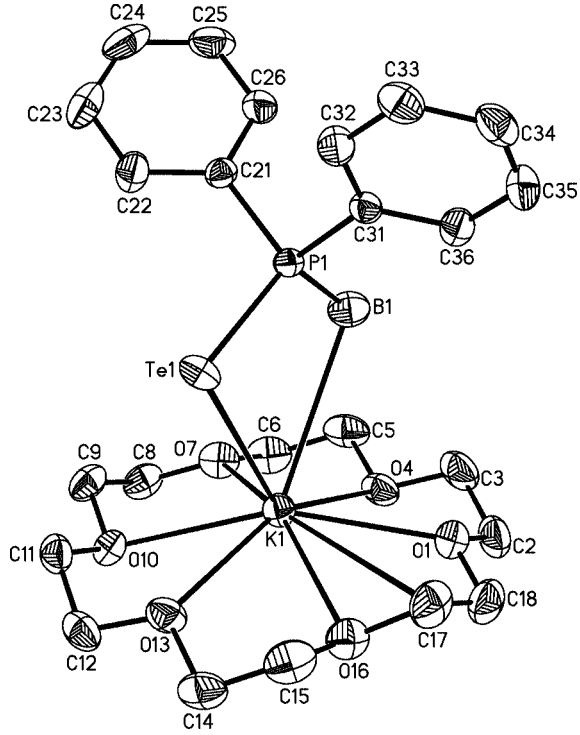


Figure 5. Molecular structure and numbering scheme of compound **5**[c]; thermal ellipsoids shown at the 50% probability level; hydrogen atoms omitted for clarity.

The vast majority of M–E–P angles in metal complexes of chalcogenophosphorylic ligands either fall in the range between 180° and 140° ($L_nM\text{-}OPR_3$) or 115° and 98° ($L_nM\text{-}EPR_3$; E = S, Se).[24] A similar trend is observed for our $[K(18\text{-c-}6)][EPR_2BH_3]$ derivatives in that the largest K–E–P angle within each of the two series is established by the oxo species. However, the *absolute* values of the K–E–P angles in $[K(18\text{-c-}6)][EPR_2BH_3]$ are generally much smaller

 © 2006 Wiley-VCH Verlag GmbH & Co. KGaA, Weinheim 

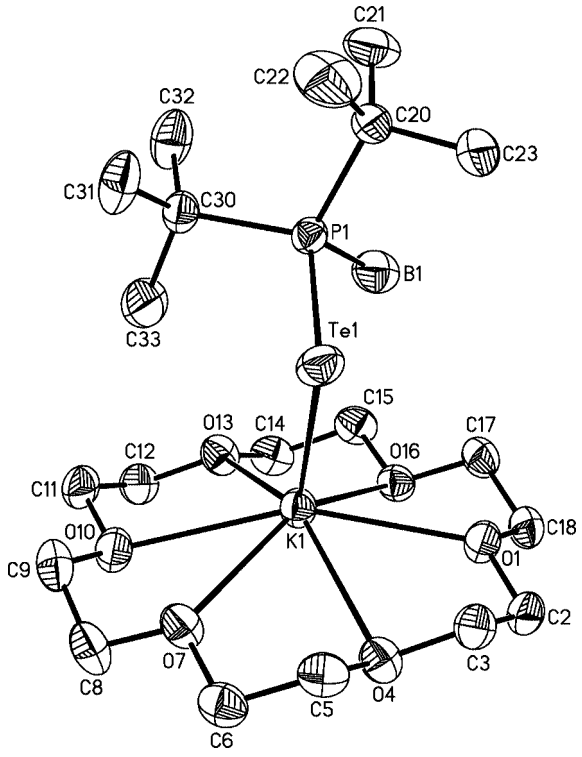


Figure 6. Molecular structure and numbering scheme of compound **10**$^{c}$; thermal ellipsoids shown at the 50% probability level; hydrogen atoms omitted for clarity.

than those of the corresponding M–E–P angles in $L_nM$-$EPR_3$, which is most likely the result of the auxiliary K–$H_3B$ interaction discussed above.

Looking at the series of compounds **2**$^{c}$–**5**$^{c}$ and **7**$^{c}$–**10**$^{c}$ as well as at related triorganylphosphane chalcogenides, it is our goal to find out whether differences in the electron density distribution at phosphorus can be correlated to systematic trends in key structural parameters such as the E–P and P–C bond lengths or the C–P–C′ bond angles. For example, it is generally accepted[25] that a tetracoordinate atom A directs hybrids of greater p character toward more electronegative substituents S and S′, which, in turn, leads to smaller S–A–S′ bond angles.

A comparison of E–P bond lengths in **2**$^{c}$–**5**$^{c}$ with those of related molecules **7**$^{c}$–**10**$^{c}$ reveals larger E–P distances in the *tert*-butyl derivatives **7**$^{c}$, **8**$^{c}$ and **10**$^{c}$ (Table 1). However, the differences are very small, and in the case of the Se compounds the order is even reversed (**9**$^{c}$ < **4**$^{c}$). Our negatively charged molecules $[EPPh_2BH_3]^-$ possess slightly longer E–P bonds than comparable neutral triorganophosphane chalcogenides (Table 2). This effect may either result from $K^+$ coordination[26] or from the presence of the electron-releasing $BH_3$ fragment in **2**$^{c}$–**5**$^{c}$. Irrespective of whether E→P backbonding via *negative hyperconjugation* or electrostatic attraction in a highly polar $^{-}E\text{-}^{+}PR_3$ adduct is the more adequate description of the E–P bond, both factors are likely less pronounced in compounds $K(EPR_2BH_3)$ than in $EPR_2CH_3$ as a consequence of the more negative formal charge on phosphorus in the $BH_3$-containing molecules. Correlations between the length of a polar bond determined in the solid state and the bond strength or bond order must, however, not be overemphasised because crystal packing effects also have to be taken into consideration. An interesting trend is evident for the C(phenyl)–P–C′(phenyl) angles, which are significantly more acute in the ionic species **2**$^{c}$, **3**$^{c}$ and **4**$^{c}$ than in the neutral triorganophosphane chalcogenides (Table 2). Replacement of one organyl substituent by the $BH_3$ group thus results in an increased p character of the two remaining P–C(phenyl) bonds, which is in agreement with the isovalent hybridisation hypothesis.[25] This conclusion is further supported by the fact that the P–C(phenyl) bond is considerably longer in **2**$^{c}$ [1.832(1) Å] than in $OPPh_2CH_3$ [**12**; 1.808(3) Å]. In the case of the heavier homologues **3**$^{c}$/$SPPh_3$ and **4**$^{c}$/$SePPh_3$, however, this bond length difference is levelled out to such an extent that it is no longer of diagnostic significance (Table 2).

Table 2. Comparison of the ionic species **2**$^{c}$, **3**$^{c}$, **4**$^{c}$, and **5**$^{c}$ with their triorganyl analogues.

| | | P–E [Å] | P–C[a] [Å] | C–P–C′ [°] |
|---|---|---|---|---|
| **2**$^{c}$ | $[K(18\text{-c-}6)][OPPh_2BH_3]$ | 1.514(1) | 1.832(1) | 100.4(1) |
| **12** | $OPPh_2CH_3$ | 1.494(2) | 1.808(3) | 105.1(1) |
| **3**$^{c}$ | $[K(18\text{-c-}6)][SPPh_2BH_3]$ | 1.987(4) | 1.822(9) | 101.9(4) |
| | $SPPh_3$[b] | 1.950(3) | 1.817(8) | 105.7(6)[a] |
| **4**$^{c}$ | $[K(18\text{-c-}6)][SePPh_2BH_3]$ | 2.182(1) | 1.828(2) | 102.3(1) |
| | $SePPh_3$[c] | 2.106(1) | 1.826(10) | 105.7(7)[a] |
| **5**$^{c}$ | $[K(18\text{-c-}6)][TePPh_2BH_3]$ | 2.398(1) | 1.830(2) | 102.5(1) |
| | $TeP\textit{i}Pr_3$[d] | 2.363(1) | – | – |
| | $TeP\textit{t}Bu_3$[e] | 2.368(4) | | |

[a] Mean value. [b] Ref.[45] [c] Ref.[46] [d] Ref.[47] [e] Ref.[48]

## NMR Spectroscopy

Characteristic NMR parameters of compounds **1**–**15** (Scheme 1) are compiled in Table 3. For comparability and solubility reasons, all NMR spectra were recorded at 300 K for thf solutions.

The phosphanylborohydrides $K(PPh_2BH_3)$ (**1**) and $K(P\textit{t}Bu_2BH_3)$ (**6**) possess $^{31}P$ NMR shifts of $\delta$ = –28.8 and 12.8 ppm, respectively, remarkably close to the values of the isoelectronic triorganylphosphanes $PPh_2CH_3$ (**11**; $\delta$ = –26.1 ppm[12]) and $P\textit{t}Bu_2CH_3$ ($\delta$ = 11.3 ppm). The pronounced deshielding of the $^{31}P$ NMR resonance upon going from the phenyl to the *tert*-butyl derivatives is attributable to the high steric demand of the alkyl substituents, which enforces a widening of the C–P–C′ angles by an increased admixture of the 3s orbital to the P–C bond.[18] As a consequence, the phosphorus lone-pair is depleted of s character and, in turn, loses some of its shielding effect. In the case of the tetra-coordinated chalcogen compounds the $^{31}P$ NMR resonances of the phenyl derivatives **2**–**5** also appear at higher field than the signals of the corresponding *tert*-butyl derivatives **7**–**10**. The shift difference lies between 30.0 ppm (**2/7**) and 64.6 ppm (**5/10**). We also note that varying the chalcogeno substituent has a much more pronounced effect on the resonance frequency of the $^{31}P$ nucleus in the

 © 2006 Wiley-VCH Verlag GmbH & Co. KGaA, Weinheim 

Table 3. Selected NMR parameters of compounds **1**–**15** in thf; upfield shifts are denoted by a minus sign and downfield shifts by a plus sign.

| | Nucleus | $\delta$ [ppm] ($^1J$ [Hz]) | | | | |
|---|---|---|---|---|---|---|
| | | $^{31}$P | $^{11}$B ($^1J_{P,B}$) | E ($^1J_{PE}$) | P-$^{13}C_i$ ($^1J_{P,C}$) | P-$^{13}C$H$_3$ ($^1J_{P,C}$) |
| **1** | K(PPh$_2$BH$_3$) | –28.8 | –30.1 (32.1) | – | 150.2 (20.1) | – |
| **2** | K(OPPh$_2$BH$_3$) | 64.0 | –35.7 (98.7) | – | 145.4 (54.0) | – |
| **3** | K(SPPh$_2$BH$_3$) | 42.1 | –31.3 (78.2) | – | 143.3 (44.3) | – |
| **4** | K(SePPh$_2$BH$_3$) | 21.8 | –30.3 (67.0) | –264.5 (544) | 141.3 (40.1) | – |
| **5** | K(TePPh$_2$BH$_3$) | –30.9 | –28.1 (51.2) | –509.3 (1249) | 139.6 (35.5) | – |
| **6** | K(P*t*Bu$_2$BH$_3$) | 12.8 | –34.7 (33.8) | – | 32.4 (12.5) | – |
| **7** | K(OP*t*Bu$_2$BH$_3$) | 94.0 | –39.4 (100.6) | – | 34.8 (30.1) | – |
| **8** | K(SP*t*Bu$_2$BH$_3$) | 76.6 | –35.3 (80.8) | – | 35.2 (21.6) | – |
| **9** | K(SeP*t*Bu$_2$BH$_3$) | 68.4 | –34.4 (72.9) | –379.8 (514) | 34.0 (17.0) | – |
| **10** | K(TeP*t*Bu$_2$BH$_3$) | 33.7 | –32.2 (64.3) | –782.0 (1170) | 32.4 (12.5) | – |
| **11** | PPh$_2$CH$_3$ | –26.1 | – | – | 140.8 (10.0) | 12.9 (12.0) |
| **12** | OPPh$_2$CH$_3$ | 28.3 | – | – | 135.8 (99.8) | 16.2 (73.2) |
| **13** | SPPh$_2$CH$_3$ | 35.8 | – | – | 135.7 (81.2) | 21.4 (60.1) |
| **14** | SePPh$_2$CH$_3$ | 24.3 | – | –305.7 (744) | 134.4 (73.1) | 21.9 (53.3) |
| **15** | TePPh$_2$CH$_3$ | 25.6 | – | –554.5 (s) | – | – |

borohydride derivatives **2**–**5** and **7**–**10** than in the triorganophosphane chalcogenides **12**–**15** (Table 3).

The $^{11}$B NMR shifts of **1**–**10** range from $\delta$ = –28.1 (**5**) to –39.4 ppm (**7**) and are typical of phosphane–borane adducts.[27]

$^1J_{P,X}$ coupling constants are valuable diagnostic tools for an assessment of the degree of s character in the P–X bonding orbitals (X = B, C, Se, Te).[28] In many cases, linear correlations between both parameters have been established. This can easily be rationalised if we assume that NMR coupling constants via a certain bond are governed by the Fermi contact term, which increases with increasing s orbital admixture to the respective bond.[28] Moreover, the magnitude of $^1J_{P,B}$ coupling constants in phosphane–borane adducts serves as a qualitative measure of the strength of the P–B bond.[13,29–31] Looking at the coupling constants via the P–B ($^1J_{P,B}$), P–CH$_3$ ($^1J_{P,C}$) and P–C(phenyl) bonds ($^1J_{P,Ci}$), there is always the same qualitative trend: all these coupling constants increase substantially upon attachment of chalcogeno substituents to the phosphorus centres of the parent molecules K(PPh$_2$BH$_3$) (**1**), K(P*t*Bu$_2$BH$_3$) (**6**) and PPh$_2$CH$_3$ (**11**). This effect is strongest for the oxo systems **2**, **7** and **12** and decreases monotonously along the series O > S > Se > Te. From these data it becomes evident that P–E bond formation is accompanied by an increase in s character of the P–BH$_3$/P–CH$_3$ and P–C(phenyl) bonds. Concomitantly, the former phosphorus lone-pair gains p character as it becomes involved in covalent bonding to the chalcogen atom. In line with Bent's rule,[25] this gain is most pronounced for compounds containing the chalcogen atom of highest electronegativity (O); it is intermediate for S and Se and least pronounced for the chalcogen atom of lowest electronegativity (Te). Interestingly, the $^1J_{P,X}$ values of the sulfur derivatives **3**, **8** and **13** are consistently larger than those of the corresponding Se-containing species **4**, **9** and **14** even though the electronegativity of S ($\chi$ = 2.44[23]) is *smaller* than the electronegativity of Se ($\chi$ = 2.48[23]). It is thus obvious that additional effects have to be taken into account for a more detailed understanding of trends in the $^1J_{P,X}$ constants and that the degree of E→P $\pi$ backbonding in particular must not be neglected. Differences in the $^1J_{P,B}$ values of species K(EPPh$_2$BH$_3$) and K(EP*t*Bu$_2$BH$_3$) bearing the same kind of atom E become larger with increasing atomic number of E. Thus, the influence of the organic substituents on the strength of the P–B bond is smallest in the oxo derivatives and most pronounced in the tellurium species.

The $^{77}$Se and $^{125}$Te NMR spectra of **4**, **5**, **9**, **10**, **14** and **15**[32] were measured and the data included in Table 3. Triorganophosphane selenides are known to possess $^1J_{P,Se}$ coupling constants in the range between 700 and 1100 Hz.[28] For SePPh$_2$CH$_3$ (**14**) we have determined a chemical shift value of –305.7 ppm with a $^1J_{P,Se}$ coupling constant of 744 Hz. Formal replacement of CH$_3$ by BH$_3$ (**14** → **4**) leads to a downfield shift of the $^{77}$Se resonance by 41.2 ppm (**4**: $\delta$ = –264.5 ppm) together with a decrease of the absolute value of the coupling constant by 200 Hz (**4**: $^1J_{P,Se}$ = 544 Hz).

## Conclusions

Two complete series of chalcogenated phosphanylborohydrides K(EPR$_2$BH$_3$) (E = O-Te; R = Ph, *t*Bu) have been synthesised and all compounds investigated by NMR spectroscopy and X-ray crystallography (in the latter case as 18-crown-6 adducts). In all cases the molecules contain a P–B bond and there is no migration of BH$_3$ from the phosphorus to the chalcogen atom. A comparison of characteristic structural [e.g. E–P bond lengths, C(phenyl)–P–C′(phenyl) bond angles] and NMR spectroscopic (e.g. $^1J_{P,X}$ coupling constants; X = B, C, Se, Te) parameters of the isoelectronic and isostructural species [EPPh$_2$BH$_3$]$^-$ and EPPh$_2$CH$_3$ leads to the conclusion that [PPh$_2$BH$_3$]$^-$ directs a $\sigma$ orbital of higher p character towards the respective chalcogen atom than PPh$_2$CH$_3$. All trends in the above mentioned parameters are nicely correlated to the changes in the electronegativities of the atoms E, as predicted by

 © 2006 Wiley-VCH Verlag GmbH & Co. KGaA, Weinheim 

Bent's rule.[25] We have already found similar correlations in pure σ adducts of $[PPh_2BH_3]^-$ and $PPh_2CH_3$,[12] which leads us to the conclusion that no influence of E→P backbonding is discernible in our study.

All structural and NMR spectroscopic data indicate the E–P bonds to be stronger with $[PPh_2BH_3]^-$ than with $PPh_2CH_3$ as ligand. This conclusion is supported by the fact that the telluride $K(TePPh_2BH_3)$ is isolable in good yield whereas $TePPh_2CH_3$ forms from a thf solution of $PPh_2CH_3$ and $Te_\infty$ only in trace amounts in a dynamic equilibrium. Moreover, displacement experiments between $K(PPh_2BH_3)$ and $EPPh_2CH_3$ (E = S, Se) resulted in the quantitative formation of $K(EPPh_2BH_3)$ and $PPh_2CH_3$. A similar reaction between $K(PPh_2BH_3)$ and $OPPh_2CH_3$ does not take place (thf, 65 °C, 18 h), most likely due to kinetic rather than thermodynamic reasons. As in triorganylphosphanes the *tert*-butyl derivative $[PtBu_2BH_3]^-$ appears to be an even better Lewis base than its counterpart $[PPh_2BH_3]^-$, most likely for both electronic (+I effect of alkyl substituents) and steric (widening of the C–P–C angle due to steric crowding) reasons.

From an inspection of the molecular structures of [K(18-c-6)][$EPPh_2BH_3$] it becomes evident that $[EPPh_2BH_3]^-$ ligands have to be considered as potentially chelating, with one donor site being the chalcogen atom E and the second the $BH_3$ moiety, which can bind to a metal centre through its hydride substituents. We are presently systematically exploring the potential of phosphanylborohydrides as anionic analogues of triorganophosphanes in coordination chemistry.

## Experimental Section

**General Considerations:** All reactions and manipulations of air-sensitive compounds were carried out under an atmosphere of dry nitrogen using standard Schlenk techniques. Solvents were freshly distilled under argon from sodium/benzophenone (thf, diethyl ether, toluene) or sodium-lead alloy (pentane, hexane) prior to use. NMR spectra were recorded with Bruker AMX 250, DPX 250, AV 300 and AV 400 spectrometers. Approximately 0.1 mL of $C_6D_6$ was added to all samples recorded in undeuterated thf (0.6 mL) to provide a lock signal. $^1H$ and $^{13}C$ NMR shifts are reported relative to tetramethylsilane and were referenced against residual solvent peaks ($C_6D_5H$: $\delta$ = 7.16, $C_6D_6$: $\delta$ = 128.06 ppm; $CHCl_3$: $\delta$ = 7.26, $CDCl_3$: $\delta$ = 77.16 ppm).[33] $^{11}B$ NMR spectra were referenced against external $BF_3{\cdot}OEt_2$, $^{31}P$ NMR spectra against external $H_3PO_4$ (85%) and $^{77}Se$ NMR spectra against external concentrated aqueous $H_2SeO_3$ ($\delta$ = 1300 ppm vs. $Me_2Se$).[34] $^{125}Te$ NMR spectra were referenced against external concentrated aqueous $H_6TeO_6$ ($\delta$ = 712 ppm vs. $Me_2Te$).[35] Abbreviations: s = singlet, d = doublet, q = quartet, dq = doublet of quartets, m = multiplet, n.r. = multiplet expected in the NMR spectrum but not resolved, *i* = *ipso*, *o* = *ortho*, *m* = *meta*, *p* = *para*. Elemental analyses were performed by the microanalytical laboratory of the J. W. Goethe-University, Frankfurt/Main, Germany.

**Materials:** Lithium, $PPh_3$, $PPh_2CH_3$, $PtBu_2H$, KH, $N_2O$, $S_8$, $Se_\infty$, $Te_\infty$, $BH_3{\cdot}THF$ solution (1 M in thf) and 18-crown-6 were purchased from Aldrich or Fluka and used as received. $HPPh_2$ was obtained by reductive cleavage of triphenylphosphane with lithium powder in thf and subsequent hydrolysis and distillation following a literature procedure.[36] The $BH_3$ adduct $HPPh_2BH_3$ was synthesised as described previously.[12] The same procedure was also used to make $HPtBu_2BH_3$.[37] The phosphane chalcogenides $EPPh_2CH_3$ (**12**–**15**) were synthesised by the reaction of $PPh_2CH_3$ with $H_2O_2$, $S_8$, grey $Se_\infty$ or $Te_\infty$ in thf at room temperature.[38–40] $TePPh_2CH_3$ could not be obtained in pure form; the $^{31}P$ NMR spectrum of the yellow reaction mixture showed a yield of approximately 6% of the target compound (dynamic equilibrium between $TePPh_2CH_3$, $Te_\infty$ and $PPh_2CH_3$).

**Synthesis of $K(PPh_2BH_3)$ (1):** A solution of $HPPh_2BH_3$ (2.29 g, 11.4 mmol) in thf (5 mL) was added to a suspension of KH (480 mg, 12.0 mmol) in thf (10 mL) with stirring at –78 °C. The mixture was then warmed to room temp. overnight. After filtration from residual KH, all volatiles were removed in vacuo. The resulting yellow oily residue solidified upon treatment with pentane. Yield: 2.40 g (88%). $^1H$ NMR (thf, 250.13 MHz): $\delta$ = 0.9 (m, 3 H, $BH_3$), 6.79–6.87 (m, 2 H, H-*p*), 6.90–6.98 (m, 4 H, H-*m*), 7.41–7.49 (m, 4 H, H-*o*) ppm. $^{11}B$ NMR (thf, 128.38 MHz): $\delta$ = –30.1 ppm (dq, $^1J_{P,B}$ = 32.1, $^1J_{B,H}$ = 89.9 Hz). $^{13}C\{^1H\}$ NMR (thf, 62.90 MHz): $\delta$ = 124.5 (n.r., C-*p*), 127.0 (d, $^3J_{P,C}$ = 5.1 Hz, C-*m*), 133.9 (d, $^2J_{P,C}$ = 14.0 Hz, C-*o*), 150.2 (d, $^1J_{P,C}$ = 20.1 Hz, C-*i*) ppm. $^{31}P\{^1H\}$ NMR (thf, 161.98 MHz): $\delta$ = –28.8 ppm (m). $C_{24}H_{37}BKO_6P$ (502.42): calcd. C 57.37, H 7.42; found C 57.25, H 7.39.

**Synthesis of $K(OPPh_2BH_3)$ (2):** A solution of **1** (479 mg, 2.01 mmol) in thf (5 mL) was stirred at room temp. under an atmosphere of $N_2O$ until the gas evolution had entirely stopped and the pale-yellow colour had disappeared (ca. 5 min). All volatiles were then removed in vacuo to give a colourless crystalline solid. Yield: 500 mg (98%). $^1H$ NMR (thf, 250.13 MHz): $\delta$ = 0.9 (m, 3 H, $BH_3$), 7.03–7.13 (m, 6 H, H-*m*,*p*), 7.64–7.75 (m, 4 H, H-*o*) ppm. $^{11}B\{^1H\}$ NMR (thf, 128.38 MHz): $\delta$ = –35.7 ppm (d, $^1J_{P,B}$ = 98.7 Hz). $^{13}C\{^1H\}$ NMR (thf, 62.90 MHz): $\delta$ = 127.8 (d, $^3J_{P,C}$ = 8.4 Hz, C-*m*), 128.7 (n.r., C-*p*), 130.7 (d, $^2J_{P,C}$ = 9.9 Hz, C-*o*), 145.4 (d, $^1J_{P,C}$ = 54.0 Hz, C-*i*) ppm. $^{31}P\{^1H\}$ NMR (thf, 101.25 MHz): $\delta$ = 64.0 ppm (m). $C_{24}H_{37}BKO_7P$ (518.42): calcd. C 55.60, H 7.19; found C 55.65, H 7.20.

**Synthesis of $K(SPPh_2BH_3)$ (3):** A solution of **1** (476 mg, 2.00 mmol) in thf (5 mL) was added to a suspension of $S_8$ (70 mg, 2.18 mmol $S_1$) in thf (6 mL) with stirring at –78 °C. The mixture was then warmed to room temp. overnight. All volatiles were removed in vacuo and the resulting pale-yellow solid was triturated with toluene (2 × 5 mL). Yield: 513 mg (95%). $^1H$ NMR (thf, 250.13 MHz): $\delta$ = 1.3 (m, 3 H, $BH_3$), 7.20–7.30 (m, 6 H, H-*m*,*p*), 8.11–8.23 (m, 4 H, H-*o*) ppm. $^{11}B\{^1H\}$ NMR (thf, 128.38 MHz): $\delta$ = –31.3 ppm (d, $^1J_{P,B}$ = 78.2 Hz). $^{13}C\{^1H\}$ NMR (thf, 62.90 MHz): $\delta$ = 127.3 (d, $^3J_{P,C}$ = 9.6 Hz, C-*m*), 128.2 (d, $^4J_{P,C}$ = 2.4 Hz, C-*p*), 131.8 (d, $^2J_{P,C}$ = 10.1 Hz, C-*o*), 143.3 (d, $^1J_{P,C}$ = 44.3 Hz, C-*i*) ppm. $^{31}P\{^1H\}$ NMR (thf, 161.98 MHz): $\delta$ = 42.1 ppm (m). $C_{24}H_{37}BKO_6PS$ (534.48): calcd. C 53.93, H 6.98; found C 53.34, H 6.52.

**Synthesis of $K(SePPh_2BH_3)$ (4):** A solution of **1** (500 mg, 2.10 mmol) in thf (5 mL) was added with stirring at –78 °C to a suspension of grey $Se_\infty$ (166 mg, 2.10 mmol $Se_1$) in thf (2 mL). The mixture was warmed to room temp. overnight whereupon the $Se_\infty$ completely dissolved. All volatiles were then removed in vacuo. The resulting pale-yellow solid was triturated with pentane (2 mL). Yield: 613 mg (92%). $^1H$ NMR (thf, 250.13 MHz): $\delta$ = 1.4 (m, 3 H, $BH_3$), 6.95–7.11 (m, 6 H, H-*m*,*p*), 7.93–8.05 (m, 4 H, H-*o*) ppm. $^{11}B\{^1H\}$ NMR (thf, 128.38 MHz): $\delta$ = –30.3 ppm (d, $^1J_{P,B}$ = 67.0 Hz). $^{13}C\{^1H\}$ NMR (thf, 62.90 MHz): $\delta$ = 127.3 (d, $^3J_{P,C}$ = 9.6 Hz, C-*m*), 128.5 (n.r., C-*p*), 132.5 (d, $^2J_{P,C}$ = 10.0 Hz, C-*o*),

 © 2006 Wiley-VCH Verlag GmbH & Co. KGaA, Weinheim 

141.3 (d, $^1J_{P,C}$ = 40.1 Hz, C-*i*) ppm. $^{31}P\{^1H\}$ NMR (thf, 161.98 MHz): $\delta$ = 21.8 ppm (m). $^{77}Se$ NMR (thf, 47.69 MHz): $\delta$ = –264.5 ppm (d, $^1J_{P,Se}$ = 544 Hz). $C_{24}H_{37}BKO_6PSe$ (581.38): calcd. C 49.58, H 6.41; found C 49.11, H 6.03.

**Synthesis of K(TePPh$_2$BH$_3$) (5):** A solution of **1** (414 mg, 1.74 mmol) in thf (6 mL) was added to a suspension of Te$_\infty$ (222 mg, 1.74 mmol Te$_1$) in thf (4 mL) with stirring at –78 °C. The mixture was then warmed to room temp. overnight. The resulting yellow solution was filtered and all volatiles removed in vacuo. The remaining yellow solid was triturated with pentane (2 mL). Yield: 605 mg (95%). $^1H$ NMR (thf, 250.13 MHz): $\delta$ = 1.8 (m, 3 H, BH$_3$), 6.93–7.09 (m, 6 H, H-*m*,*p*), 7.89–8.00 (m, 4 H, H-*o*) ppm. $^{11}B\{^1H\}$ NMR (thf, 128.38 MHz): $\delta$ = –28.1 ppm (d, $^1J_{P,B}$ = 51.2 Hz). $^{13}C\{^1H\}$ NMR (thf, 62.90 MHz): $\delta$ = 127.3 (d, $^3J_{P,C}$ = 9.5 Hz, C-*m*), 128.5 (n.r., C-*p*), 133.5 (d, $^2J_{P,C}$ = 9.6 Hz, C-*o*), 139.6 (d, $^1J_{P,C}$ = 35.5 Hz, C-*i*) ppm. $^{31}P\{^1H\}$ NMR (thf, 161.98 MHz): $\delta$ = –30.9 ppm (m). $^{125}Te\{^1H\}$ NMR (thf, 78.88 MHz): $\delta$ = –509.3 ppm (d, $^1J_{P,Te}$ = 1249 Hz). $C_{24}H_{37}BKO_6PTe$ (630.02): calcd. C 45.75, H 5.92; found C 45.53, H 5.65.

**Synthesis of K(P*t*Bu$_2$BH$_3$) (6):** A solution of HP*t*Bu$_2$BH$_3$ (1.14 g, 7.12 mmol) in thf (5 mL) was added to a suspension of KH (290 mg, 7.23 mmol) in thf (6 mL) with stirring at –78 °C. The mixture was then warmed to room temp. overnight. After filtration from residual KH all volatiles were removed in vacuo. Yield: 1.15 g (82%). $^1H$ NMR (thf, 250.13 MHz): $\delta$ = 0.28 (q, $^1J_{B,H}$ = 88 Hz, 3 H, BH$_3$), 1.16 (d, $^3J_{P,H}$ = 9.8 Hz, 18 H, CH$_3$) ppm. $^{11}B\{^1H\}$ NMR (thf, 128.38 MHz): $\delta$ = –34.7 ppm (d, $^1J_{P,B}$ = 33.8 Hz). $^{13}C\{^1H\}$ NMR (thf, 62.90 MHz): $\delta$ = 29.6 (d, $^2J_{P,C}$ = 2.8 Hz, CH$_3$), 32.4 (d, $^1J_{P,C}$ = 12.5 Hz, *C*CH$_3$) ppm. $^{31}P\{^1H\}$ NMR (thf, 161.98 MHz): $\delta$ = 12.8 ppm (m). $C_{20}H_{45}BKO_6P$ (462.44): calcd. C 51.94, H 9.81; due to the extreme air and moisture sensitivity of the compound a decent elemental analysis was not obtained, even from a single crystalline sample.

**Synthesis of K(OP*t*Bu$_2$BH$_3$) (7):** A solution of **6** (240 mg, 1.21 mmol) in thf (3 mL) was stirred at room temp. under an atmosphere of $N_2O$ until the gas evolution had entirely stopped (ca. 5 min). After all volatiles had been removed in vacuo, the product was obtained as a colourless crystalline solid. Yield: 255 mg (98%). $^1H$ NMR (thf, 250.13 MHz): $\delta$ = 0.4 (m, 3 H, BH$_3$), 1.14 (d, $^3J_{P,H}$ = 11.2 Hz, 18 H, CH$_3$) ppm. $^{11}B\{^1H\}$ NMR (thf, 128.38 MHz): $\delta$ = –39.4 ppm (d, $^1J_{P,B}$ = 100.6 Hz). $^{13}C\{^1H\}$ NMR (thf, 62.90 MHz): $\delta$ = 27.8 (d, $^2J_{P,C}$ = 2.3 Hz, CH$_3$), 34.8 (d, $^1J_{P,C}$ = 30.1 Hz, *C*CH$_3$) ppm. $^{31}P\{^1H\}$ NMR (thf, 161.98 MHz): $\delta$ = 94.0 ppm (m). $C_{20}H_{45}BKO_7P$ (478.44): calcd. C 50.21, H 9.48; found C 49.97, H 9.58.

**Synthesis of K(SP*t*Bu$_2$BH$_3$) (8):** A solution of **6** (283 mg, 1.43 mmol) in thf (3 mL) was added to a suspension of S$_8$ (48 mg, 1.50 mmol S$_1$) in thf (3 mL) with stirring at –78 °C. The mixture was then warmed to room temp. overnight. After all volatiles had been removed in vacuo, the resulting colourless solid was triturated with pentane (2 × 2 mL). Yield: 322 mg (98%). $^1H$ NMR (thf, 300.03 MHz): $\delta$ = 0.52 (q, $^1J_{B,H}$ = 92 Hz, 3 H, BH$_3$), 1.19 (d, $^3J_{P,H}$ = 12.0 Hz, 18 H, CH$_3$) ppm. $^{11}B\{^1H\}$ NMR (thf, 96.26 MHz): $\delta$ = –35.3 ppm (d, $^1J_{P,B}$ = 80.8 Hz). $^{13}C\{^1H\}$ NMR (thf, 62.90 MHz): $\delta$ = 28.5 (d, $^2J_{P,C}$ = 2.9 Hz, CH$_3$), 35.2 (d, $^1J_{P,C}$ = 21.6 Hz, *C*CH$_3$) ppm. $^{31}P\{^1H\}$ NMR (thf, 121.46 MHz): $\delta$ = 76.6 ppm (q, $^1J_{P,B}$ = 80.8 Hz). $C_{20}H_{45}BKO_6PS$ (494.50): calcd. C 48.58, H 9.17; found C 48.68, H 9.23.

**Synthesis of K(SeP*t*Bu$_2$BH$_3$) (9):** A solution of **6** (279 mg, 1.41 mmol) in thf (3 mL) was added to a suspension of grey Se$_\infty$ (111 mg, 1.41 mmol Se$_1$) in thf (2 mL) with stirring at –78 °C. The mixture was then warmed to room temp. overnight, whereupon the Se$_\infty$ dissolved completely. The reaction mixture was evaporated to dryness in vacuo and the resulting colourless solid triturated with pentane (2 mL). Yield: 357 mg (91%). $^1H$ NMR (thf, 250.13 MHz): $\delta$ = 0.75 (q, $^1J_{B,H}$ = 93 Hz, 3 H, BH$_3$), 1.27 (d, $^3J_{P,H}$ = 12.6 Hz, 18 H, CH$_3$) ppm. $^{11}B\{^1H\}$ NMR (thf, 128.38 MHz): $\delta$ = –34.4 ppm (d, $^1J_{P,B}$ = 72.9 Hz). $^{13}C\{^1H\}$ NMR (thf, 62.90 MHz): $\delta$ = 29.0 (d, $^2J_{P,C}$ = 3.0 Hz, CH$_3$), 34.0 (d, $^1J_{P,C}$ = 17.0 Hz, *C*CH$_3$) ppm. $^{31}P\{^1H\}$ NMR (thf, 161.98 MHz): $\delta$ = 68.4 ppm (m). $^{77}Se$ NMR (thf, 76.30 MHz): $\delta$ = –379.8 ppm (d, $^1J_{P,Se}$ = 514 Hz). $C_{20}H_{45}BKO_6PSe$ (541.40): calcd. C 44.37, H 8.38; found C 44.35, H 8.50.

**Synthesis of K(TeP*t*Bu$_2$BH$_3$) (10):** A solution of **6** (302 mg, 1.52 mmol) in thf (3 mL) was added to a suspension of Te$_\infty$ (195 mg, 1.53 mmol Te$_1$) in thf (3 mL) with stirring at –78 °C. The mixture was then warmed to room temp. overnight. The resulting yellow solution was filtered and all volatiles removed in vacuo. The yellow solid residue was triturated with pentane (2 × 2 mL). Yield: 490 mg (99%). $^1H$ NMR (thf, 250.13 MHz): $\delta$ = 1.2 (m, 3 H, BH$_3$), 1.34 (d, $^3J_{P,H}$ = 12.8 Hz, 18 H, CH$_3$) ppm. $^{11}B\{^1H\}$ NMR (thf, 128.38 MHz): $\delta$ = –32.2 ppm (d, $^1J_{P,B}$ = 64.3 Hz). $^{13}C\{^1H\}$ NMR (thf, 62.90 MHz): $\delta$ = 29.6 (d, $^2J_{P,C}$ = 2.8 Hz, CH$_3$), 32.4 (d, $^1J_{P,C}$ = 12.5 Hz, *C*CH$_3$) ppm. $^{31}P\{^1H\}$ NMR (thf, 161.98 MHz): $\delta$ = 33.7 ppm (m). $^{125}Te\{^1H\}$ NMR (thf, 78.88 MHz): $\delta$ = –782.0 (d, $^1J_{P,Te}$ = 1170 Hz). $C_{20}H_{45}BKO_6PTe$ (590.04): calcd. C 40.71, H 7.69; found C 40.38, H 7.27.

**OPPh$_2$CH$_3$ (12):** $^1H$ NMR (thf, 400.13 MHz): $\delta$ = 1.80 (d, $^2J_{P,H}$ = 13.4 Hz, 3 H, CH$_3$), 7.20–7.30 (m, 6 H, H-*m*,*p*), 7.66–7.74 (m, 4 H, H-*o*) ppm. $^{13}C\{^1H\}$ NMR (thf, 62.90 MHz): $\delta$ = 16.2 (d, $^1J_{P,C}$ = 73.2 Hz, CH$_3$), 128.8 (d, $^3J_{P,C}$ = 11.7 Hz, C-*m*), 130.9 (d, $^2J_{P,C}$ = 9.6 Hz, C-*o*), 131.6 (d, $^4J_{P,C}$ = 2.8 Hz, C-*p*), 135.8 (d, $^1J_{P,C}$ = 99.8 Hz, C-*i*) ppm. $^{31}P\{^1H\}$ NMR (thf, 161.98 MHz): $\delta$ = 28.3 ppm (s).

**SPPh$_2$CH$_3$ (13):** $^1H$ NMR (thf, 250.13 MHz): $\delta$ = 2.04 (d, $^2J_{P,H}$ = 13.3 Hz, 3 H, CH$_3$), 7.19–7.30 (m, 6 H, H-*m*,*p*), 7.69–7.79 (m, 4 H, H-*o*) ppm. $^{13}C\{^1H\}$ NMR (thf, 62.90 MHz): $\delta$ = 21.4 (d, $^1J_{P,C}$ = 60.1 Hz, CH$_3$), 128.7 (d, $^3J_{P,C}$ = 12.1 Hz, C-*m*), 131.2 (d, $^2J_{P,C}$ = 10.6 Hz, C-*o*), 131.3 (d, $^4J_{P,C}$ = 2.7 Hz, C-*p*), 135.7 (d, $^1J_{P,C}$ = 81.2 Hz, C-*i*) ppm. $^{31}P\{^1H\}$ NMR (thf, 161.98 MHz): $\delta$ = 35.8 ppm (s).

**SePPh$_2$CH$_3$ (14):** $^1H$ NMR (thf, 250.13 MHz): $\delta$ = 2.24 (d, $^2J_{P,H}$ = 13.6 Hz, 3 H, CH$_3$), 7.21–7.28 (m, 6 H, H-*m*,*p*), 7.71–7.79 (m, 4 H, H-*o*) ppm. $^{13}C\{^1H\}$ NMR (thf, 62.90 MHz): $\delta$ = 21.9 (d, $^1J_{P,C}$ = 53.3 Hz, CH$_3$), 128.7 (d, $^3J_{P,C}$ = 12.1 Hz, C-*m*), 131.4 (d, $^4J_{P,C}$ = 2.9 Hz, C-*p*), 131.6 (d, $^2J_{P,C}$ = 10.8 Hz, C-*o*), 134.4 (d, $^1J_{P,C}$ = 73.1 Hz, C-*i*) ppm. $^{31}P\{^1H\}$ NMR (thf, 161.98 MHz): $\delta$ = 24.3 ppm (s, $^1J_{PSe}$ = 744 Hz). $^{77}Se$ NMR (thf, 76.31 MHz): $\delta$ = –305.7 ppm (d, $^1J_{P,Se}$ = 744 Hz).

**TePPh$_2$CH$_3$ (15):** $^{31}P\{^1H\}$ NMR (thf, 161.98 MHz): $\delta$ = 25.6 ppm (s). $^{125}Te\{^1H\}$ NMR (thf, 126.19 MHz): $\delta$ = –554.5 ppm (s).

**X-ray Structural Characterisation:** Data collections were performed on a Stoe IPDS-II two-circle diffractometer with graphite-monochromated Mo-$K_\alpha$ radiation (see Tables 4 and 5). Empirical absorption corrections were performed with the MULABS option[41] in the program PLATON.[42] Equivalent reflections were averaged. The structures were solved by direct methods[43] and refined with full-matrix least-squares on $F^2$ using the program SHELXL-97.[44] Hydrogen atoms bonded to carbon and boron were placed at ideal positions and refined with fixed isotropic displacement parameters using a riding model.

CCDC-616914 (for **1**[c]), -616915 (for **2**[c]), -616916 (for **3**[c]), -616917 (for **4**[c]), -616918 (for **5**[c]), -616919 (for **6**[c]), -616920 (for

 © 2006 Wiley-VCH Verlag GmbH & Co. KGaA, Weinheim 

Table 4. Crystallographic data for compounds **1**[c]–**6**[c].

| | **1**[c] | **2**[c] | **3**[c] | **4**[c] | **5**[c] | **6**[c] |
|---|---|---|---|---|---|---|
| Formula | $C_{24}H_{37}BKO_6P$ | $C_{24}H_{37}BKO_7P$ | $C_{24}H_{37}BKO_6PS$ | $C_{24}H_{37}BKO_6PSe$ | $C_{24}H_{37}BKO_6PTe$ | $C_{20}H_{45}BKO_6P$ |
| *FW* | 502.42 | 518.42 | 534.48 | 581.38 | 630.02 | 462.44 |
| Colour, shape | yellow, plate | colourless, block | colourless, block | colourless, block | pale brown, block | colourless, block |
| Temp. [K] | 173(2) | 173(2) | 173(2) | 173(2) | 173(2) | 173(2) |
| Crystal system | orthorhombic | monoclinic | monoclinic | triclinic | triclinic | triclinic |
| Space group | $P2_12_12_1$ | $P2_1/n$ | $P2_1/n$ | $P\bar{1}$ | $P\bar{1}$ | $P\bar{1}$ |
| *a* [Å] | 9.3360(11) | 10.5434(7) | 8.5124(13) | 9.1832(6) | 9.2459(5) | 9.1609(17) |
| *b* [Å] | 10.3261(15) | 14.2860(9) | 30.376(4) | 10.7869(7) | 10.9071(6) | 16.320(3) |
| *c* [Å] | 28.178(3) | 18.4297(11) | 10.6730(17) | 14.9362(10) | 14.9509(9) | 18.428(4) |
| *α* [°] | 90 | 90 | 90 | 74.526(5) | 74.104(5) | 88.381(15) |
| *β* [°] | 90 | 100.287(5) | 99.230(13) | 81.993(6) | 83.045(5) | 81.078(15) |
| *γ* [°] | 90 | 90 | 90 | 86.034(5) | 84.802(5) | 86.627(15) |
| *V* [Å$^3$] | 2716.5(6) | 2731.3(3) | 2724.0(7) | 1411.23(16) | 1436.81(14) | 2716.5(9) |
| *Z* | 4 | 4 | 4 | 2 | 2 | 4 |
| $D_{calcd.}$ [g cm$^{-3}$] | 1.228 | 1.261 | 1.303 | 1.368 | 1.456 | 1.131 |
| *F*(000) | 1072 | 1104 | 1136 | 604 | 640 | 1008 |
| *μ* [mm$^{-1}$] | 0.289 | 0.292 | 0.366 | 1.569 | 1.270 | 0.283 |
| Cryst. size [mm] | 0.34 × 0.12 × 0.03 | 0.46 × 0.35 × 0.30 | 0.50 × 0.41 × 0.32 | 0.39 × 0.34 × 0.22 | 0.29 × 0.16 × 0.09 | 0.36 × 0.33 × 0.28 |
| Reflections collected | 19217 | 39345 | 37292 | 40557 | 54151 | 19270 |
| Indep. reflns. ($R_{int}$) | 4911 (0.1098) | 5646 (0.0567) | 5450 (0.1267) | 7317 (0.0556) | 5940 (0.0610) | 9619 (0.0896) |
| Data/restraints/params. | 4911/0/299 | 5646/0/307 | 5450/0/308 | 7317/6/326 | 5940/0/317 | 9619/0/526 |
| GOOF on $F^2$ | 0.884 | 0.969 | 1.101 | 1.023 | 0.955 | 1.146 |
| $R_1$, $wR_2$ [$I > 2\sigma(I)$] | 0.0586, 0.1148 | 0.0302, 0.0730 | 0.1773, 0.3039 | 0.033, 0.082 | 0.0195, 0.0435 | 0.1186, 0.3066 |
| $R_1$, $wR_2$ (all data) | 0.1020, 0.1304 | 0.0435, 0.0764 | 0.2006, 0.3155 | 0.0423, 0.0857 | 0.0259, 0.0468 | 0.1595, 0.3498 |
| Largest diff. peak and hole [e Å$^{-3}$] | 0.717 and –0.211 | 0.370 and –0.251 | 0.507 and –0.424 | 0.379 and –0.410 | 0.374 and –0.330 | 0.787 and –0.558 |

Table 5. Crystallographic data for compounds **7**[c]–**10**[c] and **12**.

| | **7**[c] | **8**[c] | **9**[c] | **10**[c] | **12** |
|---|---|---|---|---|---|
| Formula | $C_{20}H_{45}BKO_7P$ | $C_{20}H_{45}BKO_6PS$ | $C_{20}H_{45}BKO_6PSe$ | $C_{20}H_{45}BKO_6PTe$ | $C_{13}H_{13}OP$ |
| *FW* | 478.44 | 494.50 | 541.40 | 590.04 | 216.2 |
| Colour, shape | colourless, block | colourless, block | colourless, rod | yellow, block | colourless, plate |
| Temp. [K] | 173(2) | 173(2) | 173(2) | 173(2) | 173(2) |
| Crystal system | monoclinic | monoclinic | monoclinic | monoclinic | monoclinic |
| Space group | $P2_1/n$ | $P2_1/n$ | $P2_1/n$ | $P2_1/n$ | $P2_1/c$ |
| *a* [Å] | 9.6648(13) | 9.4050(7) | 9.3016(8) | 9.8710(7) | 8.6344(8) |
| *b* [Å] | 15.4313(16) | 14.7442(8) | 14.8982(10) | 14.8400(9) | 24.2057(18) |
| *c* [Å] | 18.745(3) | 19.9463(12) | 20.0229(17) | 19.1333(14) | 5.6957(6) |
| *α* [°] | 90 | 90 | 90 | 90 | 90 |
| *β* [°] | 100.420(11) | 98.900(5) | 97.485(7) | 92.265(6) | 108.067(7) |
| *γ* [°] | 90 | 90 | 90 | 90 | 90 |
| *V* [Å$^3$] | 2749.5(6) | 2732.6(3) | 2751.1(4) | 2800.6(3) | 1131.72(18) |
| *Z* | 4 | 4 | 4 | 4 | 4 |
| $D_{calcd.}$ [g cm$^{-3}$] | 1.156 | 1.202 | 1.307 | 1.399 | 1.269 |
| *F*(000) | 1040 | 1072 | 1144 | 1216 | 456 |
| *μ* [mm$^{-1}$] | 0.284 | 0.359 | 1.604 | 1.297 | 0.212 |
| Cryst. size [mm] | 0.38 × 0.22 × 0.20 | 0.49 × 0.44 × 0.38 | 0.38 × 0.24 × 0.22 | 0.43 × 0.35 × 0.28 | 0.2 × 0.14 × 0.04 |
| Reflections collected | 29877 | 36838 | 32382 | 37620 | 9906 |
| Indep. reflns. ($R_{int}$) | 5204 (0.0913) | 5498 (0.0698) | 5213 (0.0936) | 5609 (0.0450) | 1994 (0.0380) |
| Data/restraints/params. | 5204/0/272 | 5498/0/272 | 5213/0/272 | 5609/0/272 | 1994/46/150 |
| GOOF on $F^2$ | 0.785 | 1.036 | 0.860 | 0.866 | 1.033 |
| $R_1$, $wR_2$ [$I > 2\sigma(I)$] | 0.0374, 0.069 | 0.0369, 0.1059 | 0.0415, 0.0908 | 0.0197, 0.0419 | 0.0575, 0.1413 |
| $R_1$, $wR_2$ (all data) | 0.0845, 0.0776 | 0.0444, 0.1089 | 0.0718, 0.0979 | 0.0282, 0.0428 | 0.0642, 0.1457 |
| Largest diff. peak and hole [e Å$^{-3}$] | 0.394 and –0.289 | 0.305 and –0.580 | 0.569 and –0.720 | 0.493 and –0.344 | 0.821 and –0.497 |

**7**[c]), -616921 (for **8**[c]), -616922 (for **9**[c]), -616923 (for **10**[c]) and -616924 (for **12**) contain the supplementary crystallographic data for this paper. These data can be obtained free of charge from The Cambridge Crystallographic Data Centre via www.ccdc.cam.ac.uk/data_request/cif.

## Acknowledgments

The authors are grateful to the Deutsche Forschungsgemeinschaft (DFG) and the Fonds der Chemischen Industrie (FCI) for financial support.

 © 2006 Wiley-VCH Verlag GmbH & Co. KGaA, Weinheim 

[1] L. H. Gade, *Koordinationschemie*, Wiley-VCH, Weinheim, **1998**.
[2] C. A. Tolman, *Chem. Rev.* **1977**, *77*, 313–348.
[3] C. A. Jaska, A. J. Lough, I. Manners, *Inorg. Chem.* **2004**, *43*, 1090–1099.
[4] B. Wolfe, T. Livinghouse, *J. Am. Chem. Soc.* **1998**, *120*, 5116–5117.
[5] T. Miura, H. Yamada, S. Kikuchi, T. Imamoto, *J. Org. Chem.* **2000**, *65*, 1877–1880.
[6] B. Wolfe, T. Livinghouse, *J. Org. Chem.* **2001**, *66*, 1514–1516.
[7] J.-M. Camus, J. Andrieu, P. Richard, R. Poli, C. Darcel, S. Jugé, *Tetrahedron: Asymmetry* **2004**, *15*, 2061–2065.
[8] W. Angerer, W. S. Sheldrick, W. Malisch, *Chem. Ber.* **1985**, *118*, 1261–1266.
[9] H. Dorn, C. A. Jaska, R. A. Singh, A. J. Lough, I. Manners, *Chem. Commun.* **2000**, 1041–1042.
[10] G. Müller, J. Brand, *Organometallics* **2003**, *22*, 1463–1467.
[11] A.-C. Gaumont, M. B. Hursthouse, S. J. Coles, J. M. Brown, *Chem. Commun.* **1999**, 63–64.
[12] F. Dornhaus, M. Bolte, H.-W. Lerner, M. Wagner, *Eur. J. Inorg. Chem.* **2006**, 1777–1785.
[13] A. H. Cowley, M. C. Damasco, *J. Am. Chem. Soc.* **1971**, *93*, 6815–6821.
[14] A. E. Reed, P. v. R. Schleyer, *J. Am. Chem. Soc.* **1990**, *112*, 1434–1445.
[15] D. G. Gilheany, *Chem. Rev.* **1994**, *94*, 1339–1374.
[16] J. A. Dobado, H. Martínez-García, J. M. Molina, M. R. Sundberg, *J. Am. Chem. Soc.* **1998**, *120*, 8461–8471.
[17] D. B. Chesnut, *J. Am. Chem. Soc.* **1998**, *120*, 10504–10510.
[18] L. D. Quin, *A Guide to Organophosphorus Chemistry*, John Wiley & Sons, New York, **2000**.
[19] N. Edelstein, *Inorg. Chem.* **1981**, *20*, 297–299.
[20] J. A. Jensen, G. S. Girolami, *Inorg. Chem.* **1989**, *28*, 2107–2113.
[21] F. Takusagawa, A. Fumagalli, T. F. Koetzle, S. G. Shore, T. Schmitkons, A. V. Fratini, K. W. Morse, C.-Y. Wei, R. Bau, *J. Am. Chem. Soc.* **1981**, *103*, 5165–5171.
[22] R. D. Shannon, *Acta Crystallogr., Sect. A* **1976**, *32*, 751–767.
[23] A. F. Holleman, N. Wiberg, *Lehrbuch der Anorganischen Chemie*, 101 ed., de Gruyter, Berlin, New York, **1995**.
[24] N. Burford, *Coord. Chem. Rev.* **1992**, *112*, 1–18.
[25] H. A. Bent, *Chem. Rev.* **1961**, *61*, 275–311.
[26] The difference between the P–O bond length in free $R_3PO$ and in the corresponding $R_3PO$-$ML_n$ complexes is remarkably small and generally of the order of <0.01 Å (1%). Metal coordination to $R_3PE$ ligands (E = S, Se) also leads to only a slight elongation of the P–E bond (≈ 0.06 Å; 3%).[24].
[27] H. Nöth, B. Wrackmeyer, in *NMR Basic Principles and Progress* (Eds.: P. Diehl, E. Fluck, R. Kosfeld), vol. 14, *Nuclear Magnetic Resonance Spectroscopy of Boron Compounds*, Springer, Berlin, **1978**.
[28] S. Berger, S. Braun, H.-O. Kalinowski, *NMR-Spektroskopie von Nichtmetallen*, vol. 3, *$^{31}$P-NMR-Spektroskopie*, Thieme Verlag, Stuttgart, **1993**.
[29] R. W. Rudolph, C. W. Schultz, *J. Am. Chem. Soc.* **1971**, *93*, 6821–6822.
[30] R. Foester, K. Cohn, *Inorg. Chem.* **1972**, *11*, 2590–2593.
[31] B. Rapp, J. E. Drake, *Inorg. Chem.* **1973**, *12*, 2868–2873.
[32] Note that the $^{125}$Te NMR shift assigned to compound **15** was determined by investigating an equilibrium mixture of **11** and **15** in thf.
[33] H. E. Gottlieb, V. Kotlyar, A. Nudelman, *J. Org. Chem.* **1997**, *62*, 7512–7515.
[34] H. Duddeck, *Prog. Nucl. Magn. Reson. Spectrosc.* **1995**, *27*, 1–323.
[35] P. J. Bonasia, V. Christou, J. Arnold, *J. Am. Chem. Soc.* **1993**, *115*, 6777–6781.
[36] V. D. Bianco, S. Doronzo, *Inorg. Synth.* **1976**, *16*, 161–163.
[37] H. Dorn, R. A. Singh, J. A. Massey, J. M. Nelson, C. A. Jaska, A. J. Lough, I. Manners, *J. Am. Chem. Soc.* **2000**, *122*, 6669–6678.
[38] R. A. Zingaro, R. E. McGlothlin, *J. Chem. Eng. Data* **1963**, *8*, 226–229.
[39] R. B. King, P. R. Heckley, *Phosphorus Relat. Group V Elem.* **1974**, *3*, 209–211.
[40] G. Grossmann, B. Walther, U. Gastrock-Mey, *Phosphorus, Sulfur Relat. Elem.* **1981**, *11*, 259–272.
[41] R. H. Blessing, *Acta Crystallogr., Sect. A* **1995**, *51*, 33–38.
[42] A. L. Spek, *Acta Crystallogr., Sect. A* **1990**, *46*, C34.
[43] G. M. Sheldrick, *Acta Crystallogr., Sect. A* **1990**, *46*, 467–473.
[44] G. M. Sheldrick, *SHELXL-97. A Program for the Refinement of Crystal Structures*, University of Göttingen, Germany, **1997**.
[45] P. W. Codding, K. A. Kerr, *Acta Crystallogr., Sect. B* **1978**, *34*, 3785–3787.
[46] P. W. Codding, K. A. Kerr, *Acta Crystallogr., Sect. B* **1979**, *35*, 1261–1263.
[47] N. Kuhn, G. Henkel, H. Schumann, R. Fröhlich, *Z. Naturforsch., Teil B* **1990**, *45*, 1010–1018.
[48] N. Kuhn, H. Schumann, G. Wolmershäuser, *Z. Naturforsch., Teil B* **1987**, *42*, 674–678.


Received: August 11, 2006
Published Online: October 27, 2006

 © 2006 Wiley-VCH Verlag GmbH & Co. KGaA, Weinheim 

DOI: 10.1002/ejic.200600771

# New Chiral Ferrocene-Bridged Phosphole–Phosphane Ligands

**Jose Guadalupe Lopez Cortes,[a][‡] Olivier Ramon,[a] Sandrine Vincendeau,[a] Daniel Serra,[a] Franck Lamy,[a] Jean-Claude Daran,[a] Eric Manoury,*[a] and Maryse Gouygou*[a]**

**Keywords:** Ferrocenes / Phospholes / P,P ligands / Asymmetric catalysis / X-ray diffraction

A convenient synthesis of new chiral ferrocenene-bridged phosphole–phosphane ligands in an enantiomerically pure form has been developed. These new chiral P,P ligands have been tested in a palladium-catalysed allylic substitution reaction. High activities and moderate enantioselectivities (up to 61 %) were observed. A palladium(II) complex has been isolated and its crystal structure established.

(© Wiley-VCH Verlag GmbH & Co. KGaA, 69451 Weinheim, Germany, 2006)

## Introduction

Considerable efforts have been devoted to the development of new chiral ligands owing to the growing importance of transition-metal-catalysed asymmetric synthesis.[1] Among these chiral ligands, ferrocene-containing ligands are among the most interesting because of their stability, easy introduction of planar chirality and special electronic and stereoproperties of the ferrocene skeleton.[2] Amongst the chiral ferrocene-based ligands, enantiopure 1,2-disubstituted ferrocene derivatives, especially ferrocenediyldiphosphane ligands, played a dominant role.[3] Typical examples are Trap ligands,[4] and diphosphane Josiphos ligands,[5] in particular the industrially important Xyliphos,[6] Taniaphos[7] or Walphos-type ligands[8] (Figure 1). Common characteristics of these ligands include the ferrocenylethyl backbone and the presence of both planar and central chiralities. Little attention has been paid to ligands based on a ferrocenylmethyl backbone or more generally to those having ferrocene possessing planar chirality as their only element of chirality. Reported examples include Trap (**I**),[9] Josiphos[10] analogues (**II**) or diphosphanes (**III**)[11] developed by Kagan et al. (Figure 2).

Recently, we have extended the family of 1,2-disubstituted planar-chiral ferrocene by introduction of a phosphole group leading to planar-chiral ferrocene-bridged phosphole–amine ligands.[12] Chiral phosphole-based ligands[13] have been rather infrequently used for asymmetric catalysis,[14] despite the fact that phospholes are efficient ligands in homogeneous transition-metal catalysis.[15] However, introduction of a phosphole group, which possesses different steric and electronic effects with respect to phosphanes, may modulate the ligand properties. Other advantages of this type of ligand are related to chiral flexibility of unsymmetrically substituted phosphole due to the low inversion barrier of the phosphorus atom in phosphole.[16]

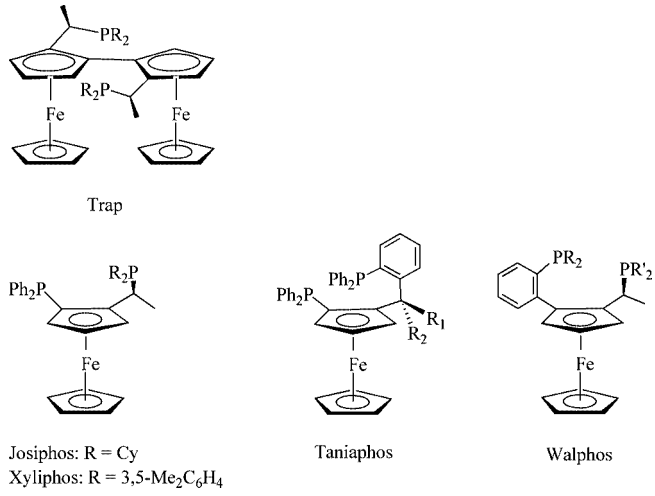


Figure 1. Well-known ferrocenyldiphosphane ligands combining both planar and central chiralities.

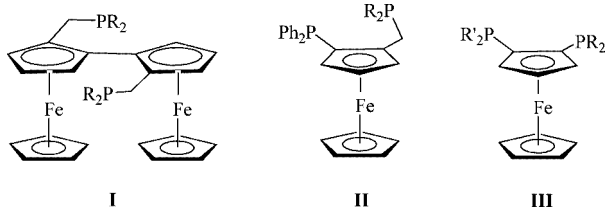


Figure 2. Ferrocenyldiphosphane ligands possessing planar chirality as their only element of chirality.

[a] Laboratoire de Chimie de Coordination, UPR-CNRS 8241, 205 Route de Narbonne, 31077 Toulouse Cedex, France
Fax: +33-5-61553131
E-mail: manoury@lcc-toulouse.fr
gouygou@lcc-toulouse.fr
[‡] Present address: Instituto de Quimica UNAM, Circuito Exterior, Ciudad Universitaria, Coyoacan, 04510 México, D. F., Mexico

 © 2006 Wiley-VCH Verlag GmbH & Co. KGaA, Weinheim 

A chirally flexible phosphole can (i) adjust the configuration to accommodate the metal centre and (ii) magnify the chiral part of the catalytic system.[17]

As part of our continuing interest in ferrocene chemistry[18] and in the design and synthesis of new chiral phosphole-based ligands,[19] we were interested in ferrocene-derived phosphole ligands with only planar chirality for asymmetric catalysis. In this paper, we describe the synthesis of new 1,2-disubstituted ferrocene-bridged phosphole–phosphane ligands involving the introduction of various phospholyl groups on Kagan's acetal derivatives. The coordination chemistry and the catalytic properties of these new chiral ferrocene-bridged phosphole–phosphane ligands are also reported.

## Results and Discussion

The synthetic approach of 1,2-disubtituted ferrocene-based phosphane by nucleophilic displacement of a leaving group (Scheme 1), as described by Hayashi et al.[20] or Togni et al.,[21] could be used to prepare the target molecules. This strategy required the introduction of the planar chirality in the first step by a stereoselective *ortho* metallation step, which required a chiral auxiliary to achieve stereochemically controlled addition of the phospholyl group on the ferrocene moiety. The stereoselective *ortho* metallations reported to date include cyclopalladation of [(dimethylamino)methyl]ferrocene, ortholithiation of ferrocenyl sulfoxides, dioxanes, amines, oxazolines, hydrazones or oxazaphospholidine oxides and so forth.[2c,22,23]

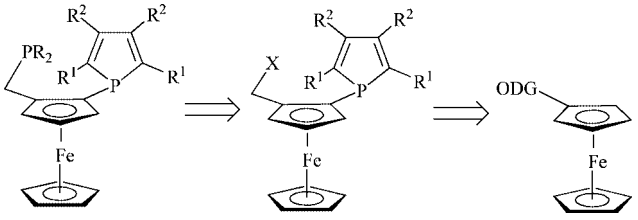


Scheme 1. Retrosynthetic synthesis of ferrocene-bridged phosphole–phosphane ligands.

To control planar chirality, we chose Kagan's method[24] starting from a chiral dioxane. So, the synthetic pathway used is based on six stereochemically controlled reactions, as shown in Scheme 2. In the first step, diastereoselective *ortho* lithiation of acetal **1** was achieved with *t*BuLi. The lithio intermediate reacted cleanly with various 1-cyanophospholes (**2a**,[25] **2b**[14k] and **2c**) as electrophilic reagents to afford the corresponding ferrocenylphosphole products. To facilitate the purification and the characterisation of these compounds, they were converted in situ into air-stable sulfur derivatives **3a–c** by using an excess of sulfur in dichloromethane at room temperature. Compounds **3a**, **3b** and **3c**, isolated after column-chromatographic purification, were obtained in each case as an enantiomerically pure diastereoisomer as confirmed by $^{1}H$, $^{31}P$ and $^{13}C$ NMR analysis and X-ray diffraction studies. The (*S*) configuration for the planar chirality, which is expected from the literature,[24] was confirmed by X-ray analysis on monocrystals in the case of **3b**. A molecular view of compounds (*S*)-**3b** is shown in Figure 3 with the atom-labelling scheme. As expected, the phosphole ring is planar, with the largest deviation [0.028(2) Å] at C11. The phosphorus atom P1 deviates slightly by 0.132(5) Å from the plane of the Cp ring to

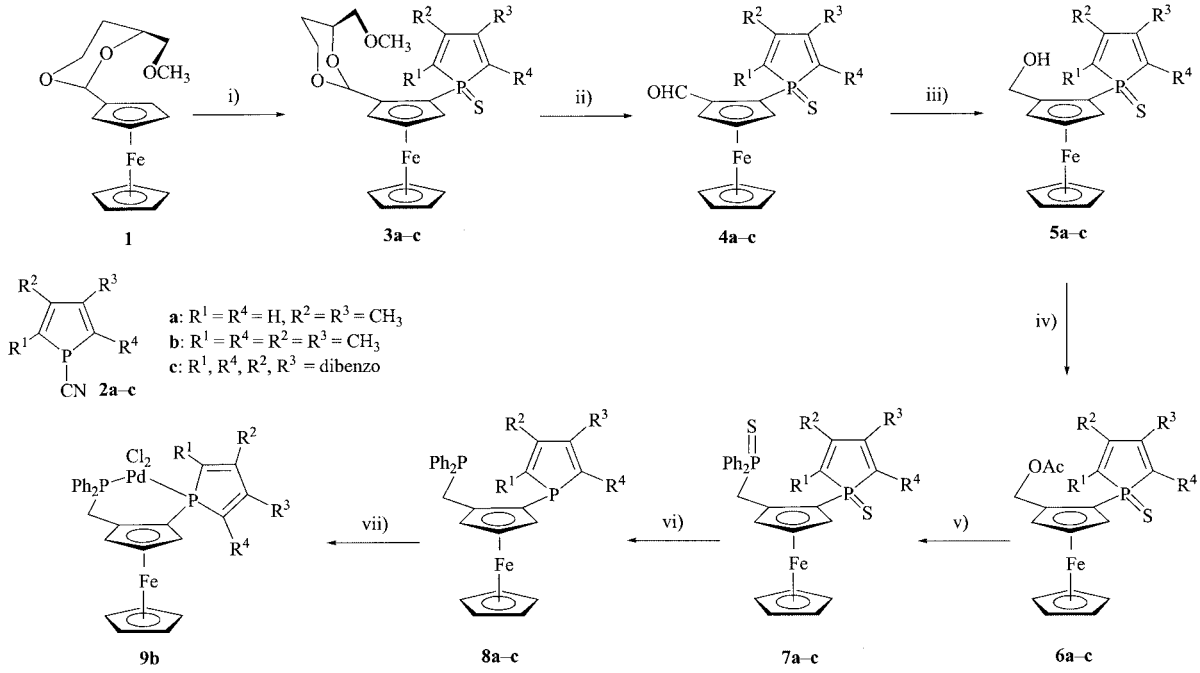


Scheme 2. Synthesis of **8**: (i) *t*BuLi, –78 °C to room temperature; 1-cyanophosphole **2**, –30 °C; $S_8$, $CH_2Cl_2$, room temperature; (ii) $H^+$, $H_2O/CH_2Cl_2$, reflux; (iii) $NaBH_4$, room temperature; (iv) AcCl/$NEt_3$, 0 °C to room temperature; $CH_2Cl_2$; (v) $R_2PH$, toluene, reflux, $S_8$, $CH_2Cl_2$, room temperature; (vi) $P(NMe_2)_3$, toluene reflux; (vii) $PdCl_2(CH_3CN)_2$, $CH_2Cl_2$, room temperature.

 © 2006 Wiley-VCH Verlag GmbH & Co. KGaA, Weinheim 

which it is attached, whereas the atom S1 is *endo* with respect to this Cp ring. The phosphole and the Cp rings are roughly perpendicular, with a dihedral angle of 83.1(1)°. The dioxane ring is distorted and the puckering parameters[26] show that its conformation is close to that of a chair: the $\theta$ and $\varphi$ angles calculated for the atom sequence C21–O22–C23–C24–C25–O26 are 177.2(3)° and 147(6)°, respectively. Owing to steric hindrance, the dioxane ring is twisted by 53.3(1)° with respect to the Cp ring. The two Cp rings are nearly eclipsed, with a twisted angle of only 2.9°.

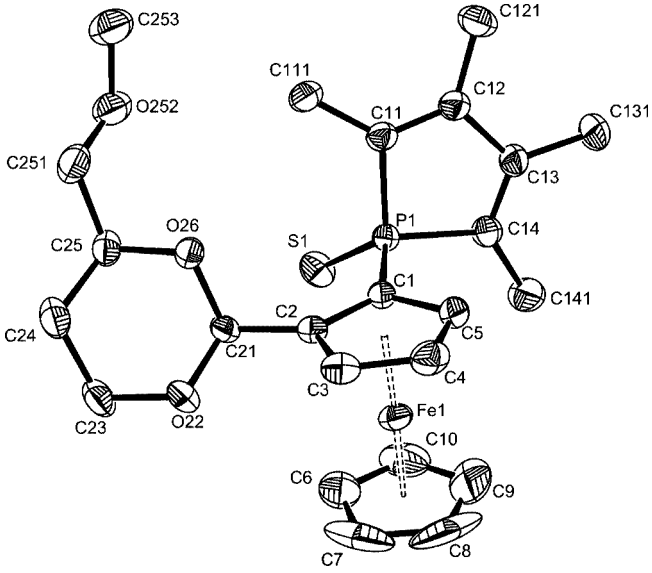


Figure 3. Molecular view of **3b** with atom-labelling scheme. Ellipsoids represent 50% probability. Selected bond lengths [Å] and bond angles [°]: P(1)–S(1) 1.9487(11), P(1)–C(1) 1.790(3), P(1)–C(11) 1.796(3), P(1)–C(14) 1.809(3), C(2)–C(21) 1.504(4), Fe(1)–Cg(1) 1.645(9), Fe(1)–Cg(2) 1.660(9); Cg(1)–Fe(1)–Cg(2) 178.2(6). Cg(1) and Cg(2) are the centroids of the (C1,C2,C3,C4,C5) Cp ring and the (C6,C7,C8,C9,C10) Cp ring, respectively.

In the next step, the acid hydrolysis of the acetal (*S*)-**3a**–**c** was performed with *p*-toluenesulfonic acid to quantitatively yield the corresponding aldehydes (*S*)-**4a**–**c**. Reduction of the crude aldehydes (*S*)-**4a**–**c** of low stabilities was then readily achieved by using an excess of sodium tetrahydroborate. The corresponding alcohols (*S*)-**5a**–**c** were obtained in good yields after column-chromatographic purification. The (*S*) configuration of compound **5b** was again confirmed by X-ray diffraction analysis. A molecular view of alcohol (*S*)-**5b** is shown in Figure 4 with the atom-labelling scheme. As previously noticed, the phosphole ring is planar, with the largest deviation [–0.022(1) Å] at C14 and a dihedral angle of 89.93(7)° with the Cp ring to which it is attached. The atom P1 deviates from the plane of the Cp ring by 0.223(3) Å, certainly minimising steric hindrance, whereas the atom S1 is slightly *endo* by 0.341(4) Å with respect to this Cp ring. The two Cp rings are twisted relative to each other by 10.7°. An interesting feature is the occurrence of an O–H···S intermolecular hydrogen bond [O–H = 0.84 Å, H···S = 2.53 Å, O···S = 3.2700(15) Å, O–H···S = 147.3°] linking the molecules to form a chain developing parallel to the *a*-axis.

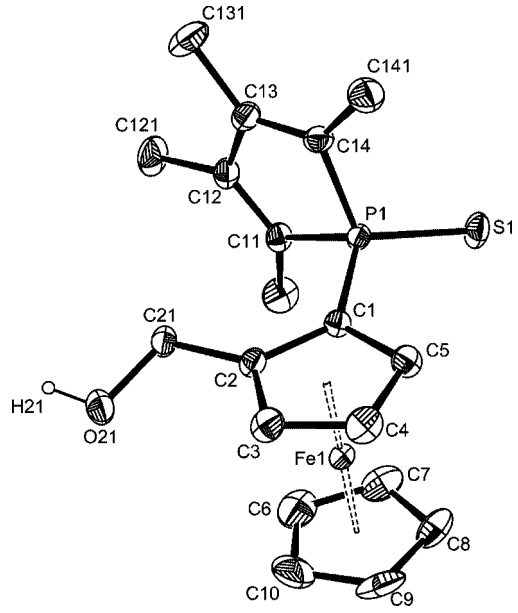


Figure 4. Molecular view of **5b** with atom-labelling scheme. Ellipsoids represent 30% probability. Selected bond lengths [Å] and bond angles [°]: P(1)–S(1) 1.9677(6), P(1)–C(1) 1.790(2), P(1)–C(11) 1.797(2), P(1)–C(14) 1.799(2), C(2)–C(21) 1.505(3), C(21)–O(21) 1.423(2), Fe(1)–Cg(1) 1.636(8), Fe(1)–Cg(2) 1.646(8), Cg(1)–Fe(1)–Cg(2) 176.6(3). Cg(1) and Cg(2) are the centroids of the (C1,C2,C3,C4,C5) Cp ring and the (C6,C7,C8,C9,C10) Cp ring, respectively.

Alcohols (*S*)-**5a**–**c** were quantitatively transformed into acetates (*S*)-**6a**–**c** by treatment with acetyl chloride. Subsequent nucleophilic substitution reactions with secondary phosphanes followed by sulfuration reaction led to ferrocene-bridged phosphole–phosphanes as disulfide derivatives **7a**–**c**. Compounds (*S*)-**7a**, (*S*)-**7b** and (*S*)-**7c**, obtained in 57%, 74% and 78% yield, respectively, were fully characterised.

In the last step, deprotection was successfully achieved with tris(dimethylamino)phosphane in refluxing toluene providing the ferrocene-bridged phosphole–phosphanes (*S*)-**8b** and (*S*)-**8c**. However, this procedure gave only low yields of (*S*)-**8a**, which could not be isolated in a pure form and was only identified by mass spectrometry. The structure of (*S*)-**8b** was determined by X-ray diffraction analysis. A molecular view of complex (*S*)-**8b** is shown in Figure 5. As already observed in free phosphole ligands,[27] the phosphorus atom is located above the butadiene fragment [0.208 (5) Å]. The atom P1 deviates from the plane of the Cp ring by 0.189(5) Å. The atom P2 is oriented *exo* with respect to the Cp ring and is located 1.518(6) Å above it. The two Cp rings are perfectly eclipsed with a twist angle of only 0.5°. The two phenyl rings are roughly perpendicular with a dihedral angle of 87.1(1)°. It is interesting to note that the lone pairs of the two phosphorus atoms are in the correct arrangement for chelating on a metal precursor.

The mode of complexation of new ligands **8** was checked by forming palladium(II) complexes. Ligand **8b** reacted in dichloromethane at room temperature with

 © 2006 Wiley-VCH Verlag GmbH & Co. KGaA, Weinheim 

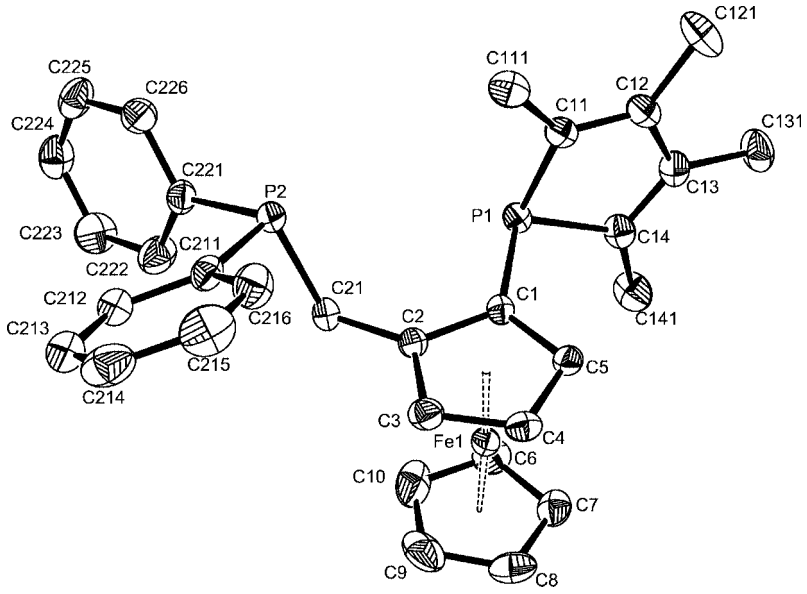


Figure 5. Molecular view of **8b** with atom-labelling scheme. Ellipsoids represent 30% probability. Selected bond lengths [Å] and bond angles [°]: P(1)–C(1) 1.809(3), P(1)–C(11) 1.800(3), P(1)–C(14) 1.807(3), C(2)–C(21) 1.515(5), C(21)–P(2) 1.842(3), P(2)–C(211) 1.835(4), P(2)–C(221) 1.842(3), Fe(1)–Cg(1) 1.6391(4), Fe(1)–Cg(2) 1.6587(4), Cg(1)–Fe(1)–Cg(2) 176.03(3). Cg(1) and Cg(2) are the centroids of the (C1,C2,C3,C4,C5) Cp ring and the (C6,C7,C8,C9,C10) Cp ring, respectively.

$[PdCl_2(CH_3CN)_2]$ in 30 min to afford complex (*S*)-**9b** (80% yield) of formula $[PdCl_2$(**8b**)] as indicated by $^1H$, $^{13}C$ and $^{31}P$ NMR spectroscopy and mass spectrometry. The molecular structure of complex (*S*)-**9b** was established by X-ray diffraction study. There are two molecules in the asymmetric unit with nearly identical geometry. A view of molecule A is depicted in Figure 6. If the phosphole and the Cp form a dihedral angle of 86.3(4)° [88.5(4) for molecule B], a value close to that observed in the free ligand, the atom P2 of the diphenylphosphanyl group is now oriented *endo* with respect to the Cp ring to accommodate the $PdCl_2$ unit. The geometry of the chelating group is closely related to the recently reported structure of {1-(diphenylphosphanyl)-2,1′-[(1-diphenylphosphanyl)butane-1,3-diyl]ferrocene}-$PdCl_2$.[28] As expected, the $Pd^{II}$ atom is square-planar coordinated, with the largest deviation from the least-squares plane being 0.016(2) Å [0.010(2) Å for molecule B] at the Pd atom. The chelating six-membered ring Pd1–P1–C1–C2–C21–P2 is folded around the P1···C21 axis with a dihedral angle of 30.0(4)° [32.8(3)° for molecule B]. The coordination results in a larger twist angle between the two Cp rings of 10.8° (12.2° for molecule B).

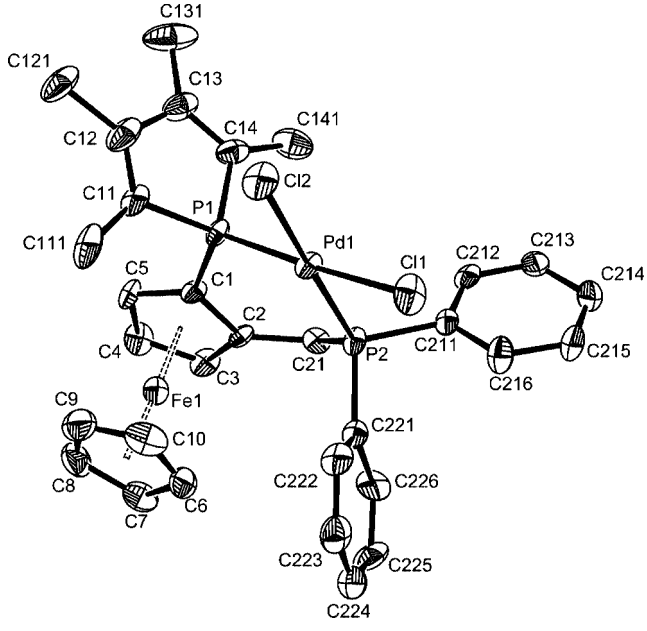


Figure 6. Molecular view of **9b** with atom labelling. Ellipsoids represent 30% probability. Selected bond lengths [Å] and bond angles [°]: Pd–Cl(1) 2.347(3) [2.348(3)], Pd–Cl(2) 2.360(3) [2.363(3)], Pd–P(1) 2.237(3) [2.245(3)], Pd–P(2) 2.261(3) [2.262(3)], P(1)–C(1) 1.791(10) [1.788(10)], C(2)–C(21) 1.487(15) [1.510(15)], P(2)–C(21) 1.828(10) [1.823(11)], Fe(1)–Cg(1) 1.656(3) [1.665(3)], Fe(1)–Cg(2) 1.669(3) [1.666(3)]; Cg(1)–Fe(1)–Cg(2) 174.8(4). Cg(1) and Cg(2) are the centroids of the (C1,C2,C3,C4,C5) Cp ring and the (C6,C7,C8,C9,C10) Cp ring, respectively. The values in square brackets refer to molecule B.

The chiral ligands (*S*)-**8b** and (*S*)-**8c** were evaluated in the palladium-catalysed asymmetric allylic substitution.[29] The reaction of 1,3-diphenylprop-2-enyl acetate (**10**) with the anion of dimethyl malonate (**11**) was carried out in the presence of $[Pd(C_3H_5)Cl]_2$ (1 mol-%) and the chiral ligands **8b**,**c** (1 mol-%) (see Scheme 3). Using the ligand (*S*)-**8b**, the allylic acetate **10** in $CH_2Cl_2$ was quantitatively converted within 1 h at room temperature to the desired product (*S*)-**12** in 38% *ee*. Under similar conditions, the ligand (*S*)-**8c**

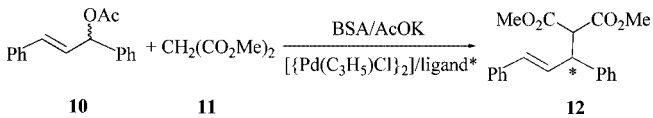


Scheme 3. Asymmetric allylic substitution reaction.

 © 2006 Wiley-VCH Verlag GmbH & Co. KGaA, Weinheim 

led also to the quantitative conversion of **10** within 1 h to (*S*)-**12**, but with a better enantioselectivity (61% *ee*).

## Conclusions

A new and convenient preparation of ferrocene-bridged phosphole–phosphane ligands in an enantiomerically pure form has been achieved. Their coordination chemistry and their abilities for catalysis in a palladium-catalysed asymmetric allylic substitution reaction have been checked. Use of these new unusual chiral P,P ligands in other asymmetric catalytic reactions as well as optimisation of ligands by modifying the phosphole ring part or the phosphane part are currently being developed in our laboratories.

## Experimental Section

**General:** All reactions were carried out under dry argon by using Schlenk glassware and vacuum-line techniques. Solvents were freshly distilled from standard drying agents. $^{1}H$, $^{13}C\{^{1}H, ^{31}P\}$ and $^{31}P\{^{1}H\}$ NMR spectra were recorded with a Bruker WMX 400 instrument operating at 400, 162 and 100 MHz respectively. Chemical shifts are reported in ppm relative to $Me_4Si$ ($^{1}H$ and $^{13}C$) or 85% $H_3PO_4$ ($^{31}P$). Mass spectra were obtained with a Nermag R10-10 instrument (DCI, FAB) and with an Applied Biosystem API 365 instrument (APCI). Elemental analysis was performed by the "Service d'Analyse du Laboratoire de Chimie de Coordination" at Toulouse. Optical rotations were measured with a Perkin–Elmer 241 polarimeter. Acetal **1**,[24b] 1-cyano-2,3,4,5-tetramethylphosphole (**2b**),[14k] 1-phenyldibenzophosphole[30] and compounds **3a**, **4a**, **5a** and **6a**[12] were prepared as described in the literature.

**1-Cyanodibenzophosphole (2c):** A solution of 1-phenyldibenzophosphole (2 g, 7.7 mmol) in THF (15 mL) was added at room temperature to a suspension of lithium (0.16 g, 23 mmol) in THF (5 mL). The reaction mixture was stirred at room temperature for 4 h. The red suspension was filtered (to remove unreacted lithium) into another Schlenk tube, cooled to –20 °C, and anhydrous $AlCl_3$ (0.35 g, 2.6 mmol) was added. The reaction mixture was warmed to 0 °C, stirred for 0.5 h and then transferred by cannula to a solution of BrCN (1.63 g, 15.4 mmol) in THF (5 mL) cooled to –78 °C. The mixture was stirred at –78 °C for 0.5 h, then warmed to room temperature and stirred overnight. The mixture was concentrated to dryness and the resulting residue was extracted with small portions of diethyl ether. The combined diethyl ether extracts were filtered through Celite and the solvents were evaporated to give crude compound **2c** as a white solid (0.93 g, 58%). This was used without purification. $^{1}H$ NMR ($CDCl_3$): $\delta$ = 7.47 (m, 2 H, Ar), 7.59 (m, 2 H, Ar), 7.90 (m, 4 H, Ar) ppm. $^{31}P$ NMR ($CDCl_3$): $\delta$ = –51.6 ppm.

**General Procedure for Synthesis of Dioxanes 3:** In a Schlenk tube, a 1.5 M solution of *tert*-butyllithium in pentane (8.1 mL, 12.1 mmol, 1.1 equiv.) was added dropwise, at –78 °C under argon, to a solution of acetal **1** (3.47 g, 11 mmol) in dry diethyl ether (40 mL). The solution was stirred at –78 °C for 15 min, then at room temperature for 2 h. The solution was cooled to –30 °C and a solution of 1-cyanophosphole **2** (1.2 equiv.) in dry diethyl ether (20 mL) was introduced by cannula. The reaction mixture was stirred at room temperature overnight. Dry triethylamine (0.5 mL) was introduced by syringe, followed by water (2 mL). Under argon, the reaction mixture was extracted with diethyl ether and washed with brine. The organic fraction was dried with sodium sulfate and the solvents were evaporated in vacuo to yield an orange oil. This oil was dissolved in dichloromethane (30 mL). Sulfur (5.7 equiv.) was added and the mixture was stirred overnight. After concentration, the mixture was chromatographed on silica gel using a pentane/dichloromethane mixture (3:7, v/v).

**(2*S*,4*S*,$S_{Fc}$)-2-[(2,3,4,5-Tetramethyl-1-thioxo-1*H*-1λ$^5$-phosphol-1-yl)-ferrocenyl]-4-(methoxymethyl)-1,3-dioxane (3b):** Yellow-orange oil (yield 68%). Crystals suitable for X-ray analysis were obtained by diffusion of pentane into a dichloromethane solution. $^{1}H$ NMR ($CDCl_3$): $\delta$ = 1.51 (br. d, $J$ = 13.3 Hz, 1 H, $CH_2CH_2CH$), 1.83 (m, 1 H, $CH_2CH_2CH$), 1.85 (br. s, 3 H, $CH_3$), 1.94 (br. s, 3 H, $CH_3$), 2.01 (d, $J_{H,P}$ = 13.3 Hz, 3 H, $CH_3$), 2.13 (d, $J_{H,P}$ = 12.8 Hz, 3 H, $CH_3$), 3.32 (s, 3 H, $OCH_3$), 3.35 (dd, ABX system, $J$ = 10.1 and 5.1 Hz, 1 H, $CH_2OCH_3$), 3.44 (dd, ABX system, $J$ = 10.1 and 5.2 Hz, 1 H, $CH_2OCH_3$), 3.95–4.10 (m, 2 H, CH, $OCH_2CH_2$), 4.02 (m, 1 H, subst. Cp), 4.25–4.30 (m, 1 H, $OCH_2CH_2$), 4.27 (m, 1 H, subst. Cp), 4.39 (s, 5 H, Cp), 4.76 (m, 1 H, subst. Cp), 6.15 (s, 1 H, OCHO) ppm. $^{13}C$ NMR ($CDCl_3$): $\delta$ = 10.5 (d, $J_{C,P}$ = 13.8 Hz, $CH_3$ α phosphole), 11.3 (d, $J_{C,P}$ = 13.1 Hz, $CH_3$ α phosphole), 14.0 (d, $J_{C,P}$ = 15.3 Hz, $CH_3$ β phosphole), 14.2 (d, $J_{C,P}$ = 15.3 Hz, $CH_3$ β phosphole), 28.5 ($CH_2CH_2CH$), 59.6 ($OCH_3$), 67.5 ($OCH_2CH_2$), 69.9 (d, $J_{C,P}$ = 10.2 Hz, subst. Cp), 71.2 (d, $J_{C,P}$ = 8.1 Hz, subst. Cp), 71.4 (Cp), 71.5 (d, $J_{C,P}$ = 79.0 Hz, quat. Cp), 71.9 (d, $J_{C,P}$ = 10.5 Hz, subst. Cp), 75.7 ($CH_2OCH_3$), 76.0 (CH), 89.1 (d, $J_{C,P}$ = 10.5 Hz, quat. Cp), 98.8 (OCHO), 128.4 (d, $J_{C,P}$ = 84.0 Hz, $CH_3$ α phosphole), 132.3 (d, $J_{C,P}$ = 82.7 Hz, $CCH_3$ α phosphole), 143.2 (d, $J_{C,P}$ = 27.1 Hz, $CCH_3$ β phosphole), 145.8 (d, $J_{C,P}$ = 27.2 Hz, $CCH_3$ β phosphole) ppm. $^{31}P$ NMR ($CDCl_3$): $\delta$ = 57.0 ppm. $[\alpha]_D$ = 3.4 ($c$ = 0.5, $CHCl_3$). MS (DCI, $NH_3$): $m/z$ (%) = 487 (100) [M + 1]. $C_{24}H_{32}FeO_3PS$ (487.40): calcd. C 59.14, H 6.62; found 59.27, H 6.42.

**(2*S*,4*S*,$S_{Fc}$)-2-[(Dibenzo-1-thioxo-1*H*-1λ$^5$-phosphol-1-yl)ferrocenyl]-4-(methoxymethyl)-1,3-dioxane (3c):** Yellow solid (yield 64%). M.p. 78 °C. $^{1}H$ NMR ($CDCl_3$): $\delta$= 1.48 (d of m, $J$ = 13 Hz, 1 H, $CH_2CH_2CH$), 1.81 (br. q of d, $J$ = 13 and 5 Hz, 1 H, $CH_2CH_2CH$), 3.42 (dd, AB system, $J$ = 10.3 and 3.9 Hz, 1 H, $CH_2OCH_3$), 3.43 (s, 3 H, $OCH_3$), 3.56 (dd, AB system, $J$ = 10.3 and 6.3 Hz, 1 H, $CH_2OCH_3$), 3.59 (m, 1 H, subst. Cp), 4.00 (td, $J$ = 11.9 and 2.5 Hz, 1 H, $OCH_2CH_2$), 4.15 (m, 1 H, subst. Cp), 4.19 (m, 1 H, CH), 4.3–4.25 (m, 1 H, $OCH_2CH_2$), 4.50 (s, 5 H, Cp), 4.80 (m, 1 H, subst. Cp), 6.40 (s, 1 H, OCHO), 7.35 (tdd, $J$ = 7.5 and 1.0 Hz, $J_{H,P}$ = 3.8 Hz, 1 H, Ar), 7.44 (tt, $J$ = 7.5 Hz, $J$ = $J_{H,P}$ = 1.2 Hz, 1 H, Ar), 7.51 (tdd, $J$ = 7.4 and 1.1 Hz, $J_{H,P}$ = 3.7 Hz, 1 H, Ar), 7.57 (tt, $J$ = 7.5 Hz, $J$ = $J_{H,P}$ = 1.3 Hz, 1 H, Ar), 7.69 (dd, $J$ = 7.6 Hz, $J_{H,P}$ = 3.1 Hz, 1 H, Ar), 7.78 (dd, $J$ = 7.6 Hz, $J_{H,P}$ = 3.0 Hz, 1 H, Ar), 7.99 (ddd, $J$ = 7.4 and 1 Hz, $J_{H,P}$ = 10.3 Hz, 1 H, Ar), $\delta$ = 8.27 (ddd, $J$ = 7.5 and 1 Hz, $J_{H,P}$ = 9.7 Hz, 1 H, Ar) ppm. $^{13}C$ NMR ($CDCl_3$): $\delta$= 28.3 ($CH_2CH_2CH$), 59.6 ($OCH_3$), 67.4 ($OCH_2CH_2$), 69.9 (d, $J_{C,P}$ = 10.9 Hz, subst. Cp), 71.4 (Cp), 71.7 (d, $J_{C,P}$ = 9.0 Hz, subst. Cp), 73.0 (d, $J_{C,P}$ = 14.1 Hz, subst. Cp), 74.0 (d, $J_{C,P}$ = 90.0 Hz, quat. Cp), 75.8 (CH), 76.0 ($CH_2OCH_3$), 89.4 (d, $J_{C,P}$ = 12.1 Hz, quat. Cp), 98.6 (OCHO), 121.3 (d, $J_{C,P}$ = 9.5 Hz, Ar), 121.8 (d, $J_{C,P}$ = 9.5 Hz, Ar), 129.5 (d, $J_{C,P}$ = 11.5 Hz, Ar), 130.0 (d, $J_{C,P}$ = 12.1 Hz, Ar), 130.1 (d, $J_{C,P}$ = 10.4 Hz, Ar), 130.9 (d, $J_{C,P}$ = 11.3 Hz, Ar), 132.5 (d, $J_{C,P}$ = 2.3 Hz, Ar), 133.1 (d, $J_{C,P}$ = 2.3 Hz, Ar), 135.7 (d, $J_{C,P}$ = 93.3 Hz, quat. Ar), 138.1 (d, $J_{C,P}$ = 91.6 Hz, quat. Ar), 139.6 (d, $J_{C,P}$ = 19.7 Hz, quat. Ar), 141.7 (d, $J_{C,P}$ = 19.7 Hz, quat. Ar) ppm. $^{31}P$ NMR ($CDCl_3$): $\delta$ = 42.9 ppm. $[\alpha]_D$ = –24 ($c$ = 0.5, $CHCl_3$). MS (DCI, $NH_3$): $m/z$ (%) = 531 (100) [M + 1]. $C_{28}H_{28}FeO_3PS$ (531.42): calcd. C 63.41, H 5.13; found C 63.43, H 5.07.

**General Procedure for the Synthesis of Ferrocenecarbaldehyde 4:** Acetal **3** (7.3 mmol), dichloromethane (120 mL) and an aqueous

 © 2006 Wiley-VCH Verlag GmbH & Co. KGaA, Weinheim 

solution (50 mL) of *p*-toluenesulfonic acid monohydrate (1.5 equiv. for **3b** or 2 equiv. for **3c**) were introduced into a round-bottomed flask equipped with a condenser and placed under argon. The reaction mixture was stirred at reflux for 26 h (**3b**) or 54 h (**3c**). After cooling to room temperature, the dark red solution was extracted with dichloromethane, washed with distilled water, dried with sodium sulfate and the solvents were evaporated. Compounds **4**, obtained quantitatively as red oils, were only characterised by $^{31}P$ and $^{1}H$ NMR spectroscopy and used without purification.

**($S_{Fc}$)-2-(2,3,4,5-Tetramethyl-1-thioxo-1*H*-1λ$^5$-phosphol-1-yl)ferrocenecarbaldehyde (4b):** $^{1}H$ NMR ($CDCl_3$): $\delta$ = 1.89 (br. s, 3 H, $CH_3$), 1.95 (br. s, 3 H, $CH_3$), 1.98 (d, $J_{H,P}$ = 13.7 Hz, 3 H, $CH_3$), 2.07 (d, $J_{H,P}$ = 13.7 Hz, 3 H, $CH_3$), 4.52 (s, 5 H, Cp), 4.61 (m, 1 H, subst. Cp), 4.72 (m, 1 H, subst. Cp), 5.16 (m, 1 H, subst. Cp), 10.58 (s, 1 H, CHO) ppm. $^{31}P$ NMR ($CDCl_3$): $\delta$ = 55.8 ppm.

**($S_{Fc}$)-2-(Dibenzo-1-thioxo-1*H*-1λ$^5$-phosphol-1-yl)ferrocenecarbaldehyde (4c):** $^{1}H$ NMR ($CDCl_3$): $\delta$ = 3.38 (m, 1 H, subst. Cp), 4.25 (m, 1 H, subst. Cp), 4.43 (s, 5 H, Cp), 5.56 (m, 1 H, subst. Cp), 7.48–7.88 (m, 8 H, Ar), 10.57 (s, 1 H, CHO) ppm. $^{31}P$ NMR ($CDCl_3$): $\delta$ = 38.6 ppm.

**General Procedure for Synthesis of Alcohols 5:** Crude compound **4** (7.3 mmol) was dissolved in methanol (200 mL) and an aqueous solution (140 mL) of sodium borohydride (2.78 g, 18.3 mmol) and sodium hydroxide (11.2 g, 280 mmol) was added. The solution turned rapidly from red to orange. After 15 min of stirring at room temperature, the reaction mixture was extracted with dichloromethane. The organic phase was washed with diluted hydrochloric acid, then water, and finally dried with sodium sulfate. After evaporation of the solvents, the crude material was purified by flash chromatography on silica gel using a pentane/diethyl ether mixture (2:8, v/v).

**($S_{Fc}$)-[2-(2,3,4,5-Tetramethyl-1-thioxo-1*H*-1λ$^5$-phosphol-1-yl)ferrocenyl]methanol (5b):** Yellow-orange oil (yield 51% from **3b**). Crystals suitable for X-ray analysis were obtained by diffusion of pentane into a dichloromethane solution. M.p. 85 °C. $^{1}H$ NMR ($CDCl_3$): $\delta$ = 1.86 (br. s, 3 H, $CH_3$ β), 1.93 (br. d, $J_{H,P}$ = 12.1 Hz, 3 H, $CH_3$ α), 1.96 (br. s, 3 H, $CH_3$ β), 2.15 (br. d, $J_{H,P}$ = 13.0 Hz, 3 H, $CH_3$ α), 3.39 (dd, $J$ = 7.8 and 5.9 Hz, 1 H, OH), 4.03 (m, 1 H, subst. Cp), 4.24 (m, 1 H, subst. Cp), 4.38 (s, 5 H, Cp), 4.47 (dd, ABX system, $J$ = 12.6 and 5.5 Hz, 1 H, $CH_2$), 4.49 (m, 1 H, subst. Cp), 4.59 (dd, ABX system, $J$ = 12.8 and 7.8 Hz, 1 H, $CH_2$) ppm. $^{13}C$ NMR ($CDCl_3$): $\delta$ = 10.6 (d, $J_{C,P}$ = 13.6 Hz, $CH_3$ α), 11.3 (d, $J_{C,P}$ = 13.3 Hz, $CH_3$ α), 14.0 (d, $J_{C,P}$ = 15.1 Hz, $CH_3$ β), 14.3 (d, $J_{C,P}$ = 15.3 Hz, $CH_3$ β), 59.4 (s, $CH_2$), 69.3 (d, $J_{C,P}$ = 10.2 Hz, subst. Cp), 70.7 (s, Cp), 71.8 (d, $J_{C,P}$ = 14.1 Hz, subst. Cp), 72.0 (d, $J_{C,P}$ = 80.2 Hz, quat. Cp), 74.4 (d, $J_{C,P}$ = 9.0 Hz, subst. Cp), 92.5 (d, $J_{CP}$ = 11.5 Hz, quat. Cp), 128.7 (d, $J_{C,P}$ = 84.2 Hz, $CCH_3$ α), 131.5 (d, $J_{C,P}$ = 82.8 Hz, $CCH_3$ α), 143.8 (d, $J_{C,P}$ = 26.9 Hz, $CCH_3$ β), 146.4 (d, $J_{C,P}$ = 27.1 Hz, $CCH_3$ β) ppm. $^{31}P$ NMR ($CDCl_3$): $\delta$ = 58.1 ppm. $[\alpha]_D$ = –125 ($CHCl_3$, $c$ = 0.5). MS (DCI, $NH_3$): $m/z$ (%) = 387 (100) [M + 1]. $C_{19}H_{23}FeOPS$ (386.28): calcd. C 59.07, H 6.00; found C 59.24, H 6.10.

**($S_{Fc}$)-[(Dibenzo-1-thioxo-1*H*-1λ$^5$-phosphol-1-yl)ferrocenyl]methanol (5c):** Yellow solid (yield 56% from **3c**). M.p. 200 °C (decomposition). $^{1}H$ NMR ($CDCl_3$): $\delta$ = 3.58 (br. t, $J \approx 6$ Hz, 1 H, OH), 3.72 (m, 1 H, subst. Cp), 4.18 (m, 1 H, subst. Cp), 4.24 (s, 5 H, Cp), 4.56–4.5 (m, 2 H, subst. Cp, $CH_2$), 5.00 (dd, $J$ = 12.6 and 5.7 Hz, 1 H, $CH_2$), 7.44 (tdd, $J$ = 7.5 and 0.9 Hz, $J_{H,P}$ = 3.8 Hz, 1 H, Ar), 7.62–7.55 (m, 2 H, Ar), 7.66 (m, 1 H, Ar), 7.82 (dd, $J$ = 7.7 Hz, $J_{H,P}$ = 3.1 Hz, 1 H, Ar), 7.88 (dd, $J$ = 7.6 Hz, $J_{H,P}$ = 3.1 Hz, 1 H, Ar), 7.94 (dd, $J$ = 7.4 Hz, $J_{H,P}$ = 10.5 Hz, 1 H, Ar), 8.11 (dd, $J$ = 7.3 Hz, $J_{H,P}$ = 10.6 Hz, 1 H, Ar) ppm. $^{13}C$ NMR ($CDCl_3$): $\delta$ = 59.9 (s, $CH_2$), 69.5 (d, $J_{C,P}$ = 10.9 Hz, subst. Cp), 70.7 (s, Cp), 73.3 (d, $J_{C,P}$ = 14.4 Hz, subst. Cp), 74.6 (d, $J_{C,P}$ = 9.8 Hz, subst. Cp), 75.1 (d, $J_{C,P}$ = 90.4 Hz, quat. Cp), 92.0 (d, $J_{C,P}$ = 13.3 Hz, quat. Cp), 121.7 (d, $J_{C,P}$ = 9.5 Hz, Ar), 121.9 (d, $J_{C,P}$ = 9.7 Hz, Ar), 129.7 (d, $J_{C,P}$ = 11.7 Hz, Ar), 129.9 (d, $J_{C,P}$ = 10.7 Hz, Ar), 130.08 (d, $J_{C,P}$ = 11.8 Hz, Ar), 130.12 (d, $J_{C,P}$ = 10.6 Hz, Ar), 133.0 (d, $J_{C,P}$ = 2.3 Hz, Ar), 133.3 (d, $J_{C,P}$ = 2.3 Hz, Ar), 136.1 (d, $J_{C,P}$ = 93.8 Hz, quat. Ar), 136.8 (d, $J_{C,P}$ = 91.5 Hz, quat. Ar), 140.2 (d, $J_{C,P}$ = 19.5 Hz, quat. Ar), 141.5 (d, $J_{C,P}$ = 19.5 Hz, quat. Ar) ppm. $^{31}P$ NMR ($CDCl_3$): $\delta$ = 44.6 ppm. $[\alpha]_D$ = –104.6 ($CHCl_3$, $c$ = 0.5). MS (DCI, $NH_3$): $m/z$ (%) = 413 (100) $[M - OH]^+$, 430 (15) $[M]^+$. $C_{23}H_{19}FeOPS$ (430.29): calcd. C 64.20, H 4.45; found C 64.11, H 4.64.

**General Procedure for Synthesis of Acetates 6:** Alcohol **5** (0.7 mmol) was dissolved in dry dichloromethane (7 mL) and anhydrous triethylamine (0.25 mL) in a Schlenk tube under argon. The solution was then cooled to 0 °C and acetyl chloride (1.5 equiv.) was added with a syringe. The solution was stirred at 0 °C for 30 min, then at room temperature for 1 h. The solution was washed with diluted hydrochloric acid then water and dried with sodium sulfate. After evaporation of the solvents, crude compound **6** was quantitatively obtained as an oil that was used without further purification in the next step.

**($S_{Fc}$)-(Acetoxy)[2-(2,3,4,5-tetramethyl-1-thioxo-1*H*-1λ$^5$-phosphol-1-yl)ferrocenyl]methane (6b):** Yellow-orange. $^{1}H$ NMR ($CDCl_3$): $\delta$ = 1.89 (d, $J$ = 10 Hz, 6 H, $CH_3$), 1.99 [s, 3 H, $C(O)CH_3$], 2.04 (d, $J$ = 13 Hz, 6 H, $CH_3$), 4.26 (m, 1 H, subst. Cp), 4.33 (m, 1 H, subst. Cp), 4.40 (m, 5 H, Cp), 4.53 (m, 1 H, subst. Cp), 5.14 (d, $J$ = 11.9 Hz, 1 H, $CH_2$), 5.33 (d, $J$ = 11.9 Hz, 1 H, $CH_2$) ppm. $^{31}P$ NMR ($CDCl_3$): $\delta$ = 53.9 ppm.

**($S_{Fc}$)-(Acetoxy)[2-(dibenzo-1-thioxo-1*H*-1λ$^5$-phosphol-1-yl)ferrocenyl]methane (6c):** Orange-red oil. $^{1}H$ NMR ($CDCl_3$): $\delta$ = 1.98 [s, 3 H, $C(O)CH_3$], 4.02 (m, 1 H, subst. Cp), 4.26 (m, 1 H, subst. Cp), 4.48 (s, 5 H, Cp), 4.51 (m, 1 H, subst. Cp), 5.11 (d, $J$ = 12.1 Hz, 1 H, $CH_2$), 5.27 (d, $J$ = 12.1 Hz, 1 H, $CH_2$), 7.3–8.1 (m, 8 H, Ar) ppm. $^{31}P$ NMR ($CDCl_3$): $\delta$ = 39.8 ppm.

**General Procedure for Synthesis of Compounds 7:** Diphenylphosphane (2.5 equiv.) was added at room temperature to a solution of crude **6** (0.7 mmol) in degassed toluene (10 mL). The reaction mixture was stirred under reflux for 24 h (**7a**, **7b**) or 36 h (**7c**) and then concentrated in vacuo to yield an orange oil. This oil was dissolved in dichloromethane (10 mL). Sulfur (5 equiv.) was added and the mixture was stirred overnight. After concentration, the mixture was chromatographed on silica gel using a pentane/diethyl ether mixture (80:20).

**($S_{Fc}$)-[2-(3,4-Dimethyl-1-thioxo-1*H*-1λ$^5$-phosphol-1-yl)ferrocenyl]-(diphenylthioxophosphanyl)methane (7a):** Yellow solid (yield 57% from **5a**). $^{1}H$ NMR ($CDCl_3$): $\delta$ = 1.95 (br. t, $J$ = 3 Hz, 3 H, $CH_3$), 2.09 (br. t, $J$ = 3 Hz, 3 H, $CH_3$), 4.11 (td, $J_{H,H}$ = 2.9 Hz, $J_{H,P1}$ = 1.5 Hz, 1 H, subst. Cp), 4.31 (s, 5 H, Cp); 4.12 (t, $J_{H,H}$ = $J_{H,P2}$ = 13.1 Hz, 1 H, $CH_2$), 4.32–4.30 (m, 1 H, subst. Cp), 4.39 (t, $J_{H,H}$ = $J_{H,P2}$ = 13.1 Hz, 1 H, $CH_2$), 4.48 (ddd, $J$ = 4.1 and 2.4 Hz, $J_{H,P1}$ = 2.8 Hz, 1 H, subst. Cp), 6.06 (br. d, $J_{H,P}$ = 30.5 Hz, 1 H, CH), 6.24 (br. d, $J_{H,P}$ = 30.6 Hz, 1 H, CH), 7.55–7.25 (m, 6 H, $PPh_2$), 7.9–7.8 (m, 4 H, $PPh_2$) ppm. $^{13}C$ NMR ($CDCl_3$): $\delta$ = 17.9 (d, $J_{C,P1}$ = 17.8 Hz, $CH_3$ phosphole), 18.0 (d, $J_{C,P1}$ = 17.8 Hz, $CH_3$ phosphole), 31.5 (d, $J_{C,P2}$ = 5 Hz, $CH_2$), 69.0 (d, $J_{C,P1}$ = 87.5 Hz, quat. Cp), 70.1 (d, $J_{C,P1}$ = 11.1 Hz, subst. Cp), 71.2 (Cp), 73.7 (d, $J_{C,P1}$ = 14.8 Hz, subst. Cp), 74.8 (d, $J_{C,P1}$ = 8.9 Hz, subst. Cp), 87.2 (dd, $J_{C,P1}$ = 11.4 Hz, $J_{C-P2}$ = 5.8 Hz, quat. Cp), 126.2 (d, $J_{C,P1}$ = 71.7 Hz, CH phosphole), 126.6 (d, $J_{C,P1}$ = 71.7 Hz, CH phosphole), 126.8 (d, $J_{C,P2}$ = 13.4 Hz, $PPh_2$), 129.1 (d, $J_{C,P2}$ = 13.1 Hz, $PPh_2$), 131.6 (d, $J_{C,P2}$ = 11.3 Hz, $PPh_2$), 132.1 (d, $J_{C,P2}$ = 3.3 Hz, $PPh_2$),

 © 2006 Wiley-VCH Verlag GmbH & Co. KGaA, Weinheim 

132.2 (d, $J_{C,P2}$ = 11.4 Hz, $PPh_2$), 132.4 (d, $J_{C,P2}$ = 3.2 Hz, $PPh_2$), 134.0 (d, $J_{C,P2}$ = 69.3 Hz, quat. $PPh_2$), 134.8 (d, $J_{C,P2}$ = 71.1 Hz, quat. $PPh_2$), 152.7 (d, $J_{C,P1}$ = 18.7 Hz, $CCH_3$ phosphole), 152.9 (d, $J_{C,P1}$ = 18.5 Hz, $CCH_3$ phosphole) ppm. $^{31}P$ NMR ($CDCl_3$): $\delta$ = 48.1 (P1, phosphole), 66.7 (P2, $PPh_2$) ppm. MS (DCI, $NH_3$): *m*/*z* (%) = 559 (100) [M + 1].

**($S_{Fc}$)-(Diphenylthioxophosphanyl)[2-(2,3,4,5-tetramethyl-1-thioxo-1*H*-1λ$^5$-phosphol-1-yl)ferrocenyl]methane (7b):** Yellow oil (yield 74% from **5b**). $^1H$ NMR ($CDCl_3$): $\delta$ = 1.85 (br. s, 3 H, $CH_3$ β phosphole), 1.91 (br. s, 3 H, $CH_3$ β phosphole), 1.92 (br. d, 3 H, $J_{H,P1}$ = 12.4 Hz, $CH_3$ α phosphole), 2.12 (br. d, 3 H, $J_{H,P1}$ = 13.1 Hz, $CH_3$ α phosphole), 3.95 (t, 1 H, $J_{H,H}$ = $J_{H,P2}$ = 13.3 Hz, $CH_2$), 4.15 (t, 1 H, $J_{H,H}$ = $J_{H,P2}$ = 13.3 Hz, $CH_2$), 4.16 (m, 1 H, subst. Cp), 4.27 (m, 1 H, subst. Cp), 4.34 (s, 5 H, Cp), 4.46 (m, 1 H, subst. Cp), 7.55–7.3 (m, 6 H, $PPh_2$), 7.9–7.5 (m, 4 H, $PPh_2$) ppm. $^{13}C$ NMR ($CDCl_3$): $\delta$ = 10.4 (d, $J_{C,P1}$ = 13.4 Hz, $CH_3$ α phosphole), 11.4 (d, $J_{C,P1}$ = 13.6 Hz, $CH_3$ α phosphole), 14.1 (d, $J_{C,P1}$ = 15.1 Hz, $CH_3$ β phosphole), 14.5 (d, $J_{C,P1}$ = 15.2 Hz, $CH_3$ β phosphole), 31.3 (s, $CH_2$), 70.3 (d, $J_{C,P1}$ = 10.6 Hz, subst. Cp), 71.1 (Cp), 71.5 (d, $J_{C,P1}$ = 79.0 Hz, quat. Cp), 73.3 (d, $J_{C,P1}$ = 13.8 Hz, subst. Cp), 73.9 (d, $J_{C,P1}$ = 7.9 Hz, subst. Cp), 85.9 (dd, $J_{C,P1}$ = 10.6 Hz, $J_{C,P2}$ = 5.6 Hz, quat. Cp), 128.8 (d, $J_{C,P2}$ = 13.3 Hz, $PPh_2$), 128.9 (d, $J_{C,P1}$ = 82.7 Hz, $CH_3$ α phosphole), 129.1 (d, $J_{C,P2}$ = 13.3 Hz, $PPh_2$), 130.2 (d, $J_{C,P1}$ = 82.7 Hz, $CH_3$ α phosphole), 131.4 (d, $J_{C,P2}$ = 11.1 Hz, $PPh_2$), 132.2 (d, $J_{C,P2}$ = 11.2 Hz, $PPh_2$), 132.3 (d, $J_{C,P2}$ = 4.7 Hz, $PPh_2$), 132.4 (d, $J_{C,P2}$ = 3.1 Hz, $PPh_2$), 134.1 (d, $J_{C,P2}$ = 71.4 Hz, quat. $PPh_2$), 134.8 (d, $J_{C,P2}$ = 71.1 Hz, quat. $PPh_2$), 134.9 (d, $J_{C,P2}$ = 73.5 Hz, quat. $PPh_2$), 144.5 (d, $J_{C,P1}$ = 26.7 Hz, $CCH_3$ β phosphole), 147.1 (d, $J_{C,P1}$ = 27.1 Hz, $CCH_3$ β phosphole) ppm. $^{31}P$ NMR ($CDCl_3$): $\delta$ = 56.7 (P1, phosphole), 66.7 (P2, $PPh_2$) ppm. MS (APCI): *m*/*z* = 587 [M + 1].

**($S_{Fc}$)-(Diphenylthioxophosphanyl)[2-(dibenzo-1-thioxo-1*H*-1λ$^5$-phosphol-1-yl)ferrocenyl]methane (7c):** Orange solid (yield 77% from **5c**). $^1H$ NMR ($CDCl_3$): $\delta$ = 3.84 (dd, $J_{H,H}$ = 16.0 Hz and $J_{H,P2}$ = 11.8 Hz, 1 H, $CH_2$), 4.06 (br. s, 1 H, subst. Cp), 4.19 (m, 1 H, subst. Cp), 4.27 (s, 5 H, Cp), 4.40 (dd, $J_{H,H}$ = 16.0 Hz and $J_{H,P2}$ = 10.8 Hz, 1 H, $CH_2$), 4.81 (br. s, 1 H, subst. Cp), 7.65–7.3 (m, 12 H, Ar), 7.82–7.74 (m, 3 H, Ar), 7.95–7.85 (m, 3 H, Ar) ppm. $^{13}C$ NMR ($CDCl_3$): $\delta$ = 33.9 (d, $J_{C,P2}$ = 54.1 Hz, $CH_2$), 71.1 (d, $J_{C,P1}$ = 11.4 Hz, subst. Cp), 71.7 (Cp), 72.6 (d, $J_{C-P1}$ = 15.0 Hz, subst. Cp), 73.7 (d, $J_{C-P1}$ = 7.8 Hz, $J_{C,P2}$ = 4.4 Hz, subst. Cp), 74.2 (dd, $J_{C,P1}$ = 78.9 Hz, $J_{C,P2}$ = 6.1 Hz, quat. Cp), 82.6 (dd, $J_{C,P1}$ = 12.1 Hz, $J_{C,P2}$ = 1.8 Hz, quat. Cp), 121.7 (d, $J_{C,P1}$ = 9.5 Hz, 2 C, benzophosphole), 129.1 (d, $J_{C,P1}$ = 12.1 Hz, 2 C, $PPh_2$), 129.9 (d, $J_{C,P1}$ = 12 Hz, benzophosphole), 130.0 (d, $J_{C,P1}$ = 11 Hz, 2 C, benzophosphole), 130.3 (d, $J_{C,P1}$ = 11.0 Hz, benzophosphole), 131.5 (d, $J_{C,P2}$ = 10.1 Hz, $PPh_2$), 131.8 (d, $J_{C,P2}$ = 2.8 Hz, $PPh_2$), 132.0 (d, $J_{C,P2}$ = 10.3 Hz, $PPh_2$), 132.1 (d, $J_{C,P2}$ = 2.7 Hz, $PPh_2$), 133.0 (d, $J_{C,P1}$ = 2.2 Hz, benzophosphole), 133.1 (d, $J_{C,P2}$ = 79.5 Hz, quat. $PPh_2$), 133.2 (d, $J_{C,P1}$ = 2.2 Hz, benzophosphole), 133.5 (d, $J_{C,P2}$ = 78.0 Hz, quat. $PPh_2$), 136.6 (d, $J_{C,P1}$ = 92.7 Hz, quat. benzophosphole), 136.8 (d, $J_{C,P1}$ = 91.3 Hz, quat. benzophosphole), 140.7 (d, $J_{C,P1}$ = 19.6 Hz, quat. benzophosphole), 141.0 (d, $J_{C,P1}$ = 19.4 Hz, quat. benzophosphole) ppm. $^{31}P$ NMR ($CDCl_3$): $\delta$ = 41.7 (P2, $PPh_2$), 43.4 (P1, phosphole) ppm. MS (DCI, $NH_3$): *m*/*z* (%) = 631 (80) [M + 1].

**General Procedure for Desulfurisation of Compounds 7:** Tris(dimethylamino)phosphane (0.2 mL, 1.2 mmol, 4 equiv.) was added at room temperature to a solution of **7** (0.3 mmol) in toluene (10 mL). The reaction mixture was stirred at reflux for 24 h. After concentration, the mixture was chromatographed on alumina using pentane and then a pentane/diethyl ether mixture (90:10).

**($S_{Fc}$)-[2-(3,4-Dimethyl-1*H*-1λ$^5$-phosphol-1-yl)ferrocenyl](diphenylphosphanyl)methane (8a):** MS (DCI, $NH_3$): *m*/*z* (%) = 495 (100) [M + 1].

**($S_{Fc}$)-(Diphenylphosphanyl)[2-(2,3,4,5-tetramethyl-1*H*-1λ$^5$-phosphol-1-yl)ferrocenyl]methane (8b):** Dark yellow solid (87%). Crystals suitable for X-ray analysis were obtained by diffusion of pentane into a dichloromethane solution. $^1H$ NMR ($CDCl_3$): $\delta$ = 1.89 (br. s, 3 H, $CH_3$ β phosphole), 1.93 (br. s, 3 H, $CH_3$ β phosphole), 2.11 (br. d, $J_{H,P1}$ = 10.7 Hz, 3 H, $CH_3$ α phosphole), 2.22 (br. d, $J_{H,P1}$ = 10.6 Hz, 3 H, $CH_3$ α phosphole), 3.15 (d, AB system, $J_{H,P2}$ = 14.5 Hz, 1 H, $CH_2$), 3.23 (dd, ABX system, $J_{H,H}$ = 1.4 Hz, $J_{H,P2}$ = 14.5 Hz, 1 H, $CH_2$), 3.86 (m, 1 H, subst. Cp), 3.97 (m, 1 H, subst. Cp), 4.12 (t, *J* = 2.5 Hz, 1 H, subst. Cp), 4.24 (s, 5 H, Cp), 7.4–7.3 (m, 8 H, $PPh_2$), 7.5–7.4 (m, 2 H, $PPh_2$) ppm. $^{13}C$ NMR ($CDCl_3$): $\delta$ = 14.0 (d, $J_{C,P1}$ = 21.0 Hz, $CH_3$ α phosphole), 14.3 (d, $J_{C,P1}$ = 3.0 Hz, $CH_3$ β phosphole), 14.5 (d, $J_{C,P1}$ = 3.0 Hz, $CH_3$ β phosphole), 14.6 (d, $J_{C,P1}$ = 21.4 Hz, $J_{C,P2}$ = 3.9 Hz, $CH_3$ α phosphole), 28.6 (dd, $J_{C,P1}$ = 4.6 Hz, $J_{C,P2}$ = 15.4 Hz, $CH_2$), 69.0 (d, $J_{C,P1}$ = 5.3 Hz, subst. Cp), 70.2 (Cp), 71.4 (dd, $J_{C,P1}$ = 2.0 Hz, $J_{C,P2}$ = 7.0 Hz, subst. Cp), 72.0 (d, $J_{C,P1}$ = 16.2 Hz, subst. Cp), 73.4 (dd, $J_{C,P}$ = 3.9 Hz, $J_{C,P}$ = 12.8 Hz, CP), 88.7 (dd, $J_{C,P}$ = 9.5 Hz, $J_{C,P}$ = 16.8 Hz, $CCH_2$), 128.6 ($CH_{Ar}$), 128.8 (d, $J_{C,P}$ = 5.7 Hz, $CH_{Ar}$), 128.9 (d, $J_{C,P}$ = 7.0 Hz, $CH_{Ar}$), 129.3 ($CH_{Ar}$), 132.5 (d, $J_{C,P}$ = 17.7 Hz, $CH_{Ar}$), 133.9 (d, $J_{C,P}$ = 20.0 Hz, $CH_{Ar}$), 134.6 (d, $J_{C,P}$ = 4.7 Hz, $CCH_{3\beta P}$), 135.5 ($CCH_{3\beta P}$), 139.8 (d, $J_{C,P}$ = 16.4 Hz, $C_{Ar}P$), 140.0 (d, $J_{C,P}$ = 16.2 Hz, $C_{Ar}P$), 142.3 (d, $J_{C,P}$ = 12.3 Hz, $CCH_{3\alpha P}$), 142.6 (d, $J_{C,P}$ = 12.5 Hz, $CCH_{3\alpha P}$) ppm. $^{31}P$ NMR ($CDCl_3$): $\delta$ = –12.3 (P2, $PPh_2$), 1.7 (P1, phosphole) ppm.

**($S_{Fc}$)-(Diphenylphosphanyl)[2-(dibenzo-1*H*-1λ$^5$-phospholyl)ferrocen-1-yl]methane (8c):** Yellow solid (94%). Crystals suitable for X-ray analysis were obtained by diffusion of pentane into a dichloromethane solution. $^1H$ NMR ($CDCl_3$): $\delta$ = 3.38 (br. d, $J_{H,H}$ = 14.2 Hz, 1 H, $CH_2$), 3.38 (br. s, 1 H, subst. Cp), 3.58 (br. d, $J_{H,H}$ = 14.2 Hz, 1 H, $CH_2$), 3.76 (br. s, 1 H, subst. Cp), 3.92 (br. s, 1 H, subst. Cp), 4.26 (s, 5 H, Cp), 7.3–7. 55 (m, 14 H, Ar), 7.90 (br. d, $J_{H,H}$ = 7.8 Hz, 1 H, Ar), 7.98 (br. d, $J_{H,H}$ = 7.4 Hz, 1 H, Ar), 8.02 (m, 1 H, Ar), 8.17 (m, 1 H, Ar) ppm. $^{13}C$ NMR ($CDCl_3$): $\delta$ = 29.3 (dd, $J_{C,P2}$ = 15.7 Hz, $J_{C,P1}$ = 8.1 Hz, $CH_2$), 68.7 (d, $J_{C,P1}$ = 2.0 Hz, subst. Cp), 69.6 (s, subst. Cp), 69.8 (s, Cp), 71.6 (dd, $J_{C,P2}$ = 5.2 Hz, $J_{C,P1}$ = 3.2 Hz, subst. Cp), 76.8 (quat. Cp), 89.3 (dd, $J_{C,P1}$ = 23.0 Hz, $J_{C,P2}$ = 16.2 Hz, quat. Cp), 121.1 (s, benzophosphole), 121.3 (s, benzophosphole), 126.9 (d, $J_{C,P1}$ = 8.3 Hz, benzophosphole), 127.4 (d, $J_{C,P1}$ = 7.4 Hz, benzophosphole), 128.26 (s, $PPh_2$), 128.30 (s, $PPh_2$), 128.4 (d, $J_{C,P2}$ = 7.1 Hz, $PPh_2$), 128.5 (d, $J_{C,P2}$ = 5.7 Hz, $PPh_2$), 128.6 (s, benzophosphole), 129.0 (s, benzophosphole), 130.9 (dd, $J_{C,P1}$ = 21.0 Hz, $J_{C,P2}$ = 11.8 Hz, benzophosphole), 131.1 (d, $J_{C,P1}$ = 21.0 Hz, benzophosphole), 132.0 (d, $J_{C,P2}$ = 17.3 Hz, $PPh_2$), 133.9 (d, $J_{C,P2}$ = 19.8 Hz, $PPh_2$), 138.5 (d, $J_{C,P2}$ = 15.7 Hz, quat. $PPh_2$), 139.3 (d, $J_{C,P2}$ = 15.3 Hz, quat. $PPh_2$), 141.8 (s, quat. benzophosphole), 142.6 (d, $J_{C,P1}$ = 3.7 Hz, quat. benzophosphole), 144.4 (d, $J_{C,P1}$ = 3.9 Hz, quat. benzophosphole), 144.8 (d, $J_{C,P1}$ = 4.0 Hz, quat. benzophosphole) ppm. $^{31}P$ NMR ($CDCl_3$): $\delta$ = –13.5 (d, $J_{P,P}$ = 6.4 Hz, P2, $PPh_2$), –26.5 (d, $J_{P,P}$ = 6.4 Hz, P1, phosphole) ppm. MS (DCI, $NH_3$): *m*/*z* (%) = 567 (100) [M + 1].

**Dichloro{($S_{Fc}$)-(diphenylphosphanyl)[2-(2,3,4,5-tetramethyl-1*H*-1λ$^5$-phospholyl)ferrocen-1-yl]methane}palladium(II) (9b):** Diphosphane **7b** (0.025 g, 0.048 mmol) was dissolved in dry dichloromethane (25 mL) in a Schlenk tube under argon and [$PdCl_2(CH_3CN)_2$] (0.015 mg, 0.058 mmol) was then added. The yellow solution turned immediately orange then deep red and finally brown. After 30 min of stirring at room temperature, the solution was partially

 © 2006 Wiley-VCH Verlag GmbH & Co. KGaA, Weinheim 

concentrated (10 mL) and dry pentane (5 mL) was added dropwise. A brown precipitate appeared. The red solution was filtered and concentrated with a high-vacuum pump to yield a red-orange solid (28 mg) (yield 80%). Crystals suitable for X-ray analysis were obtained by diffusion of pentane into a chloroform solution. $^1$H NMR ($CDCl_3$): $\delta$ = 2.00 (br. s, 3 H, $CH_3$ β phosphole), 2.066 (br. s, 3 H, $CH_3$ β phosphole), 2.07 (br. d, $J_{H,P1}$ = 13 Hz, 3 H, $CH_3$ α phosphole), 2.40 (br. d, $J_{H,P1}$ = 13.8 Hz, 3 H, $CH_3$ α phosphole), 3.40 (dd, $J_{H,P1}$ = 2.3 Hz, $J_{H,P2}$ = 10.5 Hz, 2 H, $CH_2$), 3.95 (s, 5 H, Cp), 4.13 (m, 1 H, subst. Cp), 4.26 (m, 1 H, subst. Cp), 4.34 (br. s, 1 H, subst. Cp), 7.37 (m, 2 H, $PPh_2$), 7.45 (m, 1 H, $PPh_2$), 7.6–7.5 (m, 3 H, $PPh_2$), 7.75–7.65 (m, 2 H, $PPh_2$), 8.1–8.0 (m, 2 H, $PPh_2$) ppm. $^{13}$C NMR ($CDCl_3$): $\delta$ = 14.0 (d, $J_{C,P1}$ = 15.3 Hz, $CH_3$ α phosphole), 14.3 (d, $J_{C,P1}$ = 12 Hz, $CH_3$ β phosphole), 14.5 (d, $J_{C,P1}$ = 12 Hz, $CH_3$ β phosphole), 14.7 (d, $J_{C,P1}$ = 17 Hz, $CH_3$ α phosphole), 30.6 (dd, $J_{C,P1}$ = 8.0 Hz, $J_{C,P2}$ = 28.0 Hz, $CH_2$), 63.2 (dd, $J_{C,P1}$ = 63.1 Hz, $J_{C,P2}$ = 13.4 Hz, quat. Cp), 69.1 (d, $J_{C,P1}$ = 7.1 Hz, subst. Cp), 70.7 (s, Cp), 71.5 (d, $J_{C,P1}$ = 5.7 Hz, subst. Cp), 73.0 (dd, $J_{C,P1}$ = 6.7 Hz, $J_{C,P2}$ = 4.7 Hz, subst. Cp), 85.8 (br. d, $J_{C,P1}$ = 18 Hz, quat. Cp), 128.9 (d, $J_{C,P2}$ = 11.1 Hz, $PPh_2$), 129.15 (s, $CCH_3$ β phosphole), 129.22 (s, $CCH_3$ β phosphole), 129.23 (d, $J_{C,P2}$ = 11.3 Hz, $PPh_2$), 129.7 (d, $J_{C,P2}$ = 55.8 Hz, quat. $PPh_2$), 130.8 (d, $J_{C,P2}$ = 55.3 Hz, quat. $PPh_2$), 131.8 (d, $J_{C,P2}$ = 2.7 Hz, $PPh_2$), 132.2 (d, $J_{C,P2}$ = 3.0 Hz, $PPh_2$), 133.9 (d, $J_{C,P2}$ = 10.4 Hz, $PPh_2$), 134.7 (d, $J_{C,P2}$ = 10.9 Hz, $PPh_2$), 146.9 (d, $J_{C,P1}$ = 17.8 Hz, $CCH_3$ α phosphole), 148.7 (d, $J_{C,P1}$ = 18.2 Hz, $CCH_3$ α phosphole) ppm. $^{31}$P NMR ($CDCl_3$): $\delta$ = 36.2 (P1, phosphole), 46.8 (P2, $PPh_2$) ppm. MS (FAB, MNBA): *m*/*z* (%) = 663 (100) $[M - Cl]^+$.

**General Procedure for Palladium-Catalysed Allylic Substitution:** A mixture of ligand **8**, 1,3-diphenylprop-2-enyl acetate (**10**) (0.454 g, 1.8 mmol) and $[(Pd(C_3H_5)Cl)]_2$ (3.3 mg, 0.009 mmol) in dry dichloromethane (20 mL) was stirred at room temperature for 2 h. Dimethyl malonate (**11**) (0.411 mL, 3.6 mmol), potassium acetate and BSA (0.880 mL, 3.6 mmol) were added to the resulting solution. The reaction was carried out at room temperature and monitored by TLC for the disappearance of the acetate. After the reaction was complete, the resulting mixture was diluted with diethyl ether (5 mL) and quenched with a saturated aqueous solution of ammonium chloride (5 mL). The aqueous phase was extracted with diethyl ether, the combined organic layers were dried with magnesium sulfate, filtered and the solvents evaporated. The conversion was calculated from the crude reaction mixture by $^1$H NMR spectroscopy. Subsequent purification by chromatography on silica eluting with ethyl acetate/pentane (15:85) afforded the product as a white solid. The enantiomeric excess was determined by $^1$H NMR using the chiral shift reagent $Eu(hfc)_3$.

**X-ray Structure Determinations:** A single crystal of each compound was mounted under inert perfluoropolyether at the tip of a glass fibre and cooled in the cryostream of a Stoe IPDS diffractometer for **3b**, **8b** and **9b** or an Oxford Diffraction XCALIBUR CCD diffractometer for **5b**. Data were collected using monochromatic Mo-$K_\alpha$ radiation ($\lambda$ = 0.71073). The structures were solved by direct methods (SIR97[31]) and refined by least-squares procedures on $F^2$ using SHELXL-97.[32] All H atoms were introduced in the calculation in idealised positions and treated as riding on their parent atoms. The absolute configuration was confirmed by refinement of the Flack's enantiopole parameter[33] and careful examination of sensitive reflections. Molecules were drawn with the help of ORTEP32.[34] Crystal data and refinement parameters are shown in Table 1. CCDC-605992 to -605995 contain the supplementary crys-

Table 1. Crystal data and structure refinement.

| | **3b** | **5b** | **8b** | **9b** |
|---|---|---|---|---|
| Empirical formula | $C_{24}H_{31}FeO_3PS$ | $C_{19}H_{23}FeOPS$ | $C_{31}H_{32}FeP_2$ | $C_{33}H_{34}Cl_8FeP_2Pd$ |
| Formula mass | 486.37 | 386.25 | 522.36 | 938.39 |
| Temperature [K] | 180(2) | 180(2) | 180(2) | 180(2) |
| Wavelength [Å] | 0.71073 | 0.71073 | 0.71073 | 0.71073 |
| Crystal system | monoclinic | monoclinic | orthorhombic | monoclinic |
| Space group | $P2_1$ | $P2_1$ | $P2_12_12_1$ | $P2_1$ |
| *a* [Å] | 8.4215(16) | 8.1583(6) | 11.0468(7) | 9.7972(9) |
| *b* [Å] | 11.1878(16) | 11.0794(7) | 14.4359(12) | 18.2870(13) |
| *c* [Å] | 12.490(2) | 10.0725(7) | 16.6373(13) | 21.391(3) |
| $\alpha$ [°] | 90 | 90 | 90 | 90 |
| $\beta$ [°] | 95.92(2) | 102.266(6) | 90 | 98.487(13) |
| $\gamma$ [°] | 90 | 90 | 90 | 90 |
| *V* [Å$^3$] | 1170.5(3) | 889.66(11) | 2653.2(3) | 3790.5(6) |
| *Z* | 2 | 2 | 4 | 4 |
| $D_{calcd.}$ [Mg/m$^3$] | 1.380 | 1.442 | 1.308 | 1.644 |
| $\mu$ [mm$^{-1}$] | 0.824 | 1.056 | 0.707 | 1.530 |
| *F*(000) | 276 | 404 | 1096 | 1880 |
| Crystal size [mm] | 0.76 × 0.34 × 0.16 | 0.64 × 0.54 × 0.31 | 0.38 × 0.31 × 0.28 | 0.4 × 0.32 × 0.12 |
| $\theta$ [°] | 2.43–26.11 | 3.46–28.28 | 2.21–26.04 | 2.22–24.05 |
| Reflections collected | 11372 | 6780 | 26463 | 30390 |
| Unique reflections [*R*(int)] | 4109 (0.0321) | 4105 (0.0200) | 5206 (0.0536) | 11238 (0.0526) |
| Completeness [%] | 99.2 | 99.3 | 99.3 | 93.9 |
| Absorption correction | multiscan | multiscan | empirical | multiscan |
| Max./min. transmission | 0.9247/0.8729 | 0.731/0.522 | 0.835/0.735 | 0.689/0.622 |
| Refinement method | $F^2$ | $F^2$ | $F^2$ | $F^2$ |
| Data/restraints/parameters | 4374/3/313 | 4105/1/213 | 5206/0/311 | 11238/741/820 |
| Gof on $F^2$ | 1.118 | 1.053 | 1.047 | 1.109 |
| $R_1$, $wR_2$ [$I > 2\sigma(I)$] | 0.0293, 0.0792 | 0.0238, 0.0605 | 0.0381, 0.0937 | 0.0637, 0.1560 |
| $R_1$, $wR_2$ (all data) | 0.0306, 0.0804 | 0.0246, 0.0613 | 0.0500, 0.0985 | 0.0692, 0.1590 |
| Absolute structure parameter | –0.06(5) | 0.000(10) | –0.006(19) | 0.06(3) |
| Largest diff. peak/hole [e/Å$^3$] | 0.326/–0.237 | 0.293/–0.318 | 0.999/–0.271 | 2.409/–1.177 |

 © 2006 Wiley-VCH Verlag GmbH & Co. KGaA, Weinheim 

tallographic data for this paper. These data can be obtained free of charge from The Cambridge Crystallographic Data Centre via www.ccdc.cam.ac.uk/data_request/cif.


[1] a) I. Ojima, *Catalytic Asymmetric Synthesis*, 2nd ed., Wiley-VCH, New York, **2000**; b) E. N. Jacobsen, A. Pfaltz, H. Yamamoto, *Comprehensive Asymmetric Catalysis*, Springer-Verlag, Berlin, **1999**; c) R. Noyori, *Asymmetic Catalysis in Organic Synthesis*, Wiley, New York, **1994**.

[2] a) A. Togni, T. Hayashi, *Ferrocenes*, VCH, Weinheim, **1995**; b) S. Borman, *Chem. Eng. News* **1996**, *July 22*, 38–39; c) A. Togni, *Angew. Chem. Int. Ed. Engl.* **1996**, *35*, 1475–1477; d) R. C. J. Atkinson, V. C. Gibson, N. J. Long, *Chem. Soc. Rev.* **2004**, *33*, 313–328.

[3] a) T. J. Colacot, *Chem. Rev.* **2003**, *103*, 3101–3118; b) W. Tang, X. Zhang, *Chem. Rev.* **2003**, *103*, 3029–3069; c) P. Barbaro, C. Bianchini, G. Giambiastiani, S. L. Parisel, *Coord. Chem. Rev.* **2004**, *248*, 2131–2160.

[4] a) M. Sawamura, Y. Nakayama, T. Kato, Y. Ito, *J. Org. Chem.* **1995**, *60*, 1727–1732; b) M. Sawamura, M. Sudoh, Y. Ito, *J. Am. Chem. Soc.* **1996**, *118*, 3309–3310; c) R. Kuwano, H. Miyazaki, Y. Ito, *Chem. Commun.* **1998**, 71–72; d) R. Kuwano, H. Miyazaki, Y. Ito, *Tetrahedron Lett.* **1999**, *40*, 1327–1330; e) R. Kuwano, K. Sato, T. Kurokawa, D. Karube, Y. Ito, *J. Am. Chem. Soc.* **2000**, *122*, 7614–7615.

[5] H.-U. Blaser, W. Brieden, B. Pugin, F. Spindler, M. Studer, A. Togni, *Top. Catal.* **2002**, *19*, 3–16 and references quoted therein.

[6] H.-U. Blaser, *Adv. Synth. Catal.* **2002**, *344*, 17–31 and references quoted therein.

[7] a) T. Ireland, G. Grossheimann, G. Wieser-Jeunesse, P. Knochel, *Angew. Chem. Int. Ed. Engl.* **1999**, *38*, 3212–3215; b) M. Lotz, K. Polborn, P. Knochel, *Angew. Chem. Int. Ed. Engl.* **2002**, *41*, 4708–4711; c) F. Spindler, C. Malan, M. Lotz, M. Kesselgruber, U. Pittelkow, A. Rivas-Nass, O. Briel, H.-U. Blaser, *Tetrahedron: Asymmetry* **2004**, *15*, 2299–2306.

[8] T. Sturm, W. Weissensteiner, F. Spindler, *Adv. Synth. Catal.* **2003**, *345*, 160–164.

[9] R. Kuwano, T. Uemura, M. Saitoh, Y. Ito, *Tetrahedron: Asymmetry* **2004**, *15*, 2263–2271.

[10] G. Argouach, O. Samuel, H. B. Kagan, *Eur. J. Org. Chem.* **2000**, 2885–2891.

[11] G. Argouach, O. Samuel, O. Riant, J.-C. Daran, H. B. Kagan, *Eur. J. Org. Chem.* **2000**, 2893–2899.

[12] S. Mourgues, D. Serra, F. Lamy, S. Vinceandeau, J.-C. Daran, E. Manoury, M. Gouygou, *Eur. J. Inorg. Chem.* **2003**, 2820–2826.

[13] Some recent examples of chiral phospholes: a) M. Ogasawara, K. Yoshida, T. Hayashi, *Organometallics* **2001**, *20*, 1014–1019; b) X. Sava, A. Marinetti, L. Ricard, F. Mathey, *Eur. J. Inorg. Chem.* **2002**, 1657–1665.

[14] a) T. P. Dang, J.-C. Poulin, H. B. Kagan, *J. Organomet. Chem.* **1975**, *91*, 105–115; b) G. Consiglio, S. C. A. Nefkens, *Tetrahedron: Asymmetry* **1990**, *1*, 417–420; c) J. Stille, M. Su, P. Brechot, G. Parinello, L. S. Hegedus, *Organometallics* **1991**, *10*, 1183–1189; d) G. Consiglio, S. C. A. Nefkens, A. Borer, *Organometallics* **1991**, *10*, 2046–2051; e) J.-J. Brunet, H. Hajouji, J. C. Ndjanga, D. Neibecker, *J. Mol. Catal.* **1992**, *72*, L21–L25; f) T. Langer, J. Janssen, G. Helmchen, *Tetrahedron: Asymmetry* **1996**, *7*, 1599–1602; g) T. Langer, G. Helmchen, *Tetrahedron Lett.* **1996**, *37*, 1381–1384; h) M. Peer, G. J. G. de Jong, M. Kiefer, T. Langer, H. Rieck, H. Schell, P. Sennhehn, J. Sprinz, H. Steinhagen, B. Wiese, G. Helmchen, *Tetrahedron* **1996**, *52*, 7547–7583; i) I. Toth, C. J. Elsevier, J. G. de Vries, J. Bakos, W. J. J. Smeets, A. L. Spek, *J. Organomet. Chem.* **1997**, *540*, 15–25; j) W. A. Schenk, M. Stubbe, M. Hagel, *J. Organomet. Chem.* **1998**, *560*, 257–263; k) J. Hydrio, M. Gouygou, F. Dallemer, J.-C. Daran, G. G. A. Balavoine, *Tetrahedron: Asymmetry* **2002**, *13*, 1097–1102.

[15] a) D. E. Budd, D. G. Holah, A. N. Hughes, B. C. Hui, *Can. J. Chem.* **1974**, *52*, 775–781; b) Société Nationale des Poudres et Explosifs, Patent FR 8514638, **1980**, pp. 1–19; c) D. Neibecker, R. Réau, S. Lecolier, *J. Org. Chem.* **1989**, *54*, 5208–5210; d) D. Neibecker, R. Réau, *J. Mol. Catal.* **1989**, *53*, 219–227; e) D. Neibecker, R. Réau, *J. Mol. Catal.* **1989**, *57*, 153–163; f) F. Mercier, L. Laporte, L. Ricard, F. Mathey, M. Schröder, M. Regitz, *Angew. Chem.* **1997**, *109*, 2460–2462; *Angew. Chem. Int. Ed.* **1997**, *36*, 2364–2366; g) Z. Csok, G. Keglevich, G. Petocz, L. Kollar, *J. Organomet. Chem.* **1999**, *586*, 79–84; h) P. J. Fagan, G. Li, Z. Guan, L. Wang, E. I. Du Pont De Nemours and Company, Patent WO0021970A1, **2000**; i) S. Doherty, E. G. Robins, J. G. Knight, C. R. Newman, B. Rhodes, P. A. Champkin, W. Clegg, *J. Organomet. Chem.* **2001**, *640*, 182–196; j) M. Sauthier, F. Leca, L. Toupet, R. Réau, *Organometallics* **2002**, *21*, 1591–1602; k) C. Thoumazet, M. Melaini, L. Ricard, F. Mathey, P. Le Floch, *Organometallics* **2003**, *22*, 1580–1581.

[16] In phospholes, the inversion barrier for the pyramidal phosphorus atom is reduced, relative to that in phosphanes, as a result of the increase in the aromatic character of the phosphorus atom in the transition state.

[17] a) P. J. Walsh, A. E. Lurain, J. Basells, *Chem. Rev.* **2003**, *103*, 3297–3344; b) K. Mikami, K. Aikawa, Y. Yusa, J. J. Jodry, M. Yamanaka, *Synlett.* **2002**, *10*, 1561–1578 and references cited therein.

[18] a) G. Iftime, C. Moreau-Bossuet, E. Manoury, G. G. A. Balavoine, *Chem. Commun.* **1996**, 527–528; b) G. Iftime, J.-C. Daran, C. Moreau-Bossuet, E. Manoury, G. G. A. Balavoine, *Organometallics* **1996**, *15*, 4808–4815; c) G. Iftime, J.-C. Daran, E. Manoury, G. G. A. Balavoine, *Angew. Chem. Int. Ed.* **1998**, *37*, 1698–1700; d) E. Manoury, J. Fossey, H. Aït-Haddou, J.-C. Daran, G. G. A. Balavoine, *Organometallics* **2000**, *19*, 3736–3739; e) J. Chiffre, Y. Coppel, G. G. A. Balavoine, J.-C. Daran, E. Manoury, *Organometallics* **2002**, *21*, 4552–4555; f) L. Routaboul, S. Vincendeau, J.-C. Daran, E. Manoury, *Tetrahedron: Asymmetry* **2005**, *16*, 2685–2690.

[19] a) O. Tissot, M. Gouygou, J.-C. Daran, G. G. A. Balavoine, *Chem. Commun.* **1996**, 2287–2288; b) O. Tissot, M. Gouygou, F. Dallemer, J.-C. Daran, G. G. A. Balavoine, *Angew. Chem. Int. Ed. Engl.* **2001**, *40*, 1076–1078; c) O. Tissot, M. Gouygou, F. Dallemer, J.-C. Daran, G. G. A. Balavoine, *Eur. J. Inorg. Chem.* **2001**, 2385–2389; d) J. Hydrio, M. Gouygou, F. Dallemer, G. G. A. Balavoine, J.-C. Daran, *Eur. J. Org. Chem.* **2002**, 675–685; e) E. Robé, C. Ortega, M. Mikina, M. Mikolajczyk, J.-C. Daran, M. Gouygou, *Organometallics* **2005**, *24*, 5549–5559.

[20] See for example: T. Hayashi, T. Mise, M. Fukushima, M. Kagotani, N. Nagashima, Y. Hamada, A. Matsumoto, S. Kawakami, M. Konishi, K. Yamamoto, M. Kumada, *Bull. Chem. Soc. Jpn.* **1980**, *53*, 1138–1151.

[21] a) A. Togni, C. Breutel, A. Schnyder, F. Spindler, H. Landert, A. Tijani, *J. Am. Chem. Soc.* **1994**, *116*, 4062–4066; b) A. Schnyder, L. Hintermann, A. Togni, *Angew. Chem. Int. Ed. Engl.* **1995**, *34*, 931–933.

[22] For recent reviews: a) C. J. Richards, A. J. Locke, *Tetrahedron: Asymmetry* **1998**, *9*, 2377–2407; b) G. G. A. Balavoine, J.-C. Daran, G. Iftime, E. Manoury, C. Moreau-Bossuet, *J. Organomet. Chem.* **1998**, *567*, 191–198; c) O. Riant, H. B. Kagan, in *Advances in Asymmetric Synthesis* (Ed.: A. Hassner), JAI Press, Greenwich, CT, **1997**, vol. 2, pp. 189–235; d) A. Togni, *Angew. Chem. Int. Ed. Engl.* **1996**, *35*, 1475–1477.

[23] For recent papers: a) Y. J. Wu, L. Ding, W. L. Wang, C. X. Du, *Tetrahedron: Asymmetry* **1998**, *9*, 4035–4041; b) X. L. Cui, Y. J. Wu, C. X. Du, L. R. Yang, Y. Zhu, *Tetrahedron: Asymmetry* **1999**, 1255–1262; c) M. Wildhalm, K. Mereiter, M. Bourghida, *Tetrahedron: Asymmetry* **1998**, *9*, 2983–2986; d) C. Bolm, M. Kesselgruber, K. Muniz, G. Raabe, *Organometallics* **2000**, *19*, 1648–1651; e) D. Enders, R. Peters, R. Lochtman, J. Runsink, *Eur. J. Org. Chem.* **2000**, 2839–2850; f) U. Neetekoven, M. Wildhalm, P. C. J. Kamer, P. W. N. M. van Leeuwen, K. Mere-


 © 2006 Wiley-VCH Verlag GmbH & Co. KGaA, Weinheim 

iter, M. Lutz, A. L. Spek, *Organometallics* **2000**, *19*, 2299–2309; g) L. Xiao, R. Kitsler, W. Weissensteiner, *J. Org. Chem.* **2001**, *66*, 8912–8919; h) D. Vinci, N. Mateus, X. Wu, F. Hancock, A. Steiner, J. Xiao, *Org. Lett.* **2006**, *8*, 215–218.
[24] a) O. Riant, O. Samuel, H. B. Kagan, *J. Am. Chem. Soc.* **1993**, *115*, 5835–5836; b) O. Riant, O. Samuel, T. Flessner, S. Taudien, H. B. Kagan, *J. Org. Chem.* **1997**, *62*, 6733–6745.
[25] S. Holand, F. Mathey, *Organometallics* **1988**, *7*, 1796–1801.
[26] D. Cremer, J. A. Pople, *J. Am. Chem. Soc.* **1975**, *97*, 1354–1358.
[27] a) P. Coggon, A. T. Mc Phail, *J. Chem. Soc., Dalton Trans.* **1973**, 1888–1891; b) O. Tissot, J. Hydrio, M. Gouygou, F. Dallemer, J.-C. Daran, G. G. A. Balavoine, *Tetrahedron* **2000**, *56*, 85–93; c) J. Hydrio, M. Gouygou, F. Dallemer, J.-C. Daran, G. G. A. Balavoine, *J. Organomet. Chem.* **2000**, *595*, 261–267; d) E. Mattmann, D. Simonutti, L. Ricard, F. Mercier, F. Mathey, *J. Org. Chem.* **2001**, *66*, 755–758; e) M. Ogasawara, K. Yoshida, T. Hayashi, *Organometallics* **2001**, *20*, 1014–1019; f) J. Hydrio, M. Gouygou, F. Dallemer, G. G. A. Balavoine, J.-C. Daran, *Eur. J. Org. Chem.* **2002**, 675–685; g) M. Melaimi, L. Ricard, F. Mathey, P. Le Floch, *Org. Lett.* **2002**, *4*, 1245–1247.
[28] P. Liptau, T. Seki, G. Kehr, A. Abele, R. Fröhlich, G. Erker, S. Grimme, *Organometallics* **2003**, *22*, 2226–2232.
[29] a) B. M. Trost, D. L. van Vranken, *Chem. Rev.* **1996**, *96*, 395–422; b) A. Pfalz, M. Lautens, in *Comprehensive Asymmetric Catalysis* (Eds.: E. N. Jacobsen, A. Pfaltz, H. Yamamoto), Springer-Verlag, Berlin, **1999**, pp. 834–884; c) B. M. Trost, M. L. Crawley, *Chem. Rev.* **2003**, *103*, 395–342.
[30] S. Affandi, R. L. Green, B. T. Hsich, M. S. Holt, J. H. Nelson, E. C. Alyena, *Synth. React. Inorg. Met.-Org. Chem.* **1987**, *17*, 307–308.
[31] SIR97 – a program for automatic solution of crystal structures by direct methods: A. Altomare, M. C. Burla, M. Camalli, G. L. Cascarano, C. Giacovazzo, A. Guagliardi, A. G. G. Moliterni, G. Polidori, R. Spagna, *J. Appl. Crystallogr.* **1999**, *32*, 115.
[32] G. M. Sheldrick, *SHELXL97, Program for crystal structure refinement*, University of Göttingen, Germany, **1997**.
[33] a) H. D. Flack, *Acta Crystallogr., Sect. A: Found. Crystallogr.* **1983**, *39*, 876; b) G. Bernardinelli, H. D. Flack, *Acta Crystallogr., Sect. A: Found. Crystallogr.* **1985**, *41*, 500.
[34] ORTEP3 for Windows: L. J. Farrugia, *J. Appl. Crystallogr.* **1997**, *30*, 565.

Received: August 18, 2006
Published Online: October 27, 2006

 © 2006 Wiley-VCH Verlag GmbH & Co. KGaA, Weinheim 

DOI: 10.1002/ejic.200600813

# "Inhibition" of the Enzyme Model $Tp^{Ph,Me}Zn$–OH by Diketo Compounds

Teame Tekeste[a] and Heinrich Vahrenkamp*[a]

**Keywords:** Zinc / Bioinorganic chemistry / Enzyme inhibition / Diketo compounds

In order to gain a structural understanding of zinc enzyme inhibition, the model complex $Tp^{Ph,Me}Zn$–OH was treated with various diketo compounds. α-Keto carboxylic acids were attached to the zinc ion as anionic O,O-chelate ligands, of which benzoylformate was oxidatively decarboxylated in air to form the benzoate complex. Two functionalized β-diketones did not use their functionality in forming the β-diketonate complexes. Of the α-diketones, 2,3-pentanedione formed the α-keto enolate complex, while 1-phenyl-1,2-propanedione underwent oxidative C–C coupling resulting in a red dinuclear bis(α-keto enolato) complex. Of the diaryl-α-diketones, benzil did not react, but pyridil underwent hydrolytic cleavage to pyridine-2-carbaldehyde and picolinate, of which the latter was bound to the zinc ion as an N,O-chelate ligand.

(© Wiley-VCH Verlag GmbH & Co. KGaA, 69451 Weinheim, Germany, 2006)

## Introduction

The inhibition of zinc enzymes is an active field of drug research, as it may be relevant for the treatment of such diseases as arthritis, high blood pressure, multiple sclerosis, and even cancer.[1,2] Studies towards this end can benefit from the fact that not only are a large number of zinc enzymes known, but many of them have been fully characterized by structure determinations.[3,4] Thus, there is an excellent basis for target-oriented drug design for zinc-enzyme-related diseases.

Despite this, development in this field is still mostly a matter of trial and error, and the number of zinc-specific inhibitor types is still relatively small.[2,5,6] The oldest of them, which have been successful in various fields, are the sulfonamides.[5] The best investigated are the hydroxamates.[2] They are attractive because the hydroxamate function is a very good zinc-binding group, but until now none of them has made it through all clinical tests, which is due in part to their unsuitability for oral administration as well as their potential chronic toxicity.[1,2,7]

It is therefore attractive to investigate inhibitors with other zinc-binding groups.[1,2] Studies of this kind have been reported for carboxylates,[8] β-keto enolates,[2,5] and some thiolate-containing chelators.[2,9] Considering the state of the art in the coordination chemistry of zinc and the large number of well-established zinc-binding functions, one must say that amazingly little of the knowledge accumulated has reached the field of drug design.

[a] Institut für Anorganische und Analytische Chemie der Universität Freiburg,
Albertstr. 21, 79104 Freiburg, Germany
Fax: +49-761-203-6001
E-mail: vahrenka@uni-freiburg.de

We have tackled this subject sporadically. After some basic studies of zinc complexes of drug substances,[10–14] we used our enzyme models, the TpZn–OH complexes, to study the interactions between zinc and pharmaceutically relevant substrates.[15–19] From these studies we found a striking structural similarity between the geometries at the zinc centers of the enzyme and the model complex in the hydroxamate-bound state,[20] and this enabled our mechanistic proposal for the zinc-enzyme-catalyzed hydrolysis of esters and peptides.[21,22]

Until recently, none of our investigations in this field was focused on a systematic survey of zinc-binding groups against a background of enzyme inhibition. Yet, one of our enzyme models, the $Tp^{Ph,Me}Zn$–OH complex, was used by Cohen et al. for studies of this kind, addressing the interactions between zinc and hydroxamates, pyridinones, chelating Schiff bases, and various kinds of bidentate thiolates.[23–27] This provided quite a diverse structural chemistry and some important aspects of the stability of enzyme model inhibitor complexes.

Independent of Cohen's work, we also started a systematic study scanning potentially bidentate zinc-binding groups and using the same enzyme model $Tp^{Ph,Me}Zn$–OH (**1**). Fortunately, so far the parallel work in both groups (with one exception, complex **11**, see below) has not produced any overlap. After some variations of the theme of hydroxamates and oximates,[28] we turned to zinc-binding groups that should be expected to bind through oxygen atoms only and which should be good chelators. This paper describes our results with such ligands containing two carbonyl functions: α-keto carboxylates, β-diketonates, α-diketones, and ligands derived from them.

 InterScience © 2006 Wiley-VCH Verlag GmbH & Co. KGaA, Weinheim 

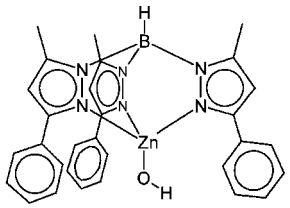

**1**

## Results and Discussion

### α-Keto Carboxylic Acids

After the hydroxamic acids, the carboxylic acids are the second most investigated group of zinc enzyme inhibitors.[1] However, at physiological pH the carboxylate function binds 100–2000 times less efficiently to the zinc centers than the hydroxamate function.[1,29] It therefore seems suitable to enhance the carboxylates' binding capacity by introducing additional donor functions that make the carboxylate function part of a bidentate chelating ligand. With this in mind we applied pyruvic acid, benzoylformic acid, and oxamidic acid as inhibitor models.

The reaction between pyruvic acid and **1** was quantitative and yielded the pyruvate complex **2**. As expected, the pyruvato ligand in **2** is bound in a bidentate fashion, forming a five-membered chelate ring. This was already evident from the $^1$H NMR spectrum, in which the pyruvate's methyl resonance experienced a high-field shift of 1 ppm upon coordination, indicating that it was embedded between the Tp's phenyl rings. This was confirmed by the structure determination (see Figure 1).

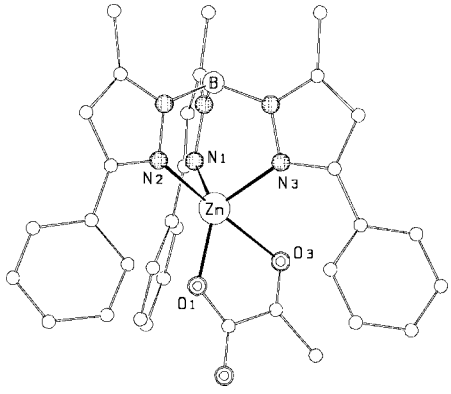

Figure 1. Molecular structure of complex **2**. Selected bond lengths [Å] and angles [°]: Zn–N1 2.020(3), Zn–N2 2.138(3), Zn–N3 2.017(3), Zn–O1 1.901(3), Zn–O3 2.397(3); O3–Zn–O1 75.6(1), O3–Zn–N1 89.7(1), O3–Zn–N3 87.7(1), O3–Zn–N2 177.5(1).

The major zinc–pyruvate interaction lies in the Zn–O bond to the carboxylate oxygen atom, which is 0.5 Å shorter than the other Zn–O bond. In part, this lengthening of the Zn–O3 bond can be ascribed to the fact that it represents the axis of a trigonal bipyramid around the zinc ion, with the Zn–N2 bond, which has also been lengthened, as the other axis. According to the Holmes definition,[30] the complex is 75% trigonal-bipyramidal and 25% square-pyramidal. Thereby **2** is one of the best examples of trigonal-bipyramidal coordination in TpZn complexes.[21]

We are not aware of any other zinc complexes of α-keto carboxylato ligands. There is, however, an iron–pyruvate complex of the $Tp^{Ph,Ph}$ ligand, the geometry of which is very similar to that of **2**.[31]

The reactions of **1** with benzoylformic acid and oxamidic acid proceeded equally straightforwardly and yielded complexes **3** and **4**. Their spectroscopic data indicate that their α-keto carboxylate functions are bound to the zinc ion in a chelating fashion, like in **2**. The main pieces of evidence are again the $^1$H NMR resonances of the phenyl group in **3** and one of the $NH_2$ hydrogen atoms in **4**, which have experienced significant high-field shifts. There is a second NH signal for **4**, 2 ppm down-field from the first one. We take this as an indication that this second hydrogen atom is involved in an N–H···O hydrogen bond, as indicated in the formula drawing. Support for our structural assignments comes from two structurally characterized related complexes: a TpFe complex of benzoylformate[31] and an aqua–zinc complex of oxamidate.[32]

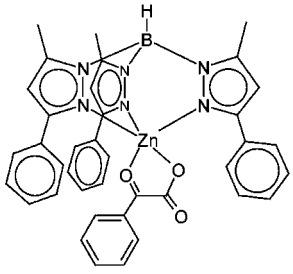

**3**

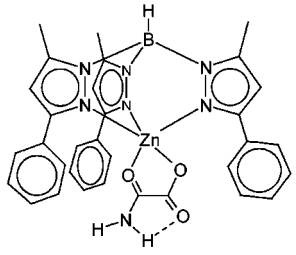

**4**

When solutions of **3** were exposed to air they turned yellow. $^1$H NMR spectroscopy indicated that **3** was consumed and replaced by another complex. Rigorous stirring in dichloromethane completed this process within hours and led to the isolation of the benzoate complex **5** in good yields. Complex **5** was identified by a structure determination (see Exp. Sect.), which is not discussed here as it revealed no unusual features.

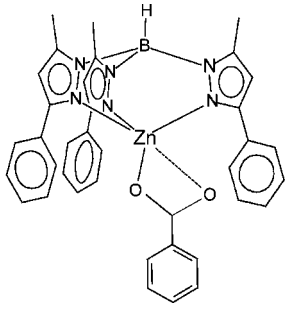

**5**

The conversion of **3** to **5** is an oxidative decarboxylation, a very typical reaction of α-keto carboxylic acids, which in organic chemistry is performed in the presence of $Fe^{II}$ and

 © 2006 Wiley-VCH Verlag GmbH & Co. KGaA, Weinheim 

in biology by Fe-containing enzymes.[33] It is not known whether zinc enzymes catalyze such a reaction. The model complex $Tp^{Ph,Ph}$Fe–benzoylformate, a close relative of **3**, was found, however, to undergo the same reaction with concomitant hydroxylation of one of the Tp's phenyl groups.[31]

### β-Diketones

Until now the reactions of TpZn complexes with β-diketones have yielded, without exception, the expected TpZn–β-diketonate complexes with the classical six-membered chelate rings.[20,21,34,35] In the present work we tried to find out whether additional functionality on the β-diketones changes this picture. For this purpose we chose methyl 2,4-dioxopentanoate, which is prone to ester cleavage by $Tp^{Ph,Me}$Zn–OH, and 2-acetylcyclohexanone, which has an unusually low p$K_a$ of the acidic CH function. Both diketones, however, behaved conventionally toward **1**, producing complexes **6** and **7** in good yields.

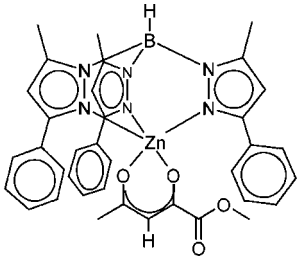

**6**

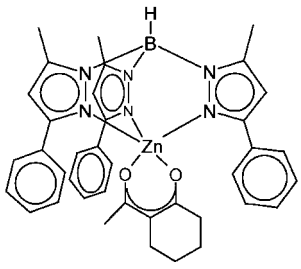

**7**

Both complexes were identified by structure determinations, the results of which are summarized in Table 1. In both cases the geometry around the zinc ion is square-pyramidal to a very high degree (96 and 93%, respectively, according to Holmes' definition[30]). In both cases the uniformity of the Zn–O bond lengths demonstrates the symmetrical attachment of the β-diketonates, despite their unsymmetrical nature. This, together with the high stability of the complexes, qualifies the β-diketones as particularly reliable chelators for zinc ions, which deserve intensified use in enzyme inhibitor studies.

Table 1. Structural details of **6** and **7**.

| | **6** | **7** |
|---|---|---|
| Zn–O1 | 2.005(4) | 1.988(5) |
| Zn–O2 | 2.039(4) | 2.000(4) |
| Zn–N1 | 2.088(4) | 2.133(6) |
| Zn–N2 | 2.137(5) | 2.123(6) |
| Zn–N3 | 2.088(5) | 2.079(5) |
| O1–Zn–N1 | 155.6(2) | 158.2(2) |
| O2–Zn–N2 | 155.8(2) | 155.6(2) |
| N3–Zn–O1 | 108.1(2) | 106.3(2) |
| N3–Zn–O2 | 110.5(2) | 111.0(2) |
| N3–Zn–N1 | 95.2(2) | 94.9(2) |
| N3–Zn–N2 | 93.7(2) | 93.0(2) |

### Aliphatic α-Diketones

Unlike the β-diketones, the α-diketones cannot form resonance-stabilized anions after deprotonation, and their reactive anionic four-electron three-center enolate systems are not favorable as ligands. Accordingly, there seem to be no zinc–α-keto enolate complexes so far. Nevertheless, the attachment of both oxygen atoms of an α-keto enolate should lead to a complex with a favorable five-membered chelate ring. With this in mind we tested diacetyl, 2,3-pentanedione, and 1-phenyl-1,2-propanedione.

Diacetyl did not react with **1**. However, in boiling methanol, **1** and 2,3-pentanedione underwent the desired elimination of water and formation of the chelate complex **8**. Complex **8** could easily be identified by its $^1$H NMR spectrum (see Exp. Sect.), and its constitution was confirmed by a structure determination (see Figure 2).

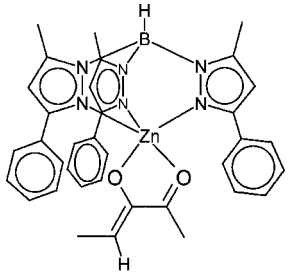

**8**

The enolate ligand in **8** is bound in a reasonably symmetrical five-membered chelate ring. Like in **2**, the Zn–O bond to the formally anionic oxygen atom is considerably shorter than the other one. The geometry at the zinc center is halfway between trigonal-bipyramidal and square-pyramidal (52% according to the Holmes definition[30]). In the trigonal bipyramid N2 and O2 would be the axial donor atoms, and in the square pyramid N1 would be at the apex.

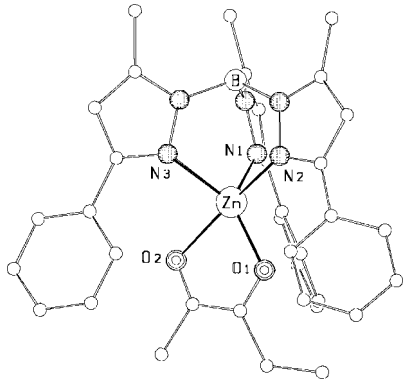


Figure 2. Molecular structure of complex **8**. Selected bond lengths [Å] and angles [°]: Zn–N1 2.067(4), Zn–N2 2.138(4), Zn–N3 2.064(4), Zn–O1 1.900(4), Zn–O2 2.255(4); N2–Zn–O2 169.0(1), N3–Zn–O1 141.7(2).

The course of the reaction between **1** and 1-phenyl-1,2-propanedione allows the assumption that its initial product is complex **9**, which is analogous to **8**. However, **9** could not be isolated, being consumed quickly by two consecutive reactions.

 © 2006 Wiley-VCH Verlag GmbH & Co. KGaA, Weinheim 

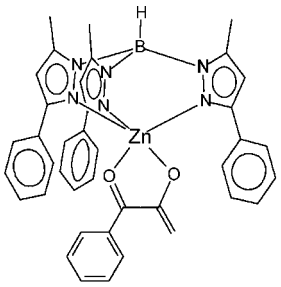

**9**

The reaction mixture turned red even in the absence of air. In the presence of air the color quickly became red-purple. Only after this could the two reaction products be isolated by fractional crystallization. One of them is the benzoate complex **5**. Its formation requires the oxidative cleavage of **9** with release of ketene, which is probably oxidized at the same time.

The second product is the red dinuclear complex **10**. Its formation can also be described as an oxidation of **9**: removal of one hydrogen atom from the vinyl group leaves a radical, the natural fate of which is dimerization leading to **10**. Although organic chemistry knows many radical dimerizations, we are not aware of an oxidative one that compares with this. Like in the formation of **5** from **4**, zinc seems to have a role here that is normally reserved for the redox-active metals.

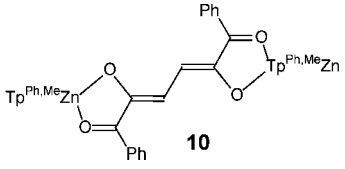

**10**

The identification of **10** came from a structure determination (see Figure 3). In **10**, which is centrosymmetrical, the ligand environment of the zinc ions and its geometry is practically identical to that in **8**: in both complexes the zinc ions are attached to vinyl-substituted α-diketonato ligands. The interesting part of **10** is the conjugated system of four (*E*)-oriented double bonds (2 C=C and 2 C=O). Its eight atoms are coplanar to a good approximation (maximum deviation 0.18 Å), and the conjugation along the chain is obvious from the slight shortening of the single bonds. This delocalization is also the reason for the intense color of the complex.

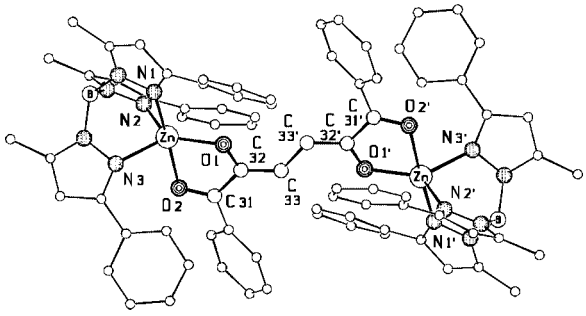

Figure 3. Molecular structure of the centrosymmetrical complex **10**. Selected bond lengths [Å]: Zn–O1 1.934(2), Zn–O2 2.281(3), Zn–N1 2.159(3), Zn–N2 2.078(3), Zn–N3 2.057(3), O1–C32 1.301(4), O2–C31 1.241(4), C31–C32 1.481(4), C32–C33 1.382(4), C33–C33′ 1.421(4).

### Aromatic α-Diketones

Unlike the aliphatic α-diketones, benzil and pyridil cannot form enolates. If they react at all with a TpZn–OH complex, they can either function as uncharged donor ligands or suffer nucleophilic attack by the strong Zn–OH nucleophiles. It turned out that the former does not happen, but the latter is the case.

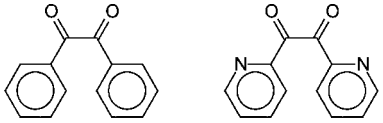

benzil pyridil

There was no reaction between **1** and benzil. Complex **1** and pyridil did react in dichloromethane at room temperature. The isolated product of this reaction was the picolinato complex **11**, which was obtained previously directly from **1** and picolinic acid.[9] The second product, pyridine-2-carbaldehyde, was identified by $^1$H NMR spectroscopy in the reaction solution. Thus, the course of the reaction is the unusual hydrolysis of pyridil at its central C–C bond, during which the oxygen atom of the Zn–OH function ends up in the picolinate while the hydrogen atom becomes the aldehydic hydrogen atom of the pyridinecarbaldehyde. Again we are not aware that there is precedence for such a hydrolytic reaction, and again it must be assumed that initial coordination of the substrate to the zinc ion (this time through the pyridyl nitrogen atom) is an essential part of its mechanism.

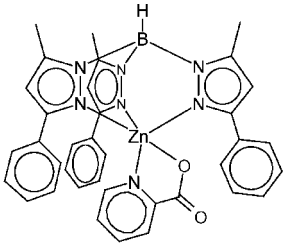

**11**

The favorable attachment of the picolinato ligand to the zinc ion by a five-membered chelate ring was confirmed by a structure determination (see Figure 4). The coordination geometry of the zinc ion is very close to trigonal-bipyramidal (73% according to the Holmes definition[30]) with the pyridine nitrogen atom and one Tp nitrogen atom on the axis. All atoms of the picolinato ligand are coplanar (strongest deviation 0.12 Å), and the short Zn–O bond indicates a quite strong zinc–picolinate interaction. Considering this, it is somewhat surprising that **11** is the first TpZn chelate complex of this kind, particularly as it is known that the complex $[Tp^{Cum,Me}Zn\text{-}Py]^+$ exists,[36] which demonstrates the strength of the TpZn–pyridine interaction by being a rare example of the cationic TpZn–X complexes.

 © 2006 Wiley-VCH Verlag GmbH & Co. KGaA, Weinheim 

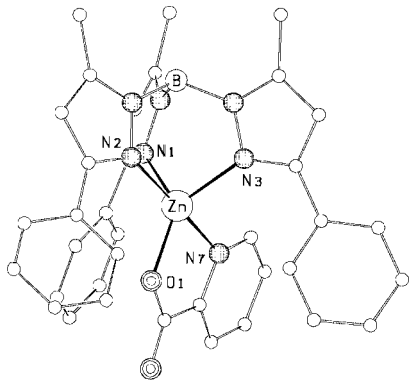


Figure 4. Molecular structure of complex **11**. Selected bond lengths [Å] and angles [°]: Zn–N1 2.051(3), Zn–N2 2.226(3), Zn–N3 2.052(3), Zn–N7 2.193(3), Zn–O1 1.966(3); N2–Zn–N7 177.5(1).

## Conclusions

A general rule for zinc complexes of 3,5-substituted Tp ligands is that the Tp ligand is a "tetrahedral enforcer", that is, four-coordinate TpZn–X complexes are preferred. This paper, however, has shown again that with suitable chelating ligands this rule is broken and very stable TpZn(X,Y) complexes are obtained. In the present case the chelators were mostly bidentate O,O donors forming five-membered chelate rings.

In the context of zinc enzyme inhibition the new complexes give further support to the hypothesis that the enzyme–inhibitor complexes are transition-state analogs, as the transition state of a zinc-enzyme-catalyzed hydrolysis has the zinc ion in a fivefold coordination with a geometry halfway between trigonal-bipyramidal and square-pyramidal.[22] As we have shown here and before,[21] the TpZn complexes of O,O chelators are very variable in their geometry, covering almost the whole range of geometries for $ZnL_5$ systems.

Of the chelate ligands employed here, the α-keto carboxylates and the α-diketo enolates have not been used before in zinc chemistry. Their stable TpZn complexes, and the even more stable TpZn complexes of the β-diketonates and the picolinate, indicate that it should be worthwhile studying compounds with these donor groups more thoroughly as potential inhibitors for zinc enzymes. It is altogether surprising how few donor functions have been employed in such studies so far.[1,2]

An unexpected, but welcome, byproduct of these investigations were the three substrate cleavage reactions. Both the two oxidative ones leading to **5** and **10** and the hydrolytic one leading to **11** are unprecedented in zinc chemistry, and one can only guess about their mechanisms. They please the zinc chemist by demonstrating once again that the "boring element" is not so boring after all.

## Experimental Section

**General:** For general working and measuring procedures see ref.[37] Complex **1** was prepared as described.[38] Organic reagents were obtained commercially. All IR spectra were recorded from KBr pellets. All $^1$H NMR spectra were obtained from $CDCl_3$ solutions. The resonances of the $Tp^{Ph,Me}$ ligands in all complexes were observed at practically identical positions: $\delta$ = 2.5 [s, 9 H, Me(pz)], 6.2 [s, 3 H, H(pz)], 7.2–7.4 [m, 9 H, Ph(3,4,5)], 7.5–7.7 [m, 6 H, Ph(2,6)] ppm. Hence, only the $^1$H NMR resonances of the co-ligands are reported here.

**Complex 2:** A solution of pyruvic acid (24 mg, 0.35 mmol) in methanol (5 mL) was added to a solution of **1** (200 mg, 0.35 mmol) in dichloromethane (20 mL). After stirring for 3 h, all volatiles were removed in vacuo. Crystallization by slow concentration from dichloromethane/methanol yielded **2** (199 mg, 81%) as colorless crystals, m.p. 186 °C. $C_{33}H_{31}BN_6O_3Zn$ (653.86): calcd. C 62.34, H 4.91, N 13.22; found C 62.10, H 5.02, N 13.22. IR (KBr): $\tilde{\nu}$ = 2552 m (BH), 1701 s, 1687 s (CO) cm$^{-1}$. $^1$H NMR: $\delta$ = 1.33 (s, 3 H, $CH_3$) ppm.

**Complex 3:** A solution of benzoylformic acid (80 mg, 0.53 mmol) in methanol (20 mL) was added to a solution of **1** (300 mg, 0.53 mmol) in dichloromethane (20 mL). After stirring for 3 h, the volume of the solution was reduced to one half in vacuo. The resulting colorless precipitate was filtered off and washed with methanol (5 mL). Crystallization by slow concentration from dichloromethane/methanol yielded **3** (314 mg, 85%) as colorless crystals, m.p. 190 °C. $C_{38}H_{33}BN_6O_3Zn$ (697.92): calcd. C 65.40, H 4.77, N 12.04; found C 65.23, H 4.85, N 11.94. IR (KBr): $\tilde{\nu}$ = 2539 m (BH), 1676 vs, 1645 s (CO) cm$^{-1}$. $^1$H NMR: $\delta$ = 7.01–7.18 [m, 12 H, Ph(Tp) and Ph], 7.42–7.53 [m, 8 H, Ph(Tp) and Ph] ppm.

**Complex 4:** As for **3**, from oxamidic acid (31 mg, 0.35 mmol) and **1** (200 mg, 0.35 mmol). Yield: **4** (161 mg, 72%) as colorless crystals, m.p. 210 °C. $C_{32}H_{30}BN_7O_3Zn$ (636.84): calcd. C 60.35, H 4.75, N 15.40; found C 59.51, H 4.84, N 15.18. IR (KBr): $\tilde{\nu}$ = 2544 m (BH), 1666 vs (CO) cm$^{-1}$. $^1$H NMR: $\delta$ = 4.45 (s, 1 H, NH), 6.51 (s, 1 H, NH) ppm.

**Complex 5:** A solution of **4** (100 mg, 0.14 mmol) in dichloromethane (20 mL) was stirred in an open flask for 2 h. The solvent was removed in vacuo and the residue crystallized by slow concentration from dichloromethane/methanol, yielding **5** (59 mg, 62%) as yellowish crystals, m.p. 224 °C. $C_{37}H_{33}BN_6O_2Zn$ (669.91): calcd. C 65.46, H 5.05, N 12.38; found C 65.36, H 5.06, N 12.37. IR (KBr): $\tilde{\nu}$ = 2541 m (BH), 1615 s, 1438 s (CO) cm$^{-1}$. $^1$H NMR: $\delta$ = 7.12–7.25 [m, 12 H, Ph(Tp) and Ph], 7.61–7.67 [m, 8 H, Ph(Tp) and Ph] ppm.

**Complex 6:** As for **2**, from methyl 2,3-dioxopentanoate (39 mg, 0.27 mmol) and **1** (150 mg, 0.27 mmol). Yield: **6** (155 mg, 83%) as colorless crystals, m.p. 187 °C. $C_{36}H_{35}BN_6O_4Zn$ (691.88): calcd. C 62.49, H 5.10, N 12.15; found C 62.19, H 5.39, N 12.03. IR (KBr): $\tilde{\nu}$ = 2540 m (BH), 1743 s, 1617 s (CO) cm$^{-1}$. $^1$H NMR: $\delta$ = 1.09 (s, 3 H, $CH_3$), 3.38 (s, 3 H, $OCH_3$), 4.75 (s, 1 H, CH) ppm.

**Complex 7:** As for **3**, from 2-acetylcyclohexanone (49 mg, 0.35 mmol) and **1** (200 mg, 0.35 mmol). Yield: **7** (161 mg, 67%) as colorless crystals, m.p. 191 °C. $C_{38}H_{39}BN_6O_2Zn{\cdot}CH_2Cl_2$ (687.97 + 84.93): calcd. C 60.61, H 5.35, N 10.87; found C 60.89, H 5.49, N 11.09. IR (KBr): $\tilde{\nu}$ = 2541 m (BH), 1593 vs (CO) cm$^{-1}$. $^1$H NMR: $\delta$ = 1.11 (s, 3 H, $CH_3CO$), 1.14–2.07 (m, 8 H, cyclohexyl), 5.29 (s, 2 H, $CH_2Cl_2$) ppm.

**Complex 8:** A solution of 2,3-pentanedione (44 mg, 46 μL, 0.44 mmol) in methanol (10 mL) was added to a suspension of **1** (250 mg, 0.44 mmol) in methanol (30 mL). After refluxing for 4 h, all volatiles were removed in vacuo. Crystallization by slow concentration from dichloromethane/methanol yielded **8** (225 mg, 79%) as yellow crystals, m.p. 172 °C. $C_{35}H_{35}BN_6O_2Zn$ (647.90): calcd. C 64.88, H 5.44, N 12.97; found C 64.29, H 5.51, N 12.85. IR (KBr):

 © 2006 Wiley-VCH Verlag GmbH & Co. KGaA, Weinheim 

Table 2. Crystallographic details.

| | **2** | **5** | **6** | **7** | **8** | **10** | **11** |
|---|---|---|---|---|---|---|---|
| Empirical formula | $C_{33}H_{31}BN_6O_3Zn$ | $C_{37}H_{33}BN_6O_2Zn$ | $C_{36}H_{35}BN_6O_4Zn$ | $C_{39}H_{41}BN_6O_2Zn\cdot CH_2Cl_2$ | $C_{35}H_{35}BN_6O_2Zn$ | $C_{39}H_{34}BN_6O_2Zn\cdot 2.5CH_2Cl_2$ | $C_{36}H_{32}BN_7O_2Zn\cdot CH_3OH$ |
| Formula mass | 635.85 | 669.91 | 691.88 | 772.90 | 647.98 | 907.27 | 702.94 |
| Crystal size [mm] | 0.35×0.12×0.12 | 0.32×0.17×0.09 | 0.14×0.12×0.03 | 0.24×0.14×0.05 | 0.32×0.22×0.18 | 0.5×0.4×0.4 | 0.30×0.18×0.10 |
| Space group | $P2_1/n$ | $P2_1/c$ | $P\bar{1}$ | $P\bar{1}$ | $P2_1/c$ | $P\bar{1}$ | $P2_1/n$ |
| $Z$ | 4 | 4 | 2 | 2 | 4 | 2 | 4 |
| $a$ [Å] | 10.209(2) | 10.085(2) | 9.941(1) | 11.604(13) | 14.824(9) | 13.019(5) | 15.537(2) |
| $b$ [Å] | 15.936(3) | 23.410(3) | 12.870(2) | 11.803(13) | 13.215(8) | 13.715(5) | 12.636(2) |
| $c$ [Å] | 18.995(4) | 13.800(1) | 13.877(2) | 16.342(18) | 16.998(10) | 13.897(5) | 17.607(3) |
| $\alpha$ [°] | 90 | 90 | 101.062(2) | 72.146(18) | 90 | 106.341(7) | 90 |
| $\beta$ [°] | 93.393(4) | 99.904(3) | 100.023(2) | 78.961(19) | 105.09(1) | 99.543(7) | 93.361(3) |
| $\gamma$ [°] | 90 | 90 | 92.213(2) | 60.974(16) | 90 | 112.945(6) | 90 |
| $V$ [Å$^3$] | 3085(1) | 3209(1) | 1711.0(4) | 1860(16) | 3215(3) | 2083(1) | 3451(1) |
| $\rho_{calcd.}$ [g cm$^{-3}$] | 1.37 | 1.39 | 1.34 | 1.38 | 1.34 | 1.45 | 1.34 |
| $\mu$(Mo-$K_\alpha$) [mm$^{-1}$] | 0.84 | 0.81 | 0.77 | 0.85 | 0.81 | 0.95 | 0.76 |
| $h$ | –13 to 14 | –13 to 13 | –12 to 12 | –15 to 15 | –20 to 19 | –16 to 17 | –21 to 14 |
| $k$ | –13 to 21 | –31 to 31 | –16 to 17 | –15 to 15 | –17 to 17 | –18 to 18 | –16 to 17 |
| $l$ | –22 to 26 | –18 to 18 | –18 to 17 | –21 to 22 | –22 to 22 | –18 to 18 | –21 to 22 |
| Measured reflections | 20403 | 28772 | 25879 | 16869 | 28147 | 18701 | 21303 |
| Independent reflections | 8437 | 7797 | 7996 | 8729 | 7819 | 9689 | 8241 |
| Observed reflections [$I > 2\sigma(I)$] | 3482 | 4079 | 4574 | 1527 | 3513 | 6755 | 4051 |
| Parameters | 401 | 428 | 1089 | 464 | 410 | 508 | 447 |
| Refined reflections | 8437 | 7797 | 7996 | 8729 | 7819 | 9689 | 8241 |
| $R_1$ (observed reflections) | 0.054 | 0.052 | 0.076 | 0.065 | 0.071 | 0.059 | 0.056 |
| $wR_2$ (all reflections) | 0.161 | 0.151 | 0.179 | 0.126 | 0.204 | 0.178 | 0.165 |
| Residual electron density [e Å$^{-3}$] | +0.6/–0.5 | +0.5/–0.7 | +0.7/–0.8 | +0.4/–0.7 | +0.6/–0.7 | +1.2/–1.9 | +0.9/–0.8 |

$\tilde{\nu}$ = 2541 m (BH), 1635 vs (CO) cm$^{-1}$. $^1$H NMR: $\delta$ = 1.11 (s, 3 H, $CH_3CO$), 1.83 (d, $J$ = 7.0 Hz, 3 H, $CH_3$), 5.27 (q, $J$ = 7.0 Hz, 1 H, CH) pm.

**Complex 10:** A solution of 1-phenyl-1,2-propanedione (52 mg, 47 μL, 0.35 mmol) in methanol (20 mL) was added to a solution of **1** (200 mg, 0.35 mmol) in dichloromethane (20 mL). After stirring in an open flask for 6 h, all volatiles were removed in vacuo. The residue was dissolved in a mixture of methanol (10 mL) and dichloromethane (5 mL) and subjected to slow concentration until most of the dichloromethane was evaporated. The resulting precipitate, which was filtered off, washed with methanol (3 mL), and dried in vacuo, consisted of **10** (78 mg, 32%) as a red powder, m.p. 230 °C. $C_{78}H_{68}B_2N_{12}O_4Zn_2\cdot 1.5CH_2Cl_2$ (1389.88 + 127.40): calcd. C 62.93, H 4.72, N 11.08; found C 62.52, H 4.62, N 11.15. IR (KBr): $\tilde{\nu}$ = 2541 m (BH), 1613 vs (CO) cm$^{-1}$. $^1$H NMR: $\delta$ = 5.29 (s, 3 H, $CH_2Cl_2$), 6.73 (s, 2 H, CH) ppm.

**Complex 11:** A solution of pyridil (74 mg, 0.35 mmol) in dichloromethane (10 mL) was added to a solution of **1** (200 mg, 0.35 mmol) in dichloromethane (10 mL). After stirring for 3 h, the mixture was filtered and the filtrate treated dropwise with methanol until a precipitate started forming. After stirring for another 30 min, the precipitate was filtered off and washed with methanol (5 mL). Recrystallization from hot methanol yielded **11** (132 mg, 56%) as yellow crystals, m.p. 226 °C. $C_{36}H_{32}BN_7O_2Zn\cdot CH_3OH$ (670.90 + 32.04): calcd. C 63.82, H 4.99, N 14.27; found C 63.21, H 4.75, N 13.97. IR (KBr): $\tilde{\nu}$ = 2539 m (BH), 1665 m and 1646 vs (CO and Py) cm$^{-1}$. $^1$H NMR: $\delta$ = 3.48 (s, 3 H, $CH_3OH$), 6.49 [t, $J$ = 7.0 Hz, 1 H, Py(4)], 6.96 [d, $J$ = 7.0 Hz, 1 H, Py(3)], 7.23 [t, $J$ = 7.0 Hz, 1 H, Py(5)], 7.62 [d, $J$ = 6.9 Hz, 1 H, Py(6)] ppm.

**Structure Determinations:** Crystals of **10** were obtained by recrystallization from dichloromethane. All other crystals were obtained as described above. Diffraction data were recorded at 240 K with a Bruker Smart CCD diffractometer with Mo-$K_\alpha$ radiation and subjected to empirical absorption corrections (program SADABS). The structures were solved with direct methods and refined anisotropically with the SHELX program suite.[39] Drawings were produced with SCHAKAL.[40] Table 2 lists the crystallographic data. CCDC-614607 (for **2**), -614608 (for **5**), -614609 (for **6**), -614610 (for **7**), -614611 (for **8**), -614612 (for **10**), and -614613 (for **11**) contain the supplementary crystallographic data for this paper. These data can be obtained free of charge from The Cambridge Crystallographic Data Centre via www.ccdc.cam.ac.uk/data_request/cif.

## Acknowledgments

This work was supported by the Fonds der Chemischen Industrie. We are indebted to Drs. H. Brombacher, G. Steinfeld, and W. Deck for advice and technical assistance, and to Ms. M. Handloser for help in the laboratory.

[1] R. E. Babine, S. L. Bender, *Chem. Rev.* **1997**, *97*, 1359–1472.
[2] M. Whittaker, C. D. Floyd, P. Brown, A. J. H. Gearing, *Chem. Rev.* **1999**, *99*, 2735–2776.
[3] D. W. Christianson, *Adv. Protein Chem.* **1991**, *42*, 281–355.
[4] W. N. Lipscomb, N. Sträter, *Chem. Rev.* **1996**, *96*, 2375–2433.
[5] C. T. Supuran, A. Scozzafava, A. Casini, *Med. Res. Rev.* **2003**, *23*, 146–189.
[6] J. I. Levin, *Curr. Top. Med. Chem.* **2004**, *4*, 1289–1310; T. S. Rush, R. Powders, *Curr. Top. Med. Chem.* **2004**, *4*, 1311–1327.
[7] L. M. Coussens, B. Fingelton, L. M. Matrisian, *Science* **2002**, *295*, 2387–2392.
[8] S. Pikul, N. E. Ohler, G. Ziszewski, M. C. Laufersweiler, N. G. Almstead, B. De, M. G. Natchus, L. C. Hsieh, M. C. Januzs, *J. Med. Chem.* **2001**, *44*, 2499–2502.

 © 2006 Wiley-VCH Verlag GmbH & Co. KGaA, Weinheim 

[9] D. T. Puerta, J. A. Lewis, S. M. Cohen, *J. Am. Chem. Soc.* **2004**, *126*, 8388–8389; F. E. Jacobsen, J. A. Lewis, S. M. Cohen, *J. Am. Chem. Soc.* **2006**, *128*, 3156–3157.
[10] U. Hartmann, H. Vahrenkamp, *Inorg. Chem.* **1991**, *30*, 4676–4677.
[11] U. Hartmann, H. Vahrenkamp, *Bull. Pol. Acad. Sci., Chem.* **1994**, *42*, 155–161.
[12] U. Hartmann, H. Vahrenkamp, *Z. Naturforsch., B: Chem. Sci.* **1994**, *42*, 1725–1730.
[13] U. Hartmann, H. Vahrenkamp, *Chem. Ber.* **1994**, *127*, 2381–2385.
[14] A. Koppenhöfer, U. Hartmann, H. Vahrenkamp, *Chem. Ber.* **1995**, *128*, 779–785.
[15] M. Ruf, K. Weis, H. Vahrenkamp, *Inorg. Chem.* **1997**, *36*, 2130–2137.
[16] K. Weis, M. Rombach, H. Vahrenkamp, *Inorg. Chem.* **1998**, *37*, 2470–2475.
[17] J. Seebacher, M. Shu, H. Vahrenkamp, *Inorg. Chem.* **2001**, *40*, 4022–4029.
[18] D. Badura, H. Vahrenkamp, *Inorg. Chem.* **2002**, *41*, 6020–6027.
[19] D. Badura, H. Vahrenkamp, *Eur. J. Inorg. Chem.* **2003**, 3723–3730.
[20] M. Ruf, K. Weis, I. Brasack, H. Vahrenkamp, *Inorg. Chim. Acta* **1996**, *250*, 271–281.
[21] M. Rombach, C. Maurer, K. Weis, E. Keller, H. Vahrenkamp, *Chem. Eur. J.* **1999**, *5*, 1013–1027.
[22] H. Vahrenkamp, *Acc. Chem. Res.* **1999**, *32*, 589–596.
[23] D. T. Puerta, S. M. Cohen, *Inorg. Chem.* **2002**, *41*, 5075–5082.
[24] D. T. Puerta, S. M. Cohen, *Inorg. Chem.* **2003**, *42*, 3423–3430.
[25] F. E. Jacobsen, S. M. Cohen, *Inorg. Chem.* **2004**, *43*, 3038–3047.
[26] D. T. Puerta, J. R. Schames, R. H. Henchman, J. A. McCammon, S. M. Cohen, *Angew. Chem.* **2003**, *115*, 3902–3904; *Angew. Chem. Int. Ed.* **2003**, *42*, 3772–3774.
[27] H. He, D. T. Puerta, S. M. Cohen, K. R. Rodgers, *Inorg. Chem.* **2005**, *44*, 7431–7442.
[28] T. Tekeste, H. Vahrenkamp, *Inorg. Chim. Acta*, in press.
[29] M. F. Browner, W. W. Smith, A. L. Castelhano, *Biochemistry* **1995**, *34*, 6602–6609.
[30] R. R. Holmes, *Prog. Inorg. Chem.* **1984**, *32*, 119–235.
[31] E. L. Hegg, R. Y. N. Ho, L. Que, *J. Am. Chem. Soc.* **1999**, *121*, 1972–1973.
[32] A. Braibanti, M. A. Pelinghelli, A. Tiripicchio, M. Tiripicchio Camellini, *Acta Crystallogr., Sect. B: Struct. Sci.* **1971**, *27*, 1240–1244.
[33] See textbooks of organic chemistry or biochemistry.
[34] A. Kremer-Aach, W. Kläui, R. Bell, A. Strerath, H. Wunderlich, D. Mootz, *Inorg. Chem.* **1997**, *36*, 1552–1563.
[35] H. Brombacher, H. Vahrenkamp, *Inorg. Chem.* **2004**, *43*, 6054–6060.
[36] T. Brandsch, F. A. Schell, K. Weis, M. Ruf, B. Müller, H. Vahrenkamp, *Chem. Ber. Recl.* **1997**, *130*, 283–289.
[37] M. Förster, R. Burth, A. K. Powell, T. Eiche, H. Vahrenkamp, *Chem. Ber.* **1993**, *126*, 2643–2648.
[38] M. Ruf, R. Burth, K. Weis, H. Vahrenkamp, *Chem. Ber.* **1996**, *129*, 1251–1257.
[39] *SHELXTL, Program Package of the Bruker Smart CCD Diffractometer*, version 5.1, **2002**.
[40] E. Keller, *SCHAKAL for Windows*, University of Freiburg, **1999**.

Received: September 3, 2006
Published Online: October 24, 2006

 © 2006 Wiley-VCH Verlag GmbH & Co. KGaA, Weinheim 